Copyrighted Material

Enhanced
DIGITAL
VERSION
Included

Editor-in-Chief
Susan Standring

GRAY'S
Anatomy
THE ANATOMICAL BASIS OF CLINICAL PRACTICE

Forty-Second Edition

ELSEVIER

Copyrighted Material

Publisher: Jeremy Bowes
Senior Content Development Specialist: Trinity Hutton
Deputy Content Development Manager: Joanne Scott
Project Managers: Julie Taylor, Joanna Souch
Production Manager: Deena Burgess
Designer: Amy Buxton
Illustration Manager: Paula Catalano
Illustrators: Antbits (Paul Richardson, Richard Tibbitts), Edanart (Ethan Danielson)
Copyeditor: Elaine Leek
Proofreaders: Glenys Norquay and Susan Stuart
Indexer: Jan Ross, Merrall-Ross International
Marketing Manager: Michele Milano

GRAY'S Anatomy

THE ANATOMICAL BASIS OF CLINICAL PRACTICE

Editor-in-Chief
Susan Standring MBE, PhD, DSc, FKC, Hon FAS, Hon FRCS
Emeritus Professor of Anatomy
King's College London
London, UK

SECTION EDITORS

Neel Anand MD
Clinical Professor of Surgery
Director, Spine Trauma,
Minimally Invasive Spine
Surgery
Spine Center
Cedars Sinai Medical Center
Los Angeles, CA, USA

Marco Catani MD, PhD
Professor of Neuroanatomy &
Psychiatry
NatBrainLab
Department of Forensic and
Neurodevelopmental Sciences
Institute of Psychiatry,
Psychology and Neuroscience
King's College London
London, UK

Patricia Collins BSc, PhD, FHEA
Emeritus Professor of Anatomy
AECC University College
Bournemouth, UK

Alan R Crossman BSc, PhD,
DSc
Emeritus Professor of Anatomy
The University of Manchester
Manchester, UK

Michael Gleeson MD, FRCS,
FRACS, FDS
Professor of Skull Base Surgery
University College London
The National Hospital for
Neurology and Neurosurgery
London, UK

Alistair Ross MB, FRCS
Consultant Orthopaedic Surgeon
The Bath Clinic
Bath, UK

R Shane Tubbs MS, PA-C, PhD
Professor
Departments of Neurosurgery,
Neurology and Structural and
Cellular Biology
Tulane University School of
Medicine
New Orleans, LA, USA
Professor of Human Gross and
Developmental Anatomy
Department of Anatomical
Sciences
St George's University
Grenada, West Indies
Faculty
National Skull Base Foundation
Thousand Oaks, CA, USA
Faculty
Department of Neurosurgery
and Ochsner Neuroscience
Institute
Ochsner Health System
New Orleans, LA, USA

Richard Tunstall BMedSci,
PhD, FHEA
Professor of Clinical Anatomy
and Imaging
Warwick Medical School
University of Warwick, UK
Professor of Clinical Anatomy
West Midlands Surgical
Training Centre
UHCW NHS Trust
Coventry, UK
Applied Surgical Anatomy Lead
Royal College of Surgeons
London, UK

Caroline B Wigley BSc, PhD
Retired Preclinical Tutor
University of Exeter Medical
School
Exeter, UK

Stephanie J Woodley PhD,
MSc, BPhty
Associate Professor
Department of Anatomy
School of Biomedical Sciences
University of Otago
Dunedin, New Zealand

SPECIAL EDITORS

Surface Anatomy

**Richard Tunstall BMedSci,
PhD, FHEA**

Imaging

**Tom Turmezei MPhil, MA,
BMBCh, PhD, FRCR**
Consultant Radiologist
Norfolk and Norwich
University Hospital
Norwich, UK
Honorary Senior Lecturer
University of East Anglia, UK
Royal College of Radiologists
2020 Roentgen Professor

Cell and Tissue Microstructure

Caroline B Wigley BSc, PhD

ELSEVIER

Forty-Second Edition

© 2021, Elsevier Limited. All rights reserved.

Forty-first edition published 2016

Fortieth edition published 2008

First edition JW Parker & Son 1858

No part of this publication may be reproduced or transmitted in any form or by any means, electronic or mechanical, including photocopying, recording, or any information storage and retrieval system, without permission in writing from the publisher. Details on how to seek permission, further information about the Publisher's permissions policies and our arrangements with organizations such as the Copyright Clearance Center and the Copyright Licensing Agency, can be found at our website: www.elsevier.com/permissions.

This book and the individual contributions contained in it are protected under copyright by the Publisher (other than as may be noted herein).

Notices
Practitioners and researchers must always rely on their own experience and knowledge in evaluating and using any information, methods, compounds or experiments described herein. Because of rapid advances in the medical sciences, in particular, independent verification of diagnoses and drug dosages should be made. To the fullest extent of the law, no responsibility is assumed by Elsevier, authors, editors or contributors for any injury and/or damage to persons or property as a matter of products liability, negligence or otherwise, or from any use or operation of any methods, products, instructions, or ideas contained in the material herein.

Although all advertising material is expected to conform to ethical (medical) standards, inclusion in this publication does not constitute a guarantee or endorsement of the quality or the value of such product or the claims made of it by its manufacturer.

ISBN: 978-0-7020-7705-0
9780702077067

Printed in China

Last digit is the print number: 9 8 7 6 5 4 3 2 1

ELSEVIER Book Aid International
Working together
to grow libraries in
developing countries
www.elsevier.com • www.bookaid.org

Get the most out of your Gray's Anatomy
FORTY-SECOND EDITION

Included in your purchase is a rich variety of BONUS electronic content, to supplement and enhance the printed book.

Look out for this icon ↗, indicating where there is related further electronic text, images, tables, labelled imaging or video material.

In addition, you can access 21 'Gray's Commentaries': especially written (electronic only) articles on new and emerging topics related to anatomy. This icon C highlights where one relates directly to a topic in the printed book. S Chapters 80 and 81 (electronic only) contain descriptions of the systematic anatomy of the peripheral nervous system and vascular system, respectively.

For an extended historical bibliography, all references from the thirty-eighth edition (which includes all references cited in earlier editions, up to and including the thirty-eighth edition) are also available in the e-book that accompanies *Gray's Anatomy*.

Don't miss out on any of this additional electronic content – see the inside front cover for your access instructions.

COVER IMAGE

The cover image for this edition is a cinematically rendered 3D reconstruction of a normal heart from a contrast-enhanced computed tomography (CT) coronary angiography study performed at the Royal Papworth Hospital, Cambridge, UK. Image reconstruction and post-processing was performed on a SIEMENS syngo.via Frontier workstation by Dr Julia Sun (Clinical Fellow in Radiology, Royal Papworth Hospital) with further editing by Dr Jonathan Weir-McCall (Honorary Consultant Radiologist, Royal Papworth Hospital) and Dr Tom Turmezei (Consultant Radiologist, Norfolk and Norwich University Hospital).

PREFACE

A common definition of a preface is that it is '*an introduction to a book, typically stating its subject, scope or aims*'. It is often the only place where an author or editor speaks directly to their readership, and in this respect, a preface is akin to an actor breaking the conceptual 'fourth wall' in the theatre or on film. In the Preface to the first edition in 1858 Henry Gray wrote that '*This Work is intended to furnish the Student and Practitioner with an accurate view of the Anatomy of the Human Body, and more especially the application of this science to Practical Surgery*'. Subsequent editions of *Gray's Anatomy* not only upheld that intention, but developed it, in order to embrace and engage a wider readership.

The first two editors to succeed Gray were Timothy Holmes (1863–1880) and Thomas Pickering Pick (1883–1905). They both wondered in their Prefaces whether it was appropriate to include findings from the burgeoning discipline of anatomical science in a book intended specifically for students of surgery: '*so long as the Examining Bodies do not exact a knowledge of this branch of science as a necessary part of Medical Education, it would be unwise to encumber the pages of a work designed specifically for students with matter which, however interesting and valuable in itself, could hardly be regarded as essential*' (Holmes, 3rd edition, 1863). Pickering Pick pointed out that microscopical anatomy had been revised in the 10th edition '*in order to keep pace with the ever-increasing activity of research in the branch of the science of Anatomy*' (1883), and while not intending the 13th edition for the 'scientific anatomist', he was anxious not '*to disparage, for an instant, the study of Philosophical or Scientific Anatomy*' (1893).

Future editions slowly assimilated findings in the fields of cell biology, embryology, neuroanatomy and imaging: just as the discipline it describes has evolved, so a book originally intended for students of surgery has morphed into the great reference book that is published today. Our current view of the detailed internal landscape of the body, from molecular to whole body and from conception onwards, owes much to the enormous technological advances that have taken place in the last half century. Our 'anatomical gaze' has been enlightened by progress in bioinformatics, molecular biology, experimental genetics, light and electron microscopy, diagnostic imaging (including X-rays, magnetic resonance imaging, computed tomography and ultrasonography), and the use of 'soft' perfusion techniques and frozen–thawed, unembalmed cadavers for dissection-based studies and surgical training. That gaze is not only informed by, but also informs, the design and negotiation of minimally invasive surgical access routes to structures and regions that were once regarded as inaccessible 'tiger territories'. The momentum created by these changes powered the radical modernizing revisions seen in the 36th to 38th editions under the editorship of Roger Warwick and Peter Williams: '*The discipline of Anatomy has changed out of all recognition because it is no longer just "Descriptive and Applied"*' (Editorial team, Preface to the 38th edition, 1995), and has continued to drive subsequent editions.

Terminological disputes have long entertained anatomists: '*one cynic has commented that anatomists would rather use each other's toothbrushes than employ their terminology*' (Tansey 1995).[1] Henry Gray's anatomical terminology in the first edition can be little different from the language he used when teaching and operating at St George's Hospital: his words were written long before the publication of the *Basle Nomina Anatomica* (BNA) in 1895. The exasperated comments of TB Johnston, in his Preface to the 25th edition, have a familiar ring almost 90 years later: '*It is my earnest hope that before another edition of this work is published, the question of terminology will have been settled and an unproductive subject will have ceased to occupy attention*' (Johnston 1932). These hopes have not been entirely satisfied. An early attempt to reconcile differing terminologies in *Gray's Anatomy* was described as 'stultifying' (Tansey 1995).[1] The text of the 42nd edition of *Gray's Anatomy* is almost entirely *Terminologia Anatomica* 2-compliant.[2] However, on occasion the preferred term that is used is a synonym that may not be TA2-compliant: it has been chosen either because it is the agreed term in the relevant clinical consensus document or, as my editors frequently remind me, because it enjoys widespread clinical usage, whereas the TA-compliant term does not.[3] Wherever this occurs, all terms are included at first meeting, with synonyms in parentheses.

The use of eponyms is contentious: detractors argue that they are inherently inaccurate, non-scientific and often undeserved, while proponents point out that eponyms are deeply embedded in the anatomical and clinical literature and that they remind us of the giants on whose shoulders we stand. On balance, I believe that *Gray's Anatomy* is an appropriate repository for anatomical eponyms: they are cited in parentheses on first usage of a preferred term in the text and an updated list of eponyms is available in the e-book for reference purposes. I recognize the irony in the exclusion of Henry Vandyke Carter's name from the eponymous title of *Gray's Anatomy*, particularly since Carter's drawings invariably attracted praise: '*those excellent images which have … contributed so materially to smooth the thorny path of the student of human anatomy*' (Carter's obituary, BMJ May 15 1897); '*The splendid illustrations in Gray have long been known as the most effective and intelligible presentations of anatomical structure ever produced …*' (Preface to the American 15th edition, 1901).

As a general rule, the orientation of diagrams and photographs throughout the book has been standardized to show the left side of the body, irrespective of whether a lateral or medial view is presented. Transverse sections have been drawn from below to facilitate comparison with axial clinical images: the conventional 'top down' orientation has been retained in diagrams in Section 3 (neuroanatomy). Clinicopathological examples have been selected where the pathology is either a direct result, or a consequence, of the anatomy, or where the anatomical features are instrumental in the diagnosis/treatment/management of the condition. Unless otherwise indicated, the photomicrographs illustrate human histology and embryology.

In the Preface to the 39th edition I explained that the editorial team had decided that, in order to provide the greatest benefit to clinicians, *Gray's Anatomy* would better mirror their daily practice if anatomy was described in the way that they use it, i.e. regionally. That said, including regional and systematic descriptions of topographical anatomy has remained my goal and I am therefore delighted that the anatomy of the nervous and vascular and lymphatic systems is included in the online version of the 42nd edition (in Chapters 80 and 81).

Neel Anand, Marco Catani, Pat Collins, Alan Crossman, Michael Gleeson, Alistair Ross, Shane Tubbs, Richard Tunstall, Caroline Wigley and Stephanie Woodley brought a wealth of scholarship and experience as anatomists, cell biologists, research scientists, educators and clinicians to their roles as Section Editors. They recognize that a knowledge of clinically relevant and evidence-based anatomy is essential for safe and effective clinical practice across all specialisms. It is with great pleasure that I thank them for their dedication and enthusiastic support, both in selecting and interacting with the authors in their Sections and in meeting Elsevier's deadlines, despite the ever-increasing demands on their time from their university and/or clinical managers. Richard

---

[1] Tansey EM 1995 A brief history of Gray's Anatomy. In Gray's Anatomy 38th ed (Williams PL et al eds). pp. xvii–xx. Edinburgh: Churchill Livingstone.

[2] Terminologia Anatomica 2, 2019 https://fipat.library.dal.ca/TA2/; Terminologia Histologica, Philadelphia: Lippincott Williams & Wilkins, 2008; Terminologia Embryologica, 2017 https://FIPAT.library.dal.ca; Terminologia Neuroanatomica, 2017 https://FIPAT.library.dal.ca.

[3] Jeppson PC, Balgobin S, Washington BB et al 2018 Recommended standardized terminology of the anterior female pelvis based on a structured medical literature review. Am J Obstet Gynecol 219:26–39.

Tunstall and Caroline Wigley also worked closely with many authors to update the text and artworks for evidence-based surface anatomy and microstructure, respectively, across Sections 3 to 9. Tom Turmezei has been an enthusiastic 'go to' editor for sourcing images throughout the book: Tom and his team have produced a superb collection of additional labelled images (see **Bonus imaging collection**). Owen Arthurs and his colleagues at Great Ormond Street Hospital provided microCT images for Section 2 (Embryogenesis and development). Over a hundred highly experienced clinicians and anatomists have contributed new text and/or artworks, original micrographs or other images to individual chapters and I thank them all for their input – as ever, it has been an enriching experience to read their revisions.

I offer my sincere thanks to the editorial team at Elsevier, under the leadership of Jeremy Bowes, for their guidance, professionalism, good humour and unfailing support at all times. I particularly thank Trinity Hutton, Joanna Souch, Julie Taylor and Elaine Leek, for being at the end of a phone or available by e-mail whenever I needed advice or support. I thank the artists who have worked to produce new artworks under Richard Tibbitts' leadership, continuing the tradition of Henry Vandyke Carter, the first great illustrator of *Gray's Anatomy.*

I dedicate my work on this edition of *Gray's Anatomy* to my daughters, Helen and Caroline.

Susan Standring
February 2020

PROFESSOR EMERITUS KARL ZILLES (1944–2020)

It was with great sadness that we learned that Professor Emeritus Karl Zilles, who co-authored the updated chapter on the cerebral hemispheres (Chapter 32), died while the proofs of this edition of *Gray's Anatomy* were being finalized. He was an outstanding neuroscientist and '*…his dedication, rigor, and scientific approaches have been transformative in the field of neuroanatomy…*' (Zaborszky 2020). The quantitative histological methods that he developed have played a significant role in bridging the gap between classical post-mortem neuroanatomy and neuroimaging of the living human brain.

Karl Zilles graduated in medicine from the Johann-Wolfgang-Goethe University in Frankfurt in 1971 and received a PhD in Anatomy from the Medical School of Hannover in 1977. He became full Professor of Anatomy and Neuroanatomy at the University of Cologne in 1981 and was Director of the prestigious Cécil and Oscar Vogt Institute for Brain Research at Heinrich Heine University in Düsseldorf from 1991 to 2012 and the Institute of Neurosciences and Medicine at the Forschungszentrum in Jülich from 1998 to 2012.

During a long and highly productive career, Karl Zilles explored the structural, molecular and functional organization of the marsupial, rodent, non-human primate and human cerebral cortices. Very early, he introduced TV cameras connected to a microscope for extracting quantitative morphometric parameters from histological sections (Zilles et al 1978). The realization of the existence of significant inter-individual differences in brain architecture led him to propose and establish the use of 3D cytoarchitectonic probabilistic maps of cortical areas (Amunts et al 1999, Schormann et al 1995). The rapid development of *in vivo* neuroimaging methods combined with a quantitative probabilistic approach to cytoarchitectonic brain mapping produced reference atlases and digital databases for the precise localization of cortical areas and functions in the human brain (Zilles and Amunts 2010).

He developed a method for the quantitative autoradiograpical analysis of the laminar and regional distribution of multiple transmitter receptors. He introduced neurotransmitter fingerprints, which reflect the balance between different receptors and neurotransmitter systems that characterize each cortical area. He demonstrated that receptor fingerprints differ across species and between healthy and diseased brains, and therefore represent a very powerful tool to study the molecular architecture of each area under different conditions (Zilles et al 1986, Zilles and Palomero-Gallagher 2017).

In the last 15 years, Karl Zilles and his collaborators introduced an ultra-high resolution method for axon and white matter fibre visualization based on polarized light imaging (Axer et al 2011). Future developments and applications of this technique will offer an invaluable tool with which to describe the organization of neural connections in the brain and to validate current descriptions of white matter tracts based on *in vivo* diffusion MRI tractography.

To his students, collaborators and friends, Professor Karl Zilles was an inspirational and encouraging figure, always ready to converse and write about neuroanatomy, history of neuroscience, epistemology, philosophy and ethics: he will be deeply missed.

References

Amunts K, Schleicher A, Bürgel U, Mohlberg H, Uylings HBM, Zilles K 1999 Broca's region revisited: Cytoarchitecture and intersubject variability. J Comp Neurol 412: 319–341.

Axer M, Amunts K, Grässel D, Palm C, Dammers J, Axer H, Pietrzyk U, Zilles K 2011 A novel approach to the human connectome: Ultra-high resolution mapping of fiber tracts in the brain. NeuroImage 54: 1091–1101.

Schormann T, Dabringhaus A, Zilles K 1995 Statistics of deformations in histology and application to improved alignment with MRI. IEEE Transactions on Medical Imaging 14: 25–35.

Zaborszky L 2020 Karl Zilles (1944–2020): a personal tribute. Brain Struct Funct 225:1185–1187. https://doi.org/10.1007/s00429-020-02088-5.

Zilles K, Schleicher A, Kretschmann HJ 1978 A quantitative approach to cytoarchitectonics. I. The areal pattern of the cortex of Tupaia belangeri. Anat Embryol 153:195–212.

Zilles K, Amunts K 2010 Centenary of Brodmann's map – conception and fate. Nature Rev Neurosci 11:139–145.

Zilles K, Schleicher A, Rath M et al 1986 Quantitative autoradiography of transmitter binding sites with an image analyzer. J Neurosci Meth 18: 207–220.

Zilles K, Palomero-Gallagher N 2017 Multiple transmitter receptors in regions and layers of the human cerebral cortex. Front Neuroanat 11:78.

ACKNOWLEDGEMENTS

Elsevier and the *Gray's Anatomy* 42nd edition editorial team would like to offer sincere thanks to the Department of Radiology at the Norfolk and Norwich University Hospital, Norwich, UK, for their support in sourcing and preparing over 140 superb new radiological imaging figures for this edition. Guided by Imaging Editor Dr Tom Turmezei, these include cutting-edge images that showcase the impact of radiology on anatomical education, harnessing different modalities and image processing techniques to show living internal human anatomy in detail. In particular, we would like to thank consultant radiologists Tariq Ali, Phyllis Mezue and Iztok Caglic; musculoskeletal radiology clinical fellow Elliott Rees; and radiology trainees Julia Sun, Ramona-Rita Barbara, Fatma Eminaga, Amr Moussa, Nathan Chan and Emily Pearlman.

The following images were sourced by the Department of Radiology at the Norfolk and Norwich University Hospital:

33.1B,C; 33.2B; 33.3B; 34.1C; 34.2B; 34.3B; 34.4C; 35.4C; 35.24H-L; 37.11B; 37.40B,C; 37.41; 37.45D,E; 38.14C–E; 39.6B–F; 40.2B; 41.6B; 44.5B; 44.6C; 44.7B; 44.13B–E; 46.6B,C; 46.20C; 46.23B; 46.25B,C; 46.27B,C; 46.44B; 46.45; 46.46A–C; 46.51C–G; 46.60B–D; 46.63B,C; 46.66B; 46.74; 47.1G; 48.3B–D; 48.4B–E; 48.7B–G; 49.15B; 49.22C; 49.23A,B; 49.30B; 50.13E–G; 50.16; 50.17B; 50.27B; 50.31B; 50.32B; 51.19D; 51.20A–D; 52.2B; 53.12B; 54.4C–H; 54.5B; 54.6F–O; 55.1B–E; 56.9B–E; 57.4F; 57.7BC; 57.17B; 57.21B; 57.27B; 57.46; 57.47; 57.48; 57.49; 57.50; 57.51; 57.59C; 58.3; 59.5B; 60.1B; 60.3C; 60.9C,D; 63.10B,C; 64.14A–C; 65.37A,B; 65.44C; 66.9B; 66.12; 67.10; 71.5B; 71.6B; 72.6A–D; 73.1B; 73.2D; 73.15C;76.3C; 77.2B; 77.17B; 77.24B; 77.28B; 77.43C,D; 77.48B,C; 78.6C; 78.14B; 78.24B; 79.4B; 79.8B; 79.9D,E; 79.10B; 79.15B; 79.17B; 79.19B

Elsevier and the *Gray's Anatomy* 42nd edition editorial team would also like to offer sincere thanks to Mr Peter Helliwell (Head Biomedical Scientist, Department of Cellular Pathology, Royal Cornwall Hospitals Trust, Truro, UK) for contributing numerous high resolution photomicrographs of specially prepared histological sections of human tissues for the 40th, 41st and 42nd editions of *Gray's Anatomy*, many prepared in collaboration with the late Dr Joseph Mathew.

CONTRIBUTORS to the forty-second edition

The editor(s) acknowledge and offer grateful thanks for the input of all contributors to previous editions, without whom this new edition would not have been possible.

Michael A Adams BSc, PhD
Professor of Biomechanics, and
Senior Research Fellow
Centre for Applied Anatomy
University of Bristol
Bristol, UK

Mohamad E Allaf MD
Professor of Urology
Johns Hopkins University School of Medicine
Baltimore, MD, USA

Neel Anand MD
Clinical Professor of Surgery
Director, Spine Trauma, Minimally Invasive Spine Surgery
Spine Center
Cedars Sinai Medical Center
Los Angeles, CA, USA

Praveen Anand MD, MRCP, FRCP
Professor of Clinical Neurology
Faculty of Medicine
Department of Brain Sciences
Head, Centre for Clinical Translation
Imperial College London, Hammersmith Hospital
London, UK

Nihal Apaydin MD, PhD
Professor of Anatomy
Department of Anatomy, Faculty of Medicine
Department of Neuroscience, Institute of Health Sciences
AU Brain Research Center
Ankara University
Ankara, Turkey

Tipu Zahed Aziz FMedSci
Professor of Neurosurgery
John Radcliffe Hospital
University of Oxford
Oxford, UK

Stuart Ballantyne MBChB, FRCS, FRCR
Department of Radiology
Gartnavel General Hospital;
Queen Elizabeth University Hospital
Glasgow, UK

Winfried Banzer
Institute of Sports Science
Goethe-Universität Frankfurt am Main
Germany

Eli Baron MD
Associate Professor of Neurosurgery
Co-Director Spine Trauma Program
Spine Surgeon
Cedars-Sinai Spine Center
Los Angeles, CA, USA

Barry KB Berkovitz BDS, MSc, PhD, FDS
Emeritus Reader in Dental Anatomy
King's College London
London, UK

Christopher D Bernard MD
Department of Orthopedic Surgery
Mayo Clinic
Rochester, MN, USA

Ranjeev Singh Bhangoo MBChB (Hons), FRCS (Eng), FRCS (SN)
Clinical Director of Neuroscience and Consultant Neurosurgeon
Department of Neurosurgery
King's College NHS Foundation Trust
London, UK

Jasneet Singh Bhullar MD, MS, FACS, FASCRS
Colorectal Surgeon
UPMC Susquehanna
Williamsport, PA, USA

Rolfe Birch MChir, FRCPS(Glasg), FRCS(Ed), FRCS(Eng)
Faculty of Medicine
Imperial College London
Hammersmith Hospital
London, UK

Kelly Brown MBBS, MRCPCH
Consultant Neonatologist
University Hospital Southampton NHS Foundation Trust
Southampton, UK

Graham J Burton MD, DSc, FMedSci
Mary Marshall and Arthur Walton Professor of the Physiology of Reproduction
Department of Physiology, Development and Neuroscience
University of Cambridge
Cambridge, UK

Andrew Bush MB BS MD FHEA FRCP FRCPCH FERS FAPSR ATSF
Professor of Paediatrics and Paediatric Respirology, and Consultant Paediatric Chest Physician
Paediatric Respiratory Medicine
Imperial College and Royal Brompton Harefield NHS Foundation Trust
London, UK

Kevin Gerard Byrnes MB BCh BAO, MCh, MRCS, PhD
Graduate Entry Medical School
University of Limerick
University Hospitals Group Limerick
Dooradoyle, Ireland

Alison Campbell BSc (Hons), M Med Sci, Dip RCPath
Group Director of Embryology
CARE Fertility Group
Nottingham, UK

Marco Catani MD, PhD
Professor of Neuroanatomy & Psychiatry
NatBrainLab
Department of Forensic and Neurodevelopmental Sciences
Institute of Psychiatry, Psychology and Neuroscience
King's College London
London, UK

Carmen Cavada MD, PhD
Professor, Human Anatomy and Neuroscience
Director, Chair in Neuroscience UAM-Fundación Tatiana Pérez de Guzmán el Bueno
Department of Anatomy, Histology and Neuroscience
Universidad Autónoma de Madrid
Madrid, Spain

Paul H Chung MD
Assistant Professor of Urology
Sidney Kimmel Medical College
Thomas Jefferson University
Philadelphia, PA, USA

John Calvin Coffey BSc, B MedSci, MB, PhD, AFRSCI, FRCSI
Foundation Chair of Surgery
Graduate Entry Medical School
University of Limerick
University Hospitals Group Limerick
Dooradoyle, Ireland

Patricia Collins BSc, PhD, FHEA
Emeritus Professor of Anatomy
AECC University College
Bournemouth, UK

Gerardo Conesa Bertran MD, PhD
Director of the Neurosurgical Department
Hospital de Sant Pau and Hospital del Mar
Barcelona, Spain

Claudius Conrad MD, PhD
Department of Surgery
Saint Elizabeth Medical Center
Boston, MA, USA

Declan Costello MA, MBBS, FRCS (ORL-HNS)
Consultant Ear Nose and Throat Surgeon specializing in voice disorders
Wexham Park Hospital
Slough, UK

Alan R Crossman BSc, PhD, DSc
Emeritus Professor of Anatomy
The University of Manchester
Manchester, UK

Craig Andrew Cunningham BSc (Hons), PhD, FRAI
Senior Lecturer of Human Anatomy
Centre for Anatomy and Human Identification
University of Dundee
Dundee, UK

Anthony V D'Antoni MS, DC, PhD
Assistant Professor of Anatomy in Radiology
Division of Anatomy, Department of Radiology
Weill Cornell Medicine
New York, NY, USA

Ignacio Delgado-Martínez MD, PhD
Department of Neurosurgery
Hospital del Mar Medical Research Institute (IMIM)
Barcelona, Spain

Emmanuel D'Heygere MD
Otolaryngologist
Department of Otolaryngology
AZ Groeninge Hospital,
Kortrijk, Belgium

Peter Dockery BSc, PhD
Established Professor of Anatomy
Anatomy School of Medicine
National University of Ireland, Galway
Galway, Ireland

Ronald H Douglas BSc, PhD, FLS
Professor of Visual Science
Division of Optometry and Visual Science
City, University of London
London, UK

Klaus D Engel MSc, PhD
Senior Principal Key Expert Visualization
Siemens Healthcare GmbH, SHS TE DTI,
Erlangen, Germany

Jaeike Welmoed Faber MD, MSc PhD candidate
Department of Medical Biology
Amsterdam University Medical Centers
Amsterdam, The Netherlands

Juan C Fernandez-Miranda MD
Associate Professor of Neurological Surgery;
Associate Director, Center for Cranial Base Surgery;
Director, Surgical Neuroanatomy Laboratory
University of Pittsburgh Medical Center
Pittsburgh, PA, USA

Erin P Fillmore BA, MPH, PhD
Associate Professor of Clinical Anatomy
Warwick Medical School, University of Warwick
Coventry, UK

Roland A Fleck FRCPath, FRMS
Professor of Ultrastructural Imaging
Centre for Ultrastructural Imaging
King's College London
London, UK

Quentin Fogg BSc (Hons), PhD, FRCPS (Glasg)
Associate Professor
Department of Anatomy and Neuroscience
The University of Melbourne
Melbourne, VIC, Australia

Matthew J Forshaw MA, MSc, MB, BChir, FRCS
Consultant Upper Gastrointestinal and General Surgeon
Glasgow Royal Infirmary
Glasgow, UK

David Nicholas Furness BSc, PhD
Professor of Cellular Neuroscience
School of Life Sciences
Keele University
Newcastle-under-Lyme, UK

Donna Geddes DMU, PostGrad Dip (Sci), PhD
Professor
School of Molecular Sciences
Faculty of Science
The University of Western Australia
Perth, WA, Australia

Andrew George MBE, MA, PhD, DSc, FRCPath, FHEA, FRSA, FRSB
Emeritus Professor of Immunology
Brunel University London
London, UK

Michael Gleeson MD, FRCS, FRACS, FDS
Professor of Skull Base Surgery
University College London
The National Hospital for Neurology and Neurosurgery
London, UK

James J Going MB, ChB, PhD, MRCP, FRCPath
Consultant Pathologist
Queen Elizabeth University Hospital
Glasgow, Scotland

Leonard G Gomella MD, FACS
Professor and Chair
Department of Urology
Thomas Jefferson University
Philadelphia, PA, USA

Michael A Gorin MD
Assistant Professor of Urology
Johns Hopkins University School of Medicine
Baltimore, MD, USA

Michael A Hall MB ChB, FRCPCH, FRCP, DCH
Visiting Professor of Neonatology
School of Health Sciences
University of Southampton
Southampton, UK

Nobutaka Hirokawa MD, PhD
Project Professor
Department of Cell Biology and Anatomy
Graduate School of Medicine, University of Tokyo
Tokyo, Japan

Andrea Hofbauer MA
Global Product Manager
Siemens Healthcare GmbH
Erlangen, Germany

Simon Holmes BDS, MBBS, FDS, RCS, FRCS
Professor of Craniofacial Traumatology
Department of Oral and Maxillofacial Surgery
Royal London Hospital, Queen Mary University of London
London, UK

Claire Hopkins MA (Oxon), FRCS (ORLHNS), DM
Consultant Ear, Nose and Throat Surgeon
Guy's and St Thomas' Hospitals;
Professor of Rhinology
King's College London
London, UK

Joe Iwanaga DDS, PhD
Associate Professor
Department of Neurosurgery
Tulane University School of Medicine
New Orleans, LA, USA

Eric Jauniaux MD, PhD, FRCOG
Professor in Obstetrics and Fetal Medicine
EGA Institute for Women's Health
Faculty of Population Health Sciences,
University College London
London, UK

Bjarke Jensen PhD
Assistant Professor
Department of Medical Biology
Amsterdam University Medical Centers
Amsterdam, The Netherlands

Mickey Karram MD
Director of Urogynecology
The Christ Hospital
Clinical Professor of Obstetrics and Gynecology
University of Cincinnati
Cincinnati, OH, USA

Abraham L Kierszenbaum MD, PhD
Emeritus Medical (Clinical) Professor of Cell Biology and Anatomy
The City University of New York School of Medicine/Sophie Davis Biomedical Education Program
New York, NY, USA

Uday Kishore PhD
Brunel University London
Uxbridge, London, UK

Aaron J Krych MD
Professor
Orthopedic Surgery and Sports Medicine
Mayo Clinic
Rochester, MN, USA

Shigeru Kuratani PhD
Chief Scientist
Evolutionary Morphology Laboratory
RIKEN Cluster for Pioneering Research (CPR)
Kobe, Japan

Joey Edward Lai-Cheong BMedSci (Hons), MBBS, PhD, FRCP
Consultant Dermatologist
Frimley Health NHS Foundation Trust
Windsor, UK

Simon Lambert BSc, MBBS, FRCS, FRCSEdOrth
Consultant Orthopaedic Surgeon
Department of Trauma and Orthopaedics
University College London Hospital NHS Foundation Trust
Honorary Consultant Orthopaedic Surgeon
Great Ormond Street Hospital for Children
London, UK

CONTRIBUTORS

Robert F LaPrade MD, PhD
Complex Knee Surgeon
Twin Cities Orthopedics
Edina, MN, USA

John Gerard Lawrenson BSc, MSc (Oxon), PhD, FCOptom
Professor of Clinical Visual Science
Division of Optometry and Visual Science
City, University of London
London, UK

Roger Lemon BSc, PhD, MA, FMedSci
Sobell Professor of Neurophysiology
Queen Square Institute of Neurology
University College London
London, UK

James Logan MBBS, BSc, PGDip (SEM), FRCS (Tr and Orth)
Orthopaedic Hand Surgeon
Royal Surrey County Hospital
Guildford, UK

Marios Loukas MD, PhD
Professor of Anatomy, Dean of Basic Sciences
Department of Anatomical Sciences
St George's University
Grenada, West Indies;
Department of Anatomy
University of Warmia and Mazury
Olsztyn, Poland

Ellen A Lumpkin PhD
Professor of Cell & Developmental Biology and of Neurobiology
Department of Molecular & Cell Biology
Helen Wills Neuroscience Institute
University of California, Berkeley
Berkeley, CA, USA

Andrew Macdonald BSc (Hons), MB BS, MPhil, FRCSEd (Gen)
Consultant Upper Gastrointestinal Surgeon
Glasgow Royal Infirmary
Glasgow, UK

M Makarova MD
Institute of Microbiology and Infection
University of Birmingham
Birmingham, UK

John A McGrath MD, FRCP, FMedSci
Mary Dunhill Chair in Cutaneous Medicine
St John's Institute of Dermatology
King's College London
London, UK

Seyed Ali Mirjalili MD, PhD, PGDipSurg
Senior Lecturer of Anatomy
Anatomy and Medical Imaging Department
University of Auckland
Auckland, New Zealand

Zoltán Molnár MD, DPhil
Professor of Developmental Neurobiology
Department of Physiology, Anatomy and Genetics and St John's College
University of Oxford
Oxford, UK

Garrett D Moore MFA, DPM
Instructor
Department of Orthopedics
University of Colorado, Anschutz Medical Campus
Aurora, CO, USA

Antoon FM Moorman PhD
Emeritus Professor of Embryology
Department of Medical Biology
Amsterdam University Medical Centers
Amsterdam, The Netherlands

Gillian Morriss-Kay DSc, Hon FAS
Emeritus Professor of Developmental Anatomy
Department of Physiology, Anatomy and Genetics
Emeritus Fellow of Balliol College
University of Oxford
Oxford, UK

Thomas P Naidich MD, FACR
Professor of Radiology, Neurosurgery & Pediatrics
Irving and Dorothy Regenstreif Research Professor of Neuroscience (Neuroimaging)
Department of Radiology
Icahn School of Medicine at Mt Sinai
New York, NY, USA

Donald Anthony Neumann PT, PhD, FAPTA
Professor, Physical Therapy Program
Marquette University
Milwaukee, WI, USA

Shigeo Okabe MD, PhD
Department of Cellular Neurobiology
The University of Tokyo
Tokyo, Japan

Dylan M Owen MSci, MRes, PhD
Department of Physics;
Randall Division of Cell and Molecular Biophysics
King's College London
London, UK

Eric M Pauli MD, FACS, FASGE
Professor of Surgery
Director of Endoscopic Surgery
Chief, Division of Minimally Invasive and Bariatric Surgery
Department of Surgery
Penn State Hershey Medical Center
Hershey, PA, USA

Erlick AC Pereira MA, BM, BCh, DM, FRCS (Neuro Surg), SFHEA
Senior Lecturer in Neurosurgery, Honorary Consultant Neurosurgeon
St George's University of London
St George's University Hospitals
London, UK

Jeffrey L Ponsky MD
Professor of Surgery
Department of General Surgery
Cleveland Clinic Lerner College of Medicine;
Professor of Surgery
School of Medicine
Case Western Reserve University
Cleveland, OH, USA

Eitan Prisman MD, MA, FRCSC
Otolaryngology Head and Neck Surgery
University of British Columbia
Vancouver, BC, Canada

Ruth Richardson MA, DPhil, FRHistS
Senior Visiting Research Fellow
Centre for Life-Writing Research
King's College London;
Affiliated Scholar in the History and Philosophy of Science, University of Cambridge, UK

Charles B Rosen MD
Professor of Surgery
Division of Transplantation Surgery
Mayo Clinic
Rochester, MN, USA

Alistair Ross MB, FRCS
Consultant Orthopaedic Surgeon
The Bath Clinic
Bath, UK

Martin Scaal PhD
Professor of Anatomy and Developmental Biology
University of Cologne
Cologne, Germany

Jeremy D Schmahmann MD, FAAN, FANA, FANPA
Professor of Neurology
Harvard Medical School;
Founding Director, Massachusetts General Hospital Ataxia Center
Director, Laboratory for Neuroanatomy and Cerebellar Neurobiology
Cognitive Behavioral Neurology Unit
Senior Clinical Neurologist
Department of Neurology
Massachusetts General Hospital
Boston, MA, USA

Justine Schober MD
Director of Academic Research
Department of Medical Education
Pediatric Urologist
Department of Urology
UPMC Hamot
Erie, PA, USA

Andrew J Sidebottom BDS, FDSRCS (Eng), MBChB, FRCS (Eng), FRCS (OMFS)
Consultant Oral and Maxillofacial Surgeon
Nottingham University Hospitals
Honorary Assistant (Consultant) Professor
University of Nottingham
Nottingham, UK

Jonathan MW Slack FMedSci
Emeritus Professor of Developmental Biology
Department of Biology and Biochemistry
University of Bath
Bath, UK

Guirish Solanki MBBS, FRCSI, FRCS (SN)
Consultant Neurosurgeon
BMI The Priory & Edgbaston Hospital
Birmingham, UK

Jane C Sowden PhD
Professor of Developmental Biology and Genetics
National Institute of Health Research (NIHR) Senior Investigator
Head of Stem Cells and Regenerative Medicine Section
UCL Great Ormond Street Institute of Child Health
University College London
London, UK

Robert J Spinner PhD
Chair, Department of Neurologic Surgery
Burton M Onofrio MD Professor of Neurosurgery
Professor of Orthopedics and Anatomy
Mayo Clinic
Rochester, MN, USA

Jonathan D Spratt MA(Cantab), FRCS(Eng), FRCR
Clinical Director of Diagnostic Radiology
City Hospitals Sunderland NHS Foundation Trust
Sunderland, UK;
Visiting Professor of Anatomy
Former Anatomy Examiner for the Royal College of Surgeons of England and Royal College of Radiologists

Susan Standring MBE, PhD, DSc, FRBS, FKC, Hon FAS, Hon FRCS
Emeritus Professor of Anatomy
King's College London
London, UK

Mark D Stringer MS, FRCP, FRCS, FRCSEd, FRACS
Honorary Professor,
University of Otago Wellington
Paediatric Surgeon
Wellington Children's Hospital
Wellington, New Zealand

Julia Sun MB BCh BAO, BSc, FRCR
Clinical Fellow in Cardiothoracic Radiology
Royal Papworth Hospital
Cambridge, UK

Andrew T Strong MD
Clinical Instructor in Surgery
Department of General Surgery
Cleveland Clinic Lerner College of Medicine of Case Western Reserve University
Cleveland, OH, USA

Yosuke Takei MD, PhD
Professor
Department of Anatomy and Neuroscience
Faculty of Medicine
University of Tsukuba
Tsukuba, Japan

Cheryll Tickle CBE, FRS, FRSE, FMedSci, HonFRSB, HonFAS
Emeritus Professor
University of Bath
Bath, UK

Andoni P Toms MBBS, PhD, FRCR
Honorary Professor of Radiology
Department of Radiology
Norfolk & Norwich University Hospital
Norwich, UK

Kimberly S Topp PT, PhD, FAAA, Hon FAS
Professor and Chair Emeritus
Physical Therapy and Rehabilitation Science
University of California San Francisco
San Francisco, CA, USA

R Shane Tubbs MS, PA-C, PhD
Professor
Departments of Neurosurgery, Neurology and Structural and Cellular Biology
Program Director of Anatomical Research
Clinical Neuroscience Research Center
Director of Surgical Anatomy
Tulane University School of Medicine
New Orleans, LA, USA;
Professor of Human Gross and Developmental Anatomy
Department of Anatomical Sciences
St George's University
Grenada, West Indies;
Faculty
National Skull Base Foundation
Thousand Oaks, CA, USA;
Professor
Institute for Systems Biology
Seattle WA, USA
Faculty
Department of Neurosurgery and Ochsner Neuroscience Institute, Ochsner Health System
New Orleans, LA, USA

Abigail Saffron Tucker DPhil, MA, BA
Professor of Development & Evolution
Centre for Craniofacial and Regenerative Biology
King's College London
London, UK

Richard Tunstall BMedSci, PhD, FHEA
Professor of Clinical Anatomy and Imaging
Warwick Medical School
University of Warwick, UK;
Professor of Clinical Anatomy
West Midlands Surgical Training Centre
UHCW NHS Trust
Coventry, UK;
Applied Surgical Anatomy Lead
Royal College of Surgeons
London, UK

Tom Turmezei MPhil, MA, BMBCh, PhD, FRCR
Consultant Radiologist
Norfolk and Norwich University Hospital
Norwich, UK
Honorary Senior Lecturer, University of East Anglia, UK
Royal College of Radiologists 2020 Roentgen Professor

Albert van Schoor BSc MedSci, BSc (Hons) Neuroanatomy, MSc, PhD
Professor
Department of Anatomy
University of Pretoria
Pretoria, South Africa

Francesco Vergani MD, PhD, FRCS (Surg Neurol)
Consultant Neurosurgeon
King's College Hospital
London, UK

Andry Vleeming PhD
Professor of Clinical Anatomy
University of New England
College of Osteopathic Medicine
Biddeford, ME, USA;
Department of Rehabilitation Sciences and Physiotherapy
Faculty of Medicine and Health Sciences
Ghent University
Ghent, Belgium

Dara Walsh BSc
Biomedical Communicator
Graduate Entry Medical School
University Hospitals Limerick Group
University of Limerick
Limerick, Ireland

Jeremy PT Ward PhD, FTPS
Emeritus Professor of Respiratory Cell Physiology
King's College London
London, UK

Peter J Ward PhD
Professor of Anatomy
Department of Biomedical Sciences
West Virginia School of Osteopathic Medicine
Lewisburg, WV, USA

David Warwick MD, BM, Dip IMC, Eur Dip Hand Surg, FRCS FRCS (Orth)
Consultant Hand Surgeon and Honorary Professor, Faculty of Medicine
University Hospital Southampton,
Southampton, UK

Koichi Watanabe MD, PhD
Professor of Anatomy
Department of Anatomy
Kurume University School of Medicine
Kurume, Japan

John C Watkinson MSC, MS, FRCS, FRCS(ENT), DLO
Honorary Senior Lecturer and Consultant ENT
Queen Elizabeth Hospital, University of Birmingham NHS Trust
Royal Marsden and Brompton Hospitals
Honorary Consultant Head and Neck and Thyroid Surgeon
University Hospital, Coventry, Warwick NHS Trust
Honorary Consultant ENT/Head and Neck and Thyroid Surgeon
Great Ormond Street Hospital
Honorary Senior Anatomy Demonstrator
University College London
Business Director, Endocrine MDT
The BUPA Cromwell Hospital
London, UK

Adam C Watts MBBS, BSc, FRCS Ed (Tr and Ortho)
Consultant Elbow Surgeon
Upper Limb Unit
Wrightington Hospital
Wigan, UK

Jonathan Weir-McCall MBChB, PhD, FRCR
University Lecturer and Consultant in Cardiothoracic Radiology in the Royal Papworth Hospital and University of Cambridge
Cambridge, UK

Caroline B Wigley BSc, PhD
Retired Preclinical Tutor
University of Exeter Medical School
Exeter, UK

Jan Wilke
Department of Sports Medicine
Goethe-Universität Frankfurt am Main
Germany

Frank H Willard PhD
Professor of Anatomy
University of New England College of Osteopathic Medicine
Biddeford, ME, USA

Stephanie J Woodley PhD, MSc, BPhty
Associate Professor
Department of Anatomy, School of Biomedical Sciences
University of Otago
Dunedin, New Zealand

Patrick J Woodman DO, MS, FACOOG (Dist.), FACS
Clinical Professor of Osteopathic Surgical Specialties
Department of Obstetrics & Gynecology
Urogynecology Division
Michigan State University College of Osteopathic Medicine
East Lansing, MI, USA

Hoi Tik Hyde Yuen MD
Fellow
Female Pelvic Medicine and Reconstructive Surgery
The Christ Hospital
Cincinnati, OH, USA

Karl Zilles MD, PhD, ML†
Professor of Neuroanatomy
Institute of Neuroscience and Medicine
Research Center Jülich
Jülich, Germany

HISTORICAL INTRODUCTION

Gray's Anatomy is now more than 160 years old. The book is a rarity in textbook publishing in having been in continuous publication on both sides of the Atlantic Ocean since 1858, an exceptionally long era for a textbook. Of course, the volume now is very different from the one Mr Henry Gray first created with his colleague Dr Henry Vandyke Carter in mid-Victorian London. In this introductory essay, I shall explain the long history of *Gray's*, from those Victorian days right up to today.

The shortcomings of existing anatomical textbooks probably impressed themselves on Henry Gray when he was still a student at St George's Hospital Medical School, near London's Hyde Park Corner, in the early 1840s. He began thinking about creating a new anatomy textbook a decade later, while war was being fought in the Crimea. New legislation was being planned that would establish the General Medical Council (1858) to regulate professional education and standards.

Gray was 28 years old, and a teacher himself at St George's. He was very able, hard-working and highly ambitious, already a Fellow of the Royal Society and of the Royal College of Surgeons. Although little is known about his personal life, his was a glittering career so far, achieved while he served and taught on the hospital wards and in the dissecting room (**Fig. 1**) (Anon 1908).

Gray shared the idea for the new book with a talented clinical colleague on the teaching staff at St George's, Henry Vandyke Carter, in November 1855. Carter was from a family of Scarborough artists, and was himself a talented artist and experienced microscopist (**Fig. 2**). He had produced fine illustrations for Gray's scientific publications before, but could see that this idea was a much more complex project. Carter recorded in his diary:

> *'Little to record. Gray made proposal to assist by drawings in bringing out a Manual for students: a good idea but did not come to any plan … too exacting, for would not be a simple artist'* (Carter 1855).

Neither of these young men was interested in producing a pretty book, or an expensive one. Their purpose was to supply an affordable, accurate teaching aid for people like their own students, who might soon be required to operate on real patients, or on soldiers injured at Sebastopol or some other battlefield. The book they planned together was a practical one, designed to encourage youngsters to study anatomy, help them pass exams and assist them as budding surgeons. It was not simply an anatomy textbook, but a guide to dissecting procedure, and to the major operations.

Gray and Carter belonged to a generation of anatomists ready to infuse the study of human anatomy with a new, and respectable, scientificity. Disreputable aspects of the profession's history, acquired during the days of body-snatching, were assiduously being forgotten. The Anatomy Act of 1832 had legalized the requisition of unclaimed bodies from workhouse and hospital mortuaries, and the study of anatomy (now with its own Inspectorate) was rising in respectability in Britain. The private anatomy schools that had flourished in the Regency period were closing their doors, and the major teaching hospitals were erecting new, purpose-built dissection rooms (Richardson 2000).

The best-known student works when Gray and Carter had qualified were probably Erasmus Wilson's *Anatomist's Vade Mecum*, and *Elements of Anatomy* by Jones Quain. Both works were small – pocket-sized – but Quain came in two thick volumes. Their small pages of dense type, and even smaller illustrations, were somewhat daunting, seeming to demand much nose-to-the-grindstone effort from the reader.

The planned new textbook's dimensions and character were serious matters. Pocket manuals were commercially successful because they appealed to students by offering much knowledge in a small compass. But pocket-sized books had button-sized illustrations. Knox's *Manual of Human Anatomy*, for example, was only 6 inches by 4 (15 × 10 cm) and few of its illustrations occupied more than one-third of a page. Gray and Carter must have discussed this matter between themselves, and with Gray's publisher, JW Parker & Son, before decisions were taken about the size and girth of the new book, and especially the size of its illustrations. While Gray and Carter were working on the book, a new edition of *Quain's* was published; this time it was a 'triple-decker' – in three volumes – of 1740 pages in all.

The two men were earnestly engaged for the following 18 months in work for the new book. Gray wrote the text, and Carter created the illustrations; all the dissections were undertaken jointly. Their working days were long – all the hours of daylight, eight or nine hours at a stretch – right through 1856, and well into 1857. We can infer from the

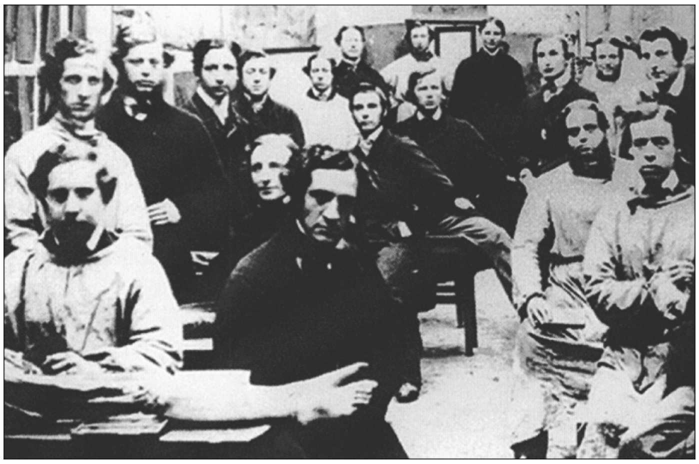

Fig. 1 Henry Gray (1827–1861) is shown here in the foreground, seated by the feet of the cadaver. The photograph was taken by a medical student, Joseph Langhorn. The room is the dissecting room of St George's Hospital Medical School in Kinnerton Street, London. Gray is shown surrounded by staff and students. When the photo was taken, on 27 March 1860, Carter had left St George's, to become Professor of Anatomy and Physiology at Grant Medical College, in Bombay (nowadays Mumbai). The second edition of *Gray's Anatomy* was in its proof stages, to appear in December 1860. Gray died just over a year later, in June 1861, at the height of his powers.

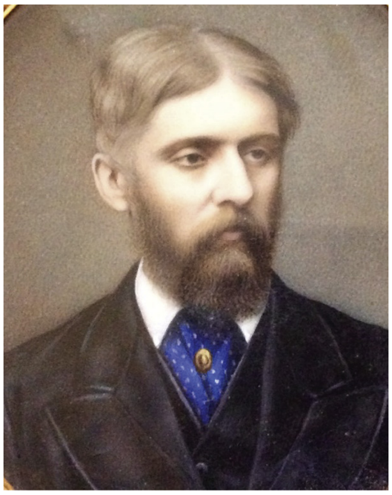

Fig. 2 Henry Vandyke Carter (1831–1897). Carter was appointed Honorary Physician to Queen Victoria in 1890. (Self portrait painted while Carter was in India, courtesy of Professor Susan Standring.)

warmth of Gray's appreciation of Carter in his published acknowledgements that their collaboration was a happy one.

> *'The Author gratefully acknowledges the great services he has derived in the execution of this work, from the assistance of his friend, Dr. H. V. Carter, late Demonstrator of Anatomy at St George's Hospital. All the drawings from which the engravings were made, were executed by him,* (Gray 1858).

With all the dissections completed, and Carter's inscribed woodblocks at the engravers, Gray took six months' leave from his teaching at St George's to work as a personal doctor for a wealthy family. It was probably as good a way as any to get a well-earned break from the dissecting room and the dead-house (Nicol 2002).

Carter sat the examination for medical officers in the East India Company, and sailed for India in the spring of 1858, when the book was still in its proof stages. Gray had left a trusted colleague, Timothy Holmes, to see it through the press. Holmes's association with the first edition would later prove vital to its survival. Gray looked over the final galley proofs, just before the book finally went to press.

THE FIRST EDITION

The book Gray and Carter had created together, *Anatomy, Descriptive and Surgical*, appeared at the very end of August 1858, to immediate acclaim. Reviews in *The Lancet* and the *British Medical Journal* were highly complimentary, and students flocked to buy.

It is not difficult to understand why it was a runaway success. *Gray's Anatomy* knocked its competitors into a cocked hat. It was considerably smaller and more slender than the doorstopper with which modern readers are familiar. The book held well in the hand, it felt substantial, and it contained everything required. To contemporaries, it was small enough to be portable, but large enough for decent illustrations: 'royal octavo' – 9½ × 6 inches (24 × 15 cm) – about two-thirds of modern A4 size. Its medium-size, single-volume format was far removed from *Quain's*, yet double the size of Knox's *Manual*.

Simply organized and well designed, the book explains itself confidently and well; the clarity and authority of the prose are manifest. But what made it unique for its day was the outstanding size and quality of the illustrations. Gray thanked the wood engravers Butterworth and Heath for the 'great care and fidelity' they had displayed in the engravings, but it was really to Carter that the book owed its extraordinary success.

The beauty of Carter's illustrations resides in their diagrammatic clarity, quite atypical for their time. The images in contemporary anatomy books were usually 'proxy-labelled': dotted with tiny numbers or letters (often hard to find or read) or bristling with a sheaf of numbered arrows, referring to a key situated elsewhere, usually in a footnote, which was sometimes so lengthy it wrapped round on to the following page. Proxy labels require the reader's eye to move to and fro: from the structure to the proxy label to the legend and back again. There was plenty of scope for slippage, annoyance and distraction. Carter's illustrations, by contrast, unify name and structure, enabling the eye to assimilate both at a glance. We are so familiar with Carter's images that it is hard to appreciate how incredibly modern they must have seemed in 1858. The volume made human anatomy look new, exciting and accessible.

The first edition was covered in a brown bookbinder's cloth embossed all over in a dotted pattern, and with a double picture-frame border. Its spine was lettered in gold blocking:

GRAY'S
ANATOMY

with 'DESCRIPTIVE AND SURGICAL' in small capitals underneath. *Gray's Anatomy* is how it has been referred to ever since. Carter was given credit with Gray on the book's title page for undertaking all the dissections on which the book was based, and sole credit for all the illustrations, though his name appeared in a significantly smaller type, and he was described as the 'Late Demonstrator in Anatomy at St George's Hospital' rather than being given his full current title, which was Professor of Anatomy and Physiology at Grant Medical College, Bombay. Gray was still only a Lecturer at St George's and he may have been aware that his words had been upstaged by the quality of Carter's anatomical images. He need not have worried: Gray is the famous name on the spine of the book.

Gray was paid £150 for every thousand copies sold. Carter never received a royalty payment, just a one-off fee at publication, which may have allowed him to purchase the long-wished-for microscope he took with him to India.

The first edition print-run of 2000 copies sold out swiftly. A parallel edition was published in the United States in 1859, and Gray must have been deeply gratified to have to revise an enlarged new English edition in 1859–60, though he was surely saddened and worried by the death of his publisher, John Parker junior, at the young age of 40, while the book was going through the press. The second edition came out in the December of 1860 and it too sold like hot cakes.

The following summer, in June 1861, at the height of his powers and full of promise, Henry Gray died unexpectedly at the age of only 34. Gray had contracted smallpox while nursing his nephew. A new strain of the disease was more virulent than the one with which Gray had been vaccinated as a child; the disease became confluent, and Gray died in a matter of days.

Within months, the whole country would be pitched into mourning for the death of Prince Albert. The creative era over which he had presided – especially the decade that had flowered since the Great Exhibition of 1851 – would be history.

THE BOOK SURVIVES

Anatomy Descriptive and Surgical could have died too. With Carter in India, the death of Gray, so swiftly after that of the younger Parker, might have spelled catastrophe. Certainly, at St George's there was a sense of calamity. The grand old medical man Sir Benjamin Brodie, Sergeant-Surgeon to the Queen, and to whom *Anatomy* had been dedicated, was a great supporter of Gray and cried forlornly: 'Who is there to take his place?' (Anon 1908).

But old JW Parker ensured the survival of *Gray's* by inviting Timothy Holmes, the doctor who had helped proof-read the first edition, and who had filled Gray's shoes at the medical school, to serve as Editor for the next edition. Other long-running anatomy works, such as that of Quain, remained in print in a similar way, co-edited by other hands (Quain 1856).

Holmes (1825–1907) was another gifted St George's man, a scholarship boy who had won an exhibition to Cambridge, where his brilliance was recognized. He was a Fellow of the Royal College of Surgeons at 28. John Parker junior had commissioned him to edit *A System of Surgery* (1860–64), an important essay series by distinguished surgeons on subjects of their own choosing. Many of Holmes's authors remain important figures, even today: John Simon, James Paget, Henry Gray, Ernest Hart, Jonathan Hutchinson, Charles-Édouard Brown-Séquard and Joseph Lister. Holmes had lost an eye in an operative accident, and he had a gruff manner that terrified students, yet he published a lament for young Parker that reveals him capable of deep feeling (Holmes 1860).

John Parker senior's heart, however, was no longer in publishing. His son's death had closed down the future for him. The business, with all its stocks and copyrights, was sold to Messrs Longman and Parker retired to the village of Farnham, where he later died.

With Holmes as editor, and Longman as publisher, the immediate future of *Gray's Anatomy* was assured. The third edition appeared in 1864 with relatively few changes, Gray's estate receiving the balance of his royalty after Holmes was paid £100 for his work.

THE MISSING OBITUARY

Why no obituary appeared for Henry Gray in *Gray's Anatomy* is curious. Gray had referred to Holmes as his 'friend' in the preface to the first edition, yet it would also be true to say that they were rivals. Both had just applied for a vacant post at St George's, as Assistant Surgeon. Had Gray lived, it is thought that Holmes may not have been appointed, despite his seniority in age (Anon 1908).

Later commentators have suggested, as though from inside knowledge, that Holmes's 'proof-reading' included improving Gray's writing style. This could be a reflection of Holmes's own self-regard, but there may be some truth in it. There can be no doubt that, as Editor of seven subsequent editions of *Gray's Anatomy* (third to ninth editions, 1864–1880), Holmes added new material, and had to correct and compress passages, but it is also possible that, back in 1857, Gray's original manuscript had been left in a poor state for Holmes to sort out. In other works, Gray's writing style was lucid, but he always seems to have paid a copyist to transcribe his work prior to submission. The original manuscript of *Gray's Anatomy*, sadly, has not survived, so it is impossible to be sure how much of the finished version had actually been written by Holmes.

It may be that Gray's glittering career, or perhaps the patronage that unquestionably advanced it, created jealousies among his colleagues, or that there was something in Gray's manner that precluded affection, or that created resentments among clever social inferiors like Carter and Holmes, especially if they felt their contributions to Gray's brilliant career were not given adequate credit. Whatever the explanation, no reference to Gray's life or death appeared in *Gray's Anatomy* itself until the twentieth century (Howden et al 1918).

A SUCCESSION OF EDITORS

Holmes expanded areas of the book that Gray himself had developed in the second edition (1860), notably in 'general' anatomy (histology) and 'development' (embryology). In Holmes's time as Editor, the volume grew from 788 pages in 1864 to 960 in 1880 (ninth edition), with the histological section paginated separately in roman numerals at the front of the book. Extra illustrations were added, mainly from other published sources.

The connections with Gray and Carter, and with St George's, were maintained with the appointment of the next editor, T. Pickering Pick, who had been a student at St George's in Gray's time. From 1883 (tenth edition) onwards, Pick kept up with current research, rewrote and integrated the histology and embryology into the volume, dropped Holmes from the title page, removed Gray's preface to the first edition, and added bold subheadings, which certainly improved the appearance and accessibility of the text. Pick said he had *'tried to keep before himself the fact that the work is intended for students of anatomy rather than for the Scientific Anatomist'* (thirteenth edition, 1893).

Pick also introduced colour printing (in 1887, eleventh edition) and experimented with the addition of illustrations using the new printing method of half-tone dots: for colour (which worked) and for new black-and-white illustrations (which did not). Half-tone shades of grey compared poorly with Carter's wood engravings, still sharp and clear by comparison.

What Henry Vandyke Carter made of these changes is a rich topic for speculation. He returned to England in 1888, having retired from the Indian Medical Service full of honours, and in 1890 he was made Honorary Physician to Queen Victoria. Carter had continued researching throughout his clinical medical career in India, and became one of India's foremost bacteriologists/tropical disease specialists before there was really a name for either discipline. He made some important discoveries, including the fungal cause of mycetoma, which he described and named, and he was a key figure in confirming scientifically in India some major international discoveries, such as Hansen's discovery of the cause of leprosy, Koch's discovery of the organism causing tuberculosis and Laveran's discovery of the organism that causes malaria. Carter married late in life, and his wife was left with two young children when he died in Scarborough in 1897, aged 65. Like Gray, he received no obituary in the book, but unlike Gray, Carter received an obituary in the *British Medical Journal* that celebrated not only his achievements in India but also *'those excellent illustrations for Gray's Anatomy which have … contributed so materially to smooth the thorny path of the student of human anatomy'* (BMJ 1897).

When Pick was joined on the title page by Robert Howden (a professional anatomist from the University of Durham) in 1901 (fifteenth edition), the volume was still easily recognizable as the book Gray and Carter had created. Although many of Carter's illustrations had been revised or replaced, many others still remained. Sadly, though, an entire section (embryology) was again separately paginated, because its revision had taken longer than anticipated. *Gray's Anatomy* had grown, seemingly inexorably, and was now quite thick and heavy: 1244 pages, weighing 5 lb 8 oz/2.5 kg. Both co-editors, and perhaps also its publisher, were dissatisfied with it.

KEY EDITION: 1905

Serious decisions were taken well in advance of the next edition, which turned out to be Pick's last with Howden. Published 50 years after Gray had first suggested the idea to Carter, the 1905 (sixteenth) edition was a landmark one.

The period 1880–1930 was a difficult time for anatomical illustration, because the new techniques of photo-lithography and half-tone were not as yet perfected, and in any case could not provide the bold simplicity of line required for a book like *Gray's*, which depended so heavily on clear illustration and clear lettering. Recognizing the inferiority of half-tone illustrations by comparison with Carter's wood-engraved originals, Pick and Howden courageously decided to jettison the second-rate half-tones altogether. Most of the next edition's illustrations were either Carter's, or old supplementary illustrations inspired by his work, or newly commissioned wood engravings or line drawings, intended 'to harmonize with Carter's original figures'. They successfully emulated Carter's verve. Having fewer pages and lighter paper, the 1905 (sixteenth edition) weighed less than its predecessor, at 4 lb 11 oz/2.1 kg. Typographically, the new edition was superb.

Howden took over as sole editor in 1909 (seventeenth edition) and immediately stamped his personality on *Gray's*. He excised 'Surgical' from the title, changing it to *Anatomy Descriptive and Applied*, and removed Carter's name altogether. He also instigated the beginnings of an editorial board of experts for *Gray's*, by adding to the title page 'Notes on Applied Anatomy' by AJ Jex-Blake and W Fedde Fedden, both St George's men. For the first time, the number of illustrations exceeded one thousand. Howden was responsible for the significant innovation of a short historical note on Henry Gray himself, nearly 60 years after his death, which included a portrait photograph (1918, twentieth edition).

THE NOMENCLATURE CONTROVERSY

Howden's era, and that of his successor TB Johnston (of Guy's), was overshadowed by a cloud of international controversy concerning anatomical terminology. European anatomists were endeavouring to standardize anatomical terms, often using Latinate constructions, a move resisted in Britain and the United States. *Gray's* became mired in these debates for over 20 years. The attempt to be fair to all sides by using multiple terms doubtless generated much confusion amongst students, until a working compromise was at last arrived at in 1955 (thirty-second edition, 1958).

Johnston oversaw the second retitling of the book (in 1938, twenty-seventh edition): it was now, officially, *Gray's Anatomy*, finally ending the fiction that it had ever been known as anything else. *Gray's* suffered from paper shortages and printing difficulties in World War II, but successive editions nevertheless continued to grow in size and weight, while illustrations were replaced and added as the text was revised.

Between Howden's first sole effort (1909, seventeenth edition) and Johnston's last edition (1958, thirty-second edition), *Gray's* expanded by over 300 pages – from 1296 to 1604 pages, and almost 300 additional illustrations brought the total to over 1300. Johnston also introduced X-ray plates (1938) and, in 1958 (thirty-second edition), electron micrographs by AS Fitton-Jackson, one of the first occasions on which a woman was credited with a contribution to *Gray's*. Johnston felt compelled to mention that she was 'a blood relative of Henry Gray himself', perhaps by way of mitigation.

AFTER WORLD WAR II

The editions of *Gray's* issued in the decades immediately following World War II give the impression of intellectual stagnation. Steady expansion continued in an almost formulaic fashion, with the insertion of additional detail. The central historical importance of innovation in the success of *Gray's* seems to have been lost sight of by its publishers and editors: Johnston (1930–1958, twenty-fourth to thirty-second editions), J Whillis (co-editor with Johnston, 1938–1954), DV Davies (1958–1967, thirty-second to thirty-fourth editions) and F Davies (co-editor with DV Davies 1958–1962, thirty-second to thirty-third editions). *Gray's* had become so pre-eminent that perhaps complacency crept in, or editors were too daunted or too busy to confront the 'massive undertaking' of a root and branch revision (Tansey 1995). The unexpected deaths of three major figures associated with *Gray's* in this era, James Whillis, Francis Davies and David Vaughan Davies – each of whom had been ready to take the editorial reins – may have contributed to retarding the process. The work became somewhat dull.

KEY EDITION: 1973

DV Davies had recognized the need for modernization, but his unexpected death left the work to other hands. Two Professors of Anatomy at Guy's, Roger Warwick and Peter Williams, the latter of whom had been involved as an indexer for *Gray's* for several years, regarded it as an honour to fulfil Davies's intentions.

Their thirty-fifth edition of 1973 was a significant departure from tradition. Over 780 pages (of 1471) were newly written, almost a third of the illustrations were newly commissioned, and the captions for the illustrations were freshly written throughout. With a complete re-typesetting of the text in larger double-column pages, a new index and the innovation of a bibliography, this edition of *Gray's* looked and felt quite unlike its 1967 (thirty-fourth edition) predecessor, and much more like its modern incarnation.

This 1973 edition departed from earlier volumes in other significant ways. The editors made explicit their intention to try to counter the impetus towards specialization and compartmentalization in twentieth-century medicine, by embracing and attempting to reintegrate the complexity of the available knowledge. Warwick and Williams openly renounced the pose of omniscience adopted by many textbooks, believing it important to accept and mention areas of ignorance or uncertainty. They shared with the reader the difficulty of keeping abreast in the sea of research, and accepted with a refreshing humility the impossibility of fulfilling their own ambitious programme.

Warwick and Williams's 1973 edition had much in common with Gray and Carter's first edition. It was bold and innovative – respectful of its heritage, while also striking out into new territory. It was visually attractive and visually informative. It embodied a sense of a treasury of information laid out for the reader (Williams and Warwick 1973). It was published simultaneously in the United States (the American *Gray's* had developed a distinct character of its own in the interval), and sold extremely well there (Williams and Warwick 1973).

The influence of the Warwick and Williams edition was forceful and long-lasting, and set a new pattern for the following quarter-century. As has transpired several times before, wittingly or unwittingly, a new editor was being prepared for the future: Professor Susan Standring (of Guy's and subsequently King's College London), who created the new bibliography for the 1973 edition of *Gray's*, went on to serve on the editorial board, and has served as Editor-in-Chief for the last three editions before this one (2005–2016, thirty-ninth, fortieth and forty-first editions). These editions are important for different reasons.

For the thirty-ninth edition, the entire content of *Gray's* was reorganized, from systematic to regional anatomy. This great sea-change was not just organizational but historic, because, since its outset, *Gray's* had prioritized bodily systems, with subsidiary emphasis on how the systems interweave in the regions of the body. Professor Standring explained that this regional change of emphasis had long been asked for by readers and users of *Gray's*, and that new imaging techniques had raised the clinical importance of regional anatomy (Standring 2005). The change was facilitated by an enormous collective effort on the part of the editorial team and the illustrators. The subsequent and current editions, now also containing a substantial online-only component including an imaging library, consolidate that momentous change (see **Table 1**).

TABLE 1 ***Gray's Anatomy*** **Editions**

Edition	Date	Author/Editor(s)	Publisher	Title
1st	1858	Henry Gray	JW Parker & Son	*Anatomy Descriptive and Surgical*
		The drawings by Henry Vandyke Carter. The dissections jointly by the author and Dr Carter		
2nd	1860	Henry Gray	JW Parker & Son	
3rd	1864	T Holmes	Longman	
4th	1866	T Holmes	Longman	
5th	1869	T Holmes	Longman	
6th	1872	T Holmes	Longman	
7th	1875	T Holmes	Longman	
8th	1877	T Holmes	Longman	
9th	1880	T Holmes	Longman	
10th	1883	TP Pick	Longman	
11th	1887	TP Pick	Longman	
12th	1890	TP Pick	Longman	
13th	1893	TP Pick	Longman	
		Gray's preface removed		
14th	1897	TP Pick	Longman	
15th	1901	TP Pick & R Howden	Longman	
16th	1905	TP Pick & R Howden	Longman	
17th	1909	Robert Howden	Longman	*Anatomy Descriptive and Applied*
		Notes on applied anatomy by AJ Jex-Blake & W Fedde Fedden		
18th	1913	Robert Howden & Blake & Fedden	Longman	
19th	1916	Robert Howden & Blake & Fedden	Longman	
20th	1918	Robert Howden & Blake & Fedden	Longman	
		First edition to feature a photograph and obituary of Henry Gray		
21st	1920	Robert Howden	Longman	
		Notes on applied anatomy by AJ Jex-Blake & John Clay		
22nd	1923	Robert Howden	Longman	
		Notes on applied anatomy by John Clay & John D Lickley		
23rd	1926	Robert Howden	Longman	
24th	1930	TB Johnston	Longman	
25th	1932	TB Johnston	Longman	
26th	1935	TB Johnston	Longman	
27th	1938	TB Johnston & J Whillis	Longman	*Gray's Anatomy*
28th	1942	TB Johnston & J Whillis	Longman	
29th	1946	TB Johnston & J Whillis	Longman	
30th	1949	TB Johnston & J Whillis	Longman	
31st	1954	TB Johnston & J Whillis	Longman	
32nd	1958	TB Johnston & DV Davies & F Davies	Longman	

Continued

TABLE 1 ***Gray's Anatomy*** **Editions—cont'd**

Edition	Date	Author/Editor(s)	Publisher	Title
33rd	1962	DV Davies & F Davies	Longman	
34th	1967	DV Davies & RE Coupland	Longman	
35th	1973	Peter L Williams & Roger Warwick	Longman	
		With a separate volume: *Functional Neuroanatomy of Man* – being the neurology section of *Gray's Anatomy*, 35th edition, 1975		
36th	1980	Roger Warwick & Peter L Williams	Churchill Livingstone	
37th	1989	Peter L Williams	Churchill Livingstone	
38th	1995	Peter L Williams & Editorial Board	Churchill Livingstone	
39th	2005	Susan Standring & Editorial Board	Elsevier	*The Anatomical Basis of Clinical Practice*
40th	2008	Susan Standring & Editorial Board	Elsevier	*The Anatomical Basis of Clinical Practice*
41st	2016	Susan Standring & Editorial Board	Elsevier	*The Anatomical Basis of Clinical Practice*
42nd	2021	Susan Standring & Editorial Board	Elsevier	*The Anatomical Basis of Clinical Practice*

THE DOCTORS' BIBLE

Neither Gray nor Carter, the young men who – by their committed hard work between 1856 and 1858 – created the original *Gray's Anatomy*, would have conceived that so many years after their deaths their book would not only be a household name, but also be regarded as a work of such pre-eminent importance that a novelist half a world away would rank it as cardinal – alongside the Bible and Shakespeare – to a doctor's education (Sinclair Lewis 1925, Richardson 2008). From this forty-second edition of *Gray's Anatomy*, we can look back to appraise the long-term value of their efforts. We can discern how the book they created triumphed over its competitors, and has survived pre-eminent. *Gray's* is a remarkable publishing phenomenon. Although the volume now looks quite different to the original, and contains so much more, its kinship with the *Gray's Anatomy* of 1858 is easily demonstrable by direct descent, every edition updated by Henry Gray's successor. Works are rare indeed that have had such a long history of continuous publication on both sides of the Atlantic, and such a useful one.

Ruth Richardson, MA, DPhil, FRHistS
Senior Visiting Research Fellow, Centre for Life-Writing Research, King's College London;
Affiliated Scholar in the History and Philosophy of Science, University of Cambridge, UK

ACKNOWLEDGEMENTS

For their assistance while I was undertaking the research for this essay, I should like to thank the Librarians and Archivists and Staff at the British Library, Society of Apothecaries, London School of Hygiene and Tropical Medicine, Royal College of Surgeons, Royal Society of Medicine, St Bride Printing Library, St George's Hospital Tooting, Scarborough City Museum and Art Gallery, University of Reading, Wellcome Institute Library, Westminster City Archives and Windsor Castle; and the following individuals: Anne Bayliss, Gordon Bell, David Buchanan, Dee Cook, Arthur Credland, Chris Hamlin, Victoria Killick, Louise King, Keith Nicol, Sarah Potts, Mark Smalley and Nallini Thevakarrunai. Above all, my thanks to Brian Hurwitz, who has read and advised on the evolving text.

References

Anon 1908 Henry Gray. St George's Hospital Gazette 16:49–54.
BMJ 1897 Henry Vandyke Carter, M.D.Lond. [Obiturary]. Br Med J 1:1256.
Carter HV 1855 Diary. Wellcome Western Manuscript 5818; 25 Nov.
Gray H 1858 Preface. In: Anatomy: Descriptive and Surgical. London: JW Parker & Son.
Holmes T (ed.) 1860 I: Preface. In: A System of Surgery. London: JW Parker & Son.
Howden R, Jex-Blake AJ, Fedde Fedden W (eds) 1918 Gray's Anatomy, 20th ed. London: Longman.
Nicol KE 2002 Henry Gray of St George's Hospital: a Chronology. London: published by the author.
Quain J 1856 Elements of Anatomy. Edited by Sharpey W, Ellis GV. London: Walton & Maberly.
Richardson R 2000 Death, Dissection and the Destitute. Chicago: Chicago University Press; pp. 193–249, 287, 357.
Richardson R 2008 The Making of Mr Gray's Anatomy. Oxford: Oxford University Press.
Sinclair Lewis H 1925 Martin Arrowsmith. New York: Harcourt Brace; p. 4.
Standring S (ed) 2005 Preface. In: Gray's Anatomy, 39th ed. London: Elsevier.
Tansey EM 1995 A brief history of Gray's Anatomy. In: Williams PL (ed), Gray's Anatomy, 38th ed. London: Churchill Livingstone.
Williams PL, Warwick R (eds) 1973 Preface. In: Gray's Anatomy, 35th ed. London: Churchill Livingstone.

ANATOMICAL NOMENCLATURE

Anatomy is the study of the structure of the body. Conventionally, it is divided into topographical (macroscopic or gross) anatomy (which may be further divided into regional anatomy, surface anatomy, neuroanatomy, endoscopic and imaging anatomy); developmental anatomy (embryogenesis and subsequent organogenesis); and the anatomy of microscopic and submicroscopic structure (histology).

Anatomical language is one of the fundamental languages of medicine. The unambiguous description of thousands of structures is impossible without an extensive and often highly specialized vocabulary. Ideally, these terms, which are often derived from Latin or Greek, should be used to the exclusion of any other, and eponyms should be avoided. In reality, this does not always happen. Many terms are vernacularized and, around the world, synonyms and eponyms still abound in the literature, in medical undergraduate classrooms and in clinics and operating theatres. The 2nd edition of the *Terminologia Anatomica*,[1] drawn up by the Federative Committee on Anatomical Terminology (FCAT) and newly published in 2019, continues to serve as our reference source for the terminology for macroscopic anatomy, and the text of the 42nd edition of *Gray's Anatomy* is almost entirely TA2-compliant. However, where terminology is at variance with, or, more likely, is not included in, the TA, the alternative term used either is cited in the relevant consensus document or position paper, or enjoys widespread clinical usage. Synonyms and eponyms are given in parentheses on first usage of a preferred term and not shown thereafter in the text; an updated list of eponyms and short biographical details of the clinicians and anatomists whose names are used in this way is available in the e-book for reference purposes (see Preface, p. ix, for further discussion of the use of eponyms).

When medical students begin dissection classes they are often surprised by the range of anatomical variation that they encounter amongst the cadavers in the laboratory. As they progress to clinical examination and study their patients' X-ray, CT, MRI or ultrasound images, they encounter further variations that prompt the age-old question, 'what is normal, and what is beyond the range of anatomical normality?' The interested reader is directed to *Bergman's Comprehensive Encyclopedia of Human Anatomic Variation*, which 'attempts to capture many of the known variants of the human form'.[2]

PLANES, DIRECTIONS AND RELATIONSHIPS

To avoid ambiguity, all anatomical descriptions assume that the body is in the conventional 'anatomical position', i.e. standing erect and facing forwards, upper limbs by the side with the palms facing forwards, and lower limbs together with the toes facing forwards (Fig. 1). Descriptions are based on four imaginary planes – median, sagittal, coronal and horizontal – applied to a body in the anatomical position. The median plane passes longitudinally through the body and divides it into right and left halves. The sagittal plane is any vertical plane parallel with the median plane; although often employed, 'parasagittal' is therefore redundant and should not be used. The coronal (frontal) plane is orthogonal to the median plane and divides the body into anterior (front) and posterior (back). The horizontal (transverse) plane is orthogonal to both median and sagittal planes. Radiologists refer to transverse planes as (trans)axial; convention dictates that axial anatomy is viewed as though looking from the feet towards the head.

Structures nearer the head are superior, cranial or (sometimes) cephalic (cephalad), whereas structures closer to the feet are inferior; caudal is most often used in embryology to refer to the hind end of the embryo. Medial and lateral indicate closeness to the median plane, medial being closer than lateral; in the anatomical position, the little finger is medial to the thumb, and the great toe is medial to the little toe. Specialized terms may also be used to indicate medial and lateral. Thus, in the upper limb, ulnar and radial are used to mean medial and lateral, respectively; in the lower limb, tibial and fibular (peroneal) are used to mean medial and lateral, respectively. Terms may be based on embryological relationships; the border of the upper limb that includes the thumb, and the border of the lower limb that includes the great toe are the pre-axial borders, whilst the opposite borders are the post-axial borders. Various degrees of obliquity are acknowledged using compound terms, e.g. posterolateral.

When referring to structures in the trunk and upper limb, we have freely used the synonyms anterior, ventral, flexor, palmar and volar, and posterior, dorsal and extensor. We recognize that these synonyms are not always satisfactory, e.g. the extensor aspect of the leg is anterior with respect to the knee and ankle joints, and superior in the foot and digits; the plantar (flexor) aspect of the foot is inferior. Dorsal (dorsum) and ventral are terms used particularly by embryologists and neuroanatomists; they therefore feature most often in Sections 2 and 3.

Distal and proximal are used particularly to describe structures in the limbs, taking the datum point as the attachment of the limb to the trunk (sometimes referred to as the root), such that a proximal structure is closer to the attachment of the limb than a distal structure. However, proximal and distal are also used in describing branching structures, e.g. bronchi, vessels and nerves. External (outer) and internal (inner) refer to the distance from the centre of an organ or cavity, e.g. the layers of the body wall, or the cortex and medulla of the kidney. External and internal can also describe rotation that is lateral or medial, respectively, e.g. at the hip or shoulder joints. Superficial and deep are used to describe the relationships between adjacent structures. Ipsilateral refers to the same side (of the body, organ or structure), bilateral to both sides, and contralateral to the opposite side.

Teeth are described using specific terms that indicate their relationship to their neighbours and to their position within the dental arch; these terms are described on page 646.

---

[1] *Terminologia Anatomica 2* (2019) is the joint creation of the Federative Committee on Anatomical Terminology (FCAT) and the Member Associations of the International Federation of Associations of Anatomists (IFAA).

[2] Tubbs RS, Shoja MM, Loukas M 2016 Bergman's Comprehensive Encyclopedia of Human Anatomic Variation. Hoboken, NJ: Wiley–Blackwell.

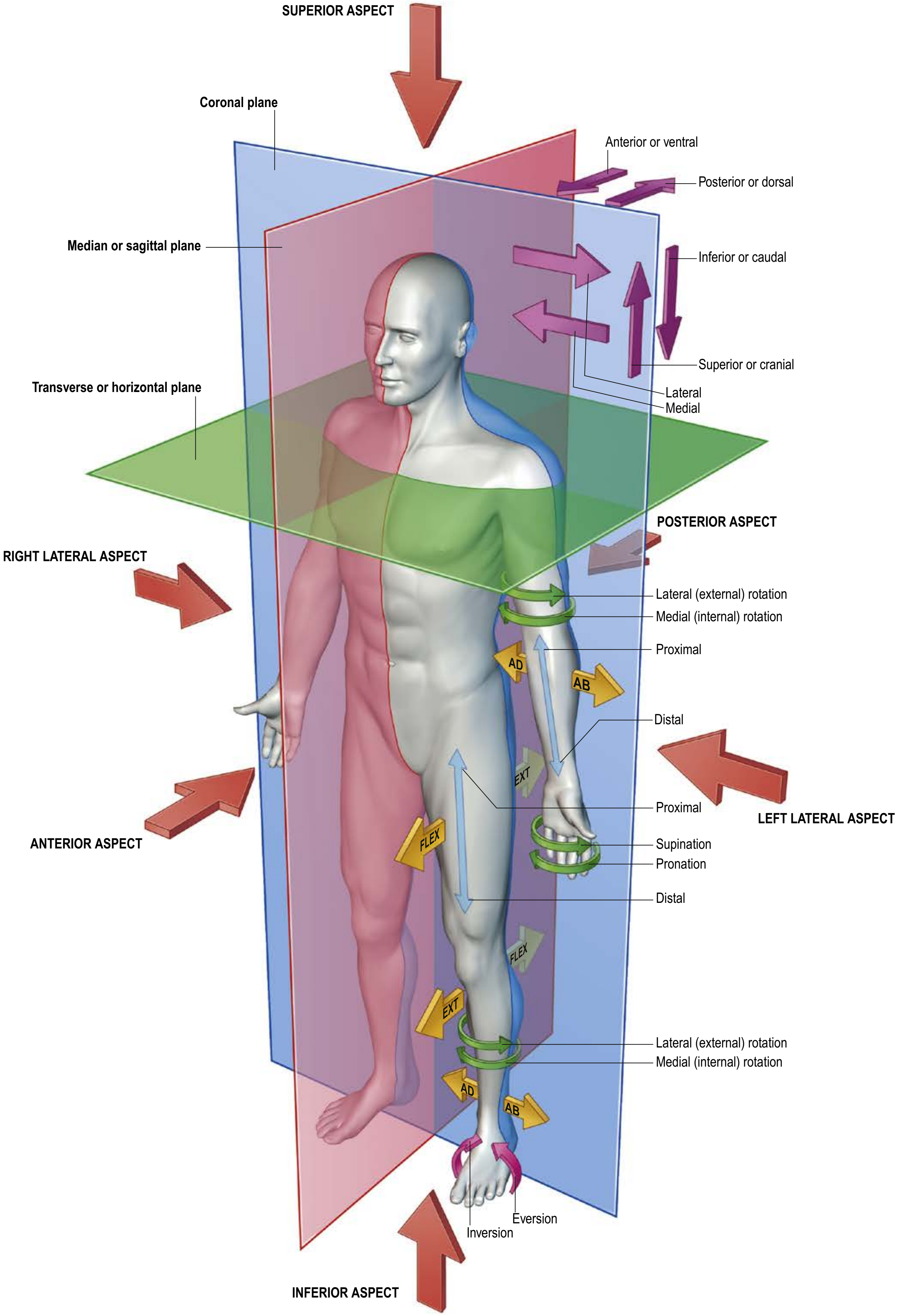
SUPERIOR ASPECT
Coronal plane
Anterior or ventral
Posterior or dorsal
Median or sagittal plane
Inferior or caudal
Superior or cranial
Transverse or horizontal plane
Lateral
Medial
POSTERIOR ASPECT
RIGHT LATERAL ASPECT
Lateral (external) rotation
Medial (internal) rotation
Proximal
AD
AB
Distal
EXT
LEFT LATERAL ASPECT
Proximal
ANTERIOR ASPECT
FLEX
Supination
Pronation
Distal
FLEX
EXT
Lateral (external) rotation
Medial (internal) rotation
AD
AB
Eversion
Inversion
INFERIOR ASPECT

Fig. 1 The terminology widely used in descriptive anatomy. Abbreviations shown on arrows: AD, adduction; AB, abduction; FLEX, flexion (of the thigh at the hip joint); EXT, extension (of the leg at the knee joint).

CHAPTER

1

Basic structure and function of cells

CELL STRUCTURE

General characteristics of cells

The shapes of mammalian cells vary widely depending on their interactions with each other, their extracellular environment and internal structures. Their surfaces are often highly folded when absorptive or transport functions take place across their boundaries. Cell size is limited by rates of diffusion, either that of material entering or leaving cells, or that of diffusion within them. Movement of macromolecules can be much accelerated and also directed by processes of active transport across the plasma membrane and by transport mechanisms within the cell. According to the location of absorptive or transport functions, apical microvilli (Fig. 1.1) or basolateral infoldings create a large surface area for transport or diffusion.

Motility is a characteristic of most cells, in the form of movements of cytoplasm or specific organelles from one part of the cell to another. It also includes: the extension of parts of the cell surface such as pseudopodia, lamellipodia, filopodia and microvilli; locomotion of entire cells, as in the amoeboid migration of tissue macrophages; the beating of flagella or cilia to move the cell (e.g. in spermatozoa) or fluids overlying it (e.g. in respiratory epithelium); cell division; and muscle contraction. Cell movements are also involved in the uptake of materials from their environment (endocytosis, phagocytosis) and the passage of large molecular complexes out of cells (exocytosis, secretion).

Epithelial cells rarely operate independently of each other and commonly form aggregates by adhesion, often assisted by specialized intercellular junctions. They may also communicate with each other, either by generating and detecting molecular signals that diffuse across intercellular spaces, or more rapidly by generating interactions between membrane-bound signalling molecules. Cohesive groups of cells constitute tissues, and more complex assemblies of tissues form functional systems or organs.

Most cells are between 5 and 50 µm in diameter: e.g. resting lymphocytes are 6 µm across, red blood cells 7.5 µm and columnar epithelial cells 20 µm tall and 10 µm wide (all measurements are approximate). Some cells are much larger than this: e.g. megakaryocytes of the bone marrow and osteoclasts of the remodelling bone are more than 200 µm in diameter. Neurones and skeletal muscle cells have relatively extended shapes, some of the former being over 1 m in length.

Cellular organization

Each cell is contained within its limiting plasma membrane, which encloses the cytoplasm. All cells, except mature red blood cells, also contain a nucleus that is surrounded by a nuclear membrane or envelope (see Fig. 1.1; Fig. 1.2). The nucleus includes: the genome of the cell contained within the chromosomes; the nucleolus; and other subnuclear structures. The cytoplasm contains cytomembranes and several membrane-bound structures, called organelles, which form separate

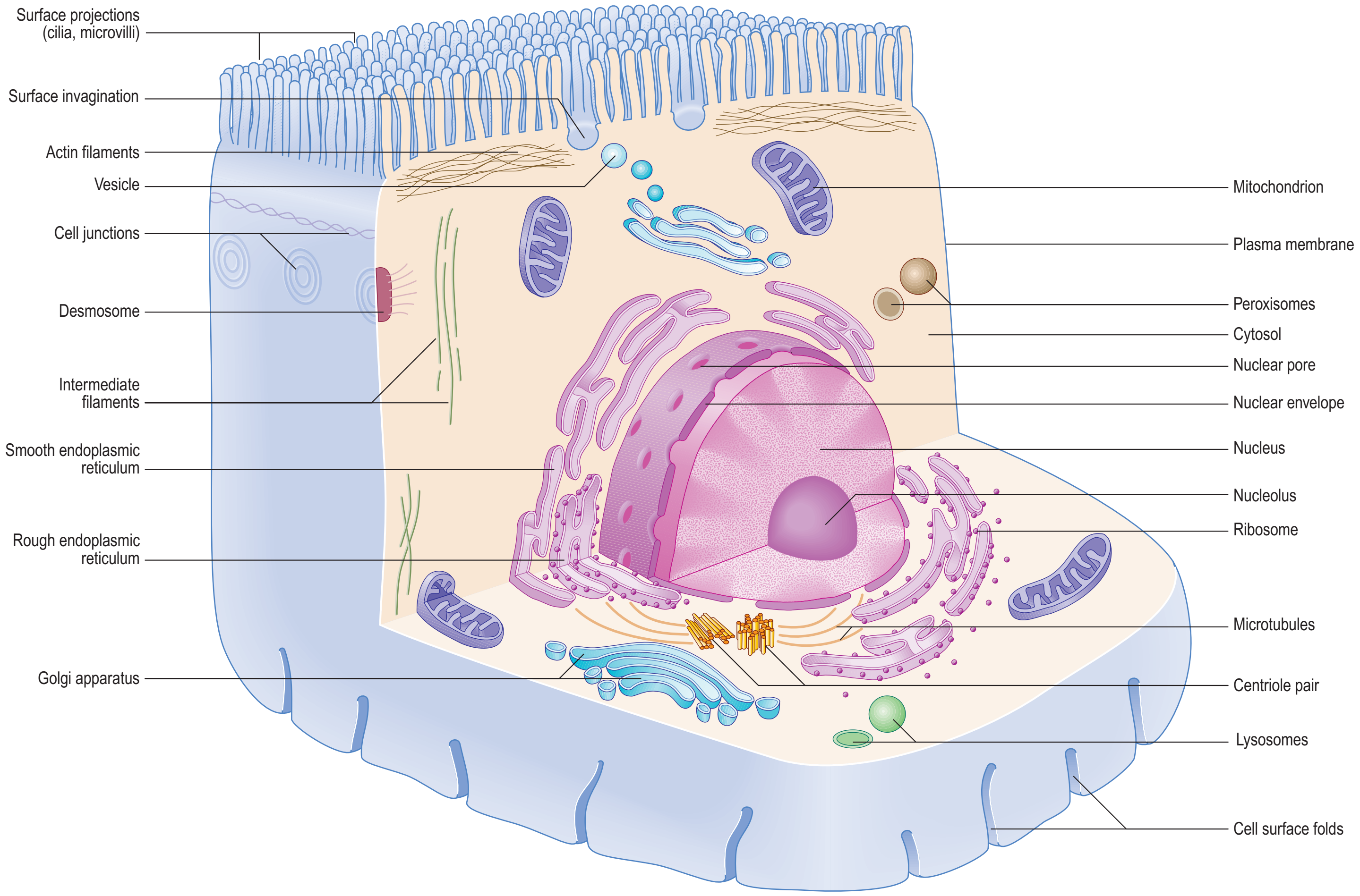
Surface projections (cilia, microvilli)
Surface invagination
Actin filaments
Vesicle
Cell junctions
Desmosome
Intermediate filaments
Smooth endoplasmic reticulum
Rough endoplasmic reticulum
Golgi apparatus
Mitochondrion
Plasma membrane
Peroxisomes
Cytosol
Nuclear pore
Nuclear envelope
Nucleus
Nucleolus
Ribosome
Microtubules
Centriole pair
Lysosomes
Cell surface folds

Fig. 1.1 The main structural components and internal organization of a generalized cell.

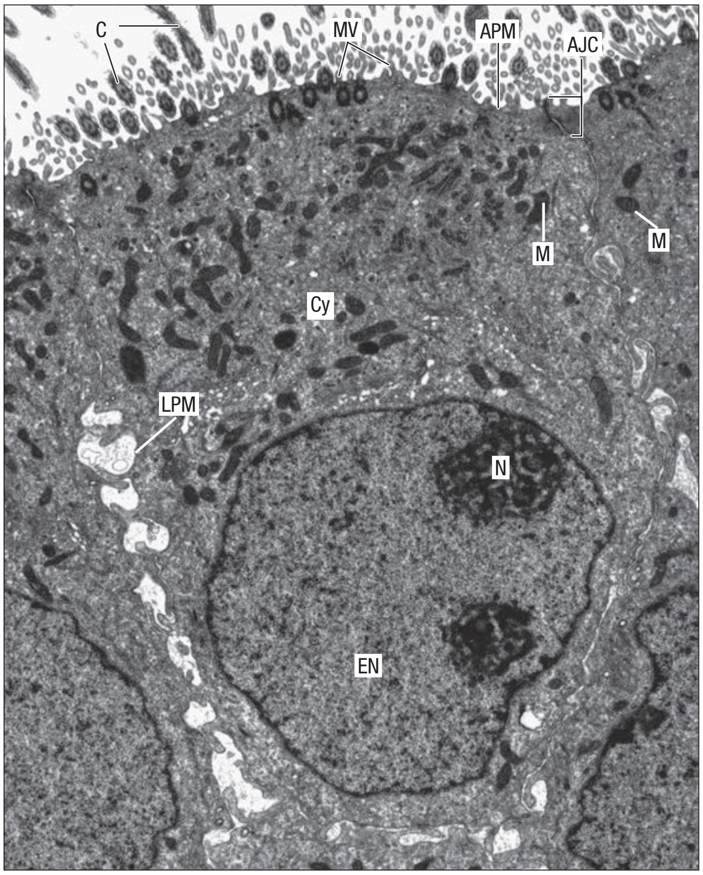

Fig. 1.2 The structural organization and some principal organelles of a typical cell. This example is a ciliated columnar epithelial cell from human nasal mucosa. The central cell, which occupies most of the field of view, is closely apposed to its neighbours along their lateral plasma membranes. Within the apical junctional complex, these membranes form a tightly sealed zone (tight junction) that isolates underlying tissues from, in this instance, the nasal cavity. Abbreviations: AJC, apical junctional complex; APM, apical plasma membrane; C, cilia; Cy, cytoplasm; EN, euchromatic nucleus; LPM, lateral plasma membrane; M, mitochondria; MV, microvilli; N, nucleolus. (Courtesy of Dr Bart Wagner, Histopathology Department, Sheffield Teaching Hospitals, UK.)

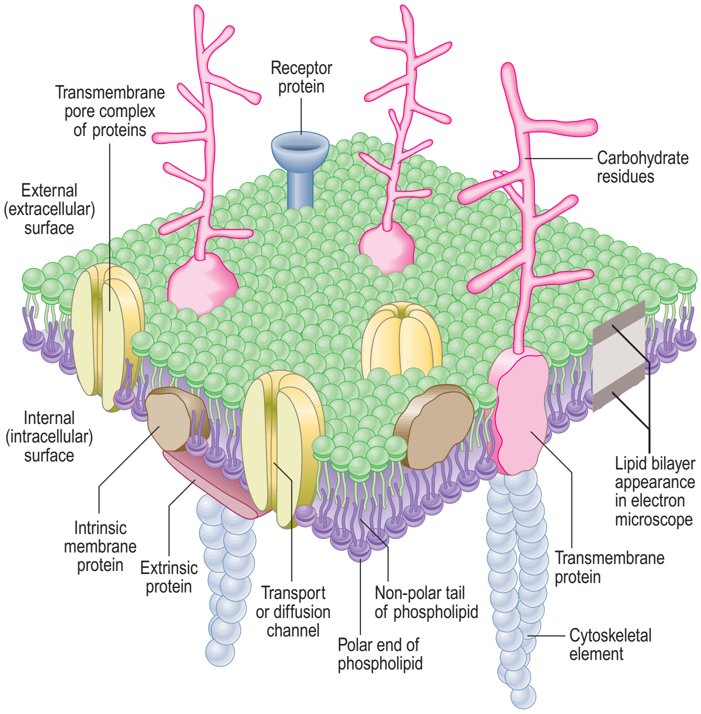
Transmembrane pore complex of proteins
Receptor protein
Carbohydrate residues
External (extracellular) surface
Internal (intracellular) surface
Lipid bilayer appearance in electron microscope
Intrinsic membrane protein
Extrinsic protein
Transport or diffusion channel
Non-polar tail of phospholipid
Polar end of phospholipid
Transmembrane protein
Cytoskeletal element

Fig. 1.3 The molecular organization of the plasma membrane, according to the fluid mosaic model of membrane structure. Intrinsic or integral membrane proteins include diffusion or transport channel complexes, receptor proteins and adhesion molecules. These may span the thickness of the membrane (transmembrane proteins) and can have both extracellular and cytoplasmic domains. Transmembrane proteins have hydrophobic zones, which cross the phospholipid bilayer and allow the protein to 'float' in the plane of the membrane. Some proteins are restricted in their freedom of movement where their cytoplasmic domains are tethered to the cytoskeleton.

and distinct compartments within the cytoplasm. Cytomembranes include the rough and smooth endoplasmic reticulum and Golgi apparatus, as well as vesicles derived from them. Organelles include lysosomes, peroxisomes and mitochondria. The nucleus and mitochondria are enclosed by a double-membrane system; lysosomes and peroxisomes have a single bounding membrane. There are also non membrane-bound structures, called inclusions, which lie free in the cytosolic compartment. They include glycogen aggregates and pigments (e.g. lipofuscin). In addition, ribosomes and several filamentous protein networks, known collectively as the cytoskeleton, are found in the cytosol. The cytoskeleton determines general cell shape and supports specialized extensions of the cell surface (microvilli, cilia, flagella). It is involved in the assembly of specific structures (e.g. centrioles) and controls cargo transport in the cytoplasm. The cytosol contains many soluble proteins, ions and metabolites.

Plasma membrane

Cells are enclosed by a distinct plasma membrane, which shares features with the cytomembrane system that compartmentalizes the cytoplasm and surrounds the nucleus. All membranes are composed of lipids (mainly phospholipids, cholesterol and glycolipids) and proteins, in approximately equal ratios. Plasma membrane lipids form a lipid bilayer, a layer two molecules thick. The hydrophobic ends of each lipid molecule face the interior of the membrane and the hydrophilic ends face outwards. Most proteins are embedded within, or float in, the lipid bilayer as a fluid mosaic. Some proteins, because of extensive hydrophobic regions of their polypeptide chains, span the entire width of the membrane (transmembrane proteins), whereas others are only superficially attached to the bilayer by lipid groups. Both are integral (intrinsic) membrane proteins, as distinct from peripheral (extrinsic) membrane proteins, which are membrane-bound only through their association with other proteins. Carbohydrates in the form of oligosaccharides and polysaccharides are bound either to proteins (glycoproteins) or to lipids (glycolipids), and project mainly into the extracellular domain (Fig. 1.3).

Combinations of biochemical, biophysical and biological techniques have revealed that lipids are not homogeneously distributed in membranes, but that some are organized into microdomains in the bilayer, called 'detergent-resistant membranes' or lipid 'rafts', rich in sphingomyelin and cholesterol. The ability of select subsets of proteins to partition into different lipid microdomains has profound effects on their function, e.g. in T-cell receptor and cell–cell signalling. The highly organized environment of the domains provides a signalling, trafficking and membrane fusion environment.

In the electron microscope, membranes fixed and contrasted by heavy metals such as osmium tetroxide appear in section as two densely stained layers separated by an electron-translucent zone – the classic unit membrane. The total thickness of each layer is about 7.5 nm. The overall thickness of the plasma membrane is typically 15 nm. Freeze–fracture cleavage planes usually pass along the hydrophobic portion of the bilayer, where the hydrophobic tails of phospholipids meet, and split the bilayer into two leaflets. Each cleaved leaflet has a surface and a face. The surface of each leaflet faces either the extracellular surface (ES) or the intracellular or protoplasmic (cytoplasmic) surface (PS). The extracellular face (EF) and protoplasmic face (PF) of each leaflet are artificially produced during membrane splitting. This technique has also demonstrated intramembranous particles embedded in the lipid bilayer; in most cases, these represent large transmembrane protein molecules or complexes of proteins. Intramembranous particles are distributed asymmetrically between the two half-layers, usually adhering more to one half of the bilayer than to the other. In plasma membranes, the intracellular leaflet carries most particles, seen on its face (the PF). Where they have been identified, clusters of particles usually represent channels for the transmembrane passage of ions or molecules between adjacent cells (gap junctions).

Biophysical measurements show the lipid bilayer to be highly fluid, allowing diffusion in the plane of the membrane. Thus proteins are able to move freely in such planes unless anchored from within the cell. Membranes in general, and the plasma membrane in particular, form boundaries selectively limiting diffusion and creating physiologically distinct compartments.

Transport across cell membranes

Most biological molecules cannot diffuse through the phospholipid bilayer. Specific transport proteins, such as carrier proteins and channel proteins, mediate the selective passage of molecules across the membrane, thus allowing the cell to control its internal composition. Molecules (such as oxygen and carbon dioxide) can cross the plasma membrane down their concentration gradients by dissolving first in the phospholipid bilayer and then in the aqueous environment at the cytosolic or extracellular side of the membrane. This mechanism, known as passive diffusion, does not involve membrane proteins. Lipid and lipid-soluble (e.g. steroid) substances can also cross the bilayer.

Other biological molecules (such as glucose, charged molecules and small ions H+, Na+, K+ and Cl−) are unable to dissolve in the hydrophobic interior of the phospholipid bilayer. They require the help of specific transport proteins (**Fig. 1.4**) and channel proteins, which facilitate the passage or facilitated diffusion of most biological molecules. Facilitated diffusion requires carrier proteins, which can bind specific molecules to be transported, or channel proteins, which form open gates through the membrane. Carrier proteins transport sugars, amino acids and nucleosides. Channel proteins are ion channels involved in the rapid transport of ions (faster transport than that mediated by carrier proteins), are highly selective of molecular size and electrical charge, and are not continuously open. Ligand-gated channels open 'gates' in response to the binding of a signalling molecule, whereas voltage-gated channels open in response to changes in electric potential across the membrane. Similar to passive diffusion, facilitated diffusion of biological molecules is determined by concentration and electrical gradients across a membrane.

There are three types of transport protein: uniporter, symporter, and antiporter (see Fig. 1.4). Uniporter transport proteins can be either channel proteins or carrier proteins. They are involved in facilitated diffusion and carry a single molecule at a time from one side of the membrane to the other along its concentration gradient. Symporter and antiporter transport proteins are involved in active transport, where the transporter utilizes energy, in the form of adenosine triphosphate (ATP) to mobilize molecules against their concentration gradient in order to maintain the correct concentrations of ions and molecules in cells. Symporter transport proteins are co-transporters (such as the glucose–sodium co-transporter): they carry two molecules simultaneously or sequentially in the same direction. Antiporter transport proteins, such as the sodium–potassium pump, carry two molecules simultaneously or sequentially in the opposite direction to each other.

Translocation of proteins across intracellular membranes

Proteins are generally synthesized on ribosomes in the cytosol or on the rough endoplasmic reticulum: a few are made on mitochondrial ribosomes. Once synthesized, many proteins remain in the cytosol, where they carry out their functions. Others, such as integral membrane proteins or proteins for secretion, are translocated across intracellular membranes for post-translational modification and targeting to their destinations. This is achieved by the signal sequence, an addressing system contained within the protein sequence of amino acids, which is recognized by receptors or translocators in the appropriate membrane. Proteins are sorted by their signal sequence (or set of sequences that become spatially grouped as a signal patch when the protein folds into its tertiary configuration), in order that they are recognized by and enter the correct intracellular membrane compartment.

Plasma membrane proteins also provide surfaces for the attachment of enzymes; sites for the receptors of external signals, including hormones and other ligands; and sites for the recognition and attachment of other cells. Internally, plasma membranes can act as points of attachment for intracellular structures, in particular those concerned with cell motility and other cytoskeletal functions. Cell membranes are synthesized by the rough endoplasmic reticulum in conjunction with the Golgi apparatus.

Cell coat (glycocalyx)

The external surface of a plasma membrane differs structurally from internal membranes in that it possesses an external, fuzzy, carbohydrate-rich coat, the glycocalyx, composed of the carbohydrate portions of glycoproteins and glycolipids embedded in the plasma membrane (see Fig. 1.3). The cell coat forms an integral part of the plasma membrane, projecting as a diffusely filamentous layer 2–20 nm or more from the lipoprotein surface.

The precise composition of the glycocalyx varies with cell type; many tissue and cell type-specific antigens are located in the coat, including the major histocompatibility complex of the immune system and, in the case of erythrocytes, blood group antigens. The glycocalyx therefore plays a significant role in organ transplant compatibility. The glycocalyx found on the apical microvilli of enterocytes, the cells forming the lining epithelium of the intestine, consists of enzymes involved in the digestive process. Intestinal microvilli are cylindrical projections (1–2 μm long and about 0.1 ts}μm in diameter) forming a closely packed layer called the brush border that increases the absorptive function of enterocytes (see Fig. 1.26).

Cytoplasm

Compartments and functional organization

The cytoplasm consists of the cytosol and two cytomembrane systems, the endoplasmic reticulum and Golgi apparatus, all enclosed by the cell or plasma membrane. The cytosol is a gel-like material made up of colloidal proteins such as enzymes, carbohydrates and small protein molecules, together with ribosomes and ribonucleic acids. The cytoplasm also contains membrane-bound organelles (lysosomes, peroxisomes and mitochondria), membrane-free inclusions (glycogen and pigments) and the cytoskeleton. The nuclear contents, the nucleoplasm, are separated from the cytoplasm by the nuclear envelope.

Endoplasmic reticulum

The endoplasmic reticulum is a system of interconnecting membrane-lined channels within the cytoplasm (**Fig. 1.5**). These channels take various forms, including cisternae (flattened sacs), tubules and vesicles. The membranes divide the cytoplasm into two major compartments. The intramembranous compartment, or cisternal space, is where secretory products are stored or transported to the Golgi complex and cell exterior: it is continuous with the perinuclear space.

Structurally, the channel system can be divided into rough or granular endoplasmic reticulum (RER), which has ribosomes attached to its outer, cytosolic surface, and smooth or agranular endoplasmic reticulum (SER), which lacks ribosomes. The functions of the endoplasmic reticulum vary greatly and include the synthesis, folding and transport of proteins; the biosynthesis and transport of phospholipids and

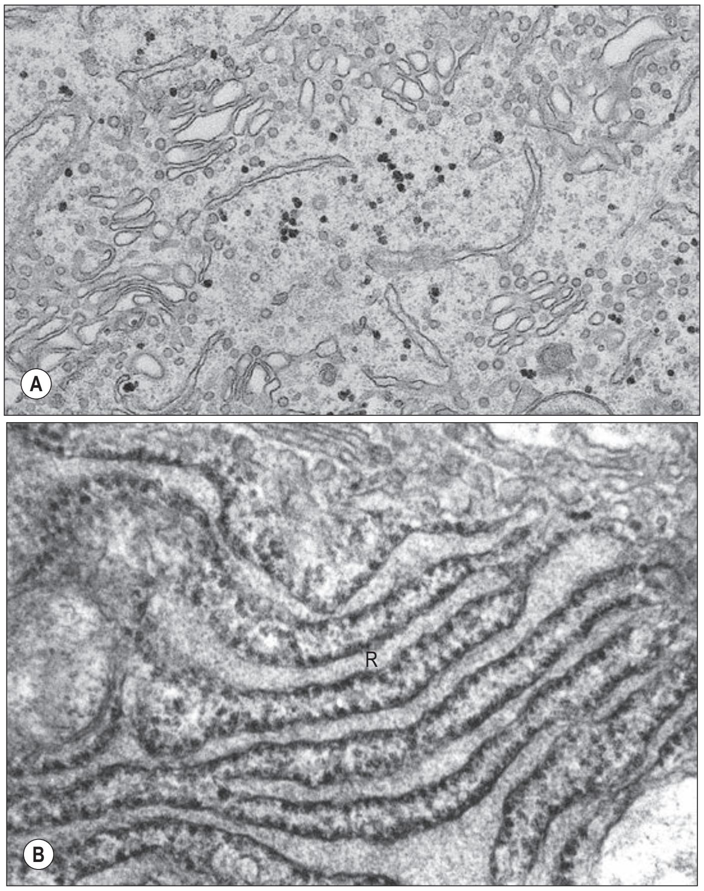

Fig. 1.5 **A**, Smooth endoplasmic reticulum with associated vesicles. The dense particles are glycogen granules. **B**, Rough endoplasmic reticulum (R), where enclosed cisternae of endoplasmic reticulum are studded with ribosomes on their cytoplasmic surfaces. (A, Courtesy of Rose Watson, Cancer Research UK. B, Courtesy of Dr Bart Wagner, Histopathology Department, Sheffield Teaching Hospitals, UK.)

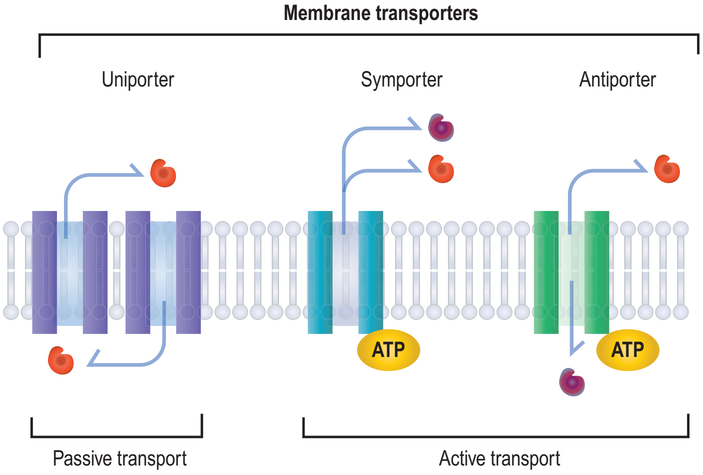

Fig. 1.4 Transporter proteins. Uniporter transport proteins are involved in facilitated diffusion (passive transport without an energy source). They carry a single molecule at a time from one side of the membrane to the other along its concentration gradient. Symporter and antiporter transport proteins are involved in active transport. In active transport, unlike passive transport, the transporter utilizes energy, in the form of adenosine triphosphate (ATP) to mobilize molecules against their concentration gradient. Symporter transport proteins are co-transporters (such as the glucose–sodium co-transporter); they carry two molecules simultaneously or sequentially in the same direction. Antiporter transport proteins, such as the sodium–potassium pump, carry two molecules simultaneously or sequentially in the opposite direction. (With permission from Kierszenbaum AL, Tres LL Histology and Cell Biology: An Introduction to Pathology, 5th ed. Elsevier. Copyright 2019.)

The glycocalyx plays a significant role in maintenance of the integrity of tissues and in a wide range of dynamic cellular processes, e.g. serving as a vascular permeability barrier and transducing fluid shear stress to the endothelial cell cytoskeleton (Weinbaum et al 2007). Disruption of the glycocalyx on the endothelial surface of large blood vessels precedes inflammation, a conditioning factor of atheromatosis (e.g. deposits of cholesterol in the vascular wall leading to partial or complete obstruction of the vascular lumen).

steroids; the degradation of glycogen; and the maintenance of calcium homeostasis. Endoplasmic reticulum (ER)-associated degradation (ERAD) is part of the cellular protein quality control system and is responsible for the clearance of misfolded proteins from the ER for cytosolic proteasomal degradation.

In general, RER is well developed in cells that produce abundant proteins, whereas SER is abundant in steroid-producing cells and muscle cells. The sarcoplasmic reticulum is a variant of the endoplasmic reticulum in muscle cells: it is involved in calcium storage and release for muscle contraction. For further reading on the endoplasmic reticulum, see Bravo et al (2013).

Smooth endoplasmic reticulum

The smooth endoplasmic reticulum (**Fig. 1.5A**) is associated with carbohydrate metabolism and many other metabolic processes, including detoxification and synthesis of lipids, cholesterol and steroids. The membranes of the smooth endoplasmic reticulum serve as surfaces for the attachment of many enzyme systems, e.g. the enzyme cytochrome P450, which is involved in important detoxification mechanisms and is thus accessible to its substrates, which are generally lipophilic. The smooth endoplasmic reticulum in hepatocytes (which are able to store glycogen) contains the enzyme glucose-6-phosphatase, which converts glucose-6-phosphate to glucose, a step in gluconeogenesis. The membranes also cooperate with the rough endoplasmic reticulum and the Golgi apparatus to synthesize new membranes; the protein, carbohydrate and lipid components are added in different structural compartments.

Rough endoplasmic reticulum

The rough endoplasmic reticulum is a site of protein synthesis; its cytosolic surface is studded with ribosomes (**Fig. 1.5B**). Ribosomes only bind to the endoplasmic reticulum when proteins targeted for secretion begin to be synthesized. Most proteins pass through its membranes and accumulate within its cisternae, although some integral membrane proteins, e.g. plasma membrane receptors, are inserted into the rough endoplasmic reticulum membrane, where they remain. After passage from the rough endoplasmic reticulum, proteins remain in membrane-bound cytoplasmic organelles such as lysosomes, become incorporated into new plasma membrane, or are secreted by the cell. Some carbohydrates are also synthesized by enzymes within the cavities of the rough endoplasmic reticulum and may be attached to newly formed protein (glycosylation). Vesicles are budded off from the rough endoplasmic reticulum for transport to the Golgi as part of the protein-targeting mechanism of the cell

Ribosomes, polyribosomes and protein synthesis

Ribosomes are macromolecular machines that catalyse the synthesis of proteins from amino acids; synthesis and assembly into subunits takes place in the nucleolus and includes the association of ribosomal RNA (rRNA) with ribosomal proteins translocated from their site of synthesis in the cytoplasm. The individual subunits are then transported into the cytoplasm, where they remain separate from each other when not actively synthesizing proteins. Ribosomes are granules approximately 25 nm in diameter, composed of rRNA molecules and proteins assembled into two unequal subunits. The subunits can be separated by their sedimentation coefficients (S) in an ultracentrifuge into larger 60S and smaller 40S components. These are associated with 73 different proteins (40 in the large subunit and 33 in the small), which have structural and enzymatic functions. Three small, highly convoluted rRNA strands (28S, 5.8S and 5S) make up the large subunit, and one strand (18S) is in the small subunit.

A typical cell contains millions of ribosomes. They may form groups (polyribosomes or polysomes) attached to messenger RNA (mRNA), which they translate during protein synthesis for use outside the system of membrane compartments, e.g. enzymes of the cytosol and cytoskeletal proteins. Some of the cytosolic products include proteins that can be inserted directly into (or through) membranes of selected organelles, such as mitochondria and peroxisomes. Ribosomes may be attached to the membranes of the rough endoplasmic reticulum (see Fig. 1.5B).

In a mature polyribosome, all the attachment sites of the mRNA are occupied as ribosomes move along it, synthesizing protein according to its nucleotide sequence. Consequently, the number and spacing of ribosomes in a polyribosome indicate the length of the mRNA molecule and hence the size of the protein being made. The two subunits have separate roles in protein synthesis. The 40S subunit is the site of attachment and translation of mRNA. The 60S subunit is responsible for the release of the new protein and, where appropriate, attachment to the endoplasmic reticulum via an intermediate docking protein that directs the newly synthesized protein through the membrane into the cisternal space.

Protein synthesis on ribosomes may be suppressed by a class of RNA molecules known as small interfering RNA (siRNA) or silencing RNA. These molecules are typically 20–25 nucleotides in length and bind (as a complex with proteins) to specific mRNA molecules via their complementary sequence. This triggers the enzymatic destruction of the mRNA or prevents the movement of ribosomes along it. Synthesis of the encoded protein is thus prevented. Their normal function may have antiviral or other protective effects; there is also potential for developing artificial siRNAs as a therapeutic tool for silencing disease-related genes.

Golgi apparatus (Golgi complex)

The Golgi apparatus is a distinct cytomembrane system located near the nucleus and the centrosome. It is particularly prominent in secretory cells and can be visualized when stained with silver or other metallic salts. Traffic between the endoplasmic reticulum and the Golgi apparatus is bidirectional and takes place via carrier vesicles derived from the donor site that bud, tether and fuse with the target site. Carrier vesicles in transit from the endoplasmic reticulum to the Golgi apparatus (anterograde transport) are coated by coat protein complex II (COPII), whereas COPI-containing vesicles function in the retrograde transport route from the Golgi apparatus (reviewed in Spang (2013)).

Golgins are long coiled-coil proteins attached to the cytoplasmic surface of cisternal membranes, forming a fibrillar matrix surrounding the Golgi apparatus to stabilize it; they have a role in vesicle trafficking (Witkos and Lowe 2015). The Golgi apparatus has several functions: it links anterograde and retrograde protein and lipid flow in the secretory pathway; it is the site where protein and lipid glycosylation occurs; and it provides membrane platforms to which signalling and sorting proteins bind.

Ultrastructurally, the Golgi apparatus (**Fig. 1.6A**) displays a continuous ribbon-like structure consisting of a stack of several flattened membranous cisternae, together with clusters of vesicles surrounding its surfaces. Cisternae differ in their enzymatic content and activity. Small transport vesicles from the rough endoplasmic reticulum are received at one face of the Golgi stack, the convex *cis*-face (entry or forming surface). Here, they deliver their contents to the first cisterna in the series by membrane fusion. The protein is transported from the edges of this cisterna to the next cisterna by vesicular budding and then fusion, and this process is repeated across medial cisternae until the final cisterna at the concave *trans*-face (exit or condensing surface) is reached. Here, larger vesicles are formed for delivery to other parts of the cell.

The *cis*-Golgi and *trans*-Golgi membranous networks form an integral part of the Golgi apparatus (**Fig. 1.6B**). The *cis*-Golgi network is a region of complex membranous channels interposed between the rough endoplasmic reticulum and the Golgi *cis*-face, which receives and transmits vesicles in both directions. Its function is to select appropriate proteins synthesized on the rough endoplasmic reticulum for delivery by vesicles to the Golgi stack, while inappropriate proteins are shuttled back to the rough endoplasmic reticulum.

The *trans*-Golgi network, at the other side of the Golgi stack, is also a region of interconnected membrane channels engaged in protein sorting. Here, modified proteins processed in the Golgi cisternae are packaged selectively into vesicles and dispatched to different parts of the cell. The packaging depends on the detection, by the *trans*-Golgi network, of particular amino acid signal sequences, leading to their enclosure in membranes of appropriate composition that will further modify their contents, e.g. by extracting water to concentrate them (vesicles entering the exocytosis pathway) or by pumping in protons to acidify their contents (lysosomes destined for the intracellular sorting pathway). The membranes contain specific signal proteins that may allocate them to microtubule-based transport pathways and allow them to dock with appropriate targets elsewhere in the cell, e.g. the plasma membrane in the case of secretory vesicles. Vesicle formation and budding at the *trans*-Golgi network involves the addition of clathrin on their external surface, to form coated pits.

Within the Golgi stack proper, proteins undergo a series of sequential chemical modifications by Golgi resident enzymes synthesized in the rough endoplasmic reticulum. These include glycosylation (changes in glycosyl groups, e.g. removal of mannose, addition of *N*-acetylglucosamine and sialic acid); sulphation (addition of sulphate groups to glycosaminoglycans); and phosphorylation (addition of phosphate groups). Some modifications serve as signals to direct proteins and lipids to their final destination within cells, including lysosomes and plasma membrane. Lipids formed in the endoplasmic reticulum are also routed for incorporation into vesicles.

Exocytic (secretory) pathway

Secreted proteins, lipids, glycoproteins, small molecules such as amines, and other cellular products destined for export from the cell are transported to the plasma membrane in small vesicles released from the *trans*-face of the Golgi apparatus. This pathway is either constitutive, in which transport and secretion occur more or less continuously, as with immunoglobulins produced by plasma cells, or it is regulated by external signals, as in the control of salivary secretion by autonomic neural stimulation. In regulated secretion, the secretory product is stored temporarily in membrane-bound secretory granules or vesicles. Exocytosis is achieved by fusion of the secretory vesicular membrane with the plasma membrane and release of the vesicle contents into the extracellular domain. In polarized cells, e.g. most epithelia, exocytosis occurs at the apical plasma membrane. Glandular epithelial cells secrete into a duct lumen, as in the pancreas, or on to a free surface, such as the lining of the stomach. In hepatocytes, bile is secreted across a very small area of plasma membrane forming the wall of the bile canaliculus. This region, the apical plasma membrane, is the site of exocrine secretion, whereas secretion of hepatocyte plasma proteins into the blood stream is targeted to the basolateral surfaces facing the sinusoids. Packaging of different secretory products into appropriate vesicles takes place in the *trans*-Golgi network. Delivery of secretory vesicles to their correct plasma membrane domains is achieved by sorting sequences in the cytoplasmic tails of vesicular membrane proteins.

Endocytic (internalization) pathway

The endocytic pathway begins at the plasma membrane and ends in lysosomes (see below) involved in the degradation of the endocytic cargo through the enzymatic activity of lysosomal hydrolases. Endocytic cargo is internalized from the plasma membrane to early endosomes and then to late endosomes. Late endosomes transport their cargo to lysosomes, where the cargo material is degraded following fusion and mixing of contents of endosomes and lysosomes. Early endosomes derive from endocytic vesicles (clathrin-coated vesicles and caveolae). Once internalized, endocytic vesicles shed their coat of adaptin and clathrin, and fuse to form an early endosome, where the receptor molecules release their bound ligands. Membrane and receptors from the early endosomes can be recycled to the cell surface as exocytic vesicles.

Clathrin-dependent endocytosis occurs at specialized patches of plasma membrane called coated pits: this mechanism is also used to

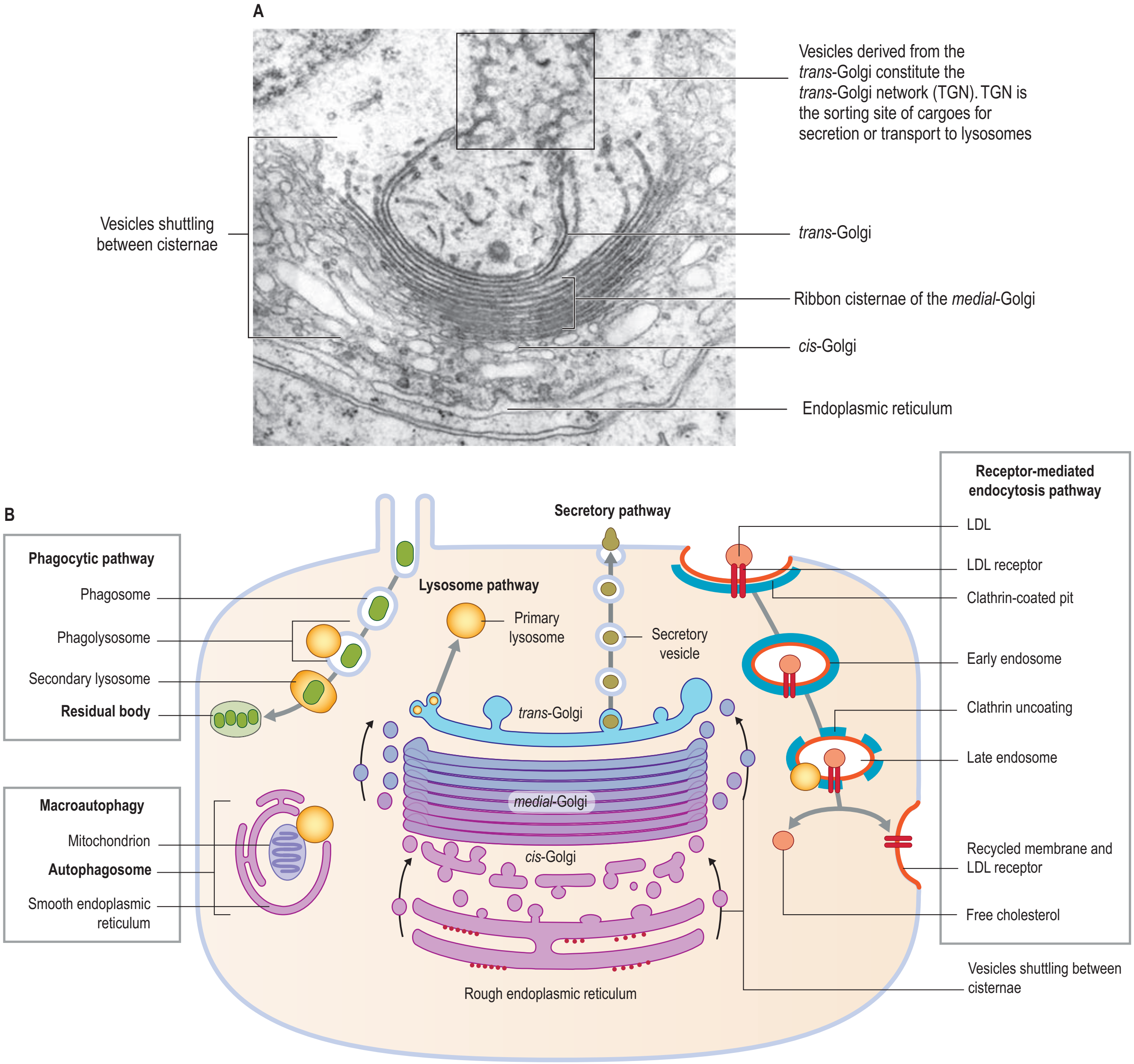
A
Vesicles derived from the trans-Golgi constitute the trans-Golgi network (TGN). TGN is the sorting site of cargoes for secretion or transport to lysosomes
Vesicles shuttling between cisternae
trans-Golgi
Ribbon cisternae of the medial-Golgi
cis-Golgi
Endoplasmic reticulum
B
Phagocytic pathway
Phagosome
Phagolysosome
Secondary lysosome
Residual body
Lysosome pathway
Primary lysosome
Secretory pathway
Secretory vesicle
trans-Golgi
medial-Golgi
cis-Golgi
Rough endoplasmic reticulum
Macroautophagy
Mitochondrion
Autophagosome
Smooth endoplasmic reticulum
Receptor-mediated endocytosis pathway
LDL
LDL receptor
Clathrin-coated pit
Early endosome
Clathrin uncoating
Late endosome
Recycled membrane and LDL receptor
Free cholesterol
Vesicles shuttling between cisternae

Fig. 1.6 **A**, The Golgi apparatus consists of four major functionally distinct compartments. Products derived from the endoplasmic reticulum enter the Golgi apparatus at the *cis*-Golgi. Cargoes exit at the *trans*-Golgi. The *medial*-Golgi is a stack of ribbon-like cisternae interposed between the *cis*-Golgi and the *trans*-Golgi. Cargoes destined for transport to lysosomes or secretion (exocytosis) are sorted in the *trans*-Golgi network (TGN). **B**, There are three major pathways for the intracellular degradation of materials. Extracellular particles can be taken up by phagocytosis and receptor-mediated endocytosis. Aged intracellular components are degraded by macroautophagy, a non-selective process. The Golgi apparatus releases vesicles for secretion or lysosome-containing vesicles that remain in the cell. Lysosomes are organelles that contain about 40 types of hydrolytic enzymes active in an acidic environment (pH approximately 5.0).

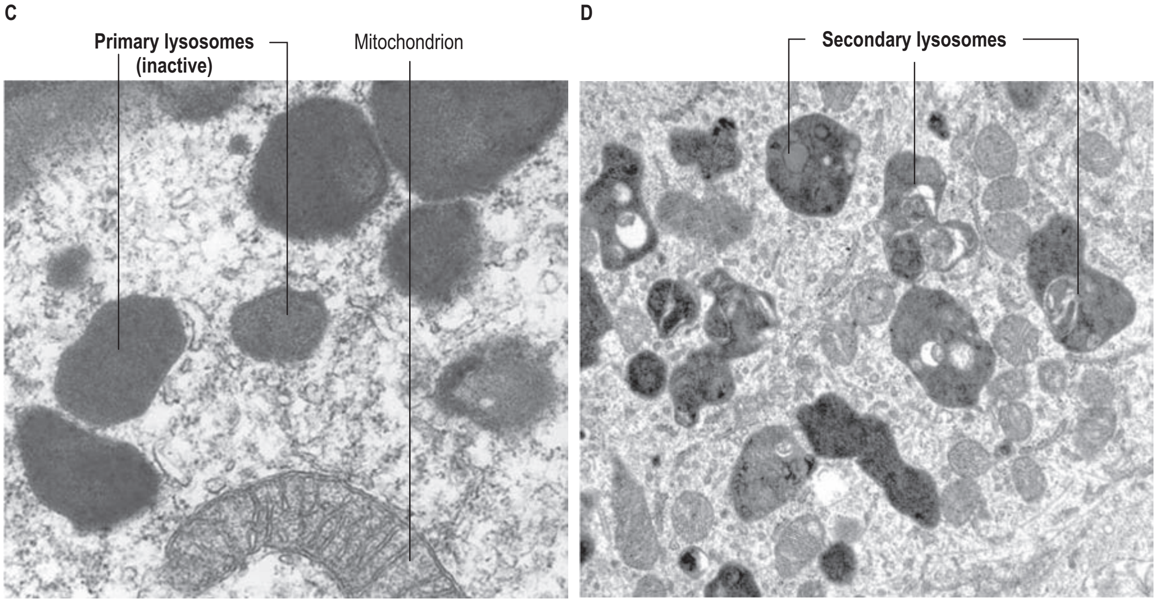

Fig. 1.6, cont'd C, Primary lysosomes are inactive storage sites for hydrolytic enzymes. **D**, Secondary lysosomes are engaged in degradation and contain remnants of the degraded structures. (A, C and D with permission from Kierszenbaum AL, Tres LL Histology and Cell Biology: An Introduction to Pathology, 5th ed. Elsevier. Copyright 2019.)

internalize ligands bound to surface receptor molecules and is also termed receptor-mediated endocytosis. Caveolae are structurally distinct pinocytotic vesicles most widely used by endothelial and smooth muscle cells, where they are involved in transcytosis, signal transduction and possibly other functions. In addition to late endosomes, lysosomes can also fuse with phagosomes, autophagosomes and plasma membrane patches for membrane repair. Lysosomal hydrolases process or degrade exogenous materials (phagocytosis or heterophagy) as well as endogenous material (autophagy). Phagocytosis consists of the cellular uptake of invading pathogens, apoptotic cells and other foreign material by specialized cells. Lysosomes are numerous in actively phagocytic cells, e.g. macrophages and neutrophil granulocytes, where they are responsible for destroying phagocytosed particles, e.g. bacteria. These cells may contain phagosomes, vesicles that potentially contain a pathogenic microorganism and that may fuse with several lysosomes.

Specialized cells of the immune system, antigen-presenting cells (APCs), degrade protein molecules (antigens) transported by the endocytic pathway for lysosomal breakdown, and expose their fragments to the cell exterior to elicit an immune response, that is mediated initially by helper T cells.

Late endosomes receive lysosomal enzymes from primary lysosomes (**Fig. 1.6C**) derived from the Golgi apparatus after late endosome–lysosome membrane tethering and fusion followed by diffusion of lysosomal contents into the endosomal lumen. The pH inside the fused hybrid organelle, now called a secondary lysosome, is low (about 5.0): this activates lysosomal acid hydrolases to degrade the endosomal contents. The products of hydrolysis are either passed through the membrane into the cytosol, or they may be retained in the secondary lysosome (**Fig. 1.6D**). Secondary lysosomes may grow considerably in size by vesicle fusion to form multivesicular bodies; the enzyme concentration may increase greatly to form large lysosomes.

Lysosomes

Lysosomes are membrane-bound organelles 80–800 nm in diameter, often with complex inclusions of material undergoing hydrolysis (secondary lysosomes). Two classes of protein participate in lysosomal function, namely soluble acid hydrolases and integral lysosomal membrane proteins. Each of the 60 or more known acid hydrolases (including proteases, lipases, carbohydrases, esterases and nucleases) degrades a specific substrate. There are about 25 lysosomal membrane proteins participating in the acidification of the lysosomal lumen, protein import from the cytosol, membrane fusion and transport of degradation products to the cytoplasm. Material that has been hydrolysed within secondary lysosomes may be completely degraded to soluble products, e.g. amino acids, which are recycled through metabolic pathways. However, degradation is usually incomplete and some debris remains. A debris-laden vesicle is called a residual body or tertiary lysosome (see Fig. 1.6B), and may be passed to the cell surface, where it is ejected by exocytosis; alternatively, it may persist inside the cell as an inert residual body. Considerable numbers of residual bodies can accumulate in long-lived cells, often fusing to form larger dense vacuoles with complex lamellar inclusions. As their contents are often darkly pigmented, this may change the colour of the tissue; e.g. in neurones, the end-product of lysosomal digestion, lipofuscin (neuromelanin or senility pigment), gives ageing brains a brownish-yellow coloration. Lysosomal enzymes may also be secreted – often as part of a process to alter the extracellular matrix, as in osteoclast-mediated erosion during bone resorption. For further reading on lysosome biogenesis, see Saftig and Klumperman (2009).

Lysosomal dysfunction

The transcription factor EB (TFEB) is responsible for regulating lysosomal biogenesis and function, lysosome-to-nucleus signalling and lipid catabolism (for further reading, see Settembre et al (2013)). If there is a failure of any of the actions of lysosomal hydrolases, of the lysosome acidification mechanism or of lysosomal membrane proteins, there is progressive lysosomal dysfunction in several tissues and organs. This may be due to faulty degradation and recycling of extracellular substrates delivered to lysosomes by the late endosome or the defective degradation and recycling of intracellular substrates by autophagy.

Lysosomal storage disorders (LSDs) are a consequence of lysosomal dysfunction. Approximately 60 different types of LSD have been identified on the basis of the type of material accumulated in cells (such as mucopolysaccharides, sphingolipids, glycoproteins, glycogen and lipofuscins).

Peroxisomes

Peroxisomes are small (0.2–1 μm in diameter) membrane-bound organelles present in most mammalian cells. They contain more than 50 enzymes responsible for multiple catabolic and synthetic biochemical pathways, in particular the β-oxidation of very-long-chain fatty acids (>C22) and the metabolism of hydrogen peroxide (hence the name peroxisome). Peroxisomes may be derived from pre-existing peroxisomes that divide by fission. Alternatively, they may arise *de novo* by budding as pre-peroxisomal vesicles from the endoplasmic reticulum and possibly from mitochondria (Farré et al 2019). All matrix proteins and some peroxisomal membrane proteins are synthesized by cytosolic ribosomes and contain a peroxisome targeting signal that enables them to be imported by proteins called peroxins (Braverman et al 2013, Theodoulou et al 2013).

Peroxisomes often contain crystalline inclusions composed mainly of high concentrations of the enzyme urate oxidase. Oxidases use molecular oxygen to oxidize specific organic substrates (such as L-amino acids, D-amino acids, urate, xanthine and very-long-chain fatty acids) and produce hydrogen peroxide that is detoxified (degraded) by peroxisomal catalase. Peroxisomes are important in the oxidative detoxification of various substances taken into or produced within cells. They are particularly numerous in hepatocytes.

LSDs are characterized by severe neurodegeneration, mental decline, and cognitive and behavioural abnormalities. Autophagy impairment caused by defective lysosome–autophagosome coupling triggers a pathogenic cascade by the accumulation of substrates that contribute to neurodegenerative disorders, including Parkinson's disease, Alzheimer's disease, Huntington's disease and several tau-opathies. In Tay–Sachs disease (GM2 gangliosidosis), a faulty β-hexosaminidase A leads to the accumulation of the glycosphingolipid GM2 ganglioside in neurones, causing death during childhood. In Danon disease, a vacuolar skeletal myopathy and cardiomyopathy with neurodegeneration in hemizygous males, lysosomes fail to fuse with autophagosomes because of a mutation of the lysosomal membrane protein LAMP-2 (lysosomal-associated membrane protein-2).

Peroxin mutation is a characteristic feature of Zellweger syndrome (craniofacial dysmorphism and malformations of brain, liver, eye and kidney; cerebrohepatorenal syndrome). Neonatal leukodystrophy is an X-linked peroxisomal disease affecting mostly males, caused by deficiency in β-oxidation of very-long-chain fatty acids.

The build-up of very-long-chain fatty acids in the nervous system and suprarenal glands determines progressive deterioration of brain function and suprarenal insufficiency (Addison's disease). For further reading, see Braverman et al (2013).

Mitochondria

Mitochondria appear in the light microscope as long, thin structures in the cytoplasm of most cells, particularly those with a high metabolic rate, e.g. secretory cells in exocrine glands. In the electron microscope, mitochondria usually appear as round or elliptical bodies 0.5–2.0 µm long (**Fig. 1.7**), consisting of an outer mitochondrial membrane; an inner mitochondrial membrane, separated from the outer membrane by an intermembrane space; cristae, infoldings of the inner membrane that harbour ATP synthase to generate ATP; and the mitochondrial matrix, a space enclosed by the inner membrane and numerous cristae. The permeability of the two mitochondrial membranes differs considerably: the outer membrane is freely permeable to many substances because of the presence of large non-specific channels formed by proteins (porins), whereas the inner membrane is permeable to only a narrow range of molecules. The presence of cardiolipin, a phospholipid, in the inner membrane may contribute to this relative impermeability.

Mitochondria are the principal source of chemical energy in most cells. They are the site of the citric acid (Krebs') cycle and the electron transport (cytochrome) pathway by which complex organic molecules are finally oxidized to carbon dioxide and water. This process provides the energy to drive the production of ATP from adenosine diphosphate (ADP) and inorganic phosphate (oxidative phosphorylation). The various enzymes of the citric acid cycle are located in the mitochondrial matrix, whereas those of the cytochrome system and oxidative phosphorylation are localized chiefly in the inner mitochondrial membrane. The intermembrane space houses cytochrome *c*, a molecule involved in activation of apoptosis.

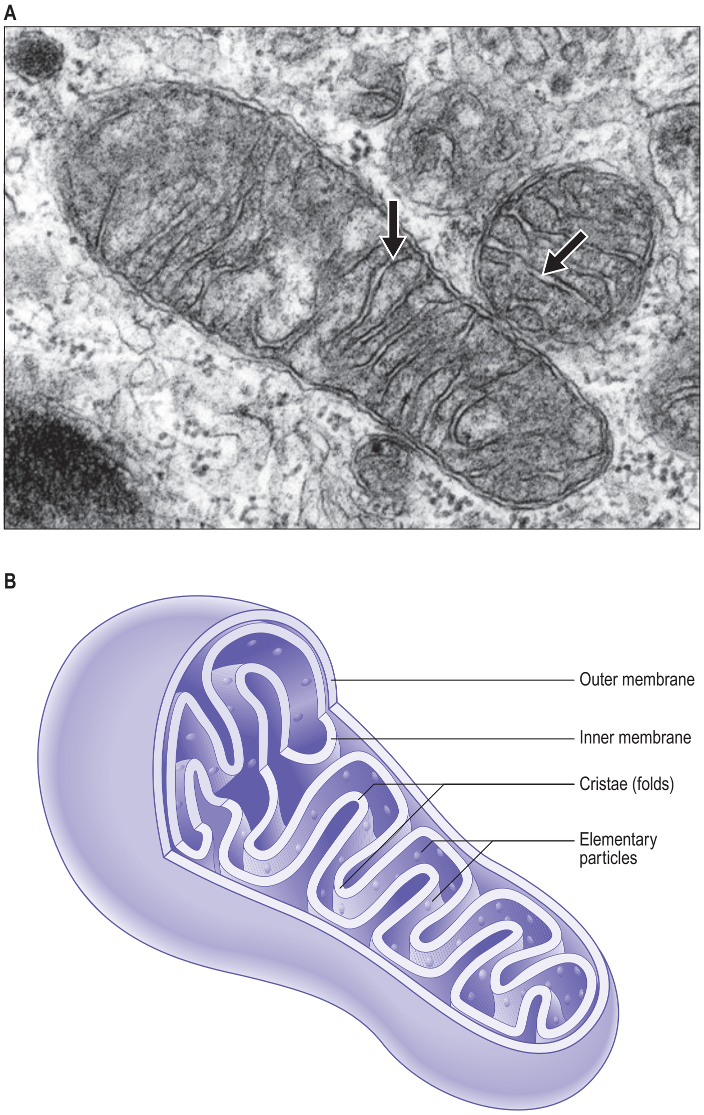

Fig. 1.7 **A**, Mitochondria in human cardiac muscle. The folded cristae (arrows) project into the matrix from the inner mitochondrial membrane. **B**, The location of the elementary particles that couple oxidation and phosphorylation reactions. (A, Courtesy of Dr Bart Wagner, Histopathology Department, Sheffield Teaching Hospitals, UK.)

The number of mitochondria in a particular cell reflects its general energy requirements; e.g. in hepatocytes there may be as many as 2000, whereas in resting lymphocytes there are usually very few. Mature erythrocytes lack mitochondria altogether. Cells with few mitochondria generally rely largely on glycolysis for their energy supplies. These include some very active cells, e.g. fast-twitch skeletal muscle fibres, which are able to work rapidly but for only a limited duration. Mitochondria are distributed within a cell according to regional energy requirements, e.g. near the bases of cilia in ciliated epithelia, in the basal domain of the cells of proximal convoluted tubules in the renal cortex (where considerable active transport occurs) and around the proximal segment, called the middle piece, of the flagellum in spermatozoa. In living cells, mitochondria constantly change shape and intracellular position; they multiply by growth and fission, and may undergo fusion.

Mitochondria may be involved in tissue-specific metabolic reactions, e.g. various urea-forming enzymes are found in liver cell mitochondria. Moreover, a number of genetic diseases of mitochondria affect particular tissues exclusively, e.g. mitochondrial myopathies (skeletal muscle) and mitochondrial neuropathies (nervous tissue).

The mitochondrial matrix is an aqueous environment. It contains a variety of enzymes, and strands of mitochondrial DNA with the capacity for transcription and translation of a unique set of mitochondrial genes (mitochondrial mRNAs and transfer RNAs, mitochondrial ribosomes with rRNAs). The DNA forms a closed loop, about 5 µm across and several identical copies are present in each mitochondrion. The ratio between its bases differs from that of nuclear DNA; the RNA sequences also differ in the precise genetic code used in protein synthesis. At least 13 respiratory chain enzymes of the matrix and inner membrane are encoded by the small number of genes along the mitochondrial DNA (mtDNA). The great majority of mitochondrial proteins are encoded by nuclear genes and made in the cytosol, then inserted through special channels in the mitochondrial membranes to reach their destinations. Their membrane lipids are synthesized in the endoplasmic reticulum.

Mitochondrial ribosomes are smaller and quite distinct from those of the rest of the cell in that they (and mitochondrial nucleic acids) resemble those of bacteria. This similarity underpins the theory that mitochondrial ancestors were oxygen-utilizing bacteria that existed in a symbiotic relationship with eukaryotic cells unable to metabolize the oxygen produced by early plants.

It has been shown that mitochondria are of maternal origin because the mitochondria of spermatozoa are not generally incorporated into the ovum at fertilization. As mitochondria are formed only from previously existing ones, it follows that all mitochondria in the body are descended from those in the cytoplasm of the ovum. Thus mitochondria (and mitochondrial genetic variations and mutations) are passed only through the female line. For further information on mitochondrial genetics and disorders, see Chinnery and Hudson (2013).

Mitochondrial replacement therapies

Available with the *Gray's Anatomy* e-book

Cytosolic inclusions

The aqueous cytosol surrounds the membranous organelles described above. It also contains various non-membranous inclusions, including free ribosomes, components of the cytoskeleton, and other inclusions, such as storage granules (e.g. glycogen), pigments (such as lipofuscin granules, remnants of the lipid oxidative mechanism seen in the suprarenal cortex).

Lipid droplets

Lipid droplets are spherical bodies of various sizes found within many cells, but are especially prominent in the adipocytes (fat cells) of adipose connective tissue. They do not belong to the Golgi-related vacuolar system of the cell. Lipid droplets, suspended in the cytosol, are surrounded by perilipin proteins, which regulate lipid storage and lipolysis. (See Smith and Ordovás (2012) for further reading on obesity and perilipins.) In cells specialized for lipid storage, the vacuoles reach 80 µm or more in diameter. They function as stores of chemical energy, thermal insulators and mechanical shock absorbers in adipocytes. In many cells, they may represent end-products of other metabolic pathways, e.g. in steroid-synthesizing cells, where they are a prominent feature of the cytoplasm. They may also be secreted, as in the alveolar epithelium of the lactating breast.

Cristae are abundant in mitochondria within cardiac muscle cells and in steroid-producing cells (in the suprarenal cortex, corpus luteum and Leydig cells). The protein, steroidogenic acute regulatory protein (StAR), regulates the synthesis of steroids by transporting cholesterol across the outer mitochondrial membrane. A mutation in the gene encoding StAR causes defective suprarenal and gonadal steroidogenesis.

Mitochondrial replacement therapies have been developed to resolve mitochondrial disorders of maternal origin, e.g. by transplantating the pronucleus from an egg containing mutant mtDNA from a carrier mother to an enucleated egg from an unaffected donor (Fig. 1.8). This procedure can be performed after in vitro fertilization using sperm from the intended father. Soon after fertilization, the haploid maternal and paternal nuclei are assembled as a pronucleus. Because it is difficult to distinguish between male and female pronuclei, pronuclear transfer (PNT) involves transplantation of both the maternal and paternal pronuclei, clearly visualized by light microscopy. mtDNA resides within mitochondria, separately from the genes housed in each cell nucleus. Since mitochondria are inherited only through the maternal germline, mutated mitochondria are thus replaced with normal mitochondria from enucleated oocytes provided by the unaffected donor. An alternative procedure involves transfer of the nuclear genetic material from the affected female (maternal spindle transfer, MST) into an enucleated donor egg with normal mitochondria, prior to fertilization.

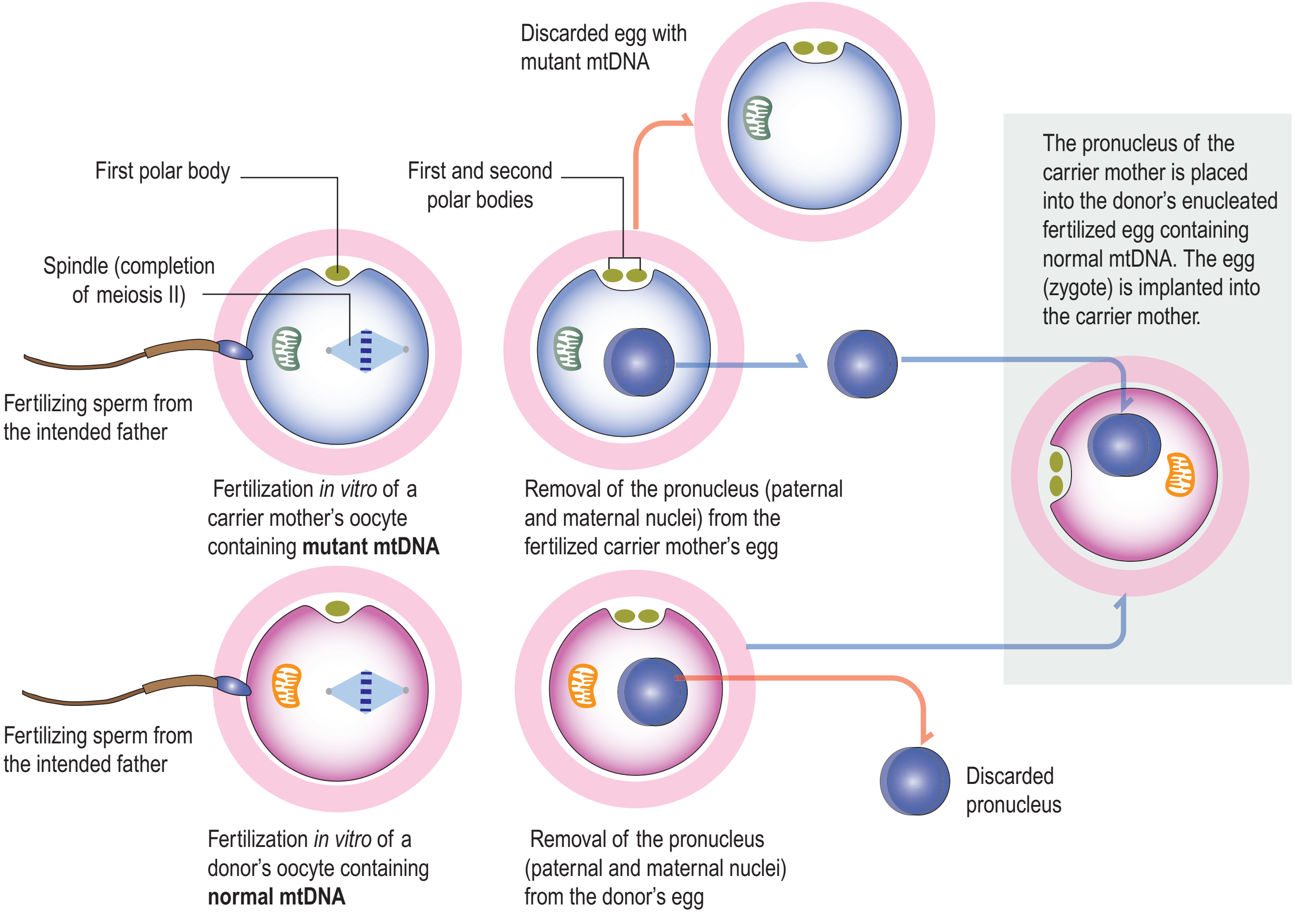
Discarded egg with mutant mtDNA
First polar body
First and second polar bodies
Spindle (completion of meiosis II)
Fertilizing sperm from the intended father
Fertilization *in vitro* of a carrier mother's oocyte containing **mutant mtDNA**
Removal of the pronucleus (paternal and maternal nuclei) from the fertilized carrier mother's egg
The pronucleus of the carrier mother is placed into the donor's enucleated fertilized egg containing normal mtDNA. The egg (zygote) is implanted into the carrier mother.
Fertilizing sperm from the intended father
Fertilization *in vitro* of a donor's oocyte containing **normal mtDNA**
Removal of the pronucleus (paternal and maternal nuclei) from the donor's egg
Discarded pronucleus

Fig. 1.8 Mitochondrial replacement by pronuclear transfer. Mitochondrial DNA (mtDNA) is transmitted by the mother (maternal inheritance). Both males and females can be affected by mitochondrial diseases, but males do not transmit the disorder to their offspring. One mitochondrial replacement therapy involves the transplantation of the pronucleus from an egg containing mutant mtDNA from a carrier mother to an enucleated egg from an unaffected donor. This can be performed after in vitro fertilization using sperm from the intended father. (With permission from Kierszenbaum AL, Tres LL Histology and Cell Biology: An Introduction to Pathology, 5th ed. Elsevier. Copyright 2019.)

Cell signalling

Cellular systems in the body communicate with each other to coordinate and integrate their functions, through a variety of processes known collectively as cell signalling, in which a signalling molecule produced by one cell is detected by another, almost always by means of a specific receptor protein molecule. The recipient cell transduces the signal, which it most often detects at the plasma membrane, into intracellular chemical messages that change cell behaviour.

The signal may act over a long distance, e.g. endocrine signalling through the release of hormones into the blood stream, or neuronal synaptic signalling via electrical impulse transmission along axons and subsequent release of chemical transmitters of the signal at synapses or neuromuscular junctions. A specialized variation of endocrine signalling (neurocrine or neuroendocrine signalling) occurs when neurones or paraneurones (e.g. chromaffin cells of the suprarenal medulla) secrete a hormone into interstitial fluid and the blood stream. Alternatively, signalling may occur at short range through a paracrine mechanism, in which cells of one type release molecules into the interstitial fluid of the local environment, to be detected by nearby cells of a different type that express the specific receptor protein.

Neurocrine cell signalling uses chemical messengers found also in the central nervous system, which may act in a paracrine manner via interstitial fluid or reach more distant target tissues via the blood stream. Cells may generate and respond to the same signal. This is autocrine signalling, a phenomenon that reinforces the coordinated activities of a group of like cells, which respond together to a high concentration of a local signalling molecule. The most extreme form of short-distance signalling is contact-dependent (juxtacrine) signalling, where one cell responds to transmembrane proteins of an adjacent cell that bind to surface receptors in the responding cell membrane. Contact-dependent signalling also includes cellular responses to integrins on the cell surface binding to elements of the extracellular matrix. Juxtacrine signalling is important during development and in immune responses. These different types of intercellular signalling mechanism are illustrated in Fig. 1.9.

Signalling molecules and their receptors

The majority of signalling molecules (ligands) are hydrophilic and so cannot cross the plasma membrane of a recipient cell to effect changes inside the cell unless they first bind to a plasma membrane receptor protein. Ligands are mainly proteins (usually glycoproteins), polypeptides or highly charged biogenic amines. They include classic peptide hormones of the endocrine system; cytokines, which are mainly of haemopoietic cell origin and involved in inflammatory responses and tissue remodelling (e.g. the interferons, interleukins, tumour necrosis factor, leukaemia inhibitory factor); and polypeptide growth factors (e.g. the epidermal growth factor superfamily, nerve growth factor, platelet-derived growth factor, the fibroblast growth factor family, transforming growth factor beta and the insulin-like growth factors). Polypeptide growth factors are multifunctional molecules with more widespread actions and cellular sources than their names suggest. They and their receptors are commonly mutated or aberrantly expressed in certain cancers. The cancer-causing gene variant is termed a transforming oncogene and the normal (wild-type) version of the gene is a cellular oncogene or proto-oncogene. The activated receptor acts as a transducer to generate intracellular signals, which are either small diffusible second messengers (e.g. calcium, cyclic adenosine monophosphate or the plasma membrane lipid-soluble diacylglycerol), or larger protein complexes that amplify and relay the signal to target control systems.

Some signals are hydrophobic and able to cross the plasma membrane freely. Classic examples are the steroid hormones, thyroid hormones, retinoids and vitamin D. Steroids, for instance, enter cells non-selectively, but elicit a specific response only in those target cells that express specific cytoplasmic or nuclear receptors. Light stimuli also cross the plasma membranes of photoreceptor cells and interact intracellularly, at least in rod cells, with membrane-bound photosensitive receptor proteins. Hydrophobic ligands are transported in the blood stream or interstitial fluids, generally bound to carrier proteins, and they often have a longer half-life and longer-lasting effects on their targets than do water-soluble ligands.

A separate group of signalling molecules that are able to cross the plasma membrane freely is typified by the gas, nitric oxide. The principal target of short-range nitric oxide signalling is smooth muscle, which relaxes in response. Nitric oxide is released from vascular endothelium as a result of the action of autonomic nerves that supply the vessel wall, causing local relaxation of smooth muscle and consequent dilation of the vessel. This mechanism is responsible for penile erection. Nitric oxide

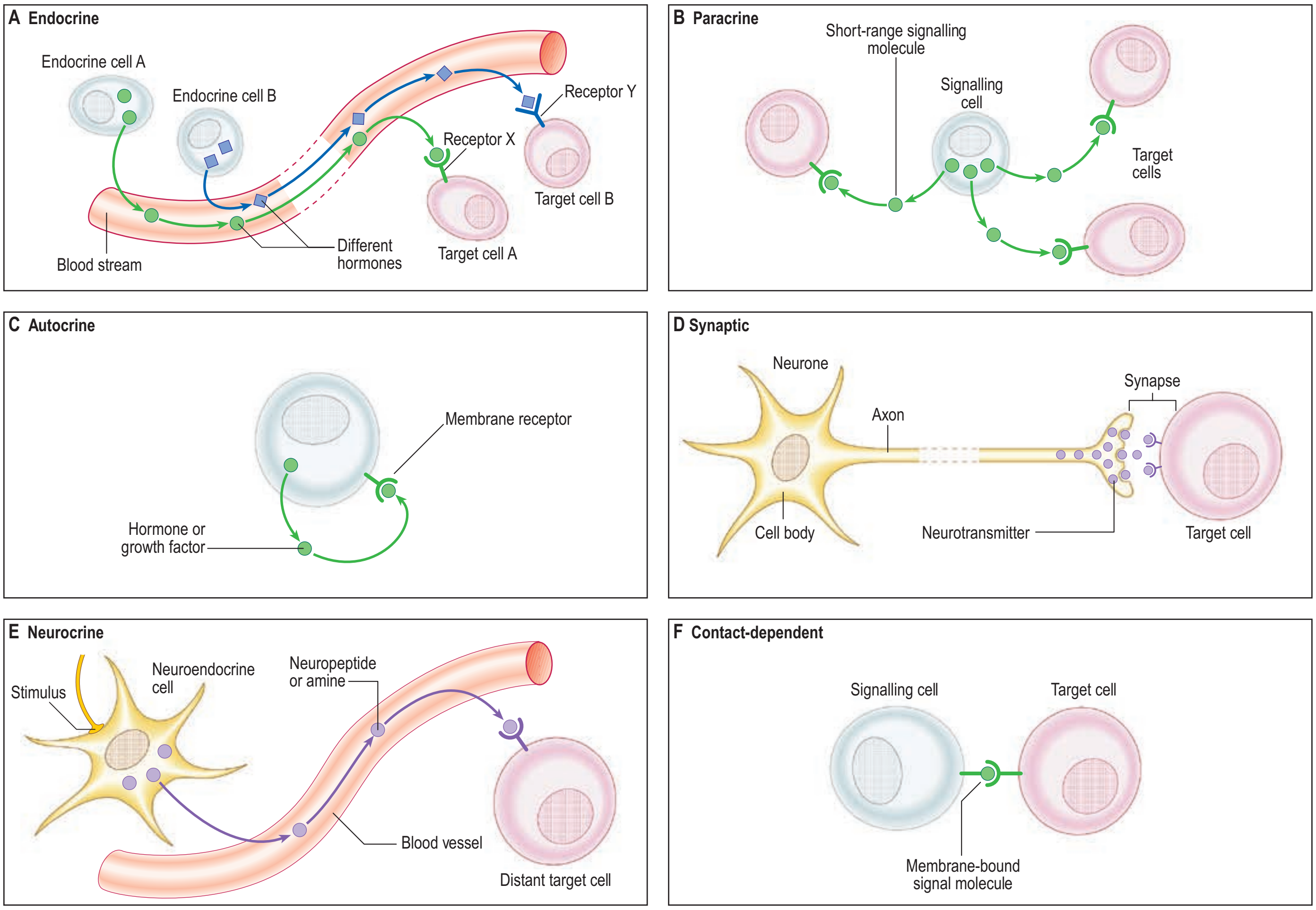

Fig. 1.9 The different modes of cell–cell signalling.

is unusual among signalling molecules in having no specific receptor protein; it acts directly on intracellular enzymes of the response pathway.

Receptor proteins

There are some 20 different families of receptor proteins, each with several isoforms responding to different ligands. The great majority of these receptors are transmembrane proteins. Members of each family share structural features that indicate either shared ligand-binding characteristics in the extracellular domain or shared signal transduction properties in the cytoplasmic domain, or both. There is little relationship either between the nature of a ligand and the family of receptor proteins to which it binds and activates, or the signal transduction strategies by which an intracellular response is achieved. The same ligand may activate fundamentally different types of receptor in different cell types.

Cell surface receptor proteins are generally grouped according to their linkage to one of three intracellular systems: ion channel-linked receptors; G-protein coupled receptors; or receptors that link to enzyme systems. Other receptors do not fit neatly into any of these categories. All the known G-protein-coupled receptors belong to a structural group of proteins that pass through the membrane seven times in a series of serpentine loops: these receptors are thus known as seven-pass transmembrane receptors or, because the transmembrane regions are formed from α-helical domains, as seven-helix receptors. The best known of this large group of phylogenetically ancient receptors are the odorant-binding proteins of the olfactory system; the light-sensitive receptor protein, rhodopsin; and many of the receptors for clinically useful drugs. A comprehensive list of receptor proteins, their activating ligands and examples of the resultant biological function is given in Pollard et al (2016).

Major signalling pathways

Most cell surface receptors stimulate intracellular target enzymes to transmit and amplify a signal upon ligand binding. A signalling pathway can activate a series of intracellular targets located downstream of the receptor, in particular the activity of intracellular proteins, or, like neurotransmitter receptors, control the flow of water (aquaporins) and electrolytes across ligand-gated ion channels located on the plasma membrane. An amplified signal can be propagated to the nucleus to regulate gene expression in response to an external cell stimulus.

The cyclic adenosine monophosphate (cAMP) pathway is a major intracellular signalling pathway. For example, there is an increase in the intracellular concentration of cAMP when adrenaline (epinephrine) binds to its receptor. Adrenaline breaks down glycogen into glucose before muscle contraction. cAMP is formed from ATP by the action of the enzyme adenylyl cyclase and degraded to adenosine monophosphate (AMP) by the enzyme cAMP phosphodiesterase. This mechanism led to the concept of a first messenger (adrenaline) mediating a cell-signalling effect by a second messenger, cAMP.

Signalling pathways play important roles in embryonic and fetal development, body axis patterning, cell migration and cell proliferation. They all contain components subject to diverse regulatory steps and crosstalk mechanisms and some use different downstream effectors activated by specific transcription factors. The following signalling pathways have clinical relevance: the JAK–STAT, Hedgehog (Hh), Wingless (Wnt) and transforming growth factor (TGF)-β signalling pathways. For example, erythropoietin stimulates the development of the erythroid lineage (red blood cell formation) in bone marrow by a mechanism that involves the JAK–STAT pathway (**Fig. 1.11**).

Cytoskeleton

The cytoskeleton is a three-dimensional network of filamentous intracellular proteins of different shapes, sizes and composition distributed throughout the cytoplasm. It provides mechanical support, maintains cell shape and rigidity, and enables cells to adopt highly asymmetric or irregular profiles. It plays an important part in establishing structural polarity and different functional domains within a cell. It also provides mechanical support for permanent projections from the cell surface (see below), including persistent microvilli and cilia, and transient processes, such as the thin finger-like protrusions called filopodia (0.1–0.3 µm) and lamellipodia (0.1–0.2 µm). Filopodia consist of parallel bundles of actin filaments and have a role in cell migration, wound healing and neurite growth. The protrusive thin and broad lamellipodia, found at the leading edge of a motile cell, contain a branched network of actin filaments.

The cytoskeleton restricts specific structures to particular cellular locations. For example, the Golgi apparatus is near the nucleus and endoplasmic reticulum, and mitochondria are near sites of energy requirement. In addition, the cytoskeleton provides tracks for intracellular transport (e.g. shuttling vesicles and macromolecules, called cargoes, among cytoplasmic sites), the movement of chromosomes during cell division (mitosis and meiosis) or movement of the entire cell during embryonic morphogenesis or the chemotactic extravascular migration of leukocytes during homing. Examples of highly developed and specialized functions of the cytoskeleton include the contraction of the sarcomere in striated muscle cells and the bending of the axoneme of cilia and flagella.

The catalogue of cytoskeletal structural proteins is extensive and still increasing. The major filamentous structures found in non-muscle cells are microfilaments (7 nm thick), microtubules (25 nm thick) and intermediate filaments (10 nm thick). Other important components are proteins that bind to the principal filamentous types to assemble or disassemble them, regulate their stability or generate movement. These include actin-binding proteins such as myosin, which in some cells can assemble into thick filaments, and microtubule-associated proteins. Pathologies involving cytoskeletal abnormalities include ciliopathies (resulting from the abnormal assembly and function of centrioles, basal bodies and cilia); neurodegenerative diseases (a consequence of defective anterograde transport of neurotransmitters along microtubules in axons); and sterility (determined by defective or absent microtubule-associated dynein in axonemes, e.g. Kartagener's syndrome).

Actin filaments (microfilaments)

Actin filaments are flexible filaments, 7 nm thick (**Fig. 1.13A**). Within most cell types, actin constitutes the most abundant protein and in some motile cells its concentration may exceed 200 µM (10 mg protein per ml cytoplasm). The filaments are formed by the ATP-dependent polymerization of actin monomer (with a molecular mass of 43 kDa) into a characteristic string of beads in which the subunits are arranged in a linear tight helix with a distance of 13 subunits between turns (Dominguez 2010). The polymerized filamentous form is termed F-actin (filamentous actin) and the unpolymerized monomeric form is known as G-actin (globular actin). Each monomer has an asymmetric structure. When monomers polymerize, they confer a defined polarity on the filament: the plus or barbed end favours monomer addition, and the minus or pointed end favours monomer dissociation.

Treadmilling designates the simultaneous polymerization of an actin filament at one end and depolymerization at the other end to maintain its constant length.

See Bray (2001) for further reading.

Actin-binding proteins

A wide variety of actin-binding proteins are capable of modulating the form of actin within the cell. These interactions are fundamental to the organization of cytoplasm and to cell shape. The actin cytoskeleton is organized as closely packed parallel arrays of actin filaments forming bundles or cables, or loosely packed criss-crossed actin filaments forming networks (**Fig. 1.14A**). Actin-binding proteins hold together bundles and networks of actin filaments. Actin-binding proteins can be grouped into G-actin (monomer) binding proteins and F-actin (polymer) capping, cross-linking and severing proteins. Actin-binding proteins may have more than one function.

Capping proteins bind to the ends of the actin filament either to stabilize an actin filament or to promote its disassembly (see Fig. 1.13A).

Cross-linking or bundling proteins tie actin filaments together in longitudinal arrays to form bundles, cables or core structures. The bundles may be closely packed in microvilli and filopodia, where parallel filaments are tied tightly together to form stiff bundles orientated in the same direction. Cross-linking proteins of the microvillus actin bundle core include fimbrin and villin.

Other actin-bundling proteins form rather looser bundles of filaments that run antiparallel to each other with respect to their plus and minus ends. They include myosin II, which can form cross-links with ATP-dependent motor activity, and cause adjacent actin filaments to slide on each other in the striated muscle sarcomere, and either change the shape of cells or (if the actin bundles are anchored into the cell membrane at both ends), maintain a degree of active rigidity. Filamin interconnects adjacent actin filaments to produce loose filamentous gel-like networks composed of randomly orientated F-actin.

F-actin can branch. The assembly of branched filamentous actin networks involves a complex of seven actin-related proteins 2/3 (Arp2/3) that is structurally similar to the barbed end of actin.

See Rotty et al (2013) for further reading.

Branched actin generated by the Arp2/3 protein complex localizes at the leading edge of migrating cells, lamellipodia and phagosomes (required for the capture by endocytosis and phagocytosis of particles and foreign pathogens by immune cells). Formin can elongate pre-existing actin filaments by removing capping proteins at the barbed end.

The adrenaline receptor is linked to adenylyl cyclase by G protein, which stimulates cyclase activity upon adrenaline binding. In the adrenaline-dependent regulation of glycogen metabolism, the intracellular signalling effects of cAMP are mediated by the enzyme cAMP-dependent protein kinase (or protein kinase A). In its inactive form, protein kinase A is a tetramer composed of two regulatory subunits (to which cAMP binds) and two catalytic subunits. Binding of cAMP results in the dissociation of the catalytic subunits. Free catalytic subunits can phosphorylate serine residues on target proteins (Fig. 1.10).

This pathway links a protein with tyrosine kinase activity (JAK) to a transcription factor (STAT) that becomes activated by this event. STAT (Signal Transducers and Activators of Transcription) proteins are transcription factors with an SH2 domain. They are present in the cytoplasm in an inactive state. Stimulation of a receptor by ligand binding recruits STAT proteins, which bind to the cytoplasmic portion of the receptor-associated JAK protein tyrosine kinase through their SH2 domain and become phosphorylated. Phosphorylated STAT proteins then dimerize and translocate into the nucleus, where they activate the transcription of target genes (Fig. 1.11).

The Hh signalling pathway (Fig. 1.12A) is involved in switching Gli (Glioma) factors from transcriptional repressors into activators in the cytoplasm to allow Hh-specific transcriptional events. Hh proteins bind to the receptor PTCH1 (PaTCHed Homologue 1) and then signal through SMO (SMOothened), a transmembrane protein, to regulate gene transcription by repressing or activating Gli3, the transcription factor. If SMO is not present, Sufu (SUppressor of FUsed) permits the truncated Gli3 repressor to block Hh-specific gene expression. If SMO is present, activated full-length Gli2A translocates to the cell nucleus to regulate Hh-specific gene expression (the expression of cyclin D, cyclin E, Myc and Patched). Hh ligands include Sonic (Shh), Indian (Ihh) and Desert (Dhh). Dysfunctions of the Hh signalling pathway include Gorlin syndrome, basal cell carcinoma in the skin and medulloblastoma.

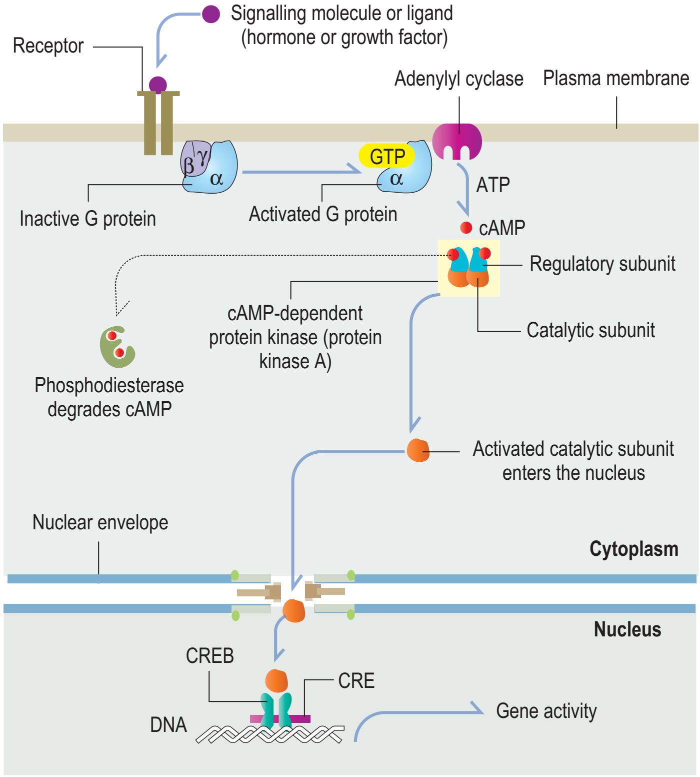
Signalling molecule or ligand (hormone or growth factor)
Receptor
Adenylyl cyclase
Plasma membrane
β γ
α
GTP
α
ATP
Inactive G protein
Activated G protein
cAMP
Regulatory subunit
cAMP-dependent protein kinase (protein kinase A)
Catalytic subunit
Phosphodiesterase degrades cAMP
Activated catalytic subunit enters the nucleus
Nuclear envelope
Cytoplasm
Nucleus
CREB
CRE
DNA
Gene activity

Fig. 1.10 The cAMP signalling pathway. Ligand binding to a cell receptor leads to the activation of adenylyl cyclase by the guanosine triphosphate (GTP)-bound G protein subunit to form cAMP from ATP. cAMP, the second messenger, binds to the regulatory subunits of cAMP-dependent protein kinase (protein kinase A) and releases the catalytic subunits. cAMP is eventually degraded by a cAMP-dependent phosphodiesterase. The activated catalytic subunit translocates into the nucleus and phosphorylates the transcription factor CREB (CRE-binding protein) bound to the cAMP response element (CRE): specific gene expression of inducible genes occurs. (With permission from Kierszenbaum AL, Tres LL Histology and Cell Biology: An Introduction to Pathology, 5th ed. Elsevier. Copyright 2019.)

The Wingless (Wnt) signalling pathway (Fig. 1.12B) relies on Wnt proteins controlling tissue organization and body-axis formation during embryogenesis and the regulation of stem cells in adult tissue. Wnt protein binding to FZD (frizzled) receptor is regulated by several interacting proteins, including leucine-rich repeat containing G protein-coupled receptor (Lgr) 5 or 6; R-spondin (Rspo) 1 to 4 and E3 ubiquitin ligase enzyme (Znrf3 or Rnf43). In the absence of Rspos, the ubiquitin ligase catalyses FZD degradation, thus preventing Wnt protein binding. Rspo prevents enzyme activity, FZD receptors accumulate and Wnt signalling increases. β-catenin then translocates to the nucleus and stimulates the transcription of Wnt target genes by interacting with the co-activators LEF1 (Lymphoid Enhancer-binding Factor 1) and TCF (T Cell Factor) 1, TCF3 and TCF4 (not shown in Fig. 1.12B). In the β-catenin independent pathway, Wnt protein induces G protein-coupled phosphatidylinositol to activate protein kinase C (PKC). Wnt signalling has direct implications for regenerative medicine and Wnt-associated cancers. Regeneration, in contrast to repair, is a steady-state condition, for example of the normal epidermis and the gastrointestinal lining. The possibility of restoring function to damaged tissue following disease, injury or ageing depends on its capacity for tissue repair.

TGF-β signalling is associated with the bone morphogenetic protein (BMP) signalling pathway (Fig. 1.12C). BMPs are members of the TGF-β superfamily and regulate cell growth, differentiation and development in a wide range of biological processes by activating SMAD transcription factor proteins.

BMP/TGF-β ligands induce the dimerization and then heteromerization of serine/threonine receptor kinases and phosphorylation of the cytoplasmic signalling molecules SMAD2 and SMAD3 for the TGF-β pathway, or SMAD1/5/8 for the BMP pathway. The common SMAD4 transducer translocates to the nucleus. Activated SMADs regulate several biological processes by cell-specific modulation of transcription. TGF-β is a tumour suppressor of premalignant cells but enhances invasion and metastasis of more advanced carcinomas. Mutations of *SMAD4* genes are frequent in gastrointestinal and pancreatic tumours. For further reading on cell signalling pathways, see Kierszenbaum and Tres (2019).

Septins are emerging as a novel cytoskeletal element because of their filamentous organization and association with actin filaments and microtubules. They are guanosine triphosphate (GTP)-binding proteins that form hetero-oligomeric complexes (see Mostowy and Cossart 2012 for additional information).

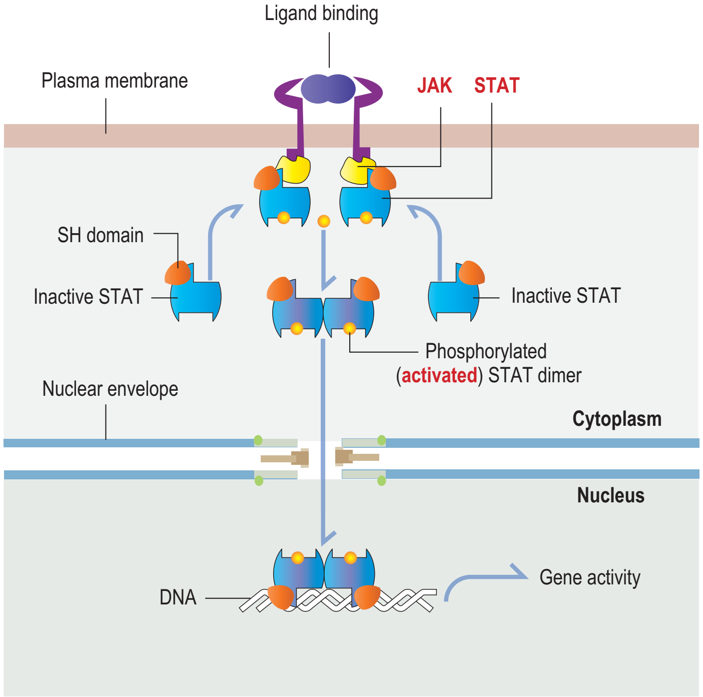

Fig. 1.11 The JAK–STAT signalling pathway. Ligand binding to a receptor leads to the attachment of the inactive transcription factor STAT, present in the cytosol, to the receptor-associated JAK protein tyrosine kinase via their SH2 domains. Phosphorylated STAT dimerizes and translocates to the nucleus where it activates transcription of target genes (With permission from Kierszenbaum AL, Tres LL Histology and Cell Biology: An Introduction to Pathology, 5th ed. Elsevier. Copyright 2019.)

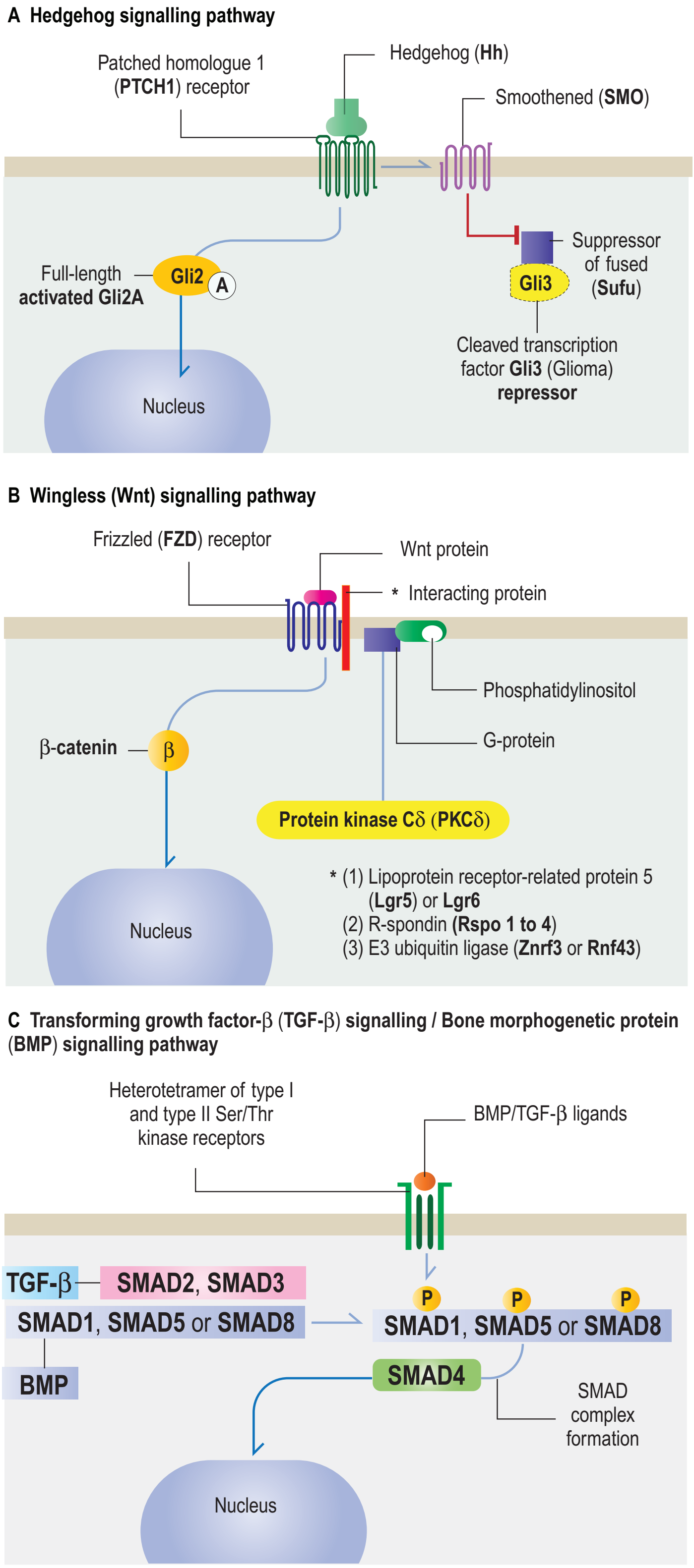
A Hedgehog signalling pathway
Patched homologue 1 (PTCH1) receptor
Hedgehog (Hh)
Smoothened (SMO)
Suppressor of fused (Sufu)
Full-length activated Gli2A
Gli2
A
Gli3
Cleaved transcription factor Gli3 (Glioma) repressor
Nucleus
B Wingless (Wnt) signalling pathway
Frizzled (FZD) receptor
Wnt protein
* Interacting protein
Phosphatidylinositol
G-protein
β-catenin
β
Protein kinase Cδ (PKCδ)
Nucleus
* (1) Lipoprotein receptor-related protein 5 (Lgr5) or Lgr6
(2) R-spondin (Rspo 1 to 4)
(3) E3 ubiquitin ligase (Znrf3 or Rnf43)
C Transforming growth factor-β (TGF-β) signalling / Bone morphogenetic protein (BMP) signalling pathway
Heterotetramer of type I and type II Ser/Thr kinase receptors
BMP/TGF-β ligands
TGF-β
SMAD2, SMAD3
SMAD1, SMAD5 or SMAD8
BMP
P
P
P
SMAD1, SMAD5 or SMAD8
SMAD4
SMAD complex formation
Nucleus

Fig. 1.12 **A**, The Hedgehog (Hh) signalling pathway. Hh proteins bind to the receptor PTCH1 and then signal through SMO, a transmembrane protein, to regulate gene transcription by repressing or activating Gli3, a transcription factor. If SMO is not present, Sufu permits the truncated Gli3 repressor to block Hh-specific gene expression. If SMO is present, activated full-length Gli2A translocates to the cell nucleus to regulate Hh-specific gene expression. Hh ligands include Sonic (Shh), Indian (Ihh) and Desert (Dhh) hedgehog proteins. **B**, The Wingless (Wnt) signalling pathway. Wnt protein binding to FZD receptor is regulated by interacting proteins (*): Leucine-rich repeat containing G protein-coupled receptor (Lgr) 5 or 6; R-spondin (Rspo) 1 to 4 and E3 ubiquitin ligase enzyme (Znrf3 or Rnf43). In the absence of Rspos, the ubiquitin ligase catalyses FZD degradation and so prevents Wnt protein binding. Rspo prevents enzyme activity, FZD receptors accumulate and Wnt signalling increases; β-catenin translocates to the nucleus and stimulates the transcription of Wnt target genes. **C**, The transforming growth factor-β (TGF-β) signalling/Bone morphogenetic protein (BMP) signalling pathway. BMP/TGF-β ligands induce the dimerization and then heteromerization of serine/threonine receptor kinases and phosphorylation of the cytoplasmic signalling molecules SMAD2 and SMAD3 for the TGF-β pathway, or SMAD1/5/8 for the BMP pathway. The common SMAD4 transducer translocates to the nucleus. Activated SMADs regulate several biological processes by cell-specific modulation of transcription. (With permission from Kierszenbaum AL, Tres LL Histology and Cell Biology: An Introduction to Pathology, 5th ed. Elsevier. Copyright 2019.)

This polarity can be visualized in negatively stained images by allowing F-actin to react with fragments containing the active head region of myosin. Myosins bind to filamentous actin at an angle to give the appearance of a series of arrowheads pointing towards the minus end of the filament, with the barbs pointing towards the plus end.

It involves the addition of ATP-bound G-actin monomers at the barbed end (fast-growing plus end) and removal of ADP-bound G-actin at the pointed end (slow-growing minus end). Actin filaments grow or shrink by addition or loss of G-actin monomer at both ends. Essentially, actin polymerization *in vitro* proceeds in three steps: nucleation (aggregation of G-actin monomers into a 3–4-monomer aggregate), elongation (addition of G-actin monomers to the aggregate) and a dynamic steady state (treadmilling). Specific toxins (e.g. cytochalasins, phalloidins and lantrunculins) bind to actin and affect its polymerization. Cytochalasin D blocks the addition of new G-actin monomers to the barbed end of F-actin; phalloidin binds to the interface between G-actin monomers in F-actin, thus preventing depolymerization; and lantrunculin binds to G-actin monomers, blocking their addition to an actin filament.

Profilin and thymosin β4 are G-actin binding proteins. Profilin binds to G-actin bound to ATP; it inhibits addition of G-actin to the slow-growing (pointed) end of F-actin but enables the fast-growing (barbed) end to grow faster and then dissociates from the actin filament. In addition, profilin participates in the conversion of ADP back to the ATP–G-actin bound form. Thymosin β4 binds to the ATP–G-actin bound form, preventing polymerization by sequestering ATP–G-actin into a reserve pool.

Members of the F-actin capping protein family are heterodimers consisting of an α subunit (CPα) and a β subunit (CPβ) that cap the barbed end of actin filaments within all eukaryotic cells. Gelsolin has a dual role: it severs F-actin and caps the newly formed barbed end, blocking further filament elongation.

Fascin is an additional cross-linking protein. Villin is also a severing protein, causing the disassembly of actin filaments and the collapse of the microvillus.

In the presence of activated nucleation promotion factors, such as Wiskott–Aldrich syndrome protein (WASP) and WASP family verprolin-homologous protein (WAVE, also known as SCAR), the Arp2/3 protein complex binds to the side of an existing actin filament (mother filament) and initiates the formation of a branching actin daughter filament at a 70° angle relative to the mother filament utilizing G-actin delivered to the Arp2/3 complex site.

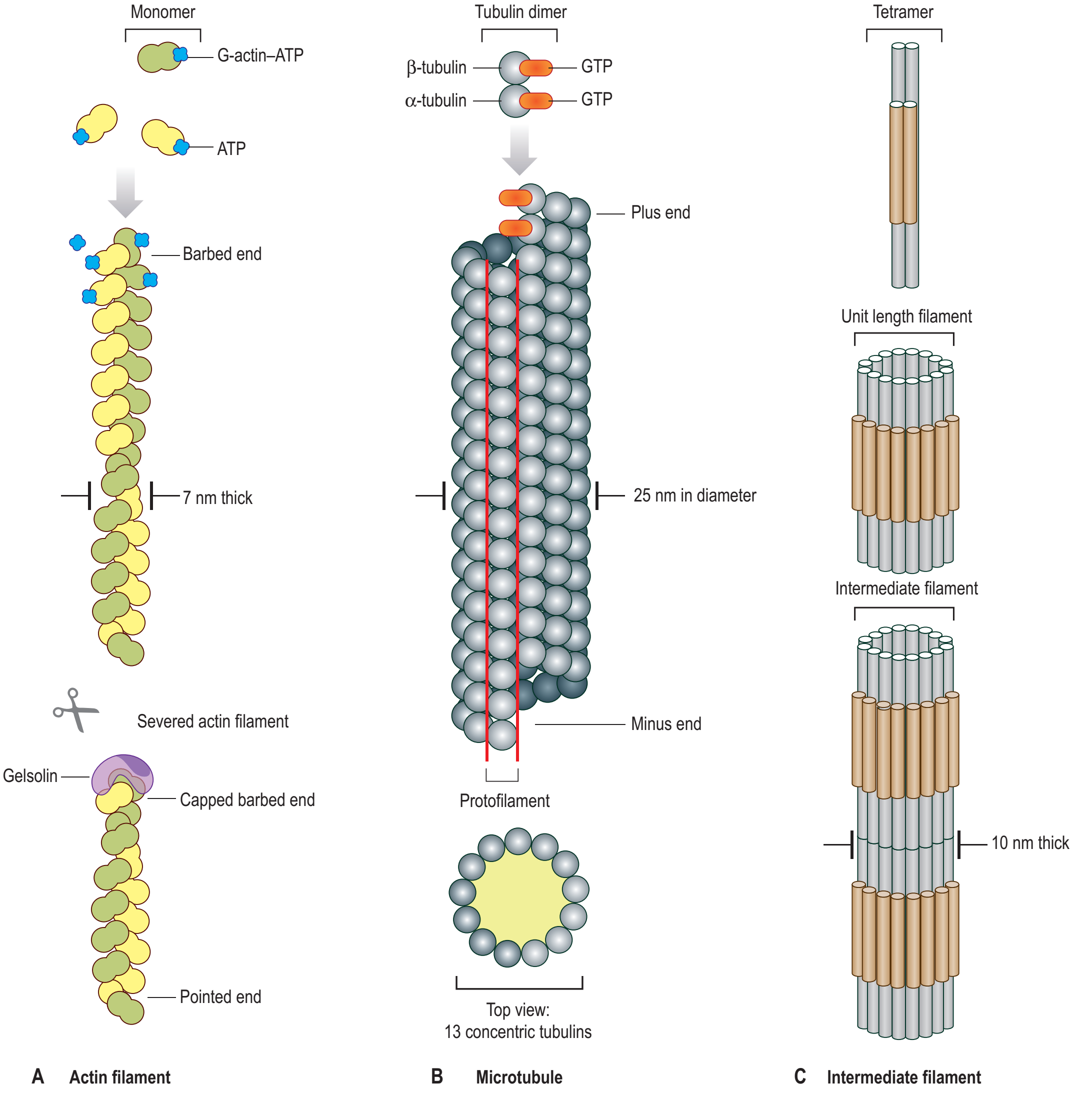

Fig. 1.13 Structural and molecular features of cytoskeletal components. **A**, The actin filament (F-actin) is a 7 nm thick polymer chain of ATP-bound G-actin monomers. F-actin consists of a barbed (plus) end, the initiation site of F-actin, and a pointed (minus) end, the dissociation site of F-actin. F-actin can be severed and capped at the barbed end by gelsolin. **B**, The microtubule is a 25 nm diameter polymer of GTP-bound α-tubulin and GTP-bound β-tubulin dimers. The dimer assembles at the plus end and depolymerizes at the minus end. A linear chain of α-tubulin/β-tubulin dimers is called a protofilament. In the end-on (top) view, a microtubule displays 13 concentrically arranged tubulin subunits. **C**, Tetrameric complexes of intermediate filament subunits associate laterally to form a unit length filament consisting of eight tetramers. Additional unit length filaments anneal longitudinally and generate a mature 10 nm thick intermediate filament.

Other classes of actin-binding protein link the actin cytoskeleton to the plasma membrane either directly or indirectly through a variety of membrane-associated proteins. The latter may also create links via transmembrane proteins to the extracellular matrix. Best known of these is the family of spectrin-like molecules, which can bind to actin and also to each other and to various membrane-associated proteins to create supportive networks beneath the plasma membrane. Tetramers of spectrin α and β chains line the intracellular side of the plasma membrane of erythrocytes and maintain their integrity by their association with short actin filaments at either end of the tetramer.

Class V myosins (see below) are unconventional motor proteins transporting cargoes (such as vesicles and organelles) along actin filaments. Class I myosins are involved in membrane dynamics and actin organization at the cell cortex, thus affecting cell migration, endocytosis, pinocytosis and phagocytosis. Tropomyosin, an important regulatory protein of muscle fibres, is also present in non-muscle cells, where its function may be primarily to stabilize actin filaments against depolymerization.

Myosins, the motor proteins

The myosin family of microfilaments is often classified within a distinct category of motor proteins. Myosin proteins have a globular head region consisting of a heavy and a light chain. The heavy chain bears an α-helical tail of varying length. The head has an ATPase activity and can bind to and move along actin filaments – the basis for myosin function as a motor protein. The best-known class is myosin II, which occurs in muscle and in many non-muscle cells. Its molecules have two heads and two tails, intertwined to form a long rod. The rods can bind to each other to form long, thick filaments, as seen in striated and smooth muscle fibres and myoepithelial cells. Myosin II molecules can also assemble into smaller groups, especially dimers, which can cross-link individual actin microfilaments in stress fibres and other F-actin arrays. The ATP-dependent sliding of myosin on actin forms the basis for muscle contraction and the extension of microfilament bundles, as seen in cellular motility or in the contraction of the ring of actin and myosin around the cleavage furrow of dividing cells. There are a number of known subtypes of myosin II; they assemble in different ways and have different dynamic properties. In skeletal muscle the myosin molecules form bipolar filaments 15 nm thick. Because these filaments have a symmetric antiparallel arrangement of subunits, the midpoint is bare of head regions. In smooth muscle the molecules form thicker, flattened bundles and are orientated in random directions on either face of the bundle. These arrangements have important consequences for the contractile force characteristics of the different types of muscle cell.

Related molecules include the myosin I subfamily of single-headed molecules with tails of varying length. Functions of myosin I include the movements of membranes in endocytosis, filopodial formation in neuronal growth cones, actin–actin sliding and attachment of actin to membranes as seen in microvilli. As indicated above, molecular motors of the myosin V family are implicated in the movements of cargoes on actin filaments. So, for example, myosin Va transports vesicles along F-actin tracks in a similar manner to kinesin and cytoplasmic dynein-related cargo transport along microtubules. Each class of motor protein has different properties, but during cargo trafficking they often function together in a coordinated fashion. (See Hammer and Sellers 2012 for further reading on class V myosins.)

Other thin filaments

A heterogeneous group of filamentous structures with diameters of 2–4 nm occurs in various cells. The two most widely studied forms, titin and nebulin, constitute around 13% of the total protein of skeletal muscle (Ch. 5). They are amongst the largest known molecules and have subunit weights of around 10^6; native molecules are about 1 μm in length. Their repetitive bead-like structure gives them elastic properties that are important for the effective functioning of muscle, and possibly for other cells.

Microtubules

Microtubules are polymers of tubulin with the form of hollow, relatively rigid cylinders, approximately 25 nm in diameter and of varying length (up to 70 μm in spermatozoan flagella). They are present in most

Spectrin-related molecules are present in many other cells. For instance, fodrin is found in neurones and dystrophin occurs in muscle cells, linking the contractile apparatus with the extracellular matrix via integral membrane proteins. Proteins such as ankyrin (which also binds actin directly), vinculin, talin, zyxin and paxillin connect actin-binding proteins to integral plasma membrane proteins such as integrins (directly or indirectly), and thence to focal adhesions (consisting of a bundle of actin filaments attached to a portion of a plasma membrane linked to the extracellular matrix).

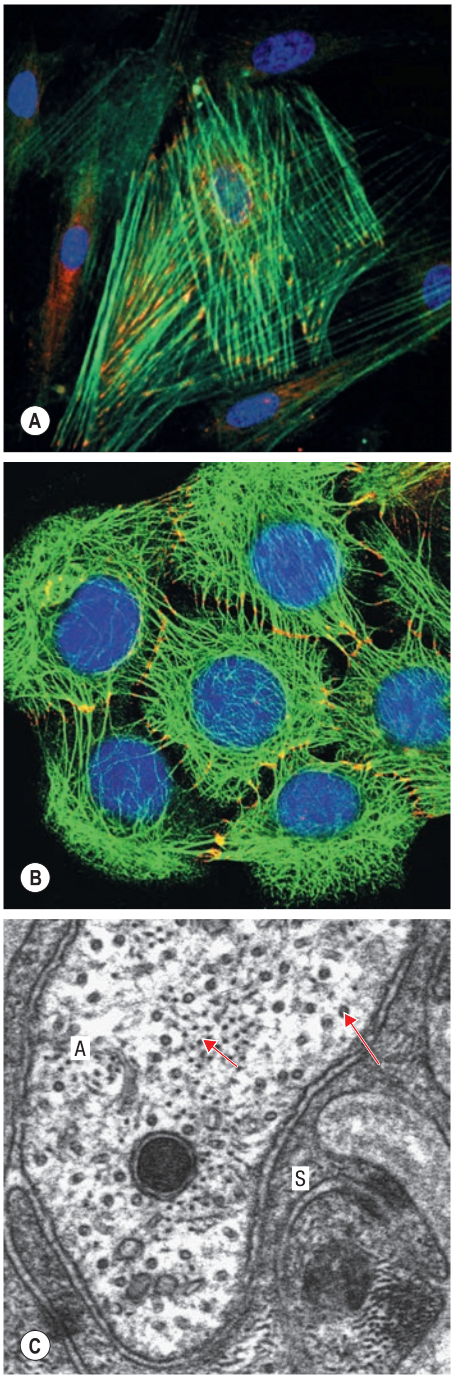

Fig. 1.14 The cytoskeleton. **A**, An immunofluorescence micrograph of α-actin microfilaments (green) in human airway smooth muscle cells in culture. The actin-binding protein, vinculin (red), is localized at the ends of actin filament bundles; nuclei are blue. **B**, An immunofluorescence micrograph of keratin intermediate filaments (green) in human keratinocytes in culture. Desmosome junctions are labelled with antibody against desmoplakin (red). Nuclei are stained blue (Hoechst). **C**, An electron micrograph of human nerve showing microtubules (small, apparently hollow structures in cross-section, long arrow) in a transverse section of an unmyelinated axon (A), engulfed by a Schwann cell (S). Neuronal intermediate filaments (neurofilaments) are the solid, electron-dense profiles, mainly in transverse section (short arrow). (A, Courtesy of Dr T Nguyen, Professor J Ward, Dr SJ Hirst, King's College London. B, Courtesy of Professor Dr WW Franke, German Cancer Research Centre, Heidelberg. C, Courtesy of Dr Bart Wagner, Histopathology Department, Sheffield Teaching Hospitals, UK.)

cell types, being particularly abundant in neurones, leukocytes and blood platelets. Microtubules are the predominant constituents of the mitotic spindles of dividing cells and also form part of the axoneme of cilia, flagella and centrioles.

Microtubules consist of tubulin dimers and microtubule-associated proteins. There are two major classes of tubulin: α- and β-tubulins. Before microtubule assembly, tubulins are associated as dimers with a combined molecular mass of 100 kDa (50 kDa each). Each protein subunit is approximately 5 nm across and is arranged along the long axis in straight rows of alternating α- and β-tubulins, forming protofilaments (Fig. 1.13B). Typically, 13 protofilaments (the number can vary between 11 and 16) associate in a ring to form the wall of a hollow cylindrical microtubule (Fig. 1.14C). Each longitudinal row is slightly out of alignment with its neighbour, so that a spiral pattern of alternating α and β subunits appears when the microtubule is viewed from the side. There is a dynamic equilibrium between the dimers and assembled microtubules: dimeric asymmetry creates polarity (α-tubulins are all orientated towards the minus end, β-tubulins towards the plus end). Tubulin is added preferentially to the plus end; the minus end is relatively slow-growing. Microtubules frequently grow and shrink at a rapid and constant rate, a phenomenon known as dynamic instability, in which growing tubules can undergo a 'catastrophe', abruptly shifting from net growth to rapid shrinkage. The primary determinant of whether microtubules grow or shrink is the rate of GTP hydrolysis. Tubulins are GTP-binding proteins; microtubule growth is accompanied by hydrolysis of GTP, which may regulate the dynamic behaviour of the tubules. Microtubule growth is initiated at specific sites, the microtubule-organizing centres, of which the best known are centrosomes (from which most cellular microtubules polymerize) and the centriole-derived basal bodies (from which cilia grow). Microtubule-organizing centres include a specialized tubulin isoform known as γ-tubulin that is essential for the nucleation of microtubule growth.

Various drugs (e.g. colcemid, vinblastine, griseofulvin, nocodazole) cause microtubule depolymerization by binding the soluble tubulin dimers and so shifting the equilibrium towards the unpolymerized state. Microtubule disassembly causes a wide variety of effects, including the inhibition of cell division by disruption of the mitotic spindle. Conversely, the drug paclitaxel (taxol) is a microtubule depolymerization inhibitor because it stabilizes microtubules and promotes abnormal microtubule assembly. Although this can cause a peripheral neuropathy, paclitaxel is widely used as an effective chemotherapeutic agent in the treatment of breast and ovarian cancer.

Microtubule-associated proteins

Various proteins that can bind to assembled tubulins may be concerned with structural properties or associated with motility. One important class of microtubule-associated proteins (MAPs) consists of proteins that associate with the plus ends of microtubules. They regulate the dynamic instability of microtubules as well as interactions with other cellular substructures. Structural MAPs form cross-bridges between adjacent microtubules or between microtubules and other structures such as intermediate filaments, mitochondria and the plasma membrane. Microtubule-associated proteins found in neurones include: MAPs 1A and 1B, which are present in neuronal dendrites and axons; MAPs 2A and 2B, found chiefly in dendrites; and tau, found only in axons. MAP 4 is the major microtubule-associated protein in many other cell types. Structural microtubule-associated proteins are implicated in microtubule formation, maintenance and disassembly, and are therefore of considerable significance in cell morphogenesis, mitotic division, and the maintenance and modulation of cell shape.

Transport-associated microtubule-associated proteins are found in situations in which movement occurs over the surfaces of microtubules, e.g. cargo transport, bending of cilia and flagella, and some movements of mitotic spindles. They include a large family of motor proteins, the best known of which are the dyneins and kinesins. Another protein, dynamin, is involved in endocytosis. The kinetochore proteins assemble at the chromosomal centromere during mitosis and meiosis. They attach (and thus fasten chromosomes) to spindle microtubules; some of the kinetochore proteins are responsible for chromosomal movements in mitotic and meiotic anaphase.

All of these microtubule-associated proteins bind to microtubules and either actively slide along their surfaces or promote microtubule assembly or disassembly. Kinesins and dyneins can simultaneously attach to membranes such as transport vesicles and convey them along microtubules for considerable distances, thus enabling selective targeting of materials within the cell. Such movements occur in both directions along microtubules. Kinesin-dependent motion is usually towards the plus ends of microtubules, e.g. from the cell body towards the axon terminals in neurones, and away from the centrosome in other cells. Conversely, dynein-related movements are in the opposite direction, i.e. to the minus ends of microtubules. The transport of cargoes along microtubules is the means by which neurotransmitters are delivered along axons within synaptic vesicle precursors towards neuronal synapses (anterograde axonal transport, utilizing kinesins) and membrane-bound vesicles are returned for recycling to the neuronal soma (retrograde axonal transport, utilizing dyneins).

Dyneins also form the arms of peripheral microtubules in cilia and flagella, where they make dynamic cross-bridges to adjacent microtubule pairs. When these tethered dyneins try to move, the resulting shearing forces cause the axonemal array of microtubules to bend, generating ciliary and flagellar beating movements. Kinesins form a large and diverse family of related microtubule-stimulated ATPases. Some kinesins are motors that move cargo and others cause microtubule disassembly, whilst still others cross-link mitotic spindle microtubules to push the two centriolar poles apart during mitotic prophase. See Bray (2001) for further reading.

Centrioles, centrosomes and basal bodies

Centrioles are microtubular cylinders 0.2 μm in diameter and 0.4 μm long (Fig. 1.15). They are formed by a ring of nine microtubule triplets linked by a number of other proteins. At least two centrioles occur in all animal cells that are capable of mitotic division (eggs, which undergo meiosis instead of mitosis, lack centrioles). See Gönczy (2012) for further reading on the structure and assembly of the centriole. They usually lie close together, at right angles or, most usually, at an oblique angle to each other (an arrangement often termed a diplosome), within the centrosome, a densely filamentous region of cytoplasm at the centre of the cell. The centrosome is the major microtubule-organizing centre of most cells; it is the site at which new microtubules are formed and the mitotic spindle is generated during cell division.

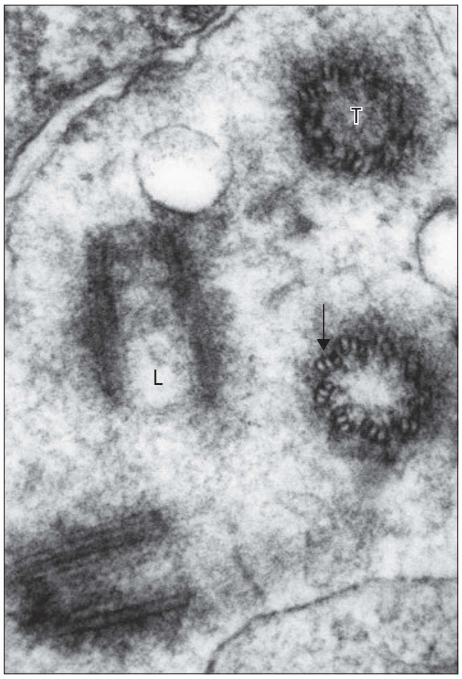

Fig. 1.15 A duplicated pair of centrioles in a human carcinoma specimen. Each centriole pair consists of a mother and daughter, orientated approximately at right angles to each other so that one is sectioned transversely (T) and the other longitudinally (L). The transversely sectioned centrioles are seen as rings of microtubule triplets (arrow). (Courtesy of Dr Bart Wagner, Histopathology Department, Sheffield Teaching Hospitals, UK.)

Centriole biogenesis is a complex process (Fig. 1.16) At the beginning of the S phase (DNA replication phase) of the cell cycle (see below), a new daughter centriole forms at right-angles to each separated maternal centriole. Each mother–daughter pair forms one pole of the next mitotic spindle, and the daughter centriole becomes fully mature only as the progeny cells are about to enter the next mitosis. Because centrosomes are microtubule-organizing centres, they lie at the centre of a network of microtubules, all of which have their minus ends proximal to the centrosome.

The microtubule-organizing centre contains complexes of γ-tubulin that nucleate microtubule polymerization at the minus ends of microtubules. Basal bodies are microtubule-organizing centres that are closely related to centrioles, and are believed to be derived from them. They are located at the bases of cilia and flagella, which they anchor to the cell surface. The outer microtubule doublets of the axoneme of cilia and flagella originate from two of the microtubules in each triplet of the basal body.

Intermediate filaments

Intermediate filaments are about 10 nm thick and are formed by a heterogeneous group of filamentous proteins. In contrast to actin filaments and microtubules, which are assembled from globular proteins with nucleotide-binding and hydrolysing activity, intermediate filaments consist of filamentous monomers lacking enzymatic activity. Intermediate filament proteins assemble to form linear filaments in a three-step process. First, a pair of intermediate filament protein subunits, each consisting of a central α-helical rod domain of about 310 amino acids flanked by head and tail non-α-helical domains of variable size, form a parallel dimer through their central α-helical rod domains coiled around each other. The variability of intermediate filament protein subunits resides in the length and amino-acid sequence of the head and tail domains, thought to be involved in regulating the interaction of intermediate filaments with other proteins. Second, a tetrameric unit is formed by two antiparallel half-staggered coiled dimers. Third, eight tetramers associate laterally to form a 16 nm thick unit length filament (ULF). Individual ULFs join end to end to form short filaments that continue growing longitudinally by annealing to other ULFs and existing filaments. Filament elongation is followed by internal compaction leading to the 30 nm thick intermediate filament (Figs 1.13C, 1.14B). The tight association of dimers, tetramers and ULFs provides intermediate filaments with high tensile strength

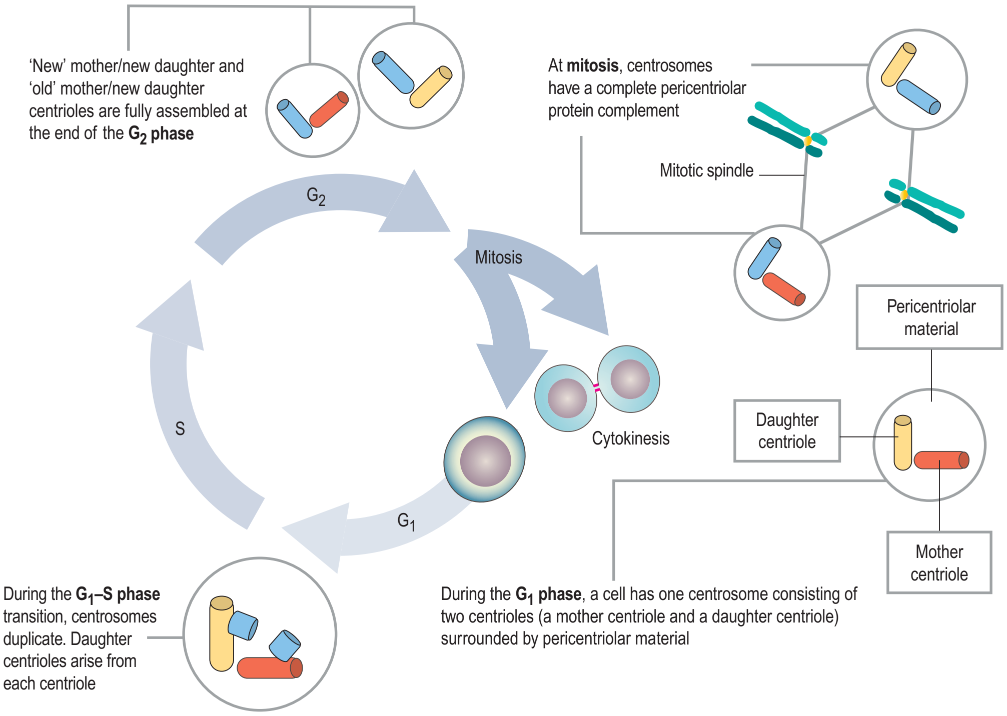

'New' mother/new daughter and 'old' mother/new daughter centrioles are fully assembled at the end of the **G_2 phase**

At **mitosis**, centrosomes have a complete pericentriolar protein complement

During the **G_1–S phase** transition, centrosomes duplicate. Daughter centrioles arise from each centriole

During the **G_1 phase**, a cell has one centrosome consisting of two centrioles (a mother centriole and a daughter centriole) surrounded by pericentriolar material

Fig. 1.16 A centriolar pair consists of a mother and a daughter centriole that duplicates once every cell cycle in preparation for cell division. Each centriole generates a daughter centriole, which means that there are two new daughter centrioles. The previous daughter centriole becomes the 'new' mother and the previous mother centriole remains as the 'old' mother centriole, i.e. an 'old' mother centriole is connected to one of the new daughter centrioles and a 'new' mother centriole is linked to the other new daughter centriole. (Adapted with permission from Kierszenbaum AL, Tres LL Histology and Cell Biology: An Introduction to Pathology, 5th ed. Elsevier. Copyright 2019.)

The association of membrane vesicles with dynein motors means that certain cytomembranes (including the Golgi apparatus) concentrate near the centrosome. This is relevant because the microtubules provide a means of targeting Golgi vesicular products to different parts of the cell.

and resistance to stretching, compression, twisting and bending forces. In contrast to actin filaments and microtubules, intermediate filaments are non-polar (because of the antiparallel alignment of the initial tetramers) and do not bind nucleotides (as in G-actin and tubulin dimers), and ULFs anneal end to end to each other (in contrast to the polarized F-actin and microtubules, with one end, the plus end, growing faster than the other end, the minus end). See Herrmann et al (2007) for further reading.

Intermediate filaments are found in different cell types and are often present in large numbers, either to provide structural strength where it is needed (see Figs 1.14B, 1.14C) or to provide scaffolding for the attachment of other structures. Intermediate filaments form extensive cytoplasmic networks extending from cage-like perinuclear arrangements to the cell surface. Intermediate filaments of different molecular classes are characteristic of particular tissues or states of maturity and are therefore important indicators of the origins of cells or degrees of differentiation, as well as being of considerable value in histopathology.

Intermediate filament proteins have been classified into five distinct types on the basis of their primary structure and tissue-specific expression. Of the different classes of intermediate filaments, keratin (cytokeratin) proteins are found in epithelia, where keratin filaments are always composed of equal ratios of type I (acidic) and type II (basic to neutral) keratins to form heteropolymers. About 20 types of each of the acidic and basic/neutral keratin proteins are known. For further reading on keratins in normal and diseased epithelia, see Pan et al (2012). Within the epidermis, expression of keratin heteropolymers changes as keratinocytes mature during their transition from basal to superficial layers. Genetic abnormalities of keratins are known to affect the mechanical stability of epithelia. For example, the disease epidermolysis bullosa simplex is caused by lysis of epidermal basal cells and blistering of the skin after mechanical trauma. Defects in genes encoding keratins 5 and 14 produce cytoskeletal instability leading to cellular fragility in the basal cells of the epidermis. When keratins 1 and 10 are affected, cells in the spinous (prickle) cell layer of the epidermis lyse, and this produces the intraepidermal blistering of epidermolytic hyperkeratosis. See Porter and Lane (2003) for further reading.

Type III intermediate filament proteins, including vimentin, desmin, glial fibrillary acidic protein and peripherin, form homopolymer intermediate filaments. Vimentin is expressed in mesenchyme-derived cells of connective tissue and some ectodermal cells during early development; desmins in muscle cells; glial fibrillary acidic protein in glial cells; and peripherin in peripheral axons. Type IV intermediate filaments include neurofilaments, nestin, syncoilin and α-internexin. Neurofilaments are a major cytoskeletal element in neurones, particularly in axons (see Fig. 1.14C), where they are the dominant protein. Neurofilaments (NF) are heteropolymers of low (NF–L), medium (NF–M) and high (NF–H) molecular weight (the NF–L form is always present in combination with either NF–M or NF–H forms). Abnormal accumulations of neurofilaments (neurofibrillary tangles) are characteristic features of a number of neuropathological conditions. Nestin resembles a neurofilament protein, which forms intermediate filaments in neurectodermal stem cells in particular. The type V intermediate filament group includes the nuclear lamins A, lamin B1 and lamin B2 lining the inner surface of the nuclear envelope of all nucleated cells. Lamin C is a splice variant of lamin A. Lamins provide a mechanical framework for the nucleus and act as attachment sites for a number of proteins that organize chromatin at the periphery of the nucleus. They are unusual in that they form an irregular anastomosing network of filaments rather than linear bundles. See Burke and Stewart (2013) for further reading.

Nucleus

The nucleus (see Figs 1.1–1.2) is generally the largest intracellular structure and is usually spherical or ellipsoid in shape, with a diameter of 3–10 µm. Conventional histological stains, such as haematoxylin or toluidine blue, detect the acidic components (phosphate groups) of deoxyribonucleic acid (DNA) and ribonucleic acid (RNA) in cells and tissue sections. DNA and RNA molecules are said to be basophilic because of the binding affinity of their negatively charged phosphate groups to basic dyes such as haematoxylin. A specific stain for DNA is the Feulgen reaction.

Nuclear envelope

The nucleus is surrounded by the nuclear envelope, which consists of an inner nuclear membrane (INM) and an outer nuclear membrane (ONM), separated by a 40–50 nm perinuclear space that is spanned by nuclear pore complexes (NPCs). The perinuclear space is continuous with the lumen of the endoplasmic reticulum. The ONM has multiple connections with the endoplasmic reticulum, with which it shares its membrane protein components. The INM contains its own specific integral membrane proteins (lamin B receptor and emerin, both providing binding sites for chromatin bridging proteins). A mutation in the gene encoding emerin causes X-linked Emery–Dreifuss muscular dystrophy (EDMD), characterized by skeletal muscle wasting and cardiomyopathy.

The nuclear lamina, a 15–20 nm thick, protein-dense meshwork, is associated with the inner face of the INM. The major components of the nuclear lamina are lamins, the type V intermediate filament proteins consisting of A-type and B-type classes.

The nuclear lamina reinforces the nuclear membrane mechanically, determines the shape of the nucleus and provides a binding site for a range of proteins that anchor chromatin to the cytoskeleton. Nuclear lamin A, with more than 350 mutations, is the most mutated protein linked to human disease. These are referred to as laminopathies, characterized by nuclear structural abnormalities that cause structurally weakened nuclei, leading to mechanical damage. Lamin A mutations cause a surprisingly wide range of diseases, from progeria to various dystrophies, including an autosomal dominant form of EDMD. A truncated farnesylated form of lamin A, referred to as progerin, leads to defects in cell proliferation and DNA damage of mesenchymal stem cells and vascular smooth muscle cells. Affected patients display cardiovascular disease and die at an early age. Mice lacking lamin B1 and lamin B2 survive until birth; however, neuronal development is compromised when lamin B1 or lamin B2 is absent. Overexpression of lamin B1 is associated with autosomal dominant leukodystrophy characterized by gradual demyelination in the central nervous system. See Worman (2012) and Burke and Stewart (2013) for additional reading on lamins and laminopathies.

Condensed chromatin (heterochromatin) tends to aggregate near the nuclear envelope during interphase. At the end of mitotic and meiotic prophase (see below), the lamin filaments disassemble by phosphorylation, causing the nuclear membranes to vesiculate and disperse into the endoplasmic reticulum. During the final stages of mitosis (telophase), proteins of the nuclear periphery, including lamins, associate with the surface of the chromosomes, providing docking sites for membrane vesicles. Fusion of these vesicles reconstitutes the nuclear envelope, including the nuclear lamina, following lamin dephosphorylation. See Simon and Wilson (2011) for further reading on the nucleoskeleton.

The transport of molecules between the nucleus and the cytoplasm occurs via specialized nuclear pore structures that perforate the nuclear membrane (**Fig. 1.17A**). They act as highly selective directional molecular filters, permitting proteins such as histones and gene regulatory proteins (which are synthesized in the cytoplasm but function in the nucleus) to enter the nucleus, and molecules that are synthesized in the nucleus but destined for the cytoplasm (e.g. ribosomal subunits, transfer RNAs and messenger RNAs) to leave the nucleus.

Ultrastructurally, nuclear pores appear as disc-like structures with an outer diameter of 130 nm and an inner pore with an effective diameter for free diffusion of 9 nm (**Fig. 1.17B**). The nuclear envelope of an active cell contains up to 4000 such pores. The nuclear pore complex has an octagonal symmetry and is formed by an assembly of more than 50 proteins, the nucleoporins. The inner and outer nuclear membranes fuse around the pore complex (see Fig. 1.17A). Nuclear pores are freely permeable to small molecules, ions and proteins up to about 17 kDa. See Raices and D'Angelo (2012) for further reading on nuclear pore complex composition. Most proteins that enter the nucleus do so as complexes with specific transport receptor proteins known as importins. Importins shuttle back and forth between the nucleus and cytoplasm. Binding of the cargo to the importin requires a short sequence of amino acids known as a nuclear localization sequence (NLS), and can either be direct or take place via an adapter protein. Interactions of the importin with components of the nuclear pore move it, together with its cargo, through the pore by an energy-independent process. A complementary cycle functions in export of proteins and RNA molecules from the nucleus to the cytoplasm using transport receptors known as exportins.

A small GTPase called Ras-related nuclear protein (Ran) regulates the import and export of proteins across the nuclear envelope.

For further reading on the Ran pathway and exportins/importins, see Clarke and Zhang (2008) and Raices and D'Angelo (2012).

Chromatin

DNA is organized within the nucleus in a DNA–protein complex known as chromatin. The protein constituents of chromatin are the histones and the non-histone proteins. Non-histone proteins are an extremely heterogeneous group that includes structural proteins, DNA and RNA polymerases, and gene regulatory proteins. Histones are the most abundant group of proteins in chromatin, primarily responsible for the packaging of chromosomal DNA into its primary level of organization, the nucleosome. There are four core histone proteins – H2A, H2B, H3 and H4 – which vary in amino acid sequence and post-translational modifications

A-type lamins include lamin A (interacting with emerin), lamin C, lamin C2 and lamin AΔ10 encoded by a single gene (*LMNA*). Lamin A and lamin C are the major A-type lamins expressed in somatic cells, whereas lamin C2 is expressed in testis. B-type lamins include lamin B1 and lamin B2 (expressed in somatic cells), and testis-specific lamin B3. Lamin B1 is encoded by the *LMNB1* gene; lamin B2 is encoded by the *LMNB2* gene.

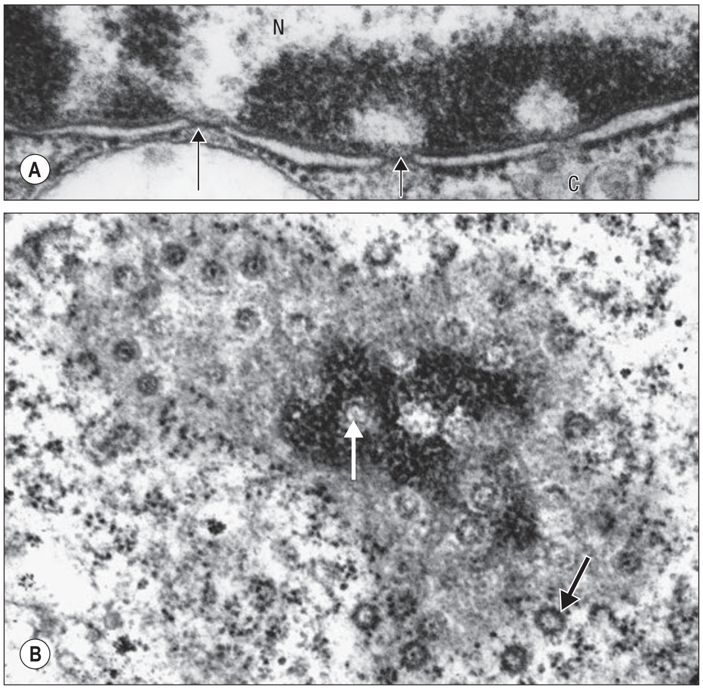

Fig. 1.17 **A**, The nuclear envelope with nuclear pores (arrows) in transverse section, showing the continuity between the inner and outer phospholipid layers of the envelope on either side of the pore. The fine 'membrane' appearing to span the pore is formed by proteins of the pore complex. Note that the chromatin is less condensed in the region of nuclear pores. Abbreviations: N, nucleus; C, cytoplasm. **B**, Nuclear pores seen '*en face*' as spherical structures (arrows) in a tangential section through the nuclear envelope. The appearance of the envelope varies in electron density as the plane of section passes through different regions of the curved double membrane, which is interrupted at intervals by pores through the envelope (see also Fig. 1.1). The surrounding cytoplasm with ribosomes is less electron dense. Human tissues. (Courtesy of Dr Bart Wagner, Histopathology Department, Sheffield Teaching Hospitals, UK.)

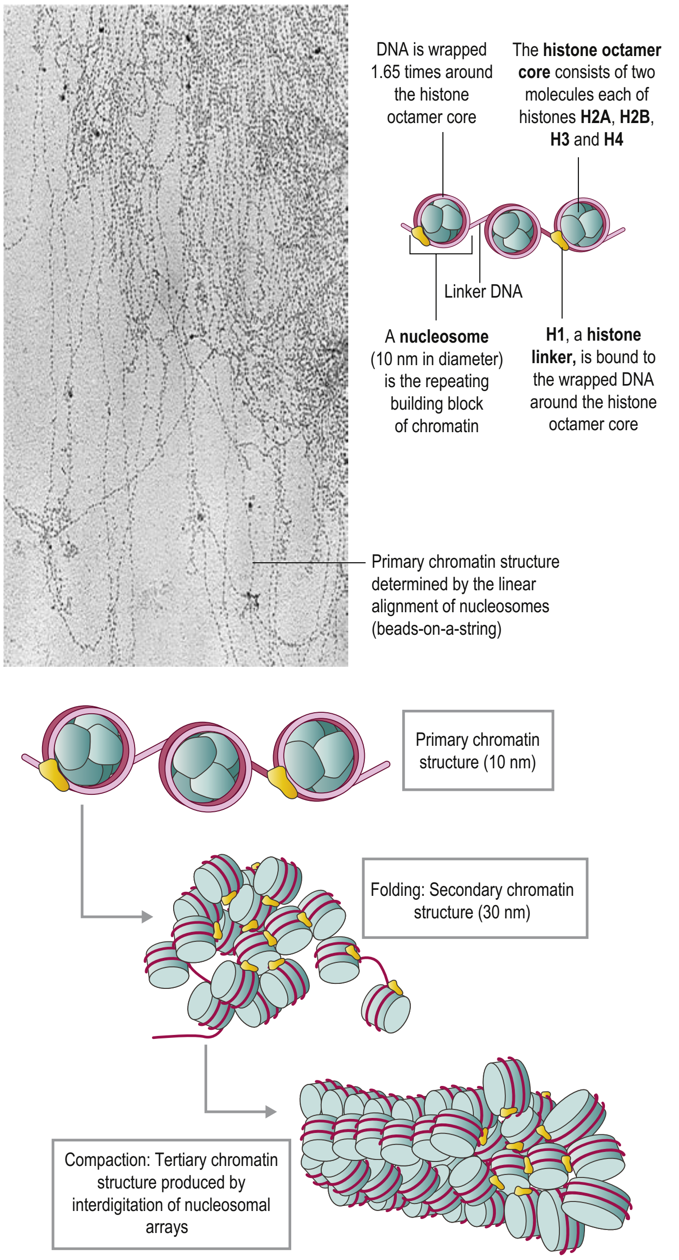
DNA is wrapped 1.65 times around the histone octamer core
The **histone octamer core** consists of two molecules each of histones **H2A**, **H2B**, **H3** and **H4**
Linker DNA
A **nucleosome** (10 nm in diameter) is the repeating building block of chromatin
H1, a **histone linker,** is bound to the wrapped DNA around the histone octamer core
Primary chromatin structure determined by the linear alignment of nucleosomes (beads-on-a-string)
Primary chromatin structure (10 nm)
Folding: Secondary chromatin structure (30 nm)
Compaction: Tertiary chromatin structure produced by interdigitation of nucleosomal arrays

Fig. 1.18 The nucleosome is the repeating building block of chromatin and consists of DNA wrapped around a histone core. Each nucleosome contains two molecules of each histone H2A, H2B, H3 and H4. Histone variability has an effect on the condensation of the chromatin fibre and the interaction of nucleosomes with non-histone proteins. Nucleosomes connected in a linear array by a short DNA segment (linker DNA) form the primary structure of chromatin. The side-by-side interaction of the primary chromatin structure (electron micrograph, left) determines a secondary order of folding. The interaction between secondary chromatin fibres producing tertiary structures accounts for the compact chromatin state seen in the condensed metaphase chromosome and in heterochromatin. (Adapted with permission from Kierszenbaum AL, Tres LL Histology and Cell Biology: An Introduction to Pathology, 5th ed. Elsevier. Copyright 2019.)

(including acetylation, methylation and phosphorylation). They combine in equal ratios to form a compact octameric nucleosome core. A fifth histone, H1, is involved in further compaction of the chromatin (Fig. 1.18). The DNA molecule (one per chromosome) winds twice around each nucleosome core, taking up 145–147 base pairs. This packaging organizes the DNA into a chromatin fibre 10 nm in diameter, and imparts to this form of chromatin the electron microscopic appearance of beads on a string, in which each bead is separated by a variable length of DNA, typically about 35 nucleotide pairs long. The nucleosome core region and one of the linker regions constitute the nucleosome proper, which is typically about 200 nucleotide pairs in length. However, chromatin rarely exists in this simple form and is usually packaged further into a 30 nm thick fibre, involving a single H1 histone per nucleosome, which interacts with both DNA and protein to impose a higher order of nucleosome packing. Usually, 30 nm thick fibres are further coiled or folded into larger domains. Individual domains are believed to decondense and extend during active transcription. In a typical interphase nucleus, euchromatin (nuclear regions that appear pale in appropriately stained tissue sections, or relatively electron-lucent in electron micrographs; see Fig. 1.2) is likely to consist mainly of 30 nm fibres and loops, and contains the transcriptionally active genes. Transcriptionally active cells, such as most neurones, have nuclei that are predominantly euchromatic. See Luger et al (2012) for further reading on the nucleosome and chromatin structure.

Heterochromatin (nuclear regions that appear dark in appropriately stained tissue sections or electron-dense in electron micrographs) is characteristically located mainly around the periphery of the nucleus, except over the nuclear pores (see Fig. 1.17A), and adjacent to the nucleolus (see Fig. 1.2). It is a relatively compacted form of chromatin in which the histone proteins carry a specific set of post-translational modifications, including methylation at characteristic residues. This facilitates the binding of specific heterochromatin-associated proteins. Heterochromatin includes non-coding regions of DNA, such as centromeric regions, which are known as constitutive heterochromatin. DNA becomes transcriptionally inactive in some cells as they differentiate during development or cell maturation, and contributes to heterochromatin; it is known as facultative heterochromatin. The inactive X chromosome in females is an example of facultative heterochromatin and can be identified in the light microscope as the deeply staining Barr body often located near the nuclear periphery or a drumstick extension of a nuclear lobe of a mature multilobed neutrophil leukocyte.

In transcriptionally inactive cells, chromatin is predominantly in the condensed, heterochromatic state, and may comprise as much as 90% of the total. Examples of such cells are mature neutrophil leukocytes (in which the condensed chromatin is present in a multilobular, densely staining nucleus) and the highly condensed nuclei of orthochromatic erythroblasts (late-stage erythrocyte precursors). In most mature cells, a mixture of the two occurs, indicating that only a proportion of the DNA is being transcribed. A particular instance of this is seen in the B lymphocyte-derived plasma cell, in which much of the chromatin is in the condensed condition and is arranged in regular masses around the perimeter of the nucleus, producing the so-called 'clock-face' nucleus (see Figs 4.6, 4.12). Although this cell is actively transcribing, much of its protein synthesis is of a single immunoglobulin type, and consequently much of its genome is in an inactive state.

During mitosis, the chromatin is further reorganized and condensed to form the much-shortened chromosomes characteristic of metaphase. This shortening is achieved through further levels of close packing of the chromatin. The condensed chromosomes are stabilized by protein complexes known as condensins. Progressive folding of the chromosomal DNA by interactions with specific proteins can reduce 5 cm of chromosomal DNA by 10,000-fold, to a length of 5 μm in the mitotic chromosome.

Chromosomes and telomeres

The nuclear DNA of eukaryotic cells is organized into linear units called chromosomes. The DNA in a normal human diploid cell contains 6×10^9 nucleotide pairs organized in the form of 46 chromosomes (44 autosomes and 2 sex chromosomes). The largest human chromosome (number 1) contains 2.5×10^8 nucleotide pairs, and the smallest (the Y chromosome) 5×10^7 nucleotide pairs.

Each chromosomal DNA molecule contains a number of specialized nucleotide sequences that are associated with its maintenance. One is the centromeric DNA region. During mitosis, a disc-shaped structure composed of a complex array of proteins, the kinetochore, forms as a substructure at the centromeric region of DNA to which kinetochore microtubules of the spindle attach. Another region, the telomere, defines the end of each chromosomal DNA molecule. Telomeres consist of hundreds of repeats of the nucleotide sequence $(TTAGGG)_n$. The very ends of the chromosomes cannot be replicated by the same DNA polymerase as the rest of the chromosome, and are maintained by a specific enzyme called telomerase, which contains an RNA subunit acting as the template for lengthening the TTAGGG repeats. See Nandakumar and Cech (2013) for further reading on the recruitment of telomerase to telomeres. Thus telomerase is a specialized type of polymerase known as a reverse transcriptase that turns sequences in RNA back into DNA. The number of tandem repeats of the telomeric DNA sequence varies. The telomere appears to shorten with successive cell divisions because telomerase activity reduces or is absent in differentiated cells with a finite lifespan. In mammals, telomerase is active in the germ-cell lineage and in stem cells, but its expression in somatic cells may lead to or prompt cancer. A lack of telomere maintenance determines the shrinking of telomeres in proliferating cells to the point when cells stop dividing, a condition known as replicative senescence. See Sahin and DePinho (2012) for further reading on telomeres and progressive DNA damage.

The role of the telomere in ageing and cell senescence is further discussed at the end of this chapter.

Karyotypes: classification of human chromosomes

A number of genetic abnormalities can be directly related to the chromosomal pattern. The characterization or karyotyping of chromosome number and structure is therefore of considerable diagnostic importance. The identifying features of individual chromosomes are most easily seen during metaphase, although prophase chromosomes can be used for more detailed analyses.

Lymphocytes separated from blood samples, or cells taken from other tissues, are used as a source of chromosomes. Diagnosis of fetal chromosome patterns is generally carried out on samples of amniotic fluid containing fetal cells aspirated from the uterus by amniocentesis, or on a small piece of chorionic villus tissue removed from the placenta. Whatever their origin, the cells are cultured *in vitro* and stimulated to divide by treatment with agents that stimulate cell division. Mitosis is interrupted at metaphase with spindle inhibitors. The chromosomes are dispersed by first causing the cells to swell in a hypotonic solution, then the cells are gently fixed and mechanically ruptured on a slide to spread the chromosomes. They are subsequently stained in various ways to allow the identification of individual chromosomes by size, shape and distribution of stain (**Fig. 1.19**). General techniques show the obvious landmarks, e.g. lengths of arms and positions of constrictions. Banding techniques demonstrate differential staining patterns, characteristic for each chromosome type. Fluorescence staining with quinacrine mustard and related compounds produces Q bands, and Giemsa staining (after treatment that partially denatures the chromatin) gives G bands (see Fig. 1.19A). Other less widely used methods include: reverse Giemsa staining, in which the light and dark areas are reversed (R bands); the staining of constitutive heterochromatin with silver salts (C-banding); and T-banding to stain the ends (telomeres) of chromosomes. Collectively, these methods permit the classification of chromosomes into numbered autosomal pairs in order of decreasing size, from 1 to 22, plus the sex chromosomes.

A summary of the major classes of chromosome is given in **Table 1.1**.

Methodological advances in banding techniques improved the recognition of abnormal chromosome patterns. These include a reciprocal translocation between chromosomes 9 and 22, the latter being characteristically short and known as the Philadelphia (Ph^1) chromosome; it

TABLE 1.1 Summary of the major classes of chromosome

Group	Features
1–3 (A)	Large metacentric chromosomes
4–5 (B)	Large submetacentric chromosomes
6–12 + X (C)	Metacentrics of medium size
13–15 (D)	Medium-sized acrocentrics with satellites
16–18 (E)	Shorter metacentrics (16) or submetacentrics (17, 18)
19–20 (F)	Shortest metacentrics
21–22 + Y (G)	Short acrocentrics; 21, 22 with satellites, Y without

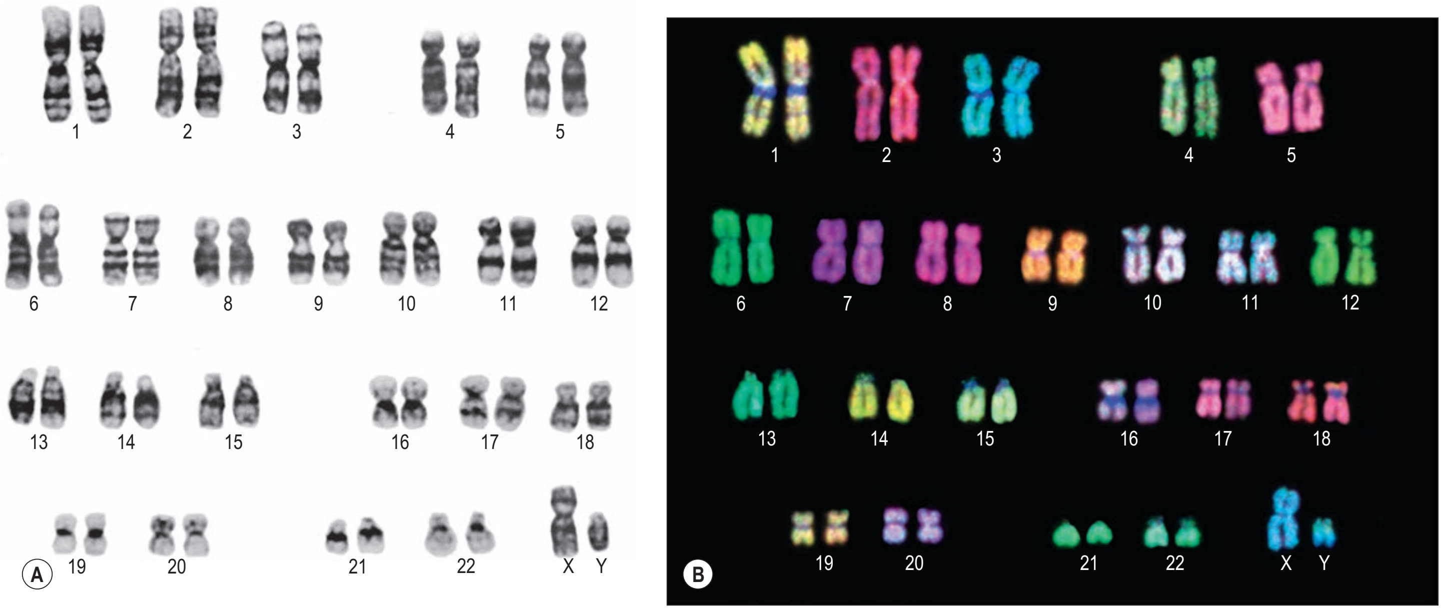

Fig. 1.19 Chromosomes from normal males, arranged as karyotypes. **A**, G-banded preparation. **B**, Preparation stained by multiplex fluorescence *in situ* hybridization to identify each chromosome. (Courtesy of Dr Denise Sheer, Cancer Research UK.)

Telomerase has been associated with ageing and cell senescence because a gradual loss of telomeres may lead to tissue atrophy, stem cell depletion and deficient tissue repair or regeneration. Mutations causing loss of function of telomerase or the RNA-containing template have been associated with dyskeratosis congenita (characterized by abnormal skin pigmentation, nail dystrophy and mucosal leukoplasia), aplastic anaemia and pulmonary fibrosis.

is a hallmark of chronic myeloid leukaemia and some cases of acute lymphoblastic leukaemia.

The use of *in situ* hybridization with fluorescent DNA probes specific for each chromosome (see Fig. 1.19B) permits the identification of even very small abnormalities.

Nucleolus

Nucleoli are a prominent feature of an interphase nucleus (see Fig. 1.2). They are the site of most of the synthesis of ribosomal RNA (rRNA) and assembly of ribosome subunits. Nucleoli organize at the end of mitosis and consist of repeated clusters of ribosomal DNA (rDNA) genes and processing molecules responsible for producing ribosome subunits. The initial step of the assembly of a ribosome subunit starts with the transcription of rDNA genes by RNA polymerase I. The rDNA genes, arranged in tandem repeats called nucleolar organizing regions (NORs), are located on acrocentric chromosomes. There are five pairs of acrocentric chromosomes in humans. The initial 47S rRNA precursor transcript is cleaved to form the mature 28S, 18S and 5.8S rRNAs, assembled with the 5S rRNA (synthesized by RNA polymerase III outside the nucleolus) and coupled to small nucleolar ribonucleoproteins and other non-ribosomal proteins to form 60S (containing 28S rRNA, 5.8S rRNA and 5S rRNA) and 40S (containing 18S rRNA) preribosome subunits. These are then exported to the cytoplasm across nuclear pores as mature ribosome subunits. About 726 human nucleolar proteins have been identified by protein purification and mass spectrometry. For further reading on nucleolar functions, see Boisvert et al (2007).

Ribosomal biogenesis occurs in distinct subregions of the nucleolus, visualized by electron microscopy. The three nucleolar subregions are fibrillar centres (FCs), dense fibrillar components (DFCs) and granular components (GCs). Transcription of the rDNA repeats takes place at the FC–DFC boundary; pools of RNA polymerase I reside in the FC region; processing of transcripts and coupling to small nucleolar ribonucleoproteins take place in DFC; and the assembly of ribosome subunits is completed in the GC region.

The nucleolus is disassembled when cells enter mitosis and transcription becomes inactive. It reforms after nuclear envelope reorganization in telophase, in a process associated with the onset of transcription in nucleolar organizing centres on each specific chromosome, and becomes functional during the G_1 phase of the cell cycle. An adequate pool of ribosome subunits during cell growth and cell division requires steady nucleolar activity to support protein synthesis. Several DNA helicases, a conserved group of enzymes that unwind DNA, accumulate in the nucleolus under specific conditions such as Bloom's syndrome (an autosomal recessive disorder characterized by growth deficiency, immunodeficiency and a predisposition to cancer) and Werner's syndrome (an autosomal recessive condition characterized by the early appearance of various age-related diseases).

CELL DIVISION AND THE CELL CYCLE

During prenatal development, most cells undergo repeated division (**Video 1.1**) as the body grows in size and complexity. As cells mature, they differentiate structurally and functionally. Some cells, such as neurones, lose the ability to divide. Others may persist throughout the lifetime of the individual as replication-competent stem cells, e.g. cells in the haemopoietic tissue of bone marrow. Many stem cells divide infrequently, but give rise to daughter cells that undergo repeated cycles of mitotic division as transit (or transient) amplifying cells. Their divisions may occur in rapid succession, as in cell lineages with a short lifespan and similarly fast turnover and replacement time. Transit amplifying cells are all destined to differentiate and ultimately to die and be replaced, unlike the population of parental stem cells, which self-renews.

Patterns and rates of cell division within tissues vary considerably. In many epithelia, such as the crypts between intestinal villi, the replacement of damaged or ageing cells by division of stem cells can be rapid. Rates of cell division may also vary according to demand, as occurs in the healing of wounded skin, in which cell proliferation increases to a peak and then returns to the normal replacement level. The rate of cell division is tightly coupled to the demand for growth and replacement. Where this coupling is faulty, tissues either fail to grow or replace their cells, or they can overgrow, producing neoplasms.

The cell cycle is an ordered sequence of events, culminating in cell growth and division to produce two daughter cells. It generally lasts a minimum of 12 hours, but in most adult tissues can be considerably longer, and is divided into four distinct phases, which are known as G_1 (for gap 1), S (for DNA synthesis), G_2 (for gap 2) and M (for mitosis). The combination of G_1, S and G_2 phases is known as interphase. M is the mitotic phase, which is further divided into four phases (see below). G_1 is the period when cells respond to growth factors directing the cell to initiate another cycle; once made, this decision is irreversible. It is also the phase in which most of the molecular machinery required to complete another cell cycle is generated. Centrosomes duplicate during S phase in preparation for mitosis. Cells that retain the capacity for proliferation, but which are no longer dividing, have entered a phase called G_0 and are described as quiescent even though they may be quite active physiologically. Growth factors can stimulate quiescent cells to leave G_0 and re-enter the cell cycle, whereas the proteins encoded by certain tumour suppressor genes (e.g. the gene mutated in retinoblastoma, *Rb*) block the cycle in G_1. DNA synthesis (replication of the genome) occurs during S phase, at the end of which the DNA content of the cell has doubled. During G_2, the cell prepares for division; this period ends with the onset of chromosome condensation and breakdown of the nuclear envelope. The times taken for S, G_2 and M are similar for most cell types, and occupy 6–8, 2–4 and 1–2 hours respectively. In contrast, the duration of G_1 shows considerable variation, sometimes ranging from less than 2 hours in rapidly dividing cells to more than 100 hours, within the same tissue.

The passage of a cell through the cell cycle is controlled by proteins in the cytoplasm: cyclins and cyclin-dependent kinases (Cdks; **Fig. 1.21**). Cyclins include G_1 cyclins (D cyclins), S-phase cyclins (cyclins E and A) and mitotic cyclins (B cyclins). Cdks, protein kinases, which are activated by binding of a cyclin subunit, include G_1 Cdk (Cdk4), an S-phase Cdk (Cdk2) and an M-phase Cdk (Cdk1). Cell cycle progression is driven in part by changes in the activity of Cdks. Each cell cycle stage is characterized by the activity of one or more Cdk–cyclin pairs. Transitions between cell cycle stages are triggered by highly specific proteolysis by the 26S proteasome of the cyclins and other key components. The targets for proteolysis are marked for destruction by E3 ubiquitin ligases, which decorate them with polymers of the small protein ubiquitin, a sign for recognition by the 26S proteasome.

To give one example, the transition from G_2 to mitosis is driven by activation of Cdk1 by its partners, the A- and B-type cyclins; the characteristic changes in cellular structure that occur as cells enter mitosis are largely driven by phosphorylation of proteins by active Cdk1-cyclin A and Cdk1-cyclin B. Cells exit from mitosis when an E3 ubiquitin ligase, the anaphase promoting complex, also called cyclosome (APC/C), marks the cyclins for destruction. In addition, APC/C prompts

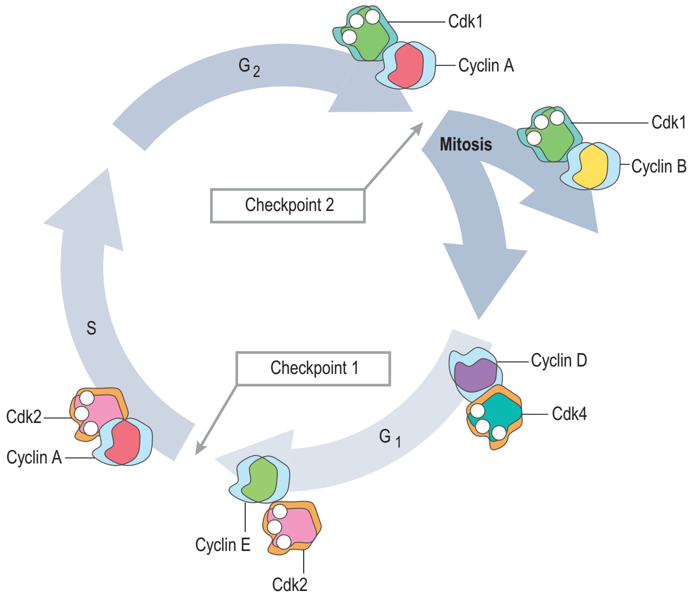

Fig. 1.21 The cell cycle consists of an interphase (G_1 phase, S phase and G_2 phase) followed by mitosis. The cyclin D/Cdk4 complex assembles at the beginning of G_1; the cyclin E/Cdk2 complex assembles near the end of G_1 as the cell is preparing to cross checkpoint 1 to start DNA synthesis (during S phase). The cyclin A/Cdk2 complex assembles as DNA synthesis starts. Completion of G_2 is indicated by the assembled cyclin A/Cdk1 complex. A cell crosses checkpoint 2 to initiate mitosis when the cyclin B/Cdk1 complex assembles. The cyclin B/Cdk1 complex is degraded by the 26S proteasome and an assembled cyclin D/Cdk4 marks the start of the G_1 phase of a new cell cycle. For details, see text. (Adapted with permission from Kierszenbaum AL, Tres LL Histology and Cell Biology: An Introduction to Pathology, 5th ed. Elsevier, Mosby. Copyright 2019.)

In this translocation, the ABL1 (cABL) cellular oncogene on chromosome 9 is relocated to a region adjacent to the *BCR* (break-point cluster) gene on chromosome 22. The resulting fusion gene codes for a hybrid protein with constitutively active tyrosine kinase signalling function. This drives uncontrolled proliferative activity in affected cells (Fig. 1.20).

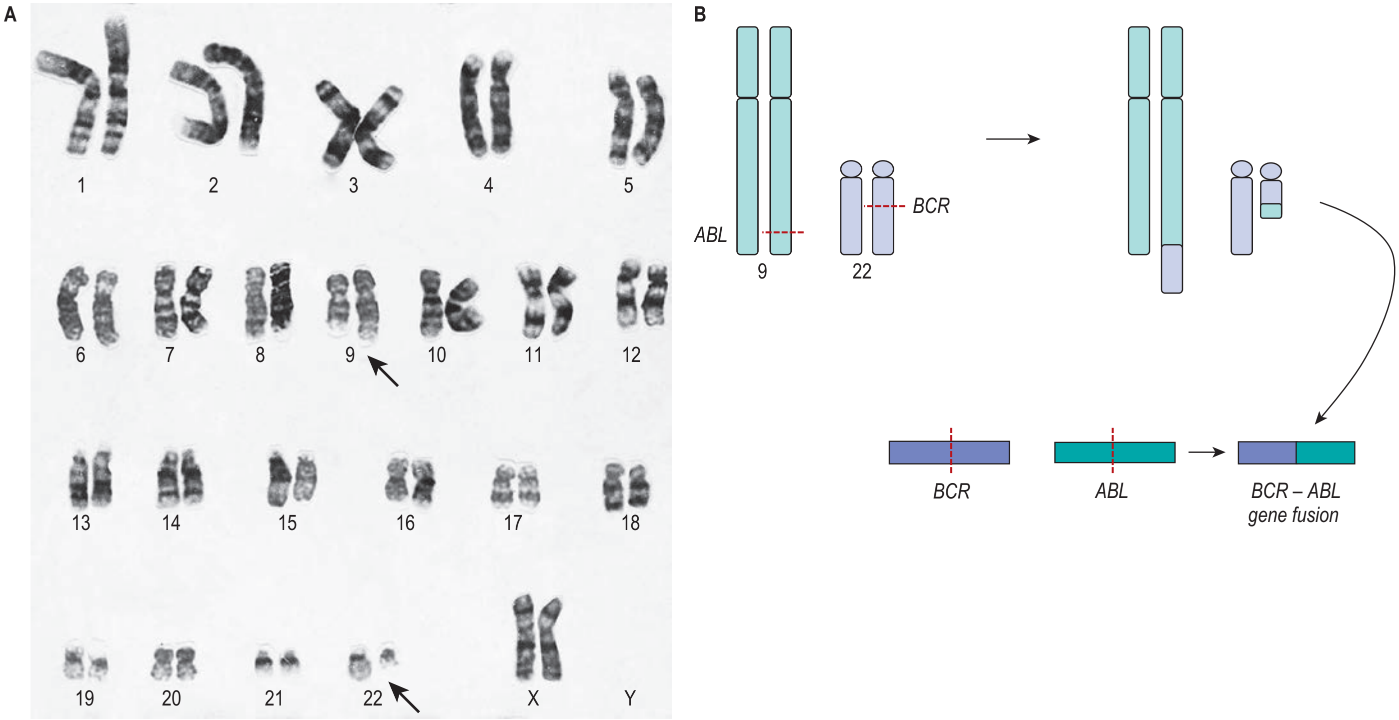

Fig. 1.20 **A**, G-banded karyotype of chronic myeloid leukaemia (CML) cells, showing a reciprocal translocation between chromosome 9 (creating the longer 9q+ chromosome) and chromosome 22. The shorter chromosome 22 is characteristic of CML and is known as the Philadelphia (Ph^1) chromosome. **B**, Representation of the Philadelphia translocation which creates a fusion gene (*BCR–ABL*). See text for details. (Courtesy of Professor Denise Sheer, Queen Mary University of London.)

the degradation of the mitotic cyclin B and the destruction of cohesins, thus allowing sister chromatids to separate.

There are important checkpoints in the cell cycle (see Fig. 1.21). Checkpoint 1 requires G_1 cyclins to bind to their corresponding Cdks to signal the cell to prepare for DNA synthesis. S-phase promoting factor (SPF; cyclin A bound to Cdk2) enters the nucleus to stimulate DNA synthesis. Checkpoint 2 requires M-phase promoting factor (mitotic cyclin B bound to M-phase Cdk1) to trigger the assembly of the mitotic spindle, breakdown of the nuclear envelope, arrest of gene transcription and condensation of chromosomes. During metaphase of mitosis, M-phase promoting factor activates APC/C, which determines the breakdown of cohesins, the protein complex holding sister chromatids together. Then, at anaphase, separated chromatids move to the opposite poles of the spindle. Finally, B cyclins are destroyed following their attachment to ubiquitin, targeting them for destruction by the 26S proteasome. As G_1 starts, cyclins D, bound to Cdk4, start preparation for a new cell cycle.

Quality control checkpoint 2 operates to delay cell-cycle progression when DNA has been damaged by radiation or chemical mutagens. Cells with checkpoint defects, such as loss of the protein p53, which is a major negative control element in the division cycle of all cells, are commonly associated with the development of malignancy. An example is Li Fraumeni syndrome, where a defective *p53* gene leads to a high frequency of cancer in affected individuals. In cells, p53 protein binds DNA and stimulates another gene to produce p21 protein, which interacts with Cdk2 to prevent S-phase promoting activity. When mutant p53 can no longer bind DNA to stimulate production of p21 to stop DNA synthesis, cells acquire oncogenic properties. The *p53* gene is an example of a tumour suppressor gene. For further reading on *p53* mutations and cancer, see Muller and Vousden (2013).

Mitosis and meiosis

Mitosis is the process that results in the distribution of identical copies of the parent cell genome to the two daughter somatic cells. In meiosis, the divisions immediately before the final production of gametes halve the number of chromosomes to the haploid number, so that at fertilization the diploid number is restored. Moreover, meiosis includes a phase in which exchange of genetic material occurs between homologous chromosomes. This allows a rearrangement of genes to take place, which means that the daughter cells differ from the parental cell in both their precise genetic sequence and their haploid state. Mitosis and meiosis are alike in many respects, and differ principally in chromosomal behaviour during the early stages of cell division. In meiosis, two divisions occur in succession, without an intervening S phase. Meiosis I is distinct from mitosis, whereas meiosis II is more like mitosis.

Mitosis

New DNA is synthesized during the S phase of the cell cycle interphase. This means that the amount of DNA in diploid cells has doubled to the tetraploid value by the onset of mitosis, although the chromosome number is still diploid. During mitosis, this amount is halved between the two daughter cells, so that DNA quantity and chromosome number are diploid in both cells. The cellular changes that achieve this distribution are conventionally divided into four phases called prophase, metaphase, anaphase and telophase (**Figs 1.22–1.23**; see Video 1.1) .

Prophase

During prophase, the strands of chromatin, which are highly extended during interphase, shorten, thicken and resolve themselves into recognizable chromosomes. Each chromosome is made up of duplicate chromatids (the products of DNA replication) joined at their centromeres. Outside the nucleus, the two centriole pairs begin to separate, and move towards opposite poles of the cell. Parallel microtubules are assembled between them to create the mitotic spindle, and others radiate to form the microtubule asters, which come to form the spindle poles or mitotic centre. As prophase proceeds, the nucleoli disappear, and the nuclear envelope suddenly disintegrates to release the chromosomes, an event that marks the end of prophase.

Prometaphase–metaphase

As the nuclear envelope disappears, the spindle microtubules extend into the central region of the cell, attaching to the chromosomes, which subsequently move towards the equator of the spindle (prometaphase). The spindle consists of kinetochore microtubules attached to the kinetochore, a multiprotein structure assembled at the centromeric DNA region, and polar microtubules, which are not attached to chromosomes but instead overlap with each other at the centre of the cell. The grouping of chromosomes at the spindle equator is called the metaphase or equatorial plate. The chromosomes, attached at their centromeres, appear to be arranged in a ring when viewed from either pole of the cell, or to lie linearly across this plane when viewed from above. Cytoplasmic movements during late metaphase effect the approximately

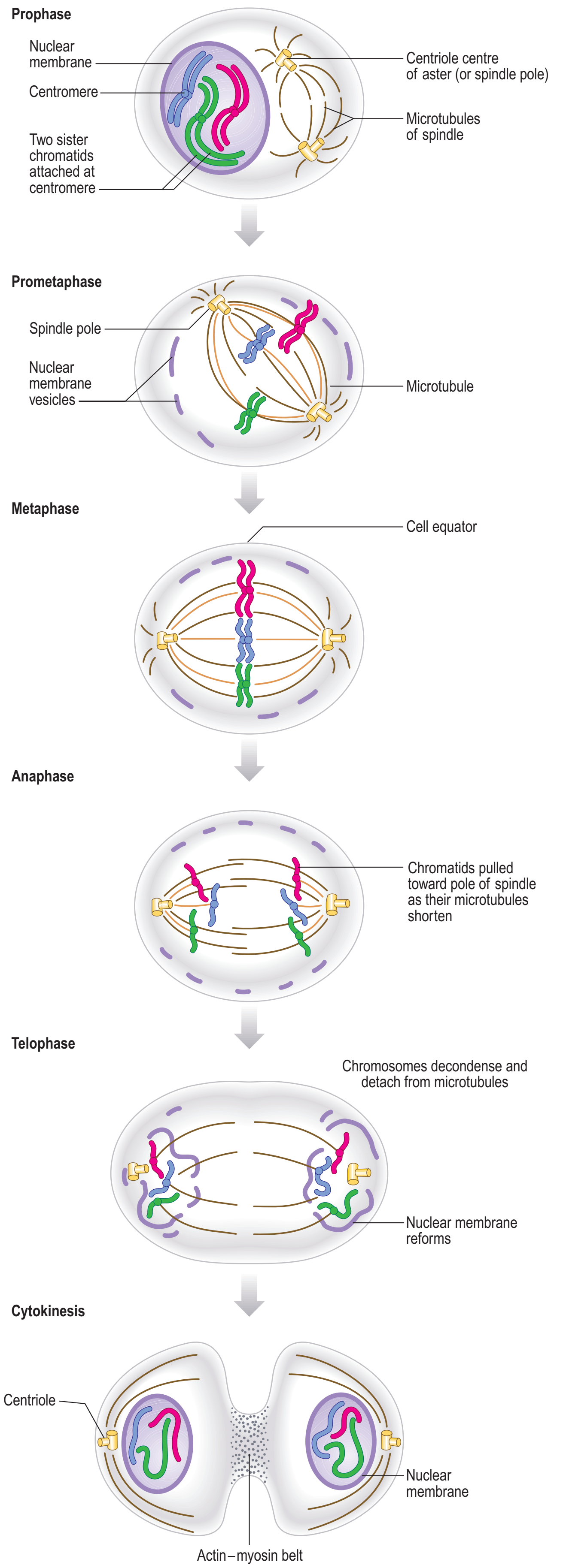
Prophase
Nuclear membrane
Centromere
Two sister chromatids attached at centromere
Centriole centre of aster (or spindle pole)
Microtubules of spindle
Prometaphase
Spindle pole
Nuclear membrane vesicles
Microtubule
Metaphase
Cell equator
Anaphase
Chromatids pulled toward pole of spindle as their microtubules shorten
Telophase
Chromosomes decondense and detach from microtubules
Nuclear membrane reforms
Cytokinesis
Centriole
Nuclear membrane
Actin–myosin belt

Fig. 1.22 The stages in mitosis, including the appearance and distribution of the chromosomes.

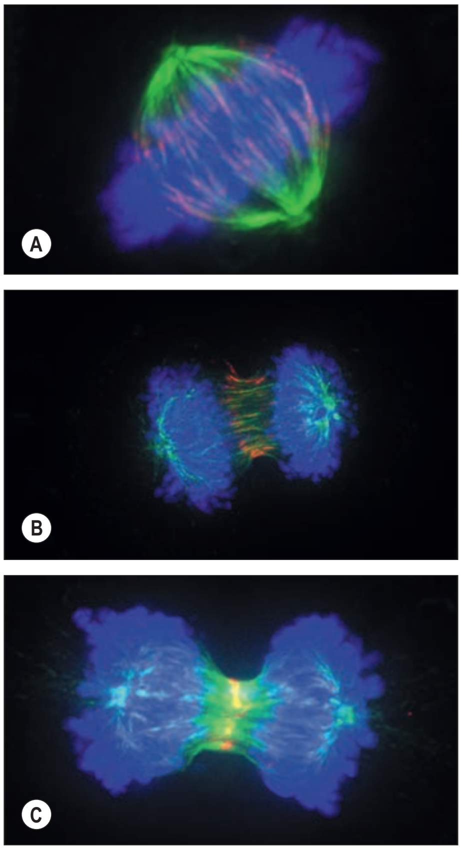

Fig. 1.23 Immunofluorescence images of stages in mitosis in human carcinoma cells in culture. **A**, Metaphase, with spindle microtubules (green), the microtubule-stabilizing protein (HURP; red) and chromosomal DNA (blue). **B**, Anaphase, with spindle microtubules (green), the central spindle (Aurora-B kinase, red) and segregated chromosomes (blue). **C**, Late anaphase, with spindle microtubules (green), the central spindle (Plk1 kinase, red, appearing yellow where co-localized with microtubule protein) and segregated chromosomes (blue). (Courtesy of Dr Herman Silljé, Max-Planck-Institut für Biochemie, Martinsried, Germany.)

equal distribution of mitochondria and other cell structures around the cell periphery.

Anaphase

By the end of metaphase every chromosome consists of a pair of sister chromatids attached to opposing spindle poles by bundles of microtubules associated with the kinetochore. The onset of anaphase begins with the proteolytic cleavage by the enzyme separase of a key subunit of protein complexes known as cohesins. The latter hold the replicated sister chromatids together to resist separation even when exposed to microtubule-dependent pulling forces. Proteolytic cleavage releases the cohesion between sister chromatids, which then move towards opposite spindle poles while the microtubule bundles attached to the kinetochores shorten and move polewards. At the end of anaphase the sister chromatids are grouped at either end of the cell, and both clusters are diploid in number. An infolding of the cell equator begins, deepening during telophase as the cleavage furrow.

Telophase

During telophase the nuclear envelopes reform, beginning with the association of membranous vesicles with the surface of the chromosomes. Later, after the vesicles have fused and the nuclear envelope is complete, the chromosomes decondense and the nucleoli reform. At the same time, cytoplasmic division, which usually begins in early anaphase, continues until the new cells separate, each with its derived nucleus. The spindle remnant now disintegrates. While the cleavage furrow is active, a peripheral band or belt of actin and myosin appears in the constricting zone; contraction of this band is responsible for furrow formation.

Failure of disjunction of chromatids, so that sister chromatids pass to the same pole, may sometimes occur. Of the two new cells, one will have more, and the other fewer, chromosomes than the diploid number. Exposure to ionizing radiation promotes non-disjunction and may, by chromosomal damage, inhibit mitosis altogether. A typical symptom of radiation exposure is the failure of rapidly dividing epithelia to replace lost cells, with consequent ulceration of the skin and mucous membranes.

Mitosis can also be disrupted by chemical agents, particularly vinblastine, paclitaxel (taxol) and their derivatives. These compounds either disassemble spindle microtubules or interfere with their dynamics, so that mitosis is arrested in metaphase.

Meiosis

There are two consecutive cell divisions during meiosis: meiosis I and meiosis II (Fig. 1.24). Details of this process differ at a cellular level for male and female lineages.

Meiosis I

Prophase I

Meiotic prophase I is a long and complex phase that differs considerably from mitotic prophase and is customarily divided into five substages, called leptotene, zygotene, pachytene, diplotene and diakinesis. There are three distinctive features of male meiotic prophase that are not seen during mitotic prophase: the pairing, or synapse, of homologous chromosomes of paternal and maternal origin to form bivalent structures; the organization of nucleoli by autosomal bivalents; and significant non-ribosomal RNA synthesis by autosomal bivalents (in contrast to the transcriptional inactivity of the XY chromosomal pair) (see Tres 2005). In the female, meiotic prophase I starts during fetal gonadogenesis, is arrested at the diplotene stage, and resumes at puberty. In the male, meiosis starts at puberty.

Leptotene stage During leptotene, homologous chromosomes (maternal and paternal copies of the same chromosome), replicated in a preceding S phase and each consisting of sister chromatids joined at the centromere (see above), locate one another within the nucleus, and the process of genetic recombination is initiated. Cytologically, chromosomes begin to condense, appearing as individual threads that are attached via their telomeres to the nuclear envelope. They often show characteristic beading throughout their length.

Zygotene stage During zygotene, the homologous chromosomes initiate pairing or synapsis, during which they become intimately associated with one another. Synapsis may begin near the telomeres at the inner surface of the nuclear membrane, and during this stage the telomeres often cluster to one side of the nucleus (a stage known as the bouquet because the chromosomes resemble a bouquet of flowers). The pairs of synapsed homologues, also known as bivalents, are linked together by a tripartite ribbon, the synaptonemal complex, which consists of two lateral dense elements and a central, less dense, linear element.

The sex chromosomes also start to synapse during zygotene. In males, with distinct X and Y chromosomes, synapsis involves a region of shared DNA sequence known as the pseudoautosomal region. The XY bivalent adopts a special condensed structure, known as the sex vesicle, which becomes associated later at pachytene with migratory nucleolar masses originating in the autosomal bivalents.

Chromosome behaviour in meiosis is intimately linked with the process of genetic recombination. This begins during leptotene, as homologous chromosomes first locate one another at a distance. Synapsis, stabilized by the synaptonemal complex, facilitates recombination, as sites of genetic exchange are turned into specialized structures known as chiasmata, which are topological crossing-over points that hold homologous chromosomes together.

Pachytene stage When synapsis is complete for all chromosomes, the cell is said to be in pachytene. Each bivalent looks like a single thick structure, but is actually two pairs of sister chromatids held together by the synaptonemal complex. Genetic recombination between non-sister chromatids is completed at this point, with sites where it has occurred (usually one per chromosome arm) appearing as recombination nodules in the centre of the synaptonemal complex.

Diplotene stage During diplotene, the synaptonemal complex disassembles and pairs of homologous chromosomes, now much shortened, separate, except where crossing over has occurred (chiasmata): this process is called disjunction. At least one chiasma forms between each homologous pair, exchanging maternal and paternal sequences; up to five have been observed. In the ovaries, primary oocytes become diplotene by the fifth month *in utero* and each remains at this stage until the period before ovulation (up to 50 years).

Diakinesis Diakinesis is the prometaphase of the first meiotic division. The chromosomes, still as bivalents, become even shorter and thicker. They gradually attach to the spindle and become aligned at a metaphase plate. In eggs, the spindle forms without centrosomes. Microtubules first

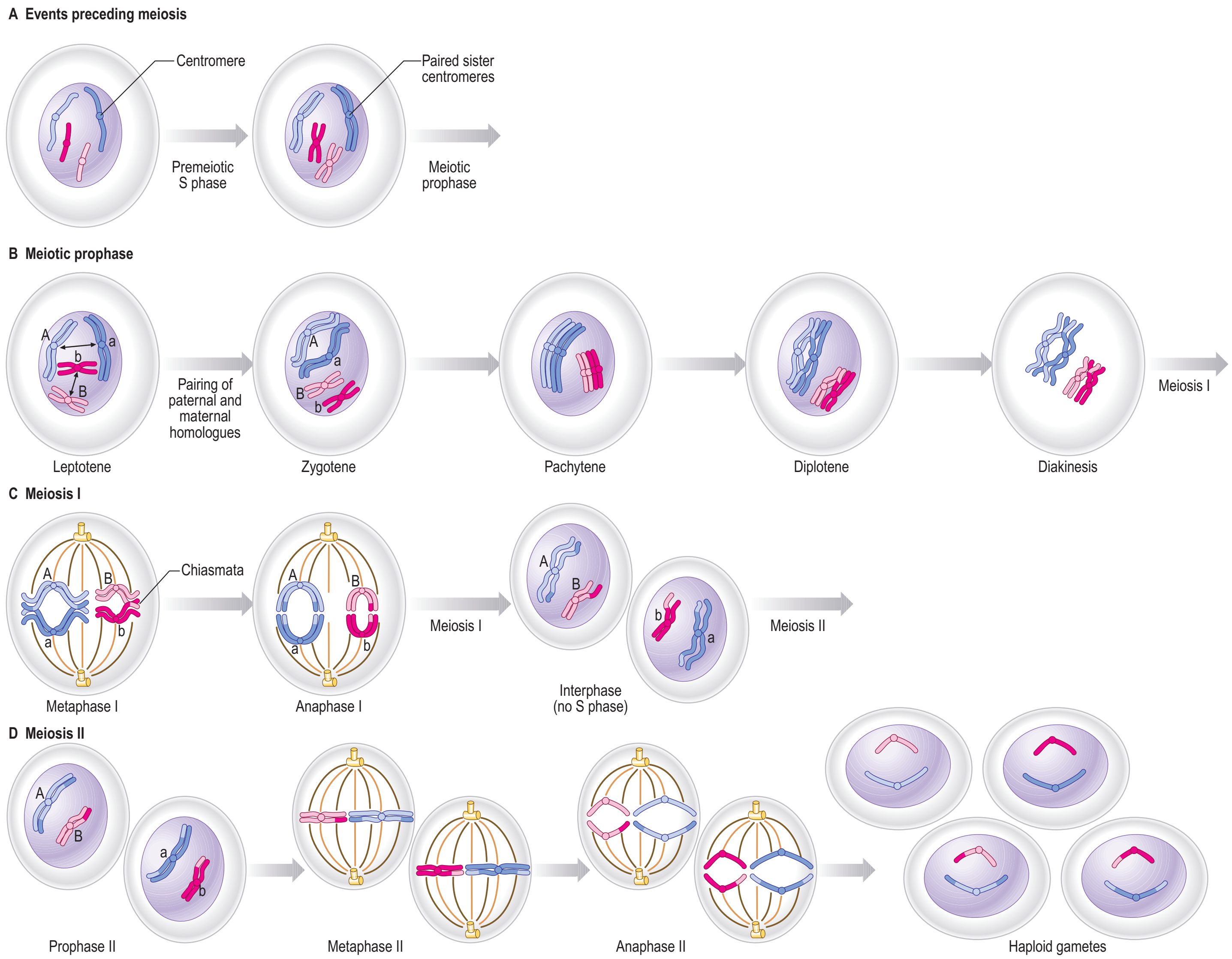

Fig. 1.24 The stages in meiosis, depicted by two pairs of maternal and paternal homologues (dark and pale colours). DNA and chromosome complement changes and exchange of genetic information between homologues are indicated.

nucleate and are stabilized near the chromosomes; the action of various motor molecules eventually sorts them into a bipolar spindle. Perhaps surprisingly, this spindle is as efficient a machine for chromosome segregation as the spindle of mitotic cells with centrosomes at the poles.

Metaphase I

Metaphase I resembles mitotic metaphase, except that the bodies attaching to the spindle microtubules are bivalents, not single chromosomes. They become arranged so that the homologous pairs occupy the equatorial plane of the spindle. The centromeres of each pair of sister chromatids function as a single unit, facing a single spindle pole. Homologous chromosomes are pulled towards opposite spindle poles, but are held paired at the spindle midzone by chiasmata. Errors in chromosome segregation (non-disjunction) lead to the production of aneuploid progeny. Most human aneuploid embryos are non-viable and this is the major cause of fetal loss (spontaneous abortion), particularly during the first trimester of pregnancy. The most common form of viable aneuploid progeny in humans is Down's syndrome (trisomy for chromosome 21): the prevalence exhibits a dramatic increase with maternal age.

Anaphase and telophase I

Anaphase I of meiosis begins with the release of cohesion between the arms of sister chromatids, much as it does during mitosis. As positioning of bivalent pairs is random, assortment of maternal and paternal chromosomes in each telophase nucleus is also random. Critically, sister centromeres, and thus chromatids, do not separate during anaphase I.

During meiosis I, cytoplasmic division occurs by specialized mechanisms. In females, the division is highly asymmetric, producing one egg and one tiny cell known as a polar body. In males, the process results in production of spermatocytes that remain joined by small cytoplasmic bridges.

Meiosis II

Meiosis II commences after only a short interval during which no DNA synthesis occurs. The centromeres of sister chromatids remain paired, but rotate so that each one can face an opposite spindle pole. Onset of anaphase II is triggered by loss of cohesion between the centromeres, as it is in mitosis. This second division is more like mitosis, in that chromatids separate during anaphase, but, unlike mitosis, the separating chromatids are genetically different (the result of genetic recombination). Cytoplasmic division also occurs and thus, in the male, four haploid cells, interconnected by cytoplasmic bridges, result from meiosis I and II.

CELL POLARITY AND DOMAINS

Epithelia are organized into sheets or glandular structures with very different environments on either side. The cells they contain actively transfer macromolecules and ions between the two surfaces and are thus polarized in structure and function. Polarized cells, particularly in epithelia, are generally subdivided into domains that reflect the activities that occur within them. The free surface, e.g. facing the intestinal lumen or airway, is the apical surface: its adjacent cytoplasm is the apical cell domain, where the cell interfaces with a specific body compartment (or, in the case of the epidermis, with the outside world). The apical surface is therefore specialized to act as a barrier, restricting access of substances from this compartment to the rest of the body. Specific components are selectively absorbed from, or added to, the external compartment by the active processes of active transport and endocytosis inwardly or exocytosis and secretion outwardly, respectively. The apical surface is often covered with microvilli, small protrusions of the cell surface which increase the surface area, particularly for absorption.

The surface of the cell opposite to the apical surface is the basal surface; its associated cytoplasm is the basolateral cell domain. In a single-layered epithelium, this surface faces the basal lamina. The other cell surfaces are known as the lateral cell surfaces: the lateral and basal surfaces often perform similar functions and their shared cellular domain is termed the basolateral domain. Cells actively transport substances, such as digested nutrients from the intestinal lumen or endocrine secretions, across their basal (or basolateral) surfaces into the subjacent connective tissue matrix and the blood capillaries that run within it. Dissolved non-polar gases (oxygen and carbon dioxide) diffuse freely between the cell and the blood stream across the basolateral surface. Apical and basolateral surfaces are separated by a tight intercellular seal, the tight junction (occluding junction, zonula adherens), which prevents the passage of even small ions through the space between adjacent cells, and thus maintains the difference between environments on either side of the epithelium.

Cell surface apical differentiations

The surfaces of many different types of cell are specialized to form structures that project from the surface. These projections may permit movement of the cell itself (flagella), or of fluids across the apical cell surface (cilia), or increase the surface area available for absorption (microvilli). Infoldings of the basolateral plasma membrane also increase the area for transport across this surface of the cell. In most non-dividing epithelial cells, the centriole-derived basal body gives rise to a non-motile primary cilium, which has an important mechanosensory role.

Cilia and flagella

Cilia and flagella are motile, hair-like projections of the cell surface. They create currents in the surrounding fluid or movements of the cell to which they are attached, or both. There are two categories of cilia: single non-motile primary cilia and multiple motile cilia. Primary cilia are non-motile but can detect physical and biochemical signals. Motile cilia are present in large numbers on the apical domains of the epithelia of the upper respiratory tract and oviducts, and beat in a wave-like motion to generate fluid movement. Cilia also occur, in modified form, at the dendritic endings of olfactory receptor cells, vestibular hair cells (kinocilia), and the photoreceptor rods and cones of the retina. Flagella have a primary function in cell locomotion. They are found on single cell eukaryotes and on spermatozoa, which each possess a single flagellum 70 μm long.

A cilium or flagellum has a shaft (0.25 μm diameter) that constitutes most of its length, a tapering tip and a basal body at its base, lying within the surface cytoplasm of the cell (**Fig. 1.25**). Other than at its base, the entire structure of a cilium is covered by plasma membrane. The core of a cilium is the axoneme, a cylinder of nine microtubule doublets surrounding a central pair of single microtubules (see Fig. 1.25). Ciliogenesis of primary and motile cilia involves distinct steps. A centriole-derived basal body migrates to the apical cell domain and axonemal microtubule doublets emerge from its distal region (the transition zone). The continued elongation of the cilium requires the import and intraciliary transport of tubulin dimers to the distal tip by bidirectional motor-driven proteins of the intraflagellar transport (IFT) complex. The constant length of cilia is maintained by a steady-state balance between tubulin turnover and the addition of new tubulin dimers at the ciliary tip.

Several filamentous structures are associated with the 9 + 2 doublet microtubule of the axoneme in the shaft of a cilium or flagellum. They include radial spokes that extend inwards from the outer doublet microtubules towards the central pair, surrounded by an inner sheath (see Fig. 1.25). The outer doublet microtubules bear two rows of tangential dynein arms attached to the complete A subfibre of the doublet (consisting of 13 protofilaments), that point towards the incomplete B subfibre of the adjacent doublet (consisting of 10–11 protofilaments). Adjacent doublets are also linked by thin nexin filaments. Tektins are scaffolding filamentous proteins that extend along the axonemal microtubules.

In motile cilia, arrays of dynein arms with ATPase activity cause outer microtubule doublets to move past one another, resulting in a large-scale bending motion: microtubules do not change in length. Movements of cilia and flagella are broadly similar. In addition to the axoneme, spermatozoan flagella have outer dense fibres and a fibrous sheath surrounding the axoneme. Flagella move by rapid undulation, passing from the attached to the free end. There is an additional helical component to this motion in human spermatozoa. In cilia, the beating is planar but asymmetric. In the effective stroke, the cilium remains stiff except at its base, where it bends to produce an oar-like stroke. During the recovery stroke that follows, the bend passes from base to tip, returning the cilium to its initial position for the next cycle. The activity of groups of cilia is usually coordinated so that the bending of one is rapidly followed by the bending of the next and so on, resulting in long travelling waves of metachronal synchrony that pass over the tissue surface in the same direction as the effective stroke. Ciliary motion is important in clearing mucus from airways, moving eggs along oviducts, and circulating cerebrospinal fluid in brain ventricles. In the node of the developing embryo, cilium-driven flow is essential for determining left–right visceral asymmetry (developing patterning). Cilia also have a sensory function, determined by the presence of receptor and channel proteins on the ciliary membrane, thus primary cilia in the collecting ducts of the uriniferous tubule sense the flow of urine and also modulate duct morphogenesis. Cilia are essential for signalling through the Hedgehog pathway, a mechanism involved in organizing the body plan, organogenesis and tumorigenesis in vertebrates. For additional reading on Hedgehog signalling and primary cilia, see Briscoe and Thérond (2013).

There is a group of genetic diseases in which cilia beat either ineffectively or not at all, e.g. Kartagener's immotile cilia syndrome. Affected cilia exhibit deficient function or a lack of dynein arms. Males are typically sterile because of the loss of spermatozoan motility, and half have an alimentary tract that is a mirror image of the usual pattern (*situs inversus*), because it rotates in the opposite direction during early development. Defects in ciliary motility disrupt airway mucus clearance, leading to chronic sinusitis and bronchiectasis. Defects in sensory cilia determine polycystic kidney disease, anosmia and retinal degeneration.

Intraflagellar and intraciliary transport mechanisms

In addition to anterograde and retrograde motor proteins, the assembly and maintenance of all cilia and flagella involves the participation of non-membrane-bound macromolecular protein complexes called IFT particles that are localized along the polarized microtubules of the axoneme, beneath the ciliary and flagellar membranes (reviewed in Scholey (2008)). IFT particles consist of two protein subcomplexes: IFT-A (required for retrograde transport of cargoes from the tip of the axoneme to the cell body for turnover) and IFT-B (participates in intraciliary/intraflagellar anterograde transport of cargoes from the cell body to the tip of the axoneme, a step essential for the assembly and maintenance of cilia and flagella). The movement of IFT proteins along microtubules is catalysed by kinesin-2 (towards the ciliary tip; anterograde direction) and cytoplasmic dynein-2 motor proteins (towards the cell body; retrograde direction). A cargo may include axonemal components, ciliary/flagellar membrane proteins (including the BBSome, for Bardet–Biedl syndrome, an obesity/retinopathy ciliopathy) and ciliary signal transduction proteins. For further reading on the BBSome, see Jin and Nachury (2009) and Ye et al (2018). For further reading on ciliogenesis, see Baldari and Rosenbaum (2010) and on IFT, see Hao and Scholey (2009).

The transport of the BBSome in cilia occurs in association with anterograde IFT-B and retrograde IFT-A particles.

Microvilli

Microvilli are finger-like cell surface extensions usually 0.1 μm in diameter and up to 2 μm long (**Fig. 1.26**).

When arranged in a regular parallel series, as typified by the absorptive surfaces of the epithelial enterocytes of the small intestine and the proximal convoluted tubule of the nephron of the kidneys, microvilli acquire a fuzzy appearance like the bristles of a paintbrush (termed brush border or striated border at the light microscope level).

Microvilli are covered by plasma membrane and supported internally by closely packed bundles of actin filaments linked by cross-bridges of the actin-bundling proteins, fascin and fimbrin. Other bridges composed of myosin I and calmodulin connect the filament bundles to the plasma membrane. At the tip of each microvillus, the free ends of microfilaments are inserted into a dense mass that includes the protein, villin. The actin filament bundles of microvilli are embedded in the apical cytoplasm amongst a meshwork of transversely running actin filaments stabilized by spectrin to form the terminal web, which is underlain by keratin intermediate filaments. The web is anchored laterally to the tight junctions and zonula adherens of the apical epithelial junctional complex. Myosin II and tropomyosin are also found in the terminal web, which may explain its contractile activity.

Microvilli greatly increase the area of cell surface (up to 40 times), particularly at sites of active absorption. In the small intestine, they have a very thick cell coat or glycocalyx, which reflects the presence of integral membrane glycoproteins, including enzymes concerned with digestion and absorption. Irregular microvilli, filopodia, are also found on the surfaces of many types of cell, particularly free macrophages and fibroblasts, where they may be associated with phagocytosis and cell motility. For further reading on the cytoskeleton of microvilli, see Brown and McKnight (2010).

Long and branching microvilli are called stereocilia, an early misnomer, because they are not motile and lack microtubules: an appropriate

Ciliopathies, many related to the defective sensory and/or mechanical function of cilia, include retinal degeneration and polycystic kidney disease, Bardet–Biedl syndrome, Jeune syndrome (asphyxiating thoracic dystrophy), respiratory disease and defective determination of the left–right axis. The seven-protein complex designated BBSome is a component of the basal body and participates in the formation of the primary cilium by regulating the export and/or import of ciliary proteins (see Fig. 1.25).

During ciliogenesis, IFT requires the anterograde kinesin-2 motor and the retrograde IFT-dynein motor to transport IFT particles–cargo complexes in opposite directions along the microtubules, from the basal body to the tip of the ciliary axoneme and back again (intraciliary transport). IFT is not restricted to the microtubules of cilia and flagella. During development of the spermatid tail, IFT particles–motor protein–cargo complexes appear to utilize microtubules of the manchette, a transient microtubule-containing structure, to deliver tubulin dimers and other proteins by intramanchette transport (Kierszenbaum et al 2011). IFT also occurs along the modified cilium of photoreceptor cells of the retina. Mutations in IFT proteins lead to the absence of cilia and are lethal during embryogenesis.

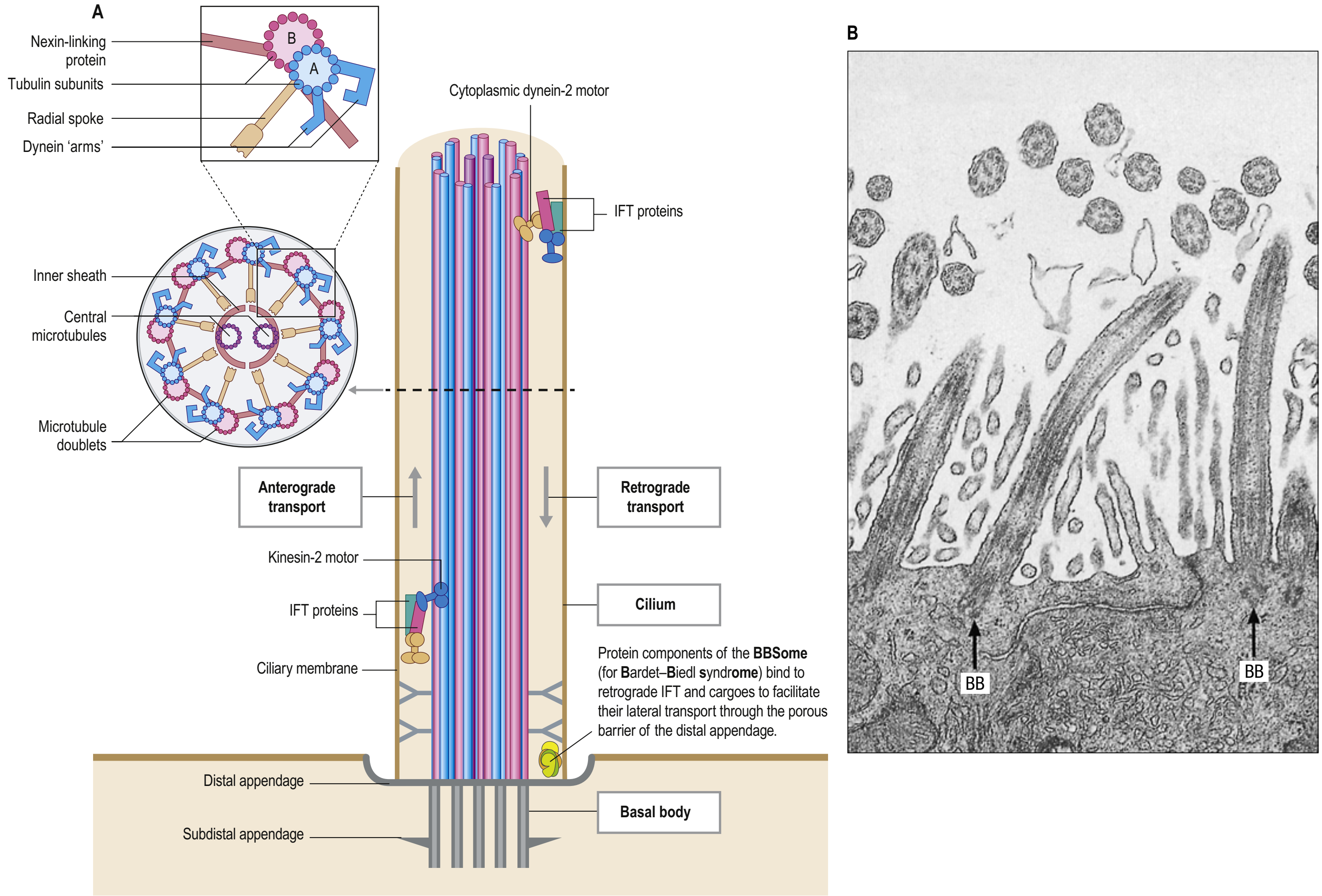

Protein components of the **BBSome** (for **B**ardet–**B**iedl **s**yndr**ome**) bind to retrograde IFT and cargoes to facilitate their lateral transport through the porous barrier of the distal appendage.

Fig. 1.25 **A**, The structure of a cilium shown in transverse (left) and longitudinal (right) section. A and B are subfibres of the peripheral microtubule doublets (see text); the basal body is structurally similar to a centriole, but with microtubule triplets. The cilium is formed and maintained by the transport of tubulins along the axoneme mediated by proteins of the intraflagellar transport (IFT) system. IFT trafficking from the base of the cilium to the tip (anterograde transport; to the microtubule plus end) is mediated by kinesin-2 motor proteins mobilizing IFT protein complexes. Cytoplasmic dynein-2 motor proteins participate in retrograde transport (to the microtubule minus end; base of the cilium). IFT proteins form a platform for transporting cargo between the base and tip of the cilium. Proteins of the Hedgehog signalling pathway participate in intraciliary and intraflagellar transport (not shown). Disruption of the kinesin-2 motor or IFT proteins blocks cilia formation. Basal body proteins influence ciliary trafficking: they include components of the BBSome, named after their association with Bardet-Biedl syndrome (BBS). BBSome proteins, bound to ciliary proteins, facilitate their crossing through the distal appendage. All motile and non-motile cilia extend from a basal body consisting of a microtubule triplet and distal and subdistal appendages. Distal appendages (also known as transition fibres) and Y-shaped structures anchor and connect the basal body to the base of the ciliary membrane. **B**, The apical region of respiratory epithelial cells, showing the proximal parts of three cilia sectioned longitudinally, anchored into the cytoplasm by basal bodies (BB). Other cilia project out of the plane of section and are cut transversely, showing the '9+2' arrangement of microtubules. (A, Adapted with permission from Kierszenbaum AL, Tres LL Histology and Cell Biology: An Introduction to Pathology, 5th ed. Elsevier, Saunders. Copyright 2019. B, With permission from Young B, Heath JW Wheater's Functional Histology, 4th ed. Elsevier, Churchill Livingstone. Copyright 2000.)

name is stereovilli. They are found on cochlear and vestibular receptor cells, where they act as sensory transducers, and also in the absorptive epithelium of the epididymis.

Intercellular junctions

The basolateral region of the plasma membrane of epithelial cells establishes junctions with adjacent cells and with structural components of the extracellular matrix. Intercellular junctions are resilient and dynamic, and prevent epithelial tissues from dissociating into their component cells. In adults, the epidermis withstands imposed deformations because of the interplay of two components of intercellular junctions, the junctional cytoskeleton and cell adhesion molecules (Fig. 1.27). The establishment and maintenance of cell polarity in an epithelial layer depends on two circumferential apical belts, the tight junctions and the zonulae adherentes, running in parallel to each other and associated with F-actin. These two belts control epithelial permeability and determine epithelial cell polarity. The apical cell domain resides above the belts; the basolateral cell domain resides below the belts. Desmosomes (maculae adherentes) are a third class of spot-like intercellular adhesion. In contrast to tight junctions and the zonulae adherentes, desmosomes do not form belts and link instead to intermediate filaments. The hemidesmosome, anchoring epithelial cells to the basal lamina, also links to intermediate filaments. Gap junctions are unique: they provide direct connection between adjacent cells and are not linked to the cytoskeleton. Molecular aspects of cell adhesion molecules will be considered first and then integrated with the junctional cytoskeleton to define specific structural and molecular aspects of different intercellular junctions.

Cell adhesion molecules

Cell adhesion molecules are transmembrane or membrane-anchored glycoproteins that bridge the intercellular space from the plasma membrane to form adhesive contacts. There are a number of molecular subgroups, which are broadly divisible on the basis of their dependence on calcium for function. Calcium-dependent cell adhesion molecules include cadherins and selectins. Calcium-independent cell adhesion

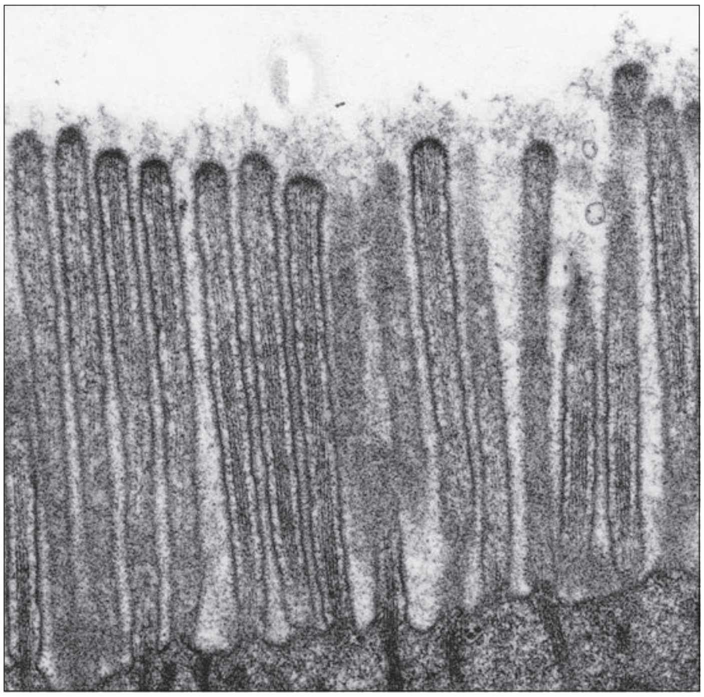

Fig. 1.26 Microvilli sectioned longitudinally in the striated border of an intestinal absorptive cell in a human duodenal biopsy specimen. Actin filaments fill the cores of the microvilli and insert into the apical cytoplasm. A prominent glycocalyx (formed by the extracellular domains of plasma membrane glycoproteins) is seen as a fuzzy coat at the tips of and between microvilli; it includes enzymes concerned with the final stages of digestion. (Courtesy of Dr Bart Wagner, Histopathology Department, Sheffield Teaching Hospitals, UK.)

molecules include the immunoglobulin-like superfamily of cell adhesion molecules (Ig-CAMs), including nectins, and integrins, the only cell adhesion molecules consisting of two subunits (α and β subunits).

Calcium-dependent cell adhesion molecules: cadherins and selectins

Cadherins are single-pass transmembrane glycoproteins, with five heavily glycosylated calcium-binding external domains and an intracellular catenin-binding cytoplasmic tail. Catenins are intracellular proteins linking cadherins to F-actin in the zonula adherens. The extracellular segment of cadherins participates in calcium-dependent homophilic *trans*-interactions in which a cadherin molecule on one cell binds to an identical cadherin molecule on an adjacent cell. After binding, cadherins cluster laterally (*cis*-interaction) at cell–cell junctions to form a zipper-like structure that stabilizes tight adhesion between cells.

Different cell types possess different members of the cadherin family, e.g. N-cadherins in nervous tissue, E-cadherins in epithelia and P-cadherins in the placenta. Two further members of the cadherin family are the desmogleins and the desmocollins. Cadherins are present in maculae adherentes and desmosomes but not in tight junctions or hemidesmosomes (see below). Alterations in the expression of cadherins in the epidermis produce pathological conditions such as blisters and ulcerations. See Brieher and Yap (2013) for further reading on cadherins and their associated cytoskeleton.

As with cadherins, selectins are calcium-dependent. In contrast to cadherins, selectins do not establish homophilic *trans*-interactions. Instead, they bind to carbohydrates and belong to the group of lectins. Each selectin has an extracellular carbohydrate recognition domain (CRD) with binding affinity to a specific oligosaccharide attached to a protein or lipid. The molecular configuration and binding affinity of the CRD to carbohydrate moieties is calcium-dependent. Selectins participate in the homing of leukocytes circulating in blood towards tissues by extravasation across the endothelium. For additional reading on the significance and mechanism of homing, see Girard et al (2012).

Three major types of selectin are L-selectin (for lymphocytes), E-selectin (for endothelial cells) and P-selectin (for platelets).

Calcium-independent cell adhesion molecules: Ig-CAMs, nectins and integrins

Ig-CAMs are cell-surface glycoproteins with an extracellular domain characterized by a variable number of immunoglobulin-like loops. Most Ig-CAMs have a transmembrane domain; others are attached to the cell surface by a glycophosphatidyl inositol (GPI) anchor. As in cadherins, Ig-CAMs establish homophilic interactions contributing to cell–cell adhesion, although in a calcium-independent manner. The cytoplasmic tail of Ig-CAMs also interacts with cytoskeletal components such as F-actin, ankyrins and spectrin. Ig-CAMs can directly or indirectly bind growth factor receptors and control their internalization.

Different types are expressed in different tissues. Neural cell adhesion molecules (N-CAMs) are found on a number of cell types but are expressed widely by neural cells. Intercellular adhesion molecules (ICAMs) are expressed on vascular endothelial cells. Cell adhesion molecule binding is predominantly homophilic, although some use a heterophilic mechanism, e.g. vascular intercellular adhesion molecule (VCAM), which can bind to integrins.

Nectins and nectin-like molecules (Necls) are members of the Ig-CAM superfamily (see Takai et al (2008) for further reading on nectins and Necls). They have an extracellular domain with three Ig-like loops, a transmembrane segment and a cytoplasmic tail. The nectins and Necls consist of four and five members, respectively. These are present in the belt-like tight junctions and zonula adherens.

The nectin–afadin complex initiates the formation of a zonula adherens; after cell–cell contacts are formed between adjacent cells, cadherins are recruited to these contact sites. Afadin and α-catenin interact with one another and also with F-actin through adaptor proteins.

Integrins mediate cell–extracellular matrix and cell–cell interactions, and integrate extracellular signals with the cytoskeleton and cellular signalling pathways. Because integrins can be activated by proteins binding to their extracellular or their intracellular domains, they can function in a bidirectional fashion by transmitting information from either outside-in (cues from the extracellular environment) or inside-out (cues from the intracellular environment) of the cell. The integrin family of proteins consists of α subunits and β subunits forming transmembrane heterodimers. The amino-acid sequence arginine–glycine–aspartic acid, or RGD motif, on target ligands (such as fibronectin, laminin and other extracellular matrix proteins) has binding affinity to the extracellular binding head of integrins. For further reading on properties of integrins and their ligands, see Barczyk et al (2010).

Specialized intercellular junctions

Specialized cell–cell junctions are the hallmark of all epithelial tissues. There are two major categories: symmetric junctions and asymmetric junctions. Symmetric junctions may be subdivided into three types: tight junctions (also known as occluding junctions or zonulae occludentes); anchoring junctions (including zonulae adherentes, or belt desmosomes, and maculae adherentes, or spot desmosomes); and communication junctions, represented by gap junctions. Tight junctions and anchoring junctions are components of the epithelial apical junctional complex. Hemidesmosomes are asymmetric junctions (see Fig. 1.27).

Tight junctions (occluding junctions, zonulae occludentes)

Tight junctions are the most apical component of the epithelial apical junctional complex. The main functions of tight junctions are the regulation of the paracellular permeability of the epithelial layer and the formation of an apical–basolateral intramembrane diffusion barrier, the hallmark of epithelial cell polarity. Tight junctions form a continuous belt (zonula) around the cell perimeter, near the apical domain of epithelial cells, and are connected to the actin cytoskeleton. At the site of the tight junction, the plasma membranes of adjacent cells come into close contact, so that the space between them is obliterated. Freeze-fracture electron microscopy shows that the contact between these membranes is represented by branching and anastomosing sealing strands of protein particles on the P (protoplasmic) face of the lipid bilayer (**Figs 1.27A, 1.27B**). A tight junction contains numerous proteins: occludins and claudins, members of the tetraspanin family of proteins, containing four transmembrane domains, two loops and two cytoplasmic tails – occludins and tetraspanins provide the molecular basis for the formation of the branching and anastomosing strands seen in freeze-fracture preparations; the afadin–nectin complex and junctional adhesion molecules (JAMs), each forming *cis*-homodimers and interacting with each other through their extracellular domains (forming *trans*-homodimers) – nectins and JAMs are members of the immunoglobulin superfamily, and the afadin component of the afadin–nectin complex interacts with F-actin; and cytosolic zonula occludens proteins 1, 2 and 3 (ZO-1, ZO-2 and ZO-3). ZO-1 protein is associated with afadin and the intracellular domain of JAMs. All three ZO proteins facilitate the reciprocal interaction of occludins, claudins and JAMs with F-actin. Defects in paracellular magnesium permeability and reabsorption in kidneys occur when there is a mutation in claudin 16 and claudin 19 (renal magnesium wasting).

The cytoplasmic tail recruits proteins of the catenin complex: β-catenin is the first to be recruited. The cadherin–β-catenin complex rapidly recruits α-catenin which binds directly to F-actin and coordinates the activity of actin-nucleating proteins and actin-binding partners (such as vinculin and α-actinin) to provide the dynamic forces that modulate cell–cell adhesion: p120-catenin binds to the cytoplasmic tail of cadherin and becomes a positive regulator of cadherin function.

Homing, a process that also enables thymus-derived T cells (Ch. 4) to home in on lymph nodes, consists of two phases. In the first, selectin phase, carbohydrate ligands on the surface of leukocytes adhere loosely to selectins present on the surface of endothelial cells. During the second, cooperative sequential integrin phase, strong adhesion permits the transendothelial migration of leukocytes into the extravascular space in cooperation with cell adhesion molecules of the Ig-CAM superfamily.

Nectins can interact homophilically or heterophilically with other nectins to mediate, primarily, adhesion. The intracellular domain of nectins binds to the cytoplasmic adaptor protein afadin, which links to actin, whereas Necls interact with scaffolding proteins but not to afadin. Necls are involved in a large variety of cellular functions, including axon–glial interaction, Schwann cell differentiation and myelination.

In humans there are about 18 α-subunit subtypes and 8 β-subunit subtypes, and 24 integrin heterodimers. The subunits are associated by non-covalent interactions and consist of an extracellular ligand-binding head, two multidomain segments, two single-pass transmembrane segments and two cytoplasmic tails. Upon binding of extracellular ligands, integrins undergo a conformational change (integrin activation), that allows the recruitment of several cytoplasmic F-actin activator proteins (such as talin, vinculin, α-actinin and kindlins) to their short cytoplasmic domain, forming a protein complex that interacts with the actin cytoskeleton.

The actin-binding protein talin binds the cytoplasmic domain of integrin β subunit and activates integrins. Vinculin interacts with talin and α-actinin and cross-links two filaments of actin. Kindlins, named after the gene mutated in Kindler's syndrome, a skin blistering disease, interact with talin to activate integrins.

The protein complex also promotes the recruitment and activation of several protein kinases (such as focal adhesion kinase), leading to the activation of signalling pathways essential for cellular activities such as cell migration, proliferation, survival and gene expression.

Genetic mutations in integrins or integrin regulators have been associated with Glanzmann's thrombasthenia (caused by mutations in integrin β3 subunit); the immunodeficiency disorder leukocyte adhesion deficiency types I and III (determined by mutations in integrin β2 subunit and kindlin 3, respectively); and skin diseases (caused by mutations in kindlin 1 and integrin α2, α6 and β3 subunits). Integrins are essential in the leucocyte homing process, following the selectin phase, and are also involved in tumour progression and metastasis.

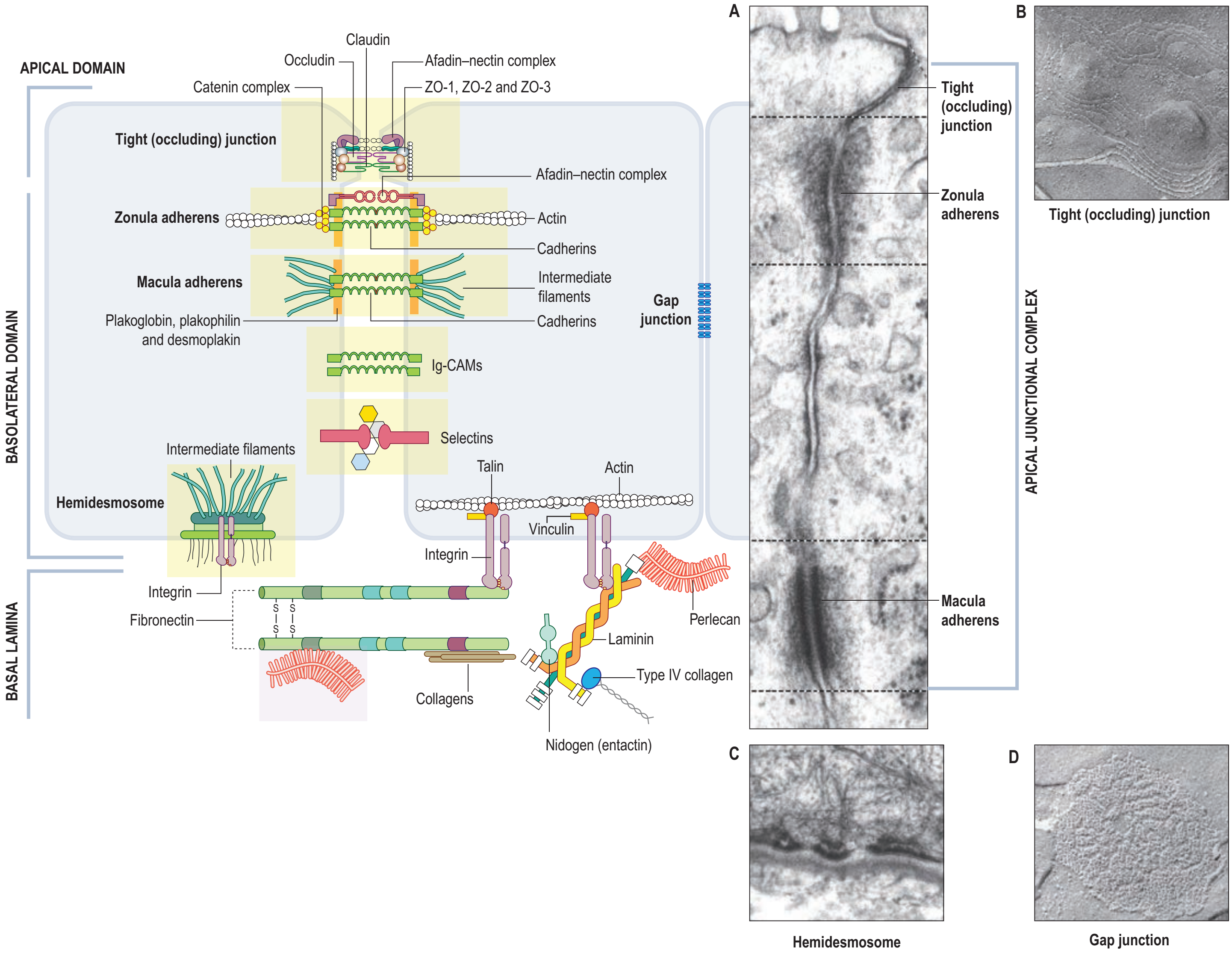
APICAL DOMAIN
Claudin
Occludin
Afadin–nectin complex
Catenin complex
ZO-1, ZO-2 and ZO-3
Tight (occluding) junction
Afadin–nectin complex
Zonula adherens
Actin
Cadherins
Macula adherens
Intermediate filaments
Cadherins
Gap junction
Plakoglobin, plakophilin and desmoplakin
Ig-CAMs
Selectins
BASOLATERAL DOMAIN
Intermediate filaments
Talin
Actin
Hemidesmosome
Vinculin
Integrin
Integrin
Fibronectin
Perlecan
Laminin
Type IV collagen
Collagens
Nidogen (entactin)
BASAL LAMINA
A
B
Tight (occluding) junction
Zonula adherens
Macula adherens
APICAL JUNCTIONAL COMPLEX
Tight (occluding) junction
C
D
Hemidesmosome
Gap junction

Fig. 1.27 Intercellular junctions: the apical junctional complex and other junctional specializations, illustrating the protein components of each junction and of the basal lamina. An anastomotic network of contacts between adjacent cell membranes forms a tight occluding junction. Basal plasma membrane is attached to a basal lamina at a hemidesmosome. In a gap junction, numerous channels (pores within connexons) are clustered to form a plaque-like junctional region between adjacent plasma membranes. (**A** and **C** are transmission electron micrographs; **B** and **D** are freeze-fractured preparations.) **A**, An apical junctional complex. **B**, A tight junction. **C**, A hemidesmosome. **D**, A gap junction. (B, Courtesy of Dr Andrew Kent, King's College London. D, Courtesy of Professor Dieter Hülser, University of Stuttgart. A, C, From human tissue, courtesy of Dr Bart Wagner, Histopathology Department, Sheffield Teaching Hospitals, UK. Figure adapted with permission from Kierszenbaum AL, Tres LL Histology and Cell Biology: An Introduction to Pathology, 3rd ed. Elsevier, Mosby. Copyright 2011.)

For further reading on claudins, see Escudero-Esparza et al (2011). For further reading on JAMs, see Bazzoni (2003).

Anchoring junctions

In contrast to tight junctions, zonulae adherentes and maculae adherentes are characterized by the presence, along the cytosolic sides of the plasma membranes of adjacent epithelial cells, of symmetric dense plaques connected to each other across the intercellular space by cadherins. They differ in that F-actin is associated with plaques in zonulae adherentes and intermediate filaments are linked to plaques in maculae adherentes.

Zonula adherens (belt desmosome)

A zonula adherens is a continuous belt-like zone of adhesion parallel and just basal to a tight junction and also encircling the apical perimeter of epithelial cells. Calcium-dependent cell adhesion molecules (members of the desmoglein and desmocollin families of cadherins) are key components of a zonula adherens. In addition to the cadherin–catenin complex, a zonula adherens also houses the afadin–nectin complex.

Essentially, two molecules, cadherins and afadin, link to the actin cytoskeleton. In cultured cells, nectins appear to initiate the formation of a zonula adherens before the involvement of cadherins.

A specific component of a zonula adherens is a cytoplasmic dense plaque attached to the cytosolic side of the plasma membrane. It consists of desmoplakin, plakophilin and plakoglobin proteins (the latter is also known as γ-catenin). A similar plaque is seen in a macula adherens or spot desmosome (see below).

Fascia adherens

A fascia adherens is similar to a zonula adherens, but is more limited in extent and forms a strip or patch of adhesion, e.g. between smooth muscle cells, in the intercalated discs of cardiac muscle cells and between glial cells and neurones. The junctions involve cadherins attached indirectly to actin filaments on the inner side of the membrane.

Desmosomes (maculae adherentes)

Desmosomes are limited, plaque-like areas of particularly strong intercellular contact. In epithelial cells, they may be located subjacent to the tight junction and zonula adherens belts, forming collectively the epithelial apical junctional complex (see Fig. 1.27A). The intercellular gap is approximately 25 nm; it is filled with electron-dense filamentous material (the intercellular cadherins) running transversely across it and is also marked by a series of densely staining bands (the cytoplasmic dense plaques) running parallel to the cell surfaces. Adhesion is mediated by calcium-dependent cadherins, desmogleins and desmocollins. Within the cells on either side, each cytoplasmic dense plaque underlies the plasma membrane and consists of the proteins plakophilin, desmoplakin and plakoglobin (γ-catenin), into which the ends of intermediate filaments are inserted. The type of intermediate filament depends on the cell type, e.g. keratins are found in epithelia and desmin filaments are found in cardiac muscle cells. Desmosomes form strong anchorage points, likened to spot-welds, between cells subject to mechanical stress, e.g. in the prickle cell layer of the epidermis, where they are extremely numerous and large.

Hemidesmosomes

Hemidesmosomes are asymmetric anchoring junctions found between the basal side of epithelial cells and the associated basal lamina. The latter is a component of the basement membrane and contains laminin, an integrin ligand. The other component of the basement membrane is the reticular lamina, a collagen-containing layer produced by fibroblasts that also contains fibronectin, another integrin ligand. Hemidesmosomes resemble a single-sided desmosome, anchored on one side to the plasma membrane, and on the other to the basal lamina and adjacent collagen fibrils (**Fig. 1.27C**). The plaque has distinct proteins not seen in the plaques of a zonula adherens or a macula adherens: BPAG1 (bullous pemphigoid antigen 1), a member of the plakin family, and BPAG2 (bullous pemphigoid antigen 2), which possesses an extracellular collagenous domain. BPAG1 and BPAG2 were initially detected in patients with bullous pemphigoid, an autoimmune blistering disease. On the cytoplasmic side of the dense plaque there is a less dense plate into which keratin filaments are inserted, where they interact with the protein plectin associated with integrin $\alpha6\beta4$. Hemidesmosomes use integrins and anchoring filaments (laminin 5) as their adhesion molecules anchored to the basal lamina, whereas desmosomes use cadherins.

Focal adhesion plaques

Less highly structured attachments with a similar arrangement exist between many other cell types and their surrounding matrices, e.g. between smooth muscle cells and their matrix fibrils, and between the ends of skeletal muscle cells and tendon fibres. The smaller, punctate adhesions resemble focal adhesion plaques, which are regions of local attachment between cells and the extracellular matrix. They are typically situated at or near the ends of actin filament bundles (stress fibres), anchored through intermediary proteins to the cytoplasmic domains of integrins. In turn, these are attached at their external ends to collagen or other filamentous structures in the extracellular matrix. They are usually short-lived; their formation and subsequent disruption are part of the motile behaviour of migratory cells. See Geiger et al (2009) for further reading on focal adhesions.

Gap junctions (communicating junctions)

Gap junctions resemble tight junctions in transverse section, but the two apposed lipid bilayers are separated by an apparent gap of 3 nm, which is bridged by a cluster of transmembrane channels (connexons). Each connexon is formed by a ring of six connexin proteins whose external surfaces meet those of the adjacent cell in the middle. A minute central pore links one cell to the next (**Fig. 1.27D**). Larger assemblies of many thousands of channels are often packed in hexagonal arrays. Gap junctions occur between numerous cells, including hepatocytes and cardiac myocytes.

AGEING, CELLULAR SENESCENCE, CANCER AND APOPTOSIS

Ageing is a universal feature of biological organisms, defined by a gradual decline over time in cell and tissue function that often, but not always, decreases the longevity of an individual. The hallmarks of ageing are reviewed in Kubben and Misteli (2017).

Cellular senescence is defined by an irreversible arrest in cell proliferation when cells experience DNA damage at telomeres and a decrease in mitogenic signalling. In contrast to reversibly arrested quiescent cells in G_0 of the cell cycle, senescent growth arrest is irreversible; cells in this state cannot be stimulated to proliferate by known stimuli and cannot be prompted to re-enter the cell cycle by physiological mechanisms. For further reading on senescence and the cell cycle, see Chandler and Peters (2013). Senescent cells can cause or foster degenerative diseases. In old age, cellular senescence in humans determines typical pathologies, including atherosclerosis leading to stroke, osteoporosis, macular degeneration, cardiopulmonary and renal failure, and neurodegenerative diseases such as Alzheimer's and Parkinson's disease.

Senescent cells undergo changes in gene expression, which result in the secretion of proinflammatory cytokines, growth factors and proteases, activities that collectively define a senescence-associated secretory phenotype capable of triggering angiogenesis, inflammatory responses, stem cell renewal and differentiation, and which may also determine resistance to cancer chemotherapy. Senescent cells can be identified histochemically by their expression of either senescence-associated β-galactosidase, a lysosomal marker which is overexpressed in these cells, or the tumour suppressor protein $p16^{INK4a}$, which promotes the formation of senescence-associated chromatin. For further reading on ageing, cellular senescence and cancer, see Campisi (2013).

Cellular senescence can be caused by a disruption of metabolic signalling pathways, derived from mitogens and proliferation factors, and the activation of tumour suppressors, combined with telomere shortening and genomic damage. See Sahin and DePinho (2012) and Kubben and Misteli (2017) for further reading.

Cellular senescence suppresses tumorigenesis because cell proliferation is required for cancer development. However, senescent cells can stimulate the proliferation and malignant progression of adjacent premalignant cells by the release of senescence-inducing oncogenic stimuli. Cancer cells must harbour mutations to prevent telomere-dependent and oncogene-induced senescence, such as in the p53 and p16-retinoblastoma protein pathways. See Kubben and Misteli (2017) for further reading on the pathogenesis of premature ageing and ageing-associated diseases.

Apoptosis

Cells die as a result of either tissue injury (necrosis) or the internal activation of a 'suicide' programme (apoptosis) in response to extrinsic or intrinsic cues. Apoptosis (programmed cell death) is defined by the controlled demolition of cellular constituents and the ultimate uptake of apoptotic cell fragments by other cells to prevent immune responses. Some senescent cells become resistant to cell-death signalling, i.e. they are apoptosis-resistant. In effect, senescence blocks growth of damaged or stressed cells, whereas apoptosis quickly disposes of them. Apoptosis is a central mechanism controlling multicellular development. During morphogenesis, apoptosis mediates activities such as the separation of the developing digits, and plays an important role in regulating the number of neurones in the nervous system (the majority of neurones die during development). Apoptosis also ensures that inappropriate or inefficient T cells are eliminated in the thymus during clonal selection.

The morphological changes exhibited by necrotic cells are very different from those seen in apoptotic cells. Necrotic cells swell and subsequently rupture, and the resulting debris may induce an inflammatory response. Apoptotic cells shrink, their nuclei and chromosomes fragment, forming apoptotic bodies, and their plasma membranes undergo conformational changes that act as a signal to local phagocytes. The dead cells are removed rapidly, and as their intracellular contents are not released into the extracellular environment, inflammatory reactions are avoided; the apoptotic fragments also stimulate macrophages to release anti-inflammatory cytokines.

Apoptosis and cell proliferation are intimately coupled; several cell cycle regulators can influence both cell division and apoptosis. The signals that trigger apoptosis include withdrawal of survival factors or exposure to inappropriate proliferative stimuli. Three main routes to the induction of apoptosis have been established (**Fig. 1.28**). Two, the Fas ligand (FasL) pathway and the granzyme B pathway, are extrinsic, whereas the mitochondrial route is intrinsic. The FasL pathway involves binding of FasL to death receptors on the plasma membrane and recruitment of adaptor proteins, such as the Fas-associated death domain proteins, followed by the recruitment and activation of caspase 8. The granzyme B pathway involves creation of a perforin plasma membrane channel enabling the caspase-like granzyme B to enter the cell. The intrinsic mitochondrial route involves the release of cytochrome *c* from the space between the inner and outer mitochondrial membranes into the cytosol. Extrinsic and intrinsic pathways work cooperatively in the subsequent activation of a family of initiator-effector proteases, known as caspases (cysteine aspartic acid-specific proteases), which are present in healthy cells as inactive precursor enzymes or zymogens. Activation of caspases 3, 6 and 7 mediates apoptosis by initiating a cascade of degradative processes that target major constituents of the cell cytoskeleton, producing membrane blebbing, a distinctive feature of apoptosis caused by cytosolic and nuclear fragments flowing into the developing apoptotic bodies. Caspase cleavage inactivates many systems that normally promote damage repair and support cell viability, and activates a number of proteins that promote the death and disassembly of the cell. For further reading on apoptosis, see Taylor et al (2008).

The ends of the chromosomes, or telomeres, become shorter and more dysfunctional with each DNA replication round. Telomere shortening has been shown to activate DNA damage responses, leading to mitochondrial dysfunction (a decrease in production of ATP and an increase in reactive oxygen species) and the activation of p53, which induces growth arrest, apoptosis and senescence of stem cells and progenitor cells. p53 interconnects with different longevity metabolic signalling pathways, including the insulin, insulin-like growth factor I (IGFI) and mammalian target of rapamycin (mTOR) pathways, which are known to regulate lifespan by increasing the expression of genes involved in stress resistance and energy balance. Mutations in TERC (the RNA component of telomerase) and TERT (the catalytic component of telomerase) are found in patients with dyskeratosis congenita (an example of a premature ageing syndrome), a bone marrow failure syndrome classically associated with a triad of mucocutaneous features: nail dystrophy, oral leukoplakia and abnormal reticulate skin pigmentation. Other important contributors to cell senescence are dysregulated autophagy and lack of disposal of misfolded proteins by the ubiquitin–26S proteasome machinery. These responses are collectively designated telomere-initiated cellular senescence.

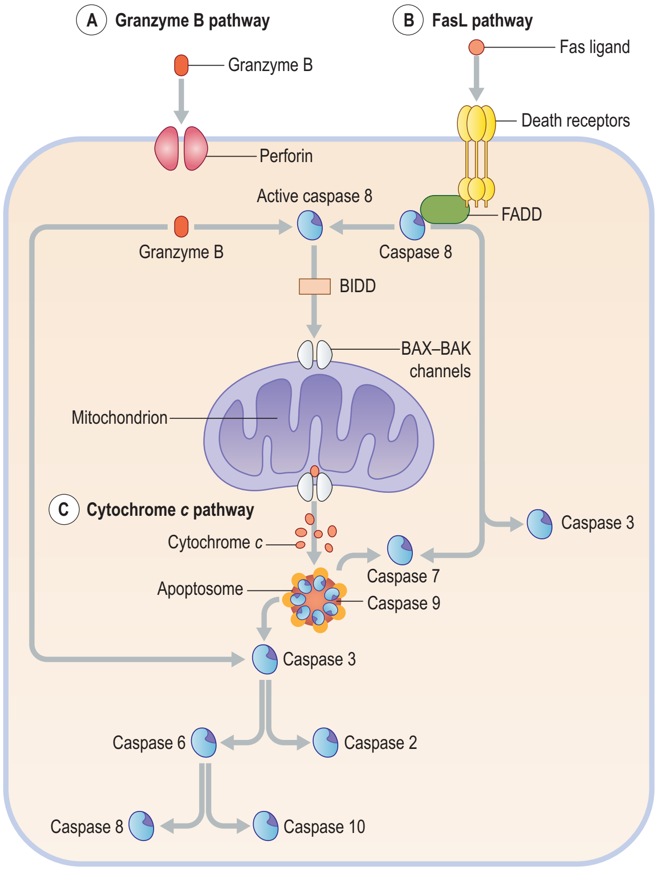

Fig. 1.28 Caspase activation pathways during apoptosis. **A**, The granzyme B extrinsic pathway activates caspase 8 and caspase 3 following entry of granzyme B across the plasma membrane pore-forming protein, perforin. This pathway is observed in cytotoxic T cells or natural killer cells for delivery of the protease granzyme B to target cells. **B**, The Fas ligand (FasL) extrinsic pathway is initiated by binding of FasL to clustered transmembrane death receptors that recruit adaptor proteins, such as the Fas-associated death-domain protein (FADD), to their intracellular domain which in turn recruits and aggregates caspase 8 molecules, which become activated. Activated caspase 8 activates caspase 7 and caspase 3. **C**, The cytochrome *c* intrinsic pathway is initiated when granzyme B or activated caspase 8 causes the proteolytic truncation of the protein BIDD (BH3-interacting domain death agonist) that penetrates a mitochondrion through BAX–BAK (BCL-2 associated X protein–BCL-2 antagonist killer) channel proteins on the outer mitochondrial membrane, causing the release of cytochrome *c*. Cytochrome *c* enables the assembly of the apoptosome (consisting of seven molecules of apoptosis protease-activating factor-1 (APAF1) and seven molecules of caspase 9), which in turn activates caspase 3 and caspase 7. Finally, the proteolytic activation cascade of caspase 6, caspase 2, caspase 8 and caspase 10 executes cell deconstruction.

Intracellular proteolytic mechanisms

The intracellular degradation of organelles and residual or misfolded proteins can be mediated by the autophagy pathway, the ubiquitin-proteasome pathway and the mitophagy signalling pathway (Fig. 1.29). The autophagy pathway involves the sequestration of cytoplasmic components within autophagosomes. Progressive dysfunction of autophagy is likely to lead to ageing. The ubiquitin-proteasome pathway utilizes a catalytic multi-subunit structure, the 26S proteasome, that recognizes ubiquitinated proteins for degradation. This pathway (Fig. 1.29B) directs the degradation of proteins that have already accomplished a specific function (such as specific cyclins during the cell cycle) or proteins that have folded incorrectly because of faulty translation or are encoded by defective genes. The mitophagy signalling pathway (Fig. 1.29C) specifically eliminates damaged mitochondria to maintain normal cell function.

The apoptosis pathway is concerned with the turnover of entire cells. While apoptosis and the ubiquitin-proteasome activities take place in the cytosol, autophagy occurs within a sealed compartment, the autophagosome, with the assistance of lysosomes. Defects in mitochondrial function are the cause of reactive oxidative stress and specific neurodegenerative disorders, such as some familial forms of Parkinson's disease.

Bonus e-book content

Fig. 1.4 Transporter proteins.

Fig. 1.8 Mitochondrial replacement by pronuclear transfer.

Fig. 1.10 cAMP signalling pathway.

Fig. 1.11 JAK–STAT signalling pathway.

Fig. 1.12 **A**, Hedgehog (Hh) signalling pathway. **B**, Wingless (Wnt) signalling pathway. **C**, Transforming growth factor-β (TGF-β) signalling/Bone morphogenetic protein (BMP) signalling pathway.

Fig. 1.20 **A**, G-banded karyotype of chronic myeloid leukaemia (CML) cells, showing the Philadelphia (Ph^1) chromosome. **B**, Representation of the Philadelphia translocation which creates a fusion gene (*BCR–ABL*).

Fig. 1.29 **A**, The autophagy pathway. **B**, The ubiquitin-proteasome pathway. **C,** Mitophagy.

Video 1.1 Mitosis in a cell with fluorescently labelled chromosomes and microtubules.

Key references

Bray D 2001 Cell Movements. New York: Garland.
A comprehensive presentation of the structural and molecular features of the cytoskeleton, including its properties and behaviour in cell and organelle movement in living cells.

Burke B, Stewart CL 2013 The nuclear lamins: flexibility in function. Nat Rev Mol Cell Biol 14:13–24.
An up-to-date, detailed description of the nuclear lamina and its major components, lamins, members of the intermediate filament protein family.

Chinnery PF, Hudson G 2013 Mitochondrial genetics. Br Med Bull 106:135–59.
A detailed survey of the involvement of mitochondrial DNA (mtDNA) defects in human disease, with a specific focus on the mechanisms controlling mtDNA inheritance.

Girard JP, Moussion C, Förster R 2012 HEVs, lymphatics and homeostatic immune cell trafficking in lymph nodes. Nat Rev Immunol 12:762–73.
A comprehensive description of the continuous trafficking of immune cells across the vascular endothelium (homing) engaging cell adhesion molecules.

Kierszenbaum AL, Tres LL 2019 Histology and Cell Biology: An Introduction to Pathology. Philadelphia: Elsevier.
An integrated visual view of histology, cell biology and basic pathology focused on structure and function, including human pathological examples from a molecular viewpoint.

Kubben N, Misteli T 2017 Shared molecular and cellular mechanisms of premature ageing and ageing-associated diseases. Nat Rev Mol Cell Biol 18:595-609.
A review of recent advances in the pathogenesis of ageing, defined by a gradual loss of physiological integrity leading to major human pathological conditions. Defects in genetic, epigenetic and metabolic pathways; mitochondrial and protein homeostasis; cell cycle; and stem cell-regenerative capacity are considered.

Pollard TD, Earnshaw WC, Lippincott-Schwartz J, et al 2016 Cell Biology. Philadelphia: Elsevier.
A detailed and comprehensive account of structural and molecular aspects of cell biology, including abnormalities related to human disease.

Porter RM, Lane EB 2003 Phenotypes, genotypes and their contribution to understanding keratin function. Trends Genet 19:278–85.
A correlation of human epithelial pathological conditions with mouse mutant studies focused on keratin diversity required for cells to attune to mechanical and biochemical signalling.

Saftig P, Klumperman J 2009 Lysosome biogenesis and lysosomal membrane proteins: trafficking meets function. Nat Rev Mol Cell Biol 10:623–35.
The participation of lysosomes in the degradation of extracellular material internalized by endocytosis and lysosomal sorting pathways, reviewed within the context of human diseases resulting from defective lysosomal biogenesis.

Ye F, Nager AR, Nachury MV 2018 BBSome trains remove activated GPCRs from cilia by enabling passage through the transition zone. J Cell Biol 217:1847–68.
The active transport of proteins inside cilia, designated intraflagellar transport (IFT), is powered by microtubule motors moving along axonemal microtubules and by proteins selected for ciliary exit.

The autophagy pathway (Fig. 1.29A) is a self-degradation and cytoprotective process involved in the turnover of cytoplasmic organelles as an adaptation to declining nutrient resources or as a form of cell death (when the intensity and duration of stress are excessive). The process of autophagy starts with the phagophore, a cytomembrane derived from the endoplasmic reticulum, Golgi or plasma membrane. The phagophore expands, surrounds and encloses a cytoplasmic component (such as a mitochondrion) that is captured within a double membrane structure, the autophagosome. Autophagy is a cellular cleansing and recycling pathway; apoptosis often occurs in the same cell, when autophagy precedes apoptosis.

The 26S proteasome is a multicatalytic protease found in the cytosol and the nucleus that degrades intracellular proteins conjugated to a polyubiquitin chain by an enzymatic cascade. The 26S proteasome consists of several subunits arranged into two 19S polar caps, where protein recognition and adenosine 5′-triphosphate (ATP)-dependent target processing occur, flanking a 20S central barrel-shaped structure with an inner proteolytic chamber (Tomko and Hochstrasser 2013). The 26S proteasome participates in the removal of misfolded or abnormally assembled proteins, the degradation of cyclins involved in the control of the cell cycle, the processing and degradation of transcription regulators, cellular-mediated immune responses, and cell cycle arrest and apoptosis.

The mitophagy signalling pathway involves two enzymes: Parkin, a ubiquitin ligase that is located in the cytoplasm in an inactive form, and PINK1, a protein kinase, associated with the outer mitochondrial membrane. In response to mitochondrial damage, PINK1 recruits and activates Parkin: activated Parkin exerts its ubiquitin ligase activity by transferring polyubiquitin to proteins attached to the outer mitochondrial membrane. Ubiquitin-tagged proteins are recognized by the proteasomal proteolytic machinery to initiate mitochondrial degradation. The goal of the Parkin–PINK1 complex is to eliminate defective mitochondria. If the Parkin–PINK1 complex is defective, dysfunctional mitochondria are not cleared and cell function is compromised. Parkinson's disease is an example of a neurodegenerative disease caused by mitochondrial dysfunction determined by mutations in the ubiquitin ligase Parkin and protein kinase (PINK1). There is a clear difference between the lysosome-based autophagy pathway and the ubiquitin-proteasome-based mitophagy signalling pathway that is recruited in the removal of aged or damaged mitochondria.

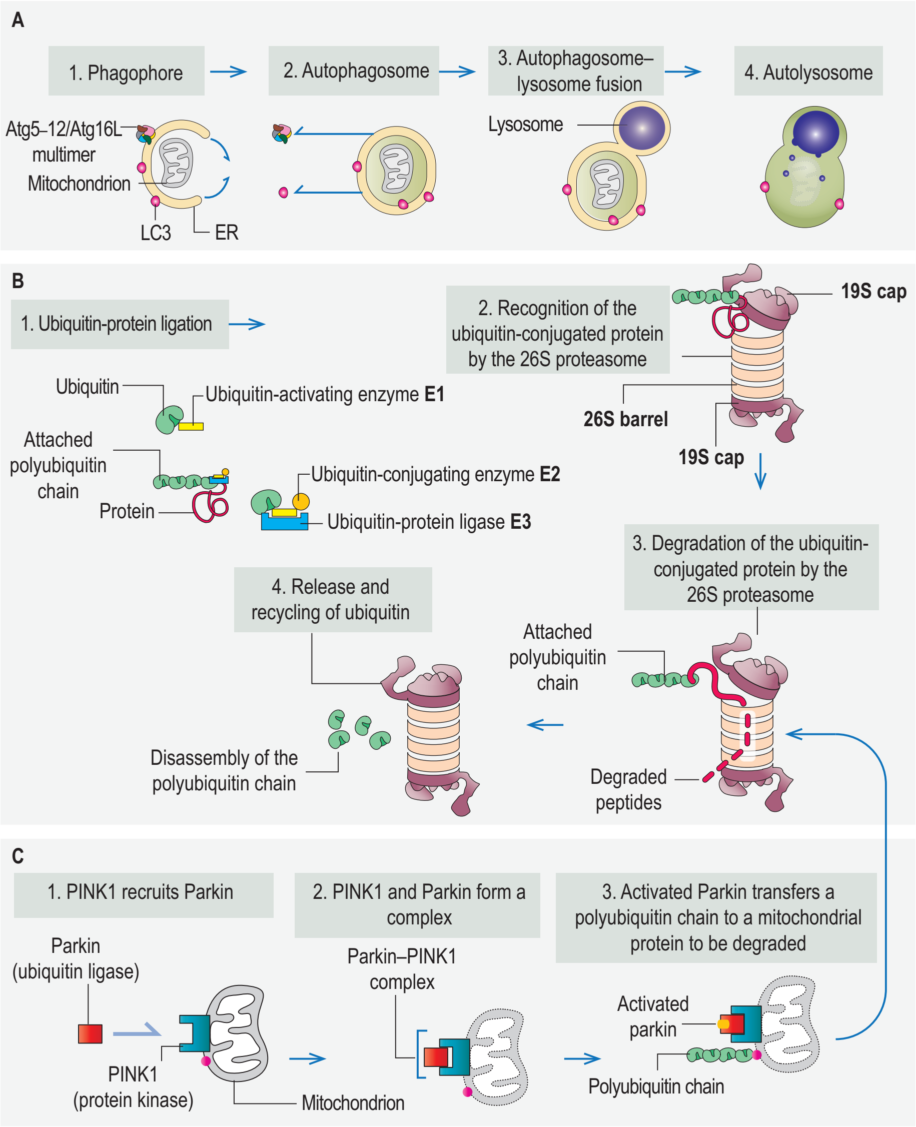
A
1. Phagophore
2. Autophagosome
3. Autophagosome–lysosome fusion
4. Autolysosome
Atg5–12/Atg16L multimer
Mitochondrion
LC3
ER
Lysosome
B
1. Ubiquitin-protein ligation
2. Recognition of the ubiquitin-conjugated protein by the 26S proteasome
19S cap
26S barrel
19S cap
Ubiquitin
Ubiquitin-activating enzyme E1
Attached polyubiquitin chain
Protein
Ubiquitin-conjugating enzyme E2
Ubiquitin-protein ligase E3
3. Degradation of the ubiquitin-conjugated protein by the 26S proteasome
4. Release and recycling of ubiquitin
Attached polyubiquitin chain
Disassembly of the polyubiquitin chain
Degraded peptides
C
1. PINK1 recruits Parkin
2. PINK1 and Parkin form a complex
3. Activated Parkin transfers a polyubiquitin chain to a mitochondrial protein to be degraded
Parkin (ubiquitin ligase)
PINK1 (protein kinase)
Mitochondrion
Parkin–PINK1 complex
Activated parkin
Polyubiquitin chain

Fig. 1.29 **A**, The autophagy pathway. 1. Assembly of a phagophore involves a membrane of the endoplasmic reticulum (ER), the conjugation of Atg (autophagy)5–Atg12 proteins interacting with Atg16L, and the insertion of LC3 (light chain 3). 2. The presence of LC3 in the extended and fused membranes of the autophagosome facilitates enclosure of a mitochondrion for degradation. The Atg5–12/Atg16L multimeric complex and some LC3 are then recycled. 3. A lysosome fuses with the autophagosome: LC3 remains associated with double membrane-containing autophagosomes. 4. The mitochondrion is proteolytically degraded within the autolysosome by hydrolytic lysosomal enzymes. Note that the autolysosome (autophagolysosome) has a single membrane. **B**, The ubiquitin-proteasome pathway. 1. The degradation process is initiated by the attachment of ubiquitin to a protein targeted for degradation. Ubiquitin-activating enzyme E1 attaches the first ubiquitin molecule to the target protein, followed by the construction of an attached polyubiquitin chain involving ubiquitin-conjugating enzyme E2 and ubiquitin-ligating enzyme E3. 2. The polyubiquitin chain-tagged protein is recognized by the 26S proteasome which consists of two 19S polar caps flanking a 25S barrel. An open 19S cap is the entry site to the 25S barrel. 3. Protein degradation takes place within the 26S barrel. 4. The polyubiquitin chain disassembles and the ubiquitin components recycle when protein degradation is completed. **C,** Mitophagy. 1. In contrast to the autophagy pathway, no autophagosome is assembled to degrade a mitochondrion. Instead, the ubiquitin ligase Parkin (like E3 in the ubiquitin-proteasome pathway) is recruited by the protein kinase PINK1 that is present in the outer membrane of a mitochondrion, close to a target protein for degradation. 2. A Parkin–PINK1 complex is formed. 3. Activated Parkin transfers a polyubiquitin chain to a mitochondrial protein to initiate the degradation process. The 26S proteasome, called into action, degrades the polyubiquitin-conjugated protein, leading to the destruction of the mitochondrion. (With permission from Kierszenbaum AL, Tres LL Histology and Cell Biology: An Introduction to Pathology, 5th ed. Elsevier. Copyright 2019.)

References

Baldari CT, Rosenbaum J 2010 Intraflagellar transport: it's not just for cilia any more. Curr Opin Cell Biol 22:75–80.

Barczyk M, Carracedo S, Gullberg D 2010 Integrins. Cell Tissue Res 339:269–80.

Bazzoni G 2003 The JAM family of junctional adhesion molecules. Curr Opin Cell Biol 15:525–30.

Boisvert FM, van Koningsbruggen S, Navascués J et al 2007 The multifunctional nucleolus. Nat Rev Mol Cell Biol 8:574–85.

Braverman NE, D'Agostino MD, Maclean GE 2013 Peroxisome biogenesis disorders: biological, clinical and pathophysiological perspectives. Dev Disabil Res Rev 17:187–96.

Bravo R, Parra V, Gatica D et al 2013 Endoplasmic reticulum and the unfolded protein response: dynamics and metabolic integration. Int Rev Cell Mol Biol 301:215–90.

Bray D 2001 Cell Movements. New York: Garland.

A comprehensive presentation of the structural and molecular features of the cytoskeleton, including its properties and behaviour in cell and organelle movement in living cells.

Brieher WM, Yap AS 2013 Cadherin junctions and their cytoskeleton(s). Curr Opin Cell Biol 25:39–46.

Briscoe J, Thérond PP 2013 The mechanisms of Hedgehog signalling and its roles in development and disease. Nat Rev Mol Cell Biol 14:418–31.

Brown JW, McKnight CJ 2010 Molecular model of the microvillar cytoskeleton and organization of the brush border. PLoS One 5:e9406.

Burke B, Stewart CL 2013 The nuclear lamins: flexibility in function. Nat Rev Mol Cell Biol 14:13–24.

An up-to-date, detailed description of the nuclear lamina and its major components, lamins, members of the intermediate filament protein family.

Campisi J 2013 Aging, cellular senescence and cancer. Annu Rev Physiol 75:685–705.

Chandler H, Peters G 2013 Stressing the cell cycle in senescence and aging. Curr Opin Cell Biol 25:765–71.

Chinnery PF, Hudson G 2013 Mitochondrial genetics. Br Med Bull 106:135–59.

A detailed survey of the involvement of mitochondrial DNA (mtDNA) defects in human disease, with a specific focus on the mechanisms controlling mtDNA inheritance.

Clarke PR, Zhang C 2008 Spatial and temporal coordination of mitosis by Ran GTPase. Nat Rev Mol Cell Biol 9:464–77.

Dominguez R 2010 Structural insights into de novo actin polymerization. Curr Opin Struct Biol 20:217–25.

Escudero-Esparza A, Jiang WG, Martin TA 2011 The Claudin family and its role in cancer and metastasis. Front Biosci 16:1069–83.

Farré J-C, Mahalingam SS, Proietto M, Subramani S 2019 Peroxisome biogenesis, membrane contact sites, and quality control. EMBO Reports 20:e46864.

Geiger B, Spatz JP, Bershadsky AD 2009 Environmental sensing through focal adhesions. Nat Rev Mol Cell Biol 10:21–33.

Girard JP, Moussion C, Förster R 2012 HEVs, lymphatics and homeostatic immune cell trafficking in lymph nodes. Nat Rev Immunol 12:762–73.

A comprehensive description of the continuous trafficking of immune cells across the vascular endothelium (homing) engaging cell adhesion molecules.

Gönczy P 2012 Towards a molecular architecture of centriole assembly. Nat Rev Mol Cell Biol 13:425–35.

Hammer JA 3rd, Sellers JR 2012 Walking to work: roles for class V myosins as cargo transporters. Nat Rev Mol Cell Biol 13:13–26.

Hao L, Scholey JM 2009 Intraflagellar transport at a glance. J Cell Sci 122:889–92.

Herrmann H, Bär H, Kreplak L et al 2007 Intermediate filaments: from cell architecture to nanomechanics. Nat Rev Mol Cell Biol 8:562–73.

Jin H, Nachury MV 2009 The BBSome. Curr Biol 19:R472–3.

Kierszenbaum AL, Rivkin E, Tres LL 2011 Cytoskeletal track selection during cargo transport in spermatids is relevant to male fertility. Spermatogenesis 1:221–30.

Kierszenbaum AL, Tres LL 2019 Histology and Cell Biology: An Introduction to Pathology, 5th ed. Philadelphia: Elsevier.

An integrated visual view of histology, cell biology and basic pathology focused on structure and function, including human pathological examples from a molecular viewpoint.

Kubben N, Misteli T 2017 Shared molecular and cellular mechanisms of premature ageing and ageing-associated diseases. Nat Rev Mol Cell Biol 18:595–609.

A review of recent advances in the pathogenesis of ageing, defined by a gradual loss of physiological integrity leading to major human pathological conditions.. Defects in genetic, epigenetic and metabolic pathways; mitochondrial and protein homeostasis; cell cycle; and stem cell-regenerative capacity are considered.

Luger K, Dechassa ML, Tremethick DJ 2012 New insights into nucleosome and chromatin structure: an ordered state or a disordered affair? Nat Rev Mol Cell Biol 13:436–47.

Mostowy S, Cossart P 2012 Septins: the fourth component of the cytoskeleton. Nat Rev Mol Cell Biol 13:183–94.

Muller PA, Vousden KH 2013 p53 mutations in cancer. Nat Cell Biol 15:2–8.

Nandakumar J, Cech TR 2013 Finding the end: recruitment of telomerase to telomeres. Nat Rev Mol Cell Biol 14:69–82.

Pan X, Hobbs RP, Coulombe PA 2012 The expanding significance of keratin intermediate filaments in normal and diseased epithelia. Curr Opin Cell Biol 25:1–10.

Pollard TD, Earnshaw WC, Lippincott-Schwartz J, et al 2016 Cell Biology. Philadelphia: Elsevier.

A detailed and comprehensive account of structural and molecular aspects of cell biology, including abnormalities related to human disease.

Porter RM, Lane EB 2003 Phenotypes, genotypes and their contribution to understanding keratin function. Trends Genet 19:278–85.

A correlation of human epithelial pathological conditions with mouse mutant studies focused on keratin diversity required for cells to attune to mechanical and biochemical signalling.

Raices M, D'Angelo MA 2012 Nuclear pore complex composition: a new regulator of tissue-specific and developmental functions. Nat Rev Mol Cell Biol 13:687–99.

Rotty JD, Wu C, Bear JE 2013 New insights into the regulation and cellular functions of the ARP2/3 complex. Nat Rev Mol Cell Biol 14:7–12.

Saftig P, Klumperman J 2009 Lysosome biogenesis and lysosomal membrane proteins: trafficking meets function. Nat Rev Mol Cell Biol 10:623–35.

The participation of lysosomes in the degradation of extracellular material internalized by endocytosis and lysosomal sorting pathways, reviewed within the context of human diseases resulting from defective lysosomal biogenesis.

Sahin E, DePinho RA 2012 Axis of ageing: telomeres, p53 and mitochondria. Nat Rev Mol Cell Biol 13:397–404.

Scholey JM 2008 Intraflagellar transport motors in cilia: moving along the cell's antenna. J Cell Biol 180:23–9.

Settembre C, Fraldi A, Medina DL et al 2013 Signals from the lysosome: a control centre for cellular clearance and energy metabolism. Nat Rev Mol Cell Biol 14:283–96.

Simon DN, Wilson KL 2011 The nucleoskeleton as a genome-associated dynamic 'network of networks'. Nat Rev Mol Cell Biol 12:695–708.

Smith CE, Ordovás JM 2012 Update on perilipin polymorphisms and obesity. Nutr Rev 70:611–21.

Spang A 2013 Traffic COPs: rules of detection. The EMBO J 32:915–16.

Takai Y, Miyoshi J, Ikeda W et al 2008 Nectins and nectin-like molecules: roles in contact inhibition of cell movement and proliferation. Nat Rev Mol Cell Biol 9:603–15.

Taylor RC, Cullen SP, Martin SJ 2008 Apoptosis: controlled demolition at the cellular level. Nat Rev Mol Cell Biol 9:231–41.

Theodoulou FL, Bernhardt K, Linka N et al 2013 Peroxisome membrane proteins: multiple trafficking routes and multiple functions? Biochem J 451:345–52.

Tomko RJ Jr, Hochstrasser M 2013 Molecular architecture and assembly of the eukaryotic proteasome. Annu Rev Biochem 82:415–45.

Tres LL 2005 XY chromosomal bivalent: nucleolar attraction. Mol Reprod Dev 72:1–6.

Weinbaum S, Tarbell JM, Damiano ER 2007 The structure and function of the endothelial cell glycocalyx layer. Annu Rev Biomed Eng 9:121–67.

Witkos TM, Lowe M. The golgin family of coiled-coil tethering proteins. Front Cell Dev Biol. 2015;3:86.

Worman HJ 2012 Nuclear lamins and laminopathies. J Pathol 226:316–25.

Ye F, Nager AR, Nachury MV 2018 BBSome trains remove activated GPCRs from cilia by enabling passage through the transition zone. J Cell Biol 217:1847-68.

The active transport of proteins inside cilia, designated intraflagellar transport (IFT), is powered by microtubule motors moving along axonemal microtubules and by proteins selected for ciliary exit.

CHAPTER
2

Integrating cells into tissues

Cells evolved as single, free-living organisms, but natural selection favoured more complex communities of cells, multicellular organisms, where groups of cells specialize during development to carry out specific functions for the body as a whole. This allowed the emergence of larger organisms with greater control over their internal environment and the evolution of highly specialized organic structures such as the brain. The human body contains more than 200 different cell types, sharing the same genome but with different patterns of gene expression.

Some cells in the body are essentially migratory, but most exist as cellular aggregates in which individual cells carry out similar or closely related functions in a coordinated manner. These aggregates are termed tissues, and can be classified into a fairly small number of broad categories on the basis of their structure, function and molecular properties. On the basis of their structure, most tissues are divided into four major types: epithelia, connective or supporting tissue, muscle and nervous tissue. Epithelia are continuous layers of cells with little intercellular space, which cover or line surfaces, or have been so derived. In connective tissues, the cells are embedded in an extracellular matrix, which, typically, forms a substantial and important component of the tissue. Muscle consists largely of specialized contractile cells. Nervous tissue consists of cells specialized for conducting and transmitting electrical and chemical signals and the cells that support this activity.

There is molecular evidence that this structure-based scheme of classification has validity. Thus the intermediate filament proteins characteristic of all epithelia are keratins (Pan et al 2012); those of connective tissue are vimentins; those of muscle are desmins; and those of nervous tissue are neurofilament and glial fibrillary acidic proteins. However, cells such as myofibroblasts, neuroepithelial sensory receptors and ependymal cells of the central nervous system have features of more than one tissue type. Despite its anomalies, the scheme is useful for descriptive purposes; it is widely used and will be adopted here.

In this chapter, two of the major tissue categories, epithelia and general connective and supporting tissues, will be described. Specialized skeletal connective tissues, i.e. cartilage and bone, together with skeletal muscle, are described in detail in Chapter 5 as part of the musculoskeletal system overview. Smooth muscle and cardiac muscle are described in Chapter 6. Nervous system tissues are described in Chapter 3. Specialized defensive cells, which also form a migrant population within the general connective tissues, are considered in more detail in Chapter 4, with blood, lymphoid tissues and haemopoiesis.

EPITHELIA

The term epithelium is applied to the layer or layers of cells that cover the body surfaces or line the body cavities that open on to it. The fate of embryonic epithelial populations is illustrated in Fig. 12.3. Epithelia function generally as selective barriers that facilitate, or inhibit, the passage of substances across the surfaces they cover. In addition, they may: protect underlying tissues against dehydration, chemical or mechanical damage; synthesize and secrete products into the spaces that they line; and function as sensory surfaces. In this respect, many features of nervous tissue can be regarded as those of a modified epithelium and the two tissue types share an origin in embryonic ectoderm.

Epithelia (**Fig. 2.1**) are predominantly cellular and the little extracellular material they possess is limited to the basal lamina. Intercellular junctions, which are usually numerous, maintain the mechanical cohesiveness of the epithelial sheet and contribute to its barrier functions. A series of three intercellular junctions forms a typical epithelial junctional complex: in sequence from the apical surface, this consists of a tight junctional zone, an adherent (intermediate) junctional zone and a region of discrete desmosome junctions. Epithelial cell shape is most usually polygonal and partly determined by cytoplasmic features such as secretory granules. The basal surface of an epithelium lies in contact with a thin layer of filamentous protein and proteoglycan termed the basal lamina, which is synthesized predominantly by the epithelial cells. The basal lamina is described on p. 35.

Epithelia can usually regenerate when injured. Indeed, many epithelia continuously replace their cells to offset cell loss caused by mechanical abrasion (reviewed in Blanpain et al 2007). Blood vessels do not penetrate typical epithelia and so cells receive their nutrition by diffusion from capillaries of neighbouring connective tissues. This arrangement limits the maximum thickness of living epithelial cell layers. Epithelia, together with their supporting connective tissue, can often be removed surgically as one layer, which is collectively known as a membrane. Where the surface of a membrane is moistened by mucous glands it is called a mucous membrane or mucosa (see p. 41), whereas a similar layer of connective tissue covered by mesothelium is called a serous membrane or serosa.

Classification

Epithelia can be classified as unilaminar (single-layered, simple), in which a single layer of cells rests on a basal lamina; or multilaminar, in which the layer is more than one cell thick. The latter includes: stratified squamous epithelia, in which flattened superficial cells are constantly replaced from the basal layers; urothelium (transitional epithelium), which serves special functions in the urinary tract; and other multilaminar epithelia such as those lining the largest ducts of some exocrine glands, which, like urothelium, are replaced only very slowly under normal conditions. Seminiferous epithelium is a specialized multilaminar tissue found only in the testis.

Unilaminar (simple) epithelia

Unilaminar epithelia are further classified according to the shape of their cells, into squamous, cuboidal, columnar and pseudostratified types. Cell shape may, in some cases, be related to cell volume. Where little cytoplasm is present, there are generally few organelles and therefore there is low metabolic activity and cells are squamous or low cuboidal. Highly active cells, e.g. secretory epithelia, contain abundant mitochondria and endoplasmic reticulum, and are typically tall cuboidal or columnar. Unilaminar epithelia can also be subdivided into those that have special functions, such as those with cilia, numerous microvilli, secretory vacuoles (in mucous and serous glandular cells) or sensory features. Myoepithelial cells, which are contractile, are found as isolated cells associated with glandular structures, e.g. salivary and mammary glands.

Squamous epithelium

Simple squamous epithelium is composed of flattened, tightly apposed, polygonal cells (squames). This type of epithelium is described as tessellated when the cells have complex, interlocking borders rather than straight boundaries. The cytoplasm may in places be only 0.1 μm thick and the nucleus usually bulges into the overlying space (**Fig. 2.2A**). These cells line the alveoli of the lungs, where their surface area is huge and cytoplasmic volume correspondingly large, and they also form the outer capsular wall of renal corpuscles, the thin segments of the renal tubules and various parts of the inner ear. Because it is so thin, simple squamous epithelium allows rapid diffusion of gases and water across its surface; it may also engage in active transport, as indicated by the presence of numerous endocytic vesicles in these cells. Tight junctions (occluding junctions, zonulae occludentes) between adjacent cells ensure that materials pass primarily through cells, rather than between them.

Cuboidal and columnar epithelia

Cuboidal and columnar epithelia consist of regular rows of cylindrical cells (**Figs 2.2B–C**). Cuboidal cells are approximately square in vertical section, whereas columnar cells are taller than their diameter, and both are polygonal when sectioned horizontally. Commonly, microvilli are found on their free surfaces, considerably increasing the absorptive area, e.g. in the epithelia of the small intestine (columnar cells with a striated border of very regular microvilli), the gallbladder (columnar cells with a brush border of microvilli); proximal convoluted tubules of the kidney (large cuboidal to low columnar cells with brush borders); and the

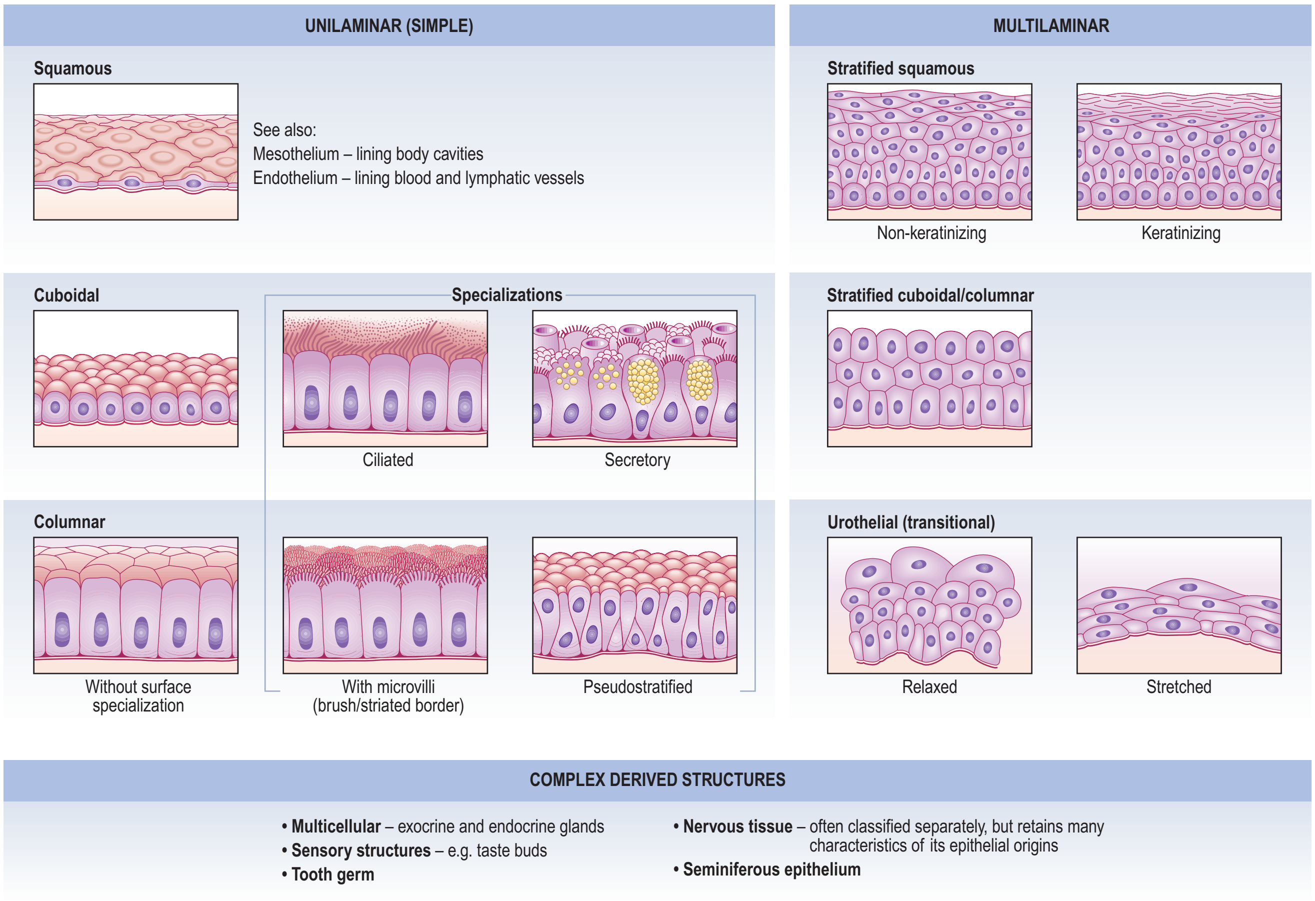
UNILAMINAR (SIMPLE)
MULTILAMINAR
Squamous
See also:
Mesothelium – lining body cavities
Endothelium – lining blood and lymphatic vessels
Stratified squamous
Non-keratinizing
Keratinizing
Cuboidal
Specializations
Ciliated
Secretory
Stratified cuboidal/columnar
Columnar
Without surface specialization
With microvilli (brush/striated border)
Pseudostratified
Urothelial (transitional)
Relaxed
Stretched
COMPLEX DERIVED STRUCTURES
• Multicellular – exocrine and endocrine glands
• Sensory structures – e.g. taste buds
• Tooth germ
• Nervous tissue – often classified separately, but retains many characteristics of its epithelial origins
• Seminiferous epithelium

Fig. 2.1 Classification of epithelial tissues and cells.

epididymis (columnar cells with extremely long microvilli, erroneously termed stereocilia).

Ciliated columnar epithelium lines most of the respiratory tract, except for the lower pharynx and vocal folds, and is pseudostratified (Fig. 2.2D) as far as the larger bronchioles. It also lines some of the tympanic cavity and auditory tube, the uterine tube and the efferent ductules of the testis. Submucosal mucous glands and mucosal goblet cells secrete mucus on to the luminal surface of much of the respiratory tract, and cilia sweep a layer of mucus, trapped dust particles and so on from the lung towards the pharynx in the mucociliary rejection current, which clears the respiratory passages of inhaled particles. Cilia in the uterine tube assist the passage of oocytes and fertilized ova to the uterus.

Some columnar cells are specialized for secretion, and aggregates of such cells may be described as glandular tissue. Their apical domains typically contain mucus- or protein-filled (zymogen) vesicles, e.g. mucin-secreting and chief cells of the gastric epithelium. Where mucous cells lie among non-secretory cells, e.g. in the intestinal epithelium, their apical cytoplasm and its secretory contents often expand to produce a characteristic cell shape, and they are known as goblet cells (see Fig. 2.2D). For further details of glandular tissue, see p. 33, and for the characteristics of mucus, see p. 42.

Pseudostratified epithelium

Pseudostratified epithelium is a single-layered (simple) columnar epithelium in which nuclei lie at different levels in a vertical section (see Fig. 2.2D). All cells are in contact with the basal lamina throughout their lifespan, but not all cells extend through the entire thickness of the epithelium. Some constitute an immature basal cell layer of smaller cells, which are often mitotic and able to replace damaged mature cells. Migrating lymphocytes and mast cells within columnar epithelia may also give a similar, pseudostratified appearance because their nuclei are found at different depths. Much of the ciliated lining of the respiratory tract is of the pseudostratified type, and so is the sensory epithelium of the olfactory area.

Sensory epithelia

Sensory epithelia are found in special sense organs of the olfactory, gustatory and vestibulocochlear receptor systems. All of these contain sensory cells surrounded by supportive non-receptor cells. Olfactory receptors are modified neurones and their axons pass directly to the brain, but the other types are specialized epithelial cells that synapse with terminals of afferent (and sometimes efferent) nerve fibres.

Myoepithelial cells

Myoepithelial cells (sometimes termed basket cells) are fusiform or stellate in shape (Fig. 2.3), contain actin and myosin filaments, and contract when stimulated by nervous or endocrine signals. They surround the secretory portions and ducts of some glands, e.g. mammary, lacrimal, salivary, prostate and sweat glands, and lie between the basal lamina and the glandular or ductal epithelium. Their contraction assists the initial flow of secretion into larger conduits. Ultrastructurally, myoepithelial cells are similar to smooth muscle cells in the arrangement of their actin and myosin, but differ from them because they originate, like the glandular cells, from embryonic ectoderm or endoderm. They can be identified immunohistochemically on the basis of the co-localization of myofilament proteins (which signify their contractile function; Fig. 2.4) and keratin intermediate filaments (which accords with their epithelial lineage) (Balachander et al 2015).

Multilaminar (stratified) epithelia

Multilaminar epithelia are found at surfaces subjected to mechanical damage or other potentially harmful conditions. They can be divided into those that continue to replace their surface cells from deeper layers, designated stratified squamous epithelia, and others in which replacement is extremely slow except after injury.

Stratified squamous epithelia

Stratified squamous epithelia are multilayered tissues in which the formation, maturation and loss of cells is continuous, although the rates of these processes can change, e.g. after injury. New cells are formed in the most basal layers by the mitotic division of stem cells and transit (or transient) amplifying cells. The daughter cells move more superficially, changing gradually from a cuboidal shape to a more flattened form, and are eventually shed from the surface as a highly flattened squame. Typically, the cells are held together by numerous desmosomes to form strong, contiguous cellular sheets that provide protection to the underlying tissues against mechanical, microbial and chemical damage. Stratified

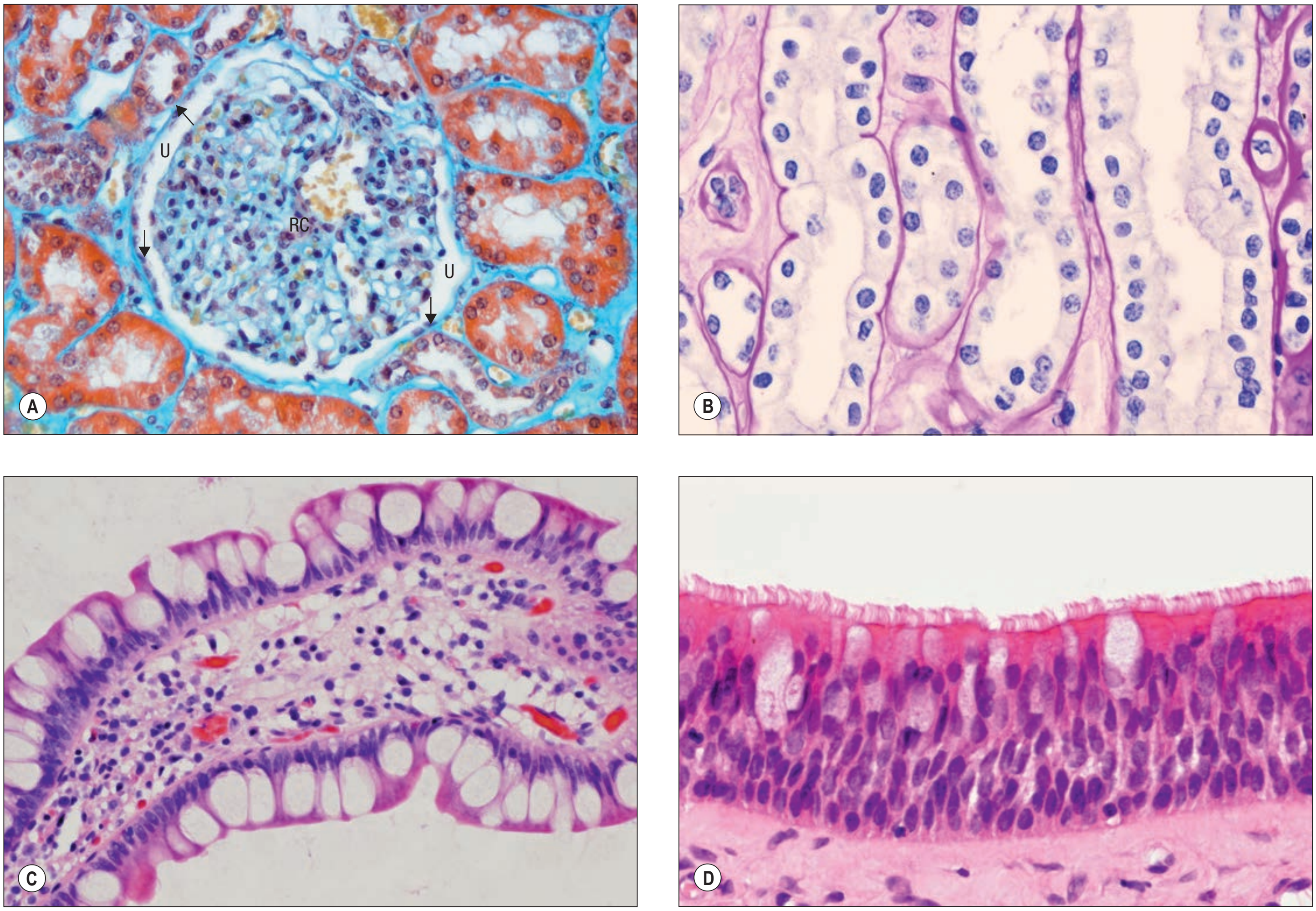

Fig. 2.2 **A**, Simple squamous epithelium lining the outer parietal layer (arrows) of a Bowman's capsule in the renal corpuscle (RC), stained with the trichrome, Martius Scarlet Blue (MSB). Oval epithelial nuclei project into the urinary space (U), within a highly attenuated cytoplasm. **B**, Simple cuboidal epithelium lining a group of collecting ducts sectioned longitudinally in the renal medulla. The basement membranes are stained magenta with periodic–acid Schiff (PAS) reagent. **C**, Simple columnar epithelium covering the tip (off field, right) of a villus in the ileum. Tall, columnar absorptive cells with oval, vertically orientated nuclei bear a striated border of microvilli, just visible as a deeper-stained apical fringe. Numerous interspersed goblet cells are present, with pale apical cytoplasm filled with mucinogen secretory granules and dark, flattened, basally situated nuclei. **D**, Ciliated columnar pseudostratified epithelium in the respiratory tract, and interspersed goblet cells, with pale, mucinogen granule-filled apical cytoplasm. All human tissues. (Courtesy of Mr Peter Helliwell and the late Dr Joseph Mathew, Department of Histopathology, Royal Cornwall Hospitals Trust, UK.)

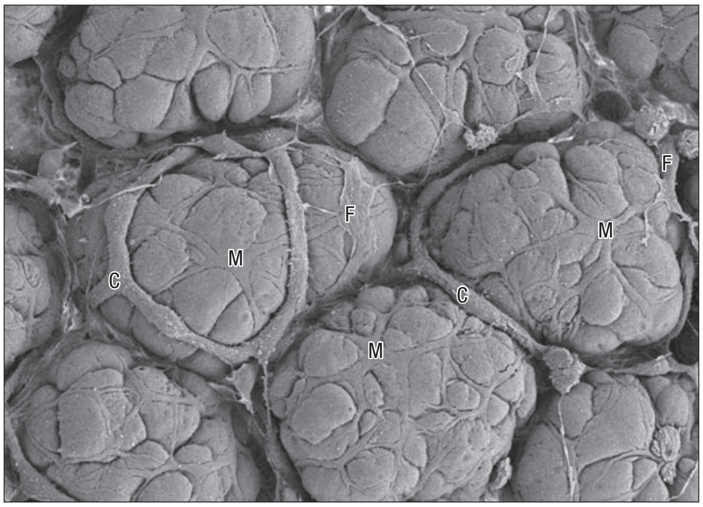

Fig. 2.3 Stellate myoepithelial cells (M) wrapped around secretory acini in the lactating mouse mammary gland, seen in the scanning electron microscope after enzymatic depletion of extracellular matrix. Blood capillaries (C) and fibroblasts (F) are also indicated. (Courtesy of Professor Toshikazu Nagato, Fukuoka Dental College, Japan.)

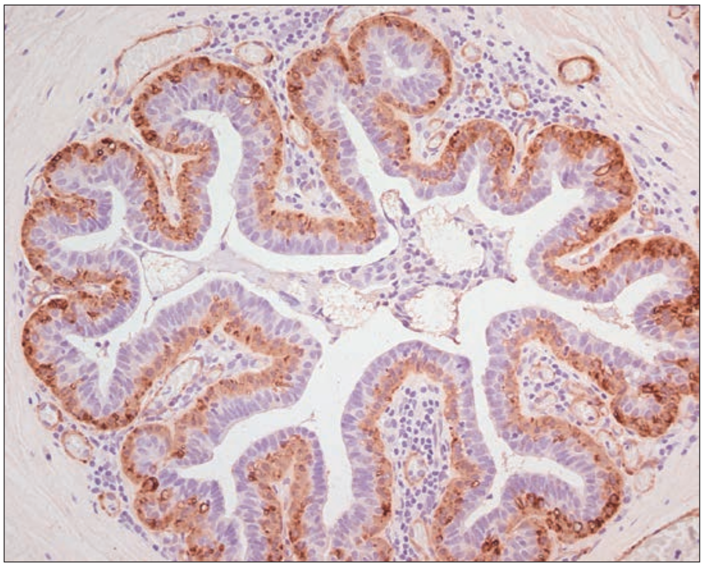

Fig. 2.4 Myoepithelial cells (stained brown), in a human breast duct, demonstrated immunohistochemically using antibody to smooth muscle actin. (Courtesy of Mr Peter Helliwell and the late Dr Joseph Mathew, Department of Histopathology, Royal Cornwall Hospitals Trust, UK.)

squamous epithelia may be broadly subdivided into keratinized and non-keratinized types.

Keratinized epithelium

Keratinized epithelium (Fig. 2.5A) is found at surfaces that are subject to drying or mechanical stresses, or are exposed to high levels of abrasion. These include the entire epidermis and the mucocutaneous junctions of the lips, nostrils, distal anal canal, outer surface of the tympanic membrane and parts of the oral lining (gingivae, hard palate and filiform papillae on the anterior part of the dorsal surface of the tongue). Their cells, keratinocytes, are described in more detail on p. 146. A distinguishing feature of keratinized epithelia is that cells of the superficial layer, the stratum corneum, are anucleate, dead, flattened squames that eventually flake off from the surface. In addition, the tough keratin intermediate filaments become firmly embedded in a matrix protein. This unusual combination of strongly coherent layers of living cells and more superficial strata made of plates of inert, mechanically robust protein complexes, interleaved with water-resistant lipid, makes this type of epithelium an efficient barrier against different types of injury, microbial invasion and water loss.

Non-keratinized epithelium

Non-keratinized epithelium is present at surfaces that are subject to abrasion but protected from drying (Fig. 2.5B). These include: the buccal cavity (except for the areas noted above); oropharynx and laryngopharynx; oesophagus; part of the anal canal; vagina; distal uterine cervix; distal urethra; cornea; inner surfaces of the eyelids; and the vestibule of the nasal cavities. Cells go through the same transitions in general shape as are seen in the keratinized type, but they do not fill completely with keratin or secrete glycolipid, and they retain their nuclei until they desquamate at the surface. In sites where considerable abrasion occurs, e.g. parts of the buccal cavity, the epithelium is thicker and its most superficial cells may partly keratinize, so that it is referred to as parakeratinized, in contrast to the orthokeratinized state of fully keratinized epithelium. Diets deficient in vitamin A may induce keratinization of such epithelia, and excessive doses may lead to its transformation into mucus-secreting epithelium.

Stratified cuboidal and columnar epithelia

Two or more layers of cuboidal or low columnar cells (Fig. 2.5C) are typical of the walls of the larger ducts of some exocrine glands, e.g. the pancreas, salivary glands and the ducts of sweat glands, and they presumably provide more strength than a single layer. Parts of the male urethra are also lined by stratified columnar epithelium. The layers are not continually replaced by basal mitoses and there is no progression of form from base to surface, but they can repair themselves if damaged.

Urothelium (urinary or transitional epithelium)

Urothelium (Fig. 2.5D) is a specialized epithelium that lines much of the urinary tract and prevents its rather toxic contents from damaging surrounding structures. It extends from the ends of the collecting ducts of the kidneys, through the ureters and bladder, to the proximal portion of the urethra. In males it lines the urethra as far as the ejaculatory ducts, then becomes intermittent and is finally replaced by stratified columnar epithelium in the membranous urethra. In females it extends as far as the urogenital membrane.

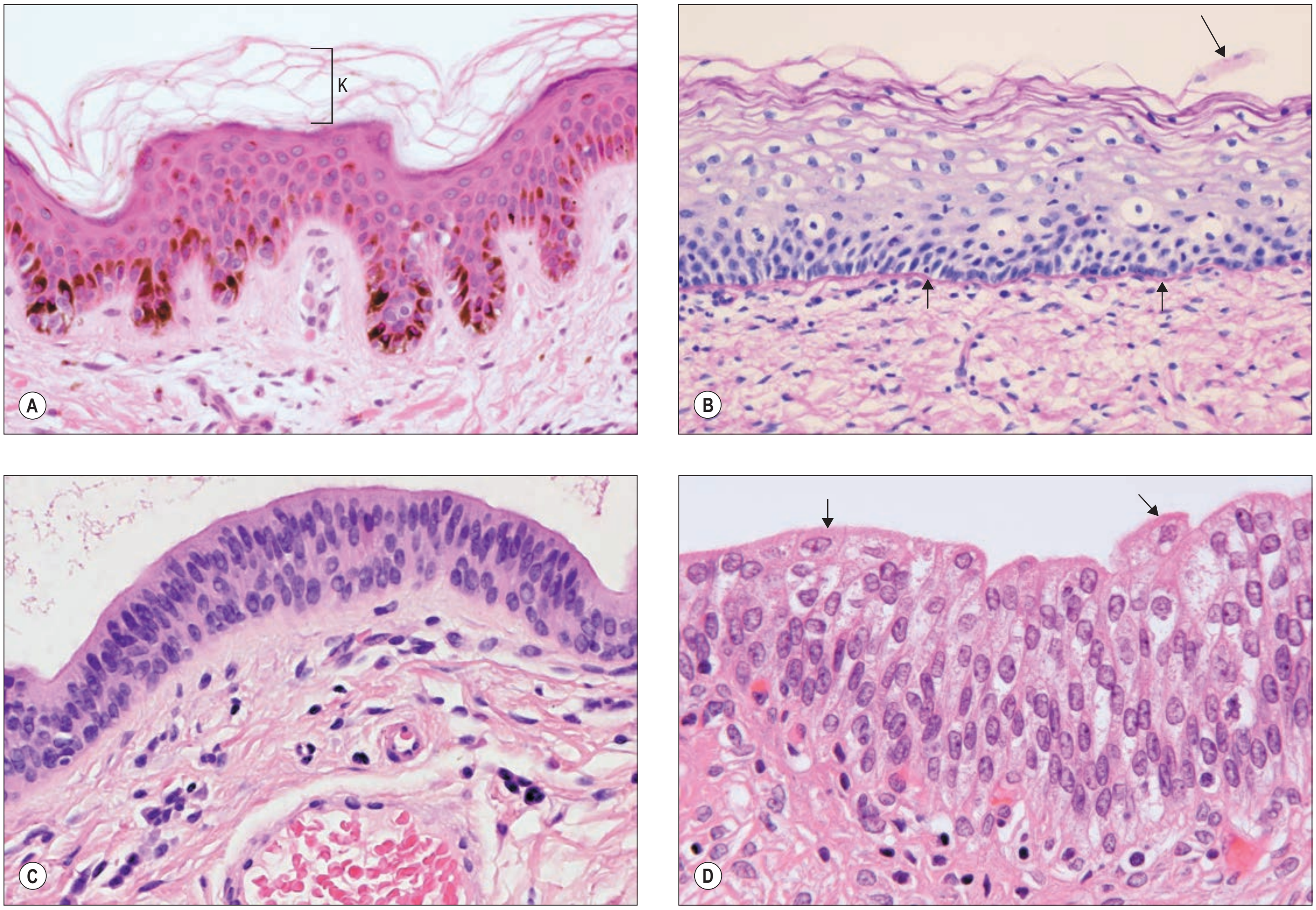

Fig. 2.5 **A**, Keratinized stratified squamous epithelium in thin skin. Pigmented melanocytes are seen in the basal layer and a few keratinocytes of the prickle cell layer also contain melanin granules. The dead, keratinized layer (K) lacks nuclei. **B**, Non-keratinized stratified squamous epithelium of the uterine ectocervix, stained with periodic–acid Schiff (PAS) reagent. The basement membrane (short arrows) and superficial squames, which retain their nuclei, are PAS-positive; squames sloughing off the surface are indicated (long arrow). **C**, Stratified low columnar epithelium of an interlobular excretory duct of the sublingual salivary gland. **D**, Urothelium (transitional epithelium) lining the relaxed urinary bladder. The most superficial cells have a thickened plasma membrane as a result of the presence of intramembranous plaques, which give an eosinophilic appearance to the luminal surface (arrows). All human tissues. (Courtesy of Mr Peter Helliwell and the late Dr Joseph Mathew, Department of Histopathology, Royal Cornwall Hospitals Trust, UK.)

The epithelium appears to be 4–6 cells thick and lines organs that undergo considerable distension and contraction. It can therefore stretch greatly without losing its integrity. In stretching, the cells become flattened without altering their positions relative to each other, because they are firmly connected by numerous desmosomes. However, the urothelium appears to be reduced to only 2–3 cells thick. The epithelium is called transitional because of the apparent transition from a stratified cuboidal epithelium to a stratified squamous epithelium, which occurs as it is stretched to accommodate urine, particularly in the bladder. The basal cells are basophilic and contain many ribosomes; they are uninucleate (diploid), and cuboidal when relaxed. More apically, they form large binucleate or, more often, polyploid uninucleate cells. The surface cells are the largest and may even be octoploid; in the relaxed state they typically bulge into the lumen as dome-shaped cells with a thickened, eosinophilic glycocalyx or cell coat. Their luminal surfaces are covered by a specialized plasma membrane in which plaques of intramembranous glycoprotein particles are embedded to stiffen the membrane. When the epithelium is relaxed, the surface area of the cells is reduced and the plaques are partially internalized by the hinge-like action of the more flexible interplaque membrane regions. The plaques re-emerge on to the surface when it is stretched.

Normally, cell turnover is very slow; cell division is infrequent and is restricted to the basal layer. However, when damaged, the epithelium regenerates quite rapidly (Balsara and Li 2017).

Seminiferous epithelium

Seminiferous epithelium is a highly specialized, complex stratified epithelium. It consists of a heterogeneous population of cells that form the lineage of the spermatozoa (spermatogonia, spermatocytes, spermatids), together with supporting cells (Sertoli cells). It is described in detail on page 1295.

GLANDS

One of the features of many epithelia is their ability to alter the environment facing their free surfaces by the directed transport of ions, water or macromolecules. This is particularly well demonstrated in glandular tissue, in which the metabolism and structural organization of the cells are specialized for the synthesis and secretion of macromolecules, usually from the apical surface. Such cells may exist in isolation amongst other non-secretory cells of an epithelium, e.g. goblet cells in the absorptive lining of the small intestine, or may form highly coherent sheets of epithelium with a common secretory function, e.g. the mucous lining of the stomach and, in a highly invaginated structure, the complex salivary glands.

Glands are conventionally subdivided into exocrine glands and endocrine glands. Exocrine glands secrete, usually via a duct, onto surfaces that are continuous with the exterior of the body, including the gastrointestinal and respiratory tracts, urinary and genital ducts and their derivatives, and the skin. Endocrine glands are ductless and secrete hormones directly into interstitial fluid and thence the circulatory system, to be conveyed throughout the body to affect the activities of other cells. The suprarenal (adrenal) medulla and the neurohypophysis are neurosecretory.

Paracrine glandular cells are similar to endocrine cells but their secretions diffuse locally to cellular targets in the immediate vicinity: many are classed as neuroendocrine cells because they secrete molecules active elsewhere in the nervous system as neurotransmitters or neuromodulators. Modes of signalling by secretory cells are illustrated in Fig. 1.9.

Exocrine glands

Types of secretory process

Secretory mechanisms vary. Secretions that are initially packaged into membrane-bound vesicles are conveyed to the cell surface, where they are discharged by exocytosis. This is merocrine secretion, which is by far the most common secretory mechanism, where vesicle membranes fuse with the plasma membrane to release their contents to the exterior (**Fig. 2.6**). Specialized transmembrane molecules in the secretory vesicle wall recognize marker proteins on the cytoplasmic side of the plasma membrane and bind to them. This initiates interactions with other proteins that cause the fusion of the two membranes and the consequent release of the vesicle contents. The stimulus for secretion varies with the type of cell but often appears to involve a rise in intracellular calcium. Glands such as the simple sweat glands of the skin, where ions and water are actively transported from plasma as an exudate, were once classified as eccrine glands. They are now known to synthesize and secrete small amounts of protein by a merocrine mechanism, and have been reclassified as merocrine glands.

In apocrine glands, some of the apical cytoplasm is pinched off with the contained secretions, which are stored in the cell as membrane-free droplets (see Fig. 2.6). The best understood example is the secretion of milk fat by mammary gland cells, where a small amount of cytoplasm is incorporated into the plasma membrane-bound lipid globule as it is released from the cell. Larger amounts of cytoplasm are included in secretions by specialized apocrine sweat glands in the axilla (Stoeckelhuber et al 2011) and anogenital regions of the body. A combination of different types of secretion occurs in some tissues, e.g. mammary gland cells secrete milk fat by apocrine secretion and milk protein, casein, by merocrine secretion.

In holocrine glands, the cells first fill with secretory products after which the entire cell disintegrates to liberate the accumulated mass of secretion into the adjacent duct or, more usually, hair follicle, e.g. sebaceous glands in the skin (see Fig. 2.6).

Structural and functional classification

Exocrine glands may be unicellular or multicellular. The latter may be in the form of simple sheets of secretory cells, e.g. the lining of the stomach, or may be structurally more complex and invaginated to a variable degree. Such glands may be simple units or their connection to the surface may be branched (see Fig. 2.6). Simple unbranched tubular glands exist in the walls of many of the hollow viscera, e.g. the small intestine and uterus, whereas some simple glands have expanded, flask-like ends (acini or alveoli). Such glands may consist entirely of secretory cells, or may have a blind-ending secretory portion that leads through a non-secretory duct to the surface, in which case the ducts may modify the secretions as they pass along them.

Glands with ducts may be branched (compound) and sometimes form elaborate ductal trees. Such glands generally have acinar or alveolar secretory lobules, as in the exocrine pancreas, but the secretory units may alternatively be tubular or mixed tubulo-acinar. More than one type of secretory cell may occur within a particular secretory unit, or individual units may be specialized to just one type of secretion (e.g. serous acini of salivary glands).

Exocrine glands are also classified by their secretory products. Secretory cells in mucus-secreting or mucous glands have frothy cytoplasm and basal, flattened nuclei. They stain deeply with metachromatic stains and periodic acid–Schiff (PAS) methods that detect carbohydrate residues. However, in general (i.e. non-specific) histological preparations, they are weakly stained because much of their content of water-rich mucin has been extracted by the processing procedures. Secretory cells in serous glands have centrally placed nuclei and eosinophilic secretory storage granules in their cytoplasm. They secrete mainly glycoproteins (including lysozyme) and digestive enzymes.

Some glands are almost entirely mucous (e.g. the sublingual salivary gland), whereas others are mainly serous (e.g. the parotid salivary gland). The submandibular gland is mixed, in that some lobules are predominantly mucous and others serous. Mucous acini may share a lumen with clusters of serous cells (seen in routine preparations as serous demilunes). Although this simple approach to classification is useful for general descriptive purposes, the diversity of molecules synthesized and secreted by glands is such that complex mixtures often exist within the same cell.

Endocrine glands

Endocrine glands secrete directly into connective tissue interstitial fluid and thence the circulation. Their cells are grouped around beds of capillaries or sinusoids, typically lined by fenestrated endothelia to allow the rapid passage of macromolecules through their walls. Endocrine cells may be arranged in clusters within vascular networks, in cords between parallel vascular channels or as hollow structures (follicles) surrounding their stored secretions. In addition to the cells of specialized ductless endocrine glands (e.g. pituitary, pineal, thyroid and parathyroid), hormone-producing cells also form components of other organ systems. These include the cells of the pancreatic islets; thymic epithelial cells; renin-secreting cells of the kidney juxtaglomerular apparatus; erythropoietin-secreting cells of the kidney; cells of the circumventricular organs; interstitial testicular (Leydig) cells; interstitial follicular and luteal ovarian cells; and placental cells (in pregnancy). Some cardiac myocytes, particularly in the walls of the atria, also have endocrine functions. These cells are all described in detail within the appropriate regional sections.

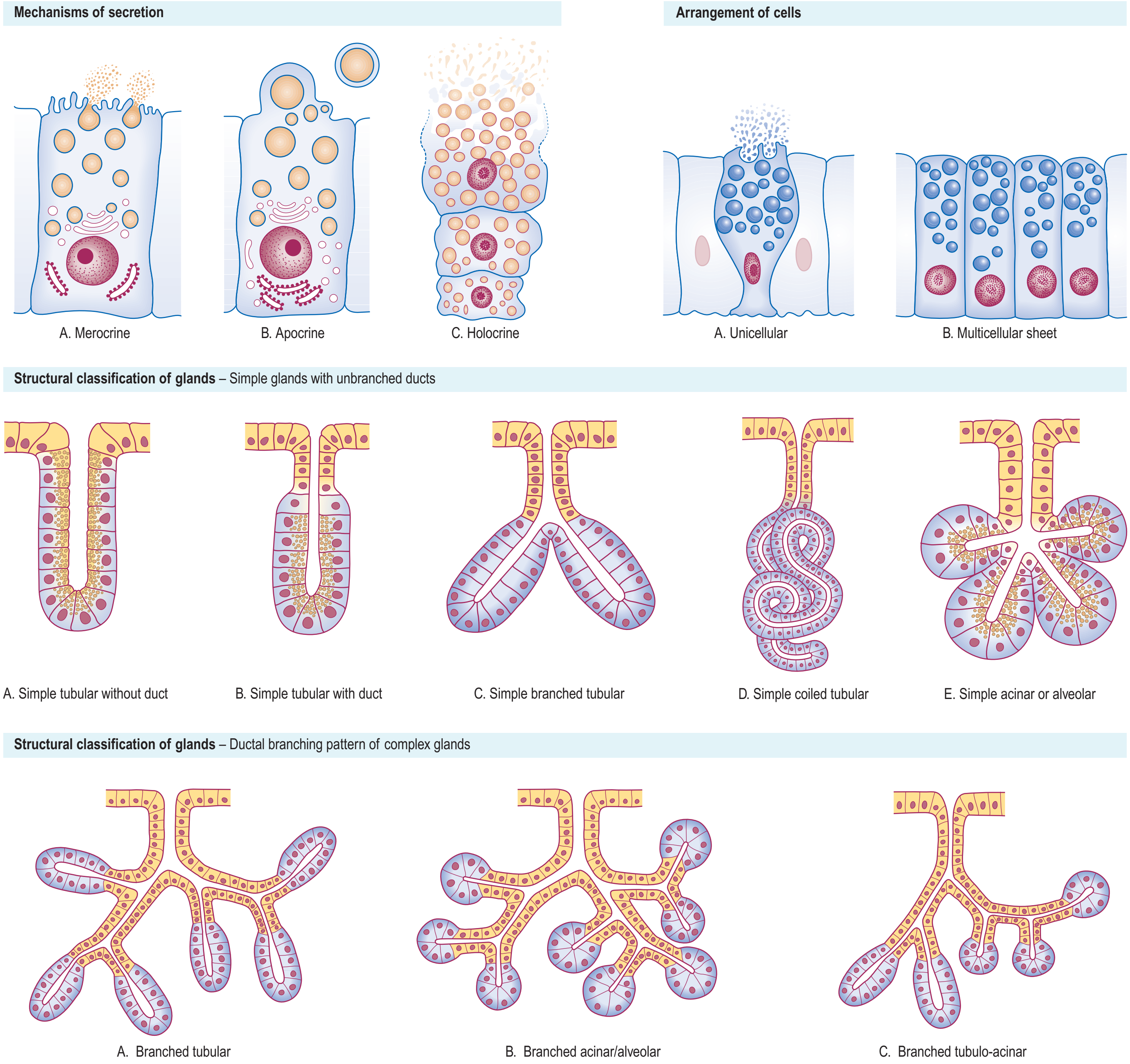
Mechanisms of secretion
Arrangement of cells
A. Merocrine
B. Apocrine
C. Holocrine
A. Unicellular
B. Multicellular sheet
Structural classification of glands – Simple glands with unbranched ducts
A. Simple tubular without duct
B. Simple tubular with duct
C. Simple branched tubular
D. Simple coiled tubular
E. Simple acinar or alveolar
Structural classification of glands – Ductal branching pattern of complex glands
A. Branched tubular
B. Branched acinar/alveolar
C. Branched tubulo-acinar

Fig. 2.6 Classification of the different types of epithelial gland.

Isolated endocrine cells scattered amongst other tissues form part of the dispersed neuroendocrine system, e.g. throughout the alimentary and respiratory tracts. They produce peptide hormones, many of which may function as neurotransmitters: they can express neurone-specific enolase, synaptophysin, secretogranins and chromogranins as well as enzymes involved in peptide hormone synthesis and processing (Asa and Mete 2018). Neuroendocrine cells are generally situated within a mucosal epithelium and their bases often rest on the basal lamina. In response to an external stimulus, they secrete their product basally into interstitial fluid. They typically have a well-developed rough endoplasmic reticulum for peptide synthesis, large Golgi complexes for packaging their hormones, and numerous secretory granules that store and also transport the hormones to the cell surface for release by exocytosis (Fig. 2.7). The secretory granules vary in shape, size and ultrastructure according to cell type. Neuroendocrine cells often take the name of the secretion they produce, e.g. gastrin-secreting G cells of the small intestine.

Control of glandular secretion

The activities of cells in the various tissue and organ systems of the body are tightly regulated by the coordinated activity of the endocrine and autonomic nervous systems. Endocrine (and paracrine) signals reach target cells in interstitial fluid, often via blood plasma, and together with autonomic nervous signals they ensure that the body responds to normal physiological stimuli and adjusts to changes in the external environment. Hormone secretion is itself controlled in a number of ways, e.g. by neural control, regulatory feedback loops or according to various cyclical, rhythmical or pulsatile patterns of release. Endocrine glands have a rich vascular supply and their blood flow is controlled by autonomic vasomotor nerves, which can thus modify glandular activity.

Glandular activity may also be controlled directly by autonomic secretomotor fibres, which may either form synapses on the bases of gland cells (e.g. in the suprarenal medulla) or release neuromediators in the vicinity of the glands and reach them by diffusion. Alternatively, the autonomic nervous system may act indirectly on gland cells, e.g. on neuroendocrine G cells via histamine, released neurogenically from another neuroendocrine cell in the gastric lining. Such paracrine activities of neuroendocrine cells are also important in the respiratory system.

Circulating hormones from the adenohypophysis stimulate synthesis and secretion by target cells in many endocrine glands. Such signals, mostly detected by receptors at the cell surface and mediated by second messenger systems, may increase the synthetic activity of gland cells, and may cause them to discharge their secretions by exocytosis. Secretions from certain exocrine glandular cells are expressed rapidly from those glands by the contraction of associated myoepithelial cells (see Figs 2.3–2.4) that enclose the secretory units and smaller ducts. Myoepithelial cells may be under direct neural control, as in the salivary glands, or they may respond to circulating hormones, as in the mammary gland, where they respond to the concentration of circulating oxytocin.

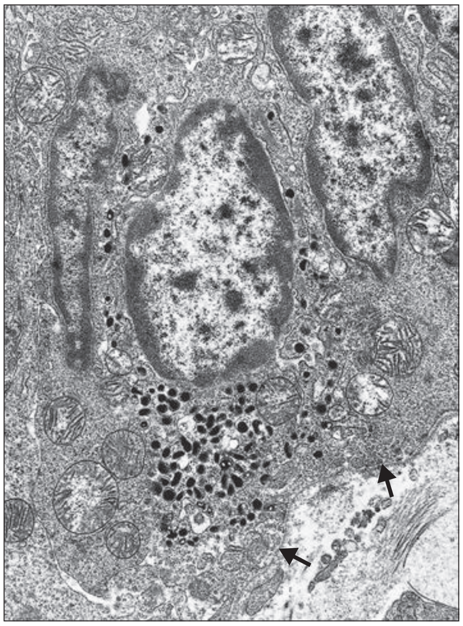

Fig. 2.7 An electron micrograph of a neuroendocrine cell between two absorptive cells in the colon (rat tissue). Dense neurosecretory granules are seen in the basal cytoplasm, apposed to the basal lamina (arrows). (Courtesy of Michael Crowder MD.)

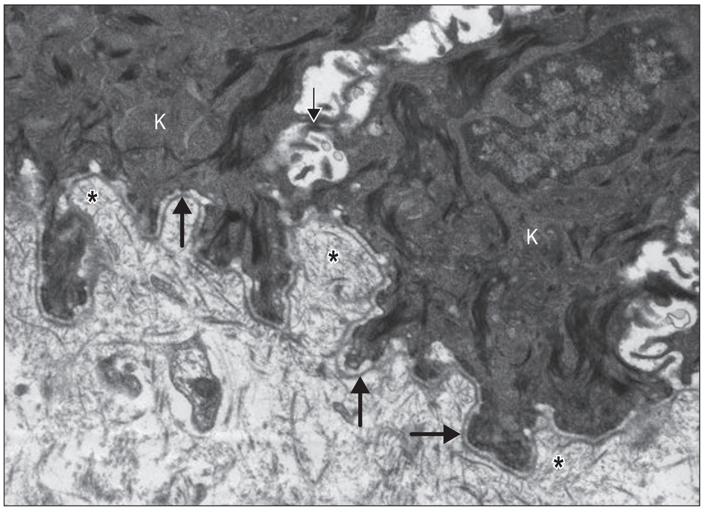

Fig. 2.8 The basal lamina as seen in an electron micrograph, underlying the basal epithelial layer of human skin (see Fig. 7.3). The finely fibrillar dense layer (thick arrows) corresponds to the lamina densa, and fine collagen fibrils (*) lie in the subjacent connective tissue. These contribute to the appearance of the basement membrane in light microscope preparations stained for carbohydrate-rich structures. The two cells seen in the upper field are basal keratinocytes (K), joined by desmosomes (thin arrow), with dense keratin filaments in their cytoplasm. (Courtesy of J McMillan MD, St John's Institute of Dermatology, St Thomas' Hospital, London.)

Feedback loops and endocrine axes

The pituitary gland, in particular the adenohypophysis, is often termed the master gland because of its central role in endocrine physiological processes (Ch. 30). It provides the means by which the central nervous system regulates and integrates, by non-neural mechanisms, the widespread functions of the body, including the activities of other endocrine glands and, often indirectly, exocrine glands such as the breast. Regulatory hormones from the adenohypophysis stimulate synthesis and secretion in target cells of many endocrine glands; these glands therefore respond to, as well as generate, hormonal signals.

The hypothalamus and the adenohypophysis in the brain are central to most regulatory feedback loops within the endocrine system. Loops can be either positive or negative, e.g. the hypothalamus stimulates release of follicle-stimulating hormone (FSH) by the adenohypophysis, which in turn stimulates ovarian follicular maturation and secretion of oestradiol, which acts on breast and endometrial target tissues. Oestradiol, in this case, also acts back on the adenohypophysis and hypothalamus to reinforce their function positively in a feedback loop. In contrast, hypothalamic and adenohypophysial stimulation of testicular production of testosterone, which acts on targets such as skeletal muscle, is negatively regulated in a feedback loop generated by circulating testosterone. Such negative feedback regulation is a widely utilized physiological mechanism.

BASEMENT MEMBRANE AND BASAL LAMINA

In early histological texts a narrow planar assembly of extracellular matrix proteins forming a two-dimensional layer that stained strongly for carbohydrates, and occurred at the interface between connective and other tissues, e.g. between epithelia and their supporting connective tissues, was termed the basement membrane. As almost all of its components are synthesized by the epithelium or other tissues, rather than the adjacent connective tissue, it will be discussed here.

As seen by electron microscopy, the basement membrane is composed of two distinct components: a thin, finely fibrillar layer, the basal lamina, associated closely with the basal cell surface (Fig. 2.8), and a reticular lamina of larger fibrils and glycosaminoglycans of the extracellular matrix that underlies the basal lamina and is continuous with the connective tissue proper. This reticular layer may be much reduced or largely absent in some tissues, e.g. surrounding muscle fibres, Schwann cells and capillary endothelia. In other tissues, the basal lamina separates two layers of cells and there are no intervening typical connective tissue elements, e.g. in the thick basal lamina of the renal glomerular filter and the basal lamina of the thin portions of the lung interalveolar septa across which gases exchange between blood and air.

The basal lamina is usually about 80 nm thick, varying between 40 and 120 nm, and consists of a sheet-like fibrillar layer, the lamina densa (20–50 nm wide), separated from the plasma membrane of the cell it supports by a narrow electron-lucent zone, the lamina lucida. The lamina lucida is absent from tissues prepared by rapid freezing and so may be an artefact. In many tissues this zone is crossed by integral plasma membrane proteins, e.g. keratinocyte hemidesmosomes are anchored into the lamina densa in the basal lamina of the epidermis. The basal lamina is a delicate felt-like network composed largely of two glycoprotein polymers, laminin and type IV collagen. The adhesive glycoprotein laminin is essential for the initial self-assembly of basal laminae into two-dimensional sheets interwoven with each other. Early embryonic basal lamina is formed only of the laminin polymer. Two other molecules cross-link and stabilize the network: nidogen (entactin), which crosslinks laminin to collagen IV and perlecan (a large heparan sulphate proteoglycan).

Although all basal laminae have a similar form, their thickness and precise molecular composition vary between tissues and even within a tissue, e.g. between the crypts and villi of the small intestine. The isoforms of laminin and collagen type IV differ in various tissues; thus Schwann cells and muscle cells express laminin-2 (merosin) rather than the prototypical laminin-1. Laminin-5, although not itself a basal lamina component, is found in the hemidesmosomes of the basal epidermis and links the basal lamina with epidermal transmembrane proteins, $\alpha_6\beta_4$ integrin and collagen type XVII (BPAG2, bullous pemphigoid antigen 2, one of the targets of the autoimmune blistering skin disease, bullous pemphigoid; Ch. 7). The particular isoform of collagen type IV in the basal lamina of different tissues is reflected in tissue-specific disease patterns. Mutations in certain collagen genes expressed in kidney glomeruli (and a few other tissues) cause Alport's syndrome, a heritable form of renal failure that can be either X-linked or autosomally transmitted (Savige et al 2016). Renal failure also occurs in Goodpasture's syndrome, in which renal basal lamina collagen is targeted by autoantibodies to a collagen domain that is normally unexposed but which may be revealed to the immune system by damaging events (Foster 2016).

In Descemet's membrane (posterior limiting lamina) in the cornea, collagen type VIII replaces collagen type IV in the much thickened (increasing with age up to 10 μm,) endothelial basal lamina. The basal lamina of the neuromuscular junction contains agrin, a heparan sulphate proteoglycan, which plays a part in the clustering of muscle acetylcholine receptors in the plasma membrane at these junctions (Rogers and Nishimune 2017).

Reticular lamina

The reticular lamina consists of a dense extracellular matrix that contains collagen. In skin, it contains fibrils of type VII collagen (anchoring fibrils), that bind the lamina densa to the adjacent connective tissue. The high concentration of proteoglycans in the reticular lamina is responsible for the positive reaction of the entire basement membrane to stains for carbohydrates, as seen in sections prepared for light microscopy (see Fig. 2.2B).

Functions of basal lamina

Basal laminae perform a number of important roles. They form selectively permeable barriers (anionic filters) between adjacent tissues, e.g. in the glomerular filter of the kidney; anchor epithelial and connective tissues, and so stabilize and orientate the tissue layers; may exert instructive effects on adjacent tissues, and so determine their polarity, rate of cell division, cell survival, etc.; and regulate angiogenesis. In addition, they may act as pathways for the migration and pathfinding activities of growing cell processes, both in development and in tissue repair, e.g. in guiding the outgrowth of axons and the re-establishment of neuromuscular junctions during regeneration after injury in the peripheral nervous system. Changes in basal lamina thickness are often associated with pathological conditions, e.g. the thickening of the glomerular basal lamina in glomerulonephritis and diabetes.

CONNECTIVE AND SUPPORTING TISSUES

The connective tissues are defined as those composed predominantly of intercellular material, the extracellular matrix, which is secreted mainly by the connective tissue cells. Extracellular matrix is composed of fibrous proteins and a relatively amorphous ground substance (**Fig. 2.9**): the cells may be widely dispersed within the matrix. Many of the special properties of connective tissues are determined by the composition of the matrix and their classification is also largely based on its characteristics. In some types of connective tissue the cellular component eventually dominates the tissue, even though the original matrix cell ratio is high, e.g. adipose tissue.

Connective tissues play several essential roles in the body. These include structural roles, which largely reflect the special mechanical properties of the extracellular matrix components; defensive roles, where the cellular component has the dominant role; and trophic and morphogenetic roles in organizing and influencing the growth and differentiation of surrounding tissues, e.g. in the development of glands from an epithelial surface.

Structural connective tissues are divided into ordinary (or general) types, which are widely distributed and special skeletal types (cartilage and bone) (Ch. 5). Haemolymphoid tissues (peripheral blood cells, lymphoid tissues and their precursors), are often grouped with other types of connective tissue because of their similar mesenchymal origins and because the various defensive cells of the blood also form part of a typical connective tissue cell population that reaches connective tissues via the blood circulation, migrating into them through the endothelial walls of vessels (Ch. 4).

Cells of general connective tissues

Cells of general connective tissues can be separated into the resident cell population (fibroblasts, adipocytes, mesenchymal progenitor cells, etc.) and a population of migrant cells with various defensive functions (macrophages, lymphocytes, mast cells, neutrophils and eosinophils), which may change in number and moderate their activities according to demand. Embryologically, fibroblasts and adipocytes arise from mesenchymal progenitor cells, some of which may remain in the tissues to provide a source of replacement cells postnatally. As noted above, the cells of haemopoietic origin (Ch. 4) migrate into the tissue from bone marrow and lymphoid tissue.

Resident cells

Fibroblasts

Fibroblasts are usually the most numerous resident cells. They are flattened and irregular in outline, with extended processes, and in profile they appear fusiform or spindle-shaped (**Fig. 2.10**; see Fig. 2.13). Fibroblasts synthesize most of the extracellular matrix of connective tissue (see Fig. 2.10); accordingly, they have all the features typical of cells active in the synthesis and secretion of proteins. Their nuclei are relatively large and euchromatic, and possess prominent nucleoli. In young, highly active cells, the cytoplasm is abundant and basophilic (reflecting the high concentration of rough endoplasmic reticulum), mitochondria are abundant and several sets of Golgi apparatus are present. In old and relatively inactive fibroblasts (often termed fibrocytes), the cytoplasmic volume is reduced, the endoplasmic reticulum is sparse and the nucleus is flattened and heterochromatic.

Fibroblasts are usually adherent to the fibres of the matrix (collagen and elastin), which they lay down. In some highly cellular structures, e.g. liver, kidney and spleen, and in most lymphoid tissue, fibroblasts and delicate collagenous fibres (type III collagen; reticular fibres) form fibrocellular networks, which are often called reticular tissue. The fibroblasts may then be termed reticular cells or reticulocytes.

Fibroblasts are particularly active during wound repair following traumatic injury or inflammation, when tissue mass is lost through cell death. They proliferate and lay down a fibrous matrix that becomes invaded by numerous blood vessels (granulation tissue). Contraction of wounds is, at least in part, caused by the shortening of myofibroblasts, specialized contractile fibroblast-like cells with properties (α-smooth muscle actin isoform expression) in common with vascular smooth muscle cells. It was thought that myofibroblasts differentiated from fibroblasts or their mesenchymal progenitor cells (see below) in granulation tissue. However, recent evidence suggests that in wound healing and in many fibrotic disease processes the myofibroblast develops as a phenotypic variant of a wider number of cell types, including fibroblasts, cardiac smooth muscle cells, vascular pericytes, hepatic perisinusoidal stellate (Ito) cells, mesenchymal progenitor cells or cells derived from epithelial or endothelial/mesenchymal transitions (reviewed in Bochaton-Piallat et al (2016)).

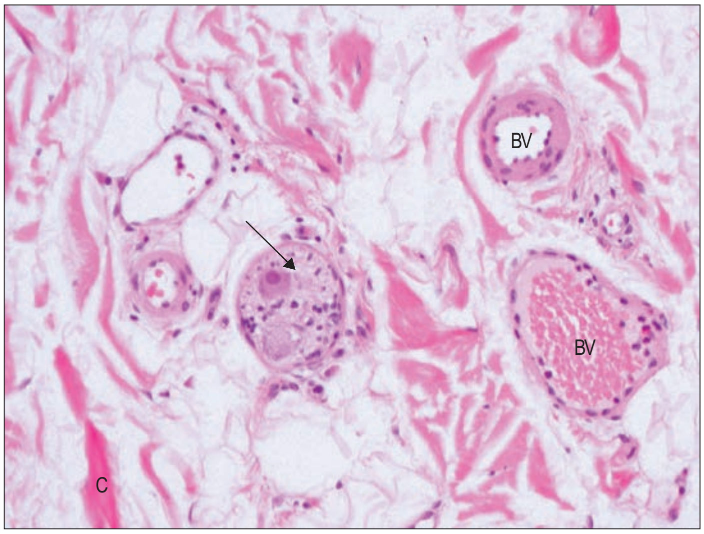

Fig. 2.9 General loose connective tissue (human), with bundles of collagen fibres (C) within an amorphous ground substance, penetrated by a neurovascular bundle of blood vessels (BV), lymphatics and nerves. A small autonomic ganglion is arrowed. (Courtesy of Mr Peter Helliwell and the late Dr Joseph Mathew, Department of Histopathology, Royal Cornwall Hospitals Trust, UK.)

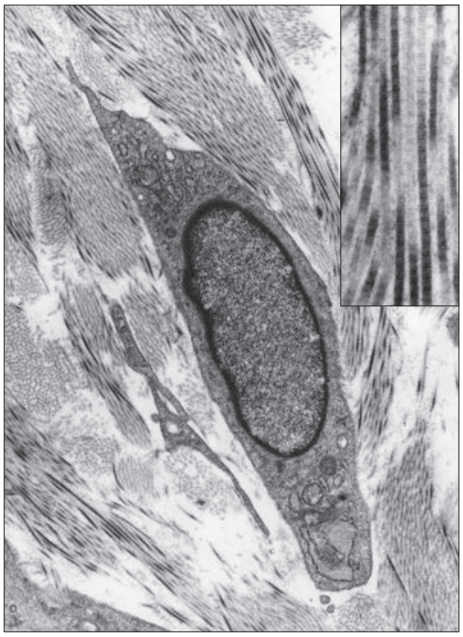

Fig. 2.10 An electron micrograph of a fibroblast in human connective tissue, surrounded by bundles of finely banded collagen fibrils (shown at high magnification in the insert), which they secrete. (Courtesy of Dr Bart Wagner, Histopathology Department, Sheffield Teaching Hospitals, UK.)

In fibrotic disease (including keloid scar formation, hepatic cirrhosis, pulmonary interstitial fibrosis), normal repair processes become dysregulated and excessive. Inflammatory macrophages communicate with myofibroblasts using soluble biochemical and cell contact-mediated signals, and physical and chemical signals transmitted through the extracellular matrix. In fibrosis, this signalling is temporally and spatially aberrant, such that the extracellular matrix of scar tissue fails to co-ordinate the normal healing process. Prolonged persistence of inflammatory cells and myofibroblasts, due at least in part to their failure to die through apoptosis, underlies the development of organ fibrosis. For further reading see Kendall and Feghali-Bostwick (2014), Pakshir and Hinz (2018).

In cases where the specialized cells of the damaged region cannot divide and regenerate functional tissue, e.g. cardiac muscle cells after infarction, connective tissue fibroblasts and their extracellular matrix fill the void to form a scar. An exception is the central nervous system, where glial scars are formed after injury. Fibroblast activity is influenced by various factors such as steroid hormone concentration, dietary content and prevalent mechanical stresses. Collagen formation is impaired in vitamin C deficiency.

Adipocytes (lipocytes, fat cells)

Adipocytes occur singly or in groups in many, but not all, connective tissues: as their name suggests, they are numerous in adipose tissue (**Fig. 2.11**). Individually, the cells are oval or spherical in shape, but when packed together they are polygonal. They vary in diameter, averaging 50 µm. Each cell consists of a peripheral rim of cytoplasm, in which the nucleus is embedded, surrounding a single large central globule of fat, which consists of glycerol esters of oleic, palmitic and stearic acids. There is a small accumulation of cytoplasm around the oval nucleus, which is typically compressed against the cell membrane by the lipid droplet, as is the Golgi complex. Many cytoskeletal filaments, some endoplasmic reticulum and a few mitochondria lie around the lipid droplet, which is in direct contact with the surrounding cytoplasm and not enclosed within a membrane. In sections of tissue not specially treated to preserve lipids, the lipid droplet is usually dissolved out by the solvents used in routine preparations, so that only the nucleus and the peripheral rim of cytoplasm surrounding a central empty space remain.

Another form of adipose tissue, brown fat, occurs in the interscapular region of neonates, a location it shares with the classic brown fat of rodents. Brown fat is characterized by the presence of large cells, each of which contains several separate droplets of fat (multilocular adipose tissue) rather than a single globule (typical of unilocular adipose tissue; see above), and by mitochondria in which the cristae are unusually large and numerous. White fat cells are specialized to store chemical energy, whereas the physiological role of brown adipose tissue (BAT) cells is to metabolize fatty acids and generate heat; BAT cells uncouple cellular respiration via the mitochondrial uncoupling protein UCP1. Although BAT cells are abundant in infancy but regress in adulthood, bioactive brown/beige adipocytes have been detected by positron emission tomography (PET) scanning in adults, mainly in the supraclavicular region, in the neck and along the spine. Beige fat cells, a distinctive subtype of thermogenic BAT, develop postnatally and are highly inducible; their recruitment is mediated by mechanisms that include *de novo* beige adipogenesis and white-to-brown adipocyte transdifferentiation (Wu et al 2012, Wang and Seale 2016, Rui 2017). They may represent an evolutionarily conserved cellular mechanism to provide flexibility in adaptive thermogenesis.

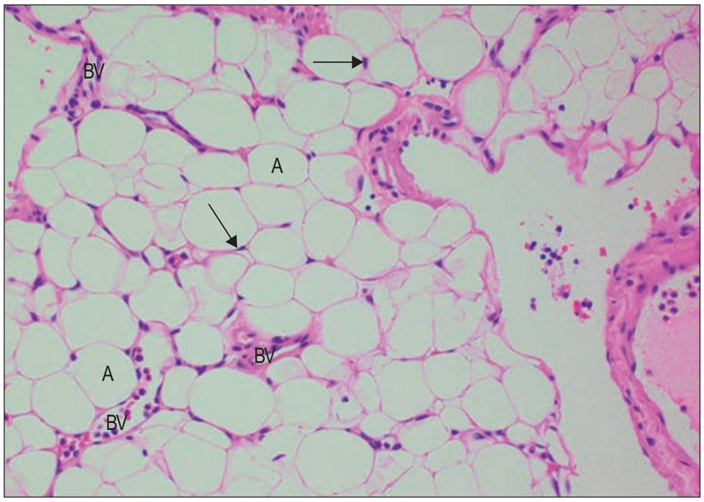

Fig. 2.11 Adipose tissue (human, from a lymph node specimen). Adipocytes (A) are distended polygonal cells filled with lipid, which has been extracted by the tissue processing. This leaves only the plasma membranes with scant cytoplasm and nuclei (arrows), occasionally visible compressed against the cell periphery. Small blood vessels (BV) penetrate the adipose tissue; a larger vessel is seen on the right. (Courtesy of Mr Peter Helliwell and the late Dr Joseph Mathew, Department of Histopathology, Royal Cornwall Hospitals Trust, UK.)

It has long been recognized that adipose tissue is central to the control of energy balance and lipid homeostasis. There is a growing view that it may play a similarly important role as an endocrine organ, secreting a class of peptides, including leptin, called adipokines which may enter the blood via capillaries or lymph. Different types of adipose tissue display functional and regional heterogeneity and differ in their involvement with disease processes (reviewed in Fasshauer and Blüher (2015)). The mobilization of fat is under nervous or hormonal control; noradrenaline (norepinephrine) released at sympathetic nerve endings in adipose tissue is particularly important in this respect. No new adipose tissue is thought to form after the immediate postnatal period, and accumulation of body fat, as in obesity, is due to excessive accumulation of lipid in existing adipocytes, which become very large. Conversely, weight loss results from the mobilization and metabolism of lipid from adipocyte stores, with the consequent shrinkage of the cells.

Mesenchymal progenitor cells

Mesenchymal progenitor cells are normally inconspicuous cells in connective tissues. They are derived from embryonic mesenchyme and are able to differentiate into the mature cells of connective tissue during normal growth and development, in the turnover of cells throughout life and, most conspicuously, in the repair of damaged tissues in wound healing. There is emerging evidence that, even in mature tissues, mesenchymal progenitor cells remain pluripotent and able to give rise to all the resident cells of connective tissues in response to local signals and cues. The potential therapeutic use of postnatal mesenchymal progenitor cell-based therapy for a wide range of autoimmune disorders and degenerative diseases is reflected in a burgeoning literature in the field of translational medicine. Much remains to be determined concerning the identity and regenerative potential of mesenchymal progenitor cells from different connective tissue sources (e.g., bone marrow and adipose tissue) before their clinical usefulness can be rigorously assessed (Ankrum and Karp 2010, Robey 2017).

Migrant cells

Macrophages

Macrophages are numerous in connective tissues, where they are either attached to matrix fibres or are motile and migratory (**Fig. 2.12**). They are relatively large cells, 15–20 µm in diameter, with indented and relatively heterochromatic nuclei and a prominent nucleolus. Their cytoplasm is

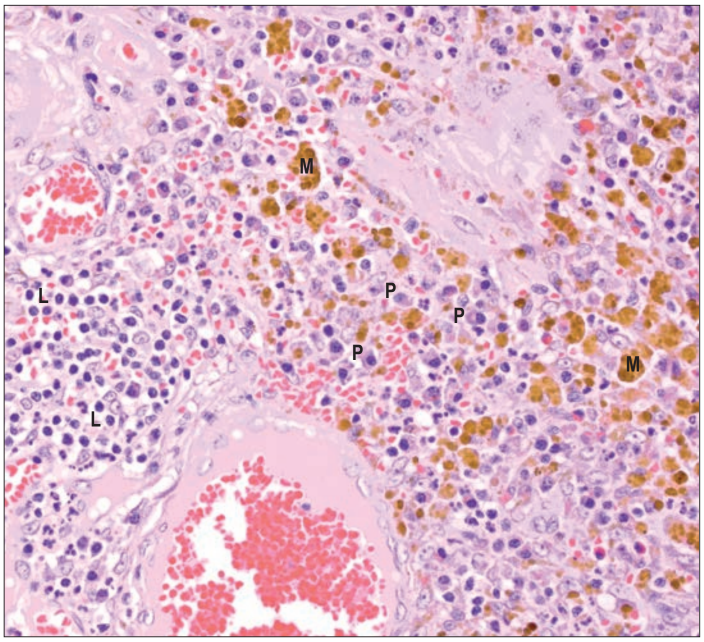

Fig. 2.12 Macrophages (M) in chronically inflamed human connective tissue, showing prominent pigmented, haemosiderin-containing cytoplasmic granules derived from ingested erythrocytes. Many are multinucleate. Also seen are plasma cells (P), small lymphocytes (L) and other haemopoietic cells. (Courtesy of Mr Peter Helliwell and the late Dr Joseph Mathew, Department of Histopathology, Royal Cornwall Hospitals Trust, UK.)

slightly basophilic, contains many lysosomes and typically has a foamy appearance under the light microscope. Macrophages are important phagocytes and form part of the mononuclear phagocyte system. They can engulf and digest particulate organic materials, such as bacteria, and are able to clear dead or damaged cells from a tissue too. They are also the source of a number of secreted cytokines that have profound effects on many other cell types. Macrophages are able to proliferate in connective tissues to a limited extent, but are derived and replaced primarily from haemopoietic stem cells in the bone marrow, which circulate in the blood as monocytes before migrating through vessel walls into connective tissues, where they differentiate.

Many properties of macrophages in general connective tissue are similar to those of related cells in other sites. These include: circulating monocytes, from which they are derived; alveolar macrophages in the lungs, which take up inhaled particles not cleared by the mucociliary rejection current; phagocytic cells in the lymph nodes, spleen and bone marrow; Kupffer cells of the liver sinusoids; and microglial cells (Ch. 3) of the central nervous system.

Lymphocytes

Lymphocytes are normally present in small numbers; they are numerous in general connective tissue only in pathological states, when they migrate in from adjacent lymphoid tissue or from the circulation. The majority are small cells (6–8 μm) with highly heterochromatic nuclei but they enlarge when stimulated. Two major functional classes exist, termed B and T lymphocytes. B lymphocytes originate in the bone marrow, then migrate to various lymphoid tissues, where they proliferate. When antigenically stimulated, they undergo further mitotic divisions, then enlarge as they mature, commonly in general connective tissues, to form plasma cells that synthesize and secrete antibodies (immunoglobulins). Mature plasma cells are rounded or ovoid, up to 15 μm across, and have an extensive rough endoplasmic reticulum. Their nuclei are spherical, often eccentrically situated, and have a characteristic 'clock-face' configuration of heterochromatin (see Fig. 4.12) that is regularly distributed in peripheral clumps. The prominent Golgi complex is visible with a light microscope as a pale region to one side of the nucleus and the remaining cytoplasm is deeply basophilic because of the abundant rough endoplasmic reticulum. Mature plasma cells do not divide.

T lymphocytes originate from precursors in bone marrow haemopoietic tissue but later migrate to the thymus, where they develop T-cell identity, before passing into the peripheral lymphoid system, where they continue to multiply. When antigenically stimulated, T cells enlarge and their cytoplasm becomes filled with free polysome clusters. The functions of T lymphocytes are numerous: different subsets recognize and destroy virus-infected cells, tissue and organ grafts, or interact with B lymphocytes and several other defensive cell types.

Mast cells

Mast cells are important defensive cells. They occur particularly in loose connective tissues and in the fibrous capsules of certain organs such as the liver, and are numerous around blood vessels. Mast cells are round or oval, approximately 20 μm in diameter, with many filopodia extending from the cell surface. The nucleus is centrally placed and relatively small. The cytoplasm contains large numbers of prominent vesicles and a well-developed Golgi apparatus, but scant endoplasmic reticulum. The vesicles have a high content of glycosaminoglycans and show a strongly positive reaction with the PAS stain for carbohydrates. They are membrane-bound, vary in size and shape (mean diameter 0.5 μm) and also have a rather heterogeneous content of dense, lipid-containing material, which may be finely granular, lamellar or in the form of membranous whorls.

The major granule components, many of them associated with inflammation, are the proteoglycan heparin, histamine, tryptase, superoxide dismutase, aryl sulphatase, β-hexosaminidase and various other enzymes, including chymase in connective tissue but not mucosal mast cells, together with chemotactic factors for neutrophil and eosinophil granulocytes. There are functional differences between mast cells found in different tissues.

Mast cells may be stimulated to release some or all of their contents, either by direct mechanical or chemical trauma, or after contact with particular antigens to which the body has previously been exposed. The consequences of granule release include alteration of capillary permeability, smooth muscle contraction, and activation and attraction to the locality of various other defensive cells. Responses to mast cell degranulation may be localized, e.g. urticaria, or there may occasionally be a generalized response to the release of large amounts of histamine into the circulation (anaphylactic shock). Mast cells closely resemble basophil granulocytes of the general circulation but are thought to develop as distinct descendants of an earlier myeloid lineage precursor. It is believed that they are generated in the bone marrow and circulate to the tissues as immature basophil-like cells, migrating through the capillary and venule walls to their final destination. For further reading, see Yamanishi and Karasuyama (2016).

Granulocytes (polymorphonuclear leukocytes)

Neutrophil and eosinophil granulocytes are immigrant cells from the circulation. Relatively infrequent in normal connective tissues, their numbers may increase dramatically in infected tissues, where they are important components of cellular defence. Neutrophils are highly phagocytic, especially towards bacteria. The functions of eosinophils are less well understood. These cells are described further in Chapter 4.

Cells of specialized connective tissues

Skeletal tissues, cartilage and bone are generally classified with the connective tissues, but their structure and functions are highly specialized and they are described in Chapter 5. As with the general connective tissues, these specialized types are characterized by their extracellular matrix, which forms the major component of the tissues and is responsible for their properties. The resident cells are different from those in general connective tissues. Cartilage is populated by chondroblasts, which synthesize the matrix, and by mature chondrocytes. Bone matrix is elaborated by osteoblasts. Their mature progeny, osteocytes, are embedded within the matrix, which they help to mineralize, turn over and maintain. A third cell type, the osteoclast, has a different lineage origin and is derived from haemopoietic tissue; osteoclasts are responsible for bone degradation and remodelling in collaboration with osteoblasts.

Extracellular matrix

The term extracellular matrix is applied collectively to the extracellular components of connective and supporting tissues. Essentially, it consists of a system of insoluble protein fibres, adhesive glycoproteins and soluble complexes composed of carbohydrate polymers linked to protein molecules (proteoglycans and glycosaminoglycans) that bind water. The extracellular matrix distributes the mechanical stresses on tissues and also provides the structural environment of the cells embedded in it, forming a framework to which they adhere and on which they can move (reviewed in Even-Ram and Yamada (2005),Wolf and Friedl (2011), Mouw et al (2014)). With the exception of bone matrix, it provides a highly hydrated medium, through which metabolites, gases and nutrients can diffuse freely between cells and the blood vessels traversing it or, in the case of cartilage, passing nearby.

There are many complex interactions between connective tissue cells and the extracellular matrix. The cells continually synthesize, secrete, modify and degrade extracellular matrix components, and respond to contact with the matrix in the regulation of cell metabolism, proliferation and motility. Degradation of the matrix is an important feature of embryonic development, morphogenesis, angiogenesis, tissue repair and remodelling (Mott and Werb 2004). Various types of proteinase are involved, principally metalloproteinases such as matrix metalloproteinases (MMPs), and those with a disintegrin and metalloproteinase domain (ADAMs) that include ADAMs with a thrombospondin domain (ADAMTS). Tissue remodelling depends on the controlled degradation of the extracellular matrix by secreted MMPs, regulated by their specific inhibitors (tissue inhibitors of metalloproteinases, TIMPs), as occurs, for instance, during involution of the postpartum uterus or during menstrual lysis and shedding of the endometrium (Gaide Chevronnay et al 2012). In the process of matrix degradation, bioactive peptides are liberated that act as growth factors, cytokines and other signalling molecules to change the behaviour of cells in the vicinity. While precisely regulated under physiological conditions, pathologically dysregulated extracellular matrix degradation is a cause of many diseases, such as atherosclerosis, emphysema, both rheumatoid and osteoarthritis, and diabetic vascular complications.

The insoluble fibres are mainly of two types of structural protein: members of the collagen family, and elastin (**Fig. 2.13**). The interfibrillar matrix (ground substance) includes a number of adhesive glycoproteins that perform a variety of functions in connective tissues, including cell–matrix adhesion and matrix–cell signalling. These glycoproteins include fibronectin, laminin, tenascin and vitronectin, in addition to a number of other less well characterized proteins. The glycosaminoglycans of the interfibrillar matrix are, with one notable exception, post-translationally modified proteoglycan molecules in which long polysaccharide side chains are added to short core proteins during transit through the secretory pathway between the rough endoplasmic reticulum and the *trans*-Golgi network. The exception, the polymeric disaccharide hyaluronan, has no protein core and is synthesized entirely by cell surface enzymes. For further reading on extracellular matrix molecules, see Pollard et al

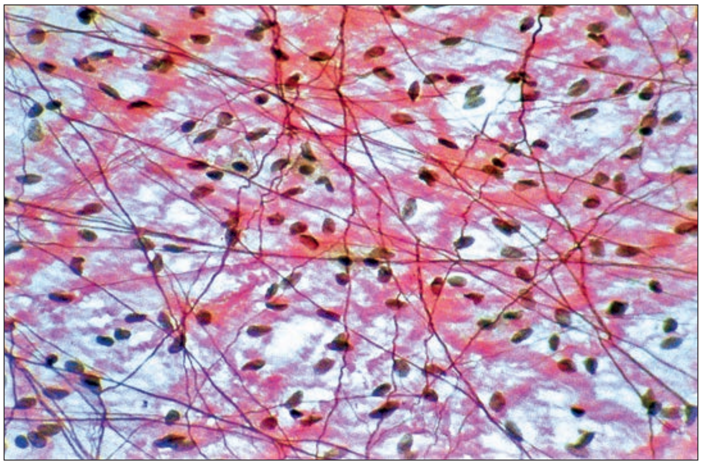

Fig. 2.13 Elastic fibres, seen as fine, dark, relatively straight fibres in a whole-mount preparation of mesentery, stained for elastin. The wavy pink bands are collagen bundles and oval grey nuclei are mainly of fibroblasts.

(2017). Functional attributes of connective tissues vary and depend on the abundance of its different components. Collagen fibres resist tension, whereas elastin provides a measure of resilience to deformation by stretching. The highly hydrated, soluble polymers of the interfibrillar material (proteoglycans and glycosaminoglycans, mainly hyaluronan) generally form a stiff gel resisting compressive forces. Thus tissues that are specialized to resist tensile forces (e.g. tendons) are rich in collagen fibrils; tissues that accommodate changes in shape and volume (e.g. mesenteries) are rich in elastic fibres; and those that absorb compressive forces (e.g. cartilages) are rich in glycosaminoglycans and proteoglycans. In bone, mineral crystals take the place of most of the soluble polymers and endow the tissue with incompressible rigidity.

Fibrillar matrix

Collagens

Collagens make up a very large proportion (approximately 30%) of all the proteins of the body. They consist of a wide range of related molecules that have various roles in the organization and properties of connective (and some other) tissues. The first collagen to be characterized was type I, the most abundant of all the collagens and a constituent of the dermis, fasciae, bone, tendon, ligaments, blood vessels and the sclera of the eyeball. The characteristic collagen of cartilage and the vitreous body of the eye, with a slightly different chemical composition, is type II, whereas type III is present in several tissues, including the dermis and blood vessels, and type IV is in basal lamina. The other types are widely distributed in various tissues. Five of the collagens, types I, II, III, V and XI, form fibrils; types IV, VIII and X form sheets or meshworks; types VI, VII, IX, XII, XIV and XVIII have an anchoring or linking role; and types XIII and XVII are transmembrane proteins. Ehlers-Danlos syndrome is a diverse group of disorders resulting from defective structure or synthesis of different collagens. Typical features include hyperelasticity of skin and hypermobility of joints. The loss of tensile strength imparted by collagen leads to vulnerability to damage in joints, blood vessels and internal organs. For further reading see Kierszenbaum and Tres (2019).

Biochemically, all collagens have a number of features in common. Unlike most other proteins, they contain high levels of hydroxyproline and all are composed of three polypeptides that form triple helices and are substantially modified post-translationally. After secretion, individual molecules are further cross-linked to form stable polymers. Functionally, collagens are structural proteins with considerable mechanical strength. Just a few of their distinguishing structural features are described below. For further reading on the molecular structure and functions of the collagens, see Pollard et al (2017).

Type I collagen

Type I collagen is very widely distributed. It forms inextensible fibrils in which collagen molecules (triple helices) are aligned side by side in a staggered fashion, with three-quarters of the length of each molecule in contact with neighbouring molecules. The fibril has well-marked bands of charged and uncharged amino acids arranged across it; these stain with heavy metals in a banding pattern that repeats every 65 nm in longitudinal sections viewed in the electron microscope (see Fig. 2.10 insert).

Fibril diameters vary between tissues and with age. Developing tissues often have thinner fibrils than mature tissues. Corneal stroma fibrils are of uniform and thin diameter, whereas tendon fibrils may be up to 20 times thicker and quite variable. Tissues in which the fibrils are subject to high tensile loading tend to have thicker fibrils. Thick fibrils are composites of uniform thin fibrils with a diameter of 8–12 nm. The fibrils themselves are relatively flexible, but when mineralized (as in bone) or surrounded by high concentrations of proteoglycan (as in cartilage), the resulting fibre-reinforced composite materials are rigid.

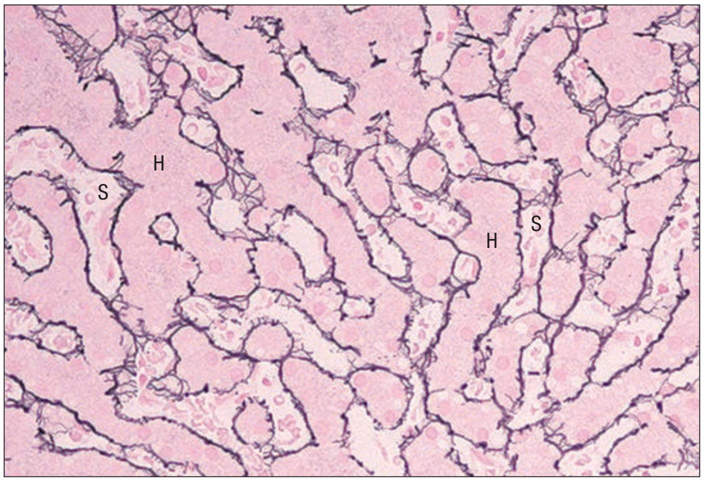

Fig. 2.14 Reticular fibres (type III collagen/reticulin demonstrated by silver staining) in human liver, forming a delicate meshwork within the space of Disse between hepatocyte (H) plasma membranes and the sinusoidal endothelia (S). (Courtesy of Mr Peter Helliwell and the late Dr Joseph Mathew, Department of Histopathology, Royal Cornwall Hospitals Trust, UK.)

Fresh type I collagen fibres are tightly packed assemblies of parallel fibrils and are white and glistening. They form variably wavy (crimped) bundles of various sizes that are generally visible at the light microscope level. The component fibres may leave one bundle and interweave with others. In some situations, collagen fibrils are laid down in precise geometrical patterns, in which successive layers alternate in direction, e.g. corneal stroma, where the high degree of order is essential for transparency. Tendons, aponeuroses and ligaments are also highly ordered tissues (Ch. 5).

Types II, III, V and XI collagens

Types II, III, V and XI collagens can also aggregate to form linear fibrils. Type II collagen occurs in extremely thin (10 nm), short fibrils in the vitreous humour of the eye and in very thick fibrils in ageing human cartilage. The amino-acid sequence and banding pattern are very similar to those of type I collagen, as are the post-translational modifications of the triple helical protein molecule. The fine fibrils in the vitreous may fuse into thicker aggregates in older tissue.

Type III collagen is very widely distributed, particularly in young and repairing tissues. It usually co-localizes with type I collagen, and covalent links between type I and type III collagen have been demonstrated. In skin, many fibrils are probably composites of type I and type III collagens.

Reticular fibres

Fine branching and anastomosing reticular fibres form the supporting mesh framework of many glands, including the liver (**Fig. 2.14**), the kidney and lymphoreticular tissue (lymph nodes, spleen, etc.). Classically, these fibres stained intensely with silver salts, although they are poorly stained using conventional histological techniques. They associate with basal laminae and are often found in the neighbourhood of collagen fibre bundles. Reticular fibres are formed principally of type III collagen.

Elastin

Elastin is a 70 kDa protein, rich in the hydrophobic amino acids valine and alanine. Elastic fibrils, which also contain fibrillin, are highly cross-linked via two elastin-specific amino acids, desmosine and iso-desmosine, which are formed extracellularly from lysine residues. They are less widely distributed than collagen, yellowish in colour, typically cross-linked and usually thinner (10–20 nm) than collagen fibrils. They can be thick, e.g. in the ligamenta flava and ligamentum nuchae. Unlike collagen type I, they show no banding pattern in the electron microscope. They stain poorly with routine histological stains but are visible when stained with orcein-containing preparations (see Fig. 2.13). They sometimes appear as sheets, as in the fenestrated elastic lamellae of the aortic wall. Elastin-rich structures stretch easily with almost perfect recoil, although they tend to calcify with age and lose elasticity. Elastin is highly resistant to attack by acid and alkali, even at high temperatures. Autosomal dominant mutations in the fibrillin I gene lead to the defects in elastic tissue seen in Marfan syndrome, affecting mainly the ocular, skeletal and cardiovascular systems.

Interfibrillar matrix

Glycosaminoglycans

The structural soluble polymers characteristic of the extracellular matrix are the acidic glycosaminoglycans, which are unbranched chains of repeating disaccharide units, each unit carrying one or more negatively charged groups (carboxylate or sulphate esters, or both). The anionic charge is balanced by cations (Na^+, K^+, etc.) in the interstitial fluid. Their polyanionic character endows the glycosaminoglycans with high osmotic activity, which helps to keep the fibrils apart, confers stiffness on the porous gel that they collectively create, and gives the tissue a varying degree of basophilia. Glycosaminoglycans are named according to the tissues in which they were first found, e.g. hyaluronan (vitreous body), chondroitins (cartilage), dermatan (skin), keratan (cornea), heparan (liver). This terminology is no longer relevant, as most glycosaminoglycans are very widely distributed, whereas, conversely, some corneas contain little or no keratan sulphate. Of the glycosaminoglycans, all except hyaluronan have short protein cores and are highly variable in their carbohydrate side-chain structure.

Hyaluronan

Hyaluronan was formerly called hyaluronic acid (or hyaluronate, as only the salt exists at physiological pH). It is a very large, highly hydrated molecule (25,000 kDa). Hyaluronan is found in all extracellular matrices and in most tissues, and is a prominent component of embryonic and developing tissues.

Hyaluronan is important in the aggregation of proteoglycans and link proteins that possess specific hyaluronan-binding sites (e.g. laminin). Indeed, the very large aggregates that are formed may be the essential compression-resisting units in cartilage. Hyaluronan also forms very viscous solutions, which are probably the major lubricants in synovial joints. Because of its ability to bind water, it is often present in semi-rigid structures (e.g. vitreous humour in the eye), where it cooperates with sparse but regular meshworks of thin collagen fibrils.

Proteoglycans

Proteoglycan nomenclature is based on cellular and subcellular location, gene and protein homologies and the presence of specific core proteins (Iozzo and Schaefer 2015): the same core protein can bear different glycosaminoglycan side chains in different tissues. The functions of many proteoglycans are poorly understood. Some of the better-known proteoglycans are: aggrecan in cartilage, perlecan in basal laminae, decorin associated with fibroblasts in collagen fibril assembly, and syndecan in embryonic tissues.

Adhesive glycoproteins

These proteins include molecules that mediate adhesion between cells and the extracellular matrix, often in association with collagens, proteoglycans or other matrix components. All of them are glycosylated and they are, therefore, glycoproteins. General connective tissue contains the well-known families of fibronectins (and osteonectin in bone), laminins and tenascins; there is a rapidly growing list of other glycoproteins associated with extracellular adhesion (Pollard et al 2017). They possess binding sites for other extracellular matrix molecules and for cell adhesion molecules, especially the integrins; in this way they enable cells selectively to adhere to and migrate through, appropriate matrix structures (reviewed in Jacquemet et al (2013)). They also function as signalling molecules, which are detected by cell surface receptors and initiate changes within the cytoplasm (e.g. to promote the formation of hemidesmosomes or other areas of strong adhesion; reorganize the cytoskeleton; and promote or inhibit locomotion and cell division).

Fibronectin

Fibronectin is a large glycoprotein consisting of a dimer joined by disulphide links. Each subunit is composed of a string of large repetitive domains linked by flexible regions. Fibronectin subunits have binding sites for collagen, heparin, heparan sulphate, and cell surface receptors, especially integrins, and so can promote adhesion between all these elements. In connective tissues, the molecules are able to bind to cell surfaces in an orderly fashion, to form short fibronectin filaments. The liver secretes a related protein, plasma fibronectin, into the circulation. The selective adhesion of different cell types to the matrix during development and in postnatal life is mediated by numerous isoforms of fibronectin generated by alternative splicing. Isoforms found in embryonic tissues are also expressed during wound repair, when they facilitate cellular proliferation and cell movements; the adult form is re-expressed once repair is complete.

Laminin

Laminins are a family of large, mosaic glycoproteins composed of globular, laminin-type epidermal growth factor (EGF)-like repeats and α-helical domains that are found mainly in the basal laminae. Laminin is a large (850 kDa) flexible molecule composed of three polypeptide chains (designated α, β and γ). There are many isoforms of the different chains, and at least 18 types of laminin. The prototypical molecule has a cruciform shape, in which the terminal two-thirds are wound round each other to form the stem of a cross, and the shorter free ends form the upright and transverse members. Interactions between modular domains within the laminin molecule and other proteins enable laminins to mediate intercellular interactions via cell surface receptors (e.g. integrins and dystroglycan) and other components of the ECM (e.g. nidogens [also known as entactins], heparan sulphate, type IV collagen and perlecans). Laminin molecules can assemble themselves into flat regular meshworks, e.g. in the basal lamina.

Tenascin

Tenascin is large glycoprotein composed of six subunits that are joined at one end to form a structure that resembles the spokes of a wheel. There is a family of tenascin molecules, generated by alternative splicing of the tenascin gene transcript. Tenascin is abundant in embryonic tissues but its distribution is restricted in the adult. It appears to be important in guiding cell migration and axonal growth in early development: it may either promote or inhibit these activities, depending on the cell type and tenascin isoform. For further reading on extracellular matrix molecules, their regulation and clinical conditions involving disorders of connective tissues, see Pollard et al (2017: Ch. 29).

Classification of connective tissues

Connective and supporting tissues differ considerably in appearance, consistency and composition in different regions. These differences reflect local functional requirements and are related to the predominance of the cell types; the concentration, arrangement and types of fibre; and the characteristics of the interfibrillar matrix. On these bases, general connective tissues can be classified into irregular and regular types, according to the degree of orientation of their fibrous components.

Irregular connective tissues

Irregular connective tissues can be further subdivided into loose, dense and adipose connective tissue.

Loose (areolar) connective tissue

Loose connective tissue is the most generalized form and is extensively distributed. Its chief function is to bind structures together, while still allowing a considerable amount of movement to take place. It constitutes the submucosa in the digestive tract and other viscera lined by mucosae, and the subcutaneous tissue in regions where this is devoid of fat (e.g. eyelids, penis, scrotum and labia), and it connects muscles, vessels and nerves with surrounding structures. It is present in the interior of organs, where it binds together the lobes and lobules of glands, forms the supporting layer (lamina propria) of mucosal epithelia and vascular endothelia, and lies within and between fascicles of muscle and nerve fibres.

Loose connective tissue consists of a meshwork of thin collagen and elastin fibres interlacing in all directions (see Fig. 2.13) to give a measure of both elasticity and tensile strength. The large meshes contain the soft, semi-fluid interfibrillar matrix or ground substance, and different connective tissue cells scattered along the fibres or in the meshes. It also contains adipocytes, usually in small groups, and particularly around blood vessels.

A variant of loose connective tissue occurs in the choroid and the sclera of the eye, where large numbers of pigment cells (melanocytes) are also present (Ch. 45).

Dense irregular connective tissue

Dense irregular connective tissue is found in regions that are under considerable mechanical stress and where protection is given to ensheathed organs. The matrix is relatively acellular and contains a high proportion of collagen fibres organized into thick bundles interweaving in three dimensions and imparting considerable strength. There are few active fibroblasts, which are usually flattened with heterochromatic nuclei. Dense irregular connective tissue occurs in: the reticular layer of the dermis; the superficial connective tissue sheaths of muscle and nerves, and the adventitia of large blood vessels; and the capsules of various glands and organs (e.g. testis, sclera of the eye, periostea and perichondria).

Adipose tissue

A few adipocytes occur in loose connective tissue in most parts of the body. However, they constitute the principal component of adipose tissue (see Fig. 2.11), where they are embedded in a vascular loose connective tissue, usually divided into lobules by stronger fibrous septa carrying the larger blood vessels. Adipose tissue only occurs in certain regions. In particular it is found: in subcutaneous tissue; in the mesenteries and omenta; in the female breast; in bone marrow; as retro-orbital fat behind the eyeball; around the kidneys; deep to the plantar skin of the foot; and as localized pads in the synovial membrane of many joints. Its distribution in subcutaneous tissue shows characteristic age and sex differences. Fat deposits serve as energy stores, sources of metabolic lipids, thermal insulation (subcutaneous fat) and mechanical shock-absorbers (e.g. soles of the feet, palms of the hands, gluteal region and synovial membranes).

Regular connective tissues

Regular connective tissues include highly fibrous tissues in which fibres are regularly orientated, either to form sheets such as fasciae and aponeuroses, or as thicker bundles such as ligaments or tendons (**Fig. 2.15**). The direction of the fibres within these structures is related to the stresses to which they are subjected: fibrous bundles display considerable interweaving, even within tendons, which increases their structural stability and resilience.

The fibroblasts that secrete the fibres may eventually become trapped within the fibrous structure as tenocytes (tendon cells), compressed, relatively inactive cells with stellate profiles and small heterochromatic nuclei. Fibroblasts on the external surface may be active in continued fibre formation and they constitute a pool of cells available for repair of injured tissue.

Although regular connective tissue is predominantly collagenous, some ligaments contain significant amounts of elastin, e.g. the ligamenta flava of the vertebral laminae and the vocal folds. The collagen fibres may form precise geometrical patterns, as in the cornea.

Mucoid tissue

Mucoid tissue is found chiefly as a stage in the development of connective tissue from mesenchyme. It exists in Wharton's jelly, which forms the bulk of the umbilical cord, and consists substantially of extracellular matrix, largely made up of hydrated mucoid material and a fine meshwork of collagen fibres, in which nucleated, fibroblast-like cells with branching processes are found. Fibres are usually rare in typical mucoid tissue, although the full-term umbilical cord contains perivascular collagen fibres. Postnatally, mucoid tissue is seen in the pulp of a developing tooth, the vitreous body of the eye (a persistent form of mucoid tissue that contains few fibres or cells) and the nucleus pulposus of the intervertebral disc.

TRANSDIFFERENTIATION AND METAPLASIA

Transitions occur between populations of cells forming an epithelium (sheets of polarized cells) and mesenchymal types (where the cells lack polarity) during normal development. In postnatal life, most well-described transitions between morphologically different cell types do not cross an epithelial–mesenchymal boundary but are transitions between types of epithelial cell or, less frequently, between mesenchymal (connective tissue) cell types. Most instances of such transdifferentiation (metaplasia, see Commentary 1.3) are adaptive, to changing environmental conditions or trauma, and almost all are pathological; the altered cells are termed metaplastic. A very common and physiologically normal example is the squamous metaplasia of columnar secretory epithelium of the distal endocervical canal, when exposed to the hormonally stimulated vaginal environment. Gastric metaplasia of the lower oesophagus may occur when chronic reflux of gastric juices exposes its stratified squamous epithelial lining to acid, and the original epithelium is replaced by a mucus-secreting columnar epithelium typical of the stomach (Barrett's oesophagus); this is pathological and susceptible to malignant change. Similarly, the respiratory epithelium (see Fig. 2.2D) of the upper airway often develops foci of stratified squamous metaplasia in response to irritants in cigarette smoke. Mesenchymal (osseous) metaplasia can occur, for example, in the fibrous connective tissue of muscles subjected to repeated damage, where trabeculi of bone develop. It is thought that stem cells (rather than the differentiated cells) in the affected tissue respond to changes in their environment by altering their differentiation pathway, a process that may be reversible if the stimulus is removed. There is evidence suggesting that cellular plasticity, known for many years to occur experimentally in the laboratory, may be more widespread in life than has been appreciated, playing a role in normal tissue homeostasis and repair after injury as well as in the development of malignancy. For a review, see Merrell and Stanger (2016).

MUCOSA (MUCOUS MEMBRANE)

A mucosa or mucous membrane (**Fig. 2.16**) lines many internal hollow organs in which the inner surfaces are moistened by mucus, such as the intestines, conducting portions of the airway, and the genital and urinary tracts. A mucosa proper consists of an epithelial lining, which may have the ducts of mucosal, submucosal or extrinsic glands opening

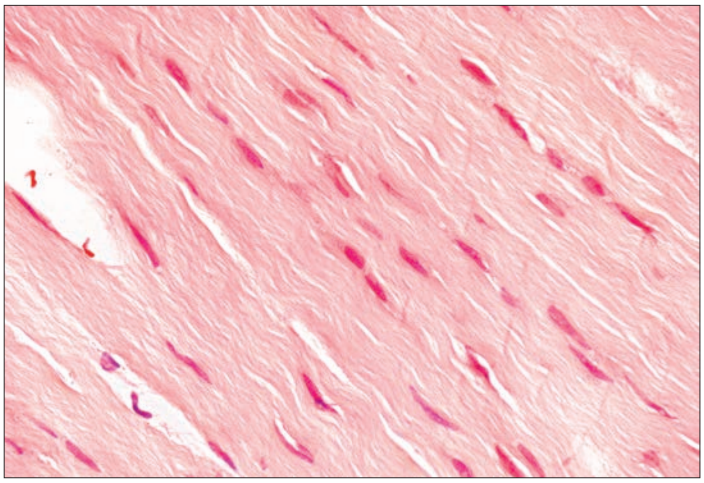

Fig. 2.15 Dense regular connective tissue in a tendon. Thick parallel bundles of type I collagen (here stained pink) present as wavy fibres in tissue sections; they give tendon its white colour in life. The elongated nuclei of inactive fibroblasts (tendon cells) are visible between collagen bundles. (Courtesy of Mr Peter Helliwell, Department of Histopathology, Royal Cornwall Hospitals Trust, UK.)

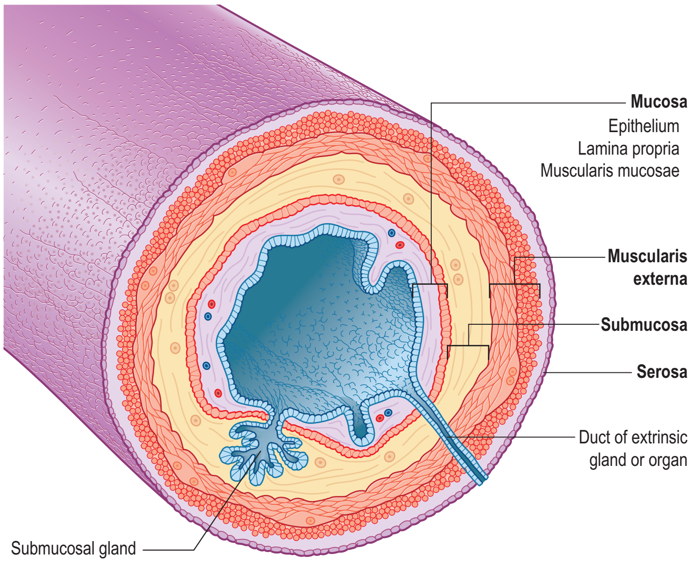

Fig. 2.16 A generalized mucosa and supporting tissues. For details and variations, see text.

onto its surface; an underlying loose connective tissue, the lamina propria; and a thin layer of smooth muscle, the muscularis mucosae. This last layer may be absent from some mucosae, or may be replaced by a layer of elastic fibres. The term mucous membrane reflects the fact that these tissues can all be peeled away as a sheet or membrane from underlying structures; the plane of separation occurs along the muscularis mucosae.

Submucosa is a layer of supporting connective tissue that usually lies below the muscularis mucosae. It may contain mucous or seromucous submucosal glands. Inflammation of the viscera involves, primarily, the connective tissues of the submucosa and lamina propria, and is characterized by dilated vessels, oedema, and accumulations of extravasated immune defence cells. Most mucosae are also supported by one or more layers of smooth muscle, the muscularis externa. Contraction of this muscle may constrict the mucosal lumen (e.g. in the airway) or, where there are two or more muscle layers orientated in opposing directions (e.g. in the intestines), cause peristaltic movement of the viscus and the contents of its lumen. The outer surface of the muscle may be covered by a serosa or, where the structure is retroperitoneal or passes through the pelvic floor, by a connective tissue adventitia.

MUCUS

Mucus is a viscous suspension of complex glycoproteins (mucins) of various kinds, and is secreted by scattered individual epithelial (goblet) cells, a secretory surface epithelium (e.g. the stomach lining) or mucous and seromucous glands. Its elasticity and viscosity play major roles in regulating the transport of food, drugs, particles (including nanoparticles and larger micron-scale particles), and infectious organisms, across mucosal linings (Bansil and Turner 2018).

The precise composition of the mucus varies with the tissue and secretory cells that produce it: all mucins consist of filamentous core proteins with attached carbohydrate chains that are usually branched; salivary mucins contain nearly 600 chains. Carbohydrate residues include glucose, fucose, galactose and *N*-acetylglucosamine (sialic acid). The terminals of some carbohydrate chains are identical to the blood group antigens of the ABO group in the majority of the population (secretors, bearing the secretor gene S^e), and can be detected in salivary mucus by means of appropriate clinical tests. The long polymeric carbohydrate chains bind water and protect surfaces against drying; they also provide good lubricating properties. In concentrated form, mucins form viscous layers that protect the underlying tissues against damage. Mucins may also exist as transmembrane glycoproteins and bind to selectins on complementary cell surfaces.

Synthesis of mucus starts in the rough endoplasmic reticulum, and progresses to the Golgi complex, where it is conjugated with sulphated carbohydrates to form the glycoprotein, mucinogen. This is exported in small, dense, membrane-bound vesicles that swell as they approach the cell surface, with which they fuse before releasing their contents. Secreted mucus is hydrated through the action of epithelial ion channels that transport chloride extracellularly and take up sodium; water follows the movement of chloride by osmosis and dilutes mucus. In this way, mucus gains more fluid and exhibits less viscous properties. In individuals with cystic fibrosis, the cystic fibrosis transmembrane conductance regulator (*CFTR*) gene is defective, impairing the transport of chloride and hydration of mucus, which therefore remains thick and sticky, traps bacteria and leads to infection as well as causing obstruction of passages such as airways and ducts.

SEROSA (SEROUS MEMBRANE)

Serosa consists of a single layer of squamous mesothelial cells, expressing keratin intermediate filaments, supported by an underlying layer of loose connective tissue that contains numerous blood and lymphatic vessels. Serosa lines the pleural, pericardial and peritoneal cavities, and covers the external surfaces of organs lying within those cavities and, in the abdomen, the mesenteries that envelop them. A potential space, filled with a small amount of protein-containing serous fluid, largely an exudate of interstitial fluid, exists between the outer parietal and the inner visceral layers of the serosa.

FASCIA

Fascia is a generic term applied to sheaths, sheets or other dissectible masses of connective tissue that are large enough to be visible to the unaided eye. Deeper-lying condensations of connective tissue have been defined according to their location, e.g. investing muscles (fascia musculorum) or viscera (fascia visceralis). (See Commentary 1.6). Loosely packed connective tissue surrounds peripheral nerves, blood and lymph vessels as they pass between other structures, often linking them together as neurovascular bundles. Some large vessels, e.g. the common carotid and femoral arteries, are invested by a dense connective tissue sheath that may be functionally significant, aiding venous return by approximating large veins to pulsating arteries.

Key references

Bochaton-Piallat M-L, Gabbiani G, Hinz B 2016 The myofibroblast in wound healing and fibrosis: Answered and unanswered questions. F1000Research 5:752.
This review summarizes current understanding of the origins of tissue myofibroblasts and their roles in wound healing and pathological fibrosis. It provides a comprehensive source of reference literature.

Fasshauer M, Blüher M 2015 Adipokines in health and disease. Trends in Pharmacol Sci 36:461–70.
This issue reviews adipose tissue function and the roles of secreted adipokines in obesity-related disease processes.

Kierszenbaum AL, Tres LL 2019 Histology and Cell Biology. An Introduction to Pathology, 5th ed. Elsevier.
An authoritative text on pathological aspects of connective tissues and many other topics covered in this chapter.

Pollard TD, Earnshaw WC, Lippincott-Schwartz J et al 2017 Cell Biology, 3rd ed. Philadelphia: Elsevier. Ch. 29, Extracellular matrix molecules
A comprehensive text on the molecular structures and functions of matrix molecules.

Robey PG 2017 Mesenchymal stem cells: fact or fiction, and implications in their therapeutic use. F1000Res 6:524.
A considered review of the nature of mesenchymal stem cells in mature connective tissues and their potential usefulness in regeneration therapies.

Wolf K, Friedl P 2011 Extracellular matrix determinants of proteolytic and non-proteolytic cell migration. Trends Cell Biol 21:736–44.
A review of cell migration through extracellular matrices in wound healing and pathological processes, using proteolytic and other mechanisms.

Yamanishi Y, Karasuyama H 2016 Introduction to basophils and mast cells in immunity and inflammation. Semin Immunopathol 38:535–7.
This introduces a number of reviews on aspects of the topic, published in subsequent articles in the issue.

References

Ankrum J, Karp JM 2010 Mesenchymal stem cell therapy: two steps forward, one step back. Trends Mol Med 16:203–9.

Asa SL, Mete O 2018 Endocrine pathology: past, present and future. Pathology 50:111–18.

Balachander N, Masthan KM, Babu NA et al 2015 Myoepithelial cells in pathology. J Pharm Bioallied Sci 7(Suppl 1):S190–S193.

Balsara ZR, Li X 2017 Sleeping beauty: awakening urothelium from its slumber. Am J Physiol Renal Physiol 312:F732–F743.

Bansil R, Turner BS 2018 The biology of mucus: composition, synthesis and organization. Adv Drug Deliv Rev 15:3–15.

Blanpain C, Horsley V, Fuchs E 2007 Epithelial stem cells: turning over new leaves. Cell 128:445–8.

Bochaton-Piallat M-L, Gabbiani G, Hinz B 2016 The myofibroblast in wound healing and fibrosis: answered and unanswered questions. F1000Research 5:752.

This review summarizes current understanding of the origins of tissue myofibroblasts and their roles in wound healing and pathological fibrosis. It provides a comprehensive source of reference literature.

Even-Ram S, Yamada KM 2005 Cell migration in 3D matrix. Curr Opin Cell Biol 17:524–32.

Fasshauer M, Blüher M 2015 Adipokines in health and disease. Trends Pharmacol Sci 36: 461–70.

This issue reviews adipose tissue function and the roles of secreted adipokines in obesity-related disease processes.

Foster MH 2016 Basement membranes and autoimmune diseases. Matrix Biol 57–58:149–168.

Gaide Chevronnay HP, Selvais C, Emonard H et al 2012 Regulation of matrix metalloproteinases activity studied in human endometrium as a paradigm of cyclic tissue breakdown and regeneration. Biochim Biophys Acta 1824:146–56.

Iozzo RV, Schaefer L 2015 Proteoglycan form and function: A comprehensive nomenclature of proteoglycans. Matrix Biol 42:11–55.

Jacquemet G, Humphries MJ, Caswell PT 2013 Role of adhesion receptor trafficking in 3D cell migration. Curr Opin Cell Biol 25:1–6.

Kendall RT, Feghali-Bostwick CA 2014 Fibroblasts in fibrosis: novel roles and mediators. Front Pharmacol 5:123.

Kierszenbaum AL, Tres LL 2019 Histology and Cell Biology. An Introduction to Pathology, 5th ed. Elsevier.

An authoritative text on pathological aspects of connective tissues and many other topics covered in this chapter.

Merrell AJ, Stanger BZ 2016 Adult cell plasticity in vivo: trans-differentiation is back in style. Nat Rev Mol Cell Biol 17:413-41.

Mott JD, Werb Z 2004 Regulation of matrix biology by matrix metalloproteinases. Curr Opin Cell Biol 16:558–564.

Mouw JK, Ou G, Weaver VM 2014 Extracellular matrix assembly: a multiscale deconstruction. Nat Rev Mol Cell Biol 15:771–85.

Pakshir P, Hinz B 2018 The big five in fibrosis: macrophages, myofibroblasts, matrix, mechanics, and miscommunication. Matrix Biol 68–69:81–93.

Pan X, Hobbs RP, Coulombe PA 2012 The expanding significance of keratin intermediate filaments in normal and diseased epithelia. Curr Opin Cell Biol 25:1–10.

Pollard TD, Earnshaw WC, Lippincott-Schwartz J et al 2017 Cell Biology, 3rd ed. Philadelphia: Elsevier. Ch. 29, Extracellular matrix molecules.

A comprehensive text on the molecular structures and functions of matrix molecules.

Robey PG 2017 Mesenchymal stem cells: fact or fiction, and implications in their therapeutic use. F1000Research 6:524.

A considered review of the nature of mesenchymal stem cells in mature connective tissues and their potential usefulness in regeneration therapies.

Rogers RS, Nishimune H 2017 The role of laminins in the organization and function of neuromuscular junctions. Matrix Biol 57–58: 86–105.

Rui L 2017 Brown and beige adipose tissues in health and disease. Compr Physiol 7:1281–306.

Savige J, Colville D, Rheault M et al 2016 Alport syndrome in women and girls. Clin J Am Soc Nephrol 11:1713–20.

Stoeckelhuber M, Schubert C, Kesting MR et al 2011 Human axillary apocrine glands: proteins involved in the apocrine secretory mechanism. Histol Histopathol 26:177–84.

Wang W, Seale P 2016 Control of brown and beige fat development. Nat Rev Mol Cell Biol 17:691–702.

Wolf K, Friedl P 2011 Extracellular matrix determinants of proteolytic and non-proteolytic cell migration. Trends Cell Biol 21:736–44.

A review of cell migration through extracellular matrices in wound healing and pathological processes, using proteolytic and other mechanisms.

Wu J, Bostro P, Sparks LM et al 2012 Beige adipocytes are a distinct type of thermogenic fat cell in mouse and human. Cell 150:366–76.

Yamanishi Y, Karasuyama H 2016 Introduction to basophils and mast cells in immunity and inflammation. Semin Immunopathol 38:535–37.

This introduces a number of reviews on aspects of the topic, published in subsequent articles in the issue.

CHAPTER

3

Nervous system

The nervous system has two major divisions, the central nervous system (CNS) and the peripheral nervous system (PNS). The CNS consists of the brain, spinal cord, optic nerve and retina, and contains the majority of neuronal cell bodies. The PNS includes all nervous tissue outside the CNS and consists of the cranial and spinal nerves, the peripheral autonomic nervous system (ANS) and the special senses (taste, olfaction, vision, hearing and balance). It is composed mainly of the axons of sensory and motor neurones that pass between the CNS and the body. The ANS is subdivided into sympathetic and parasympathetic components. It consists of neurones that innervate secretory glands and cardiac and smooth muscle, and is concerned primarily with control of the internal environment. Neurones in the wall of the gastrointestinal tract form the enteric nervous system (ENS) and are capable of sustaining local reflex activity that is independent of the CNS. The ENS contains as many intrinsic neurones in its ganglia as the entire spinal cord and is often considered as a third division of the nervous system (Gershon 1998).

In the CNS, the cell bodies of neurones are often grouped together in discrete areas termed nuclei, or they may form more extensive layers or masses of cells; collectively they constitute the grey matter. Neuronal dendrites and synaptic contacts are mostly confined to areas of grey matter and form part of its meshwork of neuronal and glial processes, termed the neuropil. Their axons join bundles of nerve fibres that tend to be grouped separately to form tracts. In the spinal cord, cerebellum, cerebral cortices and some other areas, concentrations of tracts constitute the white matter, so called because the axons are often ensheathed in lipid-rich sheaths of myelin, which is white when fresh (**Fig. 3.1**).

The PNS is composed of the efferent axons (fibres) of motor neurones situated inside the CNS, and the cell bodies of sensory neurones (grouped together as ganglia) and their afferent processes. Sensory cells in dorsal root ganglia give off both centrally and peripherally directed processes; there are no synapses on their cell bodies. Also included are ganglionic neurones of the ANS, which receive synaptic contacts from the peripheral fibres of preganglionic autonomic neurones whose cell bodies lie within the CNS.

When the neural tube is formed during prenatal development (Sanes et al 2011), its walls thicken greatly but do not completely obliterate the cavity within. The latter remains in the spinal cord as the narrow central canal and becomes greatly expanded in the brain to form a series of interconnected cavities called the ventricular system. In the fore- and hindbrains, parts of the neural tube roof do not generate neurones but become thin, folded sheets of secretory tissue, which are invaded by blood vessels and are called the choroid plexuses. The latter secrete cerebrospinal fluid (CSF), which fills the ventricles and subarachnoid spaces, and penetrates the intercellular spaces of the brain and spinal cord to create their interstitial fluid. The CNS has a rich blood supply, which is essential to sustain its high metabolic rate. The blood–brain barrier places considerable restrictions on the substances that are able to diffuse from the blood stream into the neuropil.

Neurones encode information, conduct it over considerable distances, and then transmit it to other neurones or to various non-neural targets such as muscle cells. The propagation of this information within the nervous system depends on rapid electrical signals, the action potentials. Transmission to other cells is mediated by secretion of neurotransmitters at special junctions, either with other neurones (synapses), or with cells outside the nervous system, e.g. muscle cells at neuromuscular junctions, gland cells or adipose tissue, and causes changes in the behaviour of the target cells.

The nervous system contains large populations of non-neuronal cells, termed neuroglia or glia. These cells do not generate action potentials, but convey information encoded as transient changes in intracellular calcium concentration, termed calcium signalling. Glia interact with neurones in many different ways; their two-way communication is essential for normal brain activity.

It was thought for many years that glia outnumbered neurones by 10 times in the CNS, but studies using the isotropic fractionator method challenged that popular view, suggesting instead that the two cell populations are rather similar in size (Azevedo et al 2009). That said, the glia : neurone ratio has been reported to be as high as 17 : 1 in the thalamus (Pakkenberg and Gundersen 1988).

The glial population in the CNS consists of microglia and macroglia; the latter are subdivided into oligodendrocytes and astrocytes. The principal glial cell in the PNS is the Schwann cell. Satellite cells surround each neuronal soma in ganglia.

NEURONES

Most of the neurones in the CNS are either clustered into nuclei, columns or layers, or dispersed within grey matter. Neurones in the PNS are confined to ganglia. Irrespective of location, neurones share many general features, which are discussed here in the context of central neurones. Special characteristics of ganglionic neurones and their adjacent tissues are discussed on p. 60.

Neurones exhibit great variability in their size (cell bodies range from 5 to 100 μm diameter) and shape (Spruston 2008). Their surface areas are extensive because most neurones display numerous branched cell processes. They usually have a rounded or polygonal cell body (perikaryon or soma). This is a central mass of cytoplasm that encloses a nucleus and gives off long, branched extensions with which most intercellular contacts are made. Typically, one of these processes, the axon, is much longer than the others, the dendrites (**Fig. 3.2**). Generally, dendrites conduct electrical signals towards a soma and axons conduct impulses away from it.

Neurones can be classified according to the number and arrangement of their processes (Bota and Swanson 2007). Multipolar neurones (**Fig. 3.3**) are common; they have an extensive dendritic tree that arises either from a single primary dendrite or directly from the soma, and a single axon. Bipolar neurones, which typify neurones of the special sensory systems, have only a single dendrite that emerges from the soma

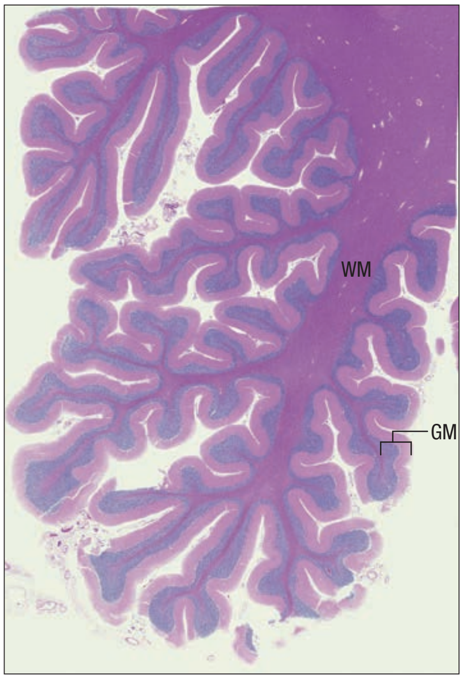

Fig. 3.1 A section through the human cerebellum stained to show the arrangement of the central white matter (WM, deep pink) and the highly folded outer grey matter (GM). In the cerebellum, GM consists of an inner granular layer of tightly packed small neurones (blue) and an outermost molecular layer (pale pink) where neuronal processes make synaptic contacts. (Courtesy of Mr Peter Helliwell and the late Dr Joseph Mathew, Department of Histopathology, Royal Cornwall Hospitals Trust, UK.)

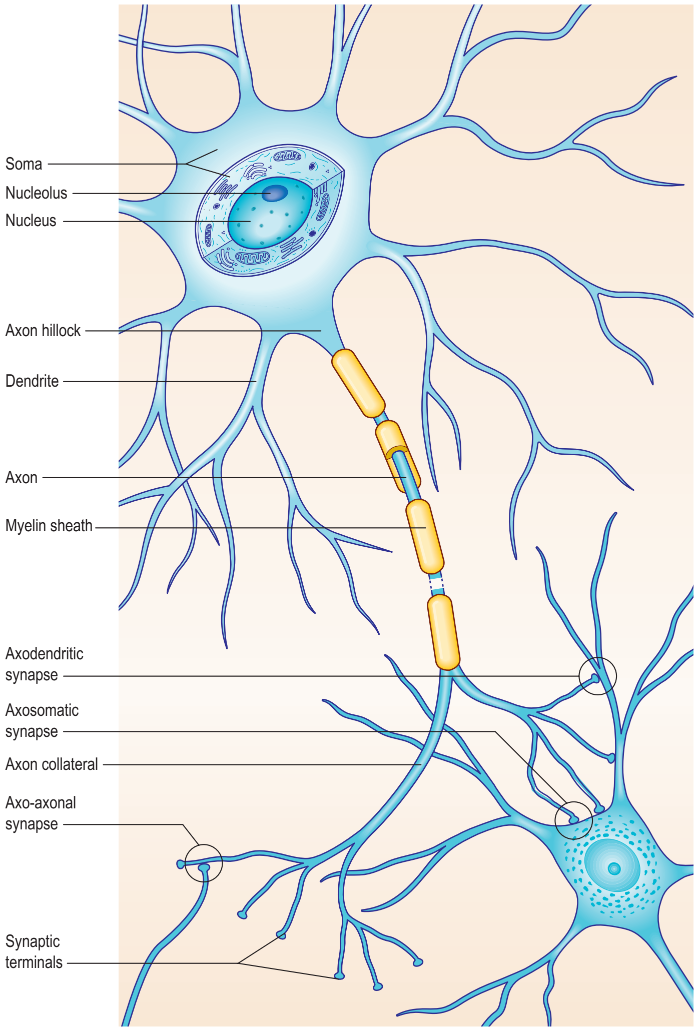

Fig. 3.2 A schematic view of typical neurones featuring one with the soma cut away to show the nucleus and cytoplasmic organelles, dendritic trees with synaptic contacts, other types of synapse, the axon hillock and a myelinated axon.

opposite the axonal pole. Unipolar neurones, which transmit general sensation, e.g. dorsal root ganglion neurones, have a single short process that bifurcates into a peripheral and a central process. This arrangement arises by the fusion of the proximal axonal and dendritic processes of a bipolar neurone during development, and so such neurones can also be termed pseudounipolar. Neurones may also be classified according to whether their axons terminate locally on other neurones (interneurones), or transmit impulses over long distances, often to distinct territories via defined tracts (projection neurones).

Neurones are postmitotic cells and, with few exceptions, they are not replaced when lost.

Soma

The plasma membrane of the soma is generally unmyelinated and is contacted by both inhibitory and excitatory axosomatic synapses; very occasionally, somasomatic and dendrosomatic contacts may be made. The non-synaptic surface may contain gap junctions and is partly covered by either astrocytic or satellite oligodendrocyte processes.

The cytoplasm of a typical soma (see Fig. 3.2) is rich in rough and smooth endoplasmic reticulum and free polyribosomes, indicating a high level of protein synthetic activity. Free polyribosomes often congregate in large groups associated with the rough endoplasmic reticulum. These aggregates of RNA-rich structures are visible by light microscopy as basophilic Nissl bodies or granules. They are distributed throughout the cell body and large dendrites; the axon hillock is conspicuously ribosome-free. Nissl bodies are more obvious in large, highly active cells, such as spinal motor neurones (**Fig. 3.4**), which contain large stacks of rough endoplasmic reticulum and polyribosome aggregates. Maintenance and turnover of cytoplasmic and membranous components are necessary activities in all cells; the huge total volume of cytoplasm within the soma and processes of many neurones requires a considerable commitment of protein synthetic machinery. Neurones also synthesize other proteins (enzyme systems, G-protein coupled receptors, scaffold proteins) involved in the production of neurotransmitters and in the reception and transduction of incoming stimuli. Various transmembrane channel proteins and enzymes are located at the surfaces of neurones, where they are associated with movements of ions.

The nucleus is characteristically large and euchromatic, and contains at least one prominent nucleolus; these are features typical of all cells engaged in substantial levels of protein synthesis. The cytoplasm contains many mitochondria and moderate numbers of lysosomes. Golgi complexes are usually close to the nucleus, near the bases of the main dendrites and opposite the axon hillock.

The neuronal cytoskeleton is a prominent feature of its cytoplasm and gives shape, strength and support to the dendrites and axons. A number of neurodegenerative diseases are characterized by abnormal aggregates of cytoskeletal proteins (reviewed in Cairns et al (2004)). Neurofilaments (the intermediate filaments of neurones) and microtubules are abundant in the soma and along dendrites and axons; the proportions vary with the type of neurone and cell process. Bundles of neurofilaments constitute neurofibrils, which can be seen by light microscopy in silver-stained or immunolabelled sections. Neurofilaments are heteropolymers of proteins assembled from three polypeptide subunits, NF-L (68 kDa), NF-M (160 kDa) and NF-H (200 kDa). NF-M and NF-H have long C-terminal domains that project as side arms from the assembled neurofilament and bind to neighbouring filaments. They can be heavily phosphorylated, particularly in the highly stable neurofilaments of mature axons, and are thought to give axons their tensile strength. Some axons are almost filled by neurofilaments.

Microtubules are important in axonal transport, although dendrites usually have more microtubules than axons. Centrioles persist in mature postmitotic neurones, where they are concerned with the generation of microtubules rather than cell division. Centrioles are associated with cilia on the surfaces of developing neuroblasts. Their significance, other than at some sensory endings (e.g. the olfactory mucosa), is unclear but recent experimental evidence suggests a complex signalling function (Guemez-Gamboa et al 2014).

Pigment granules (**Fig. 3.5**) appear in certain regions, e.g. neurones of the substantia nigra contain neuromelanin, which is probably a waste product of catecholamine synthesis. A similar pigment gives a bluish colour to the neurones in the locus coeruleus. Some neurones are unusually rich in metals, which may form components of enzyme systems, e.g. zinc in the hippocampus and iron in the red nucleus. Ageing neurones, especially in spinal ganglia, accumulate granules of lipofuscin (senility pigment) in residual bodies, which are lysosomes packed with partially degraded lipoprotein material.

Dendrites

Dendrites are highly branched, usually short processes that project from the soma (Shah et al 2010). The branching patterns of many dendritic arrays are probably established by random adhesive interactions between dendritic growth cones and afferent axons that occur during development. There is an overproduction of dendrites in early development, and this is pruned in response to functional demand as the nervous system matures and information is processed through the dendritic tree. There is evidence that dendritic trees may be plastic structures throughout adult life, expanding and contracting as the traffic of synaptic activity varies through afferent axodendritic contacts (see Wong and Ghosh (2002)). Groups of neurones with similar functions have a similar stereotypic tree structure (**Fig. 3.6**), suggesting that the branching patterns of dendrites are important determinants of the integration of the afferent inputs that converge on the tree (see Kulkarni and Firestein (2012)).

Dendrites differ from axons in many respects. They represent the afferent rather than the efferent system of the neurone, and receive both excitatory and inhibitory axodendritic contacts. They may also make dendrodendritic and dendrosomatic connections (see Fig. 3.9), some of which are reciprocal. Synapses occur either on small projections called dendritic spines or on the smooth dendritic surface. Dendrites contain ribosomes, smooth endoplasmic reticulum, microtubules, neurofilaments, actin filaments and Golgi complexes. Their neurofilament proteins are poorly phosphorylated and their microtubules are interconnected by the microtubule-associated protein (MAP)-2 almost exclusively in comparison with axons.

The shapes of dendritic spines range from simple protrusions to structures with a slender stalk and expanded distal end. Most spines are not more than 2 μm long, and have one or more terminal expansions; they can also be short and stubby, branched or bulbous. Large mushroom spines are assumed to have differentiated in response to afferent activity

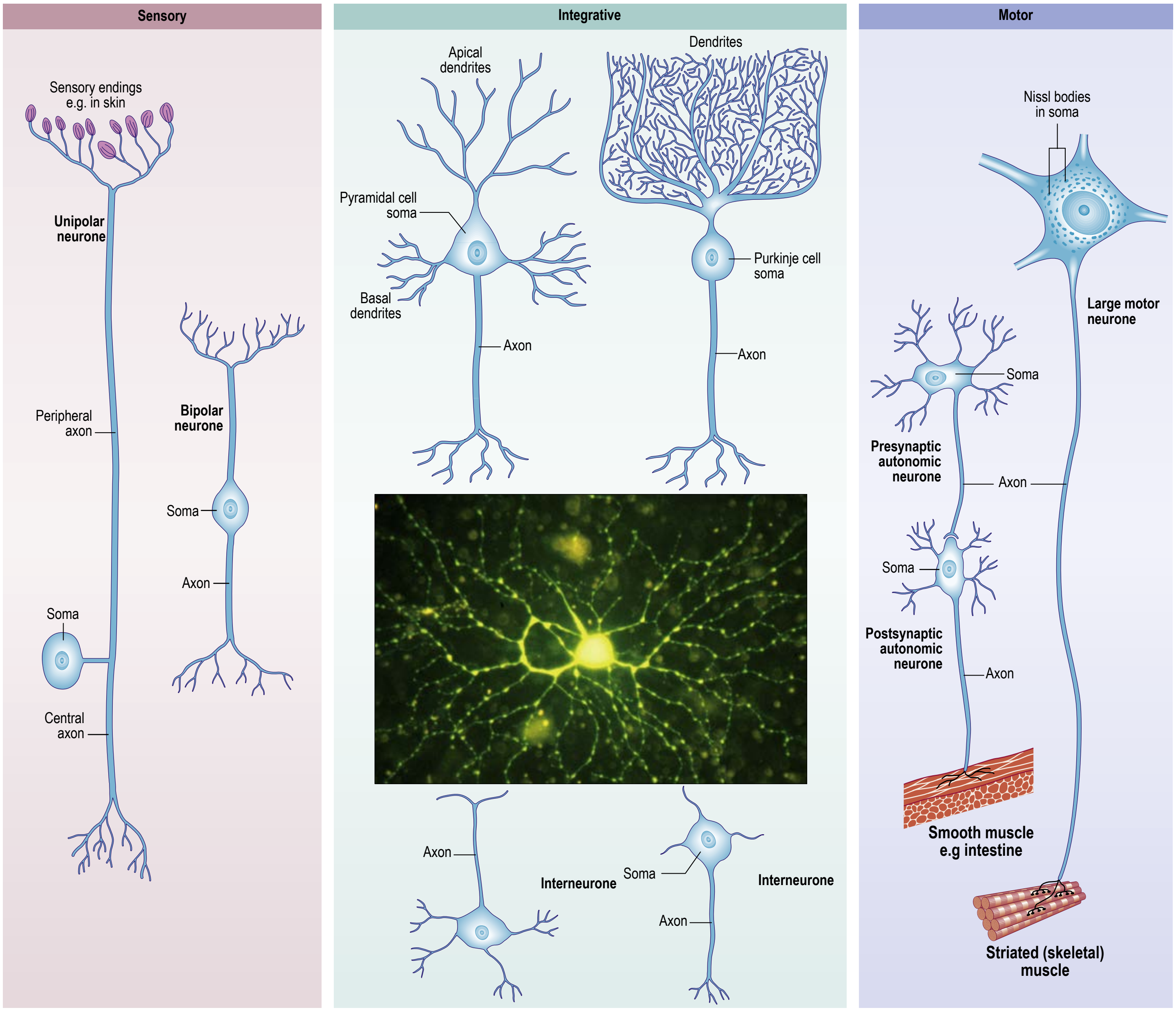
Sensory
Integrative
Motor
Sensory endings e.g. in skin
Unipolar neurone
Peripheral axon
Soma
Central axon
Bipolar neurone
Soma
Axon
Apical dendrites
Pyramidal cell soma
Basal dendrites
Axon
Dendrites
Purkinje cell soma
Axon
Axon
Interneurone
Soma
Interneurone
Axon
Nissl bodies in soma
Large motor neurone
Soma
Presynaptic autonomic neurone
Axon
Soma
Postsynaptic autonomic neurone
Axon
Smooth muscle e.g intestine
Striated (skeletal) muscle

Fig. 3.3 The variety of shapes of neurones and their processes. The inset shows a human multipolar retinal ganglion cell, filled with fluorescent dye by microinjection. (Inset, Courtesy of Drs Richard Wingate, James Morgan and Ian Thompson, King's College, London.)

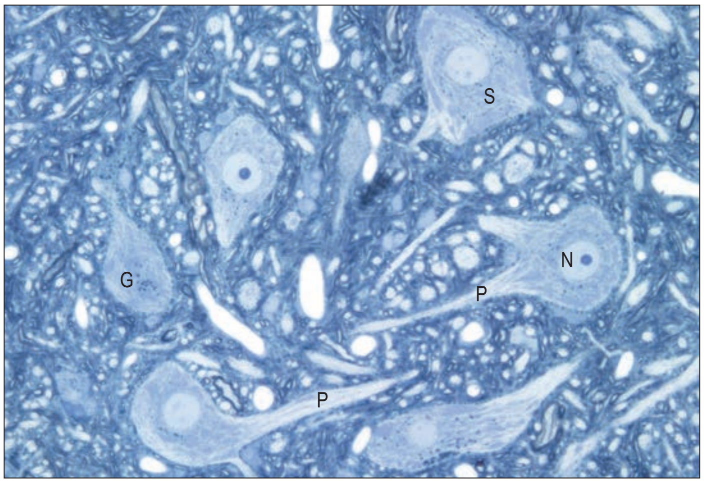

Fig. 3.4 Spinal motor neurones (toluidine blue stained resin section, rat tissue) showing a group of cell bodies (somata, S), some with the proximal parts of axonal and dendritic processes (P) visible. Their nuclei (N) typically have prominent, deeply staining nucleoli, indicative of metabolically highly active cells; two are visible in the plane of section. Nissl granules (G) are seen in the cytoplasm. Surrounding the neuronal somata is the neuropil, consisting of the interwoven processes of these and other neurones and of glial cells.

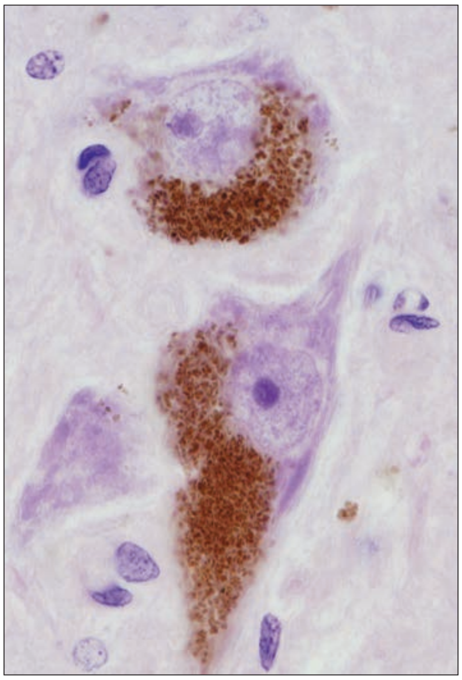

Fig. 3.5 Neurones in the substantia nigra of the human midbrain, showing cytoplasmic granules of neuromelanin pigment. (Courtesy of Mr Peter Helliwell and the late Dr Joseph Mathew, Department of Histopathology, Royal Cornwall Hospitals Trust, UK.)

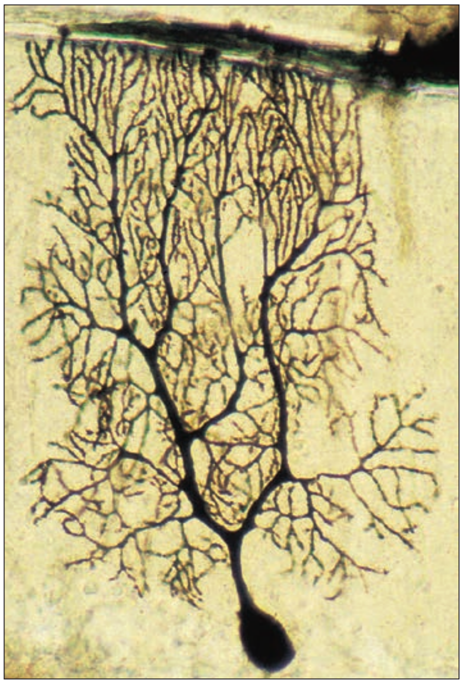

Fig. 3.6 A Purkinje neurone from the cerebellum of a rat stained by the Golgi–Cox method, showing the extensive two-dimensional array of dendrites. (Courtesy of Dr Martin Sadler and Professor M Berry, Division of Anatomy and Cell Biology, GKT School of Medicine, London.)

('memory spines'; Matsuzaki et al 2004). These large spines often contain a spine apparatus, an organelle consisting of small sacs of endoplasmic reticulum interleaved by electron-dense bars (Gray 1959, Segal et al 2010). Mouse mutants deficient in these organelles show memory deficits (Deller et al 2003). Free ribosomes and polyribosomes are concentrated at the base of the spine. Ribosomal accumulations near synaptic sites provide a mechanism for activity-dependent synaptic plasticity through the local regulation of protein synthesis (see Petralia et al 2016).

Axons

The axon originates either from the soma or from the proximal segment of a dendrite at a specialized region free of Nissl granules, the axon hillock. Action potentials are initiated here, at the junction with the proximal axon (axon initial segment) (Lörincz and Nusser 2010). The axonal plasma membrane (axolemma) is undercoated at the hillock by a concentration of cytoskeletal molecules, including spectrin and actin fibrils, which are important in anchoring numerous voltage-sensitive channels to the membrane (see Bender and Trussell (2012)). The axon hillock is unmyelinated and often participates in inhibitory axo-axonal synapses. It is unique because it contains ribosomal aggregates immediately below the postsynaptic membrane (Kole and Stuart 2012).

In the CNS, small, unmyelinated axons lie free in the neuropil, whereas in the PNS they are embedded in Schwann cell cytoplasm. Myelin, which is formed around almost all axons of >2 μm diameter by oligodendrocytes in the CNS and by Schwann cells in the PNS, begins at the distal end of the axon hillock. Nodes of Ranvier are specialized regions of myelin-free axon where action potentials are generated and where an axon may branch. In both CNS and PNS, the territory of a myelinated axon between adjacent nodes is called an internode; the region close to a node, where the myelin sheath terminates, is called the paranode; and the region just beyond that is the juxtaparanode. Myelin thickness and internodal lengths are, in general, positively correlated with axon diameter. The density of sodium channels in the axolemma is highest at nodes of Ranvier, and very low along internodal membranes; sodium channels are spread more evenly within the axolemma of unmelinated axons. Fast potassium chanels are present in the paranodal regions of myelinated axons. Fine processes of glial cytoplasm (astrocytic in the CNS, Schwann cell in the PNS) surround the nodal axolemma.

The terminals of an axon are unmyelinated. Most expand into presynaptic boutons, which may form connections with axons, dendrites, neuronal somata or, in the periphery, muscle fibres, glands and lymphoid tissue. Exceptions include the free afferent sensory endings in, for example, the epidermis, which are unspecialized structurally, and the peripheral terminals of afferent sensory fibres with encapsulated endings (see Fig. 3.29). Axon terminals contain abundant small clear synaptic vesicles and large dense-core vesicles. The former contain a neurotransmitter (e.g. glutamate, γ-aminobutyric acid (GABA), acetylcholine) that is released into the synaptic cleft on the arrival of an action potential at the terminal and which then binds to cognate receptors on the postsynaptic membrane. Depending on the nature of the transmitter and its receptors, the postsynaptic neurone will become excited or inhibited. The dense-core vesicles contain neuropeptides, including brain-derived neurotrophic factor (BDNF; Dieni et al 2012). Axon terminals may themselves be contacted by other axons, forming axo-axonal presynaptic inhibitory circuits (Veres et al 2014, Burke et al 2017).

Axons contain microtubules, neurofilaments, mitochondria, membrane vesicles, cisternae and lysosomes. They do not usually contain ribosomes or Golgi complexes, other than at the axon hillock; exceptionally, the neurosecretory fibres of hypothalamo-hypophysial neurones contain the mRNA of neuropeptides. Organelles are differentially distributed along axons, e.g. there is a greater density of mitochondria and membrane vesicles in the axon hillock, at nodes and in presynaptic endings. Axonal microtubules are interconnected by cross-linking MAPs, of which tau is the most abundant. Microtubules have an intrinsic polarity, and in axons all microtubules are uniformly orientated with their rapidly growing ends directed away from the soma towards the axon terminal. The microtubule binding protein tau plays an important role in Alzheimer's disease (Cairns et al 2004; Iqbal et al 2010): formation of tau oligomers and the subsequent pathological filament arrays are critical steps in the aetiopathogenesis of this condition. Neurofilament proteins ranging from high to low molecular weights are highly phosphorylated in mature axons, whereas growing and regenerating axons express a calmodulin-binding membrane-associated phosphoprotein, growth-associated protein-43 (GAP-43), as well as poorly phosphorylated neurofilaments. In dendrites, microtubules are the major cytoskeletal element, forming microtubule fascicles associated with filamentous MAPs such as MAP2 and MAP1B (Hirokawa 1994).

Neurones respond differently to injury, depending on whether the damage occurs in the CNS or the PNS. The glial microenvironment of a damaged central axon does not facilitate axonal regrowth; consequently, reconnection with original synaptic targets does not normally occur. In marked contrast, the glial microenvironment in the PNS is capable of facilitating axonal regrowth. However, functional outcome of clinical repair of a large mixed peripheral nerve, especially if the injury occurs some distance from the target organ, or produces a long defect in the damaged nerve, is frequently unsatisfactory (Birch 2011; see Commentary 1.5).

Axoplasmic flow

Neuronal organelles and cytoplasm are in continual motion. Bidirectional streaming of vesicles along axons results in a net transport of materials from the soma to the terminals, with more limited movement in the opposite direction. Two major types of transport occur, slow and relatively fast. Slow axonal transport is a bulk flow of axoplasm only in the anterograde direction, carrying cytoskeletal proteins and soluble, non-membrane-bound proteins from the soma to the terminals at a rate of approximately 0.1–3 mm a day. In contrast, fast axonal transport carries membrane-bound vesicular material (endosomes and lysosomal autophagic vacuoles) and mitochondria at approximately 200 mm a day in the retrograde direction (towards the soma) and approximately 40 mm per day anterogradely (in particular, precursors of synaptic vesicles and plasma membranes).

Rapid flow depends on microtubules. Vesicles with side projections line up along microtubules and are transported along them by molecular motors. Two microtubule-based motor proteins with adenosine 5′-triphosphatase (ATPase) activity are involved in fast transport: kinesin family proteins (KIFs) are responsible for the fast component of anterograde transport, and cytoplasmic dynein is responsible for retrograde transport (**Fig. 3.7**). Anterograde transport conveys synaptic vesicle precursors, vesicles containing neurotrophic factor receptors and mitochondria. Retrograde transport mediates the movement of neurotropic viruses. Specific pools of endocytic organelles, signalling endosomes, mediate the long-distance axonal transport of growth factors, such as neurotrophins and their signalling receptors. In dendrites, vesicles including transmitter receptors such as *N*-methyl-D-aspartate (NMDA) and α-amino-3-hydroxy-5-methyl-4-isoxazolepropionic acid (AMPA) receptors, mRNAs and mitochondria are transported along microtubules. Defects in axonal and dendritic transport have been linked to various neurodegenerative processes. (See Hirokawa et al (2010), Hinckelmann et al (2013) and Schmieg et al (2014) for reviews of axonal transport in health and disease.)

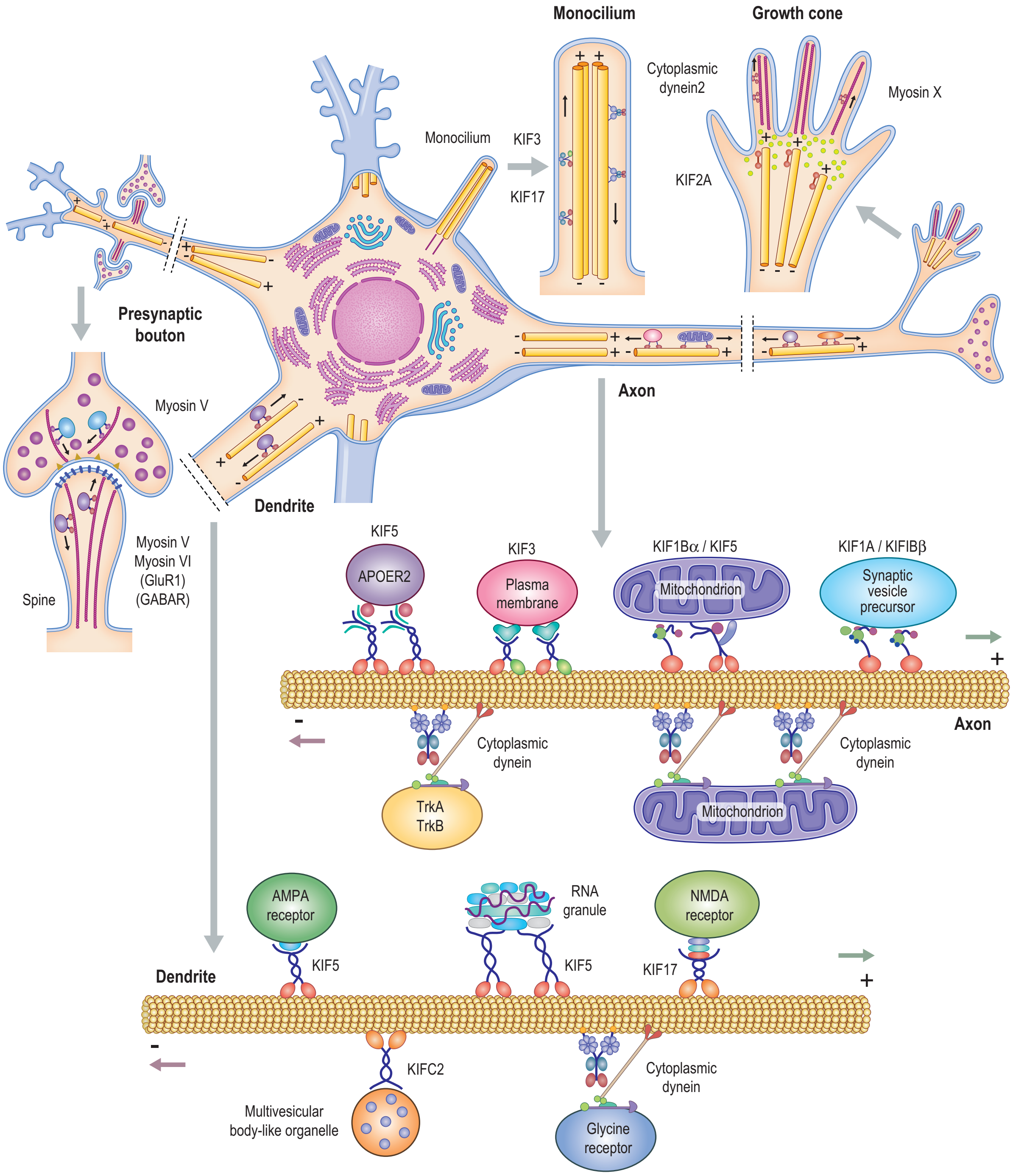
Monocilium
Growth cone
Cytoplasmic dynein2
Myosin X
Monocilium
KIF3
KIF17
KIF2A
Presynaptic bouton
Myosin V
Axon
Dendrite
Myosin V
Myosin VI
(GluR1)
(GABAR)
Spine
KIF5
APOER2
KIF3
Plasma membrane
KIF1Bα / KIF5
Mitochondrion
KIF1A / KIFIBβ
Synaptic vesicle precursor
+
-
Axon
Cytoplasmic dynein
TrkA
TrkB
Mitochondrion
Cytoplasmic dynein
AMPA receptor
RNA granule
NMDA receptor
KIF5
KIF5
KIF17
Dendrite
+
-
KIFC2
Multivesicular body-like organelle
Cytoplasmic dynein
Glycine receptor

Fig. 3.7 Intracellular transport in neurones. Various kinesin family proteins (KIFs) transport membranous organelles anterogradely in axons and dendrites, whereas cytoplasmic dynein 1 and KIFC2 transport retrograde cargoes. In neuronal cilia, anterograde transport is performed by KIF3 and KIF17, while retrograde transport is performed by cytoplasmic dynein 2. In short-range transport, such as transport in pre- and post-synapses and growth cone filopodia, the myosin family proteins function as the molecular motors. APOER2, apolipoprotein E receptor2; GluR1, glutamate receptor1; GABAR, GABA receptor. For further details, see text and source reference. (Adapted with permission from Hirokawa N, Noda Y, Tanaka Y et al 2009 Kinesin superfamily motor proteins and intracellular transport. Nature Rev Mol Cell Biol 10:682–96.)

Intraflagellar transport (IFT)

Almost all vertebrate cell types, including neurones, have primary cilia that emanate from the cell surface. They lack motility and have critical functions in sensing the extracellular environment and in coordinating signalling pathways in brain development. Primary ciliary axonemes contain nine doublet microtubules (9+0 configuration). Protein complexes and membrane organelles are bidirectionally conveyed on axonemes by intraflagellar transport (IFT). Molecular motor proteins KIF3 and KIF17 and cytoplasmic dynein have functions in IFT (see Fig. 3.7).

Synapses

Transmission of impulses across specialized junctions (synapses) between two neurones is largely chemical and depends on the release of neurotransmitters from the presynaptic terminal. These neurotransmitters bind to cognate receptors in the postsynaptic neuronal membrane, resulting in a change of membrane conductance and leading to either a depolarization or a hyperpolarization (Ryan and Grant 2009).

The patterns of axonal termination vary considerably. A single axon may synapse with one neurone (e.g. climbing fibres ending on cerebellar Purkinje neurones), or more often with many neurones (e.g. cerebellar parallel fibres, which provide an extreme example of this phenomenon). In synaptic glomeruli (e.g. in the olfactory bulb), groups of synapses between two or many neurones form interactive units encapsulated by neuroglia (**Fig. 3.8**; Perea et al 2009).

Electrical synapses (direct communication via gap junctions) are rare in the human CNS and are confined largely to groups of neurones with tightly coupled activity, e.g. the inspiratory centre in the medulla. They will not be discussed further here.

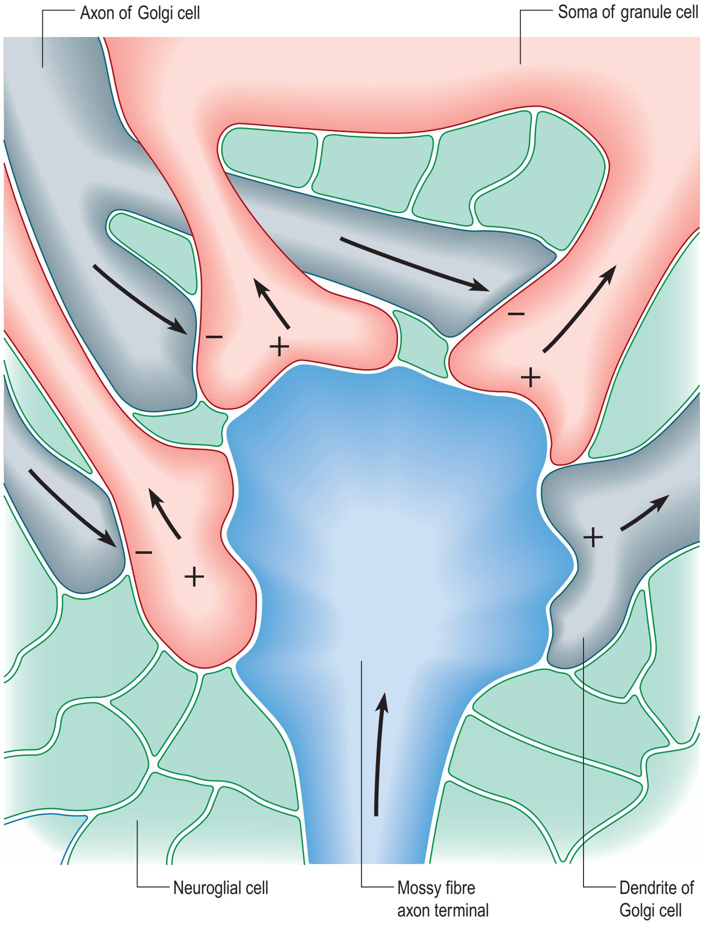

Fig. 3.8 The arrangement of a complex synaptic unit. A cerebellar synaptic glomerulus with excitatory ('+') and inhibitory ('–') synapses grouped around a central axonal bouton. The directions of transmission are shown by the arrows.

Classification of chemical synapses

Chemical synapses have an asymmetric structural organization in keeping with the unidirectional nature of their transmission (**Figs 3.9–3.10**) (Pereda 2014). Typical chemical synapses share a number of important features. They all display an area containing a presynaptic density apposed to a corresponding postsynaptic density; the two are separated by a narrow (20–30 nm) gap, the synaptic cleft. Synaptic vesicles containing the appropriate neurotransmitter are found on the presynaptic side, clustered near the presynaptic density at the presynaptic membrane. Together these define the active zone, the area of the synapse where neurotransmission takes place (Gray 1959, Eggermann et al 2012).

Chemical synapses can be classified according to a number of different parameters, including the neuronal regions forming the synapse, their ultrastructural characteristics, the chemical nature of their neurotransmitter(s) and their effects on the electrical state of the postsynaptic neurone. The following classification is limited to associations between neurones. Neuromuscular junctions share many (though not all) of these parameters, and are often referred to as peripheral synapses. They are described separately on p. 66.

Synapses can occur between almost any surface regions of the participating neurones. The most common type occurs between an axon and either a dendrite or a soma, when the axon is expanded as a small bulb or bouton (see Figs 3.9–3.10). This may be a terminal of an axonal branch (terminal bouton) or one of a row of bead-like endings, when the axon makes contact at several points, often with more than one neurone (bouton de passage). Boutons may synapse with dendrites, including thorny protrusions named dendritic spines (**Fig. 3.11**) or the flat surface of a dendritic shaft; a soma (usually on its flat surface, but occasionally on spines); the axon hillock; and the terminal boutons of other axons.

The connection is classified according to the direction of transmission, and the incoming terminal region is named first. Most common are axodendritic synapses, although axosomatic connections are frequent. All other possible combinations are found but are less common, i.e. axo-axonal, dendro-axonal, dendrodendritic, somatodendritic or somatosomatic. Axodendritic and axosomatic synapses occur in all regions of the CNS and in autonomic ganglia, including those of the ENS. The other types appear restricted to regions of complex interaction between larger sensory neurones and microneurones, e.g. in the thalamus.

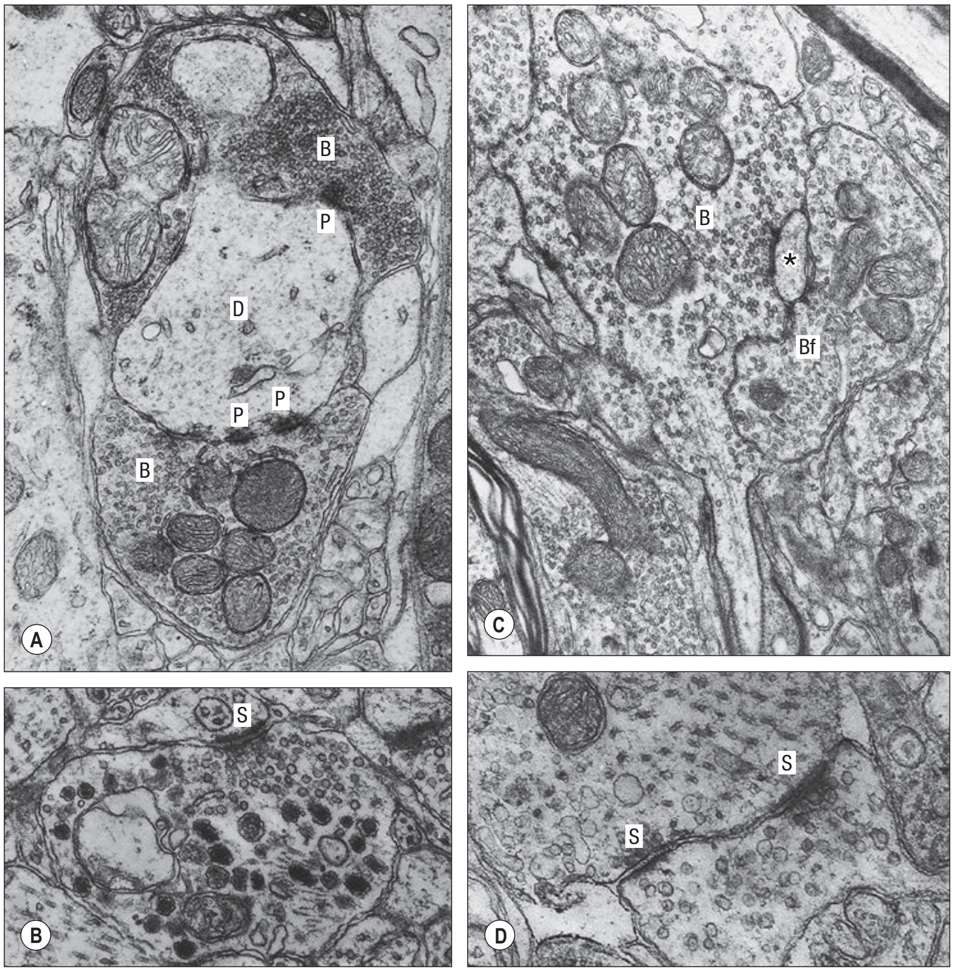

Fig. 3.9 Electron micrographs demonstrating various types of synapse. **A**, A cross-section of a dendrite (D) on which two synaptic boutons (B) end. The upper bouton contains round vesicles, and the lower bouton contains flattened vesicles of the small type. A number of pre- and postsynaptic (P) thickenings mark the specialized zones of contact. **B**, A type I synapse (S, postsynaptic site) containing both small, round, clear vesicles and also large, dense-cored vesicles of the neurosecretory type. **C**, A large terminal bouton (B) of an optic nerve afferent fibre, which is making contact with a number of postsynaptic processes, in the dorsal lateral geniculate nucleus of the rat. One of the postsynaptic processes (*) also receives a synaptic contact from a bouton (Bf) containing flattened vesicles. **D**, Reciprocal synapses (S) between two neuronal processes in the olfactory bulb. (Courtesy of Professor AR Lieberman, Department of Anatomy, University College, London.)

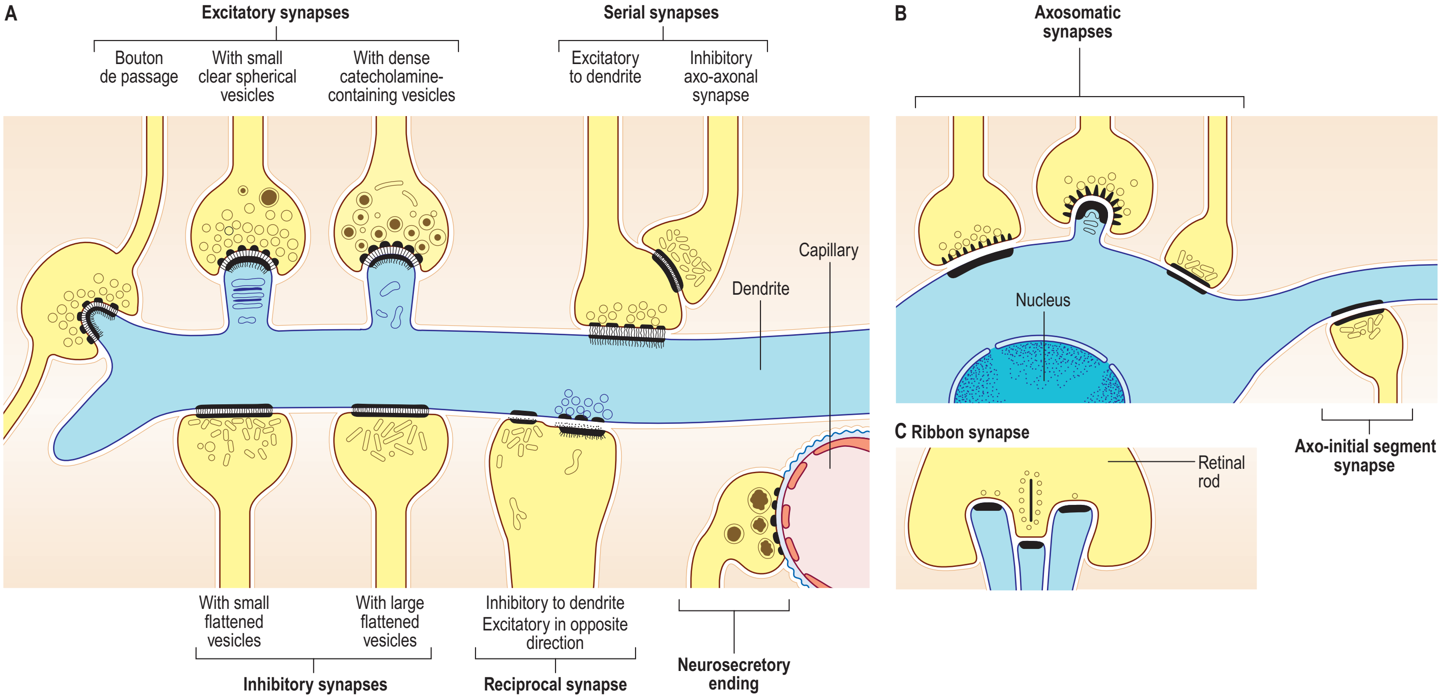
A
Excitatory synapses
Bouton de passage
With small clear spherical vesicles
With dense catecholamine-containing vesicles
Serial synapses
Excitatory to dendrite
Inhibitory axo-axonal synapse
Capillary
Dendrite
With small flattened vesicles
With large flattened vesicles
Inhibitory synapses
Inhibitory to dendrite
Excitatory in opposite direction
Reciprocal synapse
Neurosecretory ending
B
Axosomatic synapses
Nucleus
Axo-initial segment synapse
C Ribbon synapse
Retinal rod

Fig. 3.10 The structural arrangements of different types of synaptic contact.

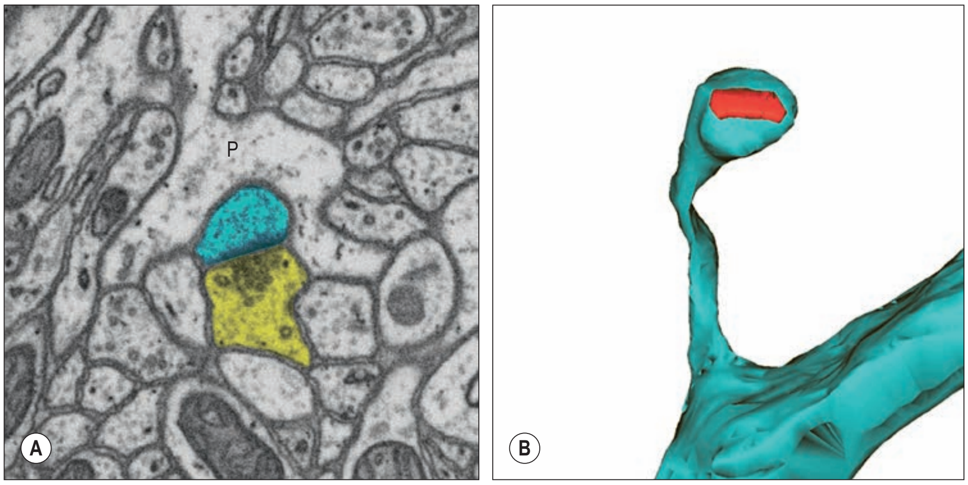

Fig. 3.11 An electron micrograph of a spine synapse in mouse cerebral cortex and its three-dimensional reconstruction. **A**, Cross-section of a presynaptic bouton (yellow) and a dendritic spine (cyan). The presynaptic bouton is in contact with an astrocytic process (P). **B**, Reconstructed image of a dendritic spine (cyan) and the postsynaptic density (red) within the spine head. (Adapted with permission from Hirokawa N, Noda Y, Tanaka Y et al 2009 Kinesin superfamily motor proteins and intracellular transport. Nature Rev Mol Cell Biol 10:682–96.)

Ultrastructurally, synaptic vesicles may be internally clear or dense, and of different size (loosely categorized as small or large) and shape (round, flat or pleomorphic, i.e. irregularly shaped). The submembranous densities may be thicker on the postsynaptic than on the presynaptic side (asymmetric synapses), or equivalent in thickness (symmetric synapses), and can be perforated or non-perforated. Synaptic ribbons are found at sites of neurotransmission in the retina and inner ear. They have a distinctive morphology, in that the synaptic vesicles are grouped around a ribbon- or rod-like density orientated perpendicular to the cell membrane (see Fig. 3.10).

Synaptic boutons make obvious close contacts with postsynaptic structures but many other terminals lack specialized contact zones. Areas of transmitter release occur in the varicosities of unmyelinated axons, where effects are sometimes diffuse, e.g. the aminergic pathways of the basal ganglia, and in autonomic fibres in the periphery. In some instances, such axons may ramify widely throughout extensive areas of the brain and affect the behaviour of very large populations of neurones, e.g. the diffuse cholinergic innervation of the cerebral cortices. Pathological degeneration of these pathways can therefore cause widespread disturbances in neural function.

Neurones express a variety of neurotransmitters, either as one class of neurotransmitter per cell or more often as several. Good correlations exist between some types of transmitter and specialized structural features of synapses. In general, asymmetric synapses with relatively small spherical vesicles are associated with acetylcholine (ACh), glutamate, serotonin (5-hydroxytryptamine, 5-HT) and some amines; those with dense-core vesicles include many peptidergic synapses and other amines (e.g. noradrenaline (norepinephrine), adrenaline (epinephrine), dopamine). Symmetric synapses with flattened or pleomorphic vesicles have been shown to contain either GABA or glycine. Flattening of synaptic vesicles was claimed to be an artefact of aldehyde fixation (Walberg 1968), but this has not been supported in the subsequent literature. It appears that the shape and orientation of synaptic vesicles may be influenced by their movement toward the active zone of a synapse: a study using adult mouse brain tissue analysed by focused ion beam scanning electron microscopy (FIB-SEM) found that synaptic vesicles were not spherical but oblate or cigar-shaped ellipsoids (Khanmohammadi et al 2015).

Neurosecretory endings found in various parts of the brain and in neuroendocrine glands and cells of the dispersed neuroendocrine system share many features with presynaptic boutons. They all contain peptides or glycoproteins within dense-core vesicles. The latter are of characteristic size and appearance: they are often ellipsoidal or irregular in shape, and relatively large, e.g. oxytocin and vasopressin vesicles in the neurohypophysis may be up to 200 nm in diameter.

Synapses may cause depolarization or hyperpolarization of the postsynaptic membrane, depending on the neurotransmitter released and the classes of receptor molecule in the postsynaptic membrane. Depolarization of the postsynaptic membrane results in excitation of the postsynaptic neurone, whereas hyperpolarization has the effect of transiently inhibiting electrical activity. Subtle variations in these responses may also occur at synapses where mixtures of neuromediators are present and their effects are integrated. For details of the synaptic organization of the brain, see Shepherd (2003).

Type I and II synapses

There are two broad categories of synapse, type I and type II. In active zones of type I synapses the cytoplasmic density is thicker on the postsynaptic side. In type II synapses the pre- and postsynaptic densities are thinner and more symmetric. Type I boutons contain a predominance of small spherical vesicles approximately 50 nm in diameter, and type II boutons contain oval or flattened vesicles. Throughout the CNS, type I synapses are generally excitatory and type II are inhibitory. In a few instances, types I and II synapses are found in close proximity, orientated in opposite directions across the synaptic cleft (a reciprocal synapse).

Mechanisms of synaptic activity

Synaptic activation begins with arrival of one or more action potentials at the presynaptic bouton, which causes the opening of voltage-sensitive calcium channels in the presynaptic membrane. The response time in typical fast-acting synapses is then very rapid; classic neurotransmitter (e.g. ACh, glutamate or GABA) is released in less than a millisecond. Release-ready synaptic vesicles are docked to the presynaptic membrane and primed through processes not yet fully understood. On calcium ion influx through voltage-sensitive channels, their membranes fuse to open a pore through which neurotransmitter diffuses into the synaptic cleft (Gray 1959, Eggermann et al 2012).

Once the vesicle has discharged its contents, its membrane is incorporated into the presynaptic plasma membrane and is then recycled back into the bouton by endocytosis near the edges of the active zone. The recycling time for a synaptic vesicle may be in the range of a few seconds to minutes; newly recycled vesicles may be used instantly for the next cycle of neurotransmitter release (cycling pool of vesicles). The fusion of vesicles with the presynaptic membrane is responsible for the observed quantal behaviour of neurotransmitter release, both during neural activation and spontaneously, in the slightly leaky resting condition (Neher and Sakaba 2008, Suedhof 2012).

Postsynaptic events vary greatly, depending on the receptor molecules and their related molecular complexes (Murakoshi and Yasuda 2012). Receptors are generally classed as either ionotropic (ligand-gated channels) or metabotropic (membrane receptors that act through a second messenger).

Ionotropic receptors can be activated by conformational changes induced when neurotransmitter molecules bind to the receptor complex, causing a voltage change within the postsynaptic cell. Examples are the nicotinic ACh receptor and the related $GABA_A$ receptor, which are formed from five subunits, the tetrameric ionotropic glutamate receptors, such as the NMDA receptor or the AMPA receptor.

In metabotropic receptors, the receptor and ion channel may be separate molecules, coupled by G-proteins, some via a complex cascade of chemical interactions (a second messenger system), e.g. the adenylate cyclase pathway. Postsynaptic effects are generally rapid and short-lived, because the transmitter is quickly inactivated either by an extracellular enzyme (e.g. acetylcholinesterase, AChE), or by uptake into neurones or glial cells. Examples of such metabotropic receptors are the muscarinic ACh receptor and the dopamine receptor.

Neurohormones

Neurohormones are included in the class of molecules with neurotransmitter-like activity. They are synthesized in neurones and released into the blood circulation by exocytosis at synaptic bouton-like structures. As with classic endocrine gland hormones, they may act at great distances from their site of secretion. Neurones secrete into the CSF or local interstitial fluid to affect other cells, either diffusely or at a distance. To encompass this wide range of phenomena the general term neuromediation has been used, and the chemicals involved are called neuromediators.

Neuromodulators

Some neuromediators do not appear to affect the postsynaptic membrane directly but they can affect its responses to other neuromediators, either enhancing their activity (by increasing or prolonging the immediate response), or perhaps limiting or inhibiting their action. These substances are called neuromodulators. A single synaptic terminal may contain one or more neuromodulators in addition to a neurotransmitter, usually (though not always) in separate vesicles. Neuropeptides (see below) are nearly all neuromodulators, at least in some of their actions. They are stored within dense granular synaptic vesicles of various sizes and appearances.

Development and plasticity of synapses

The density of synapses in the human cerebral cortex increases dramatically in the first years of life, reaches its peak in adolescence and starts to decline gradually thereafter. Immature synapses are either maintained and reinforced to become stable mature synapses or eliminated from the neural circuit (Okabe 2017). This process, synapse pruning, is thought to be important in eliminating unnecessary connections between neurones for proper and effective information processing in mature neuronal networks in the adult brain (Kano et al 2018), although even in the adult brain, a fraction of synapses in the cerebral cortex and the hippocampus can be newly formed or eliminated. Although less drastic in the magnitude of alteration, synapses in neural circuits related to memory formation can change their functional strength according to the previous history of synaptic activity and firing frequency of presynaptic and postsynaptic neurones (Squire and Kandel 2008). This process, synaptic plasticity, includes both increased or decreased synaptic strength for some hours or longer (long-term potentiation, LTP, or long-term depression, LTD, respectively). Impaired memory is a hallmark of dementia such as Alzheimer's disease, where a reduction in the number of dendritic spines, together with pathological changes such as neurofibrillary tangles and deposits of amyloid-β protein, suggests that reduced synaptic connectivity impairs cognitive function in affected individuals (Tampellini 2015).

Neurotransmitter molecules

Until relatively recently, the molecules known to be involved in chemical synapses were limited to a fairly small group of classic neurotransmitters, e.g. ACh, noradrenaline (norepinephrine), adrenaline (epinephrine), dopamine and histamine, all of which had well-defined rapid effects on other neurones, muscle cells or glands. However, many synaptic interactions cannot be explained on the basis of classic neurotransmitters, and other substances, particularly some amino acids such as glutamate, glycine, aspartate, GABA and the monoamine serotonin, also function as transmitters. Substances first identified as hypophysial hormones or as part of the dispersed neuroendocrine system (see below) of the alimentary tract, can be detected widely throughout the CNS and PNS, often associated with functionally integrated systems. Many of these are peptides: more than one hundred (together with other candidates) function mainly as neuromodulators and influence the activities of classic transmitters.

Acetylcholine

Acetylcholine (ACh) is perhaps the most extensively studied neurotransmitter of the classic type. Its precursor, choline, is synthesized in the neuronal soma and transported to the axon terminals, where it is acetylated by the enzyme choline acetyl transferase (ChAT), and stored in clear spherical vesicles 40–50 nm in diameter. ACh is synthesized by motor neurones and released at all their motor terminals on skeletal muscle. It is released by preganglionic fibres at synapses in parasympathetic and sympathetic ganglia, and many parasympathetic, and some sympathetic, ganglionic neurones are cholinergic. ACh is also associated with the degradative extracellular enzyme AChE, which inactivates the transmitter by converting it to choline.

The effects of ACh on nicotinic receptors (i.e. those in which nicotine is an agonist) are rapid and excitatory. In the CNS, the nicotinic ACh receptor mediates the effect of tobacco (for review, see Albuquerque et al (2009)). In the peripheral autonomic nervous system, the slower, more sustained excitatory effects of cholinergic autonomic endings are mediated by muscarinic receptors via a second messenger system.

Monoamines

Monoamines include the catecholamines (noradrenaline (norepinephrine), adrenaline (epinephrine) and dopamine), the indoleamine serotonin (5-hydroxytryptamine, 5-HT) and histamine (Haas et al 2008). They are synthesized by neurones in sympathetic ganglia and by their homologues, the chromaffin cells of the suprarenal medulla and paraganglia. Within the CNS, the somata of monoaminergic neurones lie mainly in the brainstem, although their axons ramify widely into all parts of the nervous system. Monoaminergic cells are also present in the retina.

Noradrenaline is the chief transmitter present in sympathetic ganglionic neurones with endings in various tissues, notably smooth muscle and glands, and in other sites including adipose and haemopoietic tissues and the corneal epithelium. It is also found at widely distributed synaptic endings within the CNS; many of their neuronal somata are situated in the locus coeruleus in the medullary floor. The actions of noradrenaline depend on its site of action and vary with the type of postsynaptic receptor, e.g. it strongly inhibits neurones of the submucosal plexus of the intestine and of the locus coeruleus via α_2-adrenergic receptors, whereas it mediates depolarization, producing vasoconstriction, via β-receptors in vascular smooth muscle. Adrenaline is present in central and peripheral nervous pathways and occurs with noradrenaline in the suprarenal medulla. Both adrenaline and noradrenaline are found in dense-cored synaptic vesicles approximately 50 nm in diameter.

Dopamine is a neuromediator of considerable clinical importance, found mainly in neurones with cell bodies in the telencephalon, diencephalon and mesencephalon. A major dopaminergic neuronal population in the midbrain constitutes the substantia nigra, so called because its cells contain neuromelanin, a black granular by-product of dopamine synthesis (Ch. 31). Dopaminergic endings are particularly numerous in the corpus striatum, limbic system and cerebral cortex. Structurally, dopaminergic synapses contain numerous dense-cored vesicles that resemble those containing noradrenaline. Pathological reduction in dopaminergic activity has widespread effects on motor control, affective behaviour and other neural activities, as seen in Parkinson's syndrome.

Serotonin and histamine are found in neurones mainly within the CNS. Serotonin is typically synthesized in small midline neuronal clusters in the brainstem, mainly in the raphe nuclei; the axons from these neurones ramify extensively throughout the entire brain and spinal cord. Synaptic terminals contain rounded, clear vesicles approximately 50 nm in diameter and are of the asymmetric type. Histaminergic neurones appear to be relatively sparse and are restricted largely to the hypothalamus.

Amino acids

Three major amino acids: GABA, glutamate and glycine, bind to specific receptors (Barrera and Edwardson 2008). GABA is a major inhibitory transmitter released at the terminals of local circuit neurones within the brainstem and spinal cord (e.g. the recurrent inhibitory loop), cerebellum (where it is the main transmitter of Purkinje cells), basal ganglia, cerebral cortex, thalamus and subthalamus. It is stored in flattened or pleomorphic vesicles within symmetric synapses. GABA may be inhibitory to postsynaptic neurones, or may mediate either presynaptic inhibition or facilitation, depending on the synaptic arrangement (Gassmann and Bettler 2012).

Glutamate is the major excitatory transmitter present widely within the CNS, including the major projection pathways from the cortex to the thalamus, tectum, substantia nigra and pontine nuclei. It is found in the central terminals of the auditory and trigeminal nerves, and in the terminals of parallel fibres ending on Purkinje cells in the cerebellum. Structurally, glutamate is associated with asymmetric synapses containing small (approximately 30 nm), round, clear synaptic vesicles (Contractor et al 2011). For further reading, see Willard and Koochekpour (2013).

Glycine is a well-established inhibitory transmitter of the CNS, particularly the lower brainstem and spinal cord, where it is mainly found in local circuit neurones. Evidence suggests that glycine may also be released from glutamatergic axon terminals to participate in activation of NMDA receptors, and from astrocytes into the synaptic cleft via activation of non-NMDA-type glutamatergic ionotropic receptors in the glial cell membrane. For further reading see Harsing and Matyus (2013).

ATP and adenosine

ATP serves not only as a universal energy substrate, but also as an extracellular signalling molecule; an extensive literature has shown ATP acts as a co-transmitter with all the classical neurotransmitters in most, perhaps all, nerves in the peripheral and central nervous systems. There are two families of receptors for purines, P1 receptors for adenosine and P2 receptors for ATP and adenosine 5′-diphosphate (ADP). Multiple P1 (adenosine), P2X (ion channel) and P2Y (G protein-coupled) nucleotide receptor subtypes are now known to be expressed by astrocytes, oligodendrocytes and microglia (Burnstock et al 2011, Burnstock 2016).

Nitric oxide

Nitric oxide, NO, is a ubiquitous gasotransmitter (Shefa et al 2018), able to diffuse freely through cell membranes, and so not under such tight quantal control as vesicle-mediated neurotransmission. NO is thought to play a role in synaptic plasticity, for example acting presynaptically at both glutamatergic and GABAergic synapses to alter the synaptic machinery involved in transmitter release. NO has also been implicated in hippocampal long-term potentiation (LTP), when it may act as a retrograde messenger after postsynaptic NMDA receptor activation. Acting at autonomic and enteric synapses NO mediates smooth muscle relaxation. Its influence in the gastrointestinal tract is significant: NO plays an important regulatory role in gut homeostasis, affecting gut motility, vascular tone, blood supply, mucosal barrier function, secretions and immunity (Savidge 2014, Sharkey and Savidge 2014).

Neuropeptides

Many neuropeptides coexist with other neuromediators in the same synaptic terminals. As many as three peptides often share a particular ending with a well-established neurotransmitter, in some cases within the same synaptic vesicles. Some peptides occur in both the CNS and the PNS, particularly in the ganglion cells and peripheral terminals of the ANS, whilst others are entirely restricted to the CNS. Only a few examples are given here.

Most of the neuropeptides are classified according to the site where they were first discovered. For example, the gastrointestinal peptides were initially found in the gut wall, and a group that includes releasing hormones, adenohypophysial and neurohypophysial hormones was first associated with the pituitary gland. Some of these peptides are closely related to each other in their chemistry because they are derived from the same gene products (e.g. the pro-opiomelanocortin group), which are cleaved to produce smaller peptides.

Substance P (SP) was the first of the peptides to be characterized as a gastrointestinal neuromediator and is considered to be the prototypic neuropeptide. It is an 11-amino-acid polypeptide that belongs to the tachykinin neuropeptide family, and is a major neuromediator in the brain and spinal cord (Mashaghi et al 2016). Contained within large granular synaptic vesicles, SP is found in approximately 20% of dorsal root and trigeminal ganglion cells, in particular in small nociceptive neurones, and in some fibres of the facial, glossopharyngeal and vagal nerves. Within the CNS, SP is present in several apparently unrelated major pathways, and has been described in the limbic system, basal ganglia, amygdala and hypothalamus. Its known action is prolonged postsynaptic excitation, particularly from nociceptive afferent terminals, which sustains the effects of noxious stimuli. SP is one of the main neuropeptides that trigger an inflammatory response in the skin and has also been implicated in the vomiting reflex, changes in cardiovascular tone, stimulation of salivary secretion, smooth muscle contraction, and vasodilation.

Vasoactive intestinal polypeptide (VIP), another gastrointestinal peptide, is widely present in the CNS, where it is probably an excitatory neurotransmitter or neuromodulator. It is found in distinctive bipolar neurones of the cerebral cortex; small dorsal root ganglion cells, particularly of the sacral region; the median eminence of the hypothalamus, where it may be involved in endocrine regulation; intramural ganglion cells of the gut wall; and sympathetic ganglia.

Somatostatin (ST, somatotropin release inhibiting factor) has a broad distribution within the CNS, and may be a central neurotransmitter or neuromodulator. It also occurs in small dorsal root ganglion cells. Beta-endorphin, leu- and metenkephalins, and the dynorphins belong to a group of peptides called the naturally occurring opiates that possess analgesic properties. They bind to opiate receptors in the brain where, in general, their action seems to be inhibitory. Enkephalins have been localized in many areas of the brain. Their particular localization in the septal nuclei, amygdaloid complex, basal ganglia and hypothalamus suggests that they are important mediators in the limbic system and in the control of endocrine function. They have also been implicated strongly in the central control of pain pathways, because they are found in the periaqueductal grey matter of the midbrain, a number of reticular raphe nuclei, the spinal nucleus of the trigeminal nerve and the substantia gelatinosa of the spinal cord. The enkephalinergic pathways exert an important presynaptic inhibitory action on nociceptive afferents in the spinal cord and brainstem. Like many other neuromediators, enkephalins also occur widely in other parts of the brain in lower concentrations.

Adult neurogenesis

In mammalian brains, generation of neurones has been considered to occur only during embryonic and perinatal stages. That concept changed in the 1960s, when the presence of lifelong neurogenesis was identified by using infusions of the thymidine analogue bromodeoxyuridine (BrdU) in rodents and primates. After infusion, BrdU is incorporated into dividing precursor cells and can be immunocytochemically detected in neurones in postmortem tissues. The first report of adult neurogenesis in human brains appeared in 1998, using brains of cancer patients who had received BrdU while they were alive. Adult neurogenesis was reported to be regionally restricted to the subgranular zone of the hippocampal dentate gyrus (Eriksson et al 1998). In both human and rodent brains, the primary progenitor cells were identified as a subpopulation of astrocytes with stem-cell-like features (Gonzalez-Peres 2012). The persistence of adult neurogenesis in human brains remains controversial, with opposing claims that neurogenesis does not continue, or is extremely rare, in adult humans (Sorrells et al 2018) or that hippocampal neurogenesis not only occurs in adult humans but does not appear to decline with ageing (Boldrini et al 2018).

CENTRAL GLIA

Glial (neuroglial) cells vary considerably in type and number in different regions of the CNS (**Fig. 3.12**). There are two major groups, macroglia (astrocytes and oligodendrocytes) and microglia, classified according to origin. Macroglia arise within the neural plate, in parallel with neurones, and constitute the great majority of glial cells. Their functions are diverse and are now known to extend beyond a passive supporting role (reviewed in Kettenmann and Ransom (2012)). Microglia have a small soma (see Fig. 3.21) and are derived from a distinct lineage of monocytic cells originating from the yolk sac.

Astrocytes

Astrocytes are the most abundant and diverse glial cell type but their identity is not well defined (Matyash and Kettenmann 2010). There is no common marker that labels all astrocytes, in the way that myelin basic protein is a marker for oligodendrocytes or the calcium-binding protein Iba1 is a marker for microglia. A commonly used marker is the expression of glial fibrillary acidic protein (GFAP), which forms intermediate filaments, but GFAP is not expressed in all astrocytes.

Classically, two forms of astrocytes were distinguished: protoplasmic and fibrous astrocytes. Protoplasmic astrocytes (star-shaped cells) are found in grey matter, possess several stem processes that branch further into a very complex network, and contact synapses, blood vessels, and the pial surface (as the glia limitans) . Fibrous astrocytes are predominantly found in white matter and their processes are often orientated in parallel with the axons. However, while all astrocytes share common properties, evidence from recent physiological and gene expression profiling studies has shown that they comprise a far more diverse cell population than was previously appreciated (Allen and Eroglu 2017).

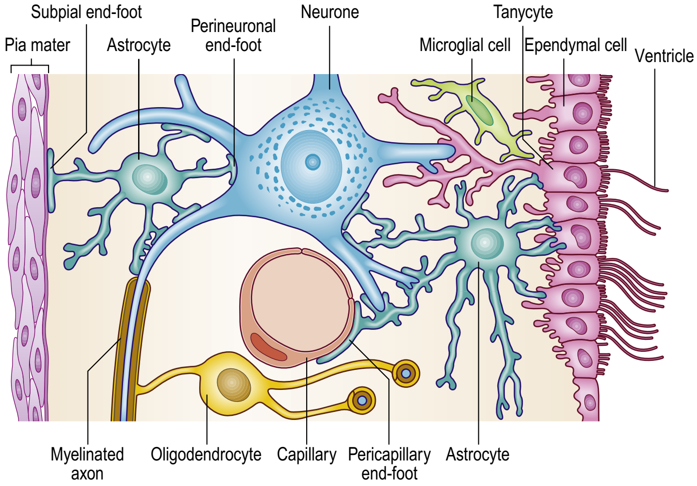

Fig. 3.12 The different types of non-neuronal cell in the CNS and their structural organization and interrelationships with each other and with neurones.

Radial glial cells are found early in development and serve as stem cells for neurones and glial cells. They may be categorized as astrocytes because they transform later in development into typical astrocytes. There are a number of other types of astrocyte with specialized morphologies. Bergmann glial cells in the cerebellum have somata in the Purkinje cell layer, processes that intermingle with the dendritic trees of the Purkinje neurones and terminal end-feet at the pial surface. Müller cells in the retina have a radial morphology and span the entire retina. Other astrocytic cells are tanycytes, velate astrocytes (cerebellum) and pituicytes (infundibulum and neurohypophysis of the pituitary gland). Pituicyte processes end mostly on endothelial cells in the neurohypophysis and tuber cinereum.

Astrocyte complexity and morphological diversity has reached the highest evolutionary level in humans (**Fig. 3.13**). A single astrocyte may enwrap several neuronal somata and make contacts with tens of thousands of individual synapses; bipolar astrocytes located in layer 5 and 6 of the cortex may extend processes up to 1 mm long.

Astrocytes in grey matter form a syncytium in which cells are interconnected by gap junctions, permitting the exchange of ions (e.g. calcium, propagated in waves) and small molecules such as ATP or glucose. They are the only cells in the brain capable of converting glucose into glycogen, which serves as an energy store. Before re-releasing glucose, astrocytes convert it to lactate, which is taken up by neurones; failure in glucose flow through the astrocytic network results in impairment of neuronal function.

Astrocytes not only respond to neuronal activity but also modulate that activity. They enwrap all penetrating and intracerebral arterioles and capillaries, control the ionic and metabolic environment of the neuropil and mediate neurovascular coupling. They form specialized structures that contact blood vessels; their end-feet entirely enwrap blood vessels and are instrumental in the establishment of the blood–brain barrier.

Traumatic injury to the CNS induces astrogliosis, seen as a local increase in the number and size of GFAP-positive cells and a characteristic extensive meshwork of processes. The microenvironment of this glial scar, which may also include cells of oligodendrocyte lineage and myelin debris, plays an important role in inhibiting regrowth of damaged CNS axons (Seifert et al 2006; Robel et al 2011) and is a significant barrier to the long-term success of chronically implanted neural electrodes (Spencer et al 2017).

Blood–brain barrier

Proteins circulating in the blood enter most tissues of the body except those of the brain, spinal cord and peripheral nerves. This concept of a blood–brain or a blood–nerve barrier applies to many substances – some

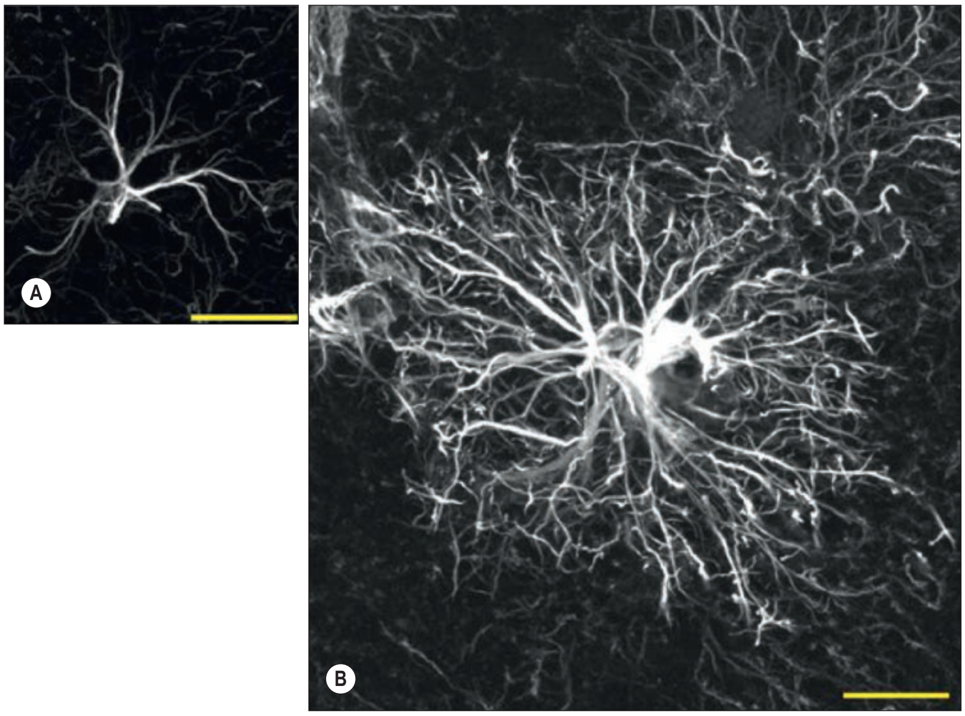

Fig. 3.13 Human protoplasmic astrocytes are larger and more complicated than their rodent counterparts. **A**, A typical mouse protoplasmic astrocyte. Glial fibrillary acidic protein (GFAP) immunostain; white. Scale bar = 20 µm. **B**, A typical human protoplasmic astrocyte to the same scale. Scale bar = 20 µm. (From Oberheim NA, Takano T, Han X et al 2009 Uniquely hominid features of adult human astrocytes. J Neurosci 29:3276–87.)

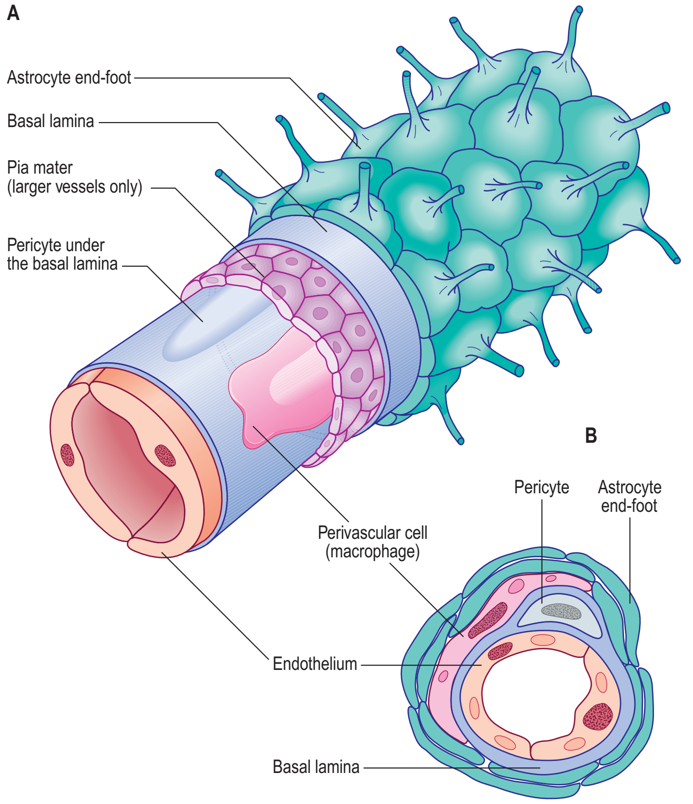

Fig. 3.14 The relationship between the glia limitans, perivascular cells and blood vessels within the brain, in longitudinal (**A**) and transverse (**B**) sections. A sheath of astrocytic end-feet wraps around the vessel and, in vessels larger than capillaries, its investment of pial meninges. Vascular endothelial cells are joined by tight junctions and supported by pericytes; perivascular macrophages lie outside the endothelial basal lamina (light blue).

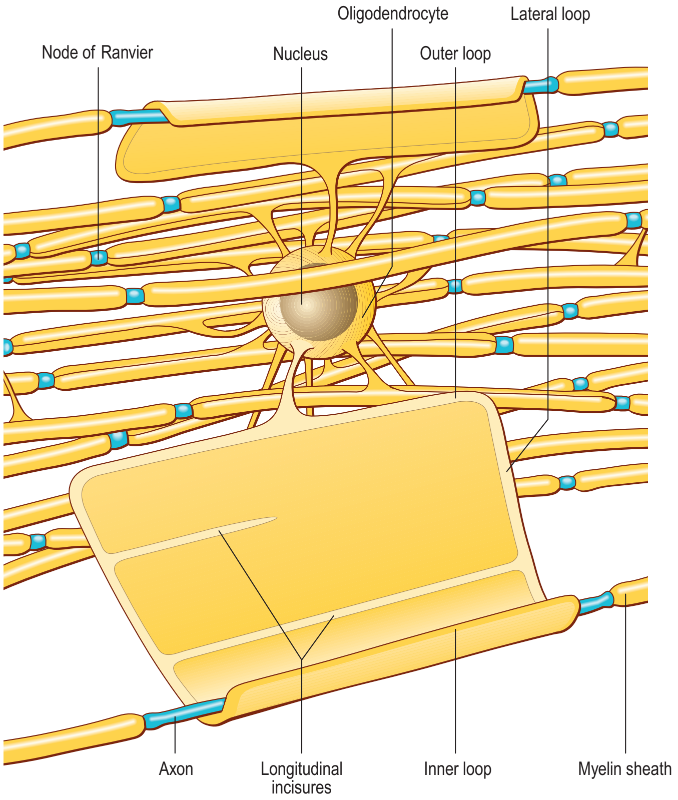

Fig. 3.15 The ensheathment of a number of axons by the processes of an oligodendrocyte. The oligodendrocyte soma is shown in the centre and its myelin sheaths are unfolded to varying degrees to show their extensive surface area. (Adapted with permission from Morell P, Norton WT 1980 Myelin. Scientific American 242(5):88–90, 92, 96; and Raine CS 1984 Morphology of myelin and myelination. In Morell P (ed) Myelin, 2nd ed. New York: Plenum Press.)

are actively transported across the blood–brain barrier, others are actively excluded. The blood–brain barrier is located at the capillary endothelium within the brain and is dependent on the presence of tight junctions (occluding junctions, zonulae occludentes) between endothelial cells coupled with a relative lack of transcytotic vesicular transport. The tightness of the barrier is substantially supported by the close apposition of astrocytes, which direct the formation of endothelial tight junctions, to blood capillaries (Abbott et al 2006, Cardoso et al 2010) (Fig. 3.14).

The blood–brain barrier develops during embryonic life but may not be fully completed by birth. There are certain areas of the adult brain where the endothelial cells are not linked by tight junctions, which means that a free exchange of molecules occurs between blood and adjacent brain. Most of these areas are situated close to the ventricles and are known as circumventricular organs; these areas make up less than 1% of the total area of the brain. Elsewhere, unrestricted diffusion through the blood–brain barrier is only possible for substances that can cross biological membranes because of their lipophilic character. Lipophilic molecules may be actively re-exported by the brain endothelium.

Breakdown of the blood–brain barrier occurs when the brain is damaged by ischaemia or infection, and is also associated with primary and metastatic cerebral tumours. Reduced blood flow to a region of the brain alters the permeability and regulatory transport functions of the barrier locally; the increased stress on compromised endothelial cells results in leakage of fluid, ions, serum proteins and intracellular substances into the extracellular space of the brain. The integrity of the barrier can be evaluated clinically using computed tomography and functional magnetic resonance imaging. Breakdown of the blood–brain barrier may be seen at postmortem in jaundiced patients who have had an infarction. Normally, the brain, spinal cord and peripheral nerves remain unstained by the bile post mortem, although the choroid plexus is often stained a deep yellow. However, areas of recent infarction (1–3 days) will also be stained by bile pigment because of the localized breakdown of the blood–brain barrier.

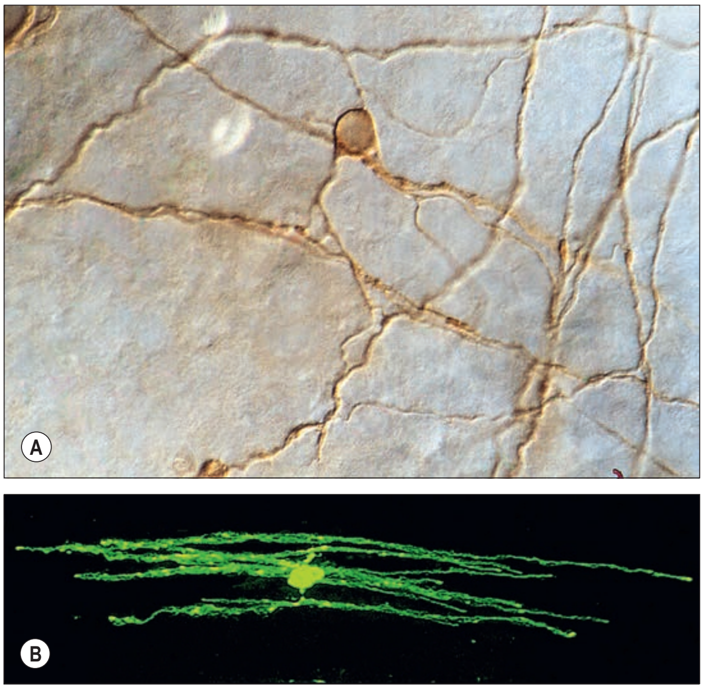

Fig. 3.16 **A**, An oligodendrocyte enwrapping several axons with myelin, demonstrated in a whole-mounted rat anterior medullary velum, immunolabelled with antibody to an oligodendrocyte membrane antigen. **B**, A confocal micrograph of a mature myelin-forming oligodendrocyte in an adult rat optic nerve, iontophoretically filled with an immunofluorescent dye by intracellular microinjection. (A, Courtesy of Fiona Ruge. B, Prepared by Professor A Butt, Portsmouth, and Kate Colquhoun, formerly Division of Physiology, GKT School of Medicine, London.)

Oligodendrocytes

Oligodendrocytes myelinate CNS axons and are most commonly seen as intrafascicular cells in myelinated tracts (Figs 3.15–3.16). They usually have round nuclei and their cytoplasm contains numerous mitochondria, microtubules and glycogen. They display a spectrum of morphological variation, from cells with large euchromatic nuclei and pale cytoplasm, to cells with heterochromatic nuclei and dense cytoplasm. In contrast to Schwann cells, which myelinate only one axonal segment, individual oligodendrocytes myelinate up to 50 axonal segments. Some oligodendrocytes are not associated with axons, and are either precursor cells or perineuronal (satellite) oligodendrocytes with processes that ramify around neuronal somata.

Within tracts, interfascicular oligodendrocytes are arranged in long rows interspersed at regular intervals with single astrocytes. Since oligodendrocyte processes are radially aligned to the axis of each row, myelinated tracts typically consist of cables of axons myelinated by a row of oligodendrocytes running down the axis of each cable.

Oligodendrocytes originate from the ventricular neurectoderm and the subependymal layer in the fetus, and continue to be generated from the subependymal plate postnatally. Stem cells migrate and seed into white and grey matter to form a pool of adult progenitor cells, which can later differentiate to replenish defunct oligodendrocytes, and possibly remyelinate axons in pathologically demyelinated regions. Several different names have been used to describe these cells since they were first recognized (NG2 glia; polydendrocyte (Nishiyama et al 2009); synantocyte (Butt et al 2005)). NG2 glia display a highly branching morphology and are widely distributed throughout the developing and mature mammalian CNS. In the postnatal CNS they either self-renew or diffeetate into myelinating and non-myelinating oligodendrocytes and are thus often designated oligodendrocyte precursor cells (OPCs). They express a complex set of voltage-gated channels and ionotropic receptors for glutamate and GABA and form direct synapses with axons, enabling transient activation of these receptors (Hill and Nishiyama 2014). They also express two OPC signature proteins, NG2 (Cspg4 gene product) and platelet-derived growth factor receptor α (Pdgfra), which are downregulated when they terminally differentiate into postmitotic oligodendrocytes (Zuo et al 2018). There is considerable support for the view that the NG2 cell is a distinct glial type.

Nodes of Ranvier and incisures of Schmidt–Lanterman

The territory ensheathed by an oligodendrocyte (or Schwann cell) process defines an internode, the interval between internodes is called a node of Ranvier (**Fig. 3.17**) and the territory immediately adjacent to the nodal gap is a paranode, where loops of oligodendrocyte cytoplasm abut the axolemma. The paranode acts as a diffusion barrier separating the voltage-gated sodium channels (Nav) channels in the node of Ranvier from the Kv1 channels in the juxtaparanodes. It also "glues" myelin to the axon, restricting membrane proteins to the node of Ranvier and reducing current flow under the myelin sheath and it is thought to direct protein traffic to the nodes via a neurofilamentous network. The strong interaction between myelin and the axolemma is achieved by a complex of axonal contactin-1 and contactin-associated protein 1 (Caspr1) and oligodendrocyte NF155. Nodal axolemma is often closely associated with astrocytic processes; their function is unknown.

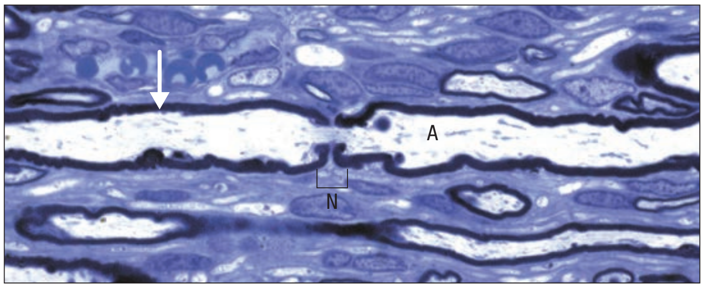

Fig. 3.17 A node of Ranvier (N) in the central nervous system of a rat. The pale-staining axon (A) is ensheathed by oligodendrocyte myelin (arrow), apart from a short, exposed region at the node. Toluidine blue stained resin section. (Courtesy of Dr Clare Farmer, King's College, London.)

Schmidt–Lanterman incisures are helical decompactions of internodal myelin where the major dense line of the myelin sheath splits to enclose a spiral of oligodendrocyte cytoplasm. Their structure suggests that they may play a role in the transport of molecules across the myelin sheath, but their function is not known.

Myelin and myelination

Myelin is formed by oligodendrocytes (CNS) and Schwann cells (PNS). A single oligodendrocyte may ensheathe up to 50 separate axon segments, depending on calibre, whereas myelinating Schwann cells ensheathe axons on a 1 : 1 basis.

In general, myelin is laid down around axons above 2 µm in diameter. However, the critical minimal axon diameter for myelination is smaller and more variable in the CNS than in the PNS (approximately 0.2 µm in the CNS compared with 1–2 µm in the PNS). There is considerable overlap between the size of the smallest myelinated and the largest unmyelinated axons, and so axonal calibre is unlikely to be the only factor in determining myelination. Moreover, the first axons to become ensheathed ultimately attain larger diameters than those that are ensheathed at a later date. There is a reasonable linear relationship between axon diameter and internodal length and myelin sheath thickness: as the sheath thickens from a few lamellae to up to 200, the axon may also grow from 1 to 15 µm in diameter. Internodal lengths increase about 10-fold during the same time (Nave 2010).

It is not known precisely how myelin is formed in either PNS or CNS. Akt/mTOR (mammalian (or mechanistic) target of rapamycin) signalling has emerged as one of the major pathways involved in myelination; it has been implicated in the regulation of several steps during the development of myelinating Schwann cells and oligodendrocytes (Norrmén and Suter 2013). In the CNS, myelination also depends in part on expression of a protein (Wiskott–Aldrich syndrome protein family verprolin homologous, WAVE), which influences the actin cytoskeleton, oligodendrocyte lamellipodia formation and myelination (Kim et al 2006). The ultrastructural appearance of myelin is usually explained in terms of the spiral wrapping of an extensive, flat glial process (lamellipodium) around an axon, and the subsequent extrusion of cytoplasm from the sheath at all points other than incisures and paranodes. In this way, the compacted external surfaces of the plasma membrane of the ensheathing glial cell are thought to produce the minor dense lines, and the compacted inner cytoplasmic surfaces, the major dense lines, of the mature myelin sheath (**Fig. 3.18**). These lines, first described in early electron microscope studies of the myelin sheath, correspond to the intraperiod and period lines respectively, defined in X-ray studies of myelin. The inner and outer zones of occlusion of the spiral process are continuous with the minor dense line and are called the inner and outer mesaxons. For further reading on aspects of myelination, see Bakhti et al (2014).

There are significant differences between central and peripheral myelin, reflecting the fact that oligodendrocytes and Schwann cells express different proteins during myelinogenesis. The basic dimensions of the myelin membrane are different. CNS myelin has a period repeat thickness of 15.7 nm whereas PNS myelin has a period to period line thickness of 18.5 nm, and the major dense line space is approximately

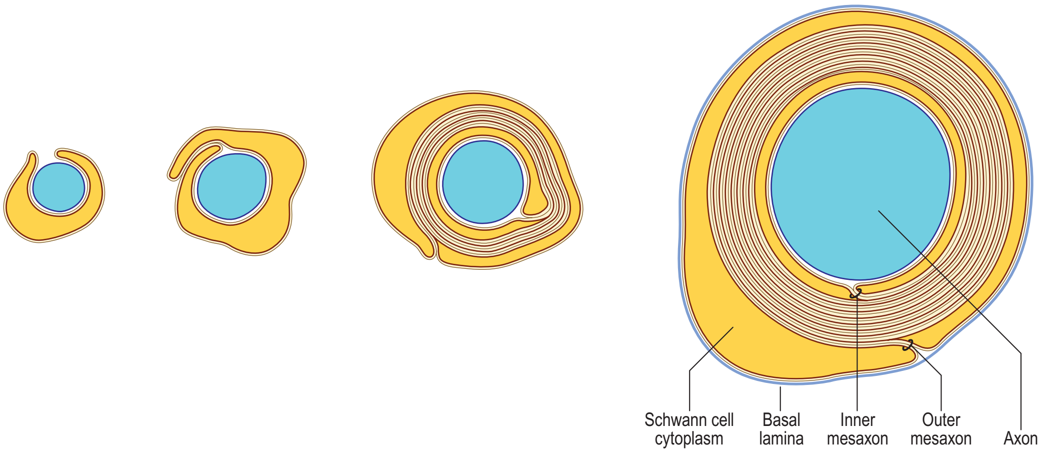

Fig. 3.18 Suggested stages in myelination of a peripheral axon by an ensheathing Schwann cell.

1.7 nm in CNS myelin, compared with 2.5 nm in PNS myelin. Myelin membrane contains protein, lipid and water, which forms at least 20% of the wet weight. It is a relatively lipid-rich membrane and contains 70–80% lipid. All classes of lipid have been found; perhaps not surprisingly, the precise lipid composition of PNS and CNS myelin is different. The major lipid species are cholesterol (the most common single molecule), phospholipids and glycosphingolipids. Minor lipid species include galactosylglycerides, phosphoinositides and gangliosides. The major glycolipids are galactocerebroside and its sulphate ester, sulphatide; these lipids are not unique to myelin but they are present in characteristically high concentrations. CNS and PNS myelin also contain low concentrations of acidic glycolipids, which constitute important antigens in some inflammatory demyelinating states. Gangliosides, which are glycosphingolipids characterized by the presence of sialic acid (*N*-acetylneuraminic acid), account for less than 1% of the lipid in myelin.

A relatively small number of protein species account for the majority of myelin protein. Some of these proteins are common to both PNS and CNS myelin, but others are different. Proteolipid protein (PLP) and its splice variant DM20 are found only in CNS myelin, whereas myelin basic protein (MBP) and myelin associated glycoprotein (MAG) occur in both. MAG is a member of the immunoglobulin supergene family, and is localized specifically at those regions of the myelin segment where compaction starts: namely, the mesaxons and inner periaxonal membranes, paranodal loops and incisures, in both CNS and PNS sheaths. It is thought to have a functional role in membrane adhesion.

In the developing CNS, axonal outgrowth precedes the migration of oligodendrocyte precursors, and oligodendrocytes associate with and myelinate axons after their phase of elongation; oligodendrocyte myelin gene expression is not dependent on axon association. In marked contrast, Schwann cells in the developing PNS are associated with axons during the entire phase of axonal growth. Myelination does not occur simultaneously in all parts of the body in late fetal and early postnatal development. White matter tracts and nerves in the periphery have their own specific temporal patterns that relate to their degree of functional maturity.

Mutations of the major myelin structural proteins have now been recognized in a number of inherited human neurological diseases. As would be expected, these mutations produce defects in myelination and in the stability of nodal and paranodal architecture that are consistent with the suggested functional roles of the relevant proteins in maintaining the integrity of the myelin sheath.

Ependyma

Ependymal cells line the ventricles (Fig. 3.19) and central canal of the spinal cord. They form a single-layered epithelium that varies from squamous to columnar in form. At the ventricular surface, cells are joined by gap junctions and occasional desmosomes. Their apical surfaces have numerous microvilli and/or cilia, the latter contributing to the flow of CSF. There is considerable regional variation in the ependymal lining of the ventricles but four major types have been described. These are: general ependymal, which overlies grey matter; general ependymal, which overlies white matter; specialized areas of ependyma in the third and fourth ventricles; and choroidal epithelium.

The ependymal cells overlying areas of grey matter are cuboidal. Each cell bears approximately 20 central apical cilia, surrounded by short microvilli. The cells are joined by gap junctions and desmosomes. Beneath them there may be a subependymal (or subventricular) zone, from two to three cells deep, consisting of cells that generally resemble ependymal cells. In rodents, the subventricular zone contains neural progenitor cells, which can give rise to new neurones, but the existence of these stem cells in the adult human brain is controversial (Kempermann 2011, Sanai et al 2011). The capillaries beneath the ependymal cells have no fenestrations and few transcytotic vesicles, which is typical of the CNS. Where the ependyma overlies myelinated tracts of white matter, the cells are much flatter and few are ciliated. There are gap junctions and desmosomes between these cells, but their lateral margins interdigitate, unlike their counterparts overlying grey matter. No subependymal zone is present.

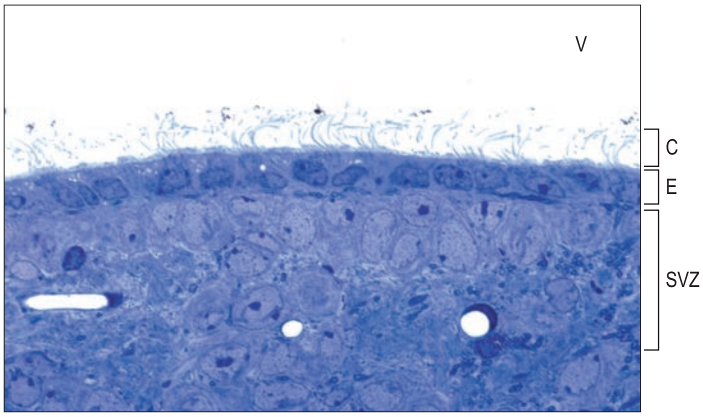

Fig. 3.19 Ciliated columnar epithelial lining of the lateral ventricle (V), overlying the subventricular zone (SVZ). C, cilia; E, ependymal cells. Mouse tissue, toluidine blue stained resin section.

Specialized areas of ependymal cells called the circumventricular organs are found in four areas around the margins of the third ventricle: namely, the lining of the median eminence of the hypothalamus; the subcommissural organ; the subfornical organ; and the vascular organ of the lamina terminalis. The area postrema, at the inferoposterior limit of the fourth ventricle, has a similar structure. In all of these sites the ependymal cells are only rarely ciliated and their ventricular surfaces bear many microvilli and apical blebs. They have numerous mitochondria, well-formed Golgi complexes and rather flattened basal nuclei. They are joined laterally by tight junctions, which form a barrier to the passage of materials across the ependyma, and by desmosomes. Many of the cells are tanycytes (ependymal astrocytes) and have basal processes that project into the perivascular space surrounding the underlying capillaries. Significantly, these capillaries are fenestrated and therefore do not form a blood–brain barrier. It is believed that neuropeptides can pass from nervous tissue into the CSF by active transport through the ependymal cells in these specialized areas, and so access a wide population of neurones via the permeable ependymal lining of the rest of the ventricle.

The ependyma is highly modified where it lies adjacent to the vascular layer of the choroid plexuses.

Motile cilia

Ependymal cells generate unidirectional flow in CSF by beating their motile cilia in a coordinated, whip-like manner. They have a highly ordered structure of nine peripheral microtubule doublets arranged around a pair of single microtubules, forming the axoneme. Various multiprotein complexes including radial spokes and dynein arms interconnect the microtubules: the dynein arms bind to the peripheral microtubules and are responsible for producing the force for the beating of the cilia.

Ependymal cells are arranged in a polarized manner within the plane of the epithelial sheets. Planar cell polarity (PCP) is the basis for generating the directed flow of CSF, by which various signalling molecules and trophic factors, such as insulin-like growth factors (IGFs), Sonic hedgehog (Shh), retinoic acid (RA), bone morphogenic proteins (BMPs), and others, are distributed throughout the ventricles. Disturbance of CSF flow through the ventricles and into the subarachnoid space results in hydrocephalus (Ch. 25).

Choroid plexus

The choroid plexus forms the CSF and actively regulates the concentration of molecules in the CSF (Ch. 25). It consists of highly vascularized masses of pia mater enclosed by pockets of ependymal cells. The ependymal cells resemble those of the circumventricular organs, except that they lack basal processes, and form a cuboidal epithelium that rests on a basal lamina adjacent to the enclosed fold of meningeal pia mater and its capillaries (Fig. 3.20). The cells possess numerous long microvilli with only a few cilia interspersed between them, many mitochondria, large Golgi complexes and basal nuclei, which are all features consistent with their secretory activity: they produce most components of the CSF. They are linked by tight junctions forming a transepithelial barrier (a component of the blood–CSF barrier), and by desmosomes. Their lateral margins are highly folded.

The choroid plexus has a villous structure where the stroma is composed of pial meningeal cells, and contains fine bundles of collagen and blood vessels. Choroidal capillaries are lined by a fenestrated endothelium. During fetal life, erythropoiesis occurs in the stroma, which is occupied by bone marrow-like cells. In adult life, the stroma contains phagocytic cells, which, together with the cells of the choroid plexus epithelium, phagocytose particles and proteins from the ventricular lumen.

Age-related changes occurring in the choroid plexus can be detected by neuroimaging. Calcification of the choroid plexus can be detected

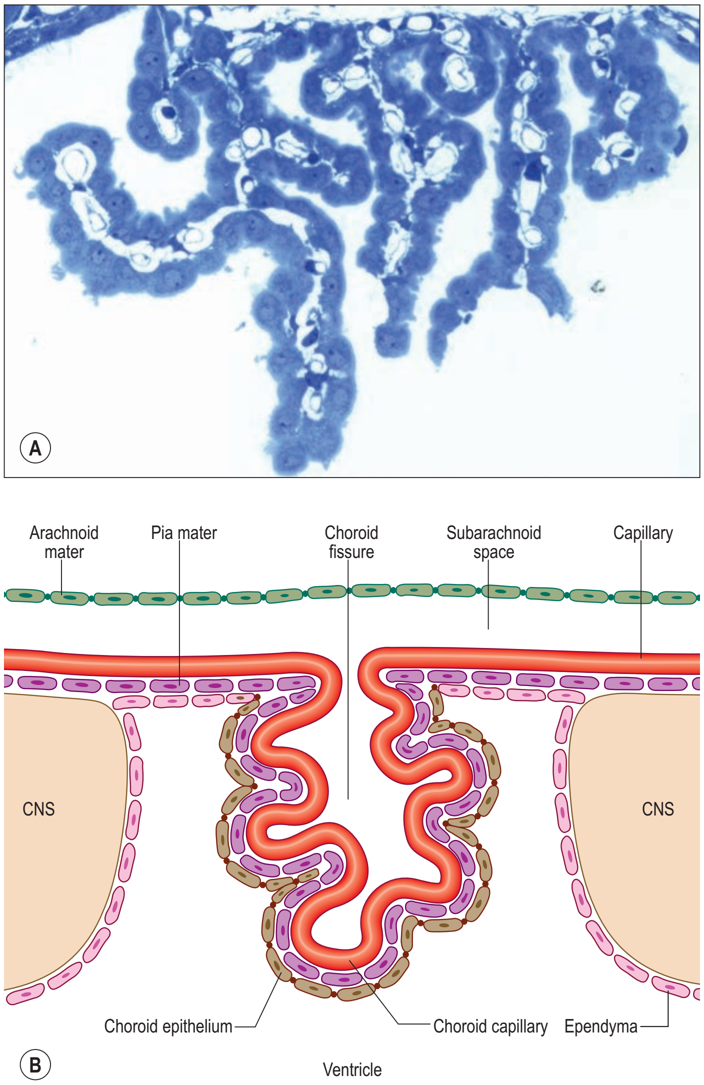

Fig. 3.20 **A**, A choroid plexus within the lateral ventricle. Frond-like projections of vascular stroma derived from the pial meninges are covered with a low columnar epithelium that secretes cerebrospinal fluid. Mouse tissue, toluidine blue stained resin section. **B**, The arrangement of tissues forming the choroid plexus.

by X-ray or CT scan very rarely in individuals in the first decade of life and in the majority in the eighth decade. The incidence of calcification rises sharply, from 35% of CT scans in the fifth decade to 75% in the sixth decade. Visible calcification is usually restricted to the glomus region of the choroid plexus, i.e. the vascular bulge in the choroid plexus as it curves to follow the anterior wall of the lateral ventricle into the temporal horn.

Microglia

Microglia are the primary innate immune cells of the brain (Kettenmann et al 2011, Eggen et al 2013, Butovsky and Weiner 2018). They originate from an embryonic monocyte precursor and invade the brain early during development. While the invading cells have an ameboid morphology, microglial cells in a mature brain are highly ramified cells. They have elongated nuclei, scant cytoplasm and several highly branched processes.

Microglia represent about 5–12% of total CNS cells in the healthy brain and the spinal cord. They occupy a defined territory in the brain parenchyma and are found in all areas of the CNS including optic nerve, retina and spinal cord. They comprise a heterogeneous community: different subpopulations in specific brain regions exhibit differing capacities and functions (Szepesi et al 2018).

Resting microglia, a term used to refer to microglia in the normal brain, should more accurately be described as surveying microglia. Microglial processes are fast-moving structures that rapidly scan their territory while the soma remains fixed in position (Shafer and Stevens 2015).

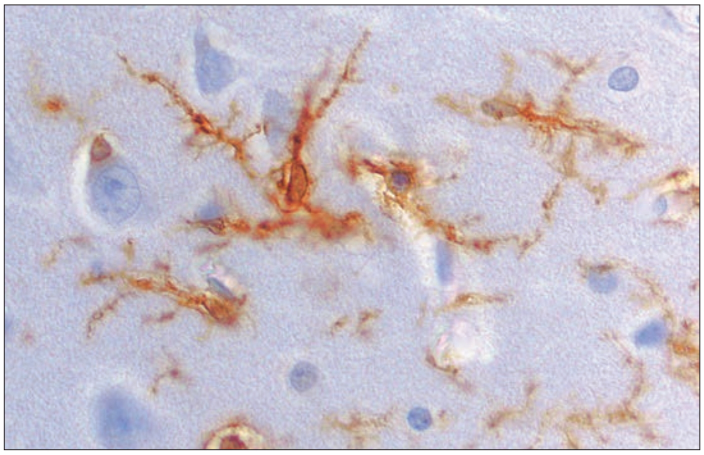

Fig. 3.21 Activated microglial cells in the human central nervous system, in a biopsy from a patient with Rasmussen's encephalitis, visualized using MHC class II antigen immunohistochemistry. (Courtesy of Dr Norman Gregson, Division of Neurology, GKT School of Medicine, London.)

All pathological changes in the brain result in the activation of microglial cells (Fig. 3.21), e.g. activated microglia are found in the brain tissue of multiple sclerosis, Alzheimer's disease and stroke patients. The most common indication of their activation is a change from a ramified to an ameboid morphology, which may occur within a few hours of the onset of injury or disease process.

In general, microglia respond to two types of signal: 'on' signals, which either appear *de novo* or are strongly upregulated, e.g. cell wall components of invading bacteria; and 'off' signals, which are normally present but disappear or decrease in pathological states, e.g. defined cytokines or neurotransmitters. Both types of event are interpreted as signals for activation. The functional repertoire of activated microglia includes proliferation; migration to the site of injury; expression of major histocompatibility complex (MHC) II molecules to interact with infiltrating lymphocytes; and the release of a variety of different substances including chemokines, cytokines and growth factors. These cells are therefore capable of significantly influencing ongoing pathological processes.

Microglial cells are the professional phagocytes of the nervous system and actively migrate through tissue. A number of factors such as ATP and complement factors act as chemoattractants. This behaviour is relevant not only in pathology but also during development where microglial cells remove apoptotic cells. After a pathological insult, microglial cells revert to their surveying phenotype, re-acquiring a ramified morphology.

Entry of inflammatory cells into the brain

Although the CNS has long been considered to be an immunologically privileged site, lymphocyte and macrophage surveillance of the brain may be a normal, but very low-grade, activity that is enhanced in disease. Lymphocytes can enter the brain in response to virus infections and as part of the autoimmune response in multiple sclerosis. Activated, but not resting, lymphocytes pass through the endothelium of small venules, a process that requires the expression of recognition and adhesion molecules (induced following cytokine activation), and subsequently migrate into the brain parenchyma. Within the CNS, microglia can be induced by T-cell cytokines to act as efficient antigen-presenting cells. After leaving the CNS, lymphocytes probably drain along lymphatic pathways to regional cervical lymph nodes.

Monocytes enter the CNS in the early stages of infarction and autoimmune disease and, in particular, in pyogenic infections, probably by passing through the endothelium of local vessels. Once in the brain, monocytes are difficult to distinguish from intrinsic microglia because both cell types express a similar marker profile. During the inflammatory phase of meningitis, polymorphonuclear leukocytes and lymphocytes pass into the CSF through the endothelium of large veins in the subarachnoid space.

Interaction between glial cells and synapses

Astrocytes in grey matter are classified as protoplasmic astrocytes and make contacts with a large number of synapses and regulate their functions. Neurotransmitters released from presynaptic boutons are effectively taken up by membrane transporters expressed in either neurones or astrocytes. Glutamate transporters in astrocytic processes in contact with synapses efficiently maintain low levels of extracellular glutamate, which is excitotoxic. Internalized glutamate is converted into glutamine and transferred to local neurones and reconverted to glutamate via the glutamate–glutamine cycle. Astrocytes play a similar role in controlling extracellular GABA levels via expression of GABA transporters. Three synaptic components, i.e. pre- and postsynaptic neuronal elements and astrocytic processes, function as a unit for appropriate transmission of impulses, constituting a'tripartite synapse' (Haydon and Carmignoto 2006).

Astrocytes can also modulate synaptic transmission and neuronal activity by releasing neuroactive substances such as D-serine, ATP or glutamate and express neurotransmitter receptors and increase intracellular calcium in response to the activation of nearby neurones and synapses. These bidirectional interactions between neurones and astrocytes may be important in information processing by the brain.

Microglial cells express receptors for neurotransmitters and thus can sense neuronal activity. Resting microglia have highly branched and motile processes, which continuously survey synapses within their territories (Nimmerjahn et al 2005). Microglial cells are involved in synapse pruning, which is required for appropriate neuronal connections, including axonal projections of retinal ganglion cells to the visual thalamus (Hammond et al 2018). Active phagocytosis of synaptic structures by microglia is proposed to be the mechanism of synaptic pruning in the visual thalamus.

PERIPHERAL NERVES

Afferent nerve fibres connect peripheral receptors to the CNS; they are derived from neuronal somata located either in special sense organs (e.g. the olfactory epithelium) or in the sensory ganglia of the craniospinal nerves. Efferent nerve fibres connect the CNS to the effector cells and tissues and are the peripheral axons of neurones with somata in the central grey matter.

Peripheral nerve fibres are grouped in widely variable numbers into bundles (fasciculi). The size, number and pattern of fasciculi vary in different nerves and at different levels along their paths (**Fig. 3.22**). Their number increases and their size decreases some distance proximal to a point of branching. Where nerves are subjected to pressure, e.g. deep to a retinaculum, fasciculi are increased in number but reduced in size, and the amount of associated connective tissue and degree of vascularity also increase. At these points, nerves may occasionally show a pink, fusiform dilation, sometimes termed a pseudoganglion or gangliform enlargement.

Classification of peripheral nerve fibres

Classification of peripheral nerve fibres is based on various parameters such as conduction velocity, function and fibre diameter. Of two classifications in common use, the first divides fibres into three major classes, designated A, B and C, corresponding to peaks in the distribution of their conduction velocities. In humans, this classification is used mainly for afferent fibres from the skin. Group A fibres are subdivided into α, β, γ and δ subgroups; fibre diameter and conduction velocity are proportional in most fibres. Group Aα fibres are the largest and conduct most rapidly, and C fibres are the smallest and slowest.

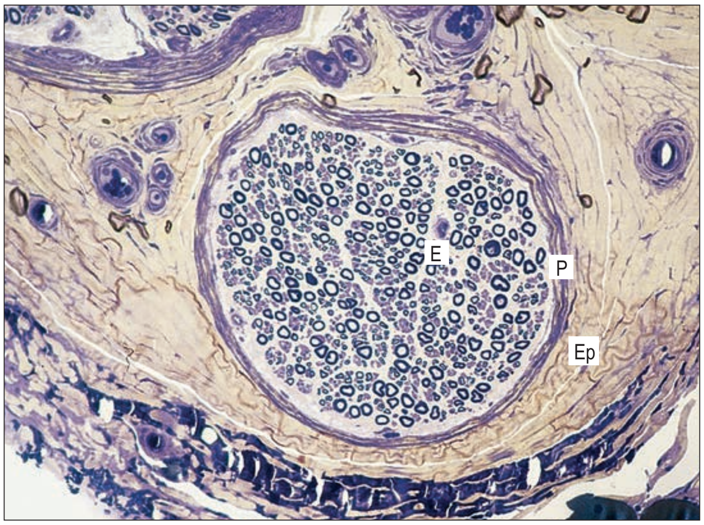

Fig. 3.22 A transverse section of a biopsied human sural nerve, showing the arrangement of the connective tissue sheaths. Individual axons, myelinated and unmyelinated, are arranged in a small fascicle bounded by a perineurium. Abbreviations: P, perineurium; Ep, epineurium; E, endoneurium. (Courtesy of Professor Susan Standring, GKT School of Medicine, London.)

The largest afferent axons (Aα fibres) innervate encapsulated cutaneous mechanoreceptors, Golgi tendon organs and muscle spindles, and some large alimentary enteroceptors. Aβ fibres form secondary endings on some muscle spindle (intrafusal) fibres and also innervate cutaneous and joint capsule mechanoreceptors. Aδ fibres innervate thermoreceptors, stretch-sensitive free endings, hair receptors and nociceptors, including those in dental pulp, skin and connective tissue. Aγ fibres are exclusively fusimotor to plate and trail endings on intrafusal muscle fibres. B fibres are myelinated autonomic preganglionic efferent fibres. C fibres are unmyelinated and have thermoreceptive, nociceptive and interoceptive functions, including the perception of slow, burning pain and visceral pain. This scheme can be applied to fibres of both spinal and cranial nerves except perhaps those of the olfactory nerve, where the fibres form a uniquely small and slow group. The largest somatic efferent fibres (Aα) innervate extrafusal muscle fibres (at motor endplates) exclusively and conduct at a maximum of 120 m/s. Fibres to fast twitch muscles are larger than those to slow twitch muscle. Smaller (Aγ) fibres of gamma motor neurones, and autonomic preganglionic (B) and postganglionic (C) efferent fibres conduct, in order, progressively more slowly (40 m/s to less than 10 m/s).

A different classification, used for afferent fibres from muscles, divides fibres into groups I–IV on the basis of their calibre; groups I–III are myelinated and group IV is unmyelinated. Group I fibres are large (12–22 μm), and include primary sensory fibres of muscle spindles (group Ia) and smaller fibres of Golgi tendon organs (group Ib). Group II fibres are the secondary sensory terminals of muscle spindles, with diameters of 6–12 μm. Group III fibres, 1–6 μm in diameter, have free sensory endings in the connective tissue sheaths around and within muscles and are nociceptive and, in skin, also thermosensitive. Group IV fibres are unmyelinated, with diameters below 1.5 μm; they include free endings in skin and muscle, and are primarily nociceptive.

Connective tissue sheaths

Nerve trunks, whether uni- or multifascicular, are limited externally by an epineurium, which is connected to surrounding tissues by mesoneurium. Mesoneurium is a loose connective tissue sheath containing the extrinsic, segmental blood supply of the nerve, and so is of clinical importance in nerve injury. Individual fasciculi of the nerve trunk are enclosed by a multilayered perineurium, which in turn surrounds the endoneurium or intrafascicular connective tissue (see Fig. 3.22).

Epineurium

Epineurium is a condensation of loose (areolar) connective tissue derived from mesoderm. As a general rule, the more fasciculi present in a peripheral nerve, the thicker the epineurium. Epineurium contains fibroblasts, collagen (types I and III) and variable amounts of adipose tissue, and it cushions the nerve it surrounds. Loss of this protective layer may be associated with pressure palsies seen in wasted, bedridden patients. The epineurium also contains lymphatics (which probably pass to regional lymph nodes) and blood vessels, vasa nervorum, that pass across the perineurium to communicate with a network of fine vessels within the endoneurium, forming the intrinsic system of vascular plexuses.

Perineurium

Perineurium extends from the CNS–PNS transition zone to the periphery, where it is continuous with the capsules of muscle spindles and encapsulated sensory endings, but ends openly at unencapsulated endings and neuromuscular junctions. It consists of alternating layers of flattened polygonal cells, once thought to be related to fibroblasts, but now believed to include glial cells derived from the CNS (Kucenas 2015) (Ch. 14). The perineurium can often contain 15–20 layers, each layer enclosed by a basal lamina up to 0.5 μm thick and separated by varying amounts of collagen (Ushiki and Ide 1990).Within each layer the cells interdigitate along extensive tight junctions; their cytoplasm typically contains vesicles and bundles of microfilaments and their plasma membrane often shows evidence of pinocytosis. These features are consistent with the function of the perineurium as a metabolically active diffusion barrier; together with the blood–nerve barrier, the perineurium is thought to play an essential role in maintaining the osmotic milieu and fluid pressure within the endoneurium (Liu et al 2018). There is experimental evidence that a subpopulation of perineurial glial cells may participate in the development and regeneration of peripheral nerves (Morris et al 2017).

Endoneurium

Strictly speaking, the term endoneurium is restricted to intrafascicular connective tissue and excludes the perineurial partitions within fascicles. Endoneurium consists of a fibrous matrix composed predominantly of type III collagen (reticulin) fibres, characteristically organized in fine bundles lying parallel to the long axis of the nerve, and condensed around individual Schwann cell–axon units and endoneurial vessels. The fibrous and cellular components of the endoneurium are bathed in endoneurial fluid at a slightly higher pressure than that outside in the surrounding epineurium. The major cellular constituents of the endoneurium are Schwann cells and endothelial cells; minor components are fibroblasts (constituting approximately 4% of the total endoneurial cell population), resident macrophages and mast cells. Schwann cell–axon units and blood vessels are enclosed within individual basal laminae and therefore isolated from the other cellular and extracellular components of the endoneurium.

Endoneurial arterioles have a poorly developed smooth muscle layer and do not autoregulate well. In sharp contrast, epineurial and perineurial vessels have a dense perivascular plexus of peptidergic, serotoninergic and adrenergic nerves. There are free nerve endings in all layers of neural connective tissue sheaths and there are some encapsulated (Pacinian) corpuscles in the endoneurium. These probably contribute to the acute sensitivity of nerves trapped in fibrosis after injury or surgery.

Schwann cells

Schwann cells are the major glial type in the PNS (Kidd et al 2013). *In vitro* they are fusiform in appearance. Both *in vitro* and *in vivo*, Schwann cells ensheathe peripheral axons, and myelinate those greater than 2 μm in diameter. In a mature peripheral nerve, they are distributed along the axons in longitudinal chains; the geometry of their association depends on whether the axon is myelinated or unmyelinated. In myelinated axons the territory of a Schwann cell defines an internode.

The molecular phenotype of mature myelin-forming Schwann cells is different from that of mature non-myelin-forming Schwann cells. Adult myelin-forming Schwann cells are characterized by the presence of several myelin proteins, some, but not all, of which are shared with oligodendrocytes and central myelin. In contrast, expression of the low-affinity neurotrophin receptor ($p75^{NTR}$) and GFAP intermediate filament protein (which differs from the CNS form in its post-translational modification) characterizes adult non-myelin-forming Schwann cells.

Schwann cells arise from Schwann cell precursors that, in turn, are generated from multipotent cells of the neural crest. Neuronal signals regulate many aspects of Schwann cell behaviour in developing and postnatal nerves. Axon-associated signals appear to control the proliferation of developing Schwann cells and their precursors; the developmentally programmed death of those precursors in order to match numbers of axons and glia within each peripheral nerve bundle; the production of basal laminae by Schwann cells; and the induction and maintenance of myelination. Axonal neuregulin 1 signalling via ErbB2/B3 receptors on Schwann cells is essential for Schwann cell myelination and also determines myelin thickness. An extensive literature supports the view that Schwann cells are key players in the acute injury response in the PNS (see Commentary 1.5), helping to provide a microenvironment that facilitates axonal regrowth (Birch 2011). Few Schwann cells persist in chronically denervated nerves.

Unmyelinated axons

Unmyelinated axons are commonly 1.0 μm in diameter, although some may be 1.5 μm or even 2 μm in diameter. Groups of up to 10 or more small axons (0.15–2.0 μm in diameter) are enclosed within a chain of overlapping Schwann cells that is surrounded by a basal lamina. Within each Schwann cell, individual axons are usually sequestered from their neighbours by delicate processes of cytoplasm. It seems likely, on the basis of quantitative studies in subhuman primates, that axons from adjacent cord segments may share Schwann cell columns; this phenomenon may play a role in the evolution of neuropathic pain after nerve injury. In the absence of a myelin sheath and nodes of Ranvier, action potential propagation along unmyelinated axons is not saltatory but continuous, and relatively slow (0.5–4.0 m/s).

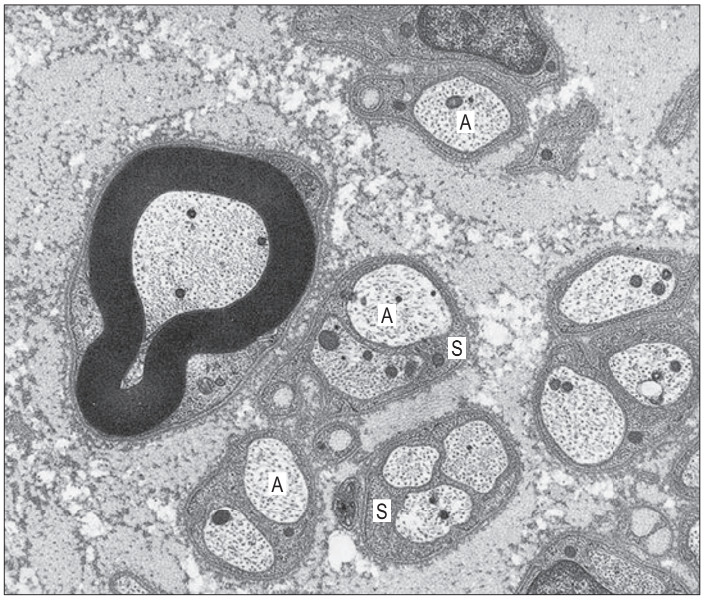

Fig. 3.23 An electron micrograph of a transverse section of biopsied human sural nerve, showing a myelinated axon and several unmyelinated axons (A), ensheathed by Schwann cells (S). (Courtesy of Professor Susan Standring, GKT School of Medicine, London.)

Myelinated axons

Myelinated axons (**Fig. 3.23**) have a 1 : 1 relationship with their ensheathing Schwann cells. The territorial extent of individual Schwann cells varies directly with the diameter of the axon they surround, from 150 to 1500 μm. Specialized domains of axo-glial interaction define nodes of Ranvier and their neighbouring compartments, paranodes and juxtaparanodes (Pereira et al 2012; **Fig. 3.24**). These domains contain multiprotein complexes characterized by unique sets of transmembrane and cytoskeletal proteins and clusters of ion channels; the mechanisms regulating channel clustering and node formation remain a subject of intense scrutiny (Peles and Salzer 2000, Poliak and Peles 2003, Horresh et al 2008). The region under the compact myelin sheath that extends between two juxtaparanodes is the internode. The molecular domains of myelinated axons, including that of the axon initial segment are reviewed in Buttermore et al (2013).

Schwann cell cytoplasm forms a continuous layer only in the perinuclear (mid-internodal) and paranodal regions, where it forms a collar from which microvilli project into the nodal gap substance. Elsewhere it is dispersed as a lace-like network over the inner (adaxonal) and outer (abaxonal) surfaces of the myelin sheath.

Nodes of Ranvier

The nodal compartment consists of a short length of exposed axolemma, typically 0.8–1.1 μm long, surrounded by a nodal gap substance composed of various extracellular components, some of which may possess nerve growth-repulsive characteristics. Multiple processes (microvilli) protrude into the gap substance from the outer collar of Schwann cytoplasm and contact the nodal axolemma. Voltage-gated sodium channels, the cell adhesion molecules NrCAM and neurofascin-186, the cytoskeletal adaptor ankyrin G25,26 and the actin-binding protein spectrin βIV are clustered at nodes. The calibre of the nodal axon is usually significantly less than that of the internodal axon, particularly in large-calibre fibres. For further reading on the molecular organization of nodes of Ranvier, paranodes and juxtaparanodes, see D'Este et al (2016).

Paranodes

The axolemma on either side of a node is contacted by paranodal loops of Schwann cell cytoplasm via specialized septate junctions that spiral around the axon. The junctions are thought to form a partial diffusion barrier into the peri-axonal space; restrict the movement of potassium channels from under the compact myelin; and limit lateral diffusion of membrane components. Caspr, contactin and their putative ligand NF155 (an isoform of neurofascin) are concentrated in paranodes.

Juxtaparanodes

The region of the axon lying just beyond the innermost paranodal junction is now recognized as a distinct domain defined by the localization

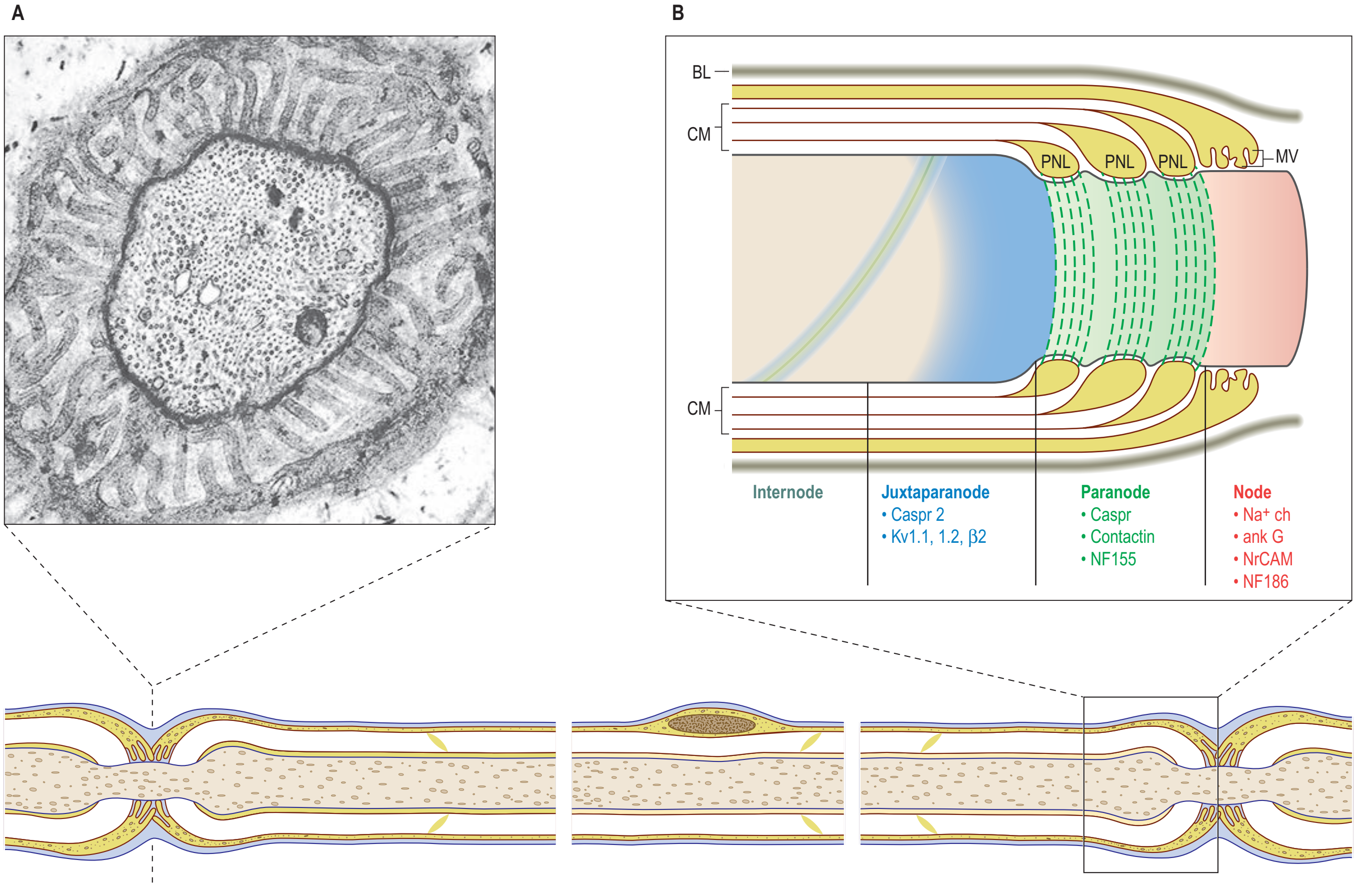

Fig. 3.24 The general plan of a peripheral myelinated nerve fibre in longitudinal section, including one complete internodal segment and two adjacent paranodal bulbs, used as a key for the more detailed microarchitecture of specific subregions. **A**, A transverse electron microscope section through the centre of a node of Ranvier, with numerous finger-like processes of adjacent Schwann cells converging towards the nodal axolemma. Many microtubules and neurofilaments are visible within the axoplasm. **B**, The arrangement of the axon, myelin sheath and Schwann cell cytoplasm at the node of Ranvier, in the paranodal bulbs and in the juxtaparanodal region. The axon is myelinated by a Schwann cell surrounded by a basal lamina (BL). Only a portion of the internode, which is located beneath the compact myelin (CM) sheath, is shown. A spiral of paranodal (green) and juxtaparanodal (blue) proteins extends into the internode; this spiral is apposed to the inner mesaxon of the myelin sheath (not shown). K^+ channels and Caspr2 are concentrated in the juxtaparanodal region. In the paranodal region, the compact myelin sheath opens up into a series of paranodal cytoplasmic loops (PNL) that invaginate and closely appose the axon, forming a series of septum-like junctions that spiral around the axon. Caspr, contactin and an isoform of neurofascin (NF155) are concentrated in this region. At the node, numerous microvilli (MV) project from the outer collar of the Schwann cell to contact the axolemma. The axon is enormously enriched in intramembranous particles at the node that correspond to Na^+ channels (Na^+ ch). Ankyrin G (ank G) isoforms and the cell adhesion molecules NrCAM and NF186 are also concentrated in this region. (A, Courtesy of Professor Susan Standring, GKT School of Medicine, London. B, Adapted with permission from Peles E, Salzer JL 2000 Molecular domains of myelinated axons. Curr Opin Neurobiol 10:558–65.)

of voltage-gated potassium channels (delayed-rectifier potassium channels Kv1.1, Kv1.2 and their Kvb2 subunit). Clustering of Kv1 channels at the juxtaparanodal region depends on their association with the Caspr2/TAG-1 adhesion complex.

Schmidt–Lanterman incisures

Schmidt–Lanterman incisures are helical decompactions of internodal myelin that appear as funnel-like profiles in teased fibre preparations labelled for markers of non-compacted myelin (e.g. MAG, Cx32). At an incisure the major dense line of the myelin sheath splits to enclose a continuous spiral band of cytoplasm passing between abaxonal and adaxonal layers of Schwann cell cytoplasm. The minor dense line of incisural myelin is also split, creating a channel connecting the peri-axonal space with the endoneurial extracellular fluid. The function of incisures is not known; their structure suggests that they may participate in transport of molecules across the myelin sheath.

Satellite cells

Many non-neuronal cells of the nervous system have been called satellite cells, including small, round extracapsular cells in peripheral ganglia, ganglionic capsular cells, Schwann cells, any cell that is closely associated with neuronal somata, and precursor cells associated with striated muscle fibres (Hanani 2010). Within the nervous system, the term is most commonly reserved for flat, epithelioid cells (ganglionic glial cells, capsular cells) that surround the neuronal somata of peripheral ganglia (see Fig. 3.25). Their cytoplasm resembles that of Schwann cells, and their deep surfaces interdigitate with reciprocal infoldings in the membranes of the enclosed neurones.

Enteric glia

Enteric nerves lack an endoneurium and so do not have the collagenous coats of other peripheral nerves. The enteric ganglionic neurones are supported by glia that closely resemble astrocytes; they contain more GFAP than non-myelinating Schwann cells and do not produce a basal lamina. Evidence for their roles in the local regulation of gastrointestinal motility and epithelial barrier function and in enteric neuroinflammation is emerging (Gulbransen and Sharkey 2012, Grubišić and Gulbransen 2017, Grundmann et al 2019).

Olfactory ensheathing glia

The olfactory system is unusual because it supports neurogenesis throughout life. Olfactory receptor neurones are continuously renewed from horizontal basal stem cells in the olfactory epithelium (Leung et al 2007, Forni and Wray 2012). They extend new axons through the lamina propria and cribriform plate into the CNS environment of the olfactory bulb, where they synapse with second-order neurones. Olfactory ensheathing cells (OECs, also known as olfactory ensheathing glia) accompany olfactory axons from the lamina propria of the olfactory epithelium to their synaptic contacts in the glomeruli of the olfactory bulbs and are thought to play a role in directing them to their correct position in the olfactory bulb (Higginson and Barnett 2011). This unusual arrangement is unique; elsewhere in the nervous system the territories of peripheral and central glia are clearly demarcated at CNS–PNS transition zones. OECs and the end-feet of astrocytes lying between the bundles of olfactory axons both contribute to the glia limitans at the pial surface of the olfactory bulbs.

OECs share many properties with Schwann cells and express some similar antigenic and morphological properties (Oprych et al 2016). They ensheathe olfactory sensory axons in a manner comparable to the relationship that exists transitorily between Schwann cells and axons in very immature peripheral nerves, i.e. they surround, but do not segregate, bundles of up to 50 fine unmyelinated axons to form approximately 20 fila olfactoria. Both OECs and Schwann cells can myelinate axons, even though normally none of the axons in the olfactory nerve is myelinated. It was thought that OECs shared a common origin with olfactory receptor neurones in the olfactory placode, but fate-mapping experiments in chicken embryos and genetic linkage-tracing studies in mice have shown that OECs are derived from neural crest cells (Forni and Wray 2012).

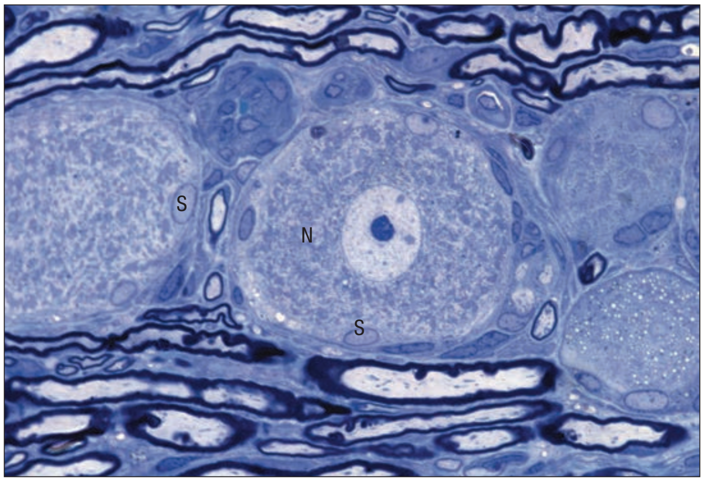

Fig. 3.25 Sensory neurones in a dorsal root ganglion (rat). Neurones (N) are typically variable in size but all are encapsulated by satellite cells (S). Myelinated axons are seen above and below the neuronal somata. Toluidine blue stained resin section. (Courtesy of Dr Clare Farmer, King's College, London.)

Blood supply of peripheral nerves

The blood vessels supplying a nerve end in a capillary plexus that pierces the perineurium. The branches of the plexus run parallel with the fibres, connected by short transverse vessels, forming narrow, rectangular meshes similar to those found in muscle. The blood supply of peripheral nerves is unusual because endoneurial capillaries have atypically large diameters and intercapillary distances that are greater than in many other tissues. Peripheral nerves have two separate, functionally independent vascular systems: an extrinsic system (regional nutritive vessels and epineurial vessels, the latter dominated by arteriovenous, AV, shunts) and an intrinsic system (longitudinally running microvessels in the endoneurium with fewer AV shunts). Anastomoses between the two systems produce considerable overlap between the territories of the segmental arteries. This unique pattern of vessels, together with a high basal nerve blood flow relative to metabolic requirements, means that peripheral nerves possess a high degree of resistance to ischaemia and probably explains why surgical mobilization of segments of a nerve does not inevitably produce ischaemic damage (Zochodne 2018).

Blood–nerve barrier

The endoneurial microenvironment is strictly regulated in two ways. Perineurial myofibroblasts provide a critical interface between the endoneurium and epineurial interstitial fluid. The blood–nerve barrier offers a restrictive microvascular barrier that operates at the level of the endoneurial capillary walls, where the endothelial cells are joined by tight junctions, are non-fenestrated and surrounded by continuous basal laminae (Palladino et al 2017, Liu et al 2018). The barrier is much less efficient in dorsal root ganglia and autonomic ganglia and in the distal parts of peripheral nerves.

Ganglia

Ganglia are aggregations of neuronal somata and are of varying form and size. They occur in the dorsal roots of spinal nerves; in the sensory roots of the trigeminal, facial, vestibulocochlear, glossopharyngeal and vagal cranial nerves; and in the peripheral autonomic nervous system (ANS). Each ganglion is enclosed within a capsule of fibrous connective tissue and contains neuronal somata and neuronal processes. Enteric ganglia are an exception to this rule; they resemble the CNS in both structure and function, and are not covered by a connective tissue capsule. Some ganglia, particularly in the ANS, contain axons that originate from neuronal somata that lie elsewhere in the nervous system and which pass through the ganglia without synapsing.

Sensory ganglia

The sensory ganglia of dorsal spinal roots (Fig. 3.25) and the ganglia of the trigeminal, facial, glossopharyngeal and vagal cranial nerves are enclosed in a periganglionic connective tissue capsule that resembles the perineurium surrounding peripheral nerves. Ganglionic neurones are unipolar: they have spherical or oval somata of varying size, aggregated in groups between fasciculi of myelinated and unmyelinated nerve fibres. For each neurone, a single axodendritic process bifurcates into central and peripheral processes; in myelinated fibres the junction occurs at a node of Ranvier. The peripheral process terminates in a sensory ending and, because it conducts impulses towards the soma, it functions as an elongated dendrite, strictly speaking. However, it has the typical structural and functional properties of a peripheral axon, and is conventionally described as an axon.

Each neuronal soma is surrounded by a sheath of satellite glial cells (SGCs) (Pannese 2010). (A notable exception is the spiral, or cochlear, ganglion, where most neuronal somata are myelinated, presumably contributing to fast electrical transmission.) The axodendritic process and its peripheral and central divisions, ensheathed by Schwann cells, lie outside the SGC sheath. All the cells in the ganglion lie within a highly vascularized connective tissue that is continuous with the endoneurium of the nerve root. In dorsal root ganglia there is no clear regional mapping of the innervated body regions. There is evidence from animal experimental studies of some somatotopic organization within the trigeminal ganglion, but as yet, there is no evidence that this is the case in the human trigeminal ganglion (Wei et al 2017). Although sensory neurones receive no synapses, they are endowed with receptors for numerous neurotransmitters and hormones, and can thus communicate chemically amongst themselves and with SGCs.

SGCs are the main type of glial cell in sensory ganglia. They share several properties with astrocytes, including expression of glutamine synthetase and various neurotransmitter transporters. In addition, like astrocytes, the SGCs that surround a neurone are coupled by gap junctions and express receptors for ATP. Unlike astrocytes, SGCs completely surround individual sensory neurones (and more rarely two or three neurones) in a glial sheath. They undergo major changes as a result of injury to peripheral nerves, and appear to contribute to chronic pain in a number of animal pain models.

Herpes zoster

Primary infection with the varicella zoster virus causes chickenpox. Following recovery, the virus remains dormant within dorsal root ganglia or trigeminal ganglia, mostly in the neurones, and less commonly in the SGCs. Reactivation of the virus leads to herpes zoster (shingles), which involves the dermatome(s) supplied by the affected sensory nerve(s). Diagnostic signs are severe pain, erythema and blistering as occurs in chickenpox, often confined to one of the divisions of the trigeminal nerve or to a spinal nerve dermatome. Herpes zoster involving the geniculate ganglion compresses the facial nerve and results in a lower motor neurone facial paralysis, known as Ramsay Hunt syndrome. Occasionally, if the vestibulocochlear nerve becomes involved, there is vertigo, tinnitus and some deafness. The most important complication of herpes zoster is post-herpetic neuralgia, a severe and persistent pain that is highly refractory to treatment.

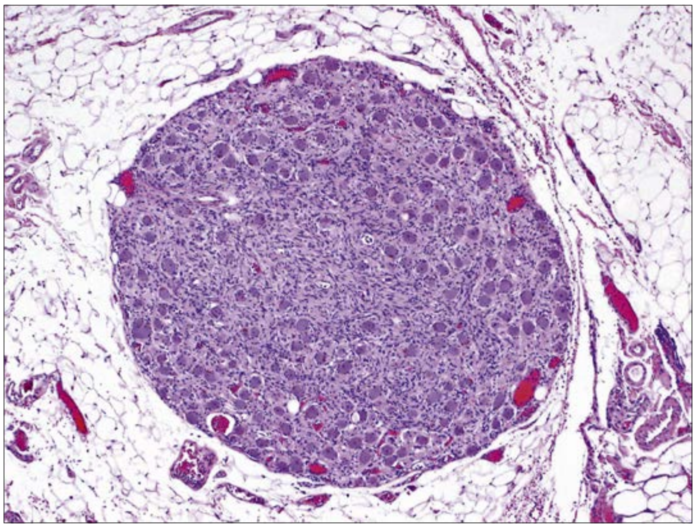

Fig. 3.26 A parasympathetic ganglion. Large neuronal somata, some with nuclei and prominent nucleoli in the plane of section, are encapsulated by satellite cells and surrounded by nerve fibres and non-neuronal cells. (Courtesy of Mr Peter Helliwell and the late Dr Joseph Mathew, Department of Histopathology, Royal Cornwall Hospitals Trust, UK.)

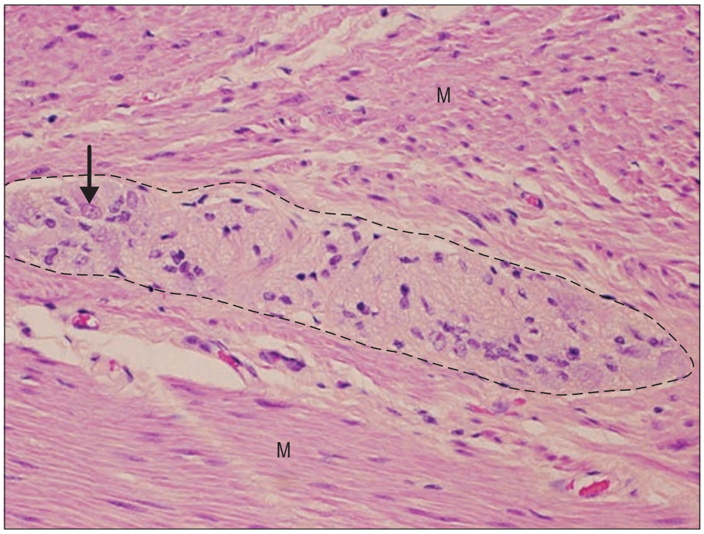

Fig. 3.27 An enteric ganglion (outlined) of the myenteric (Auerbach's) plexus between the inner circular and outer longitudinal layers of smooth muscle (M) in the wall of the human intestine. An enteric ganglionic neurone is arrowed. (Courtesy of Mr Peter Helliwell and the late Dr Joseph Mathew, Department of Histopathology, Royal Cornwall Hospitals Trust, UK.)

Autonomic ganglia

The main types of cell in autonomic ganglia are the ganglionic neurones, small intensely fluorescent (SIF) cells and satellite glial cells (SGCs) (Fig. 3.26). Most of the neurones have somata ranging from 25 to 50 µm and complex dendritic fields; dendritic glomeruli have been observed in ganglia in experimental animals. Ganglionic neurones receive many axodendritic synapses from preganglionic axons; axosomatic synapses are less numerous. Postganglionic fibres commonly arise from the initial stem of a large dendrite and produce few or no collateral processes. Given their close relationship to the ganglionic neurones, autonomic SGCs may have the potential to influence synaptic transmission. SIF cells are characterized by being smaller than the neurones and by having numerous granules that contain noradrenaline (norepinephrine), dopamine and serotonin. They are almost completely invested by a sheath of SGCs and receive and make synapses; their physiological role is currently obscure, but they lend credence to the idea that autonomic ganglia are far more than simple relay stations.

Sympathetic neurones are multipolar and their dendritic trees, on which preganglionic motor axons synapse, are more elaborate than those of parasympathetic neurones. The neurones are surrounded by a mixed neuropil of afferent and efferent fibres, dendrites, synapses and non-neural cells. There is considerable variation in the ratio of pre- and postganglionic fibres in different types of ganglion. Preganglionic sympathetic axons may synapse with many postganglionic neurones for the wide dissemination and perhaps amplification of sympathetic activity, a feature not found to the same degree in parasympathetic ganglia. Dissemination may also be achieved by connections with ganglionic interneurones or by the diffusion within the ganglion of transmitter substances produced either locally (paracrine effect) or elsewhere (endocrine effect). Some axons within a ganglion may be efferent fibres en route to another ganglion, or afferents from viscera and glands. These fibres may synapse with neurones in the ganglion, e.g. substance P-containing axons of dorsal root neurones synapse on neurones in prevertebral ganglia, thereby enabling interactions between the sensory system and the ANS.

Enteric ganglia

The enteric nervous system (ENS) lies within the walls of the gastrointestinal tract (see Fig. 59.9) and includes the myenteric and submucosal plexuses and associated ganglia (Furness 2012, Neunlist et al 2013). The ganglionic neurones (Fig. 3.27) serve different functions, including the regulation of gut motility (in conjunction with interstitial cells of Cajal (Huizinga et al 2009)), mucosal transport and mucosal blood flow. Unlike the other two divisions of the ANS, the ENS is largely independent of the CNS, and the extrinsic autonomic fibres that supply the gut wall exert only modulatory effects on it. Submucosal neurones, together with sympathetic axons, regulate the local blood flow.

Hirschsprung's disease is a congenital disease in which dysfunctional neural crest migration means that the ganglia of both the myenteric and submucosal plexuses in the distal bowel fail to develop (Nagy et al 2017). The resulting lack of propulsive activity in the aganglionic bowel leads to functional obstruction and megacolon, which can be life-threatening. Around 1 in 5000 infants is born with the condition and is typically diagnosed in the neonatal period. Treatment usually consists of removing the diseased intestinal segment.

The enteric plexuses consist of sensory neurones, interneurones and a variety of motor neurones. These neurones are endowed with receptors for a large number of neurotransmitters and also release a variety of neurotransmitters. All classes of enteric neurone are equally distributed along the entire ganglionic network; consequently the ENS consists of numerous repeating modules.

The myenteric plexus contains the motor neurones that control the movements of gastrointestinal smooth muscle. The main excitatory neurotransmitter is acetylcholine, which may be co-localized with an excitatory peptide (usually a tachykinin, such as substance P). The main inhibitory neurotransmitter is nitric oxide (NO), released from neurones that may also release the inhibitory peptide vasoactive intestinal peptide (VIP).

An important function of myenteric neurones is to mediate the peristaltic reflex, which is induced by intestinal wall distension or by mechanical stimulation of the mucosa. These stimuli initiate contraction oral to the site of the stimulus, and relaxation anal to the site, creating a pressure gradient that propels the intestinal contents. Interstitial cells of Cajal (ICC) are pacemaker cells believed to integrate neuronal signals with rhythmic oscillations of muscle contraction; disturbance of ICC function may be a factor in a number of gastrointestinal disorders (Huizinga et al 2009).

Enteric glia are the main type of glial cell in the ENS. In some respects they resemble astrocytes, e.g. they form end-feet with blood vessels, respond to numerous chemical mediators, and are extensively coupled among themselves by gap junctions. They appear to play an important role in neuroprotection and in maintaining the integrity of the intestinal mucosal barrier.

DISPERSED NEUROENDOCRINE SYSTEM

Although the nervous, neuroendocrine and endocrine systems all operate by intercellular communication, they differ in the mode, speed and degree or localization of the effects produced (Day and Salzet 2002). The autonomic nervous system uses impulse conduction and neurotransmitter release to transmit information, and the responses induced are rapid and localized. The dispersed neuroendocrine system uses only secretion. It is slower and the induced responses are less localized, because the secretions, e.g. neuromediators, can act either on contiguous cells, or on groups of nearby cells reached by diffusion, or on distant cells via the blood stream. Many of its effector molecules operate in both the nervous system and the neuroendocrine system. The endocrine system proper, which consists of clusters of cells and discrete, ductless, hormone-producing glands, is even slower and less localized, although its effects are specific and often prolonged. These regulatory systems overlap in function, and can be considered as a single neuroendocrine regulator of the

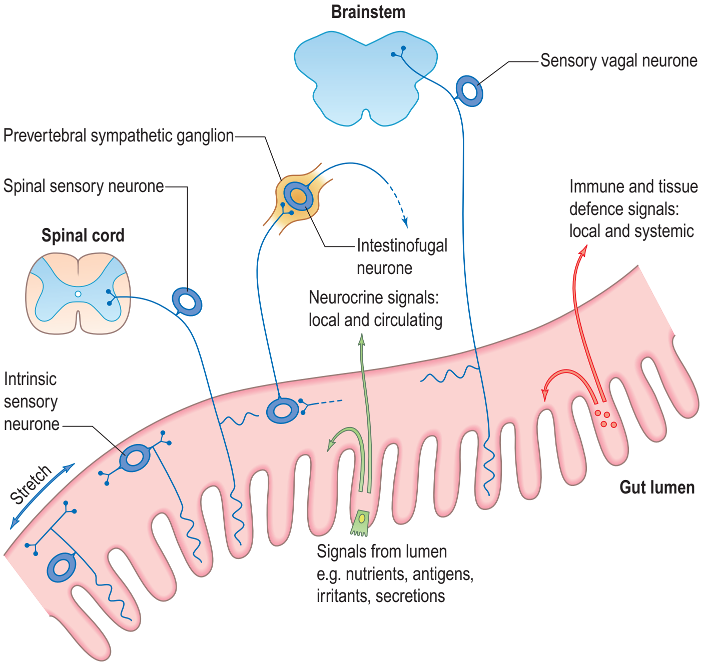
Brainstem
Sensory vagal neurone
Prevertebral sympathetic ganglion
Spinal sensory neurone
Spinal cord
Intestinofugal neurone
Immune and tissue defence signals: local and systemic
Neurocrine signals: local and circulating
Intrinsic sensory neurone
Stretch
Gut lumen
Signals from lumen e.g. nutrients, antigens, irritants, secretions

Fig. 3.28 The ways in which the nervous system, neuroendocrine system and immune system are integrated, demonstrated in the intestine. Neurocrine signals from enteric neuroendocrine cells and signals from immune defence cells (e.g. lymphocytes, macrophages and mast cells) act on other cells of those systems and on neurones with sensory endings in the intestinal wall, either locally or at a distance. Some neuronal soma lie within enteric ganglia in the gut wall; others have their bodies in peripheral ganglia. Neuronal signals may act locally, be transmitted to the CNS or enter a reflex pathway via sympathetic ganglia.

metabolic activities and internal environment of the organism, acting to provide conditions in which it can function successfully. Mediators of multi-directional crosstalk within a neuroimmune network of vessels, circulating hormones and nerve fibres that link the brain with all viscera, include the sympathetic innervation of immune tissue, cytokine activation of microglia and endocrine cells, the hormonal regulation of immunity and the activation and modulation of hypothalamic–pituitary units (Ashley and Demas 2016) (**Fig. 3.28**).

Some cells can take up and decarboxylate amine precursor compounds (amine precursor uptake and decarboxylation, or APUD, cells). They are characterized by dense-core cytoplasmic granules, similar to the neurotransmitter vesicles seen in some types of neuronal terminal. The group includes cells described as chromaffin cells (phaeochromocytes), derived from neuroectoderm and innervated by preganglionic sympathetic nerve fibres. Chromaffin cells synthesize and secrete catecholamines (dopamine, noradrenaline (norepinephrine) or adrenaline (epinephrine)). Their name refers to the finding that their cytoplasmic store of catecholamines is sufficiently concentrated to give an intense yellow–brown coloration, the positive chromaffin reaction, when they are treated with aqueous solutions of chromium salts, particularly potassium dichromate. Classic chromaffin cells include clusters of cells in the suprarenal medulla; the para-aortic bodies, which secrete noradrenaline; paraganglia; certain cells in the carotid bodies; and small groups of cells irregularly dispersed among the paravertebral sympathetic ganglia, splanchnic nerves and prevertebral autonomic plexuses.

The alimentary tract contains a large population of cells of a similar type (previously called neuroendocrine or enterochromaffin cells) in its wall. These cells act as sensory transducers, activating intrinsic and extrinsic primary afferent neurones via their release of 5-hydroxytryptamine (5-HT, serotonin). Communications between gut microbiota, the neuroendocrine system and the brain are mediated via humoral, immune and neural pathways that involve microbial metabolites, gut hormones, the enteric nervous system, the vagus nerve and spinal afferents (Farzi et al 2018). The neonatal respiratory tract contains a prominent system of neuroendocrine cells, both dispersed and aggregated (neuroepithelial bodies); the numbers of both types decline during childhood. Merkel cells in the basal epidermis of the skin store neuropeptides, which they release to associated nerve endings or other cells in a neuroendocrine role, in response to pressure and possibly other stimuli (Lucarz and Brand 2007). Experimental animal studies have revealed 5-HT-containing intraepithelial paraneurones in the urothelial lining of the urethra; these cells are thought to relay information from the luminal surface of the urethra to underlying sensory nerves.

A number of descriptions and terms have been applied to cells of this system in the older literature. They include: clear cells (so named because of their poor staining properties in routine preparations); argentaffin cells (reduce silver salts); argyrophil cells (absorb silver); small intensely fluorescent cells; peptide-producing cells (particularly of the hypothalamus, hypophysis, pineal and parathyroid glands, and placenta); Kulchitsky cells in the lungs; and paraneurones. Many cells of the dispersed (or diffuse) neuroendocrine system are derived embryologically from the neural crest. Some, particularly cells from the gastrointestinal system, are now known to be endodermal in origin.

SENSORY ENDINGS

General features of sensory receptors

There are three major forms of sensory receptor: neuroepithelial, epithelial and neuronal (**Fig. 3.29**).

A neuroepithelial receptor is a neurone with a soma lying near a sensory surface and an axon that conveys sensory signals into the CNS to synapse on second-order neurones. This is an evolutionarily primitive arrangement, and the only examples remaining in humans are the sensory neurones of the olfactory epithelium.

An epithelial receptor is a cell that is modified from a non-nervous sensory epithelium and innervated by a primary sensory neurone with a soma lying near the CNS, e.g. auditory receptors and taste buds. When activated, this type of receptor excites its neurone by neurotransmission across a synaptic gap.

A neuronal receptor is a primary sensory neurone that has a soma in a craniospinal ganglion and a peripheral axon ending in a sensory terminal. All cutaneous sensors and proprioceptors are of this type; their sensory terminals may be encapsulated or linked to special mesodermal or ectodermal structures to form a part of the sensory apparatus. The extraneural cells are not necessarily excitable, but create an appropriate environment for the excitation of the neuronal process.

The receptor stimulus is transduced into a graded change of electrical potential at the receptor surface (receptor potential), and this initiates an all-or-none action potential that is transmitted to the CNS. This may occur either in the receptor, when this is a neurone, or partly in the receptor and partly in the neurone that innervates it, in the case of epithelial receptors. Transduction varies with the modality of the stimulus, and usually causes depolarization of the receptor membrane (or hyperpolarization, in the retina). In mechanoreceptors, transduction may involve the deformation of membrane structure, which causes either strain or stretch-sensitive ion channels to open. In chemoreceptors, receptor action may resemble that for ACh at neuromuscular junctions. Visual receptors share similarities with chemoreceptors: light causes changes in receptor proteins, which activate G proteins, resulting in the release of second messengers and altered membrane permeability.

The quantitative responses of sensory endings to stimuli vary greatly and increase the flexibility of the functional design of sensory systems. Although increased excitation with increasing stimulus level is a common pattern ('on' response), some receptors respond to decreased stimulation ('off' response). Even unstimulated receptors show varying degrees of spontaneous background activity against which an increase or decrease in activity occurs with changing levels of stimulus. In all receptors studied, when stimulation is maintained at a steady level, there is an initial burst (the dynamic phase) followed by a gradual adaptation to steady level (the static phase). Though all receptors show these two phases, one or other may predominate, providing a distinction between rapidly adapting endings that accurately record the rate of stimulus onset, and slowly adapting endings that signal the constant amplitude of a stimulus, e.g. position sense. Dynamic and static phases are reflected in the amplitude and duration of the receptor potential and also in the frequency of action potentials in the sensory fibres. The stimulus strength necessary to elicit a response in a receptor, i.e. its threshold level, varies greatly between receptors, and provides an extra level of information about stimulus strength. For further reading, see Vanderah (2018).

Functional classification of receptors

Receptors have been classified in several ways. They may be classified by the modalities to which they are sensitive, such as mechanoreceptors (which are responsive to deformation, e.g. touch, pressure, sound waves, etc.), chemoreceptors, photoreceptors and thermoreceptors. Some receptors are polymodal, i.e. they respond selectively to more than one modality; they usually have high thresholds and respond to damaging stimuli associated with irritation or pain (nociceptors).

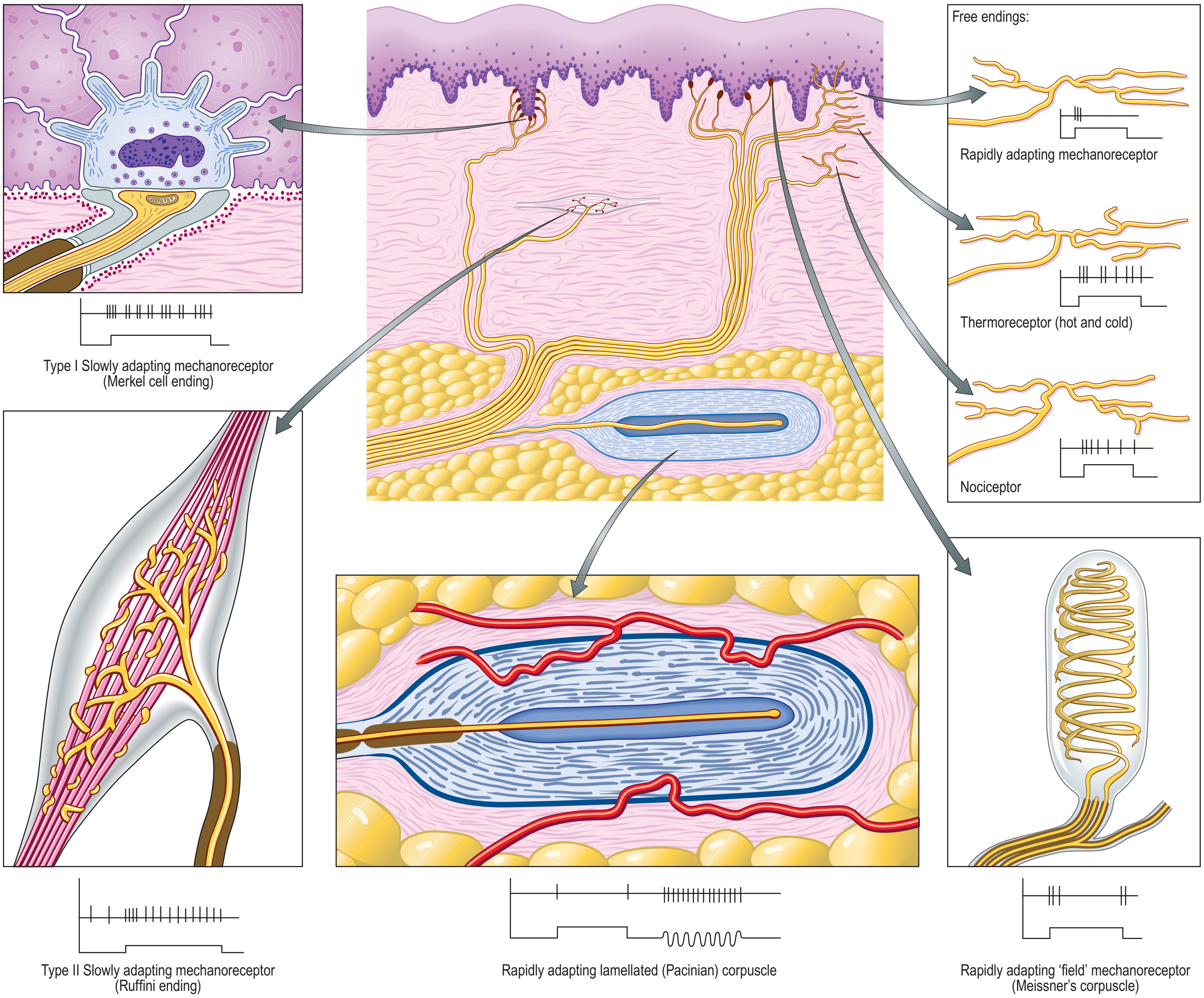
Free endings:
Rapidly adapting mechanoreceptor
Thermoreceptor (hot and cold)
Nociceptor
Type I Slowly adapting mechanoreceptor (Merkel cell ending)
Type II Slowly adapting mechanoreceptor (Ruffini ending)
Rapidly adapting lamellated (Pacinian) corpuscle
Rapidly adapting 'field' mechanoreceptor (Meissner's corpuscle)

Fig. 3.29 Some major types of sensory ending of general afferent fibres (omitting neuromuscular, neurotendinous and hair-related types). The traces below each type of ending indicate (top) their response (firing rate (vertical lines) and adaption with time) to an appropriate stimulus (below) of the duration indicated. The response of the Pacinian corpuscle to vibration (rapid sequence of on–off stimuli) is also shown.

Another widely used classification divides receptors on the basis of their distribution in the body into exteroceptors, proprioceptors and interoceptors. Exteroceptors and proprioceptors are receptors of the somatic afferent components of the nervous system, while interoceptors are receptors of the visceral afferent pathways.

Exteroceptors respond to external stimuli and are found at, or close to, body surfaces. They can be subdivided into the general or cutaneous sense organs and special sensory organs. General sensory receptors include free and encapsulated terminals in skin and near hairs; none of these has absolute specificity for a particular sensory modality. Special sensory organs are the olfactory, visual, acoustic, vestibular and taste receptors.

Proprioceptors respond to stimuli to deeper tissues, especially of the locomotor system, and are concerned with detecting movement, mechanical stresses and position. They include Golgi tendon organs, muscle spindles, Pacinian corpuscles, other endings in joints, and vestibular receptors. Proprioceptors are stimulated by the contraction of muscles, movements of joints and changes in the position of the body. They are essential for the coordination of muscles, the grading of muscular contraction, and the maintenance of equilibrium.

Interoceptors are found in the walls of the viscera, glands and vessels, where their terminations include free nerve endings, encapsulated terminals and endings associated with specialized epithelial cells. Nerve terminals are found in the layers of visceral walls and the adventitia of blood vessels, but the detailed structure and function of many of these endings are not well established. Encapsulated (lamellated) endings occur in the heart, adventitia and mesenteries. Free terminal arborizations occur in the endocardium, the endomysium of all muscles, and connective tissue generally. Tension produced by excessive muscular contraction or by visceral distension often causes pain, particularly in pathological states, which is frequently poorly localized and of a deep-seated nature. Visceral pain is often referred to the corresponding dermatome (see Fig. 24.10). Polymodal nociceptors (irritant receptors) respond to a variety of stimuli such as noxious chemicals or damaging mechanical stimuli. They are mainly the free endings of fine, unmyelinated fibres that are widely distributed in the epithelia of the alimentary and respiratory tracts; they may initiate protective reflexes.

Interoceptors include vascular chemoreceptors, e.g. the carotid body, and baroceptors, which are concerned with the regulation of blood flow and pressure and the control of respiration.

Free nerve endings

Sensory endings that branch to form plexuses occur in many sites (see Fig. 3.29). They occur in all connective tissues, including those of the dermis, fasciae, capsules of organs, ligaments, tendons, adventitia of blood vessels, meninges, articular capsules, periosteum, perichondrium, Haversian systems in bone, parietal peritoneum, walls of viscera and the endomysium of all types of muscle. They also innervate the epithelium of the skin, cornea, buccal cavity, and the alimentary and respiratory tracts and their associated glands. Within epithelia, free sensory endings lack Schwann cell ensheathment and are enveloped instead by epithelial cells. Afferent fibres from free terminals may be myelinated or unmyelinated but are always of small diameter and low conduction velocity. When afferent axons are myelinated, their terminal arborizations lack a myelin sheath. These terminals serve several sensory modalities. In the dermis, they may be responsive to moderate cold or heat (thermoreceptors); light mechanical touch (mechanoreceptors); damaging heat, cold or deformation (unimodal nociceptors); and damaging stimuli of several kinds (polymodal nociceptors). Similar fibres in deeper tissues may also signal extreme conditions, which are experienced, as with all nociceptors, as ache or pain. Free endings in the cornea, dentine and periosteum may be exclusively nociceptive.

Special types of free ending are associated with epidermal structures in the skin. They include terminals associated with hair follicles (peritrichial receptors), which branch from myelinated fibres in the deep dermal cutaneous plexus; the number, size and form of the endings are related to the size and type of hair follicle innervated. These endings respond mainly to movement when hair is deformed and belong to the rapidly adapting mechanoreceptor group.

C Merkel tactile endings (see Commentary 1.4) lie either at the base of the epidermis or around the apical ends of some hair follicles, and most are innervated by large myelinated axons. Each axon expands into a disc that is applied closely to the base of a Merkel cell in the basal layer of the epidermis. The cells are believed to be derived from the epidermis, although a neural crest origin remains possible. They contain many large (50–100 nm) dense-core vesicles, presumably containing transmitters. Merkel endings are thought to be slow-adapting mechanoreceptors, responsive to sustained pressure and sensitive to the edges of applied objects. Their functions are controversial, however, and likely to be more varied.

Encapsulated endings

Encapsulated endings are a major group of special endings that includes lamellated corpuscles of various kinds (e.g. Meissner's, Pacinian), Golgi tendon organs, neuromuscular spindles and Ruffini endings (see Fig. 3.29). They exhibit considerable variety in their size, shape and distribution but share a common feature: namely, that each axon terminal is encapsulated by non-excitable cells (Proske and Gandevia 2012).

Meissner's corpuscles

Meissner's corpuscles (Wagner–Meissner corpuscles; tactile corpuscle-like bodies) are found in the dermal papillae of all parts of the hand and foot, the anterior aspect of the forearm, the lips, palpebral conjunctiva and mucous membrane of the apical part of the tongue. They are most concentrated in thick hairless skin, especially of the finger pads, where there may be up to 24 corpuscles per cm^2 in young adults. Mature corpuscles are cylindrical in shape, approximately 80 µm long and 30 µm across, with their long axes perpendicular to the skin surface. Each corpuscle has a connective tissue capsule and central core composed of a stack of flat modified Schwann cells (**Fig. 3.30**). Meissner's corpuscles are rapidly adapting mechanoreceptors, sensitive to shape and textural changes in exploratory and discriminatory touch; their acute sensitivity provides the neural basis for reading Braille text. Tactile corpuscle-like bodies have been reported in the oesophagus, stomach, gastroesophageal junction, and colorectum as incidental findings in samples taken during endoscopic procedures (Huber et al 2017).

Pacinian corpuscles

Pacinian corpuscles are situated subcutaneously in the palmar and plantar aspects of the hand and foot and their digits, the external genitalia, arm, neck, nipple, periosteal and interosseous membranes, and near joints and within the mesenteries (**Fig. 3.31**). They are oval, spherical or irregularly coiled and measure up to 2 mm in length and 100–500 µm or more across; the larger ones are visible to the naked eye. Each corpuscle has a capsule, an intermediate growth zone and a central core that contains an axon terminal. The capsule is formed by approximately 30 concentrically arranged lamellae of flat cells approximately 0.2 µm thick. Adjacent cells overlap and successive lamellae are separated by an amorphous proteoglycan matrix that contains circularly orientated collagen fibres, closely applied to the surfaces of the lamellar cells. The amount of collagen increases with age. The intermediate zone is cellular and its cells become incorporated into the capsule or core, so that it is not clearly defined in mature corpuscles. The core consists of approximately 60 bilateral, compacted lamellae lying on both sides of a central nerve terminal.

Each corpuscle is supplied by a myelinated axon, which initially loses its myelin sheath and subsequently loses its ensheathing Schwann cell at its junction with the core. The naked axon runs through the central axis of the core and ends in a slightly expanded bulb. It is in contact with the innermost core lamellae, is transversely oval and sends short projections of unknown function into clefts in the lamellae. The axon contains numerous large mitochondria, and minute vesicles, approximately 5 nm in diameter, which aggregate opposite the clefts. The cells of the capsule and core lamellae are thought to be specialized fibroblasts but some may be Schwann cells. Elastic fibrous tissue forms an overall external capsule to the corpuscle. Pacinian corpuscles are supplied by capillaries that accompany the axon as it enters the capsule.

Pacinian corpuscles act as very rapidly adapting mechanoreceptors. They respond only to sudden disturbances and are especially sensitive to very-high-frequency vibration. The rapidity may be partly due to the lamellated capsule acting as a high pass frequency filter, damping slow distortions by fluid movement between lamellar cells. Groups of corpuscles respond to pressure changes, e.g. on grasping or releasing an object.

Ruffini endings

Ruffini endings are slowly adapting mechanoreceptors. They are found in the dermis of thin, hairy skin, where they function as dermal stretch receptors and are responsive to maintained stresses in dermal collagen. They consist of the highly branched, unmyelinated endings of myelinated afferents. They ramify between bundles of collagen fibres within a spindle-shaped structure, which is enclosed partly by a fibrocellular

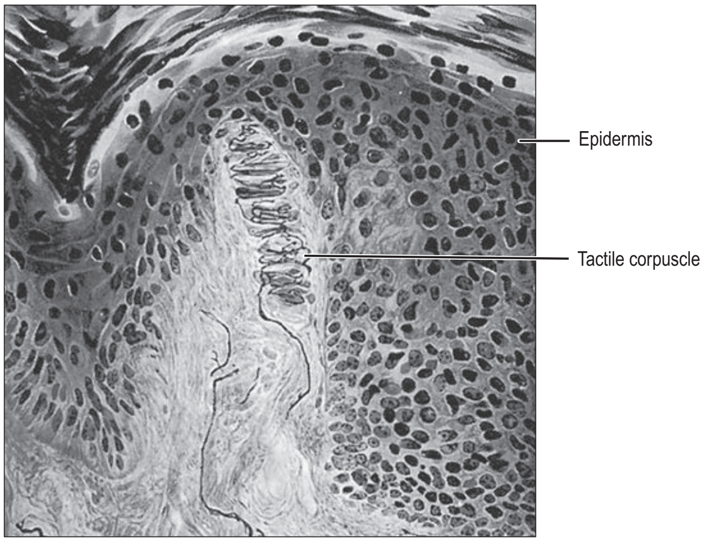

Fig. 3.30 A tactile Meissner's corpuscle in a dermal papilla in the skin, demonstrated using the modified Bielschowsky silver stain technique. (Courtesy of Professor N Cauna, University of Pittsburgh.)

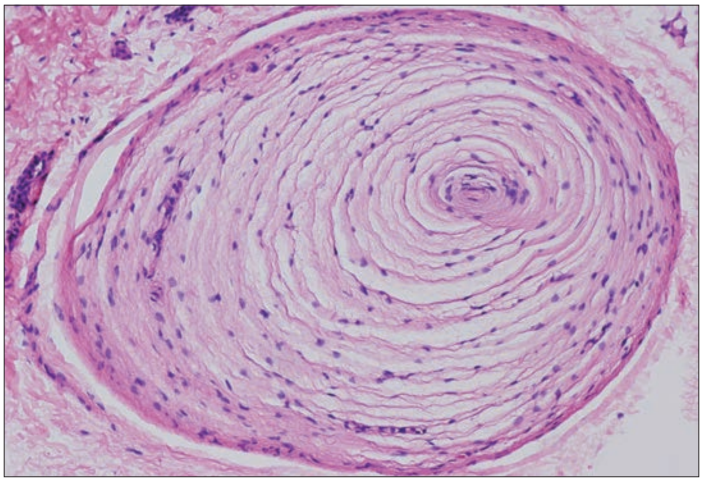

Fig. 3.31 A Pacinian corpuscle in human dermis. (Courtesy of Mr Peter Helliwell and the late Dr Joseph Mathew, Department of Histopathology, Royal Cornwall Hospitals Trust, UK.)

sheath derived from the perineurium of the nerve. Ruffini endings appear electrophysiologically similar to Golgi tendon organs, which they resemble, although they are less organized structurally; they are also found in joint capsules where they are thought to signal static joint position, changes in intra-articular pressure, and the direction, amplitude and velocity of joint movements (see below).

Golgi tendon organs

Golgi tendon organs are found mainly near musculotendinous junctions (Fig. 3.32), where more than 50 may occur at any one site. Each terminal is closely related to a group of muscle fibres (up to 20) as they insert into the tendon. Golgi tendon organs are approximately 500 μm long and 100 μm in diameter, and consist of small bundles of tendon fibres enclosed in a delicate capsule. The collagen bundles (intrafusal fasciculi) are less compact than elsewhere in the tendon, the collagen fibres are smaller and the fibroblasts larger and more numerous. A single, thickly myelinated 1b afferent nerve fibre enters the capsule and divides. Its branches, which may lose their ensheathing Schwann cells, terminate in leaf-like enlargements containing vesicles and mitochondria, which wrap around the tendon. A basal lamina or process of Schwann cell cytoplasm separates the nerve terminals from the collagen bundles that constitute the tendon. Golgi tendon organs are activated by passive stretch of the tendon but are much more sensitive to active contraction of the muscle. They are important in providing proprioceptive information that complements the information coming from neuromuscular spindles. Their responses are slowly adapting and they signal maintained tension.

Neuromuscular spindles

Neuromuscular spindles are mechanosensors essential for proprioception (Boyd 1985, Banks 2015). Each spindle contains a few small, specialized intrafusal muscle fibres, innervated by both sensory and motor nerve fibres (Figs 3.33–3.34). The whole is surrounded equatorially by a fusiform spindle capsule of connective tissue, consisting of an outer perineurium-like sheath of flattened fibroblasts and collagen, and an inner sheath that forms delicate tubes around individual intrafusal fibres (Fig. 3.35). A gelatinous fluid rich in glycosaminoglycans fills the space between the two sheaths.

There are usually 5–14 intrafusal fibres (the number varies between muscles) and two major types of fibre, nuclear bag and nuclear chain fibres, which are distinguished by the arrangement of nuclei in their sarcoplasm. In nuclear bag fibres, an equatorial cluster of nuclei makes the fibre bulge slightly, whereas the nuclei in nuclear chain fibres form a single axial row. Nuclear bag fibres are subdivided into bag1 and bag2 fibres, are greater in diameter than chain fibres and extend beyond the surrounding capsule to the endomysium of nearby extrafusal muscle fibres. Nuclear chain fibres are attached at their poles to the capsule or to the sheaths of nuclear bag fibres.

The intrafusal fibres resemble typical skeletal muscle fibres, except that the zone of myofibrils is thin around the nuclei. Dynamic bag1 fibres generally lack M lines, possess little sarcoplasmic reticulum, and have an abundance of mitochondria and oxidative enzymes, but little glycogen. Static bag2 fibres have distinct M lines and abundant glycogen. Nuclear chain fibres have marked M lines, sarcoplasmic reticulum and T-tubules, and abundant glycogen, but few mitochondria. Each

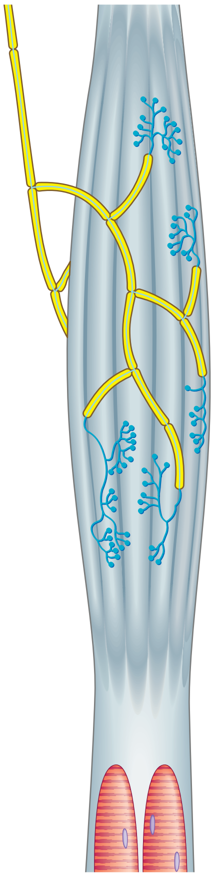

Fig. 3.32 The structure and innervation of a Golgi tendon organ. For clarity, the perineurium and endoneurium have been omitted to show the distribution of nerve fibres ramifying between the collagen fibre bundles of the tendon.

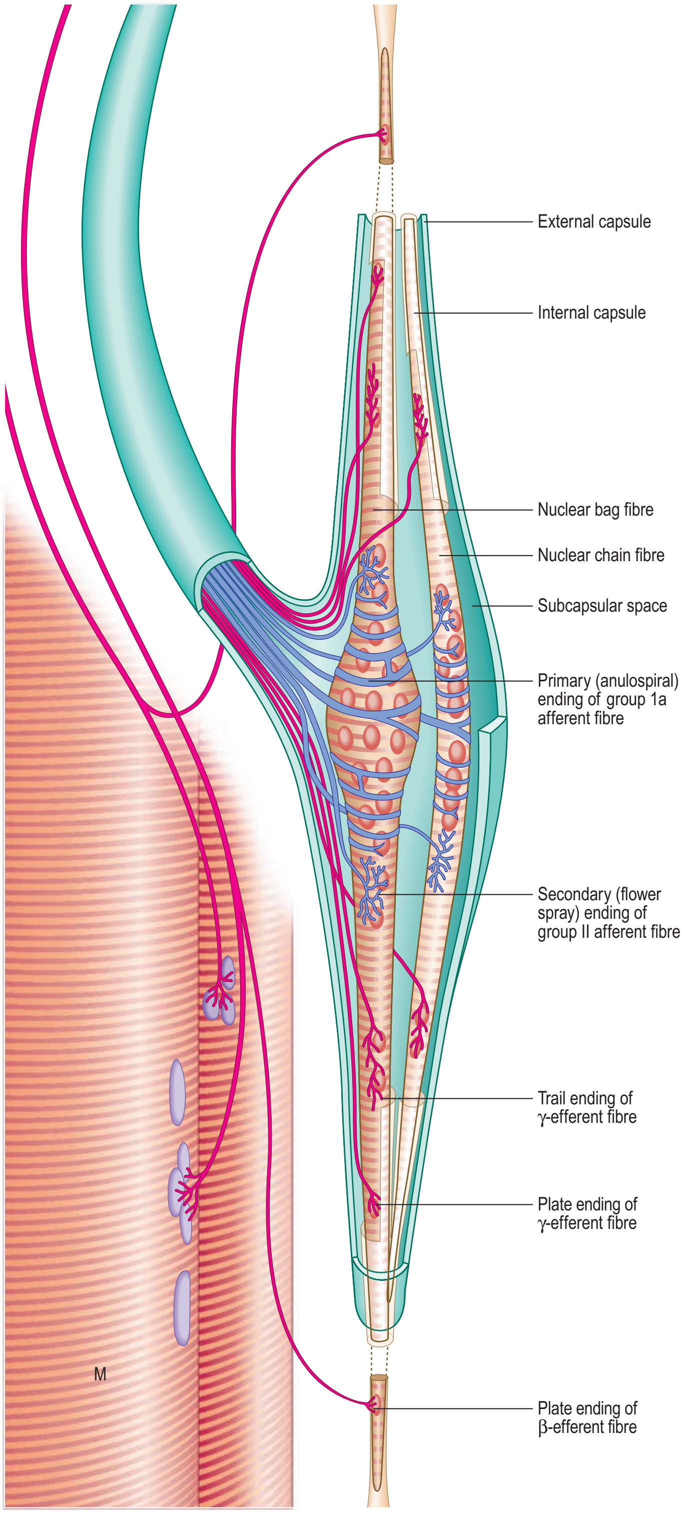
External capsule
Internal capsule
Nuclear bag fibre
Nuclear chain fibre
Subcapsular space
Primary (anulospiral) ending of group 1a afferent fibre
Secondary (flower spray) ending of group II afferent fibre
Trail ending of γ-efferent fibre
Plate ending of γ-efferent fibre
M
Plate ending of β-efferent fibre

Fig. 3.33 A neuromuscular spindle, showing nuclear bag and nuclear chain fibres within the spindle capsule (green); these are innervated by the sensory anulospiral and 'flower spray' afferent fibre endings (blue) and by the γ and β fusimotor (efferent fibre) endings (red). The β efferent fibres are collaterals of fibres innervating extrafusal slow twitch muscle cells (M).

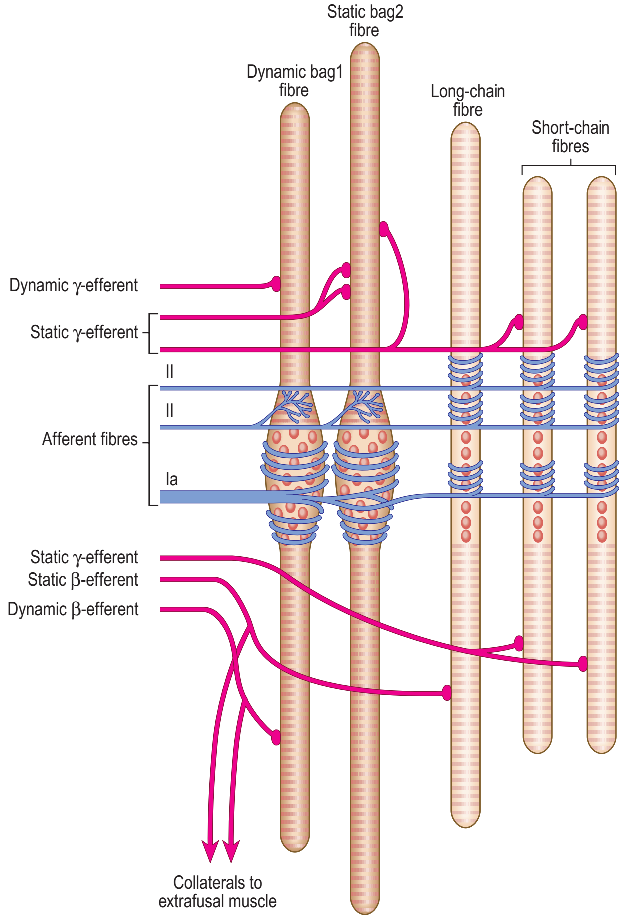

Fig. 3.34 Nuclear bag and nuclear chain fibres in a neuromuscular spindle. Dynamic β- and γ-efferents innervate dynamic bag1 intrafusal fibres, whereas static β- and γ-efferents innervate static bag2 and nuclear chain intrafusal fibres.

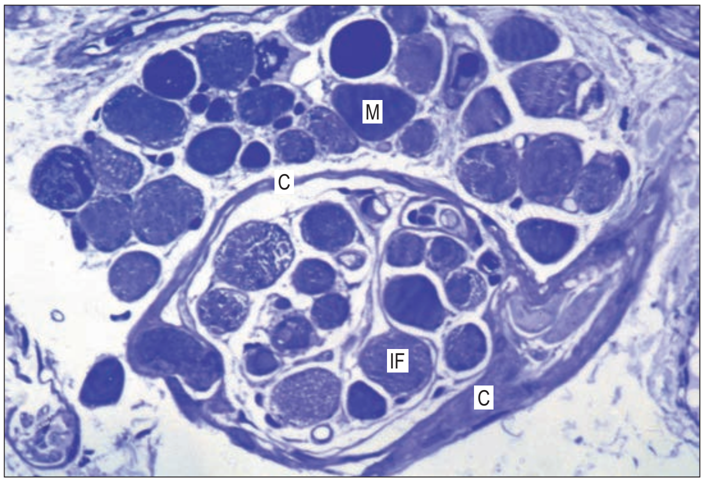

Fig. 3.35 A neuromuscular spindle in transverse section in a human extraocular muscle. The spindle capsule (C) encloses intrafusal fibres (IF) of varying diameters. Typical muscle fibres (M) in transverse section are shown above the spindle. Toluidine blue stained resin section.

fibre type carries distinct myosin heavy chain isoforms. These variations reflect the contractile properties of different intrafusal fibres.

Muscle spindles receive two types of sensory innervation via the unmyelinated terminations of large myelinated axons. Primary (anulospiral) endings are equatorially placed and form spirals around the nucleated parts of intrafusal fibres. They are the endings of large sensory fibres (group Ia afferents), each of which sends branches to a number of intrafusal muscle fibres. Each terminal lies in a deep sarcolemmal groove in the spindle plasma membrane beneath its basal lamina. Secondary (flower spray) endings, which may be spray-shaped or anular, are largely confined to bag2 and nuclear chain fibres, and are the branched terminals of somewhat thinner myelinated (group II) afferents. They are varicose and spread in a narrow band on both sides of the primary endings. They lie close to the sarcolemma, though not in grooves. In essence, primary endings are rapidly adapting, while secondary endings have a regular, slowly adapting response to static stretch.

There are three types of motor endings in muscle spindles. Two are from fine, myelinated, fusimotor (γ) efferents and one is from myelinated (β) efferent collaterals of axons that supply extrafusal slow twitch muscle fibres. The fusimotor efferents terminate nearer the equatorial region, where their terminals either resemble the motor end-plates of extrafusal fibres (plate endings) or are more diffuse (trail endings). Stimulation of the fusimotor and β-efferents causes contraction of the intrafusal fibres and, consequently, activation of their sensory endings.

Muscle spindles signal the length of extrafusal muscle both at rest and throughout contraction and relaxation, the velocity of their contraction and changes in velocity. These modalities may be related to the different behaviours of the three major types of intrafusal fibre and their sensory terminals. The sensory fusimotor endings of one type of nuclear bag fibre (dynamic bag1) are particularly concerned with signalling rapid changes in length that occur during movement, whilst those of the second bag fibre type (static bag2) and of chain fibres are less responsive to movement. These elements can therefore detect complex changes in the state of the extrafusal muscle surrounding spindles and can signal fluctuations in length, tension, velocity of length change and acceleration. Moreover, they are under complex central control; efferent (fusimotor) nerve fibres, by regulating the strength of contraction, can adjust the length of the intrafusal fibres and thereby the responsiveness of spindle sensory endings. In summary, the organization of spindles allows them to monitor muscle conditions actively in order to compare intended and actual movements, and to provide a detailed input to spinal, cerebellar, extrapyramidal and cortical centres about the state of the locomotor apparatus.

Joint receptors

The arrays of receptors situated in and near articular capsules provide information on the position, movements and stresses acting on joints. Structural and functional studies have demonstrated at least four types of joint receptor; their proportions and distribution vary with site. Three are encapsulated endings, the fourth a free terminal arborization.

Type I/Ruffini endings are encapsulated corpuscles of the slowly adapting mechanoreceptor type, equivalent to Ruffini endings in the dermis of skin. They lie in the superficial layers of the fibrous capsules of joints in small clusters and are innervated by myelinated afferent axons. Being slowly adapting, they provide awareness of joint position and movement, and respond to patterns of stress in articular capsules. They are particularly common in joints where static positional sense is necessary for the control of posture (e.g. hip, knee).

Type II endings are lamellated receptors and resemble small versions of the large Pacinian corpuscles found in general connective tissue. They occur in small groups throughout joint capsules, particularly in the deeper layers and other articular structures (e.g. the fat pad of the temporomandibular joint). They are rapidly adapting, low-threshold mechanoreceptors, sensitive to movement and pressure changes, and they respond to joint movement and transient stresses in the joint capsule. They are supplied by myelinated afferent axons but are probably not involved in the conscious awareness of joint sensation.

Type III endings are identical to Golgi tendon organs in structure and function; they occur in articular ligaments but not in joint capsules. They are high-threshold, slowly adapting receptors and may serve, at least in part, to prevent excessive stresses at joints by reflex inhibition of the adjacent muscles. They are innervated by large myelinated afferent axons.

Type IV endings are free terminals of myelinated and unmyelinated axons that ramify in articular capsules and the adjacent fat pads, and around the blood vessels of the synovial layer. They are high-threshold, slowly adapting receptors and are thought to respond to excessive movements, providing a basis for articular pain.

NEUROMUSCULAR JUNCTIONS

Skeletal muscle

The most intensively studied effector endings are those that innervate muscle, particularly skeletal muscle. All neuromuscular (myoneural) junctions are axon terminals of motor neurones. They are specialized for the release of neurotransmitter on to the sarcolemma of skeletal muscle fibres, causing a change in their electrical state that leads to

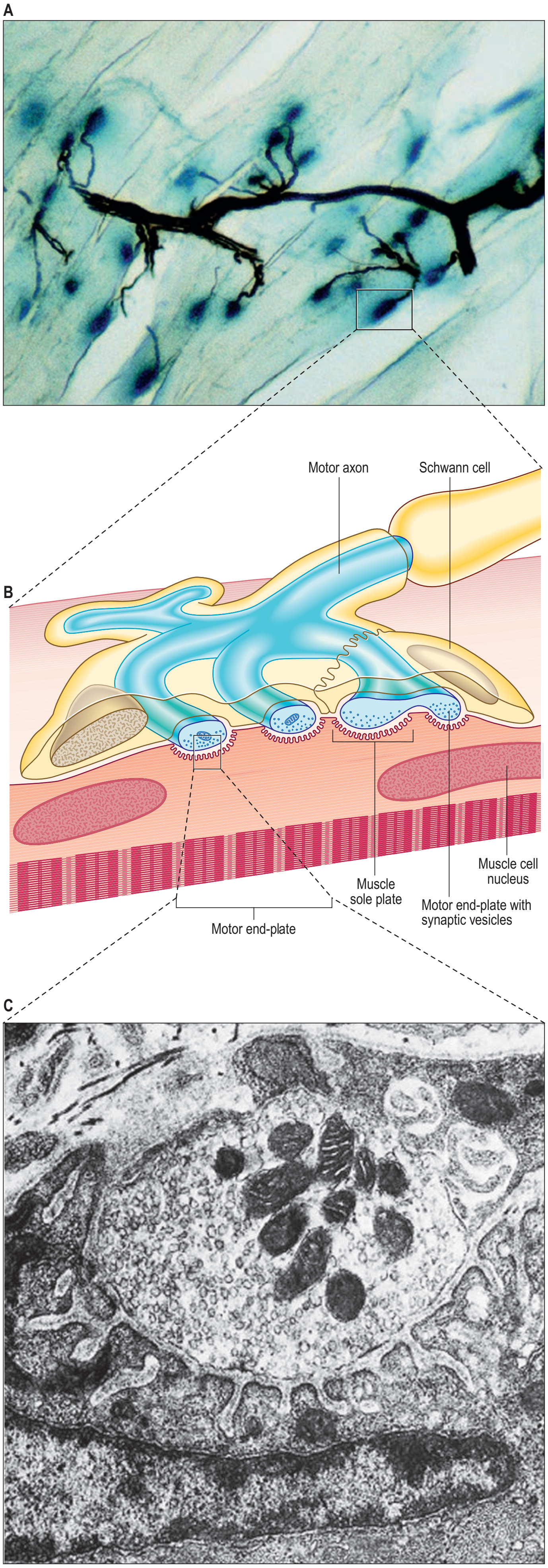

Fig. 3.36 The neuromuscular junction. **A**, Whole-mount preparation of teased skeletal muscle fibres (pale, faintly striated, diagonally orientated structures). The terminal part of the axon (silver-stained, brown) branches to form motor end-plates on adjacent muscle fibres. The sole plate recesses in the sarcolemma, into which the motor end-plates fit, are demonstrated by the presence of acetylcholinesterase (shown by enzyme histochemistry, blue). **B**, The axonal motor end-plate and the deeply infolded sarcolemma. **C**, Electron micrograph showing the expanded motor end-plate of an axon filled with vesicles containing synaptic transmitter (ACh) (above); the deep infoldings of the sarcolemmal sole plate (below) form subsynaptic gutters. (A, Courtesy of Dr Norman Gregson, Division of Neurology, GKT School of Medicine, London. C, Courtesy of Professor DN Landon, Institute of Neurology, University College London.)

contraction. Each axon branches near its terminal to innervate from several to hundreds of muscle fibres, the number depending on the precision of motor control required (Shi et al 2012).

The detailed structure of a motor terminal varies with the type of muscle innervated. Two major types of ending are recognized, innervating either extrafusal muscle fibres or the intrafusal fibres of neuromuscular spindles. In the former type, each axonal terminal usually ends midway along a muscle fibre in a discoidal motor end-plate (Fig. 3.36A), and usually initiates action potentials that are rapidly conducted to all parts of the muscle fibre. In the latter type, the axon gives off numerous branches that form a cluster of small expansions extending along the muscle fibre; in the absence of propagated muscle excitation, these excite the fibre at several points. Both types of ending are associated with a specialized receptive region of the muscle fibre, the sole plate, where a number of muscle cell nuclei are grouped within the granular sarcoplasm.

The sole plate contains numerous mitochondria, endoplasmic reticulum and Golgi complexes. The terminal branches of the axon are plugged into shallow grooves in the surface of the sole plate (primary clefts), from where numerous pleats extend for a short distance into the underlying sarcoplasm (secondary clefts) (Fig. 3.36B–C). The axon terminal contains mitochondria and many clear, 60 nm spherical vesicles similar to those in presynaptic boutons, which are clustered over the zone of membrane apposition. It is ensheathed by Schwann cells whose cytoplasmic projections extend into the synaptic cleft. The plasma membranes of the axon terminal and the muscle cell are separated by a 30–50 nm gap and an interposed basal lamina, which follows the surface folding of the sole-plate membrane into the secondary clefts. Endings of fast and slow twitch muscle fibres differ in detail: the sarcolemmal grooves are deeper, and the presynaptic vesicles more numerous, in the fast fibres.

Junctions with skeletal muscle are cholinergic: the release of ACh changes the ionic permeability of the muscle fibre (Sine 2012). Clustering of ACh receptors at the neuromuscular junction depends in part on the presence in the muscle basal lamina of agrin, which is secreted by the motor neurone, and is important in establishing the postjunctional molecular machinery. When the depolarization of the sarcolemma reaches a particular threshold, it initiates an action potential in the sarcolemma, which is then propagated rapidly over the whole cell surface and also deep within the fibre via the invaginations (T-tubules) of the sarcolemma, causing contraction. The amount of ACh released by the arrival of a single nerve impulse is sufficient to trigger an action potential. However, because ACh is very rapidly hydrolysed by the enzyme AChE, present at the sarcolemmal surface of the sole plate, a single nerve impulse only gives rise to one muscle action potential, i.e. there is a one-to-one relationship between neuronal and muscle action potentials. Thus the contraction of a muscle fibre is controlled by the firing frequency of its motor neurone.

Neuromuscular junctions are partially blocked by high concentrations of lactic acid, as in some types of muscle fatigue.

Autonomic motor terminations

Autonomic neuromuscular junctions differ in several important ways from the skeletal neuromuscular junction and from synapses in the CNS and PNS. There is no fixed junction with well-defined pre- and postjunctional specializations. Unmyelinated, highly branched, postganglionic autonomic axons become beaded or varicose as they reach the effector smooth muscle. These varicosities are not static but move along axons. They are packed with mitochondria and vesicles containing neurotransmitters, which are released from the varicosities during conduction of an impulse along the axon. The distance (cleft) between the varicosity and smooth muscle membrane varies considerably depending on the tissue, from 20 nm in densely innervated structures such as the vas deferens to 1–2 µm in large elastic arteries. Unlike skeletal muscle, the effector tissue is a muscle bundle rather than a single cell. Gap junctions between individual smooth muscle cells are low-resistance pathways that allow electronic coupling and the spread of activity within the effector bundle; they vary in size from punctate junctions to junctional areas of more than 1 µm in diameter.

Adrenergic sympathetic postganglionic terminals contain dense-cored vesicles. Cholinergic terminals, which are typical of all parasympathetic and some sympathetic endings, contain clear spherical vesicles like those in the motor end-plates of skeletal muscle. A third category of autonomic neurones has non-adrenergic, non-cholinergic endings that contain a wide variety of chemicals with transmitter properties. ATP is a neurotransmitter at these terminals, which express purinergic receptors (Burnstock et al 2011). The axons typically contain large, 80–200 nm, dense opaque vesicles, congregated in varicosities at intervals along their length. These terminals are formed in many sites, including the lungs, blood vessel walls, the urogenital tract and the external muscle layers and sphincters of the gastrointestinal tract. In the intestinal wall, neuronal somata lie in the myenteric plexus, and their axons spread caudally for a few millimetres, mainly to innervate circular muscle. Purinergic neurones are under cholinergic control from preganglionic sympathetic neurones. Their endings mainly hyperpolarize smooth muscle cells, causing relaxation, e.g. preceding peristaltic waves, opening sphincters and, probably, causing reflex distension in gastric filling. Autonomic efferents innervate exocrine glands, myoepithelial cells, adipose tissue (noradrenaline (norepinephrine) released from postganglionic sympathetic axons binds to β_3-receptors on adipocytes to stimulate lipolysis) and the vasculature and parenchymal fields of lymphocytes and associated cells in several lymphoid organs, including the thymus, spleen and lymph nodes.

CNS–PNS TRANSITION ZONE

The transition between CNS and PNS usually occurs some distance from the point at which nerve roots emerge from the brain or the spinal cord. The segment of root that contains components of both CNS and PNS tissue is called the CNS–PNS transition zone (TZ; Redlich–Obersteiner's zone). All axons in the PNS, other than postganglionic autonomic neurones, cross such a TZ. Macroscopically, as a nerve root is traced towards the spinal cord or the brain, it splits into several thinner rootlets that may, in turn, subdivide into minirootlets. The TZ is located within either rootlet or minirootlet (**Fig. 3.37**). The arrangement of roots and rootlets varies according to whether the root trunk is ventral, dorsal or cranial. Thus, in dorsal roots, the main root trunk separates into a fan of rootlets and minirootlets that enter the spinal cord in sequence along the dorsolateral sulcus. In certain cranial nerves, the minirootlets come together central to the TZ and enter the brain as a stump of white matter.

Microscopically, the TZ is characterized by an axial CNS compartment surrounded by a PNS compartment. The zone lies more peripherally in sensory nerves than in motor nerves, but in both, the apex of the TZ is described as a glial dome, whose convex surface is usually directed distally. The centre of the dome consists of fibres with a typical CNS organization, surrounded by an outer mantle of astrocytes (corresponding to the glia limitans). From this mantle, numerous glial processes project into the endoneurial compartment of the peripheral nerve, where they interdigitate with its Schwann cells. The astrocytes form a loose reticulum through which axons pass. Peripheral myelinated axons usually cross the zone at a node of Ranvier, which is here termed a PNS–CNS compound node.

Boundary cap (BC) cells are neural crest derivatives that form transient, discrete clusters localized at the presumptive dorsal root entry zones and motor exit points of the embryonic spinal cord (Golding and Cohen 1997). They are thought to prevent cell mixing at these interfaces not only by helping dorsal root ganglion afferents navigate their path to targets in the spinal cord but also by preventing motoneurone cell bodies from exiting to the periphery (Maro et al 2004). In experimental studies in zebra fish, radial glial cells have been implicated as cellular gatekeepers controlling the unidirectional movement of glial cell types across the motor exit point transition zone (Smith et al 2016).

CONDUCTION OF THE NERVOUS IMPULSE

All cells generate a steady electrical potential across their plasma membrane (the membrane potential). This potential is generated by an uneven distribution of potassium ions across the membrane (higher in the intracellular compartment than in the extracellular compartment), and by a selective permeability of the membrane for potassium (**Fig. 3.38**). The distribution of sodium ions is opposite to that for potassium ions, but at rest the sodium conductance of the membrane is low. In neurones this membrane potential is known as the resting potential, and amounts to approximately −60 mV (potential inside the cell measured relative to the outside of the cell). Non-excitable cells have an even higher membrane potential. Neurones receive, conduct and transmit information by changes in membrane conductance for sodium, potassium, calcium or chloride ions. Increase in the sodium or calcium conductance causes an influx of these ions and results in a depolarization of the cell, while chloride influx or potassium efflux results in hyperpolarization. Plasma membrane permeability to these ions is altered by the opening or closing of ion-specific transmembrane channels, triggered by voltage changes or chemical signals such as transmitters (Catterall 2010).

Chemically triggered ionic fluxes may be either direct, where the chemical agent (neurotransmitter) binds to the channel itself to cause it to open, or indirect, where the neurotransmitter is bound by a transmembrane receptor molecule that activates a complex second messenger system within the cell to open separate transmembrane channels. Electrically induced changes in membrane potential depend on the presence of voltage-sensitive ion channels, which, when the transmembrane potential reaches a critical level, open to allow the influx or efflux of specific ions. In all cases, the channels remain open only transiently, and the numbers that open and close determine the total flux of ions across the membrane (Bezanilla 2008).

The types and concentrations of transmembrane channels and related proteins, and therefore the electrical activity of the membranes, vary in different parts of the cell. Dendrites and neuronal somata depend mainly on neurotransmitter action and show graded potentials, whereas axons have voltage-gated channels that give rise to action potentials.

In graded potentials, a flow of current occurs when a synapse is activated; the influence of an individual synapse on the membrane potential of neighbouring regions decreases with distance. Thus synapses on the distal tips of dendrites may, on their own, have relatively little effect on the membrane potential of the cell body. The electrical state of a neurone therefore depends on many factors, including the numbers and positions of thousands of excitatory and inhibitory synapses, their

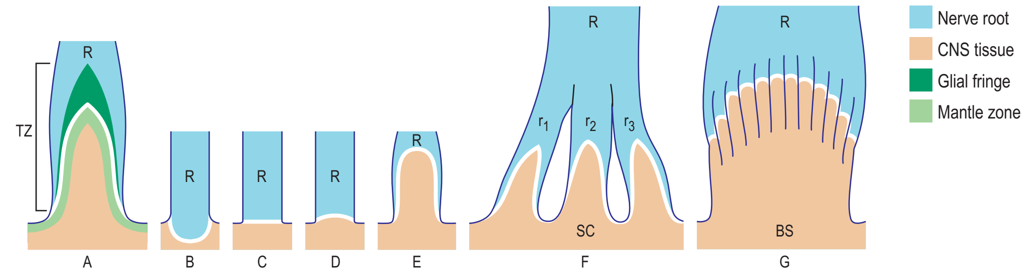

Fig. 3.37 The nerve root–spinal cord junction. **A**–**G**, Different CNS–PNS borderline arrangements. **A**, A pointed borderline. The extent of the transitional zone (TZ) is indicated. **B**–**G**, Glial fringe omitted. **B**, A concave borderline (white line) and inverted TZ. **C**, A flat borderline situated at the level of the root (R)–spinal cord junction. **D** and **E**, A convex, dome-shaped borderline; the CNS expansion into the rootlet is moderate in D and extensive in E. **F**, The root (R) splits into rootlets (r), each with its own TZ and attaching separately to the spinal cord (SC). **G**, The arrangement found in several cranial nerve roots (e.g. vestibulocochlear nerve). The PNS component of the root separates into a bundle of closely packed minirootlets, each equipped with a TZ. The minirootlets reunite centrally. BS, brainstem. (Adapted with permission from Dyck PJ, Thomas PK, Griffin JW et al (eds) Peripheral Neuropathy, 3rd ed. Philadelphia: Saunders, 1993.)

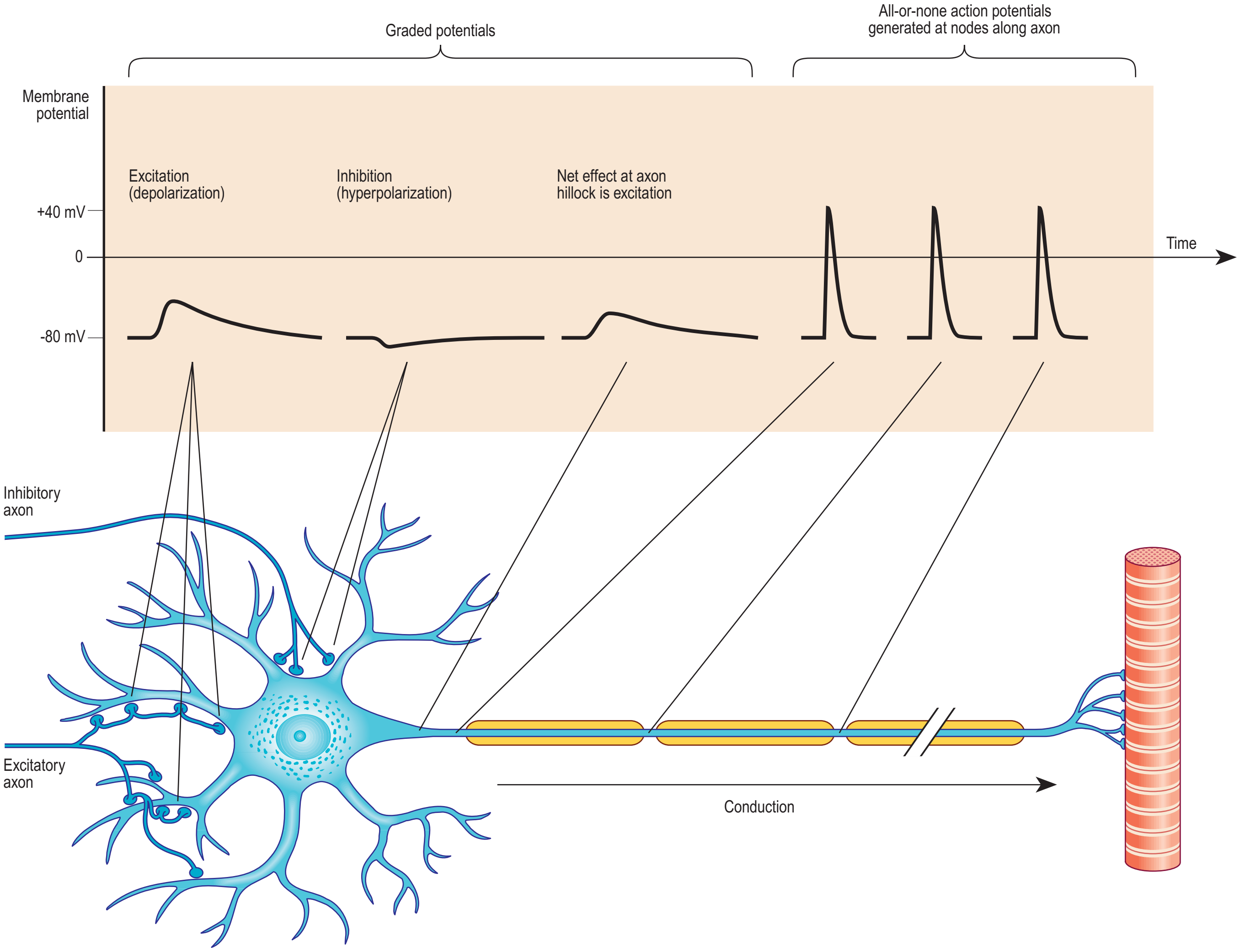
Graded potentials
All-or-none action potentials generated at nodes along axon
Membrane potential
Excitation (depolarization)
Inhibition (hyperpolarization)
Net effect at axon hillock is excitation
+40 mV
0
-80 mV
Time
Inhibitory axon
Excitatory axon
Conduction

Fig. 3.38 The types of change in electrical potential that can be recorded across the cell membrane of a motor neurone at the points indicated. Excitatory and inhibitory synapses on the surfaces of the dendrites and soma cause local graded changes of potential that summate at the axon hillock and may initiate a series of all-or-none action potentials, which in turn are conducted along the axon to the effector terminals.

degree of activation, and the branching pattern of the dendritic tree and geometry of the cell body. The integrated activity directed towards the neuronal cell body is converted to an output directed away from the soma at the site where the axon leaves the cell body, at its junction with the axon hillock. Voltage-sensitive channels are concentrated at this trigger zone, the axon initial segment, and when this region is sufficiently depolarized, an action potential is generated and is subsequently conducted along the axon.

Action potential

The action potential is a brief, self-propagating reversal of membrane polarity. It depends on an initial influx of sodium ions, which causes a reversal of polarity to about +20 mV, followed by a rapid return towards the resting potential as potassium ions flow out. The rapid reversal process is completed in approximately 0.5 msec, followed by a slower recovery phase of up to 5 msec, when the resting potential is even hyperpolarized. Once the axon hillock reaches threshold, propagation of the action potential is independent of the initiating stimulus; thus the size and duration of action potentials are always the same (described as all-or-none) for a particular neurone, no matter how much a stimulus may exceed the threshold value.

Once initiated, an action potential spreads spontaneously and at a relatively constant velocity, within the range of 4–120 m/s. Conduction velocity depends on a number of factors related to the way in which the current spreads, e.g. axonal cross-sectional area, the numbers and positioning of ion channels, and membrane capacitance (influenced particularly by the presence of myelin). In axons lacking myelin, action potential conduction is analogous to a flame moving along a fuse. Just as each segment of fuse is ignited by its upstream neighbour, each segment of axon membrane is driven to threshold by the depolarization of neighbouring membrane. Sodium channels within the newly depolarized segment open and positively charged sodium ions enter, driving the local potential inside the axon towards positive values. This inward current in turn depolarizes the neighbouring, downstream, non-depolarized membrane, and the cyclic propagation of the action potential is completed. Several milliseconds after the action potential, the sodium channels are inactivated, a period known as the refractory period. The length of the refractory period determines the maximum frequency at which action potentials can be conducted along a nerve fibre; it varies in different neurones and affects the amount of information that can be carried by an individual fibre.

Myelinated fibres are electrically insulated by their myelin sheaths along most of their lengths, except at nodes of Ranvier. The distance between nodes, referred to as the internodal distance, is directly related to axon diameter and varies between 0.2 and 2.0 mm. Voltage-gated sodium channels are clustered at nodes, and the nodal membrane is the only place where high densities of inward sodium current can be generated across the axon membrane. Conduction in myelinated axons is self-propagating, but instead of physically adjacent regions of membrane acting to excite one another (as occurs along unmyelinated axons), it is the depolarization occurring in the neighbouring upstream node that excites a node to threshold. Reaching threshold causes the sodium channels at the node to open and generate inward sodium current, but instead of this acting on the adjacent membrane, the high resistance and low capacitance of the myelin sheath directs the current towards the next downstream node, exciting it to threshold and completing the cycle. The action potential thus jumps from node to node, a process known as saltatory conduction, which greatly increases the conduction velocity.

A number of disorders of the CNS and PNS include demyelination as a characteristic feature (Arancibia-Carcamo and Attwell 2014). Perhaps most common amongst these is multiple sclerosis, which is characterized by primary demyelination at scattered sites within the CNS (it is now recognized that axonal loss also contributes to the progression of multiple sclerosis). Primary demyelination is the loss of the myelin sheath with axonal preservation, and is usually segmental, i.e. it rarely extends along the entire length of an affected axon. The phenomenon is associated with conduction block because the newly exposed, previously internodal, axolemma contains relatively few voltage-sensitive sodium channels. There is experimental and clinical evidence that remyelinated axons can conduct at near-normal speeds, because even though their sheaths are thinner than the original myelin sheaths, the safety factor (i.e. the factor by which the outward current at a quiescent node next to an excited node exceeds the minimum current required to evoke a response) is greater than 1. The myelin loss that occurs in the early stages of Wallerian degeneration in both CNS and PNS, usually distal to a site of trauma but also in response to a prolonged period of ischaemia or exposure to a neuronotoxic substance, is accompanied by axonal degeneration (the term secondary demyelination is sometimes used to describe this form of myelin loss) (see Commentary 1.5).

Axonal conduction is naturally unidirectional, from dendrites and soma to axon terminals. When an action potential reaches the axonal terminals, it causes depolarization of the presynaptic membrane, and as a result, quanta of neurotransmitter (which correspond to the content of individual vesicles) are released to change the degree of excitation of the next neurone, muscle fibre or glandular cell.

Key references

Kempermann G 2011 Adult Neurogenesis 2. New York: Oxford University Press.
A summary of the knowledge on adult neurogenesis.

Kettenmann H, Ransom BR 2012 Neuroglia. New York: Oxford University Press.
A comprehensive textbook on glial cells.

Sanes DH, Reh TA, Harris WA 2011 Development of the Nervous System, 3rd ed. Oxford: Elsevier, Academic Press.
A textbook on developmental neurobiology.

Shepherd GM 2003 The Synaptic Organization of the Brain. New York: Oxford University Press.
A description of the circuitry of the brain.

References

Abbott NJ, Rönnbäck L, Hansson E 2006 Astrocyte-endothelial interactions at the blood-brain barrier. Nature Rev Neurosci 7:41-53.

Albuquerque EX, Pereira EFR, Alkondon M et al 2009 Mammalian nicotinic acetylcholine receptors: from structure to function. Phys Rev 89:73-120.

Allen NJ, Eroglu C 2017 Cell biology of astrocyte-synapse interactions. Neuron. 96:697-708.

Arancibia-Carcamo IL, Attwell D 2014 The node of Ranvier in CNS pathology. Acta Neuropathol 128:161-75.

Ashley NT, Demas GE 2016 Neuroendocrine-immune circuits, phenotypes, and interactions. Horm Behav 87:25-34.

Azevedo FA, Carvalho LR, Grinberg LT et al 2009 Equal numbers of neuronal and nonneuronal cells make the human brain an isometrically scaled-up primate brain. J Comp Neurol 513:532-41.

Bakhti M, Aggarwal S, Simons M 2014 Myelin architecture: zippering membranes tightly together. Cell Mol Life Sci 71:1265-77.

Banks RW 2015 The innervation of the muscle spindle: a personal history. J Anat 227:115-35.

Barrera NP, Edwardson JM 2008 The subunit arrangement and assembly of ionotropic receptors. Trends Neurosci 31:569-76.

Bender KJ, Trussell LO 2012 The physiology of the axon initial segment. Annu Rev Neurosci 35:249-65.

Bezanilla F 2008 Ion channels: from conductance to structure. Neuron 60:456-68.

Birch R 2011 Surgical Disorders of the Peripheral Nerves, 2nd ed. Berlin: Springer.

Boldrini M, Fulmore CA, Tartt AN et al 2018. Human hippocampal neurogenesis persists throughout aging. Cell Stem Cell 22:589-599.e5.

Bota M, Swanson LW 2007 The neuron classification problem. Brain Res Rev 56:79-88.

Boyd IA 1985 Muscle spindles and stretch reflexes. In: Swash M, Kennard C (eds) Scientific Basis of Clinical Neurology. Edinburgh: Churchill Livingstone, pp. 74-97.

Burke DA, Rotstein HG, Alvarez VA 2017 Striatal local circuitry: a new framework for lateral inhibition. Neuron 96:267-84.

Burnstock G, Kruegel U, Abbracchio MP et al 2011 Purinergic signalling: from normal behaviour to pathological brain function. Prog Neurobiol 95:229-74.

Burnstock G 2016 P2X ion channel receptors and inflammation. Purinergic Signal 12:59-67.

Butovsky O, Weiner HL 2018 Microglial signatures and their role in health and disease. Nature Rev Neurosci 19:622-35.

Butt AM, Hamilton N, Hubbard P et al 2005 Synantocytes: the fifth element. J Anat 207:695-706.

Buttermore ED, Thaxton CL, Bhat MA 2013 Organization and maintenance of molecular domains in myelinated axons. J Neurosci Res 91:603-22.

Cairns NJ, Lee VM-Y, Trojanowski JQ 2004 The cytoskeleton in neurodegenerative disease. J Pathol 204:438-49.

Cardoso FL, Brites D, Brito MA 2010 Looking at the blood-brain barrier: molecular anatomy and possible investigation approaches. Brain Res Rev 64:328-63.

Catterall WA 2010 Ion channel voltage sensors: structure, function, and pathophysiology. Neuron 67:915-28.

Contractor A, Mulle C, Swanson GT 2011 Kainate receptors coming of age: milestones of two decades of research. Trends Neurosci 34:154-63.

Day R, Salzet M 2002 The neuroendocrine phenotype, cellular plasticity, and the search for genetic switches: redefining the diffuse neuroendocrine system. Neuroendocrinol Lett 23:379-84.

Deller T, Korte M, Chabanis S et al 2003 Synaptopodin-deficient mice lack a spine apparatus and show deficits in synaptic plasticity. Proc Natl Acad Sci U S A 100:10494-9.

D'Este E, Kamin D, Balzarotti F et al 2016 Ultrastructural anatomy of nodes of Ranvier in the peripheral nervous system as revealed by STED microscopy. PNAS E191-9.

Dieni S, Matsumoto T, Dekkers M et al 2012 BDNF and its pro-peptide are stored in presynaptic dense core vesicles in brain neurons. J Cell Biol 196:775-88.

Eggen BJ, Raj D, Hanisch UK 2013 Microglial phenotype and adaptation. J Neuroimmune Pharmacol 8:807-23.

Eggermann E, Bucurenciu I, Goswami SP et al 2012 Nanodomain coupling between Ca^{2+} channels and sensors of exocytosis at fast mammalian synapses. Nature Rev Neurosci 13:7-21.

Eriksson PS, Perfilieva E, Bjork-Eriksson T et al 1998 Neurogenesis in the adult human hippocampus. Nature Med 4:1313-7.

Farzi A, Frohlich EE, Holzer P 2018 Gut microbiota and the neuroendocrine system. Neurotherapeutics 15:5-22.

Forni PE, Wray A 2012 Neural crest and olfactory system: new prospective. Mol Neurobiol 46:349-60.

Furness JB 2012 The enteric nervous system and neurogastroenterology. Nat Rev Gastroenterol Hepatol 9:286-94.

Gassmann M, Bettler B 2012 Regulation of neuronal GABA(B) receptor functions by subunit composition. Nature Rev Neurosci 13:380-94.

Gershon MD 1998 The Second Brain. New York: HarperCollins.

Golding JP, Cohen J 1997 Border controls at the mammalian spinal cord: late-surviving neural crest boundary cap cells at dorsal root entry sites may regulate sensory afferent ingrowth and entry zone morphogenesis. Mol Cell Neurosci 9:381-96.

Gonzalez-Perez O 2012 Neural stem cells in the adult human brain. Biol Biomed Rep 2:59-69.

Gray EG 1959 Axo-somatic and axo-dendritic synapses of the cerebral cortex: an electron microscopic study. J Anat 83:420-33.

Grubišić V, Gulbransen BD 2017 Enteric glia: the most alimentary of all glia. J Physiol 15:557-570.

Grundmann D, Loris E, Maas-Omlor S et al 2019 Enteric glia: S100, GFAP, and beyond. Anat Rec 302:1333-1344.

Guemez-Gamboa A, Coufal NG, Gleeson JG 2014 Primary cilia in the developing and mature brain. Neuron 82:511-21.

Gulbransen BD, Sharkey KA 2012 Novel functional roles for enteric glia in the gastrointestinal tract. Nat Rev Gastroenterol Hepatol 9:625-32.

Haas HL, Sergeeva OA, Selbach O 2008 Histamine in the nervous system. Phys Rev 88:1183-241.

Hammond TR, Robinton D, Stevens B 2018 Microglia and the brain: complementary partners in development and disease. Annu Rev Cell Dev 34:523-44.

Hanani M 2010 Satellite glial cells in sympathetic and parasympathetic ganglia: in search of function. Brain Res Rev 64:304-27.

Harsing LG, Matyus P 2013 Mechanisms of glycine release, which build up synaptic and extrasynaptic glycine levels: the role of synaptic and non-synaptic glycine transporters. Brain Res Bull 93:110-19.

Haydon PG, Carmignoto G 2006 Astrocyte control of synaptic transmission and neurovascular coupling. Physiol Rev 86:1009-31.

Higginson JR, Barnett SC 2011 The culture of olfactory ensheathing cells (OECs) - a distinct glial cell type. Exp Neurol 229:2-9.

Hill RA, Nishiyama A 2014 NG2 cells (polydendrocytes): listeners to the neural network with diverse properties. Glia 62:1195-210.

Hinckelmann M-V, Zala D, Saudou F 2013 Releasing the brake: restoring fast axonal transport in neurodegenerative disorders. Trends Cell Biol 23:634-43.

Hirokawa N 1994 Microtubule organization and dynamics dependent on microtubule-associated proteins. Curr Opin Cell Biol 6:74-81.

Hirokawa N, Noda Y, Tanaka Y et al 2009 Kinesin superfamily motor proteins and intracellular transport. Nature Rev Mol Cell Biol 10:682-96.

Hirokawa N, Niwa S, Tanaka Y 2010 Molecular motors in neurons: transport mechanisms and roles in brain function, development, and diseases. Neuron 68:610-38.

Horresh I, Poliak S, Grant S et al 2008 Multiple molecular interactions determine the clustering of Caspr2 and Kv1 channels in myelinated axons. J Neurosci 28:14213-22.

Huber AR, Agostini-Vulaj D, Drage MG et al 2017 Tactile corpuscle-like bodies (Wagner-Meissner corpuscles) of the colorectum: a series of 5 cases. Int J Surg Pathol 25:684-7.

Huizinga JD, Zarate N, Farrugia G 2009 Physiology, injury and recovery of interstitial cells of Cajal: basic and clinical science. Gastroenterology 137:1548-56.

Iqbal K, Liu F, Gong CX et al 2010 Tau in Alzheimer disease and related tauopathies. Curr Alzheimer Res 7:656-64.

Kano M, Watanabe T, Uesaka N et al 2018 Multiple phases of climbing fiber synapse elimination in the developing cerebellum. Cerebellum 17(6):722-34.

Kempermann G 2011 Adult Neurogenesis 2. New York: Oxford University Press.

A summary of the knowledge on adult neurogenesis.

Kettenmann H, Hanisch UK, Noda M et al 2011 Physiology of microglia. Phys Rev 91:461-553.

Kettenmann H, Ransom BR 2012 Neuroglia. New York: Oxford University Press.

A comprehensive textbook on glial cells.

Khanmohammadi M, Waagepetersen RP, Sporring J 2015 Analysis of shape and spatial interaction of synaptic vesicles using data from focused ion beam scanning electron microscopy (FIB-SEM). Front Neuroanat 9:116.

Kidd GJ, Ohno N, Trapp BD 2013 Biology of Schwann cells. Handb Clin Neurol 115:55-79.

Kim H-J, DiBernardo AB, Sloane JA et al 2006 TK WAVE1 is required for oligodendrocyte morphogenesis and normal CNS myelination. J Neurosci 26:5849-59.

Kole MH, Stuart GJ 2012 Signal processing in the axon initial segment. Neuron 73:235-47.

Kucenas S 2015 Perineurial glia. Cold Spring Harb Perspect Biol 7:a020511.
Kulkarni VA, Firestein BL 2012 The dendritic tree and brain disorders. Mol Cell Neurosci 50:10-20.
Leung CT, Coulombe PA, Reed RR 2007 Contribution of olfactory neural stem cells to tissue maintenance and regeneration. Nat Neurosci 10:720-26.
Liu Q, Wang X, Yi S 2018 Pathophysiological changes of physical barriers of peripheral nerves after injury. Front Neurosci 12:597.
Lörincz A, Nusser Z 2010 Molecular identity of dendritic voltage-gated sodium channels. Science 328: 906-9.
Lucarz A, Brand G 2007 Current considerations about Merkel cells. Eur J Cell Biol 86:243-51.
Mashaghi A, Marmalidou A, Tehrani M et al 2016 Neuropeptide substance P and the immune response. Cell Mol Life Sci 73:4249-64.
Maro GS, Vermeren M, Voiculescu O et al 2004 Neural crest boundary cap cells constitute a source of neuronal and glial cells of the PNS. Nat Neurosci 7:930-8.
Matsuzaki M, Honkura N, Ellis-Davies GC et al 2004 Structural basis of long-term potentiation in single dendritic spines. Nature 429:761-6.
Matyash V, Kettenmann H 2010 Heterogeneity in astrocyte morphology and physiology. Brain Res Rev 63:2-10.
Morris AD, Lewis GM, Kucenas S 2017 Perineurial glial plasticity and the role of TGF-β in the development of the blood-nerve barrier. J Neurosci 37:4790-807.
Murakoshi H, Yasuda R 2012 Postsynaptic signaling during plasticity of dendritic spines. Trends Neurosci 35:135-43.
Nagy N, Goldstein AM 2017 Enteric nervous system development: a crest cell's journey from neural tube to colon. Semin Cell Dev Biol 66:94-106.
Nave KA 2010 Myelination and support of axonal integrity by glia. Nature 468:244-52.
Neher E, Sakaba T 2008 Multiple roles of calcium ions in the regulation of neurotransmitter release. Neuron 59:861-72.
Neunlist M, Van Landeghem L, Mahe MM et al 2013 The digestive neuronal-glial-epithelial unit: a new actor in gut health and disease. Nat Rev Gastroenterol Hepatol 10:90-100.
Nimmerjahn A, Kirchhoff F, Helmchen F 2005 Resting microglial cells are highly dynamic surveillants of brain parenchyma in vivo. Science 308:1314-8.
Nishiyama A, Komitova M, Suzuki R et al 2009 Polydendrocytes (NG2 cells): multifunctional cells with lineage plasticity. Nature Rev Neurosci 10:9-22.
Norrmén C, Suter U 2013 Akt/mTOR signalling in myelination. Biochem Soc Trans 41:944-50.
Okabe S 2017 Fluorescence imaging of synapse dynamics in normal circuit maturation and in developmental disorders. Proc Japan Acad Series B 93:483-97.
Oprych K, Cotfas D, Choi D 2016 Common olfactory ensheathing glial markers in the developing human olfactory system. Brain Struct Funct 222:1877-95.
Pakkenberg B, Gundersen HJG 1988 Total number of neurons and glial cells in human brain nuclei estimated by the disector and the fractionator. J Microsc 150:1-20.
Palladino SP, Helton ES, Jain P et al 2017 The human blood-nerve barrier transcriptome. Sci Rep 7:17477.
Pannese E 2010 The structure of the perineuronal sheath of satellite glial cells (SGCs) in sensory ganglia. Neuron Glia Biol 6:3-10.
Peles E, Salzer JL 2000 Molecular domains of myelinated axons. Curr Opin Neurobiol 10:558-65.
Perea G, Navarrete M, Araque A 2009 Tripartite synapses: astrocytes process and control synaptic information. Trends Neurosci 32:421-31.
Pereda AE 2014 Electrical synapses and their functional interactions with chemical synapses. Nat Rev Neurosci 15:250-63.
Pereira JA, Lebrun-Julien F, Suter U 2012 Molecular mechanisms regulating myelination in the peripheral nervous system. Trends Neurosci 35:123-34.
Petralia RS, Wang YX, Mattson MP et al 2016 The diversity of spine synapses in animals. Neuromolecular Med 18:497-539.
Poliak S, Peles E 2003 The local differentiation of myelinated axons at nodes of Ranvier. Nat Rev Neurosci 4:968-80.
Proske U, Gandevia SC 2012 The proprioceptive senses: their roles in signaling body shape, body position and movement, and muscle force. Physiol Rev 92:1651-97.
Robel S, Berninger B, Goetz M 2011 The stem cell potential of glia: lessons from reactive gliosis. Nature Rev Neurosci 12:88-104.
Ryan TJ, Grant SGN 2009 The origin and evolution of synapses. Nature Rev Neurosci 10:701-26.
Sanai N, Nguyen T, Ihrie RA et al 2011 Corridors of migrating neurons in the human brain and their decline during infancy. Nature 478:382-6.
Sanes DH, Reh TA, Harris WA 2011 Development of the Nervous System, 3rd ed. Oxford: Elsevier, Academic Press.
A textbook on developmental neurobiology.
Savidge TC 2014 Importance of NO and its related compounds in enteric nervous system regulation of gut homeostasis and disease susceptibility. Curr Opin Pharmacol 19:54-60.
Schmieg N, Memendez G, Schiavo G et al 2014 Signalling endosomes in axonal transport: travel updates on the molecular highway. Semin Cell Dev Biol 27:32-43.
Segal V, Vlachos A, Korkotian E 2010 The spine apparatus, synaptopodin, and dendritic spine plasticity. Neuroscientist 16:125-31.
Seifert G, Schilling K, Steinhauser C 2006 Astrocyte dysfunction in neurological disorders: a molecular perspective. Nature Rev Neurosci 7:194-206.
Shah MM, Hammond RS, Hoffman DA 2010 Dendritic ion channel trafficking and plasticity. Trends Neurosci 33:307-16.
Shafer DP, Stevens B 2015 Microglia function in central nervous system development and plasticity. Cold Spring Harbor Perspect Biol 7: a020545.
Sharkey KA, Savidge TC 2014 Role of enteric neurotransmission in host defense and protection of the gastrointestinal tract. Auton Neurosci 182:70-82.
Shefa U, Kim D, Kim MS et al 2018 Roles of gasotransmitters in synaptic plasticity and neuropsychiatric conditions. Neural Plast 2018:1824713. Published 2018 May 6. doi:10.1155/2018/1824713.
Shepherd GM 2003 The Synaptic Organization of the Brain. New York: Oxford University Press.
A description of the circuitry of the brain.
Shi L, Fu AKY, Ip NY 2012 Molecular mechanisms underlying of the vertebrate neuromuscular junction. Trends Neurosci 35:441-53.
Sine SM 2012 End-plate acetylcholine receptor: structure, mechanism, pharmacology, and disease. Phys Rev 92:1189-234.
Smith CJ, Johnson K, Welsh TG et al 2016 Radial glia inhibit peripheral glial infiltration into the spinal cord at motor exit point transition zones. Glia 64:1138-53.
Sorrells SF, Paredes MF, Cebrian-Silla A et al 2018 Human hippocampal neurogenesis drops sharply in children to undetectable levels in adults. Nature 555:377-81.
Spencer KC, Sy JC, Falcon-Banchs R 2017 A three dimensional in vitro glial scar model to investigate the local strain effects from micromotion around neural implants. Lab Chip 17:795-804.
Spruston N 2008 Pyramidal neurons: dendritic structure and synaptic integration. Nature Rev Neurosci 9:206-21.
Squire L, Kandel E 2008 Memory: From Mind to Molecules. Greenwood Village, CO: Roberts.
Suedhof TC 2012 The presynaptic active zone. Neuron 75:11-25.
Szepesi Z, Manouchehrian O, Bachiller S et al 2018 Bidirectional microglia-neuron communication in health and disease. Front Cell Neurosci 12:323.
Tampellini D 2015 Synaptic activity and Alzheimer's disease: a critical update. Front Neurosci 9:423.
Ushiki T, Ide C 1990 Three-dimensional organization of the collagen fibrils in the rat sciatic nerve as revealed by transmission- and scanning electron microscopy. Cell Tissue Res 260:175-84.
Vanderah TW 2018 Nolte's Essentials of the Human Brain, 2nd ed. Elsevier. ch. 9.
Veres JM, Nagy GA, Vereczki VK et al 2014 Strategically positioned inhibitory synapses of axo-axonic cells potently control principal neuron spiking in the basolateral amygdala. J Neurosci 34:16194-206.
Walberg F 1968 Morphological correlates of postsynaptic inhibitory processes. In: von Euler C, Skoglund S, Söderberg U (eds) Structure and Function of Inhibitory Neuronal Mechanisms. Oxford: Pergamon Press. pp. 7-14.
Wei W, Han Z, Chen M et al 2017 Three-dimensional reconstruction of the distribution of neurons contributing to ophthalmic, maxillary, and mandibular nerves in the trigeminal ganglion of experimental model. J Craniofac Surg 28:2104-7.
Willard SS, Koochekpour S 2013 Glutamate, glutamate receptors, and downstream signaling pathways. Int J Biol Sci 9:948-59.
Wong RO, Ghosh A 2002 Activity-dependent regulation of dendritic growth and patterning. Nature Rev Neurosci 10:803-12.
Zochodne DW 2018 Local blood flow in peripheral nerves and their ganglia: resurrecting key ideas around its measurement and significance. Muscle Nerve 57:884-95.
Zuo H, Wood WM, Sherafat A et al 2018 Age-dependent decline in fate switch from NG2 cells to astrocytes after Olig2 deletion. J Neurosci 38:2359-71.

CHAPTER

4

Blood, lymphoid tissues and haemopoiesis

Blood is an opaque fluid with a viscosity greater than that of water (mean relative viscosity 4.75 at 18 °C), and a specific gravity of 1.06 at 15 °C. It is bright red when oxygenated, as in the systemic arteries, and dark red to purple when deoxygenated, in systemic veins. Blood is a mixture of a clear liquid, plasma, and cellular elements, and consequently the hydrodynamic flow of blood in vessels behaves in a complex manner that is not entirely predictable by simple Newtonian equations.

Plasma is a clear, yellowish fluid that contains many substances in solution or suspension: low-molecular-weight solutes give a mean freezing-point depression of 0.54 °C. Plasma contains high concentrations of sodium and chloride ions, as well as potassium, calcium, magnesium, phosphate, bicarbonate and traces of many other ions; also present are glucose, amino acids and vitamins. It also includes high molecular weight plasma proteins, e.g. clotting factors, particularly prothrombin; immunoglobulins and complement proteins involved in immunological defence; glycoproteins, lipoproteins, polypeptide and steroid hormones, and globulins for the transport of hormones and iron. The plasma is involved in the transport of most molecules that are released or secreted by cells in response to pathological or physiological stimuli and so the routine chemical analysis of plasma is of great diagnostic importance. There is increasing interest in using metabolomics approaches for the high-throughput analysis of small molecules or metabolites in the serum, as a potential aid to diagnosis and understanding of disease (Psychogios et al 2011, James and Parkinson 2015).

The precipitation of the protein fibrin from plasma to form a clot (**Fig. 4.1**) is initiated by the release of specific materials from damaged cells and blood platelets in the presence of calcium ions. If blood or plasma samples are allowed to stand, they will separate into a clot and a clear yellowish fluid, the serum. Clot formation is prevented by removal of calcium ions, e.g. by addition of citrate, oxalate or various calcium chelators (EDTA, EGTA) to the sample. Heparin is also widely used as an anticlotting agent because it interferes with fibrin clot formation.

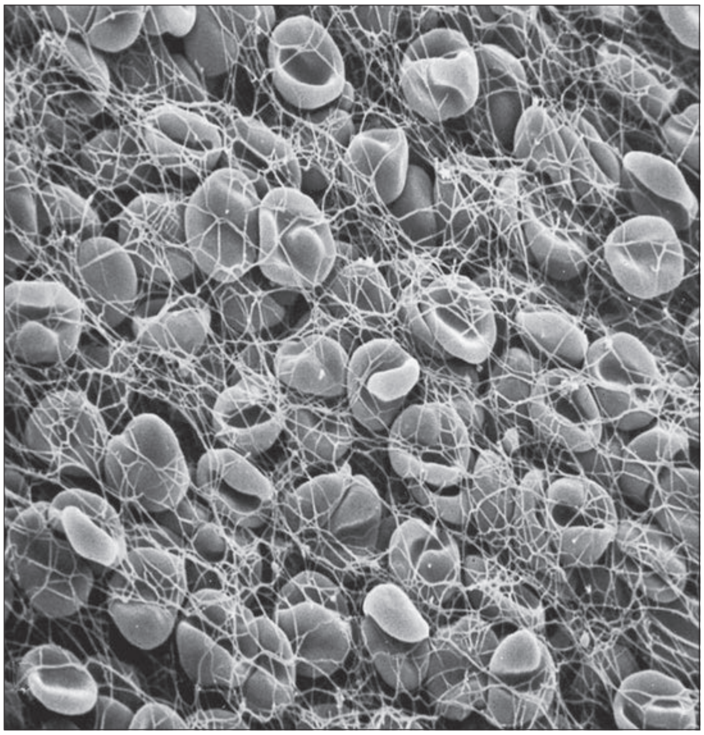

Fig. 4.1 Erythrocytes enmeshed in filaments of fibrin in a clot. (Courtesy of Michael Crowder MD.)

In postnatal life, blood cells are formed in the bone marrow. Haemopoiesis produces red cells (erythrocytes) and a wide variety of immune defense cells (white blood cells, or leukocytes). The latter include neutrophil, eosinophil and basophil granulocytes, B lymphocytes and monocytes. T lymphocytes develop in the thymus from bone marrow-derived progenitors. These cells all contribute to the immune system (for an overview of the immune system, see Murphy and Weaver (2016)). Platelets are produced in the bone marrow as cellular fragments of megakaryocytes. Only erythrocytes and platelets are generally confined to the blood vascular system, whereas all leukocytes can leave the circulation and enter extravascular tissues. The numbers of cells doing so increases greatly during inflammation caused by local infections or tissue damage.

The lymphoid tissues are the thymus, lymph nodes, spleen and the lymphoid follicles associated mainly with the alimentary and respiratory tracts. Lymphocytes populate lymphoid tissues and are concerned with immune defence. Lymphoid tissue also contains supportive stromal cells, which are non-haemopoietic in origin (e.g. thymic epithelium); non-haemopoietic follicular dendritic cells of lymph nodes and splenic follicles; haemopoietically derived dendritic cells; and macrophages of the mononuclear phagocyte system. Dendritic cells and blood monocyte-derived macrophages are found additionally in most tissues and organs, where they function as antigen-presenting cells (APCs).

CELLS OF PERIPHERAL BLOOD

Erythrocytes

Erythrocytes (red blood cells, RBCs) account for the largest proportion of blood cells (99% of the total number), with normal values of 4.1–6.0 × 10^6/μl in adult males and 3.9–5.5 × 10^6/μl in adult females. Polycythaemia (increased red cell mass) can occur in individuals living at high altitude, or pathologically in conditions resulting in arterial hypoxia. Reduction in red cell mass (anaemia) has many underlying causes but in rare instances can be due to structural defects in erythrocytes (see below).

Each erythrocyte is a biconcave disc (see Fig. 4.1; **Fig. 4.2**) with a mean diameter in dried smear preparations of 7.1 μm; in fresh preparations the mean diameter is 7.8 μm, decreasing slightly with age. Mature

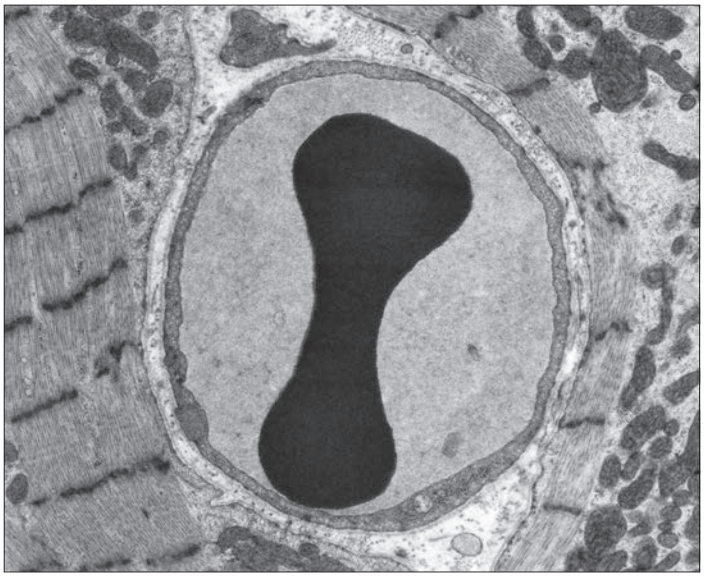

Fig. 4.2 A human heart muscle biopsy specimen, showing an erythrocyte within a capillary. The erythrocyte biconcave disc is typically electron-dense and almost fills the capillary lumen. (Courtesy of Dr Bart Wagner, Histopathology Department, Sheffield Teaching Hospitals, UK.)

In normal blood, five types of haemoglobin polypeptide chain can occur: namely, α, β and two β-like polypeptides, γ and δ. A third, β-like η chain is restricted to early fetal development. Each haemoglobin molecule contains two α-chains and two others, so that several combinations, and hence a number of different types of haemoglobin molecule, are possible. For example, haemoglobin A (HbA), which is the major adult class, contains 2 α- and 2 β-chains; a variant, HbA_2 with 2 α- and 2 δ-chains, accounts for only 2% of adult haemoglobin. Haemoglobin F (HbF), found in fetal and early postnatal life, consists of 2 α- and 2 γ-chains. Adult red cells normally contain less than 1% of HbF.

Mutations in the haemoglobin chains can result in a range of pathologies (Forget and Bunn 2013).

In the genetic condition thalassaemia, only one type of chain is expressed normally, the mutant chain being absent or present at much reduced levels. Thus, a molecule may contain 4 α-chains (β-thalassaemia) or 4 β-chains (α-thalassaemia). In haemoglobin S (HbS) of sickle-cell disease, a point mutation in the β-chain gene (valine substituted for glutamine) causes the haemoglobin to polymerize under conditions of low oxygen concentration, thus deforming the red blood cell.

erythrocytes lack nuclei. They are pale red by transmitted light, with paler centres because of their biconcave shape. The properties of their cell coat cause them to adhere to one another by their rims to form loose piles of cells (rouleaux). In normal blood, a few cells assume a shrunken, star-like, crenated form; this shape can be reproduced by placing normal biconcave erythrocytes in a hypertonic solution, which causes osmotic shrinkage. In hypotonic solutions erythrocytes take up water and become spherical; they may eventually lyse to release their haemoglobin (haemolysis), leaving red-cell ghosts.

Erythrocytes have a plasma membrane that encloses mainly a single protein, haemoglobin, as a 33% solution. The plasma membrane of erythrocytes is 60% lipid and glycolipid, and 40% protein.

More than 15 classes of protein are present, including two major types. Glycophorins A and B (each with a molecular mass of approximately 50 kDa) span the membrane, and their negatively charged carbohydrate chains project from the outer surface of the cell. Their sialic acid groups confer most of the fixed charge on the cell surface. A second transmembrane macromolecule, band 3 protein, forms an important anion channel, exchanging bicarbonate for chloride ions across the membrane and allowing the release of CO_2 in the lungs.

The filamentous protein, spectrin, is responsible for maintaining the shape of the erythrocyte. A dimer is formed of α1 and β1 spectrin monomers, and two dimers then come together to form a tetramer (Machnicka et al 2013). These are joined by junctional complexes that contain (among other proteins) ankyrin, short actin filaments, tropomyosin and protein 4.1, forming a hexagonal lattice that supports the plasma membrane (Mankelow et al 2012). The junctional complex also interacts with transmembrane proteins. This structure gives the membrane great flexibility; red cells are deformable but regain their biconcave shape and dimensions after passing through the smallest capillaries, which are 4 μm in diameter (Mohandas and Gallagher 2008). Erythrocyte membrane flexibility also contributes to the normally low viscosity of blood. Molecular defects in the cytoskeleton result in abnormalities of red cell shape, membrane fragility, premature destruction of erythrocytes in the spleen and haemolytic anaemia (Iolascon et al 1998).

Fetal erythrocytes up to the fourth month of gestation differ markedly from those of adults, in that they are larger, are nucleated and contain a different type of haemoglobin (HbF). After this time they are progressively replaced by the adult type of cell.

Haemoglobin

Haemoglobin (Hb) is a globular protein with a molecular mass of 67 kDa. It consists of globulin molecules bound to haem, an iron-containing porphyrin group. The oxygen-binding power of Hb is provided by the iron atoms of the haem groups, and these are maintained in the ferrous (Fe^{++}) state by the presence of glutathione within the erythrocyte. The Hb molecule is a tetramer, made up of four subunits, each a coiled polypeptide chain holding a single haem group.

Lifespan

Erythrocytes last between 100 and 120 days before being destroyed. As erythrocytes age, they become increasingly fragile, and their surface charge decreases as their content of negatively charged membrane glycoproteins diminishes. The lipid content of their membranes also reduces. Aged erythrocytes are taken up by the macrophages of the spleen (Mebius and Kraal 2005) and liver sinusoids, usually without prior lysis, and are hydrolysed in phagocytic vacuoles where the haemoglobin is split into its globulin and porphyrin moieties. Globulin is further degraded to amino acids, which pass into the general amino-acid pool. Iron is removed from the porphyrin ring and either transported in the circulation bound to transferrin and used in the synthesis of new haemoglobin in the bone marrow, or stored in the liver as ferritin or haemosiderin. The remainder of the haem group is converted in the liver to bilirubin and excreted in the bile. Haemoglobin that is released by destruction of erythrocytes in the body binds to haptoglobin, and is taken up via CD (antigenic Cluster of Differentiation marker of cell type)163 receptors expressed on the surface of macrophages (Kristiansen et al 2001).

The recognition of effete erythrocytes by macrophages takes place by a number of mechanisms. These include the exposure extracellularly of phospholipids (such as phosphatidyl serine) that are normally found on the inner leaflet of the membrane bilayer, alterations in the carbohydrates expressed by the cells (most notably the loss of sialic acid) and the binding of autoantibodies to antigens exposed on the aged erythrocyte. These lead to the cells being recognised and taken up by macrophages. Red cells are destroyed at the rate of 5×10^{11} cells a day (or nearly 6 million a second) and are normally replaced from the bone marrow (see Fig. 4.12) at the same rate.

Blood groups

Over 300 red cell antigens are recognizable with specific antisera. They can interact with naturally occurring or induced antibodies in the plasma of recipients of an unmatched transfusion, causing agglutination and lysis of the erythrocytes. Erythrocytes of a single individual carry several different types of antigen, each type belonging to an antigenic system in which a number of alternative antigens are possible in different persons. So far, 19 major groups have been identified. They vary in their distribution frequencies between different populations, and include the ABO, Rhesus, MNS, Lutheran, Kell, Lewis, Duffy, Kidd, Diego, Cartwright, Colton, Sid, Scianna, Yt, Auberger, Ii, Xg, Indian and Dombrock systems. Clinically, the ABO and Rhesus groups are of most importance.

Leukocytes also bear highly polymorphic antigens encoded by allelic gene variants. These belong to the group of major histocompatibility complex (MHC) antigens, also termed human leukocyte antigens (HLA) in humans. HLA class I antigens are expressed by all nucleated cells. Class II antigens are expressed on antigen-presenting cells (APCs) of the immune system, but can also be induced on many parenchymal cell types, e.g. after exposure to interferon. HLA class I and II antigens play important roles in cell–cell interactions in the immune system, particularly in the presentation of antigens to T lymphocytes by APCs.

Leukocytes

Leukocytes (white blood cells) belong to at least five different categories (see Fig. 4.12) and are distinguishable by their size, nuclear shape and cytoplasmic inclusions. In practice, leukocytes are often divided into two main groups: namely, those with prominent stainable cytoplasmic granules, the granulocytes, and those without.

Granulocytes

This group consists of eosinophil granulocytes, with granules that bind acidic dyes such as eosin; basophil granulocytes, with granules that bind basic dyes strongly; and neutrophil granulocytes, with granules that stain only weakly with either type of dye. Granulocytes (**Fig. 4.3**) all possess irregular or multilobed nuclei and belong to the myeloid series of blood cells (see Fig. 4.12).

Neutrophil granulocytes

Neutrophil granulocytes (neutrophils) are also referred to as polymorphonuclear leukocytes (polymorphs) because of their irregularly segmented (multilobed) nuclei. They form the largest proportion of the white blood cells (40–75% in adults, with a normal count of 2500–7500/μl) and have a diameter of 12–14 μm. The cells may be spherical in the circulation, but they can flatten and become actively motile within the extracellular matrix of connective tissues.

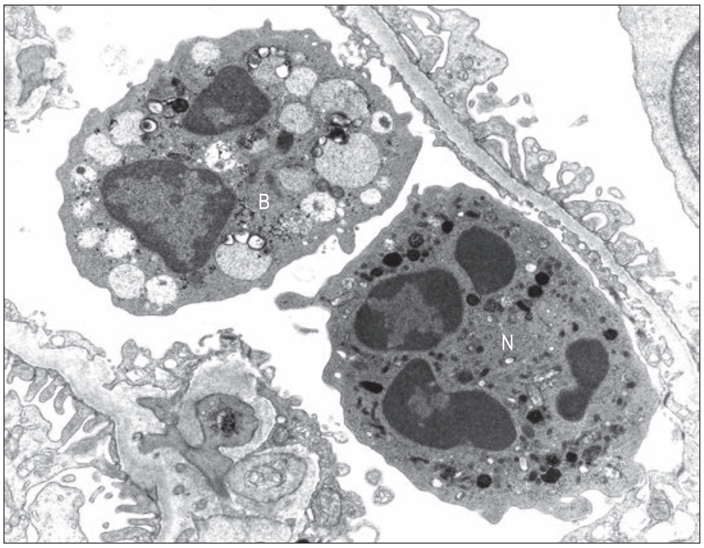

Fig. 4.3 Neutrophil (N) and basophil (B) granulocytes within a renal glomerular capillary in a human kidney biopsy. The neutrophil nucleus is more segmented (four lobes are visible) and the granules are smaller and more electron-dense than in the basophil. (Courtesy of Dr Bart Wagner, Histopathology Department, Sheffield Teaching Hospitals, UK.)

In the ABO system, two allelic genes are inherited in simple Mendelian fashion. Thus the genome may be homozygous and carry the AA complement, the blood group being A, or the BB complement, which gives blood group B, or it may carry neither (OO), producing blood group O. In the heterozygous condition the following combinations can occur: AB (blood group AB), AO (blood group A) and BO (blood group B). The ABO blood group antigens are all membrane glycolipids.

Individuals with group AB blood lack antibodies to both A and B antigens, and so can be transfused with blood of any group; they are termed universal recipients. Conversely, those with group O, universal donors, can give blood to any recipient, since anti-A and anti-B antibodies in the donated blood are diluted to insignificant levels. Normally, however, blood is only transfused between persons with corresponding groups because anomalous antibodies of the ABO system are occasionally found in blood and may cause agglutination or lysis. The anti-ABO agglutinins, unlike those of the Rhesus system, belong to the immunoglobulin M (IgM) class and do not cross the placenta during pregnancy.

The Rhesus antigen system is determined by three sets of alleles: namely, Cc, Dd and Ee. The most important clinically is Dd. Inheritance of the Rh factor also obeys simple Mendelian laws; it is therefore possible for a Rhesus-negative mother to bear a Rhesus-positive child. Under these circumstances, fetal Rh antigens can stimulate the production of anti-Rh antibodies by the mother; as these belong to the IgG class of antibody they are able to cross the placenta. For most of the pregnancy the stroma stops the blood group antibodies from crossing into the fetal circulation. However, immediately prior to birth, the antibodies can cross this barrier and cause destruction of fetal erythrocytes. In the first such pregnancy little damage usually occurs because anti-Rh antibodies have not been induced, but in subsequent Rh-positive pregnancies massive destruction of fetal red cells may result, causing fetal or neonatal death (haemolytic disease of the newborn). Sensitization of the maternal immune system can also result from abortion or miscarriage, or occasionally even from amniocentesis, which may introduce fetal antigens into the maternal circulation. Treatment is by exchange transfusion of the neonate or, prophylactically, by giving Rh-immune (anti-D) serum to the mother after the first Rh-positive pregnancy, which destroys the fetal Rh antigen in her circulation before sensitization can occur.

The numerous cytoplasmic granules are heterogeneous in size, shape and content, but all are membrane-bound and contain hydrolytic and other enzymes. Two major types can be distinguished according to their developmental origin and contents. Non-specific or primary (azurophilic) granules are formed early in neutrophil maturation. They are relatively large (0.5 µm) spheroidal lysosomes containing myeloperoxidase, acid phosphatase, elastase and several other enzymes. Specific or secondary granules are formed later, and occur in a wide range of shapes including spheres, ellipsoids and rods. These contain strong bacteriocidal components including alkaline phosphatase, lactoferrin and collagenase, none of which is found in primary granules. Conversely, secondary granules lack peroxidase and acid phosphatase. Some enzymes, e.g. lysozyme, are present in both types of granule.

In mature neutrophils the nucleus is characteristically multilobed with up to six (usually three or four) segments joined by narrow nuclear strands; this is known as the segmented stage. Less mature cells have fewer lobes. The earliest to be released under normal conditions are juveniles (band or stab cells), in which the nucleus is an unsegmented crescent or band. In certain clinical conditions, even earlier stages in neutrophil formation, when cells display indented or rounded nuclei (metamyelocytes or myelocytes) may be released from the bone marrow. In mature cells the edges of the nuclear lobes are often irregular. In females 3% of the nuclei of neutrophils show a conspicuous 'drumstick' formation, which represents the sex chromatin of the inactive X chromosome (Barr body). Neutrophil cytoplasm contains few mitochondria but abundant cytoskeletal elements, including actin filaments, microtubules and their associated proteins, all characteristic of highly motile cells.

Neutrophils are important in the defence of the body against microorganisms. They can phagocytose microbes and small particles in the circulation and, after extravasation, they carry out similar activities in other tissues. They function effectively in relatively anaerobic conditions, relying largely on glycolytic metabolism, and they fulfil an important role in the acute inflammatory phase of tissue injury, responding to chemotaxins released by damaged tissue. Phagocytosis of cellular debris or invading microorganisms is followed by fusion of the phagocytic vacuole with granules, which results in bacterial killing and digestion. Actively phagocytic neutrophils are able to reduce oxygen enzymatically to form reactive oxygen species including superoxide radicals and hydrogen peroxide, which enhance bacterial destruction probably by activation of some of the granule contents (Segal 2005, Nathan 2006). Neutrophils can also produce neutrophil extracellular traps (NETs), which are web-like structures composed of DNA and proteolytic enzymes that can trap bacteria and kill them (Kaplan and Radic 2012).

Phagocytosis is greatly facilitated by circulating antibodies to molecules such as bacterial antigens, which the body has previously encountered. Antibodies (acting as opsonins) coat the antigenic target and bind the plasma complement protein, C1, to their non-variable Fc regions. This activates the complement cascade via the classical pathway, which involves some 20 plasma proteins synthesized mainly in the liver, and completes the process of opsonization. The complement cascade involves the sequential cleavage of the complement proteins into a large fragment, which generally binds to the antigenic surface, and a small bioactive fragment, which is released. The final step is the recognition of complement by receptors on the surfaces of neutrophils and macrophages, which promotes phagocytosis of the microorganism.

Complement activation can be triggered via three pathways: classical, lectin and alternative. The classical pathway is activated by C1q binding to antigen-bound antibodies. The lectin pathway is triggered by mannan-binding lectin (MBL) interacting with carbohydrate patterns on the microbial surface. The alternative pathway relies on autoactivation of complement component C3 on the microbial surface. The products of complement activation have functions of opsonization, cytotoxicity and recruitment of infiltrating cells to the site of infection or injury.

Neutrophils are short-lived; they spend some 6–7 hours circulating in the blood and a few days in connective tissues. The number of circulating neutrophils varies, and often rises during episodes of acute bacterial infection. They die after carrying out their phagocytic role; dead neutrophils, bacteria, tissue debris (including tissue damaged by neutrophil enzymes and toxins) and interstitial fluid form the characteristic, greenish-yellow pus of infected tissue. The colour is derived from the natural colour of neutrophil myeloperoxidase.

Granules may also be released inappropriately from neutrophils. Their enzymes are implicated in various pathological conditions, e.g. rheumatoid arthritis, where tissue destruction and chronic inflammation occur.

Eosinophil granulocytes

Eosinophil granulocytes (eosinophils; for a review, see Rothenberg and Hogan (2006)) are similar in size (12–15 µm), shape and motile capacity to neutrophils, but are present only in small numbers in normal blood (100–400/µl). The nucleus has two prominent lobes connected by a thin strand of chromatin. Their cytoplasmic specific granules are uniformly large (0.5 µm) and give the living cell a slightly yellowish colour. The cytoplasm is packed with granules, which are spherical or ellipsoid and membrane-bound. The core of each granule is composed of a lattice of major basic protein, which is responsible for its strong eosinophilic staining properties. The surrounding matrix contains several lysosomal enzymes including acid phosphatase, ribonuclease, phospholipase and a myeloperoxidase unique to eosinophils.

Like other leukocytes, eosinophils are motile. When suitably stimulated, they are able to pass into the extravascular tissues from the circulation. They are typical minor constituents of the dermis, and of the connective tissue components of the bronchial tree, alimentary tract, uterus and vagina. The total lifespan of these cells is a few days, of which some 10 hours is spent in the circulation, and the remainder in the extravascular tissues.

Eosinophil numbers rise (eosinophilia) in worm infestations and also in certain allergic disorders, and it is thought that they evolved as a primary defence against parasitic attack. They have surface receptors for IgE that bind to IgE-antigen complexes, triggering phagocytosis and release of granule contents. However, they are only weakly phagocytic and their most important function is the destruction of parasites too large to phagocytose. This antiparasitic effect is mediated via toxic molecules released from their granules (e.g. eosinophil cationic protein and major basic protein). They also release histaminase, which limits the inflammatory consequences of mast cell degranulation. High local concentrations of eosinophils, e.g. in bronchial asthma and in cutaneous contact hyper sensitivity and allergic eczema, can cause tissue destruction as a consequence of the release of molecules such as collagenase from their granules.

Basophil granulocytes

Slightly smaller than other granulocytes, basophil granulocytes are 10–14 µm in diameter, and form only 0.5–1% of the total leukocyte population of normal blood, with a count of 25–200/µl. Their distinguishing feature is the presence of large, conspicuous basophilic granules. The nucleus is somewhat irregular or bilobed, and is usually obscured in stained blood smears by the similar colour of the basophilic granules. The granules are membrane-bound vesicles that display a variety of crystalline, lamellar and granular inclusions: they contain heparin, histamine and several other inflammatory agents, and closely resemble those of tissue mast cells. Both basophils and mast cells have high-affinity membrane receptors for IgE and are therefore coated with IgE antibody. If this binds to its antigen it triggers degranulation of the cells, causing vasodilation, increased vascular permeability, chemotactic stimuli for other granulocytes, and the symptoms of immediate hypersensitivity, e.g. in allergic rhinitis (hay fever). Despite these similarities, basophils and mast cells develop as separate lineages in the myeloid series, from haemopoietic stem cells in the bone marrow. Evidence from experimental animal models suggests that they are closely related (see Fig. 4.12) but studies on mast cell disorders in humans indicate that their lineages diverge from a more distant ancestral progenitor (Kocabas et al 2005). The role of mast cells in the regulation of responses to pain is of interest clinically as a therapeutic target (Chatterjea and Martinov 2015).

Mononuclear leukocytes

Monocytes

Monocytes are the largest of the leukocytes (15–20 µm in diameter) but they form only a small proportion of the total population (2–8% with a count of 100–700/µl of blood). The nucleus, which is euchromatic, is relatively large and irregular, often with a characteristic indentation on one side. The cytoplasm is pale-staining, particulate and typically vacuolated. Near the nuclear indentation it contains a prominent Golgi complex and vesicles. Monocytes are actively phagocytic cells and contain numerous lysosomes. Phagocytosis is triggered by recognition of opsonized material, as described for neutrophils. Monocytes are highly motile and possess a well-developed cytoskeleton.

Monocytes express class II MHC antigens and share other similarities to tissue macrophages and dendritic cells. Most monocytes are thought to be in transit via the blood stream from the bone marrow to the peripheral tissues, where they give rise to macrophages and dendritic cells; different monocyte subsets may target inflamed tissues. Like other leukocytes, they pass into extravascular sites through the walls of capillaries and venules.

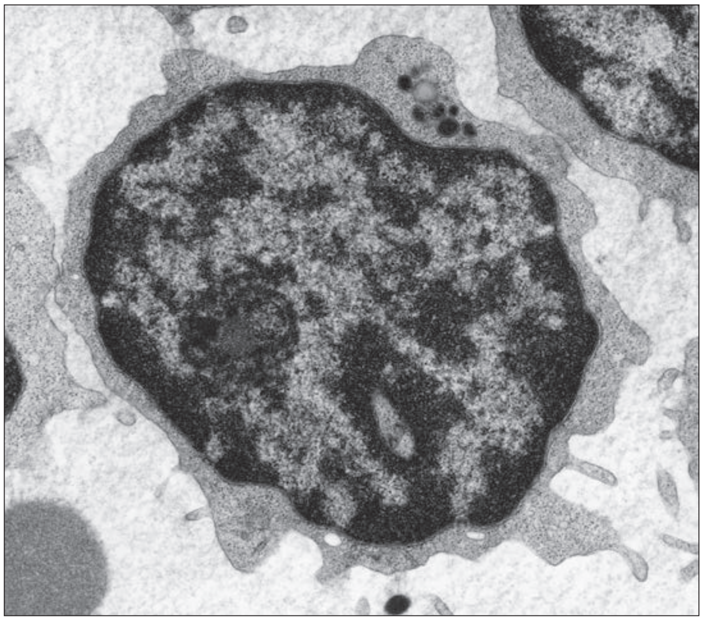

Fig. 4.4 A small, resting lymphocyte in human peripheral blood (electron micrograph). The nuclear:cytoplasmic ratio is high and the cytoplasm contains few organelles, indicative of its quiescent state. (Courtesy of Dr Bart Wagner, Histopathology Department, Sheffield Teaching Hospitals, UK.)

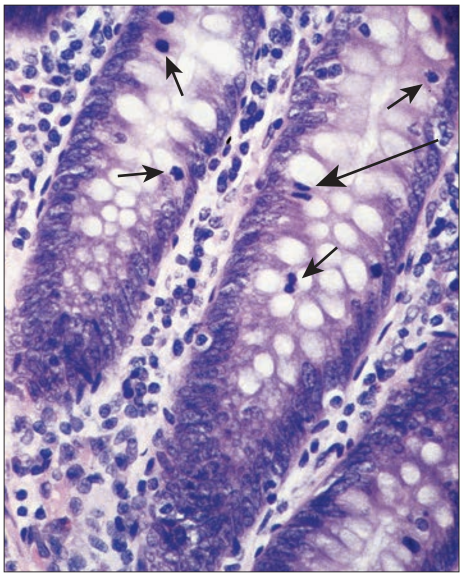

Fig. 4.5 Tubular glands in the appendix, showing intraepithelial lymphocytes (short arrows). A lymphocyte in anaphase is indicated (long arrow).

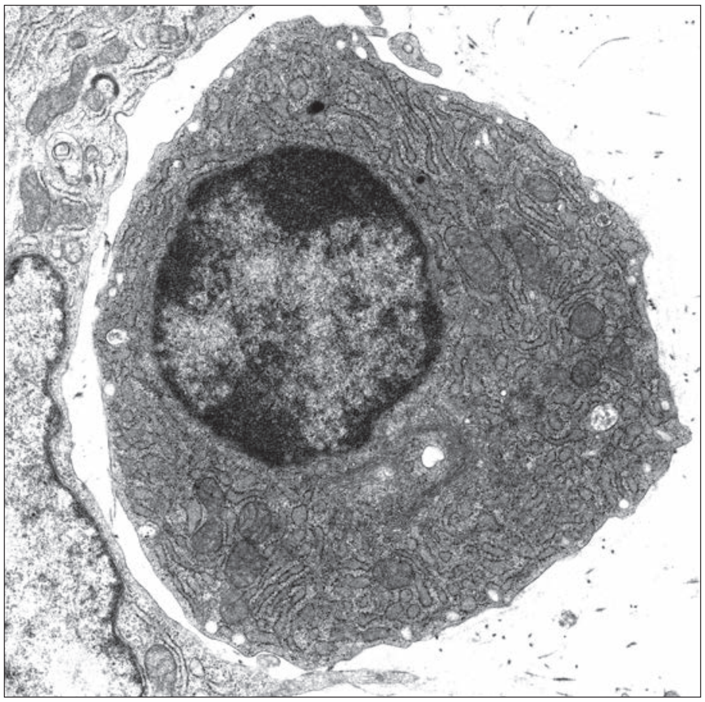

Fig. 4.6 A mature B cell (plasma cell) in human connective tissue. The abundant rough endoplasmic reticulum is typical of a cell actively synthesizing secretory protein, in this case immunoglobulin. The cell to the left is a fibroblast. (Courtesy of Dr Bart Wagner, Histopathology Department, Sheffield Teaching Hospitals, UK.)

Lymphocytes

Lymphocytes (Fig. 4.4; see Figs 4.6, 4.12) are the second most numerous type of leukocyte in adulthood, forming 20–30% of the total population (1500–2700/μl of blood). In young children they are the most numerous blood leukocyte. Most circulating lymphocytes are small, 6–8 μm in diameter; a few are medium-sized and have an increased cytoplasmic volume, often in response to antigenic stimulation. Occasionally, cells up to 16 μm are seen in peripheral blood. Lymphocytes, like other leukocytes, are found in extravascular tissues (including lymphoid tissue); however, they are the only white blood cells that return to the circulation. The lifespan of lymphocytes ranges from a few days (short-lived) to many years (long-lived). Long-lived lymphocytes are necessary for the maintenance of immunological memory.

Blood lymphocytes are a heterogeneous collection, mainly of B and T cells. About 85% of all circulating lymphocytes in normal blood are T cells. Primary immunodeficiency diseases can result from molecular defects in T and B lymphocytes that provide targets for gene therapy for these conditions (Cunningham-Rundles and Ponda 2005, Thrasher and Williams 2017).

Small lymphocytes (both B and T cells) contain a rounded, densely staining nucleus that is surrounded by a very narrow rim of cytoplasm, barely visible in the light microscope. By transmission electron microscopy (see Fig. 4.4), few cytoplasmic organelles can be seen apart from a small number of mitochondria, single ribosomes, sparse profiles of endoplasmic reticulum and occasional lysosomes; these features indicate a low metabolic rate and a quiescent phenotype. However, these cells become motile when they contact solid surfaces, and can pass between endothelial cells to exit from, or re-enter, the vascular system. They migrate extensively within various tissues, including epithelia (Fig. 4.5).

Larger lymphocytes include T and B cells that are functionally activated or proliferating after stimulation by antigen, and NK cells. They contain a nucleus, which is, at least in part, euchromatic; a basophilic cytoplasm, which may appear granular; and numerous polyribosome clusters, consistent with active protein synthesis. The ultrastructural appearance of these cells varies according to their class and is described below.

B cells

B cells and the plasma cells that develop from them synthesize and secrete antibodies that can specifically recognize and neutralize foreign (non-self) macromolecules (antigens), and can direct various non-lymphocytic cells (e.g. neutrophils, macrophages and dendritic cells) to phagocytose pathogens. B cells differentiate from haemopoietic stem cells in the bone marrow. After deletion of autoreactive cells, the selected B lymphocytes then leave the bone marrow and migrate to peripheral lymphoid sites (e.g. lymph nodes). Here, following stimulation by antigen, they undergo further proliferation and selection, forming germinal centres in the lymphoid tissues. Following this, some B cells differentiate into large basophilic (RNA-rich) plasma cells, either within or outside the lymphoid tissues. Plasma cells produce antibodies in their extensive rough endoplasmic reticulum (Fig. 4.6) and secrete them into the adjacent tissues. They have a prominent pale-staining Golgi complex adjacent to an eccentrically placed nucleus, typically with peripheral blocks of condensed heterochromatin resembling the numerals of a clock (clock-faced nucleus) (see Fig. 4.12). Other germinal centre B cells develop into long-lived memory cells capable of responding to their specific antigens not only with a more rapid and higher antibody output, but also with an increased antibody affinity compared with the primary response.

Antibodies are immunoglobulins, grouped into five classes according to their heavy polypeptide chain. Immunoglobulin G (IgG) forms the bulk of circulating antibodies. Immunoglobulin M (IgM) is normally synthesized early in immune responses. Immunoglobulin A (IgA) is present in breast milk, tears, saliva and other secretions of the alimentary tract, coupled to a secretory piece (a 70 kDa protein) that is synthesized by the epithelial cells. The secretory piece (or component) is a cleavage product of the epithelial plasma membrane Ig receptor, following internalization of the receptor–IgA complex and processing during transcytosis. It protects the immunoglobulin from proteolytic degradation after secretion: secretory IgA (sIgA) contributes to mucosal immunity (Brandtzaeg 2013). IgA deficiency is relatively common, particularly in some ethnic groups (reviewed in Woof and Kerr (2006)). Immunoglobulin E (IgE) is an antibody that binds to receptors on the surfaces of mast cells, eosinophils and blood basophils, and is found only at low concentrations in the circulation. IgE is mostly associated with type I hypersensitivity (allergic) reactions. Immunoglobulin D (IgD) is found together with IgM as a major membrane-bound immunoglobulin on mature, immunocompetent but naïve (prior to antigen exposure) B cells, acting as the cellular receptor for antigen. IgG and IgM, when bound to self or microbial antigens, can activate the classical complement pathway, leading to a cascade of cytolytic and proinflammatory consequences.

When circulating antibodies bind to antigens they form immune complexes. If present in abnormal quantities, these may cause pathological damage to the vascular system and other tissues, either by interfering mechanically with the permeability of the basal lamina (e.g. some types of glomerulonephritis), or by causing local activation of the complement system that generates inflammatory mediators (e.g. C5a), attacks cell membranes and causes vascular disease. In pregnancy, maternal IgG crosses the placenta and confers passive immunity on the fetus. Maternal milk contains secretory immunoglobulins (IgA) that help to combat bacterial and viral organisms in the alimentary tract of the baby during the first few weeks of postnatal life.

T cells

There are a number of subsets of T (thymus-derived) lymphocytes, all progeny of haemopoietic stem cells in the bone marrow. They develop and mature in the thymus, and subsequently populate peripheral secondary lymphoid organs, which they constantly leave and re-enter via the circulation. As recirculating cells, their major function is immune surveillance. Their activation and subsequent proliferation and functional maturation are under the control of APCs. T cells undertake a wide variety of cell-mediated defensive functions that are not directly dependent on antibody activity, and which constitute the basis of cellular immunity. T-cell responses focus on the destruction of cellular targets such as virus-infected cells, certain bacterial infections, fungi, some protozoal infections, neoplastic cells and the cells of grafts from other individuals (allografts, when the tissue antigens of the donor and recipient are not sufficiently similar). Targets may be killed directly by cytotoxic T cells, or indirectly by accessory cells (e.g. macrophages) that have been recruited and activated by cytokine-secreting helper T cells. A third group, regulatory T cells, acts to regulate or limit immune responses.

Functional groups of T cells are classified according to the molecules they express on their surfaces. The majority of cytokine-secreting helper T cells express CD4, while cytotoxic T cells are characterized by CD8. Regulatory T cells co-express CD4 and CD25. The CD (cluster of differentiation) prefix provides a standard nomenclature for all cell-surface molecules. At present, more than 330 different CD antigens have been designated; each one represents a cell surface molecule that can be identified by specific antibodies. Further details of the classification are beyond the scope of this publication and are given in Male et al (2012).

Structurally, T lymphocytes present different appearances depending on their type and state of activity. When resting, they are typically small lymphocytes and are morphologically indistinguishable from B lymphocytes. When stimulated, they become large (up to 15 μm), moderately basophilic cells, with a partially euchromatic nucleus and numerous free ribosomes, rough and smooth endoplasmic reticulum, a Golgi complex and a few mitochondria, in their cytoplasm. Cytotoxic T cells contain dense lysosome-like vacuoles that function in cytotoxic killing.

Cytotoxic T cells

Cytotoxic T lymphocytes (CTLs) express CD8. They are responsible for the direct cytotoxic killing of target cells (e.g. virus-infected cells); the requirement for direct cell–cell contact ensures the specificity of the response. Recognition of antigen, presented as a peptide fragment on MHC class I molecules, triggers the calcium-dependent release of lytic granules by the CTLs. These lysosome-like granules contain perforin (cytolysin), which forms a pore in the target cell membrane, very similar to the membrane attack complex generated at the end of complement activation. They also contain several different serine protease enzymes (granzymes), which enter the target cell via the perforin pore and induce programmed cell death (apoptosis; p. 27) of the target. $CD8^+$ CTLs protect their own membranes from lysis by perforin and granzymes using cathepsin B, which is bound to the granules, and which can degrade their suicidal contents. CTLs and natural killer (NK) cells of the innate immune system have similar effector functions in IFN-γ production and cytotoxicity (see below).

Helper T cells

Helper T (Th) cells express CD4 and are characterized by the secretion of cytokines. Two major populations have been identified according to the range of cytokines produced. Th1 helper T cells (a part of cell-mediated adaptive immunity) typically secrete interleukin (IL)-2, tumour necrosis factor alpha (TNF-α) and interferon gamma (IFN-γ). Th2 helper T cells (a part of humoral adaptive immunity) produce cytokines such as IL-4, IL-5 and IL-13. These two CD4-expressing populations are termed Th cells because one aspect of their function is to help, i.e. stimulate, the proliferation and maturation of B lymphocytes and CTLs (mediated via cytokines such as IL-4, IL-2 and IFN-γ), thus enabling and enhancing the immune responses mediated by those cells. Th1 cells activate phagocytic cells via production of IFN-γ and TNF-α in order to eliminate pathogens. Macrophage activation by IFN-γ involves upregulation of MHC class II surface expression and enhancement of their antigen-capturing and presenting potency. IFN-γ also promotes the generation of specialized tumour necrosis factor/inducible nitric oxide synthase- (TNF/iNOS) producing dendritic cells, facilitating swift destruction of intracellular pathogens such as *Mycobacterium tuberculosis*.

Th cells are important in directing the destruction of pathogens by recruiting accessory cells (e.g. macrophages, neutrophils, eosinophils) to the site of infection and by activating their effector functions. This process is tightly coordinated. For example, Th1 helper T cells secrete cytokines that not only attract and activate macrophages but also provide help for B cells and guide their immunoglobulin production to the subclasses that fix complement. Thus, these antibodies opsonize the pathogen target, which can then be recognized, ingested and destroyed by the macrophage accessory cells that bear receptors for complement and the Fc region of IgG. These Th1 cells are sometimes referred to as delayed-type hypersensitivity T cells. In contrast, Th2 cells secrete cytokines that induce the development and activation of eosinophils, and also induce B cells to switch their immunoglobulins to non-complement-fixing classes (e.g. IgE). Pathogens such as parasitic worms can then be coated with IgE antibody and hence recognized and destroyed by the effector functions of the eosinophil accessory cells, which bear receptors for the Fc region of IgE.

If helper T-cell activities are non-functional, a state of immunodeficiency results. This means that potentially pathogenic organisms, normally kept in check by the immune system, may proliferate and cause overt pathology, e.g. in acquired immune deficiency syndrome (AIDS), where a virus (human immunodeficiency virus, HIV) specifically infects and kills (predominantly) helper T cells, though some APCs are also killed. Dysregulated Th1 immune responses can result in organ damage and autoimmune disease due to a sustained chronic inflammatory state. In general, most effector cells die within about two weeks following antigen stimulation.

Regulatory T cells

A third population of T cells, regulatory T or Treg cells, are important in controlling the immune response. These $CD4^+$, $CD25^+$ cells have an immunomodulatory function and can dampen the effector functions of both cytotoxic and helper T cells. Regulatory T cells (natural or central Tregs) are produced in the thymus and are an important additional mechanism for maintaining self-tolerance because their T cell receptors are directed in the thymus to recognize self-antigens (Safinia et al 2015). Treg function is antigen-specific and depends on direct cell–cell contact. Molecules secreted or induced by Treg cells, such as IL-10 or transforming growth factor beta (TGF-β), also play an important role in mediating Treg suppressive effects on the immune system. Similar regulatory T cells can be induced in the periphery by TGF-β (induced Tregs) and may be important in the induction of oral tolerance to ingested antigens, as well as tolerance to tissue-specific molecules that are not expressed in the thymus (Schmitt and Williams 2013). Induced Tregs are usually generated in response to microbial antigens, as opposed to central Tregs. Tregs are long-lived and constitute about 10% of circulating $CD4^+$ T cells.

Specialized lymphocytes

The adaptive immune response involving B and T lymphocytes becomes effective following clonal expansion and differentiation of plasma cells, Th2 or Th1 cells. Specialized lymphocytes that contain receptors of limited repertoire and recognize molecular patterns on non-self antigens or pathogen surfaces immediately play an important role in connecting innate and adaptive immune mechanisms. These cells include NK cells, NKT cells, γδ T cells, intestinal intraepithelial lymphocytes (IEL), mucosal-associated invariant T (MAIT) cells, B1 cells, and marginal zone B cells (see Fig. 4.15).

Other subsets of helper T cells have been described. They include Th17 cells which secrete the cytokine IL-17, implicated in autoimmune diseases such as rheumatoid arthritis and multiple sclerosis (Stockinger and Veldhoen 2007). Th17 cells are always present in small bowel tissues where they are likely to interact with commensal gut bacteria. Since Th17 cells bear IL-23 receptors, they can recruit neutrophils very quickly in response to IL-23 produced by activated macrophages. Further subsets (Th9, Th22) have been designated and many more subsets will likely be characterized in the future (Jiang and Dong 2013, Hirahara and Nakayama 2016).

NK cells have functional similarities to cytotoxic T cells. They secrete the proinflammatory cytokine IFN-γ, but lack other typical lymphocyte features and do not express antigen-specific receptors. NK cells are found in the circulation, and in organs such as liver, spleen, lungs and bone marrow, but not in lymph nodes. They normally form only a small percentage of all lymphocyte-like cells and usually have a large granular lymphocyte morphology. When mature, NK cells have a mildly basophilic cytoplasm. Ultrastructurally, their cytoplasm contains ribosomes, rough endoplasmic reticulum and dense, membrane-bound vesicles 200–500 nm in diameter with crystalline cores that contain the protein perforin, which is capable of inserting holes in the plasma membranes of target cells, and granzymes, which trigger subsequent target cell death by apoptosis. NK cells are activated to kill target cells by a number of factors, such as type I interferons (IFN-α/β) secreted by virus-infected cells. They can recognize and kill antibody-coated target cells via antibody-dependent cell-mediated cytotoxicity (ADCC) and express activating as well as inhibitory receptors on their surface. They also have receptors that inhibit NK cell destructive activity when they recognize MHC class I on normal cells (molecular signature of self). When NK cells detect the loss or downregulation of MHC class I antigens on certain virus-infected cells and some tumour cells (missing self), they activate apoptosis-inducing mechanisms that enable them to attack these abnormal cells, albeit relatively non-specifically. For further reading, see Vivier et al (2008) and Chan et al (2015).

There are a few additional types of specialized lymphocyte with limited recognition capacity that act to bridge the time gap between innate and adaptive immune responses. NKT cells are found in blood, bone marrow, spleen and liver. They express both NK and T cell receptors on their cell surface, recognize glycolipids in conjunction with CD1d, and are activated by Gram-negative bacteria. They retain cytolytic properties, can activate NK cells, and produce IL-4 and IFN-γ cytokines. γδ T cells are distinct from αβ T cell receptor-bearing $CD4^+$ and $CD8^+$ cells, can constitute up to 5% of the circulating lymphocyte population, and their activation can lead to IFN-γ production. They are capable of producing tissue growth factors that may be helpful in tissue repair following pathogen clearance and inflammation. Intraepithelial lymphocytes (IEL) containing αβ and γδ T cell receptors, are found in the lungs and bowel, where they behave similarly to $CD8^+$ CTLs. Mucosal associated invariant T cell (MAIT) cells are relatively rare and recognize non-canonical MHC I molecules presenting microbial components: they are considered to have a regulatory role in the lamina propria of mucosae. B1 cells are made in the fetus and produce natural antibodies without antigenic stimulation. They offer protection against pathogens during the early part of neonatal life and can produce IgM and IgA antibodies in response to conserved patterns on bacterial surfaces without requiring the participation of T cells. Marginal zone B cells can generate IgM and IgG3 antibody responses against blood-borne pathogens.

Platelets

Blood platelets, also known as thrombocytes, are relatively small (2–4 µm across) irregular or oval discs present in large numbers (200,000–400,000/µl) in blood. In freshly harvested blood samples they readily adhere to each other and to all available surfaces, unless the blood is treated with citrate or other substances that reduce the availability of calcium ions. Platelets are anucleate cell fragments, derived from megakaryocytes in the bone marrow. They are surrounded by a plasma membrane with a thick glycoprotein coat, which is responsible for their adhesive properties. A band of 10 microtubules lies around the perimeter of the platelet beneath the plasma membrane; the microtubules are associated with actin filaments, myosin and other proteins related to cell contraction. The cytoplasm also contains mitochondria, glycogen, scant smooth endoplasmic reticulum, tubular invaginations of the plasma membrane, and three major types of membrane-bound vesicle, designated α, δ and λ granules. Alpha granules are the largest (up to 500 nm diameter) and contain platelet-derived growth factor (PDGF), fibrinogen and other substances. Delta granules (up to 300 nm) contain 5-hydroxytryptamine (5-HT, serotonin) that has been endocytosed from the blood plasma. Lambda granules (up to 250 nm) contain lysosomal enzymes.

Platelets play an important role in haemostasis. When a blood vessel is damaged, platelets become activated, evert their membrane invaginations to form lamellipodia and filopodia, and aggregate at the site of injury, plugging the wound. They adhere to each other (agglutination) and to other tissues. Adhesion is a function of the thick platelet coat and is promoted by the release of adenosine diphosphate (ADP) and calcium ions from the platelets in response to vessel injury. The contents of released α granules, together with factors released from the damaged tissues, initiate a complex sequence of chemical reactions in the blood plasma, which leads to the precipitation of insoluble fibrin filaments in a three-dimensional meshwork, the fibrin clot (see Fig. 4.1). More platelets attach to the clot, inserting extensions of their surfaces, filopodia, deep into the spaces between the fibrin filaments, to which they adhere strongly. The platelets then contract (clot retraction) by actin–myosin interactions within their cytoplasm, thus concentrating the fibrin clot and pulling the walls of the blood vessel together, limiting any further leakage of blood. After repair of the vessel wall, which may be promoted by the mitogenic activity of PDGF, the clot is dissolved by enzymes such as plasmin, formed by plasminogen activators in the plasma, probably assisted by lysosomal enzymes derived from the γ granules of platelets. Platelets typically circulate for 10 days before they are removed, mainly by splenic macrophages.

LYMPHOID TISSUES

Lymphocytes are located in many sites in the body, most obviously at strategic sites that are liable to infection, e.g. the oropharynx. The main areas of lymphocyte concentration are classified as primary or secondary lymphoid organs, according to whether they are involved in *de novo* lymphocyte generation (primary lymphoid organs, e.g. bone marrow, thymus) or are the site of mature lymphocyte activation and initiation of an immune response (secondary lymphoid organs, e.g. lymph nodes, spleen).

All lymphocytes arise from pluripotent haemopoietic stem cells in the bone marrow. The B lymphocyte lineage develops through a series of differentiation stages within the bone marrow. The newly formed B cells then leave through the circulation and migrate to peripheral sites. In contrast, T-lymphocyte development requires the thymus; the bone marrow-derived stem cells must therefore migrate via the blood circulation to the thymus. After their differentiation and maturation into immunocompetent T cells that have survived thymic selection processes (1–3%), they re-enter the circulation and are transported to peripheral sites where they join the pool of naïve lymphocytes that recirculate through the secondary lymphoid organs via blood and lymphatic circulation systems.

The secondary or peripheral lymphoid organs are the specialized sites where B and T lymphocytes and APCs come together to initiate immune responses to foreign antigens (Malhotra et al 2013). They include lymph nodes, spleen, and lymphoid tissue associated with epithelial surfaces (mucosa-associated lymphoid tissue, MALT), e.g. the palatine and nasopharyngeal tonsils, Peyer's patches in the small intestine, lymphoid nodules in the respiratory and urogenital systems, the skin. The microstructure of lymph nodes and of MALT in general is described below. Details of all other lymphoid tissues and organs are included in the descriptions of the appropriate regional anatomy.

Most lymphocytes enter secondary lymphoid tissues from the blood, usually by migration through the walls of capillaries or high endothelial venules, HEVs (Ch. 6) and leave by the lymphatic system. In the spleen, lymphocyte entry and exit take place via the marginal zone and venous drainage respectively. APCs (dendritic cells) enter via the lymphatics, bringing with them antigen from peripheral infected sites. In all the secondary tissues there are specific areas where either B or T cells are concentrated. After activation, functionally competent lymphocytes migrate to other sites in the body, where they combat the original infection. Organized lymphoid structures, termed tertiary lymphoid organs, can also develop at sites of chronic inflammation (Stranford and Ruddle 2012).

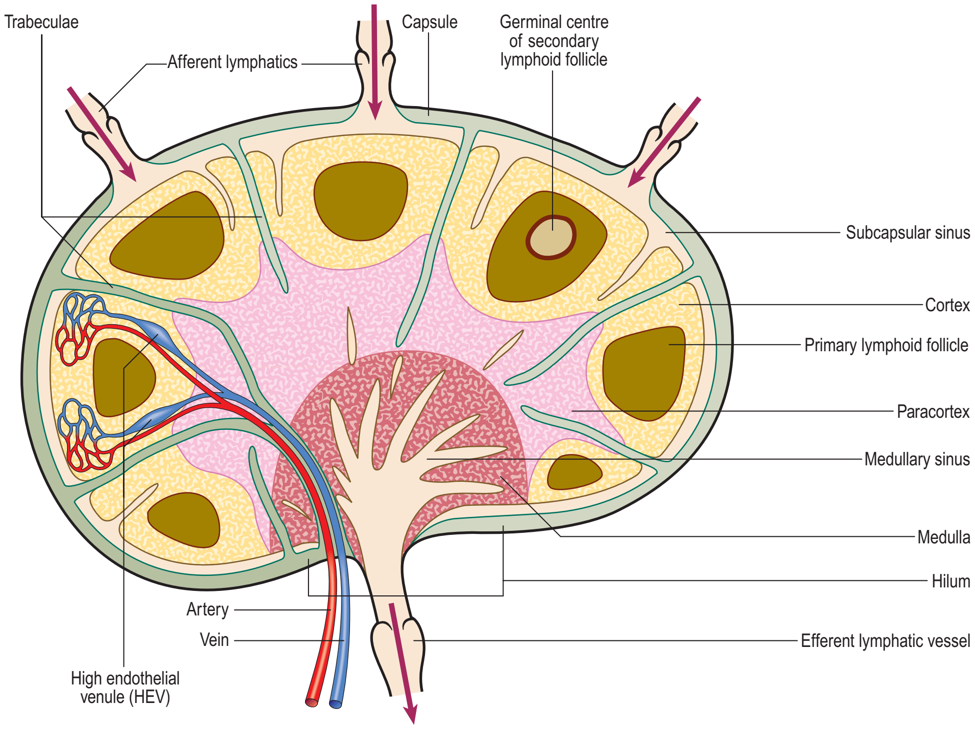
Trabeculae
Afferent lymphatics
Capsule
Germinal centre of secondary lymphoid follicle
Subcapsular sinus
Cortex
Primary lymphoid follicle
Paracortex
Medullary sinus
Medulla
Hilum
Artery
Vein
Efferent lymphatic vessel
High endothelial venule (HEV)

Fig. 4.7 The structure of a lymph node.

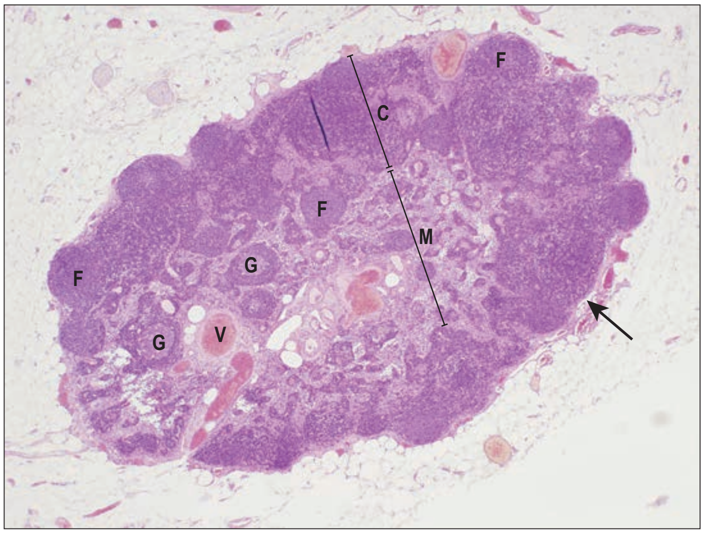

Fig. 4.8 A lymph node (human) showing cortex (C) and medulla (M), and lymphoid follicles (F), some with germinal centres (G). Also shown are the subcapsular sinus (arrow) and medullary blood vessels (V). The dark line (top, centre) is a small crease in the tissue section and is an artefact. (Courtesy of Mr Peter Helliwell and the late Dr Joseph Mathew, Department of Histopathology, Royal Cornwall Hospitals Trust, UK.)

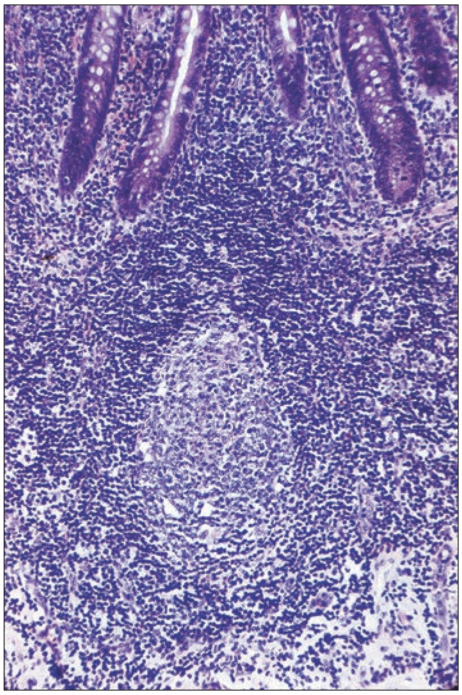

Fig. 4.10 A germinal centre in a follicle of mucosa-associated lymphoid tissue (MALT) in the mucosa and submucosa of the appendix. The bases of tubular glands of the mucosal epithelium are seen in the upper field.

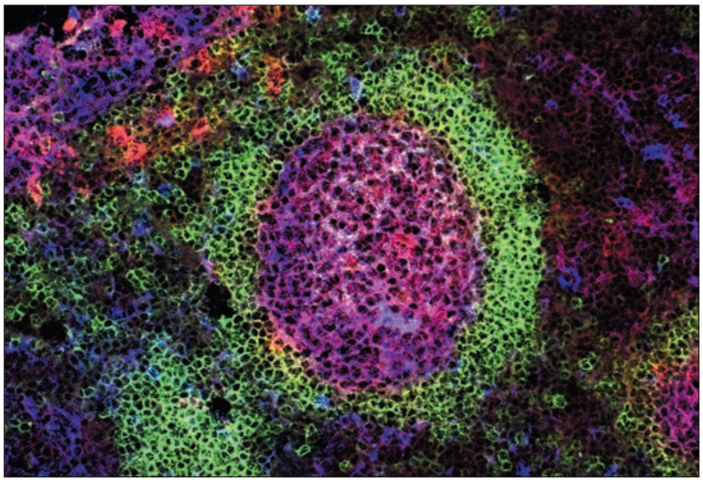

Fig. 4.9 A germinal centre in a lymphoid follicle of the human palatine tonsil, immunolabelled to show CD38-positive B cells in the germinal centre (red), IgD-positive naïve B cells (green) in the mantle zone and activated, transferrin receptor (CD71)-positive cells of various lineages (blue). (Courtesy of Dr Cécile Chalouni, Ludwig Institute for Cancer Research, Yale University School of Medicine, USA.)

Lymph nodes

Lymph nodes (Fig. 4.7) are small encapsulated, oval or kidney-shaped bodies, 0.1–2.5 cm long, lying along the course of the lymphatic vessels. A normal young adult body contains up to 450 lymph nodes, of which 60–70 are found in the head and neck, 100 in the thorax and as many as 250 in the abdomen and pelvis: they are particularly numerous in the neck, mediastinum, posterior abdominal wall, abdominal mesenteries, pelvis and proximal regions of the limbs (axillary and inguinal lymph nodes). By far the greatest number lie close to the viscera, especially in the mesenteries.

Microstructure

The capsule is composed mainly of collagen fibres, elastin fibres (especially in the deeper layers) and a few fibroblasts. Lymph nodes may be subdivided into cortex, paracortex and medulla (Girard et al 2012). Trabeculae of dense connective tissue extend radially into the interior of a node from the capsule and are continuous with a network of fine type III collagen (reticulin) fibrils that branch and interconnect to form a very dense network in the cortex. Reticulin and the associated proteoglycan matrix are produced by fibroblasts associated with the fibrous network. There are fewer fibres in the germinal centres of follicles (see below). The medulla contains a network of minute lymphatic channels (sinuses) through which lymph from the afferent lymphatics is filtered.

Lymphatic and vascular supply

Each lymph node usually has a slight indentation on one side, the hilum, where blood vessels enter or leave, and the efferent lymphatic vessel leaves (Fig. 4.8). Several afferent lymphatic vessels enter the capsule around the periphery. Afferent lymphatic vessels enter at many points on the periphery, branch to form a dense intracapsular plexus, and then open into the subcapsular sinus, a cavity that is peripheral to the whole cortex except at the hilum (see Fig. 4.7) (Roozendaal et al 2008). Numerous radial cortical sinuses lead from the subcapsular sinus to the medulla, where they coalesce as larger medullary sinuses. The latter become confluent at the hilum with the efferent vessel that drains the node. All of these spaces are lined by a continuous endothelium and traversed by fine reticular fibres.

Arteries and veins serving lymph nodes pass through the hilum, giving off straight branches that traverse the medulla and send out minor branches as they do so. In the cortex, arteries form dense arcades of arterioles and capillaries in numerous anastomosing loops, eventually returning to highly branched venules and veins. Capillaries are especially profuse around the follicles, which contain fewer vessels. Postcapillary HEVs are abundant in the paracortical zones. They form an important site of lymphocyte extravasation into lymphoid tissue, apparently by transcellular migration or paracellular transit through labile endothelial tight junctions (occluding junctions) and adherent junctions. The density of the capillary beds increases greatly when lymphocytes multiply in response to antigenic stimulation. Veins leave a node through its principal trabeculae and capsule, and drain them and the surrounding connective tissue.

Cells and cellular zones of lymph nodes

Although most of the cells in a lymph node are B and T lymphocytes, their distribution is not homogeneous. In the cortex, cells are densely packed and in the outer cortical area they form lymphoid follicles or nodules (see Fig. 4.8) populated mainly by B cells and specialized follicular dendritic cells (FDCs) (see Fig. 4.15). The number, degree of isolation and staining characteristics of follicles vary according to their state of antigenic stimulation. A primary follicle is uniformly populated by small, quiescent lymphocytes, whereas a secondary follicle has a germinal centre (Fig. 4.9), composed mainly of antigen-stimulated B cells, which are larger, less deeply staining and more rapidly dividing than those at its periphery.

The role of the germinal centre is to provide a microenvironment that allows the affinity maturation of the B-cell response, so that as the immune response progresses, the affinity or strength with which antibodies bind their antigen increases (Shlomchik and Weisel 2012, Victora and Nussenzweig 2012). B cells (centroblasts) undergo rapid proliferation in the 'dark zone', which is associated with hypermutation of the genes encoding the variable regions of their antibody molecules. They then move into the 'light zone' (as centrocytes), where they can interact with the FDCs, which carry intact unprocessed antigen on their surface in the form of immune complexes (Rezk et al 2013). The centrocytes compete for binding to the antigen; only those expressing antibody with the highest affinity survive. T cells are also present, helping the survival of the B cells and inducing class switching. Macrophages in the germinal centre phagocytose apoptotic lymphocytes (the B cells that die as part of the process of affinity maturation), and their cytoplasm becomes filled with engulfed lipid and nuclear debris forming intracellular inclusions (hence the alternative name, tingible body macrophage).

The mantle zone (see Fig. 4.9) is produced as surrounding cells are marginalized by the rapidly growing germinal centre. It is populated by cells similar to those found in primary follicles: mainly quiescent B cells with condensed heterochromatic nuclei and little cytoplasm (hence the deeply basophilic staining of this region in routine preparations; **Fig. 4.10**), a few helper T cells, FDCs and macrophages. After numerous mitotic divisions the selected B cells give rise to small lymphocytes, some of which become memory B cells and leave the lymph node to join the recirculating pool, while others leave to mature as antibody-secreting plasma cells either in the lymph node medulla or in peripheral tissues.

The paracortex (deep cortex) lies between the cortical follicles and the medulla. It is populated mainly by T cells, both $CD4^+$ and $CD8^+$ T-cell subsets, which are not organized into follicles. It also contains interdigitating dendritic cells, including Langerhans cells from the skin and other squamous epithelia, which have migrated as veiled cells via the afferent lymphatics into the draining lymph nodes (see Fig. 4.14). Their role is to present processed antigen to T cells. The region expands greatly in T cell-dominated immune responses, when its cells are stimulated to proliferate and disperse to peripheral sites.

In the medulla, lymphocytes are much less densely packed and form irregular, branching medullary cords within the reticulin network. Other cells present include macrophages, which are more numerous than in the cortex, plasma cells and a few granulocytes.

Mucosa-associated lymphoid tissue (MALT)

Unencapsulated lymphoid tissue exists in the walls of the gastrointestinal, respiratory, reproductive and urinary tracts, and in the skin. Collectively, it is termed mucosa-associated lymphoid tissue (MALT): most is found in the gut as gut-associated lymphoid tissue (GALT) (Koboziev et al 2010).

Lymphoid cells are located in the lamina propria and in the submucosa as discrete follicles or nodules. More scattered cells, derived from these follicles, are found throughout the lamina propria and in the base of the epithelium (see Figs 4.5, 4.10). MALT includes macroscopically visible lymphoid masses, notably the peripharyngeal lymphoid ring of tonsillar tissue (palatine, nasopharyngeal, tubal and lingual), and the Peyer's patches of the small intestine, all of which are described elsewhere. Most MALT consists of unencapsulated microscopic aggregates of lymphoid tissue, where the lymphocyte populations are supported mechanically by a network of fine type III collagen (reticulin) fibres and associated fibroblasts, as they are in lymph nodes.

In common with lymph nodes, MALT provides centres for the activation and proliferation of B and T lymphocytes in its follicles and parafollicular zones, respectively. The function of cells in these zones, including APCs (follicular dendritic cells and interdigitating dendritic cells) and macrophages, as well as T and B cells, is similar to that found in lymph nodes. The close proximity of lymphocytes within MALT to an epithelial surface facilitates their access to pathogens. MALT lacks afferent lymphatic vessels. Lymphocytes migrate into MALT through its HEVs and leave mainly via its efferent lymphatics, which drain interstitial fluid as lymph. The lymphocyte population in MALT is not fixed. Migration from MALT follows a different route from the major peripheral route of recirculation. After antigen activation, lymphocytes travel via the regional lymph nodes to disperse widely along mucosal surfaces to provide protective T- and B-cell immunity.

Follicle-associated epithelium

The epithelium covering MALT varies in type according to its location. It is unusual in possessing cells that are involved in sampling antigens and transferring them to APCs in the underlying tissues; appropriate clones of T and B cells in local lymphoid tissues are then activated and amplified prior to their exit via the lymphatics. Specialized epithelial cells in the small and large intestine have characteristic short microvilli on their luminal surfaces and are known as microfold (M) cells (Kraehenbuhl and Neutra 2000); in the palatine tonsils they include modified stratified squamous reticulated epithelial cells (see p. 708). The main function of B lymphocytes in MALT is to produce IgA for secretion into the lumen of the tracts that they line (Cerutti et al 2011).

Many of the lymphocytes migrating between cells in the basal regions of epithelia (see Fig. 4.5) are effector cytotoxic and helper T cells that have already been selected in lymphoid nodules and are engaged in immune responses. Similar cells, and activated IgA-producing B cells and plasma cells, are also scattered throughout the entire mucosal lamina propria.

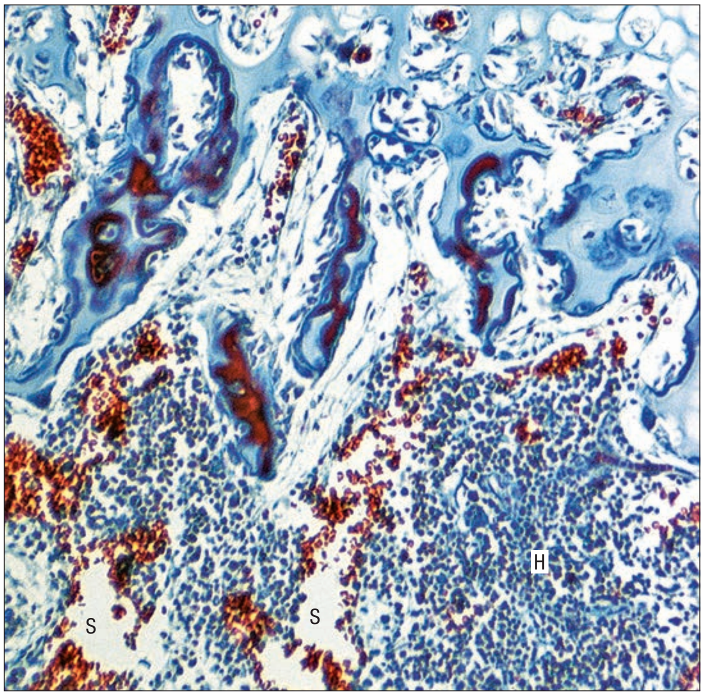

Fig. 4.11 Haemopoietic tissue (H) in the marrow cavity of a fetal long bone undergoing endochondral ossification (top). Islands of densely packed nucleated haemopoietic cells of different lineages are separated by large vascular sinusoids (S), which are filled with mature red blood cells in the general circulation.

HAEMOPOIESIS

Postnatally, blood cells are formed primarily in the bone marrow. Other tissues, particularly the spleen and liver, may develop haemopoietic activity once more, if production from the marrow is inadequate.

Bone marrow

Bone marrow is a soft pulpy tissue that is found in the marrow cavities of all bones (**Fig. 4.11**) and even in the larger Haversian canals of lamellar bone. It consists of vascular and extravascular compartments, both enclosed within a bony framework from which they are separated by a thin layer of endosteal cells. It differs in composition in different bones and at different ages, and occurs in two forms: yellow and red marrow.

Yellow marrow

Yellow marrow consists of a framework of connective tissue that supports numerous blood vessels and cells, most of which are adipocytes. A small population of typical red marrow cells persists and may be reactivated when the demand for blood cells becomes sufficiently great.

Red marrow

Red marrow is found throughout the skeleton in the fetus and during the first years of life. After about the fifth year, the red marrow, which represents actively haemopoietic tissue, is gradually replaced in the long bones by yellow marrow. The replacement starts earlier, and is generally more advanced, in the more distal bones. By 20–25 years of age, red marrow persists only in the vertebrae, sternum, ribs, clavicles, scapulae, pelvis and calvaria, and in the proximal ends of the femur and humerus.

Red bone marrow consists of a network of loose connective tissue, the stroma, supporting clusters of haemopoietic cells (haemopoietic cords or islands). The rich blood supply is derived from the nutrient

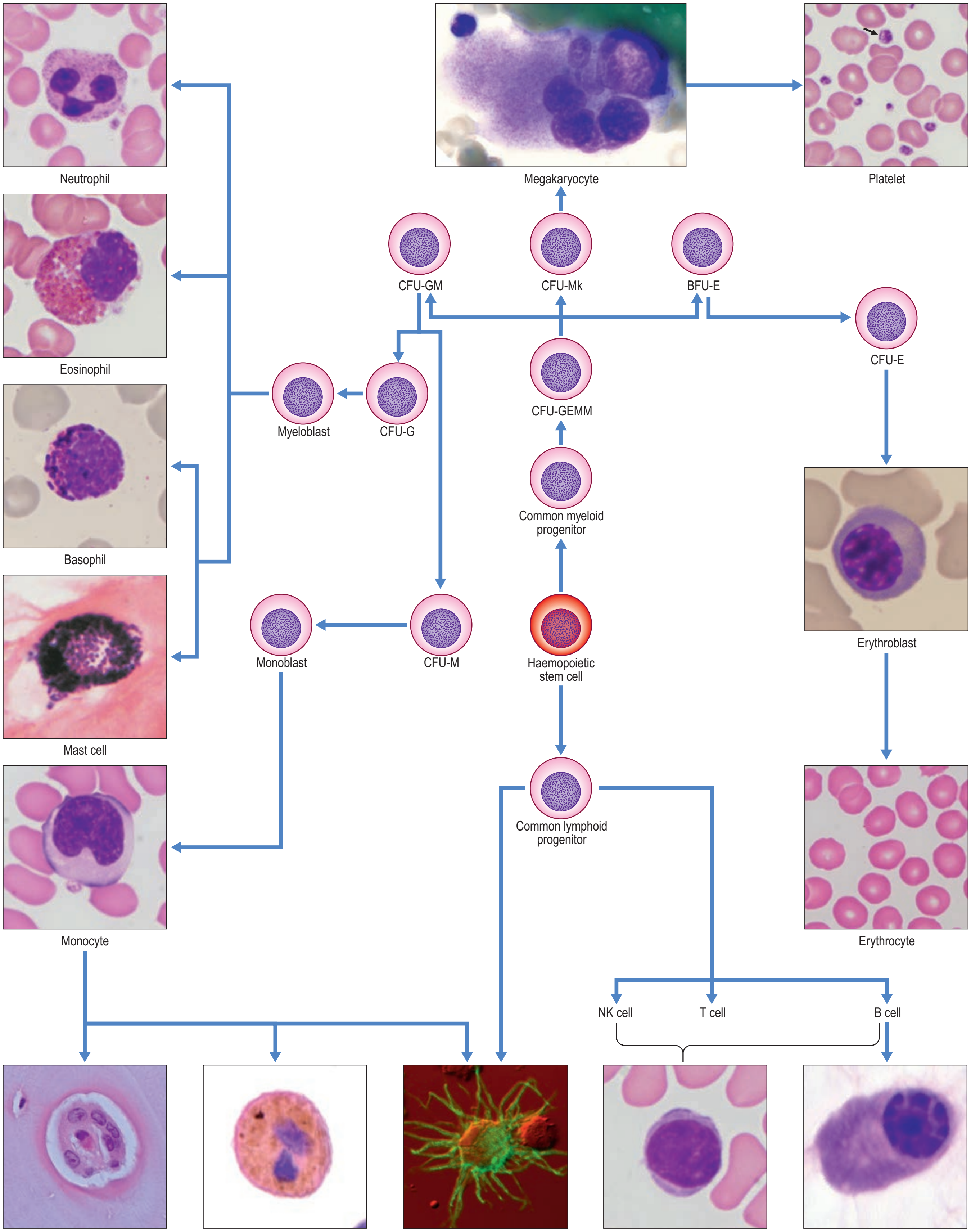
Neutrophil
Megakaryocyte
Platelet
Eosinophil
CFU-GM
CFU-Mk
BFU-E
CFU-E
Myeloblast
CFU-G
CFU-GEMM
Common myeloid progenitor
Basophil
Erythroblast
Monoblast
CFU-M
Haemopoietic stem cell
Mast cell
Common lymphoid progenitor
Monocyte
Erythrocyte
NK cell
T cell
B cell
Osteoclast
Macrophage
Dendritic cell
Lymphocyte
Plasma cell

Fig. 4.12 The origins and lineage relationships of haemopoietically derived cells of the immune system. Mature cells and selected progenitors (all human) are illustrated (magnifications vary). The dendritic cell was cultured from peripheral blood, immunolabelled to show HLA-DR and photographed using Nomarski optics. The megakaryocyte and erythroblast are from a bone marrow smear, stained with May–Grünwald–Giemsa (MGG); the remaining cells illustrated are from peripheral blood smears (Wright's stain), sections of connective tissue (plasma cell, mast cell), bone (osteoclast, in Haversian canal) and lung alveolus (macrophage). Platelets (one is arrowed) are subcellular fragments of bone marrow megakaryocytes. Note that circulating small lymphocytes cannot be classified further with routine staining methods. For further explanation of cellular structure and staining properties, along with abbreviations, see the text. (Dendritic cell image courtesy of Dr Cécile Chalouni, Ludwig Institute for Cancer Research, Yale University School of Medicine, USA. All other images courtesy of Mr Peter Helliwell and the late Dr Joseph Mathew, Department of Histopathology, Royal Cornwall Hospitals Trust, UK.)

artery to the bone. Vessels ramify in the bone marrow, becoming thin-walled arterioles from which sinusoids arise and drain into disproportionately large veins (see Fig. 4.11). The stroma contains a variable amount of fat, depending on site and the age and haematological status of the individual. Lymphatic vessels are absent from bone marrow but small patches of lymphoid tissue are present in the stroma.

Stroma

Stroma is composed of a delicate network of fine type III collagen (reticulin) fibres secreted by highly branched, specialized fibroblast-like cells (reticular cells) derived from embryonic mesenchyme. When haemopoiesis stops, as occurs in most limb bones in adult life, these cells (or closely related cells) become distended with lipid droplets and fill the marrow with yellow fatty tissue (yellow marrow). If there is a later demand for haemopoiesis, the stellate stromal cells reappear. The stroma also contains numerous macrophages attached to extracellular matrix fibres. These cells actively phagocytose cellular debris created by haemopoietic development, especially the extruded nuclei of erythroblasts, remnants of megakaryocytes and cells that have failed the B-lymphocyte selection process. Stromal cells play a major role in the control of haemopoietic cell differentiation, proliferation and maturation.

Marrow sinusoids are lined by a single layer of endothelial cells, supported by reticulin on their basal surfaces. Although the endothelial cells are interconnected by tight junctions, their cytoplasm is extremely thin in places, and the underlying basal lamina is discontinuous. The passage of newly formed blood cells from the haemopoietic compartment into the blood stream appears to occur through an interactive process with the endothelium, producing temporary apertures (large fenestrae) in their attenuated cytoplasm.

Haemopoietic tissue

Cords and islands of haematogenous cells consist of clusters of immature blood cells in various stages of development; several different cell lineages are typically represented in each focal group. One or more macrophages lie at the core of each such group of cells. These macrophages engage in phagocytic functions, are important in transferring iron to developing erythroblasts for haemoglobin synthesis, and may play a role, with other stromal cells, in regulating the rate of cell proliferation and maturation of the neighbouring haemopoietic cells.

Cell lineages

Haemopoietic stem cells

There is a very small number (0.05% of haemopoietic cells) of self-renewing, pluripotent stem cells within adult marrow capable of giving rise to all blood cell types, including lymphocytes (**Fig. 4.12**). Although they cannot be identified morphologically in the marrow, they can be recognized in aspirates by their expression of specific cell-surface marker proteins (e.g. CD34). It is thought that haemopoietic stem cells occupy specific environmental niches in the marrow associated with the endosteum of trabecular bone or with sinusoidal endothelium, and that their microenvironment is important in homeostasis, the balance between self-renewal and differentiation. Stem cells can also be found (at lower concentrations) in the peripheral blood, particularly after treatment with appropriate cytokines.

Progressively more lineage-restricted committed progenitor cells develop from these ancestors to produce the various cell types found in peripheral blood (Laiosa et al 2006). The committed progenitor cells are often termed colony-forming units (CFU) of the lineage(s), e.g. CFU-GM cells give rise, after proliferation, to neutrophil granulocytes, monocytes and certain dendritic cells, whereas CFU-E produce only erythrocytes. Each cell type undergoes a period of maturation in the marrow, often accompanied by several structural changes, before release into the general circulation. In some lineages, e.g. the erythroid series, the final stages of maturation take place in the circulation, whereas in the monocytic lineage, they occur after the cells have left the circulation and entered peripheral tissues where they differentiate into macrophages and some dendritic cells.

To generate a complete set of blood cells from a single pluripotent cell may take some months. The later progenitor cells form mature cells of their particular lineages more quickly. However, because they are not self-renewing, grafts of these later cells eventually fail because the cells they produce all ultimately die. This is of considerable importance in bone marrow replacement therapy. The presence of pluripotent stem cells in the donor marrow is essential for success; only 5% of the normal number are needed to repopulate the marrow. Following replacement therapy, T lymphocytes reconstitute more slowly than the other haemopoietic lineages, reflecting the progressive reduction in size of the thymus with age (chronic involution).

Within the bone marrow there is also a population of mesenchymal progenitor cells that can differentiate into a wide variety of non-haemopoietic cells. These pluripotent progenitor cells can also be found in the circulation, and are being investigated for their use in repairing damaged organs.

Lymphocytes

Lymphocytes are a heterogeneous group of cells that may share a common ancestral lymphoid progenitor cell, distinct from the myeloid progenitor cell (see Fig. 4.12). The first identifiable progenitor cell is the lymphoblast, which divides several times to form prolymphocytes; both cells are characterized by a high nuclear:cytoplasmic ratio. B cells undergo differentiation to their specific lineage subset entirely within the bone marrow and migrate to peripheral or secondary lymphoid tissues as naïve B cells, ready to respond to antigen. However, T cells require the specialized thymic microenvironment for their development. During fetal and early postnatal life, and subsequently at lower levels throughout life, progenitor cells migrate to the thymus where they undergo a process of differentiation and selection as T cells, before leaving to populate secondary lymphoid tissues.

B-cell development

B cells start their development in the subosteal region of the bone marrow and move centripetally as differentiation progresses. Their development entails the rearrangement of immunoglobulin genes to create a unique receptor for antigen on each B cell, and the progressive expression of cell-surface and intracellular molecules required for mature B-lymphocyte function. Autoreactive cells that meet their self-antigen within the bone marrow are eliminated. Overall, some 25% of B cells successfully complete these developmental and selection processes; those that fail die by apoptosis and are removed by macrophages. Bone marrow stromal cells (fibroblasts, fat cells and macrophages) express cell-surface molecules and secrete cytokines that control B-lymphocyte development. The mature naïve B lymphocytes leave via the central sinuses. They express antigen receptors (immunoglobulin) of IgM and IgD classes. Class switching to IgG, IgA and IgE occurs in the periphery following antigen activation in response to signals from T helper cells (see Fig. 4.15).

T-cell (thymocyte) development

T cells develop within the thymus from blood-borne, bone marrow-derived progenitors that enter the thymus via HEVs at the corticomedullary junction. They first migrate to the outer (subcapsular) region of the thymic cortex and then, as in the bone marrow, move progressively inwards towards the medulla as development continues. T-cell development involves gene rearrangements in the T-cell receptor (TcR) loci to create unique receptors for antigen on each cell, together with the progressive expression of molecules required for mature T-cell function. Selection of the receptor repertoire is more stringent for T cells than for B cells because of the way in which mature T cells recognize peptides derived from protein antigens presented in conjunction with specific molecules of the major histocompatibility complex (MHC) expressed on the surfaces of cells. Thus mature CD8$^+$ (cytotoxic) T cells recognize antigen in the form of short peptides complexed with the polymorphic MHC class I molecules, while CD4$^+$ (helper/regulatory) T cells recognize the peptides in the context of MHC class II molecules. As the TcR recognizes both the peptide and the MHC molecule, the T cell will only recognize peptides bound to their own (self) type of MHC; it will not ‘see’ peptides in combination with allelically different MHC molecules (i.e. those from other individuals). This is termed MHC restriction of T-cell recognition. Selection of T cells in the thymus must ensure the survival of those T cells that can respond only to foreign antigens, bound to their own (self) class of MHC molecule. Cells that are incapable of binding to self MHC molecules, or which bind to self-antigens, are eliminated by apoptotic cell death; it is estimated that up to 95% of T-cell progenitors undergo apoptosis in this way. Cells that express an appropriate TcR and have effective MHC-restricted binding properties survive to become mature, naïve T cells that leave the thymus and populate the periphery.

Thymic stromal cells play a crucial role in T-cell development and selection. Thymic epithelial cells in the cortex express both MHC class I and II molecules and are unique in their ability to select T cells that recognize self MHC with a moderate affinity (positive selection). Deletion of self-antigen reactive cells (negative selection) is mainly controlled by thymic dendritic cells located at the corticomedullary junction and in the medulla, although the epithelium can also perform this function. Apoptotic thymocytes are removed by thymic macrophages. The role of the thymic epithelium in thymocyte differentiation is complex and involves cell–cell contact as well as the secretion of soluble mediators such as cytokines, chemokines, neuroactive peptides (e.g. somatostatin) and thymic hormones (e.g. thymulin). Thymic fibroblasts and the extracellular matrix also play a role.

Erythrocytes

Erythrocytes and granulocytes belong to the myeloid lineage. The earliest identifiable erythroid progenitor cells are capable of rapid bursts of cell division to form numerous daughter cells; they have thus been named burst-forming units of the erythroid line (BFU-E; see Fig. 4.12). They give rise to the CFU-E, which, with their immediate progeny, are sensitive to the hormone erythropoietin. This hormone, produced in the kidney, induces further differentiation along the erythroid line.

The first readily identifiable cell of the erythroid series is the proerythroblast, which is a large cell (about 20 μm) with a large euchromatic nucleus and a moderately basophilic cytoplasm. It responds to erythropoietin. The proerythroblast contains small amounts of ferritin and bears some of the protein spectrin on the cytoplasmic surface of its plasma membrane. Proerythroblasts proliferate to produce smaller (12–16 μm) basophilic erythroblasts, rich in ribosomes, in which haemoglobin RNA synthesis begins. The cytoplasm becomes partially, and then uniformly, eosinophilic (the polychromatic erythroblast and orthochromatic erythroblast, respectively). These cells are only 8–10 μm in diameter and contain very little cytoplasmic RNA. Their nuclei become pyknotic (dense, deep-staining, shrunken) and are finally extruded, leaving anucleate reticulocytes, which enter sinusoids. Their reticular staining pattern, visible using special stains, is a consequence of residual cytoplasmic RNA, which is usually lost within 24 hours of entering the peripheral blood circulation: reticulocyte numbers in peripheral blood are therefore a good indicator of the rate of red cell production. The whole process of erythropoiesis takes 5–9 days.

Granulocytes

Granulocyte formation involves major changes in nuclear morphology and cytoplasmic contents, which are best known for the neutrophil. Initially, myeloid progenitor cells transform into large myeloblasts (10–20 μm) that are similar in general size and appearance to proerythroblasts. These proliferative cells have large euchromatic nuclei and lack cytoplasmic granules. They differentiate into slightly larger promyelocytes, in which the first group of specialized proteins is synthesized in the rough endoplasmic reticulum and Golgi apparatus. The proteins are stored in large (0.3 μm) primary (non-specific) granules, which are large lysosomes containing acid phosphatase. Smaller secondary (specific) granules are formed in the smaller myelocyte, which is the final proliferative stage. Myelocyte nuclei are typically flattened or slightly indented on one side.

The next stage produces a metamyelocyte: the cell size decreases (10–15 μm), the nucleus becomes heterochromatic and horseshoe-shaped, and protein synthesis almost stops. As the neutrophil is released, the nucleus becomes first heavily indented (the juvenile stab or band form), and subsequently segmented into up to six lobes, characteristic of the mature neutrophil. The whole process usually takes 7 days to complete (3 days proliferating and 4 days maturing). Neutrophils may then be stored in the marrow for a further 4 days, depending on demand, before their final release into the circulation.

Eosinophils and basophils pass through a similar sequence but their nuclei do not become as irregular as that of the neutrophil. It is thought that these cells each arise from distinct colony-forming units, which are separate from the CFU-GM.

Monocytes

Monocytes are formed in the bone marrow. Monocytes and neutrophils appear to be closely related cells: together with some of the antigen-presenting dendritic cells, they arise from a shared progenitor, the colony-forming unit for granulocytes and macrophages (CFU-GM). Different colony-stimulating factors (CSF) act on the common progenitor to direct its subsequent differentiation pathway. Monocyte progenitors pass through a proliferative monoblast stage (14 μm) and then form differentiating promonocytes, which are slightly smaller cells in which production of small lysosomes begins. After further divisions, monocytes (up to 20 μm) are released into the general circulation. Most migrate into perivascular and extravascular sites that they populate as macrophages, while others may give rise to certain dendritic cells, including Langerhans cells.

Platelets

Platelets arise in a unique manner by the shedding of thousands of cytoplasmic fragments from the tips of processes of megakaryocytes in the bone marrow. The first detectable cell of this line is the highly basophilic megakaryoblast (15–50 μm), followed by a promegakaryocyte stage (20–80 μm), in which synthesis of granules begins. Finally, the fully differentiated megakaryocyte, a giant cell (35–160 μm) with a large, dense, polyploid, multilobed nucleus, appears. Once differentiation is initiated from the CFU-Meg, DNA replicates without cytoplasmic division (endoreduplication), and the chromosomes are retained within a single polyploid nucleus that may contain up to 256n chromosomes (where n is the haploid complement present in gametes).

The cytoplasm contains fine basophilic granules. It becomes partitioned into proplatelets by invaginations of the plasma membrane, that appear ultrastructurally as a network of tubular profiles which coalesce to form cytoplasmic islands 3–4 μm in diameter. Individual platelets are shed into the circulation from a long, narrow process of megakaryocyte cytoplasm that is protruded through an aperture in the sinusoidal endothelium.

PHAGOCYTES AND ANTIGEN-PRESENTING CELLS

Macrophages and neutrophils are specialized phagocytes. Certain dendritic cells (see Fig. 4.12), e.g. Langerhans cells of the skin and other stratified squamous epithelia, are 'professional' antigen-presenting cells (APCs); they take up foreign material by endocytosis and macropinocytosis, and are uniquely capable of efficiently activating naïve as well as mature T lymphocytes. Macrophages are able to process and present antigen to lymphocytes, but are less effective than dendritic cells. They also play an important role in the effector arm of the immune response, clearing the infectious agent by phagocytosis. The third major cell type involved in antigen presentation and T-cell activation is the B lymphocyte, which is particularly efficient at taking up antigen that binds to its surface immunoglobulin. Follicular dendritic cells (FDCs) of lymph nodes, MALT and the spleen are capable of presenting non-processed antigen to B lymphocytes, but are not classic APCs because they cannot present antigen to helper T cells.

APCs endocytose antigen, digest it intracellularly, mostly to peptide fragments, and present the fragments on their surfaces, generally in conjunction with MHC class II molecules. (Class II molecules are normally found only on APCs, although many other cells can express class II molecules in inflammatory situations.) Recognition of foreign antigen is controlled by a variety of APC cell-surface receptors: Fc and complement receptors mediate uptake of opsonized material, while pattern recognition receptors of the innate immune system, e.g. Toll-like receptors and scavenger receptors, directly recognize pathogen-derived molecules.

Macrophages

The mononuclear phagocyte system consists of the blood monocytes, from which the other types are derived, and various tissue macrophages, some of which have tissue-specific names. Certain dendritic cells are

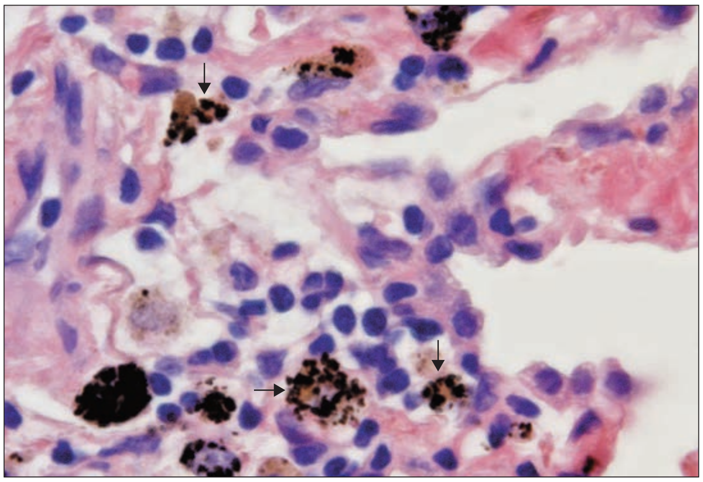

Fig. 4.13 Alveolar macrophages (dust cells, arrows) containing ingested carbon particles, in alveoli and interalveolar septa of the human lung. (Courtesy of Mr Peter Helliwell and the late Dr Joseph Mathew, Department of Histopathology, Royal Cornwall Hospitals Trust, UK.)

sometimes included in the mononuclear phagocyte system;: they share a common lineage ancestor but appear to form a discrete branch of the family tree. Most monocytes and macrophages express class II MHC molecules.

Macrophages are very variable in size (generally 15–25 µm) and are found in many tissues of the body, where they constitute a heterogeneous family of cells (Gordon and Taylor 2005). They are migrant cells in all general connective tissues, in bone marrow and all lymphoid tissues, and include alveolar macrophages in the lung and Kupffer cells in liver sinusoids. They often aggregate in subserous connective tissue of the pleura and peritoneum, where they are visible as milky spots near small lymphatic trunks, and cluster around the terminations of small (penicillar) arterioles in the spleen, where they are also distributed, more diffusely, throughout the splenic cords.

Osteoclasts in bone are closely related to macrophages; they are syncytial cells derived from the fusion of up to 30 progenitor monocytes in bone tissue, where they differentiate further. Microglia of the central nervous system originate from an embryonic monocyte precursor and migrate into the central nervous system during its development. They differ from macrophages in that normally they are quiescent cells in which MHC class II expression is downregulated, and they display little phagocytic activity.

Macrophages vary in structure depending on their location in the body. All have a moderately basophilic cytoplasm containing some rough and smooth endoplasmic reticulum, an active Golgi complex and a large, euchromatic and somewhat irregular nucleus. These features are consistent with an active metabolism: synthesis of lysosomal enzymes continues in mature cells. All macrophages have irregular surfaces with protruding filopodia and they contain varying numbers of endocytic vesicles, larger vacuoles and lysosomes. Some macrophages are highly motile, whereas others tend to remain attached and sedentary, e.g. in hepatic and lymphoid sinuses. Within connective tissues, macrophages may fuse to form large syncytia (giant cells) around particles that are too large to be phagocytosed, or when stimulated by the presence of infectious organisms, e.g. *Mycobacterium tuberculosis,* leading to granuloma formation.

When blood-borne monocytes enter the tissues through the endothelial walls of capillaries and venules, they can undergo a limited number of rounds of mitosis as tissue macrophages before they die and are replaced from the bone marrow, typically after several weeks. There is some evidence that alveolar macrophages of the lung are able to undergo many more mitoses than other macrophages.

Phagocytosis

The uptake of particulate material and microorganisms is carried out by macrophages in many tissues and organs. When present in general connective tissues, they ingest and kill invading microorganisms and remove debris that has been produced as a consequence of tissue damage. They recognize, engulf and rapidly ingest apoptotic cells in all situations. The mechanism of apoptotic cell uptake does not activate the phagocyte for antigen presentation, and so the process is immunologically silent. In the lung, alveolar macrophages constantly patrol the respiratory surfaces, to which they migrate from pulmonary connective tissue (Fig. 4.13). They engulf inhaled particles, including bacteria, surfactant and debris, and many enter the sputum (hence their alternative names, dust cells or, in patients with left heart failure or chronic pulmonary oedema, heart failure cells, which are full of extravasated erythrocytes). They perform similar scavenger functions in the pleural and peritoneal cavities. In lymph nodes, macrophages line the walls of sinuses and remove particulate matter from lymph as it percolates through them. In the spleen and liver, macrophages are involved in particle removal and in the detection and destruction of aged or damaged erythrocytes. They begin the degradation of haemoglobin for recycling iron and amino acids.

Phagocytes recognize molecular patterns on the pathogen surface (pathogen-associated molecular patterns, PAMPs) via their PAMP-recognising receptors (PRRs). Some PRRs are phagocytic receptors (mannose and scavenger receptors) while others can act as sensors (Toll-like receptors), causing macrophages to secrete proinflammatory cytokines, such as TNF-α.

Macrophages bear surface receptors for the Fc portions of antibodies and for the fragments of the C3 component of complement. Phagocytic activity is greatly increased when the target has been coated in antibody (opsonized) or complement, or both. Once phagocytosis has occurred, the vacuole bearing the ingested particle fuses with endosomal vesicles, which contain a wide range of lysosomal enzymes, including many hydrolases, and oxidative systems capable of rapid bacteriocidal action. These activities are much enhanced when macrophages are stimulated (activated macrophages) by cytokines, e.g. IFN-γ, which are secreted by other cells of the immune system, especially T lymphocytes.

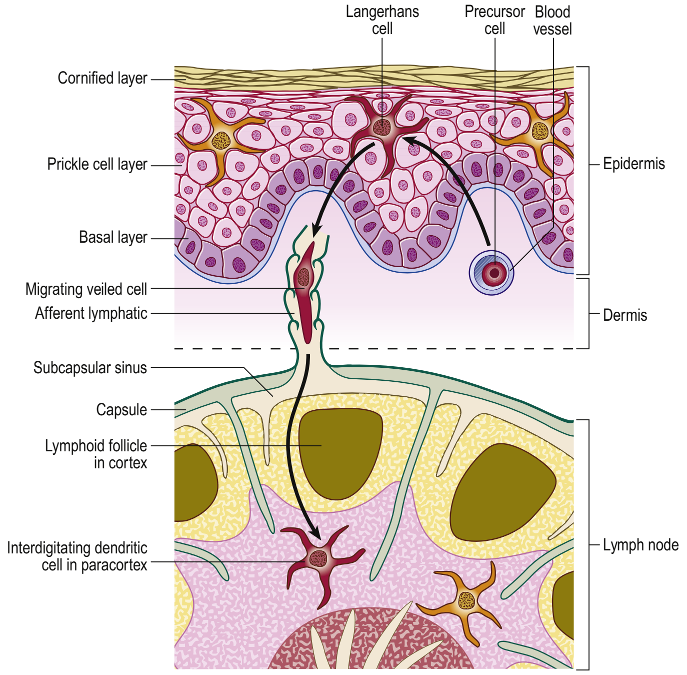

Fig. 4.14 Dendritic cells in the skin and lymphoid tissues. Their migratory routes are shown: from blood-borne, marrow-derived precursors to immature dendritic cells (Langerhans cells) in skin, and then to migrating veiled cells in afferent lymphatic vessels and interdigitating dendritic cells in lymph nodes. An example of each cell in the sequence (arrowed) is shown in red.

Close antibody-mediated binding may initiate the release of lysosomal enzymes onto the surfaces of the cellular targets to which the macrophages bind. This process of cytotoxicity is also used by other cells, including neutrophils and eosinophils, particularly if the targets are too large to be phagocytosed (e.g. nematode worm parasites).

Secretory activities

Activated macrophages can synthesize and secrete various bioactive substances, e.g. IL-1, which stimulate the proliferation and maturation of other lymphocytes, greatly amplifying the reaction of the immune system to foreign antigens. They also synthesize TNF-α, which is able to kill small numbers of neoplastic cells. TNF-α depresses the anabolic activities of many cells in the body, and may be a major factor mediating cachexia (wasting), which typically accompanies more advanced cancers. Other macrophage products include plasminogen activator, which promotes clot removal; various lysosomal enzymes; several complement and clotting factors; and lysozyme (an antibacterial protein). In pathogenesis, these substances may be released inappropriately and damage healthy tissues, e.g. in rheumatoid arthritis and various other inflammatory conditions.

Dendritic cells

There are two distinct groups of dendritic cells: myeloid dendritic cells (also known as classic dendritic cells) and plasmacytoid dendritic cells (Liu 2001, Merad et al 2013, Gerlach et al 2013). These cells can arise from common lymphoid progenitors and common myeloid progenitors. Both groups of cells are involved in antigen presentation, although they have somewhat different functional roles in controlling both the adaptive and innate immune systems. Myeloid dendritic cells are able to process and present antigen to T lymphocytes, including naïve T cells. They are present as immature dendritic cells in the epidermis of the skin (Fig. 4.14) and other stratified squamous epithelia, e.g. the oral mucosa (Langerhans cells), and in the dermis and most other tissues (tissue resident or interstitial dendritic cells), where they are concerned with immune surveillance. Immature dendritic cells have an antigen-capturing function. They can remain in the tissues for days to weeks before undergoing maturation.

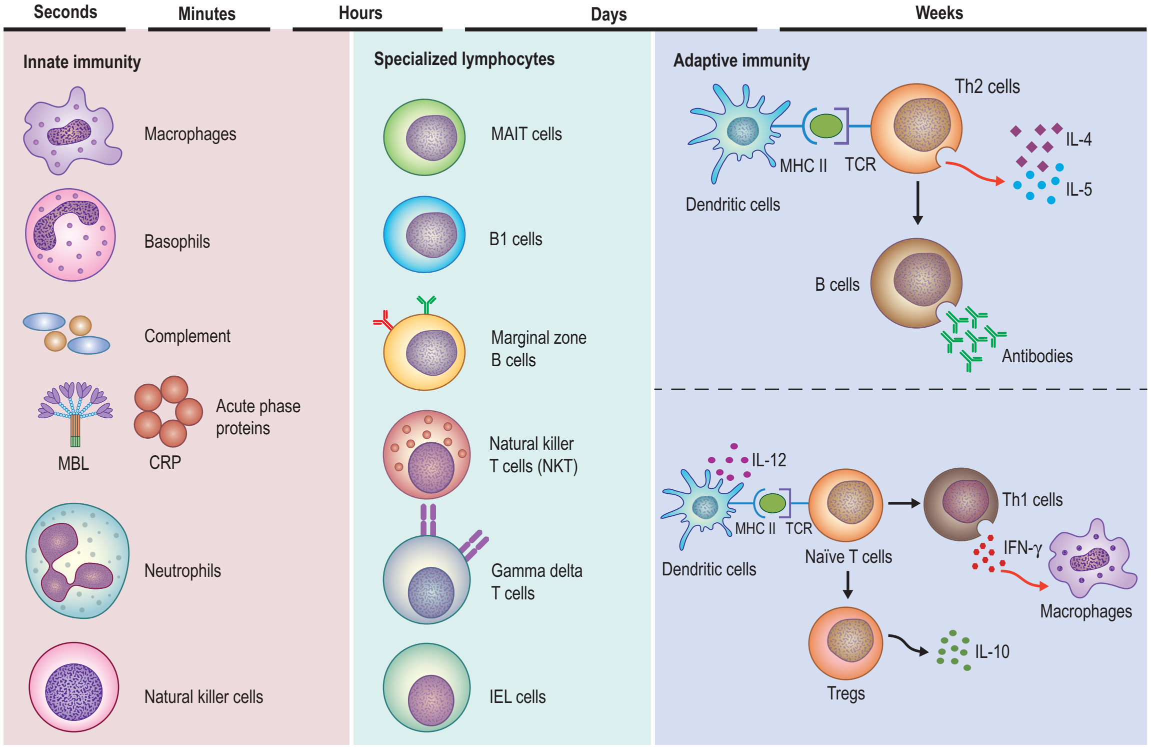
Seconds
Minutes
Hours
Days
Weeks
Innate immunity
Macrophages
Basophils
Complement
MBL
CRP
Acute phase proteins
Neutrophils
Natural killer cells
Specialized lymphocytes
MAIT cells
B1 cells
Marginal zone B cells
Natural killer T cells (NKT)
Gamma delta T cells
IEL cells
Adaptive immunity
Dendritic cells
MHC II
TCR
Th2 cells
IL-4
IL-5
B cells
Antibodies
IL-12
Dendritic cells
MHC II
TCR
Naïve T cells
Th1 cells
IFN-γ
Macrophages
Tregs
IL-10

Fig. 4.15 The immune system has two well-developed arms: innate and adaptive**.** The innate immune response against invading pathogens is induced very swiftly, involving opsonization, phagocytosis, complement activation and pro-inflammatory cytokine production. Adaptive immunity develops within a few weeks, involving MHC class II loaded peptide presentation by dendritic cells to CD4$^+$ T cells. Subsequently, a Th2 response involving IL-4 and IL-5 instructs B cells to produce antibodies targeting extracellular pathogens, whereas a Th1 response, involving IFN-γ production, activates macrophages to eliminate intracellular pathogens. Specialized lymphocytes with limited recognition and effector properties act during the time between triggering of innate and adaptive immune responses, thus acting as a bridge between the two arms of the immune system. Abbreviations: CRP, C-reactive protein; IEL, intraepithelial lymphocyte; MAIT, mucosal-associated invariant T cell; MBL, mannan-binding lectin. (Adapted with permission from an illustration by Dr Iesha Singh, Imperial College London.)

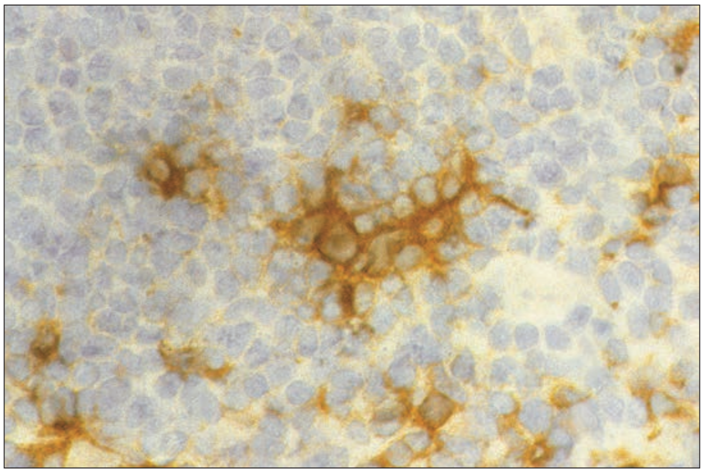

Fig. 4.16 Follicular dendritic cells (brown) in a germinal centre of the human palatine tonsil (immunoperoxidase-labelled). (Courtesy of Marta Perry MD, UMDS, London.)

Dendritic cells respond to chemotactic signals, e.g. defensins released by epithelial cells in the small intestine, and they express pattern recognition receptors (e.g. Toll-like receptors) on their surface. Binding of PAMPs derived from bacteria (e.g. carbohydrate, lipopolysaccharide or DNA) to these receptors stimulates the dendritic cells to become activated and migrate via the lymphatics to nearby secondary lymphoid tissues, where they can present antigen to T cells. They can also be activated by recognition of damage-associated molecular patterns (DAMPs), such as ATP, DNA, heat-shock proteins and high-mobility group box 1 (HMGB1) released from injured or necrotic cells.

Mature dendritic cells are known as veiled cells when in the afferent lymphatics and the subcapsular sinuses of lymph nodes, and as interdigitating dendritic cells once they are within the lymphoid tissue proper. Their function within the secondary lymphoid tissue is to present their processed antigen to T lymphocytes, and thus to initiate and stimulate the immune response. With maturation, innate immune receptors (PRRs) and phagocytic capabilities are lowered, while they start to express receptors that facilitate their migration to the T cell zones of the lymph nodes.

Dendritic cells are the most potent antigen-capturing and antigen-presenting immune cells. They are stimulated via PAMP-recognizing Toll-like receptors leading to upregulation of MHC class II molecules and expression of specialized co-stimulatory molecules required for naïve T cell proliferation. Thus, dendritic cells can act as a link between innate and adaptive immunity (**Fig. 4.15**).

Langerhans cells

Langerhans cells (see Fig. 4.14) are one of the best studied types of immature dendritic cell (Berger et al 2006, Chopin and Nutt 2015). They are present throughout the epidermis of skin, where they were first described, but are most clearly identifiable in the stratum spinosum. They have an irregular nucleus and a clear cytoplasm, and contain characteristic elongated membranous vesicles (Birbeck granules). Langerhans cells endocytose and process antigens, undergoing a process of maturation from antigen-capturing to antigen-presenting cells that express high levels of MHC class I and II molecules, co-stimulatory molecules and adhesion molecules. They migrate to lymph nodes to activate T lymphocytes.

Interdigitating dendritic cells

Immature dendritic cells are found all over the body, including peripheral blood, and function in antigen-processing and immune surveillance.

Mature dendritic cells are present in T-cell-rich areas of secondary lymphoid tissue (paracortical areas of lymph nodes, interfollicular areas of MALT, peri-arteriolar sheaths of splenic white pulp), where they are frequently referred to as interdigitating dendritic cells. Within the secondary lymphoid tissues, they are involved in the presentation to T lymphocytes of antigens associated with either MHC class I ($CD8^+$ T cells) or MHC class II ($CD4^+$ T cells) molecules. Naïve T cells can only respond to antigen presented by dendritic cells. T cells are stimulated by recognition of the antigen–MHC complex by the TcR, by interaction with co-stimulatory molecules expressed by the dendritic cells, and by cytokines secreted by the cells. These cytokines not only help activate the T cell but can also direct the nature of the T-cell response (e.g. Th1 or Th2). Appropriate T cells are thus activated to proliferate and are primed for carrying out their immunological functions. Once primed, T cells can then be stimulated by any APC, including macrophages and B cells.

Follicular dendritic cells

Follicular dendritic cells (FDCs; Fig. 4.16) are a non-migratory population of cells found in the follicles of secondary lymphoid tissues, where they attract and interact with B cells. Unlike other dendritic cells, FDCs are not haemopoietic in origin but are probably derived from the stromal cells of lymphoid tissues. They are unable to endocytose and process antigen, and they lack MHC class II molecules. However, Fc receptors and complement receptors CD21 and CD35 on FDCs allow the cells to bind immune complexes to their surface for subsequent presentation, as unprocessed antigen, to germinal centre B cells. Interactions between B cells, $CD4^+$ helper T cells and FDCs in the germinal centres are important in the selection of high-affinity B cells and their maturation to either plasma cells or memory B lymphocytes (Liu 2001).

Key references

Girard JP, Moussion C, Förster R 2012 HEVs, lymphatics and homeostatic immune cell trafficking in lymph nodes. Nat Rev Immunol 12:762–73.

A discussion of how the movement of immune cells into, through and out of the lymph node is controlled.

Kaplan MJ, Radic M 2012 Neutrophil extracellular traps: double-edged swords of innate immunity. J Immunol 189:2689–95.

A summary of our current understanding of how NETs operate.

Kristiansen M, Graversen JH, Jacobsen C et al 2001 Identification of the haemoglobin scavenger receptor. Nature 409:198–201.

A demonstration that CD163, which is expressed at the cell surface of macrophages, is a scavenger receptor for haemoglobin and haptoglobin-bound haemoglobin. This provides insight into a molecular mechanism of iron recycling by macrophages.

Liu Y-J 2001 Dendritic cell subsets and lineages, and their functions in innate and adaptive immunity. Cell 106:259–62.

A review of current research and a re-evaluation of the lineage of and functional relationships between different dendritic cell types.

Male D, Brostoff J, Roth DB et al 2012 Immunology, 8th ed. London: Elsevier, Mosby.

An explanation of the scientific principles of clinical immunology, integrated with histology, pathology and clinical examples.

Malhotra D, Fletcher AL, Turley SJ 2013 Stromal and hematopoietic cells in secondary lymphoid organs: partners in immunity. Immunol Rev 251:160–176.

The role of stromal cells in the 'architecture' of secondary lymphoid organs, as well as the control and regulation of dendritic cells and lymphocytes, and the delivery of antigen to the right site.

Mankelow TJ, Satchwell TJ, Burton NM 2012 Refined views of multi-protein complexes in the erythrocyte membrane. Blood Cells Mol Dis 49:1–10.

A summary of recent models of how protein components of the red cell membrane interact to give the membrane its required properties.

Merad M, Sathe P, Helft J et al 2013 The dendritic cell lineage: ontogeny and function of dendritic cells and their subsets in the steady state and the inflamed setting. Annu Rev Immunol 31:563–604.

A summary of recent data that has changed our understanding of how dendritic cells subsets arise and function.

Murphy K, Weaver C 2016 Janeway's Immunobiology, 9th ed. New York: Garland Science.

The unifying principles of structure and function of the immune system in health and disease.

Psychogios N, Hau DD, Peng J et al 2011 The human serum metabolome. PLoS ONE 6:e16957.

An analysis of more than 4000 serum components and their concentrations in health and disease.

Victora GD, Nussenzweig MC 2012 Germinal centers. Annu Rev Immunol 30:429–57.

A comprehensive review of germinal centres, integrating recent findings on the role of cellular dynamics in affinity maturation.

References

Berger CL, Vasquez JG, Shofner J et al 2006 Langerhans cells: mediators of immunity and tolerance. Int J Biochem Cell Biol 38:1632–6.

Brandtzaeg P 2013 Secretory IgA: designed for anti-microbial defense. Front Immunol 4:222. doi: 10.3389/fimmu.2013.00222.

Cerutti A, Chen K, Chorny A 2011 Immunoglobulin responses at the mucosal interface. Annu Rev Immunol 29:273–93.

Chan CJ, Smyth MJ, Martinet L 2015 Molecular mechanisms of natural killer cell activation in response to cellular stress. Cell Death Diff 21:5–14.

Chatterjea D, Martinov T 2015 Mast cells: versatile gatekeepers of pain. Mol Immunol 63:38–44.

Chopin M, Nutt SL 2015 Establishing and maintaining the Langerhans cell network. Semin Cell Dev Biol. 41:23-9.

Cunningham-Rundles C, Ponda PP 2005 Molecular defects in T- and B-cell primary immunodeficiency diseases. Nat Rev Immunol 5:880–92.

Forget BG, Bunn HF 2013 Classification of the disorders of hemoglobin. Cold Spring Harb Perspect Med 3:a011684.

Gerlach C, Thiriot A, von Andrian UH 2013 Of origins and pedigrees: lineage tracing of dendritic cells. Cell 154:720–2.

Girard JP, Moussion C, Förster R 2012 HEVs, lymphatics and homeostatic immune cell trafficking in lymph nodes. Nat Rev Immunol 12:762–73.

A discussion of how the movement of immune cells into, through and out of the lymph node is controlled.

Gordon S, Taylor PR 2005 Monocyte and macrophage heterogeneity. Nat Rev Immunol 5:953–64.

Hirahara K, Nakayama T 2016 $CD4^+$ T-cell subsets in inflammatory diseases: beyond the Th1/Th2 paradigm. Int Immunol 28:163–71.

Iolascon A, Miraglia del Giudice E, Perrotta S 1998 Hereditary spherocytosis: from clinical to molecular defects. Haematologica 83:240–57.

James EL, Parkinson EK 2015 Serum metabolomics in animal models and human disease. Curr Opin Clin Nutr Metab Care 18:478–83.

Jiang S, Dong C 2013 A complex issue on $CD4^+$ T-cell subsets. Immunol Rev 252:5–11.

Kaplan MJ, Radic M 2012 Neutrophil extracellular traps: double-edged swords of innate immunity. J Immunol 189:2689–95.

A summary of our current understanding of how NETs operate.

Koboziev I, Karlsson F, Grisham MB 2010 Gut-associated lymphoid tissue, T cell trafficking, and chronic intestinal inflammation. Ann N Y Acad Sci 1207 Suppl 1:E86–93.

Kocabas CN, Yavuz AS, Lipsky PE et al 2005 Analysis of the lineage relationship between mast cells and basophils using the c-kit D816V mutation as a biologic signature. J Allergy Clin Immunol 115:1155–61.

Kraehenbuhl JP, Neutra MR 2000 Epithelial M cells: differentiation and function. Annu Rev Cell Dev Biol 16:301–32.

Kristiansen M, Graversen JH, Jacobsen C et al 2001 Identification of the haemoglobin scavenger receptor. Nature 409:198–201.

A demonstration that CD163, which is expressed at the cell surface of macrophages, is a scavenger receptor for haemoglobin and haptoglobin-bound haemoglobin. This provides insight into a molecular mechanism of iron recycling by macrophages.

Laiosa CV, Stadtfelt M, Graf T 2006 Determinants of lymphoid–myeloid lineage diversification. Ann Rev Immunol 24:705–38.

Liu Y-J 2001 Dendritic cell subsets and lineages, and their functions in innate and adaptive immunity. Cell 106:259–62.

A review of current research and a re-evaluation of the lineage of and functional relationships between different dendritic cell types.

Machnicka B, Czogalla A, Hryniewicz-Jankowska A et al 2013 Spectrins: a structural platform for stabilization and activation of membrane channels, receptors and transporters. Biochim Biophys Acta 1838:620–34.

Male D, Brostoff J, Roth DB et al 2012 Immunology, 8th ed. London: Elsevier, Mosby.

An explanation of the scientific principles of clinical immunology, integrated with histology, pathology and clinical examples.

Malhotra D, Fletcher AL, Turley SJ 2013 Stromal and hematopoietic cells in secondary lymphoid organs: partners in immunity. Immunol Rev 251:160–76.

The role of stromal cells in the 'architecture' of secondary lymphoid organs, as well as the control and regulation of dendritic cells and lymphocytes, and the delivery of antigen to the right site.

Mankelow TJ, Satchwell TJ, Burton NM 2012 Refined views of multi-protein complexes in the erythrocyte membrane. Blood Cells Mol Dis 49:1–10.

A summary of recent models of how protein components of the red cell membrane interact to give the membrane its required properties.

Mebius RE, Kraal G 2005 Structure and function of the spleen. Nat Rev Immunol 5:606–16.

Merad M, Sathe P, Helft J et al 2013 The dendritic cell lineage: ontogeny and function of dendritic cells and their subsets in the steady state and the inflamed setting. Annu Rev Immunol 31:563–604.

A summary of recent data that has changed our understanding of how dendritic cells subsets arise and function.

Mohandas N, Gallagher PG 2008 Red cell membrane: past, present, and future. Blood 112:3939–48.

Murphy K, Weaver C 2016 Janeway's Immunobiology, 9th ed. New York: Garland Science.

The unifying principles of structure and function of the immune system in health and disease.

Nathan C 2006 Neutrophils and immunity: challenges and opportunities. Nat Rev Immunol 6:173–82.

Psychogios N, Hau DD, Peng J et al 2011 The human serum metabolome. PLoS ONE 6:e16957.

An analysis of more than 4000 serum components and their concentrations in health and disease.

Rezk SA, Nathwani BN, Zhao X et al 2013 Follicular dendritic cells: origin, function, and different disease-associated patterns. Hum Pathol 44:937–50.

Roozendaal R, Mebius RE, Kraal G 2008 The conduit system of the lymph node. Int Immunol 20:1483–7.

Rothenberg ME, Hogan SP 2006 The eosinophil. Annu Rev Immunol 24:147–74.

Safinia N, Scotta C, Vaikunthanathan T, et al 2015 Regulatory T cells: serious contenders in the promise for immunological tolerance in transplantation. Front Immunol 6: 438.

Schmitt EG, Williams CB 2013 Generation and function of induced regulatory T cells. Front Immunol 2013 4:152.

Segal AW 2005 How neutrophils kill microbes. Annu Rev Immunol 23:197–223.

Shlomchik MJ, Weisel F 2012 Germinal center selection and the development of memory B and plasma cells. Immunol Rev 247:52–63.

Stockinger B, Veldhoen M 2007 Differentiation and function of Th17 T cells. Curr Opin Immunol 19:281–6.

Stranford S, Ruddle NH 2012 Follicular dendritic cells, conduits, lymphatic vessels, and high endothelial venules in tertiary lymphoid organs: parallels with lymph node stroma. Front Immunol 3:350.

Thrasher AJ, Williams DA 2017 Evolving gene therapy in primary immunodeficiency. Mol Ther 25:1132–41.

Victora GD, Nussenzweig MC 2012 Germinal centers. Annu Rev Immunol 30:429–57.

A comprehensive review of germinal centres, integrating recent findings on the role of cellular dynamics in affinity maturation.

Vivier E, Tomasello E, Baratin M et al 2008 Functions of natural killer cells. Nat Immunol 9:503–10.

Woof JM, Kerr MA 2006 The function of immunoglobulin A in immunity. J Pathol 208:270–82.

CHAPTER

5

Functional anatomy of the musculoskeletal system

The musculoskeletal system comprises the specialized connective tissues of the articulated bony skeleton (including bone, cartilage and tendon) and the skeletal muscles that act across the articulations. Connective tissues are characterized by a sparse population of cells within an abundant and physically durable extracellular matrix. All of the specialized cells of the musculoskeletal system are related members of the connective tissue family and are derived from embryonic mesenchymal stem cells.

CARTILAGE

Cartilage is the fetal precursor tissue in the development of many bones. In the adult skeleton it persists at almost all joints between bones and in structures that must be deformable as well as strong, e.g. in the respiratory tract.

Microstructure of cartilage

Cartilage is a pliant, load-bearing connective tissue, covered by a fibrous perichondrium except at its junctions with bones and over the articular surfaces of synovial joints. It has a capacity for rapid interstitial and appositional growth in young and growing tissues. Three types of cartilage (hyaline cartilage, white fibrocartilage and yellow elastic cartilage) can be distinguished on the basis of the composition and structure of their extracellular matrices, but many features of the cells and matrix are common to all three types, and these features will be considered first.

Extracellular matrix

The matrix is mostly comprised of collagen (and, in some cases, elastic) fibres, embedded in a highly hydrated proteoglycan gel (**Fig. 5.1**). Large proteoglycan molecules have numerous side chains of glycosaminoglycans (GAGs), carbohydrates with remarkable water-binding properties. A preponderance of fixed negative charges on the surface of GAGs strongly attract polarized water molecules, causing wet cartilage to swell until restricted by tension in the collagen network, or by external loading. In this way, cartilage develops a compressive turgor that enables it to distribute loading evenly on to subchondral bone, rather like a water bed. Effectively, water is held in place by proteoglycans, which are themselves held in place by the collagen network. Cartilage proteoglycans are similar to those found in general, i.e. non-specialized, connective tissue. The most common GAG side chains in cartilage are chondroitin sulphate and keratan sulphate. The most common proteoglycan molecule, aggrecan, forms huge molecular aggregates with other proteoglycans and with hyaluronan (see Fig. 5.1). Other constituents of cartilage include dissolved salts, non-collagenous proteins and glycoproteins.

Collagens are described on p. 39. The collagen network varies in different types of cartilage and with age. Collagen type I forms large fibres with a wavy 'crimped' structure: it is common in most fibrous tissues, but in cartilage it occurs only in the outer layers of the perichondrium, and in white fibrocartilage. More typical of cartilage is collagen type II, which forms very thin fibrils dispersed between the proteoglycan molecules so that they do not clump together to form larger fibres. Collagen type II fibrils are often less than 50 nm in diameter and are too small to be seen by light microscopy. Transmission electron microscopy reveals that they have a characteristic cross-banding (65 nm periodicity) and are interwoven to create a three-dimensional meshwork. The length of collagen fibres and fibrils in cartilage is unknown, but even relatively short fibrils can reinforce the matrix by interacting physically and chemically with each other, and with other matrix constituents including proteoglycans (Hukins and Aspden 1985), reflecting the fact that the word collagen means 'glue-maker'. Collagen type II is found in hyaline cartilage, the notochord, the nucleus pulposus of an intervertebral disc, the vitreous body of the eye, and the primary corneal stroma.

Cartilage cells

The cells of cartilage are chondroblasts and chondrocytes. Chondroblasts are actively dividing cells, often flattened and irregular in shape, and are abundant in growing tissue where they synthesize the extracellular matrix (**Fig. 5.2**). Small projections arising from the cell membrane (**Fig. 5.3**) can form gap junctions with adjacent cells (Bruehlmann et al 2002), but these junctions may be lost when interstitial growth causes greater cell separation. As chondroblasts mature and lose the ability to divide, they develop into the larger but metabolically less active chondrocytes. These oval-shaped cells form sparse populations that maintain the extensive matrix of adult cartilage. The name 'chondrocyte' is commonly employed, as it is here, to denote all of the cartilage cells embedded in an extensive matrix. Chondrocytes are normally in close contact with their dense matrix (see Fig. 5.3); however, artefacts of tissue processing can sometimes give the illusion of an empty space or 'lacuna' surrounding

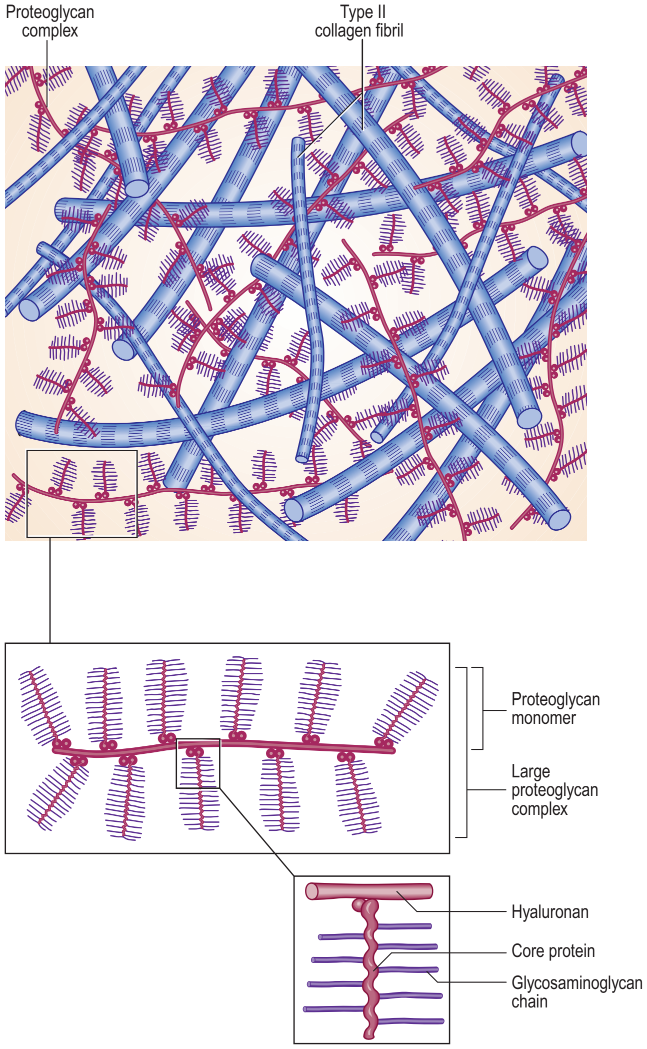

Fig. 5.1 The fine structural organization of hyaline cartilage matrix. Large proteoglycan complexes and type II collagen fibres (cross-banded and of different diameters) are depicted. Proteoglycan complexes bind to the surface of these fibres via their monomeric side chains and link them together. The arrangement of glycosaminoglycans and core protein of the proteoglycan monomer is illustrated in the expansion.

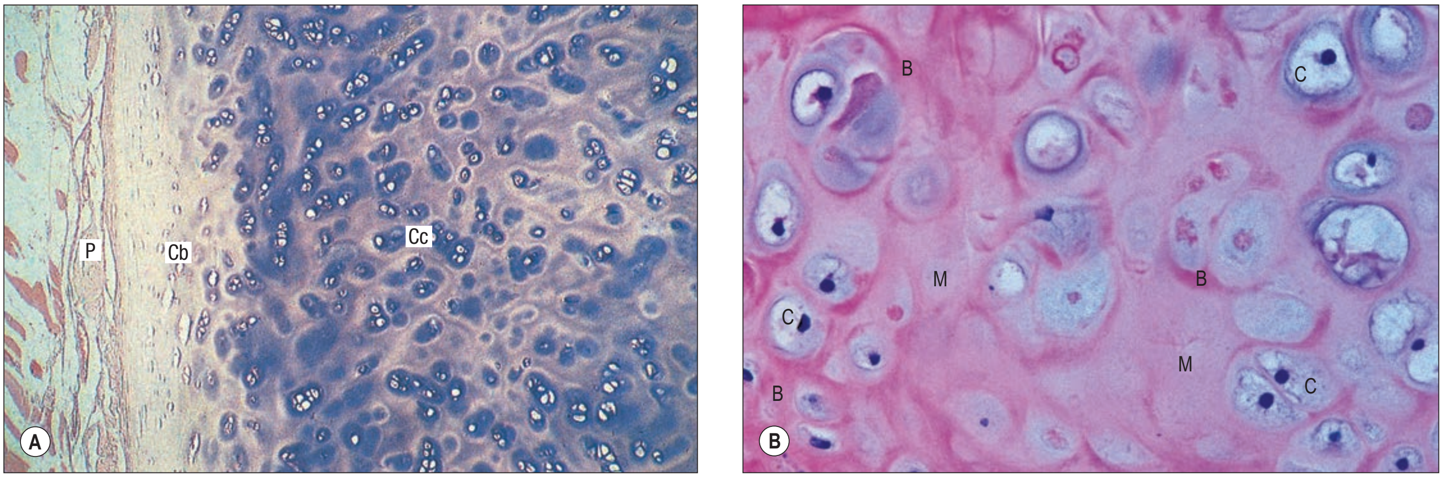

Fig. 5.2 Sections through hyaline cartilage. **A**, A low-power view of human rib, showing perichondrium (P), young chondroblasts (Cb) embedded in pale-staining interterritorial matrix, and mature chondrocytes (Cc) embedded in the basophilic interterritorial matrix (centre and right). **B**, Higher magnification of hyaline cartilage in human bronchial wall, showing isogenous groups of chondrocytes (C). Note the more deeply stained basophilic zones (B) (rich in acidic proteoglycans) around the cell clusters, with older, paler-staining matrix (M) between clusters. (B, Courtesy of Mr Peter Helliwell and the late Dr Joseph Mathew, Department of Histopathology, Royal Cornwall Hospitals Trust, UK.)

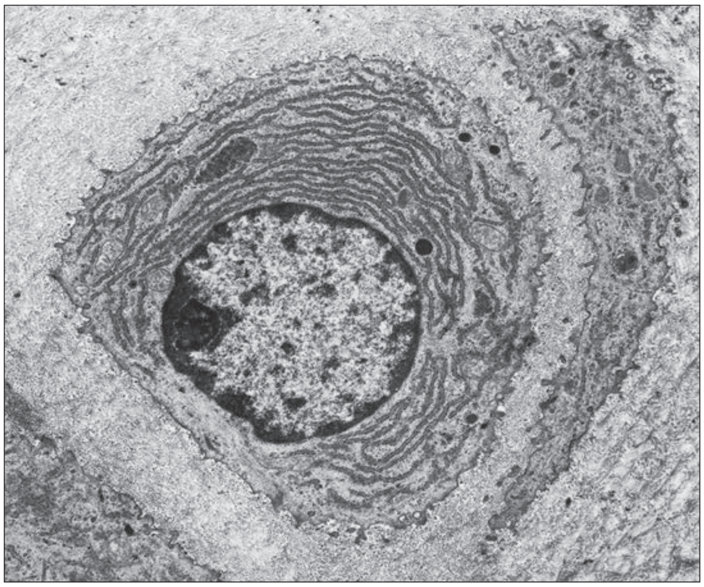

Fig. 5.3 An electron micrograph of chondroblasts in rabbit femoral condylar cartilage. The central cell has an active euchromatic nucleus with a prominent nucleolus, and its cytoplasm contains concentric cisternae of rough endoplasmic reticulum, scattered mitochondria, lysosomes and glycogen aggregates. The plasma membrane bears numerous short filopodia which project into the surrounding matrix. The latter shows a delicate feltwork of collagen fibrils within finely granular interfibrillary material. No pericellular lacuna is present; the matrix separates the central chondroblast from the cytoplasm of two adjacent chondroblasts (left, and crescentic profile). (Preparation courtesy of Susan Smith, Department of Anatomy, GKT School of Medicine, London.)

each cell or group of cells in histological sections. One or more chondrocytes can form a chondron, which consists of the cells and their pericellular matrix (**Fig. 5.2B**), surrounded by a protective basket of collagen (Roberts et al 1991, Youn et al 2006).

Cartilage cells synthesize and secrete all of the major components of their matrix, and their ultrastructure is typical of cells that are active in making and secreting proteins. The nucleus is round or oval, appears euchromatic and possesses one or more nucleoli. The cytoplasm is filled with rough endoplasmic reticulum, transport vesicles and Golgi complexes, and contains many mitochondria and frequent lysosomes, together with numerous glycogen granules, intermediate filaments (vimentin) and pigment granules. When these cells mature to the relatively inactive chondrocyte stage, the nucleus becomes heterochromatic, the nucleolus smaller and the protein synthetic machinery much reduced; the cells may also accumulate large lipid droplets.

Collagen is synthesized within the rough endoplasmic reticulum in the same way as it is in fibroblasts. Polypeptide chains are assembled into triple helices, and some carbohydrate is added. After transport to the Golgi apparatus, where further glycosylation occurs, the resulting procollagen molecules are secreted into the extracellular space. Terminal registration peptides are cleaved from their ends, forming tropocollagen molecules, and the final assembly into collagen fibrils takes place. Core proteins of the proteoglycan complexes are also synthesized in the rough endoplasmic reticulum and addition of GAG chains begins; the process is completed in the Golgi complex. Hyaluronan, which lacks a protein core, is synthesized by enzymes on the surface of the chondrocyte; it is not modified post-synthetically, and is extruded directly into the matrix without passing through the endoplasmic reticulum.

Matrix turnover is much slower in cartilage than in more metabolically active tissues. Collagen turnover is particularly slow, leaving it vulnerable to the slow process of non-enzymatic glycation, which makes the tissue yellow, stiff and vulnerable to injury (DeGroot et al 2004). Proteoglycans are turned over faster than collagen, with an estimated turnover time of 5 years for adult humans.

Cartilage is often described as avascular. Certainly, the ability of the matrix to deform under load makes it difficult for hollow blood vessels to persist in the tissue beyond early childhood, but a limited vascular supply is often found on the cartilage surface, from where it can revascularize the tissue following injury or degeneration (Lama et al 2018). Metabolite transport to cartilage cells is mostly by the process of diffusion down a concentration gradient from the cartilage surface, although fluid 'pumping' as a result of changing mechanical loading can contribute under certain circumstances. Metabolite transport severely limits cell density and metabolic rate in adult tissue, and this in turn restricts cartilage thickness to a few millimetres (Junger et al 2009). Cartilage cells situated further than this from a nutrient vessel do not survive, and their surrounding matrix typically becomes calcified. In the larger cartilages, and during the rapid growth of some fetal cartilages, vascular cartilage canals penetrate the tissue at intervals, providing an additional source of nutrients. In some cases these canals are temporary structures but others persist throughout life.

Hyaline cartilage

Hyaline (glassy) cartilage has a homogeneous, opalescent appearance, sometimes appearing bluish. It is firm and smooth to the touch and shows considerable deformability. The size, shape and arrangement of chondrocytes vary at different sites and with age. They are flat near the surface perichondrium, and rounded or angular deeper in the tissue (**Fig. 5.2A**). Groups of two or more cells frequently form a cell nest (isogenous cell group) surrounded by a basket of fine collagen fibrils (see Fig. 5.2B). Within such a 'chondron', daughter cells of a common chondroblast often meet at a straight line. The pericellular matrix closest to the cells is typically lacking in collagen fibrils, but rich in proteoglycans that can exhibit basophilic and metachromatic staining. More distant and older interterritorial matrix appears paler and is mostly collagen type II (75% of dry weight) and proteoglycans (22%).

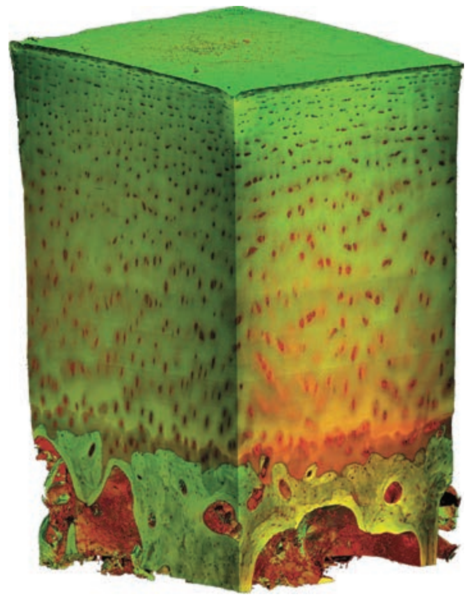

Fig. 5.4 Articular cartilage from the anterior region of the lateral femoral condyle of a young adult human female. Three-dimensional digital volumetric fluorescence imaging of serially sectioned, eosin-Y and acridine orange-stained tissue. Articular surface (top), articular cartilage and subchondral bone (below). Note the changes in size and spatial distribution of articular chondrocytes through the thickness of the cartilage. (Courtesy of Professor Robert L. Sah, Drs Won C. Bae, Kyle D. Jadin, Benjamin L. Wong, Kelvin W. Li and Mrs Barbara L. Schumacher, Department of Bioengineering and Whitaker Institute of Biomedical Engineering, University of California, San Diego.)

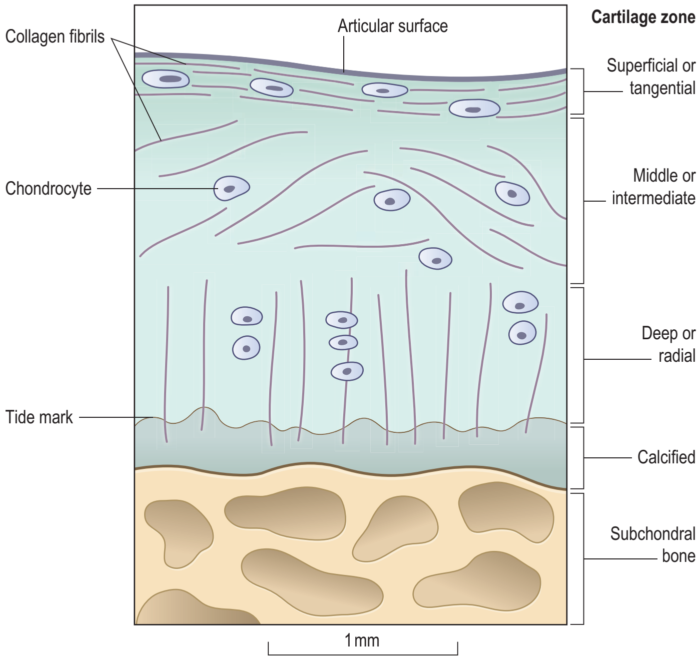

Fig. 5.5 Articular cartilage is not homogeneous: the various zones are different in terms of cell size and shape, and the orientation of the collagen fibril network.

After adolescence, hyaline cartilage may become calcified, either as part of the normal process of bone development, or as an age-related, degenerative change. In costal cartilage, the matrix tends to fibrous striation, especially in old age when cellularity diminishes. The xiphoid process and the cartilages of the nose, larynx and trachea (excepting the elastic cartilaginous epiglottis and corniculate cartilages) resemble costal cartilage in microstructure. Hyaline cartilage is the prototypical form, but it varies more with age and location than either elastic or fibrocartilage. Its regenerative capacity following injury is poor.

Articular cartilage, which covers the articular surfaces of synovial joints, is a specialized hyaline cartilage that lacks a perichondrium (**Fig. 5.4**). The synovial membrane overlaps and then merges into its structure circumferentially (see Fig. 5.32). The thickness of articular cartilage varies from 1 to 7 mm (typically 2 mm) in different joints, and decreases from middle to old age. Thickness does not increase in response to increased mechanical loading, at least in adults, although matrix composition and stiffness can adapt somewhat (Gahunia and Pritzker 2012). Central regions tend to be thickest on convex osseous surfaces, and thinnest on concave surfaces.

Articular cartilage provides an extremely smooth, firm yet deformable layer that increases the contact area between bones and thereby reduces contact stress (see Fig. 5.61). Microscopic undulations on the cartilage surface help to trap synovial fluid (see Fig. 5.60) and enable fluid-film lubrication to reduce friction and wear. Articular cartilage is generally too thin and stiff to be a good shock absorber, although shock absorption may be significant where there are multiple cartilage-covered surfaces, as in the carpus and tarsus.

Adult articular cartilage shows a structural zonation defined by its network of fine collagen type II fibrils (**Fig. 5.5**). Embedded in the deep calcified zone, fibrils rise vertically through the radial zone towards the cartilage surface, where they appear to reorientate to run parallel to the surface in the tangential zone. These collagen arcades can be visualized using phase-contrast microscopy (Thambyah and Broom 2007) but it is likely that each arcade represents numerous discrete fibrils rather than a single fibre. Their three-dimensional orientation can be appreciated by repeatedly piercing the cartilage surface with a needle; this creates a series of permanent elongated splits in the surface, which can be stained by Indian ink. The resulting split line pattern (Meachim el al 1974) reveals the predominant directions of collagen fibrils in the tangential zone, which may be related to internal lines of tension generated during joint movement.

Each zone of articular cartilage (see Fig. 5.5) has a distinct cell morphology and matrix composition. The tangential (or superficial) zone has relatively small, elongated cells orientated parallel to the surface. (Properties of the articular surface are described below under ‘Synovial joints’, p. 102). Deeper within the tangential zone, the collagen fibrils increase in diameter and density, and gradually merge with those of the transitional (or intermediate) zone. Here, the chondrocytes are large and rounded, and surrounded by collagen fibrils in a range of oblique orientations. Deeper still, in the radial zone, the cells are often disposed in vertical columns, interspersed with vertical collagen fibrils. The matrix in this zone contains collagen types IX and XI, as well as type II. An undulating band known as the tidemark indicates the start of the deepest zone, the zone of calcified cartilage, which has mechanical properties intermediate between cartilage and bone. This calcified zone is keyed into the subchondral bone by fine ridges and interdigitations, which serve to prevent shearing (gliding) movements between cartilage and bone. With age, articular cartilage thins by upward advancement of the tidemark, and gradual replacement of calcified cartilage by bone.

Cells of articular cartilage are capable of cell division, but mitosis is rarely observed in adult tissue and cartilage damage is not repaired. Superficial cells are lost progressively from normal young joint surfaces, to be replaced by cells from deeper layers. Age-related reductions in cell number and activity, and biochemical changes in the extracellular matrix, particularly affect the superficial zone of articular cartilage, increasing the risk of mechanical failure and of osteoarthritis (Lotz and Loeser 2012).

Articular cartilage derives nutrients by diffusion from vessels of the synovial membrane, synovial fluid and hypochondral vessels of an adjacent medullary cavity, some capillaries from which penetrate and occasionally traverse the calcified cartilage zone. The contributions from these sources are uncertain and may change with age. Small molecules freely traverse articular cartilage, with diffusion coefficients about half those in aqueous solution. Larger molecules have diffusion coefficients inversely related to their molecular size. The permeability of cartilage to large molecules is greatly affected by variations in its GAG (and hence water) content: a three-fold increase in GAGs increases the diffusion coefficient 100-fold.

Cartilaginous growth plates (see below under ‘Bone’, pp. 96–99) are also composed of hyaline cartilage, and there are similarities between active growth plates and growing articular cartilage on the epiphyses of long bones. In both cases, chondrocytes undergo a sequence of cell divisions and hypertrophy (with cells forming into columns) followed by cell death, and ossification by invading osteoblasts.

Fibrocartilage

Fibrocartilage is a dense, whitish tissue with a distinct fibrous texture. It forms the intervertebral discs of the spine and menisci of the knee,

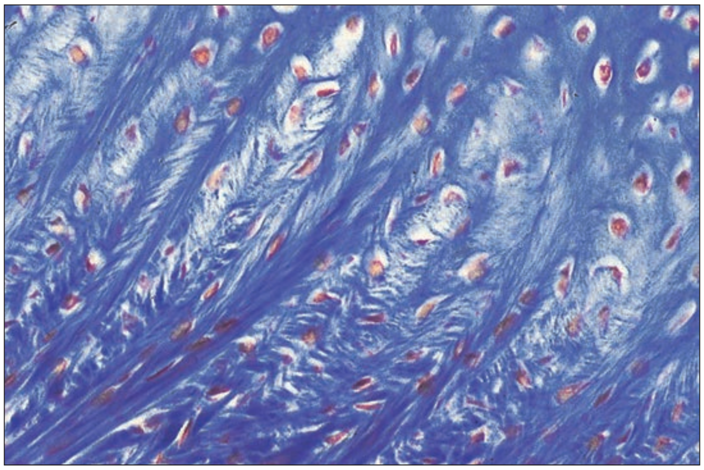

Fig. 5.6 White fibrocartilage in a late human fetal intervertebral disc. Chondroblasts lie between coarse collagen type I fibres (blue) derived from the anulus fibrosus. Mallory's triple stain.

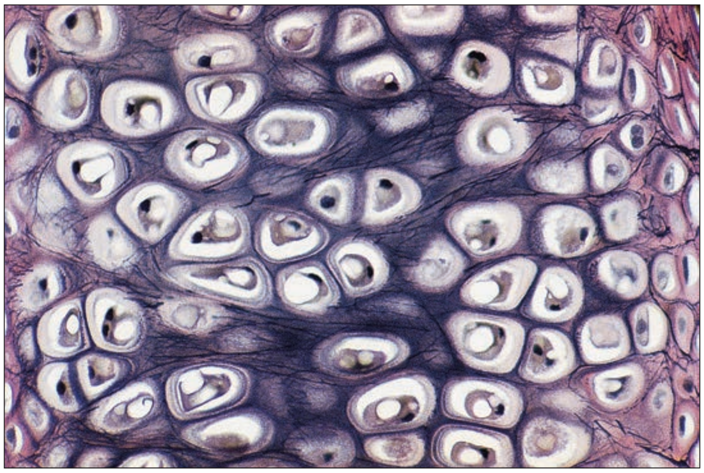

Fig. 5.7 Elastic cartilage, stained to demonstrate elastin fibres (blue–black). Chondroblasts and larger chondrocytes are embedded in the matrix, which also contains collagen type II fibres.

as well as smaller structures such as the glenoid and acetabular labra, and the lining of bony grooves for tendons. It is a versatile and tough material that combines considerable tensile strength with the ability to resist high compressive forces and to distribute them evenly on to underlying bone (Adams et al 2013). Histologically, fibrocartilage is intermediate between dense fibrous connective tissues such as tendon and ligaments, and hyaline cartilage. In some structures such as intervertebral discs, matrix composition and cell types vary from one location to another, reflecting varying mechanical properties.

Regions of fibrocartilage that are loaded predominantly in tension consist of large crimped fibres of collagen type I embedded in a hydrated proteoglycan gel. Cells are rounded in young tissue (Fig. 5.6), but become elongated and fibroblast-like with age. They may be linked by gap junctions (Bruehlmann et al 2002). Regions of fibrocartilage that are loaded predominantly in compression appear more homogeneous, contain a high proportion of fine collagen type II fibrils in an abundant proteoglycan gel, and contain rounded, chondrocyte-like cells. Fibrocartilage could therefore be regarded as a mingling of two types of tissue rather than a separate type of cartilage. However, no other tissue combines high proportions of proteoglycans with collagen type I, suggesting that fibrocartilage should be regarded as a distinct class of connective tissue.

The articular surfaces of bones that ossify in mesenchymal membranes (e.g. squamous temporal, mandible and clavicle) are covered by white fibrocartilage. The deep layers, adjacent to hypochondral bone, resemble calcified regions of the radial zone of hyaline articular cartilage. The superficial zone contains dense parallel bundles of thick collagen fibres, interspersed with typical dense connective tissue fibroblasts and little ground substance. Fibre bundles in adjacent layers alternate in direction, as they do in the cornea. A transitional zone of irregular bundles of coarse collagen and active fibroblasts separates the superficial and deep layers. The fibroblasts are probably involved in elaboration of proteoglycans and collagen, and may also constitute a germinal zone for deeper cartilage. Fibre diameters and types may differ at different sites according to the functional load.

Elastic cartilage

Elastic cartilage occurs in the external ear, corniculate cartilages, epiglottis and apices of the arytenoids. Like hyaline cartilage, it contains typical chondrocytes, either singly or in small groups, surrounded by a matrix rich in type II collagen fibrils. However, the more distant interterritorial matrix is pervaded by very fine yellow elastic fibres (Fig. 5.7) containing the protein elastin, which show no periodic banding structure under the electron microscope (as collagen fibrils do). A structure is termed 'elastic' if it returns to its original shape when loaded and then unloaded; elastic fibres (and cartilage) have the special property of being able to do this even after being subjected to deformations greater than 15%, which would damage collagen fibres. This characteristic is termed elastic recoil. Most sites in which elastic cartilage occurs have vibrational functions, such as laryngeal sound-wave production, or the collection and transmission of sound waves in the ear. Elastic cartilage is resistant to degeneration, and its capacity for limited regeneration following traumatic injury can be appreciated from the distorted repair of a cauliflower ear, as seen in participants of some contact sports.

Development and growth of cartilage

Cartilage is usually formed in embryonic mesenchyme. Mesenchymal cells proliferate and become tightly packed; the shape of their condensation foreshadows that of the future cartilage. They also become rounded, with prominent round or oval nuclei and a low cytoplasm : nucleus ratio. Each cell differentiates into a chondroblast as it secretes a basophilic halo of matrix, composed of a delicate network of fine type II collagen fibrils, type IX collagen and proteoglycan core protein. At some sites, continued secretion of matrix separates the cells, producing typical hyaline cartilage. Elsewhere, many cells become fibroblasts; collagen synthesis predominates and chondroblastic activity appears only in isolated groups or rows of cells that become surrounded by dense bundles of collagen fibres to form white fibrocartilage. In yet other sites, the matrix of early cellular cartilage is permeated first by anastomosing oxytalan fibres, and later by elastin fibres. In all cases, developing cartilage is surrounded by condensed mesenchyme, which differentiates into a bilaminar perichondrium. The cells of the outer layer become fibroblasts and secrete a dense collagenous matrix lined externally by vascular mesenchyme. The cells of the inner layer contain differentiated, but mainly resting, chondroblasts or prechondroblasts.

Cartilage grows by interstitial and appositional mechanisms. Interstitial growth is the result of continued mitosis of early chondroblasts throughout the tissue mass and is obvious only in young cartilage, where plasticity of the matrix permits continued expansion. When a chondroblast divides, its descendants temporarily occupy the same chondron. They are soon separated by a thin septum of secreted matrix, which thickens and further separates the daughter cells. Continuing division produces isogenous groups. Appositional growth is the result of continued proliferation of the cells that form the internal, chondrogenic layer of the perichondrium. Newly formed chondroblasts secrete matrix around themselves, creating superficial lacunae beneath the perichondrium. This continuing process adds additional surface, while the entrapped cells participate in interstitial growth. Apposition is thought to be most prevalent in mature cartilages, but interstitial growth must persist for long periods in growth-plate cartilage. Relatively little is known about the factors that determine the overall shape of cartilage structures.

BONE

Bone is a strong and rigid connective tissue that has evolved to enable fast terrestrial locomotion. Its strength provides support and protection for the body, while its rigidity enables it to create precisely shaped articular surfaces that do not distort under load, and ensures that forceful muscle contractions result in rapid limb movements rather than bending of bones. Unlike cartilage, bone is a highly vascular tissue with a high cell density; high cellularity enables it to adapt to changing mechanical demands, and to regenerate following injury.

Macroscopic anatomy of bone

Macroscopically, living bone is white. Its texture is either dense like ivory (compact bone) or honeycombed by large cavities (trabecular,

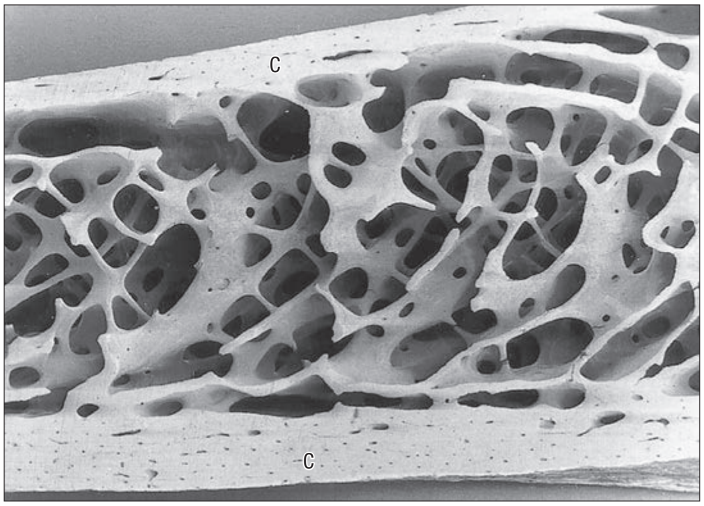

Fig. 5.8 A vertical section 2 cm below the anterosuperior border of the iliac crest (female, 42 years). The cancellous bone consists of intersecting curved plates and struts. Osteonal (Haversian) canals can just be seen in the two cortices (C) at this magnification.

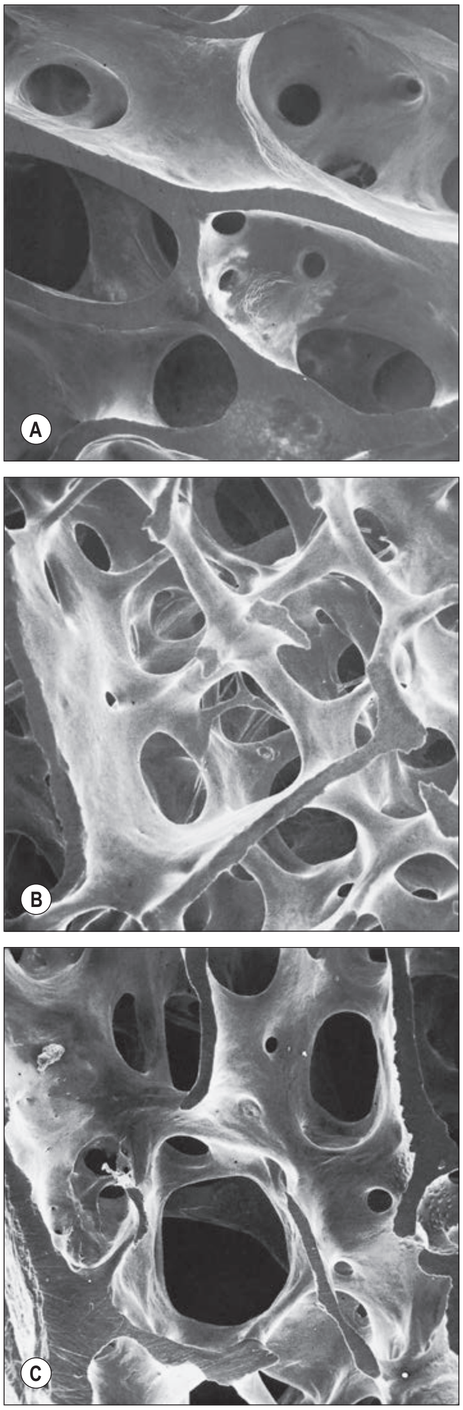

Fig. 5.9 Trabecular bone at different sites in the proximal part of the same human femur. All fields are shown at the same scale. **A**, Subcapital part of the neck. **B**, Greater trochanter. **C**, Rim of the articular surface of the head. Note the wide variation in thickness, orientation and spacing of the trabeculae. (From Whitehouse WJ, Dyson ED 1974 Scanning electron microscope studies of trabecular bone in the proximal end of the human femur. J Anat 118:417–44, by permission from Blackwell Publishing.)

cancellous or spongy bone), where the bony element is reduced to a latticework of bars and plates known collectively as trabeculae (Figs 5.8–5.9). Compact bone is usually limited to the outer shell or cortex of mature bones, where it is important in determining their strength and providing rigid articular surfaces. Cortical thickness and architecture vary between and within bones, and generally decrease with age in adults. Trabecular bone provides support to the cortex while minimizing weight. The presence of a large central medullary canal in long bones also helps to reduce their weight. Spaces within bones provide convenient and secure locations for the storage of haemopoietic tissues and fat. Bone forms a reservoir of metabolic calcium (99% of body calcium is in the bony skeleton) and of phosphate, which is under hormonal and cytokine control.

The proportions of compact to cancellous bone vary between and within bones. Generally, a thick cortex is required to provide strength in bending, e.g. in the mid-diaphysis of a long bone (see Fig. 5.20). Trabecular bone provides strength in compression and so is abundant in the epiphyses of long bones, and in the vertebral bodies of the spine. In flat bones such as the ribs, the interior is uniformly cancellous, and compact bone forms the surface. Internal cavities are usually filled with marrow, either red haemopoietic or yellow adipose, according to age and site. However, in some bones of the skull, notably the mastoid process of the temporal bone and the paranasal sinuses of the frontal, maxilla, sphenoid and ethmoid bones, many of the internal cavities are filled with air, i.e. they are variably pneumatized.

Bones vary not only in their primary shape but also in lesser surface details (secondary markings) that appear mainly in postnatal life. Most bones display features such as elevations and depressions, smooth areas and rough ridges. Broad elongated depressions are called fossae (e.g. the glenoid fossa); lengthy depressions are grooves or sulci (e.g. the humeral bicipital sulcus); a notch is an incisura; and an actual gap is a hiatus. A large projection is termed a process or, if elongated and slender or pointed, a spine. A curved process is a hamulus or cornu (e.g. the pterygoid hamuli of the sphenoid bone and the cornua of the hyoid). A rounded projection is a tuberosity or tubercle, and occasionally a trochanter. Long elevations are crests, or lines if they are less developed; crests are wider and present boundary edges or lips. An epicondyle is a projection close to a condyle and is usually a site where the common tendon of a superficial muscle group or a collateral ligament of the adjacent joint is attached. The terms protuberance, prominence, eminence and torus are occasionally applied to specific bony projections. The expanded proximal end of a long bone is often termed the 'head' or caput (e.g. humerus, radius, femur). A hole in a bone is a foramen and becomes a canal when lengthy. A large hole may be called an aperture or, if covered largely by connective tissue, a fenestra. Clefts in or between bones are fissures. A lamina is a thin plate; larger laminae may be called squamae (e.g. the temporal squama). Large areas on many bones are featureless and as smooth as articular surfaces, from which they differ by being pierced by visible vascular foramina.

Tendons are usually attached at roughened bone surfaces. Wherever any aggregation of collagen in a muscle reaches bone, surface irregularities correspond in form and extent to the pattern of tendinous fibres. Such markings are almost always elevated above the general surface, as if ossification advanced into the collagen bundles from periosteal bone. How such secondary markings are induced is uncertain but they may result from the continued incorporation of new collagen fibres into the bone, perhaps necessary for minor functional adjustment. There is evidence that their prominence may be related to the power of the muscles involved, and they increase with advancing years as if the pull of muscles and ligaments exercised a cumulative effect over a limited area. Surface markings delineate the shape of attached connective tissue structures, e.g. an obvious tendon, intramuscular tendon or septum, aponeurosis, or tendinous fibres mediating what is otherwise a direct muscular attachment. These markings may be facets, ridges, nodules, rough areas or complex mixtures; they afford accurate indications of the junctions of bone with muscles, tendons, ligaments or articular capsules.

Muscle fibres do not attach directly to periosteum or bone. Force transmission is through the connective tissue that encapsulates (epimysium) and pervades (perimysium and endomysium) all muscles. These two forms of attachment of muscles, which are at the extremes of a range of admixtures, differ in the density of collagen fibres between muscle and bone. Where collagen is visibly concentrated, markings appear on the bone surface. In contrast, the multitude of microscopic connective tissue ties of direct attachment that occur over a larger area do not visibly mark the bone, and so it appears smooth to unaided vision and touch.

Many bones articulate with their neighbours at synovial joints. Small articular surfaces are termed facets or foveae; larger, knuckle-shaped surfaces are condyles; a trochlea is grooved like a pulley. Articular surfaces are smooth and covered by articular cartilage, which means that they lack the vascular foramina typical of the surfaces of most other bones.

Microstructure of bone

Bone contains a mineralized collagenous extracellular matrix surrounding a range of specialized cells including osteoblasts, osteocytes and osteoclasts. Periosteum, endosteum and marrow are closely associated tissues. All of these components will be described first individually, and then their overall organization will be considered.

Bone organic matrix

Approximately 10–20% of bone mass is water. A significant proportion (30–40%) of the remaining dry weight is made up of the organic component of the extracellular matrix. Approximately 30% of this organic matrix is collagen; the remainder includes various non-collagenous proteins, glycoproteins and carbohydrates. The proportions of these components vary with age, location and metabolic status.

Most of the collagen in bone is an ordered branching network of type I fibres (**Fig. 5.10**). Although type I collagen fibres are found in most connective tissues, their molecular structure in bone is atypical: internal cross-linking between component fibrils is stronger and chemically more inert, and transverse spacings between collagen molecules within each fibril are larger, allowing more space for the deposition of minerals. A small amount of type V collagen is also present, probably to help regulate fibrillogenesis. Collagen fibres contribute greatly to the cohesive mechanical strength of bone, and also to its toughness (which is reflected in the energy required to break a bone).

Collagen is synthesized in bone by osteoblasts. Newly secreted molecules of tropocollagen lose part of their non-helical terminal regions, thus allowing them to polymerize in the extracellular matrix to form fibrils, which then associate to form fibres. These structures are stabilized by various cross-links, which increase in number and strength as the tissue matures. In primary bone, collagen fibres form a complex interwoven meshwork that incorporates other organic molecules; this 'osteoid' material is then mineralized to form woven (non-lamellar) bone. In time, primary bone is almost entirely replaced by regular laminar arrays of nearly parallel collagen fibres, which form the basis of lamellar bone (Currey 2002). Partially mineralized collagen networks can be seen within osteoid on the outer and internal surfaces of bone, and in the endosteal linings of vascular canals. Collagen fibres from the periosteum are incorporated in cortical bone (extrinsic fibres) and anchor this fibrocellular layer at its surface. Terminal collagen fibres of tendons and ligaments are incorporated deep into the matrix of cortical bone. They may be interrupted by new osteons during cortical drift (modelling) and turnover (remodelling), and remain as islands of interstitial lamellae or even trabeculae.

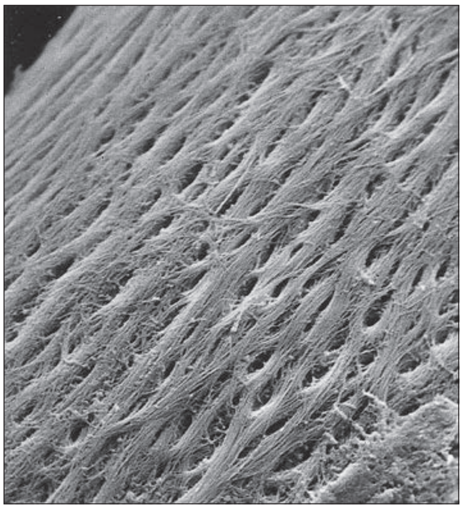

Fig. 5.10 A scanning electron micrograph of collagen fibres on the surface of human trabecular bone. Note the branching fibres (female, 2 months, sixth rib).

Bone organic matrix includes small amounts of various macromolecules attached to collagen fibres and surrounding bone crystals. They are secreted by osteoblasts and young osteocytes, and include osteonectin, osteocalcin, the bone proteoglycans biglycan and decorin, the bone sialoproteins osteopontin and thrombospondin, many growth factors including transforming growth factor beta (TGF-β), proteases and protease inhibitors, often in a latent form. The functions of some of these molecules are described with osteoblasts (see below).

Bone minerals

Approximately 60–70% of bone dry weight is made up of inorganic mineral salts in the form of microcrystalline hydroxyapatite ($Ca_{10}(PO_4)_6(OH)_2$). The microcrystals confer hardness and much of the rigidity of bone, and are the main reason why bone is easily seen on radiographs. (Bone must be 50% mineralized to be visible on radiographs produced with a standard X-ray unit.) Bone mineral also has an important carbonate content, and a lower Ca:P ratio than pure hydroxyapatite, together with a small amount of calcium phosphate. Bone crystals are extremely small (which gives them a high surface : volume ratio). They take the form of thin plates or leaf-like structures. The largest are 150 nm long × 80 nm wide × 5 nm thick, although most are half that size. Up to two-thirds of the mineral content of bone is thought to be located within collagen fibrils, where the crystals are packed closely together, with their long axes nearly parallel to the fibrils; crystal formation is probably initiated in the gaps between individual collagen molecules. Narrow spaces between the crystals contain water and organic macromolecules. The mineral substances of bone are mostly acid-soluble. If they are removed, using calcium chelators such as citrates or ethylene diamine tetra-acetic acid (EDTA), the bone retains its shape but becomes highly flexible.

The major ions in bone mineral include calcium, phosphate, hydroxyl and carbonate. Less numerous ions are citrate, magnesium, sodium, potassium, fluoride, chloride, iron, zinc, copper, aluminium, lead, strontium, silicon and boron, many of which are present only in trace quantities. Fluoride ions can substitute for hydroxyl ions, and carbonate can substitute for either hydroxyl or phosphate groups. 'Group IIA cations', such as radium, strontium and lead, all readily substitute for calcium and are therefore known as bone-seeking cations. Since they can be either radioactive or chemically toxic, their presence in bone, where they may be close to haemopoietic bone marrow, may cause illness and characteristic appearances on X-rays.

Mineralization of newly synthesized osteoid is a gradual process that slows over time; it typically reaches 70–80% in 3 weeks (Fuchs et al 2008: data for rabbits). Immature woven bone mineralizes faster and so may be distinguished from adjacent lamellar bone by its higher degree of mineralization. In cortical bone, lamellae mostly take the form of cylindrical osteons (see Fig. 5.16). These structures mineralize from inside to out, so that the concentration of mineral is highest in the older, more peripheral, lamellae. Although new osteons are less mineralized than old ones, they may show one or more highly mineralized 'arrest lines' within their walls. Mineral distribution is most uniform in established, highly mineralized osteons. Overall, mineralization increases with age, even though bone mass decreases.

Osteoblasts

Osteoblasts are derived from osteoprogenitor (stem) cells of mesenchymal origin present in bone marrow and other connective tissues. They proliferate and differentiate into osteoblasts prior to bone formation, stimulated by bone morphogenetic proteins (BMPs). A layer of osteoblasts covers the forming surfaces of growing or remodelling bone (**Fig. 5.11**). In relatively quiescent adult bone, they appear to be present mostly on endosteal rather than periosteal surfaces, but they also occur deep within compact bone wherever osteons are being remodelled. Osteoblasts are responsible for the synthesis, deposition and mineralization of the bone matrix, which they secrete. Once embedded in the matrix, they become osteocytes.

Osteoblasts are basophilic, roughly cuboidal mononuclear cells 15–30 μm across. They contain prominent bundles of actin, myosin and other cytoskeletal proteins associated with the maintenance of cell shape, attachment and motility. Their plasma membranes display

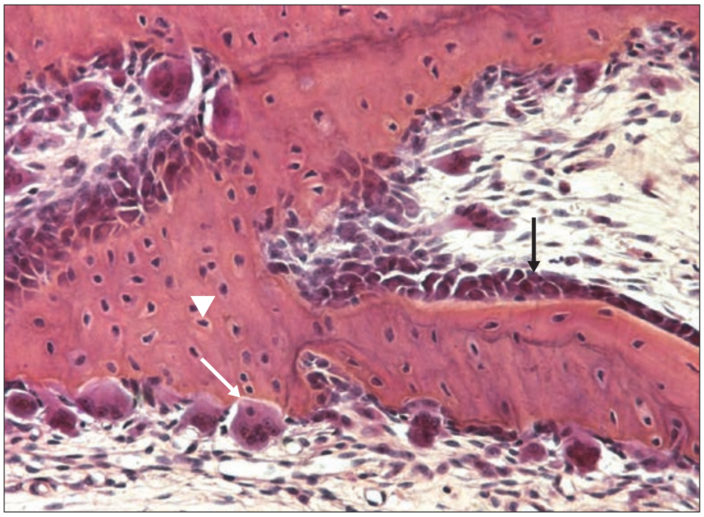

Fig. 5.11 Bone cells actively remodelling alveolar bone to accommodate a developing tooth. Large multicellular osteoclasts (white arrow) are actively resorbing bone on one surface, while a layer of osteoblasts (black arrow) is depositing osteoid on another. Osteoblasts that have become trapped in the matrix to form osteocytes are shown in the centre (white arrowhead). (Courtesy of Professor Tim Arnett, University College London.)

many extensions, some of which contact neighbouring osteoblasts and embedded osteocytes at intercellular gap junctions. This arrangement facilitates coordination of the activities of groups of cells, e.g. in the formation of large domains of parallel collagen fibres.

Ultrastructurally, osteoblasts are typical protein-secreting cells. They synthesize and secrete collagens and a number of glycoproteins. Osteocalcin is required for bone mineralization, binds hydroxyapatite and calcium, and is used as a marker of new bone formation. Osteonectin is a phosphorylated glycoprotein that binds strongly to hydroxyapatite and collagen; it may play a role in initiating crystallization and may be a cell adhesion factor. RANKL is the cell surface ligand for RANK (receptor for activation of nuclear factor kappa B), an osteoclast progenitor receptor (see below). Osteoprotegerin is a soluble, high-affinity decoy ligand for RANKL, which restricts osteoclast differentiation. Biglycan and decorin are bone proteoglycans that attract water; decorin also binds the growth factor TGF-β. The bone sialoproteins, osteopontin and thrombospondin, mediate osteoclast adhesion to bone surfaces by binding to osteoclast integrins. In addition, osteoblasts secrete latent proteases and growth factors including BMPs and TGF-β (which is also secreted by osteoclasts and which may be a coupling factor for stimulating new bone formation at resorption sites).

Although extracellular fluid is generally supersaturated with respect to the basic calcium phosphates, mineralization does not occur in most tissues. In bone, osteoblasts secrete osteocalcin (which binds calcium at levels sufficient to concentrate the ion locally) and contain membrane-bound vesicles full of alkaline phosphatase (cleaves phosphate ions from various molecules to elevate concentrations locally) and pyrophosphatase (degrades inhibitory pyrophosphate in the extracellular fluid). The vesicles bud off from the osteoblast surface into newly formed osteoid, where they initiate hydroxyapatite crystal formation. Some alkaline phosphatase reaches the blood circulation, where it can be detected in conditions of rapid bone formation or turnover.

Osteoblasts also play a key role in the hormonal regulation of bone resorption. They express receptors for parathyroid hormone (PTH), 1,25-dihydroxy vitamin D_3 (calcitriol) and other promoters of bone resorption. When activated, osteoblasts promote osteoclast differentiation via PTH-activated expression of cell surface RANKL, which binds to RANK on immature osteoclasts, establishes cell–cell contact and triggers contact-dependent osteoclast differentiation. In the presence of PTH, osteoblasts also downregulate secretion of osteoprotegerin, a soluble decoy ligand with higher affinity for RANKL. In conditions favouring bone deposition, secreted osteoprotegerin blocks RANKL binding to RANK, restricting the number of mature osteoclasts.

Bone-lining cells are flattened epithelial-like cells that cover the free surfaces of adult bone not undergoing active deposition or resorption. Generally considered to be quiescent osteoblasts or osteoprogenitor cells, they line the periosteal surface and the vascular canals within osteons, and form the outer boundary of the marrow tissue on the endosteal surface of marrow cavities.

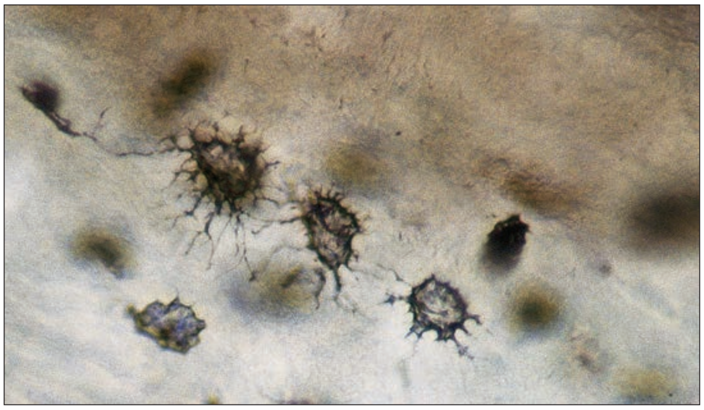

Fig. 5.12 Osteocyte lacunae shown at high magnification in a dry ground section of lamellar bone. The territories of three osteocytes are shown. Their branching dendrites contact those of neighbouring cells via the canaliculi seen here within the bone matrix. Several other osteocyte lacunae are present, out of the focal plane in this section, and tangential to the osteon axis.

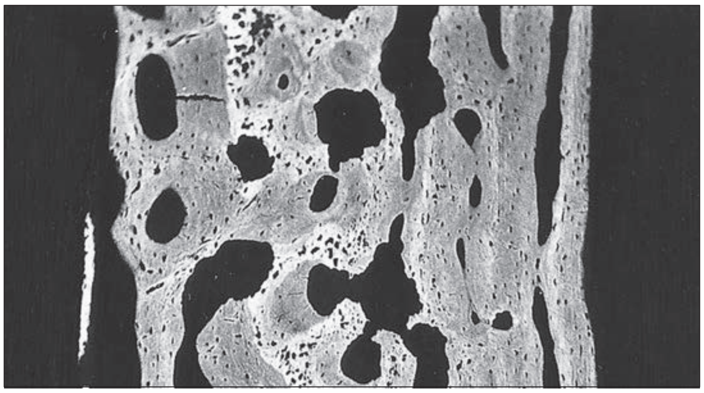

Fig. 5.13 Human parietal bone (male neonate) showing primary osteonal bone (grey) and woven bone (white) containing many connecting osteocyte lacunae (black). Internal resorption of the bone has produced large, irregular dark spaces (trabecularization).

Osteocytes

Osteocytes are the major cell type of mature bone and are distributed throughout its matrix, interconnected by numerous dendritic processes to form a complex cellular network (Fig. 5.12). They are derived from osteoblasts that have become enclosed within their rigid matrix (see Fig. 5.11) and so have lost the ability to divide or to secrete new matrix. (The rigidity of mineralized bone matrix prevents interstitial growth, so that new bone must always be deposited on pre-existing surfaces.) Osteocytes retain contact with each other and with cells at the surfaces of bone (osteoblasts and bone-lining cells) throughout their lifespan.

Mature, relatively inactive osteocytes have an ellipsoid cell body with their longest axis (approximately 25 μm) parallel to the surrounding lamellae. The rather narrow rim of cytoplasm is faintly basophilic, contains relatively few organelles and surrounds an oval nucleus. Osteocytes in woven bone are larger and more irregular in shape (Fig. 5.13). Numerous fine branching processes containing bundles of microfilaments and some smooth endoplasmic reticulum emerge from each cell body. At their distal tips, these processes form gap junctions with the processes of adjacent cells (osteocytes, osteoblasts and bone-lining cells) so that they are in electrical and metabolic continuity.

Extracellular fluid fills the small, variable spaces between osteocyte cell bodies and their rigid lacunae, which may be lined by a variable (0.2–2 μm) layer of unmineralized organic matrix. The same fluid fills the narrow channels or canaliculi that surround the long processes of the osteocytes. Approximately 0.25–0.5 μm wide, the canaliculi provide a route for the diffusion of nutrients, gases and waste products between osteocytes and blood vessels. Canaliculi do not usually extend through and beyond the reversal line surrounding each osteon and so do not communicate with neighbouring systems.

In well-vascularized bone, osteocytes are long-lived cells that actively maintain the bone matrix. The average lifespan of an osteocyte varies

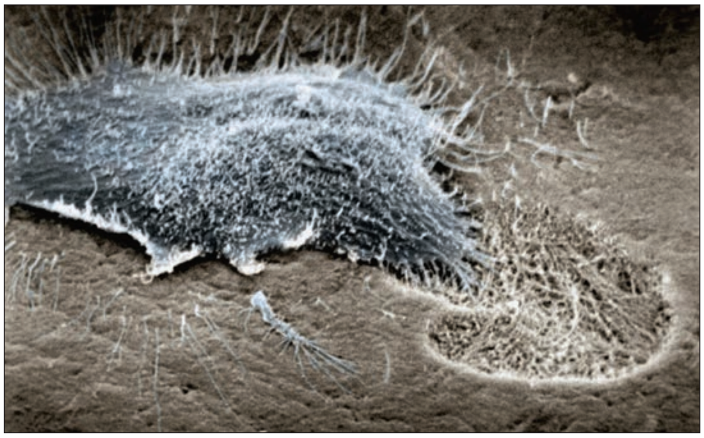

Fig. 5.14 A scanning electron micrograph of a neonatal rabbit osteoclast actively resorbing bone *in vitro* from the surface of sperm whale dentine. (Courtesy of Professor Alan Boyde, Queen Mary University of London.)

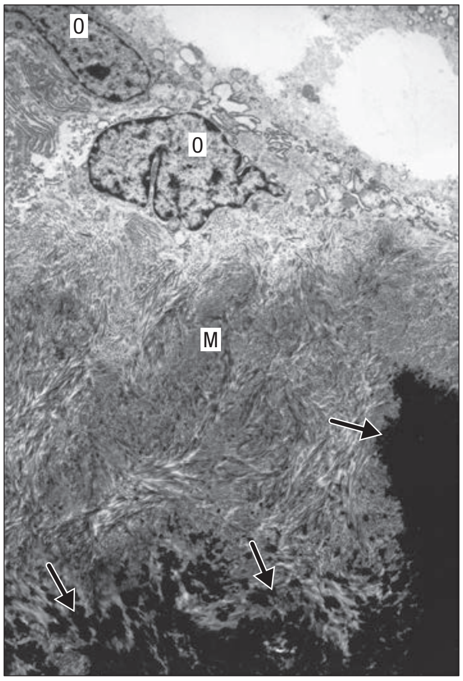

Fig. 5.15 An electron micrograph of woven bone from a failed fracture of human distal tibia. Two osteoblasts (O) lie on the free surface (top). Newly synthesized collagenous osteoid matrix (M) is seen in the centre field, with a mineralization front (electron-dense area) below (arrows). (Courtesy of Dr Bart Wagner, Histopathology Department, Sheffield Teaching Hospitals, UK.)

with the metabolic activity of the bone and the likelihood that it will be remodelled, but is measured in years. Old osteocytes may retract their processes from the canaliculi; when they die, their lacunae and canaliculi may become plugged with cell debris and minerals, which hinders diffusion through the bone. Dead osteocytes occur commonly in interstitial bone (between osteons) and in central regions of trabecular bone that escape surface remodelling. They are particularly noticeable by the second and third decades. Bones that experience little turnover, e.g. the auditory ossicles, are most likely to contain aged osteocytes and have low osteocyte viability. Osteocyte death leads to matrix resorption by osteoclast activity. Osteocytes themselves are often mineralized.

Osteoclasts

Osteoclasts are large (diameters of 40 μm or more) polymorphic cells containing up to 20 oval, closely packed nuclei (see Fig. 5.11). They lie in close contact with the bone surface in resorption bays (Howship's lacunae). Their cytoplasm contains numerous mitochondria and membrane-bound organelles, many of which are acid phosphatase-positive lysosomes. Rough endoplasmic reticulum is relatively sparse but the Golgi complex is extensive. The cytoplasm also contains numerous coated transport vesicles and microtubule arrays involved in vesicle transport between the Golgi stacks and the cell's ruffled border (the highly infolded region of plasma membrane of an active osteoclast at a site of bone resorption). A well-defined zone of actin filaments and associated proteins occurs beneath the ruffled border around the circumference of a resorption bay, in a region termed the sealing zone.

Functionally, osteoclasts are responsible for the local removal of bone during bone growth and remodelling (**Fig. 5.14**). They dissolve bone minerals by proton release to create an acidic local environment, and they remove organic matrix by secreting lysosomal (cathepsin K) and non-lysosomal (e.g. collagenase) enzymes. Osteoclasts are stimulated to resorb bone by signals from local cells (including osteoblasts, macrophages and lymphocytes) and by blood-borne factors such as PTH and 1,25-dihydroxy vitamin D_3 (calcitriol). Calcitonin, produced by C cells of the thyroid follicle, reduces osteoclast activity.

Osteoclasts differentiate from myeloid stem cells via macrophage-colony-forming units. Differentiation is primarily regulated by two cytokines: macrophage-colony stimulating factor, secreted by osteoblasts, and RANKL, expressed by osteoblasts (see above). The mononuclear precursors fuse to form terminally differentiated multinuclear osteoclasts (Väänänen and Laitala-Leinonen 2008). Osteoclast differentiation inhibitors are potential therapeutic agents for bone loss-associated disorders, e.g. osteoporosis, rheumatoid arthritis, Paget's disease, periodontal disease and osteosarcoma.

Woven and lamellar bone

The mechanical properties of bone depend not only on matrix composition, as described above, but also on the manner in which the matrix constituents are organized. Woven bone and lamellar bone represent two quite distinct types of organization.

In woven (or bundle) bone, the collagen fibres and bone crystals are irregularly arranged. The diameters of the fibres vary, so that fine and coarse fibres intermingle, producing the appearance of the warp and weft of a woven fabric. Woven bone is typical of young fetal bones, but is also seen in adults during excessively rapid bone remodelling and during fracture repair (**Fig. 5.15**). It is formed by highly active osteoblasts during development, and is stimulated in the adult by fracture, growth factors or prostaglandin E_2.

Lamellar bone, which makes up almost all of an adult skeleton, is more organized and is produced more slowly. The precise arrangement of lamellae (bone layers) varies from site to site. In trabeculae and the outer (periosteal) and inner (endosteal) surfaces of cortical bone, a few lamellae form continuous circumferential layers that are more or less parallel to the bony surfaces. However, in more central regions of cortical bone, the lamellae are arranged in concentric cylinders around neurovascular channels called Haversian canals (**Fig. 5.16**). This interconnecting, three-dimensional, laminated construction increases the toughness of lamellar bone because the interfaces between lamellae are effective in stopping the growth of cracks; more energy is therefore required to propagate cracks that are sufficiently extensive to fracture the bone.

Each lamella consists of a sheet of mineralized matrix containing collagen fibres of similar orientation locally, running in branching bundles 2–3 μm thick and often extending the full width of a lamella. The orientation of collagen fibres and crystals differs between 0° and 90° in adjacent lamellae, as may be demonstrated by polarized light microscopy (see Fig. 5.19B). At the borders of lamellae, packing of collagen fibres into bundles is less perfect and intermediate and random orientations of collagen predominate.

Cortical bone

The cylindrical structural units that comprise most cortical bone are termed Haversian systems or osteons (**Fig. 5.17**). Osteons usually lie parallel with each other (**Fig. 5.18**); in long bones, they lie parallel with the long axis of the bone. Adjacent osteons may encroach on one another because they are usually formed at different times, during successive periods of bone remodelling. Irregular gaps between osteons are filled with interstitial lamellae (**Fig. 5.17A**), which are the fragmentary remains of older osteons and circumferential lamellae. Osteons may be spiral or they may branch, and some end blindly. They are round or ellipsoidal in cross-section. The main direction of collagen fibres within osteons varies: in the shaft of long bones, fibres are more longitudinal at sites that are subjected mainly to tension, and more oblique at sites subjected mostly to compression. Peripheral lamellae of osteons contain more transverse fibres.

It has been estimated that there are 21 million osteons in a typical adult skeleton. Their diameter varies from 100 to 400 μm, and they usually contain 5–20 lamellae. Each osteon is permeated by the canaliculi

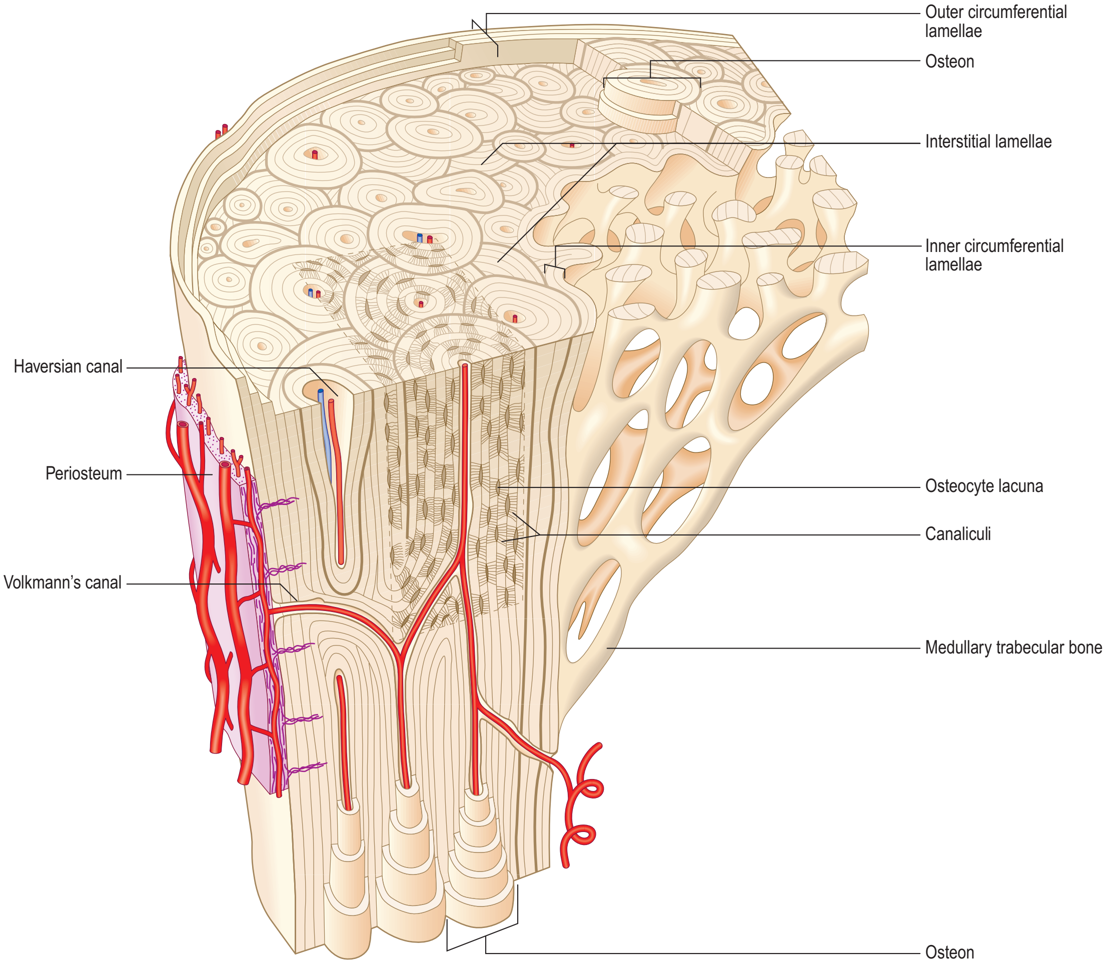

Fig. 5.16 The main features of the microstructure of mature lamellar bone. Areas of compact and trabecular (cancellous) bone are included. Note the general construction of the osteons; distribution of the osteocyte lacunae; Haversian canals and their contents; resorption spaces; and different views of the structural basis of bone lamellation.

of its resident osteocytes, which form pathways for the diffusion of metabolites between osteocytes and blood vessels. The maximum diameter of an osteon ensures that no osteocyte is more than 200 μm from a blood vessel, a distance that may be a limiting factor in their survival.

The central Haversian canals of osteons vary in size, with a mean diameter of 50 μm; those near the marrow cavity are somewhat larger. Each canal contains one or two capillaries lined by fenestrated endothelium and surrounded by a basal lamina, which also encloses typical pericytes. They usually contain a few unmyelinated and occasional myelinated axons. The bony surfaces of osteonic canals are perforated by the openings of osteocyte canaliculi and are lined by collagen fibres.

Haversian canals communicate with each other and directly or indirectly with the marrow cavity via vascular (nutrient) channels called Volkmann's canals, which run obliquely or at right-angles to the long axes of the osteons (see Fig. 5.18). The majority of these channels appear to branch and anastomose, but some join large vascular connections with vessels in the periosteum and the medullary cavity.

Osteons are distinguished from their neighbours by a cement line that contains little or no collagen, and is strongly basophilic because it has a high content of glycoproteins and proteoglycans. Cement lines are also known as reversal lines because they mark the limit of bone erosion prior to the formation of a new osteon. Canaliculi occasionally pass through cement lines, and so provide a route for exchange between interstitial bone lamellae and vascular channels within osteons. Basophilic resting lines can occur in the absence of erosion; they indicate where bony growth has been interrupted and then resumed.

Trabecular bone

The organization of trabecular bone (also known as cancellous or spongy bone) is basically lamellar, as shown most clearly under polarized light (**Fig. 5.19**). Trabeculae take the form of branching bars and curved plates of varying width, length and thickness (50–400 μm) (see Fig. 5.9). They are covered in endosteal tissue because they are adjacent to marrow cavities. Thick trabeculae and regions close to compact bone may contain small osteons, but blood vessels do not otherwise lie within trabeculae; osteocytes therefore rely on canalicular diffusion from adjacent medullary vessels. In young bone, calcified cartilage may occur in the cores of trabeculae, but this is generally replaced by bone during subsequent remodelling.

Periosteum, endosteum and bone marrow

The outer surface of bone is covered by a condensed collagenous layer, the periosteum. The inner surface is lined by a thinner, more cellular endosteum. Osteoprogenitor cells, osteoblasts, osteoclasts and other cells important in the turnover and homeostasis of bone tissue lie in these layers.

The periosteum is tethered to underlying bone by thick collagen fibres (Sharpey's fibres), which penetrate deep into the outer cortical bone tissue. It is absent from articular surfaces, and from the points of insertion of tendons and ligaments (entheses) (see Fig. 5.51). The periosteum is highly active during fetal development, when it generates osteoblasts for the appositional growth of bone. These cells form a layer, 2–3 cells deep, between the fibrous periosteum and new woven bone matrix. Osteoprogenitor cells within the mature periosteum are indistinguishable morphologically from fibroblasts. Periosteum is important in the repair of fractures; where it is absent (e.g. within the joint capsule of the femoral neck) fractures are slow to heal.

Quiescent osteoblasts and osteoprogenitor cells act as the principal reservoir of new bone-forming cells for remodelling or repair on the endosteal surfaces of resting adult bone. Bone endosteum is likely to be important in calcium homeostasis because it provides a total surface area of approximately 7.5 m^2. It is formed by flattened osteoblast precursor cells and reticular (type III collagen) fibres, and lines all the internal cavities of bone, including the Haversian canals. It overlies the endosteal circumferential lamellae and encloses the medullary cavity.

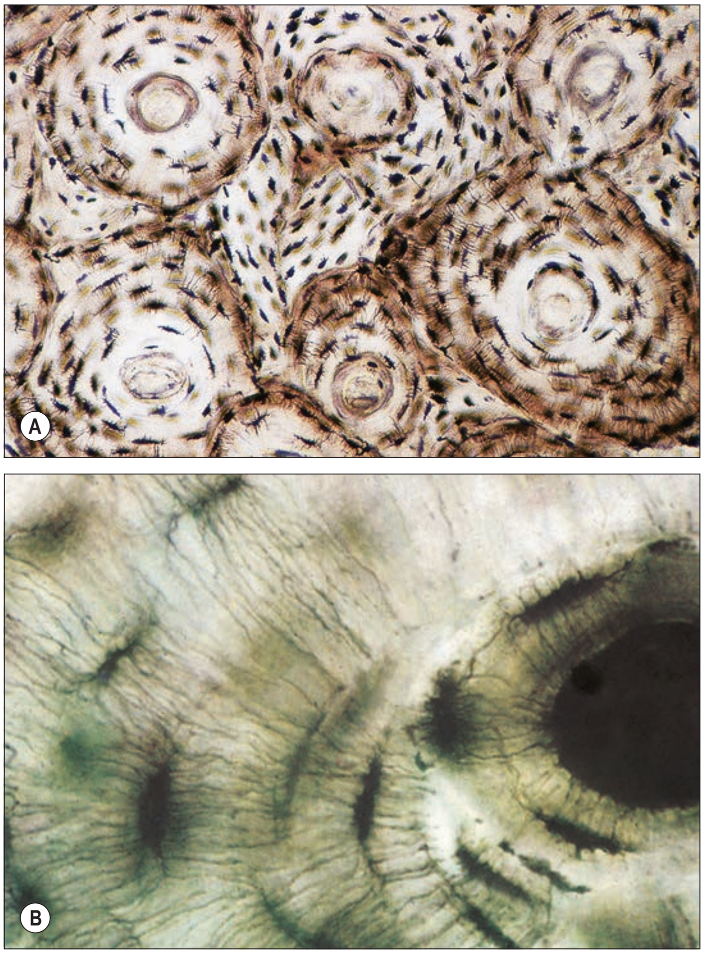

Fig. 5.17 **A**, Osteons in a dry ground transverse section of bone. Concentric lamellae surround the central Haversian canal of each complete osteon; they contain the dark lacunae of osteocytes and the canaliculi, which are occupied in life by their dendrites. These canaliculi interconnect with canaliculi of osteocytes in adjacent lamellae. Incomplete (interstitial) lamellae (e.g. centre field) are the remnants of osteons remodelled by osteoclast erosion. **B**, A high-power view of osteocytes within lamellae; a Haversian canal is seen on the right. (B, Courtesy of Sarah-Jane Smith.)

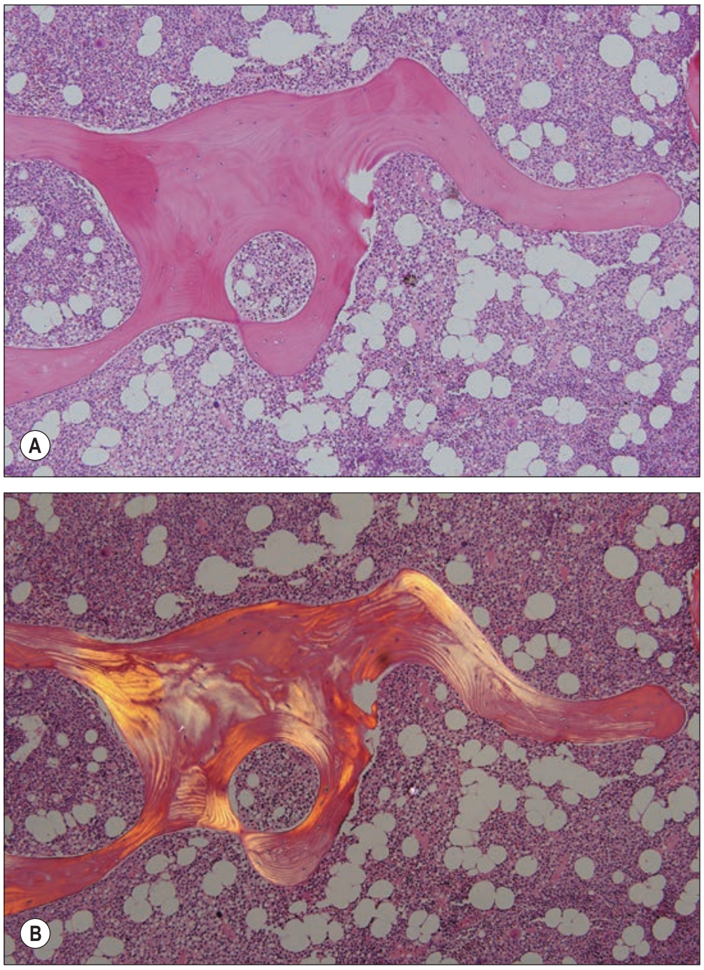

Fig. 5.19 Trabecular bone in a bone marrow sample taken from human posterior iliac crest. **A**, Irregular trabeculae of bone, surrounded by bone marrow haemopoietic and adipose tissue (haematoxylin and eosin stain). **B**, The same field viewed under polarized light, demonstrating lamellar, non-osteonic bone with lamellae orientated in different directions in different regions. Osteocytes are just visible, embedded in the solid matrix. (Courtesy of Mr Peter Helliwell and the late Dr Joseph Mathew, Department of Histopathology, Royal Cornwall Hospitals Trust, UK.)

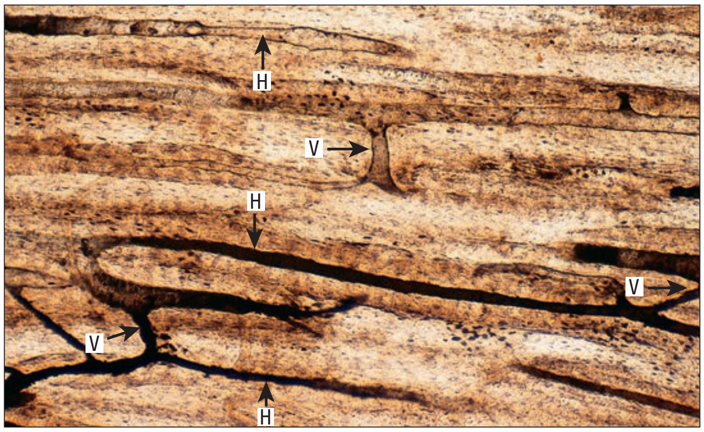

Fig. 5.18 Osteons in a dry ground longitudinal section of bone. The central Haversian canals (H; tubular structures, mainly dark) show transverse nutrient canals (Volkmann's canals, V), which form bridges between adjacent osteons and their blood vessels.

Neurovascular supply of bone

Vascular supply

The osseous circulation supplies bone tissue, marrow, perichondrium, epiphysial cartilages in young bones, and, in part, articular cartilages. The vascular supply of a long bone depends on several points of inflow that feed complex and regionally variable sinusoidal networks within the bone. The sinusoids drain to venous channels that leave through all surfaces that are not covered by articular cartilage. The flow of blood through cortical bone in the shafts of long bones is mainly centrifugal (Fig. 5.20).

One or two main diaphysial nutrient arteries enter the shaft obliquely through nutrient foramina, which lead into nutrient canals. Their sites of entry and angulation are almost constant and characteristically directed away from the dominant growing epiphysis. Nutrient arteries do not branch in their canals but divide into ascending and descending branches in the medullary cavity; these approach the epiphyses, dividing repeatedly into smaller helical branches close to the endosteal surface. The endosteal vessels are vulnerable during surgical operations, such as intramedullary nailing, which involve passing metal implants into the medullary canal. Near the epiphyses, diaphysial vessels are joined by terminal branches of numerous metaphysial and epiphysial arteries (see Fig. 5.20). The former are direct branches of neighbouring systemic vessels; the latter come from peri-articular vascular arcades formed on non-articular bone surfaces. Numerous vascular foramina penetrate bones near their ends, often at fairly specific sites; some are occupied by arteries but most contain thin-walled veins. Within bone, the arteries are unusual in consisting of endothelium with only a thin layer of supportive connective tissue. The epiphysial and metaphysial arterial supply is richer than the diaphysial supply.

Medullary arteries in the shaft give off centripetal branches, which feed a hexagonal mesh of medullary sinusoids that drain into a wide, thin-walled central venous sinus. They also possess cortical branches, which pass through endosteal canals to feed fenestrated capillaries in Haversian systems. The central sinus drains into veins that retrace the paths of nutrient arteries, sometimes piercing the shaft elsewhere as independent emissary veins. Cortical capillaries follow the pattern of Haversian canals, and are mainly longitudinal with oblique connections

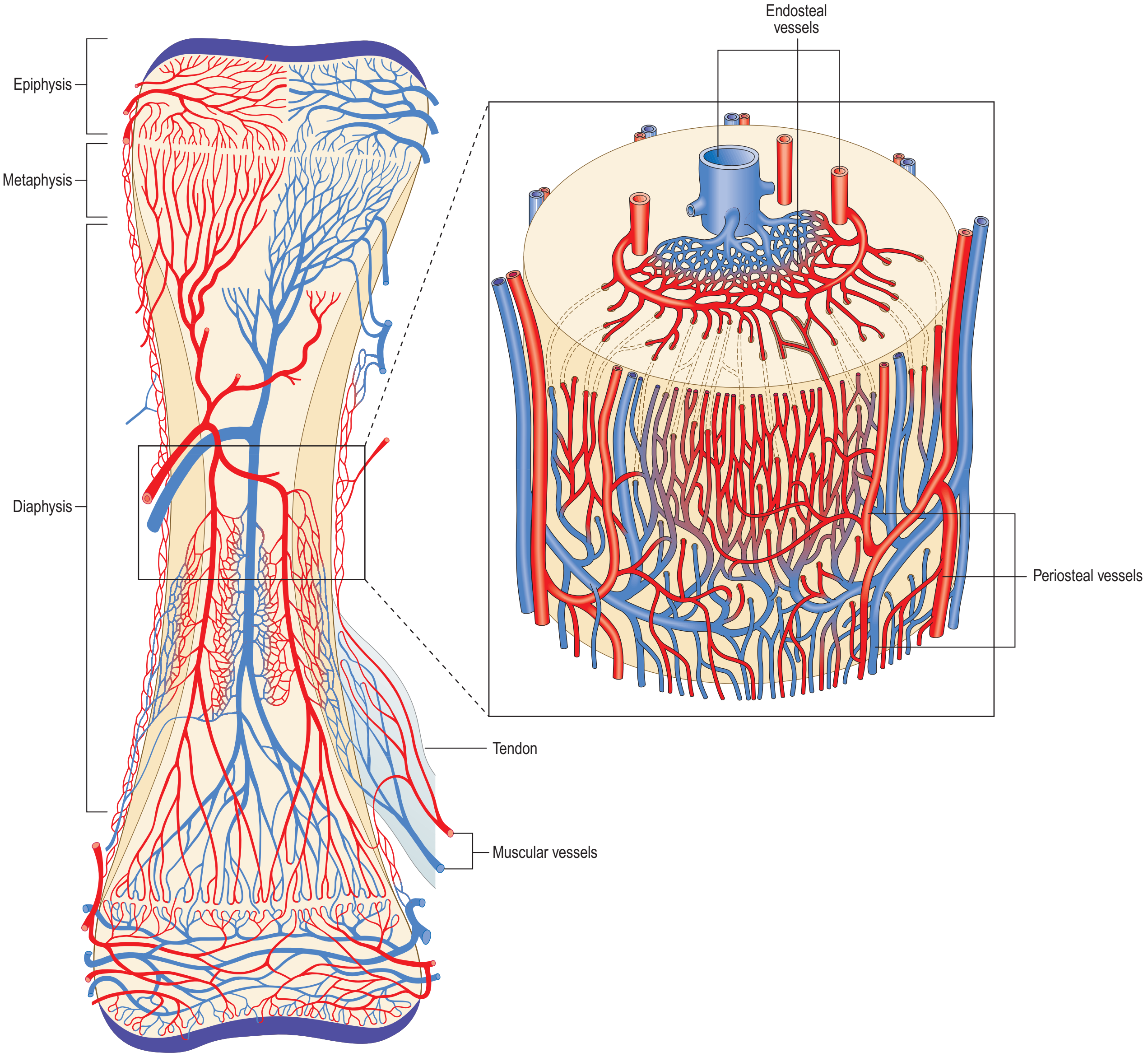

Fig. 5.20 The main features of the blood supply of a long bone. Note the contrasting supplies of the diaphysis, metaphysis and epiphysis, and their connections with periosteal, endosteal, muscular and peri-articular vessels. The expansion shows part of the diaphysis in more detail. The marrow cavity contains a large central venous sinus, a dense network of medullary sinusoids, and longitudinal medullary arteries and their circumferential rami. Longitudinally oblique transcortical capillaries emerge through minute 'cornet-shaped' foramina to become confluent with the periosteal capillaries and venules. The obliquity of the cortical capillaries is emphasized for clarity. Not to scale.

via Volkmann's canals (see Fig. 5.18). At bone surfaces, cortical capillaries make capillary and venous connections with periosteal plexuses (see Fig. 5.20) formed by arteries from neighbouring muscles that contribute vascular arcades with longitudinal links to the fibrous periosteum. A capillary network permeates the deeper, osteogenic periosteum from this external plexus. At muscular attachments, periosteal and muscular plexuses are confluent and the cortical capillaries then drain into interfascicular venules.

In addition to the centrifugal supply of cortical bone, there is an appreciable centripetal arterial flow to outer cortical zones from periosteal vessels. The large nutrient arteries of epiphyses form many intraosseous anastomoses, their branches passing towards the articular surfaces within the trabecular spaces of the bone. Near the articular cartilages, these form serial anastomotic arcades (e.g. there are three or four in the femoral head), which give off end-arterial loops. The latter often pierce the thin hypochondral compact bone to enter, and sometimes traverse, the calcified zone of articular cartilage, before returning to the epiphysial venous sinusoids.

In immature long bones, the supply is similar but the epiphysis is a discrete vascular zone. Epiphysial and metaphysial arteries enter on both sides of the growth cartilage and rarely, if ever, anastomose. Growth cartilages are probably supplied from both sources, and from an anastomotic collar in the adjoining periosteum. Occasionally, cartilage canals are incorporated into a growth plate. Metaphysial bone is nourished by terminal branches of metaphysial arteries and by primary nutrient arteries of the shaft, which form terminal blind-ended sprouts or sinusoidal loops in the zone of advancing ossification. Young periosteum is more vascular; its vessels communicate more freely with those of the shaft than their adult counterparts and give off more metaphysial branches.

Large, irregular bones such as the scapula and innominate not only receive a periosteal supply but are also often supplied by large nutrient arteries that penetrate directly into their cancellous bone, the two systems anastomosing freely. Short bones receive numerous fine vessels that supply their compact and cancellous bone and medullary cavities from the periosteum. Arteries enter vertebrae close to the base of their transverse processes (see Fig. 46.20). Each vertebral medullary cavity drains to two large basivertebral veins, which converge to a foramen on the posterior surface of the vertebral body (see Fig. 46.21). Flatter cranial bones are supplied by numerous periosteal or mucoperiosteal vessels. Large, thin-walled veins run tortuously in cancellous bone. Lymphatic vessels accompany periosteal plexuses but have not been convincingly demonstrated in bone. (For further reading on the role of the vasculature in bone development, function and regeneration, see Filipowska et al 2017).

Innervation

Nerves are most numerous in periosteum, the articular extremities of long bones, vertebrae and the larger flat bones. The nutrient blood vessels are richly innervated by postganglionic sympathetic axons. Periosteum is innervated by myelinated axons with encapsulated nerve endings and by unmyelinated axons with free endings typical of nociceptors. Many of these afferents are mechanically sensitive and respond rapidly to mechanical distortion, some can be activated by multiple stimuli and may be polymodal, and some may be stretch receptors.

Fine myelinated (Aδ) and unmyelinated (C) axons with free fibre endings accompany nutrient vessels into bone and marrow, and lie in the perivascular spaces of Haversian canals. Animal studies have revealed that many of these sensory neurones have a nociceptive phenotype, e.g. they express substance P, alpha calcitonin gene-related peptide (αCGRP), tropomyosin receptor kinase A (TrkA), and transient receptor potential cation channel subfamily V member 1 (TRPV1) and respond to noxious chemical and mechanical stimuli such as raised intraosseous pressure (Ivanusic 2017). Osteoblasts and osteoclasts possess receptors for several of the neuropeptides found in these nerves; there is increasing experimental evidence that neuropeptide-mediated signalling plays a role in modulating bone cell metabolism (Niedermair et al 2018). Pathological changes that cause the release of inflammatory mediators in bone marrow and/or raised intraosseous pressure or mechanical compression or distortion of bone and periosteum can all trigger bone pain by activating nociceptors in bone.

Development and growth of bone

Some of the bones in the skull are laid down within a fibrocellular mesenchymal membrane, by a process known as intramembranous ossification. Most bones are formed by a process of endochondral ossification, in which preformed cartilage templates (models) define their initial shapes and positions, and the cartilage is replaced by bone in an ordered sequence.

Intramembranous ossification

Intramembranous ossification is the direct formation of bone (membrane bone) within highly vascular sheets or 'membranes' of condensed primitive mesenchyme. At centres of ossification, mesenchymal stem cells differentiate into osteoprogenitor cells, which proliferate around the branches of a capillary network, forming incomplete layers of osteoblasts in contact with the primitive bone matrix. The cells are polarized, and secrete osteoid only from the surface that faces away from the blood vessels. The earliest crystals appear in association with extracellular matrix vesicles produced by the osteoblasts. Crystal formation subsequently extends into collagen fibrils in the surrounding matrix, producing an early labyrinth of woven bone, the primary spongiosa. As layers of calcifying matrix are added to the early trabeculae, osteoblasts become enclosed within primitive lacunae. These new osteocytes retain intercellular contact by means of their fine cytoplasmic processes (dendrites) and, as these elongate, matrix condenses around them to form canaliculi.

As matrix secretion and calcification proceed, trabeculae thicken and vascular spaces become narrower. Where bone remains trabecular, the process slows and the spaces between trabeculae become occupied by haemopoietic tissue. Where compact bone is forming, trabeculae continue to thicken and vascular spaces continue to narrow. Meanwhile, the collagen fibres of the matrix, secreted on the walls of the narrowing spaces between trabeculae, become organized as parallel, longitudinal or spiral bundles, and the cells they enclose occupy concentric sequential rows. These irregular, interconnected masses of compact bone each have a central canal and are called primary osteons (primary Haversian systems). They are later eroded, together with the intervening woven bone, and replaced by generations of mature (secondary) osteons.

While these changes are occurring, mesenchyme condenses on the outer surface to form a fibrovascular periosteum. Bone is laid down increasingly by new osteoblasts, which differentiate from osteoprogenitor cells in the deeper layers of the periosteum. Modelling of the growing bone is achieved by varying rates of resorption and deposition at different sites.

Endochondral ossification

The hyaline cartilage model that forms during embryogenesis is a miniature template of the bone that will subsequently develop. It becomes surrounded by a condensed, vascular mesenchyme or perichondrium, which resembles the mesenchymal 'membrane' in which intramembranous ossification occurs. Its deeper layers contain osteoprogenitor cells.

The first appearance of a centre of primary ossification (Fig. 5.21) occurs when chondroblasts deep in the centre of the primitive shaft enlarge greatly, and their cytoplasm becomes vacuolated and accumulates glycogen. The intervening matrix is compressed into thin, often perforated, septa. The cells degenerate and may die, leaving enlarged and sometimes confluent lacunae (primary areolae) whose thin walls become calcified during the final stages (Fig. 5.22). Type X collagen is produced in the hypertrophic zone of cartilage. Matrix vesicles originating

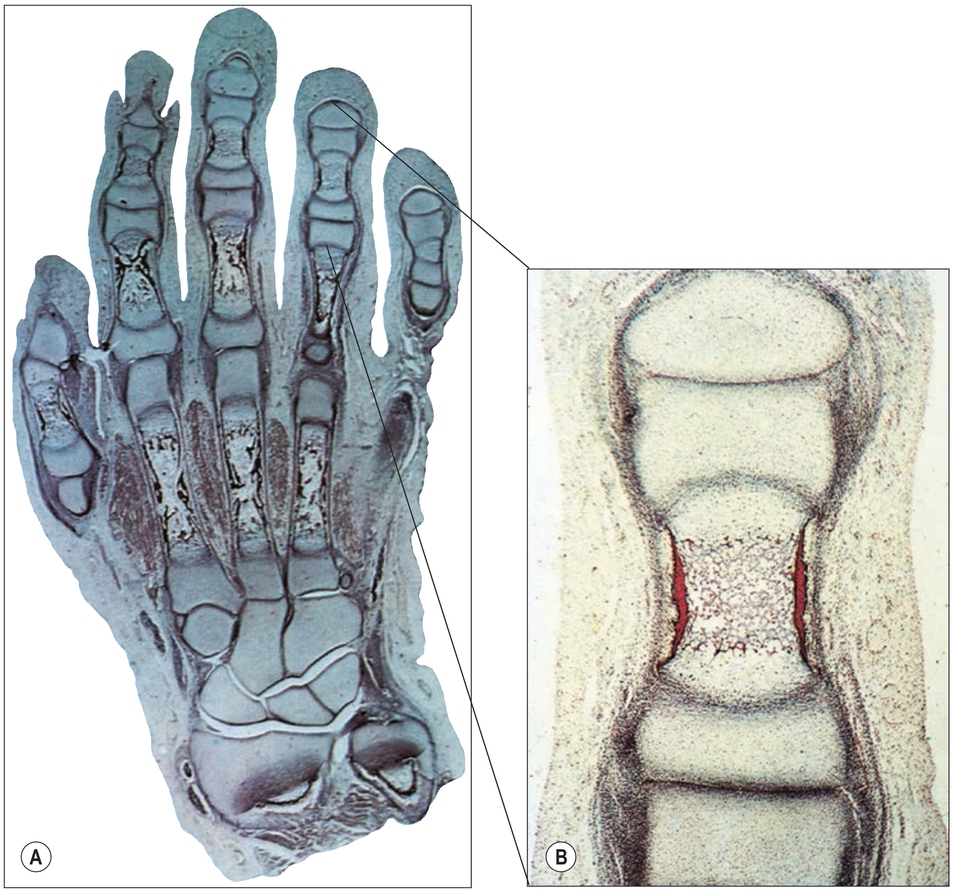

Fig. 5.21 A, A section of a human fetal hand showing cartilaginous models of the carpal bones and the primary ossification centres, which display varying stages of maturity, in the metacarpals and phalanges. Note that none of the carpal elements shows any evidence of ossification. **B,** A higher-power view of an early primary ossification centre. The cartilage cells in the shaft have hypertrophied and this region is surrounded by a delicate tube or collar of subperiosteal bone (red). (Photographed by Kevin Fitzpatrick on behalf of GKT School of Medicine, London.)

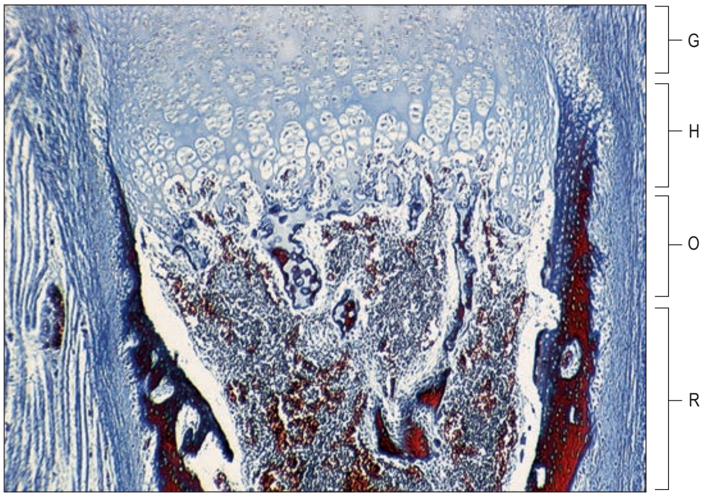

Fig. 5.22 The sequence of cellular events in endochondral ossification. This low-magnification micrograph shows the primary ossification centre in a human fetal bone. See Fig. 5.24 for further details. Abbreviations: G, growth zone; H, hypertrophic zone; O, ossification zone; R, remodelling zone.

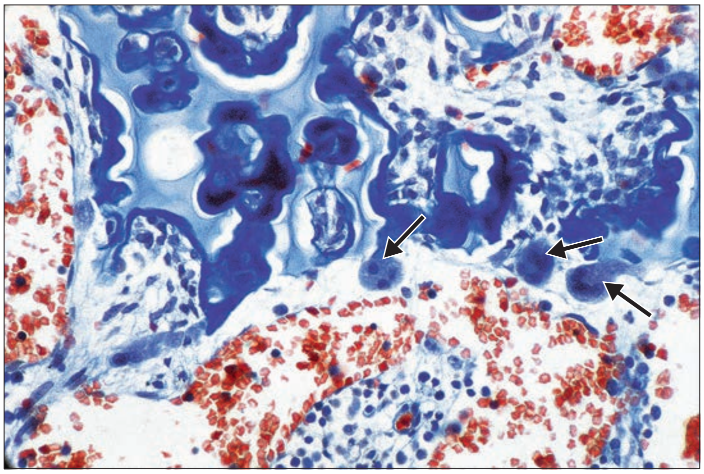

Fig. 5.24 Endochondral ossification in human fetal bone. Spicules of cartilaginous remnants (pale blue) serve as surfaces for the deposition of osteoid (dark blue), shown in the upper half of the field. Mineralized, woven bone is stained red. Three large multinucleate osteoclasts (arrows) are seen centre right, further eroding cartilage and remodelling the developing bone. Blood sinusoids and haemopoietic tissue (below) fill the spaces between areas of ossification. Heidenhain's azan trichrome preparation.

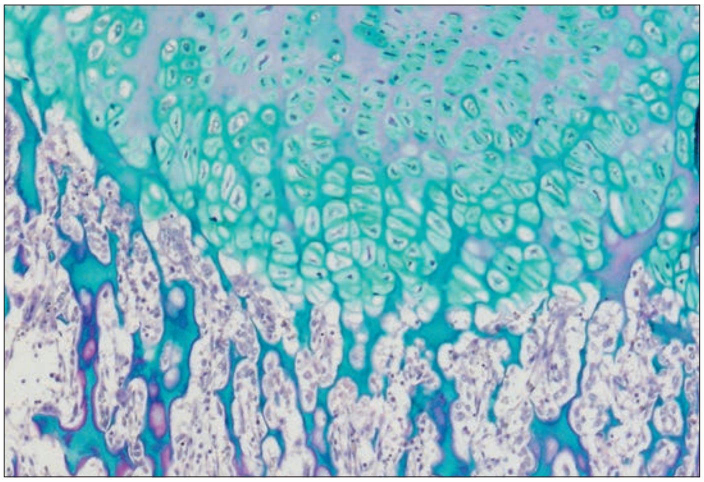

Fig. 5.23 An Alcian-blue periodic acid–Schiff (PAS)-stained section of human fetal femur showing the hypertrophy and palisading of cartilage cells as the ossifying (mineralizing) front of an early primary centre of ossification is approached (below). Lacunae are enlarged, and matrix partitions are reduced in width and exhibit increased staining density following cartilage calcification. (Courtesy of Mr Peter Helliwell and the late Dr Joseph Mathew, Department of Histopathology, Royal Cornwall Hospitals Trust, UK.)

from chondrocytes in the proliferation zone are most evident in the intercolumnar regions, where they appear to initiate crystal formation. At the same time, cells in the deep layer of perichondrium around the centre of the cartilage model differentiate into osteoblasts and form a peripheral layer of bone. Initially, this periosteal collar, formed by intramembranous ossification within the perichondrium, is a thin-walled tube that encloses and supports the central shaft (see Figs 5.21–5.22). As it increases in diameter, it also extends towards both ends of the shaft.

The periosteal collar, which overlies the calcified cartilaginous walls of degenerate chondrocyte lacunae, is invaded from the deep layers of the periosteum (formerly perichondrium) by osteogenic buds. These are blind-ended capillary sprouts that are accompanied by osteoprogenitor cells and osteoclasts. The latter excavate newly formed bone to reach adjacent calcified cartilage, where they continue to erode the walls of primary chondrocyte lacunae (**Figs 5.23–5.24**). This process leads to their fusion into larger, irregular communicating spaces, secondary areolae, which fill with embryonic medullary tissue (vascular mesenchyme, osteoblasts and osteoclasts, haemopoietic and marrow stromal cells, etc.). Osteoblasts attach themselves to the delicate residual walls of calcified cartilage and lay down osteoid, which rapidly becomes confluent, forming a continuous lining of bone. Further layers of bone are added, enclosing young osteocytes in lacunae and narrowing the perivascular spaces. Bone deposition on the more central calcified cartilage ceases as the formation of subperiosteal bone continues.

Osteoclastic erosion of the early bone spicules then creates a primitive medullary cavity in which only a few trabeculae, composed of bone with central cores of calcified cartilage (see Fig. 5.23), remain to support the developing marrow tissues. These trabeculae soon become remodelled and replaced by more mature bone or by marrow. Meanwhile, new, adjacent, cartilaginous regions undergo similar changes. Since these are most advanced centrally, and the epiphyses remain cartilaginous, the intermediate zones exhibit a temporospatial sequence of changes when viewed in longitudinal section (**Fig. 5.25**). This region of dynamic change from cartilage to bone persists until longitudinal growth of the bone ceases.

Expansion of the cartilaginous extremity (usually an epiphysis; see Fig. 5.20) keeps pace with the growth of the rest of the bone by both appositional and interstitial growth. The growth zone expands in all dimensions. Lateral growth of a developing long bone is caused by occasional transverse mitosis in its chondrocytes, and by appositional growth as a result of matrix deposition by cells from the perichondrial collar or ring at this level. The future growth plate therefore expands in concert with the shaft and adjacent future epiphysis. A zone of relatively quiescent chondrocytes (the resting zone) lies on the side of the plate closest to the epiphysis. An actively mitotic zone of cells faces towards the shaft of the bone; the more frequent divisions in the long axis of the bone soon create numerous longitudinal columns (palisades) of disc-shaped chondrocytes, each in a flattened lacuna (see Fig. 5.25). Proliferation and column formation occur in this zone of cartilage growth (the proliferative zone), and its continued longitudinal interstitial expansion provides the basic mode of elongation of a bone.

The columns of cells show increasing maturity towards the centre of the shaft, as their chondrocytes increase in size and accumulate glycogen. In the hypertrophic zone, energy metabolism is depressed at the level of the mineralizing front (see Fig. 5.23). The lacunae are now separated by transverse and longitudinal walls, and the latter are impregnated with apatite crystals in what has become the zone of calcified cartilage (or ossification zone; see Fig. 5.22). The calcified partitions enter the zone of bone formation and are invaded by vascular mesenchyme containing osteoblasts, osteoclasts, etc. The partitions, especially the transverse ones, are then partly eroded while osteoid deposition, bone formation and osteocyte enclosure occur on the surfaces of the longitudinal walls. Lysis of calcified partitions is mediated by osteoclast action, aided by cells associated with the terminal buds of vascular sinusoids that occupy, and come into close contact with, each incomplete columnar trabecular framework.

Continuing cell division in the growth zone adds to the epiphysial ends of cell columns, and the bone grows in length as this sequence of changes proceeds away from the diaphysial centre. The bone also grows in diameter as further subperiosteal bone deposition occurs near the epiphyses, and its medullary cavity enlarges transversely and longitudinally. Internal erosion and remodelling of the newly formed bone tissue continues.

Growth continues in this way for many months or years in different bones, but eventually one or more secondary centres of ossification

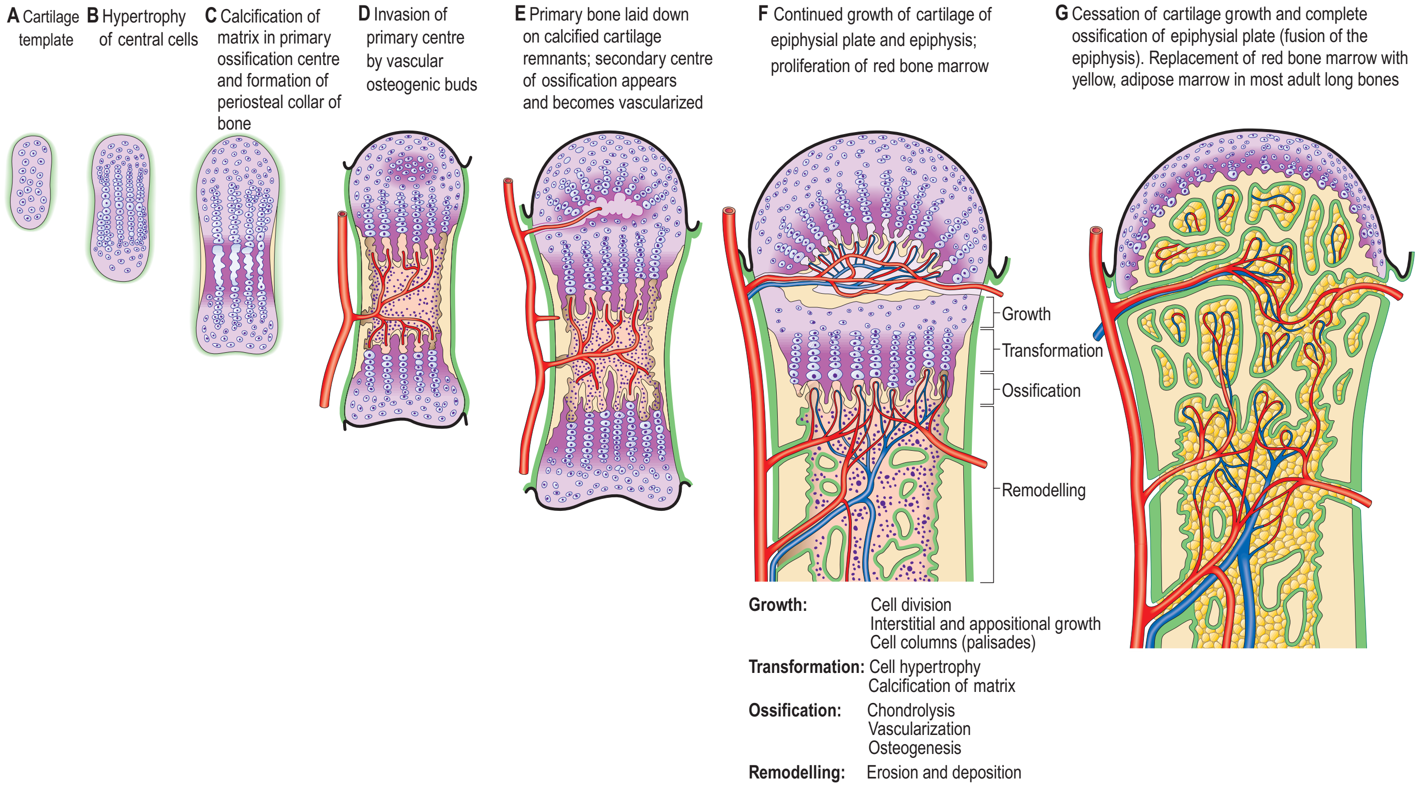
A Cartilage template
B Hypertrophy of central cells
C Calcification of matrix in primary ossification centre and formation of periosteal collar of bone
D Invasion of primary centre by vascular osteogenic buds
E Primary bone laid down on calcified cartilage remnants; secondary centre of ossification appears and becomes vascularized
F Continued growth of cartilage of epiphysial plate and epiphysis; proliferation of red bone marrow
G Cessation of cartilage growth and complete ossification of epiphysial plate (fusion of the epiphysis). Replacement of red bone marrow with yellow, adipose marrow in most adult long bones
Growth
Transformation
Ossification
Remodelling
Growth: Cell division
Interstitial and appositional growth
Cell columns (palisades)
Transformation: Cell hypertrophy
Calcification of matrix
Ossification: Chondrolysis
Vascularization
Osteogenesis
Remodelling: Erosion and deposition

Fig. 5.25 The stages of endochondral ossification in a long bone.

usually appear in the cartilaginous extremities. Initially, these epiphysial centres (or the ends of bones that lack epiphyses) do not display cell columns. Instead, isogenous cell groups hypertrophy, with matrix calcification, and are then invaded by osteogenic vascular mesenchyme, sometimes from cartilage canals. Bone is formed on calcified cartilage, as described above. As an epiphysis enlarges, its cartilaginous periphery (perichondrium) also forms a zone of proliferation in which cell columns are organized radially; hypertrophy, calcification, erosion and ossification occur at increasing depths from the surface. The early osseous epiphysis is thus surrounded by a superficial growth cartilage, and the growth plate adjacent to the metaphysis soon becomes the most active region.

As a bone reaches maturity, epiphysial and metaphysial ossification processes gradually encroach upon the cartilaginous growth plate from either side; when they meet, bony fusion of the epiphysis occurs and longitudinal growth of the bone ceases. The events that take place during fusion are broadly as follows. As growth ceases, the cartilaginous plate becomes quiescent and gradually thins; proliferation, palisading and hypertrophy of chondrocytes stop, and the cells form short, irregular, conical masses. Patchy calcification is accompanied by resorption of calcified cartilage and some of the adjacent metaphysial bone, forming resorption channels that are invaded by vascular mesenchyme.

Some endothelial sprouts pierce the thin plate of cartilage, and the metaphysial and epiphysial vessels unite. Ossification around these vessels spreads into the intervening zones and results in fusion of epiphysis and metaphysis. This bone is visible in radiographs as a radiodense epiphysial line (a term that is also used to describe the level of the perichondrial collar or ring around the growth cartilage of immature bones, or the surface junction between epiphysis and metaphysis in a mature bone). In smaller epiphyses, which unite earlier, there is usually one initial eccentric area of fusion, and thinning of the residual cartilaginous plate. The original sites of fusion are subsequently resorbed and replaced by new bone. Medullary tissue extends into the whole cartilaginous plate until union is complete and no epiphysial 'scar' persists. In larger epiphyses, which unite later, similar processes also involve multiple perforations in growth plates, and islands of epiphysial bone often persist as epiphysial scars. Calcified cartilage coated by bone forms the epiphysial scar, and is also found below articular cartilage. It has been called metaplastic bone, a term also applied to sites of attachments of tendons, ligaments and other dense connective tissues to bone.

The cartilaginous surfaces of epiphyses that form synovial joints remain unossified, but the typical sequence of cartilaginous zones persists in them throughout life. A similar developmental sequence occurs at synchondroses, except that the proliferative rates of chondrocytes and the replacement of cartilage by bone are similar, although not identical, on either side of the synchondrosis.

Postnatal growth and maintenance of bone

Modelling, by which is meant changes in general shape, occurs in all growing bones. The process has been studied mainly in cranial and long bones with expanded extremities.

During calvarial growth, a bone such as the parietal thickens and expands, but also decreases in curvature. Accretion continues at its edges by proliferation of osteoprogenitor cells at sutures; periosteal bone is mainly added externally and eroded internally, but not at uniform rates or at all times. The rate of formation increases with radial distance from the centre of ossification (in this case, the future parietal eminence). Bone formation may also occur endocranially as well as ectocranially, so changing the curvature of the bone. The relative positions of the original centres of ossification change in three dimensions as the skull bones thicken and grow at the sutures and as the calvaria (vault) of the skull expands to accommodate the growth of the brain. Development of the outer and inner cortical plates is accompanied by internal development of trabeculae and marrow spaces.

Long bones increase in length mainly by endochondral ossification at the epiphysial growth plates. Simultaneous increase in width occurs by subperiosteal deposition and endosteal erosion. Growth at different locations can occur at different rates, or even be replaced by resorption, resulting in a change in the shape of a bone. This explains how, for example, the tibia changes its cross-sectional shape from tubular to triangular. Similarly, the waisted contours of metaphyses are preserved by differential rates of periosteal erosion and endosteal deposition, as metaphysial bone becomes diaphysial in position. The junction between a field of resorption and one of deposition on the surface of a growing bone is called a surface reversal line. The relative position of such a line may remain stable over long periods of growth and shape change.

Lamellar bone forms and is remodelled at variable rates throughout adult life (see below).

Normal development and maintenance of bone requires adequate intake and absorption of calcium, phosphorus and vitamins A, C and D, and a balance between growth hormone (GH, somatotropin), thyroid hormones, oestrogens and androgens. Other biological influences include prostaglandins and glucocorticoids. Vigorous mechanical loading is important for the maintenance of adequate bone mass. Prolonged deficiency in any of these factors can lead to loss of bone tissue (osteopaenia); if bone loss is severe (osteoporosis), it can lead to fracture and deformity.

Vitamin D influences intestinal transport of calcium and phosphate, and therefore affects circulatory calcium levels. In adults, prolonged deficiency (with or without low intake) produces bones that contain regions of deformable, uncalcified osteoid (osteomalacia). During growth, vitamin D deficiency can lead to severe disturbance of growth cartilages and ossification, such as reductions of regular columnar organization in growth plates, and failure of cartilage calcification even though chondrocytes proliferate. Growth plates also become thicker and irregular, as exemplified in classic rickets or juvenile osteomalacia. In rickets, the uncalcified or poorly calcified cartilaginous trabeculae are only partially eroded; osteoblasts secrete layers of osteoid but these fail to ossify in the metaphysial region, and ultimately gravity deforms these softened bones.

Vitamin C is essential for the adequate synthesis of collagen and matrix proteoglycans in connective tissues. When vitamin C is deficient, growth plates become thin, ossification almost stops, and metaphysial trabeculae and cortical bone are reduced in thickness, causing fragility and delayed healing of fractures.

Vitamin A is necessary for normal growth and for a correct balance between deposition and removal of bone. Deficiency retards growth as a result of the failure of internal erosion and remodelling, particularly in the cranial base. Foramina are narrowed, sometimes causing pressure atrophy of the nerves that pass through them. The cranial cavity and spinal canal may fail to expand at the same rate as the developing central nervous system, impairing nervous function. Conversely, excess vitamin A stimulates vascular erosion of growth cartilages, which become thin or totally lost, and longitudinal growth ceases. Retinoic acid, a vitamin A derivative, is involved in pattern formation in limb buds and in the differentiation of osteoblasts.

Balanced endocrine functions are also essential to normal bone maturation, and disturbances in this balance may have profound effects. In addition to its role in calcium metabolism, excess parathyroid hormone (primary hyperparathyroidism) stimulates unchecked osteoclastic erosion of bone, particularly subperiosteally and later endosteally (osteitis fibrosa cystica). Growth hormone (GH) is required for normal interstitial proliferation in growth cartilages, ensuring normal increase in stature. Termination of normal growth is imperfectly understood, but may involve a fall in hormone production or in the sensitivity of chondroblasts to insulin-like growth factors regulated by GH. Reduction of GH production in the young leads to quiescence and thinning of growth plates and hence pituitary dwarfism. Conversely, continued hypersecretion in the immature leads to gigantism, and in the adult results in thickening of bones by subperiosteal deposition; the mandible, hands and feet are the most affected, a condition known as acromegaly.

While continued longitudinal growth of bones depends on adequate levels of GH, effective remodelling to achieve a mature shape also requires the action of thyroid hormones. Moreover, growth and skeletal maturity are closely related to endocrine activities of the ovaries, testes and suprarenal cortices. High oestrogen levels increase deposition of endosteal and trabecular bone; conversely, osteoporosis in postmenopausal women reflects reduced ovarian function. In men, fluctuations in the rate of growth, and the timing of skeletal maturation, depend on circulating levels of suprarenal and testicular androgens. In hypogonadism, growth-plate fusion is delayed and the limbs therefore elongate excessively; conversely, in hypergonadism, premature fusion of the epiphyses results in diminished stature.

Bone remodelling

Stiff materials (including bone) are vulnerable to the accumulation of microdamage during repeated loading. In metals this can result in crack propagation and 'fatigue failure'. Bone reduces the risk of such failure by periodically renewing itself, one small region of tissue at a time. This process is referred to as 'remodelling' because the volume and orientation of newly replaced matrix are not necessarily the same as the old; instead, bone takes this opportunity to adapt its mass and architecture to prevailing mechanical demands. Remodelling affects the local balance between resorption and deposition of bone. Its primary purpose is to renew bone rather than increase its mass, and the process continues throughout life, replacing approximately 10% of bone each year in adults (Brandi 2009).

Internal remodelling continuously supplies young osteons with labile calcium reserves, and provides a malleable bony architecture that is responsive to changing patterns of stress. A bone-remodelling unit consists of an advancing cutting cone and a closing cone. Activated osteoclasts form a cutting cone that excavates a cylindrical tunnel of bone (resorption canal) and advances ahead of a central growing blood vessel at a rate of 50 µm/day. A cutting cone is typically 2 mm long and takes 1–3 months to form; a similar period is required to create the new (secondary) osteon by completing the closing cone (**Fig. 5.26**). Osteoblasts follow the osteoclasts, filling in the space created with new osteoid, starting at the peripheral surface or walls of the tunnel. Successive layers of bone are deposited on the surface of the previous layer as cohorts of osteoblasts become embedded (as osteocytes) in the matrix they secrete, until the most central lamella is close to the blood vessel at the axis of the cylinder. The 'closing cone' (see Fig. 5.26) may contain 4000 osteoblasts per mm^2. In this way, the walls of resorption canals are lined with new lamellar matrix and the vascular channels are progressively narrowed. A hypermineralized basophilic cement (or growth-reversal) line marks the edge of a new osteon, indicating the border between the resorptive activity of the cutting cone and the bony matrix not remodelled by this activity. Remnants of the circumferential lamellae of old osteons form interstitial lamellae between newer osteons (see Fig. 5.17A).

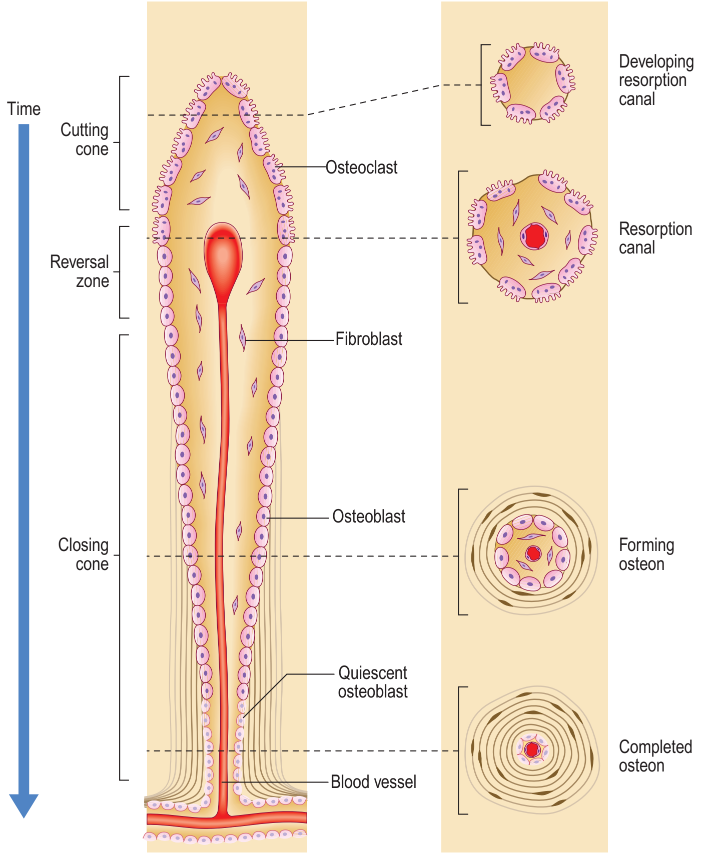

Fig. 5.26 Bone remodelling. Longitudinal and cross-sections of a time line illustrating the formation of an osteon. Osteoclasts cut a cylindrical channel through bone. Osteoblasts follow, laying down bone on the surface of the channel until matrix surrounds the central blood vessel of the newly formed osteon (closing cone of a new osteon).

The remodelling unit in cancellous bone, equivalent to the secondary osteon of compact bone, is the basic (or bony) structural unit; it has an average thickness of 40–70 µm and an average length of 100 µm, but may be more extensive and irregular in shape. Separate structural units can sometimes be visualized in microradiographs because of differences in their age and extent of mineralization (Farlay et al 2005).

Adult bone shape and mass are partly determined by genetic inheritance (Sigurdsson et al 2008). However, the pattern and extent of remodelling are largely dictated by the mechanical loading applied to the bone. Bone resorption occurs when muscle or gravitational forces are reduced, as occurs in bed rest, or in zero gravity conditions in space (Shackelford et al 2004). Reduced activity in old age is another major cause of bone loss. The rate of remodelling decreases with age, which means that numbers of osteons and osteon fragments can be used to estimate the age of skeletal material at death. Conversely, increased sporting or occupational loading of the skeleton can cause bone hypertrophy, as exemplified by the 35% increase in cortical thickness in the racket arm of elite tennis players (Jones et al 1977). Bones appear to respond to the maximum deformation they experience (see Fig. 5.68), rather than to cumulative load. Bone subjected to constant pressure can actually resorb, a response that underpins much orthodontic treatment, because teeth can be made to migrate slowly through alveolar bone by the application of steady lateral or medial pressure.

Growth of individual bones

Ossification centres appear over a long period during bone growth: many in embryonic life, some in prenatal life, and others well into the postnatal growing period. Ossification centres are initially microscopic

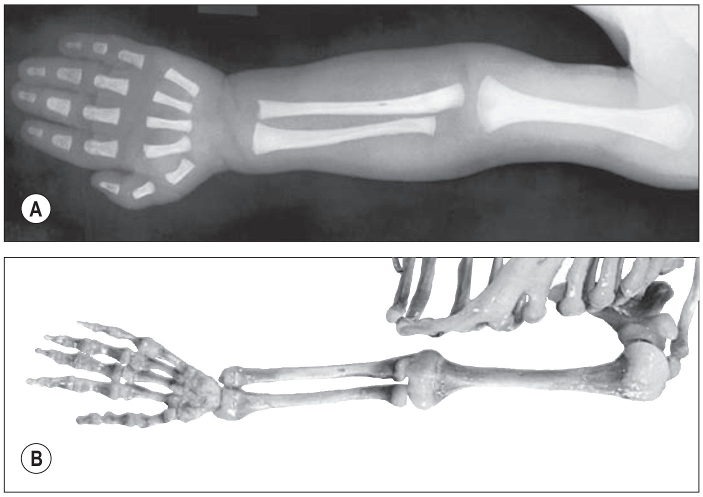

Fig. 5.27 **A**, A radiograph of a neonatal arm. Ossification from primary centres is well advanced in all of the limb bones except the carpals, which are still wholly cartilaginous. The gaps by which individual elements appear to be separated are filled by radiolucent hyaline cartilage, in which epiphysial or carpal ossification will subsequently occur. Note the flaring contours, narrow midshaft and relatively expanded metaphyses of the long bones, and the proportions of the limb segments – in particular, the relatively large hand – that are characteristic of this age. **B**, The bones and cartilages of a neonatal left arm. Compare the radiolucent areas in the radiograph (**A**) with the preserved cartilaginous epiphyses and carpal elements in this specimen. (B, Prepared by Michael C.E. Hutchinson; photographed by Kevin Fitzpatrick on behalf of GKT School of Medicine, London.)

but soon become macroscopic, which means that their growth can then be followed by radiological and other scanning techniques.

Some bones, including carpal, tarsal, lacrimal, nasal and zygomatic bones, inferior nasal conchae and auditory ossicles, ossify from a single centre, which may appear between the eighth intrauterine week and the tenth year: a wide interval for studying growth or estimating age. Most bones ossify from several centres, one of which appears in the centre of the future bone in late embryonic or early fetal life (seventh week to fourth month). Ossification progresses from the centres towards the ends, which are still cartilaginous at birth (Fig. 5.27). These terminal regions ossify from separate centres, which are sometimes multiple, and which appear between birth and the late teens; they are therefore secondary to the earlier primary centre from which much of the bone ossifies. This is the pattern in long bones, as well as in some shorter bones such as the metacarpals and metatarsals, and in the ribs and clavicles.

At birth, a bone such as the tibia is typically ossified throughout its diaphysis from a primary centre that appears in the seventh intrauterine week, whereas its cartilaginous epiphyses ossify from secondary centres. As the epiphyses enlarge, almost all the cartilage is replaced by bone, except for a specialized layer of articular (hyaline) cartilage that persists at the joint surface, and a thicker zone between the diaphysis and epiphysis. Persistence of this epiphysial growth plate, or growth cartilage, allows increase in bone length until the usual dimensions are reached, by which time the epiphysial plate has ossified. The bone has then reached maturity. Coalescence of the epiphysis and diaphysis is fusion, the amalgamation of separate osseous units into one.

Many long bones have epiphyses at both their proximal and their distal extremities, whereas metacarpals, metatarsals and phalanges have only one epiphysis. Typical ribs have epiphyses for the head and articular tubercle and another for the non-articular area. The costal cartilages represent the unossified hyaline cartilage of the developing rib and therefore do not display epiphyses. Epiphysial ossification is sometimes complex, e.g. the proximal end of the humerus is wholly cartilaginous at birth, subsequently developing three centres during childhood that coalesce into a single mass before they fuse with the diaphysis. Only one of these centres forms an articular surface, and the others form the greater and lesser tubercles, to which muscles are attached. Similar composite epiphyses occur at the distal end of the humerus and in the femur, ribs and vertebrae.

Many cranial bones ossify from multiple centres. The sphenoid, temporal and occipital bones are almost certainly composites of multiple elements in their evolutionary history;: some show evidence of fusion between membrane and cartilage bones that unite during growth.

If bone growth rate were uniform, ossification centres would appear in a strict descending order of bone size. However, disparate rates of ossification occur at different sites and do not appear to be related to bone size. The appearance of primary centres for bones of such different sizes as the phalanges and femora are separated by, at most, a week of embryonic life. Those for carpal and tarsal bones show some correlation between size and order of ossification, from largest (calcaneus in the fifth fetal month) to smallest (pisiform in the ninth to twelfth postnatal year). In individual bones, succession of centres is related to the volume of bone that each centre produces. The largest epiphyses, e.g. the adjacent ends of the femur and tibia, are the earliest to begin to ossify (immediately before or after birth) and are of forensic interest. At epiphysial plates, the rate of growth is initially equal at both ends of those bones that possess two epiphyses. However, experimental observations in other species have revealed that one epiphysis usually grows faster than the other after birth. Since the faster-growing end also usually fuses later with the diaphysis, its contribution to length is greater. Though faster rate has not been measured directly in human bones, later fusion has been documented radiologically. The more active end of a long limb bone is often termed the growing end but this is a misnomer.

The rate of increase in stature, which is rapid in infancy and again at puberty, demonstrates that rates of growth at epiphyses vary. The spurt at puberty, or slightly before, decreases as epiphyses fuse in post-adolescent years.

Growth cartilages do not grow uniformly at all points, which presumably accounts for changes such as the alteration in angle between the humeral shaft and its neck. The junctions between epiphysis and diaphysis at growth plates are not uniformly flat on either surface. Osseous surfaces usually become reciprocally curved by differential growth, and the epiphysis forms a shallow cup over the convex end of the shaft, with cartilage intervening – an arrangement that may resist shearing forces at this relatively weak region. Reciprocity of bone surfaces is augmented by small nodules and ridges, as can be seen when the surfaces are stripped of cartilage. These adaptations emphasize the formation of many immature bones from several elements held together by epiphysial cartilages. Most human bones exhibit these complex junctions, at which bone is bonded to bone through cartilage, throughout the active years of childhood and adolescence.

Forces at growth cartilages are largely compressive but with an element of shear. Interference with epiphysial growth may occur as a result of trauma but more frequently follows disease; the resulting changes in trabecular patterns of bone are visible radiographically as dense transverse lines of arrested growth (Harris's growth lines). Several such lines may appear in the limb bones of children afflicted by successive illnesses.

Variation in skeletal development occurs between individuals, sexes and possibly also races. The timing rather than the sequence of events varies, and females antedate males in all groups studied. Differences that are perhaps insignificant before birth may be as great as two years in adolescence.

JOINTS

Joints are the regions of the skeleton where two or more bones meet and articulate. These junctions are supported by a variety of soft tissue structures, and their prime functions are either to facilitate growth or to allow movement between bones. The simplest classifications of joints relate to either the range of movement possible or the nature of the intervening soft tissues; there is no satisfactory single classification. Free movement occurs at synovial joints, whereas restricted movement occurs at synarthroses, which can be subdivided into fibrous and cartilaginous joints. The general characteristics of each type of joint will be considered next. Features that are specific to individual joints are discussed in the relevant topographical chapters.

Fibrous joints

Bones in fibrous joints are joined by fibrous connective tissue that allows little movement. Three definable subtypes are sutures, gomphoses and syndesmoses (Fig. 5.28).

Suture

Sutures are restricted to the skull (see Chapter 34 for descriptions of individual sutures). In a suture, the two bones are separated by a layer of membrane-derived connective tissue. The sutural aspect of each bone is covered by a layer of osteogenic cells (cambial layer) overlaid by a capsular lamella of fibrous tissue that is continuous with the periosteum on both

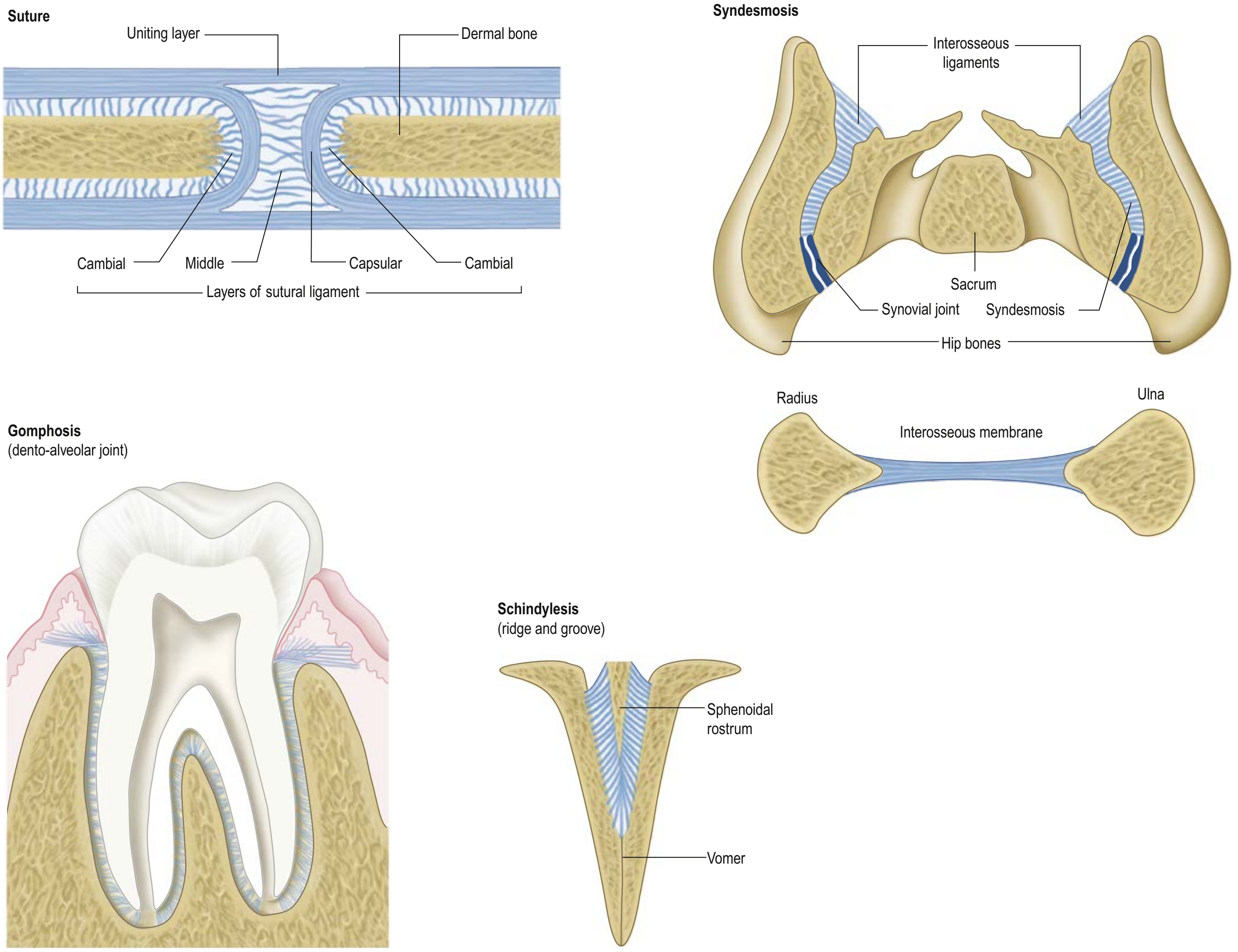

Fig. 5.28 Examples of the principal varieties of fibrous joints, each shown in section.

the endo- and ectocranial surfaces. The region between the capsular coverings contains loose fibrous connective tissue and decreases with age, so that the osteogenic surfaces become apposed. On completion of growth, many sutures synostose and are obliterated. Synostosis occurs normally as the skull ages; it can begin in the early twenties and continues into advanced age. A schindylesis is a specialized suture in which a ridged bone fits into a groove on a neighbouring element, e.g. where the cleft between the alae of the vomer receives the rostrum of the sphenoid (see Fig. 5.28).

Gomphosis

A gomphosis is a peg-and-socket junction between a tooth and its socket, where the two components are maintained in intimate contact by the collagen of the periodontium connecting the dental cement to the alveolar bone. Strictly speaking, a gomphosis is not an articulation between two skeletal structures.

Syndesmosis

A syndesmosis is a truly fibrous connection between bones. It may be represented by an interosseous ligament (e.g. the interosseous membrane between the radial and ulnar shafts), a slender fibrous cord, or a denser fibrous membrane (e.g. the posterior region of the sacroiliac joint: see Fig. 5.28).

Cartilaginous joints

Cartilaginous joints may be classified as primary (synchondrosis) or secondary (symphysis), depending on the nature of the intervening cartilage. While the distinction between fibrous and cartilaginous joints is usually clear, some degree of admixture can occur in which either a predominantly fibrous articulation contains occasional islands of cartilage, or a predominantly cartilaginous articulation contains aligned dense bundles of collagen. These joints tend to be less rigid than the fibrous articulations and some permit restricted movement (**Figs 5.29–5.30**).

Primary cartilaginous joints

Primary cartilaginous joints or synchondroses occur where advancing centres of ossification remain separated by an area of hyaline (but non-articular) cartilage (**Fig. 5.29A**). They are present in all postcranial bones that form from more than one centre of ossification. Since hyaline cartilage retains the capability to ossify with age, synchondroses tend to synostose when growth is complete. Primary cartilaginous joints are almost exclusively associated with growth plates (see above).

Secondary cartilaginous joints

Secondary cartilaginous joints, or symphyses, are largely defined by the presence of an intervening pad or disc of fibrocartilage interposed between the articular (hyaline) cartilage that covers the ends of two articulating bones (**Fig. 5.29B**). Intervertebral discs are prime examples. The pad or disc varies from a few millimetres to over a centimetre in thickness, and the whole region is generally bound by strong, tightly adherent, dense connective tissues. Collagenous ligaments extend from the periostea of the articulating bones across the symphysis. The ligaments blend with the hyaline and fibrocartilaginous perichondria but do not form a complete capsule. They contain plexuses of afferent nerve terminals, which also penetrate the periphery of the fibrocartilage. The combined strength of the ligaments and fibrocartilage can exceed that of the associated bones. A symphysis is designed to withstand a range of stresses (compression, tension, shear, bending and torsion) but the range of movement is generally limited, both by the physical nature of the articulation and by adjacent bones. Tears are

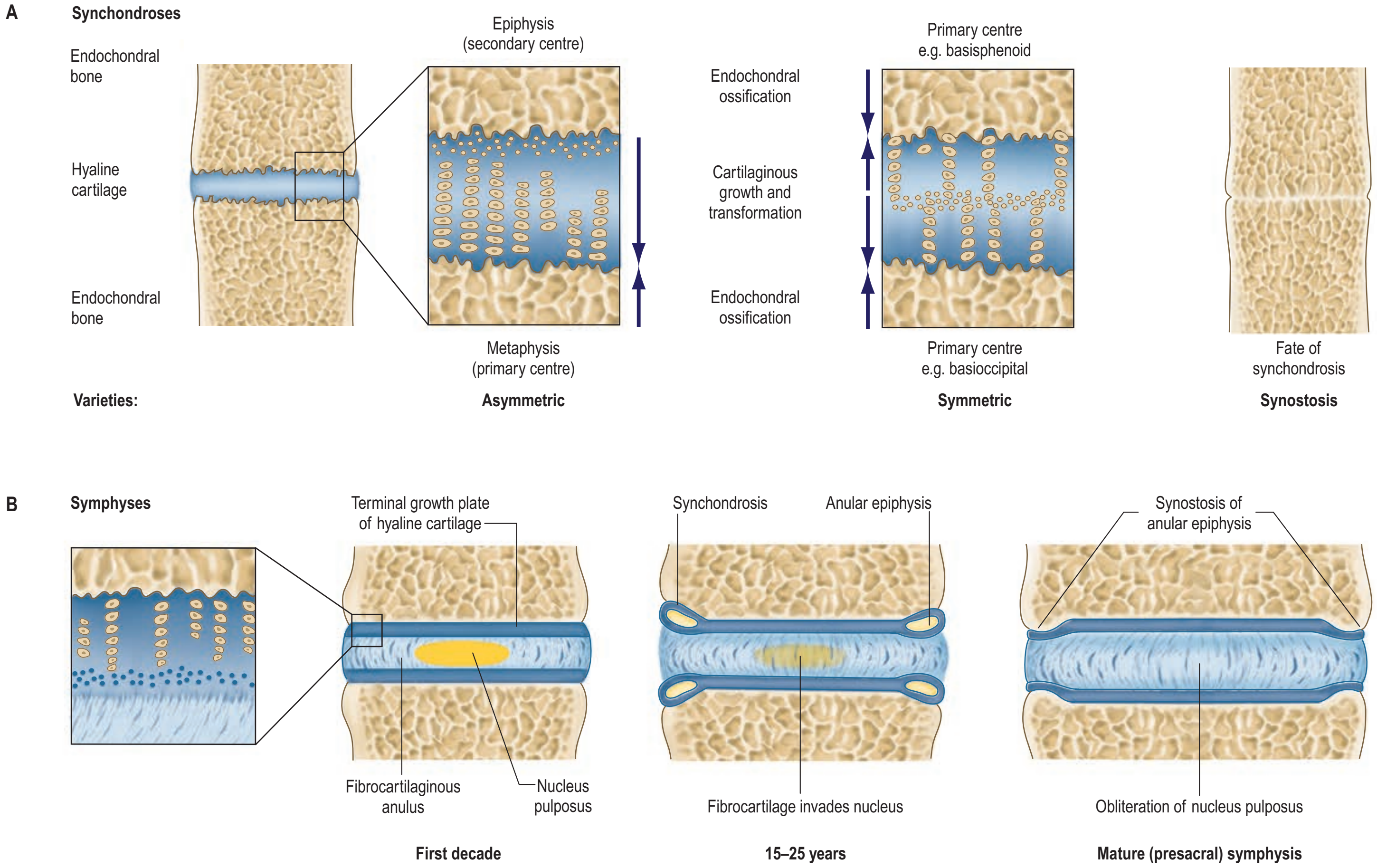
A
Synchondroses
Endochondral bone
Hyaline cartilage
Endochondral bone
Epiphysis (secondary centre)
Metaphysis (primary centre)
Endochondral ossification
Cartilaginous growth and transformation
Endochondral ossification
Primary centre e.g. basisphenoid
Primary centre e.g. basioccipital
Fate of synchondrosis
Varieties:
Asymmetric
Symmetric
Synostosis
B
Symphyses
Terminal growth plate of hyaline cartilage
Fibrocartilaginous anulus
Nucleus pulposus
Synchondrosis
Anular epiphysis
Fibrocartilage invades nucleus
Synostosis of anular epiphysis
Obliteration of nucleus pulposus
First decade
15–25 years
Mature (presacral) symphysis

Fig. 5.29 Examples of varieties of cartilaginous joints (see also Fig. 5.30). **A**, A sectional view of the principal tissues involved, more detailed architecture and main growth patterns of symmetric and asymmetric synchondroses. Lesser degrees of asymmetry occur in some locations. Synostosis is the normal fate of almost all synchondroses when endochondral growth has ceased. **B**, Intervertebral symphyses (presacral), shown in section, displaying age-related changes. Partial or complete synostosis is the normal fate of sacral and coccygeal symphyses.

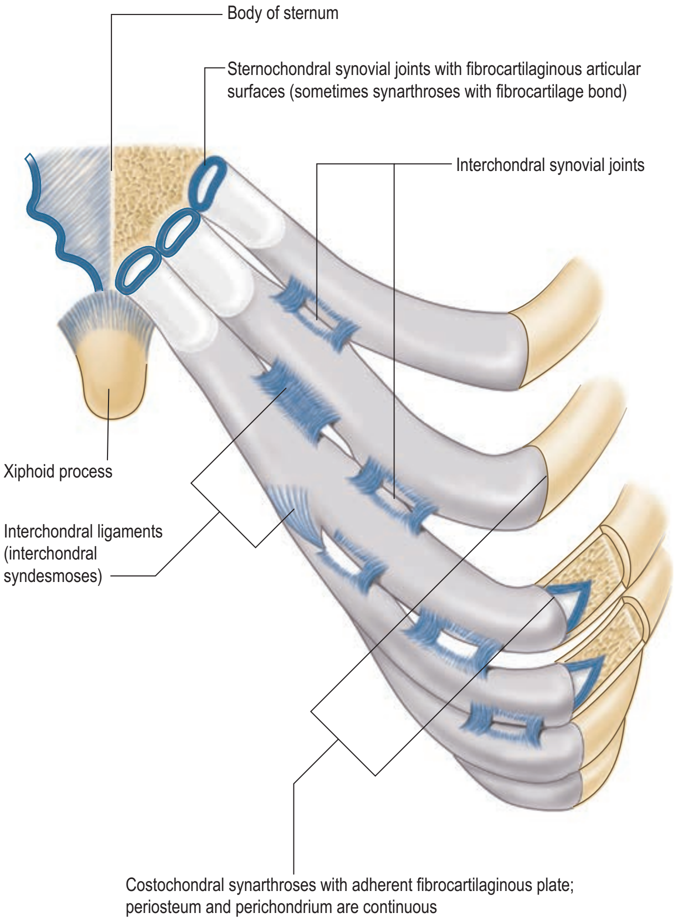
Body of sternum
Sternochondral synovial joints with fibrocartilaginous articular surfaces (sometimes synarthroses with fibrocartilage bond)
Interchondral synovial joints
Xiphoid process
Interchondral ligaments (interchondral syndesmoses)
Costochondral synarthroses with adherent fibrocartilaginous plate; periosteum and perichondrium are continuous

Fig. 5.30 Less common interchondral and osseochondral junctions: see text for other locations. General periosteum and perichondrium omitted.

usually the result of sudden stresses that occur when the body is in an inappropriate posture.

All symphyses occur in the midline (mandibular, manubriosternal, pubic and intervertebral) and all except the mandibular symphysis occur in the postcranial skeleton and resist synostosis. The mandibular symphysis (symphysis menti) is histologically different from the other symphyses; however, the widespread use of this descriptive term ensures that it remains, perhaps inappropriately, within this category.

The concept that synchondroses are temporary and concerned with growth, whereas symphyses are permanent and concerned with movement, is an oversimplification and only partly correct. Both types of joint must be strong, both are sites at which growth occurs, and both contribute either directly or indirectly to the total movement patterns of the parts involved. Movements that occur at a symphysis often depend on more than the mechanical properties of the fibrocartilaginous pad or disc, e.g. movements between vertebrae depend not only on the deformability of the intervertebral disc but also on the morphology of the apophysial joints and the properties of associated ligaments (Adams et al 2013).

The prominent role of synchondroses in skeletal growth is widely recognized, whereas growth of symphyses has received less attention. Symphysial growth may, for convenience, be considered from two interrelated aspects: namely, intrinsic growth of the fibrocartilaginous disc, and growth of the hyaline cartilaginous plates into which endochondral ossification progresses.

Synovial joints

These are freely moving joints in which the articulating bony surfaces are covered in smooth (hyaline) articular cartilage and separated by a film of viscous synovial fluid that serves as a lubricant (Fig. 5.31). Joint stability is provided by a fibrous capsule (which usually has intrinsic ligamentous thickenings), and often by internal or external accessory ligaments. Synovial fluid, which also aids metabolite transport to cells in the articular cartilages, is synthesized by the synovial membrane that lines the joint capsule.

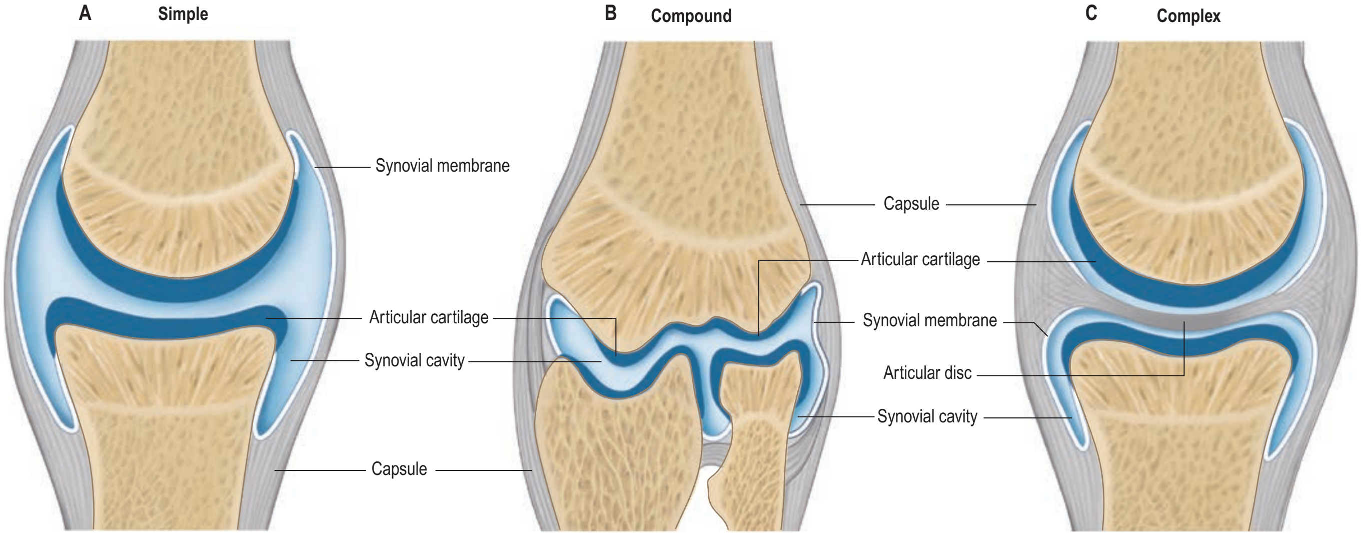

Fig. 5.31 Synovial joints, some main structural features and one elementary type of classification: **A**, simple; **B**, compound; **C**, complex joints. For clarity, the articular surfaces are artificially separated. **A** and **C** are purely diagrammatic and not related to particular joints; **B**, however, is a simplified representation of some features of an elbow joint: the complicated contours due to the olecranon, coronoid and radial fossae, and profiles of articular fat pads have been omitted for clarity.

Articular surfaces

Articular cartilage comprises a specialized type of hyaline cartilage, reflecting its origin as part of the cartilaginous 'model' of bone in embryonic life. Exceptions include the sternoclavicular, acromioclavicular and temporomandibular joints, where articulating surfaces are covered by dense fibrous tissue containing isolated groups of chondrocytes with little proteoglycan in their surrounding matrix, presumably reflecting their formation by intramembranous ossification.

The deformability of articular cartilage enables opposing cartilage surfaces to flatten slightly at their area of contact, increasing contact area and decreasing contact stress (see Fig. 5.57). This load-distributing property of articular cartilage depends on the congruence of opposing joint surfaces (see Fig. 5.61). Slight undulations in the surface trap synovial fluid so that fluid-film lubrication is possible under most circumstances; effectively, the bones 'aqua-plane' on each other (Fig. 5.60). This ensures very low friction and, consequently, low wear of the cartilage.

The most superficial layer of articular cartilage, directly adjacent to the synovial fluid, is acellular and approximately 3 μm thick. It contains fine collagen fibrils running parallel to the surface, and functions as an elastic and protective 'skin' for the underlying layers. It can appear to recoil under tension when damaged.

The acellular surface layer is coated with a large glycoprotein, lubricin, which projects from the surface so that a hydrophobic region of the molecule lies in the joint space, where it repels its counterpart on the opposing articular surface. In this way, lubricin acts in the manner of a lubricant such as grease to reduce friction and wear of the surfaces. This 'boundary lubrication' mechanism becomes important when the fluid film has been squeezed out, e.g. after sustained forceful loading of the joint, and loss of lubricin can lead to cartilage degeneration (Waller et al 2013). Transmission electron microscopy shows this lubricant layer as an interrupted electron-dense surface coat 0.03–0.1 μm thick. Synovial fluid and membranous debris, the product of chondrocytic necrosis, may contribute to this surface coat, which is transient in nature. A 'lamina splendens' is sometimes identified as a bright line at the free surface of articular cartilage when oblique sections are examined by negative phase contrast microscopy: it may be a microscopical artefact at the border between regions of different refractive index, rather than an anatomically distinct surface layer. Deeper zones of articular cartilage are described on p. 87.

With advancing age, undulations on the articular surfaces deepen and develop minute, ragged projections, perhaps as a consequence of wear and tear. These changes occur extremely slowly in healthy joints, but can be accelerated in pathologically 'dry' joints, or where synovial fluid viscosity is altered, or following injury.

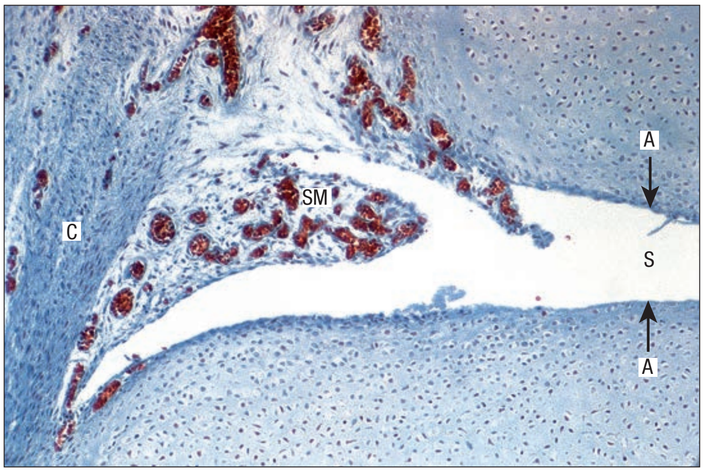

Fig. 5.32 A section of a synovial joint and its associated highly vascular synovial membrane in a human fetal hand. The two articular cartilage surfaces (A, arrows) are separated on the right by a layer of synovial fluid (S) secreted by the synovial membrane (SM), which extends a short distance into the joint space from the capsule (C).

Fibrous capsule

A fibrous capsule completely encloses each synovial joint except where it is interrupted by synovial protrusions (see descriptions of individual joints for details). It is composed of interlacing bundles of parallel fibres of collagen type I, and is attached continuously round the ends of the articulating bones. In small bones this attachment is usually near the periphery of the articular surfaces, but in long bones it varies considerably, and part or all of the attachment may be a significant distance from the articular surface. The joint capsule is perforated by vessels and nerves, and may contain apertures through which synovial membrane protrudes as bursae.

A fibrous capsule usually exhibits local thickenings of parallel bundles of collagen fibres, called capsular (intrinsic) ligaments, and named by their attachments. Some capsules are reinforced or replaced by tendons of nearby muscles, or expansions from them. Accessory ligaments are distinct structures that may be located inside or outside the joint capsule. All ligaments, although stiff in tension, are pliant in bending. They can rebound elastically from being stretched by up to 10–15%, and are protected from injury by reflex contraction of appropriate muscles. They do little to resist normal movements but become taut at the end of each normal range of movement.

Synovial membrane

Synovial membrane lines the fibrous joint capsule and exposed osseous surfaces, intracapsular ligaments, bursae and tendon sheaths (**Fig. 5.32**). It does not cover intra-articular discs or menisci, and stops at the margins of articular cartilages in a transitional zone that occupies the peripheral few millimetres of cartilage. Where a tendon is attached to bone inside a synovial joint, an extension of the synovial membrane usually accompanies it beyond the capsule. Some extracapsular tendons are separated from the capsule by a synovial bursa that is continuous with the interior of the joint. All of these protrusions are potential routes for the spread of infection into joints.

Synovial membrane secretes and absorbs a fluid that lubricates the movement between the articulating surfaces.

Pink, smooth and shining, the internal synovial surface displays a few small synovial villi that increase in size and number with age. Folds and fringes of membrane may also project into a joint cavity; some are sufficiently constant to be named, e.g. the alar folds and ligamentum mucosum of the knee. Synovial villi are more numerous near articular margins and on the surfaces of folds and fringes, and become prominent in some pathological states.

Accumulations of adipose tissue (articular fat pads) occur within the synovial membrane in many joints. These pads, together with synovial folds and fringes, are deformable cushions that occupy potential spaces and irregularities in joints that are not wholly filled by synovial fluid. During movement they accommodate to the changing shape and volume of the irregularities, a function they share with intra-articular discs and menisci. They also increase the area of synovial membrane, and may help to spread synovial fluid over the articular surfaces.

Synovial membrane consists of a highly cellular intimal layer resting on a fibrous and vascular subintimal layer (subsynovial tissue). The subintima is often composed of loose, irregular connective tissue, but also contains organized collagen and elastin fibres lying parallel to the membrane surface, interspersed with occasional fibroblasts, macrophages, mast cells and fat cells. The elastic component may prevent formation of redundant folds during joint movement. Subintimal adipose cells form compact lobules surrounded by highly vascular fibroelastic interlobular septa that provide firmness and compressive turgor.

The intimal layer consists of pleomorphic synovial cells embedded in a granular, amorphous matrix. In normal human joints, synovial cells form an interlacing, discontinuous layer, 1–3 cells and 20–40 µm thick, between the subintima and the joint cavity. They are not separated from the subintima by a basal lamina, and are distinguished from subintimal cells only because they associate to form a superficial layer. In many locations, but particularly over loose subintimal tissue, areas are commonly found that are free from synovial cells. The synovial cells over fibrous subintimal tissue may be flattened and closely packed, forming endothelium-like sheets. Human synovial cells are generally elliptical, with numerous cytoplasmic processes. Neighbouring cells are often separated by gaps, but their processes may interdigitate where they lie close together. There is considerable regional variation in cell morphology and numbers.

There are at least two morphologically distinct populations of synovial cells or synoviocytes: type A macrophage-like synoviocytes (MLS) and type B fibroblast-like synoviocytes (FLS) (Iwanaga et al 2000). The phenotype of type A synoviocytes is similar to that of other tissue resident macrophage populations: morphologically they are characterized by surface ruffles or lamellipodia, plasma membrane invaginations and associated pinocytotic vesicles, a prominent Golgi apparatus but little rough endoplasmic reticulum. They probably synthesize and release lytic enzymes and phagocytose joint debris from synovial fluid. Type B synoviocytes, which predominate, resemble fibroblasts and have abundant rough endoplasmic reticulum but fewer vacuoles and vesicles, and a less ruffled plasma membrane than type A synoviocytes. They probably synthesize some of the hyaluronan of synovial fluid, the boundary lubricant lubricin, and inhibitors of the degradative enzymes synthesized by type A cells, limiting their potential to damage joint tissues. Synoviocytes do not divide actively in normal synovial membranes, but may do so in response to trauma and haemarthrosis. Under such conditions, type B synoviocytes divide *in situ*, while the population of type A cells increases by immigration of bone marrow-derived precursors. FLS and MLS play essential roles in the joint pathology of rheumatoid arthritis (Tu et al 2018).

Synovial fluid

Synovial fluid occupies synovial joints, bursae and tendon sheaths. In synovial joints it is clear or pale yellow, viscous and slightly alkaline at rest (the pH lowers during activity), and contains a small mixed population of cells and metachromatic amorphous particles. Fluid volume is low: usually less than 0.5 ml can be aspirated from a large joint such as the knee.

The composition of synovial fluid is consistent with it being mainly a transudate of blood plasma: it contains protein (approximately 0.9 mg/100 ml) derived from the blood. It also contains hyaluronan, which is thought to be a significant determinant of its viscoelastic and thixotropic (flow rate-dependent) properties. Approximately 2% of synovial fluid protein differs from plasma protein and is probably produced by type B synoviocytes. Approximately one-quarter of this appears to be a specialized lubricating glycoprotein, lubricin. Synovial fluid contains a few cells (approximately 60 per ml in resting human joints), including monocytes, lymphocytes, macrophages, synovial intimal cells and polymorphonuclear leukocytes; higher counts are found in young individuals. The amorphous metachromatic particles and fragments of cells and fibrous tissue found in synovial fluid are presumed to be the by-products of wear and tear.

Intra-articular menisci, discs and fat pads

An articular disc or meniscus can occur between articular surfaces where congruity (conformity of opposing articular surfaces) is low. The term meniscus should be reserved for incomplete discs, like those in the knee joint and, occasionally, in the acromioclavicular joint. Complete discs, such as those in the sternoclavicular and inferior radio-ulnar joints, extend across a synovial joint, and so divide it structurally into two synovial cavities; they often have small perforations. The disc in the temporomandibular joint may be complete or incomplete (Ch. 38).

The main part of a disc is relatively acellular, but the surface may be covered by an incomplete stratum of flat cells, continuous at the periphery with adjacent synovial membrane. Discs are usually connected to their fibrous capsule by vascularized connective tissue, so that they become invaded by blood vessels and afferent and vasomotor postganglionic sympathetic nerves. The union between disc and capsule can be close and strong, as occurs in the knee and temporomandibular joints. Discs and menisci are composed of fibrocartilage containing crimped type I collagen fibres, and are not covered by synovial membrane.

The functions of intra-articular fibrocartilages are uncertain. Evidence from structural or phylogenetic data, aided by mechanical analogies, suggests that their functions include the improvement of fit between articulating surfaces; deployment of weight over larger surface areas; shock absorption; facilitation of combined movements; limitation of translational (gliding) movements at joints such as the knee; protection of articular margins; facilitation of rolling movements; and spread of lubricant. The temporomandibular disc has attracted particular attention because of its exceptional, perhaps unique, design and biomechanical properties.

The functions of labra and fat pads, two other quite common types of intra-articular structure, are also uncertain. A labrum is a fibrocartilaginous anular lip, usually triangular in cross-section, attached to an articular margin such as the glenoid fossa or acetabulum. It deepens the socket and increases the area of contact between articulating surfaces, and may act as a lubricant spreader. Unlike menisci, labra are not compressed between articular surfaces. Small fibrous labra have been described along the ventral or dorsal margins of the zygapophysial joints at lumbar levels, as have meniscus-shaped fibroadipose meniscoids at the superior or inferior poles of the same joints. Fat pads are soft and change shape to fill joint recesses that vary in dimension according to joint position.

Vascular supply and lymphatic drainage

Numerous branches from peri-articular arterial plexuses pierce the fibrous capsules to form subsynovial vascular plexuses. Some synovial vessels end near articular margins in an anastomotic fringe, the circulus articularis vasculosus. A lymphatic plexus in the synovial subintima drains along blood vessels to the regional deep lymph nodes.

Articular cartilage, intra-articular menisci and cartilaginous discs are all avascular, presumably because high mechanical pressures in these deformable tissues would collapse any blood vessels inside them. Laboratory experiments show that proteoglycans inhibit vascular growth, so the high concentration of proteoglycans in the cartilaginous tissues of joints may help to exclude blood vessels. Injury and disease can alter both the mechanical and chemical environment within cartilage, and may allow revascularization in peripheral and disrupted regions. The blood supply to subchondral bone is described on p. 95.

Innervation

A movable joint is innervated by articular branches of the nerves that supply the muscles acting on the joint and that also supply the skin covering the joint (Hilton's law). Although there is overlap between the territories of different nerves, each nerve innervates a specific part of the capsule. The region made taut by muscular contraction is usually innervated by nerves that supply the antagonists. For example, during abduction, stretching the portion of the capsule of the hip joint supplied by the obturator nerve elicits reflex contraction of the adductors that is usually sufficient to prevent damage.

Myelinated axons in articular nerves innervate Ruffini endings, lamellated articular corpuscles, and structures resembling Golgi tendon organs. Ruffini endings respond to stretch and adapt slowly, whereas lamellated corpuscles respond to rapid movement and vibration, and adapt rapidly; both types of receptor register the speed and direction of movement. Golgi tendon organs, innervated by the largest myelinated axons (10–15 μm diameter), are slow to adapt; they mediate position sense and also are concerned in stereognosis, i.e. recognition of shape of held objects. Simple endings are numerous at the attachments of capsules and ligaments, and are thought to be the terminals of unmyelinated and thinly myelinated nociceptive axons (see p. 62 for an account of sensory receptors).

Many unmyelinated postganglionic sympathetic axons terminate near vascular smooth muscle, and are presumably either vasomotor or vasosensory. The nerve endings in synovial membrane are believed to supply blood vessels exclusively, from which it is assumed that synovial membrane is normally relatively insensitive to pain.

Cartilaginous structures within joints normally have no nerve supply, partly because they are avascular and partly because axonal growth is inhibited by a high concentration of proteoglycans. However, when fibrocartilage is injured or diseased, nerves can accompany the consequent ingrowth of blood vessels (Lama et al 2018) and may give rise to pain. Subchondral bone is normally innervated and is a likely source of pain in the spine (Wang et al 2012).

Classification

Synovial joints can be classified according to their shape (Fig. 5.33). While this has some practical value, it should be remembered that they are merely variations, sometimes extreme, of basic forms. Articular surfaces are never truly flat, or complete spheres, cylinders, cones or ellipsoids.

Plane joints

Plane joints, such as intermetatarsal and some intercarpal joints, have almost flat surfaces. Slight curvature is often disregarded, although it is usual, and movements are considered to be pure translations (sliding) between bones.

Hinge joints

Movement takes place about a single stationary axis, and so is largely restricted to one plane. Examples are the interphalangeal and humero-ulnar joints. However, the surfaces of biological hinges are not truly cylindrical, and actual motion can occur in more than one plane. Hinge joints possess strong collateral ligaments.

Bicondylar joints are predominantly uniaxial hinge joints, but the presence of two condyles side by side allows limited rotation about a second axis orthogonal to the first. These joints are formed from two convex condyles that articulate with concave or flat surfaces. The condyles may lie within a common fibrous capsule (as in the knee), or in separate capsules that necessarily cooperate in all movements as a condylar pair (as in the temporomandibular joints).

Pivot joints

These are uniaxial joints in which an osseous pivot inside an osteoligamentous ring allows rotation (twisting) only around the axis of the pivot. Pivots may rotate in rings (e.g. the head of the radius rotates within the anular ligament and ulnar radial notch), or rings may rotate around pivots (e.g. the atlas rotates around the dens of the axis).

Ellipsoid joints

Ellipsoid joints are biaxial, and consist of an oval, convex surface that is apposed to an elliptical concavity. Examples are the radiocarpal and

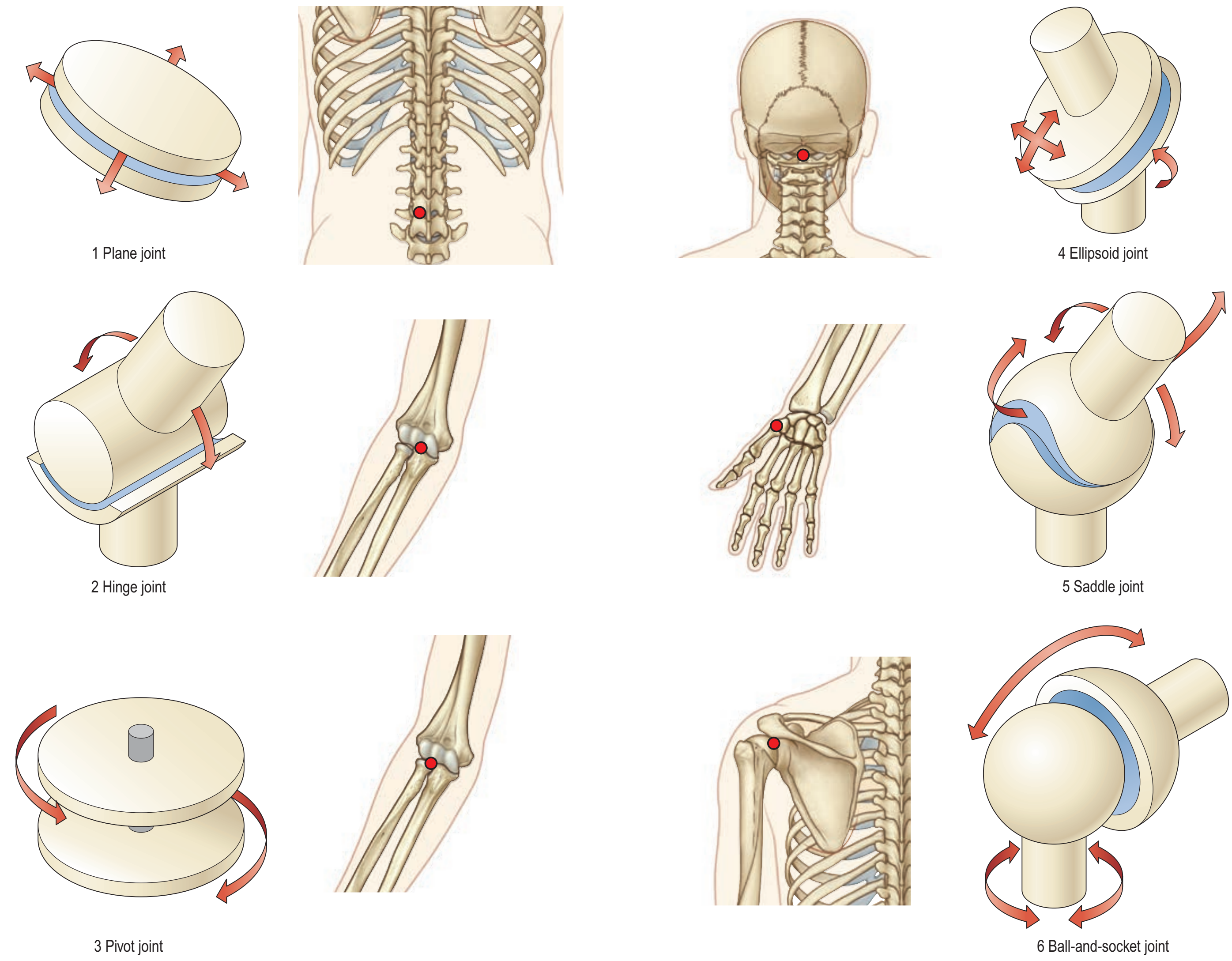
1 Plane joint
4 Ellipsoid joint
2 Hinge joint
5 Saddle joint
3 Pivot joint
6 Ball-and-socket joint

Fig. 5.33 Types of synovial joint, with selected examples.

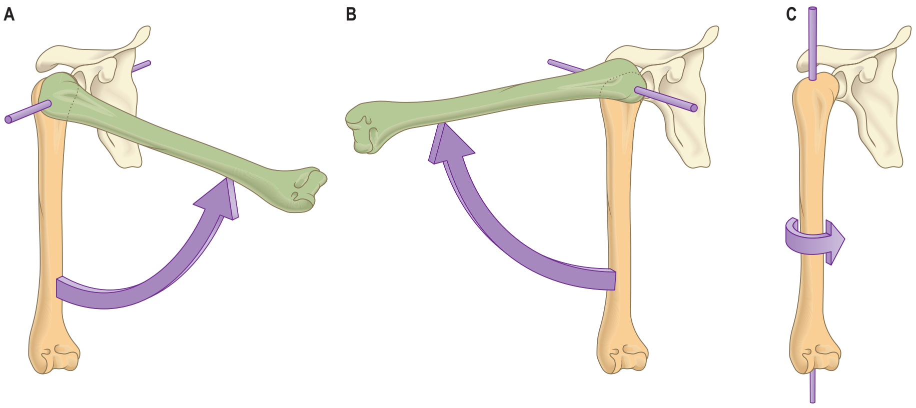

Fig. 5.34 The shoulder joint is multiaxial and possesses three degrees of freedom. The three mutually perpendicular axes are shown, around which the principal movements of flexion–extension (**A**), abduction–adduction (**B**) and medial and lateral rotation (**C**) occur. Note that these axes are referred to the plane of the scapula and not to the coronal and sagittal planes of the erect body. Although an infinite variety of additional movements may occur at such a joint, e.g. movements involving intermediate planes or combinations, they can always be resolved mathematically into components related to the three axes illustrated.

metacarpophalangeal joints. Primary movements such as flexion–extension and abduction–adduction occur around two orthogonal axes and may be combined as circumduction. Rotation around the third axis is largely prevented by general articular shape.

Saddle joints

Saddle joints are biaxial joints in which the articular surfaces have both concave and convex regions. Each surface is maximally convex in one direction and maximally concave in another, at right-angles to the first. The convexity of the larger surface is apposed to the concavity of the smaller surface and vice versa. Primary movements occur in two orthogonal planes but articular shape also causes axial rotation of the moving bone. Such 'coupled' rotation is never independent, and can be functionally significant in habitual positioning and limitation of movement. The most familiar saddle joint is the carpometacarpal joint of the thumb; other examples include the ankle and calcaneocuboid joints.

Ball-and-socket joints

These multiaxial joints are formed by a globoid 'head' articulating with an opposing cup. Prime examples are the hip and shoulder joints. Although their surfaces resemble parts of spheres, they are not strictly spherical but slightly ovoid, and consequently congruence is not perfect in most positions: it occurs in only one position, at the end of the most common movement.

Factors influencing movement

Movements at synovial joints depend on a number of factors, including the complexity and number of articulating surfaces, and the number and position of the principal axes of movement.

Complexity of form

Most synovial joints are simple articulations between two articular surfaces. A joint with more than two articular surfaces is called a compound joint, e.g. the knee and the elbow (see Fig. 5.31). In all compound joints, articulating territories remain distinct. A synovial joint that contains an intra-articular disc or meniscus is called a complex joint, e.g. the tibiofemoral joint of the knee, and the temporomandibular joint.

Degrees of freedom

Joint motion can be described by rotation and translation about three orthogonal axes. There are three possible rotations (axial, abduction–adduction, flexion–extension) and three possible translations (proximodistal, mediolateral, anteroposterior). Each is a degree of freedom. For most joints, translations are small and can be neglected (Fig. 5.34). A few joints have minor but pure translatory movements, but most joint motion is by rotation.

When movement is practically limited to rotation about one axis (e.g. the elbow), a joint is termed uniaxial and has one degree of freedom. If independent movements can occur around two axes (e.g. flexion–extension and axial rotation in the knee), the joint is biaxial and has two degrees of freedom. Since there are three axes for independent rotation, joints may have up to three degrees of freedom. Even though a true 'ball-and-socket' joint can rotate about many chosen axes, for each position there is a maximum of three orthogonal planes, which means that it can have, as a maximum, three degrees of freedom.

For a uniaxial hinge joint with a single degree of freedom, a single unchanging axis of rotation would be predicted. However, the complex shapes of joint surfaces can lead to a variable radius of curvature (Fig. 5.35), and consequently a variable axis of rotation, as joint movement progresses. If the variation is minor, as in the elbow, it is often appropriate to describe a mean position for the axis. Motion in one direction is often linked to motion in another. Coupled (or conjunct) movements occur as an integral and inevitable accompaniment of the main movement. Adjunct movements can occur independently and may or may not accompany the principal movement.

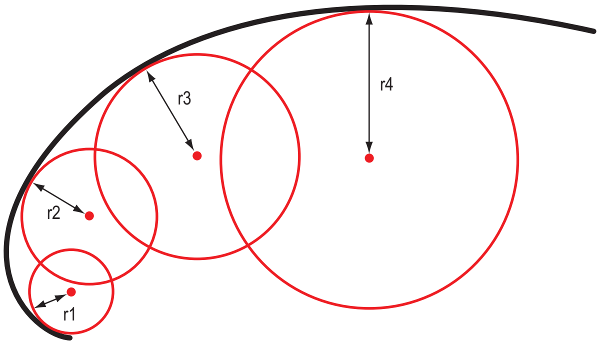

Fig. 5.35 A profile of a section through an ovoid surface showing that it may be considered as a series of segments of circles of changing radius. The radius of curvature of joint surfaces often changes from one location to another.

Types of joint movement

Joint surfaces usually move by a combination of translation (gliding) and angulation (rotation). Where movements are slight, the reciprocal surfaces are of similar size, but where they are substantial, the bone that is habitually more mobile has the larger articular surface.

Translation

Translation is the simplest motion and involves gliding or sliding without appreciable angulation. Although frequently combined with other movements, it is often considered the only motion permitted in some carpal and tarsal articulations. However, cineradiography reveals that considerable angulation occurs during movements of the small carpal and tarsal bones.

Flexion

Flexion is an example of angulation, where there is a change in angle between the topographical axes of the articulating bones. Although a widely used term, flexion is difficult to define. It often means approximation of two ventral surfaces around a transverse axis. However, the thumb is almost at right angles to the fingers: its 'dorsal' surface faces laterally so that flexion and extension at its joints occur around anteroposterior axes. At the shoulder, flexion is referred to an oblique axis through the centre of the humeral head in the plane of the scapular body, the arm moving anteromedially forwards and hence nearer to the ventral aspect of the trunk. At the hip, which has a transverse axis, flexion brings the morphologically dorsal (but topographically ventral) surface of the thigh to the ventral aspect of the trunk. Description of flexion at the ankle joint is complicated by the fact that the foot is set at a right-angle to the leg. Elevation of the foot diminishes this angle and is usually termed flexion, but because it involves the approximation of two dorsal surfaces it might equally be called extension. Since the terms 'dorsal' and 'plantar' are used to denote the superior and inferior surfaces, respectively, of the foot, dorsiflexion and plantar flexion are the terms used to describe ankle movements.

Abduction and adduction

Abduction and adduction occur around anteroposterior axes except at the first carpometacarpal and shoulder joints. The terms generally imply lateral or medial angulation, except in digits, where arbitrary planes are chosen (midlines of the middle digit of the hand and second digit of the foot), because these are least mobile in this respect. Abduction of the thumb occurs around a transverse axis and away from the palm. Similarly, abduction of the humerus on the scapula occurs in the scapular plane around an oblique axis at right-angles to it.

Axial rotation

Axial rotation is a widely, but often imprecisely, used term. Its restricted sense denotes movement around some notional 'longitudinal' axis, which may even be in a separate bone, e.g. the dens of the second cervical vertebra, on which the atlas rotates. An axis may approximate to the centre of the shaft of a long bone, as in medial and lateral humeral rotation (see Fig. 5.34). Alternatively, the axis may be at an angle to the topographical axis of a bone, as in movement of the radius on the ulna in pronation and supination, where the axis joins the centre of the radial head to the base of the ulnar styloid process. In these examples, rotations can be independent adjunct motions, constituting a degree of freedom, or obligatory (coupled) rotations, which always accompany some other main movement as a consequence of articular geometry.

Circumduction

Circumduction combines successive flexion, abduction, extension and adduction, and occurs when the distal end of a long bone circumscribes the base of a cone that has its apex at the joint in question. Examples are circular movements of the hand and foot about the shoulder and hip joints, respectively.

Development of joints

The development of joints is described in the context of limb development on page 305.

MUSCLE

Most cells possess cytoskeletal elements that are capable of lengthening or shortening and so enable the cell to change its shape. This capacity is important in a variety of cellular functions, including locomotion, phagocytosis and mitosis. Slow movements can be effected by polymerization–depolymerization mechanisms involving actin and tubulin, but much faster and more forceful movements can be created by the so-called 'motor proteins', which use energy from the hydrolysis of adenosine 5′-triphosphate (ATP). Of these ATP-dependent systems, one of the most widespread is based on the interaction of the motor protein myosin with actin.

In muscle cells the filaments of actin, myosin and other associated proteins are so abundant that they almost fill the interior of the cell. Moreover, they align predominantly in one direction, so that interactions at the molecular level are translated into forceful linear contraction of the whole cell. The ability of these specialized cells to change shape has thus become their most important property. Assemblies of contractile muscle cells, the muscles, are machines for converting chemical energy into mechanical work. Muscle forces move limbs and drive many of the functions of the human body, and muscle tissue constitutes 40–50% of body mass.

Classification of muscle

Muscle cells ('fibres') are also known as myocytes (the prefixes myo- and sarco- are frequently used in naming structures associated with muscle). They differentiate along one of three main pathways to form skeletal, cardiac or smooth muscle. Both skeletal and cardiac muscle (Ch. 6) may be called striated muscle, because their myosin and actin filaments are organized into regular, repeating structures (sarcomeres), which give the cells a finely cross-striated appearance when viewed microscopically. Cardiac muscle fibres are relatively short, with branched ends, and are joined to adjacent fibres at intercellular junctional complexes called intercalated discs, which skeletal muscle lacks. Smooth muscle cells (Ch. 6) lack striations because their actin and myosin are not organized into sarcomeres.

Other contractile cells, including myofibroblasts and myoepithelial cells, are different in character and developmental origin. They contain smooth muscle-like contractile proteins and are found singly or in small groups.

Skeletal muscle

Skeletal muscle ('striated, voluntary') is the most common muscle tissue. It consists of long, parallel multinucleate cells bundled together by collagenous sheaths. Its regular organization enables skeletal muscle to generate powerful contractions, with a power output of approximately 100 watts per kilogram of tissue. However, the price paid for this organization is a limited contractile range: skeletal muscle can shorten by only 30%. If a larger range of movement is required, it must be achieved through the amplification provided by lever systems, as described in Fig. 5.63. Skeletal muscle is innervated by somatic motor nerves and is sometimes referred to as voluntary muscle, because its contractions are often initiated under conscious control. However, this is a misleading term because skeletal muscle is involved in many movements, such as breathing, blinking and swallowing, which are often initiated at an unconscious level.

Microstructure of skeletal muscle

Skeletal muscle fibres are enormous multinucleate cells (**Figs 5.36–5.37**) which develop by fusion of individual myoblasts (see below). Individual fibres are long, cylindrical structures that tend to be consistent in size within a given muscle, but in different muscles may range from 10 to 100 μm in diameter, and from a few millimetres to many centimetres in length. The cytoplasm of each fibre, the sarcoplasm, is surrounded by a plasma membrane often called the sarcolemma. The bulk of the sarcoplasm comprises the contractile machinery, organized into myofibrils (see Fig. 5.37) 1–2 μm in diameter, which extend the length of the fibre. Numerous moderately euchromatic, oval nuclei usually occupy a thin transparent rim of sarcoplasm between the myofibrils and the sarcolemma, and are especially numerous in the region of the neuromuscular junction (see Fig. 3.36). In transverse section, a muscle fibre may reveal only one or two nuclei, but it may contain several hundred along its entire length. Myogenic satellite cells lie between the sarcolemma and the surrounding basal lamina (see below).

Sarcomeres

Although myofibrils are too tightly packed to be visible by routine light microscopy, their presence can be inferred from transverse striations across the tissue. Cross-striations may be demonstrated more effectively using special stains (see Fig. 5.36) or under polarized light, which can differentiate dark, anisotropic A-bands (which are birefringent and rotate the plane of polarized light strongly) from lighter, isotropic I-bands (rotate the plane of polarized light to a negligible degree). In transverse

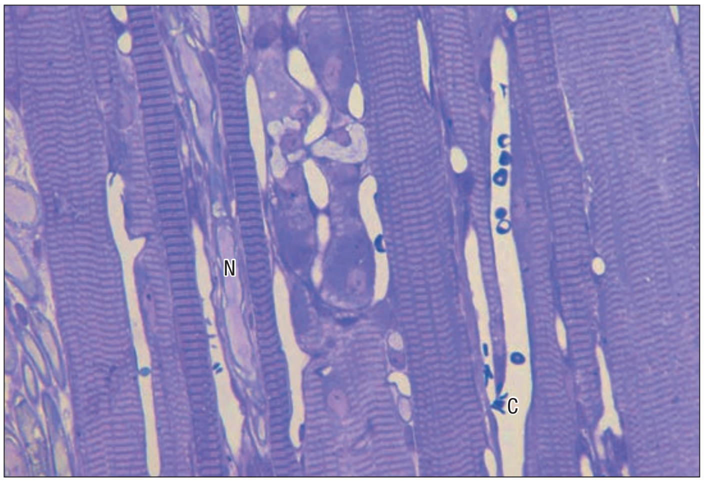

Fig. 5.36 Skeletal muscle fibres from human lateral rectus in longitudinal section, showing transverse striations representing the sarcomeric organization of actin and myosin filaments. The variation in fibre diameter is typical of extraocular muscles. Capillaries (C) and nerves (N) lie between the fibres, orientated mainly in parallel and so are also sectioned longitudinally. Toluidine blue stained resin section. (Courtesy of the Department of Optometry and Visual Science, City University, London.)

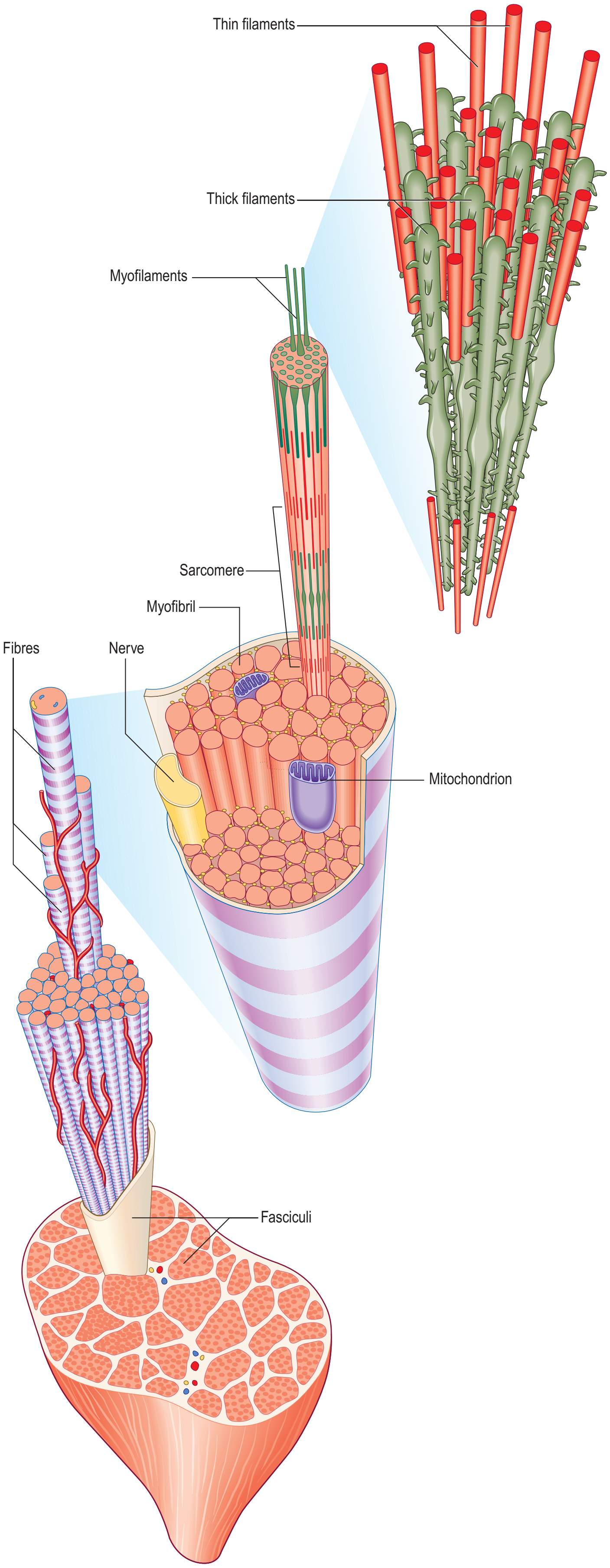

Fig. 5.37 Levels of organization within a skeletal muscle, from whole muscle to fasciculi, single fibres, myofibrils and myofilaments.

section, skeletal muscle fibres are usually polygonal (Fig. 5.38) and their sarcoplasm often has a stippled appearance, because transversely sectioned myofibrils are resolved as dots. The packing density of muscle fibres varies, from low (in the extrinsic muscles of the larynx) to high (in the group of muscles that elevate the mandible).

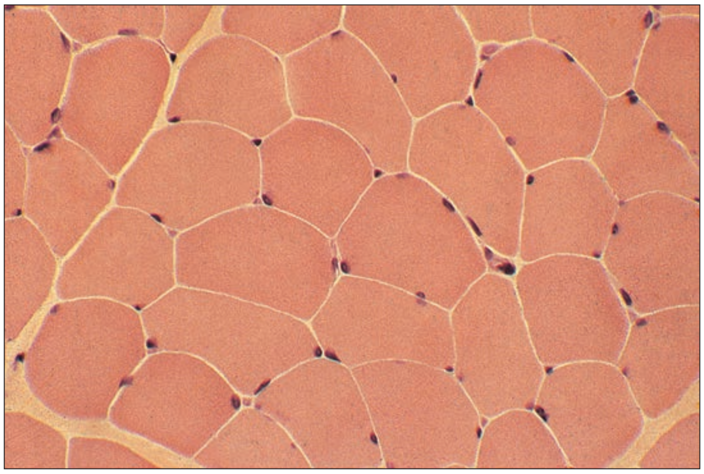

Fig. 5.38 A transverse cryostat section of adult human skeletal muscle. Note the tight packing of the fibres and the peripheral location of the dark-stained nuclei. (Photograph by Professor Stanley Salmons, from a specimen provided courtesy of Tim Helliwell, Department of Pathology, University of Liverpool.)

Most detail is revealed by transmission electron microscopy (**Fig. 5.39**). Myofibrils, approximately 1 μm in diameter, are the dominant ultrastructural feature. In longitudinal sections they appear as ribbons that are interrupted at regular intervals by thin dark transverse lines, which correspond to discs in the parent cylindrical structure. These are the Z-lines or, more properly, Z-discs (Zwischenscheiben) that divide each myofibril into a linear series of repeating contractile units, the sarcomeres. A sarcomere is typically 2.2 μm long in resting muscle. At higher power, it can be seen to consist of two types of filament, thick and thin, organized into regular arrays (see Figs 5.37 and 5.39). Thick filaments, which are approximately 15 nm in diameter, are composed mainly of myosin. Thin filaments, which are 8 nm in diameter, are composed mainly of actin. The arrays of thick and thin filaments form a partially overlapping structure in which electron density (as seen in the electron microscope) varies according to the amount of protein present. The A-band consists of the thick filaments, together with lengths of thin filaments that interdigitate with, and thus overlap, the thick filaments at either end (see Fig. 5.39; **Fig. 5.40**). The central, paler region of the A-band, which is not penetrated by the thin filaments, is called the H-zone (Helle = light). At their centres, the thick filaments are linked together transversely by material that constitutes the M-line (Mittelscheibe = middle [of] disc), which is visible in most muscles. The I-band consists of the adjacent portions of two neighbouring sarcomeres in which the thin filaments are not overlapped by thick filaments. The thin filaments of adjacent sarcomeres are anchored in the Z-disc, which bisects the I-band.

The high degree of organization of thick and thin filaments is equally evident in transverse sections (see Fig. 5.40; **Fig. 5.41**). The thick myosin filaments form a hexagonal lattice. In the regions where they overlap the thin filaments, each myosin filament is surrounded by six actin filaments at the trigonal points of the lattice. In the I-band, the thin filament pattern changes from hexagonal to square as the filaments approach the Z-disc, where they are incorporated into a square lattice structure.

The banded appearance of individual myofibrils is a function of the regular alternation of the thick and thin filament arrays. The size of myofibrils places them at the limit of resolution of light microscopy; cross-striations are only visible at that level because of the alignment in register of the A- and I-bands in adjacent myofibrils across the width of the whole muscle fibre. In suitably stained relaxed material, the A-, I- and H-bands are quite distinct, whereas the Z-discs, which are such a prominent feature of electron micrographs, are thin and much less conspicuous in the light microscope, and M-lines cannot be resolved.

Muscle proteins

Myosin, the protein of the thick filament is the most abundant contractile protein (60% of the total myofibrillar protein). The thick filaments of skeletal and cardiac muscle are 1.5 μm long. Their composition from myosin heavy and light chain assemblies is described on page p. 13. The other components of myosin, the regulatory proteins tropomyosin and troponin, play a major part in the control of contraction.

Actin constitutes 20% of the total myofibrillar protein mass: its filamentous form, F-actin, is the principal protein of the thin filaments.

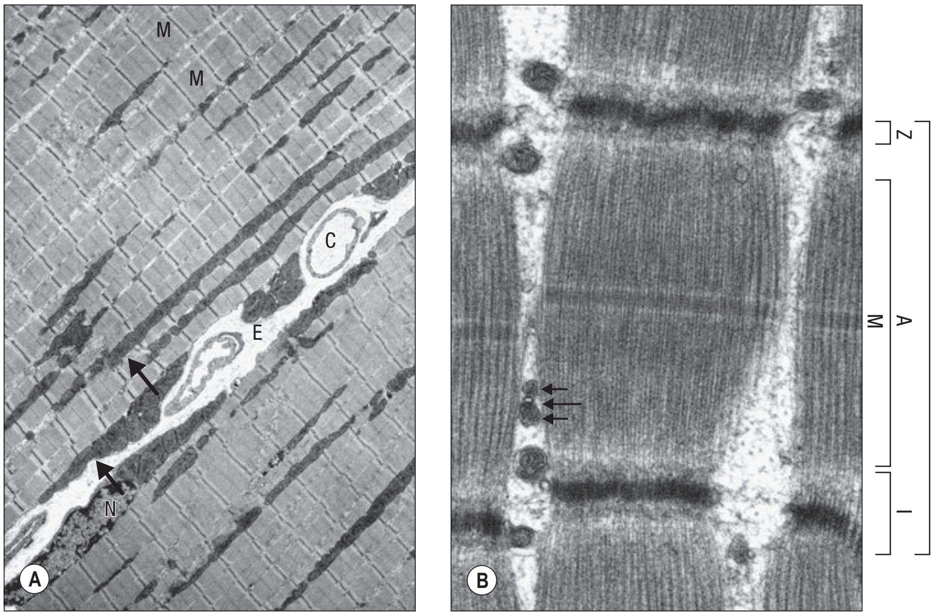

Fig. 5.39 The electron microscopic appearance of skeletal muscle in longitudinal section. **A**, A low-power view of parts of two adjacent muscle fibres, separated by endomysium (E) containing capillaries (C) and a peripherally placed nucleus (N) in the fibre. Mitochondria (arrows) are situated peripherally and between myofibrils (M). Myofibrils pack the cytoplasm, with their sarcomeres (contractile units) in register, as seen by the alignment of Z-discs (dark transverse lines) across each muscle fibre. **B**, A sarcomere within a myofibril, and parts of two others. (A sarcomere is the distance between adjacent Z-discs.) Also seen are the A-band, bisected by the M-line, and I-band, which here is almost obliterated in the contracted state (see Fig. 5.40). A triad is visible between myofibrils, comprised of a T-tubule (long arrow) and two terminal cisternae of sarcoplasmic reticulum (short arrows). (A, Courtesy of Professor Hans Hoppeler, Institute of Anatomy, University of Bern, Switzerland.)

A number of congenital myopathies result from gene mutations in components of the thin filament assembly (Clarkson et al 2004).

A third type of long sarcomeric filament (see Fig. 5.40) connects the thick filaments to the Z-disc, and is formed by the giant protein, titin, which has a molecular weight in the millions (Gregorio et al 1999). Single titin molecules span the half-sarcomere between the M-lines and the Z-discs, into which they are inserted. They have a tethered portion in the A-band, where they are attached to thick filaments as far as the M-line, and an elastic portion in the I-band. The elastic properties of titin endow the relaxed muscle fibre with passive resistance to stretching, and with elastic recoil.

A number of proteins that are neither contractile nor regulatory are responsible for the structural integrity of the myofibrils, particularly their regular internal arrangement. A component of the Z-disc, α-actinin, is a rod-shaped molecule that anchors the plus-ends of actin filaments from adjacent sarcomeres to the Z-disc. Nebulin inserts into the Z-disc, associated with the thin filaments, and regulates the lengths of actin filaments. Desmin, an intermediate filament protein characteristic of muscle, encircles the myofibrils at the Z-disc and, with the linking molecule plectrin, forms a meshwork that connects myofibrils together within the muscle fibre and to the sarcolemma. Myomesin holds myosin filaments in their regular lattice arrangement in the region of the M-line. Dystrophin is confined to the periphery of the muscle fibre, close to the cytoplasmic face of the sarcolemma. It binds to actin intracellularly and is also associated with a large oligomeric complex of glycoproteins, the dystroglycan/sarcoglycan complex that spans the membrane and links specifically with merosin, the α_2-laminin isoform of the muscle basal lamina. This stabilizes the muscle fibre and transmits forces generated internally on contraction to the extracellular matrix.

Dystrophin is the product of the gene affected in Duchenne muscular dystrophy, a fatal disorder that develops when mutation of the gene leads to the absence of the protein (Batchelor and Winder 2006). A milder form of the disease, Becker muscular dystrophy, is associated with a reduced size and/or abundance of dystrophin. Female carriers (heterozygous for the mutant gene) of Duchenne muscular dystrophy may also have mild symptoms of muscle weakness. At about 2500 kb, the gene is one of the largest yet discovered, which may account for the high mutation rate of Duchenne muscular dystrophy (approximately 35% of cases are new mutations). Other muscular dystrophies may involve deficiencies in proteins functionally associated with dystrophin, such as the dystroglycan/sarcoglycan complex or α_2-laminin; they may also be the result of mutations in proteins of the inner nuclear membrane (Azibani et al 2014, Koch and Holaska 2014).

Other sarcoplasmic structures

Although myofibrils are the dominant ultrastructural feature, skeletal muscle fibres contain other organelles essential for cellular function. Ribosomes, Golgi apparatus and mitochondria are located around the nuclei, between the myofibrils and the sarcolemma, and, to a lesser extent, between the myofibrils. Mitochondria, lipid droplets and glycogen provide the metabolic support needed by active muscle. The mitochondria are elongated and their cristae are closely packed. The number of mitochondria in an adult muscle fibre is not fixed, but can increase or decrease quite readily in response to sustained changes in activity. Spherical lipid droplets, approximately 0.25 µm in diameter, are distributed uniformly throughout the sarcoplasm between myofibrils. They represent a rich source of energy that can be tapped only by oxidative metabolic pathways; they are therefore more common in fibres that have a high mitochondrial content and good capillary blood supply. Small clusters of glycogen granules are dispersed between myofibrils and among the thin filaments. During brief bursts of activity, they provide an important source of anaerobic energy that is not dependent on blood flow to the muscle fibre.

Tubular invaginations of the sarcolemma penetrate between the myofibrils in a transverse plane at the limit of each A-band (see Fig. 5.39; **Fig. 5.42**). The lumina of these transverse (T-) tubules are thus in continuity with the extracellular space. At the ends of the muscle fibre, where force is transmitted to adjacent connective tissue structures, the sarcolemma is folded into numerous finger-like projections that strengthen the junctional region by increasing the area of attachment.

The sarcoplasmic reticulum (SR) is a specialized form of smooth endoplasmic reticulum and forms a plexus of anastomosing membrane cisternae that fills much of the space between myofibrils (see Fig. 5.42). The cisternae expand into larger sacs, junctional sarcoplasmic reticulum or terminal cisternae, where they come into close contact with T-tubules, forming structures called triads (see Figs 5.39, 5.42). The membranes of the SR contain calcium–ATPase pumps that transport calcium ions into the terminal cisternae, where the ions are bound to calsequestrin, a protein with a high affinity for calcium, in dense storage granules. In this way, calcium can be accumulated and retained in the terminal cisternae at a much higher concentration than elsewhere in the sarcoplasm. Calcium-release channels (ryanodine receptors) are concentrated mainly in the terminal cisternae and form one-half of the junctional 'feet' or 'pillars' that bridge the SR and T-tubules at the triads. The other half of the junctional feet is the T-tubule receptor that constitutes the voltage sensor.

Connective tissues of muscle

The endomysium is a delicate network of connective tissue that surrounds muscle fibres and forms their immediate external environment. It is the site of metabolic exchange between muscle and blood, and contains capillaries and bundles of small nerve fibres. Ion fluxes associated with the electrical excitation of muscle fibres take place across its proteoglycan matrix. The perimysium is a more substantial connective tissue structure that is continuous with the endomysium: it ensheathes groups of muscle fibres to form parallel bundles, or fasciculi. It carries larger blood vessels and nerves, and accommodates neuromuscular spindles. Perimysial septa are the inward extensions of a collagenous sheath, the epimysium, which forms part of the fascia that invests whole muscle groups.

Epimysium consists mainly of type I collagen; perimysium contains type I and type III collagen; endomysium contains collagen types III and IV. Collagen type IV is associated particularly with the basal lamina that invests each muscle fibre. The epimysial, perimysial and endomysial sheaths coalesce where the muscles connect to adjacent structures at tendons, aponeuroses and fasciae (see below).

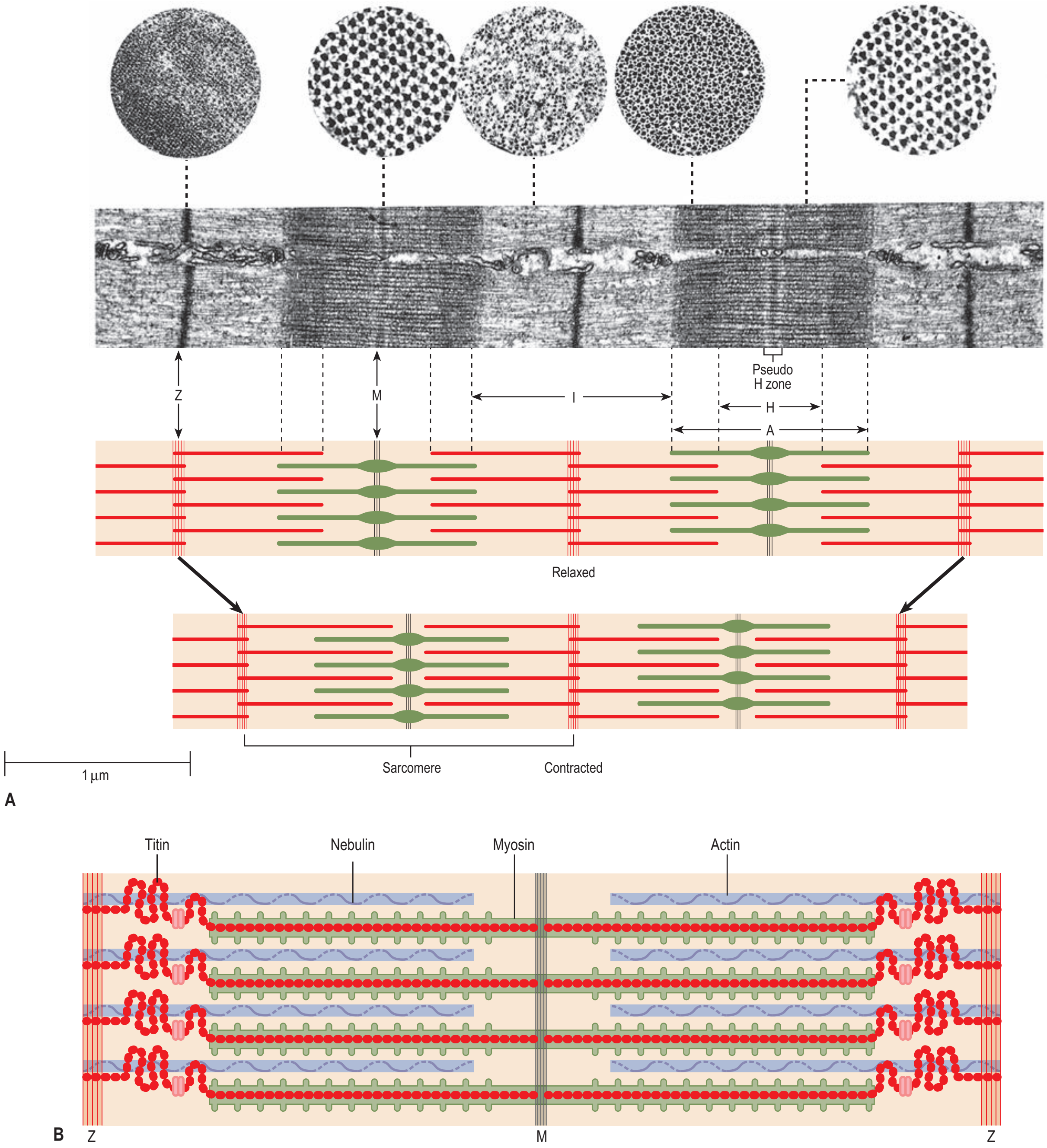

Fig. 5.40 **A**, Sarcomeric structures. The drawings below the electron micrograph (of two myofibrils sectioned longitudinally and with their long axes orientated transversely) indicate the corresponding arrangements of thick and thin filaments. Relaxed and contracted states are shown to illustrate the changes that occur during shortening. Insets at the top depict the electron micrographic appearance of transverse sections through the myofibril at the levels shown. Note that the packing geometry of the thin filaments changes from a square array at the Z-disc to a hexagonal array where they interdigitate with thick filaments in the A-band. **B**, The arrangement of titin and nebulin in a skeletal muscle sarcomere. A single titin molecule spans from the Z-disc to the M-band and contains a spring-like 'elastic' region that develops force when the sarcomere is stretched. Nebulin extends from the Z-disc for the full length of each actin filament. (A, Courtesy of Professor Brenda Russell, Department of Physiology and Biophysics, University of Illinois at Chicago. B, With permission from Prado LG et al 2005 Isoform diversity of giant proteins in relation to passive and active contractile properties of rabbit skeletal muscles. J Gen Physiol 126:461–80.)

Neurovascular supply of muscle

Vascular supply and lymphatic drainage

In most muscles, the major source artery enters on the deep surface, frequently in close association with the principal vein and nerve, at the neurovascular hilum. The vessels subsequently course and branch within the connective tissue framework of the muscle. Smaller arteries and arterioles ramify in the perimysial septa and give off capillaries that run in the endomysium. The smaller vessels lie mainly parallel to the muscle fibres, but also branch and anastomose around the fibres, forming an elongated mesh.

The gross vascular anatomy of muscles has been classified into five types according to the number and relative dominance of vascular pedicles that enter the muscle (Mathes and Nahai 1981) (Fig. 5.43). This classification has important surgical relevance in determining which muscles will survive and therefore be useful for pedicled or free tissue transfer procedures in plastic and reconstructive surgery. Type I muscles possess a single vascular pedicle supplying a muscle belly, e.g. tensor fasciae latae (supplied by the ascending branch of the lateral circumflex femoral artery) and gastrocnemius (supplied by the sural artery). Type II muscles are served by a single dominant vascular pedicle and several minor pedicles, and can be supported on a minor pedicle as well as the dominant pedicle, e.g. gracilis (supplied by the medial circumflex femoral artery in the dominant pedicle). Type III muscles are supplied by two separate dominant pedicles, each from different source arteries, e.g. rectus abdominis (supplied by the superior and inferior epigastric arteries)

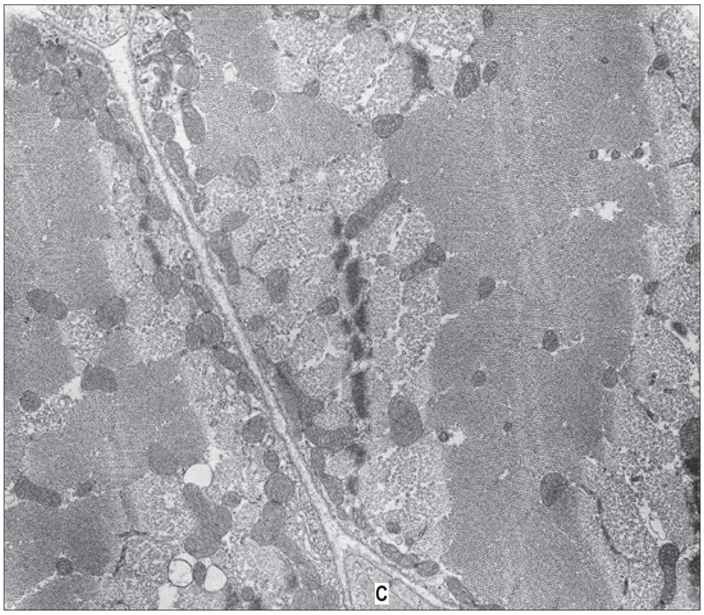

Fig. 5.41 An electron micrograph of skeletal muscle in transverse section, showing parts of two muscle fibres. Part of a capillary (C) is seen in transverse section in the endomysial space. The variation in the appearance of myofibrils in cross-section is explained in Fig. 5.40. (Courtesy of Professor Brenda Russell, Department of Physiology and Biophysics, University of Illinois at Chicago.)

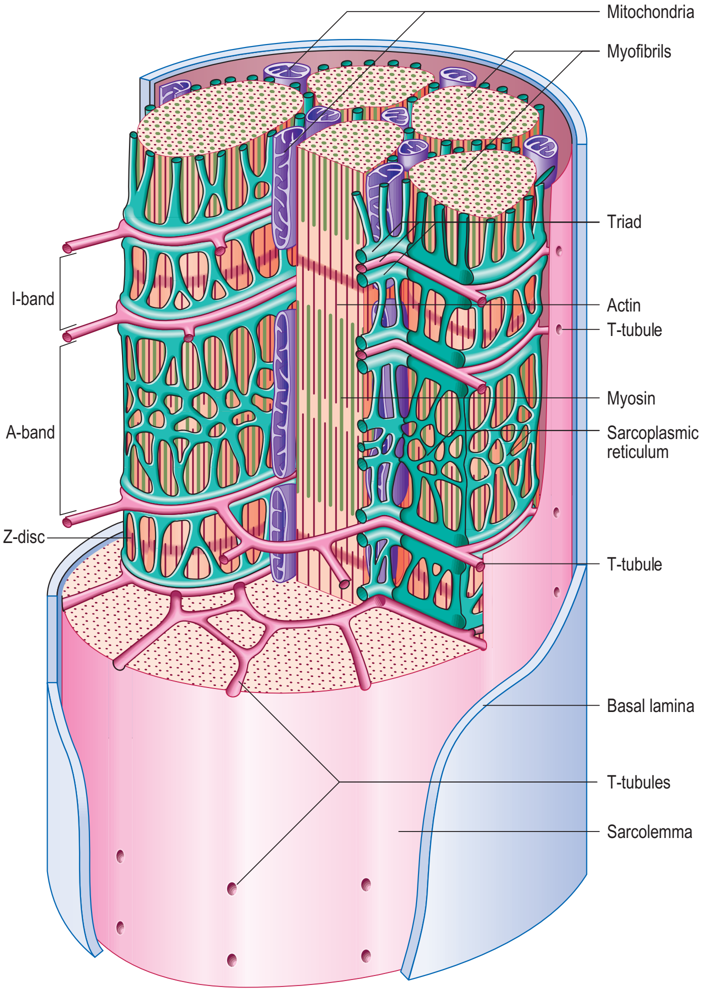

Fig. 5.42 A three-dimensional reconstruction of a mammalian skeletal muscle fibre, showing in particular the organization of the transverse (T) tubules and sarcoplasmic reticulum. Mitochondria lie between the myofibrils. Note that transverse tubules are found at the level of the A/I junctions, where they form triads with the terminal cisternae of the sarcoplasmic reticulum.

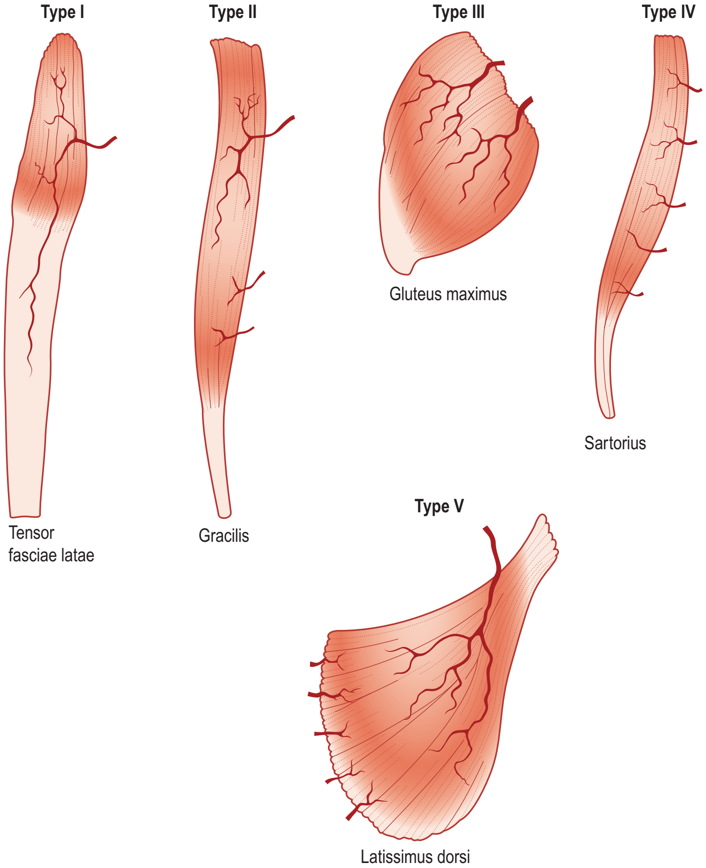

Fig. 5.43 Classification of muscles according to their blood supply. (With permission from Cormack GC, Lamberty BGH 1994 The Arterial Anatomy of Skin Flaps, 2nd ed. Edinburgh: Churchill Livingstone.)

and gluteus maximus (supplied by the superior and inferior gluteal arteries). Type IV muscles have multiple small pedicles that, in isolation, are not capable of supporting the whole muscle, e.g. sartorius and tibialis anterior; about 30% survive reduction on to a single vascular pedicle. Type V muscles have one dominant vascular pedicle and multiple secondary segmental pedicles, e.g. latissimus dorsi (supplied by the thoracodorsal artery as the primary pedicle, thoracolumbar perforators from the lower six intercostal arteries and the lumbar arteries as the segmental supply) and pectoralis major (supplied by the pectoral branch of the thoraco-acromial axis as the dominant pedicle, and anterior perforators from the internal thoracic vessels as the segmental supply).

In cross-sections of muscle, the number of capillary profiles found adjacent to fibres usually varies from 0 to 3. Muscle fibres involved in sustained activities, such as maintenance of posture, are served by a denser capillary network than fibres that are recruited only infrequently. It is common for muscles to receive their arterial supply via more than one route. The accessory arteries penetrate the muscle at places other than the hilum, and ramify in the same way as the principal artery, forming vascular territories. The boundaries of adjacent territories are spanned by anastomotic vessels, sometimes at constant calibre, but more commonly through reduced-calibre arteries or arterioles that are referred to as 'choke vessels'. These arterial arcades link the territories into a continuous network.

Veins branch in a similar way, forming venous territories that correspond closely to the arterial territories. In the zones where the arterial territories are linked by choke vessels, the venous territories are linked by anastomosing veins – in this case, without change of calibre. On either side of these venous bridges, the valves in the adjacent territories direct flow in opposite directions towards their respective pedicles, but the connecting veins themselves lack valves and therefore permit flow in either direction.

Because of the potential for relative movement within muscle groups, vessels tend not to cross between muscles, but radiate to them from more stable sites or cross at points of fusion. Where a muscle underlies the skin, blood vessels bridge between the two. These may be primarily cutaneous vessels, which supply the skin directly but contribute small branches to the muscle as they pass through it, or they may be the terminal branches of intramuscular vessels, which leave the muscle to supplement the cutaneous blood supply. The latter are less frequent where the muscle is mobile under the deep fascia. Correspondence between the vascular territories in the skin and underlying tissues gave rise to the concept of angiosomes, which are composite blocks of tissue supplied by named distributing arteries and drained by their companion veins (see Taylor and Pan (1998), Taylor (2013) for further analyses of muscle angiosomes).

Pressure exerted on valved intramuscular veins during muscle contraction functions as a 'muscle pump' that promotes venous return to the heart. In some cases this role appears to be amplified by veins that pass through the muscle after originating elsewhere in superficial or deep tissues. The extent to which the muscle capillary bed is perfused can be varied in accordance with functional demand. Arteriovenous anastomoses, through which blood can be returned directly to the venous system without traversing the capillaries, provide an alternative, regulated pathway.

The lymphatic drainage of muscles begins as lymphatic capillaries in epimysial and perimysial, but not endomysial, sheaths. These converge to form larger lymphatic vessels that accompany the veins and drain to the regional lymph nodes.

Innervation

Every skeletal muscle is supplied by one or more nerves. Muscles in the limbs, face and neck are usually innervated by a single nerve, even though the axons it contains may be derived from neurones located in several spinal cord segments and their associated sensory and sympathetic ganglia. Muscles such as those of the abdominal wall, which originate from several embryonic segments, are supplied by more than one nerve. In most cases, the nerve travels with the principal blood vessels within a neurovascular bundle (see Fig. 2.9), approaches the muscle near to its least mobile attachment, and enters the deep surface at a position that is more or less constant for each muscle.

Nerves supplying muscle are frequently referred to as 'motor nerves' but they contain both motor and sensory components. The motor component is mainly composed of large myelinated α-efferent axons that supply the muscle fibres; small, thinly myelinated γ-efferents, or fusimotor fibres, that innervate the intrafusal muscle fibres of neuromuscular spindles (see p. 65); and fine, unmyelinated postganglionic sympathetic fibres that innervate vascular smooth muscle. The sensory component consists of large, myelinated IA and smaller group II afferents from the neuromuscular spindles, large myelinated IB afferents from the Golgi tendon organs (see p. 65), and fine myelinated and unmyelinated axons that convey pain and other sensations from free terminals in the connective tissue sheaths of the muscle.

Within muscles, nerves travel through the epimysial and perimysial septa before entering the fine endomysial tissue around muscle fibres. Alpha motor axons branch repeatedly before they lose their myelinated sheaths to terminate in a narrow zone towards the centre of the muscle belly, known as the motor point. Clinically, this is the place on a muscle from which it is easiest to elicit a contraction with stimulating electrodes. Long muscles generally have two or more terminal (end-plate) bands because many muscle fibres do not run the full length of an anatomical muscle. The terminal branch of an α motor axon contacts a muscle fibre at a specialized synapse, the neuromuscular junction (see Fig. 3.36). It gives off several short, tortuous branches that each end in an elliptical area, the motor end-plate. The underlying discoidal patch of sarcolemma, the sole plate or subneural apparatus, is thrown into deep synaptic folds. This discrete type of neuromuscular junction (*en plaque* ending) is found on muscle fibres that are capable of propagating action potentials. A different type of ending is found on slow tonic muscle fibres that do not have this capability, e.g. in the extrinsic ocular muscles, where slow tonic fibres form a minor component of the anatomical muscle. In this case, the propagation of excitation is taken over by the nerve terminals, which branch over an extended distance to form a number of small neuromuscular junctions (*en grappe* endings). Some muscle fibres of this type receive the terminal branches of more than one motor neurone. The terminals of the γ-efferents that innervate the intrafusal muscle fibres of the neuromuscular spindle also take a variety of different forms.

The terminal branches of α motor axons are normally in a 'one-to-one' relationship with their muscle fibres: a muscle fibre receives only one branch, and any one branch innervates only one muscle fibre. When a motor neurone is excited, an action potential is propagated along the axon and all of its branches to all of the muscle fibres that it supplies. The motor neurone and the muscle fibres that it innervates can therefore be regarded as a functional unit: the 'motor unit'. This arrangement accounts for the more or less simultaneous contraction of a number of fibres within the muscle. The size of a motor unit varies considerably. In muscles used for precision tasks, such as the extraocular and intrinsic laryngeal muscles, each motor neurone innervates perhaps ten muscle fibres, whereas in a large limb muscle, a motor neurone may innervate several hundred muscle fibres. Within a muscle, fibres belonging to one motor unit are distributed over a wide territory without regard to fascicular boundaries, and they intermingle with the fibres of other motor units. Motor units become larger in cases of nerve damage because denervation induces collateral or terminal sprouting of the remaining axons. Each new branch can potentially reinnervate a fibre, thus increasing the territory of its parent motor neurone (see Commentary 1.5).

Muscle contraction

The arrival of an action potential at the motor end-plate of a neuromuscular junction causes acetylcholine (ACh) to be released from storage vesicles into the highly infolded 30–50 nm synaptic cleft that separates the nerve ending from the sarcolemma (see Fig. 3.36). ACh is rapidly bound by receptor molecules located in the junctional folds, triggering an almost instantaneous increase in the permeability, and hence conductance, of the postsynaptic membrane. This generates a local depolarization (the end-plate potential), which initiates an action potential in the surrounding sarcolemma. The activity of the neurotransmitter is rapidly terminated by the enzyme acetylcholinesterase (AChE), which is bound to the basal lamina in the sarcolemmal junctional folds. The sarcolemma is an excitable membrane, and action potentials generated at the neuromuscular junction propagate rapidly over the entire surface of the muscle fibre.

Action potentials are conducted radially into the interior of the fibre via extensions of the sarcolemma, the T-tubules, ensuring that all parts of the muscle fibre are activated rapidly and almost synchronously. Excitation–contraction coupling is the process whereby an action potential triggers the release of calcium from the terminal cisternae of the sarcoplasmic reticulum into the cytosol. This activates a calcium-sensitive switch in the thin filaments and so initiates contraction. At the end of excitation, the T-tubular membrane repolarizes, calcium release ceases, calcium ions are actively transported back to the calsequestrin stores in the sarcoplasmic reticulum by the calcium–ATPase pumps, and the muscle relaxes.

The lengths of the thick and thin filaments do not change during muscle contraction. The sarcomere shortens by the sliding of thick and thin filaments past one another, drawing the Z-discs towards the middle of each sarcomere (see Fig. 5.40). As the overlap increases, the I- and H-bands narrow to near-extinction, while the width of the A-bands remains constant. Filament sliding depends on the making and breaking of bonds (cross-bridge cycling) between myosin head regions and actin filaments. Myosin heads 'walk' or 'row' along actin filaments using a series of short power strokes, each resulting in a relative movement of 5–10 nm. Actin filament binding sites for myosin are revealed only by the presence of calcium, which is released into the sarcoplasm from the sarcoplasmic reticulum, causing a repositioning of the troponin–tropomyosin complex on actin: this is the calcium-sensitive switch. Myosin head binding and release are both energy-dependent and require ATP. In the absence of ATP (as occurs post mortem) the bound state is maintained, and is responsible for the muscle stiffness known as rigor mortis.

The summation of myosin power strokes leads to an average sarcomere shortening of up to 1 μm; an anatomical muscle shortens by a centimetre or more, depending on the muscle, because each muscle has thousands of sarcomeres in series along its length.

Slow-twitch versus fast-twitch fibres

The passage of a single action potential through a motor unit elicits a twitch contraction where peak force is reached within 25–100 ms, depending on the motor unit type involved. However, the motor neurone can deliver a second nervous impulse in less time than it takes for the muscle fibres to relax. When this happens, the muscle fibres contract again, building the tension to a higher level. Because of this mechanical summation, a sequence of impulses can evoke a larger force than a single impulse and, within certain limits, the higher the impulse *frequency*, the more force is produced ('rate recruitment'). An alternative strategy is to recruit more motor units. In practice, the two mechanisms appear to operate in parallel, but their relative importance may depend on the size and/or function of the muscle; in large muscles with many motor units, motor unit recruitment is probably the more important mechanism.

With the exception of rare tonic fibres, skeletal muscles are composed entirely of fibres of the twitch type. These fibres can all conduct action potentials but they differ in other respects. Some fibres obtain their energy very efficiently by aerobic oxidation of substrates, particularly of fats and fatty acids. They have large numbers of mitochondria; contain myoglobin, an oxygen-transport pigment related to haemoglobin, and are supported by a well-developed network of capillaries that maintains a steady nutrient supply of oxygen and substrates. Such fibres are well suited to functions such as postural maintenance, in which moderate forces need to be sustained for prolonged periods. At the other end of the spectrum, some fibres have few mitochondria, little myoglobin and a sparse capillary network, and store energy as cytoplasmic glycogen granules. Their immediate energy requirements are met largely through anaerobic glycolysis, a route that provides prompt access to energy but that is less sustainable than oxidative metabolism. They are capable of brief bursts of intense activity that must be separated by extended quiescent periods during which intracellular pH and phosphate concentrations are restored to normal values, and glycogen and other reserves are replenished.

In some animals, different types of muscle fibre tend to be segregated into different muscles. This causes some muscles to have a conspicuously red appearance, reflecting their rich blood supply and high myoglobin content associated with a predominantly aerobic metabolism, whereas other muscles have a much paler appearance, reflecting a more anaerobic character. These variations in colour led to the early classification of muscle into red and white types; this classification has now been largely superseded by myosin-based typing and the presence of specific disease-related enzymes.

In humans, all muscles are mixed, with fibres specialized for aerobic working conditions intermingling with fibres of a more anaerobic or intermediate metabolic character. Different types of fibre are not readily distinguished in routine histological preparations but are clear when specialized enzyme histochemical techniques are used. On the basis of metabolic differences, individual fibres can be classified as oxidative slow-twitch (red) fibres, or glycolytic fast-twitch (white) fibres. Muscles composed mainly of oxidative slow-twitch fibres correspond to the red muscles of classical descriptions. Muscles that are predominantly oxidative in their metabolism contract and relax more slowly than muscles relying on glycolytic metabolism. This difference in contractile speed is due in part to the activation mechanism (volume density of the sarcotubular system and proteins of the calcium 'switch' mechanism), and in part to molecular differences between the myosin heavy chains of these types of muscle. These differences affect the ATPase activity of the myosin head, which in turn alters the kinetics of its interaction with actin, and hence the rate of cross-bridge cycling. Differences between myosin isoforms can be detected histochemically, and ATPase histochemistry continues to play a significant role in diagnostic typing (Table 5.1). Two main categories have been described: type I fibres, which are slow-contracting, and type II, which are fast-contracting. Molecular analyses have revealed that type II fibres can be further subdivided according to their content of myosin heavy-chain isoforms into types IIA and IIX. Muscle fibres may contain only one (i.e. a pure fibre) or a combination (i.e. a hybrid fibre) of these isoforms; the five most prevalent muscle fibre types in humans are I, I/IIA, IIA, IIA/IIX, IIX. (For further reading, see Galpin et al (2012), Holland and Ohlendieck (2013).) There is a correlation between categories and fatigue resistance, such that type I fibres are generally oxidative (slow oxidative) and resistant to fatigue; type IIA are moderately oxidative, glycolytic (fast oxidative glycolytic) and fatigue-resistant; and type IIX largely rely on glycolytic metabolism (fast glycolytic) and so are easily fatigued.

TABLE 5.1 Physiological, structural and biochemical characteristics of the major histochemical fibre types

	Fibre types		
Characteristic	**Type I**	**Type IIA**	**Type IIX**
Physiological			
Function	Sustained forces, as in posture	Powerful, fast movements	
Motor neurone firing threshold	Low	Intermediate	High
Motor unit size	Small	Large	Large
Firing pattern	Tonic, low-frequency	Phasic, high-frequency	
Maximum shortening velocity	Slow	Fast	Fast
Rate of relaxation	Slow	Fast	Fast
Resistance to fatigue	Fatigue-resistant	Fatigue-resistant	Fatigue-susceptible
Power output	Low	Intermediate	High
Structural			
Capillary density	High		Low
Mitochondrial volume	High	Intermediate	Low
Z-disc	Broad	Narrow	Narrow
T-tubule and sarcoplasmic reticulum systems	Sparse		Extensive
Biochemical			
Myosin ATPase activity	Low		High
Oxidative metabolism	High	Intermediate	Low
Anaerobic glycolysis	Low	Intermediate	High
Calcium transport ATPase	Low		High

Fibre type transformation

Fibre type proportions in a named muscle may vary between individuals of different age or athletic ability. Fibre type grouping, where fibres with similar metabolic and contractile properties aggregate, increases after nerve damage and with age. Grouping occurs as a result of reinnervation episodes, where denervated fibres are 'taken over' by a sprouting motor neurone and adopt its type properties. If the nerves to fast white and slow red muscles are cut and cross-anastomosed in experimental animals, so that each muscle is reinnervated by the other's nerve, the fast muscle becomes slower-contracting, and the slow muscle faster-contracting. There is evidence that such fibre type transformation may be a response to the patterns of impulse traffic in the nerves innervating the muscles (Minetto et al 2013). If fast muscles are stimulated continuously for several weeks at 10 Hz, a pattern similar to that normally experienced by slow muscles, they develop slow contractile characteristics and acquire a red appearance and a resistance to fatigue even greater than that of slow muscles.

The initial phase of slowing can be explained by less rapid cycling of calcium, resulting from reduced sarcoplasmic reticulum and changes in the amount and molecular type of proteins involved in calcium transport and binding. Chronic stimulation also triggers the synthesis of myosin heavy and light chain isoforms of the slow muscle type; the associated changes in cross-bridge kinetics result in a lower intrinsic speed of shortening. The muscle becomes more resistant to fatigue through changes in the metabolic pathways responsible for the generation of ATP and a reduced dependence on anaerobic glycolysis. There is a switch to oxidative pathways, particularly those involved in the breakdown of fat and fatty acids, and an associated increase in capillary density and in the fraction of the intracellular volume occupied by mitochondria. If stimulation is discontinued, the sequence of events is reversed and the muscle regains, over a period of weeks, all of its original characteristics. The reversibility of transformation is one of several lines of evidence that the changes take place within existing fibres, and not by a process of degeneration and regeneration.

Many of the changes in the protein profile of a muscle that are induced by stimulation are now known to be the result of transcriptional regulation. For example, analysis of the messenger RNA species encoding myosin heavy chain isoforms shows that expression of the fast myosin heavy chain mRNA is downregulated within a few days of the onset of chronic stimulation, while the slow myosin heavy chain mRNA is upregulated. Although myosin isoform expression is responsive to the increase in use induced by chronic stimulation, it tends to be stable under physiological conditions unless these involve a sustained departure from normal postural or locomotor behaviour.

Development and growth of skeletal muscle

Most information about the early development of the skeletal musculature in humans has been derived from other vertebrate species. However, where direct comparisons with the developing human embryo have been made, the patterns and mechanisms of muscle formation have been found to be the same.

The majority of the skeletal muscle in the body develops from paraxial mesenchyme and its segmental derivatives, the somites. A small portion forming the extraocular muscles is derived from prechordal mesenchyme, which joins with the most rostral paraxial mesenchyme and which has been demonstrated to have a myogenic fate. Skeletal muscle precursor myoblasts delaminate from dermomyotomes, the lateral portion of the somites (see Fig. 18.2). Those destined for the limbs migrate into the appropriate limb bud, proliferate, express myogenic determination factors and ultimately differentiate into skeletal muscle (Ch. 19). Myogenic regulatory factors are a family of transcription factors consisting of Myogenic factor 5 (Myf5), myogenin (MyoG), Myogenic Differentiation 1 (MyoD) and Myogenic Regulatory Factor 4 (MRF4, also known as Myf-6 (herculin) in man): they activate transcription of a wide variety of muscle-specific genes and play a crucial role in myogenesis and in the specification of muscle satellite cell lineage (Buckingham et al 2003, Zammit 2017).

Formation of muscle fibres

In both myotomes and limb buds, myogenesis proceeds in the following way. Myoblasts become spindle-shaped and begin to express muscle-specific proteins. The mononucleate myoblasts aggregate and fuse to form multinucleate cylindrical syncytia, or myotubes, in which the nuclei are aligned in a central chain (**Fig. 5.44**). These primary myotubes attach at each end to the tendons and developing skeleton. The initiation of fusion does not depend on the presence of nerve fibres, since these do not penetrate muscle primordia until after the formation of primary myotubes.

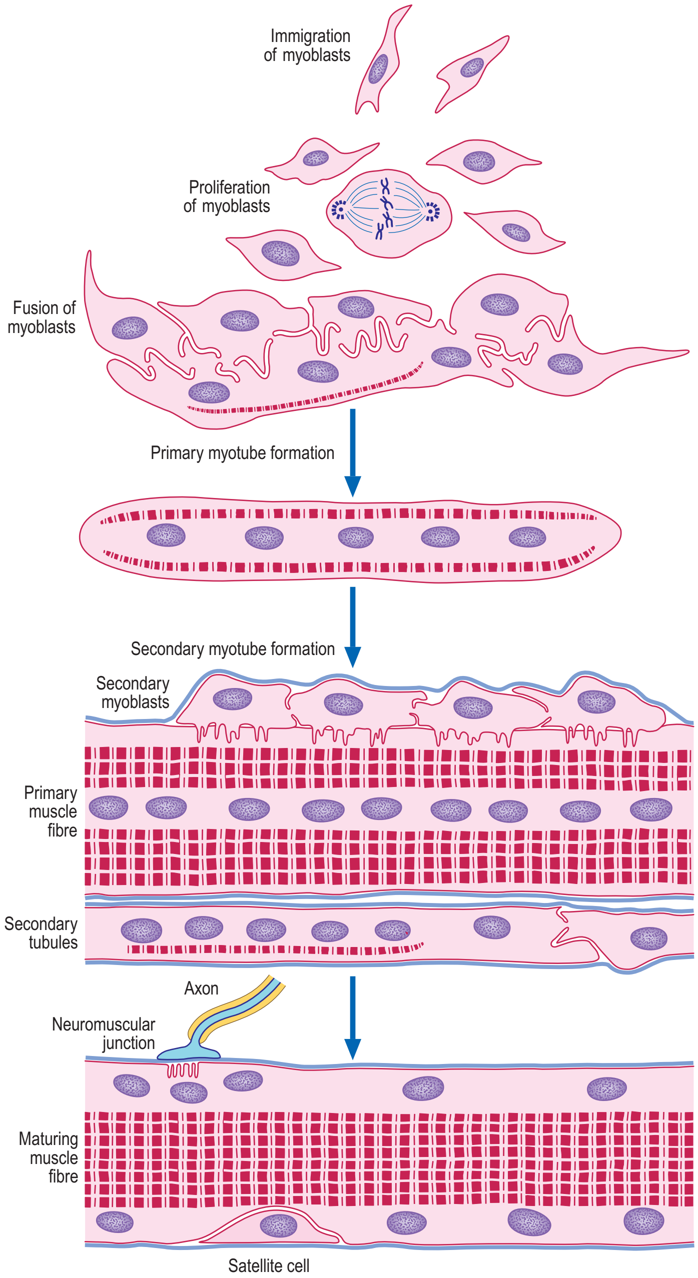

Fig. 5.44 Stages in formation of skeletal muscle. Mononucleate myoblasts fuse to form multinucleate primary myotubes, characterized initially by central nuclei. Subsequently, other myoblasts align along the primary myotubes and begin to fuse with one another, forming secondary myotubes. In large animals, such as humans, further generations of new muscle fibres are similarly formed. As the contractile apparatus is assembled, the nuclei move to the periphery, cross-striations become visible and primitive features of the neuromuscular junction emerge. Later, small adult-type myoblasts – satellite cells – can be seen lying between the basal lamina and the sarcolemma of the mature muscle fibre. These too appear to be derived from cells that originated in the somites during early development. (Adapted with permission from Terry Partridge, Department of Genetic Medicine, Children's National Medical Center, Washington DC.)

Although synthesis of the contractile machinery is not dependent on fusion of myoblasts, it proceeds much more rapidly after fusion. Sarcomere formation begins at the Z-disc, which binds actin filaments constituting the I-band to form I–Z–I complexes. The myosin filaments assemble on the I–Z–I complexes to form A-bands. Nebulin and titin are among the first myofibrillar proteins to be incorporated into the sarcomere, and may well determine the length and position of the contractile filaments. Desmin intermediate filaments connect the Z-discs to the sarcolemma at an early stage, and these connections are retained.

Myogenic cells continue to migrate and to divide, and from postfertilization weeks 7–9 there is extensive *de novo* myotube formation. Myoblasts aggregate near the midpoint of the primary myotubes and fuse with each other to form secondary myotubes, a process that may be related to early neural contact. Several of these smaller-diameter myotubes may be aligned in parallel with each of the primary myotubes. Each develops a separate basal lamina and makes independent contact with the tendon. Initially, the primary myotube provides a scaffold for the longitudinal growth of the secondary myotubes but eventually they separate. At the time of their formation, the secondary myotubes express an 'embryonic' isoform of the myosin heavy chains, whereas the primary myotubes express a 'slow' muscle isoform apparently identical to that found in adult slow muscle fibres. In both primary and secondary myotubes, sarcomere assembly begins at the periphery of the myotube and progresses inwards towards its centre. Myofibrils are added constantly and lengthen by adding sarcomeres to their ends. T-tubules are formed and grow initially in a longitudinal direction; since they contain specific proteins not found in plasma membranes, they are probably assembled via a different pathway from that which supports the growth of the sarcolemma. The sarcoplasmic reticulum wraps around the myofibrils at the level of the I-bands.

By the end of the embryonic period, the primordia of most muscle groups are well defined, contractile proteins have been synthesized and the primitive beginnings of neuromuscular junctions can be observed, confined initially to the primary myotubes. Although some secondary fibre formation can take place in the absence of a nerve, most is initiated at sites of innervation of the primary myotubes. The pioneering axons branch and establish contact with the secondary myotubes. By postmenstrual week 11 these nerve–muscle contacts have become functional neuromuscular junctions and the muscle fibres contract in response to impulse activity in the motor nerves. Under this new influence, the secondary fibres express fetal (sometimes referred to as neonatal) isoforms of the myosin heavy chains. At this stage, several crucial events take place, which may be dependent on, or facilitated by, contractile activity. As the myofibrils encroach on the centre of the myotube, the nuclei move to the periphery and the characteristic morphology of the adult skeletal muscle myofibre is established. The myofibrils become aligned laterally, and A- and I-bands in register across the myotube produce cross-striations that are visible at the light microscopic level. T-tubules change from a longitudinal to a transverse orientation and adopt their adult positions; they may be guided in this process by the sarcoplasmic reticulum, which is more strongly bound to the myofibrils.

The myotubes and myofibres are grouped into fascicles by growing connective tissue sheaths, and fascicles are assembled to build up entire muscles. As development proceeds, the increase in intramuscular volume is accommodated by remodelling of the connective tissue matrix.

At about postmenstrual week 15, primary myotubes are still in the majority, but by postmenstrual week 20 the secondary myotubes predominate. During postmenstrual weeks 16–17, tertiary myotubes appear; they are small and adhere to the secondary myotubes, with which they share a basal lamina. They become independent by postmenstrual weeks 18–23, their central nuclei move to the periphery, and they contribute a further generation of myofibres. The secondary and tertiary myofibres are always smaller and more numerous than the primary myofibres. In some large muscles, higher-order generations of myotubes may be formed.

Late in fetal life, a final population of myoblasts appears, and will become the satellite cells of adult muscle. These normally quiescent cells lie outside the sarcolemma beneath the basal lamina (see Fig. 5.44; Fig. 5.45). M-cadherin, a cell adhesion protein of possible regulatory significance, occurs at the site of contact between a satellite cell and its muscle fibre. In a young individual, there is one satellite cell for every 5–10 muscle fibre nuclei. The latter are incapable of DNA synthesis and mitosis, and satellite cells are therefore important as the sole source of additional muscle fibre nuclei during postnatal growth of muscle (to maintain the ratio of cytoplasmic volume per nucleus as fibres increase in mass). After satellite cells divide, one of the daughter cells fuses with the growing fibre, the other remaining as a satellite cell capable of further rounds of division. In adult skeletal muscle, satellite cells provide a reservoir of cells that enable exercise-induced hypertrophy, and regeneration of muscle after damage (see below).

Development of fibre types

Developing myotubes express an embryonic isoform of myosin that is subsequently replaced by fetal and adult myosin isoforms. The major isoform of sarcomeric actin in fetal skeletal muscle is cardiac α-actin; only later is this replaced by skeletal α-actin. The significance of these developmental sequences is not known.

The pattern of expression is fibre-specific and changes over time. In primary myotubes, embryonic myosin is replaced by adult slow myosin from stage 23 onwards (postfertilization days 53-58). In secondary and higher-order myotubes, the embryonic myosin isoform is superseded first by fetal and then by adult fast myosin, and a proportion go on to express adult slow myosin. Other fibre-specific, tissue-specific and species-specific patterns of myosin expression have been described in mammalian limb muscles and jaw muscles.

The origin of this diversity in the temporal patterns of expression of different fibres, even within the same muscle, is far from clear. It has been suggested that intrinsically different lineages of myoblast emerge at different stages of myogenesis or in response to different extracellular cues. If this is the case, their internal programmes may be retained or overridden when they fuse with other myoblasts or with fibres that have already formed. The fibres that emerge from this process go on to acquire a phenotype that will depend on the further influence of hormones and neural activity.

In humans, unlike many smaller mammals, muscles are histologically mature at birth, but fibre type differentiation is far from complete. In postural muscles, the expression of type I ('slow') myosin increases significantly over the first few years of life. During this same period, the proportions of fibre types in other muscles become more divergent. The presence in adult muscles of a small proportion of fibres with an apparently transitional combination of protein isoforms reinforces the view that changes in fibre type continue to some extent in all muscles and throughout adult life. Fibre type transitions also occur in relation to damage or neuromuscular disease; under these conditions, the developmental sequence of myosins may be recapitulated in regenerating fibres.

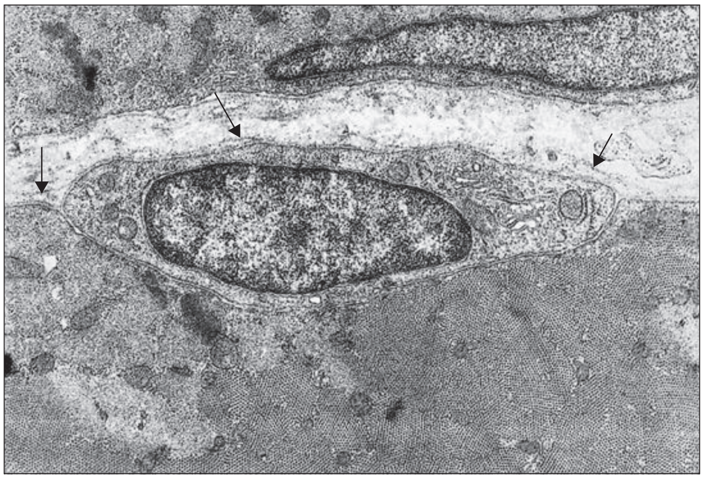

Fig. 5.45 An electron micrograph of a satellite cell. Note the two plasma membranes that separate the cytoplasm of the satellite cell from that of the muscle fibre, and the basal lamina (arrows) of the transversely sectioned muscle fibre, which continues over the satellite cell (see also Fig. 5.39A). Compare this appearance with the normal muscle nucleus, which is seen in the adjacent fibre at the top of the micrograph. (Courtesy of Dr Michael Cullen, School of Neurosciences, University of Newcastle upon Tyne.)

Growth and regulation of fibre length

Muscle fibres grow in length by addition of sarcomeres to the ends of myofibrils. In order for the mean sarcomere length, and hence filament overlap, to be optimized for maximum force, the number of sarcomeres must be regulated throughout life. This is achieved by the addition or removal of sarcomeres in response to any prolonged change of length. For example, if a limb is immobilized in a plaster cast, the fibres of muscles that have been fixed in a shortened position lose sarcomeres, while those that have been fixed in a lengthened position add sarcomeres; the reverse process occurs after the cast has been removed.

Satellite cells and muscle repair

Until the mid-twentieth century, the mechanisms responsible for maintenance and repair of skeletal muscle were unclear. These issues were largely resolved by the discoveries that multinucleated muscle fibres were formed by the fusion of mononucleated precursors, myoblasts, and that a population of satellite cells, so called because of their position on the edge of the fibre, exist between the basal lamina of the mature muscle fibre and its sarcolemma, where they constitute 2–5% of the nuclei enclosed by the basal lamina.

Studies in mouse models, where genetic analysis is possible, have shown that the functional properties of postnatal satellite cells depend on the expression of the *Pax7* gene, whereas the prenatal development of muscle is not similarly dependent. This implies that satellite cells are not simply the relics of prenatal myogenic cells, even though they appear to be derived from the same embryonic source in the somites. Moreover, satellite cells are not a homogeneous population: no two differentiation markers concur completely. This is also the situation in human tissue (**Fig. 5.46**). It has yet to be determined whether this variation reflects a difference in position in the lineage, functional status or adjacent environment.

The satellite cell has been established rigorously in experimental animal models as being both necessary and sufficient for effective regeneration of damaged skeletal muscle (Relaix and Zammit 2012, Järvinen et al 2014, Laumonier and Menetrey 2016, Segalés et al 2016). These cells proliferate to replace their resident region of muscle in 3–4 days and to replenish the quiescent satellite cell population. In humans, there is histological evidence of the rapid accumulation of myoblasts, presumably derived from local satellite cells, at sites of muscle damage. The presumed central role of satellite cells in muscle growth and adaptation has, however, been questioned by some recent research. Satellite cells are undoubtedly important during early postnatal development and growth, and in muscle regeneration following acute injury or eccentric damage. In other situations, however, regulation of protein synthesis and degradation may be more important determinants of muscle mass (Schiaffino et al 2013).

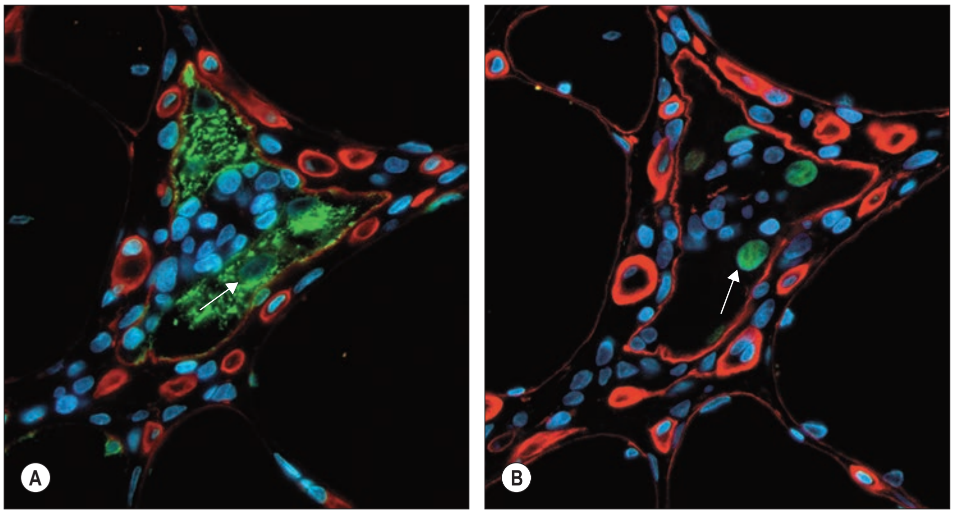

Fig. 5.46 Two adjacent sections, fluorescence-immunolabelled, of a regenerating muscle fibre in a power lifter's trapezius. **A**, Anti-laminin antibody (red) shows basal lamina. Anti-CD56 (green) is a marker of myogenic cells and of newly formed myotubes. **B**, Basal lamina (red) and myogenin-positive nuclei (green). Basal laminae outline transversely sectioned muscle fibres, including the original outline of the regenerating fibre (centre field). Numerous small blood vessels, also outlined by basal laminae, are present and probably reflect local inflammation. Within the CD56-positive zone, several nuclei (one arrowed) are positive for myogenin, indicating their terminally differentiated status. Numerous other nuclei (Hoechst dye, blue) within the basal lamina surrounding the area of regeneration probably include proliferating myogenic cells and inflammatory cells. (Courtesy of Ms Mona Lindström and Professor Lars-Eric Thornell, Department of Anatomy, Umeå University, Sweden.)

A detail of wide pathological interest is the demonstration that the failing regenerative potency of satellite cells in ageing muscle seems in large part to be attributable to age-related changes in the systemic environment rather than a decline in the intrinsic capabilities of the satellite cells themselves (Conboy et al 2005).

Regulation of muscle mass

Muscles respond to resistance exercise in training, or rehabilitation following illness or injury, by increasing in mass. This process is termed hypertrophy, particularly when applied to the increased muscle bulk that occurs in response to intense physical activity. Individual muscle fibres increase in size by the synthesis of new myofibril proteins, increased protein turnover rates and the recruitment of satellite cells to provide new nuclei for existing fibres or to form new myotubes. In inactivity, as seen in those confined to bed or wheelchair, in immobilized limbs, and in patients with disorders of voluntary movement, muscles decrease in mass. This is termed atrophy, or disuse atrophy, in contrast to the pathological wasting of skeletal muscle associated with some disease states, including cancer cachexia, heart failure, diabetes and obesity. It is also recognized that loss of skeletal muscle mass and function may be a consequence of reduced physical activity in normal healthy ageing, when it is termed sarcopenia. There is experimental evidence that this process may be associated with apoptosis of satellite cells and capillary endothelial cells (Wang et al 2014).

Form and function of skeletal muscle

The names given to individual muscles are usually descriptive and are based on their shape, size, number of heads or bellies, position, depth, attachments or actions. The meanings of some of the terms used are summarized in **Table 5.2**. The functional roles implied by the names should be interpreted with caution because they are often oversimplified, and terms denoting action may emphasize only one of a number of usual actions. A given muscle may play different roles in different movements and these roles may change if the movements are assisted or opposed by gravity.

TABLE 5.2 Terms used in naming muscles

Shape
Deltoid (triangular) Quadratus (square) Rhomboid (diamond-shaped) Teres (round) Gracilis (slender) Rectus (straight) Lumbrical (worm-like)
Size
Major, minor, longus (long) Brevis (short) Latissimus (broadest) Longissimus (longest)
Number of heads or bellies
Biceps (two heads) Triceps (three heads) Quadriceps (four heads) Digastric (two bellies)
Depth
Superficialis (superficial) Profundus (deep) Externus/externi (external) Internus/interni (internal)
Attachment
Sternocleidomastoid (from sternum and clavicle to mastoid process) Coracobrachialis (from the coracoid process to the arm)
Position
Anterior, posterior, medial, lateral, superior, inferior, supra-, infra- Interosseus (between bones) Dorsi (of the back) Abdominis (of the abdomen) Pectoralis (of the chest) Brachii (of the arm) Femoris (of the thigh) Oris (of the mouth) Oculi (of the eye)
Action
Extensor, flexor Abductor, adductor Levator, depressor Supinator, pronator Constrictor, dilator

Fibre architecture

Muscles can be classified according to their general shape and the predominant orientation of their fibres relative to the direction of pull (**Fig. 5.47**). Muscles with fibres (cells) that are largely parallel to the line of pull vary in form from flat, short and quadrilateral (e.g. thyrohyoid) to long and strap-like (e.g. sternohyoid, sartorius). In such muscles, individual fibres may run for the entire length of the muscle, or over shorter segments when there are transverse, tendinous intersections at intervals (e.g. rectus abdominis). In a fusiform muscle, the fibres may be close to parallel in the 'belly', but converge to a tendon at one or both ends. Where fibres are oblique to the line of pull, muscles may be triangular (e.g. temporalis, adductor longus) or pennate (feather-like) in construction. The latter vary in complexity from unipennate (e.g. flexor pollicis longus) and bipennate (e.g. rectus femoris, dorsal interossei) to multipennate (e.g. deltoid). Fibres may pass obliquely between deep and superficial aponeuroses, in a type of 'unipennate' form (e.g. soleus), or they may start from the walls of osteofascial compartments and converge obliquely on a central tendon in circumpennate fashion (e.g. tibialis anterior). Muscles may exhibit a spiral or twisted arrangement (e.g. sternocostal fibres of pectoralis major or latissimus dorsi, which undergo a 180°-twist between their medial and lateral attachments). Muscles may spiral around a bone (e.g. supinator, which winds obliquely around the proximal radial shaft), or contain two or more planes of fibres arranged in differing directions, a type of spiral sometimes referred to as cruciate (sternocleidomastoid, masseter and adductor magnus are all partially spiral and cruciate). Many muscles display more than one of these major types of arrangement, and show regional variations that correspond to contrasting, and in some cases independent, actions.

Direction of force

Although muscles differ in their internal architecture, the resultant force must be directed along the line of the tendon, so forces transverse to this direction must be in balance (see Fig. 5.47; **Fig. 5.48**). In strap-like muscles, the transverse component is negligible. In fusiform, bipennate and multipennate muscles, symmetry in the arrangement of the fibres produces a balanced opposition between transverse components, whereas in asymmetric muscles (e.g. unipennate muscles), the fibres generate an unopposed lateral component of force that is balanced by intramuscular pressure.

Muscles that incorporate a twist in their geometry unwind it as they contract, so that they tend not only to approximate their attachments but also to bring them into the same plane. Muscles that spiral around a bone tend to reduce the spiral on contraction, causing rotation.

Force versus range of contraction

Muscle fibre architecture varies because some muscles are required to develop a large force on their tendinous insertion, whereas other muscles are required to move their insertion through a considerable distance. These demands are largely incompatible and require different muscle architecture.

The force developed by an active muscle depends on the tension developed in each muscle fibre. If all of the muscle fibres are parallel (as in the strap-like muscle in Fig. 5.47), then the muscle force is equal to the sum of the tension in each fibre, and so will be proportional to the total cross-sectional area of those fibres. The range of contraction generated by an active muscle depends on the relative motion that can take place between the overlapping proteins in the sarcomere, and this sets a natural limit (approximately 30%) to the amount of fibre shortening that can take place. Hence, the movement of the tendinous insertion is proportional to the length of the muscle fibres.

If these principles are applied to a long, strap-like muscle in which the fibres are predominantly parallel to the line of pull (see Fig. 5.47), it will be evident that the whole muscle will be able to contract by 30% of its length (the same as each muscle fibre). However, such a strap-like muscle contains relatively few muscle fibres, so the maximum tension it can develop will not be great. Compare this to the bipennate muscle in **Fig. 5.49**, which contains perhaps three times as many muscle fibres, all set at an angle (typically 30°) to the axis of the tendon. Each short fibre will not be able to contract very far, and the contraction of the tendon will be even less, because the muscle fibres are pulling on it

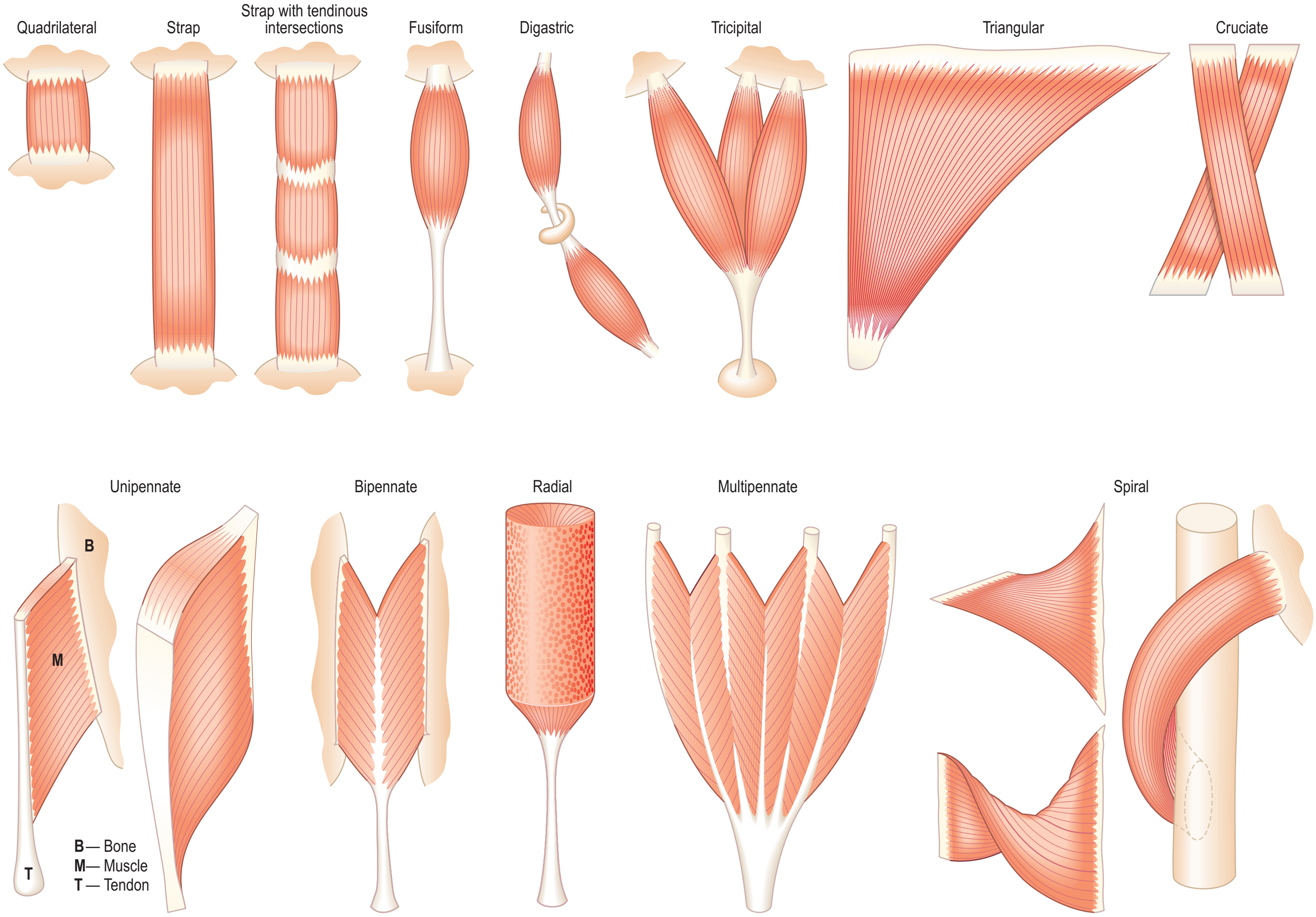
Quadrilateral
Strap
Strap with tendinous intersections
Fusiform
Digastric
Tricipital
Triangular
Cruciate
Unipennate
B
M
T
B— Bone
M— Muscle
T— Tendon
Bipennate
Radial
Multipennate
Spiral

Fig. 5.47 Morphological ‘types’ of muscle based on their general form and fascicular architecture.

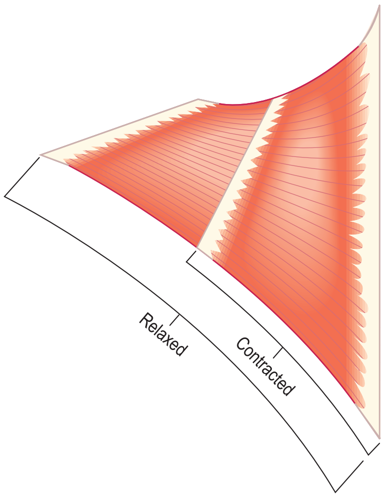
Relaxed
Contracted

Fig. 5.48 The ‘detorsion’ or untwisting that results from the contraction of a spirally arranged muscle.

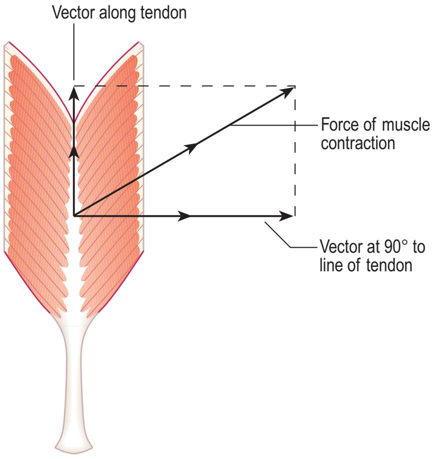
Vector along tendon
Force of muscle contraction
Vector at 90° to line of tendon

Fig. 5.49 Force vectors in an idealized pennate muscle. The increase in effective cross-sectional area made possible by this architecture outweighs the small reduction in the component of force acting in the direction of the tendon.

obliquely. So, the bipennate muscle has a poor contraction distance. However, the total force its fibres can generate will be approximately three times as great as the tension in the strap-like muscle. Even after this force is reduced to allow for its obliquity (in this case by cos 30°, which equals 0.87), the overall tension in the direction of the tendon will exceed that in the strap-like muscle by a factor of 2.6 (3×0.87). So, the bipennate muscle sacrifices contraction distance for greater maximum force. This effect would be much greater in the multipennate muscle shown in Fig. 5.47.

Force, strength and power

In descriptions of muscle performance, ‘force’, ‘strength’ and ‘power’ are often used interchangeably but these terms are not synonymous. When considering human performance, it is possible for strength to increase without a concomitant increase in the true force-generating capacities of the muscles involved. Strength is usually measured under circumstances that require the participation of several muscles, and so depends on skilful coordination of these muscles as well as the forces they generate. This disparity can be marked during the early stages of physical training.

Power is the rate at which a muscle can perform external work, and is equal to force multiplied by contraction velocity. Since force depends on the total cross-sectional area of muscle fibres, and velocity (the rate of muscle shortening) depends on muscle fibre length, powerful muscles tend to be long as well as fat. A prime example is the quadriceps, which is the prime mover when someone stands up from a seated position. A lack of power in this and other muscles is the critical factor that limits the ability of many elderly people to live independently (Reid and Fielding 2012).

Actions of muscles

Historically, the actions of specific muscles were estimated from simple observation. Muscle attachments were identified by dissection, and their probable action deduced from the line of pull. With the use of localized electrical stimulation it became possible to study the actions of selected muscles systematically in the living subject. This approach was pioneered by Duchenne de Boulogne in the mid-nineteenth century. However, the study of isolated muscles cannot reveal the manner in which they interact during voluntary movements. Duchenne appreciated this, and supplemented electrical stimulation with observations of patients with partial paralysis to make more accurate deductions about the way in which muscles cooperate. Manual palpation can be used to detect muscle contraction, but only in superficial muscles under quasi-static conditions. Modern knowledge of muscle action has been acquired almost entirely by recording the electrical activity that accompanies mechanical contraction, a technique known as electromyography (EMG). This technique can be used to study activation of deep as well as superficial muscles, under static and dynamic conditions. Multiple channels of EMG can reveal coordination between different muscles that participate in a movement. These data can be further supplemented by monitoring joint angle and ground reaction force, and by recording the movement on camera or with a three-dimensional motion analysis system.

Conventionally, the action of a muscle is defined as the movement that takes place when it contracts. However, this is an operational definition: equating 'contraction' with shortening, and 'relaxation' with lengthening is too simple in the context of whole muscles and real movements. Whether a muscle approximates its attachments on contraction depends on the degree to which it is activated, and the forces against which it has to act.

Movements that involve shortening of an active muscle are termed concentric, e.g. contraction of biceps/brachialis while raising a weight and flexing the elbow. Movements in which the active muscle undergoes lengthening are termed eccentric, e.g. in lowering the weight previously mentioned, biceps/brachialis 'pays out' length as the elbow extends. Eccentric contractions stretch the collagenous tissue sheaths within muscle (see below), which increases the risk of tears in muscles such as the hamstrings, and of a more general delayed-onset muscle soreness (Proske and Morgan 2001). Muscle contraction that does not involve change in muscle length is isometric.

Natural movements are accomplished by groups of muscles. Each muscle may be classified, according to its role in the movement, as a prime mover, antagonist, fixator or synergist. It is usually possible to identify one or more muscles that are consistently active in initiating and maintaining a movement: these are its prime movers. Muscles that wholly oppose the movement, or initiate and maintain the opposite movement, are antagonists. For example, brachialis is the prime mover in elbow flexion, and triceps is the antagonist. To initiate a movement, a prime mover must overcome passive and active resistance and impart an angular acceleration to a limb segment until the required angular velocity is reached; it must then maintain a level of activity sufficient to complete the movement.

When prime movers and antagonists contract together they behave as fixators, stabilizing the corresponding joint by increased transarticular compression, and creating an immobile base on which other prime movers may act. For example, flexors and extensors of the wrist co-contract to stabilize the wrist when an object is grasped tightly in the fingers.

Acting across a uniaxial joint, a prime mover produces a simple movement. Acting at multiaxial joints, or across more than one joint, prime movers may produce more complex movements that contain elements that have to be eliminated by contraction of other muscles. The latter assist in accomplishing the movement and are considered to be synergists, although they may act as fixators, or even as partial antagonists of the prime mover. For example, flexion of the fingers at the interphalangeal and metacarpophalangeal joints is brought about primarily by the long flexors, superficial and deep. However, these also cross intercarpal and radiocarpal joints, and if movement at these joints were unrestrained, finger flexion would be less efficient. Synergistic contraction of the carpal extensors eliminates this movement, and even produces some carpal extension, which increases the efficiency of the desired movement at the fingers.

In the context of different movements, a given muscle may act as a prime mover, antagonist, fixator or synergist. Even the same movement may involve a muscle in different ways if it is assisted or opposed by gravity. For example, in thrusting out the hand, triceps is the prime mover responsible for extending the forearm at the elbow, and the flexor antagonists are largely inactive. However, when the hand lowers a heavy object, the extensor action of the triceps is replaced by gravity, and the movement is controlled by active lengthening (eccentric 'contraction') of the flexors. It is important to remember that all movements take place against the background of gravity and its influence must not be overlooked.

TENDONS AND LIGAMENTS

Forces developed by skeletal muscles are transferred to bone by tendons, aponeuroses and fasciae, whereas ligaments prevent excessive separation of adjacent bones. All of these force-transmitting structures comprise dense fibrous connective tissues containing a high proportion of type I collagen (see Commentary 1.6).

Tendons

Gross structure and function

Tendons take the form of whitish-looking cords or straps, usually with a round or oval cross-section. They are composed of dense, regular connective tissue, with 60% of their dry weight comprising large crimped fibres of collagen type I (**Fig. 5.50**; see Fig. 2.15). Other components of their matrix include collagen types II and V, elastin, glycoproteins and proteoglycans (Wang 2006). Fascicles (bundles) of collagen fibres are orientated mainly parallel to the long axis of the tendon but are to some extent interwoven; they may be conspicuous enough to give tendons a longitudinally striated appearance to the unaided eye. Tendons generally have smooth surfaces, although large tendons may be ridged longitudinally by coarse fasciculi (as in the osseous aspect of the angulated tendon of obturator internus). Loose connective tissue between fascicles provides a conduit for small vessels and nerves; it condenses on the surface as a sheath or epitendineum, which may contain elastin and irregularly arranged collagen fibres. The loose attachments between this sheath and the surrounding tissue present little resistance to movements of the tendon. In situations where greater freedom of movement is required, a tendon is separated from adjacent structures by a synovial sheath.

Tendons can be stretched by 6–15% of their length without damage (Wang 2006). Some of this extensibility is attributable to the reorientation of collagen type I fibres, some to the straightening of the crimped (wave-like) structure of these fibres, and some to sliding between adjacent collagen fibrils and fibres (Screen et al 2004). Sliding is possible because discrete collagen fibres appear to reinforce connective tissue in the manner of a 'chopped fibre-composite' material such as fibre glass (Hukins and Aspden 1985), rather than by forming a fixed scaffold (which would make growth difficult). It takes a great deal of energy to stretch a long and strong tendon, and most of this 'strain energy' can be recovered when the tension is released. During locomotion, the rhythmic storing and releasing of strain energy in stretched tendons helps to smooth the movement, so that tendons (rather than cartilage) act as the body's

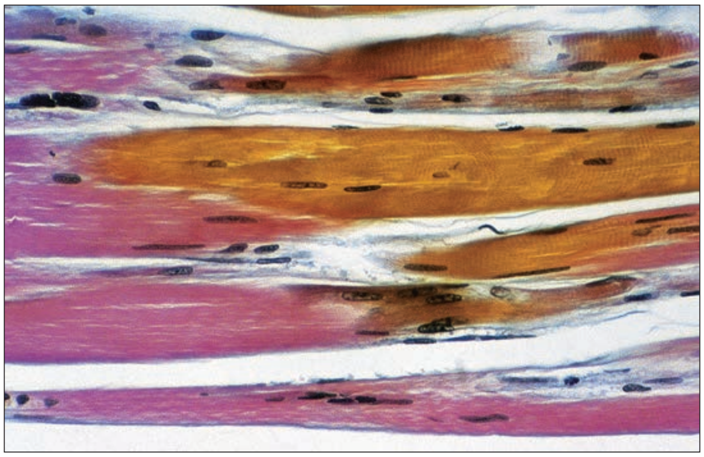

Fig. 5.50 The attachment of a tendon (pink) to skeletal muscle (orange). The regular dense connective tissue of the tendon consists of parallel bundles of type I collagen fibres, which are orientated in the long axes of the tendon and the muscle to which it is attached. A few elongated fibroblast nuclei are visible in the tendon. Trichrome stain.

natural shock absorbers. This energy storage and release also reduces the metabolic cost of locomotion. Tendons are sufficiently flexible that they can be diverted around osseous surfaces or deflected under retinacula to redirect the angle of pull.

The vascular supply of tendon is sparse but not negligible. Small arterioles from adjacent muscle tissue pass longitudinally between the fascicles, branching and anastomosing freely, and are accompanied by venae comitantes and lymphatic vessels. This longitudinal plexus is augmented by small vessels from adjacent loose connective tissue or synovial sheaths. Blood vessels rarely pass between bone and tendon at osseous attachments, and the junctional surfaces are usually devoid of foramina. A notable exception is the calcaneal (Achilles) tendon, which does receive a blood supply across its osseotendinous junction. During postnatal development, tendons enlarge by interstitial growth, particularly at myotendinous junctions, where there are high concentrations of fibroblasts. Growth decreases along a tendon from the muscle to the osseous attachments. The thickness finally attained by a tendon depends on the size and strength of the associated muscle, but also appears to be influenced by additional factors such as the degree of pennation of the muscle. The cellularity, and hence the metabolic rate, of large adult tendons is very low, but increases during infection or injury. Repair involves an initial proliferation of fibroblasts followed by interstitial deposition of new collagen fibres (Wang 2006). Complete turnover (replacement) of the tissue, as seen in bone, does not occur in adult tendons, so healed tendons do not quite recover their original strength. Tendons can adapt their stiffness and strength to match prevailing mechanical demands, but the process is slow and may be incomplete (Rumian et al 2009).

The nerve supply to tendons is largely sensory and there is no evidence of any capacity for vasomotor control. Golgi tendon organs, specialized endings that are sensitive to force, are found near myotendinous junctions; their large myelinated afferent axons run within branches of muscular nerves or in small rami of adjacent peripheral nerves. They play an important role in 'tendon reflexes', which serve to protect the musculoskeletal system from injury.

Tendon attachments

Muscles connect to bones by means of tendons, aponeuroses and fasciae. The epimysial, perimysial and endomysial sheaths within muscle coalesce at these attachments, and interdigitate with adjacent collagenous structures to form strong connections in which force transmission is aided by shear stress transfer.

At the myotendinous junction, muscle fibres separate into finger-like processes separated by insertions of tendinous collagen fibres. Although there are no desmosomal attachments at these junctions, other specializations assist in the transmission of force from the interior of the fibre to the extracellular matrix. Actin filaments from the adjacent sarcomeres, which would normally insert into a Z-disc at this point, instead penetrate a dense, subsarcolemmal filamentous matrix that provides attachment to the plasma membrane. This matrix is similar in character to the cytoplasmic face of an adherens junction. The structure as a whole is homologous to the intercalated discs of cardiac muscle. Integrins at the extracellular surface of the junctional sarcolemma provide contact with the basal lamina, which adheres closely to collagen and reticular fibres (type III collagen) of the adjacent tendon or other connective tissue structure.

Tendinous attachments to bone (also known as entheses or osteotendinous junctions) have been broadly categorized as either fibrocartilaginous or fibrous (Benjamin et al 2006). In fibrocartilaginous entheses, four zones of tissue can be distinguished: pure dense fibrous connective tissue (continuous with and indistinguishable from the tendon), uncalcified fibrocartilage, calcified fibrocartilage, and bone (continuous with and indistinguishable from the rest of the bone). There are no sharp boundaries between zones, and the proportions of each component vary between entheses. A largely fibrocartilaginous enthesis is usually found where a tendon approaches the bone at a high angle, e.g. triceps brachii (**Fig. 5.51A–B,D**). At fibrous entheses, which are characteristic of the shafts of long bones, the tendon approaches the bone at an acute angle and merges with the periosteum before attaching to bone by dense fibrous connective tissue, e.g. pronator teres (**Fig. 5.51C**). Fibrous entheses generally attach to a greater area of bone compared to fibrocartilaginous entheses, enabling them to reduce stress.

For further reading on tendons see Magnusson and Kjaer (2019).

Ligaments

The microstructure and biology of ligaments is broadly similar to that of tendons (Rumian et al 2007). Ligaments consist mostly of large crimped fibres of collagen type I, and their cells are predominantly elongated fibroblasts. However, there are two major differences between tendons

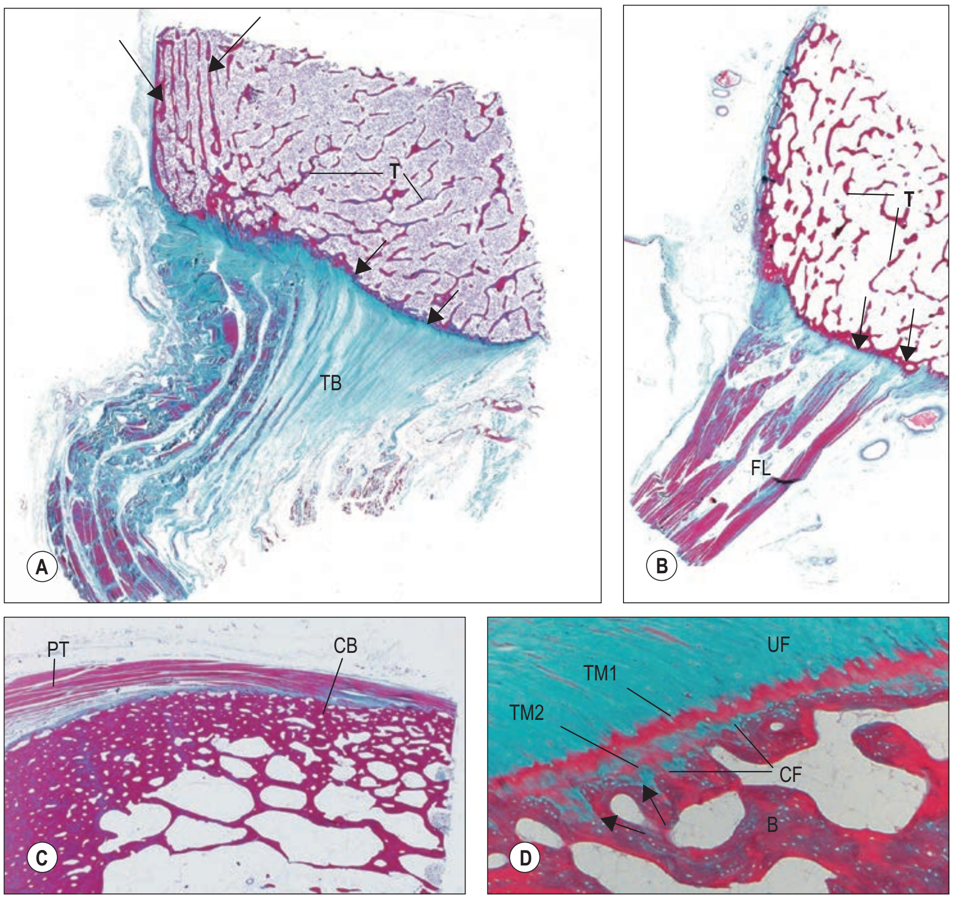

Fig. 5.51 The microstructure of bone at entheses. **A**, **B**, The cortical shell of bone (short arrows) is very thin at fibrocartilaginous attachment sites. In these examples showing the attachment of the tendons of triceps brachii (TB) and of fibularis longus (FL), the cortical shell is approximately the same thickness as the underlying trabeculae (T). Note that in **A**, the superficial trabeculae (long arrows) are aligned along the direction of pull of the tendon of triceps. **C**, In marked contrast, the layer of cortical bone (CB) at the fibrous attachment site of pronator teres (PT) to the mid-shaft of the radius, is much thicker. **D**, Higher-power view of the cortical calcified shell of tissue at a fibrocartilaginous attachment site (the calcaneal or Achilles tendon), which consists of bone (B) and calcified fibrocartilage (CF). In this specimen, there are two tidemarks, TM1 and TM2, associated with the cortical shell of calcified tissue. TM1 is adjacent to the zone of uncalcified fibrocartilage (UF), and marks the mechanical boundary between hard and soft tissues. TM2 lies nearer the bone and indicates an earlier phase of calcification. Note the relative straightness of the tidemarks but the highly irregular interface between calcified fibrocartilage and bone (arrows), which is important in anchoring the tendon to the bone. Sections of human cadaveric bone stained with Masson's trichrome. (Courtesy of Professor Michael Benjamin, Cardiff University, from sections cut and stained by S. Redman.)

and ligaments, relating to gross structure and to composition. Structurally, ligaments tend to have fibres orientated in a range of directions because they must resist the separation of bones in more than one direction, whereas collagen fibres in a tendon must simply align with tension in the adjacent muscle. More diverse mechanical roles of ligaments are also reflected in their composition. For example, the ligamentum flavum, which joins adjacent vertebrae in the spine, has a very high elastin content that enables it to be stretched more than 80% when the spine is flexed, and yet remain under tension in all postures. Maintaining tension is important because this ligament lies adjacent to the spinal cord, and could impinge on it if it became slack (and buckled) when the spine was moved into extension.

BIOMECHANICS

The purpose of this section is to explain, in a non-mathematical way, how mechanical principles shape the human musculoskeletal system. Mechanical considerations explain why bones are stiff and tendons are tough, why the surfaces of some synovial joints are imperfectly matched, and why some tendons insert closer to joints than others. The emerging subject of 'mechanobiology' considers how cells adapt their matrix to prevailing mechanical demands and explains why some tissues are better at doing this than others.

Mechanical concepts

Forces, moments and torques

A force is an action that deforms an object, or that causes it to move, and can be termed compressive, tensile or shear, according to the manner in which it deforms that object (Fig. 5.52). A force F acting at the end of a lever of length L will generate a bending moment (F × L) acting about the pivot point of the lever. A torsional moment or torque (Fig. 5.52F) can be quantified in similar terms. The combined influence of several forces can be calculated as shown in Fig. 5.53. If the forces all act in the same direction, they may be added. However, if they act in different directions, each force must be resolved into two imaginary components that act in two anatomically convenient directions at 90° to each other, using simple trigonometry. All components acting in the same direction are added to form two forces (S and C in Fig. 5.53), that can be used to calculate the magnitude and direction of the single 'resultant' force which has a similar effect to all of the individual forces combined. Forces acting on a stationary object are analysed according to the principle that all forces acting in any given direction must balance each other (i.e. add to zero), and all moments or torques acting about a given pivot point must also balance each other.

Mechanical properties of structures

Most anatomical structures deform readily when a sufficient force is applied to them, but their resistance to deformation increases steadily as the magnitude of the force increases. The resulting graph of force against deformation usually resembles the one shown in Fig. 5.54. Stiffness is the ratio of force to deformation (typical units N/mm) and so is represented by the gradient of the graph. The initial region of low stiffness, or 'toe region', is followed by a stiffer region in which the graph is almost linear. In many biological structures, the 'toe region' can be explained by the straightening out of the zig-zag 'crimped' structure of collagen type I fibres, whereas the linear region represents direct stretching of the straightened collagen fibres (and some slipping between them). If the deformed structure springs back immediately to its original dimensions when the deforming force is removed, the deformation is termed 'elastic'; a deformation that shows no sign of recovering is plastic;

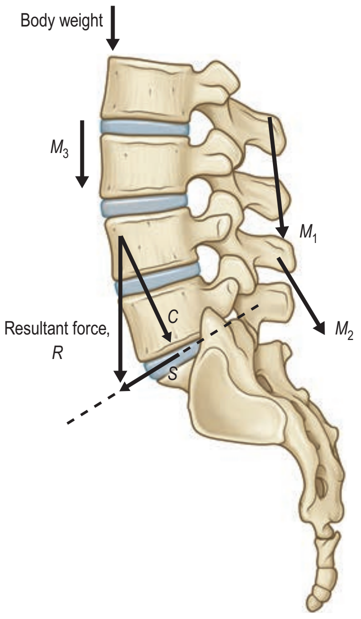

Fig. 5.53 The combined effect of several muscle forces (M_1–M_3) and body weight can be calculated by resolving each force into two components acting in two anatomically meaningful directions (in this case parallel and perpendicular to the mid plane of the lumbosacral intervertebral disc). The components acting in these two directions are then summed to give the total compressive (C) and shear (S) forces acting on the disc. The magnitude and direction of the resultant force (R), which represents the combined effect of all four forces, can be calculated using trigonometry.

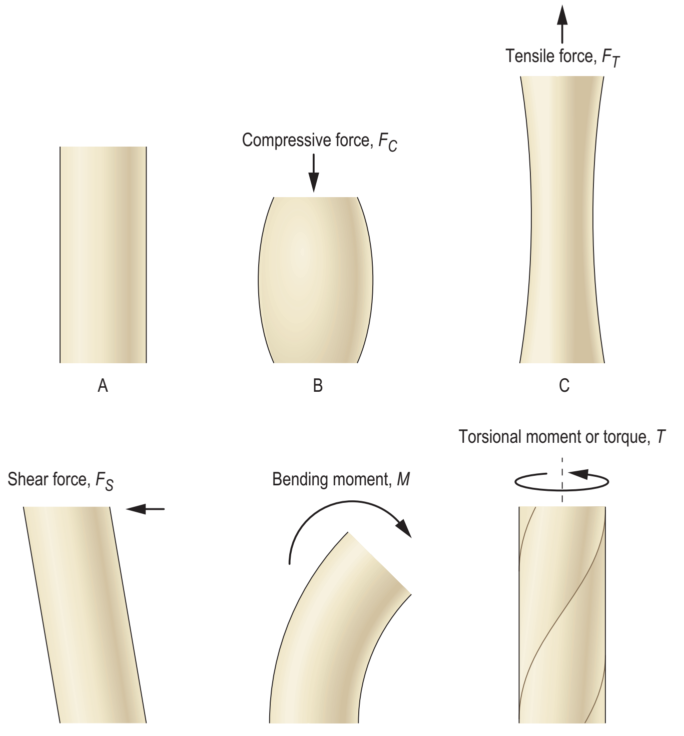

Fig. 5.52 The effects of different types of loading on a solid object (**A**) are illustrated in **B–F**.

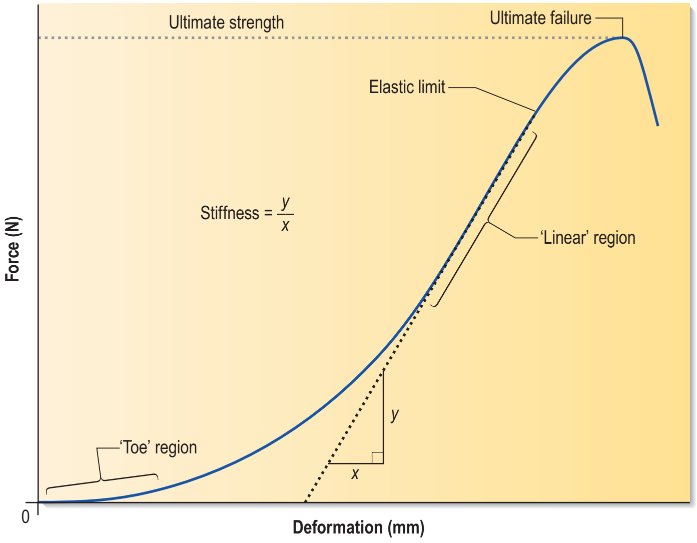

Fig. 5.54 A typical force–deformation graph for a skeletal structure subjected to mechanical loading. In the initial 'toe region', deformation increases rapidly with force, but this is followed by a linear region in which the deformation increases more slowly, and in proportion to the applied force. The gradient of the graph indicates the stiffness of the structure at any given load. Strength is the force at which an object becomes damaged, and this is usually interpreted either as the force at which the gradient first reduces (the elastic limit) or as the force when the gradient falls to zero (the ultimate strength).

a deformation that recovers eventually, but gradually, is viscoelastic (see below). 'Strength' is the force at which an object becomes damaged, and is usually interpreted either as the force at which the gradient of the graph first reduces (the elastic limit) or as the force when the gradient falls to zero (the ultimate strength).

Properties of materials

The properties of materials must be expressed in such a way that they are independent of the size and shape of the structure they constitute. A force divided by the area over which that force is applied gives a stress value (force per unit area) and the resulting deformation divided by the original length of the object gives a strain value (fractional or percentage deformation). Stress divided by strain is the size-independent material equivalent of the stiffness of an object, and is an important physical property termed the 'modulus' (sometimes 'Young's modulus'). There are different types of moduli but essentially they are measures of the stiffness, or resistance to deformation, of a material or tissue.

Energy and shock absorption

Deforming an object may require a considerable expenditure of energy. Technically, the work done (i.e. energy expended) is proportional to the average force exerted, multiplied by the distance moved. This is mathematically equivalent to the area under the graph in **Fig. 5.55**, and is referred to as the strain energy, i.e. the energy expended in deforming the object. If the object has elastic properties, it will spring back to its original shape when the deforming force is removed, and all the strain energy is then released. (This release of strain energy explains why a stretched rope can recoil violently if it snaps.) Structures such as coiled springs, which can resist high forces and also deform extensively, are capable of storing large amounts of energy, and so can act as shock absorbers when they are continually compressed and stretched. Tendons act in a similar manner during locomotion: they store strain energy when they are stretched by muscle contraction, and release most of this energy when the muscles relax later in the gait cycle. Internal friction between matrix components means that a small fraction of the stored strain energy, the hysteresis energy, is dissipated as heat (see Fig. 5.55). This heat can cause the temperature to rise by several degrees centigrade in large tendons that are involved in vigorous repetitive activity. Any material or structure that is capable of absorbing large amounts of strain energy before failure is termed tough; otherwise it is brittle. From Fig. 5.55 it is apparent that tough materials must be both strong and extensible. In contrast, brittle materials such as glass and tooth enamel undergo minimal deformation and so absorb little strain energy, even though they are strong. The shock-absorbing characteristics of tendons are important during locomotion, making movements smoother and reducing metabolic cost (Alexander 1988).

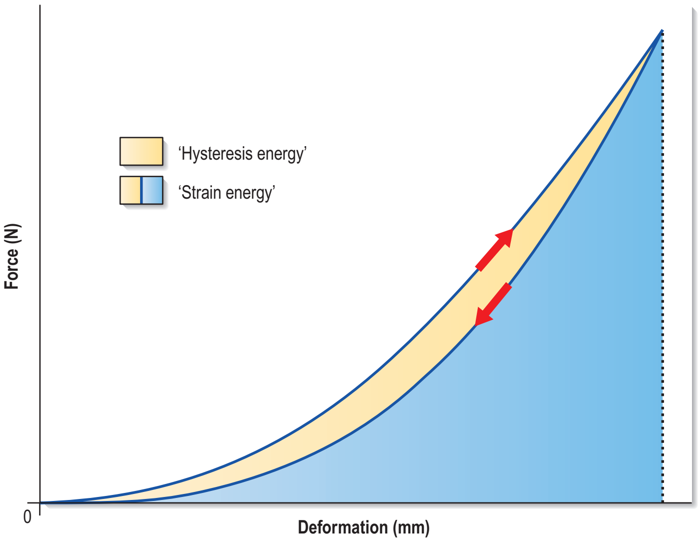

Fig. 5.55 This force–deformation graph shows how an object deforms when a force is applied to it (upward arrow) and how it recovers its shape when the force is gradually released (downward arrow). The area under the loading curve represents the strain energy that has been expended in deforming the object. The area under the unloading curve represents the energy that is given up when the object is allowed to spring back to its original shape. The small area in between represents energy that cannot be recovered but is dissipated as heat. This is the hysteresis energy.

Liquids

A liquid has negligible rigidity and so deforms readily to take the shape of its container. When compressed, it maintains practically the same volume, but it flows to equalize the intensity of loading within it. As a result, a static liquid under load exhibits a single internal stress (force per unit area) that does not vary with location or direction: this is 'pressure'. Even delicate objects are not deformed when immersed in a high-pressure liquid if they themselves are filled with liquid, because the internal and external pressures on them are exactly equal; this explains why cells can survive high pressures in liquids without damage to their delicate plasma membrane. Of the musculoskeletal tissues, only the nucleus pulposus of intervertebral discs exhibits a true fluid pressure (Adams et al 2013). Some other tissues, including bone and cartilage, contain liquid that is able to move through pores in the solid matrix.

Viscoelasticity

Materials are said to be viscoelastic if they behave partly like a thick (viscous) fluid and partly like an elastic solid. Viscoelastic deformations change with time, even when the deforming stress is constant, and complete recovery from such deformations also takes some time after the stress is removed (**Fig. 5.56**). In most biological materials, viscous behaviour occurs because applied loading causes fluid to flow from the most heavily loaded regions to the least loaded, by percolating through very small (nanometre-scale) pores in the matrix, a process that can take hours; for this reason, the term poroelastic is often preferred to viscoelastic when referring to tissues such as cartilage.

Creep and stress relaxation are two important manifestations of viscoelasticity. Creep may be described as continuing deformation under constant load (see Fig. 5.56), whereas stress relaxation is a gradual decrease in force resisted by a viscoelastic material when it is initially deformed by a certain amount, and then held with the same constant deformation. Creep can reduce the thickness of loaded articular cartilage and intervertebral discs, typically by 20% in 5 minutes and 3 hours, respectively. Creep deformation is reversed over a comparable timescale when the compressive loading is reduced and water is reabsorbed. Bone creeps at a much slower rate, but in old osteoporotic vertebrae, creep probably contributes significantly to vertebral deformity (Luo et al 2012).

Material properties of skeletal tissues

The material properties of several skeletal tissues are compared in **Table 5.3**.

Bone

Bone consists mainly of collagen type I and microcrystals of the mineral hydroxyapatite. Collagen gives bone considerable tensile strength, and

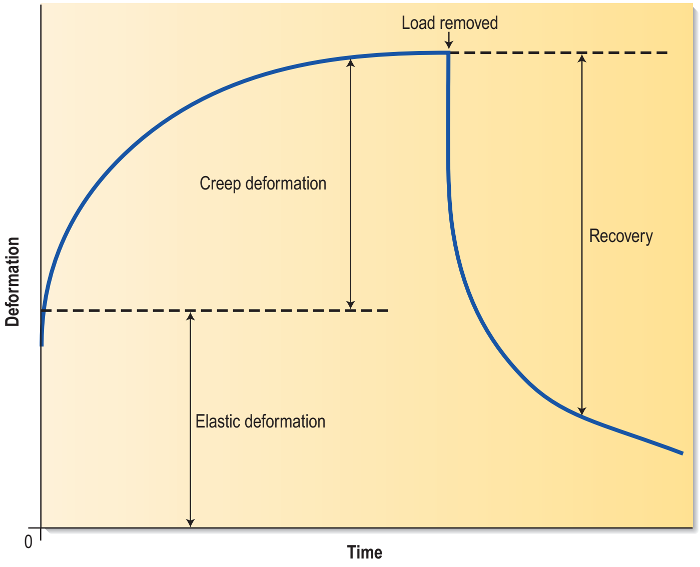

Fig. 5.56 The deformation of viscoelastic materials varies with time. In this example, a load is applied at zero time, which causes an immediate elastic deformation, followed by a slowly increasing time-dependent deformation (creep). When the load is removed, some deformation is recovered immediately, but full recovery is achieved only slowly.

TABLE 5.3 Tensile material properties of skeletal tissues*

	Cortical bone	Tendon (ligament)	Articular cartilage
Strength (MPa)	130	50–110	5–20?
Modulus (MPa)	17,000	500–1800 (150–800)	4–10
Failure strain (%)	1–2.5	10–20	30–100

**For comparison, alloy steel has a strength of 600 MPa and a modulus of 20,000 MPa.*

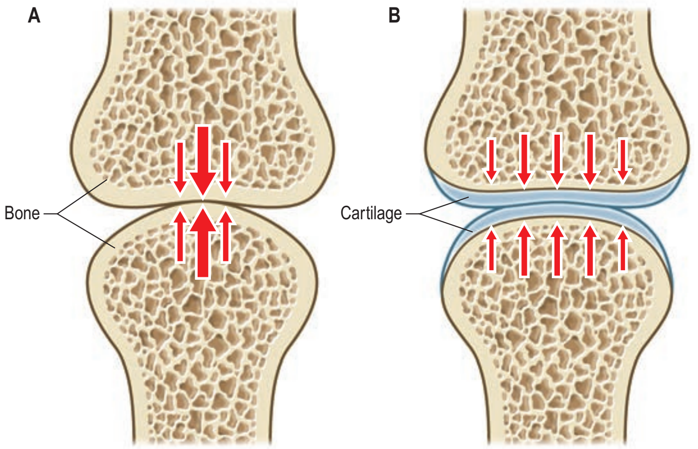

Fig. 5.57 Articular cartilage in a synovial joint is not as stiff as the underlying bone, so the presence of cartilage in a loaded joint increases the area of contact (**B**) compared to a joint without cartilage (**A**).

renders it very tough when fractured, whereas the mineral component gives bone a very high compressive modulus and high compressive strength. Rigidity (high stiffness or modulus) is the defining characteristic of bone; it enables the tissue to provide precisely shaped surfaces in synovial joints that will deform very little under load, and it also enables fast locomotion when muscles pull on bones. If bones were strong and tough but not rigid, rapid muscle contractions would cause them to bend alarmingly and would slow the angular movement of limbs.

Tendon, ligament and fascia

Tendons, ligaments and fascia consist primarily of densely packed collagen type I fibres, giving these tissues high tensile strength. The crimped nature of the collagen fibres allows them to be stretched by 10–15% before failure, and this combination of strength and extensibility enables tendons, ligaments and fascia to absorb more strain energy per unit weight than any other biological material. An important difference between tendons and ligaments is that ligaments often contain bundles of collagen fibres orientated in a range of directions, presumably because bones can be moved apart in a range of directions, whereas the fibres in a tendon are all aligned with the direction of muscle tension. Fascia usually contains collagen fibres aligned in adjacent sheets to resist forces in at least two different directions.

Hyaline cartilage

Hyaline cartilage consists mainly of very fine collagen type II fibrils and large proteoglycan molecules, which have the property of attracting water and swelling. Collagen gives cartilage its tensile stiffness and strength, and the proteoglycans give the tissue a high water content that confers compressive 'turgor'. During growth and healing, proteoglycans enable cartilage to swell and occupy space that later will be strengthened by other components of the matrix. Articular cartilage is a particular type of hyaline cartilage that covers the ends of articulating bones; its high water content enables it to distribute loading evenly on the underlying bone. Because cartilage is softer than bone, it deforms more when loaded, increasing the area of contact between articular surfaces and reducing contact stress (Fig. 5.57). Cartilage creep (see above) causes the area of contact to increase, and further reduces contact stress. Creep in articular cartilage also causes water to be exuded into the joint cavity, assisting in fluid-film lubrication (see below). Articular cartilage 'wear' (loss of material) during high and repetitive loading is minimized because the collagen type II fibrils in the superficial zone are aligned parallel to the surface, an arrangement that provides maximal resistance to surface splitting and the subsequent loss of tissue.

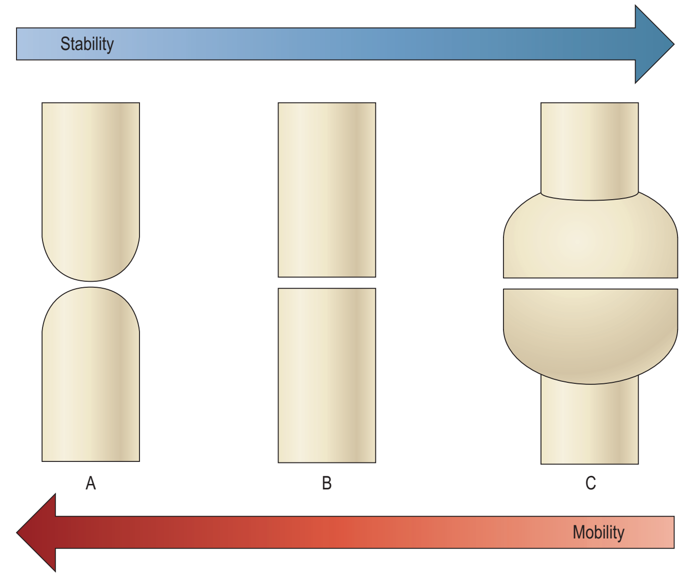

Fig. 5.58 In synovial joints, the shapes of the opposing bone ends largely determine how much movement is possible, and the stability of the joint. Curved bone ends (**A**) lead to high mobility but low stability (in the plane of the page). Conversely, very wide bone ends (**C**) lead to low mobility and high stability. Some joints resemble (**A**) in one plane but (**B**) or (**C**) in others.

Fibrocartilage and elastic cartilage

Fibrocartilage and elastic cartilage combine the high proteoglycan and water content that characterizes cartilage with a high proportion of either collagen type I (fibrocartilage) or elastin (elastic cartilage). Collagen type I confers extra tensile strength and toughness, whereas elastin fibres provide elastic recoil, i.e. the ability to spring back into shape after large deformations.

Mechanical properties of skeletal structures

Long bones

Long bones are characterized by enlarged ends covered in cartilage, a long hollow shaft and various bony protuberances. The enlarged ends serve to reduce contact stress where long bones meet in synovial joints, and to increase the stability of such joints (Fig. 5.58). A different relationship between stability and mobility can exist in different anatomical planes, even for the same joint, e.g. the knee joint favours stability in the frontal plane and mobility in the sagittal plane. The hollow shaft of a long bone minimizes bone mass and so increases the speed of movement. However, it also maximizes the bone's strength in bending for a given mass of material, because bending strength is increased by having as much bone as possible far from the axis of bending (Fig. 5.59). The precise cross-sectional shape of a long bone therefore gives a clear indication of the planes in which the shaft is most likely to be subjected to severe bending. Bony prominences or processes on long bones serve to increase the lever arm of the muscles attached to them: if a large prominence is close to the centre of rotation of a joint, then it can increase the lever arm by over 100%, and the maximum torque developed by the muscle about that centre of rotation would increase by the same amount.

Synovial joints

Typically, synovial joints are designed for full and free movements, but they must also provide some stability in specific planes (see Fig. 5.58). In a joint with a small range of movement, the intrinsic stability provided by its articular surfaces and ligaments may be more important than the extrinsic stability provided by surrounding muscles. Low-friction movement is facilitated by the smooth surfaces of articular cartilage being made slippery by the presence of the boundary lubricant lubricin, which is bound to the cartilaginous surfaces. This boundary lubrication reduces friction during slow movements, especially when forces are high. During rapid movements, microscopic undulations in the cartilage surface trap small quantities of synovial fluid between the articular surfaces, so that fluid-film lubrication (akin to aquaplaning) can also occur (Fig. 5.60), and friction and wear are greatly reduced. The sticky, viscous nature of

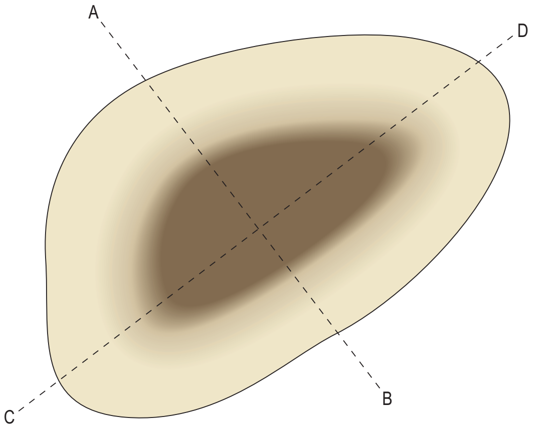

Fig. 5.59 A cross-section through the shaft of a long bone, showing how the irregular shape gives information about the bone's strength in bending about different axes. Strength will be greatest about the axis A–B because a high proportion of bone mass is located a long distance from this axis, and so will resist bending very strongly. Strength will be minimal about the axis C–D for a similar reason.

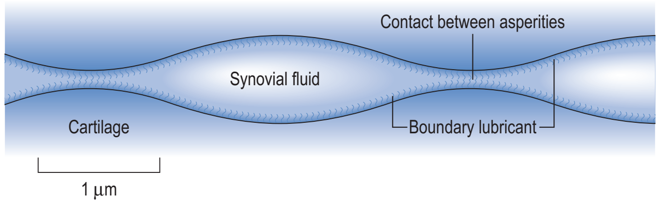

Fig. 5.60 The articular cartilage surfaces of synovial joints contain microscopic undulations that trap small quantities of synovial fluid between the surfaces, enabling fluid-film lubrication to occur. Boundary lubrication at the points of contact between cartilage asperities (roughness) is facilitated by lubricants adhering to the cartilage surface.

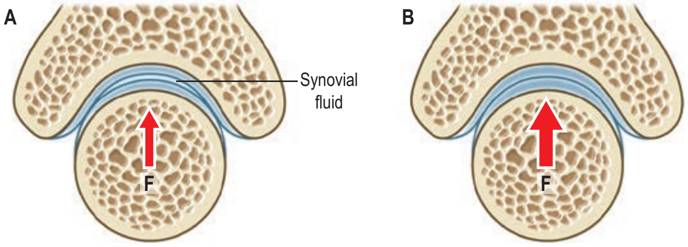

Fig. 5.61 Some synovial joints are incongruent in the sense that the opposing articular surfaces have slightly different curvatures. This ensures that there is a fluid-filled gap between them when the joint is subjected to low loading (**A**). Under high loading (**B**) this gap disappears, but peak loading at the apex of the joint remains lower than it would be if the surfaces had the same curvature, and this is a major advantage for an incongruent joint. The shape of the concave articular surface is sometimes referred to as a Gothic arch. Abbreviation: F, loading force.

synovial fluid enables it to persist between the cartilage surfaces for longer than water, which would be squeezed out much too quickly. Fluid-film lubrication is assisted by joint incongruity, in which the opposing articular surfaces have slightly different curvatures (Fig. 5.61), producing a potential fluid-filled gap that moves as the joint moves, washing synovial fluid across the cartilage surfaces. Incongruity can also help to reduce peak loading on the apex of the joint.

Intervertebral discs

Intervertebral discs are composed of three tissues: the anulus fibrosus (fibrocartilage), the nucleus pulposus (a hydrated collagen–proteoglycan gel) and the cartilage end-plates (hyaline cartilage) (Ch. 46). The water content of the nucleus pulposus can reach 90% in children and young adults, enabling the tissue to behave like a fluid. When compressive loading is applied to the vertebral column, the fluid pressure in the nucleus presses evenly on the adjacent vertebral bodies, even when they are orientated at small angles to each other. The anulus resists radial expansion of the nucleus and can deform vertically to facilitate spinal bending in various planes. The relatively dense hyaline cartilage end-plate helps to maintain a fluid pressure in the nucleus by slowing down water loss into the vertebral body through perforations in the vertebral end-plate. Nevertheless, discs lose approximately 20% of their water gradually, in the course of each day. This net loss of water is regained at night when, in recumbency, the load on the spine is relieved. Diurnal variations in disc water content cause adults to be approximately 2 cm taller in the early morning, and more flexible in the evening (Adams et al 2013).

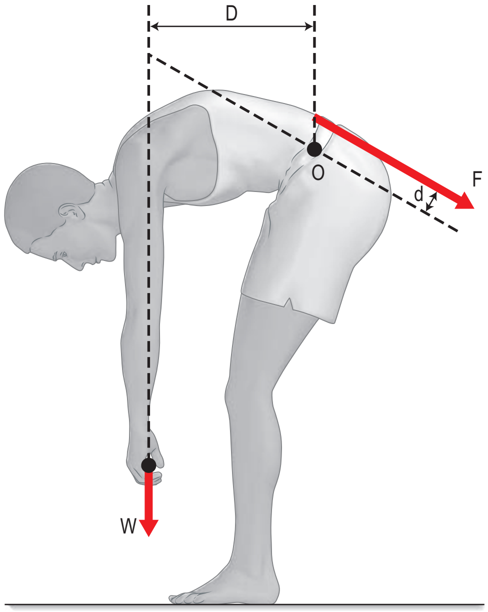

Fig. 5.62 During manual labour, muscle tension often rises to high levels in order to generate sufficient bending moment to move external objects. In this example, the back muscles act only a short distance (d) from the pivot point in the intervertebral discs (O), whereas the weight being lifted acts on a much bigger lever arm (D). In order for the moments to balance, the back muscle tension (F) must exceed the weight being lifted (W) by the ratio of D/d. In practice, this can lead to the lumbar spine being compressed by approximately 500 kg during moderate manual handling. (For simplicity, the above analysis disregards the weight of the upper body.)

Muscles and lever systems

Collagenous architecture of muscle

Muscles are supported by a hierarchy of collagenous sheaths (endomysium, perimysium and epimysium) that surround individual muscle fibres, fascicles and whole muscles, respectively. Muscles are also bound together into functional groups by collagenous fasciae. Together, these sheaths create a strong honeycomb structure that contributes to the muscle's resistance to tension. When muscle is stretched during eccentric (lengthening) contractions, high tensile forces in the collagenous structures add to the tension generated by muscle fibre contraction, leading to high and potentially damaging forces at the musculotendinous junction.

Internal muscle forces

Generally speaking, muscle forces exert greater mechanical loading on the skeleton than does body weight. For example, during relaxed standing, 50% of the compressive force acting on the lumbar spine arises from the antagonistic activity of the muscles of the back and abdomen, and 50% comes from superincumbent body weight (Adams et al 2013). However, when bending the trunk to lift weights from the ground, more than 90% of the high compressive force acting on the spine can be attributed to muscle tension (Fig. 5.62). Similarly, muscle forces acting on the knee can exceed body weight by a factor of 200–400% during stair climbing and during deep squatting movements. Muscle forces can exceed the strength of adjacent bones if they contract in alarm, so that normal inhibitory reflexes are suppressed; it is not uncommon for vertebrae to be crushed by muscle tension during major epileptic fits. According to Newton's Second Law of motion (force = mass × acceleration), muscle forces rise to high levels when attempting to accelerate body parts, e.g. during jumping or throwing: it follows that any attempt to achieve maximum acceleration will naturally require maximal muscle

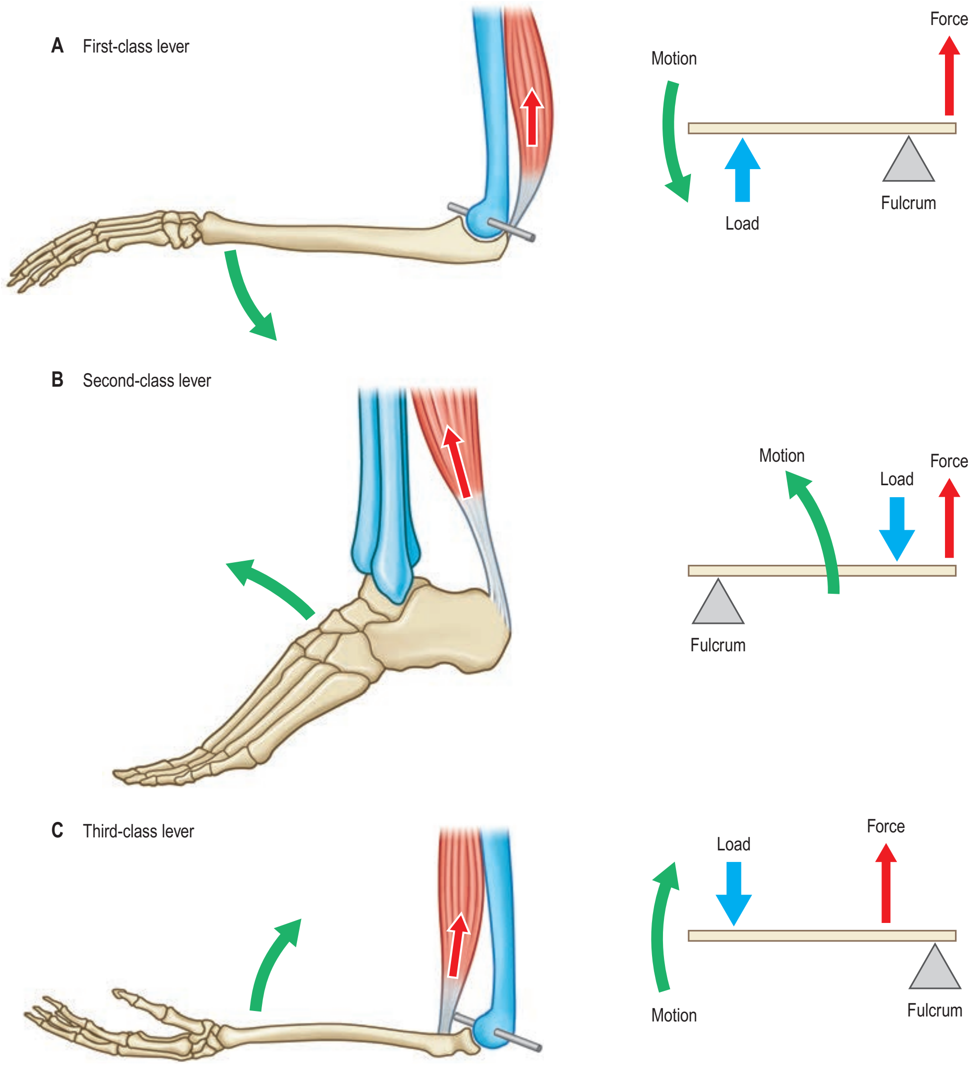

Fig. 5.63 Muscle lever systems can be classified as first-class (**A**), second-class (**B**) or third-class (**C**), according to the relative positions of the fulcrum (or pivot), the muscle insertion and the externally applied load.

tension. The size and potential dangers of internal muscle forces are often overlooked, leading some authors to draw spurious distinctions between weight-bearing and non-weight-bearing joints, and to suggest erroneously that only the former are subjected to high loading. It is likely that a watchmaker's finger joints are subjected to stresses as high, and as often, as those applied to his ankles.

Muscle lever systems

Muscle tension generates bending moments and torques about joints. Moments and torques depend on lever arms as well as muscle forces. It is conventional (although not particularly illuminating) to distinguish between three types of muscle lever system (Fig. 5.63). Generally, the length of the lever arm (the perpendicular distance between the line of action of the muscle and the centre of rotation of the joint) is more important than lever type (Fig. 5.64). If the lever arm is short, then a given muscle contraction will move the joint through a large angle, so the lever system is suited to large and/or rapid movements of that joint. Conversely, a long lever arm leads to small and/or slow movements but greater moment generation. Elite weightlifters may have muscle attachments with particularly large lever arms about particular joints.

Movements

Movements of bones

Movement of a bone is referred to as translation if it does not involve any change in orientation relative to a fixed frame of reference (or to another bone). A pure rotation involves no translation, merely a pivoting of the bone about some fixed point or centre of rotation. Spin (twisting) is the rotation of a bone about its mechanical axis, which for a long bone would coincide with its long axis. Spin can occur in conjunction with other joint rotations (Fig. 5.65). Most body movements combine rotation, translation and spin, although the translational component is often small.

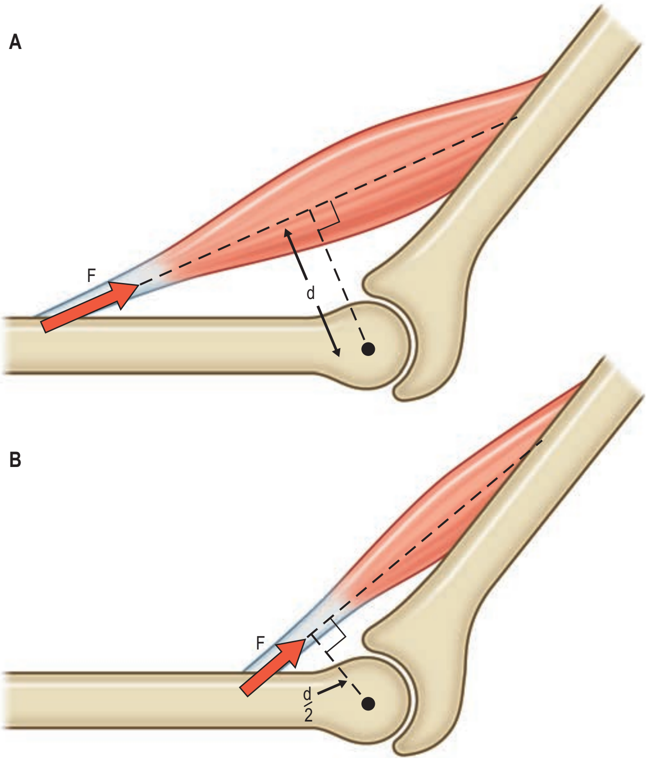

Fig. 5.64 The precise location of a muscle insertion relative to a joint greatly influences the function of that joint. **A**, If the perpendicular distance (d) between the muscle's line of action and the centre of rotation of the joint (•) is large, then the joint is suited to slow but forceful movements. **B**, If d is small, then the joint is suited to rapid but less forceful movements. Abbreviation: F, force, showing line of muscle action.

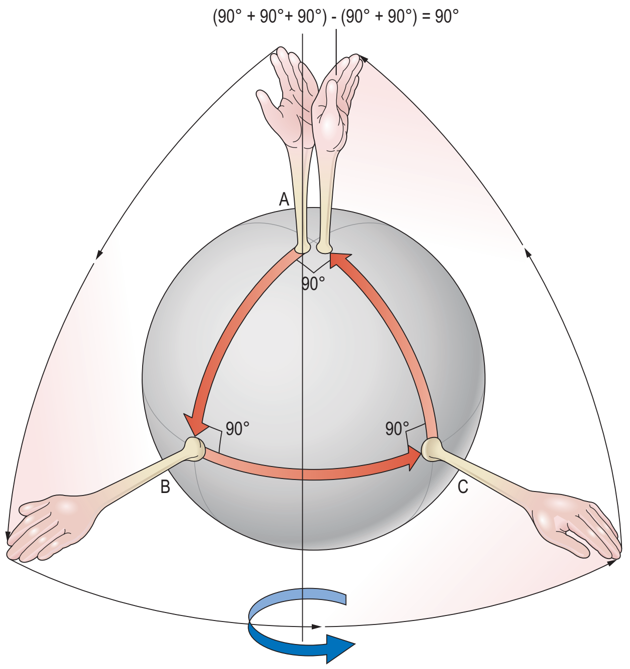

Fig. 5.65 Complex movements of the body's joints are sometimes required to produce apparently simple movements of the limbs. In this example, moving the hand as shown from A to B to C requires a hidden 'spin' movement of the arm of 90° about its mechanical (long) axis.

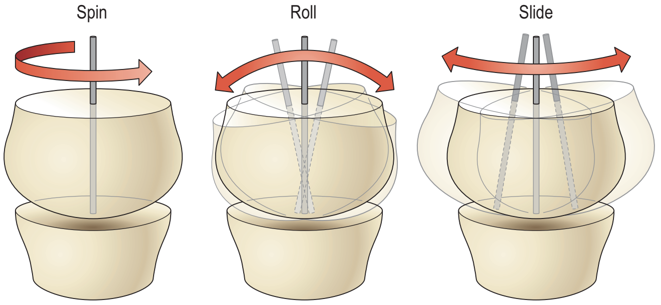

Fig. 5.66 The surfaces of incongruent joints move relative to each other by various combinations of spin, roll and slide.

Movements at articular surfaces

Opposing joint surfaces are never perfectly congruent, but substantial regions of these surfaces may fit together closely in a certain position known as the close-packed position, in which the joint is most stable. For example, the close-packed position of the knee joint corresponds to full extension. In other (loose-packed) positions, the surfaces of incongruent joints are less closely matched, and are able to move relative to each other by a combination of spin, roll and slide (Fig. 5.66). In final close-packing, when surfaces are most congruent and in maximal contact, the fibrous capsule and joint ligaments are maximally 'spiralized' and tensed, so no further movement is possible. The joint is said to be 'screwed home'. Close-packed surfaces cannot be separated by normal external force (as they may be in other positions), and bones can be regarded as temporarily locked, as if no joint existed. Any force that tends to further movement can only be resisted by contraction of appropriate muscles, and if these fail, the joint is vulnerable to injury. Therefore, movement just short of close-packing is physiologically desirable.

In symmetric standing, the knee and hip joints approach close-packed positions sufficiently to maintain an erect posture with minimal energy. Close- and loose-packed positions of several major joints are shown in Table 5.4 (see MacConaill and Basmajian (1977)). Opinions may vary in connection with some of these positions e.g. a close-packed position may possibly occur in some joints at both extremes of the range of movement. It is difficult to assess the situation in small tarsal and carpal joints and the first carpometacarpal joints.

TABLE 5.4 The close- and loose-packed positions of joints

Joint	Close-packed position	Loose-packed position
Shoulder	Abduction + lateral rotation	Semi-abduction
Ulnohumeral	Extension	Semi-flexion
Radiohumeral	Semi-flexion + semi-pronation	Extension + supination
Wrist	Dorsiflexion	Semi-flexion
2nd–5th metacarpophalangeal	Full flexion	Semi-flexion + ulnar deviation
Interphalangeal (fingers)	Extension	Semi-flexion
1st carpometacarpal	Full opposition	Neutral position of thumb
Hip	Extension + medial rotation	Semi-flexion
Knee	Full extension	Semi-flexion
Ankle	Dorsiflexion	Neutral position
Tarsal joints	Full supination	Semi-pronation
Metatarsophalangeal	Dorsiflexion	Neutral position
Interphalangeal (toes)	Dorsiflexion	Semi-flexion
Intervertebral	Extension	Neutral position

Data from MacConaill MA, Basmajian JV 1977 Muscles and Movements, 2nd ed. New York: Kriger.

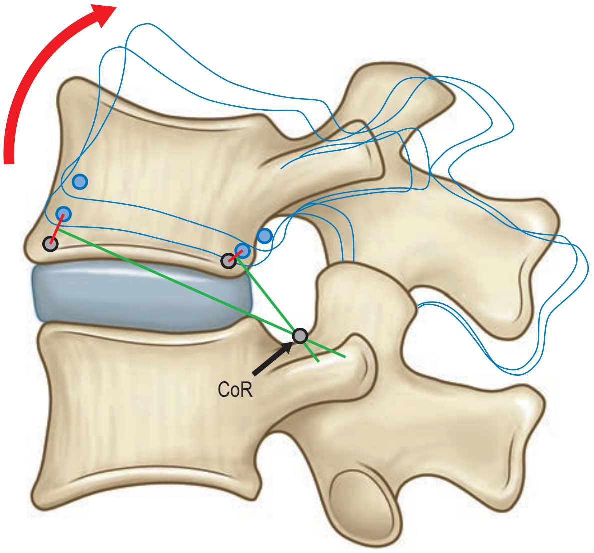

Fig. 5.67 When a bone is rotated, the centre of rotation (CoR) can be located by drawing lines between the initial and final positions of anatomical landmarks on the bone, and then determining where the perpendicular bisectors of these lines meet. The CoR may not correspond to a precise anatomical landmark.

Centre of rotation

The centre of rotation is a theoretical concept and may not correspond closely to any anatomical landmark or natural pivot. For a finite movement of one bone relative to a fixed reference (perhaps an anatomical plane), the centre of rotation can be located by drawing theoretical lines between the initial and final positions of two anatomical landmarks on the bone, and determining where the perpendicular bisectors of these two lines meet (Fig. 5.67). Real movements of real joints often involve varying combinations of rotation and translation as the movement progresses. It can be instructive to break the whole movement down into a series of small movements, calculate the centre of rotation for each one, and then join up the centres to create the locus of the instantaneous centre of rotation for the whole movement. Joint disease sometimes leads to an abnormally long and tortuous locus of the centre of rotation, because degenerative changes can reduce the restraint to motion offered by one or more tissues.

Coupled movements

An attempt to move a joint in one plane sometimes causes articular surfaces to meet at an oblique angle, creating small rotations in other planes. These secondary rotations, which are usually smaller than the

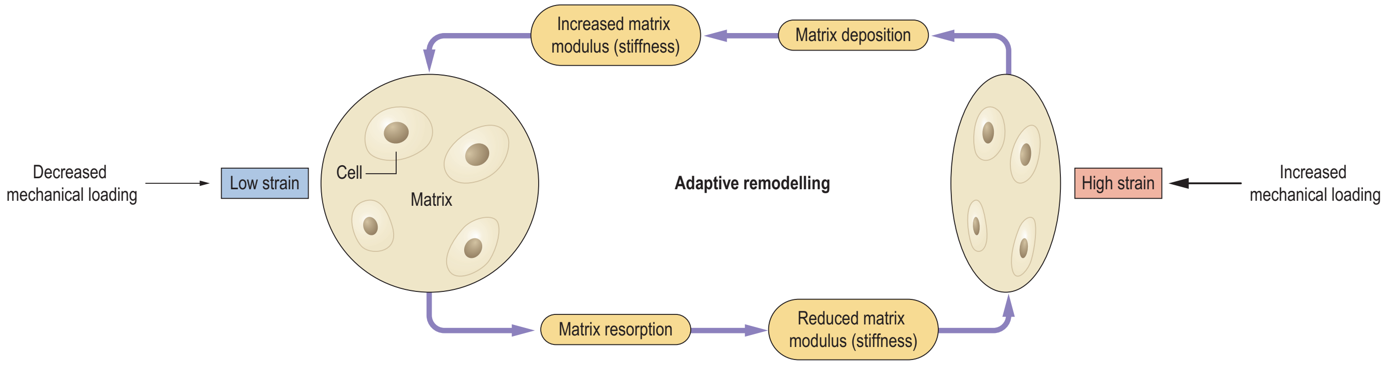
Increased matrix modulus (stiffness)
Matrix deposition
Decreased mechanical loading
Low strain
Cell
Matrix
Adaptive remodelling
High strain
Increased mechanical loading
Matrix resorption
Reduced matrix modulus (stiffness)

Fig. 5.68 Adaptive remodelling is the process by which musculoskeletal tissues adapt to prevailing mechanical demands. If a tissue is subjected to increased mechanical loading (right), it deforms more. Cells respond to this increased strain by depositing more matrix and increasing its modulus (stiffness) until strain levels return to normal. Similarly, reduced loading leads to reduced tissue strain (left), reduced matrix deposition and reduced modulus until strain levels rise to normal.

primary rotations, are referred to as coupled movements, e.g. lateral bending of the lumbar spine normally produces coupled axial rotations. Joint pathology can lead to abnormal coupled movements.

Mechanobiology

Adaptive remodelling

Skeletal tissues are generally able to adapt their mechanical properties to match the forces applied to them. This process is understood by bone biologists who refer to the general principle as Wolff's law. As illustrated in **Fig. 5.68**, the deformation of a tissue (i.e. the strain) depends on mechanical loading. Cells detect any change in maximum strain and respond by producing more (or less) extracellular matrix, which increases (or decreases) the modulus (stiffness) of the tissue until peak strain returns to normal levels. This negative feedback ensures that bone adapts (remodels) to suit its immediate mechanical environment (Currey 2002). Bone responds to maximal rather than time-averaged loading, and bone hypertrophy increases linearly with increasing maximum strain (Sugiyama et al 2012).Only 36 relatively severe loading cycles per day are sufficient to produce a maximal hypertrophic response, whereas four loading cycles per day are enough to prevent bone resorption (Rubin and Lanyon 1984). Articular cartilage adapts similarly to its mechanical environment (Hall et al 1991): anabolic changes are more evident in children whereas catabolic changes predominate increasingly with age (Gahunia and Pritzsker 2012). Therefore the mechanical properties of adjacent tissues remain suitably matched. However, different tissues cannot adapt at the same rate: highly vascularized tissues such as muscle and bone can adapt rapidly, whereas poorly vascularized tissues such as tendon do not. Avascular tissues such as articular cartilage and intervertebral discs adapt so slowly that turnover times for some matrix macromolecules can exceed 100 years. Consequently large differences in adaptive potential between adjacent musculoskeletal tissues could lead to problems in the less well-vascularized tissue when levels of mechanical loading increase abruptly (Adams and Dolan 1997).

Mechanotransduction

Various mechanisms have been proposed to explain how cells in musculoskeletal tissues detect mechanical loading. Cells in bone respond to tissue strain, possibly by detecting fluid flow within the microscopic canaliculi of the matrix. Cells in cartilage and ligaments also detect tissue strain, possibly because it deforms the cells in shear (**Fig. 5.52D**). Cells in articular cartilage and in the nucleus pulposus of intervertebral discs appear to detect hydrostatic pressure in their surrounding matrices, although only nucleus pulposus cells would normally experience a fluid pressure in life. (The pore pressure in a 'biphasic' solid such as articular cartilage can vary from place to place and is not equivalent to a single fluid pressure.) Muscle cells respond to strain and microinjury, which may disturb intracellular proteins such as titin. In general, mechanotransduction appears to be mediated by matrix molecules such as fibronectin pulling on transmembrane proteins such as integrins, which in turn disturb the cell cytoskeleton.

Injury and degeneration

Injured tissue is, by definition, less able to resist external forces. It deforms more readily under load, so that a higher proportion of any applied load must be resisted by surrounding intact tissue. This explains why focal tissue damage (and also cracking in engineering materials) naturally spreads outwards from the region of initial damage. Experiments on cadaveric intervertebral discs confirmed that measured compressive stresses decrease markedly in the immediate vicinity of damage and increase greatly in adjacent intact tissue (Adams et al 2013). The biological significance of this finding is that cartilage cells are most active and synthesize most matrix when they are subjected to moderate compressive stresses; matrix synthesis falls in response to low *and* to high stress (Hall et al 1991). Very high stress causes cartilage cells to secrete more matrix-degrading enzymes. Cartilage injury therefore creates a focal region of weakened tissue that spreads outwards and degrades progressively over time.

Key references

Adams MA, Bogduk N, Burton K et al 2013 The Biomechanics of Back Pain, 3rd ed. Edinburgh: Elsevier, Churchill Livingstone.
A detailed account of the biomechanics, biology and pathology of spinal tissues, including the origins of back pain.

Alexander RM 1988 Elastic Mechanisms in Animal Movement. Cambridge: Cambridge University Press.
A classic account of the biomechanics of animal movement by one of the founding fathers of biomechanics.

Currey JD 2002 Bones: Structure and Mechanics. Woodstock, Oxfordshire: Princeton University Press.
An authoritative account of bone structure, mechanics and adaptation.

Gahunia HK, Pritzker KP 2012 Effect of exercise on articular cartilage. Orthop Clin North Am 43:187–99
A comprehensive review of the subject.

MacConaill MA, Basmajian JV 1977 Muscles and Movements: A Basis for Human Kinesiology, 2nd ed. New York: Krieger.
A classic and detailed account of its subject by two leading researchers.

Proske U, Morgan DL 2001 Muscle damage from eccentric exercise: mechanism, mechanical signs, adaptation and clinical applications. J Physiol 537:333–45.
An influential review that explains delayed-onset muscle soreness following exercise.

Relaix F, Zammit PS 2012 Satellite cells are essential for skeletal muscle regeneration: the cell on the edge returns centre stage. Development 139:2845–56.
A review of recombination-based studies of satellite cell biology.

References

Adams MA, Dolan P 1997 Could sudden increases in physical activity cause degeneration of intervertebral discs? Lancet 350(9079):734–5.

Adams MA, Bogduk N, Burton K et al 2013 The Biomechanics of Back Pain, 3rd ed. Edinburgh: Elsevier, Churchill Livingstone.

A detailed account of the biomechanics, biology and pathology of spinal tissues, including the origins of back pain.

Alexander RM 1988 Elastic Mechanisms in Animal Movement. Cambridge: Cambridge University Press.

A classic account of the biomechanics of animal movement by one of the founding fathers of biomechanics.

Azibani F, Muchir A, Vignier N et al 2014 Striated muscle laminopathies. Semin Cell Dev Biol 29:107–15.

Batchelor CL, Winder SJ 2006 Sparks, signals and shock absorbers: how dystrophin loss causes muscular dystrophy. Trends Cell Biol 16:198–205.

Benjamin M, Toumi H, Ralphs JR et al 2006 Where tendons and ligaments meet bone: attachment sites ('entheses') in relation to exercise and/or mechanical load. J Anat 208:471–90.

Brandi ML 2009 Microarchitecture, the key to bone quality. Rheumatology 48 Suppl 4:iv3–8.

Bruehlmann SB, Rattner JB, Matyas JR et al 2002 Regional variations in the cellular matrix of the annulus fibrosus of the intervertebral disc. J Anat 201:159–71.

Buckingham M, Bajard L, Chang T et al 2003 The formation of skeletal muscle: from somite to limb. J Anat 202:59–68.

Clarkson E, Costa CF, Machesky LM 2004 Congenital myopathies: diseases of the actin cytoskeleton. J Pathol 204:407–17.

Conboy IM, Conboy MJ, Wagers AJ et al 2005 Rejuvenation of aged progenitor cells by exposure to a young systemic environment. Nature 433:760–4.

Currey JD 2002 Bones: Structure and Mechanics. Woodstock, Oxfordshire: Princeton University Press.

An authoritative account of bone structure, mechanics and adaptation.

DeGroot J, Verzijl N, Wenting-Van Wijk MJ 2004 Accumulation of advanced glycation end products as a molecular mechanism for aging as a risk factor in osteoarthritis. Arthritis Rheum 50:1207–15.

Farlay D, Boivin G, Panczer G et al 2005 Long-term strontium ranelate administration in monkeys preserves characteristics of bone mineral crystals and degree of mineralization of bone. J Bone Miner Res 20:1569–78.

Filipowska J, Tomaszewski KA, Niedźwiedzki Ł et al 2017 The role of vasculature in bone development, regeneration and proper systemic functioning. Angiogenesis 20: 291-302.

Fuchs RK, Allen MR, Ruppel ME et al 2008 In situ examination of the time-course for secondary mineralization of Haversian bone using synchrotron Fourier transform infrared microspectroscopy. Matrix Biol 27(1):34–41.

Gahunia HK, Pritzker KP 2012 Effect of exercise on articular cartilage. Orthop Clin North Am 43:187–99.

A comprehensive review of the subject.

Galpin AJ, Raue U, Jemiolo B et al 2012 Human skeletal muscle fiber type specific protein content. Anal Biochem 425:175–82.

Gregorio CC, Granzier H, Sorimachi H 1999 Muscle assembly: a titanic achievement? Curr Opin Cell Biol 11:18–25.

Hall AC, Urban JP, Gehl KA 1991 The effects of hydrostatic pressure on matrix synthesis in articular cartilage. J Orthop Res 9:1–10.

A classic experiment concerning cartilage mechanobiology that has not been bettered.

Holland A, Ohlendieck K 2013 Proteomic profiling of the contractile apparatus from skeletal muscle. Expert Rev Proteomics 10:239–57.

Hukins DWL, Aspden RM 1985 Composition and properties of connective tissue. Trends Biochem Sci 10:260–4.

Ivanusic JJ 2017 Molecular mechanisms that contribute to bone marrow pain. Front Neurol. 8:458.

Iwanaga T, Shikichi M, Kitamura H et al 2000 Morphology and functional roles of synoviocytes in the joint. Arch Histol Cytol 63:17–31.

Järvinen TA, Järvinen M, Kalimo H 2014 Regeneration of injured skeletal muscle after the injury. Muscles Ligaments Tendons J 3:3374–5.

Jones HH, Priest JD, Hayes WC et al 1977 Humeral hypertrophy in response to exercise. J Bone Joint Surg [Am] 59:204–8.

Junger S, Gantenbein-Ritter B, Lezuo P et al 2009 Effect of limited nutrition on in situ intervertebral disc cells under simulated-physiological loading. Spine 34:1264–71.

Koch AJ, Holaska JM 2014 Emerin in health and disease. Semin Cell Dev Biol 29:95–106.

Lama P, Le Maitre CL, Harding IJ et al 2018 Nerves and blood vessels in degenerated intervertebral discs are confined to physically disrupted tissue. J Anat 233(1):86–97.

Laumonier T, Menetrey J 2016 Muscle injuries and strategies for improving their repair. J Exp Orthop 3:15.

Lotz M, Loeser RF 2012 Effects of aging on articular cartilage homeostasis. Bone 51:241–8.

Luo J, Pollintine P, Gomm E et al 2012 Vertebral deformity arising from an accelerated 'creep' mechanism. Eur Spine J 21:1684–91.

MacConaill MA, Basmajian JV 1977 Muscles and Movements: A Basis for Human Kinesiology, 2nd ed. New York: Krieger.

A classic and detailed account of its subject by two leading researchers.

Magnusson SP, Kjaer M 2019 The impact of loading, unloading, ageing and injury on the human tendon. J Physiol 597:1283–98.

A recent comprehensive review of tendon structure, biology and mechanics.

Mathes SJ, Nahai F 1981 Classification of the vascular anatomy of muscles: experimental and clinical correlation. Plast Reconstr Surg 67:177–87.

Meachim G, Denham D, Emery IH et al 1974 Collagen alignments and artificial splits at the surface of human articular cartilage. J Anat 118:101–18.

Minetto MA, Botter A, Bottinelli O et al 2013 Variability in muscle adaptation to electrical stimulation. Int J Sports Med 34:544–53.

Niedermair T, Schirner S, Seebröker R et al 2018 Substance P modulates bone remodeling properties of murine osteoblasts and osteoclasts. Nature Sci Rep Article No. 9199.

Proske U, Morgan DL 2001 Muscle damage from eccentric exercise: mechanism, mechanical signs, adaptation and clinical applications. J Physiol 537:333–45.

An influential review that explains delayed-onset muscle soreness following exercise.

Reid KF, Fielding RA 2012 Skeletal muscle power: a critical determinant of physical functioning in older adults. Exerc Sport Sci Rev 40:4–12.

Relaix F, Zammit PS 2012 Satellite cells are essential for skeletal muscle regeneration: the cell on the edge returns centre stage. Development 139:2845–56.

A technical review of satellite cell biology.

Roberts S, Menage J, Duance V et al 1991 Collagen types around the cells of the intervertebral disc and cartilage end plate: an immunolocalization study. Spine 16:1030–8.

Rubin CT, Lanyon LE 1984 Regulation of bone formation by applied dynamic loads. J Bone Joint Surg [Am] 66:397–402.

A classic animal experiment concerning bone mechanobiology, which is still widely cited.

Rumian AP, Wallace AL, Birch HL 2007 Tendons and ligaments are anatomically distinct but overlap in molecular and morphological features – a comparative study in an ovine model. J Orthop Res 25:458–64.

Rumian AP, Draper ER, Wallace AL et al 2009 The influence of the mechanical environment on remodelling of the patellar tendon. J Bone Joint Surg Br 91:557–64.

Schiaffino S, Dyar KA, Ciciliot S et al 2013 Mechanisms regulating skeletal muscle growth and atrophy. FEBS J 280:4294–314.

Screen HR, Lee DA, Bader DL et al 2004 An investigation into the effects of the hierarchical structure of tendon fascicles on micromechanical properties. Proc Inst Mech Eng [H] 218:109–19.

Segalés J, Perdiguero E, Muñoz-Cánoves P 2016 Regulation of muscle stem cell functions: a focus on the p38 MAPK signaling pathway. Front Cell Dev Biol. 4:91.

Shackelford LC, LeBlanc AD, Driscoll TB et al 2004 Resistance exercise as a countermeasure to disuse-induced bone loss. J Appl Physiol 97:119–29.

Sigurdsson G, Halldorsson BV, Styrkarsdottir U et al 2008 Impact of genetics on low bone mass in adults. J Bone Miner Res 23:1584–90.

Sugiyama T, Meakin LB, Browne WJ et al 2012 Bones' adaptive response to mechanical loading is essentially linear between the low strains associated with disuse and the high strains associated with the lamellar/woven bone transition. J Bone Miner Res 27(8):1784–93.

Taylor GI 2013 The Angiosome Concept and Tissue Transfer. New York: Thieme,

Taylor GI, Pan WR 1998 Angiosomes of the leg: anatomic study and clinical implications. Plast Reconstr Surg 102:599–616.

Thambyah A, Broom N 2007 On how degeneration influences load-bearing in the cartilage-bone system: a microstructural and micromechanical study. Osteoarthritis Cartilage 15:1410–23.

Tu J, Hong W, Zhang P et al 2018. Ontology and function of fibroblast-like and macrophage-like synoviocytes: how do they talk to each other and can they be targeted for rheumatoid arthritis therapy? Front Immunol 9:1467.

Väänänen HK, Laitala-Leinonen T 2008 Osteoclast lineage and function. Arch Biochem Biophys 473:132–8.

Waller KA, Zhang LX, Elsaid KA et al 2013 Role of lubricin and boundary lubrication in the prevention of chondrocyte apoptosis. Proc Natl Acad Sci U S A 110:5852–7.

Wang JH 2006 Mechanobiology of tendon. J Biomech 39:1563–82.

Wang Y, Videman T, Battie MC 2012 Lumbar vertebral endplate lesions: associations with disc degeneration and back pain history. Spine (Phila Pa 1976) 37(17):1490–6.

Wang H, Listrat A, Meunier B et al 2014 Apoptosis in capillary endothelial cells in ageing skeletal muscle. Aging Cell 13:254–62.

Youn I, Choi JB, Cao L et al 2006 Zonal variations in the three-dimensional morphology of the chondron measured in situ using confocal microscopy. Osteoarthritis Cartilage 14:889–97.

Zammit PS 2017 Function of the myogenic regulatory factors Myf5, MyoD, Myogenin and MRF4 in skeletal muscle, satellite cells and regenerative myogenesis. Semin Cell Dev Biol 72:19–32.

CHAPTER

6

Smooth muscle and the cardiovascular and lymphatic systems

The cardiovascular system carries blood from the heart to all parts of the body through a series of tubes, all but the smallest of which are muscular. The muscle in these tubes is of two types: smooth muscle is characteristic of the walls of blood vessels, whereas cardiac muscle provides the walls of the heart chambers with their powerful contractile pumping action. The general characteristics and classification of muscle tissues are given on p. 107. Smooth muscle also forms an important contractile element in the walls of many other organ systems, e.g. the gastrointestinal tract and airways.

SMOOTH MUSCLE

In smooth muscle tissue, the contractile proteins actin and myosin are not organized into regular sarcomeres, visible as transverse striations, and so the cytoplasm has a smooth (unstriated) appearance. Smooth muscle is also referred to as involuntary muscle because its activity is neither initiated nor monitored consciously. It is much more variable, in both form and function, than either striated or cardiac muscle, a reflection of its varied roles in different systems of the body.

Smooth muscle is typically found in the walls of tubular structures and hollow viscera. It regulates diameter (e.g. in blood vessels, and branches of the bronchial tree); propels liquids or solids (e.g. in the ureter, hepatic duct and intestines); or expels contents (e.g. in the urinary bladder and uterus). The actual arrangement of the cells varies with the tissue. The account that follows will therefore be concerned with the generic properties of smooth muscle. The more specialized morphologies of smooth muscle are described in the appropriate regional chapters.

Microstructure of smooth muscle

Smooth muscle cells (fibres) are smaller than those of striated muscle. Their length can range from 15 μm in small blood vessels to 200 μm, and even to 500 μm or more in the uterus during pregnancy. The cells are spindle-shaped, tapering towards the ends from a central diameter of 3–8 μm (Fig. 6.1). The nucleus is single, located at the midpoint, and often twisted into a corkscrew shape by the contraction of the cell. Smooth muscle cells align with their long axes parallel and staggered longitudinally, so that the wide central portion of one cell lies next to the tapered end of another. Such an arrangement achieves both close packing and a more efficient transfer of force from cell to cell. In transverse section, smooth muscle is seen as an array of circular or slightly polygonal profiles of very varied size, and nuclei are present only in the centres of the largest profiles (Fig. 6.2). This appearance contrasts markedly with that of skeletal muscle cells, which show a consistent diameter in cross-section and peripherally placed nuclei throughout their length.

Smooth muscle has no attachment structures equivalent to the fasciae, tendons and aponeuroses associated with skeletal muscle. There is a special arrangement for transmitting force from cell to cell and, where necessary, to other soft tissue structures. Cells are separated by a gap of 40–80 nm. Each cell is covered almost entirely by a prominent basal lamina, which merges with a reticular layer consisting of a network of fine elastin, reticular fibres (collagen type III) and type I collagen fibres (Fig. 6.3). These elements bridge the gaps between adjacent cells and provide mechanical continuity throughout the fascicle. The cell attaches to components of this extracellular matrix at dense plaques (Fig. 6.3A, Fig. 6.4), where the basal lamina is thickened; cell–cell attachment occurs at intermediate junctions or small desmosome-like junctions, formed of two adjacent dense plaques. At the boundaries of fascicles, the connective tissue fibres become interwoven with those of interfascicular septa, so that the contraction of different fascicles is communicated throughout the tissue and to neighbouring structures. The components of the reticular network, the ground substance and collagen and elastic fibres, are synthesized by the smooth muscle cells themselves, not by fibroblasts or other connective tissue cells, which are rarely found within fasciculi.

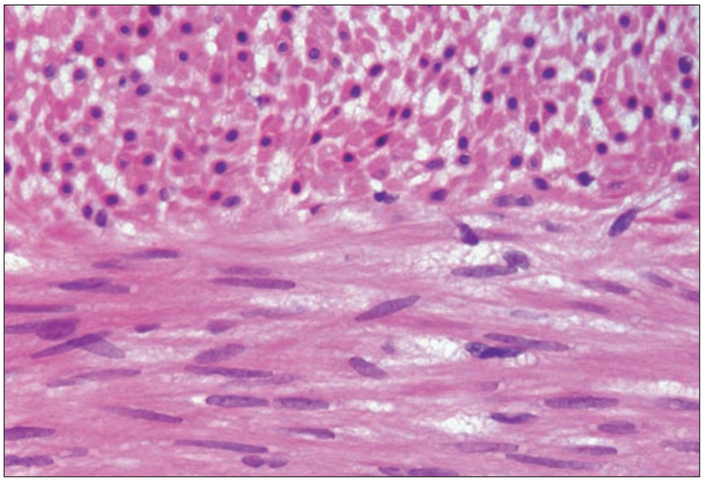

Fig. 6.1 Smooth muscle cells (fibres) in longitudinal (bottom) and transverse (top) section at the boundary of circular and longitudinal muscle layers in the human intestinal wall. Individual cells are spindle-shaped with a single central nucleus, aligned in parallel with neighbouring cells in a fasciculus. (Courtesy of Mr Peter Helliwell and the late Dr Joseph Mathew, Department of Histopathology, Royal Cornwall Hospitals Trust, UK.)

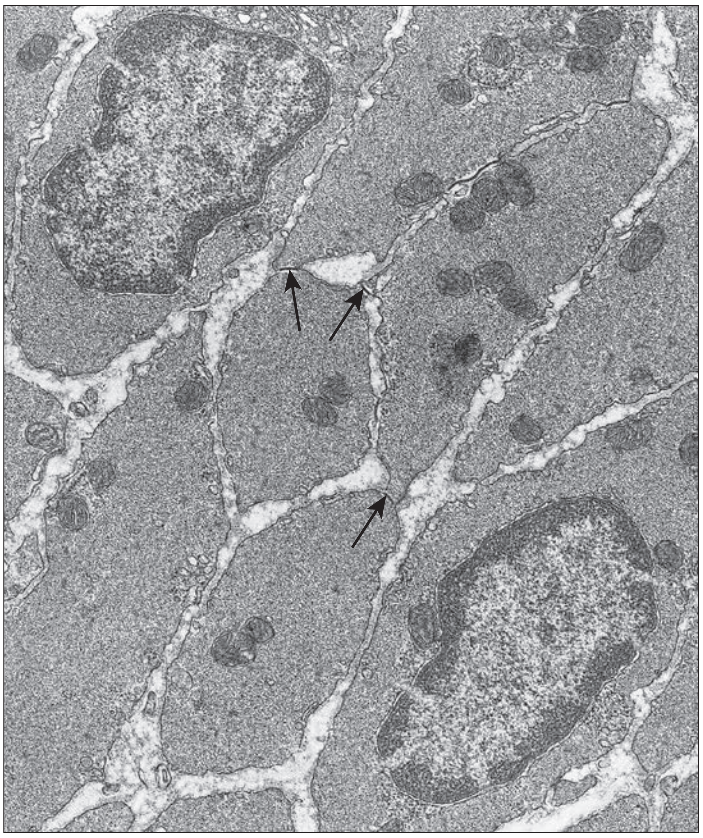

Fig. 6.2 A transmission electron micrograph showing smooth muscle fibres in transverse section, two at the level of their single central nucleus. In several places, the plasma membranes of adjacent cells are closely approximated at gap junctions (arrows).

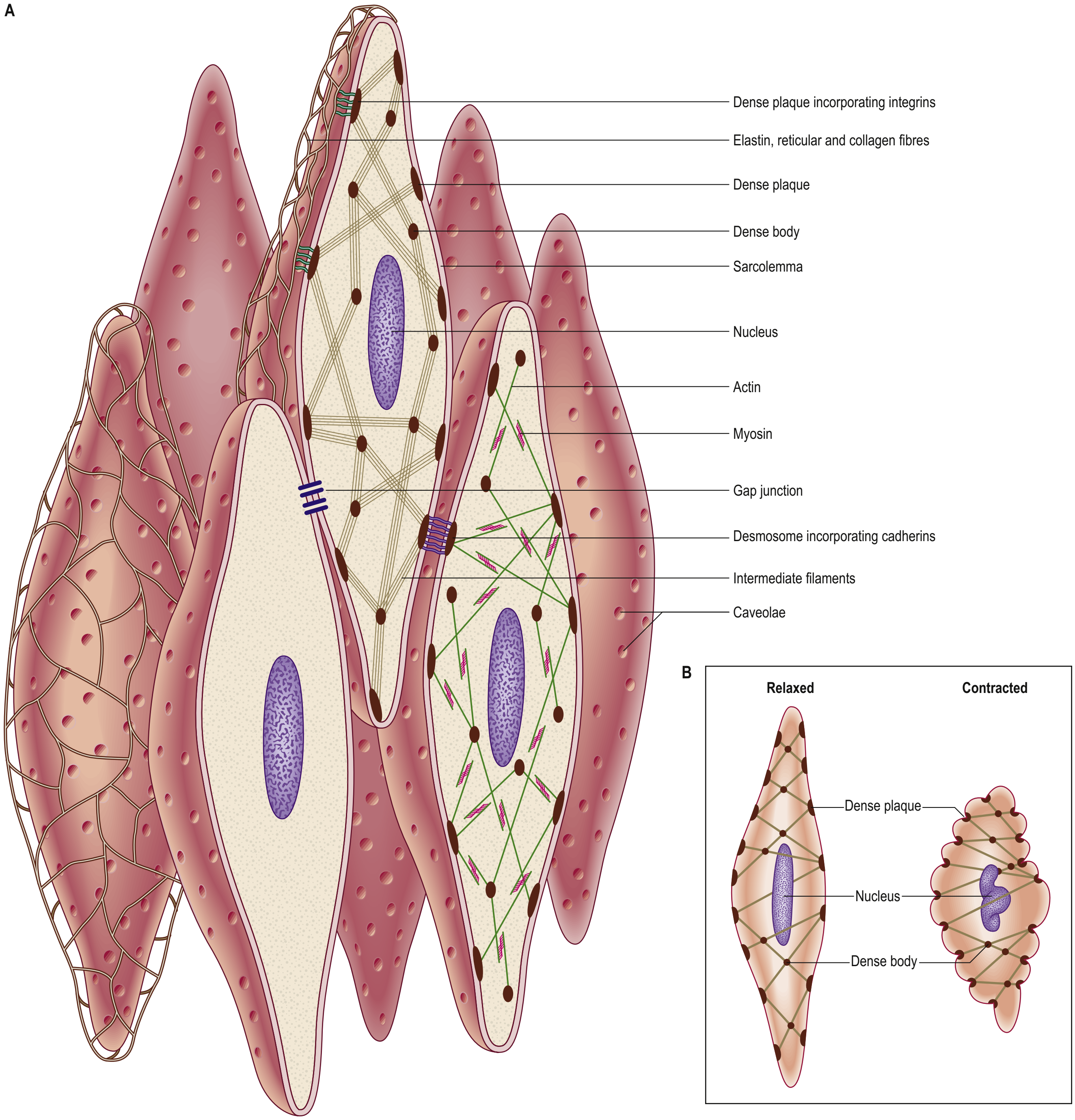

Fig. 6.3 A, A three-dimensional representation of smooth muscle cells. For clarity, some structural features have been separated for illustration in different cells. The spindle-shaped cells interdigitate with their long axes parallel; mechanical continuity between the cells is provided by a reticular layer of elastin and collagen fibres. The cytoskeletal framework consists of intermediate filament arrays (mainly longitudinal) and bundles of actin and myosin filaments (shown in separate cells) inserted into cytoplasmic dense bodies and submembraneous dense plaques to form a three-dimensional network. The sarcolemma contains anchoring desmosome-like (adheren) junctions, gap junctions and caveolae. **B**, The concertina-like change in shape of smooth muscle cells as they contract.

The membrane of smooth muscle cells contains molecules such as proteoglycans, glycoproteins and glycolipids on its exterior surface that form a thin, negatively charged network, the glycocalyx. Whilst less studied than that of endothelial cells, the smooth muscle cell glycocalyx has been shown to be important for mechanotransduction in small blood vessels. There are also a number of cell membrane-spanning proteins that extend through the glycocalyx and interact with the extracellular matrix, including cadherins and integrins. These provide structural and signalling links with the extracellular matrix and other cells, e.g. at desmosomes. The cytosolic ends of these proteins interact with components of the cytoskeleton via a complex of other proteins and kinases, and provide an important signalling pathway linking cell function to the exterior, which can modulate, for example, gene transcription and phenotype (Stegemann 2005).

Discontinuities occur in the basal lamina between adjacent cells, and here the cell membranes approach to 2–4 nm of one another to form a gap junction (see Fig. 6.2). These junctions are structurally similar to their counterparts in cardiac muscle, and are formed by binding of adjacent connexon complexes on the surface of the two cells. They provide a low-resistance channel through which electrical excitation and small molecules can pass, e.g. enabling a coordinated wave of contraction. The incidence of gap junctions varies with the anatomical site of the tissue: they appear more abundant in the type of smooth muscle that generates rhythmic (phasic) activity. In addition, they link the endothelium functionally with the underlying smooth muscle (via myoendothelial gap junctions) in small resistance arteries and arterioles.

Caveolae, cup-like invaginations of the plasma membrane with a resemblance to endocytotic vesicles, are a characteristic feature of smooth muscle cells, and may form up to 30% of the membrane (see Fig. 6.4). They are associated with many receptors, ion channels, kinases and the peripheral sarcoplasmic reticulum, and may thus act as highly localized

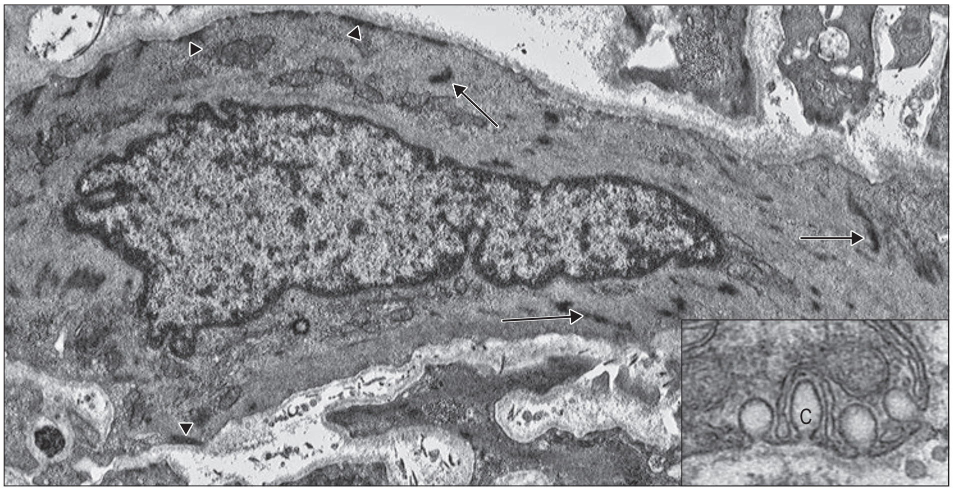

Fig. 6.4 Transmission electron micrographs showing the characteristic features of smooth muscle cells. Vascular smooth muscle in human kidney tissue, showing a cytoplasm packed densely with microfilaments (actin and myosin), cytoplasmic dense bodies (arrows) and submembraneous dense plaques (arrowheads). A basal lamina encloses the cell. The inset shows four caveolae (C) (vesicular invaginations of the cell surface at high magnification). These are associated with receptors, enzymes and ion channels important in smooth muscle function. (Courtesy of Dr Bart Wagner, Histopathology Department, Sheffield Teaching Hospitals, UK. Inset courtesy of Professor Chun Y Seow, University of British Columbia.)

signalling microdomains. They may also act as specialized pinocytotic structures involved in fluid and electrolyte transport into the cell. Other organelles (mitochondria, ribosomes, etc.) are largely confined to the filament-free perinuclear cytoplasm, although in some smooth muscle types, including vascular smooth muscle, peripheral mitochondria, sarcoplasmic reticulum and sarcolemma form important signalling microdomains.

Neurovascular supply of smooth muscle

Vascular supply

The blood supply of smooth muscle is less extensive than that of striated muscle. Where the tissue is not too densely packed, afferent and efferent vessels gain access via connective tissue septa, and capillaries run in the connective tissue between small fascicles. However, unlike striated muscle, capillaries are not found in relation to individual cells.

Innervation

Smooth muscle may contract in response to nervous or hormonal stimulation, mechanical deformation, or electrical depolarization transferred from neighbouring cells. Some muscles receive a dense innervation to all cells and are often referred to as multi-unit smooth muscles: most blood vessels are of this type. Such innervation can precisely define contractile activity, e.g. in the iris, specific nervous control can produce either pupillary constriction or dilation. Other muscles are more sparsely innervated and have been referred to as unitary smooth muscles. They tend to display myogenic activity, initiated spontaneously or in response to stretch, which may be markedly influenced by hormones. In these muscles, which include those in the walls of the gastrointestinal tract, urinary bladder, ureter, uterus and uterine tube, innervation tends to exert a more global influence on the rate and force of intrinsically generated contractions. The terms multi-unit and unitary smooth muscles are widely used, but in practice such distinctions are better regarded as the extremes of a continuous spectrum.

Smooth muscles are innervated by unmyelinated axons with cell bodies located in autonomic ganglia, either in the sympathetic chain or, in the case of parasympathetic fibres, closer to the point of innervation (Fig. 6.5). They ramify extensively, spreading over a large area of the muscle and sending branches into the muscle fasciculi. The terminal portion of each axonal branch is beaded and consists of expanded portions, varicosities, packed with vesicles and mitochondria, separated by thin, intervaricose portions. Each varicosity is regarded as a transmitter release site and may be considered as a nerve ending in the functional sense. In this way the axonal arborization of a single autonomic neurone bears a very large number of nerve endings (up to tens of thousands), as opposed to a maximum of a few hundred in somatic motor neurones. The neuromuscular terminals of autonomic efferents are considered in more detail on p. 67.

The neuromuscular junctions in smooth muscles do not show the consistent appearance seen in skeletal muscles. The neurotransmitter diffuses across a gap that can vary from 10 to 100 nm; even separations of up to 1 μm may still allow neuromuscular transmission to take place, although more slowly. The nerve ending is packed with vesicles but the adjacent area of the muscle cell is not structurally differentiated from that of non-junctional regions, i.e. there is no distinct synapse.

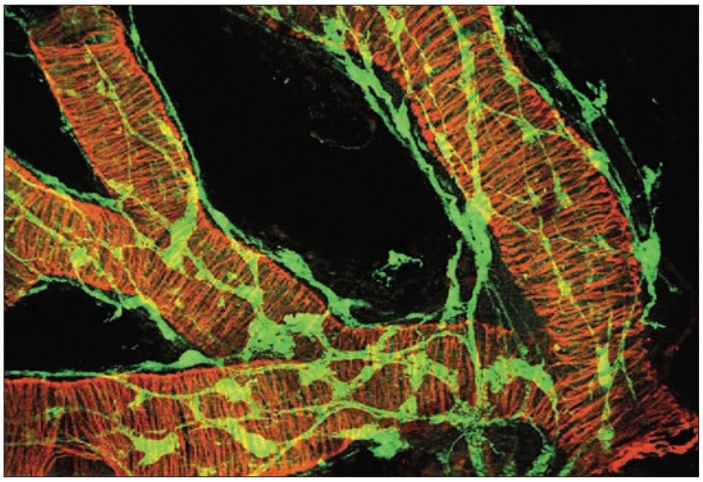

Fig. 6.5 A confocal fluorescence micrograph illustrating the innervation of airway smooth muscle in the developing human lung. Smooth muscle cells are arranged circumferentially and are labelled for actin (red); nerves and ganglia form a loose network around the smooth muscle, separated from it by up to 40 μm. Nervous tissue is labelled for PGP 9.5 (green). (With permission from Sparrow MP, Weichselbaum M, McCray PB Jr 1999 Development of the innervation and airway smooth muscle in human fetal lung. Am J Respir Cell Mol Biol 20:550–60.)

Intramuscular afferent nerves are the peripheral processes of small sensory neurones in the dorsal root ganglia. Since they are unmyelinated, contain axonal vesicles and have a beaded appearance, they are difficult to distinguish from efferent fibres, except by differential staining for neurotransmitters.

Structural basis of contraction

High-resolution immunocytochemistry of the internal architecture of the smooth muscle cell suggests a structural model for contractile function, which is illustrated in Fig. 6.3. This depends on the interaction of two systems of filaments, one forming the cytoskeleton and the other the contractile apparatus.

Excluding the perinuclear region, the cytoplasm of a smooth muscle cell effectively consists of two structural domains. The cytoskeleton forms a structural framework that maintains the spindle-like form of the cell and provides an internal scaffold with which other elements can interact. Its major structural component is the intermediate filament desmin, with the addition of vimentin (which may also be present alone) in vascular smooth muscle. The intermediate filaments are arranged mainly in longitudinal bundles, but some filaments interconnect the bundles with each other and with the sarcolemma to form a three-dimensional network. The bundles of intermediate filaments insert into focal, electron-dense bodies, approximately 0.1 μm in diameter, which are distributed uniformly throughout the cytoplasm and also attach to dense plaques underlying the plasma membrane (see Fig. 6.3A). The cytoplasmic dense bodies and submembraneous dense plaques are equivalent to the Z-discs of striated muscle cells. They contain the actin-binding protein α-actinin

In some blood vessels, notably those of the pulmonary circulation, and in the airways and probably in other smooth muscle types, there is evidence for heterogeneity of cell phenotype. The smooth muscle cells of small blood vessels and bronchioles exhibit different functional properties from those in larger vessels and airways, and may differ in morphology, expression of signalling proteins such as ion channels, and excitation–contraction coupling mechanisms. Even within individual tissues there is evidence of heterogeneity. Some myofibroblast-like cells have a function that is more secretory than contractile. The secretory phenotype is often increased in disease (e.g. chronic severe asthma, pulmonary hypertension) and is associated with increased proliferation and remodelling, and with secretion of cytokines and other mediators. Many smooth muscles seem to exhibit considerable phenotypic plasticity between these contractile and secretory phenotypes (Halayko and Solway 2001).

and thus also anchor the actin filaments of the contractile apparatus. These form a lattice of obliquely arranged bundles throughout the cytoplasm, which transmit force to the plasma membrane and thus the basal lamina and extracellular matrix via dense plaques. These are associated with a highly structured arrangement of ancillary proteins, including vinculin and talin, which in turn attach to integrins that cross the membrane and provide attachment to components of the extracellular matrix (Gunst and Zhang 2008).

An analogous arrangement underlies cell–cell attachment at desmosomes, but here the attachment between dense plaques is provided by transmembrane cadherin glycoproteins and intracellular catenins instead of integrins and talin. Mechanical deformation of the cell may be linked to cell signalling mechanisms via focal adhesion kinase (FAK) and its substrate paxillin; phosphorylation of talin and paxillin may modulate the deformability of the smooth muscle cell. Other regulatory proteins also associate specifically with actin, such as caldesmon and calponin. The cytoskeleton is not a passive structure. It adapts dynamically to load and is modulated by cell surface receptors including integrins and agonist binding to G-protein coupled receptors, and so contributes to contraction (Gunst and Zhang 2008). This presumably contributes to the low energy requirements of smooth muscle contraction because dynamic reorganization of the cytoskeleton following active contraction allows cell shortening to be maintained without further energy expenditure.

The ratio of actin to myosin is about eight times greater in smooth compared to striated muscle, reflecting the greater length of actin filaments in smooth muscle. Smooth muscle myosin filaments are 1.5–2 μm long, somewhat longer than those of striated muscle, and are formed of a slower isoform of myosin. Although smooth muscle cells contain less myosin, the longer filaments are capable of generating considerable force. The myosin filaments of smooth muscle are also assembled differently, such that their head regions lie symmetrically on either side of a ribbon-like filament, rather than imposing a bipolar organization on the filament. Actin filaments, to which they bind, can thus slide along the whole length of the myosin filament during contraction. In addition, dynamic polymerization of both myosin and actin monomers during activation can alter the length of the contractile filaments. These differences underpin the ability of smooth muscle to undergo much greater changes in length than striated muscle. Actin–myosin filament sliding generates tension, which transmits to focal regions of the plasma membrane, changing the cell to a shorter, more rounded shape (**Fig. 6.3B**) and often deforming the nucleus to a corkscrew-like profile.

Although some smooth muscles can generate as much force per unit cross-sectional area as skeletal muscle, the force develops much more slowly. Smooth muscle can contract by more than 80%, much greater than the 30% or so to which striated muscle is limited. The significance of this is illustrated by the urinary bladder, which is capable of emptying completely from an internal volume of 300 ml or more. Smooth muscles can maintain tension for long periods with very little expenditure of energy. Many smooth muscle structures are able to generate spontaneous contractions, examples are found in the walls of the intestines, ureter and uterine tube.

Excitation–contraction coupling in smooth muscle

Excitation–contraction coupling in smooth muscle is more complex than in skeletal or cardiac muscle, and may be electromechanical or pharmacomechanical. Electromechanical coupling involves depolarization of the cell membrane by an action potential, and may be generated when a membrane receptor, usually linked with an ion channel, is occupied by a neurotransmitter, hormone or other blood-borne substance. It is most commonly seen in unitary and phasic smooth muscles such as those of the viscera, with transmission of electrical excitation from cell to cell via gap junctions. In some types of smooth muscle depolarization may be the consequence of other stimuli, such as cooling, stretch and even light.

Pharmacomechanical coupling is a receptor-mediated and G-protein coupled process, and is the major mechanism in tonic smooth muscles such as in the vasculature and airways. It may involve several pathways, including formation of inositol trisphosphate, which triggers intracellular calcium release from the sarcoplasmic reticulum, activation of voltage-independent calcium channels in the sarcolemma, and depolarization causing activation of voltage-dependent calcium channels (reviewed in Berridge (2008)). Many receptors also couple to kinases that modulate contraction in a calcium-independent fashion, either via myosin phosphatase (see below) or via the actin cytoskeleton (see above). The extent to which any of these pathways contributes to activation varies between different types of smooth muscle.

Whilst the regulation of contraction of smooth muscle is largely calcium-dependent, the effects of an elevation of intracellular calcium are mediated via myosin, not actin/tropomyosin as in cardiac and skeletal muscle. Most smooth muscles contain little or no troponin, and instead calcium binds to calmodulin. The calcium–calmodulin complex regulates the activity of myosin light chain kinase, which phosphorylates myosin regulatory light chains and initiates the myosin–actin adenosine 5′-triphosphatase (ATPase) cycle. The enzymatic activation process is therefore inherently slow. Myosin phosphatase dephosphorylates myosin and thus promotes relaxation. The degree of myosin phosphorylation and therefore contraction depends on the relative activities of myosin light chain kinase and myosin phosphatase. Thus inhibition of the phosphatase, e.g. by Rho kinase, increases phosphorylation for any level of calcium (i.e. increases calcium sensitivity). The latter is a central component of the response to many constrictor agonists.

Regulation of smooth muscle intracellular calcium

Intracellular calcium is a key determinant of smooth muscle function, including contraction and also proliferation, migration and secretion of mediators. Its regulation in smooth muscle is particularly complex, and involves calcium entry via both voltage-dependent and independent ion channels, release from and reuptake into intracellular stores such as the sarcoplasmic reticulum, and modulation by mitochondria.

Origin of smooth muscle

Smooth muscle cells develop from a range of mesenchymal sources: the muscularis layer of visceral tubular systems, e.g. gut, airways etc. derive from local splanchnopleuric mesenchyme, whereas the smooth muscle of the sphincter and dilator pupillae is derived from neurectoderm. The origin of the tunica media of blood and larger lymphatic vessels varies throughout the body; sources include local splanchnopleuric mesenchyme condensing around endothelial networks and, within and around the vertebrae and muscles of the back and the descending aorta, from local somites (Wiegreffe et al 2007).

Following a period of proliferation, clusters of myoblasts become elongated in the same orientation. Dense bodies, associated with actin and cytoskeletal filaments, appear in the cytoplasm, and the surface membrane starts to acquire its specialized features, i.e. caveolae, adherens junctions and gap junctions. Cytoskeletal filaments extend to insert into the submembraneous dense plaques and cytoplasmic dense bodies. Thick filaments are seen a few days after the first appearance of thin filaments and intermediate filaments, and from this time the cells are able to contract. During development, dense bodies increase in number and further elements of the cytoskeleton are added. In addition to synthesizing the cytoskeleton and contractile apparatus, the differentiating cells express and secrete components of the extracellular matrix.

In a developing smooth muscle, all the cells express characteristics of the same stage of differentiation and there are no successive waves of differentiation. From its earliest appearance to maturity, a smooth muscle increases several hundred-fold in mass, partly by a 2–4-fold increase in the size of individual cells, but mainly by a very large increase in cell number. Growth occurs by division of cells in every part of the muscle, not just at its surface or ends. Mitosis occurs in cells in which differentiation is already well advanced, as evidenced by the presence of myofilaments and membrane specializations. Mitotic smooth muscle cells may be found at any stage of life but their numbers peak before birth, at a time that differs for different muscles; they are rare in the adult unless the tissue is stimulated to hypertrophy (as in the pregnant uterus) or to repair. The ability of mature cells to undergo mitosis therefore differs between the three major types of muscle: skeletal muscle cells cannot divide at all after differentiation; cardiac muscle cells can divide but only before birth; and smooth muscle cells appear to remain capable of division throughout life.

During the early stages of development, smooth muscle expresses embryonic and non-muscle isoforms of myosin. The proportions of these isoforms decrease progressively. Initially, SM-1 is the dominant or exclusive smooth muscle heavy chain isoform and the SM-2 isoform becomes more established later. For a review of the development of vascular smooth muscle, see Wang et al (2015).

Smooth muscle remodelling in disease

The ability of smooth muscle cells to divide and change phenotype throughout life means that smooth muscle has significant plasticity and can adapt to changing needs and stimuli, e.g. in the walls of the uterus

The arrangement of peripheral signalling microdomains (see above) is vital to this process. Sequential release from inositol trisphosphate receptors and calcium-sensitive ryanodine receptors (calcium release channels) in the sarcoplasmic reticulum, together with reuptake via the sarco-endoplasmic reticulum calcium ATPase (SERCA), give rise to slow calcium oscillations; it is now thought that the rate of oscillations, rather than the average level of calcium, is the prime driver for smooth muscle function, including contraction and activation of gene transcription (Berridge 2008).

during pregnancy. This can, however, have detrimental consequences in disease.

CARDIOVASCULAR AND LYMPHATIC SYSTEMS

General organization

Cells of peripheral blood, suspended in plasma, circulate through the body in the blood vascular system. Fluid and solutes exchange between the plasma and interstitium across capillaries and small venules. Excess interstitial fluid from peripheral tissues returns to the blood vascular system via the lymphatic system, which also provides a channel for the migration of leukocytes and the absorption of certain nutrients from the gut.

The cardiovascular system carries nutrients, oxygen, hormones, etc. throughout the body and the blood redistributes and disperses heat. As a consequence of the hydrostatic pressure, the system also has mechanical effects, such as maintaining tissue turgidity. Blood circulates within a system made up of the heart, the central pump and main motor of the system; arteries, which lead away from the heart and carry the blood to the periphery; and veins, which return the blood to the heart. The heart is essentially a pair of muscular pumps, one feeding the pulmonary circulation, which is responsible for gas exchange in the lungs and has a low hydrostatic pressure, and the other feeding the systemic circulation, which has a high hydrostatic pressure and serves the rest of the body. With limited exceptions, both circulations form a closed system of tubes, so that blood *per se* does not usually leave the circulation.

From the centre to the periphery, the vascular tree shows three main modifications. The arteries increase in number by repeated bifurcation and by sending out side branches, in both the systemic and the pulmonary circulation. For example, the aorta, which carries blood from the heart to the systemic circulation, gives rise to about 4×10^6 arterioles and four times as many capillaries. The arteries also decrease in diameter, although not to the same extent as their increase in number, so that a hypothetical cross-section of all the vessels will show an increase in total area with increasing distance from the heart. At its emergence from the heart, the aorta of an adult man has an outer diameter of approximately 30 mm (cross-sectional area of nearly 7 cm^2). The diameter decreases along the arterial tree until it is as little as 10 µm in arterioles (each with a cross-sectional area of about 80 μm^2). However, given the enormous number of arterioles, the total cross-sectional area at this level is approximately 150 cm^2, more than 200 times that of the aorta. As a result, blood flow is faster near the heart than at the periphery.

The walls of arteries decrease in thickness towards the periphery, although this is not as substantial as the reduction in vessel diameter. Consequently, in the smallest arteries (arterioles), the thickness of the wall represents about half the outer radius of the vessel, whereas in a large vessel it represents between one-fifteenth and one-fifth, e.g. in the thoracic aorta the radius is approximately 17 mm and the wall thickness 1.1 mm.

Venules, which return blood from the capillaries, converge on each other, forming a progressively smaller number of veins of increasingly large size. As with arteries, the hypothetical total cross-sectional area of all veins at a given level reduces nearer to the heart. Eventually, only the two largest veins, the superior and inferior venae cavae, open into the heart from the systemic circulation. A similar pattern is found in the pulmonary circulation but here the vascular loop is shorter and has fewer branch points, and consequently, the number of vessels is smaller than in the systemic circulation. The total end-to-end length of the vascular network in a typical adult is twice the circumference of the earth.

Large arteries, such as the thoracic aorta and subclavian, axillary, femoral and popliteal arteries, lie close to a single vein that drains the same territory as that supplied by the artery. Other arteries are usually flanked by two veins, satellite veins (venae comitantes), which lie on either side of the artery and have numerous cross-connections; the whole is enclosed in a single connective tissue sheath. The artery and the two satellite veins are often associated with a nerve, and when they are surrounded by a common connective tissue sheath they form a neurovascular bundle.

The close association between the larger arteries and veins in the limbs allows counterflow exchange of heat. This mechanism promotes heat transfer from arterial to venous blood and thus helps to preserve body heat. Counterflow heat exchange systems are found in certain organs, e.g. in the testis, where the pampiniform plexus of veins surrounds the testicular artery (this arrangement not only conserves body heat, but also maintains the temperature of the testis below average body temperature). Counterflow exchange mechanisms are found in the microcirculation, as in the vasa recta in the renal medulla. Here, countercurrent exchange retains solutes at a high concentration in the medullary interstitium, with efferent venous blood transferring solutes to the afferent arterial supply; this mechanism is essential for concentration of the urine.

Arteries and veins are named primarily according to their anatomical position. In functional terms, four main classes of vessel are described: conducting and distributing vessels (large arteries), resistance vessels (small arteries but mainly arterioles), exchange vessels (capillaries, sinusoids and small venules) and capacitance vessels (veins). Structurally, arteries can also be divided into elastic and muscular types. Although muscle cells and elastic tissue are present in all arteries, the relative amount of elastic material is greatest in the largest vessels, whereas the relative amount of smooth muscle increases progressively towards the smallest arteries.

The large conducting arteries that arise from the heart, together with their main branches, are characterized by the predominantly elastic properties of their walls. Distributing vessels are smaller arteries supplying the individual organs, and their walls are characterized by a well-developed muscular component. Resistance vessels include the smallest arteries and arterioles, and are highly muscularized. They provide the major part of peripheral resistance to blood flow and so cause the largest drop in blood pressure before the blood flows into the tissue capillary beds.

Capillaries, sinusoids and small (postcapillary) venules are collectively termed exchange vessels. Their thin walls allow exchange between blood and the interstitial fluid that surrounds all cells: this is the essential function of a circulatory system. Arterioles, capillaries and venules constitute the microvasculature, the structural basis of the microcirculation.

Larger venules and veins form an extensive but variable, large-volume, low-pressure system of vessels conveying blood back to the heart. Their high capacitance is due to the significant distensibility (compliance) of their walls, so that the content of blood is high even at low pressures. Veins contain the greatest proportion of blood, reflecting their large relative volume.

Blood from the gastrointestinal tract (with the exception of the lower part of the anal canal) and from the spleen, pancreas and gallbladder drains to the liver via the portal vein. The portal vein ramifies within the substance of the liver like an artery and ends in the hepatic sinusoids. These drain into the hepatic veins, which in turn drain into the inferior vena cava. Blood supplying the abdominal organs thus passes through two sets of capillaries before it returns to the heart. The first provides the organs with oxygenated blood, and the second carries deoxygenated blood, rich in absorption products from the intestine, through the liver parenchyma. A venous portal circulation also connects the median eminence and infundibulum of the hypothalamus with the adenohypophysis. In essence, a venous portal system is a capillary network that lies between two veins, instead of between an artery and a vein, which is the more usual arrangement in the circulation. A capillary network may also be interposed between two arteries, e.g. in the renal glomeruli, where the glomerular capillary bed lies between afferent and efferent arterioles. This maintains a relatively high-pressure system, which is important for renal filtration.

A parallel circulatory system is provided by the lymphatic vessels and lymph nodes. Lymphatic vessels originate in peripheral tissues as blind-ended endothelial tubes that collect excess fluid from the interstitial spaces between cells and conduct it as lymph. Lymph is returned to the blood vascular system via lymphatic vessels, which converge on the large veins in the root of the neck.

Certain pathologies of the cardiovascular and lymphatic systems are described below; for information on vascular tumours, see Sepulveda and Buchanan (2014). The development of blood vessels is described in Chapter 13.

General features of vessel walls

All blood vessels, with the exception of capillaries and venules, have walls consisting of three concentric layers (tunicae) (see Fig. 6.8). The intima (tunica intima) is the innermost layer. Its main component, the endothelium, lines the entire vascular tree, including the heart and lymphatic vessels. The media (tunica media) contains muscle cells, elastic fibres and collagen. While it is by far the thickest layer in arteries, the media is absent in capillaries and is comparatively thin in veins. The adventitia (tunica adventitia) is the outer coat of the vessel and consists of connective tissue, nerves and vessel capillaries (vasa vasorum). It links the vessels to the surrounding tissues. Vessels differ in the relative thicknesses and detailed compositions of these layers.

Sustained stress (physical or oxidative), tissue damage, inflammatory mediators and other stimuli can promote enhanced growth, apoptosis (programmed cell death, p. 27) and switching to a more secretory phenotype (see above). Increased mediator release by the more secretory phenotype can potentiate such changes and attract inflammatory cells, resulting in a positive feedback loop. Chronic disease and inflammation can therefore lead to extensive smooth muscle remodelling, a major contributing factor to, for example, chronic asthma and pulmonary hypertension, which significantly worsens conditions (Stenmark et al 2006, Mahn et al 2010). Peripheral vascular remodelling may also occur in essential hypertension and diabetes.

Large elastic arteries

The aorta and its largest branches (brachiocephalic, common carotid, subclavian and common iliac arteries) are large elastic arteries that conduct blood to the medium-sized distributing arteries.

The intima is made of an endothelium, resting on a basal lamina, and a subendothelial connective tissue layer. The endothelial cells are flat, elongated and polygonal in outline, with their long axes parallel to the direction of blood flow (see Fig. 6.17). The subendothelial layer is well developed, contains elastic fibres and type I collagen fibrils, fibroblasts and small, smooth muscle-like myointimal cells. The latter accumulate lipid with age, and in an extreme form this contributes to atherosclerosis (see below). Thickening of the intima progresses with age and is more marked in the distal than in the proximal segment of the aorta.

A prominent internal elastic lamina, sometimes split, lies between intima and media. This lamina is smooth, measures about 1 μm in thickness, and, with the elastic lamellae of the media, is stretched under the effect of systolic pressure, recoiling elastically in diastole. Elastic arteries can thus sustain continuous blood flow despite the pulsatile cardiac output, and smooth out the cyclical pressure wave. The media has a markedly layered structure, in which fenestrated layers of elastin (elastic lamellae) alternate with interlamellar smooth muscle cells (**Fig. 6.6**), collagen and fine elastic fibres. The arrangement is very regular, such that each elastic lamella and adjacent interlamellar zone is regarded as a 'lamellar unit' of the media. In the human aorta there are approximately 52 lamellar units, measuring about 11 μm in thickness. Number and thickness of lamellar units increases during postnatal development, from 40 at birth.

The adventitia is well developed. In addition to collagen and elastic fibres, it contains flattened fibroblasts with extremely long, thin processes, macrophages and mast cells, nerve bundles and lymphatic vessels. The vasa vasorum is usually confined to the adventitia.

Muscular arteries

Muscular arteries are characterized by the predominance of smooth muscle in the media (**Fig. 6.7**). The intima consists of an endothelium, similar to that of elastic arteries, which rests on a basal lamina and subendothelial connective tissue. The internal elastic lamina (see Fig. 6.7; **Fig. 6.8**) is a distinct, thin layer, sometimes duplicated and occasionally absent. It is thrown into wavy folds as a result of contraction of smooth muscle in the media. Some 75% of the mass of the media consists of smooth muscle cells that run spirally or circumferentially around the vessel wall. The relative amount of extracellular matrix is therefore less than in large arteries, although fine elastic fibres that run mainly parallel to the muscle cells are present. An external elastic lamina, composed of sheets of elastic fibres, forms a less compact layer than the internal lamina, and separates the media from the adventitia in larger muscular arteries. The adventitia is made of fibroelastic connective tissue, and can be as thick as the media in the smaller arteries. The inner part of the adventitia contains more elastic than collagen fibres.

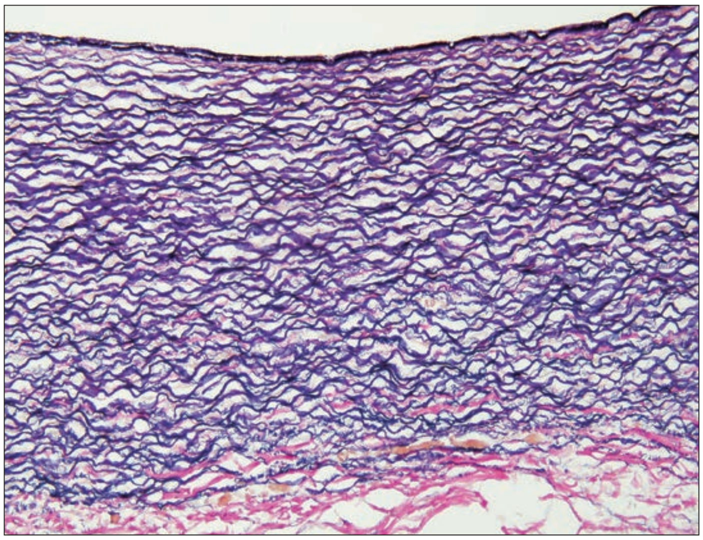

Fig. 6.6 Elastic artery (human aorta), stained for elastic fibres. The dense staining of the internal elastic lamina is seen close to the luminal surface (top); elastic lamellae fill the tunica media and merge with the external elastic lamina at its junction with the collagenous adventitia (red fibres, below). Compare with Fig. 6.20. van Gieson stain. (Courtesy of Mr Peter Helliwell and the late Dr Joseph Mathew, Department of Histopathology, Royal Cornwall Hospitals Trust, UK.)

Arterioles

The endothelial cells in arterioles are smaller than in large arteries, but their nuclear region is thicker and often projects markedly into the lumen (**Figs 6.9–6.10**). The nuclei are elongated and orientated parallel to the vessel length, as is the long axis of the cell. The basal surface of the endothelium contacts a basal lamina, but an internal elastic lamina is either absent or highly fenestrated and traversed by cytoplasmic processes of muscle or endothelial cells. The muscle cells are larger in cytoplasmic volume than those in the walls of large arteries and form a layer one or two cells thick. They are arranged circumferentially and are tightly wound around the endothelium. In the smallest arterioles each cell makes several turns, producing extensive apposition between parts of the same cell. Contraction of the muscle constricts the lumen, and so controls blood flow into the capillary bed; arterioles thus act functionally as precapillary sphincters, even though the absence of an anatomically delineated sphincter means that the term is no longer commonly used. Contraction of arterioles is primarily regulated by local vasoactive and metabolic factors, but can also be controlled by central mechanisms.

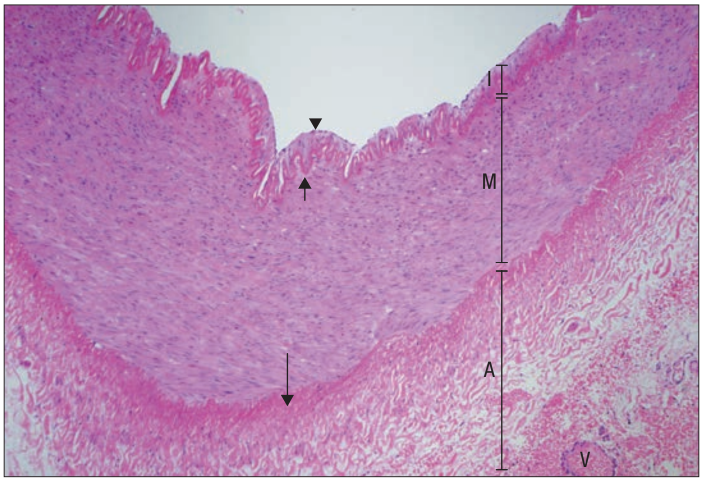

Fig. 6.7 The wall of a human muscular artery. The intima (I) forms the innermost layer, lined by an endothelium (arrowhead) and separated from the middle muscular layer, the media (M), by an internal elastic lamina (short arrow). A more diffuse external elastic lamina (long arrow) divides the media from the outermost collagenous adventitia (A), within which lie the vasa vasorum (V). (Courtesy of Mr Peter Helliwell and the late Dr Joseph Mathew, Department of Histopathology, Royal Cornwall Hospitals Trust, UK.)

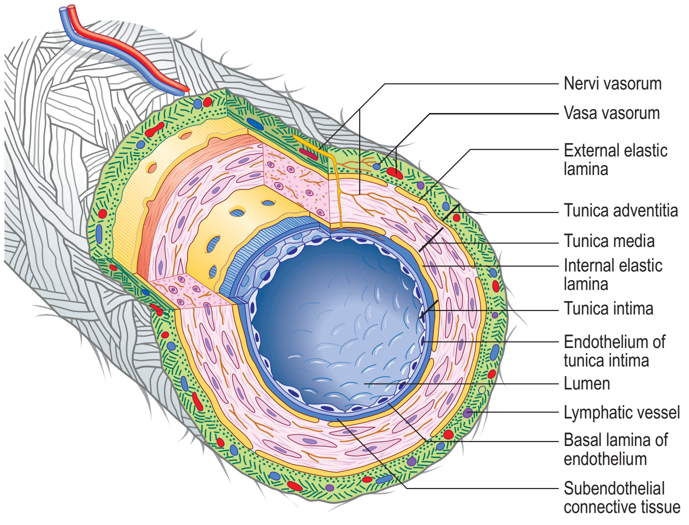

Fig. 6.8 The principal structural features of the larger blood vessels as seen in a muscular artery.

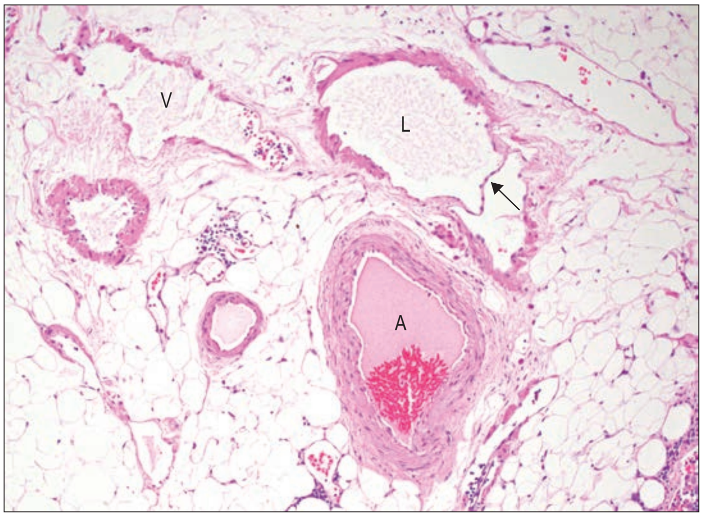

Fig. 6.9 An arteriole (A) and accompanying venule (V) and lymphatic vessel (L) (with a valve, arrow) in adipose tissue around a lymph node (human). Note the relative thicknesses of the vessel walls, in comparison with the diameters of their lumens. (Courtesy of Mr Peter Helliwell and the late Dr Joseph Mathew, Department of Histopathology, Royal Cornwall Hospitals Trust, UK.)

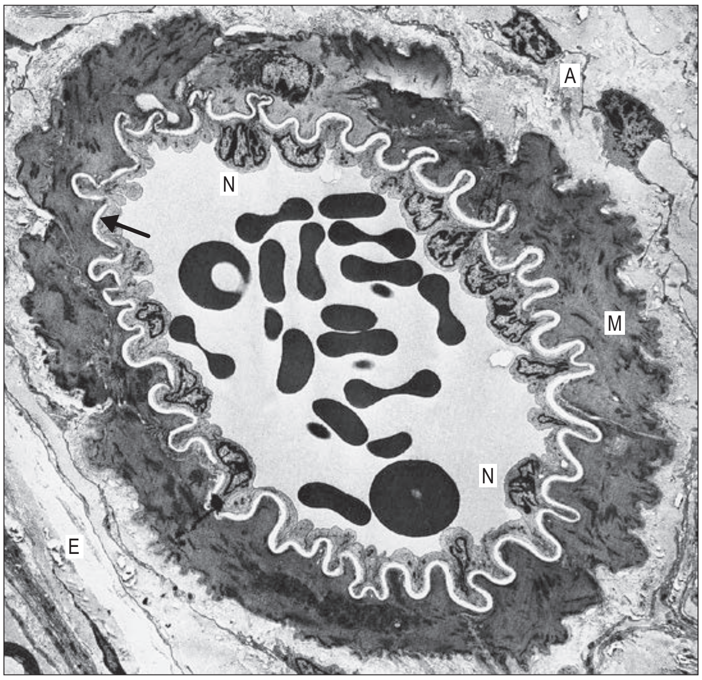

Fig. 6.10 A transmission electron micrograph of a small arteriole in the epineurium of a peripheral nerve. The vessel lumen contains erythrocytes and is lined by endothelial cells (with nuclei, N, projecting into the lumen); note the electron-lucent internal elastic lamina (pale, wavy line, arrow), the media containing densely filamentous smooth muscle cells (M) and the connective tissue of the adventitia (A) merging with that of the epineurium (E). (Courtesy of Dr Bart Wagner, Histopathology Department, Sheffield Teaching Hospitals, UK.)

Arterioles are usually densely innervated by sympathetic fibres, via small bundles of varicose axons packed with transmitter vesicles, mostly of the adrenergic type. The distance between axolemma and muscle cell membrane can be as little as 50–100 nm and the gap is occupied only by a basal lamina. Autonomic neuromuscular junctions are very common in arterioles. Arteriolar adventitia is very thin.

Capillaries

The capillary wall (Fig. 6.11) is formed by an endothelium and its basal lamina, plus a few isolated pericytes. Capillaries are the vessels closest to the tissue they supply and their wall constitutes a minimal barrier between blood and the surrounding tissues. Capillary structure varies in different locations. Capillaries measure 4–8 µm in diameter (much more in the case of sinusoids) and are hundreds of microns long. Their lumen is just large enough to admit the passage of single blood cells, usually with considerable deformation. Typically a single endothelial cell forms the wall of a capillary, and there are junctional complexes between extensions of the same cell.

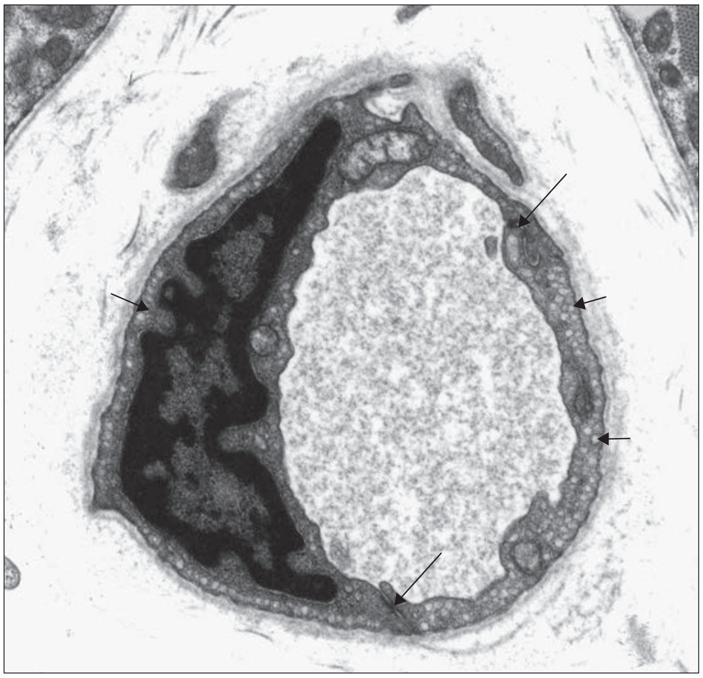

Fig. 6.11 Transmission electron micrograph of a capillary in a human muscle biopsy specimen. An endothelial cell with its nucleus in the plane of section forms adherens junctions (long arrows) with either a second cell or an extension of itself. The cytoplasm contains numerous transcytotic vesicles (short arrows). A basal lamina surrounds the capillary. (Courtesy of Dr Bart Wagner, Histopathology Department, Sheffield Teaching Hospitals, UK.)

Endothelial cells are joined by tight junctions (occluding junctions, zonulae occludentes), forming a diffusion barrier. Capillary permeability varies greatly among tissues and is correlated largely with the type of endothelium. The majority of tissues, including brain, muscle, lung and connective tissues, contain capillaries with a continuous, unbroken layer of endothelium (continuous endothelium). This is impermeable to proteins, although electrolytes can diffuse through the tight junctions, albeit relatively slowly. Their passage is further limited in brain, thymic cortex and testis by particularly tight junctions.

Endothelial cells of some capillaries have fenestrations (pores) through their cytoplasm that facilitate diffusion. Fenestrations are approximately circular and 50–100 nm in diameter, and at their edge the luminal and abluminal membranes of the endothelial cell come into contact. The fenestration itself is usually occupied by a thin, electron-dense diaphragm containing glycoprotein PV-1, which restricts passage of large molecules such as proteins. Fenestrated capillaries occur in intestinal mucosae, endocrine and exocrine glands, and renal glomeruli, where they may lack a diaphragm. Fenestrations are almost invariably present in capillaries that lie close to an epithelium, including the skin.

Sinusoids

Sinusoids are expanded capillaries (Fig. 6.12), and are large and irregular in shape. They have true discontinuities in their walls, allowing intimate contact between blood and the parenchyma. The discontinuities are formed by gaps between fenestrated endothelial cells, such that the sinusoidal lining, and sometimes also the basal lamina, is incomplete. Sinusoids occur in large numbers in the liver (where a basal lamina is completely absent), spleen, bone marrow, adenohypophysis (see Fig. 6.12) and suprarenal medulla.

Venules

When two or more capillaries converge, the resulting vessel is larger (10–30 µm) and is known as a venule (postcapillary venule). Venules (see Fig. 6.9) are essentially tubes of flat, oval or polygonal endothelial cells surrounded by basal lamina and, in the larger vessels, by a delicate adventitia of a few fibroblasts and collagen fibres mainly running longitudinally. Pericytes (see Fig. 6.21) support the walls of these venules.

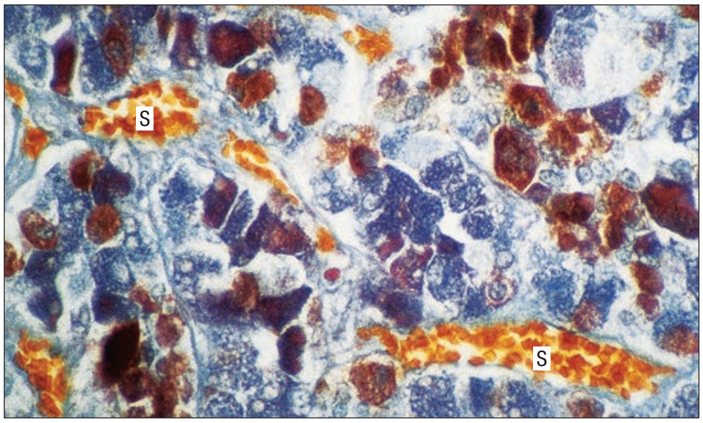

Fig. 6.12 Expanded sinusoids (S), typical of endocrine glands and certain other tissues, are seen here containing erythrocytes (orange) in the adenohypophysis. Endocrine cells stain either blue or reddish-brown, or are poorly stained in this trichrome preparation.

Postcapillary venules are sites of leukocyte migration. In venules of mucosa-associated lymphoid tissue (MALT), particularly of the gut and bronchi, and in the lymph nodes and thymus, endothelial cells are taller and have intercellular junctions through which lymphocytes and other blood components can readily pass. These are known as high endothelial venules (HEVs) (see Figs 6.18–6.19). Elsewhere, venules are believed to be a major site where migration of neutrophils, macrophages and other leukocytes into extravascular spaces occurs, and where neutrophils may temporarily attach, forming marginated pools.

In general, the endothelium of venules has few tight junctions and is relatively permeable. The intercellular junctions of venules are sensitive to inflammatory agents, which increase their permeability to fluids and defensive cells, and facilitate leukocyte extravasation by diapedesis.

Venules do not acquire musculature until they are about 50 µm in outer diameter, when they are known as muscular venules. This distinction is important because postcapillary venules, which lack muscle in their walls, are as permeable to solutes as capillaries and are thus part of the microcirculatory bed. The cross-sectional area of the vascular tree is at its maximum at the level of the postcapillary venule, and there is a dramatic fall in pressure (from 25 mmHg in the capillary to approximately 5 mmHg). Muscular venules converge to produce a series of veins of progressively larger diameter. Venules and veins are capacitance vessels because they have thin distensible walls that can hold a large volume of blood and accommodate luminal pressure changes.

Fluid exchange in the microvasculature

The microvasculature is important for the creation and maintenance of the interstitial fluid that bathes the cells. The thin walls of capillaries and small venules allow easy diffusion of fluid and most small molecules, but the endothelial barrier prevents movement of proteins; consequently, plasma and interstitial fluid have almost identical compositions, except that the latter contains very little protein. Fluid transfer across these exchange vessels is driven by the balance between the hydrostatic pressure (i.e. blood pressure within them) forcing fluid into the tissues, and the oncotic pressure (colloidal osmotic pressure, reflecting the difference in protein concentrations) drawing fluid back into the vessels. These ‘Starling forces’ are normally closely balanced, so differences in hydrostatic pressure mean that fluid tends to be filtered into the tissue at the arterial side of the exchange vessels and largely reabsorbed at the venous side. The balance forms lymph. Disruption of the balance (e.g. high venous pressure in the feet) can lead to accumulation of tissue fluid (oedema) and swelling.

Inflammation and endothelial permeability

Inflammatory mediators increase the permeability of capillaries and small venules by causing contraction of endothelial cells and so loosening tight junctions. This facilitates leukocyte extravasation by diapedesis but also disrupts normal barrier function, allowing extravasation of protein and fluids. The consequence is tissue oedema and the swelling that is commonly associated with inflammation. There is considerable cross-talk between endothelial cells and cells of the immune system.

Veins

Veins are characterized by relatively thin walls in comparison to arteries of similar size and by a large capacitance. Wall thickness is not correlated exactly with the size of the vein and varies in different regions, e.g. the wall is thicker in veins of the leg than it is in veins of a similar size in the arm.

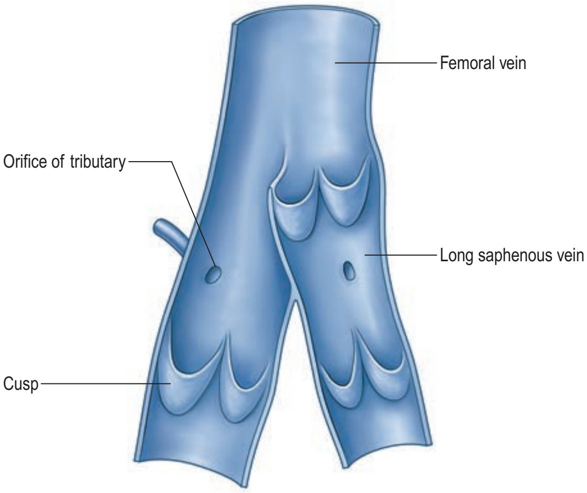

Fig. 6.13 The upper portions of the femoral and long saphenous veins laid open to show the valves, at about two-thirds of their natural size.

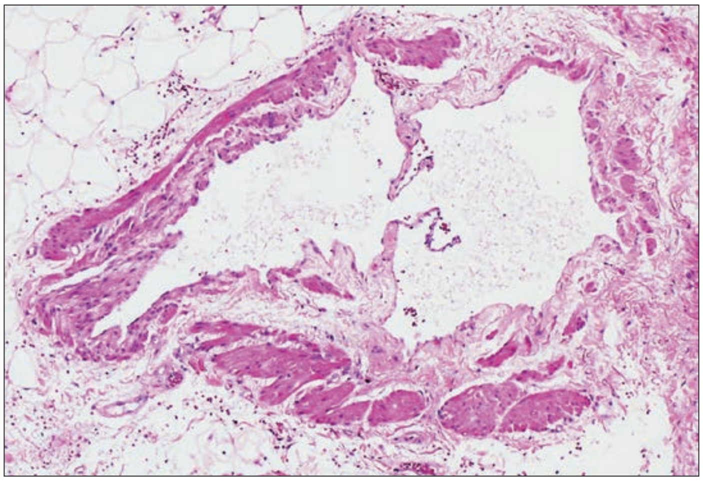

Fig. 6.14 A valve in a human small vein, formed from flap-like extensions of the intima that close when pressure increases on the proximal side, preventing backflow. (Courtesy of Mr Peter Helliwell and the late Dr Joseph Mathew, Department of Histopathology, Royal Cornwall Hospitals Trust, UK.)

The structural plan of the wall is similar to that of other vessels, except that the amount of muscle is considerably less than in arteries, while collagen and, in some veins, elastic fibres, predominate. In most veins, e.g. those of the limbs, the muscle is arranged approximately circularly. Longitudinal muscle is present in the iliac, brachiocephalic, portal and renal veins and in the superior and inferior venae cavae. Muscle is absent in the maternal placental veins, dural venous sinuses, pial and retinal veins, veins of trabecular bone and the venous spaces of erectile tissue: these veins consist of endothelium supported by variable amounts of connective tissue. Distinction between the media and adventitial layers is often difficult, and a discrete internal elastic lamina is absent.

Tethering of some veins to connective tissue fasciae and other surrounding tissues may prevent collapse of the vessel even under negative pressure (e.g. in the cranium). Pressure within the venous system does not normally exceed 5 mmHg, and it decreases as the veins grow larger and fewer in number, approaching zero close to the heart. As they contain only a small amount of muscle and commonly have a large calibre, veins have limited influence on blood flow. However, venoconstriction is an important component of the baroreceptor reflex because it reduces vein compliance and therefore capacity, effectively mobilizing blood to maintain or increase central venous pressure, and hence cardiac output. A sudden fall in blood volume, e.g. following a haemorrhage, also initiates the elastic recoil and reflex constriction of veins, in order to compensate for the blood loss and maintain central venous pressure and venous return to the heart. Vasoconstriction in cutaneous veins in response to cooling is important in thermoregulation.

Most veins have valves to prevent reflux of blood (Figs 6.13–6.14). A valve is formed by an inward projection of the intima, strengthened by collagen and elastic fibres, and covered by endothelium that differs in orientation on its two surfaces. Surfaces facing the vessel wall have transversely arranged endothelial cells, whereas on the luminal surface of the valve, over which the main stream of blood flows, cells are arranged longitudinally in the direction of flow. Most commonly two, or occasionally three, valves lie opposite one another; sometimes only one is present. They are found in small veins or where tributaries join larger veins. The valves are semilunar (cusps) and attached by their convex edges to the venous wall. Their concave margins are directed with the flow and lie against the wall as long as flow is towards the heart. When blood flow reverses, the valves close and blood fills an expanded region of the wall, a sinus, on the cardiac side of the closed valve. This may give a 'knotted' (varicose) appearance to the distended veins, if these have many valves. In the limbs, especially the legs where venous return is against gravity, valves are of great importance in aiding venous flow. Blood is moved towards the heart by the intermittent pressure produced by contractions of the surrounding muscles (the muscle pump). Valves are absent in the veins of the thorax and abdomen.

Vascular shunts and anastomoses

Arteriovenous shunts and anastomoses

Communications between the arterial and venous systems are found in many regions of the body. In some parts of the microcirculation (e.g. in the mesenteries), the capillary circulation can be bypassed by wider thoroughfare channels formed by metarterioles (Fig. 6.15A). These have similarities to both capillaries and the smallest arterioles, and have a discontinuous layer of smooth muscle in their walls. Metarterioles can deliver blood directly to venules or to a capillary bed, according to local demand and conditions. When functional demand is low, blood flow is largely limited to the bypass channel. Periodic opening and closing of different arterioles irrigates different parts of the capillary network. The number of capillaries in individual microvascular units and the size of their mesh determine the degree of vascularity of a tissue; the smallest meshes occur in the lungs and the choroid of the eye.

Arteriovenous anastomoses (Fig. 6.15B) are direct connections between smaller arteries and veins. Connecting vessels may be straight or coiled, and often possess a thick muscular tunic. Under sympathetic control, the vessel is able to close completely, diverting blood into the capillary bed. When patent, the vessel carries blood from artery to vein, partially or completely excluding the capillary bed from the circulation. Simple arteriovenous anastomoses are widespread and occur notably in the skin of the nose, lips and ears, nasal and gastrointestinal mucosae, erectile tissue, tongue, thyroid gland and sympathetic ganglia. There are few arteriovenous anastomoses in the neonate, but they develop rapidly during the early years. In old age they atrophy, sclerose and diminish in number. These factors may contribute to the less efficient temperature regulation that occurs at the two extremes of age.

In the skin of the hands and feet, especially in digital pads and nail beds (see Fig. 7.27), anastomoses form a large number of small units termed glomera. Each glomus organ has one or more afferent arteries, stemming from branches of cutaneous arteries that approach the surface. The afferent artery gives off a number of fine periglomeral branches and then immediately enlarges, makes a sinuous curve, and narrows again into a short, funnel-shaped vein that opens at right-angles into a collecting vein (Fig. 6.16).

Arterial anastomoses

Arteries can be joined to each other by an anastomosis, so that one can supply the territory of the other. An end-to-end anastomosis occurs when two arteries communicate directly, e.g. the uterine and ovarian arteries, the right and left gastro-epiploic arteries, the ulnar artery and the superficial palmar branch of the radial artery. Anastomosis by convergence occurs when two arteries converge and merge, as happens when the vertebral arteries form the basilar artery at the base of the brain. A transverse anastomosis occurs when a short arterial vessel links two large arteries transversely, e.g. the anastomoses between the two anterior cerebral arteries; the posterior tibial artery and the fibular artery; and the radial and ulnar arteries at the wrist.

The angiosome concept and vascular territories

The blood supply to the skin and underlying tissues has been mapped using ink injection studies, corrosion casts, dissection, perforator

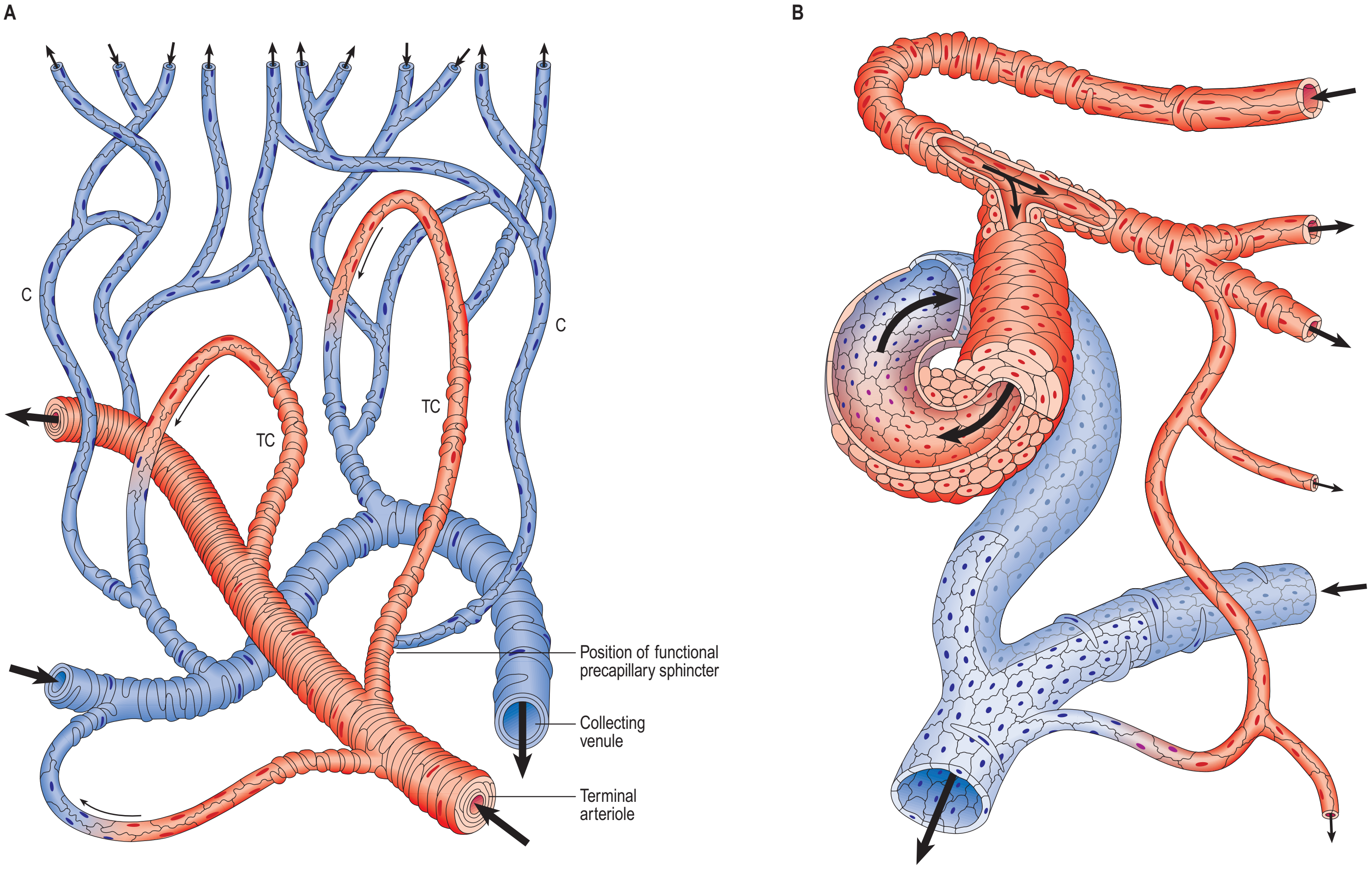

Fig. 6.15 **A**, A microcirculatory unit, showing a terminal arteriole, thoroughfare channels (TC) formed of metarterioles, capillaries (C) and collecting venule. The distribution of smooth muscle cells and one of the precapillary sites where perfusion of the capillary bed is regulated are also shown. **B,** An arteriovenous anastomosis. Note the thick wall of the anastomotic channel composed of layers of modified smooth muscle cells.

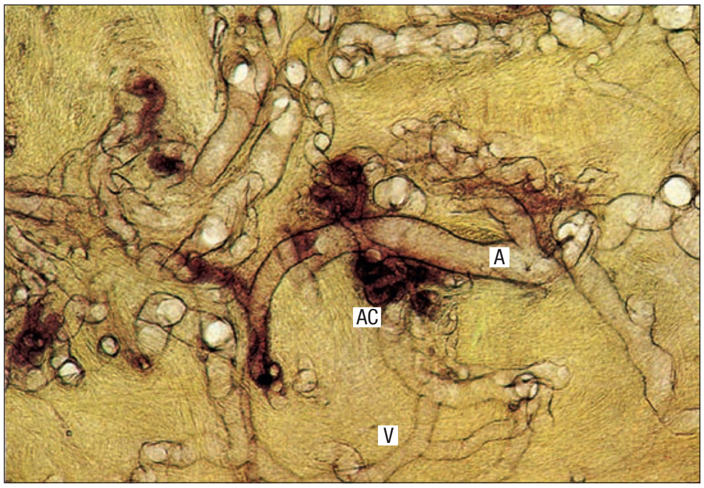

Fig. 6.16 A digital arteriovenous anastomosis, prepared by intravascular perfusion of stain in a full-thickness specimen of skin, followed by clearance. The heavily stained, thick-walled, tortuous anastomotic channels (AC) contrast with the central arterial stem (A) and the thin-walled venous (V) outflow channels. (Courtesy of the late Professor RT Grant, GKT School of Medicine, London.)

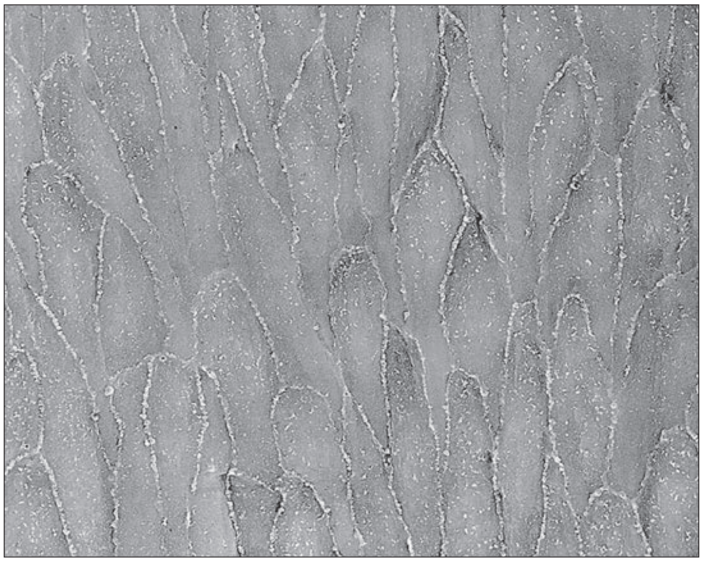

Fig. 6.17 A scanning electron micrograph of the luminal surface of the basilar artery. The tightly packed endothelial cells are elongated in the direction of blood flow. (Courtesy of Masoud Alian, University College, London.)

mapping and two- and three-dimensional radiographic analyses of fresh cadavers and isolated limbs injected with solutions containing lead oxide.

Findings from these different studies all support the clinically important concept of the angiosome, a three-dimensional block of tissue supplied by a source artery, its perforating branches and their accompanying veins (Taylor and Palmer 1987, Levy et al 2003, Taylor 2003, Pan and Taylor 2009). Angiosomes form a complex three-dimensional jigsaw puzzle; some pieces have a predominantly cutaneous component while others are predominantly muscular. Each consists of arteriosomes and venosomes linked to neighbouring angiosomes by either similar calibre (true) or reduced calibre (choke) anastomoses. Anastomoses between adjacent angiosomes may occur within the skin or within muscle. Some muscles are supplied by a single artery and its accompanying veins and therefore lie within one angiosome, while other muscles are supplied by more than one vessel and therefore cross more than one angiosome. A detailed knowledge of anatomical vascular territories and spatial angiosome architecture is essential in designing, evaluating and raising axial flaps based on vascular connections in plastic and reconstructive surgery.

Microstructure of blood vessels

Intima

The intimal lining of blood vessels consists of an endothelium, and a variable amount of subendothelial connective tissue, depending on the vessel.

Endothelium

Endothelium is a monolayer of flattened polygonal cells that extends continuously over the luminal surface of the entire vascular tree; its structure varies in different regions of the vascular bed (see Fig. 6.10; **Fig. 6.17**).

As a key component of the vessel wall, endothelium subserves several major physiological roles. Endothelial cells are in contact with the blood stream and thus influence blood flow. They regulate the diffusion of substances and migration of cells out of and into the circulating blood. In the brain, endothelial cells of small vessels actively transport substances, e.g. glucose, into the brain parenchyma. Endothelial cells play an important role in haemostasis because they produce von Willebrand factor, which promotes platelet adhesion (see below); secrete prostacyclin and thrombomodulin, which limits clot formation; and promote fibrinolysis by secreting tissue plasminogen activator. They have selective phagocytic activity and are able to extract substances from the blood. For example, the endothelium of pulmonary vessels removes and inactivates several polypeptides, biogenic amines, bradykinin, prostaglandins and lipids from the circulation, and converts the precursor of angiotensin II to its active form.

Endothelial cells secrete vasoconstrictor (thromboxane) and vasodilator (prostacyclin) prostaglandins, nitric oxide (NO) and endothelin (a vasoconstrictor). They respond to stretch (e.g. increased pressure) and the shear effect of blood flow via stretch-sensitive ion channels in the cell membrane. Endothelial cells synthesize components of the basal lamina. They proliferate to provide new cells during growth of blood vessels, to replace damaged endothelium, and to provide solid cords of cells that develop into new blood vessels (angiogenesis). Angiogenesis, which may be stimulated by local production of autocrine growth factors in response to tissue hypoxia, is important in wound healing and in the growth of tumours. Endothelial cells are also active participants in, and regulators of, inflammatory processes (Pober and Sessa 2007).

Although endothelial cells are thin, they extend over a relatively large surface area. They are thickest at the nucleus, where they can reach 2–3 µm, causing a slight bulge into the lumen (see Fig. 6.10). Elsewhere, they are thin and laminar, and are often as little as 0.2 µm thick in capillaries. They are generally elongated in the direction of blood flow, especially in arteries (see Fig. 6.17).

Except in sinusoids, endothelial cells usually adhere to each other at their edges, so there is no discontinuity in the lining of the lumen. They adhere to adjacent cells through the junctional complex, an area of apposition where adherent and tight junctions are found. They also communicate via gap junctions, which are most marked in continuous capillaries. Cell contacts and myoendothelial gap junctions between endothelial and smooth muscle cells are common in small resistance arteries and arterioles, where the separation between endothelium and media is reduced and the inner elastic lamina is either very thin or absent. Myoendothelial gap junctions play an important role in the integration and regulation of vascular function (Figueroa and Duling 2009).

Transcytotic (pinocytotic) vesicles (see Fig. 6.11) are present in all endothelial cells but are particularly numerous in exchange vessels; they include caveolae (see Fig. 6.4) typical of smooth muscle cells. They shuttle small amounts of interstitial fluid or plasma across the endothelial cytoplasm and thus facilitate bulk exchange of nutrients and metabolites between these compartments. They are normally the only means by which protein can cross the endothelium. Endothelial cells secrete many factors but they do not have the morphological characteristics of secretory cells.

The Wiebel–Palade body is characteristic of endothelial cells. It is an elongated cytoplasmic vesicle, 0.2 × 2–3 µm in length, which contains regularly spaced tubular structures parallel to its long axis. Wiebel–Palade bodies play a role in both inflammation and haemostasis because they store the adhesion molecule P-selectin (see below) and von Willebrand factor (vWF), which mediates platelet adhesion to the extracellular matrix after vascular injury.

Von Willebrand factor

Available with the *Gray's Anatomy* e-book.

Endothelial cell–leukocyte interactions

The luminal surface of endothelial cells does not normally support the adherence of leukocytes or platelets. However, many functions of human

Von Willebrand factor is a very large, multimeric glycoprotein consisting of at least 80 monomers of 250 kDa each, responsible for the characteristic appearance of Wiebel–Palade bodies. Its function is to bind to other proteins and provide a bridge between them.

On release from endothelial cells, vWF binds to collagen in the subendothelial matrix; when this is exposed following vascular damage, vWF facilitates platelet adhesion by binding to platelet glycoprotein receptors. This is particularly efficient in high-flow/shear-stress conditions, when it also causes platelet activation. Although the major source of vWF is probably endothelial cells, it is also produced by megakaryocytes and stored in platelet α-granules. vWF is present in plasma, where it binds and stabilizes factor VIII, a clotting protein secreted into the blood stream by hepatocytes. Hereditary deficiency or defective function of vWF causes defective haemostasis and a tendency to bleed (von Willebrand disease) (reviewed in Sadler (2005)).

vascular endothelial cells are dynamic rather than fixed. Activated endothelial cells and the characteristic endothelium of high endothelial venules (HEVs) of lymphoid tissues are sites of leukocyte attachment and diapedesis (see below).

HEVs (**Fig. 6.18**) are located within the T-cell domains, between and around lymphoid follicles in all secondary lymphoid organs and tissues except the spleen. They are specialized venules of 7–30 μm diameter, which possess a conspicuous cuboidal endothelial lining. The luminal aspect of HEVs shows a cobblestone appearance. The endothelial cells rest on a basal lamina and are supported by pericytes and a small amount of connective tissue (**Fig. 6.19**). They are linked by discontinuous adhesive junctions at their apical and basal aspects; the junctions are circumnavigated by migrating lymphocytes. Ultrastructurally, the endothelial cells have the characteristics of metabolically active secretory cells. Thus they contain large, rounded, euchromatic nuclei with one or two nucleoli, prominent Golgi complexes, many mitochondria, ribosomes and pinocytotic vesicles. Typically, they also possess Wiebel–Palade bodies (see above).

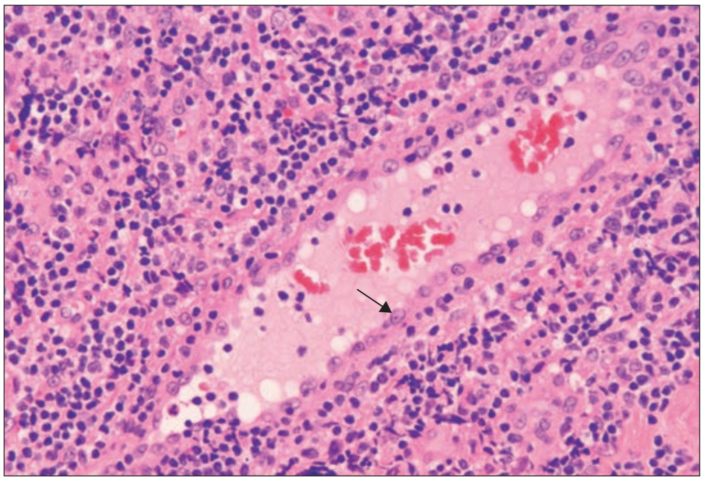

Fig. 6.18 A high endothelial venule in a human lymph node, sectioned longitudinally, lined by cuboidal endothelium (arrow). Erythrocytes and leukocytes (mainly lymphocytes and neutrophils) are seen in the lumen. (Courtesy of Mr Peter Helliwell and the late Dr Joseph Mathew, Department of Histopathology, Royal Cornwall Hospitals Trust, UK.)

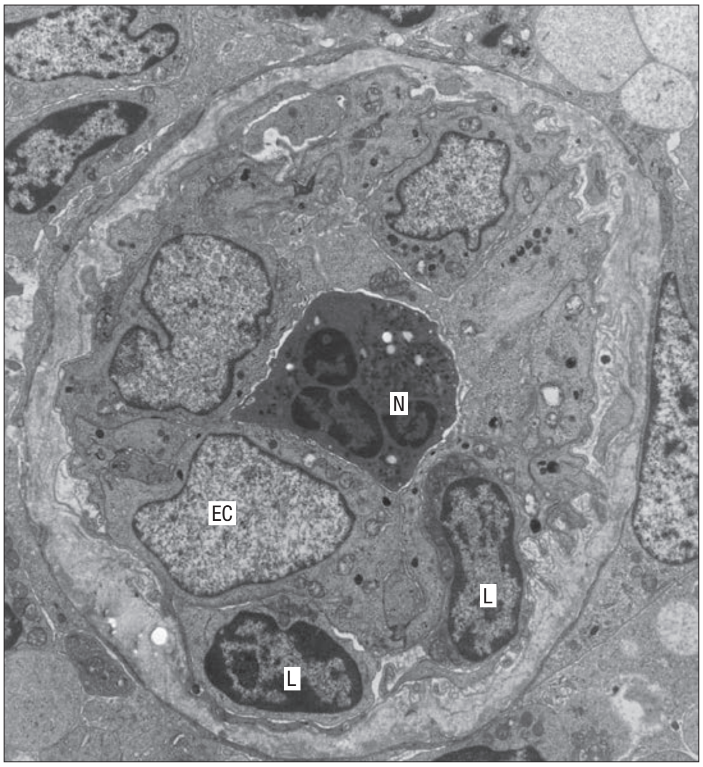

Fig. 6.19 A transmission electron micrograph of a high endothelial venule in transverse section in a human palatine tonsil. The lumen is completely filled by a neutrophil (N). Cuboidal endothelial cells (EC) line the vessel. Two lymphocytes (L) with heterochromatic nuclei are seen below, in transit within the wall of the vessel. (Courtesy of Dr Marta Perry, Department of Anatomy, St Thomas's Hospital Medical School, London.)

The adhesion molecules that mediate interactions between blood leukocytes and HEVs or cytokine-activated endothelium can be divided into three general families: selectins, integrins and the immunoglobulin supergene family. Selectins and integrins are expressed on leukocytes and mediate adhesion of circulating cells to the endothelium, which expresses selectins and members of the immunoglobulin supergene family. Regulated expression of these molecules by both cell types provides the means by which leukocytes recognize the vessel wall (leukocyte homing antigens and vascular addressins), adhere to it and subsequently leave the circulation.

The first step in this cascade is the loose binding or tethering of leukocytes, and this is initiated via L-, P- or E-selectin. This weak, reversible adhesion allows leukocytes to roll along the endothelial surface of a vessel lumen at low velocity, making and breaking contact, and sampling the endothelial cell surfaces. Recognition of chemokines (chemotactic signalling molecules) presented by the endothelium leads to 'inside-out' signalling and conversion of integrins at the leukocyte surface into actively adhesive configurations that bind strongly to their endothelial ligands, resulting in stable arrest. Finally, the leukocyte migrates through the vessel wall (diapedesis), passing either between (paracellular migration) or across (transcellular migration) endothelial cells. Transcellular migration is thought to be the preferred pathway; endothelial transcytotic vesicles (caveolae), intermediate filaments (vimentin) and F-actin are important in the creation of transient transcellular channels through which leukocytes pass. They then cross the basal lamina and migrate into the surrounding tissue by mechanisms that involve CD31 antigen and matrix metalloproteinases (reviewed in Vestweber (2007)).

Cell adhesion molecules

Available with the *Gray's Anatomy* e-book.

Subendothelial connective tissue

The subendothelial connective tissue, also termed the lamina propria, is a thin but variable layer. It is largely absent in the smallest vessels, where the endothelium is supported instead by pericytes (see Fig. 6.21). It contains a typical fibrocollagenous extracellular matrix, a few fibroblasts and occasional smooth muscle cells. Endothelial von Willebrand factor concentrates in this layer and participates in haemostasis and platelet adhesion when the overlying endothelium is damaged.

Media

The media consists chiefly of concentric layers of circumferentially or helically arranged smooth muscle cells with variable amounts of elastin and collagen.

Smooth muscle

Smooth muscle forms most of the media of arteries (see Fig. 6.7) and arterioles. A thinner layer of smooth muscle is also found in venules and veins; small segments of the pulmonary veins nearest to the heart contain striated cardiac muscle. Contraction of the smooth muscle in arteries and arterioles reduces the calibre of the vessel lumen, reducing blood flow through the vessel. This is particularly effective in small resistance vessels, where the wall is thick relative to the diameter of the vessel. Smooth muscle activation also increases the rigidity of the vessel wall, reducing its compliance. In arteries this affects propagation of the pulse, whereas in veins it effectively reduces their capacity.

The smooth muscle cells synthesize and secrete elastin, collagen and other extracellular components of the media, which bear directly on the mechanical properties of the vessels. The mechanics of the musculature of the media are complex. Distensibility, strength, self-support, elasticity, rigidity, concentric constriction, etc. are interrelated functions and are finely balanced in the different regions of the vascular bed.

In large arteries, where the blood pressure is high, the muscle cells are shorter (60–200 μm) and smaller in volume than in visceral muscle. In arterioles and veins, smooth muscle cells more closely resemble those from the viscera. The cells are packed with myofilaments and other elements of the cytoskeleton, including intermediate filaments. Vascular muscle cells contain intermediate filaments of either vimentin alone or both vimentin and desmin, whereas the intermediate filaments of visceral smooth muscle are exclusively of desmin. Intercellular junctions are mainly of the adhesive (adherens) type, coupling cells mechanically. Gap junctions couple cells electrically and allow passage of small signalling

There are three known members of the selectin family of adhesive proteins: L-selectin (also known as lymphocyte homing receptor), E-selectin and P-selectin. L-selectin is expressed on most leukocytes. Endothelial cells of HEVs in lymphoid organs express its oligosaccharide ligand, although other molecules such as mucins may be alternative ligands. L-selectin mediates homing of lymphocytes, especially to peripheral lymph nodes, but also promotes the accumulation of neutrophils and monocytes at sites of inflammation. E-selectin is an inducible adhesion molecule that mediates adhesion of leukocytes to inflammatory cytokine-activated endothelium, and is only transiently expressed on endothelium. P-selectin is rapidly mobilized from Wiebel–Palade bodies, where it is stored, to the endothelial surface after endothelial activation. It binds to ligands expressed on neutrophils, platelets and monocytes, and, like E-selectin, tethers leukocytes to endothelium at sites of inflammation. P-selectin is quickly endocytosed by the endothelial cells and so its expression is short-lived.

The integrins are a large family of molecules that mediate cell-to-cell adhesion as well as interactions of cells with extracellular matrix. Certain β_1 integrin heterodimers are expressed on lymphocytes 2–4 weeks after antigenic stimulation (very late antigens, VLAs) and bind to the extracellular matrix. Additionally, VLA-4, present on resting lymphocytes (expression increases after activation), monocytes and eosinophils, binds to the vascular cell adhesion molecule-1 (VCAM-1), the ligand on activated endothelium. In contrast to β_1 integrins, which many cells express, the expression of β_2 integrins is limited to white blood cells. Although the leukocyte integrins are not constitutively adhesive, they become highly adhesive after cell activation and therefore play a key role in the events required for cell migration. The endothelial ligands for one such β_2 integrin are the intercellular adhesion molecules-1 and 2 (ICAM-1 and ICAM-2), which belong to the immunoglobulin superfamily.

Three members of the large immunoglobulin superfamily of proteins are involved in leukocyte–endothelial adhesion, providing integrin counter-receptors on the endothelial cell membrane. ICAM-1 and ICAM-2 are constitutively expressed but upregulated by inflammatory cytokines. VCAM-1 is absent from resting endothelium but is induced by cytokines on activated endothelium and promotes extravasation of lymphocytes at sites of inflammation.

molecules. Junctions between muscle cells and the connective tissue matrix are particularly numerous, especially in arteries.

The muscle cells of the arterial media can be regarded as multifunctional mesenchymal cells. After damage to the endothelium, muscle cells migrate into the intima and proliferate, forming bundles of longitudinally orientated cells that reform the layer. In certain pathological conditions, muscle cells (and macrophages) undergo fatty degeneration and participate in the formation of atheromatous plaques.

Collagen and elastin

Components of the extracellular matrix (Ch. 2) are major constituents of vessel walls; in large arteries and veins they make up more than half of the mass of the wall, mainly in the form of collagen and elastin. Other fibrous components such as fibronectin, and amorphous proteoglycans and glycosaminoglycans, are present in the interstitial space.

Elastin is found in all arteries and veins and is especially abundant in elastic arteries (see Fig. 6.6). Individual elastic fibres (0.1–1.0 μm in diameter) anastomose with each other to form net-like structures, which extend predominantly in a circumferential direction. More extensive fusion produces lamellae of elastic material, which, though usually perforated and thus incomplete, separate the layers of muscle cells. The internal elastic lamina is a conspicuous elastic lamella in arteries, between intima and media, which allows the vessel to recoil after distension. When the intraluminal pressure falls below physiological limits (post mortem), it is compressed and coils up into a regular corrugated shape (**Fig. 6.20**; see Figs 6.7, 6.10), reducing but not obliterating the lumen; the profile of the artery remains circular. Fenestrations in the elastic lamina, which may also be split in thickness, allow materials to diffuse between intima and media. An outer elastic lamina, similar in appearance to, but markedly less well developed and less compact than, the internal elastic lamina, lies at the outer aspect of the media at its boundary with the adventitia (see Fig. 6.7). These laminae are less evident in elastic arteries, where elastic fibres occupy much of the media (see Fig. 6.6).

Collagen fibrils are found in all three layers of the vessel wall. Type III collagen (reticulin) occupies much of the interstitial space between the muscle cells of the media and is also found in the intima. Collagen is abundant in the adventitia, where type I collagen fibres form large bundles that increase in size from the junction with the media to the outer limit of the vessel wall. In veins, collagen is the main component of the vessel wall and accounts for more than half its mass.

In general, collagen and elastic fibres in the media run parallel to, or at a small angle to, the axes of the muscle cells, and they are therefore arranged mainly circumferentially. In contrast, the predominant arrangement of collagen fibres in the adventitia is longitudinal. This arrangement imposes constraints on length change in large vessels under pressure, e.g. in large arteries, in which the radial distension under the effect of the pulse far exceeds the longitudinal distension. The outer sheath of type I collagen in the adventitia therefore has a structurally supportive role. The more delicate type III collagen network of the media provides attachment to the muscle cells and its role is to transmit force around the circumference of the vessel. In a distended vessel, the elastic fibres store energy and, by recoiling, help to restore the resting length and calibre.

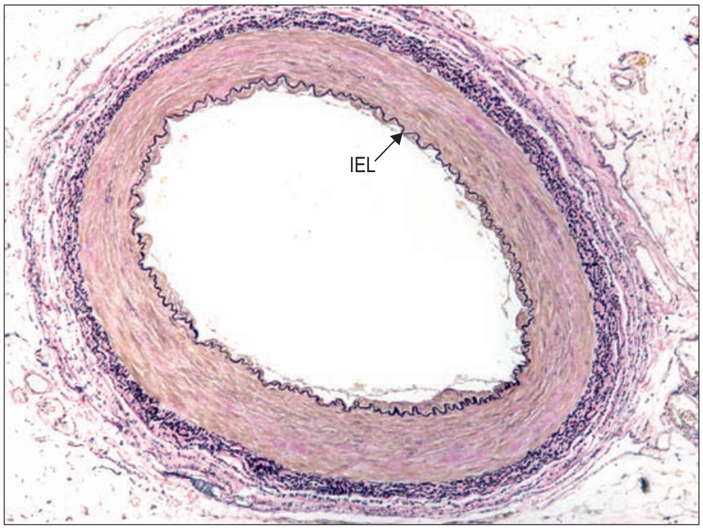

Fig. 6.20 The wall of a human muscular artery, stained for elastin (black), showing the internal elastic lamina (IEL). Fine, incomplete elastic lamellae are interspersed between smooth muscle cells of the tunica media. The endothelium is partly detached in this postmortem specimen. van Gieson stain.

The extracellular material of the media, including collagen and elastin, is produced by the muscle cells. Its turnover is slow compared to that in other tissues. In the adventitia, collagen is synthesized and secreted by fibroblasts, as it is in other connective tissues. During postnatal development, while vessels are increasing in diameter and wall thickness, there is a concomitant increase in elastin and collagen content. Subsequent changes in vessel structure, seen during ageing, include an increase in the ratio of collagen to elastin, with a reduction in vessel elasticity.

Adventitia

The adventitia is formed of general connective tissue: the thickness and density of its collagen fibre bundles vary.

Vasa vasorum

In smaller vessels, the nourishment of the tissues of the vessel wall is provided by diffusion from the blood circulating in the vessel itself. The wall thickness at which simple diffusion from the lumen becomes insufficient is 1 mm; larger vessels have their own vascular supply within the adventitia, in the form of a network of small vessels, the vasa vasorum (see Fig. 6.8). These originate from, and drain into, peripheral branches of the vessel they supply. They ramify within the adventitia and, in the largest of arteries, penetrate the outermost part of the media. The vasa vasorum of the pulmonary arteries arise from adjacent systemic arteries. The larger veins are also supplied by vasa vasorum but these may penetrate the wall more deeply, perhaps because of the lower oxygen tension.

Nervi vasorum

Blood vessels are innervated by efferent autonomic fibres that regulate the state of contraction of the musculature (muscular tone) and thus the diameter of the vessels and the resistance of arteries and arterioles. Perivascular nerves branch and anastomose within the adventitia of an artery, forming a meshwork around it. Nerves are occasionally found within the outermost layers of the media in some of the large muscular arteries.

Nervi vasorum are small bundles of axons which are almost invariably unmyelinated and typically varicose. Most are postganglionic axons derived from neurones in sympathetic ganglia. The density of innervation varies in different vessels and in different areas of the body; it is usually sparser in veins and larger lymphatic vessels, whereas large veins with a pronounced muscle layer, such as the hepatic portal vein, are well innervated. Some vessels in the brain may be innervated by intrinsic cerebral neurones, although neural control of brain vessels is of minor importance compared with metabolic and autoregulation (local response to stretch stimuli).

The control of vascular smooth muscle is complex. Vasoconstrictor adrenergic fibres release noradrenaline (norepinephrine), which acts on α-adrenergic receptors in the muscle cell membrane. In addition, circulating hormones and factors such as nitric oxide, prostaglandins and endothelin, which are released from endothelial cells, exert a powerful effect on the muscle cells. Neurotransmitters reach the muscle from the adventitial surface of the media, whereas hormonal and endothelial factors diffuse from the intimal surface. In a few tissues, sympathetic cholinergic fibres inhibit smooth muscle contraction and induce vasodilation. Vascular smooth muscle exhibits endogenous (myogenic) activity in response to stretch and shear.

Most arteries are accompanied by nerves that travel in parallel with them to the peripheral organs that they supply: these paravascular nerves do not innervate the vessels they accompany.

Pericytes

Pericytes are present at the outer surface of capillaries and the smallest venules (postcapillary venules), where an adventitia is absent and there are no muscle cells. They are elongated cells, with long cytoplasmic processes that wrap around the endothelium. They are usually absent from fenestrated capillaries, scattered in a discontinuous layer around the outer circumference of capillaries and form a more continuous layer around postcapillary venules (**Fig. 6.21**). They are gradually replaced by smooth muscle cells as vessels converge and increase in diameter.

Pericytes are enclosed by their own basal lamina, which merges in places with that of the endothelium. Most display areas of close apposition with endothelial cells, and occasionally form adherens junctions where their basal laminae are absent. Pericyte cytoplasm contains actin, myosin, tropomyosin and desmin, which suggests that they are capable of contractile activity. They also have the potential to act as connective

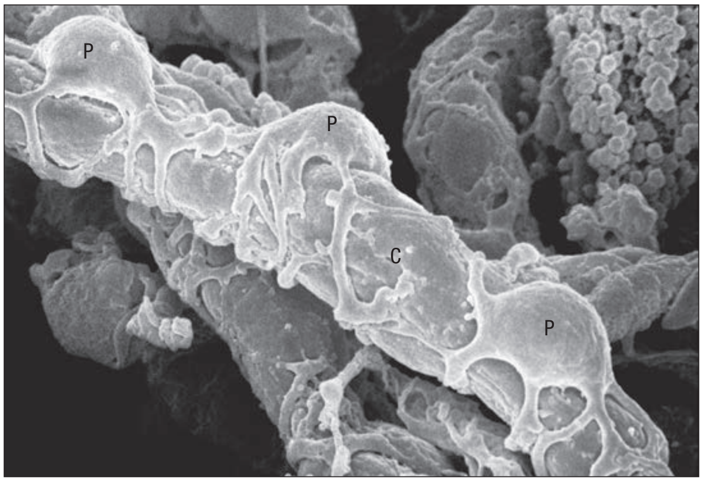

Fig. 6.21 A scanning electron micrograph of a capillary (C) and pericytes (P) supporting the vessel wall. (Courtesy of T. Fujiwara and Y. Uehara, Department of Anatomy, Ehime University School of Medicine, Japan.)

tissue progenitor cells, and participate in repair processes by proliferating and giving rise to new blood vessel and connective tissue cells.

Pericytes, or closely related cells, may be one source of myofibroblasts that contribute to fibrosis in disease processes (reviewed in Duffield (2012); see also Chapter 2). The role of pericytes is becoming recognized in other disease states with a component of vascular pathology, e.g. diabetes, where complications include retinopathy, nephropathy and neuropathy. Pericytes respond to aberrant local cues, including high glucose levels, such that their role in supporting the microvasculature is compromised: leaky vessels and the ensuing inflammation contribute to tissue damage and impaired function. There is evidence that pericytes may influence the tumour microenvironment in cancer, with detrimental consequences (reviewed in Ferland-McCollough et al (2017)).

Regional adaptations

Cerebral vasculature

Cerebral function is critically dependent on an adequate blood supply and tight regulation of the composition of cerebrospinal fluid. All cerebral vessels except capillaries have a thin outer coating of meningeal cells, usually one layer thick, with adjacent meningeal cells joined by desmosomes and gap junctions. Cerebral capillaries, the site of the blood–brain barrier, are lined by endothelial cells joined by particularly tight junctions. The endothelial cytoplasm contains a few pinocytotic vesicles. The cells are surrounded by a basal lamina (see Fig. 3.14); at points of contact with perivascular astrocytes, the intervening basal lamina is formed by fusion of the endothelial and glial basal laminae. Pericytes, completely surrounded by basal lamina, are present around capillaries (see Fig. 3.14); recent evidence suggests that relaxation of pericytes and thus dilation of capillaries is the major determinant of increased blood flow in response to increased neuronal activity (Hall et al 2014). Perivascular macrophages are attached to the outer walls of capillaries and to other vessels; they are phenotypically distinct from parenchymal microglia, which are also of monocytic origin. For further descriptions of the cerebral vasculature, see Chapter 26.

Pulmonary vasculature

The pulmonary circulation is a low pressure/high flow system. It receives the whole cardiac output, and thus must accommodate a wide range of blood flows (e.g. as occur in rest and exercise). Unlike arterioles in the systemic circulation, pulmonary arterioles smaller than 50–100 µm in diameter have little or no smooth muscle, and pulmonary vascular blood flow is largely independent of neural, local metabolic and myogenic mechanisms. Hypoxia produces hypoxic pulmonary vasoconstriction (HPV), when small pulmonary arteries constrict rather than dilate (as occurs in the systemic vasculature). This mechanism diverts blood away from poorly ventilated areas of the lung, and so optimizes ventilation/perfusion matching (Sylvester et al 2012). However, in hypoxic lung disease or at altitude, this can lead to pulmonary hypertension; if sustained, this can lead to extensive vascular remodelling, and eventually to right heart failure. Other causes of pulmonary hypertension include left heart failure, thromboembolism, and more rarely, dysfunction of the pulmonary vasculature itself. For further descriptions of the pulmonary vasculature, see Chapter 54.

Renal vasculature

Regulation of body water and solutes by the kidney depends on ultrafiltration of plasma in the glomeruli. The renal vasculature exhibits a high degree of autoregulation. Afferent arterioles leading to the glomerular capillaries in Bowman's capsule have a fenestrated endothelium (and thus a high permeability) and a specialized basement membrane, and are covered by podocytes (modified epithelial cells). The basement membrane and podocyte processes form the ultrafiltration membrane (see Figs 72.15, 72.18). The capillaries are surrounded by phagocytic mesangial cells. Glomerular capillary pressure is higher than elsewhere, and is regulated via differential constriction of the afferent and efferent arterioles. The efferent arterioles lead to peritubular capillaries which surround the cortical nephron, and to the vasa recta which descend deep into the medulla. The vasa recta help to maintain the medullary osmotic gradient essential for concentration of urine. Decreased pressure and/or stimulation by the sympathetic nerves innervating the afferent arterioles causes release of renin from granular cells in the endothelium: renin then activates the precursor of angiotensin 2, an important hormone for regulation of blood pressure and volume. Renal artery obstruction, e.g. in atherosclerosis, can cause hypertension; essential hypertension may also originate in renal dysfunction, and renal sympathetic nerve ablation has been promoted as a treatment for resistant hypertension (Papademetriou et al 2014). For further descriptions of the renal vasculature, see Chapter 72.

Cutaneous vasculature

Thermoregulation is a primary function of the skin. Heat transfer from blood to the surface is facilitated by vascular plexuses, and in the extremities (hands, feet, ears, lips, nose) arteriovenous anastomoses (see above and Chapter 7). Skin blood flow and thus heat loss are primarily controlled centrally by the hypothalamus (Ch. 30) and sympathetic nervous system, but are also affected by local mechanisms. In moderate conditions (the thermoneutral zone), changes in skin blood flow alone are sufficient to maintain body core temperature.

Raynaud's phenomenon

Raynaud's phenomenon (or syndrome) is an exaggerated and episodic vasoconstrictor response to cold or stress in the skin of the extremities, especially the fingers.

Diseases of the vasculature

Available with the *Gray's Anatomy* e-book.

Lymphatic vessels

Lymphatic capillaries form wide-meshed plexuses in the extracellular matrices of most tissues. They begin as dilated, blind-ended tubes with larger diameters and less regular cross-sectional appearances than those of blood capillaries. Their basal laminae are incomplete or absent and they lack associated pericytes. The smaller lymphatic vessels are lined by endothelial cells, which have numerous transcytotic vesicles within their cytoplasm and so resemble blood capillaries. However, unlike capillaries, their endothelium is generally quite permeable to much larger molecules: they are readily permeable to large colloidal proteins and particulate material such as cell debris and microorganisms, and also to cells. Permeability is facilitated by gaps between the endothelial cells, which lack tight junctions (discontinuous endothelium), and by pinocytosis. The lymphatic system provides an important transport pathway for leukocytes and defence against infection (reviewed in Saharinen et al (2004)).

Lymph is formed from interstitial fluid, which is derived from blood plasma via filtration in the microcirculation. Much of the filtered fluid is reabsorbed by the time the blood leaves the venules, but about 15% or 8 litres per day enters the lymphatics. Lymphatic vessels take up this residual fluid by passive diffusion and the transient negative pressures in their lumina, that are generated intrinsically by contractile activity of smooth muscle in the largest lymphatic vessel walls, and extrinsically by compression of the lymph vessels as a result of contraction of adjacent muscle or arterial pulsation. The unidirectional flow of lymph is maintained by the presence of valves in the larger vessels (**Fig. 6.27**). Lymphatic capillaries are prevented from collapsing by anchoring filaments, which tether their walls to surrounding connective tissue structures and exert radial traction.

In most tissues, lymph is clear and colourless; in the lymphatic capillaries it has an identical composition to interstitial fluid. In contrast, lymph from the small intestine is dense and milky, reflecting the presence

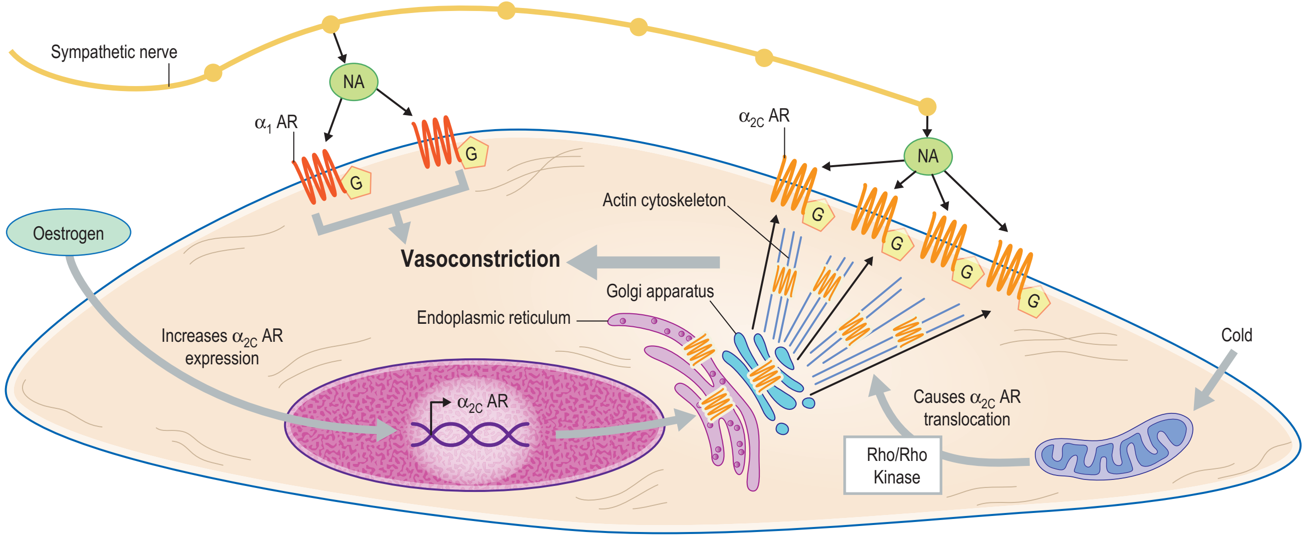

Fig. 6.22 Mechanisms underlying the response of cutaneous vascular smooth muscle to cold. Central control is mediated by release of noradrenaline (NA) from sympathetic nerves, which activates G-protein coupled α_1- and α_{2c}-adrenergic receptors (AR) to initiate vasoconstriction. Local cooling, sensed by mitochondria, causes translocation of α_{2c} AR from the Golgi and endoplasmic reticulum (ER) to the membrane via a Rho/Rho kinase and actin cytoskeleton-mediated mechanism, augmenting vasoconstriction. The female hormone oestrogen increases expression of α_{2c} AR, so enhancing the response. Raynaud's phenomenon may involve dysregulation of these processes (see Fardoun et al 2016).

Under such conditions adrenergic sympathetic activity maintains a level of tonic vasoconstriction via release of noradrenaline, which activates α_1- and α_2-adrenergic receptors on vascular smooth muscle cells. Arteriovenous anastomoses are particularly sensitive to noradrenaline and are normally strongly vasoconstricted. A fall in temperature increases sympathetic activity and thus cutaneous vasoconstriction. This is augmented locally by cold-induced and cytoskeleton-facilitated translocation of endoplasmic reticulum/Golgi associated α_{2C}-adrenergic receptors to the vascular smooth muscle cell membrane, effectively increasing sensitivity to noradrenaline (Fig. 6.22) (Fardoun et al 2016). The combined effects can reduce cutaneous blood flow by 90% in cold conditions. Conversely, an increase in temperature reduces sympathetic activity resulting in vasodilation and opening of arteriovenous anastomoses, greatly increasing blood flow and heat loss. Further increases occur at higher temperatures as sympathetic cholinergic neurones activate sweat glands (Ch. 7) which secrete bradykinin (a powerful vasodilator), and also release vasodilator co-transmitters (nitric oxide, substance P). Skin blood flow can increase 30-fold in very hot conditions.

Raynaud's phenomenon is characterized by a classic, often clearly demarcated, triphasic colour change of intense pallor (white, ischaemia), cyanosis (deoxygenation), and red (reperfusion), with associated pain and occasionally ulceration. Prevalence is 5–10% of the general population, but varies geographically: the condition is more common in premenopausal women than in men. Most cases are idiopathic (primary Raynaud's phenomenon), but about 15% are secondary to a clinical condition, especially connective tissue disorders such as scleroderma and systemic lupus erythematosus, or are induced by drugs (e.g. chemotherapy, β-adrenergic receptor antagonists), environmental/occupational exposure (e.g. smoking, vinyl chloride, arsenic), or sustained mechanical vibration of the fingers (Fardoun et al 2016, Khouri et al 2016).

The causes of Raynaud's phenomenon may be multiple, but are clearly associated with abnormalities of the cutaneous microcirculation (or possibly peripheral sympathetic nerves). There is some evidence for genetic predisposition in primary Raynaud's phenomenon. Recent studies have focused on mechanisms underlying the translocation of α_{2C}-adrenergic receptors to the vascular smooth muscle cell membrane. Interestingly, the female hormone oestrogen has been shown to potentiate expression, translocation and activity of α_{2C}-adrenergic receptors in vascular smooth muscle of the skin, suggesting a reason for the increased prevalence of Raynaud's phenomenon in premenopausal women (Fardoun et al 2016).

For a review of vascular disease and the role of extracellular matrix proteins in the vascular wall in a number of disease states, see Xu and Shi (2014).

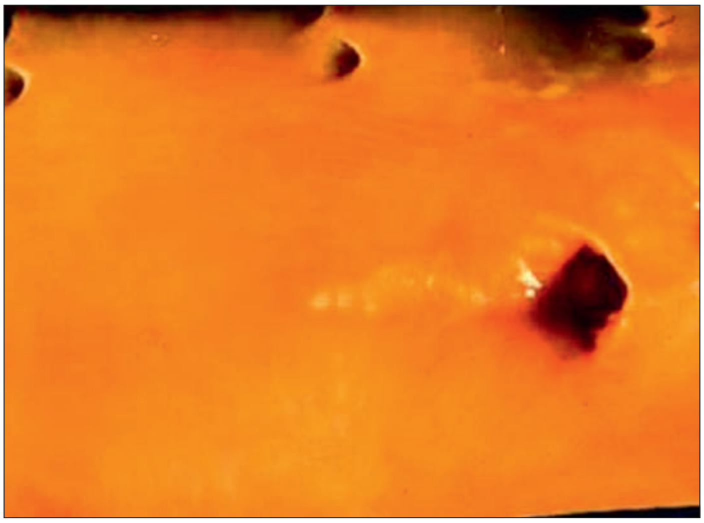

Fig. 6.23 A fatty streak (yellow) on the intimal surface of the aorta close to an arterial branch. (Courtesy of Professor Mary Sheppard, CRY Centre for Cardiac Pathology, St George's University of London, UK.)

Atherosclerosis and arteriosclerosis

Atherosclerosis is by far the most important arterial disease. It is the principal cause of death and disability in many Western countries, primarily due to ischaemic heart disease and stroke. Atherosclerosis arises and progresses as an inflammatory response of the vessel wall to chronic multifactorial injury due to hyperlipidaemia, hypertension, smoking or diabetes mellitus. It is a focal intimal disease of medium-to-large arteries, including the aorta, and carotid, coronary, iliofemoral, and cerebral arteries. Some medium-sized arteries, e.g. internal thoracic artery, are spared, as are pulmonary arteries and veins.

Low-density lipoprotein (LDL) from the plasma moves freely in and out of the intima. Within the intima a small proportion of the LDL undergoes oxidative change. The oxidized LDL acts as an inflammatory stimulus, which invokes adhesion molecule expression by endothelial cells, monocyte migration, and cytokine production. Once oxidized, the LDL is taken up by macrophage scavenger receptors, and lipid uptake continues until the cytoplasm is packed with lipid to form macrophage-derived foam cells. This influx of lipid into macrophages results in infiltration of the vessel wall by T lymphocytes, with smooth muscle proliferation, and deposition of collagen and elastin in the intima, extending into the media. The earliest visible lesion is the fatty streak which consists of raised intimal areas full of lipid-filled foam cells (macrophages) and features of inflammation (Fig. 6.23). As these intimal lesions develop, they acquire combinations of extracellular lipid, intracellular lipid within foam cells, and collagen and other connective tissue matrix components produced by smooth muscle cells. The resulting larger intimal lesions are termed atherosclerotic plaques (Fig. 6.24), with a collagen cap, a core of variable lipid with calcium deposits, and vascularization from the vasa vasorum. These plaques can increase in size and narrow the lumen of blood vessels leading to ischaemia. Progression of disease leads to further luminal narrowing and changes in the plaques, including surface ulceration, intraplaque haemorrhage, rupture and thrombosis.

Involvement of the coronary arteries results in major clinical complications, namely myocardial infarction, i.e. sudden cardiac death. Involvement of the cerebral circulation results in transient ischaemic attacks or cerebral infarcts (stroke). Atherosclerosis in the aorta results in aneurysm, rupture (particularly in the abdominal aorta), and narrowing of the iliofemoral vessels, which leads to gangrene of the lower extremities.

Arteriosclerosis means hardening of an artery. It differs from atherosclerosis as there is no intimal lipid deposition with resultant inflammation; it can affect both arteries and arterioles. Arteriosclerosis is due to gradual replacement of smooth muscle cells by collagen and deposition of plasma proteins in the smooth muscle to produce hyaline change. This process is accelerated by age, hypertension and diabetes mellitus. Arteriosclerosis lowers the compliance of the arterial tree and contributes to the age-related increase in systolic blood pressure. The lack of vascular compliance greatly increases susceptibility to hypotension which accounts for the increased mortality of shock in elderly and hypertensive patients. The term 'intimal hyperplasia' is used to describe the intimal thickening associated with arteriosclerosis, in which smooth muscle cells, collagen and elastic fibres infiltrate the intima (Fig. 6.25). This is also a feature of ageing and hypertension.

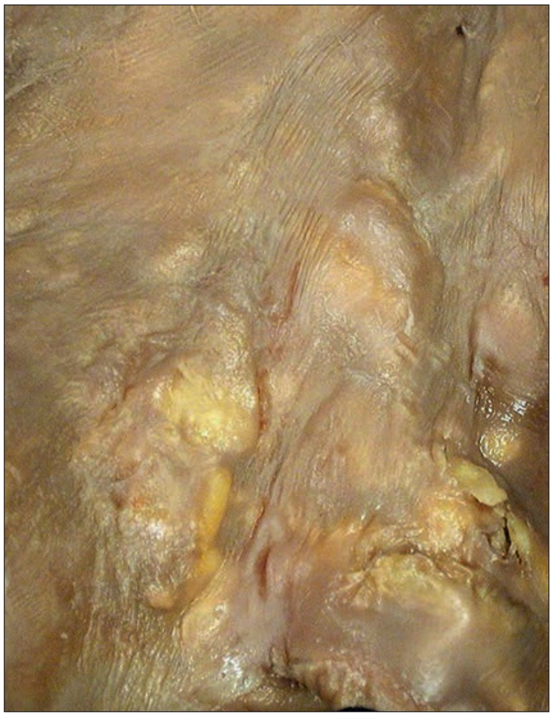

Fig. 6.24 A raised fibrofatty atheromatous plaque on the intimal surface of the aorta. (Courtesy of Professor Mary Sheppard, CRY Centre for Cardiac Pathology, St George's University of London, UK.)

Venous disease

Venous thrombosis is common and due to slow blood flow, especially in the veins of the legs. It is often due to obesity combined with immobility and is common after surgical operations or long haul flights. Leg or pelvic vein thrombosis is the principal cause of pulmonary thromboembolism. Thrombosis starts at the valves of the deep calf veins, causing deep vein thrombosis. It may propagate into the posterior tibial, popliteal, femoral, or iliac veins and into the inferior vena cava. The outcomes of venous thrombosis include: massive pulmonary embolism and sudden death; asymptomatic pulmonary embolism; pulmonary infarction; pulmonary hypertension. Sudden death is seen with total occlusion of the right side of the heart, and/or one or both left and right pulmonary arteries (Fig. 6.26). Occlusion of smaller vessels is survivable with or without pulmonary infarction. Occlusion of more than half the pulmonary arterial tree results in pulmonary hypertension and right ventricular failure. Occlusion of many vessels by showers of small emboli over months or years results in chronic pulmonary hypertension (see above).

Thrombophlebitis refers to thrombosis of veins with associated inflammation. Migrating thrombophlebitis is thrombosis and inflammation of superficial veins in association with cancer, particularly of the pancreas and gastrointestinal tract. Infected thrombi may cause pyaemia or embolism to form distant abscesses, e.g. an appendix abscess may give rise to liver abscess formation.

Varicosities (varicose veins) are caused by venous hypertension, which leads to dilated tortuous veins with failure of the venous valves, usually in the lower limbs. Standing, obesity, old age, cardiac failure and pregnancy predispose to varicose leg veins, which are very common. Although thrombosis occurs in varicose veins, the thrombi do not usually lead to embolization because they adhere to the vein wall. Varicose veins may lead to bleeding and infection, but the usual complication is poor wound healing with venous ulceration, a cause of widespread morbidity in elderly people. Oesophageal varices complicate portal hypertension in cirrhosis of the liver (usually alcohol-related): bleeding from ruptured oesophageal varices is often the terminal event in such patients. Haemorrhoids (piles) are caused by venous hypertension in the pelvic and abdominal veins as a result of constipation, obesity and pregnancy. A varicocele is a mass formed by varicosity of the pampiniform venous plexus in the testicle.

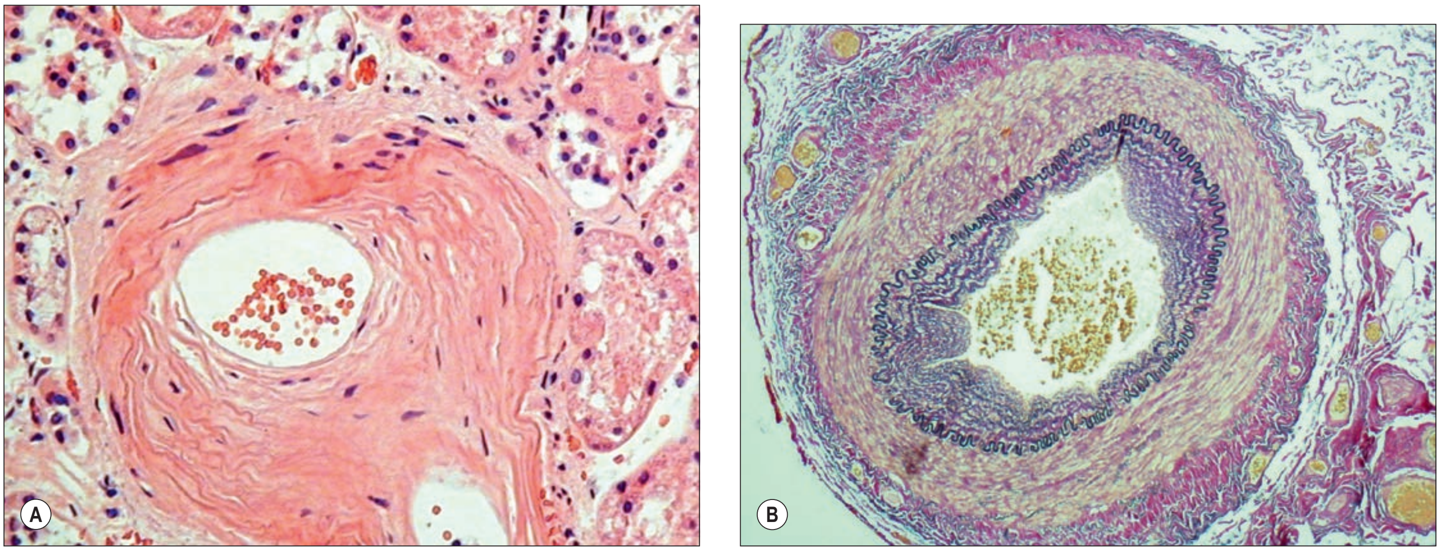

Fig. 6.25 A, Intimal fibroblastic proliferation with reduction in lumen diameter in an arteriole in the kidney. **B**, Intimal fibroelastic proliferation with reduplication of the internal elastic lamina and reduction in lumen diameter in an artery in the heart. Elastic van Gieson stain for elastic tissue. (Courtesy of Professor Mary Sheppard, CRY Centre for Cardiac Pathology, St George's University of London, UK.)

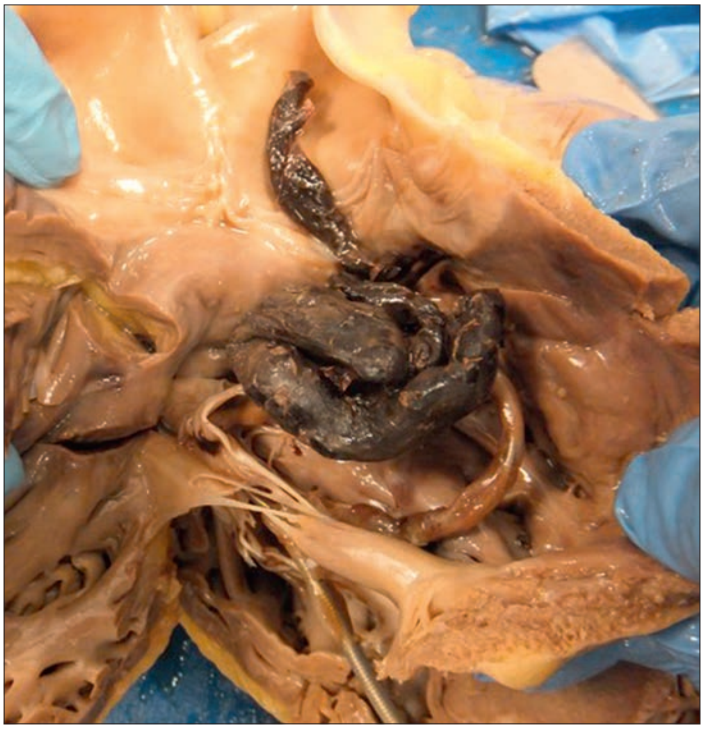

Fig. 6.26 The right ventricular outflow tract of the right ventricle showing a coiled up pulmonary embolus blocking the right ventricular outflow tract and the main pulmonary artery. (Courtesy of Professor Mary Sheppard, CRY Centre for Cardiac Pathology, St George's University of London, UK.)

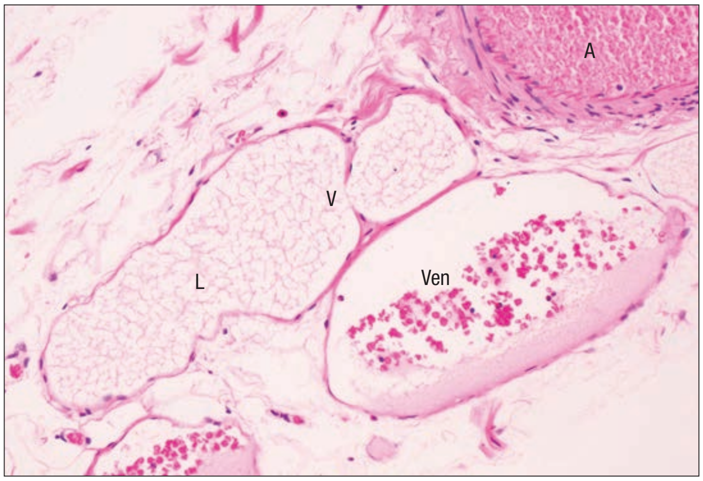

Fig. 6.27 A valve (V) in a lymphatic vessel (L), accompanying a small venule (Ven) and arteriole (A) in human connective tissue. (Courtesy of Mr Peter Helliwell and the late Dr Joseph Mathew, Department of Histopathology, Royal Cornwall Hospitals Trust, UK.)

of lipid droplets (chylomicrons) derived from fat absorbed by the mucosal epithelium. The terminal lymphatic vessels in the mucosa of the small intestine are known as lacteals and the lymph as chyle. Lymphatic capillaries are not ubiquitous: they are not present in cornea, cartilage, thymus, the central or peripheral nervous systems or bone marrow, and there are very few in the endomysium of skeletal muscles.

Lymphatic capillaries join into larger vessels that pass to local lymph nodes. Typically, lymph percolates through a series of nodes before reaching a major collecting duct. There are exceptions to this arrangement: the lymph vessels of the thyroid gland and oesophagus, and of the coronary and triangular ligaments of the liver, all drain directly to the thoracic duct without passing through lymph nodes. In the larger vessels, a thin external connective tissue coat supports the endothelium. The largest lymphatic vessels (200 μm) have three layers, like small veins, although their lumen is considerably larger than that of veins with a similar wall thickness. The tunica media contains smooth muscle cells, mostly arranged circumferentially. Elastic fibres are sparse in the tunica intima, but form an external elastic lamina in the tunica adventitia.

The larger lymphatic vessels differ from small veins in having many more valves (see Fig. 6.27). The valves are semilunar, generally paired and composed of an extension of the intima. Their edges point in the direction of the current, and the vessel wall downstream is expanded into a sinus, which gives the vessels a beaded appearance when they are distended. Valves are important in preventing the backflow of lymph.

Deep lymphatic vessels usually accompany arteries or veins, and almost all reach either the thoracic duct or the right lymphatic duct, which usually joins the left or right brachiocephalic veins respectively at the root of the neck.

The thoracic duct is structurally similar to a medium-sized vein but the smooth muscle in its tunica media is more prominent. Most lymphatic vessels anastomose freely. Larger vessels have their own plexiform vasa vasorum and accompanying nerve fibres. If their walls are acutely infected (lymphangitis) this vascular plexus becomes congested, marking the paths of superficial vessels by red lines that are visible through the skin and tender to the touch.

Lymphatic vessels repair easily. New vessels form readily after damage, beginning as solid cellular sprouts from the endothelial cells of persisting vessels that subsequently become canalized.

Diseases of the lymphatics

Lymphoedema occurs when insufficient lymphatic drainage leads to accumulation of fluid in the tissues (oedema) and swelling, typically in the limbs. In the developed world, secondary lymphoedema is most commonly the consequence of treatment for cancer, particularly breast cancer, following either surgical removal of lymph nodes and vessels, or their damage by radiation therapy. Tumours can themselves cause lymphoedema if they compress and block lymph vessels. Lymphangiectasia refers to a pathological dilation of lymph vessels, often caused by lymphatic obstruction; both can be primary or acquired. Acute lymphangitis is usually caused by invasion by virulent bacteria, e.g. *Streptococcus pyogenes*, causing subcutaneous red streaks draining an infected area: it leads to lymphadenitis and may herald septicaemia.

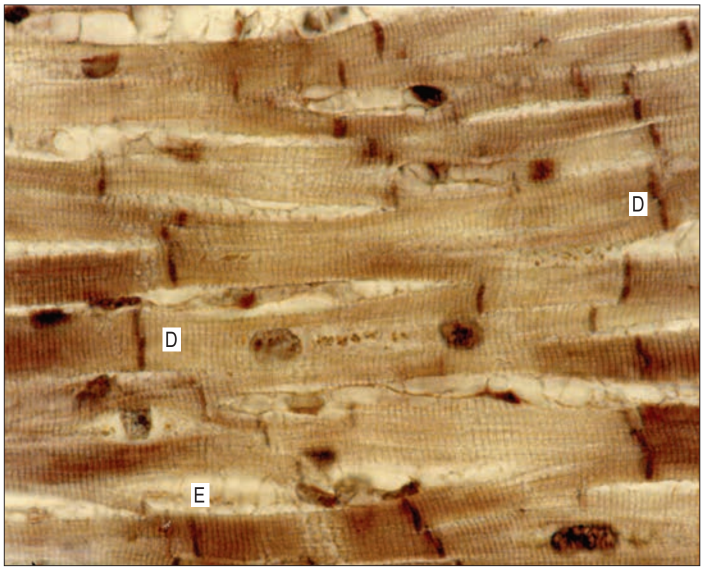

Fig. 6.28 Cardiac muscle fibres in human myocardium, sectioned longitudinally. Cell branching and fine cross-striations are clearly visible and indicate the intracellular organization of sarcomeres. The dark transverse lines are intercalated discs (D). Endomysium (E) contains nuclei of endothelial cells and fibroblasts.

CARDIAC MUSCLE

In cardiac muscle, as in skeletal muscle, the contractile proteins are organized structurally into sarcomeres that are aligned in register across the fibres, producing fine cross-striations that are visible in the light microscope. Both types of muscle contain the same contractile proteins (although commonly different isoforms), which are assembled in a similar way. The molecular basis for contraction, but not its regulation, is the same. Elevation of cytosolic calcium triggers contraction, corresponding to cardiac systole and the pumping phase of the heart cycle. Removal of cytosolic calcium induces relaxation, corresponding to diastole and cardiac filling. Despite the similarities, there are major functional, morphological and developmental differences between cardiac and skeletal muscle.

Microstructure of cardiac muscle

The myocardium, the muscular component of the heart, constitutes the bulk of its tissues. It consists predominantly of cardiac muscle cells, which are usually 120 μm long and 20–30 μm in diameter in a normal adult. Each cell has one or two large nuclei occupying the central part of the cell, whereas skeletal muscle has multiple, peripherally placed nuclei. The cells are branched at their ends, and the branches of adjacent cells are so tightly associated that their appearance under light microscopy is of a network of branching and anastomosing fibres (**Fig. 6.28**). Cells are bound together by elaborate junctional complexes, the intercalated discs (**Fig. 6.29**; see Fig. 6.31).

Fine fibrocollagenous connective tissue is found between cardiac muscle fibres. Although this is equivalent to the endomysium of skeletal muscle, it is less regularly organized because of the complex three-dimensional geometry imposed by the branching cardiac cells. Numerous capillaries and some nerve fibres are found within this layer. Coarser connective tissue, equivalent to the perimysium of skeletal muscle, separates the larger bundles of muscle fibres, and is particularly well developed near the condensations of dense fibrous connective tissue that form the 'skeleton' of the heart. The ventricles of the heart are composed of spiralling layers of fibres that run in different directions. Consequently, microscope sections of ventricular muscle inevitably contain the profiles of cells cut in a variety of orientations. A linear arrangement of cardiac muscle fibres is found only in the papillary muscles and trabeculae carneae.

Electron micrographs of cardiac muscle cells in longitudinal section show that the myofibrils separate before they pass around the nucleus, leaving a zone that is occupied by organelles, including sarcoplasmic reticulum, Golgi complex, mitochondria, lipid droplets and glycogen (**Fig. 6.30**). At the light microscopic level, these zones appear in longitudinal sections as unstained areas at the poles of each nucleus.

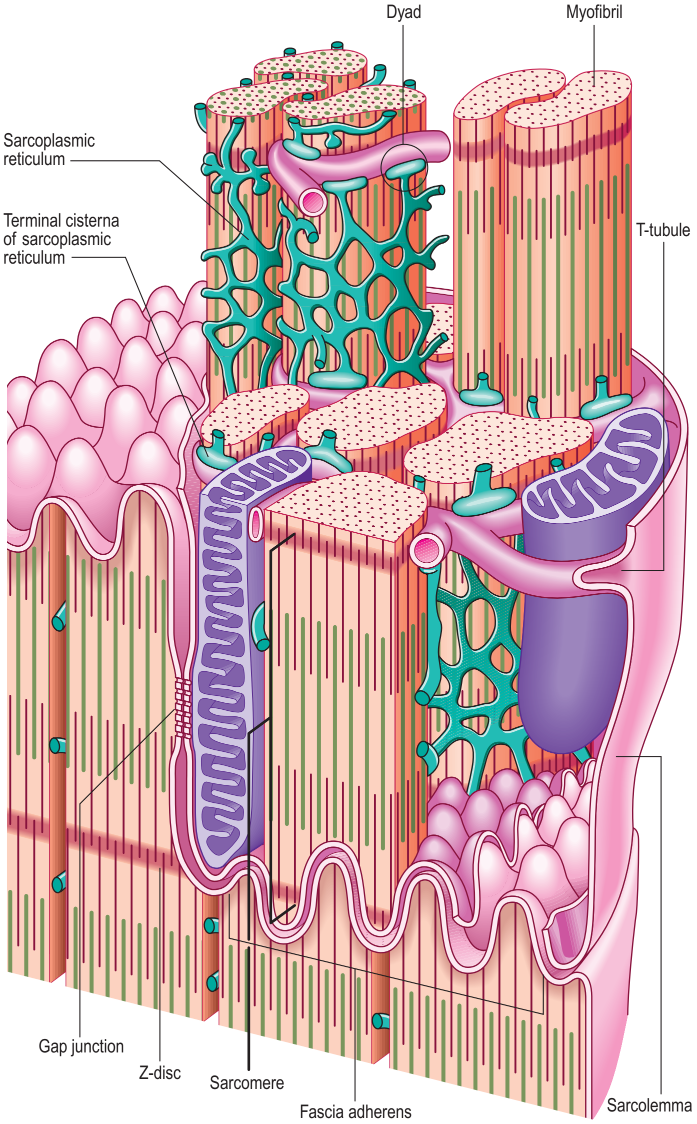

Fig. 6.29 A three-dimensional reconstruction of cardiac muscle cells in the region of an intercalated disc, a junctional complex between neighbouring cells. The interdigitating transverse parts of the intercalated disc form a fascia adherens, with numerous desmosomes; gap junctions are found in the longitudinal parts of the disc. The organization of the transverse tubules and sarcoplasmic reticulum is also shown.

They often contain lipofuscin granules, which accumulate there in individuals over the age of 10; the reddish-brown pigment may be visible even in unstained longitudinal sections.

The cross-striations of cardiac muscle are less conspicuous than those of skeletal muscle because the contractile apparatus of cardiac muscle lies within a mitochondria-rich sarcoplasm. The myofibrils are also less well delineated in cardiac muscle; in transverse sections they often fuse into a continuous array of myofilaments, irregularly bounded by mitochondria and longitudinal elements of sarcoplasmic reticulum. The large mitochondria, with their closely spaced cristae, reflect the highly developed oxidative metabolism of cardiac tissue. The proportion of the cell volume occupied by mitochondria (approximately 35%) is even greater in cardiac muscle than it is in slow twitch skeletal muscle fibres. The high demand for oxygen is also reflected in high levels of myoglobin and an exceptionally rich network of capillaries around the fibres.

The force of contraction is transferred through the ends of the cardiac muscle cells via the junctional strength provided by the intercalated discs. As in skeletal muscle, force is also transmitted laterally to the sarcolemma and extracellular matrix via vinculin-containing elements that bridge between the Z-discs of peripheral myofibrils and the plasma membrane. The actin-binding proteins spectrin and dystrophin, important components of the cardiac muscle cell cytoskeleton, associate independently with the sarcolemma to provide mechanical support. Both protein complexes form components of the costamere (Samarel 2005, Peter et al 2011), which, in addition to transmitting force from sarcomeres to the sarcolemma and extracellular matrix, is central to mechanically generated signalling mechanisms.

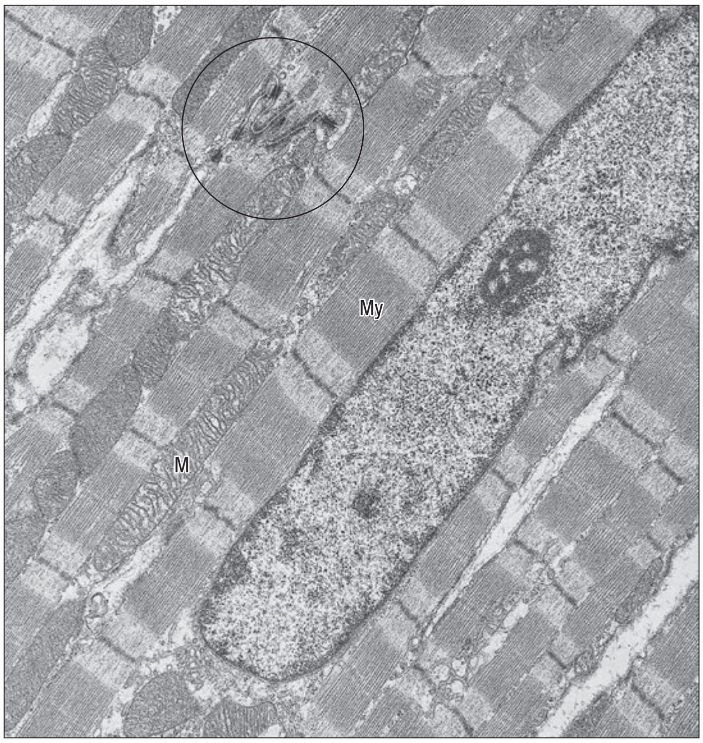

Fig. 6.30 A low-power transmission electron micrograph of cardiac muscle in longitudinal section, including the perinuclear zone of one of the fibres. Note the abundant large mitochondria (M) between myofibrils (My), and an intercalated disc (circled). (Courtesy of Professor Brenda Russell, Department of Physiology and Biophysics, University of Illinois at Chicago.)

Atrial muscle cells are smaller than ventricular cells. The cytoplasm near the Golgi complexes at the poles of the nuclei exhibits dense membrane-bound granules that contain the precursor of atrial natriuretic peptide. This hormone promotes loss of sodium and water in the kidneys, reducing blood volume and thereby lowering blood pressure. It is released into the blood in response to stretch of the atrial wall. Atrial natriuretic peptide and aldosterone have antagonistic effects on renal sodium and water handling, via independent mechanisms.

The sarcolemma of ventricular cardiac muscle cells invaginates to form T-tubules with a wider lumen than those of skeletal muscle; atrial muscle cells have few or no T-tubules. Unlike skeletal muscle, most T-tubules penetrate the sarcoplasm at the level of the Z-discs (see Fig. 6.29). The T-tubules are interconnected at intervals by longitudinal branches to form a complex network. They serve a similar function in skeletal and cardiac muscle, i.e. to carry the wave of depolarization into the cores of the cells.

The sarcoplasmic reticulum is a membrane-bound tubular plexus that surrounds and defines, sometimes incompletely, the outlines of individual myofibrils. Its main role, as in skeletal muscle, is the storage, release and re-accumulation (sequestration) of calcium ions. The calcium-binding protein calsequestrin allows large amounts of calcium to be stored within the sarcoplasmic reticulum and modulates activity of the calcium release channels (ryanodine receptors) (Györke and Terentyev 2008). The sarcoplasmic reticulum is separated from the T-tubules by a 15 nm gap spanned by structures termed junctional processes, which are thought to be the cytoplasmic part of the calcium release channels; similar processes are found in skeletal muscle at the junctional surface of the terminal cisternae. Sarcoplasmic reticulum bearing junctional processes is termed junctional sarcoplasmic reticulum to distinguish it from free sarcoplasmic reticulum, which forms a longitudinal network. Junctional sarcoplasmic reticulum makes contact with both the T-tubules and the sarcolemma (of which the T-tubules are an extension). Sarcoplasmic reticulum forms small globular extensions (corbular sarcoplasmic reticulum) in the vicinity of the Z-discs, but not in immediate relation to T-tubules or the sarcolemma. Since the junctions between T-tubules and sarcoplasmic reticulum usually involve only one structure of each type, the corresponding profiles in electron micrographs are referred to as dyads, rather than triads as in skeletal muscle.

Intercalated discs

Intercalated discs are unique, complex junctions between cardiac myocytes. In the light microscope they are seen as transverse lines crossing the

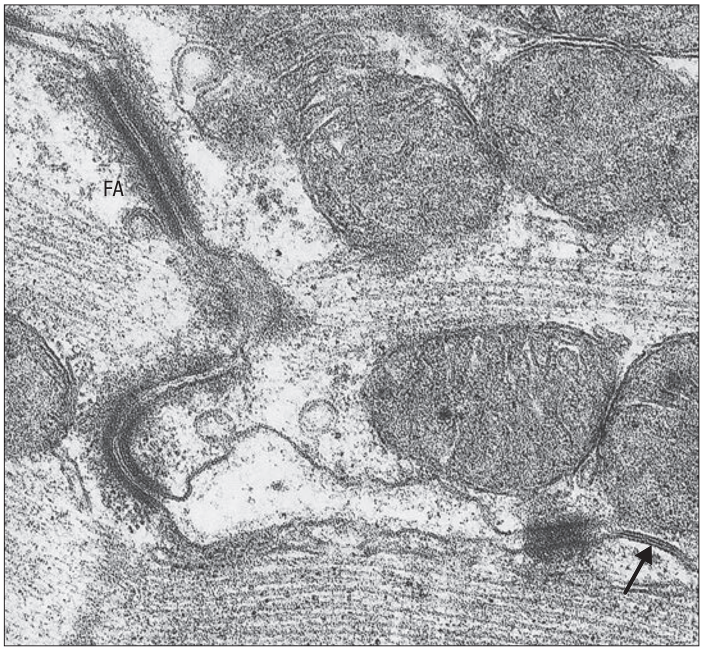

Fig. 6.31 An intercalated disc in cardiac muscle, with several zones of electron-dense fascia adherens (FA) and a gap junction (arrow). (Courtesy of Professor Brenda Russell, Department of Physiology and Biophysics, University of Illinois at Chicago.)

tracts of cardiac cells (see Fig. 6.28). They may step irregularly within or between adjacent tracts, and may appear to jump to a new position as the plane of focus is altered. Ultrastructurally, they are seen to have transverse and lateral portions (see Fig. 6.29; **Fig. 6.31**). The transverse portions occur wherever myofibrils abut the end of the cell, and each takes the place of the last Z-disc. At this point, the actin filaments of the terminal sarcomere insert into a dense subsarcolemmal matrix that anchors them, together with other cytoplasmic elements such as intermediate filaments, to the plasma membrane. Prominent desmosomes, often with a dense line in the intercellular space, occur at intervals along each transverse portion. This junctional region is homologous with, and probably similar in composition to, the structure found on the cytoplasmic face of the myotendinous junction, and is a type of fascia adherens junction. It provides firm adhesion between cells, and a route for the transmission of contractile force from one cell to the next.

The lateral portions of an intercalated disc run parallel to the myofilaments and the long axis of the cell, for a distance that corresponds to one or two sarcomeres before turning again to form another transverse portion. They are therefore responsible for the stepwise progression of the intercalated disc, which is seen microscopically. The lateral portions contain gap junctions between adjacent cells (see Fig. 6.31), which provide electrical coupling and so enable the electrical impulse to propagate from one cell to the next, spreading excitation and contraction rapidly along the branching tracts of interconnected cells. The activity of the individual cells of the heart is thus coordinated so that they function as if they were a syncytium.

Contractile protein isoforms of cardiac muscle

As in skeletal muscle, the contractile proteins of cardiac muscle exist in a number of tissue- and stage-specific forms.

The cardiac isoform of α-actin is not identical to the skeletal muscle form and is encoded by a different gene, although the two are so similar as to be functionally interchangeable. Both skeletal and cardiac isoforms of sarcomeric actin are expressed in fetal ventricular muscle. Cardiac muscle α-actin increases postnatally and exceeds that of the skeletal isoform by 4:1 in the adult.

The myosin heavy chain of human cardiac muscle exists in two isoforms, α and β, both of which are present in the fetal heart. The α-form persists as the adult isoform in atrial muscle, whereas the β-form (which is associated with a slower rate of contraction) predominates in ventricular muscle. Interestingly, the β-form of myosin heavy chain in cardiac muscle is identical to the isoform in slow twitch skeletal muscle. This identity between cardiac and slow twitch skeletal protein isoforms is true of several proteins, including ventricular myosin light chains and cardiac troponin-C. Other proteins, such as troponin-I and T, exist in cardiac-specific forms in the adult, although skeletal isoforms are expressed in the fetus and neonate. The appearance of cardiac-specific isoforms of troponin-I and T in the blood, following their release from damaged cardiac cells, is now a standard diagnostic test for myocardial infarction.

Mutations in genes encoding cardiac contractile proteins, often exhibiting autosomal dominant inheritance, are associated with several cardiomyopathies.

Hypertrophic cardiomyopathy is relatively common (1 in 500) and normally asymptomatic. However, it is the foremost cause of sudden cardiac death in young athletes. Most cases show mutations in β myosin heavy chain and cardiac myosin binding protein C. Disordered myocardial growth leads to left ventricular hypertrophy, often asymmetric, and commonly valve obstruction and arrhythmias.

Dilated cardiomyopathy involves dilation of all cardiac chambers and impaired systolic function, and is the third most common cause of heart failure. About 30–40% of cases have been positively associated with mutations in genes for sarcomere and cytoskeletal proteins, e.g. β myosin heavy chain, troponin and dystrophin. However, dilated cardiomyopathy can also be acquired via infections (myocarditis), substance abuse (alcohol, cocaine), and around childbirth (peripartum cardiomyopathy).

Arrhythmogenic right ventricular cardiomyopathy is rare (1 in 5000), but can cause sudden cardiac death, especially in young adults. Right ventricular muscle exhibits an abnormal structure and electrical conduction, potentially causing fatal re-entrant ventricular tachycardias and arrhythmias. Mutations in genes for desmosome proteins have been implicated.

Endocardium

The whole inner surface of the heart is covered by a thin layer of cells forming the endocardium, which separates the myocardium from the blood. These cells are very similar to the endothelial cells that line blood vessels, with a similar biological activity and embryological origin. They are now recognized as playing an important signalling role in cardiac muscle function (reviewed in Brutsaert (2003)).

Neurovascular Supply of Cardiac Muscle

Vascular supply

The activity of the heart is equivalent to a constant power expenditure of 1.3 watts under basal conditions, and escalates to 3 watts or more during physical exertion. Cardiac muscle cells contain glycogen, which is a reserve during peaks of activity, but the majority of their energy requirement is continuous and supplied only through a highly developed oxidative metabolism, as is evident from the high proportion of the cell volume that is occupied by mitochondria. This metabolism has to be supported by a rich blood supply. Myocardium has a very high perfusion rate of 0.5 ml/min/g of tissue (5 times that of liver and 15 times that of resting skeletal muscle). No cardiac muscle cell is more than 8 μm from a capillary, and vascular channels occupy a high proportion of the total interstitial space. Cardiac muscle is supplied by the coronary vessels. Although there is some variation in the detailed distribution of the arterial branches, the left ventricle, which has the highest workload and largest mass, receives the highest arterial blood flow. Branches run in the myocardium along the coarser aggregations of connective tissue and ramify extensively in the endomysial layer, creating a rich plexus of anastomosing vessels. This plexus includes lymphatic as well as blood capillaries, which is not the case in skeletal muscle.

The high oxygen requirement of the myocardium makes it vulnerable to ischaemic damage arising from atheroma or embolism in the coronary arteries. This vulnerability is exacerbated in the left ventricle because embedded coronary arteries are compressed by contraction of the myocardium, limiting perfusion during systole. Arterial anastomoses, often more than 100 μm in diameter, are found throughout the heart and are an important factor in determining whether an adequate collateral circulation may develop after a coronary occlusion.

Innervation

Although the impulse-generating and conducting system of the heart establishes an endogenous rhythm, the rate and force of contraction are under neural influence. Both divisions of the autonomic nervous system supply unmyelinated postganglionic fibres to the heart. The innervation is derived bilaterally but it is functionally asymmetric. Activation of the left stellate ganglion (sympathetic) has little effect on heart rate but increases ventricular contractility, whereas activation of the right stellate ganglion influences both rate and contractility. Activation of the right vagus nerve (parasympathetic) slows heart rate mainly through its influence on the pacemaker region, the sinuatrial (SA) node, whereas activation of the left vagus slows propagation of the impulse mainly through its effect on the atrioventricular (AV) node. Vagal activity has little direct effect on ventricular contractility.

Postganglionic sympathetic nerve fibres from the cervical sympathetic ganglia reach the heart via the recurrent cardiac nerves. Parasympathetic fibres in the heart are derived from ganglion cells in the cardiac plexuses and atrial walls that are innervated by preganglionic cardiac branches of the vagus. Adrenergic, cholinergic and peptidergic endings have been demonstrated in the myocardium. Fibres often end close to muscle cells and blood vessels, but junctional specializations are not seen, and a gap of at least 100 nm remains between myocyte and axon. It is probable that neurotransmitters diffuse across this gap to the adjacent cells. Some of the endings represent efferent nerve terminals, while others function as pain receptors, mechanoreceptors or chemoreceptors.

Excitation–contraction coupling in cardiac muscle

The molecular interaction between actin and myosin that underlies the generation of force is initiated by elevation of cytosolic calcium in both cardiac and skeletal muscle. However, there are significant differences in both the mechanisms by which this occurs and the physical arrangement and molecular composition of the contractile elements (reviewed in Bers (2002)).

One of the major functional differences between cardiac and skeletal muscle is the way in which contractile force is regulated. Smoothness and gradation of contraction in skeletal muscle depend on recruitment and asynchronous firing of different numbers of motor units. Individual motor units can also build up a contraction through a brief series of re-excitations. In the heart, the entire mass of muscle must be activated almost simultaneously, and mechanical summation by re-excitation is not possible, because the cells are electrically refractory until mechanical relaxation has taken place (see below).

As in skeletal muscle, cardiac muscle contraction is initiated when calcium binds to troponin-C, a component of the regulatory protein complex on the thin filaments. During basal activity of the heart, the amount of calcium bound to troponin-C during each systole induces less than half-maximal activation of the contractile apparatus. Contractile force can therefore be increased by increasing cytosolic calcium and thus the amount bound to troponin-C. This is achieved by controlling the amount of free calcium that is released into the cytosol during systole.

A special feature of the cardiac muscle cell is the long duration of its action potential. This is due to activation of voltage-dependent L-type calcium channels in the sarcolemma by the initial depolarization, through which calcium enters the cell, sustaining the depolarization and so causing a long-lasting electrical plateau of equivalent length to the contraction. However, calcium influx during the plateau only accounts for about 25% of the elevation of cytosolic calcium; the rest is released from the sarcoplasmic reticulum.

Action potentials are conducted into the T-tubules, where they activate L-type channels and calcium influx. This causes a localized increase in free calcium in the narrow space between the T-tubules and junctional sarcoplasmic reticulum, which activates calcium release channels on the latter, causing calcium to flood out into the cytosol. This 'calcium-induced calcium release' is a vital component of cardiac muscle activation and is the principal or only mechanism by which calcium can be released from the sarcoplasmic reticulum in the myocardium. This major difference between cardiac and skeletal muscle is reflected in tissue-specific isoforms of calcium release channels.

Systolic activation is terminated on repolarization of the action potential by reuptake (sequestration) of calcium from the cytosol back into the sarcoplasmic reticulum. This is mediated by a high-affinity sarco-endoplasmic reticulum calcium ATPase (SERCA), which rapidly reduces cytosolic free calcium to resting levels. The activity of this ATPase controls the rate of decay of the calcium transient and is therefore a determinant of the rate of relaxation of the heart. The sarcoplasmic reticulum contains a cardiac form of calsequestrin, a homologue of the proteins found in skeletal and smooth muscle. This calcium-binding protein buffers the free calcium concentration inside the sarcoplasmic reticulum, allowing it to store considerable amounts of total calcium without increasing the gradient against which SERCA must pump. It may also modulate the activity of the calcium release channels (Györke and Terentyev 2008).

Whilst SERCA therefore allows rapid relaxation of the myocardium, the calcium that entered the cell during the action potential must also be transported out again to prevent calcium overload. This is accomplished primarily by a sodium–calcium exchanger (NCX) in the sarcolemma, and to a much lesser extent by a sarcolemmal calcium ATPase. These act more slowly than SERCA, continuously removing calcium from the cell during the diastolic interval as calcium slowly leaks from the sarcoplasmic reticulum.

The extent of the elevation of cytosolic calcium and therefore force generation during systole is determined by both the size of the initial stimulus (amount of calcium entering through L-type channels) and the amount of calcium stored within the sarcoplasmic reticulum. The greater the amount stored, the more is available for release. This provides an intrinsic mechanism for matching any increase in heart rate with a progressive increase in contractile force. At higher heart rates, more calcium enters per unit time, but as the diastolic interval is reduced there is less time for calcium to be removed from the cell by the sarcolemmal sodium–calcium exchanger. The amount of calcium stored in the sarcoplasmic reticulum therefore increases, so more can be released during systole. Increased heart rate is therefore coupled with an increase in force, a phenomenon called the staircase response.

The most potent physiological means of enhancing cardiac contractility is through the action of β-adrenergic agents, specifically the sympathetic neurotransmitter noradrenaline (norepinephrine) and circulating adrenaline (epinephrine). Activation of β-adrenergic receptors produces cyclic adenosine monophosphate (cAMP), which enhances calcium influx via L-type calcium channels during depolarization, so stimulating greater release from the sarcoplasmic reticulum. In addition, cyclic AMP enhances the activity of SERCA via promoting phosphorylation of an associated protein, phospholamban. This enables a more rapid reduction of the cytosolic calcium pump and accelerated relaxation, which is important when the heart rate is increased. Phosphorylation of troponin-I on the thin filaments also increases the rate of cross-bridge cycling, further accelerating relaxation.

Dysfunction of cardiac muscle excitation–contraction coupling in disease

In coronary heart disease the myocardium may be inadequately perfused (myocardial ischaemia), leading to energy deficit, loss of contractility and eventually cell death. The process may culminate in irretrievable myocardial damage and progress to heart failure, which is the inability to provide adequate cardiac output for the tissues.

Channelopathies are conditions associated with mutations in genes encoding cardiac muscle ion channels (Webster and Berul 2013). They are mostly autosomal dominant, inherited conditions which increase the likelihood of arrhythmias, fainting and sudden cardiac death, especially in young otherwise healthy adults.

Origin of cardiac muscle

Cardiac myocytes differentiate from the splanchnopleuric coelomic epithelial cells of the pericardium initially subjacent to the endoderm (see Fig. 13.2). As the primitive heart tube is formed, the presumptive myocardial cells start to express genes that encode characteristic myocardial proteins, including myosin, actin, troponin and other components of the contractile apparatus. Myofibrils begin to appear in the developing myoblasts, and the first functional heart beats start soon afterwards.

Committed cardiac myoblasts do not fuse to form multinucleated myotubes, as occurs in skeletal muscle, but remain as single cells coupled physically and electrically through intercellular junctions. Differentiated cardiac myocytes continue to divide during fetal development and withdraw from the cell cycle only after birth. This is markedly different from skeletal muscle development, when differentiation, including the activation of muscle-specific genes, coincides with withdrawal from the cell cycle. During fetal maturation, successive changes in gene expression give rise to the characteristics of fetal, neonatal and adult myocardium, and are responsible for the divergence of the properties of atrial and ventricular muscle cells.

The regulatory mechanisms underlying differentiation of cardiac muscle appear to be distinct from those of skeletal muscle. It is anticipated that counterparts will be found for the transcriptional factors Myf-5, myogenin, MyoD and Myf-6, which are responsible for inducing differentiation of skeletal muscle. It is known that Tbx5 and Nkx2–5 are required for formation of atrial and ventricular myocardium (see Fig. 13.6).

The body responds to this challenge with a variety of neurohumoral mechanisms, including increased sympathetic stimulation to the heart, increasing heart rate and contractility via noradrenaline (norepinephrine; see above). Treatment includes administration of positive inotropic agents (drugs that increase contractility) such as β-adrenergic agonists and phosphodiesterase inhibitors that prevent the breakdown of cyclic AMP. The classic positive inotropic drug is digitalis (digoxin), which at therapeutic doses causes partial inhibition of the sodium pump (sodium–potassium ATPase) that maintains the ionic gradient across the sarcolemma. This leads to a reduced sodium concentration gradient, impairing operation of the sarcolemmal sodium–calcium exchanger. Less calcium is therefore extruded from the cell, so more is left in the sarcoplasmic reticulum for release during systole, increasing force. However, positive inotropes are now only used in the short term because, if used chronically, they can hasten progression of the disease. The following explains why this is the case.

An energy deficit has far-reaching consequences beyond the inhibition of actin and myosin interactions. ATP is vital for many cellular processes, in particular, the activities of the sodium pump and SERCA. Impaired operation of the sodium pump leads to reduced extrusion of calcium (see above). Inhibition of SERCA impairs calcium reuptake into the sarcoplasmic reticulum and relaxation at the end of systole. The net effect is calcium overload. Mitochondria can mitigate the effects by taking up calcium, but eventually this causes mitochondrial damage and so worsens the energy deficit. As ATP falls further, operation of the sodium pump declines, the ionic gradient is dispersed and the cell depolarizes, causing calcium entry through L-type channels, which worsens the calcium overload and leads to cell death. Positive inotropes, by increasing both cytosolic calcium and energy requirements, will clearly worsen the situation.

This sequence of events has led to development of agents that act via increasing the binding of troponin-C to calcium, rather than by increasing calcium. However, therapy for chronic heart failure is still currently focused on limiting disease progression, largely by interrupting neurohumoral compensation mechanisms. Paradoxically, this includes β-adrenergic receptor antagonists, and also antagonists to angiotensin II and aldosterone (reviewed in Francis (2001)), which may inhibit cardiac remodelling (see below).

Concurrent with the development of contractile proteins, cardiac myocytes develop numerous specific intracellular vesicles containing substances shown to induce natriuresis and diuresis, and a family of polypeptides generally known as atrial natriuretic peptides. These vesicles develop from the Golgi complex in both atria and ventricles during fetal life but become restricted to atrial muscle in the adult. Atrial natriuretic peptide is measurable when the heart is recognizably four-chambered; almost all cells within the atria are capable of its synthesis.

The impulse-generating (AV node) and conducting systems of the heart (AV node; bundle of His, Purkinje fibres) are formed from cardiac myocytes that differ in their morphology from the working myocardium of the heart chambers. Cells of the SA and AV nodes tend to be smaller with slow cell-to-cell electrical conduction, whilst those of the bundle of His and Purkinje fibres are larger in diameter with very rapid electrical conduction.

Cardiac plasticity and regeneration of cardiac muscle

The heart exhibits a significant degree of plasticity. Physiological and pathophysiological stimuli can initiate cardiac remodelling (reviewed in Hill and Olson (2008)). For example, increased loads as a result of exercise training or pregnancy induce physiological hypertrophy of the heart, where the ventricular walls thicken due to an increase in the size (but not number) of cardiac muscle cells. Conversely, hypertrophy resulting from cardiac damage, high blood pressure and/or extended activation of neurohumoral compensatory mechanisms (e.g. sympathetic stimulation, production of angiotensin II and aldosterone) can be maladaptive, increasing the risk and rate of progression of heart failure and sudden death due to arrhythmias.

Both increased mechanical stress and circulating or local mediators can initiate the gene transcription and protein synthesis associated with cardiac hypertrophy and remodelling. At least part of the response is mediated through calcium-dependent mechanisms involving calcineurin, and isoforms of protein kinase C and calcium–calmodulin-dependent kinase, but growth factors, inflammatory cytokines and other humoral mediators also activate complex signalling cascades that modify activity of transcription factors. Notably, physiological and pathological cardiac remodelling show significant differences in gene transcription and expression of certain proteins; pathological hypertrophy is associated with phenotypic switching towards fetal and less efficient isoforms of contractile proteins such as myosin heavy chain (Hill and Olson 2008).

Chronic heart failure is regarded as irreversible and progressive, and pathological cardiac remodelling plays a major role in its progression. Therapy is largely focused on agents that suppress pro-remodelling pathways (e.g. β-blockers, angiotensin-converting enzyme inhibitors, aldosterone antagonists) and therefore slow progression (Francis 2001). However, recent developments have raised hope for future treatments that might reverse cardiac damage.

In skeletal muscle, a population of precursor cells (satellite cells) is retained in adult life, constituting a pool of myoblasts capable of dividing, fusing with existing muscle fibres and initiating regeneration after damage. It was thought that cardiac muscle lacked an equivalent population of cells and was therefore incapable of regeneration. There is some evidence that the heart does contain endogenous progenitor cells capable of regenerating myocardial function (Oh et al 2004), although to a very limited extent compared to skeletal muscle and insufficient to restore heart function after ischaemic or other injury. It has been suggested that there is a slow but continuous renewal of cardiac muscle cells throughout life even in healthy individuals, with a turnover of between 0.4 and 1% per year (Bergmann et al 2009).

Bonus e-book content

Fig. 6.22 Mechanisms underlying the response of cutaneous vascular smooth muscle to cold.

Fig. 6.23 A fatty streak on the intimal surface of the aorta close to an arterial branch.

Fig. 6.24 A raised fibrofatty atheromatous plaque on the intimal surface of the aorta.

Fig. 6.25 A, Intimal fibroblastic proliferation with reduction in lumen diameter in an arteriole in the kidney. **B**, Intimal fibroelastic proliferation with reduplication of the internal elastic lamina and reduction in lumen diameter in an artery in the heart.

Fig. 6.26 The right ventricular outflow tract of the right ventricle showing a coiled up pulmonary embolus blocking the right ventricular outflow tract and the main pulmonary artery.

Key references

Berridge MJ 2008 Smooth muscle cell calcium activation mechanisms. J Physiol 586:5047–61.

A review of the mechanisms contributing to regulation of smooth muscle cell intracellular calcium, including sub-sarcolemmal signalling microdomains and calcium oscillations.

Bers DM 2002 Cardiac excitation–contraction coupling. Nature 415:198–205.

A review of the cellular mechanisms underlying cardiac muscle activation by an action potential and the elevation of cytosolic calcium.

Brutsaert DL 2003 Cardiac endothelial–myocardial signaling: its role in cardiac growth, contractile performance and rhythmicity. Physiol Rev 83:59–115.

A review of the important contributions that the endocardium and microvascular endothelial cells make to the regulation of cardiac muscle function.

Figueroa XF, Duling BR 2009 Gap junctions in the control of vascular function. Antioxid Redox Signal 11:251–66.

A review of the structure and role of smooth muscle, endothelial cell and myoendothelial gap junctions in the regulation of vascular function.

Gunst SJ, Zhang W 2008 Actin cytoskeletal dynamics in smooth muscle: a new paradigm for the regulation of smooth muscle contraction. Am J Physiol 295:C576–C87.

A review of the smooth muscle cytoskeleton and its component proteins, with particular reference to its dynamic properties and role in contractile function.

Pober JS, Sessa WC 2007 Evolving functions of endothelial cells in inflammation. Nat Rev Immunol 7:803–15.

A review of endothelial cells as active participants in and regulators of inflammatory processes and cells, and their phenotypic changes during transition from innate to adaptive immunity.

Saharinen P, Tammela T, Karkkainen MJ et al 2004 Lymphatic vasculature: development, molecular regulation and role in tumor metastasis and inflammation. Trends Immunol 25:387–95.

A comprehensive but concise review of the role, regulation and development of the lymphatic system.

Vestweber D 2007 Adhesion and signaling molecules controlling the transmigration of leukocytes through endothelium. Immunol Rev 218:178–96.

A review of the range of endothelial cell surface adhesion and signalling proteins and their interaction with leukocytes.

References

Bergmann O, Bhardwaj RD, Bernard S et al 2009 Evidence for cardiomyocyte renewal in humans. Science 324:98–102.

Berridge MJ 2008 Smooth muscle cell calcium activation mechanisms. J Physiol 586:5047–61.

A review of the mechanisms contributing to regulation of smooth muscle cell intracellular calcium, including sub-sarcolemmal signalling microdomains and calcium oscillations.

Bers DM 2002 Cardiac excitation–contraction coupling. Nature 415:198–205.

A review of the cellular mechanisms underlying cardiac muscle activation by an action potential and the elevation of cytosolic calcium.

Brutsaert DL 2003 Cardiac endothelial–myocardial signaling: its role in cardiac growth, contractile performance and rhythmicity. Physiol Rev 83:59–115.

A review of the important contributions that the endocardium and microvascular endothelial cells make to the regulation of cardiac muscle function.

Duffield JS 2012 The elusive source of myofibroblasts: problem solved? Nature Med 18:1178–80.

Fardoun MM, Nassif J, Issa K et al 2016 Raynaud's phenomenon: a brief review of the underlying mechanisms. Front Pharmacol 7:438.

Ferland-McCollough D, Slater S, Richard J et al 2017 Pericytes, an overlooked player in vascular pathobiology. Pharmacol Ther 171:30-42.

Figueroa XF, Duling BR 2009 Gap junctions in the control of vascular function. Antioxid Redox Signal 11:251–66.

A review of the structure and role of smooth muscle, endothelial cell and myoendothelial gap junctions in the regulation of vascular function.

Francis GS 2001 Pathophysiology of chronic heart failure. Am J Med 110:37S–46S.

Gunst SJ, Zhang W 2008 Actin cytoskeletal dynamics in smooth muscle: a new paradigm for the regulation of smooth muscle contraction. Am J Physiol 295:C576–C87.

A review of the smooth muscle cytoskeleton and its component proteins, with particular reference to its dynamic properties and role in contractile function.

Györke S, Terentyev D 2008 Modulation of ryanodine receptor by luminal calcium and accessory proteins in health and cardiac disease. Cardiovasc Res 77:245–55.

Halayko AJ, Solway J 2001 Molecular mechanisms of phenotypic plasticity in smooth muscle cells. J App Physiol 90:358–68.

Hall CN, Reynell C, Gesslein B et al 2014 Capillary pericytes regulate cerebral blood flow in health and disease. Nature 508:55–60.

Hill JA, Olson EN 2008 Cardiac plasticity. N Engl J Med 358:1370–80.

Khouri C, Blaise S, Carpentier P et al 2016 Drug-induced Raynaud's phenomenon: beyond β-adrenoceptor blockers. Br J Clin Pharmacol 82(1):6–16.

Levy SM, Taylor GI, Baudet J et al 2003 Angiosomes of the brachial plexus: an anatomical study. Plast Reconstr Surg 112:1799–806.

Mahn K, Ojo OO, Chadwick G et al 2010 Ca^{2+} homeostasis and structural and functional remodelling of airway smooth muscle in asthma. Thorax 65:547–52.

Oh H, Chi X, Bradfute SB et al 2004 Cardiac muscle plasticity in adult and embryo by heart-derived progenitor cells. Ann N Y Acad Sci 1015:182–9.

Pan WR, Taylor GI 2009 The angiosomes of the thigh and buttock. Plast Reconstr Surg 123:236–49.

Papademetriou V, Rashidi AA, Tsioufis C et al 2014 Renal nerve ablation for resistant hypertension. Circulation 129:1440–51.

Peter AK, Cheng H, Ross RS et al 2011 The costamere bridges sarcomeres to the sarcolemma in striated muscle. Prog Pediatr Cardiol 31:83–8.

Pober JS, Sessa WC 2007 Evolving functions of endothelial cells in inflammation. Nat Rev Immunol 7:803–15.

A review of endothelial cells as active participants in and regulators of inflammatory processes and cells, and their phenotypic changes during transition from innate to adaptive immunity.

Sadler JE 2005 von Willebrand factor: two sides of a coin. J Thromb Haemost 3:1702–9.

Saharinen P, Tammela T, Karkkainen MJ et al 2004 Lymphatic vasculature: development, molecular regulation and role in tumor metastasis and inflammation. Trends Immunol 25:387–95.

A comprehensive but concise review of the role, regulation and development of the lymphatic system.

Samarel AM 2005 Costameres, focal adhesions, and cardiomyocyte mechanotransduction. Am J Physiol Heart Circ Physiol 289:2291–301.

Sepulveda A, Buchanan EP 2014 Vascular tumors. Semin Plast Surg 28(2):49-57

Simonneau G, Robbins IM, Beghetti M et al 2009 Updated Clinical Classification of Pulmonary Hypertension. J Am Coll Cardiol 54: S43-S54.

Stegemann JP 2005 Mechanical, biochemical, and extracellular matrix effects on vascular smooth muscle cell phenotype. J Appl Physiol 98:2321–7.

Stenmark KR, Fagan KA, Frid MG 2006 Hypoxia-induced pulmonary vascular remodeling: cellular and molecular mechanisms. Circ Res 99:675–91.

Sylvester JT, Shimoda L, Aaronson PI et al 2012 Hypoxic pulmonary vasoconstriction. Physiol Rev 92:367-520.

Taylor GI 2003 The angiosomes of the body and their supply to perforator flaps. Clin Plast Surg 30:331–42.

Taylor GI, Palmer JH 1987 The vascular territories (angiosomes) of the body: experimental studies and clinical applications. Br J Plast Surg 40:113–41.

Vestweber D 2007 Adhesion and signaling molecules controlling the transmigration of leukocytes through endothelium. Immunol Rev 218:178–96.

A review of the range of endothelial cell surface adhesion and signalling proteins and their interaction with leukocytes.

Wang G, Jacquet L, Karamariti E et al 2015 Origin and differentiation of vascular smooth muscle cells. J Physiol 593: 313–30.

Webster G, Berul CI 2013 An update on channelopathies: from mechanisms to management. Circulation 127:126–40.

Wiegreffe C, Christ B, Huang R et al 2007 Sclerotomal origin of smooth muscle cells in the wall of the avian dorsal aorta. Dev Dyn 236:2578–85.

Xu J, Shi G-P 2014 Vascular wall extracellular matrix proteins and vascular diseases. Biochim Biophys Acta 1842:2106–119.

CHAPTER 7

Skin and its appendages

In this chapter, the types and functions of skin in different parts of the body are described first, followed by the microstructure of the epidermis and dermis, and the appendages of skin, including the pilosebaceous units, sweat glands and nails. The development of skin, natural skin lines and age-related changes, and clinical aspects of skin, e.g. grafts, surgical skin flaps and wound healing, are also described. The integumental system includes the skin and its derivatives, hairs, nails, sweat and sebaceous glands; subcutaneous fat and deep fascia; the mucocutaneous junctions around the openings of the body orifices; and the breasts. Mucocutaneous junctions and breast tissues are covered in the appropriate regional sections.

TYPES AND FUNCTIONS OF SKIN

The skin is the largest organ of the human body and constitutes approximately 15% of the total body weight. In an average 70 kg person, the skin weighs approximately 13 kg and has a surface area of about 2 m^2. It covers the entire external surface of the body, including the external acoustic meatus, the lateral aspect of the tympanic membrane and the vestibule of the nose. It is continuous with the mucosae of the alimentary, respiratory and urogenital tracts, and fuses with the conjunctiva at the margins of the eyelids, and with the lining of the lacrimal canaliculi at the lacrimal puncta. The thickness of the skin ranges from 1.5 to 5.0 mm and depends mainly on its location.

The skin forms a self-renewing interface between the body and its environment. It provides an effective barrier against microbial organisms, and protects against mechanical, chemical, osmotic, thermal and ultraviolet radiation damage. It is an important site of immune surveillance against the entry of pathogens and the initiation of primary immune responses. For instance, the skin produces various antimicrobial peptides such as human cathelicidin LL-37, a small cationic peptide that can prevent the immunostimulatory effects of bacterial wall molecules such as lipopolysaccharide and therefore protect against endotoxaemia. It can inhibit neutrophil apoptosis and stimulate angiogenesis, tissue regeneration and release of cytokines such as interleukin (IL)-8. Specific innate immune defenses in the skin are present throughout the epidermis, dermis, hair follicles and appendages, and in the absence of skin diseases or trauma, provide a resilient buffer against external microorganisms (Tikoo et al 2018).

Skin performs many biochemical synthetic processes, including the formation of vitamin D under the influence of ultraviolet B (UVB) radiation and synthesis of cytokines and growth factors. Skin is the target of a variety of hormones such as thyroxine, androgens and oestrogens. These activities can affect the appearance and function of individual skin components, such as the sebaceous glands, the hairs and the pigment-producing cells.

Control of body temperature is an important function of skin, and is effected mainly by regulation of heat loss from the cutaneous circulation through the rapid increase or reduction in the flow of blood to an extensive external surface area. This process is also assisted by sweating. In disorders such as erythroderma, in which more than 90% of the skin is inflamed and red, insensible fluid losses can exceed several litres per day and can result in shock if treatment is not initiated promptly. Skin is involved in socio-sexual communication and can signal emotional states by means of muscular and vascular responses. It is a major sensory organ, richly supplied by nerve terminals and specialized receptors for touch, temperature, pain and other stimuli.

Skin has good frictional properties, assisting locomotion and manipulation by its texture. It is elastic, and can be stretched and compressed within limits. The outer surface is covered by skin lines, some of which are large and conspicuous while others are microscopic, or are only revealed after manipulation or incision of the skin.

The colour of human skin is derived from, and varies with, the amount of blood (and its degree of oxygenation) in the cutaneous circulation, the thickness of the cornified layer and the ratio of eumelanin (brown/black) to pheomelanin (red/yellow). Melanin has a protective role against UV radiation and acts as a scavenger of harmful free radicals. Ethnic variations in colour are mainly due to differences in the amount, type and distribution of melanin and are genetically determined. These genetic variants may also determine the prevalence of benign skin lesions such as freckles, as well as susceptibility to common forms of non-melanoma skin cancers and skin ageing (Law et al 2017).

The appearance of skin is affected by many other factors, e.g. size, shape and distribution of hairs and of skin glands (sweat, sebaceous and apocrine), and changes associated with maturation, ageing, metabolism and pregnancy. The general state of health is reflected in the appearance and condition of the skin, and the earliest signs of many systemic disorders may be apparent in the skin.

Skin microbiome

Available with the *Gray's Anatomy* e-book.

Classification of skin

Although skin in different parts of the body is fundamentally of similar structure, there are many local variations in parameters such as thickness, mechanical strength, softness, flexibility, degree of keratinization (cornification), size and number of hairs, frequency and types of glands, pigmentation, vascularity and innervation (**Figs 7.1–7.4**). Human skin is divided into two main types: hairless (glabrous) skin and hair-bearing skin. Hairless skin is found on the palms and soles where it has a grooved surface, with alternating ridges and sulci giving rise to the dermatoglyphics (fingerprints). In palmar and plantar skin, there is a compact cornified layer which may be up to 10 times thicker than in other body sites: this skin is thus also termed thick skin. There are, however, sites such as the lips and nipples, where hairless skin has a relatively thin cornified layer.

Regional variations in skin

Available with the *Gray's Anatomy* e-book.

MICROSTRUCTURE OF SKIN AND SKIN APPENDAGES

Epidermis

The epidermis (see Figs 7.2–7.3) is a self-renewing stratified epithelial tissue consisting mainly of keratinocytes. Other cells within the epidermis include melanocytes (pigment-forming cells from the embryonic neural crest), Langerhans cells (immature antigen-presenting dendritic cells derived from bone marrow), lymphocytes and Merkel cells. Merkel cells may function as sensory mechanoreceptors or possibly as part of the dispersed neuroendocrine system and many are associated with nerve endings. Free sensory nerve endings are sparsely present within the epidermis.

The population of keratinocytes undergoes continuous renewal throughout life (Gonzales and Fuchs 2017). Turnover is mediated by epidermal stem cells in the basal layer of the epidermis which generate daughter cells that undergo a series of biochemical and physical changes as they migrate towards the surface of the skin to form the various layers of the epidermis. They transform from polygonal living cells to non-viable flattened squames full of intermediate filament proteins (keratins) embedded in a dense matrix of cytoplasmic proteins to form mature keratin.

The epidermis consists of several layers. The innermost layer, the basal layer (stratum basale) is succeeded by the spinous or prickle cell layer (stratum spinosum), granular layer (stratum granulosum), clear layer (stratum lucidum) and cornified layer (stratum corneum), which is the most superficial (see Fig. 7.4). The first three of these layers are metabolically active compartments through which cells pass and change their morphology as they undergo cellular differentiation. The more superficial layers of cells undergo terminal keratinization

Each square centimetre of skin contains approximately one million bacteria (comprising hundreds of distinct species) forming a complex community that also contains viruses and fungi. The exact composition of the community of these organisms varies across different body sites and depends on several factors, including sebaceous gland concentration, moisture content and temperature, host genetics and exogenous environmental factors. The multiple organisms are not just commensals but play a much bigger role in immune modulation and epithelial health (Chen et al 2018). Dissecting the nature of microbe–host interactions and discovering the factors that drive microbial colonization are likely to provide greater insight into the pathogenesis of skin diseases such as atopic dermatitis, and inform the development of potential new therapies.

Hairless skin has numerous encapsulated sensory endings within the dermis, but lacks hair follicles and associated sebaceous glands. Hair-bearing skin (most thin skin bears hairs) has both hair follicles and sebaceous glands associated with the follicles. Hair follicle size, structure and density can vary between different body sites. Notably, scalp has large hair follicles whereas the forehead has only small, vellus hair-producing follicles. Some hair-bearing sites, such as the axilla, contain apocrine glands as well as eccrine sweat glands. Sebaceous gland function varies with age, being active in neonates, and from puberty onwards: the relative activity influences the composition of the skin surface lipids and the skin microbiome. There are regional variations in the structure of the dermal–epidermal junction, with more hemidesmosomes and anchoring fibrils in the skin of the leg than in the skin of the arm. In the dermis, the arrangement and size of elastic fibres varies, e.g. they are very large in perianal skin, whereas there are almost none in the scrotum. Cutaneous blood supply varies markedly between areas such as the eyelid and more rigid areas such as the fingertips.

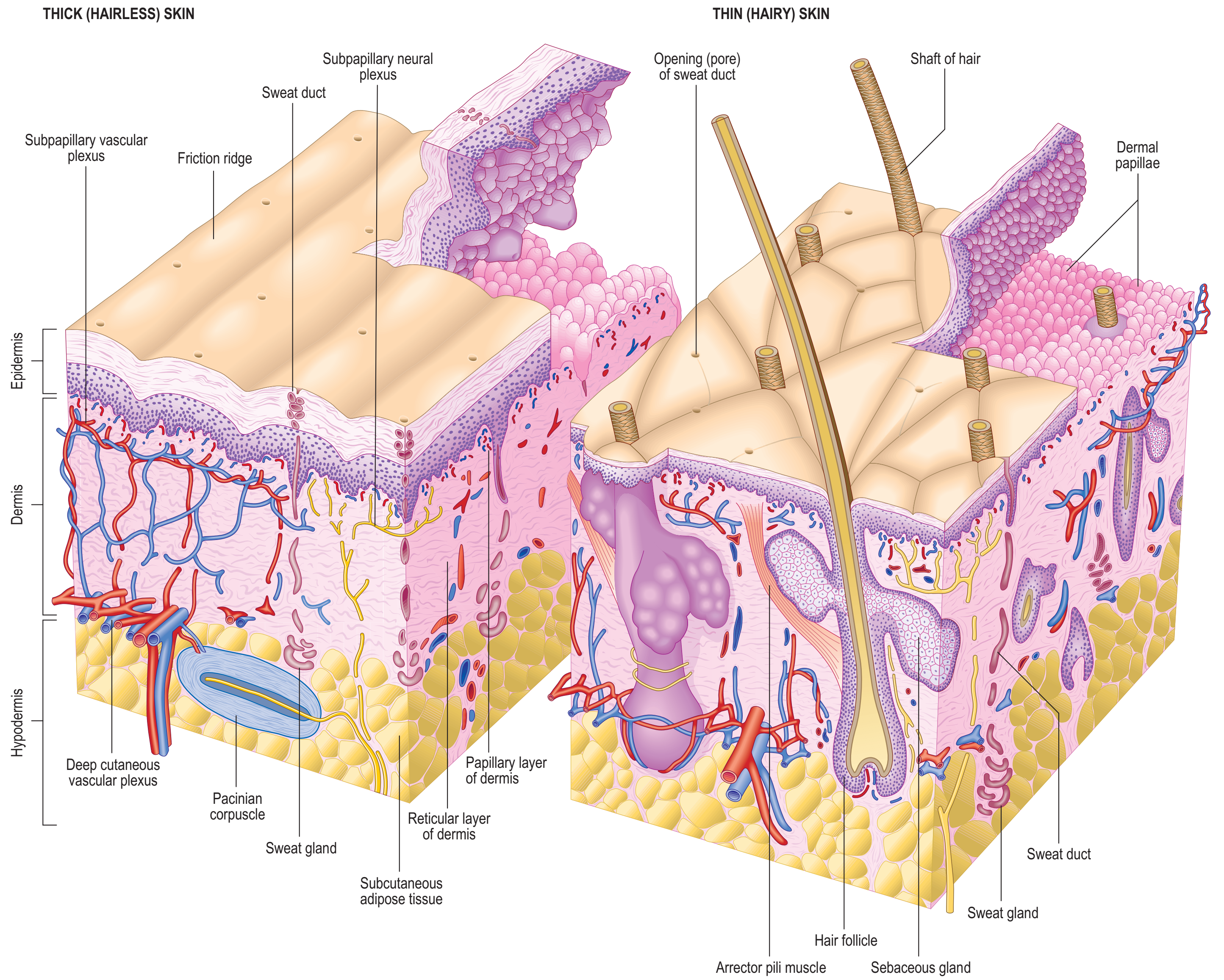
THICK (HAIRLESS) SKIN
THIN (HAIRY) SKIN
Subpapillary neural plexus
Sweat duct
Subpapillary vascular plexus
Friction ridge
Epidermis
Dermis
Hypodermis
Deep cutaneous vascular plexus
Pacinian corpuscle
Sweat gland
Subcutaneous adipose tissue
Reticular layer of dermis
Papillary layer of dermis
Opening (pore) of sweat duct
Shaft of hair
Dermal papillae
Sweat duct
Sweat gland
Hair follicle
Arrector pili muscle
Sebaceous gland

Fig. 7.1 The organization of skin, comparing the structures found in thick, hairless (plantar and palmar) skin with thin, hairy (hirsute) skin. The epidermis has been partially peeled back to show the interdigitating dermal and epidermal papillae.

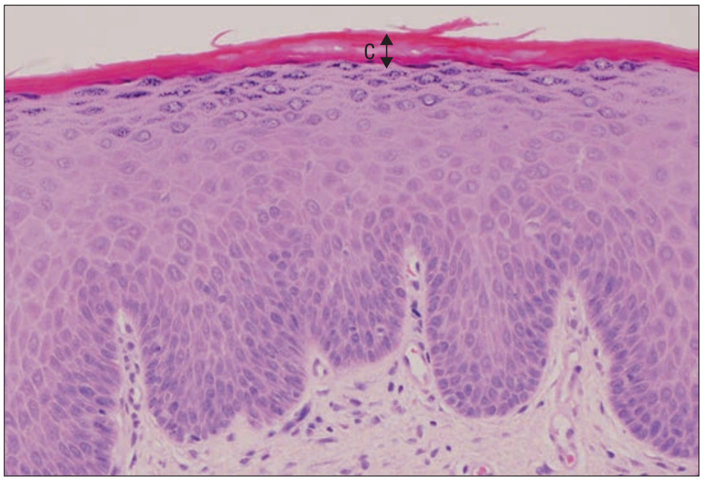

Fig. 7.2 The interfollicular epidermis of human thin skin. Note the thin cornified layer (C) in comparison with the thick cornified layer in Fig. 7.4 (which is at a lower magnification). (Courtesy of Mr Peter Helliwell and the late Dr Joseph Mathew, Department of Histopathology, Royal Cornwall Hospitals Trust, UK.)

(cornification), which involves not only structural changes in keratinocytes, but also molecular and biochemical changes within the cells and their surroundings.

The epidermal appendages (pilosebaceous units, sweat glands and nails) are formed developmentally by the ingrowth of the epidermis.

Keratinocytes

Basal layer

The basal layer is the innermost layer of the epidermis, next to the dermis and is the site of epidermal cellular proliferation. It is in contact with a basal lamina, which is a thin layer of specialized extracellular matrix not usually visible by light microscopy (**Fig. 7.5**; see Fig. 2.8). By transmission electron microscopy, the basal lamina consists of a clear lamina lucida adjacent to the basal cell plasma membrane and a darker electron-dense lamina densa (**Fig. 7.6**). The basal plasma membranes of the basal keratinocytes, the extracellular basal laminae and the anchoring fibrils of type VII collagen within the subjacent dermal matrix (lamina fibroreticularis) which insert into the lamina densa, collectively form the basement membrane zone (BMZ) at the dermal–epidermal junction. This is a highly convoluted interface, particularly in thick, hairless skin, where dermal papillae (rete ridges) project into the epidermis, interlocking with adjacent downward projections of the epidermis (rete pegs) (see Fig. 7.4).

The majority of basal keratinocytes are columnar to cuboidal in shape, with large (relative to their cytoplasmic volume), mainly euchromatic nuclei and prominent nucleoli (see Fig. 7.3). The cytoplasm contains variable numbers of melanosomes and keratin filament bundles corresponding to the keratin tonofilaments of classical electron microscopy. In the basal keratinocytes, these keratins consist mostly of keratin 5 (K5) and keratin 14 (K14) proteins. The plasma membranes of interconnecting cells are coupled by desmosomes; those of the basal keratinocytes are linked to the basal lamina by hemidesmosomes (see Figs 7.5–7.6, 1.26). Melanocytes (see Fig. 7.13), Langerhans cells (see Figs 7.16–7.17) and Merkel cells (see Fig. 3.29) are interspersed among the basal keratinocytes. Merkel cells are connected to keratinocytes by desmosomes,

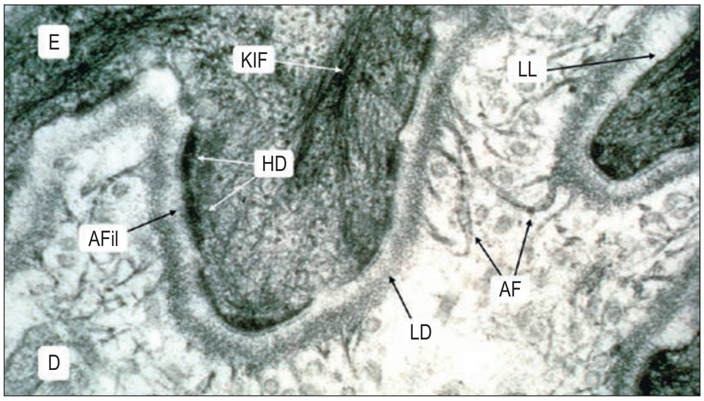

Fig. 7.6 Transmission electron micrograph of the dermal–epidermal junction. Abbreviations: AF, anchoring fibrils; AFil, anchoring filaments; D, dermis; E, epidermis; HD, hemidesmosomes; KIF, keratin intermediate filaments; LD, lamina densa; LL, lamina lucida.

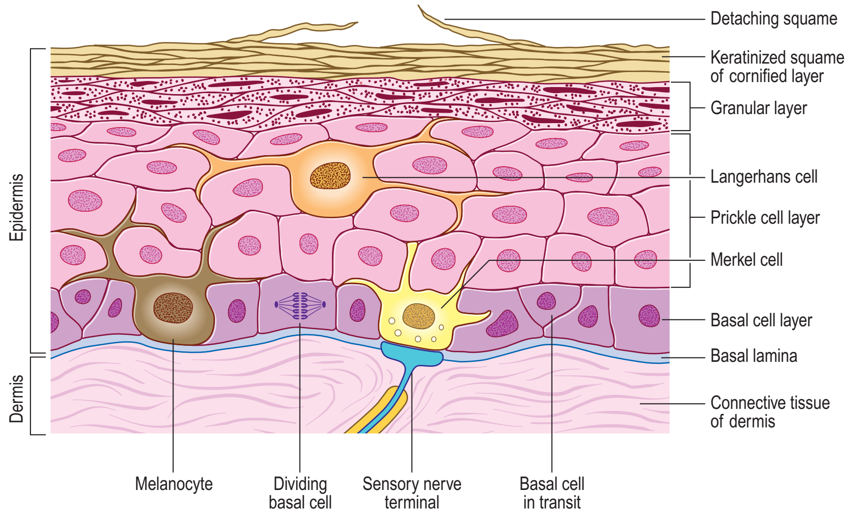
Epidermis
Dermis
Detaching squame
Keratinized squame of cornified layer
Granular layer
Langerhans cell
Prickle cell layer
Merkel cell
Basal cell layer
Basal lamina
Connective tissue of dermis
Melanocyte
Dividing basal cell
Sensory nerve terminal
Basal cell in transit

Fig. 7.3 The main features of the epidermis, including its cell layers and different cell types.

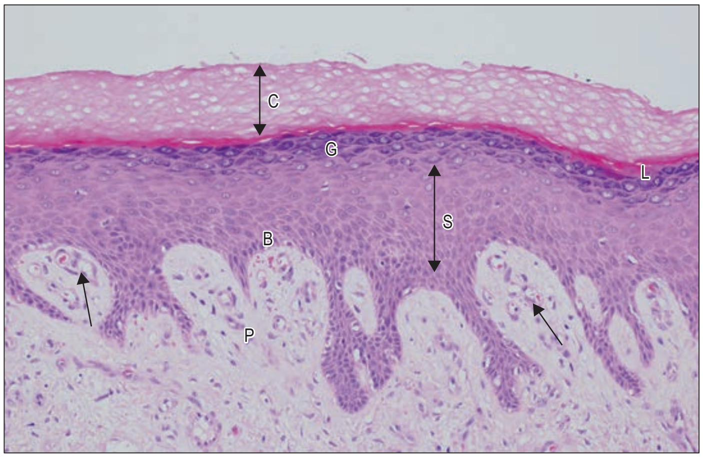

Fig. 7.4 The epidermis and papillary dermis (P) of human thick skin, showing the thick cornified layer (C, stratum corneum), the eosinophilic clear layer (L, stratum lucidum), the granular layer (G, stratum granulosum), the prickle cell layer (S, stratum spinosum) and the basal layer (B, stratum basale). Capillary loops (arrows) are seen entering the deep papillae (rete ridges) of the dermis, between downward-projecting epidermal rete pegs. (Courtesy of Mr Peter Helliwell and the late Dr Joseph Mathew, Department of Histopathology, Royal Cornwall Hospitals Trust, UK.)

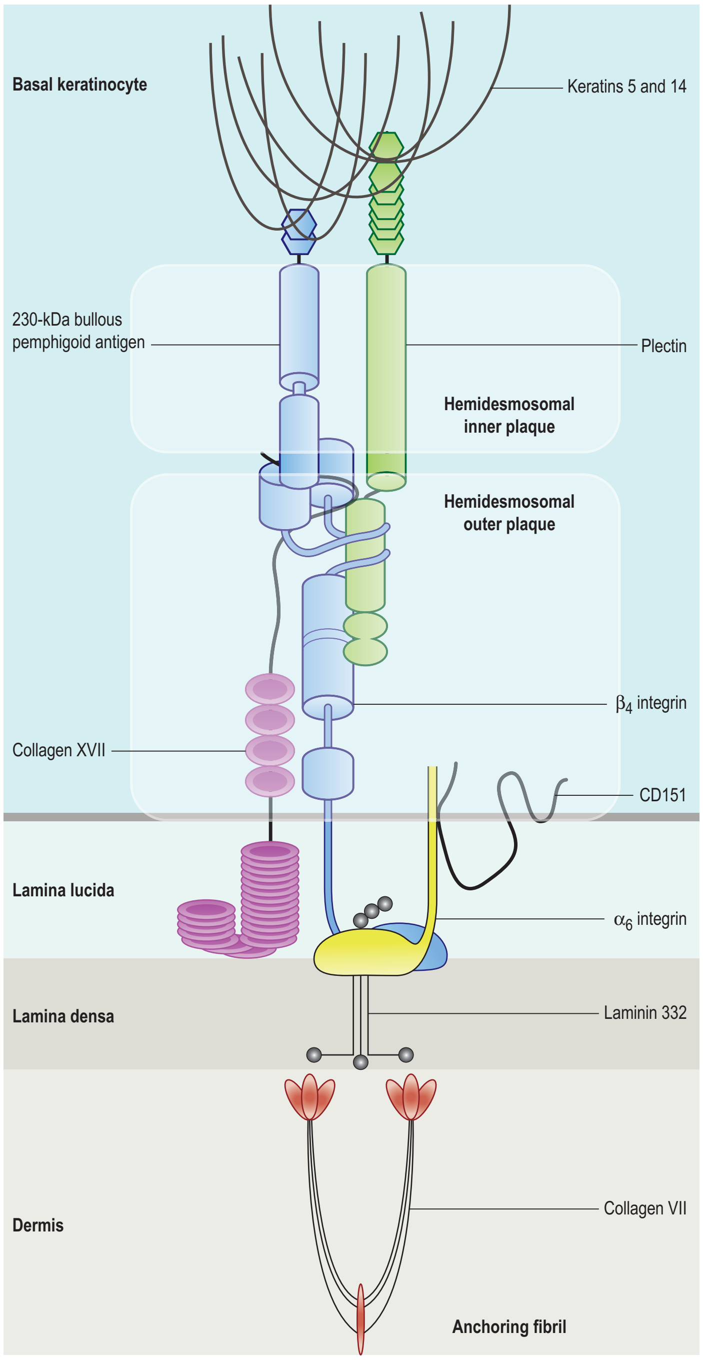
Basal keratinocyte
Keratins 5 and 14
230-kDa bullous pemphigoid antigen
Plectin
Hemidesmosomal inner plaque
Hemidesmosomal outer plaque
β_4 integrin
Collagen XVII
CD151
Lamina lucida
α_6 integrin
Lamina densa
Laminin 332
Dermis
Collagen VII
Anchoring fibril

Fig. 7.5 The major features of a hemidesmosome in the basement membrane zone (BMZ) of skin, including some of the important molecular components. Note that laminin 332 was formerly laminin 5. (Courtesy of Masatomo Kawano.)

but melanocytes and Langerhans cells lack these specialized contacts. Intraepithelial lymphocytes are present in small numbers.

Keratinocyte stem cells are found within the basal layer of the epidermis (Fuchs 2016): they are thought to reside mainly in the interfollicular epidermis in the troughs of rete pegs, and in the outer root sheath bulge of the hair follicle and in sebaceous glands. Their progeny, called transit (or transient) amplifying cells, also reside within the basal layer and pass through a few rounds of proliferation before terminally differentiating. The activity of epidermal stem cells and transit amplifying cells in the basal layer provides a continuous supply of differentiating cells that move suprabasally, eventually forming the cornified (corneocyte) layer of the epidermis.

Epidermal stem cells and their differentiated progeny are organized into columns, the epidermal proliferation units. Several layers of prickle and granular cells overlie a cluster of 6–8 basal cells, forming a columnar proliferative unit. Each group of basal cells consists of a central stem cell with an encircling ring of transit amplifying proliferative cells and postmitotic maturing cells. From the periphery of this unit, postmitotic cells transfer into the prickle cell layer. The normal total epidermal turnover time is between 52 and 75 days. In some skin disorders, the turnover rates and transit times are significantly shortened, e.g. in psoriasis, the total epidermal turnover time may be as little as 8 days. In homeostatic conditions, the multiple stem cell populations in skin generally contribute only to the differentiation programme of restricted local cells. However, following injury that inflicts systemic and local environmental change, the various stem cell populations, e.g. those in hair follicles, may display remarkable plasticity, responding to wound-induced stimuli by exiting their niche and participating in re-epithelializing damaged tissue. This

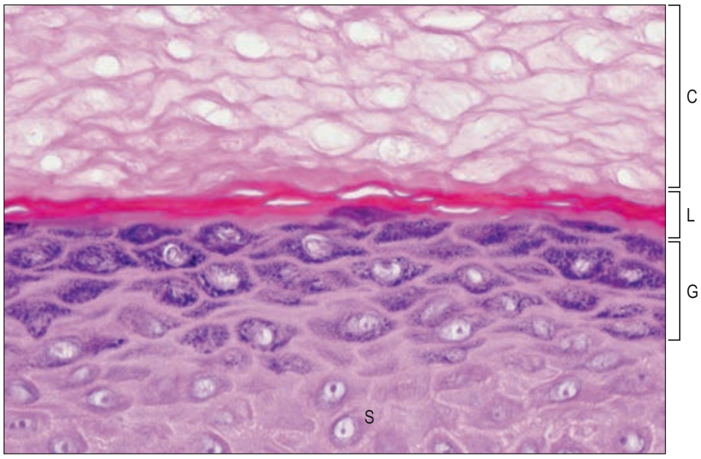

Fig. 7.7 The superficial layers of human thick skin, showing the deeply stained keratohyalin granule-containing cells of the granular layer (G) between the prickle cell or spinous layer (S) and the clear (or lucid, L) and cornified (C) layers above. Note that the clear layer is only translucent in unstained preparations and appears eosinophilic, as here, after staining. (Courtesy of Mr Peter Helliwell and the late Dr Joseph Mathew, Department of Histopathology, Royal Cornwall Hospitals Trust, UK.)

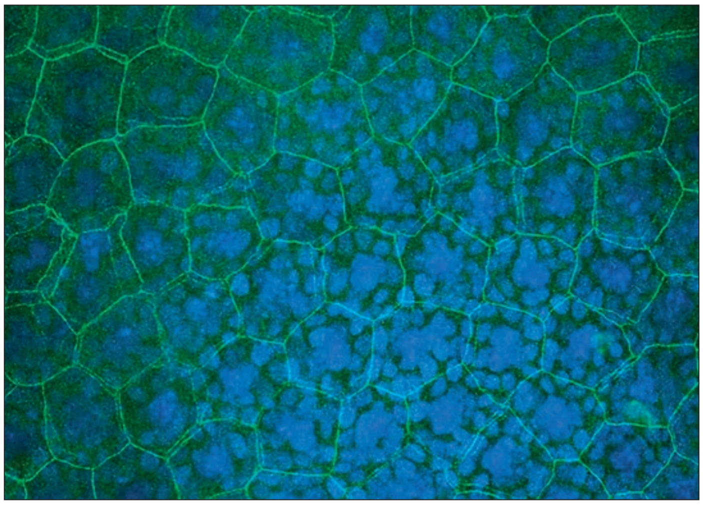

Fig. 7.9 Immunofluorescence labelling of tight junctions (green) in mouse epidermis viewed from above. Some cells are surrounded by a double layer of junctions as the keratinocytes transition across the granular layer. (Courtesy of Dr Akiharu Kubo, Keio University, Japan.)

process may involve a transient or permanent switch of their tissue regeneration programme depending upon the particular type of wound. Understanding the molecular basis of the 'switch' is likely to have considerable relevance to improving wound healing and developing the field of regenerative medicine.

Prickle cell layer

The prickle cell layer (stratum spinosum) (see Fig. 7.3; **Fig. 7.7**), consists of several layers of closely packed keratinocytes that are connected to each other by desmosomes, the specialized cell–cell junctions that provide tensile strength and cohesion to the layer. When a section of skin is stained by haematoxylin and eosin and viewed by routine light microscopy, intercellular bridges corresponding to the locations of the desmosomes are seen between the dehydrated keratinocytes, giving these suprabasal cells their characteristic spiny appearance. However, ultrastructurally, the desmosome junctions have a tight laminated appearance (**Fig. 7.8**). The cytoplasm of these keratinocytes contains prominent bundles of cytokeratin filaments, mostly cytokeratins 1 (K1) and 10 (K10), arranged concentrically around a euchromatic nucleus and attached to the dense plaques of the desmosomes and melanosomes, either singly or aggregated within membrane-bound organelles (compound melanosomes). Langerhans cells (see Fig. 7.16) and occasional lymphocytes are present in the prickle cell layer.

Granular layer

Extensive changes in keratinocyte structure occur in the 3–4 layers of flattened cells in the granular layer, also known as the stratum granulosum (Yokouchi et al. 2016). The nuclei become pyknotic and begin to disintegrate. Organelles such as ribosomes and membrane-bound mitochondria and Golgi bodies degenerate. Cytokeratin filament bundles become more compact and associated with irregular, densely staining keratohyalin granules (see Fig. 7.7). Small round granules (100 ×300 nm) with a lamellar internal structure (lamellar granules, Odland bodies, keratinosomes) also appear in the cytoplasm. Keratohyalin granules contain a histidine-rich, sulphur-poor protein, profilaggrin, which becomes modified to filaggrin as the cell reaches the cornified layer. Defects in the filaggrin protein, as a result of loss-of-function mutations in the filaggrin (*FLG*) gene, have been shown to cause ichthyosis vulgaris, a common dry scaly skin condition, as well as being a major risk factor for atopic eczema (Irvine et al 2011). In addition, copy number variation in the *FLG* gene may influence the amount of filaggrin in the skin and also contribute to the pathogenesis of both dry skin and eczema (Weidinger et al. 2018). The degradation products of filaggrin, including urocanic acid, contribute to the formation of natural moisturizing factor, a key component of the epidermal barrier function.

The lamellar granules release their hydrophobic glycophospholipid contents into the intercellular space both within the granular layer and between the granular and the cornified layers. These glycophospholipids form an important component of the permeability barrier of the epidermis: permeability is also regulated by tight junctions within the middle and upper parts of the granular layer (**Fig. 7.9**).

Clear layer

The clear layer is only found in thick palmar or plantar skin. It stains more strongly than the cornified layer with acidic dyes (see Fig. 7.6), is more optically refractile and often contains nuclear debris. Ultrastructurally, the cells contain compacted keratin filaments and resemble the incompletely keratinized cells that are occasionally seen in the innermost part of the cornified layer of thin skin.

Cornified layer

The cornified layer (see Figs 7.3, 7.7) is the final product of epidermal differentiation (Akiyama 2017). It consists of closely packed layers of flattened polyhedral squames or corneocytes (**Fig. 7.10**), ranging in surface area from 800 to 1100 μm^2. These cells overlap at their lateral margins and interlock with cells of apposed layers by ridges, grooves and microvilli. In thin skin, this layer may be a few cells deep, but in thick skin it may be more than 50 cells deep. The plasma membrane of the corneocytes appears thicker than that of other keratinocytes, partly due to the cross-linking of a soluble precursor, involucrin, at the cytoplasmic face of the plasma membrane, in the complex insoluble cornified envelope. The outer surface is also covered by a monolayer of bound lipid. The intercellular region contains extensive lamellar sheets of glycolipid derived from the lamellar granules of the granular layer. The cells lack a nucleus and membranous organelles, and consist entirely of a dense array of keratin filaments embedded in a cytoplasmic matrix composed partly of filaggrin derived from keratohyalin granules. The cornified layer has physical and chemical properties that vary across the layer, providing different amounts of absorption, hydration and mechanical defence (**Fig. 7.11**).

Under normal conditions, the production of epidermal keratinocytes in the basal layer is matched by the loss of corneocytes from the cornified layer. Desquamation of these cells is normally imperceptible. When excessive, it may appear as dandruff on the scalp or the flaking or peeling skin that follows sunburn. The thickness of the cornified layer can be influenced by local environmental factors including chronic scratching, which can lead to a considerable thickening of the whole epidermis including the cornified layer.

Keratins

Keratins are the intermediate filament proteins found in all epithelial cells. There are two types: type I (acidic) and type II (neutral/basic). They form heteropolymers, are co-expressed in specific pairs and are assembled into 10 nm intermediate filaments. Fifty-four different functional keratin genes are recognized in humans (Coulombe 2017). They are expressed in highly specific patterns according to the stage of cellular differentiation. Antibodies to individual keratins are useful analytical tools (**Fig. 7.12**). Keratins K5 and K14 are expressed by basal keratinocytes. Keratins K1 and K10 are synthesized suprabasally. In the granular layer the filaments become associated with keratohyalin granules containing profilaggrin, a histidine-rich phosphorylated protein. As the cells pass into the cornified layer, profilaggrin is cleaved by phosphatases into filaggrin, which causes aggregation of the filaments and forms the matrix in which they are embedded. Other types of keratin expression

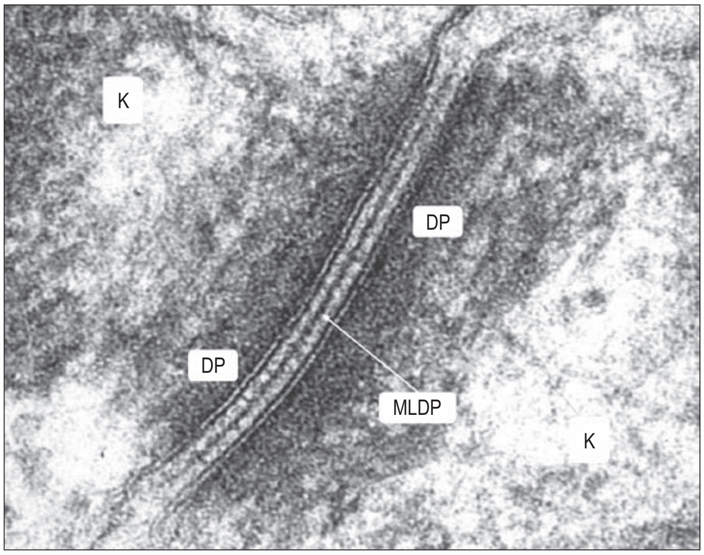

Fig. 7.8 Transmission electron micrograph of a skin desmosome junction. Abbreviations: DP, desmosomal plaque; K, keratinocyte; MLDP, midline dense plate.

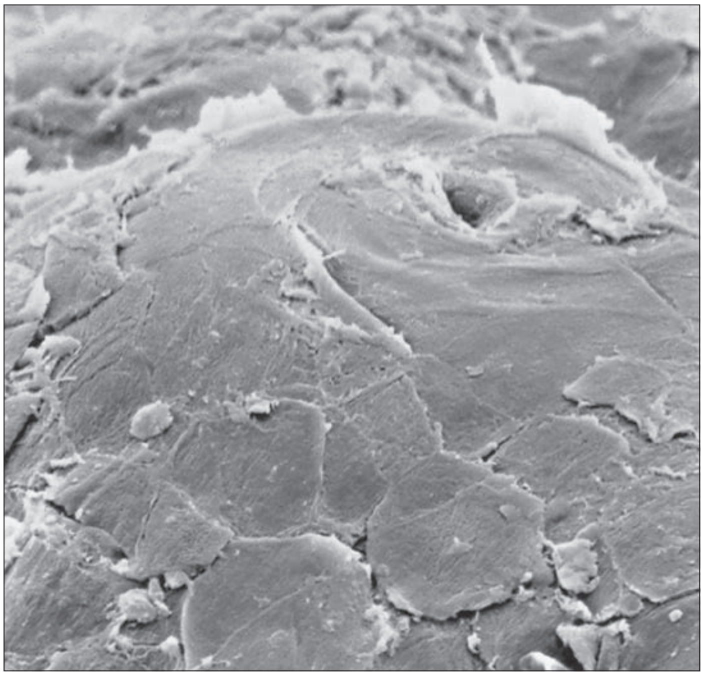

Fig. 7.10 A scanning electron micrograph showing the epidermal surface surrounding the aperture of a sweat duct. Note the polygonal, scale-like keratinocytes (squames) of the superficial cornified layer.

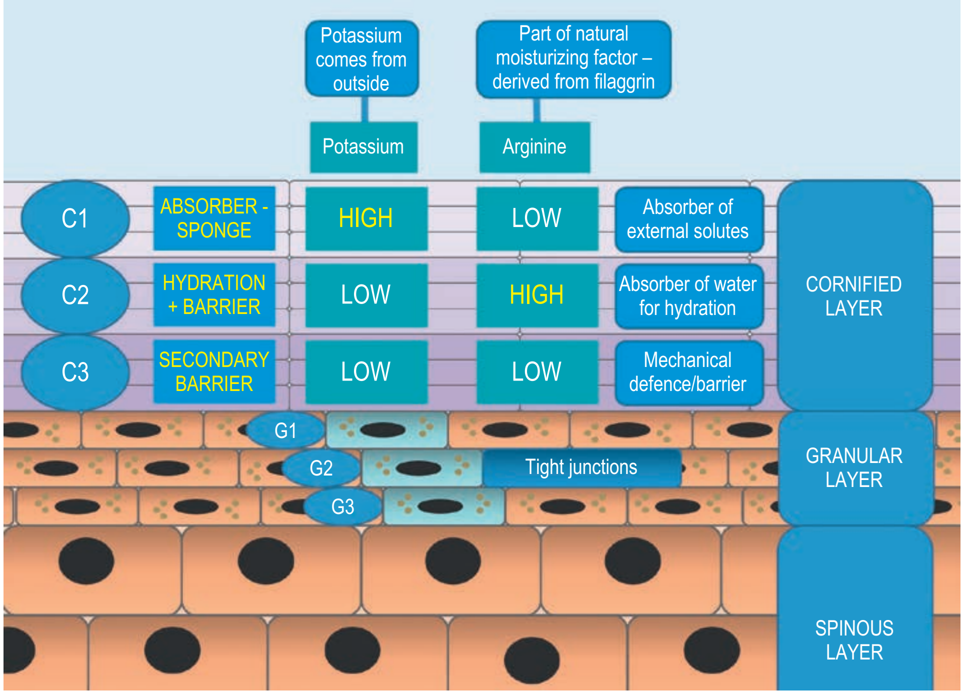
Potassium comes from outside
Part of natural moisturizing factor – derived from filaggrin
Potassium
Arginine
C1
ABSORBER - SPONGE
HIGH
LOW
Absorber of external solutes
C2
HYDRATION + BARRIER
LOW
HIGH
Absorber of water for hydration
C3
SECONDARY BARRIER
LOW
LOW
Mechanical defence/barrier
CORNIFIED LAYER
G1
G2
G3
Tight junctions
GRANULAR LAYER
SPINOUS LAYER

Fig. 7.11 Schematic representation of the cornified layer and upper epidermis to illustrate the physical and chemical properties of different parts of each layer. The cornified layer (C) is subdivided into three layers, as is the granular layer (G).

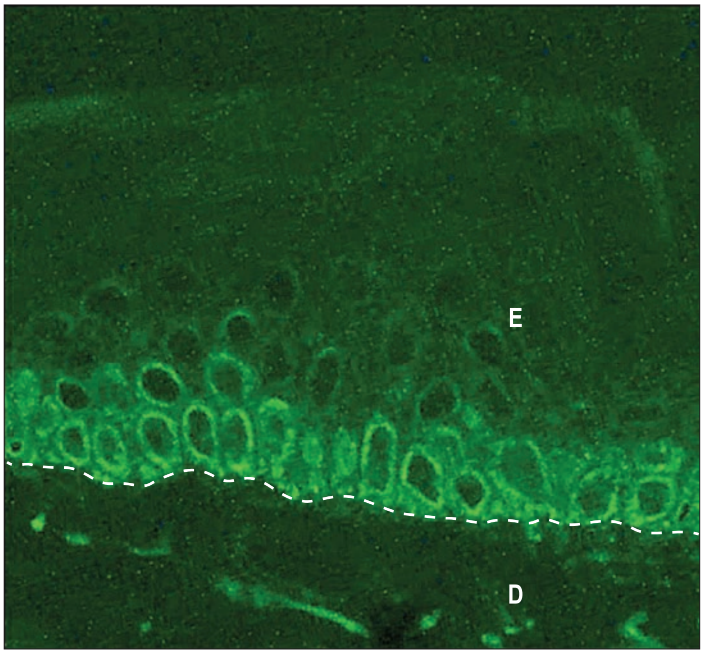

Fig. 7.12 Immunofluorescence microscopy of human skin showing the epidermis (E), cytokeratin 14 (green staining) in the basal layer, the dermis (D) and the dermal–epidermal junction (dotted line).

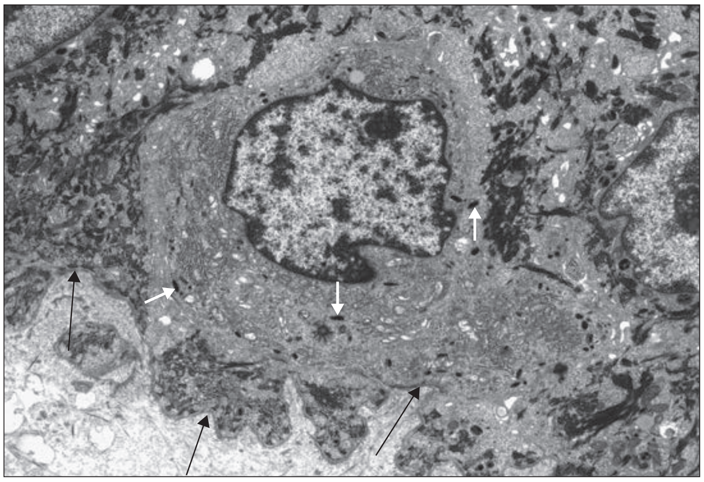

Fig. 7.14 An electron micrograph of a basal epidermal melanocyte, showing its nucleus and cytoplasm containing melanosomes (white arrows). There are no desmosomes connecting it with apposed keratinocytes. The cytoplasm of the keratinocytes is full of dense keratin filaments (which are absent from the melanocyte) and transferred melanosomes. The dermal–epidermal junction is indicated (black arrows). Human tissue. (Courtesy of Dr Bart Wagner, Histopathology Department, Sheffield Teaching Hospitals, UK.)

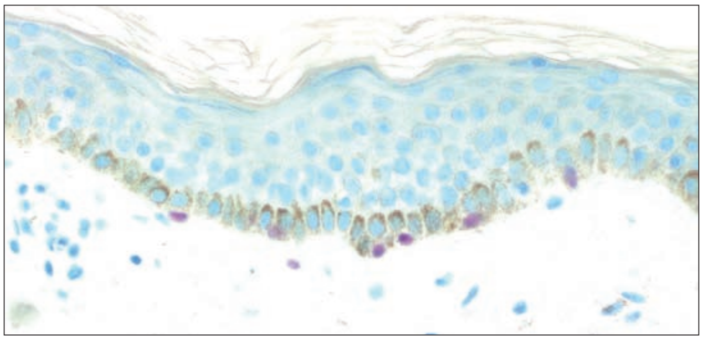

Fig. 7.13 Melanocytes in human skin revealed by Sox-9 immunostaining (pink). The brown staining is melanin in keeping with dark human skin. (Courtesy of Dr Eduardo Calonje, St John's Institute of Dermatology, London, UK.)

occur elsewhere, particularly in hair and nails, where highly specialized hard keratin is expressed. This becomes chemically modified and is much tougher than in the general epidermis.

Epidermal lipids

The epidermis serves as an important barrier to trans-epidermal loss of water and other substances through the body surface (apart from in sweating and sebaceous secretion). This is possible in part because of the presence of an epidermal lipid layer that consists of a variety of lipids that are synthesized in the epidermis. These include triglycerides, fatty acids, phospholipids, cholesterol, cholesterol esters, glycosphingolipids and ceramides. Furthermore, 7-dehydrocholesterol, an intermediate molecule in the cholesterol biosynthesis pathway and a precursor of vitamin D, is synthesized in the skin. The content and composition of epidermal lipids change with differentiation (Elias et al 2014). Phospholipids and glycolipids first accumulate within keratinocytes above the basal layer, but higher up they are broken down and are practically absent from the cornified layer. Cholesterol and its esters, fatty acids and ceramides accumulate towards the surface and are abundant in the cornified layer. The lamellar arrangement of the extracellular lipids is a major factor in their barrier function.

Melanocytes

Melanocytes are melanin pigment-producing cells derived from the neural crest (Figs 7.13–7.14). They are present in the epidermis and its appendages, oral epithelium, some mucous membranes, uveal tract (choroid coat) of the eyeball, parts of the middle and internal ear, and in the pial and arachnoid meninges, principally over the ventrolateral surfaces of the medulla oblongata. The cells of the retinal pigment epithelium, developed from the outer wall of the optic cup, also produce melanin, and neurones in different locations within the brainstem (e.g. the locus coeruleus and substantia nigra) synthesize a variety of melanin called neuromelanin. In humans there are two classes, the brown–black eumelanin and the red–yellow pheomelanin, both derived from the substrate tyrosine. Most natural melanins are mixtures of eumelanin and pheomelanin; pheomelanic pigments, trichochromes, occur in red hair.

Melanocytes are dendritic cells and lack desmosomal contacts with apposed keratinocytes, although hemidesmosomal contacts with the basal lamina are present. In routine tissue preparations, melanocytes appear as clear cells in the basal layer of the epidermis. The numbers per unit area of epidermis range from 2300 per mm^2 in cheek skin to 800 per mm^2 in abdominal skin. It is estimated that a single melanocyte may be in functional contact via its dendritic processes with up to 30 keratinocytes. The nucleus is large, round and euchromatic, and the cytoplasm contains intermediate filaments, a prominent Golgi complex and vesicles and associated rough endoplasmic reticulum, mitochondria and coated vesicles, together with a characteristic organelle, the melanosome.

The melanosome is a membrane-bound structure that undergoes a sequence of developmental stages during which melanin is synthesized and deposited within it by a tyrosine–tyrosinase reaction. Mature melanosomes move into the dendritic processes along the surfaces of microtubules and are transferred to keratinocytes through their phagocytic activity (Wu and Hammer 2014). Keratinocytes engulf and internalize the tip of the dendrite, so that the contained melanosomes are pinched off into the keratinocyte cytoplasm. Here, they may exist as individual granules in heavily pigmented skin, or be packaged within secondary lysosomes as melanosome complexes in lightly pigmented skin. In basal keratinocytes they can be seen to accumulate in a crescent-shaped cap over the distal part of the nucleus. As the keratinocytes progress towards the surface of the epidermis, melanosomes undergo degradation, and melanin remnants in the cornified layer form dust-like particles. Melanosomes are degraded more rapidly in light-skinned than in dark-skinned individuals, in whom melanosomes persist in cells of the more superficial layers. Melanosomes are acidic, which explains why the larger melanosomes present in dark skin types are associated with a more acidic skin surface (pH 4.3), compared to lighter skin types (pH 5.3). Melanosomes (and their melanin content) are mainly found in basal keratinocytes (Fig. 7.15).

Melanin protects the skin against the harmful effects of UV radiation on DNA and is also an efficient scavenger of damaging free radicals. However, a high concentration of melanin may adversely affect synthesis of vitamin D in darker-skinned individuals living in northern latitudes. Melanin pigmentation is both constitutive and facultative. Constitutive pigmentation is the intrinsic level of pigmentation and is genetically determined, whereas facultative pigmentation represents reversible changes

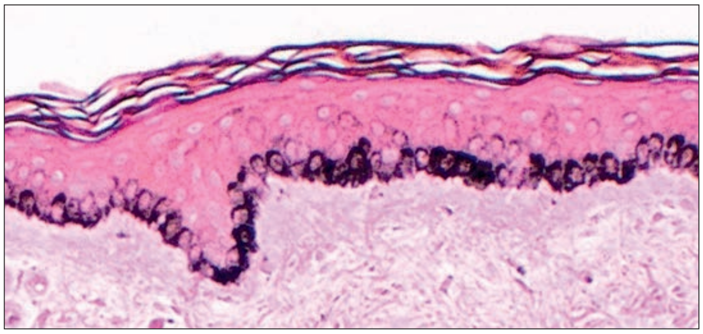

Fig. 7.15 Melanin distribution in basal keratinocytes of the epidermis in dark human skin highlighted by a Masson–Fontana stain. (Courtesy of Dr Eduardo Calonje, St John's Institute of Dermatology, London, UK.)

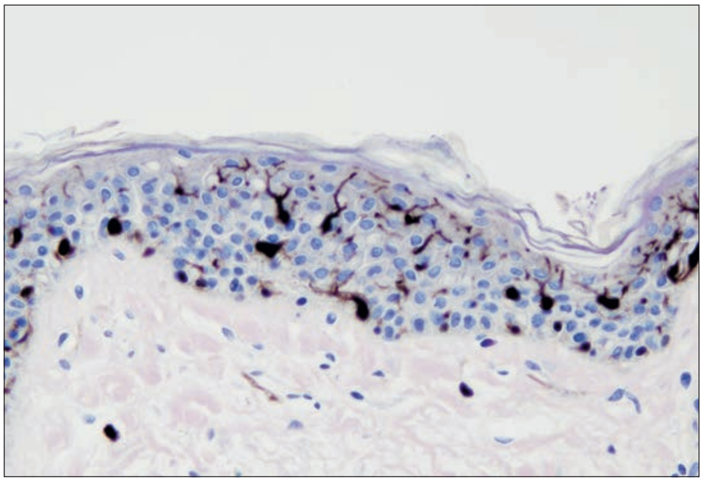

Fig. 7.16 Langerhans cells immunolabelled using a peroxidase method for the marker protein S100, extending dendrites between keratinocytes, mainly in the prickle cell layer of human thin skin. Basal layer melanocytes and scattered dermal cells (possibly of neural origin) are also positive for S100. (Courtesy of Mr Peter Helliwell and the late Dr Joseph Mathew, Department of Histopathology, Royal Cornwall Hospitals Trust, UK.)

induced by environmental agents, e.g. UV and X-radiation, chemicals and hormones. Racial variations in pigmentation are due to differences in melanocyte morphology and activity rather than to differences in number or distribution. In skin with naturally heavy pigmentation, the cells tend to be larger and more dendritic and to contain more large, late-stage melanosomes than the melanocytes of paler skins. The keratinocytes in turn contain more melanosomes, individually dispersed, whereas in light skins the majority are contained within secondary lysosomes to form melanosome complexes (D'Mello et al 2016).

The response to UV light includes immediate tanning with pigment darkening and can occur within minutes as a result of photo-oxidation of pre-existing melanin. Delayed tanning occurs after about 48 hours, and involves stimulation of melanogenesis within the melanocytes, and transfer of additional melanosomes to keratinocytes. There may also be some increase in size of active melanocytes, and in their apparent numbers, mainly through activation of dormant cells.

Langerhans cells

Langerhans cells are dendritic antigen-presenting cells that are distributed throughout the basal and prickle cell layers of the epidermis and its appendages, although their dendritic processes extend between tight junctions in the granular layer (Kubo et al 2014, Deckers et al 2018) (Figs 7.16–7.17). They are also present in other stratified squamous epithelia, including the buccal, tonsillar and oesophageal epithelia, as well as the cervical and vaginal mucosae, and the transitional epithelium of the bladder. In the eye, they are found in the conjunctiva but not in the cornea. In routine haematoxylin and eosin histological preparations, they appear as clear cells. They enter the epidermis from the bone marrow during development to establish the postnatal population (460–1000/mm^2, 2–3% of all epidermal cells, with regional variations), which is maintained by continual replacement from the marrow.

The nucleus is euchromatic and markedly indented, and the cytoplasm contains a well-developed Golgi complex, lysosomes (which often contain ingested melanosomes) and a characteristic organelle, the Birbeck granule, which is the ultrastructural hallmark of the Langerhans cell. The latter are discoid or cup-shaped, or have a distended vesicle resembling the head of a tennis racket; in section they often appear as a cross-striated rod 0.5 µm long and 30 nm wide. When stimulated by antigen, Langerhans cells migrate out of the epidermis to lymphoid tissues (see Fig. 4.14). Their numbers are increased in chronic skin inflammatory disorders, particularly of an immune aetiology, such as some forms of dermatitis.

Merkel cells

Merkel cells (see Commentary 1.4) are present as clear oval cells, singly or in groups, in the basal layer of the epidermis and in the outer root sheath of some large hair follicles. They are thought to be derived embryologically from the epidermis, although a neural crest origin has been considered. They can only be distinguished histologically from other clear cells (melanocytes and Langerhans cells) by immunohistochemical and ultrastructural criteria.

The plasma membrane of a Merkel cell has short, stiff processes that interdigitate with the adjacent basal keratinocytes to which it is attached by small desmosomes. The cytoplasm contains numerous closely packed intermediate filaments (mostly K8 and K18, but also K19 and K20) and characteristic 80–110 µm dense-core granules. The basal plasma membranes of many Merkel cells are closely opposed to the membrane of an axonal terminal that conveys the sensation of touch. They are slowly adapting mechanoreceptors that respond to directional deformations of the epidermis and the direction of hair movement by releasing a transmitter from their dense-core cytoplasmic granules. There is evidence that a subpopulation of Merkel cells lacks axonal contact and may serve a neuroendocrine function locally.

Merkel cells can undergo malignant transformation and give rise to a rare and aggressive tumour called a Merkel cell carcinoma (see Commentary 1.4) that typically presents with a painless, rapidly growing nodule on sun-exposed sites. The Merkel cell polyomavirus is clonally integrated in about 80% of Merkel cell carcinomas; the remaining 20% have a large number of ultraviolet-associated mutations.

Dermis

The dermis lies beneath the epidermis and is 15–40 times thicker than the epidermis, depending on the anatomical site (see Figs 7.1, 7.4). It is vital for the survival of the epidermis: important morphogenetic signals are exchanged at the interface between the two both during development and postnatally.

The dermis is an irregular, moderately dense connective tissue composed of an interwoven collagenous and elastic network in an amorphous ground substance of glycosaminoglycans, glycoproteins and bound water. It also contains nerves, blood vessels, lymphatics and epidermal appendages. Mechanically, the dermis provides considerable strength to the skin by virtue of the number and arrangement of its collagen fibres (which give it tensile strength) and its elastic fibres (which allow it to stretch and recoil). The density of its fibre meshwork, and therefore its physical properties, varies with different parts of the body, and with age and gender.

The dermis can be divided into two zones: a narrow, superficial papillary layer and a deeper reticular layer. The boundary between these two zones is indistinct. Fibroblasts, the main cell type of human dermis, are heterogeneous and at least four distinct sub-populations have been defined (Philippeos et al 2018). At a cellular level, different types of fibroblasts may have different properties with regard to Wnt (wingless gene family) signalling and responsiveness to interferon-γ. Their roles in the organisation of the extracellular matrix and tissue morphogenesis are only partially characterized: from a clinical perspective, future strategies involving *ex vivo* expansion or *in vivo* ablation of specific types of fibroblasts may have therapeutic applications in improving wound healing and reducing tissue fibrosis (Lynch and Watt 2018).

Adult dermal collagen is mainly of types I and III, in proportions of 80–85% and 15–20% respectively. Type I collagen fibres are coarse and found predominantly in the deeper reticular dermis, and the finer type III collagen is found in the papillary dermis and around blood vessels. Type IV collagen is found in the basal lamina between epidermis and dermis, and around Schwann cells of peripheral nerves and endothelial cells of vessels. Types V, VI and VII are minor collagenous components of the dermis. Elastic fibres form a fibrous network interwoven between the collagen bundles throughout the dermis and are more prominent in some regions, e.g. the axilla.

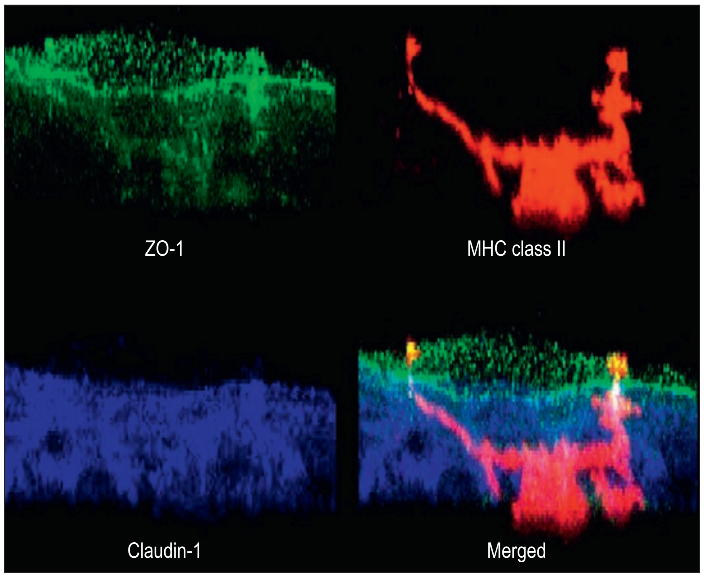

Fig. 7.17 Langerhans cell with dendritic processes extending through tight junctions (mouse skin). ZO-1 (zonula occludens-1; green) and claudin-1 (blue) are tight junction proteins; the Langerhans cell is positive for MHC class II antigen (red). The merged image reveals the close association of the Langerhans cell with tight junctions in antigen presentation. (Courtesy of Dr Akiharu Kubo, Keio University, Japan.)

Two major categories of cell are present in postnatal dermis, permanent and migrant, as is typical of all general connective tissues (Ch. 2). The permanent resident cells include cells of organized structures such as nerves, vessels, cells of the arrector pili muscles, and fibroblasts, which synthesize all components of the dermal extracellular matrix. The migrant cells originate in the bone marrow (see Fig. 4.12) and include macrophages, mast cells, eosinophils, neutrophils, T and B cells (including antibody-secreting plasma cells), and dermal interstitial dendritic cells, which are capable of immune surveillance and antigen presentation.

Layers of the dermis

Papillary layer

The papillary layer is a relatively thin zone immediately subjacent to the dermal–epidermal junction. It provides mechanical anchorage, metabolic support and trophic maintenance to the overlying epidermis, as well as supplying sensory nerve endings and blood vessels. The cytoskeleton of the basal epidermal keratinocytes is linked to the fibrous matrix of the papillary dermis through the attachment of keratin filament bundles to hemidesmosomes, then via anchoring filaments of the basal lamina, to the anchoring fibrils of type VII collagen, which extend into the papillary dermis. This arrangement provides a mechanically stable substratum for the epidermis.

The superficial surface of the dermis is shaped into numerous papillae or rete ridges, which interdigitate with rete pegs in the base of the epidermis and form the dermal–epidermal junction at their interface. The papillae have round or blunt apices, which may be divided into several cusps. In thin skin, especially in regions with little mechanical stress and minimal sensitivity, papillae are few and very small, while in the thick skin of the palm and sole of the foot they are much larger, closely aggregated, and arranged in curved parallel lines following the pattern of ridges and grooves on these surfaces (see Fig. 7.1). Lying under each epidermal surface ridge are two longitudinal rows of papillae, one on either side of the epidermal rete pegs, through which the sweat ducts pass on the way to the surface. Each papilla contains densely interwoven and fine bundles of types I and III collagen fibres. Elastic fibres are not fully formed in the papillary dermis. Also present is a capillary loop (see Fig. 7.4), and in some sites, especially in thick hairless skin, Meissner's corpuscle nerve endings. (see Figs 3.29, 3.30)

Reticular layer

The reticular layer is much thicker than the papillary dermis. Its bundles of collagen fibres are coarser and more compacted and form a strong but deformable three-dimensional lattice that contains a variable number of elastic fibres. The mostly parallel orientation of the collagen fibres may be related to local mechanical forces on the dermis and may be involved in the development of skin lines. In the reticular dermis, the elastic fibres are composed of amorphous elastin surrounding microfibrils within the centre of the elastic fibres. The elastic fibres lose their elastin component at the intersection of the reticular and papillary dermis, whereas the microfibrils continue into the papillary dermis as naked microfibrils that organize horizontally as elaunin fibres and vertically as oxytalan fibres.

Hypodermis

The hypodermis (subcutaneous tissue) is a layer of loose connective tissue of variable thickness that merges with the deep aspect of the dermis. It is often adipose, particularly between the dermis and musculature of the body wall (**Fig. 7.18**). It mediates the increased mobility of the skin, and its adipose component contributes to thermal insulation, acts as a shock absorber and constitutes a store of metabolic energy. Subcutaneous nerves, vessels and lymphatics travel in the hypodermis, their main trunks lying in its deepest layer, where adipose tissue is sparse. In the head and neck the hypodermis also contains striated muscles, e.g. platysma, which are remnants of more extensive sheets of skin-associated musculature found in other mammals (panniculus adiposus).

The amount and distribution of subcutaneous fat varies according to gender: it is generally more abundant and more widely distributed in females, whereas it diminishes from the trunk to the extremities in males. The total amount of subcutaneous fat tends to increase in both males and females in middle age. (At any age, the amount of adipose tissue reflects the quantity of lipid stored in adipocytes rather than a change in the number of cells.) There is an association with climate (rather than ancestry): superficial fat is more abundant in colder geographical regions. The hypodermis is most distinct on the lower anterior abdominal wall, where it is rich in elastic tissue and appears many-layered as it passes through the inguinal regions into the thighs. It is well differentiated in the limbs and the perineum, but is thin where it passes over the dorsal aspects of the hands and feet, the sides of the neck and face, around the anus, and over the penis and scrotum. It is almost absent from the external ears and atypical in the scalp and in the palms and soles.

The layers of the skin, including the subcutaneous tissues are tethered tightly together by connective tissue bands, the retinacula cutis (**Fig. 7.19**), forming densely packed ligament-like structures in some parts (Herlin et al 2014).

Pilosebaceous unit

The pilosebaceous unit consists of the hair and its follicle with an associated arrector pili muscle, sebaceous gland and sometimes an apocrine gland (see Fig. 7.1; **Fig. 7.20**). Not all elements of the unit occur together in all body regions.

Hairs

Hairs are filamentous cornified structures present over almost the entire body surface. They grow out of the skin at an angle (see Fig. 46.1), as is evident in the sloping of the hairs on the dorsum of forearm, hand and fingers towards the ulnar side. Hairs are absent from several areas of the body, including the thick skin of the palms, soles, the flexor surfaces of the digits, the thin skin of the lip, umbilicus, nipples, glans penis and clitoris, the labia minora and the inner aspects of the labia majora and prepuce. The presence, distribution and relative abundance of hair in certain regions such as the face (in males), pubis and axillae, are secondary sexual characteristics that play a role in socio-sexual communication. There are individual variations in density, form, distribution and pigmentation. Hairs assist in thermoregulation, e.g. on the scalp they provide some protection against injury and the harmful effects of solar radiation. They also have a sensory function.

Hair density varies from approximately 600 per cm^2 on the face to 60 per cm^2 on the rest of the body. In length, hairs range from less than a millimetre to more than a metre, and in width from 0.005 to 0.6 mm. They can be straight, coiled, helical or wavy, and differ in colour depending on the type and degree of pigmentation. Curly hairs tend to have a flattened cross-section, and are weaker than straight hairs. Over most of the body surface, hairs are short and narrow (vellus hairs) and in some areas these hairs do not project beyond their follicles, e.g. in eyelid skin. In other regions they are longer, thicker and often heavily pigmented (terminal hairs); these include the hairs of the scalp, the eyelashes and eyebrows, and the postpubertal skin of the axillae and pubis, and the moustache, beard and chest hairs of males. The presence in females of coarse terminal hairs in a male-like pattern is termed hirsutism and can be familial or a sign of an endocrine disorder involving excess androgen production.

Hair follicle

The hair follicle (see Figs 7.1, 7.20; **Fig. 7.21A**) is a downgrowth of the epidermis containing a hair. It may extend deep (3 mm) into the hypodermis, or may be superficial (1 mm) within the dermis. Typically, the long axis of the follicle is oblique to the skin surface; with curly hairs it is also curved. There are cycles of hair growth and loss, during which the follicle presents with different appearances. In the anagen phase, the hair is actively growing and the follicle is at its maximal extent of development. In the involuting or catagen phase, hair growth ceases and the follicle shrinks. During the resting or telogen phase, the inferior segment of the follicle is absent. This is succeeded by the next anagen phase. Further details of the hair growth cycle are given below.

Anagen follicle

The anagen follicle has several regions. The innermost part is the inferior segment, which includes the hair bulb region extending up to the level of attachment of the arrector pili muscle at the follicular bulge. Between this point and the site of entry of the sebaceous duct is the isthmus, above which is the infundibulum, or dermal pilary canal, which is continuous with the intraepidermal pilary canal. Below the sebaceous duct, the hair shaft and follicular wall are closely connected, and towards the upper end of the isthmus the hair becomes free in the pilary canal. Below the infundibulum, the follicle is surrounded by a thick perifollicular dermal coat containing type III collagen, elastin, sensory nerve fibres and blood vessels, and into which the arrector pili muscle fibres blend. A thick, specialized basal lamina, the glassy membrane, marks the interface between dermis and the epithelium of large hair follicles.

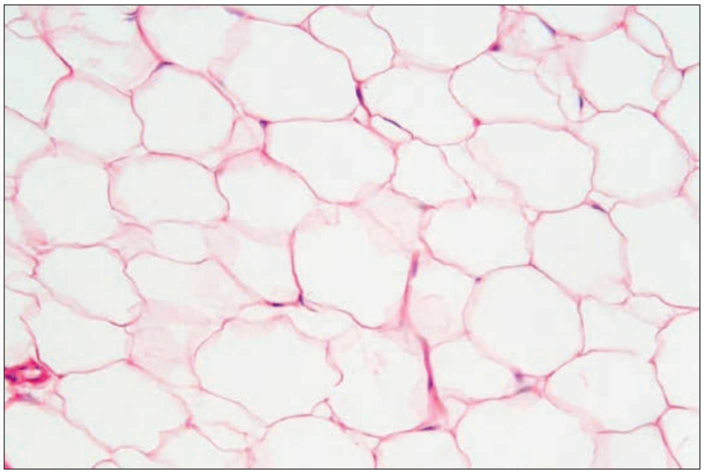

Fig. 7.18 Adipocytes (fat cells) in human skin.

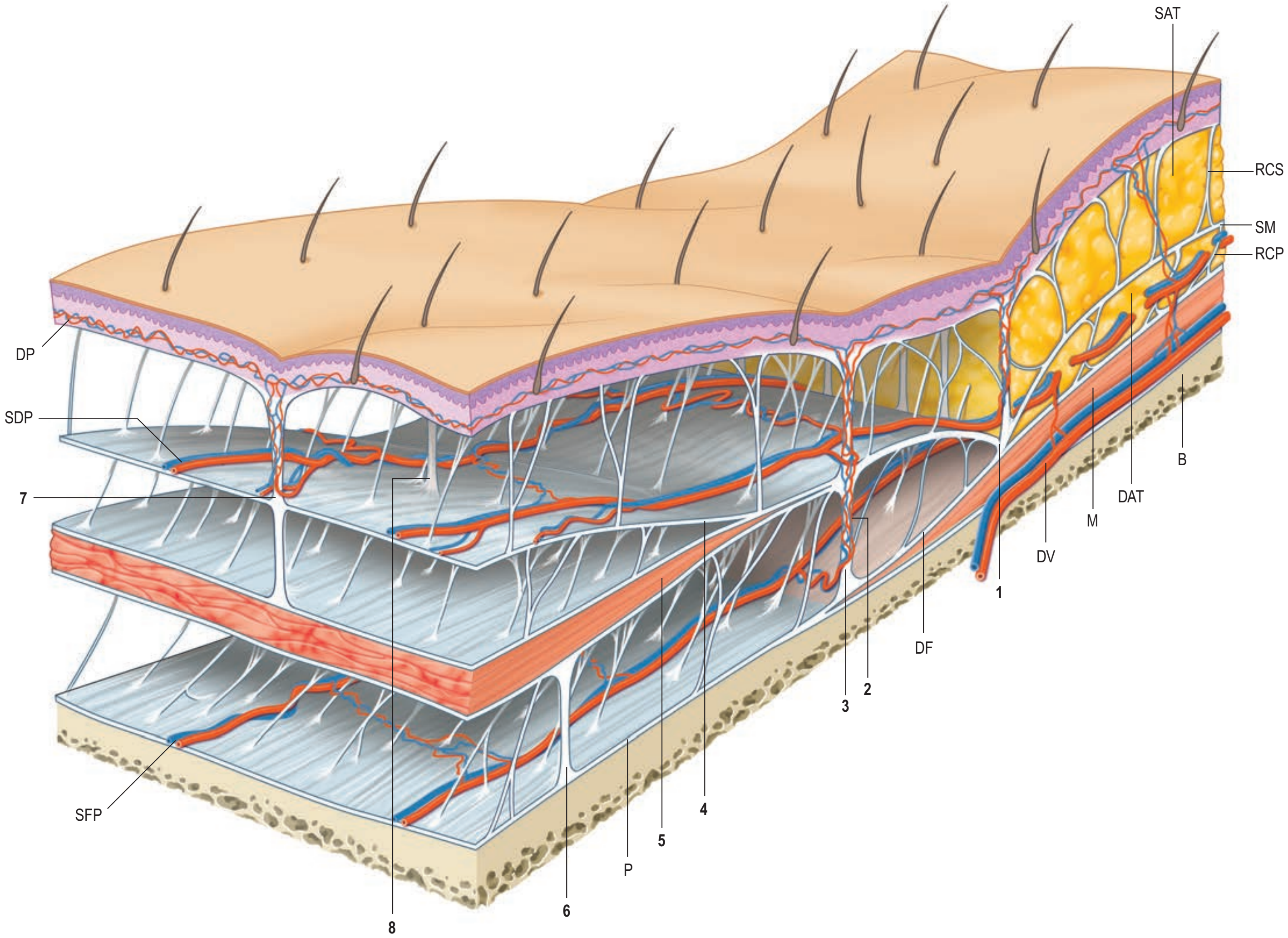

Fig. 7.19 Generic model of the skin/subcutaneous tissue complex. Note retinacula cutis. Interlobular septa are not shown. Abbreviations: B, bone; DAT, deep adipose tissue; DF, deep fascia; DP, dermal plexus; DV, deep vessels; M, muscle; P, periosteum; RCP, retinaculum cutis profondus; RCS, retinaculum cutis superficialis; SAT, superficial adipose tissue; SM, stratum membranosum (superficial fascia) SDP, sub-dermal plexus; SFP, suprafascial plexus. Key: 1, region of adhesion between the SM and the DP (opposite the sternum or the iliac crest); 2, perforating vessels running with RCP and RCS thickening; 3, skin 'ligaments' consisting of combined densification of the RCS and RCP (e.g. Furnas' ligament, McGregor's patch, Cooper's ligaments); 4, SM duplication that appears mostly in fatty areas (e.g. cheeks, lower back, breasts, thighs); 5, superficial fascia containing smooth muscle (e.g. superficial musculo-aponeurotic system (SMAS), dartos, areolar muscle, corrugator cutis ani, palmaris brevis); 6, thickening of the RCP connecting the SM and SMAS at a deep level; 7 and 8, thickening of the RCSs connecting the SM and SMAS to the skin. (Adapted from Herlin et al 2015 Three-dimensional study of the skin/subcutaneous complex using in vivo whole body 3T MRI: review of the literature and confirmation of a generic pattern of organization.)

Hair bulb

The hair bulb forms the lowermost portion of the follicular epithelium and encloses the dermal hair papilla of connective tissue cells (Fig. 7.21B). The dermal hair papilla is an important cluster of inductive mesenchymal cells, which is required for hair follicle growth in each cycle throughout adult life; it is a continuation of the layer of adventitious mesenchyme that follows the contours of the hair follicle. The hair bulb generates the hair and its inner root sheath. A hypothetical line drawn across the widest part of the hair bulb divides it into a lower germinal matrix and an upper bulb. The germinal matrix is formed of closely packed, mitotically active pluripotential keratinocytes, among which are interspersed melanocytes and some Langerhans cells. The upper bulb consists of cells arising from the matrix. These migrate apically and differentiate along several lines. Those arising centrally form the hair medulla. Radially, successive concentric rings of cells give rise to the cortex and cuticle of the hair and, outside this, to the three layers of the inner root sheath. The latter are, from innermost to outer, the cuticle of the inner root sheath, Huxley's layer and Henle's layer. Henle's layer is surrounded by the outer root sheath, which forms the cellular wall of the follicle (see Fig. 7.21). Differentiation of cells in the various layers of the hair and its inner root sheath begins at the level of the upper bulb and is asynchronous, beginning earliest in Henle's layer and Huxley's layer.

Structure of hair and its sheaths

A fully developed hair shaft consists of three concentric zones, which are, from outermost to inner, the cuticle, cortex and medulla. Each has different types of keratin filament proteins and different patterns of cornification. In finer hairs the medulla is usually absent. The cuticle forms the hair surface and consists of several layers of overlapping cornified squames directed apically and slightly outwards (Fig. 7.22). Immature cuticle cells have dense amorphous granules aligned predominantly along the outer plasma membrane with a few filaments. The cortex forms the greater part of the hair shaft and consists of numerous closely packed, elongated squames, which may contain nuclear remnants and melanosomes. Immature cortical cells contain bundles of closely packed filaments but no dense granules, and when fully cornified, they have a characteristic thumbprint appearance with filaments arranged in whorls. The medulla, when present, is composed of loosely aggregated and often discontinuous columns of partially disintegrated cells containing vacuoles, scattered filaments, granular material and melanosomes. Air cavities lie between the cells or even within them.

Henle's layer and Huxley's layer of the inner root sheath contain irregular dense keratohyalin granules and associated filaments in the precornified state. At the level of the upper bulb, Henle's layer begins to cornify, as does Huxley's layer at the middle of the inferior follicle. When fully differentiated, cells of both layers have a thickened cornified envelope enclosing keratin filaments embedded in a matrix. The cells of the inner root sheath cuticle undergo terminal differentiation at a level closer to the hair bulb than that of Huxley's layer, but lack a clear-cut filament pattern such as is seen in the cortical cells of the hair shaft. As they cornify, the cuticle cells of the inner root sheath and hair become interlocked. At about the level of entry of the sebaceous duct, above the isthmus, the inner root sheath undergoes fragmentation, and the hair then lies free in the pilary canal.

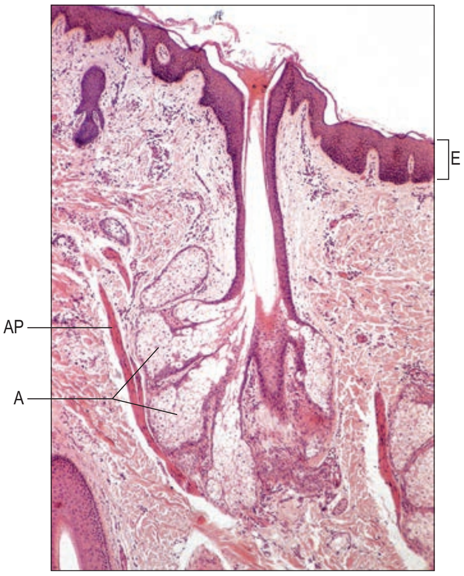

Fig. 7.20 A pilosebaceous unit in thin, hairy skin seen at low magnification. The hair follicle, hair shaft and hair root extend almost vertically through the field, the follicle joining the interfollicular epidermis (E). The acini (A) of a sebaceous gland, which are also sectioned tangentially through their capsules (centre bottom, below the portion of the hair follicle in section), open into the follicle in centre field. Note the associated arrector pili smooth muscle (AP).

The outer root sheath, beginning at the level of the upper bulb, is a single or double layer of undifferentiated cells containing glycogen. Higher up the follicle it becomes multilayered. At the isthmus all remaining cell layers of the follicle sheath become flattened, compressed and attenuated. On emerging from the isthmus, the outer root sheath assumes the stratified, differentiating characteristics of interfollicular epidermis, with which it becomes continuous. At the level of entry of the sebaceous duct, it forms the wall of the pilary canal.

Hair cycle and growth of hair

Recurrent cyclic activity of hair follicles involves growth rest, and shedding of hair in phases (Purba et al 2016). In humans, these occur in irregular cycles of variable duration; there are regional and other variations in the length of the individual phases. In the growing or anagen phase, follicle and hair are as described above. Melanocytes are active only in mid-anagen, and are capable of producing both pheo- and eumelanosomes, which they pass to precortical and medullary keratinocytes. Changes in hair colour of an individual, usually in adolescence, are due to alterations in the dominant type of melanosome produced.

Anagen is followed by the involuting or catagen phase, during which mitotic activity of the germinal matrix ceases, the base of the hair condenses into a club that moves upwards to the level of the arrector pili muscle, and the whole inferior segment of the follicle degenerates. The dermal papilla also ascends and remains close to the base of the shortened follicle and its enclosed club hair, a situation that persists during the resting or telogen phase. During telogen, melanocytes become amelanotic and can be identified only ultrastructurally. At the beginning of the next anagen, the epithelial cells at the base of the follicle divide to form a secondary hair rudiment, which envelops the dermal papilla to form a new hair bulb. This grows downwards, reforming the inferior segment of the follicle, from which a new hair grows up alongside the club hair, which is eventually shed.

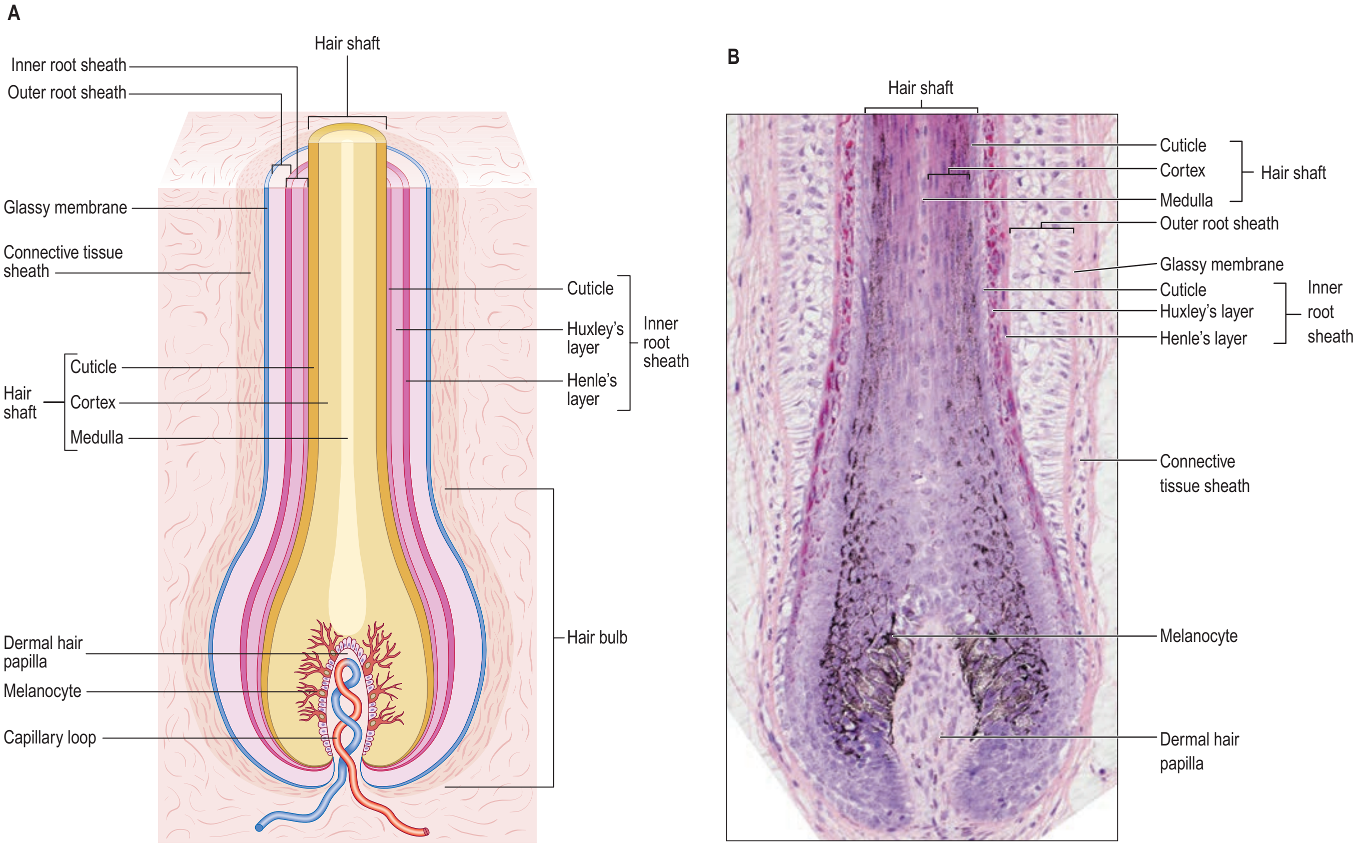

Fig. 7.21 **A**, The major structural features of the base of a hair follicle, showing the organization of the major layers of the hair and surrounding sheath, arising from the hair bulb. A dermal hair papilla invaginates the bulb, and along the basal layer of the epidermis, at its interface with the dermis, melanocytes insert their dendrites among the keratinocytes forming the hair. **B**, The hair bulb at the base of the human hair follicle. The dermal hair papilla invaginates the bulb from its fibrous outer sheath, carrying a loop of capillaries. Melanocytes in the germinal matrix (equivalent to the basal layer of interfollicular epidermis) extend dendrites into the adjacent layers of keratinocytes, to which they pass melanosomes. The layers of the hair shaft and root sheaths are also indicated. (B, Courtesy of Mr Peter Helliwell and the late Dr Joseph Mathew, Department of Histopathology, Royal Cornwall Hospitals Trust, UK.)

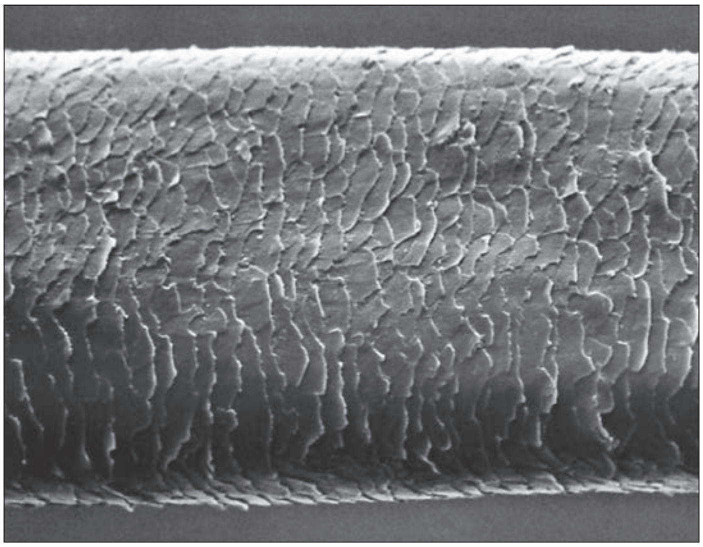

Fig. 7.22 A scanning electron micrograph of a scalp hair, showing details of its surface structure. Note that the cuticular cells overlap each other; their free ends point towards the apex of the hair. (Courtesy of Michael Crowder MD.)

Postnatally, hairs exhibit regional asynchrony of cycle duration and phase leading to an irregular pattern of growth and replacement. In some regions, such as the scalp, the cycle is measured in years; in others, such as general body hair, the cycle is much shorter and hairs are therefore limited in length. At puberty, hair growth and generation of much thicker hairs occurs on the pubes and axillae in both sexes, and on the face and trunk in males. The actions of hormones on hair growth are complex, and involve not only sex hormones, but also those of the thyroid, suprarenal cortex and pituitary glands. Androgens stimulate facial and general body hair formation. After about the first 30 years, they tend to cause the thick terminal hairs of the scalp to change to small vellus hairs, which produces recession from the forehead and sometimes almost complete male pattern baldness. In females, oestrogens tend to maintain vellus hairs; postmenopausal reduction of oestrogens may permit stronger facial and bodily hair growth. In mid-pregnancy, hair growth may be particularly active but later, often post partum, an unusually large number of hairs enter the telogen phase and are shed before the growth cycle recommences. In older males, growth of hairs on the eyebrows and within the nostrils and external acoustic meatus increases, whereas elsewhere on the body, growth slows and the hairs become much finer.

Measurements of the rate of growth of individual hairs vary considerably, probably because of the influence of the factors mentioned above. A rate of 0.2–0.44 mm per 24 hours in males is usually given; the higher rate occurs on the scalp.

Sebaceous glands

Sebaceous glands are small saccular structures (see Figs 7.1, 7.20; **Fig. 7.23**) found in the dermis. Most associate with the hair follicle and arrector pili muscle to form the pilosebaceous unit. They are present over the whole body except the thick, hairless skin of the palm, soles and flexor surfaces of digits. Typically, they consist of a cluster of secretory acini, which open by a short common duct into the dermal pilary canal of the hair follicle. They release their lipid secretory product, sebum, into the canal by a holocrine mechanism (see below). In some areas of thin skin that lack hair follicles, their ducts open instead directly onto the skin surface, e.g. on the lips and corners of the mouth, the buccal mucosa, nipples (Montgomery's glands), areolae of the female breast, penis, inner surface of the prepuce, clitoris and labia minora. At the margins of the eyelids, the large, complex palpebral tarsal glands (Meibomian glands) are of this type. They are also present in the external acoustic meatus (ceruminous glands).

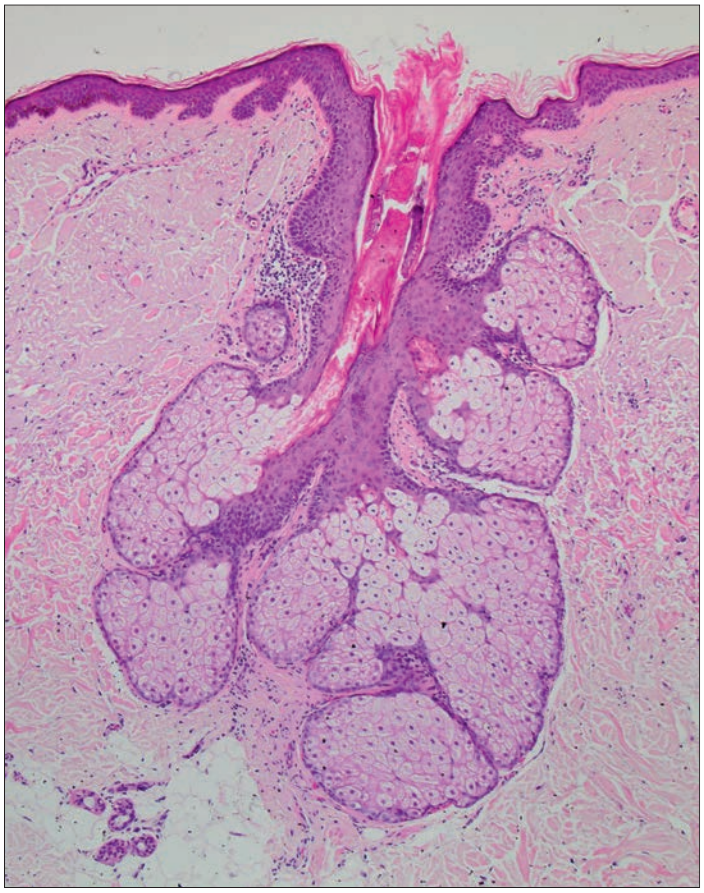

Fig. 7.23 A sebaceous gland, showing a group of secretory acini opening into a hair follicle (top). The distended sebocytes are filled with their oily secretion (sebum), which is discharged into the hair follicle by the holocrine disintegration of secretory cells. (Courtesy of Mr Peter Helliwell, Department of Histopathology, Royal Cornwall Hospitals Trust, UK.)

In general, the numbers of sebaceous glands in any given area reflect the distribution of hair follicles, ranging from an average of 100/cm^2 over most of the body to as many as 400–900/cm^2 on the face and scalp. They are also numerous in the midline of the back. Individual sebaceous glands are particularly large on the face, around the external acoustic meatus, chest and shoulders, and on the anogenital surfaces. Those on the face are often related to very small vellus hairs whose follicles have particularly wide apertures (Zouboulis et al 2016).

Microscopically, the glandular acini are enclosed in a basal lamina supported by a thin dermal capsule and a rich capillary network. Each acinus is lined by a single layer of small, flat, polygonal epithelial cells (sebocytes), which, when terminally differentiated, produce and accumulate sebum. They possess euchromatic nuclei and large nucleoli, scattered keratin filaments, free ribosomes, smooth endoplasmic reticulum and rounded mitochondria, and are attached to each other by desmosomes. Mitotically active cells give rise to progeny that move gradually towards the centre of the acinus, increasing in volume and accumulating increasingly large lipid vacuoles. The nuclei become pyknotic as the cells mature. The huge distended cells ultimately disintegrate, filling the central cavity and its duct with a mass of fatty cellular debris (holocrine secretion; see Figs 2.6, **7.23**). The process takes 2–3 weeks. The secretory products pass through a wide duct lined with keratinized stratified squamous epithelium into the infundibulum of the hair follicle and then to the surface of the hair and the general epidermis.

While its full range of functions in the skin remains to be clarified, sebum is a key component of the epidermal barrier, as well as having a key role in the skin's immune system. Sebum also contributes to a characteristic body odour. When first formed, sebum is a complex mixture of over 50% di- and triglycerides, with smaller proportions of wax esters, squalene, cholesterol esters, cholesterol and free fatty acids. At birth, sebaceous glands are quite large, regressing later until stimulated again at puberty. At that time, sebaceous gland growth and secretory activity increase greatly in both males and females, under the influence of androgens (testicular and suprarenal), which act directly on the gland. Excessive amounts of sebum may become impacted within the duct and this, associated with hyperkeratinization, may lead to blockage and formation of a comedone. This may become inflamed, and is the primary lesion of acne. Acne is the most common disease caused by dysfunction of the sebocyte. Oestrogens have an effect opposite to that of androgens; sebum secretion is considerably lower in women, and usually decreases significantly after the menopause (Piérard-Franchimont and Piérard 2002).

Apocrine glands

Apocrine glands are particularly large glands found in the dermis or subcutaneous fat. They are conventionally classed as a type of sweat gland. In the adult, they are present in the axillae, perianal region, areolae, periumbilical skin, prepuce, scrotum, mons pubis and labia minora.

An apocrine gland consists of a basal secretory coil and a straight duct that opens into either the pilary canal above the duct of the sebaceous gland, or directly onto the skin surface if there is no associated hair. The secretory region may be as much as 2 mm wide and its coils often anastomose to form a labyrinthine network. Each coil is lined by cuboidal secretory cells whose apical cytoplasm projects into the lumen and basally is in contact with a layer of myoepithelial cells within a thick basal lamina. The secretory cells contain vacuoles, vesicles and dense granules of varying size and internal structure; the numbers and character vary with the cycle of synthesis and discharge. The mechanism of secretion is still not clear but may involve merocrine secretion of granules, apocrine secretion or complete holocrine disintegration of the cells (see Fig. 2.6).

Apocrine activity is minimal before puberty, after which it is androgen-dependent and responsive to emotional stimuli. It is controlled by adrenergic nerves and is sensitive to adrenaline (epinephrine) and noradrenaline (norepinephrine). The secretion is initially sterile and odourless, but it undergoes bacterial decomposition to generate odorous and musky compounds, including short-chain fatty acids, and steroids such as 5α-androstenone. In many animals these are potent pheromonal signals but their role in humans is less certain.

Arrector pili muscles

The arrector pili muscles are small bundles of closely packed smooth muscle cells that form oblique links between the dermal sheaths of hair follicles and the papillary layer of the dermis (see Figs 7.1, 7.20). They show the typical features of smooth muscle cells and are separated by narrow spaces containing collagen fibres and unmyelinated noradrenergic sympathetic axons. The muscles are attached to the bulge region of the follicles by elastin fibrils, and are directed obliquely and towards the side to which the hair slopes superficially. The sebaceous gland occupies the angle between the muscle and the hair follicle: muscle contraction helps to expel the gland contents. Contraction tends to pull the hair into a more vertical position and to elevate the epidermis surrounding it into a small hillock (goose bump), dimpling the skin surface where the muscle is inserted superficially. Arrector pili muscles are absent from facial, axillary and pubic hairs, eyelashes and eyebrows, and from the hairs around the nostrils and the external acoustic meatus.

Sweat glands

The vast majority of sweat glands (**Figs 7.24–Fig. 7.25**) are classically termed eccrine, although their mode of secretion includes typical merocrine mechanisms. The glands are long, unbranched, tubular structures, each with a highly coiled, secretory portion up to 0.4 mm in diameter, situated deep in the dermis or hypodermis. From there, a narrower, straight or slightly helical ductal portion emerges (see Fig. 7.1). The walls of the duct fuse with the base of an epidermal rete peg and the lumen passes between the keratinocytes, often in a tight spiral, particularly in thick hairless skin (**Fig. 7.26**), and opens via a rounded aperture (pore) onto the skin surface (see Fig. 7.7). In thick hairless skin, sweat glands discharge along the centres of friction ridges, incidentally providing fingerprint patterns for forensic analysis. Sweat glands have an important thermoregulatory function, and their secretion enhances the grip and sensitivity of the palms and soles (Shiohara et al 2016).

Eccrine sweat glands are absent from the tympanic membrane, margins of the lips, nail bed, nipple, inner preputial surface, labia minora, penis and clitoris, all sites where apocrine glands are located. They are numerous elsewhere, their frequency ranging from 80 to over 600/cm^2, depending on position and genetic variation. The total number is estimated to be between 1.6 and 4.5 million, with the greatest density in plantar skin.

Microscopically, the secretory coil consists of a pseudostratified epithelium enclosing a lumen. Three types of cell have been described: clear cells, from which most of the secretion is derived; dark cells, which share the same lumen; and myoepithelial cells. Clear cells are approximately pyramidal in shape, and their bases rest on the basal lamina or are in contact with the myoepithelial cells. Their apical plasma membranes line lateral intercellular canaliculi that connect with the main lumen. The basolateral plasma membranes are highly folded, and interdigitate with apposed clear cells; they have the basal membrane infoldings typical of cells involved in transcytotic fluid and ion transport from the interstitial fluid to the glandular lumen. Their cytoplasm contains glycogen granules, mitochondria, rough endoplasmic reticulum and a small Golgi complex, but few other organelles. The nucleus is round and moderately euchromatic. Dark cells are pyramidal and lie closer to the lumen, such that their broad ends form its lining. Their cytoplasm contains a well-developed Golgi complex, numerous vacuoles and vesicles, and dense glycoprotein granules, which they secrete by a typical merocrine mechanism. Myoepithelial cells (see Figs 2.3–2.4) resemble those associated with secretory acini of the salivary glands and breast, and contain abundant myofilaments.

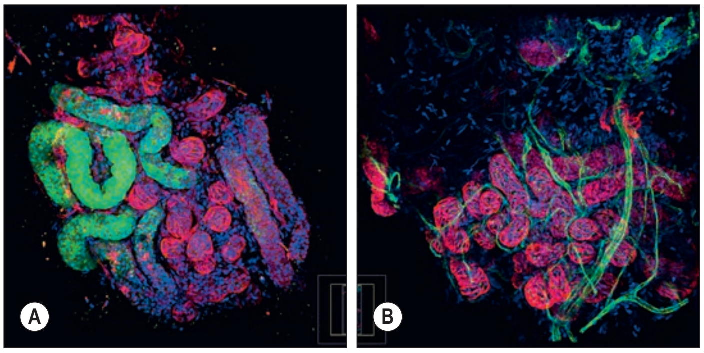

Fig. 7.25 Whole mount, 3D images of human sweat glands. **A**, The coiled secretory portion is identified by the presence of elongated myoepithelial cells labelled with anti-smooth muscle actin (red). Ducts are labelled with anti-calcium binding protein (S100) A2 (green). Nuclei are stained blue with Hoechst 33342 dye. **B**, Elongated myoepithelial cells, labelled with anti-keratin 5 (red) wrap around the coiled secretory portion of the gland. Blood vessels are labelled with anti-CD31 (green). Nuclei are stained blue, as above. (Courtesy of Dr Ryuichiro Kurata and Professor Kiyotoshi Sekiguchi, Osaka University.)

The intradermal sweat duct is composed of an outer basal layer and an inner layer of luminal cells connected by numerous desmosomes. The intraepidermal sweat duct (acrosyringium) is coiled and consists of two layers of cells, which, developmentally, are different from the surrounding keratinocytes and can be distinguished from them by the presence of keratin K19. The outer cells near the surface contain keratohyalin granules and lamellar granules, and undergo typical cornification. The inner cells, from a mid-epidermal level, contain numerous vesicles, undergo an incomplete form of cornification, and are largely shed into the lumen at the level of the cornified epidermal layer. For further details of the structure and immunocytochemical profile of sweat glands, see Kurata et al (2017).

Sweat is a clear, odourless fluid, hypotonic to tissue fluid, and contains mainly sodium and chloride ions, but also potassium, bicarbonate, calcium, urea, lactate, amino acids, immunoglobulins and other proteins. Excessive sweating can lead to salt depletion. Heavy metals and various organic compounds are eliminated in sweat. When first secreted, the fluid is similar in composition to interstitial fluid. It is modified as it passes along the duct by the action mainly of the basal cells, which resorb sodium, chloride and some water: the hormone aldosterone enhances this activity. The sweat glands are capable of producing up to 10 litres of sweat per day, in response to thermal, emotional and taste stimuli, mediated by unmyelinated sympathetic cholinergic fibres. The glands also respond to adrenaline (epinephrine). Thermoregulation is coordinated via a heat centre in the preoptic region, in and near the rostral hypothalamus, which reacts to changes in blood temperature and afferent stimuli from the skin by initiating appropriate responses such as controlling cutaneous blood supply, the rate and volume of sweat secretion (for evaporation at the surface) and shivering.

Nail apparatus

Nails (**Fig. 7.27**) are homologous with the cornified layer of the general epidermis. They consist of compacted, anucleate, keratin-filled squames in two or three horizontal layers. Ultrastructurally, the squames contain closely packed filaments that lie transversely to the direction of proximodistal growth, and are embedded in a dense protein matrix. Unlike the general epidermis, squames are not shed from the nail plate surface. A variety of mineral elements including calcium are present in nail. The hardness of nail is determined by the arrangement and cohesion of the layers of squames and their internal fibres, and not by the calcium content. Although the water content of nail is low, nail is 10 times more permeable

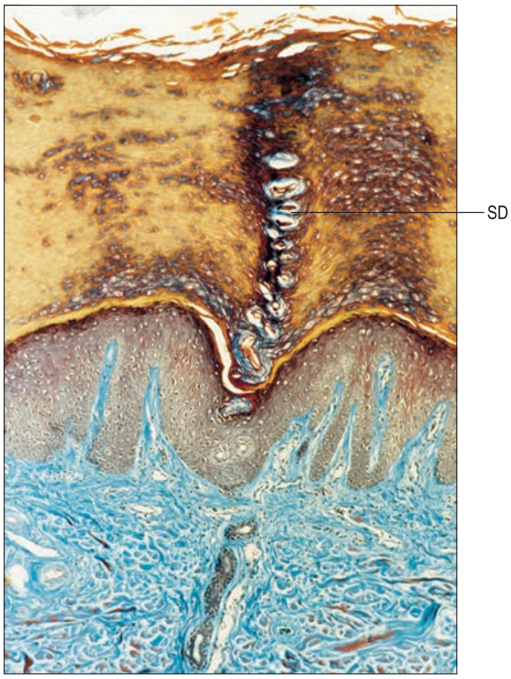

Fig. 7.26 A sweat duct in a trichrome-stained section of thick skin. The duct (SD) spirals through the dermis and epidermis, and is visible most clearly in the cornified superficial layer.

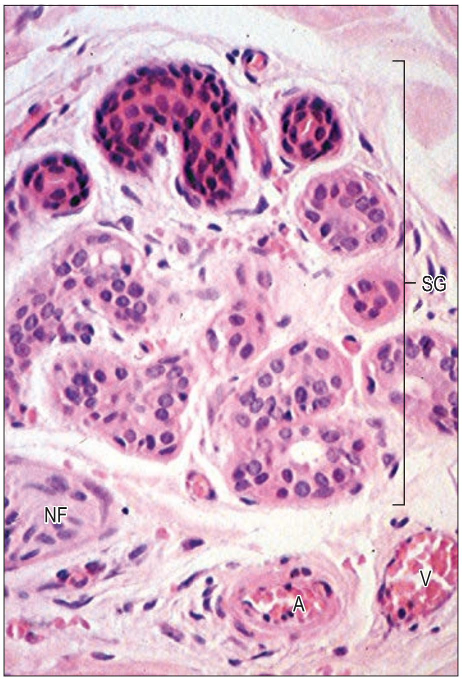

Fig. 7.24 The coiled secretory portion of a sweat gland (SG) in the reticular dermis. The deeper-stained profiles (above) are the origins of the duct. An autonomic nerve fibre (NF) and accompanying arteriole (A) and venule (V) are seen below.

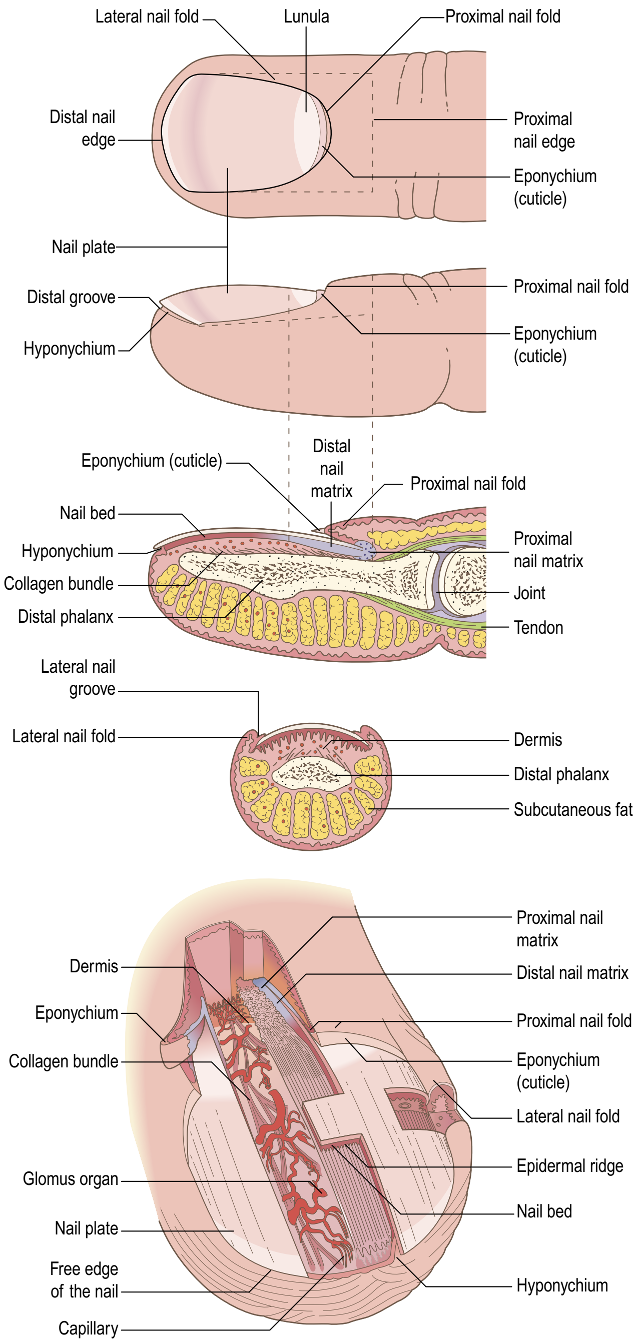

Fig. 7.27 The organization and terminology of the structures associated with a fingernail. (With permission from Paus R, Peker S 2003 Biology of hair and nails. In: Bolognia JL, Jorizzo JL, Rapini RP (eds) Dermatology. London: Mosby.)

to water than the general epidermis: the softness and elasticity of the nail plate are related to its degree of hydration.

The nail apparatus consists of the nail plate, proximal and lateral nail folds, nail matrix, nail bed and hyponychium.

Nail plate

The nail plate is embedded within the proximal and lateral nail folds. It is approximately rectangular in shape and is mostly convex in both longitudinal and transverse axes. There is considerable inter- and intra-individual variation (see Fig. 7.27). The thickness of the plate increases proximodistally from about 0.7 mm to 1.6 mm, although the terminal thickness varies between individuals. The surface of the nail plate may show fine longitudinal ridges, and its undersurface is grooved by corresponding ridges in the nail bed. Disturbances of growth pattern or disease may lead to transverse ridging or grooves. Minute trapped air bubbles may produce white flecks that move distally with the growth of the nail plate.

The nail plate arises from compacted cornified epithelial cells derived from the dorsal, intermediate and ventral nail matrices. It is densely adherent to the matrices on its undersurface but becomes a free structure distal to the onychodermal band, where it separates from the nail bed. The dorsal aspect of the nail plate originates from the more proximal regions of the germinal matrix, i.e. dorsal and intermediate matrices, whereas the deeper, palmar (volar) aspect of the plate originates from the ventral matrix.

Nail folds

The sides of the nail plate are bordered by the lateral nail folds, which are continuous with the proximal fold (see Fig. 7.27). They are bounded by the attachment of the skin to the lateral aspect of the distal phalanx margin and the lateral nail. The proximal nail fold provides the visible proximal border to the nail apparatus. It consists of superficial and deep epidermal layers separated by a core of dermis. The epidermis of the superficial layer lacks hair follicles and epidermal ridges, and its cornified distal margin extends over the nail plate as the cuticle or eponychium. The deep layer merges with the nail matrix. The eponychium is bounded by the fascial attachment of the skin to the base of the distal phalanx, distal to the insertion of the extensor tendon, and its distal free edge. It adheres to the dorsal aspect of the nail plate and overlies the root of the nail.

Nail matrix

The nail matrix is the main source of the nail plate and can be subdivided into three parts. Proximally, it is defined as the palmar or volar surface (undersurface) of the proximal nail fold. The intermediate matrix (germinal matrix) starts where the dorsal matrix folds back on itself and extends as far as the distal portion of the lunula (lunule). The ventral matrix (sterile matrix) is the remainder of the nail bed; it starts at the distal border of the lunula and ends at the hyponychium.

The matrix epithelium consists of typical basal and prickle layer keratinocytes, among which are scattered melanocytes and Langerhans cells. Cornified cells of the dorsal and ventral aspects of the matrix are steadily extruded distally to form the nail plate. The proximal 50% of the nail matrix contributes approximately 80% of the nail plate. This process continues into the nail bed at the distal edge of the lunula, which is formed where the distal portion of the ventral matrix underlies the nail plate.

The lunula is pale, opaque and convex, and is most prominent in the thumb nail. It is not known why the lunula is so pale compared with the more distal translucent pink nail bed. The lack of colour may reflect the thickness of the epidermis in the lunula and/or a paucity of capillaries in the dermis of the lunula.

Nail bed

The epidermis of the nail bed extends from the distal margin of the lunula to the hyponychium. The distal margin of the nail bed, which is the point where the nail plate becomes free of the nail bed, is called the onychodermal band. The surface of the nail bed is ridged and grooved longitudinally, corresponding to a similar pattern on the undersurface of the nail plate. This arrangement results in a tight interlocking between the nail plate and the underlying nail bed, protecting against microbial invasion and the collection of debris underneath the nail. The epidermis of the nail bed is thin and lacks a granular layer. It consists of 2–3 layers of nucleated cells that lack keratohyalin granules, and a thin cornified layer that moves distally with the growing nail plate. It contains an occasional sweat gland distally.

The dermis of the nail bed is anchored to the periosteum of the distal phalanx without an underlying subcutaneous layer. It forms a tight compartment, which means that infections involving the nail bed or an increase in pressure, e.g. resulting from a haematoma, may cause severe pain that may be relieved by the removal of part or all of the nail plate. The dermis of the nail bed is richly vascularized. The blood vessels are arranged longitudinally and display numerous glomus bodies, which are encapsulated arteriovenous anastomoses involved in the physiological control of peripheral blood flow in relation to temperature. The dermis of the nail bed is well innervated by numerous sensory nerve endings, including Merkel endings and Meissner's corpuscles. Nail bed cells differentiate towards the nail plate and contribute to its thickness ventrally.

Hyponychium

The hyponychium is the area under the free nail between the onychodermal band proximally and the distal groove. It is an epidermal ridge that demarcates the junction between the finger pulp and the subungual structures.

Nail growth

Nail growth is determined by the turnover rate of the matrix cells, which varies with digit, age, environmental temperature and season, time of day, nutritional status, trauma and various pathologies. Generally, the rate of growth is related to the length of the digit, being fastest in the middle finger of the hand (approximately 0.1 mm per day) and slowest in the little finger. Fingernails grow 3–4 times faster than toenails, more quickly in summer than in winter, and faster in the young than in the old. A fingernail grows out in about 6 months, whereas a toenail is replaced, on average, in 18 months.

VASCULAR SUPPLY, LYMPHATIC DRAINAGE AND INNERVATION

Vascular supply and lymphatic drainage

Cutaneous blood flow amounts to approximately 5% of the cardiac output. The cutaneous circulation has an important thermoregulatory function, and is organized so that its capacity can be rapidly increased or decreased by as much as 20 times, in response to a need to lose or conserve body heat. The ability to control skin blood flow decreases with ageing, making older adults less able to thermoregulate adequately. Lifestyle factors, such as physical activity, diet and smoking, might interact with the ageing process to modulate 'normal' age-associated changes in the cutaneous microcirculation.

The blood supply to the skin originates from the direct cutaneous, musculocutaneous and fasciocutaneous systems. The direct cutaneous system of vessels is derived from the main arterial trunks and accompanying veins. These vessels course in the subcutaneous fat parallel to the skin surface and are confined to certain areas of the body, e.g. the supraorbital artery, the superficial circumflex iliac artery and the dorsalis pedis artery. The musculocutaneous perforators arise from the intramuscular vasculature, pass through the surface of the muscle, and pierce the deep fascia to reach the skin by spreading out in the subcutaneous tissues. The fasciocutaneous system consists of perforating branches from deeply located vessels (deep to the deep fascia) that pass along intermuscular septa and then fan out at the level of the deep fascia to reach the skin. Examples include the fasciocutaneous perforating vessels from the radial and ulnar arteries.

The direct cutaneous vessels, musculocutaneous perforators and fasciocutaneous perforators each contribute to six anastomosing horizontal reticular plexuses of arterioles (**Fig. 7.28**), which have vascular connections between them and which ultimately provide the blood supply to the skin. Three plexuses are located in the skin itself and supply all elements including the sweat glands and pilosebaceous units. The subpapillary plexus is located at the junction of the papillary and reticular layers of the dermis and gives off small branches that form perpendicular capillary loops in the dermal papillae (usually one loop per papilla) (see Figs 7.1, 7.4; **Fig. 7.29**). The reticular dermal plexus is located in the middle portion of the dermis and is primarily venous. The deep dermal plexus is located in the deepest part of the reticular dermis and on the undersurface of the dermis. The close association between arteriolar and venous plexuses allows countercurrent heat exchange between bloods at different temperatures.

The remaining three plexuses are the subcutaneous plexus, and two plexuses associated with the deep fascia. The deep fascia has a plexus on its deep surface and a more extensive plexus superficially, an arrangement that is much more pronounced in the limbs than it is in the trunk.

The general structure and arrangement of the microvasculature is described in detail in Chapter 6 and so only features particular to skin will be considered here. In the deeper layers of the dermis, arteriovenous anastomoses are common, particularly in the extremities (hands, feet, ears, lips, nose), where vessels are surrounded by thick muscular coats. Under autonomic vasomotor control, these vascular shunts, when relaxed, divert blood away from the superficial plexus and so reduce heat loss, while at the same time ensuring maintenance of some deep cutaneous circulation and preventing anoxia of structures such as nerves. Extensive capillary anastomoses are present. Generally, cutaneous blood flow is regulated according to thermoregulatory need and also, in some areas of the body, according to emotional state. In very cold conditions, the peripheral circulation is greatly reduced by vasoconstriction, but intermittent spontaneous vasodilation results in periodic increases in temperature that prevent cooling to the level at which frostbite might occur.

The lymphatics of the skin, as elsewhere, are small terminal vessels that collect interstitial fluid and macromolecules for return to the circulation via larger vessels. They also convey lymphocytes, Langerhans cells and macrophages to regional lymph nodes. They begin as blind-ended, endothelial-lined tubes or loops just below the papillary dermis. These drain into a superficial plexus below the subpapillary venous plexus, which drains via collecting vessels into a deeper plexus at the junction of the reticular dermis and subcutis, and this, in turn, drains into larger subcutaneous channels.

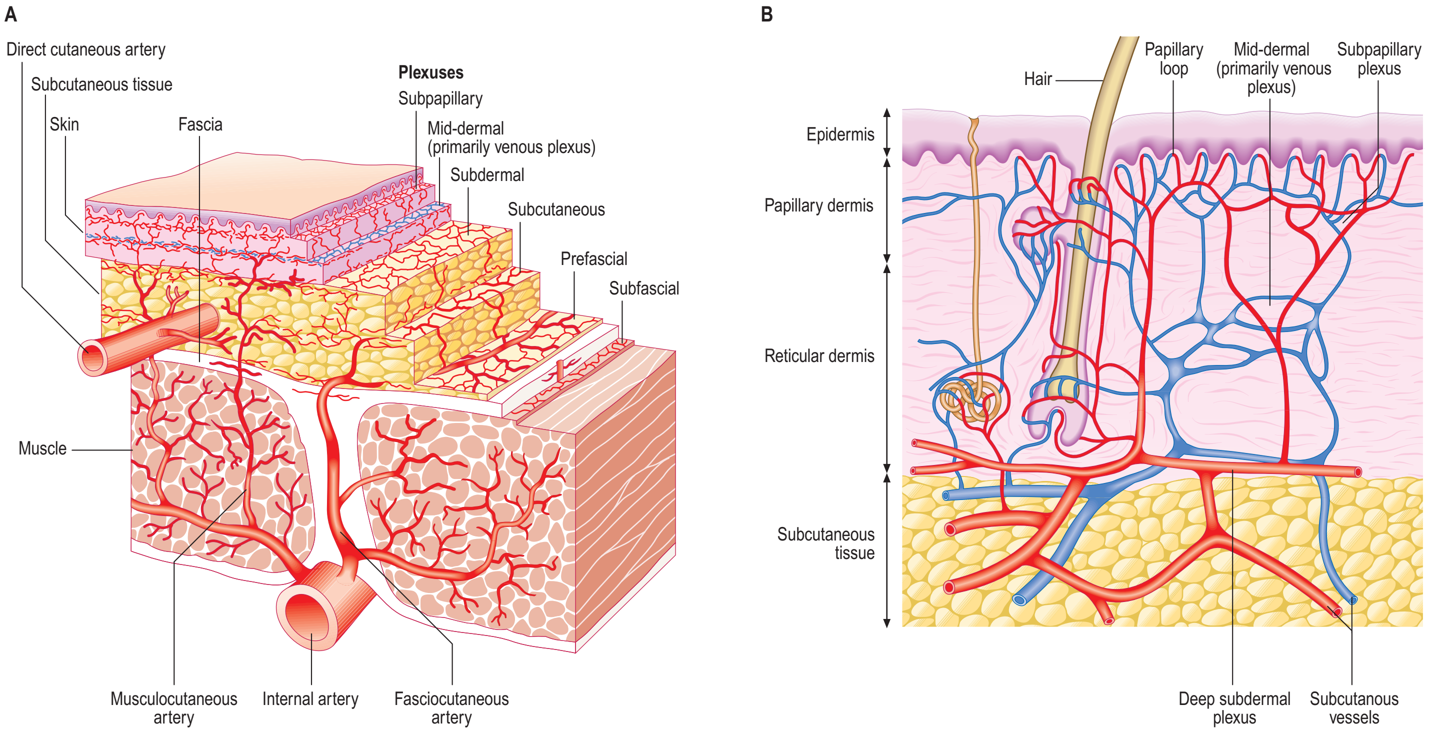

Fig. 7.28 Vascular supply to the skin. **A**, Note the various horizontal plexuses fed by direct cutaneous, fasciocutaneous and musculocutaneous arteries. **B**, Higher magnification of vascular supply. (A, Adapted with permission from McCarthy JG (ed) 1990 Plastic Surgery, Vol 1: ch. 9. Philadelphia: Saunders. B, Adapted with permission from Cormack GC, Lamberty BGH 1994 The Arterial Anatomy of Skin Flaps, 2nd ed. Edinburgh: Churchill Livingstone.)

Genetic keratin disorders (Knöbel et al 2015) may lead to nail dystrophies such as pachyonychia congenita, where the nails become grossly thickened. Germline mutations in the *RSPO4* gene, which encodes R-spondin 4, have been shown to cause recessive anonychia (absence of all fingernails and toenails). Mutations in the *FZD6* gene, which encodes the Wnt receptor protein frizzled 6, have been shown to underlie the molecular basis of autosomal recessive nail dysplasia, as well as twenty-nail dystrophy (a condition that affects the nails of all the fingers and toes).

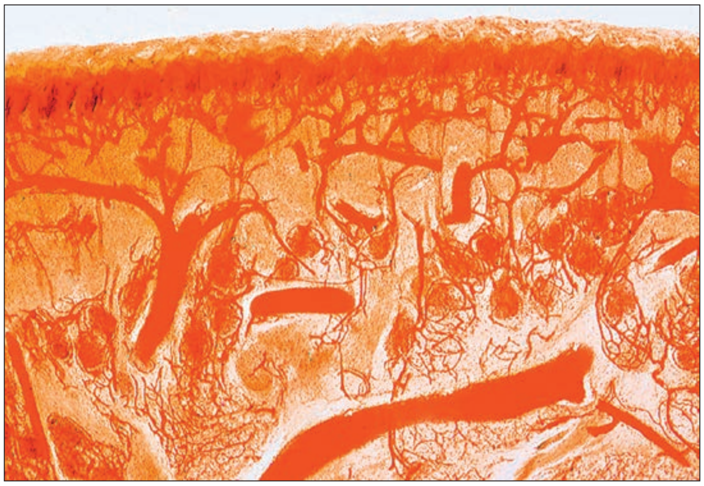

Fig. 7.29 A thick vertical section through palmar skin: the arteries, arterioles and capillaries have been injected with red gelatin to demonstrate the pattern of dermal vascularization. At the base of the dermis a broad, flat arterial plexus supplies a more superficial papillary plexus, which in turn gives off capillary loops that enter the dermal papillae.

Innervation

Skin is a richly innervated, major sensory organ. Information about the external environment is relayed through receptors responsive to various stimuli, whether mechanical (rapid or sustained touch, pressure, vibration, stretching, bending of hairs, etc.), thermal (hot or cold) or noxious (perceived as itching, discomfort or pain). Pacinian corpuscles detect deep pressure and vibrational sensation, and are located deep in the dermis or in the hypodermis, particularly of the digits. Meissner's corpuscles are rapidly adapting mechanoreceptors found in hairy and hairless skin in dermal papillae close to the dermal–epidermal junction. They are responsible for sensing light touch, and are numerous in the finger pads, being particularly suited to detecting shape and texture during active exploratory touch (Ch. 3).

Afferent sensory nerves may be myelinated or unmyelinated and are derived from neuronal cell bodies in cranial or spinal sensory ganglia. On reaching the dermis, nerve fasciculi branch extensively to form a deep reticular plexus that innervates much of the dermis, including most sweat glands, hair follicles and the larger arterioles. Many small fasciculi pass from this plexus to ramify in another superficial papillary plexus at the junction between the reticular and papillary layers of the dermis. Branches from this pass superficially into the papillary layer, ramifying horizontally and vertically, and terminate either in relation to encapsulated receptors, or as terminals reaching the level of the basal lamina. In some instances, they enter the epidermis as free endings that are responsive to light pressure and touch sensation or to nociceptive stimuli. As these fasciculi terminate, they lose their epineurial and perineurial sheaths, leaving the Schwann cell–axonal complexes or naked axons enveloped only by basal lamina, in direct contact with the matrix. These naked distal axonal terminals may be vulnerable to pathogens entering via a skin abrasion. The structure and classification of sensory endings are described in detail on p. 62.

The segmental arrangement of the spinal nerves is reflected in the sensory supply of the skin: a dermatome is the area supplied by all the cutaneous branches of an individual spinal nerve through its dorsal and ventral rami (see Fig. 24.10). Typically, dermatomes extend round the body from the posterior to the anterior median line, the upper half of each zone being supplemented by the nerve above, the lower half by the nerve below. Dermatomes of adjacent spinal nerves overlap markedly, particularly in the segments least affected by development of the limbs. In marked contrast, in the upper and lower limbs, discontinuous dermatomes meet along discrete sensory boundaries (axial lines) (Ladak et al 2014).

Efferent autonomic fibres are unmyelinated and can be either noradrenergic or cholinergic. They innervate the arterioles, arrector pili muscles, and the myoepithelial cells of sweat and apocrine glands. In the scrotum, labia minora, perineal skin and nipples they also supply the smooth muscle fasciculi of the dermis and adjacent connective tissue. Except in the nipples and genital area, the activity of the autonomic efferent nerves is mainly concerned with regulation of heat loss by vasodilation and vasoconstriction, sweat production and pilo-erection (although this is a minor function in humans).

DEVELOPMENT OF SKIN AND SKIN APPENDAGES

The skin develops from the surface ectoderm and its underlying mesenchyme. The surface ectoderm gives rise to the epidermis and its appendages such as the pilosebaceous units, sweat glands and nail units. Interactions between ectoderm and mesenchyme give rise to the oral and nasal epithelia, as well as teeth. Ectodermal cells differentiate mainly into the keratinocytes and probably Merkel cells. Melanocytes are derived from the neural crest while Langerhans cells and lymphocytes originate from the bone marrow.

The dermis is derived from the somatopleuric mesenchyme (in the limbs and trunk), and possibly the somitic mesenchyme (covering the epaxial musculature), and from the neural crest (in the head). Angiogenic mesenchyme gives rise to the blood vessels of the dermis. Nerves and associated Schwann cells, which are derived from the neural crest, enter and traverse the dermis during development.

Epidermis and appendages

General (interfollicular) epidermis

In postfertilization weeks 4–5, embryonic skin consists of a single layer of ectodermal cells overlying a mesenchyme containing cells of stellate dendritic appearance interconnected by slender processes and sparsely distributed in a loosely arranged microfibrillar matrix (Fig. 7.30). By postfertilization week 7, two epidermal cell layers are present and the highly cellular nature of the developing dermis, containing fibroblasts and stellate cells, is evident (Fig. 7.31). The interface between ectoderm and mesenchyme, known as the basement membrane zone (BMZ), is an important site of mutual interactions on which the maintenance of the two tissues depends, both in prenatal and postnatal life. Ectodermal cells, which characteristically contain glycogen deposits, contact each other at gap and tight junctions (occluding junctions, zonae occludentes). The layer so formed soon develops into a bilaminar epithelium, and desmosomes also appear. The basal germinative layer gives rise to the postnatal epidermis, and the superficial layer to the periderm, a transient layer confined to fetal life. The periderm maintains itself, expresses different keratin polypeptides, and grows by the mitotic activity of its own cells, independent of those of the germinative layer. Originally flattened, the periderm cells increase in depth; the central area containing the nucleus becomes elevated and projects as a globular elevation towards the amniotic cavity (Fig. 7.32). The plasma membrane develops numerous surface microvilli with an extraneous coat of glycosaminoglycans, and cytoplasmic vesicles become prominent deep to it. These developments reach a peak between postmenstrual weeks 12–18, at which time the periderm is a major source of the amniotic fluid to which it may contribute glucose; it also has an absorptive function. From about postmenstrual week 20 onwards, the globular protrusions become undermined and pinched off to float free in the amniotic fluid. The now-flattened periderm cells undergo terminal differentiation to form a temporary protective layer for the underlying developing epidermis, against an amniotic fluid of changing composition as a result of the accumulation of products of fetal renal excretion. Up to parturition, the periderm squames continue to be cast off into the amniotic fluid and they contribute to the vernix caseosa, a layer of cellular debris that covers the fetal skin at birth.

Proliferation in the germinative layer leads to a stratified appearance with successive layers of intermediate cells between it and the periderm. From an early stage, cells of all layers are packed with glycogen granules. Differentiation of these layers is not synchronous throughout all regions of the developing skin, being more advanced cranially than caudally, and progressing on the body from the mid-axillary line ventrally. Reduction in glycogen content of the cells is associated with a shift towards biosynthetic activity connected with terminal (cornifying) differentiation, manifested by the presence of different enzymes and expression of keratins. Simple epithelial keratins present from before implantation (K8 and K18) are replaced by typical keratinocyte basal cell keratins (K5 and K14), followed in the first suprabasal cell layer by those of higher molecular weight associated with differentiation (K1 and K10) at postfertilization weeks 10–12. This is soon followed by the expression of profilaggrin and filaggrin, and the appearance of keratohyalin granules among filamentous bundles of the uppermost intermediate layer cells at approximately postmenstrual week 20. The first fully differentiated keratinocytes appear shortly afterwards. By postmenstrual weeks 24–26, a definite cornified layer exists in some areas, and by approximately postmenstrual week 30, apart from some residual glycogen in intermediate cells, the interfollicular epidermis is essentially similar to its postnatal counterpart.

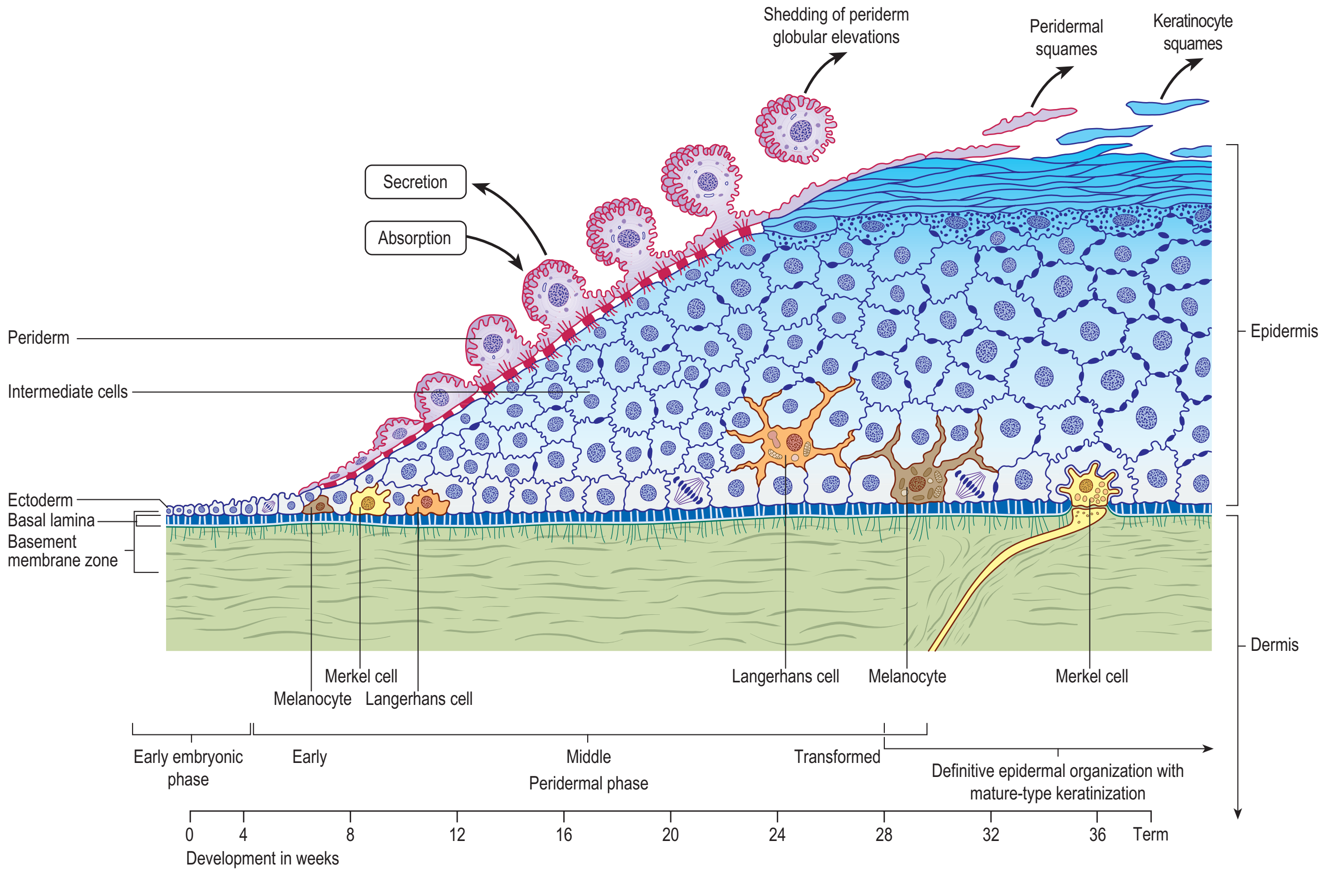
Shedding of periderm globular elevations
Peridermal squames
Keratinocyte squames
Secretion
Absorption
Periderm
Intermediate cells
Epidermis
Ectoderm
Basal lamina
Basement membrane zone
Dermis
Merkel cell
Melanocyte
Langerhans cell
Langerhans cell
Melanocyte
Merkel cell
Early embryonic phase
Early
Middle
Peridermal phase
Transformed
Definitive epidermal organization with mature-type keratinization
0
4
8
12
16
20
24
28
32
36
Term
Development in weeks

Fig. 7.30 Development of the skin.

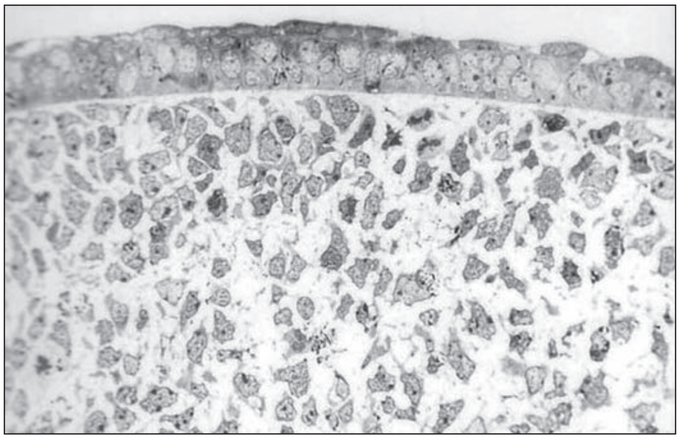

Fig. 7.31 Light microscopy of human embryonic skin at postfertilization week 7, revealing a flat two-cell layer epidermis overlying a very cellular dermis containing numerous fibroblasts and stellate cells. (Courtesy of Dr James McMillan, St John's Institute of Dermatology.)

Non-keratinocytes are present in developing epidermis from about postfertilization week 8. Langerhans cells can be seen in the epidermis by postfertilization weeks 5–6 and are fully differentiated by postfertilization weeks 12–14. Their numbers increase at least partially by mitotic division *in situ*, but at 6 months are only 10–20% of those in the adult. It is not known if Langerhans cells function in immune surveillance in fetal skin. Melanocytes are present in the bilaminar epidermis of cephalic regions as early as postfertilization week 8. By postfertilization weeks 12–14 they can reach a density of 2300 per mm^2, reducing to 800 per mm^2 just before birth. Keratinocytes regulate the final ratio between themselves and melanocytes via growth factors, cell-surface molecules and other signals. Fetal melanocytes produce melanized melanosomes and transfer them to keratinocytes. This is an intrinsic activity independent of UV irradiation and suggests that melanin has functions other than photoprotection.

Merkel cells begin to appear in the epidermis of the palm and sole of the foot between postfertilization weeks 8 and 12, and later in association with some hairs and with dermal axonal–Schwann cell complexes.

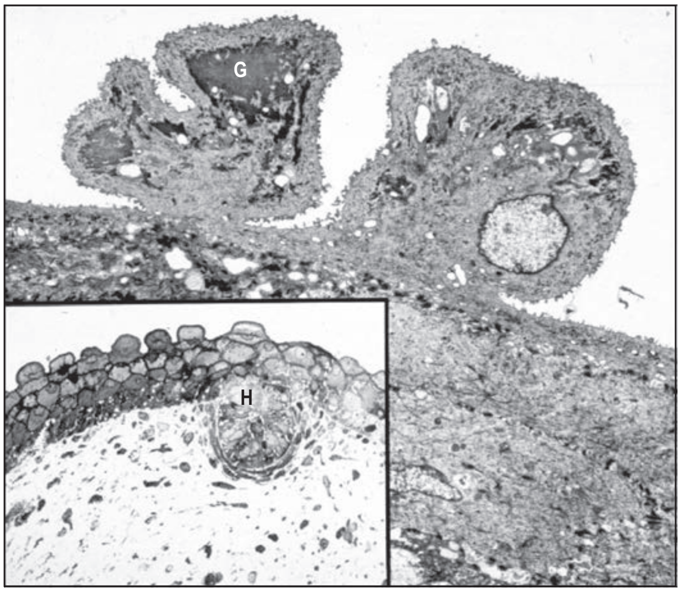

Fig. 7.32 Transmission electron micrograph of human fetal skin at postmenstrual week 21, showing the outer periderm layer (cell contents include glycogen, G); the inset shows early human hair follicle formation with a hair peg (H) projecting from the epidermis and extending into the dermis. The pale area above each photo contains amniotic fluid. (Courtesy of Dr James McMillan, St John's Institute of Dermatology.)

Pilosebaceous unit

Pilosebaceous units develop in a cranio–caudal direction from about postfertilization week 9, first in the regions of the eyebrows, lips and chin. The hair placode is a collection of cells in the basal layer of the epidermis and develops adjacent to a local concentration of mesenchymal cells, which will eventually become the dermal papilla. Further proliferation and elongation of the cells lead to a hair germ, which protrudes downwards into the mesenchyme in association with the primitive dermal papilla around postmenstrual weeks 13–15. The hair germ becomes a hair peg as it migrates downwards within the developing skin, and when its bulbous lower portion envelops the dermal papilla it becomes known as a bulbous peg. Melanocytes are individually present at the hair peg stage, and abundantly so and quite active in the bulbous peg. At this stage (approximately postmenstrual week 15), two or three swellings appear on the posterior wall. The uppermost is the rudiment of the apocrine gland (present only in some follicles), the middle forms the sebaceous gland and the lower swelling is the bulb, to which the arrector pili muscle (arising from underlying mesenchyme) later becomes attached. The cells of the lowermost region of the bulb, the matrix, divide actively and produce a pointed hair cone. This grows upwards to canalize a developing hair tract, along which the fully formed hair, derived by further differentiation of cells advancing from the matrix, reaches the surface at approximately postmenstrual week 18. The hair of the scalp lengthens during postmenstrual weeks 25–28, and the eyebrow hairs and eyelashes are well developed.

Sebaceous glands develop independently of hair follicles in the nostrils, eyelids (as tarsal glands) and the anal region. Apocrine sweat glands are formed at the same time as eccrine (merocrine) sweat glands and are at first widely distributed over the body. Their number diminishes from about postmenstrual week 20, producing the distribution seen in adult skin, and they become active at this time. The sebum that is created blends with the desquamated epidermal cells to form a cheesy covering over the skin, the vernix caseosa, which is usually considered to protect the skin from maceration by the amniotic fluid.

Hairs produced prenatally are called lanugo hairs, which are short and downy, lack a medulla, and in certain parts of the body are arranged in a vortex-like manner into tracts (Domagala et al 2017). During postmenstrual weeks 21–24 (6 months), the lanugo darkens, the vernix caseosa is more abundant and the skin becomes markedly wrinkled. Throughout the remaining postmenstrual weeks, there is a progressive loss of lanugo, except for the hairs on the eyelids (eyelashes), eyebrows and scalp. Just prior to birth, lanugo hairs are replaced by vellus hairs, and these are replaced in turn by intermediate hairs, which are the predominant type until puberty. New follicles do not develop in postnatal skin.

Eccrine sweat glands

Eccrine (merocrine) sweat glands are one type of sudoriferous gland. Sweat gland rudiments appear late in the first trimester as cell buds associated with the primary epidermal ridges of the finger and toe pads of the terminal segments of the digits. They elongate into the dermis and by postmenstrual week 16 the lower portion begins to form the secretory coil; secretory and myoepithelial cells are present within the secretory coil by postmenstrual week 22. The solid cord of cells connecting the coil to the epidermis becomes the intradermal duct, and the lumina of both are formed by dissolution of desmosomal contacts between the cells. The intraepidermal duct is foreshadowed by a column of concentrically arranged inner and outer cells within which a lumen is formed that opens on the surface at postmenstrual week 22. As with hair follicles, no new eccrine sweat glands develop postnatally. Emotional sweating occurs in preterm infants from 29 postmenstrual weeks.

Epidermal ridges

The primary epidermal ridges develop as regularly spaced, small downgrowths of epidermal cells separated by corresponding dermal ridges during the second and third months of gestation. From postmenstrual week 20, secondary ridges develop; the pattern becomes evident on the surface and is finalized through further remodelling postnatally.

Nails

Fields of proliferative ectoderm appear on the tips of the terminal segments of the digits. They progressively reach a dorsal position, where, at approximately postfertilization week 9, a flattened nail field limited by proximal, distal and lateral nail grooves is apparent. The nail field ultimately forms the nail bed, and the primordium of the nail is formed of a wedge of cells that grows diagonally, proximally and deeply into the mesenchyme from the proximal groove towards the underlying terminal phalanx. The deeper cells of this wedge form the primordium of the matrix, which gives rise to the nail plate. The latter emerges from under the now proximal nail fold at about postmenstrual week 14 and grows distally over an already keratinized nail bed. The nail matrix is usually considered to have dorsal and ventral (intermediate) components, but there are conflicting opinions as to the extent to which each contributes to the nail, both in ontogeny and postnatally. It is generally agreed that the ventral matrix contributes the major part.

At postmenstrual week 20, the nail plate entirely covers the nail field (nail bed), now limited distally by a distal ridge, which, when the plate projects beyond the tip, becomes the hyponychium beneath it. At birth, the microstructure of the main nail unit components is similar to that postnatally.

Dermis

The embryonic dermis is more cellular than the adult dermis, and many of these mesenchymal cells are involved in signalling pathways that regulate ectodermal differentiation. The mesenchymal cells underlying the surface ectoderm and early bi- and trilaminar epidermis contact each other by slender processes to form an intercommunicating network. They secrete a matrix that is rich in ions, water and macromolecules, proteoglycan/glycosaminoglycans, fibronectin, collagenous proteins of various types and elastin. Further development of these intrinsic components involves the differentiation of individual cell types, fibroblasts, endothelial cells, mast cells and the assembly of matrix components into organized fibrillar collagen fibres and elastic fibres. During embryogenesis, the matrix is heterogeneous with regard to its biochemical and macromolecular components. The main glycosaminoglycans of embryonic and fetal skin are glycuronic acid and dermatan sulphate. Types I, III, V and VI collagens are distributed more or less uniformly, regardless of fetal age, with some local concentrations of type III and V collagens, the levels of which are higher than in postnatal skin. Collagens of types IV and VII are found predominantly in the BMZ.

The progressive morphological differentiation of the dermis involves its separation from the subcutis at about the end of the first trimester; changes in the composition and size of collagen fibrils and their organization into bundles, amongst which cells become relatively fewer; downgrowth of epidermal appendages; the organization of nervous and vascular plexuses; and the relatively late appearance of elastic networks. The papillary and reticular regions are present as early as postmenstrual week 14 and the formation of the two layers of the dermis could be the result of two lineages of dermal fibroblasts (Driskell et al 2013). One lineage forms the papillary dermis and the dermal papillae that regulate hair follicle growth and arrector pili muscles, while the second fibroblast lineage forms the reticular dermis and the underlying subcutis.

Vascular supply and lymphatic drainage

The dermal vasculature is generally thought to be developed *in situ* by the transformation of angiogenic mesenchymal cells. Closed channels lined with endothelium and containing nucleated red cells are present by about postfertilization week 6 underneath the ectoderm, and by postfertilization week 8 are arranged in a single plane parallel to the epidermis: they ultimately form the subpapillary plexus. A second, deeper horizontal plexus is evident by postmenstrual weeks 12–13. Both plexuses extend by budding and give rise to the final patterns of arterioles, venules and capillaries that are established shortly after birth. Pericytes also develop from mesenchymal cells. Lymphatic vessels are formed by mesenchymal cells, which become organized to enclose pools of proteinaceous fluid leaking from the developing capillaries.

Innervation

Sensory cutaneous nerves (axons and Schwann cells) are derived from the neural crest (via dorsal root and cranial sensory ganglia). Motor fibres to vessels and glands arise from postganglionic neurones in sympathetic ganglia. As individual parts of the embryo grow, the nerves grow and lengthen with them. Small axons are present superficially at a stage when the epidermis is bilaminar. By postfertilization week 8, a functioning cutaneous plexus is already present, and by about postmenstrual week 16, the dermal plexuses are richly developed and Meissner and Pacinian corpuscles have appeared.

Epithelial–mesenchymal interactions in developing skin

Epidermal–mesenchymal (dermal) interactions at the BMZ occur during development and throughout life. At the ectodermal stage, the BMZ consists of the basal plasma membrane of an ectodermal cell, paralleled on its cytoplasmic side by various cytoskeletal filaments, and beneath it by a layer (0.1–0.2 μm) of microfibrillar amorphous material deposited by the cell. At the bilaminar stage, a continuous lamina densa is present, separated from the basal plasma membrane by a lamina lucida traversed by loosely fibrillar material; similar filaments extend from the lamina densa into the mesenchymal matrix.

Hemidesmosomes (see Fig. 1.27C) begin to appear at postfertilization week 8 as stratification begins, and anchoring fibrils appear at postfertilization weeks 9–10. By the end of the first trimester, the basic morphology of the interfollicular BMZ is essentially similar to that of the postnatal BMZ.

Laminin and type IV collagen are present in the developing basal lamina at postfertilization week 6; bullous pemphigoid antigen (BPAG, in hemidesmosomes) and anchoring fibril proteins are expressed later. These immunocytochemical and morphological observations are of importance for the prenatal diagnosis of genetically determined diseases such as epidermolysis bullosa. The basal lamina provides a physical supporting substrate and attachment for the developing epidermis, and is thought to be selectively permeable to macromolecules and soluble factors regulating epidermal–dermal morphogenetic interactions. For details of the conserved signalling pathways operating in the development of skin, see Driskell et al (2013) and Veltri et al (2017).

Neonatal growth

The surface area of the skin increases with growth. It is estimated that the surface area of a premature neonate weighing 1505 g is approximately 1266 cm^2, whereas a neonate of 2980 g has a surface area of 2129 cm^2. The skin of the neonate is thinner than that of older infants and children: it cornifies over a period of 2–3 weeks, which provides protection. In the premature infant the even thinner epidermal layer allows absorption of a variety of substances such as chlorhexidine and permits a significantly higher transepidermal water loss than occurs in full-term neonates.

At birth the skin is richly vascularized by a dense subepidermal plexus. The mature pattern of capillary loops and the subpapillary venous plexus is not present but it develops as a result of capillary budding with migration of endothelia at some sites and the absorption of vessels from other sites. Some regions mature faster than others. With the exception of the palmar and plantar skin and nail beds, the skin of the neonate has almost no papillary loops, unlike the adult (Fig. 7.28B). Instead, it has a disordered capillary network, which becomes more orderly from postnatal week 2 when papillary loops appear; defined loops are not present until postnatal weeks 4–5, and all areas possess loops by postnatal weeks 14–17.

Neonates exhibit a regional sequence of eccrine gland maturation. The earliest sweating occurs on the forehead, followed by the chest, upper arm and, later, more caudal areas. Acceleration of maturation of the sweating response occurs in premature babies after delivery. The postnatal maturation of skin and differences from adult skin are given in Stamatas et al (2011) and Liu et al (2018).

The skin microbiome rapidly becomes established in the neonate, although in hospitalized preterm infants the range of species is lower and shaped by the microbiota acquired from the hospital environment (Pammi et al 2017, Younge et al 2018).

NATURAL SKIN CREASES AND WRINKLES

Skin lines

The surface of the skin and its deeper structures show various linear markings, seen as grooves, raised areas and preferred directions of stretching.

Surface pattern lines, tension lines and skin creases

Externally visible skin lines are related to various patterns of epidermal creasing, ridge formation, scarring and pigmentation. A simple lattice pattern of lines occurs on all major areas of the body except the thick palmar and plantar skin. The lattice pattern typically consists of polygons formed by relatively deep primary creases visible to the naked eye that are irregularly divided by finer secondary creases into triangular areas (Fig. 7.33). These, in turn, are further subdivided by tertiary creases limited to the cornified layer of the epidermis and, finally, at the microscopic level, by quaternary lines, which are simply the outlines of individual squames (see Fig. 7.7). Apart from the quaternary lines, all the others increase the surface area of the skin, permit considerable stretching and recoil, and distribute stresses more evenly. Details of the patterns vary according to the region of the body, e.g. primary creases radiate from the hair follicles on the cheek, form hexagons on the scalp, and form parallelograms on the calf and thigh. There is a relationship between the type of pattern and the range of local skin extensibility.

Wrinkle lines

Wrinkle lines are caused by the contraction of underlying muscles and are usually perpendicular to their axis of shortening. On the face they are known as lines of expression; they become permanent with age as the skin progressively loses its elasticity. Occupational lines are creases produced by repeated muscular contractions associated with particular trades or skills. Contour lines are lines of division at junctions of body planes, e.g. the cheek with the nose. Lines of dependency are produced by the effect of gravity on loose skin or fatty tissue, e.g. the creases associated with the pendulous fold beneath the chin in older age.

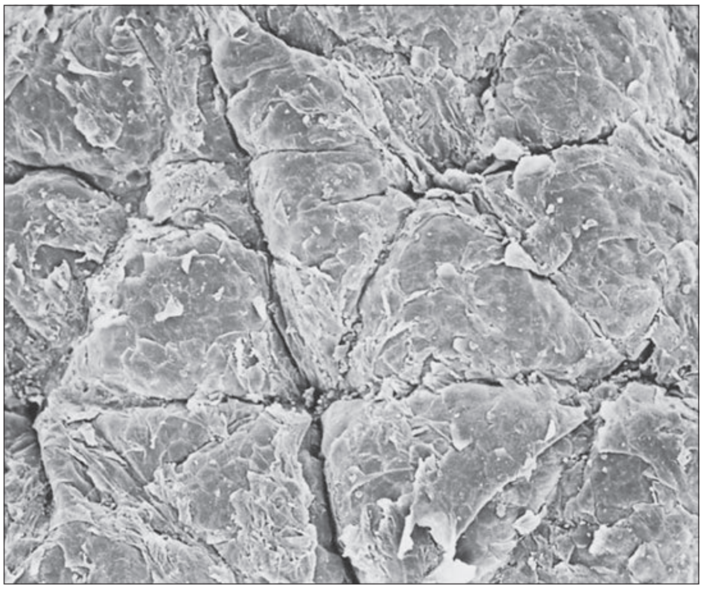

Fig. 7.33 A scanning electron micrograph of the surface of thin skin of the back, showing an interlacing network of fine creases and predominantly triangular areas between them.

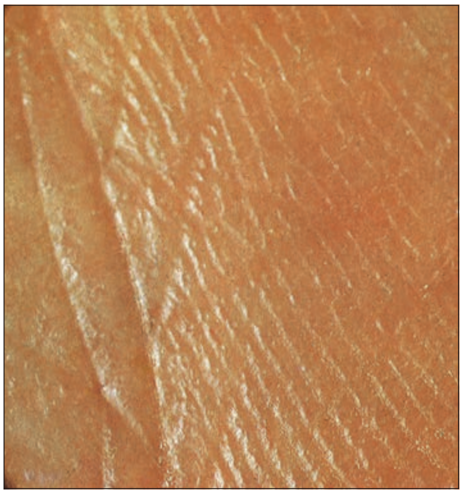

Fig. 7.34 The surface of hairless skin from the palm of the hand, showing epidermal friction (papillary) ridges and larger flexure lines (left).

Flexure (joint) lines

Flexure (joint) lines are major markings found in the vicinity of synovial joints, where the skin is attached strongly to the underlying deep fascia (Fig. 7.34). They are conspicuous on the flexor surfaces of the palms, soles and digits: in combination with associated skin folds they facilitate movement. The skin lines do not necessarily coincide with the associated underlying joint line. For example, the flexure lines demarcating the extended fingers from the palm lie approximately 12 mm distal to the metacarpophalangeal joints, the positions of which are more closely related to the distal palmar crease. The patterns of flexure lines on the palms and soles may vary and are, to some extent, genetically determined.

Papillary ridges

Papillary ridges are confined to the palmar and plantar skin and the flexor surfaces of the digits, where they form narrow parallel or curved arrays separated by narrow furrows (Figs 7.35–7.36). The apertures of sweat ducts open at regular intervals along the summit of each ridge. The epidermal ridges correspond to an underlying interlocking pattern of dermal papillae, an arrangement that helps to anchor the two layers firmly together. The pattern of dermal papillae determines the early development of the epidermal ridges. This arrangement is stable

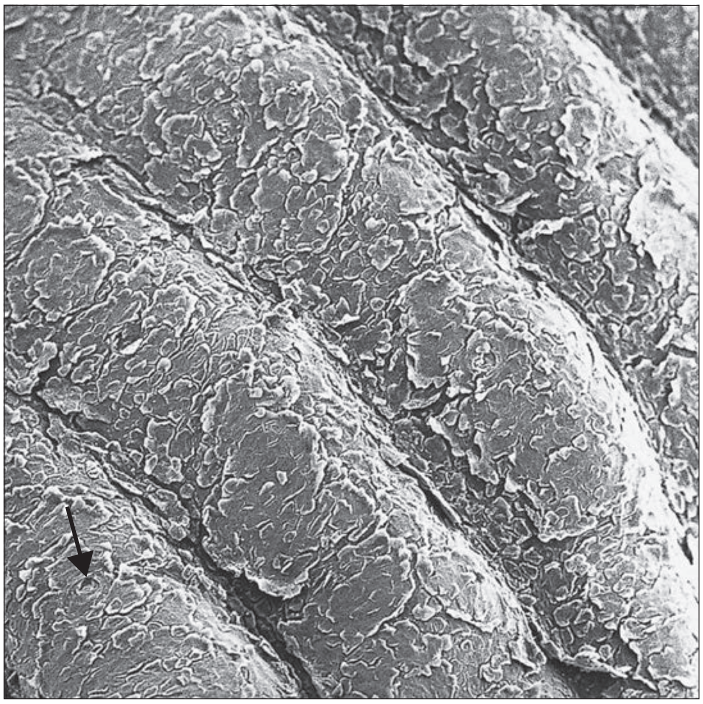

Fig. 7.36 A scanning electron micrograph of the surface of thick hairless skin from the palmar (volar) surface of a human digit, showing friction ridges along which lines of sweat ducts open as pores (one pore is arrowed). (Courtesy of Professor Lawrence Bannister and Dr Caroline Wigley.)

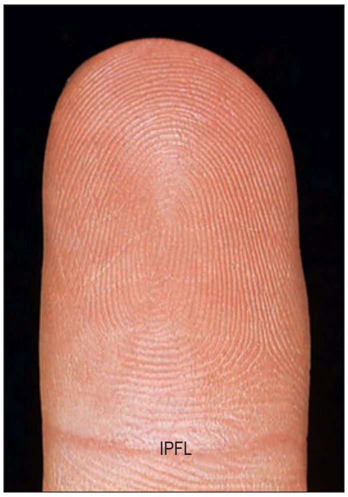

Fig. 7.35 The palmar aspect of a terminal phalanx to show fingerprint ridges. Note the interphalangeal flexure line (IPFL).

throughout life, unique to the individual, and therefore significant as a means of identification. The ridge pattern can be affected by certain abnormalities of early development, including genetic disorders such as Down's syndrome, and skeletal malformations such as polydactyly: absence of epidermal ridges is extremely rare. Functionally, epidermal ridges increase the gripping ability of hands and feet, preventing slipping. The great density of tactile nerve endings beneath them means that they are also important sensory structures.

If the mechanical demands placed on the skin are greater than the skin creases and the dermis can accommodate, the lateral cohesion of dermal collagen fibres becomes disrupted with associated haemorrhage and cellular reaction, and, eventually, the formation of poorly vascularized scar tissue. These changes are termed intrinsic to distinguish them from scars formed by external wounding. Sites of dermal rupture are visible externally as lines or striae. They are initially pink in colour, later widen and become a vivid purple or red (striae rubrae), and eventually fade, becoming paler than the surrounding intact skin (striae albae). They sometimes develop on the anterior abdominal wall during pregnancy, when they are termed striae gravidarum (stretch marks).

Lines detectable after manipulation or incision

In certain regions of the body, surgical wounds heal with a better and less conspicuous scar if they are orientated in a particular direction. This finding is related to a number of factors including skin tension and naturally formed wrinkle lines. Skin is normally under tension; the direction in which the tension is greatest varies regionally. Tension is dependent on the protrusion of underlying structures, the direction of underlying muscles, and on joint movements. Many anatomists and surgeons have therefore attempted to produce a body map to indicate the best direction in which to make an elective incision to obtain the most aesthetic scar. These maps frequently differ, especially in the region of the face. Out of the multitude of described cleavage lines, the most commonly referred to are relaxed skin tension lines (RSTLs), Langer's lines and Kraissl's lines (see Fig. 36.1). Of these, the RSTLs and Kraissl's lines are probably more appropriate lines for surgical incision.

Relaxed skin tension lines

Relaxed skin tension lines (RSTLs) are those that correspond to the directional pull (which forms furrows) when the skin is relaxed; they do not always correspond to wrinkle lines. The tension across RSTLs is constant even during sleep, but can be altered (increased, decreased or abolished) by underlying muscle contraction. The direction of the RSTLs can be determined by pinching the skin in different directions. Pinching at right-angles to the RSTLs will result in fewer and higher furrows than pinching parallel to these lines.

Blaschko's lines

Blaschko's lines represent a pattern of cutaneous mosaicism that can be observed in a range of congenital and acquired skin conditions. They do not appear to correspond to the distribution of the cutaneous vessels or nerves, and may be related to earlier developmental boundaries of a 'mosaic' nature.

Age-related skin changes

Two main factors, chronological and environmental, are involved in skin ageing (Orioli and Dellambra 2018). Chronological changes are physiological or intrinsic in origin. A major environmental factor is chronic exposure to the sun, photoageing, which is to some extent preventable.

Intrinsic ageing

From about the third decade onwards, gradual changes occur in the appearance, microstructure and mechanical properties of the skin as a result of epidermal and dermal atrophy. They become very marked in old age. Alterations include wrinkling, dryness, loss of elasticity, thinning and easy bruising. Epidermal atrophy is manifested by general thinning and loss of the basal rete pegs and flattening of the dermal–epidermal junction. Flattening of the junction decreases resistance to shear, leading to poor adhesion of epidermis and its separation following minor injury. The thickness of the cornified layer is not reduced in old age, and its permeability characteristics seem little affected. Epidermal proliferative activity and rate of cell replacement decline with age, being reduced by up to 50% in elderly skin. Synthesis of vitamin D is also reduced. After middle age, there is a 10–20% decline in the number of melanocytes, and Langerhans cells become sparser, a change associated with a reduction in immune responsiveness. Depigmentation and loss of hair, as well as some local increases (eyebrows, nose and ears in males, and face and upper lip in females), are commonly observed. Alterations in non-keratinocytes may be aggravated by chronic exposure to UV irradiation.

Dermal changes are mainly responsible for the appearance of aged skin, particularly its stiffness, flaccidity and wrinkling, as well as loss of extensibility and elasticity. Its general, thickness diminishes as a result of the decline in collagen synthesis by a reduced population of fibroblasts, though the relative proportion of type III collagen increases. Senile elastosis is a degenerative condition of collagen, which may be partly due to excessive exposure to sun. Vascularization of the skin is reduced, the capillary loops of the dermal papillae are particularly affected, and the tendency towards small spontaneous purpuric haemorrhages indicates a general fragility of the cutaneous microvasculature. There is a decrease in the sensitivity of sensory perception, associated with some loss of specialized receptors. Ageing is also associated with fat redistribution, which may contribute to the physical characteristics of loose, sagging skin.

Photoageing

Skin ageing is also influenced by external factors, such as tobacco exposure, malnutrition, airborne particulate matter and UV radiation. Photoageing, also known as extrinsic skin ageing, occurs as a result of the hazardous effect of UV radiation on human skin, and is a major concern because of an association with skin cancer. Ultraviolet light B (UVB) is primarily absorbed in the epidermis and has been shown to induce angiogenesis and lymphatic dysfunction in skin. It causes DNA damage by generating cyclobutane pyrimidine dimers and 6,4-photoproducts, all of which are photocarcinogenic. Ultraviolet A is absorbed by cellular chromophores such as melanin, riboflavin and urocanic acid, resulting in the formation of reactive oxygen species, which in turn damage lipids, DNA and proteins (Schuch et al 2017).

CUTANEOUS WOUND HEALING AND SCARRING

The end-point of healing of mammalian skin wounds is usually scar formation. This type of healing is called reparative wound healing as opposed to regenerative wound healing which can be seen in lower animals (such as the newt), where wounds can heal without scarring and with functional skin appendages.

Cutaneous scars result from injury to both the epidermis and the underlying dermis. The epidermis largely regenerates, but dermal architecture is abnormal after repair and the undulating pattern of rete ridges at the dermal–epidermal junction is not reproduced. Scar tissue is biomechanically inferior to unwounded skin. Appendages such as hair follicles, sebaceous and sweat glands, which are derived from the epidermis, do not regenerate after wounding.

The molecular biology of cutaneous repair involves the coordination of numerous cell types, signalling molecules and matrix proteins. Many of these signalling molecules have pleiotropic effects and it is the complex balance of these mediators, rather than their individual action, that determines events in wound repair. Wound healing is often considered in four overlapping temporal phases, haemostasis, inflammation, proliferation and remodelling (Fig. 7.36) (Landén et al 2016).

Haemostasis

Haemostasis occurs within minutes to hours of injury. Wounding causes vascular injury and initiates fibrin–fibronectin clot formation. The clot

The analysis of ridge patterns by studying prints of them (fingerprints) is known as dermatoglyphics and is of considerable forensic importance. Measurable parameters include the frequency of ridges in particular patterns and the disposition of tri-radii, which are junctional areas where three sets of parallel ridges meet. Fingerprint ridge patterns can be separated into three major types (see Fig. 7.35): arches (5%), loops (70%) and whorls (25%). Arches have no tri-radii, loops have one tri-radius, and whorls have two or more. Whorl finger patterns are more common on the right hand, and males generally have more whorls and fewer arches than females, in whom the ridges are relatively narrower. The frequency of individual patterns varies with particular fingers. Similar patterns are seen on the toes. Adermatoglyphia is an extremely rare autosomal dominant condition in which fingerprint ridges are absent, and is caused by mutations in the *SMARCAD1* gene. Other genetic disorders may also have reduced or absent dermatoglyphics as part of the clinical features.

Variation in pigmentation can produce visible pigmentary demarcation lines on the skin of the arms and legs. Five types (A–E) have been described. Type A, Futcher's or Voigt's lines, are the most common and occur along the anterior axial lines, extending from the sternum to the wrist, delineating the darker extensor and paler flexor surfaces of the arms.

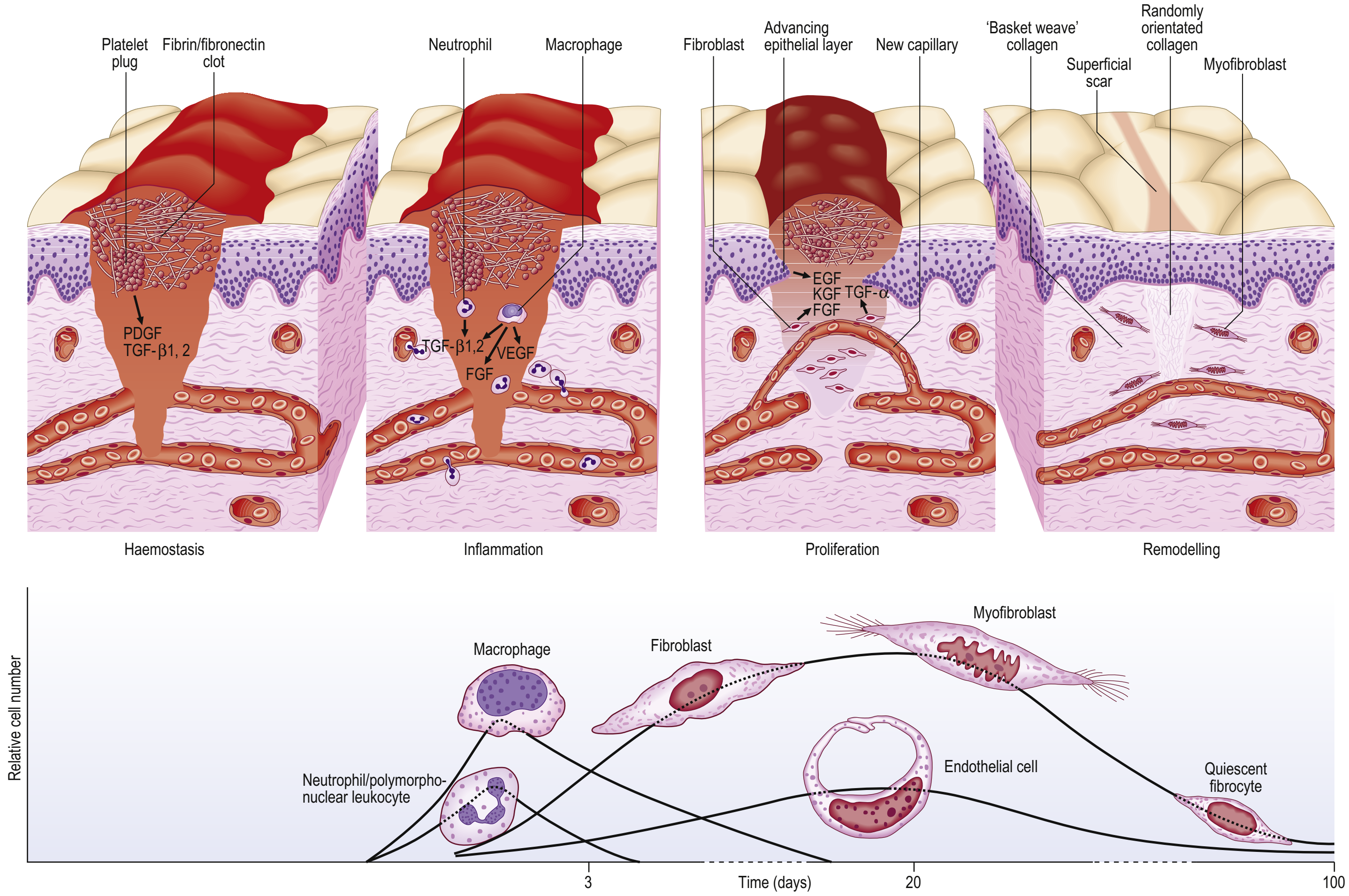

Fig. 7.36 The processes involved in the healing of a normal cutaneous wound. Abbreviations: EGF, epidermal growth factor; FGF, fibroblast growth factor; KGF, keratinocyte growth factor; PDGF, platelet-derived growth factor; TGF, transforming growth factor; VEGF, vascular endothelial growth factor.

consists of platelets (promoted to aggregate by fibrillar collagens type I and III) embedded in a mesh of cross-linked fibrin and fibronectin fibres. It serves as a haemostatic plug, protects the denuded wound with a temporary physical shield, and provides an initial wound bed that allows the surrounding fibroblasts to start laying down new collagen and extracellular matrix proteins to form the neodermis. The clot also acts as a reservoir of growth factors and cytokines that are released as platelets degranulate, and that contribute to inflammatory cell recruitment.

Inflammation

The inflammatory phase of wound healing occurs within the first 72 hours of injury and serves mainly to clear bacteria and debris from the wound and to prepare the wound bed for repair. Neutrophils and monocytes are recruited to wound sites within minutes of injury by a variety of chemotactic signals, including complement factors, bacterial polysaccharides, cytokines and growth factors such as tumour necrosis factor alpha (TNF-α), interleukin (IL)-1, IL-8, platelet-derived growth factor (PDGF), transforming growth factor alpha (TGF-α) and TGF-β1,2, basic fibroblast growth factor (bFGF/FGF-2), serotonin and monocyte chemotactic protein-1 (MCP-1). Complement, thrombin and mast cell mediators cause vasodilatation of the local capillaries and increase blood flow to facilitate the migration of inflammatory cells. Neutrophils are active against contaminating bacteria. Monocytes differentiate into macrophages that phagocytose not only pathogenic organisms, but also expended neutrophils, and cellular and matrix debris. Neutrophils and macrophages act as a source of cytokines and growth factors that amplify stimuli already present in the wound site. Macrophages are also a source of actors such as TGF-α, FGF and vascular endothelial growth factor (VEGF) that activate resident fibroblasts, endothelial cells and keratinocytes, which, in turn, are central to the processes of re-epithelialization and formation of granulation tissue.

Proliferation

The proliferative phase occurs in the first 2–3 weeks, and involves continued re-epithelialization and the formation of granulation tissue to fill the defects caused by the wound.

Re-epithelialization

Re-epithelialization begins within hours of wounding as a result of keratinocyte migration and proliferation from the wound edges and skin appendages. Cytokines such as epidermal growth factor (EGF), FGF, keratinocyte growth factor (KGF/FGF-7), insulin-like growth factor-1 (IGF-1) and TGF-α are released by activated fibroblasts and keratinocytes, and stimulate the re-epithelialization process. Advancing keratinocytes are capable of debriding the wound surface through phagocytosis of debris and dead cells and keratinocyte expression of matrix metalloproteinases (MMPs) appears to be associated with re-epithelialization. During this phase of cutaneous wound healing, keratinocyte proliferation is thought to be upregulated after migration has started; dividing and migrating cells are found in the first suprabasal as well as basal keratinocyte layers. MMP activity is regulated by the production of tissue inhibitors of MMPs (TIMPs). A relative imbalance between MMPs and TIMPs, e.g. upregulation of certain MMPs, may be associated with impaired wound healing. When the denuded wound surface has been covered by a monolayer of keratinocytes, migration ceases. A stratified epidermis with an underlying basal lamina is re-established from the margins of the wound inwards. Anchoring fibrils linking the basal lamina to the underlying connective tissue mark neo-epidermal maturity. For further reading on re-epithelialization see Belokhvostova et al (2018).

Granulation tissue formation

The term granulation tissue refers to the macroscopic appearance of wound connective tissue, which appears pink and granular. It contains numerous capillaries that invade the initial wound clot and become organized into a microvascular network (angiogenesis), together with the cells and molecules necessary to stimulate neo-matrix deposition. Angiogenesis starts 2 days after injury and is a complex process, promoted by dynamic interactions between endothelial cells, angiogenic cytokines (including FGF-2), VEGF (mainly from keratinocytes), PDGF and TGF-β1,2, MMP and the extracellular matrix environment.

Electron microscopic studies have shown that the epidermis, basal lamina and papillary dermis all develop on the surface of the granulation tissue. Wounds that fail to granulate do not heal satisfactorily, suggesting that granulation tissue formation is a key aspect of wound repair. Excessive granulation is also associated with delayed re-epithelialization.

Activated fibroblasts in the healing wound proliferate in response to growth factors, notably TGF-β1, IGF-1, PDGF, FGF and EGF. Within 72 hours of injury, these fibroblasts synthesize components of the new extracellular matrix, which are deposited in an orderly sequence. The neo-matrix initially includes fibronectin and hyaluronan, which form a provisional substratum for cellular migration. Fibronectin acts as an initiation site for collagen fibrillogenesis, and as anchorage for myofibroblasts to effect wound contraction. Hyaluronan forms a highly hydrated matrix that is easily penetrated by migrating cells. Ultimately this and other neo-matrix components are replaced, first by collagen type III, and subsequently by collagen type I, which imparts strength to the mature scar. Non-structural proteins such as tenascin are also found in the neo-matrix of healing wounds and provide signals that orchestrate the repair process. Cellularity decreases during the evolution of granulation tissue into a mature scar (and during other phases of wound healing), mainly as a result of apoptosis.

Remodelling

Remodelling of the extracellular matrix is important throughout the wound healing process and can last for months to over a year. Fibroblasts are responsible for matrix deposition and remodelling. Initially they replace hyaluronan in the neo-matrix with sulphated proteoglycans, such as decorin, biglycan and versican, which contribute to tissue resilience. Increased wound strength coincides with new collagen deposition. Approximately 3 weeks after injury, collagen breakdown and synthesis equilibrate; subsequent, more gradual increases in wound strength reflect collagen remodelling, with the formation of intermolecular cross-links and larger collagen bundles. Scar maturation is associated with proportional increases in collagen type I relative to collagen type III, associated with more organized orientation of the collagen fibrils. Scarred skin only reaches a maximum tensile strength of about 70% that of unwounded skin.

Wound contraction

An important part of remodelling is wound contraction. Once granulation tissue has been laid down, a proportion of activated fibroblasts (or other mesenchymal cells) transform into myofibroblasts, which play a key role in wound contraction; they are thought to generate forces that pull normal dermal and adipose tissue into the wound defect.

Scarless wound healing

Wounds heal with reduced or absent scarring in certain circumstances, notably cutaneous wounds in the early fetus. The transition from scarless to scarring healing is seen at 24 weeks of gestation. The development of a major inflammatory response at a wound site appears to be a significant determinant of whether scarring occurs. Scarless fetal wound healing is characterized by fewer inflammatory cells (which are less differentiated than their adult counterparts and which remain in the wound for a shorter time), rapid re-epithelialization, reduced angiogenesis and restoration of the connective tissue architecture in which collagen is arranged in the normal reticular pattern. Fetal healing is characterized by low levels of IL-6, IL-8, TGF-β1 and TGF-β2, and high levels of IL-10 and TGF-β3. TGF-β1 and 2 are produced from degranulating platelets and subsequently from monocytes and macrophages: the low levels of TGF-β1 seen in fetal wounds have been attributed to a relative lack of platelet degranulation and fibrin clot formation. The main sources of TGF-β3 are fibroblasts and keratinocytes.

Excessive scar formation

In some individuals, collagenous scar tissue forms which covers a greater area than the original wound, forming a keloid scar or keloid. This is an area of raised, hairless skin overlying the site of a wound which may have been relatively minor. Keloids are more common in darker-pigmented skins, on the upper body and in those with a familial history of keloid formation.

SKIN GRAFTS AND FLAPS

A graft is a piece of tissue that has been detached from its blood supply and therefore needs to regain a blood supply from the bed in which it is placed in order to survive. A flap is a piece of tissue that is surgically raised and transferred from one location in the body to another while maintaining its blood supply.

Grafts

Grafts can be composed of skin, fat, fascia or bone, either separately or together as a composite piece of tissue. Skin grafts can be either full-thickness grafts or split-thickness grafts. Full-thickness grafts consist of the epidermis and the full thickness of the dermis. Split-thickness grafts consist of the epidermis and a variable quantity of the dermis. An essential difference is that the donor site following the harvest of a full-thickness graft has no epidermal elements from which new skin can regenerate. These grafts therefore tend to be taken from sites of the body where the donor defect can be primarily closed. The donor site from split-thickness grafting contains adnexal remnants (hair follicles in particular), that have the propensity to divide and regenerate new epidermis, and so resurface the donor defect.

Revascularization of grafts is dependent on early and direct connection between host and graft vessels (inosculation); in the time that elapses before this occurs, graft survival depends on fluid absorption (imbibition). Revascularization, which occurs as early as 48 hours post-transplantation, is achieved by anastomosis, where the severed ends of pre-existing graft vessels are sutured to vessels of the underlying host wound bed, and/or by neovascularization, which involves the *de novo* angiogenic ingrowth of vessels from the wound bed into the graft. During the first two weeks, blood vessels from the recipient (host) site invade the graft edges along previous vascular channels in the direction of an ischaemic stimulus, while the donor graft vasculature begins to regress. Endothelial progenitor cells appear to play an important role in blood vessel formation, attracted by ischaemic gradients. Inosculation occurs, restoring blood flow to the graft microcirculation. By the start of the third week, complete blood flow in the graft vasculature has been established and, in the absence of a continuing ischaemic stimulus, neovascularization ends.

Flaps

Flaps are named according to the type of tissue transferred, e.g. a fasciocutaneous flap contains skin and fascia, and a musculocutaneous flap contains both muscle and the overlying skin, whereas a skin flap, fascial flap and muscle flap contain only the separate elements that their names imply. The blood supply to a skin flap can be randomly orientated, which limits the flap length-to-breadth proportions to no more than 2 : 1 (except on the face, where longer flaps can be performed). Much longer skin flaps can be raised elsewhere if the blood supply to the flap is a direct cutaneous artery and vein (axial pattern flaps) and are usually based on the local angiosome. An angiosome is an anatomical territory supplied by a source artery and drained by accompanying veins and lymphatic vessels (Taylor et al 2011) (see p. 135). It may include fascia, nerve, muscle and bone, as well as skin. The concept is important in the analysis of patterns of ischaemia and in planning incisions, and enables the raising of free, composite, vascularized tissue flaps.

A free flap (free tissue transfer) is a specific type of flap in which the tissue, whether skin, fascia, muscle or bone, or a combination of these, is completely removed from its original location in the body along with a single identifiable artery and vein, and transferred to a remote site. The blood vessels in the flap are anastomosed to vessels located in the new site using microsurgical techniques. This often allows for greater flexibility in performing reconstructive surgery.

SKIN STEM CELLS

To maintain, repair and regenerate itself, the skin contains stem cells that reside in various parts of the hair follicles, including the bulge area and isthmus; the basal layer of the interfollicular epidermis; the base of sebaceous glands and within sweat glands. Epidermal stem cells are able to self-renew, as well as give rise to differentiating cells. However, it is not clear whether every basal keratinocyte, or only a proportion of these cells, is a stem cell. Two hypotheses have emerged concerning epithelial renewal. One theory, known as symmetric cell division, envisages basal keratinocytes within epidermal proliferation units that contain one self-renewing stem cell and about 10 tightly packed transit amplifying cells, each of which is capable of dividing a limited number of times before exiting the basal layer to undergo terminal differentiation. This unit gives rise to a column of larger and flatter cells that culminates in a single hexagonal surface. The alternative theory, known as asymmetric cell division, is that some interfollicular stem cells (perhaps up to 70% of cells) can shift their spindle orientation from lateral to perpendicular, such that one daughter cell is committed to terminal differentiation while the other maintains its proliferative capacity, thus obviating the need for transit amplifying cells.

Hair follicle stem cells are found in the bulge regions below the sebaceous glands but also in other parts of the hair follicle (Fuchs 2018). These stem cells undergo varying degrees of growth, degeneration and rest, which are governed, in part, by Wnt signalling and bone morphogenetic protein (BMP) inhibition. The bulge area stem cells generate cells of the outer root sheath, which drive the highly proliferative matrix cells next to the mesenchymal papillae. After proliferating, matrix cells differentiate to form the hair channel, the inner root sheath and the hair shaft. Hair follicle stem cells can also differentiate into sebocytes and interfollicular epidermis. Despite this multipotency, the follicle stem cells only function in pilosebaceous unit homeostasis and do not contribute to the interfollicular epidermis unless the skin is wounded. Stem cells are also found in the base of sebaceous glands: their progeny differentiate into lipid-filled sebocytes. Stem cells in sweat glands can differentiate into epithelial, luminal or myoepithelial daughter cells to maintain skin integrity and homeostasis.

Other cells in the dermis and subcutis may have stem cell-like properties. Dermal sheath cells lie close to hair follicles; MUSE (multi-lineage differentiating stress-enduring) cells are pluripotent progenitor cells. Trauma and/or hypoxia in the skin, e.g. during wound healing or skin grafting, may induce recruitment of epithelial and endothelial progenitors from stem cell sources beyond the skin, such as the bone marrow, predominantly from the mesenchymal stromal cell pool; this is an area of much debate and current research.

Bonus e-book content

Fig. 7.6 Transmission electron micrograph of the dermal–epidermal junction.

Fig. 7.8 Transmission electron micrograph of a skin desmosome junction.

Fig. 7.10 A scanning electron micrograph showing the epidermal surface surrounding the aperture of a sweat duct.

Fig. 7.11 Schematic representation of the cornified layer and upper epidermis to illustrate the physical and chemical properties of different parts of each layer.

Fig. 7.17 Langerhans cell with dendritic processes extending though tight junctions.

Fig. 7.18 Adipocytes in human skin.

Fig. 7.22 A scanning electron micrograph of a scalp hair, showing details of its surface structure.

Fig. 7.24 The coiled secretory portion of a sweat gland (SG) in the reticular dermis.

Fig. 7.36 A scanning electron micrograph of the surface of thick hairless skin from the palmar (volar) surface of a human digit, showing friction ridges along which lines of sweat ducts open as pores (one pore is arrowed).

Key references

Chen YE, Fischbach MA, Belkaid Y 2018 Skin microbiota–host interactions. Nature 553:427–36.

This review examines the complex interaction between skin microbes and the host, and its consequences for health and disease.

D'Mello SA, Finlay GJ, Baguley BC et al 2016 Signaling pathways in melanogenesis. Int J Mol Sci 17:pii: e1144.

This review provides information about melanin and its synthesis and regulation in skin.

Elias PM, Gruber R, Crumrine D et al 2014 Formation and functions of the corneocyte lipid envelope (CLE). Biochim Biophys Acta 1841:314–318.

An update on the structure, composition and functions of the corneocyte lipid envelope with new insights from inherited and acquired disorders of lipid metabolism.

Fuchs E 2016 Epithelial skin biology: three decades of developmental biology, a hundred questions answered and a thousand new ones to address. Curr Top Dev Biol 116:357–74

This review explores how skin stem cells maintain tissue homeostasis and repair wounds and how they regulate the delicate balance between proliferation and differentiation.

Gonzales KAU, Fuchs E 2017 Skin and its regenerative powers: an alliance between stem cells and their niche. Dev Cell 43:387–401.

This well-illustrated review focuses on the epithelial stem cells of skin, where they come from, where they reside, and how they function in normal homeostasis and wound repair.

Knöbel M, O'Toole EA, Smith FJ 2015 Keratins and skin disease. Cell Tissue Res 360:583–9.

A compact description of keratin intermediate filament biology and diseases associated with keratin gene mutations.

Lynch MD, Watt FM 2018 Fibroblast heterogeneity: implications for human disease. J Clin Invest 128:26–35.

This review provides insight into how new knowledge on fibroblast heterogeneity in human skin has relevance to wound healing, scarring, malignancy, and ageing.

Philippeos C, Telerman SB, Oulès B et al 2018 Spatial and single-cell transcriptional profiling identifies functionally distinct human dermal fibroblast subpopulations. J Invest Dermatol 138:811–25.

Original study on human skin that defines multiple subpopulations of dermal fibroblasts with differential functional roles.

Weidinger S, Beck LA, Bieber T et al 2018 Atopic dermatitis. Nat Rev Dis Primers 4:1. doi: 10.1038/s41572-018-0001.

This review covers normal skin barrier structure and function and shows how mechanical and immunological disruption of its integrity leads to the common skin disorder, atopic dermatitis.

Yokouchi M, Atsugi T, Logtestijn MV et al 2016 Epidermal cell turnover across tight junctions based on Kelvin's tetrakaidecahedron cell shape. Elife 5. pii:e19593.

This study defines optimal keratinocyte shape in skin barrier formation and how tight junctions maintain skin integrity despite the mechanics of epithelial differentiation.

References

Akiyama M 2017 Corneocyte lipid envelope (CLE), the key structure for skin barrier function and ichthyosis pathogenesis. J Dermatol Sci 88:3–9.

Belokhvostova D, Berzanskyte I, Cujba AM et al 2018 Homeostasis, regeneration and tumour formation in the mammalian epidermis. Int J Dev Biol. 62(6-7-8):571–82.

Chen YE, Fischbach MA, Belkaid Y 2018 Skin microbiota–host interactions. Nature 553:427–36.

This review examines the complex interaction between skin microbes and the host, and its consequences for health and disease.

Coulombe PA 2017 The molecular revolution in cutaneous biology: keratin genes and their associated disease: diversity, opportunities, and challenges. J Invest Dermatol 137:e67–e71.

Deckers J, Hammad H, Hoste E 2018 Langerhans cells: sensing the environment in health and disease. Front Immunol 9:93. doi: 10.3389/fimmu.2018.00093. eCollection 2018.

D'Mello SA, Finlay GJ, Baguley BC et al 2016 Signaling pathways in melanogenesis. Int J Mol Sci 17. pii:e1144.

This review provides information about melanin and its synthesis and regulation in skin.

Domagała Z, Dąbrowski P, Kurlej W et al 2017 Sequence of lanugo pattern development on the trunk wall in human fetuses. Adv Clin Exp Med 26:967–72.

Driskell RR, Lichtenberger BM, Hoste E et al 2013 Distinct fibroblast lineages determine dermal architecture in skin development and repair. Nature 504:227–281.

Elias PM, Gruber R, Crumrine D et al 2014 Formation and functions of the corneocyte lipid envelope (CLE). Biochim Biophys Acta 1841:314–18.

An update on the structure, composition and functions of the corneocyte lipid envelope with new insights from inherited and acquired disorders of lipid metabolism.

Fuchs E 2016 Epithelial skin biology: three decades of developmental biology, a hundred questions answered and a thousand new ones to address. Curr Top Dev Biol 116:357–74.

This review explores how skin stem cells maintain tissue homeostasis and repair wounds and how they regulate the delicate balance between proliferation and differentiation.

Fuchs E 2018 Skin stem cells in silence, action, and cancer. Stem Cell Reports 10:1432–8.

Gonzales KAU, Fuchs E 2017 Skin and its regenerative powers: an alliance between stem cells and their niche. Dev Cell 43:387–401.

This well-illustrated review focuses on the epithelial stem cells of skin, where they come from, where they reside, and how they function in normal homeostasis and wound repair.

Herlin C, Chica-Rosa A, Subsol G 2015 Three-dimensional study of the skin/subcutaneous complex using in vivo whole body 3T MRI: review of the literature and confirmation of a generic pattern of organization. Surg Radiol Anat 37:731-41.

Irvine AD, McLean WH, Leung DY 2011 Filaggrin mutations associated with skin and allergic diseases. N Engl J Med 365:1315–27.

Knöbel M, O'Toole EA, Smith FJ 2015 Keratins and skin disease. Cell Tissue Res 360:583–9.

A compact description of keratin intermediate filament biology and diseases associated with keratin gene mutations.

Kubo A, Nagao K, Yokouchi M et al 2014 External antigen uptake by Langerhans cells with reorganization of epidermal tight junction barriers. J. Exp. Med. 206:2937–2946.

Kurata R, Futaki S, Nakano I, et al 2017 Three-dimensional cell shapes and arrangements in human sweat glands as revealed by whole-mount immunostaining. PLoS One 12(6): e0178709.

Ladak A, Tubbs RS, Spinner RJ 2014 Mapping sensory nerve communications between peripheral nerve territories. Clin Anat 27:681–90.

Landén NX, Li D, Stahle M 2016 Transition from inflammation to proliferation: a critical step during wound healing. Cell Mol Life Sci 73:3861–85.

Law MH, Medland SE, Zhu G et al 2017 Genome-wide association shows that pigmentation genes play a role in skin aging. J Invest Dermatol 137:1887–94.

Liu Q, Zhang Y, Danby SG 2018. Infant skin barrier, structure, and enzymatic activity differ from those of adult in an East Asian cohort. Biomed Res Int Jul 12;2018:1302465. doi: 10.1155/2018/1302465. eCollection 2018.

Lynch MD, Watt FM 2018 Fibroblast heterogeneity: implications for human disease. J Clin Invest 128:26–35.

This review provides insight into how new knowledge on fibroblast heterogeneity in human skin has relevance to wound healing, scarring, malignancy, and ageing.

Orioli D, Dellambra E 2018 Epigenetic regulation of skin cells in natural aging and premature aging diseases. Cells 7:268.

Pammi M, O'Brien JL, Ajami NJ et al 2017 Development of the cutaneous microbiome in the preterm infant: a prospective longitudinal study. PLoS ONE 12:e0176669.

Philippeos C, Telerman SB, Oulès B et al 2018 Spatial and single-cell transcriptional profiling identifies functionally distinct human dermal fibroblast subpopulations. J Invest Dermatol 138:811–25.

Original study on human skin that defines multiple subpopulations of dermal fibroblasts with differential functional roles.

Piérard-Franchimont C, Piérard GE 2002 Postmenopausal aging of the sebaceous follicle: a comparison between women receiving hormone replacement therapy or not. Dermatology 204:17–22.

Purba TS, Brunken L, Hawkshaw NJ 2016 A primer for studying cell cycle dynamics of the human hair follicle. Exp Dermatol 25:663–8.

Schuch AP, Moreno NC, Schuch NJ et al 2017 Sunlight damage to cellular DNA: focus on oxidatively generated lesions. Free Radic Biol Med 107:110–24.

Shiohara T, Sato Y, Komatsu Y et al 2016 Sweat as an efficient natural moisturizer. Curr Probl Dermatol 51:30–-41.

Stamatas GN, Nikolovski J, Mack MC et al 2011 Infant skin physiology and development during the first years of life: a review of recent findings based on in vivo studies. Int J Cos Sci 33:17–24.

Taylor GI, Corlett RJ, Dhar SC et al 2011 The anatomical (angiosome) and clinical territories of cutaneous perforating arteries: development of the concept and designing safe flaps. Plast Reconstr Surg 127:1447–59.

Tikoo S, Jain R, Kurz AR et al 2018 The lymphoid cell network in the skin. Immunol Cell Biol 96:485–96.

Veltri A, Lang C, Lien W 2018. Concise review: Wnt signalling pathways in skin development and epidermal stem cells. Stem Cells 36:22–35.

Weidinger S, Beck LA, Bieber T et al 2018 Atopic dermatitis. Nat Rev Dis Primers 4:1. doi: 10.1038/s41572-018-0001.

This review covers normal skin barrier structure and function and shows how mechanical and immunological disruption of its integrity leads to the common skin disorder, atopic dermatitis.

Wu X, Hammer JA 2014 Melanosome transfer: it is best to give and receive. Curr Opin Cell Biol 29:1–7.

Yokouchi M, Atsugi T, Logtestijn MV et al 2016 Epidermal cell turnover across tight junctions based on Kelvin's tetrakaidecahedron cell shape. Elife 5. pii:e19593.

This study defines optimal keratinocyte shape in skin barrier formation and how tight junctions maintain skin integrity despite the mechanics of epithelial differentiation.

Younge NE, Araújo-Pérez F, Brandon D et al 2018 Early-life skin microbiota in hospitalized preterm and full-term infants. Microbiome 6:98. doi: 10.1186/s40168-018-0486-4.

Zouboulis CC, Picardo M, Ju Q et al 2016 Beyond acne: current aspects of sebaceous gland biology and function. Rev Endocr Metab Disord 17:319–34.

COMMENTARY

1.1

Fluorescence microscopy today: a perspective

Dylan M. Owen, M. Makarova

Fluorescence microscopes are some of the most widely used tools in current cell biology, either as systems within individual laboratories, or increasingly commonly, within centralized core facilities. The largely non-invasive nature of fluorescence imaging is its major strength, in that it allows the distribution of individual, specific protein species to be mapped at submicron resolution in living cells, tissues and even whole living organisms. Techniques developed in the 1990s and early years of the twenty-first century, including the development of fluorescent fusion protein constructs based on genetically encoded fluorescent proteins, advances in excitation and detector technology allowing new levels of specificity, speed and signal-to-noise ratio, and new image analysis and computing techniques for the manipulation and quantification of the resulting data, the most modern of which now use artificial intelligence and machine learning approaches, have collectively made fluorescence a standard research tool found within most laboratories working in the biological sciences.

A new wave of technological developments that have appeared in the past decade is being adopted by the biological sciences community. New fluorescent probes, optical technology and image processing algorithms have underpinned the development of super-resolution microscopy in which fluorescence images can be obtained with resolution approaching the molecular scale. In effect, this allows the mapping of all fluorescent molecules in a sample with nanometre accuracy, a possibility that is changing the way we think about what microscope images mean. Another major advance has been light-sheet-based imaging (**Fig. 1.1.1**). Its fundamental origins go back decades, but it is only now that light-sheet technology is becoming a vital tool that is especially useful for imaging large samples such as embryos and whole organisms, and in so doing, is threatening the status of the confocal microscope as the go-to system for most bio-imaging.

Fluorescent fusion constructs allow a protein species of interest to be genetically fused to a fluorescent protein so that it can be visualized in a microscope (Chudakov et al 2010). Originally, this meant fusion to the green fluorescent protein (GFP) from the Pacific jellyfish *Aequoria victoria* (Tsien 1998). For the development of this technology, the 2008 Nobel Prize for Chemistry was shared between Osamu Shinomura, who identified and purified GFP; Martin Chalfie, who created and imaged the first fluorescent fusion (Chalfie et al 1994); and Roger Tsien, who mutated GFP to create a whole palate of possible colours – a palate that is now vast (Shaner et al 2005, Giepmans et al 2006). Unlike immunostaining, in which fluorescently tagged antibodies to the protein of interest are introduced into a cell, GFP is genetically encoded and is therefore compatible with live cell imaging, so allowing the investigation of protein dynamics under physiological conditions. The newest fluorescent protein technology includes photoactivatable and colour-switchable proteins, which are useful for tracking intracellular events (Patterson and Lippincott-Schwartz 2002). In parallel with the advances in fluorescent protein technology, work is ongoing on new, small organic dye molecules for use in immunostaining and other applications: the Janelia series of JF dyes are excellent examples of rationally designed fluorophores with superior photophysical properties that have largely rendered traditional dyes, such as FITC, obsolete.

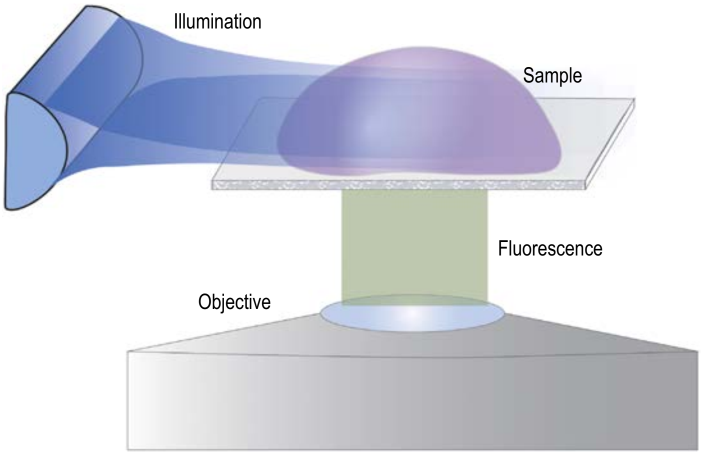

Fig. 1.1.1 Light-sheet microscopy, where the whole plane, and only that plane, is illuminated at any time; the imaging is fast but there is minimal toxicity from the laser because the peak power density is low.

Concomitant with the developments in labelling technology, detectors have become faster and more sensitive. The charge-coupled device (CCD) camera evolved into the electron-multiplying CCD (EM-CCD) camera, sensitive enough to detect individual photons and therefore to image and track single molecules within cells. Currently, compound metal-oxide semiconductor (CMOS) camera technology with very high frame rates and huge fields of view is transforming microscopy. Increases in sensitivity mean that scientific CMOS cameras are now even replacing EM-CCDs for single-molecule imaging applications. For point detectors such as those used on confocal and multiphoton systems, new hybrid detectors are being implemented, offering the Holy Grail of extremely high sensitivity and large dynamic range.

In conventional fluorescence microscopy methods (widefield epi-fluorescence, confocal, spinning disk, total internal reflection, etc.), the resolution of the final fluorescence image is limited to 200–300 nm by the diffraction of light, which means that two fluorescent objects separated by less than this distance would not be distinguishable as two separate entities. In 2014, the Nobel Prize for Chemistry was awarded to W. E. Moerner, Eric Betzig and Stefan Hell for developing super-resolution fluorescence microscopy methods. The diffraction limit was circumvented by three new methodologies that combined new fluorophores, optics and image analysis. Broadly speaking, these techniques are based on structured illumination microscopy (SIM) (**Fig. 1.1.2A**), in which a grid pattern of excitation light is projected on to the sample (Gustafsson 2000); stimulated emission depletion (STED) microscopy (**Fig. 1.1.2B**), in which a ‘doughnut’-shaped depletion beam is used to de-excite fluorophores and narrow the excitation spot used in confocal microscopy (Hell and Wichmann 1994, Vicidomini et al 2011); or single-molecule localization microscopy (SMLM) techniques (**Fig. 1.1.2C**) in which individual molecules are imaged and localized in sequence (Betzig and Chichester 1993). SMLM can be subdivided depending on the types of fluorophore used and how the signal is separated from the ensemble in order to achieve single-molecule imaging.

SIM achieves resolutions of around 100 nm and is compatible with conventional fluorophores and live cell imaging. STED typically achieves 50–100 nm resolution in biological samples, but is more challenging for live cell imaging because of the damaging laser powers used. SMLM delivers the highest resolution of 20–30 nm, but is relatively slow and therefore mainly used on fixed cells where new switchable fluorophores allow fluorescent molecules to be turned on stochastically. Individual molecules are then imaged and their coordinates recorded before the fluorophores are bleached and a new subset of molecules is activated. In this way, all molecules in the sample can be imaged in sequence, circumventing the diffraction limit. Using SMLM, the ability to acquire tables of the x, y and z coordinates of all individual fluorescent molecules, rather than images *per se*, requires new ways of thinking about the analysis and quantification of data sets, a challenge that is only just beginning. One of the newest implementations of SMLM uses complimentary DNA oligos to label molecules in the sample with fluorophores. Termed DNA points-accumulation for imaging by nanoscale topography (DNA-PAINT), it allows the serial imaging of target species and hence many-colour SMLM (Schnitzbauer et al 2017).

The newest developments in *in vivo* imaging are based on light-sheets (see Fig. 1.1.2). Originally termed SPIM (selective plane illumination microscopy), a flat sheet of excitation light is projected through

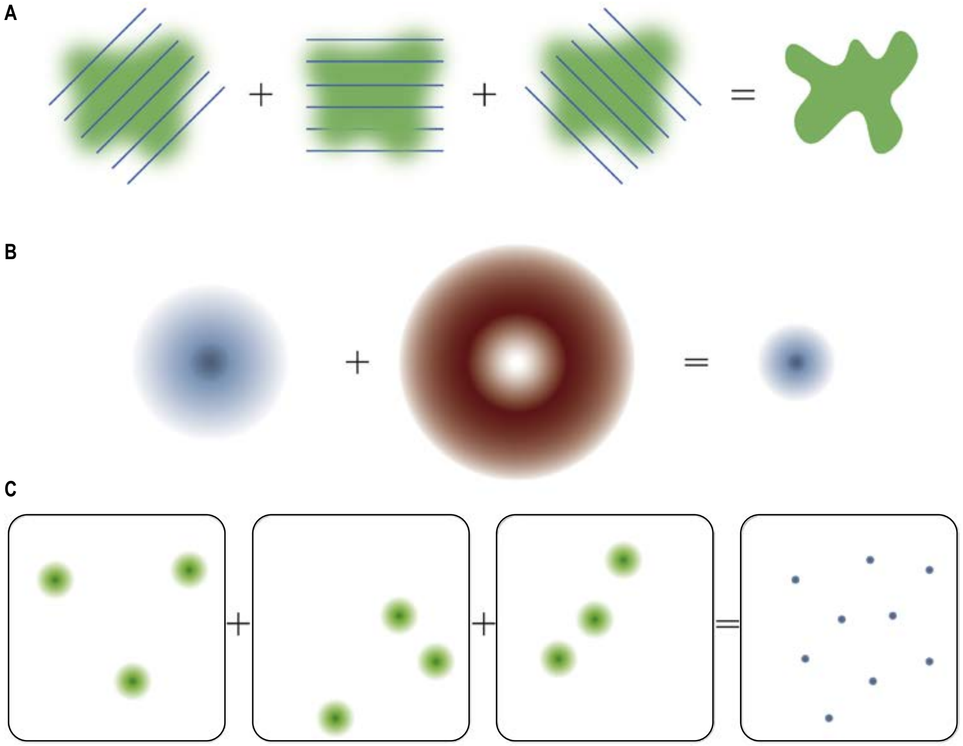

Fig. 1.1.2 In SIM, the sample is illuminated with a stripe or grid pattern which is then rotated and shifted over the sample. **A**, Mathematical reconstruction can combine these individual raw images to create a sharper picture with double the original resolution. **B**, STED works on confocal microscopes and uses a red, doughnut-shaped 'depletion beam' to shrink the size of the original illumination spot, creating a sharper image with a spot size that is dependent on the red laser power. **C**, In SMLM, molecules are imaged a few at a time, sparsely separated so that the location of each can be pinpointed with nanometre accuracy; these are then summed over thousands of frames until the position of every fluorescent molecule has been mapped.

the sample and imaged by a perpendicularly arranged lens (Huisken et al 2004), allowing high-resolution three-dimensional imaging at high speed and with minimal photo-damage to the sample. Modern implementations of light-sheet offer the advantages of confocal microscopy (e.g. optical sectioning) but with dramatically increased imaging speeds and low phototoxicity. Light-sheet therefore has numerous applications in whole, live organism imaging such as in fly embryos, nematodes and zebrafish development (Chen et al 2014). Light-sheet-based imaging is now being combined with super-resolution methods such as SIM and SMLM, with improvements in resolution, image quality, live-cell compatibility and imaging speed.

While work on new improved fluorophores, laser technology, optical components and processing algorithms continues, more radical breakthroughs in microscopic techniques and data analysis are likely. They will focus on further enhancements to resolution, e.g. the recently developed MINimal emission FLUXes (MINFLUX) method (Balzarotti et al 2017), imaging speeds and applicability to whole-organism imaging, e.g. Photoactivated Localization Microscopy (PALM), which is beginning to be applied to live cells when the biological structure is relatively stable (Shroff et al 2008) and the speed of STED has been greatly improved (Chmyrov et al 2013). There is no doubt that these advances will make fluorescence microscopy an even more valuable tool within the biological sciences.

References

Balzarotti F, Eilers Y, Gwosch KC et al 2017 Nanometer resolution imaging and tracking of fluorescent molecules with minimal photon fluxes. Science 355:606–12.

Betzig E, Chichester RJ 1993 Single molecules observed by near-field scanning optical microscopy. Science 262:1422–5.

Chalfie M, Tu Y, Euskirchen G et al 1994 Green fluorescent protein as a marker for gene expression. Science 263:802–5.

Chen B, Legant W, Wang K et al 2014 Lattice light-sheet microscopy: imaging molecules to embryos at high spatiotemporal resolution. Science 346(6208):1257998.

Chmyrov A, Keller J, Grotjohann T et al 2013 Nanoscopy with more than 100,000 'doughnuts'. Nat Meth 10:737–40.

Chudakov DM, Matz MV, Lukyanov S et al 2010 Fluorescent proteins and their applications in imaging living cells and tissues. Physiol Rev 90:1103–163.

Denk W, Strickler JH, Webb WW 1990 Two-photon laser scanning fluorescence microscopy. Science 249:72–6.

Giepmans BNG, Adams SR, Ellisman MH et al 2006 The fluorescent toolbox for assessing protein location and function. Science 312:217–24.

Gustafsson MGL 2000 Surpassing the lateral resolution limit by a factor of two using structured illumination microscopy. J Microsc 198:82–7.

Heilemann M, van de Linde S, Schüttpelz M et al 2008 Subdiffraction resolution fluorescence imaging with conventional fluorescent probes. Angew Chem Int Ed 47:6172–6.

Hell SW, Wichmann J 1994 Breaking the diffraction resolution limit by stimulated emission: stimulated-emission-depletion fluorescence microscopy. Opt Lett 19:780–2.

Huisken J, Swoger J, Del Bene F et al 2004 Optical sectioning deep inside live embryos by selective plane illumination microscopy. Science 305:1007–9.

Patterson GH, Lippincott-Schwartz J 2002 A photoactivatable GFP for selective photolabeling of proteins and cells. Science 297:1873–7.

Rust MJ, Bates M, Zhuang X 2006 Sub-diffraction-limit imaging by stochastic optical reconstruction microscopy (STORM). Nat Meth 3:793–6.

Schnitzbauer J, Strauss M, Schlichthaerle T et al 2017 Super-resolution microscopy with DNA-PAINT. Nat Prot 12:1198–1228.

Shaner NC, Steinbach PA, Tsien RY 2005 A guide to choosing fluorescent proteins. Nat Meth 2:905–9.

Shroff H, Galbraith CG, Galbraith JA et al 2008 Live-cell photoactivated localization microscopy of nanoscale adhesion dynamics. Nat Meth 5:417–23.

Tsien RY 1998 The green fluorescent protein. Annu Rev Biochem 67:509–44.

Vicidomini G, Moneron G, Han KY et al 2011 Sharper low-power STED nanoscopy by time gating. Nat Meth 8:571–3.

Wurm C, Kolmakov K, Gottfert F et al 2012 Novel red fluorophores with superior performance in STED microscopy. Opt Nanosc 1:7.

Xu K, Babcock HP, Zhuang X 2012 Dual-objective STORM reveals three-dimensional filament organization in the actin cytoskeleton. Nat Meth 9:185–8.

York AG, Parekh SH, Nogare DD et al 2012 Resolution doubling in live, multicellular organisms via multifocal structured illumination microscopy. Nat Meth 9:749–54.

COMMENTARY

1.2

Electron microscopy in the twenty-first century

Roland A. Fleck

INTRODUCTION

Biological electron microscopy (EM) is pivotal in life science research. A measure of its ubiquity is the diversity of its capacity, e.g. three-dimensional structural information about proteins and viruses at Å resolution; three-dimensional reconstructions of cellular organelles and tissues (from a few tens of nanometres to hundreds of micrometres); and two-dimensional and topographic information and elemental microanalysis at subcellular resolution. The capacity of EM can be further enhanced by correlative light and electron microscopy (CLEM) workflows, where light microscopy (LM) events are co-localized with underlying ultrastructure. In its simplest form, LM generates a 'Google Earth'-like map to identify areas of interest, which are then studied at the ultrastructural level by EM, so overcoming both the physical size limitations imposed on samples by EM and the diffraction limits of resolution imposed by LM (Williams and Carter 2009). CLEM can also be combined with advanced EM sample preparation and imaging techniques to provide previously unheralded levels of cytoarchitectural insight into biological systems (Sartori et al 2007, McDonnald 2009, Plitzko et al 2009). Pioneering groups now employ correlation in workflows which allow single particle cryo-EM techniques to be applied directly to structures in cells and tissues. Electron tomography is required to first determine the 3D structures of irregular samples such as cells and organelles. Once good tomograms are available, it is possible to extract multiple copies of a structure of interest and then apply single particle methods to obtain averages with greatly improved signal-to-noise ratios.

However, biological EM is not without its challenges. The electron beam is generated under vacuum at pressures and temperatures that are nominally incompatible with liquid water, yet water is the most abundant cellular constituent. Moreover, carbon-based life forms also have poor contrast in the electron microscope because they are composed mainly of light elements. In fact, carbon is so 'transparent' in the electron microscope that it is often employed as a film to support biological samples. To overcome these caveats, hydrated 'live' tissue is converted to a 'fixed' state; conventional protocols employ a series of steps, including chemical fixation, alcohol dehydration and resin infiltration. Heavy metal salts are added for positive staining of fixed and embedded specimens or as negative stains of whole structures that have been deposited on a support film (Glauert and Lewis 1998). More recently, cryo-fixation has been adopted to allow the 'solidification of a biological specimen by cooling with the aim of minimal displacement of its components' (Steinbrecht and Zierold 1987). By using low temperature as a physical fixation strategy, the morphology and dimensions of the living material are retained and soluble cellular components are not displaced, which means that processing artefacts commonly encountered in more conventional room-temperature EM techniques are either reduced or removed. Cryo-EM often allows direct observation of specimens that have not been stained or chemically fixed.

EM IN PATHOLOGY

Although the use of EM in diagnostic histopathology has declined from the height of its popularity in the 1980s, EM remains an important diagnostic tool in several well-defined areas. Indeed, guidance issued by the UK's Royal College of Pathologists cites and supports the Association of Clinical Pathologists Best Practice No. 160, which states that 'Many respondents [to a review of laboratory practice in renal pathology] expressed the opinion that to carry out evaluation of renal biopsy specimens without at least having the availability of electron microscopy is negligent' (de Haro and Furness 2012). Other specialized areas include the diagnosis of primary ciliary dyskinesia; certain skin/connective tissue disorders, e.g. inherited bullous lesions and Ehlers–Danlos syndrome; and specialized areas of ophthalmic pathology (de Haro and Furness 2012). Despite its continued value and capacity to inform, diagnostic transmission electron microscopy (TEM) has been largely stagnant in the clinical setting; there has been little change in procedures or application for decades. In marked contrast, TEM in the research setting has experienced an explosion in capacity and capability: there is a considerable opportunity for twenty-first century EM to translate to, and to advance, clinical research and diagnostic pathology (**Fig. 1.2.1**, **Video 1.2.1**).

LIMITATIONS OF TRADITIONAL PROCESSING TECHNIQUES AND CURRENT PROTOCOLS

Traditional EM processing strategies introduce artefacts (perturbations to structure) (**Fig. 1.2.2**) that affect tissue structure, e.g. by shrinkage or swelling of the tissue under examination, the shrinkage of cellular organelles, and/or the extraction or redistribution of cellular constituents such as lipids, proteins and DNA (Boyde and Maconnachie 1979). Most chemical fixatives react with proteins and cross-link peptide chains as part of their action (Glauert and Lewis 1998). These reactions can be highly deleterious to epitopes, significantly compromising immunohistochemical studies.

Cryo-fixation has two distinct advantages over chemical fixation (Nermut and Frank 1971, Nermut 1991). It is rapid (measured in milliseconds), which means that the sample is preserved, hydrated and in a 'close-to-life' state at the point of initiating fixation, and it ensures simultaneous immobilization of all macromolecular components (Robards and Sleytr 1995). Many protein networks are labile and prone to disruption with even a slight osmotic or temperature change; cryo-fixation minimizes these deleterious effects. Cryo-techniques allow the study of biological samples with improved ultrastructural preservation and may facilitate the study of dynamic processes. Rapid freezing prevents artefactual aggregations of proteins because tissue fixation and processing can be performed with no or minimal use of cross-linking fixatives, which means that samples retain higher antigenicity (Kellenberger 1991, Hayat 2000, Claeys et al 2004).

This level of preservation relies on vitrification (the transformation of water from a liquid to an amorphous state without inducing the nucleation of ice crystals). The nucleation of ice crystals is

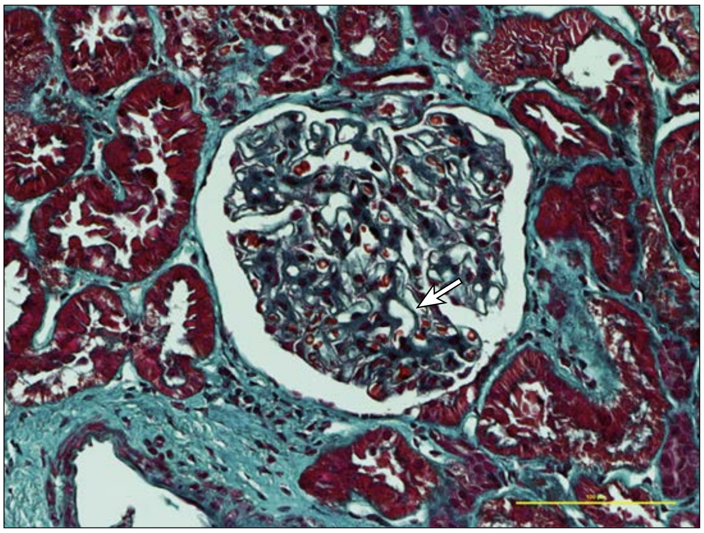

Fig. 1.2.1 A Masson trichrome stain of a renal biopsy taken for diagnostic histopathology. The arrow highlights a glomerular capillary, fringed with foot processes, which would be selected for investigation at higher resolution by transmission electron microscopy (see Video 1.2.1). For diagnostic pathology, the whole glomerulus would be examined. Key: red, keratin; blue/green, collagen; light red/pink, cytoplasm. (Courtesy of M Balys.)

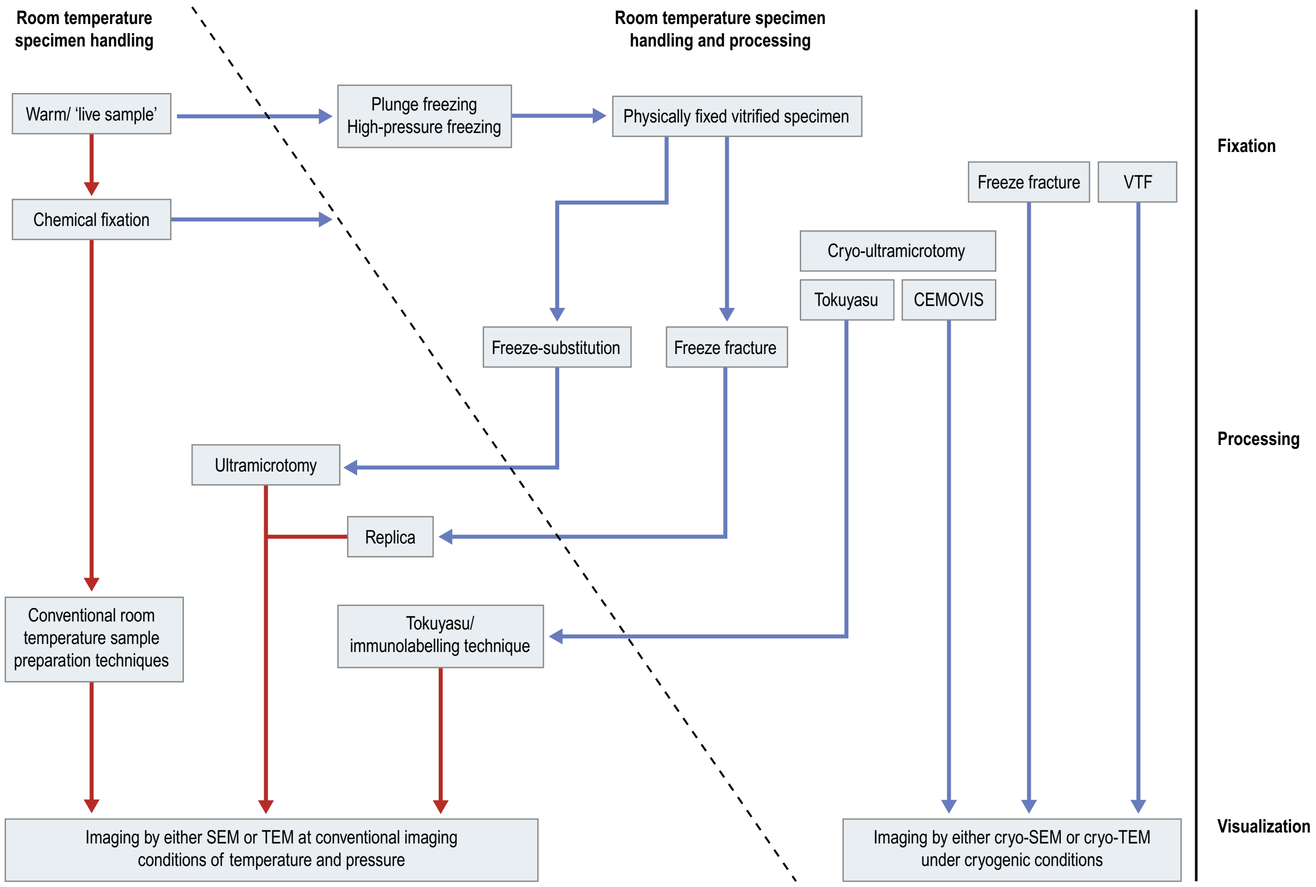
Room temperature specimen handling
Room temperature specimen handling and processing
Warm/ 'live sample'
Plunge freezing
High-pressure freezing
Physically fixed vitrified specimen
Fixation
Chemical fixation
Freeze fracture
VTF
Cryo-ultramicrotomy
Tokuyasu
CEMOVIS
Freeze-substitution
Freeze fracture
Processing
Ultramicrotomy
Replica
Conventional room temperature sample preparation techniques
Tokuyasu/ immunolabelling technique
Imaging by either SEM or TEM at conventional imaging conditions of temperature and pressure
Imaging by either cryo-SEM or cryo-TEM under cryogenic conditions
Visualization

Fig. 1.2.2 An overview of electron microscopy specimen preparation workflow. Areas to the left of the dashed line are at room temperature, indicating that samples can be handled without the requirement for specialist cryo-operating procedures. Samples to the right of the dashed line must be handled in a manner suitable for vitreous biological samples, taking specific care to pre-cool tools before approaching or manipulating samples. Arrows denote the direction of workflow and key stages required to process a sample from 'living/close to life' state to final image. Vitreous thin film (VTF) is a technique in which a liquid sample is pipetted (4–6 µl) onto a transmission electron microscopy (TEM) grid and blotted to create a thin, even liquid film across the surface of the grid. Ideally, the TEM grid should have a holey carbon film and, following blotting, the liquid sample will be held as a monolayer (approximately 12 nm thick) of particles supported within the holes. This film is then plunged rapidly into a liquid cryogen (ethane) to vitrify the sample, generating a vitreous ice film that is amorphous (no long-range structure) and thus a desirable support phase for cryo-electron microscopy of the encased particles (Cheng et al 2012). Other abbreviations: CEMOVIS, cryo-electron microscopy of vitreous sections; SEM, scanning electron microscopy. (Adapted with permission from Fleck RA 2015 Low-temperature electron microscopy. In: Wolkers W, Oldenhof H (eds) Methods in Cryopreservation and Freeze-Drying Protocols. Methods in Molecular Biology. Berlin: Springer.)

temperature- and pressure-dependent. Crystallization depends on the cooling rate, itself dependent on the thermal properties of water, the sample thickness and the heat extraction flow at the surface of the specimen. Freezing is a time-dependent process. Vitrification sits at the beginning of a workflow where the sample is either subsequently processed to a stable room-temperature state for imaging or maintained in its vitreous state throughout (see Fig. 1.2.2) (Fleck 2015).

There are a variety of methods for rapid freeze fixation of tissues. However, the depth of vitrification is often limited (e.g. a few microns for samples plunged into liquid cryogen). Of the available technologies, high-pressure freezing (HPF) is by far the most effective. First introduced by Moor and Riehle in 1968, HPF exploits the physical benefit of high pressure (210 MPa) to reduce the cooling rate required for the vitrification of water from several 100,000 K.s^{-1} to a few 1,000 K.s^{-1}, making vitrification of relatively thick samples practicable (Moor and Riehle 1968, Studer et al 2008). HPF machines synchronize the pressurization and cooling of a sample to below the glass transition temperature (Tg) within 20 ms, in a highly reproducible manner (Müller and Moor 1984, Riehle 1968, Studer et al 2001), extending the depth of vitrification to as much as 200 µm (Studer et al 1995, Studer et al 2008). These machines are now incorporating added functionality to achieve a high degree of temporal resolution. For example, light-sensitive cation channels can be expressed in cells and tissues, stimulated in the HPF pressure chamber at different time intervals (ranging from ms to s) and immediately cryo-immobilized. Electron micrographs acquired from many time points reveal in minute detail sequences of morphological changes with ms precision. Using this approach, the process of ultrafast endocytosis has been characterized during neurotransmission (Watanabe 2016). Electrical stimulation has also been adapted to HPF technology, allowing electron microscopy to reveal complex events previously identified by electrophysiology.

Tissue samples prepared in this way require further modification to make them compatible with the transmission electron microscope. They must either be converted to a room-temperature stable state (e.g. by freeze substitution into a resin), or be sectioned whilst remaining below the glass transition temperature (T_g); when this is achieved, images close to the native structure of biological specimens can be obtained. Despite its benefits, cryo-electron microscopy of vitreous sections (CEMOVIS) has not been routinely adopted, principally because of the technical difficulty in producing a ribbon of frozen sections and transferring it to an EM grid. A double micromanipulator tool that guides the ribbon using an electrically conductive fibre, and then positions and attaches the ribbon to an EM grid has been developed (Studer et al 2014) (**Fig. 1.2.3**).

ADVANCES IN INSTRUMENTATION AND DETECTOR TECHNOLOGY

EM has undergone a revolution in recent years, largely coincident with the advent of digital charge-couple device (CCD) cameras and increasing personal computer (PC) processing power. What was principally a two-dimensional technique now readily embraces three dimensions by electron tomography (Gan and Jensen 2011). In this technique, a specimen is tilted through the incident beam, sequential images are acquired, and, after alignment, a weighted back-projection is used to generate a three-dimensional tomographic volume (see Video 1.2.1). These techniques have stimulated instrument changes. In conventional TEM, low

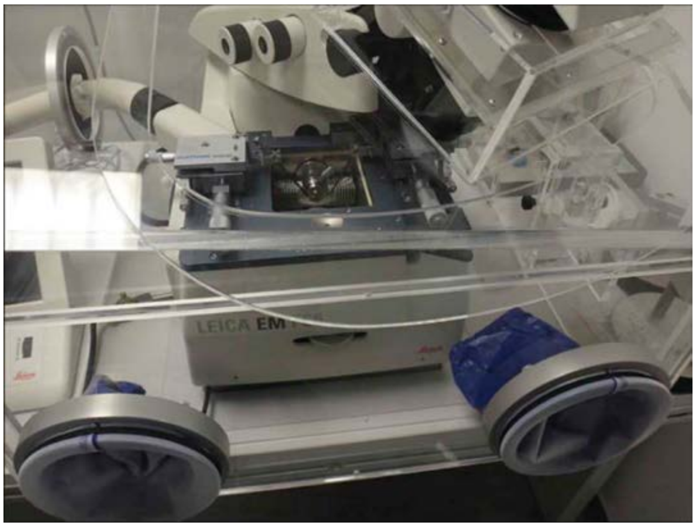

Fig. 1.2.3 Cryo-electron microscopy of vitreous sections (CEMOVIS) performed using a cryo-ultramicrotome. The cryo-chamber (Leica EM FC6, Leica Microsystems, Austria) is mounted on a conventional room-temperature ultramicrotome (Leica EM UC6, Leica Microsystems, Austria). The double manipulators (Manip, Diatome, Switzerland) are then attached to the top of the cryo-chamber, allowing precise control of both the vitreous ribbon and the transmission electron microscopy grid. The system is located within a glove box to maintain a low-humidity environment around the sample that will reduce contamination during sectioning.

accelerating voltages (80–120 keV) provide a strong beam-to-specimen interaction in order to increase contrast from electron scattering. Cryo-TEM and tomography require higher accelerating voltages (200–300 keV), which reduce the beam-to-specimen interaction; the contribution of chromatic aberration to the image is also reduced, theoretically improving resolution (Williams and Carter 2009).

Changing the emission source has been another major technical advance. A field emission gun (FEG) is becoming the preferred source of the electron beam because it provides a beam of smaller diameter, higher coherence and a current density (brightness) of up to three orders of magnitude greater than was achieved with conventional thermionic emitters (e.g. tungsten or lanthanum hexaboride (LaB_6)-tipped filaments) (Kersker 2001). The net results for both scanning electron microscopy (SEM) and TEM have been greatly improved signal-to-noise ratio and spatial resolution, coupled with a significant increase in emitter life and reliability. FEG has had a major impact on the practicality of cryo-SEM and resolution in cryo-TEM studies, although these higher accelerating voltages carry the penalty of decreased contrast.

Overcoming the challenges of contrast in the transmission electron microscope

Zero-loss energy filtering is employed to improve image contrast in the transmission electron microscope. The filter may be positioned either in-column or post-column. Increased scattering contrast and the exclusion of the blurred background (as a consequence of the interception of inelastically scattered electrons) allow specimens to be imaged closer to focus, and increase high-resolution contrast and image resolution (Grimm et al 1997, Grimm et al 1998).

Energy-filtered transmission electron microscopy (EFTEM) imaging to remove the contributions of inelastically scattered electrons is advantageous when imaging thick biological samples. Han et al (1995) demonstrated that only elastically scattered electrons contributed to the coherent image component when imaging biological specimens of more than 0.5 μm thick at 200 keV; optimization of the zero-loss signal required operation at intermediate to high primary accelerating voltages (over 200 keV). The gain due to EFTEM increases with specimen thickness, with a linear dependence for light-scattering elements (Grimm et al 1998). These results are important for the accurate recording of images of thick biological specimens by tomography and to demonstrate the increasing importance of high accelerating voltages in biological TEM (Grimm et al 1998).

New technologies are overcoming previous limitations imposed by low contrast in the transmission electron microscope. Zernike phase plates (ZP), which are well accepted for imaging with the light microscope, represent a novel approach to imaging in the transmission electron microscope. Despite technical hurdles in their use, the potential reward in greater contrast has driven research into this technology (Fukuda et al 2009, Glaeser 2013). An approximate five-fold increase in contrast is possible with a $\{\pi/2\}$ ZP that shifts the phase of only the scattered electrons (these phase-shifted electrons interfere with the unscattered electrons in the image plane), resulting in amplitude contrast rather than phase contrast. Indirect scintillator-coupled charge-coupled device (SCCD) cameras replaced film cameras and revolutionized EM because they provided a near-instant digital readout and obviated the physical limitation of a fixed number of image plates. Direct detection devices (DDD) avoid the fundamental inefficiencies of the electron-to-light conversion process of a scintillator and achieve unmatched sensitivity and resolution with superior detective quantum efficiency (DQE) relative to a conventional CCD camera (Milazzo et al 2010). Moreover, direct exposure to the incident electron beam significantly improves the signal-to-noise ratio in comparison to a SCCD (Milazzo et al 2010). Perhaps more importantly, DDD allow images to be recorded as movies, which means that movement caused by the electron beam can be corrected computationally (Grigorieff 2013). As an example, images of ribosomes of sufficient quality to permit alignment at an accuracy that approaches near-atomic resolution have been obtained using approximately 30,000 images (Bai et al 2013).

When combined, ZP, EFTEM and DDD offer a paradigm shift in the capability of the transmission electron microscope and are likely to drive further advances in EM-based research. Whether in isolation or combination, these techniques will translate from cutting edge to routine instrumentation, heralding generic benefits to the field. Phase contrast electron microscopy utilizing ZP has already been applied to histochemically stained strong-phase (high-contrast heavy-metal-stained) biological specimens (Atsuzawa et al 2009). In sections of various thicknesses specifically stained for the Golgi apparatus, a high-contrast gain was observed even for strong-phase objects, indicating that phase contrast electron microscopy has an application for traditional strong-phase-contrasted biological specimens (Atsuzawa et al 2009), as well as for low-phase cryo-fixed biological specimens (e.g. the visualization of cyanophage Syn5 inside its host, *Synechococcus*, using ZP in combination with cryo-tomography (cryo-ET) to enhance image contrast over conventional cryo-ET) and will permit direct identification of subcellular components (Dai et al 2013).

ADVANCES IN THE SCANNING ELECTRON MICROSCOPE

Cryo-FEGSEM has become well established as a research tool. The stability and emitter life of a FEG source, coupled with the stability and low keV sensitivity of a modern scanning electron microscope, is a powerful tool (Fleck and Humbel 2019). Unlike TEM, in which high accelerating voltages are used to transmit the electrons through the specimen, SEM benefits from low accelerating voltages that limit beam interaction with the specimen. This is key to successful cryo-SEM but creates a challenge around generating sufficient signal for high-resolution imaging. Modern FEGSEM systems (with improved detector sensitivity and signal-to-noise ratios) are now achieving sub-nm resolution at 1 keV, making them highly capable tools for life science research, particularly when combined with high-resolution coating and fracture techniques (Fleck 2015) (see Fig. 1.2.2; **Fig. 1.2.4**).

Large three-dimensional volumes may be generated by the assembly of sequential two-dimensional images acquired in the scanning electron microscope. There are essentially three strategies, each with unique strengths and weaknesses: focused ion beam (FIB), serial block face SEM (SBFSEM) and array tomography (AT). FIB involves milling of material in a dual-beam scanning electron microscope using a focused beam of gallium ions to cut (mill) away layers of material. After each cut, the surface is imaged, ultimately producing a stack of two-dimensional images that can be aligned to generate a three-dimensional volume. Although FIB can be combined with cryo-preparation techniques, elemental microanalysis and the range of imaging modes available within the SEM, it can be challenging (problems include achieving registry between slices, gallium contamination of the sample, and damage to structural information caused by the milling process).

SBFSEM takes a different approach from FIB and incorporates a microtome within the scanning electron microscope chamber (Denk and Horstmann 2004). The microtome cuts a thin section from the block, an image is taken and the procedure is repeated until a three-dimensional volume is generated (**Video 1.2.2**). SBFSEM is less prone to registration issues because the sample essentially remains locked in position below the detector. However, like FIB, this technique is destructive since, once sectioned, the sample is lost. SBFSEM uses room

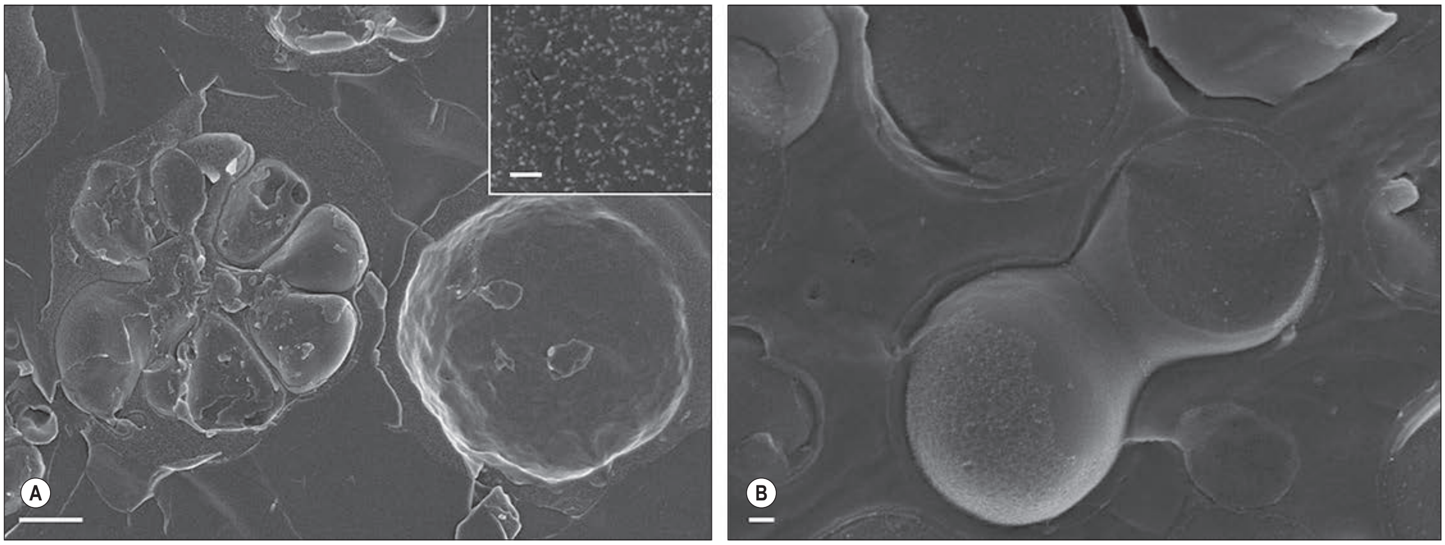

Fig. 1.2.4 Cryo-scanning electron microscopy (SEM) images. **A**, Fractured *Plasmodium falciparum*-infected erythrocytes. A cross-fractured infected erythrocyte is shown; the insert depicts a high-magnification image of the p-face of the infected erythrocyte with membrane proteins visible on the fracture plane. The scale bar represents 1 μm (main image) and 100 nm (inset). **B**, Cross-fractured *Neisseria meningitidis* showing surface membrane protein organization and polysaccharide coat. The scale bar represents 100 nm. Images were taken with a cold-field emission gun cryo-SEM (JSM-7401F, JEOL, Japan), equipped with a Baltec/Leica VCT100 vacuum transfer system and cryo-stage. Coating was applied after fracturing (3 nm Pt/C) using multi-angle rotational coating (BAF060, Baltec/Leica Microsystems, Austria).

temperature processing techniques with high levels of *en bloc* heavy metal staining that are required to generate a sufficiently robust back-scattered electron signal to form an image. The processing steps, and the limitations of the back-scattered electron detector, mean that SBFSEM is currently incompatible with elemental microanalysis or cryo-techniques. However, this is a nascent technology that is advancing rapidly. Novel applications will emerge with advances in detectors, improved resins (e.g. conductive resins) and the exploitation of charge suppression approaches in the SEM (e.g. beam deceleration).

Unlike FIB and SBFSEM, AT is not destructive and material may be recovered and re-imaged. The technique allows samples to be prepared by any TEM preparation strategy. Material is sectioned at room temperature by ultramicrotomy; the sections are collected in order as a ribbon and may then be stained to enhance contrast, or are immunolabelled. Ribbons may be imaged by LM or SEM; individual sections can be identified, recovered and imaged at the higher spatial resolution of the transmission electron microscope. Successful AT requires high-precision x-y-z sample stages that can perform programmed, sequential (in focus) imaging of serial sections. Arguably the most challenging aspect of the workflow is the serial sectioning of the sample; to date, this is undertaken almost exclusively by highly skilled operators. To simplify the process of collecting a large number of sequential sections a number of innovative solutions have been developed. The ATUMtome (RMC, USA) employs a tape system to automate the serial sectioning process by collecting hundreds of individual sections sequentially on a tape (Fig. 1.2.5) and the ARTOS3D (Leica-microsystems, Vienna) automatically creates and collects hundreds of serial-section ribbons on a carrier (silicon wafer or slide) ready for AT using a SEM equipped with software able to automate imaging of each section (or region of interest contained within a section) for all the sections loaded into the SEM. New multibeam-multidetector SEMs (e.g. 61 concurrent beams) have been developed that allow images of up to 1.2 billion pixels to be acquired in 1 s (Marx 2013) further speeding data acquisition.

Access to the cell interior enables structural studies *in situ* within otherwise unperturbed cellular environments and is an emerging frontier of life science electron microscopy. Although FIB milling is slow, it is uniquely able to produce, in a precise and controlled way, undistorted layers of suitable thickness for electron tomography. The alternative method for thinning specimens, cryo-sectioning of vitrified samples (CEMOVIS), is limited by knife damage, which compresses cryo samples by ~30% and limits usable section thickness to 50–80 nm, barely retaining any relevant 3D context. A cryo TEM operating at 200 or 300 kV or in STEM mode can readily acquire tomograms from sections up to 600 nm thickness. A minimum section depth of at least 200 nm is required to completely include major cell structures such as the nuclear pore complex (~120 nm), and malarial knob structures (~150 nm). A cryo-focused ion beam field emission scanning electron microscope (cryo FIB SEM) can be used for the preparation of vitrified lamellae of cellular material to be imaged by cryo-electron tomography in a cryo TEM. This allows three-dimensional (3D) structures of cell and tissue regions at nanoscale resolution to be determined, in order to understand biological machinery in its native, cellular context. Electron tomography generates the 3D structures of irregular samples such as cells and organelles. Once good tomograms are available, it is possible to extract multiple copies of a structure of interest and apply single particle methods to obtain high resolution 3D structures. This approach has been demonstrated for membrane coat complexes in FIB lamellae (Bykov et al 2017). There are few currently published tomography studies of FIB milled cells, however, each is reinforcing cryo FIB milling as a key preparative step in the workflow for cellular structural biology (Engel et al 2015, Mahamid et al 2015, Arnold et al 2016, Mahamid et al 2016). Its ability to precisely target and prepare electron-transparent volumes, from areas identified using CLEM approaches that harbour molecular machines in their functional context, is becoming increasingly important for cell biology. When combined with automated tomographic data acquisition in the TEM, the potential for quantitative investigation of 3D cellular structures is truly realized.

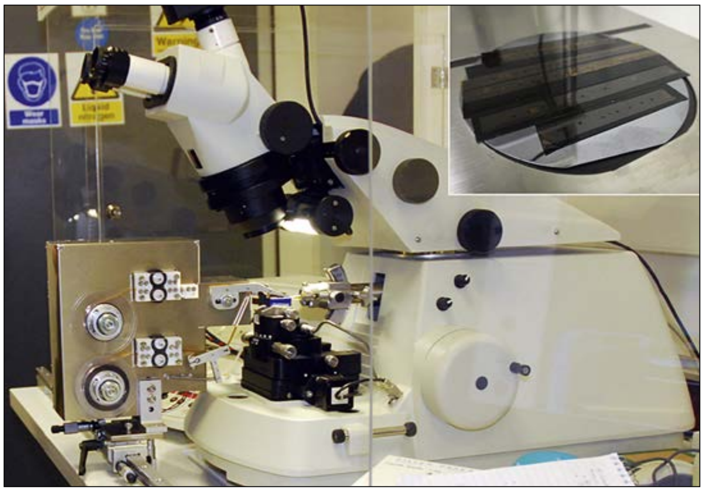

Fig. 1.2.5 ATUMtome and tape. The ATUMtome is mounted on a PT-PC PowerTome (RMC, USA), showing the tape being transferred from a delivery spool (top) to receiving spool (bottom) through the boat, which maintains a water reservoir behind the edge of the diamond knife (blue) to float the sections and allow their capture by tape. Tape tension is maintained throughout by a series of tensioning springs and guides. The inset shows individual sections on tape mounted on carbon tape and silicon wafer (to help dissipate specimen charging during imaging) ready for viewing in the scanning electron microscope.

Future trends

Developments in thin-film technology and microfabrication are facilitating the design of liquid cells that will permit improved imaging of samples in the liquid phase (de Jonge and Ross 2011). In combination with recent advances in ZP, EFTEM and DDD, the new generation of liquid cells offers considerable potential for the study of complex dynamic cellular processes. These may be further enhanced by the translation of emerging trends in material science to the life sciences which proffer higher resolution and a capacity to address transient structures. These include pulsed source TEM, compressive sensing, 4D STEM, ptychographic phase reconstruction (Dömer and Bostanjoglo 2003, Barwick et al 2008, Zewail 2010, Browning et al 2012, Stevens et al 2014, Yang et al 2015).

References

Arnold J, Mahamid J, Lucic V et al 2016 Site-specific cryo-focused ion beam sample preparation guided by 3D correlative microscopy. Biophys J 110:860–9.

Atsuzawa K, Usuda N, Nakazawa A et al 2009 High-contrast imaging of plastic-embedded tissues by phase contrast electron microscopy. J Electron Microscopy 58:35–45.

Bai XC, Fernandez IS, McMullan G et al 2013 Ribosome structures to near-atomic resolution from thirty thousand cryo-EM particles. Elife 2:e00461.

Barwick B, Park HS, Kwon O et al 2008 4D Imaging of transient structures and morphologies in ultrafast electron microscopy. Science 322:1227–31.

Boyde A, Maconnachie E 1979 Volume changes during preparation of mouse embryonic tissue for scanning electron microscopy. Scanning 2:149–63.

Browning ND, Bonds MA, Campbell GH et al 2012 Recent developments in dynamic transmission electron microscopy. Curr Opin Solid State Mater Sci 16:23–30.

Bykov YS, Schaffer M, Dodonova SO et al 2017 The structure of the COPI coat determined within the cell. Elife 6:e32493.

Cheng D, Mitchell DRG, Shieh D-B et al 2012 Practical considerations in the successful preparation of specimens for thin-film cryo-transmission electron microscopy. In: Méndez-Vilas A (ed) Current Microscopy Contributions to Advances in Science and Technology, Microscopy Series no. 5 (vol. 2). Badajoz: Formatex, pp. 880–90.

Claeys M, Vanhecke D, Couvreur M et al 2004 High-pressure freezing and freeze substitution of gravid Caenorhabditis elegans (Nematoda: Rhabditida) for transmission electron microscopy. Nematology 6:319–27.

Dai W, Fu C, Raytcheva D et al 2013 Visualizing virus assembly intermediates inside marine cyanobacteria. Nature 502:707–10.

de Haro T, Furness P 2012 Current and future delivery of diagnostic electron microscopy in the UK: results of a national survey. J Clin Pathol 65:357–61.

de Jonge N, Ross F 2011 Electron microscopy of specimens in liquid. Nat Nanotechnol 6:695–704.

Denk W, Horstmann H 2004 Serial block-face scanning electron microscopy to reconstruct three-dimensional tissue nanostructure. PLoS Biol 2:e329.

Dömer H, Bostanjoglo O 2003 High-speed transmission electron microscope. Rev Sci Instrum 74:4369.

Engel BD, Schaffer M, Kuhn Cuellar L et al 2015 Native architecture of the *Chlamydomonas* chloroplast revealed by in situ cryo-electron tomography. Elife 4:e04889.

Fleck RA 2015 Low-temperature electron microscopy. In: Wolkers W, Oldenhof H (eds) Methods in Cryopreservation and Freeze-Drying. Lab Protocol Series, Methods in Molecular Biology. Berlin: Springer, pp. 243–74.

Fleck RA, Humbel BM (eds) 2019 Biological field emission scanning electron microscopy. Oxford: Wiley–Blackwell.

Fukuda Y, Fukazawa Y, Danev R et al 2009 Tuning of the Zernike phase-plate for visualization of detailed ultrastructure in complex biological specimens. J Struct Biol 168:476–84.

Gan L, Jensen GJ 2011 Electron tomography of cells. Q Rev Biophys 45:27–56.

Glaeser RM 2013 Methods for imaging weak-phase objects in electron microscopy. Rev Sci Instrum 84:111101.

Glauert AM, Lewis PR 1998 Biological specimen preparation for transmission electron microscopy. London: Portland Press.

Grigorieff N 2013 Structural biology: direct detection pays off for electron cryo-microscopy. Elife 2:e00573.

Grimm R, Bärmann M, Häckl D et al 1997 Energy-filtered electron tomography of ice-embedded actin and vesicles. Biophys J 72:482–89.

Grimm R, Typke D, Baumeister W 1998 Improving image quality by zero-loss energy filtering – quantitative assessment by means of image cross-correlation. J Microsc-Oxford 190:339–49.

Han KF, Sedat JW, Agard DA 1995 Mechanism of image formation for thick biological specimens: exit wavefront reconstruction and electron energy-loss spectroscopic imaging. J Microsc-Oxford 178:107–19.

Hayat MA 2000 Chemical fixation. In: Principles and Techniques of Electron Microscopy: Biological Applications, 4th ed. Cambridge: Cambridge University Press, pp. 4–80.

Kellenberger E 1991 The potential of cryofixation and freeze substitution: observations and theoretical considerations. J Microsc-Oxford 161:183–203.

Kersker MM 2001 The modern microscope today. In: Zhang X-F, Zhang Z (eds) Progress in Transmission Electron Microscopy 1: Concepts and Techniques. Berlin: Springer, pp. 1–34.

Mahamid J, Pfeffer S, Schaffer M et al 2016 Visualizing the molecular sociology at the HeLa cell nuclear periphery. Science 351:969–72.

Mahamid J, Schampers R, Persoon H et al 2015 A focused ion beam milling and lift-out approach for site-specific preparation of frozen-hydrated lamellas from multicellular organisms. J Struct Biol 192:262–9.

Marx V 2013 Brain mapping in high resolution. Nature 503:147–52.

McDonnald KL 2009 A review of high-pressure freezing preparation techniques for correlative light and electron microscopy of the same cells and tissues. J Microsc-Oxford 235:273–81.

Milazzo AC, Moldovan G, Lanman J et al 2010 Characterization of a direct detection device imaging camera for transmission electron microscopy. Ultramicroscopy 110:744–47.

Moor H, Riehle U 1968 Snap-freezing under high pressure: a new fixation technique for freeze-etching. Proc Fourth Europ Reg Conf Elect Microsc 2:33–4.

Müller M, Moor H 1984 Cryofixation of thick specimens by high pressure freezing. In: Revel JP, Barnard T, Haggis GH (eds) Science of Biological Specimen Preparation. AMF O'Hare, Chicago: SEM, pp. 131–8.

Nermut MV 1991 Unorthodox methods of negative staining. Micron Microsc Acta 22:327–39.

Nermut MV, Frank H 1971 Fine structure of Influenza A2 (SINGAPORE) as revealed by negative staining, freeze-drying and freeze-etching. J Gen Virol 10:37–51.

Plitzko JM, Rigort A, Leis A 2009 Correlative cryo-light microscopy and cryo-electron tomography: from cellular territories to molecular landscapes. Curr Opin Biotechnol 20:83–9.

Riehle U 1968 Über die Vitrifizierung verdünnter wässriger Lösungen. Dissertation No. 4271: Eidgenössiche Technische Hochschule. Zurich: Federal Institute of Technology (ETH).

Robards AW, Sleytr UB 1995 Low temperature methods in biological electron microscopy. In: Glauert AM (ed) Practical Methods in Electron Microscopy, vol. 10. Amsterdam: Elsevier, pp. 5–146.

Sartori A, Gatz R, Beck F et al 2007 Correlative microscopy: bridging the gap between fluorescence light microscopy and cryo-electron tomography. J Struct Biol 160:135–145.

Steinbrecht RA, Zierold K 1987 Cryotechniques in biological electron microscopy. Berlin: Springer.

Stevens A, Yang H, Carin L et al 2014 The potential for Bayesian compressive sensing to significantly reduce electron dose in high-resolution STEM images. Microscopy 63(1):41–51.

Studer D, Michel M, Wohlwend M et al 1995 Vitrification of articular cartilage by high-pressure freezing. J Microsc-Oxford 179:321–32.

Studer D, Graber W, Al-Amoudi A et al 2001 A new approach for cryofixation by high-pressure freezing. J Microsc-Oxford 203:285.

Studer D, Humbel BM, Chiquet M 2008 Electron microscopy of high pressure frozen samples: bridging the gap between cellular ultrastructure and atomic resolution. Histochem Cell Biol 130:877–89.

Studer D, Klein A, Iacovache I et al 2014 A new tool based on two micromanipulators facilitates the handling of ultrathin cryosection ribbons. J Struct Biol 185:125–8.

Watanabe S 2016 Flash-and-freeze: coordinating optogenetic stimulation with rapid freezing to visualize membrane dynamics at synapses with millisecond resolution. Front Synaptic Neurosci 8:24.

Williams DB, Carter CB 2009 Transmission Electron Microscopy: A Textbook for Materials Science. Berlin: Springer.

Yang H, Jones L, Ryll H et al 2015 4D STEM: High efficiency phase contrast imaging using a fast pixelated detector. J Phys Conf Ser 644: conf 1. doi: 10.1088/1742-6596/644/1/012032.

Zewail AH 2010 Four-dimensional electron microscopy, Science 328:187–93.

COMMENTARY

1.3

Metaplasia

Jonathan M.W. Slack

Metaplasia is the appearance, in adult life, of a patch of tissue that normally belongs elsewhere in the body (Slack 1985, 2007). Generally it is understood that a metaplasia has originated *in situ* and has not migrated from elsewhere; so, for example, metastatic tumour deposits are not considered to be metaplasias, nor are tissues misplaced during embryonic development, such as thyroid residues in the thyroglossal duct.

Metaplasias are very diverse (Willis 1962). They include ectopic bone and cartilage arising from connective tissue, squamous metaplasia of glandular epithelia, and substitution of one glandular epithelial tissue for another. The latter group is of particular interest from a biological point of view. These transformations are normally between tissue types that originated in embryonic development as neighbours in a common cell sheet. Such tissues may remain neighbours into adult life or may become separated. An example of metaplasia between tissues that are still neighbours in the adult is intestinal metaplasia of the stomach, involving patches of small intestine-like epithelium which are found in the stomach (Stemmerman and Hayashi 1968, Gutierrez-Gonzalez and Wright 2008). An example of metaplasia between tissues that have become anatomically separated is intestinal metaplasia found in the urinary bladder that typically comprises cell types and markers normally found in the colon (Sung et al 2006). The bladder is no longer part of a common cell sheet with the intestine in the adult, but it is in the embryo, where it originates from the allantoic diverticulum of the hind gut. Metaplasias of glandular epithelia are particularly common in the gastrointestinal tract and in the female reproductive tract (Kurita 2011), perhaps because these are both examples of structures in which a number of different tissue types arise from a simple epithelial tube in the embryo.

The metaplasias are clinically important because they often predispose to cancer: for example, carcinomas of the bronchus usually arise within areas of squamous metaplasia (Auerbach 1961, Rigden 2016) and carcinomas of the stomach usually arise in regions of intestinal metaplasia (Correa 1992, Busuttil and Boussioutas 2009, Spence et al 2017). Metaplasias arise because the combination of gene activities that normally defines the tissue type in embryonic development becomes altered in adult life. The genes in question encode a limited number of key transcription factors. For example, the transcription factor p63 is essential for the formation of squamous epithelia (Koster et al 2004) and is always found to be expressed in patches of squamous metaplasia. The transcription factor CDX2 is required for the formation of intestinal epithelium, and is expressed in patches of intestinal metaplasia (Barros et al 2012). Epithelial tissues like these are maintained by continuous renewal from a population of stem cells, and the initiating event, which may be a somatic mutation or an epigenetic change of gene expression, changes the character of the stem cells: once the change has occurred, it is normally irreversible.

Barrett's metaplasia, also known as Barrett's oesophagus, is a well-studied example of metaplasia (Falk 2002, Gilbert et al 2011, Naini 2016, Colleypriest et al 2017) (**Fig. 1.3.1**). It is characterized by the

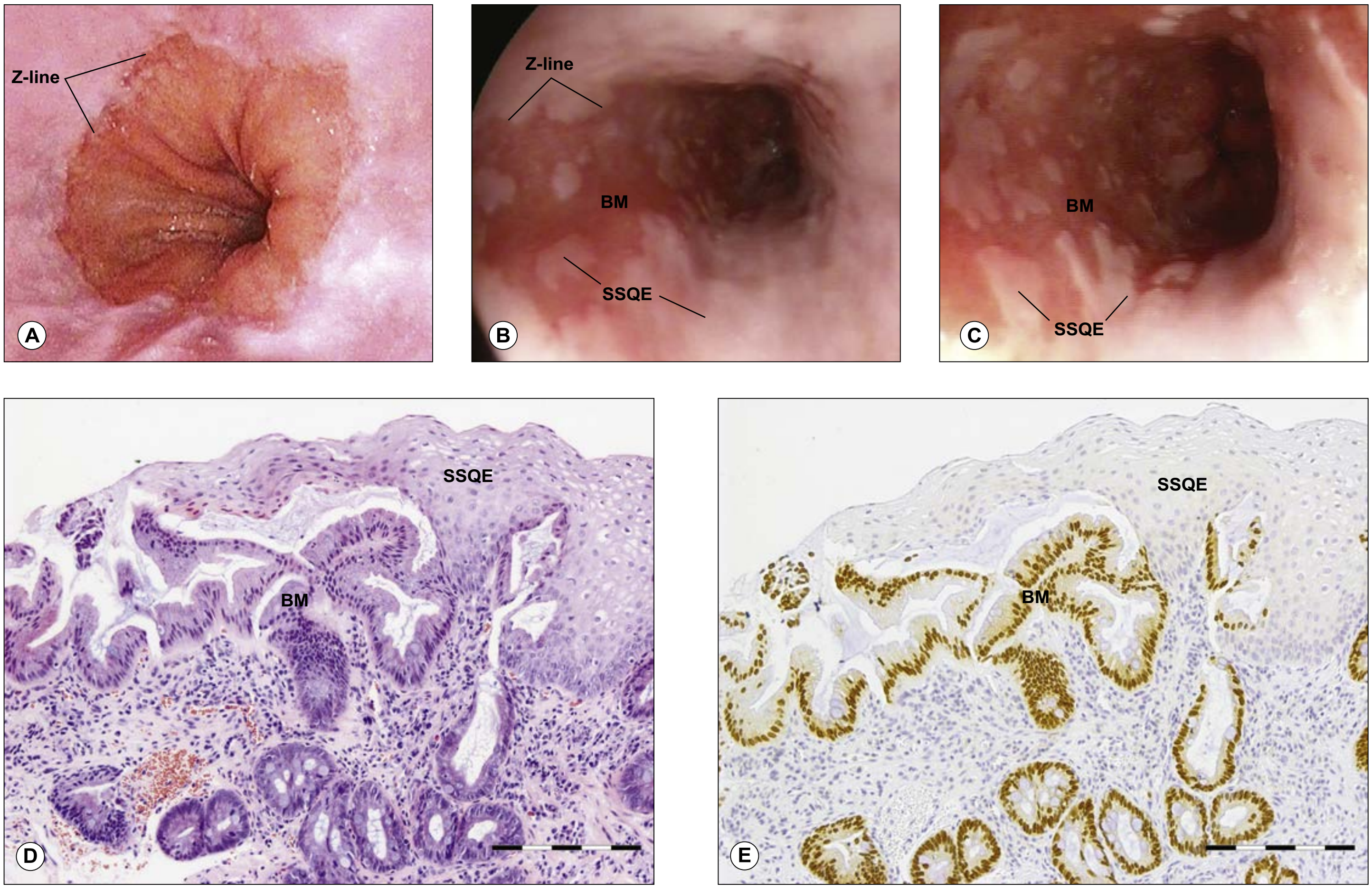

Fig. 1.3.1 Barrett's metaplasia. **A–C**, Endoscopy. **A**, Normal appearance showing the junction between gastric columnar and oesophageal squamous epithelium (Z-line). **B–C**, Two cases of Barrett's oesophagus. The Z-line has moved proximally and is very irregular. There are islands of squamous tissue within the columnar region. Abbreviations: SSQE, squamous epithelium; BM, metaplastic epithelium. **D–E**, Histological views. **D**, Hematoxylin and eosin staining. **E**, Immunostained for CDX2 (brown). Scale bar 200 µm.

presence of columnar epithelium in the distal oesophagus, some of which resembles intestinal epithelium because of the presence of goblet cells. Barrett's metaplasia is a risk factor for the development of oesophageal adenocarcinoma, a cancer whose incidence rose considerably in the late twentieth century (Hvid-Jensen et al 2011). In less developed countries most oesophageal cancers are squamous cell carcinomas, arising from the normal squamous lining of the oesophagus, but in the Western world adenocarcinomas are now more common.

Some metaplasias are monoclonal, meaning that a particular focus of ectopic tissue is derived exclusively from a single cell, as would be expected if the cause is the somatic mutation of key transcription factor genes. Monoclonality has been demonstrated for individual foci of intestinal metaplasia of the stomach, where neighbouring metaplastic crypts arise by fission (Gutierrez-Gonzalez et al 2011). In Barrett's metaplasia, patches of crypts are also monoclonal (Nicholson et al 2012) although the lesion as a whole is polyclonal, being derived from several original progenitors, with various combinations of abnormalities arising from somatic mutation (Leedham et al 2008). A key property of metaplastic foci is that the new tissue is in a situation of competitive growth with the old tissue that surrounds it. Unless the metaplastic tissue can outgrow the surrounding tissue then the transformation of a single stem cell would not give rise to a macroscopic lesion: this aspect of epithelial biology remains poorly understood.

The exact cell of origin of Barrett's metaplasia is still not known (McDonald et al 2015). Theories include a migration of glandular tissue from the stomach; an origin from transitional or primitive cells located at the squamo-columnar junction; metaplasia of the squamous epithelium of the oesophagus; an origin from submucosal oesophageal glands. The plausibility of transformation of the squamous epithelium or the oesophageal glands is increased by the fact that the normal oesophagus originates from an endodermal tube lined with columnar epithelium that becomes squamous between about 6–7 weeks of gestation (Yu et al 2005, Zhang et al 2017).

The predisposing cause of Barrett's metaplasia is gastro-oesophageal reflux, in which stomach acid and bile from the intestine enters the oesophagus (Souza 2010). It is known that this environment can induce expression of some of the key genes involved in intestinal development, such as those encoding CDX factors and hepatocyte nuclear factors, in oesophageal cells (Eda et al 2003, Debruyne et al 2006, Piessen et al 2007). Obesity is a well-known risk factor for reflux, partly because of effects on intra-abdominal pressure and probably also through the effects of cytokines released from fat (Corley et al 2007). Barrett's metaplasia may progress to dysplasia and to adenocarcinoma. Progression is associated with loss of the tumour suppressor gene *CDKN2A*, encoding the protein p16 which is an inhibitor of cell division, and *TP53*, encoding the protein p53 required for death of abnormal cells (Spechler et al 2010, Chen et al 2011).

Gastro-oesophageal reflux is normally treated with proton pump inhibitors that reduce the levels of stomach acid. This improves associated oesophagitis but does not usually result in regression of any Barrett's metaplasia. Barrett's metaplasia as such is not normally treated: if it progresses to dysplasia, it may be extirpated by a variety of endoscopic techniques of which radiofrequency ablation has become the most usual (Lim and Fitzgerald 2013, Spechler and Souza 2014).

References

Auerbach O, Stout AP, Hammond EC et al 1961 Changes in bronchial epithelium in relation to cigarette smoking and cancer of the lung. N Engl J Med 265:253–67.

Barros R, Freund JN, David L, Almeida R 2012 Gastric intestinal metaplasia revisited: function and regulation of cdx2. Trends Mol Med 18:555–63.

Busuttil RA, Boussioutas A 2009 Intestinal metaplasia: a premalignant lesion involved in gastric carcinogenesis. J Gastroenterol Hepatol 24:193–201.

Chen H, Fang Y, Tevebaugh W et al 2011 Molecular mechanisms of Barrett's esophagus. Dig Dis Sci 56:3405–20.

Colleypriest BJ, Burke ZD, Griffiths LP et al 2017 Hnf4α is a key gene that can generate columnar metaplasia in oesophageal epithelium. Differentiation 93:39–49.

Corley DA, Kubo A, Levin TR et al 2007 Abdominal obesity and body mass index as risk factors for Barrett's esophagus. Gastroenterology 133:34–41.

Correa P 1992 Human gastric carcinogenesis: a multistep and multifactorial process – first American Cancer Society award lecture on cancer epidemiology and prevention. Cancer Research 52:6735–40.

Debruyne PR, Witek M, Gong L et al 2006 Bile acids induce ectopic expression of intestinal guanylyl cyclase c through nuclear factor-kappa b and cdx2 in human esophageal cells. Gastroenterology 130:1191–206.

Eda A, Osawa H, Satoh K et al 2003 Aberrant expression of cdx2 in Barrett's epithelium and inflammatory esophageal mucosa. J Gastroenterol 38:14–22.

Falk GW 2002 Barrett's esophagus. Gastroenterology 122:1569–91.

Gilbert EW, Luna RA, Harrison VL et al 2011 Barrett's esophagus: a review of the literature. J Gastrointest Surg 15:708–18.

Gutierrez-Gonzalez L, Wright NA 2008 Biology of intestinal metaplasia in 2008: more than a simple phenotypic alteration. Dig Liver Dis 40:510–22.

Gutierrez-Gonzalez L, Graham TA, Rodriguez-Justo M 2011 The clonal origins of dysplasia from intestinal metaplasia in the human stomach. Gastroenterology 140:1251–60.

Hvid-Jensen F, Pedersen L, Drewes AM et al 2011 Incidence of adenocarcinoma among patients with barrett's esophagus. N Engl J Med 365:1375–83.

Koster MI, Kim S, Mills AA et al 2004 P63 is the molecular switch for initiation of an epithelial stratification program. Genes Dev 18:126–31.

Kurita T 2011 Normal and abnormal epithelial differentiation in the female reproductive tract. Differentiation 82:117–26.

Leedham SJ, Preston SL, McDonald SAC et al 2008 Individual crypt genetic heterogeneity and the origin of metaplastic glandular epithelium in human barrett's oesophagus. Gut 57:1041–8.

Lim YC, Fitzgerald RC 2013 Diagnosis and treatment of Barrett's oesophagus. Br Med Bull 107:117–32.

McDonald SAC, Lavery D, Wright NA et al 2015 Barrett oesophagus: lessons on its origins from the lesion itself. Nature Rev Gastroenterol Hepatol 12:50–60.

Naini BV, Souza RF, Odze RD 2016 Barrett's esophagus a comprehensive and contemporary review for pathologists. Am J Surg Pathol 40:E45–E66.

Nicholson AM, Graham AM, Simpson A et al 2012 Barrett's metaplasia glands are clonal, contain multiple stem cells and share a common squamous progenitor. Gut 61:1380–9.

Piessen G, Jonckheere N, Vincent A et al 2007 Regulation of the human mucin muc4 by taurodeoxycholic and taurochenodeoxycholic bile acids in oesophageal cancer cells is mediated by hepatocyte nuclear factor 1 alpha. Biochem J 402:81–91.

Rigden HMA, Alias T, Havelock R et al 2016 Squamous metaplasia is increased in the bronchial epithelium of smokers with chronic obstructive pulmonary disease. PloS ONE 11: e0156009.

Slack JMW 1985 Homeotic transformations in man: implications for the mechanism of embryonic development and for the organization of epithelia. J Theor Biol 114:463–90.

Slack JMW 2007 Metaplasia and transdifferentiation: from pure biology to the clinic. Nature Rev Mol Cell Biol 8:369–78.

Souza RF 2010 The role of acid and bile reflux in oesophagitis and Barrett's metaplasia. Biochem Soc Trans 38:348–52.

Spechler SJ, Fitzgerald RC, Prasad GA et al 2010 History, molecular mechanisms, and endoscopic treatment of Barrett's esophagus. Gastroenterology 138:854–69.

Spechler SJ, Souza RF 2014 Barrett's esophagus. N Engl J Med 371:836–45.

Spence AD, Cardwell CR, McMenamin UC et al 2017 Adenocarcinoma risk in gastric atrophy and intestinal metaplasia: a systematic review. BMC Gastroenterol 17:157.

Stemmermann GN, Hayashi T 1968 Intestinal metaplasia of the gastric mucosa. A gross and microscopic study of its distribution in various disease states. J Natl Cancer Inst 41:627–34.

Sung M-T, Lopez-Beltran A, Eble JN et al 2006 Divergent pathway of intestinal metaplasia and cystitis glandularis of the urinary bladder. Mod Pathol 19:1395–401.

Willis RA 1962 The Borderland of Embryology and Pathology. London: Butterworths.

Yu WY, Slack JMW, Tosh D 2005 Conversion of columnar to stratified squamous epithelium in the developing mouse oesophagus. Dev Biol 284:157–70.

Zhang Y, Jiang M, Kim E et al 2017 Development and stem cells of the esophagus. Semin Cell Develop Biol 66:25–35.

COMMENTARY

1.4

Merkel cells

Ellen A. Lumpkin

The epidermis, our outermost layer of skin, serves as a protective barrier and sensory interface with the world. In vertebrates, these functions are accomplished through the work of only four conserved cell types. Keratinocytes form a water-tight barrier, melanocytes protect against ultraviolet damage and Langerhans cells perform immune surveillance. Merkel cells, which constitute less than 1% of the epidermis, are an enigmatic cell type whose function and developmental origin have long been debated; however, recent advances show that mammalian Merkel cells are epithelial derivatives that signal to sensory neurones to initiate touch sensation.

As early as the nineteenth century, Merkel cells were proposed to contribute to skin's sensory function. These cells were first described by Friedrich Sigmund Merkel, who named them touch cells (*Tastzellen*), based on contacts with nerve terminals (Merkel 1875). Merkel cells cluster in highly touch-sensitive skin areas, including glabrous (hairless) skin of fingertips and lips, some hair follicles and touch domes on the trunk (**Fig. 1.4.1**). Most Merkel cells are innervated by a particular class of myelinated (Aβ) sensory neurones called slowly adapting type I (SAI) afferents (Iggo and Muir 1969). These touch receptors are unusual because they produce biphasic discharges of electrical impulses that send two types of information to the brain (see Fig. 1.4.1): dynamic responses to moving stimuli represent an object's spatial features (e.g. edges and curvature), whereas sustained volleys of electrical activity signify steady pressure (e.g. contact with clothing; Johnson 2001).

Merkel cells were initially proposed to serve as sensory receptor cells based on their synapse-like contacts with nerve terminals and dense-core vesicles filled with neurotransmitters (Halata et al 2003). Sensory receptor cells, such as taste-bud cells or hair cells of the inner ear, transduce the energy of a sensory stimulus into electrical signals, which then trigger neurotransmitter release to excite sensory afferents. The hypothesis that Merkel cells are mechanosensory receptors was challenged by neurophysiological studies that reported touch sensitivity after Merkel cell loss, which suggested that Merkel cells act in a non-sensory capacity. Studies in rodent models have reconciled these views by demonstrating that Merkel cells and their sensory afferents are mechanosensory cells. Three lines of evidence support this two-receptor-site model, which was proposed almost three decades ago (Yamashita and Ogawa 1991).

First, Merkel cells are touch-sensitive. Like hair cells in the inner ear, Merkel cells display fast mechanotransduction currents that convert cellular movement into electrical signals (Ikeda et al 2014, Maksimovic et al 2014, Woo et al 2014). These currents are mediated by Piezo2 mechanosensitive ion channels, which are essential for touch and proprioception (Ranade et al 2014, Woo et al 2015, Chesler et al 2016; see Fig. 1.4.1).

Second, Merkel cells are excitatory cells. This was established with optogenetics, a technique that uses light-activated molecules derived from *Archea* to stimulate or inhibit electrical signalling in specific cells. Transgenic mice were engineered to selectively express light-activated membrane proteins in Merkel cells (Maksimovic et al 2014): when their skin is illuminated, Merkel cells are activated and their sensory afferents produce sustained trains of electrical impulses that mimic the response to pressure (see Fig. 1.4.1). Conversely, neuronal firing is inhibited when Merkel cells are optogenetically silenced. These results confirm that Merkel cells are sensory cells capable of exciting afferents.

Third, Merkel cells are necessary for sustained, but not for dynamic, firing in SAI afferents. Prototypical SAI responses are abolished in transgenic mouse strains that lack either Merkel cells or epidermal PIEZO2 expression (Maricich et al 2009, Maksimovic et al 2014, Woo et al 2014). Inhibiting the release of neurotransmitter-containing vesicles from Merkel cells also attenuated touch-evoked neural activity (Chang et al 2016, Hoffman et al 2018). In all cases, sustained touch produced only transient bursts of neuronal impulses (see Fig. 1.4.1). These findings indicate that mechanosensory signalling from Merkel cells is essential for conveying information about pressure to the nervous system. Touch-driven behaviours are compromised in rodents lacking

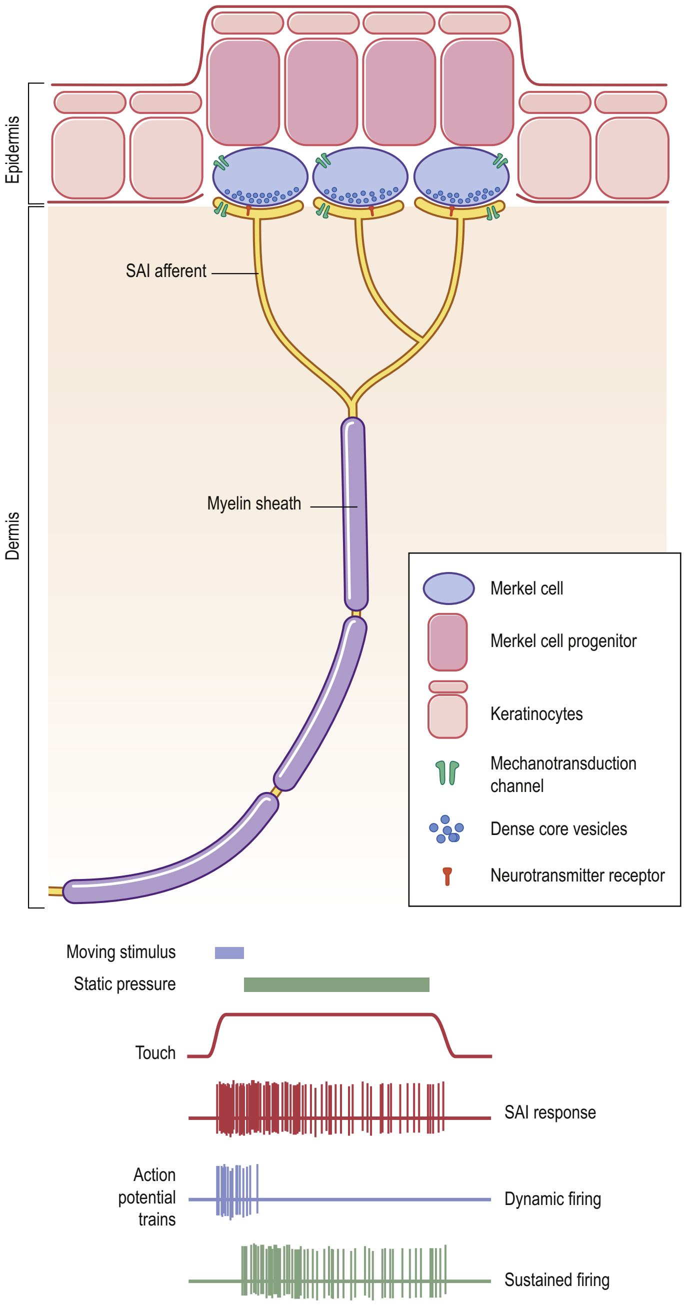

Fig. 1.4.1 The Merkel cell–neurite complex is a compound touch receptor. The schematic shows the innervation of a touch dome. Merkel cells (blue) cluster in these highly touch-sensitive spots in humans and other mammals. Merkel cells are mechanosensory receptor cells derived from epidermal progenitors. Adjacent Merkel cells are innervated by a myelinated sensory afferent fibre (yellow) that produces slowly adapting type I (SAI) responses (black electrical impulses). This response has two phases: (1) *Dynamic firing*: During a moving stimulus (blue bar), Piezo2 mechanotransduction channels (magenta) in the sensory afferent stimulate transient neuronal volleys (blue impulses). (2) *Sustained firing*: Static pressure (green bar) activates the Merkel cells' Piezo2 channels (magenta) to excite electrical signalling. Merkel cells then release monoamine-containing vesicles (black dots) to stimulate sustained electrical impulses in SAI afferent terminals (green). The intracellular signalling pathways that link G-protein coupled monoaminergic receptors (orange) to neural excitation have not been identified. (Receptor and channel symbols © motifolio.com.)

functional Merkel cells, again indicating that Merkel cells are important for the perception of touch (Maricich et al 2012, Ikeda et al 2014, Woo et al 2014). Taken together, these studies demonstrate that the Merkel cell–neurite complex is a compound touch receptor with two mechanosensory cell types arranged in series (see Fig. 1.4.1).

Which neurotransmitters convey information between Merkel cells and sensory afferents remains a key open question. In rodents, it has been proposed that whisker follicle Merkel cells signal through serotoninergic receptors (Chang et al 2016), whereas touch-dome Merkel cells have been reported to employ adrenergic synapses (Hoffman et al 2018). Both findings support the model that Merkel cells use vesicular release of monoamine neuromodulators rather than classical excitatory neurotransmitters to excite the nervous system (see Fig. 1.4.1). Since drugs that target monoamine signalling are widely used for treatment of depression (selective serotonin reuptake inhibitors) and cardiovascular disease (beta-blockers), these basic science findings may have clinical implications by suggesting new treatment avenues for peripheral sensory disturbances such as numbness and tingling.

Transgenic mouse studies have also clarified the ontogeny of the Merkel cell, which expresses an unusual assortment of epithelial and neuronal markers (Moll et al 1984, Halata et al 2003, Haeberle et al 2004). For example, although embedded in a stratified epithelium, Merkel cells express simple epithelial keratins. It was therefore unclear whether Merkel cells are derived from epithelial precursors or neural crest. These competing models were tested in transgenic mice by genetically marking specific cell lineages based on selective expression of *Cre* recombinase. *Wnt1*^{Cre}, which marks all neural crest cells, failed to label Merkel cells, whereas *Krt14*^{Cre}, a marker of keratinocyte-derived cells, labelled Merkel cells in all skin areas (Morrison et al 2009, Van Keymeulen et al 2009). Moreover, Merkel cell specification is disrupted by epithelial-specific deletion of developmental transcription factors (Morrison et al 2009, Van Keymeulen et al 2009, Bardot et al 2013, Lesko et al 2013, Perdigoto et al 2014), and Merkel cells are replenished from epidermal progenitors in mature skin (Van Keymeulen et al 2009, Woo et al 2010, Doucet et al 2013, Wright et al 2017).

The embryonic progenitor of the Merkel cell remains a matter of debate, although recent studies have identified developmental pathways that bestow this neurosensory fate in epidermis. It has been proposed that Merkel cells in mouse hair-bearing skin are derived from hair-follicle placodes, but genetic lineage tracing of hair follicle progenitors has called this model into question (Xiao et al 2016, Jenkins and Lumpkin 2017). Merkel cell progenitors have distinct molecular phenotypes in mouse hairy and glabrous skin (Nguyen et al 2019).

Despite remarkable progress in Merkel cell biology, key questions about human Merkel cells remain unanswered. Do Merkel cells serve additional, non-sensory functions? This is particularly important in human skin, where many Merkel cells lack innervation. Are human Merkel cells derived from epidermis and renewed throughout life? If so, how are these processes disrupted during ageing, which is accompanied by loss of touch receptors in extremities? This loss is thought to contribute to the decline of tactile acuity, grip strength and postural stability in the elderly. Intriguingly, a recent study linked age-related loss of Merkel cells to chronic itch, which is a prevalent clinical problem in the elderly (Feng et al 2018).

Mechanisms of Merkel cell specification may also be important in Merkel cell carcinoma (MCC). This highly aggressive, non-melanoma skin cancer has been linked to Merkel cells on the basis of ultrastructure and molecular markers (Haeberle et al 2004, Bhatia et al 2011, Harms et al 2013). An important unresolved question is whether Merkel cells or their progenitors act as cells of origin for MCC. Distinct molecular pathways appear to give rise to MCC downstream of two risk factors, namely ultraviolet (UV) irradiation or infection with Merkel cell polyoma virus (MCPyV; Feng et al 2008, Harms et al 2018). In most cases of MCC, integration of MCPyV and subsequent inhibition of retinoblastoma tumour suppressor protein give rise to MCPyV-positive tumours with a low mutational burden. By contrast, virus-negative tumours display UV mutational signatures and inactivation of tumour suppressor genes. Despite different aetiologies, virus-positive and virus-negative tumours share similar clinical presentations and treatment guidelines (Harms et al 2018).

Immune checkpoint inhibitors targeting the PD-1 pathway have been a game changer in the clinical care of MCC (Harms et al 2018, Nghiem and Park 2019). These agents are beneficial in almost half of patients with advanced MCC and overall survival at three years is dramatically improved in patients receiving immune checkpoint inhibitors compared with conventional chemotherapies (Nghiem et al 2019). Such promising clinical results have led to rapid changes in treatment guidelines, with immune checkpoint inhibitors now the recommended first-line therapy for advanced MCC in appropriate patients. Nonetheless, new therapies are needed for patients who are immunosuppressed or otherwise resistant to immune checkpoint inhibitors.

ACKNOWLEDGEMENTS

Thanks to members of the Lumpkin laboratory for helpful comments and Dr Blair Jenkins for assistance with the figure. The author is supported by the National Institutes of Health (R01 AR051219 and R01 NS105241) and the Thompson Family Foundation Initiative in CIPN and Sensory Neuroscience at Columbia University.

References

Bardot ES, Valdes VJ, Zhang J et al 2013 Polycomb subunits Ezh1 and Ezh2 regulate the Merkel cell differentiation program in skin stem cells. EMBO J 32:1990–2000.

Bhatia S, Afanasiev O, Nghiem P 2011 Immunobiology of Merkel cell carcinoma: implications for immunotherapy of a polyomavirus-associated cancer. Curr Oncol Rep 13:488–97.

Chang W, Kanda H, Ikeda R et al 2016 Merkel disc is a serotonergic synapse in the epidermis for transmitting tactile signals in mammals. Proc Natl Acad Sci U S A 113:E5491–500.

Chesler AT, Szczot M, Bharucha-Goebel D et al 2016 The role of PIEZO2 in human mechanosensation. N Engl J Med 375:1355–64.

Doucet YS, Woo SH, Ruiz ME et al 2013 The touch dome defines an epidermal niche specialized for mechanosensory signaling. Cell Rep 3:1759–65.

Feng H, Shuda M, Chang Y et al 2008 Clonal integration of a polyomavirus in human Merkel cell carcinoma. Science 319:1096–100.

Feng J, Luo J, Yang P et al 2018 Piezo2 channel-Merkel cell signaling modulates the conversion of touch to itch. Science 360:530–3.

Haeberle H, Fujiwara M, Chuang J et al 2004 Molecular profiling reveals synaptic release machinery in Merkel cells. Proc Natl Acad Sci U S A 101:14503–8.

Halata Z, Grim M, Bauman KI 2003 Friedrich Sigmund Merkel and his ‘Merkel cell’, morphology, development, and physiology: review and new results. Anat Rec 271A:225–39.

Harms PW, Patel RM, Verhaegen ME et al 2013 Distinct gene expression profiles of viral- and nonviral-associated Merkel cell carcinoma revealed by transcriptome analysis. J Invest Dermatol 133:936–45.

Harms PW, Harms KL, Moore PS et al 2018 International Workshop on Merkel Cell Carcinoma Research Working Group. The biology and treatment of Merkel cell carcinoma: current understanding and research priorities. Nat Rev Clin Oncol 15:763–76.

Hoffman BU, Baba Y, Griffith TN et al 2018 Merkel cells activate sensory neural pathways through adrenergic synapses. Neuron 100:1401–13.

Iggo A, Muir AR 1969 The structure and function of a slowly adapting touch corpuscle in hairy skin. J Physiol 200:763–96.

Ikeda R, Cha M, Ling J et al 2014 Merkel cells transduce and encode tactile stimuli to drive Aβ-afferent impulses. Cell 157:664–75.

Jenkins BA, Lumpkin EA 2017 Developing a sense of touch. Development 144:4078–90.

Johnson KO 2001 The roles and functions of cutaneous mechanoreceptors. Curr Opin Neurobiol 11:455–61.

Lesko MH, Driskell RR, Kretzschmar K et al 2013 Sox2 modulates the function of two distinct cell lineages in mouse skin. Dev Biol 382:15–26.

Maksimovic S, Nakatani M, Baba Y et al 2014 Epidermal Merkel cells are mechanosensory cells that tune mammalian touch receptors. Nature 509:617–21.

Maricich SM, Morrison KM, Mathes EL et al 2012 Rodents rely on Merkel cells for texture discrimination tasks. J Neurosci 32:3296–300.

Maricich SM, Wellnitz SA, Nelson AM et al 2009 Merkel cells are essential for light-touch responses. Science 324:1580–2.

Merkel F 1875 Tastzellen und Tastkörperchen bei den Hausthieren und beim Menschen. Archiv f mikrosk Anat 11:636–52.

Moll R, Moll I, Franke WW 1984 Identification of Merkel cells in human skin by specific cytokeratin antibodies: changes of cell density and distribution in fetal and adult plantar epidermis. Differentiation 28:136–54.

Morrison KM, Miesegaes GR, Lumpkin EA et al 2009 Mammalian Merkel cells are descended from the epidermal lineage. Dev Biol 336:76–83.

Nghiem P, Bhatia S, Lipson EJ et al 2019 Durable tumor regression and overall survival in patients with advanced Merkel cell carcinoma receiving pembrolizumab as first-line therapy. J Clin Oncol 37:693–702.

Nghiem P, Park SY 2019 Less toxic, more effective treatment: a win–win for patients with Merkel cell carcinoma. JAMA Dermatol E1–2.

Nguyen MB, Valdes VJ, Cohen I et al 2019 Dissection of Merkel cell formation in hairy and glabrous skin reveals a common requirement for FGFR2-mediated signalling. Exp Dermatol 28:374–82.

Perdigoto CN, Bardot ES, Valdes VJ et al 2014 Embryonic maturation of epidermal Merkel cells is controlled by a redundant transcription factor network. Development 141:4690–6.

Ranade SS, Woo SH, Dubin AE et al 2014 Piezo2 is the major transducer of mechanical forces for touch sensation in mice. Nature 516:121–5.

Van Keymeulen A, Mascre G, Youseff KK et al 2009 Epidermal progenitors give rise to Merkel cells during embryonic development and adult homeostasis. J Cell Biol 187:91–100.

Woo SH, Lukacs V, de Nooij JC et al 2015 Piezo2 is the principal mechanotransduction channel for proprioception. Nat Neurosci 18:1756–62.

Woo SH, Ranade S, Weyer AD et al 2014 Piezo2 is required for Merkel-cell mechanotransduction. Nature 509:622–6.

Woo SH, Stumpfova M, Jensen UB et al 2010 Identification of epidermal progenitors for the Merkel cell lineage. Development 137:3965–71.

Wright MC, Logan GJ, Bolock AM et al 2017 Merkel cells are long-lived cells whose production is stimulated by skin injury. Developmental Biol 422:4–13.

Xiao Y, Thoresen DT, Miao L et al 2016 A cascade of Wnt, Eda, and Shh signaling is essential for touch dome Merkel cell development. PLoS Genet 12:e1006150.

Yamashita Y, Ogawa H 1991 Slowly adapting cutaneous mechanoreceptor afferent units associated with Merkel cells in frogs and effects of direct currents. Somatosens Motor Res 8:87–95.

COMMENTARY

1.5

The reaction of peripheral nerves to injury

Rolfe Birch, Praveen Anand

Main nerve trunks contain many thousands of axons. When a trunk is stretched, but not ruptured, by dislocation of, say, the femoral or humeral heads, or by the nearby passage of a bullet, the axons within that nerve may respond in different ways. The degree of injury may vary along the length of a particular nerve or transversely across its cross-section: some axons will remain intact, some will sustain conduction block but recover rapidly, and yet others will degenerate throughout their entire extent distal to the injury because they have been ruptured. A proportion recover spontaneously whilst the remainder never recover.

Seddon (1943) introduced the terms neurapraxia for conduction block, axonotmesis for a degenerative lesion of favourable prognosis, and neurotmesis for a degenerative lesion of unfavourable prognosis. Sunderland (1951) expanded this classification to five degrees of peripheral nerve injury by subdividing neurapraxia according to the degree of connective tissue disruption, and Mackinnon and Dellon (1988) subsequently added a sixth category. However, the fundamental distinction between neurapraxia and either axonotmesis or neurotmesis remains the persistence of conduction in the distal segment of the nerve in neurapraxia, and the absence of conduction in axonotmesis or neurotmesis. In clinical practice, neurotmesis usually signifies transection of an entire nerve trunk, its constituent fascicles and their surrounding investments of perineurium and epineurium; the proximal and distal nerve stumps are frequently separated by an inter-stump gap of varying length (**Fig. 1.5.1**). The early disappearance of conduction indicates impending or actual critical ischaemia and is probably the most important indicator that a lesion is deepening (see below).

Neurapraxia/conduction block

Conduction block exhibits certain characteristic features: paralysis exceeds loss of sensation; proprioceptive nerves are more deeply affected than those responsible for light touch; sympathetic nerves to the smooth muscles of the blood vessels and sweat glands are least affected. There are distinct patterns of conduction block. Anoxia is important in all of them and there are often elements of mechanical deformation, inducing alterations of the nodal and paranodal apparatus in myelinated axons, and subsequent demyelination of whole internodes or of paranodes.

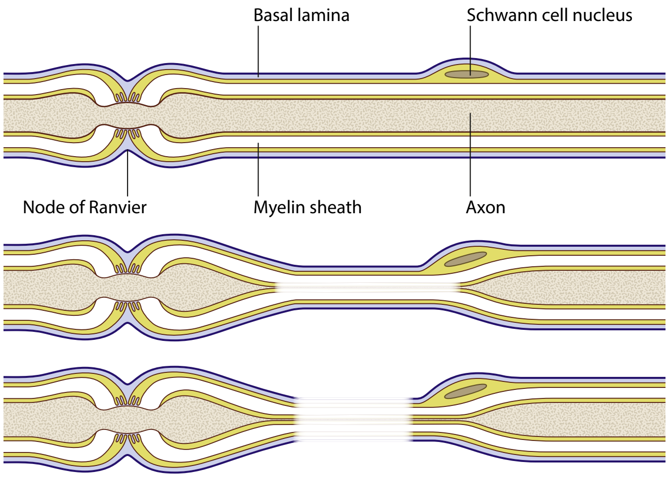

Fig. 1.5.1 Axonotmesis (centre) and neurotmesis (bottom) at the moment of injury. Note the preservation of the Schwann cell basal lamina in axonotmesis. (Courtesy of Rolfe Birch, all rights reserved, published in Birch R, Surgical Disorders of the Peripheral Nerve. 2nd edition, 2011. Springer-Verlag, London.)

Transient ischaemia

Lying in one position without moving for a long time (e.g. during coma, inebriation or anaesthesia), prolonged sitting with the legs crossed or prolonged leaning on the elbows are all situations in which a limb nerve may be transiently compressed against a bone or a hard surface. The ischaemia thus induced in the compressed nerves causes an anoxic, physiological, block of both axoplasmic transport and ion channel functions along affected axons. This is seen during operation for the exposure of limb nerves with an inflated cuff in position: stimulation of a nerve evokes a brisk muscular response by transmission through the neuromuscular junction, which then diminishes before disappearing after about 30 minutes, whereas conduction within the nerve itself can be detected for about another 30 minutes. On the other hand, direct stimulation of the muscle provokes a twitch that can be elicited for about another 2 hours; loss of this direct response signals impending muscle death. The selective vulnerability of different populations of nerve fibres is demonstrated by the classical experiment of applying an inflated cuff about the arm (Lewis et al 1931). The observer experiences first a loss of superficial sensibility, then a graduated loss of muscle power. The first pain response is lost soon after superficial sensibility fails; the delayed pain response is still detectable after 40 minutes of ischaemia. Large myelinated axons are first affected; unmyelinated axons and autonomic fibres escape, and pilomotor and vasomotor functions are scarcely affected. All modalities recover within a few minutes of release of the cuff; the unpleasant quality of the residual delayed pain sensation, and the burst of painful 'pins and needles' after release of the cuff, give an insight into the feelings of patients affected by dysaesthesiae.

Slowly progressing ischaemia

Conduction block caused by a haematoma or aneurysm, or by bleeding into compartments, produces early and deep autonomic paralysis and loss of power that extends over hours or days, whilst deep pressure sense and some joint position sense persist. These symptoms are seen in war wounds, when nerves become compressed and strangled by scar tissue or by the cicatrix deep to split skin grafts, and may progress over a period of weeks or months. The recovery of function and relief of pain are rapid – at times, dramatic – after removal of the cause in most of these cases.

Prolonged conduction block associated with focal demyelination

Severe prolonged pressure causes local demyelination and a conduction block that is not directly attributable to anoxia and that may last for weeks or months (**Fig. 1.5.2**). Compression-induced focal paranodal myelin deformation may be involved; experimental studies using a cuff inflated to high pressure around a limb produced slippage of paranodal myelin at nodes of Ranvier lying under the edges of the cuff, i.e. where the pressure gradient between compressed and non-compressed portions of the nerve was likely to be greatest (Ochoa et al 1972, Dyck et al 2005). Clinically, local demyelination and conduction block will persist until the source of the external irritation, e.g. a bony projection, is removed (Birch and St Clair Strange 1990). Relief of pain and recovery follow rapidly in lesions that have persisted for many months, or even years. Mechanical deformation is the likely explanation for the conduction block seen in cases of 'hourglass' constriction of fascicles within a nerve trunk, where axons may be focally constricted within affected fascicles (**Fig. 1.5.3**).

Prolonged conduction block of war wounds

The characteristic features of classical neurapraxia (see above), caused by the nearby passage of a missile, are likely to be provoked by a momentary displacement or stretching of the nerve trunks. However, a different pattern of conduction block may occur in recent conflicts, where the patient is exposed, at close range, to the shock wave of an explosion (e.g. blast injury), in addition to penetrating injury to the bony and soft tissues at the level of the nerve lesion. In these cases, the smallest fibres are most deeply affected and they may not recover. Pain may vary in both of these variants of conduction block (Birch et al 2012).

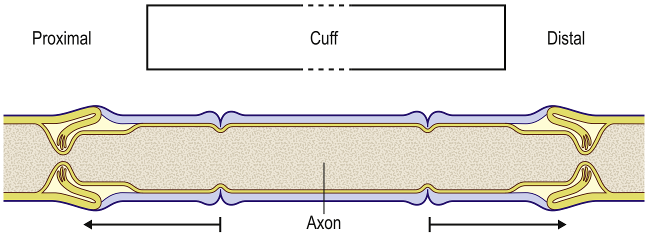

Fig. 1.5.2 The effect of mechanical compression: paranodal and juxtaparanodal myelin slippage under the edges of an inflated pressure cuff. (After Ochoa J, Fowler TJ, Gilliatt RW 1972, courtesy of Rolfe Birch, all rights reserved, published in Birch R, Surgical Disorders of the Peripheral Nerve. 2nd edition, 2011. Springer-Verlag, London.)

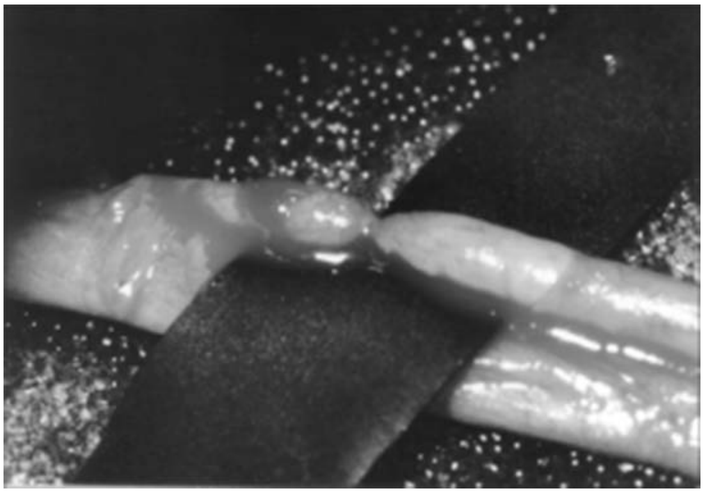

Fig. 1.5.3 Hourglass 'constriction' of the lateral root of the median nerve: the result of traction injury. There was full spontaneous recovery. (Courtesy of Rolfe Birch, all rights reserved, published in Birch R, Surgical Disorders of the Peripheral Nerve. 2nd edition, 2011. Springer-Verlag, London.)

Non-freezing cold injury (trench foot)

Trench foot, or non-freezing cold injury (NFCI), is caused by exposure to cold of sufficient severity and duration but above the freezing point. It results in abnormalities of the small sensory nerve fibres and associated vascular abnormalities which may persist for years. Based on observations of trench foot in World Wars I and II, the condition was described as a vaso-neuropathy (Ungley et al 1945). It is associated with marked degeneration of cutaneous intraepidermal nerve fibres with regeneration of disproportionate and abnormal nerve fibres along subepidermal blood vessels, causing a 'painful vaso-neuropathy' (Anand et al 2017).

Degenerative lesions

There are essentially two types of degenerative lesion, with very different potentials for recovery. In the first, which approximates to axonotmesis, the tubes of Schwann cell basal lamina that surround each axon–Schwann cell unit remain intact, which means that axons may regenerate in an orderly fashion across the lesion site and into the distal stump, providing that the causative agent is removed and that the length of the distal stump (i.e. the distance from the site of injury to the end organ) is not so long that it compromises axonal regrowth. In the second, which approximates to neurotmesis, not only the Schwann cell basal lamina tubes, but also the connective tissue sheaths around the fascicle are interrupted; spontaneous axonal regeneration following this type of injury will be imperfect and disorderly, and may not occur at all.

Deepening of a lesion in a nerve that has not been divided

Unrelieved activity of a noxious agent on an intact nerve is signified by pain and increasing neurological deficit, indicating that the lesion is deepening. Nerves within a swollen ischaemic limb or tense compartment become compressed and anoxic. Nerves displaced by an expanding haematoma become stretched and anoxic. Nerves that have become displaced into a fracture or joint are tethered and become subjected to compression, stretching and anoxia. These nerves are not severed by the initial injury; the first lesion is axonotmesis and spontaneous recovery is probable if the cause is removed. However, if this does not happen, the lesion continues to deepen into that of neurotmesis and spontaneous recovery will not occur. The speed of deepening of a lesion is related to the cause: (i) a nerve crushed by a plate or strangled by an encircling suture may recover if the cause is removed within a few minutes (Fig. 1.5.4); (ii) a nerve that has become compressed and anoxic within a swollen ischaemic limb will recover if perfusion of the tissues is restored within 3 hours; the likelihood of full spontaneous recovery diminishes with the passage of every hour after that time (Fig. 1.5.5); (iii) a nerve displaced into a fracture or joint will usually recover if it is extricated within a few days, but will be destroyed if a compression device has been used to stabilize the skeleton without retrieving the nerve (Fig. 1.5.6); (iv) function may be retained for a long time in a nerve exposed to continuing traction from a malunited fracture; (v) nerves may continue to work for months or years before failing when they are exposed to the progressing fibrosis caused by radiotherapy, by overlying split-skin graft or by other examples of deep scar; (vi) pain is the cardinal symptom of the unrelieved action of a noxious agent.

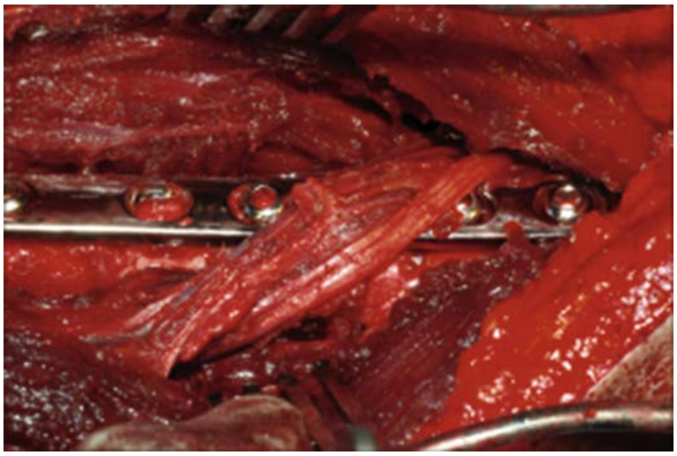

Fig. 1.5.4 The appearance of a radial nerve after extrication from beneath a compression plate 48 hours after the first operation. There was relief of pain but only incomplete recovery so that subsequent flexor to extensor transfer was necessary. (Courtesy of Rolfe Birch, all rights reserved, published in Birch R, Surgical Disorders of the Peripheral Nerve. 2nd edition, 2011. Springer-Verlag, London.)

Wallerian degeneration

Trauma that physically separates axons from their cell bodies produces Wallerian degeneration (WD). All affected axons in the extreme tip of the proximal stump and throughout the distal stump degenerate, irrespective of their calibre or functional modality; recovery is often slow and incomplete, and there may be considerable residual loss of function. Moreover, although research has tended to address issues associated with the molecular and cellular events that occur at the lesion site and target tissues, it is important to remember that injury to a peripheral nerve that induces WD also initiates significant and often long-lasting central changes in sensory ganglia and ascending and descending pathways within the spinal cord and brain; these changes also have a significant impact on the likelihood of recovery. Studies of cell bodies of human dorsal root ganglia (DRG) have revealed changes in the expression of a wide range of receptors and a remarkable alteration in the expression of genes regulating neuronal activity (Rabert et al 2004, Lawson 2005, Anand et al 2008). There is an extensive literature on WD in both central and peripheral nervous systems, and only a brief summary of the response in the peripheral nervous system is presented here (see Gordon 2015).

Neuronal cell body and proximal stump

The central and the peripheral effects of WD are profound and, in neurotmesis, ultimately irreversible. Not only is the neuronal cell body separated from its continual supply of retrogradely transported neurotrophins, but also its central connections rapidly alter; many neurones thus isolated will die. Amputation provides a model of the effect of permanent division of axons on the spinal cord: there is extensive loss of neurones in the dorsal root ganglia and in the ventral horn, and a diminution of the large myelinated axons in the ventral and dorsal roots (Dyck et al 1984, Suzuki et al 1993). Neuronal death is more severe in more proximal neurotmesis, and less marked after

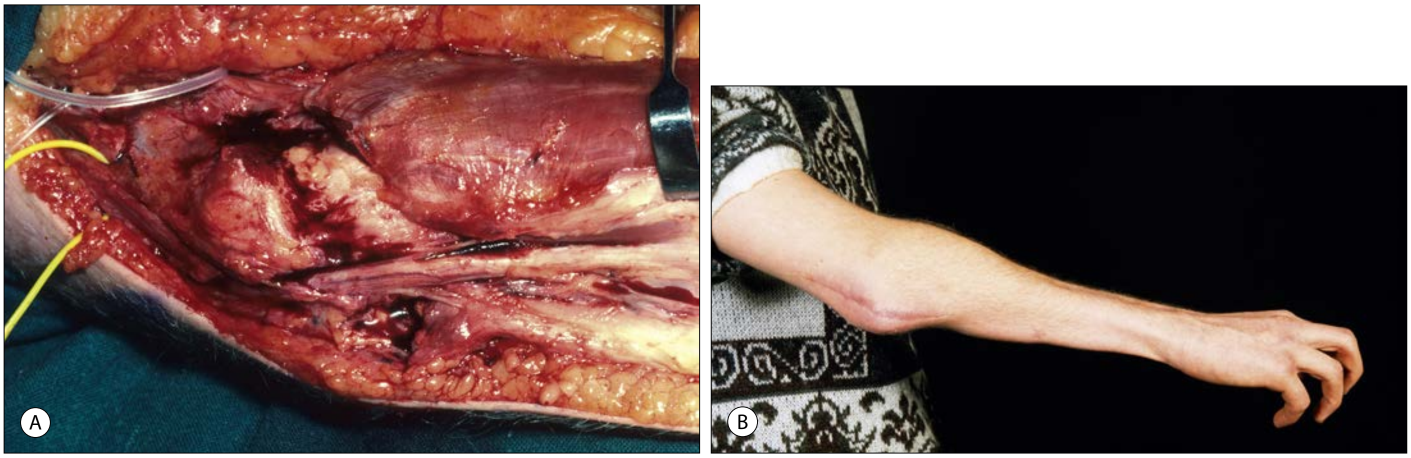

Fig. 1.5.5 Volkmann's ischaemic contracture. **A**, The ulnar nerve exposed during flexor muscle slide 8 weeks after supracondylar fracture. The epineurial vessels and also the ulnar recurrent collateral vessels are occluded, and the nerve is compressed by the swollen infarcted muscle. **B**, The appearance of the hand 14 years later. (Courtesy of Rolfe Birch, all rights reserved, published in Birch R, Surgical Disorders of the Peripheral Nerve. 2nd edition, 2011. Springer-Verlag, London.)

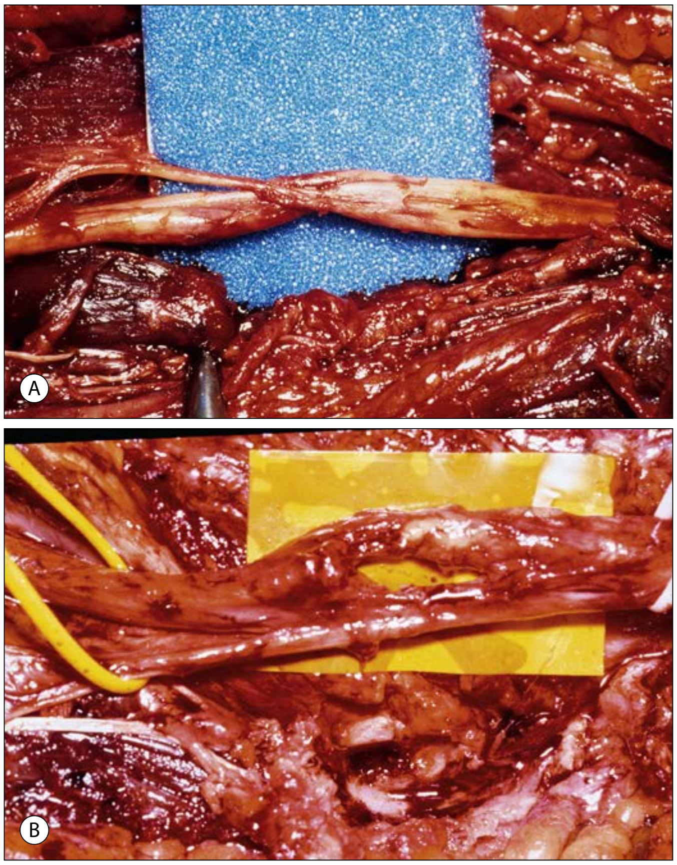

Fig. 1.5.6 Deepening of a lesion. **A**, A median nerve extricated from a supracondylar fracture in a 9-year-old girl 3 days after injury; there was complete recovery. **B**, A median nerve extricated from a supracondylar fracture in a 13-year-old girl 8 weeks after injury; there was no recovery. (Courtesy of Rolfe Birch, all rights reserved, published in Birch R, Surgical Disorders of the Peripheral Nerve. 2nd edition, 2011. Springer-Verlag, London.)

axonotmesis than after neurotmesis. Neurotmesis in the neonate produces a more rapid and much greater incidence of sensory and motor neurone death than in the adult. Surviving neurones rapidly upregulate a series of genes involved in repair and neuroprotection mechanisms following injury (repair-associated genes, RAGs), which direct many of the changes seen during WD and subsequent recovery (e.g. Calenda et al 2012). (For a review of the molecules involved in retrograde signalling to initiate expression of RAGs, particularly the family of glycoprotein 130 (gp130) cytokines, see Zigmond (2011).) Changes in the expression of ion channels and receptors in the neuronal cell bodies in human DRGs can be detected within a few minutes of an injury to the nerve (Lawson 2005).

Tip of proximal stump

Within a few hours of injury, the cut ends of a transected axon seal off, forming end bulbs. The end bulb that forms at the proximal tip of an axon in the proximal stump is transformed into a growth cone from which multiple needle-like filopodia and broader sheet-like lamellipodia grow out. The filopodia are rich in actin, and may extend or retract within a matter of minutes. Each axon forms new branches or sprouts: collateral sprouts arise from nodes of Ranvier at levels where the axons are still intact, and terminal sprouts arise from the tips of the surviving axons. The axon sprouts and fine cytoplasmic processes derived from their associated Schwann cells form clusters, regenerating units, surrounded by Schwann cell basal laminae. Sprouts within one regenerating unit represent the regenerative effort of one neurone and its axon. Within a few days of injury, the calibre of axons in the proximal stumps is reduced and nerve conduction velocity in the proximal segment falls.

Distal stump

During the first 2 or 3 weeks after injury, the constitutive tissue response within a denervated distal stump involves numerous events: some sequential, others consecutive. These include the production of debris, as axons and their myelin sheaths are degraded; an increase in local blood flow; activation of resident macrophages, and recruitment and influx of exogenous macrophages; and proliferation of fibroblasts and Schwann cells. The gliotic response produces a population of dedifferentiated daughter Schwann cells that remain within the basal lamina tubes secreted by their parent cells, forming what are now called Schwann tubes but which were previously known as bands of Büngner. They behave acutely as the 'presumed targets' of the regrowing axons until the actual targets (muscle or sensory end organ) have been reinnervated: they secrete proteins that collectively facilitate axonal regrowth, whether by providing trophic support or by establishing a supportive growth matrix (for further reading on these interactions, see Hall (2005), Webber et al (2011), Arthur-Farraj et al (2012), Gordon (2015)). There is a growing consensus that Schwann cells express distinct motor and sensory phenotypes, and that this fundamental difference affects the ability of Schwann cell tubes to selectively support regenerating neurones. For example, expression of osteopontin and clusterin is upregulated in Schwann cells in transected peripheral nerves: the two secreted factors appear to facilitate regeneration of motor or sensory neurones, respectively (Wright et al 2014).

While the microenvironment of an acutely denervated distal stump facilitates axonal regrowth because it provides a vascularized segment of longitudinally orientated, laminin-rich basal lamina tubes filled with axon-responsive Schwann cells, a chronically denervated distal stump is associated with poor axonal regeneration and poor functional recovery (Sulaiman and Gordon 2009). Biopsies taken during late repairs, especially when the injury has been complicated by arterial injury or by sepsis, often show remarkably few Schwann cells lying within a densely collagenous matrix. Myelin fragments are detectable in such cases many months after the injury. The residual Schwann cells become progressively less receptive to ingrowing regenerating axons with time; experimental studies have shown that they downregulate expression of axon-responsive receptors that are normally important in Schwann cell–axon signalling (Li et al 1997, Li et al 1998). Accordingly, injured nerves show decreased expression over time of the key Nerve Growth

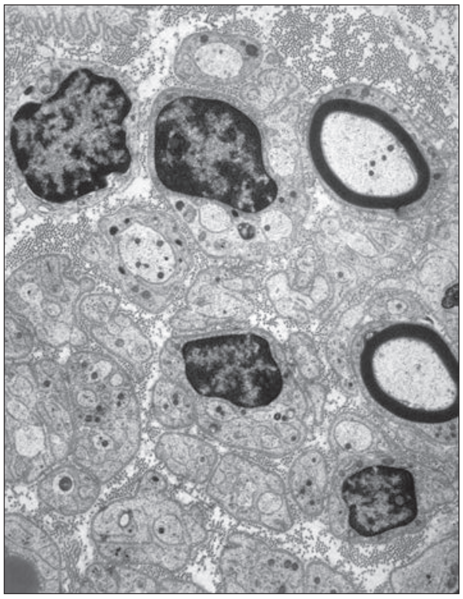

Fig. 1.5.7 Intact (afferent) myelinated and unmyelinated fibres in a suprascapular nerve, 6 weeks after an avulsion lesion of the brachial plexus; efferent fibres have degenerated. (Courtesy of Rolfe Birch, all rights reserved, published in Birch R, Surgical Disorders of the Peripheral Nerve. 2nd edition, 2011. Springer-Verlag, London.)

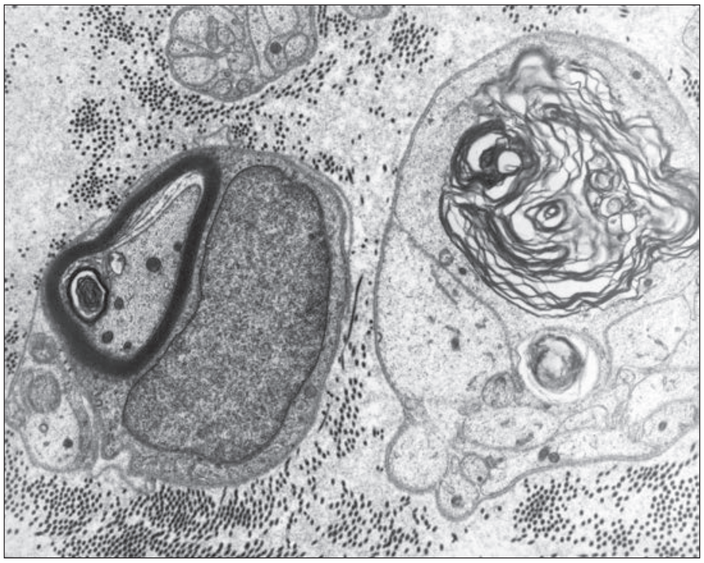

Fig. 1.5.8 Wallerian degeneration in the ventral root of the eighth cervical nerve, 6 weeks after avulsion from the spinal cord. A degenerate efferent myelinated fibre (right) compared with a healthy myelinated afferent fibre (left). (Courtesy of Rolfe Birch, all rights reserved, published in Birch R, Surgical Disorders of the Peripheral Nerve. 2nd edition, 2011. Springer-Verlag, London.)

Factor (NGF) in the residual Schwann cells of the distal stump (Anand et al 1997), which may explain, at the molecular level, the unfavourable clinical outcomes of delayed surgical nerve repair. These findings underscore the clinical observation that there is a relatively narrow window of opportunity when surgical intervention is most likely to produce positive results (Lundborg 2000, Dahlin and Wiberg 2017).

The special case of preganglionic injury

The preganglionic lesion is all too common in severe traction injuries to the brachial and lumbosacral plexuses. The roots of the spinal nerves are torn (avulsed) from the spinal cord, which means that the somatic afferent pathway is interrupted between the dorsal root ganglion and the spinal cord (see Fig. 1.5.6). The neuronal cell bodies and their axons, investing Schwann cells and associated basal laminae remain intact, healthy and conducting for a long time after the injury. The surviving axons include all those with cell bodies in the dorsal root ganglion, including many 'recurrent' fibres in the ventral root that derived from cells in the dorsal root ganglion (**Figs 1.5.7–1.5.9**). Somatic efferent fibres, being separated from their cell bodies, degenerate; postganglionic autonomic efferent axons also degenerate, as a result of damage to their grey rami communicantes. Carlstedt (2007) reckons that about one-half of all motor neurones in the affected spinal cord segment have disappeared by 2 weeks after avulsion of the ventral root and he urges 'a swift intervention to re-establish contact between the injured nerve cells and the periphery with its supply of neurotrophic substances to counteract nerve cell loss'. After avulsion injury, human dorsal root ganglion neurones show dramatic changes in the expression of genes involved in neurotransmission, trophism, cytokine function, signal transduction, myelination, transcription regulation and apoptosis (Rabert et al 2004).

Regeneration and recovery of function

> *But the journey of the axon tip to an end organ is only the most dramatic of the phases in the process of regeneration, and its arrival is alone no guarantee of the return of useful function.* **Young (1942)**

The cellular microenvironment of a normal peripheral nerve does not ordinarily support axonal regrowth; indeed, there appear to be 'molecular brakes' that prevent axonal sprouting. Somewhat counterintuitively, it appears that their expression may be upregulated after injury. WD transforms the environment throughout the distal stump of a transected nerve to one that facilitates axonal regrowth, albeit for a relatively short period (Christie and Zochodne 2013). Manipulating the many cellular and molecular responses that occur during the injury response in the peripheral nervous system remains an unachieved goal of reconstructive surgery.

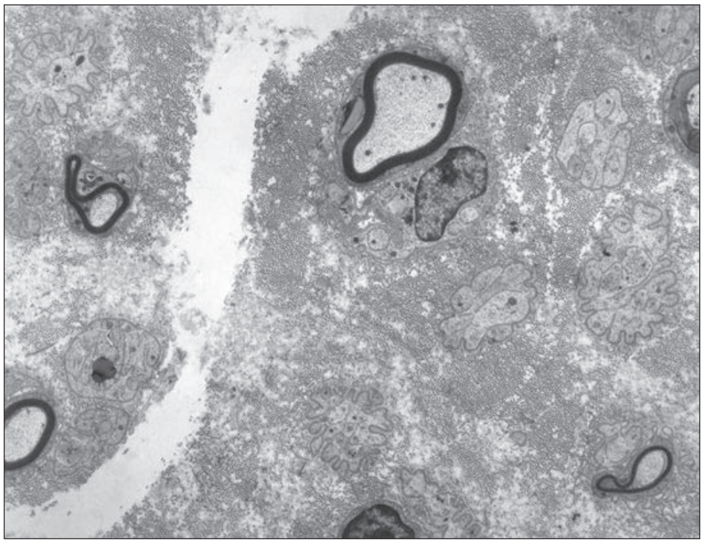

Fig. 1.5.9 Afferent and efferent fibres in a ventral root. Healthy myelinated and unmyelinated fibres in the ventral root of the eighth cervical nerve avulsed from the spinal cord 6 weeks previously. The myelinated efferent fibres have undergone Wallerian degeneration and there is a notable increase in the amount of endoneurial collagen. (Courtesy of Rolfe Birch, all rights reserved, published in Birch R, Surgical Disorders of the Peripheral Nerve. 2nd edition, 2011. Springer-Verlag, London.)

Regeneration of end organs

Reinnervation of muscle spindles and Golgi tendon receptors is generally good after crush lesions (axonotmesis). Regeneration after repair of a divided nerve is much less orderly. A muscle spindle may become reinnervated by afferents normally destined for the Golgi tendon organ; many tendon organs remain denervated and the regenerated endings are frequently abnormal in appearance. The reorganization of motor units after repair causes significant alterations in the mechanical input to an individual tendon organ.

Muscles usually exhibit weakness, impaired coordination and reduced stamina after nerve repair. There may be selective failure of regeneration of the largest-diameter fibres and of co-activation of the α and γ efferents. The normal movement of joints is brought about by smoothly coordinated and controlled activity in muscles that is precisely and delicately regulated by inhibition and facilitation of the motor neurones. The conversion of an antagonist to an agonist is the basis of musculotendinous transfer; it is common to see patients actively extending the knee or the ankle and toes as soon as the postoperative splint is removed after hamstring to quadriceps transfer or anterior transfer of tibialis posterior. Reinnervated muscles usually fail to convert after muscle transfer, irrespective of their power. Perhaps the defective reinnervation of the deep afferent pathways from the muscle

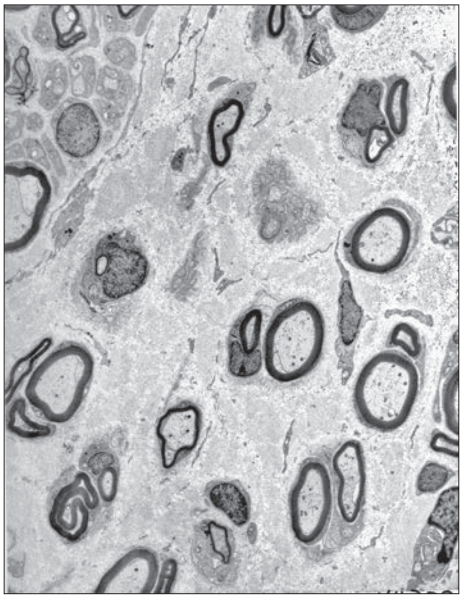

Fig. 1.5.10 Useless regeneration in a median nerve sutured 3 years previously. Proximal to the suture line, the endoneurium contains thinly remyelinated axons, some in regenerating clusters, and extensive collagenization; there was no recovery of function. (Courtesy of Rolfe Birch, all rights reserved, published in Birch R, Surgical Disorders of the Peripheral Nerve. 2nd edition, 2011. Springer-Verlag, London.)

spindles and the tendon receptors blinds muscles, which are, after all, sensory as well as effector organs.

Cutaneous sensory receptors similarly undergo a slow degenerative change after denervation and after 3 years they may disappear. Reinnervation tends to reverse these changes, although the longer the period of denervation, the less complete will be the regeneration. It is usual to find numerous myelinated axons in the tissues bridging nerve stumps in the human, even in failed sutures or in grafts coming to revision (**Fig. 1.5.10**) (Terenghi et al 1998); these findings encapsulate the difference between regeneration and recovery of function.

Plasticity in the central nervous system

Nerve transfer involves connecting the proximal stump of a healthy nerve to the distal stump of one that has been injured in such a way that direct repair is not possible.

There is considerable adaptation of the central receptor and effector mechanisms after nerve transfer (**Fig. 1.5.11**). Independent flexion of the elbow without associated activity in the flexor muscles of the forearm is usual by 24 months after transfer from the ulnar nerve to the nerve to biceps brachii. Reinnervation of the muscle spindles and corresponding reorganization and remapping of the somatosensory cortex have been confirmed after transfer of intercostal nerves to the musculocutaneous nerve in adult patients with severe lesions of the brachial plexus (Sai et al 1996, Malessy et al 2003). These central phenomena may explain the remarkably good recovery of sensation within the hand after repair of severe birth lesions of the brachial plexus. The sensory recovery is far better than that of skeletal muscle and sympathetic function: there is accurate localization to the dermatomes of avulsed spinal nerves that had been reinnervated by intercostal nerves transferred from remote spinal segments (Anand and Birch 2002).

Case report

Operation in a 6-month-old boy confirmed rupture of C5 with avulsion of C6–C8 and T1. The lesion was repaired by transfers of the accessory nerve to the suprascapular nerve, of C5–C8 and T1, and of intercostal nerves T3–T5, to the lateral cord of the brachial plexus. At the age of 5 years he was able to localize cotton wool and pinprick sensation accurately in both hands and was able to feel a pin in the affected side. Monofilament, vibration thresholds and joint position sense were identical in both hands. The thresholds for warming were 3.1 °C (C5), 0.8 °C (C6), 4.1 °C (C7), 3.6 °C (C8) and 3.3 °C (T1) on the affected side. The thresholds for cooling were 2 °C (C5), 3.9 °C (C6), 3.8 °C (C7), 2.3 °C (C8) and normal in T1. In the unaffected hand, the thresholds were less than 3.4 °C for warm sensation and less than 2.2 °C for cool sensation. Sweating was 70% of that of the intact palm. It seems likely that afferent impulses from the thumb, index and probably the middle fingers entered the spinal cord through the three intercostal nerves, whilst afferent impulses from the little and probably the ring fingers entered the spinal cord through the fifth cervical nerve as shown in **Fig. 1.5.12**. Similar findings have been observed in four other cases after transfer of intercostal nerves to the lateral cord (**Fig. 1.5.13**). The situation in the adult is very different. After transfer of the intercostal nerves to the lateral or medial cords, it is usual to find that stimulation of the reinnervated skin is referred to the chest wall and only rarely to the skin of the hand (Htut et al 2006). Concepts of the mechanisms underlying cortical plasticity following nerve injury and the importance of maintaining an active sensory map of the affected part in the somatosensory cortex during the deafferentation period are considered further by Lundborg (2003), Rosén and Lundborg (2007), Björkman et al (2009), Rosén et al (2011) and Knox et al (2015).

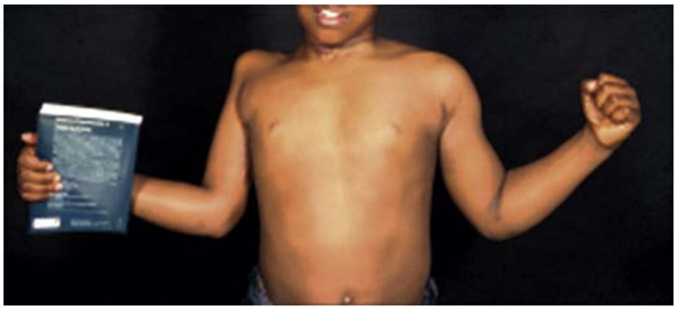

Fig. 1.5.11 A 13-year-old boy with a right-sided lesion: avulsion of C5–C7. Repair was undertaken at 2 months as follows: accessory to suprascapular transfer; one bundle of the ulnar nerve to the nerve to biceps and the nerve to the medial head of triceps; medial cutaneous nerve of the forearm to the lateral root of the median nerve. Results at 18 months show a full range of lateral rotation; abduction to 60°; power of elbow flexion, Medical Research Council (MRC) grade 4; power of elbow extension, MRC grade 3+. There is a full range of active flexion and extension without obvious co-contraction. (Courtesy of Rolfe Birch, all rights reserved, published in Birch R, Surgical Disorders of the Peripheral Nerve. 2nd edition, 2011. Springer-Verlag, London.)

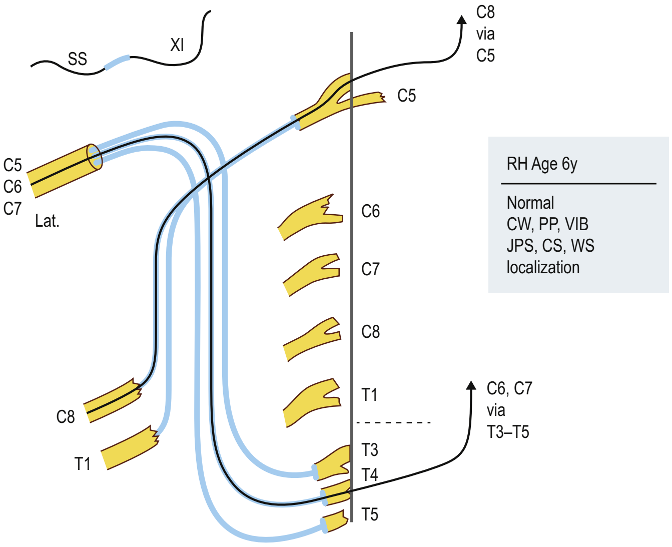

Fig. 1.5.12 The method of repair and the likely pathways for afferent function. Abbreviations: CS, cool sensation; CW, cotton wool; JPS, joint position sense; PP, pinprick; SS, suprascapular nerve; Vib, vibration threshold; WS, warm sensation; XI, accessory nerve. (Courtesy of Rolfe Birch, all rights reserved, published in Birch R, Surgical Disorders of the Peripheral Nerve. 2nd edition, 2011. Springer-Verlag, London.)

Laboratory and clinical studies

There are major differences between a laboratory investigation, in which a controlled, precise and limited lesion is inflicted on a peripheral nerve in an anaesthetized experimental animal, and the situation faced by the clinician presented with a patient with a massive wound involving soft tissues (including blood vessels and muscles) and skeletal elements, and sometimes with other injuries that threaten life and limb. That said, the fundamental cellular processes that underlie subsequent regeneration are similar in the laboratory, in the injuries of civilian practice and in the wounds of war, although in clinical practice they are

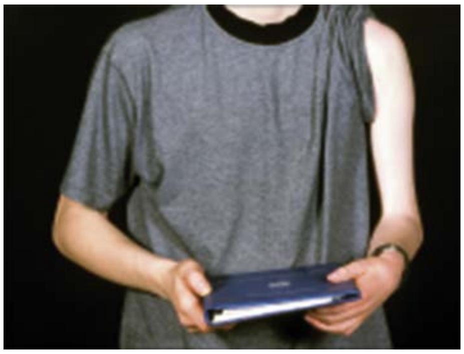

Fig. 1.5.13 Birth lesions of the brachial plexus. This boy had a group 4 lesion with rupture of C5 and avulsion of C6–C8 and T1 at birth. At 10 weeks of age, C5 was grafted to the upper trunk and to the ventral root of C8 and T1; accessory nerve was transferred to the ventral root of C7; the sensory divisions of intercostal nerves T3 and T4 were transferred to the lateral root of the median nerve. He regained a useful grasp between thumb and index finger, and is an extremely well-adjusted sportsman and musician. The photograph was taken at 10 years of age. (Courtesy of Rolfe Birch, all rights reserved, published in Birch R, Surgical Disorders of the Peripheral Nerve. 2nd edition, 2011. Springer-Verlag, London.)

modified by the violence of the injury, by the effects of injury on associated tissues and, in particular, by ischaemia and by delay before repair. Some general conclusions may be drawn from extensive clinical and laboratory studies.

The concept of retrograde degeneration of the axon extending to the first internode applies only to the most benign lesion: that of experimentally crushing the nerve between the tips of a jeweller's forceps. The extent of longitudinal damage to a nerve is greater in a rupture caused by traction than it is in 'tidy' transections caused by knife or glass; this effect worsens with increasing delay before repair, is worse still when healing has been complicated by sepsis, and worst of all in neglected ischaemia.

Failure to repair main vessels and to ensure perfusion of tissues is profoundly deleterious to regeneration and rules out worthwhile recovery of function.As time goes by, the cellular response in both stumps changes from one that facilitates regeneration to one that is less favourable. Dense collagenization, a profusion of fibroblasts and a loss of Schwann cells are characteristics of the chronically denervated distal stump and are typical of late cases. The normal architecture of a nerve is most closely restored to normal in a well-executed, tension-free primary suture. Regeneration through a graft falls away along its length and not solely at the suture lines. Delay before repair leads to increasing fibrosis and to shrinking of the distal segment so that it becomes impossible to ensure an accurate topographical match. Destruction of the target tissues, of muscle and skin, limits function even when there is strong regeneration. Chronological age plays an important role: for example, signalling mechanisms involved in the reinnervation of skeletal muscle may become impaired with age (Kawabuchi et al 2011).

References

Anand P, Birch R 2002 Restoration of sensory function and lack of long-term chronic pain syndromes after brachial plexus injury in human neonates. Brain 125:113–22.

Anand U, Otto WR, Facer P et al 2008 TRPA1 receptor localisation in the human peripheral nervous system and functional studies in cultured human and rat sensory neurons. Neurosci Lett 438:221–7.

Anand P, Privitera R, Yiangou Y et al 2017 Trench foot or non-freezing cold injury as a painful vaso-neuropathy: clinical and skin biopsy assessments. Front Neurol 8:514.

Anand P, Terenghi G, Birch R et al 1997 Endogenous NGF and CNTF levels in human peripheral nerve injury. Neuroreport 8(8):1935–8.

Arthur-Farraj PJ, Latouche M, Wilton DK et al 2012 c-Jun reprograms Schwann cells of injured nerves to generate a repair cell essential for regeneration. Neuron 75:633–47.

Birch R, Misra P, Stewart MP et al 2012 Nerve injuries sustained during warfare: part II: Outcomes. J Bone Joint Surg Br 94:529–35.

Birch R, St Clair Strange FG 1990 A new type of peripheral nerve lesion. J Bone Joint Surg Br 72:312–13.

Björkman A, Weibull A, Rosén B et al 2009 Rapid cortical reorganisation and improved sensitivity of the hand following cutaneous anaesthesia of the forearm. Eur J Neurosci 29:837–44.

Calenda G, Strong TD, Pavlovich CP et al 2012 Whole genome microarray of the major pelvic ganglion after cavernous nerve injury: new insights into molecular profile changes after nerve injury. BJU Int 109:1552–64.

Carlstedt T 2007 Central Nerve Plexus Injury. London: Imperial College Press.

Christie KJ, Zochodne D 2013 Neuroscience Forefront Review. Peripheral axon regrowth: new molecular approaches. Neuroscience 240:310–24.

Dahlin LB, Wiberg M 2017 Nerve injuries of the upper extremity and hand. EFORT Open Rev 2(5):158–70.

Dyck PJ, Nukada H, Lais CA et al 1984 Permanent axotomy: a model of chronic neuronal degeneration produced by axonal atrophy, myelin remodelling and regeneration. In: Dyck PJ, Thomas PK, Lambert EH et al (eds) Peripheral Neuropathy, 2nd ed. Philadelphia: Elsevier, Saunders, pp. 660–90.

Dyck PJ, Dyck PJB, Engelstad J 2005 Pathological alterations of nerves. In: Dyck PJ, Thomas PK (eds) Peripheral Neuropathy, 4th ed. Philadelphia: Elsevier, Saunders; Ch. 32, pp. 733–829.

Gordon T 2015 The biology, limits, and promotion of peripheral nerve regeneration in rats and humans. In: Tubbs RS et al (eds) Nerves and Nerve Injuries. Elsevier, Academic Press; Ch. 61, pp. 993–1012.

Hall S 2005 Mechanisms of repair after traumatic injury In: Dyck PJ, Thomas PK (eds) Peripheral Neuropathy, 4th ed. Philadelphia: Elsevier, Saunders; Ch. 58, pp. 1403–34.

Htut M, Misra P, Anand P et al 2006 Pain phenomena and sensory recovery following brachial plexus avulsion injury and surgical repair. J Hand Surg Br 31:596–605.

Kawabuchi M, Tan H, Wang S 2011 Age affects reciprocal cellular interactions in neuromuscular synapses following peripheral nerve injury. Ageing Res Rev 10:43–53.

Knox ADC, Goswami R, Anastakis DJ et al 2015 Cortical plasticity after peripheral nerve injury. In: Tubbs RS et al (eds) Nerves and Nerve Injuries. Elsevier, Academic Press; Ch. 64, pp. 1055–71.

Lawson SN 2005 The peripheral sensory nervous system: dorsal root ganglion neurones. In: Dyck PJ, Thomas PK (eds) Peripheral Neuropathy (2 vols), 4th ed. Philadelphia: Elsevier, Saunders; Ch. 8, pp. 163–202.

Lewis T, Pickering GW, Rothschild P 1931 Centripetal paralysis arising out of arrested bloodflow to the limb. Heart 16:1–32.

Li H, Terenghi G, Hall SM 1997 Effects of delayed re-innervation on the expression of c-erbB receptors by chronically denervated rat Schwann cells in vivo. Glia 20:333–47.

Li H, Wigley C, Hall SM 1998 Chronically denervated rat Schwann cells respond to GGF in vitro. Glia 24:290–303.

Lundborg G 2000 Brain plasticity and hand surgery: an overview. J Hand Surg Br 25:242–52.

Lundborg G 2003 Nerve injury and repair. A challenge to the plastic brain. The Bunge Memorial Lecture. J Periph Nerv Syst 8:209–26.

Mackinnon S, Dellon AL 1988 Surgery of the Peripheral Nerve. New York: Thieme.

Malessy MJ, Bakker D, Dekker AJ et al 2003 Functional magnetic resonance imaging and control over the biceps muscle after intercostal-musculocutaneous nerve transfer. J Neurosurg 98:261–8.

Ochoa J, Fowler TJ, Gilliatt RW 1972 Anatomical changes in peripheral nerves compressed by pneumatic tourniquet. J Anat 113:433–55.

Rabert D, Xiao Y, Yiangou Y et al 2004 Plasticity of gene expression in injured human dorsal root ganglia revealed by gene chip oligonucleotide microarrays. J Clin Neurosci 11:289–99.

Rosén B, Lundborg G 2007 Enhanced sensory recovery after median nerve repair using cortical audio-tactile interaction. A randomised multicentre study. J Hand Surg Eur 32:31–7.

Rosén B, Björkman A, Lundborg G 2011 Improving hand sensibility in vibration induced neuropathy: a case-series. J Occup Med Toxicol 6:13.

Sai K, Kanamura A, Sibuya M et al 1996 Reconstruction of tonic vibration reflex in the biceps brachii reinnervated by transferred intercostal nerves in patients with brachial plexus injury. Neurosci Lett 206:1–4.

Seddon HJ 1943 Three types of nerve injury. Brain 66:237–88.

Sulaiman OA, Gordon T 2009 Role of chronic Schwann cell denervation in poor functional recovery after nerve injuries and experimental strategies to combat it. Neurosurgery 65:A105–14.

Sunderland S 1951 A classification of peripheral nerve injuries producing loss of function. Brain 74:491–516.

Suzuki H, Oyanagi K, Takahishi H et al 1993 A quantitative pathological investigation of the cervical cord, roots and ganglia after long term amputation of the unilateral upper arm. Acta Neuropathol (Berl) 85:666–73.

Terenghi G, Calder JS, Birch R et al 1998 A morphological study of Schwann cells and axonal regeneration in chronically transected human peripheral nerve. J Hand Surg Br 23:583–7.

Ungley CC, Channell GD, Richards RL 1945 The immersion foot syndrome. Br J Surg 33:17–31.

Webber CA, Christie KJ, Cheng C et al 2011 Schwann cells direct peripheral nerve regeneration through the Netrin-1 receptors, DCC and Unc5H2. Glia 59:1503–17.

Wright MC, Mi R, Connor E et al 2014 Novel roles for osteopontin and clusterin in peripheral motor and sensory axon regeneration. J Neurosci 34:1689–1700.

Young JZ 1942 Functional repair of nervous tissue. Physiol Rev 22:318–74.

Zigmond RE 2011 Gp130 cytokines are positive signals triggering changes in gene expression and axon outgrowth in peripheral neurons following injury. Front Mol Neurosci 4:62.

COMMENTARY

1.6

A critical evaluation of the current status of myofascial chains

Jan Wilke, Winfried Banzer

INTRODUCTION

From a morphological point of view, most anatomy textbooks have described the skeletal muscles of the human body as being discrete actuators with clear origins and insertions (van der Wal 2009). Recent analyses of published anatomical cadaveric studies have challenged this assumption, revealing that the active components of the locomotor system are directly linked by fibrous connective tissue (Wilke et al 2016c) (**Fig. 1.6.1**). The bridging structures include: ligaments (hamstrings – sacrotuberous ligament – erector spinae muscle) (Martin 1968, Vleeming et al 1995); fascia[1] (gastrocnemius muscle – hamstrings) (Tuncay et al 2009); aponeuroses (gluteus maximus/tensor fasciae latae – iliotibial tract – calf muscles) (Wilke et al 2016b); tendons (gastrocnemius muscle – Achilles tendon – plantar aponeurosis – toe abductors) (Snow et al 1995, Stecco et al 2013).

A common feature of the listed elements is their considerable tensile strength, conferred by a large quantity of collagen type I fibres. Moreover, comparisons between samples of the fascia lata and different tendons located around the knee joint revealed that these structures share similar biomechanical, biochemical and histological properties (Butler et al 1984, Derwin et al 2008). Therefore, in addition to the classical distinctive terminology, it has been suggested that the entirety of soft collagenous connective tissues should be grouped under the umbrella terms 'fascial tissues/fascial system' when describing the body from a holistic and functional point of view (Adstrum et al 2017).

MYOFASCIAL CHAINS

Concepts of myofascial chains assume that the connectivity of muscles and stretch-resistant soft tissue creates systemic lines of pull with the potential to transmit mechanical force to distant body regions. The selection of the components of a myofascial chain is based on the criterion of continuity between their longitudinal axes (**Fig. 1.6.2**): it is assumed that this construction maximizes the amount of transmittable force. Another relevant factor is the common fibre orientation of neighbouring myofascial chain components. In tendons, the collagen fibrils are oriented parallel to each other, almost directly following the muscle's line of pull. A similar architecture with mostly parallel fibres running in a longitudinal direction can be found in ligaments. Although the investing fasciae often display a bidirectional, lattice-like fibre arrangement, biomechanical studies reveal a markedly higher longitudinal stiffness (Eng et al 2014), which might indicate a more pronounced strain transmission capacity in this direction.

Based on these thoughts, a variety of concepts have suggested body maps with hypothesized myofascial chains (**Fig. 1.6.3**) (for an overview, see Richter (2012)). Only three continuous lines, the posterior longitudinal chain, the posterior diagonal chain and the anterior diagonal chain, have been systematically verified so far (**Fig. 1.6.4A**, **Table 1.6.1**) (Wilke et al 2016c). Two other possible chains, the lateral longitudinal chain and the spiral chain, still exhibit some unresolved inconsistencies but are at least partially backed by scientific evidence (**Fig. 1.6.4B**, **Table 1.6.2**).

Limitations and perspectives

Myofascial continuity is not restricted to in-series coupling as at first glance might be implied by chain concepts. Direct morphological linkages have also been clearly documented between muscles lying parallel to each other, e.g. synergists or antagonists (Yucesoy 2010). Myofascial continuity therefore represents a global feature of body architecture, rather than a distinct hallmark of serially arranged skeletal muscles. The factors determining and influencing the amount of structural continuity are a matter of debate. While the plantar aponeurosis – also called plantar fascia or plantar ligament by other authors – fuses strongly with the Achilles tendon in young individuals, no (or only a few) bridging fibres can be detected in older persons (Snow et al 1995, Stecco et al 2013). Besides age, physical activity and gender represent other potential predictors of the degree of myofascial force transmission, but as yet have not been investigated.

MYOFASCIAL FORCE TRANSMISSION

The existence of myofascial continuity does not necessarily imply mechanical significance. Clinical relevance depends on whether or not substantial amounts of force can be transferred across the connections. In fact, although considerable inter-individual variation exists, results of biomechanical cadaveric studies suggest notable mutual interactions between serially arranged muscles and/or their connective tissue, respectively (Krause et al 2016). In the low back region, this appears

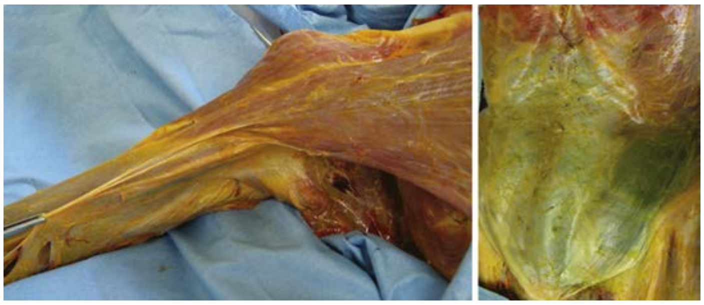
Fig. 1.6.1 The myofascial continuities of pectoralis major, which is connected to the brachial fascia (left) and the rectus abdominis sheath (right). Note that in contrast to sharply dissected muscles, no clear insertions and origins of the connective tissue can be identified. (With permission from Stecco A, Macchi V, Stecco C et al 2009 Anatomical study of myofascial continuity in the anterior region of the upper limb. J Bodyw Mov Ther 13:53–62; Stecco A, Masiero S, Macchi V et al 2009 The pectoral fascia: anatomical and histological study. J Bodyw Mov Ther 13:255–261.)

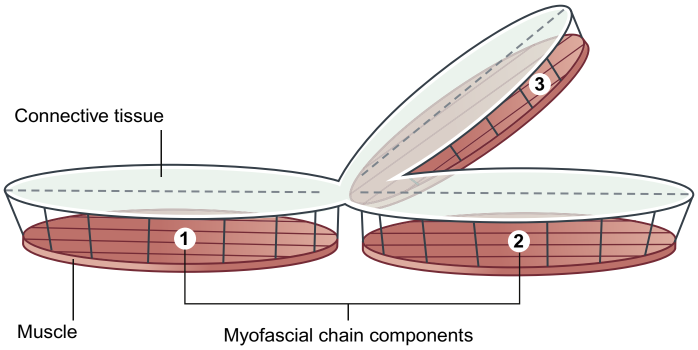

Fig. 1.6.2 A schematic drawing illustrating the selection of myofascial chain components. Although muscle 1 is connected to two other muscles (in this case through the overlying investing fasciae), the transition to muscle 2 would be preferred due to the common fibre course and the linear continuation of the longitudinal axes (grey dotted lines). Note that in this idealized model, similar tensional stiffness is assumed in all three components. If muscle 2 and its overlying connective tissue were in a slack position, force transmission could be superior between muscles 1 and 3.

---

[1] In this Commentary, the term fascia refers to the connective tissue investing the skeletal muscles, sometimes also called 'deep fascia'.

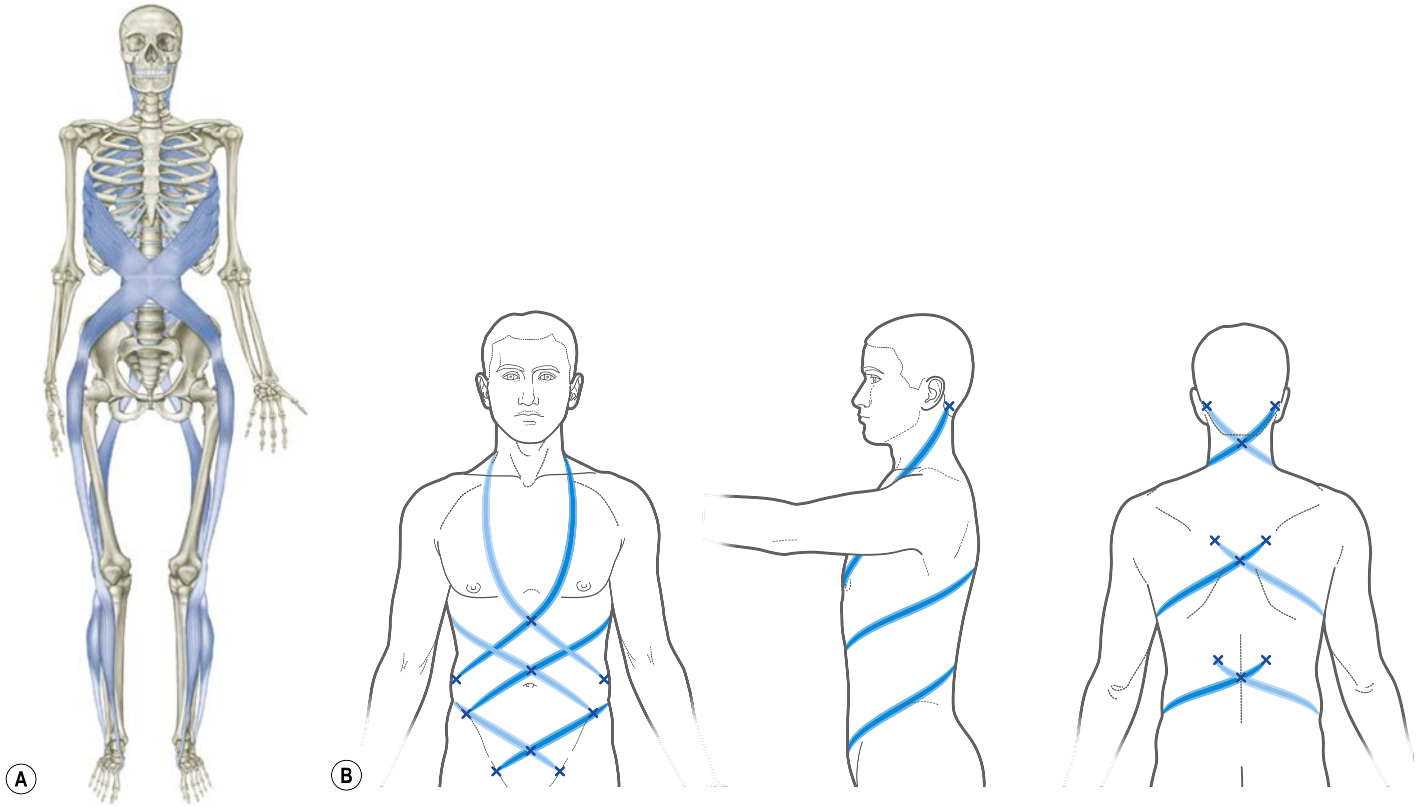

Fig. 1.6.3 Different courses and components of myofascial chains have been proposed. This figure shows two possible versions of a spiral chain wrapping around the body. **A**, Myers (1997). **B**, Dart (1950), did not include the lower leg muscles. (Adapted from Dart 1996 and reproduced with permission from Myers TW Anatomy Trains. Elsevier, Churchill Livingstone. Copyright 2014.)

to be of particular relevance: the lumbar fascia represents the mechanical hub of the posterior diagonal myofascial chain and can receive tension from both latissimus dorsi and the contralateral gluteus maximus muscle (Vleeming et al 1995, Barker et al 2004). In the posterior longitudinal chain, the lumbar fascia and erector spinae may be affected by the hamstring muscles via connectivity with the sacrotuberous ligament (Vleeming et al 1989a, 1989b, 1995). Further interactions for this chain have been demonstrated concerning the more caudal transitions between (1) the hamstrings and gastrocnemius (Cruz-Montecinos et al 2015) and (2) gastrocnemius and the plantar aponeurosis (Carlson et al 2000, Erdemir et al 2004). A mechanical force transmission has been observed between rectus abdominis and adductor longus in the anterior diagonal myofascial chain (Norton-Old et al 2013).

Limitations and perspectives

Myofascial continuity includes both parallel and serial linkages of skeletal muscles. There is evidence of mechanical force transmission in the course of myofascial chains. Numerous studies suggest strong interactions between several lower leg muscles (Wilke et al 2018). For instance, length changes of gastrocnemius at fixed ankle position are associated with substantial strains in soleus and the fibular muscles (Yaman et al 2013), indicative of a mutual interaction between these muscles. It is yet to be elucidated if in-series force transmission across myofascial chains exceeds that of structures located in parallel (**Fig. 1.6.5**).

REMOTE EXERCISE EFFECTS AND NON-LOCAL SYMPTOM MANIFESTATIONS

A few studies have attempted to translate the findings of cadaveric trials into *in vivo* conditions. Initial evidence suggests that exercise protocols based on the concept of myofascial chains lead to non-local effects: stretching of the gastrocnemius and hamstring muscles, both of which represent a part of the longitudinal posterior chain, increases the cervical range of motion (ROM) (Wilke et al 2016a, Wilke et al 2016d). Similarly, self-massage of the plantar aponeurosis enhances hamstring extensibility (Grieve et al 2015, Wilke et al 2019).

Limitations and perspectives

In most cases, non-local exercise effects have been examined using functional outcomes (e.g. ROM of neighbouring joints), which are paramount in order to estimate clinical significance. However, there is a caveat: although likely, without simultaneous imaging it cannot be concluded without doubt that a passive myofascial force transmission caused the remote effects. Alternative explanations include cortical adaptations (e.g. reduced systemic stretch tolerance) or a mechanical force transfer via peripheral neurovascular bundles that also cross multiple joints (Ellis et al 2012).

THE ROLE OF MYOFASCIAL CHAINS IN MUSCULOSKELETAL DISORDERS

Besides optimizing motor function, e.g. through enhanced ROM, force transmission across myofascial chains might contribute to musculoskeletal diseases. In some disorders, remote functional or tissue-related abnormalities can be found in addition to the typical local symptoms. Patients with sacroiliac and chronic low back pain may display hyperactivity of latissimus dorsi and the contralateral gluteus maximus, which represent the major muscular parts of the diagonal posterior chain (Mooney et al 2001, Kim et al 2014). Furthermore, although the relationship between the viscoelastic properties of the posterior thigh

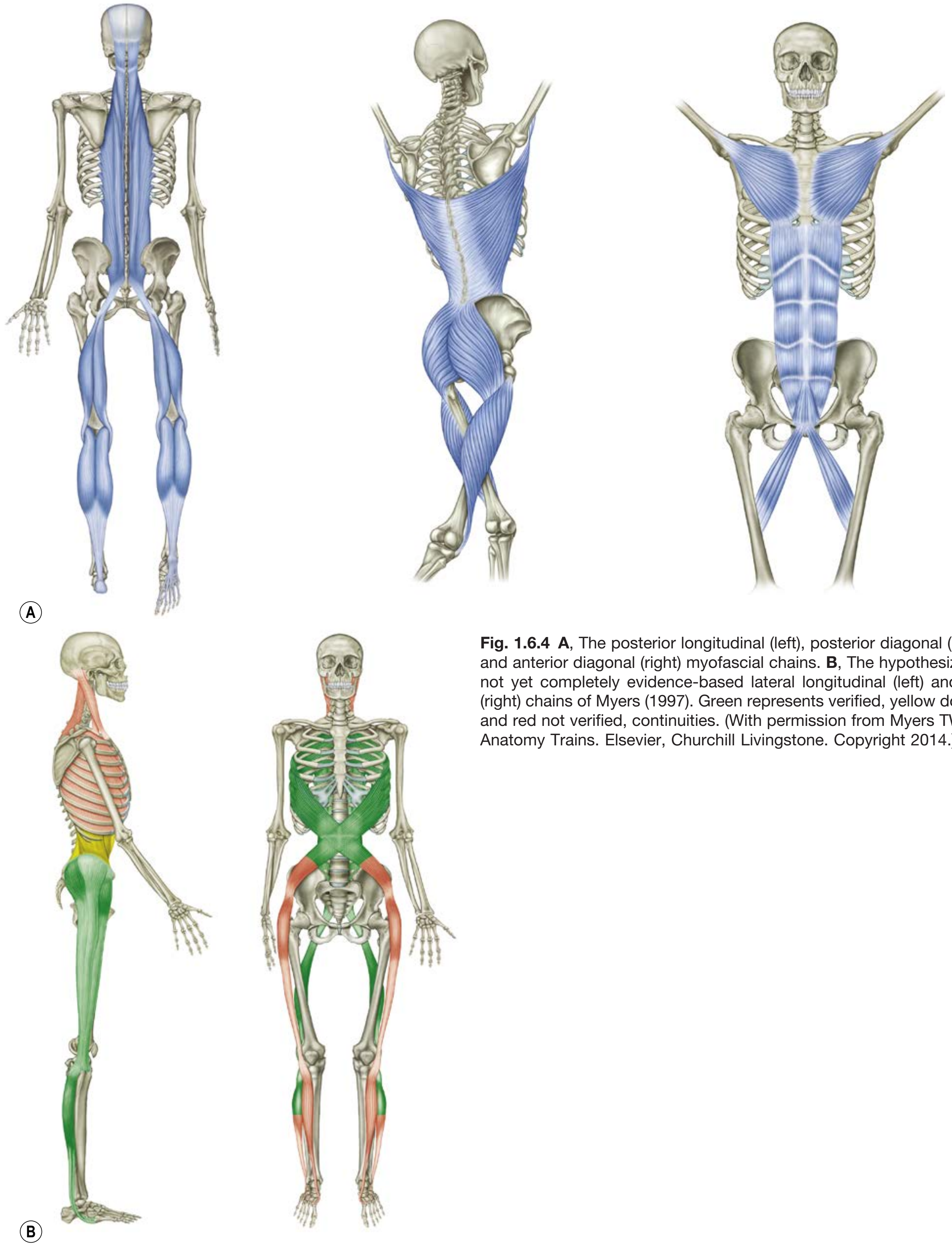

Fig. 1.6.4 **A**, The posterior longitudinal (left), posterior diagonal (middle) and anterior diagonal (right) myofascial chains. **B**, The hypothesized but not yet completely evidence-based lateral longitudinal (left) and spiral (right) chains of Myers (1997). Green represents verified, yellow doubtful, and red not verified, continuities. (With permission from Myers TW 2014 Anatomy Trains. Elsevier, Churchill Livingstone. Copyright 2014.)

muscles and back pain remains controversial (Halbertsma et al 2001), individuals with chronic lumbar pain have been reported to display decreased extensibility and increased stiffness of the hamstrings (Marshall et al 2009), a muscle group belonging to the longitudinal posterior chain. The latter chain might also be of importance in plantar fasciitis, a condition in which increased stiffness of the hamstrings and gastrocnemius has been observed (Labovitz et al 2011, Bolívar et al 2013).

Limitations and perspectives

Although cross-sectional studies indicate several non-local symptom manifestations in the course of myofascial chains, little knowledge exists regarding the success of corresponding interventions. Randomized, controlled trials of treatments of musculoskeletal disorders based on the concept of myofascial chains are therefore warranted.

TABLE 1.6.1 Components and possible functions of the three verified myofascial chains. Muscular parts include the respective investing fasciae

Myofascial chain	Soft tissue components	Assumed function	Remarks
Posterior longitudinal chain	Plantar aponeurosis Achilles tendon Gastrocnemius 'Hamstring' muscles Sacrotuberous ligament Lumbar fascia/erector spinae	Resistance to gravity, control and support of posture in the sagittal plane (e.g. upright and slumped spine), initiation and stabilization of linear vertical movements (e.g. jumps)	Continuity of plantar aponeurosis and Achilles tendon decreases with age
Posterior diagonal chain	Vastus lateralis Gluteus maximus Lumbar fascia Contralateral latissimus dorsi Brachial fascia	Connection of both body sides, interaction between upper and lower extremity, initiation and control of cross-sided movements (e.g. throwing)	In contrast to pectoralis major, the brachial fascia does not adhere strongly to the underlying muscles. This might reduce force transfer, e.g. to biceps brachii
Anterior diagonal chain	Adductor longus Rectus abdominis Pectoralis major Brachial fascia	Connection of both body sides, interaction between upper and lower extremity, initiation and control of cross-sided movements (e.g. throwing)	In contrast to latissimus dorsi, the brachial fascia does not adhere strongly to the underlying muscles. This might reduce force transfer, e.g. to triceps brachii

TABLE 1.6.2 Hypothetical components and possible functions of two not yet entirely evidence-based myofascial chains (based on the proposal of Myers 1997a, 1997b). Muscular parts include the respective investing fasciae. Unverified continuities are indicated in bold font

Myofascial chain	Soft tissue components	Assumed function
Lateral longitudinal chain	Fibularis longus/brevis/crural fascia – iliotibial tract/gluteus maximus/tensor fasciae latae Iliotibial tract/gluteus maximus/tensor fasciae latae – external/internal abdominal oblique **External/internal abdominal oblique – intercostal muscles** **Intercostal muscles – splenius capitis/sternocleidomastoid**	Stabilization and control of ankle, knee, hip and spine in the frontal plane (e.g. knee alignment/valgus/varus)
Spiral chain	Erector spinae – sacrotuberous ligament/biceps femoris Biceps femoris – fibularis longus **Fibularis longus – tibialis anterior** **Tibialis anterior – iliotibial tract/tensor fasciae latae** **Tensor fasciae latae – internal abdominal oblique** Internal – external abdominal oblique External abdominal oblique – serratus anterior Serratus anterior – rhomboid minor/major **Rhomboid minor/major – splenius capitis/cervicis**	Production and control of rotational forces (e.g. torsion of the spine or throwing in sports), stabilization and control of ankle, knee, hip and spine in the frontal plane (e.g. knee alignment/valgus/varus)

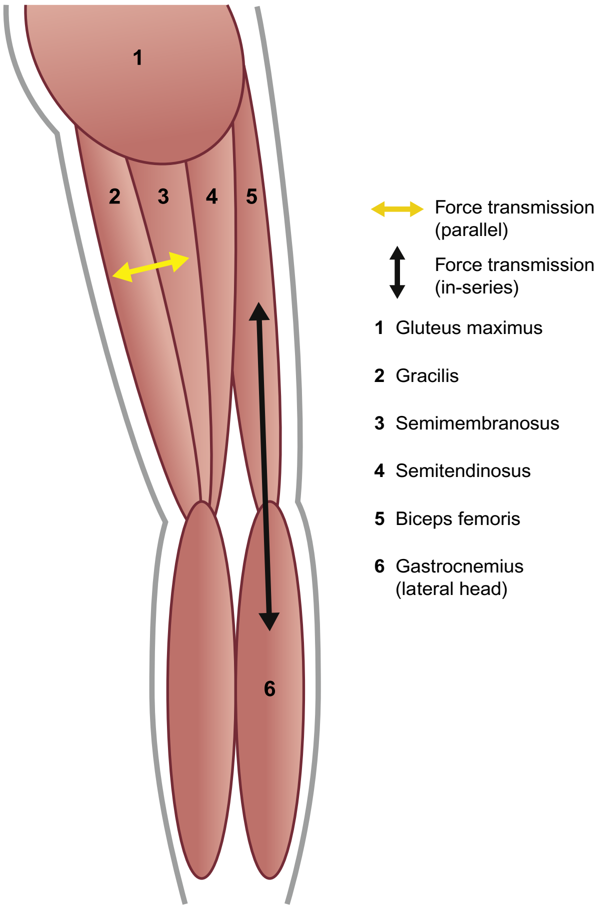
1
2
3
4
5
6
Force transmission (parallel)
Force transmission (in-series)
1 Gluteus maximus
2 Gracilis
3 Semimembranosus
4 Semitendinosus
5 Biceps femoris
6 Gastrocnemius (lateral head)

Fig. 1.6.5 A schematic representation of lower leg mechanical force transmission. In myofascial chains, mutual interactions occur between the skeletal muscles arranged in series (black arrows). However, this does not represent the only relevant pathway: forces are also transmitted to tissues located in parallel (yellow arrows).

CONCLUSION

The classical conception of skeletal muscles as independent actuators requires a thorough revision. Fascial tissue links the skeletal muscles of the body and acts as a mechanical force transmitter. Although it is not known (1) to what degree cortical adaptations play a role in the genesis of non-local exercise effects under *in vivo* conditions; and (2) whether the extent of mutual interaction between serially connected muscles exceeds that of muscles arranged parallel to each other, it is reasonable to suggest that clinical focus should not be restricted to one joint or soft tissue.

References

Adstrum S, Hedley G, Schleip R et al 2017 Defining the fascial system. J Bodyw Mov Ther 21:173–7.

Barker PJ, Briggs CA, Bogeski G 2004 Tensile transmission across the lumbar fasciae in unembalmed cadavers. Spine 29:129–38.

Bolívar YA, Munuera PV, Padillo JP 2013 Relationship between tightness of the posterior muscles of the lower limb and plantar fasciitis. Foot Ankle Int 34:42–8.

Butler DL, Grood ES, Noyes FR et al 1984 Effects of structure and strain measurement technique on the material properties of young human tendons and fascia. J Biomech 17:579–96.

Carlson RE, Fleming LL, Hutton WC 2000 The biomechanical relationship between the tendoachilles, plantar fascia and metatarsophalangeal joint dorsiflexion angle. Foot Ankle Int 21:18–25.

Cruz-Montecinos C, González Blanche A, López Sánchez D et al 2015 In vivo relationship between pelvis motion and deep fascia displacement of the medial gastrocnemius: anatomical and functional implications. J Anat 227:665–2.

Dart RA 1950 Voluntary musculature in the human body; the double-spiral arrangement. Br J Phys Med 13:265–8.

Dart RA 1996 Skill and Poise. London: STAT Books.

Derwin KA, Baker AR, Spragg RK 2008 Regional variability, processing methods, and biophysical properties of human fascia lata extracellular matrix. J Biomed Mater Res 84:500–7.

Ellis RF, Hing WA, McNair PJ 2012 Comparison of longitudinal sciatic nerve movement with different mobilization exercises: an in vivo study utilizing ultrasound imaging. J Orthop Phys Ther 42:667–75.

Eng CM, Pancheri FQ, Lieberman DE et al 2014 Directional differences in the biaxial material properties of fascia lata and the implications for fascia function. Ann Biomed Eng 42:1224–37.
Erdemir A, Hamel AJ, Fauth AR et al 2004 Dynamic loading of the plantar aponeurosis in walking. J Bone Joint Surg Am 86:546–52.
Grieve R, Goodwin F, Alfaki M et al 2015 The immediate effect of bilateral self myofascial release on the plantar surface of the feet on hamstring and lumbar spine flexibility: a pilot randomised controlled trial. J Body Mov Ther 19:544–52.
Halbertsma JP, Göeken LN, Ludwig NH et al 2001 Extensibility and stiffness of the hamstrings in patients with nonspecific low back pain. Arch Phys Med Rehabil 82:232–8.
Kim JKW, Kang MH, Oh JS 2014 Patients with low back pain demonstrate increased activity of the posterior oblique sling muscle during prone hip extension. PM R 6:400–5.
Krause F, Wilke J, Vogt L et al 2016 Intermuscular force transmission along myofascial chains: a systematic review. J Anat 228:910–18.
Labovitz JM, Yu J, Kim C 2011 The role of hamstring tightness in plantar fasciitis. Foot Ankle Spec 4:141–4.
Marshall PW, Mannion J, Murphy BA 2009 Extensibility of the hamstrings is best explained by mechanical components of muscle contraction, not behavioral measures in individuals with chronic low back pain. PM R 1:709–18.
Martin BF 1968 The origin of the hamstring muscles. J Anat 102:345–52.
Mooney V, Pozos R, Vleeming A et al 2001 Exercise treatment for sacroiliac pain. Orthopedics 24:29–32.
Myers TW 1997a The ‘anatomy trains’. J Bodyw Mov Ther 1:91–101.
Myers TW 1997b The ‘anatomy trains’: part 2. J Bodyw Mov Ther 1:135–46.
Norton-Old KJ, Schache AG, Barker PJ et al 2013 Anatomical and mechanical relationship between the proximal attachment of adductor longus and the distal rectus sheath. Clin Anat 26:522–30.
Richter P 2012 Myofascial chains: a review of different models. In: Findley TW, Chaitow L, Huijing PA et al (eds) Fascia. The Tensional Network of the Human Body. Edinburgh: Churchill Livingstone, pp. 123–31.
Snow S, Bohne W, DiCarlo E et al 1995 Anatomy of the Achilles tendon and plantar fascia in relation to the calcaneus in various age groups. Foot Ankle Int 16:418–21.
Stecco C, Corradin M, Macchi V et al 2013 Plantar fascia anatomy and its relationship with Achilles tendon and paratenon. J Anat 223:665–76.
Tuncay I, Zucuker H, Uzun I et al 2009 The fascial band from semitendinosus to gastrocnemius: the critical point of hamstring harvesting. An anatomical study of 23 cadavers. Acta Orthopaedica 78:361–3.
Van der Wal J 2009 The architecture of the connective tissue in the musculoskeletal system – an often overlooked functional parameter as to proprioception in the locomotor apparatus. Int J Ther Massage Bodyw 2:9–23.
Vleeming A, Stoeckart R, Snijders CJ 1989a The sacrotuberous ligament: a conceptual approach to its dynamic role in stabilizing the sacroiliac joint. Clin Biomech 4:201–203.
Vleeming A, Wingerden JP, Snijders CJ et al 1989b Load application to the sacrotuberous ligament; influences on sacroiliac joint mechanics. Clin Biomech 4:204–9.
Vleeming A, Pool-Goudzwaard AL, Stoeckart R et al 1995 The posterior layer of the thoracolumbar fascia. Its function in load transfer from spine to legs. Spine 20:753–8.
Wilke J, Vogt L, Niederer D et al 2016a Is remote stretching based on myofascial chains as effective as local exercise? A randomised-controlled trial. J Sport Sci 35:2021–7.
Wilke J, Engeroff T, Nürnberger F 2016b Anatomical study of the morphological continuity between iliotibial tract and the fibularis longus fascia. Surg Radiol Anat 38:349–52.
Wilke J, Krause F, Vogt L et al 2016c What is evidence-based about myofascial chains: a systematic review. Arch Phys Med Rehabil 97:454–61.
Wilke D, Niederer L, Vogt L et al 2016d Remote effects of lower limb stretching: preliminary evidence for myofascial connectivity? J Sport Sci 34:2145–8.
Wilke J, Schleip R, Yucesoy CA et al 2018 Not merely a protective packing organ? A review of fascia and its force transmission capacity. J Appl Physiol (1985) 124:234–44.
Wilke J, Kalo K, Niederer D et al 2019 Gathering hints for myofascial force transmission under in-vivo conditions: are remote exercise effects age-dependent. J Sport Rehabil 28:758–63.
Yaman A, Ozturk C, Huijing PA 2013 Magnetic resonance imaging assessment of mechanical interactions between human lower leg muscles in vivo. J Biomech Eng 135:91003.
Yucesoy CA 2010 Epimuscular myofascial force transmission implies novel principles for muscular mechanics. Exerc Sport Sci Rev 38:128–34.

CHAPTER
8

Preimplantation development

Understanding the spatial and temporal developmental processes that take place within an embryo as it develops from a single cell into a recognizable human is the challenge of embryology. The control of these processes resides within the genome; fundamental questions remain concerning the genes and interactions involved in development.

STAGING OF EMBRYOS

For the purposes of embryological study, prenatal life is divided into an embryonic period and a fetal period. The embryonic period covers the first 8 weeks of development (weeks following ovulation and fertilization resulting in pregnancy). The ages and stages of early human embryos were initially estimated by comparing their development with that of other embryos or with those of monkey embryos of known postovulatory ages. Because the external and internal development of embryos at any specified time may be different, a classification of human embryo development into 23 stages based on the internal and external features of embryos was developed by Streeter (1942), and continued by O'Rahilly and Müller (1987), from detailed histological study of approximately 600 sectioned embryos in the Carnegie collection. On the basis of correlating particular maternal menstrual histories and the known developmental ages of monkey embryos, growth tables were constructed so that the size of an embryo (specifically, the greatest length) could be used to predict its presumed age in postovulatory days (synonymous to postfertilizational days). O'Rahilly and Müller (2000, 2010) emphasize that the Carnegie embryonic stages are based on external and internal morphological criteria and are not founded on length or age. Ultrasonic examination of embryos *in vivo* has necessitated the revision of some of the ages related to stages, and embryos of stages 6–16 are now thought to be up to 3–5 days older than the embryological estimates used previously (O'Rahilly and Müller 1999, 2010). Within this staging system, embryonic life commences with fertilization at stage 1; stage 2 encompasses embryos from two cells, through compaction and early segregation, to the appearance of the blastocoele. The developmental processes occurring during the first 10 stages of embryonic life are shown in **Fig. 8.1**.

Knowledge of the early molecular processes of development is derived from experimental studies on amniote embryos, particularly the chick, mouse and rat. **Figure. 8.2** shows the comparative timescales of development of these species and human development up to stage 12 and illustrates the differences in heterochrony between the species (Ch. 11). The length and age, in post fertilization days, of human development during stages 10–23 is given in **Fig. 8.3**, the external appearance of embryos over this time is shown in Fig. 23.1 and stage is correlated to days and weeks in Fig. 23.3.

Information on developmental age after stage 23 (postfertilization days 53–58) is shown in Fig. 23.4, where the developmental staging used throughout this book is juxtaposed with the clinical obstetric estimation of pregnancy based on maternal last menstrual period. Great care should be taken when reading developmental papers to clarify the staging system used to confer age in days on any embryos. All developmental publications using the Carnegie collection prior to 2010 use earlier estimations of age. Many of the publications since 2010, when O'Rahilly and Müller revised their correlation of age in days to stage, are still using the older unrevised ages. Publications noting changes correlated to Carnegie stage (not age) still match Streeter and O'Rahilly and Müller publications. All embryonic stages in this book are corrected to postfertilization days based on O'Rahilly and Müller (2010).

FERTILIZATION

The central feature of reproduction is the fusion of the two gamete pronuclei at fertilization. In humans, the male gametes are spermatozoa, which are produced from puberty onwards. Female gametes are released as secondary oocytes in the second meiotic metaphase, usually singly, in a cyclical fashion. The signal for the completion of the second meiotic division is fertilization, which stimulates the cell division cycle to resume, completing meiosis and extruding the second polar body (the second set of redundant meiotic chromosomes).

Fertilization normally occurs in the ampullary region of the uterine tube, probably within 24 hours of ovulation. Very few spermatozoa reach the ampulla to achieve fertilization. They must undergo capacitation, a process that is still incompletely understood, and that may involve modifications of membrane sterols or surface proteins. They traverse the cumulus oophorus and corona radiata, then bind to specific glycoprotein receptors on the zona pellucida, ZP3 and ZP2. Interaction of ZP3 with the sperm head induces the acrosome reaction, in which fusion of membranes on the sperm head releases enzymes, such as acrosin, that help to digest the zona around the sperm head, allowing the sperm to reach the perivitelline space. In the perivitelline space, the spermatozoon fuses with the oocyte microvilli, possibly via two disintegrin peptides in the sperm head and integrin in the oolemma (**Figs 8.4, 8.5A**).

Fusion of the sperm with the oolemma causes a weak membrane depolarization and leads to a calcium wave, triggered by the sperm at the site of fusion, that crosses the egg within 5–20 seconds. The calcium wave amplifies the local signal at the site of sperm–oocyte interaction and distributes it throughout the oocyte cytoplasm. The increase in calcium concentration is the signal that causes the oocyte to resume cell division, initiating the completion of meiosis II and setting off the developmental programme that leads to embryogenesis. The pulses of intracellular calcium that occur every few minutes for the first few hours of development also trigger the fusion of cortical granules with the oolemma. The cortical secretory granules release an enzyme that hydrolyses the ZP3 receptor on the zona pellucida and so prevents other sperm from binding and undergoing the acrosome reaction, thus establishing the block to polyspermy. The same cortical granule secretion may also modify the vitelline layer and oolemma, making them less susceptible to sperm–oocyte fusion and providing a further level of polyspermy block.

The sperm head undergoes its protamine to histone transition as the second polar body is extruded. The two pronuclei form, the female one cortically near the site of emission of the second polar body. They move together and are juxtaposed prior to pronuclear membrane breakdown/syngamy and cleavage after approximately 24 hours after sperm and oocyte association (Coticchio et al 2018) (**Fig. 8.5B**). Pronuclear fusion as such does not occur; no true zygote containing a membrane-bound nucleus forms. The two pronuclear envelopes disappear and the two chromosome groups move together to assume positions on the first cleavage spindle. Nucleolar ribosomal ribonucleic acid (rRNA), and perhaps some messenger RNA (mRNA), are synthesized in pronuclei. A succeeding series of cleavage divisions produces eight even-sized blastomeres by approximately 55 hours, when embryonic mRNA is transcribed.

The presence of the pronuclei from both parental origins is crucial for spatial organization and the controlled growth of cells, tissues and organs. In the mouse, embryos in which the paternal pronucleus has been removed and replaced with a second maternal pronucleus develop to a relatively advanced state (25 somites), but with limited development of the trophoblast and extraembryonic tissues. In contrast, embryos in which the maternal pronucleus has been replaced by a second paternal pronucleus develop very poorly, forming embryos of only six to eight somites, but with extensive trophoblast. Thus, it seems that the maternal genome is relatively more important for the development of the embryo, whereas the paternal genome is essential for the development of the extraembryonic tissues that would lead to placental formation.

This functional inequivalence of homologous parental chromosomes is called parental imprinting. It occurs during the maturational phase of production of the haploid gametes in mammals and silences one allele by DNA methylation without changing the DNA sequence (Moore et al

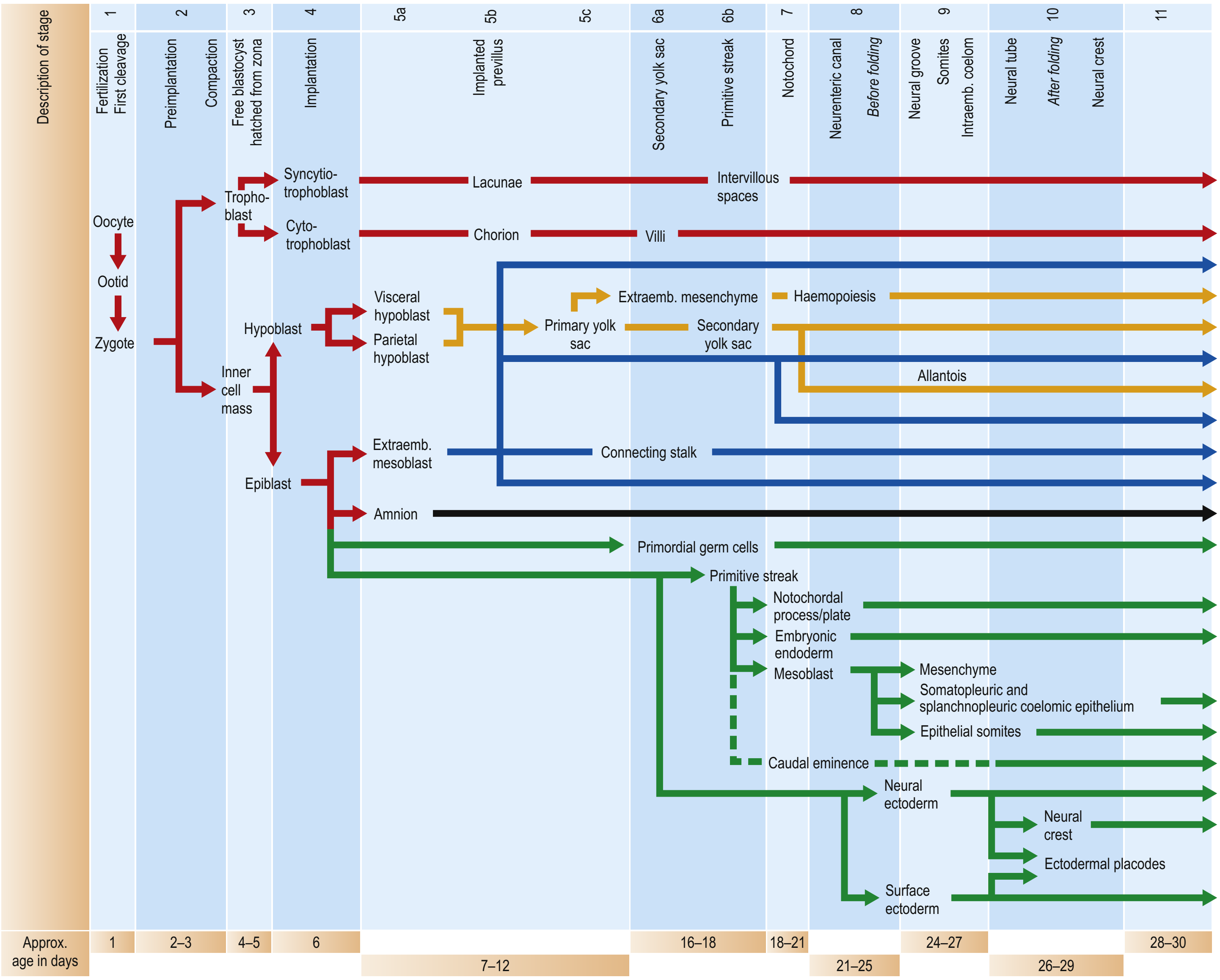
Description of stage
1
Fertilization
First cleavage
2
Preimplantation
Compaction
3
Free blastocyst
hatched from zona
4
Implantation
5a
Implanted
previllus
5b
5c
6a
Secondary yolk sac
6b
Primitive streak
7
Notochord
8
Neurenteric canal
Before folding
9
Neural groove
Somites
Intraemb. coelom
10
Neural tube
After folding
Neural crest
11
Oocyte
Ootid
Zygote
Tropho-
blast
Syncytio-
trophoblast
Cyto-
trophoblast
Lacunae
Intervillous
spaces
Chorion
Villi
Inner
cell
mass
Hypoblast
Visceral
hypoblast
Parietal
hypoblast
Extraemb. mesenchyme
Haemopoiesis
Primary yolk
sac
Secondary
yolk sac
Allantois
Epiblast
Extraemb.
mesoblast
Connecting stalk
Amnion
Primordial germ cells
Primitive streak
Notochordal
process/plate
Embryonic
endoderm
Mesoblast
Mesenchyme
Somatopleuric and
splanchnopleuric coelomic epithelium
Epithelial somites
Caudal eminence
Neural
ectoderm
Neural
crest
Ectodermal placodes
Surface
ectoderm
Approx.
age in days
1
2–3
4–5
6
7–12
16–18
18–21
21–25
24–27
26–29
28–30

Fig. 8.1 Developmental processes occurring during the first 10 stages of development. In the early stages, a series of binary choices determine the cell lineages. Generally, the earliest stages are concerned with formation of the extraembryonic tissues, whereas the later stages are concerned with the formation of embryonic tissues. The approximate age in days is taken from O'Rahilly and Müller 2010.

2015). Imprinted genes are heritable but in the next generation may be unmethylated during gametogenesis and re-established in the new germline. Between 50 and 90 imprinted genes expressed in the placenta and embryo have been identified, many concerned with embryogenesis and growth (Hanna et al 2018). Although imprinted genes represent a small proportion of the genome, they are particularly important in blastocyst implantation, placentation, developmental growth rates and the embryonic nervous system. Some epigenetic modifications can lead to congenital anomalies and syndromes (Butler 2009, Batcheller et al 2011, Fauque 2013). For example, changes to the 15q11-13 domain if paternally imprinted lead to Prader–Willi syndrome (a disorder of growth) and if maternally imprinted cause Angelman syndrome (a neurological disorder); changes to the domain 11p15 affect IGF2 if paternally expressed and H19 if maternally expressed; both of these imprinted conditions affect growth regulation and trajectory in early development, Beckwith-Wiedemann syndrome results if the region is maternally imprinted (Moore et al 2015). Generally, paternally expressed genes enhance growth and maternally expressed genes suppress growth (Butler 2009).

In vitro fertilization

In vitro fertilization (IVF) of human gametes is a successful way of overcoming most forms of infertility (**Video 8.1**). Controlled stimulation of the ovaries (e.g. pituitary downregulation using gonadotrophin-releasing hormone superactive analogues, followed by stimulation with purified, or recombinant, follicle stimulating hormone or urinary menopausal gonadotrophins) enables many preovulatory oocytes (often 10 or more) to be recruited and matured, and then aspirated transvaginally using ultrasound guidance, 34–38 hours after injection of human chorionic gonadotrophin (which is given to mimic the luteinizing hormone surge). These oocytes are then incubated overnight with motile spermatozoa in a specially formulated culture medium, in an attempt to achieve successful *in vitro* fertilization. In cases of severe male-factor infertility, in which there are insufficient normal spermatozoa to achieve conventional *in vitro* fertilization, individual spermatozoa can be directly injected into the oocyte in a process known as intracytoplasmic sperm injection (ICSI), which is as successful as routine IVF. In cases in which there are no spermatozoa in the ejaculate, suitable material can sometimes be directly aspirated from the epididymis or surgically retrieved from the testes, and the extracted sperm are then used for intracytoplasmic injection.

It is also now sometimes possible to assess embryos by preimplantation genetic testing (PGT) for the presence of monogenic/single gene diseases (PGT-M) or for structural chromosomal rearrangements (PGT-SR). A sample (biopsy) is removed from either the oocyte (polar bodies), the early cleavage stage embryo (a blastomere) or the blastocyst (small piece of trophectoderm), and subjected to specific genetic testing. Oocytes and embryos can also be biopsied and screened for errors in chromosome copy numbers using preimplantation genetic testing for aneuploidy (PGT-A). Unaffected embryos can then be identified for transfer to the recipient. Although increasingly utilized across all ages of IVF patients, there is debate over the efficacy of PGT-A. It is considered most clinically appropriate for women over 37 years of age due to increased aneuploidy levels in their oocytes. Embryos that are surplus to immediate therapeutic requirements can also be cryopreserved in liquid nitrogen for later use. Propanediol or dimethylsulphoxide are commonly used as cryoprotectants for human embryos at all stages. Conception rates per cycle using ovarian stimulation, IVF and successive transfers of fresh and cryopreserved embryos exceed those obtained during non-assisted, or natural, conception.

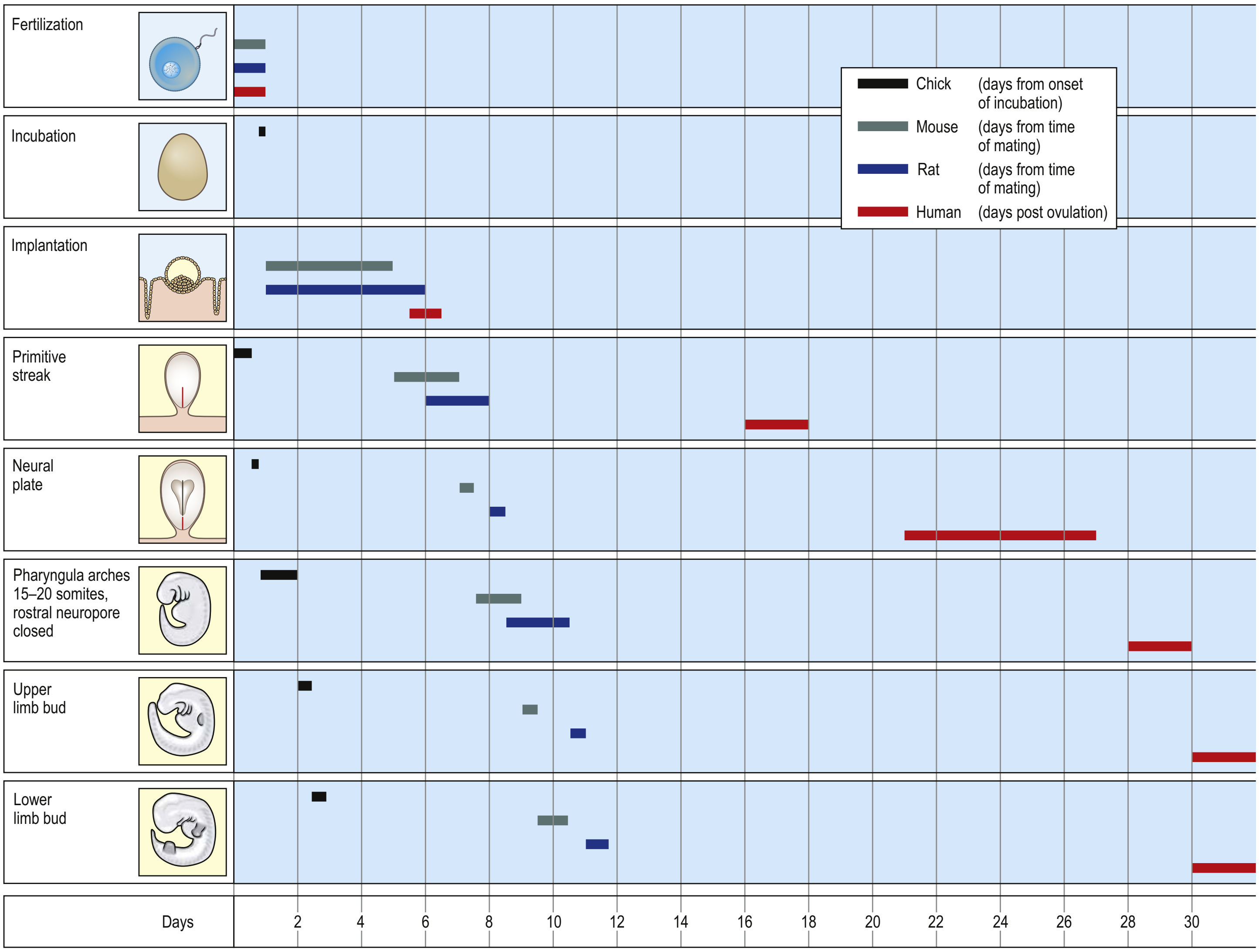

Fig. 8.2 Within developmental biology, evidence concerning the nature of developmental processes has come mainly from studies in vertebrate embryos, most commonly amniote embryos of the chick, mouse and rat. This chart illustrates the comparative timescale of development in these animals and in humans.

In 2014, some 40 years after the first IVF infant was born, more than 200,000 assisted reproductive technologies (ART) cycles were performed in the United States leading to nearly 60,000 live births. Worldwide the prevalence of ART is now extensive. For details of ART the reader should consult Kaser et al (2019).

Data collected on the longer-term effects of ART have indicated an associated increased risk of imprinting syndromes (Hanna et al 2018, Kaser et al 2019). The complexities of ART, i.e. the processes involved in collection of oocytes and sperm, *in vitro* fertilization and blastocyst culture, and the manipulation of the maternal endometrium for successful implantation, challenge many developmental conceptus–maternal interactions. It is now appreciated that the temporal conversations between oocyte/zygote/blastocyst and the mother are informed by dynamic exchange of environmental information some days before the close juxtaposition of the tissues seen in implantation, and that their effects extend into fetal growth and postnatal life (Ch. 23). These periconceptual influences are now being investigated (Moore et al 2015, Fleming et al 2018).

PREIMPLANTATION DEVELOPMENT

Cleavage

The first divisions of the zygote are termed cleavages. They distribute the cytoplasm approximately equally among daughter blastomeres, so that although the cell number of the preimplantation embryo increases, its total mass actually decreases slightly (**Fig. 8.6**). Cell division can be asynchronous and daughter cells may retain a cytoplasmic link through much of the immediately subsequent cell cycle via a midbody, as a result of the delayed completion of cytokinesis. No centrioles are present until 16–32 cells are seen, but amorphous pericentriolar material is present and serves to organize the mitotic spindles, which are characteristically more barrel-shaped than spindle-shaped at this stage.

All cleavage divisions after fertilization are dependent on continuing protein synthesis, whereas passage through the earliest cycles, up to eight cells, is independent of mRNA synthesis. Thereafter, experimental inhibition of transcription blocks further division and development, indicating that activation of the embryonic genome is required. There is also direct evidence for the synthesis of embryonically encoded proteins at this time. As the genes of the embryo first become both active and essential, the previously functional maternally derived mRNA is destroyed, although protein made on these maternal templates does persist at least during blastocyst growth. Spontaneous developmental arrest of embryos cultured *in vitro* seems to occur during the cell cycle of gene activation, but it is not caused by total failure of that activation process. Early cleavage, up to the formation of eight cells, requires pyruvate or lactate as metabolic substrates, but thereafter more glucose is metabolized and may be required. Pyruvate availability in maternal uterine tube secretions may function as an extrinsic mechanism for embryonic genome activation (Pfeffer 2018).

The earliest time at which different types of cells can be identified within the cleaving embryo is when 8–16 cells are present. Before that time cells are essentially spherical, touch each other loosely, have no specialized intercellular junctions or significant extracellular matrix and the cytoplasm in each cell is organized in a radially symmetric manner around a centrally located nucleus. Once eight cells have formed, a process of compaction occurs that creates tension between adjacent cells. Cells flatten on each other maximizing intercellular contact, this initiates the formation of gap and focal tight junctions, and radically reorganizes their cytoplasmic conformation from a radially symmetric to a highly asymmetric phenotype. This latter process includes the migration of nuclei towards the centre of the blastocyst,

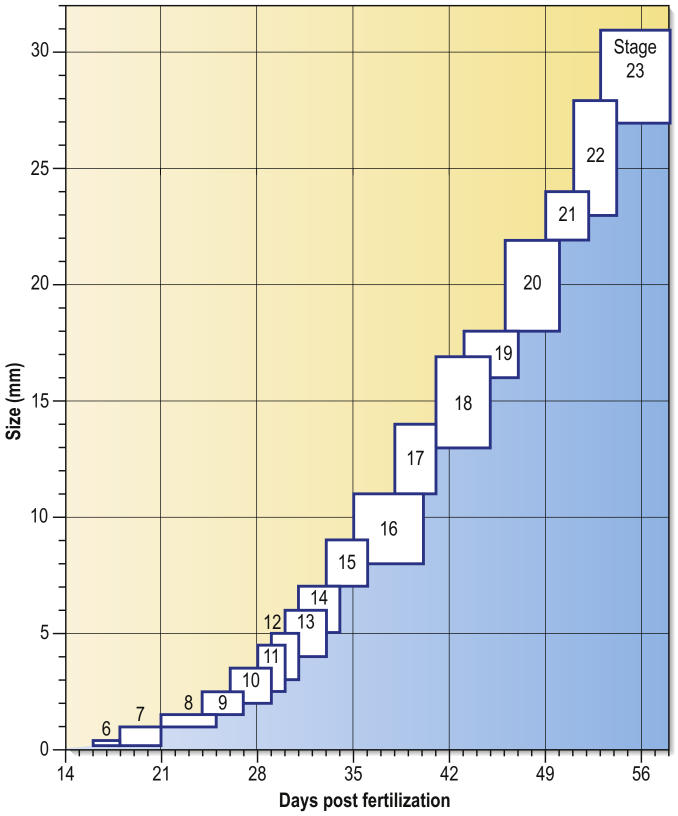

Fig. 8.3 Human developmental stages 10–23. The greatest embryonic length in mm (ordinate) is plotted against age in postfertilizational weeks (abscissa), with the stages superimposed according to current information. (Data provided by courtesy of Professor R O'Rahilly. See also O'Rahilly and Müller (2010).)

the redistribution of surface microvilli and an underlying mesh of microfilaments and microtubules to the exposed surface, and the localization of endosomes beneath the apical cytoskeletal mesh. In the mouse, blastomeres extend filopodia onto the apical surfaces of neighbouring cells between cell divisions (Fierro-González et al 2013). As a result of the process of compaction, the embryo forms a primitive proto-epithelial cyst consisting of eight polarized cells, in which the apices face outwards and basolateral surfaces face internally. The focal tight junctions, which align to become increasingly linear, are localized to the boundary between the apical and basolateral surfaces. Gap junctions form between apposed basolateral surfaces and become functional.

The process of compaction involves the cell surface and the calcium dependent cell–cell adhesion glycoprotein, E-cadherin (also called L-CAM or uvomorulin). Neutralization of its function disturbs all three elements of compaction. The entire process can function in the absence of both mRNA and protein synthesis. Post-translational controls are sufficient and seem to involve regulation through protein phosphorylation. Significantly, although E-cadherin is not synthesized and present on the surface of cleaving blastomeres, it first becomes phosphorylated when eight cells are visible, at the initiation of compaction.

Compaction is important for the generation of cell diversity in the early embryo. As each polarized cell divides, it retains significant elements of its polar organization, so that its daughter cells inherit cytocortical domains, their nature reflecting their origin and organization in the original parent cell in the eight-celled embryo. Thus, if the axis of division is aligned approximately at right-angles to the axis of cell polarity, the more superficially placed daughter cell inherits all the apical cytocortex and some of the basolateral cytocortex and is polar, whereas the more centrally placed cell inherits only basolateral cytocortex and is apolar. In contrast, if the axis of division is aligned approximately along the axis of the cell polarity, two polar daughter cells are formed. In this way, two-cell populations are formed in the 16-cell embryo that differ in phenotype (polar, apolar) and position (superficial, deep). The number of cells in each population in an individual embryo will be determined by the ratio of divisions along, and at right-angles to, the axis of eight-cell polarity. The theoretical and observed limits of the polar to apolar ratio are 16 : 0 and 8 : 8 respectively. The outer polar cells contribute largely to the trophectoderm, whereas the inner apolar cells contribute almost exclusively to the inner cell mass in most embryos.

In cleavage, the generation of cell diversity and commitment to either trophectoderm or inner cell mass, occurs in the 16-cell morula and precedes the formation of the blastocyst. During the 16-cell cycle, the outer polar cells continue to differentiate an epithelial phenotype, and display further aspects of polarity and intercellular adhesion typical of epithelial cells, while the inner apolar cells remain symmetrically organized. During the next cell division (16–32 cells), a proportion of polar cells again divide asymmetrically, as in the previous cycle, each yielding one polar and one apolar daughter cell displaying differentiation of the phenotype of the trophectoderm and inner cell mass respectively. Although such differentiative division at this time is less common than at the 8- to 16-cell transition, it has the important function of regulating an appropriate number of cells in the two cell phenotypes of the blastocyst. Thus, if differentiative divisions were relatively infrequent at the 8- to 16-cell transition, they will be more frequent at the 16- to 32-cell transition, and *vice versa*.

After division to 32 cells, the outer polar cells complete their differentiation into a functional epithelium, display structurally complete zonular tight junctions and begin to form desmosomes. The nascent trophectoderm engages in vectorial fluid transport in an apical to basal direction to generate a cavity that expands in size during the 32- to 64-cell cycles and converts the ball of cells, the morula, to a sphere, the blastocyst (**Fig. 8.7B**).

Blastocyst

Blastocysts can be broadly described by the number of cells and the extent of the blastocoele, and these can be correlated to developmental day/stage. The free, unattached blastocyst is assigned to stage 3 of development at approximately 4 days postfertilization. Early blastocysts have >35 cells and a cavity occupying <30% of the blastocyst volume; mid-blastocysts have 64–100 cells, and a cavity occupying 30–70% of the blastocyst volume; late blastocysts have 128–256 cells and the maximum cavity size within the zona pellucida. A hatched blastocyst, has >256 cells and an expanding blastocoele (Pfeffer 2018). Blastocyst 'hatching' from the zona pellucida occurs at 6–7 days, possibly assisted by an enzyme similar to trypsin (**Figs 8.7C, 8.8**). Trophoblast oozes out of a small slit and the cells assume a flattened polyhedral shape with ultrastructural features typical of a transporting epithelium. At hatching, many embryos form a figure-of-eight shape bisected by the small zona pellucida opening, especially if the zona pellucida has become hardened during oocyte maturation and cleavage. Such half-hatching could result in the formation of identical twins. Hatched blastocysts expand and differentiation of the inner cell mass proceeds.

Analysis of the transcriptome from single-cell embryo data, shows that three cell lineages are produced by blastocyst formation. Differentially expressed genes can be identified in the trophoblast (*GATA3*, *GATA2*, *KRT18*, *TEAD3*) but not in the inner cell mass. Once the inner cell mass is defined the epiblast that forms an ('upper') layer closest to the polar trophoblast expresses different genes (*NANOG*, *SOX2*, *KLF17*, *TDFG-1*) to the subjacent hypoblast (*PDGFRA*, *GATA6*, *GATA4*, *SOX17*) that gives rise to the yolk sac (Stirparo et al 2018). The appearance of epiblast and hypoblast layers in a bilaminar arrangement confers the dorsoventral axis of the developing embryo. The earliest primordial germ cells may also be defined at this stage (Chs 10, 22).

In mammals, the trophoblastic lineage becomes committed at species-specific time points related to the time of implantation, and differentiation has started by the time the blastocyst reaches the endometrial cavity. Human trophoblast commitment is noted in late blastocysts with >180 cells (Pfeffer 2018). After hatching, the trophoblast (also termed trophectoderm) surrounding the blastocyst cavity is termed mural trophoblast (cytotrophoblast) and that adjacent to the inner cell mass is termed polar trophoblast (composed of both cytotrophoblast and syncytiotrophoblast) (Ch. 9). Syncytiotrophoblast releases human chorionic gonadotrophin (hCG), which is detectable in maternal serum by 6–8 days after fertilization.

Human pregastrulation development has been studied by *in vitro* culture of donated embryos and also by culture of human embryonic stem cells derived from human embryos. The cultured cells are transcriptionally distinct from human epiblast and lose the imprinting usually established during blastocyst development. Stem cell lines of trophoblast and early endoderm are being studied and trophoblast spheroids have been generated from human embryonic stem cells (Wamaitha and Niakan 2018).

Attachment to the uterine wall

On the sixth postovulatory day, after about 72 hours in the uterine lumen, the blastocyst adheres to the uterine mucosa and the events

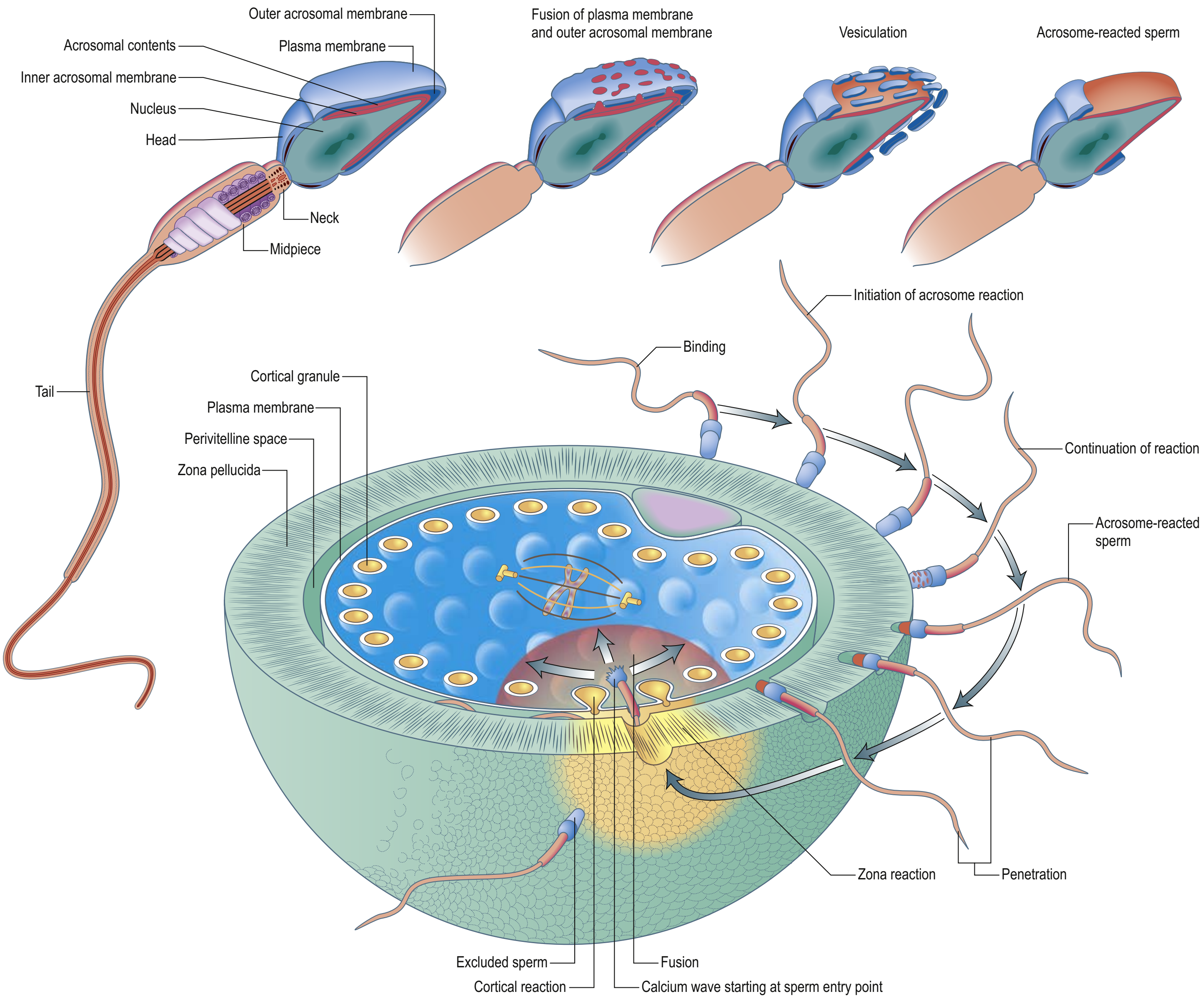
Outer acrosomal membrane
Acrosomal contents
Plasma membrane
Inner acrosomal membrane
Nucleus
Head
Neck
Midpiece
Tail
Fusion of plasma membrane and outer acrosomal membrane
Vesiculation
Acrosome-reacted sperm
Initiation of acrosome reaction
Binding
Cortical granule
Plasma membrane
Perivitelline space
Zona pellucida
Continuation of reaction
Acrosome-reacted sperm
Zona reaction
Penetration
Excluded sperm
Fusion
Cortical reaction
Calcium wave starting at sperm entry point

Fig. 8.4 The fertilization pathway: a succession of steps. After a sperm binds to the zona pellucida, the acrosome reaction takes place (see detail at top). The outer acrosomal membrane (blue), an enzyme-rich organelle in the anterior of the sperm head, fuses at many points with the plasma membrane surrounding the sperm head. Then those fused membranes form vesicles, which are eventually sloughed off from the head, exposing the acrosomal enzymes (red). The enzymes digest a path through the zona pellucida, enabling the sperm to advance. Eventually, the sperm meets and fuses with the secondary oocyte plasma membrane and this triggers cortical and zona reactions. First, enzyme-rich cortical granules in the oocyte cytoplasm release their contents (yellow) into the zona pellucida, starting at the point of fusion and progressing right and left. Next, in the zona reaction, the enzymes modify the zona pellucida, transforming it into an impenetrable barrier to sperm as a guard against polyspermy (multiple fertilization).

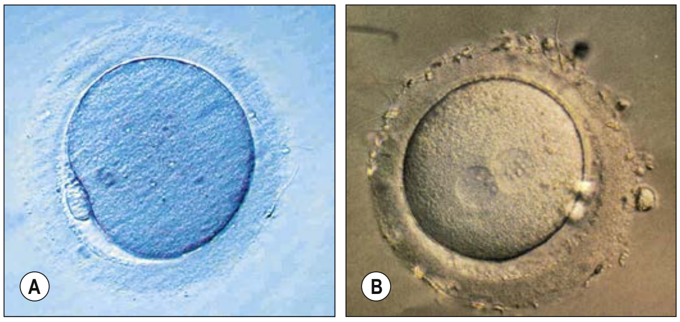

Fig. 8.5 **A**, An unfertilized human secondary oocyte surrounded by the zona pellucida; the first polar body can be seen. Spermatozoa are visible outside the zona pellucida. **B**, A fertilized human ootid before fusion of the pronuclei. Two polar bodies can be seen beneath the zona pellucida.

leading to the specialized, intimate contact of trophoblast and endometrium begin. Implantation, which is the term used for this complicated process, includes the following stages: dissolution of the zona pellucida; orientation and adhesion of the blastocyst onto the endometrium; trophoblastic penetration into the endometrium; migration of the blastocyst into the endometrium; spread and proliferation of the trophoblast, which envelops and specifically disrupts and invades the maternal tissues (Ch. 9). The interactions between the hatched blastocyst and the maternal endometrium are not well understood. Developmentally competent embryos appear to enhance the uterine environment and promote their own implantation (Brosens et al 2014, Macklon and Brosens 2014). Endometrial stromal cells and their decidualization are important for successful implantation and the interaction between the uterine wall and the blastocyst (Makieva et al 2018, Zhang et al 2018).

The site of implantation is normally in the endometrium of the posterior wall of the uterus, nearer to the fundus than to the cervix. It may be in the median plane or to one or other side, or may occur elsewhere in the uterus, or in an extrauterine or ectopic site.

Ectopic implantation

An ectopic pregnancy occurs when the blastocyst implants at a location other than the uterine endometrium. The syncytiotrophoblast and cytotrophoblast will invade any subjacent tissue, continue development and secrete hCG, with maternal serum levels lower than expected for a uterine implantation.

Almost all (95%) of ectopic implantations occur in the uterine tubes, either close to the fimbriae (11%), in the ampullae (70%), in the

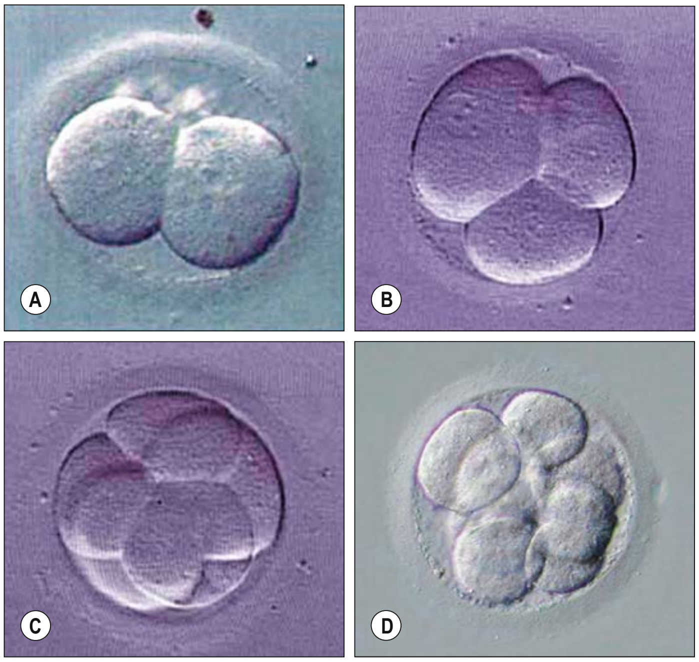

Fig. 8.6 Successive stages of cleavage of a human ootid. **A**, The two-cell stage. **B**, The three-cell stage. **C**, The five-cell stage. **D**, The eight-cell stage.

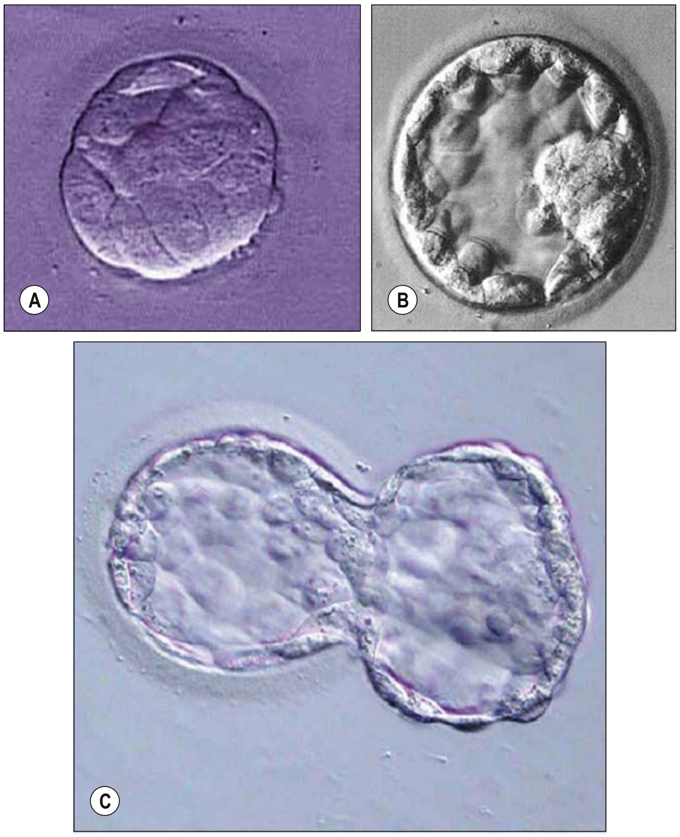

Fig. 8.7 Human embryos. Formation of a morula and blastocyst within the zona pellucida and blastocyst hatching from the zona pellucida. **A**, A ball of cells, the morula, with the cells undergoing compaction. **B**, The blastocyst cavity is developing and the inner cell mass can be seen on one side of the cavity. **C**, The blastocyst is beginning to hatch from the zona pellucida.

isthmus (2%) or in the interstitial portion of the tubes where the tubal mucosa is adjacent to the uterine myometrium (2–4%) (Coady 2011, Baltarowich and Scoutt 2017). Uterine implantations are often ipsilateral to the ovarian corpus luteum. Previous pelvic inflammatory disease, salpingitis or tubal surgery may predispose to blastocyst delay in tubal transport. The presence of an intrauterine contraceptive device or the use of progesterone-based oral contraceptives may also predispose to ectopic pregnancy, probably because of alteration in the normal tubal transport mechanisms.

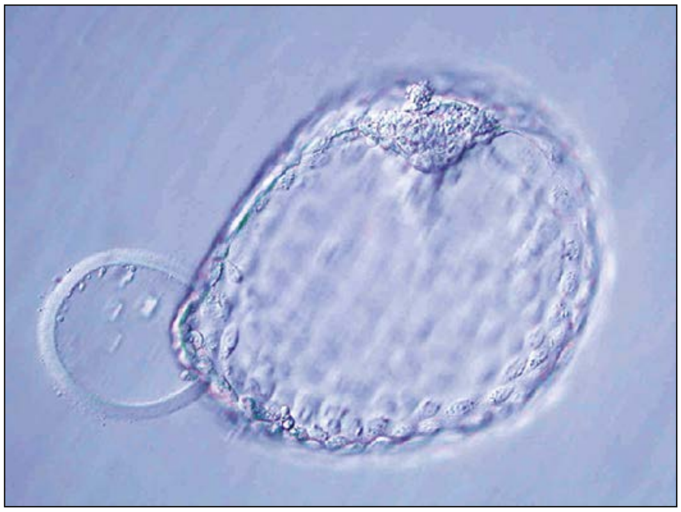

Fig. 8.8 A human blastocyst nearly completely hatched from the zona pellucida. The blastocyst can now expand to its full size.

Ovarian or abdominal pregnancies are exceptionally rare. Apart from their important clinical implications, these conditions emphasize the fact that the blastocyst can implant successfully into tissues other than a normal progestational endometrium. Prolonged development can occur in such sites and is usually terminated by a mechanical or vascular accident and not by a fundamental nutritive or endocrine insufficiency or by an immune maternal response. Abdominal implantation may occur on any organ, e.g. bowel, liver or omentum. If such a pregnancy continues, this makes removal of the placenta at delivery or abortion hazardous as a result of haemorrhage and so the placenta is usually left *in situ* to degenerate spontaneously.

Most ectopic pregnancies are anembryonic. Ectopic pregnancies with a live embryo are the most dangerous because they grow rapidly and may be detected as early as 8 weeks of pregnancy only when they have eroded the uterine tube wall and surrounding blood vessels.

In the United States approximately 2% of all pregnancies are ectopic (Baltarowich and Scoutt 2017). In the UK in 2011 the incidence was 11/1000, twice that noted between 1973–1999 (4.9/1000 (Coady 2011)). The increase in incidence is associated with an increased incidence of pelvic inflammatory disease as well as greater diagnostic accuracy. The rate of recurrent ectopic implantation is 5–20% after a single prior ectopic implantation and more than 30% after two consecutive ectopic implantations. ARTs are particularly associated with ectopic implantation. Approximately 50% of patients with ectopic implantation have no risk factors. (For details consult Baltarowich and Scoutt (2017).)

Twinning

Spontaneous twinning occurs once in approximately every 80 births. Monozygotic twins arise from a single ovum fertilized by a single sperm. At some stage up to the establishment of the axis of the embryonic area and the development of the primitive streak, the embryonic tissues separate into two parts, each of which gives rise to a complete embryo. The process of hatching of the blastocyst from the zona pellucida may result in constriction of the emerging cells and separation into two discrete entities. There is a gradual decrease in the average thickness of the zona pellucida with increasing maternal age, that may be causally related to the increase in frequency of monozygotic twinning with increased maternal age. The resultant twins have the same genotype but the description 'identical twins' is best avoided, since most monozygotic twins have differences in phenotypes. Late separation of twins from a single conceptus may result in conjoined twins; these may be equal or unequal, as in acardia. After twinning, monozygotic embryos enter a period of intense catch-up growth. Despite starting out at half the size, each twin embryo or fetus is of a size comparable to a singleton fetus in the second trimester of pregnancy, but declines in relative size in the last 10 weeks of pregnancy. The sex of monozygotic twins will be the same. Monoamniotic, monochorionic, monozygotic twins are most likely to be female, as are acardiac twins. The male to female ratio for all monozygotic twins is 0.487, and for monoamniotic, monochorionic twins it is 0.231.

Dizygotic twins represent the most frequent form of twinning. They result from multiple ovulations, which can be induced by gonadotrophins or drugs commonly used in patients with infertility. Dizygotic twins may be different sexes; like-sex pairs are more common. The male to female ratio is 0.518. The presence of two gestation sacs can be

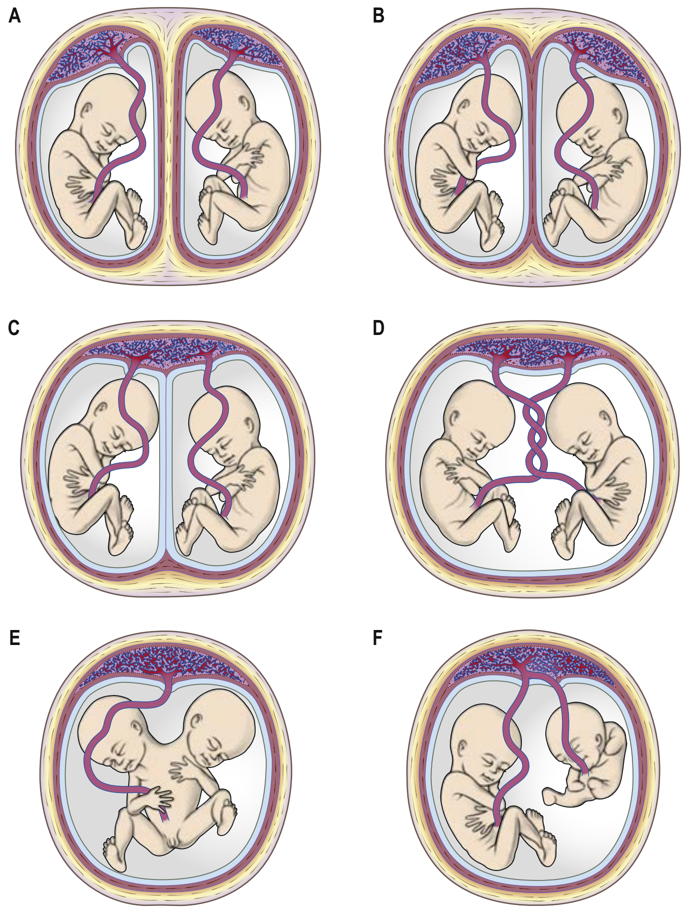

Fig. 8.9 Relationships of the extraembryonic membranes in different types of twinning. **A**, Diamnionic, dichorionic separated; i.e. separation of the first two blastomeres results in separate implantation sites. **B**, Diamnionic, dichorionic fused; here the chorionic membranes are fused but the fetuses occupy separate choria. **C**, Diamnionic, monochorionic; reduplication of the inner cell mass can result in a single placenta and chorionic sacs but separate amniotic cavities. **D**, Monoamnionic, monochorionic; duplication of the embryonic axis results in two embryos sharing a single placenta, chorion and amnion. **E**, Incomplete separation of the embryonic axis results in conjoined twins. **F**, Unequal division of the embryonic axis or unequal division of the blood supply may result in an acardiac monster.

identified on ultrasound examination at 4.5–5 postmenstrual weeks, but amniotic cavities cannot be seen clearly until 8 postmenstrual weeks. Multiple births greater than twinning, such as triplets or quadruplets, can arise from multiple ovulations, or from a single ovum, or both. It is most likely to be seen in women treated with drugs to stimulate ovulation.

The range of separation of twin embryos is reflected in the separation of the extraembryonic membranes. The types of placentation that can occur are shown in Fig. 8.9. Monoamniotic, monochorionic placentae are associated with the greatest perinatal mortality (50%), caused both by entanglement of the umbilical cords impeding the blood supply and by various vascular shunts between the placentae, which may divert blood from one fetus to the other. Artery–artery anastomoses are the most common, followed by artery–vein anastomoses. If the shunting of blood across the placentae from one twin to the other is balanced by more than one vascular connection, development may proceed unimpaired. However, if this is not the case, one twin may receive blood from the other, leading to cardiac enlargement, increased urination and polyhydramnios in the recipient, and anaemia, oligohydramnios and atrophy in the donor.

Dizygotic twins have either completely separate chorionic sacs or sacs that have fused. Such placentae are separated by four membranes, two amnia and two choria; in addition, these placentae have a ridge of firmer tissue at the base of the dividing membranes, caused by the abutting of two expanding placental tissues against each other.

FORMATION OF EXTRAEMBRYONIC TISSUES

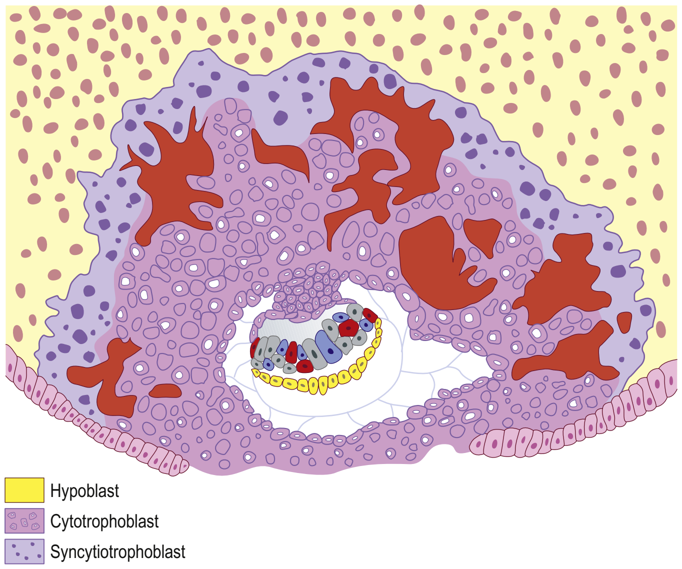

Fig. 8.10 The implanting conceptus at stage 5b. The embryo at this stage is composed only of the abutting epiblast and hypoblast layers. It is suspended within the blastocyst cavity (chorionic cavity) and surrounded by a layer of cytotrophoblast. A large mass of syncytiotrophoblast, with interconnecting lacunae, is penetrating the maternal endometrium.

The earliest developmental processes in mammalian embryos involve the production of those extraembryonic structures that will support and nourish the embryo during development. Production of these layers begins before implantation is complete. At present, it is unclear where the extraembryonic cell lines arise. Both trophoblast and inner cell mass contribute cells. Fig. 8.1 shows the sequence of development of embryonic and extraembryonic tissues in the early embryo.

Epiblast and amniotic cavity

Epiblast cells are closest to the implanting face of the trophoblast and have a definite polarity. They are arranged in a radial manner with extensive junctions near the centre of the mass of cells, supported by supranuclear organelles. A few epiblast cells are contiguous with cytotrophoblast cells: apart from this contact, a basal lamina surrounds what is initially a spherical cluster of epiblast cells isolating them from all other cells. Those epiblast cells adjacent to the hypoblast become taller and more columnar than those adjacent to the trophoblast, causing the epiblast sphere to flatten and shifting the centre of the sphere towards the polar trophoblast. Amniotic fluid accumulates at the eccentric centre of the now lenticular epiblast mass, which is bordered by apical junctional complexes and microvilli. As further fluid accumulates, an amniotic cavity forms, roofed by low cuboidal cells that possess irregular microvilli. The cells share short apical junctional complexes and associated desmosomes, and rest on an underlying basal lamina. The demarcation between true amnion cells and those of the remaining definitive epiblast is clear. The columnar epiblast cells are arranged as a pseudostratified layer with microvilli, frequently a single cilium, clefted nuclei and large nucleoli, and they have a distinct, continuous basal lamina. Cell division in the epiblast tends to occur near the apical surface, causing this region to become more crowded than the basal region. At the margins of the embryonic disc, the amnion cells are contiguous with the epiblast: there is a gradation in cell size from columnar to low cuboidal within a two- to three-cell span (Fig. 8.10; see Fig. 9.1). Further development of the amnion and amniotic fluid is described in Chapter 9.

Hypoblast and yolk sac

Hypoblast is the term used to describe the lower layer of cells of the early bilaminar disc, most commonly in avian embryos: this layer is also termed anterior, or distal, visceral endoderm in mouse embryos. Just before implantation, the hypoblast consists of a layer of squamous cells that is only slightly more extensive than the epiblast. The cells exhibit polarity, in that they show apical junctional complexes and apical microvilli that face the cavity of the blastocyst, but they lack a basal lamina. During early implantation, the hypoblast extends beyond the edges of the epiblast and can be subdivided into visceral hypoblast (cells contact the epiblast basal lamina), and parietal hypoblast (cells contact the mural trophoblast). Parietal hypoblast cells are squamous, may share adhesion junctions with the mural trophoblast and, rarely, may also share gap junctions. Visceral hypoblast cells are cuboidal, and have a uniform apical surface towards the blastocyst cavity but irregular basal and lateral regions, with flanges and projections underlying one another and extending into intercellular spaces. There is no basal lamina subjacent to the visceral hypoblast. The distance between the hypoblast cells and the epiblast basal lamina is variable.

A series of modifications of the original blastocystic cavity develops beneath the hypoblast later than those developing above the epiblast. While the amniotic cavity is enlarging within the sphere of epiblast cells, the parietal hypoblast cells are proliferating and spreading along the mural trophoblast until they extend most of the way around the circumference of the blastocyst, converging towards the abembryonic pole. At the same time, a space appears between the parietal hypoblast and the mural trophoblast that limits the circumference of the hypoblastic cavity. A variety of terms have been applied to the parietal hypoblast layer: extraembryonic hypoblast, extraembryonic endoderm and exocoelomic (Heuser's) membrane. The cavity that the layer initially surrounds is the primary yolk sac (primary umbilical vesicle), and the resultant smaller cavity lined by hypoblast is the secondary yolk sac, seen from stage 6. The method of secondary yolk sac formation may involve: cavitation of visceral hypoblast (a method similar to formation of the amnion); rearrangement of proliferating visceral hypoblast; or folding of the parietal layer of the primary yolk sac into the secondary yolk sac. Further development of the yolk sac is described in Chapter 9.

Visceral hypoblast cells are thought to be important in many aspects of the early specification of cell lines and control of the timing of early development. They induce the formation and position of the primitive streak in the midline of the embryo, thus establishing the first axis of the embryonic disc, and they influence the timing of epiblast epithelial-to-mesenchymal transition at the primitive streak. The cells remain beneath the primitive streak: their experimental removal in avian embryos causes multiple embryonic axes to form. Visceral hypoblast cells are thought to be necessary for successful induction of the head region and for the successful specification of the primordial germ cells. With the later formation of the embryonic cell layers from the epiblast, the visceral hypoblast appears to be sequestered into the secondary yolk sac wall by the expansion of the newly formed embryonic endoderm beneath the epiblast, although there is now evidence that some hypoblast cells may remain in the final endoderm layer and contribute to the gut, and that they may also play a role in the induction of cardiogenesis. For a review of the roles of hypoblast cells, see Stern and Downs (2012).

After the formation of the secondary yolk sac, a diverticulum of the visceral hypoblast, the allantois, forms towards one end of the embryonic region and extends into the local extraembryonic mesoblast. It passes from the roof of the secondary yolk sac to the same plane as the amnion. Further development of the allantois is described in Chapter 9.

Extraembryonic mesoblast

By definition, extraembryonic tissues encompass all tissues that do not contribute directly to the future body of the definitive embryo and, later, of the fetus. At stage 5, blastocysts are implanted but do not yet display trophoblastic villi (see Fig. 8.10); they range from 7 to 12 days in age. A feature of this stage is the first formation of extraembryonic mesoblast, which will eventually cover the amnion, secondary yolk sac and the internal wall of the mural trophoblast, and will form the connecting stalk of the embryo containing the allantoenteric diverticulum. The origin of this first mesoblastic extraembryonic layer has yet to be established: several sources have been proposed, including the caudal region of the epiblast, the parietal hypoblast and subhypoblastic cells. A trophoblastic origin seems unlikely because there is always a complete basal lamina underlying the trophoblast and the migration of cells out of an epithelium is usually associated with previous disruption of the basal lamina. The origin of extraembryonic cells changes over time as new germinal populations are established.

The first mesoblastic extraembryonic layer gives rise to the layer known as extraembryonic mesoblast, arranged as a mesothelium with underlying extraembryonic mesenchymal cells between the mural trophoblast and the primary yolk sac in stage 5. Later extraembryonic mesoblast populations mushroom beneath the cytotrophoblastic cells at the embryonic pole, forming the cores of the developing villus stems, and the villi and angioblastic cells that will give rise to the capillaries within them and the earliest blood cells.

Initially, the extraembryonic mesoblast connects the amnion to the chorion over a wide area. Continued development and expansion of the extraembryonic coelom means that this attachment becomes increasingly restricted until it becomes a connecting stalk between the future caudal end of the embryonic disc and the chorion, forming a permanent pathway along which vascular anastomoses around the allantois establish communication with those of the chorion.

Bonus e-book content

Video 8.1 Human *in vitro* fertilization and early development.

Key references

Brosens JJ, Walker MS, Teklenburg G 2014 Uterine selection of human embryos at implantation. Sci Reports 4:3894.

Coticchio G, Mignini Renzini M et al 2018 Focused time-lapse analysis reveals novel aspects of human fertilization and suggests new parameters of embryo viability. Hum Reprod 33(1):23–31

Fleming TP, Watkins, AJ, Velazquez MA et al 2018 Origins of lifetime health around the time of conception: causes and consequences. Lancet 391:1842–52.

Kaser DJ, Ginsburg ES, Carrell DT et al 2019 Assisted reproduction. In: Strauss J, Barbieri R, Gargiulo A (eds) Yen & Jaffe's Reproductive Endocrinology, 8th ed. Philadelphia: Elsevier. Ch. 31; pp. 779–822.

Macklon NS Brosens JJ 2014 The human endometrium as a sensor of embryo quality. Biol Reprod 91:98.

O'Rahilly R, Müller F 1987 Developmental Stages in Human Embryos. Washington, DC: Carnegie Institution. Publication 637.

O'Rahilly R, Müller F 1999 The Embryonic Human Brain: An Atlas of Developmental Stages, 2nd ed. New York: Wiley–Liss.

O'Rahilly R, Müller F 2000 Minireview: prenatal ages and stages – measures and errors. Teratology 61:382–4.

O'Rahilly R, Müller F 2010 Developmental stages in human embryos: revised and new measurements. Cells Tissues Organs 192:73–84.

Stern CD, Downs KM 2012 The hypoblast (visceral endoderm): an evo-devo perspective. Development 139:1059–69.

Streeter GL 1942 Developmental horizons in human embryos. Descriptions of age group XI, 13 to 20 somites, and age group XII, 21 to 29 somites. Contrib Embryol Carnegie Inst Washington 30:211–45.

Wamaitha SE, Niakan KK 2018 Human pre-gastrulation development. Curr Topics Dev Biol 128: 295–338.

References

Baltarowich OH, Scoutt LM 2017 Ectopic pregnancy. In: Norton ME, Scoutt LM, Feldstein VA (eds) Callen's Ultrasonography in Obstetrics and Gynecology, 6th ed. Elsevier. Ch 33.

Batcheller A, Cardozo E, Maguire M et al 2011 Are there subtle genome-wide epigenetic alterations in normal offspring conceived by assisted reproductive technologies? Fertil Steril 96:616–23.

Brosens JJ, Walker MS, Teklenburg G 2014 Uterine selection of human embryos at implantation. Sci Reports 4:3894.

Butler MG 2009 Genomic imprinting disorders in humans: a mini review. J Assist Reprod Genet 26:477–86.

Coady AM 2011 The first trimester gynaecological aspects. In: Allan PL, Baxter GM, Weston MJ (eds) Clinical Ultrasound, 3rd ed. Elsevier. Ch 39.

Coticchio G, Mignini Renzini M et al 2018 Focused time-lapse analysis reveals novel aspects of human fertilization and suggests new parameters of embryo viability. Hum Reprod 33:23–31.

Fauque P 2013 Ovulation induction and epigenetic anomalies. Fertil Steril 99:1306–1311.

Fierro-González JC, White MD, Silva JC et al 2013 Cadherin-dependent filopodia control preimplantation embryo compaction. Nat Cell Biol 15:1424–33.

Fleming TP, Watkins, AJ, Velazquez MA et al 2018 Origins of lifetime health around the time of conception: causes and consequences. Lancet 391:1842–52.

Hanna CW, Demond H, Kelsey G 2018 Epigenetic regulation in development: is the mouse a good model for the human? Hum Reprod Update 24:556–76.

Kaser DJ, Ginsburg ES, Carrell DT et al 2019 Assisted reproduction. In: Strauss J, Barbieri R, Gargiulo A (eds) Yen & Jaffe's Reproductive Endocrinology, 8th ed. Philadelphia: Elsevier. Ch. 31; pp.779–822.

Macklon NS, Brosens JJ 2014 The human endometrium as a sensor of embryo quality. Biol Reprod 91:98. doi:10.1095/biolreprod.114.122846.

Makieva S, Giacomini E, Ottolina J 2018 Inside the endometrial signalling subway: Mind the gap(s). Int J Mol Sci 19:2477.

Moore GE, Ishida M, Demetriou C et al 2015 The role and interaction of imprinted genes in human fetal growth. Phil Trans R Soc B 370:20140074.

O'Rahilly R, Müller F 1987 Developmental Stages in Human Embryos. Washington, DC: Carnegie Institution. Publication 637.

O'Rahilly R, Müller F 1999 The Embryonic Human Brain: An Atlas of Developmental Stages, 2nd ed. New York: Wiley-Liss.

O'Rahilly R, Müller F 2000 Minireview: Prenatal ages and stages – measures and errors. Teratology 61:382–4.

O'Rahilly R, Müller F 2010 Developmental stages in human embryos: revised and new measurements. Cells Tissues Organs 192:73–84.

Pfeffer PL 2018 Building principles for constructing a mammalian blastocyst embryo. Biology (Basel). 2018;7(3):41.

Stern CD, Downs KM 2012 The hypoblast (visceral endoderm): an evo-devo perspective. Development 139:1059–69.

Stirparo GG, Boroviak T, Guo G et al 2018 Integrated analysis of single-cell embryo data yields a unified transcriptome signature for the human pre-implantation epiblast. Development 145: p.ii dev158501. doi: 10.1242/dev.158501.

Streeter GL 1942 Developmental horizons in human embryos. Descriptions of age group XI, 13 to 20 somites, and age group XII, 21 to 29 somites. Contrib Embryol Carnegie Inst Washington 30:211–45.

Wamaitha SE, Niakan KK 2018 Human pre-gastrulation development. Curr Topics Dev Biol 128:295–338.

Zhang Y, Wang Y, Want X et al 2018 Crosstalk between human endometrial stromal cells and decidual NK cells promotes decidualization in vitro by upregulating IL-25. Mol Med Rep 17:286–78.

CHAPTER 9

Implantation and placentation

IMPLANTATION

Implantation involves the initial attachment of the trophoblastic wall of the blastocyst to the endometrial luminal epithelium, stimulating the decidual response. The blastocyst is present within the uterine cavity for some 72 hours prior to implantation, and during this time there is an interactive dialogue between the implanting blastocyst and endometrial decidual stromal cells (Makieva et al 2018). *In vitro* culture of human preimplantation embryos shows that normally developed preimplantation human blastocysts actively enhance the uterine environment for their implantation, whereas developmentally impaired embryos induce endoplasmic reticulum stress responses in decidual cells that inhibit implantation (Brosens et al 2014). Reponses from endometrial stromal cells also inform these interactions (Makieva et al 2018, Zhang et al 2018). Uterine surgical scars may have a long-term impact on the interactive dialogue between the implanting blastocyst and endometrial decidual stromal cells (Jauniaux et al 2018).

The trophoblast of the blastocyst gives rise to three main cell types in the human placenta: syncytiotrophoblast that forms the epithelial covering of the villous tree and is the main endocrine component of the placenta; villous cytotrophoblast cells that represent a germinative population that proliferates throughout pregnancy, fusing to generate syncytiotrophoblast; and extravillous trophoblast cells that are non-proliferative and invade the maternal endometrium. The first two cell lines can be seen from stages 4 and 5 onwards. The cytotrophoblast cells that form the mural and polar trophoblast are cuboidal. Following apposition of the blastocyst to the uterine mucosa, the polar trophoblast becomes covered externally with syncytiotrophoblast, a multinucleated tissue that penetrates between the epithelial cells (see Fig. 8.10).

Preimplantation embryos produce matrix metalloproteinases (MMPs) that mediate penetration of the maternal subepithelial basal lamina by the syncytiotrophoblast. Trophoblast cells express L-selectin (usually seen as a mediator of neutrophil rolling and tethering in inflamed endothelium), and the endometrial epithelium upregulates selectin–oligosaccharide-based ligands (Fukuda and Sugihara 2008). Thus, differentiating cytotrophoblast cells appear to use processes that also occur in vasculogenesis and during leukocyte migration from the blood into the tissues. Flanges of syncytiotrophoblast grow between the cells of the uterine luminal epithelium towards the underlying basal lamina without apparent damage to the maternal cell membranes or disruption of the intercellular junctions. Instead, shared junctions, including tight junctions, are formed with many of the maternal uterine epithelial cells.

Implantation continues with erosion of the vascular endothelium of maternal superficial capillaries and glandular epithelium and phagocytosis of the glandular secretions. There is increasing evidence that the endometrial stromal cells grow around and encapsulate the blastocyst until it occupies an uneven implantation cavity in the stroma (interstitial implantation) (**Fig. 9.1**). In the early postimplantation phase, the uterine surface is resealed by re-epithelialization and the formation of a plug that may contain fibrin. As the blastocyst burrows more deeply into the endometrium, syncytiotrophoblast forms over the mural cytotrophoblast, but never achieves the thickness of the syncytiotrophoblast over the embryonic pole.

The syncytiotrophoblast does not express either class I or class II major histocompatibility complex (MHC) antigens, but it secretes numerous hormones: human chorionic gonadotrophin (hCG) can be detected in maternal urine from as early as postfertilization day 10 and forms the basis for tests for early pregnancy. This hCG prolongs the life of the corpus luteum, which continues to secrete progesterone and oestrogens until these essential hormones are produced by the placenta. For details of postfertilization and postmenstrual ages see Fig. 23.3.

Menstruation ceases on successful implantation and the endometrium transforms into the decidua to form a suitable nidus for the conceptus. Decidualization of the endometrial stroma may occur without an intrauterine pregnancy, for example in the presence of an ectopic pregnancy, after prolonged treatment with progesterone, and in the late secretory phase of a non-conception cycle. Decidual differentiation is not evident in the stroma at the earliest stages of implantation, and it may not be until a week later that fully differentiated cells are present. During decidualization, the interglandular tissue increases in quantity (Burton et al 2010). It contains a substantial population of leukocytes (large granular lymphocytes, macrophages and T cells) distributed amongst large decidual cells.

Extracellular matrix, growth factors and protease inhibitors produced by the decidua all probably modulate the degradative activity of the trophoblast and support placental morphogenesis and placental accession to the maternal blood supply. Once implantation is complete, distinctive names are applied to different regions of the decidua (**Fig. 9.2**). The decidua capsularis covers the conceptus; the decidua basalis (where the placenta subsequently develops) lies between the conceptus and the uterine muscular wall; the decidua parietalis lines the remainder of the body of the uterus. Subsets of perivascular and stromal cells in distinct decidual layers probably mediate regulatory interactions that prevent harmful innate or adaptive immune responses at the maternal-fetal interface in early human pregnancy (Vento-Tormo et al 2018).

DEVELOPMENT OF THE PLACENTA

Formation of the human placenta requires a developmental progression that proceeds in a specific chronological order. The development of primary, secondary and anchoring villi, and the local differentiation of haemangioblast cells within them, occur concurrently with the modification of maternal blood vessels to ensure their patency. By embryonic stage 10, with the onset of the embryonic heartbeat, a primitive circulation between the embryo and the secondary yolk sac is established. Blood vessels within the walls of the allantois and connecting stalk connect the embryonic circulation to the developing placenta during postmenstrual weeks 6–12, forming a low-oxygen environment with nutrition from endometrial glands. From postmenstrual week 12, maternal blood flows into the placental intervillous spaces and a feto-placental circulation is fully established.

As the blastocyst implants, the syncytiotrophoblast invades the uterine tissues, including the glands and walls of maternal blood vessels (see Fig. 9.1; **Fig. 9.3**), and increases rapidly in thickness over the embryonic pole (**Fig. 9.4**). Microvillus-lined clefts and lacunar spaces develop within the syncytiotrophoblastic envelope (postfertilization days 9–11) and establish communications with one another. Initially, many of these spaces contain maternal blood derived from dilated uterine capillaries and veins, as the walls of the vessels are partially destroyed. As the conceptus grows, the lacunar spaces enlarge and become confluent to form intervillous spaces.

The projections of syncytiotrophoblast into the maternal decidua are the primary villi. They are invaded initially with cytotrophoblast and then with extraembryonic mesenchyme (days 13–15) to form secondary placental villi. Capillaries develop in the mesenchymal core of the villi during postfertilization week 3. The cytotrophoblast within the villi continues to grow through the invading syncytiotrophoblast and makes direct contact with the decidua basalis, forming anchoring villi. Further cytotrophoblast proliferation occurs laterally so that neighbouring outgrowths meet to form a spherical cytotrophoblastic shell around the conceptus (**Fig. 9.5**; see Fig. 9.3B). Lateral projections from the main stem villus form true villi. Elongation of growing capillaries outstrips that of the containing villi, causing vessels to loop: obtrusion of capillary loops and new sprouts results in the formation of terminal villi.

As secondary villi form, single mononuclear cells become detached from the distal (anchoring) cytotrophoblast and infiltrate the maternal decidua (**Fig. 9.6**; see Fig. 9.3B). These extravillous cells are the third lineage of the original trophoblastic cells. Extravillous trophoblast cells may be interstitial or endovascular. Interstitial extravillous trophoblast cells invade the maternal spiral arteries from their adventitia, whereas the endovascular trophoblast cells migrate along their lumens.

The most numerous are uterine natural killer (NK) cells that accumulate in the endometrium during the secretory phase of the cycle and persist until mid-pregnancy; they interact with invading extravillous trophoblast cells that express human leukocyte antigens G and C (HLA-G, HLA-C).

Decidual cells are stromal cells that contain varying amounts of glycogen, lipid and vimentin-type intermediate filaments in their cytoplasm. They are generally rounded but their shape may vary, depending on the local packing density. They may contain one, two or sometimes three nuclei, frequently display rows of club-like cytoplasmic protrusions enclosing granules, and are associated with a characteristic capsular basal lamina. Decidual cells produce a range of secretory products that may be taken up by the trophoblast, including insulin-like growth factor binding protein 1 (IGF-BP1) and prolactin. Prolactin signals to the endometrial glands to increase their secretions and may play a role in the maintenance and growth of the conceptus in the early phase of postimplantational development via histotrophic nutrition (Turco et al 2017): it can be detected in amniotic fluid in the first trimester of pregnancy.

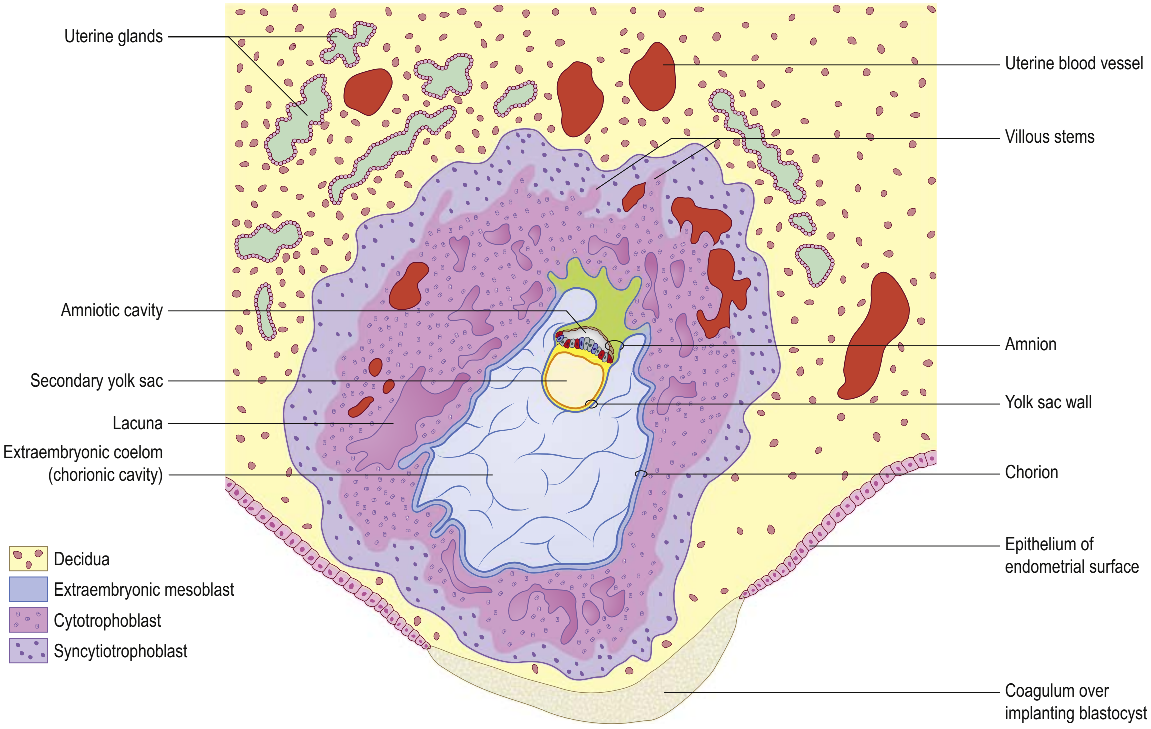
Uterine glands
Uterine blood vessel
Villous stems
Amniotic cavity
Amnion
Secondary yolk sac
Yolk sac wall
Lacuna
Extraembryonic coelom (chorionic cavity)
Chorion
Epithelium of endometrial surface
Decidua
Extraembryonic mesoblast
Cytotrophoblast
Syncytiotrophoblast
Coagulum over implanting blastocyst

Fig. 9.1 The implanting conceptus at stage 6. The embryo is composed of epiblast, with the amniotic cavity above it, and hypoblast, with the secondary yolk sac below it (see also Figs 8.10, 10.1). Both cavities are covered externally with extraembryonic mesoblast, which also lines the larger chorionic cavity. Primary villi cover the outer aspect of the conceptus and extend into the maternal endometrium, and in places, maternal blood fills the lacunae.

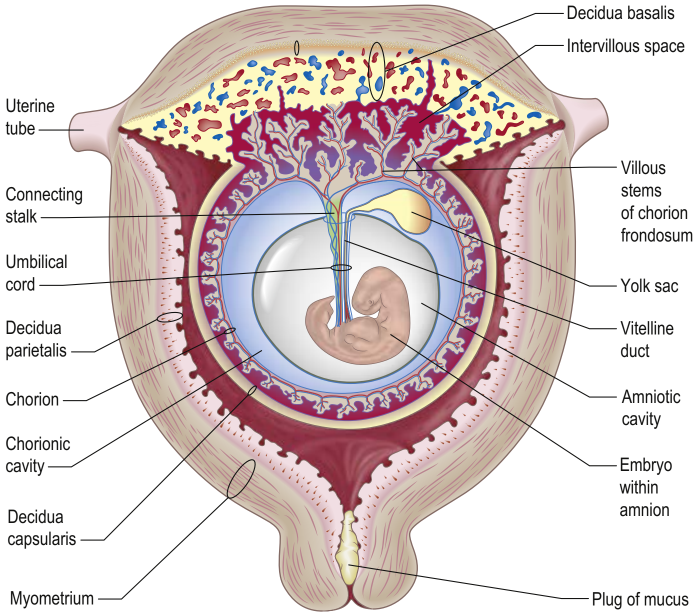
Decidua basalis
Intervillous space
Uterine tube
Villous stems of chorion frondosum
Connecting stalk
Yolk sac
Umbilical cord
Vitelline duct
Decidua parietalis
Amniotic cavity
Chorion
Chorionic cavity
Embryo within amnion
Decidua capsularis
Myometrium
Plug of mucus

Fig. 9.2 The gravid uterus at about postmenstrual week 9. A placental site precisely in the uterine fundus, as indicated on the figure, is rather unusual; the dorsal, ventral or lateral wall of the corpus uteri is more usual. The maternal endometrium is now termed decidua; different regions are distinguished.

The smooth muscle and internal elastic lamina are replaced with extracellular fibrinoid deposits (see Figs 9.3B, 9.6) (Harris 2010). In the central area of the basal plate, destined to become the definitive placenta, the endovascular trophoblast plugs block the maternal spiral arteries until the end of the first trimester, restricting inflow into the intervillous space. The cells then migrate antidromically, against the flow of maternal blood, along the spiral arteries as far as the inner myometrial region or junctional zone (Huppertz et al 2014).

The definitive placenta is composed of a chorionic plate on its fetal aspect and a basal plate on its maternal aspect, separated by an intervening intervillous space containing villous stems with branches in contact with maternal blood (see Fig. 9.5). During the first trimester, development takes place in a physiologically low-oxygen environment supported by histotrophic nutrition from the endometrial glands which discharge into the intervillous space (see Fig. 9.3A) (Burton et al 2002, Burton et al 2007, Burton and Fowden 2012). When maternal blood bathes the surfaces of the chorion bounding the intervillous space, the human placenta is defined as haemochorial. Different grades of fusion exist between the maternal and fetal tissues in many other mammals (e.g. epitheliochorial, synepitheliochorial, endotheliochorial). The chorion is vascularized by the allantoic blood vessels of the body stalk, and so the human placenta can be termed chorio-allantoic (in some mammals, a choriovitelline placenta exists either alone or supplements the chorio-allantoic variety). It can also be defined as discoidal (in contrast to other shapes in other mammals), and deciduate (because maternal tissue is shed with the placenta and membranes at parturition as part of the afterbirth).

Growth of the placenta

Expansion of the entire conceptus is accompanied by radial growth of the villi and simultaneous integrated tangential growth and expansion of the trophoblastic shell. Eventually, each villous stem forms a complex that consists of a single trunk attached by its base to the chorion, from which second- and third-order branches (intermediate and terminal villi, respectively) arise distally. Terminal villi are specialized for exchange between fetal and maternal circulations; each one starts as a syncytial outgrowth and is invaded by cytotrophoblast cells, which then develop a core of fetal mesenchyme as the villus continues to grow. The core is vascularized by fetal capillaries (each villus undergoes sequential histological differentiation forming primary, secondary and tertiary types). The germinal cytotrophoblast continues to add cells that fuse with the overlying syncytium and so contribute to the expansion of the haemochorial interface. Terminal villi continue to form and branch within the confines of the definitive placenta throughout gestation, projecting in all directions into the intervillous space (see Fig. 9.5).

Up to postmenstrual week 8 (postfertilization week 6; for comparison of postfertilization and postmenstrual ages see Fig. 23.3), the entire chorion is covered with villous stems that are thus continuous peripherally with the trophoblastic shell, which is in close apposition with the decidua capsularis and the decidua basalis. The villi adjacent to the decidua basalis are stouter and longer and show a greater profusion of villi. As the conceptus continues to expand, the decidua capsularis is progressively compressed and thinned, the circulation through it is gradually reduced, and adjacent villi slowly atrophy and disappear. This process starts at the abembryonic pole (opposite to the implantation site): by the first trimester, the abembryonic hemisphere of the conceptus is largely denuded. Eventually, the whole chorion apposed to the decidua capsularis is smooth and is now termed the chorion laeve. It will later become apposed to the amnion, forming the chorio-amnion or placental

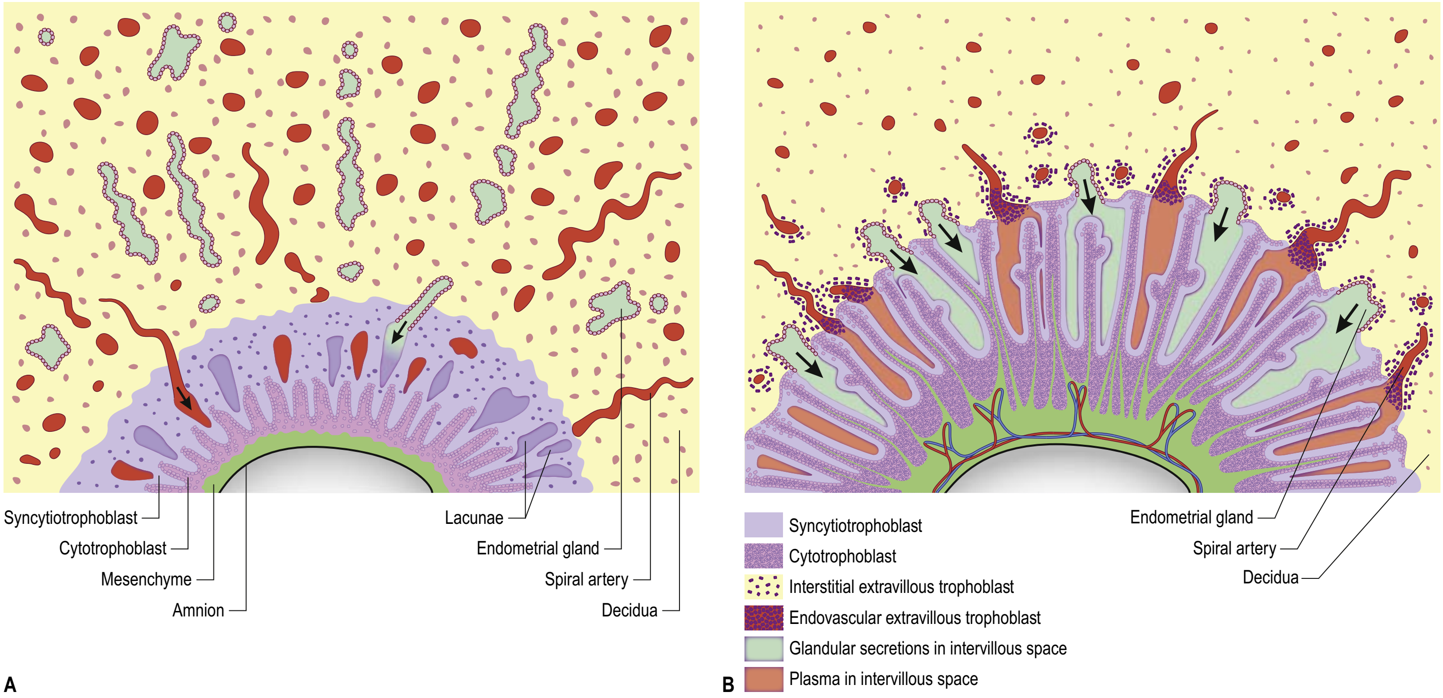

Fig. 9.3 **A**, The growing syncytiotrophoblast erodes decidual glands and spiral arteries, and their contents form lacunae within the syncytiotrophoblast. Cytotrophoblastic cells extend as villi into the syncytiotrophoblast. **B**, Cells originating from the cytotrophoblast move into the decidua, forming interstitial extravillous trophoblast cells, the third line of cytotrophoblastic cells. These surround the opened glands and spiral arteries in the decidua and inner myometrium. Cells that move through the tunicae adventitia, media and interna to enter the lumen of the vessels become endovascular extravillous trophoblast. These cells remodel the walls and plug the lumen of the spiral arteries, permitting only plasma to enter the forming intervillous space. Glandular secretions in the intervillous space provide histiotrophic nutrition to the embryo.

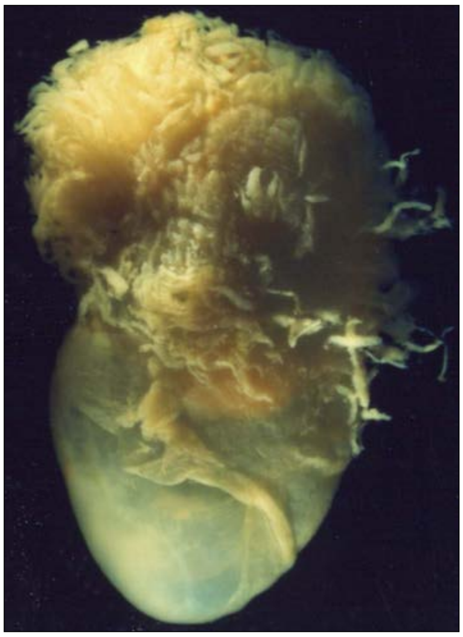

Fig. 9.4 The conceptus at about stage 14. The embryonic pole shows extensive villous formation at the chorion frondosum, whereas the abembryonic pole is smooth and villous-free at the chorion laeve. (Courtesy of P Collins.)

free membranes (see Figs 9.2, 9.10). In contrast, the villous stems of the disc-shaped region of chorion apposed to the decidua basalis increase greatly in size and complexity, and the region is now termed the chorion frondosum (see Fig. 9.4). The chorion frondosum and the decidua basalis constitute the definitive placental site (see Fig. 9.2). Abnormalities in this process may account for the persistence of villi at abnormal sites in the chorion laeve of the gestational sac and the presence of accessory or succenturiate lobes within the membranes of the definitive placenta. The presence of the entire villous ring of the primitive placenta beyond postmenstrual week 8 may lead to the development of placenta membranacea, a giant definitive placental structure surrounding the whole gestational sac during the remainder of pregnancy and covering the entire uterine cavity including the internal os of the cervix.

Coincidentally with the growth of the embryo and the expansion of the amnion, the decidua capsularis is thinned and distended, and the space between it and the decidua parietalis is gradually obliterated. The three endometrial strata recognizable in the premenstrual phase, compactum, spongiosum and basale, are better differentiated and easily distinguished. The glands in the spongiosum are compressed and appear as oblique slit-like fissures lined by low cuboidal cells. By postmenstrual week 9, the decidua capsularis and decidua parietalis are in contact. By postmenstrual weeks 17–20, the decidua capsularis is greatly thinned, and it almost disappears during the succeeding weeks.

When the placenta grows in the area of a previous uterine scar, both the extravillous trophoblast and some of the villi may develop beyond the normal junctional zone of the inner myometrium (Jauniaux et al 2018). The villi may be simply adherent to the myometrium (placenta creta) or invade more deeply inside the uterine wall (placenta increta) or beyond the uterine wall into the pelvis (placenta percreta).

Focal bleeding often occurs in the periphery of the developing placenta at the time of the formation of the membranes (postmenstrual weeks 8–12). This complication, termed threatened miscarriage, is a common clinical complication of pregnancy and can lead to a complete miscarriage if the haematoma extends to the definitive placenta (Jauniaux et al 2006).

At full term (postmenstrual week 40), the placental diameter varies from 200 to 220 mm, the mean placental weight is 500 g, its mean thickness is 25 mm and the total villous surface area is 12–14 m^2, providing an extensive and intimate interface for maternal–fetal exchange (the uteroplacental circulation carries approximately 600 ml of maternal blood per minute). There are no lymph vessels or aggregates of lymphoid cells in the placenta. Systematic evaluation and careful description of the placenta after delivery have been recommended for correlation with later neonatal neurodevelopmental outcomes (Roescher et al 2014).

Chorionic plate

The chorionic plate is covered on its fetal aspect by amniotic epithelium. A connective tissue layer carries the main branches of the umbilical vessels on the stromal side of the epithelium (see Fig. 9.5; Fig. 9.7). Subjacent to this are a diminishing layer of cytotrophoblast cells and then the syncytiotrophoblast lining the intervillous space. The connective tissue layer is formed by fusion between the mesenchyme-covered surfaces of amnion and chorion, and is more fibrous and less cellular than Wharton's jelly (of the umbilical cord), except near the larger vessels. The umbilical vessels radiate and branch from the cord attachment, with variations in the branching pattern, until

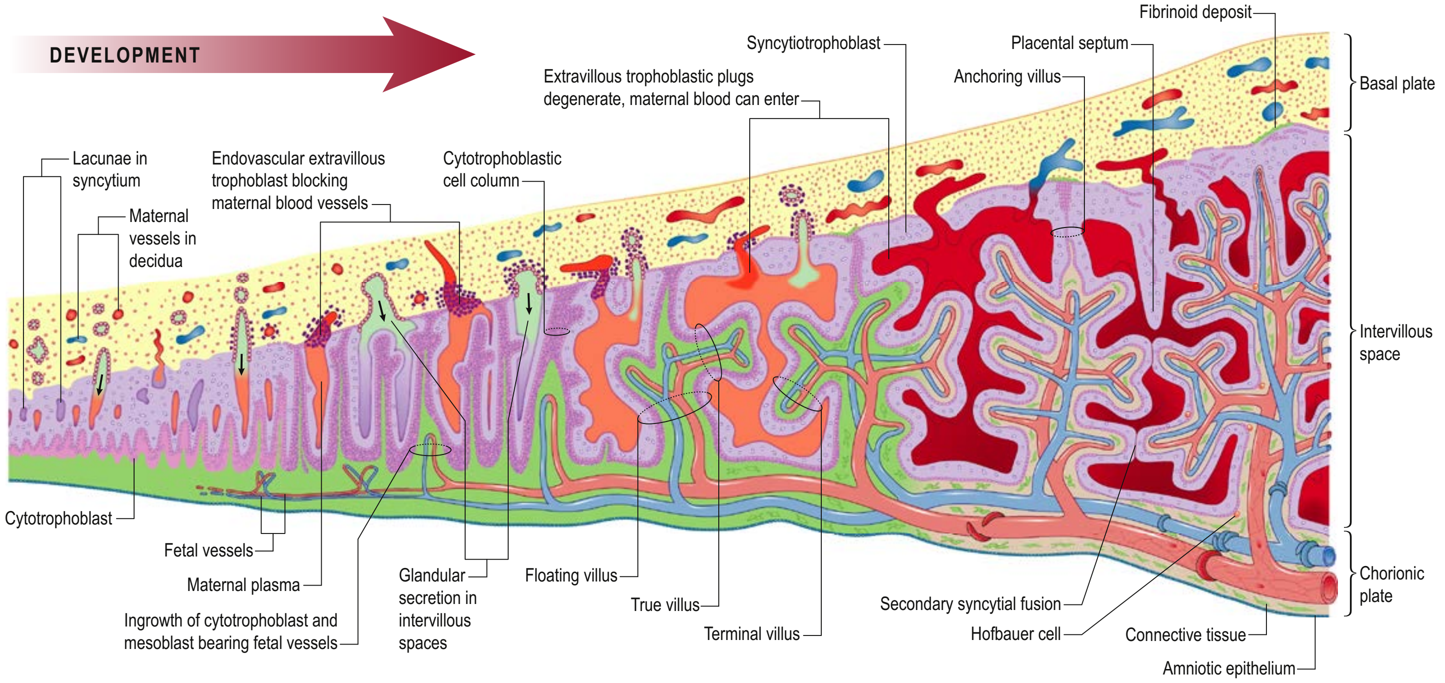
DEVELOPMENT
Fibrinoid deposit
Syncytiotrophoblast
Placental septum
Extravillous trophoblastic plugs degenerate, maternal blood can enter
Anchoring villus
Basal plate
Lacunae in syncytium
Endovascular extravillous trophoblast blocking maternal blood vessels
Cytotrophoblastic cell column
Maternal vessels in decidua
Intervillous space
Cytotrophoblast
Fetal vessels
Maternal plasma
Ingrowth of cytotrophoblast and mesoblast bearing fetal vessels
Glandular secretion in intervillous spaces
Floating villus
True villus
Terminal villus
Secondary syncytial fusion
Hofbauer cell
Connective tissue
Amniotic epithelium
Chorionic plate

Fig. 9.5 Placental development.

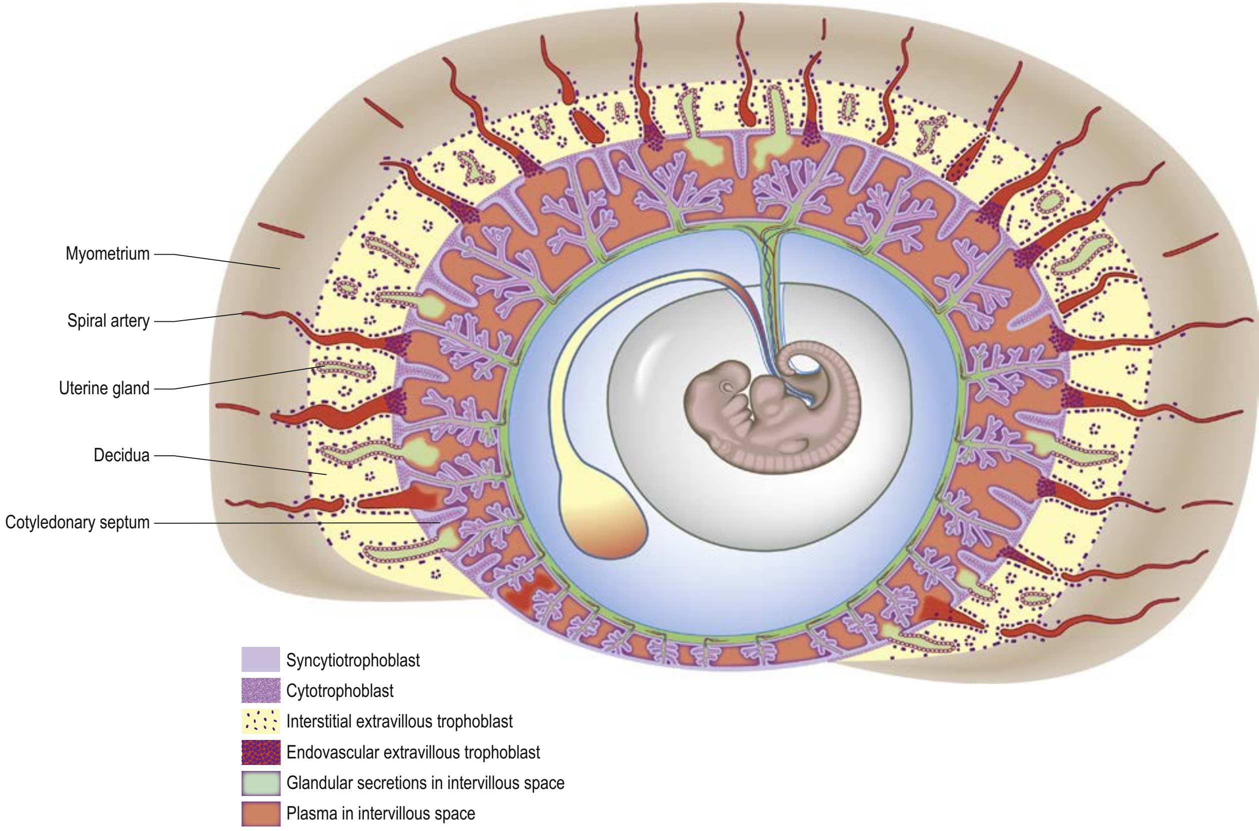
Myometrium
Spiral artery
Uterine gland
Decidua
Cotyledonary septum
Syncytiotrophoblast
Cytotrophoblast
Interstitial extravillous trophoblast
Endovascular extravillous trophoblast
Glandular secretions in intervillous space
Plasma in intervillous space

Fig. 9.6 As the placenta grows, the interstitial and endovascular extravillous trophoblast cells continue to remodel the spiral arteries into large-bore, low-resistance uteroplacental vessels. These arteries remain occluded by endovascular extravillous trophoblast until the end of the first trimester, promoting a low-oxygen environment.

they reach the bases of the trunks of the villous stem where they then arborize within the intermediate and terminal villi. The vascular trees of adjacent stems do not anastomose. The two umbilical arteries are normally joined at, or just before they enter, the chorionic plate, by some form of substantial transverse anastomosis (Hyrtl's anastomosis) (Ullberg et al 2001).

Basal plate

The basal plate, from fetal to maternal aspect, forms the outer wall of the intervillous space. The trophoblast and adjacent decidua are enmeshed in layers of fibrinoid and basement membrane-like extracellular matrix to form a complex junctional zone. In different places, the basal plate may contain syncytiotrophoblast, cytotrophoblast or fibrinoid matrix, remnants of the cytotrophoblastic shell, and, at the site of implantation, areas of necrotic maternal decidua (the so-called Nitabuch's stria) (see Figs 9.5, 9.7). Nitabuch's stria and the decidua basalis contain cytotrophoblast and multinucleated trophoblast giant cells derived from the mononuclear extravillous interstitial cytotrophoblast population that infiltrate the decidua basalis up to postmenstrual week 18. These cells penetrate as far as the inner third of the myometrium but can often be observed at or near the decidual–myometrial junction. They are not found in the decidua parietalis or the adjacent myometrium, suggesting that the placental bed giant cell represents a differentiative end stage in the extravillous trophoblast lineage. The striae of fibrinoid are irregularly interconnected and variable in prominence. Strands pass from Nitabuch's stria into the adjacent decidua

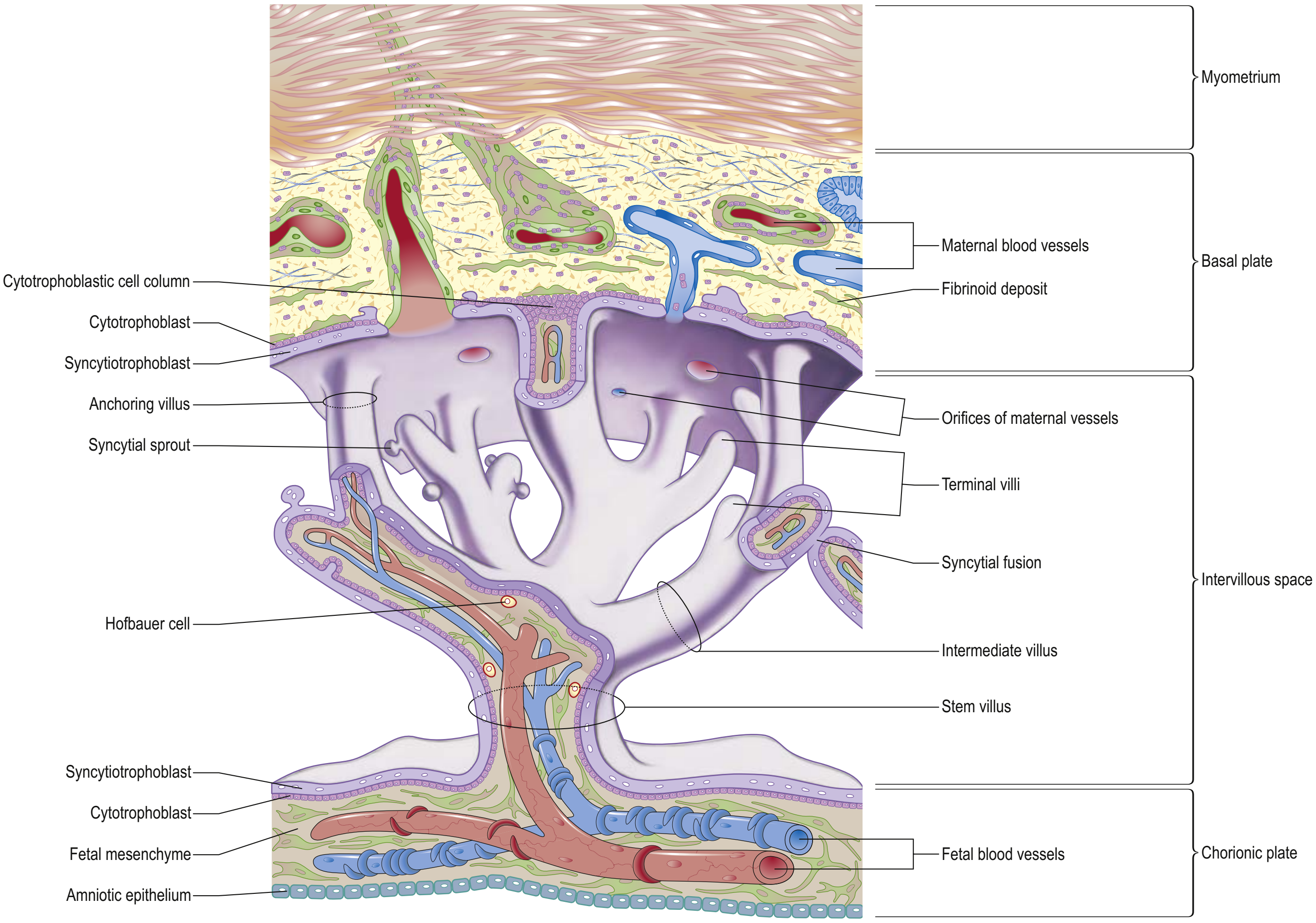

Fig. 9.7 The arrangement of the placental tissues from the chorionic plate (fetal side) to the basal plate or decidua basalis (maternal side).

which contains basal remnants of the endometrial glands and large and small decidual cells scattered in a connective tissue framework that supports an extensive venous plexus.

Initially, only the central area of a placenta contains extravillous trophoblast cells, both within and around the spiral arteries. These cells gradually migrate laterally, reaching the periphery of the placenta around mid-gestation; the extent of invasion is progressively shallower towards the periphery. Invaded maternal vessels show a 5–10-fold dilation of the vessel mouth and altered responsiveness to circulating vasoactive compounds (Hung et al 2001, Burton et al 2009).

The conversion of maternal musculoelastic spiral arteries to large-bore, low-resistance uteroplacental vessels is considered key for a successful human pregnancy. Failure to achieve these changes is a feature of common complications of pregnancy, such as early-onset pre-eclampsia, miscarriage and fetal growth restriction. The area of the basal plate is commonly smaller in these complications of pregnancy (Suri et al 2013).

Between postmenstrual weeks 9 and 12, the placental basal plate develops intercotyledonary septa, ingrowths of the cytotrophoblast covered with syncytium that grow towards, but do not fuse with, the chorionic plate (see Fig. 9.5). These septa circumscribe the uterine surface of the placenta into 15–30 lobes, often termed cotyledons, each surrounding a limited portion of the intervillous space associated with a villous trunk from the chorionic plate. From postmenstrual week 13–14, these septa are supported by tissue from the decidua basalis. Throughout the second half of pregnancy, the basal plate becomes thinned and progressively modified; there is a relative diminution of the decidual elements, increasing deposition of fibrinoid, and admixture of fetal and maternal derivatives.

Intervillous space

The intervillous space contains the main trunks of the villous stems and their arborizations into intermediate and terminal villi (see Figs 9.5, 9.7). A villous trunk and its branches may be regarded as the essential structural, functional and growth unit of the developing placenta.

At term, from the inner myometrium to the intervillous space, the walls of most spiral arteries consist of a fibrinoid matrix and embedded cytotrophoblast. This arrangement allows expansion of the arterial diameter (and so slows the rate of arterial inflow and reduces the perfusion pressure), independent of the local action of vasoconstrictive agents. Endothelial cells, where present, are often hypertrophic. The veins that drain the blood away from the intervillous space pierce the basal plate and join tributaries of the uterine veins.

In vivo studies have shown that in early pregnancy the human placenta is not truly haemochorial (**Video 9.1**) (Jauniaux et al 2003). From the time of implantation, the extravillous trophoblast not only invades the uterine tissues but also forms a continuous shell at the level of the decidua. The cells of this shell anchor the placenta to the maternal tissue and also plug the tips of the uteroplacental arteries (see Figs 9.3B, 9.6) (Burton et al 1999). The shell and the plugs form a labyrinthine interface that filters maternal blood, permitting a slow seepage of plasma but no true blood flow into the intervillous space (Burton et al 2003). This creates a low-oxygen environment that may protect the developing embryo against the deleterious and teratogenic effects of oxygen free radicals and creates a uteroplacental O_2 gradient that exerts a regulatory effect on placental tissue development and function (Jauniaux et al 2003, Burton et al 2017). In particular, it influences cytotrophoblast proliferation and differentiation along the invasive pathway, villous vasculogenesis and the formation of the chorion laeve. An O_2 gradient persists within the placental lobules throughout pregnancy; the central regions are well oxygenated compared to the periphery, reflecting the direction of maternal blood flow (Burton and Jauniaux 2011).

Formation of a well-developed cytotrophoblastic shell at the maternal–fetal interface is crucial for a successful pregnancy. Impaired formation may contribute to reduced extravillous trophoblast invasion and deficient utero-placenta remodelling (Burton and Jauniaux 2017). A thin and fragmentary shell results in premature and disorganized onset of labour and miscarriage, while in less severe cases it may predispose to haemorrhage at the interface and formation of subchorionic haematomas.

At the end of the first trimester (postmenstrual week 12), the endovascular extravillous trophoblastic plugs are progressively dislocated, allowing maternal blood to flow progressively more freely and

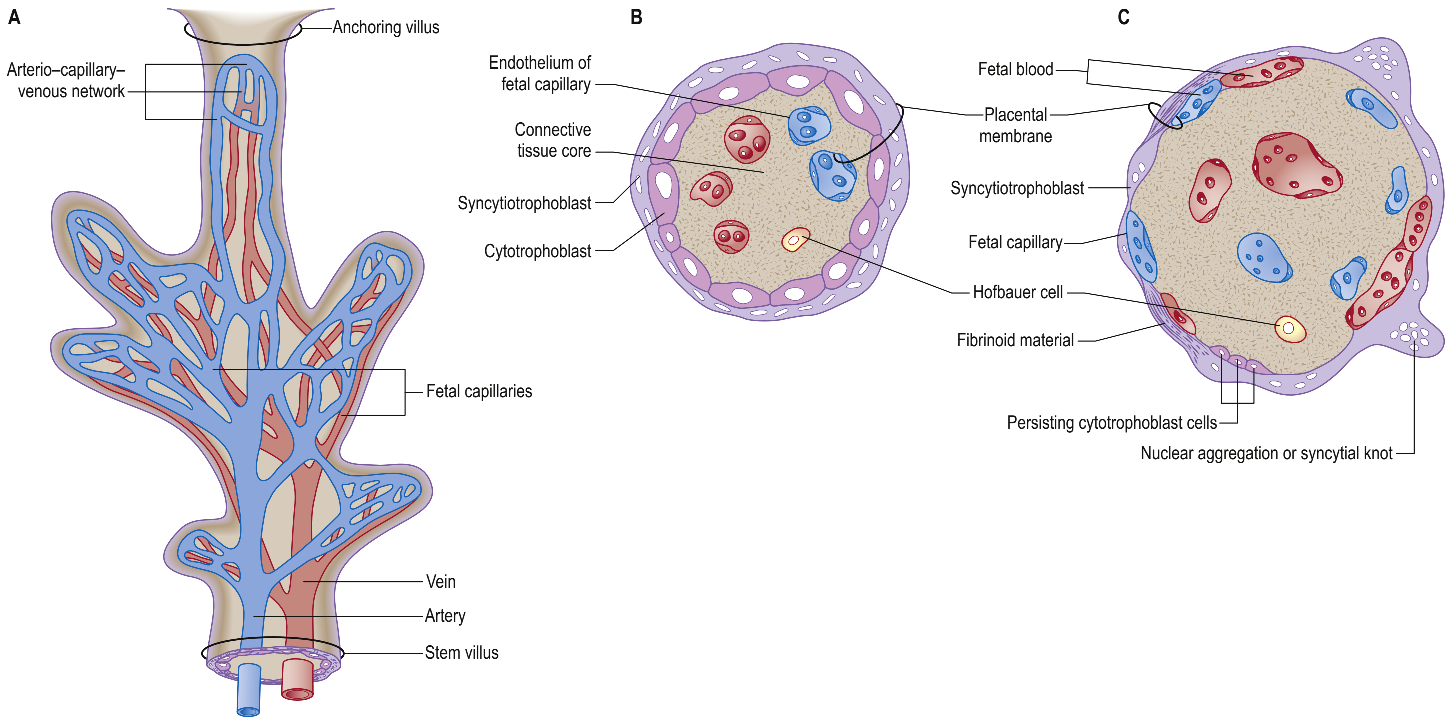

Fig. 9.8 **A**, A chorionic villus and its arterio-capillary-venous system carrying fetal blood. The artery carries deoxygenated blood and waste products from the fetus, and the vein carries oxygenated blood and nutrients to the fetus. **B–C**, Transverse sections through individual chorionic villi at about postmenstrual week 10 (**B**) and at full term (**C**). The villi would be within the intervillous space, bathed externally in maternal blood. The placental membrane, composed of fetal tissues, separates the maternal blood from the fetal blood.

continuously within the intervillous space (see Figs 9.6, 9.7, **Video 9.1**). During postmenstrual weeks 10–14, two-thirds of the primitive placenta degenerates to form the placental free membranes, the chorionic cavity (corresponding to the extraembryonic coelom) is obliterated by the growth of the amniotic sac, and maternal blood flows progressively throughout the entire placenta (Jauniaux et al 2003). These events bring the maternal blood closer to the fetal tissues, facilitating nutrient and gaseous exchange between the maternal and fetal circulations (Gutierrez-Marcos et al 2012).

Structure of a placental villus

Chorionic villi are the essential structures involved in exchanges between mother and fetus. The villous tissues separating fetal and maternal bloods are therefore crucially important functionally. From the chorionic plate, progressive branching occurs into the villous tree, as stem villi give way to intermediate and terminal villi. Each villus has a core of connective tissue containing collagen types I, III, V and VI, as well as fibronectin. Cross-banded fibres (30–35 nm) of type I collagen often occur in bundles, whereas type III collagen is present as thinner (10–15 nm) beaded fibres forming a meshwork that often encases the larger fibres. Collagens V and VI are present as 6–10 nm fibres closely associated with collagens I and III. Laminin and collagen type IV are present in the stroma associated with the basal laminae that surround fetal vessels and also in the trophoblast basal lamina. Overlying this matrix are ensheathing cytotrophoblast cells and the syncytiotrophoblast, bathed by the maternal blood in the intervillous space (see Figs 9.5, 9.7; **Fig. 9.8**). Adjacent cytotrophoblast cells and cytotrophoblast cells adjacent to the syncytium are joined by numerous desmosomes.

In earlier stages, the cytotrophoblast forms an almost continuous layer on the basal lamina. After postmenstrual weeks 13–16, it gradually expends itself producing the syncytiotrophoblast that comes to lie on the basal lamina over an increasingly large area (56% at term) and it becomes progressively thinner. Cytotrophoblastic sprouts covered in syncytium are present in the first and second trimesters and represent a stage in the development of new villi. Columns of cytotrophoblast at the tips of anchoring villi extend from the villous basal lamina to the maternal decidual stroma. Cytotrophoblastic cells persist until term but, because the increase in villous surface area outstrips their proliferation, they are usually disposed singly.

The syncytiotrophoblast is the multinucleated epithelium of the placenta. It is an intensely active tissue layer, across which most transplacental transport must occur (Ellery et al 2009). It is also a selectively permeable barrier that allows water, oxygen and other nutritive substances and hormones to pass from mother to fetus, and some of the products of excretion to pass from fetus to mother. It secretes a range of placental hormones into the maternal circulation. Syncytial cytoplasm is more strongly basophilic than that of the cytotrophoblast cells, and is packed with organelles consistent with its secretory phenotype. Where the plasma membrane adjoins basal lamina, it is often infolded into the cytoplasm, whereas the surface bordering the intervillous space is set with numerous long microvilli.

Although many nuclei are dispersed within the syncytioplasm, other are aggregated into specializations referred to as syncytial knots and syncytial sprouts (Burton et al 2003). Syncytial sprouts are markers of trophoblast proliferation. In the immature placenta, they represent the first stages in the development of new villi that later become invaded by cytotrophoblast and villous mesenchyme (Fogarty et al 2013). Occasionally, adjacent syncytial sprouts make contact and fuse to form slender syncytial bridges. The sprouts may become detached, forming maternal syncytial emboli that pass to the lungs. It has been computed that some 100,000 sprouts pass daily into the maternal circulation; deported trophoblast may be a mechanism by which the maternal immune system is maintained in a state of tolerance towards paternal antigens (Chamley et al 2011). In the lungs, syncytial sprouts provoke little local reaction and apparently disappear by lysis. However, they may occasionally form foci for neoplastic growth. Syncytial sprouts are present in the term placenta. By contrast, syncytial knots are aggregates of nuclei with particularly condensed heterochromatin, and may represent a sequestration phenomenon by which senescent nuclear material is removed from adjacent metabolically active areas of syncytium.

The core of a villus contains small and large reticulum cells, fibroblasts and macrophages (Hofbauer cells). Early mesenchymal cells differentiate initially into small reticulum cells and then into fibroblasts or large reticulum cells. The small reticulum cells appear to delimit a collagen-free stromal channel system through which Hofbauer cells migrate. Mesenchymal collagen increases from a network of fine fibres in early mesenchymal villi to a densely fibrous stroma within stem villi in the second and third trimesters. After approximately postmenstrual week 14, the stromal channels found in immature intermediate villi are infilled by collagen to give the fibrous stroma characteristic of the stem villus.

Fetal placental vessels include arterioles and capillaries but no lymphatic vessels. Pericytes may be found in close association with the capillary endothelium, and from late first trimester the vessels are surrounded externally by a basal lamina. From the second trimester (and a little later in terminal villi), dilated thin-walled capillaries are found immediately adjacent to the villous trophoblast. Their respective basal laminae apparently fuse to produce a vasculo-syncytial

The cells of the villous cytotrophoblast (Langhans cells) are pale-staining with a slight basophilia. Ultrastructurally, they have a rather electron-translucent cytoplasm and relatively few organelles and contain intermediate filaments, particularly in association with desmosomes. Between the desmosomes, the membranes of adjacent cells are separated by approximately 20 nm. Sometimes, the intercellular gap widens to accommodate microvillous projections from the cell surfaces and occasionally it contains patches of fibrinoid. A smaller population of intermediate cytotrophoblast may also be found in the chorionic villi. This postmitotic population represents a state of partial differentiation between the cytotrophoblast stem cell and the overlying syncytium.

Glycolysis is maintained in placental tissues by re-oxidation of pyridine nucleotides through the polyol pathways. The reliance on glycolysis rather than oxidative phosphorylation preserves carbon skeletons that can be utilized in the synthesis of nucleotides, cell membranes and organelles, and that would otherwise be excreted as carbon dioxide. In the placenta, this reliance may protect the embryo from free radical-mediated teratogenesis (Burton et al 2017). Glycogen is thought to be present in both layers of the trophoblast at all stages, although it is not always possible to demonstrate its presence histochemically.

Lipid droplets occur in both layers and are free in the core of the villus. In the trophoblast, they are found principally within the cytoplasm, but they also occur in the extracellular space between cytotrophoblast and syncytium, and between the individual cells of the cytotrophoblast. The droplets diminish in number with advancing age and may represent fat in transit from mother to fetus, and/or a pool of precursors for steroid synthesis. Membrane-bound granular bodies of moderate electron density occur in the cytoplasm, particularly in the syncytium, and some are probably secretion granules. Other membrane-bound bodies, lysosomes and phagosomes, are involved in the degradation of materials engulfed from the intervillous space.

Fibrinoid deposits are frequently found on the villous surface in areas lacking syncytiotrophoblast. They may constitute a repair mechanism in which the fibrinoid forms a wound surface that is subsequently re-epithelialized by trophoblast. The extracellular matrix glycoprotein tenascin has been localized in the stroma adjacent to these sites.

interface and the distance separating the maternal and fetal circulations may be reduced to as little as 2–3 µm. The endothelial cells are non-fenestrated, display numerous caveolae, and are linked by conspicuous junctional complexes incorporating tight and adherens junctions.

Transport across placental villi

The mechanism of transfer of substances across the placental barrier (membrane) is complex. The volume of maternal blood circulating through the intervillous space has been assessed at 600 ml per minute. Simple diffusion suffices to explain gaseous exchange. Transfer of ions and other water-soluble solutes is by paracellular and transcellular diffusion and transport. The relative importance of each of these for most individual solutes is unknown, and the paracellular pathway is morphologically undefined. Glucose transfer involves facilitated diffusion, while active transport mechanisms carry calcium ions and at least some amino acids. The fat-soluble and water-soluble vitamins are likely to pass across the placental barrier with differing degrees of facility (Jauniaux and Gulbis 2000a, Jauniaux et al 2004, Jauniaux et al 2005). The water-soluble vitamins B and C pass readily. Water is interchanged between fetus and mother (in both directions) at approximately 3.5 litres per hour. The transfer of substances of high molecular weight, such as complex sugars, some lipids and hormonal and non-hormonal proteins, varies greatly in rate and degree and is not well understood; energy-dependent selective transport mechanisms, including receptor-mediated transcytosis, are likely to be involved.

Lipids may be transported unchanged through and between the cells of the trophoblast to the core of the villus. The passage of maternal antibodies (immunoglobulins) across the placental barrier in late pregnancy confers some degree of passive immunity on the fetus; it is widely accepted that transfer is by micropinocytosis. Investigation of transplacental mechanisms is complicated by the fact that the trophoblast itself is the site of synthesis and storage of certain substances, e.g. glycogen.

The placenta is an important endocrine organ. Some steroid hormones, various oestrogens, β-endorphins, progesterone, hCG and human chorionic somato-mammotropin (hCS), also known as placental lactogen (hPL), are synthesized and secreted by the syncytiotrophoblast. The trophoblast contains enzyme systems that are associated with the synthesis of steroid hormones, as well as enzymes that inactivate maternal hormones, allowing the fetus to develop and mature in a protected environment; for example, the fetus is protected from 10 times higher maternal glucocorticoid levels by the placental enzyme 11beta-hydroxysteroid dehydrogenase 2 (11beta-HSD2), that converts biologically active maternal cortisol to inactive cortisone (Murphy et al 1974).

It has been suggested that leukocytes may migrate from the maternal blood through the placental barrier into the fetal capillaries. It has also been shown that some fetal and maternal red blood cells may cross the barrier, especially at the time of delivery. The former may have important consequences, e.g. in Rhesus incompatibility.

The majority of drugs are small molecules and are sufficiently lipophilic to cross the placental barrier from about postmenstrual week 6 in quantities that yield measurable concentrations in both chorionic (extraembryonic coelom) and amniotic fluid. Many are tolerated by the fetus but some may exert grave teratogenic effects on the developing embryo/fetus, depending on the gestational age and the doses used by the mother (e.g. thalidomide, cocaine). A well-documented association exists between maternal alcohol ingestion and/or drug use such as cocaine and fetal anomalies; tobacco smoke and fetal growth; and the fetus can become addicted to heroin. Among pregnant women aged 15–44 years in the United States, 5.9% report illicit drug use; 16–17% report recent cigarette use, and an annual average of about 8.5% report alcohol use during pregnancy (Ross et al 2015, Hoyme and Manning 2017).

A wide variety of bacteria (e.g. *Listeria*), protozoa (e.g. *Toxoplasma gondii*, *Trypanasoma cruzi* and *Plasmodium falciparum*), and viruses (e.g. cytomegalovirus (CMV), Zika virus (ZIKV) and rubella), are known to cross the placental barrier from mother to fetus. By contrast, group B streptococcus (GBS), herpes simplex virus (HSV) and human immunodeficiency virus (HIV) do not cross the placental barrier during pregnancy and are acquired by the fetus during delivery. Toxoplasma and CMV are transferred by cellular invasion of the villous trophoblast during the acute phase of a newly acquired maternal infection. Since the maternal circulation inside the definitive placenta only starts at the end of the first trimester, transmission of *Toxoplasma* to an embryo is rare before that time, but highly damaging to a developing fetus. *Plasmodium falciparum* (malaria) is transferred by villous sequestration of maternal infected erythrocytes or a breakdown of the villous barrier during labour. The presence of maternal rubella in the early pregnancy is of especial importance in relation to the production of congenital anomalies. For further reading about TORCH perinatal infections (**T**oxoplasmosis; **O**thers, including syphilis and listeriosis; **R**ubella; **C**MV; **H**SV) see Stegmann and Carey (2002).

FETAL MEMBRANES

The implanting conceptus consists initially of three cavities and their surrounding epithelia. The original blastocyst cavity, surrounded by trophoblast, is now termed the chorionic cavity (the extraembryonic coelom). It is a large cavity that contains the much smaller amniotic cavity and secondary yolk sac (see Fig. 9.1). The apposition of the latter two cavities delineates the extent of the early embryo. The chorionic cavity becomes lined with extraembryonic mesoblast, which is also reflected over the outer surface of the amnion and yolk sac. A fourth cavity, the allantois, develops later as a caudal hypoblastic diverticulum that becomes embedded within the extraembryonic mesenchyme, forming the connecting stalk of the embryo: it lacks a direct mesothelial covering.

Chorion

The chorion consists of developing trophoblast and extraembryonic mesothelium and varies in thickness during development, both temporally and spatially. It is thickest at the implantation site throughout gestation, initially as the chorion frondosum and then the placenta, and thinner as gestation progresses over the remainder of its surface as the chorion laeve (see Fig. 9.4). At term, the chorion consists of an inner cellular layer containing fibroblasts and a reticular layer of fibroblasts and Hofbauer cells that resembles the mesenchyme of an intermediate villus. The outer layer consists of cytotrophoblast 3–10 cells deep, resting on a pseudo-basement membrane that extends beneath and between the cells. Occasional obliterated villi within the trophoblast layer are the remnants of villi present in the chorion frondosum of the first trimester. Although the interface between the trophoblast and decidua parietalis is uneven, no trophoblast infiltration of the decidua parietalis occurs.

Yolk sac

The yolk sac is thought to be the phylogenetically oldest extraembryonic membrane. The human embryo retains a yolk sac that goes through primary and secondary phases of development. As the secondary yolk sac forms, it delineates a cavity lined with parietal, and perhaps visceral, hypoblast, continuous with the developing endoderm from the primitive streak (Ch. 10; see Fig. 10.10). The secondary yolk sac is the first structure that can be detected ultrasonographically within the chorionic cavity (Jauniaux et al 1991). Its diameter increases slightly between postmenstrual weeks 6 and 10, reaching a maximum of 6–7 mm, after which time it decreases.

The inner cells of the secondary yolk sac (denoted endoderm in many studies, although this layer is restricted to the embryo) display a few short microvilli and are linked by juxtaluminal tight junctions (Jones and Jauniaux 1995). Their cytoplasm contains numerous mitochondria, whorls of rough endoplasmic reticulum, Golgi bodies and secretory droplets, giving them the appearance of highly active synthetic cells. With further development, the epithelium becomes folded to form a series of cyst-like structures or tubules, only some of which communicate with the central cavity. The cells synthesize several serum proteins in common with the fetal lung, kidney and liver, including α-fetoprotein (AFP), α-1-antitrypsin, albumin, pre-albumin and transferrin (Gulbis et al 1998) (**Fig. 9.9**). With rare exceptions, the secretion of most of these proteins is confined to the embryonic compartments (Jauniaux and Gulbis 2000b).

The yolk sac becomes coated with extraembryonic mesenchyme, that forms mesenchymal and mesothelial layers. A diffuse capillary plexus develops between the mesothelial layer and the underlying secondary yolk sac wall, and subsequently drains through vitelline veins to the developing liver. The mesothelial layer bears a dense covering of microvilli and numerous coated pits and pinocytotic vesicles, giving it the appearance of an absorptive epithelium (Jones and Jauniaux 1995, Burke et al 2013).

The secondary yolk sac plays a major role in the early embryonic development of all mammals. In laboratory rodents, it has been demonstrated to be one of the initial sites of haemopoiesis. Human data indicate that it has an absorptive role for molecules of maternal and placental origin found in the chorionic cavity (Gulbis et al 1998) and that it mediates the main movement of molecules passing from the chorionic cavity to the embryonic gut and circulation. Conservation of

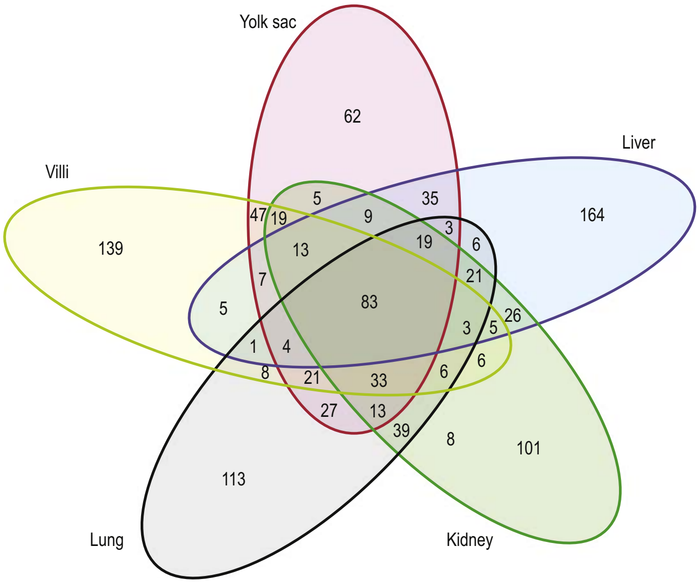

Fig. 9.9 Venn diagram comparing the most abundant 400 transcripts in the human yolk sac with first-trimester placental villi and adult liver, lung and kidney. Transcripts shared by all five tissues (*n* = 83) principally encoded housekeeping proteins, whereas those shared uniquely with liver (*n* = 35) encoded proteins involved in cholesterol and lipid metabolism, suggesting that the yolk sac may perform these functions while the fetal liver develops. By contrast, there are few transcripts shared uniquely with the kidney (*n* = 5), suggesting that the yolk sac plays little role in excretion. (With permission from Cindrova-Davies T, Jauniaux E, Elliot MG et al 2017 RNA-seq reveals conservation of function among the yolk sacs of human, mouse, and chicken. Proc Natl Acad Sci U S A 114: E4753–E4761.)

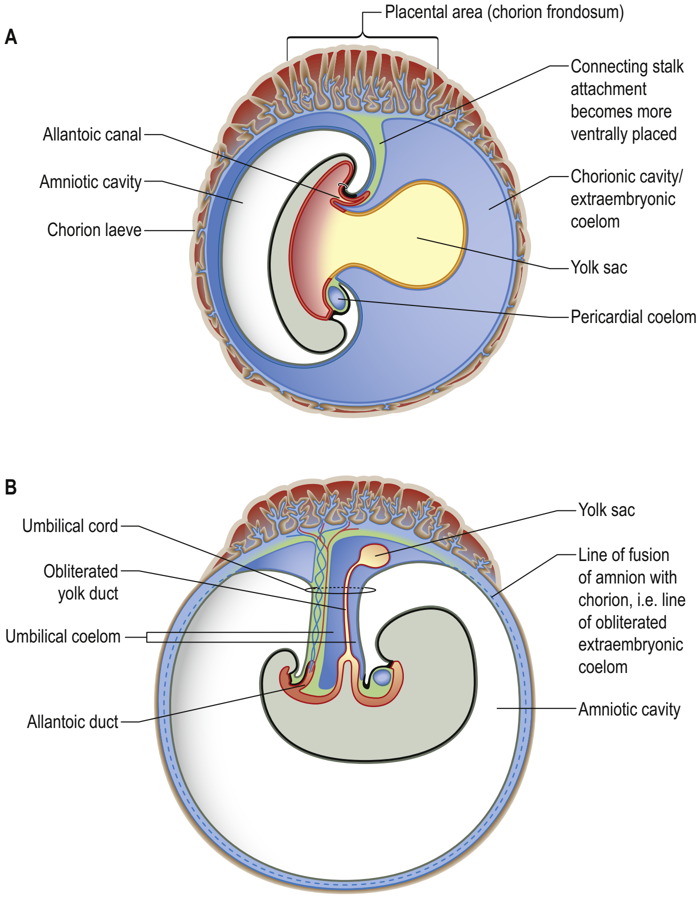
A
Placental area (chorion frondosum)
Connecting stalk attachment becomes more ventrally placed
Allantoic canal
Amniotic cavity
Chorion laeve
Chorionic cavity/ extraembryonic coelom
Yolk sac
Pericardial coelom
B
Umbilical cord
Obliterated yolk duct
Umbilical coelom
Allantoic duct
Yolk sac
Line of fusion of amnion with chorion, i.e. line of obliterated extraembryonic coelom
Amniotic cavity

Fig. 9.10 **A**, A longitudinal section of a conceptus showing the cavities associated with development. The amniotic cavity and yolk sac are both covered with extraembryonic mesoblast and are contained within the larger chorionic cavity, which is lined with extraembryonic mesoblast. The embryo is attached to the chorion frondosum by the connecting stalk into which the allantois projects. **B**, A longitudinal section of a conceptus at a later stage, showing the diminution of the chorionic cavity, expansion of the amniotic cavity, relative attenuation of the yolk sac and the structures that give rise to the umbilical cord.

transcriptomes across the species indicates that the human secondary yolk sac likely performs key functions early in development, particularly uptake and processing of macro- and micronutrients (see Fig. 9.9), many of which are found in the chorionic cavity (Cindrova-Davies et al 2017).

After postmenstrual week 9, the cellular components of the wall of the secondary yolk sac start to degenerate, and their function is subsumed into exchanges at the placental chorionic plate. With embryonic development of the midgut, the connection of the yolk sac to the embryo becomes attenuated to a slender and elongated vitelline intestinal duct. Both the yolk sac and its duct remain within the chorionic cavity (extraembryonic coelom) throughout gestation, located between the amnion and chorion as they fuse near the placental attachment of the umbilical cord.

Allantois

The allantoenteric diverticulum (see Fig. 10.10B,C) arises in stage 7 as a solid, endodermal outgrowth from the dorsocaudal part of the yolk sac into the mesenchyme of the connecting stalk. It soon becomes canalized. When the hindgut develops, the proximal (enteric) part of the diverticulum is incorporated in its ventral wall. The distal (allantoic) part remains as the allantoic duct and is carried ventrally to open into the ventral aspect of the cloaca or terminal part of the hindgut (Fig. 9.10A). The allantois is a site of angiogenesis, giving rise to the umbilical vessels that connect to the placental circulation. The extraembryonic mesenchyme around the allantois forms the connecting stalk, which is later incorporated into the umbilical cord.

In the fetus, the allantoic duct, which is confined to the proximal end of the umbilical cord, elongates and thins. However, it may persist as an interrupted series of epithelial strands at term, in which case the proximal strand is often continuous at the umbilicus with the median intra-abdominal urachus and this, in turn, continues into the apex of the bladder.

Amnion (chorio-amnion)

The original amniotic cells develop from the edges of the epiblast of the embryonic disc that ultimately form the interface with the skin at the umbilical region. Between postmenstrual weeks 10 and 12, the amniotic cavity expands until it makes contact with the chorion to form the chorio-amnion, an avascular membrane that persists to term. The amniotic membrane extends along the connecting stalk and forms the outer covering of the umbilical cord. After birth, the site of this embryonic/extraembryonic junction is important because the extraembryonic cell lines will die, causing the umbilical cord to degenerate and detach from the body wall. In cases of anomalous development of the ventral body wall, e.g. gastroschisis and exomphalos, the reflections of the amnion along the forming umbilical cord may be incomplete (see below).

The inner surface of the amnion consists of a simple cuboidal epithelium. It has a microvillous apical surface, beneath which is a cortical web of intermediate filaments and microfilaments. There are no tight junctional complexes between adjacent cells and cationic dyes penetrate between the cells as far as the basal lamina. The intercellular clefts present scattered desmosomes, but elsewhere the clefts widen and contain interlacing microvilli. These features are all consistent with selective permeability properties. The epithelium synthesizes and deposits extracellular matrix into the compact layer of acellular stroma located beneath the basal lamina, as well as into the basal lamina.

Towards full term, increasing numbers of amniotic cells undergo apoptosis, become detached from the amnion and are found in the amniotic cavity at full term. The highest incidence is in postmenstrual weeks 40–41, independent of the time of the onset of labour. Apoptosis may play a role in the fragility and rupture of the fetal membranes at term.

Human amniotic epithelial cells are thought to be pluripotent because they arise so early from the conceptus. They can be distinguished from the epiblast cells from postfertilization day 8. Amniotic cells lack the MHC antigen and so the amnion can be exposed to the maternal immune system without eliciting a maternal immune response. Cultured human amniotic epithelial cells express a range of neural and glial markers, including glial fibrillary acidic protein, myelin basic protein, vimentin and neurofilament proteins, suggesting that these cells may supply neurotrophic factors to the amniotic fluid. They also appear to have a hepatocyte gene expression profile, showing albumin production, glycogen storage and albumin secretion in organ culture: they have been shown to secrete 30-fold larger amounts of albumin than in monolayer culture, and to secrete α-1-antitrypsin (Takashina et al 2004). Amnion is used in the repair of corneas after trauma and as a graft material for reconstructing vaginas in women with cloacal abnormalities.

Prenatal changes to the chorio-amnion

At full term, the surface area of the chorio-amnion is 1000–1200 cm^2, where 30% overlies the placenta and the remaining 70% contacts the decidua (Myatt and Sun 2010). The decidual component of the chorion diminishes and chorionic apoptosis increases towards term at the supracervical site that overlies the cervical os, encompassing the site of rupture (Chai et al 2013). The amnion and choriodecidua show varying degrees of separation over the putative rupture site; the mean rupture strength of the zone is only 60% of that of the remaining membranes, associated with changes in collagen organization and an increase in MMP-9 (Strauss 2013). When compared to fetal membranes from non-labouring, elective caesarean delivery, term vaginal delivery is associated with a three-fold increase in apoptosis in the chorion close to the rupture site (Harirah et al 2012).

In preterm, premature rupture of membranes (PPROM), the chorion is reported to be thinner at all sites (Fortner et al 2014). The presence of bacteria in the chorion at term, ascending via the vagina, has been reported without concomitant chorio-amnionitis. However, chorio-amnionitis rates are higher in preterm labour and so this may be a contributing cause (Harirah et al 2012, Fortner et al 2014). Loss of chorio-amnion intracellular cytokeratins, which become downregulated in infection, is thought to make the amnion vulnerable to apoptosis, shear stress and rupture (Vanderhoeven et al 2014).

There is increasing evidence that infection and inflammation of the chorio-amnion is associated with prenatal changes to the developing brain, especially the cortex, periventricular white matter and the developing cerebral blood vessels (Harteman et al 2013, Roescher et al 2014). This association also extends to the neonatal period and postnatal gut maturation (Wynn and Neu 2012). Histologically confirmed chorio-amnionitis is associated with changes in cerebral blood flow soon after birth; male infants appear to be more affected than female (Koch et al 2014)

AMNIOTIC FLUID

Amniotic fluid (liquor amnii) provides a buoyant medium that supports the delicate tissues of the young embryo, allows free movement of the fetus up to the later stages of pregnancy and diminishes the risk to the fetus of injury from outside. Amniotic fluid is derived from multiple sources throughout gestation including secretions from amniotic epithelium, filtration of fluid from maternal vessels via the parietal decidua and amniochorion, filtration from the fetal vessels via the chorionic plate or the umbilical cord, and fetal urine and fetal lung secretions. In early pregnancy, diffusion from intracorporeal vessels via the non-keratinized fetal skin also provides a source. Once the gut is formed, fetal swallowing of amniotic fluid is a normal occurrence and the fluid is absorbed into the fetal circulation.

Amniotic fluid volume increases logarithmically during the first half of pregnancy, from less than 10 ml at postmenstrual week 8 to 30 ml at postmenstrual week 22 and 770 ml at postmenstrual week 28. After postmenstrual week 30, the volume may remain unchanged until postmenstrual week 36, after which it decreases towards the expected delivery date: volumes decrease sharply in post-term gestation, averaging 515 ml at postmenstrual week 41 (Beall et al 2007, Ross and Beall 2014).

Human fetal urine output from the metanephric kidney increases from 110 ml/kg/day at postmenstrual week 25 to almost 200 ml/kg/day at full term postmenstrual week 40, which corresponds to almost 1000 ml/day. The rate of human fetal lung secretion has not been measured but is presumed to be in the range of 60–100 ml/kg/day near full term (Callen 2008). Experimental animal studies indicate that lung fluid production is about one-third that of urine production, and that half of the fluid leaving the lungs enters the amniotic fluid and half is swallowed (Beall et al 2007, Ross and Beall 2014). It has been estimated that human fetuses swallow up to 760 ml/day of amniotic fluid near term, although this decreases in the days before delivery. The remainder of the amniotic fluid is thought to be absorbed via an intramembranous pathway directly across the amniotic cavity and fetal surface of the placenta into fetal blood vessels (Beall et al 2007, Ross and Beall 2014). Intramembranous flow is thought to reach 400 ml/day at term (Callen 2008).

Amniotic fluid volume is estimated at routine antenatal ultrasound scans, despite some concerns about its objectivity (Beattie and Rich 2007, Callen 2008, Gilbert 2017) and it may be expressed as an amniotic fluid index. A deficiency of amniotic fluid is termed oligohydramnios and absent amniotic fluid is anhydramnios. Oligohydramnios in the second or third trimester is usually the result of urinary tract malformations, e.g. bilateral renal agenesis or obstruction of the lower urinary tract, uteroplacental insufficiency or premature rupture of the membranes. The urachus may play a critical role in the resolution of oligohydramnios in lower urinary tract obstruction by acting as a fistula between the bladder and the amniotic space. The major concern with oligohydramnios at less than postmenstrual week 20 is the significant risk of pulmonary hypoplasia and neonatal death.

A volume of amniotic fluid in excess of 2 litres in the second half of pregnancy is generally considered to be abnormal and constitutes polyhydramnios (see Fig. 23.6A). Maternal causes include cardiac and renal problems and diabetes mellitus, which causes fetal hyperglycaemia and polyuria. Fetal causes include reduced fetal swallowing due to congenital anomalies, e.g. anencephaly, upper intestinal tract obstruction (oesophageal and duodenal atresia), compressive pulmonary disorders (congenital respiratory diaphragmatic hernia) and neuromuscular impairment of swallowing.

For many years amniotic fluid was regarded as a medium that physically supported the developing embryo and fetus. More recently, it has also been conceptualized as part of the embryonic and early fetal extracellular matrix, and its composition throughout pregnancy has been investigated (Tong et al 2009). Techniques for biochemical analysis have compared amniotic fluid, fetal umbilical cord blood and maternal serum. Early in development, amniotic fluid resembles blood plasma, but also demonstrates extremely low oxygen tension, reflecting the physiological placental hypoxia noted in the first trimester (Jauniaux et al 2003, Ross and Beall 2014). In the second and third trimesters, primary electrolytes are similar in amniotic fluid, umbilical cord blood and maternal serum, whereas glucose, cholesterol and some enzymes are markedly lower in amniotic fluid. Umbilical cord blood and maternal serum contain 8 and 12.5 times more protein, respectively, than amniotic fluid (Tong et al 2009). More than 100 metabolites, including cortisol and a range of cytokines, have been detected in amniotic fluid. The concentrations of most cytokines differ from those in maternal blood and reflect the physiological status of the fetus (Tong 2013). Proteomic analysis of human amniotic fluid at postmenstrual weeks 16–18 has identified more than 800 proteins and peptides (Cho et al 2007). It appears that amniotic fluid may be acting as a pathway for the transport of signalling molecules to target cells. In experimental animal studies, substances injected into the amniotic cavity were detected within the embryos within 2 minutes, demonstrating a rapid exchange with all fetal tissues in these models (Tong 2013).

UMBILICAL CORD

The umbilical cord ultimately consists of an outer covering of flattened amniotic epithelial cells and an interior mass of mesenchyme of diverse origins (see Fig. 9.10). It contains two tubes of hypoblastic origin, the vitelline-intestinal and allantoic ducts, and their associated vitelline and allantoic (umbilical) blood vessels. The yolk stalk and continuing duct extend the length of the cord, whereas the allantoic duct extends only into its proximal part. The embryonic development of the umbilical cord is considered further in Chapter 21.

The mesenchymal core is derived from the somatopleuric extraembryonic mesenchyme covering the amniotic folds; splanchnopleuric extraembryonic mesenchyme of the yolk stalk (which carries the vitelline vessels and clothes the yolk duct); and similar allantoic mesenchyme of the connecting stalk (which clothes the allantoic duct and initially carries two umbilical arteries and two umbilical veins). These various mesenchymal compartments fuse and are gradually transformed into the loose connective tissue (Wharton's jelly) that characterizes the more mature cord. The tissue consists of widely spaced elongated fibroblasts separated by a delicate three-dimensional meshwork of fine collagen fibres that contains a variety of hydrated glycosaminoglycans and is particularly rich in hyaluronic acid.

The initially symmetric vitelline and allantoic (umbilical) vessels become modified as a result of changes in the intraembryonic circulation. The vitelline vessels involute, whereas most of the allantoic (umbilical) vessels persist. The right umbilical vein disappears but the two umbilical arteries normally remain. In around 1% of pregnancies, one of the umbilical arteries may not develop or disappears at the end of the first trimester. This anomaly is often found in syndromes such as aneuploidies, acardiac fetuses or sirenomelia and when isolated can be associated with slow fetal growth. The vessels of the umbilical cord are rarely straight and are usually twisted into either a right- or left-handed cylindrical helix. The number of turns involved ranges from a few to over 300. This conformation may be produced by unequal growth of the vessels, or by torsional forces imposed by fetal

A number of clinical markers in amniotic fluid are used as predictors of fetal health, including interleukin (IL)-10, IL-6, cell free fetal DNA and cell free fetal mRNA. Genes and proteins specific to the fetal brain, lung, kidney, blood and heart have been identified in amniotic fluid; differential gene expression investigated in a range of trisomic fetuses; and lung maturity predicted by measurement of lecithin, sphingomyelin and phosphatidylglycerol (Edlow and Bianchi 2012, Ross and Beall 2014). Bacterial species have been isolated from amniotic fluid; and microbial invasion of the amniotic cavity is considered a leading cause of preterm premature delivery (DiGiulio 2012). It is thought bacteria access the amniotic cavity via the vagina and cervix, although many oral bacteria have also been identified, suggesting an alternative haematogenous route. The establishment of pathogenesis is influenced by microbial adhesion, biofilm formation, immune evasion and the maternal and fetal immune systems (DiGiulio 2012).

movements. Its functional significance is obscure: the pulsations and contractions of the helical vessels may assist the venous return to the fetus in the umbilical vein. Autonomic nerves accompanying the arteries from the pelvic plexus do not penetrate more than a third of the length of the umbilical cord.

Anomalies of the fetal anterior abdominal wall, such as exomphalos and gastroschisis can affect the arrangement of the outer covering of amnion cells along the proximal end of the umbilical cord (Ch. 21). Exomphalos arises from a failure of the lateral folds along the ventral surface of the embryo, so that the normal embryonic regression of the midgut from the umbilical stalk into the abdominal cavity fails. The abdominal contents, including intestines and liver or spleen, covered by a sac of parietal peritoneum and amnion, protrude into the base of the umbilical cord. In gastroschisis, the insertion of the umbilical cord is intact and there is evisceration of the intestine through a small abdominal wall defect that is usually located to the right of the umbilical cord, resulting in free loops of bowel in the amniotic cavity.

Mature umbilical vessels, particularly the arteries, have a strong muscular coat that contracts readily in response to mechanical stimuli. The outermost bundles pursue an interlacing spiral course, and when they contract, they produce shortening of the vessel and thickening of the media, with folding of the interna and considerable narrowing of the lumen. This action may account for the periodic sharp constrictions of contour, the valves of Hoboken, that often characterize these vessels.

The fully developed umbilical cord is, on average, some 50 cm long and 1–2 cm in diameter. Its length varies from 20 to 120 cm; exceptionally short or long cords are associated with fetal problems and complications during labour. A long umbilical cord may prolapse through the cervix into the vagina once the fetal membranes rupture and this may be exacerbated by conditions that prevent the fetal head from fully occupying the maternal pelvis, e.g. pelvic tumours (fibroids), ovarian cysts, placenta previa and prematurity. Compression of the cord by the presenting part of the fetus, or an umbilical artery spasm, will lead to fetal hypoxia and death, if untreated.

The distal end of the umbilical cord is usually attached in the central portion of the placenta. In 0.2% of pregnancies, velamentous insertion (i.e. into the membranes) occurs and may be associated with cord vessels running in the free placental membranes (vasa previa): these vessels are vulnerable to injury during delivery and may lead to fatal fetal haemorrhage.

Artificial reproductive techniques, and in particular *in vitro* fertilization and embryo transfer, are associated with a high incidence of placental and cord anatomical anomalies such as bilobate placenta, placenta previa and velamentous insertion of the cord in the membranes. These anomalies probably reflect alterations in the interactions between the blastocyst and the decidua that normally occur in spontaneous pregnancies (Jauniaux et al 1990). Damage to the uterine wall following surgery, mainly after repeat caesarean section, increases the chances of implantation in the scar area and results in a higher incidence of scar pregnancy and placenta previa accreta in subsequent pregnancies (Jauniaux et al 2018).

Bonus e-book content

Video 9.1 Ultrasound features of the maternal placental blood flow.

Key references

Brosens JJ, Salker MS, Teklenburg G et al 2014 Uterine selection of human embryos at implantation. Sci Rep 4:3894.

A study showing that developmentally impaired human embryos elicit an endoplasmic stress response in human decidual cells and suggesting that distinct positive and negative mechanisms contribute to active selection of human embryos at implantation.

Burton GJ, Jauniaux E 2011 Oxidative stress. Best Pract Res Clin Obstet Gynaecol 25:287–99.

A review of the evidence implicates oxidative stress in the pathophysiology of placental related complications of human pregnancy ranging from miscarriage to pre-eclampsia and premature rupture of the membranes.

Burton GJ, Jauniaux E, Watson AL 1999 Maternal arterial connections to the placental intervillous space during the first trimester of human pregnancy: the Boyd collection revisited. Am J Obstet Gynecol 181:718–24.

Using hysterectomy specimens from the Boyd anatomy collection, this study shows that the maternal circulation to the placenta must be extremely sluggish before the eighth week of pregnancy, supporting the concept that development of the human fetoplacental unit during most of the first trimester takes place in a low-oxygen environment.

Burton GJ, Watson AL, Hempstock J et al 2002 Uterine glands provide histiotrophic nutrition for the human fetus during the first trimester of pregnancy. J Clin Endocrinol Metab 87:2954–9.

The first study to demonstrate that the uterine glands are an important source of nutrients during organogenesis, when metabolism is essentially anaerobic. Uterine glands remain active until at least week 10 of pregnancy, and their secretions are delivered freely into the placental intervillous space, supporting the concept of histiotrophic nutrition as opposed to hemochorial nutrition.

Gilbert WM 2017 Amniotic fluid disorders. In: Gabbe SG, Niebyl JR, Simpson JL et al (eds) Obstetrics: Normal and Problem Pregnancies, 7th ed. Philadelphia, PA: Elsevier; Ch. 35.

An overview of amniotic fluid production and absorption.

Gulbis B, Jauniaux E, Cotton F et al 1998 Protein and enzyme patterns in the fluid cavities of the first trimester gestational sac: relevance to the absorptive role of secondary yolk sac. Mol Hum Reprod 4:857–62.

A study demonstrating that the secondary yolk sac membrane is an important zone of transfer between the extra-embryonic and embryonic compartments and suggesting that therapeutic protocols making use of fetal somatic gene therapy could be performed by injecting transduced cells into the exocoelomic cavity.

Jauniaux E, Gulbis B 2000a Fluid compartments of the embryonic environment. Hum Reprod Update 6:268–78.

This paper reviews the composition, biology and role of the extraembryonic coelomic or chorionic fluid cavity and its connections with the secondary yolk sac and developing placenta during the first trimester of human pregnancy.

Makieva S, Giacomini E, Ottolina J et al 2018 Inside the endometrial signalling subway: mind the gap(s). Int J Mol Sci 19, 2477; doi: 10.3390/ijms19092477.

A study that considers endometrial communication and signalling.

Ross MG, Beall MH 2014 Amniotic fluid dynamics. In: Creasy R, Resnik R, Iams JD et al (eds) Saunders' Maternal-Fetal Medicine: Principles and Practice, 7th ed. Philadelphia: Elsevier, Saunders; Ch. 3, pp. 47–52.

This chapter provides an overview of the production, circulation and absorption of amniotic fluid during gestation.

Strauss JF 2013 Extracellular matrix dynamics and fetal membrane rupture. Reprod Sci 20:140–53.

This paper presents the composition and biomechanical properties of the fetal membrane extracellular matrix. It considers the changes in extracellular matrix composition during normal pregnancy and term delivery and those seen in preterm premature rupture of membranes.

References

Beall MH, van den Wijngaard JPHM, van Gemert MJC et al 2007 Amniotic fluid water dynamics. Placenta 28:816–23.

Beattie RB, Rich DA 2007 Disorders of amniotic fluid, placenta and membranes. In: Twining P, McHugo JM, Pilling DW (eds) Textbook of Fetal Abnormalities. London: Elsevier, Churchill Livingstone; Ch 5, pp. 75–94.

Brosens JJ, Salker MS, Teklenburg G et al 2014 Uterine selection of human embryos at implantation. Sci Rep 4:3894.

A study showing that developmentally impaired human embryos elicit an endoplasmic stress response in human decidual cells and suggesting that distinct positive and negative mechanisms contribute to active selection of human embryos at implantation.

Burke KA, Jauniaux E, Burton GJ et al 2013 Expression and immunolocalisation of the endocytic receptors megalin and cubilin in the human yolk sac and placenta across gestation. Placenta 34:1105–9.

Burton GJ, Fowden AL 2012 Review: The placenta and developmental programming: balancing fetal nutrient demands with maternal resource allocation. Placenta 33 Suppl:S23–7.

Burton GJ, Jauniaux E 2011 Oxidative stress. Best Pract Res Clin Obstet Gynaecol 25:287–99.

A review of the evidence implicates oxidative stress in the pathophysiology of placental related complications of human pregnancy ranging from miscarriage to pre-eclampsia and premature rupture of the membranes.

Burton GJ, Jauniaux E 2017 The cytotrophoblastic shell and complications of pregnancy. Placenta 60:134–9.

Burton GJ, Jauniaux E, Watson AL 1999 Maternal arterial connections to the placental intervillous space during the first trimester of human pregnancy; the Boyd Collection revisited. Am J Obstet Gynecol 181:718–24.

Using hysterectomy specimens from the Boyd anatomy collection, this study shows that the maternal circulation to the placenta must be extremely sluggish before the eighth week of pregnancy, supporting the concept that development of the human fetoplacental unit during most of the first trimester takes place in a low-oxygen environment.

Burton GJ, Watson AL, Hempstock J et al 2002 Uterine glands provide histiotrophic nutrition for the human fetus during the first trimester of pregnancy. J Clin Endocrinol Metab 87:2954–9.

The first study to demonstrate that the uterine glands are an important source of nutrients during organogenesis, when metabolism is essentially anaerobic. Uterine glands remain active until at least week 10 of pregnancy, and their secretions are delivered freely into the placental intervillous space, supporting the concept of histiotrophic nutrition as opposed to hemochorial nutrition.

Burton GJ, Skepper JN, Hempstock J et al 2003 A reappraisal of the contrasting morphological appearances of villous cytotrophoblast cells during early human pregnancy; evidence for both apoptosis and primary necrosis. Placenta 24:297–305.

Burton GJ, Jauniaux E, Charnock-Jones DS 2007 Human early placental development: potential roles of the endometrial glands. Placenta 28 (Suppl A):S64–9.

Burton GJ, Woods AW, Jauniaux E et al 2009 Rheological and physiological consequences of conversion of the maternal spiral arteries for uteroplacental blood flow during human pregnancy. Placenta 30:473–82.

Burton GJ, Jauniaux E, Chernock-Jones DS 2010 The influence of the intrauterine environment on the human placental development. Int J Dev Biol 54:303–12.

Burton GJ, Jauniaux E, Murray AJ 2017 Oxygen and placental development; parallels and differences with tumour biology. Placenta 56:14–18.

Callen PW 2008 Amniotic fluid volume: its role in fetal health and disease. In: Callen PW (ed) Ultrasonography in Obstetrics and Gynecology, 5th ed. Philadelphia: Saunders; Ch. 20, pp. 758–79.

Chai M, Walker SP, Riley C et al 2013 Effect of supracervical apposition and spontaneous labour on apoptosis and matrix metalloproteinases in human fetal membranes. Biomed Res Int 2013:316146.

Chamley LW, Chen Q, Ding J et al 2011 Trophoblast deportation: just a waste disposal system or antigen sharing? J Reprod Immunol 88:99–105.

Cho CK, Shan SJ, Winsor EJ et al 2007 Proteomics analysis of human amniotic fluid. Mol Cell Proteomics 6:1406–15.

This paper presents an extensive profile of the normal human amniotic fluid proteome and considers the molecular functions of amniotic fluid including the development of biomarkers for pregnancy-associated abnormalities.

Cindrova-Davies T, Jauniaux E, Elliot MG et al 2017 RNA-seq reveals conservation of function among the yolk sacs of human, mouse, and chicken. Proc Natl Acad Sci U S A 114:E4753–61.

DiGiulio DB 2012 Diversity of microbes in amniotic fluid. Sem Fetal Neonatal Med 17:2–11.

Edlow AG, Bianchi DW 2012 Tracking fetal development through molecular analysis of maternal biofluids. Biochim Biophys Acta 1822:1970–80.

Ellery PM, Cindrova-Davies T, Jauniaux E et al 2009 Evidence for transcriptional activity in the syncytiotrophoblast of the human placenta. Placenta 30:329–34.

Fogarty NM, Ferguson-Smith AC, Burton GJ 2013 Syncytial knots (Tenney–Parker changes) in the human placenta: evidence of loss of transcriptional activity and oxidative damage. Am J Pathol 183:144–52.

Fortner KB, Grotegut CA, Ransom CE et al 2014 Bacteria localization and chorion thinning among preterm premature rupture of membranes. PLoS One 9:e83338.

Fukuda MN, Sugihara K 2008 An integrated view of L-selectin and trophinin function in human embryo implantation. J Obstet Gynaecol Res 34:129–36.

Gilbert WM 2017 Amniotic fluid disorders. In: Gabbe SG, Niebyl JR, Simpson JL et al (eds) Obstetrics: Normal and Problem Pregnancies, 7th ed. Philadelphia, PA: Elsevier; Ch. 35.

An overview of amniotic fluid production and absorption.

Gulbis B, Jauniaux E, Cotton F et al 1998 Protein and enzyme pattern in the fluid cavities of the first trimester human gestational sac: relevance to the absorptive role of the secondary yolk sac. Mol Hum Reprod 4:857–62.

A study demonstrating that the secondary yolk sac membrane is an important zone of transfer between the extra-embryonic and embryonic compartments and suggesting that therapeutic protocols making use of fetal somatic gene therapy could be performed by injecting transduced cells into the exocoelomic cavity.

Gutierrez-Marcos JF, Constância M, Burton GJ 2012 Maternal to offspring resource allocation in plants and mammals. Placenta 33 (Suppl 2):e310.

Harirah HM, Borahay MA, Zaman W et al 2012 Increased apoptosis in chorionic trophoblasts of human fetal membranes with labor at term. Int J Clin Med 3:136–42.

Harris LK 2010 Review: Trophoblast-vascular cell interactions in early pregnancy: how to remodel a vessel. Placenta 31 (Suppl):S93–8.

Harteman JC, Nikkels PGJ, Benders MJNL et al 2013 Placental pathology in full-term infants with hypoxic-ischemic neonatal encephalopathy and association with magnetic resonance imaging pattern of brain injury. J Pediatr 163:968–95.

Hoyme H, Manning M 2017 Fetal and neonatal injury as a consequence of maternal substance abuse. In: Stevenson D, Benitz W, Sunshine P et al (eds) Fetal and Neonatal Brain Injury. Cambridge: Cambridge University Press. pp. 135–61.

Hung TH, Skepper JN, Burton GJ 2001 In vitro ischemia–reperfusion injury in term human placenta as a model for oxidative stress in pathological pregnancies. Am J Pathol 159:1031–43.

Huppertz B, Weiss G, Moser G 2014 Trophoblast invasion and oxygenation of the placenta: measurements versus presumptions. J Reprod Immunol 101–2:74–9.

Jauniaux E, Gulbis B 2000a Fluid compartments of the embryonic environment. Hum Reprod Update 6:268–78.

This paper reviews the composition, biology and role of the extraembryonic coelomic or chorionic fluid cavity and its connections with the secondary yolk sac and developing placenta during the first trimester of human pregnancy.

Jauniaux E, Gulbis B 2000b In vivo investigation of placental transfer early in human pregnancy. Eur J Obstet Gynecol Reprod Biol 92:45–9.

Jauniaux E, Englert Y, Vanesse M et al 1990 Pathologic features of placentas from singleton pregnancies obtained by in vitro fertilization and embryo transfer. Obstet Gynecol 76:61–4.

Jauniaux E, Jurkovic D, Henriet Y et al 1991 Development of the secondary human yolk sac: correlation of sonographic and anatomic features. Hum Reprod 6:1160–6.

Jauniaux E, Gulbis B, Burton GJ 2003 The human first trimester gestational sac limits rather than facilitates oxygen transfer to the foetus: a review. Placenta (Suppl A)24:S86–93.

Jauniaux E, Cindrova-Davies T, Johns J et al 2004 Distribution and transfer pathways of antioxidant molecules inside the first trimester human gestational sac. J Clin Endocrinol Metab 89:1452–8.

Jauniaux E, Hempstock J, Teng C et al 2005 Polyol concentrations in the fluid compartments of the human conceptus during the first trimester of pregnancy: maintenance of redox potential in a low oxygen environment. J Clin Endocrinol Metab 90:1171–5.

Jauniaux E, Poston L, Burton GJ 2006 Placental-related diseases of pregnancy: involvement of oxidative stress and implications in human evolution. Hum Reprod Update 12:747–55.

Jauniaux E, Collins S, Burton GJ 2018 Placenta accreta spectrum: pathophysiology and evidence-based anatomy for prenatal ultrasound imaging. Am J Obstet Gynecol 218:75–87.

Jones CPJ, Jauniaux E 1995 Ultrastructure of the materno-embryonic interface in the first trimester of pregnancy. Micron 2:145–73.

Koch FR, Wagner CL, Jenkins DD et al 2014 Sex differences in cerebral blood flow following chorioamnionitis in healthy term infants. J Perinatol 34:197–202.

Makieva S, Giacomini E, Ottolina J et al 2018 Inside the endometrial signalling subway: mind the gap(s). Int J Mol Sci 19, 2477; doi: 10.3390/ijms19092477.

A study that considers endometrial communication and signalling.

Murphy BE, Clark SJ, Donald IR et al 1974 Conversion of maternal cortisol to cortisone during placental transfer to the human fetus. Am J Obstet Gynecol 118:538–41.

Myatt L, Sun K 2010 Role of fetal membranes in signaling of fetal maturation and parturition. Int J Dev Biol 54:545–53.

Roescher AM, Timmer Erwich JJ, Bos AF 2014 Placental pathology, perinatal death, neonatal outcome, and neurological development: a systematic review. PloS One 9:e89419.

Ross MG, Beall MH 2014 Amniotic fluid dynamics. In: Creasy R, Resnik R, Iams JD et al (eds) Saunders' Materna–Fetal Medicine: Principles and Practice, 7th ed. Philadelphia: Elsevier, Saunders; Ch. 3, pp. 47–52.

This chapter provides an overview of the production, circulation and absorption of amniotic fluid during gestation.

Ross EJ, Graham DL, Money KM et al 2015 Developmental consequences of fetal exposure to drugs: what we know and what we still must learn. Neuropsychopharmacology 40:61–87.

Stegmann BJ, Carey JC 2002 TORCH Infections. Toxoplasmosis, Other (syphilis, varicella-zoster, parvovirus B19), Rubella, Cytomegalovirus (CMV), and Herpes infections. Curr Womens Health Rep 2:253–8.

Strauss JF 2013 Extracellular matrix dynamics and fetal membrane rupture. Reprod Sci 20:140–53.

This paper presents the composition and biomechanical properties of the fetal membrane extracellular matrix. It considers the changes in extracellular matrix composition during normal pregnancy and term delivery and those seen in preterm premature rupture of membranes.

Suri S, Muttukrishna S, Jauniaux E 2013 2D-ultrasound and endocrinologic evaluation of placentation in early pregnancy and its relationship to fetal birthweight in normal pregnancies and pre-eclampsia. Placenta 34:745–750.

Takashina S, Ise H, Zhao P et al 2004 Human amniotic epithelial cells possess hepatocyte-like characteristics and functions. Cell Struct Funct 3:13–84.

Tong X 2013 Amniotic fluid may act as a transporting pathway for signalling molecules and stem cells during the embryonic development of amniotes. J Chin Med Assoc 76:606–10.

This paper considers the bi-directional substance exchange between amniotic fluid and fetal tissues, its role in transporting signaling molecules and the dynamic nature of amniotic fluid throughout pregnancy.

Tong X, Wang L, Gao T et al 2009 Potential function of amniotic fluid in fetal development – novel insights by comparing the composition of human amniotic fluid with umbilical cord and maternal serum at mid and late gestation. J Chin Med Assoc 72:368–73.

Turco MY, Gardner L, Hughes J et al 2017 Long-term, hormone-responsive organoid cultures of human endometrium in a chemically defined medium. Nat Cell Biol 19:568–77.

Ullberg U, Sandstedt B, Lingman G 2001 Hyrtl's anastomosis, the only connection between the two umbilical arteries. A study in full term placentas from AGA infants with normal umbilical artery blood flow. Acta Obstet Gynecol Scand 80:1-6.

Vanderhoeven JP, Bierle CJ, Kapur RP et al 2014 Group B streptococcal infection of the choriodecidua induces dysfunction of the cytokeratin network in amniotic epithelium: a pathway to membrane weakening. PLoS Pathog 10:e1003920.

Vento-Tormo R, Efremova M, Botting RA et al 2018 Single-cell reconstruction of the early maternal–fetal interface in humans. Nature 563:347–353.

Wynn JL, Neu J 2012 The neonatal gastrointestinal tract as a conduit to systemic inflammation and developmental delays. In: Neu J Gastroenterology and Nutrition: Neonatology Questions and Controversies, 2nd ed. Philadelphia: Elsevier, Saunders; Ch. 19, pp. 293–304.

Zhang Y, Wang Y, Want X et al 2018 Crosstalk between human endometrial stromal cells and decidual NK cells promotes decidualization *in vitro* by upregulating IL-25. Mol Med Rep 17:2869–78.

CHAPTER

10

Cell populations at gastrulation

CONCEPTUS WITH A BILAMINAR EMBRYONIC DISC

At stage 6 the conceptus is composed of the walls of three cavities. The large chorionic cavity is surrounded by a meshwork of trophoblast and developing villi, and lined with extraembryonic mesoblast. The chorion, trophoblast and extraembryonic mesoblast enclose the extraembryonic coelom and contain the much smaller amniotic cavity and yolk sac that abut at the embryonic bilaminar disc where the epithelial epiblast and visceral hypoblast are approximated (see Fig. 9.1). A fourth cavity, the allantois, will form as a hypoblastic diverticulum in stage 7. The 'bilaminar disc' commonly referred to in embryology texts does not yet possess the definitive layers of embryonic ectoderm and endoderm that will give rise to embryonic structures. Only the epiblast will give rise to the embryo and all other layers produced so far are extraembryonic. The amnion and chorion and surrounding extraembryonic mesoblast are part of the extraembryonic somatopleure, whereas the yolk sac, allantois and surrounding extraembryonic mesoblast constitute extraembryonic splanchnopleure. At the junctional zone surrounding the margins of the embryonic area, where the walls of the amnion and yolk sac converge, the somatopleuric and splanchnopleuric layers of extraembryonic mesoblast are continuous.

The terms epiblast and hypoblast are used to make the distinction between the earliest bilaminar disc layers and the later embryonic layers. Epiblast and hypoblast contain mixed populations of cells with little restriction, that establish the placental structures and extraembryonic tissues before the production of embryonic cell lines at gastrulation. The older terminology depicting three germ layers that give rise to the skin, gut lining and intervening tissues is therefore incorrect for the bilaminar and trilaminar embryonic disc. The persistent application of this terminology to descriptions of the early stages of embryogenesis continues to cause confusion and restricts the development of more pertinent language to describe these early events. The earliest three cell lineages, not layers, that give rise to the extraembryonic membranes and the embryo are trophoblast, hypoblast and epiblast (Ch. 8) and each expresses different lineage-specific genes for its establishment, maintenance and differentiation (Pfeffer 2018, Stirparo et al 2018).

At early stage 6 the epiblast is producing extraembryonic mesenchyme from its caudal margin. With the appearance of the primitive streak, a process is started whereby cells of the epiblast pass either deep to the epiblast layer to form the populations of cells within the embryo, or remain on the dorsal aspect of the embryo to become the embryonic ectoderm. Although human embryos do not form a 'gastrula' as such, the term gastrulation is used here to denote an early period of development during which significant rearrangements, migrations and folding of the early embryo occur. The primitive streak is the site of organizer cells analogous to those found in embryos that do undergo gastrulation. The appearance of the primitive streak therefore marks the beginning of a period when gross alterations in morphology and complex rearrangements of cell populations occur. During this time, the epiblast will give rise to a complex multilaminar structure with a defined craniocaudal axis. By the end of gastrulation, cell populations from different, often widely separated, regions of the embryonic disc will become spatially related and the embryonic shape will have been produced.

Primitive streak and node

Seen from the dorsal (epiblastic) aspect at stage 6, the embryonic disc appears elongated. At this stage the primitive streak is first seen in the caudal region of the embryonic disc as a collection of pluripotent cells, orientated along its long axis in the median position and conferring the future craniocaudal axis of the embryo (**Figs 10.1–10.2**). Although the future rostral (cranial) and caudal regions of the embryo are well within the boundaries of the embryonic disc, it has become the practice to term the region of the disc closest to the streak 'caudal', and the region of the disc furthest from the streak 'rostral'. With the development of the streak, the terms medial and lateral can be used. The relative dimensions of the primitive streak and the fates of the cells that pass through it change with the developmental stage. Thus, the streak extends half way along the disc in the stage 6 embryo, reaching its greatest relative length in stage 7 and its maximum length in stage 8.

Formation of the primitive streak is induced by the underlying visceral hypoblast, which remains beneath the streak even at later stages. The primitive streak may be considered to be generally homologous with the blastopore of lower vertebrates (e.g. amphibia), with the nodal region corresponding to the dorsal lip. Experiments clearly show the lip of the blastopore to be a dynamic wave front on which cells are carried into the interior to form the roof of the archenteron, a situation analogous to ingression through the node of the prechordal plate and endoderm. The primitive streak similarly may be considered analogous to the coapted, or fused, lateral lips of the blastopore, and the cloacal membrane and its immediate environs are considered analogous to the ventral lip of the blastopore.

At the primitive streak, epiblast cells undergo a period of intense proliferation, the rate of division being much faster than that of blastomeres during cleavage. Streak formation is associated with the local production of several cell layers, extensive disruption of the epiblast basal lamina: increase in adhesive plaques and gap junctions; synthesis of vimentin; and loss of cytokeratins by the emerging cells.

As the epiblast cells proliferate, two ridges are formed on each side of the primitive streak, which appears to sink between them. The lower midline portion of the streak is termed the primitive groove. The process by which cells become part of the streak and then migrate away from it beneath the epiblast is termed ingression and is an example of epithelial to mesenchymal transformation.

The primitive node, or Hensen's node, is the most rostral region of the primitive streak. It appears as a curved ridge of cells similar in shape to the top of an old-fashioned keyhole. Cells ingressing from the ridge pass into the primitive pit (the most rostral part of the primitive groove), and then migrate rostrally beneath the epiblast. The primitive node has been recorded in all stage 7 human embryos; it produces axial cell populations, the prechordal plate, notochord, embryonic endoderm and the medial halves of the somites. Experimental removal of the node in avian embryos results in complete absence of the notochord and a failure of neurulation.

Studies on the dynamics of ingression at the primitive streak have shown movement of the underlying extracellular tissues as well as of the overlying cells. Re-examination of the processes of cell movement relative to the surrounding extracellular molecules in embryos has found that vertical and convergent extension motion patterns, previously thought to be limited to the epiblast, also occur in sub-epiblastic extracellular matrix fibronectin fibrils (Zamir et al 2008, Szabó et al 2011).

Position and time of ingression through the primitive streak

Studies of cell fate have shown that epiblast cells that will pass through the streak are randomly located within the epiblast layer before their ingression, and that epiblast fate is determined at or before the time of ingression through the streak, indicating that passage through the primitive streak is the most important factor for future differentiation.

The position and time of ingression through either streak or node directly affect the developmental fate of cells. Passage through the streak is specified according to time and position, e.g. via the node, or rostral, middle or caudal regions of the streak. Cells that ingress through the primitive node give rise to the axial cell lines, the prechordal mesenchyme and notochord, and the endoderm and the medial halves of the somites. The rostral portion of the primitive streak produces cells for the lateral halves of the somites, whereas the middle streak produces the lateral plate mesoblast. The adjacent caudal portion of the streak gives rise to the primordial germ cells (which can be distinguished histologically and histochemically) and the most caudal portion of the streak contributes cells to the extraembryonic mesoblast until the somites are visible. A composite of the information on the position of ingression through the streak and node is shown in **Fig. 10.3**. Epiblast cells that do not pass through the streak but remain within the epiblast population give rise to the neural and surface ectoderm of the embryo.

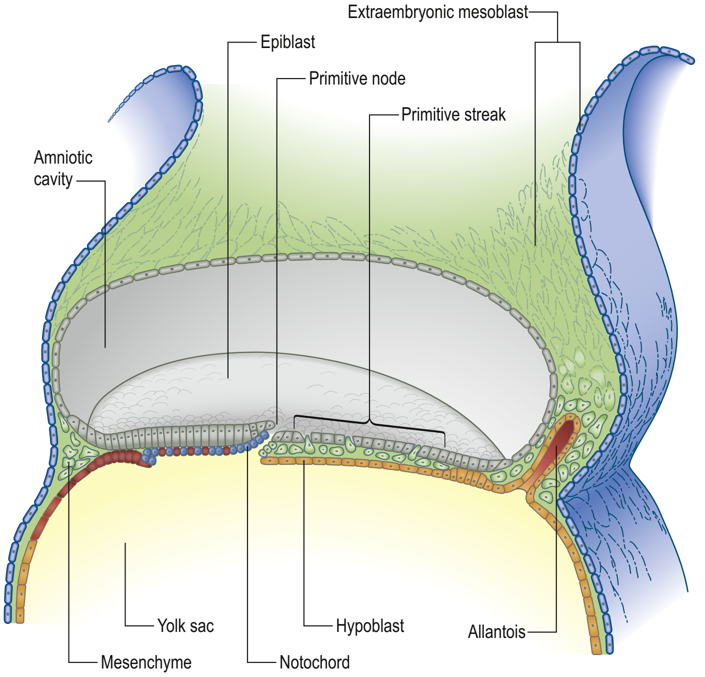

Fig. 10.1 A longitudinal section through an early conceptus. Ingression of mesoblast is occurring at the primitive streak and the notochord is ingressing via the primitive (Hensen's) node.

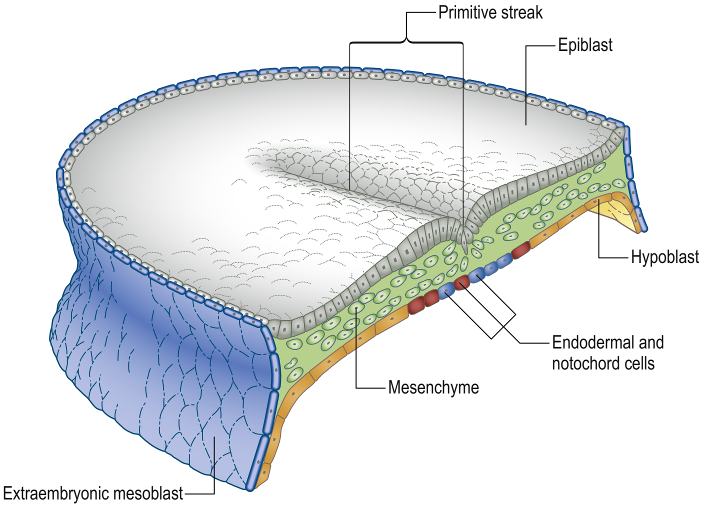

Fig. 10.2 A transverse section through the embryonic plate at the level of the primitive streak to show the early movement of mesoblast between the epiblast and underlying hypoblast.

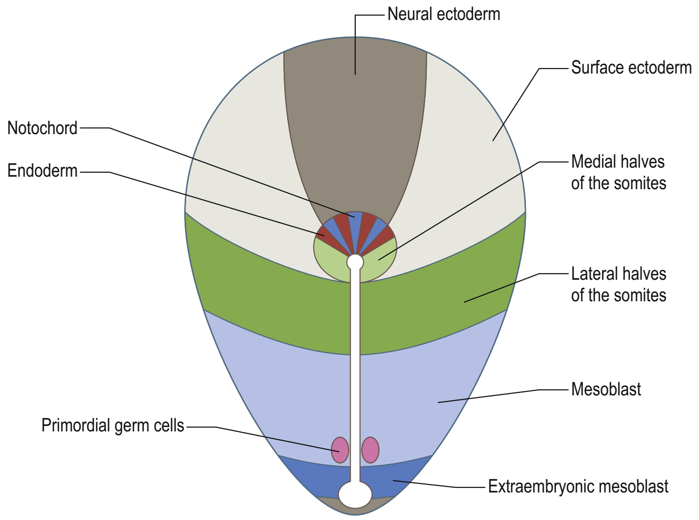

Fig. 10.3 The predictive fates of the epiblast cell population at the time the primitive streak is present.

Prechordal plate

The earliest cells migrating through the primitive node and streak give rise to both the embryonic endoderm and the notochord. The prechordal plate is first seen at stage 7. It has been defined as a localized thickening of the endoderm rostral to the notochordal process, although it is seen as a highly developed mesenchymal mass in contact with the floor of the neural groove, rostral to the notochordal process, rather than as an epithelial layer. The prechordal plate is a temporary collection of cells that underlies the neural plate during stage 9. It is composed of cells that are similar to, or larger and more spherical than, the ingressing endodermal cells (Müller and O'Rahilly 2003). In stage 8 embryos, the prechordal plate is up to eight cells deep and extends along the long axis of the embryonic disc. By stages 9 and 10 the cells at the lateral edge of the plate have begun to migrate laterally as free mesenchymal cells and the plate reduces in height to two cells deep. At stage 11 the migrating prechordal mesenchyme forms bilateral premandibular mesenchymal condensations and is no longer a median structure. The extent of prechordal cells that remain within the endoderm has yet to be established.

Notochord

The notochord (chordamesoderm, the head process or chorda) arises from epiblast cells of the medial part of the primitive node. It passes through several stages during development, i.e. notochordal process and notochordal plate, before the definitive notochord is formed (de Bree et al 2018). The cells of the early notochordal process express myogenic markers transiently as they migrate beneath the epiblast, but later they become epithelial, forming junctions and a basal lamina. The notochordal cells are intimately mixed with endodermal cells, because both cell lines ingress synchronously (see Figs 10.1–10.2; Fig. 10.4). During stage 8 the ingressing notochordal cells remain in the midline along the cephalocaudal axis. They form a rostral part composed of a cell mass continuous with the prechordal mesenchyme; a mid-portion in which cells are arranged in a tube with a central notochordal canal; and a caudal epithelial layer of cells, the notochordal plate, contiguous with the embryonic endoderm, which forms a roof to the secondary yolk sac. There is a transitory opening between the primitive node (and amniotic cavity) and the secondary yolk sac called the neurenteric canal (so named because its upper opening is in the future caudal floor of the neural groove, and its lower opening is into the archenteron, which is the primitive gut). It may still be found at stage 9 and the site of the neurenteric canal can be recognized in stage 10 embryos. The ingression of notochordal cells at the primitive node is matched by specification of the overlying neural ectodermal cells, and the notochordal plate is thus matched in length by the future neural floor plate. Both the notochord and the region of the floor plate of the neural tube may arise from a common progenitor cell. The early notochord is important for the maintenance and subsequent development of the neural floor plate and the induction of motor neurones. Experimental removal of the notochord results in elimination of the neural floor plate and motor neurones and expression of sensory neurones.

Caudal eminence

From stages 9–10 the region between the neurenteric canal and the cloacal membrane (see below), including the primitive streak, is termed the caudal eminence. It consists of the caudal region of the trunk, composed of mesenchyme derived from the primitive streak and epiblast, and covered with surface ectoderm. Whereas ingression of cells through the primitive streak gives rise to the prechordal and notochordal plates, and cells rostral to the neurenteric canal (see above), the cells of the caudal eminence arise from local division of a mesenchymal population positioned caudal to the neurenteric canal. The caudal portions of the notochord, that form later in development when secondary neurulation processes begin, arise from these cell populations, sometimes termed the caudoneural hinge or junction. This tissue is thicker and more advanced in differentiation than the tissues derived from the early primitive streak.

Embryonic endoderm

Before ingression, definitive embryonic endoderm cells are found in the epiblast, located at the primitive node and rostral primitive streak. In the mouse, the endodermal cells lie beneath the epiblast mainly in the midline, interspersed with presumptive notochordal cells, forming the roof of the secondary yolk sac. The ingressing endoderm displaces the visceral hypoblast into the secondary yolk sac wall by a dramatic

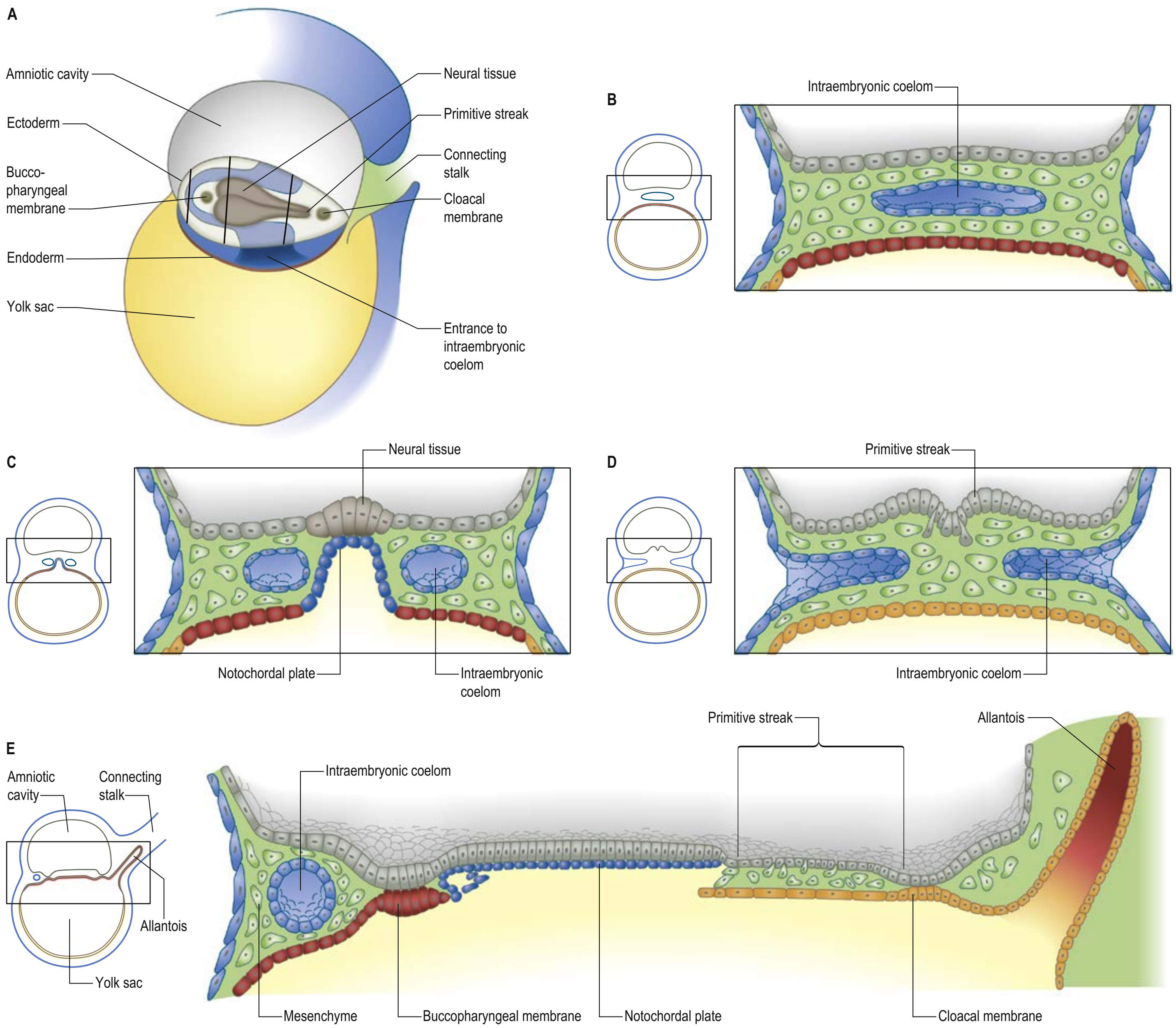
A
Amniotic cavity
Ectoderm
Bucco-
pharyngeal
membrane
Endoderm
Yolk sac
Neural tissue
Primitive streak
Connecting
stalk
Cloacal
membrane
Entrance to
intraembryonic
coelom
B
Intraembryonic coelom
C
Neural tissue
Notochordal plate
Intraembryonic
coelom
D
Primitive streak
Intraembryonic coelom
E
Amniotic
cavity
Connecting
stalk
Allantois
Yolk sac
Intraembryonic coelom
Primitive streak
Allantois
Mesenchyme
Buccopharyngeal membrane
Notochordal plate
Cloacal membrane

Fig. 10.4 **A**, The unfolded embryo, showing the disposition of the intraembryonic coelom within the embryonic disc. The three lines across the embryo show the level of transverse sections through the disc shown in **B–D**. **E**, A longitudinal section through the disc.

territorial expansion that is brought about by a change in the morphology of the cells (see Figs 10.1–10.2, 10.4). The putative endoderm cells are cuboidal epithelial cells within the node but they become squamous in the endoderm layer; this could result in a four-fold increase in the surface area covered by the cells. A complete replacement of the visceral hypoblast has not yet been confirmed and there may be a mixed population of cells in the endodermal layer in the early stages. Ingression of cells through the streak and node in the human is apparent at stage 6 and, by stage 7, a population of endoderm and notochord cells is present beneath the epiblast (see Figs 10.1–10.2, 10.4). During stages 6–11 the midline roof of the secondary yolk sac becomes populated mainly by the notochordal plate, which remains in direct lateral continuity with the endodermal cells. It is not until stage 11, after the definitive notochord is formed, that the endoderm cells can join across the midline. For the developmental fate of the embryonic endoderm, see Fig. 12.3.

Intraembryonic mesoblast (mesenchyme)

Epiblast cells undergo a transformation of cell phenotype from stage 8, ingressing through the rostral and middle parts of the streak individually, maintaining their apical epithelial contacts while elongating ventrally. The cells become flask-shaped, with thin, attenuated apical necks and broad basal regions. Their basal and lateral surfaces form lamellipodia and filopodia, and their adjacent apical contacts are released. The cells are now free mesoblast cells, their fibroblastic, stellate morphology reflecting their withdrawal from the epithelial layer. Once through the streak, the cells secrete an extracellular matrix that surrounds and separates them. The cells contact one another by filopodia and lamellipodia, with which they also contact the basal lamina of the overlying epiblast, using it for their subjacent migration. Gap junctions have been observed between filopodia and cell bodies. With the generation of mesoblast cells and their secretion of an extracellular matrix rich in glycosaminoglycans, spaces form between the epiblast and visceral hypoblast through which the mesoblast cells can move. Groups of mesoblast cells open up migration routes and the following cells seem to be pulled along behind in a coordinated mass movement. Mesoblast formed by cells migrating through the primitive node and rostral primitive streak forms the paraxial mesenchyme, whereas cells migrating later through the middle to caudal streak form the lateral plate mesenchyme (see Figs 10.1–10.2). Tissue motion of cell and extracellular matrix movement from the primitive streak has been elegantly demonstrated in avian embryos (Loganathan et al 2016).

Embryonic ectoderm

When the ingression of cells through the primitive streak is complete, the epithelial cells remaining in the epiblast layer are termed embryonic ectoderm cells. This layer still contains a mixed population because both surface ectoderm cells and neural ectoderm cells are present. It is believed that these cells were originally in the rostral half of the disc when the primitive streak first appeared, at which time the neural-fated cells were closest to the streak, and the surface ectoderm cells were most rostral (see Fig. 10.3). The process of primary neurulation relocates most of the neuroepithelial cells (see below).

Primordial germ cells

Although early studies on human embryos reported primordial germ cells, and described their development from the early endoderm of the yolk sac and allantois, results from animal experimentation indicate that primordial germ cells arise from epiblast ingressing at the caudal end of the primitive streak (see Fig. 10.3). It is not known whether these cells originate from rostral regions that migrate to the streak or from local caudal regions. Extremely early segregation of the germ cells, when the epiblast layer consists of only 10–13 cells, has been demonstrated and it has been suggested that the primordial germ cells remain sequestered in the extraembryonic mesenchyme at the caudal end of the embryo until the embryonic endoderm has been produced and gastrulation completed, and that they start to migrate along the allantoic and hindgut endoderm as the folding of the embryo begins. The formation of the tail fold brings the proximal portion of the allantois within the body, so reducing the final distance over which the cells migrate to the genital ridges. Further development of the germ cells is described in Chapter 22.

TRILAMINAR DISC

Although the stage 8 embryo is termed a trilaminar disc, the concept of three epithelial layers forming a trilaminar disc is not correct because the middle, mesoblast, layer is several cells thick with intervening extracellular matrix. The embryo at this stage, approximately 23 days after ovulation, is pear-shaped, and broader rostrally than caudally (**Fig. 10.5**). The upper epiblast cells are tall and form a pseudostratified columnar epithelial layer with a basal lamina, except at the primitive streak, where the cells are ingressing to form the other layers. The more centrally placed epiblast will give rise to neural ectoderm (neurectoderm) and the more laterally placed epiblast will give rise to surface ectoderm. The future neural ectoderm is seen as a neural plate that matches the length of the notochordal plate directly beneath, being slightly wider near the prechordal plate. The lower embryonic endoderm, a simple squamous layer with a developing basal lamina, is not always complete at this stage, particularly in the midline caudal to the prechordal plate, which is still occupied by the notochordal process or plate.

The middle, mesoblast, layer is composed of free cells migrating rostrally, laterally and caudally from the primitive streak and producing extracellular matrix: it separates the epiblast and endoderm of the embryonic area and permits their migration (see Fig. 10.4). The streams of mesoblast extend between the epiblast and endoderm throughout all of the disc area except rostrally at the buccopharyngeal membrane (where the endoderm and ectoderm become apposed once the prechordal mesenchyme has migrated laterally), and caudally at the cloacal membrane (a patch of thickened endoderm, similar to the buccopharyngeal membrane, caudal to the primitive streak). The mesoblast on each side of the notochord is termed paraxial mesenchyme.

Mesoblast that passes in a rostral direction flanks the notochordal plate and passes around the prechordal plate region, converging medially to fuse in the midline beyond its rostral border. This transmedian mass, in which the heart and pericardium will develop, is initially termed the cardiogenic mesoblast. It fuses with the junctional zone of extraembryonic mesoblast around the extreme cephalic margin of the embryonic area. This region will eventually form the septum transversum and primitive ventral mesentery of the foregut. Mesoblast passing laterally from the streak soon approaches and becomes confluent with the extraembryonic mesoblast around the margins of the disc, i.e. at the junctional zone where the splanchnic and somatic strata of extraembryonic mesoblast merge. Mesoblast that streams caudally from the primitive streak skirts the margins of the cloacal membrane and then converges towards the caudal midline extremity of the embryonic disc to become continuous with the extraembryonic mesoblast of the connecting stalk. It is unclear if the lower layer of the cloacal membrane consists of visceral hypoblast, like the more rostral primitive streak (the hypoblast is necessary for maintaining the streak), or if it is replaced by migrating embryonic endoderm, or if there is a region for ingression of endoderm at the caudal end of the streak, similar to the node rostrally.

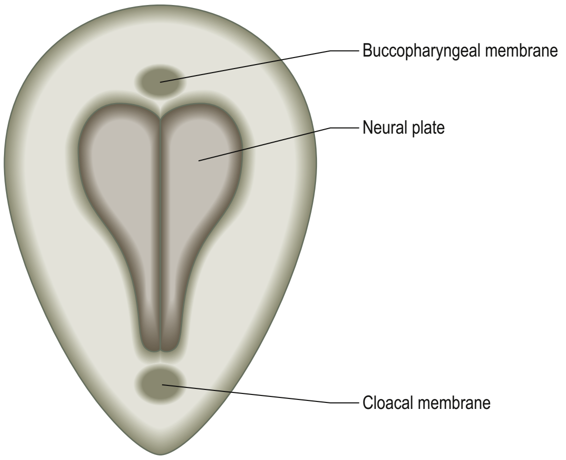

Fig. 10.5 The extent and shape of the neural plate in an unfolded embryo.

Still further caudally, the embryonic disc develops a midline diverticulum adjacent to the cloacal membrane. This diverticulum, the allantois, projects into the extraembryonic connecting stalk (see Figs 9.10, 10.4; **Fig. 10.6**). It is unclear whether the allantois is composed of visceral hypoblast, parietal hypoblast or embryonic endoderm. The allantois later develops a rich anastomotic blood supply around it, in the manner of the yolk sac.

The generation of cells at the primitive node produces midline endoderm, notochord and the floor plate of the future neural tube. As the notochord grows and elongates, there is a matched growth of neural floor plate cells until both cell lines extend to the buccopharyngeal membrane. The epiblast lateral to the midline contains both future surface and neural ectoderm. The latter becomes arranged between the primitive node and buccopharyngeal membrane; cells destined to be in the neural plate lie medially, and those destined for the neural crest lie along the junction between the neural plate and surface ectoderm (see Fig. 10.5). A smaller subpopulation of neuronal cells, the ectodermal placodes, are arranged either close to the neural crest or within the rostral limit of the neural plate itself.

FOLDING OF THE EMBRYO

In a diagrammatic representation of the trilaminar disc prior to folding and viewed from the ectodermal aspect, all of the future external surface of the body is delimited (see Fig. 10.5). The ends of the gut tube are specified on the ectodermal surface at the buccopharyngeal and cloacal membranes, regions where the ectoderm and underlying endoderm are apposed without intervening mesoblast. In the midline between these membranes, proliferation of the neural ectoderm matches the underlying migration of mesoblast from the primitive streak, so that the neural plate covers the paraxial mesenchyme on each side of the notochord (see Fig. 10.6E). As the paraxial mesenchyme segments, the formation of the epithelial somites elevates the edges of the neural plate and initiates primary neurulation (see Fig. 10.6F; **Figs 10.7–10.8**). The neural plate itself undergoes concurrent morphological changes. The most medial cells become wedge-shaped, forming the neural groove. Further elevation of the edges of the neural groove permits fusion of the neuronal populations in the dorsal midline to form the neural tube. The surface ectoderm forms the putative dorsal epidermis (see Figs 10.6G, 10.7–10.8). Cells at the lateral edge of the neural plate, neural crest cells, remain as a linearly arranged mesenchymal population between these two epithelia. Fusion of the neural tube begins in the future rhombencephalic region of the embryo and proceeds rostrally and caudally to about the level of somite 29. Neurulation is described further in Chapter 14. A population of neural epithelial cells remain within the surface ectoderm and at this stage they are termed ectodermal placodes.

The representation of a person on the trilaminar disc (**Fig. 10.9**) shows, to some extent, the way in which the positions of the main body structures are already specified in the unfolded embryo. Ectoderm lateral to the neural plate and the paraxial mesenchyme will form structures within the back. The portion of the disc between the buccopharyngeal membrane and the edge of the disc will become the ventral thoracic wall and the ventral abdominal wall rostral to the umbilicus. Further caudally, midway along the neural axis, the lateral portions of the disc will become the lateral and ventral abdominal walls of the trunk. The portion of the disc beyond the cloacal membrane will form the ventral abdominal wall caudal to the umbilicus. The circumference of the disc, where the embryonic tissue meets the extraembryonic membranes, will become restricted to the connection between the ventral abdominal wall and the umbilical cord, i.e. the umbilicus.

Head folding begins at stage 9, when the fusing rostral neural plate rises above the surface ectoderm and the portion of the disc rostral to

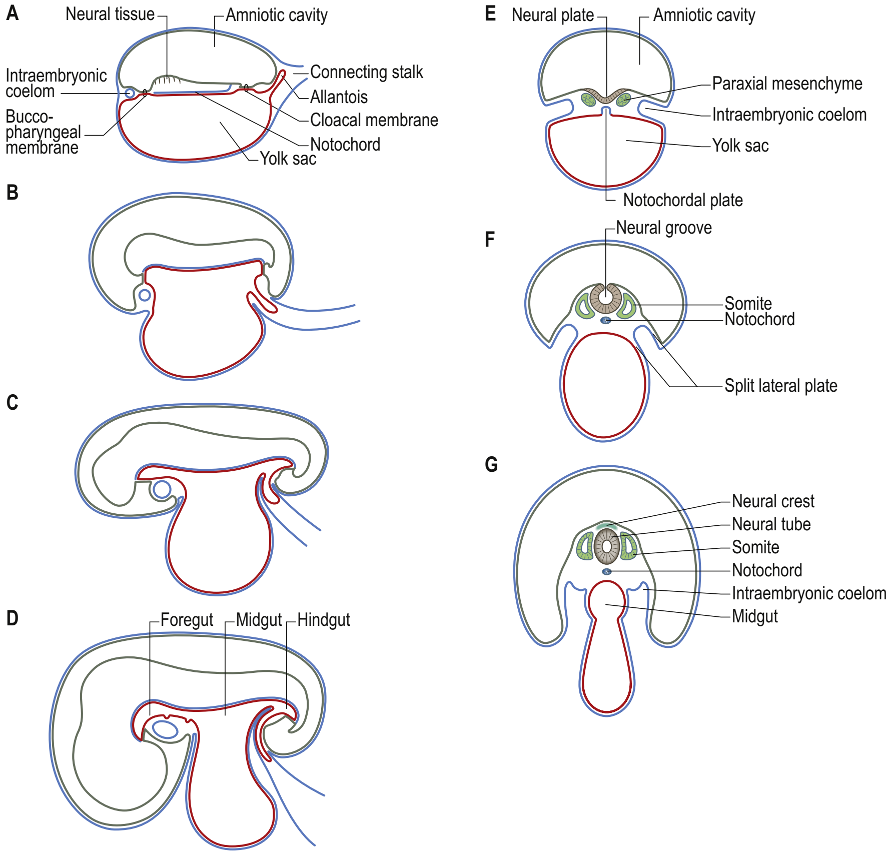

Fig. 10.6 Head and tail (**A–D**) and lateral (**E–G**) folding of the embryo. **A–D**, Median sagittal sections through the embryonic disc at successive stages; the relative positions of the buccopharyngeal and cloacal membranes have been maintained; thus, the movement of the most rostral and caudal portions of the disc can be followed. As these portions of the disc move ventrally, the initially wide-open yolk sac becomes constricted and fore- and hindgut divisions can be seen; the midgut is that region remaining in wide connection to the yolk sac. **E–G**, Transverse sections through the midpoint of the embryonic disc at successive stages to illustrate lateral folding that occurs as neurulation proceeds.

the buccopharyngeal membrane (containing the cardiogenic mesenchyme) moves to lie ventral to the developing brain (see Fig. 10.6). The prosencephalon and buccopharyngeal membrane are now the most rostral structures of the embryo. The previously flat region of endoderm, which may contain cells from the prechordal plate, is now modified into a deep tube, the primitive foregut. Tail folding can be seen in stage 10 embryos, when the entire embryo comes to rise above the level of the yolk sac. Similar movement of the part of the disc caudal to the cloacal membrane results in its repositioning ventral to the neural plate. Generally, as the embryo rises above the edges of the disc, the lateral regions of the disc are drawn ventrally and medially, contributing to the lateral folding of the embryo.

FORMATION OF THE INTRAEMBRYONIC COELOM

At and just before stage 9 (before formation of the head fold), vesicles appear between the mesenchymal cells rostral to the buccopharyngeal membrane and within the rostral lateral plate mesenchyme. At the periphery of the vesicles, the mesenchymal cells undergo mesenchymal to epithelial transformation, developing the apical polarity and junctional complexes typical of the epithelial phenotype. The vesicles become confluent to form a horseshoe-shaped tube, the intraembryonic coelom, that extends caudally to the level of the first somite and laterally into the lateral plate mesenchyme towards the extraembryonic mesenchyme. The lateral plate mesenchyme epithelium subjacent to the ectoderm is termed somatopleuric coelomic epithelium, and that adjacent to the embryonic endoderm is termed splanchnopleuric coelomic epithelium (see Fig. 12.2C(iv)). At this stage, the intra- and extraembryonic coeloms do not yet communicate.

During development of the head fold, the morphological movements that organize the foregut and buccopharyngeal membrane have a similarly profound effect on the shape of the intraembryonic coelom. The midline portion of the originally flat, horseshoe-shaped intraembryonic coelom moves ventrally, leaving the caudal arms of the horseshoe in their original position. In this way, the midline part of the coelom, which was originally just rostral to the buccopharyngeal membrane, comes to lie ventral to the foregut (caudal to the buccopharyngeal membrane), and the two lateral extensions of the coelom pass close to the lateral walls of the foregut on each side. The caudal portions of the coelom (the two arms of the horseshoe), which, in the unfolded disc, communicated laterally with the extraembryonic coelom, turn 90° to lie lateral to the gut, and communicate with the extraembryonic coelom ventrally.

Compartments of the coelom that will give rise to the body cavities later in development can already be seen. The midline ventral portion, caudal to the buccopharyngeal membrane, becomes the pericardial cavity. The canals lateral to the foregut (pericardioperitoneal canals) become the pleural cavities and the uppermost part of the peritoneal cavity. The remaining portion of the coelom becomes the peritoneal cavity. By stage 11 the intraembryonic coelom within the lateral plate mesenchyme extends caudally to the level of the caudal wall of the yolk sac. The intra- and extraembryonic coeloms communicate widely on each side of the midgut along the length of the embryo from the level of the fourth somite (**Fig. 10.10**).

In the early embryo, the intraembryonic coelom provides a route for the circulation of coelomic fluid and, with the beating of the heart tube, functions as a primitive circulation that takes nutritive fluid deep into the embryo until it is superseded by the blood vascular system. The coelomic channel, and the primitive circulation that passes through it, is of paramount importance up to stage 13. Whereas the superficial tissues of the embryo can receive nutrients via the amniotic sac and yolk sac fluids, the deeper tissues are, until the formation of the coelom, under conditions similar to those found in tissue culture. However, from stage 10 exocoelomic fluid, propelled by the first contractions of the developing heart, is brought into contact with the deeply placed mesenchyme. This early 'circulation' ensures that an adequate supply of nutrients reaches the rapidly increasing amount of embryonic tissue, and meets most of the requirements of the deeper mesenchymal derivatives. From stage 12 the endothelial system expands and fills rapidly with plasma, which passes across the locally thinned coelomic epithelium into the large hepatocardiac channels that project into the pericardioperitoneal canals at the level of the seventh somite. Exocoelomic fluid (which is propelled into the intraembryonic coelom) has been collected, via coelocentesis, from the chorionic cavity (see Fig. 10.10)

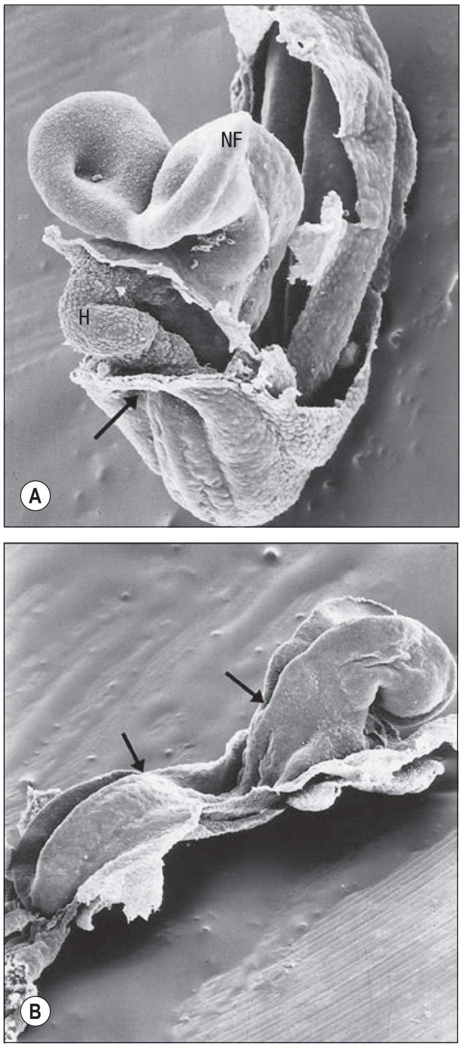

Fig. 10.7 Scanning electron micrographs of rat embryos at the time of neurulation. **A**, Ventral view, showing the neural fold (NF), and the heart (H), with the somatopleuric pericardial membrane and surface ectoderm removed; the arrow indicates the entrance to the foregut via the rostral intestinal portal. **B**, Dorsolateral view; the arrows indicate the extent of rostral (to the right) and caudal (to the left) neural tube formation. (Photographs by P Collins; printed by S Cox, Electron Microscopy Unit, Southampton General Hospital.)

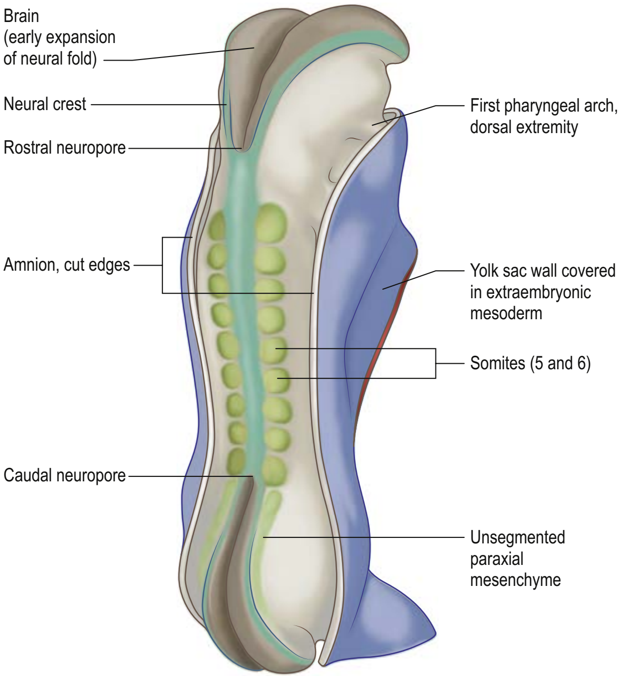

Fig. 10.8 A human embryo at stage 10, 2.1 mm long, with nine somites: right lateral and dorsal aspects. Nearly all the yolk sac and the caudal amnion have been excised.

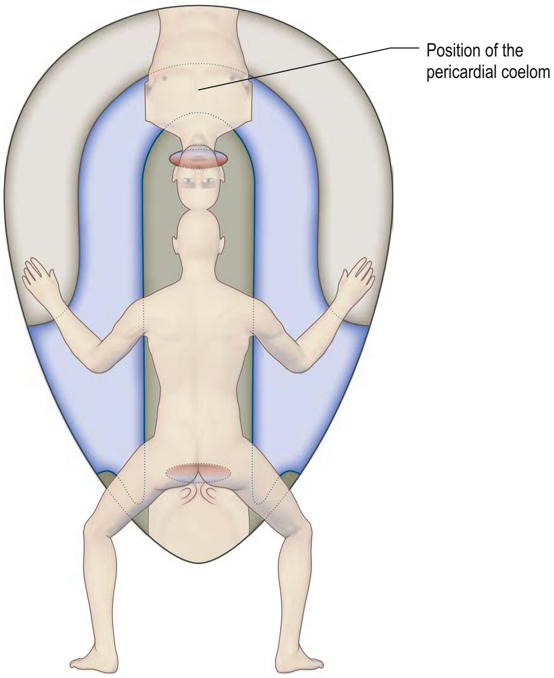

Fig. 10.9 A representation of a person on the flat embryonic disc. The position of the central nervous system has been matched to the dimensions of the neural plate, and the position of the heart in the thorax to the position of the pericardial coelom. The limbs, although represented in this diagram, are not present on the disc at this stage. The usefulness of this diagram lies in its illustration of the extent of the anterior body wall both rostral to the buccopharyngeal membrane and caudal to the cloacal membrane. The future dorsal regions of the body are found medially on the disc, while the ventral regions of the body are situated laterally and peripherally on the disc. After head and tail folding and lateral folding, the peripheral edge of the disc becomes constricted as the edge of the umbilicus.

of embryos at stages 9–14; its total protein content is 54 times higher than that in amniotic fluid, but 18 times lower than in maternal serum (Aiello et al 2018).

In spite of the importance of the coelom in defining the body cavities, and of the coelomic epithelium in the production of the major mesenchymal populations of the trunk (Streeter 1942, Langemeijer 1976, O'Rahilly and Müller 1987) (see Fig. 12.2), until recently the overall contribution of the epithelial coelomic walls to the embryo has received relatively little attention (Carmona et al 2013). The coelom is a single, tubular organ that may be compared to the neural tube, in that it possesses a specialized wall that encloses a cavity. Like neural ectoderm, proliferating coelomic epithelium is a pseudostratified columnar epithelium with a germinal layer displaying interkinetic nuclear migration, matching the timing of the cell cycle, from which cellular progeny migrate. After the germinal phase, which occurs in the fetal period, both epithelia ultimately form the lining of a cavity, ependyma for the neural epithelium, and mesothelium for the coelomic epithelium. Coelomic epithelium, like neural epithelium, produces cells destined for different fates from different sites and at different developmental times. Coelomic cells are like the neural epithelium, in that they have apical epithelial specializations and tapering basal processes that are in direct contact with the underlying mesenchyme, without an intervening basal lamina. The possibility of the tapering processes forming directional signals for migrating progeny, similar to the radial glia of the neural tube, has not been examined.

EMBRYONIC CELL POPULATIONS AT GASTRULATION

After gastrulation, the cells of the embryo contribute to two fundamental types of tissue, epithelia and mesenchyme. Differentiation of specialized circulating blood cells and other cell types occurs in sequence. Embryonic and fetal cell types are replaced later in development or after birth.

Epithelia

Epithelial populations in the embryo have many of the morphological characteristics of differentiated epithelia, i.e. they are composed of

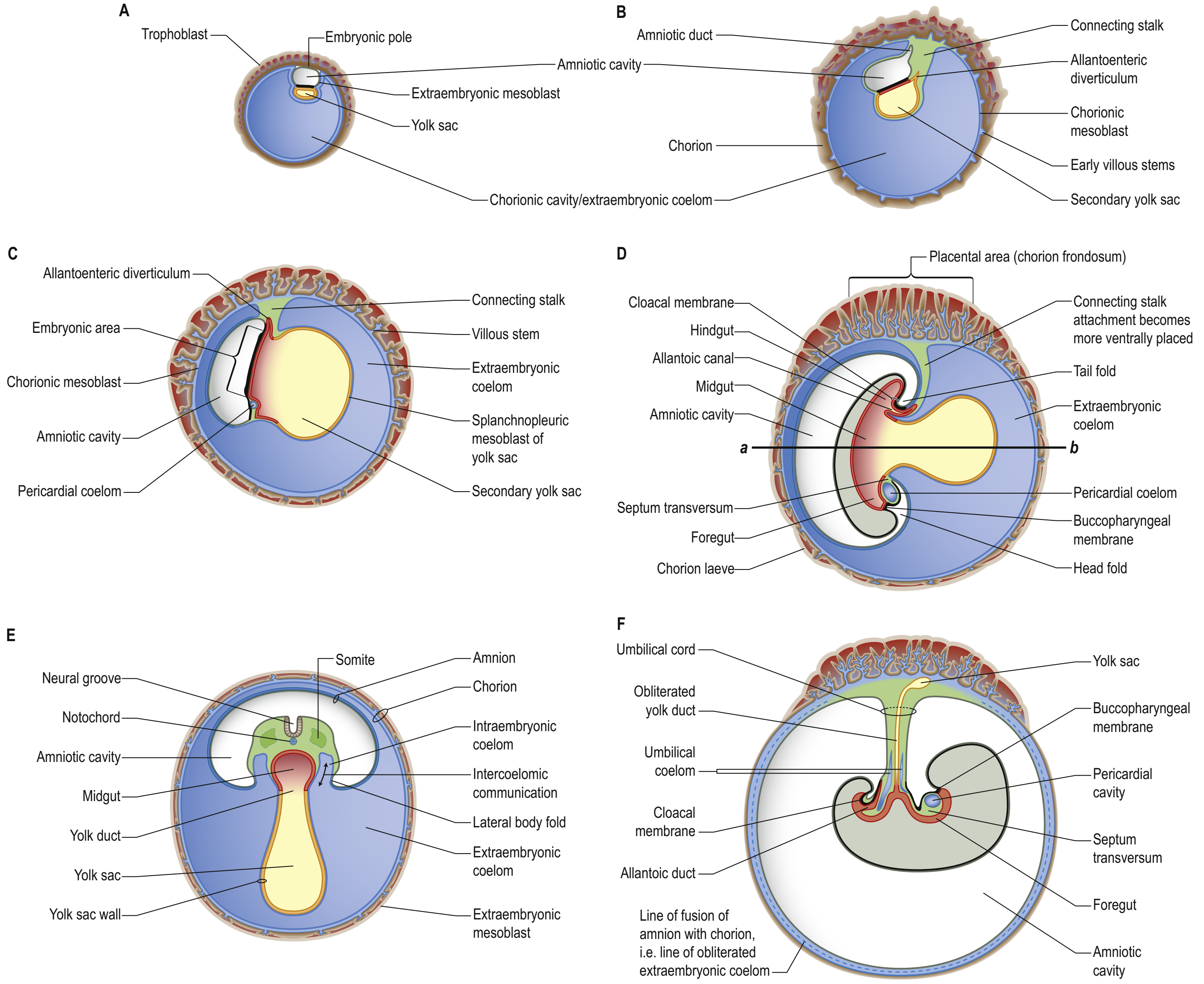
A
Trophoblast
Embryonic pole
Amniotic cavity
Extraembryonic mesoblast
Yolk sac
Chorionic cavity/extraembryonic coelom
B
Amniotic duct
Connecting stalk
Allantoenteric diverticulum
Chorionic mesoblast
Chorion
Early villous stems
Secondary yolk sac
C
Allantoenteric diverticulum
Embryonic area
Chorionic mesoblast
Amniotic cavity
Pericardial coelom
Connecting stalk
Villous stem
Extraembryonic coelom
Splanchnopleuric mesoblast of yolk sac
Secondary yolk sac
D
Placental area (chorion frondosum)
Cloacal membrane
Hindgut
Allantoic canal
Midgut
Amniotic cavity
a
b
Septum transversum
Foregut
Chorion laeve
Connecting stalk attachment becomes more ventrally placed
Tail fold
Extraembryonic coelom
Pericardial coelom
Buccopharyngeal membrane
Head fold
E
Neural groove
Notochord
Amniotic cavity
Midgut
Yolk duct
Yolk sac
Yolk sac wall
Somite
Amnion
Chorion
Intraembryonic coelom
Intercoelomic communication
Lateral body fold
Extraembryonic coelom
Extraembryonic mesoblast
F
Umbilical cord
Obliterated yolk duct
Umbilical coelom
Cloacal membrane
Allantoic duct
Line of fusion of amnion with chorion, i.e. line of obliterated extraembryonic coelom
Yolk sac
Buccopharyngeal membrane
Pericardial cavity
Septum transversum
Foregut
Amniotic cavity

Fig. 10.10 **A**, An early stage in development of a human blastocyst. **B**, A blastocyst sectioned through the longitudinal axis of an embryo, showing the early formation of the allantois and the connecting stalk. **C**, A longitudinal section of an embryo at a later stage of development; the pericardial cavity can be seen at the most rostral part of the embryonic area. **D**, A longitudinal section of an embryo at a later stage, showing formation of the head and tail folds, the expansion of the amnion and the delimitation of the umbilicus. **E**, A transverse section along the line a–b in **D**; observe that the intraembryonic coelom communicates freely with the extraembryonic coelom. **F**, A longitudinal section of an embryo at a later stage, showing full expansion of the amniotic cavity and the umbilical cord.

sheets of closely packed, polarized cells, with narrow intercellular clefts containing minimal extracellular material, and a developed basal lamina containing specific proteins synthesized by the epithelium itself. The cells usually show juxtaluminal lateral surface specializations, (e.g. desmosomes, tight junctions or gap junctions) and specializations of the apical surface (e.g. microvilli or cilia).

Epithelial polarity factors establish the extent of the apical, lateral and basal domains of the individual cells forming an epithelium. Three main control pathways have been identified in maintaining apicobasal polarity (St Jonston and Sanson 2011). The apical domain is specified by the Crumbs transmembrane protein; Baz/PAR-3 specifies the position and extent of the intercellular junction; and Scribble restricts the size of the junctional domains. Once established with an underlying basal lamina, the basal surface displays integrins. Changes in the morphology of an epithelial sheet will involve relative changes in the apical, lateral and basal domains of all the cells in the sheet. Planar polarity of epithelia is driven by intercellular cortical actin and myosin. Epithelial cells are contiguous via actomyosin contractile networks, that contact the lateral cell membrane through E-cadherin adhesion (Gorfinkiel and Blanshard 2011). Wnt/planar cell polarity signalling pathways are involved in these epithelial morphogenetic movements and also in orientated cell division that occurs in epithelial sheets (Tao et al 2009).

Embryonic epithelia differ from those in the fetus and adult. Two distinct types can be identified. Early germinal epithelia, that give rise to epithelial or mesenchymal populations of the embryo and confer their early patterning are termed organizers, e.g. the primitive streak. Later germinal epithelia give rise to system-specific progenitor populations, e.g. the ventricular zone of the neural tube. All epithelia other than special germinal epithelia divide to produce embryonic growth throughout development and may retain stem cells that will divide throughout life.

Characteristically, epithelia clothe internal and external surfaces as simple or compound cellular sheets that separate phases of differing composition (e.g. the external environment and the subepithelial tissue fluids; intravascular and extravascular fluids). Traffic of materials in the intercellular clefts is limited. Traffic occurs across the cells because their limiting membranes, which function as energy-dependent selective barriers, enhance the passage of some materials and impede the passage of others.

Mesenchyme

The terms mesoblast and mesenchyme are used in this text in a specific manner and are not interchangeable. Previously, cells generated by the primitive streak, forming a population between the epiblast and hypoblast were termed mesoderm and, more recently, mesenchyme. The terms primary and secondary mesenchyme have been used to distinguish between those cells that arise from ingression through the primitive streak and those that arise from neural crest ingression from the edges of the neural plate, respectively. Primary mesenchymal cells revert to epithelia at their destinations. However, whereas some primary mesenchymal cells may become epithelial within a short timeframe, e.g. somites and lateral plate, other cells may transform later, e.g. the epithelium lining blood vessels. To address these terminological conflicts, the mixed population of epiblast cells that ingress through the primitive streak and come to lie between the epiblast and embryonic endoderm is termed mesoblast until the cells have migrated to their final position, at which time the populations of mesenchyme can be identified and their fates inferred.

Mesoblastic and mesenchymal cells have no polarity. They form junctional complexes, which are not exclusively juxtaluminal, and they produce extracellular matrix molecules and fibres from the entire cell surface. Mesenchymal populations are formed from a range of germinal epithelia and by proliferation of mesenchymal cells directly, and occupy all the regions between the various epithelial layers described above. The term mesoderm is reserved for the coelomic epithelia that later form mesothelia.

Mesenchymal cells support epithelia throughout the developing body, both locally where they contribute to the basement membrane and form the lamina propria and smooth muscle of tubes, and generally where they differentiate into connective tissue. Specific mesenchymal populations control the patterning of local regions of epithelium (e.g. the zone of polarizing activity on the postaxial limb border posterior to the apical ectodermal ridge).

Extracellular matrix

The space beneath epithelia and between mesenchyme cells is filled with extracellular matrix. Epithelial and mesenchymal cells synthesize extracellular matrix molecules and their receptors. Epithelial cells produce two-dimensional basal laminae that contain a variety of matrix molecules, including laminin, fibronectin, type IV collagen and various proteoglycans. The particular molecules can vary during development according to spatial and temporal patterns, resulting in changes in the behaviour of the underlying mesenchymal cells (e.g. in patterning of the basal regions of the skull). Mesenchymal cells produce extracellular matrix molecules in three dimensions. Those adjacent to an epithelial layer will connect with its basal lamina, forming a basement membrane that secures the epithelial layer to the underlying tissue. Cells deep within a mesenchymal population may synthesize matrix molecules (fibrillar or granular) to separate cells locally, open up migration routes or leave information within the matrix to act on cell populations passing at a later time (see Fig. 11.1).

Molecules of the extracellular matrix are complex. They include more than 19 individual types of collagen (some capable of being individually spliced to give more than 100 variants), proteoglycans and glycoproteins (which come in a wide variety of forms, with and without binding proteins), and elastic fibres (Ch. 2). Hyaluronic acid, a glycosaminoglycan, has a vast capacity to bind water molecules and so create and structure the space between the mesenchymal cells, thereby producing much of the overall shape of an embryo. Experimental removal of hyaluronic acid prevents the formation of cell migration routes, removes the support for overlying epithelia, and disrupts the normal branching of glandular systems.

Fibronectin deposited extracellularly along a migration pathway will affect cells that touch it later, causing realignment of their intracellular actin filaments and thus of their orientation, and it also induces cell migration. The receptors for extracellular matrix molecules such as fibronectin and laminin were originally termed integrins because they integrate extracellular proteins and intracellular cytoskeletal elements (via α and β subunits that span the cell membrane), allowing them to act together; the binding preference of integrins depends on their combination of subunits and environmental conditions.

Extracellular matrix is structured rather than random. Epithelial and mesenchymal cell populations can structure the space around them by secretion of particular matrix molecules or growth factors, which, in turn, can organize the cells that contact them. Cell–matrix interactions and matrix–cell interactions control the position of migration routes and cellular ‘decisions’ to migrate or to begin to differentiate. Matrix molecules propagate developmental instructions from cell to cell and form a far-reaching four-dimensional (spatial and temporal) mechanism of communication. Mapping the molecular pathways and the biomechanical processes that underlie morphogenesis, the dynamic epigenetics of early mesenchyme cells and their secreted three-dimensional extracellular matrices, and the mechanisms by which the stiffness of the surrounding matrix affects the actions of the cells within it, and how the specific deposition of fibrillary proteins creates tissue boundaries and zones of tension, remain the subject of ongoing research (e.g. Davidson et al 2010, Loganathan et al 2012, Loganathan et al 2016).

Transition between epithelial and mesenchymal states

Transformations of cell morphology from epithelium to mesenchyme, and *vice versa*, occur in specific places and times during development, and can be seen as ways of dispersing germinal centres with increasing cell restriction. The first epithelial-to-mesenchymal transition occurs at the primitive streak, a germinal epithelium that confers embryonic specification on the resultant mesoblast population. The mesoblast so formed migrates and the cells undergo mesenchymal-to-epithelial transitions when they reach their final destinations. Series of small epithelial germinal centres, the somites, are formed, as are larger, more extensive, germinal epithelial sheets that line the walls of the intraembryonic coelom. The coelomic walls, especially those derived from somatopleure and splanchnopleure, form germinal epithelia that give rise to the major mesenchymal populations that form the viscera. The early epithelial somites undergo further local epithelial-to-mesenchymal transitions to form the sclerotomes, and subsequently form several germinal epithelia in the epithelial plate of each somite. Later mesenchymal-to-epithelial transitions are not associated with the formation of germinal epithelia; the most common involve the transition of mesenchyme into the endothelium of the vascular system. The nephrons of the mesonephric and metanephric systems also form from mesen chymal-to-epithelial transition. The generation of epithelial layers supported by underlying mesenchyme are widespread throughout the developing embryo and important for cellular interactions. The generation of two abutting epithelia with adjoining basal laminae is rare and seen within particular organs (Ch. 11).

Key references

Müller F, O’Rahilly R 2003 The prechordal plate, the rostral end of the notochord and nearby median features in staged human embryos. Cells Tissues Organs 173:1–20.

This paper describes the specific population of cells that are derived from the earliest invagination of cells rostral to the primitive streak.

O’Rahilly R, Müller F 1987 Developmental Stages in Human Embryos. Washington, DC: Carnegie Institution.

Ronan O’Rahilly and Fabiola Müller continued the work of George Streeter in examining the Carnegie Collection of human embryos and they published extensively on the development of many specific systems and organs. This text provides the overview of the stages, and contains photographs of the external and internal features of a range of embryos at each stage. It should be noted that the authors revised their correlation of age from post-fertilization days to stages in 2010.

St Jonston D, Sanson B 2011 Epithelial polarity and morphogenesis. Curr Opin Cell Biol 23:540–6.

The establishment and maintenance of epithelial cell polarity is of fundamental importance for the future interaction of these cells with each other and with underlying, non-polarized, mesenchymal cells. This paper describes the genes and transmembrane proteins that specify the apical, lateral and basal domains of epithelial cells and the organization and regulation of the cell cytoskeleton to which they are attached.

Streeter GL 1942 Developmental horizons in human embryos. Descriptions of age group XI, 13 to 20 somites, and age group XII, 21 to 29 somites. Contrib Embryol Carnegie Inst Washington 30:211–45.

George Streeter collated the internal and external features of human embryos held in the Carnegie Collection into stages that he termed ‘developmental horizons’; they formed the basis for the Carnegie Staging systems of human embryos. Streeter decided that horizon 23 (now termed stage 23), when bone marrow formation could be seen in the humerus, was the end of the embryonic period and the beginning of the fetal period of intrauterine development. This paper describes embryonic development during stages 11 and 12.

References

Aiello D, Giambona A, Leto F et al 2018 Human coelomic fluid investigation: a MS-based analytical approach to prenatal screening. Sci Rep 8(1):10973. doi: 10.1038/s41598-018-29384-9.

Carmona R, Cano E, Mattiotti A et al 2013 Cells derived from the coelomic epithelium contribute to multiple gastrointestinal tissues in mouse embryos. PLoS One 8:e55890.

de Bree K, de Bakker BS, Oostra RJ 2018 The development of the human notochord. PLoS One 13(10):e0205752.

Davidson LA, Joshi SD, Kim HY et al 2010 Emergent morphogenesis: elastic mechanics of a self-deforming tissue. J Biomech 43:63.

Gorfinkiel N, Blanshard GB 2011 Dynamics of actomyosin contractile activity during epithelial morphogenesis. Curr Opin Cell Biol 23:531–539.

Langemeijer RA 1976 Le Coelome et son revêtement comme organoblastème. Bull Assoc Anat 60:547–558.

Loganathan R, Potetz BR, Rongish BJ et al 2012 Spatial anisotropies and temporal fluctuations in extracellular matrix network texture during early embryogenesis. PLoS One 7:e38266.

Loganathan R, Rongish BJ, Smith CM et al 2016 Extracellular matrix motion and early morphogenesis. Development 143:2056–2065.

Müller F, O'Rahilly R 2003 The prechordal plate, the rostral end of the notochord and nearby median features in staged human embryos. Cells Tissues Organs 173:1–20.

This paper describes the specific population of cells that are derived from the earliest invagination of cells rostral to the primitive streak.

Pfeffer PL 2018 Building principles for constructing a mammalian blastocyst embryo. Biology (Basel) 7(3). pii: E41. doi: 10.3390/biology7030041.

O'Rahilly R, Müller F 1987 Developmental Stages in Human Embryos. Washington, DC: Carnegie Institution.

Ronan O'Rahilly and Fabiola Müller continued the work of George Streeter in examining the Carnegie Collection of human embryos and they published extensively on the development of many specific systems and organs. This text provides the overview of the stages, and contains photographs of the external and internal features of a range of embryos at each stage. It should be noted that the authors revised their correlation of age from post-fertilization days to stages in 2010.

St Jonston D, Sanson B 2011 Epithelial polarity and morphogenesis. Curr Opin Cell Biol 23:540–6.

The establishment and maintenance of epithelial cell polarity is of fundamental importance for the future interaction of these cells with each other and with underlying, non-polarized, mesenchymal cells. This paper describes the genes and transmembrane proteins that specify the apical, lateral and basal domains of epithelial cells and the organization and regulation of the cell cytoskeleton to which they are attached.

Stirparo GG, Boroviak T, Guo G et al 2018 Integrated analysis of single-cell embryo data yields a unified transcriptome signature for the human pre-implantation epiblast. Development 145:dev158501. (Additional supplementary data was added to this article in Development 145:dev169672).

Streeter GL 1942 Developmental horizons in human embryos. Descriptions of age group XI, 13 to 20 somites, and age group XII, 21 to 29 somites. Contrib Embryol Carnegie Inst Washington 30:211–45.

George Streeter collated the internal and external features of human embryos held in the Carnegie Collection into stages that he termed 'developmental horizons'; they formed the basis for the Carnegie Staging systems of human embryos. Streeter decided that horizon 23 (now termed stage 23), when bone marrow formation could be seen in the humerus, was the end of the embryonic period and the beginning of the fetal period of intrauterine development. This paper describes embryonic development during stages 11 and 12.

Szabó A, Rupp PA, Rongish BJ et al 2011 Extracellular matrix fluctuations during early embryogenesis. Phys Biol 8:045006.

Tao H, Suzuki M, Klyonarl H et al 2009 Mouse prickle 1, the homolog of a PCP gene is essential for epiblast apical-basal polarity. PNAS 106:14426–31.

Zamir EA, Rongish BJ, Little CD 2008 The ECM moves during primitive streak formation – computation of ECM versus cellular motion. PLoS Biol 6:e247.

CHAPTER 11

Overarching concepts in development

GENES IN DEVELOPMENT

Study of secondary oocytes before and after fertilization, and of the selection of embryos for implantation after *in vitro* fertilization, has identified the range of maternal genes ready for expression to ensure cleavage, morula and blastocyst formation. Embryonic genome activation occurs in the 4–8 cells stage (Niakan et al 2012) when embryonic cells express polarity genes, initiating cell–cell interaction (Mihajlović and Bruce 2017); by 6 days post fertilization the hatched blastocyst is able to interact with maternal tissue. A simplistic but useful concept likens these early developmental processes to a series of binary choices (see Fig. 8.1). Two cell phenotypes, epithelial and non-epithelial cells, are specified during cleavage and early compaction within the zona pellucida. All the relevant genes required to maintain these cell shapes and behaviours are upregulated at these very early stages.

Three lineages are set up at this time with the specification of trophoblast, hypoblast (primitive endoderm) and epiblast. Cells subsequently respond locally to their environment, specifically to other cells that are positioned lateral and basal to them. In the mouse embryo, the genes operating at these early times are given in Takaoka and Hamada (2012). The implanting blastocyst also expresses and secretes miRNAs (involved in post-translational gene expression) involved in interactions with the maternal endometrium which secretes similar molecules (Lian et al 2017): successful embryo–maternal cross-talk is vital for implantation.

Two related themes have emerged from experimental studies of development: the control of embryonic morphology has been highly conserved in evolution between vertebrates and invertebrates; this control involves families of genes coding for proteins that act as transcriptional regulators. Homeobox genes are believed to be responsible, at least in part, for the evolutionary origin of the embryonic body plan (Irie and Kuratani 2014) and for appropriate axial elongation of the embryo and limb specification (Deschamps and Duboule 2017). Experimental studies of transgenic animals in which the homeobox genes have been knocked out provide some evidence of their function. However, because developmental processes permit significant recovery from insult, some of the outcomes cannot be directly interpreted as demonstrating the effect of such gene loss. Other gene families required for normal development include the T-box family (helix–loop–helix transcription factors and *Sox* genes) and the signalling factors transforming growth factor beta (TGF-β), bone morphogenetic proteins (BMPs), fibroblast growth factor family (FGF), the Wnt family and Hedgehog signalling molecules. A range of cell receptor molecules are also required. For details on individual members within this range of factors, see Carlson (2014).

The successful culture of embryonic stem cells, the techniques of single-cell RNA-sequencing, analysis of all proteins expressed by early embryonic cells, the transcription factors they express, the molecules they secrete and those produced as metabolites, have generated extensive data on early genes and the control of sequential expression of genes specific to diverging cell phenotypes (Giacomini et al 2017).

Signalling between embryonic cells and tissues

Within the developing blastocyst, the position of cells relative to each other leads to epigenetic change. The acquisition of cell polarity is fundamental, because this specifies apical and basolateral domains, cell surface specializations, the positioning of intracellular organelles and cytoskeletal elements, and the position and nature of cell–cell junctions. The establishment cell junctional complexes between the outer, polarized, cells of the morula within the zona pellucida are the earliest embryonic cell interactions. The signals received by adjacent cells induces a change in their subsequent behaviour. Cellular signalling between cells and tissues occur via: direct cell–cell contact (gap junctions); cell adhesion molecules and their receptors; extracellular matrix molecules and their receptors; and growth factors and their receptors. The production of a basal lamina by epithelial cells (containing, e.g., laminin and fibronectin) and its attachment to underlying extracellular matrix molecules (collagen, proteoglycans and glycosaminoglycans) synthesized by mesenchyme cells constructs the tissues in which reciprocal signalling occurs (**Fig. 11.1**). In most developing tissues an epithelium and its basal lamina are supported by underlying mesenchymal cells, each contributing to developmental interactions. However, there are a few sites where two epithelial layers, a special epithelium and an endothelium, generate a shared basement membrane to which both epithelial phenotypes contribute. This arrangement is seen between type-1 pneumocytes and endothelium in the developing lung alveoli; between the podocytes and endothelium in the glomerulus of the developing kidney; and between astrocyte end feet and pial-derived endothelium in the developing brain (**Fig. 11.2**).

Combinations of all of these signalling routes are involved in development and their perturbation may result in developmental aberration. The transient production of, e.g., gap junctions is seen as epithelial somites are formed; between neuroepithelial cells within rhombomeres; and in the tunica media of the outflow tract of the heart. Mutations of the genes that code for extracellular matrix molecules give rise to a number of congenital disorders, e.g. mutations in type I collagen produce osteogenesis imperfecta; mutations in type II collagen produce disorders of cartilage; and mutations in fibrillin are associated with Marfan syndrome

Growth factors are distinguished from extracellular matrix molecules. They can be delivered to, and act on, cells in a variety of ways, namely: endocrine, autocrine, paracrine, intracrine, juxtacrine or matricrine (**Fig. 11.3**). Many growth factors are secreted in a latent form, e.g. associated with a propeptide (latency-associated peptide) in the case of transforming growth factor beta, or attached to a binding protein, in the case of insulin-like growth factors.

Other signalling mechanisms occurring between these cell arrangements include the transduction of the biomechanics of mesenchyme cell synthesized matrix. Stiffness of the matrix leads cells towards an osteoblastic developmental phenotype, whereas soft matrix leads to an adipocyte lineage (Heisenberg and Bellaïche 2013). Endogenous electrical fields are also believed to have a role in cell–cell communication and have been demonstrated in a range of amphibian embryos, and in vertebrate embryos during primitive streak ingression. Neuroepithelial cells are electrically coupled, regardless of their position relative to inter-rhombomeric boundaries.

The spatial and temporal distribution of a variety of cell adhesion molecules has been localized in the early embryo and displayed within the 3D tissue arrangement of embryos at a variety of stages (MGI mouse gene expression data search: eMAGE). The temporal appearance of these molecules correlates with a variety of morphogenetic events that involve cell aggregation or disaggregation.

It is important to realize that while developmental studies on laboratory species and *in vitro* studies of animal tissues indicate the range of factors operating in embryos, the spatial and temporal expression of these factors in human embryos will be different. Figure 8.2 illustrates the temporal differences in external features between human and some animal species. Differences in heterochrony (the time at which genes are expressed and specific structures develop), are easily appreciated between mammals and marsupials, where marsupial embryos are born with facial and upper limb development well in advance of mammals of a similar developmental age (Chew et al 2014). Although not so extreme, differences in heterochrony are significant between human and mouse embryos and any extrapolation of animal developmental sequences to human development should be avoided. Somite generation frequency is 5 hours in humans and 2 hours in mice, and other processes, such as progenitor cell population expansion, have different time lines, e.g. generation of motor neurones takes 2–3 weeks in humans but a few days in mice (Ebisuya and Briscoe 2018). The way in which embryonic cells and tissues count time is not yet clear, but analyses and correlation of specific heterochronic interspecies differences are now being investigated at the molecular level.

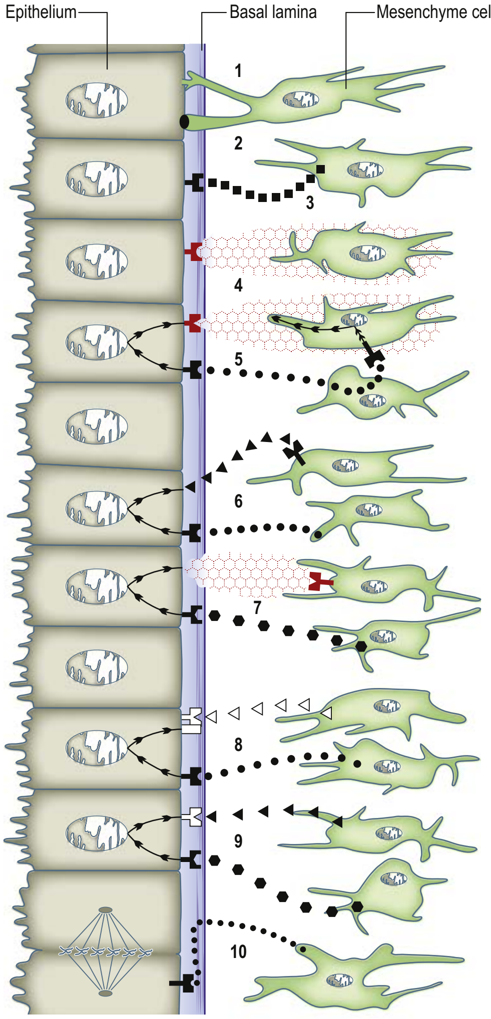

1 Direct cell–cell contact by gap junctions.

2 Cell–cell contact by cell adhesion molecules.

3 A soluble factor (growth factor) reacting with a receptor for that factor on the epithelial cells.

4 Extracellular matrix molecule secreted by the mesenchyme cells interacting with a receptor on the epithelial cell.

5 A soluble factor (growth factor) secreted by a mesenchymal cell having a biphasic action interacting (i) with a receptor on an epithelial cell, causing it to express a specific extracellular matrix molecule receptor; (ii) with a receptor on a mesenchyme cell, causing it to secrete a specific extracellular matrix molecule which then interacts with the induced epithelial receptor.

6 A soluble factor (growth factor) secreted by a mesenchyme cell interacting with a receptor on an epithelial cell, causing it to express a receptor or secrete a factor, which interacts with another factor synthesized, or receptor expressed, by another mesenchyme cell.

7 A soluble factor secreted by a mesenchyme cell interacting with a receptor on an epithelial cell, causing it to synthesize an extracellular matrix molecule (or a receptor for such a molecule) which then interacts with a specific receptor for that molecule on another mesenchyme cell.

8 A soluble factor secreted from a mesenchyme cell interacting with a receptor on an epithelial cell, causing it to synthesize a molecule which stabilizes or enhances the interaction between a mesenchymal-derived factor and its epithelial receptor.

9 A soluble factor secreted by a mesenchyme cell interacting with a receptor on an epithelial cell, causing the inhibition of synthesis/assembly of a factor or receptor.

10 A soluble factor secreted by a mesenchyme cell binding to the extracellular matrix of the basal lamina, where it remains active and subsequently interacts with a receptor on an epithelial cell which appears at a later developmental time.

Fig. 11.1 The many ways by which mesenchyme cells could signal to epithelial cells. Precisely the same mechanisms can operate in reverse, i.e. epithelium to mesenchyme.

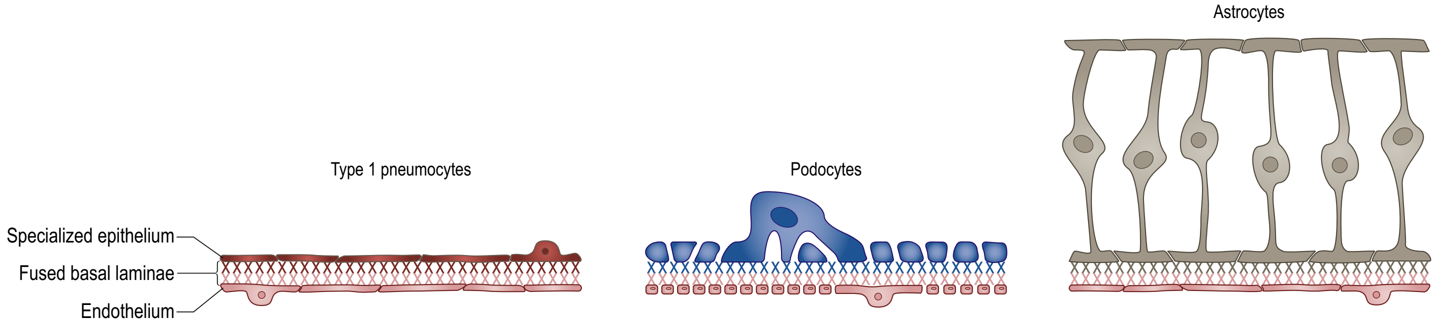

Lung alveoli – Fused basal laminae between endoderm-derived Type 1 pneumocytes and pulmonary endothelium forms thin part of interalveolar septa.

Kidney glomeruli – Fused basal laminae between podocytes, derived from mesenchyme to epithelium transformation, and fenestrated systemic endothelium forms the glomerular basement membrane.

Brain – Fused basal laminae between neurectoderm-derived astrocyte end feet and pial-derived endothelium forms part of the blood:brain barrier.

Fig. 11.2 Sites where specialized epithelial cells form shared basal laminae with endothelium.

Induction and interactions

All cell signalling events form the basis of induction and are involved in cell–cell and tissue interactions. The sequential consequents of induction are described using specific terminology. The ability of a cell population (or tissue) to respond to an inductive signal is called *competence* and denotes the ability of the population to alter its initial behaviour as a result of the induction. After a cell population has been induced to develop along a certain pathway, it loses competence and becomes *restricted*. Once restricted, cells are set on a particular pathway of development and after a number of binary choices (further restrictions), they are said to be *determined*. Determined cells are programmed to follow a process of development that will lead to *differentiation*. The determined state is a heritable characteristic of cells and is the final step in restriction. Once a cell has become determined, it will progress to a differentiated phenotype if the environmental factors are suitable.

The process of determination and differentiation within embryonic cell populations is reflected by the ability of these populations to produce specific proteins. Primary proteins (colloquially termed housekeeping proteins) are considered essential for cellular metabolism, whereas proteins synthesized as cells become determined, and are therefore specific to the state of determination, are termed secondary proteins; e.g. liver and kidney cells produce arginase, but muscle cells do not. Fully differentiated cells produce tertiary proteins, that no other cell line can synthesize, e.g. haemoglobin in erythrocytes. The range of housekeeping, regulatory, and tissue-specific proteomes in adult cells is presented in the Human Protein Atlas (www.proteinatlas.org).

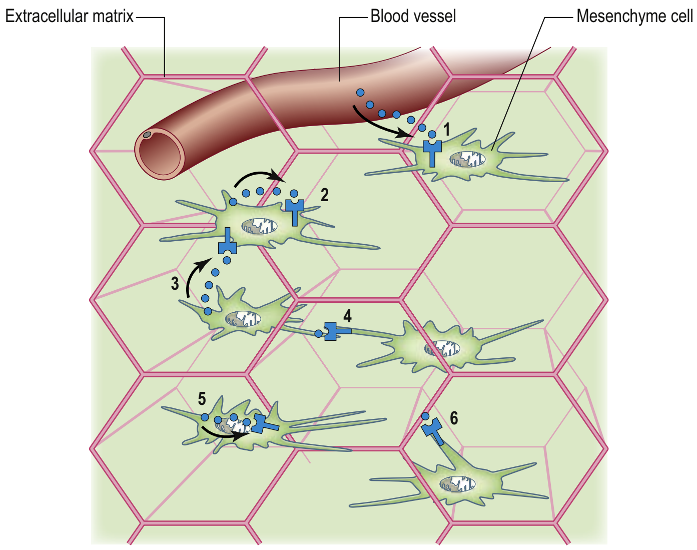

1 **Endocrine** Delivery of growth factor by the blood stream from a distant biosynthetic site to the target mesenchyme cell.

2 **Autocrine** Synthesis of growth factor by the cell, its secretion, binding and activation of a surface receptor elsewhere on its own surface.

3 **Paracrine** Synthesis of growth factor by the cell, its secretion and diffusion to an adjacent cell (or group of cells) where it binds to and activates a cell surface receptor.

4 **Juxtacrine** Synthesis of growth factor by the cell. The growth factor remains on the cell surface and binds to and activates a receptor on an immediately adjacent cell.

5 **Intracrine** Synthesis of growth factor within the cytoplasm of the cell. The growth factor moves to the nucleus and binds to and activates its own nuclear receptors.

6 **Matricrine** Synthesis and export of growth factor from the cell. The growth factor binds to the extracellular matrix where it remains active and subsequently binds to and activates a receptor for that growth factor on the same or a different cell.

Fig. 11.3 In addition to the mechanisms described in Fig. 11.1, cells may also communicate by the reception, production and secretion of growth factors. A typical embryonic mesenchyme cell may receive and produce growth factors in this way.

Permissive and instructive tissue interactions

Classically two types of cell and tissue interaction have been described, namely, permissive and instructive (Wessells 1977).

In a permissive interaction, a signal from an adjacent tissue is necessary for the successful self-differentiation of the responding tissue. This means that a particular cell population (or the matrix molecules secreted by the cells that it contains) will maintain mitotic activity in an adjacent cell population. Since a variety of different cell populations may permit a specific cell population to undergo mitosis and cell differentiation, no specific instruction or signal that might limit the developmental options of the responding tissue is involved; this signal therefore does not influence the developmental pathway selected and there is no restriction. The responding tissue has the intrinsic capacity to develop, and only needs appropriate environmental conditions in order to express this capacity. Permissive interactions often occur later in development, when a tissue whose fate has already been determined is maintained and stabilized by another.

An instructive (directive) interaction (induction) changes the cell type of the responding tissue, so that the cell population becomes restricted. Wessells (1977) proposed four general principles in most instructive interactions: in the presence of tissue A, responding tissue B develops in a certain way; in the absence of tissue A, responding tissue B does not develop in that way; in the absence of tissue A, but in the presence of tissue C, tissue B does not develop in that way; and in the presence of tissue A, a tissue D, which would normally develop differently, is changed to develop like tissue B.

These principles are exemplified during induction of the lens vesicle by the optic cup (see Fig. 15.1). An example of D is the experimental association of chicken flank ectoderm with mouse mammary mesenchyme, which results in the morphogenesis of mammary gland-like structures even though chickens do not normally develop mammary glands Wessells (1977).

Tissue interactions continue into adult life and are probably responsible for maintaining the functional heterogeneity of adult tissues and organs, as exemplified by the complex tissue heterogeneity, with sharply compartmentalized boundaries, that occurs in the oral cavity. The junctions between the mucosa of the vestibule and the lip, and between the vermillion border and the facial skin, are distinct boundaries of specific epithelial and mesenchymal differentiation, and are almost certainly maintained by continuing epithelial–mesenchymal interactions in adult life. Perturbation of these interactions throughout the body may underlie a wide variety of adult diseases, including susceptibility to cancer and proliferative disorders.

The interactions between adjacent epithelia and underlying connective tissue continue throughout embryonic and fetal life and extend into postnatal life. In the adult, these interactions also permit the metaplastic changes that tissues can undergo in response to local environmental conditions

Cell fates and stem cells

As populations of cells become progressively determined, they can be described within a hierarchy of cellular development as stem cells, progenitor cells, and terminally differentiated cells.

Stem cells The definition of a *stem cell* has changed as newer methods for producing such cells *in vitro* have expanded. Within an embryo the earliest cells are totipotent and become restricted as development proceeds. In the adult, populations of stem cells remain within most tissues able to replenish the temporal loss of senescent cells and to respond to changes in environmental conditions by asymmetric division, where one daughter cell remains as a stem cell, while the other proceeds along a differentiation pathway. In proliferative cell division, which may be symmetric, the derived cells have identical determination.

Stem cell populations have been developed from a range of embryonic, fetal and adult cells (**Fig. 11.4**) and are now routinely used in *in vitro* culture for exploration of their properties and their reactions to possible therapeutic agents. Human embryonic stem cells (hESC) were first established in culture by Thomson et al (1998); embryonic and adult *induced* pluripotent stem cells (iPSCs) were established by Takahashi and Yamanaka (2006). All stem cells undergo passaging in culture (cells are grown to confluence then split into subcultures and regrown many times); specific growth factors are added to the culture media to promote cell restriction and determination. Precise control of levels of oxygen tension and growth factors *in vitro* (retroviral transduction of OCT4, KLF4m, c-MYC and SOX2), and forced changing of cell phenotype (mesenchyme to epithelial) have been used to produce a range of human *induced* pluripotential stem cell (hiPSC) types, e.g. cardiac myocytes, hepatocytes, neurones etc. (Takahashi and Yamanaka 2016, Chhabra 2017).

Progenitor cells Progenitor cells are already determined along a particular pathway. They may individually follow that differentiation pathway or may proliferate and produce large numbers of similarly determined progenitor cells that subsequently differentiate; neuroblasts or myoblasts are examples of progenitor cells.

Terminally differentiated cells By virtue of their extreme specialization, terminally differentiated cells can no longer divide, e.g. erythrocytes and neurones. Apoptosis is a particular variety of terminal differentiation in which the final outcome is the death of the individual cells or cell populations. It occurs in the developing limb, where cells die along the pre- and postaxial limits of the apical ectodermal ridge, limiting its extent, and also between the digits, permitting their separation (see Ch. 19).

MORPHOGENESIS AND PATTERN FORMATION

The outcomes of embryonic studies show that the process of expression of specific genes and transcription factors, the consequent synthesis of proteins, and movements of local cells or cell populations, is repeated in many different locations and at different times within an embryo. Correlation of these different but related processes informs overarching concepts of development that are applicable to many different cell populations and regions of an embryo. Over time, the meaning and use of some of the terms that describe such concepts have changed: the most recent ways of defining these terms are presented and attributed in what follows.

Interactions between cells are inferred when a change in the initial status of the cell (cells) is noted, e.g. the cell may undergo mitosis or apoptosis, change its glycocalyx protein receptors, or show signs of differentiation. The outcomes of any interaction can be specified by

Initial cell culture studies were usually in 2D systems. Cultured cells are now grown in 3D in specific gels, on microfluidic chips, or in bioprinted shapes, where the culture medium and oxygen tension can be controlled. The metabolic products of such cultures have been analysed through proteomic analysis (metabolome or secretome). Cells grown in 3D culture will form organoids, where epithelial cells, supported by outer mesenchymal cells form hollow spheres. If these self-organizing cell lines are implanted into animals they continue to grow; if maintained in 3D culture they can be used for drug testing or examination of transcription factors they release. Exploration of the cellular interactions in such systems gives insights into how cells self-organize temporally and spatially (Simunovic and Brivanlou 2017). 3D culture of mouse embryonic stem cells with trophoblastic and hypoblastic (extraembryonic endoderm) cell lines has produced gastrulating embryo-like structures *in vitro* (Sozen et al 2018). These structures allow the exploration of gene expression, spatio-temporal modifications, transcriptional profiling, and comparison with *in vitro* embryonic development.

It is worth reflecting that changes from a perceived 'normal' behavioural repertoire seen in stem cell culture, as a result of changes to the culture conditions may lead to the misinterpretation of experimental results. Undifferentiated embryonic cells are seen only transiently in developing embryos (De Paepe et al 2014), yet hiPSCs, generated by resetting their epigenetic landscapes are used as 'embryonic' stem cells that can be pushed into specific developmental pathways by factors in the culture media. It has been noted that some of the epigenetic memories of such hiPSCs are not eradicated by their preparation and this may obfuscate hypotheses to explain their behaviours (Noguchi et al 2018). Such memory may also include a developmental clock. Heterochronic species-specific differences were conserved when hiPSC-derived neural progenitors were implanted into neonatal mouse brain: the hiPSCs divided for longer and took much longer to differentiate, reflecting their epigentic timeline for *in vivo* human corticogenesis (Espuny-Canacho et al 2013). The results from studies using implanted stem cell-derived tissues or from *in vitro* organoids, or the outcomes of metabolome and secretome analyses of stem cell-derived 'gastrulating embryo-like structures' (Sozen et al 2018), may provide answers to specific questions but these should not be extrapolated to represent what happens in whole embryo development.

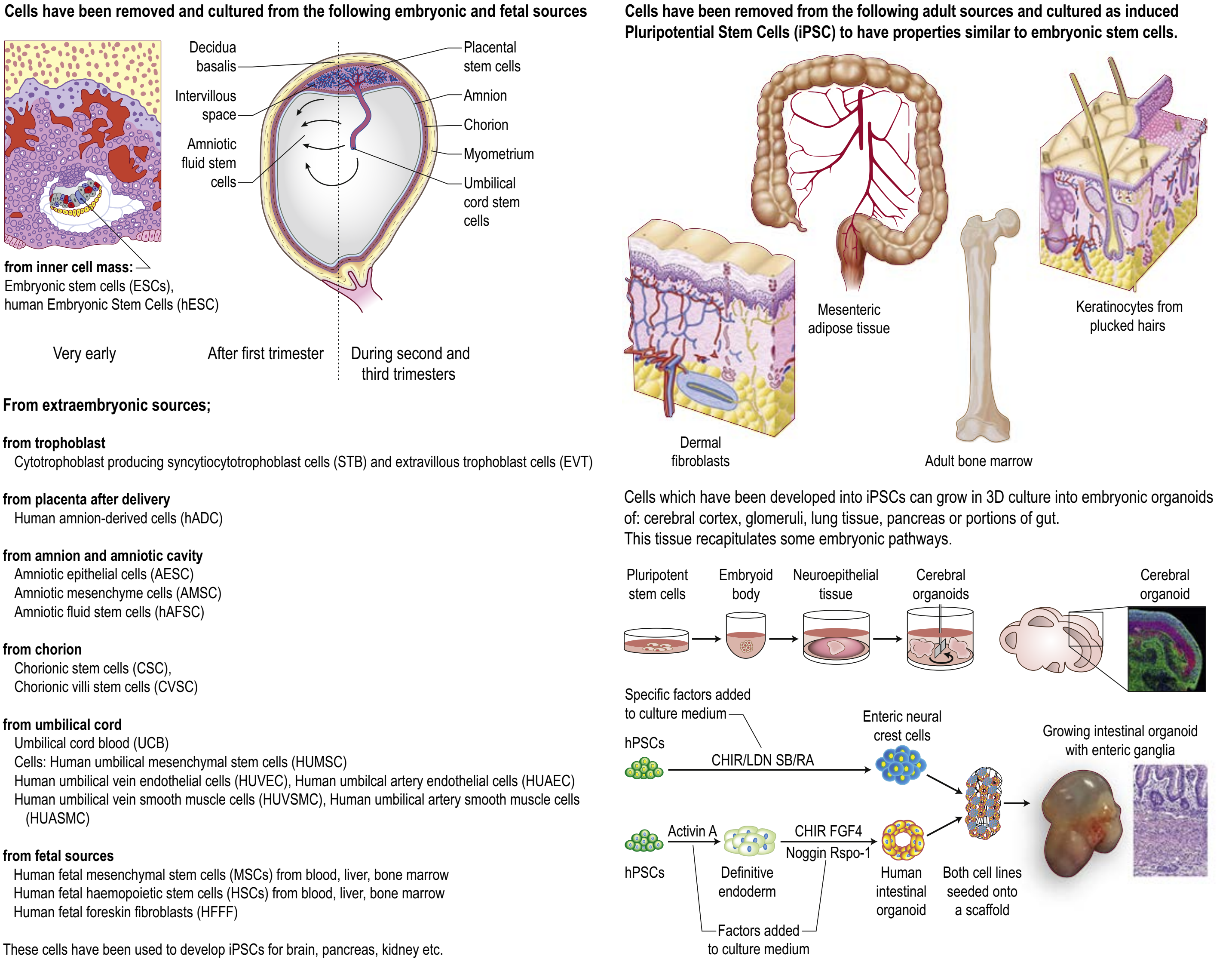
Cells have been removed and cultured from the following embryonic and fetal sources
Decidua basalis
Intervillous space
Amniotic fluid stem cells
Placental stem cells
Amnion
Chorion
Myometrium
Umbilical cord stem cells
from inner cell mass:
Embryonic stem cells (ESCs),
human Embryonic Stem Cells (hESC)
Very early
After first trimester
During second and third trimesters
From extraembryonic sources;
from trophoblast
Cytotrophoblast producing syncytiocytotrophoblast cells (STB) and extravillous trophoblast cells (EVT)
from placenta after delivery
Human amnion-derived cells (hADC)
from amnion and amniotic cavity
Amniotic epithelial cells (AESC)
Amniotic mesenchyme cells (AMSC)
Amniotic fluid stem cells (hAFSC)
from chorion
Chorionic stem cells (CSC),
Chorionic villi stem cells (CVSC)
from umbilical cord
Umbilical cord blood (UCB)
Cells: Human umbilical mesenchymal stem cells (HUMSC)
Human umbilical vein endothelial cells (HUVEC), Human umbilcal artery endothelial cells (HUAEC)
Human umbilical vein smooth muscle cells (HUVSMC), Human umbilical artery smooth muscle cells (HUASMC)
from fetal sources
Human fetal mesenchymal stem cells (MSCs) from blood, liver, bone marrow
Human fetal haemopoietic stem cells (HSCs) from blood, liver, bone marrow
Human fetal foreskin fibroblasts (HFFF)
These cells have been used to develop iPSCs for brain, pancreas, kidney etc.
Cells have been removed from the following adult sources and cultured as induced Pluripotential Stem Cells (iPSC) to have properties similar to embryonic stem cells.
Mesenteric adipose tissue
Keratinocytes from plucked hairs
Dermal fibroblasts
Adult bone marrow
Cells which have been developed into iPSCs can grow in 3D culture into embryonic organoids of: cerebral cortex, glomeruli, lung tissue, pancreas or portions of gut.
This tissue recapitulates some embryonic pathways.
Pluripotent stem cells
Embryoid body
Neuroepithelial tissue
Cerebral organoids
Cerebral organoid
Specific factors added to culture medium
hPSCs
CHIR/LDN SB/RA
Enteric neural crest cells
Growing intestinal organoid with enteric ganglia
Activin A
CHIR FGF4
Noggin Rspo-1
hPSCs
Definitive endoderm
Human intestinal organoid
Both cell lines seeded onto a scaffold
Factors added to culture medium

Fig. 11.4 Origins of stem cell populations from embryos, fetuses and adults.

considering three subsequent characteristics of the cells involved: their spatial arrangement, i.e. where cells are in relation to other cells within their 3D cell population; their temporal state, i.e. the time since they were produced or expressed particular factors; their state of restriction or determination, i.e. their individual state at any one time, as a response to their neighbouring cells

Over time, the consequences of interactions are movements of cell populations that change the shape of an embryo. This overarching process is termed morphogenesis. It denotes the assumption of, and change in, form by the whole or part of a developing embryo: it is apparent in the whole embryo during gastrulation and in local cell population movements in branching morphogenesis, which occurs in developing lungs, kidneys and most glandular organs.

The development of branches from a tubular duct occurs over a period of time. Reciprocal interaction between the proliferating epithelium of the duct and its surrounding mesenchyme and extracellular matrix results in a series of clefts that produce a characteristic branching pattern (Fig. 11.5). During tubular and acinar development, hyaluronidase secreted by the underlying mesenchymal cells breaks down the basal laminae produced by the epithelial cells, which increases epithelial mitoses locally and results in an expanding acinus. Cleft formation is initiated by the mesenchyme, which produces collagen III fibrils within putative clefts. (If the collagen is removed experimentally, no clefts develop, whereas if excess collagen is not removed, supernumerary clefts appear.) The collagen acts to protect the basal lamina from the effects of the hyaluronidase, which means that the overlying epithelia have a locally reduced rate of mitosis. The region of rapid mitoses at the tip of the acinus is split into two, and two branches develop from this point.

Experimental approaches to embryology

Study of the development of chimeric embryos, where small portions of an embryo are excised and replaced with similar portions of an embryo from a different species at the same stage, has provided significant advances in the understanding of conserved genes and interactive pathways. The technique was particularly effective in early chick/quail chimeric embryonic experiments because the nucleolus is especially prominent in quail but not in chick cells, allowing easy identification of quail cells within a chick embryo (Le Douarin 1969). Chimeric embryo experimentation confirmed the reciprocity of tissue interaction between the embryonic species, a phenomenon that had previously been illustrated, for a limited period, in co-cultures of embryonic avian and mammalian tissues. Somite development and vertebral formation have been studied in mouse–chick chimeras (Fontaine-Pérus 2000). The production, *in vitro*, of human–animal chimeric cell lines has also provided new ways of studying cellular pathways, as has the introduction of human artificial chromosome vectors into animal cells to study their interaction.

Techniques in which specific genes were targeted, removed or replaced (knock-out and knock-in studies) provided significant information on the actions of genes and the result of their perturbation in *in vivo* and *in vitro* experimentation. Culture of embryos, embryonic tissues and embryonic cells permitted investigation of the products of cell metabolism via perturbation of the culture media and analysis of culture metabolites, seen in proteomic, metabolome and secretome studies. Such techniques have also been used to study extraembryonic membranes, e.g. amnion and yolk sac.

The current production of human *induced* pluripotent stem cells which can be encouraged along any line of development by the provision of specific growth factors in the culture media has expanded the possibilities of embryonic research. Specified cell phenotypes can be produced in culture and encouraged, within 3D systems, to form organoids with the view to further study of interactive developmental sequences, to implant such organoids back into animals to study their ability to grow *in vivo*, or to promote continued growth *in vitro* to produce portions of organs which could be transplanted into humans as future treatments.

Branching morphogenesis is an example of pattern formation, the process whereby the individual members of a mass of cells follow a number of different responses that are precisely related to each other, in an orderly manner in space and time. Conceptually, two separate components of pattern formation within branching morphogenesis have been noted (Salazar-Ciudad et al 2003): inductive mechanisms, which pattern via cell signalling, and mophogenetic mechanisms, which act on cell populations to change the spatial distribution of cells (a change of form) without changing the cell states (e.g. degree of restriction).

Inductive mechanisms seem to have a hierarchy, based on sequential gene expression; patterns generated in this way are similar to one another and limited in complexity. In contrast, morphogenetic mechanisms, which include the epigenetic context of cell populations, mechanical interactions between cells and also the ECM, and also the local properties of the ECM and its response to the local stresses, appear to generate more complex patterns using fewer genes.

A cell population with equivalent states of gene expression, noted as a genetic territory (Salazar-Ciudad et al 2003) can undergo an overall change in form. This has been termed a morphostatic mechanism: the population follows an autonomous and specific temporal sequence of behavioural changes specified by the expression of a new range of transcription factors, e.g. the meristematic growth of the developing limb bud (Ch. 19).

Morphodynamic mechanisms denote cell populations where genetic territories are changing at the same time as the cells are sending and receiving inductive molecular signals. Inductive and morphogenetic mechanisms are working synchronously and interdependently. Cells are acquiring positional information dynamically and, because of the different relative positions of each cell to its neighbour, the local interpretations of any inductive signals to a cell population is complex, as cells interact with changing molecular and biomechanical microenvironments over time. Such mechanisms can be seen in cerebral development (Ch. 14). For details of patterning in vertebrate development, see Tickle (2003).

The concept of pattern formation is used throughout all branches of embryology and development. It can be identified across species and used to explore the evolution of conserved cell interactions (Schlosser et al 2014). The prediction of patterning described mathematically by Turing (1952) where a cell producing two morphogens with different diffusion rates, one an activator and the other an inhibitor, has been applied to many developmental scenarios such as hair follicle patterning in developing skin, villous patterning in the gut and the development of stripes (Maini et al 2006, Heller and Fuchs 2015). Pattern formation can also be seen within *in vitro* culture of organoids (Deglincerti et al 2016, Ishihara et al 2017), demonstrating that the sequences of interactions, gene expression and signalling of cells in culture continue to follow the epigenetic programming of stem cells within their specified culture microenvironment.

Buckling morphogenesis is a process integrating further complexity, where two epithelia contribute to inductive interactions in three and four dimensions, with the transductive effects of the biomechanical properties of the combined tissues effecting subsequent developmental outcomes. This type of interaction is seen particularly in gut development, where joined linear sequences of epithelial: mesenchyme interactions are covered by a second epithelium. The elongation of the first tube is informed by its own genetic programme and also confined by the dynamic relationship with the outer epithelium. The biomechanical tension produced in the system informs regional lengthening, rate of growth of the original epithelial–mesenchyme interaction, and the local formation of complex looping. Differential growth between the epithelial layers in this system can give rise to complex coiling of the gut which can then slide into and pack closely within a restricted space. Although aspects of buckling morphogenesis can be predicted mathematically, the parameters for inclusion are extremely complex and not all of the mechanical properties of the tissues involved can yet be specified (Nerurkar et al 2017, Nerurkar et al 2019).

Co-culture of different embryonic cell phenotypes has provided further information on the factors involved in instructive interactions between epithelial and mesenchymal cells, and has also allowed experimental examination of the extracellular matrix and its biomechanical properties (Hadden et al 2017). Three-dimensional cell culture has highlighted the self-organizing properties of mixed phenotypic embryonic cell populations and given rise to a plethora of studies where portions of embryos or embryonic stem cells are grown in mini-culture conditions with full control of the liquid and gaseous environment. Such ‘organ on chips’ culture systems are producing high volumes of data on the conditions under which such cell systems will flourish and the metabolites that are produced. However, these experimental results cannot be extrapolated to any *in vivo* embryonic development and care must be taken in generalizing the knowledge gained from them.

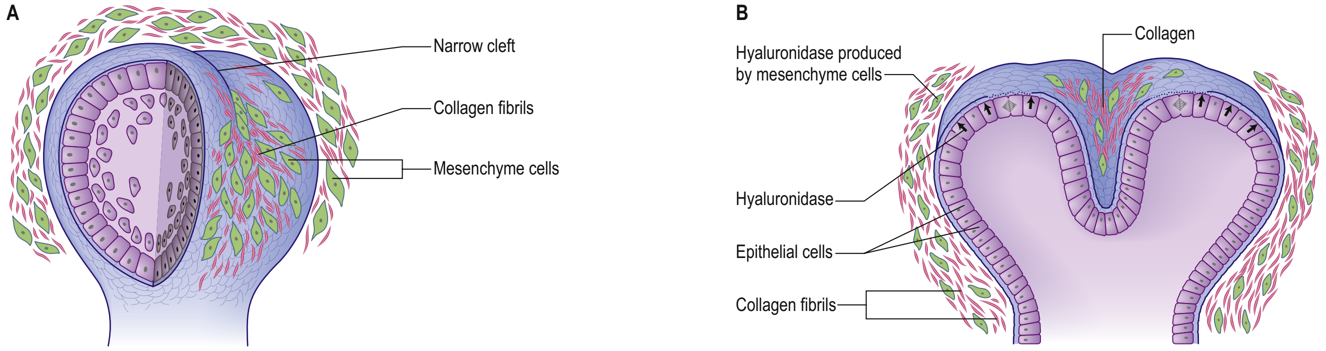

Fig. 11.5 Branching of a tubular duct may occur as a result of an interaction between the proliferating epithelium of the duct and its surrounding mesenchyme and extracellular matrix. **A**, Mesenchymal cells initiate cleft formation by producing collagen III fibrils locally within the development clefts and hyaluronidase over other parts of the epithelium. Collagen III prevents local degradation of the epithelial basal lamina by hyaluronidase and slows the rate of mitosis of the overlying epithelial cells. **B**, In regions where no collagen III is produced, hyaluronidase breaks down the epithelial basal lamina and locally increases epithelial mitoses, forming an expanded acinus (arrows). (Adapted with permission from Gilbert SF 1991 Developmental Biology. Sunderland, MA: Sinauer Associates.)

Answers from these studies should not be assumed to add to our knowledge of normal development. Human embryos must not be grown *in vitro* for longer than 14 days after the point of fertilization; the present 14-day rule advocated in the UK by the Warnock Committee (Department of Health and Social Security 1984) was established at a time when human embryos could only be grown *in vitro* for a few days. Today, the purposeful culture of '*synthetic human entities with embryo-like features*' (SHEEFs) (Aach et al 2017), multi-phenotype self-organizing gastruloids/organoids of gut, kidney or cerebral cortex (which can model diverse brain regions) created from hiPSCs, with the very real possibility of maintaining growth beyond the 14-day limit, poses significant ethical problems (Chan 2018). The International Society for Stem Cell Research (ISSCR) produced guidelines for the review, by a proposed human Embryo Research Oversight (EMRO) process, of '*embryo-like structures that might manifest human organismal potential*' (ISSCR 2016). The production of these organoids enables researchers to study portions of embryos, in effect, at developmental stages much later than those at present permitted (Aach et al 2017). How the transnational dimension of any regulatory change ought to be managed and how this would affect the global dynamic of science needs careful thought and discussion (Chan 2018).

DEVELOPMENT OF HIERARCHICAL ONTOLOGIES AND COMPUTER MODELLING OF DEVELOPMENT

Bioinformatic databases use embryological ontologies to trace the lineage of organs and tissues to the earliest time and provide a temporal and spatial framework against which the sequential activation of genes preceding changes in cell and tissue morphology can be matched. They also provide a means of viewing all of the complex partonomy, lineage data and temporal information occurring within embryos within a specific timeframe and of linking these to adult anatomical tissue types. As understanding of the complexity of early developmental events expands, the use of ontological databases provide methods to correlate embryological information (limitations are discussed in Bard 2012).

Computer models have so far focused on single attributes of cells, such as their position, movement or forces transmitted through layers, e.g. cell position relative to a lattice, or the contact surfaces of a cell with other cells in 3D. Such models are more suited to densely packed epithelial cell populations than to mesenchymal populations where the viscoelastic properties of the glycosaminoglycans can be changed in three dimensions by mesenchymal cell–cell interaction or epithelial–mesenchymal interaction. Quantifying the development of complexity time in specific embryonic regions offers the opportunity to compare features such as gene expression, cell lineage and territories (Salvador-Martinez and Salazar-Ciudad 2017).

The exploration of data derived from analysis of the genomes of a range of animals including humans has benefited from ontologies and powerful computing algorithms. Internet websites contain the databases of genomes, spatial and temporal gene expressions, metabolomes and secretomes throughout the development of a range of invertebrate and vertebrate species (including Wormbase, Flybase, Mouse eMAP, KOMP (Knockout Mouse Project), and Human Developmental Studies Network – HUDSEN). Such ontologies assist embryological study, reveal explicit similarities in interspecies developmental processes and enhance the production of taxonomies of vertebrate evolution.

Outcomes of studies based on analyses of Big Data in embryological studies and how they fit into the sum of knowledge may need caution in their interpretation (Hutter and Moerman 2015). If the input data (and underlying concepts) used to solve a problem are based on obfuscated and confused understanding, then the output may not answer the question investigated.

Key references

Aach J, Lunshof J, Iyer E et al 2017 Addressing the ethical issues raised by synthetic human entities with embryo like features. Elife 6:pii: e20674. doi: 10.7554/eLife.20674.

Bard J 2012 A new ontology (structured hierarchy) of human developmental anatomy for the first 7 weeks (Carnegie stages 1–20). J Anat 221:406–16.

Chhabra A 2017 Derivation of human induced pluripotent stem cell (iPSC) lines and mechanism of pluripotency: historical perspective and recent advances. Stem Cell Rev 13:757–73.

Fontaine-Pérus J 2000 Mouse–chick chimera: an experimental system for study of somite development. Curr Top Dev Biol 48:269–300.

Le Douarin NM 1969 Particularités du noyau interphasique chez la caille japonaise (*Coturnix coturnix japonica*). Utilisation de ces particularités comme 'marquage biologique' dans les recherches sur les interactions tissulaires et les migrations cellulaires au cours de l'ontogenèse. Bull Biol Fr Belg 103:435–52.

Simunovic M, Brivanlou AH 2017 Embryoids, organoids and gastruloids: new approaches to understanding embryogenesis. Development 144:976–85.

Wessells NK 1977 Tissue Interaction and Development. Menlo Park, CA: Benjamin.

Until fairly recently the study of embryology has been based on detailed examination of histological sections of embryos at different developmental stages: an understanding of cells, tissues and extracellular spaces in 3D; and the use of specific staining techniques to compare sections of normal, perturbed or chimeric embryos. Today many computer programs based on cell or gene ontologies, devised and specified some years ago, are making predictions about developmental mechanisms. New research outcomes are curated and updated in the main by other computer algorithms, with human curation of only a small proportion of the uploaded data. The concepts used to explain developmental processes have evolved in step with an increased understanding of gene expression, common embryonic mechanisms, cell–cell and cell–matrix interactions, and newly discovered transitory embryonic cell populations. However, it is perhaps now no longer possible to modify how embryonic processes are (re) conceptualized in the light of new knowledge, because the language used when computer ontologies were first devised cannot be revised. The earlier freedom for exploration of concepts and theories, their revision in the light of new discoveries and the development of new thoughts and language, may no longer be possible. As computers are now able to devise their own algorithms, learning from their past searches, the original concepts and thoughts concerning embryological mechanisms and interaction may become changed in ways not yet apparent, and certainly not transparent.

References

Aach J, Lunshof J, Iyer E et al 2017 Addressing the ethical issues raised by synthetic human entities with embryo like features. Elife 6:pii: e20674. doi: 10.7554/eLife.20674.

Bard J 2012 A new ontology (structured hierarchy) of human developmental anatomy for the first 7 weeks (Carnegie stages 1–20). J Anat 221:406–16.

Carlson BM 2014 Human Embryology and Developmental Biology, 5th ed. Philadelphia: Elsevier, Saunders; Ch. 4.

Chan S 2018 How and why to replace the 14 day rule. Curr Stem Cell Rep 4:288–34.

Chew KY, Shaw G, Yu H et al 2014 Heterochrony in the regulation of the developing marsupial limb. Dev Dyn 243:324–8.

Chhabra A 2017 Derivation of human induced pluripotent stem cell (iPSC) lines and mechanism of pluripotency: historical perspective and recent advances. Stem Cell Rev 13:757–73.

De Paepe C, Krivega M, Cauffman G et al 2014 Totipotency and lineage segregation in the human embryo. Mol Hum Reprod 20:599–618.

Deglincerti A, Etoc F, Guerra MC et al 2016 Self-organization of human embryonic stem cells on micropatterns. Nat Protoc 11:2223–32.

Department of Health and Social Security 1984 Report of the Committee of Inquiry into Human Fertilisation and Embryology (the Warnock Report). London: Her Majesty's Stationery Office.

Deschamps J, Duboule D 2017 Embryonic timing, axial stem cells, chromatic dynamics, and the Hox clock. Genes Dev 31:1406–16.

Ebisuya M, Briscoe J 2018 What does time mean in development? Development 145: dev164368. doi: 10.1242/dev.164368.

Espuny-Camacho I, Michelsen KA, Gall D et al 2013 Pyramidal neurons derived from human pluripotent stem cells intergrate efficiently into mouse brain circuits in vivo. Neuron 77:440–56.

Fontaine-Pérus J 2000 Mouse–chick chimera: an experimental system for study of somite development. Curr Top Dev Biol 48:269–300.

Giacomini E, Vago R, Sanchez AM et al 2017 Secretome of in vitro cultured human embryos contains extracellular vesicles that are uptaken by the maternal side. Sci Rep 7(1):5210. doi: 10.1038/s41598-017-05549-w.

Hadden WJ, Young JL, Holle AW, et al 2017 Stem cell migration and mechanotransduction on linear stiffness gradient hydrogels. PNAS 114:5647–52.

Heisenberg C-P, Bellaïche Y 2013 Forces in tissue morphogenesis and patterning. Cell 153:948–62.

Heller E, Fuchs E 2015 Tissue patterning and cellular mechanics. J Cell Biol 211:219–31.

Hutter H, Moerman D 2015 Big data in Caemorhabditis elegans: quo vadis? Mol Biol Cell 26:3090–14.

ISSCR (International Society for Stem Cell Research) 2016 Guidelines for stem cell research and clinical translation. Go to ISSCR Guidelines on https://www.isscr.org/.

Irie N, Kuratani 2014 The developmental hourglass model: a predictor of the body plan? Development 141:4649–55.

Ishihara K, Ranga A, Lutolf MP et al 2017 Reconstitution of a patterned neural tube from single mouse embryonic stem cells. Methods Mol Biol 1597:43–55. doi: 10.1007/978-1-4939-6949-4_4.

Le Douarin NM 1969 Particularités du noyau interphasique chez la caille japonaise (*Coturnix coturnix japonica*). Utilisation de ces particularités comme 'marquage biologique' dans les recherches sur les interactions tissulaires et les migrations cellulaires au cours de l'ontogenèse. Bull Biol Fr Belg 103:435–52.

Lian J, Wang S, Wang Z 2017 Role of microRNAs in embryo implantation. Reprod Biol Endocrinol 15:90.

Maini P, Baker RE, Chuong C 2006 The Turing model comes of molecular age. Science 314:1397–8.

Mihajlović AI, Bruce AW 2017 The first cell-fate decision of mouse preimplantation embryo development: integrating cell position and polarity. Open Biol 7: 170210.

Nerurkar NL, Mahadevan L, Tabin CJ 2017 BMP signaling controls buckling forces to modulate looping morphogenesis of the gut. Proc Natl Acad Sci U S A 114: 2277–82.

Nerurkar NL, Lee C, Mahadevan L et al 2019 Molecular control of macroscopic forces drives formation of the vertebrate hindgut. Nature 565: 480–4.

Niakan KK, Han J, Pedersen RA et al 2012 Human pre-implantation embryo development. Development 139:829–41.

Noguchi H, Miyagi-Shiohira C, Nakashima Y 2018 Induced tissue-specific stem cells and epigenetic memory in induced pluripotent stem cells. Int J Mol Sci 19(4):pii: E930. doi: 10.3390/ijms19040930.

Salazar-Ciudad I, Jernvall J, Newman S 2003 Mechanisms of pattern formation in development and evolution. Development 130:2027–37.

Salvador-Martinez I, Salazar-Cuidad I 2017 How complexity increases in development. An analysis of the spatial-temporal dynamics of gene expression in Ciona intestinalis. Mech Dev 144:113–24.

Schlosser G, Patthey C, Shimeld SM 2014 The evolutionary history of vertebrate cranial placodes II. Evolution of ectodermal patterning. Dev Biol 389:98–119.

Simunovic M, Brivanlou AH 2017 Embryoids, organoids and gastruloids: new approaches to understanding embryogenesis. Development 144:976–85.

Sozen B, Amadei G, Cox A et al 2018 Self assembly of embryonic and two extra-embryonic stem cell types into gastrulating embryo-like structures. Nature Cell Biol 20:979–89.

Takahashi K, Yamanaka S 2006 Induction of pluripotent stem cells from mouse embryonic and adult fibroblast cultures by define factors. Cell 126:663–76.

Takahashi K, Yamanaka S 2016 A decade of transcription factor-mediated reprogramming to pluripotency. Nat Rev Mol Cell Biol 17:183–93.

Takaoka K, Hamada H 2012 Cell fate decisions and axis determination in the early mouse embryo. Development 139:3–14.

Thomson JA, Itskovitz-Eldor J, Shapiro SS et al 1998 Embryonic stem cell lines derived from human blastocysts. Science 282:1145–7.

Tickle C 2003 Patterning in Vertebrate Development. Oxford: Oxford University Press.

Turing AM 1952 The chemical basis of morphogenesis. Phil Trans R Soc B 237:37–72.

Wessells NK 1977 Tissue Interaction and Development. Menlo Park, CA: Benjamin.

CHAPTER

12

Cell populations at the start of organogenesis

SPECIFICATION OF THE BODY AXES AND THE BODY PLAN

Embryos can be thought of as being constructed with three orthogonal spatial axes (cephalocaudal, dorsoventral and laterolateral), plus a temporal axis. In mammalian embryos, axes cannot be specified at very early stages: embryonic axes can be defined only after the early extraembryonic structures have been formed and the inner cell mass can be seen. The position of the future epiblast can be predicted in human embryos when the hollow blastocyst has formed. The inner cell mass becomes (seemingly) randomly located on the inside of the trophectoderm and forms a population of epiblast cells subjacent to the trophoblast. This region implants first. It is not known whether the trophectoderm in contact with the inner cell mass initiates implantation, so that the future dorsal surface of the embryo is closest to the disrupted maternal vessels at the implantation site, or whether the inner cell mass can travel around the inside of the trophoblast to gain a position subjacent to the implantation site once implantation has started.

Axes may be conferred on the whole embryonic disc, which is initially flat and mainly two-dimensional. However, their subsequent orientation in the folded three-dimensional embryo will be completely different. The dorsal structures of the folded embryo form from a circumscribed central ellipse of the early flat embryonic disc (see Fig. 10.5). Lateral and ventral structures form from the remainder of the disc, and the peripheral edge of the disc eventually becomes constricted at the umbilicus (see Figs 10.9–10.10). Although the appearance of part of the epiblast is taken to specify the dorsal surface of the embryo, the inner layer, i.e. the hypoblast, is not, by default, a ventral embryonic structure.

The primary, cephalocaudal, axis is conferred by the appearance of the primitive streak in the bilaminar disc. The primitive streak patterns cells during ingression, and so also specifies the dorsoventral axis, which becomes apparent after embryonic folding. The position of ingression through the streak confers axial, medial or lateral characteristics on the forming mesenchyme cells. The axial and medial populations remain as dorsal structures in the folded embryo, and the surface ectoderm above them will exhibit dorsal characteristics. The lateral plate mesenchyme will assume lateral and ventral positions after embryonic folding, and the surface ectoderm above this population will gain ventral characteristics. The third and last spatial axis is the bilateral, or laterolateral, axis, which appears as a consequence of the development of the other two axes. Initially, the right and left halves of the embryonic body are bilaterally symmetric. Lateral projections, the upper and lower limbs, develop in two places on each side of the body wall (somatopleure).

With the last axis established, the temporal modification of the original embryonic axes can be seen. The segmental arrangement of the cephalocaudal axis is very obvious in the early embryo and is retained in many structures in adult life. Similarly, dorsal embryonic structures remain dorsal and undergo relatively little change. However, structures that were originally midline and ventral, especially those derived from splanchnopleuric mesenchyme, e.g. the cardiovascular system and the gastrointestinal tract and its adnexae, are subject to extensive shifts, and change from a bilaterally symmetric arrangement to an entire body that is now chiral, i.e. has distinct left and right sides.

Organogenesis, the development of all the body organs and systems, begins after the dramatic events of gastrulation, when the embryo has attained a recognizable body plan. In human embryos, this corresponds to the end of stage 10 (**Fig. 12.1**). The head and tail folds are well formed, with enclosure of the foregut and hindgut (proenteron and metenteron), although the midgut (mesenteron) is only partly constricted from the yolk sac. The forebrain projection dominates the cranial end of the embryo, and the buccopharyngeal membrane and cardiac prominence are caudal and ventral to it. The cardiac prominence contains the transmedian pericardial cavity, which communicates dorsocaudally with right and left pericardioperitoneal canals. These pass dorsally to the transverse septum mesenchyme and open caudally into the extraembryonic coelom on each side of the midgut. The intraembryonic mesenchyme has begun to differentiate and the paraxial mesenchyme is being segmented into somites. Neural groove closure is progressing caudally, so that a neural tube is forming between the newly segmenting somites. Rostrally, the early brain regions, which have not yet fused, can be discerned. The neuroepithelium is separated from the dorsal aspect of the gut by the notochord. The earliest blood vessels have appeared and a primitive tubular heart occupies the pericardium. The chorionic circulation is soon to be established, after which the embryo rapidly becomes completely dependent on the maternal blood stream for its requirements. The embryo is connected to the developing placenta by a mesenchymal connecting stalk in which the umbilical vessels develop, and that also contains the allantois, a hindgut diverticulum. The lateral body walls are still widely separated. The embryo has contact with three different vesicles, namely, the amnion, which is in contact with the surface ectoderm; the yolk sac, which is in contact with the endoderm; and the chorionic cavity, containing the extraembryonic coelom, which is in contact with the intraembryonic coelomic lining (see Fig. 10.10).

The early body plan of the embryo is segmented. The boundaries between the segments are maintained by the differential expression of genes and proteins that restrict cell migration in these regions. Organogenetic processes either retain the segmental plan, e.g. spinal nerves, or replace it locally, e.g. the modifications of somatic intersegmental vessels by the development of longitudinal anastomoses. Anomalies may result from improper specification of segments along the cephalocaudal axis and may fail to produce the appropriately modified segmental plan.

The degree to which vertebrate embryos are developmentally constrained at this period of development is controversial. Comparative studies on the timing at which specific embryonic structures appear, heterochrony, have shown that other embryonic species do not follow the same developmental sequence as humans (Richardson and Keuck 2002). Although some developmental mechanisms are highly conserved, e.g. the homeobox gene codes, others may have been dissociated and modified in different vertebrate species during evolution.

Organogenesis, the further development of body regions and organs that is described in this Section, starts from about stage 10 (postfertilization days 28–29). Although it is both conventional and convenient to consider the further development of each body system on an individual basis, not only do all systems develop simultaneously, but also they interact and modify each other as they develop. This necessary interdependence is supported by the evidence of experimental embryology and reinforced by the phenomena of growth anomalies, which cut across the artificial boundaries of systems in most instances. For these reasons, it is recommended that the development of an individual system or body region should be studied in relation to others, especially those most closely associated with it, whether spatiotemporally or causally.

EMBRYONIC CELL POPULATIONS AT THE START OF ORGANOGENESIS

The developmental processes operating in the embryo between stages 5 and 9 enabled the construction of the bi- and trilaminar embryonic disc, the intraembryonic coelom and new proliferative epithelia. From the end of stage 10 a range of local epithelial and mesenchymal populations now interact to produce viscera and appendages. The inductive influences on these tissues and their repertoire of responses are very different from those seen at the onset of gastrulation. The range of tissues present at the start of organogenesis, when the body plan is clear, is given below (see Fig. 12.1; **Fig. 12.2**). A summary of the fates of the embryonic cell populations is given in **Fig. 12.3**.

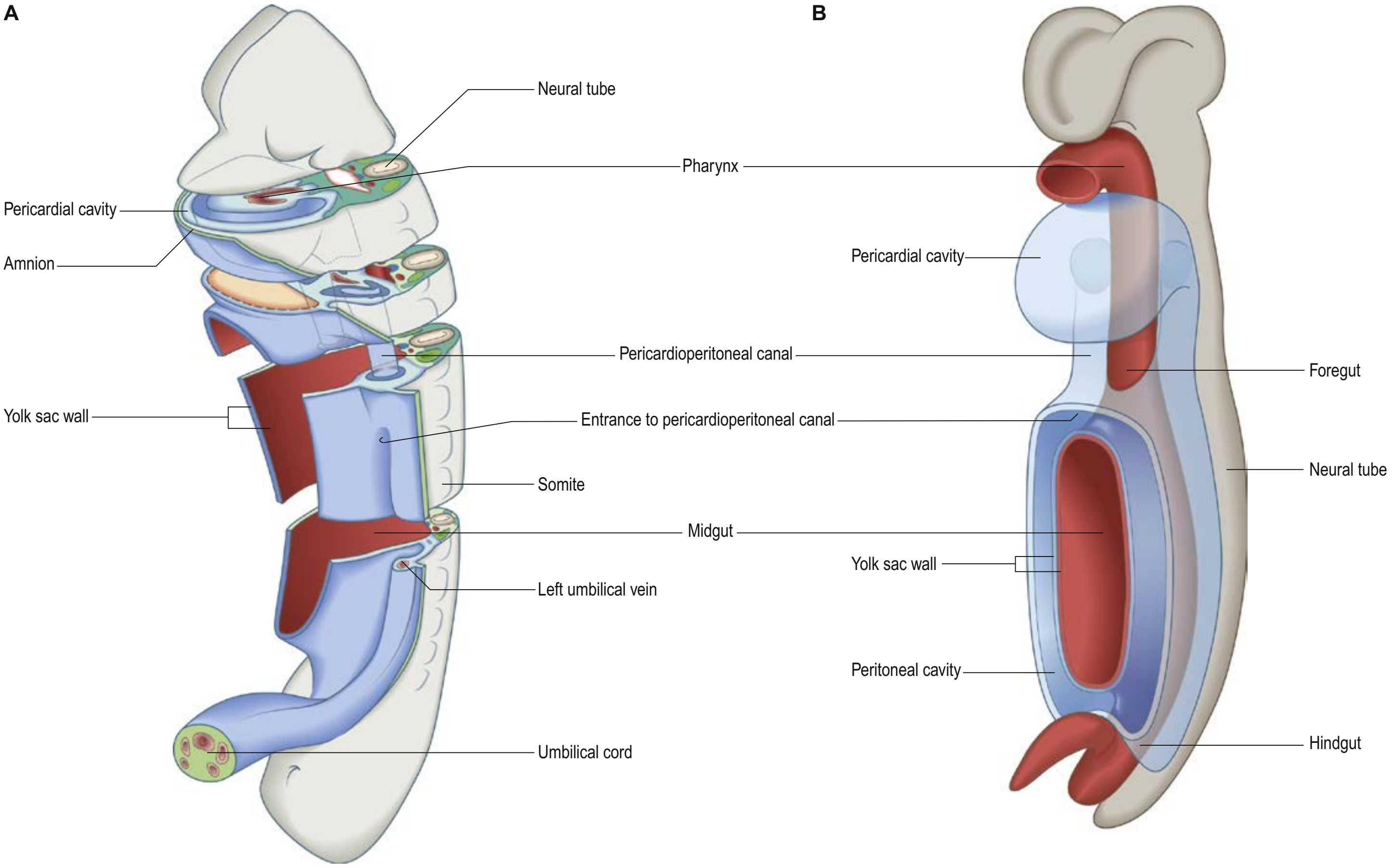

Fig. 12.1 **A**, The embryo at stage 11, showing the position of the intraembryonic coelom (contained by the walls coloured blue). **B**, The three major epithelial populations within a stage 11 embryo, viewed from a ventrolateral position. The neural tube lies dorsal to the gut. Ventrally, the intraembryonic coelom crosses the midline at the level of the foregut and hindgut, but is lateral to the midgut and a portion of the foregut.

Epithelial populations in the embryo

All epithelial populations express the cell polarity genes *Crumbs*, *Scribble* and *Baz/PAR-3* (Ch. 10). They all display apical specializations, including primary cilia and microvilli, juxtaluminal junctions and, when not actively dividing, temporally and spatially specified basal laminae. Movement of fluid or proteins is limited between epithelial populations, creating barriers between developing tissues and organs.

Surface ectoderm

During embryogenesis, the surface ectoderm shows regional differences in thickness. Ectoderm over the dorsal region of the head and trunk is thin, as is the pericardial covering; this has been interpreted as a consequence of the expansion of this epithelium over structures that are enlarging rapidly as development proceeds. After the surface ectoderm has completed a number of early interactions it forms an upper layer, the periderm, which remains throughout fetal life, and a lower layer which differentiates into epidermis.

Ectodermal ring and ectodermal placodes

The ectoderm on the head and lateral borders of the embryo shows a zone of epithelial thickening, the ectodermal ring, which can be discerned from stage 10 and is completed by stage 12. Rostrally, it contains populations of neuroectoderm that remain in the ectoderm after primary neurulation and are termed ectodermal placodes. The latter may be considered to be neuroepithelial cells that remain within the surface ectoderm until central nervous system development has progressed sufficiently for their inclusion into sensory epithelia and cranial nerve ganglia. The neuronal placodes may either invaginate *in toto* to form a vesicle, or remain as a neuronal layer, or contribute individually to neuronal structures with cells of other origins. A midline ectodermal thickening, the adenohypophysial placode, invaginates as Rathke's pouch and forms a vesicle immediately rostral to the buccopharyngeal membrane. The ectodermal ring then passes bilaterally to encompass the olfactory and optic placodes, which give rise to the olfactory sensory epithelium and the lens of the eye, respectively. It then overlays the pharyngeal arches, where it gives rise to epibranchial placodes which remove themselves individually from the ectoderm at stage 10–11 and become associated with the neural crest cells within the cranial sensory ganglia supplying the arches. It also forms specializations of the ectoderm on the frontonasal, maxillary and mandibular processes, which give rise to the tooth buds and the outer coating of the teeth. The paired otic placodes overlying the rhombencephalon at the lateral portion of the second pharyngeal arch invaginate to form the otic vesicles, which give rise to the membranous labyrinth of the ear. The ectodermal ring then passes over the occipital and cervicothoracic parts of the embryo, superficial to the four occipital somites and later to the occipitocervical junction. Further caudally, it is associated with the upper limb field, where it will give rise to the apical ectodermal ridge. O'Rahilly and Müller (1985) have called the portion of the ring between the upper and lower limbs the intermembral part. It overlies the underlying intraembryonic coelom, and later (between stages 12 and 13), the mesonephric duct and ridge. In stages 14–15 this portion of the ectodermal ring gives rise to the mammary line. In the unfolded embryo, caudal to the lower limb field, the ring passes distal to the cloacal membrane. In the folded embryo, this region becomes superior to the cloacal membrane and corresponds to the ectoderm associated with the external genitalia, particularly the genital tubercle and urogenital swellings, where it influences the internal and external descent of the testis and the formation of the inguinal canal.

Neural ectoderm

The neuroepithelium at the time of primary neurulation is pseudostratified. It has a midline hinge region, which, with concomitant wedging of the cells in the lateral wall of the neural groove, promotes neural tube formation. The processes of the neuroepithelium abut on to internal and external limiting membranes. This epithelium proliferates to form all the cell lines of the central nervous system and, via the production of neural crest, all the cell lines of the peripheral nervous system.

Notochord

During stage 10 the notochordal plate undergoes a process that is similar to, but a mirror image of, neurulation, and forms an epithelial tube from caudal to rostral, ending with the pharynx. The notochordal plate forms a deep groove, the vertical edges of the groove move medially and touch, and then the endodermal epithelium from each side fuses ventral to the notochord. The cells swell and develop an internal

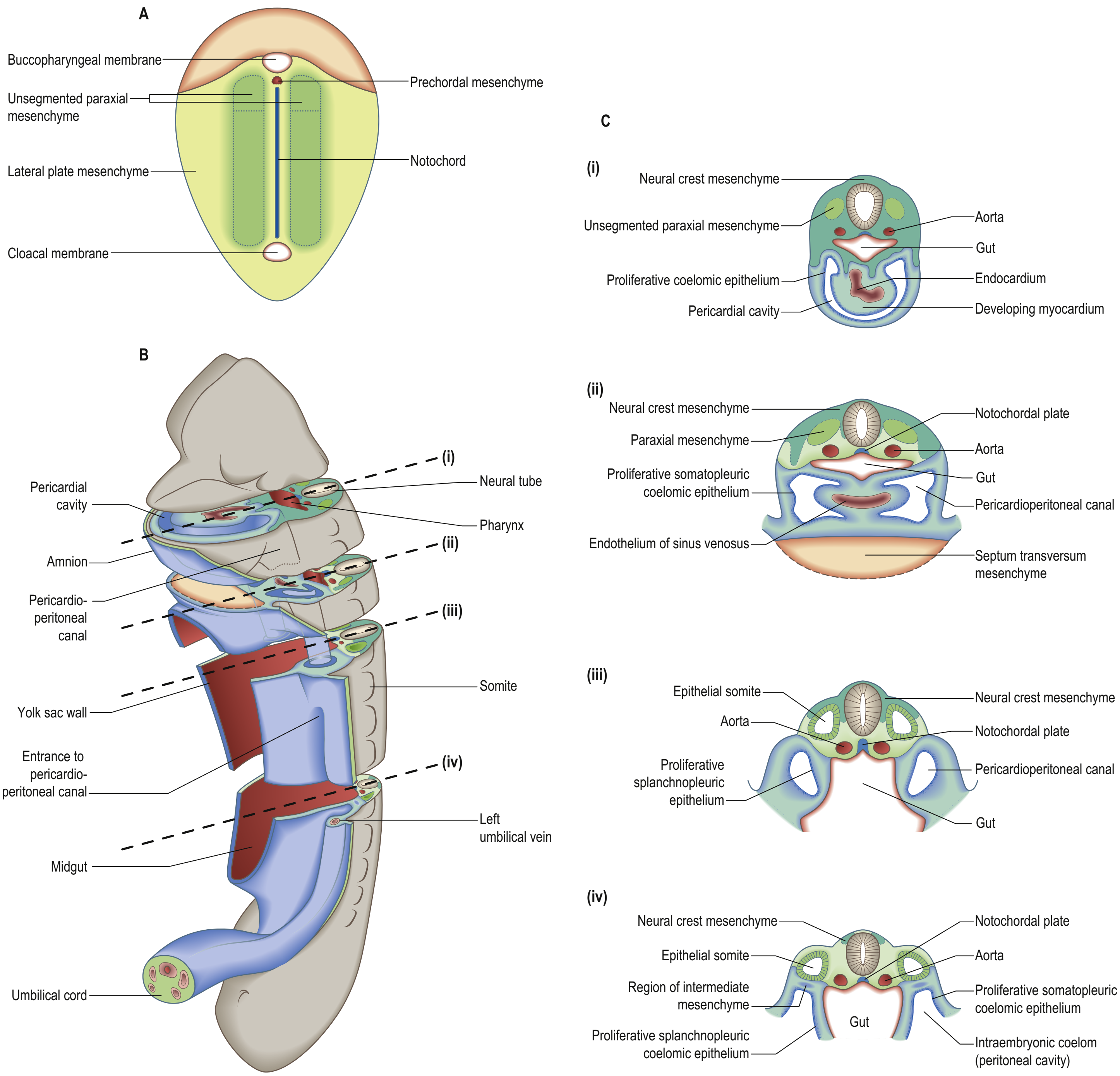
A
Buccopharyngeal membrane
Unsegmented paraxial mesenchyme
Lateral plate mesenchyme
Cloacal membrane
Prechordal mesenchyme
Notochord
B
Pericardial cavity
Amnion
Pericardio-peritoneal canal
Yolk sac wall
Entrance to pericardio-peritoneal canal
Midgut
Umbilical cord
(i)
(ii)
(iii)
(iv)
Neural tube
Pharynx
Somite
Left umbilical vein
C
(i)
Neural crest mesenchyme
Unsegmented paraxial mesenchyme
Proliferative coelomic epithelium
Pericardial cavity
Aorta
Gut
Endocardium
Developing myocardium
(ii)
Neural crest mesenchyme
Paraxial mesenchyme
Proliferative somatopleuric coelomic epithelium
Endothelium of sinus venosus
Notochordal plate
Aorta
Gut
Pericardioperitoneal canal
Septum transversum mesenchyme
(iii)
Epithelial somite
Aorta
Proliferative splanchnopleuric epithelium
Neural crest mesenchyme
Notochordal plate
Pericardioperitoneal canal
Gut
(iv)
Neural crest mesenchyme
Epithelial somite
Region of intermediate mesenchyme
Proliferative splanchnopleuric coelomic epithelium
Gut
Notochordal plate
Aorta
Proliferative somatopleuric coelomic epithelium
Intraembryonic coelom (peritoneal cavity)

Fig. 12.2 **A**, Mesoblast populations within the early embryonic disc. **B**, A stage 11 embryo, showing the position of the intraembryonic coelom (contained by the walls coloured blue) and the positions of the sections (i)–(iv) shown in **C**. **C**, Transverse sections, arranged cranial to caudal, from a stage 11 embryo; the populations of mesenchyme and the sites of mesenchymal proliferation are indicated.

pressure (turgor) that confers rigidity on the notochord. The notochord is surrounded by a basal lamina, which is initially connected to a basement membrane, referred to as a perinotochordal sheath (Trapani et al 2017); this term is subsequently applied to mesenchymal populations that surround the notochord. After stage 11 the tubular notochord is in contact with the neural tube dorsally and the endoderm ventrally. It is not a proliferative epithelium, but it has inductive effects on the overlying neural tube and the adjacent somites, and later provides a focus for sclerotomal migration.

Endoderm

The craniocaudal progression of development means that the endoderm of the early stomodeum develops ahead of other portions of the endodermal epithelium. The development of the pharyngeal arches and pouches (Ch. 17) is closely associated with the development of the neural ectoderm and proliferation of the neural crest. The respiratory diverticulum arises slightly later, when the postpharyngeal gut may also be distinguished. The endoderm gives rise to the epithelial lining of the respiratory and gastrointestinal tracts, the biliary system, and the urinary bladder and urethra.

Coelomic epithelium

The coelomic epithelium lines the intraembryonic coelom, which is subdivided into a midline pericardial cavity, two bilateral pericardioperitoneal canals, and (initially bilateral) peritoneal cavities which are continuous with the extraembryonic coelom. The coelomic epithelium is a germinal epithelium. It produces the myocardium and connective tissue populations for the viscera, and gives rise to the supporting cells for the germ cells, the epithelial lining of the urogenital tracts, and the mesothelial lining of the pericardial, pleural and peritoneal cavities.

Somites

Somites are discrete epithelial spheres formed by the transformation of paraxial mesoblast cells to epithelium once their migration is complete. Specific regions of somitic epithelium form local proliferative centres. Like neural and coelomic epithelium, somatic epithelium produces cells destined for different fates, at different developmental times. Somites can be seen on each side of the fusing neural tube in the human embryo from stage 9. Development proceeds in a craniocaudal direction: the original epithelial somites form the base of the skull and the vertebral

Endoderm epithelium	Coelomic wall epithelium	Mesenchyme
Primitive gut **Foregut** – recesses, diverticula and glands of the pharynx. General mucous glandular and duct-lining cells and the main follicular cells of the thyroid. Epithelium of pharyngeal pouches (tonsil, middle ear cavity, thymus, parathyroids 3 and 4, C cells of thyroid), adenoid, epithelial lining of the auditory tube, tympanic cavity, tympanic antrum, internal lamina of the tympanic membrane. **Respiratory tract** – epithelial lining, secretory and duct-lining cells of the trachea, bronchi, bronchioles and alveolar sacs. Epithelial lining, secretory and duct-lining cells of the oesophagus, stomach and duodenum. Hepatocytes of liver, biliary tract, exocrine and endocrine cells of the pancreas. **Midgut** – epithelial lining, glandular and duct-lining cells of the duodenum, jejunum, appendix, caecum, part of transverse colons. **Hindgut** – epithelial lining, glandular and duct-lining cells of part of the transverse, descending and sigmoid colons, rectum, upper part of anal canal. **Allantois** – urinary bladder, vagina, urethra, secretory cells of the prostate and urethral glands.	**Walls of intraembryonic coelom** **Primitive pericardium** – myocardium, parietal pericardium. **Pericardioperitoneal canals** – visceral, parietal and mediastinal pleura, pleuroperitoneal membranes contributing to diaphragm. *Splanchnopleuric epithelium* – visceral peritoneum of stomach, peritoneum of lesser and greater omenta, falciform ligament, lienorenal and gastrosplenic ligaments. *Somatopleuric epithelium* – parietal peritoneum. **Primitive peritoneal cavity** Splanchnopleuric epithelium – visceral peritoneal covering of mid- and hindgut, the mesentery, transverse and sigmoid mesocolons. Pronephros, epithelial lining of mesonephric ducts, vas deferens, epididymis, seminal vesicles, ejaculatory duct, ureters, vesical trigone. Müllerian ducts, epithelial lining of uterine tubes, body and cervix of uterus, vagina, broad ligament of uterus. Germinal epithelium of gonad (note the germ cells are not included on this chart because of their early sequestration into the extraembryonic tissues). Germinal epithelium forming cortex of suprarenal gland. *Somatopleuric epithelium* – parietal peritoneum, tunica vaginalis of testis.	**Paraxial mesenchyme (somites and somitomeres)** *Sclerotome* – vertebrae and portions of the neurocranium, axial skeleton. *Myotome* – all voluntary muscles of the head, trunk and limbs. Dermatome – dermis of skin over dorsal regions. **Intermediate mesenchyme** – connective tissue of gonads, mesonephric and metanephric nephrons, smooth muscle and connective tissues of the reproductive tracts. **Septum transversum** – epicardium, fibrous pericardium, portion of diaphragm, oesophageal mesentery, sinusoids of liver, tissue within lesser omentum and falciform ligament. **Lateral plate mesenchyme** *Splanchnopleuric layer* – smooth muscle and connective tissues of respiratory tract and associated glands. Smooth muscle and connective tissues of intestinal tract, associated glands and abdominal mesenteries. Smooth muscle and connective tissue of blood vessels (also see below). *Somatopleuric layer* – appendicular skeleton, connective tissue of limbs and trunk, including cartilage, ligaments and tendons. Dermis of ventral body wall and limbs. Mesenchyme of external genitalia. **Angiogenic mesenchyme** Endocardium of heart, endothelium of blood and lymphatic vessels, vessels of choroid plexus, sinusoids of liver and spleen, circulating blood cells, microglia, tissue macrophages.

Surface ectoderm epithelium	Neural plate epithelium	Neural crest
Ectodermal placodes Adenohypophysis. Sensory neurones of the cranial ganglia V, VII, VIII, IX, X. Olfactory receptor cells and olfactory epithelium. Epithelial walls of the membranous labyrinth, the cochlear organ of Corti. Lens of the eye. Enamel organs of the teeth. **Cranial structures** Secretory and duct-lining cells of the lacrimal, nasal, labial, palatine, oral and salivary glands. Epithelia of the cornea and conjunctiva. Epithelial lining of the external acoustic meatus and external epithelium of the tympanic membrane. Epithelial lining of the lacrimal canaliculi and nasolacrimal duct. Epithelial lining of the paranasal sinuses, lips, cheeks, gums and palate. **Epidermal structures** Most of the cutaneous epidermal cells, the secretory, duct-lining and myoepithelial cells of the sweat, sebaceous and mammary glands. Hair and nails. Proctodeal epithelium and epithelium of the terminal male urethra.	**CNS – Brain and spinal cord** Neurohypophysis. Prosencephalon (telencephalon and diencephalon) – cerebral hemispheres, basal nuclei. Mesencephalon – cerebral peduncles, tectum, tegmentum. Rhombencephalon (metencephalon and myelencephalon) – cerebellum, pons, medulla oblongata. Spinal cord. All cranial and spinal motor nerves. All CNS neurones, including preganglionic efferent neurones, that have somata within the CNS. Astrocytes and oligodendrocytes. Ependyma lining the cerebral ventricles, aqueduct and central canal of the brain and spinal cord, tanycytes, cells covering the choroid plexuses, circumventricular cells. Retina and optic nerve (II), epithelium of the iris, ciliary body and processes.	**Neural derivatives** Sensory neurones of the cranial ganglia V, VII, VIII, IX, X. Sensory neurones of the spinal dorsal root ganglia and their peripheral sensory receptors. Satellite cells in all sensory ganglia. Sympathetic ganglia and plexuses: neurones and satellite cells. Parasympathetic ganglia and plexuses: neurones and satellite cells. Enteric plexuses: neurones and glial cells. Schwann cells of all the peripheral nerves. Medulla of the suprarenal gland. Chromaffin cells. Carotid body type I cells (and type II, satellite type cells). Calcitonin-producing cells (C cells). Melanocytes. **Mesenchymal derivatives in the head** Frontal, parietal, squamous temporal, nasal, vomer and palatine bones, maxillae and mandible. Meninges. Choroid and sclera of eye. Connective tissue of lacrimal, nasal, labial, palatine, oral and salivary glands. Dentine of teeth. Connective tissues of head, including cartilage, ligaments and tendons. Connective tissues of thyroid gland and of the pharyngeal pouches, i.e. parathyroid glands, thymus. Tunica media of the outflow tract of the heart and the great vessels.

Fig. 12.3 Structures that will be derived from specific epithelial and mesenchymal populations in the early embryo. Abbreviation: CNS, central nervous system.

column and ribs and the dorsolateral portion, the dermomyotome, gives rise to the majority of the skeletal muscle of the body, including that in the limbs.

The relative dispositions of the neural, endodermal and coelomic epithelia are shown in Fig. 12.1.

Mesenchymal populations in the embryo

The term 'mesenchyme' refers to the three-dimensional arrangement of unrestricted and undetermined cell populations (expressing a range of surface signalling molecules and receptors), and the extracellular secretions of these cells (collectively producing the extracellular matrix (ECM), e.g. collagens, elastins, proteoglycans and glycosaminoglycans (GAGs)). The proportions of fibrous extracellular proteins (collagens) and the hydrophilic GAGs are important, because they confer turgidity and stiffness on developing tissues, open migration routes and provide 'signposts' for cellular interactions by facilitating the local deposition of growth factors (Ch. 11) (Loganathan et al 2016). Understanding the interactions between ECM stiffness, the mechanotransduction of forces within early mesenchymal populations, and how these interact in an epigenetic manner during development, has become an important topic of study (Hadden et al 2017).

In a stage 10 embryo the major mesenchymal populations are in place. Mesoblast is still being generated at the primitive streak and moving into the presomitic mesenchymal population adjacent to the notochord and some mesoblast is also contributing to the lateral regions of the embryo. The different mesenchymal populations within the embryo from stage 10 onwards are described below. The relative dispositions of the early mesenchymal populations are shown in Fig. 12.2.

Axial mesenchyme

The first epiblast cells to ingress through the primitive streak form the endoderm and notochord, and initially occupy a midline position. The earliest population of endodermal cells rostral to the notochordal plate is termed the prechordal plate. The notochordal cells remain medially and the endodermal cells subsequently flatten and spread laterally. The population of cells that remain mesenchymal in contact with the floor of the neural groove, just rostral to the notochordal plate, is the prechordal mesenchyme (**Fig. 12.4**). These axial mesenchyme cells are tightly packed, unlike the more lateral paraxial cells but, unlike the notochord, they are not contained in an extracellular sheath. They are displaced laterally at the time of head flexion and form bilateral premandibular mesenchymal condensations. They become associated with the local paraxial mesenchyme. Experimental orthotopic grafting has demonstrated that these cells leave the edges of the prechordal mesenchyme and migrate laterally into the periocular mesenchyme, where they give rise to all of the extraocular muscles.

Paraxial mesenchyme

Mesenchyme adjacent to the notochord and developing neural tube is termed paraxial mesenchyme. It arises from epiblast cells that undergo epithelial to mesenchymal transition and ingress through the primitive streak. This population of cells is termed paraxial mesoblast when migrating; at their final destination the cells form epithelial structures. Those cells ingressing through the primitive node will form the medial part of the paraxial mesenchyme, and cells that ingress through the rostral streak will form the lateral part (see Fig. 10.3). Before somite formation, this mesenchymal tissue is also termed presomitic or unsegmented mesenchyme in mammals (analogous to the segmental plate in birds). Paraxial mesenchyme extends rostrally from the primitive streak to the prechordal plate, which is immediately rostral to the notochord.

Caudal to the otic vesicle, the paraxial mesenchyme on each side of the rhombencephalon segments into somites as the neural folds elevate and neurulation begins; somites are therefore post-otic. During somitogenesis, mesoblastic cells show changes in shape and in cell–cell adhesion. They undergo mesenchymal to epithelial transformation and become organized into epithelial somites: this process begins at the eighth somitomere, just caudal to the midpoint of the notochordal plate (Ch. 18). Somite one is also termed the first occipital somite. The post-otic paraxial cell population is termed paraxial mesoderm in contemporary literature.

Skeletal muscle throughout the body is derived from paraxial mesoblast-derived somatic epithelium, which proliferates to form myoblastic populations that migrate to the head, body and limbs.

Septum transversum

Early mesenchyme that invaginates through the middle part of the primitive streak comes to lie rostral to the buccopharyngeal membrane, where the cells undergo mesenchymal to epithelial transformation to form the wall of the pericardial coelom. As this epithelium proliferates, the visceral pericardial wall gives rise to myocardium. The parietal pericardial wall forms mesenchyme, initially termed precardiac, or cardiac, mesenchyme, which is able to induce proliferation of hepatic endodermal epithelium. With further proliferation, the precardiac mesenchyme forms a ventral mass caudal to the heart, the septum transversum, which separates the foregut endoderm from the pericardial coelom (see Fig. 12.2). By stage 11 the septum transversum extends dorsally on each side of the developing gut and becomes continuous with the mesenchymal populations that proliferate from the walls of the pericardioperitoneal canals. Cells of the septum transversum give rise to the sinusoids of the liver, the central portions of the respiratory diaphragm and the epicardium (visceral layer of serous pericardium).

Neural crest

The neural crest is a unique mesenchymal population. It arises from stage 10 onwards from cells that lie initially at the outermost edges of the neural plate, between the presumptive epidermis and the neural tube, and become committed to a neural crest lineage before the neural plate begins to fold. The neural crest gives rise to neuronal populations in the head and trunk, and provides an extensive non-neuronal mesenchymal population in the head with attributes similar to somatopleuric mesenchyme in terms of patterning. After neurulation, neural crest cells form a transient axial population and then disperse, in some cases migrating over considerable distances, to a variety of different developmental fates. Unlike mesoblast, which is produced from the primitive streak, none of the cells that arise from the neural crest subsequently become epithelial. The development and fate of head and trunk neural crest cells are very different and therefore they will be considered separately.

Head neural crest

Head neural crest migrates before the neural tube closes: the crest cell population arising from the rostral neural plate is larger than that found at any trunk level. Each brain region has its own crest population that migrates dorsolaterally around the sides of the neural tube to reach the ventral side of the head. Crest cells surround the prosencephalic and optic vesicles, and occupy each of the pharyngeal arches (Ch. 17). They provide mesenchyme cells that will produce the connective tissue in parts of the neuro- and viscerocrania: all cartilage, bone, ligament, tendon, dermal components and glandular stroma in the head; and contribute to the tunica media of the aortic arch arteries.

Trunk neural crest

Unlike its counterpart in the head, trunk neural crest is formed as the neural tube closes rostrocaudally, which means that various stages of crest development can be found in the more caudal regions of an embryo. As the neural tube begins to fuse dorsally in the midline, the neural crest cells lose their epithelial characteristics and junctional connections, and form a band of loosely arranged mesenchyme cells immediately dorsal to the neural tube and beneath the ectoderm. Initially, most of the crest cells lie with their long axes perpendicular to the long axis of the neural tube. Later, the cell population expands laterally and around the neural tube as a sheet. Trunk neural crest cells move from their position dorsal to the neural tube via three routes: dorsolaterally, to form dorsal root ganglia throughout the trunk; ventrally, to form sympathetic ganglia, enteric nerves and the suprarenal medulla; and rostrocaudally, along the aorta, to form the pre-aortic ganglia (see Fig. 14.6). In a second migration route, crest cells pass dorsolaterally between the ectoderm and the epithelial plate of the somite into the somatopleure, where they eventually form melanocytes in the skin.

Lateral plate

Lateral plate is the term for the early unsegmented mesoblast population lateral to the paraxial mesenchyme. Mesoblastic cells that arise from the middle of the primitive streak (primary mesenchyme) migrate cranially, laterally and caudally to reach their destinations, where they undergo mesenchymal to epithelial transformation to form a continuous layer subjacent to the ectoderm dorsally and the endoderm ventrally. The epithelium faces a new intraembryonic cavity, the intraembryonic coelom, which becomes confluent with the extraembryonic coelom and provides a route for the circulation of coelomic fluid through the embryo. Once formed, the intraembryonic coelomic wall becomes a proliferative epithelium that produces new populations of mesenchymal cells. The mesenchymal population subjacent to the ectoderm is termed somatopleuric mesenchyme, produced by the somatopleuric coelomic epithelium. The mesenchymal population surrounding the endoderm is termed splanchnopleuric mesenchyme, produced by the splanchnopleuric coelomic epithelium (see Fig. 12.2).

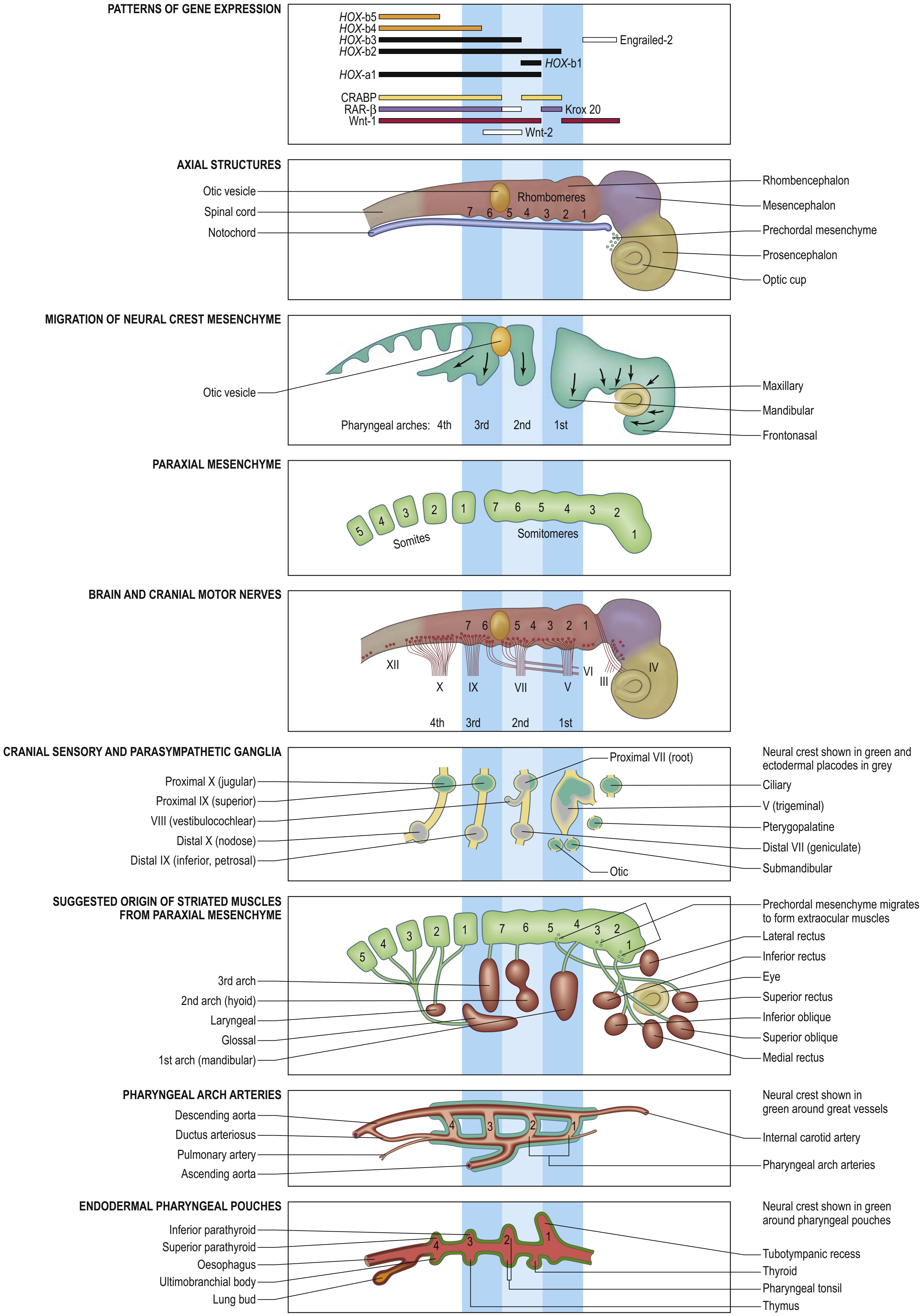
PATTERNS OF GENE EXPRESSION
HOX-b5
HOX-b4
HOX-b3
HOX-b2
Engrailed-2
HOX-b1
HOX-a1
CRABP
RAR-β
Krox 20
Wnt-1
Wnt-2
AXIAL STRUCTURES
Otic vesicle
Spinal cord
Notochord
Rhombomeres
7 6 5 4 3 2 1
Rhombencephalon
Mesencephalon
Prechordal mesenchyme
Prosencephalon
Optic cup
MIGRATION OF NEURAL CREST MESENCHYME
Otic vesicle
Pharyngeal arches: 4th 3rd 2nd 1st
Maxillary
Mandibular
Frontonasal
PARAXIAL MESENCHYME
5 4 3 2 1
Somites
7 6 5 4 3 2 1
Somitomeres
BRAIN AND CRANIAL MOTOR NERVES
7 6 5 4 3 2 1
XII
X
IX
VII
V
VI
III
IV
4th 3rd 2nd 1st
CRANIAL SENSORY AND PARASYMPATHETIC GANGLIA
Proximal X (jugular)
Proximal IX (superior)
VIII (vestibulocochlear)
Distal X (nodose)
Distal IX (inferior, petrosal)
Proximal VII (root)
Otic
Neural crest shown in green and ectodermal placodes in grey
Ciliary
V (trigeminal)
Pterygopalatine
Distal VII (geniculate)
Submandibular
SUGGESTED ORIGIN OF STRIATED MUSCLES FROM PARAXIAL MESENCHYME
5 4 3 2 1
7 6 5 4 3 2 1
3rd arch
2nd arch (hyoid)
Laryngeal
Glossal
1st arch (mandibular)
Prechordal mesenchyme migrates to form extraocular muscles
Lateral rectus
Inferior rectus
Eye
Superior rectus
Inferior oblique
Superior oblique
Medial rectus
PHARYNGEAL ARCH ARTERIES
Descending aorta
Ductus arteriosus
Pulmonary artery
Ascending aorta
4 3 2 1
Neural crest shown in green around great vessels
Internal carotid artery
Pharyngeal arch arteries
ENDODERMAL PHARYNGEAL POUCHES
Inferior parathyroid
Superior parathyroid
Oesophagus
Ultimobranchial body
Lung bud
4 3 2 1
Neural crest shown in green around pharyngeal pouches
Tubotympanic recess
Thyroid
Pharyngeal tonsil
Thymus

Fig. 12.4 The organization of the head and pharynx in an embryo at about stage 14. The individual tissue components have been separated but are aligned in register through the numbered zones.

It is important to note that these terms are relevant only caudal to the third pharyngeal arch. Rostral to this arch, there is a sparse mesenchymal population between the pharynx and the surface ectoderm prior to migration of the head neural crest, and there are no landmarks with which to demarcate lateral from paraxial mesenchyme. This unsplit lateral plate is believed to contribute to the cricoid and arytenoid cartilages, the tracheal rings and the associated connective tissue.

Somatopleuric mesenchyme

Somatopleuric mesenchyme produces a mixed population of connective tissues and has a significant organizing effect at the level of the developing limbs. The pattern of limb development is controlled by information contained in the somatopleuric mesenchyme. Regions of the limb are specified by interaction between the surface ectoderm (apical ectodermal ridge) and underlying somatopleuric mesenchyme and together these tissues form the progress zone of the limb. The somatopleuric mesenchyme in the limb bud also specifies the postaxial border of the developing limb. Somatopleuric mesenchyme gives rise to the connective tissue elements of the appendicular skeleton, including the bones, cartilages and associated ligaments and tendons of the pectoral and pelvic girdles and the limbs. It also gives rise to the dermis of the skin of the ventral and lateral body walls and of the limbs.

Splanchnopleuric mesenchyme

Splanchnopleuric mesenchyme surrounds the developing gut and respiratory tubes, contributing connective tissue cells to the lamina propria and submucosa, and smooth muscle cells to the muscularis mucosae and muscularis externa. It plays a patterning role in endodermal development, specifying the region and villus type in the gut, and the branching pattern in the respiratory tract.

Intermediate mesenchyme

Intermediate mesenchyme is a loose collection of cells found between the somites and the lateral plate (see Fig. 12.2). Its development is closely related to the progress of differentiation of the somites and the proliferating coelomic epithelium from which it is derived. Intermediate mesenchyme is not present before somitogenesis or the formation of the eighth somite. In embryos with 8–10 somites, it is present lateral to the sixth somite but does not extend cranially. The mesenchyme cells are arranged as layers, one continuous with the dorsal side of the paraxial mesenchyme and the somatopleure, the other with the ventral side of the paraxial mesenchyme and the splanchnopleure.

As development proceeds, the intermediate mesenchyme forms a loosely packed dorsolateral cord of cells that lengthens at the caudal end and ultimately joins the cloaca: it gives rise to the nephric system, gonads and reproductive ducts.

Angioblastic mesenchyme

Mesenchymal cells that give rise to the cellular elements of the blood, the endothelium and the mesenchymal layers of the tunica externa and tunica adventitia of blood and lymphatic vessels, arise initially from extraembryonic and later from intraembryonic sources. Evidence suggests that endodermal tissues are necessary for endothelial differentiation, particularly in the early foregut. Angioblastic mesenchyme forms early in postfertilization week 3 from extraembryonic mesenchyme in the splanchnopleure of the yolk sac, in the body stalk (containing the allantois), and in the somatopleure of the chorion. Later, contiguous islands merge, forming a continuous network of fine vessels. Intraembryonic blood vessels are first seen at the endoderm–mesenchyme interface within the lateral splanchnic mesenchyme at the caudolateral margins of the cranial intestinal portal. Angioblastic competence has been demonstrated within the ventral (splanchnopleuric) mesenchyme with which the endoderm interacts. The notochord and prechordal plate do not contain angiogenic cells and ectodermal tissues do not appear to give rise to angiogenic cells. Somites, derived from paraxial mesenchyme, have been shown to be a source of angioblasts that either differentiate with the somite derivatives, or migrate to the neural tube, ventrolateral body wall, limb buds, mesonephros and the dorsal part of the aorta.

The earliest angiogenic mesenchymal cells form blood vessels by vasculogenesis, a process in which new vessels (e.g. endothelial heart tubes, dorsal aortae, umbilical and early vitelline vessels) develop *in situ* (Ch. 13). Later vessels develop by angiogenesis, sprouting and branching from the endothelium of pre-existing vessels; this process is the means by which most other vessels develop. The ultimate pattern of vessels is controlled by the surrounding non-angiogenic mesenchyme: vessels become morphologically specific for the organ in which they develop, and immunologically specific, expressing organ-specific proteins. Blood cells also arise from extraembryonic tissues of the secondary yolk sac, with three overlapping waves of production as intraembryonic regions become seeded with haemopoietic stem cell precursors (Ch. 13). They are not derived from the same precursor populations that produce blood and lymphatic vessels.

Key references

O'Rahilly R, Müller F 1985 The origin of the ectodermal ring in staged human embryos of the first 5 weeks. Acta Anat 122:145–57.

Richardson MK, Keuck G 2002 Haeckel's ABC of evolution and development. Biol Rev Camb Philos Soc 77:495–528.

References

Hadden WJ, Young JL, Holle AW et al 2017 Stem cell migration and mechanotransduction on linear stiffness gradient hydrogels. Proc Natl Acad Sci U S A 114:5647–52.

Loganathan R, Rongish BJ, Smith CM et al 2016 Extracellular matrix motion and early morphogenesis. Development 143:2056–65.

O'Rahilly R, Müller F 1985 The origin of the ectodermal ring in staged human embryos of the first 5 weeks. Acta Anat 122:145–57.

Richardson MK, Keuck G 2002 Haeckel's ABC of evolution and development. Biol Rev Camb Philos Soc 77:495–528.

Trapani V, Bonaldo P, Corallo D 2017 Role of the ECM in notochord formation, function and disease. J Cell Sci 130:3203–11.

CHAPTER

13

Development of the heart and circulation

The early embryonic circulation is symmetric (Fig. 13.1). It is modified throughout development to produce a functioning heart and fetal circulation that is connected to the placenta, and changes rapidly at birth to accommodate disconnection from the placenta and the start of gaseous exchange in the lungs. Major restructuring of early vessels occurs as the embryo grows; anastomoses form and then disappear, capillaries fuse and give rise to arteries or veins, and the direction of blood flow may reverse several times before the final arrangement of vessels is completed. Embryonic cell populations arise and become restricted to a cardiovascular phenotype in spatially and temporally defined interactions during the earliest stages of development.

Cells from mesenchyme derived from the midline splanchnopleuric coelomic epithelium initially form both the myocardium and the endocardial lining. Later, this splanchnopleuric coelomic epithelium is also the source of the epicardium, the coronary arteries and the interstitial fibroblasts of the heart. (The epicardium, sometimes included in descriptions of the myocardium as 'epimyocardium', is not present at early stages of heart development.) A further cell population of head neural crest mesenchyme that arises from the region between the otic vesicle and the caudal limit of somite 3 later migrates to the arterial pole of the heart and contributes to the formation of the valves and aortic arch arteries (see Fig. 17.9).

The position of the developing myocardium is intimately related to the formation of the intraembryonic coelom and the relative movement of that tubular structure during neurulation and somitogenesis. The splanchnopleuric wall of the early midline intraembryonic coelom, directly adjacent to the endoderm, is a horseshoe-shaped proliferative epithelium that produces cardiogenic mesenchyme. It is termed the

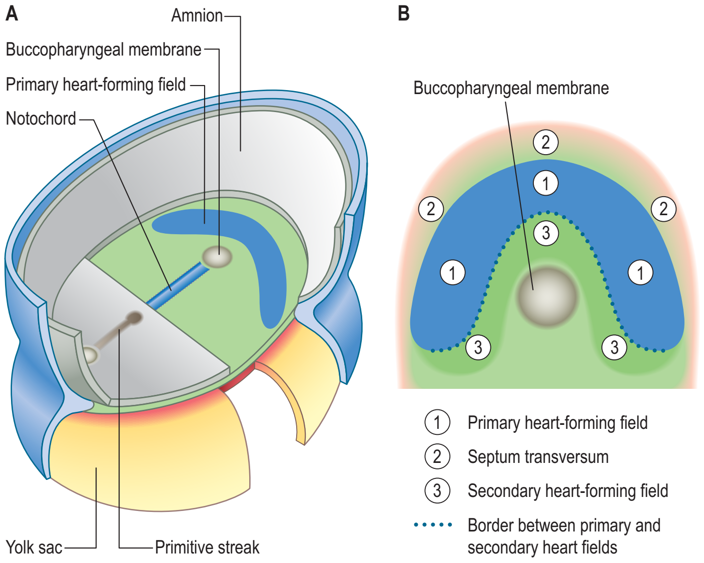
A
Amnion
Buccopharyngeal membrane
Primary heart-forming field
Notochord
Yolk sac
Primitive streak
B
Buccopharyngeal membrane
②
①
②
②
③
①
①
③
③
① Primary heart-forming field
② Septum transversum
③ Secondary heart-forming field
••••• Border between primary and secondary heart fields

Fig. 13.2 **A**, The early embryonic disc viewed from a dorsolateral perspective, showing the position of the primary heart-forming field relative to the surface ectoderm of the trilaminar disc. **B**, The rostral end of the unfolded embryonic disc from a dorsal perspective, showing the position of the mesenchymal populations that will give rise to the primary heart-forming field, septum transversum mesenchyme and second heart-forming field.

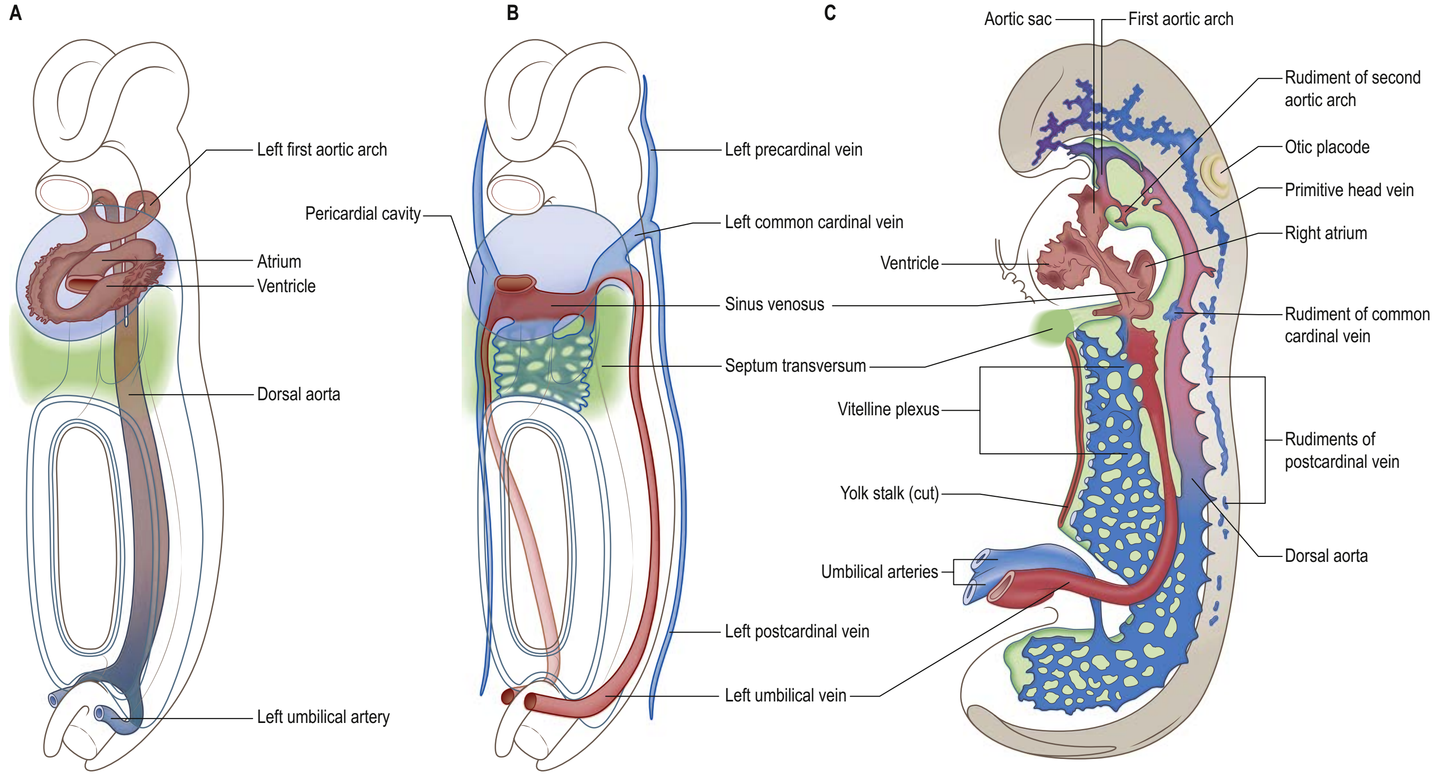
A
Left first aortic arch
Atrium
Ventricle
Dorsal aorta
Left umbilical artery
B
Pericardial cavity
Left precardinal vein
Left common cardinal vein
Sinus venosus
Septum transversum
Left postcardinal vein
Left umbilical vein
C
Aortic sac
First aortic arch
Rudiment of second aortic arch
Otic placode
Primitive head vein
Right atrium
Ventricle
Rudiment of common cardinal vein
Vitelline plexus
Rudiments of postcardinal vein
Yolk stalk (cut)
Umbilical arteries
Dorsal aorta

Fig. 13.1 The early, symmetric blood vascular system. **A**, Ventrolateral view of the endothelial profile of the heart, the first aortic arch arteries and the dorsal aorta shown in relation to the major epithelial populations. **B**, Ventrolateral view of the main venous channels shown in relation to the major epithelial populations. **C**, Left lateral view of the blood vascular system of a stage 11 human embryo; only the endothelial lining of the heart tube is shown. At this stage, the arteries and veins are in the process of development and no true circulation is yet established.

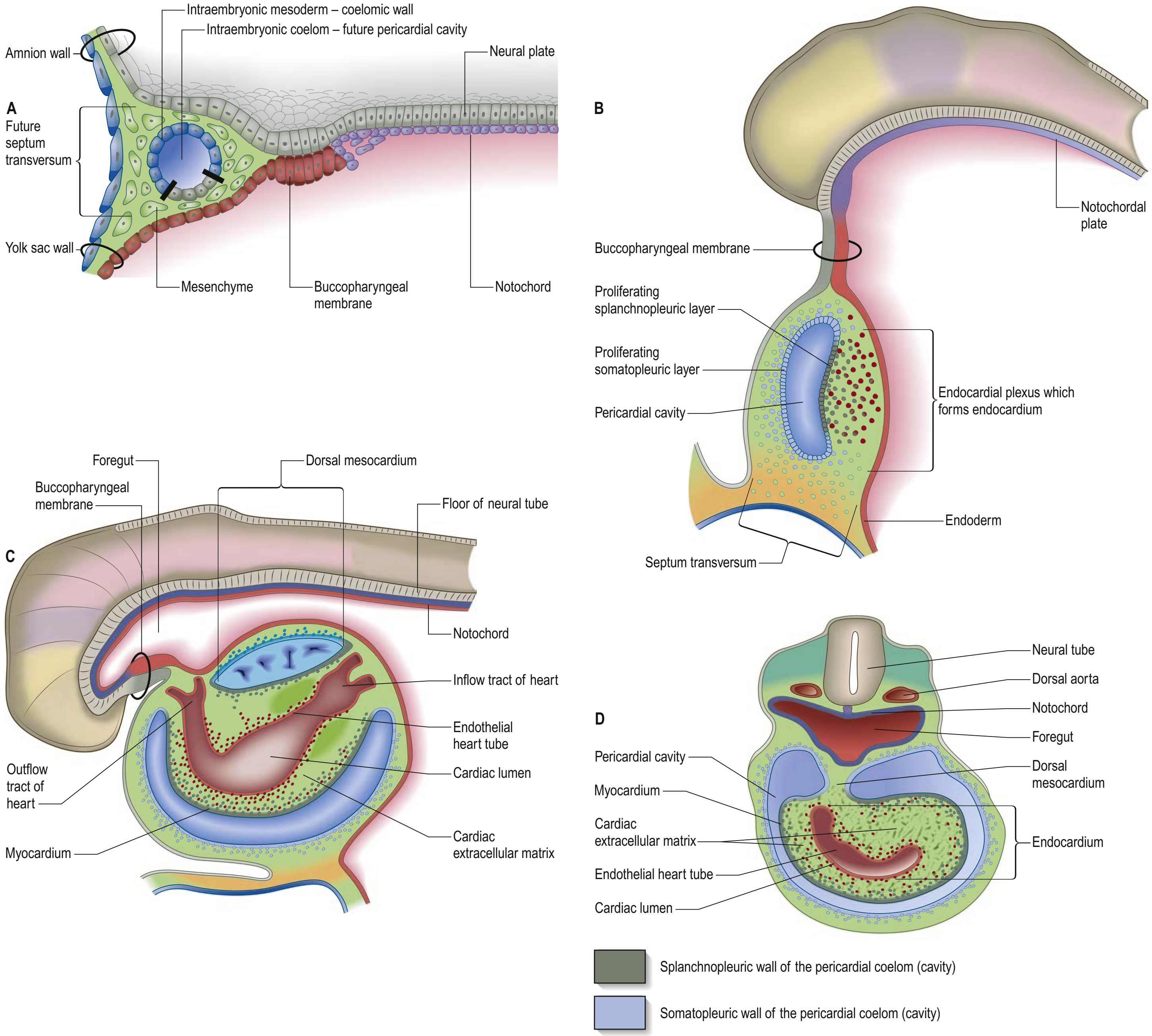
A
Amnion wall
Intraembryonic mesoderm – coelomic wall
Intraembryonic coelom – future pericardial cavity
Neural plate
Future septum transversum
Yolk sac wall
Mesenchyme
Buccopharyngeal membrane
Notochord
B
Notochordal plate
Buccopharyngeal membrane
Proliferating splanchnopleuric layer
Proliferating somatopleuric layer
Pericardial cavity
Endocardial plexus which forms endocardium
Endoderm
Septum transversum
C
Foregut
Dorsal mesocardium
Buccopharyngeal membrane
Floor of neural tube
Notochord
Inflow tract of heart
Endothelial heart tube
Cardiac lumen
Outflow tract of heart
Cardiac extracellular matrix
Myocardium
D
Neural tube
Dorsal aorta
Notochord
Foregut
Dorsal mesocardium
Pericardial cavity
Myocardium
Cardiac extracellular matrix
Endocardium
Endothelial heart tube
Cardiac lumen
Splanchnopleuric wall of the pericardial coelom (cavity)
Somatopleuric wall of the pericardial coelom (cavity)

Fig. 13.3 **A**, A median section through part of the embryonic disc to show the position of the future pericardial cavity before head folding. **B**, A median section through the cranial end of a human embryo during early head folding, showing its reversal effect on the position of the pericardium. **C**, A median section through the cranial end of a human embryo after head folding, showing the pericardial cavity and endothelial heart tube now located ventral to the foregut. **D**, A horizontal section through the pericardium and endothelial heart tube shown in **C**. The position of the dorsal mesocardium, a source of secondary heart field mesenchyme, is indicated. Circles and dots denote cells migrating away from proliferating epithelia.

cardiac crescent or primary heart-forming field (Fig. 13.2) and is characterized by the expression of myocardium-specific markers, such as cardiac myosin and the cardiac transcription factor Nkx2-5. The area of the coelomic epithelium dorsomedial to the primary heart-forming field will later also add to the forming heart tube and is therefore named the secondary heart-forming field (see Fig. 13.2). These two myocardial fields may represent distinct myocardial lineages; they both express Islet1 but they sequentially add to different parts of the heart.

The endocardium that lines the cardiac lumen develops from the coelomic splanchnopleuric epithelium during stages 8 and 9. Individual endocardial cells arise from it close to the ventrolateral edges of the cranial intestinal portal and form an endocardial plexus between the splanchnopleuric coelomic epithelium and the foregut endoderm. This plexus of cells, formed initially by vasculogenesis and subsequently from angioblastic mesenchyme, is one of the earliest intraembryonic vascular precursors to appear. The cells express molecular markers of both the myocardial and the endothelial cell lineages, indicating that the endocardium has a different origin than other endothelial populations. The cells of the endocardial plexus aggregate to form two separate endocardial epithelial tubes that fuse across the midline, from the arterial pole to the venous pole, producing a single linear heart tube.

The development of the early heart is described below, followed by the formation of the early compartments of the heart and their later septation.

FORMATION OF THE HEART TUBE

During the process of embryonic head folding, the midline splanchnopleuric coelomic epithelium (now cardiogenic epithelium) becomes positioned ventral to the foregut; the portion of the intraembryonic coelomic cavity it surrounds is the future pericardial cavity (Fig. 13.3). Populations of cardiac myocytes now arise from the ventral proliferating coelomic epithelium and surround the endocardial linear heart tube forming the early myocardium; these cells will have undergone restriction, differentiation and most will have left the cell cycle (Ch. 11). The secondary heart-forming field proliferates and adds cells to this bilaminar heart tube after embryonic head folding. It has been suggested that the secondary heart-forming field only contributes cells to those cardiac components that are required for the pulmonary circulation: namely, the right ventricle and outflow tract at the arterial pole, and the dorsal atrial wall and atrial septum at the venous pole. However, a type of secondary heart-forming field can also be distinguished in zebrafish and other chordates that lack a pulmonary circulation, implying that it is evolutionarily conserved independent of the presence of a pulmonary circulation (Sizarov et al 2016).

The pericardial cavity and myocardium gradually extend around the forming endocardial tube, leaving the dorsal mesocardium as a transient connection between the forming heart tube and the dorsal pericardial wall, analogous to the mesentery of the intestines (see Fig. 13.3C–D). The dorsal mesocardium is contiguous with the splanchnopleuric mesenchyme that surrounds the embryonic foregut and the developing lung buds and is the site of early mediastinal mesenchyme production. It disappears as a mesenteric entity in embryos with 8–12 somites. The partial breakdown of the dorsal mesocardium creates the transverse sinus of the pericardium that extends across the pericardial cavity from side to side, dorsal to the heart. Persisting dorsal mesocardium at the venous pole remains connected to the splanchnopleuric mesenchyme in which the pulmonary veins will develop; it is also confluent with the septum transversum mesenchyme, in which the liver will later develop.

By stage 10 (28–29 days postfertilization; embryonic stages 10–23 correlated to postfertilization days of development and postmenstrual weeks of pregnancy are shown in Fig. 23.3) a single endocardial tube is established that is almost completely surrounded by myocardial cells. This arrangement of an outer myocardial sleeve containing an inner endocardial tube constitutes the primary heart tube. The primary myocardium will not only give rise to the major parts of the conduction system of the heart, including the sinus node, the atrioventricular node, and the atrioventricular bundle, but also to part of the floor of the right atrium (the vestibule) and the entire atrioventricular canal. An enlarging space between the endocardial tube and the developing myocardium is filled by a meshwork of cardiac extracellular matrix proteins, produced by the cardiac myocytes, which promotes occlusion of some parts of the early heart tube during myocardial contraction and mechanical assistance for the generation of flow of early blood. There are heterochronic differences between species in these processes, for example, in the mouse, cardiac chambers start to form before a distinct linear heart tube has appeared.

Endocardial cushions

The extracellular matrix of the embryonic heart (see Fig. 13.3C–D), historically termed cardiac jelly, is composed of hyaluronic acid, hyaluronidase and fibronectin among other components. Inductive signals originating from the cardiac myocytes, such as BMP2 and TGF-β, lead to the activation of a subset of endocardial epithelial cells that will line the future atrioventricular canal and the proximal outflow tract; in the future left ventricle, endocardial cells do not undergo such an activation. The activated endocardial cells lose their cell-to-cell connections and undergo an epithelial to mesenchymal transition. Their expression of neural cell adhesion molecule (N-CAM) decreases and expression of substrate adhesion molecules such as chondroitin sulphate and fibronectin increases. Expression of type I procollagen is initiated and cytoskeletal re-arrangements facilitate cell migration into the cardiac extracellular matrix where they continue to proliferate. The cells and the locally accumulated extracellular matrix molecules, form the endocardial or cardiac cushions. Endocardial cushions initially function as valves in the embryonic heart: they give rise to the valves of the atrioventricular canal and the outflow tract and also supply the mesenchyme that is needed to complete the septation of the atria, ventricles and the outflow tract. This particular epithelial to mesenchymal transition may be the only example of a mesenchymal population derived from an endothelial lineage; endothelial to mesenchymal transformation may be relevant to later circulatory pathologies (Suzuki et al 2018, Kovacic et al 2019).

Looping of the heart tube

The early primary heart tube is initially bilaterally symmetric and has the form of an inverted 'Y'. The caudal 'legs' of the Y are positioned on either side of the cranial intestinal portal, where they form the venous pole of the heart (**Fig. 13.4A–C**). The rostral 'stem' of the Y connects cranially with the future aortic arch arteries, forming the arterial pole of the heart. From the start, both poles are connected with the systemic vessels that run from the embryo, yolk sac and placenta. The pulmonary veins form later, their initial venous primordium becoming evident in the dorsal mesocardial mesenchyme. Myocardium from the secondary heart-forming field continues to be added to the heart, forming the smooth dorsal wall of the left atrium, and providing the site where the primary atrial septum will form.

The putative cardiac segments are not present in the early linear heart tube. The definitive cardiac chambers are formed by local differentiation and expansion, or 'ballooning', of the myocardial walls of the primary heart tube, indicating that cardiac myocyte identity is dependent on genetic, spatial and temporal signals and lacks a fixed ontogeny. Genetic fate map studies have shown that the primary heart tube will contribute to only two compartments: the legs of the inverted Y of the primary heart tube contain precursor cells of the atrioventricular canal, while the stem of the inverted Y contains myocardial precursor cells of the left ventricle (van Eif et al 2018). The atrioventricular canal precursors finally reside in the left ventricular free wall and the cells of the original embryonic left ventricle largely end up in the left face of the ventricular septum. The embryonic outflow tract contributes to the right ventricle.

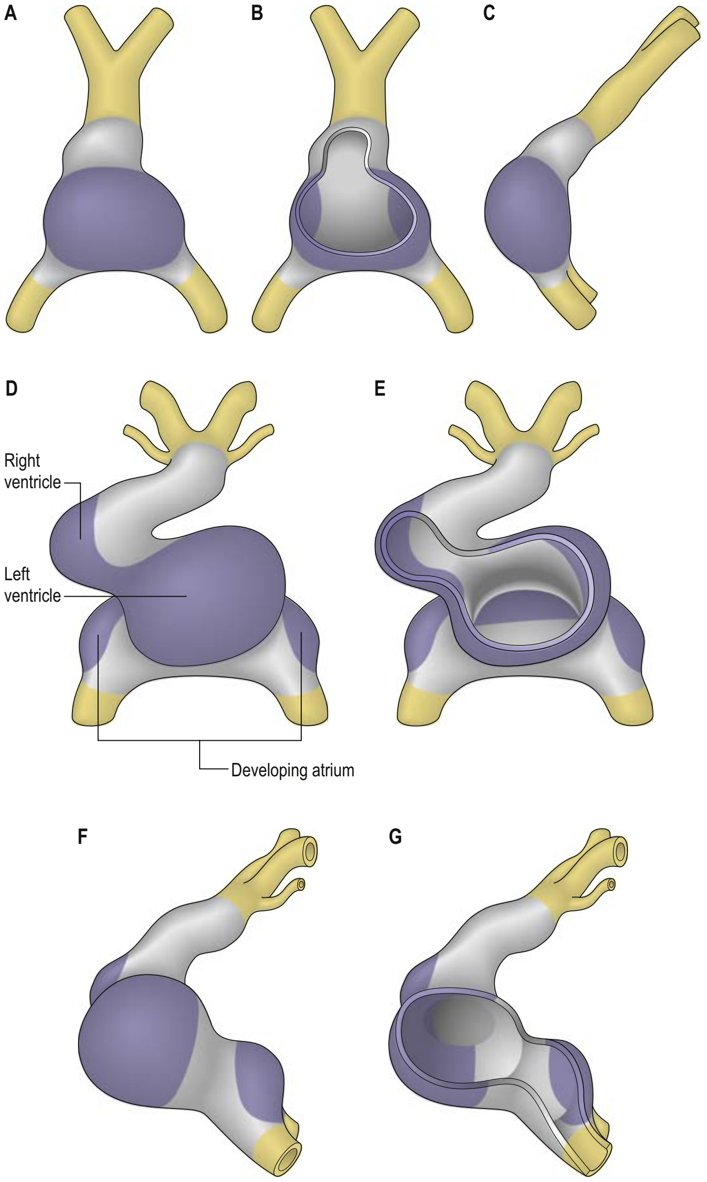

Fig. 13.4 Local expansion of the myocardial wall of the early heart tube and heart tube looping. **A**, Ventral view. **B**, The ventral wall has been removed to show the inner aspect of the early heart tube. **C**, Left lateral view. The early heart tube is shaped like an inverted 'Y'. The legs of the Y pass caudal to each side of the cranial intestinal portal. In the early heart tube, the myocardium of the stem of the Y (purple) contains only precursor cells for the left ventricle. The remaining myocardium (grey) contains only precursor cells for the atrioventricular canal and atria. The precursor left ventricular cells expand first. **D–G**, The later heart tube, showing looping. **D**, Ventral view. **E**, The ventral wall has been removed to show the inner aspect of the folding heart tube. **F**, Left lateral view. **G**, The lateral wall has been removed to show the inner aspect of the heart from the left. In **D** and **E**, the expansion of the right ventricle can be seen and the heart tube has elongated to the right. The developing atrium can be seen dorsolaterally in **D**–**G**.

The nodal/pitx2/cited-2 signalling pathway that determines the formation of the morphologically left-sided or right-sided features in the lungs, bronchial tree, liver and spleen is also expressed in the heart outflow tract and atrial appendages (Ocaña et al 2017). The lengthening heart tube bends ventrally and rightwards, concomitant with the partial breakdown of the dorsal mesocardium. This bend is now named the ventricular loop because the left ventricle will balloon from its outer

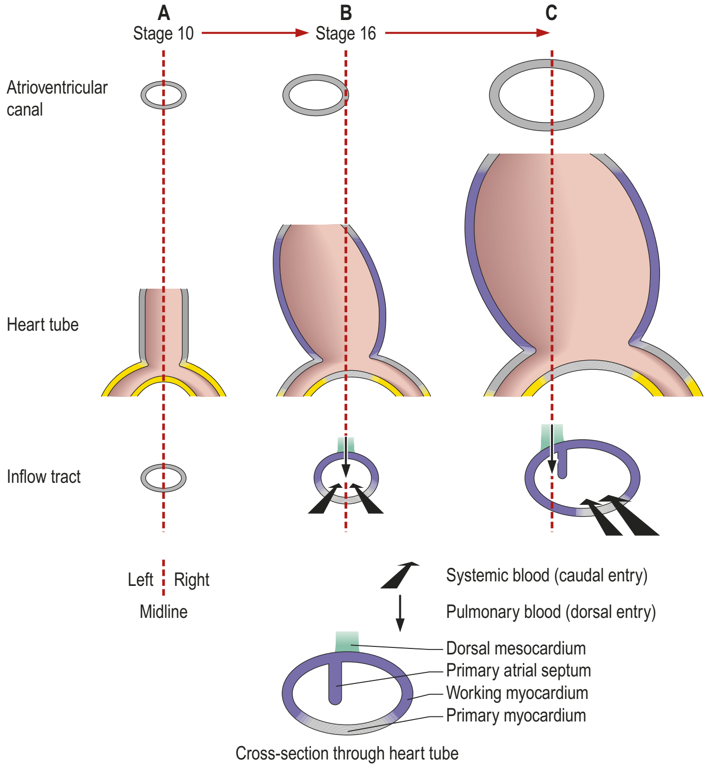

Fig. 13.5 Movements of the atrioventricular canal relative to the midline during early heart development. **A**, The primary heart tube (primary myocardium, grey) is found at the body midline; it receives bilateral veins (yellow) from the body and placenta. **B**, Working myocardium (purple) is present between the inflow tract and the atrioventricular canal. The atrioventricular canal moves to the left; the inflow tract remains in the midline. The pulmonary vein develops within the dorsal mesocardium. **C**, The atrioventricular canal moves to the right, returning toward the midline.

curvature, the original ventral side of the straight tube; the inner curvature of this loop is the original dorsal side.

At the start of stage 10 the venous pole, the atrioventricular canal, the developing left ventricle and the outflow tract are all positioned symmetrically around the midline (Fig. 13.5A). As a result of the subsequent rapid lengthening of the cardiac tube, the atrioventricular canal moves in its entirety to the left (Fig. 13.5B), and the ventricular part of the heart tube loops to the right, thus placing the developing left ventricle on the left and the forming right ventricle on the right side of the midline of the body. The atrial floor, including the developing systemic sinus venosus and the atrioventricular canal moves to the right (Fig. 13.5C). The developing pulmonary vein remains anchored in the midline and after these manoeuvres, the atrioventricular canal again becomes positioned in the midline; these movements facilitate the appropriate connections of the developing muscular ventricular septum with the atrioventricular and outflow cushions. The orifice of the sinus venosus is now positioned to the right. From the outset, the muscular ventricular septum develops in line with the right side of the dorsal atrioventricular cushion so that the right atrium always has direct access to the developing right ventricle.

Cardiac gene expression, differentiation, contraction, conduction and automaticity

Cardiac differentiation and morphogenesis are intimately related processes, achieved by a still obscure transcriptional network. It is known that the cardiac transcription factor Nkx2–5, which has a homogeneous distribution over the embryonic heart tube, is generally important for cardiac-specific gene expression. In the human, mutations in this factor cause atrial septal defects and disturbances of atrioventricular conduction; in *Drosophila*, the heart will not form in its absence. The discovery of the involvement of locally expressed T-box transcription factors, provides some evidence of the further complexity of the patterning of the heart (Fig. 13.6). For example, whereas Tbx5 confers caudocranial positional information over the heart tube, determining the regional development of the cardiac chambers along these axes, Tbx2 and Tbx3 prevent regional formation of the cardiac chambers, permitting the myocardium in these regions to differentiate into the conduction system. Tbx18 is involved in the development of the sinus venosus while Tbx1 is necessary for the development of the outflow tract of the heart.

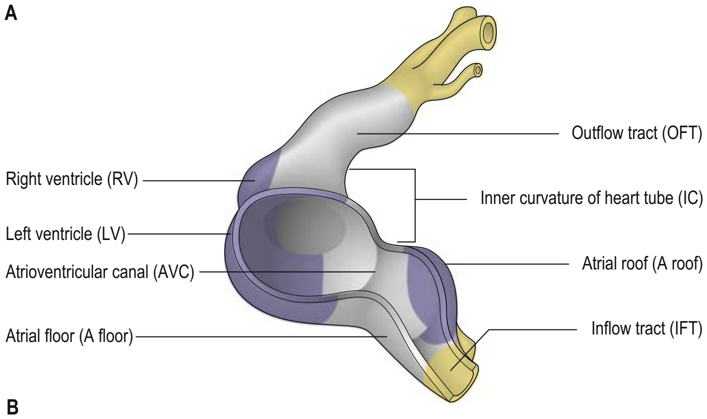

B

	IFT	A roof	A floor	AVC	IC	LV	RV	OFT
Tbx1	–	–	–	–	–	–	–	+
Tbx2	+	–	+	+	+	–	–	+
Tbx3	–	–	+	+	+	–	–	–
Tbx5	+	+	+	+	+	+	+/–	–
Tbx18	+	–	–	–	–	–	–	–
Tbx20	+	+	+	+	+	+	+	+

Fig. 13.6 **A**, Lateral view of the early heart tube showing the developing regions. **B**, The distribution of the T-box transcription factors in the early heart. Primary myocardium (grey) is found in the inner curvature of the heart, the atrioventricular canal and the atrial floor. Working myocardium (purple) makes up the ventricles and the atrial roof.

TABLE 13.1 Basic phenotypes of cardiac myocytes

Feature	Type of myocardium			
	'Primary'	'Nodal'	'Conducting'	'Working'
Automaticity	High	High	High	Low
Conduction velocity	Low	Low	High	High
Contractility	Low	Low	Low	High
Sarcoplasmic reticulum	Low	Low	Low	High

Nodal myocardium as found in the sinus node and AV node derives directly from primary myocardium. The working myocardium as found in the bodies of the atria and ventricles has an opposite phenotype. The conducting myocardium exhibits an intermediate phenotype.

Most cardiac myocytes cease to divide after their differentiation to myocardium (Ahuja et al 2007). The primary heart tube continues to elongate as additional myocytes are recruited from the secondary heart-forming field. Hypertrophy of cardiac myocytes is not thought to be part of the process in this elongation as in mouse embryos, cardiac myocyte volume remains at approximately $2 \times 10^{-3} \mu m^3$ throughout gestation (de Boer et al 2012). Cardiac myocytes share a number of characteristic features that distinguish them from other cells: they are mononuclear, have sarcomeres and a sarcoplasmic reticulum and are joined to adjacent myocytes by the gap-junctional proteins connexin 40 and 43 (van Eif et al 2018). The expression of sarcomeric proteins is seen in primitive cardiomyocytes in stage 9 embryos. All cardiac myocytes share the capacity for producing an intrinsic cycle of electrical activity, i.e. the capacity to generate and conduct a depolarizing impulse that results in contraction (the cells are myogenic): the phenomenon is called automaticity, or pacemaker activity. Because the cells are electrically coupled the fastest pacemaking activity will take the lead. In embryonic hearts, the leading pacemaker is always found at the venous pole which corresponds to the sinuatrial node in the adult heart. There is evidence for the presence of a tertiary heart-forming field specific for pacemaker formation (Liang et al 2017).

All of the cardiac conduction system is myocardial in origin. The nodes, sinuatrial and atrioventricular, and the atrioventricular bundle constitute the central conduction system, while the bundle branches and their terminal ramifications, the Purkinje fibres, represent the peripheral ventricular conduction system. The development of the conduction system of the heart is intimately related to overall heart formation and the blood flow through the heart, embryo and placenta. The underlying gene-regulatory networks have been conserved during vertebrate evolution. Each phase of heart development shows different patterns of spontaneous electrical activation and contraction (Watanabe et al 2016).

Varying degrees of differentiation seen in early populations of cardiac myocytes can be categorized as forming primary, nodal, conducting and working myocardium (**Table 13.1**). There is a relationship between the degree of apparent differentiation and extent of the coupling between myocytes, and the occurrence of slow or fast wave propagation and corresponding contraction. All regions of the early embryonic heart tube have poorly coupled cells and display intrinsic automaticity (**Video 13.1**). This produces slow wave propagation of the depolarizing impulse along the heart tube and matching peristaltic waves of contraction that push the blood in an antegrade direction. That part of the early heart tube wall termed primary myocardium retains this phenotype; it shows poorly developed sarcoplasmic reticulum and sarcomeric structures. Poor electrical coupling and slow conduction seen in nodal myocytes is an absolute requirement for effective pacemaking because it allows the cells to build up sufficient electrical charge, which is then propagated through the surrounding myocardium. Cells that differentiate into working myocardium display virtually no automaticity. They have well developed sarcomeres and sarcoplasmic reticular structures, and contiguous cells show well developed gap junctions expressing connexins 40 and 43. The cells of the putative atrioventricular and peripheral ventricular conduction system have an ambiguous phenotype: they are well coupled, thus allowing fast conduction of the depolarizing impulse, but otherwise retain an embryonic phenotype. Myocytes of the atrioventricular bundles and Purkinje fibres have a phenotype between that of working and primary myocardium. Distinguishing conduction myocardium from working myocardium may suggest that the working myocardium does not conduct, while the conduction system conducts rapidly. However, to produce powerful synchronous contractions, the working myocardium must also conduct rapidly. Unambiguous morphological markers are often lacking in the early embryonic heart, which means that it is not possible to distinguish the various cells phenotypically; automaticity and the speed of conduction have therefore become important functional parameters with which to describe the development of the different parts of the heart.

Peristaltic hearts do not need valves, whereas chambered hearts require the presence of one-way valves at the inlets to, and the outlets from, the chambers. During development, specific regions of mesenchyme and cardiac extracellular matrix fulfil this function. The sequential arrangement of slow and fast conduction portions of the early myocardium is key to its early development. The fast conducting working myocardium of the atrial and ventricular chambers permits nearly simultaneous contraction, increasing the velocity of the forward pressure of blood. The slow conducting primary myocardium within the atrioventricular junction and outflow tract is adjacent to endocardial cushions formed from locally accumulated cardiac extracellular matrix. These regions have longer, slower closure and are thus able to function as sphincteric valves, preventing retrograde flow of blood. The longer closure permits discrete and successive contraction of the atrial chambers followed by the ventricular chambers: contraction in the ventricles at these early stages passes from base to apex. Conduction myocytes originate from part of a primary interventricular ring that becomes positioned at the atrioventricular fibrous ring, close to the interventricular septum in the adult heart (see Fig. 13.10). For further reading about the electrophysiology of the developing chick heart, see Watanabe et al (2016).

COMPARTMENTS OF THE HEART

The future atrial and ventricular components of the developing heart can be distinguished once the primary heart tube has formed its ventricular loop (**Fig. 13.7**; see Figs 13.4, 13.5A). The region where the systemic venous tributaries join the primary heart tube is called the inflow tract of the heart. Within the primary heart tube, the developing atrial and ventricular chambers can be discerned as bulges that are separated by the atrioventricular canal. The ventricles connect to the outflow tract which, in a later stage, will septate and give rise to the pulmonary trunk and the aorta.

Inflow tract

Initially, blood flows into the heart via a sinus venosus, a confluence of bilateral umbilical, vitelline and cardinal venous channels (see Fig. 13.1). The sinus enlarges forming right and left sinus horns; a process under the control of the T-box transcription factor Tbx18. The common cardinal veins, the main contributors to the sinus horns, become surrounded by cardiomyocytes (van den Berg and Moorman 2011). With later development of the septum transversum and hepatic blood vessels, modifications of the cardinal system of veins and the terminal portions of the vitelline and umbilical veins form a main hepatocardiac channel that directs blood from the caudal part of the embryo towards the right horn of the sinus venosus (**Fig. 13.8**; see Figs 13.17, 13.21, 13.22). The sinus wall is thickened dorsally where the right and left sinus horns meet: this is the sinus septum that will give rise to the roof of the orifice of the future coronary sinus.

Inflow tract anomalies

Available with the *Gray's Anatomy* e-book

Sinuatrial junction

The sinus venosus becomes incorporated into the right atrium proper (see Fig. 13.8C), distinguished from the common atrium by a sinuatrial valve. The growth of the sinuatrial valve is slower than that of the surrounding myocardium and the valve leaflets lose their competence over

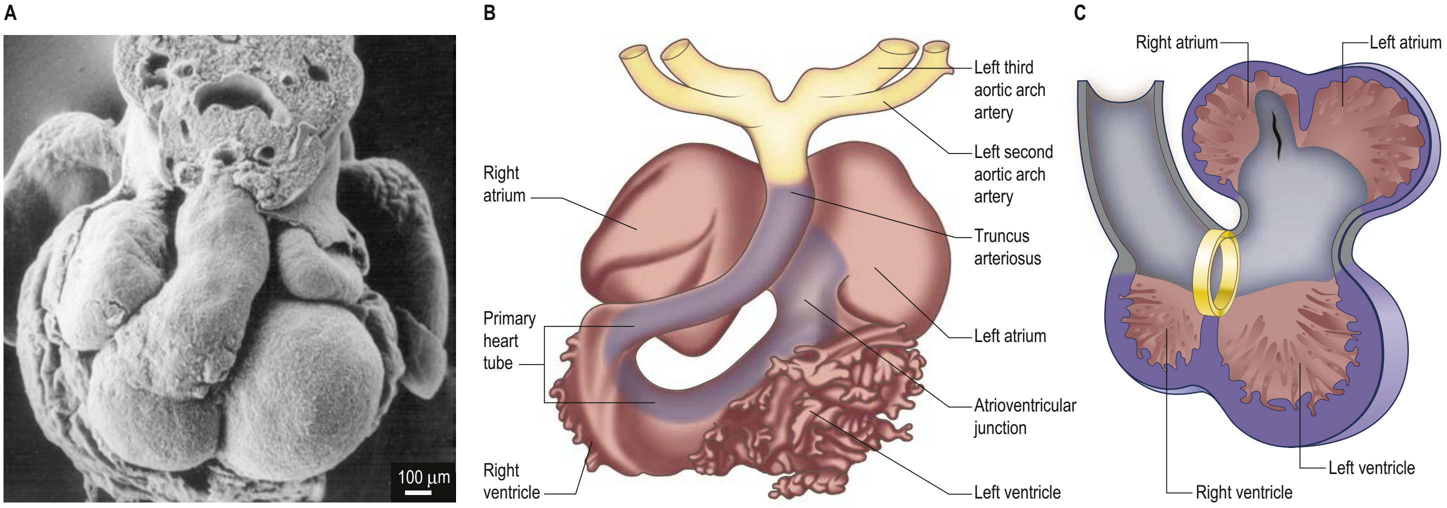

Fig. 13.7 **A**, A scanning electron micrograph of an early developing human heart, showing the external appearance of the myocardium of the right and left ventricles and the right and left atrial appendages. The truncus arteriosus passes between the atria. **B**, A reconstruction of the heart tube at stage 13, showing the endocardium. In the left and right ventricles, the endocardium interdigitates with the myocardium and appears trabeculated; at the atrioventricular canal and in the outflow tract, it is separated from the myocardium by the cardiac extracellular matrix. **C**, The heart at stage 13 with the truncus arteriosus reflected to the right. The opening of the sinus venosus into the right atrium can be seen (yellow). The region of the primary heart tube is indicated by a yellow interventricular ring. (A, With permission from Oostra RJ, Steding G, Lamers WH et al 2006 Steding's and Virágh's Scanning Electron Microscopy Atlas of the Developing Human Heart. New York: Springer-Verlag. B, Modified from O'Rahilly R, Müller F 1987 Developmental Stages in Human Embryos. Washington, DC: Carnegie Institution. Publication 637.)

The most common systemic venous anomaly is a persistent left superior vena cava that drains into the right atrium through an enlarged orifice of the coronary sinus (Povoski and Khabiri 2011): it can be caused by defects in the Robo1 and Robo2 receptors (Mommersteeg et al 2013).

The inferior vena cava can have an interrupted abdominal course and drain to the heart via the azygos or hemiazygos venous system (see Figs 13.4, 13.18), an aberration found most frequently with left isomerism of the atrial appendages.

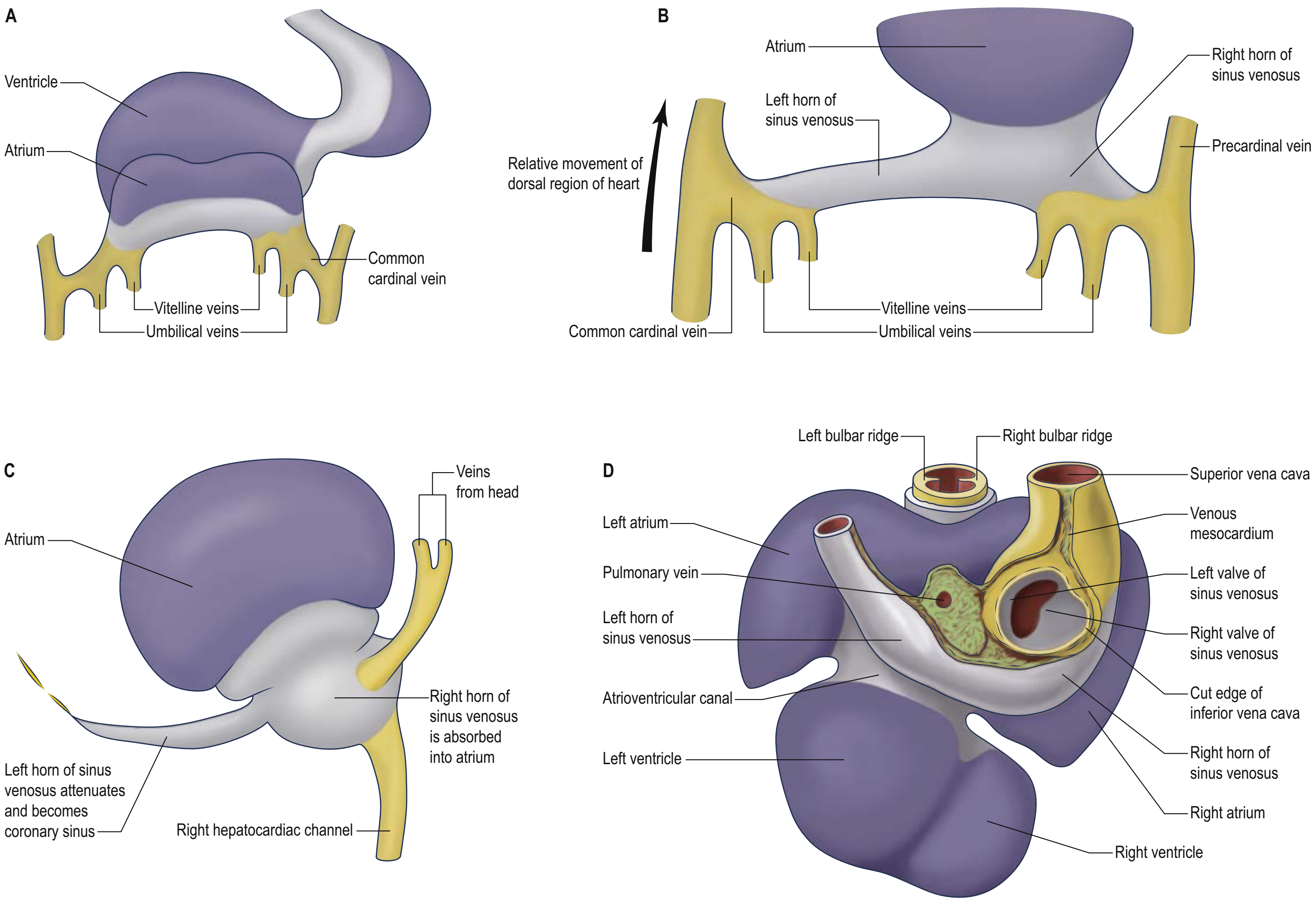
A
Ventricle
Atrium
Common cardinal vein
Vitelline veins
Umbilical veins
B
Atrium
Right horn of sinus venosus
Left horn of sinus venosus
Precardinal vein
Relative movement of dorsal region of heart
Vitelline veins
Umbilical veins
Common cardinal vein
C
Veins from head
Atrium
Right horn of sinus venosus is absorbed into atrium
Left horn of sinus venosus attenuates and becomes coronary sinus
Right hepatocardiac channel
D
Left bulbar ridge
Right bulbar ridge
Superior vena cava
Venous mesocardium
Left atrium
Pulmonary vein
Left valve of sinus venosus
Left horn of sinus venosus
Right valve of sinus venosus
Cut edge of inferior vena cava
Atrioventricular canal
Right horn of sinus venosus
Left ventricle
Right atrium
Right ventricle

Fig. 13.8 The changes to the sinus venosus. **A**, A dorsal view of the early heart tube shown in Fig. 13.4D. **B**, Changes to the circulation bring the venous circulation to the right, causing enlargement of the right horn of the sinus venosus and atrium, and attenuation of the left horn of the sinus venosus. **C**, The right horn of the sinus venosus becomes incorporated into the atrium. The left horn of the sinus venosus becomes the coronary sinus. **D**, A dorsal view of a stage 16 embryonic human heart, showing the relative changes to the sinus venosus.

time. The sinuatrial orifice becomes elongated and slit-like because of this differential growth. The two sinuatrial valve leaflets that flank it meet cranially to form the septum spurium. Later, a cranial part of the right sinuatrial valve leaflet, caudal to the septum spurium, becomes continuous with the crista terminalis, a ridge that projects from the atrial roof. More caudally, the right sinuatrial valve leaflet forms the valve of the inferior vena cava (Eustachian valve) and of the original left superior vena cava, later the valve of the coronary sinus (Thebesian valve). When this process is disturbed, a venous network (Chiari's network) can develop from the right sinuatrial valve leaflet (Figueras-Coll et al 2017).

As development proceeds, the left-sided systemic venous tributaries diminish in size. The left common cardinal vein (later the left superior vena cava) forms the oblique vein of the left atrium (also known as the oblique vein of Marshall), while the remainder of the left sinus horn is incorporated into the left atrioventricular junction forming the coronary sinus (see Fig. 13.8C). The coronary sinus retains its own myocardial wall, histologically distinct from the left atrial wall, although some merging may take place.

At the sinus venosus side of the sinuatrial junction, cardiac nodal myocytes form a specialized sinuatrial node able to initiate the electrical impulses that activate the atrial myocardium and heart, and lead to its contraction. This node consists of distinct morphological regions and is supplied by a relatively large artery. It forms under the influence of Tbx18 and its differentiation is regulated by Tbx3. Later, when the dorsal wall of the sinus venosus lies in line with the atrial myocardium, lateral to the sinuatrial valve leaflets, and the sinuatrial valve has lost its competence, this region is termed the sinus venarum: it is smooth-walled and forms the dorsal wall of the right atrium. In adult humans, the sinus venosus myocardium contracts simultaneously with that of the right atrium and can therefore be considered to be incorporated functionally into the right atrium.

Sinus venosus anomalies

Available with the *Gray's Anatomy* e-book

Common atrium

The working myocardium of the primitive atrium differentiates at the dorsal and lateral sides of the primary heart tube (Sylva et al 2013) (see Fig. 13.4D–G). The developing atrium then expands, ballooning in dorsal, lateral and cranial directions. The cranial expansion is pouch-shaped and forms the left and right atrial appendage (see Fig. 13.7A–B). Although it is possible to distinguish the left from the right atrial appendage around stage 14, the right being more extensive than the left, the atrium itself contains only a single cavity at this stage. The onset of primary septum formation is initially visible in the atrial roof. During atrial septation, the sinuatrial junction moves from a symmetric, midline position to a right-sided position (see Figs 13.5, 13.8, 13.20).

Right atrium

In the developing right atrium, the united remnants of the sinuatrial valve leaflets, caudal to the valve of the coronary sinus (Thebesian valve), continue to pass through the tissue that separates the orifice of the coronary sinus from the foramen ovale. These remnants form the tendon of Todaro (Ch. 57): the atrioventricular node of the fully formed heart is located at the end of this structure. The left sinuatrial valve leaflet blends with the right side of the atrial septum and there is usually no trace of it in the postnatal heart. The inner aspect of the sinus venosus myocardium and that of the newly forming mediastinal myocardium, derived from the dorsal mesocardium, is smooth, whereas the myocardium of the atrial appendages is ridged on its inner surface, forming the pectinate muscles.

The secondary heart-forming field myocardium of the atrial appendages is working myocardium and expresses the markers atrial natriuretic factor and connexin 40, like the ventricular myocardium at this stage. The mediastinal myocardium is connexin 40-positive but atrial natriuretic factor-negative. Connexin 40-negative primary myocardium marks the inflow to, and the outflow from, the initial atrial

Interatrial communications can occur where the venae cavae join the sinus venosus and are most frequently noted for the superior vena cava (Jensen et al 2016). These defects are usually associated with drainage of the right pulmonary veins into the sinuatrial junction. Known as sinus venosus defects, their essential feature is a bi-atrial connection of the involved vena cava (Keyte et al 2014). Defective signalling by the guidance molecule Semaphorin 3d, which normally ensures that forming pulmonary veins connect to the left atrium, could underlie this malformation (Degenhardt et al 2013). An interatrial communication can occur through the mouth of the coronary sinus when there is a deficiency or absence of the walls that usually separate the left sinus horn or future coronary sinus from the left atrium (Ootaki et al 2003).

chambers as ‘rings’. The ring at the inflow defines the sinuatrial junction, and the atrioventricular canal ring forms the atrial outlets during development. The original atrioventricular canal is present within the definitive right and left atrial chambers as the atrial vestibules. These Tbx3-positive, connexin 40-negative rings initially lie parallel in the primary heart tube, but they become separated. The atrial floor or vestibule normally becomes Tbx3-negative and connexin 40-positive as a result of the ingrowth of myocardium from the secondary heart-forming field, while the sinus node and atrioventricular node, derivatives from the primary myocardium, retain their molecular phenotype. Connexin 40-negative remnants of the primary myocardium have been reported in the atrial floor and Tbx3-positive cardiomyocytes are found around the mouth of the coronary sinus: while these cardiomyocytes do not form a separate functional tract, they might be the substrate for arrhythmias.

Left atrium

Following the formation of the left atrial appendage and the primary atrial septum, the left atrium takes shape by the incorporation of mediastinal myocardium. While the tributaries of the sinus venosus approach the right atrium caudally and cranially, the differentiating pulmonary veins gain their entrance to the left atrial cavity through the dorsal mesocardium (see Fig. 13.3). The definitive topographical relationships between vessels and heart seen postnatally are therefore only established once differentiation of the pulmonary venous portal occurs.

Around stage 14, simultaneously with atrial septation, the pulmonary vein develops as a solitary channel from angiogenic cells derived from the dorsal mesocardium. This channel establishes continuity with the vascular plexus formed in the mediastinal mesenchyme around the developing lung buds. The initially solitary pulmonary vein, guided by Semaphorin 3d signals, later opens into the caudo-dorsal wall of the atrium adjacent to the developing atrioventricular junction, where a depression termed the pulmonary pit, flanked by the pulmonary ridges, has already been established (Degenhardt et al 2013).

The primary atrial septum develops from the right pulmonary ridge, confining the pulmonary venous orifice to the developing left atrium (see Fig. 13.11). The pulmonary vein initially branches within the dorsal mediastinal mesenchyme, its tributaries draining blood from the developing lung. With continuing development, the walls of the pulmonary venous channels become surrounded by myocardium; this process occurs up to and beyond the level of the second bifurcation. The veins then expand and their walls become incorporated into the roof of the left atrium, eventually forming the greater part of its cavity. The four pulmonary veins do not achieve their separate opening into the atrial roof until well after septum formation is completed, around postmenstrual week 11. The left half of the primary atrium becomes progressively restricted to the mature appendage. The myocardial sleeves that surround the pulmonary orifices taper off distally and become intermingled with fibrous tissue. In adult life, it is likely that this intermingling of myocardial and fibrous tissues forms the substrate for some forms of atrial fibrillation. Variations in the precise pattern of pulmonary venous drainage are quite common.

Anomalous pulmonary venous connections and cor triatriatum sinistrum

Available with the *Gray’s Anatomy* e-book

Ventricles

The ventricles develop from the ventral side of the looping primary heart tube (see Figs 13.4, 13.7). The left ventricle develops from the rostral stem of the inverted, Y-shaped primary heart tube. The right ventricle develops later, downstream relative to the left ventricle, after more myocardium has been added to the cardiac tube from the secondary heart-forming field. As a consequence of the heart tube looping, the right ventricle is positioned to the right of the left ventricle, which is a prerequisite for forming the appropriate connections with the expanding atrial component of the heart. Unlike the atrial chambers, the morphological differences between the right and left ventricles are not part of the general asymmetry between the right- and left-sided organs of the body, but under the control of signalling pathways that determine caudocranial differentiation, such as retinoic acid and its downstream transcription factor Tbx5, which play a crucial role in this process. The Hand transcription factors also play a role in left ventricular growth and endocardial cushion maturation (Vincentz et al 2017).

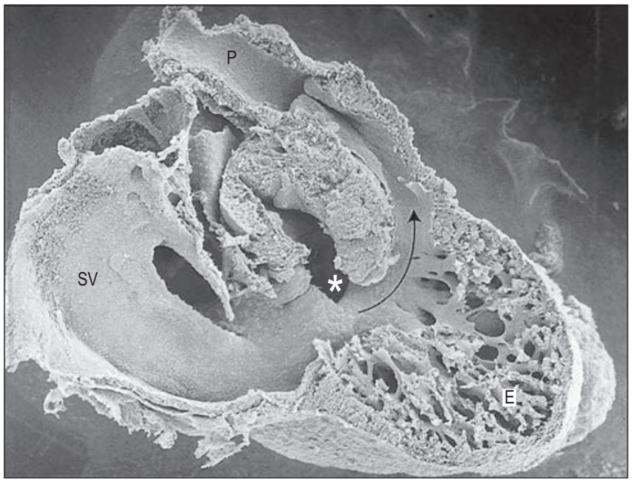

Fig. 13.9 A scanning electron micrograph of a human heart at stage 18 showing the embryonic trabeculae in the right ventricle (E). The right lateral walls of the right atrium, right ventricle and outflow tract have been removed. The sinuatrial valve (SV) is prominent in the right atrium. There is no septal cusp of the tricuspid valve guarding the inlet portion of the right ventricle. The parietal cusp has been removed. The atrioventricular cushions are fused. A small interventricular foramen is indicated (*). There is a well-developed right ventricular outflow tract (curved arrow) culminating in the pulmonary trunk (P).

Formation of the ventricular wall

The myocardium at the inner curvature of the looped heart, which is the original dorsal side of the primary heart tube, remains smooth-walled, whereas the myocardium at the outer curvature of the myocardial tube displays trabeculae as early as stage 10 (see Fig. 13.7C). By stage 17 the trabeculae have achieved a typical spatial organization, giving a sponge-like appearance to the internal aspect of both ventricles. Embryonic trabeculae are a few tens of micrometres in width, and diffusion with early luminal blood is sufficient to maintain cardiac cellular homeostasis, which means that the increase of cardiac mass by trabecular addition can continue in the absence of a coronary circulation (**Fig. 13.9**). Trabecular cardiomyocytes proliferate much less and exhibit more mitochondrial activity than compact wall cardiomyocytes, and are likely to be the main contributor to pressure generation. As development proceeds, a portion of the embryonic trabeculae on the luminal side of the ventricles stops proliferating and differentiates into the fast-conducting peripheral ventricular conduction system that includes the bundle branches and the Purkinje fibres (**Fig. 13.10**). A further portion, from the level of the atrioventricular junction to the apex of the heart, forms thicker adult trabeculae; the trabeculae in the right ventricle are coarser compared to those in the left. Over time the outer layer of ventricular myocardium will become highly proliferative and will form the thick compact layer of the ventricular wall.

Embryonic ventricular myocardium, encompassing both the trabeculae and exterior wall, possesses a specific molecular chamber phenotype: the myocytes express, among other proteins, the fast-conducting gap-junctional proteins connexin 40 and 43, and atrial natriuretic factor. During development, only the peripheral ventricular conduction system retains this molecular phenotype. The ventricular working myocardium loses connexin 40 and atrial natriuretic factor expression while retaining low expression of connexin 43. Changes in the expression of connexin 40 and 43 have been correlated with morphological development of the fetal heart. The increasing complexity of the helical disposition of ventricular myocardial fibres has been studied using high resolution diffusion tensor magnetic resonance imaging (Pervolaraki et al 2017).

Left ventricular noncompaction

Available with the *Gray’s Anatomy* e-book

Outflow tract

The outflow tract of the heart (truncus arteriosus) is formed by cells derived from the secondary heart-forming field and is confluent with the right ventricle. Initially, the outflow tract myocardium extends

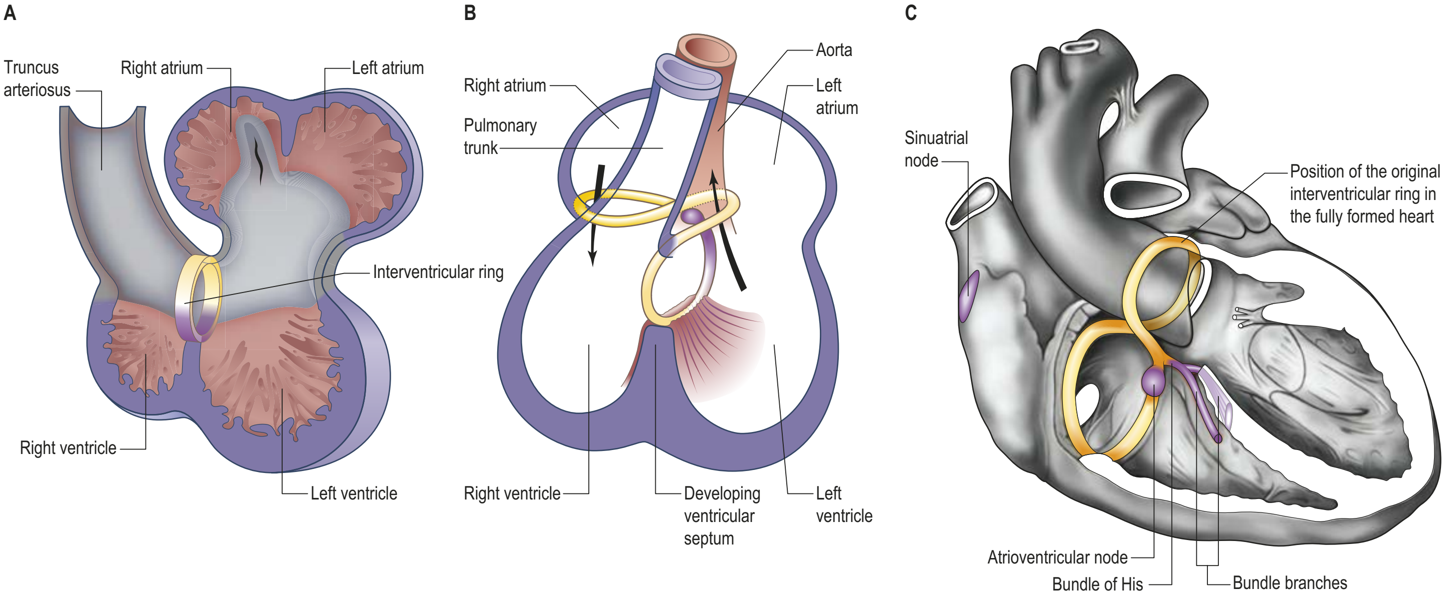

Fig. 13.10 Development of the conduction system of the heart. **A**, At stage 13 with the truncus arteriosus reflected to the right, the interventricular ring marks the region of the primary heart tube. The purple part of the interventricular ring will give rise to the atrioventricular bundle and bundle branches, whereas the yellow part of the interventricular ring will not participate in the formation of the adult conducting system. **B**, The truncus arteriosus, now divided into the pulmonary trunk and aorta, is presented between the right and left atria, which expand lateral to it. The right atrium is now positioned entirely above the right ventricle, and the outflow tract has expanded to the left; the left ventricle has access to the aorta. **C**, The position of the original primary heart tube ring indicated in the formed heart. The pulmonary trunk has been removed.

up to the pericardial reflections. As development proceeds, continuous addition of non-myocardial cells changes the position of the myocardium and cardiac extracellular matrix (cardiac jelly) relative to the outflow tract bend, a conspicuous morphological feature in the embryonic heart. The outflow tract is therefore a highly dynamic structure along which cells pass to contribute to the definitive right ventricle. By definition, the outflow tract is downstream of the ventricular loop, irrespective of the fact that, eventually, it will largely become incorporated within the definitive right ventricle (see Figs 13.4, 13.7). The method of incorporation of the outflow tract into the heart is different to that of the sinus venosus, because it involves movement of a structure, whereas the sinus venosus changes identity but otherwise shows no relative movement.

Within the inner curvature of the ventricular loop, the walls of the outflow tract and atrioventricular canal fade into one another without a clear boundary. It is within this ventricular part of the primary heart tube that the cushions of the atrioventricular canal and the outflow tract must achieve appropriate connections with the ventricular septum in order to separate the pulmonary trunk and the aorta.

Aortic arch anomalies

Available with the *Gray's Anatomy* e-book

SEPTATION OF THE EMBRYONIC CARDIAC COMPARTMENTS

The early embryonic heart is an undivided continuous tube. During development, septa are formed within the compartments of the heart. Initially they separate blood draining to the right side of the heart (oxygenated blood from the placenta and venous drainage from the body) and arterial flow from the left side of the heart (to the body and placenta); after birth they permit the smooth transfer of blood flow from the intrauterine to the extrauterine arrangement. Septa develop within the common atrium, in the atrioventricular canal, between the ventricles and within the outflow tract. Initially flow of blood on the right and left sides of the developing heart does not intermingle because flow is laminar. Pressures are similar in the right and left sides of the embryonic and fetal heart.

A number of shunts are open in the early heart and vessels because oxygenation is derived from the placenta and the pulmonary circulation is not functional in the embryo and fetus. Blood flow through the beating heart, the local pressures generated, and the shear forces created within the endocardial tube, form part of the epigenetic processes involved in heart development and the establishment of systemic and placental circulations.

Septation of the atrial chambers

Atrial septation is a process in which a valvular structure develops that initially directs the flow of placental blood to the body and allows separation of the two atrial chambers immediately after birth. It is typically described in terms of two septa that separate the endocardial and myocardial walls of the common atrium and two foramina that ensure continuous blood flow. Atrial septation starts at about stage 13 with proliferation of a crescentic ridge of mesenchyme in the atrial roof. This ridge, the septum primum, grows by active proliferation from the craniodorsal atrial roof towards the atrioventricular canal, just to the right of the entrance of the pulmonary vein (pulmonary pit) (Fig. 13.11A,D). Its leading edge is covered by a mesenchymal cap which is continuous with extracardiac mesenchyme (mediastinal mesenchyme) derived from the dorsal mesocardium that forms a dorsal mesenchymal protrusion. Under the influence of BMP signalling, the ventral horn of the crescentic septum primum will touch the ventral atrioventricular cushion, while the dorsal horn will fuse with the dorsal atrioventricular cushion. The primary atrial foramen (foramen or ostium primum) is therefore entirely surrounded by mesenchyme, subjacent to the atrial endocardium. Caudal to the advancing edge of the septum primum, the developing atrial chambers still communicate through the foramen primum (see Fig. 13.11A,D). The foramen primum diminishes in size as a result of continuous growth of the muscular primary atrial septum and the cranial part of the septum perforates by apoptosis. The perforations coalesce, producing a secondary atrial foramen (foramen, or ostium, secundum) that allows continued shunting of oxygen-enriched blood from the placenta to the left side of the heart and so to the head and brain. The foramen secundum forms during stages 15–17. The foramen primum is occluded in the median plane by stage 17, when the septum primum mesenchyme merges with the fusing atrioventricular (Fig. 13.11B,E). This tissue later differentiates to myocardium and forms a ridge that will become the limbus of the future fossa ovalis.

The secondary atrial septum (septum secundum) is reported to appear during stages 18–21 (O'Rahilly and Müller 1987), signalling the earliest development of the foramen ovale. Anderson et al (2002), however, note that invagination of the roof of the right atrium, forming a myocardial ridge, constitutes the septum secundum, and that this is not present until after stage 23 (see Fig. 13.11B,E). The free edge of the septum secundum overlaps the foramen secundum forming an oblique channel, the

The developing common pulmonary vein migrates towards the heart before connecting to the pulmonary pit, but the correct connection may not occur (van den Berg and Moorman 2011). In total anomalous pulmonary venous connection, which occurs in about 7/100,000 neonates, no pulmonary veins enter the left atrium (Wu et al 2018) and the more primitive connection between the splanchnic plexus that surrounds the lungs with the right atrial inflow tract persists (Kao et al 2017): these vessels do not become surrounded by myocardium (Douglas et al 2009). In case of a partial anomalous pulmonary venous connection, one or more connections with the left atrium will be established alongside this primitive conjunction between cardinal veins and the splanchnic plexus. It has been suggested that these anomalies occur when there is a defect in the Semaphorin 3d signalling that would normally act as a repelling guiding factor (Degenhardt et al 2013).

In cor triatriatum sinistrum, a very rare anomaly, the left atrium is subdivided into two compartments separated by a full or partial membrane. The pulmonary venous confluence is guarded from the rest of the atrial body. There is evidence that mutations in the enzyme HYAL2 can lead to cor triatriatum sinistrum in humans (Muggenthaler et al 2017). The membrane might be an outgrowth of a ridge that is naturally found between the left superior pulmonary vein and the atrial appendage. Often this defect coincides with a septal defect, anomalous pulmonary venous connections or a patent ductus arteriosus.

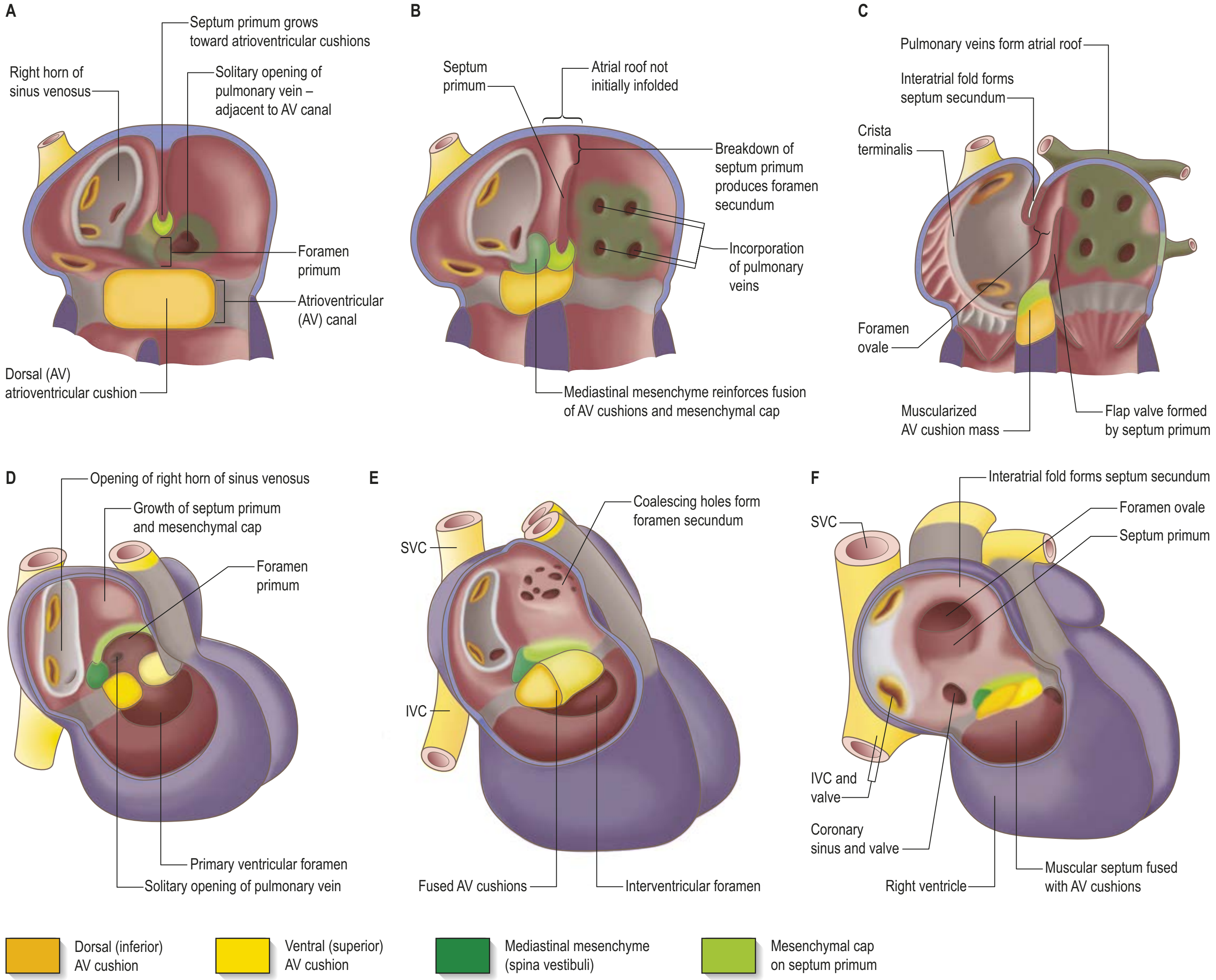
A
Septum primum grows toward atrioventricular cushions
Right horn of sinus venosus
Solitary opening of pulmonary vein – adjacent to AV canal
Foramen primum
Atrioventricular (AV) canal
Dorsal (AV) atrioventricular cushion
B
Septum primum
Atrial roof not initially infolded
Breakdown of septum primum produces foramen secundum
Incorporation of pulmonary veins
Mediastinal mesenchyme reinforces fusion of AV cushions and mesenchymal cap
C
Pulmonary veins form atrial roof
Interatrial fold forms septum secundum
Crista terminalis
Foramen ovale
Musculized AV cushion mass
Flap valve formed by septum primum
D
Opening of right horn of sinus venosus
Growth of septum primum and mesenchymal cap
Foramen primum
Primary ventricular foramen
Solitary opening of pulmonary vein
E
SVC
IVC
Coalescing holes form foramen secundum
Fused AV cushions
Interventricular foramen
F
Interatrial fold forms septum secundum
Foramen ovale
Septum primum
SVC
IVC and valve
Coronary sinus and valve
Right ventricle
Muscular septum fused with AV cushions
Dorsal (inferior) AV cushion
Ventral (superior) AV cushion
Mediastinal mesenchyme (spina vestibuli)
Mesenchymal cap on septum primum

Fig. 13.11 Three representative stages in the development of the atrial septum. **A–C**, Coronal views from the front. **D–F**, Lateral views from the right side. **A** and **D**, At stage 14 the primary atrial septum has not yet obliterated the original communication between the two atria (primary atrial foramen) and the atrioventricular endocardial cushions have not yet fused. The mediastinal mesenchyme starts to protrude into the heart. **B** and **E**, A few days later, the atrioventricular endocardial cushions have fused with each other and with the mediastinal mesenchyme and the mesenchymal cap of the primary atrial septum, which starts to exhibit openings in its cranial part that will form the secondary atrial foramen. **C** and **F**, The secondary atrial septum is forming to the right of the primary atrial septum and overlaps the secondary atrial foramen. The sinuatrial valve has lost its competence and the pulmonary veins have acquired their respective entries to the left atrium. The left superior cava now functions as the coronary sinus. Abbreviations: AV, atrioventricular; IVC, inferior vena cava; SVC, superior vena cava.

foramen ovale, between the now divided atria. Once these septa have formed, blood passes under the crescentic edge or limbus that is the crista dividens of the septum secundum, and flows obliquely towards and through the foramen secundum to the left atrium. This passage through the foramen ovale, persists throughout intrauterine life (see Videos 13.2, 23.1). In postnatal life, when left atrial pressure exceeds that in the right atrium, the septum primum will close against the septum secundum as a type of flap valve, completing atrial septation (Fig. 13.11C,F). On the right side of the foramen ovale, part of the septum primum remains underneath the rim of the septum secundum and becomes the fossa ovalis. **Fig. 13.12** summarizes all the anomalies of septation.

Atrial septal defects

Available with the *Gray's Anatomy* e-book

Septation and appropriate positioning of the atrioventricular canal

The atrioventricular canal is initially a continuation of myocardium between the common atrium and the primitive ventricle. Four cardiac cushions are formed at the margin of this canal, namely: the left and right cushions, and the much larger ventral and dorsal cushions. The single orifice of the atrioventricular canal is divided by the approximation and later merger of the ventral and dorsal cushions. The dorsal atrioventricular cushion runs along the floor of the atrium. As it extends further dorsally it meets the dorsal mesenchymal protrusion (spina vestibuli) that connects with the mesenchymal cap that runs along the leading edge of the septum primum until it meets the ventral atrioventricular cushion (see Fig. 13.11). The dorsal atrioventricular cushion has a ventricular extension to the inner curvature of the heart tube that comes to lie on top of the developing muscular ventricular septum: much of the membranous septum of the ventricles is derived from this extension.

The two atrioventricular cushions fuse during stages 14–17, at which time they become known as the central fibrous body. Relative to the canal itself, the cushions are large, leaving narrow right and left slits for the passage of blood (**Fig. 13.13**). At the same time as the cushions fuse, the canal expands. This is seen most clearly on the lateral right side where the size of the right atrioventricular opening increases. Relative to the heart, the entire atrioventricular canal also shifts to the

In left ventricular noncompaction, the left ventricle exhibits particularly prominent trabeculae as compared to the compact wall. Although most cases of left ventricular noncompaction are thought to be developmental in origin, the process behind acquisition of prominent trabeculae is not clear: variation in trabecular prominence is seen during adult life, for example in pregnant women (Gati et al 2014). The condition can reflect failure of the trabeculae to compact, or excessive trabecular formation, or hypoplasticity of the compact wall (Anderson et al 2017, Jensen et al 2017) and can be associated with heart failure. Its uncertain aetiology is reflected in the diversity of current diagnostic criteria (Ivanov et al 2017).

A series of aortic arch arteries develop from the outflow tract and conduct blood through the pharyngeal arches before joining the dorsal aortae; the temporal changes that occur in the arteries are outlined on p. 222 and described in detail in Chapter 17 (see Fig. 17.9). The persistence of a right aortic arch is caused by a failure of resorption of the embryonic fourth right pharyngeal arch artery (Kanne and Godwin 2010), and is found most frequently with Fallot's tetralogy or with a persistent truncus arteriosus. It can also exist, together with a left aortic arch, in various combinations known as arterial rings, which compress the oesophagus, causing so-called dysphagia lusoria. For example, the right subclavian artery can sometimes arise from the arch of the aorta distal to the origin of the left subclavian artery and pass to the right, behind the trachea and oesophagus. This aberrant connection can be explained by the failure of fusion of the right common carotid artery and the right subclavian artery, caused by a fault in the right aortic arch involution.

Worldwide, the reported prevalence of persistent communication between the atrial chambers through the foramen ovale is 1.64/1000 live births (13% of the most common congenital heart disease subtypes) (van der Linde et al 2011). It is often the result of failure of the flap valve (septum primum) to fuse completely with the infolded muscular rim of the septum secundum. This type of atrial septal defect is known as a persistent foramen ovale. When the flap valve is still able to overlap the rim, the communication is of little or no functional significance as long as the left atrial pressure is greater than the right, which is usually the case in healthy individuals. However, when the pressure in the right atrium increases during sneezing, when diving, or in the case of pulmonary hypertension, there is a risk of some blood entering the left atrium directly, bypassing the pulmonary circulation (Briggs et al 2012). If the flap valve (septum primum) does not cover the foramen ovale, or if it is perforated, a true septal defect exists (Geva et al 2014) (see Fig. 13.12A). A foramen secundum defect is present when the lumen of the left atrium is visible from within the right atrium; it can be the result of either a septum secundum that is too small or a foramen secundum in the septum primum that is too large. Foramen primum defects occur when the mesenchymal cap of the septum primum does not fuse with the atrioventricular cushions, resulting in an interatrial communication. Deficient growth of the dorsal mesenchymal protrusion may also result in foramen primum defects: this is an atrioventricular septal defect permitting exclusively atrial shunting (Jensen et al 2016, Wessels 2016).

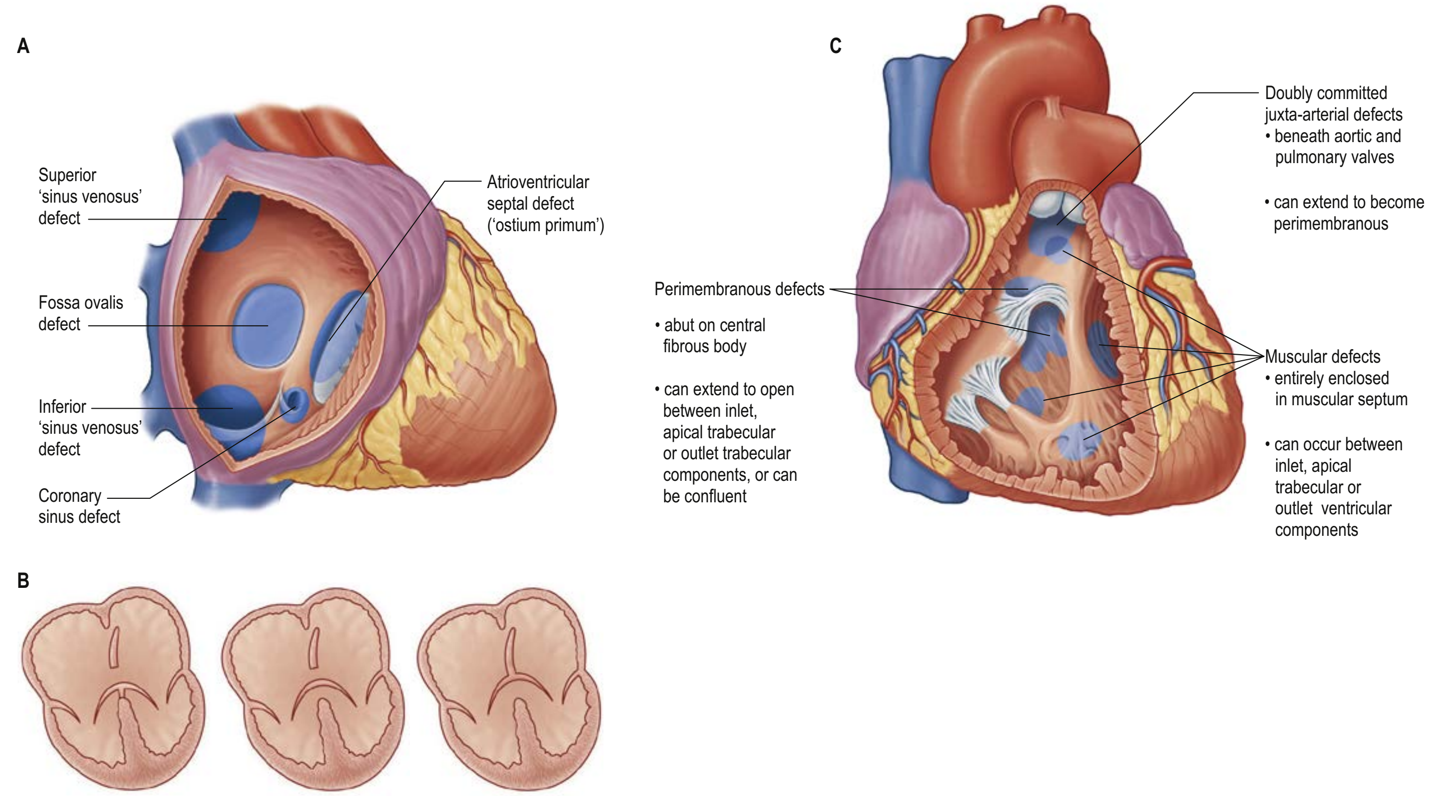
A
Superior 'sinus venosus' defect
Fossa ovalis defect
Inferior 'sinus venosus' defect
Coronary sinus defect
Atrioventricular septal defect ('ostium primum')
B
C
Doubly committed juxta-arterial defects
• beneath aortic and pulmonary valves
• can extend to become perimembranous
Perimembranous defects
• abut on central fibrous body
• can extend to open between inlet, apical trabecular or outlet trabecular components, or can be confluent
Muscular defects
• entirely enclosed in muscular septum
• can occur between inlet, apical trabecular or outlet ventricular components

Fig. 13.12 **A**, Location of the defects that produce an interatrial communication. Only defects within the fossa ovalis are true atrial septal defects. **B**, Shunting across an atrioventricular septal defect. This can be atrial (left), ventricular (right) or at both levels (middle), depending on the attachment of the bridging cusps. **C**, Ventricular septal defects. Depending on the structure of the anatomical borders seen from the right ventricle, these defects can be placed into perimembranous, muscular or doubly committed groups. (B and C, Courtesy of Professor RH Anderson, Institute of Child Health, University College, London.)

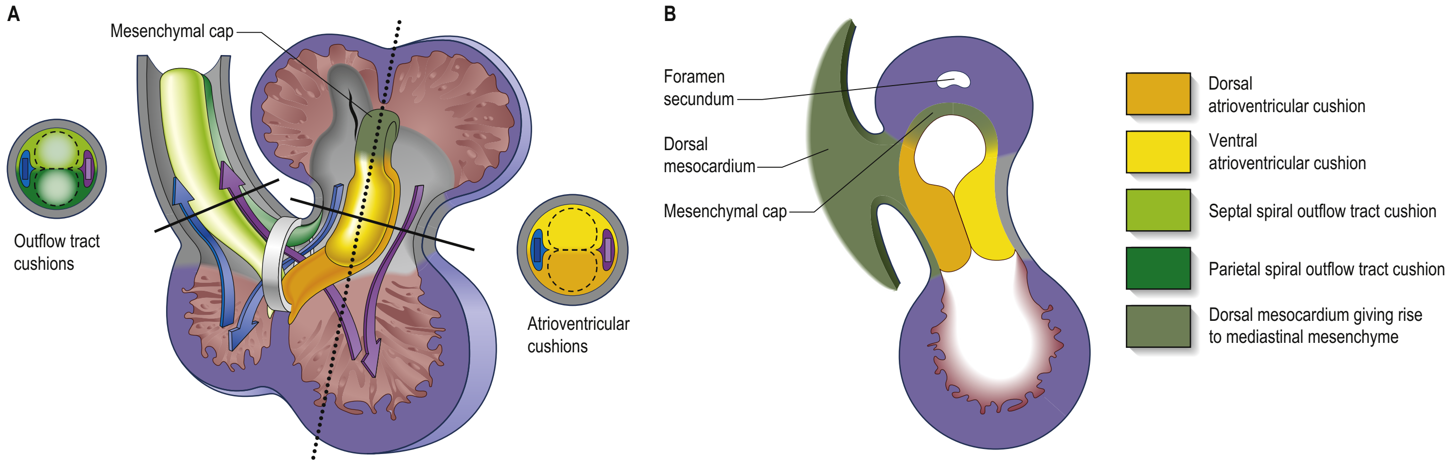
A
Mesenchymal cap
Outflow tract cushions
Atrioventricular cushions
B
Foramen secundum
Dorsal mesocardium
Mesenchymal cap
Dorsal atrioventricular cushion
Ventral atrioventricular cushion
Septal spiral outflow tract cushion
Parietal spiral outflow tract cushion
Dorsal mesocardium giving rise to mediastinal mesenchyme

Fig. 13.13 Septation of the ventricles and outflow tract. **A**, A frontal view of the heart at stage 13, with the outflow tract reflected to the right. Lines show the level of the transverse sections through the atrioventricular cushions and outflow tract. Note that blood from both atria has to pass through the embryonic primary myocardial ring at this stage. **B**, A sagittal section of heart along the dotted line in **A**, showing the atrioventricular junctional region as seen from the right side. The atrioventricular cushions extend cranially onto the leading edge of the septum primum where they are fused with the mesenchymal cap.

right (see Fig. 13.5), causing the dorsal cushion to overhang the ventricular septum into the developing right ventricle while the ventral cushion remains mostly on the left side.

Atrioventricular septal defects

Available with the *Gray's Anatomy* e-book

Septation of the ventricles

Three distinct structures contribute to the formation of the ventricular septum: the atrioventricular cushions (including the protrusion of the dorsal atrioventricular cushion that lies on the ventricular septal crest), the muscular ventricular septum and the proximal parts of the outflow cushions. Separation of the right and left ventricles is heralded by the appearance of a caudal crescentic ridge within the ventricular loop (see Fig. 13.7). This is a persisting part of the Tbx3 and G1N2-positive primary heart tube myocardium, which means that the crest of the septum is the oldest portion of the developing ventricular septum. The ventricles (especially those parts that will become the apex of the heart) become enlarged as if they were expanding like balloons on either side of the muscular ventricular septum (see Figs 13.4, 13.7). Later, the dorsal part of the crest of the septum will become the atrioventricular bundle, while the atrioventricular node will form at the dorsal atrioventricular junction (see Fig. 13.10C). The ventral parts will largely disappear except

Atrioventricular septal defects result from a failure of fusion of the endocardial atrioventricular cushions, leading to a common atrioventricular orifice and deficiencies of the adjacent septal structures (see Fig. 13.12B). Two major subgroups of atrioventricular defects are identified. The more frequent is complete atrioventricular defect, characterized by a common atrioventricular orifice and the potential for shunting through the septal defect at both atrial and ventricular levels (see Fig. 13.12B). The common atrioventricular orifice is guarded by a single common valve, with superior and inferior leaflets that bridge the scooped-out ventricular septum. The valve is tethered to both right and left ventricles. Although the left component of this valve is often interpreted as a ‘cleft mitral valve’, it bears no resemblance to the normally structured mitral valve because it has three leaflets where the ‘cleft’ forms the zone of apposition between the left ventricular components of the ventral and dorsal bridging leaflets. The less common incomplete atrioventricular septal defect has separate right and left atrioventricular orifices and shunting occurs only at the atrial level. Occasionally, when the bridging leaflets are attached to the underside of the atrial septum, shunting is minor and confined to the ventricular level (Briggs et al 2012).

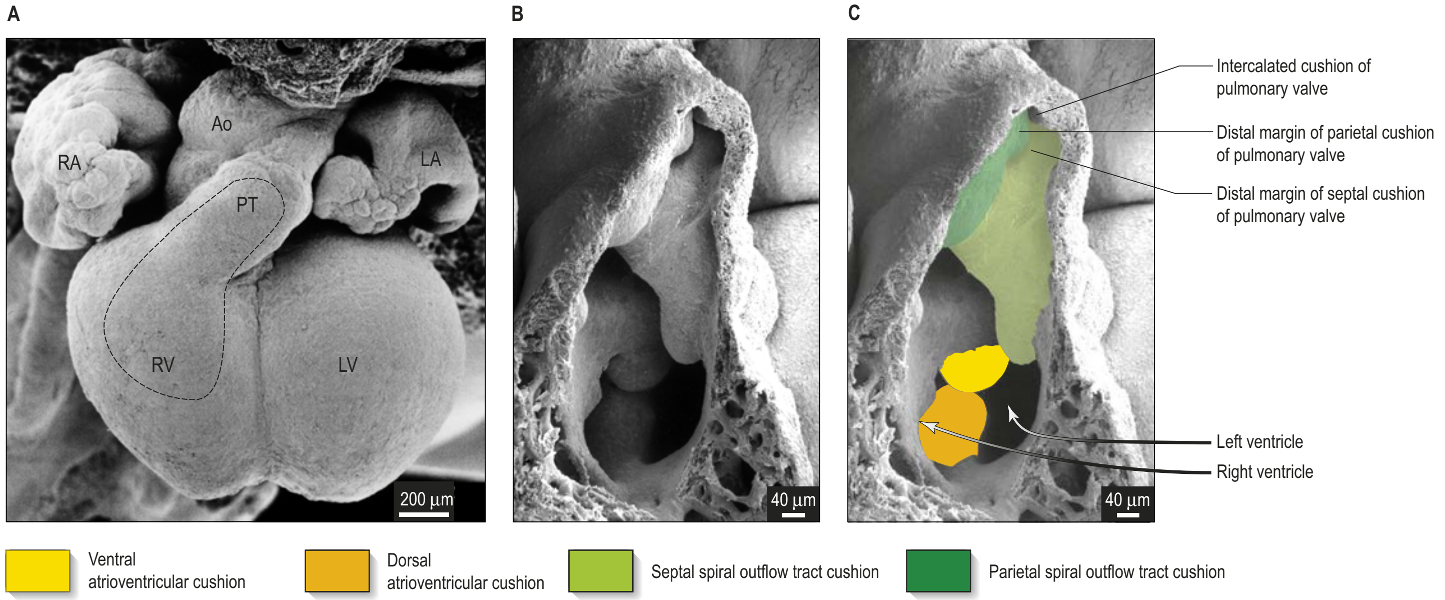
A
B
C
Ao
RA
LA
PT
RV
LV
200 µm
40 µm
40 µm
Intercalated cushion of pulmonary valve
Distal margin of parietal cushion of pulmonary valve
Distal margin of septal cushion of pulmonary valve
Left ventricle
Right ventricle
Ventral atrioventricular cushion
Dorsal atrioventricular cushion
Septal spiral outflow tract cushion
Parietal spiral outflow tract cushion

Fig. 13.14 Septation of the outflow tract. **A**, A scanning electron micrograph (SEM) of a human heart at stage 18. The pulmonary trunk is separated from the aorta. **B**, An SEM of the human heart at stage 17, showing the luminal aspect of the right ventricle and the outflow tract. The anterior and parietal walls of the outflow tract have been removed along the dotted line shown in **A**. **C**, An SEM with added colour to show the structures in **B**. The outflow cushions are unfused. The distal margins of both outflow tract cushions are contributing to the developing pulmonary valve: the third leaflet and sinus of this valve are derived from the intercalated cushion. The components of the aortic valve develop from the dorsal aspect of the outflow tract cushions. Abbreviations: Ao, aorta; LA, left atrium; LV, left ventricle; PT, pulmonary trunk; RA, right atrium; RV, right ventricle. (Courtesy of Professor G Steding, Göttingen, with permission from Oostra RJ, Steding G, Lamers WH et al 2006 Steding's and Virágh's Scanning Electron Microscopy Atlas of the Developing Human Heart. New York: Springer-Verlag.)

the so-called 'dead-end tract' (Anderson et al 2016, de Vries et al 2016). The crest of the septum, covered by an extension of the dorsal atrioventricular cushion, together with the fused atrioventricular cushions themselves, bounds the ovoid interventricular foramen. The Tbx3 and G1N2-positive myocardium that surrounds this foramen marks a ring composed of primary myocardium which is smooth (see Fig. 13.10). Completion of ventricular septation is seen after a rightward shift of the atrioventricular canal and the positioning of the outflow tract between the separating atrioventricular canals so that it too overrides the developing ventricular septum. The foramen finally closes by formation of the membranous septum that completely separates the right from the left ventricle (see Fig. 13.13). During ventricular septation, transition from the early ventricular base-to-apex conduction activation to an apex-to-base conduction is initiated. Maturation of the ventricular conduction system, with concomitant development of the fibrous rings of the heart, continues throughout fetal development (Watanabe et al 2016).

Ventricular septal defects

Available with the *Gray's Anatomy* e-book

Septation and appropriate positioning of the outflow tract

The appearance of two outflow cushions is key to the separation of the outflow tract (truncus arteriosus). Together with the myocardial wall, the cushions spiral as they extend from their septal and parietal positions at end of the right ventricle to the developing aortic sac (see Fig. 13.13; **Fig. 13.14**). Within the developing aortic sac, a transverse wedge of tissue composed of dorsal mediastinal mesenchyme, the aortopulmonary septum, initially separates the origins of the aorta and the pulmonary trunk before their individual walls are formed. Meanwhile, neural crest cells migrate from the pharyngeal mediastinal myocardium into the outflow cushions. They do not populate the septum itself, but form the larger parts of the walls of the intrapericardial portions of the truncus arteriosus (Keyte et al 2014).

The outflow cushions start to fuse from stage 15. Fusion starts in the distal part of the outflow tract and continues gradually in the direction of the ventricular septum (see Fig. 13.14; **Fig. 13.15A**). Early on, the most proximal parts of the cushions remain unfused. The arterial valves and sinuses develop distally within the myocardial sleeve that surrounds this area. When the most proximal parts of the cushions fuse, they are invaded by cardiac myocytes (myocardium) and become continuous with the muscular ventricular septum, so joining the aorta to the left ventricle. Spread of myocardial cells also gives rise to the greater part of the supraventricular crest. In the right ventricle, the wall of the proximal myocardial outflow tract persists as the smooth-walled muscular sub-pulmonary infundibulum. Some myocardium also persists distal to the pulmonary valve. There is no distinct myocardial outflow tract present within the left ventricle in the postnatal heart: the myocardium that initially surrounded the entire aortic root is lost on the side of the non-coronary leaflet because a fibrous continuity develops between the mitral valve and the aorta.

Outflow tract septal anomalies

Available with the *Gray's Anatomy* e-book

CARDIAC VALVE DEVELOPMENT

Competent mesenchymal valves develop at the atrioventricular junction and between the ventricles and outflow tract. The valvular apparatus is largely composed of endocardium-derived mesenchyme. All leaflets and the chordae tendineae and myotendinous junctions initially form from internal endocardial projections that cover a myocardial basement membrane, matrix and mesenchymal cells.

Atrioventricular valves

The mitral and tricuspid valves are formed at the site of the atrioventricular canal. The endocardial cushions are located on the inside of the canal. The cushions occupy most of the canal, save two tiny lumina that connect the right atrium to the developing right ventricle and the left atrium to the developing left ventricle. On the outside of the heart, at the level of the atrioventricular canal, a groove forms which is covered by the developing epicardium (see p. 220). As the atrioventricular valves develop, the epicardium and the endocardial cushions fuse at the ventricular margin of the canal, disrupting the

Ventricular septal defects account for approximately two-thirds of all cardiac septal defects; the worldwide prevalence is 2.6/1000 live births (34% of the most common congenital heart disease subtypes) (van der Linde et al 2011, Xie et al 2017). The inappropriate formation and connection of the atrioventricular cushions to the muscular ventricular septum results in a perimembranous ventricular septal defect (see Fig. 13.12C). The membranous septum, and by extension a perimembranous ventricular septal defect, is closely associated with the area of insertion of the septal leaflet of the tricuspid valve. A perimembranous defect can also extend further into the ventricular outlet beneath the supraventricular crest that borders the right ventricle from the outflow tract. Perimembranous ventricular septal defects are often associated with the aortic orifice overriding the crest of the muscular septum, i.e. ‘overriding aorta’. When combined with pulmonary stenosis or atresia, this forms the basis for the syndrome of Fallot’s tetralogy. The last feature of the tetralogy, right ventricular hypertrophy, which developed in infancy in the untreated child, is now usually seen in cases where an affected child does not have timely surgical repair. The condition does not cause important haemodynamic imbalance during fetal life (Wohlmuth and Gardiner 2020). When the pulmonary trunk is normal or even dilated with this combination of anomalies, it is known as the Eisenmenger complex. Perimembranous defects can also occur with abnormal ventriculoarterial connections. Taussig–Bing anomaly occurs when, in a case of transposition of the great arteries, the pulmonary trunk overrides the muscular septum, causing both arteries to connect to the right ventricle and the ventricular septum is also defective. In perimembranous ventricular septal defects, the atrioventricular bundle and its right and left branches are still always found along the dorsal and caudal margins of the defect.

Less commonly, a septal defect may be found in the ventricular outflow tract underneath the conjoined facing leaflets of the aortic and pulmonary valves. Such juxta-arterial defects are doubly committed, in that they open beneath the orifices of both aortic and pulmonary valves. They are the result of the failure of formation of the free-standing muscular sub-pulmonary infundibulum, which links them to persistent truncus arteriosus anomalies, but the ventriculoarterial junctions are appropriately separated. These defects usually have a muscular dorsocaudal rim that protects the atrioventricular bundle: the defect can sometimes extend to the membranous septum.

A third type of ventricular septal defect occurs within the musculature of the septum. Defects may affect all parts of the septum and can be multiple, producing a so-called ‘Swiss cheese’ septum (Spicer et al 2014).

A number of outflow anomalies may occur if the outflow cushions either fail to develop or fuse in an inappropriate fashion. When the cushions fail to fuse, the result is a persistent truncus arteriosus, represented by an undivided arterial channel, guarded by a common arterial valve, positioned above and astride the free margin of the muscular ventricular septum (**Fig. 13.16**). This anomaly occurs frequently in DiGeorge syndrome and can be a result of a Tbx1 deletion (Rana et al 2014). Persistent truncus arteriosus is also likely linked to abnormal development of the secondary heart-forming field, which, by means of an overall shorter heart tube, leads to poor alignment of the aorta with the left ventricle. In this condition, there is a coexisting juxta-arterial deficiency of the ventricular septum; right and left pulmonary arteries usually arise via a confluent segment but can also take independent origin from the trunk, which continues as the ascending aorta. The common valve usually has three leaflets but may also have two, four or more.

Transposition of the arterial trunks (also referred to as transposition of the great vessels) is a condition in which the aorta arises from the right ventricle and the pulmonary trunk from the left. Better described as having discordant ventriculoarterial connections, such hearts can coexist with deficiencies of cardiac septation. They can also be found with discordant connections at the atrioventricular junctions, producing a congenitally corrected transposition. The developmental history of discordant connections remains unknown but may have similar signalling pathways that are involved in right atrial isomerism, the nodal/pitx2 pathways (Nakajima 2016).

Double outlet ventricle occurs when the greater parts of both arterial valves fall within the same ventricle, almost always the right. In these cases, in order to continue the circulation of oxygenated blood after birth, it is necessary that either the ventricular septum is deficient, or the ductus arteriosus remains patent with medication; in rare cases, the septal defect can close as a secondary event.

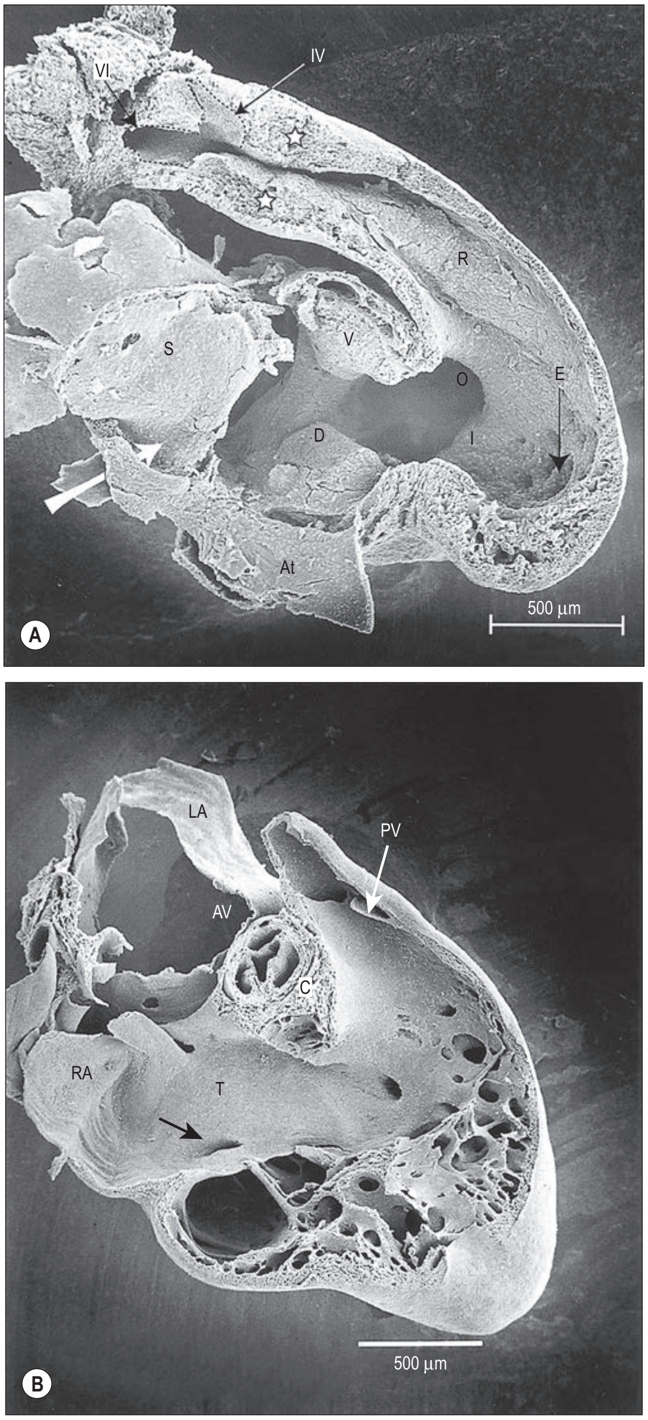

Fig. 13.15 **A**, A scanning electron micrograph (SEM) of a human heart at stage 15. The right lateral walls of the right atrium, right ventricle and the outflow tract have been removed. The primary atrial septum (S) is at a distance from the unfused ventral (V) and dorsal (D) atrioventricular cushions. There is not yet a membranous ventricular septum, leaving an opening between the left and right ventricle (O). The muscular interventricular septum (I) is visible. Note the left anterolateral ridge (R) and, at the distal margins of the truncus arteriosus, the valve swellings (*) of the putative aorta and pulmonary trunk. The white arrow marks the direction of blood flow from the systemic veins into the right atrium. Other abbreviations: At, atrium; E, embryonic trabeculae; IV, origin of fourth aortic arch; VI, origin of sixth aortic arch. **B**, The septal aspect of the right ventricle of a human heart at stage 23. Delamination of the septal cusp of the tricuspid valve (T) is taking place. A cleft (black arrow) has appeared, marking the posterior margin of the septal cusp. There are no clefts delineating the anterior margins in the region adjacent to the supraventricular crest (C), and the endocardium is continuous. No tension apparatus (chordae tendinae and papillary muscles) is visible. Other abbreviations: AV, aortic valve; LA, left atrium; PV, pulmonary valve; RA, right atrium.

myocardial continuity. Only the prospective atrioventricular conduction axis is spared from disruption. The sites of myocardial disruption later form the anulus fibrosus, a collagenous structure that physically insulates the atria from the ventricles. If anulus fibrosus formation is disrupted, accessory strands of myocardium between the atria and ventricles may persist and can become aberrantly differentiated thereby becoming able to propagate the electrical impulse. This can lead to early excitation of the ventricles and can act as a substrate for re-entry ventricular tachycardias as seen in Wolf–Parkinson–White syndrome.

Although molecular lineage studies in the mouse have demonstrated that the atrioventricular cushions are initially entirely populated by endocardium-derived mesenchymal cells, they later receive a significant epicardial contribution. For example, the fibroblasts that make up the parietal valvular leaflets and the tendinous cords in the formed heart are derived from both the endocardium and the epicardium.

The atrioventricular valves develop as shelf-like projections from the margins of the expanded atrioventricular orifices. These projections contain both myocardium and endocardial cushion mesenchyme. They grow deep into the ventricular cavity initially as trabecular ridges. Part of these trabeculae will later remodel to form papillary muscles. Each valve leaflet develops functionally significant regional variations in surface texture while its core condenses as a collagenous fibrous lamina, supported either by the fibro-fatty tissue of the atrioventricular groove, or by the anulus fibrosus. In the mitral valve, the aortic leaflet forms before the mural leaflet. Both are fully delaminated from the myocardial wall by postmenstrual week 10. The formation of the inferior leaflet of the tricuspid valve is followed by the formation of the septal and, later, the anterosuperior leaflets. This process continues until at least postmenstrual week 13 (see Fig. 13.15B).

Atrioventricular valve defects

Available with the *Gray's Anatomy* e-book

Aortic and pulmonary valves

The aortic and pulmonary valves are derived from the endocardial cushions within the myocardial outflow tract. These cushions become populated by neural crest cells, in addition to endocardial- and pharyngeal-derived mesenchymal cells, which helps them fuse across the tract. The myocardial wall surrounding the cushions then starts to split giving rise to the aortic and pulmonary roots. What remains of the fused cushions in each of the arterial roots will develop into the right and left adjacent pulmonary and coronary leaflets. The developing intercalated cushions, which form on opposite sides of the fused outflow cushions, will give rise to the non-adjacent leaflets of the aortic and pulmonary valve (see Fig. 13.14). In all these cushion-derived intrusions, the distal parts become excavated from the arterial wall to form the valvular leaflets. The valvular sinuses are found between the leaflets and the wall. The anulus fibrosus surrounding the atrioventricular valves also partially surrounds the outflow tract valves: only the pulmonary valve is not fully connected to it. The non-adjacent and left coronary leaflet of the aortic valve and the aortic leaflet of the mitral valve form a fibrous continuity with each other.

Neural crest cells play a role in the spatiotemporal regulation of the division of the outflow tract into the aortic and pulmonary arteries, and therefore of the development of the muscular sub-pulmonary infundibulum. Although proper migration of these cells is crucial for normal development of the outflow tract and the formation of arterial valve leaflets and sinuses, their exact role is largely obscure. Scarcely any neural crest cells remain in the adult heart, either in the leaflets of the arterial valves in the formed heart, or in the muscular sub-pulmonary infundibulum.

Arterial valve defects

Available with the *Gray's Anatomy* e-book

Non-myocardial additions to the developing heart

The parietal pericardial wall surrounding the heart is lined with bipotential mesothelium that will either add cells to the venous pole of the heart or differentiate towards the Tbx18-positive epicardial lineage. Bone morphogenetic proteins and fibroblast growth factors influence which lineage is ultimately followed. After heart looping and septation has started, epicardial mesenchyme is added to the external surface of the heart. The epicardium subsequently gives rise to the coronary vasculature and to the population of interstitial

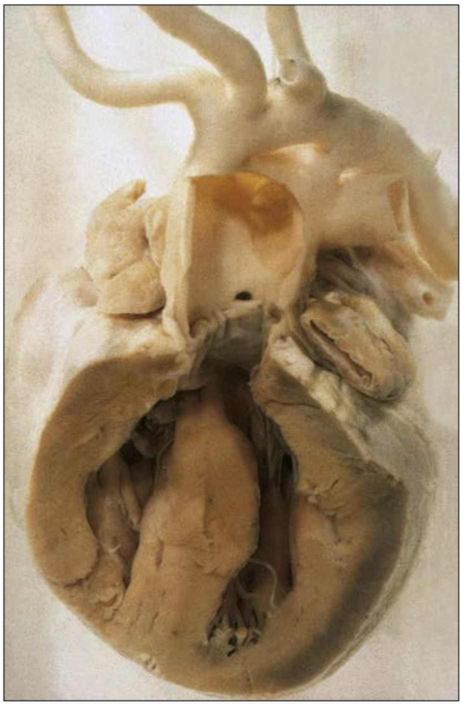

Fig. 13.16 This heart possesses a common arterial trunk, with a common truncal valve overriding a juxta-arterial deficiency of the ventricular septum, the result of failure of septation of the arterial pole of the developing heart. (Courtesy of Professor RH Anderson, Institute of Child Health, University College, London. Specimen prepared by Dr Leon M Gerlis.)

When the right atrioventricular junction (the connection between the right atrium and the right ventricle) does not expand normally during atrioventricular septation, the tricuspid valve remains atretic. Often a small dimple can still be observed within the right atrium where the connection should have been. Atresia of the tricuspid valve coincides with an atrial septal defect and a failure in right ventricle development. The left ventricle supports both the systemic and pulmonary circulation.

In Ebstein's malformation, the septal and inferior tricuspid valve leaflets are attached abnormally deep into the right ventricular chamber (Paranon and Acar 2008). This often leads to right ventricular overload and valve regurgitation (Lombardi and Pluchinotta 2018). In rare cases, Ebstein's malformation can coexist with atresia of the tricuspid valve; it does not coincide with hypoplasia of the right ventricle because the developmental process is different.

The mitral valve can exhibit several anomalies that result either in a valve stenosis or a valve regurgitation (Prakash et al 2017). Often, the papillary muscles or tensor apparatus are involved in these malformations (Séguéla et al 2011).

Bicuspid aortic valve is the most common congenital cardiac anomaly and often results from the aberrant formation of a large leaflet from two leaflets (Hoffman and Kaplan 2002, Yener et al 2002). It is linked with an ascending aorta that is prone to dilatation and dissection later in life. The aetiology is not yet fully understood but may involve different extracellular matrix composition (Siu and Silversides 2010, Rambeau et al 2017).

cardiac fibroblasts which not only produce extracellular matrix but also play a role in tissue repair and homeostasis (Tallquist and Molkentin 2017).

Epicardium

The epicardium develops from a protrusion of mesenchymal cells covered by mesothelium, the pro-epicardial organ (Simões and Riley 2018). This structure arises from the pericardial surface in the region of the sinus venosus during postfertilization week 5. The pro-epicardial cells migrate on the surface of the heart both by proliferation from their original location and by local directional outgrowth. The pro-epicardial cells successively spread over the myocardial surface of the developing atria, atrioventricular canal, ventricles and the proximal part of the outflow tract. The remnants of the pro-epicardium can be found in the area of the developing systemic venous tributaries up to stage 15 before it ultimately regresses.

After the formation of the epicardium, a distinct region, the sub-epicardial space or sub-epicardium, is formed between the developing epicardium and the outer myocardial layer. It is particularly pronounced at the atrioventricular junction and around the outflow regions of the heart tube and is populated by mesenchymal cells that are largely derived from the epicardium and that play an important role in the formation of the coronary vasculature.

Coronary blood vessels

Coronary arteries develop concomitantly with outflow tract septation during stages 14–16, by vasculogenesis from blood islands that coalesce into a plexus within the epicardial mesenchyme (Tomanek 2016). Plexus formation takes place before the formation of the arterial orifices in the aortic sinuses to which the coronary vessels ultimately connect. The coronary veins develop by a similar mechanism of plexus formation and mostly attach to the sinus venosus, although a small subpopulation will drain directly to the atrial chambers (Thebesian veins).

The coronary vessels themselves are formed by several precursor tissues. The endothelium is thought to arise from at least three different sources: the sinus venosus endothelium, the endocardium and, to a lesser extent, the pro-epicardium. The pericytes and smooth muscle cells arise from the epicardium and partially from the cushion endocardium. Neural crest cells can be traced to parts of the smooth muscle layer and fibroblasts arise mainly from the sub-epicardium.

The mature coronary vascular pattern is established by remodelling of the capillary plexuses and reduction in the number of arteriovenous anastomoses. Concomitant with the connection of the arterial plexus to the aorta, those vessels that acquire a tunica media and an adventitial covering persist and their luminal diameter increases (Sharma et al 2017), whereas those lacking a tunica media regress. Between postmenstrual weeks 16–19 the coronary arteries and veins increase in number and show thickening of the tunica media. During postmenstrual weeks 26–34 further expansion of the coronary vasculature occurs and elastic fibres are seen in the thickening tunica adventitia (Tomanek 2016).

Coronary artery anomalies

Available with the *Gray's Anatomy* e-book

EMBRYONIC BLOOD, BLOOD VESSELS AND EARLY CIRCULATION

Early formation of blood

Cellular elements

The cellular elements of the blood initially arise from the extraembryonic tissues of the secondary yolk sac (Ch. 8). The yolk sac wall is composed of an epithelial parietal hypoblast layer covered with an epithelial extraembryonic mesodermal layer, derived from extraembryonic mesoblast, and some intervening extraembryonic mesenchyme (Ch. 9). The yolk sac floats freely in the extraembryonic coelom (chorionic cavity) and after head and tail folding is continuous with the developing intraembryonic midgut within the embryo via a narrow vitelline duct (Ch. 10).

Evidence for the temporal phases of blood cell production is based mainly on experimental chick and mouse embryo studies. As both of these laboratory animals have very different developmental timescales and arrangements of extraembryonic tissues, any comparison to human development must be treated with caution. In the chick, the allantois becomes the site for gaseous exchange, and in the mouse, there is an extensive inverted visceral yolk sac and a haemotrichorial labyrinthine placenta. In humans, discoid haemochorial placentation provides gaseous and nutritional exchange and a separate yolk sac, which remains throughout gestation, can be identified at parturition.

Three overlapping waves of blood cell production have been identified, with differences between erythrocyte production and that of other cellular elements (Baron 2013). Lineage analyses of blood cells have revised some of the traditional views of the initial restriction of haemopoietic cell lines, e.g. populations of megakaryocytes and macrophages have been identified in the yolk sac wall at the same time as the earliest erythrocytes (McGrath et al 2015).

Erythrocytes arising in the first haemopoietic wave have conventionally been termed 'primitive', a term that is frequently used to indicate that embryonic cells are different from their adult counterparts: the acronym, EryP, primitive erythrocytes, is more useful. EryPs arise in the yolk sac wall within 3–4 weeks post fertilization in human embryos. The cells are nucleated and, in the mouse, very large (three times larger than fetal erythrocytes and 6 times larger than adult erythrocytes) (Kauts et al 2016). They express the zeta (ζ) and epsilon (ε) globin genes, which are consistently expressed in amniote embryos. EryPs enter the developing extraembryonic and intraembryonic circulations as a transiently amplifying pool of dividing cells, able to transport oxygen and carbon dioxide, and appear to have a role in vascular remodelling. They can leave the circulation, demonstrate surface adhesion molecules and form tight associations with other EryPs in the adjacent mesenchymal tissue surrounding early vessels. Over time, circulating EryPs continue to mature, as their cell diameter decreases and they lose nucleoli. In the mouse, EryPs undergo enucleation in the liver and remain in the fetal circulation until birth. In humans, EryPs are found in the stroma of placental villi at postfertilization week 4, and by week 5 the process of enucleation is first seen. Macrophages are present and proliferating in the chorionic plate before the fetoplacental circulation is established. In the process of EryP enucleation, groups of EryPs surround a macrophage, which contacts them via cytoplasmic projections and appears to engulf and digest their extruded nuclei (Van Handel et al 2010). The enucleated cells, reticulocytes, are found in the circulation, as are blood elements termed pyrenocytes, which are nuclei from EryPs with a surrounding cell membrane (McGrath et al 2008).

The second wave of erythrocyte production, also from the yolk sac wall, gives rise to EryD (definitive erythrocytes) from about postfertilization week 4 in humans. These cells are considered to arise from transient multipotent progenitors which will become restricted to erythroid and myeloid lineages (Baron 2013). In the mouse, EryD cells are found in the yolk sac wall, the developing liver and in the forming bone marrow. EryD cells are smaller than EryPs, they display different gene expression and requirements for erythropoietin, and different oxygen carrying capacities. Both types of early erythrocyte are present in the circulation during the second wave, and EryD cells rapidly outnumber EryPs.

The third wave of erythrocyte production of haemopoietic stem cells (HSCs), arises within the embryo at intraembryonic sites, including mesenchyme adjacent to large blood vessels, within the placental stroma and in the aorta-gonad-mesonephros (AGM) region. This latter region is subjacent to the intraembryonic coelom, particularly the lower ends of the pericardio-peritoneal canals and the upper posterior wall of the peritoneal cavity on either side of the mesentery of the midgut. It forms at the junction between somatopleuric and splanchnopleuric mesenchyme and is referred to as intermediate mesenchyme (Ch. 12).

It was always stated that the embryonic liver develops precociously to become a haemopoietic site before the medullary cavities form in developing long bones. In the mouse, both EryP and EryDs mature and enucleate in the liver. EryDs, (which are zeta-globin negative) have been identified in human embryonic liver from 6.5 weeks post fertilization, equivalent to about stage 19, and enucleating cells have been identified in sub-sinusoidal spaces at 11 weeks post fertilization. These findings suggest that the fetal human liver may not support erythroblast enucleation until later in development than was previously thought (Van Handel et al 2010). Study of haemopoietic stem cells from human fetal liver and cord blood have produced genome-wide maps of the DNA methylation profiles of developing blood cells (Farlik et al 2016).

Ultimately, only solitary right and left coronary arteries remain. There are occasional anomalies in coronary artery morphology: small accessory branches of the coronary arteries take their origin directly from the coronary sinuses in one third of human hearts. For information on coronary artery anomalies see Spicer et al (2015) and Pérez-Pomares et al (2016).

In the mouse there is some evidence that cells with a future haemopoietic lineage arise from the caudal primitive streak (Fraser 2012). Mesoblast cells arising from the caudal primitive streak migrate rostrally and laterally and differentiate into the initial epithelial lining of the intraembryonic coelomic wall (see Fig. 10.3). These cells then proliferate producing the mesenchymal populations (splanchnopleuric, somatopleuric and intermediate). It is possible that the final stem cells for late fetal and future adult haemopoiesis remain in the coelomic wall epithelium until the requisite time. These haemopoietic stem cells do not differentiate *in situ*, but seed precursor cells to the liver, thymus and bone marrow, which subsequently produce all blood lineages; they have been found in human embryos in very small numbers around 5 postfertilization weeks (Baron 2013).

Plasma

It has been suggested that the rapidly expanding early cardiovascular system is filled with plasma, reflecting the movement of fluid from the intraembryonic coelom to the veins. The intraembryonic coelomic wall is largely composed of proliferating cells that produce the splanchnopleuric and somatopleuric mesenchymal populations; when not dividing, adjacent cells form tight junctions, indicating a barrier function of the epithelium (Guo et al 2014). However, the walls of a portion of the pericardioperitoneal canals are thinner, and possibly more permeable to coelomic fluid, at the time when the canals surround the hepatocardiac channels. The latter lie between the hepatic plexus and the sinus venosus; the hepatocardiac channel on the right side is a wider vessel whereas on the left it is more plexiform, with only a transitory connection to the sinus venosus. The differentiation of this specific coelomic region occurs just in advance of the expansion and filling of the right and left atria, at about stage 12. Fluid within the extraembryonic coelomic space, the chorionic cavity, which is continuous with the intraembryonic coelom, has been collected and examined in the early human embryo (Jauniaux and Gulbis 2000). There are few, if any, studies on the synthesis and circulation of proteins including plasma proteins, although both erythropoietin and thrombopoietin are apparently needed for embryonic erythrocyte production (Baron 2013).

Early formation of blood vessels

It was thought that blood cells and blood vessels were derived from the same precursor population, initially in the extraembryonic tissues, but lineage studies have shown that EryPs and endothelial precursors do not share a common progenitor (Baron 2013). Vasculogenesis and angiogenesis are involved in the formation of blood vessels lined with endothelium. Vasculogenesis is the process where vessels arise *in situ* in extra- and intraembryonic sites: vitelline vessels form within the yolk sac wall; umbilical vessels arise within the mesenchyme surrounding the allantois; and the endocardium and dorsal aortae arise from splanchopleuric mesenchyme derived from the epithelial coelomic wall.

Angiogenesis

Further vessel development occurs by a process of angiogenesis in which endothelial precursors, angioblasts, arising in splanchnic and somitic tissues, add endothelial sprouts and branches to earlier vessels. None of the main vessels of the adult arises as a single trunk in the embryo. A capillary network is first laid down along the course of each vessel and the larger arteries and veins are defined by selection and enlargement of definite paths in this network. Lymphatic vessels develop after the main arteries and veins are formed. They arise initially by angiogenesis from the cardinal veins and subsequently by proliferation of lymphangioblasts that form lymphatic capillaries.

Five stages of angiogenesis have been described: endothelial tip cell specification and sprout initiation; sprout elongation and local guidance, where the distal tip cell extends supported by proximal stalk cells that may divide; sprout elongation in response to cues from the extracellular matrix; lumen formation, initially by the confluence of intracellular vacuoles, followed by establishment of apical basal polarity of the cells of the endothelial sprout; and fusion of the tip cell to another sprout tip so that two developing tubes join to form an early vascular plexus (Kuijper et al 2007, Chappell et al 2012). The developmental processes of angiogenesis are similar to those seen in both neoplasia and acute inflammation in adult tissue. The literature on angiogenesis is extensive and the process will not be considered in detail here; the interested reader is directed to Herbert and Stainier (2011), Senger and Davis (2011), Beets et al (2013), Eichmann and Pardanaud (2014) and Hashimoto et al (2016).

Studies have considered the development of capillary beds within the surrounding mesenchymal tissues destined to become laminae propriae, but few have looked at how capillary beds form within tissues undergoing morphogenetic movements. Czirok et al (2011) discussed the temporal imperative for free-living embryos to develop rapidly in contrast to amniote embryos, which do not have to fend for themselves. They concluded that prior to the establishment of a circulation, amniote vascular patterns of development are not predetermined by a network of patterning genes and cell signalling pathways, but rather that the tissue movements during organogenesis and the realignment and tension that develop within extracellular matrix fibres may guide cell migration and the position of early vessels.

Extracellular matrix plays a critical role in angiogenesis and vessel stabilization in the embryo and in the adult. Differences in the composition and abundance of specific extracellular matrix components between the embryo and adult mean that there are likely to be significant differences in the process at different ages. Fibronectin is required for normal vascular development; its deposition is related to interactions between endothelial cells and pericytes, and local tensional forces that occur between blood vessel basement membrane and local extracellular matrix assembly (Davis and Senger 2005, Senger and Davis 2011). Early blood vessels are initially surrounded by a fibronectin-rich matrix that is later incorporated into the endothelial basal lamina along with laminin, a particularly early constituent. Several layers of fibronectin-expressing cells are seen around larger vessels, such as the dorsal aortae. The endothelium does not synthesize a basal lamina in those regions where remodelling and angiogenesis are active, and the mesenchyme around such endothelium does not express α-actin or laminin until branching has stopped and differentiation of the tunica media begins (after a stable vascular pattern has formed). It is not known how differentiation of pericytes and smooth muscle cells is induced; the majority of arteries accumulate medial smooth muscle from the surrounding mesenchyme.

In early development, the early vessels of the embryo are disproportionately large and their walls consist of little more than a single layer of endothelium. The cardiac orifices are also relatively large and the force of the cardiac contraction is weak and, consequently, the circulation is sluggish, despite the rapid rate of contraction of the developing heart. However, the tissues are able to draw nourishment not only from the capillaries but also from the large arteries and the intraembryonic coelomic fluid. The earliest blood cells are also very large; as the embryo grows the early vascular beds become more complex and narrowed and erythrocytes also become smaller.

There is an ongoing relationship between developing blood vessels, their response to haemodynamic forces and the mechanotransduction pathways involved. The flow of blood exerts pressure on the developing vessel walls; circumferential stress is generated when vessels stretch in response to pressure, and shear stress, the tangential frictional force of flowing blood against the endothelium, is detected by and produces epigenetic changes in that epithelium (Culver and Dickinson 2010). Three principles operate in embryonic vasculature: if the flow increases or decreases the blood vessel calibre increases or decreases to normalize the shear stress; if the blood pressure in the vessel increases or decreases the vessel wall thickens or thins respectively, mainly by the modulation of the amount of smooth muscle; increase in capillary pressure leads to new capillary growth (Roman and Pekkan 2012). Endothelial cells are mechanosensitive, they are able to respond to laminar and disturbed blood flows and are sensitive to blood viscosity. Very complex interactions occur throughout the development of the circulation; cardiac rate increases with development and cardiac output increases in proportion to the weight of the embryo, so that when dorsal aortic blood flow is matched to embryonic weight, blood flow remains constant over a more than 150-fold change in the mass of the embryo. The influence of blood flow on cardiac development, and the ways that computational fluid dynamics can be used to determine developmental responses to blood flow have been studied (Courchaine and Rugonyi 2018, Courchaine et al 2018). Routine postmenstrual week 20 4D ultrasound assessments have been correlated with fluid mechanics of blood flow through fetal hearts (Wiputra et al 2016). For further information on haemodynamic forces in vascular development, remodelling and vessel specification see Culver and Dickinson (2010) and Roman and Pekkan (2012).

Embryonic arteries

Early arteries

After head folding, the embryo has bilateral primitive aortae, each consisting of ventral and dorsal parts that are continuous through the first embryonic aortic arches. The ventral aortae are fused and form a dilated aortic sac. The dorsal aortae run caudally, one on each side of the notochord, and fuse from about the level of the fourth thoracic to the fourth lumbar segment to form a single definitive descending aorta in stage 10 (**Fig. 13.17B**). In general, more mature endothelial channels are seen in the rostral, more advanced regions of the embryo. More caudally, a changing capillary plexus constantly remodels, becoming confluent with the extraembryonic vascular channels developing in the walls of the yolk sac and allantois (within the connecting stalk). The dorsal continuation of the primitive dorsal aortae forms anastomoses with the vitelline vessels around the yolk sac, and more caudally with anastomoses forming around the allantois.

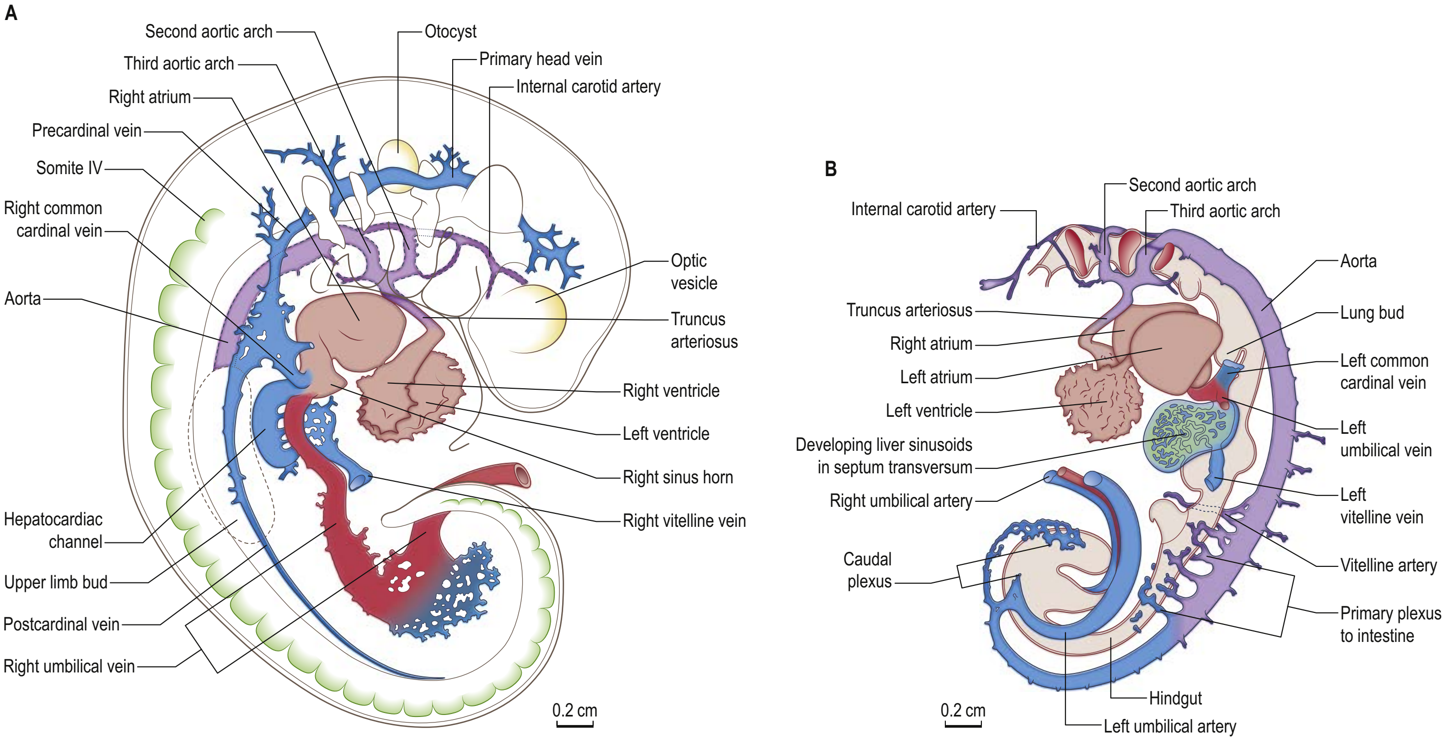
A
Second aortic arch
Third aortic arch
Right atrium
Precardinal vein
Somite IV
Right common cardinal vein
Aorta
Hepatocardiac channel
Upper limb bud
Postcardinal vein
Right umbilical vein
Otocyst
Primary head vein
Internal carotid artery
Optic vesicle
Truncus arteriosus
Right ventricle
Left ventricle
Right sinus horn
Right vitelline vein
0.2 cm
B
Internal carotid artery
Second aortic arch
Third aortic arch
Aorta
Lung bud
Left common cardinal vein
Left umbilical vein
Left vitelline vein
Vitelline artery
Primary plexus to intestine
Truncus arteriosus
Right atrium
Left atrium
Left ventricle
Developing liver sinusoids in septum transversum
Right umbilical artery
Caudal plexus
0.2 cm
Hindgut
Left umbilical artery

Fig. 13.17 Profile reconstructions of the blood vascular system of a stage 13 human embryo. The early circulation is now asymmetric; the venous vessels are enlarging on the right and diminishing on the left. **A**, Seen from the right side, showing the main venous channels to the heart. **B**, Seen from the left side, showing the aortic arch arteries, the main vessels arising from the dorsal aorta and umbilical arteries. Note that only the endothelial lining of the heart chambers is shown and, because the muscular wall has been omitted, the pericardial cavity appears much larger than the contained heart.

Initially, the dorsal aortae are the only longitudinal vessels present. Their branches all run at right-angles to the long axis of the embryo. Later, these transverse arteries become connected by longitudinal anastomosing channels that persist in part, forming arteries such as the vertebral, internal thoracic, superior and inferior epigastric, and gastroepiploic (gastro-omental). Each primitive dorsal aorta gives off somatic arteries (intersegmental branches to the body wall), a caudal continuation that passes into the body stalk (the umbilical arteries), lateral splanchnic arteries (paired segmental branches to the mesonephric ridge), and ventral splanchnic arteries (paired segmental branches to the digestive tube).

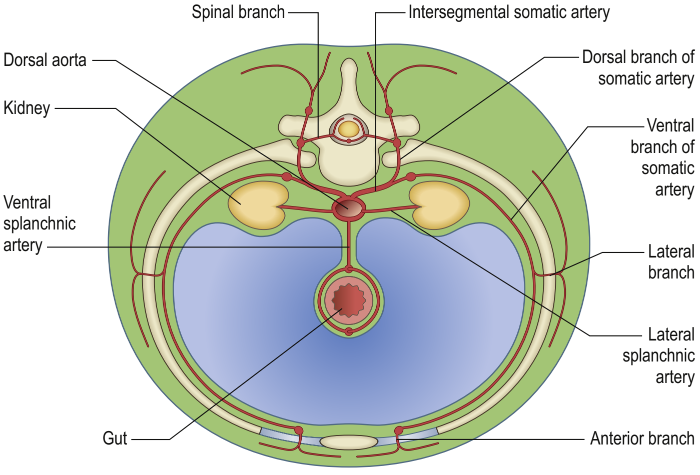
Spinal branch
Intersegmental somatic artery
Dorsal aorta
Dorsal branch of somatic artery
Kidney
Ventral branch of somatic artery
Ventral splanchnic artery
Lateral branch
Lateral splanchnic artery
Gut
Anterior branch

Fig. 13.18 The segmental and intersegmental arteries. The small red dilations indicate the positions of the longitudinal anastomoses.

Aortic arch arteries

The aortic arch arteries arise from the truncus arteriosus and pass bilaterally around the developing pharynx, to join bilateral dorsal aortae (Fig. 13.17). Details of the fates of the aortic arteries are given in Chapter 17, Fig. 17.9. The arterial vessels supplying the head and brain in stage 17 are illustrated in Fig. 17.8 and details of the maturation of cerebral arteries are given in Chapter 14 (see Fig. 14.36).

Somatic arteries

The somatic arteries are intersegmental in position. They persist, almost unchanged, in the thoracic and lumbar regions, as the posterior intercostal, subcostal and lumbar arteries. Each gives off a dorsal ramus that passes backwards in the intersegmental interval and divides into medial and lateral branches to supply the muscles and superficial tissues of the back (Fig. 13.18). The dorsal ramus also gives off a spinal branch that enters the vertebral canal and divides into a series of branches that supply the walls and joints of the osteoligamentous canal, and neural branches to the spinal cord and spinal nerve roots. After giving off its dorsal ramus, each intersegmental artery runs ventrally in the body wall, gives off a lateral branch and terminates in muscular and cutaneous rami.

Lateral splanchnic arteries

On each side the lateral splanchnic arteries supply the mesonephros, metanephros (see Fig. 22.2), testis or ovary and the suprarenal gland. All these structures develop, in whole or in part, from the intermediate mesenchyme, later termed the aorta–gonad–mesonephros region. One testicular or ovarian artery and three suprarenal arteries persist on each side. The phrenic artery branches from the most cranial suprarenal artery, and the renal artery arises from the most caudal. Additional renal arteries are frequently present and may be regarded as branches of persistent lateral splanchnic arteries.

Ventral splanchnic arteries

The ventral splanchnic arteries are originally paired (vitelline) vessels distributed to the capillary plexus in the wall of the yolk sac. After fusion of the dorsal aortae, they merge as unpaired trunks that are distributed to the increasingly defined and lengthening primitive digestive tube. Longitudinal anastomotic channels connect these branches along the dorsal and ventral aspects of the tube, forming dorsal and ventral splanchnic anastomoses (see Figs 13.17, 13.18). Above the respiratory diaphragm, a variable number of ventral splanchnic arteries persist, usually four or five, and supply the thoracic oesophagus. The dorsal splanchnic anastomosis persists in the gastro-omental (gastroepiploic), pancreaticoduodenal and primary branches of the colic arteries, whereas the ventral splanchnic anastomosis forms the right and left gastric and the hepatic arteries. Below the diaphragm, the ventral splanchnic arteries are reduced to three: the coeliac trunk and the superior and inferior mesenteric arteries. As the viscera supplied descend into the abdomen, their origins migrate caudally by differential growth. Thus the origin of the coeliac artery is transferred from the level of C7 to the level of T12; the superior mesenteric from T2 to L1; and the inferior mesenteric from T12 to L3. The superior mesenteric artery extends along the axis of the midgut loop into the extraembryonic coelom from stage 14 until 9 postfertilization weeks. As the proximal limb of the midgut loop develops secondary and tertiary loops, the artery gives rise to a series of branches. At stage 23 eight branches have arisen from the intra-abdominal portion of the artery, with the first three supplying the most proximal portion of the midgut loop. The third branch is bifurcated and supplies the midgut at the umbilical opening. The distal parts of the intra-abdominal branches 5–8 extend into the mesentery within the extraembryonic coelom, and all of the remaining branches, 9–14, supply that part of the midgut loop outside the embryonic body. The distance between the individual branches 9–14 are longer than those between branches 5–8. A colic branch arises consistently on the cranial side of the artery between branches 7 and 9 (Hikspoors et al 2015).

Early vitelline arteries

Vitelline arteries form in the vitelline arterial plexus around the secondary yolk sac and become confluent with the dorsal aortae in stage 12. By stage 13 communication between the embryonic body and yolk sac is limited to a single vitelline artery arising from the splanchnic branches of the dorsal aorta and running rostral to the narrowing vitelline duct (see Fig. 13.17). During stage 14 the artery with the vitelline duct is a landmark for the apex of the midgut loop within the splanchnopleuric mesenchyme of the dorsal mesentery. The vitelline artery is not a patent vessel at stage 16: its proximal origin becomes the origin of the superior mesenteric artery (Hikspoors et al 2015).

Early umbilical arteries

Initially, the umbilical arteries are the direct caudal continuation of the primitive dorsal aortae (see Fig. 13.17). They are present in the body stalk (connecting stalk) before any vitelline or visceral branches emerge, indicating the dominance of the allantoic over the vitelline circulation in the human embryo. (On a comparative basis, the umbilical vessels are chorio-allantoic and therefore 'somatovisceral'.) After the dorsal aortae fuse, right and left umbilical arteries arise from their ventrolateral aspects and pass lateral to the allantois in the connecting stalk (see Figs 13.17, 22.1). Later, the proximal part of each umbilical artery is joined by a new vessel that leaves the aorta at its termination and passes lateral to the allantois. This, possibly the fifth lumbar intersegmental artery, constitutes the dorsal root of the umbilical artery (the original stem forms the ventral root). The dorsal root gives off the axial artery of the lower limb, branches to the pelvic viscera and, more proximally, the external iliac artery. The ventral root disappears entirely and the umbilical artery now arises from that part of its dorsal root distal to the external iliac artery, i.e. the internal iliac artery.

Embryonic veins

Early veins

The early embryonic veins are often segregated into two groups, visceral and somatic, for convenience and apparent simplicity. The visceral group contains the derivatives of the vitelline and umbilical veins, and the somatic group includes all remaining veins. It should be noted that, with time, embryonic veins change the principal tissues they drain. They may receive radicles from obviously parietal tissues, which become confluent with drainage channels that are clearly visceral, and so form a compound vessel. The arrangement of the early embryonic veins is initially symmetric (see Fig. 13.17). The primitive tubular symmetric heart receives its venous return through the right and left horns of the sinus venosus, which are initially embedded in the mesenchyme of the septum transversum. Each horn receives vitelline, umbilical and the common cardinal veins (see Fig. 13.8). This symmetric pattern changes as the heart and gut develop and cardiac return is diverted to the right side of the heart.

Cardinal veins and somatic venous complexes

The initial venous channels in the early embryo have conventionally been termed cardinal because of their importance at this stage. The cardinal venous complexes are first represented by two large vessels on each side, the precardinal portion is rostral and the postcardinal is caudal to the heart. The two vessels unite to form a short common cardinal vein which passes ventrally to open into the corresponding horn of the sinus venosus (see Figs 13.1B, 13.17A; **Fig. 13.19B**). Further development of the precardinal veins directing the venous drainage of the head and arms to the right gives rise to the superior vena cava. Caudally, the postcardinal veins connect to a range of bilateral longitudinal anastomoses and venous confluences that cross the midline and successively direct the venous drainage from the lower limbs and body to the right, forming the inferior vena cava.

The precardinal veins join across the midline via an oblique interprecardial anastomosis (see Fig. 13.19B(i)) and undergo further remodelling as the head develops to form the dural venous sinuses (Ch. 17, p. 279; see Fig. 17.10). As the embryo increases in size, the postcardinal veins are insufficient channels to carry the venous return from the body wall and the developing mesonephros and gonads, and are supplemented by the bilateral longitudinal channels that anastomose with each other and with the posterior cardinal system. These channels are the subcardinal veins ventrally, and the subcentral, supracardinal, azygos line, and precostal veins more dorsally (**Fig. 13.19A**).

Postcardinal veins

The early postcardinal veins communicate across the midline via an interpostcardinal anastomosis (see Fig. 13.19B(ii)). This remains as an oblique transverse anastomosis between the iliac veins, and becomes the major part of the definitive left common iliac vein. It diverts an increasing volume of blood into the right longitudinal veins, which accounts for the ultimate disappearance of most of those on the left.

Subcardinal veins

Subcardinal veins (see Fig. 13.19B(i)) form in the ventromedial parts of the mesonephric ridges and become connected to the postcardinal veins by a number of vessels traversing the medial part of the ridges. They communicate by a pre-aortic intersubcardinal anastomotic plexus (the renal collar), which later forms the part of the left renal vein that crosses anterior to the abdominal aorta. On the right side, the subcardinal vein comes into intimate relationship with the developing liver. A cranial extension of the vessel establishes continuity with a corresponding new formation that is growing caudally from the right vitelline hepatocardiac (common hepatic) vein. In this way, on the right side, a more direct route is established to the heart and the prerenal (cranial) segment of the developing inferior vena cava.

Supracardinal veins

Supracardinal veins (see Fig. 13.19B(ii)) form dorsolateral to the aorta and lateral to the sympathetic trunk and take over the intersegmental venous drainage from the posterior cardinal vein. The supracardinal veins are also referred to as lateral sympathetic line veins or the thoracolumbar line. They receive the larger venous drainage of the growing body wall and communicate with the iliac veins caudally and with each other via the azygos lines and subcentral veins. The right supracardinal vein persists and forms the greater part of the postrenal segment of the inferior vena cava. The continuity of the vessel is maintained by the persistence of the anastomosis between the right supracardinal and the right subcardinal in the renal collar, a complete venous ring around the aorta below the origin of the superior mesenteric artery. The left supracardinal disappears, but some of the renal collar formed by the left supracardinal–subcardinal anastomosis persists in the left renal vein. Both supracardinal veins drain cranially into the subcardinal veins.

Azygos line veins

Azygos line veins form dorsolateral to the aorta and medial to the sympathetic trunk (see Fig. 13.19B(ii)). These channels, also referred to as the medial sympathetic line veins, gradually take over the intersegmental venous drainage from the supracardinal veins. The intersegmental veins now reach their longitudinal channel by passing medial to the sympathetic trunk, a relationship that the lumbar and intercostal veins subsequently maintain. Cranially, the azygos lines join the persistent cranial ends of the posterior cardinal veins.

Subcentral veins

Subcentral veins form directly dorsal to the aorta in the interval between the origins of the paired intersegmental arteries (see Fig. 13.19A). These veins communicate freely with each other and with the azygos line veins: these connections ultimately form the retro-aortic parts of the left lumbar veins and of the hemiazygos veins.

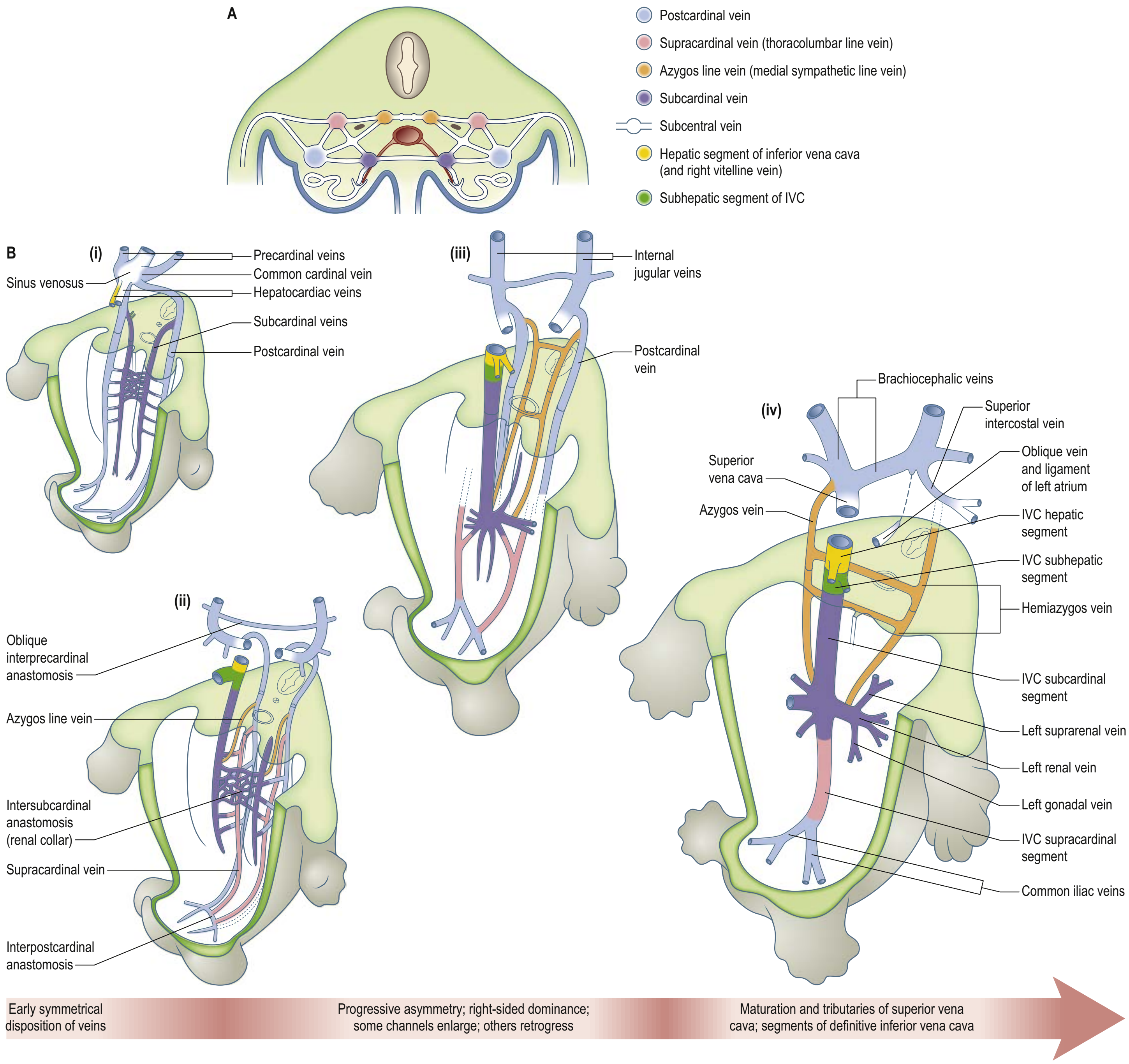
A
● Postcardinal vein
● Supracardinal vein (thoracolumbar line vein)
● Azygos line vein (medial sympathetic line vein)
● Subcardinal vein
Subcentral vein
● Hepatic segment of inferior vena cava (and right vitelline vein)
● Subhepatic segment of IVC
B
(i)
Sinus venosus
Precardinal veins
Common cardinal vein
Hepatocardiac veins
Subcardinal veins
Postcardinal vein
(ii)
Oblique interprecardinal anastomosis
Azygos line vein
Intersubcardinal anastomosis (renal collar)
Supracardinal vein
Interpostcardinal anastomosis
(iii)
Internal jugular veins
Postcardinal vein
(iv)
Brachiocephalic veins
Superior intercostal vein
Superior vena cava
Azygos vein
Oblique vein and ligament of left atrium
IVC hepatic segment
IVC subhepatic segment
Hemiazygos vein
IVC subcardinal segment
Left suprarenal vein
Left renal vein
Left gonadal vein
IVC supracardinal segment
Common iliac veins
Early symmetrical disposition of veins
Progressive asymmetry; right-sided dominance; some channels enlarge; others retrogress
Maturation and tributaries of superior vena cava; segments of definitive inferior vena cava

Fig. 13.19 Somatic venous development. **A**, A section through the embryonic trunk. Principal longitudinal veins are colour-coded. Interconnections and intersegmental veins are uncoloured. **B**, The development of the principal somatic veins, from the early symmetric state, through states of increasing asymmetry, to the definitive arrangement. Abbreviations: IVC, inferior vena cava.

Precostal or lumbocostal venous line

A precostal or lumbocostal venous line, anterior to the vertebrocostal element and posterior to the supracardinal, is recognized by some authorities. The ascending lumbar vein is a possible derivative.

Further development of the somatic veins

The final arrangement of the embryonic abdominal and thoracic longitudinal cardinal veins may be summarized as follows. The terminal part of the left postcardinal vein forms the distal part of the left superior intercostal vein. On the right side, its cranial end persists as the terminal part of the azygos vein. The caudal part of the subcardinal vein is, in part, incorporated in the testicular or ovarian vein and partly disappears. The cranial end of the right subcardinal vein is incorporated into the inferior vena cava and also forms the right suprarenal vein. The left subcardinal vein, cranial to the intersubcardinal anastomosis, is incorporated into the left suprarenal vein. The renal and testicular or ovarian veins on both sides join the supracardinal–subcardinal anastomosis. On the left side, this connects directly to the forming inferior vena cava via an intersubcardinal anastomosis; the right supracardinal vein forms much of the caudal (postrenal) segment of the inferior vena cava. The left supracardinal vein disappears entirely. The right azygos line persists in its thoracic part to form all but the terminal part of the azygos vein. Its lumbar part can usually be identified as a small vessel that leaves the azygos vein on the body of the twelfth thoracic vertebra and descends on the vertebral column, deep to the right crus of the diaphragm, to join the posterior aspect of the inferior vena cava at the upper end of its postrenal segment. The left azygos line forms the hemiazygos veins. The subcentral veins give rise to the retro-aortic parts of the left lumbar veins and of the hemiazygos veins (see Fig. 13.19B(iv)).

Inferior vena cava

The inferior vena cava (see Fig. 13.19B(iv)) is a composite vessel that develops on the posterior abdominal wall dorsal to the developing peritoneal cavity. It forms as a consequence of the temporal remodelling of the successive venous complexes described above. The precise mode of development of its postrenal segment (caudal to the renal vein) is still somewhat uncertain. Its function is initially carried out by the right and left postcardinal veins which receive the venous drainage of the

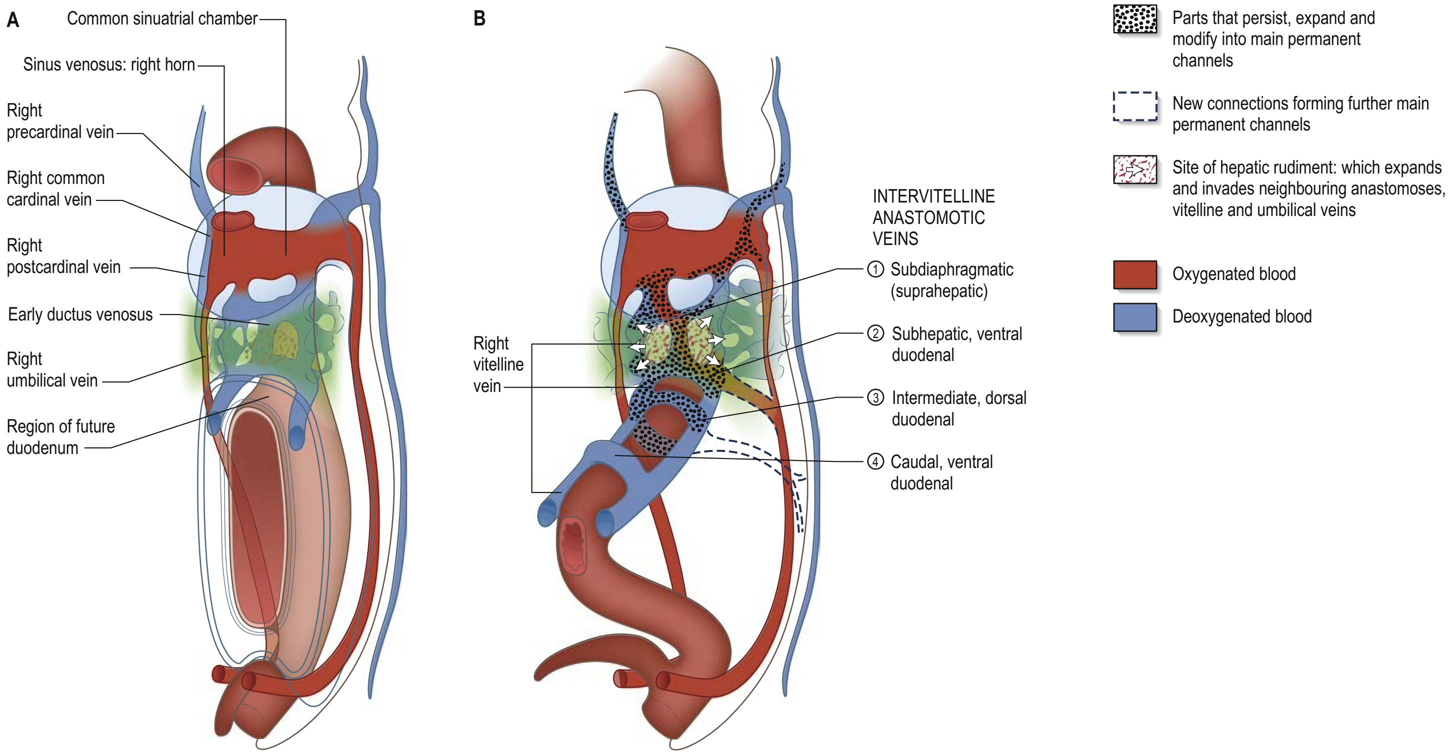
A
Common sinuatrial chamber
Sinus venosus: right horn
Right precardinal vein
Right common cardinal vein
Right postcardinal vein
Early ductus venosus
Right umbilical vein
Region of future duodenum
B
Right vitelline vein
INTERVITELLINE ANASTOMOTIC VEINS
① Subdiaphragmatic (suprahepatic)
② Subhepatic, ventral duodenal
③ Intermediate, dorsal duodenal
④ Caudal, ventral duodenal
Parts that persist, expand and modify into main permanent channels
New connections forming further main permanent channels
Site of hepatic rudiment: which expands and invades neighbouring anastomoses, vitelline and umbilical veins
Oxygenated blood
Deoxygenated blood

Fig. 13.20 Development of the vitelline, umbilical and terminal cardinal vein complexes: the early symmetric condition. **A**, The early symmetric arrangement of cardinal and umbilical veins entering the sinus venosus; blood from the yolk sac passes, via vitelline veins, through anastomoses forming in the septum transversum mesenchyme (green). **B**, The developing duodenum is surrounded by transverse duodenal intervitelline anastomoses. Changes in the developing gut and umbilical veins cause shifts in the routes taken by venous blood flowing to the sinus venosus.

lower limb buds and pelvis, and run in the dorsal part of the mesonephric ridges, receiving tributaries from the body wall (intersegmental veins) and from the derivatives of the mesonephroi. Many of the changes seen in the development of the infrahepatic caval and azygos systems in the human may result from lateral to medial movement of the vessels as a consequence of the growth of the abdominal viscera (Hikspoors et al 2015).

Descriptions of venous development are very largely based on studies on animals, where the dimensions and final disposition of visceral organs differ from those found in humans. In some animals, the right postcardinal vein constitutes a large part of the postrenal segment of the inferior vena cava. In these cases, the right ureter, on leaving the kidney, passes medially, dorsal to the vessel and then, curving round its medial side, crosses its ventral aspect. Rarely, a similar condition is found in humans, and indicates the persistence of the right postcardinal vein and failure of the right supracardinal to play its normal part in the development of the inferior vena cava.

Only the supracardinal part of the inferior vena cava receives intersegmental venous drainage. The postrenal (caudal) segment of the inferior vena cava is on a plane that lies dorsal to the plane of the prerenal (cranial) segment. Thus, the right phrenic, suprarenal and renal arteries, which represent persistent mesonephric arteries, pass behind the inferior vena cava, whereas the testicular or ovarian artery, which has a similar developmental origin, passes anterior to it.

In summary, the inferior vena cava is formed from below upwards by the confluence of: the common iliac veins, a short segment of the right postcardinal vein, the postcardinal–supracardinal anastomosis, part of the right supracardinal vein, the right supracardinal–subcardinal anastomosis, right subcardinal vein, a new anastomotic channel of double origin (the hepatic segment of the inferior vena cava) and the cardiac termination of the right vitelline hepatocardiac vein (common hepatic vein).

Visceral venous complexes, ductus venosus and the portal vein

Early vitelline veins

The early vitelline veins drain capillary plexuses that develop within the extraembryonic splanchnopleuric mesenchyme of the secondary yolk sac (see Fig. 9.10). With head, tail and lateral fold formation, elongation of the rostral endoderm forms the foregut, the allantois is brought within the body cavity with the hindgut dorsally, and the midgut remains confluent with the yolk sac (see Fig. 10.10). At stage 12, derivatives from all these levels possess a venous drainage that is originally vitelline and enters the sinus venosus as the most medial of the vessels contributing to the inflow tract of the heart (see Fig. 13.8). The intraembryonic confluence of both vitelline veins descends between stages 14 and 18 as the heart descends.

Early umbilical veins

The early umbilical veins form in the mesenchyme surrounding the allantois and in the mesenchymal connecting stalk confluent with the developing placenta (see Figs 9.2, 9.10, 13.1). The human endodermal allantois is very small, projecting only into the (proximal) embryonic end of the connecting stalk, which is therefore regarded as precociously formed allantoic mesenchyme. Peripheral venules drain the mesenchymal cores of the placental chorionic villous stems and terminal villi. They are the radicles of a single vessel, the vena umbilicalis impar, that traverses the mixed mesenchyme of the connecting stalk to reach the caudal rim of the developing umbilical cord where it divides into primitive right and left umbilical veins. Each curves rostrally in the somatopleuric lateral border of the umbilicus, i.e. where intraembryonic and extraembryonic or amniotic somatopleure are continuous, lying lateral to the communication between both the intraembryonic and the extraembryonic coeloms. Rostrolateral to the umbilicus, the two umbilical veins reach, enter and traverse the junctional mesenchyme of the septum transversum and connect with septal capillary plexuses (**Fig. 13.20**). They then continue, entering their corresponding horn of the sinus venosus lateral to the terminations of the vitelline veins.

Later vitelline veins

From stage 13 the vitelline veins passing to the embryo from the yolk sac wall enter an intervitelline anastomosis (hepatic plexus) in the caudal part of the septum transversum before reaching the sinus venosus. This network is ventral to the future subdiaphragmatic end of the oesophagus, primitive stomach, the superior (first) and descending (second) regions of the duodenum and the remainder of the duodenal tube. The channel is sometimes termed suprahepatic because of the position of the hepatic primordium; as the latter expands, it becomes partly intrahepatic. The terminations of the vitelline veins from this time are termed hepatocardiac channels.

Development of the portal circulation is initiated by changes in the disposition of the duodenum and related changes to the intervitelline anastomotic veins. The duodenum develops from the caudal part of the foregut (that part of the gut with dorsolateral pericardioperitoneal canals), and the cranial part of the midgut. All portions are surrounded

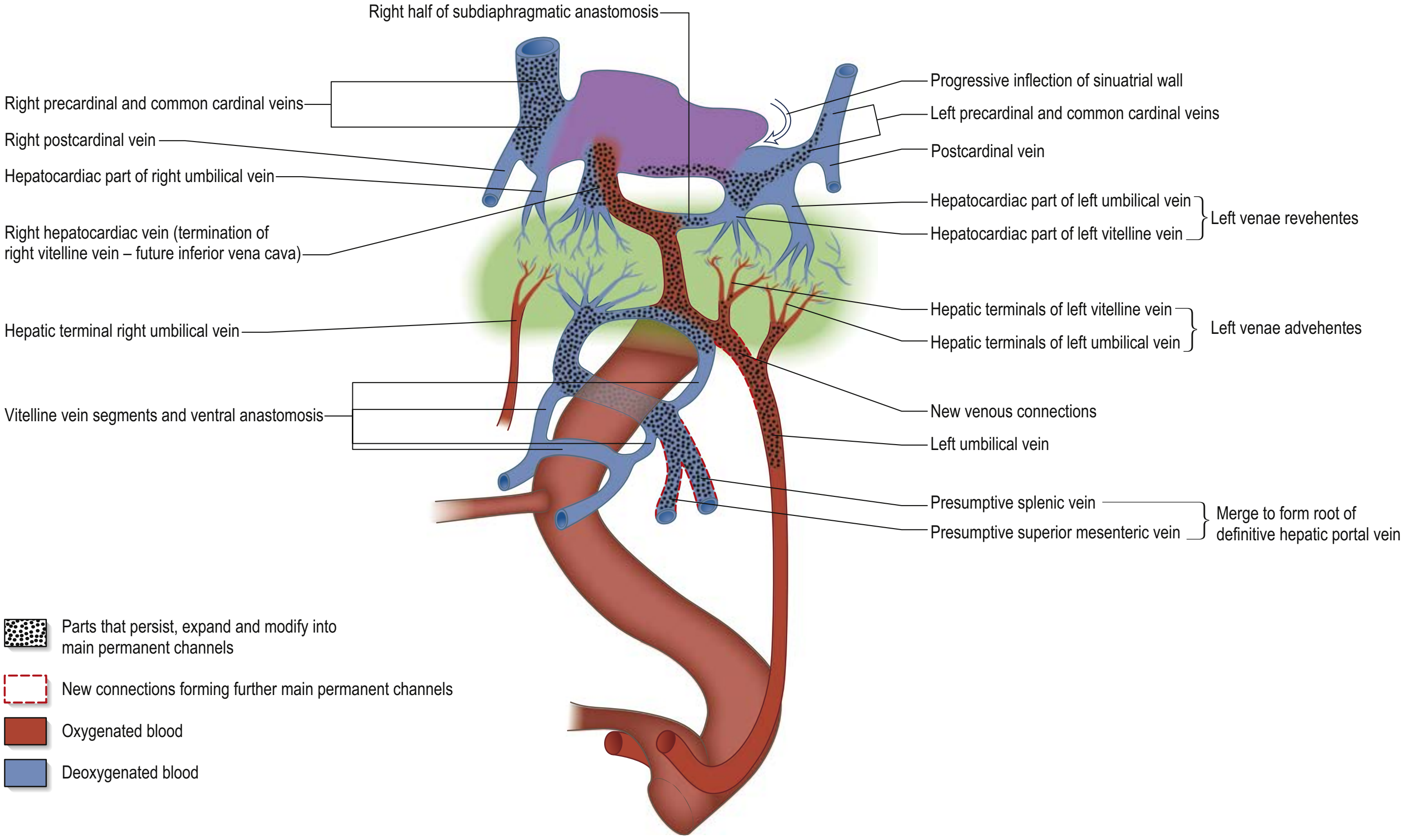
Right half of subdiaphragmatic anastomosis
Right precardinal and common cardinal veins
Right postcardinal vein
Hepatocardiac part of right umbilical vein
Right hepatocardiac vein (termination of right vitelline vein – future inferior vena cava)
Hepatic terminal right umbilical vein
Vitelline vein segments and ventral anastomosis
Progressive inflection of sinuatrial wall
Left precardinal and common cardinal veins
Postcardinal vein
Hepatocardiac part of left umbilical vein
Hepatocardiac part of left vitelline vein
Left venae revehentes
Hepatic terminals of left vitelline vein
Hepatic terminals of left umbilical vein
Left venae advehentes
New venous connections
Left umbilical vein
Presumptive splenic vein
Presumptive superior mesenteric vein
Merge to form root of definitive hepatic portal vein
Parts that persist, expand and modify into main permanent channels
New connections forming further main permanent channels
Oxygenated blood
Deoxygenated blood

Fig. 13.21 Development of the vitelline, umbilical and terminal cardinal vein complexes: a mid-stage of asymmetry has been reached between the early symmetric condition (see Fig. 13.20) and the definitive late prenatal state. The extent of the liver within the septum transversum mesenchyme is shown in green.

by splanchnopleuric mesenchyme: the portal circulation develops from angiogenic lineages in this tissue. Ventrally only the caudal part of the foregut is continuous with the ventral mesogastrium, derived from the cranial part of the septum transversum mesenchyme; the cranial midgut ventral surface lies free in the future peritoneal cavity. Dorsally, the duodenum is attached by splanchnopleuric mesenchyme to a dorsal mesoduodenum cranially and the dorsal mesentery of the midgut caudally.

Proximally a subdiaphragmatic (suprahepatic) anastomosis lies close to the foregut portion of the duodenum. As the cranial midgut portion of the duodenum lengthens, three more transverse duodenal intervitelline anastomoses, subhepatic (ventral duodenal), intermediate (dorsal duodenal) and caudal (ventral duodenal), become visible (see Fig. 13.20B). As can be inferred from their names, their relation to the duodenum alternates and it has become customary to describe the blood flow through these paraduodenal vitelline veins and their associated anastomoses as forming a figure of eight.

Distally, when the connection of the yolk sac to the midgut narrows, forming the vitelline duct, the vitelline veins also lengthen and continue on each side of the duct (see Fig. 21.2B). They lengthen even further when the midgut loop extends into the extraembryonic coelom. The left vitelline vein lies within the dorsal mesentery between the proximal and distal parts of the midgut loop. In stage 14 embryos, the right vitelline vein is cranial to the proximal midgut loop within the mesenchyme surrounding the vitelline duct; from stage 16 onwards it appears disconnected from this mesenchyme and free within the abdominal cavity alongside the vitelline duct. Its course forms the central axis of the primary midgut loop and marks the apex of the loop until the return of the herniated small intestine to the abdominal cavity (Hikspoors et al 2015).

Later umbilical veins

The further development of the vitelline veins and their anastomoses is closely interlocked with the growth of hepatic sinusoids in the septum transversum and changes to the umbilical veins. Evagination of hepatic 'cords' of presumptive hepatocytes from the endodermal foregut into the septum transversum mesenchyme initiates the formation of early plexiform connections of the hepatic sinusoids. As these expand laterally and extend caudally, they merge with the terminal connections of the vitelline and umbilical veins and subsume them within a series of complex branching vessels conducting blood in and out of the hepatic sinusoids.

Both deoxygenated and oxygenated blood enter the developing hepatic sinusoids, in the same way as the adult liver sinusoids convey portal and systemic blood. However, in the embryo and fetus, both blood supplies travel within veins. Vitelline veins from the extraembryonic yolk sac and the intraembryonic developing gut carry deoxygenated blood, and umbilical veins carry oxygenated blood from the placenta. All of these vessels branch and enter the liver via afferent hepatic veins, the venae advehentes. Blood leaves the hepatic sinusoids through four efferent hepatic veins, the venae revehentes; these are the terminal ends of the right and left vitelline veins, and the right and left umbilical veins, now termed hepatocardiac veins, all of which enter the sinus venosus (**Fig. 13.21**).

Changes to the circulation that involve returning venous blood to the right side via modifications of the cardinal system of veins occur contemporaneously with changes to the terminal portions of the vitelline and umbilical veins. The right umbilical vein regresses and atrophies during stages 14–15 (see Fig. 13.21). The hepatic terminal of the left umbilical vein retains some vessels that discharge into the sinusoids, but blood flow preferentially enlarges connections with the left half of the subhepatic (ventral duodenal) intervitelline anastomosis. These connections form a channel, the ductus venosus, which courses to the right half of the subdiaphragmatic anastomosis to join the right hepatocardiac channel (the termination of the right vitelline vein) and empty into the inferior vena cava (see Fig. 13.21; **Fig. 13.22**). The portal vein is derived from presumptive superior mesenteric and splenic veins that pass via the intermediate (dorsal duodenal) intervitelline anastomosis into the liver sinusoids via a right vena advehente. Blood in the umbilical vein supplies the left lobe of the liver and ductus venosus; the right lobe of the liver receives blood from the portal circulation. This arrangement means that the left lobe of the liver receives the most oxygenated blood returning from the placenta: the remainder (proportions change during the third trimester) passes into the ductus venosus and, via haemodynamic streaming, to the inferior vena cava and right atrium, then through the foramen ovale to the left atrium, to supply heart muscle and brain.

EMBRYONIC LYMPHATIC VESSELS

Lymphatic endothelial cells in lymphatic capillaries display a discontinuous basal lamina and basement membrane. They are held by anchoring filaments to the surrounding extracellular matrix. In the mouse, their differentiation starts with expression of Sox-18 and Prox-1,

Fig. 13.22 The condition of some main upper abdominal and intrathoracic right atrial terminal veins in the later prenatal months. The rotation of the stomach and movement of the duodenum produce relative changes in the final arrangement of the duodenal intervitelline anastomoses that form the hepatic portal vein.

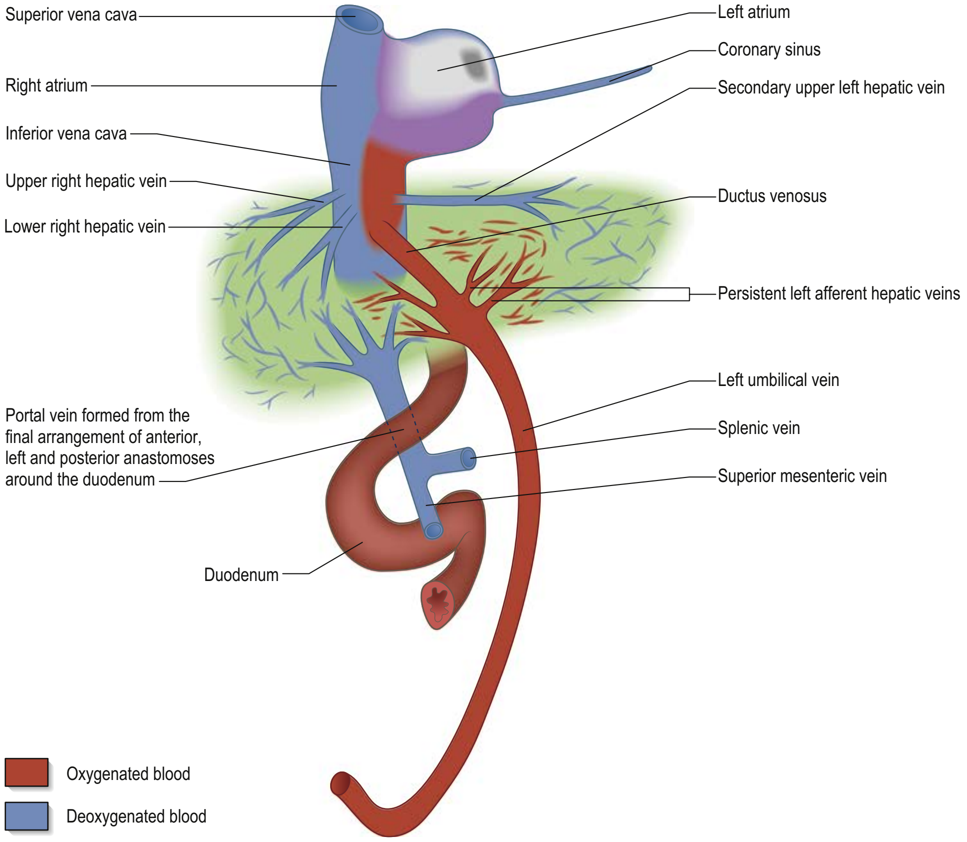
Superior vena cava
Right atrium
Inferior vena cava
Upper right hepatic vein
Lower right hepatic vein
Portal vein formed from the final arrangement of anterior, left and posterior anastomoses around the duodenum
Duodenum
Left atrium
Coronary sinus
Secondary upper left hepatic vein
Ductus venosus
Persistent left afferent hepatic veins
Left umbilical vein
Splenic vein
Superior mesenteric vein
🟥 Oxygenated blood
🟦 Deoxygenated blood

a Prospero homeobox transcription factor, in a subset of cardinal veins (Zhou et al 2010, Park et al 2011). Prox-1 is the most specific and functional lymphatic marker: its disruption leads to failure of lymphatic vessel development. Abnormal or absent lymphatic development is also seen with lack of vascular endothelial growth factor 3 (VEGFR3) and lack of angiopoietin 1, respectively (Yamashita 2007). Abnormalities of development and of remodelling of primary lymphatic vessels also occur if Akt, a serine/theonine protein kinase, is absent, possibly due to insufficient recruitment of smooth muscle cells to larger lymphatic vessels (Zhou et al 2010). An overview of the development of the mammalian lymphatic vasculature and genes involved, based on the mouse embryo, is given in Yang and Oliver (2014).

The earliest lymphatic vessels arise from budding of lymphatic endothelial cells from the cardinal veins to form lymph sacs (Eichmann et al 2005). Six early lymph sacs can be identified; two are paired (the jugular and the posterior lymph sacs) and two are unpaired (the retroperitoneal sac and the cisterna chyli). In lower mammals, an additional pair (subclavian) is present, but in the human embryo, these are merely extensions of the jugular sacs.

The jugular lymph sac is the first to appear, at the junction of the subclavian vein with the precardinal vein, with later prolongations along the internal and external jugular veins. The posterior lymph sac encircles the left common iliac vein, the retroperitoneal sac appears in the root of the mesentery near the suprarenal glands, and the cisterna chyli appears opposite the third and fourth lumbar vertebrae (**Fig. 13.23**). The lymph vessels bud out from the lymph sacs along lines that correspond more or less closely with the course of embryonic blood vessels (typically of the veins); many also arise *de novo* in the mesenchyme and establish connections with existing vessels (**Fig. 13.24**). The deeper plexuses are the first to be developed in the body wall and the wall of the intestine, and the vessels in the superficial layers are gradually formed by continued growth.

The thoracic duct is derived from left and right lymphatic trunks joined across the midline by anastomoses. The definitive duct consists of the lower portion of the right trunk, a transverse anastomosis and the upper portion of the left trunk. In contrast to the adult arrangement, the fetal thoracic duct is dilated at its origin from the cisterna chyli, and there is no associated lymphatic plexus draining the thoracic wall (Amore et al 2016). Perinatal and neonatal chylous visceral effusions are rare, but may be caused by hypoplastic or hyperplastic development of the lymphatic system. Chylothorax is the most common cause of pleural effusion in the neonate; primary chylous ascites is caused by anomalous development of the intra-abdominal lymphatic vessels (Bellini et al 2012).

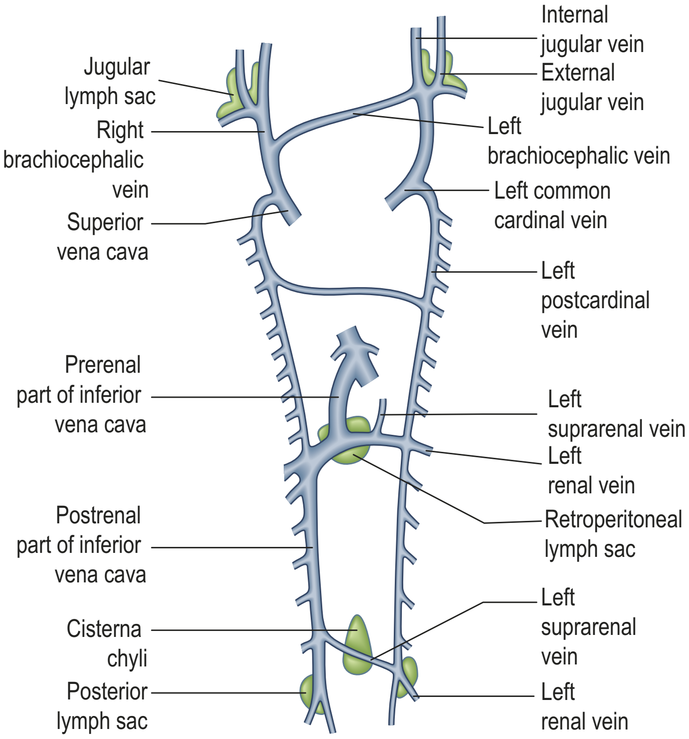
Jugular lymph sac
Right brachiocephalic vein
Superior vena cava
Prerenal part of inferior vena cava
Postrenal part of inferior vena cava
Cisterna chyli
Posterior lymph sac
Internal jugular vein
External jugular vein
Left brachiocephalic vein
Left common cardinal vein
Left postcardinal vein
Left suprarenal vein
Left renal vein
Retroperitoneal lymph sac
Left suprarenal vein
Left renal vein

Fig. 13.23 Relative positions of the primary lymph sacs (as originally determined by Sabin (1912)).

Lymph nodes and lymphoid tissues

Lymph vessels can be seen in the embryo in the cervical region from stage 16. Lymph nodes provide regional proliferative foci for lymphocytes and have been identified from week 9. Early lymph sacs become infiltrated by lymphoid cells, and the outer portion of each sac becomes the subcapsular sinus of the lymph node. Morphological differentiation of medullary and cortical compartments has not been observed until the end of postfertilization week 10 (Tonar et al 2001). At the same time as these early lymph nodes are developing, the nasopharyngeal wall is infiltrated by lymphoid cells that are believed to herald the early development of the tubal and nasopharyngeal tonsils.

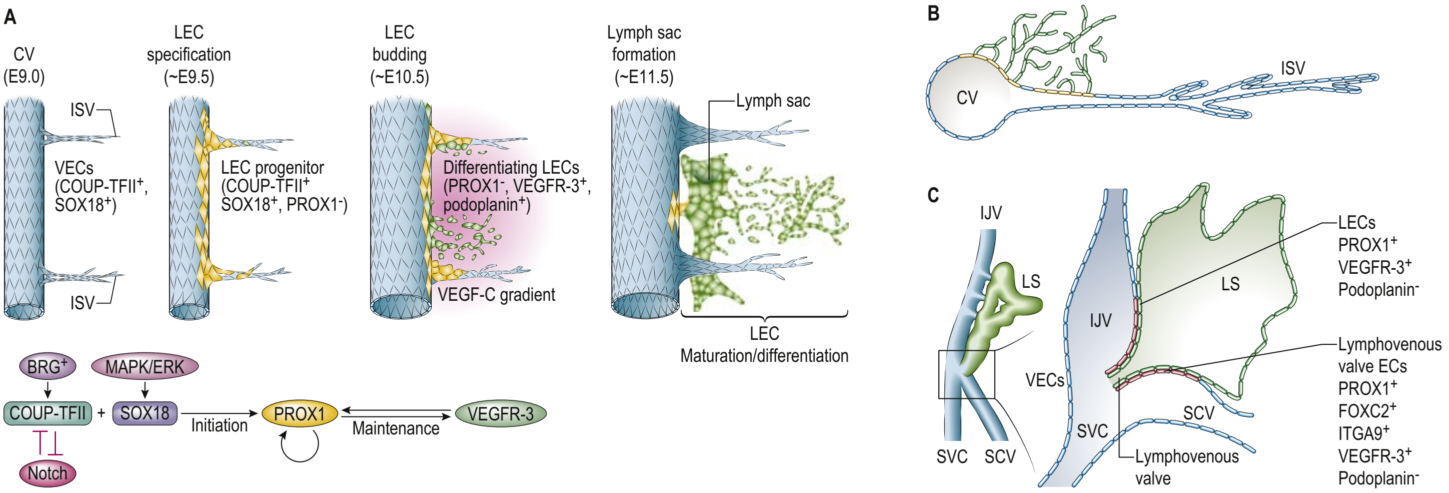

Fig. 13.24 Schematic representation of the development of the mammalian lymphatic vasculature and lymphovenous valves. **A**, A sagittal view of the formation of lymph sacs from the cardinal vein (mouse embryo, age given in days) and the genes expressed. Progenitor lymphatic endothelial cells bud off the wall of the cardinal vein, interconnect and assemble to form lymph sacs that provide the main source of future lymphatic endothelial cells. **B**, A transverse view of progenitor lymphatic endothelial cells budding from the cardinal vein. **C**, The formation of lymphovenous valves; note differences in gene expression in the valve leaflets. Abbreviations: CV, cardinal vein; EC, endothelial cell; IJV, internal jugular vein; ISV, intersomitic vein; LEC, lymphatic endothelial cell; LS, lymph sac; SCV, subclavian vein; SVC, superior vena cava; VEC, venous endothelial cell. (Adapted with permission from Yang Y, Oliver G 2014 Transcriptional control of lymphatic endothelial cell type specification. Adv Anat Embryol Cell Biol 214:5–22.)

FETAL CIRCULATION

As the cardiovascular system develops, the embryonic circulation is modified into a fetal circulation that is able to establish a separate pulmonary circulation at birth. The dorsal aortae persist on the cranial side of the third aortic arches as the internal carotid arteries (see Fig. 17.9). The dorsal aorta between the third and fourth aortic arches, the carotid duct, diminishes and ultimately disappears. From the fourth arch to the origin of the seventh intersegmental artery, the right dorsal aorta becomes part of the right subclavian artery, and caudal to the seventh intersegmental artery, the right dorsal aorta disappears up to the site where the thoracic aortae fuse. The remnants of the left carotid duct are found in the descending part of the aortic arch. The fused right and left embryonic dorsal aortae persist as the definitive descending thoracic and abdominal aorta.

Concomitant changes also occur in the early venous system. The precardinal veins enlarge as the embryo develops. They are further augmented by the subclavian veins from the upper limb buds, which become the chief tributaries of the common cardinal veins, gradually assuming a craniocaudal orientation as the thorax enlarges around the heart (see Fig. 13.19). These parts of the original precardinal vein, rostral to the subclavian veins, are now the internal jugular veins, and their confluences are the brachiocephalic veins. The right and left common cardinal veins are originally of the same diameter but the development of a large oblique transverse connection means that the left brachiocephalic vein carries more blood across from the left to the right. The part of the original right precardinal vein between the junction of the two brachiocephalic veins and the azygos veins will give rise to the upper part of the superior vena cava. The caudal part of this vessel, below the entrance of the azygos vein, is formed by the right common cardinal vein. The left precardinal and left common cardinal veins caudal to the transverse branching of the left brachiocephalic vein will disappear; the precardinal vein constitutes the terminal part of the left superior intercostal vein, while the common cardinal vein is represented by the ligament of the left superior vena cava and the oblique vein of the left atrium (vein of Marshall). The remainder of the left superior intercostal vein is developed from the cranial end of the postcardinal vein and drains the second, third and, on occasion, the fourth intercostal veins. The oblique vein of the left atrium passes downwards across the back of the left atrium to open into the coronary sinus, which represents the persistent left sinus horn.

Functioning fetal shunts

The adult circulation consists of higher pressure systemic and lower pressure pulmonary circulations, whereas the fetal circulation consists of systemic and placental circulations and a very limited high resistance pulmonary circulation (because the lung fields are not open). The ductus venosus, foramen ovale and ductus arteriosus are important conduits in the fetal circulation: the connection of a number of vascular ducts (shunts) and a valve between the atria enables the fetal circulation to change to the adult circuits within hours and days after delivery.

The placenta serves as the organ for fetal exchange of nutrients, gases and waste products of the blood, and in the second trimester receives 30% of the cardiac output (Kiserud and Haugen 2017). Fetal blood reaches the placenta via two umbilical arteries (carrying deoxygenated blood) and, in fetal life, returns by a single left umbilical vein (carrying oxygenated blood) because the right embryonic umbilical vein regresses. The left umbilical vein enters the abdomen at the umbilicus and angles upwards towards the liver in the caudal edge of the peritoneal layers of the original ventral mesentery, later termed the falciform ligament (see Fig. 21.6). The vein reaches the hepatic surface, joins the left branch of the comparatively small portal vein at the porta hepatis, and continues as the ductus venosus which ascends posterior to the liver to join the left hepatic vein near its termination in the inferior vena cava (**Fig. 13.25**; see Figs 13.20–13.22). In the second trimester about 70% of the blood in the umbilical vein passes into the liver and 30% passes into the ductus venosus (Kiserud and Haugen 2017).

The ductus venosus in the fetus does not appear to change size between postmenstrual weeks 13–17. During this time the portal sinus, which leads to the ductus venosus, has an average diameter of 2.6 mm and is lined by smooth endothelium. It ends at a thickening of subendothelial elastic fibres that form a protrusion into the ductal lumen, the shelf of the ductus venosus inlet. The ductus venosus is about 5.1 mm long (range 3.4–6.5) and has an average diameter of 1.4 mm at its inlet and outlet. It displays longitudinal endothelial corrugations supported by underlying elastin fibres and a single layer of longitudinally arranged smooth muscle cells that extends along the entire length of the ductus. Adrenergic nerve fibres have been identified in the wall of the ductus venosus at postmenstrual weeks 20–24; contraction in response to noradrenaline, acetylcholine and 5-HT has been demonstrated, as has dilation in response to NO, PGE1 and hypoxaemia (Kiserud and Haugen 2017). From the portal sinus to the subdiaphragmatic vestibulum, the ductus venosus progressively narrows and then dilates; the lumen is described as hourglass-shaped. It has been suggested that, unlike other veins, the ductus venosus acts as a high-pressure vessel: the narrowing of the inlet accelerates low-pressure, high-volume flow in the portal sinus, and the abundant elastic fibres in its wall propagate the wave by elastic recoil (Mavrides et al 2002). For details of the fetoplacental circulation see Kiserud and Haugen (2017).

Blood from the ductus venosus and hepatic veins joins the venous return from the lower limbs and abdominal wall in the inferior vena cava and enters the right atrium. The portocaval pressure gradient (blood pressure of the intra-abdominal umbilical vein) accelerates the blood in the ductus venosus to a velocity three times that of the umbilical vein and in the most favourable direction to open the foramen ovale valve and enter the left atrium (Kiserud and Haugen 2017). On ultrasound examination the foramen ovale can be seen with the septum primum, a flap-like valve, pushed to the left (see Video 13.2). From the left atrium, blood enters the left ventricle and from there flows to the aorta and is probably distributed almost entirely to the heart, head and upper limbs. Blood returning from the head and upper limbs enters the right atrium via the superior vena cava, flows through the right atrioventricular orifice into the right ventricle, together with the small amount of blood that is returned via the inferior vena cava, and then passes into the pulmonary trunk. However, because the fetal lungs are largely inactive, only a small amount of blood, 13% at week 20 and 21% at week 38, will flow from the right ventricle through the right and left pulmonary arteries to return to the left atrium via the pulmonary veins. The greater part of the outflow through the pulmonary trunk is carried by the ductus arteriosus directly to the aorta, where it mixes with any remaining blood that comes from the left ventricle. During the second half of pregnancy, the fetus maintains a combined cardiac output of 400 mL/kg/min; approximately two-thirds of the total fetal cardiac output is ejected by the right ventricle and the remaining third by the left ventricle (Kiserud and Haugen 2017, Fineman and Maltepe 2018).

The ductus arteriosus, a remnant of the left sixth pharyngeal arch artery, allows blood from the right ventricle to reach the arch of the aorta and thus bypass the fetal lungs (see Fig. 13.25; **Fig. 13.26**). In the fetus, it arises as a direct continuation of the pulmonary trunk at the point where it divides into right and left pulmonary arteries. It is 8–12 mm long, and joins the aorta at an angle of 30–35° on the left side, anterolaterally, below the origin of the left subclavian artery. The opening of the ductus arteriosus into the aorta is greatly elongated. Its diameter at its origin from the pulmonary trunk, when distended with blood, is 4–5 mm, which is nearly equal to the diameter of the adjacent ascending aorta (5–6 mm). Both arteries taper to a smaller diameter as they pass inferiorly and the aorta remains slightly larger (4 mm) (**Fig. 13.27**).

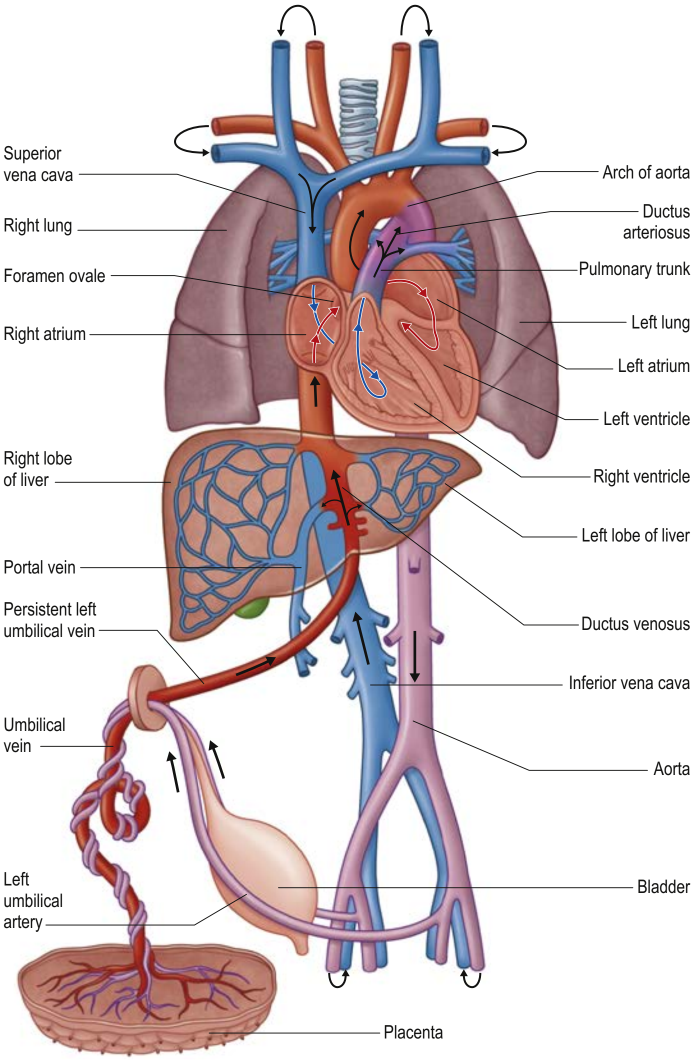

Fig. 13.25 A plan of the fetal cardiovascular circulation: the arrows indicate the direction of blood flow. The placenta is drawn to a greatly reduced scale.

The ductus arteriosus differs from the other great vessels that arise from the heart because its tunica media contains smooth muscle rather than layers of elastin. The intima of the ductus arteriosus starts to thicken by accumulation of glycosaminoglycans beneath the endothelium. The left recurrent laryngeal nerve (which, at stage 16, is very large in relation to the aortic arch system) passes inferior to the ductus arteriosus.

The ductus arteriosus remains patent during intrauterine life due to synergistic interaction of high circulating PGE2 (prostaglandin E2) and low oxygen tension (Hung et al 2018). Fetal and neonatal ductal tissue produce PGE_2 and to a lesser extent PGE_{12}. Treatment for conditions such as polyhydramnios, where indomethacin is given, may cause premature intrauterine closure of the ductus arteriosus and consequent associated problems.

Antenatal ultrasound imaging of the fetal heart and circulation

The first trimester ultrasound scan to confirm successful implantation and a live conceptus will identify an embryonic heartbeat from postmenstrual week 6 (stage 10 embryo). The embryonic heart rate is about 175 beats per minute at stage 23.

In the routine second trimester ultrasound scan at 18–20 postmenstrual weeks, the evaluation initially checks that the fetal heart and stomach are both on the left and that the liver is on the right. A specific series of sectional views of the heart are recorded. In a four-chamber view of the fetal heart (observed up to about postmenstrual week 28), the following are checked: the heart occupies about one-third of the thorax in the anterior left quadrant of the chest; the two atria are of equal size as are the two ventricles and there is an intact interventricular septum; and the apex of the heart points to the left anterior thorax. In moving images, the ventricles show equal contraction, the two atrioventricular canals open equally and the foramen ovale flap valve can be seen flickering in the left atrium (see Videos 13.2, 23.1). The function and rhythm of the heart is recorded. The heart rate is about 140 beats per minute throughout fetal life, despite the increase in heart size over this period: heart rate increase is a sign of fetal distress. The blood flow through the heart can be demonstrated with colour flow (**Fig. 13.28**). After postmenstrual week 28 the right ventricle may look dilated compared with the left. The origin of the great vessels from their respective ventricles is assessed in transverse section, and the aorta is assessed longitudinally (see Fig. 23.5); it normally arises in the centre of the thorax and the vessels to the head and neck can be seen arising from the curve of the aortic arch.

In a healthy near-term fetus the ductus venosus has an hourglass shape. Ultrasound studies have shown that 30% of umbilical venous flow enters the ductus venosus at about postmenstrual week 20 declining to 20% during the last trimester (Kiserud and Haugen 2017). Blood flow in this fetal shunt regulates inflow to the right atrium through a constricted aperture that admits umbilical venous blood via a narrow, high velocity flow directly to the foramen ovale. In healthy fetuses the ductus venosus regulates the distribution of placental nutrients and oxygen by restricting the centralization of blood flow, and it can actively dilate in hypoxaemia (Kaimal 2019). Anomalous flow in the first trimester has been reported in Down's syndrome and fetal growth restriction is associated with changes of flow through the ductus venosus. (For further details of ultrasound findings consult Coady and Bower (2015).)

Neonatal heart and circulatory changes at birth

At full term (notionally 40 postmenstrual weeks), the heart is situated midway between the crown of the head and the lower level of the buttocks and weighs about 20 g (see Fig. 23.14). Because the right ventricle has been working against the systemic pressure in the fetus, the pulmonary circulation not yet being active, the right ventricle is heavier at birth and continues to be so for up to 1–2 postnatal months. With the establishment of the pulmonary circulation, the work of the right side of the heart decreases, and the left side of the heart, particularly the ventricle, grows rapidly to meet the increased demand. The ventral surface of the heart is formed mainly by the right atrium and right ventricle, as in the adult. This surface is usually covered by the thymus, which may extend over the base of the right ventricle. Soon

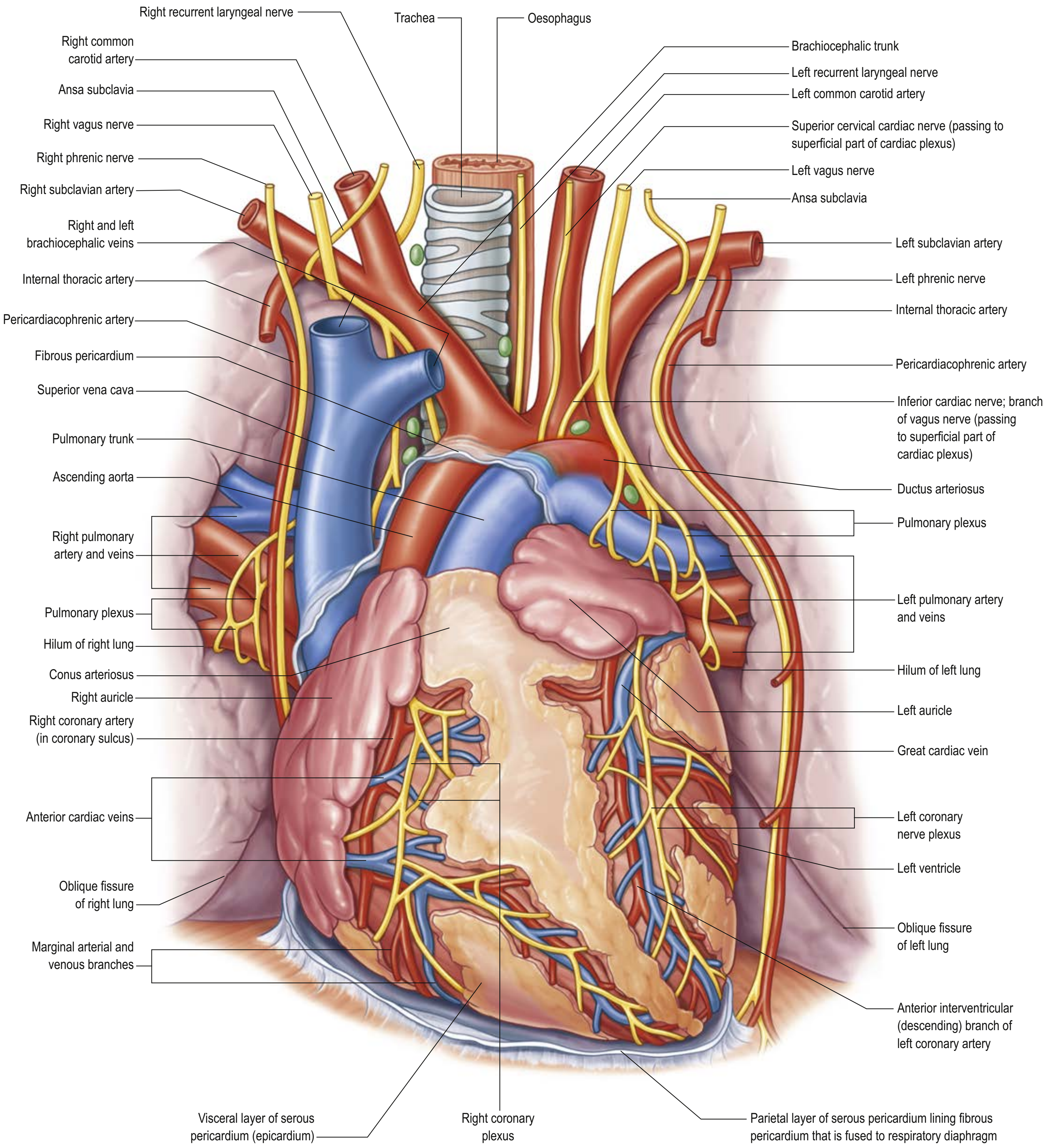
Right recurrent laryngeal nerve
Trachea
Oesophagus
Right common carotid artery
Ansa subclavia
Right vagus nerve
Right phrenic nerve
Right subclavian artery
Right and left brachiocephalic veins
Internal thoracic artery
Pericardiacophrenic artery
Fibrous pericardium
Superior vena cava
Pulmonary trunk
Ascending aorta
Right pulmonary artery and veins
Pulmonary plexus
Hilum of right lung
Conus arteriosus
Right auricle
Right coronary artery (in coronary sulcus)
Anterior cardiac veins
Oblique fissure of right lung
Marginal arterial and venous branches
Brachiocephalic trunk
Left recurrent laryngeal nerve
Left common carotid artery
Superior cervical cardiac nerve (passing to superficial part of cardiac plexus)
Left vagus nerve
Ansa subclavia
Left subclavian artery
Left phrenic nerve
Internal thoracic artery
Pericardiacophrenic artery
Inferior cardiac nerve; branch of vagus nerve (passing to superficial part of cardiac plexus)
Ductus arteriosus
Pulmonary plexus
Left pulmonary artery and veins
Hilum of left lung
Left auricle
Great cardiac vein
Left coronary nerve plexus
Left ventricle
Oblique fissure of left lung
Anterior interventricular (descending) branch of left coronary artery
Visceral layer of serous pericardium (epicardium)
Right coronary plexus
Parietal layer of serous pericardium lining fibrous pericardium that is fused to respiratory diaphragm

Fig. 13.26 An anterior view of the heart and great vessels in a neonate. The lungs have been displaced to expose the heart, and the pericardium and epicardium have been dissected off the heart and the roots of the great vessels. Note that, after birth, blood flow has reversed through the ductus arteriosus prior to its closure. (Adapted with permission from Crelin ES 1969 Anatomy of the Newborn. Philadelphia: Lea and Febiger.)

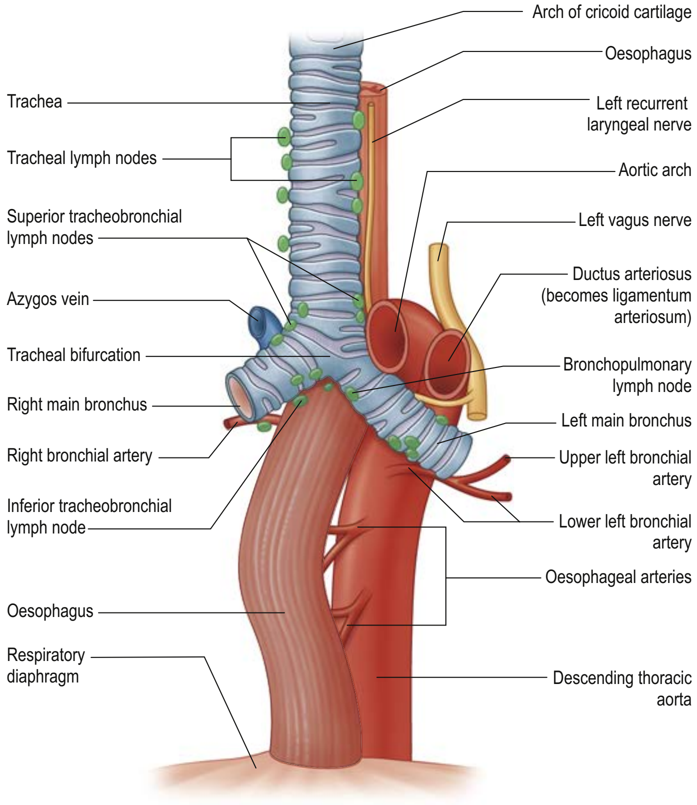
Trachea
Tracheal lymph nodes
Superior tracheobronchial lymph nodes
Azygos vein
Tracheal bifurcation
Right main bronchus
Right bronchial artery
Inferior tracheobronchial lymph node
Oesophagus
Respiratory diaphragm
Arch of cricoid cartilage
Oesophagus
Left recurrent laryngeal nerve
Aortic arch
Left vagus nerve
Ductus arteriosus (becomes ligamentum arteriosum)
Bronchopulmonary lymph node
Left main bronchus
Upper left bronchial artery
Lower left bronchial artery
Oesophageal arteries
Descending thoracic aorta

Fig. 13.27 **A**, An anterior view with the heart removed to show the relationship between the left primary bronchus, the aortic arch and the ductus arteriosus in a full-term fetus. (B, *continued online*)

after birth, the fetal shunts of the foramen ovale and the ductus arteriosus and ductus venosus will close. The umbilical vessels will also occlude as the circulation of the neonate becomes independent of maternal oxygen supply after detachment of the placenta from the uterine wall.

Congenital heart disease has an overall prevalence of 8/1000 births (Tarabit et al 2018). Neonates with congenital heart disease are at higher risk of fetal growth restriction and preterm birth; infant mortality rates are reported to be 20% for congenital heart disease and 65% for congenital heart disease and preterm delivery (Laas et al 2017). Assisted reproductive techniques have been shown to affect the incidence of preterm delivery and of congenital heart disease. The incidence of preterm birth in cases of congenital heart disease has been reported as about 13% in spontaneously conceived neonates, and about 40% in conception following infertility treatments (Tarabit et al 2018).

Closure of the umbilical vessels

Umbilical arteries

The fetal umbilical arteries are continuous with the internal iliac arteries. Their lumen is 2–3 mm in diameter at their origin, when distended. They narrow as they approach the umbilicus, where there is a reciprocal thickening of the tunica media, reflecting an increase in the number of longitudinal smooth muscle and elastic fibres. The umbilical vessels lack a nerve supply in their extra-abdominal course. Before birth, there is a proliferation of connective tissue within the vessel wall. Within minutes of delivery, blood flow within the umbilical cord vessels decreases and the vessels constrict in response to handling, stretching, cooling and altered tensions of oxygen and carbon dioxide. After the cord is severed, the umbilical arteries constrict, preventing significant blood loss; thrombi often form in the distal ends of the arteries. Full closure of the umbilical vessels is mediated by several factors including prostaglandins, endoperoxides and serotonin. As oxygen tension increases shortly after birth, bradykinin, one of the kinin polypeptide hormones that induce contraction or relaxation of smooth muscle, forms in the blood of the umbilical cord. It is also formed and released by granular leukocytes in the lungs of the neonate after exposure to adequate oxygen. Bradykinin is a potent constrictor of the umbilical arteries and veins, and of the ductus arteriosus, but is also a potent inhibitor of contraction of the pulmonary vessels. The umbilical arteries obliterate from their distal ends until, by the end of postnatal month 2–3, involution has occurred at the level of the superior vesical arteries: the proximal parts of the obliterated vessels remain as the medial umbilical ligaments (see Ch. 21).

Umbilical vein

The umbilical vein in the neonate is 2–3 cm long and 4–5 mm in diameter when distended. It passes from the umbilicus within the layers of the falciform ligament, superiorly and to the right, to the porta hepatis, where it gives off several large intrahepatic branches to the liver and then joins the left branch of the portal vein and the ductus venosus. The thin-walled umbilical vein possesses a definite internal lamina of elastic fibres at the umbilical ring but not in its intra-abdominal course. The tunica media contains smooth muscle fibres, collagen and elastic fibres.

When the cord is severed, the umbilical vein constricts, but not as vigorously as the arteries. The rapid decrease in pressure in the umbilical vein after the cord is clamped means that the elastic tissue at the umbilical ring is sufficient to arrest any retrograde flow along the vessel. Before birth, there is a subintimal proliferation of connective tissue; after birth, the contraction of the collagen fibres in the tunica media and the increased subintimal connective tissue contribute to the transformation of the vessel into the ligamentum teres hepatis (round ligament of the liver). Obliteration occurs from the umbilical ring towards the hepatic end. No thrombi are formed in the obliteration process. For up to 48 hours after birth, the intra-abdominal portion of the umbilical vein can be easily dilated. In most adults, the original lumen of the vein persists through the ligamentum teres hepatis and can be dilated to 5–6 mm in diameter.

Closure of the ductus venosus

In the fetus, the ductus venosus is a direct continuation of the umbilical vein and arises from the left branch of the portal vein, directly opposite the termination of the umbilical vein. It passes for 2–3 cm within the layers of the lesser omentum, in a groove between the left lobe and caudate lobe of the liver, before terminating in either the inferior vena cava, or in the left hepatic vein immediately before it joins the inferior vena cava. In the area of transition into the portal sinus, the vessel wall contains circularly arranged smooth muscle fibres, collagen and abundant elastic fibres and its inner surface is ridged. After birth, with the loss of the umbilical blood flow, the blood pressure in the portal sinus drops, the width of the ductus venosus decreases and the inner edges are approximated. The remaining lumen becomes filled with cell-dense connective tissue that occludes the whole vessel. The ductus venosus is already closed in about one-third of neonates, for the remainder it closes between postnatal days 4 and 6, sooner in post-term and macrosomic neonates. Obliteration begins at the portal vein end in the second postnatal week, progresses to the vena cava and is complete by postnatal month 2–3. The fibrous remnant of the ductus venosus is the ligamentum venosum.

Closure of the foramen ovale

Within the heart, considered relative to the thoracic landmarks, the foramen ovale lies at the level of the third intercostal space (see Fig. 23.14). It is approximately 4–6 mm long and 3–4 mm wide and blood passes through it from the ventrally positioned right atrium dorsally and cranially to reach the left atrium. At birth, as pulmonary respiration begins, pulmonary blood flow increases dramatically and the left atrium now receives pulmonary venous blood under a relatively high pressure. A decrease in pressure occurs in the inferior vena cava as a result of the reduction of venous return concomitant with occlusion of the umbilical vein and ductus venosus, lowering the right atrial pressure. Left atrial pressure is now greater than that of the right atrium, and the foramen ovale is closed by apposition. Subsequent fusion of the primary septum to the rims of the secondary septum occurs, likely by fibrosis mediated by transition of the endocardium into mesenchyme. Although the foramen ovale closes functionally after pulmonary respiration is established, it does not become structurally closed until later: it is obliterated in fewer than 3% of infants 2 weeks after birth. In adults, fusion is sometimes incomplete, and the foramen remains probe-patent in up to one-third of all individuals. Almost invariably, this lack of fusion has no functional effect because the inequality of atrial pressures and the valve-like arrangement of the opening do not favour right to left shunting of blood.

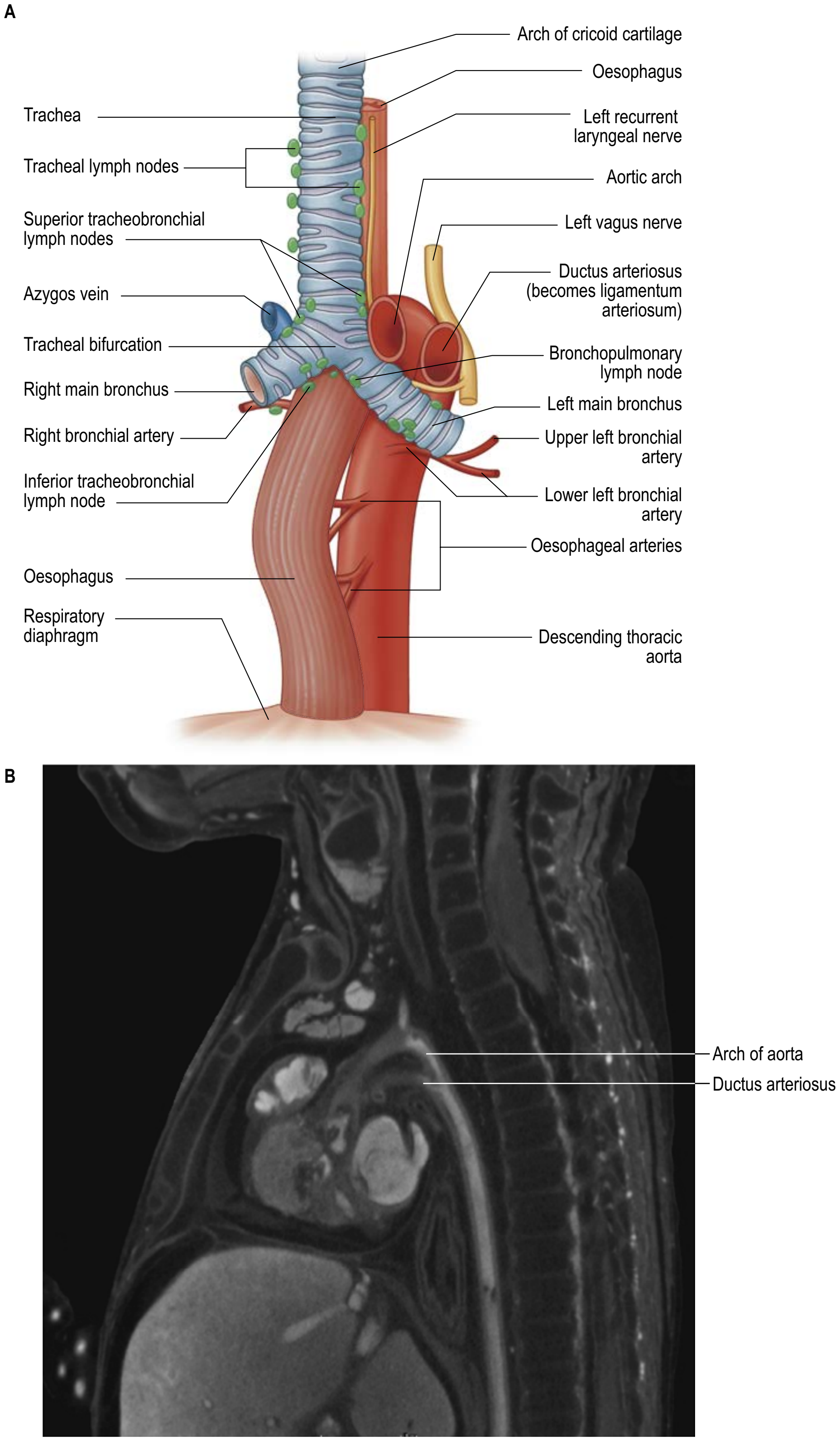
A
Arch of cricoid cartilage
Oesophagus
Trachea
Left recurrent laryngeal nerve
Tracheal lymph nodes
Aortic arch
Superior tracheobronchial lymph nodes
Left vagus nerve
Azygos vein
Ductus arteriosus (becomes ligamentum arteriosum)
Tracheal bifurcation
Bronchopulmonary lymph node
Right main bronchus
Left main bronchus
Right bronchial artery
Upper left bronchial artery
Inferior tracheobronchial lymph node
Lower left bronchial artery
Oesophageal arteries
Oesophagus
Respiratory diaphragm
Descending thoracic aorta
B
Arch of aorta
Ductus arteriosus

Fig. 13.27 **A**, An anterior view with the heart removed to show the relationship between the left primary bronchus, the aortic arch and the ductus arteriosus in a full-term fetus. **B**, MicroCT sagittal section of a fetus at 14 postmenstrual weeks. Note that the ductus arteriosus and arch of aorta have a similar calibre. (A, Adapted with permission from Crelin ES 1969 Anatomy of the Newborn. Philadelphia: Lea and Febiger. B, Courtesy of Dr Owen Arthurs and Dr Susan Shelmerdine, Great Ormond Street Hospital, London.)

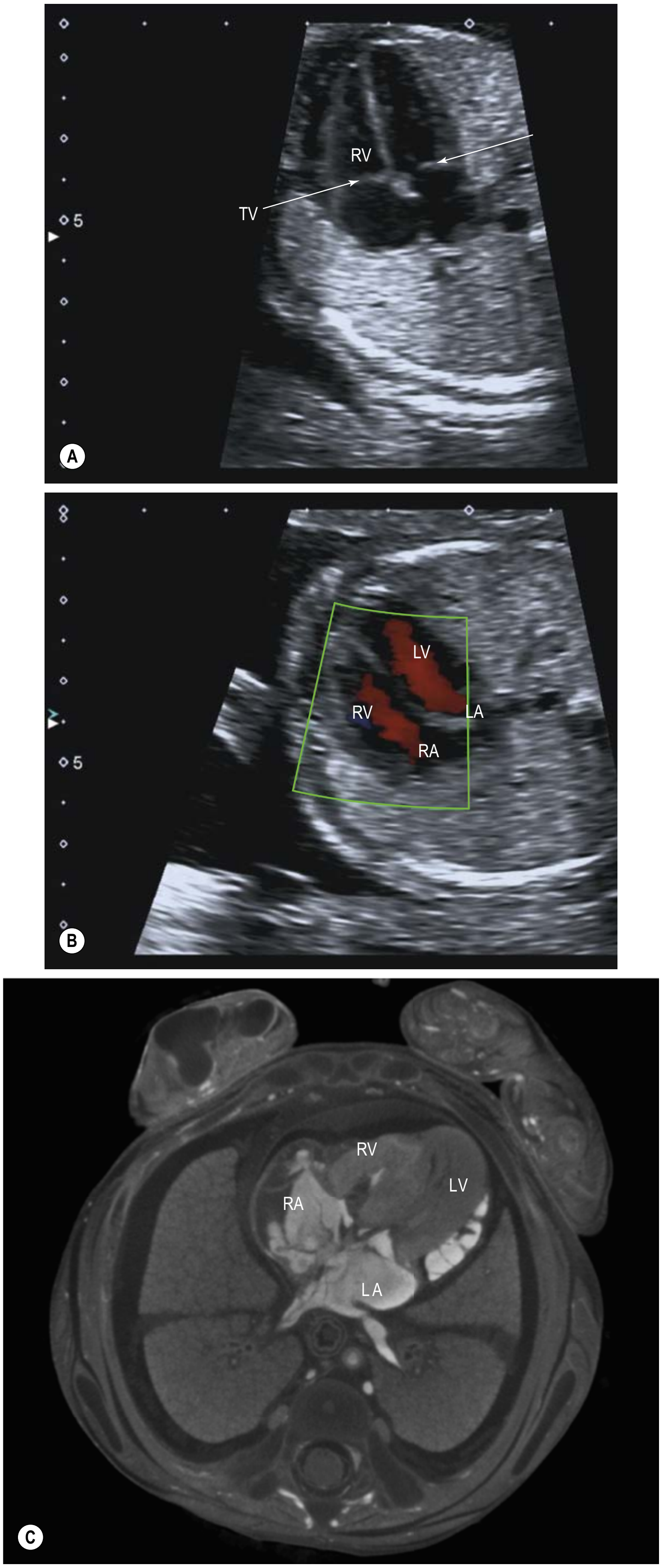

Fig. 13.28 **A**, Ultrasound image of a normal four-chamber view at 22 postmenstrual weeks. **B**, The ventricular inflow with colour flow. Flow (seen in red) is seen from each atrium to each ventricle. **C**, MicroCT axial section of a fetus at 14 postmenstrual weeks showing chambers of the heart. Abbreviations: LA, left atrium; LV, left ventricle; MV, mitral valve; RA, right atrium; RV, right ventricle; TV, tricuspid valve. (A, B, Courtesy of Professor Gurleen Sharland, Evelina London Children's Hospital. C, Courtesy of Dr Owen Arthurs and Dr Susan Shelmerdine, Great Ormond Street Hospital, London.)

Closure of the ductus arteriosus

At birth when a neonate takes its first breaths the lungs expand and the pulmonary resistance decreases. Blood flow from the right ventricle now passes along the pulmonary trunk to the lungs and the flow along the ductus arteriosus reverses, flowing from the aorta to the pulmonary trunk. Animal studies have shown that reversal of flow occurs rapidly after ventilation begins. Blood flow from the left ventricle travels via the aorta: the ductus arteriosus contributes almost 50% of total pulmonary blood flow in the neonate. The initial process of ductal closure consists of contraction of the smooth muscle cells and development of sub-endothelial oedema. Initial constriction at birth has been attributed to increased oxygen tension and decrease in prostaglandin E_2 (Hung et al 2018). Other factors in the closure process include increased plasma catecholamine concentrations; suppression of prostaglandin I2 production; unresponsive prostaglandin E receptors; a synergistic role of prostaglandin F2a and oxygen concentrations; and a decrease in plasma adenosine concentration. The high oxygen tension of the reversed blood flow through the ductus is thought to initiate the synthesis of a hydroperoxy fatty acid that suppresses prostacyclin production, thus exposing the ductus to the contractile effects of prostaglandin endoperoxide. A neural factor may also be involved; the muscular wall has afferent and efferent nerve endings and responds to adrenaline (epinephrine) and noradrenaline (norepinephrine) within 10 minutes of the onset of ventilation; after 2 postnatal hours, the response to adrenaline falls to about 25%. The turbulence and increased shear stress of blood flow through the ductus apparently releases vasoconstrictive factors from the endothelium (Crossley et al 2009). For details of the molecular mechanisms regulating ductus closure see Hung et al (2018).

The first stage of ductal closure is completed within 10–15 hours, occurring in 50% of full-term neonates at 24 hours, in 90% by 48 hours and in 100% by 72 hours. Definitive closure usually takes 2–3 weeks, but can take up to 3 months before it is considered permanent. Several mechanisms have been implicated as mediators of permanent closure, including intimal cushion formation, proliferation and migration of smooth muscle cells, endothelial cell proliferation and production of extracellular matrix (Hung et al 2018). Following functional closure, the ductal smooth muscle cells undergo apoptosis, resulting in fibrosis and the formation of the ligamentum arteriosum that connects the left pulmonary artery (near its origin) to the aortic arch.

Patent ductus arteriosus

Patent ductus arteriosus can be defined as a failure of the ductus arteriosus to close within 72 hours after birth (Dice and Bhatia 2007). It affects 1 in 2000 live births in the United States and is seen most frequently in preterm neonates and in up to 70% of those born before postmenstrual week 28 (Clyman 2013, Gillam-Krakauer and Reese 2018). Persistent patency of the ductus arteriosus should be distinguished from delayed closure. The persistently patent ductus can be an obligatory part of the circulation when associated with transposition of the great arteries since it allows shunting: the patency may be ensured by appropriate medication. Developmentally, failure to close may be related to reduced intimal thickening, the presence of a thick elastic lamina, low levels of circulating prostaglandins and a low oxygen tension after birth. The condition affects 66% of infants with congenital heart disease born at high altitude (Chun et al 2019). Rubella infection and a genetic predisposition are associated with a patent ductus arteriosus. Patent ductus arteriosus is almost always found in Char syndrome, a mutation in *TFAP2B*, encoding a transcription factor in cardiac neural crest cells (Huang et al 2008).

Coarctation of the aorta

Smooth muscle cells extending to the aortic wall rather than remaining within the wall of the ductus arteriosus may be a cause of aortic narrowing in preductal or postductal positions. A constriction, the aortic isthmus, is sometimes present in the aorta between the site of origin of the left subclavian artery and the orifice of the ductus arteriosus that can persist as a coarctation of the aorta. This can be found as an isolated lesion, with a normally closed ductus arteriosus. When the ductus arteriosus remains open coarctation is more likely to be associated with additional lesions within the heart, often a bicuspid aortic valve (O'Brien and Marshall 2015). Coarctation of the aorta has an estimated incidence of 1 in 2500 live births, affecting males more than females, and is the fifth most common heart defect (Kenny and Hijazi 2011).

Catheterization of neonatal blood vessels

In the neonate, the blood vessels of the trunk and their associated visceral branches are relatively larger than the vessels in the limbs, an arrangement that favours central pooling of blood. Neonatal peripheral vessels are particularly small, with delicate walls that can be easily damaged, and consequently their cannulation poses much more of a challenge than is the case with their adult counterparts. Large vessels are in the same relative positions as in the adult but may correspond to different vertebral levels. Thus, although the bifurcation of the common carotid artery into internal and external carotid arteries typically occurs at the level of the upper border of the thyroid cartilage in both neonate and adult, the thyroid cartilage is relatively higher in the neonatal neck than it is in the adult. The renal arteries also arise at a higher vertebral level in the neonate, often that between the twelfth thoracic and first lumbar vertebrae, whereas they arise at the level of the inferior part of the body of the first lumbar vertebra/upper border of the body of the second lumbar vertebra in the adult. The abdominal aorta bifurcates into common iliac arteries at the upper border of the body of the fourth lumbar vertebra, rather than at the lower border of the body of the fourth lumbar vertebra, as typically occurs in the adult.

Umbilical arterial catheterization

Insertion of an umbilical catheter is undertaken to provide direct access to the arterial circulation. Arterial blood can be withdrawn repeatedly for measurement of oxygen and carbon dioxide partial pressures, pH, base excess and many other parameters of blood biochemistry and haematology. The indwelling catheter also enables the continuous measurement of arterial blood pressure. The catheter is inserted directly into either the cut end or the side of one of the two umbilical arteries in the umbilical cord stump that remains attached to the baby after transection of the umbilical cord at the time of delivery. The catheter tip is then advanced along the length of the umbilical artery, through the internal iliac artery, into the common iliac artery and, from there, into the aorta. In order to keep the catheter patent, a small volume of fluid is continuously infused through it. It is important for the tip of the catheter to be located well away from arteries branching from the aorta, to avoid potentially harmful perfusion of these arteries with the catheter fluid. Thus, umbilical arterial catheter tips are placed in the descending aorta either in a 'high' position, above the coeliac trunk but well below the ductus arteriosus, or in a 'low' position, below the renal and inferior mesenteric arteries but above the point where the aorta bifurcates into the two common iliac arteries. The length of catheter to be inserted can be estimated from charts relating the required catheter length to external body measurements, or from birth weight. Positioning of the catheter is assessed by means of radiographs of the abdomen or chest: a 'high' catheter tip should be located in the descending aorta somewhere between the levels of the sixth and ninth thoracic vertebrae, while a 'low' catheter tip should be at a level between the third and fourth lumbar vertebrae. Relevant anatomical reference points are given in **Table 13.2**.

Umbilical vein catheterization

The umbilical vein may be catheterized for initial central venous access in preterm babies and in term neonates to enable exchange and transfusion of blood, for central venous pressure measurement and for emergency vascular access. The catheter is inserted into the cut end of the umbilical vein and is advanced along the length of the vein, through the ductus venosus and into the inferior vena cava; the tip is placed between the ductus venosus and the right atrium. Positioning of the catheter tip is confirmed radiologically: it should be located just above the respiratory diaphragm at a point that is level with the ninth or tenth thoracic vertebrae. Estimation of the required catheter length can be determined from standard charts.

Central venous catheterization

Small-bore catheters can be fed into large central veins, superior or inferior venae cavae, just outside the right atrium, via needles or catheters inserted in the peripheral veins. Typically, the median cubital or basilic veins are used in the upper limb, the long saphenous vein at the medial malleolus in the lower limb, and the superficial temporal vein in the scalp. The tip of the catheter is sited at the entrance to the right atrium. The required catheter length is

TABLE 13.2 **Key anatomical reference points for umbilical arterial catheterization**

Structure	Vertebral level
Ductus arteriosus	T4–T5
Coeliac artery	T12
Superior mesenteric artery	L1
Renal artery	T12–L1
Inferior mesenteric artery	L3
Aortic bifurcation	L4–L5

assessed from direct measurement of the distance between the proximal surface entry point in the limb or scalp to the right atrium, estimated at mid-sternal level.

Peripheral arterial puncture

It is common practice to insert a small-bore cannula into a peripheral artery in neonates receiving intensive care when either the umbilical artery is not accessible or there are clinical reasons to avoid cannulation of the umbilical vessels, e.g. if the umbilical cord has dried or in older neonates. Trans-illumination can be used to provide an outline of the artery to be cannulated. The peripheral arteries that are most commonly used are the radial artery, just proximal to the radiocarpal join on the palmar (volar) surface of the wrist, or the posterior tibial artery, posterior to the medial malleolus. The proximity of the ulnar nerve to the ulnar artery increases the risk of iatrogenic nerve damage associated with cannulation of the ulnar artery, and there is a higher risk of ischaemia with cannulation of this vessel. The relatively poor collateral circulation associated with the dorsalis pedis artery means that this artery is used only as a last resort. The axillary artery is now used in infants with difficult peripheral access; the brachial artery at the antecubital fossa, which was used previously, is rarely used because it has poor collateral circulation and the median nerve is in close proximity.

Confirmation that an adequate collateral circulation is present when cannulating the radial artery can be obtained by performing Allen's test (Ch. 48). Alternatively, intact arterial flow can usually be confirmed, particularly in the preterm infant, by direct visualization of the arteries using trans-illumination. A cold light source is placed on the posterior aspect of the lower forearm and the shadow of the pulsating arteries can be seen on the anterior surface of the forearm.

Bonus e-book content

Fig. 13.16 Failure of septation of the arterial pole of a developing heart.

Fig. 13.26 An anterior view of the heart and great vessels in a neonate.

Fig. 13.27 **B**, MicroCT sagittal section of a fetus at 14 postmenstrual weeks.

Fig. 13.28 **A–C**, Ultrasound and microCT images of the fetal heart.

Video 13.1 Animation of the pattern of contraction of the early heart tube.

Video 13.2 Ultrasound features of a four-chambered fetal heart.

Key references

Baron MH 2013 Early embryonic erythropoiesis …. Not so primitive after all. Stem Cells 31:849–56.

Courchaine K, Rykiel G, Rugonyi S 2018 Influence of blood flow on cardiac development. Prog Biophys Mol Biol 137:95–110.

Hung YC, Yeh J, Hsu J 2018 Molecular mechanisms for regulating postnatal ductus arteriosus closure. Int J Mol Sci 19:1861.

Jensen B, Spicer DE, Sheppard MN et al 2016 Development of the atrial septum in relation to postnatal anatomy and interatrial communications. Heart 103:456–62.

Laas E, LeLong N, Ancel P et al 2017 Impact of preterm birth on infant mortality for newborns with congenital heart defects: The EPICARD population-based cohort study. BMC Pediatr 17:124 DOI 10.1186/s12887-017-0875-z.

Liang X, Evans SM, Sun Y 2017 Development of the cardiac pacemaker. Cell Mol Life Sci 74:1247–59.

Pervolaraki E, Dachtler J, Anderson RA et al 2017 Ventricular myocardium development and the role of connexins in the human fetal heart. Sci Rep 7:12272. doi: 10.1038/s41598-017-11129-9.

Sizarov A, Baldwin HS, Srivastava D et al 2016 Development of the heart: morphogenesis, growth, and molecular regulation of differentiation. In: Allen HD, Shaddy RE, Penny JD et al (eds) Moss and Adams' Heart Disease in Infants, Children, and Adolescents, Including the Fetus and Young Adult, 9th ed. Philadelphia: Wolters Kluwer; Ch. 1, pp. 1–55.

Sylva M, van den Hoff MJ, Moorman AF 2013 Development of the human heart. Am J Med Genet A 164A:1347–71.

References

Ahuja P, Sdek P, MacLelolan WR 2007 Cardiac myocyte cell cycle control in development, disease and regeneration. Physiol Rev 87:521–44.

Amore M, Bernardez R, Enriquez R et al 2016 Anatomical variations of the thoracic duct: a preliminary report in adult and fetal specimens. Lymphology 49:205–9.

Anderson RH, Brown NA, Webb S 2002 Development and structure of the atrial septum. Heart 88:104–10.

Anderson RH, Jensen B, Mohun TJ et al 2017 Key questions relating to left ventricular noncompaction cardiomyopathy: is the emperor still wearing any clothes? Can J Cardiol 33:747–57.

Anderson RH, Spicer DE, Mori S 2016 Of tracts, rings, nodes, cusps, sinuses, and arrhythmias. J Cardiovasc Dev Dis 3(2): pii: E17. doi: 10.3390/jcdd3020017.

Baron MH 2013 Early embryonic erythropoiesis …. Not so primitive after all. Stem Cells 31:849–56.

Beets K, Huylenbroeck D, Moya IM et al 2013 Robustness in angiogenesis: notch and BMP shaping waves. Trends Genet 29:140–9.

Bellini C, Ergaz Z, Radicioni M et al 2012 Congenital fetal and neonatal visceral chylous effusions: neonatal chylothorax and chylous ascites revisited. A multicentre retrospective study. Lymphology 45:91–102.

Briggs LE, Kakarla J, Wessels A 2012 The pathogenesis of atrial and atrioventricular septal defects with special emphasis on the role of the dorsal mesenchymal protrusion. Differentiation 84:117–30.

Chappell JC, Wiley DM, Bautch VL 2012 How blood vessel networks are made and measured. Cells Tissues Organs 195:94–107.

Chun H, Yue Y, Wang Y et al 2019 High prevalence of congenital heart disease at high altitudes in Tibet. Eur J Prev Cardiol 26(7):756–9.

Clyman RI 2013 The role of patent ductus arteriosus and its treatment in the development of bronchopulmonary dysplasia. Semin Perinatol 37:102–7.

Coady AM, Bower S (eds) Twining's Textbook of Fetal Abnormalities, 3rd ed. Oxford: Elsevier.

Courchaine K, Rugonyi S 2018 Quantifying blood flow dynamics during cardiac development: demystifying computational methods. Phil Trans R Soc B 373 (1759). https://doi.org/10.1098/rstb.2017.0330.

Courchaine K, Rykiel G, Rugonyi S 2018 Influence of blood flow on cardiac development. Prog Biophy Mol Biol 137:95–110.

Crossley KL, Allison BJ, Polglase GR et al 2009 Dynamic changes in the direction of blood flow through the ductus arteriosus at birth. J Physiol 587:4695–703.

Culver JC, Dickinson ME 2010 The effects of hemodynamic force on embryo development. Microcirc 17:164–78.

Czirok A, Ronglish BJ, Little CD 2011 Vascular network formation in expanding versus state tissues: embryos and tumours. Genes Cancer 2:1072–80.

Davis GE, Senger DR 2005 Endothelial extracellular matrix. Circ Res 97:1093–107.

de Boer BA, van den Berg G, de boer PAJ et al 2012 Growth of the developing mouse heart: an interactive qualitative and quantitative 3D atlas. Dev Biol 368:203–13.

de Vries L, Hendriks A, Szili-Torok T 2016 The 'dead-end tract' and its role in arrhythmogenesis. J Cardiovasc Dev Dis 3(2): pii.

Degenhardt K, SinghMK, Aghajanian H et al 2013 Semaphorin 3D signaling defects are associated with anomalous pulmonary venous connections. Nat Med 19:760–65.

Dice JE, Bhatia J 2007 Patent ductus arteriosus: an overview. J Pediatr Pharmaol Ther 12:136–46.

Douglas YL, Jongbloed MRM, den Hartog WCE et al 2009 Pulmonary vein and atrial wall pathology in human total anomalous pulmonary venous connection. Int J Cardiol 134: 302–12.

Eichmann A, Pardanaud L 2014 Emergence of endothelial cells during vascular development. In: Feige JJ, Pagès G, Soncin F (eds) Molecular Mechanisms of Angiogenesis. From Ontogenesis to Oncogenesis. Paris: Springer-Verlag France; Ch. 1, pp. 3–23.

Eichmann A, Yuan Li, Moyon D et al 2005 Vascular development: from precursor cells to branched arterial and venous networks. Int J Dev Biol 49:259–67.

Farlik M, Halbritter F, Müller F et al 2016 DNA methylation dynamics of human hematopoietic stem cell differentiation. Cell Stem Cell 19:808-22.

Figueras-Coll M, Sabaté-Rotés A, Cañete-Abajo N et al 2017 The Chiari network – only an embryonic remnant of a confusing finding? World J Pediatr Congenit Heart Surg 2020;11(4):NP47-NP49.

Fineman JR, Maltepe E 2018 Fetal cardiovascular physiology. In: Resnik R, Lockwood C, Moore T et al (eds) Creasy and Resnik's Maternal–Fetal Medicine: Principles and Practice. Elsevier; Ch. 13, pp. 190–9.

Fraser ST 2012 The modern primitives: applying new technological approaches to explore the biology of the earliest red blood cells. ISRN Hematol 2013:568928. doi: 10.1155/2013/568928.

Gati S, Papadakis M, Papamichael ND et al 2014 Reversible de novo left ventricular trabeculations in pregnant women: implications for the diagnosis of left ventricular noncompaction in low-risk populations. Circulation 130:475–83.

Geva T, Martins JD, Wald RM 2014 Atrial septal defects. Lancet 383:1921–32.

Gillam-Krakauer M, Reese J 2018 Diagnosis and management of patent ductus arteriosus. Neoreviews 19(7):e394–e402. doi: 10.1542/neo.19-7-e394.

Guo P, Preuett B, Krishna P et al 2014 Barrier function of the coelomic epithelium in the developing pancreas. Mech Dev 134:67–79.

Hashimoto T, Tsuneki M, Foster TR et al 2016 Membrane-mediated regulation of vascular identity. Birth Defect Rec C Embryo Today 108:65–84.

Herbert SP, Stainier D 2011 Molecular control of endothelial cell behaviour during blood vessel morphogenesis. Nat Rev Mol Cell Biol 12:551–64.

Hikspoors JPJM, Soffers JHM, Mekonen HK et al 2015 Development of the human infrahepatic inferior caval and azygos venous systems. J Anat 226:113–25.

Hoffman JIE, Kaplan S 2002 The incidence of congenital heart disease. J Am Coll Cardiol 39:1890–900.

Huang J, Cheng L, Li J et al 2008 Myocardin regulates expression of contractile genes in smooth muscle cells and is required for closure of the ductus arteriosus in mice. J Clin Invest 118:515–25.

Hung YC, Yeh J, Hsu J 2018 Molecular mechanisms for regulating postnatal ductus arteriosus closure. Int J Mol Sci 19:1861.

Ivanov A, Dabiesingh DS, Bhumireddy GP et al 2017 Prevalence and prognostic significance of left ventricular noncompaction in patients referred for cardiac magnetic resonance imaging. Circ Cardiovasc Imaging 10:1–10.

Jauniaux E, Gulbis B 2000 Fluid compartment of the embryonic environment. Hum Reprod Update 6:268–78.

Jensen B, Spicer DE, Sheppard MN et al 2016 Development of the atrial septum in relation to postnatal anatomy and interatrial communications. Heart 103:456–62.

Jensen B, van der Wal AC, Moorman AFM et al 2017 Excessive trabeculations in noncompaction do not have the embryonic identity. Int J Cardiol 227:325–30.

Kaimal AJ 2019 Assessment of fetal heath. In: Resnik R, Lockwood C, Moore T et al (eds) Creasy and Resnik's Maternal–Fetal Medicine: Principles and Practice. Elsevier; Ch. 34, pp. 549–63.

Kanne JP, Godwin JD 2010 Right aortic arch and its variants. J Cardiovasc Comput Tomogr 4:293–300.

Kao C, Hsieh C, Cheng P et al 2017 Total anomalous pulmonary venous connection: from embryology to a prenatal ultrasound diagnostic update. J Med Ultrasound 25:130–7.

Kauts ML, Vink CS, Dzierzak E 2016 Hematopoietic (stem) cell development – how divergent are the roads taken? FEBS Lett 590:3975–86.

Kenny D, Hijazi ZM 2011 Coarctation of the aorta: from fetal life to adulthood. Cardiol J 18:487–95.

Keyte AL, Alonzo-Johnsen M, Hutson MR 2014 Evolutionary and developmental origins of the cardiac neural crest: building a divided outflow tract. Birth Defects Res C Embryo Today 102(3):309–23.

Kiserud T, Haugen G 2017 Umbilical circulation. In: Polin RA, Abman SH, Rowitch DH et al (eds) Fetal and Neonatal Physiology, 5th ed. Elsevier; Ch. 58, pp. 599–611.

Kovacic JC, Dimmeler S, Harvey RP et al 2019 Endothelial to mesenchymal transition in cardiovascular disease. J Am Coll Cardiol 73:190–209.

Kuijper S, Turner CJ, Adams RH 2007 Regulation of angiogenesis by Eph-Ephrin interactions. Trends Cardiovasc Med 17:145–51.

Laas E, LeLong N, Ancel P et al 2017 Impact of preterm birth on infant mortality for newborns with congenital heart defects: The EPICARD population-based cohort study. BMC Pediatr 17:124 doi: 10.1186/s12887-017-0875-z.

Liang X, Evans SM, Sun Y 2017 Development of the cardiac pacemaker. Cell Mol Life Sci 74:1247–59.

Lombardi M, Pluchinotta FR 2018 Going beyond morphology in Ebstein's anomaly. Int J Cardiol 15:257–75.

Mavrides E, Moscoso G, Carhalho JS et al 2002 The human ductus venosus between 13 and 17 weeks of gestation: histological and morphometric studies. Ultrasound Obstet Gynecol 19:39–46.

McGrath KE, Kingsley PD, Koniski AD et al 2008 Enucleation of primitive erythroid cells generates a transient population of 'pyrenocytes' in the mammalian fetus. Blood 111:2409–17.

McGrath KE, Frame JM, Pallis J 2015 Early hematopoiesis and macrophage development. Semin Immunol 27:379–87.

Mommersteeg MTM, Andrews WD, Ypsilanti AR et al 2013 Slit-roundabout signaling regulates the development of the cardiac systemic venous return and pericardium. Circ Res 112:465–75.

Muggenthaler MMA, Chowdhury B, Hasan SN et al 2017 Mutations in HYAL2, encoding hyaluronidase 2, cause a syndrome of orofacial clefting and cor triatriatum sinister in humans and mice. PLoS Genet 13:e1006470. doi: 10.1371/journal.pgen.1006470.

Nakajima Y 2016 Mechanism responsible for D-transposition of the great arteries: is this part of the spectrum of right isomerism? Congenit Anom (Kyoto) 56:196–202.

O'Brien P, Marshall AC 2015 Coarctation of the aorta. Circulation 131:e363-e365. doi: 10.1161/CIRCULATIONAHA.114.008821.

Ocaña OH, Coskun H, Minguillón C et al 2017 A right-handed signalling pathway drives heart looping in vertebrates. Nature 549:86–90.

Ootaki Y, Yamaguchi M, Yoshimura N et al 2003 Unroofed coronary sinus syndrome: diagnosis, classification, and surgical treatment. J Thorac Cardiovasc Surg 126:1655–6.

O'Rahilly R, Müller F 1987 Developmental stages in human embryos. Publication 637. Carnegie Institution of Washington.

Paranon S, Acar P 2008 Ebstein's anomaly of the tricuspid valve: from fetus to adult. Heart 94:237–43.

Park C, Lee JY, Yoon Y 2011 Role of bone marrow derived lymphatic endothelial progenitor cells for lymphatic neovascularisation. Trends Cardiovasc Med 21:135–40.

Pérez-Pomares JM, de la Pompa JL, Franco D et al 2016 Congenital coronary artery anomalies: a bridge from embryology to anatomy and pathophysiology – a position statement of the development, anatomy and pathology. ESC Working Group. Cardiovasc Res 109:204–16.

Pervolaraki E, Dachtler J, Anderson RA et al 2017 Ventricular myocardium development and the role of connexins in the human fetal heart. Sci Rep 7:12272. doi: 10.1038/s41598-017-11129-9.

Povoski SP, Khabiri H 2011 Persistent left superior vena cava: review of the literature, clinical implications, and relevance of alterations in thoracic central venous anatomy as pertaining to the general principles of central venous access device placement and venography in cancer. World J Surg Oncol 9:173.

Prakash S, Borreguero LJJ, Sylva M et al 2017 Deletion of Fstl1 (Follistatin-Like 1) from the endocardial/endothelial lineage causes mitral valve disease. Arterioscler Thromb Vasc Biol 37(2017):e116–e130.

Rambeau P, Faure E, Théron A et al 2017 Reduced aggrecan expression affects cardiac outflow tract development in zebrafish and is associated with bicuspid aortic valve disease in humans. Int J Cardiol 249:340–3.

Rana MS, Théveniau-Ruissy M, De Bono C et al 2014 Tbx1 coordinates addition of posterior second heart field progenitor cells to the arterial and venous poles of the heart. Circ Res 10;115:790–9.

Roman B, Pekkan K 2012 Mechanotransduction in embryonic vascular development. Biomech Model Mechanobiol 11:1149–68.

Sabin F 1912 On the origin of the abdominal lymphatics in mammals from the vena cava and the renal veins. Anat Rec 6:235-242.

Séguéla PE, Houyel L, Acar P 2011 Congenital malformations of the mitral valve. Arch Cardiovasc Dis 104:465–79.

Senger DR, Davis GE 2011 Angiogenesis. Cold Spring Harb Perspect Biol 3:1–19.

Sharma B, Chang A, Red-Horse K 2017 Coronary artery development, progenitor cells and differentiation pathways. Annu Rev Phyisol 79:1–19.

Simões FC, Riley PR 2018 The ontogeny, activation and function of the epicardium during heart development and regeneration. Development 145: p.ii. dev155994. doi: 10.1242/dev.155994.

Siu SC, Silversides CK 2010 Bicuspid aortic valve disease. J Am Coll Cardiol 55:2789–00.

Sizarov A, Baldwin HS, Srivastava D et al 2016 Development of the heart: morphogenesis, growth, and molecular regulation of differentiation. In: Allen HD, Shaddy RE, Penny JD et al (eds) Moss and Adams' Heart Disease in Infants, Children, and Adolescents, Including the Fetus and Young Adult, 9th ed. Philadelphia: Wolters Kluwer; Ch. 1, pp. 1–55.

Spicer DE, Hsu HH, Co-Vu J et al 2014 Ventricular septal defect. Orphanet J Rare Dis 9:144. doi: 10.1186/s13023-014-0144-2.

Spicer DE, Henderson DJ, Chaudhry B et al 2015 The anatomy and development of normal and abnormal coronary arteries. Cardiol Young 25:1493–503.

Suzuki T, Carrier EJ, Talati MH et al 2018 Isolation and characterization of endothelial-to-mesenchymal transition cells in pulmonary arterial hypertension. Am J Physiol Lung Cell Mol Physiol 314:L118–L126.

Sylva M, van den Hoff MJ, Moorman AF 2013 Development of the human heart. Am J Med Genet A 164A:1347–71.

Tallquist MD, Molkentin JD 2017 Redefining the identity of cardiac fibroblasts. Nat Rev Cardiol 14:484–91.

Tarabit K, Lelong N, Goffinet F et al EPICARD Study Group 2018 Assessing the risk of preterm birth for newborns with congenital heart defects conceived following infertility treatments: a population-based study. Open Heart 5:e000836. doi: 10.1136/ openhrt-2018-000836.

Tomanek RJ 2016 Developmental progression of the coronary vasculature in human embryos and fetuses. Anat Rec (Hoboken) 299:25–41.

Tonar Z, Kocova J, Liska V et al 2001 Early development of the jugular lymphatics. Sb Lek 102:217–25.

van den Berg G, Moorman AFM 2011 Development of the pulmonary vein and the systemic venous sinus: an interactive 3D overview. PLoS One 6:e22055.

Van der Linde D, Konings EEM, Slager MA et al 2011 Birth prevalence of congenital heart disease worldwide. J Am Col Cardiol 58:2241–7.

van Eif VWW, Devalla HD, Boink GJJ et al 2018 Transcriptional regulation of the cardiac conduction system. Nat Rev Cardiol 15:617–30.

Van Handel B, Prashad SL, Hassanzadeh-Kiabi N et al 2010 The first trimester human placenta is a site for terminal maturation of primitive erythroid cells. Blood 116:3321–30.

Vincentz JW, Toolan KP, Zhang W et al 2017 Hand factor ablation causes defective left ventricular chamber development and compromised adult cardiac function. PLoS Genet 13:e1006922. doi.org/10.1371/journal.pgen.1006922.

Watanabe M, Rollins AM, Polo-Parada L et al 2016 Probing the electrophysiology of the developing heart. J Cardiovasc Dev Dis 3. p.ii:E10. doi: 10.3390/jcdd3010010.

Wessels A 2016 Inflow tract development. In: Rickert-Sperling S, Kelly RG, Driscoll DJ eds Congenital Heart Diseases: The Broken Heart. Vienna: Springer-Verlag Vienna, pp. 55–63.

Wiputra H, Lai CQ, Lim GL et al 2016 Fluid mechanics of human fetal right ventricles from imaged-based computational fluid dynamics using 4D clinical ultrasound scans. Am J Physiol Heart Circ Physiol 311:H1498–H1508.

Wohlmuth C, Gardiner HM 2020 The heart. In: Pandya PV, Oepkes D, Sebire NJ, Wapner RJ (eds) Fetal Medicine Basic Science and Clinical Practice, Elsevier; Ch 29.

Wu Y, Wu Z, Zheng J et al 2018 Sutureless techniques versus conventional surgery in the primary treatment of total anomalous pulmonary venous connection: a systematic review and meta-analysis. J Cardiothorac Surg 13:69. doi: 10.1186/s13019-018-0756-z.

Xie D, Wang H, Liu Z et al 2017 Perinatal outcomes and congenital heart defect prognosis in 53313 non-selected perinatal infants, PLoS One 12(2017):1–10.

Yamashita JK 2007 Differentiation of arterial, venous and lymphatic endothelial cells from vascular progenitors. Trends Cardiovasc Med 17:59–63.

Yang Y, Oliver G 2014 Transcriptional control of lymphatic endothelial cell type specification. Adv Anat Embryol Cell Biol 214:5-22.

Yener N, Oktar GL, Erer MM et al 2002 Bicuspid aortic valve. Ann Thorac Cardiovasc Surg 8: 264–7.

Zhou F, Chang Z, Zhang L et al 2010 Akt/protein kinase B is required for lymphatic network formation, remodelling and valve development. Am J Pathol 177:2124–33.

CHAPTER
14

Development of the nervous system

The entire nervous system and the special sense organs originate from three sources, each derived from specific cell populations of the early epiblast termed neural ectoderm. The first source to be clearly delineated is the neural plate, which gives rise to the central nervous system (CNS), the somatic motor nerves and the preganglionic autonomic nerves. The second source is from cells at the perimeter of the neural plate, neural crest cells, which remove themselves by epithelial to mesenchymal transition from the plate and migrate away just prior to its fusion into a neural tube. These cells give rise to the majority of the neurones and glia of the peripheral nervous system (PNS), i.e. the somatic sensory nerves, the somatic and autonomic ganglia, postganglionic autonomic nerves and suprarenal and chromaffin cells, as well as significant mesenchymal populations in the head. The third source is from ectodermal placodes, focal thickenings of the ectoderm covering the embryonic head, that contribute cells to the cranial sensory neurones and form the olfactory epithelia, the epithelia of the inner ear and, by a non-neuronal contribution, the lens of the eye. Early establishment of a pial capillary network, derived from mesenchymal neural crest cells, provides cell lines for neuroepithelial:endothelial interactions throughout the developing nervous system.

NEURULATION

Primary neurulation

Primary neurulation begins at stage 9 and is completed during stage 12 (**Figs 14.1–14.2**) (embryonic stages 10–23 correlated to postfertilization days of development and postmenstrual weeks of pregnancy are shown in Fig. 23.3). The process is continuous spatially and temporally but has been envisaged as four stages. It begins with local elongation of the ectoderm cells in a midline zone of the embryonic disc and their reorganization into a pseudostratified epithelium, the neural plate. This is followed by reshaping and bending of the neural plate into a neural groove that subsequently closes to form a neural tube bidirectionally from its mid portion to its cranial and caudal ends. A continuous surface ectoderm forms dorsal to the tube. As neurulation proceeds, the neural tube elongates by convergent extension, a process where the apical surfaces of adjacent cells narrow (convergence) and there is rostrocaudal elongation (extension) (Bay and Caspary 2012, Nikolopoulou et al 2017).

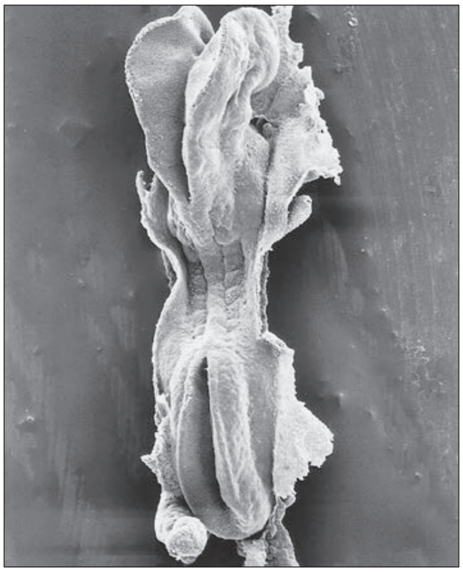

Fig. 14.1 A scanning electron micrograph of a neurulating rat embryo comparable to a stage 10 human embryo. The expanded brain region can be seen at the top of the image; somite formation occurs centrally as neurulation proceeds caudally. Caudally, the ridge of underlying neural crest cells can be seen medial to the unsegmented paraxial mesenchyme. (Photograph by P Collins; printed by S Cox, Electron Microscopy Unit, Southampton General Hospital.)

Two sites of dorsal fusion of the neural tube appear in succession in the human embryo. The initial fusion site, termed α, or the dorsal lip of the rostral neuropore, is in the rhombencephalic region from which closure extends both rostrally and caudally. A second site, termed β, or the terminal lip of the rostral neuropore, forms in the prosencephalic region and extends caudally (O'Rahilly and Müller 2002). Closure of the rostral neuropore is completed in stage 11 when about 19–20 pairs of somites are present. Continued generation of the neural plate from the primitive node adds caudal regions to the elongating and closing neural tube and generation of mesenchyme from the primitive streak adds paraxial mesenchymal populations that form somites as the neural tube closes (Ch. 18). Primary neurulation ends and the caudal neuropore starts to close in stage 12 (30–32 days postfertilization, see Fig. 23.3), when approximately 29 somites are present: the final site of closure corresponds to the level of the future somite 31 (the level of the future second sacral vertebra) (O'Rahilly and Müller 2004).

Secondary neurulation

Secondary neurulation is the process by which the caudal portion of the neural tube is formed in the absence of a neural plate. It starts from the closure of the caudal neuropore at stage 12 and ends at about stage 17. At the time of caudal neuropore closure the caudal midline cells are generically termed the caudal eminence (O'Rahilly and Müller 2004). A specific population of mesenchymal cells, the caudoneural hinge or junction, shares the same molecular markers as the primitive node. These cells aggregate at the midline and undergo mesenchymal to epithelial transition, producing a cellular cylinder that is contiguous with the caudal end of the neural tube. Further elongation of the caudal neural tube involves cavitation of the neural cylinder. In a study of human embryos, the caudal end of the forming neural tube showed multiple outpouchings of the lumen at stage 18. The most caudal part was accompanied by a notochord. Immunohistochemical staining was negative for a range of neuronal antigens: N-CAM and NeuN labelling was seen after stage 16 and neurofilament-associated protein (3A10) labelled cells were seen from stages 16 and 18 in dorsal tissues. Apoptosis was noted in the very terminal end of the caudal eminence and the caudal portion of the neural tube showed regression at stage 19 (Yang et al 2014). Neural crest cells delaminate from the dorsal surface of the cylinder in a rostrocaudal direction and the paraxial mesenchyme concurrently undergoes somitogenesis. The range of processes involved in secondary neurulation, the mechanisms of generation of caudal tissues, their further interactions within the developing cloacal region, and the formation of associated somatic and autonomic nerves, are all still as yet unknown. It may be that, as occurs in the head, where special populations of cells are required to form and provide neurological control of the oropharyngeal reflexes associated with the airway and proximal gut, a similar system occurs in the caudal region, where special cell populations provide tissues for the cloacal region and control the reflexes of the enteric, urinary and reproductive sphincters.

Failure of neurulation

Failure of neurulation produces the conditions of craniorachischisis totalis (where the entire neural tube is unfused in the dorsal midline), cranioschisis or anencephaly (where the neural tube is fused dorsally to form the spinal cord but is not fused dorsally in the brain), and spina bifida (where local regions of the spinal neural tube are unfused, or there is failure of formation of the vertebral neural arches) (**Fig. 14.3**; see Fig. 18.14). Anencephalic fetuses display severe disturbances in the shape, position and ossification of the basichondrocranium and in the course of the intracranial notochord, and so the condition is more complicated than 'simply' a failure of neural tube fusion. Spinal neural

Primary neurulation depends on cellular changes within the neural plate; and may also also involve movements of the paraxial mesenchyme in the trunk. Initial fusion of the surface ectoderm is followed by fusion of the neural ectoderm. The neural ectodermal cells become elongated and then wedge-shaped. The forces needed to shape the neural tube are intrinsic to the cells of the neurectoderm: human embryonic stem cells can self-organize into three-dimensional neural structures (Eiraku and Sasai 2012, Sasai et al 2012). Epithelial populations are established in the embryo with the formation of the epiblast. Three main control pathways that maintain epithelial apicobasal polarity have been described (Crumbs, Baz/PAR-3, Scribble) and Wnt/planar cell polarity gene expression is involved with epithelial cell movement. When the neural tube is closing, its walls consist of a pseudostratified layer of columnar neural epithelial cells (see below). The cells increase in length and develop numerous longitudinally disposed microtubules; their apical surfaces are joined by tight junctions supported by claudins and linked to the actin cytoskeleton that forms a dense paraluminal web of microfilaments. The nuclei assume basal positions and this, together with the contraction of apically arranged actin, imparts a slight wedge conformation along the midline of the neural plate, creating a median hinge point that is termed the floor plate. The apical location of Wnt and the planar polarity genes maintain the apicobasal polarity and contribute to the convergent extension movements (Baumholtz et al 2017). Movements of the cell populations on each side of the floor plate promote elevation of the layer and neural tube formation.

The position of hinge points within the neural plate confers different luminal characteristics within the formed neural tube. With a median hinge point the neural folds remain relatively straight and the tube in this position has a slit-shaped lumen, as can be seen from the initial region of fusion rostralwards. If dorsolateral hinge points are added the resulting neural tube lumen becomes rhombic, and if all neuroepithelial cells exhibit some apical narrowing then the tube has a circular lumen. Rostrally, the slit-shaped profile depends more on support from adjacent tissues than at the caudal end of the tube where secondary neurulation produces a neural tube with a circular lumen.

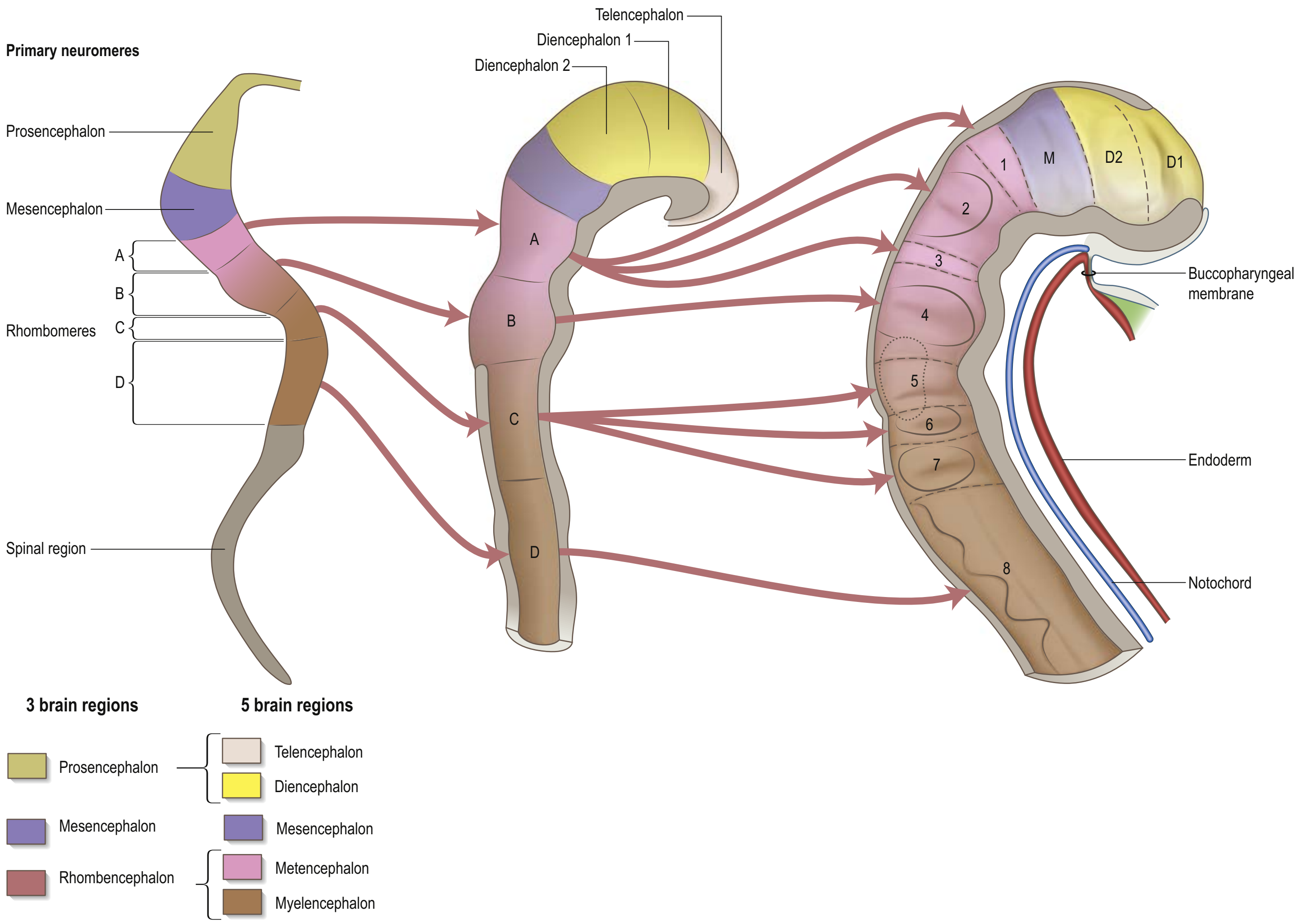

Fig. 14.2 The primary brain regions, neuromeres and their expansion during neurulation.

tube defects commonly correspond to the junctional region between primary and secondary neurulation processes (Dady et al 2014). Heterozygous mutations in the polarity gene signalling pathway have been identified in individuals with neural tube defects. Defects in the structure or function of the primary cilium (see below) are also associated with neural tube defects and with changes in cortical formation thought to underlie cognitive deficits and mental retardation in a range of recessive ciliopathies (Higginbotham et al 2013, Wheway et al 2018).

EARLY BRAIN REGIONS

Prior to the closure of the neural tube, the neural folds become considerably expanded in the head region. The first indication of a brain and its major divisions can be seen at stage 10 (see Fig. 14.2; **Fig. 14.4**). Regional expansions, the prosencephalon (forebrain), mesencephalon (midbrain) and rhombencephalon (hindbrain), have been called the three primary cerebral vesicles, although the term 'vesicle' in this context is probably inappropriate to describe localized accelerations of growth in the wall of the brain. As the neural tube closes, the neural wall appears to form a series of ridges and depressions perpendicular to its long axis. These transient repeating segments are termed primary neuromeres. Initially, six can be identified, namely, the prosencephalon, mesencephalon and four subdivisions of the rhombencephalon, rhombomeres A, B, C and D. The primary neuromeres themselves become subdivided during stages 10, 11 and 12, and a total of 16 secondary neuromeres have been identified. The prosencephalon gives rise to the telencephalon, diencephalon 1 (D1) and diencephalon 2 (D2), which has three subdivisions. The mesencephalon is subdivided into the mesencephalon 1 (M1) and mesencephalon 2 (M2). The rhombencephalon is subdivided into the isthmus rhombencephali and rhombomeres 1–8; the original rhombomere A gives rise to secondary rhombomeres 1, 2 and 3; rhombomere B gives rise to secondary rhombomere 4; rhombomere C gives rise to secondary rhombomeres 5, 6 and 7; and rhombomere D gives rise to secondary rhombomere 8 (O'Rahilly and Müller 1999). As the rhombencephalon grows, the rhombomeric boundaries become less distinct. With the early appearance of the cerebellum from the isthmus rhombencephali and rhombomere 1, the rhombencephalon is traditionally divided into the metencephalon, which extends to about rhombomere 3, and the myelencephalon, which extends to the spinomedullary junction. A summary of the derivatives of the cerebral regions is given in **Table 14.1**.

Before the closure of the neural tube the elongation of the brain occurs concurrently with the appearance of three flexures, two are concave ventrally and one is concave dorsally. During stages 13 and 14 the brain bends at the mesencephalon (mesencephalic flexure) so that the prosencephalon bends in a ventral direction around the cephalic end of the notochord and foregut until its floor lies almost parallel with that of the rhombencephalon (see Fig. 14.4). A bend (cervical flexure) also appears at the junction of the rhombencephalon and spinal cord, increasing in angulation over stages 14–20, by which time the rhombencephalon forms nearly a right-angle to the spinal cord. Extension of the head takes place after stage 20 and the cervical flexure diminishes and eventually disappears. The third bend, the pontine flexure, is directed ventrally between the metencephalon and myelencephalon and does not substantially affect the outline of the head. In this region, the roof plate thins until it is composed only of a single layer of cells and pia mater, the tela choroidea. The flexure of the neural tube at this point produces a rhombic shape in the roof that later forms the medullary velum.

NEURAL CREST

The neuronal populations of the early epiblast become arranged in the medial region of the embryonic disc as the neural plate (see Fig 10.5). Laterally, neural folds or crests indicate a transitional region between the neural and surface ectoderm. Cells in the crests undergo epithelial to mesenchymal transition and leave the epithelium just prior to its fusion with the contralateral fold in the rhombencephalic dorsal midline: their new mesenchymal phenotype means that they acquire migratory properties. Two distinct populations of neural crest cells are formed: a neuronal population produced throughout the brain and spinal cord that gives rise to sensory and autonomic neurones and associated glia, and a non-neuronal mesenchymal population that arises only from the brain (**Figs 14.5-14.6**). As development proceeds, sequential migration of these cells gives rise to four neural crest subpopulations: cranial, vagal, trunk and sacral.

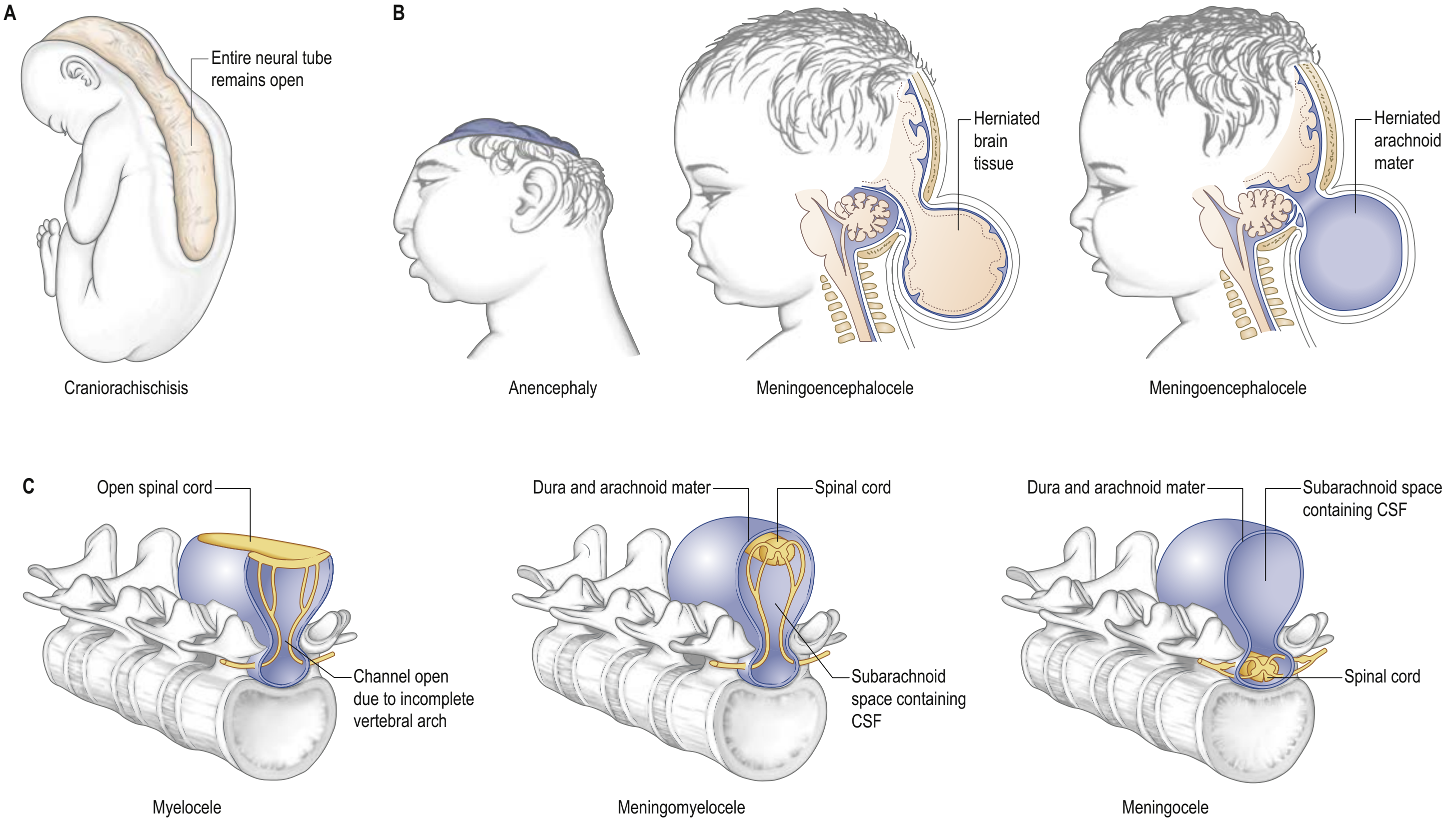
A
Entire neural tube remains open
Craniorachischisis
B
Anencephaly
Herniated brain tissue
Meningoencephalocele
Herniated arachnoid mater
Meningoencephalocele
C
Open spinal cord
Channel open due to incomplete vertebral arch
Myelocele
Dura and arachnoid mater
Spinal cord
Subarachnoid space containing CSF
Meningomyelocele
Dura and arachnoid mater
Subarachnoid space containing CSF
Spinal cord
Meningocele

Fig. 14.3 Defects caused by failure of neural tube formation. **A**, Total failure of neurulation. **B**, Failure of rostral neurulation. **C**, Failure of caudal neurulation. Abbreviation: CSF, cerebrospinal fluid.

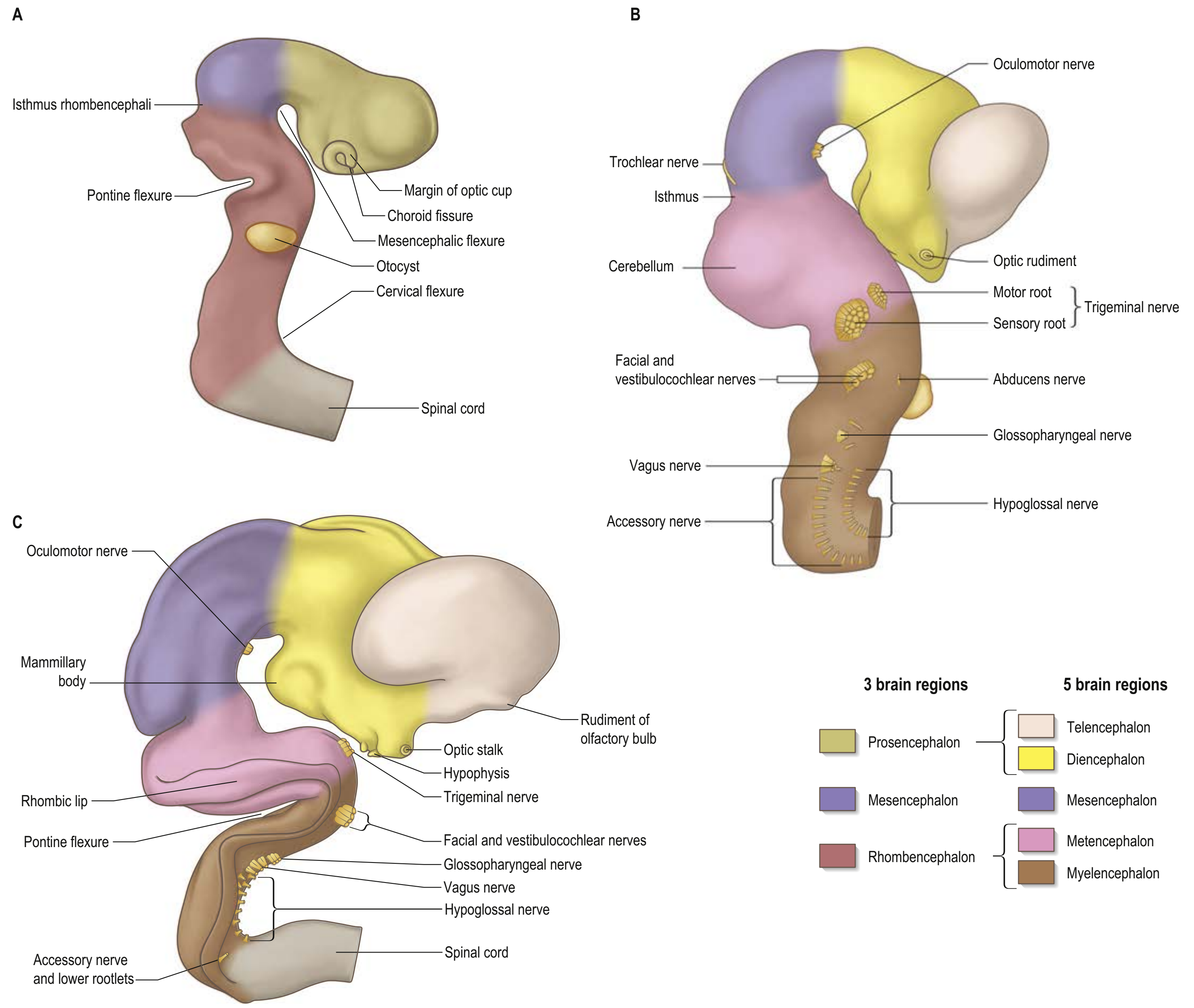
A
Isthmus rhombencephali
Pontine flexure
Margin of optic cup
Choroid fissure
Mesencephalic flexure
Otocyst
Cervical flexure
Spinal cord
B
Oculomotor nerve
Trochlear nerve
Isthmus
Cerebellum
Optic rudiment
Motor root
Sensory root
Trigeminal nerve
Facial and vestibulocochlear nerves
Abducens nerve
Glossopharyngeal nerve
Vagus nerve
Hypoglossal nerve
Accessory nerve
C
Oculomotor nerve
Mammillary body
Rudiment of olfactory bulb
Optic stalk
Hypophysis
Trigeminal nerve
Rhombic lip
Pontine flexure
Facial and vestibulocochlear nerves
Glossopharyngeal nerve
Vagus nerve
Hypoglossal nerve
Spinal cord
Accessory nerve and lower rootlets
3 brain regions
5 brain regions
Prosencephalon
Telencephalon
Diencephalon
Mesencephalon
Mesencephalon
Rhombencephalon
Metencephalon
Myelencephalon

Fig. 14.4 Formation of the mesencephalic, cervical and pontine flexures; human embryos, lateral views. The roof of the rhombencephalon has been removed in each case. **A**, Stage 16. **B**, Stage 17. **C**, Stage 18.

TABLE 14.1 Derivatives of the cerebral regions from caudal to rostral

Cerebral region	Derivatives
Rhombencephalon (or hindbrain)	
1. Myelencephalon	Medulla oblongata Caudal part of the fourth ventricle Inferior cerebellar peduncles
2. Metencephalon	Pons Cerebellum Middle part of the fourth ventricle Middle cerebellar peduncles
3. Isthmus rhombencephali	Superior medullary velum Superior cerebellar peduncles
Mesencephalon (or midbrain)	Cerebral peduncles Tegmentum Tectum Aqueduct
Prosencephalon (or forebrain)	
1. Diencephalon	Thalamus Metathalamus Subthalamus Epithalamus Caudal part of the hypothalamus Caudal part of the third ventricle
2. Telencephalon	Rostral part of the hypothalamus Rostral part of the third ventricle Cerebral hemispheres Lateral ventricles Cortex (archicortex, paleocortex, neocortex) Corpus striatum

Cells within the rostral prosencephalic neural fold and smaller populations of cells in bilateral sites lateral to the early brain do not form migratory neural crest cells but remain within the surface epithelium as ectodermal placodes. Neural crest cells arising from the diencephalon up to the level of the future pineal gland (epiphysis) contribute mesenchymal populations to the frontonasal process. From stage 10 a number of transverse subdivisions perpendicular to the long axis of the brain can be seen within the rhombencephalon, dividing it into segments termed rhombomeres (Müller and O'Rahilly 1997). Eight main rhombomeres extend from the midbrain–hindbrain boundary rostrally to the developing spinal cord caudally (see Fig. 14.2). Both non-neuronal neural crest mesenchyme and neuronal somatic sensory and autonomic ganglia are formed from rhombencephalic crest cells (see Fig. 12.4). Rhombomeres 1 and 2 produce neural crest cells that invade the first pharyngeal arch; rhombomere 4 crest cells migrate into pharyngeal arch 2; rhombomere 6 crest cells migrate into pharyngeal arch 3; rhombomeres 7 and 8 derived neural crest cells migrate into pharyngeal arches 4 and 6. Rhombomeres 3 and 5 give rise to only a very small number of neural crest cells that migrate rostrally and caudally to enter the adjacent even-numbered rhombomeres. These rostral origins give rise to cranial and vagal neural crest. Vagal neural crest migration is extensive: the cells pass ventrally into the developing heart and appear to have a particular association with organs that arise from endoderm, e.g. the thymus gland, foregut-derived respiratory tubes and the gut, where they give rise to the enteric nervous system (Hutchins et al 2018).

Trunk neural crest cells are patterned by their migration through the somites. As the crest cells move laterally and ventrally they can pass between the somites and within the rostral sclerotomal half of each somite, but they cannot penetrate the caudal portion of the sclerotomal mesenchyme. The segmental distribution of the spinal and sympathetic ganglia

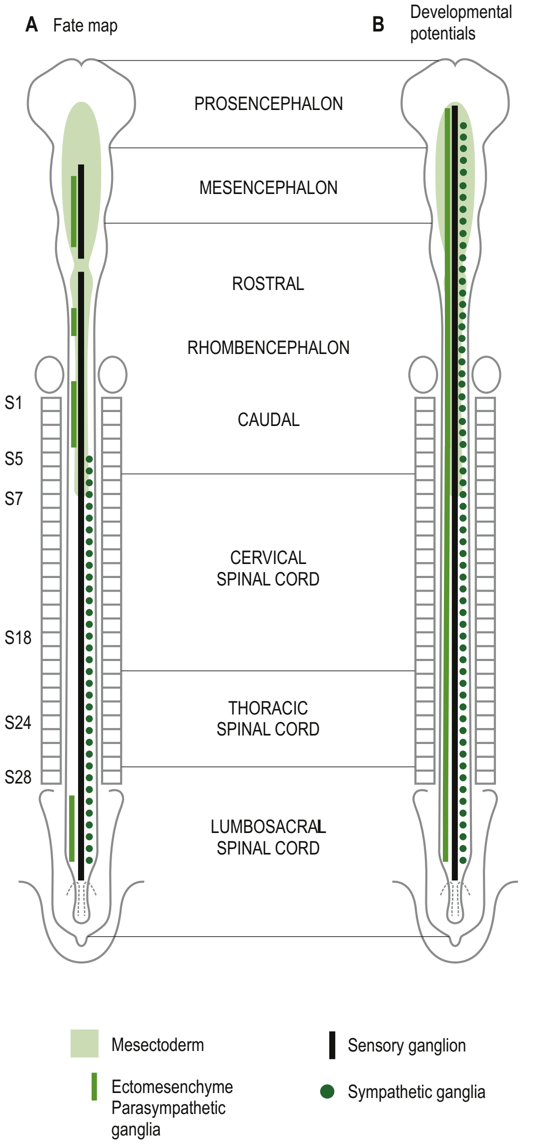

Fig. 14.5 **A**, A fate map along the neural crest of the presumptive territories that yield ectomesenchyme, sensory, parasympathetic and sympathetic ganglia, and neural crest-derived mesenchyme in normal development. **B**, Developmental potentials for the same cell types. If neural crest cells from any level of the neural axis are implanted into the appropriate sites of a host embryo, they can give rise to almost all of the cell types forming the various kinds of peripheral nervous system ganglia. This is not true for neural crest-derived mesenchyme, whose precursors are confined to the cephalic area of the crest down to the level of somite 5. Key: S, somite.

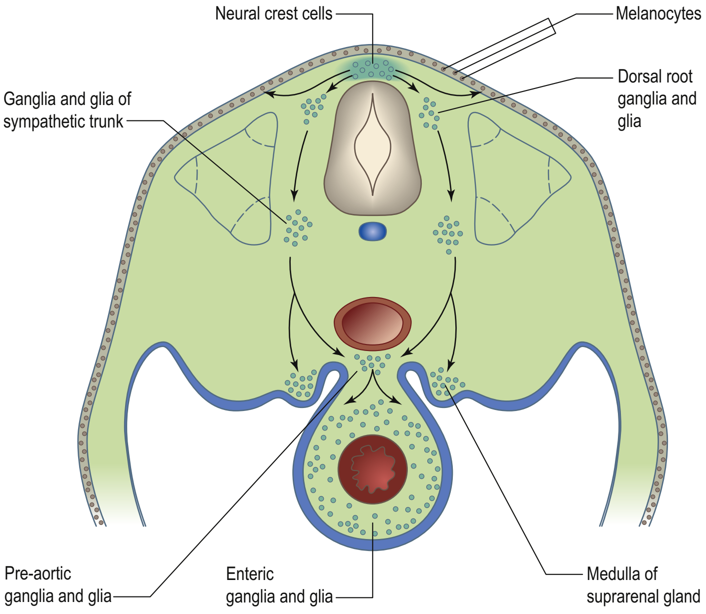
Neural crest cells
Melanocytes
Ganglia and glia of sympathetic trunk
Dorsal root ganglia and glia
Pre-aortic ganglia and glia
Enteric ganglia and glia
Medulla of suprarenal gland

Fig. 14.6 **A**, Migration routes taken by trunk neural crest cells. (B, *continued online*)

is therefore imposed on trunk neural crest cells by a pre-pattern that exists within the somitic paraxial mesenchyme (see Fig. 14.6; see Ch. 18; Figs 18.4, 18.8). Caudally, from approximately somite 29 secondary neurulation processes produce the most caudal sacral neural crest.

Melanocytes develop from lateral migration of a subpopulation of neural crest cells derived from both the head and the trunk (see Fig. 14.6). They form one of the three pigment cell types (the others being retinal pigment epithelium and the pigment cells of the pineal organ, both of which originate from the diencephalon).

ECTODERMAL PLACODES

Before the neural tube closes, the elevating neural folds contain two distinctive neuronal populations. The larger population, of neural crest cells, migrates from the neural epithelium prior to neural tube fusion. The smaller population, of neuroepithelial cells, becomes incorporated into the surface ectoderm after neural tube closure. These areas of neuroepithelium within the surface ectoderm have been termed ectodermal placodes. Although the majority of the ectodermal placodes form nervous tissue, non-neurogenic placodes also occur (Begbie and Graham 2001). After an appropriate inductive stimulus, the placodes thicken and they either generate migratory neuronal cells that will contribute to the cranial sensory ganglia, or the whole placodal region invaginates to form a vesicle beneath the remaining surface ectoderm. Neurogenic placodes undergo both processes. Paired non-neurogenic placodes invaginate to form the lens vesicles under the inductive influence of the optic vesicles (Ch. 15).

The neural folds meet in the rostral midline adjacent to the buccopharyngeal membrane. The rostral neural fold does not generate neural crest but gives rise to the hypophysial placode, i.e. the future Rathke's pouch, which remains within the surface ectoderm directly rostral to the buccopharyngeal membrane. The rostral neural fold also gives rise to the olfactory placodes that remain as paired, laterally placed placodes, and to the epithelium of the nasal cavity (**Fig. 14.7**).

Further caudally, similar neurogenic placodes, the epibranchial, otic and trigeminal placodes, can be identified (**Fig. 14.8**). The epibranchial placodes appear in the surface ectoderm immediately dorsal to the area of pharyngeal (branchial) cleft formation. The first epibranchial placode is located at the level of the first pharyngeal groove and contributes cells to the distal (geniculate) ganglion of the facial nerve. The second and third epibranchial placodes contribute cells to the petrosal and nodose ganglia of the glossopharyngeal and vagus nerves, respectively. These placodes thicken and cells begin to detach from their epithelium soon after the pharyngeal pouches have contacted the overlying ectoderm. Concurrently, the neural crest cells reach and move beyond these lateral extensions of the pharynx. Neurones migrate from the epibranchial placodes internally to the sites of ganglion formation, where they show signs of early differentiation into neurones, including the formation of neurites.

The otic placodes, located lateral to the myelencephalon, invaginate to form otic vesicles from which the membranous labyrinth of the inner ear develops (Ch. 16). Neurones of the vestibulocochlear ganglia arise from neurones that bud off the ventromedial aspect of the otic cup, after which they can be distinguished in the acoustic and vestibular ganglia.

The profundal and maxillomandibular trigeminal placodes, which fuse in humans to form a single entity, lie rostral to the otic placodes, alongside the mesencephalic–rhombencephalic junction. Prospective neuroblasts migrate from foci dispersed throughout the surface ectoderm lateral and ventrolateral to the caudal mesencephalon and metencephalon to contribute to the distal portions of the trigeminal ganglia.

A small endodermal diverticulum, Seessel's pouch, projects towards the brain from the cranial end of the foregut, immediately caudal to the buccopharyngeal membrane. In some marsupials, this pouch forms a part of the hypophysis, but it is not well defined and disappears entirely in humans.

Pituitary gland (hypophysis cerebri)

The hypophysis cerebri consists of the adenohypophysis, derived from an ectodermal placode, and the neurohypophysis, derived from the neural plate. Prior to neurulation, these cell populations are adjacent within the rostral portion of the floor of the neural plate and the contiguous midline neural fold (see Fig. 14.7). During primary neurulation the neurohypophysial cells remain within the floor of the prosencephalon but the adenohypophysial cells are displaced into the ectoderm as a placode rostral to the buccopharyngeal membrane. Both components remain in contact: there is no growth or migration of one to meet the other during subsequent development.

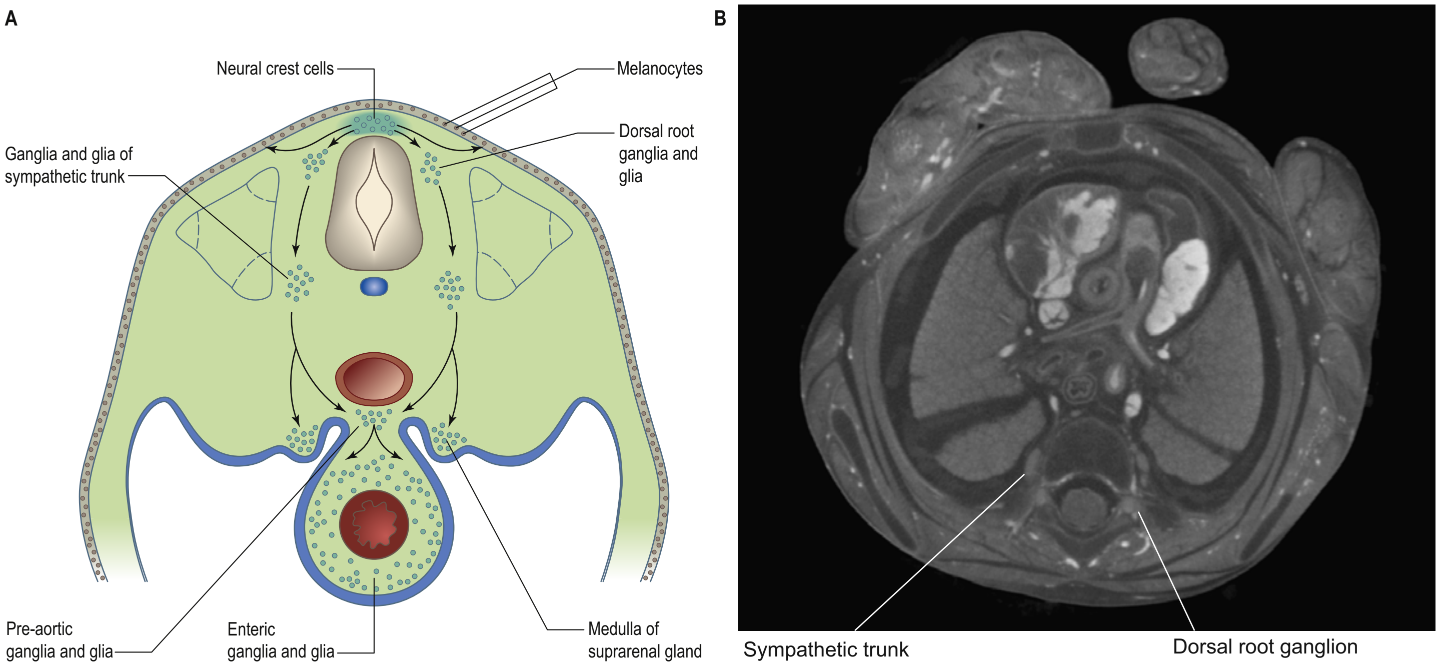
A
Neural crest cells
Melanocytes
Ganglia and glia of sympathetic trunk
Dorsal root ganglia and glia
Pre-aortic ganglia and glia
Enteric ganglia and glia
Medulla of suprarenal gland
B
Sympathetic trunk
Dorsal root ganglion

Fig. 14.6 **A**, Migration routes taken by trunk neural crest cells. **B**, MicroCT image of axial section at the level of the heart in a 14-postmenstrual-week fetus showing the neural crest cell derivatives, the bilateral dorsal root ganglia and sympathetic trunks. (B, Courtesy of Dr Owen Arthurs and Dr Susan Shelmerdine, Great Ormond Street Hospital, London.)

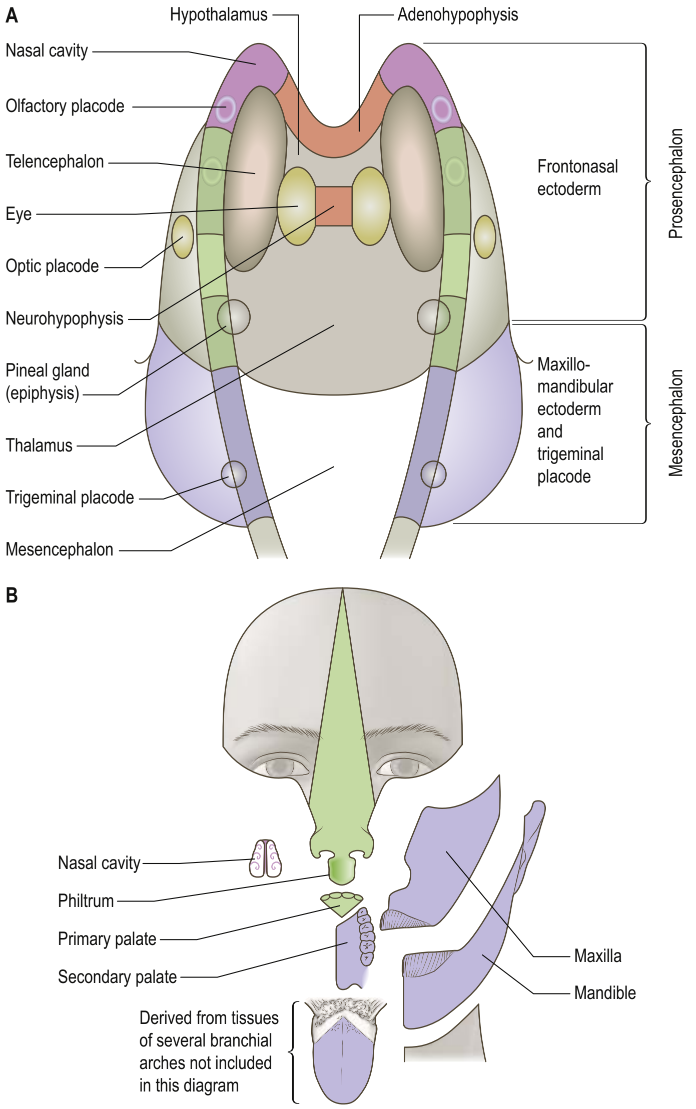
A
Hypothalamus
Adenohypophysis
Nasal cavity
Olfactory placode
Telencephalon
Eye
Optic placode
Neurohypophysis
Pineal gland (epiphysis)
Thalamus
Trigeminal placode
Mesencephalon
Frontonasal ectoderm
Maxillo-mandibular ectoderm and trigeminal placode
Prosencephalon
Mesencephalon
B
Nasal cavity
Philtrum
Primary palate
Secondary palate
Derived from tissues of several branchial arches not included in this diagram
Maxilla
Mandible

Fig. 14.7 A fate map of the rostral region of the neural primordium as established by the quail–chick chimera system. **A**, The various territories yielding rostral head are indicated on the neural plate and neural fold of a 1–3-somite embryo. **B**, The results obtained in the avian embryo have been extrapolated to the human head. For example, the neural fold area that is coloured green in **A** yields the epithelium of the nose, philtrum and primary palate.

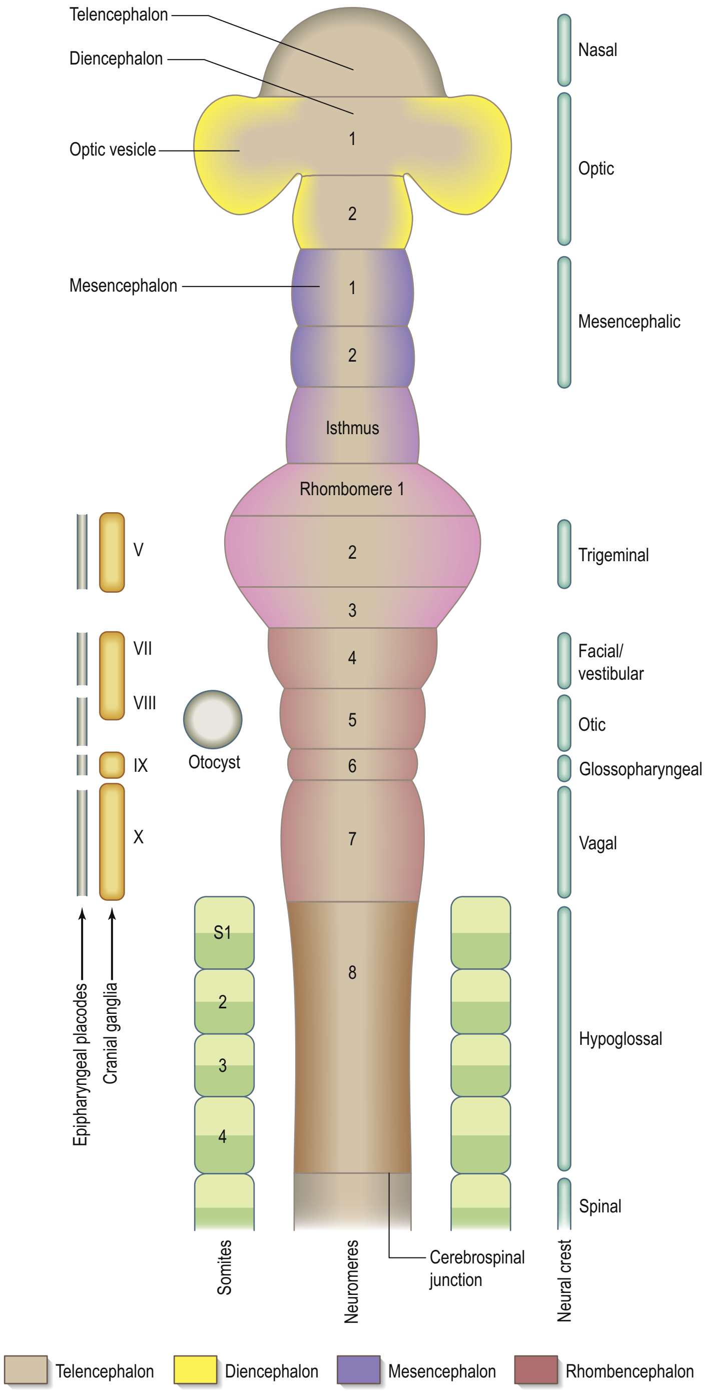
Telencephalon
Diencephalon
Optic vesicle
Mesencephalon
1
2
1
2
Isthmus
Rhombomere 1
2
3
4
5
6
7
8
V
VII
VIII
IX
X
Otocyst
S1
2
3
4
Epipharyngeal placodes
Cranial ganglia
Somites
Neuromeres
Cerebrospinal junction
Neural crest
Nasal
Optic
Mesencephalic
Trigeminal
Facial/ vestibular
Otic
Glossopharyngeal
Vagal
Hypoglossal
Spinal
Telencephalon
Diencephalon
Mesencephalon
Rhombencephalon

Fig. 14.8 A scheme of a human embryo at stage 13, rendered flat to eliminate the cerebral flexures. The cranial sensory ganglia and otocyst, derived from the epibranchial placodes, are shown on the left. The levels of origin of the neural crest that contribute to the cranial sensory ganglia and mesenchymal populations in the head are indicated on the right. This arrangement may vary in other species. (Courtesy of Professor R O'Rahilly and Dr F Müller.)

The buccopharyngeal membrane ruptures at about stage 12. By stage 13 the placodal thickening of the adenohypophysis can be seen just rostral to the edge of the now ruptured buccopharyngeal membrane and rostral to the tip of the subjacent notochord. The placode invaginates to form the roof and walls of a saccular depression, the adenohypophysial (Rathke's) pouch (Figs 14.9–14.10) that expands laterally to remain associated with the floor and sides of the overlying diencephalic wall. By stage 15 an infundibular recess in the floor of the diencephalon is present, and it evaginates to form the infundibular process and infundibular stem during stage 16. During stage 18 the adenohypophysis and neurohypophysis are closely apposed with no intervening mesenchyme: the wall of the neurohypophysis has characteristic folds. There is vascular mesenchyme between the adenohypophysis and the hypothalamic floor in stage 18 and between the adenohypophysis and neurohypophysis by stage 20. At this time, the adenohypophysial stem is solid and embedded in the chondrocranium.

The interactions between hypothalamic and oral ectoderm previously identified in cultured mouse embryos can be replicated in human embryonic stem cells grown in serum-free floating embryoid body-like aggregates. The tissues that form will generate hormone-producing cells and differentiated cell lines that respond to corticotrophic hormone and secrete ACTH, and respond to GHRH and secrete growth hormone (Ozone et al 2016). For an overview of the regulatory factors involved in pituitary embryogenesis and the conditions under which pituitary stem cells may be activated in postnatal life see Cox et al (2017).

At birth the hypophysis is about one-sixth of the weight of the adult gland. It increases in weight to become about one-half of the weight of the adult gland at 7 years, and attains adult weight at puberty. Throughout postnatal life, the gland appears larger in females, in both size and weight. Traces of the original invagination point of the adenohypophysial pouch may be present at the junction of the septum of the nose and palate. A craniopharyngeal canal is a defect of the midline of the body of the sphenoid bone that extends from the floor of the sella turcica to the roof of the nasopharynx: three types of craniopharyngeal canals have been identified based on CT and MR imaging (Abele et al 2014).

EARLY CELLULAR ARRANGEMENT AND HISTOGENESIS OF THE NEURAL TUBE

Formation of the neural tube floor plate is matched by ventral ingression of the notochord from the primitive node. Dorsoventral patterning of the neural tube is dependent on this close contact because the original floor plate and the dorsal site of fusion of the neural tube initially contain non-neural cells. Motor neurones usually develop ventrally,

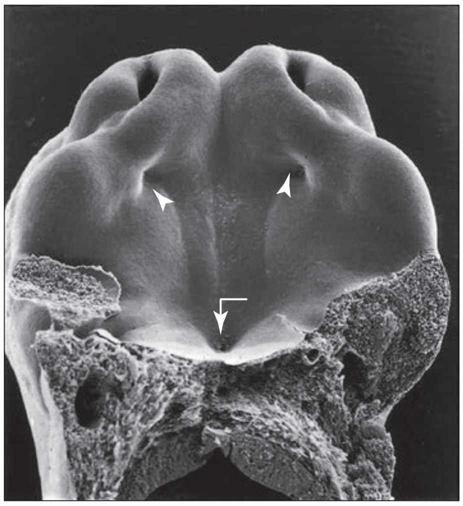

Fig. 14.9 A scanning electron micrograph of the roof of the pharynx showing the invagination of placodal ectoderm to form the adenohypophysis (Rathke's pouch, arrow) and choanal membranes (arrowheads). (Photograph by P Collins; printed by S Cox, Electron Microscopy Unit, Southampton General Hospital.)

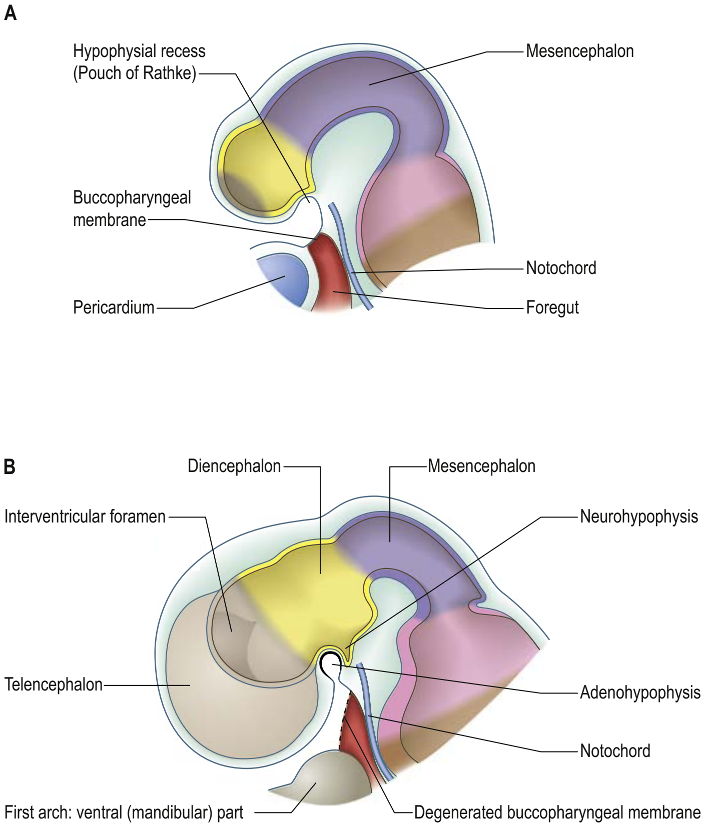

Fig. 14.10 A–B, Initial stages in the development of the hypophysis: sagittal sections of early embryo heads.

close to the notochord, and sensory neurones develop dorsally. Experimental removal of the notochord results in the elimination of the floor plate and motor neurones, and the differentiation of dorsal cell types in the ventral region of the cord (Dodd et al 1998). Experimental grafting of another notochord dorsally results in the induction of a floor plate and ectopic motor neurones close to the grafted notochord. Grafting an isolated neural floor plate dorsal to the neural tube also results in induction of ectopic motor neurones overlying the graft (Fig. 14.11). Elucidation of the specific transcription factors involved in the early patterning of the neural tube has enabled the *in vitro* culture of hPSCs and recapitulation of these early processes. Graded Shh signalling originating in the notochord and floor plate establishes discrete individual neuronal precursor domains that later give rise to specific classes of postmitotic motor neurones (Pantani 2016).

Three zones or regions can be identified within the wall of the early neural tube as the pseudostratified epithelium proliferates. Conventionally, these zones have been named ventricular, mantle and marginal, from deep to superficial (Fig. 14.12). The inner, ventricular zone (germinal, primitive ependymal or matrix layer) contains the apical, nucleated parts of the pseudostratified columnar neuroepithelial cells and rounded cells undergoing mitosis. As daughter cells migrate ventriculofugally (radially) from the ventricular zone, a middle, mantle layer (intermediate zone) is formed. Radial glial cells form early with processes extending from the ventricular surface (apical cell surface) to the pial surface (basal cell surface). The lateral connection of adjacent apical or basal surfaces give rise to layers termed the internal and external glia limitans (glial limiting membrane), respectively. The region containing the basal surfaces and cytoplasmic processes of the radial glia is termed the marginal zone; it will be invaded later by vascular endothelium, varieties of glial cells and axonal processes extending from neuroblasts.

The neural tube caudal to the developing brain is initially oval in transverse section and its lumen is narrow and slit-like (Fig. 14.13). Proliferation in the ventricular zone and migration of the resulting progeny means that the lateral walls thicken and the lumen, now the central canal, widens in its dorsal part. A longitudinal sulcus limitans develops on each side, dividing the ventricular and mantle (now also referred to as intermediate) zones in each lateral wall into a ventrolateral lamina or basal plate, and a dorsolateral lamina or alar plate, respectively. The widening central canal becomes somewhat rhombic on cross-section (Fig. 14.14).

The early spinal cord and much of the brainstem retain only the ventricular, intermediate and marginal zones. However, in the telencephalon, cellular proliferation extends deeper than the ventricular zone. A population of cells resulting from the asymmetric division of stem cells at the ventricular zone move to a subventricular zone, where they divide symmetrically. Cells from both layers continue to multiply to provide generations of neurones and glia that subsequently migrate into the intermediate and marginal zones. Those in the subventricular zone are termed intermediate neural progenitor cells or basal progenitors to emphasize the fact that they are no longer attached to the apical (ventricular) surface. They translocate their nuclei to an abventricular location for mitosis. Radially migrating cells from the ventricular zone in the developing cerebral hemispheres form a zone, the cortical plate, outside the intermediate zone. The most recently formed cells migrate to the outermost layers of the cortical plate, so that earlier derived and migrating cells become subjacent to those migrating at a later time. The subplate zone is a crucial additional transient stratum found deep to the early cortical plate in the forebrain (Molnar et al 2019).

In the cerebellar cortex, some mitotic subventricular stem cells migrate across the entire neural wall to form a subpial population and establish a new zone of cell division and differentiation. Many cells formed in this site remain subpial in position, but others migrate back towards the ventricle through the developing nervous tissue, and finish their migrations in various definitive sites where they differentiate into neurones or macroglial cells.

Segmentation in the neural tube

The early neural tube is visibly divided into segments by shallow transverse folds that extend perpendicular to its long axis. Primary neuromeres can be identified at stage 9, with 16 secondary neuromeres present at stage 14. Rhombomeres, the segments within the rhombencephalon, identified from stage 10, are crucial units of pattern formation (Tümpel et al 2009). Other brain regions are not segmented in quite the same way as the hindbrain. Morphological boundaries, domains of cell lineage restriction and of cell mixing, and regions of gene expression that abut sharp boundaries, are found in the diencephalon and telencephalon. Although these segmental units lose their morphological prominence with subsequent development, they represent the fundamental ground plan of the neuraxis, creating a series of semi-autonomous units, within which local variations in patterning can then develop. It is likely that compartmentation of cell groups with some, if not all, of the features of rhombomeres plays an important role in the formation of various brain regions.

Domains of expression of developmental control genes abut rhombomere boundaries. Single-cell labelling experiments have revealed that cells within rhombomeres form segregated non-mixing populations (Fig. 14.16). The neural crest also shows intrinsic segmentation in the rhombencephalon. It is segregated into streams at its point of origin in the dorsal neural tube, which may represent a mechanism whereby morphogenetic specification of the premigratory neural crest cells is conveyed to the pharyngeal arches (see Fig. 12.4). Developmental studies of rhombomeric fate, developmental gene expression, progeny analysis and fate mapping are calling into question the traditional

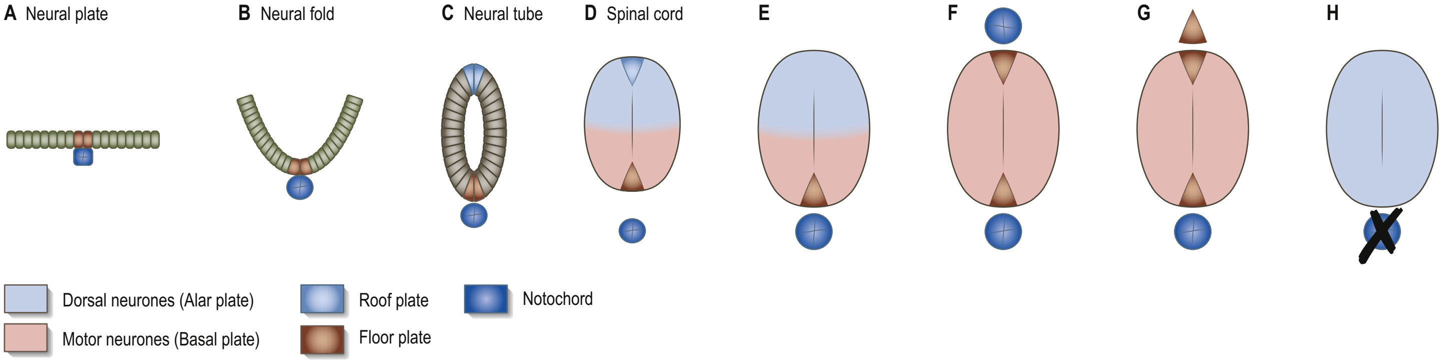

Fig. 14.11 **A–D**, Successive stages in the development of the neural tube and spinal cord. **A**, The neural plate consists of epithelial cells. Cells in the midline of the neural plate are contacted directly by the notochord. More lateral regions of the neural plate overlie the paraxial mesenchyme (not shown). **B**, During neurulation, the neural plate bends at its midline and this elevates the lateral edges of the plate as the neural folds. Contact between the midline of the neural plate and the notochord is maintained at this stage. **C**, The neural tube is formed when the dorsal tips of the neural folds fuse. Cells in the region of fusion form the roof plate, a specialized group of dorsal midline cells. **D**, Cells at the ventral midline of the neural tube retain proximity to the notochord and differentiate into the floor plate. After neural tube closure, neuroepithelial cells continue to proliferate and eventually differentiate into defined classes of neurones at different dorsoventral positions within the spinal cord. For example, sensory relay, commissural and other classes of dorsal neurones differentiate near to the roof plate, and motor neurones differentiate ventrally near the floor plate, which, by this time, is no longer in contact with the notochord. **E–H**, Summary of the results obtained from experiments in chick embryos in which either a notochord or floor plate is grafted to the dorsal midline of the neural tube, or the notochord is removed before neural tube closure. **E**, The normal condition: motor neurones are located ventrally and sensory relay neurones are located dorsally. **F**, Dorsal grafts of a notochord result in the induction of a floor plate in the dorsal midline and ectopic dorsal motor neurones. **G**, Dorsal grafts of a floor plate induce a new floor plate in the dorsal midline and ectopic dorsal motor neurones. **H**, Removal of the notochord results in the elimination of the floor plate and motor neurones, and the expression of dorsal cell types in the ventral region of the spinal cord. (Adapted with permission from Jessell TM, Dodd J 1992 Midline signals that control the dorso-ventral polarity of the neural tube. Semin Neurosci l4:317–325.)

Planar cell polarity genes are expressed by the neuroepithelium. Each cell displays an apical non-motile primary cilium (internal 9 + 0 configuration of microtubules), and a system of intraflagellar transport (Tissir and Goffinet 2010). The membrane of the primary cilium expresses receptors and ion channels and modulates signalling pathways for Shh, Wnt and PDGFα (Lee and Gleeson 2010).

Pseudostratified epithelial proliferation of neuroepithelial progenitor cells at the ventricular zone is recognized by interkinetic nuclear migration. The cells have a relatively small basal surface that generates a basal lamina, a similarly small apical surface (with a primary cilium) joined by an adherence junctional belt, and extensive lateral surfaces that span the neuroepithelial wall. Their nuclei migrate basally during G1 phase of the cell cycle; S-phase (DNA replication) occurs as the nuclei approach the basal lamina. During G2, the nuclei migrate apically (toward the neural tube lumen) where cell division occurs. The basal body of the primary cilium is anchored to the apical surface: the cilium persists through the cell cycle until the onset of mitosis when the basal body and associated second centriole form the centrosomes of the mitotic spindle (Taverna and Huttner 2010). The movement of the nuclei during proliferation is responsible for the pseudostratified appearance of the epithelium, because the nuclei move basally and then apically as they pass through a complete mitotic cycle (Fig. 14.15).

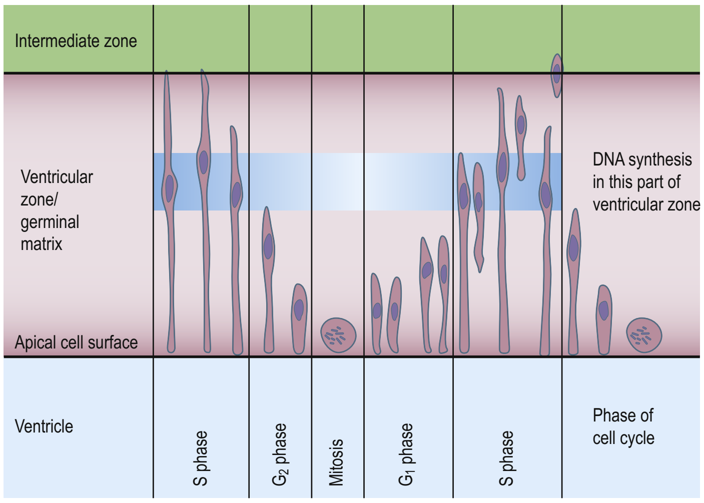

Fig. 14.15 The cell cycle in the ventricular zone of the developing neural tube. The nuclei of the proliferating stem cells show interkinetic migration. (Adapted from Fujita S 1963 The matrix cell and cytogenesis in the developing central nervous system. J Comp Neurol 120:37–42.)

The first populations formed by symmetric division become radial glial cells: through their contact with both the neural tube lumen and the outer pial surface, they provide a scaffold on which future cell progeny can migrate. Radial glial cells express GFAP, distinguishing them from neuroepithelial progenitor cells (Silver et al 2019). The Golgi apparatus in radial glial cells remains apical to the nucleus and perpendicular to the apicobasal axis of the cell and appears to have only a minor role in synthesis of constituents for the basolateral plasma membrane (Taverna et al 2016). Arl13b, a cilia-specific small guanosine triphosphatase (GTPase), is essential for the formation of radial glia (Higginbotham et al 2013). Later, asymmetric divisions produce one neuroepithelial progenitor cell and another cell that migrates radially (ventriculofugally), so producing clones of neuroblasts and glioblasts. With development of the intermediate zone, the nuclei of cells undergoing asymmetric division show interkinetic nuclear migration only within the ventricular and subventricular zones (Taverna and Huttner 2010). The heterogeneity of the radial glial cell population, which can become detached from the basal and apical surfaces as development proceeds, has yet to be elucidated (Silver et al 2019). The stem cells in the ventricular zone finally produce two postmitotic daughter cells that differentiate into ependyma that lines the ventricular system. The ventricular epithelium differentiates into choroid plexus and specialized circumventricular organs in particular sites within the third and fourth ventricles.

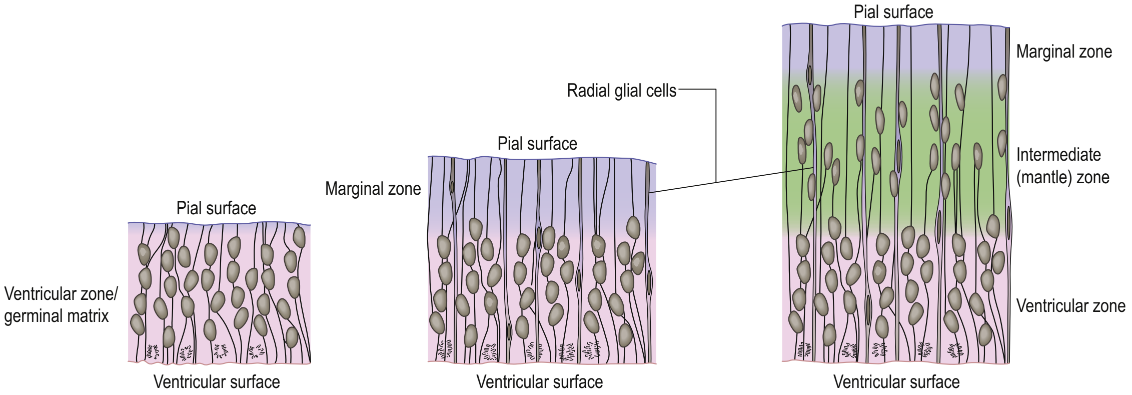
Pial surface
Radial glial cells
Marginal zone
Pial surface
Marginal zone
Pial surface
Intermediate (mantle) zone
Ventricular zone/ germinal matrix
Ventricular zone
Ventricular surface
Ventricular surface
Ventricular surface

Fig. 14.12 Early development of the neural tube: three layers are delineated in the spinal cord and brainstem.

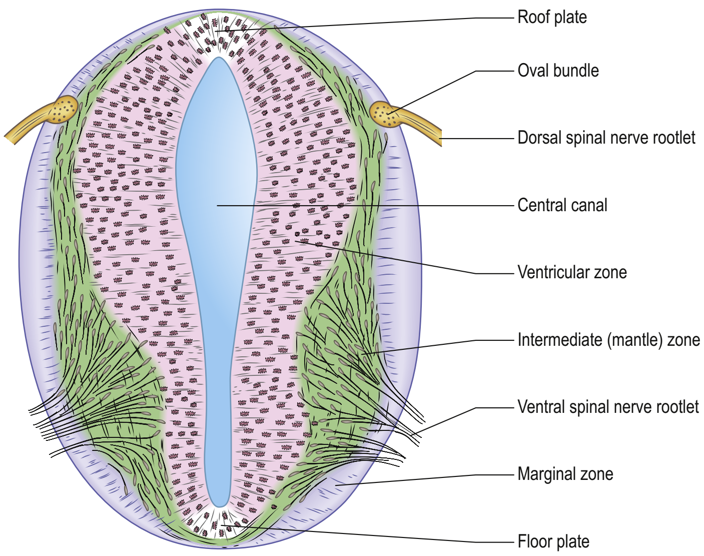
Roof plate
Oval bundle
Dorsal spinal nerve rootlet
Central canal
Ventricular zone
Intermediate (mantle) zone
Ventral spinal nerve rootlet
Marginal zone
Floor plate

Fig. 14.13 Transverse section of the spinal cord of a human embryo, stage 13.

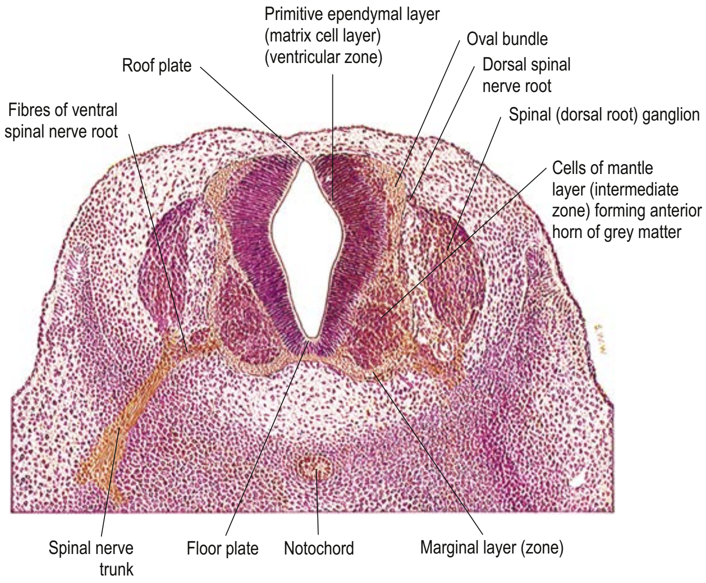
Primitive ependymal layer (matrix cell layer) (ventricular zone)
Roof plate
Oval bundle
Dorsal spinal nerve root
Fibres of ventral spinal nerve root
Spinal (dorsal root) ganglion
Cells of mantle layer (intermediate zone) forming anterior horn of grey matter
Spinal nerve trunk
Floor plate
Notochord
Marginal layer (zone)

Fig. 14.14 Transverse section of the spinal cord in the cervical region of a human embryo about stage 16.

subdivisions of the brainstem into midbrain, pons and medulla oblongata that have been based on the external appearance of the human brainstem (Watson et al 2019). The brainstem boundaries identified by these new analyses are illustrated in **Fig. 14.17** and Figs 28.25, 28.26.

The significance of intrinsic segmentation in the hindbrain is underlined by the absence of overt segmentation of the adjacent paraxial mesenchyme. There is no firm evidence for intrinsic segmentation in the spinal cord. Instead, segmentation of the neural crest, motor axons and thus, eventually, the spinal nerves, is dependent on the segmentation of the neighbouring somites. Both neural crest cell migration and motor axon outgrowth occur through only the rostral and not the caudal sclerotome of each somite, so that dorsal root ganglia form only at intervals. The caudal sclerotome possesses inhibitory properties that deter neural crest cells and motor axons from entering.

Genes such as the *Hox* and *Pax* gene families, which encode transcription factor proteins, show intriguing expression patterns within the nervous system. Genes of the *Hox-b* cluster, for example, are expressed throughout the caudal neural tube, and up to discrete limits in the hindbrain that coincide with rhombomere boundaries. The ordering of these genes within a cluster on the chromosome (5′–3′) is the same as the caudal to rostral limits of expression of consecutive genes. This characteristic pattern is surprisingly similar in fish, frogs, birds and mammals. *Hox* genes play a role in patterning not only of the neural tube but also of much of the head region, consistent with their expression in neural crest cells, and within the pharyngeal arches. Disruption of *Hox a-3* gene in mice mimics DiGeorge's syndrome, a congenital human disorder characterized by the absence (or near absence) of the thymus, parathyroid and thyroid glands, hypotrophy of the walls of the arteries derived from the aortic arches, and subsequent conotruncal cardiac malformations. Some *Pax* genes are expressed in different dorsoventral domains within the neural tube. *Pax-3* is expressed in the alar lamina, including the neural crest, while *Pax-6* is expressed in the intermediate plate. The *Pax-3* gene has the same chromosomal localization as the mouse mutation Splotch and the affected locus in the human Waardenburg's syndrome, both of which are characterized by neural crest disturbances with pigmentation disorders and occasional neural tube defects. Both *Hox* and *Pax* genes have restricted expression patterns with respect to the rostrocaudal and the dorsoventral axes of the neural tube, consistent with roles in positional specification. The expression pattern of *Hox* and other genes expressed in rhombomeres, and the transcriptional analysis of individual rhombomeres illustrate the genome-wide complexity of mid- and hindbrain patterning in animal embryos (Krumlauf et al 1993, Chambers et al 2009, Wilson and Chambers 2014).

While craniocaudal positional values are probably conferred on the neuroepithelium at the neural plate or early neural tube stage, dorsoventral positional values may become fixed later. The development of the dorsoventral axis is heavily influenced by the presence of the underlying notochord. The notochord induces the floor plate in the ventral midline of the neural tube. This specialized region consists of a strip of non-neural cells with distinctive adhesive and functional properties. Notochord and floor plate together participate in inducing the differentiation of the motor columns. Motor neurone differentiation occurs early, giving some grounds for the idea of a ventral to dorsal wave of differentiation. The notochord/floor plate complex may also be responsible for allotting the values of more dorsal cell types within the tube (see Fig. 14.11). For example, the dorsal domain of expression of *Pax-3* extends more ventrally in chick embryos experimentally deprived of notochord and floor plate, while grafting an extra notochord adjacent to the dorsal neural tube leads to a repression of *Pax-3* expression.

Cell populations of the early brain and their growth

Cells in the nervous system are derived from three embryonic sources. The neural plate and tube give rise to CNS neurones, astrocytes and oligodendrocytes, and neuronal neural crest cells and ectodermal

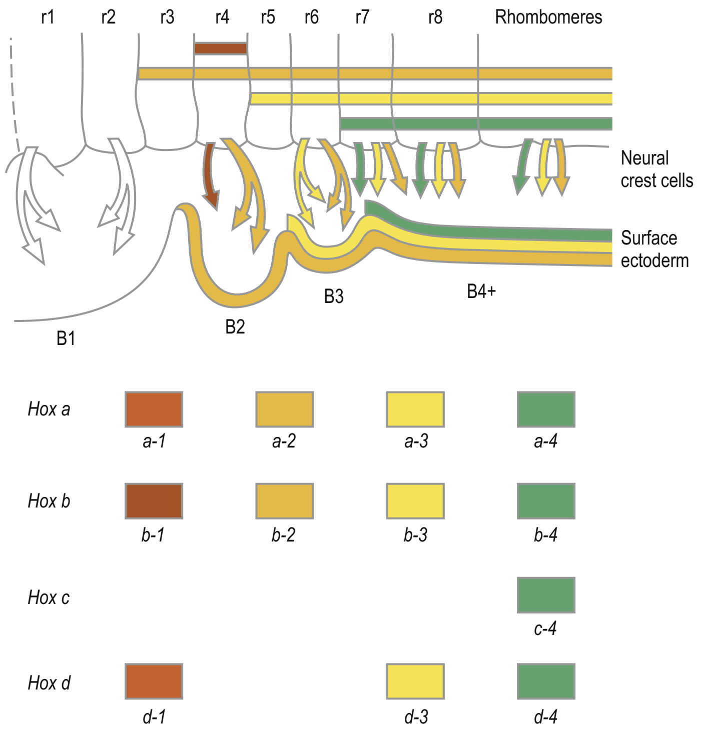

Fig. 14.16 *Hox* gene expression domains in the branchiorhombomeric area in the mouse embryo at E9.5. The arrows indicate neural crest cells migrating from the rhombencephalon and midbrain. Cells migrating from the rhombencephalon are shaded to indicate the *Hox* genes they express. The same combination of *Hox* genes is expressed in the rhombomeres and in the superficial ectoderm of the pharyngeal arches at the corresponding rostrocaudal levels. The four *Hox* clusters are represented below. (Adapted with permission from the Annual Review of Cell and Developmental Biology, Volume 8, 1992 by Annual Reviews.)

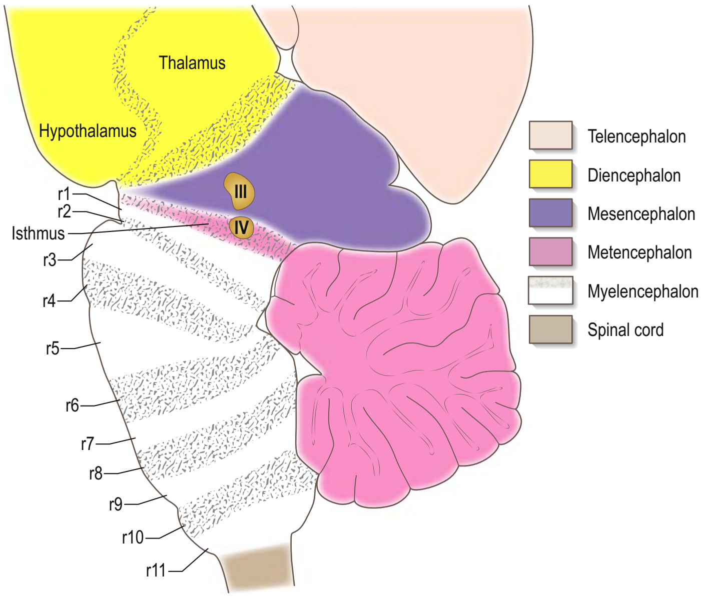

Fig 14.17 The extent of the rhombomeres in the brainstem (r1–r11). Traditionally, based on the ventral appearance of the brainstem, the mesencephalon has been described as extending from the thalamus to the rostral margin of the pons, and including the posterior commissure, the nuclei for cranial nerves III and IV, the interpeduncular nuclei and the isthmus. Studies of developmental gene expression, progeny analysis and fate mapping of the rhombomeres in the brainstem have shown that whereas the mesencephalon does include the oculomotor nerve nuclei (III), the posterior commissure is part of the diencephalon and the abducens nerve nuclei (VI) and the isthmus are part of the rhombencephalon (subdivided into metencephalon and myelencephalon). The isthmus, an important organizer of brainstem development, is now recognized as part of the rhombencephalon and designated rhombomere 0. (Adapted with permission from Watson C, Bartholomaeus C, Pueles L 2019 Time for radical changes in brain stem nomenclature – applying the lessons from developmental gene patterns. Front Neuroanat 13:10. doi.org/10.3389/fnana.2019.00010.)

placodes give rise to PNS ganglionic neurones, both somatic and autonomic, and associated astrocytes and Schwann cells. Neuronal neural crest cells also form all neurones and glia of the enteric nervous system and the chromaffin cells of the suprarenal (adrenal) cortex. Non-neuronal neural crest cells form angiogenic mesenchyme in the layers around the developing neural tube, and other haematogenic precursors give rise to microglial cells that subsequently enter the nervous system. Human neural development is now being investigated by *in vitro* studies of human pluripotent stem cells (hPSCs), 3D culture and the development of cerebral organoids from human tissue (Lee et al 2017). The latter have been used to identify cortical cell types infected by Zika virus and the screening of potential pharmacological treatments (Molnar et al 2019).

Proliferation of the ventricular zone of the early neural tube gives rise to neurones before glial cells. The timing of events differs in various parts of the CNS and between species. Most neurones are formed prenatally in mammals but postnatal neurogenesis occurs in the cerebral cortex, olfactory bulb and the small granular cells of the cerebellum. Gliogenesis continues after birth in periventricular and other sites.

Immature neurones are initially rotund or fusiform. Their cytoplasm contains a prominent Golgi apparatus, many lysosomes, glycogen and numerous unattached ribosomes. As maturation proceeds, cells send out fine cytoplasmic processes that contain neurofilaments, microtubules and other structures, often including centrioles at their bases where microtubules form. Internally, cisternae of the endoplasmic reticulum appear and attached ribosomes and mitochondria proliferate, while the glycogen content progressively diminishes.

Astrocytes differentiate into protoplasmic and fibrous phenotypes. Human cortical protoplasmic astrocytes first appear around postmenstrual week 20 and their density continues to increase into postnatal life. During early adulthood gliogenic progenitors from the subventricular zone can contribute to the generation of new astrocytes in response to injury (Krencik et al 2017).

Oligodendrocytes arise later in development and myelinate developing CNS axons over a protracted period. (For details of myelin formed by oligodendrocytes see Chapter 3.) Oligodendrocyte progenitor cells are prevalent initially in the brainstem at about postmenstrual week 22 and cortical myelination continues into postnatal life. The oligodendrocyte precursor cell population is heterogeneous; maturation appears to be both spatially and temporally controlled (Dimou and Simons 2017). Research in this area is frustrated by methodological difficulties (differentiated oligodendrocytes are very difficult to isolate): single cell transcriptome techniques have been used to study oligodendrocyte lineage (Van Bruggen et al 2017). Synapses between oligodendrocyte precusor cells and neurones have been observed. Vesicular neurotransmitter release and adenosine signalling via adenosine receptors regulate the migration of oligodendrocyte progenitor cells at the motor exit point transition zone in zebra fish embryos (Fontenas et al 2019; see p. 241).

Schwann cells are derived from neural crest cells of the head and trunk. They associate with most PNS axons and many produce myelin, responding to neuronal signals. Schwann cell precursors are multipotent embryonic progenitors that may migrate into the peripheral tissues and signpost nerve fibre migration routes; they also cling to extending axons and, in this way, spread throughout the body with the developing peripheral nervous system. Factors secreted by Schwann cell precursors may pattern the development of neurovascular bundles (Furlan and Adameyko 2018).

Microglial cells are derived from haemopoietic cells found in the yolk sac and precursor blood stem cells become seeded in various body regions (Tay et al 2017). Microglial cells enter the brain by two routes, initially via pial vessels and later also via the early cerebral circulation that supplies both the ventricular zone and the developing choroid plexuses in the lateral ventricle (Reemst et al 2016, Michell-Robinson et al 2017, Menassa and Gomez-Nicola 2018). Within the developing nervous system they have roles during late neurogenesis and gliogenesis. They remain within the CNS after the blood–brain barrier matures and are able to proliferate and respond to homeostatic disequilibrium throughout pre and postnatal life. For the time line of human microglial development see Menassa and Gomez-Nicola (2018).

Early neuronal growth

Early neuroblasts form one main process, the axon, and other processes that establish a dendritic tree. Studied in tissue culture, axons may grow as much as 1 mm per day, navigating with precision over complex courses and considerable distances to reach their targets. Eventually, axons make functional contact with their appropriate end organs (neuromuscular endings, secretomotor terminals, sensory corpuscles or synapses with other neurones). There are reciprocal interactions with the target tissues: reciprocal signalling occurs during development, postnatally and in adult life (Harris 2008, da Silva and Wang 2011).

Ramón y Cajal was the first to describe the expanded growing tips of axons, naming them growth cones. These tips are constantly active, changing shape and extending and withdrawing filopodia and lamellipodia, small protuberances that apparently 'explore' the local environment for a suitable surface over which to extend. This incessant palpatory activity depends on the organization and dynamics of actin filaments that fill the leading margin (peripheral (P–) domain) of the growth cone. It is regulated by actin-binding proteins that control all aspects of filament assembly, turnover, interactions with other filaments and cytoplasmic components, and the production of mechanical forces. Adhesive ligands and extrinsic guidance cues bind growth cone receptors to their substratum and trigger signalling activities involving Rho GTPases, kinases, phosphatases, cyclic nucleotides and Ca^{2+} fluxes. Adhesion to a substratum appears to be important for transient consolidation (stabilization) of the growth cone, elaboration of the axonal cytoskeleton in the direction of growth, and transduction of mechanical forces into traction in order to pull the axon towards its next target (Gomez and Letourneau 2014). After consolidation, the exploratory behaviour begins again, resembling the behaviour at the leading edge of migratory cells such as fibroblasts and neutrophils.

Axon extension occurs when growth cones encounter a permissive physical substrate containing short-range cues such as appropriate extracellular matrix components, transmembrane phosphatases and cadherins. Axonal repulsion requires negative cues that inhibit the progress of the growth cone. Long-range cues diffuse from distant targets down gradients of specific factors, inducing neurones to turn their axons either towards the source of an attractive signal or away from a repulsive signal. Topographic projections, such as the retinotectal pathway, are established as specific populations of growth cones follow spatial gradients of guidance cues (Kalil et al 2011).

Once growth cones have arrived in their appropriate target area, they form terminals and synapses. Extensive dendritic trees are generated and subsequently shaped by dendrite retraction and pruning. Signalling mechanisms underlying these processes are poorly understood: centrosomal CaMKIIβ signalling has been proposed as a mechanism restricting dendrite elaboration while promoting dendrite pruning (Puram et al 2011). The final shape of dendritic trees is influenced by patterns of afferent connections and their activity and is necessary for the accurate formation of neuronal circuitry. Dendritic spine density in childhood exceeds adult values by two- to three-fold and begins to decrease during puberty. However, the overproduction and later pruning of supernumerary synapses continues well into the third decade of life before stabilizing (Petanjek et al 2011, Kolb et al 2013). Successful neuronal connectivity is the product of a series of tightly regulated programmed events that include axon initiation, growth cone formation and navigation, and the formation and pruning of dendritic trees and synapses (Chiu et al 2013).

Axonal and dendritic outgrowth is initiated and supported by neurotrophins. Differential responses reflect the distribution of receptors or components of the relevant signal transduction pathways on neuronal, axonal and dendritic surfaces. Structurally and functionally related neurotrophic molecules include the nerve growth factor (NGF) superfamily and the GDNF family (Cirulli and Alleva 2009, Park and Poo 2013, West et al 2014). The NGF superfamily includes BDNF, NT-3 and NT-4/5, which exert their survival effects selectively on particular subsets of neurones. NGF is specific to sensory ganglion cells from the neural crest, sympathetic postganglionic neurones and basal forebrain cholinergic neurones. BDNF promotes the survival of retinal ganglion cells, motor neurones and some placode-derived neurones, such as those of the nodose ganglion, that are unresponsive to NGF. NT-3 has effects on motor neurones, limb proprioceptive neurones and both placode- and neural crest-derived sensory neurones. Other growth factors that influence the growth and survival of neural cells include the FGFs and ciliary neurotrophic factor (CNTF), which are unrelated in sequence to the NGF family. Members of the FGF family support the survival of embryonic neurones from many regions of the CNS. CNTF may control the proliferation and differentiation of sympathetic ganglion cells and astrocytes.

Each of the neurotrophins binds specifically to certain receptors on the cell surface. The receptor $p75^{NTR}$ binds all the neurotrophins with similar affinity, whereas members of the family of receptor tyrosine kinases (Trks) bind with higher affinity and display binding preferences for particular neurotrophins; the presence of a Trk receptor seems to be required for $p75^{NTR}$ function.

CNS/PNS zone patterning

Relatively little is known about tissue interactions at the CNS/PNS junctional zone between neural plate-derived motor neurones (with axons extending into the periphery) and neural crest-derived somatic sensory neurones (with processes entering the neuraxis from the periphery). Transition zones between the central and peripheral nervous systems show segregation of neurones and their axons and also of central and peripheral glia. Different processes appear to operate in the spinal cord at the basal plate motor exit points and alar plate dorsal root entry zones. The experimental evidence for these findings has come largely from zebrafish and mouse embryos, indicating some conservation of developmental processes.

Early in development peripheral nervous cells are apparently able to migrate in and out of the developing spinal cord before the radial glial end feet establish an external glia limitans (Smith et al 2016). Once a continuous glia limitans is in place, neural crest derivatives, termed boundary cap cells, migrate along the spinal cord and transiently cluster at transition zones that match the sites of axonal exit and entry points. In mouse embryos, where *Krox-20* is expressed early in rhombomeres 3 and 5, the expression persists in boundary cap cells and later in Schwann cells (Fontenas and Kucenas 2017). Loss of boundary cells adjacent to the basal plate results in the presence of ectopic cell bodies of motor neurones in the ventral rootlets; inactivation of *Krox-20* results in ectopic cell bodies of motor neurones within the motor ventral rootlets and ectopic oligodendrocytes, rather than Schwann cells, within the proximal parts of both motor and sensory nerve rootlets. Perineurial glia are *nkx2.2a*-expressing cells that originate from the basal plate of the spinal cord and migrate apparently exclusively into the motor exit rootlets along the motor axons, ensheathing them, forming tight junctions and differentiating into perineurium. In zebrafish, loss of *nkx2.2a* leads to motor axons exiting the CNS ectopically, cell bodies of motor neurones moving out of the spinal cord and an absence of perineurial ensheathment of motor axons peripherally (Kucenas 2015, Fontenas and Kucenas 2017). The origin of sensory perineurial glia has yet to be established.

At the alar plate a different mechanism is seen. Axons extending centrally from sensory neurones in the dorsal root ganglia form actin-rich filopodia that extend toward the dorsal root entry zone. Pioneer axons migrate along the radial glial end-feet, then cross the CNS/PNS radial glial boundary to form rostral and caudal projections within the CNS (Nichols and Smith 2019). The growth cones swell during entry and are thought to rearrange their actin filaments dynamically as they cross the glia limitans. Whether or not boundary cap cells are associated with sensory axon entry is still unclear; the temporal dynamics indicate entry of rostral growth cones before more caudal ones, and the later coalescence of peripheral glial populations (Fontenas and Kucenas 2017, Nichols and Smith 2019).

PERIPHERAL NERVOUS SYSTEM

Somatic nerves

Spinal nerves

Each spinal nerve is connected to the spinal cord by a ventral root and a dorsal root (**Fig. 14.18**). The fibres of the ventral rootlets grow out from cell bodies in the anterior and lateral parts of the intermediate zone and pass through the overlying marginal zone and external limiting membrane. Some enter the myotomes of the somites, and some penetrate the somites, reaching the adjacent somatopleure: in both sites, they ultimately form α-, β- or γ-efferents. At appropriate levels these axons are accompanied by the outgrowing axons of preganglionic sympathetic neuroblasts (segments T1–L2) or preganglionic parasympathetic neuroblasts (S2–S4).

The fibres of the dorsal rootlets extend from cell somata in dorsal root ganglia into the spinal cord and into the periphery. Neural crest cells are produced continuously along the length of the spinal cord, but gangliogenic cells migrate only into the rostral part of each somitic sclerotome, where they condense and proliferate to form a bilateral series of oval primordial spinal ganglia (dorsal root ganglia) (see Fig. 14.6; Ch. 18). Negative factors in the caudal sclerotome deter neural crest cells from entering. The rostral sclerotome has a mitogenic effect on the crest cells that settle within it. From the ventral region of each ganglion, a small part separates to form sympathochromaffin cells, while the remainder becomes a definitive spinal ganglion (dorsal root ganglion). The spinal ganglia are arranged symmetrically at the sides of the neural tube and, except in the caudal region, are equal in number to the somites. The cells of the ganglia, like the cells of the intermediate zone of the early neural tube, are glial and neuronal precursors. The glial precursors develop into satellite cells (which become closely applied to the ganglionic nerve cell somata), Schwann cells and, possibly, other cells. The neuroblasts, at first round or oval, soon become fusiform, and their extremities gradually elongate into central and peripheral processes. The central processes grow into the neural tube as the fibres of the dorsal nerve roots, while the peripheral processes grow ventrolaterally to mingle with the fibres of the ventral root, thus forming a mixed spinal nerve. As development proceeds, the original bipolar form of the cells in the spinal ganglia changes:

Several families of signalling molecules are known to be instructive guidance cues. The original canonical group of netrins, semaphorins, slits and ephrins has now been amplified by members of three families of developmental morphogens (bone morphogenetic protein (BMP), Hedgehog and Wnt families), and a number of growth factors (hepatocyte growth factor (HGF), fibroblast growth factors (FGFs) and glial cell-derived neurotrophic factor (GDNF)) for subsets of motor axons, e.g. neurotrophins (brain-derived neurotrophic factor (BDNF) and neurotrophin 3 (NT3)) for sensory axons, neuregulins for thalamocortical axons, and vascular endothelial growth factor A (VEGFA) for commissural axons (Omotade et al 2017).

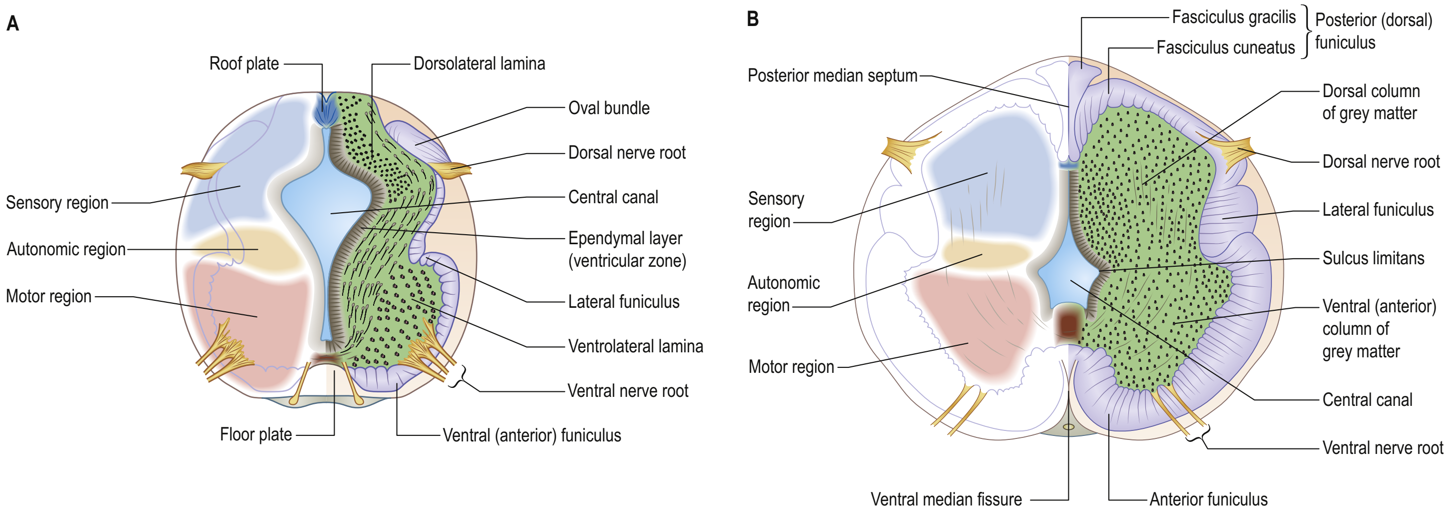
A
Roof plate
Dorsolateral lamina
Oval bundle
Dorsal nerve root
Sensory region
Central canal
Autonomic region
Ependymal layer (ventricular zone)
Motor region
Lateral funiculus
Ventrolateral lamina
Ventral nerve root
Floor plate
Ventral (anterior) funiculus
B
Fasciculus gracilis
Fasciculus cuneatus
Posterior (dorsal) funiculus
Posterior median septum
Dorsal column of grey matter
Dorsal nerve root
Sensory region
Lateral funiculus
Sulcus limitans
Autonomic region
Ventral (anterior) column of grey matter
Motor region
Central canal
Ventral nerve root
Ventral median fissure
Anterior funiculus

Fig. 14.18 The developing spinal cord, human embryos. Transverse sections. **A**, Approximately stage 17. **B**, Approximately postmenstrual week 12.

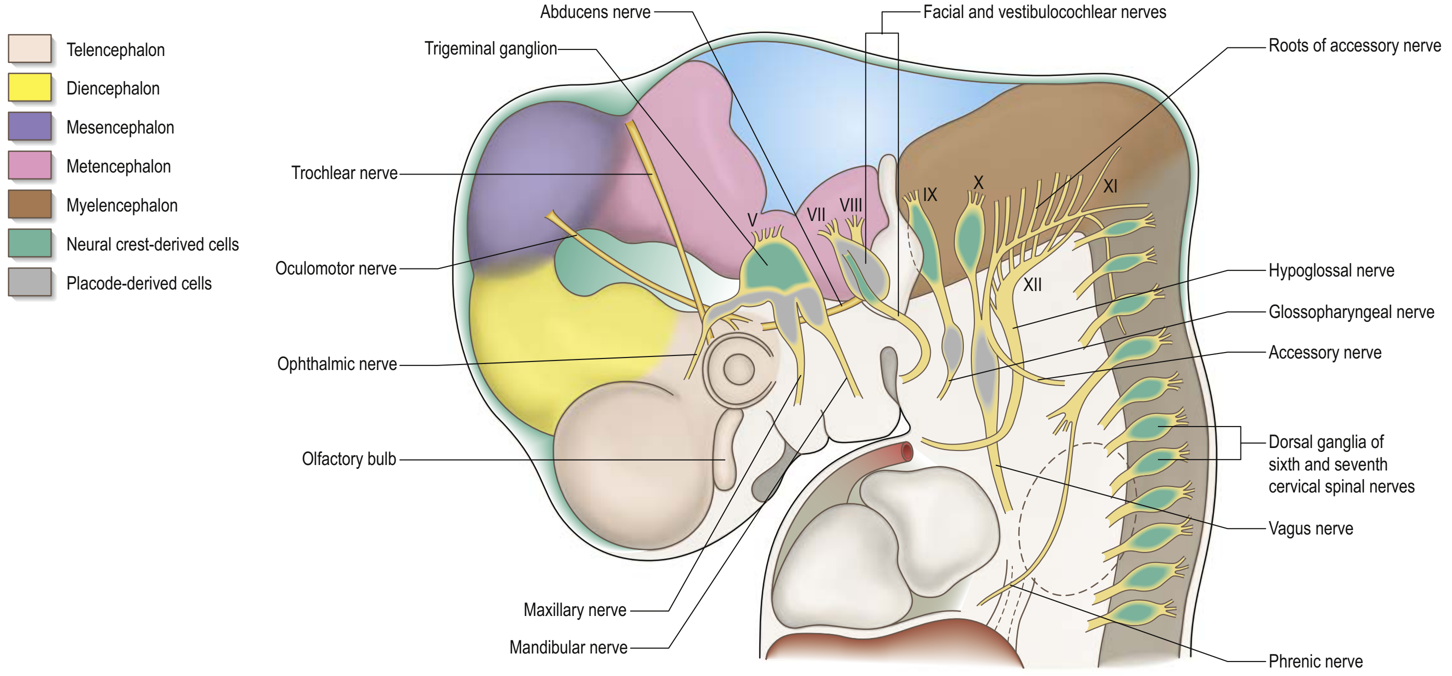
Telencephalon
Diencephalon
Mesencephalon
Metencephalon
Myelencephalon
Neural crest-derived cells
Placode-derived cells
Abducens nerve
Facial and vestibulocochlear nerves
Trigeminal ganglion
Roots of accessory nerve
Trochlear nerve
IX
X
XI
V
VII
VIII
XII
Oculomotor nerve
Hypoglossal nerve
Glossopharyngeal nerve
Accessory nerve
Ophthalmic nerve
Olfactory bulb
Dorsal ganglia of sixth and seventh cervical spinal nerves
Vagus nerve
Maxillary nerve
Mandibular nerve
Phrenic nerve

Fig. 14.19 Brain and cranial nerves, human embryo stage 16. Note the derivation of the ganglia associated with the trigeminal, facial, vestibulocochlear, glossopharyngeal, vagus and accessory nerves.

the two processes become closer and ultimately fuse to form a single stem, producing the characteristic morphology of a unipolar neurone. The bipolar form is retained in the ganglion of the vestibulocochlear nerve. For details of the timing of spinal nerve maturation, see Ashwell and Waite (2012).

Cranial nerves

Cranial nerves may contain motor or sensory fibres or both types of fibres. With the exception of the olfactory and optic nerves, cranial nerves develop in a manner that is similar, in some respects, to the development of the components of the spinal nerves. The somata of motor neuroblasts originate within the neuroepithelium, while those of sensory neuroblasts are derived from the neural crest, with the addition in the head of contributions from ectodermal placodes (Fig. 14.19).

The motor fibres of the cranial nerves that project to striated muscle are the axons of cells originating in the basal plate of the midbrain and hindbrain. The functional and morphological distinction between the neurones within these nerves is based on the types of muscle innervated. In the trunk, the motor roots of the spinal nerves all emerge from the spinal cord close to the ventral midline to supply the muscles derived from the somites.

In the head, the motor outflow is traditionally segregated into two pathways (see Figs 14.4B,C, 14.19). General somatic efferent neurones exit ventrally in a similar manner to those of the spinal cord. Thus, the oculomotor, trochlear, abducens and hypoglossal nerves parallel the organization of the somatic motor neurones in the spinal cord. The second motor component, special branchial efferent, consists of the motor components of the trigeminal, facial, glossopharyngeal and vagus nerves that supply the pharyngeal (branchial) arches, and the (spinal) accessory nerve. These nerves all have nerve exit points more dorsally placed than the somatic motor system.

The cranial nerves also contain general visceral efferent (parasympathetic preganglionic) neurones that travel in the oculomotor, facial, glossopharyngeal and vagus nerves and leave the hindbrain via the same exit points as the special branchial efferent fibres. All three categories of motor neurones probably originate from the same region of the basal plate, adjacent to the floor plate. The definitive arrangement of nuclei reflects the differential migration of neuronal somata. It is not known whether all these cell types share a common precursor within the rhombencephalon. In the spinal cord, somatic motor and preganglionic autonomic neurones are linearly related.

Motor neurone types are designated according to the types of muscles or structures they innervate. General somatic efferent nerves supply striated muscle derived from the cranial (occipital) somites and prechordal mesenchyme. Myogenic cells from the ventrolateral edge of the epithelial plate of occipital somites give rise to the intrinsic muscles of the tongue, while the prechordal mesenchyme gives rise to the extraocular muscles. Special branchial efferent nerves supply the striated muscles developing within the pharyngeal (branchial) arches, which are derived from parachordal mesenchyme rostrocaudally between the occipital somites and the prechordal mesenchyme. All the voluntary muscles of the head originate from axial (prechordal) or paraxial mesenchyme, rendering the distinction between somatic efferent supply and branchial efferent supply somewhat artificial. However, the obviously special nature of the arch musculature, its patterning by the neural crest cells, its particularly rich innervation for both voluntary and reflex activity, and the different origins from the basal plate of the branchial efferent nerves compared to the somatic efferent nerves, make the retention of a distinction between the two of some value.

The cranial sensory ganglia are derived in part from the neural crest and in part from cells of the ectodermal placodes (see Figs 14.8, 14.18). Generally, neurones distal to the brain are derived from placodes while proximal ones are derived from the neural crest (see Fig. 12.4). Supporting cells of all sensory ganglia arise from the neural crest. The most rostral sensory ganglion, the trigeminal, contains both neural crest- and placode-derived neurones that mediate general somatic afferent functions. This is also the case for more caudal cranial nerves (the facial, glossopharyngeal and vagus), but the two cell populations form separate ganglia in the case of each nerve. The proximal series of ganglia is neural crest-derived (forming the proximal root of the facial nerve, the superior ganglion of the glossopharyngeal nerve, the jugular ganglion of the vagus nerve, and associated glial precursors) while the distal series is derived from placodal cells (forming the neurones of the geniculate ganglion of the facial nerve, the petrosal ganglion of the glossopharyngeal nerve and the nodose ganglion of the vagus nerve). These ganglia contain neurones that mediate special and general visceral afferent and somatic afferent functions. The vestibular ganglion contains both crest and placodal cells, and the cochlear ganglion contains only placodal neurones; the axons from these cells are special somatic afferents and they all travel in the vestibulocochlear nerve.

The neurones and supporting cells of the cranial autonomic ganglia in the head and the trunk originate from neural crest cells. Caudal to the vagal ganglion, the occipital region of the neural crest is concerned with the 'ganglia' of the accessory and hypoglossal nerves. Rudimentary ganglion cells may occur along the hypoglossal nerve in the human embryo but they subsequently regress. Ganglion cells are found on the developing intraspinal root of the accessory nerve and are believed to persist in the adult. The central processes of the cells of these various ganglia, where they persist, enter the alar lamina of the hindbrain. Their peripheral processes join the efferent components of the nerve to be distributed to the various tissues innervated. Some incoming fibres from the facial, glossopharyngeal and vagus nerves collect to form an oval bundle, the tractus solitarius, on the lateral aspect of the myelencephalon. This bundle is the homologue of the oval bundle (of His) of the spinal cord, but in the hindbrain it becomes more deeply placed by the overgrowth, folding and subsequent fusion of tissue derived from the rhombic lip on the external aspect of the bundle. For details of the development of sensory and cranial nerve nuclei see Ashwell and Mai (2012).

Myelination of spinal and cranial nerves

PNS myelination, by Schwann cells, occurs over a protracted period that starts during the second trimester. Motor roots start to myelinate before sensory roots in the PNS, whereas sensory nerves start to myelinate before motor nerves. The cranial nerves of the midbrain, pons and medulla oblongata begin to myelinate from about postmenstrual week 22. For reviews of the molecular mechanisms regulating myelination in the CNS and PNS (including precursor specification, proliferation, migration, differentiation and myelination of appropriate axons), see Elbaz and Popko (2017) and Herbert and Monk (2017), respectively.

Autonomic nervous system

Autonomic nerves, apart from the preganglionic motor axons that arise from the CNS, are formed by the neural crest. For the purposes of the following description, the autonomic nervous system encompasses sympathetic and parasympathetic neurones and their accompanying glia in the peripheral ganglia, the chromaffin cells in the suprarenal medulla and other sites, and the neurones and glia of the enteric nervous system. Within the head, the neural crest cells migrate prior to neural fusion, generating autonomic neurones and a vast mesenchymal population. During caudal neurulation in the trunk, neural crest cells migrate from the neural epithelium to lie transitorily on the fused neural tube, they subsequently migrate laterally and then ventrally to their respective destinations (see Fig. 14.6). Four major neural crest cell populations, cranial, vagal, trunk and lumbosacral, are destined to form autonomic nerves.

Parasympathetic ganglia

Parasympathetic preganglionic (general visceral efferent) neurones innervate the sphincter pupillae and ciliaris muscles, the exocrine glands of the head, and the thoracic and abdominal viscera. From rostral to caudal, three populations of neural crest (cranial neural crest, cardiac neural crest and vagal neural crest) give rise to parasympathetic postganglionic neurones.

Neural crest cells from the caudal third of the mesencephalon and the rostral metencephalon migrate along or close to the ophthalmic branch of the trigeminal nerve and give rise to the ciliary ganglion. Cells migrating from the nucleus of the oculomotor nerve may also contribute to the ganglion; a few scattered cells are often demonstrable in postnatal life along the course of this nerve. Preotic myelencephalic neural crest cells give rise to the pterygopalatine ganglion, which may also receive contributions from the ganglia of the trigeminal and facial nerves. The otic and submandibular ganglia are also derived from myelencephalic neural crest and may receive contributions from the glossopharyngeal and facial cranial nerves, respectively (see Fig. 12.4).

Neural crest from the region located between the otic placode and the caudal limit of somite 3 has been termed cardiac neural crest. Cells derived from these levels migrate through pharyngeal arches 3, 4 and 6, where they provide, *inter alia*, support for the embryonic aortic arch arteries, cells of the aorticopulmonary septum and truncus arteriosus. Some of these neural crest cells also differentiate into the neural anlage of the parasympathetic ganglia of the heart.

The origin and migration of the sacral neural crest from the caudal eminence and the formation of the caudal parasympathetic ganglia has recently been disputed, and it has been suggested that the sacral autonomic flow is entirely sympathetic and not parasympathetic (Espinosa-Medina et al 2016, Espinosa-Medina et al 2017, Horn 2018). The distinct vasodilator and vasoconstrictor mechanisms of blood vessels in the pelvic viscera, and the complexities of control of the lower urinary tract, lower enteric sphincters and the reproductive reflexes pathways, plus their central connections to circuits in the spinal cord, brainstem, hypothalamus and cortex, are significant. The precise coordination of activity in these pathways and the distinctive functional discharge patterns that define each type of autonomic pathway inform this continuing discussion (Jänig et al 2018). Sacral postganglionic parasympathetic neurones are generated later than sympathetic neurones from sacral glial progenitor-like cells associated with the extending nerves. The analysis of transcription factors expressed by cranial, thoracolumbar and sacral autonomic neurone precursors suggest that, whereas the developmental processes of thoracolumbar and sacral autonomic neurones are similar, both differ from processes seen in the development of cranial parasympathetic precursors (Ernsberger and Rohrer 2018).

Sympathetic ganglia

Neural crest cells migrate ventrally, penetrate the underlying somites and continue to the region of the future paravertebral and prevertebral plexuses, where they form the sympathetic trunks and the major ganglia around the anterior visceral branches of the abdominal aorta (see Figs 14.6, 14.20). Neural crest cells are induced to differentiate into sympathetic neurones by the dorsal aorta through the actions of the signalling molecules Bmp-4 and Bmp-7. The sympathetic trunk appears earlier in the lower cervical and thoracic regions than in the lumbosacral regions; outflow from the lumbosacral sympathetic trunk to the sciatic nerve has been reported about postmenstrual weeks 18–21 (Ashwell and Waite 2012). In mouse embryos, the superior cervical ganglion may arise from vagal neural crest cells (Hutchins et al 2018).

Chromaffin cells

Chromaffin cells are derived from the neural crest. They are found at numerous sites throughout the body, namely the classic chromaffin cells of the suprarenal medulla, bronchial neuroepithelial cells, dispersed epithelial endocrine cells of the gut (formerly known as argentaffin cells), carotid body cells and the paraganglia. The sympathetic ganglia, suprarenal medulla and chromaffin cells are all derived from the cells of the sympathosuprarenal lineage. In the suprarenal medulla, first seen in stage 14, these cells differentiate into small and intermediate-sized neuroblasts or sympathoblasts, and larger, initially rounded phaeochromocytoblasts. Large cells with pale nuclei, thought to be the progenitors of chromaffin cells, can be detected after stage 23, and clusters of small neurones are evident from postmenstrual week 14.

Sympathetic preganglionic neuronal axons leave the spinal cord with the somatic motor rootlets at motor exit points and travel only in the ventral rootlets: the process is presumably controlled by boundary cap cells. When a postganglionic neuroblast is in place it extends axons and dendrites, and synaptogenesis occurs. The earliest axonal outgrowths from the superior cervical ganglion occur at about stage 14. The local environment plays a major role in controlling the appropriate differentiation of the presumptive autonomic ganglion neurones: the factors responsible for subsequent development of an adrenergic, cholinergic or peptidergic phenotype have not been identified. Cholinergic characteristics are acquired relatively early and the appropriate phenotypic expression may be promoted by cholinergic differentiation factor and ciliary neurotrophic factor.

Intermediate-sized neuroblasts differentiate into multipolar postganglionic sympathetic neurones that secrete noradrenaline (norepinephrine) at their terminals. The smaller neuroblasts probably correlate with the small, intensely fluorescent (SIF) cells, types I and II, that store and secrete dopamine type I and are thought to function as true interneurones, synapsing with the principal postganglionic neurones. Type II cells probably operate as local neuroendocrine cells, secreting dopamine into the ganglionic microcirculation. Both types of SIF cells can modulate synaptic transmission in the ganglionic neurones. The large cells differentiate into masses of columnar or polyhedral phaeochromocytes (classic chromaffin cells) that secrete either adrenaline (epinephrine) or noradrenaline. These cell masses are termed paraganglia and may be situated near, on the surface of, or embedded in, the capsules of the ganglia of the sympathetic chain, or in some of the large autonomic plexuses. The largest members of the latter are the para-aortic bodies that lie along the sides of the abdominal aorta in relation to the inferior mesenteric artery. During childhood, the para-aortic bodies and the paraganglia of the sympathetic trunk partly degenerate and can no longer be isolated by gross dissection; even in the adult, chromaffin tissue can still be recognized microscopically in these various sites. Both phaeochromocytes and SIF cells belong to the amine precursor uptake and decarboxylation (APUD) series of cells and are paraneuronal in nature. Suprarenal chromaffin-like cells have been derived in culture from human pluripotential stem cells (Abu-Bonsrah et al 2018). For further reading about the mechanisms of chromaffin cell development see Unsicker et al (2013) and Hockman et al (2018).

Enteric nervous system

The enteric nervous system is different from the other components of the autonomic nervous system because it can mediate reflex activity independently of control by the brain and spinal cord. The number of enteric neurones that develop is believed to be of the same magnitude as the number of neurones in the spinal cord. The mechanisms by which neuronal diversity is generated in the enteric nervous system are unclear: to date, expression patterns of a number of transcription and signalling factors have been mapped in the developing murine and human enteric nervous systems using transcriptome and histochemical analyses (Memic et al 2018).

Neuronal and glial enteric nervous system precursors are derived from vagal and sacral neural crest. The axial levels of crest origin are shown in Fig. 14.20. Rostrally, adjacent to the early rhombencephalon formed by primary neurulation, vagal neural crest cells give rise to both neuroblasts and glial support cells throughout the gut. In experimental studies on chick and mouse embryos, vagal neural crest cells destined for the gut appear to travel through the rostral half of adjacent somites and are thought to gain enteric lineage from exposure to retinoic acid within the somatic mesenchyme. Vagal neural crest cells migrate ventrally to enter the gut, then turn caudally to populate the entire length of the gut progressing at a migratory speed of about 40 μm/hour (Nagy and Goldstein 2017).

Within the gut of chick and mouse embryos, vagal neural crest cells migrate more rapidly when in contact with each other in a wave front of chain migration. The cells proliferate as they migrate, and the end of proliferation promotes the onset of differentiation. Those cells at the leading edge of the wave front move into unpopulated regions of splanchnopleuric mesenchyme that support their migration and subsequent differentiation (Lake and Heuckeroth 2013, Nagy and Goldstein 2017). The submucosal plexus is formed by a secondary radial migration from the myenteric plexus. Enteric neural crest cells differentiate into sensory and motor neurones and interneurones, and into four types of glial cells with a transcriptome that overlaps with astrocytes, oligodendrocytes and Schwann cells (Charrier and Pilon 2017). Almost all enteric glia express myelin proteolipid protein, and have more genes in common with myelinating glia than with astrocytes (Rao and Gershon 2018). Neurospheres of human postnatal enteric neural stem cells transplanted into chick or mouse embryos interact and migrate within their hosts to form chimeric enteric ganglia (Cheng et al 2017). A population of vagal neural crest cells that colonize the foregut secondarily migrate into the developing pancreatic buds and give rise to the resident ganglia and Schwann cells around the islets of Langerhans (Hutchins et al 2018).

Caudally, from somites 28 onwards, neural crest cells and somites arise by secondary neurulation processes within the caudal eminence. Sacral neural crest cells migrate through the adjacent somites and then ventrally within the mesocolon towards the hindgut (which will form the distal part of the colon, rectum and cloaca); some crest cells subsequently contribute to components of the pelvic plexus (see Fig. 14.6).

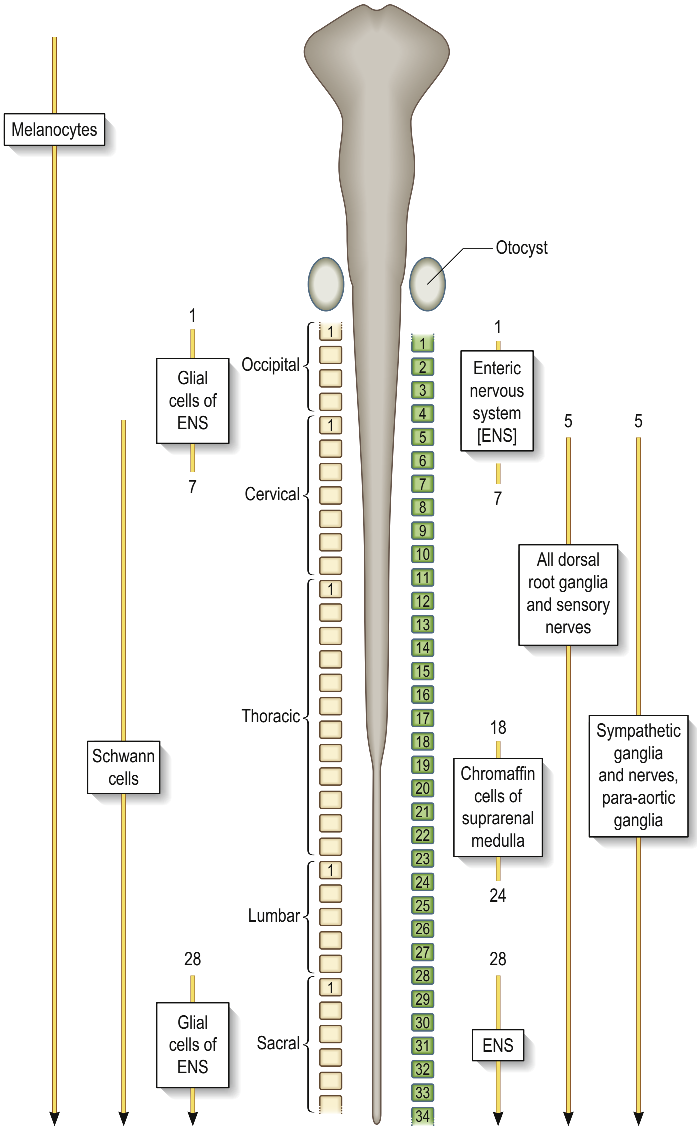

Fig. 14.20 Derivatives of neural crest cells in the trunk. The fate of crest cells arising at particular somite levels is shown.

Once within the gut wall, a regionally specific pattern of enteric ganglia formation occurs, possibly controlled by the local splanchnopleuric mesenchyme. In the mouse embryo, sacral neural crest cells do not colonize the distal colon until vagal neural crest cells are present, at which time the sacral neural crest cells migrate in a caudorostral direction (Mundell et al 2012). The cells lie initially within the developing mesentery, then transiently between the layers of the differentiating muscularis externa, and finally form a more substantial intramural plexus that is characteristic of the adult enteric nervous system.

The human gut has a partially established enteric nervous system with a full complement of enteric neurotransmitters by postmenstrual week 24. Maturation continues into the postnatal period: mucosal enteric glial cells that move into the mucosa after birth interact with the colonizing intestinal flora, suggesting a microbiota-driven homeostatic mechanism for gut function (Ashwell and Waite 2012, Kabouridis and Pachnis 2015). For details of the molecular mechanisms of enteric nervous system development see Rao and Gershon (2018).

Hirschsprung's disease appears to result from a failure of neural crest cells to colonize the gut wall appropriately. The proximal extent of the condition is variable but the rectum is always affected. This distribution suggests that Hirschsprung's disease is a failure of migration and differentiation of the most distal vagal neural crest and/or failure of migration and differentiation of the sacral neural crest derived from secondary neurulation. Histologically, ganglia and postganglionic neurones in the myenteric plexus of the affected segment of gut are either absent or reduced in number and postganglionic innervation of the muscle layers is also often defective. The condition is characterized by a dilated segment of colon proximally (or small bowel in cases of total colonic Hirschsprung's disease) and a lack of peristalsis in the segment distal to the dilation. The condition is also characterized by a transition zone with reduced innervation that may follow an asymmetric course around the circumference of the bowel, which means that a single biopsy may be unreliable. Neonates with Hirschsprung's disease show delay in the passage of meconium, constipation, vomiting and abdominal distension. The condition is often associated with other defects of neural crest development, e.g. Waardenburg type II syndrome, which includes deafness and facial clefts with megacolon.

CENTRAL NERVOUS SYSTEM

Spinal cord

In the future spinal cord, the median roof plate (dorsal lamina) and floor plate (ventral lamina) of the neural tube do not participate in the cellular proliferation that occurs in the lateral walls and so remain thin. Their cells contribute largely to the formation of the ependyma.

The neuroblasts of the lateral walls of the tube are large and, at first, round or oval (apolar). They soon develop processes at opposite poles and become bipolar neurones. One process is then withdrawn so that the neuroblast becomes unipolar, although this is not invariable in the spinal cord. On further differentiation, dendritic processes develop and the cells become typical multipolar neurones lying in clusters of neuronal clones. The development of a longitudinal sulcus limitans on each side of the central canal of the cord divides the ventricular and intermediate zones in each lateral wall into a basal (ventrolateral) plate or lamina, and an alar (dorsolateral) plate or lamina (see Fig. 14.18). This separation signifies a fundamental functional difference. Neural precursors in the basal plate include the motor cells of the anterior (ventral) and lateral grey columns, while those of the alar plate exclusively form 'interneurones', some of which will synapse with the terminals of primary sensory neurones. Caudally, the central canal of the cord ends as a fusiform dilation, the terminal ventricle.

Anterior (ventral) grey column

The cells of the ventricular zone are closely packed at this stage and arranged in radial columns (see Fig. 14.14). Their disposition may be determined in part by contact guidance along the earliest radial array of glial fibres that cross the full thickness of the early neuroepithelium. The cells of the intermediate zone are more loosely packed. They increase in number initially in the region of the basal plate. This enlargement outlines the anterior (ventral) column of the grey matter and causes a ventral projection on each side of the median plane; the floor plate remains at the bottom of the shallow groove so produced. As growth proceeds, these enlargements are further increased by the development of the anterior funiculi (tracts of axons passing to and from the brain) and encroach on the groove until it becomes converted into the slit-like anterior median fissure of the adult spinal cord. The axons of some of the neuroblasts in the anterior grey column cross the marginal zone and emerge as bundles of ventral spinal nerve rootlets on the anterolateral aspect of the spinal cord. These will eventually constitute both the α-efferents that establish motor end-plates on extrafusal striated muscle fibres and the γ-efferents that innervate the contractile polar regions of the intrafusal muscle fibres of the muscle spindles. As the ventral grey column matures the motor neurones become grouped into motor pools containing functionally coherent subsets of motor neurones that innervate individual muscles in the limb (Dewitz et al 2018). Motor neurone progenitors initially produce medial groups of neurones, later born neurones migrate radially through the medial group to settle in the lateral ventral horn. N-cadherin is required for this migration but does not specify the dorsoventral positioning of these cells (Dewitz et al 2018).

Neurones in different motor pools can be distinguished by their surface protein expression and transcription factor profiles. Motor pools that innervate limb muscles with related functions are grouped into minicolumns or columels, in a 3D organization that reflects the position of the muscles along the three main axes of the limb. Thus, for example, a dorsoventral motor columel and its resident pools displays a linear correlation with the distal-to-proximal position of its synergistic target muscles (Jessell et al 2011, Sürmeli et al 2011). *In vitro* culture of hPSCs along neuronal pathways has elucidated the developmental steps for patterning the rostrocaudal (*Hox* gene expression) and dorsoventral (Shh expression) axes of the neural tube and producing postmitotic neural precursor subtypes. Factors promoting further development of motor neurone progenitors have been established (Pantani 2016).

Lateral grey column

Some intermediate zone neuroblasts in the thoracic and upper lumbar regions in the dorsal part of the basal plate outline a lateral column. Their axons join the emerging ventral nerve roots and pass as preganglionic fibres either to the ganglia of the sympathetic trunk or related ganglia, the majority eventually myelinating to form white rami communicantes. The axons within the rami synapse on autonomic ganglionic neurones; postganglionic axons innervate smooth muscle cells, adipose tissue or exocrine glandular cells. Other preganglionic sympathetic efferent axons pass to the suprarenal medulla. An autonomic lateral column is also laid down in the mid-sacral region and gives origin to the preganglionic parasympathetic fibres that run in the pelvic splanchnic nerves, although this origin has recently been disputed (Espinosa-Medina et al 2016, Espinosa-Medina et al 2017, Horn 2018).

The ventral region of each basal plate initially forms a continuous column of cells throughout the length of the developing cord. This soon develops into two columns on each side: one is medially placed and concerned with innervation of the axial musculature, and the other is laterally placed and concerned with the innervation of the limb musculature. At limb levels, the lateral column enlarges enormously, but regresses at other levels.

Axons arising from ventral horn neurones, i.e. α-, β- and γ-efferent fibres, are accompanied at thoracic, upper lumbar and midsacral levels by preganglionic autonomic efferents from neuroblasts of the developing lateral horn. Numerous interneurones develop in these sites (including Renshaw cells); it is uncertain how many of these differentiate directly from ventrolateral lamina (basal plate) neuroblasts and how many migrate to their final positions from the dorsolateral lamina (alar plate).

In the human embryo the definitive grouping of the ventral column cells that characterizes the mature cord occurs early and by postmenstrual week 14 all the major groups can be recognized. As the anterior and lateral grey columns assume their final form, the germinal cells in the ventral part of the ventricular zone gradually stop dividing. The layer becomes reduced in thickness until it forms the single-layered ependyma that lines the ventral part of the central canal of the spinal cord.

Posterior (dorsal) grey column

The posterior (dorsal) column develops later, which means that the ventricular zone is transiently much thicker in the dorsolateral lamina (alar plate) than it is in the ventrolateral lamina (basal plate) (see Figs 14.14, 14.18). While the columns of grey matter are being defined, the dorsal region of the central canal becomes narrow and slit-like, and its walls come into apposition and fuse with each so that the central canal becomes relatively reduced in size and somewhat triangular in outline.

From about stage 13 advancing axonal sprouts invade the marginal zone. The first to develop are those destined to become short intersegmental fibres (from the neuroblasts in the intermediate zone) and fibres in the dorsal roots of spinal nerves that invade the dorsal marginal zone (from small dorsal root ganglionic neuroblasts). By about stage 16 the latter form a well-defined oval bundle near the peripheral part of the dorsolateral lamina (see Fig. 14.14). This bundle of small calibre axons increases in size and spreads towards the median plane, forming the primitive posterior funiculus. Later, fibres derived from new populations of large dorsal root ganglionic neuroblasts join the dorsal root and are destined to become larger calibre fibres. As the posterior funiculi increase in thickness, their medial surfaces come into contact, separated only by the posterior medial septum, which is ependymal in origin and neuroglial in nature. It is thought that the displaced primitive posterior funiculus may form the basis of the dorsolateral tract or fasciculus (of Lissauer). Experimental studies have shown that the connection of first order 1A afferent neurones from muscle spindles to the appropriate dorsoventral motor neurone pool is independent of the target motor neurones: these sensory afferents avoid synapsing on motor neurones that innervate antagonistic muscles at the same joint (Sürmeli et al 2011).

Maturation of the spinal cord

Long intersegmental axons begin to appear early in the second trimester; corticospinal axons are seen somewhat later. All nerve fibres initially lack myelin sheaths. Myelination starts in different groups at different times, e.g. along the ventral and dorsal nerve roots during the second trimester, and persists until overall growth of the CNS and PNS has finished. In many sites, slow growth continues for long periods, even into the postpubertal years. In the CNS, myelin is formed by oligodendrocytes derived from the ventricular zone of the neural tube, and in the PNS myelin is formed by Schwann cells derived from neural crest cells. A boundary zone controlled by neural crest-derived boundary cap cells separates these two myelin sources (see p. 241). The cervical and lumbar enlargements appear at the time of the development of their respective limb buds.

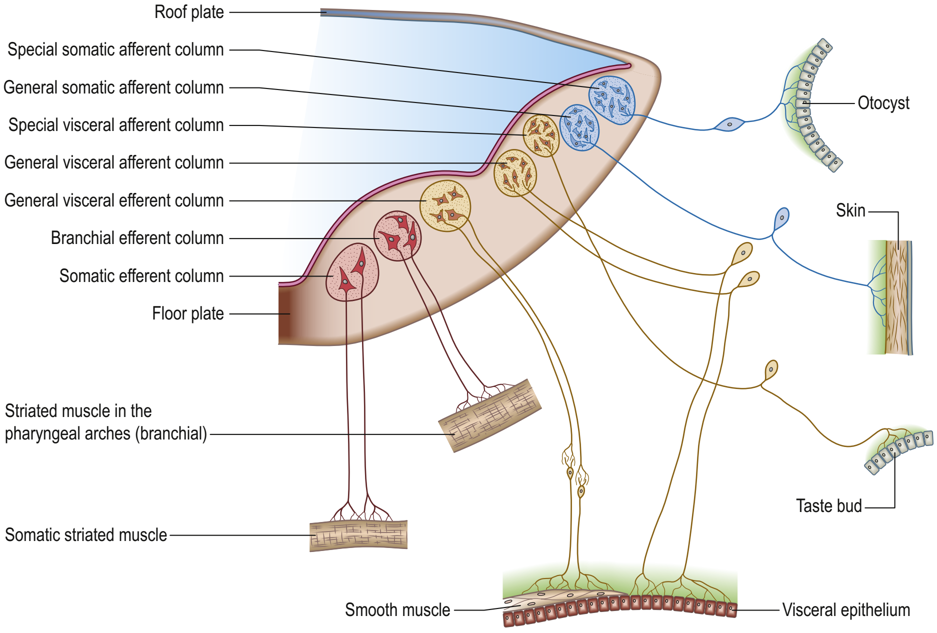
Roof plate
Special somatic afferent column
General somatic afferent column
Special visceral afferent column
General visceral afferent column
General visceral efferent column
Branchial efferent column
Somatic efferent column
Floor plate
Otocyst
Skin
Striated muscle in the pharyngeal arches (branchial)
Taste bud
Somatic striated muscle
Smooth muscle
Visceral epithelium

Fig. 14.21 Transverse section through the developing hindbrain of a human embryo about stage 16, showing the relative positions of the columns of grey matter from which the nuclei associated with the different varieties of nerve components are derived. Postganglionic neurones are associated with the general visceral efferent column; bipolar neurones are associated with the otocyst; unipolar afferent neurones are associated with the other alar plate columns.

Ascent of conus medullaris

The spinal cord occupies the entire length of the vertebral canal in early embryonic life; the spinal nerves pass at right-angles to the cord. From the second trimester, the vertebral column grows more rapidly than the spinal cord, which means that the relationship between the conus medullaris and the vertebral column changes as the conus gradually ascends to lie at higher vertebral levels (Barson 1970). Most of this relative rostral migration occurs during the first half of intrauterine life. By postmenstrual week 25 the terminal ventricle of the spinal cord has altered in level from the second coccygeal vertebra to the third lumbar, a distance of nine segments (Ch. 18, p. 300). As the change in level begins rostrally, the caudal end of the terminal ventricle, which is adherent to the overlying ectoderm, remains *in situ*, and the walls of the intermediate part of the ventricle and its covering pia mater become drawn out to form a delicate filament, the filum terminale. The separated portion of the terminal ventricle persists for a time; it usually disappears before birth, although it does occasionally give rise to congenital cysts near the coccyx. In the definitive state, the upper cervical spinal nerves retain their position roughly at right-angles to the cord: proceeding caudally, the nerve roots lengthen and become progressively more oblique. By postmenstrual week 40 the conus medullaris typically lies between the first and third lumbar vertebrae.

Determining the prenatal position of the conus medullaris relative to specific vertebrae is a widely used method of identifying the termination of the spinal cord. Studies of formalin-fixed fetuses, usually of preterm stillbirths that may be small for dates, have provided the main timescales. More recently, values have been derived from antenatal ultrasound and magnetic resonance imaging (MRI) examinations. The often wide discrepancies between published values attest to the fact that ageing preterm infants remains an inexact science. Measurements may be influenced by factors such as placental health, maternal diet, ethnic biometrical variation, fetal sex and the interpretation and correlation of results obtained using differing methodologies (cadaveric dissection, ultrasound, MRI).

Brain

A summary of the derivatives of the cerebral regions from caudal to rostral is given in Table 14.1.

Rhombencephalon

By the time the midbrain flexure appears, the length of the rhombencephalon is greater than that of the combined extent of the mesencephalon and prosencephalon. Rostrally, it exhibits a constriction, the isthmus rhombencephali (see Fig. 14.4A), best viewed from the dorsal aspect. Ventrally, the hindbrain is separated from the dorsal wall of the primitive pharynx only by the notochord, the two dorsal aortae and a small amount of mesenchyme; on each side, it is closely related to the dorsal ends of the pharyngeal arches.

The pontine flexure appears to 'stretch' the thin, epithelial roof plate, which becomes widened. The greatest increase in width corresponds to the region of maximum convexity, so that the outline of the roof plate becomes rhomboidal. By the same change, the lateral walls become separated, particularly dorsally, and the cavity of the hindbrain, (presumptive fourth ventricle), becomes flattened and somewhat triangular in cross-section. The pontine flexure becomes increasingly acute until, at the end of the first trimester, the laminae of its cranial (metencephalic) and caudal (myelencephalic) slopes are opposed to each other (see Fig. 14.22); at the same time, the lateral angles of the cavity extend to form the lateral recesses of the fourth ventricle.

At about stage 14 when the pontine flexure is first discernible, the association between the rhombomeres and the underlying motor nuclei of certain cranial nerves can be seen. The general pattern of distribution of motor nuclei is as follows: rhombomere 1 contains the trochlear nucleus, rhombomeres 2 and 3 contain the trigeminal nucleus, rhombomeres 4 and 5 contain the facial nucleus, rhombomere 5 contains the abducens nucleus, rhombomeres 6 and 7 contain the glossopharyngeal nucleus, and rhombomeres 7 and 8 contain the vagal, accessory and hypoglossal nuclei. Rhombomeric segmentation represents the ground plan of development in this region of the brainstem and is pivotal for the development of regional identity (see Figs 14.2, 12.4). With further morphogenesis, the obvious constrictions of the rhombomere boundaries disappear and the medulla once again assumes a smooth contour. The differentiation of the lateral walls of the hindbrain into basal (ventrolateral) and alar (dorsolateral) plates has a similar significance to the corresponding differentiation in the lateral wall of the spinal cord: ventricular, intermediate and marginal zones are formed in the same way.

Cell columns of the basal plate (ventrolateral lamina)

Cells of the basal plate form three elongated, discontinuous, columns: ventral, intermediate and dorsal (**Fig. 14.21**). The most ventral column is continuous with the anterior grey column of the spinal cord and will supply muscles considered 'myotomic' in origin. It is represented in the caudal part of the hindbrain by the hypoglossal nucleus, and it reappears at a higher level as the nuclei of the abducens, trochlear and oculomotor nerves (somatic efferent nuclei). The intermediate column is represented in the upper part of the spinal cord and caudal brainstem (medulla oblongata and pons), and its neurones supply branchial (pharyngeal) and postbranchial musculature. It is discontinuous, forming the elongated nucleus ambiguus in the caudal brainstem, which gives fibres to the glossopharyngeal, vagal and (cranial) accessory nerves, and continues into the cervical spinal cord as the origin of the (spinal) accessory nerve. At higher levels, parts of this column give origin to the motor nuclei of the facial and trigeminal nerves. The nucleus ambiguus and the facial and trigeminal motor nuclei are termed branchial (special visceral) efferent nuclei. Neurones in the most dorsal column of the basal plate (represented in the spinal cord by the lateral grey column) innervate viscera. This column is discontinuous in that its large caudal part forms some of the dorsal nucleus of the vagus and its cranial part forms the salivatory nucleus. These nuclei are termed general visceral (general splanchnic) efferent nuclei, and their neurones give rise to preganglionic, parasympathetic nerve fibres. The neurones of the basal plate and their three columnar derivatives are only motor in the sense that some of their number form either motor neurones or preganglionic parasympathetic neurones. The remainder greatly outnumber the former and differentiate into functionally related interneurones and, in some loci, into neuroendocrine cells.

Cell columns of the alar plate (dorsolateral lamina)

Cell columns of the alar plate are discontinuous and give rise to general visceral (general splanchnic) afferent, special visceral (special splanchnic) afferent, general somatic afferent and special somatic afferent nuclei (their relative positions, in simplified transverse section, are shown in Fig. 14.21). The general visceral afferent column is represented by a part of the dorsal nucleus of the vagus, the special visceral afferent column by the nucleus of the tractus solitarius, the general somatic afferent column by the afferent nuclei of the trigeminal nerve, and the special somatic afferent column by the nuclei of the vestibulocochlear nerve. (The relatively simple functional independence of these afferent columns implied by the foregoing classification is, in the main, an aid to elementary learning. The emergent neurobiological mechanisms are much more complex and less well understood.) Although they tend to retain their primitive positions, some of these nuclei are later displaced by differential growth patterns, by the appearance and growth of neighbouring fibre tracts, and possibly by active migration.

It has been suggested that a neurone tends to remain as near as possible to its predominant source of stimulation, and that, to achieve this aim, it will migrate around intervening structures, towards the greatest density of stimuli. The curious paths of the axons arising from the facial nucleus and the nucleus ambiguus have been regarded as exemplars of this phenomenon of so called neurobiotaxis. At stage 16 the facial nucleus lies in the floor of the fourth ventricle, occupying the position of the special visceral efferent column, and it is placed at a higher level than the abducens nucleus. As growth proceeds, the facial nucleus migrates at first caudally and dorsally, relative to the abducens nucleus, and then ventrally to reach its adult position. As it migrates, the axons to which its somata give rise elongate and their subsequent course is assumed to map out the pathway along which the facial nucleus has travelled. Similarly, the nucleus ambiguus initially arises immediately deep to the ventricular floor but, in the adult, it is more deeply placed and its efferent fibres pass first dorsally and medially before curving laterally to emerge at the surface of the medulla oblongata.

Myelencephalon

The caudal slope of the embryonic hindbrain constitutes the myelencephalon, which develops into the medulla oblongata (see Figs 14.4, 14.19, 14.22). The nuclei of the glossopharyngeal, vagal, accessory and hypoglossal cranial nerves develop in the positions already indicated: afferent fibres from the ganglia of the glossopharyngeal and vagus nerves form an oval marginal bundle in the region overlying the alar (dorsolateral) lamina. Throughout the rhombencephalon, the dorsal edge of this lamina is attached to the thin, expanded roof plate and is termed the rhombic lip. (The inferior rhombic lip is confined to the myelencephalon, the superior rhombic lip to the metencephalon.) As the walls of the rhombencephalon spread outwards, the rhombic lip protrudes as a lateral edge that becomes folded over the adjoining area. The rhombic lip may later become adherent to this area, and its cells migrate actively into the marginal zone of the basal plate. In this way, the oval bundle that forms the tractus solitarius becomes buried. Alar plate cells that migrate from the rhombic lip are believed to give rise to the olivary and arcuate nuclei and to the scattered grey matter of the nuclei pontis. While this migration is in progress, the floor plate is invaded by fibres that cross the median plane (accompanied by neurones that cluster in and near this plane), and it becomes thickened to form the median raphe. Some of the migrating cells from the rhombic lip in this region do not reach the basal plate and form an oblique ridge, the corpus pontobulbare (nucleus of the circumolivary bundle), across the dorsolateral aspect of the inferior cerebellar peduncle.

The lower part (caudal half) of the myelencephalon takes no part in the formation of the fourth ventricle and closely resembles the spinal cord in its development. The gracile and cuneate nuclei and some reticular nuclei are derived from the alar plate, and their efferent arcuate fibres and interspersed neurones play a large part in the formation of the median raphe.

The descending corticospinal fibres invade the ventral part of the medulla oblongata to initiate formation of the pyramids. Contemporaneously, the inferior cerebellar peduncle is formed dorsally by ascending fibres from the spinal cord, and by olivocerebellar, parolivocerebellar and external arcuate fibres, and two-way reticulocerebellar and vestibulocerebellar interconnections. (The reticular nuclei of the lower medulla probably have a dual origin from both basal and alar plates.) In a full-term neonate, the brainstem is more oblique and has a distinct bend as it passes through the foramen magnum to become the spinal cord.

Metencephalon

The rostral slope of the embryonic hindbrain is the metencephalon, from which both the cerebellum and the pons develop. Before formation of the pontine flexure, the dorsolateral laminae of the metencephalon are parallel with one another. After its formation, the roof plate of the hindbrain becomes rhomboidal and the dorsal laminae of the metencephalon lie obliquely. They are close at the cranial end of the fourth ventricle, but widely separated at the level of its lateral angles (see Figs 14.19, 14.22). Accentuation of the flexure approximates the cranial angle of the ventricle to the caudal, and the alar plates of the metencephalon now lie almost horizontally.

The basal plate of the metencephalon becomes the pons. Ventricular, intermediate and marginal zones are formed in the usual way, and the nuclei of the trigeminal, abducens and facial nerves develop in the intermediate layer. It is possible that the grey matter of the reticular formation is derived from the basal plate and that of the nuclei pontis from the alar plate by the active migration of cells from the rhombic lip. At about postmenstrual weeks 15–16 the pons is invaded by corticopontine, corticonuclear and corticospinal fibres, becomes proportionately thicker, and takes on its adult appearance; it is relatively smaller in the full-term neonate.

The region of the isthmus rhombencephali undergoes a series of changes that are notoriously difficult to interpret. They result in the incorporation of the greater part of the region into the caudal end of the midbrain. Only the roof plate, in which the superior medullary velum is formed, and the dorsal part of the alar plate, which becomes invaded by converging fibres of the superior cerebellar peduncles, remain as recognizable derivatives in the adult. Early in development, the decussation of the trochlear nerves is caudal to the isthmus, but it is gradually displaced rostrally until it reaches its adult position.

Fourth ventricle and choroid plexus

Caudal to the developing cerebellum, the roof of the fourth ventricle remains epithelial, and covers an approximately triangular zone from the lateral angles of the rhomboid fossa to the median obex (see Figs 14.19, 14.22). Nervous tissue fails to develop over this region and vascular pia mater is closely applied to the subjacent ependyma. At each lateral angle and in the midline caudally, the membranes break through, forming the lateral (Luschka) and median (Magendie) apertures of the roof of the fourth ventricle: they become the principal routes by which cerebrospinal fluid, produced in the ventricles, escapes into the subarachnoid space. The vascular pia mater (tela choroidea), in an inverted V formation cranial to the apertures, invaginates the ependyma to form vascular fringes that become the vertical and horizontal parts of the choroid plexuses of the fourth ventricle.

Cerebellum

The cerebellum develops from the rhombic lip (dorsal rhombomere 1 (r1)), the dorsal part of the alar plate of the metencephalon, which constitutes the rostral margin of the diamond-shaped fourth ventricle. This region is specified as the isthmus organizer (Yu et al 2013). Two rounded swellings develop and initially project partly into the ventricle, forming the rudimentary cerebellar hemispheres (**Fig. 14.22**). The most rostral part of the roof of the metencephalon originally separates the two swellings, but it becomes invaded by cells derived from the alar plate, which form the rudiments of the vermis. At a later stage, extroversion of the cerebellum occurs, its intraventricular projection is reduced and the dorsal extraventricular prominence increases. The cerebellum now consists of a bilobar (dumbbell-shaped) swelling stretched across the rostral part of the fourth ventricle (see **Fig. 14.22**). It is continuous rostrally with the superior medullary velum, formed from the isthmus rhombencephali, and caudally with the epithelial roof of the myelencephalon. With growth, a number of transverse grooves appear on the dorsal aspects of the cerebellar rudiment: they are the precursors of the numerous fissures that characterize the surface of the mature cerebellum (**Fig. 14.23**).

The first fissure to appear on the cerebellar surface is the lateral part of the posterolateral fissure, which forms the border of a caudal region corresponding to the flocculi of the adult. The right and left parts of this fissure subsequently meet in the midline, where they form the boundary between the most caudal vermian lobule, the nodule, and the rest of the vermis. The flocculonodular lobe can now be recognized as the most caudal cerebellar subdivision at this stage and it serves as the attachment of the epithelial roof of the fourth ventricle. Because of the expansion of the other divisions of the cerebellum, the flocculonodular

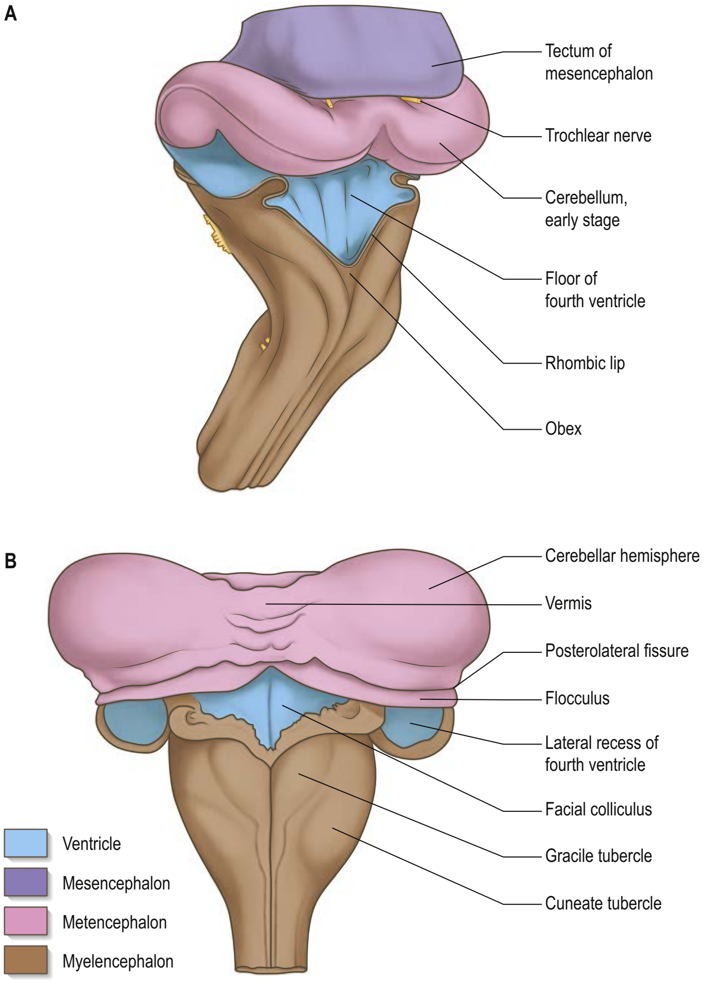

Fig. 14.22 **A**, The developing brainstem of a human fetus at approximately postmenstrual week 12, left dorsolateral aspect. **B**, The dorsal aspect of the developing cerebellum, postmenstrual weeks 17–20.

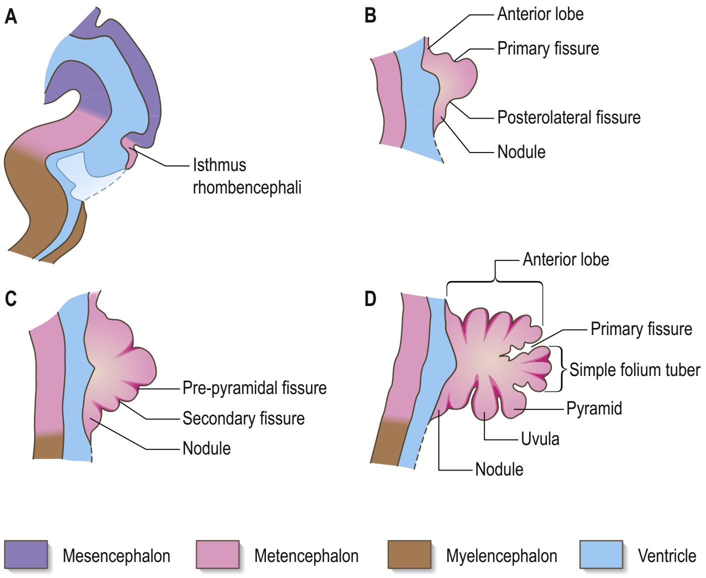

Fig. 14.23 Median sagittal sections through the developing cerebellum, at four chronologically later stages.

lobe comes to occupy an anteroinferior position in adults. At the end of the first trimester, a transverse sulcus appears on the rostral slope of the cerebellar rudiment and deepens to form the fissura prima that cuts into the vermis and both hemispheres, and forms the border between the anterior and posterior lobes. Contemporaneously, two short transverse grooves appear in the caudal vermis. The first is the fissura secunda (postpyramidal fissure), which forms the rostral border of the uvula and the second is the pre-pyramidal fissure, which demarcates the pyramid. The cerebellum now grows dorsally, rostrally, caudally and laterally, and the hemispheres expand much more than the inferior vermis, which therefore becomes buried at the bottom of a deep hollow, the vallecula. Numerous other transverse grooves develop, the most extensive being the horizontal fissure.

Cellular development of the cerebellum

The cerebellum consists of a cortex, beneath which are buried a series of deep nuclei. The organization of the cerebellar cortex is similar to that of the cerebral cortex, except that the latter typically has six layers while the former has only three. However, whereas in the cerebral cortex neuroblasts originate from the ventricular zone and migrate ventriculofugally towards the pial surface (in an 'inside-out' fashion), early in cerebellar development a layer of cells derived exclusively from the metencephalic rhombic lip initially migrates ventriculofugally to form a layer beneath the glia limitans over the surface of the developing cerebellum. These cells form the external germinative layer; later in development their progeny will migrate ventriculopetally (in an 'outside-in' manner), into the cerebellum. The cerebellum therefore has an intraventricular portion (cells proliferating from the ventricular zone) and an extraventricular portion (cells proliferating from the external germinative layer) during development. The extraventricular portion becomes larger at the expense of the intraventricular portion, the so-called extroversion of the cerebellum. Before the end of the first trimester, the main mass of the cerebellum is extraventricular.

The developed cerebellar cortex contains three layers, namely the molecular, Purkinje and granular layers. The early bilateral expansion of the ventricular surface reflects the production, by the metencephalic alar plate ventricular epithelium, of neuroblasts that will give rise to the radial glia, cerebellar nuclei and efferent neurones of the cerebellar cortex (the Purkinje cells) (Fig. 14.24). The radial glia play a role in guiding the Purkinje cells to the meningeal surface of the cerebellar anlage. During this early stage of cerebellar development, which is dominated by the production and migration of efferent cerebellar neurones, the surface of the cerebellar anlage remains smooth. The extroversion of the cerebellum begins later when cells of the external germinative layer, also termed the superficial matrix, begin proliferation and migration. These cells produce the granule cells which migrate inwards along the radial glia, through the layers of Purkinje cells, settling deep to them in the granular layer. This stage coincides with the emergences of the transverse folial pattern. Proliferation and migration of granule cells lead to a great rostrocaudal expansion of the meningeal surface of the cerebellum, forming the transverse fissures and transforming the multicellular layer of Purkinje cells into a monolayer. The development of the efferent neurones of the cerebellar cortex and nuclei precedes the development of its afferent organization: Purkinje cells and nuclear cells are formed prior to the granule cells, which are the recipients of the main afferent (mossy fibre) system of the cerebellum.

The early bilateral cerebellar anlage is changed into a unitary structure by fusion of the bilateral intraventricular bulges and the disappearance of the ependyma at this site; the merging of the left and right primitive cerebellar cortices over the midline; and the development of the cerebellar commissure by ingrowth of afferent fibres and outgrowth of efferent axons from the medial cerebellar nuclei.

The distinction between the efferent projections from the vermis and hemispheres is established at an early age. When the external germinative layer is initially formed, the multicellular Purkinje cell layer beneath is not uniform, but subdivided into clusters that form columns that extend rostrocaudally (Fig. 14.25). These clusters will give rise to Purkinje cell zones in the adult cerebellum that project to a single vestibular or cerebellar nucleus. The medial Purkinje cell clusters develop into the future vermis and their axons will synapse on neurones in the vestibular and fastigial nuclei. The lateral clusters belong to the future hemispheres and will grow axons that terminate in the interposed and dentate nuclei.

In the developing human brain, only the external germinative layer can be seen at postmenstrual weeks 17–18; the Purkinje cells become apparent between postmenstrual weeks 20 and 23. After postmenstrual week 30 four layers can be recognized: the external germinative layer (external granular layer), formed by 6–8 rows of densely packed small round cells; the Purkinje cell layer, formed by 5–6 layers of larger, round, immature neurones external to the internal granular layer; and the molecular layer, containing cells that resemble external granular layer cells in migration (Lavezzi et al 2006). The external granular layer involutes between postnatal months 5–7; it is only a discontinuous layer at postnatal month 10 and is totally absent by postnatal month 12, after which time the cerebellar cortex shows a three-layered structure. From postnatal months 5–7 the Purkinje cells are reduced in number and more widely spaced, displaying mature polygonal somata with evident axons and dendrites.

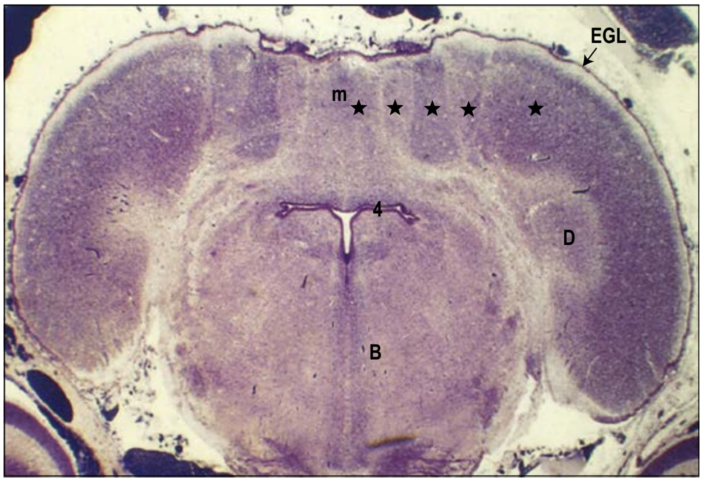

Fig. 14.25 Coronal section through the cerebellum and the brainstem of a human fetus about postmenstrual week 12. Purkinje cells are located in five multicellular clusters (stars) on both sides of the midline. The anlage of the dentate nucleus occupies the centre of the most lateral Purkinje cell cluster. Key: B, brainstem; D, dentate nucleus; EGL, external granular layer; m, midline; 4, fourth ventricle. (Courtesy of the Schenk Collection, Dr Johan M Kros, Division of Neuropathology, Department of Pathology, Erasmus Medical Centre, Rotterdam, The Netherlands.)

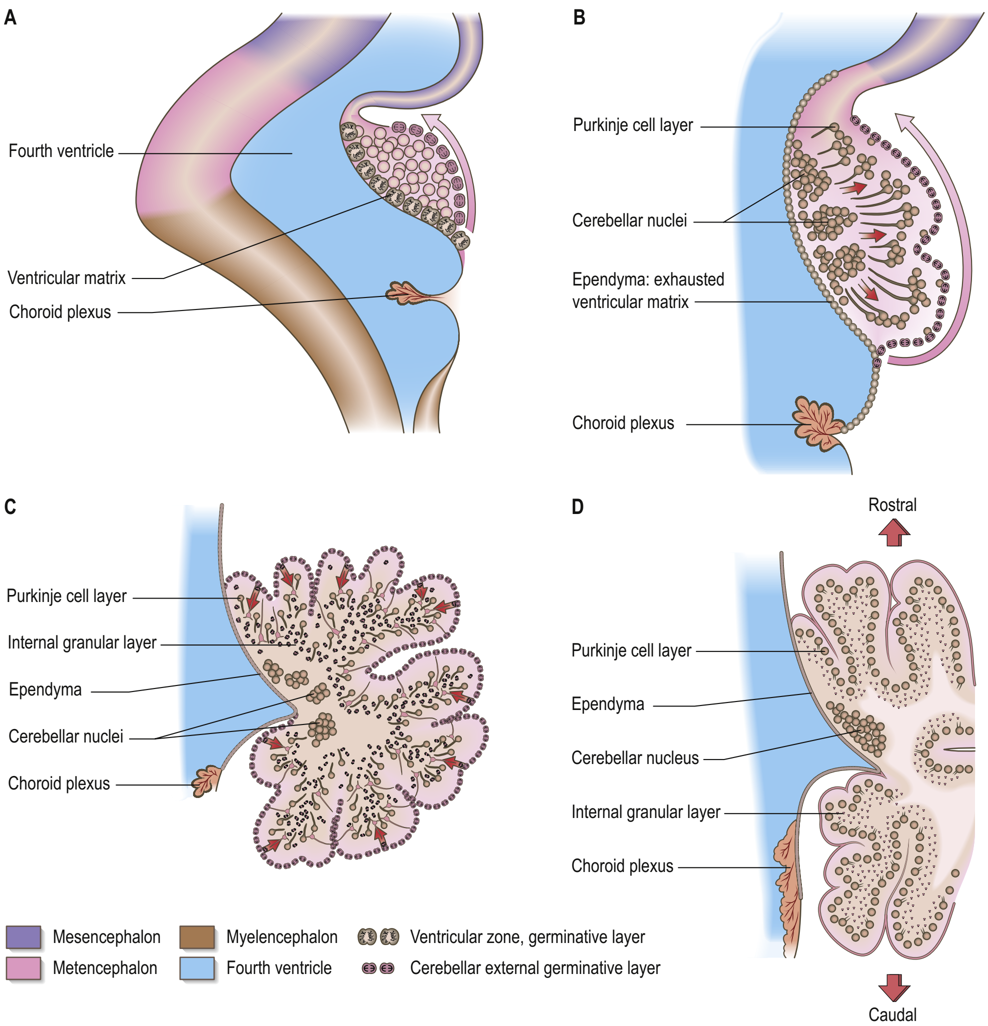

Fig. 14.24 Histogenesis of the cerebellar cortex and the cerebellar nuclei. **A**, Purkinje cells and cells of the cerebellar nuclei are produced by the ventricular zone and migrate to their future positions. The cells of the superficial matrix (the external granular layer) take their origin from the ventricular epithelium at the caudal pole of the cerebellar anlage and migrate rostrally over its surface. **B**, After migration, the Purkinje cells constitute a multicellular layer beneath the external germinative layer. Cell production in the ventricular epithelium has stopped. The remaining cells transform into ependymal cells. **C**, Granule cells produced by the external germinative layer migrate inwards through the Purkinje cell layer to their position in the internal granular layer. Purkinje cells spread into a monolayer. **D**, The adult position of cortical and nuclear neurones.

Relatively little is known about the molecular mechanisms involved in cerebellar development in the human (but see Manto and Jissendi (2012), Yu et al (2013), Martinez et al (2013)). The cerebellum undergoes its major growth during the third trimester and infancy (Leto et al 2016). Very small preterm infants are at particular risk of later cerebellar dysfunction with consequences for cognition and behaviour. Because much of cerebellar maturation occurs postnatally there is interest in therapeutic agents that may improve long-term outcomes for such infants (Manto and Jissendi 2012). A summary of mammalian cerebellar development including human cerebellar anomalies is given by Leto et al (2016).

Mesencephalon

The mesencephalon or midbrain is subdivided early in development into two neuromeres, mesencephalon 1 and mesencephalon 2. It persists for a time as a thin-walled tube enclosing a cavity of some size, separated from that of the prosencephalon by a slight constriction and from the rhombencephalon by the isthmus rhombencephali (see Fig. 14.4; **Fig. 14.26**). Later, its cavity becomes relatively reduced in diameter and, in the adult brain, it forms the cerebral aqueduct. The basal (ventrolateral) plate of the midbrain increases in thickness to form the cerebral peduncles, which are at first of small size but enlarge rapidly in the early second trimester, when their numerous fibre tracts begin to appear in the marginal zone. The neuroblasts of the basal plate of mesencephalon 2 give rise to the nuclei of the oculomotor nerve and some grey masses of the tegmentum, while the nucleus of the trochlear nerve remains in the region of the isthmus rhombencephali. The cells that give rise to the trigeminal mesencephalic nucleus arise either side of the dorsal midline, from the isthmus rhombencephali rostrally across the roof of the mesencephalon. The progenitors of these cells do not express neural crest cell markers.

The cells of the dorsal part of the alar (dorsolateral) plates proliferate and invade the roof plate, which therefore thickens and is later divided into corpora bigemina by a median groove. Caudally, this groove becomes a median ridge that persists in the adult as the frenulum veli, and the corpora bigemina are later subdivided into the superior and inferior colliculi by a transverse furrow. The red nucleus, substantia nigra and reticular nuclei of the midbrain tegmentum may first be defined at the end of the first trimester. Their origins are probably mixed, from neuroblasts of both basal and alar plates.

The detailed histogenesis of the tectum and its main derivatives, the colliculi, will not be followed here but, in general, the principles outlined for the cerebellar cortex, the paleopallium and neopallium also apply to this region. A high degree of geometric order exists in the developing retinotectal projection (the equivalent of the retinogeniculate projection) and in the tectospinal projection. (For further reading, see Cang and Feldheim (2013).)

Prosencephalon

At an early stage, a transverse section through the forebrain shows the same parts that are displayed in similar sections of the spinal cord and medulla oblongata, i.e. thick lateral walls connected by thin floor and roof plates. Each lateral wall is divided into a dorsal area and a ventral area separated internally by the hypothalamic sulcus (see Fig. 14.26). This sulcus ends rostrally at the medial end of the optic stalk. In the fully developed brain, it persists as a slight groove extending from the interventricular foramen to the cerebral aqueduct. It is analogous to, if not the homologue of, the sulcus limitans. The thin roof plate remains epithelial but invaginated by vascular mesenchyme, the tela choroidea of the choroid plexuses of the third ventricle. Later, the lateral margins of the tela undergo a similar invagination into the medial walls of the cerebral hemispheres. The floor plate thickens as the nuclear masses of the hypothalamus and subthalamus develop.

At a very early period, before the closure of the rostral neuropore, the subdivision of the prosencephalon into the most rostral telencephalon and two subdivisions of the diencephalon, D1 and D2, is heralded (see Fig. 14.2). At this early time, two eye fields are separated by the future neurohypophysis in the floor of the future D1. After head folding, the eye fields expand as two lateral optic evaginations, that will become optic vesicles, one on each side of the early brain. For a time, they communicate with the cavity of the prosencephalon by relatively wide openings. The distal parts of the optic vesicles expand, while the proximal parts become

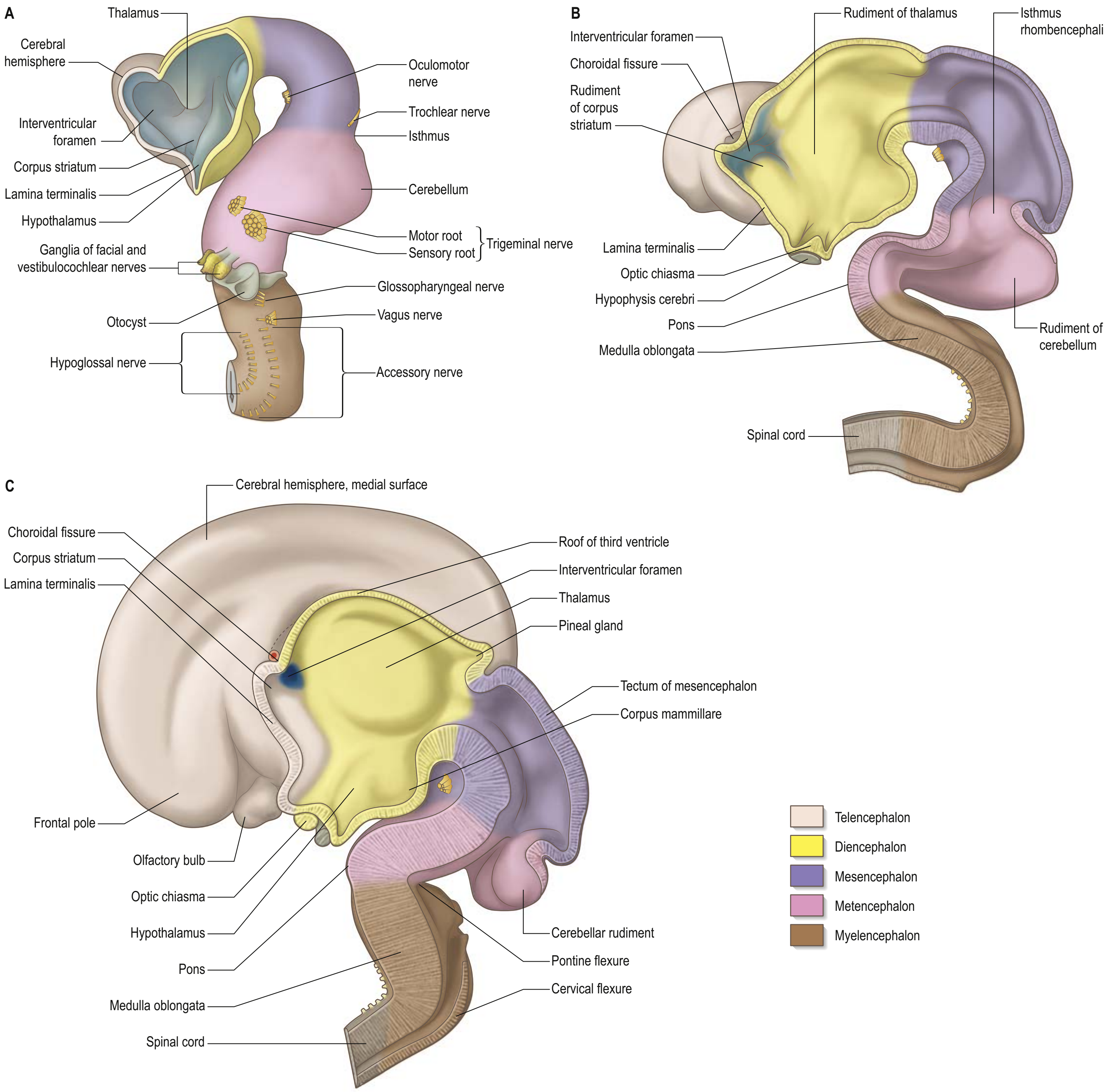
A
Thalamus
Cerebral hemisphere
Interventricular foramen
Corpus striatum
Lamina terminalis
Hypothalamus
Ganglia of facial and vestibulocochlear nerves
Otocyst
Hypoglossal nerve
Oculomotor nerve
Trochlear nerve
Isthmus
Cerebellum
Motor root
Sensory root
Trigeminal nerve
Glossopharyngeal nerve
Vagus nerve
Accessory nerve
B
Interventricular foramen
Choroidal fissure
Rudiment of corpus striatum
Rudiment of thalamus
Isthmus rhombencephali
Lamina terminalis
Optic chiasma
Hypophysis cerebri
Pons
Medulla oblongata
Rudiment of cerebellum
Spinal cord
C
Cerebral hemisphere, medial surface
Choroidal fissure
Corpus striatum
Lamina terminalis
Roof of third ventricle
Interventricular foramen
Thalamus
Pineal gland
Tectum of mesencephalon
Corpus mammillare
Frontal pole
Olfactory bulb
Optic chiasma
Hypothalamus
Pons
Medulla oblongata
Spinal cord
Cerebellar rudiment
Pontine flexure
Cervical flexure
Telencephalon
Diencephalon
Mesencephalon
Metencephalon
Myelencephalon

Fig. 14.26 The shape of the developing ventricular system and the expansion of the medial portion of the telencephalon. The roof of the metencephalon and myelencephalon has been removed in each case. **A**, A human embryo at stage 16, left lateral surface of the diencephalon and telencephalon removed. **B**, A human embryo at stage 18, median section. **C**, A human fetus, approximately postmenstrual week 12, median section.

the tubular optic stalks. The optic vesicles (described with the development of the eye in Ch. 15) are thus derived from the lateral walls of the D1 subdivision of the prosencephalon before the telencephalon can be clearly identified. The optic chiasma is often regarded as the boundary between the diencephalon and telencephalon.

As the most rostral portion of the prosencephalon enlarges, it curves ventrally, and two further diverticula expand rapidly from it, one on each side. These diverticula, rostrolateral to the optic stalks, subsequently form the cerebral hemispheres. Their cavities are the rudiments of the lateral ventricles and they communicate with the median part of the forebrain cavity by relatively wide openings that ultimately become the interventricular foramina. The rostral limit of the median part of the forebrain consists of a thin sheet, the lamina terminalis (see Fig. 14.26), which stretches from the interventricular foramina to the recess at the base of the optic stalks. The rostral part of the forebrain, including the rudiments of the cerebral hemispheres, consists of the telencephalon and the caudal part of the diencephalon; both contribute to the formation of the third ventricle, although the latter predominates. The fate of the lamina terminalis is described below.

Diencephalon

The diencephalon, D2, is broadly divided by the hypothalamic sulcus into dorsal (pars dorsalis diencephali) and ventral (pars ventralis diencephali) parts; each contributes to diverse neural structures. The dorsal part develops into the (dorsal) thalamus and metathalamus along the immediate suprasulcal area of its lateral wall, while the highest dorsocaudal lateral wall and roof form the epithalamus. The thalamus is first visible as a thickening that involves the rostral part of the dorsal area (see Fig. 14.26). Caudal to the thalamus, the lateral and medial geniculate bodies, or metathalamus, are recognizable at first as surface depressions on the internal aspect and as elevations on the external aspect of the lateral wall. As the thalami enlarge as smooth ovoid masses, the wide interval between them gradually narrows into a vertically compressed cavity that forms the greater part of the third ventricle. After a time these medial surfaces may come into contact and become adherent over a variable area, the connection (single or multiple) constituting the interthalamic adhesion or massa intermedia. The caudal growth of the thalamus excludes the geniculate bodies from the lateral wall of the third ventricle.

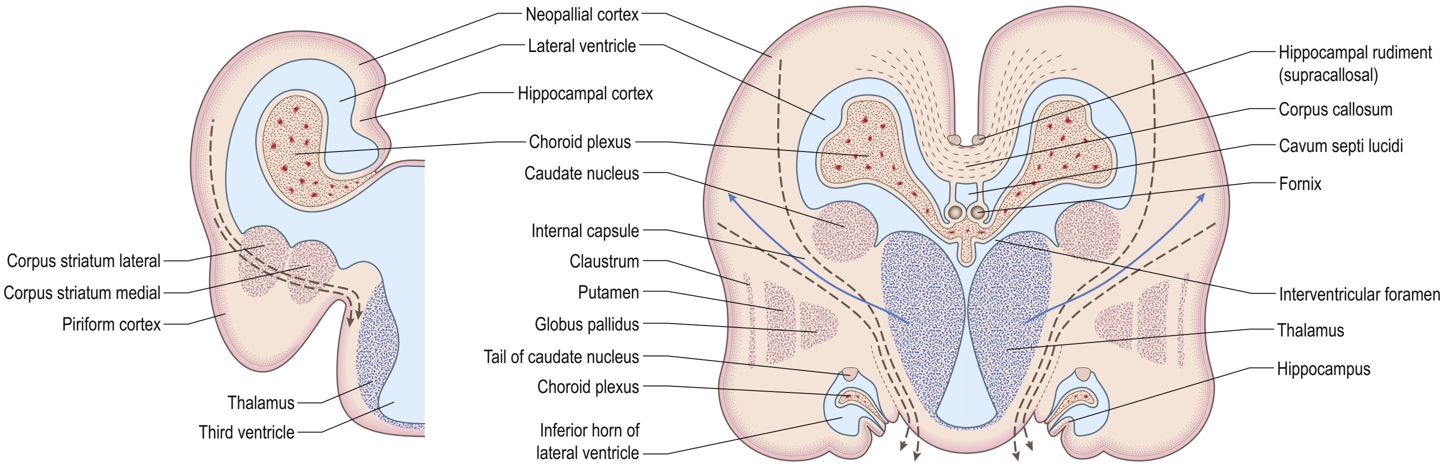

Fig. 14.27 The development of the basal nuclei and internal capsule, coronal views. (Redrawn with permission from Hamilton WJ, Boyd JD, Mossman HW 1972 Human Embryology: Prenatal Development of Form and Function. Baltimore: Williams and Wilkins.)

At first the lateral aspect of the developing thalamus is separated from the medial aspect of the cerebral hemisphere by a cleft that becomes obliterated as the thalamus fuses with the part of the hemisphere in which the corpus striatum is developing (**Fig. 14.27**). The subsequent development of the corticofugal and corticopetal projection fibres of the neocortex means that the thalamus becomes related to the internal capsule, which intervenes between it and the lateral part of the corpus striatum (lentiform nucleus). Ventral to the hypothalamic sulcus the lateral wall of the diencephalon, in addition to median derivatives of its floor plate, forms a large part of the hypothalamus and subthalamus.

The epithalamus, which includes the pineal gland, the posterior and habenular commissures and the trigonum habenulae, develops in association with the caudal part of the roof plate and the adjoining regions of the lateral walls of the diencephalon. Between stages 17–20 the epithalamus in the lateral wall projects into the third ventricle as a smooth ellipsoid mass, larger than the adjacent mass of the (dorsal) thalamus and separated from it by a well-defined epithalamic sulcus. Subsequent growth of the thalamus rapidly overtakes that of the epithalamus and the intervening sulcus is obliterated: structures of epithalamic origin become relatively diminutive topographically.

The pineal gland arises as a hollow outgrowth from the roof plate, immediately adjoining the mesencephalon. Its distal part becomes solid by cellular proliferation but its proximal stalk remains hollow and contains the pineal recess of the third ventricle. In many reptiles the pineal outgrowth consists of a rostral outgrowth (parapineal organ) that develops into the pineal or parietal eye, and a glandular caudal outgrowth that is homologous with the human pineal gland. The rostral outgrowth also develops in the human embryo but soon disappears entirely.

The nucleus habenulae, the most important constituent of the trigonum habenulae, develops in the lateral wall of the diencephalon. It is initially a close relation of the geniculate bodies, from which it is later separated by the dorsal growth of the thalamus. The habenular commissure develops in the cranial wall of the pineal recess. The posterior commissure is formed by fibres that invade the caudal wall of the pineal recess from both sides.

The ventral part of the diencephalon forms the subsulcal lateral walls of the third ventricle and takes part in the formation of the hypothalamus, including the mammillary bodies, the tuber cinereum and infundibulum of the hypophysis. The mammillary bodies arise as a single thickening that becomes divided by a median furrow during the end of the first trimester. The tuber cinereum develops rostral to the mammillary bodies as a cellular proliferation that extends forwards as far as the infundibulum. A wide-mouthed diverticulum forms in the floor of the diencephalon in front of the tuber cinereum and grows towards the stomodeal roof, coming into contact with the posterior aspect of a dorsally directed ingrowth from the stomodeum (Rathke's pouch). These two diverticula together form the hypophysis cerebri (see Fig. 14.10). An extension of the third ventricle persists in the base of the neural outgrowth as the infundibular recess. The remaining caudolateral walls and floor of the ventral diencephalon are an extension of the midbrain tegmentum, the subthalamus. This forms the rostral limits of the red nucleus, the substantia nigra, numerous reticular nuclei and a mass of interweaving, ascending, descending and oblique nerve fibre bundles.

Third ventricle and choroid plexus

The roof plate of the diencephalon rostral to the pineal gland continues over the median telencephalon, remaining thin and epithelial in character and is invaginated by the choroid plexuses of the third ventricle (see Fig. 14.27; **Fig. 14.28**). Before the development of the corpus callosum and the fornix, it lies at the bottom of the longitudinal fissure between and reaching the two cerebral hemispheres. It extends as far rostrally as the interventricular foramina and lamina terminalis. Here, and elsewhere, choroid plexuses develop by the close apposition of vascular pia mater and ependyma without intervening nervous tissue. With development, the vascular layer is infolded into the ventricular cavity and develops a series of small villous projections, each covered by a cuboidal epithelium derived from the ependyma. The cuboidal cells display numerous microvilli on their ventricular surfaces and complex folding of their basal plasma membranes. The early choroid plexuses secrete a protein-rich cerebrospinal fluid into the ventricular system, which may provide a nutritive medium for the developing epithelial neural tissues. As the latter become increasingly vascularized, the histochemical reactions of the cuboidal cells and the character of the fluid change to the adult type. Many regions of the lining of the third ventricle become highly specialized, and develop concentrations of tanycytes or other modified cells that are collectively termed the circumventricular organs, e.g. the subfornical organ, the organum vasculosum (intercolumnar tubercle) of the lamina terminalis, the subcommissural organ, and the linings of the pineal, suprapineal and infundibular recesses.

Telencephalon

The telencephalon consists of two lateral diverticula connected by a median region, the telencephalon impar. The rostral part of the third ventricle develops from the impar and is closed below and in front by the lamina terminalis. The lateral diverticula are outpouchings of the lateral walls of the telencephalon that may correspond to the alar lamina, although this is uncertain. Their cavities are the future lateral ventricles and their walls are formed by the presumptive nervous tissue of the cerebral hemispheres. The roof plate of the median part of the telencephalon remains thin and is continuous behind with the roof plate of the diencephalon (see Figs 14.26–14.27). The rostral parts of the hypothalamus, which include the optic chiasma, optic recess and related nuclei, develop in the floor plate and lateral walls of the prosencephalon, ventral to the primitive interventricular foramina. The chiasma is formed by the meeting, and partial decussation, of the optic nerves in the ventral part of the lamina terminalis. The optic tracts subsequently grow backwards from the chiasma to end in the diencephalon and midbrain.

Cerebral hemispheres

The cerebral hemispheres arise as diverticula of the lateral walls of the telencephalon, with which they remain in continuity around the margins of initially relatively large interventricular foramina, except caudally, where they are continuous with the rostral part of the lateral wall of the diencephalon (see Figs 14.4, 14.26). As growth proceeds each hemisphere enlarges forwards, upwards and backwards and acquires an oval outline, medial and superolateral walls, and a floor. As a result the medial surfaces approach, but are separated by, a vascularized mesenchyme and pia mater that fills the median longitudinal

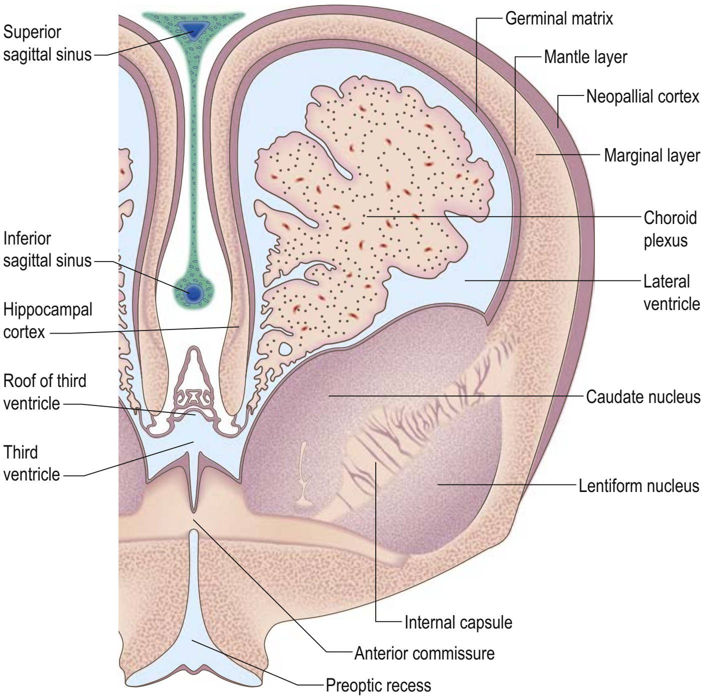

Fig. 14.28 Coronal section of the left cerebral hemisphere at postmenstrual week 13. (Redrawn with permission from Hamilton WJ, Boyd JD, Mossman HW 1972 Human Embryology: Prenatal Development of Form and Function. Baltimore: Williams and Wilkins.)

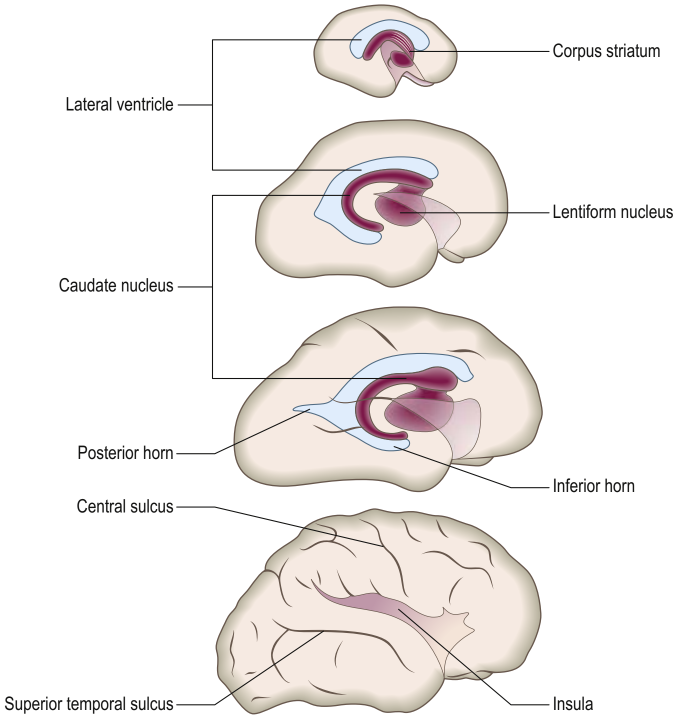

Fig. 14.29 Lateral views of developing brains show the formation of the basal nuclei and lateral ventricles as the telencephalon develops. (Redrawn with permission from Hamilton WJ, Boyd JD, Mossman HW 1972 Human Embryology: Prenatal Development of Form and Function. Baltimore: Williams and Wilkins.)

fissure (see Fig. 14.28). At this stage the floor of the fissure is the epithelial roof plate of the telencephalon, which is directly continuous caudally with the epithelial roof plate of the diencephalon.

At the early oval stage of hemispheric development, regions are named according to their future principal derivatives. The rostromedial and ventral floor becomes linked with the forming olfactory apparatus and is termed the primitive olfactory lobe. The floor (ventral wall, or base) of the remainder of each hemisphere forms the anlage of the primitive corpus striatum and amygdaloid complex, including its associated rim of lateral and medial walls (the striate part of the hemisphere). The rest of the hemisphere, i.e. the medial, lateral, dorsal and caudal regions, is the suprastriate part of the hemisphere. Although it is the largest in terms of surface area, initially it possesses comparatively thin walls. The rostral end of each oval hemisphere becomes the definitive frontal pole. As the hemisphere expands its original posterior pole moves relatively in a caudoventral and lateral direction, following a curve like a ram's horn. It curves towards the orbit in association with the growth of the caudate nucleus and other structures to form the definitive temporal pole. A new posterior part persists as the definitive occipital pole of the mature brain (**Figs 14.29-14.30**).

The migration and differentiation of neural progenitors to form nuclei is either minimal or limited throughout the brainstem and spinal cord. The progeny of these progenitors remain immediately extra-ependymal or partially displaced towards the pial exterior, and are arrested deeply embedded in the myelinating 'white matter' of the region. In marked contrast, proliferation and migration of neuroblasts in the cerebral hemispheres produce a superficial layer of grey matter in both the striate and the suprastriate regions, but not in the central areas of the original medial wall, where secondary fusion with the diencephalon occurs. The superficial layer of grey matter consists of neuronal somata, dendrites, the terminations of incoming (afferent) axons, extending outgrowing (efferent) axons, and glial and endothelial cells. Successive generations of neuroblasts migrate through the layers of earlier generations to attain subpial positions (see below and Fig. 14.33), which means that the outer, pial surface of the cerebral hemispheres expands at a rate greater than that of the hemispheres as a whole. The subpial region of grey matter is termed the cortex or pallium; a transient cortical subplate is seen. The growing hemispheres subsequently overlap, successively, the diencephalon and the mesencephalon, and then meet the rostral surface of the cerebellum. The temporal lobes embrace the flanks of the brainstem.

The terminology used to describe regions of the cortex is based on evolutionary concepts. The oldest portions of cortex receive information concerned with olfaction and are termed archicortex (archipallium) and paleocortex (paleopallium): both are subdivisions of an overall allocortex. The archicortex is the forerunner of the hippocampal lobe, and the paleocortex gives rise to the piriform area. The remaining cortical surface expands greatly in mammals, forming the neocortex that displaces the earlier cortices so that they come to lie partially internally in each hemisphere. The typically six-layered mammalian neocortex is also described as isocortex.

Lateral ventricles and choroid plexus

The early diverticulum or anlage of the cerebral hemisphere initially contains a simple spheroidal lateral ventricle continuous with the third ventricle via the interventricular foramen. The rim of the foramen is the site of the original evagination. The expanding ventricle develops the ram's horn shape of the surrounding hemisphere, becoming first roughly ellipsoid and then a curved cylinder that is convex dorsally (see Fig. 14.29). The ends of the cylinder expand towards, but do not reach, the frontal and (temporary) occipital poles; differentiating and thickening neural tissues separate the ventricular cavities and pial surfaces at all points, except along the line of the choroidal fissure. Pronounced changes in ventricular form accompany the emergence of a temporal pole. The original caudal end of the curved cylinder expands within its substance and the temporal extensions in each hemisphere pass ventrolaterally to encircle both sides of the upper brainstem (see Fig. 14.27). Another extension may develop from the root of the temporal extension in the substance of the definitive occipital pole and pass caudomedially; it is quite variable in size, often asymmetric on the two sides, and one or both may be absent. Although the lateral ventricle is a continuous system of cavities, specific parts are now given regional names. The central part (body) extends from the interventricular foramen to the level of the posterior edge (splenium) of the corpus callosum. Three cornua (horns) diverge from the body: anterior towards the frontal pole, posterior towards the occipital pole, and inferior towards the temporal pole. At these early stages of hemispheric development, in most instances the term pole is preferred to lobe: lobes are defined by specific surface topographical features that will appear over several postmenstrual weeks, and differential growth patterns persist for a considerable period.

The pia mater covers the epithelial roof of the third ventricle at this stage and is itself covered with loosely arranged mesenchyme and developing blood vessels. These vessels subsequently invaginate the roof of the third ventricle on each side of the median plane to form its choroid plexuses (see Fig. 14.27). The lower part of the medial wall of the cerebral hemisphere, which immediately adjoins the epithelial roof of the interventricular foramen and the rostral extremity of the diencephalon, also remains epithelial and consists of ependyma and pia mater. Elsewhere, the walls of the hemispheres are thickening to form the

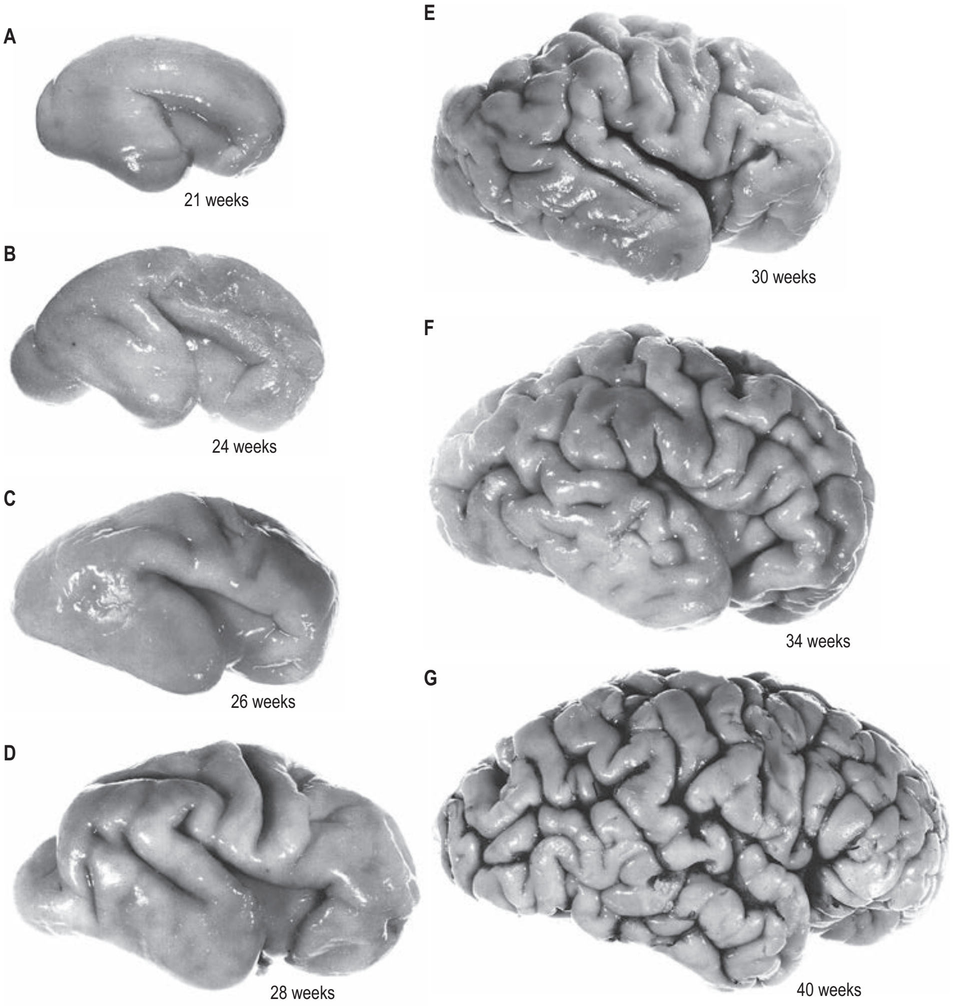

Fig. 14.30 A–G, The superolateral surfaces of human fetal cerebral hemispheres at the postmenstrual weeks indicated, showing the changes in size, profile and the emerging pattern of cerebral sulci with increasing maturation. Note the changing prominence and relative positions of the frontal, occipital and, particularly, the temporal, poles of the hemisphere. At the earliest stage **(A)**, the lateral cerebral fossa is already obvious: its floor covers the developing corpus striatum in the depths of the hemisphere and progressively matures into the cortex of the insula. The fossa is bounded by overgrowing cortical regions (frontal, temporal and parietal opercula) that gradually converge to bury the insula; their approximation forms the lateral cerebral sulcus. By the sixth month, the central, pre- and postcentral, superior temporal, intraparietal and parieto-occipital sulci are all clearly visible. In the subsequent stages shown, all the remaining principal and subsidiary sulci rapidly appear, and by postmenstrual week 40, all the features that characterize the adult hemisphere in terms of surface topography are present in miniature. (Photographs provided by Dr Sabina Strick, The Maudsley Hospital, London.)

pallium. The thin part of the medial wall of the hemisphere is invaginated by vascular tissue that is continuous in front with the choroid plexus of the third ventricle and constitutes the choroid plexus of the lateral ventricle. This invagination occurs along a line that arches upwards and backwards, parallel with and initially limited to, the rostral and upper boundaries of the interventricular foramen. This curved indentation of the ventricular wall, where no nervous tissue develops between ependyma and pia mater, is termed the choroidal fissure (see Figs 14.26C, 14.27). The subsequent assumption of the definitive form of the choroidal fissure depends on related growth patterns in neighbouring structures. Of particular importance are the relatively slow growth of the interventricular foramen; the secondary 'fusion' between the lateral diencephalon and medial hemisphere walls; the encompassing of the upper brainstem by the forward growth of the temporal lobe and its pole towards the apex of the orbit; and the massive expansion of two great cerebral commissures (the fornix and corpus callosum). The choroidal fissure is now clearly a caudal extension of the much-reduced interventricular foramen, which arches above the thalamus and is here only a few millimetres from the median plane. It diverges ventrolaterally near the caudal end of the thalamus, its curve reaching and continuing in the medial wall of the temporal lobe over much of its length (i.e. to the tip of the inferior horn of the lateral ventricle). The upper part of the arch will be overhung by the corpus callosum and it is bordered by the fornix and its derivatives throughout its convexity.

Basal nuclei

At first, growth proceeds more actively in the floor and the adjoining part of the lateral wall of the developing hemisphere, and thickenings of the ventricular zone formed by the rudimentary corpus striatum, often termed medial and lateral ganglionic (ventricular) eminences, develop from stage 18 (see Figs 14.26–14.29). The head of the caudate nucleus appears as three successive parts, medial, lateral and intermediate. Caudally, these merge to form the tail of the caudate nucleus and the amygdaloid complex, which both remain close to the temporal pole of the hemisphere. When the occipital pole grows backwards and the general enlargement of the hemisphere carries the temporal pole downwards and forwards, the tail of the caudate is continued from the floor of the central part (body) of the lateral ventricle into the roof of its temporal extension, the future inferior horn (see Fig. 14.29). The amygdaloid complex encapsulates its tip. Rostrally, the head of the caudate nucleus extends forwards to the floor of the interventricular foramen, where it is separated from the developing rostral end of the thalamus by a groove; the head subsequently expands in the floor of the anterior horn of the lateral ventricle. The lentiform nucleus develops from two cellular laminae, medial and lateral, that are continuous with both the medial and lateral parts of the caudate nucleus. The internal capsule appears first in the medial lamina and extends laterally through the lateral lamina to the cortex. It divides the laminae into two, the internal parts join the caudate nucleus and the external parts form the lentiform nucleus (see Figs 14.27–14.28): the remaining medial lamina cells give rise mainly to the globus pallidus and the lateral lamina cells to the putamen. The putamen expands concurrently with the intermediate part of the caudate nucleus.

Fusion of diencephalic and telencephalic walls

As the hemisphere enlarges, the caudal part of its medial surface overlaps and hides the lateral surface of the diencephalon (thalamic part), from which it is separated by a narrow cleft occupied by vascular connective tissue. A transverse section made caudal to the interventricular foramen would pass from the third ventricular cavity successively through the developing thalamus, the narrow cleft just mentioned, the thin medial wall of the hemisphere, and the cavity of the lateral ventricle, with the corpus striatum in its floor and lateral wall (see Fig. 14.27).

As the thalamus increases in extent it acquires a superior surface in addition to medial and lateral surfaces. The lateral part of its superior surface fuses with the thin medial wall of the hemisphere so that this part of the thalamus is finally covered with the ependyma of the lateral ventricle immediately ventral to the choroidal fissure. As a result the corpus striatum is approximated to the thalamus and is separated from it only by a deep groove that becomes obliterated by increased growth along the line of contact. The lateral aspect of the thalamus is now in continuity with the medial aspect of the corpus striatum so that a secondary union between the diencephalon and the telencephalon is effected over a wide area, providing a route for the subsequent passage of projection fibres to and from the cortex (see Fig. 14.27).

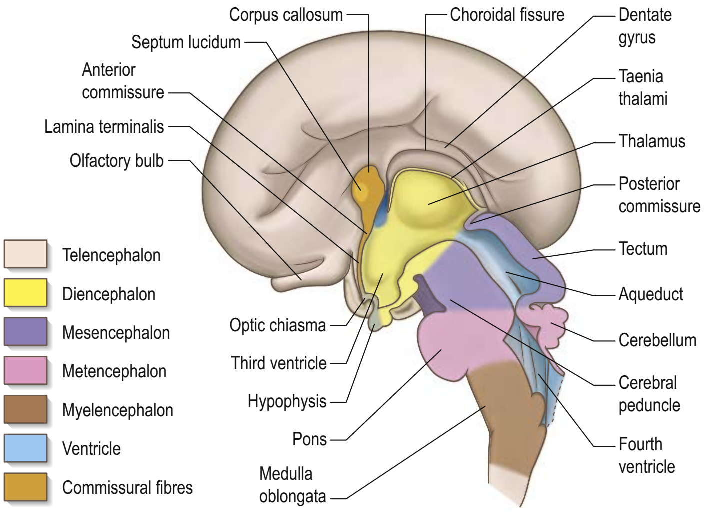

Fig. 14.31 The anterior and posterior commissures in the brain of a human fetus at postmenstrual week 16; medial aspect of the left half of the brain.

Formation of the insula

At the end of the first trimester, while the corpus striatum is developing, growth between the frontal and temporal lobes is relatively restricted. The region lateral to the striatum becomes depressed to form a lateral cerebral fossa with a portion of cortex, the insula, at its base (see Figs 14.29–14.30). As the temporal lobe continues to protrude towards the orbit, and with more rapid growth of the temporal and frontal cortices, the surface of the hemisphere expands at a rate greater than that of the hemisphere as a whole, and the cortical areas become folded, forming gyri and sulci. The insula is gradually overgrown by adjacent cortical regions that overlap it to form the opercula: the free margins of the opercula form the anterior part of the lateral fissure. This process is not completed until after birth. The lentiform nucleus remains deep to and coextensive with the insula.

Olfactory bulb

A longitudinal groove appears in the anteromedial part of the floor of each developing lateral ventricle at about the stage 17. It deepens and forms a hollow diverticulum that is continuous with the hemisphere by a short stalk. The diverticulum becomes connected on its ventral or inferior surface to the olfactory placode. Placodal cells give rise to afferent axons that terminate in the walls of the diverticulum. As the head increases in size, the diverticulum grows forwards, loses its cavity and becomes converted into the solid olfactory bulb. The forward growth of the bulb is accompanied by elongation of its stalk to form the olfactory tract. The part of the floor of the hemisphere to which the tract is attached constitutes the piriform area.

Olfactory nerve, limbic lobe and hippocampus

The growth changes in the temporal lobe that help to submerge the insula produce important changes in the olfactory and neighbouring limbic areas. The olfactory tract diverges into lateral, medial and (variable) intermediate striae as it approaches the hemispheric floor. The medial stria is clothed with a thin archicortical medial olfactory gyrus. This curves up into further archicortical areas rostral to the lamina terminalis (paraterminal gyrus, prehippocampal rudiment, parolfactory gyrus, septal nuclei) and these continue into the indusium griseum. The lateral stria, clothed by the lateral olfactory gyrus, and the intermediate stria (when present) terminate in the rostral parts of the piriform area, including the olfactory trigone and tubercle, anterior perforated substance, uncus and entorhinal area of the anterior part of the future parahippocampal gyrus. The lateral limit of the lateral stria is indicated by the rhinal sulcus. The forward growth of the temporal pole and the general expansion of the neocortex cause the lateral olfactory gyrus to bend laterally, the summit of the convexity lying at the anteroinferior corner of the developing insula. During the second trimester, much of the piriform area becomes submerged by the adjoining neocortex and, in the adult, only a part of it remains visible on the inferior aspect of the cerebrum.

The limbic lobe is the first part of the cortex to differentiate. At first it forms a continuous, almost circular, strip on the medial and inferior aspects of the hemisphere. Below and in front, where the stalk of the olfactory tract is attached, it constitutes a part of the piriform area. The portion outside the curve of the choroidal fissure constitutes the hippocampal formation (see Fig. 14.27; **Fig. 14.31**). In this region, the neural progenitors of the developing cortex proliferate and migrate. The wall of the hemisphere thickens, producing an elevation that projects into the medial side of the ventricle. The elevation is the hippocampus; it appears first on the medial wall of the hemisphere, in the area above and in front of the lamina terminalis (paraterminal area), and gradually extends backwards, curving into the region of the temporal pole, where it adjoins the piriform area. The marginal zone in the neighbourhood of the hippocampus is invaded by neurones to form the dentate gyrus. The hippocampus and the dentate gyrus extend from the paraterminal area backwards above the choroidal fissure and follow its curve downwards and forwards towards the temporal pole, where they continue into the piriform area. A shallow groove, the hippocampal sulcus, crosses the medial surface of the hemisphere throughout the hippocampal formation. The efferent fibres from the cells of the hippocampus collect along its medial edge and run forwards immediately above the choroidal fissure. Rostrally, they turn ventrally and enter the lateral part of the lamina terminalis to gain the hypothalamus, where they end in and around the mammillary body and neighbouring nuclei. These efferent hippocampal fibres form the fimbria hippocampi and the fornix.

Projection fibres, internal capsule

The growth of the neocortex, and its enormous expansion during the latter part of the first trimester, is associated with the initial appearance of corticofugal and corticopetal projection fibres and the internal capsule. The fibres follow the route provided by the apposition of the lateral aspect of the thalamus with the medial aspect of the corpus striatum. They divide the latter, almost completely, into a lateral part, the lentiform nucleus, and a medial part, the caudate nucleus; these two nuclei remain confluent only in their anteroinferior regions (see Figs 14.27–14.28). The corticospinal tracts are first identified at the end of stage 23 at the pyramidal decussation. The lateral corticospinal tracts are in the cervical cord by postmenstrual weeks 14–15 and in the anterior corticospinal tract from about postmenstrual week 16 (Jin et al 2016). The fibres destined for the cervical and upper thoracic regions, which innervate the upper limbs, are in advance of those that innervate the lower limbs, and these, in turn, are in advance of fibres that innervate the face; the timing of the appearance of reflexes associated with these three parts of the body is similarly staggered. The proportions of crossed and uncrossed fibres in each corticospinal tract vary; a dominant uncrossed corticospinal tract and a complete absence of pyramidal decussation have been found in posterior fossa anomalies such as occipital encephalocele, Dandy–Walker malformation and Joubert's syndrome. There is evidence of substantial plastic reorganization of the motor cortex and corticospinal projections following pre- or perinatal lesions to the corticospinal system (Eyre 2007). For further reading about the development of the human pyramidal tract, see ten Donkelaar et al (2004).

The majority of subcortical nuclear masses receive terminals from descending fibres of cortical origin and thalamocortical, hypothalamocortical and other afferent ascending bundles. The internal capsular fibres pass lateral to the head and body of the caudate nucleus, the anterior cornu and central part of the lateral ventricle, the rostroventral extensions and body of the fornix, the dorsal thalamus and dorsal choroidal fissure, and medial to the lentiform nucleus (see Figs 14.27–14.28).

Formation of gyri and sulci

Apart from the shallow hippocampal sulcus and the lateral cerebral fossa, the surfaces of the hemisphere remain relatively smooth and uninterrupted until postmenstrual week 21 (see Fig. 14.30). The parieto-occipital sulcus appears at about that time on the medial aspect of the hemisphere. Its appearance seems associated with an increase in the number of splenial fibres in the corpus callosum. Over the same period, the posterior part of the calcarine sulcus appears as a shallow groove extending forwards from a region near the occipital pole. It is a true infolding of the cortex in the long axis of the striate area and produces an elevation, the calcar avis, on the medial wall of the posterior horn of the ventricle.

The cingulate sulcus appears on the medial aspect of the hemisphere about postmenstrual weeks 18–20, and sulci appear on the inferior and superolateral aspects after postmenstrual week 21. The central, precentral and postcentral sulci appear, each in upper and lower parts that usually coalesce shortly afterwards, although they may remain discontinuous. The superior and inferior frontal, the intraparietal, occipital, superior and inferior temporal, occipitotemporal, collateral and rhinal sulci all make their appearance during the same period. Secondary and tertiary gyri form after neurones attain their final areal and laminar positions (Silver et al 2019). All the important sulci can be recognized by postmenstrual week 32 (see Fig. 14.30). Preterm infants developing *ex utero* have less gyrification and shallower sulci by their equivalent postmenstrual week 40 than neonates born at full-term (postmenstrual week 40) (Engelhardt et al 2016a, Shimony et al 2016). Mathematical modelling of gyral patterns has identified distinct folding patterns and sex differences in the superior temporal, inferior frontal and cingulate gyri in healthy singleton, twin, preterm and full-term neonates (Duan et al 2019).

Development of commissures

The development of the commissures causes a very profound alteration of the medial wall of the hemisphere. At the time of their appearance, the two hemispheres are connected to each other by the median part of the telencephalon. The roof plate of this area remains epithelial, while its floor becomes invaded by the decussating fibres of the optic nerves and developing hypothalamic nuclei. These two routes are thus not available for the passage of commissural fibres passing from hemisphere to hemisphere across the median plane, and these fibres therefore pass through the rostral wall of the interventricular foramen, i.e. the lamina terminalis. The first commissures to develop are those associated with the paleocortex and archicortex. Fibres of the olfactory tracts cross in the ventral or lower part of the lamina terminalis and, together with fibres from the piriform and pre-piriform areas and the amygdaloid bodies, form the rostral part of the anterior commissure (see Fig. 14.31; **Fig. 14.32**). The two hippocampi become interconnected by transverse fibres that cross from fornix to fornix in the upper part of the lamina terminalis as the commissure of the fornix (hippocampal commissure). Various other decussating fibre bundles (known as the supraoptic commissures, although they are not true commissures) develop in the lamina terminalis immediately dorsal to the optic chiasma, between it and the anterior commissure.

The commissures of the neocortex develop later and follow the pathways already established by the commissures of the limbic system. Fibres from the tentorial surface of the hemisphere join the anterior commissure and constitute its larger posterior part. All the other commissural fibres of the neocortex associate themselves closely with the commissure of the fornix and lie on its dorsal surface. These fibres increase enormously in number and the bundle rapidly outgrows its neighbours to form the corpus callosum (see Figs 14.31–14.32).

The corpus callosum originates as a thick mass connecting the two cerebral hemispheres around and above the anterior commissure. The upper end of this neocortical commissural area extends backwards to form the trunk of the corpus callosum. The rostrum of the corpus callosum develops later and separates some of the rostral end of the limbic area from the remainder of the cerebral hemisphere. Further backward growth of the trunk of the corpus callosum then results in the entrapped part of the limbic area becoming stretched out to form the bilateral septum pellucidum. As the corpus callosum grows backwards, it extends above the choroidal fissure, carrying the commissure of the fornix on its undersurface. In this way, a new floor is formed for the longitudinal fissure, and additional structures come to lie above the epithelial roof of the third ventricle. In its backward growth, the corpus callosum invades the area hitherto occupied by the upper part of the archicortical hippocampal formation, and the corresponding parts of the dentate gyrus and hippocampus are reduced to vestiges, the indusium griseum and the longitudinal striae. The posteroinferior (temporal) archicortical regions of both dentate gyrus and hippocampus persist and enlarge.

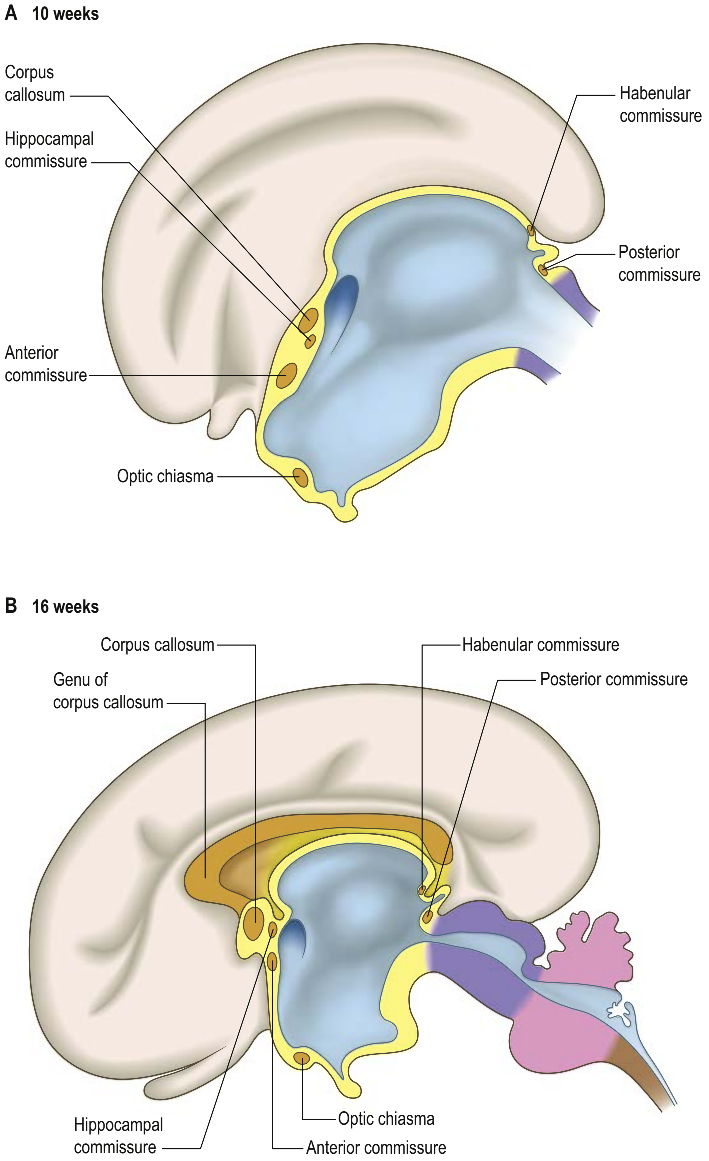

Fig. 14.32 Median sections showing the formation of the commissures. The telencephalon gives rise to commissural tracts that integrate the activities of the left and right cerebral hemispheres. These tracts include the anterior and hippocampal commissures and the corpus callosum. The small posterior and habenular commissures arise from the epithalamus.

Cellular development of the cerebral cortex

Cortical neurones are not generated within the cortex itself but in proliferative transient embryonic zones such as the ventricular (VZ) and subventricular (SVZ) zones (see Fig. 14.33). Precise patterns of cell division and the subsequent migration of the progeny of these divisions along the shafts of a transient population of radial glial cells transform the neuroepithelium of the embryonic forebrain into the adult cerebral cortex (Noctor et al 2004). Neurones are derived from a lineage of radial glia stem cells and transit amplifying intermediate progenitor cells; expansion in one or both cell populations has been proposed as a potential mechanism for neocortical expansion (Kriegstein and Gotz 2003, Lui et al 2011). The earliest-generated cortical neurones accumulate in an outside-in sequence to form the preplate. Subsequent generations of neurones migrate into the preplate, forming a series of layers called the cortical plate that splits the preplate into a superficial layer at the pial surface, the marginal zone, and a deeper layer, the subplate. Subplate neurones integrate into the intra- and extracortical circuitry and extend axons via the internal capsule towards the thalamus and superior colliculus at times before other cortical neurones have been born (Kanold and Luhmann 2010). In humans, the subplate is maximal at approximately postmenstrual week 25 and recedes after birth by postnatal month 6 (Kostovic et al 2012). The diverse cellular components of the subplate are embedded in an abundant hydrophilic extracellular matrix rich in secreted polymeric glycosaminoglycans, fibronectin and chondroitin sulphate proteoglycans that, for example, provide a major corridor for migrating GABAergic neurones (Hoerder-Suabedissen and Molnar 2015). Subplate neurones are vulnerable to injury during prenatal stages; their premature loss has been implicated in the pathogenesis of chronic deficits such as cognitive delay, behavioural problems and epilepsy associated with preterm birth (Jantzie et al 2015). They have also been implicated in the pathogenesis of cognitive developmental disorders such as autism and schizophrenia (Silver et al 2019, Molnar et al 2019).

Neurones migrate along radial glial processes (see Fig. 14.12). The migration of neuronal precursors from the ventricular and intermediate zones occurs radially towards the pial surface (Kriegstein and Noctor 2004). From the pial surface inwards, the following zones may be defined: marginal, cortical plate, subplate, intermediate, subventricular and ventricular (**Fig. 14.33**). (For a review of the nomenclature of the developing zones, see Bystron et al (2008).) The marginal zone, the outermost layer of the developing cerebral cortex, will form layer 1. The neurones of the cortical plate and subplate form the neurones of the remaining cortical laminae (2–6), the complexity varies in different locations and with further additions of neurones from the deeper zones. The intermediate zone gradually transforms into the white matter of the hemisphere. Meanwhile, other deep progenitor cells produce generations of glioblasts that also migrate into the more superficial layers. As proliferation wanes and finally ceases in the ventricular and subventricular zones, their remaining cells differentiate into general or specialized ependymal cells, tanycytes or subependymal glial cells.

The timing of proliferation of different cortical neurones varies according to their laminar destination and cell type. The first groups of

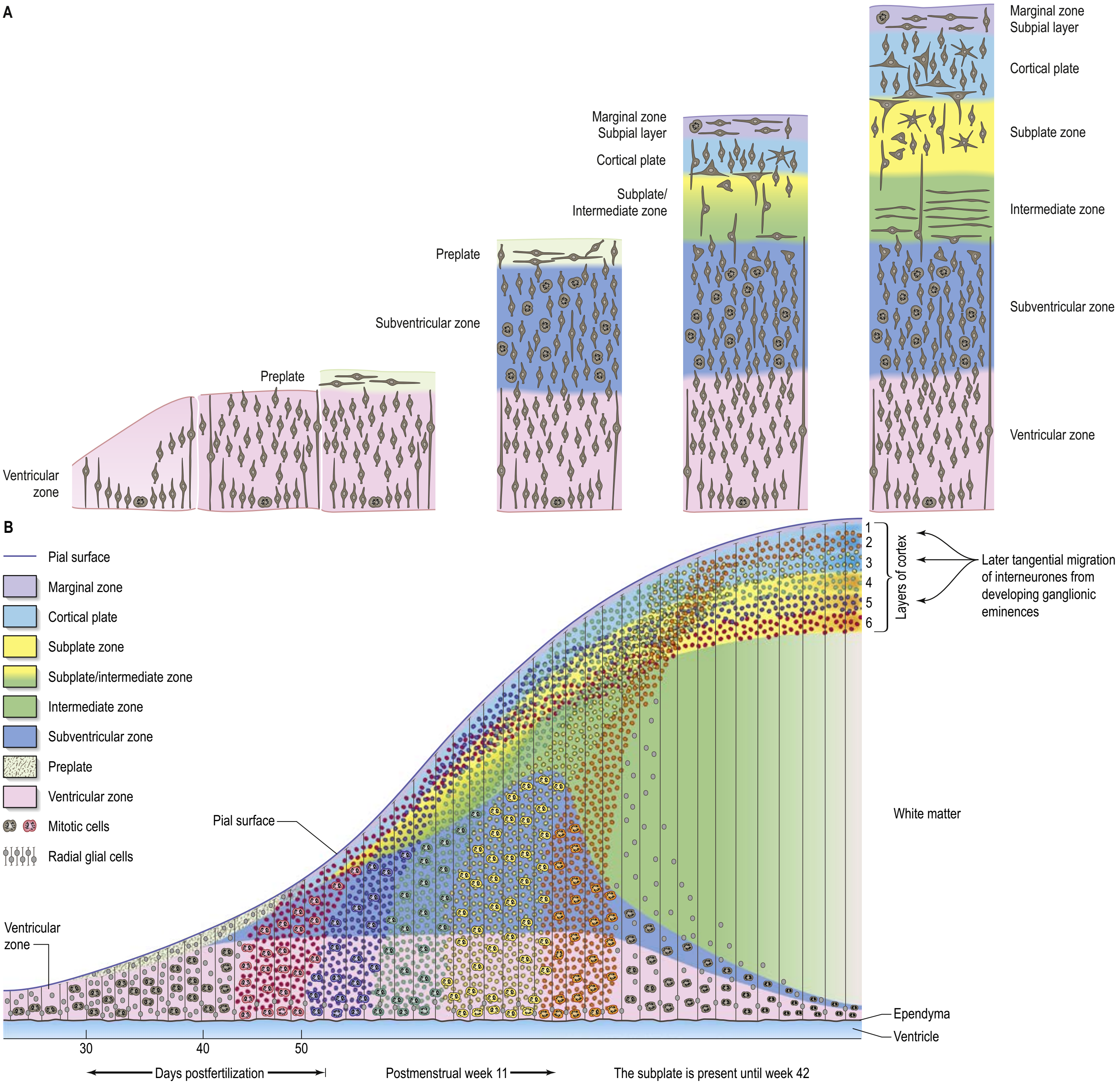
A
Ventricular zone
Preplate
Subventricular zone
Preplate
Marginal zone
Subpial layer
Cortical plate
Subplate/
Intermediate zone
Marginal zone
Subpial layer
Cortical plate
Subplate zone
Intermediate zone
Subventricular zone
Ventricular zone
B
Pial surface
Marginal zone
Cortical plate
Subplate zone
Subplate/intermediate zone
Intermediate zone
Subventricular zone
Preplate
Ventricular zone
Mitotic cells
Radial glial cells
Pial surface
Ventricular zone
1
2
3
4
5
6
Layers of cortex
Later tangential migration of interneurones from developing ganglionic eminences
White matter
Ependyma
Ventricle
30
40
50
Days postfertilization
Postmenstrual week 11
The subplate is present until week 42

Fig. 14.33 **A**, The layers of the developing telencephalon. The early pseudostratified arrangement of the neural tube is defined by radial glia that extend from the ventricular surface to the pial surface. Neuroblasts and glioblasts divide in the ventricular and subventricular zones and migrate radially along the radial glia to form a cortical plate and then a subplate. The preplate, subplate, subventricular and ultimately the ventricular zones recede during development and early postnatal life. **B**, Successive migration of neuroblasts from the ventricular and subventricular zones to the cortex. The first cells to migrate to the cortical plate and subplate zone form the deep cortical laminae. Later cells migrate radially between these cells to the outer part of the developing cortex. Note the extensive early proliferation of the subventricular zone and its later diminution as the cells it contains migrate radially to the cortex. The effect of this radial cell migration towards the developing cortical surface is expansion of the cortical area rather than an increase in cortical thickness. Axons from cells in the cortex extend through the intermediate zone which becomes cerebral white matter. Once the earliest cortical layers have formed, cells originating from the ganglionic eminences migrate tangentially into the cortical layers and form interneurones.

cells to migrate are destined for the deep cortical laminae and later groups pass through them to more superficial regions. The subplate zone exists until postmenstrual week 42 and is most prominent during mid-gestation: it contains neurones surrounded by a dense neuropil and is the site of the most intense synaptogenesis in the embryonic cortex (Molnar et al 2019). The cumulative effect of this radial and tangential growth is evident in a marked expansion of the surface area of the cortex without a comparable increase in its thickness (Rakic 1988, 2009).

The phylogenetically oldest regions in the pallial walls of the mammalian cerebral hemisphere are the first to differentiate during ontogeny: they border the interventricular foramen and its extension, the choroidal fissure, the lamina terminalis and the piriform lobe. The pallidum contributes interneurones to the formation of the cerebral cortex. A significant portion of GABAergic inhibitory (non-pyramidal) cells are generated not in the cortical ventricular zone, but along the inner curving border of the developing lateral ventricle, in the ganglionic (ventricular) eminences that will later form the lentiform and caudate nuclei (see Figs 14.27–14.28). The ganglionic eminences have three anatomical subdivisions, medial, lateral and caudal, distinguished by the molecular markers and cell

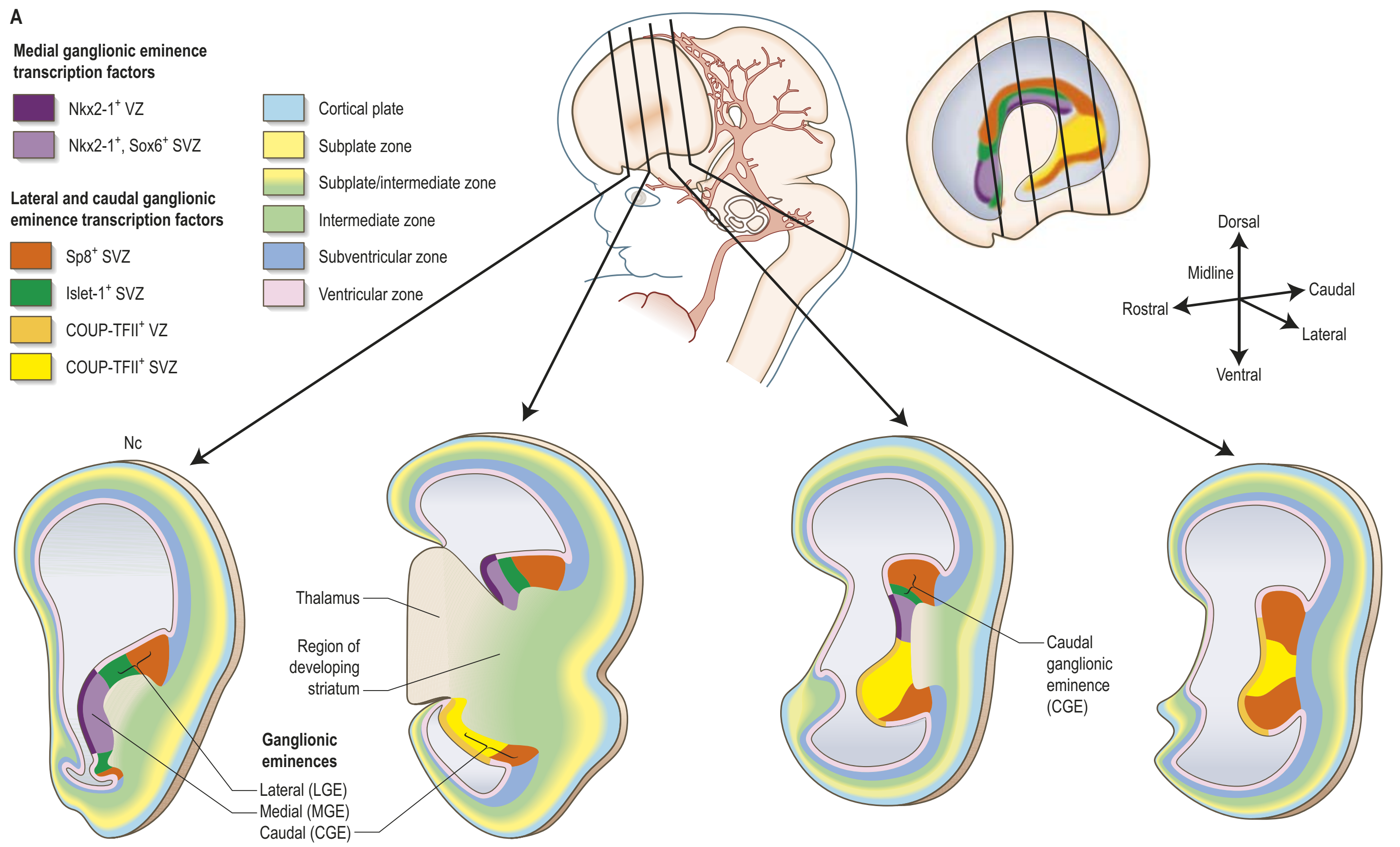

Fig. 14.34 **A**, Sections through the medial, lateral and caudal ganglionic eminences that are destined to become the caudate nucleus, part of the corpus striatum. Cells from these ganglionic eminences migrate into the subventricular zone and then to the subplate zone and cortical plate. The medial ganglionic eminence has strong Nkx2-1 expression in the ventricular (VZ) and subventricular (SVZ) zones. The lateral (LGE) and caudal (CGE) ganglionic eminences show expression patterns of Nkx2-1 and Sox6, COUP-TFII, Islet-1 (a transcription factor that marks the LGE SVZ and differentiating striatal cells in rodents) and Sp8. Sp8+ cells are mainly located in the SVZ; many of them express Ki67, a marker of proliferative cells. In the dorsal CGE, COUP-TFII+ cells are located mainly in the SVZ: most do not express Ki67. In the ventral CGE, COUP-TFII+ cells are in the VZ and SVZ, and many express Ki67. (Expression patterns as determined by Ma et al 2012.) (B–C, *continued online*)

types they produce (**Fig. 14.34**). Cortical interneurones are generated mainly in the caudal and medial parts of the ganglionic eminence and the preoptic area and migrate tangentially through the future striatocortical junction and the subplate to reach the cortex, governed by molecular cues including Semaphorin3a/f, CXCL12, Neuregulin1, Robo, and Ephrin (Métin et al 2006, Wonders and Anderson 2006, Ma et al 2012, Hansen et al 2013, Molnar and Butt 2013). Experimental evidence suggests that the developing cortical areal map is patterned in the same way as the rest of the body, by diffusible proteins (members of the FGF, Wnt, BMP and SHH families) that are released from signalling centres: in the cortex, FGF8 influences the rostrocaudal axis, and Wnts and BMP influence the dorsoventral axis. The extent to which these findings can be extrapolated from experimental animals, especially mice, to the developing human cortex remains speculative; there are indications that some mechanisms may be conserved (Silver et al 2019).

Although the biological significance of the inside-out gradient of neurogenesis is unclear, it is known that if the gradient is disturbed, by genetic or epigenetic factors, neurones display abnormal cortical function. Failure or delay in neuronal migration has been associated with a wide range of disorders, such as lissencephaly and schizophrenia (Wu et al 2014).

After the initial generation of neuroblasts the ventricular and subventricular zones give rise to glioblasts that migrate to the cortical subplate. Oligodendrocyte progenitor cells are prevalent initially in the subventricular zone and after postmenstrual weeks 19–22 in the subplate zone (Jakovcevski et al 2009). The cues that initiate myelination in some axons and not others are still unclear: regional differences in oligodendrocyte-lineage cells, which probably emerge after specification of oligodendrocyte precursors, may explain some differences in myelination between CNS regions (Osso and Chan 2017, Saab and Nave 2017). In human cerebral white matter, the oligodendrocyte lineage appears to involve three successive stages (pre-oligodendrocyte, immature oligodendrocyte and mature oligodendrocyte) from about postmenstrual week 22 (Back et al 2001). Ventrodorsal gradients of oligodendrocyte precursor cell density and of myelination have been described in the telencephalon.

The sequence of myelination of the motor pathways may explain, at least partially, the order of development of muscle tone and posture in the premature infant and full-term neonate. Myelination of the various subcorticospinal pathways (vestibulospinal, reticulospinal, olivospinal and tectospinal) starts at postmenstrual weeks 24–30 for the medial tracts, and at postmenstrual weeks 28–34 for the lateral tracts (Dubois et al 2014) (**Fig. 14.35**).

The vast species differences between invertebrate, murine, non-human primate and primate nervous systems pose particular, sometimes intractable, problems for neuroscientists exploring the evolution of the human cerebral cortex. Current understanding of the pre- and postnatal events that regulate the numbers of neurones and their associated glia; the dynamics of neuronal migration to proper layers, columns and regions; the enormous expansion of the cortical surface; and the development of connectivity, particularly networks mediating higher cognitive functions and language, remains in its infancy for the human cortex. (For further reading on the evolution of the neocortex, see Rakic (2009), Lui et al (2011), Geschwind and Rakic (2013), Lister et al (2013), Silver et al (2019).)

The Allen Human Brain Atlas (http://human.brain-map.org/) uses DNA microarrays for transcriptional profiling of several hundred locations spanning the adult human neocortex (Hawrylycz et al 2012), while the NIH Blueprint Non-Human Primate Atlas profiles individual cortical layers in the Rhesus monkey (http://www.blueprintnhpatlas.org/). Similarly, the BrainSpan Atlas of the Developing Human Brain (http://www.brainspan.org/) is a resource for studying the transcriptome across human brain development, using RNA sequencing on discrete cortical regions across an entire lifespan, and comparative DNA microarrays on laser-microdissected individual layers of different regions of the developing neocortex.

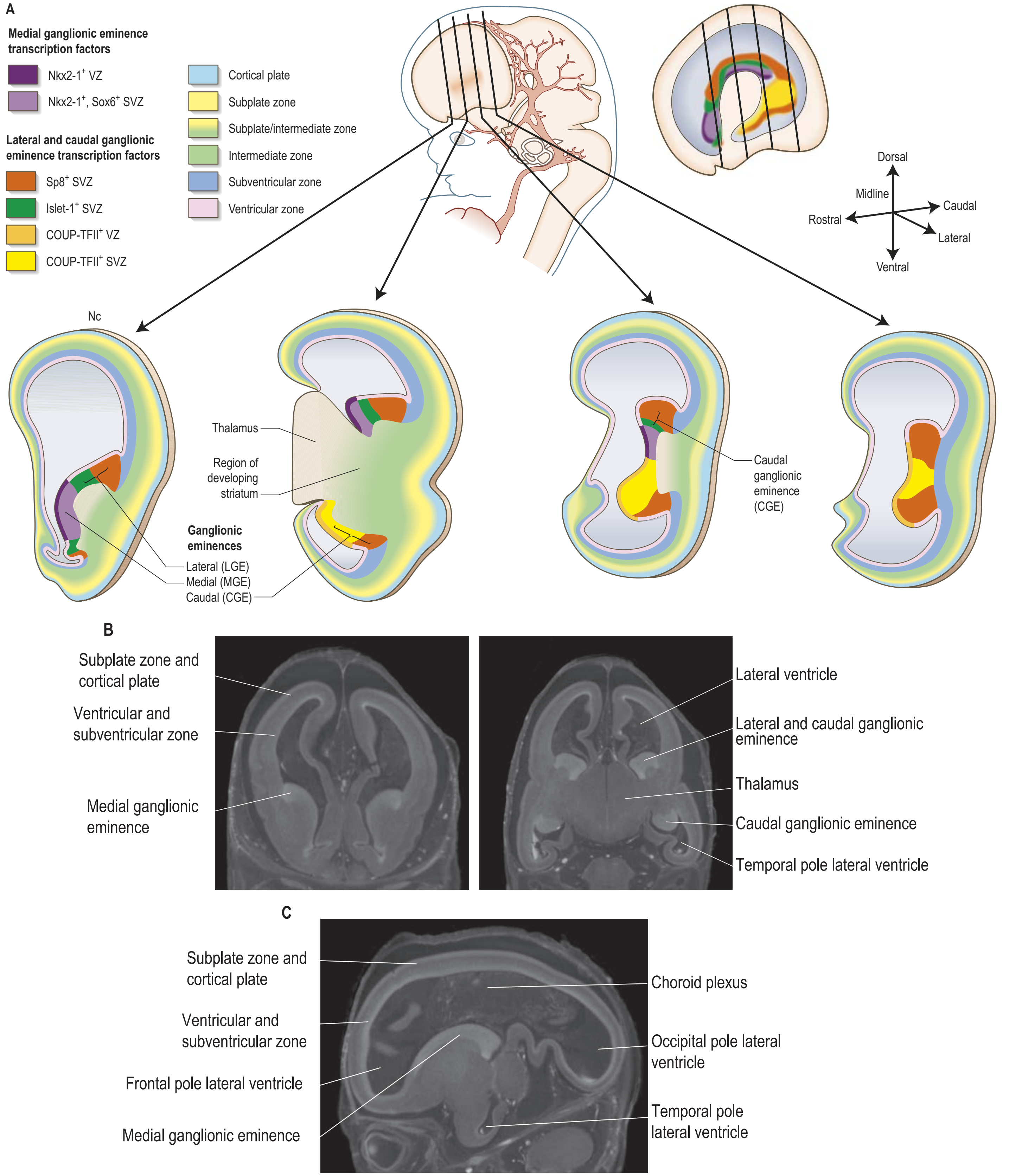
A
Medial ganglionic eminence transcription factors
Nkx2-1+ VZ
Nkx2-1+, Sox6+ SVZ
Lateral and caudal ganglionic eminence transcription factors
Sp8+ SVZ
Islet-1+ SVZ
COUP-TFII+ VZ
COUP-TFII+ SVZ
Cortical plate
Subplate zone
Subplate/intermediate zone
Intermediate zone
Subventricular zone
Ventricular zone
Dorsal
Midline
Caudal
Rostral
Lateral
Ventral
Nc
Thalamus
Region of developing striatum
Ganglionic eminences
Lateral (LGE)
Medial (MGE)
Caudal (CGE)
Caudal ganglionic eminence (CGE)
B
Subplate zone and cortical plate
Ventricular and subventricular zone
Medial ganglionic eminence
Lateral ventricle
Lateral and caudal ganglionic eminence
Thalamus
Caudal ganglionic eminence
Temporal pole lateral ventricle
C
Subplate zone and cortical plate
Ventricular and subventricular zone
Frontal pole lateral ventricle
Medial ganglionic eminence
Choroid plexus
Occipital pole lateral ventricle
Temporal pole lateral ventricle

Fig. 14.34 **A**, Diagrams of sections through the medial, lateral and caudal ganglionic eminences that are destined to become the caudate nucleus, part of the corpus striatum. Cells from these ganglionic eminences migrate into the subventricular zone and then to the subplate zone and cortical plate. The medial ganglionic eminence has strong Nkx2-1 expression in the ventricular (VZ) and subventricular (SVZ) zones. The lateral (LGE) and caudal (CGE) ganglionic eminences show expression patterns of Nkx2-1 and Sox6, COUP-TFII, Islet-1 (a transcription factor that marks the LGE SVZ and differentiating striatal cells in rodents) and Sp8. Sp8+ cells are mainly located in the SVZ; many of them express Ki67, a marker of proliferative cells. In the dorsal CGE, COUP-TFII+ cells are located mainly in the SVZ: most do not express Ki67. In the ventral CGE, COUP-TFII+ cells are in the VZ and SVZ, and many express Ki67. (Expression patterns as determined by Ma et al 2012.) **B–C**, MicroCT images of a fetus at 14 postmenstrual weeks. **B**, Rostral and further caudal coronal sections of the cerebral hemispheres and developing corpus striatum. **C**, Lateral sagittal section of the left cerebral hemisphere and developing corpus striatum. (B–C, Courtesy of Dr Owen Arthurs and Dr Susan Shelmerdine, Great Ormond Street Hospital, London.)

Culture of hPSCs (ESC and iPSCs) into 3D organoids has provided new ways to study cortical development: cells recapitulate temporal and spatial migration. Optimized culture methods have produced outer radial glial progenitor cells; self-organized cortical tissues show early-born neurones migrating to deep cortical plate layers and later-born cells migrating to the upper layers. Cerebral organoids showing discrete brain regions and tissues, including the hippocampus, midbrain/hindbrain boundary and choroid plexus, have been used to study neurodevelopmental disorders and neurodegenerative diseases (Lee et al 2017, Amin and Paşca 2018, Wang 2018). Spontaneous cellular network formation that exhibits periodic and regular oscillatory events dependent on glutamatergic and GABAergic signalling has been reported in long-term culture of cerebral organoids (Trujillo et al 2019).

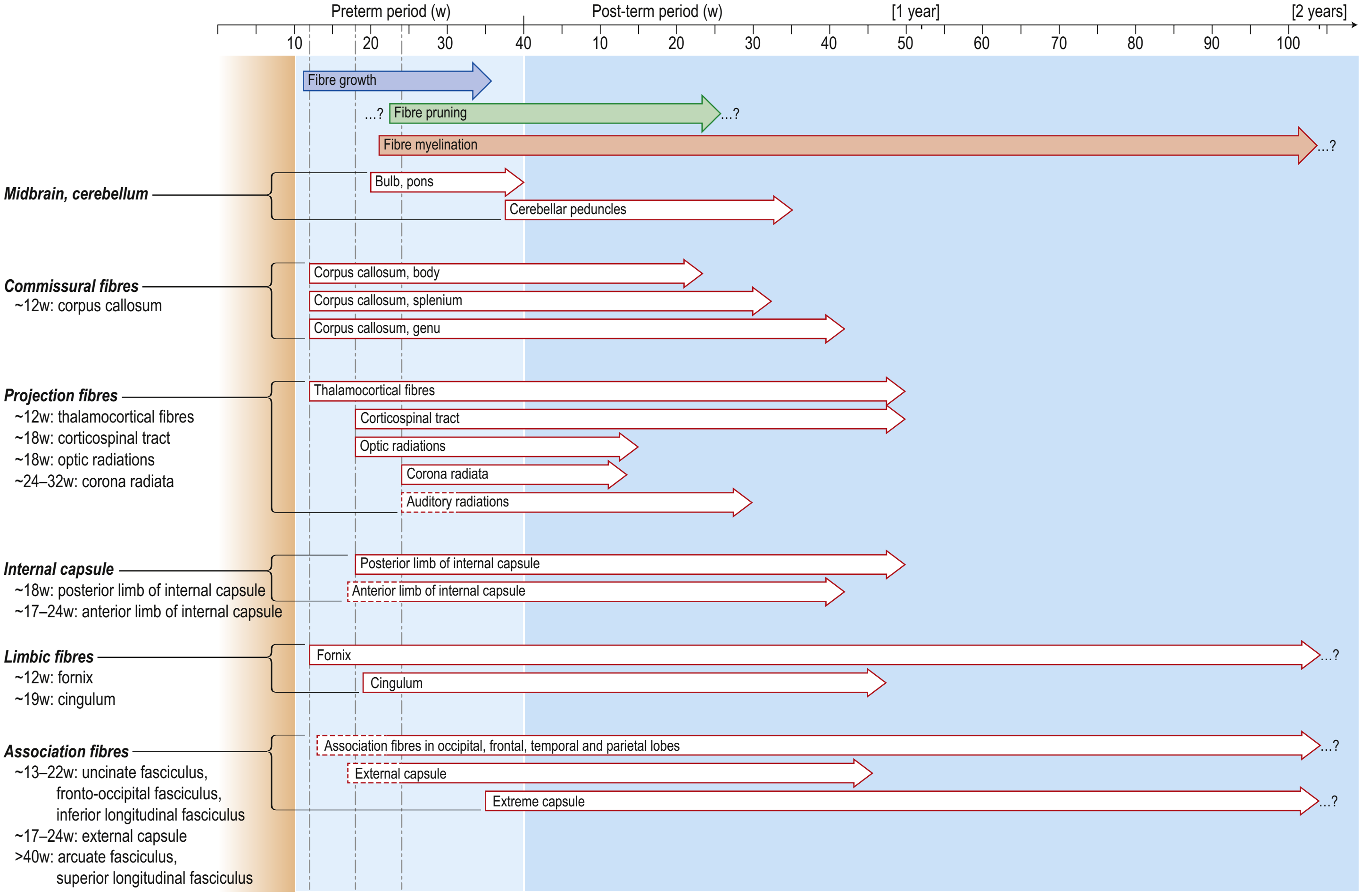

Fig. 14.35 A general timeline of white matter development. (Based on Dubois et al 2014.)

VASCULAR SUPPLY

Cerebral arteries

The cranial extensions of the dorsal aortae that supply the head receive blood entirely through the third aortic arches. The internal carotid artery is formed progressively from the third arch artery (which contributes its proximal part) (see Fig 17.9) and a further forward continuation that differentiates, at the time of regression of the first and second aortic arches, from the capillary plexus extending to the walls of the forebrain and midbrain. At its anterior extremity, this primitive internal carotid artery divides into cranial and caudal divisions. The former terminates as the primitive olfactory artery and supplies the developing regions implied (see Fig. 17.8). The latter sweeps caudally to reach the ventral aspect of the midbrain; its terminal branches are the primitive mesencephalic arteries. Simultaneously, bilateral longitudinal channels differentiate along the ventral surface of the rhombencephalon from a plexus fed by intersegmental and transitory presegmental branches of the dorsal aorta and its forward continuation. The most important of the presegmental branches is closely related to the trigeminal nerve, the primitive trigeminal artery. Otic and hypoglossal presegmental arteries occur and may persist. The longitudinal channels later connect cranially with the caudal divisions of the internal carotid arteries (each of which gives rise to an anterior choroidal artery supplying branches to the diencephalon, including the telae choroideae and midbrain), and caudally with the vertebral arteries through the first cervical intersegmental arteries. Fusion of the longitudinal channels results in the formation of the basilar artery. The caudal division of the internal carotid artery becomes the posterior communicating artery and the stem of the posterior cerebral artery. The remainder of the posterior cerebral artery develops comparatively late, probably from the stem of the posterior choroidal artery, which is annexed by the caudally expanding cerebral hemisphere, its distal portion becoming a choroidal branch of the posterior cerebral artery. The posterior choroidal artery supplies the tela choroidea at the future temporal end of the choroidal fissure; its rami advance through the tela to become confluent with branches of the anterior choroidal artery. The cranial division of the internal carotid artery gives rise to anterior choroidal, middle cerebral and anterior cerebral arteries. The stem of the primitive olfactory artery remains as a small medial striate branch of the anterior cerebral artery. The cerebellar arteries, of which the superior is the first to differentiate, emerge from the capillary plexus on the wall of the rhombencephalon.

The source of the blood supply to the territory of the trigeminal nerve varies at different stages in development. When the first and second aortic arch arteries begin to regress, the supply to the corresponding arches is derived from a transient ventral pharyngeal artery, which grows from the aortic sac and terminates by dividing into mandibular and maxillary branches.

Leptomeningeal arteries

At stages 20–23 the circle of Willis is completed. The anterior communicating arteries develop by stage 23. An anular network of leptomeningeal arteries, originating mainly from each middle cerebral artery, passes over each developing cerebral hemisphere. Caudally, similar meningeal branches arise from the vertebral and basilar arteries and embrace the cerebellum and brainstem. The further development of the telencephalon somewhat obscures this early pattern over the cerebrum.

The meningeal arteries so formed have been classified into three groups: paramedian, short circumferential and long circumferential arteries. They can be described both supratentorially and infratentorially, and all give off fine side branches and end as penetrating arteries. Of the supratentorial vessels, the paramedian arteries have a short course prior to penetrating the cerebral neuropil (e.g. branches of the anterior cerebral artery); the short circumferential arteries have a slightly longer course before becoming penetrating arteries (e.g. the striate artery); and the long circumferential arteries reach the dorsal surface of the hemispheres. Infratentorial meningeal arteries are very variable. The paramedian arteries, after arising from the basilar or vertebral arteries, penetrate the brainstem directly. The short circumferential arteries end at the lateral surface of the brain before

Fig. 14.36 Development of cerebral blood vessels. **A**, The brain is surrounded by a system of leptomeningeal arteries from afferent trunks at its base. Intracerebral arteries arise from this system and converge (ventriculopetally) towards the ventricle (the inner circle in this diagram). **B**, A few deep, penetrating vessels supply the brain close to the ventricle and send ventriculofugal arteries towards the ventriculopetal vessels without making anastomoses. **C**, The arrangement of ventriculopetal and ventriculofugal vessels around a cerebral hemisphere. **D**, The similar arrangement of vessels around the cerebellum. **E**, Changes in the arterial pattern of the human cerebrum between postmenstrual weeks 24 and 34. **F**, Arterial supply to the basal nuclei at postmenstrual week 30. (A–D, With permission from Van den Bergh R, Van der Eecken H 1968 Anatomy and embryology of cerebral circulation. Prog Brain Res 30:1–25; E–F, With permission from the BMJ Publishing Group from Hambleton G, Wigglesworth JS 1976 Origin of intraventricular haemorrhage in the preterm infant. Arch Dis Child 51:651–9.)

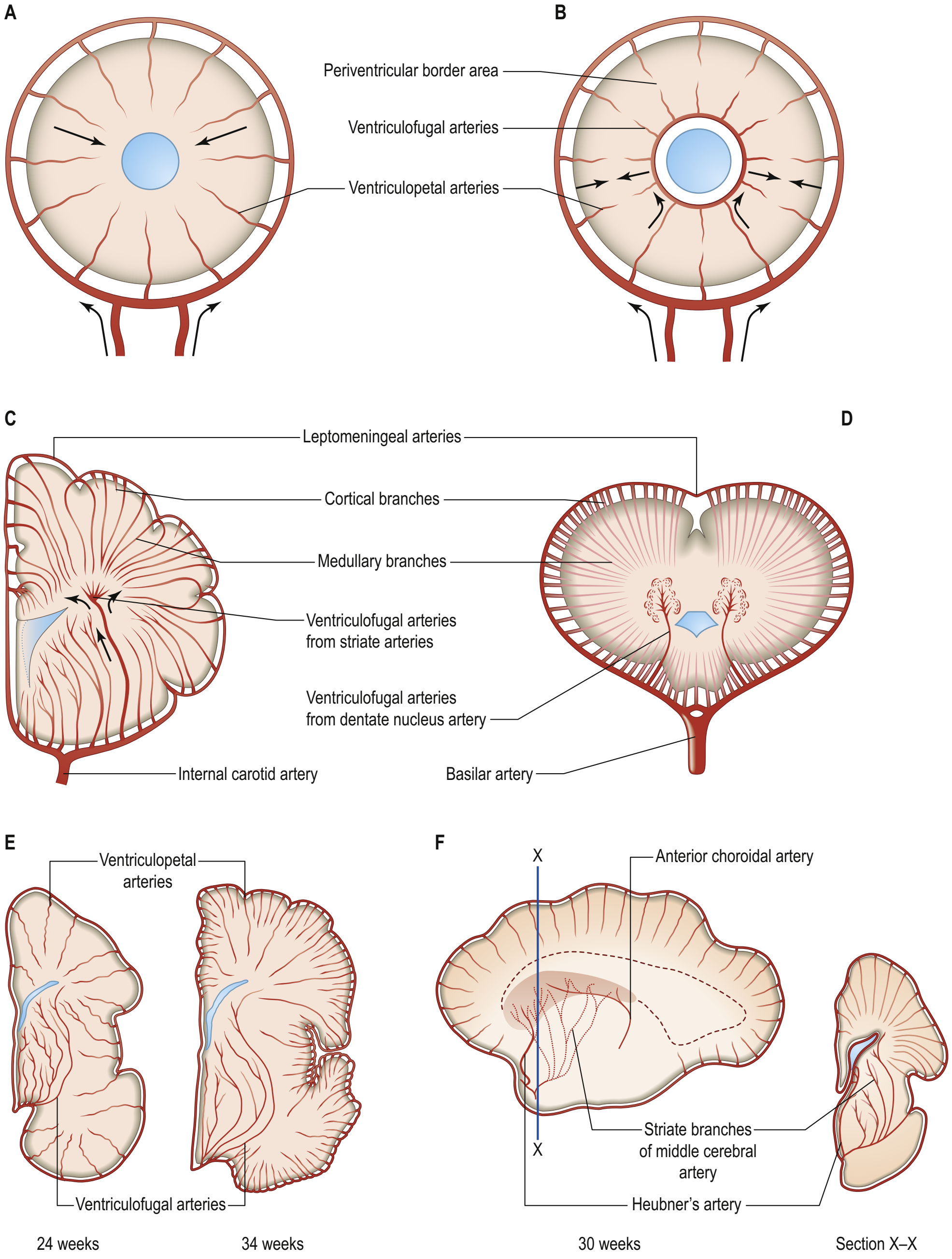
A
B
Periventricular border area
Ventriculofugal arteries
Ventriculopetal arteries
C
D
Leptomeningeal arteries
Cortical branches
Medullary branches
Ventriculofugal arteries from striate arteries
Ventriculofugal arteries from dentate nucleus artery
Internal carotid artery
Basilar artery
E
F
Ventriculopetal arteries
Ventriculofugal arteries
24 weeks
34 weeks
X
X
Anterior choroidal artery
Striate branches of middle cerebral artery
Heubner's artery
30 weeks
Section X–X

penetration and the long circumferential arteries later form the range of cerebellar arteries. These vessels, arranged as a series of loops over the brain, arise from the circle of Willis and brainstem vessels on the base of the brain.

By postmenstrual week 16 the anterior, middle and posterior cerebral arteries that contribute to the formation of the circle of Willis are well established. The leptomeningeal arteries arising from them display a simple pattern with little tortuosity and very few branches. With the increasing age of the fetus and acquisition of the gyral pattern on the surface of the brain, their tortuosity, diameter and number of branches all increase. The branching pattern is completed by postmenstrual week 28 and the number of branches does not increase further. Numerous anastomoses (varying in size from 200 to 760 μm) occur between the arteries in the depths of the developing sulci, nearly always in the cortical boundary zones of the three main cerebral arteries supplying each hemisphere. The number, diameter and location of these anastomoses change as fetal growth progresses, reflecting the regression and simplification of the complex embryonic cerebral vascular system.

Vascularization of the brain

The brain becomes vascularized by angiogenesis rather than by direct invasion by angioblasts. The first indication of pia mater, containing a plexus of blood vessels that forms on the neural surface, is seen at stage 11 around the caudalmost part of the rhombencephalon and extends to the mesencephalic level by stage 12. The pial basement membrane is formed from interaction between neural crest cells, the meningeal extracellular matrix and the basal processes (end feet) of the radial glial cells. Meningeal extracellular matrix-mediated activation of integrins promotes proliferation of basal radial glia progenitors, which in turn sustain the expression of the extracellular matrix genes (Silver et al 2019). Vessels in the pial plexus sprout and form branches that elongate at the junction between the ventricular and marginal zones; the branches project laterally within the inter-rhombomeric boundaries and longitudinally adjacent to the median floorplate. Additional sprouts later penetrate the inter-rhombomeric regions on the walls and floor of the hindbrain. Branches from the hindbrain elongate towards and join the branches in the inter-rhombomeric junctions, forming primary vascular channels between rhombomeres and longitudinally on each side of the median floorplate. Later additional sprouts invade the hindbrain within the rhombomeres, anastomosing in all directions.

Leptomeningeal perforating branches pass into the brain parenchyma as cortical, medullary and striate branches (Fig. 14.36). The cortical vessels supply the cortex via short branches that may form precapillary anastomoses, whereas the medullary branches supply the white matter. The medullary branches converge towards the ventricle but rarely reach it and often follow a tortuous course as they pass around bundles of nerves. The striate branches penetrate the brain through the anterior perforated substance and supply the basal nuclei and internal capsule via a sinuous course; they are larger than the medullary branches and the longest reach close to the ventricle. The periventricular region and basal nuclei are also supplied by branches from the tela choroidea, which develops from the early pial plexus, becoming medially and more deeply placed as the telencephalon enlarges.

The cortical and medullary branches irrigate a series of corticosubcortical cone-shaped areas, each centred around a sulcus containing an artery. They supply a peripheral portion of the cerebrum and are grouped as ventriculopetal arteries. In contrast, striate branches arborize close to the ventricle and supply a more central portion of the cerebrum. Together with branches from the tela choroidea, they give rise to ventriculofugal arteries that supply the ventricular zone (germinal matrix of the brain) and also send branches towards the cortex. The ventriculopetal and ventriculofugal arteries run towards each other but do not anastomose. The ventriculopetal arteries form networks of small arterioles (see Fig. 14.36) and supply relatively more mature regions of the brain compared to the ventriculofugal vessels. The latter are subject to constant remodelling and do not develop tunicae mediae until ventricular zone proliferation is completed. The same pattern of centripetal and centrifugal arteries develops around the fourth ventricle. The ventriculofugal circulation is more extensive in the cerebellum than in the telencephalon. The arteries arise from the various cerebellar arteries and course with the cerebellar peduncles directly to the centre of the cerebellum, bypassing the cortex. The ventriculopetal arteries are derived from the meningeal vessels over the cerebellar surface and most terminate in the white matter.

At postmenstrual week 24 the blood supply to the basal nuclei and internal capsule is relatively well developed, via a prominent Heubner's artery (arteria recurrens anterior), a branch of the anterior cerebral artery. The cortex and the white matter regions are rather poorly vascularized at this stage. The distribution of arteries and veins on the lateral aspect of the cerebral hemispheres is affected by the formation of the lateral fissure and the development of cerebral sulci and gyri. Between postmenstrual weeks 12–20 the middle cerebral artery and its branches are relatively straight, branching in an open-fan pattern. At the end of postmenstrual week 20 the arteries become more curved as the opercula begin to appear and submerge the insular cortex. The area supplied by the middle cerebral artery becomes dominant when compared to the territories supplied by the anterior and posterior cerebral arteries. Early arterial anastomoses appear around postmenstrual week 16 and increase in size with advancing fetal age. The sites of anastomoses between the middle and anterior cerebral arteries move from the convexity of the brain towards the superior sagittal sinus and anastomotic connections between the middle and posterior cerebral arteries shift towards the basal aspect of the brain.

By postmenstrual weeks 32–34 marked involution of the ventricular zone (germinal matrix) has occurred and the cortex acquires its complex gyral pattern and an increased vascular supply. Ventricular zone capillaries are gradually remodelled to blend with the capillaries of the caudate nucleus. Heubner's artery eventually supplies only a small area at the medial aspect of the head of the caudate nucleus. In the cortex, there is progressive elaboration of cortical blood vessels (see Fig. 14.36). Towards the end of the third trimester, the balance of cerebral circulation shifts from one that is central and basal nuclei-orientated, to one that predominantly serves the cortex and white matter.

Vessels of the ventricular zone (germinal matrix) and formation of the blood–brain barrier

The capillary bed of the ventricular zone is supplied mainly by Heubner's artery and terminal branches of the lateral striate arteries from the middle cerebral artery. The capillary channels in the ventricular zone open at right-angles directly into the veins. Subependymal veins (septal, choroidal, thalamostriate and posterior terminal) flow towards the interventricular foramen where there is a change of direction and the veins recurve at an acute angle to form the paired internal cerebral veins.

Vessels within the ventricular and subventricular zones have been described as less mature than cortical vessels: their apparent fragility has been implicated in the aetiopathogenesis of intraventricular haemorrhage in premature infants. A rounded contour, relative paucity of pericytes, an immature basal lamina and a deficiency of glial fibrillary acidic protein (GFAP) in the ensheathing astrocyte end feet have all been cited as indicators of the immaturity of the microvasculature of the germinal matrix (Ballabh 2010). The ventricular and subventricular zones retain an embryonic capillary bed until cell proliferation is complete, which means that the highly cellular structure of the ventricular zone is a temporary feature. The capillary beds have the capacity to remodel after the ventricular cells finally differentiate as ependyma.

The direct mutual support of two epithelial layers and their shared basal laminae, rather than support of an epithelium by a lamina propria is unique, seen elsewhere only in the kidney glomerular basement membrane and alveolar-capillary membrane (see Fig 11.2). In the nervous system the cells of the neurovascular unit, endothelial, astrocyte and pericyte, form a blood–brain barrier that matures at different times in different brain regions during development. The permissive interactions between these epithelial phenotypes via their respective basal laminal secretions may contribute towards the patterning of the brain parenchymal spaces. Endothelial cells have a complex glycocalyx and are joined by tight and gap junctions; the integral membrane protein, occludin, spans the intracellular gaps between adjacent cells and claudins increase the hydraulic and electrical resistance across the endothelium (Pearce 2018). Pericytes, sparse in fetal vessels, are required for endothelial–astrocyte barrier formation and disruption of pericyte–endothelial cell interaction may lead to barrier dysfunction. Cerebral vessels differ during development: their proximity to the great arteries; position in the cortex or white matter; reactions to fluctuating oxygen and carbon dioxide tissue levels; expression of membrane receptors; and recent vasoreactivity to a given stimulus, all contribute to their extensive functional heterogeneity (Pearce 2018). Endothelial–astrocyte interactions can affect both neuronal migration and blood–brain barrier function (Keep et al 2019) (Ch. 3). It has been suggested that interstitial fluid from the neurovascular unit flows along an intramural perivascular pathway (Engelhardt et al 2016b).

The ventricular zone operates a brain–cerebrospinal fluid barrier during development but not once the ventricular zone has ceased as a dividing layer and the cells have differentiated to form ependyma. The choroid plexuses, sites of a blood–cerebrospinal fluid barrier, function during development and control paracellular transport to the cerebrospinal fluid (Neuwelt et al 2011).

Cerebral veins

The developing venous channels in the brain direct blood from the capillary networks along two main routes, superficial and deep, from pial vessels supplying the cortical and subcortical regions, and from the ventricular zone and subependymal regions, respectively. The arterial supply is ventriculopetal in the cortical/subcortical zone and ventriculofugal in the ventricular zone, whereas the venous return is ventriculofugal in pial veins and ventriculopetal in the subependymal region.

The pial capillary plexus supplies the developing cortical plate and subjacent developing white matter. Pial veins deep within the sulci drain this region, receiving superficial medullary veins at the grey/white matter interface and numerous fine short subcortical veins that may join arcuate veins within the cortex before draining into intracortical veins. The latter join cortical veins on the cerebral cortex that may attach to the dura or run within the dural layers towards the closest dural sinus. At the superior sagittal sinus, the cortical veins join at an acute angle, against the dural blood flow: this arrangement is thought to be due to differential growth of the cerebrum in the third trimester (Pearl et al 2011). Venous vessel density in the cortex and subcortical white matter is low between postmenstrual weeks 16 and 28 and increases after postmenstrual week 36. The superior, middle, inferior, anterior and posterior cortical cerebral veins appear more tortuous than the meningeal arteries. Rapid cortical development correlates with the regression of the middle cerebral vein and its tributaries and the development of ascending and descending cortical veins. Cortical cerebral veins and the anastomoses between them can be identified from postmenstrual week 16. The inferior anastomotic vein (of Labbé), an anastomosis between the middle and inferior cerebral veins, becomes recognizable at postmenstrual week 20, and the superior anastomotic vein (of Trolard), connecting the superior and middle cerebral veins, is seen after the end of postmenstrual week 30.

The ventricular zone capillary plexus is drained by a deep venous plexus that extends to the enlarging subcortical region. This plexus forms deep medullary veins within a region filled with migrating neurones and growing axons. Vessel density is high in this region between postmenstrual weeks 16–24, transiently decreases in postmenstrual weeks 28–36 and increases after postmenstrual week 39 (Takashima et al 2009). The deep medullary veins are very long veins; the deepest join arcades of larger veins until all drain into subependymal veins

Sympathetic axons are seen in the walls of arteries supplying the rostral brain regions by about postmenstrual weeks 19–23. Unlike adult cerebral arteries, cholinergic nerves appear at the same time: fetal and neonatal cerebral arteries dilate in response to low concentrations of acetylcholine (Pearce 2018). Fetal perivascular innervation includes sensory fibres from the trigeminal ganglion (able to release vasoactive intestinal polypeptide, calcitonin gene-related peptide, substance-P, somatostatin and cholecystokinin) and, particularly around the arteries that form the circle of Willis and in the pial circulation, nerves that release neuropeptide Y (Pearce 2018). Very little is known about the functions of the neurotransmitters that act on the fetal cerebral circulation.

within the ventricular zone that become the internal cerebral veins. Early in development the invagination of pia mater to form the choroid plexuses gives rise to the tela choroideae which are drained by a transitory vessel, the median prosencephalic vein (of Markowski); this vessel gives rise to bilateral veins of the lateral choroid plexuses, bilateral internal cerebral veins and the great cerebral vein that drains into the straight sinus (Pearl et al 2011).

The development of the primary head veins, dural stems and dural sinuses is described in Chapter 17.

Developmental venous anomalies

Developmental venous anomalies include any changes to the previously described developmental pattern such that the usual balance of cortical and medullary venous drainage is not evident. Lack of cortical veins may lead to parts of the cortex draining only into the subependymal network via larger deep medullary veins, in a ventriculopetal rather than ventriculofugal matter. Conversely, a significant connection between the deep medullary veins and an intracortical vein may result in a ventriculofugal rather than ventriculopetal flow. Enlarged deep medullary veins, recognized as caput medusa, is seen in both variants. A vein of Galen aneurysmal malformation is seen in up to 30% of intracranial vascular anomalies; the early median prosencephalic vein does not regress, but remains connected to one or more choroidal arteries and enlarges as a result of the retained arteriovenous anastomosis (Pearl et al 2011, Cao and Cai 2019).

Interventricular haemorrhage

Anatomical variability of the course of the subependymal veins draining the proliferating ventricular zone (germinal matrix) is reported to be a predisposing factor for germinal matrix haemorrhage–interventricular haemorrhage (GMH–IVH), together with the level of developmental maturity of the ventricular zone capillary bed and its drainage. Each subependymal vein exhibits a U-shaped curve at the level of the interventricular foramen as it passes from the caudate–thalamic groove to its confluence with the internal cerebral vein. Increased vessel curvature (a more acute angle) is associated with blood flow alterations, increased luminal shear stress and possible venous thrombosis. Anomalous subependymal vein curvature in premature infants with GMH–IVH has been positively associated with unilateral haemorrhage occurring only in the hemisphere with a subependymal vein variant (Tortora et al 2018).

Periventricular leukomalacia

In fetuses and preterm infants of less than postmenstrual week 30 the blood vessels in the ventricular zone (germinal matrix) contain no smooth muscle, collagen or elastin fibres and have a disproportionately small number of reticulin fibres. In later preterm infants, the basal lamina surrounding the vessels is deficient in fibronectin, and thicker and more irregular than cortical vessels. In the periventricular regions at this time, the widening intermediate zone is filled with neuroblastic and glioblastic progeny from the ventricular and subventricular zones and the medial and lateral eminences migrating to the cortical subplate; axons extending from differentiating cortical neurones to the developing basal nuclei; axons extending from differentiating basal nuclei neurones to the cortex, all with their associated populations of pre-oligodendrocytes. This region represents a boundary zone between cortical and subcortical white matter supplied by superficial cortical arteries and veins, and the ventricular and subventricular zones supplied by the deeper striate arteries and deep medullary veins, and can be regarded as a watershed area between ventriculopetal and ventriculofugal circulations. Perturbation of cerebral blood flow in this watershed area can lead to a spectrum of developing white matter injury (see below).

THE NEONATAL BRAIN

Preterm neonate

Those babies born premature and with very low birth weight have been shown to have an altered cortical thickness that is still present in late teenage years (Bjuland et al 2013). It is not clear whether such changes are a consequence of preterm delivery, of perinatal brain injury or of fetal inflammatory response syndrome. Approximately 50% of preterm births are associated with clinical and subclinical chorioamnionitis (Maltepe and Penn 2018). Extremely and very preterm infants are usually stabilized by assisted ventilation, however, ventilation-induced lung injury in preterm infants also causes alveolar injury and release of cytokines that contribute to a systemic inflammatory response affecting the brain in those without prior infection (Barton et al 2015). Very preterm infants are also thought to be at risk of altered postnatal brain growth because of epigenetic regulation (DNA methylation) of the serotonin transported gene, as a consequence of early neonatal intensive care stress (Fumagalli et al 2018).

Preterm infants born before postmenstrual week 27 are at risk during early postnatal life of perturbation of the intermediate zone and the developing white matter (Ment and Sould 2012, Molnar and Rutherford 2013). Serial postnatal MRI scans of a group of infants delivered before postmenstrual week 27 (postnatal age counted sequentially in postmenstrual weeks), found increasing pathological changes with age, with about 20% showing white matter changes by 28 postmenstrual weeks, 50% showing changes during postmenstrual week 29 and about 80% exhibiting diffuse white matter signal anomalies by postmenstrual week 40 (Volpe 2017).

It was thought that in the preterm infant, where autoregulation of cerebral blood flow is limited, hypoperfusion of the intermediate zone was sufficient to cause local ischaemic lesions resulting in periventricular leukomalacia (PVL). PVL can also occur in full-term infants with congenital cyanotic heart anomalies. It is now thought that the disturbance of the differentiation of pre-oligodendrocytes (which are particularly affected by swings in cerebral ischaemia and reperfusion), accompanying astrocytosis and microgliosis, and prenatal systemic infection and inflammation cause hypomyelination (Volpe et al 2011, Back 2017). Histopathological studies now identify a spectrum of white matter injury from macroscopic lesions that are easily recognized on MRI, to microscopic focal necrotic lesions; the terms severe, moderate and mild white matter injury have been recommended to describe the condition (Volpe 2017). Studies on the long-term effects of preterm delivery note that even late preterm birth (postmenstrual weeks 34–37) has long-term effects. The late preterm brain may be unable to cope with postnatal conditions that may add to the problems of immaturity: for example, speech and language acquisition are delayed, as are school readiness and academic performance (Woythaler 2019).

Full-term neonate

Because the head is large at birth, measuring one-quarter of the total body length, the brain is also proportionally larger. The brain of a full-term (postmenstrual week 40) neonate ranges from 300 g to 400 g in weight, with an average of 350 g; the brains of neonatal males are slightly heavier than those of females. The brain occupies 97.5% of the cranial cavity from birth to 6 years of age, after which the space between the brain and skull increases in volume until the adult brain occupies only 92.5% of the cranial cavity. The cerebral ventricles are relatively larger in the neonatal brain than they are in the adult with a total of 10–15 ml of cerebrospinal fluid when delivered vaginally and 30 ml when delivered by caesarean section (as the head moves down the birth canal and is compressed, the cerebrospinal fluid is pushed out into the venous sinuses, whereas this does not happen in a caesarean delivery).

The sulci of the cerebral hemispheres appear after postmenstrual week 24. At full term, the general arrangement of sulci and gyri is present, but the insula is not completely covered, the central sulcus is situated further rostrally, and the lateral sulcus is more oblique than in the adult. The caveat here is that most of the developmental stages of sulci and gyri have been identified in the brains of premature infants where sulci are shallower at their equivalent postmenstrual week 40 than those of full-term neonates (Engelhardt et al 2016a, Shimony et al 2016). Of the cranial nerves, the olfactory nerve and the optic nerve at the chiasma are relatively much larger than they are in the adult, whereas the roots of the other cranial nerves are relatively smaller.

Reflexes present in the perinatal period

At birth mammals exhibit a range of coordinated motor movements that enhance their survival; these are species-specific. In humans, early reflex patterns, often somewhat erroneously termed ‘primitive’ reflexes, indicate the patterns of activity of multiple muscle groups present at birth (Feldman and Chaves-Gnecco 2018). Five tests of neurological development are most useful in determining developmental age. Lower limb flexor tone is detectable from about postmenstrual week 29. The pupillary reflex is consistently absent before postmenstrual week 29 and present after postmenstrual week 31; the glabellar tap, a blink in response to a tap on the glabella, is absent before postmenstrual week 32 and present after postmenstrual week 34; the neck-righting reflex appears between postmenstrual weeks 34–37; the traction response, where flexion of the neck or arms occurs when the baby is pulled up by the wrists from the supine position, appears after postmenstrual weeks 33; head-turning in response to light appears between postmenstrual weeks 32 and 36. The Babinski response, which involves extension of the great toe with spreading of the remaining toes in response to stimulation of the lateral aspect of the sole of the foot, is frequently elicited in neonates and reflects the level of myelination of the pathways. Early reflexes disappear in a predictable sequence reflecting postnatal myelination; their persistence suggests abnormal myelination of higher inhibitory pathways, seen in neurological developmental disorders and perinatal hypoxic–ischaemic brain injury (Futagi et al 2012, Feldman and Chaves-Gnecco 2018).

By full-term the neonate at rest has a strong flexor tone accompanied by adduction of all limbs. Neonates also display a distinct preference for a head position facing to the right, which appears to be independent of handling practices. The usual reflexes that can be elicited in a full-term (postmenstrual week 40) neonate include Moro, asymmetric tonic neck response, rooting–sucking, grasp, placing (contacting the dorsum of the foot with the edge of a table produces a ‘stepping over the edge’ response), stepping, and trunk incurvation (elicited by stroking down the paravertebral area with the infant in the prone position) (Futagi et al 2012). Examination of the motor system and evaluation of these reflexes allow assessment of the nervous system in relation to developmental age. The neonate also exhibits complex reflexes, such as nasal reflexes and sucking and swallowing. Early reflexes are tested during the routine examination of the newborn (Walker 2018). Production of otoacoustic emissions from sensory cell activity in the inner ear in response to sound is now routinely tested in neonates as an assessment of normal hearing. An adult-like auditory reflex (medial olivocochlear reflex) is present postnatally from about postmenstrual week 36 (Abdala and Mishra 2013).

Nasal reflexes produce apnoea via the diving reflex, sneezing, sniffing, and both somatic and autonomic reflexes. Stimulation of the face or nasal cavity with water or local irritants produces apnoea in neonates. Breathing stops in expiration, with laryngeal closure, and neonates exhibit bradycardia and a lowering of cardiac output. Blood flow to the skin, splanchnic areas, muscles and kidneys decreases, whereas flow to the heart and brain is protected. Different fluids produce different effects when introduced into the pharynx of preterm infants. A comparison of the effects of water and saline in the pharynx showed that apnoea, airway obstruction and swallowing occur far more frequently with water than with saline, suggesting the presence of an upper airway chemoreflex. Reflux of gastric content into the oesophagus is a well-recognized cause of apnoea and constitutes an acute life-threatening event in infants. Reflex responses to the temperature of the face and nasopharynx are necessary to start pulmonary ventilation: in the past, midwives often blew on the faces of neonates to induce the first breath.

Sucking and swallowing are a particularly complex set of reflexes, partly conscious and partly unconscious. As a combined reflex, sucking and swallowing require the coordination of several of the 12 pairs of cranial nerves. A neonate can, within the first couple of feeds, suck at the rate of once per second, swallow after five or six sucks, and breathe during every second or third suck. Air moves in and out of the lungs via the nasopharynx, and milk crosses the pharynx *en route* to the oesophagus without apparent interruption of breathing and swallowing, or significant misdirection of air into the stomach or fluids into the trachea. Swallowing movements are first noted at about postmenstrual week 11; *in utero* fetuses swallow 450 ml of amniotic fluid per day. Sucking and swallowing in premature infants (1700 g) is not associated with primary peristaltic waves in the intestine; however, in older babies and full-term neonates, at least 90% of swallows will initiate primary peristaltic waves.

The taste of the fluid, as well as nutrient content, affects the efficiency of nutritive sucking in the early neonatal period. There is more sucking with milk than with 5% dextrose: sucking activities increase with solutions that are determined to be sweet by adult appraisal. In full-term neonates, the placing of a spoon or food on to the anterior part of the tongue elicits an extrusion reflex: the lips are pursed and the tongue pushes vigorously against the object. By postnatal months 4–6, the reflex changes and food deposited on the anterior part of the tongue is moved to the back of the tongue, into the pharynx, and swallowed (see Ch. 40 for a description of swallowing in the adult). Rhythmic biting movements occur by postnatal months 7–9, even in the absence of teeth.

Postnatal brain maturation

Postnatal brain growth velocity is illustrated by the change in brain volume from 25% of adult volume at full-term delivery to 75% of adult volume by the end of the first postnatal year. This growth can be accounted for partly by increase in the size of neuronal cell bodies, the profusion and dimensions of their dendritic trees, axons and collaterals, and by the growth of the neuroglial cells and cerebral blood vessels, but mostly it reflects the myelination of many of the axons. During the second and subsequent years, growth proceeds much more slowly. The brain reaches 90% of its adult size by year 5, 95% by year 10, and adult size between years 17–18, largely as a result of the continuing myelination of various groups of nerve fibres.

Maturational progression of neonatal and postnatal brains can be evaluated using diffusion tensor magnetic resonance imaging (DTMRI). A number of studies have assessed the growth status of white matter tracts from prenatal ages to early childhood (Huang et al 2006, Huang et al 2009, Lodygensky et al 2010, Dubois et al 2014, Huang and Vasung 2014, Dubois et al 2016) (see Fig. 14.35). Evidence from diffusion tensor imaging (DTI) suggests that myelination is a dominant process during the first year of life, starting centrally and spreading peripherally, and spreading rostrally from the occipital to the frontal lobe (Dubois et al 2016). Myelination of the corticospinal tracts starts in full-term neonates at about postnatal days 10–14 in the internal capsule and cerebral peduncles, and then proceeds simultaneously in both regions. Myelin appears to start first around longer axons, which presumably explains why, in the preterm infant, axial extension precedes flexion, whereas finger flexion precedes extension.

Comparison of postnatal rates of myelination in human and primate brains shows that humans achieve approximately 60% of adult myelination during adolescence (compared to 96% in chimpanzees at comparable stages of growth). Myelin growth continues in humans to the end of the third decade. Miller et al (2012) suggest this schedule of neural connectivity in humans might contribute to the development of functional circuitry with greater plasticity and capacity to be shaped by postnatal environmental and social interactions. The greatest delay in myelination is seen in the prefrontal cortex, an area where many neural circuits concerned with learning and memory develop only after sexual maturity has been attained.

Autism spectrum disorders are at present viewed as a range of neurodevelopmental conditions with increasing prevalence. In China the prevalence increased from 10.3/10,000 in 2009 to 26.6/10,000 in 2013, and in the United States, it affected 1 in 152 children in 2002 and 1 in 68 in 2012 (Wang et al 2017). Prevalence in the UK showed a five-fold increase in incidence rates during the 1990s, with rates in 8-year-old children then reaching a plateau (Taylor et al 2013). The condition is thought to arise from increased proliferation of neuroprogenitor cells in the subventricular zone that leads to hyperexpansion of cortical surface areas. Early deficits in visual receptive and attention abilities are reported. At 2–4 postnatal years infants and children have increased grey matter volume, although this diminishes in adolescence and adulthood (Piven et al 2017, Wang et al 2017).

Sucking develops, generally, slightly later than swallowing, although mouthing movements have been detected in premature babies as early as postmenstrual weeks 18–24, and infants delivered at postmenstrual weeks 29–30 make sucking movements a few days after birth. Coordinated activities are not noted before postmenstrual weeks 33–34. The concept of non-nutritive and nutritive sucking has been introduced to account for the different rates of sucking seen in a neonate. Non-nutritive sucking, when rhythmic negative intraoral pressures are initiated that do not result in the delivery of milk, can be spontaneous or stimulated by an object in the mouth. This type of sucking tends to be twice as fast as nutritive sucking; the sucking frequency for non-nutritive sucking is 1.7 sucks/second in preterm infants of postmenstrual weeks 37–38, 2 sucks/second in term (postmenstrual week 40) neonates, and 2.7 sucks/second at postnatal months 7–9. Corresponding times for nutritive sucking are about 1 suck/second in term neonates, increasing to 1.5 sucks/second by postnatal month 7.

Difficulties in sucking and swallowing in infancy may be an early indication of disturbed nervous system function. There is a correlation between feeding styles of neonates and later eating habits. Children who were obese at 1 and 2 years of age, as measured by triceps skin-fold thickness, had a feeding pattern in the first month of life that was characterized by sucking more rapidly, producing higher pressures during prolonged bursts of sucking, and having shorter periods between bursts of sucking. Fewer feeds and higher sucking pressure seem to be associated with greater adiposity (Agras et al 1987). It has been noted that the levels of appetite-regulation hormones in fully breastfed infant serum are higher than in formula-fed infants at 4 postnatal months (Vásquez-Garibay et al 2019). Infants who are unable to feed orally in the first few weeks of life as a result of a congenital anomaly such as oesophageal atresia may develop food aversion.

Prior to preterm or full-term birth, the mother and fetus share circadian and other synchronized homeostatic physiological rhythms. After delivery, via processes similar to those seen in the postnatal synchronization of the optic pathways to ensure the development of the lateral geniculate nuclei and optic cortex, and of the auditory pathways to ensure postnatal maturation of hearing, the establishment of close mutual interactions between carer and neonate forms the basis for continuing infant cortical maturation and epigenetic upregulation of postnatal developmental genes. The continuing close reciprocal bond between carer and infant, with synchronization of a range of physiological rhythms, is described as the mother–infant dyad (Provenzi et al 2018).

Establishment of the mother–infant dyad initially promotes infant motor activity, skin tactile input and via establishment of oral feeding routines, autonomic sensory experiences. Synchrony of interactions, mutual eye contact, and mutual responsiveness of the mother–infant dyad appears to be set by postnatal month 4 (Navarez 2014). Later, the mother and family members encourage mirroring of behaviour (smiling and talking to the infant) and the infant becomes aware of its own sensory somatic states induced by the result of its motor actions. In this way the culturally driven rules for play and emotional display are transmitted to the infant. From psychological and sociological perspectives (i.e. through concepts of constructivist interactionism), the multiple ongoing interactions with the infant by family members (playing with the infant), and the resultant homeostatic interactions ongoing within the infant (feelings generated by their own movement), promote the development of cognitive pathways (Cantor et al 2018). The development of these ‘salience’ networks and pathways (anterior insula to anterior cingulate) in the neonate are important for normal postnatal adaptive behaviour responses (Molnar et al 2019). Failure of these postnatal processes is recognized in stress responses and withdrawn behaviours in infants; infants do not cry if they learn no one will come, inhibiting their emotional expression even when their cortisol levels are high. In later life such individuals may have difficulties regulating intense feelings. Mothers who get less support during these times are reported to demonstrate more restraint, avoidant and anxious attachment to their offspring, which subsequently affects the infant. Establishment of the mother–preterm infant dyad is difficult, with immature salience network development involved in neuropsychiatric disorders seen in adults born preterm (Molnar et al 2019). The preterm infant is less alert, hypersensitive to stimulation, inefficient at oral feeding, with lower capacity for self-regulation. Mothers of preterm infants have heightened stress and anxiety and may respond by either overstimulation or subsequent decreased stimulation; maternal anxiety is associated with preterm infants being less facially responsive and this can lead to difficulty over time with responsive maternal facial interactions (White-Traut et al 2013). For details of the mother–infant dyad and the neurobiology of postnatal development see Navarez (2014).

Bonus e-book content

Fig. 14.3 A–C, Defects caused by failure of neural tube formation.

Fig. 14.6 B, MicroCT image of axial section at the level of the heart in a 14-postmenstrual-week fetus showing the neural crest cell derivatives, the bilateral dorsal root ganglia and sympathetic trunks.

Fig. 14.11 A–D, Successive stages in the development of the neural tube and spinal cord. **E–H,** Results from experiments in chick embryos in which either a notochord or floor plate is grafted to the dorsal midline of the neural tube, or the notochord is removed before neural tube closure.

Fig. 14.15 The cell cycle in the ventricular zone of the developing neural tube.

Fig. 14.25 Coronal section through the cerebellum and the brainstem of a human fetus about postmenstrual week 12.

Fig. 14.34 B–D, MicroCT images of the cerebral hemispheres and developing corpus striatum of a fetus at 14 postmenstrual weeks.

Key references

Back SA 2017 White matter injury in the preterm infant: pathology and mechanisms. Acta Neuropath 134:331–49.

Bystron I, Blakemore C, Rakic P 2008 Development of the human cerebral cortex: Boulder Committee revisited. Nat Rev Neurosci 9:110–22.

A review of the development of the human cerebral cortex.

Fontenas L, Kucenas S 2017 Livin′ on the edge: glia shape nervous system transition zones. Curr Opin Neurobiol 47:44–51.

A review of the mechanisms by which axons and glia negotiate the transition zone between the CNS and the PNS.

Hansen DV, Lui JH, Flandin P et al 2013 Non-epithelial stem cells and cortical interneuron production in the human ganglionic eminences. Nature Neurosci 16:1576–87.

The paper presents evidence for the tangential migration of cortical neurones.

Leto K, Arancillo M, Becker EB et al 2016 Consensus paper: cerebellar development. Cerebellum 15:789–828.

Molnar Z, Clowry GJ, Sestan N et al 2019 New insights into the development of the human cerebral cortex. J Anat 235:432–51.

Nichols EL, Smith CJ 2019 Pioneer axons employ Cajal's battering ram to enter the spinal cord. Nature Comm 10:562. doi.org/10.1038/s41467-019-08421-9.

A description of the entry of pioneer axons into the dorsal root entry zone visualised using time-lapse imaging in zebrafish.

Rakic P 2009 Evolution of the neocortex: a perspective from developmental biology. Nat Rev Neurosci 10:724–35.

A review of differences in gene expression, molecular pathways and novel cellular interactions in the embryonic cerebral cortex in different mammalian species.

Volpe JJ 2017 Confusions in nomenclature: ′periventricualr leukolalacia′ and ′white matter injury′ – identical, distinct, or overlapping? Ped Neurol 73:3–6.

An update on the terminology used to describe pathological changes in white matter in the fetal period.

References

Abele TA, Salzman KL, Harnsberger HR et al 2014 Craniopharyngeal canal and its spectrum of pathology. Am J Neuroradiol 25:772–7.

Abu-Bonsrah KD, Zhang D, Bjorksten AR et al 2018 Generation of adrenal chromaffin-like cells from human pluripotent stem cells. Stem Cell Reports 10:134–50.

Abdala C, Mishra S 2013 Maturation of the human medial efferent reflex revisited. J Accoust Soc Am 133:938–50.

Agras WS, Kraemer HC, Berkowitz RI et al 1987 Does a vigorous feeding style influence early development of adiposity? J Pediatr 110:799–804.

Amin ND, Paşca S 2018 Building models of brain disorders with three-dimensional organoids. Neuron 100:389–405.

Ashwell KW, Mai JK 2012 Fetal development of the central nervous system. In: Mai JK, Paxinos G (eds) The Human Nervous System. London: Elsevier; Ch. 3, pp. 31–79.

Ashwell KW, Waite PM 2012 Development of the peripheral nervous system. In: Mai JK, Paxinos G (eds) The Human Nervous System. London: Elsevier; Ch. 2, pp. 14–30.

Back SA 2017 White matter injury in the preterm infant: pathology and mechanisms. Acta Neuropath 134:331-349

Back SA, Luo NL, Borenstein NS et al 2001 Late oligodendrocyte progenitors coincide with the developmental window of vulnerability for human perinatal white matter injury. J Neurosci 21:1302–12.

Ballabh P 2010 Intraventricular hemorrhage in premature infants: mechanism of disease. Pediatr Res 67:1–8.

Barson AJ 1970 The vertebral level of termination of the spinal cord during normal and abnormal development. J Anat 106:489–97.

Barton SK, Tolcos M, Miller SL et al 2015 Unraveling the links between the initiation of ventilation and brain injury in preterm infants. Front Pediatr 3:97. doi: 10.3389/fped.2015.00097.

Baumholtz AI, Simard A, Nikolopoulou E et al 2017 Claudins are essential for cell shape changes and convergent extension movements during neural tube closure. Dev Biol 428:25–38.

Bay SN, Caspary T 2012 What are those cilia doing in the neural tube? Cilia 1:19.

Begbie J, Graham A 2001 The ectodermal placodes: a dysfunctional family. Philos Trans R Soc Lond B Biol Sci 356:1655–60.

An account that challenges the view of ectodermal placodes as a coherent group and discusses their early development, induction and evolution.

Bjuland KJ, Løhaugen GC, Martinussen M et al 2013 Cortical thickness and cognition in very-low-birth-weight late teenagers. Early Hum Dev 89:371–380.

Bystron I, Blakemore C, Rakic P 2008 Development of the human cerebral cortex: Boulder Committee revisited. Nat Rev Neurosci 9:110–22.

A review of the development of the human cerebral cortex.

Cang J, Feldheim DA 2013 Developmental mechanisms of topographic map formation and alignment. Annu Rev Neurosci 36:51–77.

Cantor P, Osher D, Berg J et al 2018 Malleability, plasticity, and individuality: how children learn and develop in context. App Dev Sci. doi: 10.1080/10888691.2017.1398649.

Cao L, Cai C 2019 Vein of Galen aneurysmal malformation: an updated review. J Pediatr Neurol 17:45–56.

Chambers D, Wilson LJ, Alfonsi F et al 2009 Rhombomere-specific analysis reveals the repertoire of genetic cues expressed across the developing hindbrain. Neural Dev 4:6 doi: 10.1186/1749-8104-4-6.

Charrier B, Pilon N 2017 Toward a better understanding of enteric gliogenesis. Neurogenesis. 4:e1293958 (8 pages). doi.org/10.1080/23262133.2017.1293958.

Cheng L, Hotta R, Graham HK et al 2017 Postnatal human enternic neuronal progenitors can migrate, differentiate, and proliferate in embryonic and postnatal aganglionic gut environments. Pediatr Res 81:838–46.

Chiu H, Alqadah A, Chang C 2013 The role of microRNAs in regulating neuronal connectivity. Front Cell Neurosci 7:283.

Cirulli F, Alleva E 2009 The NGF saga: from animal models of psychosocial stress to stress-related psychopathology. Front Neurosci 30:379–95.

Cox B, Roose H, Vennekens A et al 2017 Pituitary stem cell regulation: who is pulling the strings? J Endocrinol 234: R135–R158.

da Silva S, Wang F 2011 Retrograde neural circuit specification by target-derived neurotrophins and growth factors. Curr Opin Neurobiol 21:61–7.

Dady A, Harris E, Escriou V et al 2014 Junctional neurulation: a unique developmental programme shaping a discrete region of the spinal cord highly susceptible to neural tube defects. J Neurosci 34:13208–21.

Dewitz C, Pimpinella S, Hackel P et al 2018 Nuclear organization in the spinal cord depends on motor neuron lamination orchestrated by catenin and afadin function. Cell Rep 22:1681–94.

Dimou L, Simons M 2017 Diversity of oligodendrocytes and their progenitors. Curr Opin Neurobiol 47:73–9.

Dodd J, Jessell TM, Placzek M 1998 The when and where of floor plate induction. Science 282:1654–7.

Duan D, Xia S, Rekik I et al 2019 Exploring folding patterns of infant cerebral cortex based on multi-view curvature features: methods and applications. Neuro Image185:575–92.

Dubois J, Dehaene-Lambertz G, Kulikova S et al 2014 The early development of brain white matter: a review of imaging studies in fetuses, newborns and infants. Neuroscience 276:48–71.

Dubois J, Adibpour P, Poupon C et al 2016 MRI and M/EEG studies of the white matter development in human fetuses and infants: review and opinion. Brain Plasticity 2:49–69.

Eiraku M, Sasai Y 2012 Self-formation of layered neural structures in three-dimensional culture of ES cells. Curr Opin Neurobiol 22:768–77.

Elbaz B, Popko B 2017 Molecular control of oligodendrocyte development Trends. Neurosci 42:263–77.

Engelhardt E, Inder TE, Alexopoulos D et al 2016a Regional impairments of cortical folding in premature infants. Ann Neurol 77:154–62.

Engelhardt B, Carare RO, Bechmann I et al 2016b Vascular, glial and lymphatic immune gateways of the central nervous system. Acta Neuropathol 132:317–38.

Ernsberger U, Rohrer H 2018 Sympathetic tales: subdivisions of the autonomic nervous system and the impact of developmental studies. Neural Dev 13:20. doi.org/10.1186/s13064-018-0117-6.

Espinosa-Medina I, Saha O, Boismoreau F et al 2016 The sacral autonomic outflow is sympathetic. Science 354: 893–7.

Espinosa-Medina I, Saha O, Boismoreau F et al 2017 The 'sacral parasympathetic': ontogeny and anatomy of a myth. Clin Auton Res 28:13–21.

Eyre JA 2007 Corticospinal tract development and its plasticity after perinatal injury. Neurosci Biobehav Rev 31:1136–49.

Feldman HM, Chaves-Gnecco 2018 Developmental/behavioural paediatrics. In: Zitelli BJ, McIntire SC, Nowalk AJ (eds) Zitelli and Davis' Atlas of Pediatric Physical Diagnosis, 7th ed. Elsevier; Ch.3.

Fontenas L, Kucenas S 2017 Livin' on the edge: glia shape nervous system transition zones. Curr Opin Neurobiol 47:44-51.

A review of the mechanisms by which axons and glia negotiate the transition zone between the CNS and the PNS.

Fontenas L, Welsh TG, Piller M et al 2019 The neuromodulator adenosine regulates oligodendrocyte migration at motor exit point transitions zones. Cell Reports 27:115–28.

Fujita S 1963 The matrix cell and cytogenesis in the developing central nervous system. J Comp Neurol 120:37–42.

Fumagalli M, Provenzi L, De Carli P et al 2018 From early stress to 12-month development in very preterm infants: preliminary findings on epigenetic mechanisms and brain growth. PLoS One 13(1): e0190602.

Furlan A, Adameyko I 2018 Schwann cell precursor: a neural crest cell in disguise? Dev Biol. doi.org/10.1016/j.ydbio.2018.02.008.

Futagi Y, Toribe Y, Suzuki Y 2012 The grasp reflex and Moro reflex in infants: hierarchy of primitive reflex responses. Int J Pediat. doi: 10.1155/2012/191562.

Geschwind DH, Rakic P 2013 Cortical evolution: judge the brain by its cover. Neuron 80:633–47.

Gomez TM, Letourneau PC 2014 Actin dynamics in growth cone motility and navigation. J Neurochem 129:221–34.

Hansen DV, Lui JH, Flandin P et al 2013 Non-epithelial stem cells and cortical interneuron production in the human ganglionic eminences. Nature Neurosci 16:1576–87.

The paper presents evidence for the tangential migration of cortical neurones.

Harris KD 2008 Stability of the fittest: organizing learning through retroaxonal signals. Trends Neurosci 31:130–6.

Hawrylycz MJ, Lein ES, Guillozet-Bongaarts AL et al 2012 An anatomically comprehensive atlas of the adult human brain transcriptome. Nature 489:391–9.

Herbert AL, Monk KR 2017 Advances in myelinating glial cell development. Curr Opin Neurobiol 42:53-60.

Higginbotham H, Guo J, Yokota Y et al 2013 Arl13b-regulated cilia activities are essential for polarized radial glial scaffold formation. Nat Neurosci 16:1000–7.

Hockman D, Adameyko I, Kaucka M et al 2018 Striking parallels between carotid body glomus cells and adrenal chromaffin cell development. Dev Biol 444(Suppl 1):S308–S324.

Hoerder-Suabedissen A, Molnar Z 2015 Development, evolution and pathology of neocortical subplate neurons. Nature Rev Neurosci 16:133–46.

Horn JP 2018 The sacral autonomic outflow is parasympathetic: Langley got it right. Clin Auton Res 28:181–5.

Huang H, Vasung L 2014 Gaining insight of fetal brain development with diffusion MRI and histology. Int J Dev Neurosci 32:11–22.

Details of the structural development of major components of the fetal brain, derived from DTI and histology, that may provide reference standards for use in the diagnostic radiology of premature newborns.

Huang H, Zhang J, Wakana S et al 2006 White and gray matter development in human fetal, newborn and pediatric brains. Neuroimage 33:27–38.

Huang H, Xue R, Zhang J et al 2009 Anatomical characterization of human fetal brain development with diffusion tensor magnetic resonance imaging. J Neurosci 29:4263–73.

Hutchins EJ, Kunttas E, Piacentino ML et al 2018 Migration and diversification of the vagal neural crest. Dev Biol 444 (Suppl 1):S98–S109.

Jakovcevski I, Filipovic R, Mo Z et al 2009 Oligodendrocyte development and the onset of myelination in the human fetal brain. Front Neuroanat 3:5. doi: 10.3389/neuro.05.005.2009.

Jänig W, McLachlan EM, Neuhuber WL 2018 The sacral autonomic outflow: against premature over simplification. Clin Autonom Res 28:5–6.

Jantzie LL, Corbett CJ, Firl DJ et al 2015 Postnatal erythropoietin mitigates impaired cerebral cortical development following subplate loss from prenatal hypoxia-ischemia. Cereb Cortex 25(9):2683–95.

Jessell TM, Dodd J 1992 Midline signals that control the dorso-ventral polarity of the neural tube. Semin Neurosci l4:317–325.

Jessell TM, Sürmeli G, Kelly JS 2011 Motor neurons and the sense of place. Neuron 72:419–24.

Jin ZW, Cho KH, Abe H et al 2016 Anterior corticalspinal tract revisited: a study using human fetuses. Pediatr Neurosurg 51:121–6.

Kabouridis PS, Pachnis V 2015 Emerging roles of gut microbiota and the imment system in the development of the enteric nervous system. J Clin Invest 125:956–64.

Kalil K, Li L, Hutchins BI 2011 Signaling mechanisms in cortical axon growth, guidance, and branching. Front Neuroanat 5:62.

Kanold PO, Luhmann HJ 2010 The subplate and early cortical circuits. Annu Rev Neurosci 33:23–48.

Keep RF, Jones HC, Drewaw LR 2019 The year in review, progress in brain barriers and brain fluid research in 2018. Fluid Barriers CNS 16(1):4.

Kolb B, Mychasiuk R, Muhammad A et al 2013 Brain plasticity in the developing brain. Prog Brain Res 207:35–64.

Kostovic I, Jovanov-Milosevic N, Rados M et al 2012 Perinatal and early postnatal reorganization of the subplate and related cellular compartments in the human cerebral wall as revealed by histological and MRI approaches. Brain Struct Funct 219:231–53.

Krencik R, van Asperen JV, Ullian EM 2017 Human astrocytes are distinct contributors to the complexity of synaptic function. Brain Res Bull 129:66–73.

Kriegstein AR, Gotz M 2003 Radial glia diversity: a matter of cell fate. Glia 432:37–43.

Kriegstein AR, Noctor SC 2004 Patterns of neuronal migration in the embryonic cortex. Trends Neurosci 27:392–9.

Krumlauf R, Marshall H, Studer M et al 1993 Hox homeobox genes and regionalisation of the nervous system. J Neurobiol 24:1328–40.

Kucenas S 2015 Perineurial glia. Cold Spring Harb Perspect Biol 2015;7:a020511.

Lake JI, Heuckeroth RO 2013 Enteric nervous system development: migration, differentiation, and disease. Am J Physiol Gastrointest Liver Physiol 305:G1–G24.

Lavezzi AM, Ottavianni G, Terni L et al 2006 Histological and biological developmental characterization of the human cerebellar cortex. Int J Dev Neurosci 24:365–71.

Lee C, Bendriem RM, Wu WW et al 2017 3D brain organoids derived from pluripotent stem cells: promising experimental models for brain development and neurodegenerative disorders. J Biomed Sci 24:59

Lee JH, Gleeson JG 2010 The role of primary cilia in neuronal function. Neurobiol Dis 38:167–72.

Leto K, Arancillo M, Becker EB et al 2016 Consensus paper: cerebellar development. Cerebellum 15:789–828.

Lister R, Mukamel EA, Nery JR et al 2013 Global epigenomic reconfiguration during mammalian brain development. Science 341:1237905.

Lodygensky GA, Vasung L, Sizonenko SV et al 2010 Neuroimaging of cortical development and brain connectivity in human newborns and animal models. J Anat 217:418–28.

Lui JH, Hansen DV, Kriegstein AR 2011 Development and evolution of the human neocortex. Cell 146:18–36.

Ma T, Zhang Q, Cai Y et al 2012 A subpopulation of dorsal lateral/caudal ganglionic eminence-derived neocortical interneurons expresses the transcription factor Sp8. Cerebral Cortex 22:2120–30.

Maltepe E, Penn AA 2018 Development, function and pathology of the placenta. In: Gleason CA, Juul SE (eds) Avery's Diseases of the Newborn, 10th ed. Elsevier; Ch. 5.

Manto MU, Jissendi P 2012 Cerebellum: links between development, developmental disorders and motor learning. Front Neuroanat 6:1–10.

Martinez S, Andreu A, Mecklenburg N et al 2013 Cellular and molecular basis of cerebellar development. Front Neuroanat 7:18.

Memic F, Knoflach V, Morarach K et al 2018 Transcription and signaling regulators in developing neuronal subtypes of mouse and human enteric nervous system. Gastroenterology 154:624–636.

Menassa DA, Gomez-Nicola D 2018 Microglial dynamics during human brain development. Front Immunol 9:1014. doi: 10.3389/fimmu.2018.01014.

Ment LR, Sould JS 2012 Injury to the developing preterm brain: intraventricular hemorrhage and white matter injury. In: Swaiman K, Ashwal S, Ferriero DM et al (eds) Swaiman's Pediatric Neurology: Principles and Practice, 5th ed. London: Elsevier; Ch. 19, pp. 77–99.

Métin C, Baudoin JP, Rakic S et al 2006 Cell and molecular mechanisms involved in the migration of cortical interneurones. Eur J Neurosci 23:894–900.

Michell-Robinson MA, Touil H, Healy LM et al 2017 Roles of microglia in brain development, tissue maintenance and repair. Brain 138:1138–59.

Miller DJ, Duka T, Stimpson CD et al 2012 Prolonged myelination in human neocortical evolution. PNAS Science Sessions 109:16480–5.

Molnar Z, Butt SJB 2013 Best-laid schemes for interneuron origin of mice and men. Nature Neurosci 16:1512–14.

Molnar Z, Rutherford M 2013 Brain maturation after preterm birth. Sci Transl Med 5:168ps2.

Molnar Z, Clowry GJ, Sestan N et al 2019 New insights into the development of the human cerebral cortex. J Anat 235:432–51.

Müller F, O'Rahilly R 1997 The timing and sequence of appearance of neuromeres and their derivatives in staged human embryos. Acta Anat (Basel) 158:83–99.

Mundell NA, Plank JL, LeGrone AW et al 2012 Enteric nervous system specific deletion of Foxd3 disrupts glial cell differentiation and activates compensatory enteric progenitors. Dev Biol 363:373–87.

Nagy N, Goldstein AM 2017 Enteric nervous system development: a crest cell's journey from neural tube to colon. Semin Cell Dev Biol 66:94–106.

Navarez D 2014 Neurobiology and the development of human morality. London: WW Norton & Co.

Neuwelt EA, Bauer B, Fahlke C et al 2011 Engaging neuroscience to advance translational research in blood brain barrier biology. Nat Rev Neurosci 12:169–82.

Nichols EL, Smith CJ 2019 Pioneer axons employ Cajal's battering ram to enter the spinal cord. Nature Comm. doi.org/10.1038/s41467-019-08421-9.

A description of the entry of pioneer axons into the dorsal root entry zone visualised using time-lapse imaging in zebrafish.

Nikolopoulou E, Gelea GL, Rolo A et al 2017 Neural tube closure: cellular, molecular and biochemical mechanisms. Development 144:552–66.

Noctor SC, Martínez-Cerdeño V, Ivic L et al 2004 Cortical neurons arise in symmetric and asymmetric division zones and migrate through specific phases. Nat Neurosci 7:136–44.

Omotade OF, Pollitt SL, Zheng JQ 2017 Actin-based growth cone motility and guidance. Mol Cell Neurosci 2017;84:4–10.

O'Rahilly R, Müller F 1999 The Embryonic Human Brain. An Atlas of Developmental Stages, 2nd ed. Chichester: Wiley–Liss.

O'Rahilly R, Müller F 2002 The two sites of fusion of the neural folds and the two neuropores in the human embryo. Teratology 65:162–70.

O'Rahilly R, Müller F 2004 The primitive streak, the caudal eminence and related structures in staged human embryos. Cells Tissues Organs 117:2–20.

Osso LA, Chan JR 2017 Architecting the myelin landscape. Curr Opin Neurobiol 27:1–7.

Ozone C, Suga H, Eiraku M et al 2016 Functional anterior pituitary generated in self-organizing culture of human embryonic stem cells. Nature Comm. doi: 10.1038/ncomms10351.

Pantani R 2016 Generating diverse spinal motor neuron subtypes from human pluripotential stem cells. Stem Cells International Article, doi.org/10.1155/2016/1036974.

Park H, Poo M 2013 Neurotrophin regulation of neural circuit development and function. Nat Rev Neurosci 14:7–23.

Pearce WJ 2018 Fetal cerebrovascular maturation: effects of hypoxia. Semin Ped Neurol 28:17–28.

Pearl M, Gregg L, Gandhi D 2011 Cerebral venous development in relation to developmental venous anomalies and vein of Galen aneurysmal malformations. Semin Ultrasound CT MRI 32:252–63.

Petanjek Z, Judas M, Simic G et al 2011 Extraordinary neoteny of synaptic spines in the human prefrontal cortex. Proc Natl Acad Sci U S A 108:13281–6.

Piven J, Elison JT, Zylka MU 2017 Toward a conceptual framework for early brain and behaviour development in autism. Mol Psychiatry 22:1385–94.

Provenzi L, Scotto di Minico G, Giusti L et al 2018 Disentangling the dyadic dance: theoretical, methodological and outcomes systematic review of mother-infant dyadic processes. Front Psychol 9:348. doi: 10.3389/fpsyg.2018.00348.

Puram SV, Kim AH, Ikeuchi Y et al 2011 A CaMKIIβ signaling pathway at the centrosome regulates dendrite patterning in the brain. Nat Neurosci 14:973–83.

Rakic P 1988 Specification of cerebral cortical areas. Science 241:170–6.

Rakic P 2009 Evolution of the neocortex: a perspective from developmental biology. Nat Rev Neurosci 10:724–35.

A review of differences in gene expression, molecular pathways and novel cellular interactions in the embryonic cerebral cortex in different mammalian species.

Rao M, Gershon MD 2018 Enteric nervous system development: what could possibly go wrong? Nat Rev Neurosci 19:552–65.

Reemst K, Noctor SC, Lucassen PJ et al 2016 The indispensable roles of microglia and astrocytes during brain development. Front Hum Neurosci 10:566. doi: 10.3389/fnhum.2016.00566.

Saab AS, Nave K 2017 Myelin dynamics: protecting and shaping neuronal functions. Curr Opin Neurobiol 47:104–12.

Sasai Y, Eiraku M, Suga H 2012 In vitro organogenesis in three dimensions: self-organising stem cells. Development 139:4111–21.

Shimony JS, Smyser CD, Wideman G et al 2016 Comparison of cortical folding measures for evaluation of developing human brain. Neuroimage 125:780–90.

Silver DL, Rakic P, Grove EA et al 2019 Evolution and ontogenetic development of cortical structures. In: The Neocortex Vol. 27, Singer W, Sejnowski TJ, Rakic P (Eds), Strüngmann Forum Reports, JR Lupp, series editor. Cambridge, MA: MIT Press.

Smith CJ, Johnson K, Welsh TG et al 2016 Radial glia inhibit peripheral glial infiltration into the spinal cord at motor exit point transition zones. Glia 64:1138–53.

Sürmeli G, Akay, Ippoloto GC et al 2011 Patterns of spinal sensory-motor connectivity prescribed by a dorsoventral positional template. Cell 147:653–65.

Takashima S, Itoah M, Oka A 2009 History of our understanding of cerebral vascular development and pathogenesis of perinatal brain damage over the past 30 years. Semin Pediatr Neurol 16:226–36.

Taverna E, Huttner WB 2010 Neural progenitor nuclei IN Motion. Neuron 67:906–14.

Taverna E, Mora-Bermudez F, Strzyz PJ, et al 2016 Non-canonical features of the Golgi apparatus in bipolar epithelial neural stem cells. Sci Rep 6:21206.

Tay TL, Savage JC, Hui CW et al 2017 Microglia across the lifespan: from origin to function in brain development, plasticity and cognition. J Physiol 95:1929–45.

Taylor B, Jick H, MacLaughlin D 2013 Prevalence and incidence rates of autism in the UK: time trend from 2004-2010 in children aged 8 years. BMJ Open2013;3:e003219. doi: 10.1136/bmjopen-2013-003219.

ten Donkelaar HJ, Lammens M, Wesseling P et al 2004 Development and malformations of the human pyramidal tract. J Neurol 251:1429–42.

Tissir F, Goffinet AM 2010 Planar cell polarity signalling in neural development. Curr Opin Neurobiol 20:572–7.

Tortora D, Severino M, Malova M et al 2018 Differences in subependymal vein anatomy may predispose preterm infants to GMH-IVH. Arch Dis Child Fetal Neonatal 103:F59–F65.

Trujillo CA, Gao R, Negraes PD et al 2019 Complex oscillatory waves emerging from cortical organoids model early human brain network development. Cell Stem Cell 25:1–12.

Tümpel S, Wiedemann LM, Krumlauf R 2009 Hox genes and segmentation of the vertebrate hindbrain. Curr Top Dev Biol 88:103–37.

Unsicker K, Huber K, Schober A et al 2013 Resolved and open issues in chromaffin cell development. Mech Dev 130:324–9.

Van Bruggen D, Agirre E, Castelo-Branco G 2017 Single-cell transcriptomic analysis of oligodendrocyte lineage cells. Curr Opin Neurobiol 47:168–75.

Vásquez-Garibay EM, Larrosa-Haro A, Guzmán-Mercado E et al 2019 Serum concentration of appetite-regulating hormones of mother–infant dyad according to the type of feeding. Food Sci Nutri 28:869–74.

Volpe JJ 2017 Confusions in nomenclature: 'periventricualr leukolalacia' and 'white matter injury' – identical, distinct, or overlapping? Ped Neurol 73:3–6.

An update on the terminology used to describe pathological changes in white matter in the fetal period.

Volpe JJ, Kinney HC, Jensen FE et al 2011 The developing oligodendrocyte: key cellular target in brain injury in the premature infant. Int J Dev Neurosci 29:423–40.

Walker VP 2018 Newborn evaluation. In: Gleason CA, Juul SE (eds) Avery's Diseases of the Newborn, 10th ed. Elsevier; Ch. 25.

Wang H 2018 Modeling neurological diseases with human brain organoids. Front Synaptic Neurosci 10:15. doi: 10.3389/fnsyn.2018.00015.

Wang J, Fu K, Chen L et al 2017 Increased gray matter volume and resting-state functional connectivity in somatosensory cortex and their relationship with autistic symptoms in young boys with autism spectrum disorder. Front Physiol 8:588. doi.org/10.3389/fphys.2017.00588.

Watson C, Bartholomaeus C, Pueles L 2019 Time for radical changes in brain stem nomenclature – applying the lessons from developmental gene patterns. Front Neuroanat 13:10. doi: 10.3389/fnana.2019.00010.

West AE, Pruunsild P, Timmusk T 2014 Neurotrophins: transcription and translation. Handb Exp Pharmacol 220:67–100.

Wheway G, Nazlamova L, Hancock JT 2018 Signaling through the primary cilium. Front Cell Dev Biol 6:8. doi: 10.3389/fcell.2018.00008.

White-Traut R, Norr KF, Fabiyi C et al 2013 Mother–infant interaction improves with a developmental intervention for mother-preterm infant dyads. Infant Behav Dev 36(4). doi: 10.1016/j.infbeh.2013.07.004.

Wilson L, Chambers D 2014 Transcriptomic analysis of midbrain and individual hindbrain rhombomeres in the chick embryo. Scientific Data 1:140014. doi: 10.1038/sdata.2014.14.

Wonders CP, Anderson SA 2006 The origin and specification of cortical interneurones. Nat Rev Neurosci 7:687–96.

Woythaler M 2019 Neurodevelopmental outcomes of the late preterm infant. Semin Fetal Neonatal Med 24:54–9.

Wu Q, Liu J, Fang A et al 2014 The dynamics of neuronal migration. Adv Exp Med Biol 800:25–36.

Yang H, Lee D, Lee Y et al 2014 Secondary neurulation of human embryos: morphological changes and the expression of neuronal antigens. Childs Nerv Syst 30:73–82.

Yu T, Meiners LC, Danielsen K et al 2013 Deregulated FGF and homeotic gene expression underlies cerebellar vermis hypoplasia in CHARGE syndrome. eLife 2:e01305.

CHAPTER
15

Development of the eye

The development of the eye involves a series of inductive interactions between neighbouring tissues in the embryonic head. These are the neurectoderm of the forebrain (which forms the sensory retina and accessory pigmented structures), the surface ectoderm (which forms the lens and the corneal epithelium) and the intervening neural crest mesenchyme (which contributes to the fibrous coats of the eye and to tissues of the anterior segment of the eye). A broad anterior domain of neurectoderm, characterized by the activation of several homeobox-containing transcriptional regulator genes, including *PAX6*, *RAX*, *SIX3* and *OTX2*, and the repression of caudalizing Wnt signalling, develops the potential to form optic vesicles. Subsequent interactions between mesenchyme and neurectoderm, involving midline expression of the gene (*SHH*) encoding the secreted protein sonic hedgehog, subdivides this eyefield region into bilateral domains at the future sites of the eyes (Chow and Lang 2001). Loss of *SHH* function causes holoprosencephaly and a range of anomalies that can include cyclopia, due to incomplete separation of the prosencephalon (Dubourg et al 2004).

In three-dimensional culture of murine embryonic stem cells supplemented with the correct growth factors and Matrigel® (to promote basement membrane formation), but in the absence of surface ectoderm or lens epithelium, a neuroepithelial vesicle develops and undergoes dynamic shape change to form a two-layered optic cup (Eiraku and Sasai 2012). The tissue so formed demonstrated interkinetic nuclear migration and a stratified architecture similar to that of postnatal retina, including appropriate synapses. Similar results, i.e. production of retinal architecture and retinal pigment epithelial cells, have been reported using human embryonic stem cells (Nakano et al 2012, Zhu et al 2013).

The parallel process of lens determination appears to depend on a brief period of inductive influence that spreads through the surface ectoderm from the rostral neural plate and elicits a lens-forming area of the head. Reciprocal interactions that are necessary for the complete development of both tissues take place as the optic vesicle forms and contacts the potential lens ectoderm (Saha et al 1992, Fuhrmann 2010, Nakano et al 2012). The vascular tissue of the developing eye forms by local angiogenesis or vasculogenesis of angiogenic mesenchyme (Hughes et al 2000). Development of the choroidal vasculature is followed by the (temporary) fetal hyaloid vasculature and then the retinal vasculature. (For further reading see O'Rahilly (1966, 1983).)

EMBRYONIC COMPONENTS OF THE EYE

The first morphological sign of eye development is a thickening of the diencephalic neural folds in stage 10 (28–29 days postfertilization, see Fig. 23.2), when the embryo has seven to eight somites. This optic primordium (eye field) extends on both sides of the neural plate and crosses the midline at the primordium chiasmatis. A slight transverse indentation, the optic sulcus, appears in the inner surface of the optic primordium on each side of the brain. During rostral neuropore closure in stage 11 the walls of the neuromere diencephalon 1 (see Fig. 14.2) begin to evaginate at the optic sulcus, projecting laterally towards the surface ectoderm and by stage 13 (postfertilization days 31–33), the optic vesicles are formed. Failure of the specification and development of the optic vesicle is associated with mutation of several transcriptional regulatory genes expressed in the eye field and leads to anophthalmia (absence of the eye) (Graw 2003). Each optic vesicle is surrounded by a sheath of mesenchymal cells derived from the head mesenchyme and neural crest; its lumen is continuous with that of diencephalon 1. Regional differentiation is apparent in each of the source tissues of the eye. The optic vesicle is visibly differentiated into its three primary parts. At the junction with the diencephalon, a thick-walled region marks the future optic stalk; laterally, the tissue that will become the sensory (neural) retina forms a flat disc of thickened epithelium in close contact with the surface ectoderm; and the thin-walled part that lies between these regions will later form the pigmented layer of the retina (retinal pigmented epithelium). The area of surface ectoderm that is closely apposed to the distal optic vesicle thickens to form the lens placode, and the mesenchymal sheath of the vesicle begins to show signs of angiogenesis. During stage 14 (postfertilization days 33–34), the lens placode and optic vesicle undergo coordinated morphogenesis. Filopodia tether the presumptive optic and lens vesicles to coordinate epithelial invagination. The lens placode invaginates, forming a pit that pinches off from the surface ectoderm to form the lens vesicle (**Fig. 15.1**). The surface ectoderm reforms a continuous layer that will become the corneal epithelium. The lateral part of the optic vesicle invaginates to form a cup, which is incompletely formed and open at the ventral surface (optic fissure); the inner layer (facing the lens vesicle) will become the sensory (neural) retina, and the outer layer, influenced by signals from the surrounding extraocular mesenchyme, becomes the retinal pigmented epithelium. As a result of these folding movements, what had been the apical (luminal) surfaces of the presumptive neural retina and retinal pigmented epithelium of the optic vesicle now face one another across a much-reduced lumen, the intraretinal space. The pigmented layer becomes attached to the mesenchymal sheath, but the junction between the pigmented and sensory layers is less firm and is the site of pathological detachment of the retina. The two layers are continuous at the lip of the cup (**Fig. 15.2**). The narrow part of the optic vesicle between the base of the cup and the brain forms the optic stalk. The distal part of the optic stalk also invaginates, forming a wide groove, the choroid (optic) fissure, through which mesenchyme migrates and differentiates to form the ingressing hyaloid artery. These infoldings involve differential growth, changes in cell shape, cell movement and high levels of proliferation in the inner neuroepithelial layer. The hyaloid artery forms part of the vasculature of the eye. It transiently supplies the developing lens and the inner part of the retina until a retinal vasculature forms and eventually regresses by apoptosis (Lutty and McLeod 2018).

As growth proceeds, the fissure closes and the artery is included in the distal part of the stalk. The fusion process is characterized by apoptosis at the margins of the fissure. Failure of the optic fissure to close is a rare anomaly that may be accompanied by a corresponding deficiency in the choroid, retina and iris (congenital coloboma) and is often associated with microphthalmia (small eyes). Reduced growth of the optic cup caused by mutation of the homeobox gene *VSX2*, important for specification and growth of the neural retina, is one known cause of microphthalmia (Graw 2003). Anophthalmia, microphthalmia and coloboma are also associated with mutation of the *SOX2* gene.

DIFFERENTIATION OF THE FUNCTIONAL COMPONENTS OF THE EYE

The developments just described bring the embryonic components of the eye into the spatial relationships necessary for the passage of light into the globe and onto the retina. The next phase of development involves further patterning and phenotypic differentiation in order to develop the specialized structures of the adult organ needed for focusing and sensing of light.

The optic cup becomes patterned, from the base to the rim, into regions with distinct functions. Several secreted factors, including bone morphogenetic proteins (BMP), retinoic acid and SHH, and transcriptional regulator genes, including *PAX6* and *PAX2*, are important for specifying each region (Chow and Lang 2001, Sinn and Wittbrodt 2013). The outer layer of the optic cup remains as a thin layer of cells, which begin to acquire pigmented melanosomes and form the pigmented epithelium of the retina at stage 17. In a parallel process that begins before invagination, the cells of the inner layer of the cup proliferate to form a thick pseudostratified neuroepithelium, the future neural retina, over the base and sides of the cup. The peripheral region around the lip of the cup extends, and is further differentiated into the components of the prospective iris at the rim, and the ciliary body a little further back, adjacent to the neural retina (see Fig. 15.2). The development of this pattern is reflected in regional differences in the expression of various genes that encode transcriptional regulators and that are therefore likely to play key roles in controlling and coordinating development. Distinct sets of genes are expressed prior to and during overt cell-type differentiation. For example, *PAX6* is expressed in the prospective ciliary and iris regions of the optic cup; individuals heterozygous for mutations in *PAX6* lack an

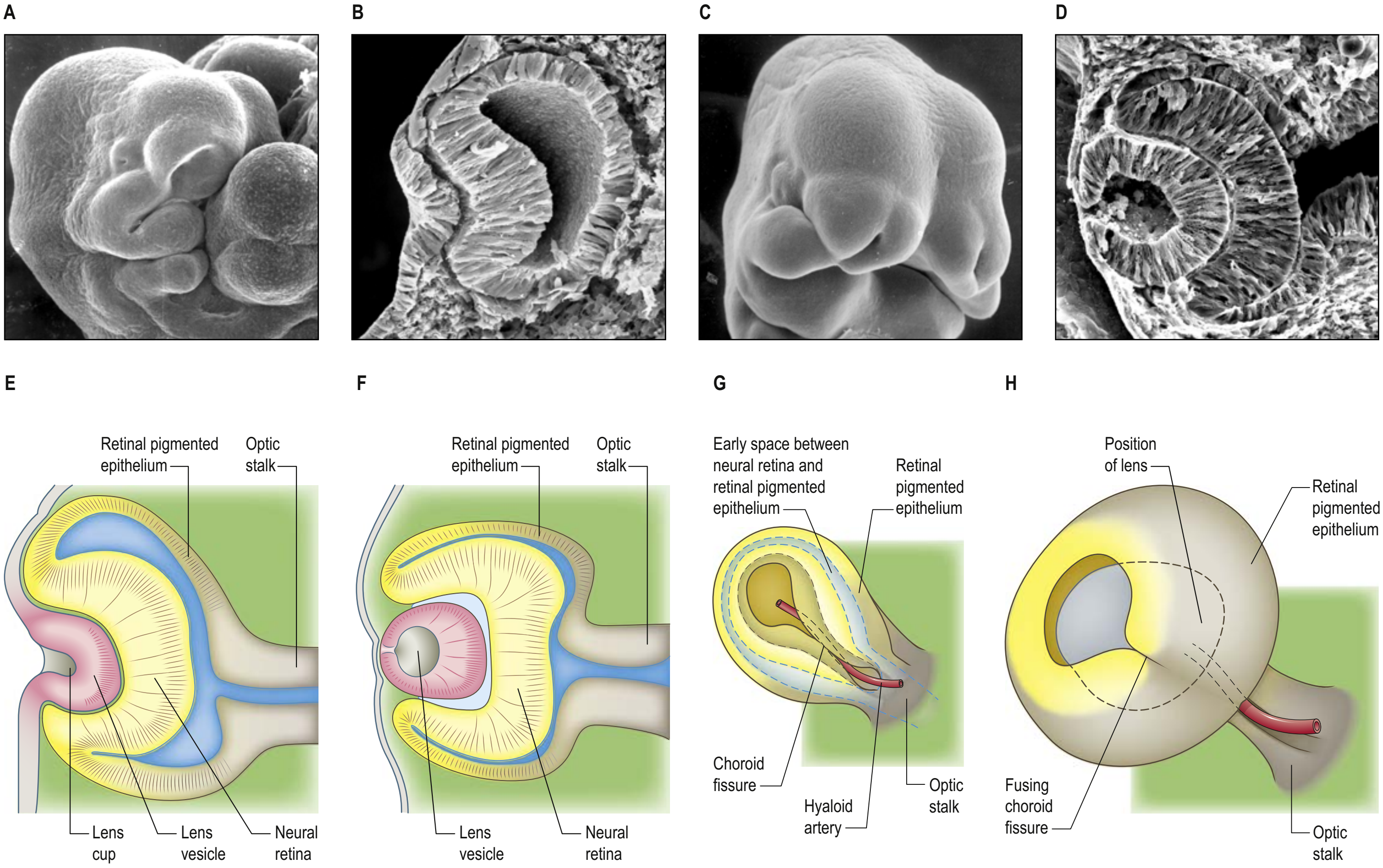
A
B
C
D
E
F
G
H
Retinal pigmented epithelium
Optic stalk
Lens cup
Lens vesicle
Neural retina
Retinal pigmented epithelium
Optic stalk
Lens vesicle
Neural retina
Early space between neural retina and retinal pigmented epithelium
Retinal pigmented epithelium
Choroid fissure
Hyaloid artery
Optic stalk
Position of lens
Retinal pigmented epithelium
Fusing choroid fissure
Optic stalk

Fig. 15.1 Development and morphogenesis of the optic cup. **A–D**, Scanning electron micrographs of early eye development, **A** and **C** showing external view, **B** and **D** showing longitudinal sections through the eye. **B** and **E** show the early invagination of the lens placode and the modification of the optic vesicle to an optic cup. **D** and **F** show the formation of the lens vesicle and the two layers of the retina (nervous and pigmented). **G** and **H** show three-dimensional images of the outer aspect of the optic cup. **G**, Early formation of the choroid fissure along the side of the optic cup and optic stalk; the layers of the retina are shown. **H**, The fused choroid fissure; the position of the lens within the optic cup is shown in dotted outline. (A–D, Courtesy of Kathleen Sulik PhD, Professor, University of North Carolina.)

iris (aniridia), suggesting a causal role for this gene in the development of the iris. The genes expressed in the eye are also often active at a variety of other specific sites in the embryo. This may, in part, account for the co-involvement of the eye and other organs in syndromes that result from single genetic lesions, e.g. *PAX2* mutation causes coloboma and kidney defects (Graw 2003).

Developing neural retina

The developing neural retina consists of an outer nuclear zone, which contains dividing neuroepithelial retinal progenitor cells, and an inner marginal zone, which is initially devoid of nuclei. At about stage 16 the cells of the nuclear zone invade the marginal zone, and by stage 18 the nervous stratum of the retina consists of inner and outer neuroblastic layers. Cell lineage analyses have shown that seven retinal cell types are all derived from a common multipotential retinal progenitor cell that undergoes mitosis at the apical (ventricular) surface. Different types of retinal cells are born (i.e. cease dividing) in a conserved sequence during development: ganglion cells, amacrine cells, cone photoreceptors and horizontal cells develop early, whereas bipolar cells, rod photoreceptors and Müller glial cells develop later (Cepko et al 1996). Newly born cells migrate from the apical (ventricular) surface to the appropriate cell layer in the developing retina, establishing its characteristic laminar structure. The developing ganglion cell layer first separates from the neuroblastic layers by formation of the inner plexiform layer. The inner nuclear layer, containing developing amacrine, horizontal, bipolar and Müller glial cells, is then separated from the outer nuclear layer, containing the developing rod and cone photoreceptors, by the formation of the outer plexiform layer. Mature retinal neurones first appear in the central part of the retina. By postmenstrual weeks 29–32 all the named layers of the retina can be identified. The photoreceptor cells continue to differentiate after birth, generating an array of increasing resolution and sensitivity; the macula does not reach maturity until 15–45 months after birth (Hendrickson and Yuodelis 1984).

The divergent differentiation of the pigmented and sensory layers of the retina from the initially bipotential neuroepithelium of the optic vesicle involves activation of region-specific regulatory genes, e.g. *VSX2* in the presumptive neural retina and *MITF* in the presumptive pigmented epithelium (Bharti et al 2006). Patterning by gene expression is an important aspect of establishing regional identity of the optic cup and the subsequent maturation of these respective tissues. Soluble factors from the retina elicit the polarized distribution of plasma membrane proteins and the formation of tight junctions in the pigmented epithelium. Neural retinal differentiation is mediated by several growth factors, including fibroblast growth factors, SHH and retinoic acid. Basic helix–loop–helix proneural transcriptional regulatory genes also play a central role in regulating retinal cell fate. However, the pigmented epithelium initially retains the potential to become neural retina and will do so if the embryonic retina is wounded, demonstrating the plasticity of the early commitment to pigment epithelium or neural retinal fate.

The retinal vasculature forms by the aggregation of spindle-shaped cells (vascular mesenchymal cells) that emanate from the optic disc by postmenstrual week 15 and form vascular cords, consistent with vessel formation by vasculogenesis, which give rise to the inner plexus of the retina. Vessel formation in the temporal and peripheral retina occurs by angiogenesis. New vessel segments sprout by endothelial cell migration from pre-existing vessels and grow tangentially by angiogenesis into the neuroepithelium (Hughes et al 2000). Three parallel interconnected vascular networks located in the nerve fibre and plexiform layers develop with arteries and veins entering and exiting through the optic nerve. The foveal area never develops a retinal vasculature (Provis and Hendrickson 2008).

Optic nerve

The optic nerve develops from the optic stalk. The centre of the optic cup, where the optic fissure is deepest, will later form the optic disc, at the transition zone where the neural retina is continuous with the corresponding invaginated cell layer of the optic stalk; the developing

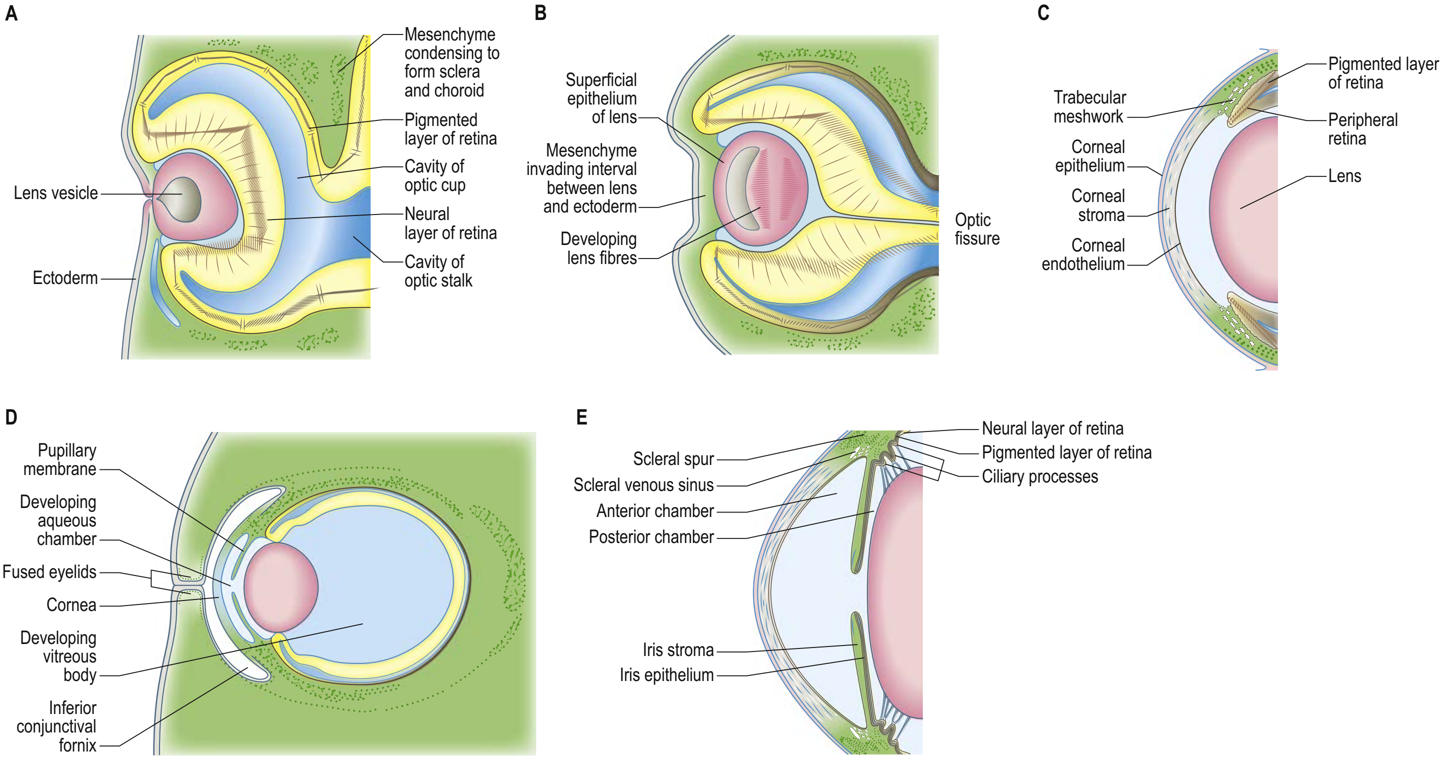
A
Mesenchyme condensing to form sclera and choroid
Pigmented layer of retina
Cavity of optic cup
Lens vesicle
Neural layer of retina
Cavity of optic stalk
Ectoderm
B
Superficial epithelium of lens
Mesenchyme invading interval between lens and ectoderm
Developing lens fibres
Optic fissure
C
Trabecular meshwork
Corneal epithelium
Corneal stroma
Corneal endothelium
Pigmented layer of retina
Peripheral retina
Lens
D
Pupillary membrane
Developing aqueous chamber
Fused eyelids
Cornea
Developing vitreous body
Inferior conjunctival fornix
E
Scleral spur
Scleral venous sinus
Anterior chamber
Posterior chamber
Iris stroma
Iris epithelium
Neural layer of retina
Pigmented layer of retina
Ciliary processes

Fig. 15.2 Sections through the developing eyes of human embryos. **A**, The thick nervous and the thinner pigmented layers of the developing retina and the lens at about stage 16. The two layers of the embryonic optic cup are separated by the cavity of the optic cup. **B**, Section through the optic cup and optic fissure by stage 17. Mesenchyme has moved between the lens and surface ectoderm and the cavity of the optic cup is reduced. **C**, Later, more detailed view of the structures anterior to the lens. Anterior growth of both the peripheral retina and the pigmented layer of the retina, together with local mesenchymal proliferation, will give rise to the ciliary body and iris. The surface ectoderm anterior to the lens forms the corneal epithelium, whereas the corneal endothelium and stroma differentiate from invading neural crest mesenchyme. **D**, The development of the eye and surrounding structures by postmenstrual week 11. The eyelids have developed and are fused; the extent of the conjunctival fornices can be seen. The aqueous chamber is developing and the vitreous body is present. The eye is surrounded by neural crest mesenchyme. **E**, Details of the developing uveal tract. The anterior and posterior aqueous chambers are separated by the iris and the lens is attached to the ciliary body.

axons of the ganglion cells, therefore, pass directly into the wall of the stalk and convert it into the optic nerve. Retinal ganglion cell axons projecting into the stalk promote the optic stalk neuroepithelium to differentiate into astrocytes. Myelination of the axons within the optic nerve begins shortly before birth but the process is not completed until some time later. The optic chiasma is formed by the meeting and partial decussation of the axons within the two optic nerves in the ventral part of the lamina terminalis (at the junction of the telencephalon with the diencephalon in the floor of the third ventricle). Beyond the chiasma, the axons continue as the optic tracts, and pass principally to the lateral geniculate bodies and to the superior tectum of the midbrain. Multiple axonal guidance molecules that influence both intraretinal and chiasmal axon guidance have been identified (Erskine and Herrera 2014). Graded expression molecules (members of the Eph family of receptor tyrosine kinase receptors and ephrin ligands) provide spatial identity to cells in the retina and target cells in the midbrain, and are important for the topographic mapping of retinal ganglion cell axons to form a projection map that is representative of visual input.

Ciliary body

The ciliary body is a compound structure. Its epithelial components are derived from the region of the inner layer of the retina, between the iris and the neural retina, and the adjacent outer layer of pigmented epithelium. The cells here differentiate in close association with the surrounding mesenchyme to form highly vascularized folds that secrete aqueous fluid into the anterior segment of the eye.

The inner surface of the ciliary body forms the site of attachment of the lens. The outer layer is associated with smooth muscle derived from mesenchymal cells in the choroid that lie between the anterior scleral condensation and the pigmented ciliary epithelium.

Iris

The iris develops from the tip of the optic cup, where the two neuroepithelial layers remain thin and are associated with pial blood vessels. The muscles of the sphincter and dilator pupillae are unusual in that they are of neurectodermal origin, developing as a result of the further growth and differentiation of the two layers of the optic cup. Mesenchymal cells, largely composed of neural crest cells that have migrated anterior to the lens, form the collagen-rich iris stroma; they overlay the pigmented epithelium of the iris, which is continuous with the ciliary body and retina and is of neurectodermal origin. The mature colour of the iris develops after birth and is dependent on the relative contributions of the pigmented epithelium on the posterior surface of the iris and the neural crest-derived melanocytes in the mesenchymal stroma of the iris. If only epithelial pigment is present, the eye appears blue, whereas if there is an additional contribution from the melanocytes, the eye appears brown. Aniridia, the absence of the iris, is commonly caused by heterozygous mutations of *PAX6*.

Lens

The lens develops from the lens vesicle (see Figs 15.1F, 15.2A). Initially, this is a hollow ball of actively proliferating epithelium, but by stage 16 there is a discernible difference between the thin anterior (i.e. outward-facing) epithelium and the thickened posterior epithelium. Cells of the posterior wall lengthen and fill the vesicle (see Fig. 15.2B,C), reducing the original cavity to a slit by about stage 18. The posterior cells lose their mitochondria and nuclei and become filled with a very high concentration of proteins (crystallins), that render them transparent; they also become densely packed within the lens as primary lens fibres. Cells at the equatorial region of the lens subsequently elongate and contribute secondary lens fibres to the body of the lens in a process that continues into adult life, sustained by continued proliferation of cells in the anterior epithelium.

The polarity and growth of the lens appear to depend on the differential distribution of soluble factors that promote either cell division or lens fibre differentiation, and are present in the anterior chamber and vitreous humour, respectively. Congenital cataracts can be associated with mutations in genes that encode structural lens proteins, particularly crystallin proteins, as well as genes that encode transcriptional regulatory factors expressed specifically in the lens, such as *MAF* and *PITX3*, which are needed for normal lens development and which also influence normal growth of the globe of the eye (Graw 2003, 2010). Complete absence of the lens (aphakia) can be caused by mutation of the transcriptional regulatory factor gene *FOXE3*.

The developing lens is surrounded by a vascular mesenchymal condensation, the vascular capsule. The posterior part of the capsule is supplied by branches from the hyaloid artery, and the anterior part, the pupillary membrane, is supplied by branches from the anterior ciliary arteries. During postmenstrual weeks 13–16 the hyaloid artery gives off retinal branches. By postmenstrual weeks 21–24 all of the vessels have atrophied, except the hyaloid artery; this becomes occluded during postmenstrual weeks 29–32, although its proximal part persists in the adult as the central artery of the retina. Atrophy of the hyaloid vasculature and of the pupillary membrane appears to be an active process of programmed tissue remodelling that is macrophage-dependent; visual impairment occurs in persistent hyperplastic primary vitreous, a condition in which normal regression of the hyaloid vasculature fails to occur. The hyaloid canal carries the vessels through the vitreous and persists after they have become occluded. In the full-term neonate, the canal extends more or less horizontally from the optic disc to the posterior aspect of the lens, but when the adult eye is examined with a slit-lamp, it can be seen to follow an undulating course, sagging downwards as it passes forwards to the lens. With the loss of its blood vessels, the vascular capsule disappears and the lens becomes dependent for its nutrition on diffusion via the aqueous and vitreous humours. The lens remains enclosed in the lens capsule, a thickened basal lamina derived from the lens epithelium. Sometimes, the pupillary membrane persists at birth, giving rise to congenital atresia of the pupil.

Vitreous humour (vitreous body)

The vitreous humour develops between the lens and the optic cup as a transparent, avascular gel of extracellular substance stabilized by collagen fibrils. The vitreous proteins are derived from surrounding tissues including the developing ciliary body. Initially the lens rudiment and the optic vesicle are in contact, but they draw apart after closure of the lens vesicle and formation of the optic cup, and remain connected by a network of delicate cytoplasmic processes. This network, derived partly from cells of the lens and partly from those of the retina, is the primitive vitreous body. At first, these cytoplasmic processes are connected to the whole of the neuroretinal area of the cup but, later, they become limited to the ciliary region, where, by a process of condensation, they form the basis of the zonular fibres (suspensory ligaments) of the ciliary zonule. The vascular mesenchyme enters the cup through the choroidal fissure and around the equator of the lens and associates locally with this reticular tissue and thus contributes to the formation of the vitreous body.

Anterior segment

Neural crest mesenchymal cells migrate ventrally around the optic cup and between the surface ectoderm and the lens to contribute to the development of anterior segment structures, including the ciliary body, the iris, the cornea and the iridocorneal angle tissues (see Fig. 15.2C–E) (Gould et al 2004). The anterior chamber initially appears as a cleft in this mesenchymal tissue. The mesenchyme superficial to the cleft forms the stroma (substantia propria) and endothelium of the cornea, and that deep to the cleft forms the stroma of the iris and the pupillary membrane. Tangentially, this early cleft extends as far as the iridocorneal angle, where communications are established with the scleral venous sinus (canal of Schlemm). Mesenchymal cells of neural crest origin lying at the angle of the anterior chamber differentiate to form a specialized meshwork of trabecular beams (collagen fibrils covered by cells). The open spaces of the meshwork become open to the anterior chamber as the beams develop. The scleral venous sinus develops deep to the trabecular meshwork. Initially a vascular structure lined by endothelial cells, the canal acts as an aqueous sinus during postmenstrual weeks 17–20 (McMenamin 1989). The forward-growing optic cup rim differentiates into the ciliary epithelium and the iris; the posterior chamber is formed between the iris, the lens capsule, the zonular fibres and the ciliary processes. The latter produce the aqueous humour that flows through the pupil and is drained in the iridocorneal angle, mainly by the trabecular meshwork and the scleral venous sinus. In this way, the walls of the anterior and posterior segment chambers furnish both the sites of production, and the channels for circulation and reabsorption, of the aqueous humour. The *FOXC1* and *PITX2* transcriptional regulatory genes are expressed in the neural crest cells migrating into the presumptive anterior segment, and regulate differentiation of the anterior segment tissues. Anterior segment dysgenesis, involving malformation of the iris, cornea and angle, occurs when these genes are mutated (e.g. Axenfeld–Rieger syndrome) and is often associated with raised intraocular pressure and glaucoma (Gould et al 2004).

Cornea

The cornea is induced in the front of the anterior chamber by the lens and optic cup. The (external) corneal epithelium is formed from surface ectoderm. The primordial corneal endothelium lining the front of the anterior chamber (inner corneal epithelium) is formed from neural crest mesenchymal cells that migrate along the inner surface of the developing cornea and differentiate to form specialized fibroblasts (keratocytes) that secrete the extracellular matrix of the corneal stroma (see Fig. 15.2C–E). A regular array of collagen fibres (lamellae) is established between inner and outer corneal epithelial layers and serves to reduce scattering of light entering the eye. The most anterior region of the stroma (Bowman's layer) develops as an acellular zone packed with collagen fibrils that confer strength on the layer. From postmenstrual weeks 9–12, the corneal endothelium is organized as a monolayer of cells and develops a strong, laminated basal lamina (Descemet's membrane) adjacent to the stroma. The endothelium maintains corneal transparency by regulating the water content of the stroma.

Choroid and sclera

The choroid and sclera differentiate as inner vascular and outer fibrous layers, respectively, from the neural crest mesenchyme that surrounds the optic cup. The choroid is continuous with the leptomeningeal internal sheath of the optic nerve, and the sclera is continuous with the outer dural sheath of the optic nerve. Choroidal vasculature can be seen by stage 18 around the retinal pigmented epithelium. It forms a complete vascular plexus by postmenstrual weeks 21–22, supplying the photoreceptor cells and the ciliary body (Lutty and McLeod 2018).

DIFFERENTIATION OF STRUCTURES AROUND THE EYE

Extraocular muscles

Development of the extrinsic ocular muscles is complex, involving coordinated juxtaposition of specific muscle precursors, cranial motor nerve outgrowth and neural crest mesenchyme. During gastrulation, when the earliest cells are migrating through the primitive node to form the prechordal plate and notochordal process, they transiently express myogenic markers. In stages 9–10 a population of prechordal mesenchyme cells migrate laterally from the lateral edge of the prechordal plate toward the unsegmented paraxial mesenchyme on each side of the notochord. After neurulation is complete, bilateral premandibular, intermediate and caudal cavities develop adjacent to the neural tube. The walls of these 'head cavities', previously termed 'preotic somites', are lined by flat or cylindrical cells that do not exhibit the characteristics of a germinal epithelium.

At the level of the premandibular head cavity, as the oculomotor nerve grows towards the developing eye, the prechordal mesenchyme becomes apparent as a condensation of premuscle cells at its ventrolateral side. This condensation later subdivides into the blastema of the superior, inferior, medial and lateral recti and inferior oblique. Similar events occur in the intermediate head cavity associated with the trochlear nerve and the premuscle cells that form superior oblique, and the caudal head cavity associated with the abducens nerve and premuscle cells that form lateral rectus (see Figs 12.4 and 17.7).

The early myogenic properties of the prechordal mesenchyme have been demonstrated experimentally. If transplanted into limb buds, these cells are able to develop into muscle tissue but their timing of expression of myosin heavy chain isoforms is different from that of limb myoblasts (Wachtler and Jacob 1986). Myotube formation starts later and progresses at a slower pace than in the limb, and coexpression of MyHCI/1st and MyHCI/2nd are both seen from the earliest stages of development, whereas only MyHCI/1st is seen in the limb. These early myoblasts retain their distinct differences from other skeletal muscles as they mature: they are smaller, loosely arranged and belong to very small motor units (Porter and Baker 1996, Pedrosa-Domellöf et al 2000). Extraocular muscle tendons derive from neural crest mesenchyme that connects to the sclera and the orbit. In cases of anophthalmia the relative location and structure of extraocular muscles can be identified (Pedrosa-Domellöf et al 2000, Bohnsack et al 2011). Abnormal development of the extraocular muscles or their motor neurones, in some cases due to single gene defects, causes congenital fibrosis of the extraocular muscles and eye movement disorders (Whitman et al 2004).

Eyelids

The eyelids are formed as small cutaneous folds of surface ectoderm with a core of neural crest mesenchyme (see Fig. 15.2D). During postmenstrual weeks 10–11 their edges come together and unite over the cornea to enclose the conjunctival sac; they usually remain united until about postmenstrual week 24. When the eyelids open, the conjunctiva lining their inner surfaces and covering the scleral region of the eye fuses with the corneal epithelium. Transforming growth factor alpha (TGF-α) and several other growth factors regulate the mesenchyme–epithelium interactions and cell migration that are required for eyelid formation; keratinization is thought to play an important role in lid separation. The eyelashes and lid glands, i.e. sebaceous glands associated with the eyelashes and tarsal (Meibomian) glands, develop from ectoderm, as do the lacrimal and accessory lacrimal glands. Orbicularis oculi, which closes the eyelids, develops on each side from skeletal myoblasts from the second pharyngeal arch that invade the developing eyelids. The muscles that widen the palpebral fissure develop within the orbit from mesenchymal cells; the superior and inferior tarsal muscles are smooth muscle, whereas levator palpebrae superioris is striated muscle that is attached to each upper eyelid by a tendon derived from the neural crest (Plock et al 2005). (For a detailed timetable for upper eyelid development in staged human embryos and fetuses see Byun et al (2011).)

Lacrimal apparatus

The ectodermal epithelium of the superior conjunctival fornix proliferates and gives rise to a series of tubular buds that form the alveoli and ducts of the lacrimal gland. The buds are arranged in two groups: one forms the gland proper and the other forms its palpebral process (de la Cuadra-Blanco et al 2003). The lacrimal sac and nasolacrimal duct are derived from ectoderm in the nasomaxillary groove (between the lateral nasal process and the maxillary process of the developing face) (see Fig. 17.12). The ectoderm thickens to form a solid cord of cells, the nasolacrimal ridge, which subsequently sinks into the mesenchyme and becomes canalized during postmenstrual weeks 9–12 to form the nasolacrimal duct. The lacrimal canaliculi arise from the cranial extremity of the cord as buds that establish openings (puncta lacrimalia) on the margins of the lids. The inferior canaliculus isolates a small part of the lower eyelid to form the lacrimal caruncle and plica semilunaris.

Neonatal and infant eye

Low birthweight and preterm infants are at risk of developing retinopathy of prematurity, a proliferative retinopathy involving proliferation of the retinal vasculature into the vitreous (Kashani et al 2014, Hartnett et al 2014, Hartnett 2015). Fetuses and preterm infants younger than postmenstrual week 30 have no pupillary light reflex or pupillary constriction, with variable responses developing until postmenstrual weeks 32–34. Fetuses are not exposed to light. Preterm neonates born at less than postmenstrual week 32 have little ability to limit the light entering the eye because their eyelids are mostly open and are very thin when closed (Graven 2004). Preterm infants appear to have better visual acuity at term equivalent age than full-term neonates (Wirth et al 2018). Retinal development in the fetus is active between postmenstrual weeks 22 and 40, becoming associated with REM sleep from about postmenstrual weeks 28–30. Eye movement activity is seen in fetuses particularly during postmenstrual weeks 28–29 and then again from postmenstrual weeks 36–37 to 38–39 (Okawa et al 2017). Preterm neonates fail to gain the normal endogenous *in utero* visual stimulation during this time and begin exogenous visual stimulation in an immature system (Wirth et al 2018). They will be susceptible to strong competing stimuli such as intense noise, pain, movement and bright light; sedation that changes sleep patterns may also affect retinal maturation (Graven 2004).

At full term (postmenstrual week 40), the eye is 65% of its adult size. It grows rapidly for the first year, slightly slower until 3 years and then more slowly until puberty. There is proportionately less growth of anterior, compared to posterior, structures and the globe of the eye becomes more spherical. The neonatal lens is more spherical than that of the adult, which helps to compensate for the relative shortness of the eye. The visual acuity of neonates is estimated to be 20/400 and can reach 20/30–20/20 by 2–3 years of age; there is a general trend for infants to be far-sighted (Olitsky et al 2011). The convergence reflex usually appears after postnatal month 4 in full-term neonates; it is seen in preterm infants at about postnatal month 4 regardless of the actual date of delivery (Wirth et al 2018). Extraocular muscle coordination is usually achieved by postnatal months 3–6 and persistent deviation of an eye requires evaluation. Preterm infants have reduced reflex and tear secretion, and tears may not be present with crying until more than 3 months of age (Olitsky et al 2011).

Key references

Fuhrmann S 2010 Eye morphogenesis and patterning of the optic vesicle. Curr Top Dev Biol 93:61–84.

This paper considers the factors involved in the patterning of the optic vesicle into neural retina and pigmented retinal epithelium.

Graw J 2010 Eye development. Curr Top Dev Biol 90:343–86.

This paper presents the transcription factors in eye development and discusses their relevance to human eye disorders.

Kashani AH, Drenser KA, Capone Jr A 2014 Retinopathy of prematurity. In: Yanoff M, Duker J (eds) Ophthalmology, 4th ed. Oxford: Elsevier, Saunders; Ch. 6.20, pp. 535–40.

This chapter reviews the genetic factors and molecular causes of retinopathy in preterm, low birthweight infants.

Olitsky SE, Hug D, Plummer LS et al 2011 Disorders of the eye. Growth and development. In: Kliegman RM, Stanton BF, St Geme JW et al (eds) Nelson Textbook of Pediatrics, 19th ed. Philadelphia: Elsevier, Saunders; Ch. 610.

This chapter considers the postnatal growth of the eye.

O'Rahilly R 1966 The early development of the eye in staged human embryos. Contrib Embryol Carnegie Inst 38:1.

This paper presents the fundamental information on the development of the human eye in staged embryos.

O'Rahilly R 1983 The timing and sequence of events in the development of the human eye and ear during the embryonic period proper. Anat Embryol (Berl) 168:87–99.

This paper presents the stages of human eye development.

Pedrosa-Domellof F, Holmgren Y, Lucas CA et al 2000 Human extraocular muscles: unique pattern of myosin heavy chain expression during myotube formation. Invest Ophthalmol Vis Sci 41:1608–16.

A study of extraocular muscle development in human embryos and fetuses.

Saha MS, Servetnick M, Grainger RM 1992 Vertebrate eye development. Curr Opin Genet Dev 2:582–8.

A review of the interactions involved in eye development and discussion of the genes responsible for development of the eye.

Sinn R, Wittbrodt J 2013 An eye of eye development. Mech of Dev 130:347–58.

This paper reviews the transcription factors that are involved in the development of the eye.

Wachtler F, Jacob M 1986 Origin and development of the cranial skeletal muscles. Bibl Anat 29:24–46.

This paper considers the origin of the extraocular muscles.

Maturation of the visual pathways occurs in early infancy and slows in childhood, with adult levels of visual acuity attained by postnatal year 4. The visual pathways, lateral geniculate body and occipital visual cortex are patterned postnatally by exposure to visual stimuli. By postmenstrual weeks 38–40 neonates focus on the edges of objects, lines, shapes and movement, and focus their attention to the human face (preferably main caregiver). Each shape patterns columns of neurones within the visual cortex; direct light into the eyes does not create columns. Colour input becomes attached to patterned directional columns from postnatal months 2–3. The critical period for visual development occurs from the end of the second trimester to postnatal year 3 (Graven 2004).

Any condition that impedes the generation of aligned, high-resolution images on the retina may result in amblyopia due to loss of appropriate patterning of these brain regions from the deprived eye, followed by progressive expansion of axonal input from the functioning eye. The visual cortex of animals dark reared from birth remains immature, whereas specific use of the affected eye promotes reversal of cortical inhibition (Stryker and Löwel 2018). Amblyopia affects about 1–5% of people, caused by strabismus and anisometropia, where the two eyes have different focusing powers. Examination of the eyes is part of neonatal screening, performed within 72 hours of delivery and again at postnatal weeks 6–8; the assessment includes the red reflex, which is the reflection of the back of the retina seen in flash photography that may be changed in congenital cataract, retinoblastoma or neuroblastic tumour. It is difficult to assess visual acuity in infants and techniques rely on assessing preferential looking. Over 90% of children with amblyopia have significant refractive error that should be treated ahead of any strabismus. Treatment of amblyopia has been occlusion of vision in the unaffected eye with a patch to force reliance on the amblyopic eye and thus patterning of the lateral geniculate body and visual cortex. Studies on the effectiveness of this treatment have shown that children benefit most from 3–6 hours of occlusion per day for a period of 3 months. Although occlusion is the usual treatment modality, atropine eye drops, causing blurring of vision by pupillary dilation, or computer games that present images separately to each eye with reduced contrast to the unaffected eye, are considered promising. These treatments have been shown to improve vision but the residual deficit in children with moderate amblyopia is 2 lines of a visual acuity chart (Jefferis et al 2015).

Growth of the eyeball and achievement of the appropriate axial length to focus correctly onto the retina is associated with daylight entering the eyes over childhood. The prevalence of myopia has increased and is now affecting 80–90% of young adults in East Asia and 40–60% in Europe and North America. This change has been correlated with less time spent outdoors in daylight (Guo et al 2017).

References

Bharti K, Nguyen MT, Skuntz S et al 2006 The other pigment cell: specification and development of the pigmented epithelium of the vertebrate eye. Pigment Cell Res 19:390–4.

Bohnsack BL, Gallina D, Thompson H et al 2011 Development of extraocular muscles requires early signals from periocular neural crest and the developing eye. Arch Ophthalmol 129:1030–1041.

Byun TH, Kim JT, Park HW et al 2011 Timetable for upper eyelid development in staged human embryos and fetuses. Anat Rec (Hoboken) 294:789–96.

Cepko CL, Austin CP, Yang X et al 1996 Cell fate determination in the vertebrate retina. Proc Natl Acad Sci USA 93:589–595.

Chow RL, Lang RA 2001 Early eye development in vertebrates. Annu Rev Cell Dev Biol 17:255–96.

de la Cuadra-Blanco C, Peces-Peña MD, Mérida-Velasco JR 2003 Morphogenesis of the human lacrimal gland. J Anat 203:531–6.

Dubourg C, Lazaro L, Pasquier L 2004 Molecular screening of SHH, ZIC2, SIX3, and TGIF genes in patients with features of holoprosencephaly spectrum: mutation review and genotype-phenotype correlations. Hum Mutat 24:43–51.

Eiraku M, Sasai Y 2012 Self-formation of layered neural structures in three-dimensional culture of ES. Curr Opin Neurobiol 22:768–77.

Erskine L, Herrera E 2014 Connecting the retina to the brain. ASN Neuro 6. pii. doi: 10.1177/1759091414562107.

Fuhrmann S 2010 Eye morphogenesis and patterning of the optic vesicle. Curr Top Dev Biol 93:61–84.

This paper considers the factors involved in the patterning of the optic vesicle into neural retina and pigmented retinal epithelium.

Gould DB, Smith RS, John SW 2004 Anterior segment development relevant to glaucoma. Int J Dev Biol 48:1015–29.

Graven SN 2004 Early neurosensory visual development of the fetus and newborn. Clin Perinatol 31:199–216.

Graw J 2003 The genetic and molecular basis of congenital eye defects. Nat Rev Genet 4:876–888.

Graw J 2010 Eye development. Curr Top Dev Biol 90:343–86.

This paper presents the transcription factors in eye development and discusses their relevance to human eye disorders.

Guo Y, Liu LJ, Tang P et al 2017 Outdoor activity and myopia progression in 4-year follow-up of Chinese primary school children: The Beijing Children Eye Study. PLoS One 12:e0175921.

Hartnett ME, Morrison MA, Smith S et al 2014 Genetic variants associated with severe retinopathy of prematurity in extremely low birth weight infants. Invest Ophthalmol Vis Sci 55:6194–203.

Hartnett ME 2015 Pathophysiology and mechanisms of severe retinopathy of prematurity. Ophthalmology 122:200–10.

Hendrickson AE, Yuodelis C 1984 The morphological development of the human fovea. Ophthalmology 91:603–12.

Hughes S, Yang H, Chan-Ling T 2000 Vascularization of the human fetal retina: roles of vasculogenesis and angiogenesis. Invest Ophthalmol Vis Sci 41:1217–1228.

Jefferis JM, Connor AJ, Clarke MP 2015 Amblyopia. BMJ 351:h5811. doi: 10.1136/bmj.h5811.

Kashani AH, Drenser KA, Capone Jr A 2014 Retinopathy of prematurity. In: Yanoff M, Duker J (eds) Ophthalmology, 4th ed. Oxford: Elsevier, Saunders; Ch. 6.20, pp. 535–40.

This chapter reviews the genetic factors and molecular causes of retinopathy in preterm, low birthweight infants.

Lutty GA, McLeod DS 2018 Development of the hyaloid, choroidal and retinal vasculatures in the fetal human eye. Prog Retin Eye Res 62:58–76.

McMenamin PG 1989 Human fetal iridocorneal angle: a light and scanning electron microscopic study. Br J Ophthalmol 73: 871–9.

Nakano T, Ando S, Takata N et al 2012 Self-formation of optic cups and storable stratified neural retina from human ESCs. Cell Stem Cell 10:771–85.

Olitsky SE, Hug D, Plummer LS et al 2011 Disorders of the eye. Growth and development. In: Kliegman RM, Stanton BF, St Geme JW et al (eds) Nelson Textbook of Pediatrics, 19th ed. Philadelphia: Elsevier, Saunders; Ch. 610.

This chapter considers the postnatal growth of the eye.

O'Rahilly R 1966 The early development of the eye in staged human embryos. Contrib Embryol Carnegie Inst 38:1.

This paper presents the fundamental information on the development of the human eye in staged embryos.

O'Rahilly R 1983 The timing and sequence of events in the development of the human eye and ear during the embryonic period proper. Anat Embryol (Berl) 168:87–99.

This paper presents the stages of human eye development.

Okawa H, Morokuma S, Maehara K et al 2017 Eye movement activity in normal human fetuses between 24 and 30 weeks gestation. PLoS One 12:e0178722.

Pedrosa-Domellöf F, Holmgren Y, Lucas CA et al 2000 Human extraocular muscles: unique pattern of myosin heavy chain expression during myotube formation. Invest Ophthalmol Vis Sci 41:1608–16.

This paper presents a study of extraocular muscle development in human embryos and fetuses.

Plock J, Contaldo C, von Lüdinghausen M 2005 Levator palpebrae superioris muscle in human fetuses: anatomical findings and their clinical relevance. Clin Anat 18:473–80.

Porter JD, Baker RS 1996 Muscles of a different 'color': the unusual properties of the extraocular muscles may predisposeor protect them in neurogenic and myogenic disease. Neurology 46:30–7.

Provis JM, Hendrickson AE 2008 The foveal avascular region of developing human retina. Arch Ophthalmo1 26:507–11.

Saha MS, Servetnick M, Grainger RM 1992 Vertebrate eye development. Curr Opin Genet Dev 2:582–8.

A review of the interactions involved in eye development and discussion of the genes responsible for development of the eye.

Sinn R, Wittbrodt J 2013 An eye of eye development. Mech Dev 130:347–58.

This paper reviews the transcription factors that are involved in the development of the eye.

Stryker MP, Löwel S 2018 Amblyopia: New molecular/pharmacological and environmental approaches. Vis Neurosci 35:E018. doi:10.1017/S0952523817000256.

Wachtler F, Jacob M 1986 Origin and development of the cranial skeletal muscles. Bibl Anat 29:24–46.

This paper considers the origin of the extraocular muscles.

Whitman M, Hunter DG, Engle EC 2004 Congenital fibrosis of the extraocular muscles. [Updated 2016, Jan 14]. In: Adam MP, Ardinger HH, Pagon RA et al (eds) GeneReviews® [Internet]. Seattle, WA: University of Washington, Seattle; 1993–2019.

Wirth M, Naud A, Schmitt E et al 2018 Visual maturation at term equivalent age in very premature infants according to factors influencing its development. Front Physiol 20. doi.org/10.3389/fphys.2018.01649.

Zhu Y, Carido M, Meinhardt A et al 2013 Three-dimensional neuroepithelial culture from human embryonic stem cells and its use for quantitative conversion to retinal pigment epithelium. PLoS One 8:e54552.

CHAPTER
16

Development of the ear

INNER EAR

The production of a precisely positioned and functionally well-tuned inner ear depends on genetic patterning and a cascade of transcription signals expressed by numerous tissues, including the developing inner ear and its surrounding periotic mesenchyme, the adjacent hindbrain, neural crest and notochord (Ohyama et al 2010, Sienknecht 2013).

The first signs of inner ear development are visible shortly after those associated with the developing eyes. Two patches of ectodermal thickening, the otic placodes, appear lateral to the hindbrain at stage 9. Each placode invaginates as an otic pit, adjacent to rhombomeres 5 and 6 of the hindbrain and dorsal to the second pharyngeal cleft (Ch. 17; see Fig. 17.1B). During stage 12 (30–32 days postfertilization, see Fig. 23.3) the pit is pinched off from the surface ectoderm to form a simple, hollow epithelial sac, the otic vesicle (otocyst or auditory vesicle) (**Fig. 16.1**).

Regions of the vesicle differentiate into prosensory domains, which give rise to the membranous labyrinth and the vestibulocochlear (statoacoustic) ganglia of the eighth cranial nerve. The first morphological evidence of this differentiation is visible during stage 14 (postfertilization days 32–34), when the otic vesicle loses its initial piriform shape. A tubular diverticulum, the endolymphatic appendage, develops from its dorsomedial rim. The remainder of the vesicle, the utriculosaccular chamber, differentiates into an expanded pars superior and a narrower pars inferior. The endolymphatic appendage elongates and its tip expands into an endolymphatic sac that is connected to the pars superior by a narrow endolymphatic duct.

Two plate-like diverticula, one vertical and one horizontal, emerge from the dorsal part of the pars superior. The epithelia in the centre of each outgrowth coalesce to form a fusion plate; the central part of this plate is eventually resorbed, leaving the anlagen of the semicircular canals. The vertical plate gives rise to the anterior and posterior semicircular canals, which share a common crural attachment to the utriculosaccular chamber, and the horizontal plate gives rise to the lateral semicircular canal. A small expansion, the ampulla, forms at one end of each semicircular canal.

The central part of the utriculosaccular chamber, which now represents the membranous vestibule, becomes divided into a small ventral saccule and a larger dorsal utricle, mainly by horizontal infolding extending from the lateral wall of the chamber towards the opening of the endolymphatic duct. In this way, communication between the utricle and saccule is restricted to a narrow utriculosaccular duct. The latter becomes acutely bent on itself; its apex is continuous with the endolymphatic duct. While this is happening, the membranous labyrinth rotates so that its long axis, which was originally vertical, becomes more or less horizontal.

The ventral tip of the pars inferior begins to elongate. A medially directed evagination, the cochlear anlagen, is evident in the ventral part of the utriculosaccular chamber by stage 15. The proximal region of this cochlear duct continues to increase in length and its distal region becomes progressively more coiled, reaching 2.5 turns by postfertilization week 10 (**Fig. 16.2**)(Pechriggl et al 2015). When the duct has achieved its final length and spiral configuration, its proximal part becomes constricted, forming the ductus reuniens by which the saccule remains connected to the cochlea. The cochlea is initially patterned into several prosensory domains. The central domain will give rise to the organ of Corti. Molecular signals regulating the induction and differentiation of the organ of Corti are complex (Kelly and Chen 2009, Chacko et al 2016): a combination of bone morphogenetic protein (BMP), fibroblast growth factor and Notch signalling is required to define the sensory and non-sensory territories in the cochlear duct (Ohyama et al 2010, Whitfield 2015).

Cells derived from the otocyst differentiate into the bipolar neurones that populate the vestibular and cochlear ganglia; sustentacular cells (Wan et al 2013); the unique endolymph-producing epithelia of the stria vascularis; the absorbing epithelia of the endolymphatic sac; the general epithelial lining of the membranous labyrinth; and specialized cells in the six sensory patches of the inner ear (crista ampullaris of the three semicircular canals, maculae of the utricle and saccule, organ of Corti in the cochlea). Each of the sensory patches consists of mechanosensory hair cells and non-sensory supporting cells arranged into mosaic patterns that are essential for normal hearing and balance. The only cells in the mature inner ear that are not of otocyst origin are melanocytes in the stria vascularis, derived from the neural crest.

The very different morphologies of the mature cristae, maculae and organ of Corti reflect the differential expression of multiple genes during their development and maturation. The formation of the utricle and saccule occurs during a time that coincides with the initiation of hair cell planar polarity. The development of core planar cell polarity in the orientation of stereocilia in the mechanosensory hair cells of the mammalian inner ear is described in an extensive and conflicting literature (Deans 2013, Ezan and Montcouquiol 2013).

At the same time as these changes are taking place, mesenchymal cells surrounding the developing membranous labyrinth undergo chondrogenesis to form an encasing cartilaginous otic capsule. Between postmenstrual weeks 16–23 the otic capsule ossifies to form almost all of the bony labyrinth of the internal ear within the petrous temporal bone; the modiolus and osseous spiral lamina ossify directly from connective tissue. The cartilaginous capsule is initially incomplete and the cochlear, vestibular and facial ganglia are temporarily exposed in the gap between its canalicular and cochlear parts. They subsequently become covered by an outgrowth of cartilage that will enclose the facial nerve.

Vacuoles filled with perilymph develop in the embryonic connective tissue between the cartilaginous capsule and the epithelial wall of the membranous labyrinth. The rudiment of the periotic cistern or vestibular perilymphatic space can be seen in the reticulum between the saccule and fenestra vestibuli by stage 17. The cochlear scalae (scala vestibuli and scala tympani) develop by fusion of these spaces; the mechanism is uncertain (Kim et al 2011). The two scalae gradually extend along each side of the cochlear duct and a communication, the helicotrema, opens between them when they reach the tip of the coiled duct. An overview of human inner ear development is given in Lim and Brichta (2016).

The rudiment of the eighth cranial nerve appears in stage 13 as the vestibulocochlear (statoacoustic) ganglion that lies between the otocyst and the hindbrain and is initially temporarily fused with the ganglion of the facial nerve. Neuroblasts (fate already specified in the ectoderm of the otic placode) delaminate from the anteroventral region of the otic vesicle, proliferate and migrate to the site of the presumptive ganglion, where they coalesce. They differentiate into mature bipolar sensory neurones and become segregated into vestibular and spiral ganglia, each associated with the corresponding division of the eighth cranial nerve. These neurones are unusual because they are exclusively placodal in origin, unlike neurones in most cranial ganglia with a dual placodal and neural crest origin, and many of their somata become enveloped in thin myelin sheaths. Their peripheral processes collectively provide the afferent innervation of the labyrinthine hair cells, relaying balance and auditory information. Tantalizing evidence about the transcriptional networks that encode the positioning of sensory hair cells and spiral ganglion neurones along a frequency (tonotopic) gradient within the developing cochlea, and that ensure that the two cell types make appropriate functional connections, is appearing in animal models (Appler and Goodrich 2011, Appler et al 2013, Coate and Kelley 2013). The olivocochlear bundle, an outgrowth of axons from neurones in the superior olivary complexes in the pons, accompanies the axons of the developing eighth cranial nerve; these axons provide the inner ear with an efferent innervation, mainly to the outer hair cells in the organ of Corti, where they are associated with modulation of hearing. *In utero*, the fetus receives sound by bone conduction. interaural sound differences are not established until birth, whether preterm or term.

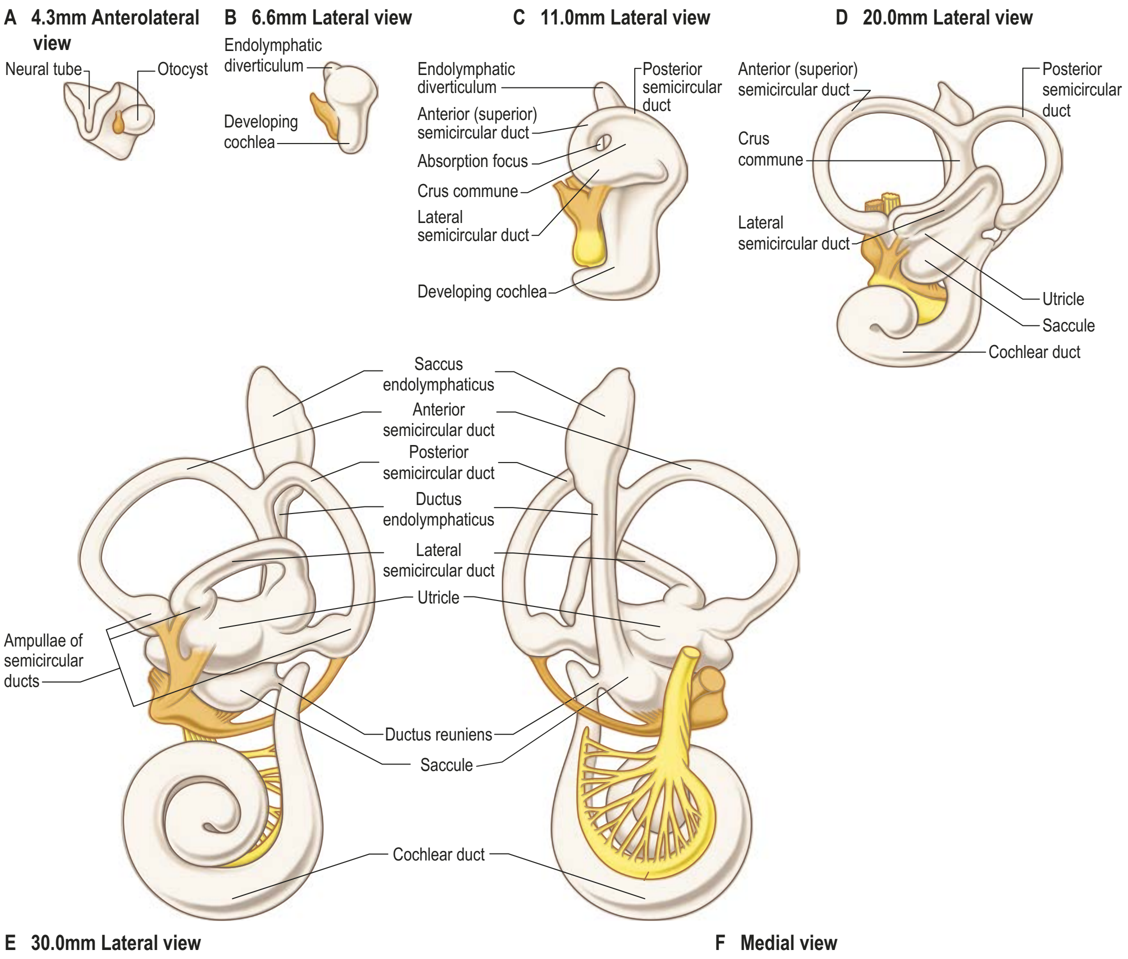
A 4.3mm Anterolateral view
Neural tube
Otocyst
B 6.6mm Lateral view
Endolymphatic diverticulum
Developing cochlea
C 11.0mm Lateral view
Endolymphatic diverticulum
Anterior (superior) semicircular duct
Absorption focus
Crus commune
Lateral semicircular duct
Developing cochlea
Posterior semicircular duct
D 20.0mm Lateral view
Anterior (superior) semicircular duct
Crus commune
Lateral semicircular duct
Posterior semicircular duct
Utricle
Saccule
Cochlear duct
Saccus endolymphaticus
Anterior semicircular duct
Posterior semicircular duct
Ductus endolymphaticus
Lateral semicircular duct
Utricle
Ampullae of semicircular ducts
Ductus reuniens
Saccule
Cochlear duct
E 30.0mm Lateral view
F Medial view

Fig. 16.1 A–F, The stages in the development of the membranous labyrinth from the otocyst, at the embryonic stages and aspects indicated. Note the relationship of the vestibular (orange) and cochlear (yellow) parts of the vestibulocochlear nerve.

MIDDLE EAR (TYMPANIC CAVITY AND PHARYNGOTYMPANIC (AUDITORY) TUBE)

All the components of the external and middle ears develop from the first and second pharyngeal arches. The pharyngotympanic tube and tympanic cavity initially form as bilateral extensions of the early pharynx (see Fig. 17.4). They become visible in stage 13 as hollow tubotympanic recesses of the first pharyngeal pouches. The more lateral part of each recess widens and develops into the early tympanic cavity. The tubotympanic recess at first lies inferolateral to the cartilaginous otic capsule (Ch. 17) but this spatial relationship alters as the capsule enlarges and the tympanic cavity becomes anterolateral. A cartilaginous process grows from the lateral part of the otic capsule to form the tegmen tympani (Rodríguez-Vázquez et al 2011). The process curves caudally to form the lateral wall of the pharyngotympanic tube, incorporating the tympanic cavity and the proximal bony third of the pharyngotympanic tube into the petrous region of the temporal bone. The mastoid antrum appears as a dorsal expansion of the tympanic cavity during the late second and early third trimester (it can be seen on ultrasound at postmenstrual week 34). The tympanic ring, a bone derived from first pharyngeal arch mesenchyme, is of particular importance in supporting the tympanic membrane (see below) (Takechi et al 2016).

The middle ear ossicles are of neural crest origin, derived from crest cells that have migrated from rhombomeres 1–4 into the mesenchyme of the first and second pharyngeal arches. The malleus and incus develop from the dorsal end of the first arch, derived from Meckel's (ventral mandibular) cartilage (Burford and Mason 2016). The incus and malleus are homologous to the quadrate and articular bones of birds and reptiles and take part in the earliest jaw articulation in suckling marsupials (Anthwal et al 2013, Maier and Ruf 2016). A transitory connection of the incus, but not the malleus, to the otic capsule has been reported (Rodríguez-Vázquez et al 2018). The stapes develops from the second arch, although possibly not from the proximal end of Reichert's cartilage (Rodríguez-Vázquez 2005). Its characteristic shape reflects the growth and elongation of the stapedial artery during stages 16–20, and the formation of a ring of cartilage (anulus stapes) around the vessel; the latter involutes by stage 21. The stapedial footplate forms within the otic capsule (paraxial mesenchyme) by stage 22; this part of the stapes has a dual origin from both paraxial and neural crest mesenchyme (Rodríguez-Vázquez 2005, Tucker 2017).

The two anlagen of each stapedius muscle appear close to the stapedial artery and facial nerve within the second arch mesenchyme in stage 18. The pyramidal eminence is formed within a condensation of mesenchyme around the bell of the stapedius muscle (Rodríguez-Vázquez 2009). Tensor tympani starts to appear near the extremity of the tubotympanic recess at almost the same time in the first arch mesenchyme.

Neural crest mesenchyme fills the early middle ear cavity and later retracts to create the true tympanic cavity. The hypotympanum (the portion of the tympanic cavity inferior to the level of the inferior margin of the external acoustic meatus) is lined by endodermal epithelium. Experimental studies on transgenic mice have shown that the epitympanic recess is lined by neural crest cells that have undergone mesenchymal to epithelial transition (Thompson and Tucker 2013, Takechi et al 2016). From stage 18 onwards the ossicles start to differentiate into cartilage, but remain embedded in the mesenchymal roof of the tympanic cavity until postmenstrual weeks 29–32, when the mesenchyme is resorbed. As this happens, the ossicles become suspended within the developing tympanic cavity, supported by forming ligaments and becoming covered by the mucosa of the middle ear as the tympanic cavity expands. The differentiation of the middle ear mucosa in the developing and postnatal mouse is described in Tucker et al (2018). The human tympanic cavity fills with air after birth and further postnatal developmental changes contribute to the functional maturation of the middle ear.

EXTERNAL EAR

The external acoustic meatus is traditionally described as developing within the first pharyngeal cleft, and is clearly visible from stage 12 on lateral views of human embryos (see Fig. 17.3). In mouse embryos, developmental studies of gene expression suggest that the external acoustic meatus forms more rostrally from invagination of the ectoderm of the first arch rather than at the first pharyngeal cleft (Minoux et al 2013, Anthwal and Thompson 2016, Tucker 2017). By the end of the embryonic period, the surface ectoderm has developed into a bilaminar epithelium: the basal germinative layer gives rise to the epidermis and the superficial layer to the periderm which grows throughout fetal life by mitotic activity independent of the developing epidermal stratum basale (see Fig. 7.30). The periderm has tight junctions and acts as a protective barrier that prevents adhesion between intimately apposed,

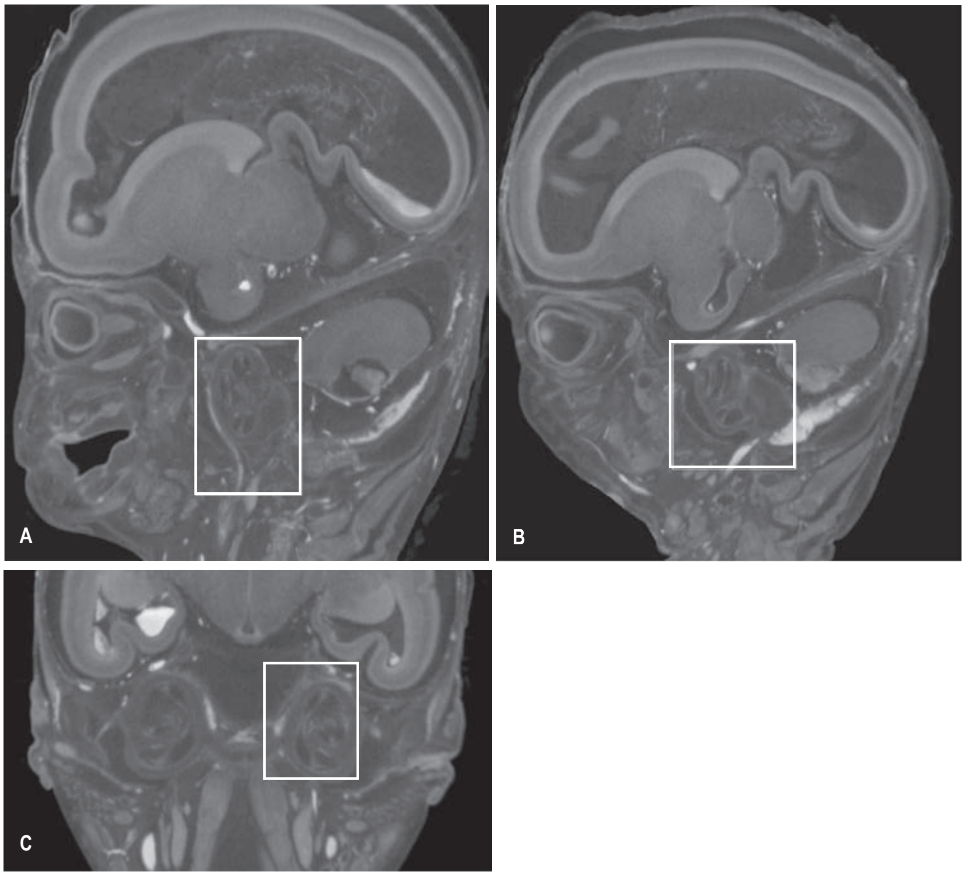

Fig. 16.2 MicroCT images of the inner ear in a 14-postmenstrual-week fetus. **A**, Semicircular ducts (white rectangle), right sagittal section. **B**, Cochlea (white rectangle), left sagittal section. **C**, Semicircular ducts (white rectangle), coronal section. (Courtesy of Dr Owen Arthurs and Dr Susan Shelmerdine, Great Ormond Street Hospital, London.)

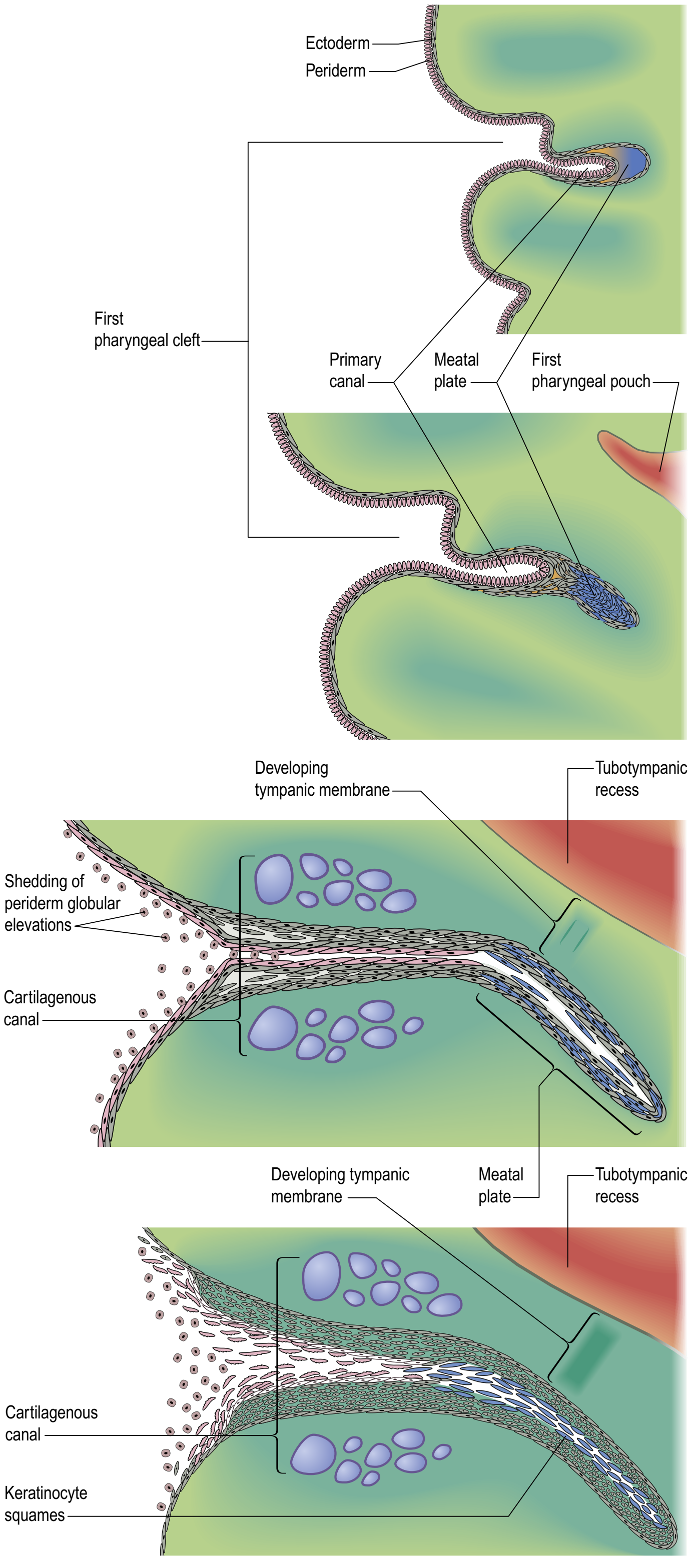

Fig. 16.3 The development of the external acoustic meatus (external auditory canal).

adhesion-competent epithelia (Hammond et al 2019). Both periderm and epidermis line the open primary external acoustic meatus (**Fig. 16.3**).

A solid epidermal meatal plate forms and extends from the edge of the open primary canal toward the developing tympanic ring, a structure that is essential for the formation of the external acoustic meatus (Takechi et al 2016). The underlying mesenchyme forms the cartilaginous part of the final canal (see Fig. 17.4). The cells within the meatal plate separate from postmenstrual weeks 13–14 and an open canal is formed by postmenstrual week 18, with ongoing epidermal mitosis generating movement of keratinous debris to the exterior (Fig. 16.3) (Michaels and Soucek 1989, Nishimura and Kumoi 1992). The osseous part of the external acoustic meatus develops postnatally from the tympanic ring of the temporal bone whereas the cartilaginous part develops much earlier, independently of the osseous part (Ikari et al 2013).

The tympanic membrane is formed from three sources, ectoderm-derived cells of the meatal plate, the endodermal-derived floor of the tubotympanic recess and the neural crest mesenchyme that intervenes between these layers. The tympanic membrane is supported by the tympanic ring which starts to ossify later than other viscerocranial bones. Four ossification centres appear about postmenstrual week 14 (see Fig. 17.6), but the bone is not completely developed until 2 years of age. In the neonate the tympanic membrane and ossicles have already reached adult size but the external acoustic meatus is much smaller than in the adult.

The first indication of auricular development is the appearance of mesenchymal proliferations beneath the ectoderm of the caudal border of the first pharyngeal arch and the cranial border of the second pharyngeal arch, at stage 15 (O'Rahilly and Müller 1987). These proliferations, traditionally termed auricular hillocks and numbered 1–6, were thought to contribute equally to the auricle, and are apparent by stages 22–23. However, 3D reconstructions of human embryonic auricles have demonstrated that the bulk of an auricle arises from second pharyngeal arch mesenchyme and that the tragus and anterior external acoustic meatus are derived from first pharyngeal arch mesenchyme (Veugen et al 2019). The lobule is the last part of the auricle to develop.

Common congenital anomalies of the auricle are described in Chapter 42.

HEREDITARY DEAFNESS

Prelingual deafness is the most common congenital anomaly, affecting 2–6/1000 newborns: at least two-thirds of cases reported in the developed world are due to genetic factors, classified as non-syndromic (typically sensorineural and accounting for approximately 70% of cases) and syndromic (may be sensorineural, conductive or mixed and accounting for approximately 30% of cases). A number of genes likely to be mediators of genetic hearing loss have been identified, including *TGFB1*, *BMP4*, *ERK1/2*, *EYA1* and many *GPCR* genes (Stamatiou and Stankovic 2013). The range of affected chromosomes and the specific genes involved in sensorineural deafness is given by Hildebrand et al (2010). The structural abnormalities resulting from absent or aberrant gene expression during the development of the inner ear include labyrinthine dysplasias (e.g. a reduction in the number of cochlear turns or an enlargement of the endolymphatic duct); disorganization of the patterns of stereocilia in sensory hair cells and loss of cytoskeletal components in these cells; and defects in K^+ recycling across gap junctions between activated hair cells. Structural anomalies resulting from altered gene expression in the middle and external ear include failure of complete cavitation of the middle ear and canal atresia, with defects in the external and middle ear impacting on each other, highlighting the close association of these structures during development.

NEONATAL AND INFANT EAR

The onset of hearing occurs from about postmenstrual week 20 with fetuses exposed to the intrauterine sound environment. Permanent hearing loss is more common in preterm infants (30/1000) than in full-term neonates: preterm infants with no hearing loss may have changes in postnatal auditory processing. The effects of early perinatal acoustic exposure are not yet known (Durante et al 2018). Two neonatal hearing tests are used in routine screening: evoked otoacoustic emissions, the detection of low-level sounds emitted by the cochlea in response to a sound stimulation; and automated auditory brainstem response, the recording via an electroencephalograph of wave generation in response to click stimuli in the external ear. The screening should occur before postnatal week 4 and it is recommended that those who fail should have further diagnostic evaluation before postnatal month 3 (Stewart and Bentley 2019).

Bonus e-book content

Fig. 16.2 MicroCT images of the inner ear in a 14-postmenstrual-week fetus.

Loss of auditory input to the temporal cortex affects its postnatal patterning and maturation, in a similar manner to the effect of loss of visual input from the retina in amblyopia. Although cortical regions are present at full-term birth, the interconnections mature during postnatal experience (Kral et al 2017). Auditory temporal resolution (i.e. the ability to detect time intervals between sound stimuli) is necessary for the auditory perception of rhythm, and to discriminate frequency and duration of phonemes (units of sound) (Durante et al 2018). Neonates can discriminate their mother's voice before postnatal month 1. They are initially sensitive to acoustic differences but later specialize and remain sensitive to distinctive phonemes in their mother language (Saito et al 2019). Congenital deafness is associated with delay in speech and language acquisition and consequent learning difficulties. Cochlear implants are an optimal therapy for prelingually deaf infants, if implanted within postnatal years 1–3 (Kral 2013) (Ch. 43). Untreated congenital deafness in animals and humans gives rise to changes to the cochlear nuclei, the inferior colliculi and reduced white matter volume in the auditory cortex (Berger et al 2017).

Key references

Appler JM, Lu CC, Druckenbrod NR et al 2013 Gata3 is a critical regulator of cochlear wiring. J Neurosci 33:3679–3691.

A study that uses conditional knockout mice to show that the transcription factor Gata3 (expressed in spiral ganglion neurones throughout their development) is apparently essential for the formation of precisely wired connectivity in the cochlea.

Burford CM, Mason MJ 2016 Early development of the malleus and incus in humans. J Anat 229: 857–870.

Deans MR 2013 A balance of form and function: planar polarity and development of the vestibular maculae. Semin Cell Dev Biol 24:490–498.

This article reviews the significance of planar polarity on vestibular system function and the molecular mechanisms associated with the development of planar polarity at three different anatomical scales (subcellular, cellular and tissue) in vestibular hair cells.

Hildebrand MS, Hussein M, Smith RJH 2010 Genetic sensorineural hearing loss. In: Flint PW, Haughey BH, Lund VJ et al (eds) Cummings Otolaryngology–Head and Neck Surgery, 5th ed. Philadelphia: Elsevier, Mosby; Ch. 147.

This chapter reviews the classification and genetics of sensorineural hearing loss.

Kral 2013 Auditory critical periods: a review from system's perspective. Neurosci 247:117–133

Lim R, Brichta AM 2016 Anatomical and physiological development of the human inner ear. Hear Res 338:9–21.

Stamatiou GA, Stankovic KM 2013 A comprehensive network and pathway analysis of human deafness genes. Otol Neurotol 34:961–970.

An in silico *analysis of deafness genes using ingenuity pathway analysis.*

References

Anthwal N, Thompson H 2016 The development of the mammalian outer and middle ear. J Anat 228:217–32.

Anthwal N, Joshi L, Tucker AS 2013 Evolution of the mammalian middle ear and jaw: adaptations and novel structures. J Anat 222:147–160.

Appler JM, Goodrich LV 2011 Connecting the ear to the brain: molecular mechanisms of auditory circuit assembly. Prog Neurobiol 93:488–508.

Appler JM, Lu CC, Druckenbrod NR et al 2013 Gata3 is a critical regulator of cochlear wiring. J Neurosci 33:3679–3691.

A study that uses conditional knockout mice to show that the transcription factor Gata3 (expressed in spiral ganglion neurones throughout their development) is apparently essential for the formation of precisely wired connectivity in the cochlea.

Berger C, Kühne D, Scheper V et al 2017 Congenital deafness affects deep layers in primary and secondary auditory cortex. J Comp Neurol 525:3110–3125.

Burford CM, Mason MJ 2016 Early development of the malleus and incus in humans. J Anat 229: 857–870.

Chacko LJ, Pechriggl EJ, Fritsch H et al 2016 Neurosensory differentiation and innervation patterning in the human fetal vestibular end organs between the gestational weeks 8–12. Front Neuroanat 10:111. doi: 10.3389/fnana.2016.00111.

Coate TM, Kelley MW 2013 Making connections in the inner ear: recent insights into the development of spiral ganglion neurons and their connectivity with sensory hair cells. Semin Cell Dev Biol 24:460–469.

Deans MR 2013 A balance of form and function: planar polarity and development of the vestibular maculae. Semin Cell Dev Biol 24:490–498.

This article reviews the significance of planar polarity on vestibular system function and the molecular mechanisms associated with the development of planar polarity at three different anatomical scales (subcellular, cellular and tissue) in vestibular hair cells.

Durante AS, Mariano S, Pachi PR 2018 Auditory processing abilities in prematurely born children. Early Hum Dev 120:26–30.

Ezan J, Montcouquiol M 2013 Revisiting planar cell polarity in the inner ear. Semin Cell Dev Biol 24:499–506.

Hammond NL, Dixon J, Dixon MJ 2019 Periderm: Life-cycle and function during orofacial and epidermal development. Semin Cell Dev Biol 91:75–83.

Hildebrand MS, Hussein M, Smith RJH 2010 Genetic sensorineural hearing loss. In: Flint PW, Haughey BH, Lund VJ et al (eds) Cummings Otolaryngology–Head and Neck Surgery, 5th ed. Philadelphia: Elsevier, Mosby; Ch. 147.

This chapter reviews the classification and genetics of sensorineural hearing loss.

Ikari Y, Katori Y, Ohtsuka A et al 2013 Fetal development and variations in the cartilages surrounding the human external acoustic meatus. Ann Anat 195:128–136.

Kelly MC, Chen P 2009 Development of form and function in the mammalian cochlea. Curr Opin Neurobiol 19:395–401.

Kim JH, Rodriguez-Vázquez JF, Verdugo-López S et al 2011 Early fetal development of the human cochlea. Anat Rec (Hoboken) 294:996–1002.

Kral 2013 Auditory critical periods: a review from system's perspective. Neurosci 247:117–133.

Kral A, Yusuf PA, Land R 2017 Higher-order auditory areas in congenital deafness: top-down interactions and corticocortical decoupling. Hearing Res 343:50–63.

Lim R, Brichta AM 2016 Anatomical and physiological development of the human inner ear. Hear Res 338:9–21.

Maier W, Ruf I 2016 Evolution of the mammalian middle ear: a historical review. J Anat 228:270–283.

Michaels L, Soucek S 1989 Development of the stratified squamous epithelium of the human tympanic membrane and external canal: the origin of auditory epithelial migration. Am J Anat 184:334-344.

Minoux M, Kratochwil CF, Ducret S et al 2013 Mouse Hoxa2 mutations provide a model for microtia and auricle duplication. Development 140:4386–97.

Nishimura Y, Kumoi T 1992 The embryologic development of the human external auditory meatus. Preliminary report. Acta Otolaryngol 112:496–503.

Ohyama T, Basch ML, Mishina Y et al 2010 BMP signaling is necessary for patterning the sensory and nonsensory regions of the developing mammalian cochlea. J Neurosci 30:15044–15051.

O'Rahilly R, Müller F 1987 Developmental Stages in Human Embryos. Washington, DC: Carnegie Institution.

Pechriggl EJ, Bitsche M, Glueckert R et al 2015 Development of the innervation of the human inner ear. Dev Neurobiol 75:683–702.

This paper presents the stages of human ear development.

Rodríguez-Vázquez JF 2005 Development of the stapes and associated structures in human embryos. J Anat 207:165–173.

Rodríguez-Vázquez JF 2009 Development of the stapedius muscle and pyramidal eminence in humans. J Anat 215:292–299.

Rodríguez-Vázquez JF, Murakami G, Verdugo-López S et al 2011 Closure of the middle ear with special reference to the development of the tegmen tympani of the temporal bone. J Anat 218:690–698.

Rodríguez-Vázquez JF, Yamamoto M, Abe S et al 2018 Development of the human incus with special reference to the detachment from the chondrocranium to be transferred into the middle ear. Anat Rec 301:1405–15.

Saito O, Nishimura T, Morimoto C et al 2019 Audiological evaluation of infants using mother's voice. Int J Ped Otorhinolaryngol 121:81–87.

Sienknecht UJ 2013 Developmental origin and fate of middle ear structures. Hear Res 301:19–26.

Stamatiou GA, Stankovic KM 2013 A comprehensive network and pathway analysis of human deafness genes. Otol Neurotol 34:961–970.

An in silico *analysis of deafness genes using ingenuity pathway analysis.*

Stewart JE, Bentley JE 2019 Hearing loss in paediatrics. Pediatr Clin North Am 66:425–36.

Takechi M, Kitazawa T, Hirasawa T et al 2016 Developmental mechanisms of the tympanic membrane in mammals and non-mammalian amniotes. Congen Anom 56:12–17.

Thompson H, Tucker AS 2013 Dual origin of the epithelium of the mammalian middle ear. Science 339:1453–1456.

Tucker AS 2017 Major evolutionary transitions and innovations: the tympanic middle ear. Phil Trans R Soc B 372:20150483.

Tucker AS, Dyer CJ, Fons Romero JM et al 2018 Mapping the distribution of stem/progenitor cells across the mouse middle ear during homeostasis and inflammation. Development 145 pii:dev154393. doi:10.1242/dev.154393.

Veugen CCAFM, Dikkers FG, de Bakker BS 2019 The developmental origin of the auricula revisited. Laryngoscope. doi: 10.1002/lary.28456 (ePub 2019 Dec 11).

Wan G, Corfas G, Stone JS 2013 Inner ear supporting cells: rethinking the silent majority. Semin Cell Dev Biol 24:448–459.

Whitfield TT 2015 Development of the inner ear. Curr Opin Genet Dev. 32:112–8.

CHAPTER
17

Development of the head and neck

Head and neck development is distinct from that of the trunk, utilizing region-specific genes, signalling mechanisms and morphogenetic processes. The boundary between the head and trunk is not always clear. The neck is contiguous rostrally with the head but it also joins and shares developmental processes caudally with the back (Ch. 18) and the upper limb (Ch. 19). Studies of developmental gene expression in vertebrate and non-vertebrate embryos are elucidating the conserved mechanisms within the tissues interacting in this region (Kuratani et al 2019) (Commentary 2.1). Studies on human embryos have necessarily been mainly descriptive but observations from lineage and genetic studies in mouse embryos together with clinical genetics studies, have provided major insights into the underlying mechanisms. The description of human development provided here is derived from the following sources, which incorporate primary data by the authors, as well as references to older primary source material: Hamilton et al (1962), Patten (1968), O'Rahilly and Müller (1987, 2001), Hinrichsen (1990), Steding (2009). References to experimental studies in the mouse and human clinical studies are provided in the text.

It is important to note that the term mesenchyme simply describes a loose cellular tissue organization with a rich extracellular matrix, in contrast to the sheets of simple epithelia that form the outer ectodermal and inner endodermal layers of early embryos. Prior to the migration of neural crest cells from the edges of the cranial neural folds to their final destinations, the only mesenchyme in the embryonic head is 'primary mesenchyme', i.e. mesenchymal cells formed by epithelial–mesenchymal transformation in the primitive streak. This is the mesodermal germ layer. There is no lateral plate mesoderm in the head; all of the cranial mesoderm is paraxial. Thus cranial mesenchyme is derived from mesodermal, neural crest and placodal sources, each of which has specific distributions and specific derivatives.

Evolution of the vertebrate head is a consequence of the origin of a novel cell population, the neural crest. Neural crest cells form a wide variety of neural derivatives throughout the body and neural and non-neural derivatives in the head (Ch. 14), where they also give rise to connective and skeletal tissues and make major contributions to the skull. In mammalian embryos, cranial neural crest cells undergo epithelial to mesenchymal transformation and emigrate from the edges of the still-open cranial neural folds. **Fig. 17.1** shows stylized views of human embryos at an early stage of neural crest migration (Fig. 17.1A) and at the end of the crest migration (Fig. 17.1B). **Fig. 17.2C–D** shows the same developmental stages in mouse embryos with neural crest cells identified by staining techniques. In the head, cranial and vagal neural crest populations are generated from the dorsal neural folds according to positional information from brain segments (rhombomeres) and the lateral migration of the neural crest cells through adjacent somites.

The first transverse division to form in the early embryonic brain is the preotic sulcus (see Fig. 17.1A; **Fig. 17.2A**), which defines the boundary between prorhombomeres A and B. This early division is of major functional and organizational significance because it separates the regions of origin of the skeletogenic neural crest populations that make a major contribution to the skull from those that form skeletal structures in the neck (hyoid bone and larynx). During cranial neurulation, the prorhombomeres undergo subdivision so that, by the time the brain region of the neural tube closes, seven rhombomeres can be clearly distinguished. The occipital region (adjacent to the four occipital somites) remains unsegmented (**Fig. 17.2B**) and by analogy with the segmented rhombencephalon, it is also referred to as prorhombomere D/rhombomere 8. The segmental organization of the embryonic head caudal to prorhombomere A is related to the expression of evolutionarily conserved *HOX* genes (written *Hox* in the mouse) that have their rostral boundaries at specific rhombomere divisions; they are also expressed in the corresponding neural crest cells (Santagati and Rijli 2003, Hutchins et al 2018). Genetic experiments in the mouse and other vertebrates have shown that skeletal patterning of the first pharyngeal arch depends on the absence of *Hox* gene expression in the neural crest cells migrating into it, whereas skeletal patterning of the second arch depends on the crest cell expression of *Hoxa2*. In marked contrast investigation of *Hox* gene expression in arches 3–6 has suggested that skeletal patterning functions reside within the environment into which the neural crest cells migrate. (See Brunskill et al 2014 for gene expression maps of neural crest, paraxial mesoderm and ectodermal populations in mouse embryos during the early stages of craniofacial development.)

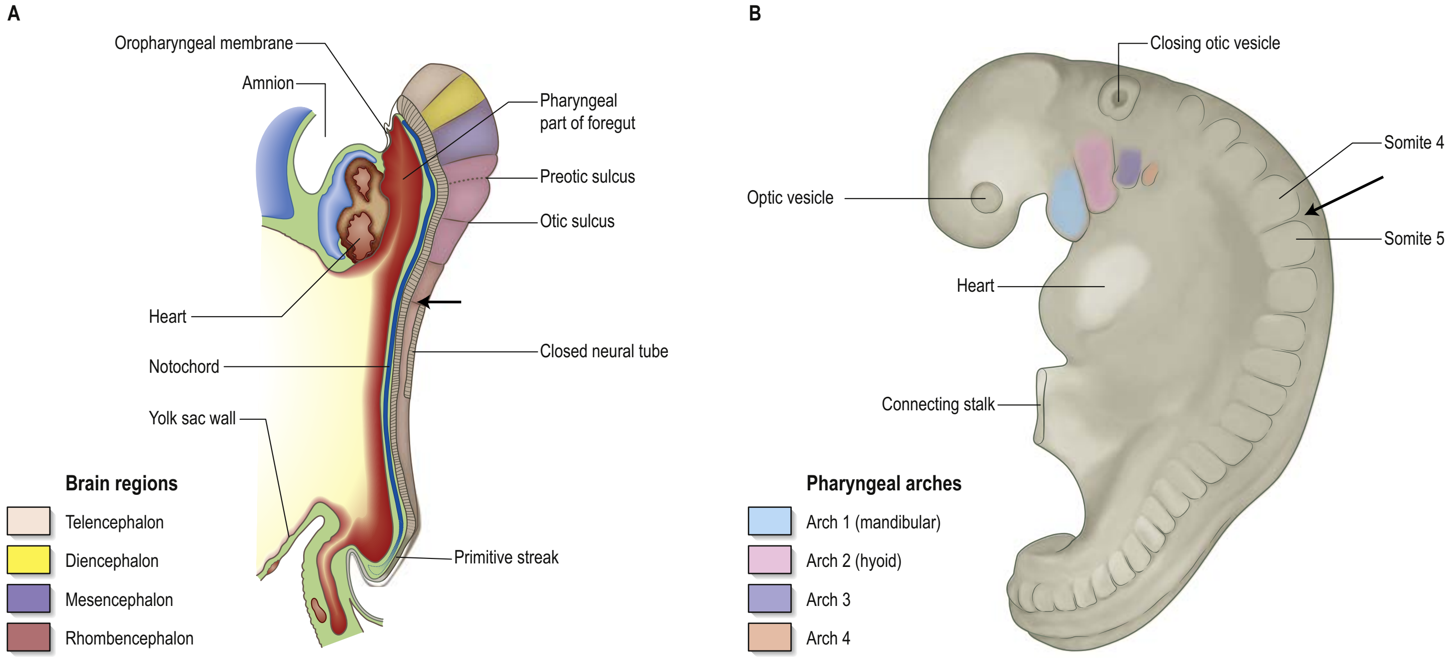

Fig. 17.1 Human embryos during the early stages of head development. The occipital–cervical boundary is indicated by an arrow in **A** and **B**. **A**, A sagittal section of a stage 10 embryo, in which neural tube closure has begun in the future occipito-cervical region. **B**, A lateral view of a stage 12 embryo (see also Fig. 14.2). (Embryonic stages 10–23 correlated to postfertilization days of development and postmenstrual weeks of pregnancy are shown in Fig. 23.3.)

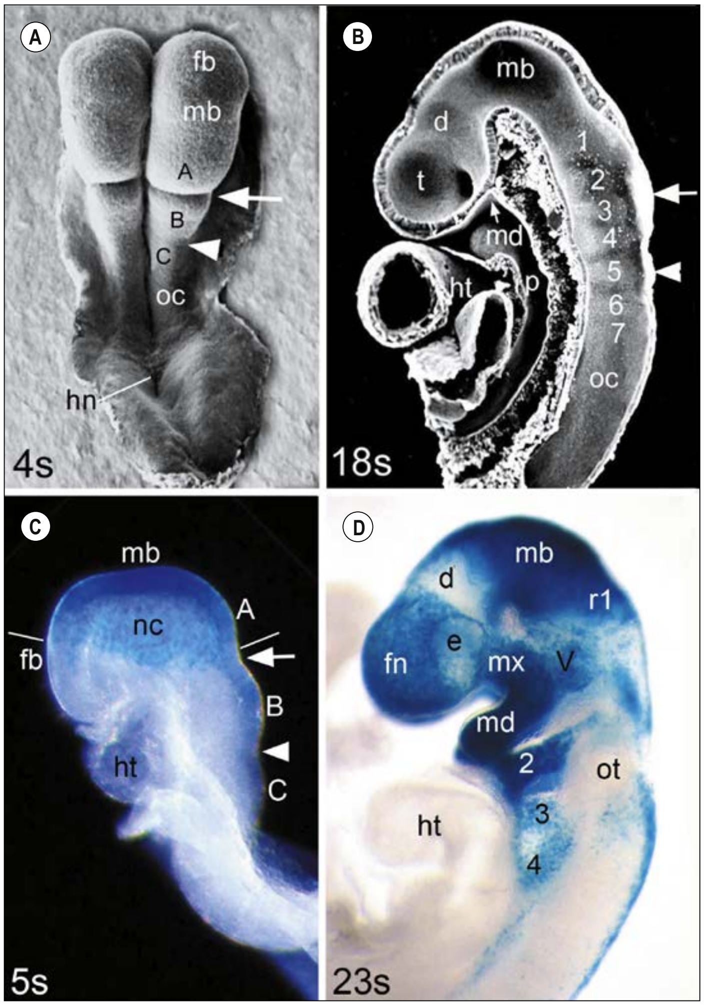

Fig. 17.2 Mouse embryo heads during the period of cranial neural crest cell migration. **A–B**, Scanning electron micrographs (**A**, dorsal view; **B**, median section) of embryos near the start (4 somite pairs) and end (18 somite pairs, interior view) of the period of neural crest cell migration. At the 4-somite stage, the neural folds are convex and the hindbrain is divided into prorhombomeres A, B and C by the preotic (arrow) and otic (arrowhead) sulci; at the 18-somite stage, the neural tube is closed and the hindbrain is divided into seven rhombomeres (numbered) and the unsegmented occipital region (oc). Rathke's pouch is indicated by a small arrow on **B**. **C–D**, Lateral views of embryos at the 5- and 23-somite stage, respectively, carrying a permanent marker for neural crest cells and the neural epithelium from which the trigeminal crest cells originate (blue stain). **C**, Trigeminal neural crest cells (nc) migrate as a veil-like mass beneath the surface ectoderm, originating as a continuous group from prorhombomere A, the midbrain and the caudal diencephalic region (d) of the forebrain, into the frontonasal region (fn) and the first arch (white lines indicate the level of the migrating edge). **D**, After migration, frontonasal neural crest cells (fn) cover the telencephalon and rostral diencephalon, surrounding the eye (e); maxillary (mx) and mandibular (md) neural crest populates the first pharyngeal arch; the trigeminal ganglion primordium (V) is also present. Hyoid neural crest cells from prorhombomere B have populated the hyoid arch and the primordium of ganglion VII/VIII, rostral to the otocyst (ot); vagal crest cells from prorhombomere C are migrating into arches 3 and 4, and starting to form the primordia of the glossopharyngeal and vagal ganglia, caudal to the otocyst. Other abbreviations: fb, forebrain; hn, Hensen's node; ht, heart; mb, midbrain; p, pharynx; r1, rhombomere 1 of the hindbrain; t, telencephalon. (A and B, With permission from Morriss-Kay GM, Wilkie AOMW 2005 Growth of the normal skull vault and its alteration in craniosynostosis. J Anat 207:637–53. C and D, With permission from Jiang X, Iseki S, Maxson RE et al 2002 Tissue origins and interactions in the mammalian skull vault. Dev Biol 241:106–16.)

In the mouse, the lineage marker Wnt1-Cre/R26R has enabled neural crest cells to be traced from the stage at which they leave the neural epithelium through to their final locations in mature tissues. These studies show three separate populations of neural crest cells migrating from the cranial neural folds; each gives rise to both neuronal and non-neuronal progeny (Jiang et al 2002). The first (trigeminal) population originates from the diencephalic region of the forebrain, the midbrain and prorhombomere A of the hindbrain (which subsequently divides to form rhombomeres 1 and 2) (see Figs 17.2A–B). The neural crest cells with a neuronal fate contribute to the trigeminal ganglion. The non-neuronal cells migrate extensively to surround the telencephalon and part of the diencephalon, forming the frontonasal mesenchymal populations and also migrate lateral to the rhombencephalon to form the mesenchyme of the maxillary and mandibular regions of the first arch (see Figs 17.2C–D).

The second (hyoid) population emigrates from prorhombomere B (which forms rhombomeres 3 and 4); some cells condense to form the otic ganglion before the main population continues into the second pharyngeal arch. The third (vagal) population has a more extensive origin, from the neural folds caudal to the otocyst, i.e. prorhombomere C. These cells will contribute to the ganglia of the glossopharyngeal and vagal nerves. The non-neuronal vagal crest cells migrate into pharyngeal arches 3, 4 and 6 and some of them continue into the heart where they contribute to the division of the cardiac outflow tract (Jiang et al 2000). The neural crest also gives rise to the parasympathetic ganglia and parasympathetic postganglionic nerves in the head and neck. For a full account of the neuronal derivatives of neural crest cells, see Chapter 14. In human embryos, histological methods have revealed equivalent cranial neural crest cell origins and migration routes to those of the mouse (O'Rahilly and Müller 2007).

Caudal to the segmented region of the cranial neural tube, neural crest cells from the occipital region (prorhombomere D/rhombomere 8) migrate with occipital myoblasts to form the hypoglossal cord. They eventually differentiate to form the connective tissue of the tongue and the occipital myoblasts form the intrinsic tongue musculature. No sensory ganglia are formed from the occipital neural crest in human embryos.

Ectodermal placodes appear as patches of columnar or pseudostratified epithelium within the otherwise squamous epithelium of the surface ectoderm. Three pairs of placodes contribute to sense organs, forming the olfactory epithelium, the lens and the otocyst. They each undergo morphogenesis to form a pit and then (for the lens and otic pits) a closed cyst (vesicle). Epibranchial (epipharyngeal) placodes are situated near the proximal end of each pharyngeal arch. Some of their cells undergo epithelial to mesenchymal transformation, joining the underlying neural crest cell condensations to form sensory neuroblasts in the ganglia of cranial nerves V, VII, IX and X. Some cells from the otocyst and an adjacent placode similarly delaminate to contribute to the ganglia of cranial nerve VIII.

EMBRYONIC PHARYNX AND PHARYNGEAL ARCHES

The most cranial portion of the foregut, the embryonic pharynx, is the scaffolding around which the face, palate and anterior neck structures are built. The development of this region from neural crest, paraxial mesoderm, surface ectoderm and foregut endoderm involves spatiotemporal coordination of cell movement, tissue growth and tissue interactions. As successive populations of neural crest cells migrate around the pharynx at progressively more caudal levels, five pairs of pharyngeal arches are formed (numbered 1, 2, 3, 4 and 6 for consistency with comparative anatomy terminology, although this numbering has been queried because it does not seem to reflect the situation across the vertebrates as a whole (Graham et al 2019)). This process is complete by stages 14–15 (**Fig. 17.3**). For details of the age in postfertilization days of the stages given see Fig. 23.3. Pharyngeal clefts (grooves) separate the arches externally and are matched internally by internal depressions, the pharyngeal pouches (see Fig. 17.3). Pharyngeal arches are also known as branchial arches, reflecting their evolutionary origin supporting the gills in the earliest vertebrates.

Each pharyngeal arch consists of an epithelial covering of ectoderm externally and endoderm internally and is filled with mesenchyme that is mainly of neural crest origin (see Fig. 17.3). Understanding the origin and fates of the structures within the pharyngeal arches is aided by considering their conformity to, or deviation from, a basic plan: the cartilages, muscles, nerves and arteries associated with each arch are summarized in **Table 17.1**. The neural crest cells of arches 1–4 form a skeletal element and associated connective tissue: in all arches they give rise to the outer walls of an aortic arch blood vessel with an endothelial lining that develops by angiogenesis from the heart outflow tract endocardium. Paraxial mesoderm also forms the muscle associated with each pharyngeal arch. Motor and sensory innervation is supplied by arch-specific cranial nerves. For an overview of the organization of these tissues in the pharynx, see Fig. 12.4; for their fate, see Figs 17.5–17.7.

The first pharyngeal arch, unlike the other arches, possesses a dorsal and ventral process, and appears C-shaped in lateral view. The main 'mandibular' component forms the lower jaw and the dorsal process contributes to maxillofacial and palatopharyngeal structures and to the middle ear. The second pharyngeal arch is termed the hyoid arch because of its

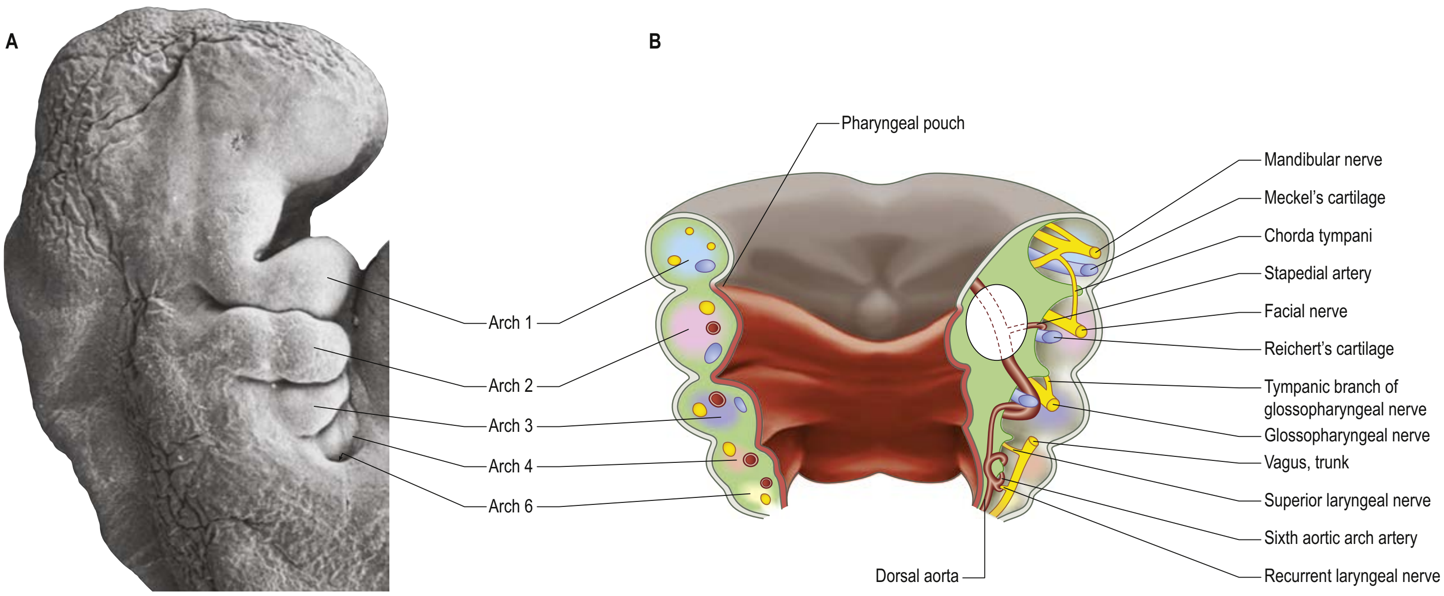

Fig. 17.3 Pharyngeal arch development. **A**, A scanning electron micrograph of a human embryo (stage 14/15), showing the right lateral aspect of the pharyngeal arches; auricular hillocks are visible on arch two. **B**, The pharyngeal region (stage 15) viewed from the dorsal aspect. The whole left side and part of the right side of the endodermal roof of the pharynx has been removed to show the grooves in its lateral walls and floor, and the nerves, arteries and cartilages of the arches. The position of the right otocyst is shown as a clear oval. (A, Courtesy of Professort G Steding, Georg-August-University of Göttingen, Göttingen, Germany.)

TABLE 17.1

Chart of derivatives of the pharyngeal arches

Arch number	Arch name	Embryonic cartilage	Cartilage derivative	Muscle	Nerve	Artery
1	Mandibular	Meckel's	Incus Malleus Anterior ligament of malleus Spine of sphenoid Sphenomandibular ligament Genial tubercle of mandible	Tensor tympani Muscles of mastication Mylohyoid Anterior belly of digastric Tensor veli palatini	Trigeminal (V) mandibular division	First aortic arch artery [transitory]
2	Hyoid	Reichert's	Stapes Styloid process of temporal bone Stylohyoid ligament Lesser horn and upper part of body of hyoid bone	Stapedius Stylohyoid Muscles of the face, auricle and scalp Buccinator Platysma Posterior belly of digastric	Facial (VII)	Stapedial artery [transitory]
3	Third		Greater horn and lower part of body of hyoid bone	Stylopharyngeus	Glossopharyngeal (IX)	Common carotid artery, first part of internal carotid artery
4	Fourth		Thyroid cartilage	Cricothyroid	Vagus (X) superior laryngeal branch	Proximal part of subclavian artery on the right Arch of aorta between origins of left subclavian arteries
6	Sixth		Other laryngeal cartilages	Other intrinsic laryngeal muscles	Vagus (X) recurrent laryngeal branch	Part between the pulmonary trunk and dorsal aorta becomes ductus arteriosus on left, disappears on right
4+6	Fourth + sixth			Pharyngeal constrictors Palatal muscles except tensor veli palatini	Pharyngeal plexus (IX, X)	

contribution to the hyoid bone (and to other parts of the hyomandibular apparatus in fishes). The third, fourth and sixth arches are not named.

The left and right mandibular arches, first seen at stage 10, grow ventromedially in the floor of the pharynx to meet in the median plane, forming the ventral border of the early mouth immediately above the developing heart. The maxillary processes are not clearly visible as surface structures until stage 13; their enlargement coincides with the proliferation of the frontonasal mesenchyme to form the nasal swellings (see Fig. 17.10A–B). The hyoid arches appear at stage 11, the third arches at stage 12 and the fourth arches by stage 13. The sixth arch can only be identified by the arrangement of the arch arteries and nerves, and by a slight projection on the pharyngeal aspect. The floor of the pharynx is formed mainly by ventral apposition of the arches of the two sides. The inferior border of the second arch grows over the lower arches and encloses an ectodermal depression termed the cervical sinus (Fig. 17.4).

Skeletal elements of the pharyngeal arches

In human embryos, neural crest mesenchyme in the first three arches gives rise to ligaments, tendons, connective tissue and cartilage that

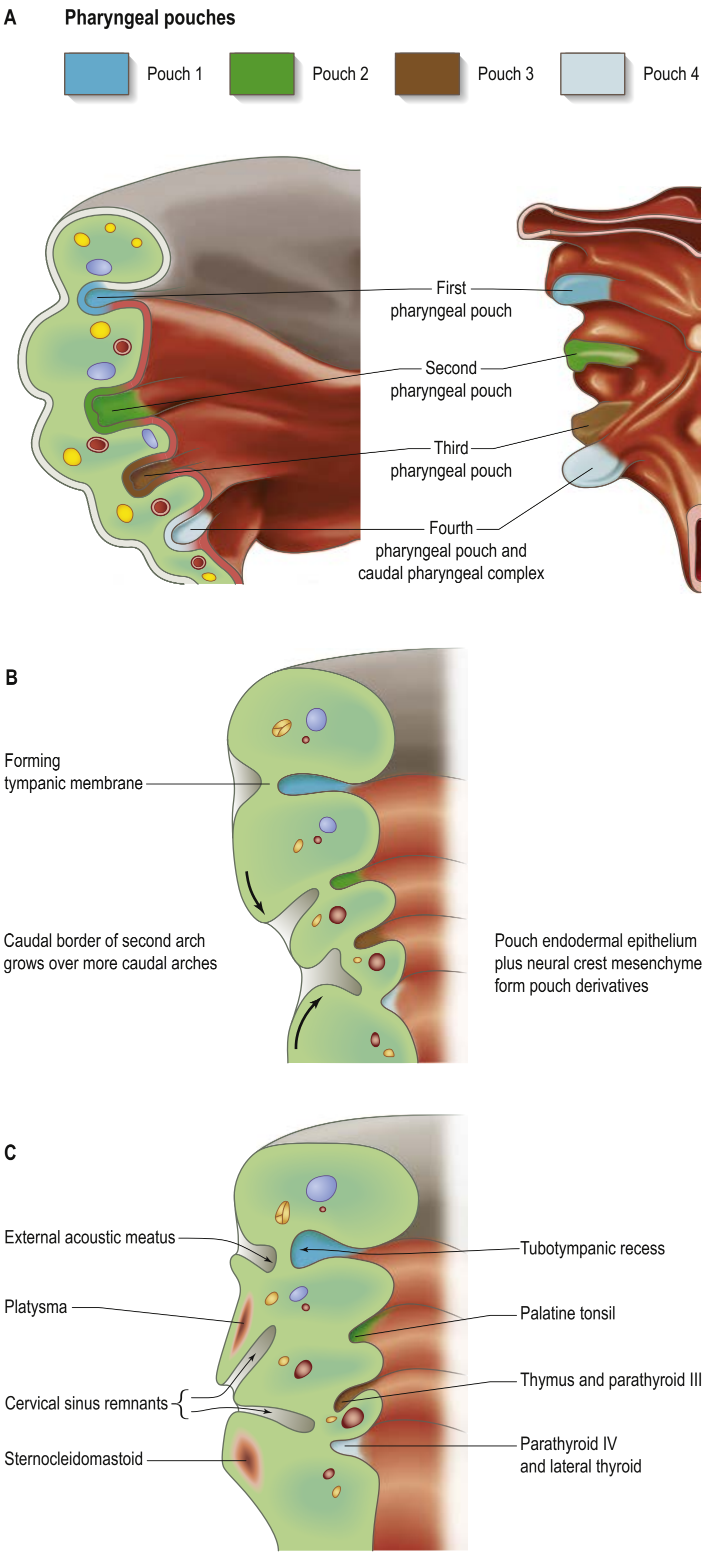
A
Pharyngeal pouches
Pouch 1
Pouch 2
Pouch 3
Pouch 4
First pharyngeal pouch
Second pharyngeal pouch
Third pharyngeal pouch
Fourth pharyngeal pouch and caudal pharyngeal complex
B
Forming tympanic membrane
Caudal border of second arch grows over more caudal arches
Pouch endodermal epithelium plus neural crest mesenchyme form pouch derivatives
C
External acoustic meatus
Platysma
Cervical sinus remnants
Sternocleidomastoid
Tubotympanic recess
Palatine tonsil
Thymus and parathyroid III
Parathyroid IV and lateral thyroid

Fig. 17.4 Pharyngeal pouch development. **A**, The arrangement of the early pharyngeal pouches: on the left, the internal aspect of the pharyngeal floor viewed from above; on the right, the external aspect of the pharyngeal floor viewed from below. **B**, A coronal section of the left side of the pharynx at stage 18, showing changes to the pharyngeal pouches internally and pharyngeal clefts externally. **C**, A coronal section of the left side of the pharynx at stage 19. See also Fig. 17.19 for further development.

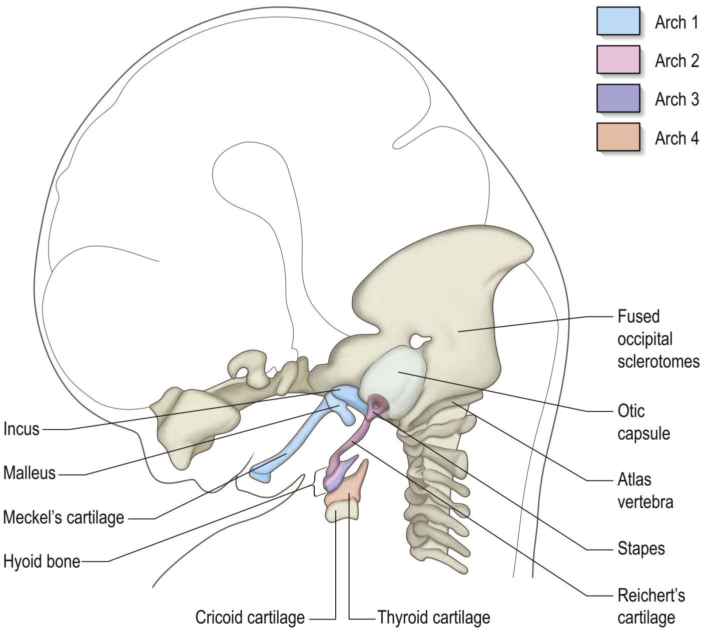
Arch 1
Arch 2
Arch 3
Arch 4
Fused occipital sclerotomes
Otic capsule
Atlas vertebra
Stapes
Reichert's cartilage
Incus
Malleus
Meckel's cartilage
Hyoid bone
Cricoid cartilage
Thyroid cartilage

Fig. 17.5 The chondrocranium and arch cartilage derivatives at stage 20.

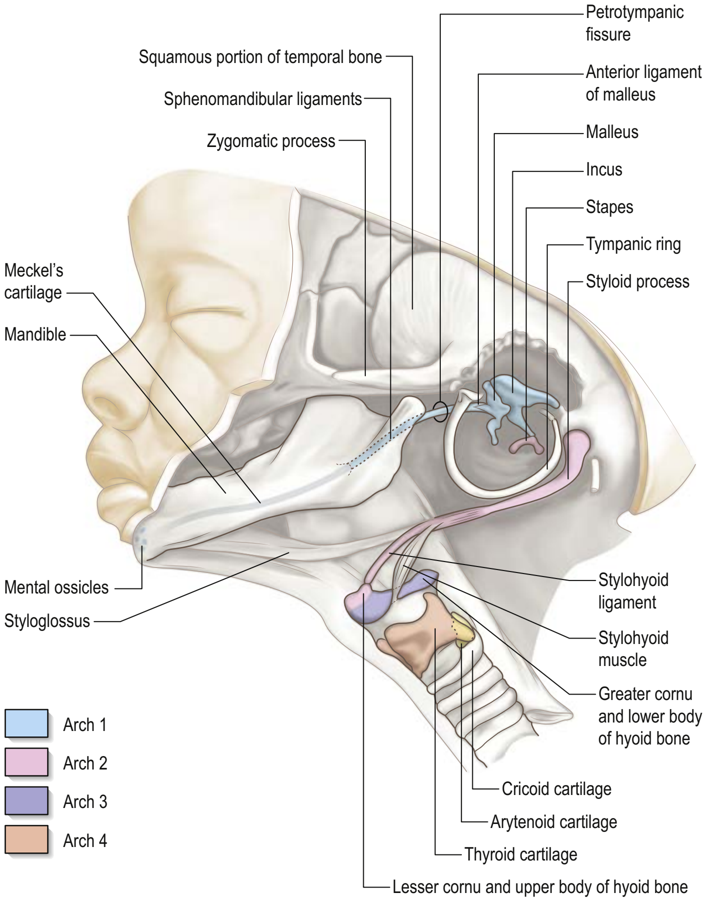
Petrotympanic fissure
Squamous portion of temporal bone
Anterior ligament of malleus
Sphenomandibular ligaments
Malleus
Zygomatic process
Incus
Stapes
Tympanic ring
Meckel's cartilage
Styloid process
Mandible
Mental ossicles
Styloglossus
Stylohyoid ligament
Stylohyoid muscle
Greater cornu and lower body of hyoid bone
Arch 1
Arch 2
Arch 3
Arch 4
Cricoid cartilage
Arytenoid cartilage
Thyroid cartilage
Lesser cornu and upper body of hyoid bone

Fig. 17.6 Derivatives of the pharyngeal arch cartilages after about post-menstrual week 15.

forms skeletal elements that subsequently chondrify in part or in their entirety. Where chondrogenesis is complete, the element contacts the skull base lateral to the hindbrain (**Figs 17.5–17.6**). No cartilages form in the fourth and sixth arches in human embryos (de Bakker et al 2018).

The first arch cartilage, Meckel's cartilage, is a structure around which the embryonic lower jaw skeleton arises. After the mandible forms by intramembranous ossification of the neural crest mesenchyme lateral to it, Meckel's cartilage degenerates but its sheath persists as the anterior malleolar and sphenomandibular ligaments. At its proximal end, endochondral ossification forms two of the middle ear bones, the malleus and incus. These are homologous with the articular and quadrate bones that form the reptilian jaw articulation, where the quadrate forms from the caudal end of the palatopterygoquadrate cartilage. The mammalian evolutionary derivatives of this cartilage are thought to include part of the greater wing of the sphenoid bone, the roots of its pterygoid plates and the incus.

The second arch cartilage, Reichert's cartilage, forms from neural crest mesenchyme that extends from the proximity of the otic capsule dorsally toward the median plane ventrally. It gives rise to the stapes, which is the most ancient of the three auditory ossicles, homologous with the rod-shaped columella auris of reptiles and birds, and the styloid process proximally and the lesser cornua of the hyoid bone distally: the stylohyoid ligament develops between these two bones (see Fig. 17.6). Cartilage in the third arch, also derived from neural crest

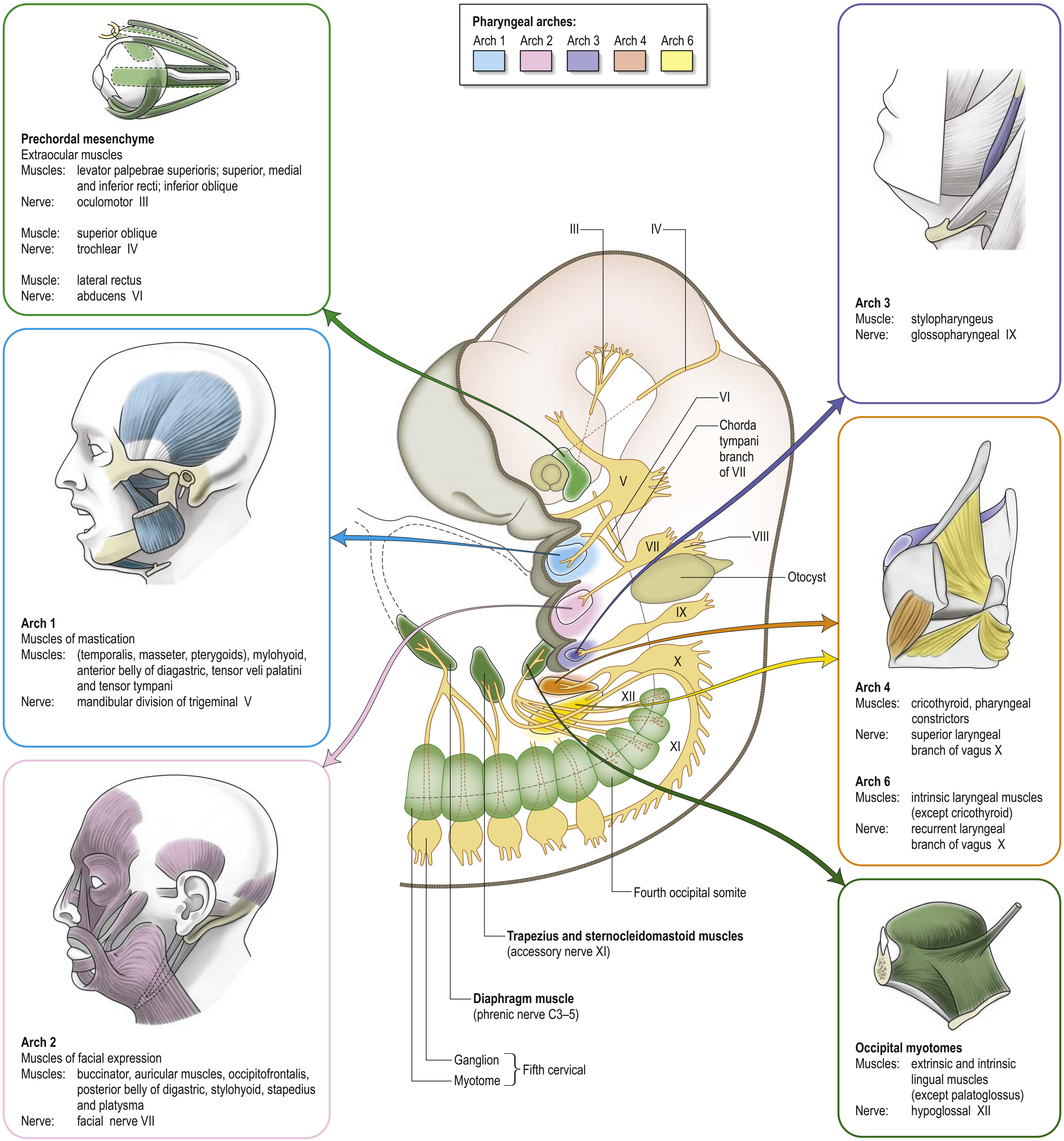
Pharyngeal arches:
Arch 1
Arch 2
Arch 3
Arch 4
Arch 6
Prechordal mesenchyme
Extraocular muscles
Muscles: levator palpebrae superioris; superior, medial and inferior recti; inferior oblique
Nerve: oculomotor III
Muscle: superior oblique
Nerve: trochlear IV
Muscle: lateral rectus
Nerve: abducens VI
Arch 1
Muscles of mastication
Muscles: (temporalis, masseter, pterygoids), mylohyoid, anterior belly of diagastric, tensor veli palatini and tensor tympani
Nerve: mandibular division of trigeminal V
Arch 2
Muscles of facial expression
Muscles: buccinator, auricular muscles, occipitofrontalis, posterior belly of digastric, stylohyoid, stapedius and platysma
Nerve: facial nerve VII
Arch 3
Muscle: stylopharyngeus
Nerve: glossopharyngeal IX
Arch 4
Muscles: cricothyroid, pharyngeal constrictors
Nerve: superior laryngeal branch of vagus X
Arch 6
Muscles: intrinsic laryngeal muscles (except cricothyroid)
Nerve: recurrent laryngeal branch of vagus X
Occipital myotomes
Muscles: extrinsic and intrinsic lingual muscles (except palatoglossus)
Nerve: hypoglossal XII
III
IV
VI
Chorda tympani branch of VII
V
VII
VIII
Otocyst
IX
X
XII
XI
Fourth occipital somite
Trapezius and sternocleidomastoid muscles
(accessory nerve XI)
Diaphragm muscle
(phrenic nerve C3–5)
Ganglion
Myotome
Fifth cervical

Fig. 17.7 The muscular derivatives of the prechordal mesenchyme, unsegmented paraxial mesoderm and rostral somites.

mesenchyme, gives rise to the greater cornua of the hyoid bone. The body of the hyoid bone develops from a ventral mesenchymal population without contributions from the distal second and third arch cartilages. The laryngeal cartilages associated with arches 4 and 6 (thyroid, cricoid and arytenoid) arise from mesenchymal condensations in the ventral neck: fourth and sixth arch cartilages are not seen in human embryos (de Bakker et al 2018).

Muscles of the pharyngeal arches

The striated muscle of each arch is derived from cranial paraxial mesoderm, which is unsegmented rostral to the occipital region, whereas more caudally segmentation gives rise to four pairs of epithelial somites that are similar to those of the trunk, except that the first pair is rather poorly defined. Myoblasts migrate from the paraxial mesoderm to sites of future muscle differentiation and form premuscle condensations prior to the development of any skeletal elements. The pattern of primary myotube alignment for any one muscle is specified by the surrounding neural crest-derived mesenchyme. The rate and pattern of muscle maturation are closely associated with the development of the skeletal elements. Fig. 17.7 illustrates the muscle masses of each arch, their innervation and their derivatives in the adult.

The muscle mass of the mandibular part of the first arch forms tensor tympani, tensor veli palatini, mylohyoid, anterior belly of digastric and the masticatory muscles. Tensor tympani retains its connection with the skeletal element of the arch through its attachments to the malleus, and tensor veli palatini remains attached to the base of the medial pterygoid process, which may itself be derived from the dorsal cartilage of the first arch. All of these muscles are supplied by the mandibular nerve, the mixed nerve of the first arch. The maxillary division of the trigeminal nerve has no motor component, because no muscles are derived from maxillary mesenchyme.

The muscles of the second arch migrate widely but retain their original nerve supply from the facial nerve. Their migration is facilitated by the early obliteration of part of the first pharyngeal cleft and pouch. Stapedius, stylohyoid and posterior belly of digastric remain attached to the hyoid bone but the facial musculature, platysma, auricular muscles and occipitofrontalis all lose their connection with it.

The muscle masses from the third and fourth arches form the musculature of the pharynx, larynx and soft palate. Stylopharyngeus is a third arch muscle, and is innervated by a branch of the glossopharyngeal nerve. All of the intrinsic laryngeal muscles are innervated by the vagus nerve: the cricothyroid by the superior laryngeal branch to the fourth arch and the others by the recurrent laryngeal nerve, which has been considered to be the sixth arch nerve. Precise arch origins are not clearly defined for the palatal muscles (except tensor veli palatini), or for the pharyngeal constrictors; these muscles all receive their nerve supply via the pharyngeal plexus (see Ch. 40). The extraocular muscles are not associated with the pharyngeal arches but are derived from mesenchyme arising from the prochordal plate that migrates to differentiate adjacent to the eyes (Ch. 15).

Nerves of the pharyngeal arches

The cranial nerves associated with each arch arise from the adjacent hindbrain (see Fig. 17.7; see also Figs 12.4, 14.19). They are the trigeminal (V), facial (VII), glossopharyngeal (IX), vagus (X) and cranial and spinal accessory (XI) nerves. The motor nerves extend from the basal plate of the hindbrain to innervate the striated muscle of the arches and are termed special visceral efferent nerves because they innervate pharyngeal musculature. Sensory nerves extend peripherally and centrally from cranial ganglia that are formed partly from neural crest and partly from cells that delaminate from epibranchial placodes; they convey general and special somatic afferent axons. Each arch is innervated by a mixed nerve, but the nerves of the first three arches also have a purely sensory branch that innervates the arch rostral to its 'own' arch; this sensory nerve is called the pretrematic branch because it extends rostral to the cleft (trema) between the two arches (see Figs 17.3, 17.7). The nerves to the mandibular arch include the mandibular division of the trigeminal nerve, which is mixed, and the chorda tympani, the purely sensory pretrematic branch of the facial nerve. The maxillary branch of the trigeminal and the tympanic branch of the glossopharyngeal are also considered to be pretrematic nerves. The ophthalmic branch of the trigeminal nerve, which supplies the frontonasal area, is not an arch nerve; in fishes, its ganglion is separate from the first arch nerve ganglion.

The vagus nerve supplies the fourth and sixth arches (see Fig. 17.7). The recurrent laryngeal branch initially loops under the sixth arch artery on both sides, but the asymmetric changes to the vascular system affect the symmetry of this nerve. On the right, when the sixth aortic arch lateral to the right pulmonary artery degenerates, the recurrent laryngeal nerve usually loops under the fourth arch-derived subclavian artery; on the left, it loops round the ductus arteriosus (which is retained as the ligamentum arteriosum in the adult). Further details of cranial nerve development and composition are provided in Chapter 14.

Blood vessels of the pharyngeal arches

Pharyngeal arch arteries

The heart outflow tract initially develops by vasculogenesis soon after neural crest cells have invaded the early pharyngeal arches. Angiogenic mesenchyme migrates into the neural crest-populated areas and forms the endothelial lining of the vessels, and neural crest contributes to the outer layers of the walls (Jiang et al 2000, Yoshida et al 2008). The first aortic arch artery is part of the original vascular circuit that links the aortic sac of the heart to the paired dorsal aortae, blood returning to the heart via the allantoic, vitelline and common cardinal veins (see Fig. 13.1C). As the heart descends relative to the forebrain and other rostral structures, the aortic sac (ventral aortic root) gives rise to paired aortic arches at successively more caudal levels, each of which passes laterally on each side of the pharynx to join the dorsal aortae. The dorsal aortae are not invested by neural crest cells, and nor are the more distal (cranial) parts of the carotid arteries, which form by angiogenesis (Ch. 13). The whole complement of aortic arches never coexists, thus the first aortic arch degenerates through remodelling of the cranial arteries before the sixth is formed.

When the first and second aortic arch arteries begin to regress, the blood supply to the corresponding pharyngeal arches is derived from a transient ventral pharyngeal artery, which terminates by dividing into mandibular and maxillary branches. The second aortic arch artery at first anastomoses with the ventral pharyngeal artery and passes through the mesenchyme of the stapedial cartilage, which condenses around it, forming the foramen of the stapes.

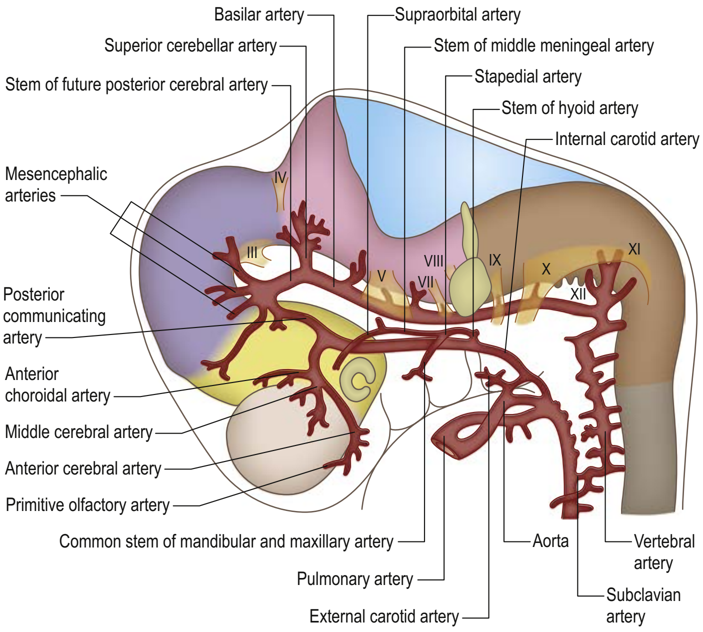

Fig. 17.8 The arterial system of the head at about stage 17.

Further development of the third, fourth and sixth aortic arches (**Figs 17.8–17.9**) produces the main arteries to the head and the great vessels arising from the heart. The common carotid artery arises from an elongation of the aortic sac, and the third arch artery becomes the proximal part of the internal carotid artery. The external carotid artery arises as a sprout from the common carotid; it incorporates the stem of the ventral pharyngeal artery, and its maxillary branch communicates with the common trunk of origin of the maxillary and mandibular branches of the stapedial artery and annexes these vessels. The proximal part of the common trunk persists as the root of the middle meningeal artery (see Fig. 17.8). More distally, the meningeal artery is derived from the proximal part of the supraorbital artery. The maxillary branch becomes the infraorbital artery and the mandibular branch forms the inferior alveolar artery. When the definitive ophthalmic artery differentiates as a branch from the terminal part of the internal carotid artery, it communicates with the supraorbital branch of the stapedial artery, which becomes the lacrimal artery distally, and retains an anastomotic connection with the middle meningeal artery. The dorsal stem of the original second arch artery remains as one or more caroticotympanic branches of the internal carotid artery.

The fourth aortic arch on the right forms the proximal part of the right subclavian artery, whereas the corresponding vessel on the left constitutes the arch of the definitive aorta between the origins of the left common carotid and left subclavian arteries. With elongation of the neck, longitudinal anastomoses in the cervical region link intersegmental arteries and their branches, and direct blood flow to the developing brain in the vertebral arteries in parallel with the internal carotid arteries (see Figs 17.8–17.9).

The sixth aortic arch is associated with the developing lung buds. Initially, each bud is supplied by a capillary plexus from the aortic sac. As the sixth aortic arch develops, it becomes the channel for blood from the aortic sac to the developing lung buds as well as to the corresponding dorsal aorta, the latter being the main channel. Soon after formation of the sixth aortic arch, the outflow tract of the heart is divided by an influx of neural crest cells, which form the spiral aorticopulmonary septum (Jiang et al 2000) that separates the aortic sac into the pulmonary trunk and ascending aorta. The part of the sixth aortic arch between the pulmonary trunk and the dorsal aorta is lost on the right but on the left becomes the ductus arteriosus which remains the main channel for blood to pass from the right ventricle to the descending aorta until the lungs and their associated blood vessels expand at birth. After birth, the ductus arteriosus is functionally closed by contraction of the circular muscle of the tunica media leaving a ligamentous remnant, the ligamentum arteriosum (Ch. 13) (see Fig. 17.9). The right dorsal aorta caudal to the right subclavian artery also degenerates, leaving the left dorsal aorta as the definitive descending aorta (see Fig. 17.9).

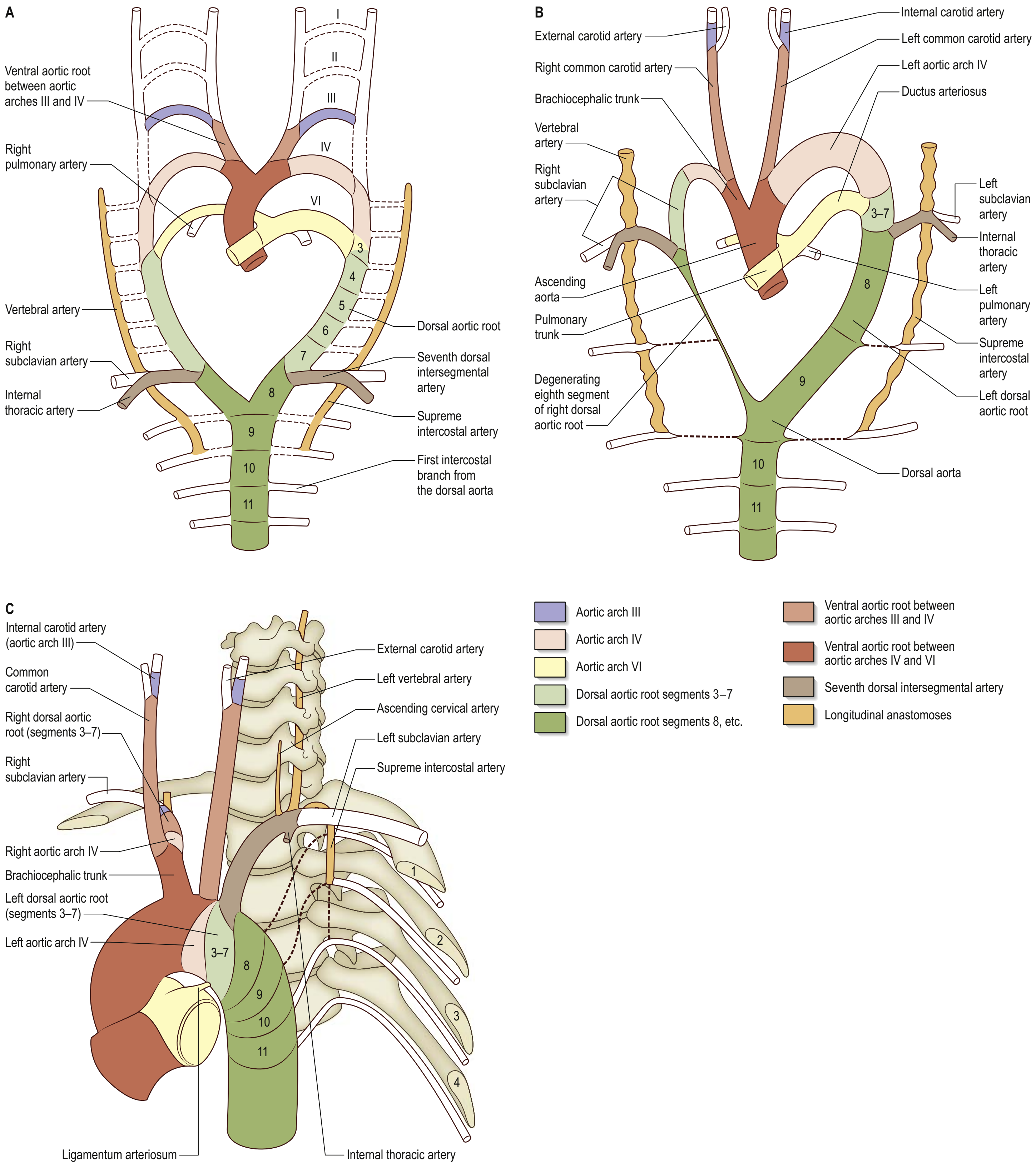
A
I
II
III
IV
VI
Ventral aortic root between aortic arches III and IV
Right pulmonary artery
Vertebral artery
Right subclavian artery
Internal thoracic artery
Dorsal aortic root
Seventh dorsal intersegmental artery
Supreme intercostal artery
First intercostal branch from the dorsal aorta
3
4
5
6
7
8
9
10
11
B
External carotid artery
Right common carotid artery
Brachiocephalic trunk
Vertebral artery
Right subclavian artery
Ascending aorta
Pulmonary trunk
Degenerating eighth segment of right dorsal aortic root
Internal carotid artery
Left common carotid artery
Left aortic arch IV
Ductus arteriosus
Left subclavian artery
Internal thoracic artery
Left pulmonary artery
Supreme intercostal artery
Left dorsal aortic root
Dorsal aorta
3–7
8
9
10
11
C
Internal carotid artery (aortic arch III)
Common carotid artery
Right dorsal aortic root (segments 3–7)
Right subclavian artery
Right aortic arch IV
Brachiocephalic trunk
Left dorsal aortic root (segments 3–7)
Left aortic arch IV
Ligamentum arteriosum
External carotid artery
Left vertebral artery
Ascending cervical artery
Left subclavian artery
Supreme intercostal artery
Internal thoracic artery
3–7
8
9
10
11
1
2
3
4
Aortic arch III
Aortic arch IV
Aortic arch VI
Dorsal aortic root segments 3–7
Dorsal aortic root segments 8, etc.
Ventral aortic root between aortic arches III and IV
Ventral aortic root between aortic arches IV and VI
Seventh dorsal intersegmental artery
Longitudinal anastomoses

Fig. 17.9 The aortic arch arteries and their derivatives.

Venous drainage of the pharyngeal arches and head

Blood returning from the early head flows into a close-meshed capillary plexus continuous cranially with a transitory primordial hindbrain channel that lies on the neural tube medial to the cranial nerve roots and later becomes the primary head vein. This vessel runs caudally from the medial side of the trigeminal ganglion, lateral to the facial and vestibulocochlear nerves and the otocyst, then medial to the vagus nerve, to become continuous with the precardinal vein and a lateral anastomosis subsequently brings it lateral to the vagus nerve (see Figs 13.1, 13.17).

The ventral pharyngeal vein drains the mandibular and hyoid arches into the common cardinal vein (Fig. 17.10A) and with neck elongation into the cranial part of the precardinal vein, which later becomes the internal jugular vein (Fig. 17.10B). The ventral pharyngeal vein receives tributaries from the face and tongue, and becomes the linguofacial vein. As the face develops, the primitive maxillary vein extends its drainage into the territories of supply of the ophthalmic and mandibular divisions of the trigeminal nerve, including the pterygoid and temporal muscles, and it anastomoses with the linguofacial vein over the lower jaw. This anastomosis becomes the facial vein: it receives blood from the retromandibular vein from the temporal region, and drains through the linguofacial vein into the internal jugular vein. The stem of the linguofacial vein is now the lower part of the facial vein, whilst the dwindling connection of the facial with the primitive maxillary vein becomes the deep facial vein.

The external jugular vein develops from a tributary of the cephalic vein within the tissues of the neck and anastomoses secondarily with

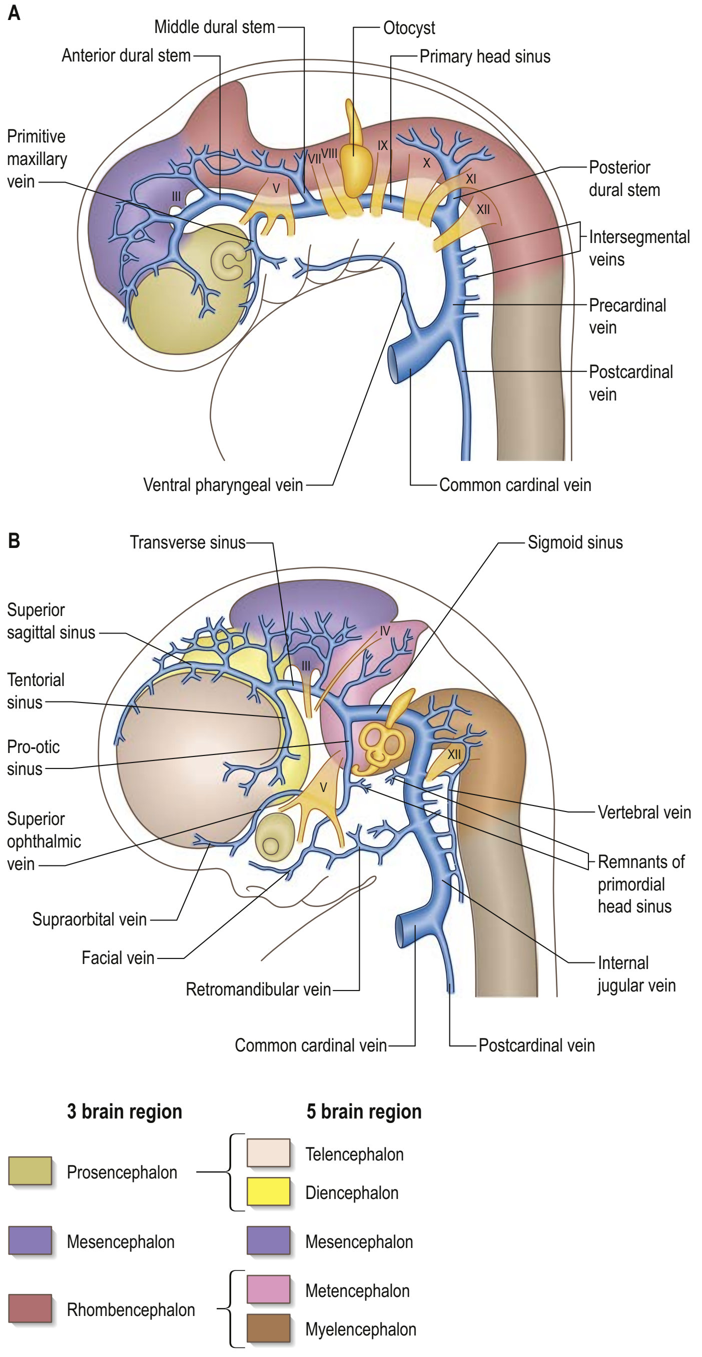

Fig. 17.10 Successive stages in the development of the veins of the head and neck: **A**, about stage 16; **B**, about stage 22.

the anterior facial vein. At this stage, the cephalic vein forms a venous ring around the clavicle, by which it is connected with the caudal part of the precardinal vein. The deep segment of the venous ring forms the subclavian vein and receives the definitive external jugular vein. The superficial segment of the venous ring dwindles, but may persist minimally in adult life. The deep aspects of the maxillomandibular facial prominences, the retrogingival oral cavity, the pharyngeal walls and their lymphoid and endocrine derivatives, and the cervicothoracic oesophagus thus all have drainage channels that connect with the precardinal complex. Laryngeal and tracheobronchial veins also drain to the precardinal complex, whilst the capillary plexuses, developed in the (splanchnopleuric) walls of the fine terminal respiratory passages and alveoli, converge on pulmonary veins of increasing calibre, finally making secondary connections with the left atrium of the heart.

Pharyngeal ectoderm and clefts

Surface ectoderm lines the roof of the embryonic pharynx from the outer margin up to and including the invagination of the adenohypophysial (Rathke's) pouch (see Figs 14.9–14.10). It also completely covers the first arch, including the lateral walls and floor of the stomodeum, unlike the more caudal arches, which are lined with endoderm. The external surface ectoderm of the first arch ultimately produces the keratinized stratified squamous epithelium of the epidermis, including hair follicles, sweat and sebaceous glands, and the specialized epithelium of the vermilion part of the lips. Within the oral cavity, first arch ectoderm forms the mucous membranes of the internal surface of the lips and cheeks, the palate, the presulcal part of the tongue, the epithelial components of the salivary and mucous glands, and the enamel organs of the developing teeth (see Figs 17.15–17.16). The first pharyngeal cleft is obliterated ventrally; its dorsal end deepens to form the external acoustic meatus, including its ceruminous glands and the outer surface of the tympanic membrane (see Fig. 17.4). Developmental studies of gene expression in the pharyngeal arches in chick and mouse embryos are calling into question the traditional view of pharyngeal cleft development based on external appearance. In mouse embryos the external acoustic meatus forms more rostrally from an invagination of the ectoderm of the first arch rather than at the first pharyngeal cleft (Minoux et al 2013; Tucker 2017). Three auricular hillocks are observed on the first and second arches each side of the first pharyngeal cleft, during stages 15–16. It was thought that these contributed equally to the auricle (pinna) of the external ear, however, 3D reconstruction in human embryos up to stage 23 has shown that cells from the second arch form almost the entire auricle, whereas the first arch ectoderm and mesenchyme give rise to the tragus and anterior part of the external auditory meatus (Veugen et al 2019) (Ch. 16).

The external contours of the arches and clefts are modified as the skeletal and muscular elements develop. During stages 18–19 the second, third and fourth pharyngeal clefts form the rostral and caudal parts of a depression, the cervical sinus. As shown in Fig. 17.4, the sinus is adjacent to extensions from the occipital myotomes that contribute to sternocleidomastoid, trapezius and platysma. Fusion of the hyoid arch with the cardiac elevation closes the cervical sinus, excluding the third, fourth and sixth arches from contributing to the skin of the neck and also results in platysma, which lies within the superficial fascia, extending along the neck to the ventral thoracic wall.

Pharyngeal endoderm and pouches

The four pharyngeal pouches appear in sequence craniocaudally during stages 10–13. The rostral pharynx is broad and dorsoventrally compressed (see Fig. 17.19). Laterally, the endoderm of the pouches approaches the ectoderm of the pharyngeal clefts to form thin closing membranes (see Fig. 17.4). The approximating ectoderm and endoderm between the first cleft and pouch form the outer and inner surfaces of the tympanic membrane. The ventral end of the first pouch is obliterated, but its dorsal end persists and expands as the head enlarges. This, together with the adjoining lateral part of the pharynx, and possibly with a contribution from the dorsal part of the second pharyngeal pouch, constitutes the tubotympanic recess. The recess forms the middle ear cavity, the pharyngotympanic tube and epitympanic recess. Expansion of the middle ear cavity around the ear ossicles occurs late during fetal life, by breakdown of the mesenchyme around the ossicles so that the cavity comes to surround them, except at their attachments to the tympanic membrane and fenestra ovalis (fenestra vestibuli, oval window).

The ectoderm of the pharyngeal clefts and the endoderm of the pouches become increasingly separated by mesenchyme. The blind recesses of the second, third and fourth pouches are prolonged dorsally and ventrally as angular, wing-like diverticula (see Fig. 17.19) and the pouch endoderm thickens and evaginates into localized neural crest-derived mesenchymal condensations. Further development of the second, third and fourth pouches is summarized in Fig. 17.19 and described in the associated text.

FACE, NASAL CAVITIES, PALATE AND MOUTH

Face

By stage 12 migration of the most rostral neural crest cell population is complete and the sequence of morphogenetic changes that will form the face begins (**Fig. 17.11**). Neural crest cells have populated the mandibular arch and its maxillary extension, and formed the frontonasal mesenchyme that covers the telencephalon and caudal diencephalon (see Fig. 17.2). They also contribute to the primordium of the trigeminal nerve, whose first fibres begin to extend at stage 13. The three divisions of the trigeminal nerve will provide sensory innervation to the frontonasal, maxillary and mandibular parts of the face, respectively.

Localized mesenchymal proliferation results in the formation of four paired processes, namely the medial and lateral nasal, maxillary and mandibular processes. The lateral and medial nasal processes surround

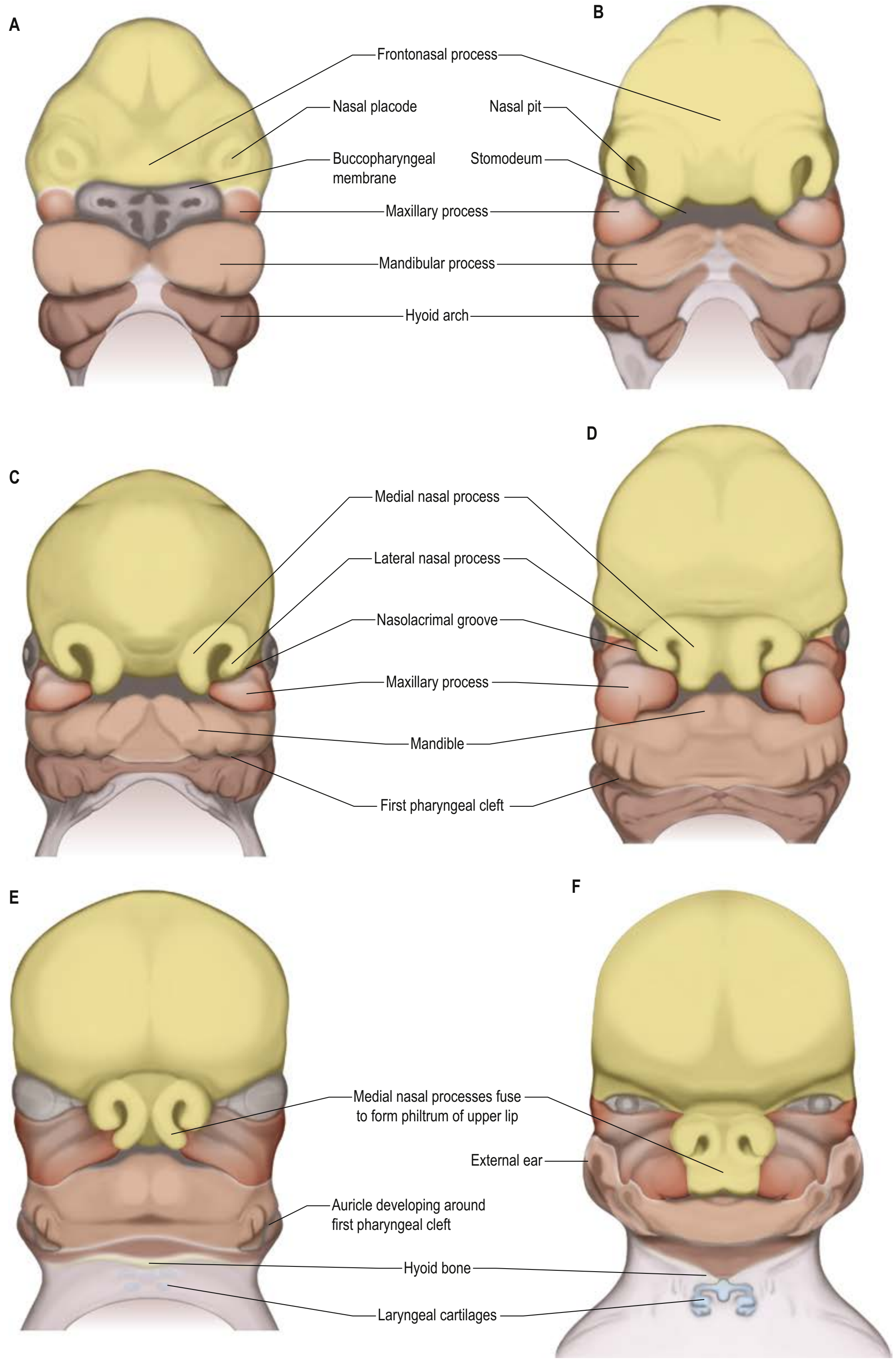
A
B
Frontonasal process
Nasal placode
Nasal pit
Buccopharyngeal membrane
Stomodeum
Maxillary process
Mandibular process
Hyoid arch
C
D
Medial nasal process
Lateral nasal process
Nasolacrimal groove
Maxillary process
Mandible
First pharyngeal cleft
E
F
Medial nasal processes fuse to form philtrum of upper lip
External ear
Auricle developing around first pharyngeal cleft
Hyoid bone
Laryngeal cartilages

Fig. 17.11 Development of the face: **A**, stage 12–13; **B**, stage 14; **C**, stage 16; **D**, stage 17; **E**, stage 20; **F**, stage 23.

the nasal placodes, causing them to sink deep to the surface, forming the nasal pits. The two medial nasal processes approach each other to form the nasal septum between them and extend downwards to form the premaxillary component of the upper lip and jaw and the primary palate. Concomitant with formation of the nasal processes, proliferation of the maxillary mesenchyme forms the maxillary processes that make contact with the medial and lateral nasal processes at stages 16–17 (see Fig. 17.11). Fusion of the maxillary processes with the medial nasal processes unites the premaxillary and maxillary parts of the upper jaw and lip; failure of this process on one or both sides causes unilateral or bilateral cleft lip (see Fig. 17.18). Superiorly, this fusion closes the cleft at the lower edge of the nasal pits, completing the future nostrils. Fusion of the maxillary with the lateral nasal processes is a much simpler process and rarely gives rise to anomalies. At stage 16 the epithelium of the groove between these fusing processes thickens to form the lacrimal lamina, the primordium of the nasolacrimal system. At stage 19 it separates from the surface ectoderm, forming the lacrimal cord beneath the surface. The cord becomes canalized to form the nasolacrimal duct in postfertilization week 10 (de la Cuadra-Blanco et al 2006). The original site of the lacrimal lamina marks the lateral division between frontonasal and maxillary contributions to the face: the sensory nerve supply of these territories is from the ophthalmic and maxillary divisions of the trigeminal nerve, respectively (**Fig. 17.12**).

At the start of facial development, the stomodeal opening extends across the whole width of the embryonic head. A wide mouth is maintained until differential growth brings the eyes and the lateral parts of the maxillary–mandibular structures from the sides to the front of the face in stages 20–23. Although differential growth makes the mouth opening proportionately smaller, progressive fusion of the lateral regions of the maxillary and mandibular processes also makes an important contribution to decreasing the width of the mouth and to forming the cheeks. Differences in mouth width within the human population are mainly due to variation in the extent of maxillomandibular fusion. The period from stages 18 to 22 is the final period of major morphogenetic change in facial development. In addition to formation of the mouth and cheeks, it is marked by further narrowing of the nasal region and philtrum, and the ascent of the ears. By stage 19 the face is recognizably human, although differential growth will continue to bring about changes in proportion and the relative position of the features. (For further reading about the genetics of normal-range variation in facial morphology see Indencleef et al (2018), Richmond et al (2018).)

The contribution made by the frontonasal process to surface epithelial derivatives extends from the skin of the forehead, over the supraorbital and glabellar regions, including the upper eyelid and conjunctiva, to the external aspect of the nose and philtrum of the upper lip. During later development, the maxillary nerve invades the skin of the philtrum and nasal alae, so that the trigeminal nerve distribution does not completely coincide with the tissue origins (compare Figs 17.11 and 17.12). A detailed 3D reconstruction of a stage 23 human embryo reported heterochronous skeletal muscle development: genioglossus, hyoglossus and styloglossus and all the extraocular muscles except levator palpebrae superioris were identified (Warmbrunn et al 2018).

Nasal cavities and palate

After formation of the nasal pits, the original olfactory placodal cells lie deep within each pit, adjacent to the underlying telencephalon. They differentiate into olfactory neuroblasts, supporting (sustentacular) cells and stem cells. Neurites begin to extend from the olfactory neuroblasts and reach the olfactory region of the telencephalon by stage 16. The earliest pioneer neurites cross a mesenchyme-filled gap between the placode and the brain. The remaining placodal cells differentiate into columnar supporting cells, rounded basal cells and, by invagination, the duct-lining and secretory acinar cells of the glands of Bowman. Basal infiltration by lymphocytes is a relatively late event.

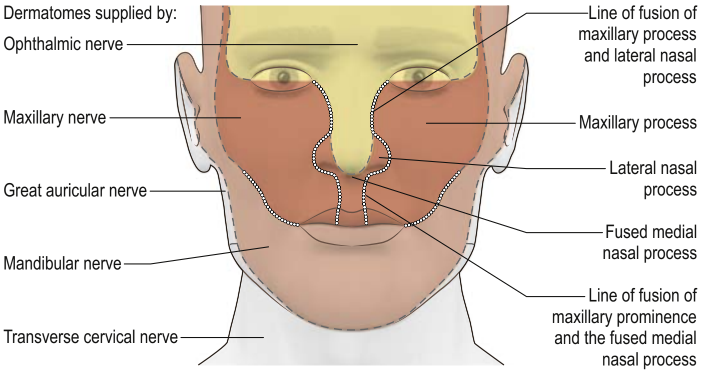
Dermatomes supplied by:
Ophthalmic nerve
Maxillary nerve
Great auricular nerve
Mandibular nerve
Transverse cervical nerve
Line of fusion of maxillary process and lateral nasal process
Maxillary process
Lateral nasal process
Fused medial nasal process
Line of fusion of maxillary prominence and the fused medial nasal process

Fig. 17.12 The parts of the adult face derived from the ophthalmic (frontonasal), maxillary and mandibular divisions of the skin of the face, showing the lines of fusion and definitive innervation.

Once the nasal cavities have formed, the roof of the oral cavity is regarded as the primitive palate (not to be confused with the primary palate, which forms from the most rostral part of the primitive palate). Each nasal cavity has an arcuate shape, extending upwards over the primary palate to the differentiating olfactory epithelium and then down again towards the oral cavity, from which it is separated by an epithelial choanal membrane. Towards the end of stage 18 the choanal membranes degenerate to form internal openings, the choanae, lateral to the primary palate; the nasal cavities are now a duct from the external environment to the oral cavity. Within the nasal cavity, the non-olfactory areas of the ectodermal lining and subjacent mesenchyme differentiate to form the mucous membrane of the nasal vestibule, conchae and paranasal sinuses.

At stage 17 the internal aspect of each maxillary process begins to bulge into the oral cavity as a palatal process; the palatal processes are the primordia of the secondary palate (**Fig. 17.13**). The tongue is well developed by this stage, and its domed form fills the space between the nascent palatal shelves laterally and the primitive palate superiorly. The mandible is still short, relative to the maxillary region, and does not extend as far as the primary palate. Further growth of Meckel's cartilages brings the mandibular region and tongue forwards, extending to a position below the primary palate. At the same time, the palatal processes continue to grow, projecting vertically downwards on either side of the tongue. At stage 23 (postfertilization days 56–58), the tongue descends and the palatal shelves rotate, bringing them to a horizontal position above the tongue (see Fig. 17.13). The rapidity of the process of shelf elevation is caused, at least in part, by swelling of the palatal mesenchyme due to accumulation and hydration of hyaluronan in the extracellular matrix (Ferguson 1991). This occurs during a period of continuous growth in head height but almost no growth in head width. This latter factor is important because, if palatal shelf elevation is delayed so that it occurs during a period of growth in facial width, the unfused processes may be unable to make contact in the midline, resulting in a cleft palate (see Fig. 17.18). Other factors affecting palatal closure include the growth in length of Meckel's cartilages and the change in position of the maxillae relative to the anterior cranial base, both having the effect of lifting the head and upper jaw away from the mandible during postfertilization weeks 9–10, facilitating withdrawal of the tongue from between the palatal shelves and creating space for their elevation. Mouth opening, tongue protrusion and hiccup movements have also been noted at this time, and it may be that these movements and their associated pressure changes assist palatal shelf elevation.

Midline fusion of the two palatal shelves involves adherence and breakdown (by apoptosis) of the apposed epithelial surfaces. The shelves also fuse with the posterior border of the primary palate, except over a small median area, where a nasopalatine canal maintains connection between the nasal and oral cavities for some time and marks the future position of the incisive fossa. During the period of palatal shelf development, a median downgrowth from the primitive palate forms the definitive nasal septum and is supported by cartilage. The fusing medial edges of the elevated palatal shelves also fuse with the free edge of the nasal

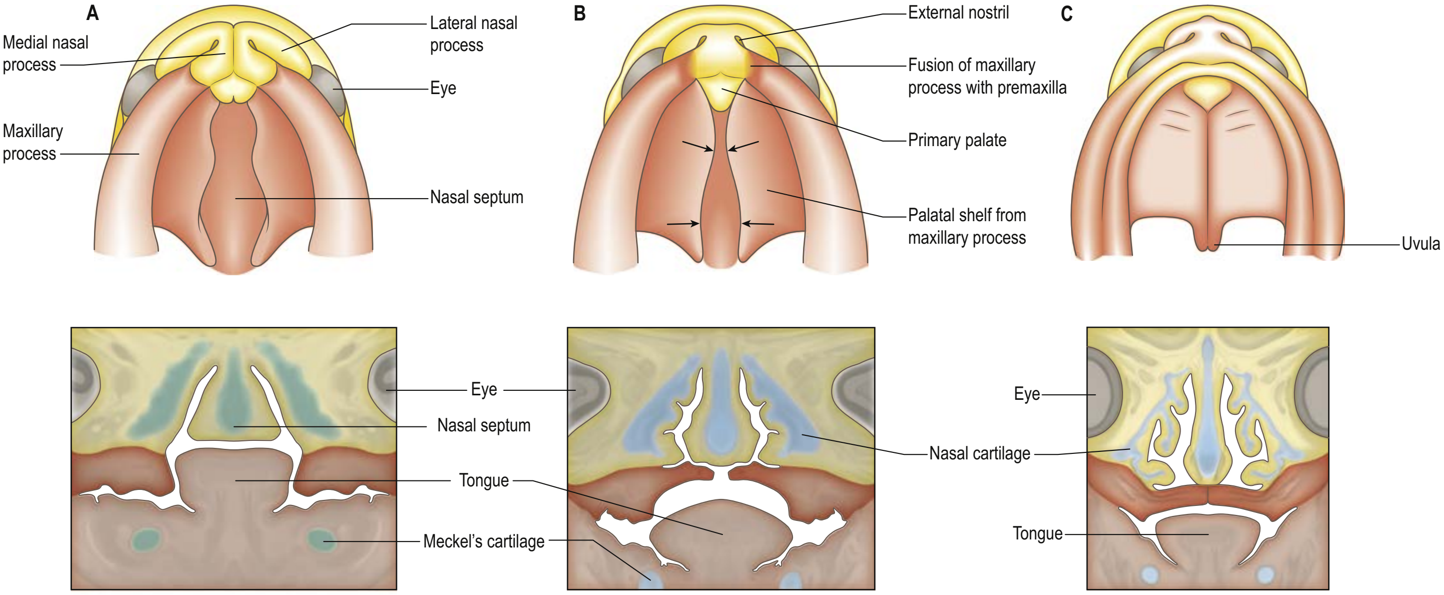

Fig. 17.13 Development of the palate. **A–C**, Developmental progression over stages 18–23; ventral views (top row) and coronal sections (bottom row).

septum, forming separate right and left nasal cavities above the secondary palate. The original positions of the choanae are now covered by the palatal shelves so that the nasal cavities extend from the nostrils to the free (caudal) edge of the palate at the nasopharynx. Bone forms by both intramembranous ossification within the palatal mesenchyme to form the hard palate, except near its caudal border, and by endochondral ossification of the cartilaginous nasal septum. At this time, the free edge of the palatal shelves lies directly below the former position of the attachment of the adenohypophysial (Rathke's) pouch to the roof of the oral cavity. Caudal to the hard palate, its free edges grow to form the soft palate and uvula, which extend into the oropharynx. Myogenic mesenchyme from the first (tensor veli palatini only) and third pharyngeal arches migrates into the soft palate and around the caudal margins of the pharyngotympanic tube. Separation of the definitive nasal and oral cavities is now complete. Three elevations appear on the lateral wall of each nasal cavity: the superior, middle and inferior conchae (see Fig. 17.13). Nasal septal deviation can be identified in the fetus within the second trimester; males are apparently affected more often than females (Salwinski et al 2010). It is thought that the magnitude of nasal septal deviation and the relationship between any septal deviation and the anterior sphenoid body is established by postnatal year 7 (Goergen et al 2017).

On either side of the septal cartilage, a pair of small diverticula, the vomeronasal organs, form at stage 17 within the nasal septum. From postmenstrual weeks 12–19 the vomeronasal organ has an olfactory epithelium-like appearance, with cells termed estheziocytes; luteinizing hormone-releasing hormone (LHRH)-immunoreactive cells are present in nerve fascicles extending from it to the olfactory bulb (Boehm et al 1994). In many species, the vomeronasal organ has a pheromonal communication function; although most adult humans have a vomeronasal organ, its olfactory-type structure and LHRH immunoreactivity are lost during later fetal life and a pheromonal function in adults has not been established (Ch. 39). It has been identified in fetuses in the second trimester and is present in childhood and adult life (Vasuki et al 2016, Stoyanov et al 2018).

Bilateral dorsal expansions of the first and second pharyngeal pouches form the tubotympanic recesses, which will become the tympanic cavities and pharyngotympanic tubes (Ch. 16). A number of focal proliferations of nasopharyngeal endoderm become invaded by lymphoid tissue.

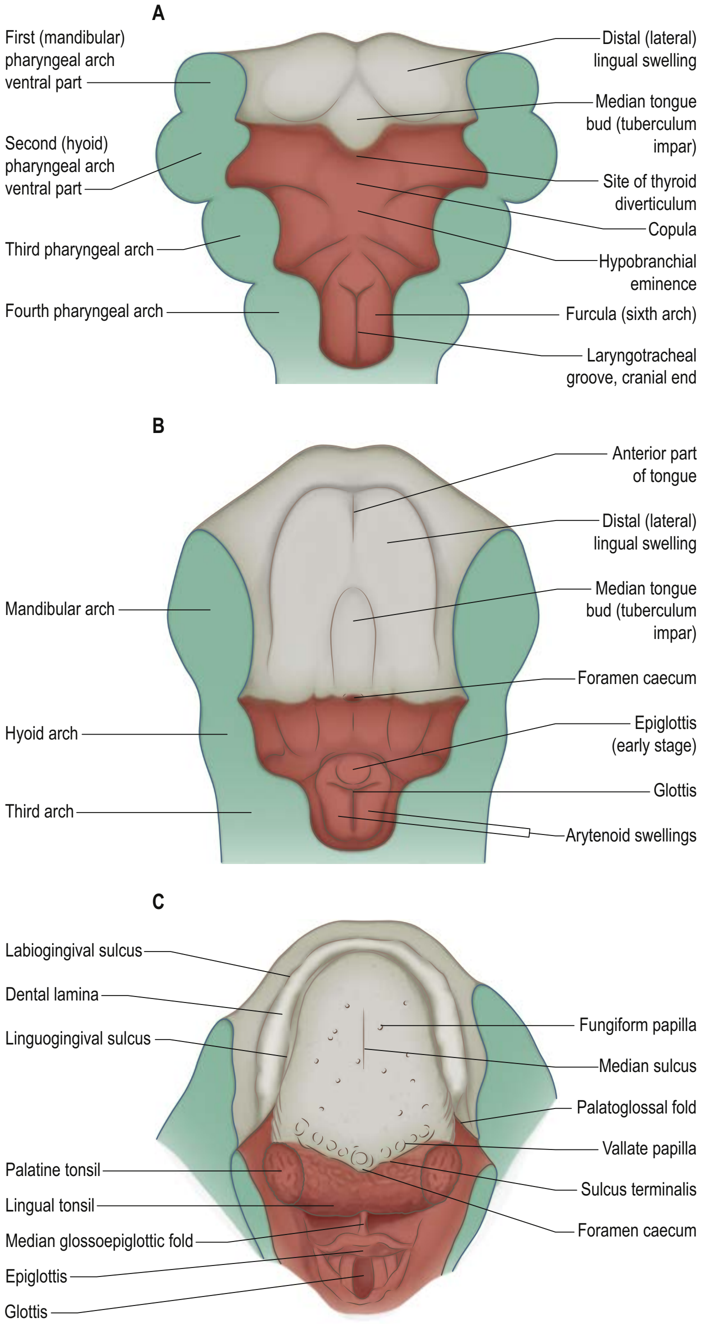
A
First (mandibular) pharyngeal arch ventral part
Second (hyoid) pharyngeal arch ventral part
Third pharyngeal arch
Fourth pharyngeal arch
Distal (lateral) lingual swelling
Median tongue bud (tuberculum impar)
Site of thyroid diverticulum
Copula
Hypobranchial eminence
Furcula (sixth arch)
Laryngotracheal groove, cranial end
B
Mandibular arch
Hyoid arch
Third arch
Anterior part of tongue
Distal (lateral) lingual swelling
Median tongue bud (tuberculum impar)
Foramen caecum
Epiglottis (early stage)
Glottis
Arytenoid swellings
C
Labiogingival sulcus
Dental lamina
Linguogingival sulcus
Palatine tonsil
Lingual tonsil
Median glossoepiglottic fold
Epiglottis
Glottis
Fungiform papilla
Median sulcus
Palatoglossal fold
Vallate papilla
Sulcus terminalis
Foramen caecum

Fig. 17.14 Development of the pharyngeal floor and tongue. **A**, Stage 14, showing median and lateral swellings in the floor of the first arch. **B**, After fusion of the swellings. **C**, The tongue and oropharynx at birth.

Mouth

The oropharyngeal membrane breaks down at stage 13 and communication is established between the ectoderm-lined (stomodeal) and the endoderm-lined (oropharyngeal) parts of the oral cavity, creating a continuous cranial foregut cavity. Formation of the hard and soft palates separates this area into the nasal cavity and nasopharynx above and the definitive oral cavity below. The oral cavity is demarcated from the oropharynx posteriorly by the oropharyngeal isthmus, which is formed by the free edge of the soft palate and uvula above, and the palatoglossal arch laterally.

Tongue

Because the mandibular arch grows more rapidly than the other arches, it makes the greatest contribution to the pharyngeal floor. By stage 14 three swellings are apparent: a small median elevation, the tuberculum impar or median tongue bud, and paired lateral lingual swellings distally (**Fig. 17.14A**). These three swellings fuse to form the anterior two-thirds (presulcal part) of the tongue (**Fig. 17.14B**). A small median diverticulum, the foramen caecum (thyroid diverticulum), invaginates immediately caudal to the median tongue bud (**Fig. 17.14B-C**; see Fig. 17.19). Caudal to the median tongue bud, a small swelling, the copula, forms in the floor of the second arch. The hypobranchial eminence forms in the floor of the third arch, grows over the second arch (which does not contribute to the tongue) and fuses with the anterior tongue rudiment along a V-shaped line, the sulcus terminalis, at stage 17. Another transverse groove separates the developing tongue from the caudal (fourth arch) swelling that will form the epiglottis. A sulcus forms along the ventral and lateral margins of the developing tongue and deepens, internal to the future dental laminae, to form the linguogingival sulcus (groove) (Fig. 17.14C).

The composite character of the mucous membrane of the tongue is reflected in its sensory innervation. The first arch-derived part is innervated by the lingual branch of the mandibular nerve, and by the chorda tympani of the facial nerve. The third arch-derived part is innervated by the glossopharyngeal nerve, which invades the tissue immediately distal to the sulcus limitans, including innervation of the (cicum)vallate papillae. The vallate papillae begin to differentiate within the mucous membrane at around postmenstrual week 10 and increase in number until the end of the second trimester. The fourth arch-derived root of the tongue, near the epiglottis, is innervated by the vagus. The motor innervation is from the pharyngeal plexus (for palatoglossus) and hypoglossal nerves, which extend around and under the pharynx together with myogenic cells migrating from the occipital myotomes during stages 14–15. Tongue development is morphologically complete by stage 23 but sensory papillae continue to differentiate

Teeth and gingivae

Demarcation of the lips begins after fusion of the facial primordia at stage 18, during the period of secondary palatal development. Two parallel epithelial thickenings, an outer labiogingival lamina and an inner dental lamina, form around the interior border of the mouth in both upper and lower jaws (see Fig. 17.14C). The linguogingival sulcus is formed as an indentation between the dental lamina and the tongue. At stage 22 each labiogingival lamina indents the underlying mesenchyme to form a shallow groove that deepens to form the labiogingival sulcus between the lips and gingivae. Laterally, the epithelial lining of the oral cavity forms the inner aspect of the cheeks.

Tooth formation involves a sequence of reciprocal interactions that are controlled by a large number of genetic factors, mediated by the extracellular matrix components of the mesenchyme and the epithelial basement membrane, including laminin, collagen IV, nidogen and

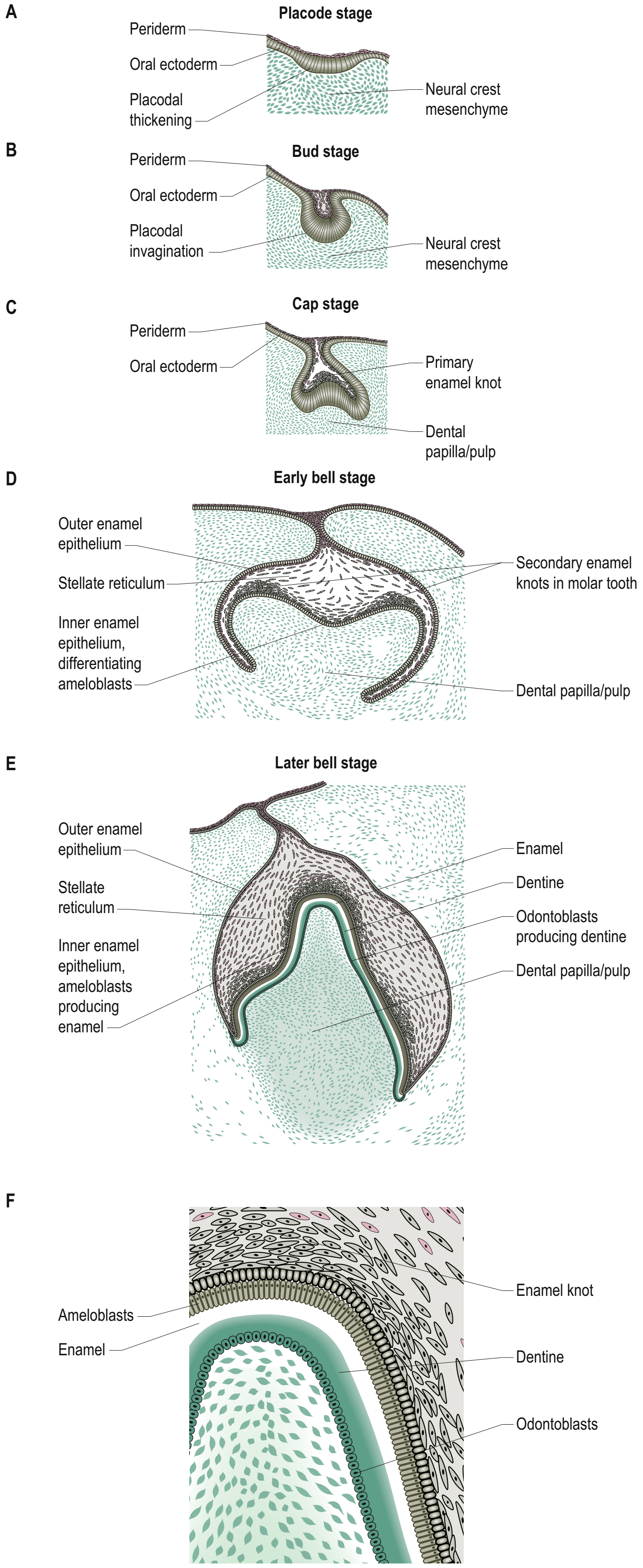
A
Placode stage
Periderm
Oral ectoderm
Placodal thickening
Neural crest mesenchyme
B
Bud stage
Periderm
Oral ectoderm
Placodal invagination
Neural crest mesenchyme
C
Cap stage
Periderm
Oral ectoderm
Primary enamel knot
Dental papilla/pulp
D
Early bell stage
Outer enamel epithelium
Stellate reticulum
Inner enamel epithelium, differentiating ameloblasts
Secondary enamel knots in molar tooth
Dental papilla/pulp
E
Later bell stage
Outer enamel epithelium
Stellate reticulum
Inner enamel epithelium, ameloblasts producing enamel
Enamel
Dentine
Odontoblasts producing dentine
Dental papilla/pulp
F
Ameloblasts
Enamel
Enamel knot
Dentine
Odontoblasts

Fig. 17.15 A–E, Stages of tooth development from placodal to late bell stage. **F**, Details of the formation of enamel and dentine by ameloblasts and odontoblasts.

sulphated proteoglycans (Thesleff 2016). During stage 22, 10 localized thickenings of the upper and lower dental laminae, the dental placodes, initiate formation of the dental epithelial components of the tooth primordia (Fig. 17.15A). They expand into dental sacs surrounded by vascular mesenchyme in the bud stage (Fig. 17.15B). The cap stage is formed around postmenstrual week 10, as the basal area of epithelium proliferates to form an enamel knot (Fig. 17.15C). This is the signalling centre that initiates formation of the tooth crown (Jernvall and Thesleff 2012); it overlies a mesenchymal condensation, the dental papilla. Collectively, this unit constitutes a tooth germ and alveolar bone forms the tooth socket around it. The tooth germ becomes bell-shaped as the lateral and basal parts of the sac (inner and outer enamel epithelia) becomes separated by the stellate reticulum, a loose group of cells with a proteoglycan-rich extracellular matrix. The inner enamel epithelium grows rapidly and is already multi-cusped for the premolars and molars (Fig. 17.15D) and single-cusped for the incisors and canines (Fig. 17.15E). During the bell stage, the cells of the inner enamel epithelium differentiate into tall columnar ameloblasts, and the underlying layer of mesenchymal cells differentiates into columnar odontoblasts (Fig. 17.15F). The odontoblasts produce and secrete dentine, which induces the ameloblasts to form enamel that is laid down in successive layers: after mineralization, it is the hardest tissue in the body. Enamel and dentine production from the bell-shaped tooth germ both begin at postmenstrual week 24 (Fig. 17.16). The dental papilla mesenchyme below the odontoblast layer forms the pulp, which becomes vascularized and innervated.

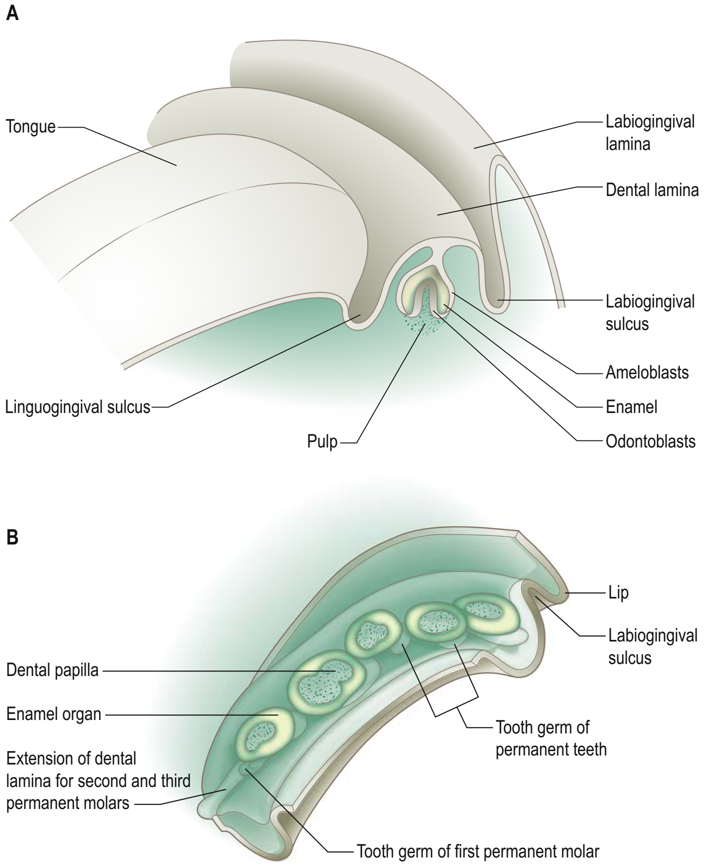
A
Tongue
Labiogingival lamina
Dental lamina
Labiogingival sulcus
Ameloblasts
Enamel
Odontoblasts
Linguogingival sulcus
Pulp
B
Lip
Labiogingival sulcus
Dental papilla
Enamel organ
Tooth germ of permanent teeth
Extension of dental lamina for second and third permanent molars
Tooth germ of first permanent molar

Fig. 17.16 The lip, gums and developing teeth after postmenstrual week 24. **A**, Oral view. **B**, The right half of the lower jaw viewed from below; the midline is upper right.

Salivary glands

The salivary glands arise bilaterally as the result of epithelial–mesenchymal interactions between the ectodermal epithelial lining of the stomodeal part of the oral cavity and the subjacent neural crest-derived mesenchyme. The parotid gland can be recognized at stage 15 as an elongated furrow running dorsally from the angle of the mouth between the mandibular and maxillary prominences. The groove, which is converted into a tube and becomes the parotid duct, loses its connection with the epithelium of the oral cavity, except at its ventral end, and extends dorsally into the soft tissue of the cheek. After fusion of the lateral parts of the maxillary and mandibular prominences, the parotid duct opens on the inside of the cheek at some distance from the angle of the mouth. As the gland develops, its branches interweave with branches of the facial nerve; it lies between the masseter and the ear by full-term and extends to cover the parotid duct during early infancy and childhood.

The submandibular and sublingual glands form as solid diverticula that undergo branching morphogenesis, each tree-like structure later acquiring a lumen. The blind ends of the branches form acini, in which cells differentiate to form serous cells initially, and mucus-secreting cells postnatally. The submandibular gland is identifiable at stage 18 as an epithelial diverticulum into the mesenchyme from the floor of the caudal part of the linguogingival sulcus. It increases rapidly in size and

Experimental studies in mice (which have only incisors and molars) have revealed that regional differences in signalling pathways within maxillary and mandibular mesenchyme govern the type of tooth produced (Tummers and Thesleff 2009). Fibronectin is present in the basement membrane of the internal enamel epithelium during the bell phase. It assists attachment of the pre-odontoblasts and is essential for their differentiation and becomes progressively more abundant during the later fetal period. Collagen I is the major supportive extracellular scaffold in the maturing dental papilla and stellate reticulum.

branches several times. At first, the connection of the submandibular gland with the floor of the mouth lies at the side of the tongue, but as the edges of the linguogingival sulcus come together, from behind forwards, they enclose the elongating duct. The orifice of the submandibular duct is thus located progressively more distally until it is below the tip of the tongue, close to the median plane. The sublingual gland arises at stage 20 as a number of small epithelial thickenings within and lateral to the linguogingival sulcus. Each thickening canalizes separately, so multiple sublingual ducts open on the summit of the sublingual fold, while others join the submandibular duct.

The minor salivary glands are distributed throughout the wall of the oral cavity, except for the gingivae and hard palate, and form in a similar manner to the major glands but undergo very little branching and remain within the submucosa.

Lymphoid tissues

Tonsils form at several sites around the oro- and nasopharynx, where focal proliferations of endoderm become invaded by lymphoid tissue. The endodermal epithelial lining grows into the surrounding mesenchyme as a number of solid buds, which are excavated by degeneration and shedding of their central cells, forming tonsillar fossae and crypts. Lymphoid cells accumulate around the crypts at about postmenstrual weeks 17–20 and become grouped as lymphoid follicle in which T- and B-cell regions can be identified. The palatine tonsils develop from the ventral parts of the second pharyngeal pouches (see Fig. 17.4). The slit-like intratonsillar cleft that extends into the upper part of the tonsil is possibly a remnant of the second pharyngeal pouch. Lymphoid tissue similar to that of the palatine tonsils is found in the first pouch (tubal tonsils), the surface of the posterior part of the tongue (lingual tonsils), and in the dorsal pharyngeal wall (adenoid or pharyngeal tonsil).

Anomalies of facial development

Available with the *Gray's Anatomy* e-book

NECK, GLANDS AND PHARYNX

By the time the facial swellings have merged to form a recognizably human face (stage 19), Meckel's cartilage has grown sufficiently to project outwards as a potential chin but the face is still orientated towards, and close to, the cardiac prominence (see Fig. 17.5). By this time formation of the posterior part of the neck is well advanced, with cartilaginous cervical vertebrae, muscles, nerves and blood vessels. The anterior neck forms gradually, as the relatively rapid growth of the anterior structures, including the larynx, trachea, oesophagus, common carotid arteries and jugular veins, takes place. Growth of the anterior neck lifts the head to a forward-facing orientation, simultaneously increasing the angle between the spinal cord and brainstem. Growth of the first pharyngeal arch occurs at a more rapid rate than the lower arches, so that Meckel's cartilage and the developing membrane bone of the mandible project further forwards. The hyoid bone primordium remains small, defining the future angle between the anterior neck and lower jaw. Lateral neck structures develop after the caudal edge of the second pharyngeal arch has fused with the ectoderm over the heart. Myoblasts derived from paraxial mesoderm invade the second pharyngeal arch as it forms and by this stage are present in the superficial connective tissue beneath the anterior neck skin; these spread out from the underside of the chin to the upper thorax and differentiate to form platysma. The muscle maintains the attachment of the skin beneath the lower jaw to the underlying tissues and is the main human remnant of the panniculus carnosus, the subcutaneous muscle that is present throughout the skin of many mammals.

Arch anomalies, predominantly second arch, represent 20% of the neck masses seen in children; remnants of lower pharyngeal clefts are seen in a spectrum of anomalies presenting as branchial cysts, fistulae or sinuses. Fistulae present typically in infants and young children, and cysts in older children and adults. Both first and second cleft anomalies are classified into subtypes; on ultrasound examination they are thin-walled, anechoic and well-circumscribed, and found along the line of the original cleft (Adams et al 2016).

There is much discussion concerning the head–trunk interface and its evolutionary progression and heterochronic development in species used in embryonic research (Commentary 2.1). The exact zones of transition between neural crest, paraxial and somatopleuric-derived mesenchymal populations are not yet established in the human embryo: it is known that zonal delimitation varies between species. The interface between cranial nerve-innervated pharyngeal arch muscles and spinal nerve-innervated trunk muscles occurs at the lower neck and the upper parts of the pectoral girdle. While deep epaxial myotomal populations are clearly derived from somites and remain associated with developing vertebrae, the myotomal populations of the shoulder and lower neck arise from the ventrolateral border of somites adjacent to the limb bud that migrate into the limb and then back to the shoulder and lower neck region (Valasek et al 2011, Mekonen et al 2016) (Chs 18–19). The more superficial muscles of the neck have various origins: parts of splenius, trapezius and sternocleidomastoid are derived from overlapping, undefined interfaces between the various myotomal origins in this region. The local mesenchymal populations that differentiate into endo-, peri- and epimysium, and the boundary zone of the myotendinous junction, as well as entheses and bone precursors, confer patterning information in these regions. Both the proximal and distal connections of trapezius are formed from post-otic neural crest cells, albeit with differences between avian and murine embryos (Matsuoka et al 2005). The neural crest generates areas of endochondral ossification in the cervical vertebral column and scapula associated with trapezius attachment. Defects in the fate choices of neural crest cells might explain a number of syndromes that have pharyngeal, laryngeal, occipital, cervical and shoulder dysmorphologies with co-occurrence of swallowing problems; related syndromes include Klippel–Feil, Sprengel deformity and cleidocranial dysplasia (Matsuoka et al 2005) (Chs 18, 19).

Glands of the neck

Further development of the pharyngeal floor and the second to fourth pharyngeal pouches gives rise to the thyroid gland, and paired palatine tonsils, parathyroid glands and thymus, i.e. glands that are ultimately disposed in the neck and anterior mediastinum.

Thyroid gland

The thyroid gland is a midline derivative of the pharynx. It is first identifiable in stage 11–12 embryos as a median thickening of endoderm lying in the floor of the pharynx between the first and second pharyngeal pouches and immediately dorsal to the aortic sac. The foramen caecum is the site of a median diverticulum that appears in the furrow immediately caudal to the median tongue bud (see Fig. 17.14B–C; **Fig. 17.19**). It extends caudally as the thyroglossal duct, passing ventral to the primordium of the hyoid bone and reaches the rostral border of the aortic sac by stage 15. The tip of the duct bifurcates and the tissue mass subsequently divides to form the isthmus and lateral lobes of the thyroid gland. The endoderm-derived epithelial tissue is invested by vagal neural crest mesenchyme, which gives rise to the connective tissue capsule and interlobular septa, and perifollicular mesenchyme, which carries the neurovascular and lymphatic supply to the gland. The gland has three stages of development: Stage 1 (postmenstrual weeks 10–18) is characterized by active folliculogenesis and gradual accumulation of colloid, into which the follicular cells release thyroglobulin, the substrate for tyrosine iodination and subsequent synthesis of the thyroid hormones T_4 and T_3. Stage 2 (postmenstrual weeks 18–29) is quiescent, with little change in the epithelium:colloid ratio and follicular size. Stage 3 (after postmenstrual week 29) is characterized by a gradual increase in the epithelium:colloid ratio and a decrease in follicular size (Bocian-Sobkowska et al 1997). This suggests that stimulation of the gland by pituitary-derived thyrotropin (TSH) is enhanced in the third trimester. T_4 is present at low levels from postmenstrual weeks 10–22, and increases during postmenstrual weeks 22–40. Normograms of fetal thyroid size from ultrasound examination between postmenstrual weeks 14–38 have been correlated to skull biparietal diameter (Gietka-Czernal et al 2012).

Failure of downgrowth of all or part of the thyroid gland from the pharyngeal floor results in ectopic thyroid tissue within the tongue (lingual thyroid), between the foramen caecum and the epiglottis. Occasionally, parts of the midline thyroglossal duct persist and may occur in lingual, suprahyoid, retrohyoid or infrahyoid positions; they may form aberrant masses of thyroid tissue, cysts, fistulae or sinuses, usually in the midline. Nodules of glandular tissue may also be found laterally, posterior to sternocleidomastoid.

Parathyroid glands

The parathyroid glands develop from interactions between the third and fourth pharyngeal pouch endoderm and local neural crest mesenchyme. Each third pharyngeal pouch has dorsal and ventral sites of proliferation (see Fig. 17.19B). The epithelium on the dorsal aspect of the pouch and the region of its duct-like connection with the cavity of

Malformations involving the neural crest

Congenital malformations of the face may be initiated early, mainly related to abnormal migration, proliferation and/or apoptosis of neural crest cells, or later, during the morphogenetic phase of facial development. Craniofrontonasal syndrome is characterized by a broad forehead and hypertelorism, premature fusion of one or both coronal sutures, a central nasal groove, and sometimes cleft lip and palate; there are also extracranial features. It is caused by deletions of the gene *EFNB1*, which is known to play essential roles in boundary formation between tissues, including those between neural crest and adjacent non-crest cells (Twigg et al 2004). Mandibulofacial dysostosis (Treacher Collins syndrome) is characterized by incomplete orbits, reduced jaws and auditory ossicles (hence conductive deafness), abnormal external ears and fistulae or cysts, suggesting involvement of the first and second arch components of the cranial neural crest. It is caused by haploinsufficiency of the gene *TCOF1*. Hemifacial microsomia (Goldenhaar's syndrome) affects only one side of the face and comprises a small mandible (sometimes with absence of the temporomandibular joint), malformed or absent ears with accessory ear tags, and facial clefts. Experimental evidence in animals suggests that it is due to haemorrhage of the stapedial artery, which may have a genetic basis. Deficient growth of the mandible (micrognathia) is usually associated with other defects. In Pierre Robin sequence (**Fig. 17.17**), the small size of the mandible obstructs descent of the tongue, resulting in a U-shaped cleft palate; a conotruncal septum defect is present in one-quarter of cases, suggesting possible involvement of the cardiac neural crest. The condition is usually an isolated genetic occurrence but can be inherited as an autosomal dominant trait and can occur as part of syndromes such as Stickler, CHARGE and velo-cardio-facial syndrome (Morice et al 2018). Further details and references for facial malformations may be found in Morriss-Kay and Wilkie (2005), Hennekam et al (2010) and Evans et al (2018).

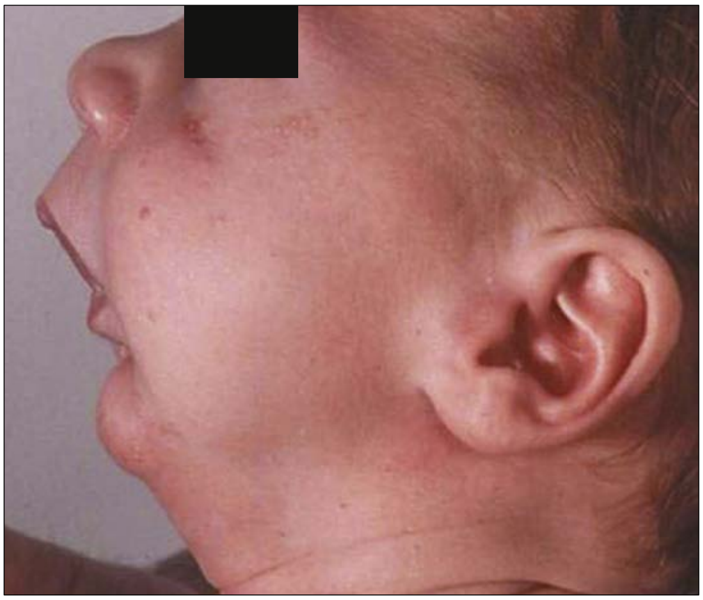

Fig. 17.17 The Pierre Robin sequence. (Courtesy of Mr T Goodacre and Oxford Radcliffe Hospitals NHS Trust.)

Clefts of the face and palate

Cleft lip occurs when one or both medial nasal processes fail to fuse with the corresponding maxillary process(es). The severity of clefting varies from a small notch in the upper lip to a double cleft extending into both nostrils (**Fig. 17.18A–D**). In a unilateral cleft lip, the nasal septum deviates to the non-cleft side. This is because the muscles on the medial side of the cleft (transverse muscles of the nose and orbicularis oris) are not inserted into either the muscles of the contralateral side (Fig. 17.18B). The three functional groups of superficial facial muscles – nasolabial (transverse nasalis, levator labii superioris and levator labii superioris alaeque nasi), bilabial (orbicularis oris) and labiomental (depressor anguli oris) – are all displaced inferiorly. A further consequence is the underdevelopment of the incisor-bearing part of the maxilla. These abnormalities in turn influence the mucocutaneous tissues, resulting in the displacement of the skin of the nostril to the upper part of the lip, retraction of the labial skin and anomalies of the soft tissues on either side of the mucocutaneous junction.

A narrow or incomplete cleft of the hard palate is likely to be due to a growth defect in the palatal shelves and/or a delay in shelf elevation, and/or to failure of fusion of the apposed palatal shelves. Broader clefts (**Figs 17.18D–E**), in which the tongue lies between the still-vertical shelves, are caused by a greater developmental delay that may be associated with abnormality of other structures in the face and elsewhere in the body. In the mildest forms of cleft palate, only the soft palate, and sometimes just the uvula, is cleft (**Fig. 17.18F**). A submucous cleft, which may be detected as a median V-shaped notch of the soft palate, can cause speech difficulties. Very rarely, muscle hypoplasia, particularly of the musculus uvulae, causes palatopharyngeal incompetence.

Cleft lip with or without cleft palate (CL/P) is multigenic or multifactorial in origin, i.e. it has both genetic and environmental components (Hennekam et al 2010). CL/P has a frequency of 0.5–3.6/1000 live births, with a 2 : 1 male to female ratio. Isolated cleft palate is genetically unrelated to CL/P, and has a frequency of 0.4/1000; it is more common in females. Clefts of the face are rare (1/50,000–1/175,000 births) and are mainly caused by pressure from amniotic bands rather than from dysmorphogenesis, although a morphogenetic component cannot be ruled out when the cleft is along a line of fusion, e.g. maxillary–mandibular. Median cleft lip (true hare lip) is also rare, because this is not a line of morphogenetic fusion. Median grooving of the nose occurs with hypertelorism in various frontonasal dysplasias, suggesting a developmentally early broadening of the median region of the face.

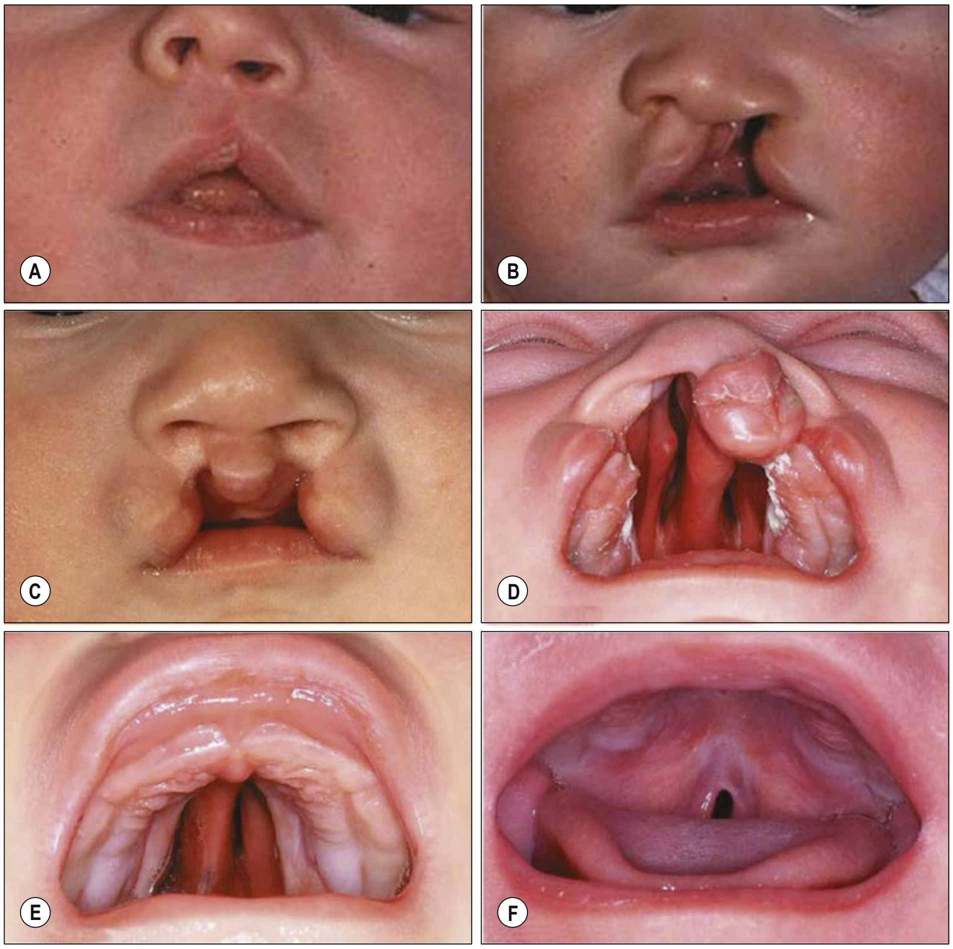

Fig. 17.18 Cleft lip and cleft palate. **A**, Incomplete unilateral cleft lip. **B**, Complete unilateral cleft lip. **C**, Incomplete bilateral cleft lip. **D**, Complete bilateral cleft lip and cleft palate (the nasal septum and both inferior nasal conchae can be seen). **E**, Cleft palate (the nasal septum and left inferior nasal concha can be seen). **F**, Cleft of the soft palate. (Courtesy of Mr T Goodacre and Oxford Radcliffe Hospitals NHS Trust.)

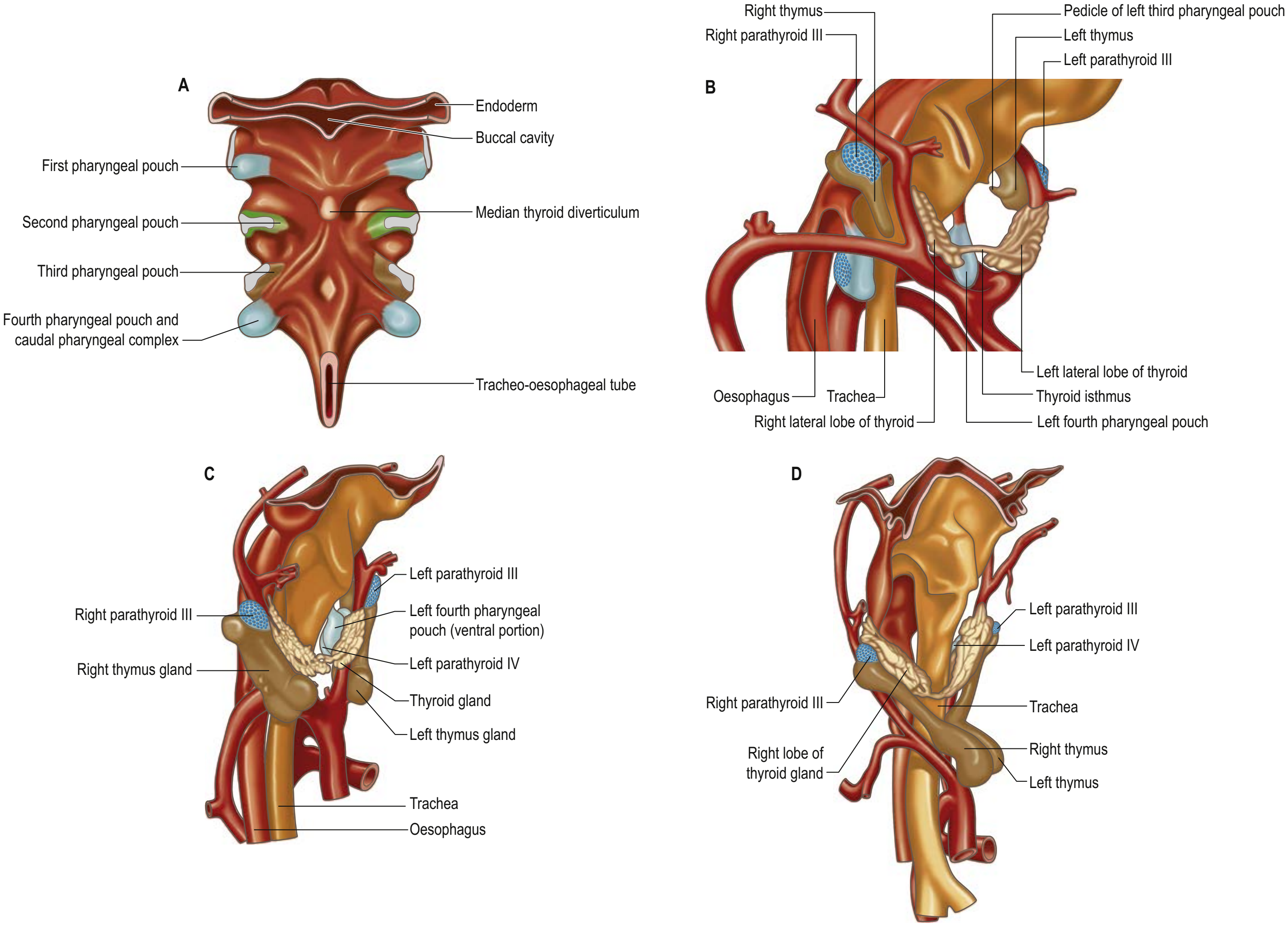
A
Endoderm
Buccal cavity
First pharyngeal pouch
Median thyroid diverticulum
Second pharyngeal pouch
Third pharyngeal pouch
Fourth pharyngeal pouch and caudal pharyngeal complex
Tracheo-oesophageal tube
B
Right thymus
Right parathyroid III
Pedicle of left third pharyngeal pouch
Left thymus
Left parathyroid III
Oesophagus
Trachea
Right lateral lobe of thyroid
Left lateral lobe of thyroid
Thyroid isthmus
Left fourth pharyngeal pouch
C
Left parathyroid III
Right parathyroid III
Left fourth pharyngeal pouch (ventral portion)
Right thymus gland
Left parathyroid IV
Thyroid gland
Left thymus gland
Trachea
Oesophagus
D
Left parathyroid III
Left parathyroid IV
Right parathyroid III
Trachea
Right lobe of thyroid gland
Right thymus
Left thymus

Fig. 17.19 **A**, The ventral aspect of the endoderm of the pharynx, showing the pharyngeal pouches. The areas of contact of the pharyngeal endoderm with the surface ectoderm are shown as flattened surfaces. Note that the colours of the pharyngeal pouches and the median thyroid diverticulum are retained in **B**, **C** and **D**. **B**, Ventral and dorsal diverticuli of the third and fourth pharyngeal pouches and midline thyroid gland at stage 16–17. **C**, The thymus, thyroid and parathyroid glands at stage 18–19. **D**, The thymus, thyroid and parathyroid glands at about stage 21. (Redrawn with permission from Hamilton WJ, Boyd JD, Mossman HW 1962 Human Embryology: Prenatal Development of Form and Function. Cambridge: Heffer.)

the pharynx becomes differentiated as the primordium of the inferior parathyroid gland (parathyroid III). Although the connection between the pouch and the pharynx is soon lost, the connection between the dorsal parathyroid and the ventral thymic rudiment of the third pharyngeal pouch persists for some time and both descend (move caudally). The superior parathyroid glands (parathyroid IV) develop from the dorsal recess of the right and left fourth pharyngeal pouches. They make contact with, and appear to be anchored by, the lateral lobes of the thyroid gland and thus remain cranial to the descended parathyroid III glands. Vagal neural crest mesenchyme provides the connective tissue elements, and invading angiogenic mesenchyme gives rise to fenestrated capillaries and lymphatics.

Thymus

The thymus gland plays a pivotal role in the development of immunological competence. It is formed from the ventral part of the third pharyngeal pouch on each side (see Fig. 17.19). It cannot be recognized prior to the differentiation of the inferior parathyroid glands at stage 16, but thereafter it is represented by two elongated diverticula that soon become solid cellular masses and grow caudally into the surrounding vagal neural crest mesenchyme. Ventral to the aortic sac, the two thymic rudiments meet but do not fuse, and they are subsequently united only by connective tissue. The thymus gland becomes located in the anterior mediastinum of the thorax once the neck is fully developed and the heart has descended (see Fig. 23.14A, J, K). The connection with the third pouch is soon lost, but the stalk may persist for some time as a solid, cellular cord.

As the thymus proliferates and descends, the local neural crest-derived mesenchyme controls the pattern and development of the gland. Defective development of the vagal neural crest, which affects the heart and peripheral neural ganglia, also results in thymic deficiencies, as seen in DiGeorge syndrome and Pierre Robin sequence. Neural crest mesenchyme forms connective tissue septa that produce the lobulated architecture of the gland (Hutchins et al 2018). Angiogenic mesenchyme, including lymphoid stem cells, invades this local mesenchyme, and by postmenstrual week 10 more than 95% of the cells in the gland belong to the T-cell lineage, with a few erythroblasts and B lymphocytes. Hassall's corpuscles are also present. By postmenstrual week 12 the mesenchymal septa, blood vessels and nerves have reached the newly differentiating medulla, which allows the entry of macrophage lineage precursors. Macrophages and interdigitating cells are first seen at postmenstrual week 14. Granulopoiesis occurs in the perivascular spaces. By postmenstrual week 17 the thymus appears fully differentiated. After this time, it produces the main type of thymocyte that is present throughout life (designated TdT$^+$). The fetal thymus shows linear growth between postmenstrual weeks 23 and 37, correlated to estimated fetal weight. Cord blood collected at term delivery indicates higher levels of regulatory T lymphocytes (Treg cells) in fetuses showing reduced thymus growth or low fetal weight; preterm infants have higher percentages of Treg cells in cord blood. It is suggested that reduced fetal thymus growth is compensated by increased release of Treg cells to ensure suppression of autoreactivity and anti-maternal immunity (Diemert et al 2016). The gland begins to atrophy shortly after puberty.

Caudal pharyngeal complex

The most caudal endodermal evaginations of the pharynx are the fourth pharyngeal pouch and the ultimobranchial body, a small diverticulum medial to the main pouch. Collectively, these diverticula are termed the caudal pharyngeal complex (see Fig. 17.19), and they are connected to the pharynx via the pharyngobranchial duct. They are surrounded by vagal neural crest and by the tissues of the developing thyroid gland. The cells of the ultimobranchial body become incorporated into the lateral thyroid lobes and give rise to the calcitonin-secreting 'C' or parafollicular cells of the thyroid gland. Parafollicular cells are seen singly early in the second trimester, and mostly in an intrafollicular position by the end of the trimester (Das et al 2017).

Pharynx, larynx, trachea and oesophagus

In human embryos, the hyoid bone is formed from five cell populations: the distal ends of mesenchymal condensations recognized as future second and third pharyngeal arch cartilages and a solitary midline condensation of mesenchyme (de Bakker et al 2018). This mesenchymal condensation forms a cylindrical structure and differentiates into cartilage between stages 15 and 20, which is earlier than cartilage formation in the distal parts of the arch cartilage anlagen. It has been suggested that the midline mesenchymal population arises from cells in the hypobranchial eminence or copula, which would mean that the body of the hyoid bone in human embryos is not derived from a pharyngeal arch cartilage (Rodríguez-Vázquez et al 2011).

Reichert's cartilage undergoes chondrogenesis only at its longer proximal (cranial) styloid segment continuous with the otic capsule, and at a distal segment in contact with the midline hyoid condensation; its intervening portion is always mesenchymal (Rodríguez-Vázquez et al 2006). The stylohyoid ligament does not arise from a cartilage anlage (Rodríguez-Vázquez et al 2015).

Chondrogenesis occurs in the proximal part of the second arch in stage 18, when the precursors of stylopharyngeus, stylohyoid and styloglossus (the three muscles that are attached to the styloid process) appear. During this stage the external carotid artery is forming between the cartilage and stylohyoid. Chondrogenesis is seen in the distal segment in stage 21, and by postfertilization week 10 the adjoining mesenchyme between the proximal and distal segments disappears, coinciding with a decrease in neck flexion and the growth of facial structures (Rodriguez-Vázquez et al 2015).

The larynx forms at the cranial end of the laryngotracheal groove, caudal to the epiglottis (see Figs 17.5–17.6, 17.14). The thyroid cartilage appears as two lateral plates, each chondrified from two centres and united in the mid-ventral line by a fibrous membrane, within which an additional centre of chondrification develops. Fourth and sixth arch cartilages have not been detected in human embryos: the thyroid and cricoid cartilages are derived from ventral mesenchymal condensations in the neck (de Bakker et al 2018).

The cricoid cartilage arises at stage 20 from two centres that soon unite ventrally, gradually extend, and ultimately fuse on the dorsal surface of the tube as the cricoid lamina, with the appearance of a modified tracheal cartilage. Paired arytenoid swellings appear within the ventral tissue of the sixth arches from stage 22, one on each side of the cranial end of the laryngotracheal groove. As they enlarge, they approximate to each other and to the caudal part of the hypobranchial eminence, where the epiglottis develops. The opening into the larynx, at first a simple slit, is converted into a T-shaped cleft by the enlargement of the arytenoid swellings. The vertical limb of the T lies between the two swellings with its horizontal limb lying between the swellings and the epiglottis. The arytenoid swellings differentiate into the arytenoid and corniculate cartilages (see Fig. 17.6), and the ridges that join them to the epiglottis become the definitive aryepiglottic folds, within which the cuneiform cartilages differentiate from the epiglottis.

The lower part of the larynx, the trachea, bronchi and lungs develop from the laryngotracheal groove (Ch. 20). This groove forms at stage 12 between two ridges extending from the floor of the caudal part of the pharynx into the mesenchyme surrounding the sinus venosus and inflow tract of the heart (see Figs 13.1C, 21.2B). Formation of the groove initiates separation of the respiratory and alimentary tubes. It remains at a constant level during the embryonic period, and the trachea lengthens distally as its bifurcation point descends. The splanchnopleuric mesoderm that surrounds the developing trachea and oesophagus induces the different histogenic pathways of the two tubes. By stage 22 the mesenchyme around the trachea is beginning to undergo chondrogenesis at regular intervals to form C-shaped cartilages whereas the mesenchyme around the oesophagus has a wide submucosal zone and muscular coats. The respiratory diverticulum becomes surrounded by angiogenic mesenchyme that forms the pulmonary blood vessels and connects to the developing sixth aortic arch artery (Chs 13, 20). Continued dorsal, sagittal connection between the enteric gut and respiratory airway, laryngo-tracheo-oesophageal cleft, is a rare anomaly that may be fatal; there may be clefting of the cricoid cartilage and along the thoracic trachea to the carina (Leboulanger and Garabédian 2011). Tracheo-oesophageal fistulae are considered in Chapter 20. For further details of tracheal development see Chapter 20, for early development of the oesophagus see Chapter 21.

MENINGES AND VENOUS SINUSES

The meninges may be divided in development into the pachymeninx (dura mater) and leptomeninges (arachnoid mater, subarachnoid space with arachnoid cells and fibres, and pia mater). The cells forming the meningeal layers originate from mesenchyme in the trunk and caudal regions of the head, and from neural crest in regions rostral to the mesencephalon. They form a loose mesenchyme, traditionally termed meninx primitiva, or primary meninx, that surrounds the early developing neural tube. (For a detailed account of the development of the meninges in the human, consult O'Rahilly and Müller (1986).)

Those mesenchymal populations projecting from the rostral end of the notochord, and those in the region of the prechordal plate, extend rostrally into the mesencephalic flexure and form the earliest cells of the tentorium cerebelli and the dura of the future chondrocranial skull base by stage 19. The medial part of the tentorium becomes thinner and disappears, leaving an incomplete partition that separates a subarachnoid area containing the telencephalon and diencephalon from one containing the cerebellum and rhombencephalon. The precursors of the venous sinuses are also present by stage 19, and the region of the future falx cerebri is seen by stage 20, although the dorsal regions of the brain are not yet covered with putative meninges. By stage 23 the dura is almost complete over the rhombencephalon and mesencephalon but is only present laterally around the telencephalon. Subarachnoid spaces and most of the cisternae are present from this time, after the arachnoid mater becomes separated from the primitive dura mater by the accumulation of cerebrospinal fluid (which now has a net movement out of the ventricular system).

The differentiation of the skull and meninges is closely associated with the development of venous channels returning blood from around the early brain and influences the final disposition and drainage routes of the venous plexuses that form bilateral primary head veins. Superficial venous channels draining the ectoderm and outer leptomeninges gain confluence with developing radicles that will ultimately drain into the external jugular venous complex. Deeper venous plexuses lateral to the brain coalesce to form anterior, middle and posterior dural stems that join the primary head vein (see Fig. 17.10). The anterior stem drains the prosencephalon and mesencephalon, and enters the primary head vein rostral to the trigeminal ganglion. The middle stem drains the metencephalon and empties into the primary head vein caudal to the trigeminal ganglion (V) and rostral to the root of the facial nerve (VII). The posterior stem drains the myelencephalon and enters caudal to the vagus nerve (X) where the primary head vein is confluent with the precardinal vein. It should be noted that the superficial venous channels retain some connections with the deeper meningeal venous channels during development, and become emissary veins.

Bilateral growth and expansion of the telencephalon gives rise to the growing cerebral hemisphere. Venous plexuses drain into networks of capillary venules along the dorsal margins of the anterior and middle dural stems and into a sagittal plexus in the position of the future falx cerebri. Rostrodorsally the sagittal plexus forms the superior sagittal sinus and ventrally it forms the inferior sagittal and straight sinuses and part of the great cerebral vein; drainage is commonly into the left transverse sinus. The convex surface of the cerebral hemispheres and the ventral aspect of the diencephalon are drained along the ventrolateral edge by a transitory tentorial sinus, to the transverse sinus. With growth of the temporal lobe, the tentorial sinus becomes elongated and attenuated, eventually disappearing; its territory is drained by enlarging anastomoses of pial vessels that become the basal veins, radicles of the great cerebral vein.

Changes to the early anterior dural stem as a consequence of early bilateral telencephalic enlargement leads to retention of the rostral part of the primary head vein medial to the trigeminal ganglion, the dwindling caudal part of which becomes the inferior petrosal sinus. The anterior dural stem receives the primitive maxillary vein which becomes the main trunk of the primitive supraorbital vein and is the superior ophthalmic vein in the adult.

The middle dural stem enlarges as the pro-otic sinus and receives the main venous drainage of the orbit and its contents and drains into the forming transverse sinus, and at a later stage, into the cavernous sinus. The cavernous sinus is formed from a secondary plexus derived from the primary head vein and lies between the otic and basioccipital cartilages. This plexus also gives rise to the inferior petrosal sinus which drains through the primordial hindbrain channel into the internal jugular vein. The superior petrosal sinus arises later from a ventral metencephalic tributary of the pro-otic sinus and communicates secondarily with the cavernous sinus. The pro-otic sinus, meanwhile, has developed a new and more caudally situated stem, the petrosquamosal sinus, which drains into the sigmoid sinus. With progressive ossification of the skull, the pro-otic sinus becomes diploic.

The development of the venous drainage and portal system of the hypophysis cerebri is closely associated with that of the venous sinuses.

SKULL

The skull has two major functional and anatomical components: the neurocranium and the viscerocranium. The neurocranium is composed of the calvaria and basicranium; it surrounds and protects the brain and the special sense organs of olfaction, vision, hearing and balance. The viscerocranium forms the skeleton of the face, palate and pharynx, and mediates the functions of feeding, breathing and facial expression; it also protects the tongue and forms the middle ear and the bony external acoustic meatus.

A conceptual plan of the skull base, viewed superiorly and laterally, and its relation to the mesenchymal condensations of the future pharyngeal arch cartilages, aids understanding of the development of the foramina at the base of the skull and the position of the cranial nerves (**Fig. 17.20**). The dorsoventral disposition of this region is shown in sagittal section in Fig. 17.22A. The position of the notochord can be seen in both figures. Adjacent to the notochord on each side paraxial mesenchymal extends laterally to the otic capsules. Rostrally the notochord ends at the site of the neurohypophsial outgrowth, caudally it is incorporated into the upper cervical vertebrae. Rostral to cartilaginous condensations around the adeno- and neurohypophyses, skull base mesoderm supports the enlarging eyes and developing olfactory structures. The cranial nerves can be enumerated rostrally from the hypoglossal canal. The position of the developing internal carotid artery and the divisions of the trigeminal nerve and nerves to the extraocular muscles can be seen between portions of the developing sphenoid bone. A lateral view of the skull base with the neural crest mesenchymal condensations forming the pharyngeal arches reveals the juxtaposition of the first and second arch condensations (producing the incus, malleus and stapes) with the otic capsule and indicates the future relationship of the developing middle ear ossicles.

The most rostral neural crest cell population makes a major contribution to the skull, forming the whole viscerocranium and the rostral part of the neurocranium (**Fig. 17.21**). The boundary between neural crest and cranial mesenchyme lies between the frontal and parietal bones (coronal suture) of the calvaria. The skull base is formed by neural crest rostral to the tip of the notochord, and is sclerotome-derived (i.e. from paraxial mesenchyme) in the notochordal region (McBratney-Owen et al 2008). The tip of the notochord lies immediately caudal to the hypophysial fossa (**Fig. 17.22A**). Broadly speaking, the bones of the skull base are formed by endochondral ossification (chondrocranium), whereas those of the calvaria and face ossify directly from mesenchymal condensations, i.e. by intramembranous ossification. The occipital, temporal and sphenoid bones and the mandible are of compound structure with respect to their tissue origins and/or type of ossification. The following account is based largely on descriptive studies on human embryos and fetuses (O'Rahilly and Müller 1987, 2001, 2007), together with details of cell lineage based on investigations in the mouse.

Chondrocranium

The first cranial skeletal structures to differentiate are the cartilages of the skull base, sensory capsules, viscerocranium and occiput (see Figs 17.5, 17.22). Development of the pharyngeal arch-related cartilages of the viscerocranium and ear ossicles is described in Chapter 16. Before any mesenchyme condenses to initiate the formation of cranial cartilage, the major cranial nerves and blood vessels are already in place, suggesting that the foramina of the skull base are specified before the bones are formed. Observations in chick embryos have demonstrated that the presence of these structures inhibits condensation and chondrogenesis of the surrounding mesenchyme, leading to the formation of foramina (Akbareian et al 2015). The adenohypophysial (Rathke's) pouch is still connected to the roof of the oral cavity as the skull base cartilage forms (dashed lines in **Fig. 17.22A**). The notochordal sheath is rich in sulphated glycosaminoglycans, which play a role in inducing condensation and chondrification of the occipital sclerotome-derived mesenchyme around it.

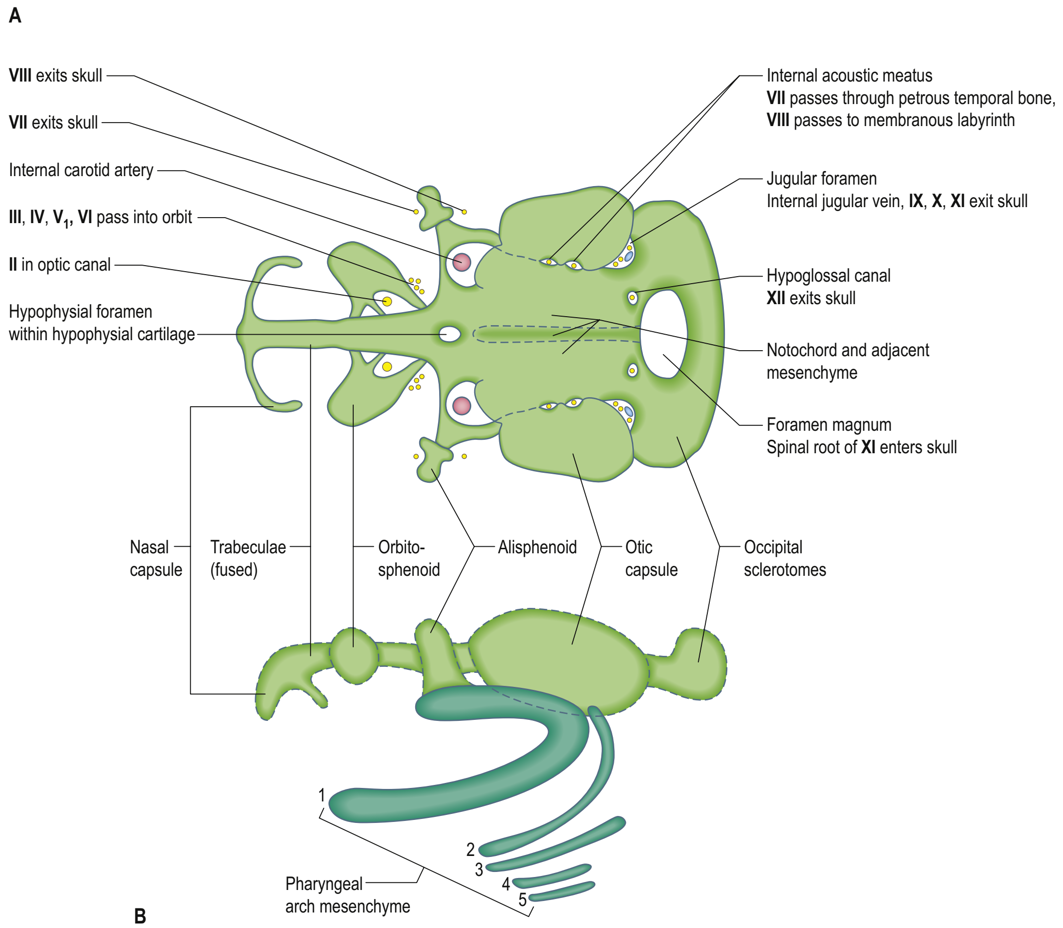
A
VIII exits skull
VII exits skull
Internal carotid artery
III, IV, V1, VI pass into orbit
II in optic canal
Hypophysial foramen within hypophysial cartilage
Internal acoustic meatus
VII passes through petrous temporal bone, VIII passes to membranous labyrinth
Jugular foramen
Internal jugular vein, IX, X, XI exit skull
Hypoglossal canal
XII exits skull
Notochord and adjacent mesenchyme
Foramen magnum
Spinal root of XI enters skull
Nasal capsule
Trabeculae (fused)
Orbito-sphenoid
Alisphenoid
Otic capsule
Occipital sclerotomes
1
2
3
4
5
Pharyngeal arch mesenchyme
B

Fig. 17.20 A diagrammatic representation of the developing skull. **A**, The skull base from a dorsal aspect to show the developing foramina and cranial nerves. **B**, A lateral view of the skull base with the relative position of mesenchyme of the pharyngeal arches.

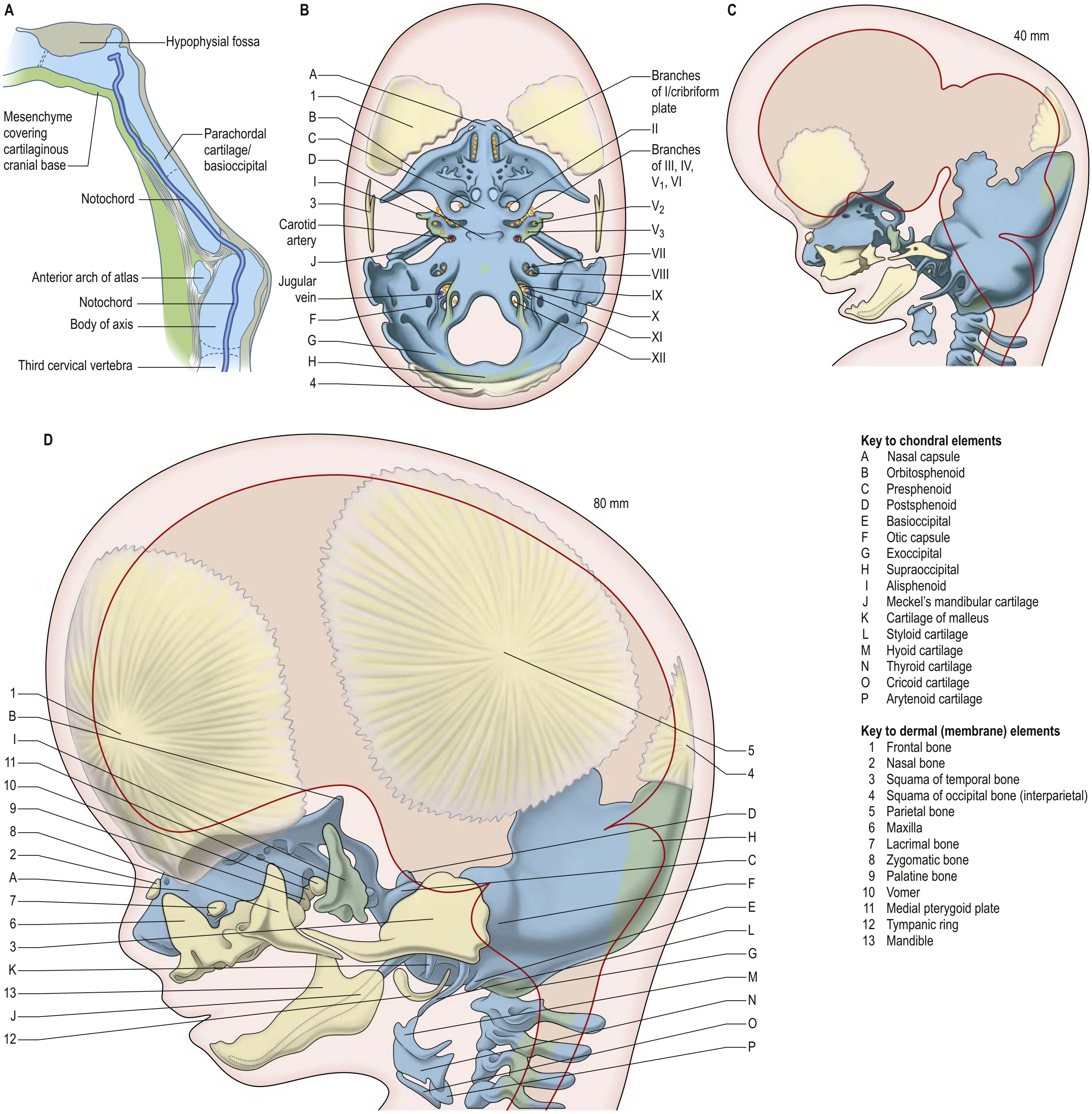
A
Hypophysial fossa
Mesenchyme covering cartilaginous cranial base
Parachordal cartilage/ basioccipital
Notochord
Anterior arch of atlas
Notochord
Body of axis
Third cervical vertebra
B
A
1
B
C
D
I
3
Carotid artery
J
Jugular vein
F
G
H
4
Branches of I/cribriform plate
II
Branches of III, IV, V1, VI
V2
V3
VII
VIII
IX
X
XI
XII
C
40 mm
D
80 mm
1
B
I
11
10
9
8
2
A
7
6
3
K
13
J
12
5
4
D
H
C
F
E
L
G
M
N
O
P

Key to chondral elements

A	Nasal capsule
B	Orbitosphenoid
C	Presphenoid
D	Postsphenoid
E	Basioccipital
F	Otic capsule
G	Exoccipital
H	Supraoccipital
I	Alisphenoid
J	Meckel's mandibular cartilage
K	Cartilage of malleus
L	Styloid cartilage
M	Hyoid cartilage
N	Thyroid cartilage
O	Cricoid cartilage
P	Arytenoid cartilage

Key to dermal (membrane) elements

1	Frontal bone
2	Nasal bone
3	Squama of temporal bone
4	Squama of occipital bone (interparietal)
5	Parietal bone
6	Maxilla
7	Lacrimal bone
8	Zygomatic bone
9	Palatine bone
10	Vomer
11	Medial pterygoid plate
12	Tympanic ring
13	Mandible

Fig. 17.22 Representative stages in the development of the cranium. In all the diagrams the chondrocranium and cartilaginous stages of vertebrae are shown in blue; ossification is indicated in green. Intramembranous bones are shown in cream. Cranial nerves are indicated by the appropriate Roman numeral. **A**, A sagittal section through the cranial end of the developing axial skeleton at about stage 16, showing the extent of the notochord. **B**, The superior aspect of the skull base at about postmenstrual week 11. **C**, The lateral aspect of **B**. **D**, The lateral aspect of the cranium at about postmenstrual week 14.

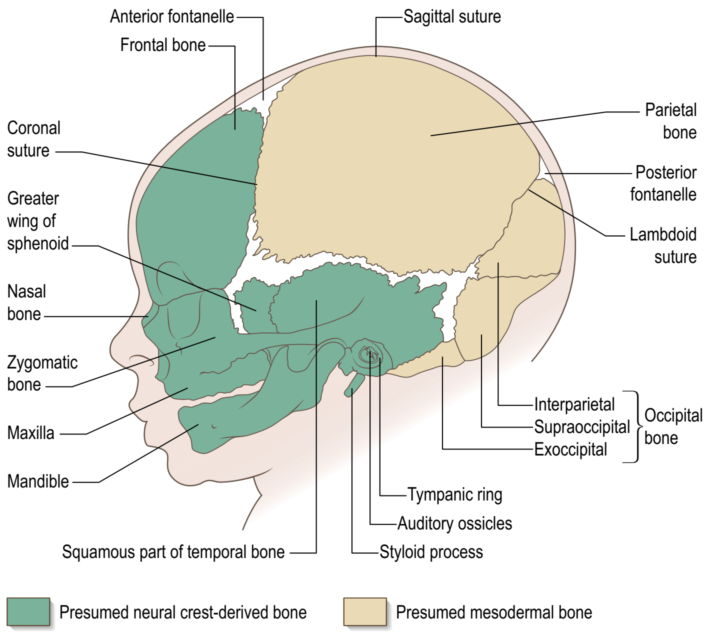

Fig. 17.21 The newborn skull, showing the presumed tissue origins of the bones (based on combined mouse and human data).

The structures referred to in the following account are illustrated in Fig. 17.22, which shows the cartilaginous skull base at about postmenstrual week 11. The central regions of all four occipital sclerotomes contribute to the parachordal cartilage, which surrounds the notochord and extends as a flat plate on either side of it by the end of the stage 20, forming the basioccipital component of the occipital bone (see also Fig. 18.13). Laterally, the exoccipital components (derived from sclerotomes 3 and 4) chondrify soon afterwards. They extend around the hindbrain to form the occipital arch, which is developmentally equivalent to the neural arch components of vertebrae. Roots of the hypoglossal nerve run between the parachordal and exoccipital cartilages, so that when the exoccipital and parachordal components fuse, they leave foramina for these nerve roots (see Figs 17.22B, 18.12). The supraoccipital part of the occipital cartilage extends dorsally from the exoccipital cartilage to complete the foramen magnum. Further development of the occipitocervical junction is considered in Chapter 18 and formation and ossification of the occipital bone is considered in Bernard et al (2015).

After formation of the exoccipital cartilages, differentiation also extends further rostrally in the medial part of the skull base, with formation of the hypophysial cartilages on either side of the hypophysial stalk. They unite in the median plane to form the primordium of the postsphenoid cartilage, cradling the hypophysis and retaining a perforation for the hypophysial stalk until postmenstrual weeks 10–12. This part of the basisphenoid cartilage will form the sella turcica and hypophysial fossa with the rostral presphenoid cartilages forming the jugum of the sphenoid body. This is the last part of the medial part of the skull base to differentiate as cartilage, bridging the gap between the postsphenoid and the nasal capsule.

At stage 17 mesenchyme begins to condense and later to chondrify around the nasal pits, forming the outer part of the nasal capsule and the nasal septum. The roof of each nasal capsule is completed slightly later, when cartilage differentiates around the olfactory nerve bundles (as they extend from the nasal placode-derived olfactory epithelium) to form the cribriform plates of the ethmoid bone. During postmenstrual weeks 9–12 cartilaginous conchae form. The whole nasal capsule is well developed by the end of postmenstrual week 12, and consists of a common median septal part, sometimes initially termed the interorbitonasal septum or mesethmoid, and the outer ectethmoid. The conchae ossify during postmenstrual weeks 17–20; the superior and middle conchae form part of the ethmoid bone, and the inferior pair become separate elements. Each lateral part of the nasal capsule becomes ossified as the orbital plate and ethmoidal labyrinth, with spaces ('cells') that communicate with the nasal cavity and become filled with air after birth (see Ch. 39). Part of the capsule remains cartilaginous as the septal and alar cartilages of the nose, and part is replaced by the intramembranous vomer and nasal bones.

Orbital cartilages surround the eye but do not undergo ossification in their entirety. The most rostral of them becomes continuous with the presphenoid cartilage by differentiation of a cartilaginous bridge that forms the caudal boundary of the optic foramen, enclosing the optic nerve; this later ossifies to form the lesser wing of the sphenoid bone (orbitosphenoid). The greater wing of the sphenoid (alisphenoid) has both intramembranous and endochondral components; the endochondral part initially differentiates as a cartilage surrounding the mandibular branch of the trigeminal nerve, forming the foramen ovale. This condensation extends medially to join the rostral edge of the hypophysial cartilage on each side. It also extends rostrally to surround the maxillary branch of the trigeminal nerve, forming the foramen rotundum. It extends laterally to join the intramembranous part of the bone, which replaces the caudal part of the orbital cartilage. The greater and lesser wings of the sphenoid are separated by the oculomotor, trochlear and abducens nerves and by the first (ophthalmic) division of the trigeminal nerve.

The otic capsule differentiates from a mesenchymal condensation around the otocyst, after its morphogenesis to form the cochlea and semicircular canals. Differentiation of cartilage begins laterally, at the same time as the hypophysial cartilages are first detectable and is complete by stage 20. Chondrogenesis around the point of exit of the vestibulocochlear nerve creates the internal acoustic meatus. Chondrogenesis of mesenchyme around the carotid arteries joins each hypophysial cartilage to the otic capsule, forming the carotid canals. A gap occupied by the jugular vein and the glossopharyngeal, vagus and accessory nerves remains between each otic capsule and the parachordal cartilage and becomes the jugular foramen. Chondrogenesis of the mesenchyme between the separate cartilages completes formation of the cartilaginous skull base and sensory capsules, which together form a continuous framework around the pre-existing blood vessels and cranial nerves by postmenstrual week 11 (see Fig. 17.22).

Establishing the dates of ossification, endochondral or intramembranous, in fetuses is not straightforward. At the transition time, when an embryo at the end of stage 23 (postfertilization days 53–58, or postfertilization weeks 8–9, see Fig. 23.3) becomes a fetus, the same age is then expressed from the date of the maternal last menstrual period, as postmenstrual weeks 10–11. Many schemes are used to age fetuses and it is not always clear what anthropometric units have been correlated to estimate an age given as postmenstrual weeks. Crown rump length is still used, although O'Rahilly and Müller (1999) recommended a move to greatest length; some studies age fetuses by femur length or foot length, but studies correlating these measurements to fetal age are limited. Variation of growth rate during the fetal period and differences in maternal ethnicity, height and weight affect fetal size. In this text, the postmenstrual age of fetuses based on publications has been carefully reviewed and crown rump length has been converted to postmenstrual weeks based on the fetal growth charts of Papageorghiou et al (2014) (see Chapter 23). For these reasons the age of appearance of ossification centres are estimations only. The process of endochondral ossification in the skull is essentially the same as that of the long bones, except that each ossification centre is equivalent to a primary centre, and follows a specific programme of growth and patterning. Growth takes place within synchondroses, the cartilaginous areas between adjacent ossification centres. The first ossification centres to appear are those of the lesser and greater wings of the sphenoid, at postfertilization weeks 8 and 9, respectively. A single basisphenoid ossification centre appears at postmenstrual week 11; three presphenoid and four postsphenoid ossification centres appear at postmenstrual week 16. Bone replaces most of the cartilage until only the major synchondroses remain; these enable the endochondral skull base and sensory capsules to continue growing until they reach their final size at puberty or earlier. At birth, unossified chondrocranium persists in the alae, lateral nasal cartilage and septum of the nose, the sphenoethmoidal junction, the spheno-occipital and sphenopetrous junctions, the apex of the petrous temporal bone (foramen lacerum), and between ossification centres of the sphenoid and occipital bones. As indicated above, parts of the chondrocranium do not ossify, but are replaced by adjacent intramembranous bone, e.g. the greater wing of the sphenoid (alisphenoid). In general, endochondral ossification centres form later than intramembranous ossification sites, which first appear after stage 19.

Calvaria

The bones of the calvaria (roof and lateral walls of the neurocranium) are formed entirely by intramembranous ossification. They are also described as dermal bones, since they are considered to be the evolutionary descendants of dermal plates formed as a protective cover for the brain in fish. In humans, as in all mammals, the major part of the calvaria is formed by paired frontal and parietal bones and the unpaired interparietal (membranous part of the occipital bone). The squamous part of the temporal bones and the alisphenoids contribute to the lateral walls. Lineage data from mouse studies indicate that the frontal bones abutting at the metopic suture, and the squamous temporal bones are of neural crest origin; the parietals are of paraxial origin; and the interparietal is mixed (Jiang et al 2002). The coronal suture forms at the neural crest/paraxial mesodermal interface, as does the sagittal suture, due to a small tongue of neural crest-derived tissue lying between the two developing bones. These tissue interfaces are significant for initiating the molecular signalling system that governs growth of the calvaria. Growth at the borders of adjacent bones, i.e. in the sutures, is the major mechanism of calvarial growth. The presence of fetal dura is not required for initial suture morphogenesis, which appears to be controlled by mesenchymal cell proliferation and fibrous extracellular matrix synthesis induced by the overlapping of the advancing osteo-inductive fronts of the calvarial bones. It is thought that a signal is transferred to the underlying dura that induces changes in localized regions beneath the sutures. Once a suture has formed, it serves as a primary site for cranial bone growth and constant interaction with the dura is required to avoid ossiferous obliteration (Opperman 2000). A sequence of events that maintains a balance between cell proliferation and osteogenic differentiation is mediated by an intercellular signalling system that includes the transcription factor TWIST and ligand–receptor interactions between fibroblast growth factors (FGFs) and their receptors (FGFRs). Mutations in the genes encoding these proteins cause premature fusion of the cranial sutures (craniosynostosis), which results in deficient growth in the plane perpendicular to the suture (**Fig. 17.23**; Morriss-Kay and Wilkie 2005, Twigg and Wilkie 2015). Mutations in an increasingly large number of skull development-related genes have been identified in a quarter of craniosynostosis cases (Wilkie et al 2017). In addition to the expansion-related growth that takes place in the sutures, appositional growth, where bone is laid down on, and resorbed from, the bone surfaces, plays an important role in remodelling the calvarial bones to maintain a degree of curvature that matches the curved surface of the growing brain. Appositional growth can also provide some compensatory expansion of the skull in craniosynostosis (see Fig. 17.23).

The frontal and parietal bones are initiated as basolateral mesenchymal primordia, that extend upwards between the dermal connective tissue and the mesenchymal dura mater. They do not, as previously thought, differentiate within the mesenchyme of an 'ectomeninx' that surrounds the brain. As the frontal and then the parietal primordia extend upwards, the differentiating osteoblasts secrete osteoid, which then undergoes mineralization. Only the mineralized parts of the bones are detected in alizarin-stained specimens and ultrasound scans. Clear frontal bone primordia are detectable in the superciliary arch region of alizarin-stained human embryos by postfertilization week 8. As they become mineralized above this level, the parietal bone primordia can also be seen. The two bones appear to be separated by a wide gap at the coronal suture, but this gap only shows the separation of the mineralized parts of the bone and the unmineralized edge of the parietal bone actually overlaps the caudal edge of the frontal bone. After the upgrowth phase, mineralization takes place centrifugally from the central points of the frontal and parietal bones, which, by this time, form convex plates over the curvature of the underlying brain (see Fig. 17.22D).

The interparietal bone (supranuchal squamous portion of the occipital bone) forms from two ossification centres that appear by stage 23. These are considered to be homologous with the paired postparietal bones of reptiles. The fact that they unite to form a single bone in mammals may be due to the interpolation of a small area of neural crest that migrates from the hindbrain after neural tube closure (Jiang et al 2002). Two further ossification centres develop laterally at postmenstrual week 12. A wide gap initially occupied by cartilage between the interparietal and parietal bones disappears as the membrane bones grow towards each other, forming the lambdoid suture when they abut. The lambdoid suture contributes growth to the caudal border of the parietal bones and to the upper part of the occipital bone. Synostosis of this suture is relatively rare (fewer than 5% of craniosynostosis cases) and has a less severe effect on overall skull growth than coronal and median fusions. Between the interparietal bone and the foramen magnum, the calvaria is completed by endochondral ossification of the supraoccipital component of the occipital bone.

In addition to the sutures that are formed where two membrane bones abut, fontanelles are formed where three or four bones meet. In the median plane, these are the anterior fontanelle, at the junction of the metopic and sagittal sutures, and the posterior fontanelle, at the junction of the sagittal and lambdoid sutures. The anterolateral fontanelle lies between the frontal, parietal, greater wing of the sphenoid and squamous temporal bones: after closure its site is the pterion. The posterolateral fontanelle lies between the parietal, petrous temporal, exoccipital and basioccipital bones; after closure, its site is the asterion. The size of the fontanelles at birth, and the timing of their closure, are highly variable. Delayed growth of the skull bones causes ossification defects, including cranium bifidum and parietal foramina, for which several genetic defects have been identified. Cleidocranial dysplasia is a defect of ossification affecting the intramembranous part of the clavicle as well as the calvaria and is caused by haploinsufficiency of the bone master gene *RUNX2*.

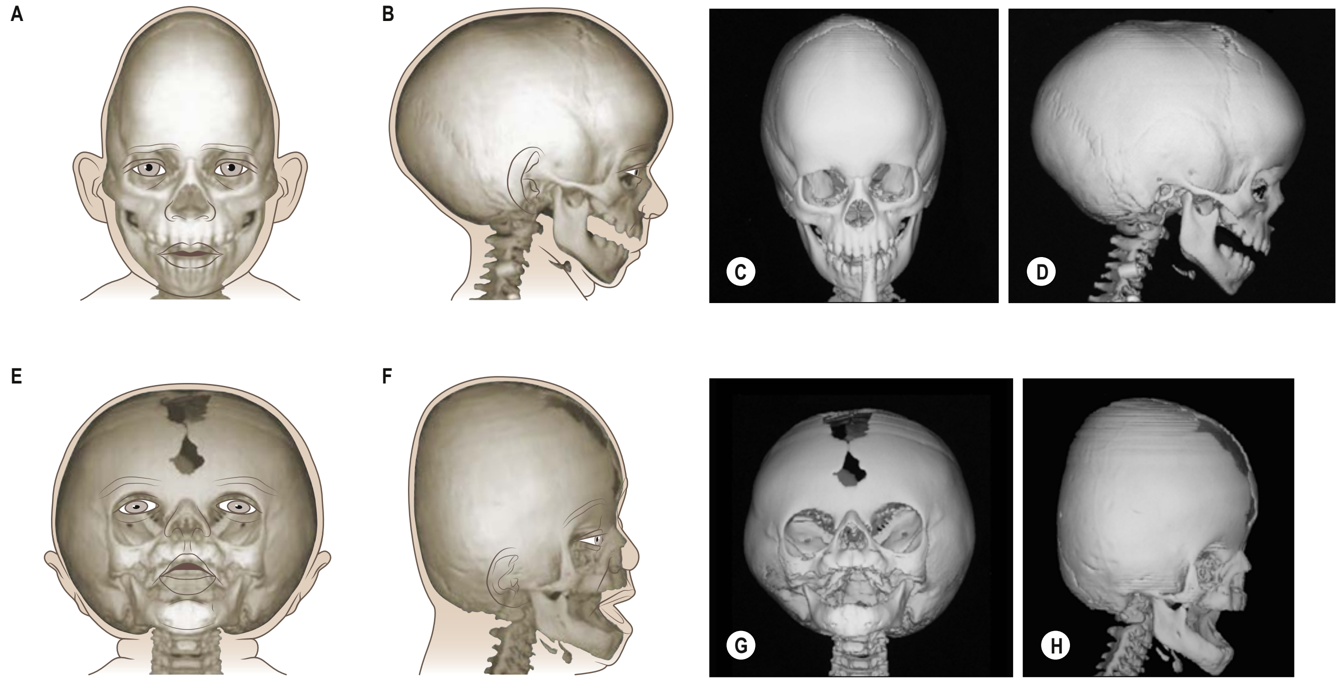

Fig. 17.23 Craniosynostosis. **A**–**B**, Line drawings of frontal and lateral views of sagittal synostosis. **C**–**D**, Three-dimensional computed tomography (3D-CT) scans. Premature fusion of the sagittal suture has restricted growth in breadth of the skull but there is compensatory growth in the fronto-occipital plane. **E**–**F**, Line drawings of frontal and lateral views of bicoronal synostosis. **G**–**H**, 3D-CT scans. Premature fusion of both coronal sutures has restricted growth in the fronto-occipital plane but there is compensatory growth in breadth. The pairs of CT scans are not from the same patients as those indicated in the line drawings; the endotracheal tube has been digitally removed from **D**. (CT scans courtesy of P Anslow.)

Membrane bones of the face and viscerocranium

The face and viscerocranium are formed from neural crest-derived membrane bones. From forehead to chin the facial skeleton includes the frontal, lacrimal and zygomatic and nasal bones and the vomer, maxilla and mandible. The maxilla and mandible form from first arch mesenchyme, as do the medial pterygoid plates of the sphenoid bone, the palatine and the tympanic bones.

During migration, the trigeminal neural crest cells divide into a frontonasal population that migrates superior to the eye and comes to surround the telencephalon and part of the diencephalon, a mandibular population that migrates into the first pharyngeal arch, and a maxillary population that forms the maxillary swelling (see Fig. 17.2). The frontal, lacrimal, nasal bones, the vomer and the premaxillary (incisor tooth-bearing) part of the maxilla are derived from the frontonasal mesenchyme; the maxilla and zygomatic bone are derived from the maxillary mesenchyme; and the mandible and tympanic ring are derived from the mandibular mesenchyme. The maxilla and premaxilla have primary ossification centres by stages 19–20, and three further ossification centres (orbitonasal, nasopalatine and zygomatic) form in the maxillary mesenchyme around stage 23. These components fuse to form a single bone in humans, in contrast to some mammals, in which the incisor-bearing premaxillary part remains separate. By stage 23 ossification centres for most of the facial and viscerocranial bones are present, except for the tympanic ring, for which four ossification centres appear at about postmenstrual week 14. They fuse to form the sickle-shaped bone that supports the tympanic membrane (see Fig. 17.6).

The mandible is the first membrane bone to begin ossification and its single ossification centre appears in stages 18–20. It is a developmentally complex bone. Although the body of the bone is formed by intramembranous ossification adjacent to Meckel's cartilage, the coronoid region and condyle are formed by endochondral ossification in cartilage that develops after formation of the membrane bone. These secondary ossification centres form between postmenstrual weeks 10–14. Distal cartilage forms two further secondary ossification centres, the mental ossicles between postmenstrual weeks 25 and 28. This complex system enables the mandible to grow at both proximal and distal ends, analogous to a long bone.

The temporomandibular joint forms later than other diarthrodial joints. Mesenchymal condensations of the mandibular condyle and zygomatic process of the squamous part of the temporal bone are present between stages 21–23. Joint capsule development begins at this stage; the inferior joint cavity appears at the end of postfertilization week 9, when the articular disc can be seen and chondrogenesis commences in the mandibular condyle. The superior joint cavity is seen from postfertilization week 11. Buccal movements, seen from postfertilization weeks 7–8, are thought to be important for the development of the joint. The posterior region of the joint is associated with the tympanosquamosal fissure; Meckel's cartilage, the discomalleolar ligament, chorda tympani nerve and anterior tympanic blood vessels pass through it. Intramembranous ossification of the area of insertion of lateral pterygoid begins during postmenstrual week 13 and endochondral ossification of the condylar cartilage is seen from postmenstrual week 17 (Carvalho de Moraes et al 2015).

Antenatal ultrasound imaging of the head and neck

The fetal head appears oval on transthalamic and transventricular planes and is symmetric and broader posteriorly (see Fig. 23.5). Biparietal skull diameter, taken through a plane of section that traverses the third ventricle and thalami, is the most accurate index of fetal age and the expected date of delivery and is routinely measured between postmenstrual weeks 15–28. Head circumference, measured through a plane that traverses the third ventricle and thalami plus the cavum septi pellucidi anteriorly and the tentorial hiatus posteriorly, is routinely measured and used to estimate pre- and post-term head growth (see Fig. 23.5). The size of the cisterna magna can be estimated to note hypoplasia of the posterior fossa of the skull. Increased thickness of the nuchal tissues at the back of the neck, measured from the outer edge of the occipital bone to the outer skin edge, is part of screening for Down's syndrome (Nafziger and Vilensky 2014). Nuchal translucency is increased in a number of trisomies and in fetuses with congenital heart defects (Chen 2010). The causes of this are complex and include an increase in hyaluronic acid in the extracellular matrix in the nuchal skin folds, aberrant jugular lymphatic flow and disturbed venous–lymphatic differentiation leading to local oedema (de Mooij et al 2010).

Prenatal diagnosis of asymmetric craniosynostosis and of craniofacial syndrome has been reported. Ultrasound evaluation of facial structures is possible by postmenstrual weeks 16–17. Standard facial views can visualize orbital size and position, eye size and nasal hypoplasia. Routine ultrasound has identified 93% of cases of cleft lip and palate, 67% of isolated cleft lip and 22% of cleft palate only (Evans et al 2018). Anomalies of the fetal neck are uncommon.

Postnatal development and growth of the skull

Available with the *Gray's Anatomy* e-book

Bonus e-book content

Fig. 17.17 Pierre Robin sequence.

Fig. 17.18 Cleft lip and cleft palate.

Fig. 17.22 Representative stages in the development of the cranium.

Fig. 17.24 Postnatal growth of the skull.

Key references

Hamilton WJ, Boyd JD, Mossman HW 1962 Hamilton, Boyd and Mossman's Human Embryology: Prenatal Development of Form and Function. Cambridge: Heffer.

The first comprehensive embryology book to add fundamental new studies to the original pioneering human embryology investigations. This work laid the foundations for later embryology textbooks and for many of the illustrations used in this chapter. It remains an important resource.

Hennekam R, Allanson J, Krantz I 2010 Gorlin's Syndromes of the Head and Neck (Oxford Monographs on Medical Genetics). New York: Oxford University Press.

This classic book describes the congenital anomalies of the head and neck.

Jiang X, Rowitch DH, Soriano P, et al 2000 Fate of the mammalian cardiac neural crest. Development 127:1607–1616.

The first publication to report the use of the Wnt1-Cre/R26R construct to trace the fate of neural crest cells in mouse embryos. Importantly, it showed that the whole of the septum that divides the outflow tract into the aortic and pulmonary arches is neural crest-derived.

McBratney-Owen B, Iseki S, Bamforth SD et al 2008 Development and tissue origins of the mammalian cranial base. Dev Biol 322:121–132.

A detailed analysis of the morphogenesis and tissue origins of the skull base. It complements the skull vault and face study by Yoshida et al (2008).

Morriss-Kay GM, Wilkie AO 2005 Growth of the normal skull vault and its alteration in craniosynostosis. J Anat 207:637–653.

This account concentrates on the role of FGFR signaling in calvarial growth and craniosynostosis. Other genetic contributions to normal and abnormal skull development are covered in the review by Wilkie et al. (2017).

O'Rahilly R, Müller F 2001 Human Embryology and Teratology, 3rd ed. New York: Wiley–Liss.

This book brings together studies on the Carnegie collection of human embryos carried out over several decades.

Thesleff I 2016 The developmental anatomy of teeth. In: Baldock R, Bard J, Davidson DR et al (eds) Kaufman's Atlas of Mouse Development Supplement. London: Elsevier; Ch. 18, pp. 231–238.

An excellent summary of tooth development in the mouse that provides all the basic morphogenetic and molecular information on epithelial–mesenchymal interactions that is also valid for human tooth development.

Twigg SRF, Wilkie AOM 2015 A genetic-pathophysiological framework for craniosynostosis. Am J Hum Genet 97(3): 359–377.

A summary of the genetic basis of human craniosynostosis, the insights gained from mouse studies and prospects for therapy.

Veugen CCA, Dikkers FG, de Bakker BS 2019 The developmental origin of the auricula revisited. Laryngoscope. doi: 10.1002/lary.28456 (ePub 2019 Dec 11).

Wilkie AOM, Johnson D, Wall SA 2017 Clinical genetics of craniosynostosis. Curr Opin Pediatr 29:622–628.

Based on a 13-year cohort of patients, this study considers the extent to which identified genetic causes of craniosynostosis can contribute to genetic counselling.

Yoshida T, Vivatbutsiri P, Morriss-Kay G et al 2008 Cell lineage in mammalian craniofacial mesenchyme. Mech Dev 125:797–808.

The availability of a mesoderm cell marker here demonstrates the completely complementary distribution of mesoderm and neural crest-derived cell populations in the mouse skull. Angiogenic and myogenic mesenchymal markers further show that these populations invade neural crest areas at early stages.

During vaginal birth, the overlap of the frontal and parietal bones enables them to slide over each other at the coronal suture. During the neonatal period, when the baby cries and intracranial pressure rises, the overlapping bones slide apart, increasing the fronto-occipital diameter of the skull. Growth at the coronal suture provides the major increase in the fronto-occipital plane of the calvaria. Premature synostosis of the coronal sutures restricts growth in this plane, causing brachycephaly; unilateral coronal synostosis leads to plagiocephaly, in which one side of the skull fails to grow in the fronto-occipital plane. Uni- and bilateral coronal synostosis comprises 20–25% of all forms of craniosynostosis.

Postnatal growth of the skull is characterized by changing proportions of its components and the extremely rapid growth of the brain in the first 2 postnatal years. The metopic and sagittal sutures are formed when the upwardly extending frontal and parietal bones, respectively, abut in the median plane. Growth within these sutures increases the breadth of the skull. The timing of fusion of the metopic suture is variable, but is complete by the end of the first year in most infants. Premature fusion of the sagittal suture results in the formation of a narrow, elongated skull. Sagittal synostosis is the most common form of craniosynostosis (40–55%). The sagittal suture continues as an active growth centre until puberty, with remodelling of the frontal bones mediated by appositional growth.

The paranasal sinuses begin to form in late fetal life as diverticula from the nasal cavity that gradually invade the maxilla, frontal, ethmoid and sphenoid bones. At birth, small ethmoidal and maxillary sinuses are present and become pneumatized during the first postnatal month; pneumatization of the sphenoid bone begins around postnatal month 4. The frontal sinus remains an out-pouching from the nasal cavity to term delivery, developing over the first 2 postnatal years; it is fully pneumatized by 14–15 years (Ma et al 2013). Thickening of the skull bones is accompanied by increasing size of the sinuses, and by a change in form of the sutures, from straight to wavy lines and, finally, to the complex interdigitations seen in the adult. After growth ceases, the skull sutures contain inert connective tissue and some cartilage; in old age, some of them are completely replaced by bone (natural synostosis).

The inner ear and the temporal bone grow very little after birth, so the increasing breadth of the skull draws the petrous temporal bone out laterally, creating the bony external acoustic meatus. The tympanic ring (with the tympanic membrane) lies at the surface of the meatus in the neonatal skull and remains at the proximal (inner) end of the deepening canal. The squamous temporal bone increases in size so that it contributes a greater proportion of the calvaria at puberty and in the adult than in the neonate (**Fig. 17.24**). By postnatal year 2 the mastoid process of the temporal bone has developed air-filled spaces (mastoid air cells) that are continuous with the middle ear cavity.

The suture between the primary (premaxilla-derived) and secondary parts of the palate is still patent in the neonate and there is a steady increase in maxillary volume postnatally, to accommodate the development and eruption of the permanent dentition (Langford et al 2003). At full-term birth, each quadrant of the jaws has five unerupted deciduous teeth and the germs of the first five permanent teeth. Permanent teeth develop in accessional positions from the lingual aspects of the deciduous tooth germs and, for the 12 permanent molar teeth, from posterior extensions of the dental laminae on each side of both jaws (see Fig. 17.16). Mineralization begins in both deciduous and permanent teeth before birth. The deciduous teeth have well-developed crowns by full term: eruption through the gingivae usually begins with the lower incisors between postnatal months 3–6. After eruption, the gingivae remain attached to the neck of each tooth by the upper part of the periodontal ligament, while the major part of the ligament attaches the tooth root to the bone of the tooth socket. The type of transition to extrauterine life is permanently recorded in the primary teeth and can be reliably demonstrated in forensic dental identification. The circadian growth rhythm of dentine and enamel deposition in tooth germs is temporarily blocked by the metabolic stress of delivery; the resultant change in enamel prism deposition is seen as a neonatal line or ring that can be detected in all deciduous teeth and permanent first molar teeth of live births. The thickness of the line is related to birth difficulties, being thinner in caesarean section and thicker in vaginal delivery (Sabel et al 2008, Canturk et al 2014).

During the first 5 years there is as much anteroposterior as vertical growth of the maxilla, after which there is relatively more vertical growth. Growth of the face occurs in the sutures between the membrane bones in a similar manner to that of the calvarial sutures. Postnatally, the face grows more rapidly than the calvaria, in contrast to the fetal period during which rapid growth of the brain has a dominant influence on regional skull growth. Habitual mouth breathing due to nasal obstruction may cause variable adaptation of facial muscles leading to anomalous maxillary or mandibular growth in children; lower anterior facial height (philtrum to midline mandibular distance), is greater in mouth breathers, in whom the mandible may be smaller with less rotation (Souki et al 2012).

In the full-term neonate there is no space between the hard palate and the tongue when the mouth is closed, which means that the entire surface of the neonatal tongue, which is short and broad, lies within the oral cavity. The oropharynx and nasopharynx join without any sharp junctional demarcation to a pharynx that is one-third of the relative length seen in the adult. By 5 years of age an oblique angle is formed at this junction, and in the adult, the nasopharynx and oropharynx join at almost a right-angle. The hyoid bone and larynx are initially relatively high and the epiglottis may extend above the soft palate with the laryngeal airway in directly continuous with the posterior nares (see Fig. 40.11). The hyoid bone and larynx descend during the first postnatal year and by the fourth or fifth year, form part of the anterior wall of the oropharynx (see Fig. 23.15). The anatomical arrangement of the laryngeal structures enables the infant to breathe while suckling, as milk passes on either side of the laryngeal opening to reach the oesophagus (see Fig. 40.12).

During breastfeeding, three oral spaces are identified, a median space between the tongue and hard palate occupied by the nipple when suckling and which bifurcates posteriorly to produce channels on each side of the soft palate and epiglottis, and two lateral spaces, the lateral arcuate cavities, that are formed between the tongue and cheeks. The upper and lower gingivae within these spaces do not touch during suckling. The hard palate is only slightly arched and its mucous membrane is corrugated by five or six irregular transverse folds (rugae) that assist with gripping the nipple. Each cheek is supported by a mass of subcutaneous fat, the suctorial pad, that lies between buccinator and masseter. Studies on the biomechanical processes of milk extraction during breastfeeding have shown that balanced postnatal muscular development is promoted by forward movement of the mandible and raising and lowering the tongue. Tongue movements can generate vacuum pressures of some −145 mmHg: tongue lowering decreases the pressure. In bottle feeding the main action the infant uses is sucking and the tongue only controls the milk outlet through bilateral contraction of buccinator. Children who have never breastfed have a greater prevalence of posterior cross bite in both mixed and permanent dentition and of abnormal swallowing patterns and mouth breathing (which may also have compromised occlusal development) than children who

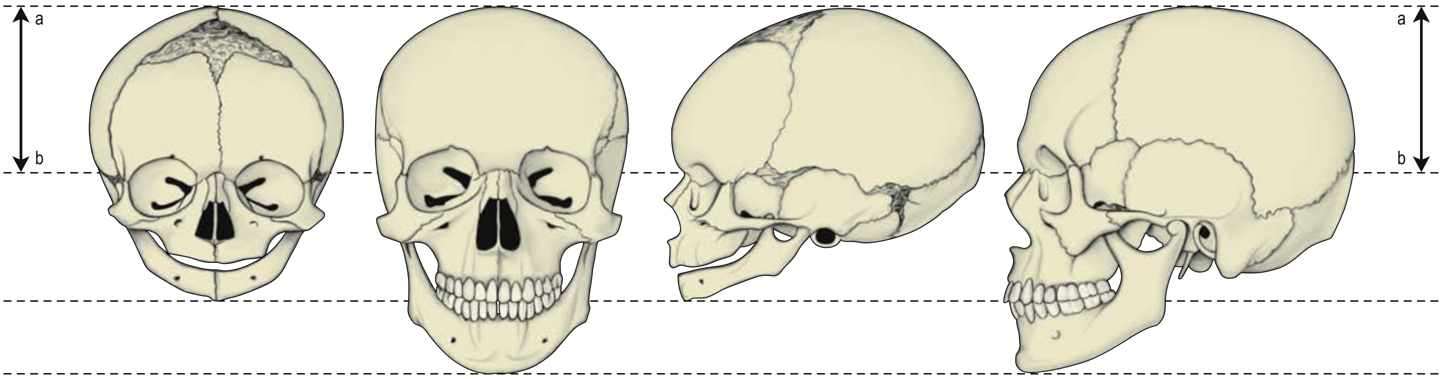

Fig. 17.24 During postnatal growth of the skull, the viscerocranium increases in size relative to the neurocranium. This diagram shows that, with the height of the cranial vault expressed as similar in newborn and adult skulls (lines a↔b), the facial skeleton increases particularly rapidly during childhood and puberty.

have breastfed for more than 6 months postnatally (Chen et al 2015, Boronat-Catalá et al 2017). Preterm infants have poor suck–swallow–breathe coordination and an inability to generate adequate vacuum strength (Geddes et al 2017).

Non-nutritive sucking does not appear to act in synergy with breastfeeding to promote malocclusion. It is seen as early at postmenstrual weeks 13–16 and considered a normal part of fetal and neonatal development. A sucking reflex remains to 12 postnatal months after which time the infant has learned to feed (Feştilă et al 2014). Infantile swallowing, with the jaws apart and lip musculature forming a tight contact around the mother's breast, is different to the adult swallowing pattern with the lips relaxed, teeth together and the tongue against the hard palate. The transition from infant to adult swallowing is usually present by 9–10 years; it is never achieved by 10–15% of the population (Feştilă et al 2014).

Structures that descend to the mediastinum are considered in Chapter 20. Within the neck in the full-term neonate, the trachea is relatively small in relation to the larynx; it has thicker walls and cartilage plates that are relatively closer together than in the adult. It commences at the upper border of the sixth cervical vertebra, a relationship that is conserved with growth. It bifurcates at the level of the thoracic vertebrae 3 or 4, descending to lie level with the upper border of the thoracic vertebra 5 in the adult (endotracheal intubation in the neonate is described in Chapter 20). In extremely preterm infants, later phonation and voice quality appears to be affected by supraglottic hyperfunction, a secondary response to structural laryngeal pathology caused by neonatal intubation (Reynolds et al 2016). The prevalence of voice anomalies is reported to be above 50% in children intubated for longer than 28 days in the neonatal period (Hseu et al 2018).

The thyroid gland is relatively large in the neonate, where it has a long, narrow isthmus connecting lobes that do not yet contact the upper part of the trachea. Thyroid volume at birth varies due to variations in maternal iodine intake; the volume is lower at postmenstrual week 36, in preterm infants delivered before postmenstrual week 28, than in infants delivered at full term (Ng et al 2018). It usually attains half the adult size by 2 years of age. The parathyroid glands are as variable in size and position as they are in the adult. They double in size between birth and puberty. Parathyroid hormone (parathormone, PTH) is produced from postmenstrual week 12. It is essential for calcium homeostasis and is involved in the remodelling of growing bones.

The oesophagus begins and ends one to two vertebral levels higher than in the adult, extending from between the fourth and sixth cervical vertebrae to the level of the ninth thoracic vertebra. The narrowest constriction is at its junction with the pharynx, where the inferior pharyngeal constrictor constricts the lumen; in this region there is a risk it may be traumatized with medical instruments or catheters. The pharyngo-oesophageal phase of swallowing is controlled by multiple afferent and efferent cranial nerves, excitatory and inhibitory neurones and central pattern generators. In the preterm infant oromotor inertia, oral pooling and delayed initiation of the pharyngeal phase of swallowing can cause cough with feeding, wet gurgly breathing and nasopharyngeal regurgitation. Laryngeal penetration and aspiration, where food passes into the laryngeal vestibule above the level of the vocal folds or between the true vocal folds, respectively, can breach airway protection reflexes. About 25% of preterm infants show dysphagia; the incidence of laryngeal aspiration ranges from 25% to 85% in infants with swallowing dysfunction. (For further reading about the factors and mechanisms of dysphagia in the high-risk infant, see Jadcherla (2016).)

References

Adams A, Mankad K, Offiah C et al 2016 Branchial cleft anomalies: a pictorial review of embryological development and spectrum of imaging findings. Insight Imag 7:69–76.

Akbareian SE, Pitsillides AA, Macharia GR et al 2015 Occipital foramina development involves localised regulation of mesenchyme proliferation and is independent of apoptosis. J Anat 226:560–74.

Bernard S, Loukas M, Rizk E et al 2015 The human occipital bone: review and update on its embryology and molecular development. Childs Nerv Syst 31:2217–23.

Bocian-Sobkowska J, Woźniak W, Malendowicz LK 1997 Morphometric studies on the development of the human thyroid gland. II. The late fetal life. Histol Histopathol 12:79–84.

Boehm N, Roos J, Gasser B 1994 Luteinizing hormone-releasing hormone (LHRH)-expressing cells in the nasal septum of human fetuses. Brain Res Dev Brain Res 82:175–80.

Boronat-Catalá M, Montiel-Company JM, Bellot-Arcís C et al 2017 Association between duration of breastfeeding and malocclusions in primary and mixed dentition: a systematic review and meta-analysis. Sci Rep 7:5048. doi: 10.1038/s41598-017-05393-y.

Brunskill EW, Potter AS, Distasio A et al 2014 A gene expression atlas of early craniofacial development. Dev Biol 391:133–46.

Canturk N, Atsu SS, Aka PS et al 2014 Neonatal line on fetus and infant teeth, an indicator of live birth and mode of delivery. Early Human Dev 90:393–7.

Carvalho de Moraes LO, Tedesco RC, Arraéz-Aybar LA et al 2015 Development of synovial membrane in the temporomandibular joint of the human fetus. Eur J Histochem 59:2569. doi: 10.4081/ejh.2015.2569.

Chen CP 2010 Pathophysiology of increased fetal nuchal translucency thickness. Taiwan J Obstet Gynecol 49:133–8.

Chen X, Xia B, Ge L 2015 Effects of breastfeeding duration, bottle-feeding duration and non-nutritive sucking habits on the occlusal characteristics of primary dentition. Pediatrics 15:46. doi 10.1186/s12887-015-0364-1.

Das SS, Mishra S, Kaul JM 2017 Development of parafollicular cells and their relationship with developing thyroid follicles in human foetuses. J Clin Diagn Res 11(7):AC01-AC04. doi: 10.7860/JCDR/2017/26211.10225.

de Bakker BS, de Bakker HM, Soerdibalie-Maikoe C et al 2018 The development of the human hyoid–larynx complex revisited. Laryngoscope 128:1829–34. doi: 10.1002/lary.26987.

de la Cuadra-Blanco C, Peces-Peña MD, Jáñez-Escalada L et al 2006 Morphogenesis of the human excretory lacrimal system. J Anat 209:127–35.

de Mooij YM, Bartelings MM, Twisk JWR et al 2010 Altered jugular vein and ductus venosus flow velocities in fetuses with increased nuchal translucency and distended jugular lymphatic sacs. Am J Obstet Gynecol 202:566–7.

Diemert A, Hartwig I, Pagenkemper M et al 2016 Fetal thymus size in human pregnancies reveals inverse association with regulatory T cell frequencies in cord blood. J Reprod Immunol 113:76-82.

Evans KN, Hing AV, Cunningham ML 2018 Craniofacial malformations. In: Gleason CA, Juul SE (eds) Avery's Diseases of the Newborn, 10th ed. Elsevier; Ch. 100.

Ferguson MW 1991 The orofacial region. In: Wigglesworth JS, Singer DB (eds) Textbook of Fetal and Perinatal Pathology. Oxford: Blackwell Scientific; Ch. 22.

Feştilă D, Ghergie M, Muntean A et al 2014 Suckling and non-nutritive sucking habit: what should we know? Clujul Med. 87:11–14.

Geddes DT, Chooi K, Nancarrow K et al 2017 Characterisation of sucking dynamics of breastfeeding preterm infants: a cross sectional study. BMC Pregnancy Childbirth 17:386. doi: 10.1186/s12884-017-1574-3.

Gietka-Czernel M, Dębska M, Kretowicz P et al 2012 Fetal thyroid in two-dimensional ultrasonography: normograms according to gestational age and biparietal diameter. Eur J Obstet Gynecol Reprod Biol 162:131–8.

Goergen MJ, Holton NE, Grünheid T 2017 Morphological interaction between the nasal septum and nasofacial skeleton during human ontogeny. J Anat 230:689–700.

Graham A, Poopalasundaram S, Shone V et al 2019 A reappraisal and revision of the numbering of the pharyngeal arches. J Anat doi: 10.1111/joa.13067 (ePub 2019 Aug 11).

Hamilton WJ, Boyd JD, Mossman HW 1962 Human Embryology (Prenatal Development of Form and Function). Cambridge: Heffer.

The first comprehensive embryology book to add fundamental new studies to the original pioneering human embryology investigations. This work laid the foundations for later embryology textbooks and for many of the illustrations used in this chapter. It remains an important resource.

Hennekam R, Allanson J, Krantz I 2010 Gorlin's Syndromes of the Head and Neck (Oxford Monographs on Medical Genetics). New York: Oxford University Press.

The most recent edition of the classic book on congenital anomalies of the head and neck. It is very comprehensive.

Hinrichsen KV (ed) 1990 Human-Embryologie. Berlin: Springer.

Hseu A, Ayele N, Kawai K et al 2018 Voice abnormalities and laryngeal pathology in preterm children. Ann Oto Rhinol Laryngol 127:508–13.

Hutchins EJ, Kunttas E, Piacentino ML et al 2018 Migration and diversification of the vagal neural crest. Dev Biol 444(Suppl 1):S98–S109.

Indencleef K, Roosenboom J, Hoskens H et al 2018. Six NSC/P loci show associations with normal-range craniofacial variation. Front Genetics 9:502. doi: 10.3389/fgene.2018.00502.

Jadcherla S 2016 Dysphagia in the high-risk infant: potential factors and mechanisms. Am J Clin Nutr 103(Suppl): 622S–628S.

Jernvall J, Thesleff I 2012 Tooth shape formation and tooth renewal: evolving with the same signals. Development 139:3487–97.

Jiang X, Rowitch DH, Soriano P et al 2000 Fate of the mammalian cardiac neural crest. Development 127:1607–16.

The first publication to report the use of the Wnt1-Cre/R26R construct to trace the fate of neural crest cells in mouse embryos. Importantly, it showed that the whole of the septum that divides the outflow tract into the aortic and pulmonary arches is neural crest-derived.

Jiang X, Iseki S, Maxson RE et al 2002 Tissue origins and interactions in the mammalian skull vault. Dev Biol 241:106–16.

Kuratani S, Kusakabe R, Hirasawa T 2019 The neural crest and evolution of the head/trunk interface in vertebrates. Dev Biol 444:60–6.

Langford RJ, Sgouros S, Natarajan K et al 2003 Maxillary volume growth in childhood. Plast Reconstr Surg 111:1591–7.

Leboulanger N, Garabédian E 2011 Laryngo-tracheo-oesophageal clefts. Orphanet J Rare Dis 6:81.

Ma YX, Zhang WJ, Yan ZH et al 2013 Normal pneumatization time of paranasal sinuses in 799 children: evaluation with magnetic resonance imaging. Zhonghua Yi Xue Za Zhi 19:816–18.

Matsuoka T, Ahlberg PE, Kessaris N et al 2005 Neural crest origins of the neck and shoulder. Nature 436:347–55.

McBratney-Owen B, Iseki S, Bamforth SD et al 2008 Development and tissue origins of the mammalian cranial base. Dev Biol 322:121–32.

A detailed analysis of the morphogenesis and tissue origins of the skull base. It complements the skull vault and face study by Yoshida et al (2008).

Mekonen H, Hikspoors JPJM, Mommen G et al 2016 Development of the epaxial muscles in the human embryo. Clin Anat 29:1031–45.

Minoux M, Kratochwil CF, Ducret S et al 2013 Mouse Hoxa2 mutations provide a model for microtia and auricle duplication. Development 140:4386–97.

Morice A, Soupre V, Mitanchez D et al 2018 Severity of retrognathia and glossoptosis does not predict respiratory and feeding disorders in Pierre Robin sequence. Front Paediatr 6:351. doi: 10.3389/fped.2018.00351. eCollection 2018.

Morriss-Kay GM, Wilkie AO 2005 Growth of the normal skull vault and its alteration in craniosynostosis. J Anat 207:637–53.

This account concentrates on the role of FGFR signaling in calvarial growth and craniosynostosis. Other genetic contributions to normal and abnormal skull development are covered in the review by Wilkie et al. (2017).

Nafziger E, Vilensky JA 2014 The anatomy of nuchal translucency at 10–14 weeks gestation in fetuses with trisomy 21: an incredible medical mystery. Clinic Anat 27:353–9.

Ng SM, Turner MA, Avula S 2018 Ultrasound measurements of thyroid gland volume at 36 weeks' corrected gestational age in extremely preterm infants born before 28 weeks' gestation. Eur Thyroid J 7:21–6.

Opperman LA 2000 Cranial sutures as intramembranous bone growth sites. Dev Dynamics 219:472–85.

O'Rahilly R, Müller F 1986 The meninges in human development. J Neuropathol Exp Neurol 45:588–608.

O'Rahilly R, Müller F 1987 Developmental Stages in Human Embryos. Washington: Carnegie Institution of Washington Publication 637.

O'Rahilly R, Müller F 1999 The Embryonic Human Brain. An Atlas of Developmental Stages, 2nd ed. New York: Wiley–Liss.

O'Rahilly R, Müller F 2001 Human Embryology and Teratology, 3rd ed. New York: Wiley–Liss.

This book brings together studies on the Carnegie collection of human embryos carried out over several decades.

O'Rahilly R, Müller F 2007 The development of the neural crest in the human. J Anat 211:335–51.

Papageorghiou AT, Ohuma EO, Altman DG et al 2014 International standards for fetal growth based on serial ultrasound measurements: the Fetal Growth Longitudinal Study of the INTERGROWTH-21st Project. Lancet 384:869–79.

Patten BM 1968 Human Embryology, 3rd ed. New York: Blakiston.

Reynolds V, Meldrum S, Simmer K et al 2016 Dysphonia in extremely preterm children: a longitudinal observation. Logoped Phoniatr Vocol. 41:154–8.

Richmond S, Howe LJ, Lewis S et al 2018 Facial genetics: a brief overview. Front Genet 9:462. doi: 10.3389/fgene.2018.00462.

Rodríguez-Vázquez JF, Mérida-Velasco JR, Verdugo-López S et al 2006 Morphogenesis of the second pharyngeal arch cartilage (Reichert's cartilage) in human embryos. J Anat 208:179–89.

Rodríguez-Vázquez JF, Kim JH, Verdugo-López S et al 2011 Human fetal hyoid body origin revisited. J Anat 219:143–9.

Rodríguez-Vázquez JF, Verdugo-López S, Abe H et al 2015 Anat Rec 298:1395–1407.

Sabel N, Johansson C, Kühnisch J et al 2008 Neonatal lines in the enamel of primary teeth. A morphological and scanning electron microscopy investigation. Arch Oral Biol 53:954–63.

Salwinski TG, Lewandowski J, Dzieciolowska-Baran E et al 2010 Nasal septum morphology in human fetuses in computed tomography images. Eur J Med Res 15 (Suppl II):202–5.

Santagati F, Rijli FM 2003 Cranial neural crest and the building of the vertebrate head. Nat Rev Neurosci 4:806–20.

Souki BQ, Lopes PB, Pereira TBJ et al 2012 Mouth breathing children and cephalometric pattern: does the stage of dental development matter? Int J Ped Otorhinolaryngol 76:837–41.

Steding G 2009 The Anatomy of the Human Embryo: A Scanning Electron-Microscopic Atlas. Basel: Karger.

Stoyanov GS, Matev BK, Valchanov P et al 2018 The human vomeronasal (Jacobson's) organ: a short review of current conceptions, with an English translation of Potiquet's original text. Cureas10:e2643. doi: 10.7759/cureus.2643.

Thesleff I 2016 The developmental anatomy of teeth. In: Baldock R, Bard J, Davidson DR et al (eds), Kaufman's Atlas of Mouse Development Supplement. London: Elsevier; Ch. 18, pp. 231–8.

An excellent summary of tooth development in the mouse that provides all the basic morphogenetic and molecular information on epithelial-mesenchymal interactions that is also valid for human tooth development.

Tucker AS 2017 Major evolutionary transitions and innovations: the tympanic middle ear. Phil Trans R Soc B 372:20150483.

Tummers M, Thesleff I 2009 The importance of signal pathway modulation in all aspects of tooth development. J Exp Zool B Mol Dev Evol 312B:309–19.

Twigg SRF, Kan R, Babbs C et al 2004 Mutations of ephrin-B1 (EFNB1), a marker of tissue boundary formation, cause craniofrontonasal syndrome. Proc Natl Acad Sci U S A 101:8652–7.

Twigg SRF, Wilkie AOM 2015 A genetic-pathophysiological framework for craniosynostosis. Am J Hum Genet 97(3): 359–77.

A summary of the genetic basis of human craniosynostosis, the insights gained from mouse studies and prospects for therapy.

Valasek P, Theis S, DeLaureir A et al 2011 Cellular and molecular investigations into the development of the pectoral girdle. Dev Biol 57:108–16.

Vasuki AK, Fenn TK, Devi MN et al 2016 Fate and development of human vomeronasal organ – a microscopic fetal study. J Clin Diagn Res 10:AC08–AC011. doi: 10.7860/JCDR/2016/15930.7373.

Veugen CCA, Dikkers FG, de Bakker BS 2019 The developmental origin of the auricula revisited. Laryngoscope. doi: 10.1002/lary.28456 (ePub 2019 Dec 11).

Warmbrunn MV, de Bakker BS, Hagoort J et al 2018 Hitherto unknown detailed muscle anatomy in an 8-week-old embryo. J Anat 233: 43–54.

Wilkie AOM, Johnson D, Wall SA 2017 Clinical genetics of craniosynostosis. Curr Opin Pediatr 29 622–8.

Based on a 13-year cohort of patients, this study considers the extent to which identified genetic causes of craniosynostosis can contribute to genetic counselling.

Yoshida T, Vivatbutsiri P, Morriss-Kay G et al 2008 Cell lineage in mammalian craniofacial mesenchyme. Mech Dev 125:797–808.

The availability of a mesoderm cell marker here demonstrates the completely complementary distribution of mesoderm and neural crest-derived cell populations in the mouse skull. Angiogenic and myogenic mesenchymal markers further show that these populations invade neural crest areas at early stages.

CHAPTER 18

Development of the back

Vertebrae and their alternating intervertebral discs are one of the main manifestations of body segmentation or metamerism. A chain of segments arranged in sequence allows the overall structure to bend when it is moved by the associated muscles. The original body segments, the somites, are formed from paraxial mesenchymal populations found lateral to the neural tube and notochord in the early embryo (Ch. 12). The somites provide the embryonic cell populations for the axial skeleton and skeletal muscle. The vertebrae form from immediately cranial and caudal somites by the recombination of two neighbouring somite halves in a process called resegmentation, while the muscles that are attached to adjacent vertebrae are derived from a single somite. Each vertebra develops from bilateral origins to form a midline centrum, two lateral arches bearing transverse processes that develop lateral and dorsal to the neural tube, and a midline fused dorsal portion with a spinous process. Individual vertebrae may be distinguished by modifications of these component parts. After resegmentation a single vertebra contains cells originating from four individual somites: the cranial and caudal halves of longitudinally abutting somites of one side of the body that unite with the corresponding two halves of the contralateral somites. The intervertebral discs have a dual origin: the anulus fibrosus develops from the sclerotome and the nucleus pulposus develops from the notochord.

SEGMENTATION OF PARAXIAL MESENCHYME

Epithelial epiblast cells that ingress through the lateral aspect of the primitive node and the rostral primitive streak (see Fig. 10.3) become committed to a somitic lineage as they undergo an epithelial to mesenchymal transition. The position of ingression of the epiblast informs the specific destination of the cells. Those ingressing through the lateral portion of Hensen's node form the medial halves of the somites, whereas those ingressing through the primitive streak, approximately 200 µm caudal to the node, form the lateral halves of the somites. The two somite halves do not appear to intermingle. After passing through the streak the mesoblastic cells retain contact with epiblast and hypoblast basal laminae both during migration and after reaching the lateral sides of the notochord. Here the cell population is referred to as paraxial mesenchyme. The unsegmented mesenchymal population (presomitic mesenchyme), also termed segmental plate, subsequently undergoes a mesenchymal to epithelial transition to form somites in a process called somitogenesis. The first pair of somites in human embryos develops at stage 9 (about 26 postfertilization days; see Fig. 23.3) and 38–39 pairs of somites are present at stage 14 (Mekonen et al 2017).

Somitogenesis is an autonomous process. Somites will form from cultured presomitic mesenchyme with or without the presence of neural tube tissue or primitive node tissue. Transcriptome profiling of human paraxial mesenchyme, presomitic and mature somite cells, derived from stage 13–14 human embryos, has identified some of the regulatory pathways in the human and highlighted specific differences from equivalent mouse embryo somitic stages (Xi et al 2017). Myogenic, osteogenic and chondrogenic cells have been grown in 3D culture from both human embryonic stem cells (hESCs) and human induced pluripotential stem cells (hiPSCs), cultured according to specific human profiling information for somitogenesis (Xi et al 2017, Nakajima et al 2018).

Bilateral segmentation of the paraxial presomitic mesoblastic populations, which divide into discrete epithelial spheres, occurs as a sequential process along the craniocaudal axis. In avian embryos, a pair of somites is formed every 90 minutes until the full number is obtained. The molecular pathway for this synchronous segmentation has been termed the segmentation clock and has been identified as a conserved process in vertebrates from fish to mammals. It is based on the rhythmic production of messenger RNAs (mRNAs) for the transcription of genes related to Notch, a large transmembrane receptor, and a number of other factors, including members of the Wnt and fibroblast growth factor (FGF) signalling pathways.

Intrinsically coordinated pulses of mRNA expression appear as a wave within the presomitic mesoblast as each somite forms. As new cells enter the paraxial mesenchyme caudally, they begin phases of upregulation of the cycling genes, followed by downregulation of these genes. During each cycle, the most cranial presomitic mesoblast will segment and undergo mesenchymal to epithelial transformation to form the next somite. Experimental evidence from chick embryos shows that newly formed paraxial mesoblast cells undergo 12 such cycles before they finally form a somite, the period from ingression through the primitive streak to segmentation into a somite taking approximately 18 hours (Pourquié and Kusumi 2001). The somite number and the rate of somite formation varies between vertebrate species, taking 2 hours in mouse and 5 hours in human embryos (Ebisuya and Briscoe 2018). Those vertebrates with elongated bodies and many somites form somites more rapidly relative to their developmental rate than those with shorter bodies, a finding that supports the concept that somite number is controlled, in part, by species-specific cyclical properties of the presomitic mesoblast (Richardson et al 1998, Gomez et al 2008).

The final determination of somitic boundary formation has not yet been fully elucidated but seems to require a periodic repression of the Notch pathway genes. The caudal presomitic mesoblastic cells are thought to be maintained in an immature state by their production of FGF8, and become competent for segmentation when FGF8 levels drop below a certain threshold. For an overview of vertebrate segmentation and its clinical implications, see Pourquié (2011) and Hubaud and Pourquié (2014).

SOMITE DEVELOPMENT

Five main stages can be identified in somitogenesis and somite development (**Figs 18.1–18.2**). A local portion of the most cranial paraxial mesoblast undergoes compaction. The compacted cells undergo a mesenchymal to epithelial transformation, resulting in an epithelial sphere of cells that surrounds free somitocoele cells. This stage marks segmentation of the paraxial mesenchyme and somite formation. Shortly after the somite boundaries have been defined, the mesenchymal sclerotome

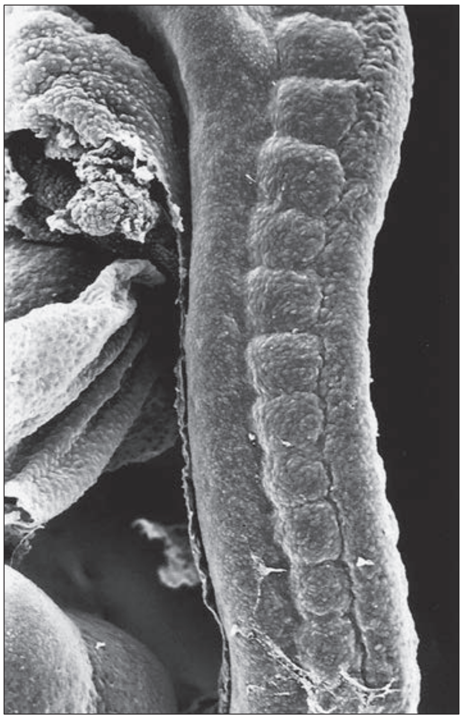

Fig. 18.1 A scanning electron micrograph of a lateral view of an embryo, showing the somites. The cranial somites are at the upper border and the more caudal somites are at the lower border. Note the change in size of the cranially more advanced somites. (Photograph by P Collins; printed by S Cox, Electron Microscopy Unit, Southampton General Hospital.)

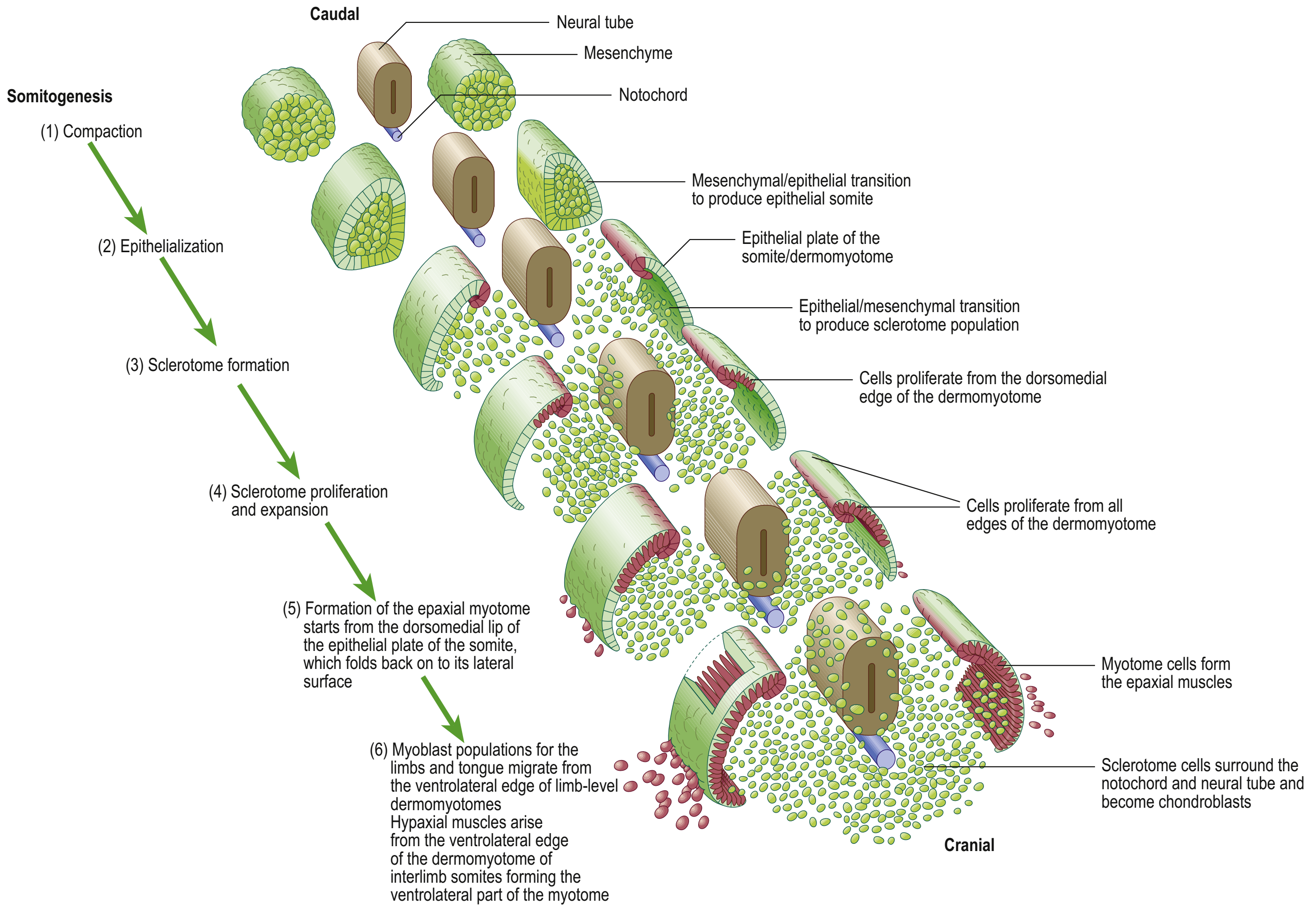
Caudal
Neural tube
Mesenchyme
Notochord
Somitogenesis
(1) Compaction
(2) Epithelialization
(3) Sclerotome formation
(4) Sclerotome proliferation and expansion
(5) Formation of the epaxial myotome starts from the dorsomedial lip of the epithelial plate of the somite, which folds back on to its lateral surface
(6) Myoblast populations for the limbs and tongue migrate from the ventrolateral edge of limb-level dermomyotomes
Hypaxial muscles arise from the ventrolateral edge of the dermomyotome of interlimb somites forming the ventrolateral part of the myotome
Mesenchymal/epithelial transition to produce epithelial somite
Epithelial plate of the somite/dermomyotome
Epithelial/mesenchymal transition to produce sclerotome population
Cells proliferate from the dorsomedial edge of the dermomyotome
Cells proliferate from all edges of the dermomyotome
Myotome cells form the epaxial muscles
Sclerotome cells surround the notochord and neural tube and become chondroblasts
Cranial

Fig. 18.2 The stages of somite development. Development occurs in a craniocaudal progression. The more cranially placed somites (at the lower right of the figure) are further developed than those caudally placed (at the upper left of the figure). The stages in somite development are given on the left of the figure; more detailed information is given on the right.

is formed by a region-specific epithelial to mesenchymal transition of the ventral and ventromedial walls of the somite. As the embryo enlarges, the sclerotomal populations on each side become contiguous with the notochord and the neural tube. The rest of the dorsal lateral somitic epithelium remains as the epithelial plate of the somite, also termed the dermomyotome, a proliferative epithelium that will give rise to (nearly) all of the striated muscles of the body. Formation of the epaxial myotome begins. Segmentation of the paraxial mesoblast, mesenchymal to epithelial transformation to form epithelial somites and the resultant somite developmental processes (epithelial to mesenchymal transformation to form the sclerotome) all occur in a craniocaudal progression caudal to the otic vesicle from stage 9.

Cells of the spherical epithelial somite are polarized. Their apical region contains Golgi apparatus, actin and α-actinin close to the luminal surface, while their basal surface, corresponding to the outer circumference of the somite, rests on a basal lamina that contains collagen, laminin and fibronectin. Basal, filopodia-like processes pass through this basal lamina to contact the basal laminae of the neural tube medially, notochord ventromedially and surface ectoderm dorsolaterally. Dorsoventral patterning of the somites is dependent on the activity of Sonic Hedgehog (SHH) from the notochord/neural tube floor plate, Wnt1 and Wnt3a from the neural tube roof plate, and Wnt6 from the overlying ectoderm. A role of somitic filopodial processes in signal transduction is likely for Wnt signalling from the surface ectoderm (Sagar et al 2015).

The diverse sclerotomal cell populations have been studied mostly in the chick embryo, where the fates of the cells have been tracked (Christ et al 2004) (**Figs 18.3–18.6**). The main mass of the sclerotome is termed the central sclerotome, the portion close to the notochord is termed the ventral sclerotome, and the portions adjacent to the dorsomedial and ventrolateral dermomyotomal margins are termed the dorsal sclerotome and lateral sclerotome, respectively. The central sclerotome remains close to the dermomyotome and will give rise to the pedicles and ventral parts of the neural arches, and the proximal ribs. The ventral sclerotomal cells that laterally abut the notochord, proliferate and fuse with their contralateral counterparts to form an axial cell population within the extracellular matrix of the perinotochordal space, now termed the perinotochordal sheath. The dorsal sclerotomal cells develop relatively late, invade the space between the surface ectoderm and growing neural tube, and form the dorsal part of the neural arches. The lateral sclerotomal cells give rise to distal parts of the ribs (Scaal 2016). Generally, there is a dorsolateral expansion of the whole sclerotome rather than the medial migration of a population of sclerotomal cells (Gasser 2006), as can be seen in Figs 18.3–18.5. Sclerotomal cells also give rise to the meninges surrounding the spinal cord, local tendons and ligaments, and endothelial cells of blood vessels (Christ et al 2004). The somitocoele cells, which remain mesenchymal throughout somite formation, give rise to the vertebral joints, intervertebral discs and the proximal ribs (Mittapalli et al 2005).

The dermomyotome is a proliferative rectangular epithelial cell sheet that releases cells from its four borders (**Fig. 18.7**). Proliferation at the dorsomedial edge produces muscle precursor cells that elongate along the cranial to caudal extent of the dermomyotome underneath its ventral (apical) surface as they move laterally. With a slight delay, cells similarly elongate from the cranial and caudal edges of the dermomyotome. The cells that are produced from these three edges are termed the epaxial myotome and will give rise to skeletal muscle dorsal to the vertebrae, i.e. the epaxial (back) musculature. Cells produced by the ventrolateral edge of the dermomyotome are termed the hypaxial myotome. Cells from occipital and cervical somites migrate ventrally, giving rise to the intrinsic muscles of the tongue and respiratory diaphragm respectively. Cells arising adjacent to the limb buds migrate laterally to enter them (Ch. 19). At interlimb levels, the ventrolateral edge of the epithelial dermomyotome extends into the body wall and gives rise to the intercostal and abdominal muscles. Dermomyotomal cells that do not form myotomal muscle fibres contribute to the dermis and subcutis of the back (Scaal and Christ 2004).

It was once thought that the somite gave rise to segmental portions of the dermis of the skin, as well as bone and muscle. However, it is now clear that the somitic contribution to the skin from the epithelial plate is limited to de-epithelialization of dermomyotomal cells over the epaxial muscles alone, a much smaller distribution than the segmental portion of skin usually implied by the term dermatome. The concept that an embryological dermatome, derived from the somite, produces all of the dermis of the skin is no longer tenable.

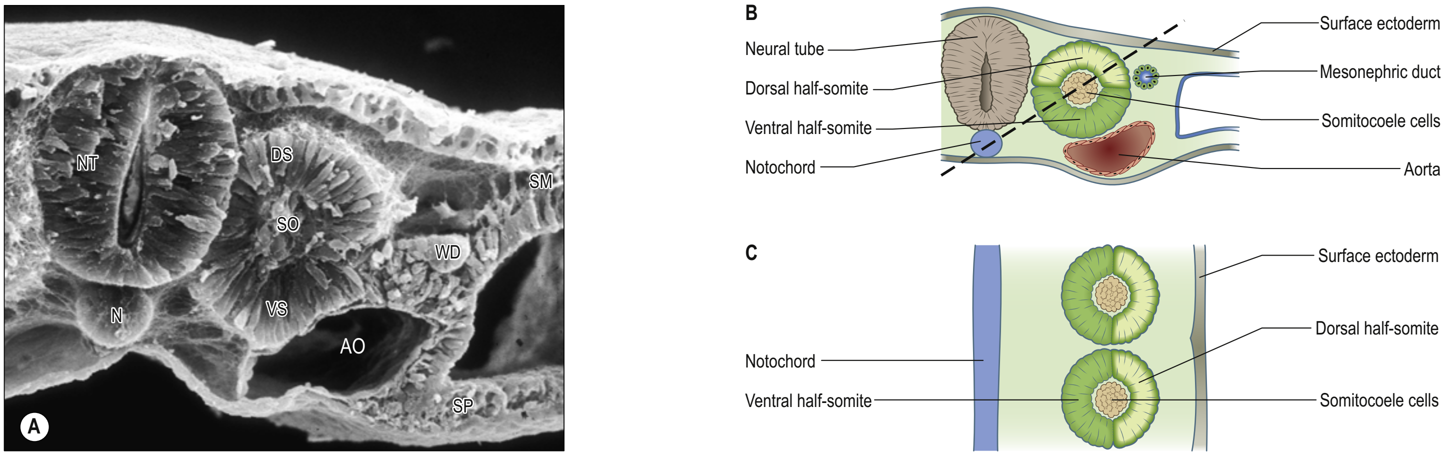
A
NT
DS
SO
VS
N
AO
WD
SM
SP
B
Neural tube
Dorsal half-somite
Ventral half-somite
Notochord
Surface ectoderm
Mesonephric duct
Somitocoele cells
Aorta
C
Notochord
Ventral half-somite
Surface ectoderm
Dorsal half-somite
Somitocoele cells

Fig. 18.3 The development of the sclerotome. **A**, A scanning electron micrograph of a transversely fractured 2-day chick embryo. **B–C**, Transverse (**B**) and longitudinal (**C**) sections through the somites; the plane in C is indicated by the dotted line in **B**. The somites here are in the epithelialization phase of somitogenesis. Abbreviations: AO, aorta; DS, dorsal somite; N, notochord; NT, neural tube; SM, somatopleure; SO, somitocoele; SP, splanchnopleure; VS, ventral somite; WD, Wolffian duct (mesonephric duct). (A, Courtesy of Dr Heinz Jürgen Jacob, Bochum, Germany.)

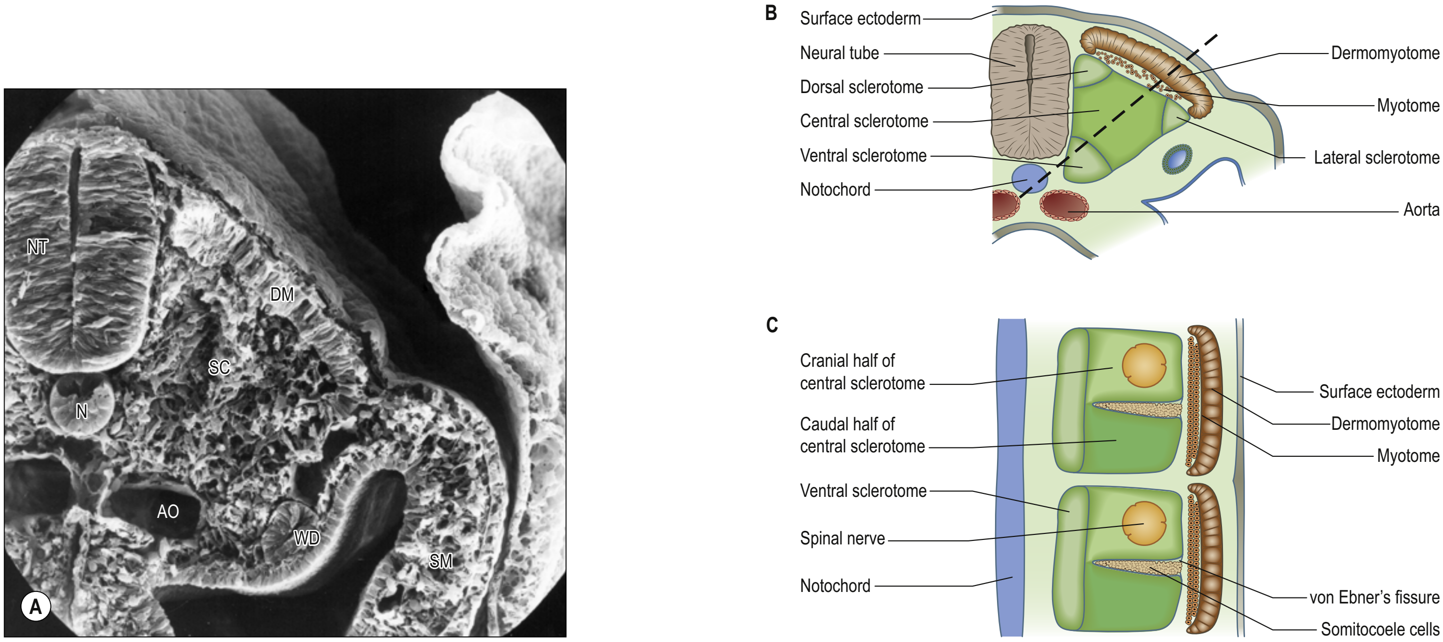
A
NT
DM
SC
N
AO
WD
SM
B
Surface ectoderm
Neural tube
Dorsal sclerotome
Central sclerotome
Ventral sclerotome
Notochord
Dermomyotome
Myotome
Lateral sclerotome
Aorta
C
Cranial half of central sclerotome
Caudal half of central sclerotome
Ventral sclerotome
Spinal nerve
Notochord
Surface ectoderm
Dermomyotome
Myotome
von Ebner's fissure
Somitocoele cells

Fig. 18.4 The development of the sclerotome. **A**, A scanning electron micrograph of a transversely fractured 3-day chick embryo. **B–C**, Transverse (**B**) and longitudinal (**C**) sections through the developing sclerotome; the plane in **C** is indicated by the dotted line in **B**. Abbreviations: AO, aorta; DM, dermomyotome; N, notochord; NT, neural tube; SC, sclerotome; SM, somatopleure; WD, Wolffian duct (mesonephric duct). (A, Courtesy of Dr Heinz Jürgen Jacob, Bochum, Germany.)

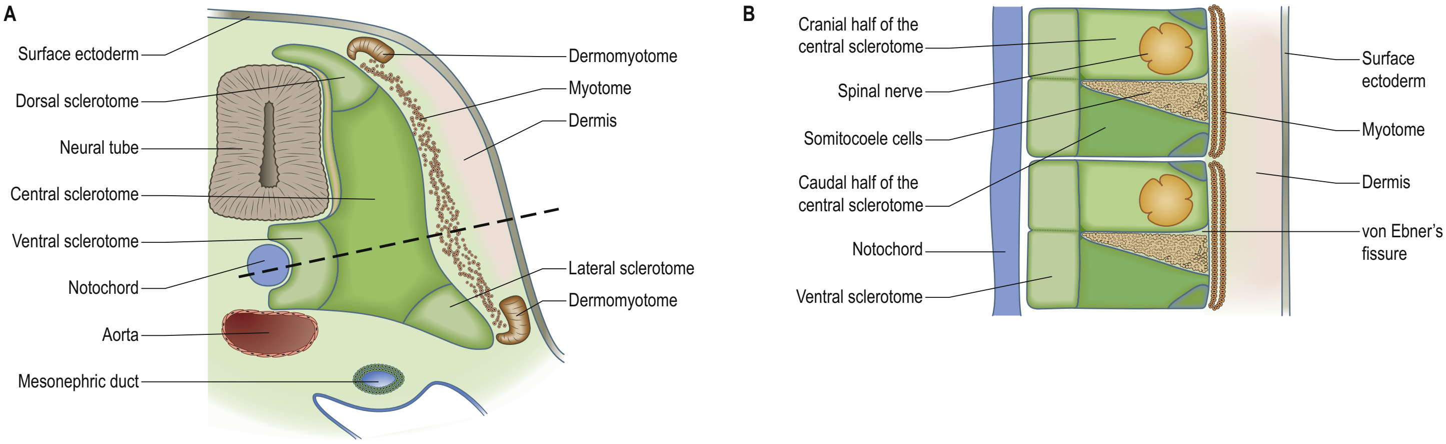
A
Surface ectoderm
Dorsal sclerotome
Neural tube
Central sclerotome
Ventral sclerotome
Notochord
Aorta
Mesonephric duct
Dermomyotome
Myotome
Dermis
Lateral sclerotome
Dermomyotome
B
Cranial half of the central sclerotome
Spinal nerve
Somitocoele cells
Caudal half of the central sclerotome
Notochord
Ventral sclerotome
Surface ectoderm
Myotome
Dermis
von Ebner's fissure

Fig. 18.5 Later development of the sclerotome. **A**, Transverse section. **B**, Longitudinal section through the dotted line indicated in **A**, showing the sclerotomal subdivisions.

The regularity of somite formation provides criteria for staging embryos. The staging scheme proposed by Ordahl (1993) noted that morphogenetic events occur in successive somites in a craniocaudal progression. The somite most recently formed from the unsegmented paraxial mesenchyme was designated as stage I, the next most recent as stage II, and so on. When the embryo has formed an additional somite, the stages of the previously formed somites increase by one Roman numeral. According to this scheme, in the chick embryo, compaction occurs at stage 0, epithelialization at stage I, formation of mesenchymal sclerotome cells from stage V, and myotome formation from stage VI. Early migration of the ventrolateral lip of the dermomyotome and production of myotome cells are still occurring at stage X.

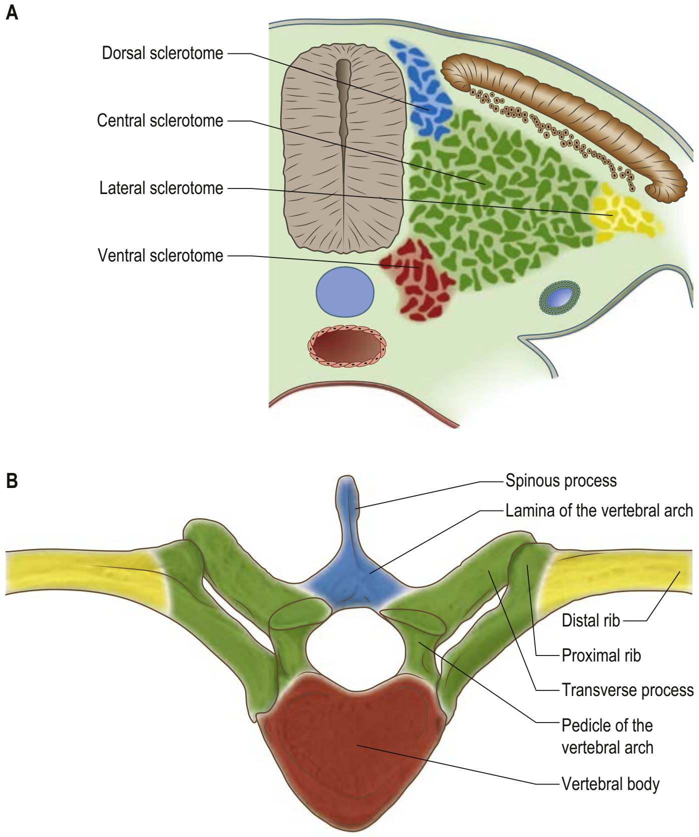

Fig. 18.6 Contributions of sclerotome cells to the vertebrae. **A**, Sclerotomal subcompartments. **B**, The derivatives of the sclerotomal subcompartments (shown in similar colours) in a thoracic vertebra. (Courtesy of Professor Martin Scaal, Germany.)

DEVELOPMENT OF SCLEROTOMES

Sclerotomal cell populations form from the ventral half of the epithelial somite. An intrasegmental boundary (fissure or cleft, sometimes termed von Ebner's fissure), initially filled with extracellular matrix and a few cells, appears within the sclerotome and divides it into loosely packed cranial and densely packed caudal halves. The dermomyotome covers both half-sclerotomes dorsally. The bilateral sclerotomal cell populations of each segment migrate towards the notochord and surround it to form the perinotochordal sheath. They undergo a matrix-mediated interaction with the notochord, differentiating chondrogenetically to form the cartilaginous precursor of the vertebral centrum. The perinotochordal sheath starts to express type II collagen, and this is believed to mark a chondrogenic fate in those mesenchyme cells that contact it. Each vertebra is formed by the combination of much of the caudal half of one bilateral pair of sclerotomes with much of the cranial half of the next caudal pair of sclerotomes, their fusion around the notochord producing the blastemal centrum of the vertebra (**Figs 18.8–18.10**). The mesenchyme adjoining the intrasegmental sclerotomic fissure now increases greatly in density to form a well-defined perichordal disc that intervenes between the centra of two adjacent vertebrae and is the future anulus fibrosus of the intervertebral symphysis ('disc') (see below).

The basic pattern of a typical vertebra is initiated by this recombination of caudal and cranial sclerotome halves (resegmentation) (see Fig. 18.9; **Fig. 18.11**), followed by differential growth and sculpturing of the sclerotomal mesenchyme that encases the notochord and neural tube. The centrum encloses the notochord and lies ventral to the neural tube. Sclerotomal differentiation starts in human embryos at about stage 10, when 10 somite pairs are present. The loosely packed cranial and densely packed caudal halves of the sclerotome can be seen at stage 15, with the neural processes extending dorsolaterally to the spinal ganglia (Mekonen et al 2017). The neural arch consists of paired bilateral pedicles (ventrolaterally) and laminae (dorsolaterally) that coalesce in the midline dorsal to the neural tube to form the spinous process. This is seen initially in the mid-thoracic region by postfertilization week 9. On each side, three further processes project cranially, caudally and laterally from the junction of the pedicle and laminae. The cranial and caudal projections are the blastemal articular processes (zygapophyses) that become contiguous with reciprocal processes of adjacent vertebrae; their junctional zones mark the future zygapophysial or facet joints. The lateral projections are the true vertebral transverse processes. Bilateral costal processes (ribs) grow anterolaterally from the ventral part of the pedicles (i.e. near the centrum) from the neighbouring perichordal disc, and, at most thoracic levels, with accessions from the next adjacent caudal pedicles. The costal processes expand to meet the tips of the transverse processes. Transverse processes are first seen in lower cervical and thoracic vertebrae during stage 18 (see Fig. 18.6). The definitive vertebral body is compound, formed from a median centrum (derived from the cells of the perinotochordal sheath), and bilaterally from the expanded pedicle ends (derived from the migrating sclerotomal populations) (see Fig. 18.11). These portions of the vertebral body fuse at the neurocentral synchondroses.

The segmental nature of the vertebrae is promoted by the notochord and neural floor plate, which induce the ventral elements of the vertebrae and repress dorsal structures such as the spinous processes.

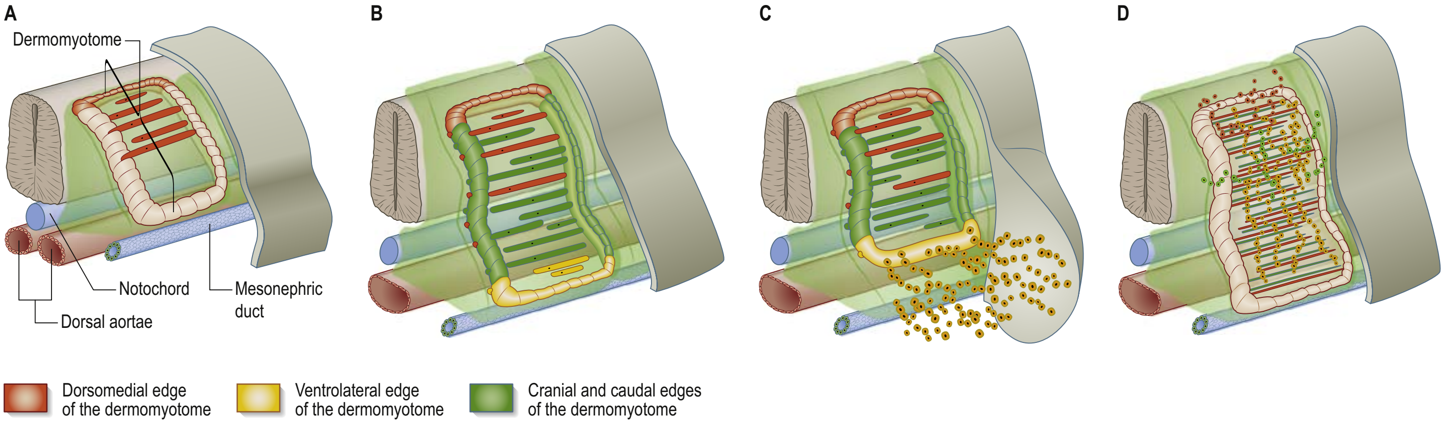
A
B
C
D
Dermomyotome
Notochord
Mesonephric duct
Dorsal aortae
Dorsomedial edge of the dermomyotome
Ventrolateral edge of the dermomyotome
Cranial and caudal edges of the dermomyotome

Fig. 18.7 A–D, Epaxial and hypaxial muscle origin from the dermomyotome. **A**, Early dermomyotome proliferation. **B**, The dermomyotome at interlimb level, producing epaxial myoblasts. **C**, The dermomyotome at limb level. Hypaxial dermomyotome cells de-epithelialize from the ventrolateral edge and migrate into the limb bud. **D**, The local dermis is formed later by superficial de-epithelialization of dermomyotome cells.

Experimental excision of the notochord in early chick embryos results in fusion of the centra and formation of a cartilaginous plate ventral to the neural tube. Dorsal segmentation is influenced by the spinal ganglia: experimental removal of the ganglia results in fusion of the neural arches and the formation of a uniform cartilaginous plate dorsal to the neural tube. Vertebrae are specified as to region very early in development. If a group of thoracic somites is transplanted to the cervical region, ribs will still develop. In marked contrast, the sclerotome is restricted and the myotome will produce muscle characteristic of its new location.

Intervertebral discs

Vertebral centra are derived from caudal and cranial sclerotomal halves. An intervertebral disc is formed from the free somitocoele cells within the epithelial somite that migrate with the caudal sclerotomal cells and from notochordal cells. Genetic labelling experiments in the mouse embryo indicate that notochordal cells act as embryonic precursors to all cells found within the nucleus pulposus of the mature intervertebral disc (McCann et al 2012). The sclerotomal mesenchyme that forms the centra of the vertebrae replaces the notochordal tissue that it surrounds. The notochord expands between the developing vertebrae as localized aggregates of cells and matrix that form the nucleus pulposus of the intervertebral disc (see Figs 18.8, 18.11). The intermediate part of each perichordal disc, forming the anulus fibrosus, surrounds the nucleus pulposus and differentiates into an external laminated fibrous zone and an internal cuff that lies next to the nucleus pulposus: the inner zone contributes to the growth of the outer. In human embryos, the growth rate of the vertebral bodies is such that the volume increases three times between stage 17 and postfertilization week 10, whereas the intervertebral discs show little volume increase until stage 23, after which their growth rate increases to match that of the vertebral bodies (Mekonen et al 2017).

The original sclerotomes are coextensive with the individual metameric body segments. Each sclerotomic fissure, perichordal disc and maturing intervertebral disc lies opposite the centre of each corresponding segment (somite). It follows therefore that the discs correspond in level to, and form the ventral boundaries of, the intervertebral foramina and their associated mixed spinal nerves, ganglia, vessels and sheaths. The foramina are bounded by the capsules of the synovial facet joints dorsally; the rims of the vertebral notches of adjacent vertebrae lie cranially and caudally. All the structures listed (and other associated structures) are therefore often designated segmental, whereas vertebral bodies are designated intersegmental. (For further discussion of resegmentation theories, see Müller and O'Rahilly (1986), Huang et al (2000) and Ward et al (2017).)

Development of vertebrae

The initial movements of sclerotomal cells round the neural tube and the expression of type II collagen signal the blastemal stage of vertebral development (see Fig. 18.11). In human embryos, vertebral bodies consist of loose mesenchyme until stage 17, and intervertebral discs are composed of dense mesenchyme continuous with the neural processes. Both mesenchymal populations show cartilage differentiation from stage 18. Each centrum chondrifies from one cartilage anlage. Each half of a neural arch is chondrified from a centre, starting in its base and extending dorsally into the laminae and ventrally into the pedicles, to meet, expand and blend with the centrum. There are 33 or 34 cartilaginous vertebrae by stage 23, but the spinous processes have not yet developed and so the overall appearance is of total spina bifida occulta. Fusion of the spines starts in the thoracic region at postfertilization week 9 and is seen in the sacral region by postfertilization week 15. For details of neural arch closure at all vertebral levels see Mekonen et al (2017). The transverse and articular processes are chondrified in continuity with the neural arches. Intervening zones of mesenchyme that do not become cartilage mark the sites of the facet joints and the complex of costovertebral joints, within which synovial cavities later appear.

A typical vertebra is ossified from three primary centres, one in each half-vertebral arch and one in the centrum (see Fig. 46.34). Centres in arches appear at the roots of the transverse processes and ossification spreads backwards into laminae and spines, forwards into pedicles and posterolateral parts of the body, laterally into transverse processes, and upwards and downwards into articular processes. Conventionally, centres in vertebral arches are said to appear first in upper cervical vertebrae and then in successively more distal vertebrae, reaching lower lumbar levels by about postmenstrual week 12. However, a radiographic study of unsexed human fetuses found a pattern that differed from such

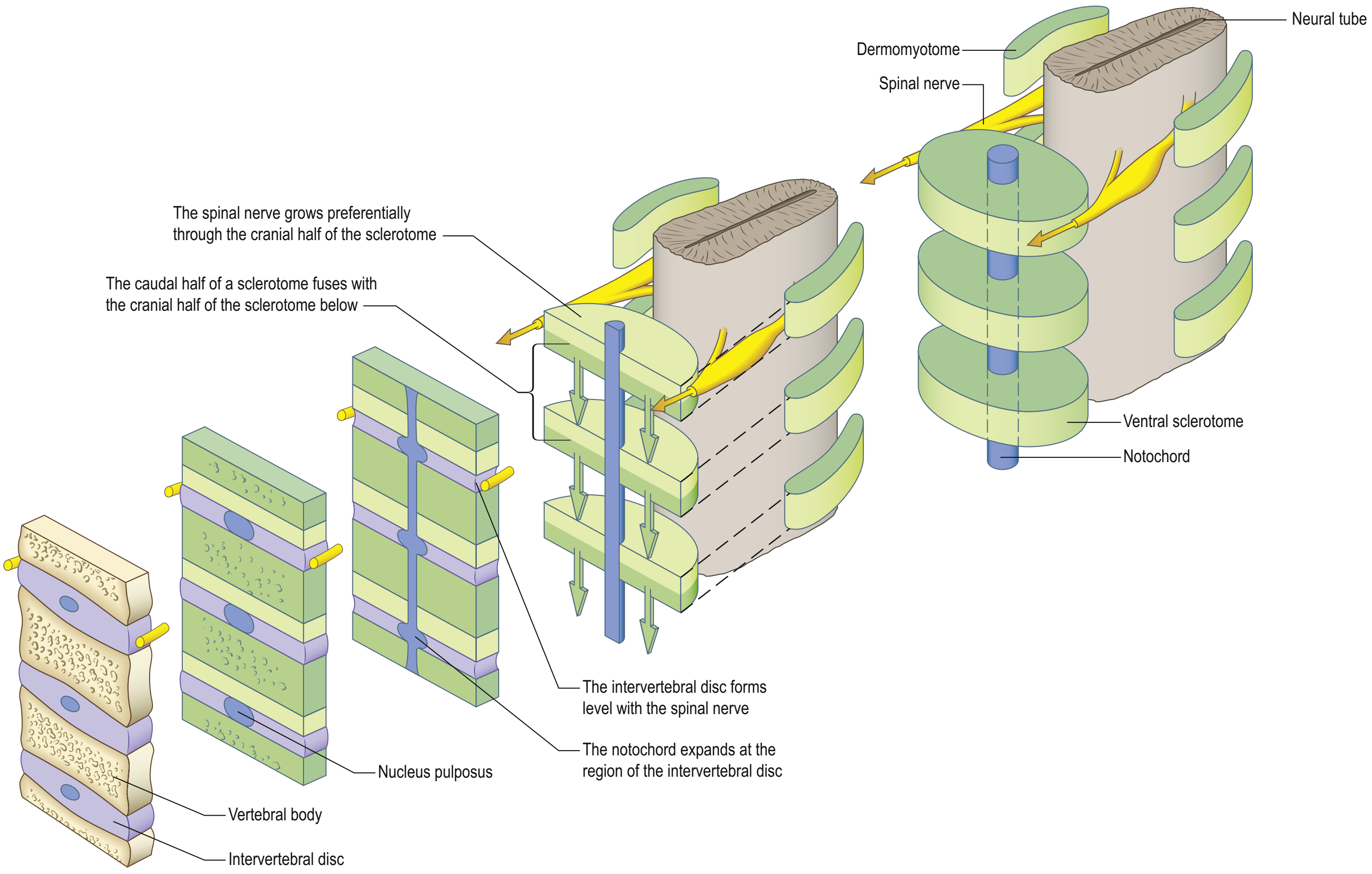
Neural tube
Dermomyotome
Spinal nerve
The spinal nerve grows preferentially through the cranial half of the sclerotome
The caudal half of a sclerotome fuses with the cranial half of the sclerotome below
Ventral sclerotome
Notochord
The intervertebral disc forms level with the spinal nerve
The notochord expands at the region of the intervertebral disc
Nucleus pulposus
Vertebral body
Intervertebral disc

Fig. 18.8 The formation of vertebrae and intervertebral discs from the mesenchymal sclerotomes. Each vertebra is formed from the cranial half of one bilateral pair of sclerotomes and the caudal half of the next pair of sclerotomes.

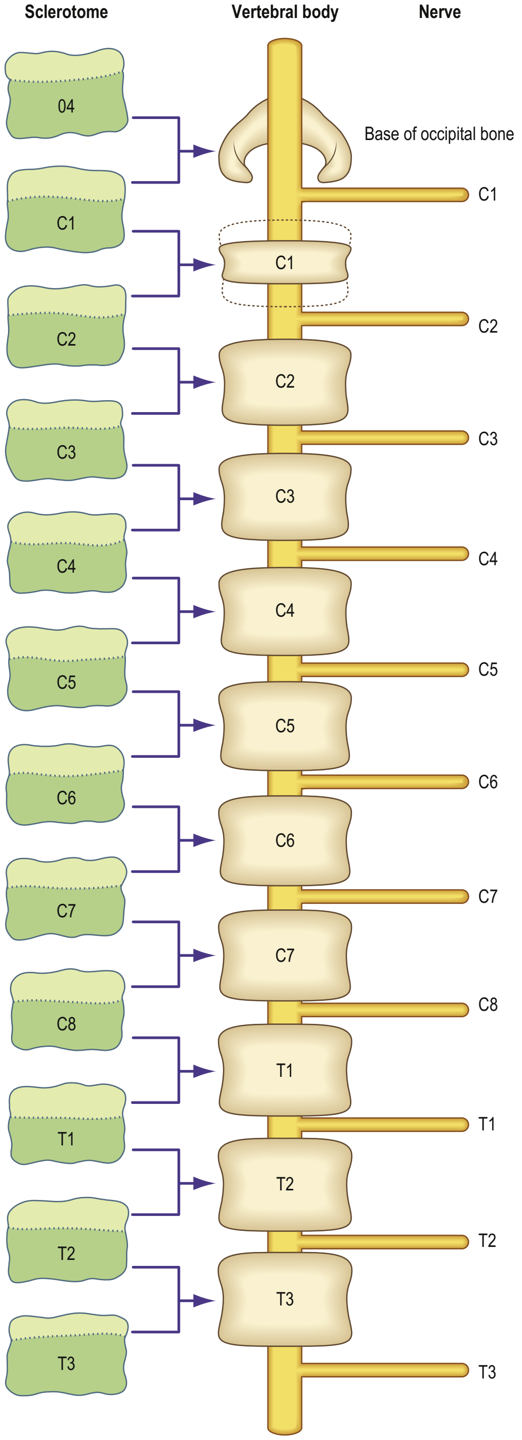

Fig. 18.9 The contribution of the somites to the vertebrae. Each somite induces a ventral root to grow out from the spinal cord. When the sclerotomes recombine, the cranial half of the first cervical sclerotome fuses with the occipital sclerotome above contributing to the occipital bone of the skull. The cervical nerves, beginning with C1, exit above the corresponding vertebra. Nerve C8 exits below the seventh cervical vertebra (C7), and thereafter nerves arise below their numbered vertebrae. (With permission from Larsen WJ 1997 Human Embryology, 2nd ed. Edinburgh: Churchill Livingstone.)

a simple craniocaudal sequence. Centres first appeared in the lower cervical/upper thoracic region, quickly followed by others in the upper cervical region. After a short interval, a third group appeared in the lower thoracolumbar region and remaining centres then appeared, spreading regularly and rapidly in craniocaudal directions (Bagnall et al 1977).

The major part of the vertebral body, the centrum, ossifies from a primary centre dorsal to the notochord. Centra are occasionally ossified from bilateral centres that may fail to unite. Suppression of one of these produces a cuneiform vertebra (hemivertebra), one cause of lateral spinal curvature (scoliosis). At birth and during the early postnatal years the centrum is connected to each half-neural arch by a synchondrosis or neurocentral joint. In thoracic vertebrae, costal facets on the bodies are posterior to neurocentral joints.

During the first year, the arches unite first in the lumbar region and then throughout the thoracic and cervical regions. In typical upper cervical vertebrae, centra unite with arches during year 3, but union is not complete in lower lumbar vertebrae until year 6. The upper and lower surfaces of the bodies and apices of the transverse and spinous processes are cartilaginous until puberty, at which time five secondary centres appear: one in the apex of each transverse and spinous process and two anular epiphyses (ring apophyses) for the circumferential parts of the upper and lower surfaces of the vertebral body. Costal articular facets are extensions of these anular epiphyses and they fuse with the rest of the bone at about 25 years. There are two secondary centres in bifid cervical spinous processes. Exceptions to this pattern of ossification are described in the appropriate subsections in Chapter 46.

Occipitocervical junction

In humans, the occipitocervical (craniovertebral, spinomedullary) junction between the head and neck is placed at the boundary between the fourth and fifth somites (Müller and O'Rahilly 1994, 2003, Hita-Contreras et al 2014). At stage 12 it is identified by the presence of hypoglossal nerve rootlets (**Fig. 18.12A**) and at stages 14–15 it lies between the hypoglossal rootlets and the first spinal ganglion (**Fig. 18.12B–C**). In avian embryos, where all embryonic stages may be obtained experimentally, the occipitocervical boundary occurs within the fifth somite (Wilting et al 1995). The onset of avian sclerotome formation in occipital and upper cervical somites is initiated simultaneously in multiple somites and occurs later than at thoracolumbar levels, in contrast to the serial cranial to caudal progression of somite maturation in the trunk (Maschner et al 2016).

The segmental pattern present in the development of the somites can be seen rostrally in the developing skull base. Occipital somites are rostral to the first cervical nerve (see Fig 17.7). The first somite, defined by its position caudal to the vagal neural crest or ganglion, can be seen between stages 9–12. Mesenchymal condensations equivalent to the centra of occipital somites 2, 3 and 4 become apparent and form the basiocciput. Occipital sclerotomes 3 and 4 are the most distinct at stage 14, by which time the first three sclerotomes have fused. The hypoglossal rootlets pass through the less dense portion of occipital sclerotome 4, accompanied by the hypoglossal artery. Occipital sclerotome 4 forms an incomplete centrum axially and exoccipital elements laterally. Exoccipital elements are regarded as corresponding to neural arches and they form the rim of the foramen magnum. The occipital condyles develop from the cranial part of sclerotome 5, derived from the first cervical somite. The centra of occipital segments 1–4 are fused by stage 15 in the human embryo and form the basiocciput. The dorsocranial boundary of the foramen magnum is formed by stage 23 (Mekonen et al 2017).

In the occipitocervical junctional region, the centra formed from sclerotomes 5, 6 and 7 have a different fate from those more caudally placed, whereas the lateral portions of these sclerotomes generally develop similarly to those of lower ones. In a study of occipitocervical segmentation in human embryos, Müller and O'Rahilly designated the three complete rostral centra that develop in the atlanto-axial region X, Y and Z (**Fig. 18.13**; Müller and O'Rahilly 1986, 2003). They noted that the height of the XYZ complex is equal to that of three centra elsewhere. X is on the level of sclerotome 5, and Y and Z are in line with sclerotome 6 and with the less dense portion of sclerotome 7. During stage 17 a temporary intervertebral disc appears peripherally between Y and Z. It begins to disappear in stage 21, although remnants may be found in the adult. No disc develops between X and Y. The origin of the anterior arch of the atlas is unclear: it is evident at stages 21–23 at the level of X or, sometimes, between X and Y. The posterior arch of the atlas arises from the dense area of sclerotome 5 at the level of X. The XYZ complex belongs to the axis, which means that the atlas does not incorporate a part of the central column (Müller and O'Rahilly 1994). The posterior arch of the axis arises from the dense area of sclerotome 6 and is at the level of Y and Z, particularly Z. XYZ correspond to the three parts of the median column of the axis, where X represents the tip of the dens, Y represents the base of the dens, and Z represents the centrum of the axis. The latter differs from other cervical vertebrae in that it is thicker and square-shaped. A review of the development and associated anomalies of this region is given in Shoja et al (2018).

Most defects of the atlas do not contribute to abnormal occipitocervical anomalies and are not associated with basilar invagination. Abnormalities of the axis are usually concerned with fusion of the dens with the centrum of the second cervical sclerotomes. Using the classification of the three complete centra that develop in the atlanto-axial region as X, Y and Z (Müller and O'Rahilly 1986, 2003), failure of fusion of X with the YZ complex produces an ossiculum terminale, a

The bony elements of the occipitocervical junction may be thought of as a central pillar (basiocciput and dens of the axis) surrounded by two rings (the rim of the foramen magnum and occipital condyles superiorly, and the anterior and posterior arches of the atlas inferiorly). Bony anomalies involving this embryologically complex region may produce altered, unstable anatomical relationships that result in the compression of underlying neural and/or vascular structures and may also compromise cerebrospinal fluid dynamics (Menezes 2008, Pang and Thompson 2011, 2014). The development of the cervical spine, particularly of the upper cervical vertebrae, is closely related to the development of the basiocciput and exocciput, and anomalous development will affect both regions. For example, abnormal prolapse of the dens into the foramen magnum, a condition termed basilar invagination, has been attributed variously to hypoplasia of the basiocciput, occipital condyles or atlas; deficiencies in the bony arches of the atlas with spreading of the lateral masses; or atlanto-occipital assimilation (Smith et al 2010). Malfusions of the caudal portion of occipital sclerotome 4 and the cranial portion of cervical sclerotome 1 may produce defects of the occipital condyles. The pro-atlas, a transient bony structure derived from the fourth occipital sclerotome, usually fuses with the three upper occipital sclerotomes to form the occipital bone and the dorsal part of the foramen magnum. Very rarely, remnants of the pro-atlas persist into adult life: several malformations and anomalies of the most caudal of the occipital sclerotomes have been attributed to failures of pro-atlas segmentation (Menezes and Fenoy 2009, Muhleman et al 2012).

Chiari malformation type I (CM-I) is defined radiographically as a displacement of the cerebellar tonsils of 5 mm or more below the foramen magnum in young adults. Classic CM-I is thought to be a congenital anomaly, in which the normally developing hindbrain is compressed within a hypoplastic posterior cranial fossa, forcing the cerebellar tonsils down through the foramen magnum. Patients with classic CM-I have a characteristically shallow posterior cranial fossa, particularly below Twining's line (a line joining the tuberculum sellae and internal occipital protuberance). Basioccipital shortness means that the foramen magnum is constricted transversely; the suggested pathogenesis is premature stenosis of the basi-exoccipital and exosupra-occipital synchondroses (Milhorat et al 2010). Tonsillar herniation is aetiologically heterogeneous and there are many causes that do not appear to be related to skull-base hypoplasia; CM-I can occur in association with disorders that appear to be unrelated to skull-base hypoplasia and may be acquired (Tubbs et al 2007).

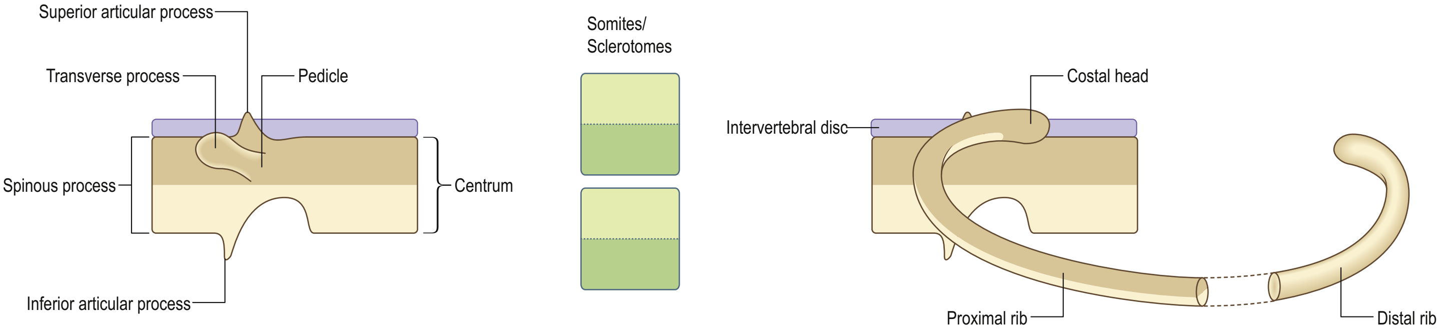

Fig. 18.10 The contribution of two adjacent somites to one vertebra and rib. The intervertebral disc and the costal head are derived from somitocoele cells from one somite, which migrate with the caudal half of the sclerotome. The proximal rib is formed from caudal and cranial somite halves with no mixing of cells; in the distal rib, there is more mixing of cranial and caudal cells as segmentation diminishes in the ventral body wall. (Redrawn with permission from Christ B, Huang R, Wilting J 2000 The development of the avian vertebral column. Anat Embryol (Berl) 202:179–94.)

dissociated apical odontoid epiphysis. Failure of fusion of the XY complex with Z at the dentocentral synchondrosis, or maintenance of the transitory intervertebral disc at this point, produces an os odontoideum, thought to be induced by excessive movement at the time of ossification of the dens (Crockard and Stevens 1995). Hypoplasia and aplasia of the X and Y centra, and aplasia of the Z centrum, will all lead to a reduced size of the dens: there are widely differing views about whether this will lead to atlanto-axial instability. For further details of the development of the human craniovertebral joints and associated ligaments, see Hita-Contreras et al (2014).

Third to seventh cervical vertebrae

The vertebral arches appose by postfertilization week 10 in the human embryo. In cervical vertebrae 3–7, the transverse process is dorsomedial to the foramen transversarium (see Fig. 18.13). The costal process, corresponding to the head, neck and tubercle of a rib, limits the foramen ventrolaterally. The distal parts of these cervical costal processes do not usually develop, but do so occasionally in the case of the seventh cervical vertebra, and may even develop costovertebral joints: these cervical ribs may reach the sternum (Ch. 20). Shifts of axial identity may also occur at more caudal levels, e.g. between lumbar and sacral vertebrae, and are based on expression anomalies of *Hox* genes, known as homeotic transfomations (Scaal 2016).

The seventh cervical vertebra is transitional in shape between typical cervical and thoracic vertebrae. The laminae are longer than other cervical vertebrae in the neonate and lie almost perpendicular to the basal plane; the inferior articular facets are more upright, and resemble those of thoracic vertebrae; and, in the lateral view, the superior articular facets extend transversely to the top of the transverse processes.

Anomalies of the lower cervical vertebrae are generally caused by inappropriate cervical vertebral fusion, collectively termed Klippel–Feil syndrome. This term includes all congenital fusions of the cervical spine, from two segments to the entire cervical spine. Affected individuals have a low posterior hairline, short neck and limitations of head and neck movement. Scoliosis and/or kyphosis is common. In both humans and mice these phenotypes have been linked to loss of expression of the homeobox gene *Meox1* (Mohamed et al 2013).

Thoracic vertebrae

At stage 23 the neural processes of thoracic vertebrae are short, slightly bifurcated and joined by collagenous fibres, the transverse processes are prominent and the three facets for articulation with the ribs at the costovertebral and costotransverse joints are present. At postfertilization week 9, the thoracic vertebral arches are the first to close (Mekonen et al 2017). In the neonate, the thoracic neurocentral and posterior synchondroses are not fused: the posterior synchondroses close within 2–3 postnatal months, and the neurocentral synchondroses remain open until 5–6 postnatal years. In general, the thoracic spine develops ahead of the cervical and lumbar spine. From postfertilization week 9, ossification begins in the cartilaginous vertebrae in a craniocaudal progression.

Ribs

Ribs usually develop in association with the thoracic vertebrae and can be identified in stage 15 embryos. Occasionally, they can arise from the seventh cervical and first lumbar vertebrae, associated with ectopic *Hox* gene expression (homeotic transformation).

The costal processes attain their maximum length as the ribs in the thoracic region. Each rib originates from lateral sclerotomal populations and forms from the caudal half of one sclerotome and the cranial half of the next subjacent sclerotome (see Fig. 18.10). The head of the rib develops from somitocoele cells from one somite that migrate with the caudal half of the sclerotome. The proximal portion of the rib forms from both caudal and cranial sclerotomal halves but there is no mixing of cells from these origins. The distal portion of the rib forms from caudal and cranial sclerotomal halves and these cells mix as the rib extends into the ventral body wall and segmentation diminishes.

The ribs arise anterolaterally from the ventral part of the pedicles and form bilateral costal processes that expand to meet the tips of the transverse processes. As they elongate laterally and ventrally they come to lie between the myotomic muscle plates. In the thorax, the costal processes grow laterally to form a series of precartilaginous ribs (Figs 18.6, 18.11). The transverse processes grow laterally behind the vertebral ends of the costal processes, at first connected by mesenchyme that later becomes differentiated into the ligaments and other tissues associated with the costotransverse joints. The capitular costovertebral joints are similarly formed from mesenchyme between the proximal ends of the costal processes and the perichordal disc, and the adjacent parts of two (sometimes one) vertebral bodies, derived from the neural arch. Ribs 1–7 (vertebrosternal) curve round the body wall to reach the developing sternal plates. Ribs 8–10 (vertebrochondral) are progressively more oblique and shorter, only reaching the costal cartilage of the rib above, and contributing to the costal arch. Ribs 11–12 are free (floating), and have cone-shaped terminal cartilages to which muscles become attached. For clear images of rib development in the human embryo and fetus see Mekonen et al (2015, 2016).

Lumbar vertebrae

The ribs do not develop distally in lumbar vertebrae (see Fig. 18.11). Their proximal parts become the 'costal processes', while the morphologically true transverse processes may be represented by the accessory processes of the vertebrae. Occasionally, movable ribs may develop in association with the first lumbar vertebra. Lumbar intervertebral discs are thicker than thoracic discs. By stage 23 the peripheral part of the anulus fibrosus can be seen, and the notochordal cells are expanding internally to form the nucleus pulposus.

Sacrum

Sacral vertebrae have lower centra and are narrower overall from side to side than their thoracic and lumbar counterparts. Each sacral vertebra is composed of a centrum and bilateral neural processes. O'Rahilly et al (1990) divided the neurocentral junctional area into two parts, anterolateral or alar and posterolateral, and found the alar element in sacral vertebra 1 to be novel, because it was absent in lumbar vertebra 5. There is support for this view if the course of the dorsal rami of the spinal nerves is used to distinguish the costal elements ventrally from the transverse elements dorsally. The alar elements of the sacral vertebrae are ventral to the sacral dorsal rami, and both costal and transverse portions are posterolateral. The alar element of S1 and S2 forms the auricular surface of the sacrum. At stage 23 the cartilaginous sacral vertebrae have joined and the outline of the future bone can be recognized. Individual pedicles and laminae are very small and can be detected in S3–S5. For images of the closure of the sacral vertebral canal see (Mekonen et al 2017).

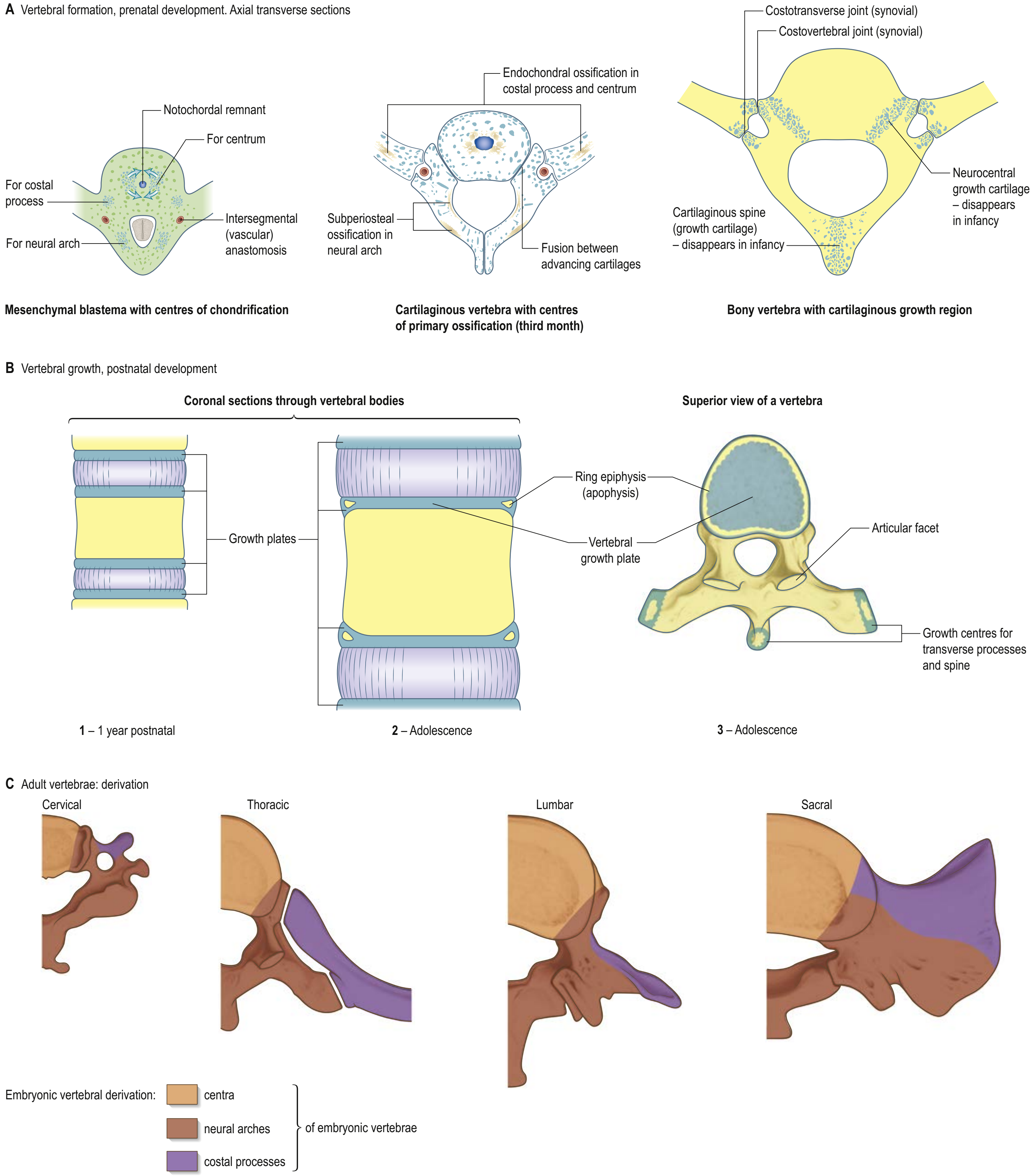
A Vertebral formation, prenatal development. Axial transverse sections
Notochordal remnant
For centrum
For costal process
For neural arch
Intersegmental (vascular) anastomosis
Mesenchymal blastema with centres of chondrification
Endochondral ossification in costal process and centrum
Subperiosteal ossification in neural arch
Fusion between advancing cartilages
Cartilaginous vertebra with centres of primary ossification (third month)
Costotransverse joint (synovial)
Costovertebral joint (synovial)
Cartilaginous spine (growth cartilage) – disappears in infancy
Neurocentral growth cartilage – disappears in infancy
Bony vertebra with cartilaginous growth region
B Vertebral growth, postnatal development
Coronal sections through vertebral bodies
Growth plates
Ring epiphysis (apophysis)
Vertebral growth plate
Superior view of a vertebra
Articular facet
Growth centres for transverse processes and spine
1 – 1 year postnatal
2 – Adolescence
3 – Adolescence
C Adult vertebrae: derivation
Cervical
Thoracic
Lumbar
Sacral
Embryonic vertebral derivation:
centra
neural arches
costal processes
of embryonic vertebrae

Fig. 18.11 **A–B**, Vertebral development through blastemal, cartilaginous and pre- and postnatal stages of ossification. **C**, The derivation of the principal morphological parts of adult vertebrae.

Ossification of the vertebral column proceeds in a craniocaudal direction and after postmenstrual week 16, it has progressed to L5. Ossification of each additional vertebra occurs over a period of 2–3 weeks; S2 is ossified by postmenstrual week 22.

The sacral vertebrae are derived by secondary neurulation processes from the caudal eminence. All tissues of the caudal region of the embryo are produced in this way and can lead to anomalies of the sacrum, pelvis, cloacal region and urogenital and enteric sphincters. Very rarely, anomalous sacral or lumbosacral vertebrae may develop, often in association with a maternal history of diabetes. When there is sacral agenesis, motor paralysis is profound below the affected vertebral level, whereas the sensory disturbance does not relate to the vertebral level so closely, and sensation may be present down to the knees. Urinary bladder involvement is a consistent feature. In cloacal anomalies and cases of classic bladder exstrophy, a range of dimensional and rotational anomalies are seen (Ch. 22). The sacrum is larger with approximately 25% more surface area and 40% larger total volume. Sacroiliac joint angles are 10° larger, i.e. more toward the coronal plane than normal, and the bony pelvis has more inferior rotation than normal. 3D CT imaging has demonstrated a range of previously unknown rotational anomalies (Ch. 19) (Gearhart and Mathews 2016).

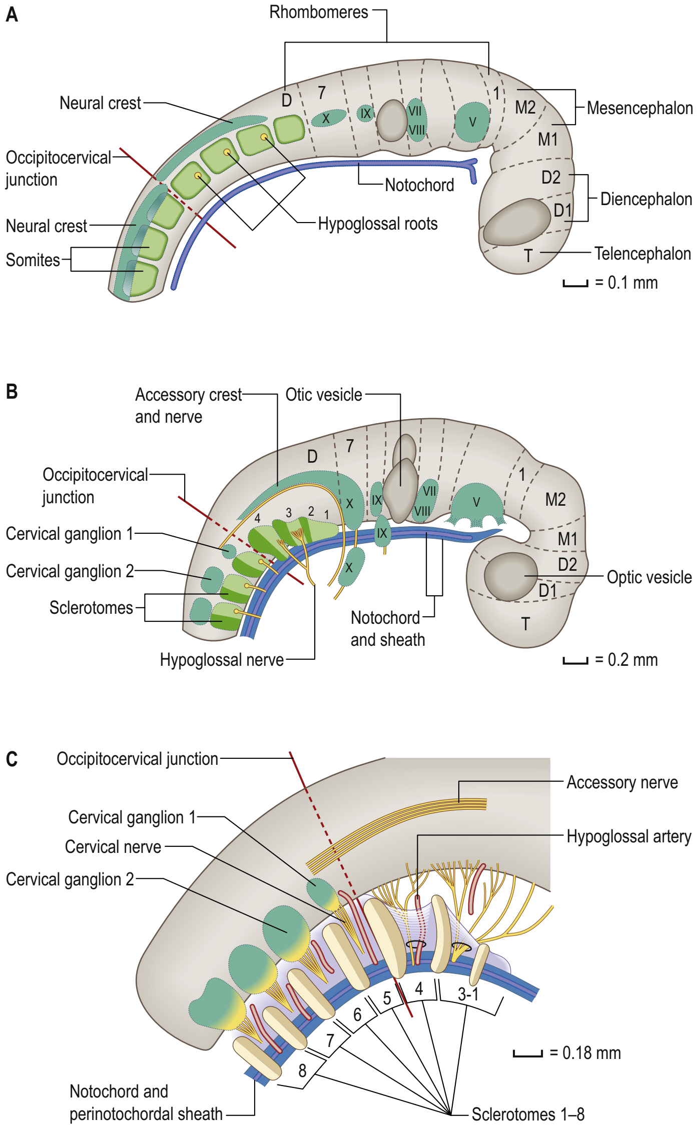
A
Rhombomeres
Neural crest
Occipitocervical junction
Neural crest
Somites
D
7
X
IX
VII
VIII
V
1
M2
Mesencephalon
M1
Notochord
D2
Diencephalon
D1
Hypoglossal roots
T
Telencephalon
= 0.1 mm
B
Accessory crest and nerve
Otic vesicle
Occipitocervical junction
Cervical ganglion 1
Cervical ganglion 2
Sclerotomes
Hypoglossal nerve
Notochord and sheath
D
7
1
4
3
2
1
X
IX
VII
VIII
V
M2
M1
D2
D1
Optic vesicle
T
= 0.2 mm
C
Occipitocervical junction
Cervical ganglion 1
Cervical nerve
Cervical ganglion 2
Accessory nerve
Hypoglossal artery
8
7
6
5
4
3-1
= 0.18 mm
Notochord and perinotochordal sheath
Sclerotomes 1–8

Fig. 18.12 Reconstructions of the occipitocervical region of human embryos. **A**, Stage 12: occipital somites innervated by hypoglossal fibres (small yellow circles). Three cervical somites are shown. The crest-derived ganglia of cranial nerves V, VII, VIII, IX and X are shown in green. Neural crest associated with the occipital somites is hypoglossal and perhaps accessory (also shown in green). **B**, Stage 14: the somites have transformed into sclerotomes and moved ventrally. The less dense cranial and dense caudal parts of the sclerotomes and occipital sclerotomes 1–4 are indicated. Hypoglossal fibres and cervical ventral rami migrate through the less dense parts of the sclerotomes. The occipital neural crest is now seen to be mostly accessory. The cervical crest is subdivided into spinal ganglia. A perinotochordal sheath can be seen extending rostrally to the termination of the notochord. **C**, Stage 15: the dense parts of sclerotomes 1–8 are shown. Intersegmental arteries are visible in the less dense areas of the sclerotomes, as are the spinal nerve fibres. In all diagrams, the occipitocervical junction is indicated by the red line. (After Müller F, O'Rahilly R 1994 Occipitocervical segmentation in staged human embryos. J Anat 185: 251–8, with permission from Blackwell Publishing.)

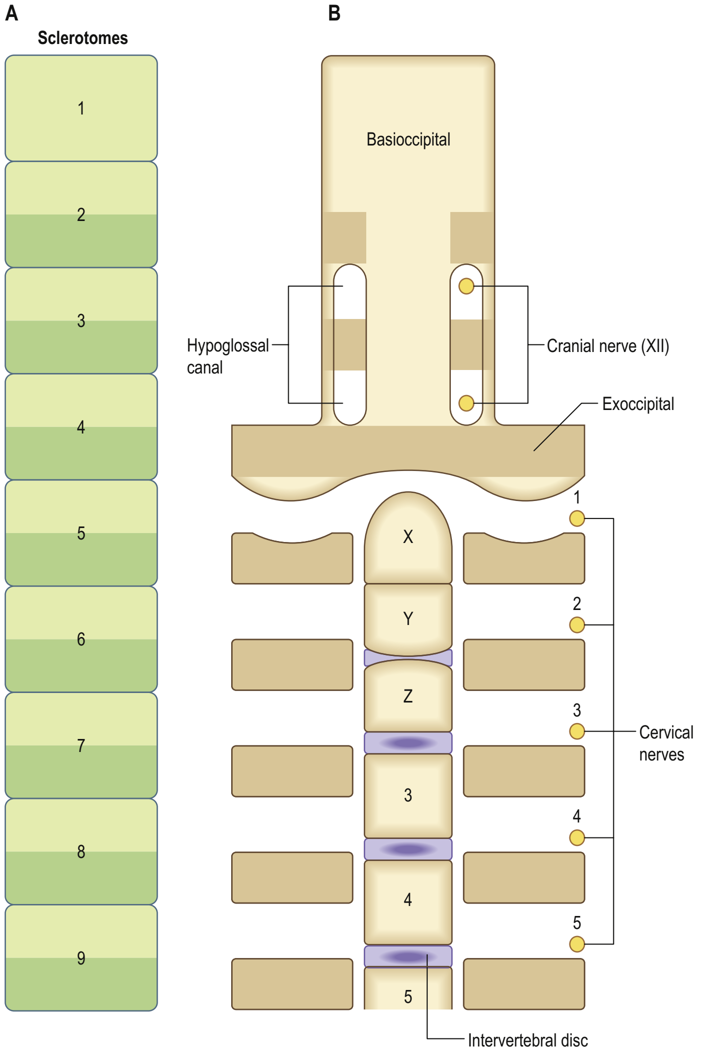
A
Sclerotomes
1
2
3
4
5
6
7
8
9
B
Basioccipital
Hypoglossal canal
Cranial nerve (XII)
Exoccipital
1
X
2
Y
Z
3
Cervical nerves
3
4
4
5
5
Intervertebral disc

Fig. 18.13 The relationship between the centra and neural arches of the vertebrae and the related spinal ganglia and nerves. A scheme of the details of the early development of the occipitocervical region. **A**, The column of sclerotomes from occipital somite 1. **B**, A dorsal view of the developing vertebrae, with the centra in the middle and the bilateral components of the neural processes laterally. X, Y and Z are three centra that will produce the tip of the dens of the axis (X), the base of the dens of the axis (Y) and the centrum of the axis (Z). An intervertebral disc appears temporarily between Y and Z during stage 17. No disc develops between X and Y. The occipital condyles are derived from the first cervical sclerotome. (After Müller F, O'Rahilly R 1994 Occipitocervical segmentation in staged human embryos. J Anat 185: 251–8, with permission from Blackwell Publishing.)

Spina bifida

Spinal dysraphism is a generic term covering a wide range of developmental anomalies of the vertebral column and spinal cord, characterized by a failure of fusion of midline structures (Sepulveda et al 2012). The spectrum of defects includes non-fusion of the entire neural tube with no vertebral arch development (craniorachischisis); non-fusion of the rostral portion of the neural tube with no calvarial or occipital development (anencephaly); and non-fusion of caudal portions of the neural tube and local failure of vertebral arch development (spina bifida) (see Fig. 14.3; Figs 18.14–18.16). Spina bifida may be obvious at birth or before (e.g. spina bifida cystica and spina bifida aperta), or not obvious at birth (spina bifida occulta). Spina bifida cystica occurs where the meninges have developed adjacent to or over the defective neural tissue. Local accumulation of cerebrospinal fluid may push a defective neural plaque or spinal cord superficial to the level of the vertebrae, so forming a meningomyelocele. Alternatively, if one or two spinous processes are absent, a meningeal sac may protrude in the midline above a formed spinal cord, producing a meningocele. In spina bifida aperta, the exposed spinal cord has no cystic covering, although it may be covered by thin membranes. Meningomyelocele occurs in thoracolumbar, lumbar or lumbosacral regions; sacral lesions are less common. The vertebral lesion usually extends cranially further than the neural lesion, with deformities of the vertebral bodies and laminae. Vertebrae may be wedge-shaped or hemivertebrae, and ribs may be fused or absent. In spina bifida occulta, dysraphism primarily affects the vertebrae; the neural and meningeal elements are not herniated to the surface and so the underlying defects are masked by the skin. This closed form of spina bifida affects about 5% of the population and usually occurs in the lumbosacral or sacral segment. Affected individuals have bifid spinous processes often at the lumbosacral junction and there may also be a pigmented naevus, angioma, hirsute patch, dimple or dermal sinus on the overlying skin.

Tethering of the cord and diastematomyelia

Available with the *Gray's Anatomy* e-book

Ultrasound antenatal imaging of the back

Antenatal ultrasound assessment of the fetal spine at postmenstrual weeks 18–20 routinely assesses the three ossification centres of each vertebra (in the centrum and bilaterally at the lamina–pedicle

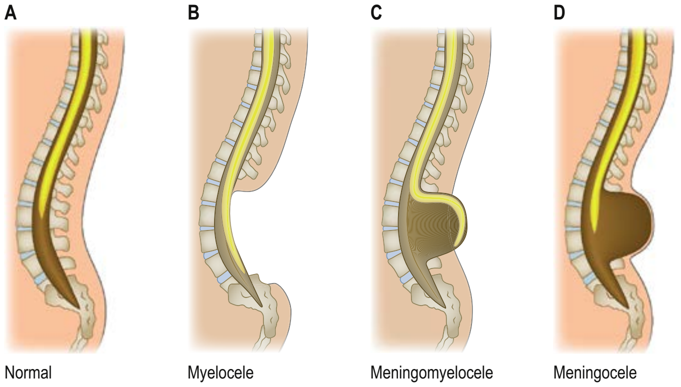

Fig. 18.14 The spectrum of spina bifida. **A**, Intact neural tube. **B**, Open spina bifida – myelocele. **C**, Open spina bifida – myelomeningocele. **D**, Closed spina bifida with meningocele. (Redrawn with permission from Tulio G et al Neural tube defects: craniorachischisis and spina bifida. In: Copel J (ed) Obstetric Imaging (Expert Radiology Series). Elsevier. Copyright 2012.)

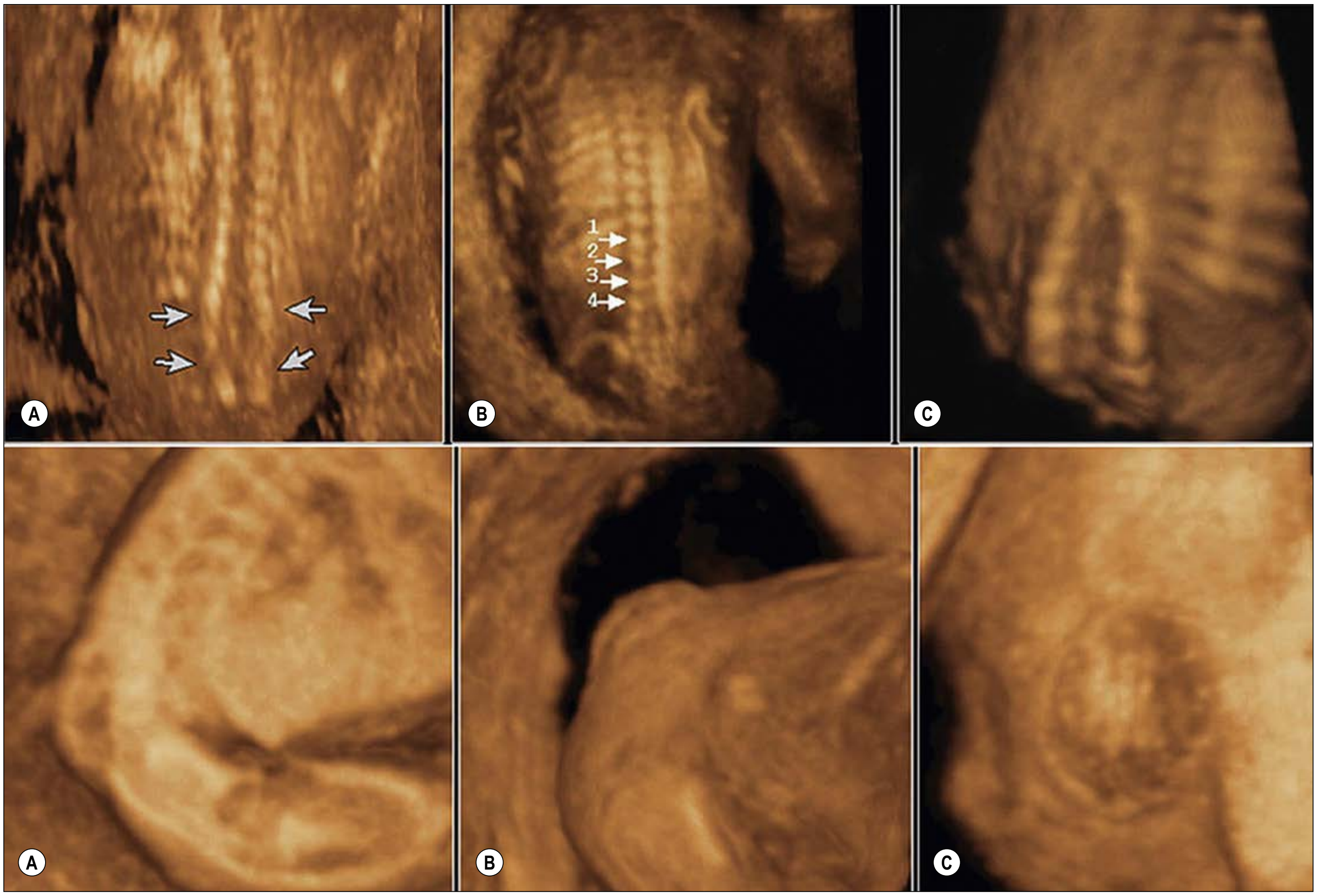

Fig. 18.15 A fetal myelomeningocele. Upper panel: three-dimensional ultrasound maximum transparency mode shows the spinal defect in the coronal (**A** and **B**) and oblique (**C**) views. Arrows in **A** depict the vertebral dysraphism. The level of the defect can be clearly established (numbers 1 to 4 in **B** show the lumbar vertebrae). Lower panel: three-dimensional ultrasound surface rendering mode shows the spinal defect in the sagittal (**A** and **B**) and coronal (**C**) views. (With permission from Sepulveda W, Ximenes R, Wong AE et al 2012 Fetal magnetic resonance imaging and three-dimensional ultrasound in clinical practice: applications in prenatal diagnosis. Best Pract Res Clin Obstet Gynaecol 26:593–624.)

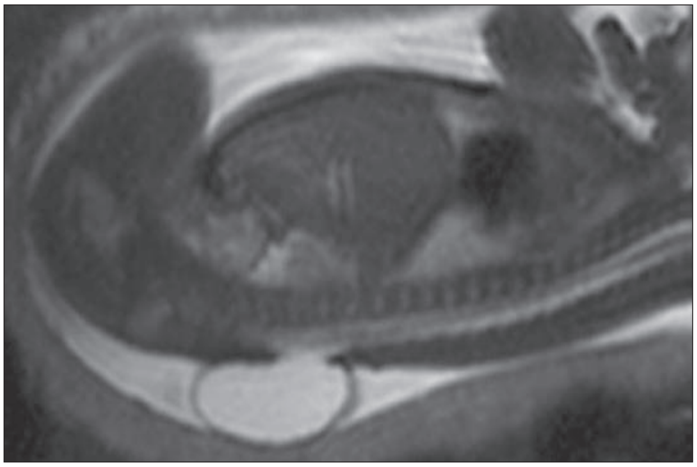

Fig. 18.16 A fetal magnetic resonance image shows a lumbar myelomeningocele in sagittal section. (With permission from Sepulveda W, Ximenes R, Wong AE et al 2012 Fetal magnetic resonance imaging and three-dimensional ultrasound in clinical practice: applications in prenatal diagnosis. Best Pract Res Clin Obstet Gynaecol 26:593–624.)

Prior to antenatal diagnosis of spina bifida by ultrasonography, most live births with spina bifida cystica had a meningomyelocele. Prenatal diagnosis of meningomyelocele and termination of affected fetuses have resulted in a significant decrease in the incidence of live births with this condition. Individuals with postnatal spina bifida repair are considered to be affected not only by the initial neurulation failure but also by the secondary effects of loss of cerebrospinal fluid into the amniotic fluid and the progressive damage to neural tissue caused by exposure to amniotic fluid. Nearly all neonates with the condition have Arnold-Chiari II malformation and over 90% will develop hydrocephalus requiring ventriculoperitoneal shunting (Saadai and Farmer 2012). Clinical trials of fetal meningomyelocele repair, between postmenstrual weeks 23–25, have found decreased hindbrain herniation after elective caesarean delivery at postmenstrual week 37 and reduction in the postnatal incidence of ventriculoperitoneal shunt-dependent hydrocephalus (Moldenhauer and Adzick 2017). The multidisciplinary surgical procedures involved are complex and not without risk to the mother (Asch and Sauerbrei 2018).

The greatest change of vertebral length occurs within the second and third trimesters. During the second trimester, the rapid relative growth of the vertebral column compared to the spinal cord results in a rostral displacement of the caudal end of the spinal cord from the second coccygeal vertebra to the third lumbar vertebra by postmenstrual week 25 (Ch. 14). When there is any degree of spina bifida, the upward movement of the caudal end of the spinal cord is limited, and the cord is said to be tethered. In neonates, neurological deficits caused by this condition become apparent soon after birth; some individuals may show degrees of urinary dysfunction later in life. Very rarely, tethering symptoms may be associated with abnormal development of the vertebral centra, e.g. when a midline cartilaginous or osseous spicule or a fibrous septum projects into the vertebral canal. These obstacles may split the spinal cord or intraspinal nerve roots into two columns, a condition termed diastematomyelia. Usually, patients with this condition have a cutaneous abnormality, such as a dimple, pigmented naevus or patch of hair, along their back at the level of the tethering.

junction), in the axial, coronal and sagittal planes. In the coronal plane, the posterior ossification centres have a characteristic 'railtrack' appearance; the twelfth rib is adjacent to the twelfth thoracic vertebra and the first sacral vertebra is level with the top of the iliac wing. Longitudinal scans of the fetal spine can demonstrate scoliosis and hemivertebrae.

DEVELOPMENT OF DERMOMYOTOMES

The dermomyotome forms from the dorsal half of the early somite and gives rise to all the skeletal muscle in the trunk and limbs and to the intrinsic muscles of the tongue. Muscles in the head arise from the unsegmented paraxial mesenchyme rostral to the occipital somites. The dorsomedial lip (border) of the dermomyotome is an infolding of the epithelial plate of the somite and becomes a proliferative epithelial site from which mediolateral growth of the dermomyotome itself occurs. The neural tube, the notochord/neural floor plate complex and the (early) dorsally placed ectoderm are all required for myogenesis. A balance between levels of Shh from the notochord and Wnts from the dorsal neural tube and ectoderm promotes myogenesis; high levels of either lead to sclerotomal or non-myogenic dermomyotomal development (Scaal and Christ 2004). Myogenic determination factors, MyoD, myogenin, Myf5 and herculin/MRF4, can first be detected in the medial half of the somite as early as stage II in chick embryos, several hours prior to the onset of myotome formation.

The mode of formation of mononucleated, postmitotic, primitive myotubes from the dermomyotome has been elucidated in the chick but not yet confirmed in mammals (Gros et al 2004) (**Fig. 18.17**). In this model, all four borders of the dermomyotome give rise to myotomal cells, produced in two phases. First, cells are produced from the dorsomedial dermomyotomal lip by direct ingression and bidirectional extension. Second, myotomal precursor cells are released by the caudal dermomyotomal border, followed, in turn, by the cranial dermomyotomal border, and lastly, by the ventrolateral dermomyotomal lip. Those myotomal cells arising from the dorsomedial dermomyotomal border contribute cells exclusively to the epaxial domain, while those from the ventrolateral border contribute cells exclusively to the hypaxial domain. The cells arising from the cranial and caudal borders move into both epaxial and hypaxial domains (Scaal and Christ 2004) (see Fig. 18.8). Later in development, proliferative muscle progenitor cells originating from the de-epithelializing dermomyotome contribute to fetal muscle growth (Gros et al 2005).

Epaxial muscle: dorsal trunk muscles

Epaxial muscles arise from the dorsomedial lip of the dermomyotome. Early myotome cells are postmitotic embryonic myoblasts. Later in development, they fuse to form syncytia that produce the intrinsic skeletal muscles of the back. They bridge the early segmental borders and join vertebrae together. The epaxial muscles are innervated by the dorsal rami of each pair of spinal nerves. At later stages, satellite cells originating from the dermomyotome enter the myotome. The mechanism of development of endo-, peri- and epimysium in relation to the epaxial muscles has not been conclusively determined.

The development of epaxial muscle in the human embryo has been studied in staged human embryos. From stage 16 epaxial myotomes merge into a longitudinally continuous muscle mass that extends from the occiput to the second lumbar vertebra. By stage 17 this longitudinal muscle mass has segregated into lateral and medial columns and the medial column further segregates into intermediate and medial columns by stage 18. Development appears to be from lateral to medial and gives rise to all of the intrinsic back muscles. Caudal to the third lumbar vertebra, the epaxial compartment does not develop the same muscle mass columns seen at more proximal levels (Mekonen et al 2016, Warmbrunn et al 2018): the caudal zone of tissues that encompass the lower lumbar and sacral vertebrae is derived by secondary neurulation processes from the caudal eminence and there is no neural plate at these levels (Ch. 14). The ways in which the neural tube, neural crest and splanchnopleuric and somatopleuric mesenchymal populations develop from this caudal zone are not yet clear: it is possible that the developmental patterning processes identified in cervical and thoracic regions do not operate at this level.

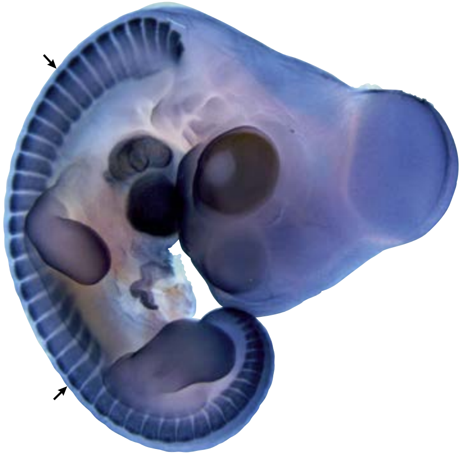

Fig. 18.17 The metameric structure of the myotomes (arrows) of a 5-day-old chick embryo, visualized by whole-mount immunohistochemistry with an antibody staining for myosin heavy chain.

Hypaxial muscle: ventrolateral trunk muscles

Two modes of production of hypaxial musculature are seen, depending on the axial level (see Fig. 18.7). At cervical and trunk levels, myotubes are produced by the ventrolateral edge of the dermomyotome in a manner similar to the production of epaxial muscles. As development proceeds, lateral growth of the dermomyotome means that the ventrolateral border extends ventrolaterally into the developing lateral and ventral body wall, in a process that depends on the homeobox-containing transcription factor Pitx2 (Eng et al 2012). The somite structures that extend into the somatopleure of the abdominal and thoracic walls thus consist of two layers, dermomyotome and myotome, that give rise to the muscle blastemata for the intercostal and abdominal oblique muscles, transversus abdominis and rectus abdominis. The number of somatopleuric mesenchymal cells within the muscle-forming zone increases, and myotubes can be seen for the first time. There is a subsequent ventral shift of the already separated muscle blastemata within the growing abdominal wall as they attain their definitive positions. Muscle differentiation continues and muscular connective tissue, tendons and aponeuroses develop. In the human embryo at stage 15 separate epaxial and hypaxial muscle compartments are evident as the hypaxial muscles extend into the lateral body wall. The interlimb hypaxial musculature is continuous with the musculature of the cervical region and upper limb and caudally extends to the lower boundary of the forming umbilical ring and lower limb mesenchyme (Mekonen et al 2015). Three muscle sheets can be identified by stage 18, corresponding to external abdominal oblique, internal abdominal oblique and transversus abdominis; these layers are homologous throughout mammalia (Hall et al 2017). Between stages 18 and 23 the infra-umbilical region expands caudally, the caudal boundaries of external abdominal oblique, internal abdominal oblique and transversus abdominis extend to the ilium and the cranial boundaries descend 6 body segments to their definitive attachments to the ribs. Rectus abdominis is seen from stage 18. For details of the formation of hypaxial muscles see (Mekonen et al 2015).

At occipital, cervical and limb levels, a ventrolateral dermomyotomal lip is not formed in the same way: cells undergo epithelial to mesenchymal transformation and migrate to their destination. Myoblasts move from the occipital dermomyotomes into the developing mandibular processes to form the intrinsic muscles of the tongue (Ch. 17), and from cervical dermomyotomes into the developing respiratory diaphragm (Ch. 20). Those opposite the early limb buds migrate into the limbs as dorsal and ventral muscle masses that give rise to the shoulder, hip and appendicular muscles (Ch. 19). The muscles of the perineal region are derived from a portion of the ventral muscle mass that migrates into the lower limb and then subsequently migrates back into the cloacal region after cloacal division by the urorectal septum. The muscle masses form layers similar to those in the ventrolateral trunk: the layers are the external anal and urethral sphincters, bulbospongiosus, ischiocavernosus, transverse superficial peroneal muscle and levator ani (Ch. 22). This arrangement is patterned by the local somatopleuric mesenchyme which regulates the extended myotomal sheets of the ventrolateral body wall and gives rise to the associated muscular connective tissues, tendons and aponeuroses (Hall et al 2017). (For a review of dermomyotomal development, see Scaal and Christ (2004).)

Other structures derived from the somites

Dermal precursors arise from the central portion of the dermomyotome and (possibly) from the dorsomedial dermomyotome lip (see Fig. 18.7). The cells undergo an epithelial to mesenchymal transformation, leave the dermomyotome and migrate to the dorsomedial subectodermal

In spina bifida, the posterior ossification centres show abnormal widening in the axial plane; forming a U or V shape, they splay outwards from each other and are no longer parallel. Anomalies of the spine (spina bifida) are among the most common fetal malformations noted on antenatal ultrasound examination (Asch and Sauerbrei 2018). The Northern Congenital Abnormality Survey reported a total prevalence at birth and termination of 17.9 cases/10,000 between 1984 and 1996 in the UK and Ireland, compared with the prevalence in Europe of 11.5 cases/10,000 over the same time period. The prevalence in the years 1991–2012 was estimated to be 12.8 cases/10,000 in England and Wales (19% live births, 81% terminations and 0.5% still birth and fetal deaths at less than postmenstrual week 20). There was little change in prevalence between the years 1998 and 2012 in the UK, whereas in the United States the introduction of mandatory fortification of flour with folic acid in 1998 was followed by a 23% reduction in the occurrence of neural tube defects (Morris et al 2016).

space overlying the dorsal neural tube. Their transformation seems to be controlled by factors from the neural tube. There is a sharp boundary between dermis that is somite-derived (covering the back) and that which is derived from the somatopleuric mesenchyme of the lateral plate (covering the limbs, part of the lateral and all of the ventral body wall).

Somitic cells are now considered to give rise to smooth muscle cells within and around the developing somites and within the tunica media of the descending aorta (Wiegreffe et al 2007). All compartments of the epithelial somite, including the somitocoele cells, give rise to angioblasts. The early ventral half of the somite gives rise to the endothelium of ventrolateral blood vessels. Angioblastic cells arising from the dorsomedial dermomyotome migrate mainly into the dorsal dermis, whereas those arising from the dorsolateral part move to the ventrolateral body wall and limbs (Scaal and Christ 2004, Christ et al 2007).

Bonus e-book content

Fig. 18.14 The spectrum of spina bifida.

Fig. 18.15 Fetal myelomeningocele.

Fig. 18.16 Fetal magnetic resonance image: lumbar myelomeningocele.

Fig. 18.17 The metameric structure of the myotomes of a 5-day-old chick embryo.

Key references

Christ B, Huang R, Scaal M 2004 Formation and differentiation of the avian sclerotome. Anat Embryol (Berl) 208:333–350.

An overview of the formation and different developmental fates of the sclerotome.

Hita-Contreras F, Roda O, Martínez-Amat A et al 2014 Embryonic and early fetal period development and morphogenesis of human craniovertebral junction. Clin Anat 27:337–45.

This paper presents first and early second trimester development of bones, joints and ligaments of the craniovertebral junction.

Mekonen H, Hikspoors JPJM, Mommen G, Köhler SE, Lamers WH 2015 Development of the ventral body wall in the human embryo. J Anat 227:673–85.

Figures 2–7 illustrate in 3D reconstructions, over stages 15–23, the lengthening and medial growth of the ribs and formation of the sternum.

Mekonen H, Hikspoors JPJM, Mommen G, Köhler SE, Lamers WH 2016 Development of the epaxial muscles in the human embryo. Clinical Anat 29:1031–45.

Figures 2, 3, 4, 6, 7 and 8 show 3D reconstructions over stages 15–23 and the formation of epaxial muscle columns.

Mekonen H, Hikspoors JPJM, Mommen G, Kruepunga N, Köhler SE, Lamers WH 2017 Closure in the vertebral canal in human embryos and fetuses. J Anat 231:260–74.

Figures 6 and 7 show the degree of closure of the neural arches of cervical, thoracic, lumbar and sacral vertebrae at postfertilization weeks 7, 8, 9, 10 and 15. The paper also gives details of the components of the occipitocervical junction at postfertilization weeks 7 and 8.

These three papers from Mekonen et al provide accurate embryonic staging, in line with O'Rahilly and Müller (2010), illustrate the conversion of serial histological sections to 3D images using computer software, and compare successive embryonic stages. They present a visual sequence of the 4D changes that take place during complex concurrent morphological changes.

Müller F, O'Rahilly 2003 Segmentation in staged human embryos: the occipitocervical region revisited. J Anat 203:297–315.

This paper clearly demonstrates the craniocervical junction in staged human embryos.

Scaal M, Christ B 2004 Formation and differentiation of the avian dermomyotome. Anat Embryol 208:411–24.

An overview of the development of the dorsal somite compartment into dermis and muscle.

Scaal M 2016 Early development of the vertebral column. Semin Cell Dev Biol 49:83–91.

A comprehensive overview of the early steps of vertebral column formation from segmentation to sclerotomal differentiation.

References

Asch E, Sauerbrei E 2018 The fetal spine. In: Rumack CM, Levine D (eds) Diagnostic Ultrasound, 5th ed. Elsevier; Ch. 35, pp. 1216–42.

Bagnall KM, Harris PF, Jones PRM 1977 A radiographic study of the human spine II. The sequence of development of ossification centres in the vertebral column. J Anat 124:791–802.

Christ B, Huang R, Scaal M 2004 Formation and differentiation of the avian sclerotome. Anat Embryol (Berl) 208:333–50.

An overview of the formation and different developmental fates of the sclerotome.

Christ B, Huang R, Scaal M 2007 Amniote somite derivatives. Dev Dyn 236:2382–96.

An overview of the formation and different developmental fates of the sclerotome.

Crockard HA, Stevens JM 1995 Craniovertebral junction anomalies in inherited disorders: part of the syndrome or caused by the disorder? Eur J Pediatr 154:504–512.

Ebisuya M, Briscoe J 2018 What does time mean in development? Development 145:dev164368. doi: 10.1242/dev.164368.

Eng D, Ma HY, Xu J et al 2012 Loss of abdominal muscle in Pitx2 mutants associated with altered axial specification of lateral plate mesoderm. PLoS 1 7:e42228.

Gasser RF 2006 Evidence that some events of mammalian embryogenesis can result from differential growth, making migration unnecessary. Anat Rec 289B:53–63.

Gearhart JP, Mathews R 2016 Exstrophy-epispadias complex. In: Wein AJ, Kavoussi LR, Partin AW (eds) Campbell-Walsh Urology, 11th ed. Elsevier; Ch. 139.

Gomez C, Ozbudak EM, Wunderlich J et al 2008 Control of segment number in vertebrate embryos. Nature 454:335–9.

Gros J, Scaal M, Marcelle C 2004 A two-step mechanism for myotome formation in chick. Dev Cell 6:875–82.

Gros J, Manceau M, Thomé V et al 2005 A common somitic origin for embryonic muscle progenitors and satellite cells. Nature 435:954–8.

Hall M, Rodriguez-Sosa JR, Plochicki JH 2017 Reorganization of mammalian body wall patterning with cloacal septation. Sci Rep 7:918. doi: 10.1038/s41598-017-09359-y.

Hita-Contreras F, Roda O, Martínez-Amat A et al 2014 Embryonic and early fetal period development and morphogenesis of human craniovertebral junction. Clin Anat 27:337–45.

This paper presents first and early second trimester development of bones, joints and ligaments of the craniovertebral junction.

Huang R, Zhi Q, Brand-Saberi B et al 2000 New experimental evidence for somite resegmentation. Anat Embryol (Berl) 202:195–200.

Hubaud A, Pourquié O 2014 Signalling dynamics in vertebrate segmentation. Nat Rev Mol Cell Biol 15:709–721. doi: 10.1038/nrm3891.

Maschner A, Krück S, Draga M et al 2016 Developmental dynamics of occipital and cervical somites. J Anat 229:601–9.

McCann MR, Tamplin OJ, Rossant J et al 2012 Tracing notochord-derived cells using a Noto-cre mouse: implications for intervertebral disc development. Dis Model Mech 5:73–82.

Mekonen H, Hikspoors JPJM, Mommen G, Köhler SE, Lamers WH 2015 Development of the ventral body wall in the human embryo. J Anat 227:673–85.

Figures 2–7 illustrate in 3D reconstructions, over stages 15–23, the lengthening and medial growth of the ribs and formation of the sternum.

Mekonen H, Hikspoors JPJM, Mommen G, Köhler SE, Lamers WH 2016 Development of the epaxial muscles in the human embryo. Clinical Anat 29:1031–45.

Figures 2, 3, 4, 6, 7 and 8 show 3D reconstructions over stages 15–23 and the formation of epaxial muscle columns.

Mekonen H, Hikspoors JPJM, Mommen G, Kruepunga N, Köhler SE, Lamers WH 2017 Closure in the vertebral canal in human embryos and fetuses. J Anat 231:260–74.

Figures 6 and 7 show the degree of closure of the neural arches of cervical, thoracic, lumbar and sacral vertebrae at postfertilization weeks 7, 8, 9, 10 and 15. The paper also gives details of the components of the occipitocervical junction at postfertilization weeks 7 and 8.

These three papers from Mekonen et al provide accurate embryonic staging, in line with O'Rahilly and Müller (2010), illustrate the conversion of serial histological sections to 3D images using computer software, and compare successive embryonic stages. They present a visual sequence of the 4D changes that take place during complex concurrent morphological changes.

Menezes AH 2008 Craniocervical developmental anatomy and its implications. Childs Nerv Syst 24:1109–22.

Menezes AH, Fenoy KA 2009 Remnants of occipital vertebrae: proatlas segmentation abnormalities. Neurosurgery 64:945–53.

Milhorat TH, Nishikawa M, Kula RW et al 2010 Mechanisms of cerebellar tonsil herniation in patients with Chiari malformations as guide to clinical management. Acta Neurochir 152:1117–27.

Mittapalli VR, Huang R, Patel K et al 2005 Arthrotome: a specific joint forming compartment in the avian somite. Dev Dyn 234:48–53.

Mohamed JY, Faqeih E, Alsiddiky A et al 2013 Mutations in MEOX1, encoding mesenchyme homeobox 1, cause Klippel–Feil anomaly. Am J Hum Genet 92:157–61.

Moldenhauer JS, Adzick NS 2017 Fetal surgery for myelomeningocele: after the Management of Myelomeningocele Study (MOMS). Semin Fet Neo Med 22:360–6.

Morris JK, Rankin J, Draper ES et al 2016 Prevention of neural tube defects in the UK: a missed opportunity. Arch Dis Child 101:604–7.

Muhleman M, Charran O, Matusz P et al 2012 The proatlas: a comprehensive review with clinical implications. Childs Nerv Syst 28:349–56.

Müller F, O'Rahilly R 1986 Somitic–vertebral correlation and vertebral levels in the human embryo. Am J Anat 177:3–19.

Müller F, O'Rahilly R 1994 Occipitocervical segmentation in staged human embryos. J Anat 185:251–8.

Müller F, O'Rahilly 2003 Segmentation in staged human embryos: the occipitocervical region revisited. J Anat 203:297–315.

This paper clearly demonstrates the craniocervical junction in staged human embryos.

Nakajima T, Shibata M, Nishio M et al 2018 Modeling human somite development and fibrodysplasia ossificans progressive with induced pluripotent stem cells. Development 145:pii: dev165431. doi: 10.1242/dev.165431.

O'Rahilly R, Müller F, Meyer DB 1990 The human vertebral column at the end of the embryonic period proper. 4. The sacrococcygeal region. J Anat 168:95–111.

Ordahl CP 1993 Myogenic lineages within the developing somite. In: Bernfield M (ed) Molecular Basis of Morphogenesis. New York: Wiley–Liss, pp. 165–76.

Pang D, Thompson DN 2011 Embryology and bony malformations of the craniovertebral junction. Childs Nerv Syst 27:523–64.

Pang D, Thompson DN 2014 Embryology, classification, and surgical management of bony malformations of the craniovertebral junction. Adv Tech Stand Neurosurg 40:19–109.

Pourquié O 2011 Vertebrate segmentation. From cyclic gene networks to scoliosis. Cell 145:650–63.

Pourquié O, Kusumi K 2001 When body segmentation goes wrong. Clin Genet 60:409–16.

Richardson MK, Allen SP, Wright GM et al 1998 Somite number and vertebrate evolution. Development 125:151–60.

Saadai P, Farmer DL 2012 Clinics in Perinatology: Fetal surgery for myelomenigocele. Clin Perinatol 39:279–88.

Sagar, Pröls F, Wiegreffe C, Scaal M 2015 Communication between distant epithelial cells by filopodia-like protrusions during embryonic development. Development 142:665–71.

Scaal M, Christ B 2004 Formation and differentiation of the avian dermomyotome. Anat Embryol 208:411–24.

An overview of the development of the dorsal somite compartment into dermis and muscle.

Scaal M 2016 Early development of the vertebral column. Semin Cell Dev Biol. 49:83–91.

A comprehensive overview of the early steps of vertebral column formation from segmentation to sclerotomal differentiation.

Sepulveda W, Ximenes R, Wong AE et al 2012 Fetal magnetic resonance imaging and three-dimensional ultrasound in clinical practice: applications in prenatal diagnosis. Best Pract Res Clin Obstet Gynaecol 26:593–624.

Shoja MM, Ramdhan R, Jensen CJ et al 2018 Embryology of the craniocervical junction and posterior cranial fossa, Part I: development of the upper vertebrae and skull. Clin Anat 31:466–87.

Smith JS, Shaffrey CI, Abel MF et al 2010 Basilar invagination. Neurosurgery 66:39–47.

A presentation of three different models of somite formation in the context of molecular data.

Tubbs RS, Lyerly MJ, Loukas M et al 2007 The pediatric Chiari I malformation: a review. Childs Nerv Syst 23:1239–50.

Ward L, Evans SE, Stern CD 2017 A resegmentation-shift model for vertebral patterning. J Anat 230:290–6.

Warmbrunn MV, de Bakker BS, Hagoort J et al 2018 Hitherto unknown detailed muscle anatomy in an 8-week-old embryo. J Anat 233:243–54.

Wiegreffe C, Christ B, Huang R et al 2007 Sclerotomal origin of smooth muscle cells in the wall of the avian dorsal aorta. Dev Dyn 236:2578–85.

Wilting J, Ebensperger C, Müller TS et al 1995 *Pax-1* in the development of the cervico-occipital transitional zone. Anat Embryol 192:221–7.

Xi H, Fujiwara W, Gonzalez K et al 2017 In vivo human somitogenesis guides somite development from hPSCs. Cell Rep 18:1573–85.

CHAPTER 19

Development of the limbs

OVERARCHING CONCEPTS

The limbs develop from permissive and instructive interactions between epithelium and mesenchyme at specified times and places along the lateral body wall. The outgrowths are initiated at defined positions along the embryonic axis where these cell lines continue to proliferate, giving rise to local thickenings that soon develop into limb buds (Gros and Tabin 2014). The early limb bud elongates and, gradually, the different limb regions become apparent. A broad plate forms at the tip and, within it, digital rays develop that mark the position of the forming digits. The digits later separate and become tipped with nails. **Fig. 19.1** shows the main stages in the development of a human upper limb; the stages in development of the lower limb are basically the same.

Upper and lower limb buds protrude laterally from the trunk, encased in an ectodermal epithelium rimmed by a longitudinal ridge of columnar epithelial cells: the apical ectodermal ridge. The ectoderm will ultimately form the epidermis of the skin. Beneath the epithelium is a mixed population of mesenchymal cells derived from the proliferating epithelial somatopleuric lateral plate (Ch. 12, p. 205); these cells have already undergone restriction to develop into upper or lower limbs before the limb buds are visible. They give rise to the connective tissues, bone, cartilage, ligament, tendon, muscle attachment and encasing layers, loose connective tissue and dermis. Muscle in the limb originates from paraxial mesenchyme cells that migrate from the somites; this cell population also contributes to some of the endothelial cells that produce an extensive vascular network in the early limb bud. Motor and sensory nerves and their associated Schwann cells, together with melanocytes destined for the skin, migrate into the developing limb somewhat later; motor neurones derive from the neural plate; sensory neurones, Schwann cells and melanocytes are derived from the neural crest.

Specification of the axes of the limbs

For descriptive, experimental and conceptual purposes, various ‘axes’, borders, surfaces and lines in relation to the developing limb bud are defined and named (**Fig. 19.2**). An imaginary line from the centre of the elliptical base of the bud, through the centre of its mesenchymal core to the centre of the apical ectodermal ridge, defines the proximodistal axis of the limb bud (previously known in descriptive embryology simply as the axis). Named in relation to the proximodistal axis, the cranially placed limb border is the preaxial border and the caudally placed limb border is the postaxial border. (In vertebrate embryos used as experimental models, e.g. chick embryos, the pre- and postaxial borders are termed anterior and posterior borders, respectively.) Any line that passes through the limb bud from preaxial to postaxial border, orthogonal to the proximodistal axis, constitutes a craniocaudal axis. The dorsal and ventral ectodermal surfaces clothe their respective aspects from preaxial to postaxial borders, and any line that passes from dorsal to ventral aspect, orthogonal to both proximodistal and craniocaudal axes, constitutes a dorsoventral axis. It should be noted here that the terms dorsal and ventral axial lines are to be used exclusively in relation to developing and definitive patterns of cutaneous innervation of the limbs and their associated levels of the trunk.

The three developmental axes (proximodistal, craniocaudal and dorsoventral) can be identified in the human developing limb bud by stage 13 (31–33 days postfertilization, see Fig. 23.3). Experiments on wing buds of chick embryos have shown that a different set of cell–cell interactions control the development of structures in relation to each of the three principal axes of the limb bud: proximodistal (e.g. humerus to fingers), craniocaudal (e.g. thumb to little finger) and dorsoventral (e.g. extensors to flexors) (see Fig. 19.2). The same sets of interactions take place in chick leg limb buds. These experiments are described in detail in Hinchcliffe and Johnson (1980).

Outgrowth of the limb bud along its proximodistal axis is controlled by interactions between the apical ectodermal ridge and underlying somatopleuric mesenchyme, and is accompanied by the sequential formation of limb structures along the proximodistal axis. Growth and development along its craniocaudal axis involves an interaction between a small population of mesenchyme cells on the postaxial border of the limb bud, termed the zone of polarizing activity, or polarizing region, and adjacent mesenchyme. The development of the dorsoventral axis of the limb involves an interaction between the surface ectoderm on the sides of the limb bud and the underlying mesenchyme. These sets of cell–cell interactions are coordinated so that the developing limb develops properly with respect to all three axes.

Early differential growth of parts of the limb bud results in two main changes to the originally symmetric axes of the limb. The dorsal aspect of the limb grows faster than the ventral, which causes the limb bud to curve around the body wall; the ventral surface of the limb (closest to the body wall) remains relatively flat, but the dorsal surface bulges into the amniotic cavity. The apical ectodermal ridge, originally facing laterally, becomes increasingly directed caudally (upper limb) and ventrally (lower limb) as the limbs extend around the body.

Apical ectodermal ridge

The apical ectodermal ridge (AER, or apical ridge) is required for limb bud outgrowth. When it is removed from a chick wing bud, outgrowth ceases and a truncated wing results with the level of truncation depending on the stage at which the ridge is removed; severe truncations result when the AER is removed from early limb buds while progressively more distal structures develop when the AER is removed at later stages. The importance of the AER is further demonstrated by grafts of a second AER to a wing bud inducing a new outgrowth that develops digits (Saunders et al 1976, Tickle 2017) (**Fig. 19.3**). The molecular basis of the cell–cell interactions between apical ridge and underlying mesenchyme is conserved between different vertebrates; the apical ectodermal ridge of a mouse limb bud can promote outgrowth of a chick wing bud.

There is evidence that the limb mesenchyme beneath the apical ectodermal ridge provides a factor that is essential for maintaining activity of the ridge (the so-called apical ectodermal ridge maintenance factor). Thus, the craniocaudal extent of production of apical ectodermal ridge maintenance factor determines the length of the apical ectodermal ridge. When cells from the proximal region of a chick leg bud are grafted to the tip of a wing bud beneath the apical ectodermal ridge, the apical ridge is maintained and outgrowth continues. It should be noted that the grafted cells produce the structures according to their new position, but because they are leg cells, they form toes rather than wing digits (Saunders and Gasseling 1959) (see Fig. 19.3). In addition, leg mesenchyme will pass information to local wing ectoderm, eliciting appropriate epidermal development: in this case, formation of scales rather than feathers.

For many years it was thought that a timing mechanism linked to limb bud outgrowth specified the pattern of structures along the proximodistal axis. The timing mechanism was postulated to operate at the tip of a developing limb bud beneath the apical ectodermal ridge in the zone of proliferating undifferentiated mesenchyme cells, which was therefore called the progress zone. It was assumed that, as cells left the progress zone during limb bud outgrowth, their proximodistal fate becomes fixed. Thus, cells spending a short time at the tip of the limb bud would be specified to form proximal structures, while cells spending a longer time would be specified to form distal structures (Summerbell et al 1973). It was suggested that the proximodistal pattern is specified in the very early limb bud (Dudley et al 2002) and that the prespecified structures are progressively elaborated as the bud grows out. It now seems that the proximal part of the limb (humerus/femur) is specified in the very early limb bud by signals from the body wall (Cooper et al 2011, Rosello-Diez et al 2011) while the more distal structures are specified as the bud grows out by a timing mechanism (Saiz-Lopez et al 2015).

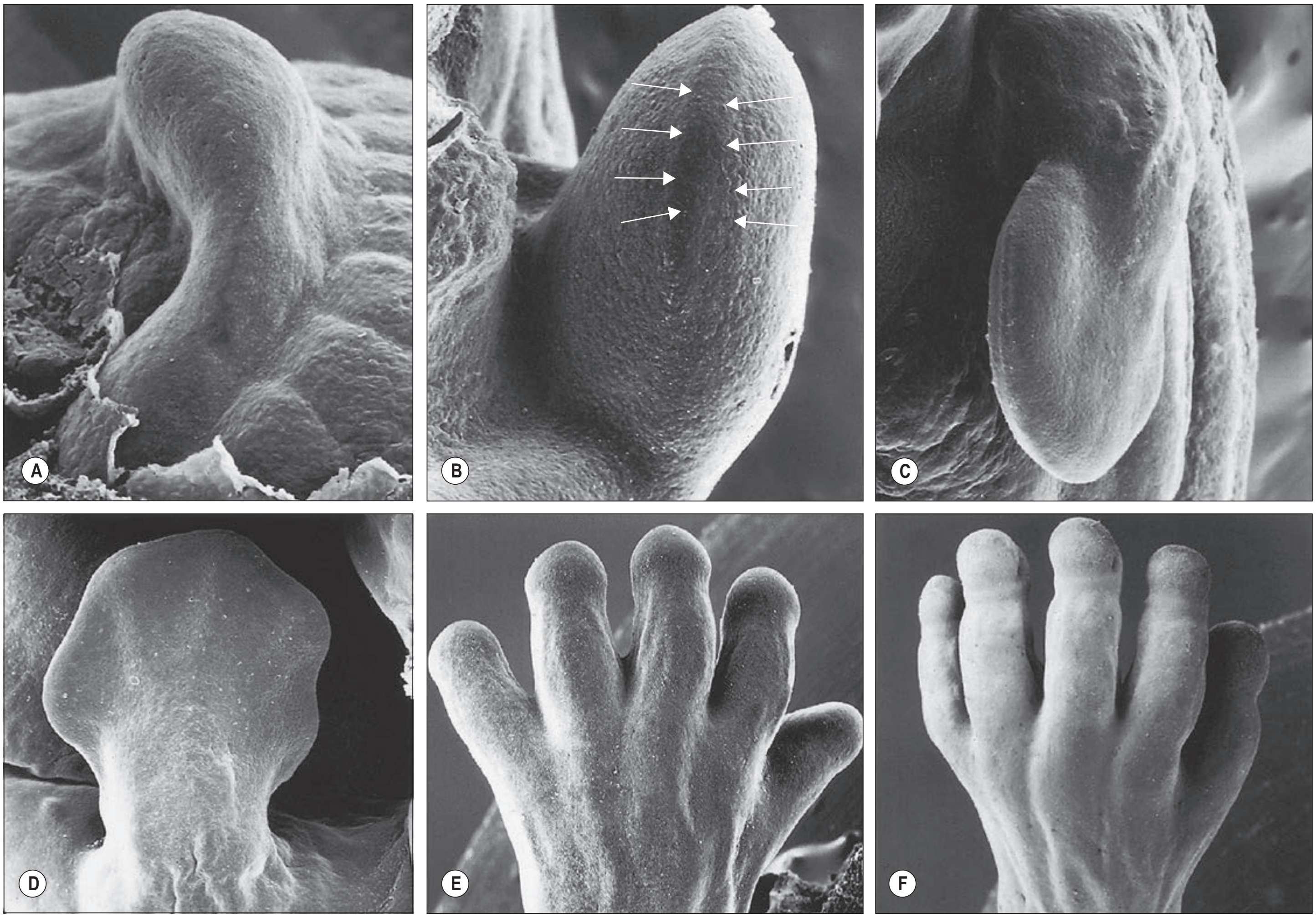

Fig. 19.1 Scanning electron micrographs to show the development of the upper limb. **A**, An early limb bud viewed from the postaxial border. **B**, A limb bud viewed from the postaxial border; the apical ectodermal ridge (arrows) can be seen. **C**, A limb bud, dorsolateral view; the shoulder and elbow region can be discerned, and a hand plate has formed. The apical ectodermal ridge is still obvious at the margin of the hand plate. **D**, Digital rays are present in the hand plate and the margin of the plate is becoming notched. **E**, The fingers are nearly separated and proliferation is commencing at the distal end of each digit to form the nail bed. **F**, The fingers each have tactile pads distally, and nail development continues. (Photographs courtesy of P Collins; printed by S Cox, Electron Microscopy Unit, Southampton General Hospital.)

Zone of polarizing activity

The zone of polarizing activity (or polarizing region) at the postaxial border was discovered by a grafting experiment on chick wing buds (Saunders and Gasseling 1968, Tickle 2017). When a polarizing region is grafted to the preaxial border of an early chick wing bud, so that there are polarizing region cells at both borders, duplication of distal limb structures occurs, with two ulnae (instead of an anterior radius and posterior ulna) and a mirror-image pattern of six digits (the normal chick wing has three digits (see Fig. 19.3)). The digit closest to the polarizing region is always the most postaxial digit (in the chick wing, traditionally designated as digit 4), while more preaxial digits develop further away. Thus, it was proposed that the polarizing region is the source of a diffusible morphogen which controls both digit pattern and digit number. Digit pattern is specified by concentration of the morphogen although timing is also important, e.g. an additional digit can be specified by a prolonged exposure to a low morphogen concentration or by a short exposure to a high morphogen concentration. Digit number is controlled by regulating the width of the limb bud: both directly, via promoting cell proliferation, and indirectly, by controlling production of the apical ectodermal ridge maintenance factor. The width of the limb bud is also limited by zones of programmed cell death on the preaxial and postaxial borders. (It should be noted that, in the literature relating to work on animal embryos, pre- and postaxial borders are termed anterior and posterior borders, respectively, and therefore the regions in which programmed cell death occurs are termed the anterior and posterior necrotic zones.) When the length of the apical ectodermal ridge is reduced, fewer digits form (oligodactyly), while, when the apical ectodermal ridge becomes longer, more digits form (polydactyly). Other regions of apoptotic cell death occur between the digits and result in separation of the digits, but these appear later than the anterior and posterior necrotic zones; the resultant debris in the necrotic zones is removed by macrophages.

Grafts of the zone of polarizing activity only generate mirror-image digit patterns when placed beneath or adjacent to the apical ectodermal ridge in a chick wing, suggesting that the apical ridge produces a factor that maintains polarizing region activity. A positive feedback loop, in which the polarizing region and the apical ectodermal ridge mutually maintain each other's activity, ensures that development of craniocaudal and proximodistal axes is coordinated. Like that of the apical ectodermal ridge, the function of the polarizing region is conserved across species and grafts of the postaxial border of limb buds from mammals, including human limb buds (Fallon and Crosby 1977), generate additional chick digits. This shows that the polarizing region produces the same molecular signal in both birds and mammals, but that the character of a digit depends on the responding cells.

Ectodermal axial specification

Signals from the ectoderm control the dorsoventral axis. It is possible to remove the surface ectodermal epithelium (like peeling off a glove) from the mesenchymal core of an early chick limb bud. When the ectodermal epithelium from a left limb bud is recombined with the mesenchymal core from a right limb bud, keeping the craniocaudal axis in register, the distal part of the limb that develops conforms to the polarity of the ectoderm rather than the polarity of the mesenchyme (MacCabe et al 1974) (see Fig. 19.3). This can be seen in the pattern of muscles, orientation of the joints and eventual characteristic differentiation of the epidermis.

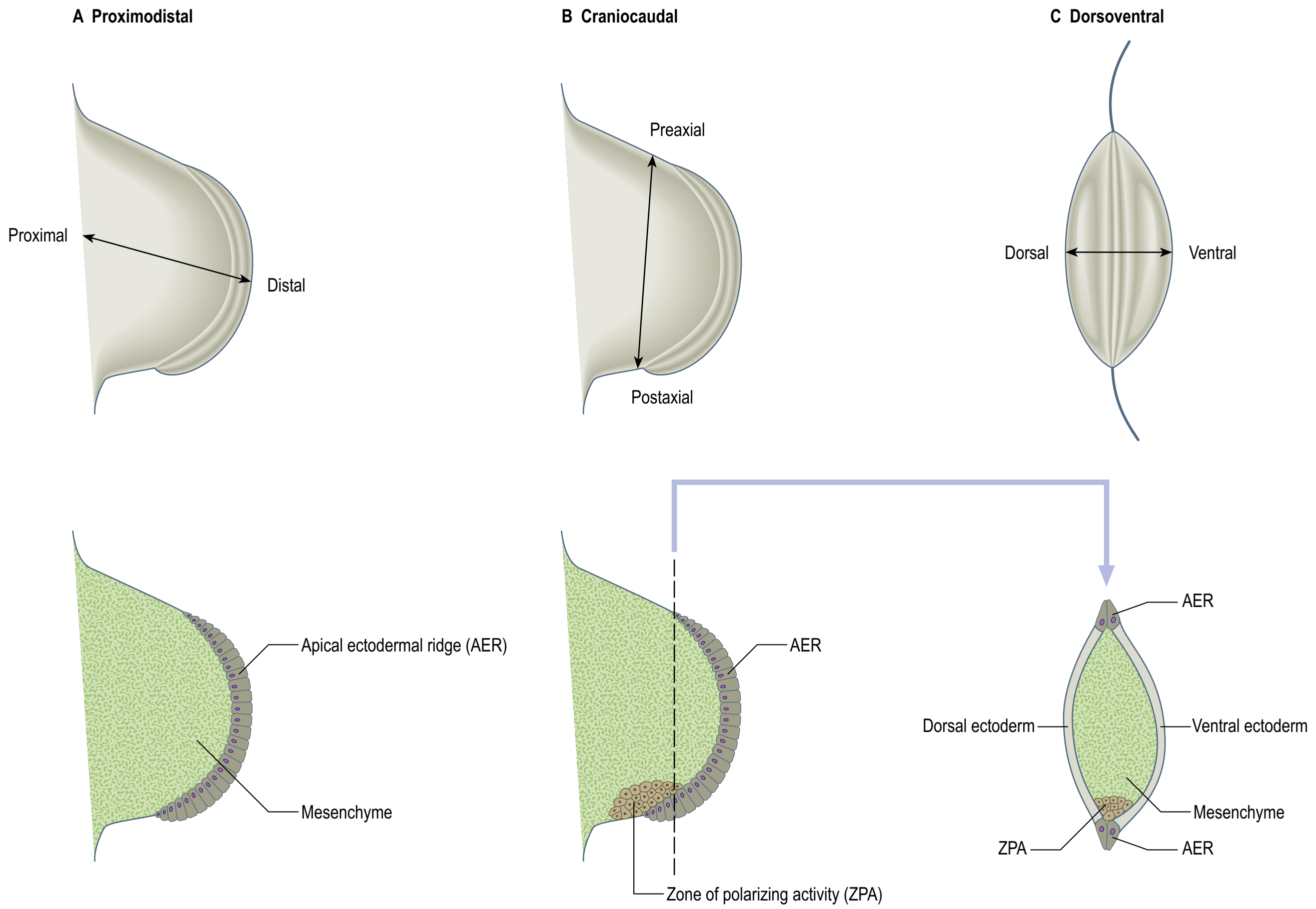

Fig. 19.2 Axes of the developing limb and specification of structures along the different axes. **A**, Proximodistal; limb bud viewed from the dorsal side. **B**, Craniocaudal; limb bud viewed from the dorsal side. **C**, Dorsoventral; limb bud viewed from the distal end. The development of limb structures and the ectodermal specializations are controlled by the limb mesenchyme. Outgrowth of limb bud is controlled by the apical ectodermal ridge and accompanied by the laying down of structures along the proximodistal axis; craniocaudal pattern is controlled by the zone of polarizing activity (polarizing region); dorsoventral pattern is controlled by signals from dorsal and ventral ectoderm, shown in cross-section; the section taken in the plane is shown by the dotted line. The limb bud in the diagram is equivalent to that of a human embryo at approximately stage 14.

Genes and molecules in limb development

The apical ectodermal ridge produces fibroblast growth factors, extracellular cell–cell signalling molecules that act on the underlying mesenchyme cells and are essential for limb bud outgrowth (Niswander et al 1993). Fibroblast growth factors also maintain the activity of the polarizing region. The latter expresses *Sonic hedgehog* (*Shh*), a gene encoding another class of secreted protein that acts as diffusible morphogen (Riddle et al 1993). Sonic hedgehog protein (Shh) plays a pivotal role in the specification of the craniocaudal digit pattern: it spreads across the chick wing bud so that cells at different positions across the craniocaudal axis are exposed to different Shh concentrations (Tickle and Towers 2017). In mouse limb buds, the two most postaxial digits (corresponding to the little finger and the ring finger in the hand) come from the polarizing region itself and are specified by the length of exposure to Shh (Harfe et al 2004). Responding cells transduce the signal through the Gli family of transcription factors. (The Gli proteins are bifunctional effectors of Shh signalling and can lead to either activation or repression of expression of target genes.) Shh secreted by the polarizing region also acts on adjacent mesenchyme cells, controlling their proliferation and maintaining the expression of the Gremlin gene, encoding an extracellular antagonist of secreted bone morphogenetic proteins (BMP). Gremlin functions as the apical ectodermal ridge maintenance factor by antagonizing BMP signalling which would otherwise inhibit fibroblast growth factor (*Fgf*) expression in the apical ectodermal ridges (Zuniga et al 1999, Zeller et al 2009). Dorsal limb ectoderm expresses *Wnt7a*, a gene encoding another extracellular signalling molecule that acts as a dorsalizing signal (Parr and McMahon 1995).

Among the genes expressed in response to cell–cell signalling molecules in the limb bud and which form dynamic and overlapping domains of expression are 5′ members of the *Hoxa* and *Hoxd* gene complexes. *Hox* genes code for transcription factors that act in a cell-autonomous fashion to control expression of many target genes. There are two phases of *Hoxd* and *Hoxa* expression in the developing limb. In the first phase in the early limb bud, the expression of 5′ *Hoxd* genes (*Hoxd9*, *d10*, *d11 d12* and *d13*) is activated sequentially and in progressively more restricted distal and proximal domains, while the expression of 5′ members of the *Hoxa* gene complex is activated similarly, but slightly later than the *Hoxd* genes, in overlapping domains along the proximodistal axis. The first phase of *Hox* gene expression establishes the growth and pattern of proximal limb structures, i.e. upper and lower arm; the second phase, which occurs in the broad digital plate, establishes the growth and pattern of distal structures, i.e. the hand/foot. Regulatory gene sequences in the DNA on either side of the *Hoxd* complex have been identified that control the switch in expression from the first phase to the second phase as the limb bud develops (Andrey et al 2013). The gene encoding the transcription factor Lmxb1 is expressed in the dorsal part of the limb, in response to Wnt7a signalling by dorsal ectoderm, and establishes the pattern of dorsal structures.

The molecular basis of limb development is conserved in humans. Mutations associated with many of the genes described above are responsible for human congenital limb malformations. Details can be found in Ferretti and Tickle (2006), Zuniga et al (2012) and Pickering and Towers (2014). There are, however, many human congenital limb anomalies for which the genes involved are not known. A global gene expression analysis of developing mouse limbs estimates that several thousand genes, maybe around 35% of the genome, participate in some aspect of limb development (Taher et al 2011), with relatively fewer genes (hundreds) preferentially expressed in either forelimb or hindlimb. The first genome-wide study on developing human limbs has documented patterns of histone modifications marking active regulatory sequences in the DNA that control gene expression, with the aim of identifying regulatory regions of genes active specifically in human limb buds (Cotney et al 2013).

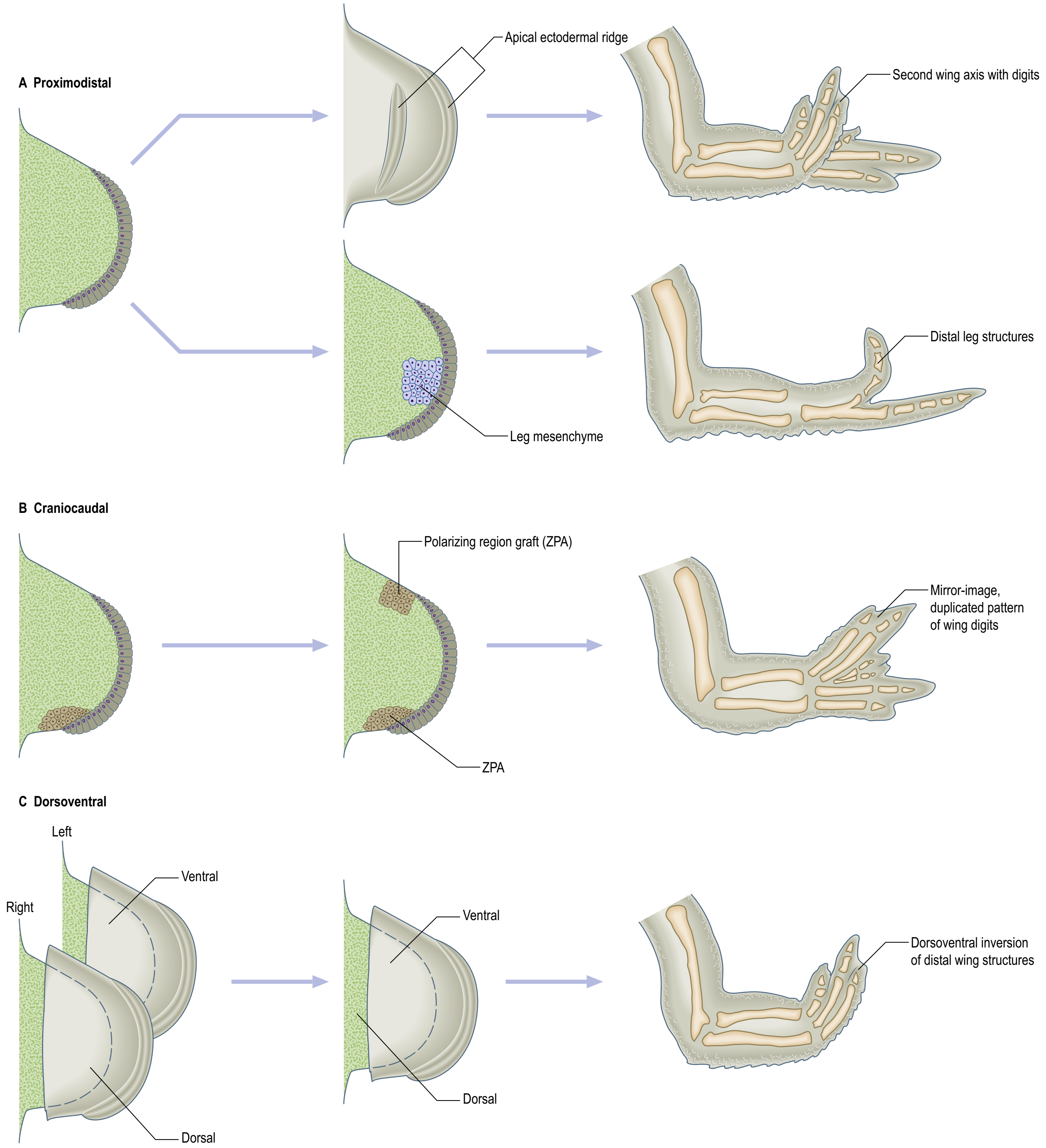
A Proximodistal
Apical ectodermal ridge
Second wing axis with digits
Distal leg structures
Leg mesenchyme
B Craniocaudal
Polarizing region graft (ZPA)
Mirror-image, duplicated pattern of wing digits
ZPA
C Dorsoventral
Left
Right
Ventral
Ventral
Dorsoventral inversion of distal wing structures
Dorsal
Dorsal

Fig. 19.3 A–C, Experimental manipulations that identified the fundamental cell–cell interactions involved in patterning the three main axes of the limb in the chick. Abbreviation: ZPA, zone of polarizing activity.

DEVELOPMENT OF LIMB TISSUES

Connective tissue and bone

Somatopleuric mesenchyme in the limb buds gives rise to the connective tissues of the limb. Cell lineage analyses in early chick limb buds show that a single mesenchyme cell can give rise to the major types of connective tissue including cartilage, perichondrium, tendon and epi-, peri- and endomysial layers around the muscles. The first signs of the formation of skeletal elements are regions of increased cell density in the core of the limb bud. The cells in these regions go on to differentiate into chondrocytes, which produce large quantities of extracellular matrix, in which they become embedded, giving rise to a cartilage model of the bone that will eventually develop. One centre of chondrogenesis forms in the proximal region of an early human limb bud; two centres of chondrogenesis then form more distally as the limb bud lengthens, followed by five centres in the broadened distal tip. The Sox9 transcription factor is essential for chondrocyte differentiation in mouse embryos; the *Sox9* gene is expressed before and during deposition of cartilage (Wright et al 1995). *Sox9* gene transcripts are expressed in the humerus and forearm skeletal elements of human embryos at approximately 44 days postfertilization, and in the carpals, metacarpals and phalanges, in addition to the more proximal elements, at approximately 52 days postfertilization (**Fig. 19.4**). Mutations in human *Sox9* are associated with campomelic dysplasia, a skeletal dysmorphology syndrome (Foster et al 1994). Some bony eminences, which are sites of entheses, have been shown to derive from chondrogenic foci which form separately and later than the cartilage model of the long bones (Blitz et al 2013). The cells co-express *Sox9* and the transcription factor *scleraxis* (*Scx*) and blockage of *Scx* arrests eminence development. Scleraxis is also expressed in the early limb subjacent to the ectoderm in tendon progenitors and later in the cells of all tendons. Studies of *Scx* knockout mice show that *Scx* is required for the differentiation of

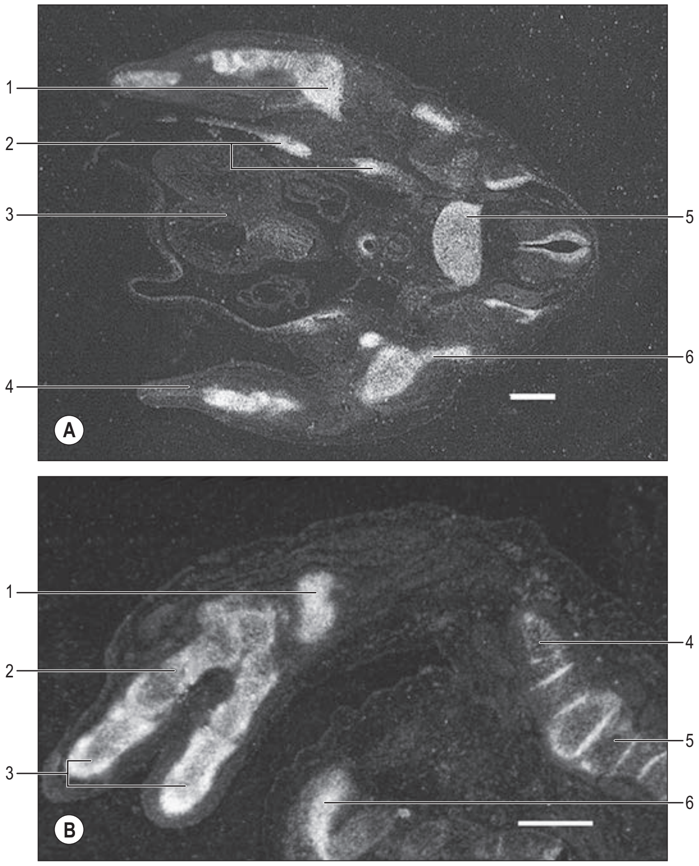

Fig. 19.4 *Sox9* expression in the skeleton of developing limbs of human embryos. **A**, Stage 18; Key: 1, humerus; 2, ribs; 3, heart; 4, forearm; 5, vertebral body; 6, scapula. **B**, Stage 21; Key: 1, carpal; 2, metacarpal; 3, phalanges; 4, humerus; 5, scapula; 6, rib. *Sox9* transcripts are detected in sections with radioactively labelled probes followed by autoradiography. Positive signal is represented by silver grains that show up as white areas. Scale bars represent 500 µm in both **A** and **B**. (The human tissue was provided by the joint MRC–Wellcome Human Developmental Biology Resource (http://www.hdbr.org) at the Institute of Human Genetics, Newcastle upon Tyne, UK. Courtesy of Dr Susan Lindsay, Institute of Human Genetics, University of Newcastle upon Tyne, UK.)

force-transmitting tendons but not for muscle-anchoring tendons (Muchison et al 2007). A population of Scx^{+}/$Sox9^{+}$ progenitor cells have been shown to give rise to Scx^{-}/$Sox9^{+}$ chondrocytes and Scx^{+}/$Sox9^{-}$ tenocytes/ligamentocytes. The Scx^{+}/$Sox9^{+}$ cells contribute particularly to establishing the enthesis organ between the cartilage and tendon. The closer the tendon is to the cartilage primordium (anchoring tendon), the more tenocytes arise from the Scx^{+}/$Sox9^{+}$ lineage. In general, the number of tenocytes derived from this lineage decreases with increasing distance from the cartilage model, although there is variation between individual force-transmitting tendons (Sugimoto et al 2013). For further details on tendon development see Delgado Caceres et al (2018).

Two methods of bone ossification occur (Ch. 5). In intramembranous ossification mesenchymal bone precursors differentiate directly into osteoblasts; in endochondral ossification, osteoprogenitor cells which give rise to osteoblasts enter the cartilage models of the long bones via vascular invasion. Initially a periosteal collar forms, and osteoblasts proliferate and secrete bone matrix within the mid-section of the future diaphysis, forming a primary ossification centre; this extends proximally and distally until it reaches the future epiphysial levels, where growth plates (epiphysial plates) will be established. For further details on the cellular development of cartilage and bone, see Chapter 5. For further details on the development of specific limb bones, see appropriate regional chapter. It should be noted that maternal nutrition and vitamin status affects fetal bone growth and that despite vitamin supplementation in Western countries, pregnant women in northern latitudes may remain vitamin D deficient in winter pregnancies. Infant femur length was shorter in pregnancies with early serum 25-hydroxyvitamin D below the median value (Walsh et al 2013).

The first evidence of bone formation in human embryos is intramembranous ossification of the clavicle (stage 18–19) followed by the mandible. Endochondral ossification of cartilage models of long bones is initially seen in the limbs in stage 21–23 human embryos (50–58 days postfertilization). By postmenstrual week 10, columns of chondrocytes can be seen at the epiphysial level of most bones. However, only the lower end of the femur and upper end of the tibia develop secondary ossification centres before birth.

Joints

Regions of developing cartilage are easily recognized histologically in the developing limb because they consist of widely spaced cells surrounded by matrix. These regions are separated by transverse bands of relatively flattened cells – interzones – which mark the sites of future joints. Their subsequent development varies according to the type of joint that is formed.

In developing fibrous joints, the interzone is converted into collagen, which is the definitive medium connecting the bones involved. In developing synchondroses, the interzone becomes growth cartilage of the modified hyaline type; in developing symphyses, it is predominantly fibrocartilage. In developing synovial joints, the interzonal mesenchyme becomes trilaminar when a more tenuous intermediate zone appears, splitting the mesenchyme into two dense strata. As the skeletal elements chondrify, and in part ossify, the dense strata of the interzonal mesenchyme also become cartilaginous; subsequent cavitation of the intermediate zone establishes the cavity of the joint. The loose mesenchyme around the cavity forms the synovial membrane and probably also gives rise to all other intra-articular structures, such as ligaments, discs and menisci. In joints containing discs or menisci, and in compound articulations, more than one cavity may appear initially, sometimes merging later into a complex single cavity. For details of the genes expressed in joint development consult Decker et al (2014). As development proceeds, thickenings in the fibrous capsule can be recognized as the specializations peculiar to a particular joint. (In some joints, such accessions to the fibrous capsule are derived from neighbouring tendons, muscles or cartilaginous elements.) Although the initial stages in the process of cavitation of joints are independent of movements, a true joint cavity can generally form only in the presence of movements (Shea et al 2015).

Muscles

It is well established that all limb myogenic precursor cells originate from the somites (Chevallier et al 1977, Kardon et al 2003). These cells are committed at an early stage and can be identified in the lateral halves of the somites. After the mesenchymal sclerotome cells have migrated from the epithelial somite, the remaining dorsolateral portion is termed the epithelial plate or dermomyotome of the somite (see Fig. 18.2). Cells from the dorsomedial edge of the dermomyotomes form the axial musculature, whereas, at limb levels, cells de-epithelialize and migrate from the ventrolateral edges of the dermomyotome into the limb bud. The myogenic precursor cells do not differentiate into muscle before their migration into the limb, probably because of inhibitory signals produced by the somatopleuric mesenchyme. Muscle differentiation depends on the key activity of the MyoD family of transcription factors (Weintraub et al 1991).

The myogenic precursor cells colonize the limb bud in a proximodistal direction but never reach the most distal portion of the limb. Experiments in chick embryos revealed that myogenic cells are still indifferent regarding their region-specific determination when they first enter the limb. Thus, when brachial-level somites are grafted opposite the leg-forming region, or when pelvic-level somites are grafted opposite the wing-forming region, a normal limb musculature develops, irrespective of the origin of the somites, i.e. putative myoblasts, unlike the somatopleuric (lateral plate) mesenchymal cells, are not specified to be wing or leg (Chevallier et al 1977). Other experiments in the chick wing show that the muscle pattern developed in the limb reflects the pattern of the skeletal elements: duplication or lack of lower arm elements is accompanied by the duplication or lack of the corresponding muscles (Robson et al 1994).

It is thought that in all classes of tetrapods the first myogenic cells to arrive in the limb bud form principal dorsal and ventral premuscle masses that undergo specific spatiotemporal sequences of divisions and subdivisions as the limb lengthens. In human embryos, this leads to the individualization of about 19 muscles in the upper limb and 14 muscles in the lower limb. In the upper limb, the premuscle masses first divide into three masses, the next division gives rise to the muscles attached to the carpus, and the final division produces the long muscles of the digits. A similar pattern is seen in the lower limb. The mechanisms that divide the muscle masses are not known; one suggestion is that they are created by invading somatopleuric cells which ultimately form the myotendinous junctions, and endo-, peri and epimyseal layers which complete the composite anatomical muscle. For details on the development of the myotendinous junction see Charvet et al (2012) and Subramanian and Schilling (2015). For further development of skeletal muscle, see Chapter 5.

The literature suggests that all musculoskeletal elements are in their appropriate positions in human limbs by postmenstrual week 10. For detailed accounts of the process, consult O'Rahilly and Gardner (1975) and Uhthoff (1990). For reviews on limb development, including tissue formation, see Lane and Tickle (2003).

Vessels

Arteries

The early limb bud receives blood via intersegmental arteries that contribute to a primitive capillary plexus. At the tip of the limb bud a terminal plexus is constantly renewed in a distal direction as the limb grows (see **Fig. 19.5**). Later, one main vessel, the axial artery, supplies the limb and the terminal plexus.

The development of the vasculature in the early limb precedes the morphological and molecular changes that occur within the limb mesenchyme as tissues begin to form. Cartilage differentiation within the early chick limb bud occurs only after local vascular regression begins, and only in areas with few or no capillaries (Hallmann et al 1987). It is not known whether the presence, or lack, of blood vessels affords different local environmental stimuli for mesenchymal cells (by varying the supply of nutrients to the tissue), or whether the local environment is controlled by the endothelial cells. Experimental work on chick wing buds suggests that the position of the central artery in the primitive limb bud vasculature depends on Shh signalling from the polarizing region (Davey et al 2007).

In the developing skin in mouse embryo limbs, although there is no initial association between sensory nerves and blood vessels, later nerve–vessel alignment is seen. The skin arterial branching pattern coincides with the branching pattern of pre-established sensory nerves. Arterial differentiation is preceded by the local action of nerve-derived vascular endothelial growth factor A (VEGF-A) (Li et al 2013).

Veins

A terminal capillary plexus develops at the tip of the early limb bud; it expands as a superficial venous plexus with radicles coalescing along the pre- and postaxial borders of the limb, as a marginal vein. As the limb enlarges, the marginal vein can be subdivided into pre- and postaxial veins, which run along their respective borders and which are the precursors of the superficial veins of the limb. Generally, the preaxial (superficial) veins join the deep veins at the proximal joint, and the postaxial (superficial) veins join the deep veins at the distal joint of the limb. Deep veins develop *in situ* alongside the arteries.

Lymphatic channels

It was thought that lymphatic vessels in the limb derived from outgrowths from the main cardinal veins. However, studies on the initiation of *Prox1* expression in lymphatic vessels in mammals have identified intersomitic vessels and the superficial venous plexus of the growing limb as additional sources of lymphatic endothelial cell progenitors, especially in the dermis (Kazenwadel and Harvey 2016).

Nerves

During development, the spinal cord opposite the limbs becomes specialized, with the formation of longitudinal minicolumns (columels) along its rostrocaudal axis. The columels consist of groups of individual pools of differentiated motor neurones, precisely organized according to function (Jessell et al 2011). Motor neurones within each individual pool innervate a particular muscle. Neurones in medial pools express the transcription factor Islet1 and their axons innervate ventral limb muscles, while neurones in lateral pools express the related transcription factor, Lim1, and innervate dorsal limb muscles. Neurones also express different Hox proteins according to their position along the rostrocaudal axis of the spinal cord, and this determines not only their identity and their position within the spinal cord but also their specificity of limb muscle innervation (Dasen et al 2005, Catela et al 2016).

Motor axons enter the developing limbs earlier than sensory axons at the time when dorsal and ventral muscle masses have started to form. Guidance of the growing axons is not dependent on the presence of migrating myoblasts; when these are absent, the main nerve trunks in the limb still form, although the smaller motor branches that would innervate individual muscles do not form (Lewis et al 1981, Honig et al 2005). Neurones entering the chick embryonic limb appear to have a heterochronic delay before multinucleated muscle fibres are formed and associated with nerve endings, whereas in mammalian embryos, although nerve contact with primary myotubes is not necessary for initial myoblast migration, muscle fibre differentiation requires nerve ending contact. The temporal shift in early myoblast expression of *Pax3* to later expression of *Pax7* coincides with interaction with nerve endings (Hurren et al 2015). Motor axons grow into the dorsal and ventral muscle masses and innervate muscle groups in a proximo–distal progression. Correct axonal routing depends on both repulsive and attractive cues. The pathfinding of motor axons is an important model system for understanding binary axon guidance decisions: glial cell (line)-derived neurotrophic factor (GDNF) attracts motor neurone growth cones, and interacts synergistically with ephrin-As to determine growth cone directionality (Drescher 2011). Experimental studies in mice and chickens have shown that axons of neurones in lateral pools grow into the dorsal part of the limb as a result of repulsive interactions between the receptor EphA4 (expressed by these motor neurones) and its ligand, ephrinA (expressed by ventral limb cells). The axons of EphB-expressing motor neurones in medial pools grow into the ventral part of the limb as a result of repulsive interactions with ephrinB-expressing cells in the dorsal limb (Drescher 2011). The dorso-ventral differences in Ephrin expression in the limb are controlled by the system that establishes the dorso-ventral axis of the limb and that results in dorsal expression of Lmxb1.

Sensory neurones in the dorsal root ganglia opposite the limbs send axons peripherally to terminate in the skin and to innervate proprioceptors in the limb muscles. The trajectories of sensory axons into the limb can be influenced by their interaction with motor axons. When sensory axons grow into a developing limb, it has already been invaded by motor axons and the environment will have been altered by any extracellular factors these axons may have secreted. If motor axons are removed before sensory axons extend into a limb, those sensory axons, that would normally terminate in muscle (Ia afferent axons), appear unable to do so and instead become cutaneous nerves (Honig et al 1986, 1998, Honig and Rutishauser 1996).

The developing skin (ectoderm and immediately underlying somatopleuric mesenchyme) is essential for the normal development of cutaneous sensory axons. If the ectoderm is removed, the cutaneous nerves that would project to it are absent. This can be prevented by applying the signalling molecule BMP4 (Honig et al 2004, 2005). Cutaneous sensory axons are not matched to particular regions of skin in the limb and can innervate regions outside their usual anatomical dermatomes, or expand into regions of skin where the cutaneous innervation is eliminated (Wang and Scott 2002).

Proprioceptive sensory neurones are characterized by expression of the transcription factor Runx3 and also express a neurotrophic factor receptor (TrkC) that binds specifically to the neurotrophic factor NT-3. NT-3 is expressed in the limb bud and may serve as a short-distance guide to the ingrowing axons (Genc et al 2004). There is a reciprocal interaction with the neuronal soma: in the absence of NT-3, proprioceptive neurones in the dorsal root ganglia die. The central processes of the proprioceptive sensory neurones innervating limb muscle form monosynaptic connections to motor neurones in the spinal cord after their peripheral axons have extended into the limbs. However, the pattern for these sensory/motor connections appears to be specified early. The proximo–distal position of the sensory endings in the limb is linked to the dorso–ventral location of the target motor neurones in the spinal cord, such that proximal sensory axons will connect to ventral motor columels (Sürmeli et al 2011). NT-3 is also expressed in ventral neural tube and, as in the periphery, may help guide the axons to the correct location in the spinal cord.

The different types of sensory endings show activation at different developmental times, thus mechanoreceptors and proprioceptors are active ahead of nociceptive neurones prenatally. A third wave of mechanosensitivity acquisition by nociceptors occurs just after birth (Lechner et al 2009).

Embryonic and fetal movements

Observations in model organisms have shown that embryonic movements are vital for development of the musculoskeletal system of the limb (Pitsillides 2006, Nowlan et al 2010). These movements generate strain and stresses on the skeletal tissues. When movement is reduced or eliminated and the limb skeleton is no longer subject to appropriate mechanical stimulation, the development of joints and endochondral ossification is abnormal. In human embryos, simple movements of an extremity have been detected sporadically as early as postfertilization week 7 by ultrasonography. Combined movements of limb, trunk and head commence between postmenstrual weeks 12 and 16, and trunk and lower limb movements are perceived consistently by the mother from about postmenstrual week 16 (quickening). Movements of the fetus often involve slow and asymmetric twisting and stretching movements of the trunk and limbs, which resemble athetoid movements. There may also be rapid, repetitive, wide-amplitude limb movements, similar to myoclonus. Forces generated by movements in human fetuses have been measured by novel cine-magnetic resonance imaging and the resultant stresses and strains on the developing limb skeleton determined *in utero* (Verbruggen et al 2018). The forces generated by fetal kicks increases between postmenstrual weeks 20 and 30, and even though this movement then decreases, the overall stresses and strains on the fetal limb skeleton rise during the third trimester.

By postmenstrual week 32, symmetric flexor movements are most frequent. By term, the quality of the movements has generally matured to smooth, alternating movement of the limbs, with medium speed and intensity. The reduced effect of gravity *in utero* may cause certain fetal movements to appear, on ultrasonography, more fluent than the equivalent movements observed postnatally. The number of spontaneous movements decreases after postmenstrual week 35 and, from this time, there is an increase in the duration of fixed postures. This restriction of normal fetal movements in late gestation reflects the degree of compliance of the maternal uterus. Movement patterns of preterm babies from postmenstrual week 27 have been observed and anomalous general movements categorized (Einspieler et al 2016). These studies add to the general knowledge of maturation of the preterm musculoskeletal system and predict later movement deficits. It is not known whether the different stresses and strains of early gravitational forces and limitations of movement imposed by medical access cause their own epigenetic effects in the preterm infant.

In addition to promoting normal musculoskeletal development, movements of the fetus encourage skin growth and flexibility indirectly. Fetuses with *in utero* muscular dystrophies, or other conditions that result in small or atrophied muscles, have webs of skin, pterygia, which pass across the flexor aspect of the joints and severely limit movement. Multiple pterygium syndrome is characterized by webbing across the neck, the axillae and antecubital fossae. Usually, the legs are maintained straight and webbing is not seen at the hip and knee. A group of congenital disorders, collectively termed 'multiple congenital contractures', may result from genetic causes, or limitations of embryonic and fetal joint mobility, or may be secondary to muscular, connective tissue, skeletal or neurological abnormalities. These conditions may be recognized on prenatal ultrasound examination by the appearance of fixed, immobile limbs in bizarre positions, or by webbing in limb flexures. Specific syndromes, lethal multiple pterygium syndrome and congenital muscular dystrophy, have been described.

PECTORAL GIRDLE

The pectoral girdle develops at an interface between the tissues forming the head and neck, the back and the upper limb. Each of these regions appears to have different cell lineages and heterochronic gene expression contributing to the development of similar tissues that reflect the evolution of the neck and shoulder region (Commentary 2.1).

Early limb development is patterned by somatopleuric mesenchyme via permissive interactions with the limb ectoderm, and cartilage differentiation to a chondrogenic phenotype is initiated by local increases in mesenchyme cell density. A number of mesenchymal populations have been suggested as giving rise to the pectoral girdle: cells adjacent to the paraxial mesenchyme of somites 1–3 (which have been described, possibly erroneously, as occipital lateral plate); somatopleuric mesenchyme; the hypaxial rather than the epaxial domain of specific somites; neural crest cells, which give rise to and pattern the connective tissues in the head. Studies on chick embryos have shown that the clavicle arises from mesenchymal populations just caudal to the pharyngeal arches at the head/trunk interface, and that lateral scapular structures are derived from the somatopleuric mesenchyme, whereas the medial border of the scapula originates from dermomyotomes of somites 17–24, which switch from a myogenic to a chondrogenic fate (Wang et al 2005, Valasek et al 2010, 2011, Nagashima 2016). The sternum is derived from somatopleuric mesenchyme, although there is evidence of neural crest within the manubrium.

Pectoral girdle muscles have a similar heterogeneous origin. Upper limb myoblasts derived from somites migrate laterally from the ventrolateral border of cervical dermomyotomes and form dorsal and ventral masses prior to migration into the limb bud. After a brief period within the limb bud, a subset of these myoblasts migrates medially, out of the limb bud and back towards the axial mesenchyme to form the pectoral muscles ventrally and latissimus dorsi dorsally. This origin of the superficial pectoral girdle muscles has been described as an 'in–out' mechanism (from the trunk into the limb and then from the limb back towards the trunk) (Valasek et al 2011). Only myoblasts undergo this second, medial, migration out of the limb bud. The somatopleuric mesenchyme remains within the proximal limb anlagen and produces the glenohumeral joint and coracoid process. The deep pectoral girdle muscles, serratus anterior and the rhomboid muscles arise from the hypaxial domain of those somites forming the medial border of the scapula (Valasek et al 2011).

Trapezius and sternocleidomastoid muscles (evolutionarily related to the cucullaris muscle in the chick), are derived from upper occipital somites and innervated by the accessory nerve (see also Pu et al 2016) (see Fig. 17.7); the myoblasts migrate into neural crest mesenchyme which forms their connective tissue. The proximal and distal attachments of trapezius, to the nuchal line of the occipital bone and the upper part of the spine of the scapula, respectively, are derived from post-otic neural crest cells, as is the attachment of sternocleidomastoid muscle to the clavicle (Matsuoka et al 2005). Gene expression of the pectoral girdle muscles reflects the myoblast origins. *Pax3* and *Pax7* are normally expressed during trunk muscle development, but not in head myogenic precursors; *Tbx5* is expressed in the upper limb but does not extend to the dorsal midline. Pharyngeal arch muscle related genes, *MyoR*, *Pitx2* and *Tbx1*, are expressed early in the myoblast populations giving rise to the trapezius and sternocleidomastoid muscles, but the muscles themselves differentiate later, in line with the head and not the trunk myogenic programme (Theis et al 2010).

A 'muscle scaffold model' proposed by Matsuoka et al (2005), which links the patterning effects of mesenchyme populations, which form endo-, per- and epimysium as well as tendons, to muscle attachment sites, may explain a range of anomalies based on defects of post-otic neural crest and which affect the pharynx and larynx as well as the shoulder region, e.g. Klippel–Feil disease, Sprengel deformity and cleidocranial dysplasia.

UPPER LIMB

In human embryos, the upper limb bud is first visible as a thickening along the lateral longitudinal axis of the body wall opposite somites 8–10, at the level of the entrance to the cranial intestinal portal during stage 12 (30–32 days postfertilization). It enlarges, protruding laterally from its elliptical base at the body wall as a symmetric bud, with a curved border and an apical ectodermal ridge forming its distal tip. Initially, it has equal and relatively flat dorsal and ventral ectodermal surfaces and a somatopleuric mesenchymal core. By stage 13 the upper limb bud is curved ventrally. By stage 14 it has elongated and is opposite the developing ventricles of the heart; it is directed caudally because of preferential elongation of the preaxial part of the bud. At stage 15 the upper limb can be subdivided into definite regions. The proximal portion, still showing the dorsal bulge and ventral curve, is the shoulder and upper arm region; the next distal portion can now be identified as the forearm; the most distal portion is now expanded into a flattened hand plate.

At stage 16 there are the first indications of digit rays in the hand plate. The limb may be close to the body wall or may be abducted. By stage 17 the upper limb has an elbow region and well-defined digit rays; the hand plate may show a crenated rim, indicating the start of tissue removal between the digits (see Fig. 19.1). Crenation of the hand plate between the digit rays continues in stage 18 embryos (42–44 days postfertilization). Changes during stages 19–23 are concerned with growth of the limb and separation of the digits. The hands now curve over the cardiac region. The distal phalangeal portions of the fingers enlarge at stage 21, forming the nail beds. The finger tip is the only part of the human limb that can regenerate and does so as long as enough of the nail remains (Jafari et al 2017). The digit tips of mice also regenerate and have been used as an experimental model to investigate the processes involved. It is hoped that new clinical approaches can be found to promote regenerative responses in damaged limbs (Dolan et al 2018).

Most of the bones in the appendicular skeleton are derived from somatopleuric mesenchyme. Prechondroblasts are present in the upper limb at stage 13 and condensations of cartilage can be detected at stage 16, when the humeral anlage can be recognized. Cavitation of the

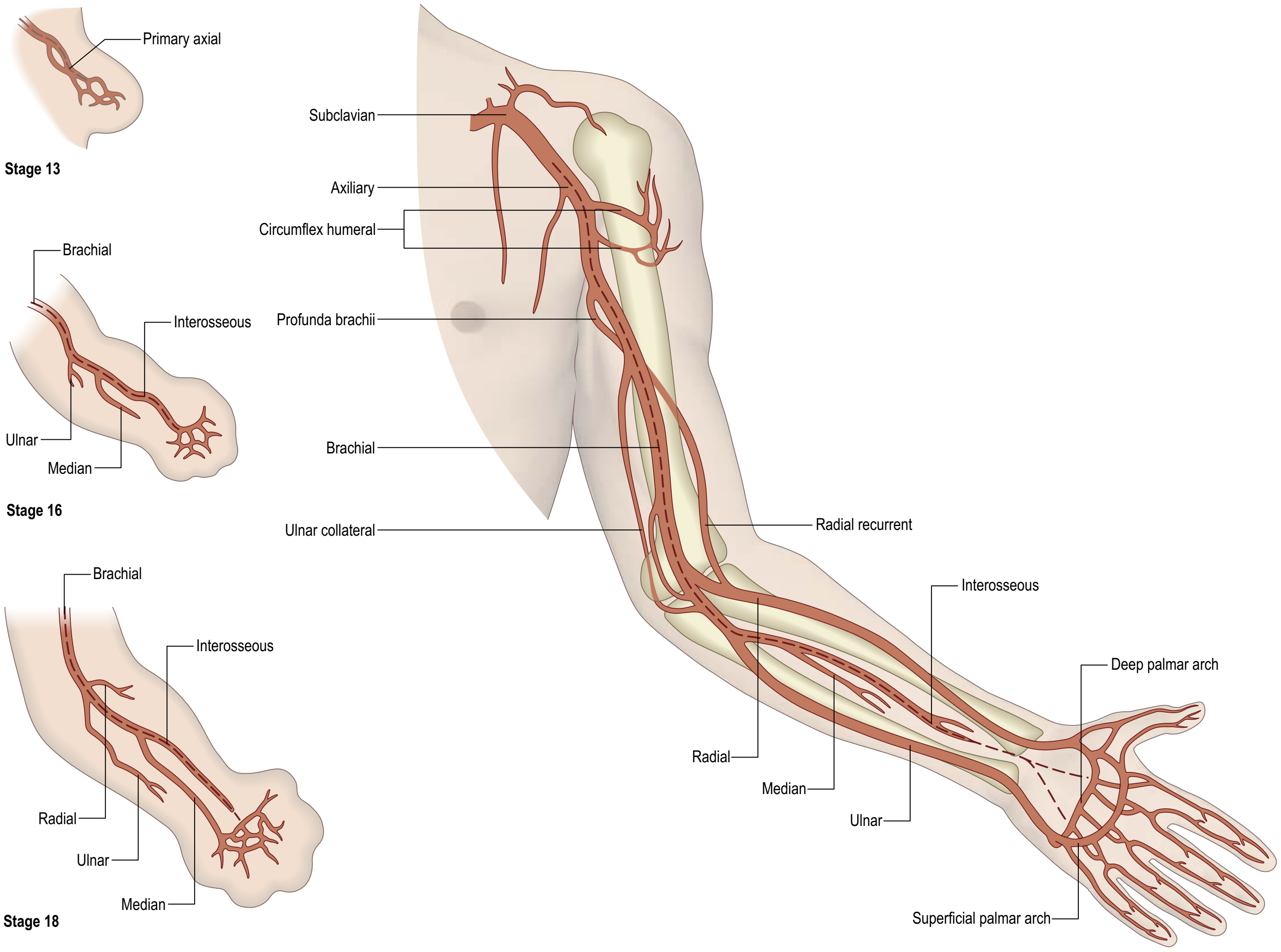

Fig. 19.5 Stages in the development of the arteries of the arm. The path of the axial artery is indicated by an interrupted line.

shoulder and elbow joints occurs at postfertilization weeks 7–8. By stage 17 when the radius and ulna chondrify, the branched tips of the radial, median and ulnar nerves have migrated to the distal hand plate. The carpals chondrify at stage 18, when the hand plate shows notching of the digital rays; the distal phalanges of the hand chondrify in stages 21 and 22. Ossification is earliest in the clavicle, between stages 18 and 20. It begins in the humerus during stages 21 and 22, in the ulna in stages 22 and 23 and in scapula and radius in stage 23. For more details see O'Rahilly and Gardner (1975), Gupta et al (2000).

Vessels

Arteries

In the upper limb, usually only one arterial trunk, the subclavian, persists; it probably represents the lateral branch of the seventh intersegmental artery. Its main continuation, the axial artery of the upper limb, becomes the axillary and brachial arteries, passes into the forearm deep to the flexor muscle mass and terminates as a deep plexus in the developing hand (Fig. 19.5). The original axial vessel ultimately persists as the anterior interosseous artery and the deep palmar arch. A branch from the main trunk passes dorsally between the early radius and ulna as the posterior interosseous artery; a second branch accompanies the median nerve into the hand, where it ends in a superficial capillary plexus. The radial and ulnar arteries are the latest arteries to appear in the forearm. Initially, the radial artery arises more proximally than the ulnar artery, crosses anterior to the median nerve, and supplies biceps brachii. Later, the radial artery establishes a new connection with the main trunk at or near the level of origin of the ulnar artery, and the upper portion of its original stem usually disappears. On reaching the hand, the ulnar artery links up with the superficial palmar plexus, from which the superficial palmar arch is derived. The median artery commonly loses its distal connections and is reduced to a small vessel. The radial artery passes to the dorsal surface of the hand, gives off dorsal digital branches, traverses the first intermetacarpal space and joins the deep palmar arch.

Anomalies of the arterial tree in the forelimb are fairly common: there are several potential causes. The arteries have multiple and plexiform sources; the principal arteries, anastomoses and periarticular networks emerge according to a temporal sequence; and some paths that are initially functionally dominant subsequently regress. In general, anomalous patterns may present as differences in the mode and proximodistal level of branching; the presence of unusual compound arterial segments; aberrant vessels that connect with other principal vessels, arcades or plexuses; vessels that occupy exceptional tissue planes (e.g. superficial fascia instead of the usual subfascial route), or vessels that have unexpected neural, myological or osteoligamentous relationships.

Veins

In the upper limb, the preaxial vein becomes the cephalic vein and drains into the axillary vein at the shoulder. The postaxial vein becomes the basilic vein, which passes deep in the arm to continue as the axillary vein.

Ultrasound antenatal imaging

In the routine, postmenstrual week 18–20 ultrasound fetal assessment, shortening of long bones below 2 standard deviations should lead to a full assessment of all bones (McHugo 2007). Whereas the majority of lethal short limb dysplasias show marked shortening by this time, non-lethal short limb dysplasias seen at birth are not apparent at postmenstrual week 20. Normally, the humerus should be slightly longer than the radius and ulna. The term rhizomelia is used where limb shortening affects the proximal bones more than the distal bones.

NEONATAL UPPER LIMB

In general, the upper limbs in the neonate are proportionately shorter than they are in the adult and extend to the upper thigh, although the trunk is much shorter in the neonate (see Fig. 23.16). At postmenstrual week 37, the arm (shoulder to elbow) is longer than the forearm (elbow to wrist); the arm is not as long as the leg (Pomeroy et al 2014). Only primary centres of ossification are present in the upper limb, apart from a secondary centre in the head of the humerus. The elbow of the newborn can flex to 145° but lacks some 10–15% of full extension. The neonate has a relatively strong reflex grasp within the first few days. The fingernails usually extend to the fingertips or just beyond. They are soft at birth but soon dry and become quite firm and sharp. For details of neonatal blood vessel cannulation in the upper limb see Chapter 13 (peripheral arterial puncture).

DEVELOPMENTAL ANOMALIES OF THE UPPER LIMB

Available with the *Gray's Anatomy* e-book

PELVIC GIRDLE

The pelvic girdle develops in close proximity to cloacal structures. The anterior portion of the pelvic girdle is intimately associated with the normal development of the caudal part of the urogenital system and the anterior body wall. Studies on the development of the lower limb in avian species and the mouse show that the perineal muscles, including the sphincters, derive from somitic myoblasts that have previously entered the hindlimb bud. Similar to the developmental process seen in the upper limb, somitic myoblasts originating from the ventrolateral edge of the dermomyotome migrate into the somatopleuric mesenchyme of the early lower limb bud. The myoblasts coalesce into a single entity before dividing into dorsal and ventral muscle masses. The cells of the ventral muscle mass then divide again, with one population continuing to develop within the limb and the other migrating ventrally towards the genital tubercle (Valasek et al 2005). In the avian embryo, myoblasts from somites 26–29 enter the limb only, and those from somites 30–33 form both cloacal and limb muscles, whereas those from somite 34 form cloacal muscles solely. Within pelvic girdle development, myoblasts do not attain their position by somitic hypaxial domain extension; all myoblasts migrate into the region. Interestingly, the population of myoblasts giving rise to perineal muscles are innervated by axons derived from neurones located in Onuf's nucleus, whereas those that remain in the limb bud gain innervation from anterior horn motor neurones (Valasek et al 2005).

The bony pelvis forms from two hemipelves, each of which develops from one cartilaginous focus. The timetable of chondrogenesis and ossification has been described (Okumuta et al 2017, Verbruggen and Nowlan 2017). Ossification of the pelvis starts with the ilium, which undergoes endochondral ossification at about postmenstrual weeks 9–10 (Baumgart et al 2018). Development of trabecular bone in the ilium is evident from about postmenstrual week 22 and a mature trabecular morphology is present at full-term birth (Cunningham and Black 2009a, 2009b). It has been suggested that the trabecular pattern, previously assumed to develop consequent to weight bearing and bipedal gait, is initiated through genetic patterning plus intrauterine muscular movements which confer biomechanical loading onto the ilium and pelvis.

The development of the superior pubic rami is related to the normal development of the cloacal membrane. In cases of bladder exstrophy (see Fig. 22.11), the superior pubic rami are shortened and do not meet at the pubic symphysis. There is a 4 cm pubic diastasis at birth, which increases to 8 cm at age 10 years, compared with a mean normal width of the pubic symphysis of 0.6 cm at all ages (Wild et al 2011). The ischiopubic segment of the pelvis is 30% shorter, the iliac wings are externally rotated and the acetabuli are retroverted (Wild et al 2011). The mechanisms suggested for this abnormal development are premature rupture of an abnormally cranially placed cloacal membrane, obstruction of medial migration of somatopleuric mesenchyme, and local apoptosis of ventral mesenchyme (Stec 2011, Gearhart and Mathews 2016). It is thought that some combination of the three is likely.

The sacroiliac joint can be recognized by postfertilization week 7; its development is slightly different from that of other synovial joints in that the development of the ilium is ahead of that of the sacrum. Reconsideration of the role of the sacroiliac joint in the transfer of load from axial to appendicular skeleton has been prompted by study of the relative growth of regional surface areas of the ilium from birth to adulthood (Yusof et al 2013). Cavitation of the hip joint has been reported at postfertilization week 7–8. Cloacal anomalies including bladder exstrophy affect the sacroiliac joints with 10° larger sacroiliac joint angles, i.e. more toward the coronal plane than sagittal, and 14.7° inferior rotation compared to unaffected individuals. 3D CT imaging has demonstrated a range of previously unknown rotational anomalies of the pelvis, including external rotation of the posterior pelvis/iliac wings; external rotation of the anterior pelvic segment; coronal rotation of the sacroiliac joint; acetabular retroversion; convergence of the iliac wings; femoral retroversion (Gearhart and Mathews 2016).

LOWER LIMB

The lower limb is first recognizable as a laterally projecting thickening in the body wall opposite somites 24–29 at stage 13 (31–33 days post fertilization); by stage 14 it lies close to the wide umbilical cord. During stages 15–17 (35–41 days post fertilization) the limb projects laterally and outgrowth is fairly symmetric. The core of mesenchymal cells is derived from both somatopleuric and paraxial mesenchyme.

By stage 17 the lower limb still has a flattened foot plate and, although a hip region can be identified, there is no true knee. In stage 18 the lower limb appears to be flexed and abducted at the hip with the knee bent, giving the appearance that the knee is facing laterally. The femur, tibia and fibula begin to chondrify in stages 17 and 18, and the sciatic nerve extends distally to the tibia by stage 18. The patella begins chondrification in stages 21 and 22. The soles of the feet face the umbilical cord, and the foot plate has digit rays. The tarsus and metatarsus start to chondrify in stages 18 and 19. During stages 20–23 (47–58 days post fertilization) the digit rays separate and toes are clearly defined by stage 23. The feet can finally touch at stage 21, when the umbilical cord becomes proportionally smaller and the embryo larger. Ossification of the femur, tibia and fibula starts in stages 22 and 23. For more details see O'Rahilly and Gardner (1975).

Vessels

Arteries

The blood supply to the lower limb is derived from the lateral branch of the fifth lumbar intersegmental artery, which arises from the dorsal root of the umbilical artery passing to the placenta, and continues into the limb bud as the axial artery. The arterial supply to the developing lower limb is thus far less oxygenated than the arterial supply to the upper limb, which receives blood directly from the heart via the subclavian artery. It is possible that the development of several arteries in the distal part of the leg in the embryonic period, some of which subsequently regress, is a reflection of the lower oxygenation of these tissues. During development, the lower limb undergoes medial rotation and extension, so that the original dorsal (extensor) portion of the limb becomes directed ventrally. This relative movement suggests that very different patterning mechanisms operate in the lower limb compared to those in the upper limb and an early complex vasculature may be a product of that difference.

There have been relatively few studies on the early development of the vasculature of the lower limb (Mandell et al 1985, Levinsohn et al 1991, Senior 1991a, 1991b). The terminology used to describe the developing vessels is specific and will be used here. **Table 19.1** describes and illustrates the changes to the axial artery, the new vessels that arise and the vessels that regress, during stages 13–20. The mature vascular pattern is established by the end of the embryonic period.

Veins

The superficial veins of the lower limb are derived from the marginal vein which runs along the periphery of the extending limb bud beneath the pre- and post-axial limb borders. The preaxial vein becomes the long saphenous vein, which drains into the femoral vein at the saphenous opening. The postaxial vein becomes the short saphenous vein, which passes deep and joins the popliteal vein. The earliest valves in the short saphenous vein have been noted at postmenstrual week 13. The number

Approximately 1 in 600 neonates will have a congenital anomaly of the hand or forearm, 30% of which will be bilateral (Goldfarb et al 2015). They occur with an approximately equal frequency in males and females. A defect is twice as likely to occur in the upper limb as in the lower limb. The most critical period for the development of anomalies is during stages 12–16.

For many years, congenital limb anomalies were grouped according to the pattern of deficiency, although the clinical picture did not always relate to the developmental process occurring in the limb (Swanson 1976). More recent classifications of upper limb anomalies are based on developmental molecular biology and pathogenetics (Oberg et al 2010, Tonkin et al 2013, Tonkin 2017).

Limb reduction defects

Limb reduction defects are categorized as failures of development. The basis of limb reductions seen in infants whose mothers took thalidomide during their pregnancy seems likely to be due to death of mesenchyme cells in the early limb bud, causing phocomelia. Proximal segments of the limb were lost, although, in some cases, normal distal segments still formed. There is evidence from experiments in chick embryos that thalidomide interferes with vascularization of the limbs (Vargesson 2009, 2015), and this could lead to mesenchymal cell death. A protein to which thalidomide binds has been identified but it is not yet clear how this is related to thalidomide teratogenicity (Ito et al 2010). Although chorionic villus sampling was reported to be associated with limb reduction defects in the 1990s, present data confirm that sampling between postmenstrual weeks 10 and 13 does not increase the risk; sampling before this time is not recommended (Wapner and Dugoff 2019).

Inheritance of autosomal dominant genes may cause anomalies of the hand. This could, for example, result in absence of the central digit ray of the distal hand plate and subsequent absence of the middle or ring finger and its metacarpals. Extra preaxial digits can result from ectopic polarizing activity due to mutations in regulatory regions in the DNA that control expression of the *Shh* gene, specifically in the developing limb bud (Anderson et al 2012). Other changes in digit number may be the result of alterations in limb bud width and the length of the apical ectodermal ridge.

Anomalies of the digits

Syndactyly, the fusion of adjacent digits, is the most common congenital anomaly of the hand and occurs in about 1 in 2000 live births; it is twice as common in males. It occurs because of failure to remove mesenchymal cells between the digit rays during stages 19–23. Third, fourth, second and first web spaces are affected in decreasing frequency and the condition is bilateral in half of cases (Jordan et al 2012). Clinodactyly is a congenital condition in which the little finger is curved towards the ring finger. It can occur in isolation, or in association with chromosomal abnormalities like Down's syndrome. Camptodactyly is a congenital condition in which the little finger, and sometimes the ring finger, are held in a fixed, flexed position. Symphalangism is a rare congenital disorder in which there is fusion of the interphalangeal joints. The affected finger is stiff, skin creases are absent over the affected joint, there is minimal joint space, and sometimes the digit is shorter than normal. Several different types of brachydactyly, shortening of the digits, can be recognized according to which digits and which parts of these digits are affected. The genetic basis of different types of brachydactyly has now been determined, which is particularly gratifying because brachydactyly was the first condition in humans to be recognized as a dominant Mendelian condition (Gao and He 2004).

TABLE 19.1 **The development of the arteries of the lower limb during stages 13–20.**

Stage	Axial artery	Developing arteries	Regressing arteries	Arterial status
11–12	First appearance of the lower limb bud. The lower limb axial artery arises from the fifth lumbar intersegmental branch of the aorta.			
13–16	The axial artery courses through the lower limb bud to the developing digital plate where it branches into a terminal plexus (future dorsal and plantar networks).			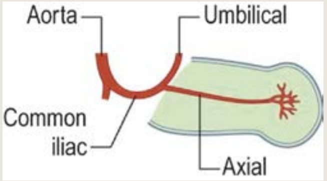
16–17	The axial artery is now described as ischiadic proximally and popliteal profunda (PP) and interossea (I) as it progresses distally.	The external iliac artery, which arises just proximal to the origin of the ischiadic artery, extends distally towards the knee as the femoral artery. A branch, the ramus communicans superior (RCS), passes dorsally to join the ischiadic artery. Perforating branches of the profunda femoris artery initially anastomose with the proximal part of the ischiadic artery.		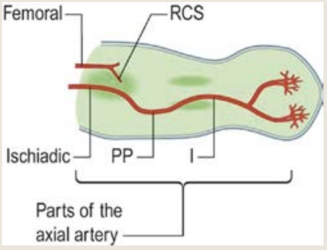 Femoral RCS Ischiadic PP I Parts of the axial artery
18	Elongation of the axial artery forms the popliteal superficialis (PS) between the popliteal profunda and interossea arteries.	Two new vessels arise from the popliteal superficialis artery. These are the tibialis posterior superficialis (TPS) and the peronea posterior superficialis (PPS). Both vessels join the plantar network. There are now three arteries in the leg.	The proximal portion of the ischiadic artery starts to regress. Parts persist in the adult as the inferior gluteal artery and the arteria comitans nervi ischiadici.	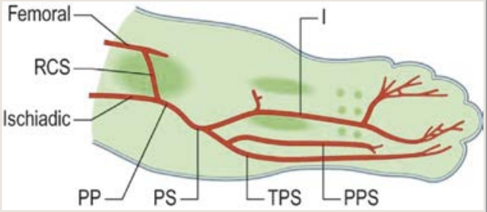
19		Two further vessels arise. They are the tibialis anterior pars distalis (TApd) from the interossea artery and the ramus communicans inferior (RCI) from the peronea posterior superficialis. The original plantar network is remodelled into a medial plantar artery (from the distal part of tibialis posterior superficialis) and a lateral plantar artery (from the distal continuation of the confluence of the interossea, ramus communicans inferior and the peronea posterior superficialis) which together form the plantar arch. There are now five arteries in the leg.		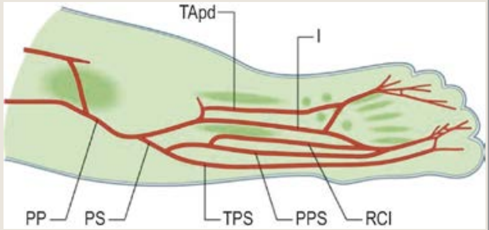
20		The arteries in the leg at this stage are the tibialis anterior (TA), tibialis posterior (TP) and the ramus communicans inferior. The latter is confluent with the peronea posterior superficialis in the tarsal region and becomes the fibular (peroneal) artery. The plantar arch is now supplied solely by the tibialis posterior. There are now three arteries in the leg.	Popliteal profunda, interossea artery and peronea posterior superficialis arteries.	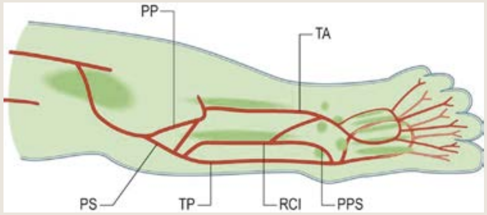

of valves increases from 1 to 8 between postmenstrual weeks 13–18; there are more valves in the proximal than in the distal portion of the short saphenous vein (Czarniawska-Grzesińska and Bruska 2002).

Ultrasound antenatal imaging

Femur length is routinely measured to assess growth velocity (along with head circumference and abdominal circumference) and to predict the expected date of delivery. The longest axis of the ossified diaphysis is identified with soft tissue noted beyond both ends. The distal epiphysis is excluded (Fig. 19.6). Overall limb length correlates to the ecogeographic principles, Bergmann's and Allen's rules, that mammalian species have greater body mass in colder climates and limbs tend to be shorter in cold environments and longer in warm environments (Bogin 2012). Appropriate fetal biometry comparison charts are necessary for accurate evaluation (Ogasawara 2009). Identification of short femur length is associated with a higher risk of chromosomal abnormalities (Mathiesen et al 2014) and a significantly higher likelihood of the fetus being small for gestational age and at risk of early preterm delivery

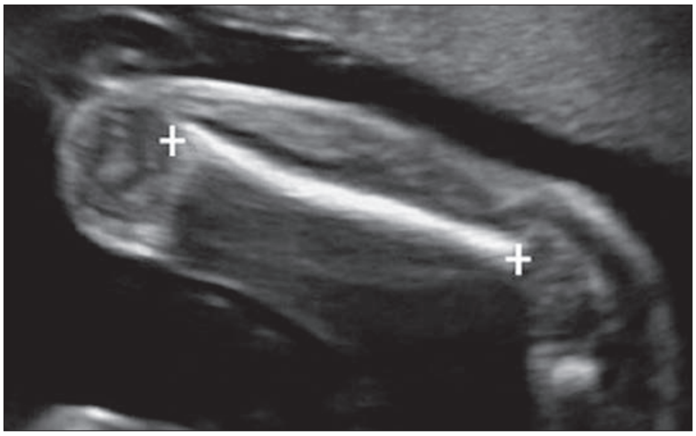

Fig. 19.6 An ultrasound image showing femur length. (With permission from To M, Pereira S Routine fetal anomaly scan. In: Coady AM (ed) Twining's Textbook of Fetal Abnormalities, 3rd ed. Elsevier, Churchill Livingstone. Copyright 2015.)

(Özlü and Ozcan 2013, Mathiesen et al 2014). It has been estimated that identification of isolated short femur length below the 10th or 5th percentile at mid-gestation is associated with more than a three-fold risk of the development of fetal growth restriction and increased risk of early preterm birth before postmenstrual weeks 34–37 (Goetzinger et al 2012). Although the cause of this relationship must be multifactorial, it has been suggested that changes in placentation and chronic fetal hypoxia may lead to a fetal adaptive response in which highly oxygenated blood is diverted to the brain and heart at the expense of the extremities.

NEONATAL LOWER LIMB

In the neonate, the pelvis is cone-shaped. The transverse diameter of the true pelvis is 2.2 cm, its anteroposterior diameter is 2.8 cm and the length between the inlet and outlet is 2 cm. The sacrum is proportionately larger than in the adult and the sacral promontory is higher. When walking begins, the sacrum descends between the ilia and the promontory develops. The ilia, ischia and pubic bones are variably ossified at birth; they meet at the triradiate epiphysis in the acetabulum, which in the neonate is cartilaginous, relatively large and shallow.

In human neonates the lower limbs are less developed compared to the upper limbs. Genotypic factors have been implicated, but this disparity may also reflect the lower oxygen saturation levels in the blood that flows to the lower limb and that also passes to the umbilical arteries and placenta. Clinical evidence has shown that postnatally increased blood flow to the limbs is linked to greater growth; children living at high altitude have reduced tibial length and lower blood oxygen saturation (Bogin 2012).

At term (postmenstrual week 37), the thigh (hip to knee) is longer than the leg (knee to ankle) (Pomeroy et al 2014). The femoral neck is much shorter than in the adult and forms an acute angle with the shaft, which at this stage is quite straight: the adult curvature is acquired with walking. The head of the femur is larger than the acetabular fossa and nearly one-third remains external, which means that the ligament of the head of the femur is relatively very long. Dislocation of the hip joint is relatively easy: the femoral head can be removed from the acetabular fossa laterally but not posteriorly. The fetal position, where the lower limbs are in a flexed position, is often assumed by postnatal babies: it keeps the thighs in continuous abduction and stretches the adductors. The muscles that will be used for walking are weak and the lack of gluteal development, in particular, gives the typically diminutive buttocks of the neonate.

Although the legs appear to be bowed, the tibia and fibula are straight. The illusion of bow legs is caused by the shape of the soft tissues and the slightly more advanced development of the lateral head of gastrocnemius compared to its medial head. The calcaneus and the talus each have an ossification centre at birth, and a centre is frequently present in the cuboid. The feet are usually inverted and they have a greater degree of dorsiflexion, caused by the relatively greater area of the trochlea of the talus. Plantar flexion is limited, in part reflecting the shortness of the extensor muscles of the foot. At birth, the footprint outlines the whole plantar surface, reflecting the deposition of subcutaneous fat beneath the longitudinal and transverse arches, and so most babies appear flat-footed. For details of neonatal blood vessel cannulation in the lower limb see Chapter 13 (Peripheral arterial puncture).

DEVELOPMENTAL ANOMALIES OF THE LOWER LIMB

Available with the *Gray's Anatomy* e-book

Key references

Ferretti P, Tickle C 2006 The limbs. In: Ferretti P, Copp A, Tickle C et al (eds) Embryos, Genes and Birth Defects, 2nd ed. Chichester: Wiley, pp. 123–166.
An account of the genetic basis of limb development.

Hinchcliffe JR, Johnson DR 1980 The Development of the Vertebrate Limb. An Approach through Experiment, Genetics, and Evolution. Oxford: Clarendon Press.
A presentation of the classical experiments on limb development.

O'Rahilly R, Gardner E 1975 The timing and sequence of events in the development of the limbs in the human embryo. Anat Embryol (Berl) 148:1–23.
A description of the stages in human limb development.

Shea CA, Rolfe RA, Murphy P 2015 The importance of foetal movement for co-ordinated cartilage and bone development in utero: clinical consequences and potential for therapy. Bone Joint Res 4:105–116.
This paper discusses how embryonic and fetal movements affect cartilage, bone and joint development, including the way that mechanical transduction can influence the biomechanical properties of the extracellular matrix. Biophysical cues generated by movement constitute the feedback that maintains and remodels all skeletal tissues throughout life.

Swanson AB 1976 A classification for congenital limb malformations. J Hand Surg Am 1:8–22.
A source that sets out details of an accepted classification for congenital limb malformations.

Tickle C, Towers M 2017 Sonic hedgehog signaling in limb development. Front Cell Dev Biol 5:14.
This reference summarizes the specification of the craniocaudal axis of the developing limb and considers how positional values within the limb bud are specified over time.

Tonkin MA, Tolerton SK, Quick TJ et al 2013 Classification of congenital anomalies of the hand and upper limb: development and assessment of a new system. J Hand Surg Am 38:1845–1853.
A presentation of the Oberg, Manske and Tonkin (OMT) classification of upper limb anomalies and the challenges of incorporating the molecular mechanisms of limb anomalies into current systems.

Valasek P, Theis S, Krejci E et al 2010 Somitic origin of the medial border of the mammalian scapula and its homology to the avian scapula blade. J Anat 216:482–488.
This article establishes the avian scapular blade and medial border of the mammalian scapula as homologous structures that share the same developmental origin.

Valasek P, Theis S, DeLaureir A et al 2011 Cellular and molecular investigations into the development of the pectoral girdle. Dev Biol 357:108–116.
The study provides evidence that the formation of the muscles of the proximal limb occurs through two distinct mechanisms.

Zeller R, Lopez-Rios J, Zuniga A 2009 Vertebrate limb development; moving towards integrative analysis of organogenesis. Nat Rev Genet 10:845–858.
A review of the molecular basis of limb development particularly focusing on how cell–cell interactions are integrated.

Developmental dysplasia of the hip (previously known as congenital dislocation of the hip) refers to an abnormal configuration of, or relationship between, the femoral head and the acetabulum that occurs either before or after birth in approximately 1 in 1000 live births with a female : male ratio of 6 : 1. (In 2% of cases, hip dislocation is not evident at birth but manifests in the first few months of the life.) It covers a continuum of disorders that ranges from shallowness of the acetabulum to instability and subluxation of the femoral head and, ultimately, to frank dislocation. Acetabular anteversion may occur (Li et al 2009). The aetiology is considered to be multifactorial and is associated with first pregnancies, suggesting that both maternal and uterine musculature restricts fetal movement and puts postural strain on the fetal hips.

Developmental dysplasia of the hip is seen more frequently in breech delivery, especially if the knees are extended; breech position at any time after postmenstrual week 36 is a risk factor for the condition. The incidence is similar in preterm and term infants born in the breech position (Quan et al 2013). The left hip is more frequently affected than the right, possibly because, in breech presentation, the fetus lies with the right shoulder anterior and the left thigh closest to the maternal sacrum. The physiological effects that cause the maternal ligaments to become temporarily lax prior to delivery are also considered to affect the fetus and to contribute to laxity of the hip capsule. Risk factors are breech delivery, female gender, a positive family history, clicking of the hips and hips that can be easily dislocated at clinical examination (de Hundt et al 2012). Ultrasound is the definitive investigation used for early detection together with clinical examination; magnetic resonance imaging (MRI) may be required to identify the underlying bony and soft tissue anatomy.

The collodiaphysial angle (CDA; neck–shaft angle, Mikulicz angle) is the angle between the long axis of the femoral shaft and the head and neck of the femur; the normal adult range varies between 125° and 140° (see Fig. 77.30). Where the CDA is enhanced, usually above 135°, a coxa valga deformity occurs. Where CDA is decreased (usually defined as less than 120°), a coxa vara deformity occurs; the mechanism is thought to be a failure of medial growth of the physial plate. The resulting lower limb is shortened and abduction is restricted.

The adult femur normally aligns on the tibia obliquely, creating an angle of 174° facing laterally. A medial angulation of the leg in relation to the thigh is called genu varum, and a lateral angulation, where the upper part of the knee is displaced inwards with the lower part displaced outwards, is called genu valgum. The hip–knee (femoral–tibial) angle in children is +3.6° (varum) between the ages of 1 and 2 years, and −2.5° (valgum) between the ages of 2 and 3 years. The prevalence of lower limb deformities physiologically decreases after 5 years of age; the angle is +0.3° after the age of 7 years, which is within 1° of adult reference values (Sabharwal and Zhao 2009). Both deformities cause unequal weight distribution that hastens destruction of knee cartilages; persistence of genu varum/valgum until late childhood may require correction in order to prevent arthrosis. (For further reading, see Goldman and Green (2010).) Congenital dislocation of the patella may be noted in the neonate with flexion contracture of the knee, genu valgus, external tibial torsion and foot deformity. It is irreducible and treated surgically. The patella ossifies between postnatal years 3 and 5 and so it is not visible on X-ray in infancy and early childhood (Wada et al 2008).

The patella may be absent or hypoplastic, an anomaly that may be isolated or may be associated with other defects (Mizobuchi et al 2007).

Congenital talipes equinovarus, or club foot, derives its name from a combination of *talus* and *pes*, together with terms describing an elevated heel resembling that of a horse (*equino*), which is also turned inwards (*varus*). It is a common neonatal anomaly and occurs in approximately 1 per 1000 live births, with males affected twice as often as females. There is some degree of inheritance, so it is not entirely an effect of intrauterine positioning or of oligohydramnios (abnormally little amniotic fluid). Both bones and soft tissues are affected, which means that it is difficult to distinguish between primary and secondary effects. A number of theories have been proposed to explain the underlying pathogenetic mechanism(s), including abnormal tendon and ligament attachments, defective development of the talus and delayed muscle maturation. One theory is that the talus undergoes defective development and that all the other anomalies arise as a consequence of this initial defect. The talus is decreased in size by up to 25%. It has a foreshortened neck and decreased body/neck angle, and the subtalar facets are medially rotated. The navicular is small and medially deviated relative to the talus. The calcaneus is also small and shows varus displacement and equinus tilt; the anterior facets correspond to those of the talus (Barlow and Clarke 1994). The entire affected foot and calf are smaller than their normal counterparts. The foot is inverted and supinated, and the forefoot is adducted. The heel is small, rotated inwards and elevated. The calcaneus is inverted beneath the talus. MRI analysis of the lower legs of patients who had been treated for idiopathic congenital talipes equinovarus showed that leg muscle volume was consistently reduced (Duce et al 2013). Treatment varies between splintage and repeated complex surgery, which reflects the highly variable severity of the condition and individual response to therapy. Positional talipes equinovarus is usually attributed to intrauterine position of the foot, is passively correctable and does not require surgery, whereas fixed talipes equinovarus is not passively correctable and usually requires surgery.

‘Flat feet’ are common in childhood. The majority are ‘flexible’ and simply related to posture, whereas ‘rigid’ flat feet are caused by structural anomalies. The description of ‘rocker bottom’ foot is associated with many congenital syndromes. The foot is flat and rigid, and the plantar surface appears curved with the apex of the curve at the midtarsal joint. The condition shows an equinus position of the hindfoot. The talus may be vertical and palpable on the plantar surface. A majority of infants with this condition also have neurological anomalies.

References

Anderson E, Peluso S, Lettice LA et al 2012 Human limb abnormalities caused by the disruption of hedgehog signalling. Trends Genet 28:364–373.

Andrey G, Montavon T, Mascrez B et al 2013 A switch between topological domains underlies HoxD genes collinearity in mouse limbs. Science 340: 1234167.

Barlow I, Clarke NM 1994 Congenital talipes equinovarus. Surgery 12:211–215.

Baumgart M. Wiśniewski M, Grzonkowska M et al 2018 Quantitative anatomy of the ilium's primary ossification center in the human fetus. Surg Radiol Anat 340:1047–1054.

Blitz E, Sharir A, Akiyama H et al 2013 Tendon–bone attachment unit is formed modularly by a distinct pool of Scx- and Sox-positive progenitors. Development 140:2680–2690.

Bogin B 2012 Leg length, body proportion, health and beauty. In: Cameron N, Bogin B (eds) Human Growth and Development, 2nd ed. London: Academic Press Elsevier; Ch. 13.

Catela C, Shin MM, Lee DH et al 2016 Hox proteins coordinate motor neuron differentiation and connectivity programs through Ret/Gfrα genes. Cell Rep 14:1901–1915.

Charvet B, Ruggiero F, Le Guellec D 2012 The development of the myotendinous junction. A review. Muscle Ligaments Tendons J 2:53–63.

Chevallier A, Kieny M, Mauger A 1977 Limb–somite relationship: origin of the limb musculature. J Embryol Exp Morphol 41:245–258.

Cooper KL, Hu JK, ten Berge D et al 2011 Initiation of proximo–distal patterning in the vertebrate limb by signals and growth. Science 332: 1083–1086.

Cotney J, Leng J, Yin J et al 2013 The evolution of lineage-specific regulatory activities in the human embryonic limb. Cell 154:185–196.

Cunningham CA, Black SM 2009a Development of the fetal ilium – challenging concepts of bipedality. J Anat 214:91–99.

Cunningham CA, Black SM 2009b Anticipating bipedalism: trabecular organization in the newborn ilium. J Anat 214:897–929.

Czarniawska-Grzesińska M, Bruska M 2002 Development of valves in the small saphenous vein in human fetuses. Folia Morphol (Warsz) 61:37–42.

Dasen JS, Tice BC, Brenner-Morton S et al 2005 A Hox regulatory network establishes motor neuron pool identity and target-muscle connectivity. Cell 123:477–491.

Davey MG, James J, Paton IR et al 2007 Analysis of talpid3 and wild-type chicken embryos reveals roles for Hedgehog signalling in development of the limb bud vasculature. Dev Biol 301:155–165.

de Hundt M, Vlemmix F, Bais JM et al 2012 Risk factors for developmental dysplasia of the hip: a meta-analysis. Eur J Obstet Gynecol Reprod Biol 165:8–17.

Decker RS, Koyama E, Pacifici M 2014 Genesis and morphogenesis of limb synovial joints and articular cartilage. Matrix Biol 39:5–10

Delgado Caceres M, Pfeifer CG, Docheva D 2018 Understanding tendons: lessons from transgenic mouse models. Stem Cells Dev 27:1161–1174.

Dolan CP, Dawson LA, Muneoka K 2018 Digit tip regeneration: merging regeneration biology with regenerative medicine. Stem Cells Transl Med 7:262–270.

Drescher U 2011 Axon guidance: push and pull with ephrins and GDNF. Curr Biol 21:R30–R32.

Duce SL, D'Alessandro M, Du Y et al 2013 3D MRI analysis of the lower legs of treated idiopathic congenital talipes equinovarus (clubfoot). PLoS One 8:e54100.

Dudley AT, Ros MA, Tabin CJ 2002 A re-examination of proximodistal patterning during vertebrate limb development. Nature 418:539-544.

Einspieler C, Marschik PB, Urlesberger B et al 2016. The general movement optimality score – a detailed assessment of general movements during preterm and term age. Dev Med Child Neurol 58:361–368.

Fallon JF, Crosby GM 1977 Polarizing activity in limb buds of amniotes. In: Ede DA, Hinchliffe JR, Balls M (eds) Vertebrate Limb and Somite Morphogenesis. Cambridge: Cambridge University Press, pp. 55–70.

Ferretti P, Tickle C 2006 The limbs. In: Ferretti P, Copp A, Tickle C et al (eds) Embryos, Genes and Birth Defects, 2nd ed. Chichester: Wiley, pp. 123–166.

An account of the genetic basis of limb development.

Foster JW, Dominguez-Steglich MA, Guioli S et al 1994 Campomelic dysplasia and autosomal sex reversal caused by mutations in an SRY-related gene. Nature 372:525–530.

Gao B, He L 2004 Answering a century old riddle: brachydactyly type A1. Cell Res 14:179–187.

Gearhart JP, Mathews R 2016 Exstrophy–epispadias complex. In: Wein AJ, Kavoussi LR, Partin AW (eds) Campbell-Walsh Urology, 11th ed. Elsevier; Ch. 139.

Genc B, Ozdinler PH, Mendoza AE et al 2004 A chemoattractant role for NT-3 in proprioceptive axon guidance. PloS Biol 12:e403.

Goetzinger KR, Cahill AG, Macones GA et al 2012 Isolated short femur length on mid-trimester ultrasound: a marker for fetal growth restriction and other adverse perinatal outcomes. J Ultrasound Med 31:1935–1941.

Goldfarb CA, Wall LB, Bohn DC et al 2015 Epidemiology of congenital upper limb anomalies in a midwest United States population: an assessment using the Oberg, Manske, and Tonkin classification. J Hand Surg Am 40:127–132.

Goldman V, Green DW 2010 Advances in growth plate modulation for lower extremity malalignment (knock knees and bow legs). Curr Opin Pediatr 22:47–53.

Gros J, Tabin CJ 2014 Vertebrate limb bud formation is initiated by localized epithelial-to-mesenchymal transition. Science 343: 1253–1256.

Gupta A, Kay SPJ, Scheker LR 2000 The Growing Hand. London: Harcourt.

A source that includes articles on embryology, growth and congenital anomalies of the hand.

Hallmann R, Feinberg RN, Latker CH et al 1987 Regression of blood vessels precedes cartilage differentiation during chick limb development. Differentiation 34:98–105.

Harfe BD, Scherz PJ, Nissim S et al 2004 Evidence for an expansion-based temporal Shh gradient in specifying vertebrate digit identities. Cell 118: 517–528.

Hinchcliffe JR, Johnson DR 1980 The Development of the Vertebrate Limb. An Approach through Experiment, Genetics, and Evolution. Oxford: Clarendon Press.

A presentation of the classical experiments on limb development.

Honig MG, Rutishauser UR 1996 Changes in the segmental pattern of sensory neuron projections in the chick hindlimb under conditions of altered cell adhesion molecule function. Devel Biol 175:325–337.

Honig MG, Lance-Jones C, Landmesser L 1986 The development of sensory projection patterns in embryonic chick hindlimb under experimental conditions. Dev Biol 118:532–548.

Honig MG, Frase PA, Camilli SJ 1998 The spatial relationships among cutaneous, muscle sensory and motoneuron axons during development of the chick hindlimb. Development 125:995–1004.

Honig MG, Camilli SJ, Xue QS 2004 Ectoderm removal prevents cutaneous nerve formation and perturbs sensory axon growth in the chick hindlimb. Dev Biol 266:27–42.

Honig MG, Camilli SJ, Surineni KM et al 2005 The contributions of BMP4, positive guidance cues, and repulsive molecules to cutaneous nerve formation in the chick. Dev Biol 282:257–273.

Hurren B, Collins JJP, Duxson MJ et al 2015 First neuromuscular contact correlated with onset of primary myogenesis in rat and mouse limb muscles. PLoS One 10(7): e0133811. doi: 10.1371/journal.pone.0133811.

Ito T, Ando H, Suzuki T et al 2010 Identification of a primary target of thalidomide teratogenicity. Science 327:1345–1350.

Jafari P, Muller C, Grognuz A et al 2017 First insights into human fingertip regeneration by echo-Doppler imaging and wound microenvironment assessment. Int J Mol Sci 18:1054. doi: 10.3390/ijms18051054.

Jessell TM, Sürmeli G, Kelly JS 2011 Motor neurons and the sense of place. Neuron 72:419–424.

Jordan D, Hindocha S, Dhital M et al 2012 The epidemiology, genetics and future management of syndactyly. Open Orthopaed J 6 (Suppl 1:M2) 14027.

Kardon G, Campbell JK, Tabin C 2003 Local extrinsic signals determine muscle and endothelial cell fate and patterning in the vertebrate limb. Dev Cell 3:533–545

Kazenwadel J, Harvey NL 2016 Morphogenesis of the lymphatic vasculature: a focus on the new progenitors and cellular mechanisms important for constructing lymphatic vessels. Dev Dyn 245:209–219.

Lane EB, Tickle C 2003 How to make a hand: a 3 day symposium held at the University of Dundee. J Anat 202:1.

A collection of reviews on limb development and human limb malformations.

Lechner SG, Frenzel H, Wang R et al 2009 Developmental waves of mechanosensitivity acquisition in sensory neuron subtypes during embryonic development. EMBO J 28:1479–1491.

Levinsohn EM, Hootnick DR, Packard DS 1991 Consistent arterial abnormalities associated with a variety of congenital malformations of the human lower limb. Invest Radiol 26:364–373.

Lewis J, Chevallier A, Kieny M et al 1981 Muscle nerve branches do not develop in chick wings devoid of muscle. J Embryol Exp Morph 64:211–232.

Li LY, Zhang LJ, Zhao Q et al 2009 Measurement of acetabular anteversion in developmental dysplasia of the hip in children by two- and three-dimensional computed tomography. J Int Med Res 37:567–575.

Li W, Kohara H, Uchida Y et al 2013 Peripheral nerve-derived CXCL12 and VEGF-A regulate the patterning of arterial vessel branching in developing limb skin. Dev Cekk 24:359–371.

MacCabe JA, Errick J, Saunders JW 1974 Ectodermal control of the dorsoventral axis of the leg bud of the chick embryo. Dev Biol 39:69–82.

Mandell VS, Jaques PF, Delany DJ et al 1985 Persistent sciatic artery: clinical, embryologic, and angiographic features. Am J Roentgenol AJR 144:245–249.

Mathiesen JM, Aksglaede L, Skibsted L et al 2014 Outcome of fetuses with short femur length detected at second-trimester anomaly scan: a national survey. Ultrasound Obstet Gynecol 44:160–165.

Matsuoka T, Ahlberg PE, Kessaris N et al 2005 Neural crest origins of the neck and shoulder. Nature 436:347–355.

This paper considers the development of the transition zones between the head and neck, the back and the pectoral girdle.

McHugo JM 2007 Skeletal anomalies. In: Twining P, McHugo JM, Pilling DW (eds) Textbook of Fetal Abnormalities, 2nd ed. Edinburgh: Elsevier, Churchill Livingstone; Ch. 12.

Mizobuchi RR, Galbiatti JA, Quirici Neto F et al 2007 Ultrasonographic study of the femoropatellar joint and its attachments in normal infants from birth to 24 months of age: part I. J Pediatr Orthop 16:262–265.

Muchison ND, Proce BA, Conner SDA et al 2007 Regulation of tendon differentiation by scleraxis distinguishes force-transmitting tendons from muscle-anchoring tendons. Development 134:2697–2708.

Nagashima H, Sugahara F, Watanabe K et al 2016 Developmental origins of the clavicle, and its implications for the evolution of the neck and paired appendages in vertebrates. J Anat 229:536–548.

Niswander L, Tickle C, Vogel A et al 1993 FGF-4 replaces the apical ectodermal ridge and directs outgrowth and patterning of the limb. Cell 75:579–587.

Nowlan NC, Sharpe J, Roddy KA et al 2010 Mechanobiology of embryonic skeletal development: insights from animal models. Birth Defects Res C Embryo Today 90:203–213.

An account that reviews and contrasts recent work on both chick and mouse models on the importance of movement in the development of the locomotor apparatus.

Oberg KC, Feenstra JM, Manske PR et al 2010 Developmental biology and classification of congenital anomalies of the hand and upper extremity. J Hand Surg 35:2066–2076.

Ogasawara KK 2009 Variation in fetal ultrasound biometry based on differences in fetal ethnicity. Am J Obstet Gynecol 200:676–678.

Okumuta M, Ishikawa A, Aoyama T et al 2017 Cartilage formation in the pelvic skeleton during the embryonic and early-fetal period. PLoS ONE 12(4): e0173852. https://doi.org/10.1371/journal. pone.0173852.

O'Rahilly R, Gardner E 1975 The timing and sequence of events in the development of the limbs in the human embryo. Anat Embryol (Berl) 148:1–23.

A description of the stages in human limb development.

Özlü T, Ozcan T 2013 Fetal isolated short femur in the second trimester and adverse pregnancy outcomes. Prenat Diagn 33:1063–1069.

Parr BA, McMahon AP 1995 Dorsalizing signal Wnt-7a required for normal polarity of D-V and A-P axes of mouse limb. Nature 374:350–353.

Pickering J, Towers M 2014 Molecular genetics of human congenital limb malformations. eLS. https://doi.org/10.1002/9780470015902.a0025686.

Pitsillides AA 2006 Early effects of embryonic movement: 'a shot out of the dark'. J Anat 208:417–431.

A review of recent work using chicken embryos to explore the importance of movement in development of the locomotor apparatus.

Pomeroy E, Stock JT, Cole TJ et al 2014 Relationships between neonatal weights, limb lengths, skinfold thicknesses, body breadths and circumferences in an Australian cohort. PLoS ONE 9(8): e105108. doi: 10.1371/journal.pone.0105108.

Pu Q, Huang R, Brand-Saberi B 2016 Development of the shoulder girdle musculature. Dev Dyn 245:342–350.

Quan T, Kent AL, Carlisle H 2013 Breech preterm infants are at risk of developmental dysplasia of the hip. J Paediatr Child Health 49:658–663.

Riddle RD, Johnson RL, Laufer E et al 1993 Sonic hedgehog mediates the polarizing activity of the ZPA. Cell 75:1401–1416.

Robson LG, Kara T, Crawley A et al 1994 Tissue and cellular patterning of the musculature in chick wings. Development 120:1265–1276.

Rosello-Diez A, Ros MA, Torres M 2011 Diffusible signals not autonomous mechanisms determine the main proximodistal limb subdivision. Science 332: 1086–1088.

Sabharwal S, Zhao C 2009 The hip–knee–ankle angle in children: reference values based on a full-length standing radiograph. J Bone Joint Surg Am 91:2461–2468.

Saiz-Lopez P, Chinnaiya K, Campa VM et al 2015 An intrinsic timer specifies distal structures of the vertebrate limb. Nat Commun 6:8108.

Saunders JW, Gasseling MT 1959 The differentiation of prospective thigh mesoderm grafted beneath the apical ectodermal ridge of the wing bud in the chick embryo. Dev Biol 1:281–301.

Saunders JW, Gasseling MT 1968 Ectodermal-mesenchymal interactions in the origin of limb symmetry. In: Fleischmajer R, Billingham RE (eds) Epithelial–Mesenchymal Interactions. Baltimore: Williams & Wilkins, pp. 78–97.

Saunders JW, Gasseling MT, Errick JE 1976 Inductive activity and enduring cellular constitution of a supernumerary apical ectodermal ridge grafted to the limb bud of the chick embryo. Dev Biol 50:16–25.

Senior HD 1991a The development of the arteries of the human lower extremity. Am J Anat 25:54–95.

Senior HD 1991b An interpretation of the recorded arterial anomalies of the human leg and foot. J Anat 53:130–171.

Shea CA, Rolfe RA, Murphy P 2015 The importance of foetal movement for co-ordinated cartilage and bone development in utero: clinical consequences and potential for therapy. Bone Joint Res 4:105–116.

This paper discusses how embryonic and fetal movements affect cartilage, bone and joint development, including the way that mechanical transduction can influence the biomechanical properties of the extracellular matrix. Biophysical cues generated by movement constitute the feedback that maintains and remodels all skeletal tissues throughout life.

Stec AA 2011 Embryology and bony and pelvic floor anatomy in the bladder exstrophy-epispadias complex. Semin Pediatr Surg 20:66–70.

Subramanian A, Schilling TF 2015 Tendon development and musculoskeletal assembly: emerging roles for the extracellular matrix. Development 142:4191–4204.

Sugimoto Y, Takimoto A, Akiyama H et al 2013 Scx+/Sox9+ progenitors contribute to the establishment of the junction between cartilage and tendon/ligament. Development 140:2280–2288.

Summerbell D, Lewis J, Wolpert L 1973 Positional information in chick limb morphogenesis. Nature 244:492–496.

Sürmeli G, Akay T, Ippolito G et al 2011 Patterns of spinal sensory-motor connectivity prescribed by a dorsoventral positional template. Cell 147:653–665.

Swanson AB 1976 A classification for congenital limb malformations. J Hand Surg Am 1:8–22.

A source that sets out details of an accepted classification for congenital limb malformations.

Taher L, Collette NM, Murugesh D et al 2011 Global gene expression analysis of murine limb development. PLoS One 6:e28358.

Theis S, Patel K, Valasek P et al 2010 The occipital lateral plate mesoderm is a novel source for vertebrate neck musculature. Development 137:2961–2971.

Tickle C 2017 An historical perspective on the pioneering experiments of John Saunders. Dev Biol 429:374-381.

Tickle C, Towers M 2017 Sonic hedgehog signaling in limb development. Front Cell Dev Biol 5:14.

This reference summarizes the specification of the craniocaudal axis of the developing limb and considers how positional values within the limb bud are specified over time.

Tonkin MA 2017 Classification of congenital anomalies of the hand and upper limb. J Hand Surg Eur 42:448–456.

Tonkin MA, Tolerton SK, Quick TJ et al 2013 Classification of congenital anomalies of the hand and upper limb: development and assessment of a new system. J Hand Surg Am 38:1845–1853.

A presentation of the Oberg, Manske and Tonkin (OMT) classification of upper limb anomalies and the challenges of incorporating the molecular mechanisms of limb anomalies into current systems.

Uhthoff HK 1990 The Embryology of the Human Locomotor System. Berlin: Springer.

A description of embryonic limb development.

Valasek P, Evans DJ, Maina F et al 2005 A dual fate of the hindlimb muscle mass: cloacal/perineal musculature develops from leg muscle cells. Development 132:447–458.

Valasek P, Theis S, Krejci E et al 2010 Somitic origin of the medial border of the mammalian scapula and its homology to the avian scapula blade. J Anat 216:482–488.

This article establishes the avian scapular blade and medial border of the mammalian scapula as homologous structures that share the same developmental origin.

Valasek P, Theis S, DeLaureir A et al 2011 Cellular and molecular investigations into the development of the pectoral girdle. Dev Biol 357:108–116.

This study provides evidence that the formation of the muscles of the proximal limb occurs through two distinct mechanisms.

Vargesson N 2009 Thalidomide-induced limb defects: resolving a 50-year-old puzzle. Bioessays 31:1327–1336.

Vargesson N 2015 Thalidomide-induced teratogenesis: history and mechanisms. Birth Defects Res C Embryo Today 105:140–156.

Verbruggen SW, Nowlan NC 2017 Ontogeny of the human pelvis. Anat Rec 300:643–52

Verbruggen SW, Kainz B, Shelmerdine SC et al 2018 Stresses and strains on the human fetal skeleton during development. J R Soc Interface 15:pii: 20170593.

Wada A, Fujii T, Takamura K et al 2008 Congenital dislocation of the patella. J Child Orthop 2:119–123.

Walsh JM, Kilbane M, McGowan CA et al 2013 Pregnancy in dark winters: implications for fetal bone growth? Fertil Steril 99:206–211.

Wang B, He L, Ehehalt F et al 2005 The formation of the avian scapular blade takes place in the hypaxial domain of the somites and requires somatopleure-derived BMP signals. Dev Biol 287:11–18.

Wang G, Scott SA 2002 Development of 'normal' dermatomes and somatotopic maps by 'abnormal' populations of cutaneous neurons. Dev Biol 251:424–433.

Wapner RJ, Dugoff L 2019 Prenatal diagnosis of congenital disorders. In Resnik R, Lockwood C, Moore T et al Creasy and Resnik's Maternal–Fetal Medicine: Principles and Practice. Elsevier. Ch 32; pp. 493–538.

Weintraub H, Davis R, Tapscott S et al 1991 The MyoD gene family: nodal point during specification of the muscle cell lineage. Science 251:761–766.

Wild AT, Sponseller PD, Stec AA et al 2011 The role of osteotomy in surgical repair of bladder exstrophy. Semin Pediatr Surg 20:71–78.

Wright E, Hargrave MR, Christiansen J et al 1995 The Sry-related gene Sox9 is expressed during chondrogenesis in mouse embryos. Nat Genet 9:15–20.

Yusof N, Soames RW, Cunningham CA et al 2013 Growth of the human ilium: the anomalous sacroiliac junction. Anat Rec 296:1688–1694.

Zeller R, Lopez-Rios J, Zuniga A 2009 Vertebrate limb development; moving towards integrative analysis of organogenesis. Nat Rev Genet 10:845–858.

A review of the molecular basis of limb development particularly focusing on how cell–cell interactions are integrated.

Zuniga A, Haramis AG, McMahon AP et al 1999 Signal relay by BMP antagonism controls the SHH/FGF-4 feedback loop in vertebrate limb buds. Nature 401:598–602.

Zuniga A, Zeller R, Probst S 2012 The molecular basis of human congenital limb malformations. WIREs Dev Biol 1:803–822.

A presentation of genes involved in limb development and their relevance to human congenital limb defects.

CHAPTER

20

Development of the lungs, thorax and respiratory diaphragm

DEVELOPMENT OF THE RESPIRATORY TREE

The development of the respiratory system can be conceptualized as the growth of six intertwined trees: the bronchial tree of conducting airways and terminal gas-exchanging sacs; the systemic arterial and venous trees that perfuse and drain the airways; the pulmonary arterial and venous trees that supply and drain the alveolar membrane, anastomose with the systemic and venous trees, and are pivotal in the provision of blood oxygenation and carbon dioxide excretion after birth; and the lymphatic tree. Development of each tree is related to that of the others and all proceed proximo-distally in terms of growth and expansion. Uniquely, the lungs develop while not fulfilling their postnatal function, but they must function efficiently immediately after birth or the neonate will require respiratory support and may die of respiratory failure. (For overviews of lung developmental biology, see Roth-Kleiner and Post 2005, Kimura and Deutsch 2007, Maeda et al 2007, Morrisey and Hogan 2010, Warburton 2017). Knowledge of the molecular basis of lung development is based on studies of the *in vitro* growth of human and animal (usually mouse and rat) explants, and using knockout and transgenic mice. Anomalous lung development is an important factor in the aetiogenesis of airway diseases such as asthma and COPD (Bush 2016).

The development of the respiratory diverticulum can first be seen at stage 12 (approximately 30–31 days postfertilization; see Fig. 23.3) when there is a sharp onset of epithelial proliferation within the foregut at regions of the endoderm tube destined to become the lungs, stomach, liver and dorsal pancreas. The specialized respiratory epithelium forms from the endoderm and the other elements of the airway wall are of mesenchymal origin. The future respiratory epithelium bulges ventrally into the investing splanchnopleuric mesenchyme, then grows caudally as a bulb-shaped tube (**Figs 20.1–20.2**; see Fig. 21.3). By stage 13 the caudal end of the tube has divided asymmetrically to form the future primary bronchi. The right primary bronchus becomes orientated more caudally as it grows, whereas the left extends more transversely. The trachea is clearly recognizable at stage 14 and from this time the origin of the trachea remains close to its site of evagination from the future oesophagus. Longitudinal growth of the trachea causes the region of the future carina to descend, until ultimately it lies within the thorax. Failure of complete separation between trachea and oesophagus will result in the baby being born with one of the variants of tracheo-oesophageal fistula (see below).

Trachea

The trachea and oesophagus arise from the foregut just caudal to the pharyngeal pouches. Tracheal development starts at stage 12 as a ventral outgrowth from the endodermal foregut into the mesenchyme that surrounds the sinus venosus and inflow tract of the heart (**Figs 20.1B–C**; see Figs 21.3, 21.5). The point at which the original respiratory diverticulum buds from the foregut, the laryngotracheal groove, remains at a constant level during the embryonic period, and the trachea lengthens distally as the point of bifurcation descends. The respiratory diverticulum generally becomes surrounded by angiogenic mesenchyme which connects to the developing sixth aortic arch artery and is essential for airway branching. By stage 17 the mesenchyme around the trachea is beginning to condense to form cartilage.

Initially, the tracheal mesenchyme is continuous with that surrounding the ventral wall of the oesophagus (see Fig. 20.2). Progressive lengthening and continued division of the tracheal bud, together with deviation of the lung buds dorsally, isolates the oesophagus and trachea within tissue-specific mesenchyme and facilitates regional differentiation, not only between the trachea and lungs, but also within the lungs themselves, i.e. the number of lobes, or the degree of growth and maturity of a particular lung. Each lung develops by a process of dichotomous branching. For branching to occur, a cleft must develop in the tip (or side) of the epithelial tube, the epithelium then evaginates each side of the cleft, forming new branches that lengthen, and the process is then repeated. The mesenchyme is flattened and densely packed at the tips of the developing epithelial buds, whereas it forms an ordered row of cuboidal cells along the side of the bud and in the clefts. Cells in both arrangements send processes towards the epithelial basal lamina, which is thicker in the clefts but so attenuated as to be almost indistinguishable on the tips of the buds where the epithelium and mesenchymal cells form intimate contacts. Tenascin, an extracellular matrix molecule, is present in the budding and distal tip regions, but absent in the clefts. Conversely, fibronectin, an extracellular matrix molecule found commonly in basal laminae, is found in the clefts and along the sides of the developing bronchi, but not on the budding and distal tips. It is likely that branching morphogenesis is not rigidly pre-specified after the first 'stereotypical' generation and adapts to the space available within the mesenchyme (Blanc et al 2012, Lang et al 2018).

The splanchnopleuric mesenchyme controls the branching pattern of the respiratory tree. Experimental recombination of tracheal mesenchyme with bronchial respiratory endoderm results in inhibition of bronchial branching, whereas recombination of bronchial mesenchyme with tracheal epithelium induces bronchial outgrowths from the trachea. Experimental exposure of rat fetal airway to chick mesenchyme produces a branching pattern typical of a chick airway.

Smooth muscle and nerves are found outside the airways at this early developmental stage. Airway smooth muscle is innervated and contractile: there is experimental evidence that GDNF (glial derived neurotrophic factor) may play a role in the early innervation of developing airways (Tollet et al 2002). Phasic contraction and relaxation of airways is important in growth factor release and moving secreted fluid from distal to proximal regions of the bronchial tree.

Failure of separation of the oesophagus and trachea is described below under disorders of the proximal airways. The development of the oesophagus is described in Chapters 17 and 21.

Lungs

Branching morphogenesis of the conducting airways is generally complete by postmenstrual week 16: the airways subsequently increase in size, but not in number. Alveolar development is largely (but not completely) a postnatal phenomenon. The development of pre-acinar blood vessels follows the conducting airway development. The airways act as a template for blood vessel development by *de novo* vasculogenesis driven by epithelial-derived VEGF. Development of intra-acinar blood vessels follows the development of the alveolar ducts and alveolar sacs. Vascular development is also complex and has been recently reviewed (Cornett et al 2013, Lange et al 2014, Bolte et al 2018). Lung development is described histologically as progressing through embryonic, pseudoglandular, canalicular, saccular and alveolar phases. (For further details see Bush 2005.)

Embryonic phase (0–7 postfertilization weeks: appearance of lung buds and main pulmonary arteries)

The endodermal epithelial lung buds grow dorsally, passing each side of the relatively smaller oesophagus, and bulge into the splanchnopleuric mesenchyme of the medial walls of the laterally situated pericardio-peritoneal canals (see Figs 20.2, 21.5). Proliferation of this splanchnopleuric coelomic epithelium, which is especially evident in stage 13 and decreases in stage 14, produces splanchnopleuric mesenchyme that becomes arranged in zones around the developing endoderm. This investing mesenchyme will eventually produce the supporting walls of the conducting airways, differentiating into the mucosal and submucosal laminae propriae (containing fibrocytes that

Lung development depends on the balanced expression of transcription factors that are also expressed in other developing organs (Xu et al 2012, Morrisey et al 2013). The early lung develops by branching morphogenesis (see Fig. 11.5). An early transcription factor, NKX2.1 (TTF-1), is involved in regulating pulmonary immune function, and mutations in this gene lead to combinations of lung, brain and thyroid disease (Hamvas et al 2013). BMP-4 and fibronectin induce the formation of a cleft between two branches. Branching is promoted by receptor tyrosine kinase and their ligands and by inhibition of FGF10 in mesenchymal MMPs. It is inhibited by Gremlin (a BMP4 antagonist), transforming growth factor β (TGFβ) family members and Sonic Hedgehog (Shh) produced in the distal epithelial cells (Stabile et al 2007). Lung morphogenesis is also regulated by interactions between the canonical Wnt/β-catenin and Kras/ERK/Foxm1 signalling pathways that control the regional and developmental expression of the transcription factor SOX9 (Ustiyan et al 2016). (For further information on miRNAs and RNA binding proteins, see Wang et al (2015) and Ameis et al (2017)). Understanding the genetic control of lung development is now informed by molecular techniques (Kho et al 2010) and proteomic analyses. Surfactant protein genes are expressed from postmenstrual week 13 (Ardini-Poleske et al 2017, Moghieb et al 2018). Epigenetic influences on lung development that have been identified include passive tobacco smoking (Li et al 2005, Magnus et al 2015).

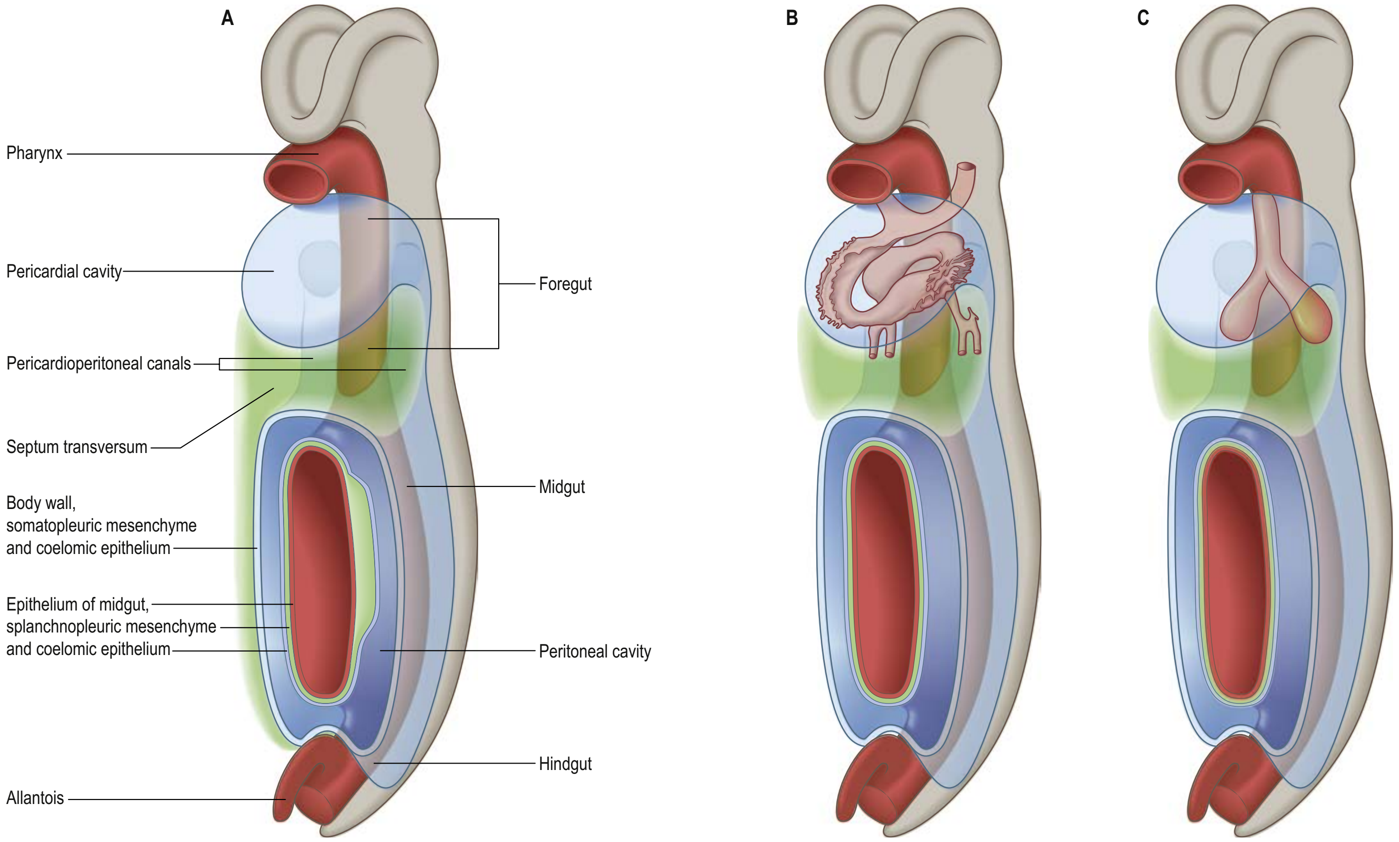
A
B
C
Pharynx
Pericardial cavity
Pericardioperitoneal canals
Septum transversum
Body wall, somatopleuric mesenchyme and coelomic epithelium
Epithelium of midgut, splanchnopleuric mesenchyme and coelomic epithelium
Allantois
Foregut
Midgut
Peritoneal cavity
Hindgut

Fig. 20.1 **A**, The arrangement of the epithelial populations in an embryo at about stage 11. The future thoracic region lies caudal to the pharynx and extends to the upper part of the septum transversum. **B**, The heart is shown in situ within the pericardial cavity. Venous tributaries return blood from the body, yolk sac and placenta, and arterial trunks pass each side of the pharynx. **C**, The respiratory diverticulum arises in the midline from the lower portion of the pharynx, and lung buds extend dorsally into the pericardioperitoneal canals.

synthesize the type I and II collagen, elastin, proteoglycans and glycosaminoglycans of the extracellular matrix) and smooth muscle cells.

Angiogenic mesenchyme is apparent around the primary bronchi at stage 15. It forms an extensive capillary network around each lung bud, receiving blood from the developing sixth aortic arch artery and draining it into an anastomosis connected to the dorsal surface of the left atrium in the mediastinal mesenchyme (Ch. 13). The pulmonary arteries arise from the sixth aortic arch arteries and the pulmonary veins develop from a solitary channel derived from the dorsal mesocardium that establishes continuity with the vascular plexus formed in the mediastinal mesenchyme. The pulmonary veins become surrounded by myocardium to the level of the second bifurcation; the veins themselves expand and are incorporated into the roof of the left atrium, which means that cardiac muscle is found in the central branches of the pulmonary venous tree (Hislop 2005).

After stage 15 the coelomic epithelium projecting into the pericardioperitoneal canals and covering the lung buds will follow a differentiation pathway to form the visceral pleura. Lobar or secondary bronchi can be seen at stage 16 and bronchopulmonary segments are present at stage 17 (see Fig. 21.3E). Later stages of respiratory development involve the repeated division of the bronchial tree to form the subsegmental bronchi.

Pseudoglandular phase (5–17 postfertilization weeks: development of airways and blood vessels to the level of acinus)

By stage 17 the separation of the lungs from the digestive system is complete and the pseudoglandular phase of pulmonary development, including the development of the lower conducting airways and the appearance of the acinar structures, begins. During this period, virtually the complete branching structure of the future bronchial tree is laid down in 20 generations.

The growth and branching of the endoderm epithelium is controlled by the local investing splanchnopleuric mesenchyme. The airways begin to differentiate during this stage. Primitive ciliated cells appear at about postfertilization week 7, initially in the region of the membranous trachea, and in the cartilaginous region by postfertilization week 12; ciliogenesis is complete at birth in humans. The proximal airways develop basal cells from postfertilization week 11. Mucous glands develop by postfertilization week 12 and enlarge in the submucosa: secretory activity has been identified in the trachea at postfertilization week 14. The splanchnopleuric mesenchyme condenses around the epithelium, and from stages 16–17 it differentiates into connective tissue cell types and smooth muscle proximal to the tips of the developing airways. Smooth muscle cells are innervated from stage 23. Human tracheal smooth muscle cells have a fluctuating resting membrane potential associated with the spontaneous development of tone and peristalsis-like contractions of the airway of a myogenic nature, probably modified by neuro-humoral factors. Club cells develop in the peripheral airways during the pseudoglandular period and produce a surfactant apoprotein and a10-kDa protein (CC10) with immunomodulatory and anti-inflammatory activity. Cartilage also develops during this period, and is found in the airways in an adult distribution by postmenstrual week 24. By the end of this period, airway branching and pre-acinar vascular patterns are mature. A normal airway ‘template’ is essential for normal alveolar formation: a degree of pulmonary alveolar hypoplasia is inevitable in conditions characterized by an anomalous airway branching pattern (e.g. both ipsilateral and contralateral to a respiratory diaphragmatic hernia).

Further endothelial proliferation is seen in the pseudoglandular phase when capillary networks form around the developing lung buds; they will become capillary anastomoses around the future alveoli. The splanchnopleuric mesenchyme differentiates into myointimal cells and the tunica media of the developing blood vessels. Vimentin is expressed in the cells around developing vessels in the pseudoglandular stage, and is replaced by desmin in the saccular phase.

Canalicular phase (17–27 postmenstrual weeks: formation of respiratory airways and blood–gas barrier thins)

Two to three generations of branching occur during the canalicular phase, after which the amount of mesenchyme around the branching tips of the dividing respiratory tree decreases and the distal airspaces widen. At 23 postmenstrual weeks, longitudinal histological sections of

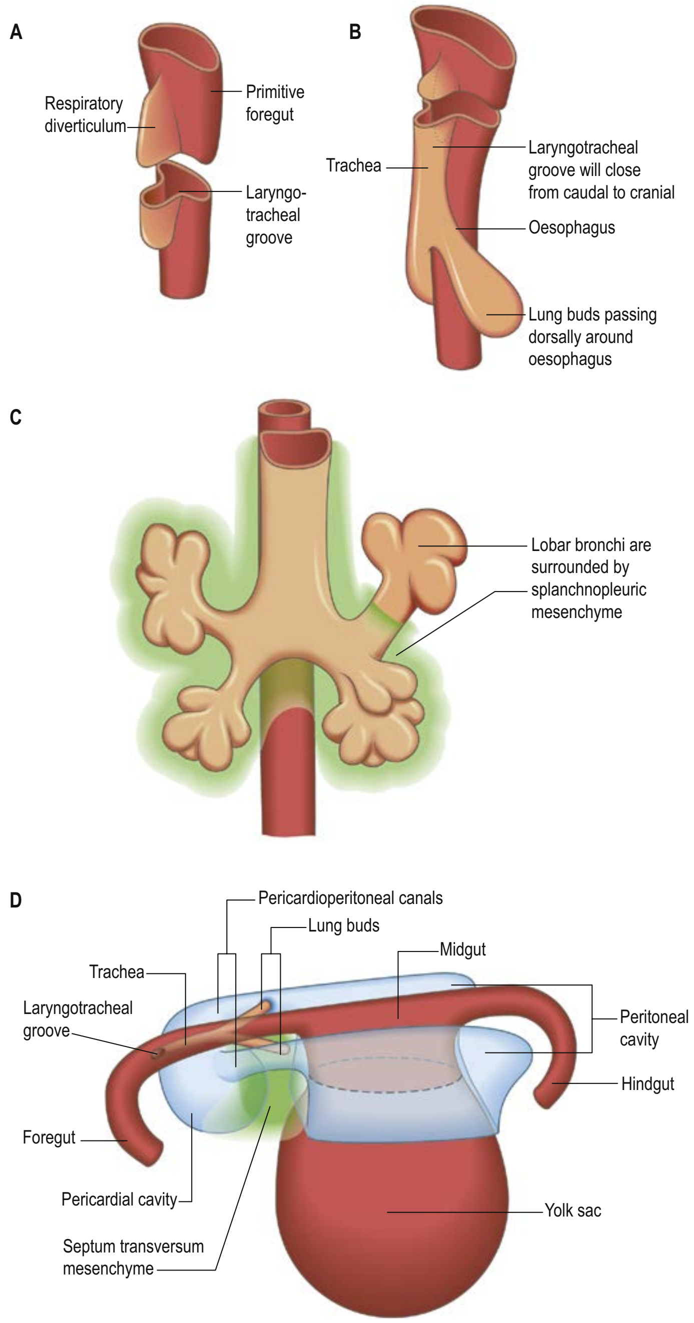
A
Respiratory diverticulum
Primitive foregut
Laryngo-tracheal groove
B
Trachea
Laryngotracheal groove will close from caudal to cranial
Oesophagus
Lung buds passing dorsally around oesophagus
C
Lobar bronchi are surrounded by splanchnopleuric mesenchyme
D
Pericardioperitoneal canals
Lung buds
Midgut
Trachea
Laryngotracheal groove
Peritoneal cavity
Hindgut
Foregut
Pericardial cavity
Yolk sac
Septum transversum mesenchyme

Fig. 20.2 Development of the respiratory tree and diaphragm. **A–C**, Development of the endodermal respiratory tree. **D**, Major epithelial populations in the early embryo from a left dorsolateral view: the lung buds are bulging into the laterally placed pericardioperitoneal canals.

the future distal regions show a sawtooth margin, which may indicate the site of further acini. Peripheral growth is accompanied by an increase in the capillary network around the distal airspace: in many places, the capillaries are in close contact with the respiratory cuboidal epithelium. The primitive endodermal cuboidal epithelial cells, previously the predominant cell in this part of the lung, differentiate into type I epithelial cells (pneumocytes) and type II epithelial cells (pneumocytes) containing lamellar bodies that form the intracellular storage bodies of surfactant. Type II pneumocytes are believed to be the stem cells of the alveolar epithelium. Apposition of the capillary networks to the thin type I pneumocytes and reduction of the interstitial tissue of the lung are prerequisites for future effective gas exchange. By postmenstrual week 24, the histological characteristics of the airways, including cartilage distribution, are the same as in the adult.

Saccular/alveolar phase (28 postmenstrual weeks–term: first appearance of alveoli in humans)

Thin-walled terminal saccules are apparent at the saccular stage and will become alveolar ducts as development proceeds. The expansion of the prospective respiratory airspaces that occurs during this period is accompanied by a further decrease in the amount of mesenchymal interstitial tissue, and the capillary networks become ever more closely opposed to the pneumocyte epithelium. Secondary crests develop from the invaginations of the saccule walls, although this may be an apparent movement when the saccule walls expand each side of a subjacent blood vessel. As an alveolar crest protrudes into a saccule, part of the capillary network becomes drawn into it. After the later expansion of the saccules on each side of the crest, a double capillary layer becomes annexed between what are now alveolar walls. During the saccular stage, elastin is deposited beneath the epithelium (an important step for future alveolar formation), and surfactant production, from type II pneumocytes, matures (essential for the survival of a preterm neonate).

Alveolar phase

An epithelial layer is usually supported by an underlying lamina propria, as in the conducting airways. The mutual support of two epithelial layers, a specialized epithelium and an endothelium, where both contribute to the generation of mutual basal laminal proteins, is very unusual and seen elsewhere only in the kidney glomerular basement membrane and in the brain (see Fig. 11.2). This close relationship develops during the alveolar phase between type I pneumocytes and pulmonary endothelium. A number of genes and growth factors are expressed during the formation and maturation of the type I pneumocyte:endothelium interface (alveolar–capillary membrane; blood–gas barrier) and in the final fibrocyte deposition of matrix molecules between developing alveoli. Retinoic acid regulates the expression of a number of growth signalling molecules, homeobox genes and lung epithelial genes. TGF-β, platelet- derived growth factor (PDGF) and fibroblast growth factor are involved in the final stages of conducting airway branching. TGFβ is also involved in septal formation and the induction of myofibroblasts which co-localize at ridges signalling the start of alveolar crest development. Myofibroblasts are found later at the tips of alveoli and play a particular role in production of elastin: their failure to produce elastin leads to a lack of alveoli. PDGF also stimulates myofibroblasts: PDGF-null mice fail to form secondary septa. Mechanical stretching of developing lung tissue stimulates human smooth muscle cell differentiation and increases tropoelastin content. Elastin gene expression, possibly modulated through retinoic acid, appears to play a pivotal role. (For further reading about factors controlling alveogenesis, see Hind et al (2009), Chao et al (2016), Ng-Blichfeldt et al (2017).)

Exactly when the saccular structure of the lung can be termed alveolar is not yet clear: estimates range from postmenstrual weeks 28 to 32. The formation of millions of alveoli is accomplished by a complex process of folding and division of type I pneumocytes. Mechanical stretch drives type II to type I cell differentiation. The existing walls of the alveoli become thinner as type I pneumocyte cells flatten, forming primitive alveoli. Septa (ridges) initially form where the type I pneumocytes meet subjacent capillaries and myofibroblasts. Subsequent areal expansion of type I pneumocytes, of more than ten times, and increased capillary development, combine to form new alveoli. Mouse embryo studies indicate that each type I pneumocyte may form the walls of multiple adjacent alveoli (Yang et al 2016). Vessels remain within the developing secondary septa whereas the myofibroblasts are temporary. The process of remodelling of the final capillary network between adjacent alveoli is not yet elucidated, however, it has been noted that type I pneumocytes secrete VEGF (Yang et al 2016).

The distal airspaces expand during late gestation and continue to do so after birth. The number of alveoli present at birth (variously estimated as between none to 5 x10^7) is controversial; the number probably increases particularly rapidly over postmenstrual weeks 41–64 (postnatal months 0–6). This process is accompanied by fusion of adjacent capillary networks, so that shortly after birth there is an extensive double capillary net. Fusion of these layers is apparent at postnatal day 28, extensive at 1.5 years and probably complete by 5 years. The alveolar stage is now considered to continue beyond infancy and throughout childhood (whereas heterochronic differences in rat and mouse development show that alveolar formation is exclusively post-natal in these animals).

Development of the intrapulmonary vasculature and lymphatics

Two vascular circulations arise in the developing lungs, bronchial and pulmonary. Two or three bronchial arteries grow from the descending aorta from stages 21–22. They enter the lung at the hilum and branch, the airways acting as a template for their development. The vessels extend adjacent to the developing airways and eventually form subepithelial and adventitial plexuses that reach the distal portions of the bronchioles by birth. Bronchial arteries also supply the pleura near the hilum and form vasa vasorum in the adventitia of the large arteries and veins. The bronchial veins from the periphery of the lungs drain into the pulmonary veins. Postnatally, inflammatory lung conditions such as asthma, cystic fibrosis and bronchiectasis cause hypertrophy of the bronchial circulation and these vessels may bleed, sometimes giving rise to massive haemoptysis (McCullagh et al 2010). Some congenital thoracic anomalies have a systemic arterial blood supply.

The earliest pulmonary vessels form in the mesenchyme by vasculogenesis: the capillaries coalesce to form small blood vessels alongside the branching airways. Pulmonary arteries form adjacent to the conducting airways, joining the angiogenic mesenchyme of the sixth aortic arch arteries. Pulmonary veins develop from mediastinal mesenchyme in the dorsal mesocardium and become separated from the airways by the growth of alveoli and lymphatic vessels. By stage 15 a circulation is present from the aortic sac through a branching network of pulmonary arteries into capillary plexuses around the two lung buds, and returning via pulmonary veins to the developing left atrium. As each new distal airway forms in the mesenchyme, a new angiogenic plexus forms as a halo around it, and coalesces with the pulmonary vessel already alongside the proximal airway. In this way, addition of the newly formed tubules to the existing pulmonary vessels is sustained. Vessel formation occurs at least until the end of the pseudoglandular stage and has been shown to be controlled by production of VEGF from type I pneumocytes (Yang et al 2016). As the arteries increase in size they acquire a muscular wall, initially from the bronchial smooth muscle of the adjacent airway and then from the splanchnopleuric mesenchyme. The muscle layer is thick relative to the lumen, and this in part increases resistance to blood flow. Although only 10% of blood flow goes through the pulmonary circulation during intrauterine life, it is important for normal lung development. By postmenstrual week 20, the structure of the pulmonary vessels is the same as it is in the adult. Vascular innervation follows muscularization; the vasoactive peptides contained in these nerves are predominantly vasoconstrictor.

As the pulmonary veins enlarge, they become separated from the airways by the lymphatic vessels that lie within the mesenchyme. At around postmenstrual week 12, the peripheral veins develop a single layer of smooth muscle cells in their walls. This layer is derived exclusively from the splanchnopleuric mesenchyme and not from bronchial smooth muscle (as occurs in the arteries). The lumen of each vein is relatively large and the wall is relatively thin at all levels. Arteries and veins continue to develop in the canalicular phase, probably by angiogenesis (dividing cells are seen in the peripheral capillaries). The epithelium of the most peripheral conducting airways flattens when the developing capillaries come to lie immediately subjacent to it. (For a review of the development of the pulmonary circulation see Hislop (2005)).

Lymphatic capillaries and vessels run within bronchovascular bundles. Lymphatic channels develop from outgrowths of vascular endothelial cells: the molecular trigger for lymphatic sprouting is VEGF-C and D, acting through the VEGF receptor 3 (Janér et al 2006). See Kulkarni et al (2011) for a review of lymphatic development.

Intrauterine maturation of the lungs

More than 30 different cell types found within the adult lung mature during development. Only a few important changes relevant to human disease will be highlighted here.

Pulmonary surfactant is produced by type II alveolar epithelial cells, and stored in lamellar bodies; surfactant production is under complex molecular control (Xu et al 2010). Surfactant proteins (Sp) B and C are surface active, whereas A and D are part of the collectin family of pattern recognition receptors. Surfactant is crucial for maintaining the functional integrity of alveoli: the main morbidity of extreme prematurity reflects surfactant deficiency causing neonatal respiratory distress syndrome (treatment has been transformed by the availability of exogenous surfactant). Mutations in the genes encoding *SpB* and *SpC*, *ABCA3* (responsible for surfactant processing) and the transcription factor *NKX2.1* (controlling *SpB*, *SpC* and *ABCA3* expression) can all present in the neonatal period in full-term babies (notionally 40 postmenstrual weeks) with relentlessly progressive respiratory distress and diffuse ground glass shadowing on imaging studies (Spagnolo and Bush 2016). Fetal breathing movements appear to be important in surfactant synthesis: the functional maturation of the surfactant system can be accelerated therapeutically by the administration of steroids to the mother with important benefits to the preterm baby (Roberts et al 2017).

Normal lung development requires sufficient intrathoracic space, normal fetal breathing movements and sufficient amniotic fluid. There is evidence that perturbation of fetal lung blood flow also affects lung growth, even though most of the right ventricular output of the heart is shunted away from the lungs through the ductus arteriosus: pulmonary valve stenosis is associated with pulmonary hypoplasia. Although many fetal organs are able to grow to normal proportions even if they are in abnormal locations, this is not the case for the lungs. Lung growth becomes impaired by restricted expansion. Absence or impairment of fetal breathing movements, and defects affecting respiratory diaphragmatic activity, are all associated with pulmonary hypoplasia. Distension of the developing lung may provide a major stimulus to growth during normal development. It is believed that normal fetal breathing movements increase the lung volume and stimulate growth of the distal airspaces. Fetal breathing movements involve rhythmic activation of the respiratory diaphragm and the muscles of the upper respiratory tract. Even though such movements are necessarily very small compared with those seen after birth, because the fetal airways are filled with lung fluid, there is evidence that these phasic movements are important in the release of growth factors. Fetal breathing becomes more prominent in the second and third trimesters, by which time the fetus spends nearly one-third of the time breathing (Hagen-Ansert 2018). One effect of the absence of fetal breathing movements, for example in severe neuromuscular diseases of antenatal origin such as severe (type I) spinal muscular atrophy and spinal muscular atrophy with respiratory distress, is pulmonary hypoplasia (Inanlou et al 2005).

During development, the mucous glands of the trachea and bronchi secrete a chloride-rich fluid that usually passes up the respiratory tract to mix with the amniotic fluid secreted by the fetal kidneys. Amniotic fluid volume, pressure and, possibly, content significantly influence lung development by maintaining appropriate lung distension. Renal agenesis, severe congenital urinary obstruction and oligohydramnios (Potter's syndrome; Potter's sequence), leads to pulmonary hypoplasia at birth. In renal agenesis, reduced bronchial branching occurs as early as postmenstrual weeks 12–14 (i.e. at a time before amniotic fluid is produced by the metanephric kidneys), which suggests that a direct renal factor supports lung development. Later, the presence of amniotic fluid is necessary for normal fetal lung development. The fetal lung is a net fluid secretor, the output of fluid reaching as high as 5 ml/kg/hour shortly before birth. Most of the fluid produced within the lungs remains there because of the mechanical effect exerted by amniotic fluid pressure, and normally only a small amount of this fluid contributes to the amniotic fluid. The normal functioning of the kidneys regulates the volume and pressure of the lung airway fluid and may in turn provide the pressure needed for expansion and enlargement of the bronchial and pulmonary systems. Interestingly, obstruction to the fetal airway causes accelerated maturation of alveoli, a finding that has been used therapeutically in congenital diaphragmatic hernia, based on studies showing that intermittent inflation and deflation of an intra-tracheal balloon in a lamb model resulted in better lung growth and maturation (Ruano et al 2014). This treatment is the subject of interventional trials in human fetuses (https://www.totaltrial.eu/; Van der Veeken et al 2018).

Two other cell types that participate in normal lung development, neuroendocrine cells and pulmonary lipofibroblasts, have been implicated in postnatal paediatric interstitial lung disease with early onset of respiratory distress (Spagnolo and Bush 2016).

Antenatal influences on intrauterine lung development

There is increasing evidence from epidemiological studies that antenatal factors have long-lasting effects on lung development. The earliest major effect is congenital respiratory diaphragmatic hernia (see below): this leads to both ipsilateral and contralateral abnormalities in branching patterns in the first 16 postmenstrual weeks that cannot be corrected subsequently, even by intrauterine tracheal balloon occlusion. Inevitably abnormal branching leads to abnormal alveolarization. The most important influence on later development is maternal smoking; there is evidence that maternal exposure to pollution is also an important cause of subsequent airflow obstruction (Morales et al 2015). Animal studies have confirmed that antenatal nicotine exposure leads to structural changes in the fetal lung (Bush 2016), and it should be remembered that e-cigarettes contain nicotine. Other factors that may be important include maternal hypertension in pregnancy and maternal antibiotic and paracetamol usage (Rusconi and Gagliardie 2018).

Congenital anomalies of the trachea, bronchi and lungs

Available with the *Gray's Anatomy* e-book

Neuroendocrine cells are found in the normal developing airway: neuroendocrine cell hyperplasia of infancy (NEHI) is characterized by persistence of bombesin-positive neuroendocrine cells. Abnormal glycogen-containing cells derived from lipofibroblasts (Deutsch and Young 2016) result in pulmonary interstitial glycogenosis (PIG), which is not related to any of the systemic glycogen storage diseases. Both conditions tend to remit over time, and in neither case is it known whether the abnormal cells are of pathophysiological significance or merely markers of another process. These likely represent part of a spectrum of pulmonary dysmaturation syndromes, including alveolar capillary dysplasia-congenital alveolar dysplasia, see Bush et al (2018) and Bush et al (2019).

The concept of the lung as six 'trees' has been mentioned earlier; all except the systemic venous tree may contribute to a congenital thoracic malformation (Bush et al 2018). Congenital anomalies of the heart and great vessels, and of the chest and abdominal walls, may adversely impact lung development. It is somewhat artificial to describe airway malformations in isolation. The possibility of associated vascular abnormalities must always be considered and descriptions of what is seen clinically should be kept separate from speculations about the putative developmental origins of an anomaly.

Disorders of the proximal airways

Tracheomalacia and bronchomalacia

Abnormalities in cartilage development lead to the affected airways being 'floppy', and collapsing during inspiration or expiration, depending on whether they are outside or inside the bony thorax, respectively: these anomalies are termed tracheomalacia when the trachea is affected, and bronchomalacia when the bronchi are involved. The abnormality may involve a small, localized area, or may be more generalized (e.g. Williams–Campbell syndrome, a congenital deficiency of the airway cartilage, in which there is diffuse bronchomalacia from the second to the seventh generation of bronchi). Tracheobronchomalacia usually presents in early infancy with cough, tachypnoea, stridor and wheeze; it may also be associated with cardiac or respiratory anomalies, such as absent pulmonary valve syndrome, or tracheo-oesophageal fistula, respectively (Wallis et al 2019). Patients with significant obstruction and apnoea may be treated by the insertion of airway stents if the disease is localized, although there is only limited long-term experience in children with stents; generalized disease may mandate respiratory support, either with non-invasive mask ventilation during sleep, or via a tracheostomy, depending on severity. Surgical treatment by aortopexy is controversial.

Tracheo-oesophageal fistulae

Laryngo-tracheo-oesophageal clefts are very rare retained connections between the enteric gut and trachea (Leboulanger and Garabédian 2011). Tracheo-oesophageal atresia is rare, with an incidence of 1 in 3000 to 1 in 4500 births. Oesophageal atresia with or without tracheo-oesophageal fistula may present antenatally with polyhydramnios due to failure of movement of amniotic fluid into the gut after fetal swallowing, and choking and inability to swallow saliva in the neonatal period. Tracheo-oesophageal fistulae are the most common abnormalities of the lower respiratory tract, and occur in about 1 in 3000 births. They are diagnosed antenatally if associated with oesophageal atresia, polyhydramnios and an absent or small stomach. In the neonate they present with recurrent respiratory distress and choking spells and attempts to pass a gastric tube are unsuccessful. Later presentation in adult life has been described.

Five types of tracheo-oesophageal fistulae may be recognized (**Fig. 20.3**). Prenatally, polyhydramnios may be a clinical feature, but may not be apparent until the third trimester. In almost all cases, the oesophagus ends blindly and the stomach is connected to the lower end of the trachea. Because of this connection, the abdomen becomes rapidly distended with air once the baby is delivered and starts breathing. In two of the five types of tracheo-oesophageal fistulae there is no communication between the stomach and the upper gut. Such cases are identifiable on ultrasound, because the stomach should always be visible at a postmenstrual week 20 ultrasound examination, and its absence should prompt further evaluation.

Tracheo-oesophageal fistula is commonly associated with other congenital anomalies, including cardiovascular defects (30%), anorectal (15%) and genitourinary (15%) anomalies. These defects may be combined in the VATER, VACTER and VACTERL associations, which involve varying combinations of vertebral defects, anorectal atresia, cardiac anomalies, trachea-oesophageal fistula and oesophageal atresia, together with radial aplasia and other limb abnormalities, renal abnormalities and the presence of a single umbilical artery (Gottlieb and Andropoulos 2018).

Complete cartilage rings

The normal large airway cartilages are horseshoe-shaped, with the ends of the horseshoes joined by the membranous part of the trachea. Meyerholz et al (2010) suggested that tracheal cartilage shape is abnormal in cystic fibrosis in both human infants and the pig model; however, the rings are not continuous in this condition. Complete cartilage rings may develop in the trachea and large airways, and the posterior membranous part of the airway may be absent in a single cartilage or in long segments of the airway. This anomaly may be associated with vascular anomalies such as pulmonary artery sling (where the left pulmonary artery originates from the right pulmonary artery and not from the main pulmonary trunk). Extensive severe disease may present with neonatal respiratory distress; later presentations include apparently steroid-resistant asthma. Tracheal transplantation has been used to treat long segment tracheal stenosis.

Disorders of the distal airways

Agenesis and aplasia of the lungs

Agenesis and aplasia of the lungs are extremely rare congenital anomalies, where there may be unilateral or bilateral absence of the lung. In agenesis, the airway stump is absent, i.e. the trachea is absent in bilateral disease, or the primary bronchus is absent in unilateral disease. In aplasia, there is a rudimentary airway stump, but no distal lung; the contralateral lung is enlarged, with a greater number of alveoli, but has a normal bronchial branching pattern. Individuals with aplasia may present with recurrent infection, dyspnoea and reduced exercise capacity, and there may be pooling of bronchial secretions, with secondary infection and overspill of infected secretions into the contralateral normal lung.

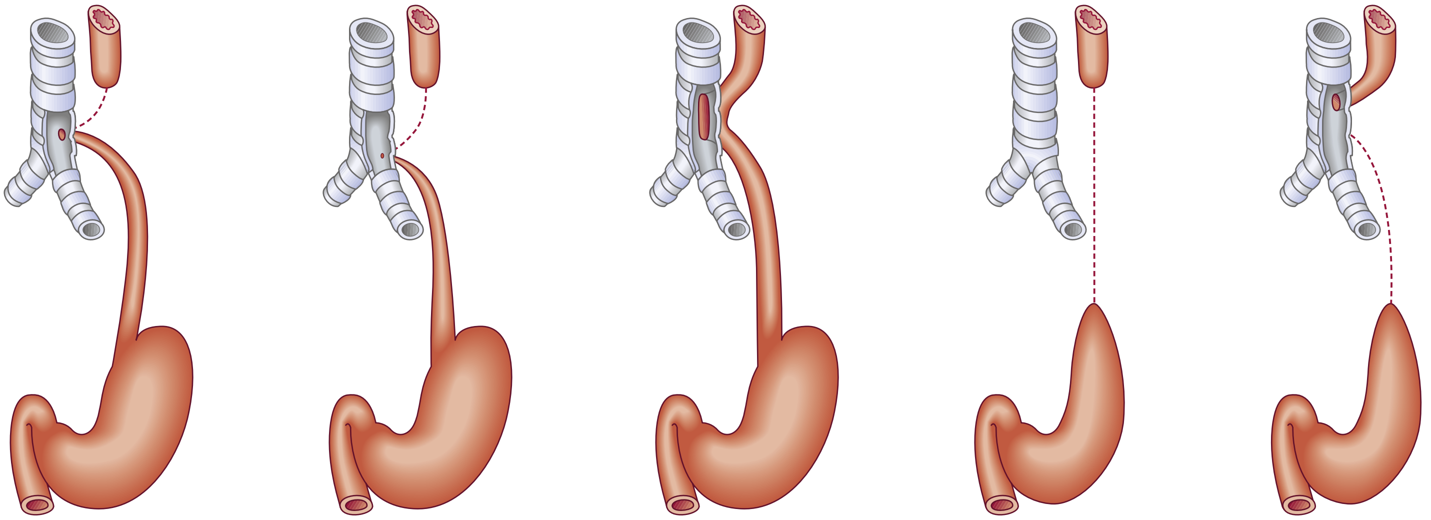

Fig. 20.3 Examples of tracheo-oesophageal fistulae and oesophageal atresia.

Bronchial atresia

Bronchial atresia is a congenital condition in which a major bronchus or segmental airway ends blindly or with a thin membrane. Pulmonary development normally occurs distally, and over time this tissue becomes distended with debris and mucus (bronchocele), with adjacent overinflated lung tissue. Bronchial atresia characteristically affects the left upper lobe (64% of cases): the chest radiographic findings are of a perihilar ovoid density with strands projecting into a localized area of hyperlucent lung. The left lower lobe is affected in 14% of cases and the right lower and right middle lobe in 8% of cases. The majority of cases are asymptomatic and are revealed as incidental findings on chest radiographs. However, many eventually become the seat of recurrent infection and require operative removal. Some infants may show a congenital large hyperlucent pulmonary lobe (CLHL), a condition termed 'congenital lobar emphysema' although it has nothing to do with adult emphysema. Presentation in severe cases is with neonatal respiratory distress, in which case early surgery is required, otherwise it may be a chance radiographic finding later in life, in which case no action is needed.

Bronchogenic and other cysts

Cysts of various types, by order of frequency, may be found in the carinal (51%), right para-tracheal (19%), para-oesophageal (14%), hilar (9%) and pericardial, retrosternal and para-vertebral (7%) regions. Clinically they are part of the spectrum of congenital thoracic anomalies and can only be classified in more detail pathologically when the wall of the cyst is examined. They may have a systemic blood supply and venous drainage. Multicystic abnormalities, described as various types of congenital cystic adenomatous malformations (CCAM) and sequestrations (intra- and extrapulmonary), are best considered generically as CTM spectrum, at least until examined pathologically, and even then, features of CCAM and sequestration may be found in the same malformation, rendering classification difficult. Presentation may be with a range of problems, from intractable neonatal respiratory distress to a chance finding in adult life. If the infant is symptomatic, then surgical resection is indicated. Treatment of the asymptomatic malformation is controversial; some centres would operate electively on all but the tiniest malformations, because of fears of missing a pleuropulmonary blastoma or malignant transformation, whereas others would manage even large asymptomatic cystic malformations conservatively. Evidence for and against these approaches is summarized in Bush et al (2018).

DEVELOPMENT OF THE THORACIC WALL AND RESPIRATORY DIAPHRAGM

Postnatal function of the lungs requires development of the pleural cavities, respiratory diaphragm and thoracic wall, all structures that will generate the negative intrathoracic pressure required to pull air into the lungs when the thoracic cavity enlarges. The thorax as an entity is not apparent in embryos until the end of the embryonic stage of development (stage 23, 53–58 days post fertilization).

In stage 14 embryos, the heart is at the level of the upper cervical somites, above the upper limb buds and undergoing septation of its compartments (Ch. 13), and the thoracic somites are opposite the midgut. Caudal to the heart, septum transversum mesenchyme (see Figs 20.1, 21.5) is being invaginated by endodermal epithelial cells from the foregut hepatic primordium.

Pleural cavities

The pleural cavities develop from parts of the intraembryonic coelom, an epithelial tube that develops within the embryo from stage 9 and gives rise to all of the body. Embryonic head folding brings this original planar intraembryonic structure into a 3D tube with a large, ventral, pericardial cavity, smaller dorsolateral pericardioperitoneal canals on each side of the foregut, and a peritoneal cavity confluent with the extraembryonic coelom (chorionic cavity) that surrounds the midgut and yolk sac (see Figs 13.1, 20.2, 20.4). The walls of the pericardioperitoneal canals are composed of a germinal epithelium that changes spatially and temporally giving rise to populations of mesenchyme which surround and support adjacent structures. The medial walls of the pericardioperitoneal canals proliferate to form splanchnopleuric mesenchyme that surrounds the developing endodermal foregut, trachea and lung buds, the lateral walls give rise to somatopleuric mesenchyme adjacent to the somites and lateral body wall ectoderm. In stage 12 embryos the luminal walls of the pericardioperitoneal canals are separate. The canals are filled with fluid, continuous with that in the extraembryonic coelom which provides a primitive type of circulation up to stage 13, enabling transfer of oxygen and nutrients to the deeper embryonic structures. Sampling of this fluid from the chorionic cavity via coelocentesis has provided a source of fetal stem cells and proteomic analysis has revealed the differences between coelomic and amniotic fluid (Aiello et al 2018). In stage 12 embryos, the epithelium at the caudal ends of the pericardioperitoneal canals is not proliferative, but very thin and permeable to fluid movement between the intraembryonic coelom and the developing hepatocardiac channels, thus providing a route for the transfer of fluid into the developing blood circulation.

At stage 13 the trachea can be seen as a midline projection from the foregut that extends caudally and bifurcates forming lung buds (see Fig. 21.3). During stage 15 right and left lung buds project dorsally, lateral to the oesophagus, pushing into the splanchnopleuric mesenchyme and displacing the medial walls of the pericardioperitoneal canals (**Fig. 20.4**). The presence and continuing dichotomous growth of the lung buds subdivides the pericardioperitoneal canals into primary pleural coeloms around the lung buds cranially, and paired peritoneal coeloms caudally, contiguous with the wider peritoneal coelom around the mid- and hindguts. The communications with the pericardial and peritoneal coeloms are termed the pleuropericardial and pleuroperitoneal canals, respectively. The descent of the heart as the pharyngeal arches form, together with the changes to the inflow tract of the heart, result in morphological shifts in the relative position of the common cardinal veins that affect the craniocaudal and dorsoventral position of the lung buds. As the lung buds continue to grow and expand, the primary pleural cavities and their cranial and caudal connections become increasingly smaller and eventually separate by different morphological processes. Separation of the pleural cavities from the pericardial and peritoneal cavities is expedited by concomitant changes to the venous system and growth of other thoracic and abdominal viscera.

Growth and movement of the common cardinal veins produces a curved elevation of tissue, the pulmonary ridge, on the lateral wall of each pericardioperitoneal canal partially encircling it. The ridge is continuous with the dorsolateral edge of the septum transversum. As it enlarges into the adjacent pericardioperitoneal canal, each developing lung bud abuts on the ridge and expands caudal to the common cardinal vein, causing the growing ridge to hollow, forming two diverging membranes that meet at the septum transversum. The cranially placed ridge, containing the common cardinal vein, is now termed the pleuropericardial membrane (see Fig. 20.4A). It also contains the elongating phrenic nerve, which reaches the septum transversum by this route. The secondary pleural cavity forms by excavation of the somatopleuric mesenchyme of the body wall (**Fig. 20.5**). The apical part of the lung forms by local invasion and splitting of the body wall cranially on the lateral aspect of the common cardinal vein, which means that the common cardinal vein and the phrenic nerve come to lie medially in the mediastinum. The remaining connection with the pericardial cavity, which lies medial to the vein, is gradually narrowed to a slit and soon obliterated by the apposition and fusion of its margins. Closure occurs early and is mainly effected by the growth and expansion of the surrounding viscera (heart and great vessels, lungs, trachea and oesophagus), and not by active growth of the pleuropericardial membrane across the opening to the root of the lung. As the right common cardinal vein is larger than the left (because of changes to the venous return to the heart; see Figs 13.1, 13.8, 13.19), closure occurs first on this side; failure of closure is usually found on the left side.

The caudal part of the hollowed pulmonary ridge is termed the pleuroperitoneal membrane (pleuroperitoneal fold) (see Fig. 20.4). It contains mesenchymal populations from the cephalic pole of the mesonephros as well as the septum transversum. As the lungs expand into the pleural coelom, the ridge grows dorsolaterally to ventromedially across the pleuroperitoneal canal, abutting and fusing with the opposite wall and separating the now complete pleural cavity from the peritoneal cavity. The pleuroperitoneal membrane contributes to the respiratory diaphragm (see below). The right pleuroperitoneal canal closes earlier than the left, which presumably explains why an abnormal communication persisting between the pleural and peritoneal cavities is more frequently encountered on the left. In addition to extension of the

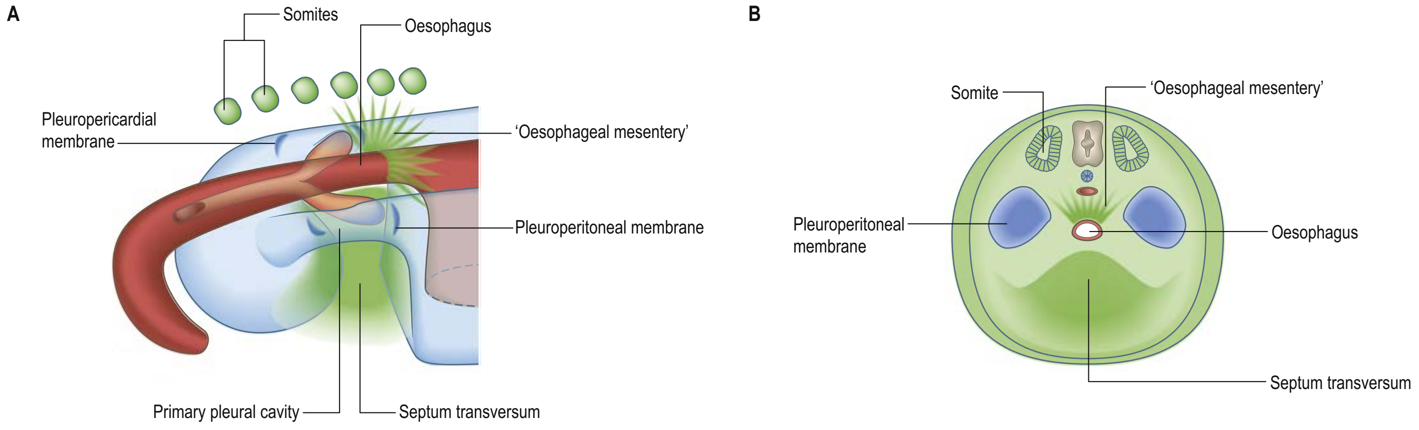

Fig. 20.4 **A**, Dorsolateral view of the foregut between the pericardioperitoneal canals. The respiratory diverticulum arises from the ventral side of the pharynx and grows caudally. Bilateral lung buds extend dorsally and the most lateral parts project into the dorsolateral pericardioperitoneal canals. Later changes in position of the common cardinal veins contribute to the formation of the pericardiopleural membranes cranial to the developing lungs, whereas folds of coelomic epithelium (pleuroperitoneal membranes) separate the pleural cavities from the peritoneal cavity. **B**, Components of the respiratory diaphragm.

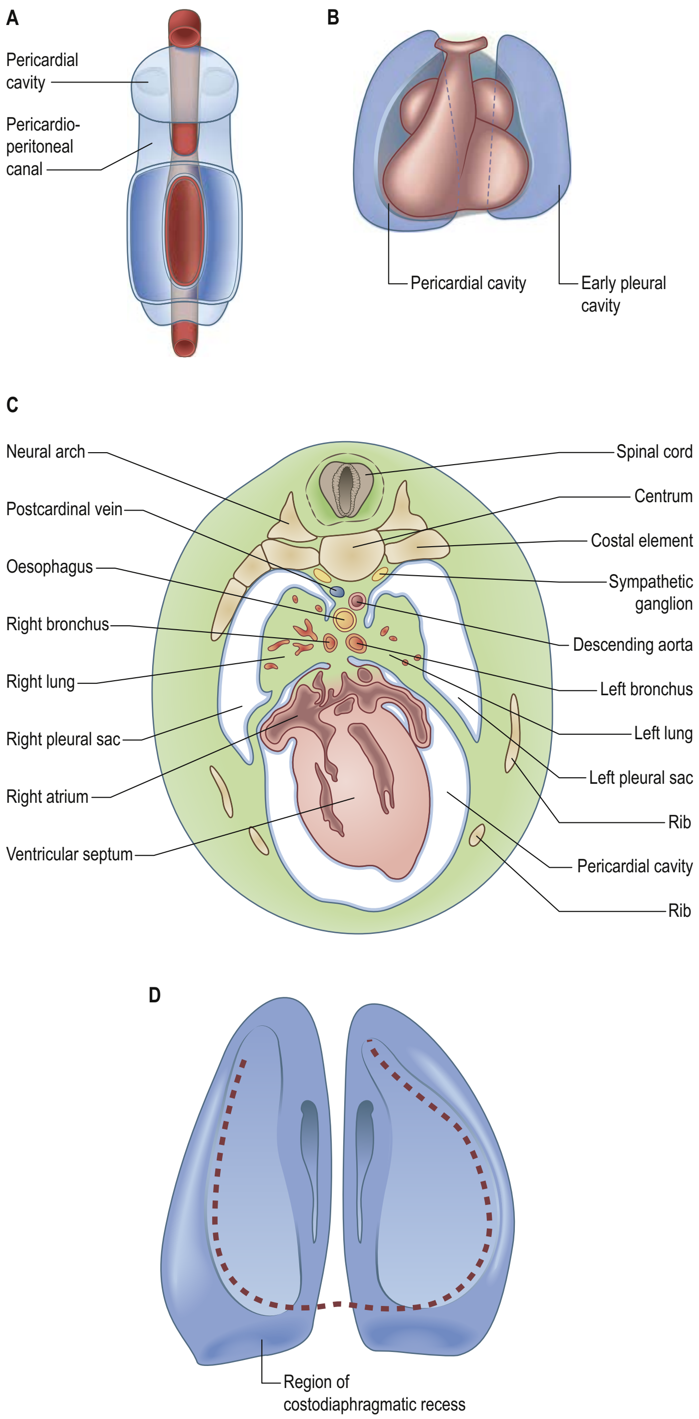

Fig. 20.5 **A**, Ventral view of the intraembryonic coelom forming early body cavities. **B**, The parietal pericardium is shown surrounding the developing heart ventrally, with the parietal pleura of the lungs dorsal and lateral on each side. **C**, A transverse section through the thoracic region, showing the ventral extensions of the pleural sacs on each side of the pericardium that split the body wall mesenchyme. **D**, An anterior view of the pleural sacs. The position of the pericardium is shown by a dotted line. Dorsolateral growth of the pleural sacs also splits the body wall dorsocaudally, defining the costodiaphragmatic recess.

pleural cavities in a cranial direction, the lungs and their associated visceral and parietal pleurae also enlarge ventromedially and dorsocaudally. In the ventromedial extension, the lungs and pleurae excavate and split the somatopleuric mesenchyme covering the pericardium, separating the latter from the ventral and lateral thoracic walls (see Fig. 20.5B–D). The ventrolateral fibrous pericardium, parietal serous pericardium and mediastinal parietal pleura, although topographically deep, are therefore somatopleuric in origin. In the caudodorsal extension, the expanding pleural cavities extend into the mesenchyme dorsal to the suprarenal glands, the gonads and (degenerating) mesonephric ridges. The somatopleuric mesenchyme is peeled off the dorsal body wall to form a substantial portion of the dorsolumbar part of the diaphragm (see Fig. 20.5C).

Until the end of the embryonic period the shape of the early pleural cavities is determined by the growing lungs. The somatopleuric pleural walls form the parietal (costal, diaphragmatic and mediastinal) pleurae and the splanchnopleuric pleural walls, the visceral pleurae. As the pleural mesothelium differentiates, subpleural tissue is thicker where it is associated with superficial veins, and is generally thicker over the basal areas of the lungs than the apices (Yamamoto et al 2018). Differentiated mesothelial cells display pinocytotic vesicles and microvilli, at higher density in visceral than parietal pleura, and in caudal than cranial regions. They secrete glycosaminoglycans, proteoglycans and phospholipids which contribute to a glycocalyx that is non-adhesive for intracoelomic movements. The parietal pleural mesothelial cells are involved in drainage of pleural liquid to underlying lymphatic channels, via stomata between the mesothelial cells (in a manner similar to the parietal peritoneum). Anomalous development of this drainage route may negatively affect prenatal or perinatal control of pleura fluid volume and lead to congenital chylothorax (Bellini et al 2013).

Respiratory diaphragm

The respiratory diaphragm develops as a composite mesenchymal structure that is invaded by myoblast from cervical somites 3–5 (see Figs 17.7, 20.4). The majority of the early diaphragm is formed from a portion of the septum transversum mesenchyme above the developing liver. The septum transversum is a population of mesenchyme cells that arise from the coelomic wall of the caudal part of the pericardial cavity. As this population proliferates, it forms a condensation of mesenchyme, caudal to the pericardial cavity and extending from the ventral and lateral regions of the body wall to the foregut. The endodermal hepatic bud grows into the caudal part of the septum transversum, whereas the cranial portion forms the respiratory diaphragm (see Fig. 21.5).

The oesophagus and developing stomach are dorsal to the septum transversum and the pleuroperitoneal canals are dorsolateral (see Figs 20.1, 20.4, 20.5). As development proceeds, the lower portion of the oesophagus inclines ventrally, ventral to the descending thoracic aorta. Although the oesophagus has no true ventral or dorsal mesentery within the developing thorax, in descriptions of respiratory diaphragmatic development, the portion of mesenchyme between the oesophagus and aorta at the level of the forming diaphragm is often homologized with part of a dorsal meso-oesophagus.

The later extension of the pleural cavities ventromedially and dorsolaterally into the somatopleuric mesenchyme of the body wall enlarges the area of the developing respiratory diaphragm, particularly dorsally when the costodiaphragmatic recesses develop. The pleuroperitoneal membranes contribute relatively small bilateral areas to the diaphragm, however, as they are the only portion that closes the connection between the pleural and peritoneal cavities, anomalous development will cause a diaphragmatic hernia.

After the septum transversum has undergone a progressive change in its relative position, skeletal muscle myoblasts migrate into the respiratory diaphragm from occipital myotomes from about stage 13. The dorsal border of the septum transversum, which initially lies opposite the second cervical segment, migrates caudally as the embryo grows and the heart enlarges. At first the ventral border moves more rapidly than the dorsal, but after the embryo has attained a length of 5 mm (about stage 13, 31–33 days post fertilization), the dorsal border migrates more rapidly. When the dorsal border of the septum transversum lies opposite the fourth cervical segment, the phrenic nerve (derived from spinal cord segments C3, C4 and C5) and portions of the corresponding myotomes grow into it and accompany it in its later migrations. The dorsal border of the septum transversum does not come to lie opposite the last thoracic and first lumbar segments, the final position occupied by some of the dorsal attachments of the diaphragm, until the end of the second month. The main derivatives of the central part of the respiratory diaphragm lie at considerably more cranial levels. The cervical myoblasts populate the outer rim of the mesenchymal area and the dorsolateral part which extends caudally behind the developing suprarenal (adrenal) glands. Although histological sections of this region provide clear images of adjacent structures, the curvature of embryos and the difficulty of accurately aligning sectional planes make this developmental process particularly difficult to visualize in 3 dimensions. For details of the closure of the pleuroperitoneal canals in human embryos and fetuses see Hayashi et al (2011).

Respiratory diaphragmatic herniae

Available with the *Gray's Anatomy* e-book

Respiratory diaphragmatic herniae may result from failure of fusion of the component parts or from a primary defect. Posterolateral defects (Bochdalek's hernia) are the most common (85–90%) and may be bilateral (5%) or unilateral. Of the unilateral defects, the left side is more commonly affected (80%) (Chandrasekharan et al 2017). Although these hernias have been attributed to failure of fusion of the pleuroperitoneal membrane, there is increasing evidence that the primary abnormality is lung hypoplasia, and the herniation of the abdominal contents is secondary, which has important implications for treatment (Jesudason 2002). A non-muscular membranous sac, possibly derived from the pleuroperitoneal canal wall is present in 10–15% of cases, signifying the early occurrence of this lesion prior to closure of the pleuroperitoneal canal. Hernias between the costal and sternal origins (Morgagni hernia) are rare (1–2%) (**Fig. 20.6**). Midline defects in the central tendon arise from septum transversum defects. The incidence of congenital diaphragmatic hernias is about 1 : 3000 to 1 : 5000 in neonates, with a prenatal incidence of 1 : 2000.

Respiratory diaphragmatic hernias can usually be diagnosed by antenatal ultrasound examination. The presence of bowel in the thorax and mediastinal shift may be seen sonographically and radiographically (**Fig. 20.7**). The main causes of death in babies with diaphragmatic hernias are pulmonary hypoplasia and pulmonary hypertension. Pulmonary hypoplasia is related to the abnormal branching of the airways both ipsilaterally and contralaterally and the resulting reduced numbers of alveoli. Pulmonary hypertension is related to pulmonary hypoplasia, and to the increased muscularization and reactivity of the pulmonary circulation. There may be associated anomalies, including trisomy 13 and 18, and diaphragmatic hernia may be part of a number of syndromes, many of which may lead to termination of the pregnancy or to death of the neonate. For a review summarizing the recurrent genetic causes of congenital diaphragmatic hernias, see Wynn et al (2014).

Diaphragmatic eventration is a condition in which an abnormal diaphragmatic silhouette is seen on X-ray with an abnormal medial bulge into the thorax; it is associated with paradoxical motion of the diaphragm during respiratory movements. It may be a benign condition, often a chance finding, requiring no treatment or it may lead to respiratory symptoms, requiring plication, and it is occasionally associated with rib and cardiac anomalies.

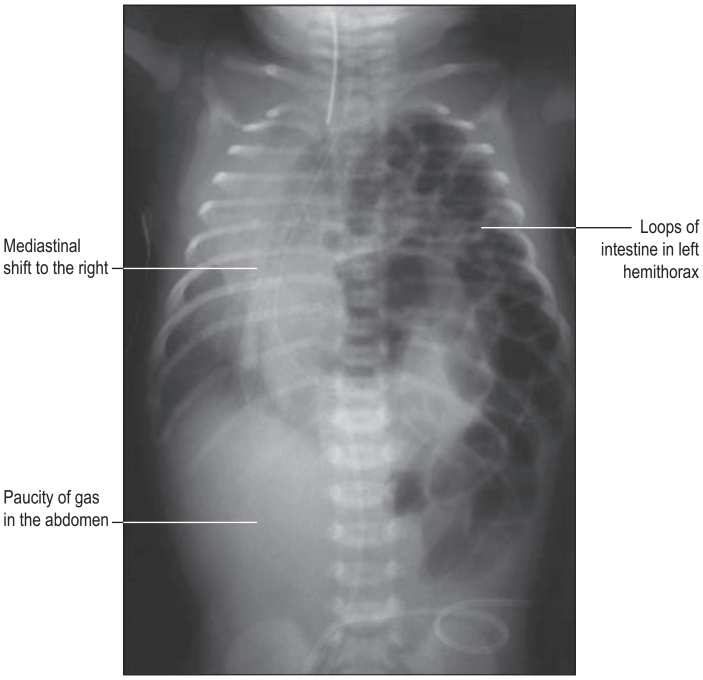
Mediastinal shift to the right
Paucity of gas in the abdomen
Loops of intestine in left hemithorax

Fig. 20.7 Plain radiograph of the chest and abdomen in a 1-day-old neonate with left posterolateral congenital respiratory diaphragmatic hernia. (Courtesy of Mr G Jawaheer, Great North Children's Hospital, Newcastle upon Tyne.)

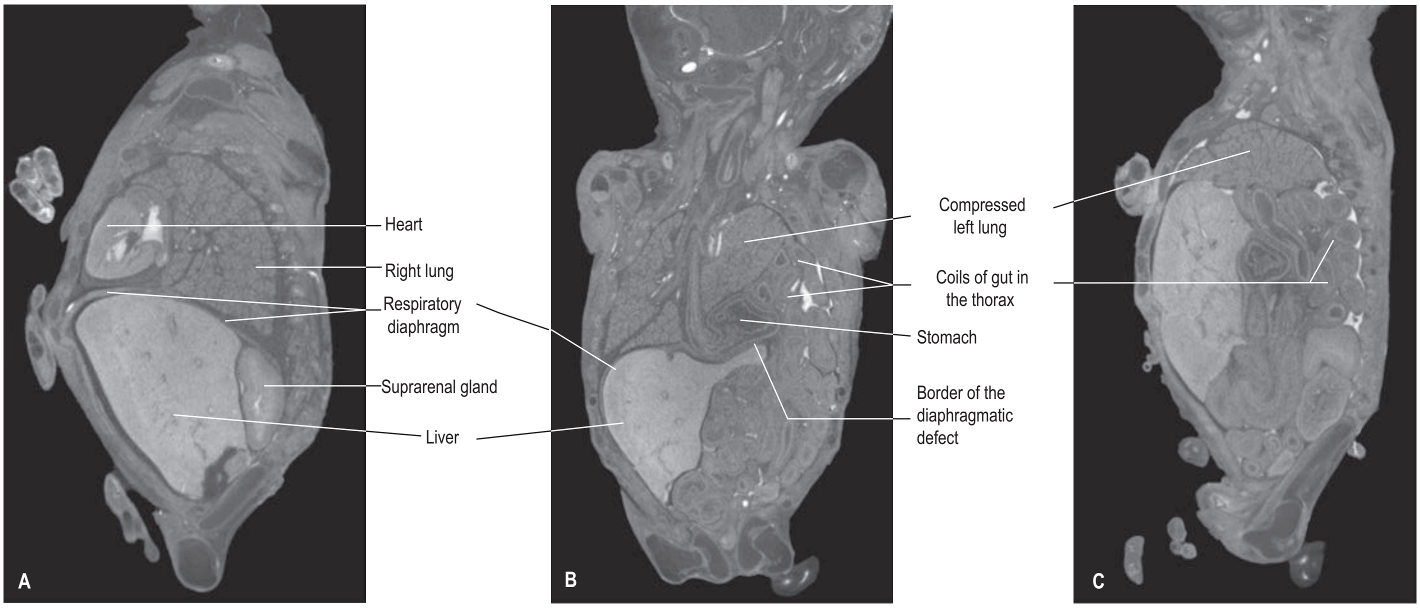

Fig. 20.6 MicroCTs of a 13-postmenstrual-weeks fetus with a left-sided congenital diaphragmatic hernia. **A**, Right sagittal section: respiratory diaphragm is intact. **B**, Coronal section: respiratory diaphragm is intact on the right but not on the left, where the stomach is in the thorax. **C**, Left sagittal section: coils of gut in the thorax. (Courtesy of Dr Owen Arthurs and Dr Susan Shelmerdine, Great Ormond Street Hospital, London.)

Thoracic wall, ribs, sternum

The ventral thoracic wall of the embryo consists of minimal amounts of mesenchyme between the ectoderm and pericardial cavity. The ribs and intercostal muscles develop from thoracic somites adjacent to the neural tube (Ch. 18). Hypaxial portions of the myotomes at these levels migrate ventrally between stages 14–18, and the spinal nerves follow marginally later. The intercostal muscles form as the hypaxial myotomal sheet grows around the body wall, separating into three layers, still in continuity with myoblasts that will give rise to the abdominal muscles once the umbilical cord origin becomes proportionally smaller.

Rib primordia are identifiable in stage 15 and grow into the hypaxial muscle sheet. The vertebral column is bent ventrally in a primary, concave curve. The origin of the umbilical cord (umbilical ring) is proportionately large at stage 15 and is opposite ribs 5–11; by stage 17 the umbilical ring is opposite ribs 11 and 12 because the trunk has lengthened. During stages 15–17, ribs 1–7 are of a similar length and extend half way along the lateral body wall; ribs 8–12 are shorter. In stage 18 the ribs begin to bend ventrally and by stage 20 ribs 1–8 also bend mediocranially towards the putative sternum. Although the ribs do not change their orientation from this time, by stage 23 they have increased in length three-fold as the thorax and upper abdomen circumference increases (Mekonen et al 2015).

The sternum is first visible in stage 18 as a presternal condensation above the first rib, and a pair of lateral sternal bars. The presternal condensation forms the manubrium and extends to the second rib by stage 23, at which time the sternal bars are caudal to the putative manubrium. The sternal bars join with ribs 2–5 and approach each other at the ventral midline. The sternal bars extend to connect with the lower ribs in stage 23 and remain bifid until postfertilization week 10 (Mekonen et al 2015). For details of postnatal development of the sternum see Bayaroğullari et al (2014).

Congenital anomalies of the thoracic wall

Vertebral anomalies, including formation of hemivertebrae and block vertebrae (where cranial and caudal sclerotomal halves do not separate), may contribute to scoliosis. Five per cent of scoliosis is congenital and it may be associated with numerous other anomalies, e.g. the VACTERL (Vertebral; Anorectal; Cardiac; Tracheal; Esophageal; Renal; Limb) association or with congenital syndromes such as Marfan syndrome and congenital neurofibromatosis. The diagnosis may be missed at birth. Syndromes in which the chest wall does not develop properly and the lungs are hypoplastic include Jeune syndrome, asphyxiating thoracic dystrophy (an autosomal recessive condition that may be associated with short limb dwarfism and polydactyly) and Poland's syndrome, which consists of unilateral pectoral aplasia and dysdactylia (Martin and Hackam 2017). Rib cage anomalies also occur in thanatrophic dwarfism, achondroplasia, chondroectodermal dysplasia and giant exomphalos. Many of these conditions are fatal soon after birth; milder forms may improve with time, but affected individuals may need prolonged respiratory support. Ellis van Creveld and Sesenbrenner's syndromes also affect chest wall and rib development and are related to mutations in primary (non-motile) cilia genes.

Anomalies of the sternum and ventral body wall include ectopia cordis, a condition in which the heart is outside the body without a surrounding pericardium. This very rare condition is thought to be caused by failure of the heart to descend into the thorax: cervical, cervicothoracic, thoracic, thoracoabdominal and abdominal types have been classified (Engum 2008). The condition can be detected on second trimester ultrasound examination. Less serious and more prevalent sternal anomalies include pectus excavatum, the most common, seen in 1 in 300–400 live births (male : female ratio 3 : 1) and pectus carinatum, seen 1 in 10,000 live births (male : female ratio 6 : 1) (Gottlieb et al 2018).

Ultrasound antenatal imaging of the thorax and fetal lungs

The fetal thorax is symmetrically bell-shaped on coronal section and almost circular in axial section. Fetal chest size is estimated by measuring the chest circumference on axial section at the level of the four-chamber-heart view. Such measurement can confirm or exclude reduced chest volume (Karl and Chaoui 2015). The relative circumference of the thorax and heart remains the same in the second and third trimesters. The respiratory diaphragm is best viewed in sagittal view as a dome on each side of the body with no difference in its height on either side. Diaphragmatic hernias can be diagnosed from about postmenstrual week 18 by the presence of the stomach bubble or gut within the thoracic cavity and mediastinal shift; the liver may also herniate into the chest (Bulas 2018).

Pulmonary hypoplasia, an absolute decrease in lung volume and weight for gestational age, may be identified but cannot be confirmed. It is normally associated with oligohydramnios and renal agenesis. Unilateral hypoplasia may be suggested by rotation and displacement of the heart on ultrasound examination. In bilateral pulmonary hypoplasia the heart appears relatively large with a reduced chest volume. However, intrauterine growth retardation may also cause similar findings. Increased echogenicity of the lungs indicates conditions that prevent the normal circulation of lung fluid (for further details consult Coady and Bower (2015)). Details of prenatal lung anomalies and their detection are given in Epelman et al (2013) and of ultrasound examination of the fetal thorax in Hagen-Ansert (2018). Fetal breathing movements become more prominent in the second and third trimesters; at least 30 seconds of continuous, rhythmic breathing movements are considered normal within a 30 minute sonography examination (Benson and Doubilet 2018). Maternal activity affects fetal breathing; it is stimulated by increased sugar and decreased by maternal cigarette smoking (Hagen-Ansert 2018).

Other thoracic structures are noted in the ultrasound examination. The fetal thymus can be identified in the anterior mediastinum at 14 postmenstrual weeks. The normal thymus has an average transverse diameter of 12 mm at 19 postmenstrual weeks and 33 mm at 33 postmenstrual weeks; the normal, average thymic perimeter is 128 mm at 38 postmenstrual weeks. Although imaging and measurement of the thymus is not routinely performed, acute thymic involution has been noted in association with chorioamnionitis, and thymic measurements showing aplasia or hypoplasia may be seen in DiGeorge syndrome (Bulas 2018). Pleural effusion, an accumulation of fluid within the pleural cavity can be bilateral or unilateral; when unilateral and right-sided it is commonly a chylothorax caused by an anomaly of the thoracic duct (Hagen-Ansert 2018).

Postnatal development of the respiratory system

Functional changes in the lungs at birth

Just prior to birth, the placenta is the organ of respiration. Virtually all the venous return to the right heart is shunted away from the lungs through the foramen ovale and the ductus arteriosus. Pulmonary vascular resistance is maintained at a very high level by the muscular precapillary pulmonary vessels. At birth, the umbilical cord is tied and cut, and within seconds the lungs must take over all respiratory function in order to maintain life. In the non-compromised full-term neonate, it is advised that cord clamping should be delayed for at least one minute to enhance venous return of blood to the lungs during the first few postnatal breaths.

With the onset of postnatal breathing the lung must change from secreting fluid to absorbing it. The mechanisms that mediate these dramatic changes are obscure. However, it is clear that the first breath results in pulmonary vasodilatation by at least two mechanisms. First, the mechanical effect of traction on the vasculature: as the chest wall expands, it pulls open the pulmonary vessels. Second, oxygen entering the lungs for the first time produces pulmonary vasodilatation. The demonstration that pulmonary vascular resistance (PVR) falls, even if an experimental animal fetus is delivered into an atmosphere of pure nitrogen, implies that other mediators, including cyclo-oxygenase metabolites, are important. The gene for cyclo-oxygenase 1 (but not 2) in endothelium and vascular smooth muscle shows enhanced expression in late fetal and early post-natal life. Endothelin receptor expression increases around the time of birth, implying a role for this system in postnatal adaptation. The role of nitric oxide in postnatal adaptation is controversial, and there are likely to be important species differences. Nitric oxide synthase (NOS) is more abundant in young compared with mature animals, and smooth muscle sensitivity to nitric oxide may be greater at birth than in older animals. The effects of mediators may differ ante- and postnatally, e.g. endothelin (ET)-1 causes vasodilatation in fetal sheep, but vasoconstriction postnatally in lambs.

Most arteries and veins are present and the morphology of the blood–gas barrier is the same as in adults, however, until lung alveoli become filled with air and stretched by the first breaths the functional relationship between the expanding pulmonary capillary endothelial cells and the type I pneumocytes is not yet fully established. The endothelial cells of the precapillary arteries are still squat and have narrow bases on the subendothelium, a low surface : volume ratio and many surface projections. Five minutes after birth, the endothelial cells are thinner and gradually show less cell overlap, the surface : volume ratio increases, fewer cell projections are seen, the vessel wall becomes thinner and the lumen diameter increases (**Fig. 20.8**).

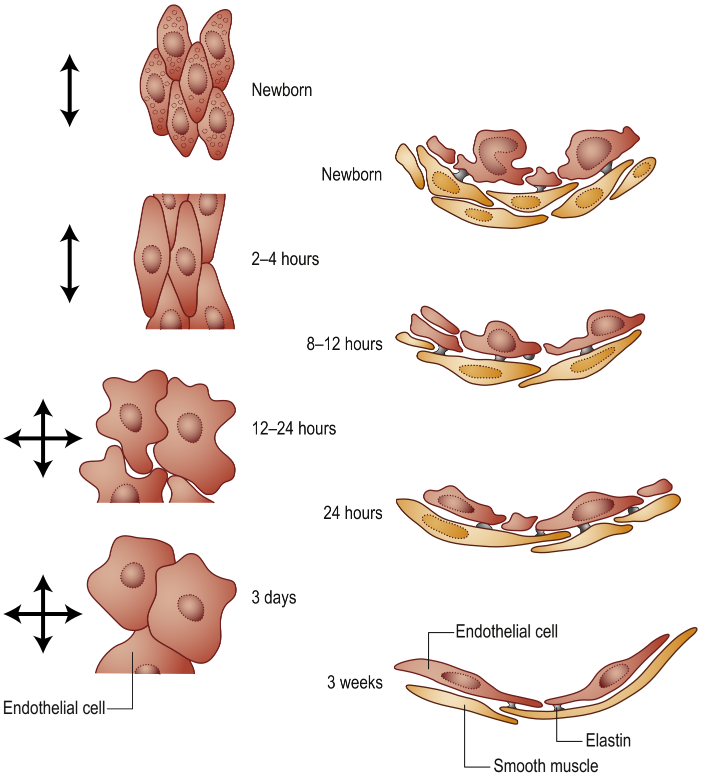

Fig. 20.8 *En face* views (left) and transverse sections (right) showing the changes in the endothelial and smooth muscle cells of small muscular pulmonary arteries accompanying terminal bronchi from the neonatal period to postnatal week 3. (With permission from Haworth SG 1992 Pathophysiological and metabolic manifestations of pulmonary vascular disease in children. Herz 17:254–61.)

As respiration is established but before structural remodelling has taken place, pulmonary vascular resistance may rise steeply if the neonate becomes even minimally hypoxic or acidaemic. The fetal shunts (foramen ovale and ductus arteriosus) reopen and right to left shunting causes profound hypoxaemia, 'persistent fetal circulation'. At full-term delivery the lung volume is small but related to body weight. All airways are present and differentiated (cartilage, glands, muscle, nerves) with one-third to one-half of the adult complement of alveoli present, giving sufficient surface area for gas exchange.

Lungs at birth in preterm infants

There appears to be a relationship between those organs with specialized epithelia abutting endothelium with fused basal laminae and their sensitivity to damage by prematurity and haemodynamic shifts (see Fig 11.2). The alveolar–capillary membrane, the glomerular basement membrane and the blood–brain barrier are specifically affected by preterm birth, where changes in oxygen tension and blood pressure can change the normal developmental trajectory, and any one of these sites is affected by changes in the others. These sites are also particularly affected by postnatal haemodynamic shifts within the still embryonic blood vessels, such that either the tissue becomes more hypoxic than the fetal environment, or hyperoxic when cardiac shunts change postnatally. Either change can cause damage, resulting in acute inflammation and healing, with cytokines entering the fetal circulation and affecting other vulnerable developing organs.

Extremely premature babies, who are treated with surfactant and ventilated using low-pressure, high-rate strategies, show arrest of alveolar development and pulmonary hypoplasia. Arrest of development is also seen in outer cortical glomeruli and in the migration of neuroblasts and glioblasts to the cortical plate in preterm infants. However, in the kidney and brain the connection between the specialized epithelia and adjacent endothelium is stable in some mature areas, for example, the glomerular basement membrane in the kidney functions prenatally and does not undergo significant mechanical change at birth. In contrast, lung alveoli and pulmonary capillaries expand during the first postnatal breaths, initiating postnatal maturation of ventilation perfusion matching. In the preterm infant the initial extent of lung expansion is crucial. As few as three large assisted ventilatory breaths may cause sufficient damage to the expanding alveolar type I pneumocytes and associated pulmonary alveolar capillaries to initiate an inflammatory response and cytokine release triggering a systemic inflammatory response (Barton et al 2015). Ventilation-induced lung injury contributes to subsequent healing processes and leads to bronchopulmonary dysplasia (also known as chronic lung disease). Impaired haemodynamic autoregulation effects the cerebral blood flow and leads to either hypoxia/ischaemia or cerebral haemorrhage, and affects the permeability of the blood–brain barrier (Barton et al 2015, Volpe 2017).

Preterm males may have worse respiratory distress than females after control for other risk factors, such as degree of prematurity; it is possible that in male fetuses surfactant production is delayed (Anadkat et al 2012, Jackson 2018). Androgens delay fetal lung maturation while stimulating fetal lung growth: type II cells in males are less mature than in females during the canalicular phase.

More than half of preterm infants develop respiratory distress syndrome due to lung immaturity and surfactant deficiency. Shear stress in the alveoli and terminal bronchi, caused by repetitive reopening of collapsed alveoli and overdistention of open alveoli, leads to type I pneumocyte damage and protein exudate into the alveoli and terminal airways (this is the basis of hyaline membranes). The exudate may impair the function of the limited surfactant that is present in immature lungs. Reopening collapsed alveoli requires the generation of highly negative intrathoracic pressure, thus the preterm infant shows retractions of the thoracic wall and use of accessory muscles during inspiration. Expiratory grunting, caused by partial closure of the glottis, helps maintain end-expiratory pressure and patency of unstable alveoli (Jackson 2018). Hyperoxia or dexamethasone treatment of experimental rats during the alveolarization period permanently abrogates alveolar development, suggesting that iatrogenic damage to the developing alveoli when ventilating a preterm baby with oxygen-enriched mixtures is probably irreversible, and ventilation-induced lung injury may now be the basis of bronchopulmonary dysplasia (Voynow 2017). The long-term effects of preterm birth and its treatment are changing over the years. Survivors from the pre-surfactant era have disease dominated by airflow obstruction. Importantly even babies born at 33–34 postmenstrual weeks have persistent postnatal airflow obstruction (Kotecha et al 2012).

Neonatal thorax

In the normal full-term neonate, the trachea is relatively small in relation to the larynx. The walls of the trachea are relatively thick and the tracheal cartilages are relatively closer than they are in the adult. The trachea begins level with the upper border of the sixth cervical vertebra, a relationship that is conserved with growth, and it bifurcates at the level of the third or fourth thoracic vertebra.

A number of differences between the neonatal and adult thorax and respiratory diaphragm are significant in early postnatal life, especially in the preterm infant. The full-term neonatal thorax has a rounded circumference whereas the adult profile is dorsoventrally flattened. The compliance of the adult chest wall and lung are approximately equal, but the neonatal chest wall is up to five times more compliant than the lungs and so is easily deformable: indrawing of the chest wall is an important sign of increased work of breathing in the neonate. The respiratory diaphragm is relatively flat at birth and gains its dome shape as the thorax and abdominal viscera grow. The arrangement of the ribs and diaphragm in the neonate means that contraction of the diaphragm pulls the compliant ribs inwards. This does not contribute to inspiration and leads to chest distortion: it may be opposed by the stabilizing action of the expiratory muscles. The neonatal respiratory diaphragm exhibits an exaggerated asymmetric movement: the posterior portion shows a considerably greater excursion than the anterior portion.

A neonate undertakes relatively greater work in order to breathe, and is much more vulnerable to developing respiratory muscle fatigue and respiratory muscle failure than an adult. Experimental animal studies suggest that neonates may be especially vulnerable to respiratory muscle failure because of the initial immaturity of synapses. Moreover, myosin isoforms are developmentally regulated in the diaphragm, and the reduced power output and work performance of the neonatal diaphragm may reflect these molecular differences. In expiration, there may be active braking of airflow, caused by inspiratory muscle activity and partial constriction of the larynx.

At all ages, there is a reduction, if not loss, of tonic intercostal activity during rapid eye movement (REM) sleep. The mechanism is believed to be related to a descending spinal inhibition of the muscle spindle system. In addition, although during REM sleep the respiratory diaphragm descends further, this inspiratory effort is dissipated in sucking in the ribs and enlarging the abdomen, such that the rib cage and abdominal ventilatory movements become out of phase. The neonate is at particular risk in this respect, because the chest wall is flexible, and much of the infant sleep activity is of the REM type. Furthermore, the upper airway musculature may lose tone during REM sleep, so that the soft tissues of the pharynx are sucked in during inspiration, limiting the cross-sectional area of the upper airway and further increasing the work of breathing.

Endotracheal intubation in the neonate

The insertion of an endotracheal tube is a procedure that may be required for resuscitation of the neonate at birth and subsequently to enable artificial ventilation. The larynx is more funnel-shaped than in the adult. It is located at the level of the middle of the body of the third cervical vertebra in preterm infants, and at the interspace between the third and fourth cervical vertebrae in full-term infants (Fiadjoe et al 2018). Visualization of the infant larynx is difficult because, unlike the adult, the angle between the plane of the tongue and the plane of the glottic opening is more acute; the epiglottis is omega-shaped and narrow and angled away from the axis of the trachea; and the vocal cords are angled with a higher attachment ventrally than dorsally. The cricoid cartilage is functionally the narrowest portion of the upper airway in infants.

An endotracheal tube is introduced, usually orally initially, and guided through the vocal cords under direct vision using a laryngoscope. The length of the trachea (vocal cords to carina) in full-term neonates and infants to 1 year of age varies from 5 to 9 cm. Once in place, the tip of the tube should be in the mid-trachea, well above the carina. The required length of the tube can be estimated according to birth weight; although correlation to foot length has also been noted to be as accurate as weight (Fiadjoe et al 2018). Confirmation of correct positioning of the endotracheal tube is obtained from a chest X-ray (Schmölzer et al 2013). Long-term endotracheal intubation in extremely preterm infants is associated with subglottic stenosis and later dysphonia. Voice anomalies have been reported in more than 50% of children born preterm with endotracheal intubation longer than 28 days, and in those with prolonged admission to a neonatal intensive care unit (Hseu et al 2018).

Postnatal lung development

Available with the *Gray's Anatomy* e-book

Normal postnatal pulmonary arterial development

Immediately after birth, dramatic remodelling of the pulmonary vasculature occurs to effect an abrupt reduction of pulmonary vascular resistance. This process continues at a rapid rate throughout the first 1–2 postnatal months, while the lungs adapt to extrauterine life, and then more slowly throughout childhood. Failure to remodel in the presence of an anatomically normal heart leads to persistent pulmonary hypertension. Normal postnatal pulmonary arterial development in the full-term neonate can be divided into three stages:

Stage one lasts from birth to about postnatal day 4, and concerns the immediate adaptation to extrauterine life. The endothelial cells expand and the vessel wall becomes thinner (see Fig. 20.8). The smooth muscle cells show a significant reduction in diameter during this time.

Stage two lasts from around day 4 to 3–4 postnatal weeks, and is the time when the cells deposit matrix around themselves to fix their new positions. At birth, the internal elastic lamina of the small muscular arteries consists only of amorphous elastin in a basal lamina-like matrix. By 3 postnatal weeks, a definitive elastic lamina is evident, although it is heavily fenestrated, permitting contact between the endothelial cells and the smooth muscle cells.

Stage three continues into adulthood. The intrapulmonary arteries increase in size and their walls increase in thickness. However, the maturation of all of the pulmonary vascular smooth muscle cells, from the hilum to the precapillary bed, is not advanced until 2 years. As the distal airspaces expand, the capillary networks fuse from one alveolus to another, forming, for a period, an extensive double capillary net: this process can be seen from postnatal day 28, becomes more extensive by 1.5 years, and it is believed to be complete by 5 years.

The first 4-6 years of life seem to be a key time window, after which there is no catch-up growth in lung function (Bush 2016). Postnatal lung development is also impaired by exposure to tobacco smoke, and there is increasing evidence that air pollution, early polysensitization to aeroallergens and attacks of severe wheeze also adversely impact on normal lung growth.

Bonus e-book content

Fig. 20.3 Tracheo-oesophageal fistulae and oesophageal atresia.

Fig. 20.6 MicroCTs of a 13-postmenstrual-weeks fetus with a left-sided congenital diaphragmatic hernia.

Fig. 20.7 Plain radiograph of the chest and abdomen in a 1-day-old neonate with left posterolateral congenital respiratory diaphragmatic hernia.

Key references

Barton SK, Tolcos M, Miller SL et al 2015 Unraveling the links between the initiation of ventilation and brain injury in preterm infants. Front Pediatr 3:97. doi: 10.3389/fped.2015.00097.

Consideration of the initial ventilation needs of the preterm infant and links to the pathogenesis of brain injury.

Bush A 2016 Lung development and aging. Ann Am Thorac Soc 13(Suppl 5): S438–S446.

An overview of the pre- and postnatal lung.

Martin L, Hackam D 2017 Congenital chest wall deformities. In: Cameron JL, Cameron AM (eds) Current Surgical Therapy, 12th ed. Elsevier, pp. 891–8.

This chapter gives an overview of the anomalies of chest wall development.

Mekonen HK, Hokspoors JPJM, Mommem G, Köhler SE, Lamers WH 2015 Development of the ventral body wall in the human embryo. J Anat 227:673–85.

Figures 2–7 illustrate in 3D reconstructions, over stages 15–23, the lengthening and medial growth of the ribs and formation of the sternum. Hypaxial muscle growth is shown and the closure of the ventral body wall discussed. This paper provides accurate embryonic staging, in line with O'Rahilly and Müller (2010), illustrates the conversion of serial histological sections to 3D images using computer software and compares successive embryonic stages.

Morrisey EE, Hogan BL 2010 Preparing for the first breath: genetic and cellular mechanisms in lung development. Dev Cell 18:8–23.

This paper presents an overview of the molecular mechanisms of lung development.

The amount and type of connective tissue in the lung change after birth. The neonatal lung has abundant type III and type IV collagen, but little type I collagen. Types III and IV collagen are not mechanically strong, suggesting that the neonatal lung has a phenotype that facilitates the changes in cell shape and orientation that characterize adaptation to extrauterine life. It is probable that the rapid deposition of type I collagen postnatally contributes structural stiffness to the blood vessel walls.

Conducting airways undergo profound postnatal changes, and exhibit increased smooth muscle and bronchoconstrictor responsiveness. Although the precise molecular signalling for these processes is unknown, it appears to be tightly developmentally regulated.

Lung volume increases most rapidly during the first year of life and also increases more rapidly than airway calibre during this time, a finding which is consistent with the concept of dysanaptic lung growth, i.e. a dissociation between the growth of the lung parenchyma and the airways. It was thought that most of the alveoli were formed by two years of age, with subsequent lung growth primarily resulting from an increase in the size of individual alveoli. However, measurements of alveolar size throughout childhood and adolescence using hyperpolarized helium have shown that neo-alveolarization as well as an increase in alveolar size continues through childhood and adolescence (Narayanan et al 2012). This has important implications for diseases characterized by neonatal arrest of alveolarization, for example after ventilation of the extreme preterm baby there is more scope for recovery than previously thought, but also more potential harm from childhood perturbations. Forced vital capacity measured by the raised volume, rapid thoracoabdominal compression technique is reported to be the same in male and female infants and very young children (Jones et al 2000), which is consistent with post mortem morphometric measurements. By the second year of life the rate of increase in forced vital capacity is similar to that reported in older children.

The best data on the evolution of spirometry over the life course are from the Global Lung Initiative (Quanjer et al 2012), based on more than 160,000 data points. Briefly, spirometry rises to reach a plateau at age 20–25 years and thereafter declines steadily. During childhood, lung volumes and flow rates increase linearly with height, with a greater intercept and more positive slope in boys compared to girls (Stanojevic et al 2008). The linearity of these changes is interrupted by puberty (Rosenthal et al 1993a, 1993b, Rosenthal and Bush 2002), when important shape changes occur in the thorax, particularly in boys, and are mirrored by changes in the size of the underlying lung (and in particular the alveoli) as manifest by an abrupt increase in vital capacity, forced expired volume in one second, and total lung capacity. Thereafter, the change in lung size again proceeds in a linear fashion. High resolution CT scanning has been used to measure airway dimensions (de Jong et al 2006), although this technique should be used with caution because of the radiation exposure.

There is little in the way of structural data to set alongside epidemiology. The reticular basement membrane is first detected at about 30 postmenstrual weeks, thickens throughout childhood and adolescence, and plateaus or possibly declines in thickness with age (Tsartsali et al 2011). In terms of airway smooth muscle, limited data from endobronchial biopsies suggested that this did not change from age three years throughout childhood (O'Reilly et al 2013). Autopsy data suggest an increase in airway smooth muscle over the first two years of life. Goblet cells also increase over the same timeframe (Hislop and Haworth 1989).

References

Aiello D, Giambona A, Leto F et al 2018 Human coelomic fluid investigation: a MS-based analytical approach to prenatal screening. Sci Rep. 8:10973. doi: 10.1038/s41598-018-29384-9.

Ameis D, Khoshgoo N, Iwasiow BM et al 2017 MicroRNAs in lung development and disease. Paediatr Respir Rev 22:38–43.

Anadkat JS, Kuzniewicz MW, Chaudhari BP et al 2012 Increased risk for respiratory distress among white, male, late preterm and term infants. J Perinatol 32:780–5.

Ardini-Poleske ME, Clark RF, Ansong C et al MAP Consortium 2017 Lung MAP: The Molecular Atlas of Lung Development Program. Am J Physiol Lung Cell Mol Physiol 313: L733–L740.

Barton SK, Tolcos M, Miller SL et al 2015 Unraveling the links between the initiation of ventilation and brain injury in preterm infants. Front Pediatr 3:97. doi: 10.3389/fped.2015.00097.

Consideration of the initial ventilation needs of the preterm infant and links to the pathogenesis of brain injury.

Bayaroğullari H, Yengil E, Davran R et al 2014 Evaluation of the postnatal development of the sternum and sternal variations using multidetector CT. Diagn Interv Radiol 20:82–9.

Bellini C, Ergaz Z, Boccardo F et al 2013 Dynamics of pleural fluid effusion and chylothorax in the fetus and newborn: role of the lymphatic system. Lymphology 46:75–84.

Benson CB, Doubilet PM 2018 Fetal measurement: normal and abnormal fetal growth and assessment of fetal well-being. In: Rumack CM, Levine D (eds) Diagnostic Ultrasound, 5th ed. Elsevier; Ch. 42, pp. 1443–64.

Blanc P, Coste K, Pouchin P et al 2012 A role for mesenchyme dynamics in mouse lung branching morphogenesis. PLoS One 7:e41643.

Bolte C, Whitsett JA, Kalin TV et al 2018 Transcription factors regulating embryonic development of pulmonary vasculature. Adv Anat Embryol Cell Biol 228:1–20.

Bulas D 2018 The fetal chest. In: Rumack CM, Levine D (eds) Diagnostic Ultrasound, 5th ed. Elsevier; Ch. 36, pp. 1243–69.

Bush A 2005 Asthma research: the real action is in children. Paediatr Respir Rev 6:101–10.

A review of how early problems with lung growth and development impact on later lung disease.

Bush A 2016 Lung development and aging. Ann Am Thorac Soc 13(Suppl 5):S438–S446.

An overview of the pre- and postnatal lung.

Bush A, Abel R, Chitty L et al 2018 Congenital lung disease. In: Wilmott R, Deterding R, Li A et al (eds) Kendig's Disorders of the Respiratory Tract in Children, 9th ed. Elsevier, pp. 289–337

Bush A, Griese M, Seidl E et al 2019 Early onset children's interstitial lung diseases: discrete entities or manifestations of pulmonary dysmaturity? Paediatr Respir Rev 2019 30:65–71.

Chandrasekharan PK, Rawat M, Madappa R et al 2017 Congenital diaphragmatic hernia – a review. Matern Health Neonatol Perinatol 3:6–32.

Chao CM, Moiseenko A, Zimmer KP et al 2016 Alveologenesis: key cellular players and fibroblast growth factor 10 signaling. Mol Cell Pediatr 3:17.

Coady AM, Bower S (eds) 2015 Twining's Textbook of Fetal Abnormalities, 3rd ed. Oxford: Elsevier.

Cornett B, Snowball J, Varisco BM et al 2013 Wntless is required for peripheral lung differentiation and pulmonary vascular development. Dev Biol. 379:38–52.

de Jong PA, Long FR, Wong JC et al 2006 Computed tomographic estimation of lung dimensions throughout the growth period. Eur Respir J 27:261–7.

Deutsch GH, Young LR 2016 Lipofibroblast phenotype in pulmonary interstitial glycogenosis. Am J Respir Crit Care Med 193:694–6.

Engum SA 2008 Embryology, sternal clefts, ectopia cordis, and Cantrell's pentalogy. Semin Ped Surg 17:154–60.

Epelman M, Daltro P, Soto G et al 2013 Congenital lung anomalies. In: Coley BD (ed) Caffey's Pediatric Diagnostic Imaging, 12th ed. Philadelphia: Elsevier, Saunders; Ch. 53.

Fiadjoe JE, Litman RS, Serber JF et al 2018 The pediatric airway. In: Coté CJ, Lerman J, Anderson B (eds). A Practice of Anesthesia for Infants and Children, 6th ed. Philadelphia: Elsevier Saunders; Ch. 14, pp. 297–339.

Gottlieb EA, Andropoulos DB 2018 Pediatrics. In: Pardo MC, Miller RD (eds) Basics of Anesthesia, 7th ed. Elsevier; Ch. 34, pp. 587–609.

Gottlieb LJ, Reid RR, Slidell MB 2018 Pediatric chest and trunk defects. In: Rodriguez ED, Losee JE, Neligan PC (eds) Plastic Surgery: Volume 3: Craniofacial, Head and Neck Surgery and Pediatric Plastic Surgery, 4th ed. Philadelphia: Elsevier; Ch. 40.

Hagen-Ansert SL 2018 Fetal thorax. In: Hagen-Ansert S (ed), Textbook of Diagnostic Sonography. Elsevier; Ch. 61, pp. 1406–18.

Hamvas A, Deterding RR, Wert SE et al 2013 Heterogeneous pulmonary phenotypes associated with mutations in the thyroid transcription factor gene NKX2-1. Chest 144:794–804.

Hayashi S, Fukuzawa Y, Rodrigues-Vazquex JF et al 2011 Pleuroperitoneal canal closure and the fetal adrenal gland. Anat Rec 294:633–44.

Hind M, Gilthorpe A, Stinchcombe S et al 2009 Retinoid induction of alveolar regeneration: from mice to man? Thorax 64:451–7.

Hislop A 2005 Developmental biology of the pulmonary circulation. Paediatr Respir Rev 6:35–43.

Hislop AA, Haworth SG 1989 Airway size and structure in the normal fetal and infant lung and the effect of premature delivery and artificial ventilation. Am Rev Respir Dis 140:1717–26.

Hseu A, Ayele N, Kawai K et al 2018 Voice abnormalities and laryngeal pathology in preterm children. Ann Oto Rhinol Laryngol 127:508–13.

Inanlou MR, Baguma-Nibasheka M, Kablar B 2005 The role of fetal breathing-like movements in lung organogenesis. Histol Histopathol 20:1261–6.

Jackson 2018 Respiratory disorders in the preterm infant. In: Gleason CA, Juul SE (eds), Avery's Diseases of the Newborn, 10th ed. Elsevier; Ch. 46.

Janér J, Lassus P, Haglund C et al 2006 Pulmonary vascular endothelial growth factor-C in development and lung injury in preterm infants. Am J Respir Crit Care Med 174:326–30.

Jesudason EC 2002 Challenging embryological theories on congenital diaphragmatic hernia: future therapeutic implications for paediatric surgery. Ann R Coll Surg Engl 84:252–9.

This paper considers the evidence for anomalous lung development underpinning the development of diaphragmatic hernia.

Jones M, Castile R, Davis S et al 2000 Forced expiratory flows and volumes in infants: normative data and lung growth. Am J Respir Crit Care Med 161:353–9.

Karl K, Chaoui R 2015 Pulmonary abnormalities. In: Coady AM, Bower (eds) Twining's Textbook of Fetal Abnormalities, 3rd ed. Oxford: Elsevier; pp. 394–416.

Kho AT, Bhattacharya S, Tantisira KG et al 2010 Transcriptomic analysis of human lung development. Am J Respir Crit Care Med 181:54–63.

Kimura J, Deutsch GH 2007 Key mechanisms of early lung development. Pediatr Dev Pathol 10:335– 47.

Kotecha SJ, Watkins WJ, Paranjothy S et al 2012 Effect of late preterm birth on longitudinal lung spirometry in school age children and adolescents. Thorax 67:54–61.

Kulkarni RM, Herman A, Ikegami M et al 2011 Lymphatic ontogeny and effect of hypoplasia in developing lung. Mech Dev 128:29–40.

Lang C, Conrad L, Michos O 2018 Mathematical approaches of branching morphogenesis. Front Genet 9:673. doi:10.3389/fgene.2018.00673.

Lange AW, Haitchi HM, LeCras TD et al 2014 Sox17 is required for normal pulmonary vascular morphogenesis. Dev Biol 387:109–20.

Leboulanger N, Garabédian E 2011 Laryngo-tracheo-oesophageal clefts. Orphanet J Rare Dis 6:81. doi: 10.1186/1750-1172-6-81.

Li YF, Langholz B, Salam MT et al 2005 Maternal and grandmaternal smoking patterns are associated with early childhood asthma. Chest 127:1232–41.

Maeda Y, Davé V, Whitsett JA, 2007 Transcriptional control of lung morphogenesis. Physiol Rev 87:219–44.

Magnus MC, Håberg SE, Karlstad Ø et al 2015 Grandmother's smoking when pregnant with the mother and asthma in the grandchild: the Norwegian Mother and Child Cohort Study. Thorax 70:237–43.

Martin L, Hackam D 2017 Congenital chest wall deformities. In: Cameron JL, Cameron AM (eds) Current Surgical Therapy, 12th ed. Elsevier; pp. 891–8.

This chapter gives an overview of the anomalies of chest wall development.

McCullagh A, Rosenthal M, Wanner A et al 2010 The bronchial circulation – worth a closer look: a review of the relationship between the bronchial vasculature and airway inflammation. Pediatr Pulmonol 45:1–13.

Mekonen HK, Hokspoors JPJM, Mommem G, Köhler SE, Lamers WH 2015 Development of the ventral body wall in the human embryo. J Anat 227:673–85.

Figures 2–7 illustrate in 3D reconstructions, over stages 15–23, the lengthening and medial growth of the ribs and formation of the sternum. Hypaxial muscle growth is shown and the closure of the ventral body wall discussed. This paper provides accurate embryonic staging, in line with O'Rahilly and Müller (2010), illustrates the conversion of serial histological sections to 3D images using computer software and compares successive embryonic stages.

Meyerholz DK, Stoltz DA, Namati E et al 2010 Loss of cystic fibrosis transmembrane conductance regulator function produces abnormalities in tracheal development in neonatal pigs and young children. Am J Respir Crit Care Med 182:1251–61.

Moghieb A, Clair G, Mitchell H et al 2018 Time-resolved proteome profiling of normal lung development. Am J Physiol Lung Cell Mol Physiol 315(1):L11–L24.

Morales E, Garcia-Esteban R, de la Cruz OA et al 2015 Intrauterine and early postnatal exposure to outdoor air pollution and lung function at preschool age. Thorax 70:64–73.

Morrisey EE, Hogan BL 2010 Preparing for the first breath: genetic and cellular mechanisms in lung development. Dev Cell 18:8–23.

This paper presents an overview of the molecular mechanisms of lung development.

Morrisey EE, Cardoso WV, Lane RH et al 2013 Molecular determinants of lung development. Ann Am Thorac Soc 10:S12–16.

Narayanan M, Owers-Bradley J, Beardsmore CS et al 2012 Alveolarization continues during childhood and adolescence: new evidence from helium-3 magnetic resonance. Am J Respir Crit Care Med 185:186–91.

Ng-Blichfeldt JP, Alcada J, Montero MA, Dean CH, Griesenbach U, Griffiths MJ, Hind M 2017 Deficient retinoid-driven angiogenesis may contribute to failure of adult human lung regeneration in emphysema. Thorax 72:510–21.

O'Rahilly R, Müller F 2010 Developmental stages in human embryos: revised and new measurements. Cells Tissues Organs 192:73–84.

O'Reilly R, Ullmann N, Irving S et al 2013 Increased airway smooth muscle in preschool wheezers who have asthma at school age. J Allergy Clin Immunol 131:1024–32.

Quanjer PH, Stanojevic S, Cole TJ et al ERS Global Lung Function Initiative 2012 Multi-ethnic reference values for spirometry for the 3–95-yr age range: the global lung function 2012 equations. Eur Respir J 40:1324–43.

Roberts D, Brown J, Medley N et al 2017 Antenatal corticosteroids for accelerating fetal lung maturation for women at risk of preterm birth. Cochrane Database Syst Rev 3:CD004454. doi: 10.1002/14651858.CD004454.pub3.

Rosenthal M, Bain SH, Cramer D et al 1993a Lung function in white children aged 4–19 years: I. Spirometry. Thorax 48:794–802.

Rosenthal M, Cramer D, Bain SH et al 1993b Lung function in white children aged 4–19 years: II. Single breath analysis and plethysmography. Thorax 48:803–8.

Rosenthal M, Bush A 2002 The growing lung: normal development, and the long-term effects of pre- and post-natal insults. In: Bush A, Zach M, Carlsen K-H (eds) Growing up with lung disease: the lung in transition to adult life. Eur Respir Monograph 7:1–24.

Roth-Kleiner M, Post M 2005 Similarities and dissimilarities of branching and septation during lung development. Pediatr Pulmonol 40:113–34.

An account of the molecular mechanisms underlying normal lung development.

Ruano R, Ali RA, Patel P et al 2014 Fetal endoscopic tracheal occlusion for congenital diaphragmatic hernia: indications, outcomes, and future directions. Obstet Gynecol Surv 69:147–58.

Rusconi F, Gagliardie L 2018 Pregnancy complications and wheezing and asthma in childhood. Am J Respir Crit Care Med 197:580–8.

Schmölzer GM, O'Reilly M, Davis PG et al 2013 Confirmation of correct tracheal tube placement in newborn infants. Resuscitation 84:731–7.

Spagnolo P, Bush A 2016 Interstitial lung disease in children younger than 2 years. Pediatrics 137(6): pii: e20152725.

Stabile H, Mitola S, Moroni E et al 2007 Bone morphogenic protein antagonist Drm/gremlin is a novel proangiogenic factor. Blood 109:1834–40.

Stanojevic S, Wade A, Stocks J et al 2008 Reference ranges for spirometry across all ages: a new approach. Am J Respir Crit Care Med 177:253–60.

Tollet J, Everett AW, Sparrow MP 2002 Development of neural tissue and airway smooth muscle in fetal mouse lung explants: a role for glial-derived neurotrophic factor in lung innervation. Am J Respir Cell Mol Biol 26:420–9.

Tsartsali L, Hislop AA, McKay K et al 2011 Development of the bronchial epithelial reticular basement membrane: relationship to epithelial height and age. Thorax 66:280–5.

Ustiyan V, Zhang Y, Perl AK et al 2016 β-catenin and Kras/Foxm1 signaling pathway are critical to restrict Sox9 in basal cells during pulmonary branching morphogenesis. Dev Dyn 245:590–604.

Van der Veeken L, Russo FM, De Catte L et al 2018 Fetoscopic endoluminal tracheal occlusion and reestablishment of fetal airways for congenital diaphragmatic hernia. Gynecol Surg 15(1):9.

Volpe JJ 2017 Confusions in nomenclature: 'periventricular leukolalacia' and 'white matter injury' – identical, distinct, or overlapping? Ped Neurol 73:3–6.

Voynow JA 2017 'New' bronchopulmonary dysplasia and chronic lung disease. Paed Resp Rev 24:17–18.

Wallis C, Alexopoulou E, Antón-Pacheco JL et al 2019 ERS Statement on Tracheomalacia and Bronchomalacia in Children. Eur Respir J Jul 18. pii: 1900382. doi: 10.1183/13993003.00382-2019.

Wang Y, Huang C, Chintagari NR et al 2015 miR-124 regulates fetal pulmonary epithelial cell maturation. Am J Physiol Lung Cell Mol Physiol 309:L400–13.

Warburton D 2017 Overview of lung development in the newborn human. Neonatology 111:398–401.

Wynn J, Yu L, Chung WK 2014 Genetic causes of congenital diaphragmatic hernia. Semin Fetal Neonatal Med 19:324–30.

Xu Y, Zhang M, Wang Y et al 2010 A systems approach to mapping transcriptional networks controlling surfactant homeostasis. BMC Genomics 11:451.

Xu Y, Wang Y, Besnard V et al 2012 Transcriptional programs controlling perinatal lung maturation. PLoS One 7:e37046.

Yamamoto M, Wilting J, Abe H et al 2018 Development of the pulmonary pleura with special reference to the lung surface morphology: a study using human fetuses. Anat Cell Biol 51:150–7.

Yang J, Hemandez BJ, Martinez-Alanis DM et al 2016 The development and plasticity of alveolar type 1 cells. Development 143:54–65.

CHAPTER
21

Development of the peritoneal cavity, gastrointestinal tract and its adnexae

POSTPHARYNGEAL FOREGUT

The primitive gut is divided by head- and tail-folding into three main compartments. The foregut extends from the buccopharyngeal membrane to its continuation into the central midgut region via the cranial intestinal portal. The midgut extends between the intestinal portals and, in the early embryo, is in wide communication with the yolk sac. The hindgut extends from the caudal intestinal portal to the cloacal membrane. The cranial end of the foregut, the embryonic pharynx, is intimately associated with head and neck development (Ch. 17). The portion of foregut that passes dorsal to the pericardial cavity gives rise to the respiratory diverticulum and oesophagus within the thorax (Chs 17 and 20). Caudal to the developing respiratory diaphragm, the enteric gut is conventionally subdivided into three embryological portions: fore-, mid- and hindgut. There are no corresponding fundamental morphological and cytological distinctions between the three parts (**Fig. 21.1**), and so the foregut produces a portion of the duodenum, as does the midgut, and the midgut similarly produces large intestine, as does the hindgut. The differences between the portions of the gut develop as a result of interactions between the three embryonic tissue layers that give rise to the gut: namely, the endodermal inner epithelium, the thick layer of splanchnopleuric mesenchyme and the outer layer of proliferating splanchnopleuric coelomic epithelium.

The mucosal epithelial layer and connected ducts and glands are derived from the endodermal epithelium. The lamina propria and muscularis mucosa, the connective tissue of the submucosa, the muscularis externa and the future serosal lamina propria are all derived from the splanchnopleuric mesenchyme. The outer splanchnopleuric coelomic epithelium forms the epithelial component of the serosa (peritoneum, a mesothelium). Both epithelia, inner and outer, express cell polarity markers and form specific apical junctional complexes; they are highly proliferative and appear histologically as pseudostratified epithelia with interkinetic nuclear migration matching the timing of the cell cycle. In the endodermal layer, this proliferation results in lengthening of the inner endodermal epithelium. In the splanchnic coelomic epithelium, which acts as a barrier throughout development to contain locally secreted morphogens, proliferation not only increases the surface area and gives rise to the subjacent mesenchymal population, but also generates biomechanical tension across the whole composite tube, which by differentiative temporo-spatial patterning contributes to regional gut development (Grosse et al 2011, Guo et al 2014, Ariza et al 2016, Chevalier et al 2018).

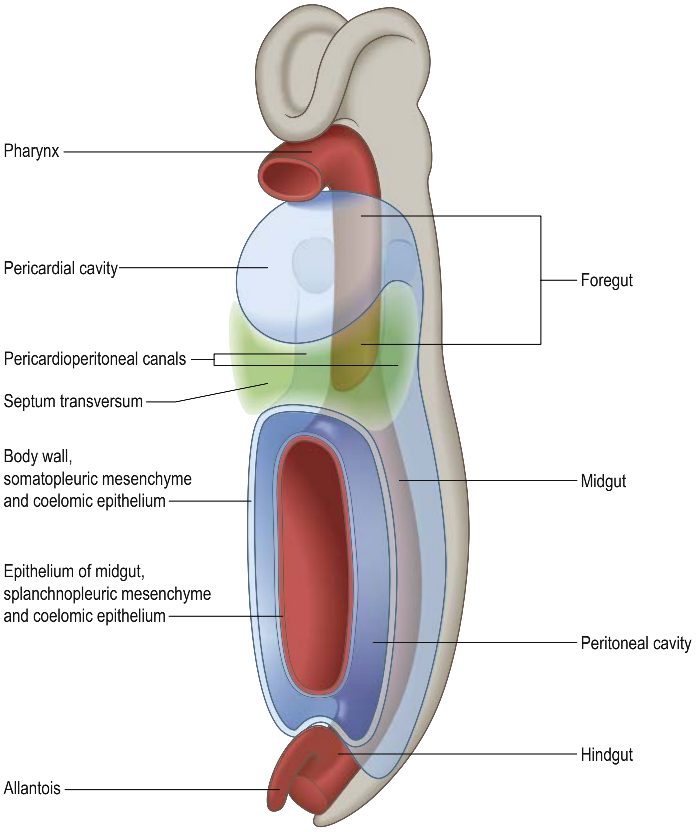
Pharynx
Pericardial cavity
Pericardioperitoneal canals
Septum transversum
Body wall, somatopleuric mesenchyme and coelomic epithelium
Epithelium of midgut, splanchnopleuric mesenchyme and coelomic epithelium
Allantois
Foregut
Midgut
Peritoneal cavity
Hindgut

Fig. 21.1 Major epithelial populations within the early embryo. The early gut tube is close to the notochord and neural tube dorsally. The splanchnopleuric layer of the intraembryonic coelomic epithelium is in contact with the foregut ventrally and laterally, with the midgut laterally, and the hindgut ventrally and laterally.

Throughout the gut, blood vessels, lymphatics and lymph nodes develop from local populations of angiogenic mesenchyme. The nerves, which are distributed within the enteric and autonomic systems, are derived from the neural crest. There is a craniocaudal developmental gradient along the gut, in that the stomach and small intestine develop in advance of the colon.

Fig. 21.1 shows the fundamental relationship of the intraembryonic coelom to the developing gut. **Fig. 21.2** shows the gut in a stage 12 embryo in relation to the other developing viscera, especially the heart and liver. **Fig. 21.3** shows the overall development of the gut from stages 13 to 17. These diagrams should be compared. See Fig. 23.3 for a comparison of stages to postfertilzation days and the clinical scale of postmenstrual weeks.

All regions of the gut develop from epithelial–mesenchymal interactions that are dependent on the sequential expression of a range of basic and specific genes; on the regulation of the developmental clock, seen in all areas of development; and on endogenous regulatory mechanisms and local environmental influences (Lebenthal 1989). Although all these factors pertain to the whole range of developing tissues, local differences in any one of these factors along the length of the developing gut promote the differentiation of, for example, the gastric mucosa and hepatocytes; the rotation of the midgut; and the final disposition of the sessile portions of the fully formed gastrointestinal tract. The Hedgehog (Hh) ligands, Shh, Ihh and Dhh, are expressed in the developing gut: Shh and Ihh in the endodermal epithelium and Dhh in endothelial cells. These ligands bind to the Patched receptors (Ptch-1 and Ptch-2), which activate the transcription factor Gli3. Knockout of Shh and Ihh has been associated with oesophageal atresia, gut malrotation, decreased development of the muscularis propria, enteric neurone anomalies and imperforate anus (Kolterud et al 2009). The gut is functional prior to birth and able to interact with the extrauterine environment in preterm infants.

Oesophagus

The oesophagus can be distinguished from the stomach at stage 13 (31–33 days postfertilization). It elongates during successive stages and its absolute length increases more rapidly than the embryo as a whole. By stage 15 it is surrounded by splanchnopleuric mesenchyme derived from the walls of the pericardioperitoneal canals. Cranially, it is dorsal to the developing trachea and the two tubes share the mesenchymal population between them; more caudally it is medial to the developing lung buds (Fig. 21.3). The terminal, pregastric segment of the oesophagus is surrounded ventrally by the most cranial part of the septum transversum mesenchyme and dorsally by splanchopleuric mesenchyme, which forms a short, thick, dorsal meso-oesophagus with the lower medial walls of the pericardioperitoneal canals. Caudally these mesenchymal populations are continuous with their respective primitive dorsal and ventral mesogastria. Although the oesophagus has only limited areas related to a primary coelomic epithelium at its caudal end, it is important to note the subsequent development of the para-oesophageal right

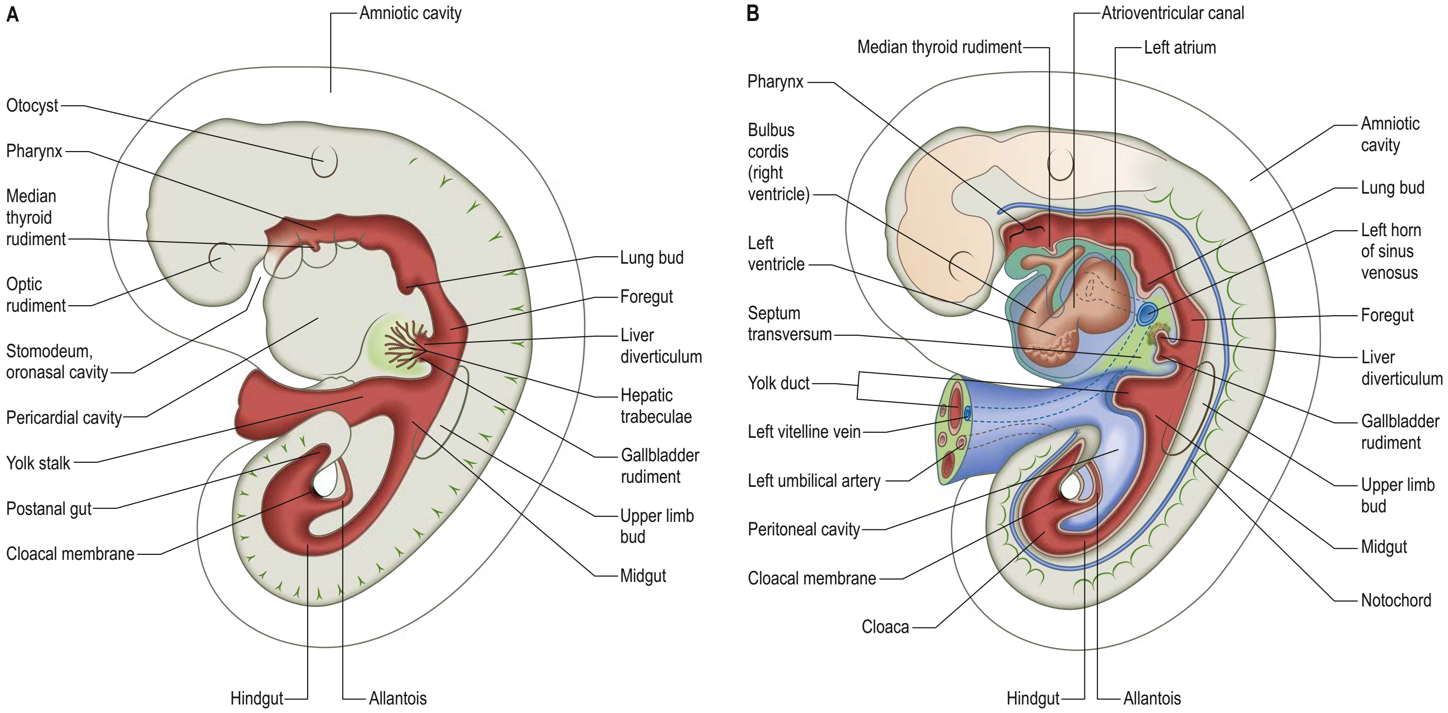

Fig. 21.2 **A**, The developing gut of a human embryo at stage 12. (Pharyngeal development is followed further in Fig. 17.19). **B**, Reconstruction of the gut and its outgrowths in median section. The brain is shown in outline but the spinal cord has been omitted. The heart is shown in perspective, and the left horn of the sinus venosus is cut just medial to the entrance of the common cardinal vein (see Figs 13.8A-B, 13.17). The somites are indicated in outline.

and left pneumatoenteric recesses (see Fig. 21.7), the relation of the ventral aspect of the middle third of the oesophagus to the oblique sinus of the pericardium, and the relation of its lateral walls in the lower thorax to the mediastinal pleura. All the foregoing are secondary extensions from the primary coelom.

The oesophageal mucosa consists of two layers of cells by stage 15, but the proliferation of the mucosa does not occlude the lumen at any time. The mucosa becomes ciliated at 10 postfertilization weeks, and stratified squamous epithelium is present after postmenstrual week 20; occasionally, patches of ciliated epithelium may be present at birth. Circular muscle can be seen at stage 15 but longitudinal muscle has not been identified until stage 21. Neuroblasts can be demonstrated in the early stages; the myenteric plexuses have cholinesterase activity by 9.5 postfertilization weeks and ganglion cells are differentiated by 13 postfertilization weeks. It has been suggested that the oesophagus is capable of peristalsis in the first trimester. Pharyngeal phase swallowing activity has been identified from 11 postmenstrual weeks on ultrasound examination; oesophageal motor function is well developed by 26 postmenstrual weeks (Neu 2012, Jadcherla et al 2015). The volume of amniotic fluid ingested increases during the third trimester to more than 500 ml/day.

Oesophagus at birth

At birth, the oesophagus extends 8–10 cm from the cricoid cartilage to the gastric cardiac orifice. It starts and ends one to two vertebrae, respectively, higher than in the adult, extending from between the fourth to the sixth cervical vertebra to the level of the ninth thoracic vertebra (see Fig. 23.15). Its average diameter is 5 mm and it possesses the constrictions seen in the adult. The narrowest constriction is at its junction with the pharynx, where the inferior pharyngeal constrictor functions to constrict the lumen; this region may be easily traumatized with instruments or catheters. In the neonate, the mucosa may contain scattered areas of ciliated columnar epithelium but these disappear soon after birth. Complex swallowing and oesophageal reflexes are present in the full-term neonate (Ch. 14). A coordinated relaxation of the upper oesophageal sphincter is followed sequentially by oesophageal peristalsis and relaxation of the lower oesophageal sphincter (Jadcherla 2016). Air or liquid can be distinguished in the oesophagus and result in different swallowing patterns. Maturational changes are seen in the lower oesophageal sphincter relaxation reflex in the postnatal development of preterm infants (Jadcherla et al 2015). In term and preterm infants, transient lower oesophageal sphincter relaxations, unrelated to swallowing, permit gastro-oesophageal reflux resulting in frequent regurgitation of food in the newborn period, with a peak prevalence at 4 postnatal months, declining thereafter (Neu 2012).

Stomach

The stomach can be recognized, at stage 13, as a fusiform dilation cranial to the wide opening of the midgut into the yolk sac (see Fig. 21.3). By stage 14 this opening has narrowed into a tubular vitelline intestinal duct, which will lose its connection with the digestive tube. At this time, the stomach is median in position and separated cranially from the pericardium by the septum transversum (see Fig. 21.5A), which extends caudally on to the cranial side of the vitelline intestinal duct and ventrally to the somatopleure. Dorsally, the stomach is related to the aorta and connected to the body wall by a short dorsal mesentery, the dorsal mesogastrium, formed by the medial walls of the pleuroperitoneal canals and intervening splanchnopleuric mesenchyme (see Figs 21.5B, 21.6). The latter is directly continuous with the dorsal mesentery (mesenteron) of almost all of the remainder of the intestine, except its caudal short segment.

The characteristic gastric curvatures are already recognizable in human embryos during stages 15–16. Growth is more active along the dorsal border of the viscus; its convexity markedly increases and the rudimentary fundus appears. Because of more rapid growth along the dorsal border, the pyloric end of the stomach turns ventrally and the concave lesser curvature becomes apparent (see Figs 21.3, 21.6). The stomach is now displaced to the left of the median plane and becomes physically rotated, such that its original right surface becomes dorsal and its left surface becomes ventral. Accordingly, the right vagus nerve is distributed mainly to the dorsal, and the left vagus mainly to the ventral, surfaces of the stomach. The dorsal mesogastrium increases in depth and becomes folded on itself. The ventral mesogastrium becomes more coronal than sagittal. The pancreaticoenteric recess (see Fig. 21.7B(ii)), until this point conventionally described as a simple depression on the right side of the dorsal mesogastrium, becomes dorsal to the stomach and excavates downwards and to the left between the folded layers: it may now be termed the inferior recess of the bursa omentalis. To summarize, the stomach has undergone relative morphological movements, traditionally referred to as two ‘rotations’. The first is 90° clockwise, about a longitudinal axis viewed from the cranial end; the second is 90° clockwise, about a dorsoventral axis viewed ventrally. The displacement, morphological changes and apparent ‘rotation’ of the stomach have been attributed to differential growth changes of the stomach itself; extension of the pancreaticoenteric recess with changes in its mesenchymal walls; and pressure, particularly that exerted by the rapidly growing liver. Whether the ‘rotations’, which are conventionally used to aid understanding, occur only in the axes described is unclear; differential regional growth and some ‘rotation’ in the transverse plane have also been invoked. The angula insura and the cardia of the stomach

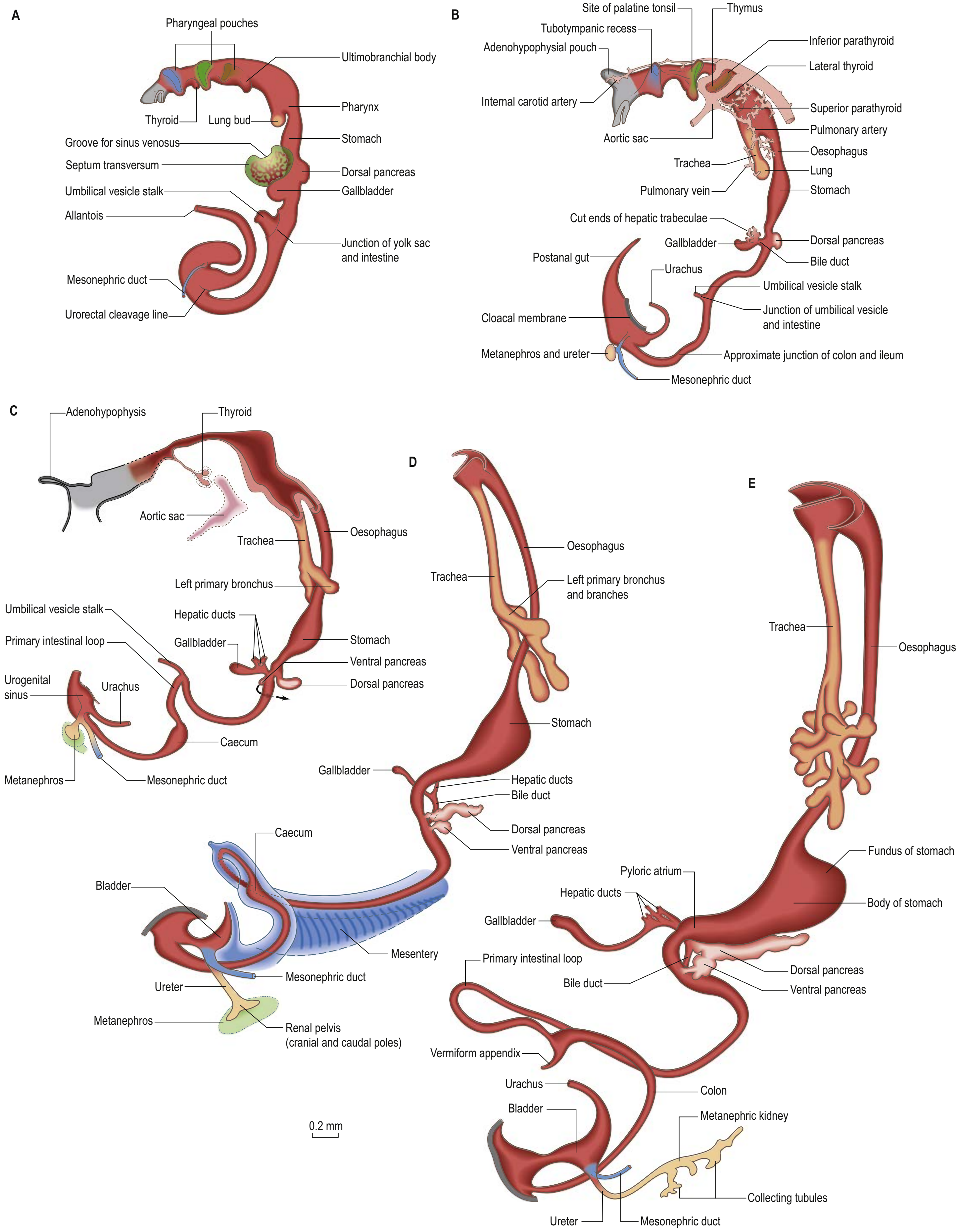
A
Pharyngeal pouches
Ultimobranchial body
Thyroid
Lung bud
Pharynx
Groove for sinus venosus
Stomach
Septum transversum
Dorsal pancreas
Umbilical vesicle stalk
Gallbladder
Allantois
Junction of yolk sac and intestine
Mesonephric duct
Urorectal cleavage line
B
Site of palatine tonsil
Thymus
Tubotympanic recess
Adenohypophysial pouch
Inferior parathyroid
Lateral thyroid
Internal carotid artery
Superior parathyroid
Pulmonary artery
Aortic sac
Oesophagus
Trachea
Lung
Pulmonary vein
Stomach
Cut ends of hepatic trabeculae
Gallbladder
Dorsal pancreas
Postanal gut
Bile duct
Urachus
Umbilical vesicle stalk
Junction of umbilical vesicle and intestine
Cloacal membrane
Metanephros and ureter
Approximate junction of colon and ileum
Mesonephric duct
C
Adenohypophysis
Thyroid
Aortic sac
Trachea
Oesophagus
Left primary bronchus
Umbilical vesicle stalk
Hepatic ducts
Primary intestinal loop
Gallbladder
Stomach
Ventral pancreas
Dorsal pancreas
Urogenital sinus
Urachus
Caecum
Metanephros
Mesonephric duct
D
Oesophagus
Trachea
Left primary bronchus and branches
Stomach
Gallbladder
Hepatic ducts
Bile duct
Dorsal pancreas
Ventral pancreas
Caecum
Bladder
Mesentery
Mesonephric duct
Ureter
Metanephros
Renal pelvis (cranial and caudal poles)
0.2 mm
E
Trachea
Oesophagus
Fundus of stomach
Pyloric atrium
Hepatic ducts
Body of stomach
Gallbladder
Primary intestinal loop
Dorsal pancreas
Bile duct
Ventral pancreas
Vermiform appendix
Urachus
Colon
Bladder
Metanephric kidney
Collecting tubules
Ureter
Mesonephric duct

Fig. 21.3 The shape of the endodermal epithelium of the gut at succeeding stages. The scale is constant, illustrating the enormous growth of the gut over a 13-day period. **A**, Stage 13. **B**, Stage 14. **C**, Stage 15. **D**, Stage 16. **E**, Stage 17. Note the separation of the respiratory diverticulum; the elongation of the foregut and expansion of the stomach; the formation of the hepatic and pancreatic diverticula; the lengthening of the midgut loop, which protrudes into the umbilical cord; and the separation of the cloaca into enteric and allantoic portions. (Modified from O'Rahilly R, Müller F 1987 Developmental Stages in Human Embryos. Carnegie Institution of Washington. Pub 637.)

can be seen in stage 18 and the fundus, body and pylorus are evident at stage 20 (Kaigai et al 2014).

Mucosa

Mucosal and submucosal development can be seen in postfertilization weeks 8–9. No villi form in the stomach, unlike in the small intestine; instead, glandular pits can be seen in the body and fundus. These develop in the pylorus and cardia by postfertilization weeks 10–11, when parietal cells can be demonstrated. Although the embryo generally matures in a proximo-distal direction, gastric glands form slightly later than villi in the midgut. Murine embryos show a sharp boundary between the mucosal epithelium of the stomach and the first duodenal crypt. It is suggested that repression of the determination of the stomach endodermal epithelium until a later time, when instructive signals from the surrounding mesenchyme specify a glandular rather than villous mucosal fate, could be part of the patterning of the pylorus and the first part of the duodenum (Li et al 2009).

Chief cells can be identified after postfertilization weeks 12–13, although pepsinogen has not been demonstrated until term (40 postmenstrual weeks). Mucous neck cells actively produce mucus from 16 postmenstrual weeks. Acid secretion has not been demonstrated in the fetal stomach before 32 postmenstrual weeks, however, preterm infants from 26 postmenstrual weeks onwards, are able to secrete acid soon after birth. Intrinsic factor, also from parietal cells, has been detected after postfertilization week 11; it increases during postmenstrual weeks 14–15, at which time the pylorus, which contains more parietal cells than it does in the adult, also contains a relatively larger quantity of intrinsic factor. The significance of the early production of intrinsic factor and the late production of acid by the parietal cells is not known. Gastrin-producing cells have been demonstrated in the antrum between postmenstrual weeks 19 and 20, and gastrin levels have been measured in cord blood and in the plasma at term. Cord serum contains gastrin levels 2–3 times higher than those in maternal serum. Smooth muscle cells of the muscularis mucosae are first visible by 14 postmenstrual weeks and this layer is well defined by 22 postmenstrual weeks.

Muscularis

The muscularis externa can initially be seen at 10 postmenstrual weeks, when neural plexuses are developing in the body and fundus. At postmenstrual week 16, the oblique muscle layer can be seen and by postmenstrual week 26 all three muscularis externa layers are present. The pyloric musculature is thicker than that of the rest of the stomach; its layers develop within the same timescale as those in the fundus, cardia and body (Pangtey et al 2017).

Serosa

The serosa of the stomach is derived from the splanchnopleuric coelomic epithelium. No part of this serosa undergoes absorption. The original left side of the gastric serosa faces the greater sac; the right side faces the lesser sac.

Stomach at birth

The stomach exhibits fetal characteristics until just after birth, when the initiation of pulmonary ventilation, the reflexes of coughing and swallowing, and crying cause the ingestion of large amounts of air and liquid. Once postnatal swallowing has started, the stomach expands to four or five times its contracted state, and shifts its relative position accommodating the status of expansion and contraction of the other abdominal viscera, and to the position of the body. Gastric emptying is slower in the preterm infant than in the term infant (Jadcherla and Berseth 2012). In the neonate, the anterior surface of the stomach is generally covered by the left lobe of the liver, which extends nearly as far as the spleen (see Fig. 23.14B). Only a small portion of the greater curvature of the stomach is visible anteriorly. The capacity of the stomach is 30–35 ml in the full-term neonate, rising to 75 ml in the second postnatal week and 100 ml by the fourth postnatal week (adult capacity is, on average, 1000 ml). The mucosa and submucosa are relatively thicker than in the adult; however, the muscularis is only moderately developed and peristalsis is not coordinated. At birth, gastric acid secretion is low, which means that gastric pH is high for the first 12 postnatal hours. It falls rapidly with the onset of gastric acid secretion, usually after the first feed. Acid secretion usually remains low for the first 10 postnatal days. Gastric emptying and transit times are delayed in the neonate.

Duodenum

The duodenum develops from the caudal part of the foregut and the cranial part of the midgut. A ventral mesoduodenum, which is continuous cranially with the ventral mesogastrium, is attached only to the foregut portion. Posteriorly, the duodenum has a thick dorsal mesoduodenum, which is continuous with the dorsal mesogastrium cranially and the dorsal mesentery of the midgut caudally. Anteriorly, the extreme caudal edge of the ventral mesentery of the foregut extends on to the short initial segment of the duodenum. The liver arises as a diverticulum from the ventral surface of the duodenum at the foregut–midgut junction, i.e. where the midgut is continuous with the yolk sac wall (the cranial intestinal portal). The ventral pancreatic bud also arises from this diverticulum. The dorsal pancreatic bud evaginates posteriorly into the dorsal mesoduodenum slightly more cranially than the hepatic diverticulum. The rotation, differential growth, and cavitations related to the developing stomach and omenta cause corresponding movements in the duodenum, which forms a loop directed to the right, with its original right side now adjacent to the posterior abdominal wall (see Fig. 21.6). This shift is compounded by the migration of the bile duct and ventral pancreatic duct around the duodenal wall. Their origin shifts until it reaches the medial wall of the second part of the fully formed duodenum; the bile duct passes posteriorly to the duodenum and travels in the free edge of the ventral duodenum and ventral mesogastrium. Local adherence of part of the duodenal serosa and the parietal peritoneum result in almost the whole of the duodenum, other than a short initial segment, becoming sessile.

Foregut anomalies

Available with the *Gray's Anatomy* e-book.

Special glands of the postpharyngeal foregut

Pancreas

The pancreas develops from two evaginations of the foregut that fuse to form a single organ. A dorsal pancreatic bud can be seen in stage 13 embryos as a thickening of the endodermal tube that proliferates into the dorsal mesogastrium (see Fig. 21.3; **Fig. 21.4**). A ventral pancreatic bud evaginates in close proximity to the liver primordium but cannot be clearly identified until stage 14, when it appears as an evagination of the bile duct itself. At stage 16 differential growth of the wall of the duodenum results in movement of the ventral pancreatic bud and the bile duct to the right side and, ultimately, to a dorsal position. It is not clear whether there is a corresponding shift of mesenchyme during this rotation. However, the ventral pancreatic bud and the bile duct rotate from a position within the ventral mesogastrium (ventral mesoduodenum) to one in the dorsal mesogastrium (dorsal mesoduodenum), which is destined to become fixed on to the posterior abdominal wall. By stage 17 the ventral and dorsal pancreatic buds have fused, although the origin of the ventral bud from the bile duct is still obvious. Three-dimensional reconstruction of the ventral and dorsal pancreatic buds has confirmed that the dorsal pancreatic bud forms the anterior part of the head, the body and the tail of the pancreas, and the ventral pancreatic bud forms the posterior part of the head and the posterior part of the uncinate process. The ventral pancreatic bud does not form all of the uncinate process (Collins 2002a).

The developing pancreatic ducts usually fuse in such a way that most of the dorsal duct drains into the proximal part of the ventral duct (see Figs 21.3–21.4). The proximal portion of the dorsal duct usually persists as an accessory duct. The fusion of the ducts takes place late in development or in the postnatal period; 85% of infants have patent accessory ducts, as compared to 40% of adults. Fusion may not occur in 10% of individuals, in which case separate drainage into the duodenum is maintained: so-called pancreatic divisum (pancreas divisum). Failure of the ventral pancreatic diverticulum to migrate will result in an anular pancreas, which may constrict the duodenum locally.

Developmental movements of the pancreas in the dorsal mesoduodenum and dorsal mesogastrium are considered below (see p. 338).

Cellular development of the pancreas

The early specification of pancreatic endoderm requires the proximity of the notochord to the dorsal endoderm, which locally represses the expression of Shh transcription factor. Endoderm caudal to the pancreatic region does not respond to notochordal signals. The ventral pancreatic endoderm does not seem to undergo the same induction. Expression of pancreatic duodenal homeobox 1 transcription factor (PDX-1) is seen in the developing endodermal epithelial cells and in

Oesophageal atresia is one of the more common obstructive conditions of the alimentary tract and may be indicated by polyhydramnios. It may be related to trachea-oesophageal fistulae or other associations of vertebral defects, anal atresia, cardiac defects, renal and limb anomalies (VACTERL) (Ch. 20). Infantile hypertrophic pyloric stenosis has a prevalence of 2/1000 live births, with male sex and a family history being the most common associations. It presents between 3 to 8 postnatal weeks with projectile vomiting of milk feeds. Risk factors are first born, caesarean section delivery, preterm birth, formula feeding in the neonatal period; exclusive breast-feeding is noted to be protective (Zhu et al 2017). No clear aetiology has been found, however the transition from a fetal gut receiving only amniotic fluid, with immature parietal cell function and neutral gastric pH, plus slow maturation of gastrin feedback mechanisms, is suggested to contribute to acid over secretion which stimulates pyloric sphincter hypertrophy (Rogers 2015). Duodenal atresia is a developmental defect found in 1 in 5000 live births (Whittle 1999). It may be associated with an anular pancreas, which may compress the duodenum externally (20% of duodenal atresia), or with anomalies of the bile duct. In 40–60% of cases, the atresia is complete and pancreatic tissue fills the lumen. The condition can be diagnosed on abdominal X-ray and ultrasound examination, which reveal a typical double bubble appearance, caused by fluid antenatally and air postnatally enlarging the stomach and the proximal duodenum. Polyhydramnios is invariably present and often is the indication for the scan. Duodenal atresia commonly occurs with other developmental defects, e.g. cardiac and skeletal anomalies, and in Down's syndrome.

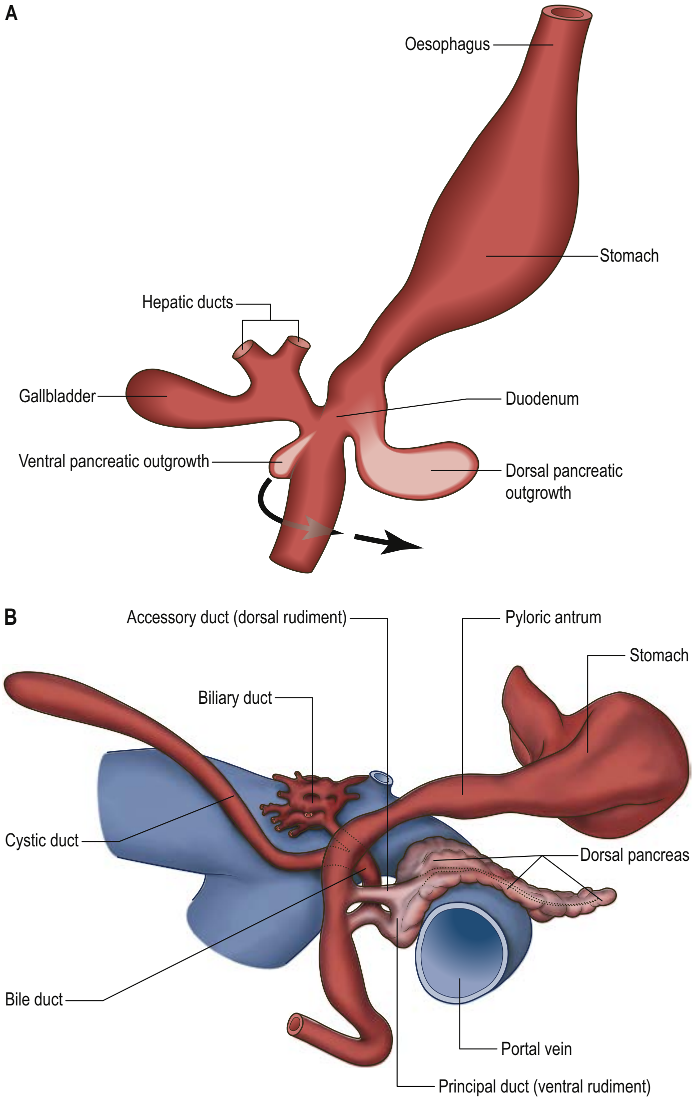

Fig. 21.4 Development of the pancreas in a human embryo. **A**, Stage 14: lateral view. **B**, Stage 17: ventral view.

the maturing postnatal pancreas (Hayes et al 2016, Byrnes et al 2018). Pancreatic mesenchyme is derived from two regions. The mesenchyme that surrounds the dorsal pancreatic bud proliferates from the splanchnopleuric coelomic epithelium of the medial walls of the pericardioperitoneal canals, whereas the ventral pancreatic bud is invested by septum transversum mesenchyme and by mesenchyme derived from the lower ventral walls of the pericardioperitoneal canals.

The primitive endodermal ductal epithelium provides the stem cell population for all the secretory cells of the pancreas. Initially, endocrine cells are located in the duct walls or in buds developing from them; later, they accumulate in pancreatic islets. The remaining primitive duct cells will differentiate into definitive ductal cells. In the fetus, they develop microvilli and cilia but lack the lateral interdigitations seen in the adult. Branches of the main duct become interlobular ductules, which terminate as blind-ending acini or as tubular, acinar elements.

The ductal branching pattern and acinar structure of the pancreas are determined by the pancreatic mesenchyme derived from the coelomic epithelium (Landsman et al 2011, Byrnes et al 2018). This mesenchyme gives rise to connective tissue between the ducts, which, in the fetus, appears to be important in stimulating pancreatic proliferation and maintaining the relative proportions of acinar, α and β cells during development. It also provides cell lines for smooth muscle within the pancreas. Angiogenic mesenchyme invades the developing gland to produce blood and lymphatic vessels. Mouse pancreas endoderm grown in culture without coelomic epithelium does not show normal branching morphogenesis and exhibits higher endocrine/acinar pancreatic markers (Guo et al 2014).

The process of islet differentiation is divided into two phases (Collins 2002a). Phase I, characterized by proliferation of polyhormonal cells, occurs from postmenstrual week 9 to week 15. Phase II, characterized by differentiation of monohormonal cells, is seen from postmenstrual week 16 onwards. The β cells, producing insulin and amylin, differentiate first, followed by α cells, which produce glucagon. The δ cells, which produce somatostatin, are seen after 30 postmenstrual weeks. The dorsal bud gives rise mostly to α cells, and the ventral bud to most of the pancreatic polypeptide-producing cells. The β cells develop from the duct epithelium throughout development and into the neonatal period. Later, in postmenstrual weeks 10–15, some of the primitive ducts differentiate into acinar cells, in which zymogen granules or acinar cell markers can be detected at 12–16 postmenstrual weeks.

The role of the medial coelomic walls of the lower ends of the pleuroperitoneal canals in pancreatic development has other interesting aspects, beyond that of a proliferative epithelium. This specific portion of coelomic epithelium forms tight junctions with adjacent cells and a basement membrane with the underlying mesenchyme, suggesting that it may function as a barrier preventing loss of intrapancreatic morphogens outwards and spread of extrapancreatic morphogens, e.g. from the mesenchyme surrounding the aorta, inwards, maintaining a boundary function between adjacent viscera (Guo et al 2014). This has been demonstrated *in vitro* using mouse embryonic tissue. Developing pancreatic and lung buds from which the coelomic epithelium had been removed fused into a single chimeric tissue mass, whereas no fusion occurred if the coelomic epithelium remained intact. When pancreas without coelomic epithelium was co-cultured with pancreas with intact coelomic epithelium, the epithelium engulfed both explants, extending over the entire surface, forming a larger pancreas. This is reminiscent of the process of dorsal and ventral pancreatic bud fusion. Fusion does not occur in co-culture of lung and pancreatic buds, or two pancreatic buds, when they are surrounded by the relevant coelomic epithelia (Guo et al 2014). This suggests that the maturing coelomic epithelium creates region-specific barriers between portions of gut and its evaginations with two distinct functions: maintenance of local internal environments which express specific and different morphogenetic molecules and maintenance of a barrier, ensuring lack of fusion, between closely apposed regions of gut and developing derived viscera.

Pancreas at birth

The pancreas in the neonate has all of the normal subdivisions of the adult. The pancreatic head is proportionately large in the newborn and there is a smooth continuation between the body and the tail. The inferior border of the head of the pancreas is found at the level of the second lumbar vertebra. The body and tail pass cranially and to the left, and the tail is in contact with the spleen.

Liver

The liver develops from an endodermal evagination of the foregut and from septum transversum mesenchyme, which is derived from the proliferating coelomic epithelium in the protocardiac region. The development of the liver is intimately related to the development of the heart. The vitelline veins, succeeded by the umbilical veins passing to the sinus venosus, are disrupted by the enlarging septum transversum to form a hepatic plexus, the forerunner of the hepatic sinusoids. (See Collins (2002b) for a detailed account of hepatic development.)

Early liver development

As the head fold and early intraembryonic coelom form, the ventral parietal wall of the pericardial cavity gives rise to populations of cells termed precardiac or cardiac mesenchyme. Hepatic endoderm is induced to proliferate by this mesenchyme, although all portions of the early heart tube, truncus arteriosus, atria, ventricle, both endocardium and myocardium, have hepatic induction potency that is tissue-specific but not species-specific. As the heart and foregut become separated by the accumulation of the cardiac mesenchyme, the mesenchyme itself is renamed septum transversum. It is seen as a ventral mass, caudal to the heart, which passes dorsally on each side of the developing gut to join the mesenchyme proliferating from the walls of the pericardioperitoneal canals. The majority of the cells within the septum transversum are destined to become hepatic mesenchyme. For details of the molecular signalling of early hepatic development, see Lemaigre (2009), Gordillo et al (2015).

In the stage 11 embryo, the hepatic endoderm is located at the superior boundary of the rostral intestinal portal. By stage 12 the hepatic endodermal primordium is directed ventrally and begins to proliferate as a diverticulum. There are two parts: a caudal part, which will produce the cystic duct and gallbladder; and a cranial part, which forms the liver biliary system (see Fig. 21.3; **Fig. 21.5A**). The cells start to express liver-specific molecular markers and glycogen storage.

The basal lamina around the cranial portion of the hepatic diverticulum is progressively disrupted and individual epithelial cells migrate

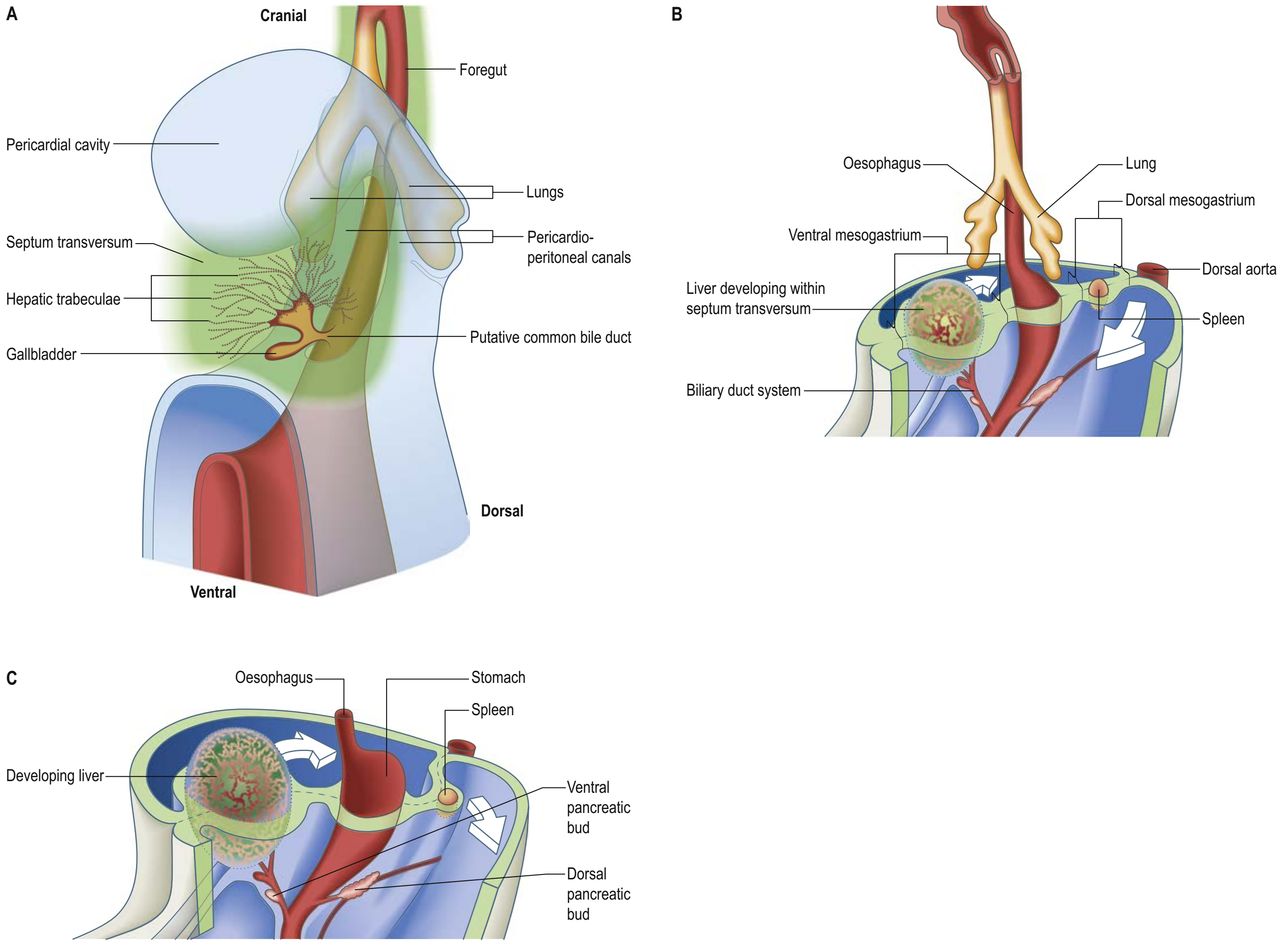

Fig. 21.5 Early development of the liver and the supra-umbilical peritoneal cavities. **A**, The hepatic endodermal primordium proliferates ventrally into the septum transversum mesenchyme. The endodermal cells forming the hepatic trabeculae will become hepatocytes; the septum transversum mesenchymal cells will become the endothelium of the liver sinusoids and early blood cells. The developing lung buds can be seen expanding into the pericardioperitoneal cavities. **B**, The septum transversum mesenchyme and the stomach become enclosed by the right and left pericardioperitoneal canals (shown on transverse section). The apposition of the medial pericardioperitoneal walls forms the dorsal and ventral mesogastria. The proximity of the lung buds to the developing stomach can be seen. The pleural and supra-umbilical peritoneal cavities are transiently, and bilaterally, symmetric above the umbilicus. **C**, The lower border of the ventral mesogastrium denotes the connection between the supra-umbilical peritoneal cavities: pleuroperitoneal canals, which can be identified by the position of the ventral pancreatic bud and common bile duct. The white arrows in **B** and **C** indicate the direction of movement of the dorsal and ventral mesogastria.

into the surrounding septum transversum mesenchyme. The previously smooth contour of the diverticulum merges into columnar extensions of endoderm, the epithelial trabeculae, which stimulate the hepatic mesenchymal cells to form blood islands and endothelium. The advance of the endodermal epithelial cells promotes the conversion of progressively more hepatic mesenchyme into endothelium and blood cells, and only a little remains to form the scanty liver capsule and interlobular connective tissue. This invasion by the hepatic epithelium is completed in stage 13, when it approaches the caudal surface of the pericardial cavity from which it is separated by only a thin lamina of mesenchyme that will give rise to part of the respiratory diaphragm.

During this early phase of development, the liver is far more highly vascularized than the rest of the gut. The hepatic capillary plexus is connected bilaterally with the right and left vitelline veins. Dorsolaterally, these veins empty by multiple channels into enlarged hepatocardiac channels, that lead to the right and left horns of the sinus venosus (see Fig. 13.20); usually, the channel on the right side is more developed. Both left and right channels bulge into the pericardioperitoneal canals, forming sites for the exchange of fluid from the coelom into the vascular channels. The ingrowths of hepatic tissue in these regions are sometimes referred to as the left and right horns of the liver.

The liver remains proportionately large during its development and constitutes a sizeable organ dorsal to the heart at stage 14, then more caudally placed by stage 16. By this stage, hepatic ducts can be seen separating the hepatic epithelium from the extrahepatic biliary system, but, even at stage 17, the ducts do not penetrate far into the liver. The definitive arrangement of the portal and hepatic veins becomes established over stages 18–20. The quadrate and caudate lobes become identifiable in stages 16 and 17 (Hikspoors et al 2017).

Maturation of the liver

The cellular maturation of hepatocytes and hepatic sinusoids corresponds to a complex cell sorting of early endodermal epithelial hepatoblasts, which differentiate into cholangiocytes and hepatocytes, angiogenic mesenchyme from the heart and developing gut which becomes organized into hepatic sinusoids, and septum transversum mesenchymal cells which give rise to the fibroblastic populations, and are thought to control the patterning of liver development with the angiogenic mesenchyme. The cellular arrangements within the liver are complex with sheets of epithelial hepatocytes, with apical biliary canaliculi between adjacent cells, arranged adjacent to sinusoids conveying portal and arterial blood to central veins. Epithelial hepatocytes do not secrete a continuous basal lamina but are able to interact with the endothelium of the sinusoids without direct contact via shared basal lamina proteins. The vascular perfusion and generated shear stress through the developing liver induces the proliferation of hepatocytes both *in vivo* and *in vitro* (Beckwitt et al 2018, Lorenz et al 2018). Specific white blood cells, Kupffer cells, migrate later into the liver sinusoids. The usual functions of the liver in the production of plasma proteins and metabolism of nutrients is undertaken by the placenta; fetal hepatocytes are glycolytic and have low mitochondrial activity.

After stage 19, EryD cells (definitive erythrocytes), part of the second wave of haemopoiesis, are seen within the liver; their terminal maturation by enucleation occurs from postfertilization week 11 (Van Handel et al 2010) (Ch. 13). The third wave of erythrocyte production, from haemopoietic stem cells in a number of regions (including the placental stroma and aorta-gonad-mesonephros region), seeds precursor cells to the liver, thymus and bone marrow, and subsequently give rise to all blood lineages. Although the liver has been considered a main site of haemopoiesis, a study at 15–16 postmenstrual weeks found that fewer lymphocytes were present in the liver than in abdominal lymph nodes (Hwang et al 2014). In a comparison of adult and fetal patterns of gene expression in the liver, haemopoietic genes had low expression at 20–22 postmenstrual weeks, perhaps because by this time blood cell production is established in the bone marrow (Huse et al 2015).

At the end of the first trimester the liver almost fills the abdominal cavity, and its left lobe is nearly as large as its right (see Figs 23.14D–E and Figs 23.15B–E). It remains relatively larger than in the adult throughout fetal life. The increase in fetal liver volume is linear between 18–30 postmenstrual weeks, with no sex differences. In diabetic mothers, fetal liver volume is increased by 20% or more, and it is also enlarged in fetuses with trisomy 21. In cases of fetal growth restriction, liver volume is decreased (Szpinda et al 2015).

Development of intrahepatic biliary ducts

The development of the intrahepatic biliary ducts follows the branching pattern of the portal vein radicles (Collins 2002b). The cranial hepatic diverticulum gives rise to the liver hepatoblasts, the intrahepatic large bile ducts (right and left hepatic ducts, segmental ducts, area ducts and their first branches) and the small bile ducts (septal bile ducts, interlobular ducts and bile ductules). The portal and hepatic veins arise together from the vitelline veins. Early in development, the accumulation of mesenchyme around these veins is similar, whereas later mesenchyme increases around the portal veins; this accumulation is a prerequisite for bile duct development. Primitive hepatoblasts surround the portal vein branches and associated mesenchyme, and form a sleeve of cells termed the ductal plate. Individual cells of the ductal plate are termed cholangiocytes. Local hepatoblasts that are adjacent to the cholangiocytes arrange themselves to delineate a bile duct lumen and then also switch to a cholangiocyte lineage (Lemaigre 2009). As the bile ducts develop, angiogenic mesenchymal cells form blood vessels that connect to the hepatic artery from postfertilization week 10. Thus, the portal triads are patterned by the portal vein radicles, which initially induce bile duct formation and then artery formation. The development of the biliary system extends from the hilum to the periphery. Anomalies of the biliary tree are associated with abnormalities of the branching pattern of the portal vein. The developing bile ducts remain patent throughout development (Tan and Moscoso 1994).

Development of extrahepatic biliary ducts

The caudal part of the hepatic endodermal diverticulum forms the extrahepatic biliary system, the common hepatic duct, gallbladder, cystic duct and common bile duct.

The bile duct, which originated from the ventral wall of the foregut (now duodenum), migrates with the ventral pancreatic bud, first to the right and then dorsomedially into the dorsal mesoduodenum. The right and left hepatic ducts arise from the cranial end of the common hepatic duct from postfertilization week 12.

Liver and biliary ducts at birth

In the neonate, the liver constitutes 4% of the body weight, compared to 2.5–3.5% in adults. It is in contact with the greater part of the respiratory diaphragm and extends below the costal arch anteriorly, and, in some cases, to within 1 cm of the iliac crest posteriorly. The left lobe covers much of the anterior surface of the stomach and constitutes nearly one-third of the liver (see Fig. 23.14A). Fetal liver haemopoiesis ceases before birth, whereas enzymatic and synthetic functions are not completely mature at birth. Hepatocytes remain a heterogeneous population with different gene expressions and metabolic functions within different hepatic lobule locations: metabolic zonation becomes fully established after birth (Lemaigre 2009).

In the neonate, the gallbladder has a smaller peritoneal surface than in the adult, and its fundus often does not extend to the liver margin. It is generally embedded in the liver and, in some cases, may be covered by bands of liver. After the second year, the gallbladder assumes the relative size it has in the adult. Normal sonographic measurements of liver and biliary ducts for neonates and infants is given in Zale (2018).

Atresia of the extrahepatic bile ducts in neonates occurs alone or in conjunction with a range of other anomalies, including situs inversus, malrotation, polysplenia and cardiac defects. In such cases, the intrahepatic bile ducts have a mature tubular shape but also show features of ductal plate malformation. Biliary atresia is seen more commonly in males (Zale 2018). Elevated bile acids in infants with biliary atresia has been reported and that postnatal biliary duct inflammatory process may be involved (Davenport 2016).

MIDGUT

The midgut forms the third and fourth parts of the duodenum, jejunum, ileum and two-thirds of the way along the transverse colon; its development produces most of the small, and a portion of the large, intestine. In amniote embryos the midgut, which is connected to a narrowing vitelline intestinal duct to the yolk sac, forms a loop which projects away from the body ventrally, with a proximal cranial limb and a distal caudal limb; in mammals it enters the extraembryonic coelom. The usual explanation for this movement is that rotation of the loop can only occur out of the abdominal cavity, however, studies have shown that biomechanical transduction may promote gut lengthening, and suggest that the formation of the complex secondary and tertiary loops are controlled by genetic regulation. Experimental studies in chick embryo have indicated that the mechanical tension transmitted by the lengthening vitelline duct and the arteries passing to it along the dorsal mesentery, drive the proliferation and elongation of the midgut loop. In the absence of tension gut did not grow, i.e. there was no increase in volume or cell number (Chevalier et al 2018). The differential contribution of the endodermal core, the surrounding mesenchyme, or the outer coelomic epithelial layer which is continuous with the dorsal mesentery, remains to be elucidated.

In human embryos at stages 10–11 the midgut extends from the cranial to the caudal intestinal portals and communicates directly with the yolk sac over its entire length: it has a dorsal wall, but the lateral walls have not yet formed. By stage 12 the connection with the yolk sac has narrowed, such that the midgut has ventral walls cranially and caudally. This connection is reduced to a yolk stalk containing the vitello-intestinal duct during stage 13, at which time the yolk sac appears as a sphere in front of the embryo. Dorsal to the midgut, the splanchnopleuric coelomic epithelia converge, and form the dorsal mesentery with intervening mesenchyme. Ventrolaterally, the intraembryonic coelom is in wide communication with the extraembryonic coelom. At stage 14 the midgut has increased in length more than the axial length of the embryonic body and, with elongation of the dorsal mesentery, it bulges ventrally, deviating from the median plane (see Fig. 21.3).

The following description focuses on the movements of the elongating endodermal epithelial tube, surrounding splanchnopleuric mesenchyme and outer coelomic epithelium. For the later consequences of these movements, focusing on the coelomic epithelium and the fates of the elongating mesenteries relative to the dorsal wall of the developing peritoneal cavity, see p. 338. There is consequently some repetition in these two accounts.

Primary intestinal (midgut) loop

Formation of primary, secondary and tertiary looping of the midgut has been studied in human embryos to determine which parts of the process may be genetically determined and to provide 3D measurements of the movements of the midgut (Soffers et al 2015, Ueda et al 2016). The midgut starts to loop ventrally during stage 14 when the cranial end is level with somites 11–12 (this corresponds to putative thoracic vertebral levels 4–6), and the caudal end with somites 17–18 (putative thoracic vertebral levels 10–11). The caecal bud can be discerned on the lower limb of the loop, caudal to the yolk stalk (which arises from the apex or summit of the loop). The embryonic body is slightly helical at this time, so that the caudal portion of the embryo is more likely to be to the right of the head, and the midgut loop is midsagittal, following the helical body axis. The vitelline veins and the vitelline artery are landmarks for the apex of the midgut loop at stage 14, but from stage 16 the remaining proximal part of the artery gives rise to the superior mesenteric artery. The root of this vessel descends from somite level 13 to 19 (from putative thoracic vertebral levels T6 to T12).

The longest (dorsoventral) portion of the dorsal mesentery is at the level of the yolk stalk: there is less relative lengthening near the caudal end of the duodenum or the cranial half of the colon. When midgut length has increased sufficiently to extend the apex of the loop into the umbilical coelom, the proximal, cranial limb has moved to the right and the distal, caudal limb to the left relative to the midline (see Fig. 21.3C). This relative position is approximately maintained so long as the protrusion persists, during which time the proximal limb that forms the small intestine elongates even further. It becomes coiled developing secondary loops in a strict spatiotemporal pattern during postfertilization weeks 6–7, and its adjacent mesentery adopts a pleated appearance. Tertiary loops form after the end of postfertilization week 8 when there is an acceleration of the longitudinal growth of this part of the midgut. The origin of the root of the mesentery is initially both median and vertical, while, at its intestinal attachment, it is elongated like a ruffle and folded along a horizontal zone. The distal, colic, part of the loop elongates less rapidly and has no tendency to become coiled. Between stages 16 and 23, the crown–rump length of the embryo increases 3.6 times. The increase in relative length of the gut over this time shows that the duodenum is 3.5 times longer, the large intestinal part of the midgut loop is 8 times longer, and the small intestinal part of the loop 20 times longer (Ueda et al 2016). By 10 postfertilization weeks the peritoneal cavity has enlarged and the relative size of the liver and mesonephroi is much less. The re-entry of the gut occurs rapidly, the umbilical ring being sufficiently large to permit multiple loops to return, and in a particular sequence. The proximal loop returns first, with the jejunum mainly on the left and the ileum mainly on the right of the subhepatic abdominal cavity. As they re-enter the abdominal cavity, the coils of jejunum and ileum slide inwards over the right aspect of the descending mesocolon, and so displace the putative descending colon to the left. The transverse colon passes superiorly to the origin of the root of the mesentery (**Fig. 21.6**). The caecum is the last to re-enter and, at first, lies on coils of ileum on the right. Later development of the colon leads to its elongation and to the establishment of the hepatic and splenic flexures. Timetables for intestinal rotation in staged human embryos is given by Kim et al (2003), Soffers et al (2015), Ueda et al (2016).

The development of the midgut has been described and taught for many years in terms of a rotation of the gut around a dorsoventral axis of some 300°, anticlockwise viewed from the ventral aspect. This concept has recently been challenged. Soffers et al (2015) and Hikspoors et al (2019) reviewed the movement of the midgut using computer generated reconstructions of staged human embryos. They found that several factors contribute to the relative movements of the midgut loop: the helical disposition of the early embryonic body; the extreme longitudinal growth of portions of the midgut loop (the small intestine growth is double that of the colon); the descent of the origins of the cranial and caudal limits of the loop together with the origins of the vessels remained in the loop axis. While the midgut is in the umbilical coelom, secondary loops develop (excluding the intra-abdominal duodenojejunal loop) at three places along the midgut (proximal jejunal, distal jejunal and ileocaecum). Tertiary looping also occurs in these sites although with no predictable pattern of distribution. Resolution of the physiological herniation of the midgut, without any growth of the dorsal mesentery, is achieved once the dorsoventral depth of the abdomen increases, by proximodistal sequential movement of the extra-abdominal loops in a 'slide and stack' manner. This conclusion was supported by the observation of intermediate stages where only secondary, or secondary and tertiary, loops of small intestine had returned. The distal ileum and caecum enter the abdomen by sliding from the umbilical orifice to the lower-right abdominal cavity.

Umbilical cord

During the embryonic stages the umbilical cord is formed as the amniotic cavity expands and amnion encases the connecting stalk, allantois and embedded umbilical vessels caudally, and the extraembryonic coelom surrounding the vitelline duct and vessels cranially (Figs 9.10, 10.10). From stage 14 the umbilical cord occupies all of the ventral body wall between the pericardial bulge and the developing external genitalia, with similar linear dimensions as the heart; by stage 16 it is proportionally smaller than, and distinguishable from the thorax; at stage 23 it forms about one quarter of the ventral abdominal wall. Caudally, there is no infraumbilical region before stage 15; it becomes apparent by 9 postfertilization weeks. Somatic (hypaxial) mesenchyme, that will form the ventral body wall musculature, migrates into the somatopleuric mesenchyme and passes ventrally towards the midline and the lateral borders of the umbilical cord (Mekonen et al 2015). A portion of the extraembryonic coelom (chorionic cavity), the umbilical coelom, remains in the forming umbilical cord into which the lengthening midgut loop protrudes. The midgut loop returns to the abdominal cavity at about 10 postfertilization weeks, and the umbilical coelom remains in the cord for at least one week longer (Soffers et al 2015). The following changes to the maturing cord then occur: the vitellointestinal duct and vessels involute; the cranial end of the allantois becomes thinned and its lumen partially obliterated, forming the urachus. The mesenchymal core of the umbilical cord is derived by coalescence of somatopleuric amniotic mesenchyme, splanchnopleuric vitellointestinal (yolk sac) mesenchyme and splanchnopleuric allantoic (connecting stalk) mesenchyme. These various layers become fused and are gradually transformed into the viscid, mucoid, connective tissue (Wharton's jelly) that characterizes the more mature cord. The changes in the circulatory system result in a large, cranially orientated, left umbilical vein (the right umbilical vein regresses), and two caudally orientated, spirally disposed umbilical arteries (see Fig. 13.25). There is a clear distinction between skin, derived from ectoderm and underlying somatopleuric mesenchyme, and the tissues within the umbilical cord. After birth all tissues within the umbilical cord undergo involution and the cord itself will detach from the skin, regardless of its dimensions.

Anomalies of midgut rotation

Available with the *Gray's Anatomy* e-book.

Maturation of the small intestine

Mucosa

The exact timing of the cellular morphogenesis of the gut is difficult to establish, especially as it undergoes a proximodistal gradient in maturation. Developmental differences between parts of the small intestine or colon have not yet been correlated with age. The endodermal cells of the small intestine proliferate and form pseudostratified layers exhibiting interkinetic nuclear migration with mitotic figures. The formation of villi occurs in a proximodistal progression from the duodenum to the ileocaecal junction in Turing-like pattern formation (Ch. 11). It is not clear how vilification is eventually suppressed in the future colon. For details of the comparative development of the interactions between epithelial endoderm and the local splanchnic mesenchyme see Walton et al (2018). In the human, blunt projections of the endoderm form in the duodenum and proximal jejunum from postfertilization week 7; these developing villi increase in length until, in the duodenum, the lumen becomes difficult to discern. The concept of occlusion of the lumen and subsequent recanalization, described in many accounts of development, is not supported by the cytodifferentiation that occurs in the gut epithelia, challenging the belief that secondary recanalization of the gut lumen occurs (Grosse et al 2011). By 9 postfertilization weeks, the duodenum, jejunum and proximal ileum have villi, and the remaining distal portion of ileum develops villi by 11 postfertilization weeks. The villi are covered by a simple epithelium. Primitive crypts, epithelial downgrowths into the mesenchyme between the villi, appear during postfertilization weeks 10–12, and similarly follow a craniocaudal progression. Brunner's glands are present in the duodenum from postmenstrual week 15 and the muscularis mucosa can be seen in the small intestine from postmenstrual week 18.

Whereas mitotic figures are initially seen throughout the pseudostratified endodermal layer of the small intestine prior to villus formation, by 10–12 postfertilization weeks they are limited to the intervillous regions and the developing crypts. It is believed that an 'adult' turnover of cells may exist when rounded-up cells can be observed at the villus tips, in position for exfoliation. The absorptive enterocytes have microvilli at their apical borders before postfertilization week 9. An apical tubular system appears at this time, and is composed of deep invaginations of the apical plasma membrane and membrane-bound vesicles and tubules; many lysosomal elements (meconium corpuscles) appear in the apical cytoplasm. These latter features are more developed in the ileum than jejunum, are most prominent at 16 postmenstrual weeks, and diminish by 21 postmenstrual weeks. There are abundant deposits of glycogen in the fetal epithelial cells, and it has been suggested that, prior to the appearance of hepatic glycogen, the intestinal epithelium serves as a major glycogen store. Goblet cells are present in small numbers by postfertilization week 8, Paneth cells differentiate at the base of the crypts from postfertilization week 11, and enteroendocrine cells appear between postfertilization weeks 9–11. M cells (membrane or microfold cells) are present from about 14 postmenstrual weeks.

Intestinal subepithelial myofibroblasts have been described within the villus cores and adjacent to the intervillous space at the base of the crypts from postmenstrual week 21. They are arranged as a syncytium between the epithelium and the muscularis mucosae, where they

If the midgut loop fails to return to the abdominal cavity at the appropriate time, a number of ventral defects can result. Failure of obliteration of the vitellointestinal duct connecting the midgut to the yolk sac produces Meckel's diverticulum. This may present as a short segment of vitelline duct attached to the original ventral side of the ileum; it may remain attached to the umbilicus as a fistula; or it may remain as a ligamentous attachment to the umbilicus. The position and configuration of the duodenal loop are of particular importance in children. The normal duodenal loop has a U-shaped configuration. The suspensory ligament of the duodenum (ligament of Treitz) is usually found to the left of the body of the first or second lumbar vertebral body after normal gut rotation; any other position of this ligament may indicate some degree of gut malrotation. On barium studies, the duodenojejunal flexure should, thus, lie to the left of the upper lumbar spine at the level of the pylorus.

If the caecum has remained in the right upper quadrant, it may become fixed in that position by peritoneal attachments passing to the right, the so-called Ladd's bands. These may compress the underlying duodenum and give rise to duodenal stenosis. The high positioning of the caecum close to the duodenal jejunal flexure, in some cases, in the midline, is associated with later development of small intestinal volvulus.

An umbilical hernia occurs when loops of gut protrude into a widened umbilical cord at term. The degree of protuberance may increase when the infant cries, which raises the intra-abdominal pressure; these hernias usually resolve without treatment. Larger anomalies can be detected on routine antenatal ultrasound examination.

Exomphalos is a ventral wall defect with midline herniation of the gut into the base of the umbilical cord. It is frequently associated with genetic and chromosomal anomalies. Herniated viscera are covered by the visceral peritoneum, and parietal peritoneum lines the amniotic covering of the umbilical cord externally. The omphalocele so formed ranges in size from a large umbilical hernia to a very large mass containing most of the visceral organs. Even after the exomphalos has been repaired, these babies will still have a deficient anterior abdominal wall.

Gastroschisis is a paraumbilical defect (usually to the right) of the anterior abdominal wall associated with evisceration of the abdominal organs into the amniotic cavity. The organs are not enclosed in membranes which means that gastroschisis can be detected by prenatal ultrasonography and differentiated from exomphalos (see Fig. 23.6B). Gastroschisis has increased in incidence worldwide over the past 25 years, from 0.1 : 10,000 to 1.0 : 10,000 in developed countries and from 3.0 : 10,000 to 5.0 : 10,000 in underdeveloped countries (Campbell and Copel 2018). Women younger than 25 years of age have 2–3 times higher risk, and since the mid-1990s the incidence in women under 20 years of age has increased from 8 : 10,000 to 18 : 10,000. Low socioeconomic status and vasoactive drug use are risk factors in this population (Wolf 2018). Gastroschisis is not regarded as a genetic condition, although familial occurrences have been reported. It is not usually associated with other visceral anomalies. A number of proposed mechanisms have been suggested, initially periumbilical ischaemia, caused by vascular compromise of either the umbilical vein or arteries; anomalous development of the somatopleuric mesenchyme of the ventral body wall, similar to that in ectopia cordis and cloacal exstrophy; other scenarios permitting coils of intestine to enter the amniotic cavity, rather than stay in contact only with the extraembryonic coelomic fluid within the chorionic cavity and umbilical coelom, include amniotic membrane rupture, possibly at the base of the umbilical ring (Wolf 2018). Nearly all cases of gastroschisis are associated with elevated levels of maternal serum alpha-fetoprotein, which prior to ultrasound screening was the sole indicator of the condition (Campbell and Copel 2018). Oligohydramnios is a common association.

Congenital volvulus arises if the midgut loop does not rotate appropriately. A number of types of this condition are identified. Left-sided colon occurs if the midgut loop has not rotated at all; mixed rotation results in the caecum lying inferior to the pylorus; and failure of appropriate attachment of the peritoneum may result in the small intestine being attached at only two points on the posterior abdominal wall. All of these arrangements lead to a risk of volvulus, which may result in necrosis of the gut. The identification of intestinal malrotation can be made by contrast radiography investigation. However, ultrasonography has the advantage of showing the position of the superior mesenteric vein and artery. The vein should lie to the right of the artery. Most cases of volvulus will show inversion of this normal relationship but malrotation can occur with apparently normally related vessels, particularly in malrotation with bowel obstruction due to Ladd's bands and not volvulus.

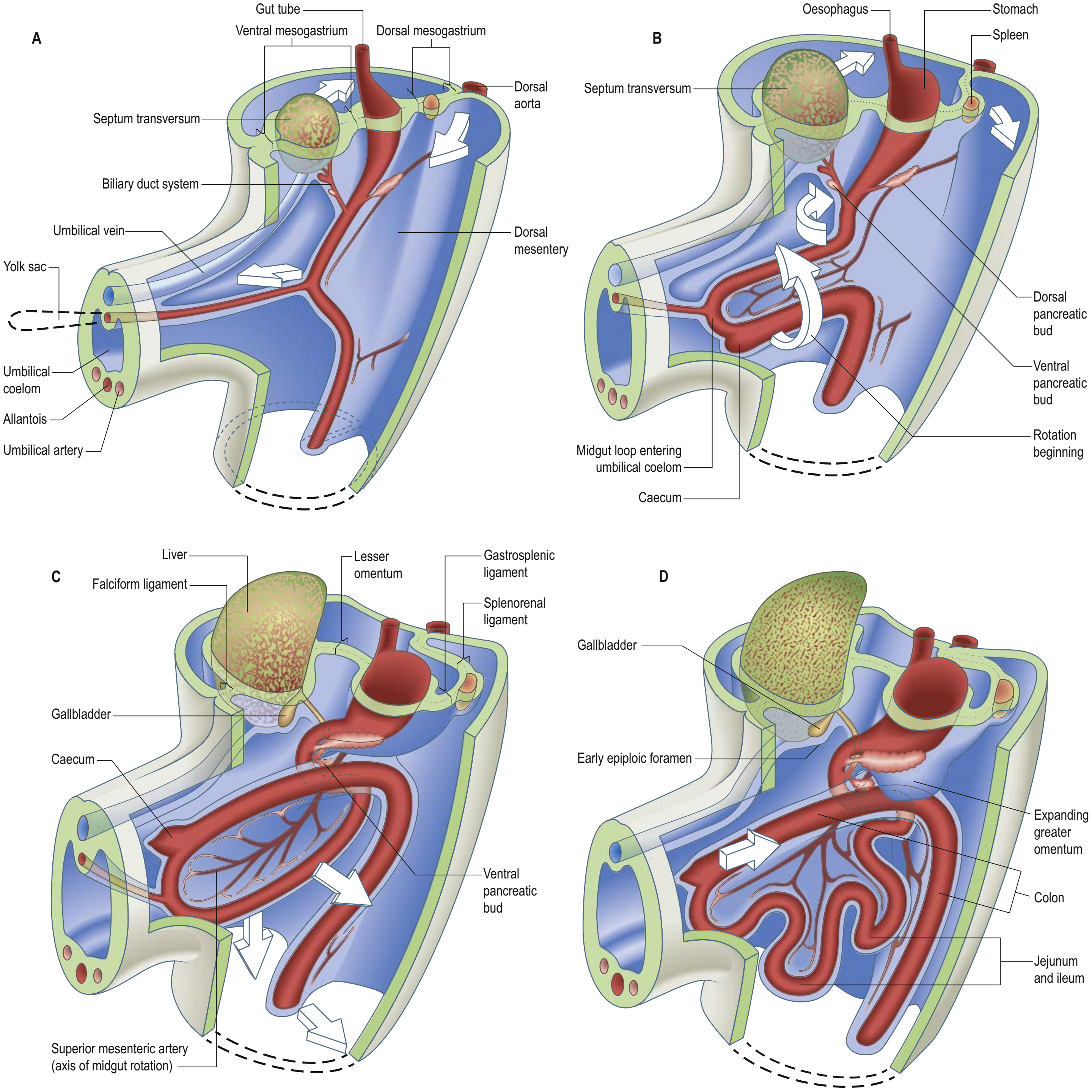
A
Gut tube
Ventral mesogastrium
Dorsal mesogastrium
Dorsal aorta
Septum transversum
Biliary duct system
Umbilical vein
Dorsal mesentery
Yolk sac
Umbilical coelom
Allantois
Umbilical artery
B
Oesophagus
Stomach
Spleen
Septum transversum
Dorsal pancreatic bud
Ventral pancreatic bud
Rotation beginning
Midgut loop entering umbilical coelom
Caecum
C
Liver
Falciform ligament
Lesser omentum
Gastrosplenic ligament
Splenorenal ligament
Gallbladder
Caecum
Ventral pancreatic bud
Superior mesenteric artery (axis of midgut rotation)
D
Gallbladder
Early epiploic foramen
Expanding greater omentum
Colon
Jejunum and ileum

Fig. 21.6 The major developmental sequences of the subdiaphragmatic gut, associated major glands, peritoneum and mesenteries: left anterolateral aspect. The developmental sequence spans the period from stage 14 when the midgut starts to loop ventrally to postmenstrual weeks 10–12 when it returns to the abdominal cavity: it assumes its final disposition between postmenstrual weeks 16–20. **A–B**, The top white arrows show the relative movements of the dorsal and ventral mesogastria that result in the longitudinal rotation of the stomach and limited entry to the lesser sac (see also Fig. 21.5). **C–D**, The lower white arrows associated with the midgut indicate the relative movements and rotation of the midgut loop within the umbilical coelom, and as it returns to the abdominal cavity.

Continued

contribute to the extracellular matrix. They demonstrate α-smooth muscle actin (SMA) expression (McLin et al 2009). It is not clear whether these cells derive from splanchnopleuric mesenchyme fibroblasts, smooth muscle precursors or neural crest. They migrate from the crypts to the villous axis in a manner similar to enterocytes.

Meconium can be detected in the lumen of the intestine by 16 postmenstrual weeks. It is derived from swallowed amniotic fluid, which contains vernix and cellular debris, salivary, biliary, pancreatic and intestinal secretions, and sloughed enterocytes. As the mixture passes along the gut, water and solutes are removed and cellular debris and proteins concentrated. Meconium contains enzymes from the pancreas and proximal intestine in higher concentrations in preterm than in full-term babies.

Muscularis layer

The muscularis layer is derived from the splanchnopleuric mesenchyme, as it is in other parts of the gut. Smooth muscle myoblasts can be identified by expression of α-SMA, with longitudinal muscle seen from 12 postfertilization weeks. At 26–30 postmenstrual weeks, the gut shows contractions without regular periodicity; from 30–33 postmenstrual weeks, repetitive groups of regular contractions have been seen in preterm neonates.

Serosa

The small intestine possesses only a dorsal mesentery. The movement of the root of this mesentery, and the extensive lengthening of its enteric

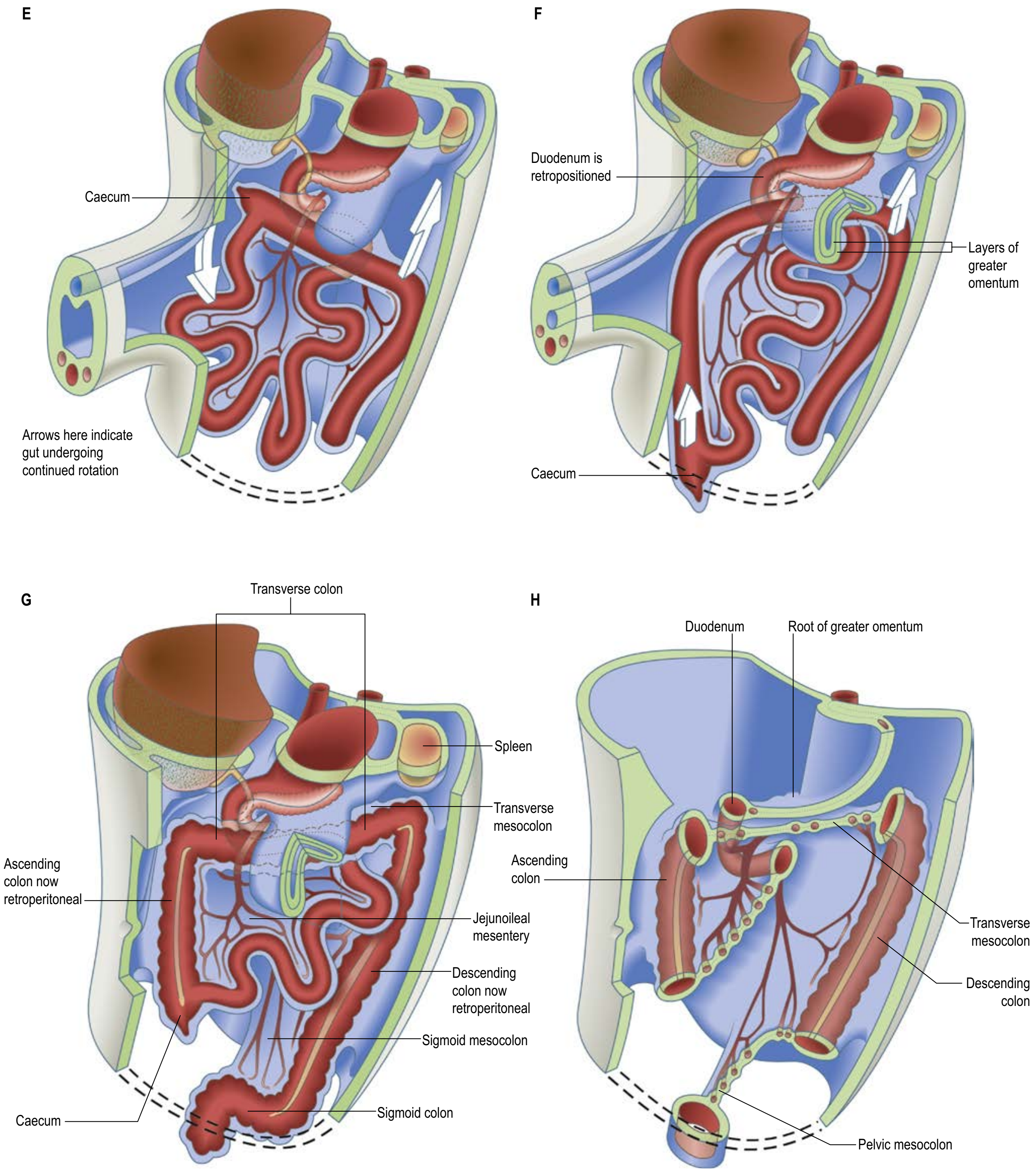
E
Caecum
Arrows here indicate gut undergoing continued rotation
F
Duodenum is retropositioned
Layers of greater omentum
Caecum
G
Transverse colon
Spleen
Transverse mesocolon
Ascending colon now retroperitoneal
Jejunoileal mesentery
Descending colon now retroperitoneal
Sigmoid mesocolon
Caecum
Sigmoid colon
H
Duodenum
Root of greater omentum
Ascending colon
Transverse mesocolon
Descending colon
Pelvic mesocolon

Fig. 21.6, **Cont'd** **E–F**, The lower white arrows associated with the midgut indicate the relative movements and rotation of the midgut loop within the umbilical coelom, and as it returns to the abdominal cavity. **G–H**, The approximate disposition in the adult abdomen of the gut (**G**) and the mesenteric roots, showing their lines of attachment and principal contained vessels (**H**).

border in order to match the longitudinal growth of the gut, reflect the spiralizing of the midgut loop in the umbilical coelom (see p. 338).

Small intestine at birth

The radial patterning of the small intestine is completed before birth, with differentiation of the crypt–villous axis. Specification of the space between villi, crypt depth and villous length is a dynamic process dependent on the establishment of the intestinal microbiota (see Postnatal development of the gut, p. 340). In the full-term neonate, the small intestine forms an oval-shaped mass with its greater diameter transversely orientated in the abdomen, rather than vertically as in the adult. The mass of the small intestine inferior to the umbilicus is compressed by the urinary bladder, which is anterior at this point. The small intestine is 300–350 cm long at birth and its width, when empty, is 1–1.5 cm. The ratio between the length of the small and large intestines at birth is similar to the adult ratio. Mucosal villi are present throughout the small intestine, however, some epithelial differentiation is incomplete. The muscularis is very thin, particularly the longitudinal layer, and there is little elastic tissue in the wall. There are few or no circular folds in the small intestine, and the jejunum and ileum have little fat in their mesentery.

PRIMITIVE HINDGUT

Just as the foregut has an extensive ventral endodermal diverticulum that contributes to a system separate from the gut, so, too, the hindgut has a ventral diverticulum, the allantois, that is destined for urogenital system development. However, unlike the respiratory diverticulum of the foregut, the allantois is formed very early in development, prior even to formation of the embryonic endoderm and tail-folding. With the reorganization of the caudal region of the embryo at stage 10, part of the allantois is drawn into the body cavity. The early embryonic hindgut thus consists of a dorsal tubular region extending from the caudal intestinal portal to the cloacal membrane, and a ventral blind-ending allantois extending from the cloacal region into the connecting stalk. The slightly dilated cavity, lined by endoderm, that cranially receives the enteric hindgut proper and the root of the allantoenteric diverticulum is termed the endodermal cloaca. It is closed ventrally by the cloacal membrane (endoderm opposed to proctodeal ectoderm), and it also has, transiently, a small recess of endoderm in the root of the tail, the postanal gut. As elsewhere, the hindgut, allantois and endodermal cloaca are encased in splanchnopleuric mesenchyme. Proliferation of the mesenchyme and endoderm in the angle of the junction of hindgut and allantois produces a urorectal septum from stage 15 (see Fig. 22.4B). Continued proliferation of the urorectal septum and elongation of the endodermal structures move the endodermal epithelium towards the cloacal membrane, with which it fuses centrally, separating the presumptive rectum and upper anal canal (dorsally) from the presumptive urinary bladder and urogenital sinus (ventrally) (see Fig. 22.4C). The cloacal membrane is thus divided into anal (dorsal) and urogenital (ventral) membranes. The nodal centre of division is the site of the future perineal body, the functional centre of the perineum. For details of the formation of the urorectal septum in human embryos see Kruepunga et al (2018).

There are few studies on the complex development of the caudal regions of the embryonic and fetal body. The skeletal and neural elements, and the lower sphincters of the enteric and urogenital systems, develop subsequent to secondary neurulation processes, within the embryonic caudal eminence. The autonomic and somatic neurological control in this region postnatally is comparable to that of the aerodigestive pharynx, even though the derivation, interactions and maturation of the caudal neural crest cells may be very different.

Enteric hindgut

The development of the large intestine, whether derived from mid- or hindgut, seems to be similar. The proximal end of the colon can be identified initially at stage 15, when an enlargement of a local portion of gut on the caudal limb of the midgut loop defines the developing caecum. An evagination of the distal portion of the caecum forms the vermiform appendix at stage 17 (see Fig. 21.3E). Apart from the embryonic studies of Streeter (1942), there is little information about the development of the large intestine in humans. The early endodermal lining of the colon is pseudostratified with interkinetic nuclear migration and mitoses in the layer. A series of longitudinal folds arise initially at the rectum and caecum, and later in the regions of colon between these two points. The folds segment into villi, with new villi forming between. The developing mucosa invaginates into the underlying mesenchyme between the villi to form glands that increase in number by splitting longitudinally from the base upwards. The villi gradually diminish in size and are absent by the time of birth.

Maturation of the large intestine

The similarity of development of the small and large intestines is further mirrored in their cytological differentiation. From 11 postfertilization weeks, dipeptidase activity in the colon as well as in the small intestine is seen. Throughout preterm development, meconium corpuscles are seen in the colon and in the small intestine; they are believed to be the phagocytosed remains of neighbouring cells that have died as a result of programmed cell death. Between 17 and 24 postmenstrual weeks, fetuses express fewer genes in the colon than adults, but like adults, there is a differential expression of genes between ascending and descending colon (Glebov et al 2003). There is little direct evidence of colonic function in the human fetus.

Mucosa

The absorption of glucose and amino acids does not take place through the colonic mucosa in adult life, but there is evidence of direct absorption of these nutrients during development. At birth, the normal cycle of bile acids is not mature. In the adult, bile is secreted by the liver, stored in the gallbladder and then secreted into the intestine, where it is absorbed by the jejunum and ileum. In the fetus and neonate, the transport of bile acids by an active process from the ileum does not occur, and so bile salts pass on into the colon. In the adult, the presence of bile salts in the colon stimulates the secretion of water and electrolytes, which results in diarrhoeal syndrome; however, the fetal and neonatal colon seems protected from this effect. The colon is not considered a site of significant nutrient absorption in the adult, and yet neonates are unable to assimilate the full lactose load of a normal breast feed from the small intestine and a large proportion of it may be absorbed from the colon. Thus, it appears that the colon fulfils a slightly different role in the preterm and neonatal period, conserving nutrient absorption and minimizing fluid loss until the neonate has adjusted to extrauterine life, oral feeding and the establishment of the symbiotic bacterial flora (see Postnatal development of the gut, p. 340).

Muscularis

The muscularis is present and functioning by the eighth postfertilization week, when peristaltic waves have been observed. The specific orientation of the longitudinal muscle layer into taeniae coli occurs in the 11–12 postfertilization weeks, when haustra appear. The enteric nerves are present in Meissner's and Auerbach's plexuses at 8 and 12 weeks postfertilization, respectively; there is a craniocaudal migration of neurones into the gut wall. A normal distribution of ganglion cells has been noted in preterm babies of 24 postmenstrual weeks, although there is a region devoid of ganglia just above the anal valves. Anomalous migration of neural crest cells to the gut may give rise to Hirschsprung's disease (see p. 334). Puborectalis appears in stage 22–23 embryos, following opening of the anal membrane.

Serosa

The development of the serosa of the intestine is considered with the development of the peritoneal cavity (see below).

Colon at birth

In the full-term (notional 40 postmenstrual weeks) neonate, the colon is typically 66 cm long and averages 1 cm in width. The caecum is relatively smaller than in the adult and it tapers into the vermiform appendix. The ascending colon is shorter in the neonate, reflecting the shorter lumbar region. The transverse colon is relatively long, whereas the descending colon is short, although twice the length of the ascending colon (see Fig. 23.14B). The sigmoid colon may be as long as the transverse colon; it often touches the inferior part of the anterior body wall on the left and, in some neonates, part of the sigmoid colon lies in the right iliac fossa. The muscularis, including the taeniae coli, is poorly developed in the colon, as it is in the small intestine. Appendices, epiploicae and haustra are not present, and so the colon has a smooth external appearance: haustra appear within the first 6 months. This means that the small and large intestines cannot be differentiated by standard radiological views. The rectum is relatively long and its junction with the anal canal forms at nearly a right-angle.

Anal canal

In stage 14 a small part of the hindgut, the postanal gut, projects caudally beyond the anal membrane (see Fig. 21.3B), but it usually disappears by the end of stage 15. Mesenchymal proliferation occurs around the rim of the ectodermal aspect of the anal membrane, which thus comes to lie at the bottom of a depression, the proctodeum (see Fig. 22.7E). With the absorption and disappearance of the anal membrane, the anorectum communicates with the exterior. The lower part of the anal canal is formed from the proctodeal ectoderm and underlying mesenchyme, but its upper part is lined by endoderm: the line of union corresponds with the edges of the anal valves. The dual origin of the anal canal is reflected in its innervation, in that the endodermal portion is innervated by autonomic nerves, and the ectodermal proctodeum is innervated by spinal nerves. The external anal sphincter has an origin from the myoblasts which migrate into the lower limb and then return to the external genital region (Chs 19, 22) (Valasek et al 2005). The anatomy of the terminal portions of the muscularis externa, adventitia, perineal body and the external anal sphincter in the fetus has been explored Wu et al (2018).

Anal canal at birth

Imperforate anus is a term that has been used to describe many different anorectal anomalies. The most common is anal agenesis, which is found in almost half of all cases of imperforate anus. The condition is usually associated with a fistula, which opens into the vulva (females) or into the urethra (males). It is rare for the anal membrane to fail to perforate. The condition cannot reliably be diagnosed prenatally by ultrasound diagnosis, and it may be confused with Hirschsprung's disease (see below) and colonic atresia. The prognosis is good for low lesions of the anal canal. In all cases, the principal concern is the degree of bowel and urinary control and, in some cases, sexual function, which is compromised by the condition. Anorectal anomalies may be indicators of other anomalies, e.g. those forming the 'VATER' syndrome (Vertebral, Anal, Tracheo-oEsophageal and Renal anomalies).

Blood supply to the gut

The development of the blood supply to the gut and the changes that occur in the formation of the portal circulation are given in Chapter 13. Three midline arteries, the coeliac trunk, superior and inferior mesenteric arteries supply the fore, mid- and hindgut, respectively: they travel in the intermesenteric space of the associated mesenteries, where they arborize.

Enteric nervous system

Enteric neurones are derived from cranial (vagal) neural crest cells at somite levels 1–7 and from level 28 onwards (see Fig. 14.20). Glial cells associated with the gut have been identified as arising from similar levels. Migrating vagal neural crest cells reach the midgut by postfertilization week 5 and the entire length of the gut is colonized by stages 18–20. Sacral neural crest cells migrate ventrally and invade the gut via the dorsal mesentery (see Fig. 14.6A). It is thought that the vagal and sacral neural crest cells have intrinsic differences in their ability to colonize the gut. The local splanchnopleuric mesenchyme patterns the crest cells, such that those that enter the gut layers attain an enteric fate, whereas those that remain outside the gut become committed as parasympathetic postganglionic neurones. The enteric neurones also migrate to the pancreas. Maturation of the myenteric plexus follows a craniocaudal progression, with enteric neurones differentiating into intrinsic primary afferent neurones, motor neurones and interneurons (Rao and Gerson 2018). The submucosal plexus arises from centripetally migrating cells from the myenteric plexus 2–3 days later (Burns et al 2009). Interstitial cells of Cajal are derived from splanchnopleuric mesenchymal cells that interact with the wavefront of migrating chains of neural crest cells along the gut. These cells express a proto-oncogene, *c-kit*, that can be identified in the gut at the end of the embryonic period along a rostrocaudal gradient. Five subtypes have been identified: the subtype ICC-MP has a pacemaker role throughout the gut, generating and propagating electrical slow waves; subtype ICC-SMP also has a pacemaker role in the colon (Radenkovic et al 2018). There is evidence that mucosal enteric glial cells, which move into the mucosa after birth, interact with the colonizing intestinal flora, suggesting a microbiota-driven homeostatic mechanism for gut function (Kabouridis et al 2015).

Hirschsprung's disease

Available with the *Gray's Anatomy* e-book

Gut-associated lymphoid tissue (GALT)

Individual lymphocytes appear in the lamina propria of the gut from about postmenstrual week 14–16, and lymphoid aggregates, Peyer's patches, can be seen from postmenstrual week 19; it is not clear whether these cells migrate in from distant sources or differentiate from the investing mesenchyme (Hoorweg and Cupedo 2008). The endodermal epithelium overlying the lymphoid aggregates is often distorted into a dome shape. The cells within the dome are a mixed population of enterocytes, endocrine cells, goblet cells and M cells. The latter are specialized to provide a mechanism for the transport of microorganisms and intact macromolecules across the epithelium to the intraepithelial space and lamina propria. They have been observed in the fetus by 17 postmenstrual weeks and it is believed that they are formed by a specialized epithelial–mesenchymal interaction of the endoderm and underlying lymphoid-type mesenchyme.

There are similarly specialized epithelial cells between the enterocytes. Intraepithelial leukocytes typically account for 15% of the epithelial cells of the gut in the adult. They have been observed at postfertilization week 11, with a distribution of 2–3 intraepithelial leukocytes per 100 gut epithelial cells. Both T and B lymphocytes have been described in the developing gut wall. For an account of the development of human innate lymphoid cells, consult Juelke and Romagnani (2016). Neonatal gut maturation continues postnatally when the gut microbiome becomes established (see Postnatal development of the gut, p. 340).

PERITONEAL CAVITY

The early development of the intraembryonic coelom, which gives rise to the peritoneal cavity, is described in Chapter 10. Figure 12.2 shows a scheme of the shape of the early peritoneal cavity and indicates the mesenchymal populations derived from its epithelial walls. Initially, the peritoneal cavity associated with the lower end of the foregut has separate right and left components: the pleuroperitoneal canals (see Fig. 21.1). At the level of the midgut, these canals join a confluent cavity surrounding the developing gut, which transitorily is in communication with the extraembryonic coelom.

The description of the development of the peritoneal cavity that follows pertains to changes that occur as a consequence of the differential growth of the gut.

Peritoneum

Peritoneum arises from the terminal differentiation of the intraembryonic coelomic walls. Initially, the intraembryonic coelomic epithelium is a pseudostratified germinal layer from which cellular progeny with different fates arise in specific sites and at specific developmental times. The portion that will give rise to the peritoneum is derived from the lower parts of the pericardioperitoneal canals, and the somatopleure and splanchnopleure associated with the lower foregut, midgut and hindgut to the future rectum (see Figs 21.1, 12.2). The proliferative splanchnopleuric epithelium of these regions of coelomic wall produces splanchnic mesenchymal cell populations that form the laminae propriae of the mucosa and submucosa, the smooth muscle in the muscularis of the gut, and the lamina propria and epithelium of the visceral peritoneum (the serosa of the gut wall). The somatopleuric epithelium gives rise to the lamina propria and epithelium of the parietal peritoneum and the underlying body wall adjacent to the ectoderm.

The coelom wall has not been a topic of specific interest in the past, however, it apparently possesses remarkable characteristics in early development. Its proliferation gives rise to mesenchymal cell populations for all gastrointestinal glands and the connective tissues of the lateral and ventral body walls. At the junction of splanchopleure and somatopleure, it contributes epithelial and mesenchymal populations to the suprarenal glands, the urinary and reproductive tracts, the gonads and the spleen (Ariza et al 2016). Most importantly for gut development, it forms an active barrier in the developing abdomen that maintains the integrity of, and separates, the developing viscera, functions that are continued by the fully developed peritoneum (Guo et al 2014). Its particular role(s) in the development of the respiratory diaphragm and the early expansions of the pleural and peritoneal cavities are as yet uncertain. Above the forming respiratory diaphragm, this putative mesothelial layer is involved in expanding the caudodorsal regions of the pleural cavities, where the somatopleuric mesenchyme of the body wall is excavated dorsal to the developing suprarenal glands, degenerating mesonephric ridges and gonads. Beneath the respiratory diaphragm it drives the development of the upper parts of the forming peritoneal cavity and the transitory formation of peritoneal cul de sacs that pass into the thorax. The most caudal parts of the coelomic wall evaginate bilaterally to create passages for, and the peritoneal coverings of, the testes, as they descend and move out of the abdominal cavity.

As the gut grows, splanchnic mesenchyme accumulates around the inner endodermal epithelium and the whole unit generally moves ventrally. There is a concomitant enlargement of the caudal ends of the developing pericardioperitoneal (pleuroperitoneal) canals and developing peritoneal cavity adjacent to the midgut. The medial walls of the intraembryonic coelom move closer and there is a relative decrease in the mesenchyme between them. The regions where the medial portions of the intraembryonic coelom come together are termed mesenteries. They are composed of two layers of splanchnopleuric coelom wall with intervening mesenchyme, and contain the neurovascular structures that pass to and from the gut. At the caudal ends of the pleuroperitoneal canals, the gut has both ventral and dorsal mesenteries, whereas, caudal to this, there is only a dorsal mesentery that extends from the third part of the duodenum to the rectum (see Fig. 21.6; **Fig. 21.7**). The arrangement of an (endodermal) epithelial tube, surrounded by splanchnopleuric mesenchyme, enclosed with a further layer of (splanchnopleuric) epithelium, permits the development of differential, regional, biomechanical tension and compressive forces along the gut and mesentery. These biomechanical forces produce a growth pattern termed buckling morphogenesis (Chevalier et al 2018). Loose loops of gut are the result of a decrease in differential growth, i.e. equal contributions of the

Hirschsprung's disease (commonly called megacolon) is usually characterized by an aganglionic portion of gut that does not display peristalsis, and a dilated segment of structurally normal colon proximal to this site. Histologically, there is either an absence or a reduction in the number of ganglia and postganglionic neurones in the myenteric plexus of the affected segment of gut; postganglionic innervation of the muscle layers is also often defective. It is believed that the condition is caused by a failure of neural crest cells to colonize the gut wall appropriately (Gershon 2010). A variable length of large intestine may be affected; the lower and mid-rectum are the most common sites but, in severe cases, the rectum, sigmoid, descending and even proximal colon can be aganglionic. Occasionally, aganglionosis affects only a very short length of rectum proximal to the anorectal junction and the degree of functional obstruction is minimal; in these cases of 'ultra-short-segment Hirschsprung's disease', clinical anomalies arise later in life. Infants with Hirschsprung's disease show delay in the passage of meconium, constipation, vomiting and abdominal distension. Culture of enteric nervous system cells derived from patients with Hirschsprung's disease have been shown to support development of enteric nerves in an aganglionic portion of gut from the same patient, indicating that the colonic tissue is still permissive for enteric neurone development and that postnatal enteric nervous system derived cells are still competent to respond (Rollo et al 2016). Suction rectal biopsy is used for histological confirmation of aganglionosis in 90% of neonates. The main surgical procedure in the UK for left-sided disease is the primary pull-through within 3 postnatal months; there is still variation in surgical practice for right-sided Hirschsprung's disease (Bradnock and Walker 2011).

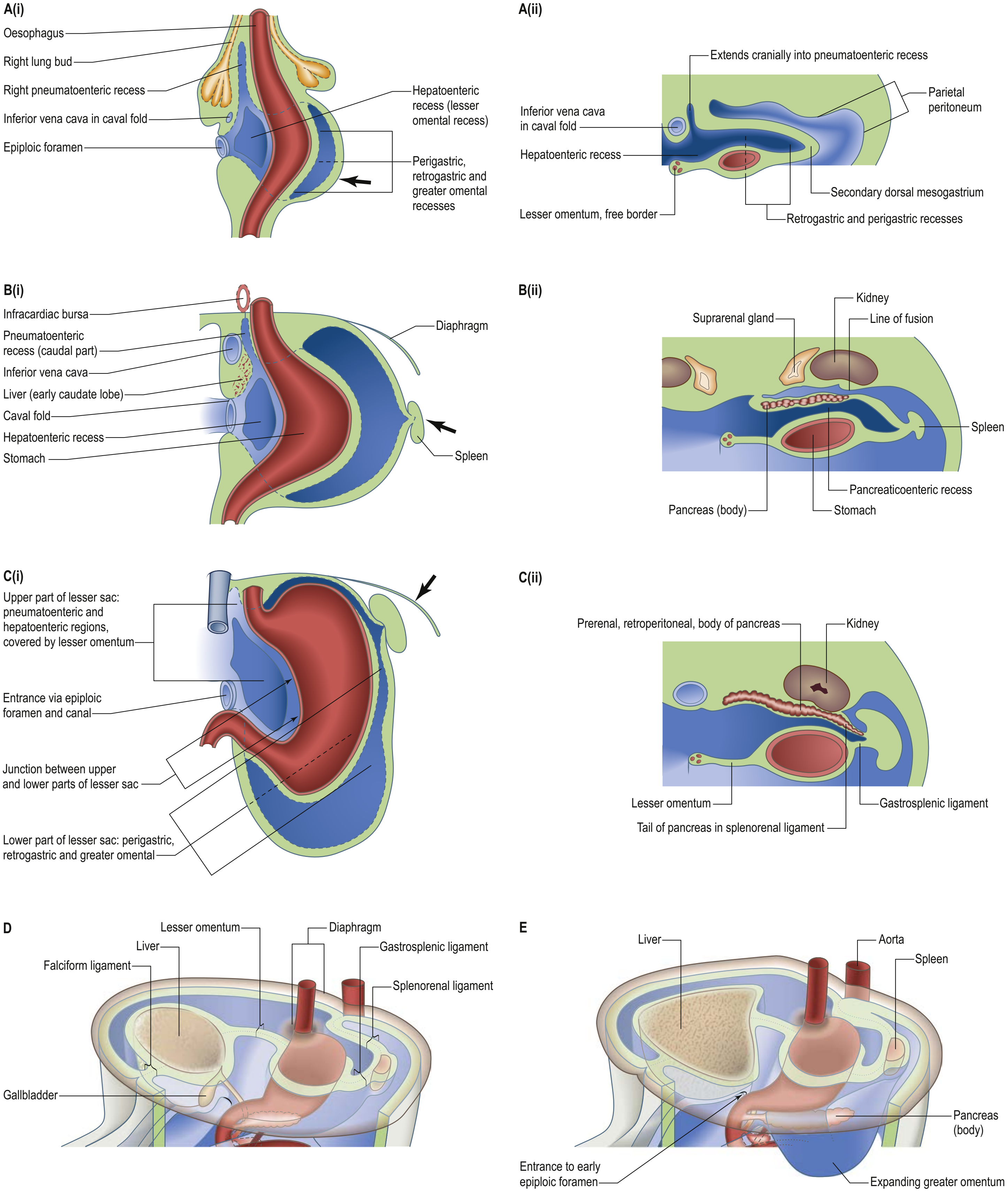
A(i)
Oesophagus
Right lung bud
Right pneumatoenteric recess
Inferior vena cava in caval fold
Epiploic foramen
Hepatoenteric recess (lesser omental recess)
Perigastric, retrogastric and greater omental recesses
A(ii)
Extends cranially into pneumatoenteric recess
Parietal peritoneum
Inferior vena cava in caval fold
Hepatoenteric recess
Secondary dorsal mesogastrium
Lesser omentum, free border
Retrogastric and perigastric recesses
B(i)
Infracardiac bursa
Pneumatoenteric recess (caudal part)
Inferior vena cava
Liver (early caudate lobe)
Caval fold
Hepatoenteric recess
Stomach
Diaphragm
Spleen
B(ii)
Kidney
Suprarenal gland
Line of fusion
Spleen
Pancreaticoenteric recess
Pancreas (body)
Stomach
C(i)
Upper part of lesser sac: pneumatoenteric and hepatoenteric regions, covered by lesser omentum
Entrance via epiploic foramen and canal
Junction between upper and lower parts of lesser sac
Lower part of lesser sac: perigastric, retrogastric and greater omental
C(ii)
Prerenal, retroperitoneal, body of pancreas
Kidney
Lesser omentum
Gastrosplenic ligament
Tail of pancreas in splenorenal ligament
D
Lesser omentum
Diaphragm
Liver
Gastrosplenic ligament
Falciform ligament
Splenorenal ligament
Gallbladder
E
Liver
Aorta
Spleen
Pancreas (body)
Entrance to early epiploic foramen
Expanding greater omentum

Fig. 21.7 A–C, Stages of development of the subdiaphragmatic foregut and the right and left pericardioperitoneal/pleuroperitoneal canals, with particular reference to the terminal oesophagus, stomach, duodenum, spleen, the lesser sac of the peritoneum and the omenta, seen in semicoronal section (left column) and transverse section at the levels indicated by the arrows (right column). **D–E**, The lesser sac and dorsal and ventral mesogastria.

increase in the endodermal tube radius and matched growth of the mesentery; tight gut coils result from an increase in differential growth, i.e. lengthening of the endodermal epithelium and surrounding mesenchyme with reduction in the elongation of the dorsal mesentery (Nerurkar et al 2017).

The mechanisms of midgut gut and dorsal mesentery protrusion from the developing abdomen, and the subsequent return and specific disposition of the gut in the abdominal cavity into regions termed intra-abdominal and retroperitoneal, does not align with observed adult pathology, and has led to a re-examination of the processes involved (Dodds et al 1986). Dodds et al (1986) suggested that the midgut could be conceptualized as a retroperitoneal organ, similar to the mesonephroi and gonads, regardless of how far its linear elongation and that of the dorsal mesentery changed its relative position. The process of fusion of specific apposed peritoneal surfaces, when part or the whole of the mesentery lies against the dorsal parietal peritoneum, has also been challenged (Dodds et al 1986, Coffey et al 2016, Haaga and Di Lorenzo 2017).

The proliferating coelomic walls undergo differential determination according to their position to become a mesothelium. Mesothelial cells mostly differentiate into simple squamous cells, however in a few specific places more complex phenotypes are seen. Cuboidal cells covering the respiratory diaphragm form specialized mesothelial:lymphatic endothelial units, with lacunae (about 120 μm wide) and smaller stomata (20 μm in size). These enable particulate matter (equivalent to the stomata size) to be absorbed from the supramesocolic compartment. Mesothelial cells express cytokines and may have an antigen presentation function (Isaza-Restrepo et al 2018). Although pleural mesothelia are described as simple squamous cells, they display stomata on their pleural surface, but at less density than on the peritoneal side. This difference between the mesothelial cells either side of the respiratory diaphragm may permit peritoneal fluid to enter the pleural space, whereas passage from the pleural space to the peritoneum does not occur (Haaga and Di Lorenzo 2017). This might be the reason for some cases of right-sided hydrothorax in patients undergoing peritoneal dialysis (identified by pleural fluid high glucose levels), although other causes have been suggested, including small diaphragmatic herniae, unspecified pleuroperitoneal communication, and remnants of the pneumatoenteric recess and the infracardiac bursa (Gagnon and Daniels 2004).

Mesenteries of the developing gut

The alimentary tube, from the respiratory diaphragm to the start of the rectum, initially possesses a sagittal dorsal mesentery. Its line of continuity with the dorsal parietal peritoneum (i.e. its 'root' or 'line of reflection') is, initially, also midline. Although all of the gut and its derived glands are associated with mesenteries, the nomenclature for some portions of the gut and glands is different. Thus, the mesenteries of the stomach (initially termed mesogastria) are called omenta and the reflections of peritoneum around the liver, which develop from a confluence of splanchnopleuric, somatopleuric and septum transversum-derived portions, are called ligaments.

The movements of the developing viscera within the peritoneal cavity occur with associated movements of the mesothelia that surround them. The descriptions of peritoneal cavity development that follow are thus describing a sequence of changes that affect a complex space and its boundaries.

Foregut mesenteries

The cervicothoracic oesophagus develops between the pericardioperitoneal canals. It is encased in prevertebral, retrotracheal and retrocardiac mesenchyme. As the pericardioperitoneal canals expand with the developing lung buds, and the respiratory diaphragm forms immediately below them, the oesophagus has no true dorsal or ventral mesentery at this level. At superior and intermediate thoracic levels, parts of the lateral aspects of the oesophagus are closely related to the secondary, mediastinal, parietal pleura. In the lower thorax, the oesophagus inclines ventrally. The dorsocaudally sloping midline mesenchyme between oesophageal and aortic orifices may be homologized with part of a dorsal meso-oesophagus, and is used in that context in descriptions of respiratory diaphragmatic development. A ventral midline mesenchymal region may also be considered to be a derivative of a ventral meso-oesophagus; however, this region is more usually thought of as septum transversum.

From the respiratory diaphragm to the future hepatopancreatic duodenal papilla, the abdominal foregut has a ventral mesentery. This extends from the ventrolateral margins of the abdominal oesophagus and as yet 'unrotated' primitive stomach and proximal duodenum, cranially to the future respiratory diaphragm and ventrally to the ventral abdominal wall at the level of the cranial rim of the umbilical cord. Caudally, between umbilicus and duodenum, it presents a crescentic free border (Figs 21.5–21.6).

The ventral and dorsal foregut mesenteries are relatively extensive compared with the slender endodermal tubes they encase. The endodermal epithelium of the stomach and duodenum does not rotate relative to its investing mesenchyme. The rotation includes the coelomic epithelial walls of the pericardioperitoneal canals, and dorsally where these layers come together, the elongating dorsal mesogastrium and the much shorter dorsal mesoduodenum. A ventral mesogastrium can be seen when the distance between the stomach and liver increases.

Consequences of rotation of the stomach

A number of processes occur concurrently, which, conceptually, can be visualized as the movement of the right pleuroperitoneal canal to a position posterior to the stomach, such that its communication with the remainder of the peritoneal cavity is reduced. These processes include the differential growth of the walls of the stomach, the formation and specific local extension of the omenta (dorsal and ventral mesogastria), and the growth of the liver and, particularly, of the vessels and ducts that enter and leave the liver.

Whereas the dorsal mesogastrium takes origin from the posterior body wall in the midline, its connection to the greater curvature of the stomach, which lengthens as the stomach grows, becomes directed to the left as the stomach undergoes its first rotation. With the second rotation, a portion of the dorsal mesogastrium now faces caudally (see Fig. 21.6). The ventral mesogastrium remains as a double layer of coelomic epithelium, which encloses mesenchyme and forms the lesser omentum (see Fig. 21.7).

These developments permit stomach expansion both anteriorly and posteriorly when food is ingested, and free movement of peristalsis. The right pleuroperitoneal canal forms a discrete region of the peritoneal cavity, the lesser sac and the remaining left pleuroperitoneal canal and the remainder of the peritoneal cavity form the greater sac. The entrance to the original right pleuroperitoneal canal (lesser sac) becomes reduced in size. It is called the epiploic foramen, foramen of Winslow, or the aditus of the omental bursa (bursa omentalis).

Early stages of lesser sac development

The lesser sac is first indicated by the appearance of multiple clefts in the para-oesophageal mesenchyme on both left and right aspects of the oesophagus. Although they may become confluent, the left clefts are transitory and soon atrophy. The right clefts merge to form the right pneumatoenteric recess that extends from the oesophageal end of the lesser curvature of the stomach as far as the caudal aspect of the right lung bud. At its gastric end, it communicates with the general peritoneal cavity and lies ventrolateral to the gut, while more rostrally it lies directly lateral to the oesophagus. It is not, as commonly stated, a simple progressive excavation of the right side of the dorsal mesogastrium. The right pneumatoenteric recess undergoes further extension, subdivision and modification (see Fig. 21.7A(i), B(i)). From its caudal end, a second process of cleft and cavity formation occurs, which produces the hepatoenteric recess. This thins and expands the splanchnopleure between the liver and the stomach and proximal duodenum, and reaches the respiratory diaphragm (see Fig. 21.7A(i), C(i)). The resulting mesenteric sheet is the lesser omentum. It is derived, cranially to caudally, from the small meso-oesophagus; the much larger ventral mesogastrium, and the most caudal free border is from the ventral mesoduodenum. As differential growth of the duodenum occurs, the biliary duct is repositioned and the duodenum is sessile. The duodenal attachment of the free border and a continuous neighbouring strip of the lesser omentum become confined to the upper border of a short segment of its superior part. The contrasting growth and positioning of its attached viscera cause the free border to change gradually from the horizontal to the vertical. It carries the bile duct, portal vein and hepatic artery, and its hepatic end is reflected around the porta hepatis. An alternative name for this part of the lesser omentum is the hepatoduodenal ligament; it forms the anterior wall of the epiploic foramen. The floor of the foramen is the initial segment of the superior part of the duodenum, its posterior wall is the peritoneum covering the immediately subhepatic part of the inferior vena cava, and its roof the caudate process of the liver. The major part of the lesser omentum from the lesser gastric curvature passes in an approximately coronal plane to reach the floor of the increasingly deep groove for the ductus venosus on the hepatic dorsum; this part is sometimes called the hepatogastric ligament.

Ligaments of the liver

The liver appears precociously large during development. Thus, the liver mass projects into the abdominal cavity with equal growth on the two sides of the peritoneal cavity. The ligaments associated with the liver develop from the ventral mesogastrium, which passes from the foregut to the ventral abdominal wall, down to the cranial rim of the intestinal portal, and from the reflections of peritoneum from the liver to the respiratory diaphragm.

The medial portions of the proliferating coelomic epithelial walls producing splanchnopleuric mesenchyme, plus the septum transversum mesenchyme and developing liver, constitute the early ventral mesogastrium (see Fig. 21.5). The mesenchyme between these layers is continuous superiorly with the septum transversum mesenchyme of the future respiratory diaphragm. The coelomic epithelial layers of the ventral mesogastrium almost touch ventrally and dorsally to the liver, and are separated by a slender layer of mesenchyme. They form the falciform ligament and the lesser omentum, respectively, and where they are in contact with the liver directly, they form visceral peritoneum (see Fig. 21.7D).

When the respiratory diaphragm is formed above the liver (Ch. 20), local cavities coalesce and open into the general coelomic cavity as extensions of the greater and lesser sacs. In this way, almost all the ventrosuperior, visceral and some of the posterior aspects of the liver become peritonealized. The process of extending the greater sac continues over the right lobe and stops when the future superior and inferior layers of the coronary ligament and the right triangular ligament are defined. Those, plus a medial boundary provided by an extension of the lesser sac, enclose the 'bare area' of the liver, where loose areolar tissue of septum transversum origin persists. Later in development, the left lobe becomes relatively smaller than the right, and this presumably accounts for the smaller size of the left triangular ligament.

Where the superior layers of the coronary and left triangular ligaments meet, they continue as a (trilaminar) ventral mesentery attached to the ventrosuperior aspects of the liver. The somewhat arched umbilicohepatic free caudal border carries the left umbilical vein. As the ventral body wall develops, this falciform ligament, which initially attaches to the early cranial intestinal portal, is drawn to the diminishing cranial rim of the umbilicus. It may be considered as the final ventral part of the ventral mesogastrium, although its free border has a ventral mesoduodenal origin. Its passage to the ventral body wall becomes increasingly oblique, curved and falciform as the umbilicus becomes more defined.

In the early embryo, the connection between the pericardioperitoneal canals is directly across the ventral surface of the cranial midgut, immediately caudal to the developing primitive ventral mesogastrium (see Fig. 21.1). By stage 14 passage from one side of the falciform ligament to the other means passing either below the greatly enlarged liver, or the curved lower edge of the falciform ligament, or the lesser omentum. The position of the falciform ligament is of clinical interest in the neonate in diagnosing pneumoperitoneum because it is silhouetted by air on abdominal X-rays.

Caval fold

The caval fold is a developing linear eminence, protruding from the dorsal wall of the pleuroperitoneal canal, produced bilaterally by morphological changes in the position of the common cardinal veins, the horns of the sinus venosus, and formation of the rostral portions of the vena cava (Ch. 13). It has divergent rostral and caudal ends. Rostrally, it becomes continuous lateromedially with the root of the developing lung bud and pleural coelom, the uppermost portion of the septum transversum mesenchyme, and the retrocardiac mediastinal mesenchyme. Caudally, it forms an arch with dorsal and ventral horns. The dorsal horn merges with the primitive dorsal mesentery of the developing heart and the mesonephric ridge and associated gonad and suprarenal (adrenal) glands developing on the dorsal walls of the intraembryonic coelom. The ventral horn is confluent with the dorsal surface of the septum transversum mesenchyme.

Thus, the caval fold is a zone where intestinal, mesenteric, intermediate, hepatic, pericardial, pulmonary and mediastinal mesenchymes meet and blend. It provides a mesenchymal route for the upper abdominal, transdiaphragmatic and transpericardial parts of the inferior vena cava, and it is also prominent in the development of parts of the liver, the lesser sac of peritoneum, and certain mesenteries. The left fold regresses whereas the right fold enlarges rapidly (see Fig. 21.7A(i), A(ii)).

The pneumatoenteric recess continues to expand to the right into the substance of the caval fold. It stops near the left margin of the hepatic part of the inferior vena cava, which remains extraperitoneal and crosses the base of the now roughly triangular bare area of the liver and this new expanded line of reflection. With closure of the pleuroperitoneal canals, the rostral part of the right pneumatoenteric recess is sequestered by the respiratory diaphragm but often persists as a small serous sac in the right pulmonary ligament. The remaining caval fold mesenchyme to the left of the inferior vena cava – which forms the right wall of the upper part of the lesser sac – becomes completely invaded by embryonic hepatic tissue and is transformed into the caudate lobe of the liver. This smooth, vertically elongated mass projects into the cavity of the lesser sac; both its posterior and much of its anterior surfaces become peritonealized as a result of the increasing depth of the groove for the ductus venosus and the attachment of the lesser omentum to its floor.

Later stages of lesser sac development

The lower (inferior) part of the lesser sac can be first seen in stage 15 embryos; the early pneumatoenteric and hepatoenteric recesses are well established. Progressive differential gastric growth produces an elliptical transverse sectional profile, with a right-sided lesser curvature, which corresponds to the original ventral border of the gastric tube. The lesser omental gastric part of the ventral mesogastrium remains attached to this border. The greater curvature of the stomach is a new, rapidly expanding, region; its convex profile projects mainly to the left, but also cranially and caudally (see Fig. 21.7A(i), B(i), C(i)). The original dorsal border of the gastric tube now traverses the dorsal aspect of the expanding rudiment, curving along a line near the lesser curvature. The primitive dorsal mesogastrium is transiently attached to it, and blends with the thick layer of compound gastric mesenchyme clothing the posterior aspect and greater curvature of the miniature stomach. Because of its thickness, the mesenchyme projects rostrally, caudally and, particularly, to the left, beyond the 'new' greater curvature of the endodermal lining of the stomach.

The processes already described in relation to the ventral mesenteries now supervene. Multiple clefts appear at various loci in the mesenchyme, with local mesenchymal to epithelial transition. The groups of clefts rapidly coalesce to form transiently isolated closed spaces, which soon join with each other and with the preformed upper part of the lesser sac; the newly formed epithelia join the coelomic epithelium. In sequence, the initial loci occur in the compound posterior gastric mesenchyme nearer the lesser curvature and along its zone of blending with the primitive dorsal mesogastrium; in the dorsal mesoduodenum; and independently, in the caudal rim, where greater curvature mesenchyme and dorsal mesogastrium blend. As these cavities become confluent and their 'reniform' expansion follows, matches and then exceeds that of the gastric greater curvature, there are several major sequelae. The primitive dorsal mesogastrium increases in area by intrinsic growth, and, as cavitation proceeds, by incorporating substantial contributions from the dorsal lamella separated by cleavage of the posterior gastric mesenchyme. It becomes the secondary dorsal mesogastrium and its gastric attachment changes progressively (see Fig. 21.7A(ii)). It may be regarded as a set of somewhat spiral lines, longitudinally disposed, that move with time to the left, from near the lesser curvature, towards and finally reaching the definitive greater curvature. The parietal mesogastrial and (cleaving) mesoduodenal attachments remain in the dorsal midline for a time, but they later undergo profound changes. With the confluence of the cavities that collectively form the lower part of the lesser sac, its communication with the upper part (which corresponds to the lesser gastric curvature and right and left gastropancreatic folds) becomes better defined. Ventral to the lower part of the cavity, post-cleavage splanchnopleure covers the posteroinferior surface of the stomach and a short proximal segment of the duodenum. This ventral wall is continued beyond the greater curvature and duodenum as the splanchnopleuric strip of visceral attachment of the secondary dorsal mesogastrium and mesoduodenum. The radial width of the strip is relatively short cranially (gastric fundus) and gradually increases along the descending left part of the greater curvature. It is longest throughout the remaining perimeter of the greater curvature as far as the duodenum; this prominent part shows continued marginal (caudoventral and lateral) growth with extended internal cavitation (its walls constitute the expanding greater omentum; see Fig. 21.6H). The margins of the cavity of the inferior part of the lesser sac are limited by the reflexed edges of the ventrally placed strata derived from the secondary dorsal mesogastrium just described. These converge to form the splanchnopleuric dorsal wall, which is initially 'free' throughout, except at its midline dorsal root. At roughly mid-gastric levels, the pancreatic rudiment grows obliquely encased in this dorsal wall; its tail ultimately reaches the left limit of the lesser sac at the level of the junction between gastric fundus and body (see Fig. 21.7C(ii)).

Greater omentum

The greater omentum continues to grow, both laterally and, particularly, caudoventrally. It covers and is closely applied to the transverse mesocolon, transverse colon and inframesocolic and infracolic coils of small intestine (see Fig. 21.6D–G). At this stage, the quadrilaminar nature of the dependent part of the greater omentum is most easily appreciated. Mesenteries may be considered trilaminar: they possess two mesothelial surfaces derived from splanchnopleuric coelomic epithelium 'sandwiching' splanchnopleuric mesenchyme between them. In the greater omentum, the gastric serosa covering its posteroinferior surface (single mesothelium) and the anterosuperior serosa (single mesothelium) converge to meet at the greater curvature and initial segment of the duodenum, with intervening mesenchyme. The resulting mesentery continues caudoventrally as the 'descending' trilaminar stratum of the omentum. This, on reaching the omental margins, is reflexed and now passes craniodorsally to its parietal root as the 'ascending' posterior, trilaminar stratum. The descending and ascending layers are, initially, in fairly close contact caudally, but are separated by a fine, fluid-containing, cleft-like extension of the lower part of the lesser sac. The posterior mesothelium of the posterior stratum makes equally close contact with the anterosuperior surface of the transverse colon, starting at the taenia omentalis, and with its transverse mesocolon.

Maturation of the lesser sac

At this stage, and subsequently, it is convenient to designate the lower part of the lesser sac as consisting of three subregions: retrogastric, perigastric and greater omental (see Fig. 21.7C(ii)). The names are self-explanatory but their confines are all modified by various factors. Two phenomena are particularly prominent: namely, gastric 'descent' relative to the liver, and adherence of peritoneal layers ultimately giving altered lines of reflection, and loss of parts of cavities.

After the first trimester, hepatic growth, particularly of the left lobe, diminishes and the whole organ fits into the upper region of the enlarging abdomen. Meanwhile, the stomach elongates and some descent occurs, despite its relatively fixed cranial and caudal ends. This produces the angular flexure of the stomach, that persists postnatally. The concavity of the lesser curvature is now directed more precisely to the right, and the lesser omentum is more exactly coronal and its free border vertical. Ventral to the liver, the free border of the falciform ligament passes steeply craniodorsally from umbilicus to liver (see disposition in the neonate in Figs 23.14 and 23.15A, D).

The mesenchymal dorsal wall of the lower part of the lesser sac has, up to this point, retained its original dorsal midline root. The mesenchymal cores of the mesenteries become thinner, and are termed fascial sheaths and septa. Overlying areas of mesentery then adhere to the original dorsal coelomic wall, by ways as yet unknown. Where sheets adhere, they remain surgically separable and no vascular anastomoses develop across the interzone.

Above the pancreas, the original left leaf of the dorsal mesoduodenum and greater omentum becomes closely applied to the original left dorsal coelomic wall covering the lower parts of the respiratory diaphragm, much of the left suprarenal gland, the ventromedial part of the upper pole of the left kidney, the initial part of the abdominal aorta, the coeliac trunk and its branches, and other vessels, nerves and lymphatics. Their peritoneal surfaces adhere.

This process is repeated at the level of the developing pancreas which is now extending into the layers of the dorsal mesoduodenum and greater omentum. As the pancreas grows dorsally, and then to the left as the mesenteries themselves move, the whole surface of the pancreas is covered by splanchnopleuric mesenchyme and developing peritoneum, except where peritoneal lines of reflection exist. The left leaf of the dorsal mesoduodenum/greater omentum becomes closely applied and adheres to the left dorsal coelomic wall covering all the posterior abdominal wall structures it crosses, but at a lower level than that described above, i.e. inferior vena cava, abdominal aorta, splenic vein, superior mesenteric vessels, inferior mesenteric vein, portal vein, left renal vessels, the caudal pole of the left suprarenal gland, a broad ventral band on the left kidney and developing muscles of the dorsal abdominal wall (see Fig. 21.7A(ii), B(ii), C(ii)). The pancreas is now sessile. The original right leaf of the dorsal mesoduodenum/greater omentum becomes the peritoneum covering the upper left part of its head, neck and the anterosuperior part of the pancreatic body forms the central part of the dorsal wall of the lesser sac. The pancreatic tail remains peritonealized by a persisting part of the secondary dorsal mesogastrium as it curves from the ventral aspect of the left kidney towards the hilum of the spleen. The infracolic parts of the pancreas are covered with greater sac peritoneum. In the greater omental subregion of the lower part of the lesser sac, two contrasting forms of mesenteric adhesion occur. The posterior 'returning' stratum of the omentum undergoes partial adhesion with the peritoneum of the transverse colon at the taenia omentalis and with its mesocolon. The layers remain surgically separable; no anastomosis occurs between omental and colic vessels.

The original dorsal midline attachment of the foregut dorsal mesentery is profoundly altered during the development of the lesser sac and its associated viscera. However, despite the extensive areas of adhesion, virtually the whole of the gastric greater curvature (other than a small suboesophageal area) and its topographical continuation (the inferior border of the first 2–3 cm of the duodenum) retain true mesenteric derivatives of the secondary dorsal mesogastrium and its continuation, the dorsal mesoduodenum. Although regional names are used to assist identification and description, it is important to emphasize that they are all merely subregions of one continuous sheet.

The upper (oesophagophrenic) part of the lesser omentum arches across the respiratory diaphragm. As this mesentery approaches the oesophageal hiatus, its epithelial laminae diverge, skirting the margins of the hiatus. They then descend for a limited distance and with variable inclination, to enclose reciprocally shaped areas on the dorsum of the gastric fundus and respiratory diaphragm. The area may be roughly triangular to quadrangular. It contains mesenchyme that becomes areolar tissue, and constitutes the bare area of the stomach or, when large, the left extraperitoneal space. Its right lower angle is the base of the left gastropancreatic fold, and its left lower angle reconstitutes the mesentery. The root of the latter arches downwards and to the left across the respiratory diaphragm and suprarenal gland, and gives the gastrophrenic ligament to the gastric fundus. It continues to arch across the ventral surface of the upper part of the left kidney, and its layers part to receive the pancreatic tail; they initially extend to the hilum of the spleen as the splenorenal ligament (see Figs 21.6C, 21.7D). The left half of this trilaminar 'ligament' provides an almost complete mesenchymal and peritoneal tunic for the developing spleen. It then reunites with its fellow at the opposite rim of the splenic hilum, and continues to the next part of the gastric greater curvature as the gastrosplenic ligament. The remaining part (perhaps two-thirds) of the gastric greater curvature and its short duodenal extension provide attachment for the anterior, 'descending', stratum of the greater omentum. Its returning, posterior, stratum continues to its parietal root (which extends from the inferior limit assigned to the splenorenal ligament), and curves caudally and to the right along the anterior border of the body of the pancreas, immediately cranial to the line of attachment of the transverse mesocolon. Crossing the neck of the pancreas, the same curve is followed for a few centimetres on to its head, the omental root then sharply recurves cranially and to the left, to reach the inferior border of the duodenum. Thus it reaches that part of the lesser sac provided by cleavage of the dorsal mesoduodenum from the greater sac. It enters the epiploic foramen, traverses the epiploic canal between the caudate hepatic process and proximal duodenum, then crosses the right gastropancreatic fold, and descends behind the proximal duodenum to enter the right marginal strip enclosed by the greater omentum.

Peritoneum associated with the midgut loop and hindgut

The midgut and hindgut have no ventral mesentery; thus, the early pleural and supra-umbilical peritoneal cavities are, initially and transiently, bilaterally symmetric above the umbilicus. Below the umbilicus, the peritoneal cavity is freely continuous across the midline ventral to the gut (see Fig. 21.5A). It is convenient to consider the mesenteries of the small and large intestine after rotation when the principal growth patterns have been achieved, and the developing pancreas is sessile. Studies of the adult parietal peritoneum, driven by surgical resection of the mesocolon, have led to the view that apposed layers of developing peritoneum adhere in some manner rather than involute dorsally, and that the final differentiation of the dorsal mesentery is of an organ in its own right, continuous from the duodenojejunal flexure to the mesorectum, as it is in the embryo (Dodds et al 1986, Sehgal and Coffey 2014, Byrnes et al 2019). The trilaminar layer of the dorsal mesentery is highlighted by consideration of the intermesenteric space; this refers to the early splanchopleuric mesenchymal layer which transmits autonomic nerves, blood and lymphatic vessels to the gut. Dodds et al (1986) considered that the endodermal epithelial gut was also part of the intermesenteric domain and could be regarded as an extraperitoneal structure. Communication between intermesenteric and the original retroperitoneal mesenchyme is via aortic and caval vessels which supply both regions. Histological examination of regions of mesenteric adhesion has shown, as predicted by Toldt in the nineteenth century, that the original (visceral) left side of the mesentery is joined to the dorsal parietal coelomic wall with a layer termed Toldt's fascia intervening (Coffey et al 2016). These sites have been termed fascial planes (Sehgal and Coffey 2014).

Although understanding the movements and sites of adhesion of the midgut dorsal mesentery is challenging, adding this to earlier, ventral layering of the dorsal mesoduodenum and greater omentum as the pancreas develops, is particularly thought-provoking. However, it does explain the many previously described retroperitoneal planes. The compartments of the retroperitoneum and the final position of the dorsal mesentery of the midgut in the infracolic compartments and the regions of adult parietal peritoneal reflection, are described in Chapters 61 and 62. In the infracolic regions, three original layers of coelomic wall form the peritoneum medial to the ascending and descending colon: the original right and left dorsal coelomic walls and both layers of the mesocolon after its rotation and final disposition. The original right leaf of the mesocolon adheres to the original dorsal coelomic walls, with Toldt's fascia intervening; the left leaf of the mesocolon is uppermost and faces the peritoneal cavity.

Mesenteric relative movements at the junction of the distal end of the foregut and beginning of the midgut are more complex and the exact fate of the overlying layers is not known. The layers over the part of the duodenum facing the lesser sac are: the left dorsal coelomic wall which adheres to the left leaf of the dorsal mesoduodenum/greater omentum; the right leaf of the dorsal mesoduodenum/greater omentum which becomes the peritoneum covering central dorsal wall of the lesser sac, covering the upper left part of its head, neck and the anterosuperior part of the body of the pancreas. The layers over the lower parts of the duodenum are more complex. The dorsal mesoduodenal layers are covered with portions of peritoneum facing the right infracolic compartment, so are part of the midgut mesocolon. Dodds et al (1986) described the layers in this region, from dorsal to ventral, as primary left dorsal peritoneum; fused leaves of the right mesoduodenum with the pancreas in the so-called pancreaticoduodenal space; left leaf mesoduodenum; right leaf mesocolon; left leaf mesocolon. The importance of understanding these early mesenteric movements was predicted some years ago and they are now informing surgical approaches to gut resection, especially in complete mesocolic excision for colon cancer (Coffey et al 2015, Zhu et al 2016). However, over the years many different terms have been applied to these epithelial and mesenchyme tissues and their final juxtapositions. Hopefully the most pertinent terms will be retained and used and eventually correlated to histological studies on the mechanisms of mesothelial adherence (Lian et al 2019).

Small intestine

Most of the duodenal loop encircles the head of the pancreas and is sessile with peritoneum noted covering its ventral and convex aspects. Areas not covered are a short initial segment of the superior (first) part, which is more completely peritonealized because it gives attachment to the right margins of the greater and lesser omenta; the sites where the transverse colon is closely apposed to the descending (second) part, or where the latter is crossed by the root of the transverse mesocolon; and the sites where the mesentery crosses the transverse (third) part, and descends across the ascending (fourth) part from its upper extremity at the duodenojejunal flexure.

From a mesenteric standpoint, the succeeding small intestine, from the duodenojejunal flexure to the ileocaecal junction, undergoes less modification of its embryonic form than other gut regions. Its early dorsal mesentery is a continuous, single (but structurally trilaminar) sheet, with a midline dorsal attachment (line of reflection) that becomes an oblique narrow band from the left aspect of the second lumbar vertebra to the cranial aspect of the right sacroiliac joint.

Ascending colon

The caecum and vermiform appendix arise as a diverticulum from the antimesenteric border of the caudal limb of the midgut loop and consequently the caecum does not possess a primitive mesocaecum. These regions of the gut undergo long periods of growth, often asymmetric, and their final positions, dimensions and general topography show considerable variation. The vermiform appendix is almost wholly clothed with visceral peritoneum, derived from the diverging layers of its rather diminutive mesoappendix. The latter should perhaps be regarded as a direct derivative of the primitive dorsal mesentery, and a similar status for the vascular fold of the caecum should be considered.

The colonic gut retains its primitive dorsal mesentery, the mesocolon, until the differential growth, rotation and circumabdominal displacement of this part of the gut nears completion. Its original root is still vertical in the dorsal midline, although the mesocolon diverges from it widely as an incomplete, flattened pyramid, to reach its colonic border at the future taenia mesocolica. During postmenstrual weeks 16–20, substantial areas of the primitive mesocolon adhere to the dorsal coelomic wall. In this way, some colonic segments become sessile while others have a shorter mesocolon with an often profoundly altered parietal line of attachment. The mesocolon of the transverse and sigmoid segments normally persists, while the ascending colon, right (hepatic) flexure and descending colon become sessile; the ascending or descending, or both, colonic segments may also retain a mesocolon, which varies from a localized 'fold' to a complete mesocolon. When sessile, the ventral, medial and lateral aspects of the ascending or descending colon are clothed with peritoneum, and the protrusion of the viscus produces medial and lateral peritoneal paracolic gutters on each side. This form of apposition to underlying structures proceeds from the ascending colon to include the right colic (hepatic) flexure, and from there it continues ventro-inferiorly to the left, so involving the right-sided initial segment of the transverse colon.

Transverse colon

The right extremity of the transverse colon is sessile, and is separated by fibro-areolar tissue from the ventral aspect of the descending (second) part of the duodenum and the corresponding aspect of most of the head of the pancreas. The remainder of the transverse colon, up to and including the left (splenic) colic flexure, is almost completely peritonealized by the diverging layers of the transverse mesocolon. The root of the latter reaches the neck and whole extent of the ventral border of the body of the pancreas. The long axis of the definitive pancreas lies obliquely. The splenic colonic flexure is considerably more rostral than the hepatic flexure and, consequently, the root of the mesocolon curves obliquely upwards as it crosses the upper abdomen from right to left. As it expands, the posteroinferior (descending) wall of the greater omental part of the lesser sac gradually covers, and then adheres to the transverse mesocolon and its contained colon, finally projecting beyond the latter. Craniocaudal adhesion now occurs between the omental wall and the pericolonic and mesocolonic layers.

Descending colon

The left colic flexure receives much of its peritoneal covering from the left extremity of the transverse mesocolon. It is also often connected to the parietal peritoneum of the respiratory diaphragm over the 10th and 11th ribs by a phrenicocolic ligament. The latter sometimes blends with a presplenic fold that radiates from the gastrosplenic ligament. The descending colon becomes sessile. The process of adhesion of both ascending and descending mesocolons starts laterally and progresses medially.

Sigmoid colon

The sigmoid colon is most variable in its length and disposition. It retains its dorsal mesocolon, but the initial midline dorsal attachment of its root is considerably modified in its definitive state.

Rectum

The rectum develops from the dorsal region of the early cloaca. The urorectal septum, a localized region of proliferating coelomic epithelium and underlying mesenchyme grows caudally towards the cloacal membrane, and concomitantly enlarges the intraembryonic coelom in a caudal direction (see Figs 21.1, 22.4). By stage 15 the cloaca is divided into enteric hindgut and urogenital sinus, and the cloacal membrane is divided into urogenital and anal parts (Ch. 22). Urorectal septal growth generates different populations of splanchnopleuric mesenchyme that contribute to the lower portions of the enteric hindgut and urethra. The overlying coelomic epithelium covers the dorsal and ventral borders of an extending peritoneal pouch until, at stages 18–20, the caudal region, where these layers are confluent, approaches mesenchyme surrounding the developing levator ani muscle. After this time the lower part of the pouch is found just caudal to the insertion of the mesonephric ducts into the urogenital sinus; segmental levels 31–32 (S2–S3). Between stages 20–23, mesenchymal proliferation increases above the levator ani muscle, and from about 11 postmenstrual weeks onwards the deepest point of the prerectal peritoneal pouch is located in the plane through S3 and the symphysis pubis (Kruepunga et al 2018). The reflection of the peritoneum in female and male neonates is shown in Figs 22.9–22.10. The proximal third of the rectum is covered by peritoneum ventrolaterally, the middle third only on its ventral surface, where it forms the posterior wall of the rectovesical or rectouterine pouch. The remaining rectum and anal canal are extraperitoneal.

Dorsal to the rectum the early splanchnopleuric mesenchyme is sometimes called the dorsal mesorectum, but this is a misnomer. With progressive skeletal development, it is reduced to a woven fibroareolar sheet that displays patterned variations in thickness and fibre orientation. The sheet is closely applied to the ventral concavity of the sacrum and coccyx, and encloses numerous fibromuscular and neurovascular elements.

The interactions between the tissue populations in this caudal body region have not yet been elucidated. Apposition and fusion of the coelomic walls between the developing rectum and urinary bladder and urethra had been suggested to account for the surgically separable fibrous stratum between these structures. However, Silver (1952) concluded that there was no direct evidence that the peritoneum contributed to the rectovesical septum in male fetuses, a view supported by Kraima et al (2015). It is likely that the patterning of the uroseptum mesenchyme is complex; this cell population is involved in interactions with ectodermal and endodermal epithelia, and the development of the external genitalia and external sphincters, which derive from the ventral muscle mass which initially migrates into the lower limb and then returns to the perineal region (Valasek et al 2005). Histological examination of rectogenital mesenchyme in fetuses from 10 to 37 postmenstrual weeks shows development of condensations of collagen, longitudinal smooth muscle and parasympathetic and sensory nerve fibres; a role in the sensory input from local sphincters is suggested (Aigner et al 2014, Kraima et al 2015). The rectogenital mesenchyme is adherent to and continuous with the ventral mesorectal fascia in the fetus; this is suggested to be the site of a surgical plane in the adult, identified in total mesorectal excision (Heald 1988, 2013, Kraima et al 2015, Sahnan et al 2018).

Peritoneal cavity at birth

The fully formed peritoneal cavity, although complex topographically, remains a single cavity with numerous intercommunicating regions, pouches and recesses (see Fig. 23.14A–E). The only small peritoneal sacs to separate completely from the main cavity are the infracardiac bursa and the tunica vaginalis testis.

In fetal life, the cavity between the anterior descending and posterior ascending layers of the greater omentum extend to the internal aspect of the caudal and lateral edges of the omentum. Postnatally, a slow but progressive adhesion of the internal surfaces occurs, with obliteration of the most dependent part of the cavity; this proceeds rostrally and, when mature, the cavity does not usually extend appreciably beyond the transverse colon. Adhesion between the posterior leaf of the greater omentum and the originally right, but now cranial leaf of the transverse mesocolon, is completed when the transverse colon attains its final position.

In the neonate, the peritoneal cavity is ovoid and fairly shallow from anterior to posterior, because the bilateral posterior extensions on each side of the vertebral column, which are prominent in the adult, are not present. Two factors lead to the protuberance of the anterior abdominal wall in the neonate and infant. The respiratory diaphragm is flatter in the newborn, which produces a caudal displacement of the viscera. The pelvic cavity is very small in the neonate, which means that organs that are normally pelvic in the adult, i.e. urinary bladder, ovaries and uterus, all extend superiorly into the abdomen (see Figs 22.9–22.10). The pelvic cavity is joined to the abdominal cavity at less of an acute angle in the neonate because there is no lumbar vertebral curve and only a slight sacral curve.

The peritoneal attachments are similar to the adult. However, the greater omentum is relatively small; its constituent layers of peritoneum may not be completely adherent, and it does not extend much below the level of the umbilicus. Generally, the relative length of the mesentery of the small intestine and of the transverse and sigmoid mesocolons is greater than in the adult, whereas the area of adherence of the ascending and descending colons is relatively smaller. The peritoneal mesenteries and omenta contain little fat.

SPLEEN

Although the spleen is not in any way related to enteric or overall mesenteric gut development, it develops within the layers of the dorsal mesogastrium. It appears during stages 15–17 as a localized thickening of the coelomic epithelium of the dorsal mesogastrium near its cranial end (see Figs 21.6–21.7). The proliferating cells invade the underlying angiogenic mesenchyme, which becomes condensed and vascularized. The process occurs simultaneously in several adjoining areas, that soon fuse to form a lobulated spleen of dual origin, i.e. from dorsal mesogastrium mesenchyme derived from the coelomic epithelium and from angiogenic mesenchyme derived from developing mesenteric blood vessels. Experimental studies in mouse embryos suggest that neural crest cells also invade the spleen via the splenic vessels and give rise to astrocyte-like glial cell populations (Barlow-Anacker et al 2017).

The splenic vascular reticulum is well developed by the end of stage 23 and contains numerous closely spaced, thin-walled, vascular loops and immature reticulocytes. From about 11 postfertilization weeks, the development of the spleen has been described in four stages: stage 0 has erythrocyte precursors, few macrophages and fewer lymphocytes; in stage I, lymphocytes begin colonization and arterial vascular lobules are seen; in stage II, T and B lymphocytes form periarteriolar clusters with B cells aggregated around the peripheral branches of splenic arterioles and T cells centrally; in stage III, before birth, the lobular arrangement is no longer discernible (Steiniger et al 2007). By postmenstrual weeks 15–16, lymphocytes have been found in the mesenteric lymph nodes, but far fewer than those found in the liver and spleen (Hwang et al 2014).

From postmenstrual week 17, α-SMA-positive reticulum cells are found around arterioles. These increase in number and form a reticular framework from 20–23 postmenstrual weeks, when a primitive white pulp can be observed around arterioles. By 24 postmenstrual weeks, T and B lymphocytes become segregated; T cells are found within the SMA-positive reticular framework, and B cells aggregate close to the periarticular lymphoid sheath, where they form lymphoid follicles (Satoh et al 2009).

Changes to the position of the developing spleen are driven by the expansion of the right pleuroperitoneal canal to the left, and the consequent lengthening of the dorsal mesogastrium and its movements caused by stomach rotation. The dorsal mesogastrium becomes the splenorenal ligament (from the dorsal abdominal wall to the spleen) and the gastrosplenic ligament (from the spleen to the stomach) (see Fig. 21.6). There is some adhesion between the original left dorsal coelomic wall and the left leaf of the dorsal mesogastrium, although this does not extend as far as the spleen. The earlier lobulated character of the spleen disappears, but is indicated by the presence of notches on its upper border in the adult.

At birth the spleen weighs, on average, 13 g. It doubles its weight in the first postnatal year and triples it by the end of the third year. The spleen displays various developmental anomalies, including complete agenesis, multiple spleens or polysplenia, isolated small additional spleniculi and persistent lobulation. Asplenia and polysplenia are associated with other anomalies, especially those involving the cardiac and pulmonary systems. For details of the anatomical variation of the spleen, see Varga et al (2018).

Ultrasound antenatal imaging of the fetal abdomen

The abdominal circumference, routinely estimated at 20 postmenstrual weeks, is calculated from the anteroposterior diameter and the transverse abdominal diameter perpendicular to it, taken at the widest part of the abdomen. The section usually includes one entire rib and the stomach cavity (termed stomach bubble) and can be confirmed on the left side of the body (see Fig. 23.5G). Anteriorly, the connection of the umbilical cord can be confirmed (see Fig. 23.5H). Anomalies of the anterior body wall, exomphalos and gastroschisis, are readily detected. In exomphalos, a mass of peritoneal organs herniate through the base of the umbilical ring; in gastroschisis, loops of small intestine and colon float free in the amniotic fluid (see Fig. 23.6B) (Ionescu et al 2014).

POSTNATAL DEVELOPMENT OF THE GUT

Available with the *Gray's Anatomy* e-book.

Key references

Guo P, Preuett B, Krishna P et al 2014 Barrier function of the coelomic epithelium in the developing pancreas. Mech Dev 134:67–79.

This paper presents the functions of the coelomic epithelium during development in the control of epithelial mesenchymal interactions.

Lebenthal E 1989 Concepts in gastrointestinal development. In: Lebenthal E (ed) Human Gastrointestinal Development. New York: Raven Press; Ch. 1.

This chapter is the first in a volume dedicated to the development of structure and function of the gut, liver and pancreas. It includes the development of the immunological surveillance mechanisms and gastrointestinal flora.

Lian J, Huang J, Chen T et al 2019 The Toldt fascia: a historic review and surgical implications in complete mesocolic excision for colon cancer. Asian J Surg 42:1–5.

This article considers the movements and adherence of the developing enteric mesentery.

Neu J (ed) 2012 Gastroenterology and Nutrition: Neonatology Questions and Controversies, 2nd ed. Philadelphia: Elsevier, Saunders.

This volume contains a comprehensive range of articles on the development and maturation of the gut.

Rao M, Gerson MD 2018 Enteric nervous system development: what could possibly go wrong? Nat Rev Neurosci 19:552–65.

A review of the genetic and environmental factors that may affect enteric nervous system development.

Soffers J, Hikspoors JPJM, Mekonen HK et al 2015 The growth pattern of the human intestine and its mesentery. Dev Biol 13:31. doi: 10.1186/s12861-015-0081-x.

This paper gives histological and 3D representations of the formation of the midgut loop.

Postnatal maturation of the gut is dependent on the establishment of an intestinal microbiota, which, in turn, is affected by term age, mode of delivery, type of feeding and any medical interventions. In cases of chorioamnionitis, preterm infants ingest bacterial products from the amniotic fluid: it has been suggested that this may be associated with preterm labour (Neu and Mai 2012). Chorioamnionitis is associated with an increased risk of necrotizing enterocolitis in preterm infants (Kallapur et al 2014). The prevalence of necrotizing enterocolitis is about 7% in infants delivered at 32 postmenstrual weeks with a birthweight between 500–1500 g. It develops after postnatal week 2, and is characterized by intestinal inflammation, systemic inflammatory response syndrome and multiorgan system failure. There is feeding intolerance, abdominal distention, and pneumatosis is seen on abdominal X-ray, showing intramural gas. It is thought to be caused by genetic predisposition, imbalanced microvascular tone, intestinal immaturity and abnormal microbial intestinal colonization (Sharma et al 2012).

Normal, term vaginal delivery establishes the initial colonization of the neonatal gut with maternal vaginal and intestinal flora. Two-way interactions between enteric microbes in a biofilm within the luminal glycocalyx of enterocytes modify intestinal permeability, increase T and B lymphocyte numbers within the mucosal lamina propria and mesenteric lymph nodes, and stimulate postnatal immune development (Martin et al 2012, Patel et al 2012, Vaarala 2012, Wynn and Neu 2012, Gritz and Bhandari 2015). Delivery by caesarean section results in the establishment of skin microbiota, different intestinal microbes and low microbiota diversity. Failure to develop an appropriate dynamic microbiota is thought to be associated with allergic and inflammatory conditions in later life (Wynn and Neu 2012). (For further reading, see Neu and Mai (2012), Bäckhed et al (2015), Rodríguez et al (2015), Dzidic et al 2018.)

The onset of feeding also contributes to gut maturity. Breast milk, considered an 'active fluid', is complex and unique, containing a range of growth factors, cytokines, chemokines and stem cells (Fanos et al 2017, Bardanzellu et al 2018). It also contains a range of breast-derived and blood derived cells which pass to the infant. Milk leukocyte composition is highest in colostrum and decreases in transition and mature milk; these maternal cells can move from the infant gut to lymph nodes, spleen and liver; an increase in breast milk leukocytes is seen when the infant has an infection, suggesting a dynamic interaction within the mother–infant dyad (Ch. 14, p. 233) (Witkowska-Zimny and Kaminska-El-Hassan 2017). Breast milk is a source of epidermal growth factor, which promotes postnatal mucosal development, helps mucosal repair, and affects the production of immunoglobulin A (IgA) in the gut mucosa (Vaarala 2012). Breast milk also contains a microbiome of about 50 different genera, contributing to the bacterial populations the neonate ingests during vaginal delivery. Sialylated human milk oligosaccharides can induce transcription responses in the intestinal microbiota, indicating the interactive nature of establishing the gut microbiome and gut maturation (Bardanzellu et al 2018). Breast feeding is associated with reduction in postnatal necrotizing enterocolitis and sepsis.

Undernutrition leads to villous atrophy: in the preterm infant, parenteral nutrition is associated with changes in intestinal structure and function that may lead to increased intestinal permeability. Antibiotic therapy within the neonatal period can lead to changes in, and the establishment of, the normal intestinal microbiota (Martin et al 2012). The normal pattern of microbiome formation is disrupted in children with undernutrition causing stunting. Human milk oligosaccharides are not absorbed in the proximal gut, but function as prebiotics for bacterial strains, enhancing gut barrier function and protecting against enteropathogen infection. Sialic acid-containing oligosaccharides are especially important for postnatal neural and musculoskeletal development: their levels are 20 times higher in human milk than bovine milk, suggesting that their use in formula milk supplementation would improve growth outcomes in undernourished infants and children (Charbonneau et al 2016).

The first passage of faeces of the newborn is termed meconium. This dark, sticky, viscid substance is formed from the passage of amniotic fluid, sloughed mucosal cells, digestive enzymes and bile salts along the fetal gut. Meconium becomes increasingly solid as gestation advances but does not usually pass out of the fetal body while *in utero*. Fetal distress produced by anoxia may induce the premature defecation of meconium into the amniotic fluid, with the risk of its inhalation. At birth, the colon contains 60–200 g of meconium. The majority of neonates defecate within the first 24 hours after birth. Delayed passage of stool beyond this time is associated with Hirschsprung's disease (see p. 334.e1) or imperforate anus. The normal passage of meconium continues for the first 2 or 3 days after birth, and is followed by a transition to faecal stools by postnatal day 7.

References

Aigner F, Zbar AP, Ludwikowski B et al 2014 The rectogenital septum: morphology, function, and clinical relevance. Dis Colon Rectum 47:131–40.

Ariza L, Carmona R, Cañete A et al 2016 Coelomic epithelium-derived cells in visceral morphogenesis. Dev Dyn 245:307–22.

Bäckhed F, Roswall J, Peng Y et al 2015 Dynamics and stabilization of the human gut microbiome during the first year of life. Cell Host Microbe 17:690–703.

Barlow-Anacker AJ, Fu M, Erickson CS et al 2017 Neural crest cells contribute an astrocyte-like glial population to the spleen. Sci Rep 7:45645. doi: 10.1038/srep45645.

Bardanzellu F, Fanos V, Strigini FAL et al 2018 Human breast milk: exploring the linking ring among emerging components. Front Pediatr 6:215. doi: 10.3389/fped.2018.00215.

Beckwitt CH, Clark AM, Wheeler S et al 2018 Liver 'organ on a chip'. Expt Cell Res 363:15–25.

Bradnock TJ, Walker GM 2011 Evolution in the management of Hirschsprung's disease in the UK and Ireland: a national survey of practice revisited. Pediatr Surg 93:34–8.

Burns AJ, Roberts RR, Bornstein JC et al 2009 Development of the enteric nervous system and its role in intestinal motility during fetal and early postnatal stages. Semin Pediatr Surg 18:196–205.

Byrnes LE, Wong DM, Subramaniam M et al 2018 Lineage dynamics of murine pancreatic development at single-cell resolution. Nat Commun 9:3922. doi: 10.1038/s41467-018-06176-3

Byrnes KG, Walsh S, Dockery P et al 2019 Anatomy of the mesentery: current understanding and mechanisms of attachment. Semin Cell Dev Biol 92:12–7.

Campbell KH, Copel JA, 2018 Gastroschisis. In: Copel JA, D'Alton ME, Feltovich H et al (eds) Obstetric Imaging: Fetal Diagnosis and Care, 2nd ed. Elsevier; Ch. 20, pp. 76–84.

Charbonneau MR, O'Donnell D, Blanton LV et al 2016 Sialylated milk oligosaccharides promote microbiota-dependent growth in models of infant undernutrition. Cell 164:859–71.

Chevalier NR, de Witt TM, Cornelissen AJM et al 2018 Mechanical tension drives elongational growth of embryonic gut. Sci Rep 8:5995. doi: 10.1038/s41598-018-24368-1.

Coffey JC, Dillon M, Sehgal R et al 2015 Mesenteric-based surgery exploits gastrointestinal, peritoneal, mesenteric and fascial continuity from duodenojejunal flexure to the anorectal junction – a review. Dig Surg 32:291–300.

Coffey JC, Culligan K, Walsh LG et al 2016 An appraisal of the computed axial tomographic appearance of the human mesentery based on mesenteric contiguity from the duodenojejunal flexure to the mesorectal level. Eur Radiol 26:714–21.

Collins P 2002a Embryology of the pancreas. In: Howard ER, Stringer MD, Colombani PM (eds) Surgery of the Liver, Bile Ducts and Pancreas in Children, Part 8. London: Arnold, pp. 479–92.

This chapter covers pancreatic morphogenesis, the timescale of development, the origin of pancreatic cell lines and factors that regulate pancreatic development.

Collins P 2002b Embryology of the liver and bile ducts. In: Howard ER, Stringer MD, Colombani PM (eds) Surgery of the Liver, Bile Ducts and Pancreas in Children, Part 3. London: Arnold, pp. 91–102.

This chapter covers morphogenesis of the liver and early hepatic circulation, the origin of hepatic cell lines and the development of the extra- and intrahepatic biliary systems.

Davenport M 2016 Biliary atresia: from Australia to the zebrafish. J Pediatr Surg 51:200–5.

Dodds WJ, Darweesh RMA, Lawson TL et al 1986 The retroperitoneal spaces revisited. Am J Radiol 147:1155–61.

Dzidic M, Boix-Amorós A, Selma-Royo M et al 2018 Gut microbiota and mucosal immunity in the neonate. Med Sci 6:56. doi: 10.3390/medsci6030056.

Fanos V, Pintus R, Reall A 2017 Miracles and mysteries of breast milk: from Egyptians to the 3 M's (metabolomics, microbiomics, multipotent stem cells). J Pediatr Neonat Individ Med 6:e060204. doi: 10.7363/060204.

Gagnon RF, Daniels E 2004 The persisting pneumatoenteric recess and the infracardiac bursa: possible role in the pathogenesis of right hydrothorax complicating peritoneal dialysis. Adv Perit Dial 20:132–6.

Gershon MD 2010 Developmental determinants of the independence and complexity of the enteric nervous system. Trends Neurosci 33:446–56.

This paper reviews the molecular basis of normal and defective enteric nervous system development.

Glebov OK, Rodriguez LM, Nakahara K et al 2003 Distinguishing right from left colon by the pattern of gene expression. Cancer Epidemiol Biomarkers Prev 12:755–62.

Gordillo M, Ev ans T, Gouon-Evans V 2015 Orchestrating liver development. Development 142:2094–108.

Gritz EC, Bhandari V 2015 The human neonatal gut microbiome: a brief review. Front Pediatr 3:17.

Grosse AS, Pressprich MF, Curley LB et al 2011 Cell dynamics in fetal intestinal epithelium: implications for intestinal growth and morphogenesis. Development 138:4423–32.

Guo P, Preuett B, Krishna P et al 2014 Barrier function of the coelomic epithelium in the developing pancreas. Mech Dev 134:67–79.

This paper presents the functions of the coelomic epithelium during development in the control of epithelial mesenchymal interactions.

Haaga JR, Di Lorenzo DR 2017 Peritoneum. In Haaga JR, Boll D (eds) CT and MRI of the whole body, 6th ed. Elsevier; Ch. 49, pp. 1558–604.

Hayes HL, Zhang L, Becker TC et al 2016 A Pdx-1 regulated soluble factor activates rat and human islet cell proliferation. Mol Cell Biol 36:2918–30.

Heald RJ 1988 The 'Holy Plane' of rectal surgery. J R Soc Med 81:503-8.

Heald RJ 2013 A new solution to some old problems: transanal TME. Tech Coloproctol 17:257–8.

Hikspoors JPJM, Peeters MMJP, Kruepunga N et al 2017 Human liver segments: role of cryptic liver lobes and vascular physiology in the development of liver veins and left-right asymmetry. Sci Reports 7:17109. doi:10.1038/s41598-017-16840-1.

Hikspoors JPJM, Kruepunga N, Mommen GMC et al 2019 The development of the dorsal mesentery in human embryos and fetuses. Semin Cell Dev Biol 92:18–26.

Hoorweg K, Cupedo T 2008 Development of human lymph nodes and Peyer's patches. Semin Immunol 20:164–170.

Huse SM, Gruppo PA, Boekelheide K et al 2015 Patterns of gene expression and DNA methylation in human fetal and adult liver. BMC Genomics 16:981. doi 10.1186/s12864-015-2066-3.

Hwang SE, Kim JH, Yu HC et al 2014 Lymphocyte subpopulations in the liver, spleen, intestines, and mesenteric nodes: an immunohistochemical study using human fetuses at 15–16 weeks. Anat Rec 297:1478–89.

Ionescu S, Mocanu M, Andrei B et al 2014 Differential diagnosis of abdominal wall defects – omphalocele versus gastroschisis. Chirurgia (Bucur) 109:7–14.

Isaza-Restrepo A, Martin-Saavedra JS, Velez-Leal JL 2018 The peritoneum: beyond the tissue – a review. Front Physiol 9:738. doi: 10.3389/fphys.2018.00738.

Jadcherla S 2016 Dysphagia in the high-risk infant: potential factors and mechanisms. Am J Clin Nutr 103(Suppl): 622S–628S.

Jadcherla SR, Berseth C 2012 Development of gastrointestinal motility reflexes. In Neu J (ed) Gastroenterology and Nutrition: Neonatology Questions and Controversies, 2nd ed. Philadelphia: Elsevier, Saunders; Ch. 3.

Jadcherla SR, Shubert TR, Gulati IK et al 2015 Upper and lower esophageal sphincter kinetics are modified during maturation: effect of pharyngeal stimulus in premature infants. Pediatr Res 77:99–106.

Juelke K, Romagnani C 2016 Differentiation of human innate lymphoid cells (ILCs). Curr Opin Immunol 38:75-85.

Kabouridis PS, Lasrado R, McCallum S 2015 Microbiota controls the homeostasis of glial cells in the gut lamina propria. Neuron 85:289–95.

Kaigai N, Nako A, Yamada S et al 2014 Morphogenesis and three-dimensional movement of the stomach during the human embryonic period. Anat Rec 297:791–7.

Kallapur SG, Presicce P, Rueda CM et al 2014 Fetal immune response to chorioamnionitis. Semin Reprod Med 32:56–67.

Kim WK, Kim H, Ahn DH et al 2003 Timetable for intestinal rotation in staged human embryos and fetuses. Birth Defects Res A Clin Mol Teratol 67:941–5.

Kolterud A, Grosse AS, Zacharias WJ et al 2009 Paracrine hedgehog signalling in stomach and intestine: new roles for hedgehog in gastrointestinal patterning. Gastroenterology 137:618–28.

Kraima AC, West NP, Treanor D et al 2015 Whole mount microscopic sections reveal that Denonvilliers' fascia is one entity and adherent to the mesorectal fascia; implications for the anterior plane in total mesorectal excision? Eur J Surg Oncol 41:738–45.

Kruepunga N, Hikspoors JPJM, Mekonen KM et al 2018 The development of the cloaca in the human embryo. J Anat 233:724–39.

Landsmann L, Nijagal A, Whitchurch TJ et al 2011 Pancreas mesenchyme regulates epithelial organogenesis throughout development. PLoS Biol 9:e1001143. doi:10.1371/journal.pbio.1001143.

Lebenthal E 1989 Concepts in gastrointestinal development. In: Lebenthal E (ed) Human Gastrointestinal Development. New York: Raven Press; Ch. 1.

This chapter is the first in a volume dedicated to the development of structure and function of the gut, liver and pancreas. It includes the development of the immunological surveillance mechanisms and gastrointestinal flora.

Lemaigre FP 2009 Mechanisms of liver development: concepts for understanding liver disorders and design of novel therapies. Gastroenterology 137:62–71.

Li X, Udager AM, Hu C et al 2009 Dynamic patterning at the pylorus; formation of an epithelial intestine-stomach boundary in later fetal life. Dev Dyn 238:3205–17.

Lian J, Huang J, Chen T et al 2019 The Toldt fascia: a historic review and surgical implications in complete mesocolic excision for colon cancer. Asian J Surg 42:1–5.

This article considers the movements and adherence of the developing enteric mesentery.

Lorenz L, Axnick J, Buschmann T et al 2018 Mechanosensing by β1 integrin induces angiocrine signals for liver growth and survival. Nature 562:128–32.

Martin CR, Caicedo RA, Walker WA 2012 Development of the intestinal mucosal barrier. In: Neu J (ed) Gastroenterology and Nutrition: Neonatology Questions and Controversies, 2nd ed. Philadelphia: Elsevier, Saunders; Ch. 4, pp. 39–58.

McLin VA, Henning SJ, Jamrich M 2009 The role of the visceral mesoderm in the development of the gastrointestinal tract. Gastroenterology 136:2074–91.

Mekonen H, Hikspoors JPJM, Mommen G et al 2015 Development of the ventral body wall in the human embryo. J Anat 227:673–85.

Nerurkar NL, Mahadevan L, Tabin CJ 2017 BMP signalling controls buckling forces to modulate looping morphogenesis of the gut. Proc Natl Acad Sci U S A 144:2277–82.

Neu J (ed) 2012 Gastroenterology and Nutrition: Neonatology Questions and Controversies, 2nd ed. Philadelphia: Elsevier, Saunders.

Contains a comprehensive range of articles on the development and maturation of the gut.

Neu J, Mai V 2012 The developing intestinal microbiome and its relationship to health and disease. In: Neu J (ed) Gastroenterology and Nutrition: Neonatology Questions and Controversies, 2nd ed. Philadelphia: Elsevier, Saunders; Ch. 5, pp. 59–65.

O'Rahilly R, Müller F 1987 Developmental Stages in Human Embryos. Washington, DC: Carnegie Institution.

Pangtey B, Kaul JM, Mishra S 2017 Histogenesis of muscularis mucosae and muscularis externa of stomach: a human foetal study. J Clin Diagn Res 11:AC01–AC03.

Patel RM, Neish AS, Lin P 2012 The developing intestine as an immune organ. In: Neu J (ed) Gastroenterology and Nutrition: Neonatology Questions and Controversies, 2nd ed. Philadelphia: Elsevier, Saunders; Ch. 6, pp. 67–89.

Radenkovic G, Radenkovic D, Velickov A 2018 Development of interstitial cells of Cajal in the human digestive tract as a result of reciprocal induction of mesenchymal and neural crest cells. J Cell Mol Med 22:778–85.

Rao M, Gerson MD 2018 Enteric nervous system development: what could possibly go wrong? Nat Rev Neurosci 19:552–65.

A review of the genetic and environmental factors that may affect enteric nervous system development.

Rodríguez JM, Murphy K, Stanton C et al 2015 The composition of the gut microbiota throughout life, with an emphasis on early life. Microb Ecol Health Dis 26:26050. doi: 10.3402/mehd.v26.26050.

Rogers IM 2015 The cause of pyloric stenosis of infancy: a hyperacidity pathogenesis. Medical Hypotheses Nov 26. pii: S0306-9877(15)00446-6. doi: 10.1016/j.mehy.2015.11.023.

Rollo BN, Zhang D, Stamp LA et al 2016. Enteric neural cells from Hirschsprung disease patients form ganglia in autologous aneuronal colon. Cell Mol Gastroenterol Hepatol 2:92–109.

Sahnan K, Pellino G, Adegbola SO et al 2018 Development of a model of three-dimensional imaging for the preoperative planning of TaTME. Tech Colonproctol 22:59–63.

Satoh T, Sakurai E, Tada H et al 2009 Ontogeny of reticular framework of white pulp and marginal zone in human spleen: immunohistochemical studies of fetal spleens from the 17th to 40th week of gestation. Cell Tissue Res 336:287–97.

Sehgal R, Coffey JC 2014 Historical development of mesenteric anatomy provides a universally applicable anatomic paradigm for complete/total mesocolic excision. Gastroent Report 2:245–50.

Sharma R, Young C, Neu J 2012 Necrotizing enterocolitis. In: Neu J (ed) Gastroenterology and Nutrition: Neonatology Questions and Controversies, 2nd ed. Philadelphia: Elsevier, Saunders; Ch 15.

Silver PHS 1952 The role of the peritoneum in the formation of the septum recto-vesicale. J Anat 90:538–46.

Soffers J, Hikspoors JPJM, Mekonen HK et al 2015 The growth pattern of the human intestine and its mesentery. Dev Biol 13:31. doi: 10.1186/s12861-015-0081-x.

This paper gives histological and 3D representations of the formation of the midgut loop.

Steiniger B, Ulfig N, Risse M et al 2007 Fetal and early post-natal development of the human spleen: from primordial arterial B cell lobules to a non-segmented organ. Histochem Cell Biol 128:205–15.

Streeter GL 1942 Developmental horizons in human embryos. Descriptions of age group XI, 13 to 20 somites, and age group XII, 21 to 29 somites. Contrib Embryol Carnegie Inst Wash 30:211–45.

Szpinda M, Paruszewska-Achtel M, Wozniak A et al 2015 Volumetric growth of the liver in the human fetus: an anatomical, hydrostatic, and statistical study. Biomed Res Int Biomed Res Int 2015:858162. doi: 10.1155/2015/858162.

Tan CE, Moscoso GJ 1994 The developing human biliary system at the porta hepatic level between 29 days and 8 weeks of gestation: a way to understand biliary atresia. Part 1. Pathol Int 44:587–99.

Ueda Y, Yamada S, Uwabe C et al 2016 Intestinal rotation and physiological umbilical herniation during the embryonic period. Anat Rec 299:197–206.

Vaarala O 2012 The developing gastrointestinal tract in relation to autoimmune disease, allergy, and atopy. In: Neu J (ed) Gastroenterology and Nutrition: Neonatology Questions and Controversies, 2nd ed. Philadelphia: Elsevier, Saunders; Ch. 7, pp. 91–9.

Valasek P, Evans DJR, Maina F et al 2005 A dual fate of the hindlimb muscle mass: cloacal/perineal musculature develops from leg muscle cells. Development 132:447–58.

Van Handel B, Prashad SL, Hassanzadeh-Kiabi N et al 2010 The first trimester human placenta is a site for terminal maturation of primitive erythroid cells. Blood 116:3321–30.

Varga I, Babala J, Kachlik D 2018 Anatomic variations of the spleen: current state of terminology, classification, and embryological background. Surg Radiol Anat 40:21–9.

Walton KD, Mishkind D, Riddle MR 2018 Blueprint for an intestinal villus: species-specific assembly required. Wiley Interdiscip Rev Dev Biol 7: e317. doi:10.1002/wdev.317.

Whittle MJ 1999 Gastrointestinal abnormalities. In: Rodeck CH, Whittle MJ (eds) Fetal Medicine: Basic Sciences and Clinical Practice. Edinburgh: Elsevier, Churchill Livingstone; Ch. 54, pp. 703–14.

This chapter reviews the diagnosis and treatment of anomalies of the gastrointestinal tract.

Witkowska-Zimny M, Kaminska-El-Hassan E 2017. Cells of human breast milk. Cell Mol Biol Lett 22:11. doi: 10.1186/s11658-017-0042-4. eCollection 2017.

Wolf RB 2018 Abdominal imaging. In: Resnik R, Lockwood C, Moore T et al (eds) Creasy and Resnik's Maternal–Fetal Medicine: Principles and Practice. Elsevier; Ch. 26, pp. 393–413.

Wu Y, Dabhoiwala NF, Hagoort J et al 2018 Architecture of structures in the urogenital triangle of young adult males; comparison with females. J Anat 233:447–59.

Wynn JL, Neu J 2012 The neonatal gastrointestinal tract as a conduit to systemic inflammation and developmental delays. In: Neu J (ed) Gastroenterology and Nutrition: Neonatology Questions and Controversies, 2nd ed. Philadelphia: Saunders; Ch. 19, pp. 293–304.

Zale KM 2018 Neonatal and pediatric abdomen. In: Hagen-Ansert S (ed) Textbook of Diagnostic Sonography. Elsevier; Ch. 25, pp. 689–720.

Zhu D, Chen X, OuYang M et al 2016 Three surgical places identified in laparoscopic complete mesocolic excition for right-sided colon cancer. World J Surg Oncol 14:7.

Zhu J, Zhu T, Lin Z et al 2017 Perinatal risk factors for infantile hypertrophic pyloric stenosis: a meta-analysis. J Pediatr Surg 52:1389–97.

CHAPTER
22

Development of the urogenital system

DEVELOPMENT OF THE POSTERIOR COELOM WALL

From stage 11 (29–30 days postfertilization; see Fig. 23.3 for comparison of postfertilzation days and the clinical scale of postmenstrual weeks) the dorsal region of the wall of the intraembryonic coelom is composed of a mesenchymal population termed intermediate mesenchyme. Predictive fates of epiblast cells that transform to mesenchyme on ingression through the primitive streak show temporally specified induction of cells that ingress later than those that form the lateral halves of the somites and earlier than mesoblast forming the lateral plate, and become epithelial coelomic wall at the end of their migration (see Fig. 10.3). The rostral limit of the intermediate mesenchymal population, in stage 10 embryos, is lateral to somite 6. It lengthens caudally during development, and is sited (in the folded embryo) at the junction between the splanchnopleuric mesenchyme (surrounding the gut medially) and the somatopleuric mesenchyme (subjacent to the ectoderm laterally). Ultimately it blends with splanchnopleuric mesenchyme around the cloaca (**Fig. 22.1**). After the early migration of mesoblast, further intermediate mesenchyme is formed by proliferation of the overlying coelomic epithelial wall to give a ventrally projecting urogenital ridge (previously termed the nephrogenic cord). Interaction between the coelomic epithelium and its mesenchymal progeny give rise, in a rostro-caudal progression, to the kidneys, suprarenal glands, gonads and reproductive ducts.

URINARY SYSTEM

In lower vertebrates, intermediate mesenchyme typically develops serial, segmental, epithelial diverticula termed nephrotomes. Each nephrotome encloses a cavity, the nephrocele, which communicates with the coelom through a peritoneal funnel, the nephrostome (**Fig. 22.2**). The dorsal wall of a nephrotome evaginates as a nephric tubule. The dorsal tips of the cranial nephric tubules bend caudally and fuse to form a longitudinal primary excretory duct, which grows caudally and curves ventrally to open into the cloaca. The more caudally placed, and therefore chronologically later, tubules open secondarily into this duct or into tubular outgrowths from it. Glomeruli, specific arrangements of capillaries and overlying coelomic epithelium, arise from the ventral wall of the nephrocele (internal glomeruli) or the coelomic wall adjacent to the peritoneal funnels (coelomic or external glomeruli), or in both situations (see Fig. 22.2). External glomeruli, composed of recognizable podocytes, facing the intraembryonic coelom, and the lateral openings of ciliated peritoneal funnels, have been described in turtle embryos (Collins 1990): it is doubtful whether external glomeruli develop in human embryos.

The renal excretory system is described as forming from three organs, the pronephros, mesonephros and metanephros, which succeed each other in time and space, such that the last to develop is retained as the permanent kidney (see Figs 22.1–22.2). It is difficult to provide reliable criteria by which to distinguish these stages or to define their precise limits in human embryos. Much of the knowledge on development of the meso- and meta-nephros comes from experimental studies of mouse embryos and more recently from *in vitro* study of human stem cell-derived kidney organoids. Although kidney development is evolutionarily conserved in mammals, there are significant heterochronic differences between murine and human development that make direct extrapolation between the species unwise; similarly, extrapolation of *in vitro* conditions to *in vivo* development should be treated with caution.

Pronephros

A pronephros is present in human embryos only as clusters of cells in the most cranial portions of the urogenital ridge (see Figs 22.1–22.2).

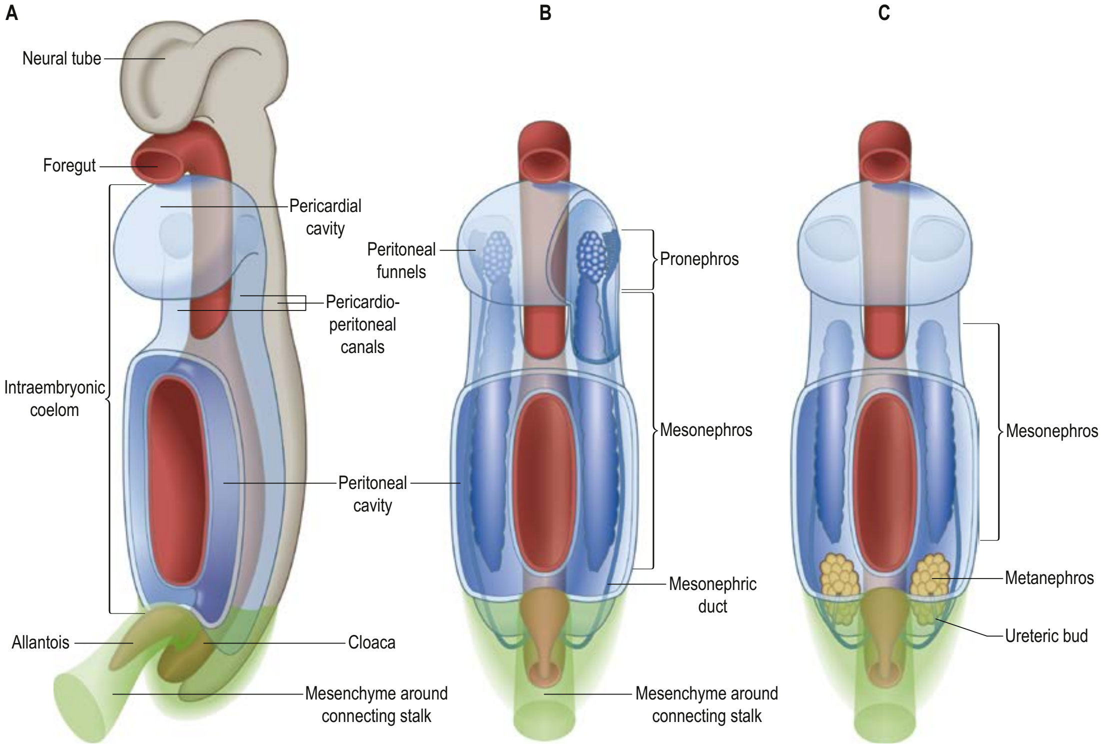

Fig. 22.1 **A**, The major epithelial populations within a stage 11 embryo, viewed from a ventrolateral position. **B**, The position of pronephros and mesonephros on the posterior thoracic and abdominal walls. **C**, The position of mesonephros and metanephros.

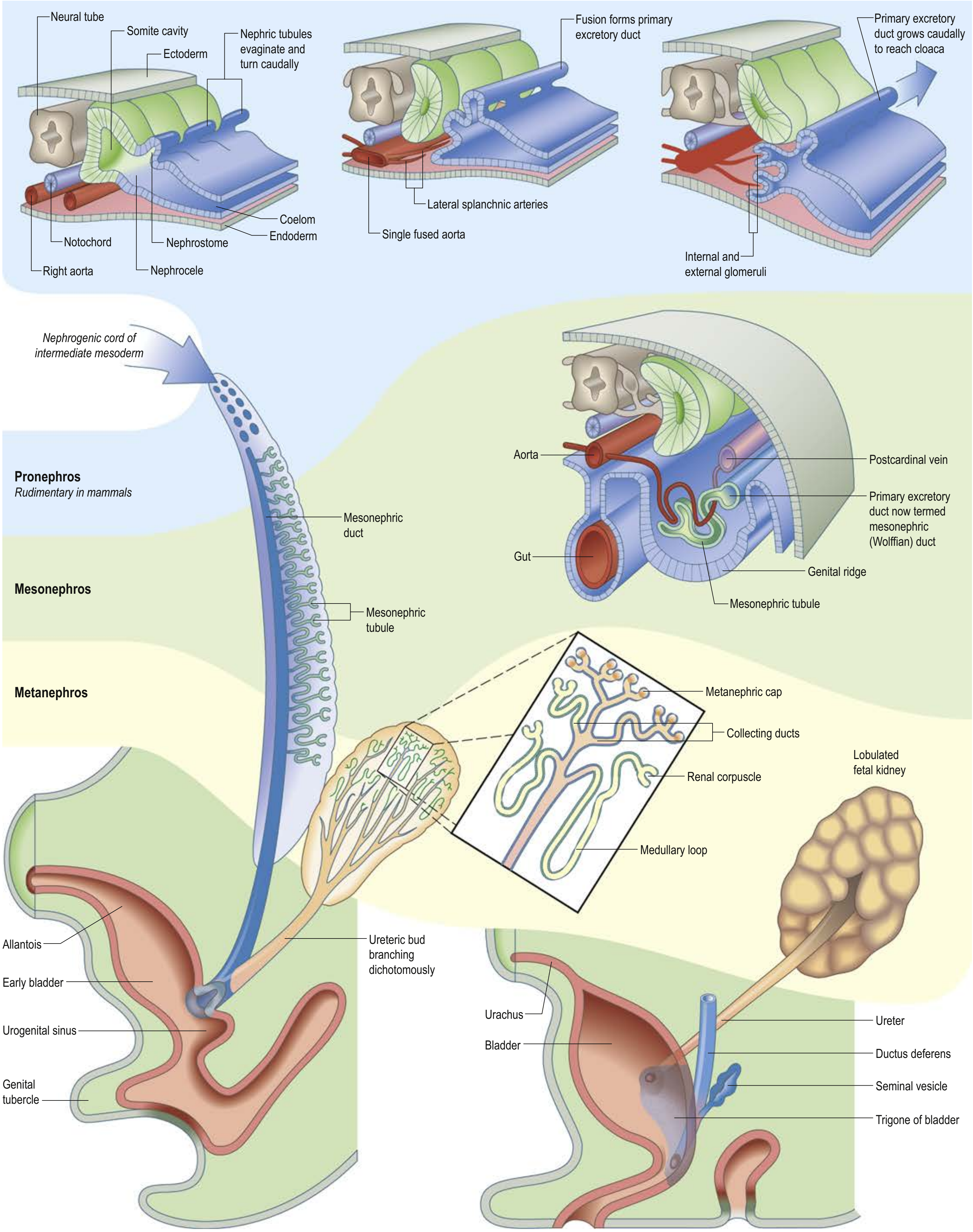
Neural tube
Somite cavity
Ectoderm
Nephric tubules evaginate and turn caudally
Coelom
Endoderm
Notochord
Nephrostome
Right aorta
Nephrocele
Fusion forms primary excretory duct
Lateral splanchnic arteries
Single fused aorta
Primary excretory duct grows caudally to reach cloaca
Internal and external glomeruli
Nephrogenic cord of intermediate mesoderm
Pronephros
Rudimentary in mammals
Mesonephric duct
Mesonephros
Mesonephric tubule
Metanephros
Aorta
Postcardinal vein
Primary excretory duct now termed mesonephric (Wolffian) duct
Gut
Genital ridge
Mesonephric tubule
Metanephric cap
Collecting ducts
Renal corpuscle
Lobulated fetal kidney
Medullary loop
Allantois
Early bladder
Urogenital sinus
Genital tubercle
Ureteric bud branching dichotomously
Urachus
Bladder
Ureter
Ductus deferens
Seminal vesicle
Trigone of bladder

Fig. 22.2 The principal features of the primitive vertebrate nephric system for comparison with the development of the human nephric system. A considerable period of embryonic and fetal life has necessarily been compressed into a single diagram. (Modified with permission from Williams PL, Wendell-Smith CP, Treadgold S 1969 Basic Human Embryology, 2nd ed. London: Pitman Medical & Scientific.)

More caudally, similar groups of cells appear and become vesicular. The dorsal ends of the most caudal of the vesicles join a primary excretory duct. Their central ends are connected with the coelomic epithelium by cellular strands that probably represent rudimentary peritoneal funnels. Glomeruli do not develop in association with these cranially situated nephric tubules, which ultimately disappear.

Primary excretory duct

In stage 11 embryos of approximately 14 somites, a primary excretory duct can be seen as a solid rod of cells in the dorsal part of the urogenital ridge. Its cranial end is about the level of somite 9 and its caudal tip merges with the undifferentiated mesenchyme of the ridge. It differentiates before any nephric tubules and, when the latter appear, it is at first unconnected with them. In older embryos, the duct has lengthened and its caudal end becomes detached from the urogenital ridge to lie beneath the ectoderm. From this level, it grows caudally, independent of the nephrogenic mesenchyme, and then curves ventrally to reach the wall of the cloaca. The lumen develops progressively from its caudal end to form a true duct, which opens into the cloaca in stage 12 embryos.

Mesonephros

From stage 12 mesonephric tubules, which develop from the intermediate (now nephrogenic) mesenchyme between somite levels 8 and 20, begin to connect to the primary excretory duct, which is now renamed the mesonephric duct. More caudally, a continuous ridge of nephrogenic mesenchyme extends to the level of somite 24. The mesonephric tubules (nephrons) are not metameric and there may be two or more mesonephric tubules opposite each somite.

Within the mesonephros, each tubule first appears as a condensation of mesenchyme cells that epithelialize and form a vesicle. One end of the vesicle grows towards and opens into the mesonephric duct, while the other dilates and invaginates. The outer stratum forms the glomerular capsule, while the inner cells differentiate into mesonephric podocytes that clothe the invaginating capillaries to form a glomerulus. The capillaries are supplied with blood through lateral branches of the aorta. It has been estimated that 70–80 mesonephric tubules and a corresponding number of glomeruli develop. However, these tubules are not all present at the same time: it is rare to find more than 30–40 in an individual embryo because the cranial tubules and glomeruli develop and atrophy before those situated more caudally have developed.

By stage 17 each mesonephros is an elongated, spindle-shaped organ that projects into the coelomic cavity, one on each side of the dorsal mesentery, from the level of the septum transversum to the third lumbar segment. This whole projection is called the mesonephric ridge, mesonephros or Wolffian body (see Fig. 22.1B–C; **Fig. 22.3**). It develops subregions, and the suprarenal gland and gonad develop on its medial surface. There are striking similarities in structure between the mesonephros and the permanent kidney or metanephros, but the mesonephric nephrons lack a segment that corresponds to the descending limb of the loop of Henle. The mesonephros is believed to produce urine by stage 17. A detailed comparison of the development and function of the mesonephros and metanephros in staged human embryos is not available.

In stage 18 embryos the mesonephric ridge extends cranially to about the level of rib 9. In both sexes, the cranial end of the mesonephros atrophies. In stage 19 embryos a mesonephros is found only in the first three lumbar segments, although it may still possess as many as 26 tubules. The most cranial one or two tubules persist as rostral aberrant ductules (see Fig. 22.13); the succeeding five or six tubules develop into either the efferent ductules of the testis and lobules of the head of the epididymis (male), or the tubules of the epoophoron (female); the caudal tubules form the caudal aberrant ductules and the paradidymis (male), or the paroophoron (female).

Mesonephric duct

Once mesonephric nephrons connect to the primary excretory duct, it is renamed the mesonephric duct. This runs caudally in the lateral part of the urogenital ridge, and projects into the cavity of the coelom in the substance of a mesonephric fold at the caudal end of the ridge (see Fig. 22.3). As the mesonephric ducts from each side approach the urogenital sinus (see below) the two mesonephric folds fuse, forming a transverse partition across the cavity of the pelvis, somewhat inappropriately called the genital cord (see Fig. 22.3). The insertion of the mesonephric duct into the urogenital sinus occurs at stage 13 and remains associated with segmental levels 31–32 (S2–S3) as the embryo lengthens (Kruepunga et al 2018). In the male, the mesonephric duct itself becomes the canal of the epididymis, ductus deferens and ejaculatory duct, whereas it involutes in the female.

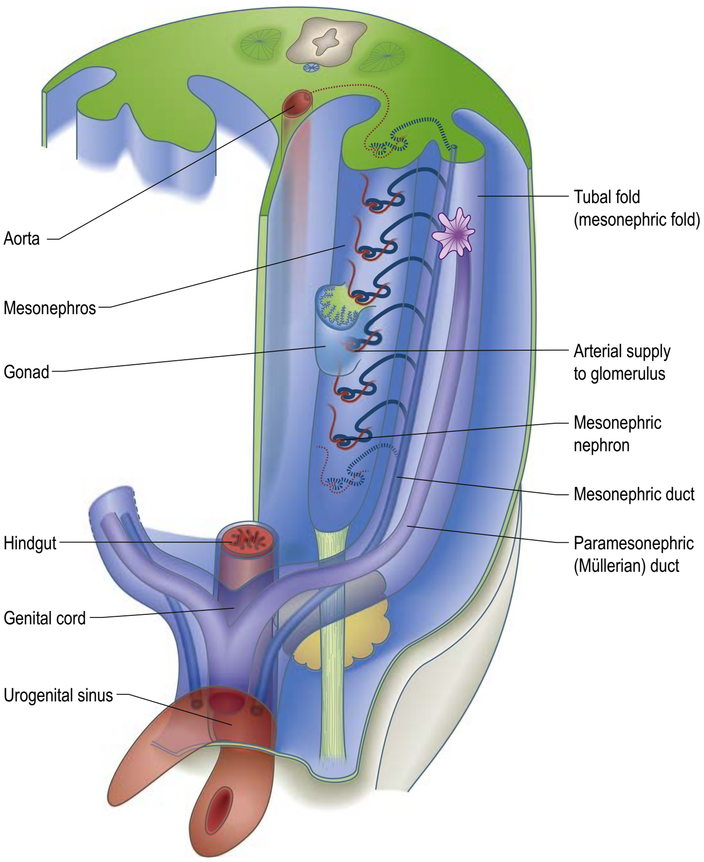

Fig. 22.3 The relative positions of the mesonephros and early gonad in the abdomen in the ambisexual stage of development. The mesonephric and paramesonephric ducts run within the tubal fold to the urogenital sinus.

Urogenital sinus and allantois

The early cloaca consists of a dorsal, tubular, enteric hindgut region extending from the caudal intestinal portal to the cloacal membrane, and a ventral, blind-ending allantois extending from the connecting stalk. It is a slightly dilated cavity, lined by endoderm (Fig. 22.1). The allantois and enteric hindgut portions of the cloaca are separated, from stage 15, by the proliferation of the urorectal septum, a partition of mesenchyme and endodermal cloacal wall in the angle of the junction of enteric hindgut and allantois (**Fig. 22.4**; see Fig. 22.7). Molecular markers of the urorectal septum mesenchyme, also termed the intercloacal mesenchyme, include *Six1* and *Six2* (Wang et al 2011, 2013). The endodermal epithelium beneath the mesenchyme of the urorectal septum moves towards the cloacal membrane and fuses centrally, separating the intraembryonic urogenital sinus and extraembryonic allantois (ventrally), bounded now by a urogenital membrane, from the presumptive rectum and upper anal canal (dorsally), bounded by the anal membrane (Kruepunga et al 2018). Both membranes break down during stages 18–20. The urogenital sinus is continuous cranially with the allantoic duct within the connecting stalk. During development it forms the vesico-urethral canal with a middle, narrow channel, the pelvic portion, and a caudal, deep, phallic section that is open to the amniotic cavity. It receives the mesonephric and paramesoneprhic ducts and will become the urinary bladder and urethra (Fig. 22.4A).

Metanephros

The pronephros and mesonephros are linear structures. They both contain stacks of tubules distributed along the craniocaudal axis of the embryo, an arrangement that results in the production of hypotonic urine in the embryo and fetus. In the mesonephric kidney, development proceeds in a craniocaudal progression, and cranial nephrons degenerate before caudal ones are produced. In the metanephric kidney, development is patterned radially such that the outer cortex is the last part to be formed, and nephrons are arranged concentrically with the loops

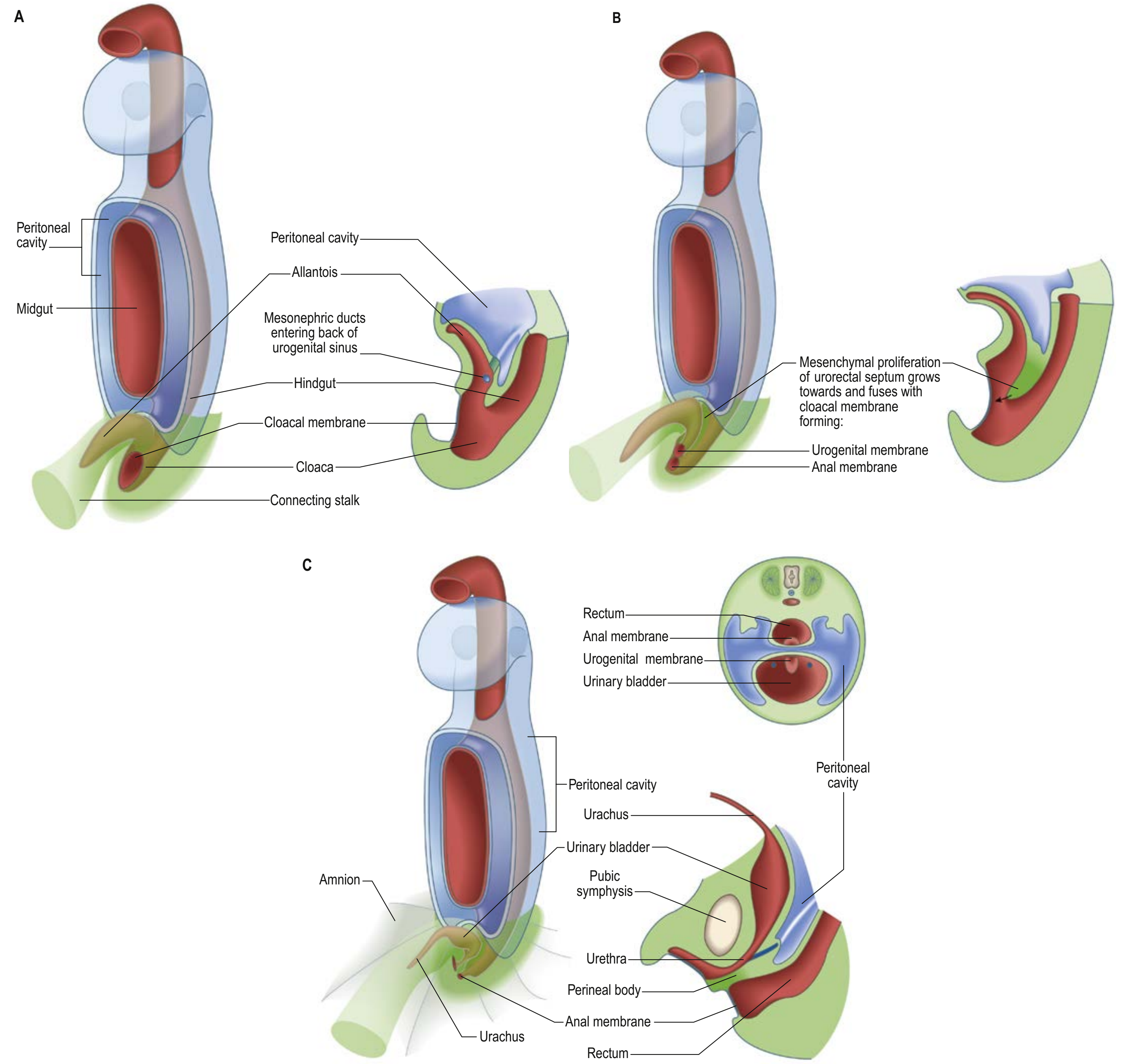
A
Peritoneal cavity
Midgut
Peritoneal cavity
Allantois
Mesonephric ducts entering back of urogenital sinus
Hindgut
Cloacal membrane
Cloaca
Connecting stalk
B
Mesenchymal proliferation of urorectal septum grows towards and fuses with cloacal membrane forming:
Urogenital membrane
Anal membrane
C
Rectum
Anal membrane
Urogenital membrane
Urinary bladder
Peritoneal cavity
Peritoneal cavity
Urachus
Urinary bladder
Amnion
Pubic symphysis
Urethra
Perineal body
Anal membrane
Urachus
Rectum

Fig. 22.4 The division of the hindgut into urinary and enteric parts: left ventrolateral view of the intraembryonic coelom and corresponding midsagittal sections. **A**, The early cloaca. **B**, Proliferation of the urorectal septum. **C**, Complete separation of the urethra and anal canal, and position of the perineal body.

of Henle directed towards the renal pelvis. This arrangement allows different concentration gradients to develop within the metanephric kidney and results in the production of hypertonic urine.

The metanephric kidney develops from three sources from stage 13. An evagination of the mesonephric duct, the ureteric bud, and a local condensation of mesenchyme, the metanephric blastema, form the nephric structures (**Fig. 22.5**). Angiogenic mesenchyme migrates into the metanephric blastema slightly later to produce the glomeruli and vasa recta. It is possible that an intact nerve supply is also required for metanephric kidney induction. A range of intra- and extracellular factors potentially involved in metanephric development have been discussed (Kanwar et al 2004).

The following interactions occur sequentially in the development of the metanephric kidney (see Fig. 22.5). Although the timing of human development differs from that in other mammalian species that have been described, similar growth and transcription factors are thought to underpin kidney development (Davidson 2009, Batchelder et al 2010, Faa et al 2012, Chai et al 2013). The ureteric bud bifurcates when it comes into contact with the metanephric blastema in response to extracellular matrix molecules synthesized by the mesenchyme. Both chondroitin sulphate proteoglycan synthesis and chondroitin sulphate glycosaminoglycan processing are necessary for branching of the ureteric bud. The proximal part of the ureteric bud elongates to form the developing ureter and the first generation of branches form the major and minor calyces of the renal pelvis (see Fig. 22.6). Further ureteric branches form the collecting ducts and as they elongate the metanephric mesenchyme condenses adjacent to each of them. An adhesion molecule, syndecan, can be detected between the mesenchymal cells in the condensate. The cells switch off expression of neural cell adhesion molecule (N-CAM), fibronectin and collagen I, and start to synthesize liver cell adhesion molecule (L-CAM; also called E cadherin) and the basal lamina constituents, laminin and collagen IV. The mesenchymal clusters are thus converted to small groups of epithelial cells that undergo complex morphogenetic changes. Each epithelial group elongates, initially forming a comma-shaped, and then an S-shaped, body, with a dilated sac at its proximal end and an elongating distal end that subsequently fuses with a collecting duct (see Fig. 22.5). Each dilated sac invaginates to form a cup: the outer cells become parietal, glomerular capsule cells, and the inner ones become visceral, epithelial podocytes. The podocytes develop in close proximity to the angiogenic

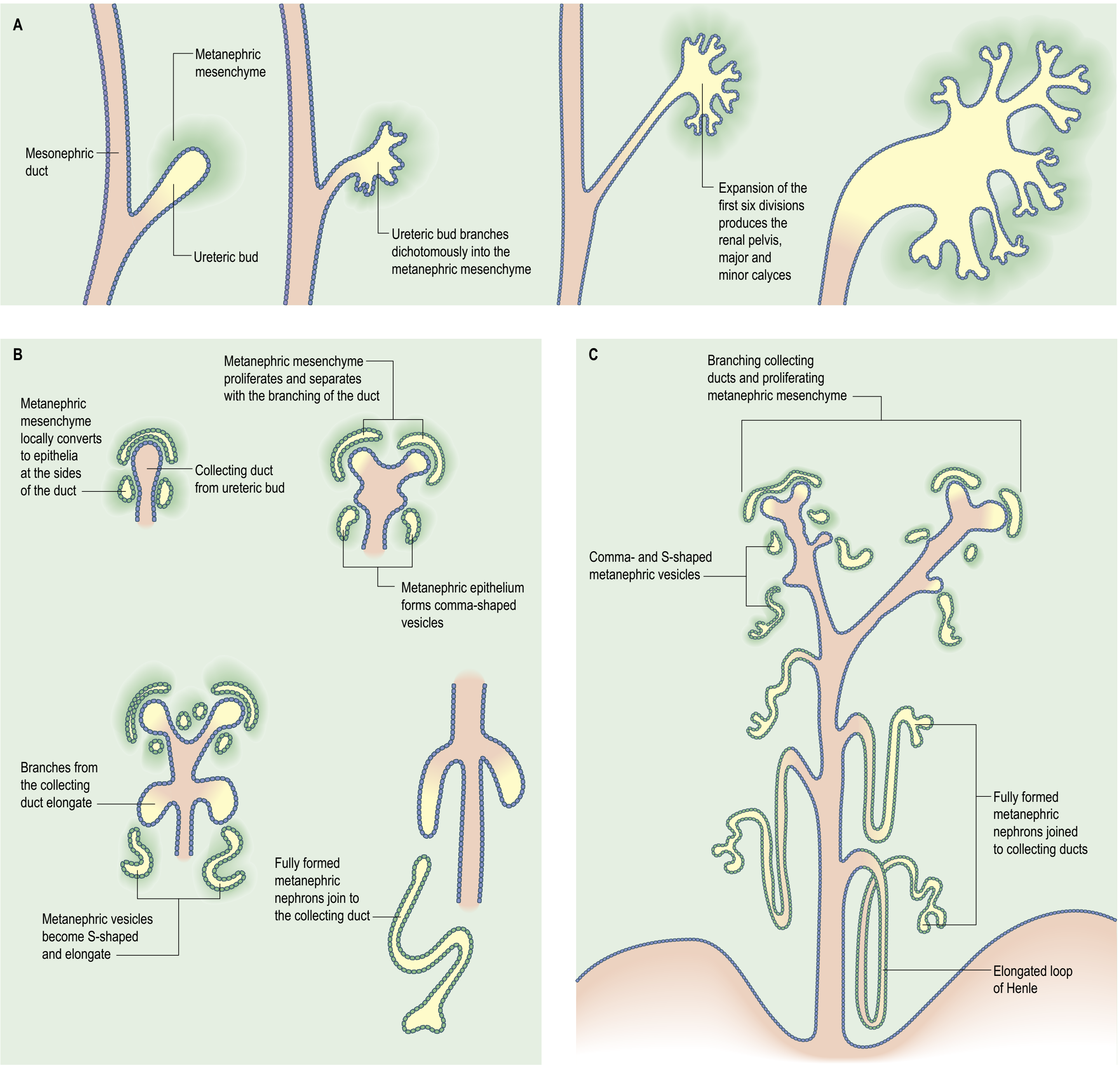
A
Metanephric mesenchyme
Mesonephric duct
Ureteric bud
Ureteric bud branches dichotomously into the metanephric mesenchyme
Expansion of the first six divisions produces the renal pelvis, major and minor calyces
B
Metanephric mesenchyme proliferates and separates with the branching of the duct
Metanephric mesenchyme locally converts to epithelia at the sides of the duct
Collecting duct from ureteric bud
Metanephric epithelium forms comma-shaped vesicles
Branches from the collecting duct elongate
Metanephric vesicles become S-shaped and elongate
Fully formed metanephric nephrons join to the collecting duct
C
Branching collecting ducts and proliferating metanephric mesenchyme
Comma- and S-shaped metanephric vesicles
Fully formed metanephric nephrons joined to collecting ducts
Elongated loop of Henle

Fig. 22.5 An overview of metanephric kidney development. **A**, The ureteric bud arises from the mesonephric duct. The metanephric mesenchyme proliferates and separates with each subdivision of the ureteric bud. **B**, The metanephric mesenchyme converts to epithelia, forming comma- and S-shaped vesicles, which become metanephric nephrons. **C**, All stages of metanephric development are present concurrently. The most recently formed nephrons are on the outer aspect of the kidney.

mesenchyme of invading capillaries which give rise to the endothelial and mesangial cells of the glomerulus. Both cell lines contribute to components of the glomerular basement membrane. The direct mutual support of two epithelial layers, rather than support of an epithelium by an underlying lamina propria, is unusual and seen only in the lung and brain (see Fig. 11.2). Podocytes and endothelial cells contribute to the generation of mutual basal laminal proteins and the formation of the glomerular basement membrane. The isoforms of type IV collagen within this layer follow a specific programme of maturation as the filtration of macromolecules from the plasma becomes restricted. Platelet-derived growth factor (PDGF) β-chain and the PDGF receptor β-subunit (PDGFR β) have been detected between stage 23 and the end of the first trimester; PDGF β-chain has been localized in the dilated epithelial sac during its comma- and S-shaped stages and PDGFR β is expressed in the undifferentiated metanephric blastema, vascular structures and interstitial cells. Both PDGF β-chain and PDGFR β are expressed by mesangial cells, which may promote further mesangial cell proliferation. Innervation is also necessary for metanephric development: nephrogenesis is completely blocked if developing kidney rudiments are incubated with antisense oligonucleotides that neutralize nerve growth factor receptor (NGF-R) mRNA. With continuing elongation of the collecting ducts and adjacent coalescence of mesenchymal cells, all stages of nephron differentiation can be seen concurrently (see Fig. 22.5C). A number of genes involved in the development of the renal medulla and vasa recta in the mouse have been identified (Song and Yosypiv 2012).

Metanephric mesenchyme will develop successfully *in vitro*, which makes experimental perturbation of non-human kidney development comparatively easy to evaluate. Early experimental studies demonstrated that other mesenchymal populations, and spinal cord, were able to induce ureteric bud division and metanephric development. Culture of hiPSC along a kidney lineage has resulted in the generation of nephron progenitor cells and kidney organoids which are being used to study aspects of podocyte development (Shamin et al 2016, Hale et al 2018). Time-lapse study of cultured mouse embryonic kidney has shown that the original branching morphogenesis of the collecting ducts (from the ureteric bud) changes during maturation such that the branching point moved centripetally. This may promote elongation of outer cortical collecting ducts, resulting in a renal pattern rather than one that would result from repeated dichotomous branching morphogenesis. Biomechanical factors generated by the outer renal capsule may contribute to these temporal specifications of epithelial mesenchymal interactions (Lindström et al 2015).

Fetal kidney maturation

Nephrons are added to the metanephric kidney throughout the fetal period with different temporal patterning. The earliest ureteric bud branches are absorbed into the renal pelvis so that an average of 44 collecting ducts open into 8 papillae. After the 13th to 15th branching, several metanephric mesenchymal to epithelial transformations can occur along adjacent collecting ducts, forming arcades of juxtaglomerular nephrons in the inner renal cortex. The mid and outer renal cortices are induced by collecting tubules that elongate towards the renal capsule. Addition of new nephrons in the outermost cortex occurs by metanephric mesenchymal induction at collecting duct tips, at a constant average of 83 µm from the inner side of the renal capsule, with only two layers of mesenchyme intervening (Minuth 2018). This subcapsular region of the developing kidney is called the nephrogenic zone. It contains angiogenic mesenchymal populations forming embryonic blood vessels, which means that the tissues are at lower oxygen tension than more central regions where endothelial glomeruli are established. It has been suggested, on the basis of animal experimentation, that increased oxygen tension promotes glomerular differentiation, whereas low oxygen tension maintains stem cell populations and continued developmental interactions (Rymer et al 2014). The addition of new nephrons normally ceases after postmenstrual week 38, although the mechanism is not known (Minuth 2018). Nephrogenesis has been reported as complete by postmenstrual week 34, presumably in fetuses with appropriate weight (Solhaug and Jose 2017). Mature renal capsules contain a constant number and proportion of podocytes relative to other glomerular cell types, whether formed early or later between postmenstrual weeks 20 and 40 (Ryan et al 2018).

The metanephric kidney is lobulated throughout fetal life, but this condition usually disappears during the first year after birth (see Fig. 22.8). Varying degrees of lobulation occasionally persist throughout life.

The growth of left and right kidneys is well matched during development: fetal kidney volume increases most during the second trimester in both sexes. Male fetuses show greater values for renal volume than female fetuses from the third trimester onwards (Geelhoed et al 2009). In neonates and infants, total renal blood flow is determined by clearance of *p*-aminohippurate (PAH), which measures effective renal plasma flow (ERPF); flow correlates with postmenstrual age. ERPF increases in infants born preterm from 20 ml/min/1.73m^2 (the latter unit is a standard measure of body surface area) at postmenstrual week 30, to 45 ml (same units) at postmenstrual week 35 and 83 ml at postmenstrual week 40. In full-term infants, during postnatal months 1–3, ERPF increases to 300 ml/min/1.73 m^2 and thereafter reaches values of 650 ml/min/1.73 m^2 by postnatal months 12–24. The full-term neonatal kidney has a greater percentage of blood flow to inner cortical and medullary areas than the adult kidney (Solhaug and Jose 2017).

At delivery of preterm and low birth weight babies nephrogenesis is still active. It has been shown to continue for up to 3 postnatal weeks in experimental non-hominids, however, there is evidence of nephrogenic perturbation resulting in oligonephropathy in 8–24% of preterm deliveries (Minuth 2017). Dilated Bowman's space and shrunken glomerular tufts have been identified in the outer renal cortex. It may be that the general increase in oxygen tension after birth causes rapid differentiation of all formed nephrons but inhibition of further development of immature outer cortical mesenchymal populations. Kidney weight is lower in infants with low (< −2 SDs) birth weight, reflecting a decreased number of nephrons. This relative smaller kidney size continues into early childhood and may be a factor in adult kidney pathology (Geelhoed et al 2009). Preterm neonates achieve a similar estimated glomerular filtration rate as term neonates soon after birth, possibly by glomerular hyperfiltration in the nephrons present (Kandasamy et al 2018).

Endocrine development of the kidney

The kidney functions not only as an excretory organ, but also as an endocrine organ, secreting hormones that are concerned with renal haemodynamics. Before birth, homeostasis is controlled by the placenta. The fetal kidney produces amniotic fluid. The kidneys of premature babies of less than 36 postmenstrual weeks are immature and contain incompletely differentiated cortical nephrons that compromise their ability to maintain homeostasis. Problems of immaturity are further compounded by the effects of hypoxia and asphyxia, which modify renal hormones.

Renal hormones include the renin–angiotensin system, renal prostaglandins, the kallikrein–kinin system and renal dopamine. Renin is found in the smooth muscle cells of arterioles, interlobular arteries and branches of the renal artery, and has also been described in the distal convoluted tubule cells. Renal dopamine is produced (mainly) by the enzymatic conversion of L-dopa to dopamine in the early segments of the proximal convoluted tubule, and is also sourced locally from dopaminergic nerves. Other renal hormones include an antihypertensive lipid produced in the interstitial cells of the renal medulla, and, possibly, histamine and serotonin. Growth factors produced by human embryonic kidney cells include erythropoietin and interleukin β (which stimulate megakaryocyte maturation) and transforming growth factor-β. For reviews of the various factors in this aspect of kidney development see Yosypiv (2009) and Kurtzeborn et al (2018). Prostaglandins may be important in the fetus in the regulation of renal blood flow (Solhaug and Jose 2017).

Ascent of the kidney

The metanephric kidney is initially sacral, but as the ureteric outgrowth lengthens and the body curvature diminishes, it becomes positioned progressively more cranially. The metanephric pelvis lies on a level with the fourth lumbar vertebra at about stage 18 (Hikspoors et al 2015). During this period the ascending kidney receives its blood supply sequentially from arteries in its immediate neighbourhood, i.e. the middle sacral and common iliac arteries. The definitive renal artery is not recognizable until the beginning of the third month. It arises from the most caudal of the three suprarenal arteries, all of which represent persistent mesonephric or lateral splanchnic arteries. Additional renal arteries are relatively common, and may enter at the hilum or at the upper or lower pole; they also represent persistent mesonephric arteries.

Ureter

At first, the distal end of the ureter is connected to the dorsomedial aspect of the mesonephric duct but, as a result of differential growth, this connection comes to lie lateral to the duct. The wall of the early ureter is initially highly permeable. Its lumen later becomes obliterated and is subsequently recanalized. Both of these processes begin in intermediate portions of the ureter and proceed cranially and caudally. Recanalization is not associated with metanephric function, but perhaps reflects the rapid elongation of the ureter as the embryo grows. Two fusiform enlargements appear at the lumbar and pelvic levels of the ureter at 5 and 9 months, respectively (the pelvic enlargement is inconstant). As a result, the ureter shows a constriction at its proximal end (pelviureteric region) and another as it crosses the pelvic brim. A third narrowing is always present at its distal end and is related to the growth of the bladder wall. Ureteric smooth muscle differentiation occurs from the ureterovesical junction to the ureteropelvic junction. The processes that occur during the development of typical and atypical smooth muscle cells that generate ureteric peristaltic waves are unknown. Interstitial cells of Cajal-like cells have been identified in mouse embryos before ureteric pacemaker activity first occurs (Rassouly and Lu 2013).

Urinary bladder

The urinary bladder develops from the cranial vesico-urethral canal, which is continuous above with the allantoic duct (see Fig. 22.4; **Figs 22.6–22.7**). The mesonephric ducts open into the urogenital sinus during stage 13. The ureters develop as branches of the mesonephric ducts, which gain their own access to the developing bladder, and their orifices open separately into the bladder on the lateral side of the opening of the mesonephric ducts during stage 17. Later, the two orifices become separated still further and, although the ureter retains its point of entry into the bladder, the mesonephric duct opens into that part of the urogenital sinus that subsequently becomes the prostatic urethra (Kruepunga et al 2018) (see Fig. 22.6E). The remainder of the vesico-urethral canal forms the body of the bladder and urethra, and its apex is prolonged to the umbilicus as a narrow canal, the urachus.

For many years, it was believed that the absorption of the mesonephric ducts into the urogenital sinus contributed a mesodermal epithelium into the endodermal bladder, limited to the trigone and the dorsal wall of the proximal half of the prostatic urethra extending to the opening of the prostatic utricle and ejaculatory ducts, or its female homologue, the whole female urethral dorsal wall. Studies on transgenic mice have demonstrated that the region of the combined ducts close to the urogenital sinus, referred to as the common nephric duct, undergoes local apoptosis as a part of the normal development of the trigone region of the bladder and the establishment of separate entry

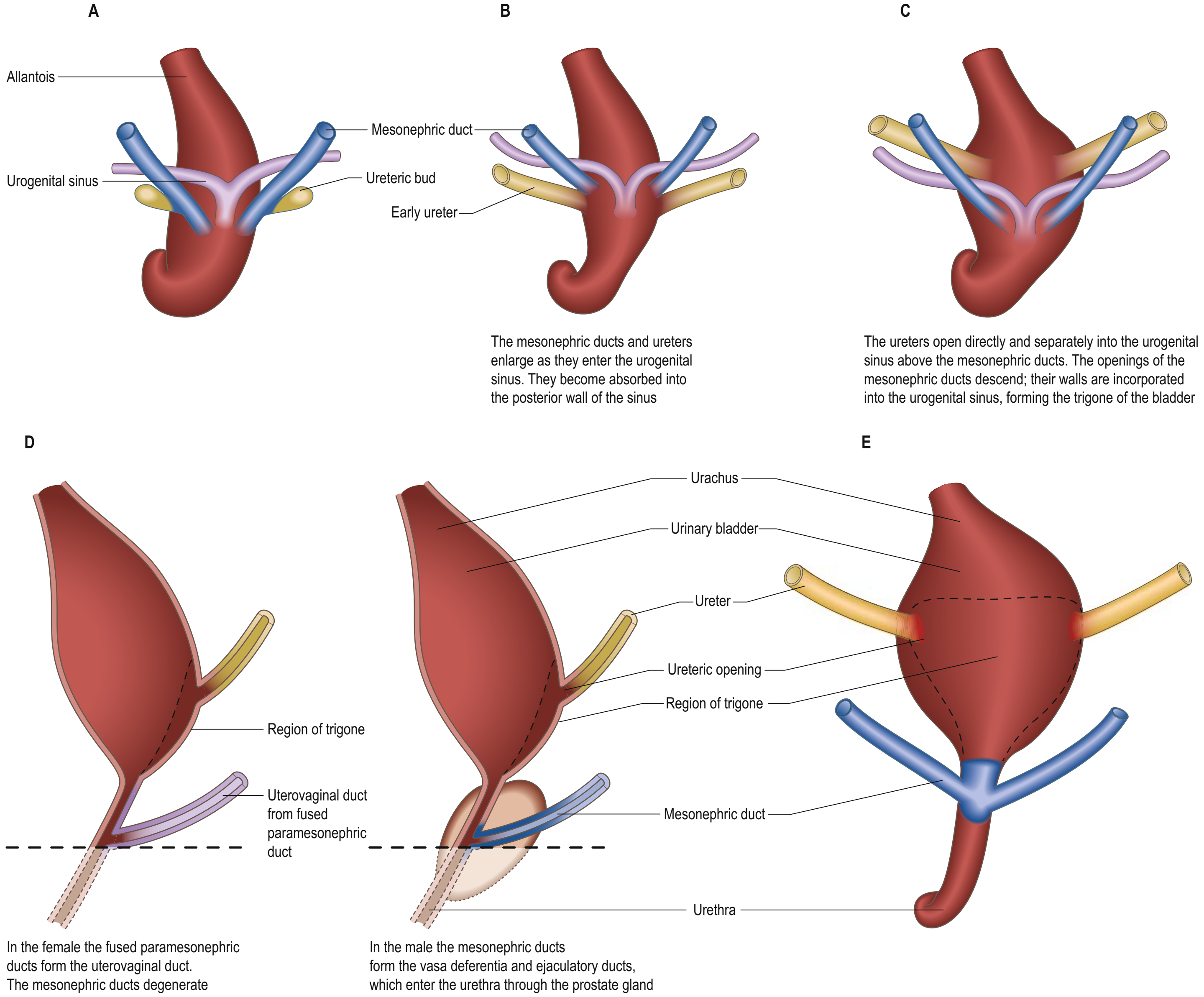

The mesonephric ducts and ureters enlarge as they enter the urogenital sinus. They become absorbed into the posterior wall of the sinus

The ureters open directly and separately into the urogenital sinus above the mesonephric ducts. The openings of the mesonephric ducts descend; their walls are incorporated into the urogenital sinus, forming the trigone of the bladder

In the female the fused paramesonephric ducts form the uterovaginal duct. The mesonephric ducts degenerate

In the male the mesonephric ducts form the vasa deferentia and ejaculatory ducts, which enter the urethra through the prostate gland

Fig. 22.6 The development of the urinary part of the urogenital sinus and formation of the trigone of the bladder. **A–C**, **E**, Posterior views. **D**, Male and female, median sagittal sections. (Based on Tuchmann-Duplessis H, Haegel P 1972 Illustrated Human Embryology, Vol 2 Organogenesis. London: Chapman and Hall. With kind permission of Springer Science+Business Media.)

points for the ureters and mesonephric ducts (Mendelsohn 2009). Retinoic acid is required for ureteric insertion into the urogenital sinus (Batourina et al 2005). There is no mesodermal epithelial contribution to the bladder at the trigone. This is supported by the observation that *in vitro*, combination of fetal urogenital sinus mesenchyme with epithelial mesoderm or endoderm produces different outcomes. Tissue recombined with endoderm gives rise to prostatic epithelium, whereas the same mesenchyme combined with epithelial mesoderm forms seminal gland epithelium. Trigone epithelium differentiates into prostatic epithelium, confirming an endoderm lineage (Tanaka et al 2010).

The previous mechanism for trigone development also suggested that the muscle in that region was derived from the ureter and contributed to the valve-like entry point that prevents urinary reflux. Studies have now shown that the ureter passes through a tunnel in the bladder wall in parallel with blood vessels and that a tunnel forms even in the absence of ureters (Viana et al 2007). Study of smooth muscle progenitors shows that the bulk of the trigone is derived from bladder muscle (detrusor); there is a limited contribution from ureteric longitudinal smooth muscle fibres at the lateral edges. Eponymous muscular tissues such as Mercier's bar (between the ureteric orifices) and Bell's muscle (extending caudally from the ureteric orifices to the apex of the trigone) that were previously thought to arise from the ureter, have been shown to be derived from urinary bladder muscle (Viana et al 2007).

Differentiation of the bladder mucosal epithelium to transitional epithelium can be seen from about postmenstrual week 10 (Rassouly and Lu 2013). Urothelium develops from both the original mesonephric duct epithelium of the ureteric bud and the endodermal epithelium of the urogenital sinus which becomes the bladder, and in places it is responsive to different local osmolarity. The cells express uroplakin, which is thought to be involved in signalling during the epithelial/mesenchyme interactions that are involved in urinary tract development. The differentiation of the urothelium is a significant element in the development of the blood–urine barrier; genetic modification of uroplakin genes suggests their perturbation is associated with the development of congenital anomalies of the urinary tract (Carpenter and McHugh 2017).

Bladder filling and emptying cycles are required for normal bladder remodelling during fetal development; in this process, detrusor smooth muscle cells undergo cyclical apoptosis and proliferation. Mechanical stretching promotes proliferation. Bladders in which the fluid is diverted do not show this cycle, and do not enlarge or undergo normal remodelling. The detrusor stops growing, producing a low-volume, low-compliance bladder, although the serosal connective tissues continue to expand (Wei et al 2012). As yet, there is little information on the development of bladder interstitial cells of Cajal, which are present within detrusor, bladder microvessels and the mucosal lamina propria (Johnston et al 2010).

Ultrasound antenatal imaging of the urinary system

The fetal bladder may be identified by ultrasound examination at postmenstrual weeks 9–11 in transverse and sagittal section. Filling and emptying over a 30–45 minute cycle can be demonstrated. The absence

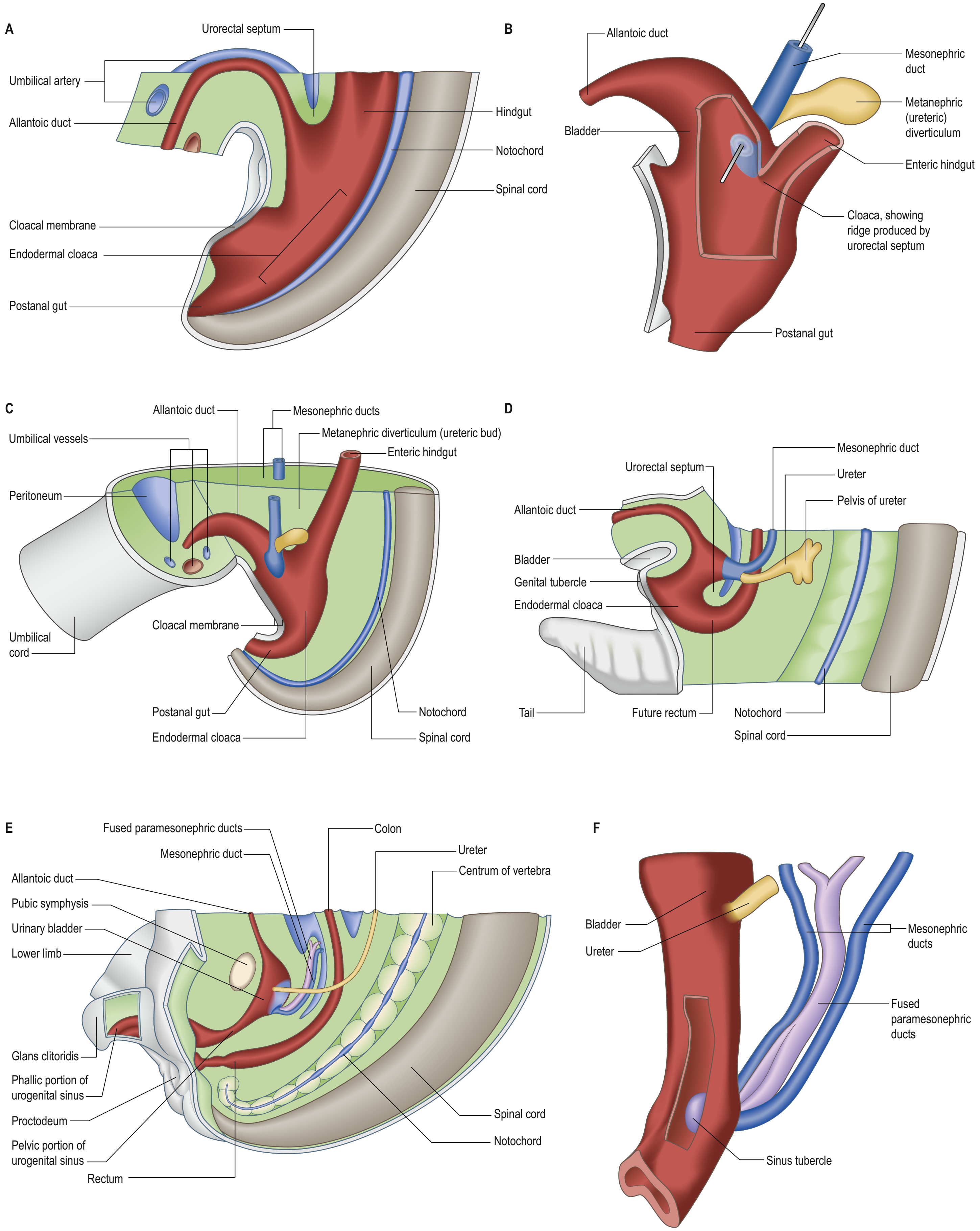
A
Urorectal septum
Umbilical artery
Allantoic duct
Hindgut
Notochord
Spinal cord
Cloacal membrane
Endodermal cloaca
Postanal gut
B
Allantoic duct
Mesonephric duct
Metanephric (ureteric) diverticulum
Bladder
Enteric hindgut
Cloaca, showing ridge produced by urorectal septum
Postanal gut
C
Allantoic duct
Mesonephric ducts
Metanephric diverticulum (ureteric bud)
Enteric hindgut
Umbilical vessels
Peritoneum
Umbilical cord
Cloacal membrane
Postanal gut
Endodermal cloaca
Notochord
Spinal cord
D
Mesonephric duct
Urorectal septum
Ureter
Pelvis of ureter
Allantoic duct
Bladder
Genital tubercle
Endodermal cloaca
Tail
Future rectum
Notochord
Spinal cord
E
Fused paramesonephric ducts
Colon
Mesonephric duct
Ureter
Centrum of vertebra
Allantoic duct
Pubic symphysis
Urinary bladder
Lower limb
Glans clitoridis
Phallic portion of urogenital sinus
Proctodeum
Pelvic portion of urogenital sinus
Rectum
Spinal cord
Notochord
F
Bladder
Ureter
Mesonephric ducts
Fused paramesonephric ducts
Sinus tubercle

Fig. 22.7 **A**, The caudal end of a human embryo about stage 11, showing the left lateral aspects of the spinal cord, notochord and endodermal cloaca. **B**, The endodermal cloaca of a human embryo about stage 13. Part of the left wall of the cloaca, including the left mesonephric duct, has been removed, together with the adjoining portions of the walls of the developing bladder and rectum. A piece of the ectoderm around the cloacal membrane has been left *in situ*. A wire is shown passing along the right mesonephric duct into the cloaca. **C**, The caudal end of a human embryo about stage 13, showing the endodermal cloaca. **D**, The caudal end of a human embryo about stage 15. The cloaca is becoming divided by the urorectal septum. **E**, The caudal end of a female human fetus about stage 23, from the left-hand side, showing structures in and near the median plane. The cloaca is now completely divided into urogenital and intestinal segments. **F**, Part of the vesico-urethral portion of the endodermal cloaca of a female human embryo about stage 23. The sinus tubercle is the elevation on the posterior wall of the urogenital sinus, caused by the fusion with the paramesonephric ducts.

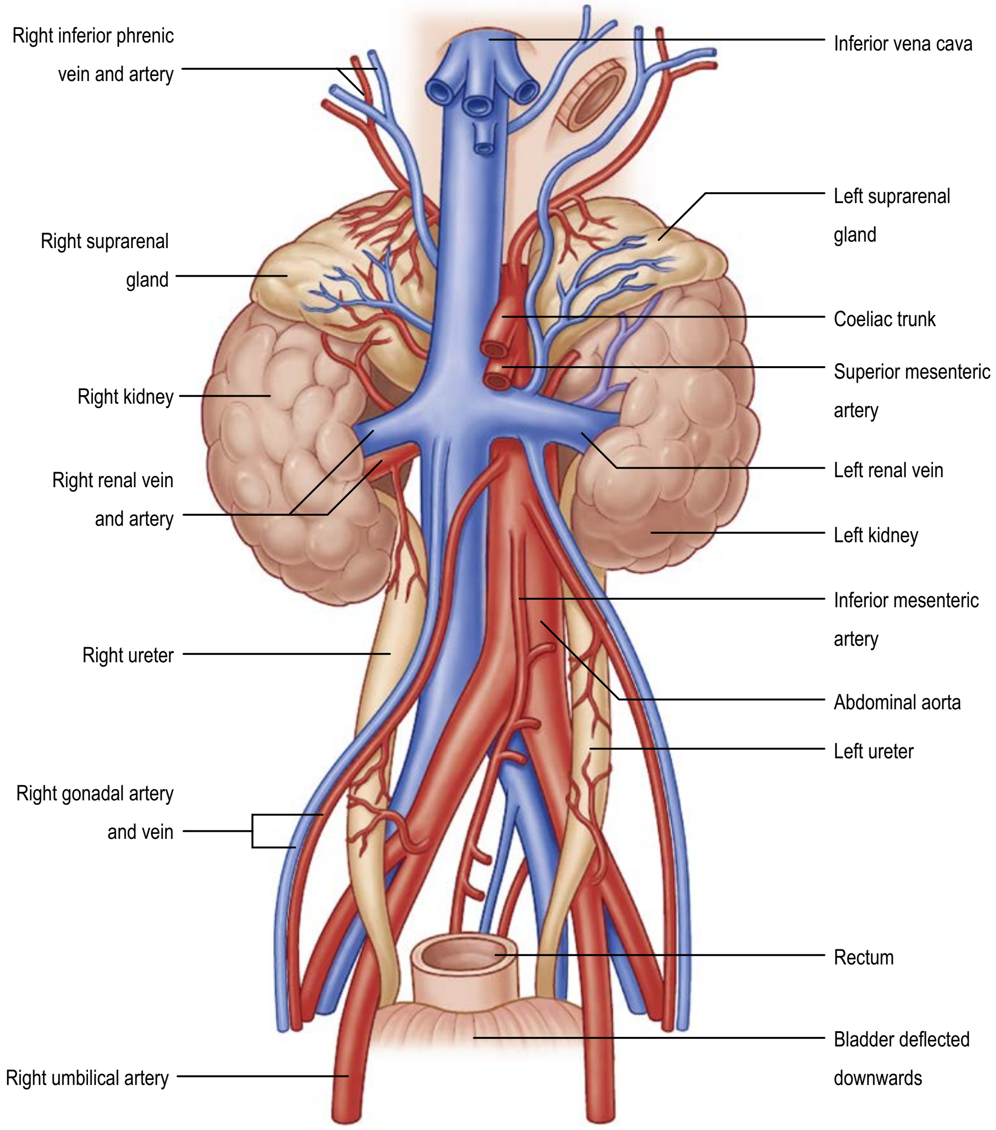

Fig. 22.8 The posterior abdominal wall of a full-term neonate. Note the lobulated kidneys and relatively wide calibre of the ureters.

of a bladder image at postmenstrual week 13 or later is considered abnormal. At postmenstrual week 20, the kidneys are best visualized in a section of the abdomen caudal to that used for abdominal circumference estimation. The diameter of the renal pelvis is reported in the anterior posterior view; 7 mm or less is considered normal around postmenstrual week 20 (To and Pereira 2015).

The routine use of ultrasound as an aid to *in utero* diagnosis of anomalies has revealed a prevalence of 1–2 abnormal fetuses per 1000 ultrasound procedures, of which 20–30% are anomalies of the genitourinary tract, detectable as early as postmenstrual weeks 12–15. The decision to be made after such a finding is by no means clear. Urinary obstruction is considered an abnormality, yet transient modest obstruction is considered normal during canalization of the urinary tract, and has been reported in 10–20% of fetuses in the third trimester. A delay in canalization, or in the rupture of the cloacal membrane, can produce a dilation. Similarly, the closure of the urachus at postmenstrual week 32 may be associated with high-resistance outflow for the system, which again produces transient obstruction. Distension of the fetal bladder, which may indicate lower urinary tract obstruction, affects 2.2/10,000 births, more commonly in males (Hodges et al 2009, Dias et al 2014). Over half of such cases are caused by the development of posterior urethral valves (a congenitally obstructing posterior urethral membrane); there may also be a dilated posterior urethra and thickened bladder wall

Urinary system at birth

The kidneys function early in development and produce the amniotic fluid that surrounds the fetus. At full-term (postmenstrual week 40), the two kidneys weigh approximately 23 g and the lobulated appearance of fetal kidneys is still present (**Fig. 22.8**; see Fig. 23.14C). Addition of new cortical nephrons continues in the first few months of postnatal life, and after this time, general growth of the glomeruli and tubules results in the disappearance of lobulation. The renal blood flow is lower in the neonate; adult values are attained by the end of the first year. The glomerular filtration rate at birth is approximately 30% of the adult value, which is attained by 3–5 months of age.

The neonatal urinary bladder is egg-shaped and the larger end is directed downwards and backwards (**Figs 22.9–22.10**; see Figs 23.14A, F–I). Although described as an abdominal organ, nearly one-half of the neonatal bladder lies below a line drawn from the promontory of the sacrum to the upper edge of the pubic symphysis, i.e. within the cavity of the true pelvis. From the bladder neck, the bladder extends anteriorly and slightly upwards in close contact with the pubis, until it reaches the ventral abdominal wall. The apex of the contracted bladder, which has a distinct interureteric fold, lies at a point midway between the pubis and the umbilicus. When the bladder is filled with urine, the apex may extend up to the level of the umbilicus: pressure on the lower abdominal wall will express urine from an infant bladder. The bladder remains connected to the umbilicus by the obliterated remains of the urachus (see Figs 22.19 and 23.15A), and so stimulation of the umbilicus can initiate micturition in babies. The elongated shape of the bladder in neonates means that the ureters are correspondingly reduced in length and they lack a pelvic portion. The bladder does not gain its adult, pelvic, position until about the sixth year.

Urine can be aspirated from the neonatal bladder into a sterile syringe, via a needle inserted through the abdominal wall about 2 cm above the pubic symphysis. The success rate of this procedure is improved by the use of ultrasound scanning to visualize urine in the bladder prior to insertion of the needle (O'Callaghan and McDougall 1987).

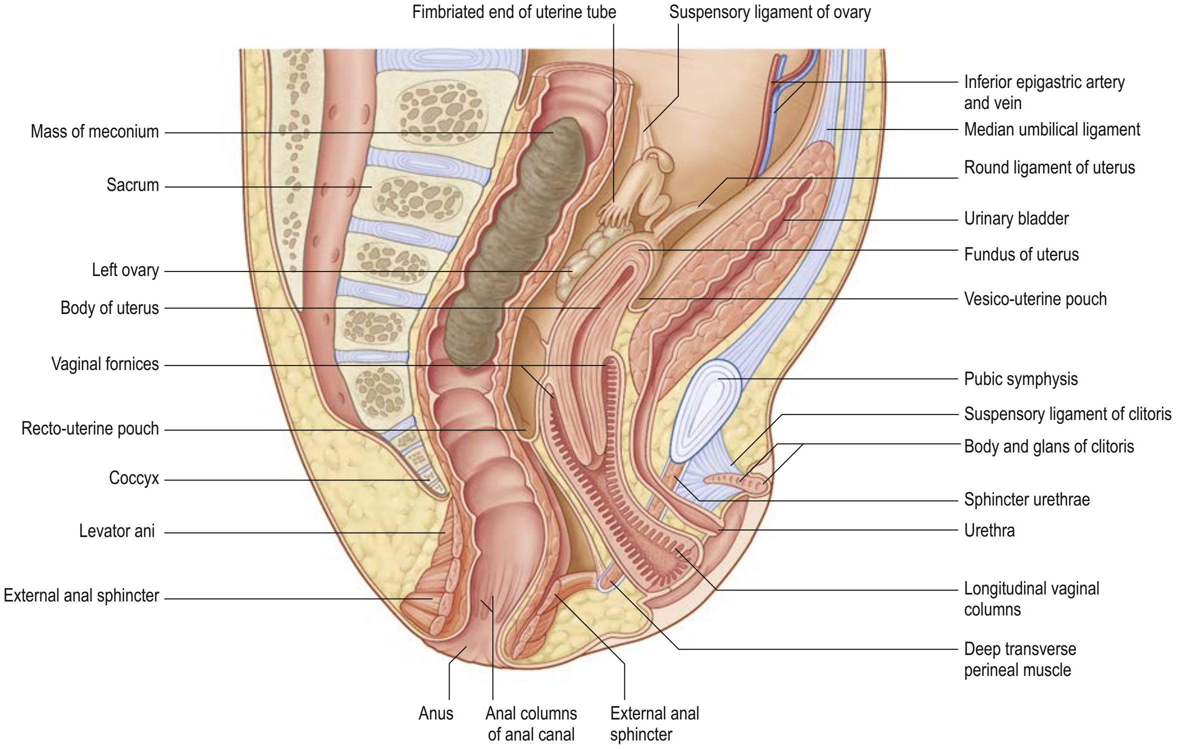
Fimbriated end of uterine tube
Suspensory ligament of ovary
Mass of meconium
Sacrum
Left ovary
Body of uterus
Vaginal fornices
Recto-uterine pouch
Coccyx
Levator ani
External anal sphincter
Inferior epigastric artery and vein
Median umbilical ligament
Round ligament of uterus
Urinary bladder
Fundus of uterus
Vesico-uterine pouch
Pubic symphysis
Suspensory ligament of clitoris
Body and glans of clitoris
Sphincter urethrae
Urethra
Longitudinal vaginal columns
Deep transverse perineal muscle
Anus
Anal columns of anal canal
External anal sphincter

Fig. 22.9 A midsagittal section through the pelvis of a full-term female neonate. Note the abdominal position of the urinary bladder and uterus. (Modified with permission from Crelin ES 1969 Anatomy of the Newborn. Philadelphia: Lea and Febiger.)

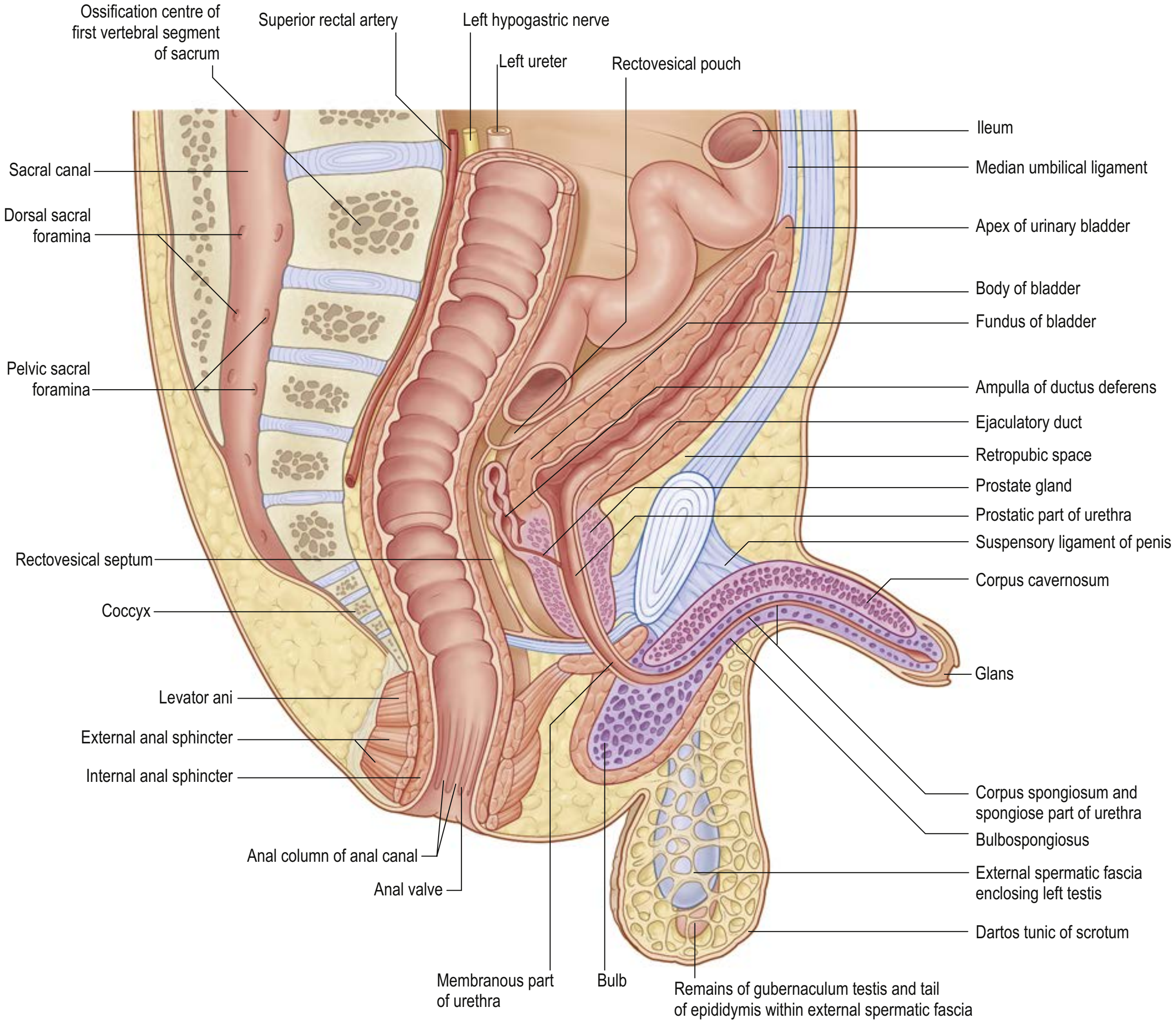
Ossification centre of first vertebral segment of sacrum
Superior rectal artery
Left hypogastric nerve
Left ureter
Rectovesical pouch
Sacral canal
Dorsal sacral foramina
Pelvic sacral foramina
Rectovesical septum
Coccyx
Levator ani
External anal sphincter
Internal anal sphincter
Anal column of anal canal
Anal valve
Membranous part of urethra
Bulb
Remains of gubernaculum testis and tail of epididymis within external spermatic fascia
Ileum
Median umbilical ligament
Apex of urinary bladder
Body of bladder
Fundus of bladder
Ampulla of ductus deferens
Ejaculatory duct
Retropubic space
Prostate gland
Prostatic part of urethra
Suspensory ligament of penis
Corpus cavernosum
Glans
Corpus spongiosum and spongiose part of urethra
Bulbospongiosus
External spermatic fascia enclosing left testis
Dartos tunic of scrotum

Fig. 22.10 A midsagittal section through the pelvis of a full-term male neonate. Note the abdominal position of the urinary bladder. (Modified with permission from Crelin ES 1969 Anatomy of the Newborn. Philadelphia: Lea and Febiger.)

Developmental anomalies of the urinary system

Available with the *Gray's Anatomy* e-book

SUPRARENAL GLANDS

The suprarenal (adrenal) gland is first seen in the human embryo at stage 14 as a specific proliferative region of the coelomic epithelium on the ventromedial surface of the urogenital ridge. Cells pass into the underlying mesenchyme between the root of the dorsal mesogastrium and the mesonephros (see Fig. 14.6A). The proliferating tissue extends from the level of the thoracic segments 6–12, and is soon disorganized dorsomedially by invasion of neural crest cells from somite levels 18–24 (see Fig. 14.20) that form the suprarenal medulla, and by the development of venous sinusoids. The latter are joined by capillaries that arise from adjacent mesonephric arteries and penetrate the cortex in a radial manner. By stage 18, the suprarenal gland is larger than the adjacent degenerating mesonephros and the developing, cranially ascending, metanephros. It remains larger than the metanephros (which touches it by stage 20), but as metanephric growth continues the suprarenal gland becomes relatively smaller by postmenstrual week 10 (see relative size at postmenstrual week 14 in Fig. 23.14F–I). As the suprarenal gland grows it is the most cranial viscus related to the developing pleuroperitoneal membrane (which contributes to the respiratory diaphragm). Initially this membrane is located on the ventral side of the suprarenal gland, gonad and mesonephros, but as the body wall is excavated during the formation of the costodiaphragmatic recess, the pleuroperitoneal membrane and associated mesenchyme become dorsal to the suprarenal gland and degenerating mesonephros during stages 16–17 (Hayashi et al 2011).

When proliferation of the coelomic epithelium stops, the cortex is enveloped ventrally, and later dorsally, by a mesenchymal capsule derived from the dorsolateral mesonephros. The subcapsular nests of cortical cells are the rudiments of the zona glomerulosa and they proliferate cords of cells that pass deeply between the capillaries and sinusoids. The cells in these cords degenerate in an erratic fashion as they pass towards the medulla; they become granular, eosinophilic and ultimately they autolyse. These cords of cells constitute the fetal cortex, which undergoes rapid involution during the first 2 postnatal years. Molecular aspects of the development of the early and fetal suprarenal gland have been reviewed (Ross and Louw 2015, Lotfi et al 2018). A comparison of the proteome of the embryonic and postnatal suprarenal gland in the rat has revealed expression of more proteins in later development and postnatal life (Dihazi et al 2015).

Functional, if not morphological zones, have been described in the fetal suprarenal gland from postmenstrual week 12. Cortisol is produced by the end of the first trimester and the gland is highly active throughout the second trimester. Early steroid synthesis provides substrates for placental oestrogen production: fetal steroid concentrations do not change after postmenstrual week 12. The fetal suprarenal gland does not produce aldosterone during the second trimester, suggesting that salt-wasting disorders, frequently seen in extreme preterm infants, may occur because of this limited early capacity for aldosterone production. Maternal smoking affects fetal suprarenal function and the development of the HPA axis, with reported alterations of placental function, reduced cortisol levels and response to stress in the first postnatal month (Johnston et al 2018).

Ultrasound examination of the suprarenal gland

A range of anthropometric studies have been published to aid identification of abnormal growth. These include fetal suprarenal gland length, recorded at 4-week intervals from postmenstrual week 15; nomograms showing linear growth of the gland between postmenstrual weeks 16 and 24; reference ranges of fetal suprarenal gland and fetal zone volumes between postmenstrual weeks 24 and 38, generated from 3D ultrasound examination (van Vuuren et al 2012, Jamigorn and Phupong 2017, Helfer et al 2017).

Suprarenal glands at birth

The suprarenal glands are large throughout development and are still relatively very large at birth (see Figs 22.8, 23.14C), constituting 0.2% of the entire body weight, compared with 0.01% in the adult. The left gland is heavier and larger than the right, as it is in the adult. At term, each gland usually weighs 4 g and the average weight of the two glands is 9 g (average in the adult is 7–12 g). Estimation of the suprarenal gland volume can provide an estimate of fetal weight; a volume of greater than 420 mm^3/kg is relevant in predicting preterm birth within 5 days of measurement (Turan et al 2007, Turan et al 2012). The glands shrink to normal infantile size within the first 2 weeks of postnatal life,. The average weight of both glands is 5 g by the end of postnatal week 2, and 4 g by 3 postnatal months; gland birth weight is not regained until puberty. This rapid involution of the glands occurs regardless of age at delivery: it is thought that parturition is the stimulus for suprarenal involution (Ben-David et al 2007). The cortex of the suprarenal gland is thicker than in the adult and the medulla of the gland is small. With normal involution, the fetal zone cells of the postnatal gland become smaller and they assume the appearance and organization typical of zona fasciculata.

Developmental anomalies of the suprarenal gland

The most common anomaly of suprarenal gland development is congenital hyperplasia (also termed congenital adrenal hyperplasia) occurring in 1 : 5000 to 1 : 15,000 births. The condition is caused by a group of autosomal recessive disorders, in which there are deficiencies in enzymes required for the synthesis of cortisol. In 90% of cases, the cause is deficiency of the enzyme 21-hydroxylase, producing an accumulation of 17-hydroxyprogesterone, which is converted to androgens. Mutations in the *CYP21A2* gene, on chromosome 6p, is found in 90–95% of affected individuals. The levels of androgens increase in this condition by several hundred times, causing female embryos and fetuses to undergo external genital masculinization ranging from clitoral hypertrophy to the formation of a phallus and scrotum. Postnatal management includes, if required, deferring gender assignment and establishment of the genetic sex of within 48 hours of delivery and monitoring serum electrolyte levels, blood glucose and blood pressure levels; 67–75% of these individuals will have salt wasting due to lack of aldosterone secretion (Rink 2016). In male embryos, the enzyme levels of 21-hydroxylase do not cause any changes in external genitalia. Suprarenal cortical growth and the molecular underpinning of anomalies has been reported (Lotfi et al 2018).

REPRODUCTIVE SYSTEM

Development of the reproductive organs from the intermediate mesenchyme starts from stage 14 (32–34 days postfertilization, see Fig. 23.3 for comparison of postfertilization days and the clinical scale of postmenstrual weeks), about 10 days later than the urinary system. Bilateral paramesonephric (Müllerian) ducts develop alongside the mesonephric ducts, and the midportion of each mesonephros undergoes thickening to form the gonadal ridge. Although the primordial germ cells are delineated very early in development, they are sequestered in the extraembryonic tissues until the gonadal ridge is ready to receive them. It was thought that development to one or other sexual phenotype occurred after migration of the primordial germ cells to the indifferent gonads. However, it is now recognized that the development of male or female gonads, genital ducts and external genitalia is far more complicated, and is the result of a complex interplay between genetic expression, timing of development and the influence of sex hormones. As development proceeds, a significant proportion of early embryonic urinary tissue is incorporated into the reproductive tracts, especially in the male. The earliest stage of reproductive development, prior to the arrival of the primordial germ cells into the gonad, is termed the indifferent or ambisexual stage.

Early gonadal development (ambisexual or indifferent stage)

Essentially, four different cell lineages contribute to the gonads. Cells are derived from: proliferating coelomic epithelium on the medial side of the mesonephros; underlying mesonephric mesenchyme; invading angiogenic mesenchyme already present in the mesonephros; and primordial germ cells that arise from the epiblast very early in development and later migrate from the allantoic wall.

The formation of the gonads is first indicated by the appearance of an area of thickened coelomic epithelium on the medial side of the mesonephric ridge in stage 16 (**Figs 22.12–22.13**; see Fig. 22.16). Elsewhere on the surface of the ridge, the coelomic epithelium is one or two cells thick, but over this gonadal area it becomes multilayered. Thickening rapidly extends in a longitudinal direction until it covers nearly the whole of the medial surface of the ridge. The thickened epithelium continues to proliferate, displacing the renal corpuscles of the

Congenital anomalies of the kidney and urinary tract are relatively common (3–6% of live births). For further reading about the genetic, epigenetic and *in utero* environmental factors in the pathogenesis of non-syndromic forms of human congenital anomalies of the kidney and urinary tract (CAKUT), see Yosypiv (2012) and Capone et al (2017).

Renal agenesis is the absence of one or both kidneys. In unilateral renal agenesis, the remaining kidney exhibits compensatory hypertrophy and produces a nearly normal functional mass of renal tissue. Atresia of the ureter during development causes a non-functional multicystic dysplastic kidney, thought to be secondary to urinary obstruction while the tubules are still forming. Problems with kidney ascent can result in a pelvic kidney. Alternatively, the kidneys may fuse together at their caudal poles, producing a horseshoe kidney that cannot ascend out of the pelvic cavity because the inferior mesenteric artery prevents its further migration. A duplex kidney arises when two ureteric buds meet the metanephros; it is characterized by two pelvicalyceal systems and is associated with ureterocele, ectopic insertion of the ureter and vesico-ureteric reflux.

It was thought that renal cysts arose from clumps of vesicular cells that persisted when the tips of branches from the ureteric diverticulum failed to fuse with metanephrogenic cap tissue. It is now believed that they are wide dilations of a part of otherwise continuous nephrons. In most cases, autosomal dominant polycystic kidney disease results from mutations of *PKD1* or *PKD2* genes, which are expressed in human embryos from postfertilization weeks 5–6 within the mesonephros and later the metanephros (Chauvet et al 2002). In this condition, the cystic dilation may affect any part of the nephron, from Bowman's capsule to collecting tubules. Less common is infantile cystic renal disease, inherited as a recessive trait, in which the proximal and distal tubules are dilated to some degree but the collecting ducts are grossly affected.

Anomalies of the ventral body wall caudal to the umbilicus, especially with inappropriate siting of the genital tubercle, can result in exstrophy of the bladder (**Fig. 22.11**) (Suzuki et al 2009, Williams 2013). In this condition, the urorectal septum (internal) is associated with the genital tubercle (external), which means that the urogenital and anal membranes are widely separated. When the urogenital membrane involutes, the posterior surface of the bladder is exposed to the ventral abdominal wall. The lower part of the abdominal wall is therefore occupied by an irregularly oval area, covered with mucous membrane, onto which the two ureters open. The periphery of this extroverted area, which is covered by urothelium, becomes continuous with the skin. The innervation of the underlying detrusor muscle seems to be normal, but the muscle has a decreased number of smooth muscle cells and an increased amount of collagen, which means that the bladder may have reduced contractile performance after reconstruction (Johal et al 2019). Bladder exstrophy is a complex condition involving the development of the pelvis, cloaca, urorectal septum, urogenital sinus, urethral plate, external genital tissues and all of the associated autonomic and somatic nerves supplying the region. For further reading about exstrophy–epispadias complex, its genetics, presentation and surgical repair, see Gearhart and Mathews (2016). Absence of the bladder, low insertion of the umbilical cord and bony pelvic anomalies on routine antenatal ultrasound examination would suggest the presence of bladder exstrophy in a fetus, however, it has been reported that only 25% of those neonates born with this condition were diagnosed antenatally. Its postnatal repair is exceedingly complex and has not been completely successful in establishing continence and a bladder capable of voluntary voiding. The accumulated experience of those surgical units undertaking these reconstructions provide hope for improved patient outcomes in the future (Dickson 2014).

Amniotic fluid is a dynamic fluid medium that changes throughout development (Ch. 9). The volume of amniotic fluid is used as an indicator of renal function but does not reflect fetal urinary output until the second trimester. Although variation in the amount of amniotic fluid may suggest anomalies of either the gut or the kidneys, it is not always possible to correlate even severe oligohydramnios (too little amniotic fluid) with renal dysfunction. There is an important relationship between the volume of amniotic fluid, lung development and maturity: oligohydramnios has been shown to be associated with pulmonary hypoplasia (Ch. 20).

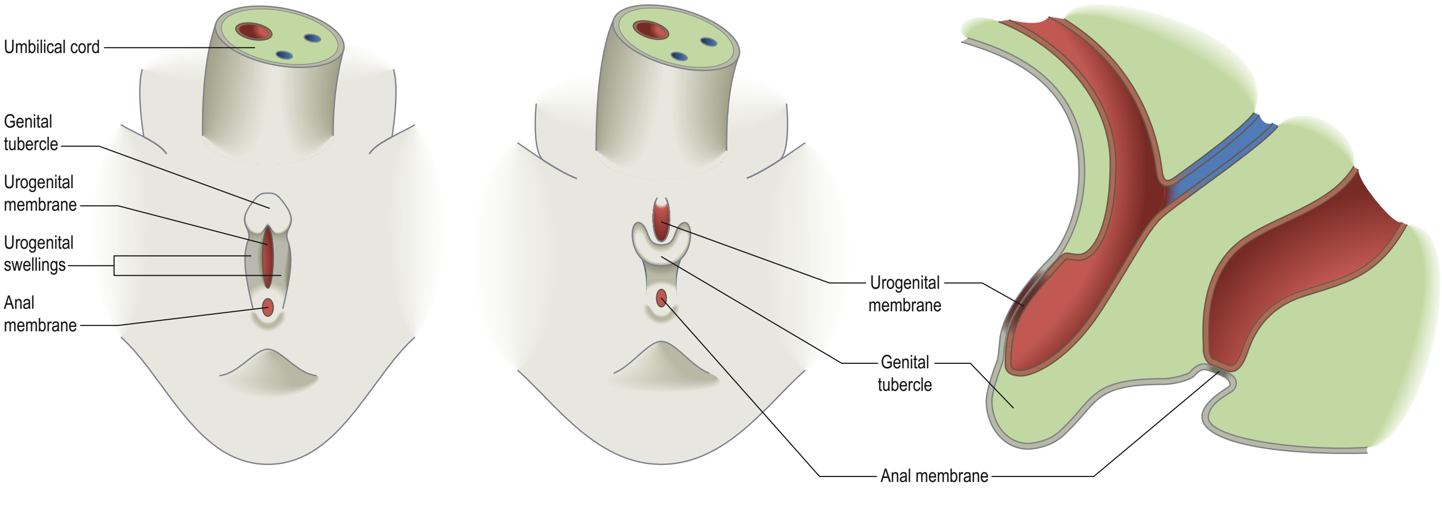

Normal

Exstrophy of the bladder and epispadias

Fig. 22.11 Bladder exstrophy. Misalignment of the genital tubercle and urogenital swellings with the urogenital membrane during early development results in subsequent malposition of the bladder, urethra and associated sphincters. The disappearance of the urogenital membrane exposes the posterior wall of the bladder, and the urethral opening is on the superior side of the penis or clitoris. (Redrawn from Tuchmann-Duplessis H, Haegel P 1972 Illustrated Human Embryology, Volume 2 Organogenesis. London: Chapman and Hall. With kind permission of Springer Science+Business Media.)

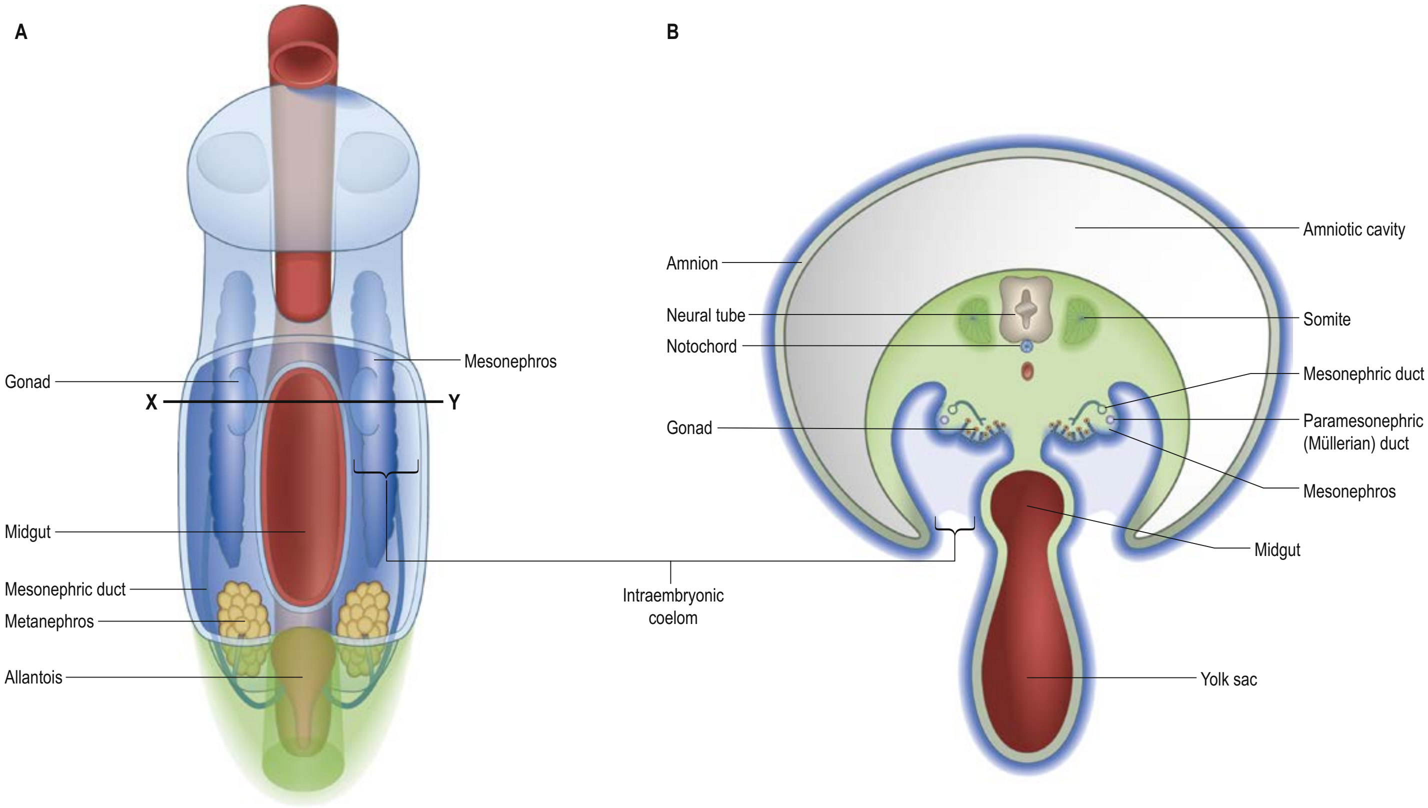

Fig. 22.12 **A**, The position of the gonads on the posterior abdominal wall, anteromedial to the mesonephros. **B**, A transverse section of figure **A**, through the line X–Y.

mesonephros in a dorsolateral direction, and forms a projection into the coelomic cavity: the gonadal ridge. Surface depressions form along the limits of the ridge, which is thus connected to the mesonephros by a broad mesentery, the mesogenitale. In this way, the mesonephric ridge becomes subdivided into a lateral part, the tubal fold, containing the mesonephric and paramesonephric ducts, and a medial part, the gonadal fold. The tubal fold also contains the nephric tubules and glomeruli at its base (see Fig. 22.3).

The ambisexual gonad possesses no sexually differentiating feature. From stage 16, the proliferating coelomic epithelium forms a number of cellular epithelial cords (sometimes called primary sex cords), separated by mesenchyme. The cords remain at the periphery of the primordium and form a cortex. Proliferation and labyrinthine cellular condensation of the mesonephric mesenchyme, including angiogenic mesenchyme, produce a central medulla. In both sexes the epithelial cells derived from the coelomic epithelium are destined to be the cell populations that support the primordial germ cells and contribute to the gonad–blood barrier. Some of the intervening mesenchyme cells have a later role in hormone production.

Reproductive ducts

The paramesonephric, Müllerian, ducts develop in embryos of both sexes, but become dominant in the development of the female reproductive system. They are not detectable until stage 16. Each begins as a linear invagination of the coelomic epithelium, the paramesonephric groove, on the lateral aspect of the mesonephric ridge near its cranial end. The blind caudal end continues to grow caudally into the substance of the ridge as a solid rod of cells that becomes canalized as it lengthens. Throughout the extent of the mesonephros, it is lateral to the mesonephric duct, which acts as a guide for it. The paramesonephric duct reaches the caudal end of the mesonephros, turns medially and crosses ventral to the mesonephric duct to enter the genital cord, where it bends caudally in close apposition with its fellow from the opposite side (see Fig. 22.13). The two ducts reach the dorsal wall of the urogenital sinus during stage 23 and their blind ends produce an elevation called the Müllerian or sinus tubercle (see Figs 22.7F, 22.19).

At the end of the indifferent stage, each paramesonephric duct consists of vertical cranial and caudal parts and an intermediate horizontal region. The mesonephric ducts course caudally, medial to the paramesonephric ducts, and both duct systems open into the urogenital sinus. The genital ducts possess an external coelomic epithelial covering; a smooth muscle muscularis, derived from underlying mesenchyme; and an internal mucosa, derived from either the mesonephric duct or from the invaginated tube of coelomic epithelium that forms the paramesonephric duct. The layers are invaded by angiogenic mesenchyme and by nerves.

Reproductive ducts in the female: uterine tubes, uterus, cervix

In the female, the mesonephric duct is vestigial. Cranially, it becomes the longitudinal duct of the epoophoron, and caudally it is referred to as Gartner's duct (**Table 22.1**). The cranial part of the paramesonephric ducts forms the uterine tubes, and the original coelomic invagination remains as the pelvic opening of the tube. The fimbriae become defined as the cranial end of the mesonephros degenerates. The caudal vertical parts of the two ducts fuse with each other during stage 23 to form the uterovaginal primordium (**Fig. 22.14**) that gives rise to the lower part of the uterus; as it enlarges, it takes in the horizontal parts to form the fundus and most of the body of the adult uterus. The stroma of the endometrium and the uterine musculature develop from the surrounding mesenchyme of the genital cord.

Failure of fusion of the two paramesonephric ducts can lead to a range of anomalies summarized in **Fig. 22.15**. These fusions can also contribute to anomalies of vaginal development. The fetal female reproductive tract is affected by maternal hormones and undergoes some enlargement in the fetus. The endocervical glands are active before birth and the cervical canal is usually filled with mucus.

At birth, the uterine tubes are relatively short and wide, the uterus is relatively large, 2.5–5 cm long (average 3.5 cm), 2 cm wide between the uterine tubes, and a little over 1 cm thick (see Figs 22.9, 23.14C, 23.15A). The body of the uterus is smaller than the uterine cervix, which forms two-thirds or more of the length. The isthmus between the body and the cervix is absent. The position of the uterus in the pelvic cavity depends, to a great extent, on the state of the bladder anteriorly and the rectum posteriorly. If the bladder contains only a small amount of urine, the uterus may be anteverted but it is often in a direct line with the vagina (see Figs 22.9, 22.19). The uterus subsequently involutes to about one-third of its length and more than half of its weight; it does not regain its neonatal size and weight until puberty.

Vagina

At approximately postmenstrual week 12, an endodermal epithelial proliferation, the sinuvaginal bulb, arises from the dorsal wall of the urogenital sinus in the region of the sinus tubercle. Its proliferation

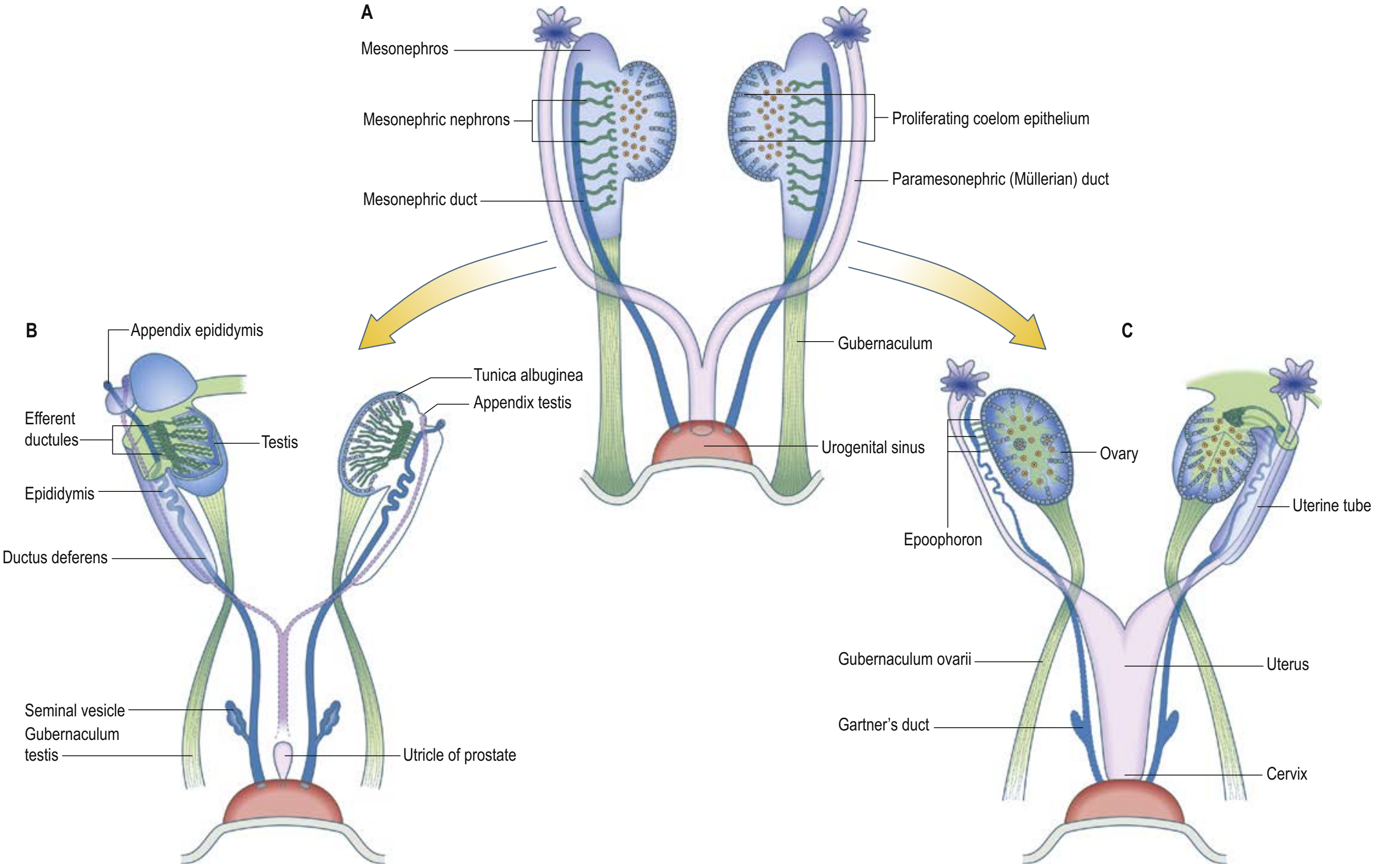

Fig. 22.13 **A**, The indifferent or ambisexual stage of development. **B**, Male. The mesonephric ducts are retained (left) and the paramesonephric ducts involute (right). **C**, Female. The paramesonephric (Müllerian) ducts are retained (right) and the mesonephric ducts involute (left).

TABLE 22.1 Homologies of the parts of the urogenital system in male and female

Gonad	Testis	Ovary
Gubernacular cord	Gubernaculum testis	Ovarian and round ligaments
Mesonephros (Wolffian body)	Appendix epididymis (?)	Appendices vesiculosae (?)
	Efferent ductules	Epoophoron
	Lobules of epididymis	
	Paradidymis	Paroophoron
	Aberrant ductules	
Mesonephric duct (Wolffian duct)	Duct of epididymis	Duct of epoophoron (Gartner's duct)
	Ductus (vas) deferens	
	Ejaculatory duct	
	Part of bladder and prostatic urethra	Part of bladder and urethra
Paramesonephric (Müllerian) duct	Appendix testis	Uterine tube
		Uterus
	Prostatic utricle	Vagina (?)
Allantoic duct	Urachus	Urachus
Cloaca:		
Dorsal part	Rectum and upper part of anal canal	Rectum and upper part of anal canal
Ventral part	Most of bladder	Most of bladder and urethra
	Part of prostatic urethra	
Urogenital sinus	Prostatic urethra distal to utricle	
	Bulbourethral glands	Greater vestibular glands
	Rest of urethra to glans	Vestibule
Genital folds	Ventral penis	Labia minora
Genital tubercle	Penis	Clitoris
	Urethra in glans	

produces a column of cells, the vaginal plate, flattened anteroposteriorly, encased within caudal splanchnopleure, that will eventually become the fibromuscular wall of the vagina, cervix and body of the uterus. This uterovaginal primordium results in elongation of the female reproductive tract, causing the caudal tip of the fused paramesonephric ducts to be displaced cranially (see Figs 22.7F, 22.14B). The origin of the sinuvaginal bulb marks the site of the future hymen. Anomalies of paramesonephric duct fusion can produce related vaginal anomalies (see Fig. 22.15).

The following sequence of events occurs between postmenstrual weeks 14–22: the exact timing of each part will vary in individual fetuses. The vaginal plate enlarges into a cylindrical structure that is gradually canalized through its whole extent, the process starting from its caudal end and extending cranially. The lower end grows caudally and approaches the developing vestibule. The vaginal lumen is complete around postmenstrual week 19 and continuous with the exterior about one week later. The boundary of the origin of the vaginal mucosa has been defined in the mouse, but there are significant heterochronic differences between murine and human development (Kurita 2010, 2011). A series of studies have demonstrated the differential expression of *PAX2* and *FOXA1* genes in the human female reproductive tract (Robboy et al 2017, Cunha, Robboy et al 2018a). Coelomic-derived paramesonephric ducts express *PAX2* along their length, whereas vaginal plate expresses *FOXA1*, an endodermal epithelial gene noted in the hindgut and urogenital sinus. At about postmenstrual week 19, *PAX2* is expressed at the lower end of the uterovaginal canal in the uterus, cervix and future vaginal fornices. By about postmenstrual week 22, the fornices and exocervix express *FOXA1*: the transition of expression is sited in the endocervical canal. The surrounding mesenchyme instructively induces the extent of vaginal epithelial differentiation.

In early fetal life the epithelium of the uterine tubes, uterus and cervix is simple columnar, with some ciliated cells. Stratified squamous epithelium is seen in the vagina at about postmenstrual week 19, and by about postmenstrual week 22, the vaginal mucosa is folded and the epithelium thickened in response to oestrogenic stimulation. This hypertrophy continues throughout the later months of fetal life under the influence of placental and maternal hormones (see Fig. 22.22). The

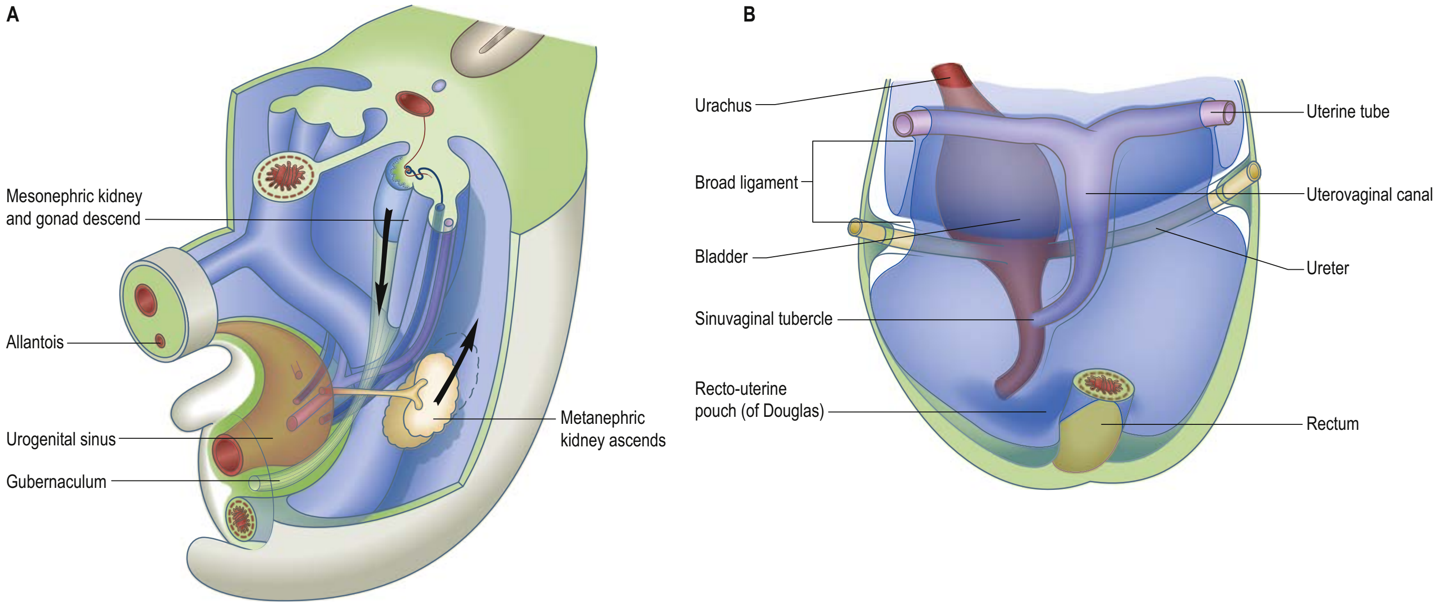
A
Mesonephric kidney and gonad descend
Allantois
Urogenital sinus
Gubernaculum
Metanephric kidney ascends
B
Urachus
Broad ligament
Bladder
Sinuvaginal tubercle
Recto-uterine pouch (of Douglas)
Uterine tube
Uterovaginal canal
Ureter
Rectum

Fig. 22.14 Relative movements of the gonads and associated tubes. **A**, Gonads and mesonephros move caudally, and the metanephros ascends. **B**, A posterior view of the mesonephric ducts (ureters) and the fused paramesonephric ducts (uterovaginal canal) in the female. For earlier development, see Fig. 22.3. (Based on Tuchmann-Duplessis H, Haegel P 1972 Illustrated Human Embryology, Volume 2 Organogenesis. London: Chapman and Hall. With kind permission of Springer Science+Business Media.)

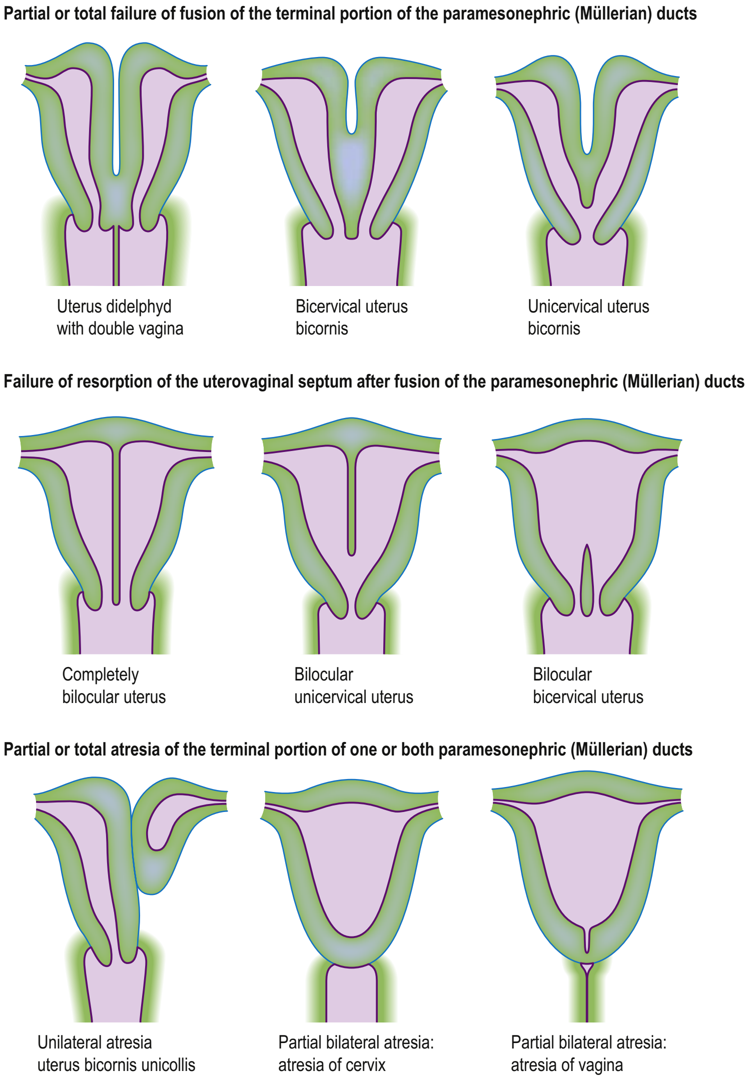
Partial or total failure of fusion of the terminal portion of the paramesonephric (Müllerian) ducts
Uterus didelphyd with double vagina
Bicervical uterus bicornis
Unicervical uterus bicornis
Failure of resorption of the uterovaginal septum after fusion of the paramesonephric (Müllerian) ducts
Completely bilocular uterus
Bilocular unicervical uterus
Bilocular bicervical uterus
Partial or total atresia of the terminal portion of one or both paramesonephric (Müllerian) ducts
Unilateral atresia uterus bicornis unicollis
Partial bilateral atresia: atresia of cervix
Partial bilateral atresia: atresia of vagina

Fig. 22.15 Uterovaginal anomalies.

vaginal epithelium assumes the inactive form of childhood after the period of mini-puberty (see p. 364).

In the neonate, the vagina is 2.5–3.5 cm long and 1.5 cm wide at the fornices, and the uterine cervix extends into the vagina for about 1 cm (Crelin 1969). The posterior vaginal wall is longer than the anterior wall, giving the vagina a distinct curve (see Figs 22.9, 22.19, 23.15A). The cavity is filled with longitudinal columns covered with a thick layer of cornified, stratified, squamous epithelium: these cells slough off after birth, when the effect exerted by maternal hormones is removed.

The orifice of the vagina is surrounded by the hymen, a thick, elliptical ring of connective tissue. During childhood, the hymen becomes a membranous fold along the posterior margin of the vaginal lumen: should the fold form a complete diaphragm across the vaginal lumen, it is termed an imperforate hymenal membrane.

Reproductive ducts in the male: epididymis, ductus deferens, seminal glands (vesicles)

In the male, most of the paramesonephric ducts atrophy (see Fig. 22.13) under the influence of anti-Müllerian hormone (AMH; also called Müllerian inhibiting substance, or MIS), which is released into the mesonephric duct by the Sertoli cells of the testis. It is thought that the epithelial cells of the paramesonephric duct initially undergo apoptosis, and that once the epithelial cells no longer secrete a basal lamina, the remaining ductal epithelial cells transform into mesenchyme that remains in the vicinity of the involuting duct (Allard et al 2000). Vestigial remnants of the paramesonephric ducts are most likely to persist cranially and/or caudally, at the limits of the local exocrine effects of AMH. A vestige of the cranial end of the duct persists as the appendix testis (see Figs 22.13, 22.19; see Table 22.1). The fused caudal ends of the two ducts are connected to the wall of the urogenital sinus by a solid utricular cord of cells that soon merges with a proliferation of sinus epithelium, the sinu-utricular cord, that is similar to, but less extensive than, the sinus proliferation in the female. The proliferating epithelium is claimed to be an intermingling of the endoderm of the urogenital sinus with the lining epithelia of the mesonephric and paramesonephric ducts, which have extended on to the surface of the sinus tubercle. As the sinu-utricular cord grows, so the utricular cord recedes from the tubercle. In the second half of fetal life, the composite cord acquires a lumen and becomes dilated to form the prostatic utricle, the lining of which consists of hyperplastic stratified squamous epithelium. The sinus tubercle becomes the colliculus seminalis.

The main reproductive ducts in the male are derived from the mesonephric ducts, which persist under the action of androgens that are probably secreted down the ducts themselves, and are subsumed into the male reproductive system as the metanephric kidney develops. The mesonephric duct gives rise to the canal of the epididymis, ductus (vas) deferens and ejaculatory duct. It is possible that the extensive lengthening and coiling of the epididymis is a local example of buckling morphogenesis produced by biomechanical tension in the surrounding tissues (Hirashima 2014). The seminal gland and the ampulla of the ductus deferens appear as a common swelling at the end of the mesonephric duct during the end of the third and into the fourth months. Their appearance coincides with degeneration of the paramesonephric ducts, although no causal relation between the two events has been established. Separation into two rudiments occurs at about 125 mm crown–heel length. The seminal gland elongates, its duct is delineated and hollow diverticula bud from its wall. Around postmenstrual weeks 22–23, the growth rate of both vesicle and ampulla is greatly increased. Fig. 22.10 shows the position of the ampulla of the ductus deferens in the neonate, possibly in response to increased secretion of prolactin by the fetal or maternal hypophysis, or to the effects of placental hormones. The tubules of the prostate show a similar increase in growth rate at this time.

Primordial germ cells

The primordial germ cells are formed very early from the epiblast (see Fig. 10.3). They are larger (12–20 μm in diameter) than most somatic cells, and are characterized by vesicular nuclei with well-defined nuclear membranes, and by a tendency to retain yolk inclusions long after these have disappeared from somatic cells. It is not yet clear whether the primordial germ cells are derived from particular blastomeres during cleavage, if they constitute a clonal line from a single blastomere, or if they are the product of a progressive concentration of the nucleus of the fertilized ovum by unequal partition at successive mitoses. Primordial germ cells spend the early stages of development within the extraembryonic tissues near the end of the primitive streak and in the connecting stalk (see Fig. 10.4E). In this situation, they are away from the inductive influences to which the majority of the somatic cells are subjected during early development.

Primordial germ cells can be identified in human embryos in stage 11, when the number of cells is probably not more than 20–30. When the tail fold has formed, they appear within the endoderm and the splanchnopleuric mesenchyme and epithelium of the hindgut, as well as in the adjoining region of the wall of the yolk sac. They migrate dorsocranially in the mesentery, by amoeboid movements and by growth displacement, and pass around the dorsal angles of the coelom (medial coelomic bays) to reach the genital ridges from stage 15 (see Fig. 22.16). It is believed that the genital ridges exert long-range effects on the migrating primordial germ cells, in terms of controlling their direction of migration and supporting the primordial germ-cell population. Primordial germ cells contact each other via long processes and retain cytoplasmic bridges when they divide. They are usually in close proximity to somatic cells, which may modify the local environment, forming junctional complexes with them. The surface of primordial germ cells displays binding sites for extracellular matrix macromolecules. A range of molecular markers associated with the migration and proliferation of primordial germ cells has been described (Soto-Suazo and Zorn 2005, Runyan et al 2006, De Felici 2013). Single-cell RNA-Seq analysis has identified the range of genes and transcription factors expressed in the first and second trimester by human primordial germ cells and their associated somatic cells (Li et al 2017).

Primordial germ cells proliferate both during and after migration to the mesonephric ridges. Cells that do not complete this migration mainly degenerate, but if they survive, they can give rise to germ cell tumours, usually in the midline (Runyan et al 2006). After segregation, when they are sometimes termed primary gonocytes, or spermatogonia and oogonia in male and female respectively, they divide to form secondary gonocytes.

Development of the gonads

Gonads in both sexes arise from local interactions along the medial side of the mesonephros, between proliferating dorsal coelomic wall epithelium and the underlying mesonephric mesenchyme and mesonephric nephrons (see Fig. 22.12). Primordial germ cells migrate into this region and are sequestered within the epithelial populations in different ways in male and female. The factors that lead to formation of either testis or ovary are described below and in **Fig. 22.16**.

Testis

The testis develops in the middle portion of the gonadal ridge, but unlike the ovary does not retain any local remnants from the cranial or caudal parts.

The proliferating coelomic epithelial cells contribute to lengthening epithelial cords which invade the underlying mesenchyme. They become determined as Sertoli cells (also called sustenocytes) and form the walls of the seminiferous tubules encroaching on and uniting with a medullary network of mesonephric mesenchyme which forms the rete testis (see Figs 22.13, 22.16). Sertoli cells proliferate throughout fetal and early postnatal life (see mini puberty, p. 364) and perhaps again at the initiation of puberty (Sharpe et al 2003); once dividing ceases the cells mature and cannot be reactivated. Primordial germ cells are incorporated into the early cords and between the dividing Sertoli cells. The number of Sertoli cells produced at this early time determines the maximal limit of adult sperm production, as each Sertoli cell can only support a fixed number of proliferating primordial germ cells (Sharpe et al 2003). Because developing and maturing spermatogonia make up the bulk of the adult testis, the number of Sertoli cells is a major determinant of the size to which the testes will grow (factors that impair the process of spermatogenesis, resulting in the loss of primordial germ cells, will also affect testicular size). Variation in Sertoli cell number is probably the most important factor in accounting for the enormous variation in sperm counts between individual males, whether fertile or infertile. Indeed, the available data for adult males indicate that Sertoli cell numbers vary across a 50-fold range (Sharpe et al 2003). Although some of this variation may result from attrition of Sertoli cell numbers because of ageing, the major differences in Sertoli cell numbers will have been determined by events in fetal life and/or childhood, with parental epigenetic effects also contributing (Sharpe 2010). In mammals, the testis–blood barrier is formed by tight junctions between adjoining Sertoli cell at the basal region of the seminiferous tubule adjacent to the epithelial basal lamina and actin-rich adherens junctions termed ectoplasmic specializations (Wen et al 2018): it is not yet known when this occurs in humans. Early blood vessels form between the seminiferous tubules and appear to form around clusters of Leydig cells.

The interstitial cells of the testis are derived from mesenchyme and, possibly, also from coelomic epithelial cells that do not become incorporated into the tubules. Among other cell lines, they form the embryonic

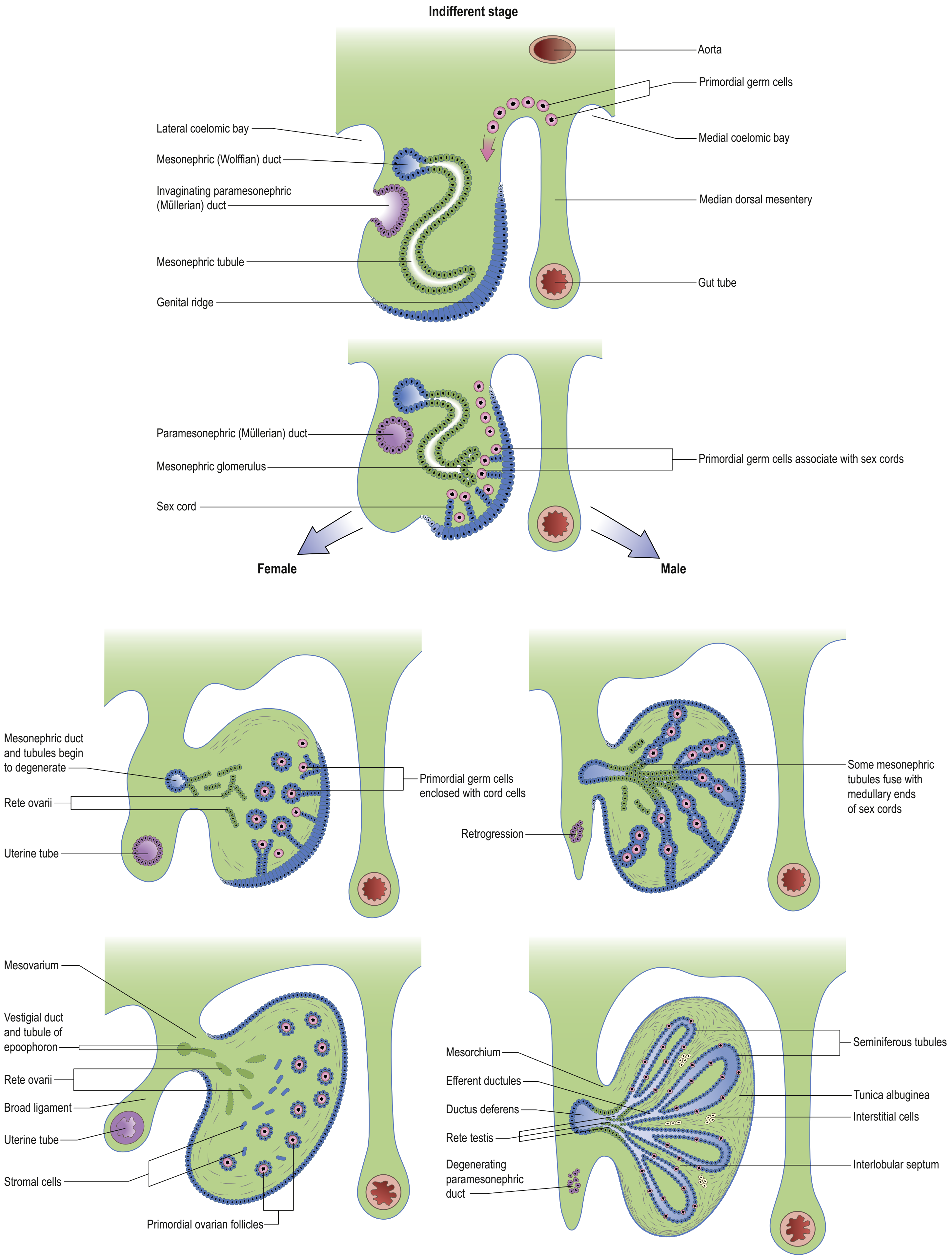
Indifferent stage
Aorta
Primordial germ cells
Lateral coelomic bay
Medial coelomic bay
Mesonephric (Wolffian) duct
Invaginating paramesonephric (Müllerian) duct
Median dorsal mesentery
Mesonephric tubule
Gut tube
Genital ridge
Paramesonephric (Müllerian) duct
Mesonephric glomerulus
Primordial germ cells associate with sex cords
Sex cord
Female
Male
Mesonephric duct and tubules begin to degenerate
Rete ovarii
Primordial germ cells enclosed with cord cells
Uterine tube
Some mesonephric tubules fuse with medullary ends of sex cords
Retrogression
Mesovarium
Vestigial duct and tubule of epoophoron
Rete ovarii
Broad ligament
Uterine tube
Stromal cells
Primordial ovarian follicles
Mesorchium
Efferent ductules
Ductus deferens
Rete testis
Degenerating paramesonephric duct
Seminiferous tubules
Tunica albuginea
Interstitial cells
Interlobular septum

Fig. 22.16 The development of the gonads and associated ducts, as seen in transverse section, to show the fate of the primordial germ cells, mesonephric duct and tubules, and paramesonephric duct in males and females. (Modified with permission from Williams PL, Wendell-Smith CP, Treadgold S 1969 Basic Human Embryology, 2nd ed. London: Pitman Medical & Scientific.)

and fetal cells of Leydig, which secrete testosterone and insulin-like factor 3 (INSL3), and peritubular myoid cells (smooth muscle cells), which surround the seminiferous tubules. Leydig cell numbers increase until postnatal month 3 and then decrease. The tunica albuginea of the testis form from a later migration of mesenchyme beneath the coelomic epithelium.

The channels of the rete testis become connected to the glomerular capsules of persisting mesonephric nephrons. Ultimately the 5–12 most cranial persisting mesonephric tubules form a connection to the mesonephric duct. They become exceedingly convoluted and form the lobules of the head of the epididymis. The mesonephric duct, which was the primitive 'ureter' of the mesonephros, becomes the canal of the epididymis and the ductus deferens of the testis. The seminiferous tubules do not acquire lumina until postmenstrual weeks 25–28; the tubules of the testicular rete become canalized somewhat earlier.

Developmental anomalies of the testis

All testicular cell lines and their developmental processes can contribute to anomalous development and limited fertility, e.g. genetic changes to the Y chromosome (Colaco and Modi 2018), imbalance of the genes required to ensure sufficient Sertoli and Leydig cell differentiation (She and Yang 2017), disorders of development and descent of the male reproductive tract (Hadziselimovic 2017). Although all of these factors are operating concordantly, disorders of descent of the male reproductive tract is considered below. Anomalies of the testis, e.g. gonadal dysgenesis and small testes, are important risk factors for the later development of testicular germ cell cancer. Testicular carcinoma-in-situ (CIS) cells arise from primordial germ cells that have failed to complete differentiation into spermatogenic germ cells (Rajpert-De Meyts 2006). The condition is seen in young males (95% of cases affect 15- to 45-year-old males) caused by activation of premalignant cells. The incidence of testicular germ cell cancer has increased over the past 60 years and appears to be caused by environmental/lifestyle causes rather than genetic factors. Risk of testicular germ cell cancers in migrant males is comparable to their original country of origin, whereas the risk to children born in a country to which their parents have emigrated is the same as in that country. The development of fewer Sertoli cells during fetal and early postnatal life and at the initiation of puberty directly affects the number of spermatogenic germ cells that the testis can support.

In the relatively recent past, prospective, well-standardized studies undertaken across Europe have documented a fall in sperm counts of around 40–50% (1% per year over the last 50 years); 15–20% of young males have an abnormally low sperm count (less than 20 million sperm per ml based on WHO standards); and only 5–15% of the sperm produced can be classified as normal (depending on the strictness of the criteria of normality used) (Cooper et al 2010, Sharpe 2010). Although this dramatic decrease is obviously manifest only in adulthood, as is the case with testicular cancer, there is growing evidence that it may reflect impaired testicular development during fetal or childhood life (Lobo et al 2019). Imbalance between the genes promoting or suppressing Sertoli/follicle cells and Leydig/theca cells that extends throughout fetal and postnatal life is noted in disorders of sex development, leading to male to female or female to male transition. These related factors, together with cryptorchidism (see below), are considered part of a testicular dysgenesis syndrome promoted by environmental factors, including exhaust fumes, smoking, parental obesity and epigenetic effects, seen particularly in Western countries (Sharpe 2010).

Ovary

The ovary develops from the middle part of the gonadal ridge: the cranial part becomes the suspensory ligament of the ovary (infundibulopelvic fold of peritoneum), and the caudal part is incorporated into the ovarian ligament.

Cellular development of the ovary occurs slightly later than the testis (see Figs 22.13, 22.16). Few, if any, epithelial cords from the proliferating coelomic epithelium invade the underlying mesenchyme. The majority of epithelial cells remain in the cortex separated by fine septa of undifferentiated mesenchyme. An ovarian rete condenses in the medullary mesenchyme and may temporarily join mesonephric glomeruli, but any connection subsequently regresses; mesenchyme and developing blood vessels form the ovarian stroma which will give rise to future thecal cells. The cortical epithelial clusters become determined as follicle cells and surround the primordial germ cells (now identified as primary oocytes) that have entered the prophase of the first meiotic division. Primary oocytes are derived from a mitotic division of the primordial germ cells (naked oogonia). Flattened epithelial follicle cells (also termed pregranulosa cells) coalesce around them producing primordial follicles from about postmenstrual week 13. Placental-derived oestrogens promote an increase in primordial follicle development after postmenstrual weeks 14–15, when about 100,000 are present; this number increases to 680,000 by postmenstrual week 34 when some of these follicles mature. The pool of primordial follicles remains stable until postnatal month 8 (Lanciotti et al 2018).

Further development of ovarian follicles in the fetus, neonate and after puberty includes the specification of a blood–follicle barrier that proteins/peptides, sugars, electrolytes and ions in fluid must cross to access the follicular antrum from the theca (Rodgers and Irving-Rodgers 2010, Siu and Cheng 2012). The barrier is composed of the surrounding endothelial cells (joined by tight and adhesion junctions and an underlying basal lamina), the thecal interstitium, the follicular basement membrane, and the membrana granulosa. The permselectivity of the subendothelial basal lamina and the follicular basement membrane differ, possibly because some of the extracellular matrix components of the follicular basement membrane change during primordial, primary and pre-antral stages (Siu and Cheng 2012). From the pre-antral stage of follicle development to maturity, those cells closest to the oocyte are termed granulosa cells.

There are temporospatial changes within the developing ovary. Neurotropins and their receptors have been shown to be expressed within the fetal ovary between postmenstrual weeks 13 and 21. NT4 is localized initially in epithelioid cells mingled with oogonia, then within oogonial mRNA, and finally in the primordial follicle cells, with lesser expression in the enclosed oocytes (Anderson et al 2002).

Expression of p450c17, a steroidogenic enzyme involved in the production of androgens, has been shown in the human fetal ovary during the second and third trimesters (Cole et al 2006). Its temporospatial expression showed a movement from the cortex to the medulla, with its presence in primary interstitial cells in the cortex from postmenstrual weeks 14 to 23, but not in hilus interstitial cells. Between postmenstrual weeks 27 and 33, few cells stained for p450c17, but there was an increase after postmenstrual week 33 in theca interstitial cells associated with pre-antral follicles. Positive-staining hilar interstitial cells were rarely seen before postmenstrual week 33. The temporospatial expression was similar in anencephalic fetuses of the same age, indicating that anterior pituitary function is not regulating this maturation. A possible role for insulin in regulating fetal ovary androgen production has been suggested. Overexpression of interstitial androgen production is a component in the pathophysiology of polycystic ovary syndrome (Cole et al 2006).

Sex determination in the embryo

It was believed that the gonads were indifferent or ambisexual until the arrival of the primordial germ cells in the gonadal ridge, at which point the sex of the embryo was 'turned on' by the presence of the male or female germ cells. However, embryos in which the genital ridges are devoid of germ cells may still undergo otherwise normal testis development. It is not clear if the germ cells are necessary for ovarian determination. They are required for the proper organization and differentiation of the ovary, and their absence results in the development of 'streak gonads', where only lines of follicular cells can be seen, as in Turner's syndrome.

The processes of sex determination and differentiation involve interacting pathways of gene activity that lead to the total patterning of the embryo as either male or female.

In the current, generally accepted, model of sex determination in humans, the female pathway is considered to be the 'set-up' programme, i.e. the course of events that will occur unless development is diverted into the testicular pathway, a process triggered by the presence of a Y chromosome. The resulting cellular changes convert the indifferent gonad into a testis, which then produces three key hormones (AMH, INSL3 and testosterone) that collectively induce masculinization of the fetus and acquisition of male secondary sexual characteristics.

The possession of a Y chromosome is usually associated with a male developmental pathway. Deletion mapping of the Y chromosome in a class of XX males arising from abnormal X–Y interchange at meiosis showed that the male-determining region of the chromosome was a conserved sequence located near its tip, termed the testis-determining factor (TDF). This sequence contains a gene that is the 'master switch' which programmes the direction of sexual development, the so-called *SRY* gene (sex-determining region on the Y chromosome). The human *SRY* gene is a single exon on Yp that encodes a protein of 204 amino acids with a conserved DNA-binding domain (Colaco and Modi 2018). The *SRY* gene acts initially within the epithelial cords of cells derived from the coelomic epithelium of the ambisexual gonad. These cells can potentially differentiate into either Sertoli or follicle (granulosa) cells, the supporting cells for the germ cells in the testis and ovary, respectively. Studies indicate that *SRY* initiates testis formation from the indifferent gonad by directing the development of supporting-cell precursors as Sertoli rather than follicle cells (Albrecht and Eicher 2001, She and Yang 2017). *SRY* gene expression is initiated in humans at postfertilization day 41; it reaches maximal expression after this time and is thereafter maintained at a low level throughout fetal, postnatal and adult life (She and Yang 2017). The expression is seen first in cells designated as pre-Sertoli, located centrally in the developing gonad, and then later in the cranial and caudal poles. Once the developmental pathway of Sertoli cells has been initiated, the differentiation of the other cell types in the testicular pathway follows: Leydig cells subsequently appear, and the connective tissue becomes organized into a male pattern. The germ cells are also affected by this environment. When they arrive, they become enclosed within the Sertoli cells, do not enter meiosis and continue to proliferate (which is characteristic of spermatogenesis), instead of ceasing proliferation and entering meiosis and meiotic arrest, as occurs in the ovary. Thus, the development of male characteristics follows the expression of *SRY*: female characteristics develop in its absence.

Studies of XY individuals with sex reversal (i.e. XY females) and corresponding gene knockout studies in mice have established that *SRY* initiates testis development by inducing the expression of another gene, *SOX9* (SRY-like HMG-box protein 9): its expression in the absence of *SRY* is sufficient for male determination. A multi-step cascade of gene expression changes essentially reinforce SOX9 expression and consolidate development along the male pathway; the genes involved include *WT1* (Wilm's tumour gene), *GATA4* (GATA-binding protein 4), *FGF9* (fibroblast growth factor 9) and *DAX-1* (orphan nuclear receptor DAX-1) (Biason-Lauber 2010, Munger et al 2013). This cascade also actively represses expression of genes that promote development along the female pathway, including *RSPO1* (R-spondin 1), *WNT4* (Wingless-type MMTV integration site family member 4) and *FOXL2* (Forkhead box L2). Activation of the female cascade of gene expression actively suppresses expression of SOX9 and/or other genes in the 'male cascade'. Development of either a testis or an ovary therefore results from a balance between activation and repression of sexually dimorphic genes: inactivating mutations in any of these genes, or their aberrant expression in the wrong sex fetus, has the potential to interfere, partially or completely, with normal gonad formation and thus with downstream sexual development (Biason-Lauber 2010, Munger et al 2013).

Gene expression balance is required throughout development and adult life. In early development, high *FGF9* and low *WNT4* is seen in the XY gonad, whereas low *FGF9* and high *WNT4* is seen in the XX gonad. In later development and throughout life, FOXL2 and DMRT1 (doublesex and mac-3 related transcription factor 1) interact: DMRT1 antagonizes FOX12 to maintain postnatal testis differentiation, and FOXL2 suppresses DMRT1 to ensure adult ovarian differentiation. *DMRT1* is found on chromosome 9, its deletion is correlated with XY male to female sex reversal (Huang et al 2017). *Foxl2* deletion in adult mouse ovary switches theca cells to Leydig-like cells and follicle (granulosa) cells to Sertoli-like cells. For details of the delicate balance of these factors and the maintenance of adult gonadal differentiation see She and Yang (2017)

Subsequent development of the male phenotype requires fetal secretion of testosterone, AMH and INSL3. Of these, testosterone is the most important, because it has body-wide effects, both on the developing reproductive system/genitalia and on numerous other organs/tissues, including the brain. The development of the appropriate cytoplasmic testosterone-binding receptor protein (the androgen receptor) is also important. Sertoli cells synthesize AMH, which causes the regression of the Müllerian ducts, and Leydig cells produce testosterone, which promotes the development of the mesonephric ducts, sets into process the development of male external genitalia, and sensitizes other tissues to testosterone. Absence of a functional androgen receptor, as occurs in the complete androgen insensitivity syndrome (CAIS), results in XY individuals who have testes and degenerated Müllerian ducts, but cannot respond to the circulating testosterone produced by their testes and therefore develop female secondary sexual characteristics.

Descent of the gonads

The gonads develop on the posterior abdominal wall bilaterally along the central portion of the mesonephros. This region receives a rich blood supply that is directed to the gonads as the mesonephros involutes. Both gonads descend, the testis to lie outside the abdominal cavity, and the ovary to the pelvis, and they both retain their early blood supply from the dorsal aorta.

Descent of the testis

The mechanism of testicular descent remains poorly understood (Barthold and Ivell 2018). It is conventionally described in two phases, transabdominal and inguinoscrotal, that are regulated by distinct morphological and endocrine factors (Barteczko and Jacob 2000).

Transabdominal phase

Each testis initially lies on the dorsal abdominal wall. As it enlarges, its cranial end degenerates and the remaining organ therefore occupies a more caudal position. It is attached to the mesonephric fold by the mesorchium (the mesogenitale of the undifferentiated gonad), a fold of the coelomic wall and underlying mesenchyme that contains the testicular vessels and nerves. It also acquires a secondary attachment to the ventral abdominal wall that has a considerable influence on its subsequent movements. At the point where the mesonephric fold bends medially to form the genital cord (see Fig. 22.3), each testis becomes connected to the lower part of the ventral abdominal wall by an inguinal fold of coelomic wall that covers a mesenchymal cord, the gubernaculum or genito-inguinal ligament (see Figs 22.3, 22.13; **Fig. 22.17**). Traditionally, regardless of sex, the proximal end of the gubernaculum has been described as extending from the lower end of the developing gonad, attached either to the mesonephric duct or to the caudal pole of the developing epididymis (Hadziselimovic 2017). The distal end of the gubernaculum seems to align to the inguinal part of the milk line that extends from the axilla to the femoral region (see Fig. 53.27). It has been suggested that this line corresponds to the original lateral edge of the embryo that expresses the apical ectodermal ridges and mesenchymal progress zones of the upper and lower limbs (Hutson 2013, Hutson et al 2014).

Up to about postmenstrual week 12, the gubernaculum in male and female embryos is similar, but then production of the non-androgenic hormone insulin-like 3 (INSL3) from Leydig cells stimulates enlargement (known as the 'swelling reaction') of the gubernaculum in males. This serves to anchor the fetal testis near the future inguinal canal as the abdominal cavity enlarges between postmenstrual weeks 12–15. By comparison, the gubernaculum in females remains thin and subsequently develops into the round ligament (see Table 22.1; p. 359). The cranial attachment of the urogenital ridge, known as the cranial suspensory ligament, regresses in males under the action of androgens. Subtle changes in Leydig cell dysfunction and changes in INSL3 production may occur in cryptorchidism (Barthold and Ivell 2018).

After postfertilization week 12 the midgut loop returns to the abdomen and the ventral abdominal wall inferior to the umbilical cord lengthens. As each umbilical artery runs ventrally from the dorsal to the ventral wall, it pulls up a falciform peritoneal fold, which forms the medial boundary of a peritoneal fossa, the saccus vaginalis of lateral inguinal fossa, into which each testis projects.

Inguinoscrotal phase

Gonadotropin releasing hormone and altering levels of FGF signalling are essential for testicular descent. The caudal end of the gubernaculum is initially associated with a specific portion of the milk line of the abdominal wall around which the future inguinal canal is formed by differentiating abdominal wall muscles. An interaction with the mammary line ectoderm and underlying mesenchyme may trigger gubernacular meristematic growth similar to that seen in the progress zone of the limb bud. Between postmenstrual weeks 25 and 35, the male gubernaculum begins to bulge out from the abdominal muscles and elongate across the pubis and into the scrotum (see Fig. 22.17). A specific evagination of the coelomic wall continuous with the peritoneal cavity, the processus vaginalis, extends into the gubernaculum, hollowing it out so that the proximal part is divided into a crescentic parietal layer within which the cremaster muscle develops, and a central column attached to the epididymis. Elongation of the soft, gelatinous end of the gubernaculum, which, in the early stage, is formed mainly of hyaluronic acid, is controlled by androgens. The exact mechanisms mediating gubernacular growth in humans are still unclear (Barthold and Ivell 2018). In rodent models, there is good evidence that androgens cause sexual dimorphism of the sensory branches of the genitofemoral nerve, which supplies the gubernaculum, the developing cremaster muscle within it, and part of the scrotum. The genital branch of the nerve releases calcitonin gene-related peptide (CGRP), which stimulates growth of the gubernacular tip along a chemotactic gradient to the scrotum.

The testis remains in apposition with the deep inguinal ring, held by the gubernaculum during postmenstrual weeks 13–24 (Barteczko and Jacob 2000). From postmenstrual week 35, the extracellular matrix of the gubernaculum is resorbed and it forms a fibrous attachment to the inside of the scrotum. Testis descent during the inguinoscrotal phase occurs relatively rapidly over postmenstrual weeks 25–28, the left testis usually descending ahead of the right. Intra-abdominal pressure acting

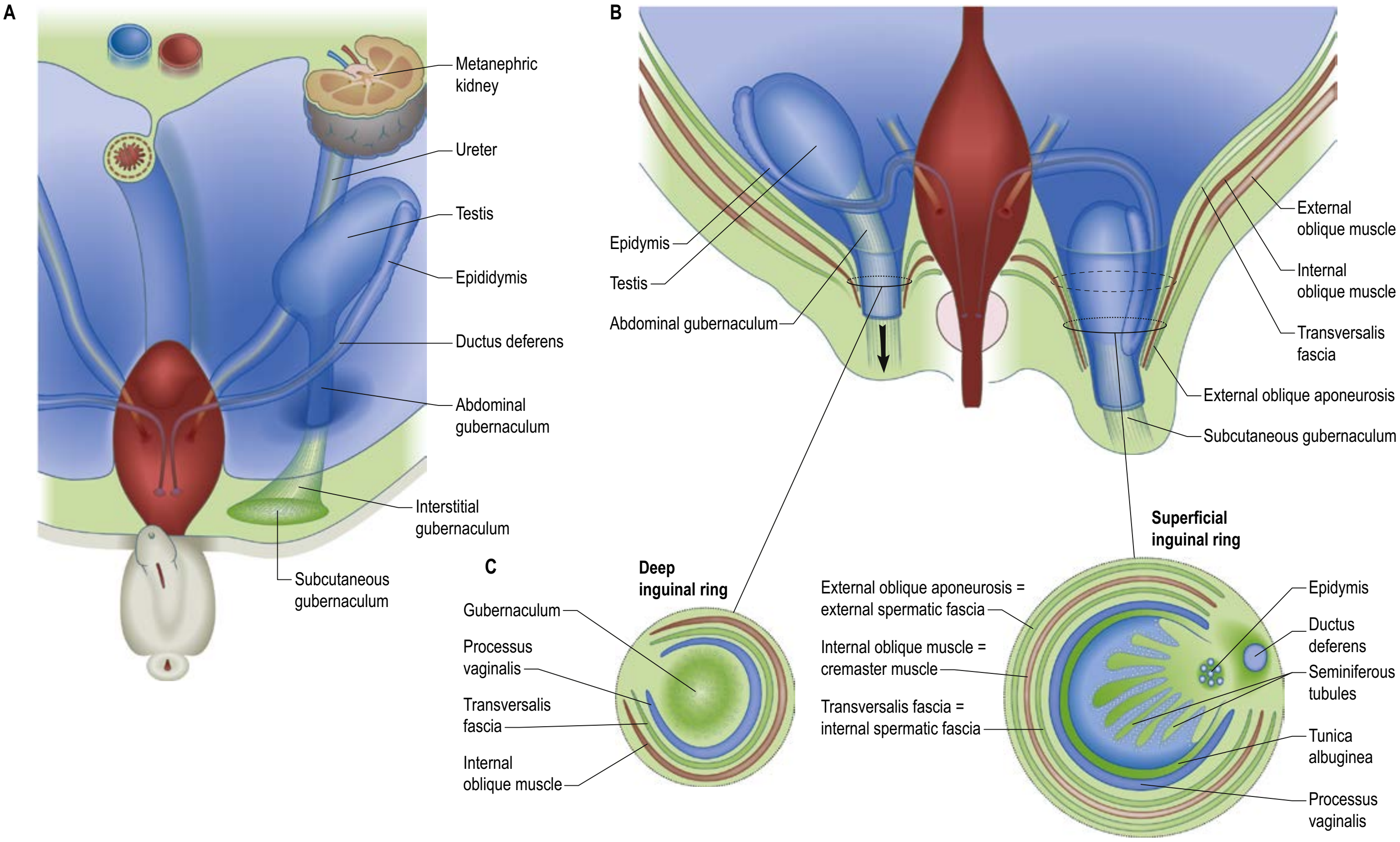
A
Metanephric kidney
Ureter
Testis
Epididymis
Ductus deferens
Abdominal gubernaculum
Interstitial gubernaculum
Subcutaneous gubernaculum
B
Epidymis
Testis
Abdominal gubernaculum
External oblique muscle
Internal oblique muscle
Transversalis fascia
External oblique aponeurosis
Subcutaneous gubernaculum
C
Gubernaculum
Processus vaginalis
Transversalis fascia
Internal oblique muscle
Deep inguinal ring
Superficial inguinal ring
External oblique aponeurosis = external spermatic fascia
Internal oblique muscle = cremaster muscle
Transversalis fascia = internal spermatic fascia
Epidymis
Ductus deferens
Seminiferous tubules
Tunica albuginea
Processus vaginalis

Fig. 22.17 The descent of the testis. The testis is retroperitoneal throughout development. It becomes obliquely orientated during abdominal descent. **A**, The gubernaculum attached to the lower part of the testis has an abdominal part covered with developing peritoneum, an interstitial part and a distal end embedded in the ventral abdominal wall at the site of the future inguinal canal. **B**, The gubernaculum swells, becoming similar in width to the testis. The distal-most portion of the gubernaculum bulges into abdominal wall muscles and grows 3–5 cm over the superior pubic ramus and into the scrotum. A crescentic column of peritoneum, the processus vaginalis, develops in the expanding gubernaculum. **C**, The testis gains a crescentic covering of visceral and parietal peritoneum (which forms the tunica vaginalis) and muscle and connective tissue layers as it passes through the deep and superficial inguinal rings. The coverings remain around the ductus deferens, whereas the proximal processus vaginalis normally becomes obliterated by postnatal week 3. (Based on data from Barteczko KJ, Jacob MI 2000 The testicular descent in human. Origin, development and fate of the gubernaculum Hunteri, processus vaginalis peritonei and gonadal ligaments. *Adv Anat Embryol Cell Biol* 156:III–X, 1–98.)

through the patent processus vaginalis likely contributes to this migration (Hutson 2012).

Although testis descent may not be complete in preterm infants, over 95% of term (postmenstrual week 40) neonates have descended testes. After descent the processus vaginalis remains patent for 2 weeks in nearly 70% of male infants; it is partially obliterated in 80% of male infants by postnatal week 3, the left side before the right. The distal processus vaginalis (with visceral and parietal layers derived from the coelomic wall) persists as the tunica vaginalis, a satellite peritoneal cavity around the testis that becomes firmly attached to the surrounding scrotum within a few weeks. Obliteration of the proximal processus vaginalis is controlled by androgens, indirectly via CGRP released from the genitofemoral nerve. Both exogenous CGRP and hepatocyte growth factor can cause obliteration *in vitro* of the processus vaginalis in hernial sacs excised from babies with indirect inguinal hernia.

Persistent patency of the processus vaginalis leads to indirect inguinal hernia (widely patent and allowing prolapse of bowel), or hydrocele (narrow patency permitting only intraperitoneal fluid to trickle down into the tunica vaginalis). During obliteration, fluid may trickle only part of the way down the processus vaginalis to produce an encysted hydrocele of the cord. This is a relatively common but transient state and usually resolves completely within a few weeks by further obliteration. The spermatic cord, scrotum, seminal glands and adjacent ampullae of the ductus deferens are all relatively large in the neonate, reflecting perinatal androgen exposure.

In aberrant testicular descent, the testis may remain in the abdomen, although this is thought to be uncommon because the hormonal and morphological features of the transabdominal phase are relatively simple. By contrast, the indirect endocrine regulation and complex migratory process of the gubernaculum during the inguinoscrotal phase is frequently abnormal: the testis lies in the inguinal or pubic region in 2–5% of neonates. Rarely, the testis may lie in the perineum, in the upper part of the thigh or at the root of the penis. Causes may be deficient prenatal and postnatal androgens, a mislocated genitofemoral nerve or inadequate CGRP production from the nerve. Testes that have descended may not remain within the scrotum if the spermatic cord does not double its length between birth and puberty (Hutson 2013). The aetiology of acquired undescended testes is probably linked to that of hydrocele and hernia.

Descent of the ovary

The relative movements of the ovary are less extensive than those of the testis and are not hormonally regulated. Like the testis, the ovary ultimately reaches a lower level than it occupies in the early months of fetal life, but it does not leave the pelvis to enter the inguinal canal, except in certain anomalies. The ovary is connected to the medial aspect of the mesonephric fold by the mesovarium (homologous with the mesorchium), and to the ventral abdominal wall by the inguinal fold (see Fig. 22.13; **Fig. 22.18**). A mesenchymatous gubernaculum develops in this fold but, as it traverses the mesonephric fold, it acquires an additional attachment to the lateral margin of the uterus near the entrance of the uterine tube. Its lower part, caudal to this uterine attachment, becomes the round ligament of the uterus, and the part cranial to the attachment becomes the ovarian ligament. Collectively, these structures are homologous with the gubernaculum testis in the male (**Fig. 22.19**). This new uterine attachment may be correlated with the restricted ovarian descent. Initially, the ovary is attached to the medial side of the mesonephric fold but, in accordance with the manner in which the two mesonephric folds form the genital cord, it is finally connected to the posterior layer of the broad ligament of the uterus. The gubernacula thus develop in the female, unlike in the male, as bilateral fibrous bands or ligaments in the absence of INSL3. They do not extend into the labia majora, but end in the connective tissue just external to the external ring of the inguinal canal: in the absence of androgens, there is no migratory phase analogous to inguinoscrotal migration in the male. The saccus vaginalis is present in the female. Its prolongation into the inguinal canal (the canal of Nuck) is normally completely obliterated, but may remain patent and form the sac of a potential indirect inguinal hernia.

Cryptorchidism is common in neonates, with a prevalence of 2–9% of all boys (Barthold and Ivell 2018, Chen et al 2018). Cryptorchidism used to be considered a relatively minor birth defect that was corrected surgically sometime during childhood. It is now considered to be a symptom of testicular dysgenesis syndrome, a spectrum that includes hypospadias, impaired semen quality and testicular germ cell cancer; it is associated with low birth weight; maternal smoking and gestational diabetes (Toppari et al 2014, Hadziselimovic 2017). Since the number of spermatogonia decreases rapidly in undescended testes, orchidopexy is now undertaken between 6–9 months of postnatal life. Further delay results in impaired testicular catch-up growth in boys: even with early orchidopexy, men with bilateral undescended testes are six times more likely to be infertile (Lee and Shortliffe 2014). The finding that males with unilateral cryptorchidism are 25 times more likely to develop azoospermia than normal males supports the premise that this is a bilateral disease. Lower levels of testosterone, AMH and inhibin B were found in male infants (about 2 postnatal years) with bilateral cryptorchidism, compared to control male infants (Hamdi et al 2017). It has been suggested that cryptorchidism and neurodevelopmental disorders may share genetic risk factors or that individual *in utero* or early postnatal risk factors may be common precursors for both cryptorchidism and neurodevelopmental disorders (Chen et al 2018).

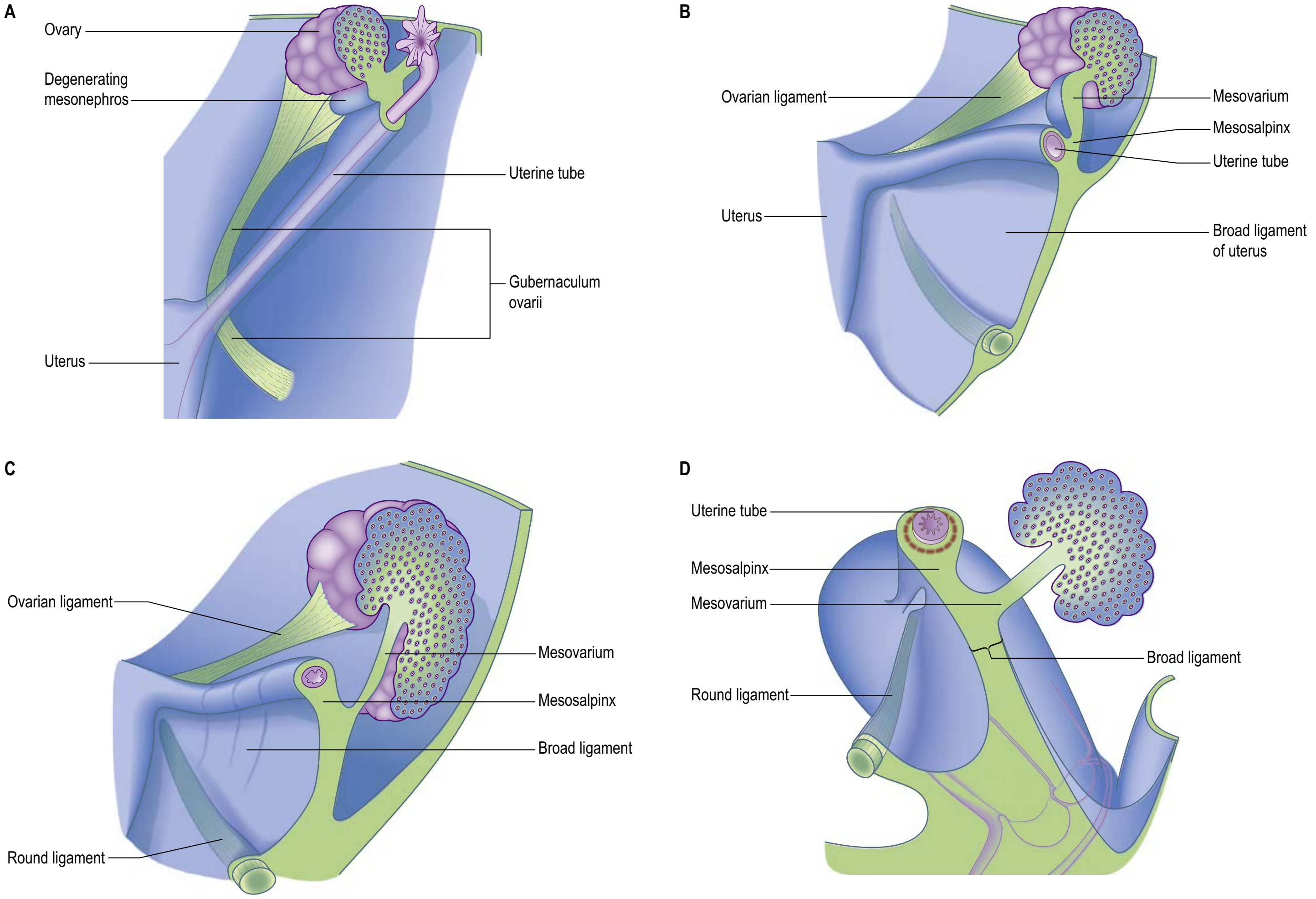

Fig. 22.18 The descent of the ovary. **A**, An early developing left ovary and uterine tube. **B**, The start of posterior movement of the ovary. **C**, The left ovary in its definitive posterior position. **D**, A sagittal section of the ligaments associated with the ovary, viewed from a left lateral position.

In the term neonate (postmenstrual week 40), the ovaries lie in the lower part of the iliac fossae. The long axis of the ovary is almost vertical. It becomes temporarily horizontal during descent, but regains the vertical when it reaches the ovarian fossa. The ovaries complete their descent into the ovarian fossae in early childhood. Thus, at birth, the ovary and the lateral end of the corresponding uterine tube lie above the pelvic brim. They do not sink into the lesser pelvis until the latter enlarges sufficiently to contain both of them and the other pelvic viscera, including the bladder. Neonatal ovaries are 1–3.6 mm long (Stranzinger and Strouse 2008) and their combined weight at birth is 0.3 g, which is relatively large, and much larger than the combined weight of the testes (see Figs 22.9, 23.14C). The ovaries double in weight during the first 6 postnatal weeks. They bear surface furrows that disappear during postnatal months 2–3. All of the primary oocytes for the reproductive life of a female are present in her ovaries by the end postmenstrual week 12. Of the 7 million primary oocytes estimated to be present at about postmenstrual week 20, 1 million remain at birth and 40,000 by puberty and only 400 are ovulated during reproductive life.

Cloaca

The cloaca is the region at the caudal end of the primitive hindgut that is continuous with the allantois (see Figs 22.4, 22.7). The allantois, a blind-ending ventral diverticulum, passes into the connecting stalk of the early embryo prior to tail-folding and is drawn into the body cavity after stage 10. In subsequent stages the distal extension within the connecting stalk is termed the allantoic duct, and the proximal end that later passes into the forming umbilical cord is termed the urachus. The cloacal cavity is slightly dilated and lined with endoderm. It is initially connected dorsocranially to the enteric hindgut, ventrally to the allantois and ventrocaudally is in contact with overlying ectoderm at the cloacal membrane. It receives and contains fluid from the mesonephric kidneys until the cloacal membrane breaks down and the cloacal and amniotic cavities become confluent. Proliferation of mesenchyme at the angle of the junction of the hindgut and allantois produces the urorectal septum (intercloacal mesenchyme), which shows passive caudal expansion with embryonic growth, promoting the movement of the endodermal epithelium towards the cloacal membrane (**Fig. 22.20**). The cloaca becomes separated into a presumptive rectum and anal canal dorsally, and a presumptive urinary bladder and urogenital sinus ventrally, and the cloacal membrane is divided into anal and urogenital parts, respectively. The nodal centre of division is the site of the future perineal body. The urogenital sinus receives the mesonephric and paramesonephric ducts. The genes involved in mouse embryo cloacal division and the morphogenetic movements of human cloacal division have been reported (Matsumaru et al 2015, Kruepunga et al 2018).

The development of the cloaca, the lower ends of the reproductive ducts and the external genitalia is complex, and associated with mesenchymal populations derived from secondary neurulation. The cranial and dorsal areas of the cloaca show less growth and enlargement than the ventrocaudal area, which matches overall embryonic growth between stages 14 and 23, when the embryonic body straightens and the region of ventral body wall between the cloaca and umbilicus lengthens. There are also regional differences in growth of the surrounding mesenchymal populations, accumulation of extracellular matrix and extent of cell apoptosis. Ventrally, during stage 14, there is concomitant expansion of the genital tubercle and increase in length of the cloacal membrane. The middle portion of the cloacal membrane, formed by close apposition of internal endoderm and external ectoderm breaks down during stage 18 (Kruepunga et al 2018).

Developmental anomalies of the cloaca

Available with the *Gray's Anatomy* e-book

Pelvic floor

The pelvic floor consists of the ligamentous supports of the cervix, and the pelvic and urogenital diaphragms. The muscles control

From a morphological perspective, the underlying mechanism of some cloacal malformations may be due to the balance of regional cloacal change: too little or absent regression of the dorsal area of the cloaca may result in its persistence, with the anal opening becoming positioned more ventrally on the perineum, whereas too much regression may lead to stenosis or atresia of the anorectal junction and insufficient development of the internal anal sphincter (Kruepunga et al 2018). Bladder exstrophy is considered with urinary tract malformations (see Fig. 22.11). Cloacal malformations include the exstrophy–epispadias complex and the range of disorders of sex development; associated genital tract anomalies are common, with paramesonephric duct duplication in 40% of those affected (see Fig. 22.15) (Rintala 2016). The broad grouping of cloacal anomalies covers persistent urogenital sinus, anorectal malformations and ambiguous external genitalia. Persistent urogenital sinus is frequently seen with congenital adrenal hyperplasia; it can occur with normal and ambiguous external genitalia. The position of the resulting confluence of urethra and vagina relative to the bladder neck is important for future surgical management; one single common urogenital sinus channel opens on the perineum and anterior displacement of the anus may be seen. In persistent cloacal anomalies confluence of genital, urinary and intestinal paths form an isolated single perineal opening (Rink 2016). Antenatal ultrasound findings of transient fetal ascites and decreased amniotic fluid have been noted from postmenstrual week 19 in cloacal anomalies, and are thought to be due to blocked urine outlet via the vagina (hydrocolpos) and secondary retrograde flow of urine through the uterus and uterine tubes to the peritoneal cavity. Hydronephrosis is common, related to the hydrocolpos and consequent compression of the bladder neck by the distended vagina (Rink 2016). Cloacal anomalies are associated with risk of renal impairment and may ultimately need renal transplant (Gupta et al 2014).

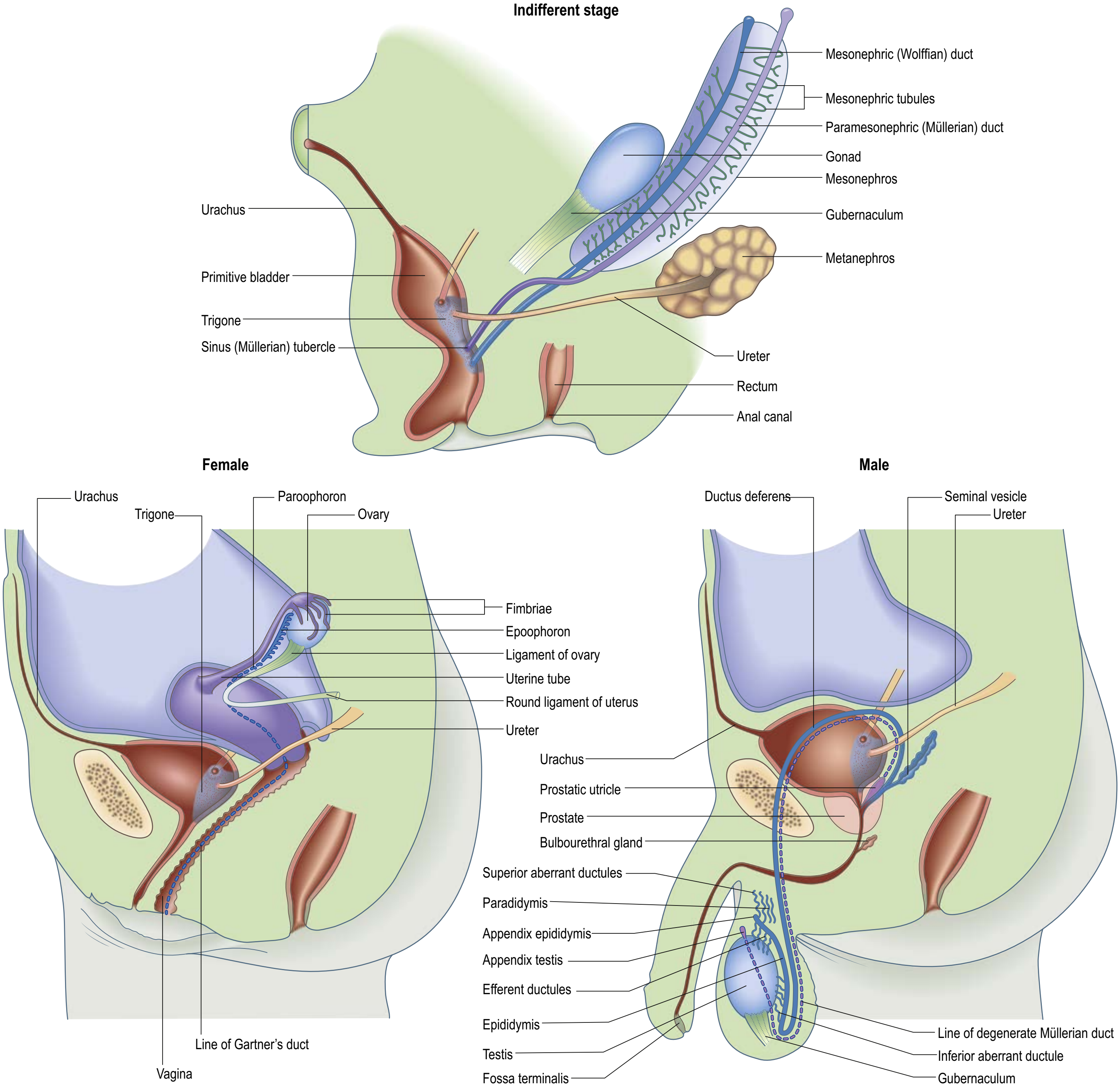
Indifferent stage
Mesonephric (Wolffian) duct
Mesonephric tubules
Paramesonephric (Müllerian) duct
Gonad
Mesonephros
Gubernaculum
Metanephros
Urachus
Primitive bladder
Trigone
Sinus (Müllerian) tubercle
Ureter
Rectum
Anal canal
Female
Urachus
Trigone
Paroophoron
Ovary
Fimbriae
Epoophoron
Ligament of ovary
Uterine tube
Round ligament of uterus
Ureter
Line of Gartner's duct
Vagina
Male
Ductus deferens
Seminal vesicle
Ureter
Urachus
Prostatic utricle
Prostate
Bulbourethral gland
Superior aberrant ductules
Paradidymis
Appendix epididymis
Appendix testis
Efferent ductules
Epididymis
Testis
Fossa terminalis
Line of degenerate Müllerian duct
Inferior aberrant ductule
Gubernaculum

Fig. 22.19 The development of the urogenital system from the indifferent stage to the definitive male and female states. (Modified with permission from Williams PL, Wendell-Smith CP, Treadgold S 1969 Basic Human Embryology, 2nd ed. London: Pitman Medical & Scientific.)

enteric and urinary sphincter mechanisms and vascular erectile tissues. The striated muscle is derived initially from individual muscle precursor cells from the ventrolateral edge of dermomyotomes adjacent to the lower limb that enter the lower limb and divide into dorsal and ventral muscle masses. The cells of the ventral mass divide again and a population migrate from the limb ventrally towards the genital tubercle (Valasek et al 2005). A migratory interaction present in other body regions has been identified in avian and murine embryos, where migratory cloacal muscle cells expressing surface CXCR4 respond to SDF-1 guiding cues expressed in cloacal tissues (Rehimi et al 2010). Although these myoblasts are derived from muscle precursor cells that migrate into the lower limb, they are later patterned by similar developmental signalling as that of trunk body wall muscles into four layers: subcutaneous, external, internal and transverse (Hall et al 2017). The muscle precursor cells give rise to the external urethral and anal sphincters, bulbospongiosus, ischiocavernosus and levator ani muscles. Striated muscle fibres can be seen from postmenstrual week 15, as can the smooth muscle of the urethral sphincter. Puborectalis appears following opening of the anal membrane.

Urethra

The urethra arises from a ventral elongation of the lower end of the urogenital sinus. It is derived, as are the prostate gland and vagina, from endodermal epithelium and local urogenital mesenchyme. Between stages 18 and 23 a solid proliferation of the endodermal epithelium forms the urethral plate which later canalizes and opens to form a urethral groove. Once the cloacal membrane proper thins and ruptures, the urethral groove is in contact with amniotic fluid. For details of the early development of the cloaca and growth of the urethral plate see Kruepunga et al (2018).

In the male, the prostatic urethra proximal to the orifice of the prostatic utricle is derived from the vesico-urethral part of the cloaca and the incorporated caudal ends of the mesonephric ducts. The remainder of the urethra is derived from the urethral groove and its later incorporation by movements of the urethral folds into the shaft of the penis as far as the glans (see Fig. 22.20). It had always been thought that the distal urethra was formed by invaginating ectoderm, however, studies have shown that the urethral plate in the glans is canalized without forming a urethral groove, and that it expresses *FOXA1*,

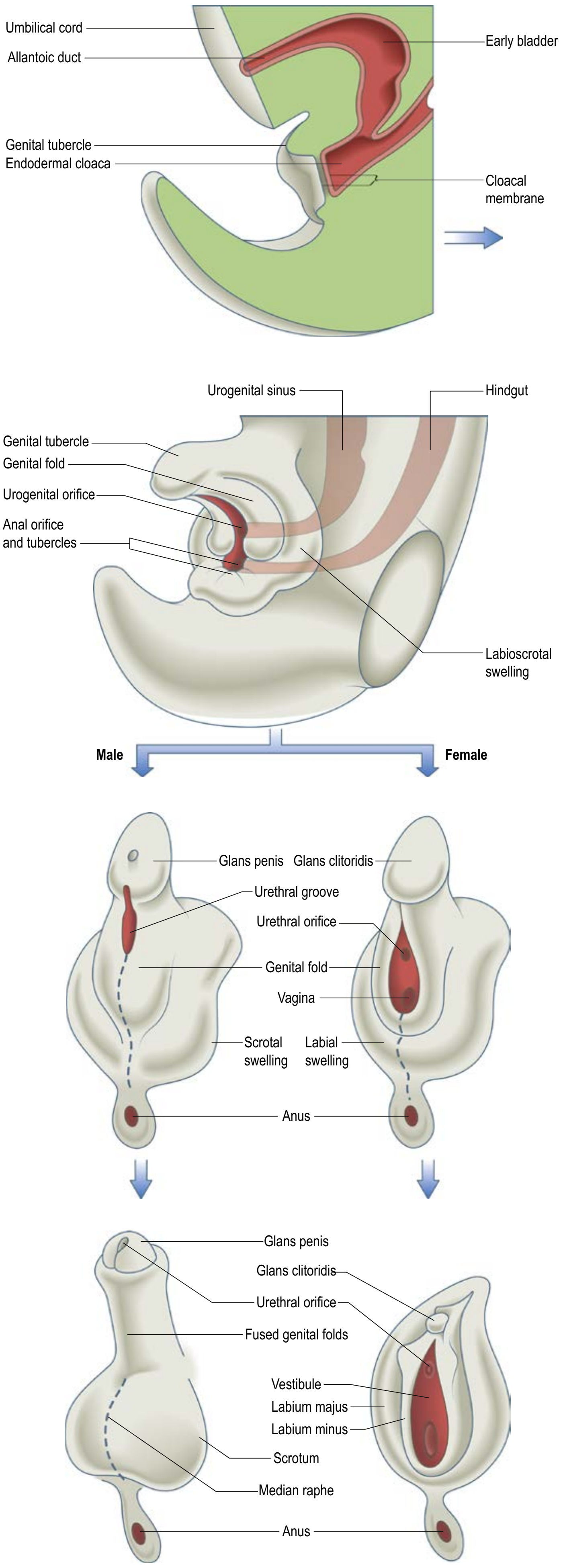

Fig. 22.20 The development of the external genitalia from the indifferent stage to the definitive male and female states.

specific for endodermal epithelium, to the distal meatus (Liu et al 2018, Baskin et al 2018). This endodermal epithelium also expresses cytokeratin 7 and uroplakin, markers of developing and mature urothelium.

In the female, the urethra is derived entirely from the vesico-urethral region of the cloaca, including the dorsal region derived from the mesonephric ducts. It is homologous with the part of the prostatic urethra proximal to the orifices of the prostatic utricle and the ejaculatory ducts. The region of the early urethra remains open to form the vestibule, into which the definitive urethra and vagina open (see Fig. 22.20). It is thought that these regions are invaded by ectoderm because they are innervated by somatic nerves.

The urethral sphincter first forms as a mesenchymal condensation around the urethra in stage 18 embryos, after division of the cloaca. The mesenchyme proliferates and becomes defined at the bladder neck after stage 23, and along the anterior part of the urethra by about postmenstrual week 13. The muscle fibres differentiate after postnatal week 15, at which time both smooth and striated fibres are present. In females, there is continuity between the smooth muscle of the bladder and urethral wall. In males, the muscle fibres are less abundant because of the local development of the prostate. Striated muscle fibres form around the smooth muscle, initially in the anterior wall of the urethra, and later encircle the smooth muscle layer. The striated muscle originates from ventral mass, lower limb myoblasts that, having entered the lower limb, then migrate to the perineal region. In the mouse embryo the myoblasts form levator ani (Valasek et al 2005). The smooth and striated components of the urethral sphincter are closely related, but there is no mixing of fibres as occurs in the anorectal sphincter.

Developmental anomalies of the urethra

Available with the *Gray's Anatomy* e-book

Prostate gland

The prostate gland arises during postmenstrual weeks 11–12 from interactions between the urogenital sinus mesenchyme associated with the mesonephric and paramesonephric ducts and the endoderm of the proximal part of the urethra. This region has been termed the Müllerian duct–urogenital sinus junction (Cai 2008). Five stages of prostatic development have been demonstrated in rodent embryos and human fetuses, each typical for an evaginating gland (Cunha et al 2018b). The endodermal urogenital epithelium surrounding the developing urethra thickens and 14–20 solid buds arise around the whole circumference of the tube, mainly on its lateral aspects and excluding the dorsal wall above the utricular plate. The buds elongate and branch into the urogenital mesenchyme, showing some differentiation into luminal and basal cells as the lumen extends. They give rise to the outer glandular zone of the prostate. Later they will complete their secretory differentiation. Smooth muscle cells are seen in the urogenital mesenchyme at about postmenstrual week 20.

In human fetuses the original entry point of the two mesonephric ducts and the (midline joined) paramesonephric ducts into the urogenital sinus produces a region of mixed epithelial derivation. An evagination of each mesonephric duct, now the ductus deferens, gives rise to the seminal glands, and thereafter it is the caudal continuation, the ejaculatory duct, that enters the developing urethra. In the embryo, the entry of the paramesonephric ducts into the urogenital sinus initiates the endodermal proliferation of the sinuvaginal bulb which will grow cranially as the vaginal plate in the female. The caudal-most remnants of the paramesonephric ducts, which involute under the effects of AMH in the male, remain as the prostatic utricle, a structure sometimes termed the male vagina (Puppo and Puppo 2016). These entry points produce an elongated dorsal prominence, the seminal colliculus (verumontanum). This has been shown, by its epithelial expression of FOXA1, to be derived from the urogenital sinus, although it patchily expresses PAX2, the gene expressed by the epithelium of the mesonephric and paramesonephric ducts (Cunha et al 2018a). Anomalous fusion and/or growth of the different tissue populations that meet at the verumontanum may result in protruberance of tissue into the urethra; the biomechanical effects of bladder filling and emptying might elongate this tissue, producing the sail-like fold(s) arising from the verumontanum that are seen in cases of posterior urethral valves. These can be identified on ultrasound examination during the second and third trimesters and are associated with hydro-ureteronephrosis (Hodges et al 2009, Siebert et al 2013).

The developing prostate gland is affected by the local hormonal environment: in response to increased androgens, experimental recombination of female vaginal mesenchyme can direct endodermal epithelium to

Urethral defects are common in the male. Epispadias is a defect in the dorsal wall of the urethra on the glans of the penis, penile shaft, or at the junction of the penis with the ventral (anterior) abdominal wall. Isolated male epispadias is rare (1 in 117,000 males); this anomaly is considered to be a less severe form of exstrophy of the bladder (Gearhart and Mathews 2016). Hypospadias is more common (1 in 250 births), with the urethral meatal opening anywhere along the line of fusion of the urogenital folds and scrotum. The incidence of hypospadias at distal sites along the penis is 94%, but also occurs in the midshaft (4%) and proximal shaft (1%). In more severe cases, the genital folds fail to fuse, and the urethra opens on the ventral aspect of a malformed penis just in front of the scrotum. The prevalence of hypospadias has increased and it is thought to be part of testicular dysgenesis syndrome. Congenital penile curvature (chordee), both dorsal or ventral, with an orthotopic meatus, is frequently associated with hypospadias and is thought to be linked to anomalous distribution of smooth muscle fibres in the dartos muscle. This condition becomes more evident after puberty (Haroun 2018).

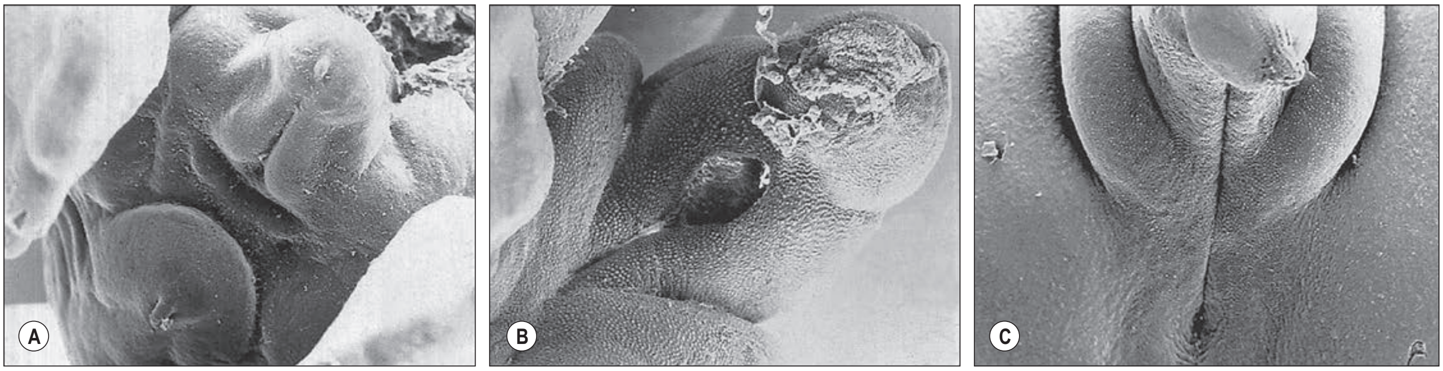

Fig. 22.21 Scanning electron micrographs of early human external genitalia. **A**, The indifferent stage in a human embryo about stage 18. **B**, A human female embryo about postmenstrual week 12. The genital folds are not fused. **C**, A human male embryo at about postmenstrual week 12. Fusion of the genital folds has occurred. (Photographs by P Collins.)

form prostate gland (Cai 2008). In the male, the early surge in androgens at postmenstrual weeks 8–10 is associated with endodermal proliferation; mesenchymal proliferation occurs later from about postmenstrual week 12, when maternal oestrogen levels increase (Cai 2008).

Similar outgrowths occur in the female but remain rudimentary in the absence of androgenic stimulation.

The bulbourethral glands in the male, and the greater vestibular glands in the female, arise as diverticula from the epithelial lining of the urogenital sinus.

External genitalia

Patterning of the external genitalia may be achieved by mechanisms similar to those that pattern the face and limb. In the cranial region, neural crest mesenchyme makes an important contribution to the organization of the pharyngeal arches and the regions around the pharyngeal constrictors and the upper oesophageal sphincter. Neural crest also arises from the tail-bud region, specifically from a population of cells termed the caudoneural hinge, which share the same molecular markers as the primitive node. The neural tube at this level is derived from a mesenchymal to epithelial transformation of caudoneural hinge cells that form a cylinder. Neural crest cells delaminate from the dorsal surface of the cylinder in a rostrocaudal direction. It is not known whether neuronal neural crest arising from secondary neurulation processes contributes to the caudal interface between endoderm and ectoderm. Many of the genes controlling external genital development have been identified (Kojima et al 2010, Blaschko et al 2012).

The external genitalia, like the gonads, pass through an indifferent state before distinguishing sexual characters appear (see Fig. 22.20). From stage 13, primordia of the external genitalia, composed of underlying proliferating mesenchyme covered with ectoderm, arise around the cloacal membrane, between the primitive umbilical cord and the caudal limit of the embryo. During stage 15, the cloacal membrane is divided by the urorectal septum into a cranial urogenital membrane and a caudal anal membrane (see Fig. 22.4). Local ectodermal–mesenchymal interactions give rise to the anal sphincter, which will develop even without the presence of the anal canal: the skeletal muscle is derived from a portion of the ventral muscle mass that initially migrates into the lower limb and then moves to the perineal region (Valasek et al 2005, Rehimi et al 2010). These myoblasts will give rise to the bulbospongiosus and ischiocavernosus muscles. A surface elevation, produced by underlying pericloacal mesenchyme, the genital tubercle, appears at the cranial end of the urogenital membrane and two lateral ridges, the genital or urethral folds, form each side of the membrane (Wang et al 2013) (see Fig. 22.20). The genital tubercle forms a distinct primordium that will become the glans of either the penis or the clitoris. Elongation of the genital folds and urogenital membrane produces a primitive phallus. As this structure grows, it is described as having a cranial surface analogous to the dorsum of the penis, and a caudal surface analogous to the perineal surface in both sexes (Isaacson et al 2018). The urogenital sinus contiguous with the internal aspect of the urogenital membrane, becomes attenuated within the elongating phallus, forming the primitive urethra. The urogenital membrane breaks down at about stage 19, allowing communication of ectoderm and endoderm at the edges of the disrupted membrane and continuity of the urogenital sinus with the amniotic cavity. Urine can escape from the urinary tract from this time. The endodermal layer of the attenuated distal portion of the urogenital sinus, which is now displayed on the caudal aspect of the phallus, is termed the urethral plate (male) and vestibular plate (female). While these changes are in progress, two labioscrotal (genital) swellings appear, one on each side of the base of the phallus, and extend caudally, separated from the genital folds by distinct grooves (see Fig. 22.20; **Fig. 22.21**). Homologies of the parts of the urogenital system are shown in Table 22.1.

As a general rule, epithelium that can be touched easily and has a somatic innervation, is derived from ectoderm. In the buccal cavity and pharynx, the ectoderm/endoderm boundary is a zone towards the posterior third of the tongue, and touch here usually elicits the gag reflex. In the anal canal, the outer portion, distal to the anal valves, is derived from ectoderm and has a somatic innervation, whereas the epithelium proximal to the valves is derived from endoderm and has an autonomic and visceral afferent innervation. The urethral meatus and vagina, although derived from endoderm, have a somatic innervation at the vestibule and so must be part of an ectodermal/endodermal boundary zone in this region.

Male genitalia

The growth of male external characteristics is stimulated by androgens regardless of the genetic sex. The male phallus enlarges to form the penis. As mesenchyme proliferates within the genital folds, the urethral plate sinks into the body of the phallus, forming a primary urethral groove. The genital folds meet proximally in a transverse ridge immediately ventral to the anal membrane. The genital swellings meet each other ventral to the anus and unite to form the scrotum (see Fig. 22.20). The genital folds fuse with each other from behind forwards, enclosing the phallic part of the urogenital sinus behind to form the bulb of the urethra, and closing the definitive urethral groove in front to form the greater part of the spongiose urethra (Shen et al 2016). Fusion of the folds results in the formation of a median raphe and occurs in such a way that the lining of the postglandular urethra is formed by closure of the urethral groove. Thus, as the phallus lengthens, the urogenital orifice is carried onwards until it reaches the base of the glans at the apex of the penis. Within the glans the urethral plate canalizes directly to the urethral meatus. Expression of FOXA1, cytokeratin 7 and uroplakin confirm the entire endodermal origin of the human penile urethra (Liu et al 2018).

The glans and shaft of the penis are recognizable by the end of the first trimester. Development of the prepuce can be seen by postmenstrual week 14, when the primary external orifice of the urethra is still at the base of the glans. A ridge consisting of a mesenchymal core covered by epithelium appears proximal to the neck of the penis and extends forwards over the glans (Isaacson et al 2018, Liu et al 2018). A solid lamella of epithelium deep to this ridge extends backwards to the base of the glans. The ventral extremities of the ridge curve backwards to become continuous with the genital folds at the margins of the urethral orifice. As the urethral folds meet to form the terminal part of the urethra, the ventral horns of the ridge fuse to form the frenulum. The epithelial lamella breaks down over the dorsum and sides of the glans to form the preputial sac, and thus free the prepuce from the surface of the glans. Thereafter, the prepuce grows as a free fold of skin, which covers the terminal part of the glans. Although the prepuce and glans begin to separate from postmenstrual weeks 17–20, they may still be joined at birth. The preputial sac may not be complete until 6–12 postnatal months or more after birth and, even then, the presence of some connecting strands may still interfere with the retractability of the prepuce (Liu et al 2018).

The mesenchymal core of the phallus is comparatively undifferentiated up to stage 17, with the blastemata of the corpora cavernosa becoming defined after stage 23. Myoblasts forming the bulbospongiosus and ischiocavernosus muscles are derived from lower limb myoblasts (Valasek et al 2005). Nerves are present in the differentiating mesenchyme from about stage 21. Despite containing less smooth muscle and elastic tissue than the adult, the neonatal penis is capable of erection.

The scrotum is formed by proliferation of the genital swellings that fuse across the midline covering the base of the penis. The testes descend into the scrotum prior to birth. The gelatinous matrix of the gubernaculum is then resorbed and the tunica vaginalis becomes adherent to the connective tissue of the scrotum. In the male neonate (postmenstrual week 40), the scrotum has a broad base that does not narrow until after the first year. The septum (i.e. the mesenchyme remaining between the tunica vaginalis on each side) and the walls of the scrotum are both relatively thicker than in adults.

There is evidence that in certain tissues, e.g. urogenital sinus and genital swellings, testosterone is converted into 5α-dihydrotestosterone. In XY individuals with a genetic deficiency of the enzyme responsible for this conversion, not only functioning testes but also female external genitalia, with an enlarged clitoris and a small vaginal pouch, are present, suggesting that external genital development is under the control of 5α-dihydrotestosterone (Kang et al 2014). Such individuals are often raised as girls; however, at puberty the external genitalia become responsive to testosterone, causing masculinization at this time.

Female genitalia

The female phallus becomes the clitoris. The vestibular plate forms a vestibular groove, but there is no midline fusion process and the vestibular groove remains open. The genital swellings remain separate as the labia majora and the genital folds remain separate as the labia minora (see Fig. 22.20). The perineal orifice of the original urogenital sinus is retained as the cleft between the labia minora, and the urethra and vagina open above it. The prepuce of the clitoris develops in the same way as its male homologue. By about postmenstrual week 16, female external genitalia can no longer be masculinized by androgens. In the female neonate (postmenstrual week 40), the distal end of the round ligament of the uterus, the gubernaculum ovarii, ends just outside the external inguinal ring and the labia majora are united by a posterior labial commissure.

Disorders of sex development

The acquisition of appropriate gonads, reproductive ducts, external genital structures and appropriate gender identity occurs through a myriad of complex processes, both local and systemic. Anomalous developmental processes, leading to differences in sex chromosomes, gonadal structure and position, retention of ductal homologues, androgen insensitivity, androgen excess, and ambivalent external genitalia requiring gender assignment, were previously described as intersexual conditions or hermaphrodism. Such terminology is nonspecific, confusing and perceived as potentially pejorative by affected individuals. Advances in the identification of molecular genetic causes of such conditions have led to proposed changes to describe them as 'disorders of sex development' (DSD): congenital conditions in which development of chromosomal, gonadal or anatomical sex is atypical (Lee et al 2006). The range of anomalous development and its management by multidisciplinary teams, as well as by the affected family, are comprehensively covered by Arboleda and Vilain (2014).

Maturation of the reproductive organs, mini-puberty and puberty

Available with the *Gray's Anatomy* e-book

Bonus e-book content

Fig. 22.11 Bladder exstrophy.

Fig. 22.22 Patterns of fetal and postnatal hormones during mini-puberty.

Fig. 22.23 The average ages at which maturation events occur in adolescent girls and boys.

Key references

Barteczko KJ, Jacob MI 2000 The testicular descent in human. Origin, development and fate of the gubernaculum Hunteri, processus vaginalis peritonei and gonadal ligaments. Adv Anat Embryol Cell Biol 156:III–X, 1–98.

This paper presents excellent images of early human testis and its descent into the scrotum.

Chai O, Song C, Park S et al 2013 Molecular regulation of kidney development. Anat Cell Biol 46:19–31.

This paper examines the molecular processes behind some of the epithelial:mesenchymal interactions occurring in the developing kidney.

Cunha GR, Robboy SJ, Kurita T et al 2018a Development of the human female reproductive tract. Differentiation 103:46–65.

This paper illustrates gene expression and histological appearance of the developing human female reproductive tract.

Hadziselimovic F 2017 On the descent of the epididymo-testicular unit, cryptorchidism, and prevention of infertility. Basic Clin Androl 27:21. doi:10.1186/s12610-017-0065-8.

A review of the processes of testicular descent.

Kruepunga N, Hikspoors JPJM, Mekonen KM et al 2018 The development of the cloaca in the human embryo. J Anat 233:724–739.

A clear interpretation of tissue movements during the development of the lower enteric and urogenital tracts.

Lanciotti L, Cofini M, Leonardi A et al 2018 Up-to-date review about minipuberty and overview of hypothalamic–pituitary–gonadal axis activation in fetal and neonatal life. Front Endocrinal 9:410. doi:10.3389/fendo.2018.00410.

A comprehensive review of hormonal status in the first 6 months of postnatal life.

Lee PA, Houk CP, Ahmed SF et al 2006 Consensus statement on management of intersex disorders. International Consensus Conference on Intersex. Paediatrics 118:e488–500.

This paper presents the recommendations in intersex disorder management.

Minuth WW 2018 Reading first coordinates from the nephrogenic zone in human fetal kidney. Nephron 138:137–146.

A consideration of the links between fetal growth restriction, preterm delivery and cessation of nephrogenesis.

Sharpe RM, McKinnell C, Kivlin C et al 2003 Proliferation and functional maturation of Sertoli cells, and the relevance to disorders of testis function in adulthood. Reproduction 125:769–784.

This paper considers the importance of Sertoli cell development and the future sperm count of adult males.

Early morphological changes in the developing gonads and ducts are affected by secretion of placental hormones. The functional development of the hypothalamus and pituitary gland is seen towards the end of the embryonic period: LH and FSH are synthesized from about postmenstrual week 9 and appear in fetal serum from postmenstrual weeks 12–14. In males up to postmenstrual week 12, placental hCG induces the differentiation of Leydig cells which secrete testosterone at a peak level similar to adults. In females, the majority of oestrogen is produced by the placenta and primordial ovarian follicles form when fetal circulating oestrogen levels are high, most rapidly after postmenstrual weeks 14–15.

Fetal pituitary secretion of GnRH peaks in mid-gestation and decreases towards birth. It is suppressed toward term by placental oestrogen secretion, which suppresses the fetal HPG axis. Serum LH and FSH are not related to GnRH mid-gestation, but are induced by it after postmenstrual weeks 30–31. Low production of LH and FSH in males coincides with the first maturation of seminiferous tubules, and high production in females coincides with the first maturation of primary ovarian, and growing antral follicles (Lanciotti et al 2018).

At birth, the level of oestradiol in cord blood is high: LH and FSH are undetectable in females and FSH levels are very low in males because of the inhibitory effects of this placental hormone. The concentration in cord blood depends on the age (postmenstrual weeks) and mode of delivery. Circulating placental hormone levels fall in the first few postnatal days. GnRH begins to rise after postnatal days 6–10 when the neonatal HPG axis is re-initiated. In males, LH level increases 10 times within a few minutes of delivery and there is a concomitant rise in testosterone that lasts about 12 hours.

Mini-puberty is the period from birth to about postnatal month 6, when changes in pituitary hormones and consequent changes in the gonads (that affect future growth) occur (Rey 2014, Hadziselimovic 2017, Lanciotti et al 2018). The changing patterns of hormones in male and female fetuses and early neonates is shown in **Fig. 22.22**.

In males Sertoli cells continue to proliferate in the first month after birth, but there is no spermatogenesis because they do not express androgen receptors. They secrete inhibin B that peaks at postnatal months 3–6 and remains elevated until postnatal month 15. Secretion of AMH is highest at postnatal month 3 and then declines to remain stable in childhood until puberty, when it declines to adult levels (3–4% of infant level). The number of Leydig cells increases until postnatal month 3 and then decreases.

In females, the labia minora, clitoris and labia majora are relatively enlarged, reflecting the effects of placental oestrogens. Levels of oestradiol increase after the first postnatal week and remain high up to 6 postnatal months, with fluctuations in the first months. During this time, some ovarian follicles mature to antral stages and some atrophy. Further development of the follicles produces a marked rise in AMH levels, secreted by granulosa cells, at postnatal month 3. The pool of primordial follicles remains stable until postnatal month 8 at which time the majority undergo atresia. The remaining follicles resume development after puberty, completing oocyte first meiotic division shortly before ovulation. The granulosa cells at this time enlarge and multiply to form the stratum granulosum; they are surrounded by thecal cells that differentiate from the stroma.

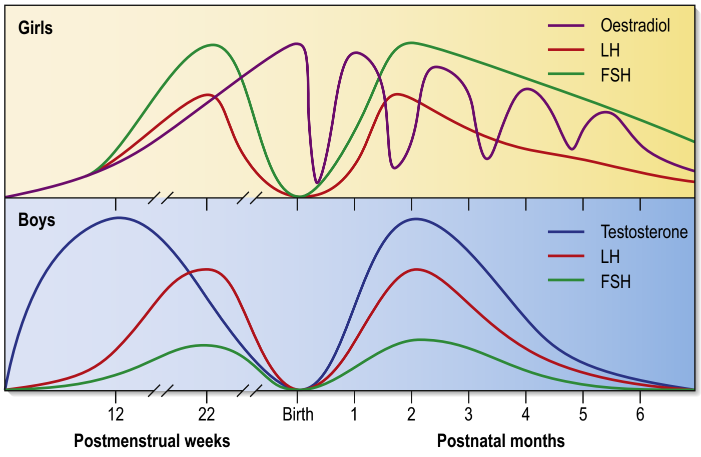

Fig. 22.22 Patterns of fetal and postnatal hormones during mini-puberty. LH, luteinizing hormone; FSH, follicle stimulating hormone. (With permission from Lanciotti L, Cofini M, Leonardi A et al 2018 Up-to-date review about minipuberty and overview of hypothalamic–-pituitary–gonadal axis activation in fetal and neonatal life. Front Endocrinol (Lausanne) 9:410.)

Most term neonates of both sexes have palpable breast tissue, larger and persisting longer in females, that reflects the high level of oestradiol in cord blood. Mammary gland diameter gradually decreases in both sexes, until postnatal month 6 in boys and over a longer time in girls, reflecting endogenous oestrogen activity (Fig. 22.22). Uterine length increases primarily during pregnancy under the influence of the hormones that cross the placental barrier. It is relatively longest at day 7 in full-term babies, then steadily involutes towards postnatal month 3, remains fairly unchanged until the second year, and does not regain its neonatal size and weight until puberty. In males, the penis and scrotum are relatively large; penile length, which is correlated with serum testosterone level, increases from birth to 3 years of age, with the highest growth velocity between birth and postnatal month 3. Testicular volume increases from birth to postnatal months 5–6, reflecting the proliferation of Sertoli cells, and then decreases from about postnatal month 9. It has been suggested that transient activation of the HPG axis causes early germ cells to differentiate into adult dark (Ad) spermatogonia, the future adult reservoir of stem cells, from postnatal month 3 (Hadziselimovic 2017).

In preterm babies the postnatal HPG axis activation is stronger and more prolonged than in full-term babies. In males, the testosterone levels are higher, with a significant difference to full-term babies at postnatal month 6. Preterm males have faster penile and testicular growth. In females the levels LH and FSH are higher, the FSH level possibly reflecting less ovarian follicle development. Antral follicles can be seen postnatally and there are increases in AMH and oestradiol from granulosa cells. The intensity of postnatal hormonal stimulation in preterm babies can cause ovarian hyperstimulation syndrome, which is self-limiting. In neonates with fetal growth restriction, males show reduced testicular volume and testosterone concentration in adult life, leading to infertility; females show adrenal and ovarian hyperandrogenism, with precocious pubarche and reduced ovulation rate, associated with lower insulin sensitivity (Lanciotti et al 2018).

Puberty is the term given to describe the time at which changes in HPG axis, gonads, reproductive organs and secondary sexual characteristics occur, along with the adolescent growth spurt (Ch. 23). The sequence of events, which is much less variable than the age at which they take place, is shown in **Fig. 22.23**. Normal puberty can be regarded as a process of innate maturation that can be modified by nutrition and stress. There is a secular trend toward early puberty in many developed and developing countries linked to the secular trend of greater adult height: faster growth in childhood/juvenile phases is associated with earlier age at puberty. The earliest change associated with puberty is the onset of sleep-related LH pulses that occur earlier in girls than boys; rising oestradiol levels reflect primary follicle recruitment in girls; rising testosterone levels in boys reflect increasing Leydig cell activity and proliferation of Sertoli cells (Ellison and Reiches 2012). Chondrocyte proliferation is stimulated in the growth plates of growing bones (Jee and Baron 2016). Androgen secretion by the suprarenal gland stimulates growth of pubic and axillary hair in both sexes, appearing earlier in girls. Body composition changes as a consequence of gonadal steroid production; oestradiol stimulates adipose tissue growth in girls particularly in the breasts and gluteofemoral region, whereas in boys, testosterone inhibits adipose tissue growth and stimulates muscle anabolism (Ellison and Reiches 2012).

The uterus and vagina develop simultaneously with the breasts. Menarche occurs after the peak of the height spurt; onset is more closely related to radiological than to chronological age. It has been suggested that the menarche occurs as a critical weight of 50 kg is attained. Sports and excessive restriction of diet, both of which may reduce weight below this level, can cause amenorrhoea in females who were previously menstruating normally. Tall girls reach sexual maturity earlier than short ones, but girls with a late adolescent growth spurt and later puberty are ultimately taller on the average than those who pass through the menarche early. A girl who has begun to menstruate can be predicted to grow a further 7.5 cm at most. Menarche marks a definitive stage of uterine development but does not mean attainment of full reproductive function: many of the early menstrual cycles may not involve ovulation.

Testis growth in boys reflects seminiferous tubule development and Sertoli cell proliferation. The volume of the testes may be estimated: the average adult volume is 20 ml, and a volume of 6 ml indicates that puberty has started. Later, the penis, prostate and seminal glands begin to enlarge. Increased testosterone levels produced by the Leydig cells of the testes promote changes in the larynx, skin and distribution of bodily hair.

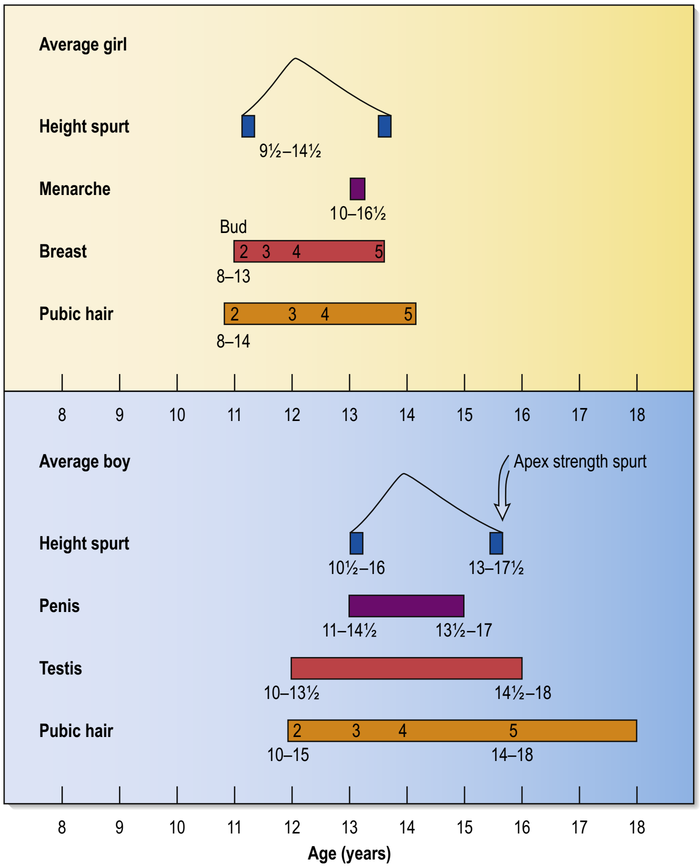

Fig. 22.23 The average ages at which maturation events occur in adolescent girls and boys. The figures beneath the bars indicate the range of ages within which each event may begin and end. Figures within the bars indicate the developmental stage. The velocity of the strength spurt peaks later than the height spurt in boys, associated with testosterone and growth hormone levels. It is appreciated that the assessment and interpretation of the strength spurt during puberty is complex (De Ste Croix 2007). (Modified with permission from Tanner JM 1962 Growth at Adolescence, 2nd ed. Oxford: Blackwell Publishing.)

References

Albrecht KH, Eicher EM 2001 Evidence that SRY is expressed in pre-Sertoli cells and Sertoli and granulosa cells have a common precursor. Dev Biol 240:92–107.

Allard S, Adin P, Gouédard L et al 2000 Molecular mechanisms of hormone-mediated Müllerian duct regression: involvement of β-catenin. Development 127:3349–60.

Anderson RA, Robinson LLL, Brooks J et al 2002 Neurotropins and their receptors are expressed in the human fetal ovary. J Clin Endocrinol Metabol 87:800–7.

Arboleda VA, Vilain E 2014 Disorders of sex development. In: Strauss JF, Barbieri RL (eds) Yen & Jaffe's Reproductive Endocrinology, 7th ed. Philadelphia: Elsevier, Saunders; Ch. 17.

This chapter considers the complexities of disorders of sex development and their management.

Barteczko KJ, Jacob MI 2000 The testicular descent in human. Origin, development and fate of the gubernaculum Hunteri, processus vaginalis peritonei and gonadal ligaments. Adv Anat Embryol Cell Biol 156:III–X, 1–98.

This paper presents excellent images of early human testis and its descent into the scrotum.

Barthold JS, Ivell R 2018 Perspective: a neurohormonal systems approach to understanding the complexity of cryptorchidism susceptibility. Front Endocrinol 9:401. doi:10.3389/fendo.2018.00401.

Baskin L, Shen J, Sinclair A et al 2018 Development of the human penis and clitoris. Differentiation 103:74–85.

Batchelder CA, Lee CCI, Martinez ML et al 2010 Ontology of the kidney and renal developmental markers in the Rhesus monkey (*Macaca mulatta*). Anat Rec 293:1971–83.

Batourina E, Tsai S, Lambert S et al 2005 Apoptosis induced by vitamin A signalling is crucial for connecting the ureters to the bladder. Nat Genet 37:1082–9.

Ben-David S, Zuckerman-Levin N, Epelman M et al 2007 Parturition itself is the basis for fetal adrenal involution. J Clin Endocrinol Metabol 92:93–97.

Biason-Lauber A 2010 Control of sex development. Best Pract Res Clin Endocrinol Metabol 24:163–86.

Blaschko SD, Cunha GR, Baskin LS 2012 Molecular mechanisms of external genitalia development. Differentiation 84:261–8.

Cai Y 2008 Participation of caudal Müllerian mesenchyme in prostate development. J Urol 180:1898–903.

Capone VP, Morello W, Taroni F et al 2017 Genetics of congenital anomalies of the kidney and urinary tract: the current state of play. Int J Mol Sci 18(4):pii: E796. doi:10.3390/ijms18040796.

Carpenter AR, McHugh KM 2017 Role of renal urothelium in the development and progression of kidney disease. Pediatr Nephrol 32:557–64.

Chai O, Song C, Park S et al 2013 Molecular regulation of kidney development. Anat Cell Biol 46:19–31.

This paper examines the molecular processes behind some of the epithelial:mesenchymal interactions occurring in the developing kidney.

Chauvet V, Qian F, Boute N et al 2002 Expression of PKD1 and PKD2 transcripts and proteins in human embryo and during normal kidney development. Am J Pathol 160:973–83.

Chen J, Sörensen HT, Miao M et al 2018 Cryptorchidism and increased risk of neurodevelopmental disorders. J Psych Res 96:153–61.

Colaco S, Modi D 2018 Genetics of the human Y chromosome and its association with male infertility. Reprod Biol Endocrinol 16:14.

Cole B, Hensinger K, Maciel GAR et al 2006 Human fetal ovary development involves the spatiotemporal expression of P450c17 protein. J Clin Endocrinol Metabol 91:3654–61.

Collins P 1990 The origin, development, and degeneration of the pronephros in *Caretta caretta*. J Morphol 205: 297–305.

Cooper TG, Noonan E, von Eckardstein S et al 2010 World Health Organization reference values for human semen characteristics. Hum Reprod Update 16:231–45.

Crelin ES 1969 Anatomy of the newborn. Philadelphia: Lea and Febiger.

Cunha GR, Robboy SJ, Kurita T et al 2018a Development of the human female reproductive tract. Differentiation 103:46–65.

This paper illustrates gene expression and histological appearance of the developing human female reproductive tract.

Cunha GR, Vezina CM, Isaacson D et al 2018b Development of the human prostate. Differentiation 103:24–45.

Davidson AJ 2009 Mouse kidney development. StemBook (ed) The Stem Cell Research Community: StemBook; doi/10.3824/stembook.1.34.1.

De Felici M 2013 Origin, migration, and proliferation of human primordial germ cells. In: Coticchio G, Albertinit DF, De Santis L (eds) Oogenesis. London: Springer; Ch. 2, pp. 19–37.

De Ste Croix M 2007 Advances in paediatric strength assessment: changing our perspective on strength development. J Sports Sci Med 6:292–304.

Dias T, Sairam S, Kumarasiri S 2014 Ultrasound diagnosis of fetal renal abnormalities. Best Pract Res Clin Obstet Gynaecol 28:403–15.

Dickson AP 2014 The management of bladder exstrophy: the Manchester experience. J Pediatr Surg 49:244–50.

Dihazi GH, Mueller GA, Asif AR et al 2015 Proteomic characterization of adrenal gland embryonic development reveals early initiation of steroid metabolism and reduction of the retinoic acid pathway. Proteome Sci 13:6.

Ellison PT, Reiches MW 2012 Puberty. In: Cameron N, Bogin B (eds) Human Growth and Development, 2nd ed. London: Academic Press. Elsevier; Ch. 4.

Faa G, Gerosa C, Fanni D et al 2012 Morphogenesis and molecular mechanisms involved in human kidney development. J Cell Physiol 227:1257–68.

Gearhart JP, Mathews R 2016 Exstrophy–epispadias complex. In: Wein AJ, Kavoussi LR, Partin AW (eds), Campbell-Walsh Urology, 11th ed. Elsevier; Ch 139.

Geelhoed JJM, Verburg BO, Nauta J et al 2009 Tracking and determinants of kidney size from fetal life until the age of 2 years: the Generation R Study. Am J Kidney Dis 53:248–58.

Gupta A, Bischoff A, Peña A et al 2014 The great divide: understanding cloacal septation, malformation, and implications for surgeons. Pediatr Surg Int 30:1089–95.

Hadziselimovic F 2017 On the descent of the epididymo-testicular unit, cryptorchidism, and prevention of infertility. Basic Clin Androl 27:21. doi:10.1186/s12610-017-0065-8.

A review of the processes of testicular descent.

Hale LJ, Howden SE, Phipson B et al 2018 3D organoid-derived human glomeruli for personalised podocyte disease modelling and drug screening. Nat Comm 4;9(1):5167. doi:10.1038/s41467-018-07594-z.

Hall MI, Rodriguez-Sosa JR, Plochocki JH 2017 Reorganzation of mammalian body wall patterning with cloacal septation. Sci Rep 7:9182 7. doi:10.1038/s41598-017-09359-y.

Hamdi SM, Almont T, Galinier P et al 2017 Altered secretion of Sertoli cells hormones in 2–year–old prepubertal cryptorchid boys: a cross–sectional study. Andrology 5: 783–9.

Haroun HSW 2018 Pathembryology of hypospadias and chordee. MOJ Anat Physiol 5(1):00155.

Hayashi S, Fukuzawa Y, Rodriguez-Vazquez JF et al 2011 Pleuroperitoneal canal closure and the fetal adrenal gland. Anat Rec 294:633–44.

Helfer TM, Rolo LC, Okasaki NA et al 2017 Reference ranges of fetal adrenal gland and fetal zone volumes between 24 and 37+6 weeks of gestation by three-dimensional ultrasound. J Matern Fetal Neonatal Med 30:568–73.

Hikspoors JP, Soffers JH, Mekonen HK et al 2015 Development of the human infrahepatic inferior caval and azygos venous systems. J Anat 226:113–25.

Hirashima T 2014 Pattern formation of an epithelial tube by mechanical instability during epididymal development. Cell Reports 9:866–73.

Hodges SJ, Patel B, McLorie G et al 2009 Posterior urethral valves. Sci World J 14:1119–26.

Huang S, Ye L, Chen H 2017 Sex determination and maintenance: the role of DMRT1 and FOXL2. Asian J Androl 19:619–24.

Hutson JM 2012 Undescended testis, torsion, and varicocele. In: Coran AG (ed) Pediatric Surgery, 7th ed. Saunders, Elsevier; Ch. 77, pp. 1003–19.

Hutson JM 2013 Undescended testis: the underlying mechanisms and the effects on germ cells that cause infertility and cancer. J Pediatr Surg 48:903–8.

This paper considers the relationships between testicular development and final testis maturity.

Hutson JM, Baskin LS, Risbridger G et al 2014 The powers and perils of animal models with urogenital anomalies: handle with care. J Ped Urol 10:699–705.

Isaacson D, Shen J, Overland M et al 2018 Three-dimensional imaging of the developing human fetal urogenital-genital tract: indifferent stage to male and female differentiation. Differentiation 103:14–23.

Jamigorn M, Phupong V 2017 Nomograms of the whole foetal adrenal gland and foetal zone at gestational age of 16–24 weeks. J Obstet Gynaecol 37:867–71.

Jee YH, Baron J 2016 The biology of stature. J Pediatr 173:32–8.

Johal NS, Arthurs C, Cuckow P et al 2019 Functional, histological and molecular characteristics of human exstrophy detrusor. J Ped Urol 15:154.e1–154.e9.

Johnston L, Woolsey S, Cunningham RM et al 2010 Morphological expression of *KIT* positive interstitial cells of Cajal in human bladder. J Urol 184:370–7.

Johnston ZC, Bellingham M, Filis P et al 2018 The human fetal adrenal produces cortisol but no detectable aldosterone throughout the second trimester. BMC Med 16(1):23. doi:10.1186/s12916-018-1009-7.

Kandasamy Y, Rudd S, Smith R et al 2018 Extrauterine development of preterm kidneys. Pediatric Nephrol 33:1007–12.

Kang H, Imperato-McGinley J, Zhu Y et al 2014 5a-reductase-2 deficiency's effect on human fertility. Fertil Steril 101:310–6.

Kanwar YS, Wada J, Lin S et al 2004 Update of extracellular matrix, its receptors, and cell adhesion molecules in mammalian nephrogenesis. Am J Physiol Renal Physiol 286:F202–15.

Kojima K, Kohri K, Hayashi Y 2010 Genetic pathway of external genitalia formation and molecular etiology of hypospadias. J Pediatr Urol 6:346–54.

Kruepunga N, Hikspoors JPJM, Mekonen KM et al 2018 The development of the cloaca in the human embryo. J Anat 233:724–39.

A clear interpretation of tissue movements during the development of the lower enteric and urogenital tracts.

Kurita T 2010 Developmental origin of vaginal epithelium. Differentiation 80:99–105.

Kurita T 2011 Normal and abnormal epithelial differentiation in the female reproductive tract. Differentiation 82:117–26.

Kurtzeborn K, Cebrian C, Kuure S 2018 Regulation of renal differentiation by trophic factors. Front Physiol 9:1588. doi: 10.3389/fphys.2018.01588.

Lanciotti L, Cofini M, Leonardi A et al 2018 Up-to-date review about minipuberty and overview of hypothalamic–pituitary–gonadal axis activation in fetal and neonatal life. Front Endocrinol (Lausanne) 9:410. doi:10.3389/fendo.2018.00410.

A comprehensive review of hormonal status in the first 6 months of postnatal life.

Lee JJ, Shortliffe LMD 2014 Undescended testes and testicular tumors. In: Holcomb GW, Murphy JP, Ostlie DJ (eds) Ashcraft's Pediatric Surgery, 6th ed. Elsevier; Ch. 51, pp. 698–701.

Lee PA, Houk CP, Ahmed SF et al 2006 Consensus statement on management of intersex disorders. International Consensus Conference on Intersex. Paediatrics 118:e488–e500.

This paper presents the recommendations in intersex disorder management.

Li L, Dong J, Yan L et al 2017 Single-cell RNA-Seq analysis maps development of human germline cells and gonadal niche interactions. Cell Stem Cell 20:858–73.

Lindström NO, Chang CH, Valerius MT et al 2015 Node retraction during patterning of the urinary collecting duct system. J Anat 226:13–21.

Liu X, Liu G, Shen J et al 2018 Human glans and preputial development. Differentiation 103:86–99.

Lobo J, Gillis AJM, Jerònimo C, et al 2019 Human germ cell tumours are developmental cancers: impact of epigenetics on pathobiology and clinic. Int J Mol Sci 20:258. doi:10.3390/ijms20020258.

Lotfi CFP, Kremer JL, Dos Santos Passaia B et al 2018. The human adrenal cortex: growth control and disorders. Clinics (Sao Paulo) 73(Suppl 1):e473s. doi:10.6061/clinics/2018/e473s.

Matsumaru D, Murashima A, Fukushima J et al 2015 Systematic stereoscopic analysis for cloacal development: the origin of anorectal malformations. Sci Reports 5:13943. doi:10.1038/srep13943.

Mendelsohn C 2009 Using mouse models to understand normal and abnormal urogenital tract development. Organogenesis 5:306–14.

Minuth WW 2017 Concepts for a therapeutic prolongation of nephrogenesis in preterm and low-birth-weight babies must correspond to structural-functional properties in the nephrogenic zone. Mol Cell Pediatr 4:12. doi:10.1186/s40348-017-0078-6.

Minuth WW 2018 Reading first coordinates from the nephrogenic zone in human fetal kidney. Nephron 138:137–46.

A consideration of the links between fetal growth restriction, preterm delivery and cessation of nephrogenesis.

Munger SC, Natarajan A, Looger LL et al 2013 Fine time course expression analysis identifies cascade of activation of repression and maps a putative regulator of mammalian sex determination. PLoS 9:1–17.

O'Callaghan C, McDougall PN 1987 Successful suprapubic aspiration of urine. Arch Dis Childhood 62:1072–3.

Puppo V, Puppo G 2016 Male vagina is a more accurate term than prostatic utricle. Int J Urol 23:108.

Rajpert-De Meyts E 2006 Developmental model for the pathogenesis of testicular carcinoma *in situ*: genetic and environmental aspects. Human Reprod Update 12:303–323.

Rassouly HM, Lu W 2013 Lower urinary tract development and disease. Wiley Interdiscip Rev Syst Biol Med 5:307–42.

Rehimi R, Khalida N, Yusuf F et al 2010 A novel role of CxXr4 and SDF-1 during migration of cloacal muscle precursors. Dev Dyn 239:1622–31.

Rey RA 2014 Mini-puberty and true puberty: differences in testicular function. Ann Endocrinol 75:58–63.

Rink RC 2016 Surgical management of disorders of sex development and cloacal and anorectal malformation. In: Wein AJ, Kavoussi LR, Partin AW et al (eds) Campbell-Walsh Urology, 11th ed. Elsevier; Ch 151.

Rintala RJ 2016 Congenital cloaca: long term follow-up results with emphasis on outcomes beyond childhood. Sem Ped Surg 25:112–6.

Robboy SJ, Kurita T, Baskin L et al 2017 New insights into human female reproductive tract development. Differentiation 97:9–22.

Rodgers RJ, Irving-Rodgers HF 2010 Formation of the ovarian follicular antrum and follicular fluid. Biol Reprod 82:1021–9.

Ross IL, Louw GJ 2015 Embryological and molecular development of the adrenal glands. Clin Anat 28:235–42.

Runyan C, Schaible K, Molyneaux K et al 2006 Steel factor controls midline cell death of primordial germ cells and is essential for their normal proliferation and migration. Development 133:4861–9.

Ryan D, Sutherland MR, Flores TJ et al 2018 Development of the human fetal kidney from mid to late gestation in male and female infants. EBioMedicine 27:275–83.

Rymer C, Paredes J, Halt K et al 2014 Renal blood flow and oxygenation drive nephron progenitor differentiation. Am J Physiol Renal Physiol 307 (3):F337-45. doi:10.1152/ajprenal.00208.2014 (ePub 2014 Jun 11).

Shamin S, Taguchi A, Kaku Y et al 2016 Human induced pluripotent stem cell-derived podocytes mature into vascularized glomeruli upon experimental transplantation. J Am Soc Nephrol 27:1778–9.

Sharpe RM 2010 Environmental/lifestyle effects on spermatogenesis. Phil Trans R Soc B 365:1697–1712.

Sharpe RM, McKinnell C, Kivlin C et al 2003 Proliferation and functional maturation of Sertoli cells, and the relevance to disorders of testis function in adulthood. Reproduction 125:769–84.

This paper considers the importance of Sertoli cell development and the future sperm count of adult males.

She Z, Yang W 2017 *Sry* and *SoxE* genes: how they participate in mammalian sex determination and gonadal development? Sem Cell Dev Biol 63:13–22.

Shen J, Overland M, Sinclair A et al 2016 Complex epithelial remodelling underlie the fusion event in early fetal development of the human penile urethra. Differentiation 92:169–82.

Siebert JR, Smith KJ, Cox LL et al 2013 Microtomographic analysis of lower urinary tract obstruction. Pediatr Dev Path 16:405–14.

Siu MKY, Cheng AY 2012 The blood-follicle barrier (BFB) in disease and in ovarian function. Adv Exp Med Biol 763:186–92.

Solhaug MJ, Jose PA 2017 Development and regulation of renal blood flow in the neonate. In: Polin RA, Abman SH, Rowitch D et al (eds) Fetal and Neonatal Physiology, 5th ed. Elsevier; Ch 101, pp. 977–83.

Song R, Yosypiv IV 2012 Development of the kidney medulla. Organogenesis 8:10–17.

Soto-Suazo M, Zorn TM 2005 Primordial germ cells migration: morphological and molecular aspects. Anim Reprod 2:147–60.

Stranzinger E, Strouse PJ 2008 Ultrasound of the pediatric female pelvis. Semin Ultrasound CT MR 29:98–113.

Suzuki K, Economides A, Yanagita M et al 2009 New horizons at the caudal embryo: coordinated urogenital/reproductive organ formation by growth factor signalling. Curr Opin Genet Dev 19:491–6.

Tanaka ST, Ishii K, Demarco RT et al 2010 Endodermal origin of bladder trigone inferred from mesenchymal–epithelial interaction. J Urol 183:386–91.

This paper presents the molecular evidence for the origin of the bladder trigone mucosa.

To M, Pereira S 2015 Routine fetal anomaly scan. In: Coady AM, Bower S (eds) Twining's Textbook of Fetal Abnormalities, 3rd ed. Elsevier, Churchill Livingstone; Ch. 3, pp. 60–80.

Toppari J, Rodprasert W, Virtanen HE 2014 Cryptorchidism – disease or symptom? Ann Endocrinol 75:72–6.

Turan OM, Turan S, Funai EF et al 2007 Fetal adrenal gland volume: a novel method to identify women at risk for impending preterm birth. Obstet Gynecol 109:855–62.

Turan OM, Turan S, Buhimschi IA et al 2012 Comparative analysis of 2-D versus 3-D ultrasound estimation of the fetal adrenal gland volume and prediction of preterm birth. Am J Perinatol 29:673–80.

Valasek P, Evans DJR, Maina F et al 2005 A dual fate of the hindlimb muscle mass: cloacal/perineal musculature develops from leg muscle cells. Development 132:447–58.

van Vuuren SH, Damen-Elias HA, Stigter RH et al 2012 Size and volume charts of fetal kidney, renal pelvis and adrenal gland. Ultrasound Obstet Gynecol 40:659–64.

Viana R, Batourina E, Huang H et al 2007 The development of the bladder trigone, the center of the anti-reflux mechanism. Development 134:3763–9.

Wang C, Gargollo P, Guo C et al 2011 *Six1* and *Eya1* are critical regulators of peri-cloacal mesenchymal progenitors during genitourinary tract development. Dev Biol 360:186–94.

Wang C, Wang JY, Borer JG et al 2013 Embryonic origin and remodelling of the urinary and digestive outlets. PLoS One 8:e55587.

This paper considers the development of the cloacal region and its separation into enteric and urogenital parts.

Wei W, Howard PS, Kogan B et al 2012 Urinary diversion results in marked decreases in proliferation and apoptosis in fetal bladder. J Urol 188:1306–12.

Wen Q, Tang EI, Gao Y et al 2018 Signaling pathways regulating blood–tissue barriers – lesson from the testis. Biochim Biophys Acta 1860:141–53.

Williams A 2013 Congenital abnormalities of the lower urinary tract. Surgery 31:371–7.

Yosypiv IV 2009 Renin–angiotensin system-growth factor cross-talk: a novel mechanism for ureteric bud morphogenesis. Pediatr Nephrol 24:1113–20.

Yosypiv IV 2012 Congenital anomalies of the kidney and urinary tract: genetic disorder? Int J 2012:909083. doi:10.1155/2012/909083 (ePub 2012 May 20).

CHAPTER

23

Pre- and postnatal growth and the neonate

PRENATAL STAGES

Development of a human from fertilization to delivery at ‘full term’ averages 266 postfertilization days, or 9.5 lunar months (28 day units). It has long been customary to compute the length of a pregnancy, whether in a normal birth or an abortion, from the first day of the last menstrual period of the mother but, as ovulation usually occurs near the fourteenth day of a menstrual cycle, this ‘menstrual age’ is an overestimate of developmental age of about 2 weeks. Estimated in this manner, pregnancy averages 280 days from the last menstrual period or 10 lunar months (40 weeks).

The development of a human from fertilization to birth is divided into two periods: embryonic and fetal. The absolute size of an embryo or fetus does not afford a reliable indication of either its chronological age or the stage of its structural organization, even though graphs based on large numbers of observations have been constructed to provide averages. All such data suffer from the difficulty of timing the moment of conception in humans; *in vitro* fertilization techniques now accurately time the start of embryonic life (Ch. 8).

The embryonic period was graded or classified into developmental stages or ‘horizons’, on the basis of the internal and external features of approximately 600 sectioned embryos, by Streeter (1942, 1945, 1948). These sections formed the basis of the Carnegie system of staging. Streeter’s work and its continuation by O’Rahilly and Müller (1987), provided, and continues to provide, a sound foundation for embryonic study and a means of comparing stages of human development with those of the animals routinely used for experimental study, namely the chick, mouse and rat.

The postfertilization developmental events in embryonic stages 1–10 are shown in detail in Fig. 8.1. The stages up to stage 5 are concerned with implantation of the blastocyst. The external appearance of representative stages from stage 6 to stage 23, correlated with the greatest length in millimetres and approximate age in days is shown in **Fig. 23.1**. Estimations of embryonic length from fixed histological specimens may be 1–5 mm less than their equivalent *in vivo* estimates, reflecting the shrinkage caused by the preparative procedures used in embryological studies. O’Rahilly and Müller (2000, 2010) revised some of the ages that had previously been assigned to early Carnegie embryonic stages, pointing out that interembryonic variation might be greater than had been thought and that, consequently, some ages might have been underestimated. They noted that, as a guide, the age of an embryo could reasonably be estimated from the embryonic length within the range 3–30 mm, by adding 29 to the length. Recent use of ultrasound for the examination

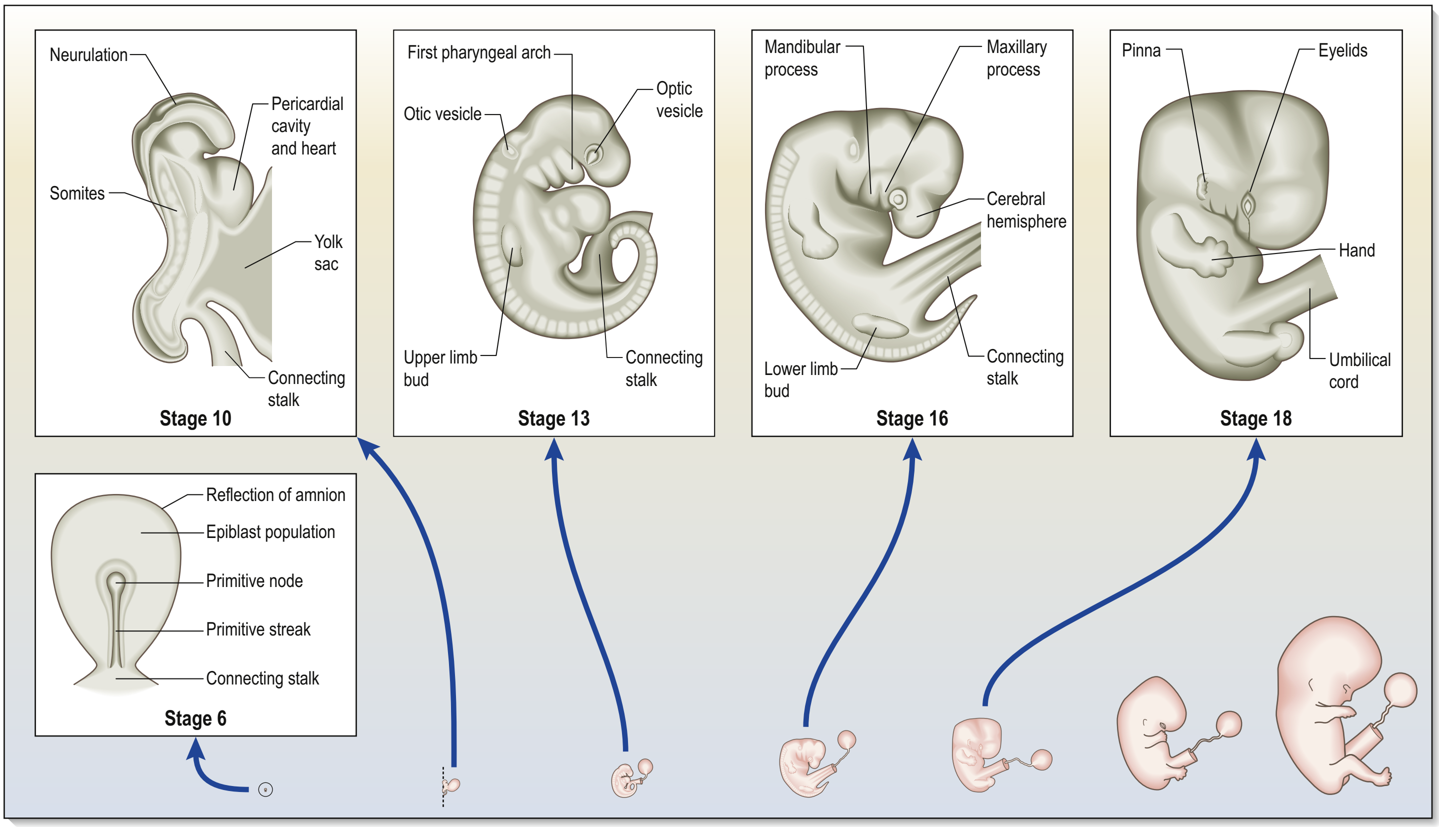
Neurulation
Pericardial cavity and heart
Somites
Yolk sac
Connecting stalk
Stage 10
First pharyngeal arch
Optic vesicle
Otic vesicle
Upper limb bud
Connecting stalk
Stage 13
Mandibular process
Maxillary process
Cerebral hemisphere
Lower limb bud
Connecting stalk
Stage 16
Pinna
Eyelids
Hand
Umbilical cord
Stage 18
Reflection of amnion
Epiblast population
Primitive node
Primitive streak
Connecting stalk
Stage 6

Embryonic stage	6	10	13	16	18	20	23
Size (mm)	0.4	1.5–3	4–6	8–11	13–17	21–23	28–30
Approximate age (days)	16–18	26–29	30–33	35–40	41–45	46–50	53–58

Fig. 23.1 The external appearance and size of embryos between stages 6 and 23. Early in development, external features are used to describe the stage, e.g. somites, pharyngeal arches or limb buds. (Adapted with permission from Pandya P, Oepkes D, Sebire N et al (eds) Fetal Medicine: Basic Science and Clinical Practice, 3rd ed. Elsevier. Copyright 2020.)

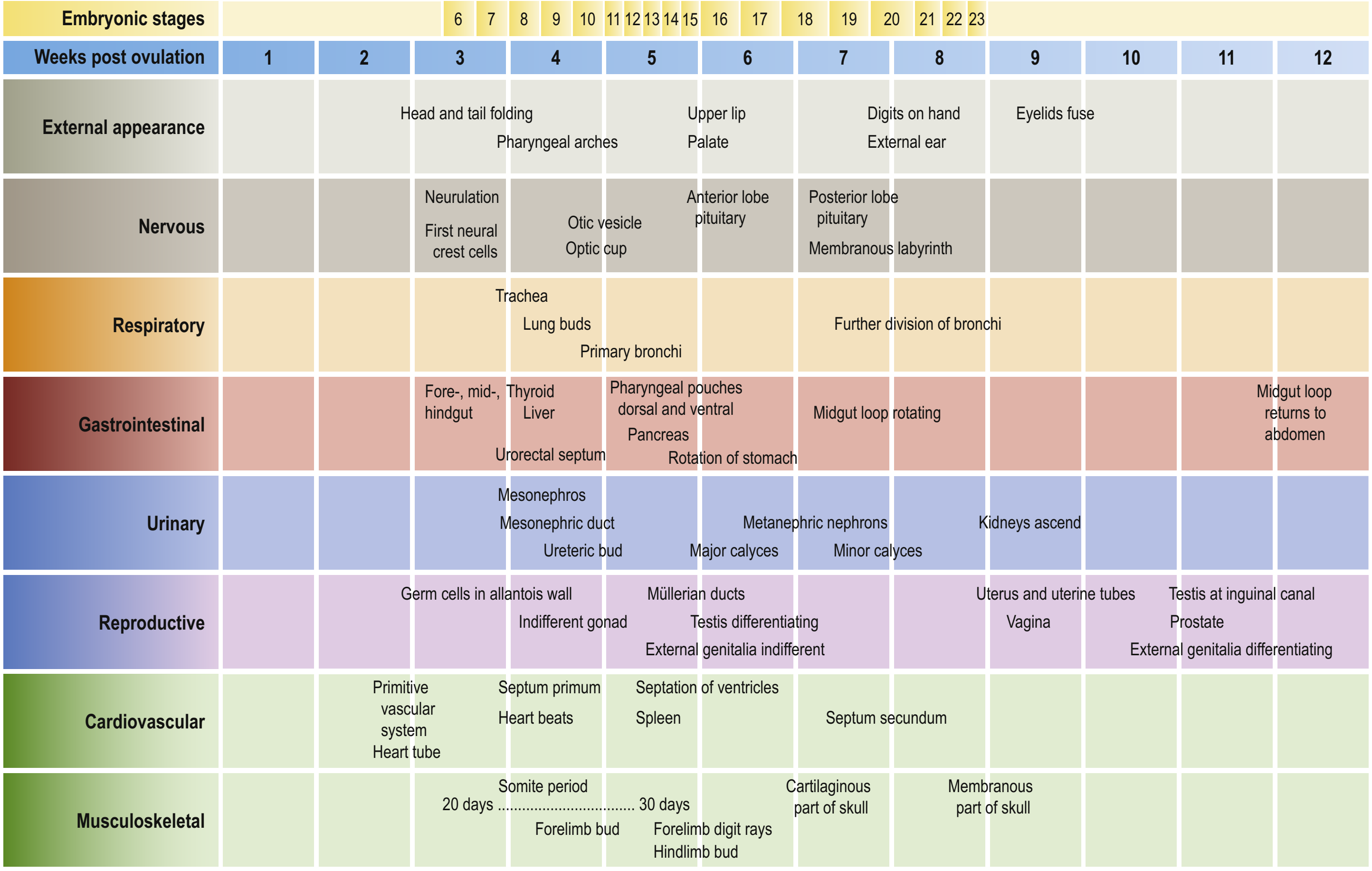

Weeks post ovulation	1	2	3	4	5	6	7	8	9	10	11	12
Embryonic stages			6 7	8 9 10	11 12 13 14 15	16 17	18 19	20 21 22 23				
External appearance			Head and tail folding	Pharyngeal arches		Upper lip Palate		Digits on hand External ear	Eyelids fuse			
Nervous			Neurulation First neural crest cells	Otic vesicle Optic cup		Anterior lobe pituitary	Posterior lobe pituitary Membranous labyrinth					
Respiratory				Trachea Lung buds	Primary bronchi			Further division of bronchi				
Gastrointestinal			Fore-, mid-, hindgut	Thyroid Liver Urorectal septum	Pharyngeal pouches dorsal and ventral Pancreas	Rotation of stomach	Midgut loop rotating					Midgut loop returns to abdomen
Urinary				Mesonephros Mesonephric duct Ureteric bud		Major calyces	Metanephric nephrons Minor calyces		Kidneys ascend			
Reproductive			Germ cells in allantois wall	Indifferent gonad	Müllerian ducts	Testis differentiating External genitalia indifferent			Uterus and uterine tubes Vagina		Testis at inguinal canal Prostate External genitalia differentiating	
Cardiovascular		Primitive vascular system Heart tube		Septum primum Heart beats	Septation of ventricles Spleen		Septum secundum					
Musculoskeletal				Somite period 20 days .... 30 days Forelimb bud	Forelimb digit rays Hindlimb bud		Cartilaginous part of skull		Membranous part of skull			

Fig. 23.2 A timetable of development of the body systems. The development of individual systems can be seen progressing from left to right. Embryonic stages and weeks of development are shown. Embryonic stages are associated with external and internal morphological features rather than embryonic length. To identify the systems and organs at risk at any time of development, follow a vertical progression from top to bottom.

of human embryos and fetuses *in utero* has confirmed much of the staging data. However, assigning embryos to a particular stage and the estimated length of days that that stage encompasses remains subject to error. The revisions of age to particular stages given by O'Rahilly and Müller (2010) are followed as closely as possible in what follows.

Obvious external features provide some guidance to the changes occurring within embryos during successive stages. Somite number is related to early embryonic stages; once the number of somites is too great to count with accuracy, the degree of development of the pharyngeal arches is often used. External staging becomes more obvious when the limb buds appear. The upper limb bud is clearly visible at stage 13 (approximately 31–33 days post fertilization) and the acquisition of a distal paddle on the upper limb bud is characteristic by stage 16 (approximately 37–38 days post fertilization). At stage 18 (approximately 42–44 days post fertilization) the lower limb bud has a distal paddle, whereas the upper limb bud has digit rays that are beginning to separate. By stage 23 (approximately 53–58 days post fertilization) the embryo has a head that is almost erect and rounded, and eyelids are beginning to form. The limbs look far more in proportion and fingers and toes are separate. At this stage the external genitalia are well developed, although they may not be sufficiently developed for the accurate determination of the sex.

Stages of embryonic development include all aspects of internal and external morphogenetic change that occur within the embryo during that stage. They are used to convey a snapshot of the status of the development of all body systems within a particular timeframe. **Fig. 23.2** gives an overview of the changes in the main body systems over time and also shows the systems and organs at risk at any specific developmental time and the range of anomalies caused by teratogenic insult at a particular time. Historically, the onset of bone marrow formation in the humerus in stage 23 was used by Streeter to indicate the end of the embryonic period and the beginning of the fetal period of prenatal life, after 53–58 days (about 8 weeks) postfertilization. **Fig. 23.3** shows embryonic stages 10–23 correlated to postfertilization days of development alongside postmenstrual weeks. The 'term' of a pregnancy, i.e. its completion resulting in delivery, is considered clinically normal between 37 and 42 weeks.

In obstetric practice, the period of pregnancy is divided into thirds, termed trimesters. Within this time scale, starting from the last menstrual period, the fetal period commences during the end of the first trimester (**Fig. 23.4**). Neonates delivered before 37 weeks are called preterm (or premature); those delivered after 42 weeks are post-term. The use of postmenstrual weeks as a timescale for development has now been extended to those fetuses that are delivered before their predicted 'term'. This terminology removes the ambiguous use of 'gestation','gestational age' or 'gestational weeks', and helpfully standardizes the terminology in studies that continue to document growth postnatally to 64 postmenstrual weeks (the equivalent of 6 postnatal months for a full-term infant born at 40 weeks). Some studies have used the term 'corrected age' for follow-up studies on preterm infants, calculated by subtracting the number of weeks born before 40 weeks' gestation from the chronological age. It is of note that this method is now standardizing 40 weeks as 'term' and it is worth considering if all studies of term babies should have their age similarly adjusted if they were born at 38, 39 or 41 weeks.

The period from postmenstrual week 24 and up to 7 days after birth is termed the perinatal period (see Fig. 23.4). In the UK fetuses that are delivered and die before postmenstrual week 24 are considered to be miscarriages of pregnancy, although technological advances in neonatal care assist the delivery and support of infants younger than postmenstrual week 24. The neonatal period is considered to extend from birth to 28 days postnatally; the early neonatal period extends from birth to 7 days and the late neonatal period from 7 to 28 days.

Ultrasound staging

The predicted date of full term and delivery is revised after routine ultrasound examination of the fetus. Early ultrasound estimation of fetal age increases the rate of reported preterm delivery (delivery at <37 weeks) compared with estimation based only on the date of the last menstrual period, possibly because delayed ovulation is more frequent than early ovulation (Yang et al 2002).

The difficulty of correlating the appearance of a chorionic sac, embryo or fetus on an ultrasound scan, with age during the first trimester is related

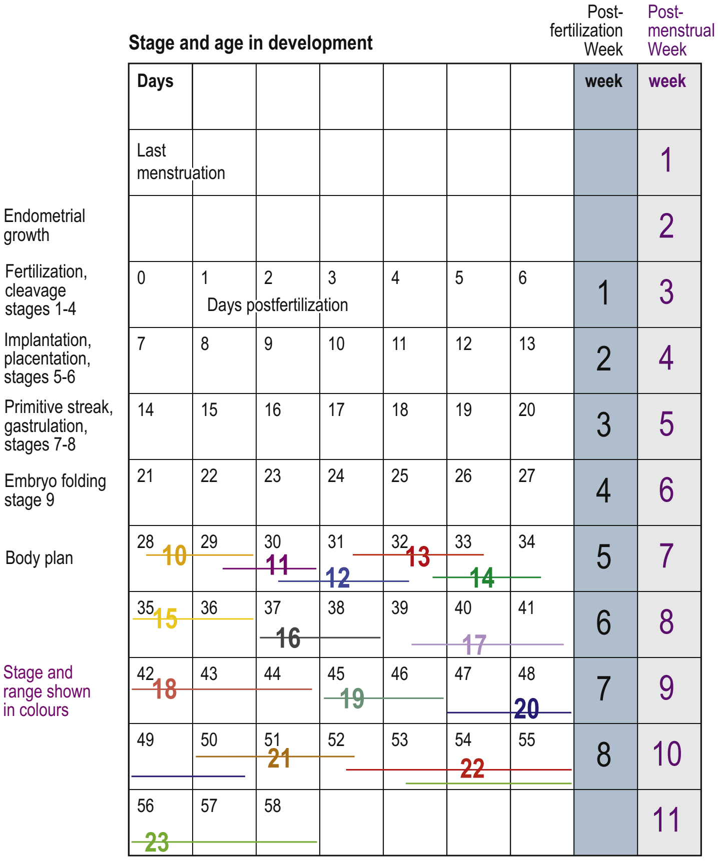
Stage and age in development
Post-fertilization Week
Post-menstrual Week
Days
week
week
Last menstruation
1
Endometrial growth
2
Fertilization, cleavage stages 1-4
0 1 2 3 4 5 6
Days postfertilization
1 3
Implantation, placentation, stages 5-6
7 8 9 10 11 12 13
2 4
Primitive streak, gastrulation, stages 7-8
14 15 16 17 18 19 20
3 5
Embryo folding stage 9
21 22 23 24 25 26 27
4 6
Body plan
28 29 30 31 32 33 34
10 11 12 13 14
5 7
35 36 37 38 39 40 41
15 16 17
6 8
Stage and range shown in colours
42 43 44 45 46 47 48
18 19 20
7 9
49 50 51 52 53 54 55
21 22
8 10
56 57 58
23
11

Stage of embryonic development counted in days from fertilization ends at stage 23, equivalent to 53-58 days.
Fetal development counted in days/weeks from the last menstrual period is used to predict the date of delivery.

Fig. 23.3 Stages of embryonic development according to O'Rahilly and Müller (2010) correlated with age in postfertilization days. Embryonic stages are based on internal and external morphogenetic change within the duration of a stage. Some stages span only 2 days and others up to 6 days. The clinical estimation of pregnancy is given in postmenstrual weeks for comparison. Note that fertilization occurs at the beginning of week 3 in this system. (Adapted with permission from Pandya P, Oepkes D, Sebire N et al (eds) Fetal Medicine: Basic Science and Clinical Practice, 3rd ed. Elsevier. Copyright 2020.)

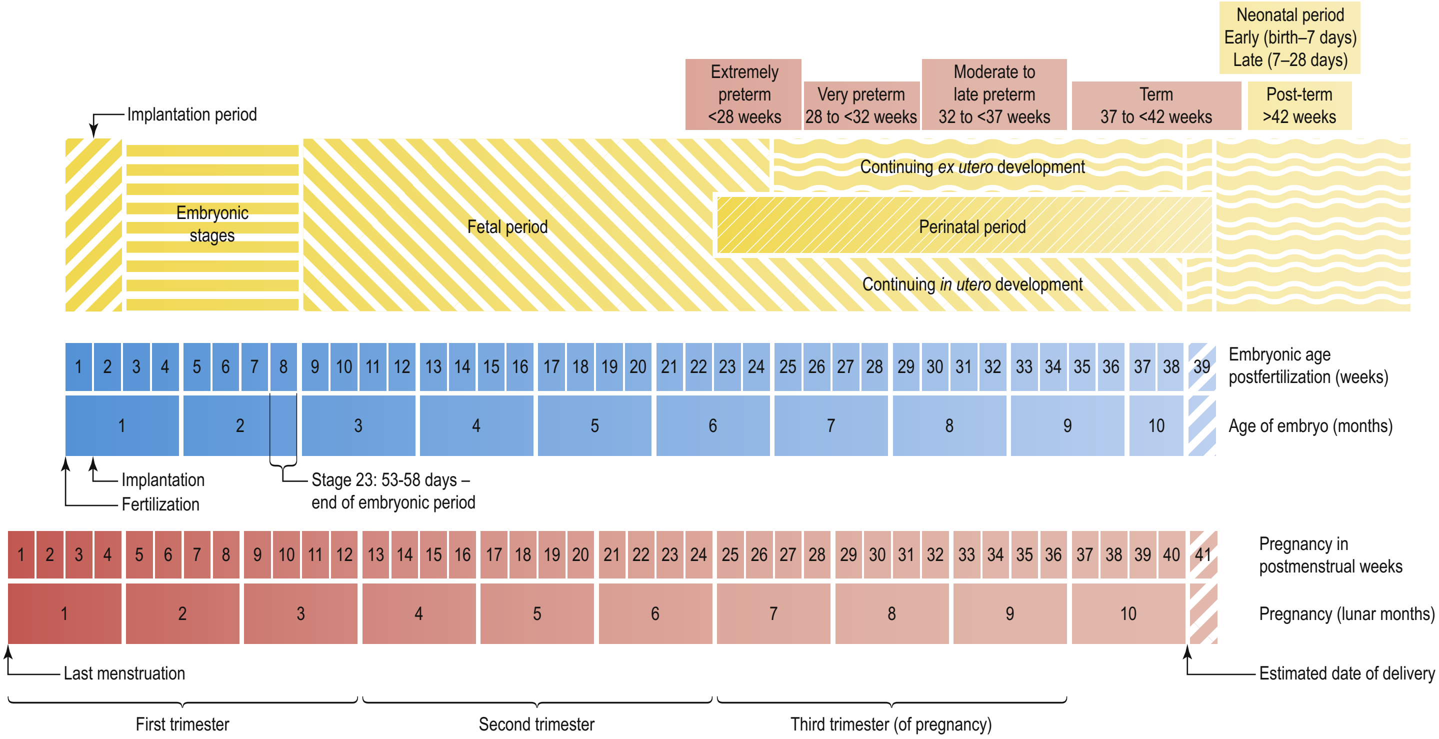
Neonatal period
Early (birth–7 days)
Late (7–28 days)
Extremely preterm <28 weeks
Very preterm 28 to <32 weeks
Moderate to late preterm 32 to <37 weeks
Term 37 to <42 weeks
Post-term >42 weeks
Implantation period
Embryonic stages
Fetal period
Continuing *ex utero* development
Perinatal period
Continuing *in utero* development
1 2 3 4 5 6 7 8 9 10 11 12 13 14 15 16 17 18 19 20 21 22 23 24 25 26 27 28 29 30 31 32 33 34 35 36 37 38 39
Embryonic age postfertilization (weeks)
1 2 3 4 5 6 7 8 9 10
Age of embryo (months)
Implantation
Fertilization
Stage 23: 53-58 days – end of embryonic period
1 2 3 4 5 6 7 8 9 10 11 12 13 14 15 16 17 18 19 20 21 22 23 24 25 26 27 28 29 30 31 32 33 34 35 36 37 38 39 40 41
Pregnancy in postmenstrual weeks
1 2 3 4 5 6 7 8 9 10
Pregnancy (lunar months)
Last menstruation
Estimated date of delivery
First trimester
Second trimester
Third trimester (of pregnancy)

Fig. 23.4 The two timescales used to depict human development. Embryonic development, in the upper scale, is counted in days from fertilization according to O'Rahilly and Müller (2010). Throughout this book, embryonic development is based on this scale. The clinical estimation of pregnancy is counted from the last menstrual period and is shown on the lower scale; throughout this book, fetal ages are described in postmenstrual weeks. Note that there is a 2-week discrepancy between these scales. The perinatal period is very long because it includes all preterm deliveries.

to the specificity of reporting the age. An age reported as within a specific postmenstrual week, e.g. week 12, will cover a period of 6 days (12 weeks 0 days up to 12 weeks 6 days, now noted as 12w0d and 12w6d). It is recommended that sonographic estimation of age should be given as postmenstrual weeks and days (i.e. 12 weeks indicates 12w0d) (Galan et al 2008).

First trimester scan

An early ultrasound scan will detect implantation and viability of the embryo once a heartbeat is detected, confirm multiple pregnancy and estimate the date of delivery. Cardiac activity can be identified by the sixth postmenstrual week (Galan et al 2008); note in Fig. 23.2 that this corresponds to approximately stage 10 (28–29 postfertilization days). Crown–rump length measurement, i.e. the greatest distance between the vertex of the skull and the ischial tuberosities, with the fetus in the natural curved position, is the most accurate predictor of the postmenstrual age of the embryo during the first trimester (Galan et al 2008). Greatest length exclusive of the lower limbs is independent of fixed points and thus simpler to measure, and was recommended by O'Rahilly and Müller (2000); it is generally taken to be the sitting height in postnatal life. Nuchal translucency is measured between 10 and 14 weeks to diagnose trisomy 21. The development of three-dimensional ultrasound scanning has enabled early detection of many anomalies that were previously diagnosed in the second trimester, including anencephaly, hydrocephalus and encephalocele (Pretorius et al 2014). Normograms of fetal spine growth constructed for a Taiwan population showed mean spine length increasing linearly between 11 and 14 weeks (Cheng et al 2010) and a tendency for spinal extension as early as 11 weeks.

Second trimester scan

Routine scanning at 18–20 postmenstrual weeks is used to confirm the delivery date and assess not only the position of the placenta but also the presence of fetal anomalies that would require special intervention following delivery, such as cardiac defects, lung immaturity, renal agenesis, polyhydramnios and defects of the anterior abdominal wall (gastroschisis and exomphalos). Estimations are made of the following: biparietal skull diameter, taken through a plane of section that traverses the third ventricle and thalami; head circumference through a plane that traverses the third ventricle and thalami plus the cavum septi pellucidi anteriorly and the tentorial hiatus posteriorly; abdominal circumference through a plane where the transverse diameter of the liver is greatest, the appearance of the lower ribs is symmetric and the junction of the left and right portal veins is identified; and femoral length, which measures the ossified portions of the diaphysis and metaphyses (**Fig. 23.5**). Between 15 and 28 postmenstrual weeks, the biparietal diameter is the most accurate index of fetal age and the expected date of delivery. Other measurements that may also be taken include the transverse cerebellar diameter and foot length. The amount and type of fetal movement, breathing movements and visceral functions, exemplified by bladder emptying, peristaltic action and colonic echogenicity, are noted. Gender can be identified later in development but this information is not always routinely passed on to parents. Three- and four-dimensional ultrasound scans are now routinely constructed (**Video 23.1**). For assessment of fetal wellbeing from ultrasound examination see Benson and Doubilet (2018).

Managing fetal anomalies

An outcome of routine ultrasound examination of embryos and fetuses for anomalies may be a change to the perinatal management, i.e. to the time, method and place of delivery of the fetus, or the parents may choose to terminate the pregnancy to minimize concerns about fetal and neonatal suffering and long-term disability. Termination may be chosen for severe, untreatable inherited metabolic disorders (e.g. Tay–Sachs disease), severe chromosomal anomalies (e.g. trisomy 13), lethal bone dysplasias, lethal anomalies such as anencephaly and other extreme neurological defects, and bilateral renal agenesis (Cass 2011). Improvements in prenatal screening and diagnosis have led to an overall increase in the prevalence of reported birth defects and overall lower perinatal mortality rates, reflecting increased early terminations of pregnancy (Cass 2011).

Magnetic resonance imaging

Advances in prenatal ultrafast magnetic resonance imaging (MRI) now provide further ways to detect fetal anomalies, capturing particularly clear images (Sepulveda et al 2012) (**Fig. 23.6**). For this reason, MRI is considered a useful adjunct to ultrasound imaging at 20–22 postmenstrual weeks because it enables better management planning for known or suspected anomalies (Reddy et al 2014).

Fetal surgery

The use of routine ultrasound examination and MRI of fetuses has led to the development of a number of prenatal surgical interventions: e.g. to correct placental or membrane anomalies resulting in twin-to-twin transfusion and the production of amniotic bands (Deprest et al 2014); or to offer improved outcomes for meningomyelocele on the basis that the neural tissue may become secondarily damaged by exposure to amniotic fluid and mechanical traumatic injury during gestation (Adzick 2013, Cohen et al 2014, Danzer and Johnson 2014). Other conditions have also been treated prenatally with limited improvement in mortality. Congenital diaphragmatic hernia has been treated by percutaneous fetoscopic endoluminal tracheal occlusion from 25 to 33 postmenstrual weeks to prevent loss of lung fluid and enhance lung growth (Deprest et al 2004). Fetal airway patency has also been preserved during birth through perinatal *ex utero* intrapartum (EXIT) treatment, where a portion of the fetus is delivered through a hysterectomy incision for surgery while the fetus remains attached to the uteroplacental circulation, and the fetus is subsequently completely delivered after the airway procedure is completed (Deprest et al 2014).

GROWTH

The changes with age seen in the fetal period are part of a continuum termed growth, which extends postnatally to adulthood. Growth, which describes the velocity of change in size, has distinct phases. It is most rapid in utero, slower but relatively rapid in infancy, steady in childhood, rapid again during adolescence and thereafter very slow as adulthood is approached. It is measured throughout these periods, in a similar manner to that used for embryonic staging, i.e. by documenting increments in height and weight over time. Both genetic and environmental influences operate in exactly the same way as in earlier stages, with one or the other being dominant at any time point. Individual genetic potential can be fully realized at any stage of growth when environmental effects are neutral; conversely, negative environmental conditions and consequent epigenetic changes can prevent an individual from reaching their full growth potential.

Growth is documented in charts that portray different attributes of growth optimally for different end users, e.g. paediatricians, midwives, health visitors, endocrinologists, researchers etc. The recorded data is subject to detailed and specific statistical methodologies that ensure any graphs presented show smooth curves and are easy to follow. Specific terminology indicates the methodology used when collecting and presenting the data. A *longitudinal study* shows the successive measurement of individuals taken for the entire period of growth. A *cross-sectional study* collects measurements from different individuals and means (with their standard deviation – SD) are calculated for each time point, sometimes also for each sex.

A cross-sectional collection of weight or height from an adult population would produce a graph with a normal distribution with the mean measurement at the highest point. To display the change in weight and height in children, growth charts are presented with the weight or height plotted against time plus standard deviations each side of the mean (1SD, 2SD and 3SD), shown also as lines. Growth charts can also be constructed to show centiles (calculated from the mean and SD), so that the 50th centile (also known as the median), in the midpoint of the distribution, is flanked by lines showing the 3rd, 10th, 25th, 75th, 90th and 97th centiles. The charts are different because SD lines are delineated equally each side of the mean, whereas centiles are more widely spaced above the median than below. Both types of chart are often colloquially termed growth curves (Cole 2003, 2012).

The data from longitudinal and cross-sectional studies can be used to plot the increments in height or weight from one age to the next. This produces a *velocity curve*, which reflects a child's state at any particular time much better than the growth curve, in which each point is dependent on the preceding one. The oldest published longitudinal study, still of great value today, was made by Count Philibert de Montbeillard on his son (**Fig. 23.7**). Comparison of the charts show clearly that although height increases over 18 years, the growth velocity decreases from birth onwards, with an acceleration between 13–15 years, during the adolescent growth spurt. Height and the corresponding growth velocity for the first 22 months of life, compiled from cross-sectional data is shown in **Fig. 23.8**.

The time at which data for growth charts were collected is important because secular change is now very apparent between older and more recent charts. Many of the growth charts acknowledged in the literature are based on meticulous studies from the 1940s and 1950s. They illustrate the reference weight and height for children born between or after the World Wars and later when food rationing was still in operation in the UK. They also reflect the social mores of those times when men were usually fed first, followed by the children, and women were fed last, factors that undoubtedly affected the growth of children at that time and the fetuses of low weight mothers.

Cross-sectional growth charts are particularly important in the management of public health issues, e.g. summarizing and comparing the nutritional status of different groups of children to explore the potential effects of socioeconomic status on growth. In this case the applicability of the chart to an individual child is less important. However, the

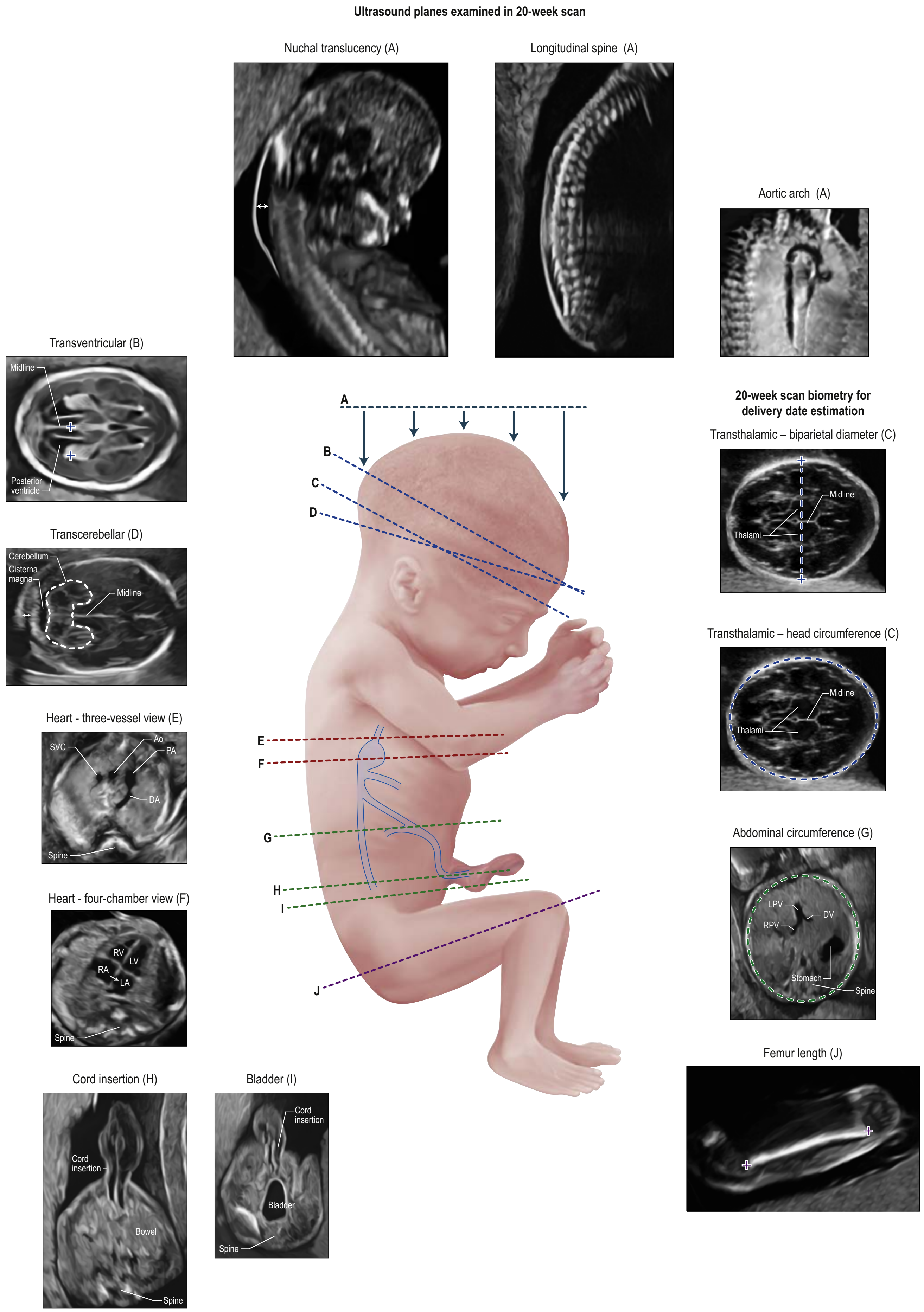
Ultrasound planes examined in 20-week scan
Nuchal translucency (A)
Longitudinal spine (A)
Aortic arch (A)
Transventricular (B)
Midline
Posterior ventricle
Transcerebellar (D)
Cerebellum
Cisterna magna
Midline
Heart - three-vessel view (E)
SVC
Ao
PA
DA
Spine
Heart - four-chamber view (F)
RV
LV
RA
LA
Spine
Cord insertion (H)
Cord insertion
Bowel
Spine
Bladder (I)
Cord insertion
Bladder
Spine
A
B
C
D
E
F
G
H
I
J
20-week scan biometry for delivery date estimation
Transthalamic – biparietal diameter (C)
Midline
Thalami
Transthalamic – head circumference (C)
Midline
Thalami
Abdominal circumference (G)
LPV
DV
RPV
Stomach
Spine
Femur length (J)

Fig. 23.5 Ultrasound planes examined in a routine second-trimester antenatal scan (left) and measurements taken to predict the estimated date of delivery (right). The top three images are in the sagittal plane (A). The other planes are transverse, apart from J, which is longitudinal. Abbreviations: Ao, aorta; DA, ductus arteriosus; DV, ductus venosus; LA, left atrium; LPV, left portal vein; LV, left ventricle; PA, pulmonary artery; RA, right atrium; RPV, right portal vein; RV, right ventricle; SVC, superior vena cava.

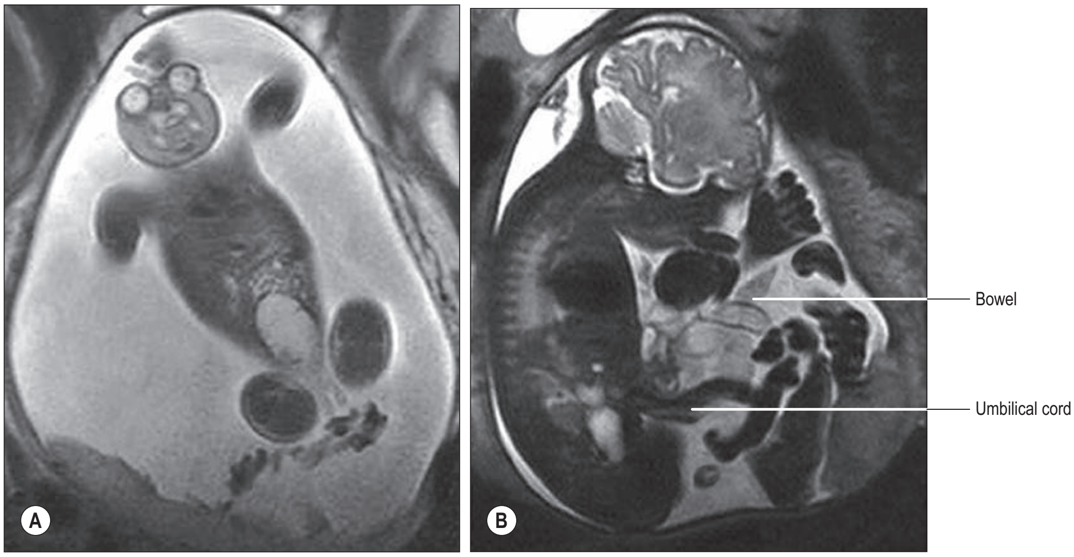

Fig. 23.6 MRI scans of fetal anomalies. **A**, Polyhydramnios may arise as a result of oesophageal compression, impaired swallowing and lack of absorption of amniotic fluid from the gut. **B**, Gastroschisis with loops of bowel in the extracellular coelom (chorionic cavity) and normal insertion of the umbilical cord. (With permission from Sepulveda W, Ximenes R, Wong AE et al 2012 Fetal magnetic resonance imaging and three-dimensional ultrasound in clinical practice: applications in prenatal diagnosis. Best Pract Res Clin Obstet Gynaecol 26:593–624.)

Fetal growth velocity has been computed from estimated fetal weight standards for singleton pregnancies undergoing ultrasound scans at 10w0d–13w6d, 16–22, 24–29, 30–33, 34–37 and 38–41 postmenstrual weeks (Grantz et al 2018). Mean EFW growth velocity at 16, 20, 30 and 35 postmenstrual weeks was 29 g/wk, 59 g/wk, 175 g/wk and 215 g/wk, with growth velocity peaking at 35 weeks (Grantz et al 2018) (**Fig. 23.11**). Considering the anthropometric measurements in this study, the average BPD growth velocity peaks at 13 postmenstrual weeks with a second slight acceleration from 19–22 weeks. Head circumference average growth velocity peaks at 14 weeks with a second acceleration from 19–21 weeks. Both decrease in growth velocity after this time. Average growth velocities for femoral and humeral length peak at about 15 weeks and then steadily decline. Abdominal circumference average growth velocity increases until 16 postmenstrual weeks, with a second acceleration from 27–31 weeks, after which growth velocity steadily declines up to 40 weeks (**Fig. 23.12A–D**).

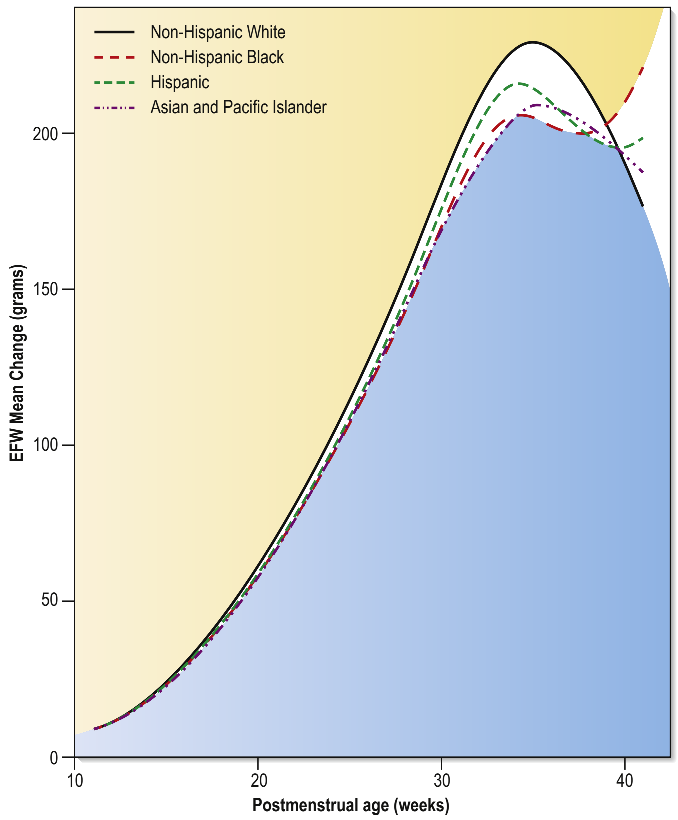

Fig. 23.11 Velocity of estimated fetal growth over postmenstrual weeks. (Data from Grantz et al 2018.)

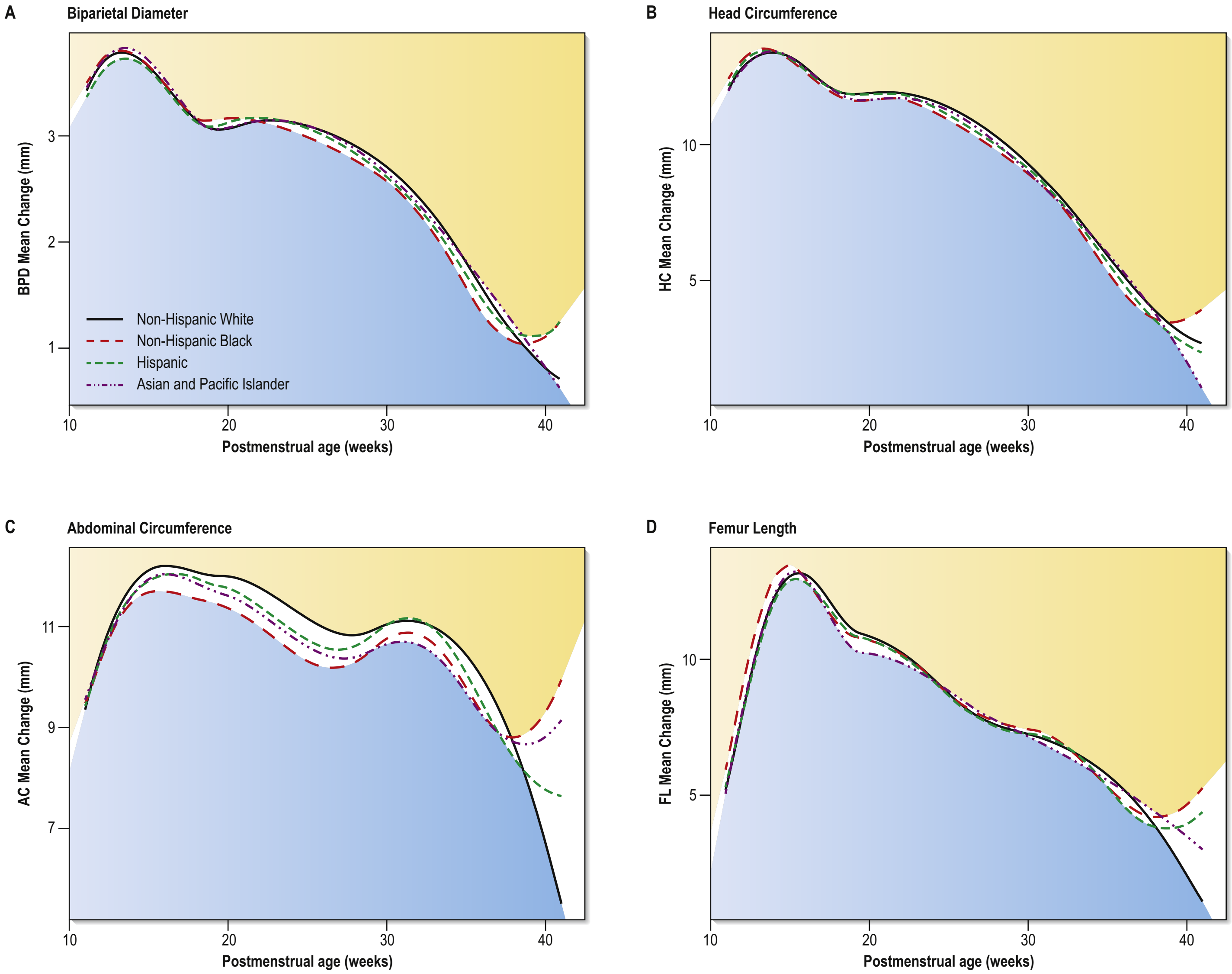

Fig. 23.12 A–D, Velocity of estimated fetal growth parameters over postmenstrual weeks. (Data from Grantz et al 2018.)

There is a correlation between short maternal stature and macrosomia; macrosomic fetuses are at risk of shoulder dystocia and brachial plexus injuries during vaginal delivery. Adiposity at birth is related to obesity and metabolic dysfunction in childhood, which may be perpetuated through adulthood in an ongoing cycle through the generations (Catalano and Hauguel-De Mouzon 2011, Poston 2012). A range of risk factors for pre-, peri- and postnatal issues in maternal obesity is given in McGuire et al (2010).

Stillbirth

Stillbirth is classified as antepartum death occurring before the initiation of labour or intrapartum death occurring during labour and delivery. It is estimated that by 28 postmenstrual weeks approximately 1 in 250 pregnancies will result in a stillbirth in high-income countries and 1 in 22 pregnancies in low- and middle-income countries (Hirst et al 2018). Maternal age of 40 years or older doubled the risk of stillbirth compared to mothers aged 18–25 years. The epidemiology of neonatal mortality in Europe and the UK is presented in Macfarlane and Mugford (2012).

Assisted reproductive technique effects

A range of assisted reproductive techniques (ART) (Ch. 8) have been used and developed over the last 40 years and account for about 2% of births annually in Europe and America (Ginod et al 2018). It is becoming apparent that the mode of conception influences the epigenetic imprinting of offspring and that ARTs affect fetal growth kinetics, postnatal growth and adult risk of pathology. ART-conceived fetuses show higher CRL and EFW than reference charts during the first and second trimesters, but decelerated growth from the second trimester onwards with increased risk of low birth weight mortality (Fleming et al 2018, Ginod et al 2018).

TRANSITION TO EXTRAUTERINE LIFE

The sudden release of a fetus into a gaseous environment of varying temperature, with full gravity and a range of microorganisms, promotes the rapid maturation of some systems and the compensatory growth of others (in terms of responses to the effect of gravity, enteral feeding and exposure to microorganisms, respectively). Maturational processes involving local interactions and pattern formation still drive development at local and body-system levels in preterm infants. For details of the cardiovascular changes at birth see Chapter 13.

The type of birth, whether for preterm or term delivery, confers developmental outcomes on the neonate that affect its subsequent growth. Caesarean section for preterm delivery appears not to be associated with improved neonatal outcomes but is associated with increased risk of respiratory distress syndrome due to slower postnatal movement of fluid out of the lungs (Bellini et al 2006, Bhatta and Keriakos 2011, Werner et al 2012). The dramatic rise of this delivery method is not necessarily driven by improved neonatal outcomes because caesarean section has been shown to increase the odds of developing asthma and type 1 diabetes in later life by 20%. Meta-analyses indicate that the endocrine milieu during caesarean section may lead to epigenetic effects on hepatic and metabolic function and so affect immune function in adult life, leading, in some instances, to food allergy and obesity (Steer and Modi 2009, Hyde and Modi 2012, Song et al 2013).

Prior to birth, the gut is exposed to hundreds of proteins, metabolites and cytokines that are swallowed in amniotic fluid, and there is some evidence for the presence of bacterial species in amniotic fluid prior to delivery. Establishment of the gut microbiota by exposure to maternal vaginal and colonic bacteria during vaginal delivery leads to normal maturation of the gut wall. Gut colonization in preterm infants is delayed (Cilieborg et al 2012). Infants born via caesarean section may have primary gut flora disturbance for up to 6 months after birth and associated delay in postnatal immune development (Neu and Rushing 2011, Neu and Mai 2012, Matamoros et al 2013).

Preterm neonate

The way in which birth at a particular postmenstrual week of delivery has been classified into preterm birth age has been more complex than might be thought. The WHO has subdivided preterm birth into the categories of postmenstrual weeks *in utero*: extremely preterm <28 weeks; very preterm 28–32 weeks; late preterm 32–<37 weeks (Howson et al 2012). Term pregnancy has been defined as within the postmenstrual weeks period 37 completed weeks to less than 42 completed weeks; early term delivery 37–38 weeks; full term 38–40 weeks and post-term >42 weeks (Quinn et al 2016). Because the processes involved in initiating parturition are so complex, Villar et al (2012) recommend that five components should be included in any consideration of preterm birth: significant maternal conditions present before delivery; significant fetal conditions present before delivery; presence of placental pathological conditions; signs of the initiation of parturition; and the type of delivery. These factors involved in the pathogenesis of spontaneous preterm birth are discussed in Buhimschi and Norman (2014). Infection of the decidua, amniotic fluid, amnion or chorion, and clinical and subclinical chorioamnionitis have been reported in approximately 50% of preterm births (Maltepe and Penn 2018) (Ch. 9), whereas sterile inflammation occurs normally in the decidua, myometrium and cervix prior to parturition (Mesiano 2019). In 2010 more than 10% of all births were premature world-wide (Simhan et al 2014), the majority in south Asia and sub-Saharan Africa. In the United States, more than 70% of preterm births occurred between 34 and 36 postmenstrual weeks and 16% of preterm births occurred before 32 postmenstrual weeks (Simhan et al 2014). Preterm birth is the most frequent cause of infant mortality and accounts for one-third of infant deaths (for details of the risk factors for preterm birth see Simhan et al (2014)).

Previously, low birth weight fetuses and neonates were grouped statistically with preterm birth infants, however, improvement in sonographic estimation of fetal age means that perinatal and infant morbidities, which vary according to maturity and weight, can be addressed separately. A new definition of preterm birth syndrome has been proposed in publications from the Global Alliance to Prevent Prematurity and Stillbirth, which includes all births (live births, stillbirths and pregnancy terminations) occurring from 16w0d to 38w6d (Villar et al 2012, Kramer et al 2012, Buhimschi and Norman 2014). The rationale for the early time is because pathologies occurring between 16 and 20 weeks also affect later gestation; the rationale for the later time because births between 37 and 39 weeks are associated with greater morbidity than births after 39 weeks. The definition aims to consider early delivery and not disturbances of growth (see p. 371). The definition is based on a clinical phenotype of: (a) one or more conditions of the mother, placenta, or fetus; (b) the presence or absence of signs of parturition; (c) the pathway to delivery (spontaneous or caregiver initiated). The Global Alliance to Prevent Prematurity and Stillbirths recommends the use of this definition world-wide and acknowledges that its use will initially lead to higher reported rates.

It was previously assumed that the trajectories for extrauterine growth of preterm neonates would mimic that of intrauterine growth of fetuses matched for gestational age and of neonatal birth weights. The Preterm Postnatal follow-up study of the INTERGROWTH-21st Project has highlighted the differences between weight and head circumference of preterm infants and the WHO Child Growth Standards for term neonates (Villar et al 2015). The prospective studies within the INTERGROWTH project collected data from heathy women, with reliable menstrual dates and confirmatory ultrasound scan dating. Singleton pregnancies born preterm between 26 and 37 postmenstrual weeks were followed. The infants were breastfed or bottle-fed maternal milk daily, initially by nasogastric tube if required. Any neonates with congenital anomalies or with birth weights less than the 3rd centile were excluded, thus these growth charts are standards of postnatal growth of healthy infants, delivered earlier than expected. The charts plot postnatal growth up to 64 postmenstrual weeks, at which time the growth trajectories are similar to the WHO Child Growth Standards for term neonates (**Fig. 23.13**).

Full-term neonate

Details of the relative positions of the viscera and the skeleton in a full-term neonate are shown in **Figs 23.14–23.16**. The newborn infant is not a miniature adult, and extremely preterm infants are not the same as full-term infants.

Just as there are differences in the anatomical relationships of structures between the 40 postmenstrual week neonate, child and adult, there are major differences between 20 postmenstrual week and 40 postmenstrual week fetuses. The study of fetal anatomy at 20, 25, 30 and 35 weeks is vital for the investigative and life-saving procedures carried out on preterm infants today.

At birth, neonatal weight reflects the maternal environment, the number of conceptuses, the sex of the baby and the parity of the mother. Generally, full-term female babies are lighter than full-term males, twins are lighter than singletons, and later children tend to be heavier than the first born. The 10th to 90th centile ranges for the weight of a full-term infant at parturition can be seen in Fig. 23.10 (Stirnemann et al 2017). Body water accounts for 75–80% of this weight and a further 15–28% is composed of adipose tissue. Heavier babies have greater fat mass that can contribute to 46% of the variance in birth weight, although the relationship between lean mass and fat mass is not clear; heavier babies have thicker skinfolds (a measurement of fat mass) proportional to their size (Pomeroy et al 2014).

The establishment of enteral feeding has profound effects on early postnatal maturation. Human breast milk contains many bioactive substances that enhance gut maturity. It improves gastric emptying, encourages the growth of the microbiome and contains a range of proteins, including large amounts of secretory immunoglobulin A and cytokines (e.g. interleukin (IL)-10) (Jakaitis and Denning 2014). Feeding preterm infants human milk is associated with less feeding intolerance and is thought to provide protection against diabetes and obesity in later life (Valentine and Morrow 2012). Metabolomic studies on human milk fed to preterm and full-term neonates have shown that preterm milk contains higher concentrations of proteins and amino acids, and that the fatty acid content is higher in colostrum from mothers with neonates lower than the 20th centile for weight. The metabolome of milk from preterm delivered mothers achieves a similar composition to full-term delivered mothers by 5–7 postnatal weeks (Bardanzellu et al 2018). The rate of growth of infants fed breast milk for the first 6 months of postnatal life is different to that of formula-fed infants. Delivery of low-weight preterm babies, followed by parenteral feeding with no enteral nutrition, disrupts normal gut maturation and may lead to necrotizing enterocolitis (Wynn and Neu 2012, Neu and Pammi 2017). However, a balance with the gut microbiome is necessary; although full-term neonates born in tropical countries have similar villous height to those born in temperate climates, villous length in the small intestine shortens within 2–12 months of birth as a consequence of tropical enteropathy (Ramakrishna et al 2006). Human milk oligosaccharides, which are not absorbed in the proximal gut, are thought to act as probiotics by establishing interactions with the early gut microbiome so that specific bacterial species, able to metabolize sialylated breast milk oligosaccharides, can flourish, enhance gut barrier function and limit the expansion of enteropathogens (Charnonneau et al 2016). The physiological effects and importance of maternal–infant dyad interactions in establishing healthy postnatal life are complex and only now being investigated.

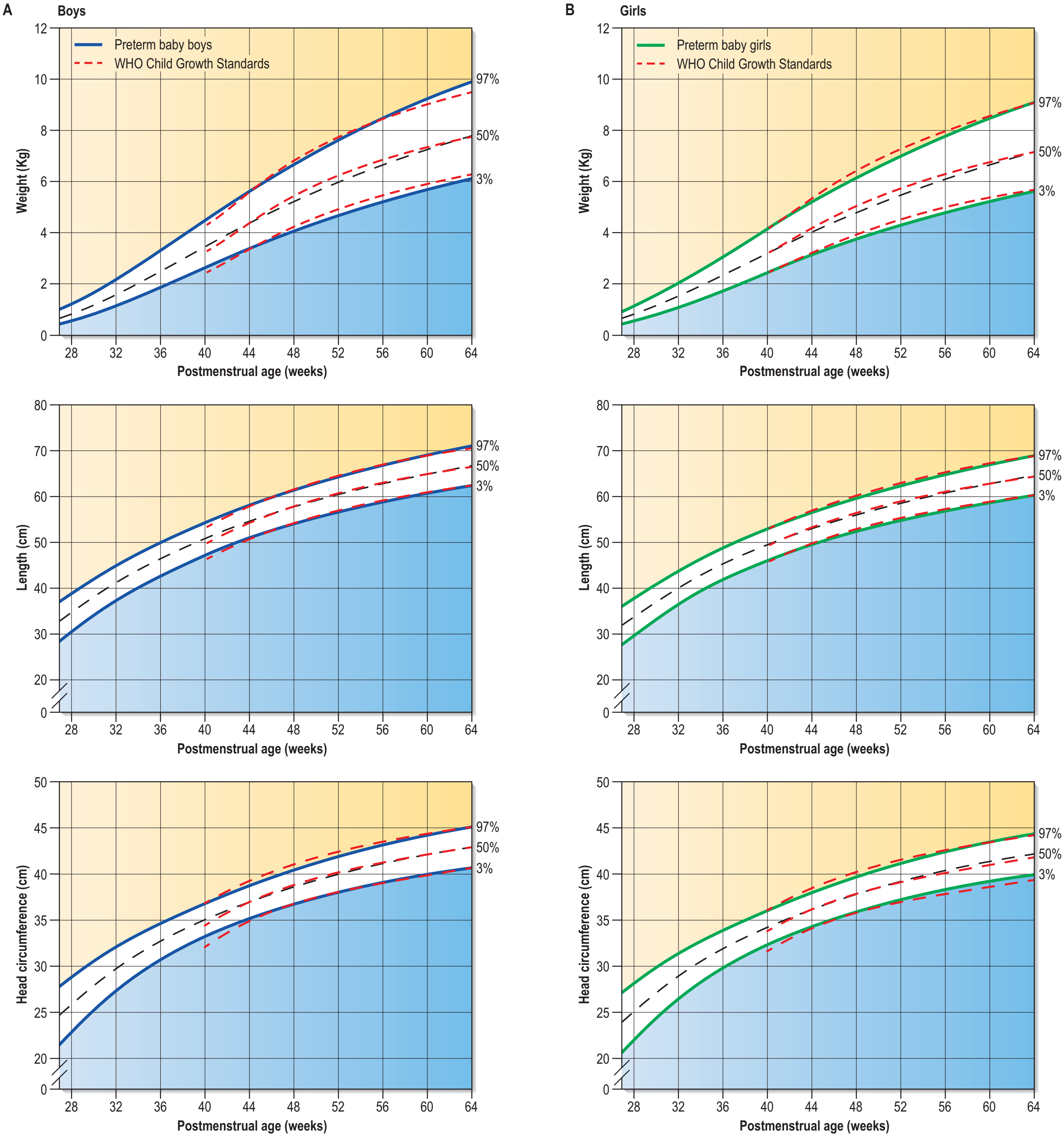

Fig. 23.13 Preterm delivered infant growth rate (red dotted lines) over a continuing scale shown in postmenstrual weeks, compared with INTERGROWTH-21st Newborn Size Standards for weight, height and head circumference in (**A**) boys (blue lines) and (**B**) girls (green lines). The trajectory for extrauterine growth of preterm infants does not match the intrauterine growth of fetuses or attain the levels of full-term (postmenstrual week 40) neonates. Growth trajectories are similar by the equivalent of postmenstrual week 64. (Data from Villar et al 2015.)

Different birth phenotypes have been correlated with different pathological sequelae. Infants who are thin at birth, with a low ponderal index (weight/length^3), tend to develop a combination of insulin resistance, hypertension, type 2 diabetes and lipid disorders, whereas those who are short in relation to head size tend to develop hypertension and high plasma fibrinogen concentrations. These associations have been reported in low weight babies, rather than in those born prematurely. Some babies of average weight also develop cardiovascular pathology; they are either thin at birth and small in relation to the size of their placenta, or of average weight but short in relation to head size and have below average weight gain during the first year (Barker et al 1993). For more views on this concept consult Godfrey and Barker (2000), Ross and Beal (2008) and Kelishadi and Poursafa (2014).

Post-term neonate

Post-term delivery has been reported to affect the subsequent growth of boys more than girls. It is estimated that 8.1% of all live births in Europe and 5.6% of live births in the United States are born post-term (Beltrand et al 2012). In a Swedish study, post-term boys were heavier and longer than term boys at birth, although with similar ponderal indices. Post-term boys showed weight velocity changes and had higher BMIs than term boys by 3 years of age. There were no differences in weight gain throughout childhood in post-term and term girls. By 16 years post-term and term boys had similar height, but post-term boys were heavier. The rate of obesity (BMI >95th centile for age; BMI >85th centile for age) was 29% and 47% respectively in post-term boys and 7% and 13% respectively for term boys (Beltrand et al 2012).

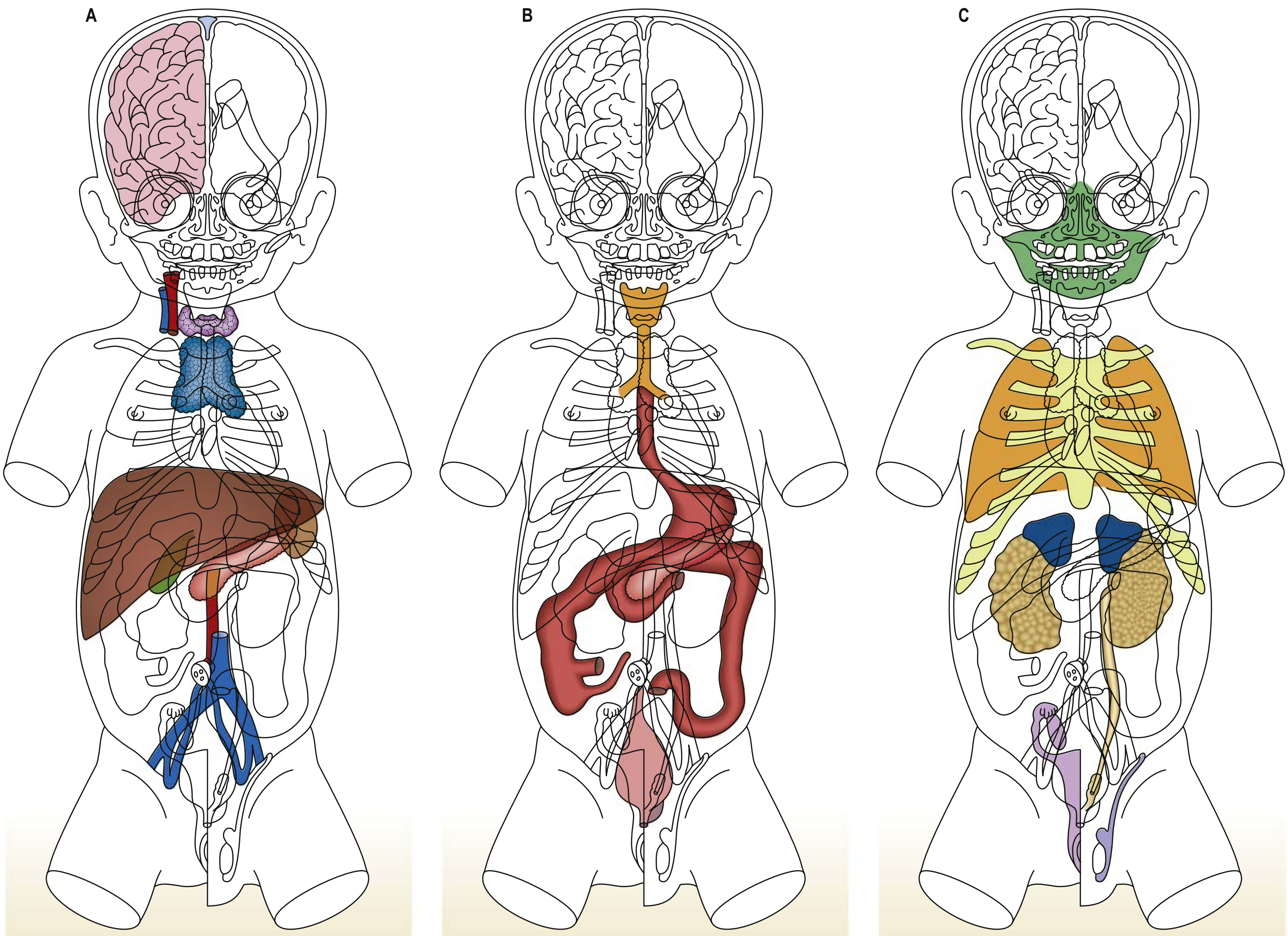

From cranial to caudal, the following structures are indicated:

🟦	Superior sagittal sinus
🟥	Brain
🟪	Thyroid gland
🟦	Thymus
🟫	Liver
🟩	Gallbladder
🟫	Spleen
🟥	Pancreas
🟥 🟦	Blood vessels

Oxygenated blood (red) is returned to the fetal heart via the umbilical vein, which passes from the umbilicus to the liver. The right atrium contains oxygenated blood, which mainly passes to the left atrium. The right ventricle receives some oxygenated blood from this flow and also the deoxygenated blood from the head and neck. Blood is returned to the placenta via two umbilical arteries.

From cranial to caudal, the following structures are indicated:

🟧	Larynx and trachea
🟥	Gastrointestinal tract
🟥	Pancreas
🟥	Urinary bladder
🟪	Prostate gland

Note that the apex of the bladder continues as the urachus to the umbilicus.

From cranial to caudal, the following structures are indicated:

🟩	Maxillae and mandible
🟨	Costal cartilages
🟧	Lungs
🟦	Suprarenal glands
🟫	Lobulated kidneys
🟨	Ureter passing to the posterior surface of the urinary bladder
🟪	Right uterine tube, uterus and vagina
🟪	Left testis and ductus deferens

Note that the lower border of the lung is below the central, upper border of the liver.
Note that the suprarenal glands are relatively large and superomedial to the lobulated kidneys.

Fig. 23.14 A–C, Topographical representations of the anatomy of a full-term neonate. The surface markings of all organs are shown, with some coloured and others only in outline. The female genital tract is shown on the right of the body, and the male tract is shown on the left. (D–K, *continued online*)

Infancy and childhood

Preadult life is divided into five stages (Bogin 2012). Term delivery is considered normal between postmenstrual weeks 37 and 40. Postnatal growth is now described to 64 postmenstrual weeks to facilitate examination of the growth trajectories of preterm infants. The normal neonatal period can be defined as the first 28 postnatal days, 40–44 postmenstrual weeks. It is followed by infancy, which commences at postmenstrual week 45 and ends at about 36 postnatal months. During infancy weaning occurs and deciduous tooth eruption is seen. The WHO define infancy as ending at 12 postnatal months and the CDC have the subdivision of toddler extending from 1 to 3 years of age. Childhood extends from 3 to 7 years; there a midgrowth spurt, and eruption of the first permanent incisor and molar teeth. A human juvenile period begins at about 7 years of age; this ends in girls at about 10 years and in boys at about 12 years. Juveniles are prepubertal and in

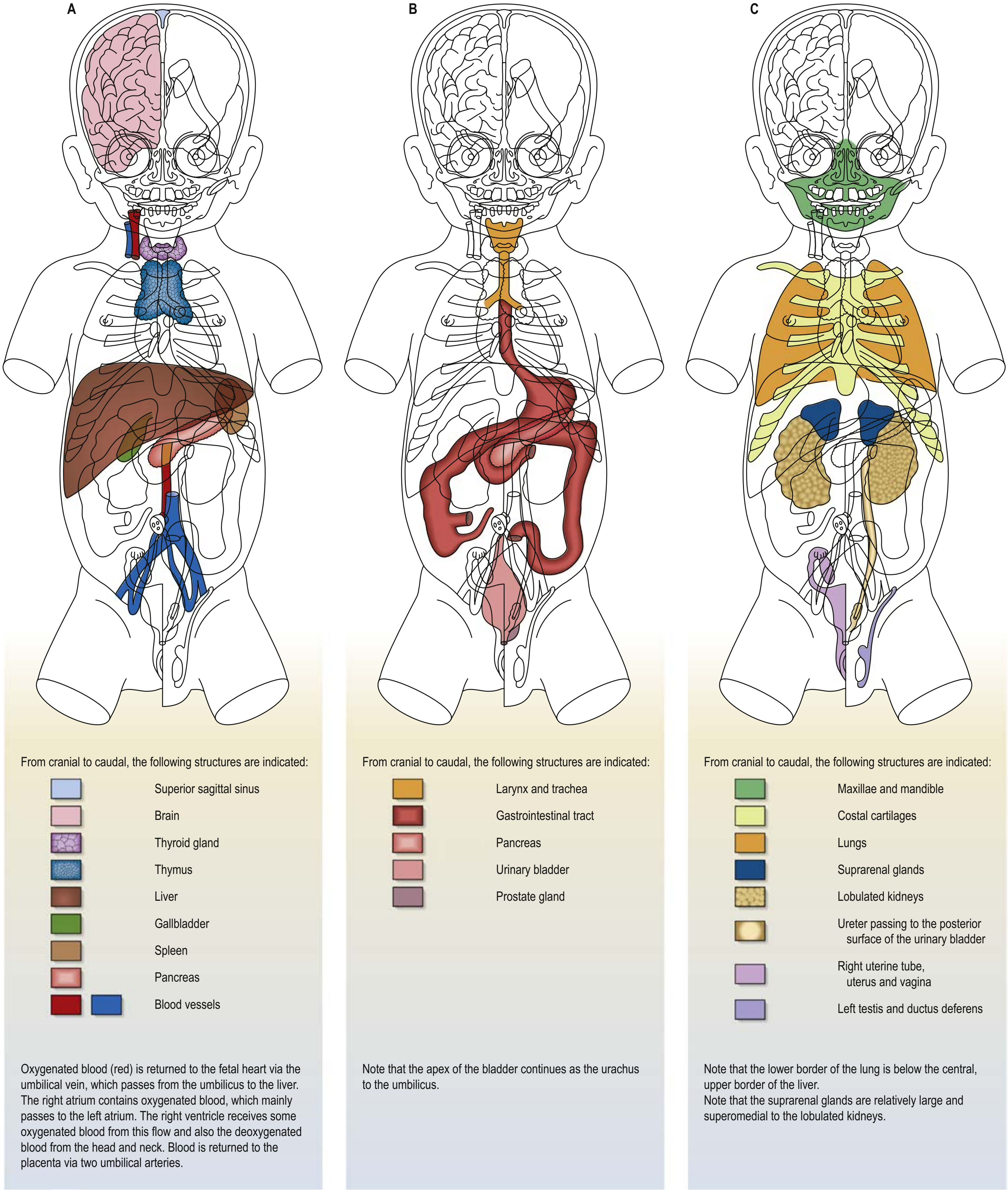

From cranial to caudal, the following structures are indicated:

- 🟦 Superior sagittal sinus
- 🟪 Brain
- 🟪 Thyroid gland
- 🟦 Thymus
- 🟫 Liver
- 🟩 Gallbladder
- 🟫 Spleen
- 🟥 Pancreas
- 🟥 🟦 Blood vessels

Oxygenated blood (red) is returned to the fetal heart via the umbilical vein, which passes from the umbilicus to the liver. The right atrium contains oxygenated blood, which mainly passes to the left atrium. The right ventricle receives some oxygenated blood from this flow and also the deoxygenated blood from the head and neck. Blood is returned to the placenta via two umbilical arteries.

From cranial to caudal, the following structures are indicated:

- 🟧 Larynx and trachea
- 🟥 Gastrointestinal tract
- 🟥 Pancreas
- 🟥 Urinary bladder
- 🟪 Prostate gland

Note that the apex of the bladder continues as the urachus to the umbilicus.

From cranial to caudal, the following structures are indicated:

- 🟩 Maxillae and mandible
- 🟨 Costal cartilages
- 🟧 Lungs
- 🟦 Suprarenal glands
- 🟨 Lobulated kidneys
- 🟨 Ureter passing to the posterior surface of the urinary bladder
- 🟪 Right uterine tube, uterus and vagina
- 🟪 Left testis and ductus deferens

Note that the lower border of the lung is below the central, upper border of the liver.
Note that the suprarenal glands are relatively large and superomedial to the lobulated kidneys.

Fig. 23.14 A–C, Topographical representations of the anatomy of a full-term neonate. The surface markings of all organs are shown, with some coloured and others only in outline. The female genital tract is shown on the right of the body, and the male tract is shown on the left.

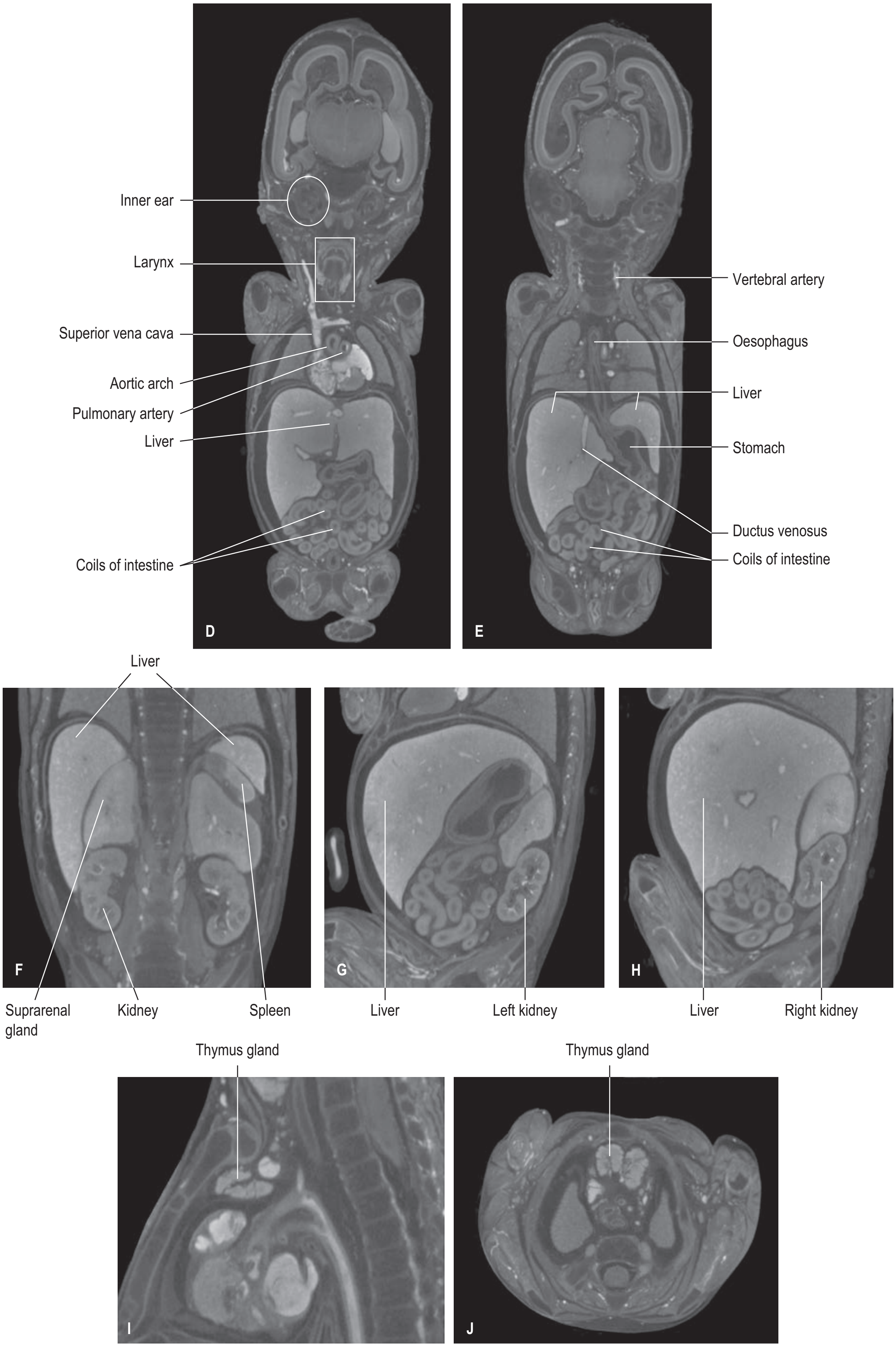
Inner ear
Larynx
Superior vena cava
Aortic arch
Pulmonary artery
Liver
Coils of intestine
D
Vertebral artery
Oesophagus
Liver
Stomach
Ductus venosus
Coils of intestine
E
Liver
F
Suprarenal gland
Kidney
Spleen
G
Liver
Left kidney
H
Liver
Right kidney
Thymus gland
I
Thymus gland
J

Fig. 23.14 cont'd D–J are microCT coronal sections through a 14-postmenstrual-week fetus. **D–E** show the extent of the liver on the left and right sides and the position of coils of intestine. **F–H**, show the kidneys and suprarenal glands. **I–J** show the thymus gland. **F**, Coronal section. **G**, Left sagittal section. **H**, Right sagittal section. **I**, Sagittal section. **J**, Axial section. (**D–J**, Courtesy of Dr Owen Arthurs and Dr Susan Shelmerdine, Great Ormond Street Hospital, London.)

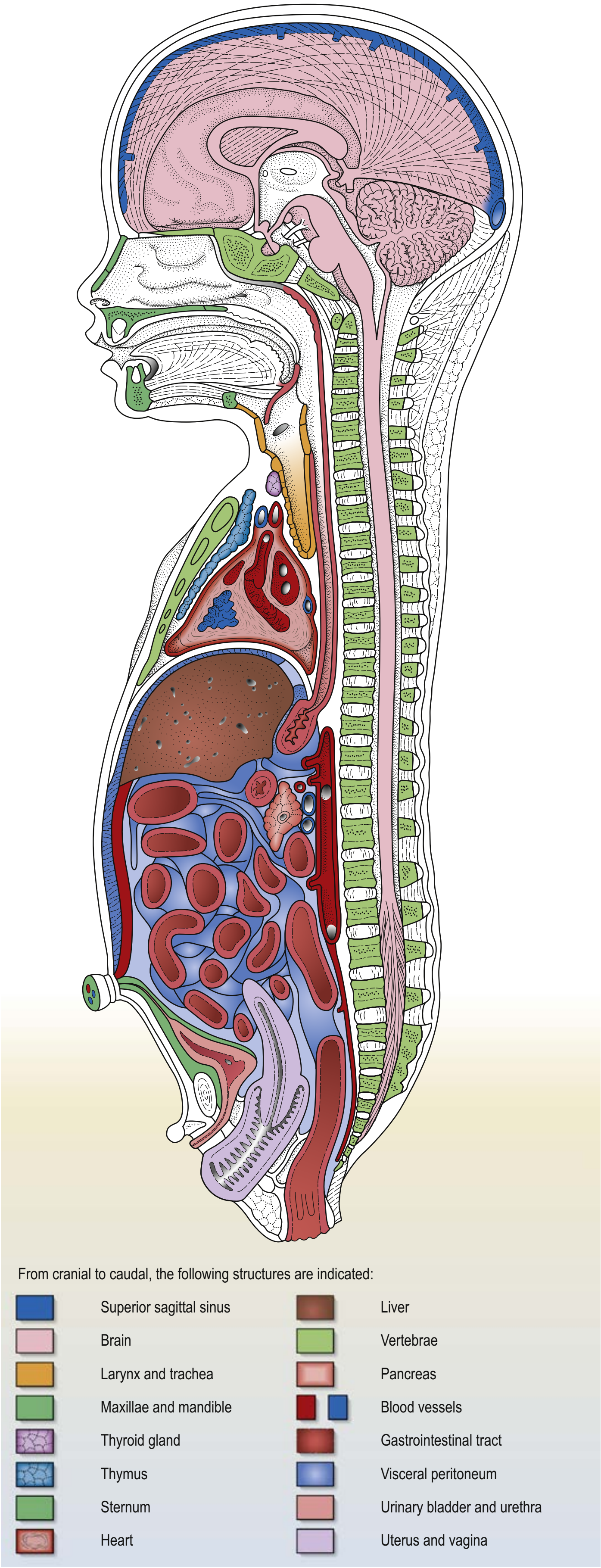
From cranial to caudal, the following structures are indicated:
Superior sagittal sinus
Brain
Larynx and trachea
Maxillae and mandible
Thyroid gland
Thymus
Sternum
Heart
Liver
Vertebrae
Pancreas
Blood vessels
Gastrointestinal tract
Visceral peritoneum
Urinary bladder and urethra
Uterus and vagina

Fig. 23.15 **A**, A topographical representation of the anatomy of a full-term female neonate. The cut surfaces of the organs are the same colours as in Fig. 23.14. (B–E, *continued online*)

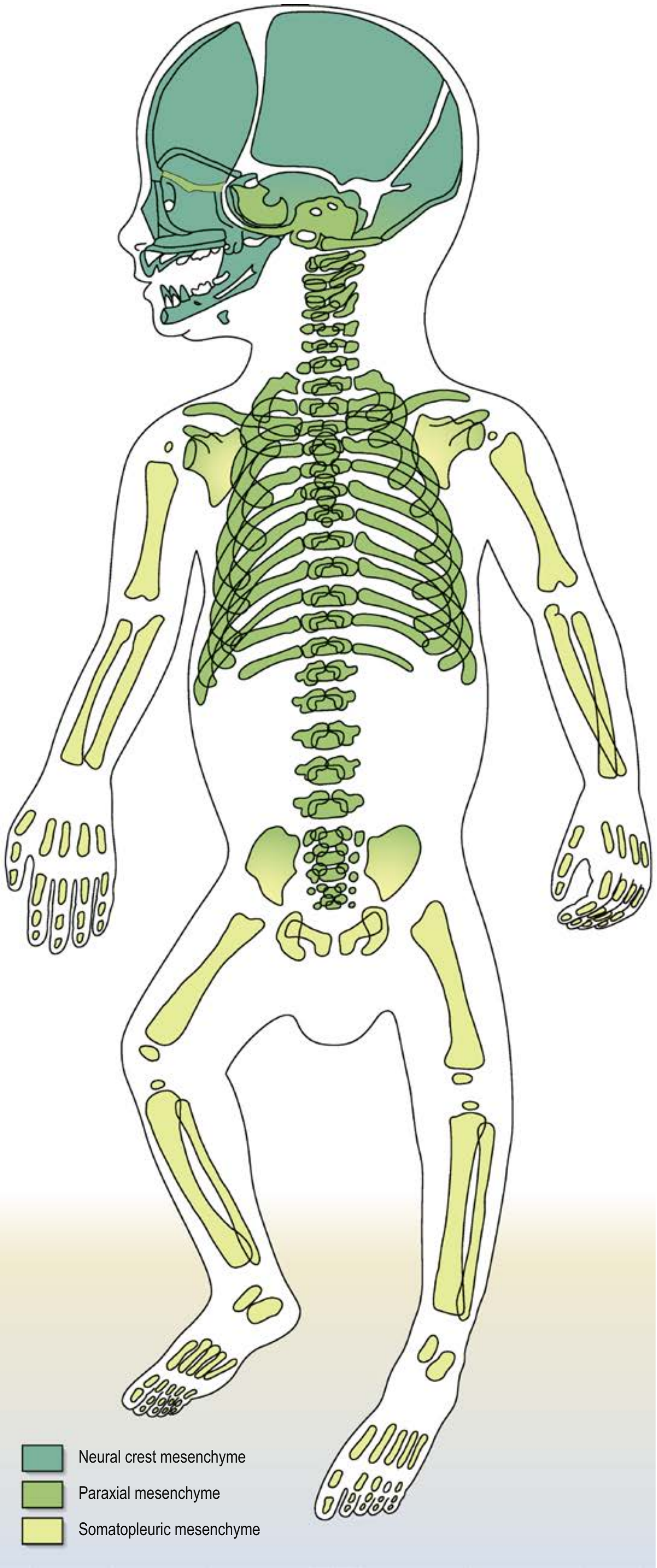
Neural crest mesenchyme
Paraxial mesenchyme
Somatopleuric mesenchyme

Fig. 23.16 The extent of the ossified skeleton in a full-term neonate. Note the derivation of the parts of the skeleton: the skull is derived from paraxial mesenchyme and neural crest mesenchyme; the axial skeleton, vertebrae and ribs are derived from paraxial mesenchyme; and the skeletal elements in the limbs are derived from somatopleuric mesenchyme, which forms the limb buds.

many industrialized nations the juvenile stage coincides with entry into traditional formal education.

After birth, there is a general decrease in total body water but a relative increase in intracellular fluid. Normally, a newborn loses about 10% of its birth weight by 3–4 days postnatally as a result of loss of excess extracellular fluid: by the end of the first year, total body water makes up 60% of the body weight. Growth in weight usually reaches its peak velocity after birth. Birth weight normally triples by the end of the first year, and quadruples by the end of the second year. Infants that have been breastfed for longer have slower weight growth velocities in the first months of life and their peak weight growth velocity occurs at

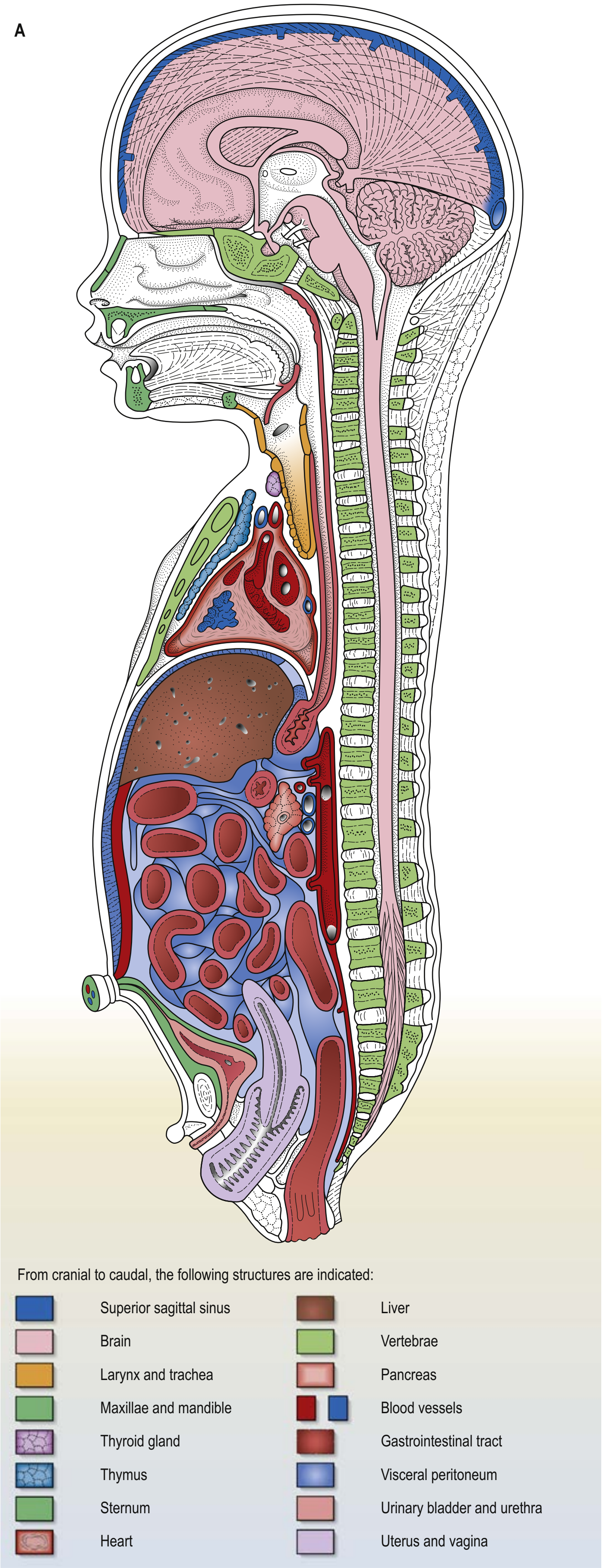
A
From cranial to caudal, the following structures are indicated:
Superior sagittal sinus
Brain
Larynx and trachea
Maxillae and mandible
Thyroid gland
Thymus
Sternum
Heart
Liver
Vertebrae
Pancreas
Blood vessels
Gastrointestinal tract
Visceral peritoneum
Urinary bladder and urethra
Uterus and vagina

Fig. 23.15 A, A topographical representation of the anatomy of a full-term female neonate. The cut surfaces of the organs are the same colours as in Fig. 23.14.

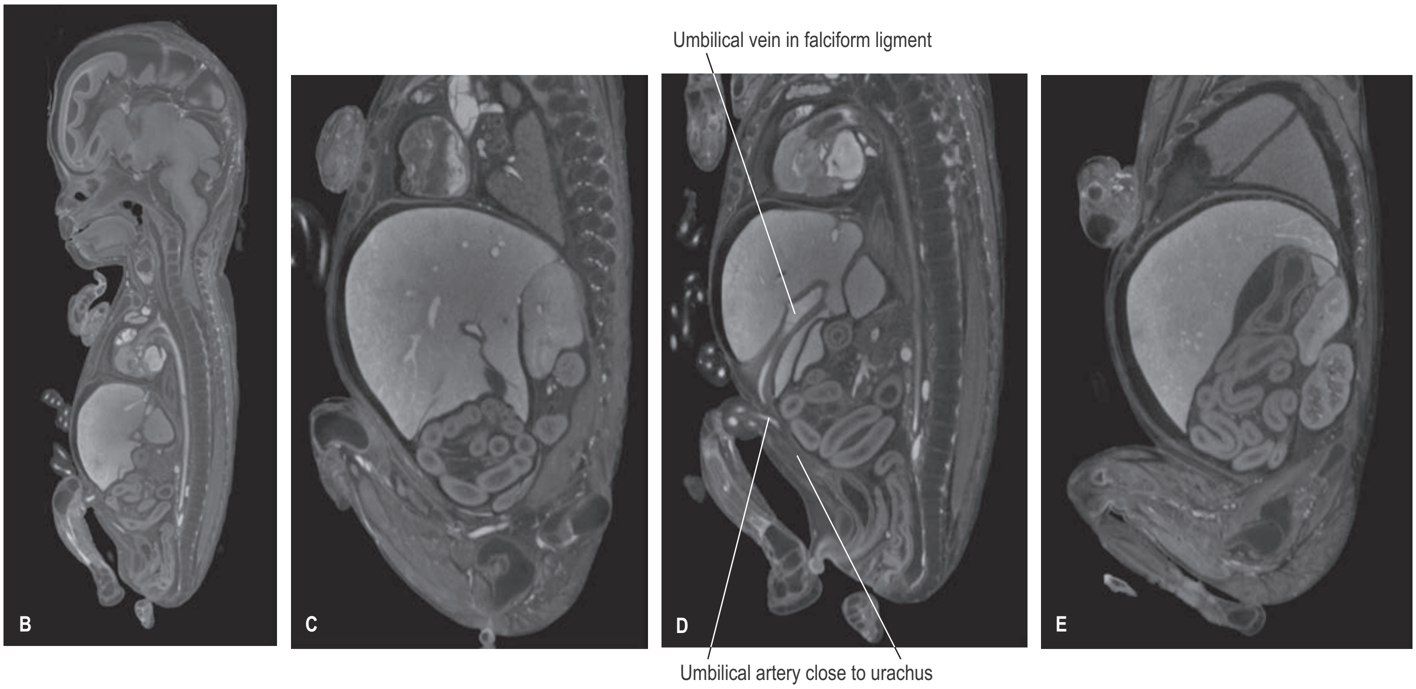
Umbilical vein in falciform ligment
B
C
D
E
Umbilical artery close to urachus

Fig. 23.15, cont'd **B–E**, MicroCT sagittal section images of a fetus at 14 postmenstrual weeks. **B**, Midline sagittal section. **C**, Liver, right sagittal section. **D**, Liver, midline sagittal section. E, Liver, left sagittal section. Note the liver is normally very large at this age and extends to the left. (B–E, Courtesy of Dr Owen Arthurs and Dr Susan Shelmerdine, Great Ormond Street Hospital, London.)

a later age (Regnault and Gillman 2014). The peak velocity for length is reached at about 4 postnatal months (see Fig. 23.7). Body length increases from a neonatal range of 48–53 cm to about 75 cm during the first year after birth, by 12–13 cm in the second year and by 5–6 cm each year thereafter until puberty.

Hormonal changes that affect early postnatal life and subsequent growth rates in infants occur from birth to 6 postnatal months. This period has been termed mini-puberty (Ch. 22). It is associated with the rapid decrease of circulating placental hormones in the neonate and the activation of the HPG axis. The early surge in circulating testosterone in males during the first postnatal months influences somatic and adipose development in childhood. The growth velocity in weight and BMI at 8 postnatal weeks in boys is faster than girls; this corresponds to the time when median testosterone levels approach pubertal male values (Lanciotti et al 2018).

In 2006 the WHO published growth charts from birth to 5 years and 5–19 years compiled from children considered to be growing under optimal environmental conditions, i.e. they were breastfed, raised in environments that minimized poor diets and infection, and had non-smoking mothers. UK reference growth charts for boys and girls aged 2–18 years were published in 2012 by the Royal College of Paediatrics and Child Health (**Fig. 23.17**). Similar growth charts have been published for specified regions around the world, addressing racial and ethnic differences (Mansourian et al 2012, Khadilkar and Khadilkar 2015, Barzin et al 2018). As an example, Khadilkar and Khadilkar (2015) stress the importance of updating growth reference charts in countries experiencing major secular change in nutritional status and an increasing incidence of obesity. Compared to previous Indian growth charts, the revised charts show that Indian boys and girls are taller at all ages than they were 7 years ago. Using WHO guidelines, Khadilkar and Khadilkar lowered the weight centiles in comparison to previous charts which had included affluent children. The revised Indian Academy of Pediatrics charts are now considered more appropriate for use with Asian children. At birth South Asian children are among the lightest with a 'thin-fat' phenotype, i.e. small abdominal viscera, low muscle mass, and a relatively large proportion of body fat (Fairley et al 2013). Lower birth weight and fast early growth in Asian populations, both in Asia and in the UK, led to increased adiposity and increased cardiometabolic risk with a lower BMI (West et al 2013).

The pattern of postnatal growth in children is considered to be predictable: deviation from these patterns suggests growth disorders. Measurement of linear growth (supine length in infants and height in children) and growth velocity (as assessed from sequential height charts) show that linear growth velocity is most rapid in infancy, averaging 15 cm/year in the first two years. Children who grow in an environment that does not constrain their growth exhibit a pattern of growth that is mainly parallel to a particular centile, a phenomenon that has been termed homeorhesis or canalization (following the same imaginary 'canal' on the growth chart). Two-thirds of infants cross centile channels on linear growth curves (Cuttler 2016). After deviation from a centile (e.g. as a consequence of chronic disease in childhood, or the adolescent growth spurt), most children return to the same centile position in adulthood, a finding that suggests that this pattern is genetically determined within individuals (Cameron and Bogin 2012). Upward crossing of 2 centile lines in the first 6 months of life is more predictive of later obesity than upward centile crossing in any other 6-month interval in the first two years of postnatal life (Regnault and Gillman 2014).

From infancy to puberty the velocity of linear growth averages about 6 cm/year (Cuttler 2016). A target height, the child's genetic potential, can be predicted by the midparental height plus 6.5 cm for boys and minus 6.5 cm for girls. (Mid-parental height is the average of both parents' heights, plotted on the height centile chart at age 18 years after adjustment for sex). Syndrome-specific growth charts have been developed for aneuploidy and genetic anomalies that cause differences in the growth trajectory of children to adulthood, although there are few new growth charts for short stature children. For growth charts for Down's syndrome consult Styles et al (2002) for UK data and Zemel et al (2015) for US data. For growth charts for Turner syndrome consult Lyon et al (1985) for UK data and Isojima et al (2010) for Japanese data.

Infants and children with chronic diseases and recurrent infections fail to achieve the genetic growth potential. 'Catch-up growth' describes growth above the normal rate expected for the specific age, seen on recovery from such conditions. It may restore the child to their original canal (channel) on the growth chart; if the disorder extends for many years and into puberty, it may not be completed. Information concerning individual growth may be retained as a memory in the epiphysial plates of long bones and in the chondrocyte resting zone and seems to influence structural and functional catch up in the epiphysial plate (Cuttler 2016).

Changes in weight during childhood can be secondary to changes in body water, muscle mass, total lean body mass and fat: weight is not synonymous with fat. Body mass index (BMI, weight/height^2) can be calculated for children. Body fat increases from about 15% to 25% by 6 months of age and decreases to about 15% by 5 years. Weaning is usually initiated after the first 6 months of postnatal life (equivalent to 64 postmenstrual weeks); there is high risk of growth delay during this process that may affect weight. By 5 years of age the sex difference in body fat is about 2% increasing to 6% by 10 years. Although growth velocity plateaus between 5 and 10 years, a mid-growth or juvenile growth spurt is seen between 6 and 8 years in both sexes. It is small in terms of height, but larger for weight and skinfolds and has been attributed to an increase in adrenal androgenic hormone secretion (Lejarraga 2012).

Low weight in infancy and childhood at a given age may result in stunting, i.e. linear growth restriction (short height for age), or wasting, i.e. low weight for height (low BMI for age or reflecting recent weight loss). In neonates, these examples of alterations in growth are considered to be two different phenotypes with different timing, duration of causal insult and different prognoses (Victora et al 2015). Although the proportion of undernourished and underweight children declined globally from 25% in 1990 to 15% in 2015, it increased by about one-third in sub-Saharan Africa between 1990 and 2015. One-third of all undernourished children globally are now in sub-Saharan Africa, 39% of those stunted and 10% wasted (Akombi et al 2017).

Adolescence and adulthood

The juvenile period ends when puberty commences. Puberty is a short time period when there is a dramatic increase in sex hormone secretions and reactivation of the CNS for sexual development. It precedes adolescence, a developmental stage of 5–10 years during which there is a growth spurt in height and weight, eruption of the remaining permanent teeth, development of secondary sexual characteristics and sociosexual maturation (Bogin 2012). Humans seem to be the only species to have a quiescent interval between the rapid growth that takes place after birth and the adolescent growth spurt, a pattern of growth termed the Infancy/Childhood/Puberty (ICP) growth model (Stevens et al 2013). It has been suggested that this quiescent interval allows the acquisition of language, cultural inheritance and complex socialization before individuals pass through puberty and become sexually active. A neotenous heterochronic shift in the transcription of specific genes in the prefrontal cortex occurs in humans from early adolescence and corresponds to a period of substantial cortical reorganization that may be associated with the development of cognitive skills (Somel et al 2009).

Development-related gene expression correlates with three phases of human growth (infancy/early childhood; childhood/puberty; final height) in a development-dependent manner in human tissues (Stevens et al 2013) (**Fig. 23.18**). The outcomes of the Human Genome Project have been linked to anthropomorphic traits in meta-analyses of genome-wide association data that have identified genetic variants at hundreds of loci relevant to growth in pre-puberty, puberty and adulthood, particularly those associated with childhood and adult obesity (Genome-wide Investigation of ANThropometric measures – GIANT). Genome-wide association studies have shown genetic loci linking pubertal timing, height and growth with childhood obesity and genes involved with increases in BMI (Cousminer et al 2013, Locke et al 2015).

It is thought that the return to long bone growth seen in adolescence is a specifically human event (Stevens et al 2013). The adolescent growth spurt occurs at different times for different individuals, which means that nearly all children will cross centiles on reference charts of cross-sectional data. In an 'early developer', the height-for-age curve rises before that of their peers and levels off early. In a 'late developer', growth appears to slow but then accelerates and so their height-for-age curve rises after their peers have either ceased or nearly ceased growing (Cameron 2012). The increase in the growth velocity occurs between 10.5 and 11 years in girls, and 12.5 and 13 years in boys (**Fig. 23.19**; see Fig. 23.17). In both sexes, this spurt lasts for 2–2.5 years. Girls gain about 16 cm in height during the spurt, with a peak velocity at 12 years of age. Boys gain about 20 cm in height (mostly by growth of the trunk), with a peak velocity at 14 years of age, during which time they may be growing at the rate of 10 cm a year.

Growth in height continues at a slower rate after the adolescent growth spurt. Noticeable growth is said to stop at 18 years in females

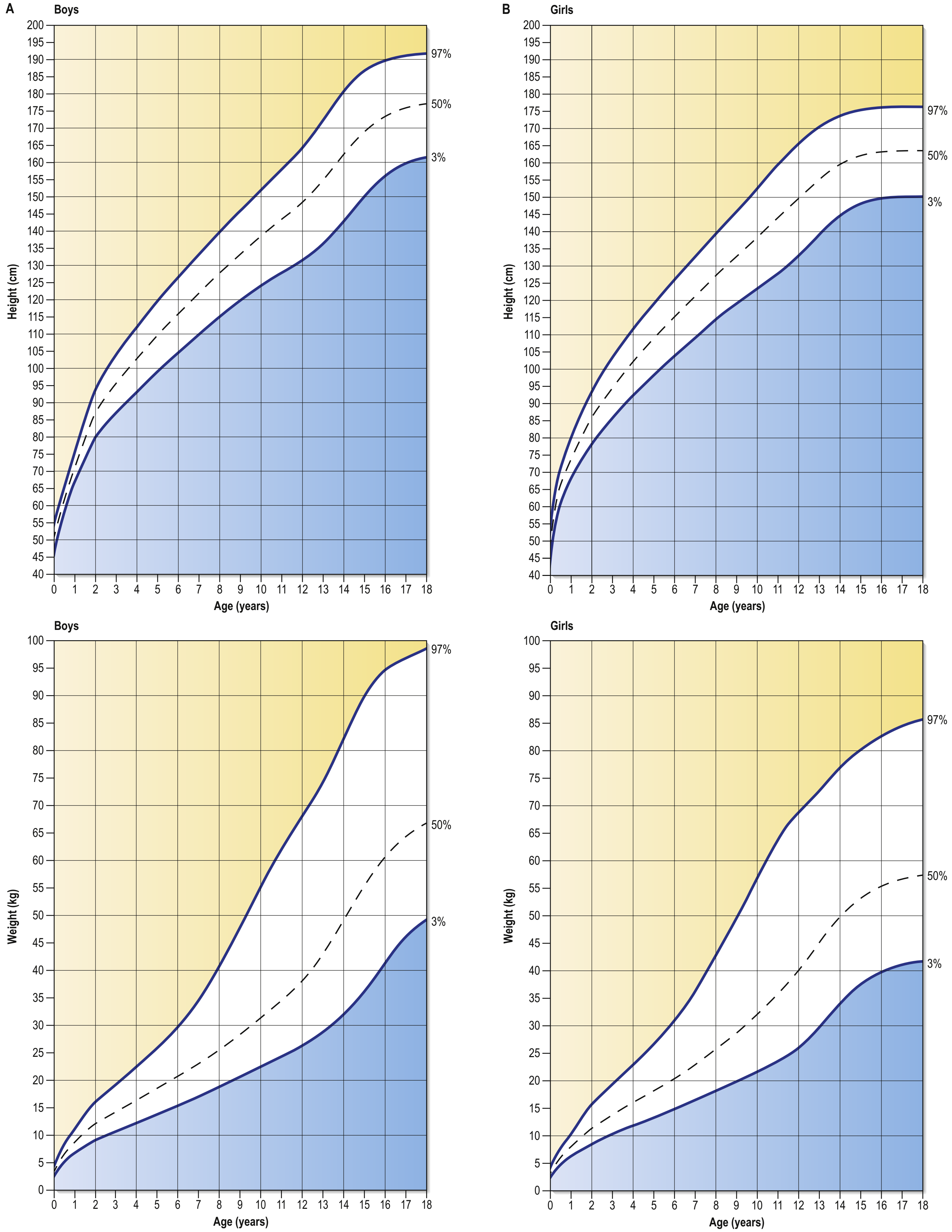

Fig. 23.17 Standard growth charts of (**A**) British boys and (**B**) girls. (Data from the Royal College of Paediatrics and Child Health 2012.)

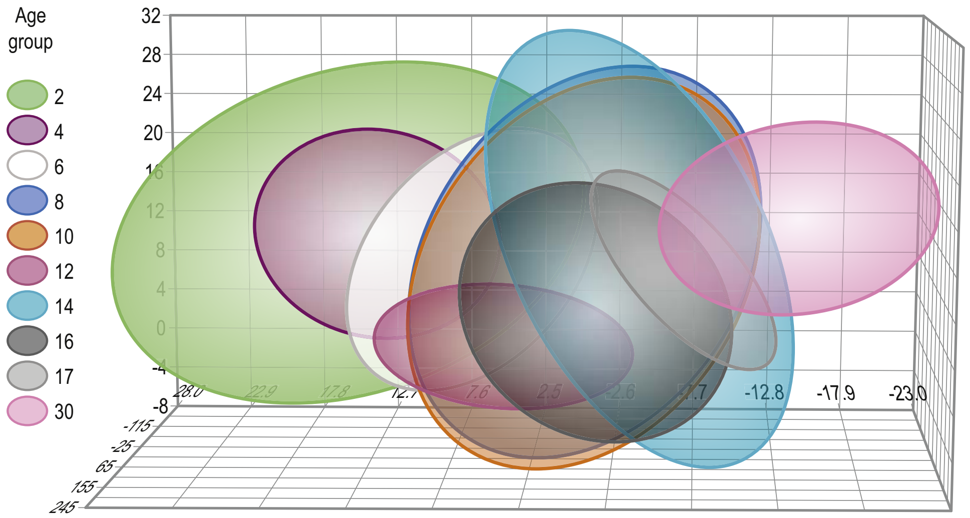

Fig. 23.18 Gene expression of 927 development-related genes by age from 2 to 30 years. Ellipsoids represent 2 standard deviations of normalized gene expression. (From Stevens A, Hanson D, Whatmore A et al 2013 Human growth is associated with distinct patterns of gene expression in evolutionarily conserved networks. BMC Genomics 14:547.)

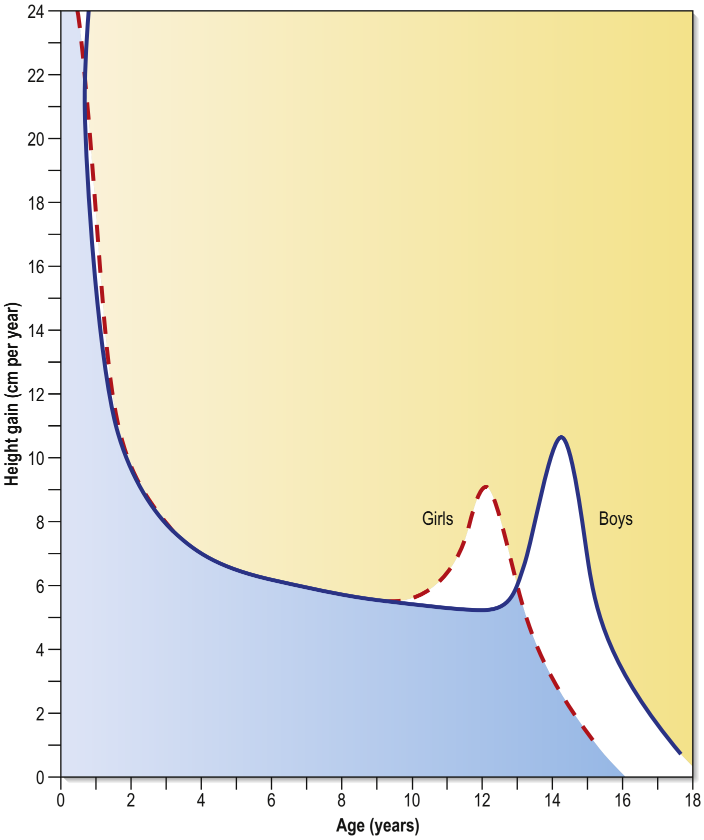

Fig. 23.19 Typical individual velocity curves for height: British boys and girls. (After Tanner JM, Whitehouse RH, Takaishi IM 1966 Standards from birth to maturity for height, weight, height velocity and weight velocity. Arch Dis Child 41:454–71, with permission from BMJ Publishing.)

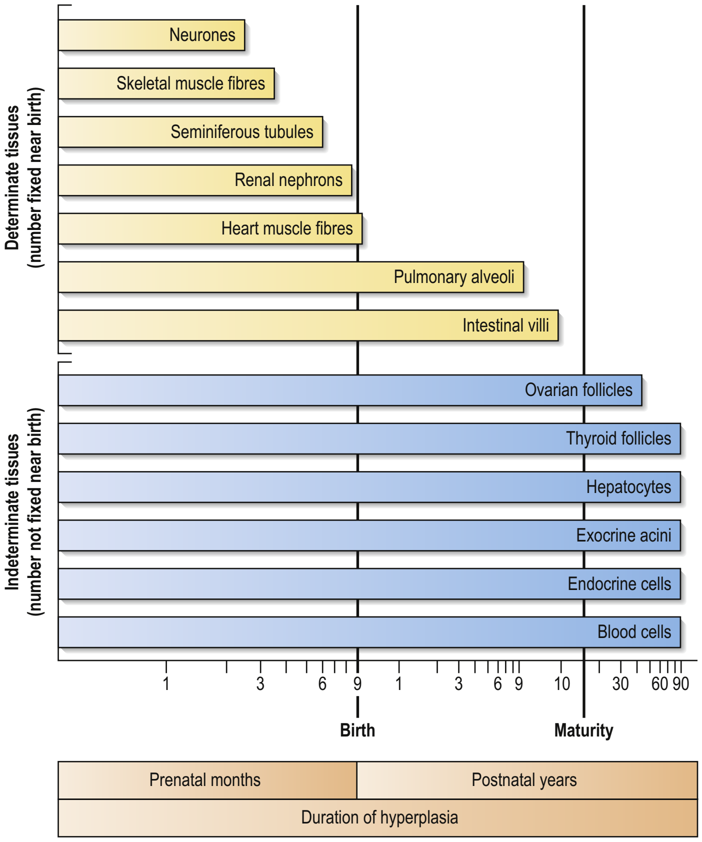

Fig. 23.20 The duration of multiplicative growth for various human tissues.

and 20 years in males; longitudinal studies have indicated an average figure of 16.25 years (females) and 17.75 years (males) with a normal variation of ± 2 years (Harrison et al 1964). Bone age is suggested to be a better predictor of pubertal milestones than chronological age (Cuttler et al 2016). A bone age of 11 years in boys and of 12 years in girls corresponds to the onset of puberty; menarche in girls occurs at a mean skeletal age of about 13 years. Second metacarpal length has been used to assess the impact of regional nutrition on development (Moro and Covino 2018).

Weight gain is more variable in the juvenile stage and adolescence. The onset of puberty is reported to be earlier in obese girls, although obesity *per se* does not affect the age of menarche (Li et al 2017). Juvenile weight increases by 2.25–2.75 kg annually until the adolescent growth spurt, when boys may add 20 kg to their weight and girls 16 kg. The peak velocity for weight gain lags behind the peak velocity for height by about 3 months. Body weight does not reach adult values until sometime after adult height is attained. Apart from the expected change in growth velocity that occurs during adolescence, it is now apparent that taller child height is prospectively associated with an elevated risk of obesity (Johnson et al 2012, Van Dommelen 2014) and that early attainment of peak height velocity may increase the risks for chronic disease in adulthood life (Regnault and Gillman 2014).

Longitudinal studies suggest that adult height peaks at the end of the third decade of life and declines with increasing velocity from the end of the fourth decade (Leon et al 1995). In a 10-year longitudinal study in England of individuals mostly aged over 55 years, physical stature declined by an annual rate of 0.08–0.10% for males and 0.12–0.14% for females, which would be a 2–4 cm reduction in height over the life course: reductions in height loss occurred simultaneously with deteriorating health (Fernihough and McGovern 2015).

INTEGRATION OF TYPES OF GROWTH DURING DEVELOPMENT AND LIFE

The complex interaction between maternal and paternal genes from the earliest stages of development has been likened to a 'parental conflict' for maternal resources. Parentally imprinted genes are only a small proportion of the genome but are important in blastocyst implantation, placentation and developmental growth rates. For example, changes in some individuals to the 11p15 domain affects the future expression of Insulin-like Growth Factor 2 (*IGF2*) gene (if paternally imprinted) or the negative growth regulator *PHLDA2* gene (if maternally imprinted); both conditions affect growth regulation and trajectory in early development (Moore et al 2015) (Ch. 8). Generally, paternally expressed genes enhance growth and maternally expressed genes suppress growth, the latter via genetic processes that prevent offspring becoming too large to be delivered normally because of obstructed labour (Butler 2009). Parental and neonatal phenotype and the prenatal environment may also affect the sexes differently; male fetuses grow faster and to a larger size and may place a greater demand on maternal physiology in stressful environments (Pomeroy et al 2015).

The various types of growth in the later prenatal months and in the postnatal period occur in differing patterns and at different rates. Under physiological conditions it appears that growth and duration of pregnancy are inversely related, with fast-growing fetuses delivering early and slower-growing fetuses having a longer time *in utero* (Kiserud and Johnsen 2009). High growth velocity at 16–22 weeks increases the likelihood for preterm birth (Lampl et al 2009). These differences in the rates of fetal growth affect the accuracy of estimations of fetal age.

The extent of tissue growth in an organ depends on the specific duration of multiplicative growth for the cell types contained within the organ (**Fig. 23.20**). Different cell populations complete their initial developmental proliferation and become differentiated at different times; the final stage of differentiation is usually the cessation of cell division.

Growth of a body can be described in two ways: isometric and allometric. Isometric growth implies a progressive proportional increase in all organs and systems with time; it does not occur in the developing embryo, which displays differential rates of growth. Allometric growth describes the differences in the relative rates of growth between one part of the body and another, and is most clearly seen in the changes in body proportion between fetuses, neonates, children and adults. Between 6 and 7 weeks after fertilization, the head is nearly one-half of the total embryonic length; it subsequently grows proportionally more slowly and it is one-quarter of the entire length at birth. During childhood, this pattern of growth continues with lengthening of the torso and limbs; in adults, the head is one-eighth of the total length of the body and lower limb length is the equivalent of four head lengths (**Fig. 23.21**). Relative limb length at birth is not associated with birth weight and growth-restricted fetuses show little difference in limb proportion. The limbs undergo accelerated

Global estimates of the numbers of adults who are overweight or obese in adult life exceed the numbers of adults who do not have sufficient food (Mascie-Taylor and Goto 2007). Some of the consequences of the high prevalence of obesity in adults on future generational growth are now apparent. Oocyte maturation in obese women is affected by higher circulating concentrations of inflammatory cytokines: these oocytes are smaller, influencing periconception quality. Elevated BMI in men is associated with altered seminal fluid composition, sperm anomalies and decreased motility (Fleming et al 2018). Approximately one-third of adults of reproductive age (20–39 years) were obese in 2015–2016 in the United States (Hales et al 2017), with an annual increase of 2% (Adibi and Zhao 2017). It has been suggested that placental metabolism buffers the lipid environment of the obese mother, limiting lipotoxic effects on the fetus by placental lipid storage (Calabuig-Navarro et al 2017).

The Fetal Origins of Adult Disease hypothesis correlated low birth weight with increased adult risk of cardiovascular diseases; due to fetal anticipation of a similar future *ex utero* environment to that *in utero* followed by a childhood obesogenic environment (Barker 2013). The adaptations of this process to fetuses and children of obese parents are still to be investigated.

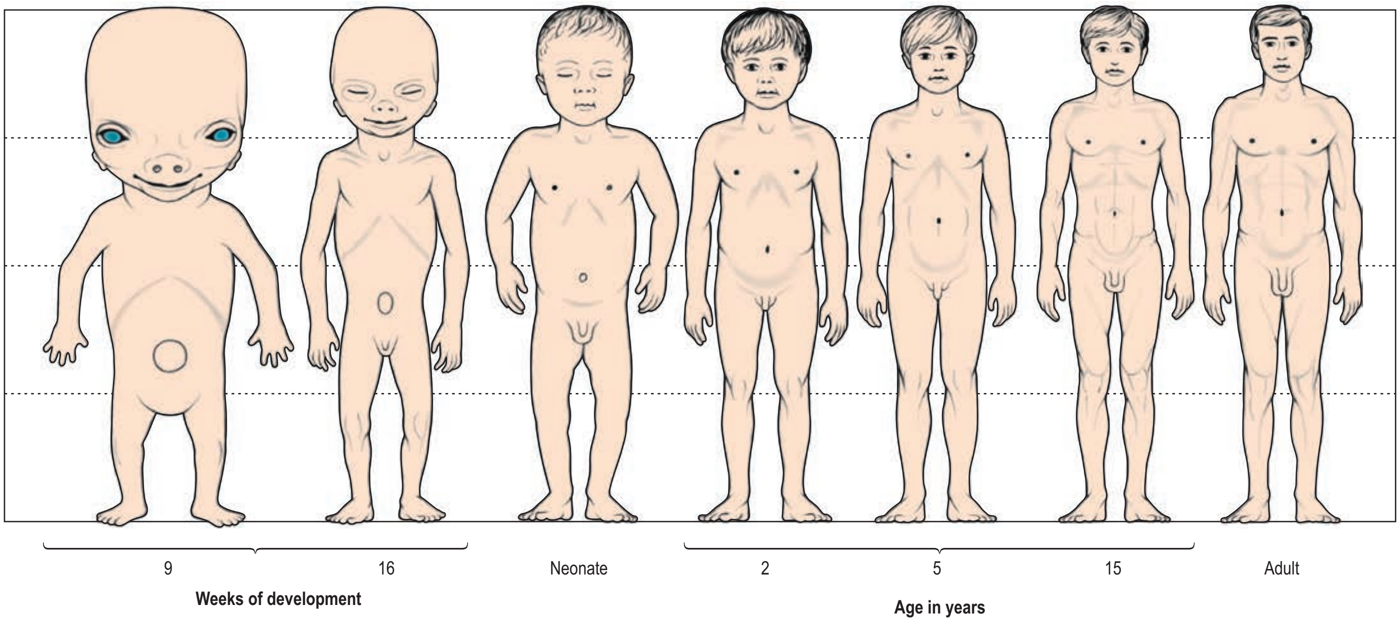

Fig. 23.21 Allometric growth in humans. The head is very large in proportion to the rest of the body during the embryonic period. After this time, the head grows more slowly than the torso and limbs and, by adulthood, the head is only one-eighth of the body length.

postnatal growth relative to the head and trunk and distal limb segment length is especially sensitive to the postnatal environment (Pomeroy et al 2014). Undernutrition between 7 and 8 years of age causes relatively short legs in adults; adults with short stature caused by relatively short legs appear to be at greater risk for coronary heart disease and diabetes than those adults with longer legs (Bogin 2012, Pomeroy et al 2014). Growth of the liver, spleen, kidneys, skeletal and muscular tissues generally follows pre- and postnatal growth curves given for the entire body, whereas other tissues have very different growth rates. The brain, skull, lymphoid tissues and reproductive organs all show differing growth rates during childhood and adolescence (Kappelou et al 2006) (**Fig. 23.22**).

Differential bone growth rates during puberty can lead to temporal-specific associated pathology. For example, 30% of childhood fractures affect the radius, mostly the distal metaphysis, during the pubertal growth spurt, but the incidence of these fractures decreases rapidly thereafter (Rauch 2012). Local differential rates of bone growth are seen in bone growth plates, peripheral and central trabecular bone, and in bone remodelling. During prepubertal growth, the distal radial growth plate adds about 9 mm to the length of the radius per year and the spaces between the peripheral trabeculae are filled with mineralized bone. It has been suggested that incomplete trabecular coalescence during this rapid growth, and not bone remodelling (which takes at least 6 months to complete), leads to lower bone mineral density (especially in boys) and higher local metaphysial cortical porosity (Wang et al 2010, Rauch 2012).

Final adult height is determined by the time at which the epiphysial growth plates fuse and appears to be controlled by a mechanism within the growth plate itself rather than by a systemic mechanism (Baron et al 2015, Jee and Baron 2016). The length of the proliferative columns of chondrocytes within growth plates is correlated with the length of the limbs in mammals, and is longer in longer limb bones: the sensitivity of growth plates changes during development (Bogin 2012). Over the juvenile and pubertal time periods chondroblast number decreases, and the rate of cell division and extent of cell hypertrophy diminishes; the process is termed growth plate senescence. When chondroblast proliferation ceases, the growth plate is resorbed and replaced by bone. Growth velocity, which is at the equivalent of 82 cm/year from postmenstrual weeks 12 to 40, decreases linearly from birth to about 5 cm/year just before the onset of puberty. During puberty a growth spurt is driven by oestrogen and androgens and followed by further linear growth velocity decrease until cessation of chondrogenesis at the growth plate. Growth plates are sensitive to oestrogen which accelerates the loss of chondrocyte progenitor cells in the growth plate; early exposure to oestrogens, as in precocious puberty, causes early epiphysial fusion. Inflammatory illness and malnutrition in children slow linear growth and the rate of growth plate senescence: if the condition resolves, the growth plates function at a more rapid rate resulting in catch-up growth (Jee and Baron 2016). Skeletal dysplasias affecting stature are thought to reflect the molecular balance of the variable spatial and temporal expression of skeletal genes (Baron et al 2015).

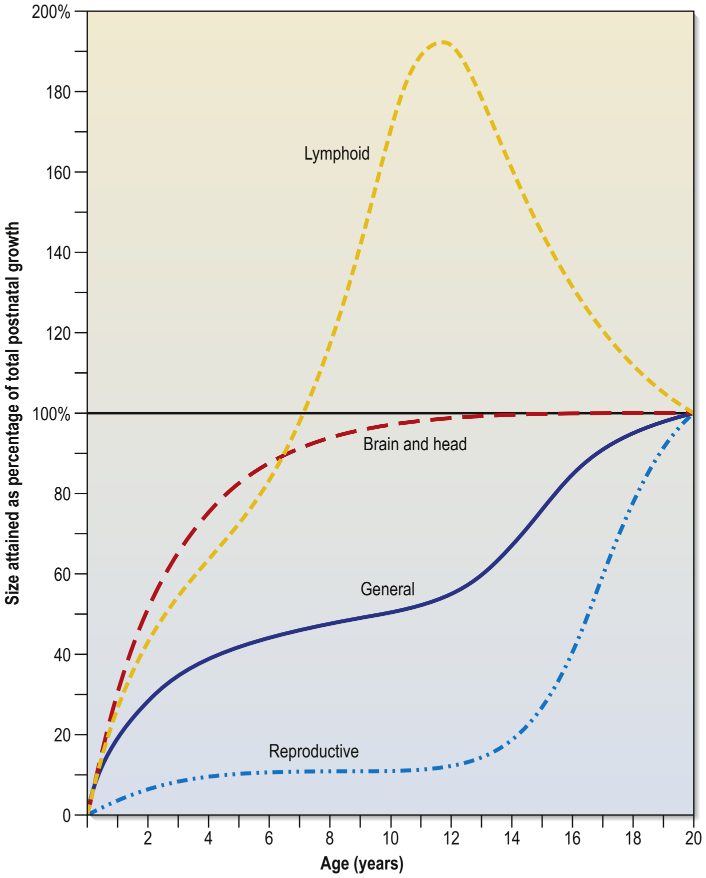

Fig. 23.22 Growth curves of different tissues, regions of the body and systems. Note that the growth of lymphoid tissue, thymus, lymph nodes and intestinal lymph masses decreases after puberty. (Adapted with permission from Tanner JM 1962 Growth at Adolescence, 2nd ed. Oxford: Blackwell Publishing.)

Bonus e-book content

Fig. 23.6 MRI scans of fetal anomalies.

Fig. 23.11 Velocity of estimated fetal growth over postmenstrual weeks.

Fig. 23.12 A–D Velocity of estimated fetal growth parameters over postmenstrual weeks.

Fig. 23.14 D–E, MicroCT coronal sections through a 14-postmenstrual-week fetus showing the extent of the liver on left and right sides and position of coils of intestine. **F–H,** MicroCT images of a 14- postmenstrual-week fetus showing the kidneys and suprarenal glands. **I–J,** MicroCT images of a 14-postmenstrual-week fetus showing the thymus gland.

Fig. 23.15 B–E, MicroCT sagittal section images of a fetus at 14 postmenstrual weeks.

Fig. 23.18 Gene expression of 927 development-related genes by age from 2 to 30 years.

Video 23.1 Ultrasound features of a fetus at 26 weeks.

Key references

Cameron N, Bogin B 2012 Human Growth and Development, 2nd ed. New York: Elsevier, Academic Press.

A fundamental text for all aspects of human growth.

Catalano PM, Hauguel-De Mouzon S 2011 Is it time to revisit the Pedersen hypothesis in the face of the obesity epidemic? Am J Obstet Gynecol 204:479–87.

This paper considers the changes in the demographics of obesity and its consequences for epigenetic changes to the feto-placental unit leading to generational chronic disease.

Cole T 2012 The development of growth references and growth charts. Ann Hum Biol 39:382–94.

A source of fundamental information for understanding growth charts.

Godfrey KM, Barker DJ 2000 Fetal nutrition and adult disease. Am J Clin Nutr 71:1344S–52S.

This paper considers the effect of maternal diet on the future risk factors for cardiovascular disease in her offspring.

Lampl M, Kusanovic JP, Erez O et al 2009 Early rapid growth, early birth: accelerated fetal growth and spontaneous late preterm birth. Am J Hum Biol 21:141–50.

This paper considers the relationship between fetal growth patterns and preterm delivery.

O'Gorman N, Salomon LJ 2018 Fetal biometry to assess the size and growth of the fetus. Best Pract Res Clin Obstet Gynaecol 49:3–15.

This paper sets out the range of fetal measurements taken with antenatal ultrasound examination and the use of fetal biometry charts to assess fetal growth.

O'Rahilly R, Müller F 1987 Developmental Stages in Human Embryos. Washington, DC: Carnegie Institution.

The most comprehensive and detailed morphological account of human development during the first 8 weeks of life; it sets out the basis for the staging system used for human embryos.

O'Rahilly R, Müller F 2010 Developmental stages in human embryos: revised and new measurements. Cells Tissues Organs 192:73–84.

This paper presents measurements that are based on accurate staging to assess embryonic age.

Papageorghiou AT, Ohuma EO, Altman DG et al 2014 International standards for fetal growth based on serial ultrasound measurements: the Fetal Growth Longitudinal Study of the INTERGROWTH-21st Project. Lancet 384:869–79.

Recommended international fetal growth standards.

Sepulveda W, Ximenes R, Wong AE et al 2012 Fetal magnetic resonance imaging and three-dimensional ultrasound in clinical practice: applications in prenatal diagnosis. Best Pract Res Clin Obstet Gynaecol 26:593–624.

This paper gives examples of the clarity of 3D MRI.

Villar J, Guiliani F, Bhutta ZA et al 2015 Postnatal growth standards for preterm infants: the preterm postnatal follow up study of the INTERGROWTH-21st Project. Lancet Global Health 3:e681–91.

Growth standard charts for postnatal growth in preterm infants up to 64 postmenstrual weeks.

References

Adibi JJ, Zhao Y 2017 Placental transfer of maternal obesity: identifying the gatekeeper. Endocrinol 158:2439–40.

Adzick NS 2013 Prospects for fetal surgery. Early Human Dev 89:881–6.

Akombi BJ, Agho KE, Hall JJ et al 2017 Stunting, wasting and underweight in sub-Saharan Africa: a systematic review. Int J Environ Res Public Health 14(8):pii: E863. doi: 10.3390/ijerph14080863.

Bardanzellu F, Fanos V, Strigini FAL et al 2018 Human breast mild. Exploring the linking ring among emerging components. Front Periatr 6:215. doi: 10.3389/fped.2018.00215.

Barker D 2013 Fetal origins of adult disease. In: BMA Board of Science (ed) Growing up in the UK. London: BMA; Ch. 8.

Barker DJP, Osmond C, Simmonds SJ et al 1993 The relation of head size and thinness at birth to death from cardiovascular disease in adult life. BMJ 306:422–6.

A source of evidence for a link between birth weight and size and predictions of later cardiovascular pathology.

Baron J, Sävendahl L, De Luca F et al 2015 Short and tall stature: a new paradigm emerges. Nat Rev Endocrinol 11:735–46.

Barzin M, Aryannezhad S, Srahati S et al 2018 Incidence of obesity and its predictors in children and adolescents in 10 years of follow up: Tehran lipid and glucose study (TLGS). BMC Pediat 18:245. doi:10.1186/s12887-018-1224-6.

Baschat AA, Galan HL 2017 Intrauterine growth restriction. In: Gabbe SG, Niebyl JR, Simpson JL (eds) Obstetrics Normal and Problem Pregnancies, 7th ed. Elsevier; Ch. 33: pp.737–69.

Bellini C, Boccardo F, Bonioli E et al 2006 Lymphodynamics in the fetus and newborn. Lymphology 39:110–17.

Beltrand J, Soboleva TK, Shorten PR et al 2012 Post-term birth is associated with greater risk of obesity in adolescent males. J Pediatr 160:769–73.

Benson CB, Doubilet PM 2018 Fetal measurements: normal and abnormal fetal growth and assessment of fetal well-being. In: Rumack CM, Levine D (eds) Diagnostic Ultrasound, 5th ed. Elsevier; Ch 42.

Bhatta SRC, Keriakos R 2011 Review of the recent literature on the mode of delivery for singleton vertex preterm babies. J Pregnancy 2011:186560.

Bogin B 2012 The evolution of human growth. In: Cameron N, Bogin B (eds) Human Growth and Development, 2nd ed. New York: Elsevier, Academic Press; Ch. 14.

Buck Louis GM, Grewal J, Albert PS 2015 Racial/ethnic standards for fetal growth, the NICHD fetal growth studies. Am J Obstet Gynecol 213:(4):449.e1-449.e41. doi:10.1016/j.ajog.2015.08.032.

Buhimschi CS, Norman JE 2014 Pathogenesis of spontaneous preterm birth. In: Creasy RK, Resnik R, Iams JD et al (eds) Creasy & Resnik's Maternal–Fetal Medicine. Principles and Practice, 7th ed. Elsevier; Ch. 39, pp. 599–623.

Butler MG 2009 Genomic imprinting disorders in humans: a mini-review. J Assist Reprod Genet 26:477–86.

Caino S, Kelmansky D, Adamo P et al 2006 Short-term growth in healthy infants, schoolchildren and adolescent girls. Ann Hum Biol 33:213–26.

Calabuig-Navarro V, Haghiac M, Minium J et al 2017 Effect of maternal obesity on placental lipid metabolism. Endocrinology 158:2543–55.

Cameron N 2012 The human growth curve, canalization and catch-up growth. In: Cameron N, Bogin B (eds) Human Growth and Development, 2nd ed. New York: Elsevier, Academic Press; Ch. 1.

Cameron N, Bogin B 2012 Human Growth and Development, 2nd ed. London: Elsevier, Academic Press.

A fundamental text for all aspects of human growth.

Cass DL 2011 Impact of prenatal diagnosis and therapy on neonatal surgery. Semin Fetal Neonatal Med 16:130–8.

Catalano PM 2014 Trying to understand gestational diabetes. Diabet Med 31:273–81.

Catalano PM, Hauguel-De Mouzon S 2011 Is it time to revisit the Pedersen hypothesis in the face of the obesity epidemic? Am J Obstet Gynecol 204:479–87.

This paper considers the changes in the demographics of obesity and its consequences for epigenetic changes to the feto-placental unit leading to generational chronic disease.

Charnonneau MR, O'Donnell D, Blanton LV et al 2016 Sialylated milk oligosaccharides promote microbiota-dependent growth in models of infant undernutrition. Cell 164:859–71.

Cheng P-J, Human S, Shaw SW et al 2010 Evaluation of fetal spine biometry between 11 and 14 weeks of gestation. Ultrasound Med Biol 36:1060–5.

Cilieborg MS, Boye M, Sangild PT 2012 Bacterial colonization and gut development in preterm neonates. Early Human Dev 88:541–9.

Ciobanu A, Wright A, Syngelaki A et al 2019 Fetal Medicine Foundation reference ranges for umbilical artery and middle cerebral artery pulsatility index and cerebroplacental ratio. Ultrasound Obstet Gynecol 53:465–72.

Cohen AR, Couto J, Cummings JJ et al 2014 Position statement on fetal myelomeningocele repair. Am J Obstet Gynecol 210:107–11.

Cole T 2003 Growth references and standards. In: Cameron N, Bogin B (eds) Human Growth and Development, 2nd ed. New York: Elsevier, Academic Press; Ch. 18, pp. 383–413.

Cole T 2012 The development of growth references and growth charts. Ann Hum Biol 39:382–94.

A source of fundamental information for understanding growth charts.

Cousminer DL, Bery DJ, Timpson NJ et al 2013 Genome-wide association and longitudinal analyses reveal genetic loci linking pubertal height growth, pubertal timing and childhood adiposity. Hum Mol Genet 22:2735–47.

Cuttler L, Misra M, Koontz M 2016 Somatic growth and maturation. In: Jameson JL, De Groot LJ, de Kretset DM (eds) Endocrinology: Adult and Pediatric, 7th ed. Elsevier; Ch. 22.

Danzer E, Johnson MP 2014 Fetal surgery for neural tube defects. Semin Fetal Neonatal Med 19:2–8.

Deprest J, Gratacos E, Nicolaides KH 2004 Fetoscopic tracheal occlusion (FETO) for severe congenital diaphragmatic hernia: evolution of a technique and preliminary results. Ultrasound Obstet Gynecol 24:121–6.

Deprest J, Hodges R, Gratacos E et al 2014 Invasive fetal therapy. In: Creasy R, Resnik R, Iams JD et al (eds) Creasy and Resnik's Maternal–Fetal Medicine: Principles and Practice, 7th ed. Philadelphia: Elsevier, Saunders; Ch. 35, pp. 516–57.

Fairley L, Petherick ES, Howe LD et al 2013 Describing differences in weight and length growth trajectories between white and Pakistani infants in the UK: analysis of the Born in Bradford birth cohort study using multilevel linear spline models. Arch Dis Child 98:274–79

Fernihough A, McGovern M 2015 Physical stature decline and the health status of the elderly population in England. Econ Hum Biol 16:30–44.

Fleming TP, Watkins, AJ, Velazquez MA et al 2018 Origins of lifetime health around the time of conception: causes and consequences. Lancet 391:1842–52.

Galan HL, Pandipati S, Filly RA 2008 Ultrasound evaluation of fetal biometry and normal and abnormal fetal growth. In: Callan PW (ed) Ultrasonography in Obstetrics and Gynecology. Philadelphia: Elsevier, Saunders; Ch. 7, pp. 225–65.

This chapter gives an overview of dating a pregnancy, measuring growth and assessing fetal status.

Ginod P, Choux C, Barberet J et al 2018 Singleton fetal growth kinetics depend on the mode of conception. Fertility and Sterility 110:1109-1117

Godfrey KM, Barker DJ 2000 Fetal nutrition and adult disease. Am J Clin Nutr 71:1344S–52S.

This paper considers the effect of maternal diet on the future risk factors for cardiovascular disease in her offspring.

Grantz KL, Hediget Ml, Liu D et al 2018 Fetal growth standards: the NICHD fetal growth study approach in context with INTERGROWTH-21st and the WHO Multicentre Growth Reference Study. Am J Obstet Gynecol 218: (2S):S641-S655.e28. doi:10.1016/j.ajog.2017.11.593 (ePub 2017 Dec 22).

Hales CM, Carroll MD, Fryar CD et al 2017 Prevalence of obesity among adults and youth: United States, 2015–2016. NCHS Data Brief no 288.

Harrison GA, Weiner JS, Tanner JM et al 1964 Human Biology. Oxford: Clarendon Press; Ch. 19.

A presentation of data on the human growth curve.

Hayward CE, Lean S, Sibley C et al 2016 Placental adaptation: what can we learn from birthweight:placental weight ratio? Front Physiol 7:28. doi:10.3389/fphys.2016.00028 (ePub 2016 Feb 5).

Hirst JE, Villar J, Victora CG et al for the International Fetal and Newborn Growth Consortium for the 21st Century (INTERGROWTH-21st) 2018 The antepartum stillbirth syndrome: risk factors and pregnancy conditions identified from the INTERGROWTH-21st Project. BJOG 125:1145–53.

Howson CP, Kinney M, Lawn JE (eds), March of Dimes, PMNCH, Save the Children, WHO 2012 Born Too Soon: The Global Action Report on Preterm Birth. Geneva: World Health Organization.

Hyde MJ, Modi N 2012 The long-term effects of birth by caesarean section: the case for a randomised controlled trial. Early Human Dev 88:943–9.

Isojima T, Yokoya S, Ito J et al 2010 Proposal of new auxological standards for Japanese girls with Turner syndrome. Clin Pediatr Endocrinol 19:69–82.

Jakaitis BM, Denning PW 2014 Human breast milk and the gastrointestinal innate immune system. Clin Perinatol 41:423–35.

Jee YH, Baron J 2016 The biology of stature. J Pediatr 173:32–8.

Johnson W, Stovitz SD, Choh AC et al 2012 Patterns of linear growth and skeletal maturation from birth to 19 years of age in overweight young adults. Int J Obes 36:535–41.

Kappelou O, Counsell SJ, Kennea N et al 2006 Abnormal cortical development after premature birth shown by altered allometric scaling of brain growth. PLoS Med 3:e265.

Kelishadi R, Poursafa P 2014 A review on the genetic, environmental, and lifestyle aspects of the early-life origins of cardiovascular disease. Curr Probl Pediatr Adolesc Health Care 44:54–72.

Khadilkar VV, Khadilkar V 2015 Revised Indian Academy of Pediatrics 2015 growth charts for height, weight and body mass index for 5–18-year-old Indian children. Indian J Endocrinol Metab 19:470–6.

Kiserud T, Johnsen SL 2009 Biometric assessment. Best Pract Res Clin Obstet Gynaecol 23:819–31.

Kiserud T, Haugen F 2017 Umbilical circulation. In: Polin RA, Abman SH, Rowitch D et al (eds) Fetal and Neonatal Physiology, 5th ed. Elsevier; Ch. 58, pp. 599–611.

Kramer MS, Papageorghiou A, Culhane J et al 2012 Challenges in defining and classifying the preterm birth syndrome. Am J Obstet Gynecol 206:108-112.

Lampl M 2002 Saltation and stasis. In: Cameron N (ed) Human Growth and Development. New York: Academic Press; Ch. 12.

A presentation of the evidence for saltatory growth in humans.

Lampl M, Kusanovic JP, Erez O et al 2009 Early rapid growth, early birth: accelerated fetal growth and spontaneous late preterm birth. Am J Hum Biol 21:141–50.

This paper considers the relationship between fetal growth patterns and preterm delivery.

Lanciotti L, Cofini M, Leonardi A et al 2018 Up-to-date review about minipuberty and overview of hypothalamic–pituitary–gonadal axis activation in fetal and neonatal life. Front Endocrinol (Lausanne) 9:410. doi:10.3389/fendo.2018.00410.

Lejarraga H 2012 Growth in infancy and childhood: a pediatric approach. In: Cameron N, Bogin B (eds) Human Growth and Development, 2nd ed. London: Elsevier, Academic Press; Ch. 2.

Leon DA, Smith GD, Shipley M et al 1995 Adult height and mortality in London: early life, socioeconomic confounding, or shrinkage? J Epidem Con Health 49:5–9.

Li W, Liu Q, Deng X et al 2017 Association between obesity and puberty timing: a systematic review and meta-analysis. Int J Environ Res Public Health 14:1266.

Locke AE, Kahali B, Berndt SI et al 2015 Genetic studies of body mass index yield new insights for obesity biology. Nature 518(7538):197–206. doi:10.1038/nature14177.

Lyon AJ, Preece MA, Grant DB 1985 Growth curve for girls with Turner syndrome. Arch Dis Child 60:932–5.

Macfarlane A, Mugford M 2012 Epidemiology. In: Rennie J (ed.) Rennie & Roberton's Textbook of Neonatology, 5th ed. Elsevier; Ch. 1.

Maltepe E, Penn AA 2018 Development, function and pathology of the placenta. In: Gleason CA, Juul SE. Avery's Diseases of the Newborn, 10th ed. Elsevier.

Mansourian M, Marateb HR, Kelishadi R et al 2012 First growth curves based on the WHO reference in a Nationally-Representative sample of pediatric population in the Middle East and North Africa (MENA): the CASPIAN-III study. BMC Pediatrics 12:149. doi:10.1186/1471-2431-12-149.

Mascie-Taylor CGN, Goto R 2007 Human variation and body mass index: a review of the universality of BMI cut-offs, gender and urban-rural differences, and secular changes. J Physiol Anthropol 26:109–12.

Matamoros S, Gras-Leguen C, Le Vacon F et al 2013 Development of intestinal microbiota in infants and its impact on health. Trends Microbiol 21:167–73.

McGuire W, Dyson L, Renfrew M 2010 Maternal obesity: consequences for children, challenges for clinicians and carers. Semin Fetal Neonatal Med 15:108–12.

Mesiano S 2019 Endocrinology of human pregnancy and fetal-placental neuroendocrine development. In: Strauss JF, Barbieri RL (eds) Yen & Jaffe's Reproductive Endocrinology, 8th ed. Elsevier; Ch 11.

Moore GE, Ishida M, Demetriou C et al 2015 The role and interaction of imprinted genes in human fetal growth. Phil Trans R Soc B 370:20140074.

Moro C, Covino J 2018 Nutrition and growth: assessing the impact of regional nutritional intake on childhood development and metacarpal parameters. Anat Cell Biol 51:31–40.

Neu J, Mai V 2012 The developing intestinal microbiome and its relationship to health and disease. In: Neu J (ed) Gastroenterology and Nutrition: Neonatology Questions and Controversies, 2nd ed. Philadelphia: Elsevier, Saunders; Ch. 5, pp. 59–65.

Neu J, Pammi M 2017 Pathogenesis of NEC: impact of an altered intestinal microbiome. Sem Perinatol 41:29–35.

Neu J, Rushing J 2011 Cesarean versus vaginal delivery: long term infant outcomes and the hygiene hypothesis. Clin Perinatol 38:321–31.

O'Gorman N, Salomon LJ 2018 Fetal biometry to assess the size and growth of the fetus. Best Pract Res Clin Obstet Gynaecol 49:3–15.

This paper sets out the range of fetal measurements taken with antenatal ultrasound examination and the use of fetal biometry charts to assess fetal growth.

O'Rahilly R, Müller F 1987 Developmental stages in human embryos. Washington, DC: Carnegie Institution.

The most comprehensive and detailed morphological account of human development during the first 8 weeks of life; it sets out the basis for the staging system used for human embryos.

O'Rahilly R, Müller F 2000 Minireview: prenatal ages and stages – measures and errors. Teratology 61:382–4.

O'Rahilly R, Müller F 2010 Developmental stages in human embryos: revised and new measurements. Cells Tissues Organs 192:73–84.

This paper presents measurements that are based on accurate staging to assess embryonic age.

Papageorghiou AT, Ohuma EO, Altman DG et al 2014 International standards for fetal growth based on serial ultrasound measurements: the Fetal Growth Longitudinal Study of the INTERGROWTH-21st Project. Lancet 384:869–79.

Recommended international fetal growth standards.

Pomeroy E, Stock JT, Cole TJ et al 2014. Relationships between neonatal weights, limb lengths, skinfold thicknesses, body breadths and circumferences in an Australian cohort. PLoS One 9(8): e105108. doi:10.1371/journal.pone.0105108.

Pomeroy E, Wells JCK, Cole TJ et al 2015 Relationships of maternal and paternal anthropometry with neonatal body size, proportions and adiposity in and Australian cohort. Am J Phys Anthropol 156:625–36.

Poston L 2012 Maternal obesity, gestational weight gain and diet as determinants of offspring long term health. Best Pract Res Clin Endocrinol Metab 26:627–639.

Pretorius DH, Aziz S, D'Agostini DA et al 2014 Clinical applications of three dimensional sonography in obstetrics. In: Creasy RK, Resnik R, Iams JD et al (eds) Creasy and Resnik's Maternal–Fetal Medicine: Principles and Practice, 7th ed. Philadelphia: Elsevier, Saunders; Ch. 19, pp. 218–33.

Quinn JA, Munoz FM, Gonik B et al 2016 Preterm birth: case definition and guidelines for data collection, analysis, and presentation of immunisation safety data Vaccine 34(49):6047–6056. doi:10.1016/j.vaccine.2016.03.045 (ePub 2016 Oct 13).

Ramakrishna BS, Venkataraman S, Mukhopadhya A 2006 Tropical malabsorption. Postgrad Med J 82:779–87.

Rauch 2012 The dynamics of bone structure development during pubertal growth. J Musculoskelet Neuronal Interact 12:1–6.

Reddy UM, Abuhamad AZ, Levine D et al 2014 Fetal imaging: Executive Summary of a Joint Eunice Kennedy Shriver National Institute of Child Health and Human Development, Society for Maternal–Fetal Medicine, American Institute of Ultrasound in Medicine, American College of Obstetricians and Gynecologists, American College of Radiology, Society for Pediatric Radiology, and Society of Radiologists in Ultrasound Fetal Imaging Workshop. Am J Obstet Gynecol 210:387–97.

Regnault N, Gillmann MW 2014 Importance of characterizing growth trajectories. Ann Nutr Metab 65:110–13

Ross EJ, Graham DL, Money KM 2015 Developmental consequences of fetal exposure to drugs: what we know and what we still must learn. Neuropsychopharmacology 40:61–87.

Ross MG, Beal MH 2008 Adult sequelae of intrauterine growth restriction. Semin Perinatol 32:213–8.

Royal College of Paediatrics and Child Health 2012 UK–WHO growth charts – 2–18 years. London: RCPCH[GB]. Available at https://www.rcpch.ac.uk/resources/uk-who-growth-charts-2-18-years.

Ruiz-Martiez S, Papageorghiou AT, Staines-Urias E et al 2019 Clinical impact of Doppler reference charts to manage fetal growth restriction: need for standardization. Ultrasound Obstet Gynecol. doi.org/10.1002/uog.20380.

Schwartz N, Quant HS, Sammel MD et al 2014 Macrosomia has its roots in early placental development. Placenta 35:684–90.

Sepulveda W, Ximenes R, Wong AE et al 2012 Fetal magnetic resonance imaging and three-dimensional ultrasound in clinical practice: applications in prenatal diagnosis. Best Pract Res Clin Obstet Gynaecol 26:593–624.

This paper gives examples of the clarity of 3D MRI.

Simhan HN, Berghella V, Iams JD 2014 Preterm labor and birth. In: Creasy RK, Resnik R, Iams JD et al (eds) Creasy & Resnik's Maternal–Fetal Medicine: Principles and Practice, 7th ed. Elsevier; Ch. 40, pp. 624–53.

Somel M, Franz H, Yan Z 2009 Transcriptional neoteny in the human brain. Proc Natl Acad Sci U S A 106:5743–8.

Song SJ, Dominquez-Bello MG, Knight R 2013 How delivery mode and feeding can shape the bacterial community in the infant gut. CMAJ 185:373–4.

Steer PJ, Modi N 2009 Elective caesarean sections – risks to the infant. Lancet 374:675–6.

Stevens A, Hanson D, Whatmore A et al 2013 Human growth is associated with distinct patterns of gene expression in evolutionarily conserved networks. BMC Genomics 14:547.

Stirnemann J, Villar J, Salomon LJ et al 2017 International estimated fetal weight standards of the INTERGROWTH-21st Project. Ultrasound Obstet Gynecol 49:478–86.

Streeter GL 1942 Developmental horizons in human embryos. Descriptions of age group XI, 13 to 20 somites, and age group XII, 21 to 29 somites. Contrib Embryol Carnegie Inst Washington 30:211–45.

Streeter GL 1945 Developmental horizons in human embryos. Description of age group XIII, embryos of about 4 or 5 millimeters long, and age group XIV, period of indentation of the lens vesicle. Contrib Embryol Carnegie Inst Washington 31:27–63.

Streeter GL 1948 Developmental horizons in human embryos. Description of age groups XV, XVI, XVII, and XVIII, being the third issue of a survey of the Carnegie collection. Contrib Embryol Carnegie Inst Washington 32:133–203.

Styles ME, Cole TJ, Dennis J et al 2002 New cross sectional stature, weight, and head circumference references for Down's syndrome in the UK and Republic of Ireland. Arch Dis Child 87:104–8.

Valentine CJ, Morrow AL 2012 Human milk feeding of the high risk neonate. In: Neu J (ed) Gastroenterology and Nutrition: Neonatology Questions and Controversies, 2nd ed. Philadelphia: Elsevier, Saunders; Ch.13, pp. 203–12.

van Dommelen P, de Kroon MLA, Cameron N et al 2014 The impact of height during childhood on the national prevalence rates of overweight. PLoS One 9:e85769.

Victora CG, Villar J, Barros FC et al 2015 Anthropometric characterization of impaired fetal growth. Risk factors and prognosis of newborns with stunting or wasting. JAMA Pediatr 2015;169(7):e151431. doi:10.1001/jamapediatrics.2015.1431.

Villar J, Papageorghiou AT, Knight HE et al 2012 The preterm birth syndrome: a prototype phenotypic classification. Am J Obstet Gynecol 206:119–23.

Villar J, Guiliani F, Bhutta ZA et al 2015 Postnatal growth standards for preterm infants: the preterm postnatal follow up study of the INTERGROWTH-21st Project. Lancet Global Health 3:e681–91. *Growth standard charts for postnatal growth in preterm infants up to 64 postmenstrual weeks.*

Walsh JM, McAuliffe FM 2012 Prediction and prevention of the macrosomic fetus. Eur J Obstet Gynecol Reprod Biol 162:125–30.

Wang Q, Wang XF, Iuliano-Burns S et al 2010 Rapid growth produces transient cortical weakness: a risk factor for metaphyseal fractures during puberty. J Bone Miner Res 25:1521–6.

Werner EF, Savitz DA, Janevic TM et al 2012 Mode of delivery and neonatal outcomes in preterm, small-for-gestational-age newborns. Obstet Gynecol 120:560–4.

West J, Lawlor DA, Fairley L et al 2013 UK-born Pakistanti-origin infants are relatively more adipose than white British infants: findings from 8704 mother–offspring pairs in the Born-in-Bradford prospective birth cohort. J Epidemiol Community Health 67:544–51.

WHO Multicenter Growth Reference Study Group 2006 WHO child growth standards based on length/height, weight and age. Acta Paediatr Suppl 450:76–85.

Wynn JL, Neu J 2012 The neonatal gastrointestinal tract as a conduit to systemic inflammation and developmental delays. In: Neu J (ed) Gastroenterology and Nutrition: Neonatology Questions and Controversies, 2nd ed. Philadelphia: Elsevier, Saunders; Ch 19, pp. 293–304.

Yang H, Kramer MS, Platt RW et al 2002 How does early ultrasound scan estimation of gestational age lead to higher rates of preterm birth? Am J Obstet Gynecol 186:433–7.

Zemel BS, Pipan M, Stallings VA et al 2015 Growth charts for children with Down syndrome in the United States. Pediatrics 136:(5):e1204–e1211. doi:10.1542/peds.2015-1652.

COMMENTARY

2.1

Head–trunk interface in the vertebrate embryo

Shigeru Kuratani

The vertebrate body is characterized by the possession of an overt head. However, the definition of 'head' in this context is enigmatic because the boundary between the head and trunk is not always self-evident. The head is usually defined as the rostral region of the vertebrate body where the brain, various sensory organs and a well-developed oral apparatus are located, but this definition can vary according to morphological context (reviewed by Kuratani 2019).

In the vertebrate embryo, the head is composed of various germ-layer derivatives. Head-specific mesodermal components include the head mesoderm in the paraxial domain, and the pharyngeal arch mesoderm in the ventrolateral domain of the pharyngula. The endoderm develops into the pharynx and the segmental pharyngeal pouches, and further head-specific ectodermal components include ectodermal placodes and populations of cranial neural crest cells (**Fig. 2.1.1A**). These head-specific components are distinct from those of the trunk, such as the unsegmented lateral plate, pharyngeal endoderm, segmented somites and trunk neural crest (TNC; see Fig. 2.1.1A).

During early embryogenesis, cranial neural crest cells migrate under the epidermis to form the ectomesenchyme, which comprises three distinct neural crest cell populations (these are, from rostral to caudal: trigeminal, hyoid and circumpharyngeal).

Dorsal migration of cranial neural crest cells is permitted by the absence of somites, which also allows the cranial neural crest cells to adhere selectively to rhombomeres 2, 4 and 6 and to the posterior region of the hindbrain, thus prefiguring the morphology of the trigeminal (V), facial (VII), glossopharyngeal (IX) and vagus (X) cranial nerves (i.e., the branchiomeric nerves that innervate pharyngeal arches). The morphological pattern of these nerves is different from that of the spinal nerves in the trunk, the precursors of which are segmented by somites.

Ventrally, the cranial neural crest cells migrate into the pharyngeal pouches, where they come into contact with the epibranchial placodes (primordia of the inferior ganglia of the branchiomeric nerves) (**Fig. 2.1.1B**). The cranial neural crest cells also migrate ventrally to fill the pharyngeal arches and craniofacial region, thereby establishing the (pseudo-)segmental organization (branchiomeres and rhombomeres) of the branchiomeric cranial nerves, pharyngeal arches and hindbrain.

The posterior boundary of the head mesoderm (at roughly the position of the otic vesicle) does not line up with the caudal-most pharyngeal arch, and so the posterior boundary of the cranial neural crest cell distribution forms an S-shape (see Fig. 2.1.1). This boundary was first recognized by Froriep (1885), who interpreted it as representing the interface between the somatic and visceral parts of the body (see Figs 17.7, 18.12). Developmentally, the interface coincides with the first few somites and lateral plates (Kuratani 1997). In other words, there is a domain in the vertebrate pharyngula (a stage in embryonic development after head and tail folding with a specified body plan, about stage 11 in human embryos, see Chapter 12) where somites and pharyngeal arches coexist at the same rostrocaudal level. This means that the somites in this domain – the suprapharyngeal somites (see Fig. 2.1.1A) – develop in a unique environment, surrounded both by cells that are unique to the head and by cells that are unique to the trunk.

During the evolutionary process, the shoulder girdle developed as the posterior-most part of the dermal shield of the head of jawless vertebrates; it arises during embryogenesis along the S-shaped head–trunk interface. In jawed vertebrates, the shoulder girdle began to move away from the head, eventually resulting in the formation of an aperture (Trinajstic et al 2013), around which several unique structures that also develop along the head–trunk interface – including the hypobranchial muscles (including the muscles of the tongue and geniohyoid and infrahyoid), vagus, hypoglossal (occipitospinal) and accessory nerves and cucullaris (trapezius and sternocleidomastoid) muscles – then form and elongate to produce the neck (**Fig. 2.1.1C**). Some somite-derived muscles are also referred to as 'neck muscles' because their connective tissues are, in part, derived from cranial neural crest cells, unlike most other postcranial skeletal muscles, the connective tissues of which are mesodermal in origin. The developmental and morphological characteristics of the cucullaris muscles remain to be elucidated (reviewed by Tada and Kuratani 2015).

The neck is particularly conspicuous in amniotes, whose hearts are shifted posteriorly (Hirasawa et al 2016). In this context, the neck can be defined as the domain between the head and the shoulder girdle, where, during embryogenesis, the posterior-most part of the ectomesenchyme contributes to organogenesis, including that of the connective tissues of the neck muscles (Noden 1983, Matsuoka et al 2005, Nagashima et al 2016; reviewed by Hirasawa and Kuratani 2015). It is important to note that the neck has partially lost its trunk-like nature, not only with respect to the distribution of cranial neural crest cells, but also because of the disappearance of the coelom, as seen in the head. Furthermore, the neck muscles are not considered to be hypaxial skeletal muscles because they are not located in the lateral body wall (see Fig. 2.1.1C).

The head–trunk interface is not present in non-vertebrate chordates such as amphioxi and tunicates. In cyclostomes (modern jawless vertebrates), lamprey and hagfish embryos both show an S-shaped interface between the prospective head and trunk, but the hagfish embryo shows an additional caudal shift of the posterior half of the pharynx. The hagfish hypoglossal nerve violates the head–trunk interface and has lost the typical shape of this nerve in vertebrates: this peculiar morphology is assumed to be a derived condition (Oisi et al 2015, Kuratani et al 2019). Despite these differences, the cyclostome hypobranchial muscles are coextensive with the pharynx, thereby being a prototype of the human neck. Thus, the head–trunk interface appears to have been already obtained by the latest common vertebrate ancestor. This interface can be seen as a synapomorphy that defines vertebrates as a unique group among chordates with a clearly differentiated head and trunk (Irie et al 2018).

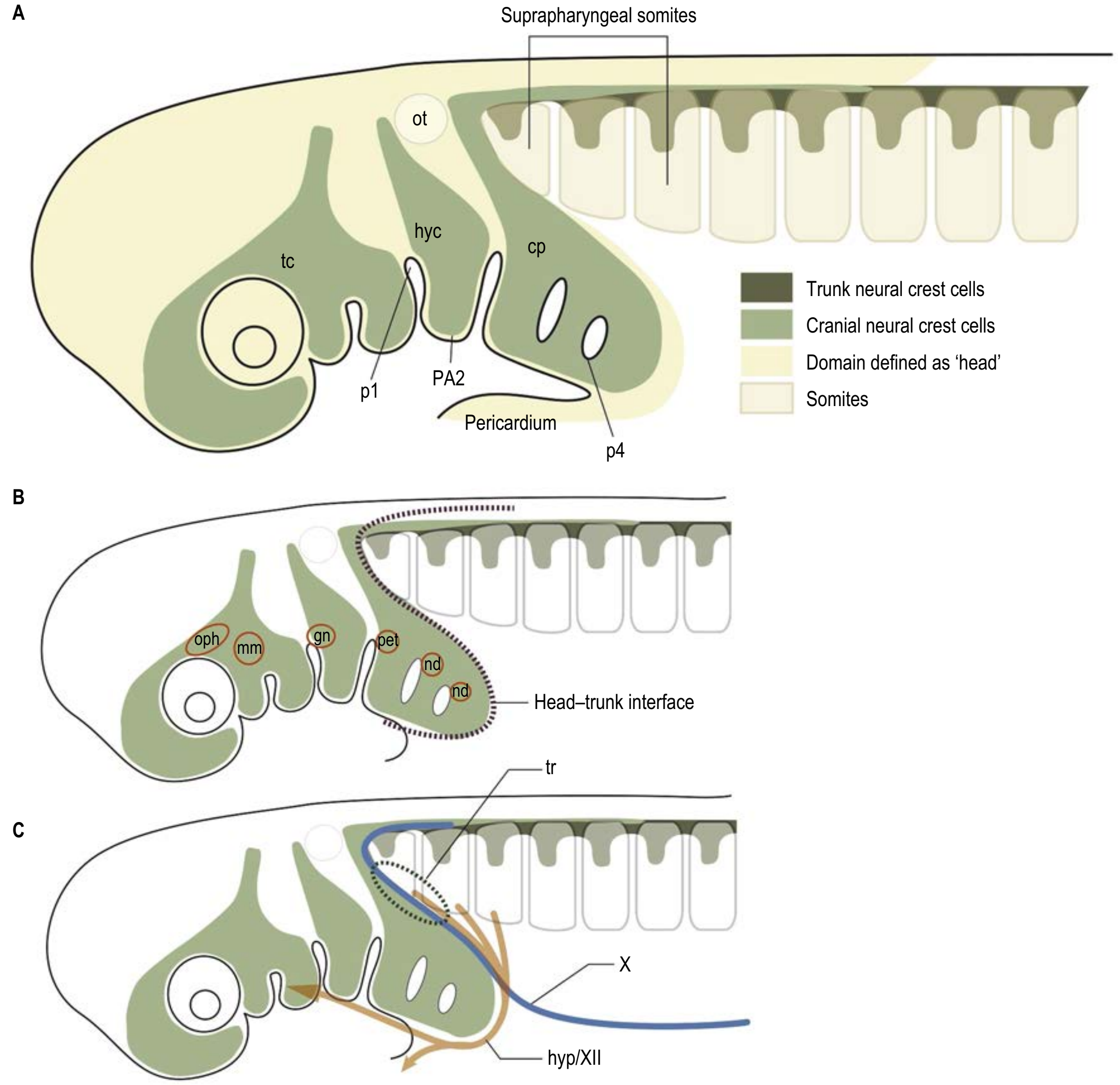

Fig. 2.1.1 The head–trunk interface in the vertebrate embryo. **A**, The ectomesenchyme that fills the pharyngeal arches and craniofacial region of the vertebrate embryo comprises three distinct cell populations of cranial neural crest cells: trigeminal (tc), hyoid (hyc) and circumpharyngeal (cp). In contrast, the TNC cell population is divided segmentally by somites that reflect the basic vertebrate body plan. The head is defined by the distribution of cranial neural crest cells. The suprapharyngeal somites are ventrally associated not with the lateral plate but with the pharyngeal arches and will form the occipital bones and hypobranchial muscles. **B**, The head–trunk interface (purple dotted line) and sensory ganglionic placodes (red circles). **C**, The vagus nerve (X), hypoglossal nerve (XII) and hypobranchial muscle primordium (hyp) follow the head–trunk interface. The trapezius muscle anlage (tr) also develops along the head–trunk interface. Other abbreviations: gn, geniculate placode; mm, maxillomandibular placode; nd, nodose placode; oph, ophthalmic placode; ot, otic vesicle; p1–p4, pharyngeal pouches or slits; PA2, second pharyngeal (hyoid) arch; pet, petrosal placode. (Adapted with permission from Kuratani S, Kusakabe R, Hirasawa T 2019 The neural crest and evolution of the head/trunk interface in vertebrates. Dev Biol 444:60–6.)

References

Froriep A 1885 Über Anlagen von Sinnesorganen am Facialis, Glossopharyngeus und Vagus, über die genetische Stellung des Vagus zum Hypoglossus, und über die Herkunft der Zungenmusculatur. Arch Anat Physiol 1885:1–55.

Hirasawa T, Kuratani S 2015 Evolution of the vertebrate skeleton: morphology, embryology, and development. Zool Lett 1:2.

Hirasawa T, Fujimoto S, Kuratani S 2016 Expansion of the neck reconstituted the shoulder-diaphragm in amniote evolution. Dev Growth Differ 58:143–53.

Irie N, Kuratani S, Satoh N 2018 The phylum Vertebrata: a way of zoological recognition. Zool Lett 4:32.

Kuratani S 1997 Spatial distribution of postotic crest cells defines the head/trunk interface of the vertebrate body: embryological interpretation of peripheral nerve morphology and evolution of the vertebrate head. Anat Embryol 195:1–13.

Kuratani S 2019 History and current theories of the vertebrate head segmentation. In: Nuno de la Rosa L, Müller G (eds) Evolutionary Developmental Biology. Cham: Springer.

Kuratani S, Kusakabe R, Hirasawa T 2019 The neural crest and evolution of the head/trunk interface in vertebrates. Dev Biol 444:60–6.

Matsuoka T, Ahlberg PE, Kessaris N et al 2005 Neural crest origins of the neck and shoulder. Nature 436:347–55.

Nagashima H, Sugahara F, Watanabe K et al 2016 Developmental origin of the clavicle, and its implications for the evolution of the neck and the paired appendages in vertebrates. J Anat 229:536–48.

Noden DM 1983 The embryonic origins of avian cephalic and cervical muscles and associated connective tissues. Am J Anat 168:257–76.

Oisi Y, Fujimoto S, Ota KG et al 2015 On the peculiar morphology and development of the hypoglossal, glossopharyngeal and vagus nerves and hypobranchial muscles in the hagfish. Zool Lett 1:6.

Tada M, Kuratani S 2015 Evolutional and developmental understanding of the spinal accessory nerve. Zool Lett 1:4.

Trinajstic K, Sanchez S, Dupret V et al 2013 Fossil musculature of the most primitive jawed vertebrates. Science 341:160–4.

CHAPTER 24

Overview of the nervous system

The human nervous system is the most complex product of evolution. The activity of its billions of neurones constitutes the physical basis of sensory experience, motor behaviour, consciousness and self-awareness. Research to elucidate the mechanisms that underlie these functions is one of the most active areas of contemporary biology and medicine and is essential for the future treatment and prevention of neurological and psychiatric disorders.

The nervous system has two major divisions, the central nervous system (CNS) and the peripheral nervous system (PNS). The CNS consists of the brain and spinal cord. The PNS consists of the cranial and spinal nerves and their peripheral ganglia and ramifications. It is composed mainly of the axons of sensory and motor neurones that pass between the CNS and the body. The autonomic nervous system (ANS) consists of neurones located within both the CNS and PNS which control secretory glands and smooth and cardiac muscle. It is subdivided into sympathetic and parasympathetic components and is concerned primarily with control of the internal environment. Neurones in the wall of the gastrointestinal tract form the enteric nervous system (ENS) and are capable of sustaining local reflex activity that is independent of the CNS.

CENTRAL NERVOUS SYSTEM

The brain and spinal cord (see Fig. 47.1A) contain the great majority of neuronal cell bodies in the nervous system. In many parts of the CNS, neuronal cell bodies are grouped together and are, more or less, segregated from axons. The generic term for such collections of cell bodies is grey matter. Small aggregations of neuronal cell bodies, which usually share common connections and functional roles, are termed nuclei. Neuronal dendrites and synaptic interactions are mostly confined to grey matter. Axons tend to be grouped together to form white matter, so named because axons are often ensheathed in myelin, which confers a paler coloration on the tissue. Axons that pass between similar origins or destinations within the CNS tend to run together in defined pathways, or tracts. These often cross the midline (decussate), which means that one half of the body is, in many respects, controlled by, and sends information to, the opposite side of the brain.

Some groups of neurones in the spinal cord and brainstem that subserve similar functions are organized into longitudinal columns. The neurones in these columns may be concentrated into discrete, discontinuous nuclei in some areas, e.g. the cranial nerve nuclei of the brainstem, or they may form more or less continuous longitudinal bands, as in much of the spinal cord (**Fig. 24.1**). Efferent neurones constitute three such columns. The axons of motor neurones in the somatic motor column innervate muscles derived from head somites. The two other columns are related to specialized features of head morphology: neurones in the branchial motor column innervate muscles derived from the wall of the embryonic pharynx (branchial muscles) and the visceral motor column supplies preganglionic parasympathetic fibres to exocrine glands and visceral smooth muscle. Four longitudinal cell columns are related to sensory functions. The general somatic sensory column essentially deals with general sensory information from the head; special somatic sensory neurones are related to the special senses and receive vestibular and auditory input; general visceral sensory neurones deal with information from widespread and varied visceral sensory endings; special visceral sensory neurones are related to the special sense of taste.

The spinal cord and brain communicate with the rest of the body via the spinal and cranial nerves, respectively. These nerves contain afferent fibres that bring information into the CNS from sensory receptors, and efferent fibres that convey instructions from the CNS to peripheral effector organs. The spinal cord and brainstem can control many aspects of bodily function by reflex action mediated via interconnections of varying complexity between the afferent and efferent components of the spinal and cranial nerves. Numerous descending connections from the brain may modulate this activity. Afferent input to the spinal cord and brainstem is channelled into various ascending pathways, some of which eventually impinge upon the cerebral cortex, conferring conscious awareness.

To provide the energy required by constant neuronal activity, the CNS has a high metabolic rate and a rich blood supply (Ch. 26). A blood–brain barrier controls the neuronal environment and restricts the types of substance that can pass from the blood stream into nervous tissue.

Spinal cord

The spinal cord lies within the vertebral column, in the upper two-thirds of the vertebral canal, and is continuous rostrally with the medulla oblongata of the brainstem. For the most part, the spinal cord receives afferent input from, and controls the functions of, the trunk and limbs. Afferent and efferent connections between the periphery and the spinal cord travel in 31 pairs of segmentally arranged spinal nerves that are attached to the cord as a linear series of dorsal and ventral rootlets. Adjacent groups of rootlets unite to form dorsal and ventral roots that combine to form the spinal nerves proper (**Fig. 24.2**). Dorsal and ventral roots are functionally distinct: dorsal roots carry primary afferent nerve fibres from neuronal cell bodies located in dorsal root ganglia, whereas ventral roots carry efferent fibres from neuronal cell bodies located in the spinal grey matter.

Internally, the spinal cord consists of a central core of grey matter surrounded by white matter. The grey matter is configured in a characteristic H, or butterfly, shape that has projections known as dorsal (posterior) and ventral (anterior) horns (**Fig. 24.3**). In general, neurones situated in the dorsal horn are primarily concerned with sensory functions whilst those in the ventral horn are mostly associated with motor activities. At thoracic and upper lumbar levels of the spinal cord a small lateral horn is additionally present, marking the location of the cell bodies of preganglionic sympathetic neurones. The central canal, a vestigial component of the ventricular system, lies at the centre of the spinal grey matter and runs the length of the cord. The white matter of the spinal cord consists of ascending and descending tracts that link spinal cord segments to one another and the spinal cord to the brain.

Brain

The brain receives information from, and controls the activities of, the trunk and limbs, mainly via connections with the spinal cord. It also possesses 12 pairs of cranial nerves through which it communicates with structures that are mostly in the head and neck.

The brain is divided into major regions on the basis of ontogenetic growth and phylogenetic principles (**Figs 24.4–24.6**). Ascending in sequence from the spinal cord, the principal divisions are the rhombencephalon (hindbrain), mesencephalon (midbrain) and prosencephalon (forebrain).

The rhombencephalon is subdivided into the myelencephalon or medulla oblongata, metencephalon or pons, and the cerebellum. The medulla oblongata, pons and midbrain are collectively referred to as the brainstem: it lies upon the basal portions of the occipital and sphenoid bones (clivus). The medulla oblongata is the most caudal part of the brainstem and is continuous with the spinal cord below the level of the foramen magnum. The pons lies rostral to the medulla and is distinguished by a mass of transverse nerve fibres that connect it to the cerebellum. The midbrain is a short segment of brainstem, rostral to the pons. The cerebellum consists of paired hemispheres united by a median vermis: it lies within the posterior cranial fossa, dorsal to the pons, medulla and caudal midbrain, with all of which it has numerous fibre connections.

The prosencephalon is subdivided into the diencephalon and the telencephalon. The diencephalon equates mostly to the thalamus and hypothalamus, but also includes the smaller epithalamus and

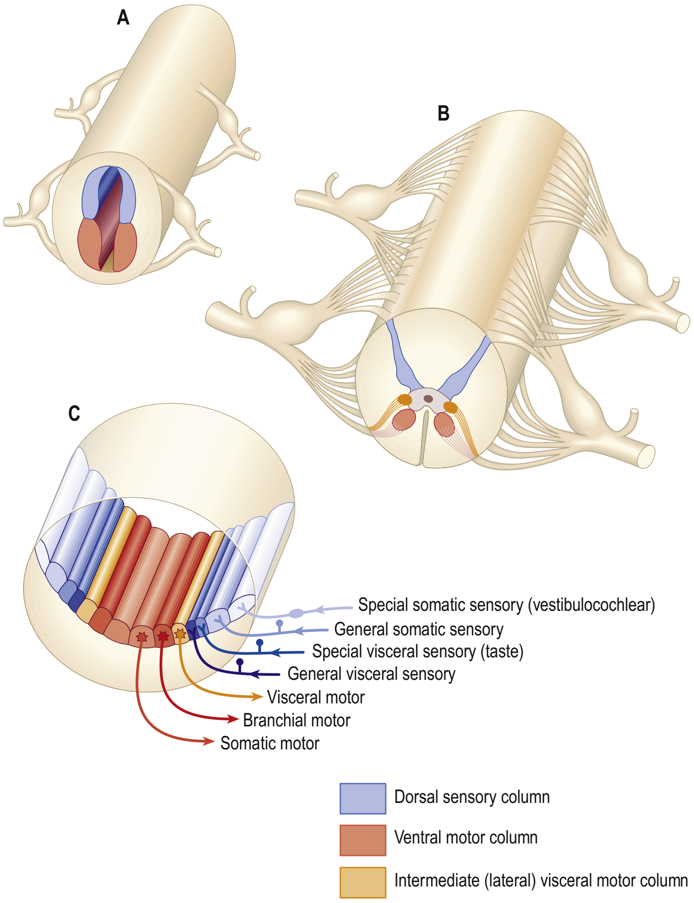
A
B
C
Special somatic sensory (vestibulocochlear)
General somatic sensory
Special visceral sensory (taste)
General visceral sensory
Visceral motor
Branchial motor
Somatic motor
Dorsal sensory column
Ventral motor column
Intermediate (lateral) visceral motor column

Fig. 24.1 The arrangement of sensory and motor cell columns in the spinal cord and brainstem. In each of parts A, B and C, dorsal is towards the top of the diagram. **A**, The organization of the primitive spinal cord with a dorsal sensory column, a ventral motor column and segmentally arranged dorsal and ventral nerve roots. **B**, The adult thoracic spinal cord with sensory and somatic motor columns and an additional intermediate (lateral) visceral motor column. **C**, The arrangement of multiple longitudinal columns in the brainstem, where the motor column is now subdivided into three, and the sensory column into four. For further information about the embryological aspects of the early nervous system, consult Chapter 17.

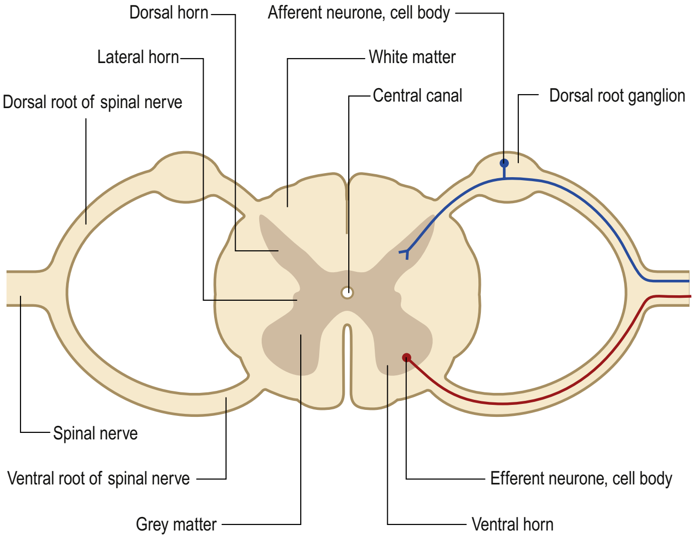
Dorsal horn
Afferent neurone, cell body
Lateral horn
White matter
Dorsal root of spinal nerve
Central canal
Dorsal root ganglion
Spinal nerve
Ventral root of spinal nerve
Efferent neurone, cell body
Grey matter
Ventral horn

Fig. 24.2 A transverse section through the spinal cord, illustrating the disposition of grey and white matter and the attachment of dorsal and ventral spinal nerve roots.

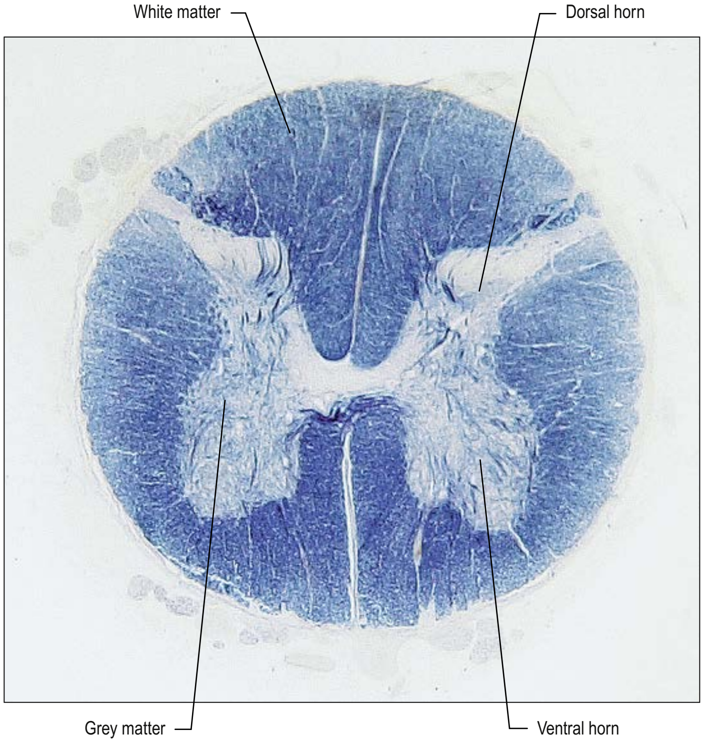
White matter
Dorsal horn
Grey matter
Ventral horn

Fig. 24.3 A transverse section through the spinal cord at lumbar level. The section has been stained for nerve fibres, leaving the grey matter relatively unstained. (Figure enhanced by B Crossman.)

subthalamus. The telencephalon is composed mainly of the cerebral hemisphere or cerebrum. The diencephalon is almost completely embedded in the cerebrum and is, therefore, largely hidden from the exterior. The human cerebrum constitutes the major part of the brain. It occupies the anterior and middle cranial fossae and is directly related to the calvaria. The surface of the cerebral hemisphere is convoluted into a complex pattern of ridges (gyri) and furrows (sulci). Internally, the hemisphere has an outer layer of grey matter, the cerebral cortex, beneath which lies a thick mass of white matter (**Fig. 24.7**). One of the most important components of the cerebral white matter, the internal capsule (see Fig. 24.9), contains nerve fibres that pass to and from the cerebral cortex and lower levels of the neuraxis. Several large nuclei of grey matter, the basal ganglia or basal nuclei, are partly embedded in the subcortical white matter. Nerve fibre connections between corresponding areas on either side of the brain cross the midline within commissures, the largest being the corpus callosum.

During prenatal development, the walls of the neural tube thicken greatly but never completely obliterate the central lumen, which remains in the spinal cord as the vestigial central canal and becomes greatly expanded in the brain to form a series of interconnected cavities or ventricles (Ch. 25). In the forebrain and hindbrain, parts of the roof of the neural tube do not generate nerve cells but become thin, folded sheets of highly vascular secretory tissue, the choroid plexuses which secrete cerebrospinal fluid into the ventricles. The cavity of the rhombencephalon becomes expanded to form the fourth ventricle dorsal to the pons and upper half of the medulla. Caudally, the fourth ventricle is continuous with a canal in the caudal medulla and, through this, with the central canal of the spinal cord. It is continuous with the subarachnoid space through three openings (the foramina of Luschka and of Magendie) and with a narrow channel, the cerebral aqueduct, at its rostral extent. The cerebral aqueduct passes through the midbrain and opens out rostrally into the third ventricle, a narrow, slit-like, midline cavity bounded laterally by the diencephalon. At the rostral end of the third ventricle, a small aperture on each side leads into the large lateral ventricle located within each cerebral hemisphere (see Fig. 24.4C).

Overview of ascending sensory pathways

Sensory modalities are conventionally described as being either special senses or general senses. The special senses are olfaction, vision, taste, hearing and vestibular function: afferent information is encoded by highly specialized sense organs and transmitted to the brain in the olfactory, optic, facial, vestibulocochlear and glossopharyngeal nerves.

The general senses include touch (ranging from light to discriminative), pressure, vibration, pain, thermal sensation and proprioception (perception of posture and movement). Stimuli from the external and internal environments activate a diverse range of receptors in the skin, fascia, viscera, muscles, bones, tendons and joints (Ch. 3). Afferent impulses from the trunk and limbs are conveyed to the spinal cord in spinal nerves, while those from the head are carried to the brain in cranial nerves. The detailed anatomy of the complex pathways by which the various general senses impinge on consciousness levels is better

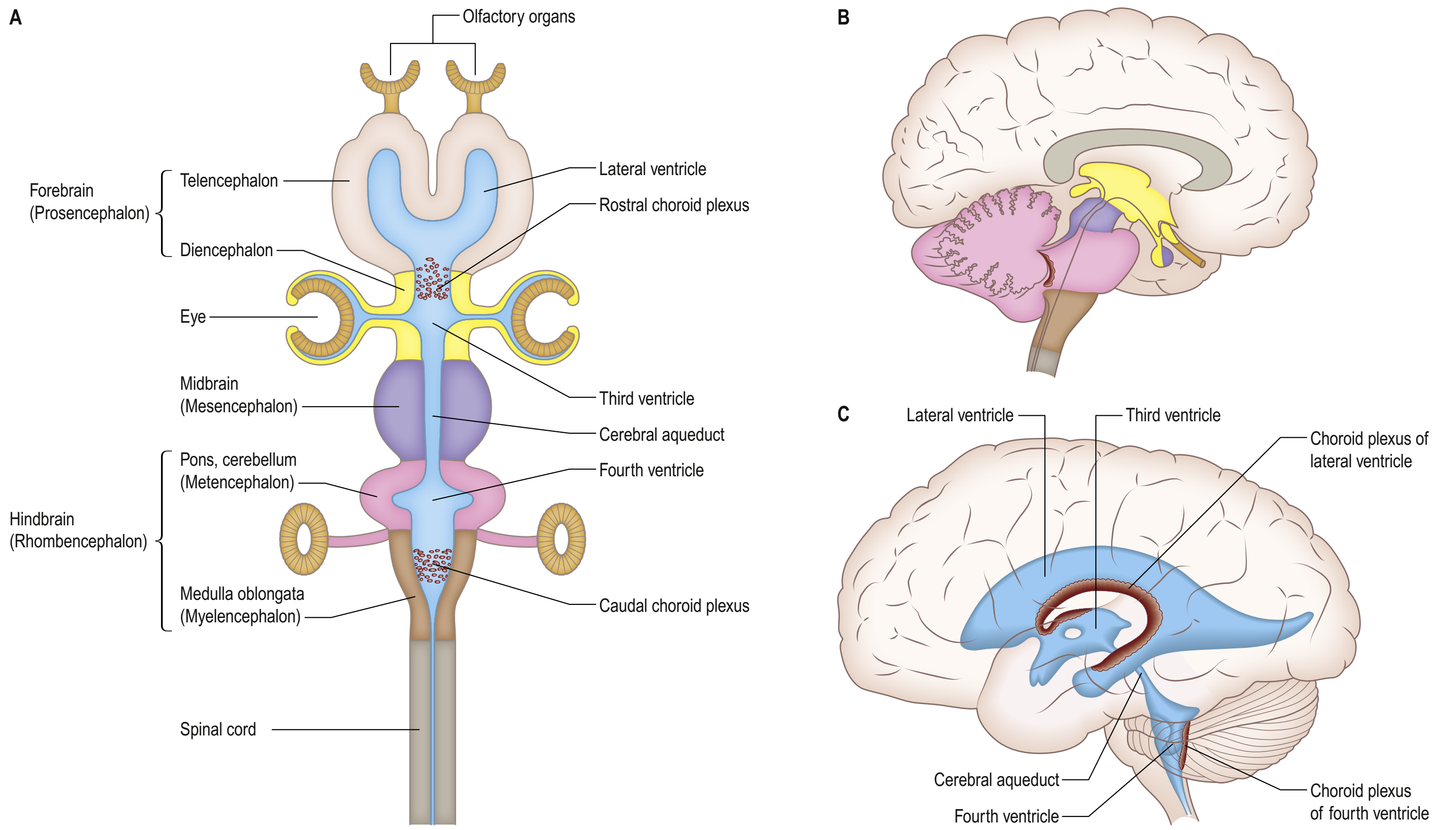
A
Olfactory organs
Forebrain (Prosencephalon)
Telencephalon
Diencephalon
Lateral ventricle
Rostral choroid plexus
Eye
Midbrain (Mesencephalon)
Third ventricle
Cerebral aqueduct
Pons, cerebellum (Metencephalon)
Fourth ventricle
Hindbrain (Rhombencephalon)
Medulla oblongata (Myelencephalon)
Caudal choroid plexus
Spinal cord
B
C
Lateral ventricle
Third ventricle
Choroid plexus of lateral ventricle
Cerebral aqueduct
Fourth ventricle
Choroid plexus of fourth ventricle

Fig. 24.4 Nomenclature and arrangement of the major divisions of the brain. **A**, The major features of the basic brain plan, including their relationships to the major special sensory organs of the head. **B**, The corresponding regions in the adult brain, seen in sagittal section. **C**, The organization of the ventricular system in the brain.

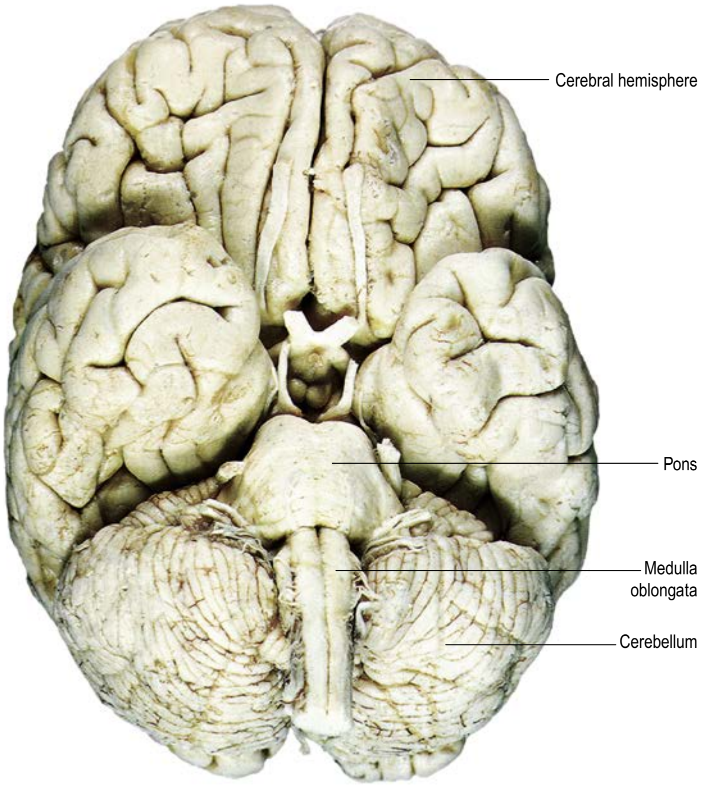
Cerebral hemisphere
Pons
Medulla oblongata
Cerebellum

Fig. 24.5 The base of the brain, showing the major divisions and cranial nerves. (Figure enhanced by B Crossman.)

understood by reference to certain common organizational principles. Whilst undoubtedly oversimplified and subject to exceptions, this schema is helpful in emphasizing the essential similarities that exist between the ascending sensory systems.

In essence, ascending sensory projections related to the general senses consist of a sequence of three neurones that extends from peripheral receptor to contralateral cerebral cortex (Fig. 24.8). These are often referred to as primary, secondary and tertiary neurones or first-, second- and third-order neurones. Primary afferents have peripherally located sensory endings and cell bodies that lie in dorsal root ganglia or the sensory ganglia associated with certain cranial nerves. Their axons enter the CNS through spinal or cranial nerves and terminate by synapsing on the cell bodies of ipsilateral second-order neurones, the precise location of which depends upon the modality.

Primary afferent fibres carrying pain, temperature and light touch/pressure information from the trunk and limbs terminate in the dorsal horn of the spinal grey matter, near their point of entry into the spinal cord. Homologous fibres from the head terminate in the spinal nucleus of the trigeminal nerve in the brainstem. The cell bodies of second-order neurones are located in either the dorsal horn or the spinal nucleus of the trigeminal nerve. Their axons decussate and ascend to the ventral posterior nucleus of the contralateral thalamus as the spinothalamic or the trigeminothalamic tract, respectively; they synapse on the cell bodies of third-order neurones in the thalamus. Axons of third-order neurones pass through the internal capsule to reach the cerebral cortex, terminating in the primary somatosensory cortex in the postcentral gyrus of the parietal lobe.

Primary afferent fibres carrying proprioceptive information and fine (discriminative) touch from the trunk and limbs ascend ipsilaterally in the spinal cord as the dorsal columns (fasciculus gracilis and fasciculus cuneatus) and end by synapsing on second-order neurones in the dorsal column nuclei (nucleus gracilis and nucleus cuneatus) of the medulla. Axons of second-order neurones decussate in the medulla and then ascend as the medial lemniscus to the ventral posterior nucleus of the contralateral thalamus, where they synapse on the cell bodies of third-order neurones. Axons of third-order neurones pass through the internal capsule and terminate in the primary somatosensory cortex. A similar homologous projection to the cortex exists for afferents derived from the head, except that primary afferent fibres carrying discriminative touch from the face and oral cavity terminate by synapsing on second-order neurones in the principal sensory nucleus of the trigeminal nerve.

Overview of descending motor pathways

Corticofugal fibres descend through the internal capsule and pass into the brainstem, where many of them terminate in various cranial nerve nuclei and other brainstem nuclei such as the red nucleus, reticular nuclei, and olivary nuclei. The term 'corticobulbar' has been used for many years to describe cortical projections to brainstem nuclei but it is

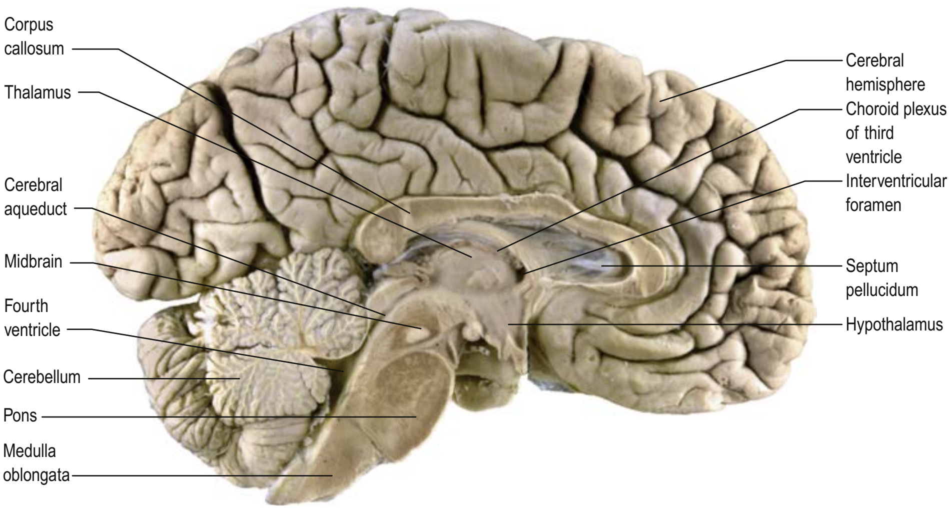
Corpus callosum
Thalamus
Cerebral aqueduct
Midbrain
Fourth ventricle
Cerebellum
Pons
Medulla oblongata
Cerebral hemisphere
Choroid plexus of third ventricle
Interventricular foramen
Septum pellucidum
Hypothalamus

Fig. 24.6 A sagittal section of the brain. (Figure enhanced by B Crossman.)

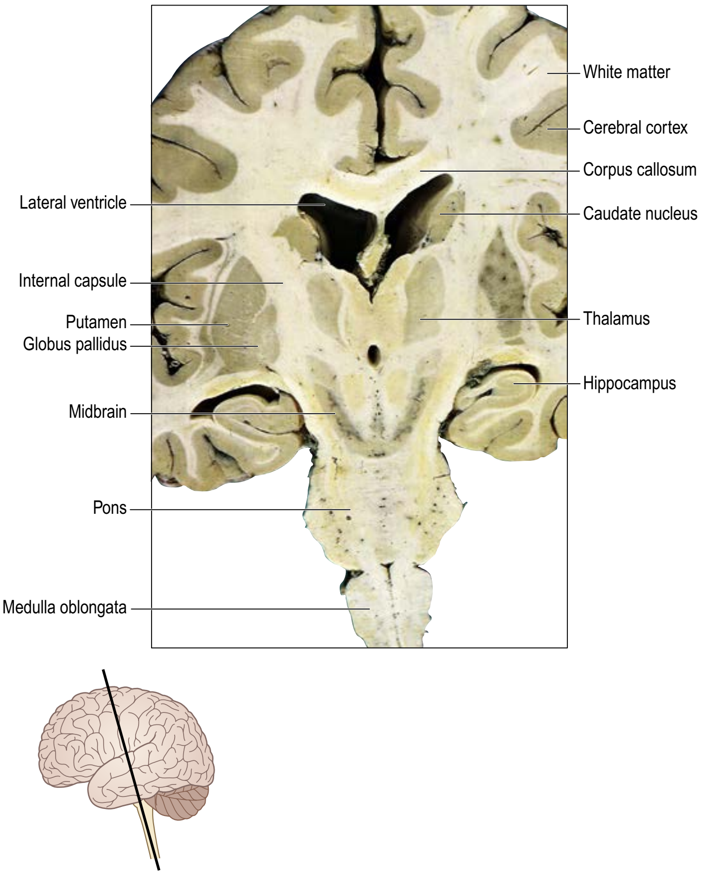
White matter
Cerebral cortex
Corpus callosum
Caudate nucleus
Lateral ventricle
Internal capsule
Putamen
Globus pallidus
Thalamus
Hippocampus
Midbrain
Pons
Medulla oblongata

Fig. 24.7 A section through the cerebral hemisphere and brainstem, showing the disposition of grey and white matter, the basal ganglia and the internal capsule. (Dissection by EL Rees; photograph by Kevin Fitzpatrick, London.)

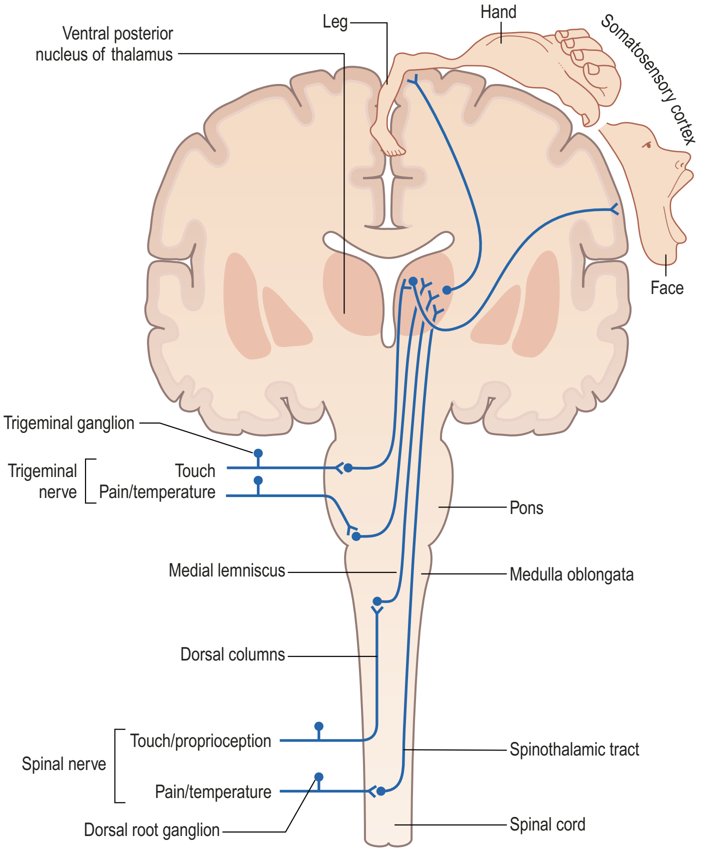
Leg
Hand
Somatosensory cortex
Ventral posterior nucleus of thalamus
Face
Trigeminal ganglion
Trigeminal nerve
Touch
Pain/temperature
Pons
Medial lemniscus
Medulla oblongata
Dorsal columns
Spinal nerve
Touch/proprioception
Pain/temperature
Spinothalamic tract
Dorsal root ganglion
Spinal cord

Fig. 24.8 The organization of general sensory pathways showing first-order, second-order and third-order neurones.

a misnomer. The suffix 'bulbar' is derived from 'bulb', an archaic name for the medulla oblongata. The term 'corticonuclear' is, therefore, more accurate to describe these connections although the term 'bulb' is still used (e.g. pseudobulbar palsy).

Corticospinal (pyramidal tract) fibres originate from widespread regions of the cerebral cortex, including the primary motor cortex of the frontal lobe where the contralateral half of the body is represented in a detailed somatotopic fashion. The fibres descend throughout the length of the brainstem and the majority then cross to the contralateral side in the decussation of the pyramids in the ventral medulla. Thereafter, the majority of fibres continue caudally as the lateral corticospinal tract of the spinal cord and terminate in association with interneurones and motor neurones of the spinal grey matter (Fig. 24.9). The principal function of the corticonuclear and corticospinal tracts is the control of fine, fractionated movements, particularly of those parts of the body where delicate muscular control is required. These tracts are particularly important in speech (corticonuclear fibres) and movements of the hands (corticospinal fibres).

The concept of 'upper' and 'lower' motor neurones is fundamental in clinical neurology because the motor signs and symptoms of damage to each category are different and are indicative of the anatomical site of the lesion. Lower motor neurones are the alpha motor neurones located in the brainstem and spinal cord that innervate the extrafusal muscle fibres of skeletal muscle. The term upper motor neurones refers collectively to all the descending pathways that impinge upon the activity of lower motor neurones but, in clinical parlance, the term is often equated with the corticonuclear and corticospinal tracts. The terms upper and lower motor neurone lesion are used clinically to distinguish, for example, between the effects of a stroke in the internal capsule (a typical upper motor neurone lesion) and those of motor neurone disease (a typical lower motor neurone lesion).

Lower motor neurone lesions cause paralysis or paresis of specific muscles because the affected muscles have lost their direct innervation. There is also loss or reduction of tendon reflex activity and reduced muscle tone. Spontaneous muscular contractions (fasciculation) occur and affected muscles atrophy over time. Upper motor neurone lesions cause paralysis or paresis of movements as a result of loss of higher control. There is increased tendon reflex activity and increased muscle

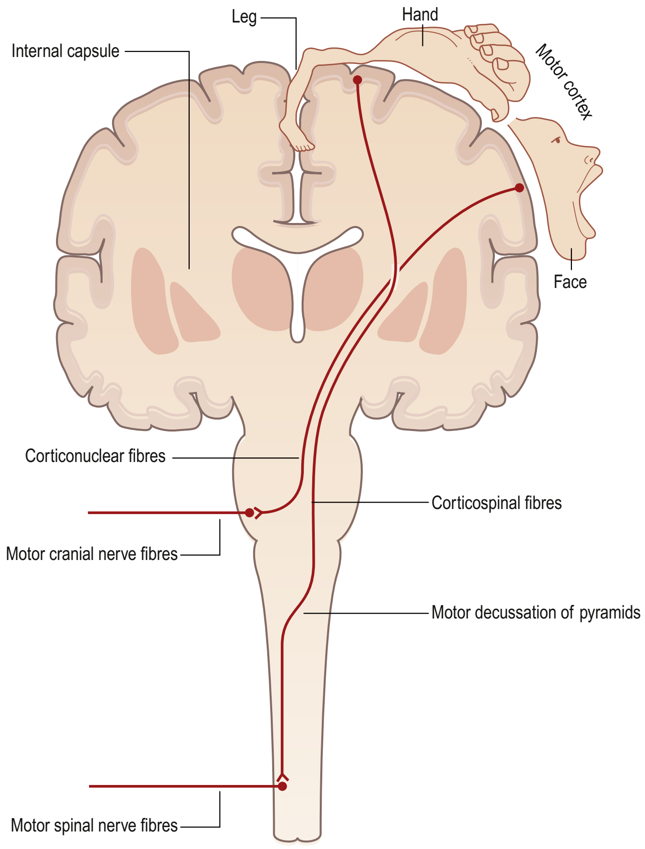
Leg
Hand
Internal capsule
Motor cortex
Face
Corticonuclear fibres
Corticospinal fibres
Motor cranial nerve fibres
Motor decussation of pyramids
Motor spinal nerve fibres

Fig. 24.9 The corticospinal and corticonuclear tracts.

tone, but no muscle atrophy. The combination of paralysis, increased tendon reflex activity and hypertonia is referred to as spasticity. A positive plantar (Babinski) reflex is present with corticospinal lesions.

The pathophysiology underlying the symptoms of upper motor neurone lesions is complex. This is because many descending pathways other than the corticonuclear and corticospinal tracts that also influence lower motor neurone activity may be compromised to varying extents, depending on the site of a lesion. These pathways include corticofugal projections to the brainstem that traverse the internal capsule (e.g. corticoreticular and corticopontine fibres), and numerous pathways that originate within the brainstem itself (e.g. reticulospinal and vestibulospinal tracts): their involvement is believed to be important in the pathophysiological mechanisms that underlie the generation of spasticity. Pure corticospinal tract lesions are exceedingly rare in humans because corticospinal tract fibres lie in close relationship to other pathways throughout most of their course: when they occur, they are believed to cause specific deficits in delicate, fractionated movements and to induce a positive plantar reflex.

Two other major systems that contribute to the control of movement are the basal ganglia (basal nuclei) and the cerebellum. The basal ganglia are a group of large subcortical nuclei, the major components being the caudate nucleus, putamen and globus pallidus (see Fig. 24.7; Ch. 31). These structures have important connections with the cerebral cortex, certain nuclei of the thalamus and subthalamus, and with the brainstem. They appear to be involved in the selection of appropriate behavioural patterns/movements and the suppression of inappropriate ones. Disorders of the basal ganglia cause either too little movement (akinesia) or abnormal involuntary movements (dyskinesias), as well as tremor and abnormalities of muscle tone (Crossman and Neary 2019). The basal ganglia are sometimes described as being part of the so-called 'extrapyramidal system'. This somewhat archaic term was introduced to distinguish between the effects of basal ganglia disease and those of damage to the 'pyramidal' (corticospinal) system. However, the progressive elucidation of the anatomy of the basal ganglia and of the pathophysiology of motor disorders has revealed the close functional interrelationship between the two 'systems', and has rendered the terms that distinguish them largely obsolete (Brodal 1981). The cerebellum (Ch. 29) has rich connections with the brainstem, particularly the reticular and vestibular nuclei, and with the thalamus. It is concerned with the coordination of movement: cerebellar disorders cause ataxia, intention tremor and hypotonia.

PERIPHERAL NERVOUS SYSTEM

The peripheral nervous system (PNS) is composed mainly of spinal nerves, cranial nerves, their ganglia and their ramifications that carry afferent and efferent neurones between the CNS and the rest of the body. It also includes the peripheral part of the autonomic nervous system (ANS), notably the sympathetic trunks and ganglia, and the enteric nervous system (ENS), composed of plexuses of nerve fibres and cell bodies in the wall of the gastrointestinal tract.

Spinal nerves

Spinal nerves are the means by which the CNS receives information from, and controls the activities of, the trunk and limbs. Spinal nerves are considered in detail elsewhere on a regional basis (Sections 4–9).

There are 31 pairs of spinal nerves (8 cervical, 12 thoracic, 5 lumbar, 5 sacral, 1 coccygeal) and these contain a mixture of sensory and motor fibres. They originate from the spinal cord in a continuous series of dorsal and ventral nerve rootlets. Adjacent groups of rootlets fuse to form dorsal and ventral roots, which then merge to form the spinal nerves proper. The dorsal roots of spinal nerves contain afferent nerve fibres from neuronal cell bodies located in dorsal root ganglia. The ventral roots of spinal nerves contain efferent fibres from motor neurones (somatic and autonomic) located in the spinal grey matter.

Spinal nerves leave the vertebral canal via their corresponding intervertebral foramina and each divides into a large ventral (anterior) ramus and a smaller dorsal (posterior) ramus. In general terms, ventral rami innervate the limbs and the muscles and skin of the anterolateral trunk: the nerve fibres serving the upper and lower limbs are redistributed within the brachial and the lumbar and lumbosacral plexuses, respectively. Dorsal rami innervate the post-vertebral (intrinsic) muscles and skin of the back.

Cranial nerves

Cranial nerves are the means by which the brain receives information from, and controls the activities of, the head and neck and the thoracic and (most of) the abdominal viscera. The component fibres, their route of exit from the cranial cavity, their subsequent peripheral course and the distribution and functions of the cranial nerves are considered in detail elsewhere on a regional basis.

There are 12 pairs of cranial nerves that are individually named and numbered (Roman numerals) in a rostrocaudal sequence (**Table 24.1**). Unlike spinal nerves, only some cranial nerves are mixed in function, and carry both sensory and motor fibres; some others are purely sensory or motor. The first cranial nerve (I; olfactory) has an ancient lineage and is derived from the forerunner of the cerebral hemisphere. It retains this unique position through the connections of the olfactory bulb, and is the only sensory cranial nerve that projects directly to the cerebral cortex rather than indirectly via the thalamus. The areas of cerebral cortex receiving olfactory input have a primitive cellular organization and are an integral part of the limbic system, which is concerned with the emotional aspects of behaviour. The second cranial nerve (II; optic) consists of the axons of second-order visual neurones and these terminate in the thalamus. Most of the component fibres of the other 10 pairs of cranial nerves originate from, or terminate in, named cranial nerve nuclei in the brainstem.

Dermatomes and myotomes

The sensory fibres in individual spinal and cranial nerves have characteristic, but often overlapping, peripheral (cutaneous) distributions. As far as the innervation of the body surface is concerned, the area of skin that is supplied by a particular spinal or cranial nerve is referred to as a dermatome (Greenberg 2003), and the areas of skin supplied by named peripheral nerves are often referred to as the peripheral nerve field (or cutaneous nerve distribution) of that nerve. There is marked overlap between dermatomes of adjacent spinal nerves, particularly for the segments least affected by development of the limbs, i.e. the second thoracic to the first lumbar segments (Ladak et al 2013). In some regions, e.g. the upper anterior thoracic wall, the cutaneous nerves that supply adjoining areas are not derived from consecutive spinal nerves and in these instances

TABLE 24.1 Summary of cranial nerves

No.	Name	Components	Cells of origin	Main central connections	Exit from skull	Distribution and function
I	Olfactory	Special somatic afferent	Olfactory receptor cells in nasal mucosa	To olfactory bulb, anterior perforated substance, piriform cortex	Foramina of cribriform plate	Olfaction
II	Optic	Special somatic afferent	Ganglion cells of retina	To lateral geniculate nucleus of thalamus, pretectal area of midbrain	Optic canal	Vision
III	Oculomotor	Somatic efferent	Oculomotor nucleus	From visual cortical areas, medial longitudinal fasciculus	Superior orbital fissure	Motor to medial rectus, inferior rectus, superior rectus, inferior oblique, levator palpebrae superioris
III	Oculomotor	General visceral efferent	Edinger–Westphal nucleus	From pretectal area of midbrain	Superior orbital fissure	Parasympathetic to sphincter pupillae and ciliary muscles, via ciliary ganglion, mediating pupillary constriction and accommodation
IV	Trochlear	Somatic efferent	Trochlear nucleus	From visual cortical areas, medial longitudinal fasciculus	Superior orbital fissure	Motor to superior oblique
Trigeminal division:						
V	Ophthalmic (V$_1$)	General somatic afferent	Trigeminal (semilunar) ganglion	To trigeminal sensory nucleus	Superior orbital fissure	Sensation from forehead, scalp, eyelids, nose and eye, including conjunctiva
	Maxillary (V$_2$)	General somatic afferent	Trigeminal (semilunar) ganglion	To trigeminal sensory nucleus	Foramen rotundum	Sensation from mid-face, lower eyelid, nasal cavity and paranasal sinuses, upper lip, maxillary teeth and palate
	Mandibular (V$_3$)	General somatic afferent	Trigeminal (semilunar) ganglion	To trigeminal sensory nucleus	Foramen ovale	Sensation from lower face and scalp, tongue and floor of mouth, mandibular teeth and part of external ear
		General somatic afferent	Mesencephalic part of trigeminal sensory nucleus	To trigeminal sensory nucleus, cerebellum	Foramen ovale	Proprioception from muscles of mastication, temporomandibular joint
	Mandibular (V$_3$)	Branchial (special visceral) efferent	Trigeminal motor nucleus	From precentral gyrus	Foramen ovale	Motor to muscles of mastication (temporalis, masseter, medial and lateral pterygoids), tensor tympani
VI	Abducens	Somatic efferent	Abducens nucleus	From visual cortical areas, medial longitudinal fasciculus	Superior orbital fissure	Motor to lateral rectus
VII	Facial	General somatic afferent	Geniculate ganglion	To trigeminal sensory nucleus, cerebellum	Internal acoustic meatus	Sensation from part of tympanic membrane, external acoustic meatus and skin behind pinna. Proprioception from facial muscles
VII	Facial	Special visceral afferent	Geniculate ganglion	To nucleus solitarius	Internal acoustic meatus	Taste from anterior two-thirds of tongue
VII	Facial	General visceral efferent	Superior salivatory nucleus	From olfactory areas, nucleus solitarius	Internal acoustic meatus	Parasympathetic to lacrimal gland and mucous membrane of nasal and oral cavities (via pterygopalatine ganglion) and submandibular and sublingual salivary glands (via submandibular ganglion) causing secretion and vasodilation
VII	Facial	Branchial (special visceral) efferent	Facial nucleus	From precentral gyrus	Internal acoustic meatus	Motor to 'muscles of facial expression', stapedius, posterior belly of digastric and stylohyoid
VIII	Vestibulocochlear					
	Vestibular division	Special somatic afferent	Vestibular ganglion	To vestibular nuclei, cerebellum	Internal acoustic meatus	Sensations of equilibrium and motion
	Cochlear division	Special somatic afferent	Spiral ganglion	To cochlear nuclei	Internal acoustic meatus	Hearing
IX	Glossopharyngeal	General somatic afferent	Glossopharyngeal ganglia	To trigeminal sensory nucleus	Jugular foramen	General sensation from posterior one-third of tongue, oropharynx and middle ear
IX	Glossopharyngeal	General visceral afferent	Glossopharyngeal ganglia	To nucleus solitarius	Jugular foramen	Sensory from carotid body (chemoreceptors) and carotid sinus (baroreceptors)
IX	Glossopharyngeal	Special visceral afferent	Glossopharyngeal ganglia	To nucleus solitarius	Jugular foramen	Taste from posterior one-third of tongue
IX	Glossopharyngeal	General visceral efferent	Inferior salivatory nucleus	From olfactory areas, nucleus solitarius	Jugular foramen	Parasympathetic to parotid salivary gland (via otic ganglion), causing secretion and vasodilation
IX	Glossopharyngeal	Branchial (special visceral) efferent	Nucleus ambiguus	From precentral gyrus	Jugular foramen	Motor to stylopharyngeus
X	Vagus	General somatic afferent	Superior (jugular) ganglion	To trigeminal sensory nucleus	Jugular foramen	General sensation from pharynx, larynx, trachea, oesophagus, part of auricle and external auditory meatus
X	Vagus	General visceral afferent	Inferior (nodose) ganglion	To nucleus solitarius	Jugular foramen	Sensory from thoracic and abdominal viscera Sensory from aortic arch (baroreceptors) and aortic bodies (chemoreceptors)
X	Vagus	General visceral efferent	Dorsal motor nucleus of vagus	From hypothalamus, nucleus solitarius	Jugular foramen	Parasympathetic to glands and smooth muscle in the pharynx, larynx, thoracic and abdominal viscera
X	Vagus	Branchial (special visceral) efferent	Nucleus ambiguus	From precentral gyrus, sensory nuclei of brainstem	Jugular foramen	Motor to pharyngeal, external laryngeal and oesophageal striated muscles
XI	*Accessory					
	Cranial root	*Branchial (special visceral) efferent*	*Nucleus ambiguus*	*From precentral gyrus, sensory nuclei of brainstem*	*Jugular foramen*	*Motor to muscles of soft palate and intrinsic muscles of larynx (distributed via vagus)*
	Spinal root	Branchial (special visceral) efferent	Spinal cord segments C1–C5	From precentral gyrus	Jugular foramen	Motor to sternocleidomastoid and trapezius
XII	Hypoglossal	Somatic efferent	Hypoglossal nucleus	From precentral gyrus	Hypoglossal canal	Motor to all intrinsic and extrinsic muscles of the tongue, except palatoglossus

Key

🟥	General somatic afferent
⬛	Special somatic afferent
🟫	General visceral afferent
🟨	Special visceral afferent
🟩	Somatic efferent
🟪	General visceral efferent
🟦	Branchial (special visceral) efferent

*The existence of a 'cranial root' of the accessory nerve, with its cell bodies in the nucleus ambiguus and a distribution as given in the table is controversial. There is a view that the 'spinal root' of the accessory nerve should be regarded as the accessory nerve proper (sometimes called the 'spinal accessory nerve') and that the vagus nerve supplies all but one of the muscles of the soft palate and all of the intrinsic muscles of the larynx.

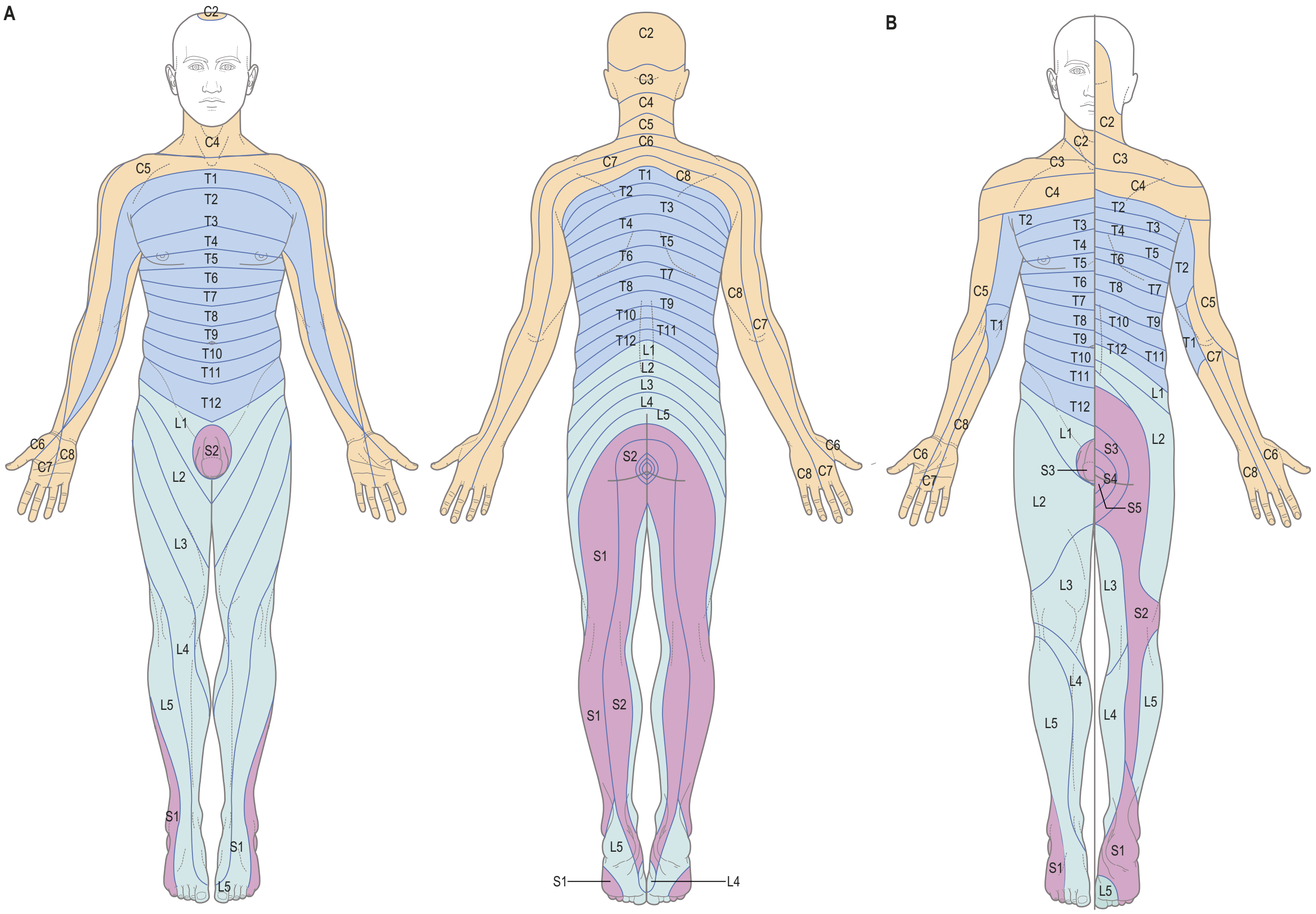

Fig. 24.10 Typical dermatome maps, illustrating some of the variations reported by different authors. **A**, Dermatome map based on Keegan JJ, Garrett FD 1948 The segmental distribution of the cutaneous nerves in the limbs of man. Anat Rec 102:409–39. Mainly used in literature in the USA. **B**, Dermatome map based on Moffat DB 1993 Lecture Notes on Anatomy, 2nd ed. Oxford: Blackwell Scientific. Mainly used in literature in the UK.

the overlap between dermatomes is minimal; these boundaries give more reliable and clinically useful borders (Apok et al 2011). Maps of dermatome distribution are useful in clinical neurology as a guide to identify the location of pathology in patients with peripheral sensory deficits, but it is important to remember that they are approximations. Dermatome maps are somewhat inconsistently reported by different authors, reflecting the fact that the maps are composites that have been compiled to a large extent by clinical observations on patients with cranial or spinal nerve pathology, and also that considerable normal individual variation exists (**Fig. 24.10**) (Lee et al 2008). Common to all published maps are areas of sensory overlap along borders of contiguous spinal nerves and axial lines where non-contiguous spinal nerves meet, and across which very little or no sensory overlap occurs. Detailed dermatome maps are described on a regional basis. The motor axons of individual spinal and cranial nerves tend to innervate anatomically and functionally related groups of skeletal muscles, referred to as myotomes.

AUTONOMIC NERVOUS SYSTEM

The autonomic nervous system represents the visceral component of the nervous system. It consists of neurones located within both the CNS and the PNS that are concerned with the control of the internal environment, through the innervation of secretory glands and cardiac and smooth muscle. Its functions are closely integrated with those of the somatic nervous system.

Visceral efferent pathways differ from their somatic equivalents because they are interrupted by peripheral synapses, which means that there is a sequence of at least two neurones between the CNS and the target structure: these are referred to as preganglionic and postganglionic neurones, respectively (Fig. 24.11). The somata of preganglionic neurones are located in the visceral efferent nuclei of the brainstem and in the lateral horn of the spinal cord. Their axons, which are usually finely myelinated, exit from the CNS in certain cranial and spinal nerves, and then pass to peripheral ganglia, where they synapse on postganglionic neurones. The axons of postganglionic neurones are usually unmyelinated. Postganglionic neurones are more numerous than preganglionic ones; one preganglionic neurone may synapse with 15–20 postganglionic neurones, which permits the wide distribution of many autonomic effects.

The autonomic nervous system is traditionally divided into two major parts: sympathetic and parasympathetic. Structures innervated by the autonomic nervous system generally receive both sympathetic and parasympathetic fibres. Neurones intrinsic to the gastrointestinal tract are regarded as a third, or enteric, division.

Two long-held dogmas are that the sympathetic and parasympathetic nervous systems are functionally antagonistic. A better concept is that the two systems constitute an integrated system for the coordinated neural regulation of visceral and homeostatic functions. In general, sympathetic activity results in the constriction of cutaneous arteries (increasing blood supply to the heart, muscles and brain), cardiac acceleration, an increase in blood pressure, contraction of sphincters and depression of peristalsis, all of which mobilize body energy stores for dealing with increased activity. Parasympathetic activity results in cardiac slowing and an increase in intestinal glandular and peristaltic activities, which may be considered to conserve body energy stores.

The classical concept of autonomic neurotransmission holds that preganglionic sympathetic and pre-and postganglionic parasympathetic neurones are cholinergic and postganglionic sympathetic neurones are mainly noradrenergic. The discovery of neurones that use neither acetylcholine nor noradrenaline as their primary transmitter, and the recognition of a multiplicity of substances in autonomic nerves that fulfil the criteria for a neurotransmitter or neuromodulator, greatly complicated neuropharmacological concepts of the autonomic nervous system (Burnstock 2013).

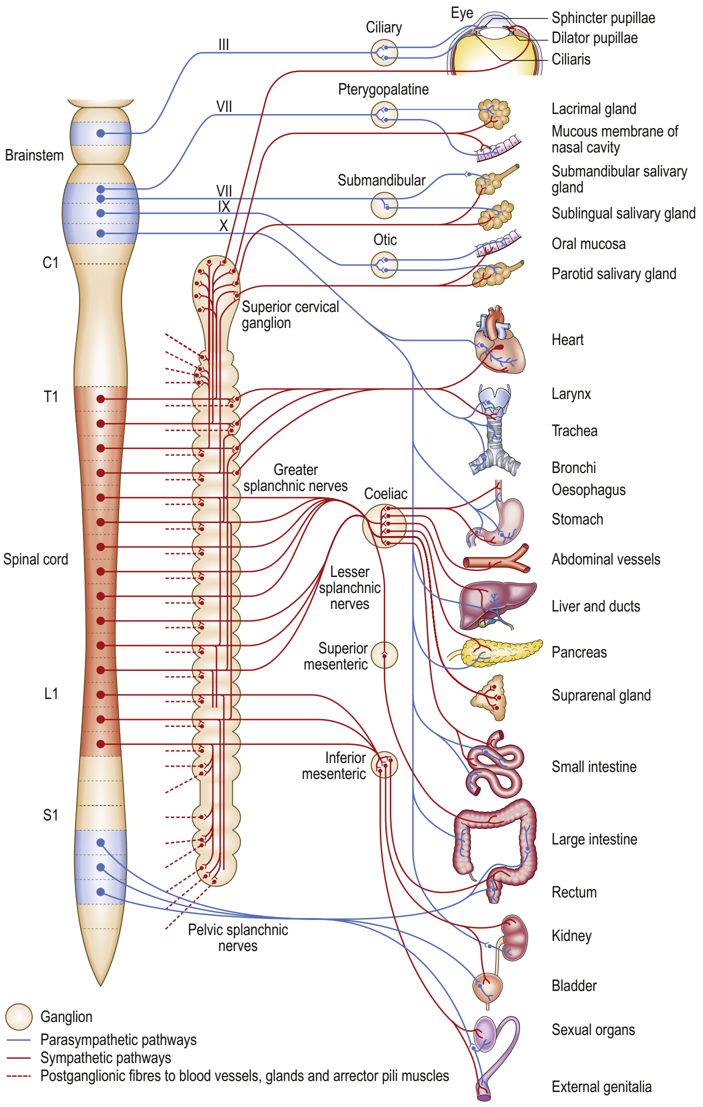
Eye
Ciliary
Sphincter pupillae
Dilator pupillae
Ciliaris
III
Pterygopalatine
VII
Lacrimal gland
Mucous membrane of nasal cavity
Brainstem
Submandibular
Submandibular salivary gland
VII
IX
X
Sublingual salivary gland
Otic
Oral mucosa
C1
Parotid salivary gland
Superior cervical ganglion
Heart
T1
Larynx
Trachea
Greater splanchnic nerves
Bronchi
Coeliac
Oesophagus
Stomach
Spinal cord
Abdominal vessels
Lesser splanchnic nerves
Liver and ducts
Superior mesenteric
Pancreas
L1
Suprarenal gland
Inferior mesenteric
Small intestine
S1
Large intestine
Rectum
Pelvic splanchnic nerves
Kidney
Bladder
Ganglion
Sexual organs
Parasympathetic pathways
Sympathetic pathways
Postganglionic fibres to blood vessels, glands and arrector pili muscles
External genitalia

Fig. 24.11 Efferent pathways of the autonomic nervous system.

Sympathetic nervous system

The sympathetic system has a much wider distribution than the parasympathetic system. It innervates all sweat glands and arrector pili muscles, the muscular walls of many blood vessels, the heart, lungs and respiratory trees, the abdominopelvic viscera, the muscles of the iris and the non-striated muscle of the eyelids, oesophagus and urogenital tract.

The cell bodies of preganglionic sympathetic neurones are located in the lateral horn of the spinal grey matter of all thoracic segments and the upper two or three lumbar segments (Fig. 24.12). The cell bodies of postganglionic sympathetic neurones are located in the paravertebral sympathetic trunk or a more peripheral plexus (e.g. coeliac plexus). The sympathetic trunk is a ganglionated cord that extends on either side of the vertebral column from the cranial base to the sacrococcygeal junction. The ganglia are joined to spinal nerves by short connecting nerves, the white and grey rami communicantes (Fig. 24.13).

In the neck, the sympathetic trunks lie posterior to the carotid sheath and anterior to the transverse processes of the cervical vertebrae. In the thorax, the trunks are anterior to the heads of the ribs, in the abdomen they lie anterolateral to the bodies of the lumbar vertebrae, and in the pelvis they are anterior to the sacrum and medial to the anterior sacral foramina. The two trunks meet in a single, median, terminal ganglion, the ganglion impar, at the level of the sacrococcygeal junction. Cervical sympathetic ganglia are usually reduced to three, superior, middle and inferior, by fusion. The internal carotid nerve, a continuation of the sympathetic trunk, issues from the cranial pole of the superior cervical ganglion and accompanies the internal carotid artery through its canal into the cranial cavity. There are between 10 and 12 (usually 11) thoracic ganglia, 4 lumbar ganglia, and 4 or 5 ganglia in the sacral region.

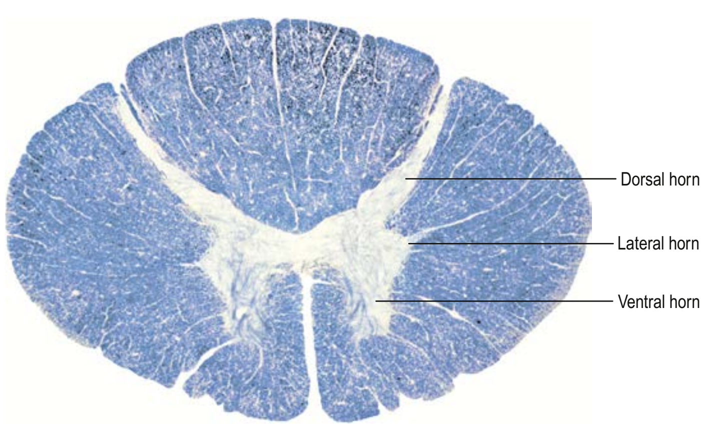
Dorsal horn
Lateral horn
Ventral horn

Fig. 24.12 A transverse section through the thoracic spinal cord. Preganglionic sympathetic neurones are located in the lateral horn. (Figure enhanced by B Crossman.)

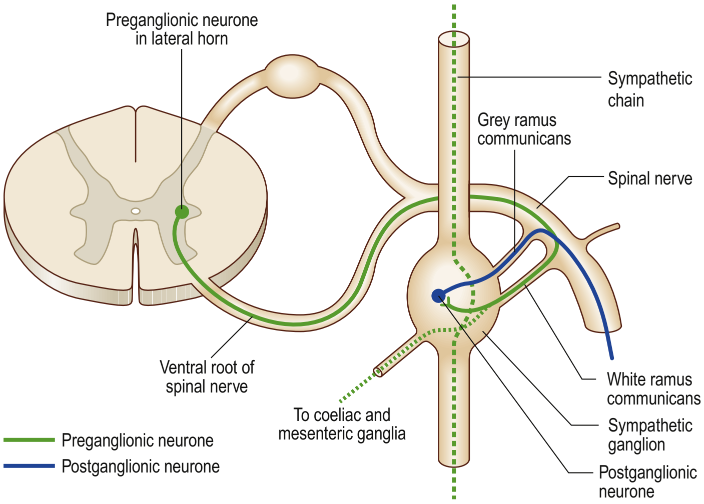
Preganglionic neurone in lateral horn
Sympathetic chain
Grey ramus communicans
Spinal nerve
Ventral root of spinal nerve
To coeliac and mesenteric ganglia
White ramus communicans
Sympathetic ganglion
Postganglionic neurone
Preganglionic neurone
Postganglionic neurone

Fig. 24.13 Outflow from preganglionic sympathetic neurones in the lateral horn of the spinal cord. Preganglionic axons may synapse on a postganglionic neurone in a sympathetic ganglion at the same segmental level, or may pass into the sympathetic chain to synapse on a postganglionic neurone in a more rostral or caudal sympathetic ganglion, or may pass to a ganglion in an autonomic plexus in the abdominal cavity, e.g. the coeliac ganglion.

Preganglionic axons are myelinated, with diameters of 1.5–4 µm, and join the sympathetic trunk through the white rami communicantes. On reaching the trunk, the axons behave in one of several ways (see Fig. 24.13). They can synapse with neurones in the nearest ganglion, or traverse the nearest ganglion and ascend or descend in the sympathetic trunk to end in another ganglion. A preganglionic fibre can terminate in a single ganglion or, through collateral branches, synapse with neurones in several ganglia. Preganglionic fibres may traverse the nearest ganglion, ascend or descend and, without synapsing, emerge in one of the medially directed branches of the sympathetic trunk to synapse in the ganglia of autonomic plexuses (mainly situated in the midline, e.g. around the coeliac and mesenteric arteries). More than one preganglionic fibre may synapse with a single postganglionic neurone. Uniquely, the suprarenal gland is innervated directly by preganglionic sympathetic neurones that traverse the sympathetic trunk and coeliac ganglion without synapsing.

The cell bodies of postganglionic sympathetic neurones are located in the ganglia of the sympathetic trunk or in ganglia in more peripheral plexuses. Postganglionic axons are unmyelinated and are distributed to target organs in various ways. Those from a ganglion in the sympathetic trunk may return to the spinal nerve of preganglionic origin through a grey ramus communicans (which usually joins the nerve just proximal to the white ramus communicans), and they are then distributed through ventral and dorsal spinal rami to blood vessels, sweat glands, hairs, etc., in their zone of supply. Segmental areas vary in extent and overlap considerably and the extent of innervation of different effector systems, e.g. vasomotor, sudomotor, etc. by a particular nerve may not be the same. Alternatively, postganglionic fibres may pass direct to particular viscera, or innervate adjacent blood vessels, or pass along them externally to their peripheral distribution. They may ascend or descend before leaving the sympathetic trunk as described above. Many fibres are distributed along arteries and ducts as plexuses to distant effectors.

Postganglionic sympathetic fibres that return to the spinal nerves are vasoconstrictor to blood vessels, secretomotor to sweat glands and motor to the arrector pili muscles within their dermatomes. Those that accompany the motor nerves to voluntary muscles are probably only dilatory. Most, if not all, peripheral nerves contain postganglionic sympathetic fibres. Those reaching the viscera are concerned with general vasoconstriction, bronchial and bronchiolar dilation, modification of glandular secretion, pupillary dilation, inhibition of gastrointestinal muscle contraction, etc. A single preganglionic fibre probably synapses with the postganglionic neurones in only one effector system, which means that effects such as sudomotor and vasomotor actions can be separate.

Parasympathetic nervous system

Preganglionic parasympathetic neuronal cell bodies are located in certain cranial nerve nuclei of the brainstem and in the lateral horn (intermediolateral column) of the second to fourth sacral segments of the spinal cord. Efferent fibres, which are myelinated, emerge from the CNS only in the oculomotor, facial, glossopharyngeal and vagus nerves, and in the second to fourth sacral spinal nerves. Preganglionic parasympathetic neurones are cholinergic.

The cell bodies of postganglionic parasympathetic neurones are mostly sited distant from the CNS, either in discrete ganglia located near the structures they innervate, or dispersed in the walls of viscera. In the cranial part of the parasympathetic system, four small peripheral ganglia (ciliary, pterygopalatine, submandibular and otic) are all described on a regional basis. These are efferent parasympathetic ganglia, unlike the trigeminal, facial, glossopharyngeal and vagal sensory ganglia, all of which are concerned exclusively with afferent impulses and contain the cell bodies of sensory neurones. The cranial parasympathetic ganglia are also traversed by afferent fibres, postganglionic sympathetic fibres and, in the case of the otic ganglion, by branchial efferent fibres, but none of these fibres synapse in the ganglia. Postganglionic parasympathetic fibres are usually unmyelinated and shorter than their counterparts in the sympathetic system because the ganglia in which the parasympathetic fibres synapse are either in or near the viscera they supply. Postganglionic parasympathetic neurones are cholinergic.

Enteric nervous system and intrinsic neurones

Many peripheral autonomic ganglia contain neurones derived from the neural crest during embryonic development that are anatomically distinct from classical sympathetic and parasympathetic neurones. Connections between these intrinsic neurones allow them to sustain and modulate visceral activities by local reflex mechanisms. The enteric nervous system consists of many millions of neurones and enteric glial cells grouped into ganglionated plexuses lying in the wall of the gastrointestinal tract; ganglia containing neuronal cell bodies and glia are connected by bundles of axons to form myenteric and submucous plexuses that extend from the oesophagus to the anal sphincter (see Fig. 59.9). This intrinsic circuitry mediates numerous reflex functions including the contractions of the muscular coats of the gastrointestinal tract, secretion of gastric acid, intestinal transport of water and electrolytes, and the regulation of mucosal blood flow (Poole and Furness 2012). Although complex interactions occur between the enteric and sympathetic and parasympathetic nervous systems, the enteric nervous system is capable of sustaining local reflex activity independent of the CNS.

Since intrinsic neurones survive after section of the extrinsic sympathetic and parasympathetic nerves, organs that are transplanted are not truly denervated. Separation from their autonomic input often has no obvious impact on the non-striated muscle or glands innervated by autonomic fibres; contraction may be unaffected and no structural changes ensue. This has been variously attributed to the continued activity of local plexuses or to the intrinsic activity of visceral muscle. In some important instances, however, denervation does result in cessation of activity, e.g. in sweat glands, pilomotor muscle, orbital non-striated muscle and the suprarenal medulla.

Visceral afferent pathways

Visceral afferent pathways in many ways resemble somatic afferent pathways. The peripheral processes of visceral afferents run through autonomic ganglia or plexuses, and possibly through somatic nerves. Their central processes accompany somatic afferent fibres through cranial nerves or dorsal spinal roots into the CNS, where they establish connections that mediate autonomic reflexes and visceral sensation.

General visceral afferent fibres from the viscera and blood vessels accompany their efferent counterparts, and are the peripheral processes of neuronal cell bodies located in the sensory ganglia of some cranial nerves and in dorsal root ganglia. They travel in the vagus, glossopharyngeal and possibly other cranial nerves; the second to fourth sacral spinal nerves, distributed with the pelvic splanchnic nerves; and thoracic and upper lumbar spinal nerves, distributed through rami communicantes and alongside the efferent sympathetic innervation of viscera and blood vessels.

The cell bodies of vagal general visceral afferent fibres are in the superior and inferior vagal ganglia. Their peripheral processes are distributed to terminals in the pharyngeal and oesophageal walls where, acting synergistically with glossopharyngeal visceral afferents in the pharynx, they are concerned with swallowing reflexes. Vagal afferents are also believed to innervate the thyroid and parathyroid glands. In the heart, vagal afferents innervate the walls of the great vessels, the aortic bodies and pressor receptors, where they are stimulated by raised intravascular pressure. In the lungs they are distributed via the pulmonary plexuses. They supply bronchial mucosa, where they are probably involved in cough reflexes; bronchial muscle, where they encircle myocytes and end in tendrils that are sometimes regarded as muscle spindles and which are believed to be stimulated by change in the length of myocytes; interalveolar connective tissue, where their knob-like endings, together with terminals on myocytes, may evoke Hering–Breuer reflexes; the adventitia of pulmonary arteries, where they may be pressor receptors; and the intima of pulmonary veins, where they may be chemoreceptors. Vagal visceral afferent fibres also end in the gastric and intestinal walls, digestive glands and the kidneys. Fibres ending in the gastrointestinal tract and its ducts respond to stretch or contraction. Gastric impulses may evoke sensations of hunger and nausea.

The cell bodies of glossopharyngeal general visceral afferents are in the glossopharyngeal ganglia. Their peripheral processes innervate the posterior lingual region, the palatine tonsils and the oropharynx, but they do not innervate taste buds. They also innervate receptors sensitive to tension and changes in the chemical composition of the blood in the carotid sinus and the carotid body: impulses from these receptors are essential to the integrity of circulatory and respiratory reflexes.

Visceral afferents that enter the spinal cord through spinal nerve roots terminate in the spinal grey matter. Almost all the central processes of vagal and glossopharyngeal afferent fibres end in the nucleus tractus solitarius of the medulla. About 5% of the vagal afferents project directly to, and terminate in, the upper cervical spinal cord (C1–C2), where they are believed to contribute to referred sensations, as well as to propriospinal mechanisms of nociceptive modulation. Visceral afferents establish connections within the CNS that mediate autonomic reflexes. They probably also mediate visceral sensations such as hunger, nausea, sexual excitement and vesical distension, etc. Visceral pain fibres may follow these routes. Although viscera are insensitive to cutting, crushing or burning, excessive tension in smooth muscle and some pathological conditions produce visceral pain. In visceral disease, vague pain may be felt near the viscus itself (visceral pain) or in a cutaneous area or other tissue from which somatic afferents enter spinal segments that also receive afferents from the viscus, a phenomenon known as referred pain. If inflammation spreads from a diseased viscus to the adjacent parietal serosa (e.g. the peritoneum), somatic afferents will be stimulated, causing local somatic pain, which is commonly spasmodic. Referred pain is often associated with local cutaneous tenderness. For further reading on visceral pain, see Bielefeldt and Gebhart (2013).

Afferent fibres in pelvic splanchnic nerves innervate pelvic viscera and the distal part of the large intestine. Vesical receptors are widespread; those in muscle strata are associated with thickly myelinated fibres and are believed to be stretch receptors, possibly activated by contraction. Pain fibres from the bladder and proximal urethra travel in both the pelvic splanchnic nerves and the inferior hypogastric plexus, hypogastric nerves, superior hypogastric plexus and lumbar splanchnic nerves to reach their cell bodies in ganglia on the lower thoracic and upper lumbar dorsal spinal roots. Lesions of the cauda equina abolish pain from vesical overdistension; hypogastric section is ineffective. Pain fibres from the uterus traverse the hypogastric plexus and lumbar splanchnic nerves to reach their cell bodies in the lowest thoracic and upper lumbar spinal ganglia; hypogastric division may relieve dysmenorrhoea. Afferents from the uterine cervix traverse the pelvic splanchnic nerves to reach their cell bodies in the upper sacral spinal ganglia; stretching the cervix uteri causes pain but cauterization and biopsy excisions do not.

In general, afferent fibres that accompany pre- and postganglionic sympathetic fibres have a segmental arrangement and end in spinal cord segments from which preganglionic fibres innervate the region or viscus concerned. General visceral afferents entering thoracic and upper lumbar spinal segments are largely concerned with pain. Nociceptive impulses from the pharynx, oesophagus, stomach, intestines, kidneys, ureter, gallbladder and bile ducts seem to be carried in sympathetic pathways. Cardiac nociceptive impulses enter the spinal cord in the first to fifth thoracic spinal nerves, mainly via the middle and inferior cardiac nerves; some fibres pass directly to the spinal nerves. Peripherally, the fibres pass through the cardiac plexuses and along the coronary arteries. Myocardial anoxia may evoke symptoms of angina pectoris in which pain is typically presternal, and is also referred to much of the left chest, and radiates to the left shoulder, the medial aspect of the left arm, along the left side of the neck to the jaw and occiput, and down to the epigastrium. Cardiac afferents carried in vagal cardiac branches are concerned with the reflex depression of cardiac activity. Ureteric pain fibres, also running with sympathetic fibres, are presumably involved in the agonizing renal colic that follows obstruction by calculi. Afferent fibres from the testis and ovary run through the corresponding plexuses to neuronal call bodies in the tenth and eleventh thoracic dorsal root ganglia.

Some of the primary afferent neurones that innervate the gut, lungs, heart and blood vessels, also appear to have an efferent function in that they release transmitters from their peripheral endings during the axon reflex. The primary substances released in this way are substance P, calcitonin gene-related peptide (CGRP) and ATP. These act on target cells to produce vasodilation, increased venular permeability, changes in smooth muscle contractility, degranulation of mast cells and a variety of effects on leukocytes and fibroblasts, a process collectively known as 'peripheral neurogenic inflammation'. The local release of such substances may play a trophic role in the maintenance of tissue integrity and repair in response to injury (for further reading, see Xanthos and Sandkühler (2014)).

Paraganglia

Paraganglia are extra-suprarenal aggregations of neuroepithelial cells. They are all derived from the neural crest and all synthesize and store catecholamines (**Fig. 24.14**). Paraganglia can be divided into two broad categories, non-chromaffin and chromaffin. Non-chromaffin paraganglia are related to the parasympathetic system, particularly in the head and neck, where they tend to be associated with the glossopharyngeal or vagus nerves (carotid body, promontory of the middle ear, tunica adventitia of the jugular bulb, facial canal, ganglion nodosum, larynx). Chromaffin paraganglia are connected with the orthosympathetic system (in the sympathetic ganglia of various viscera and a variety of thoracolumbar para-aortic retroperitoneal sites). Small paraganglia have also been reported incidentally in the urinary bladder, prostate, gallbladder, splenic capsule and mesosigmoid. Their functions differ with location: some cells act as interneurones, others as sources of neuroendocrine secretion. Paraganglionic catecholamine release occurs mainly in response to chemical rather than to neural stimuli. Extra-suprarenal chromaffin tissue is prominent in the fetus, and acts as the main source of catecholamines while the suprarenal medulla is immature. Although many paraganglia degenerate soon after birth, others persist into adulthood, often as microscopic paraganglia.

Paraganglia are well vascularized and their secretory cells are usually close to one or more fenestrated capillaries. Most have a sympathetic innervation and act as endocrine organs, e.g. suprarenal medullary chromaffin cells. Those associated with the parasympathetic system probably have activities on local nerve endings, e.g. the carotid body. Paraganglia produce regulatory peptides, particularly enkephalins, and store them as cytoplasmic granules until stimulated to release them. Their secretions may exert a local paracrine action on nearby cells, in addition to having remote endocrine effects.

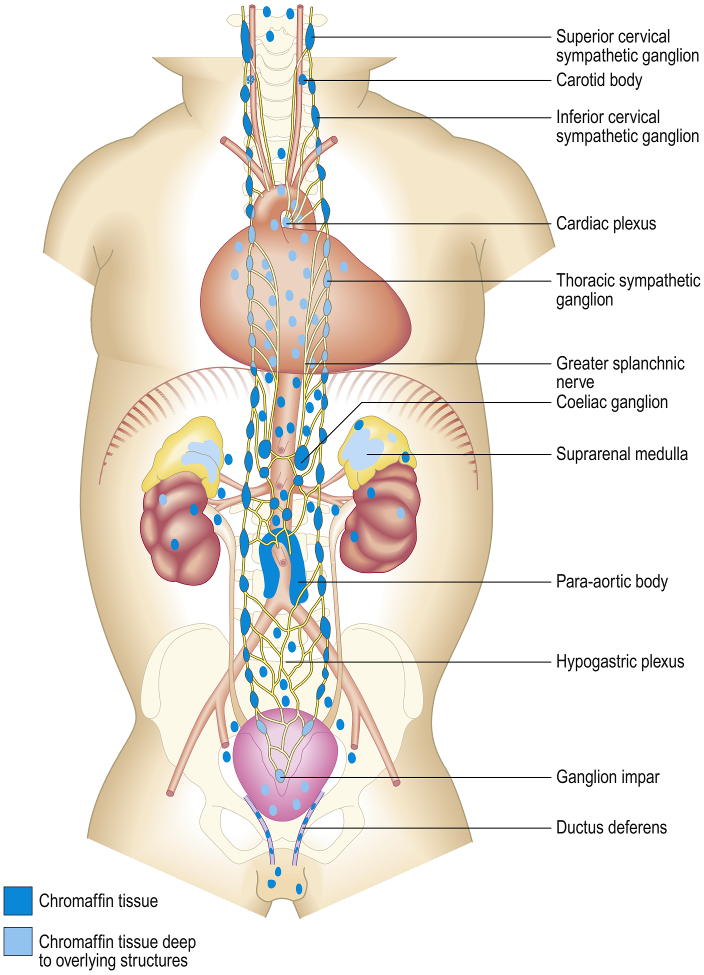

Fig. 24.14 The principal aggregations of 'classic' chromaffin tissue in the human neonate. The aggregates in pale blue lie deep to overlying structures.

Paragangliomas have been found in practically every site in which normal paraganglia are known to occur; carotid body paragangliomas are the most common and important group of extra-suprarenal paragangliomas (accounting for approximately 60% of head and neck paragangliomas). For further reading, see Rosai (2011) and Lack and Wieneke (2014).

SURFACE ANATOMY

The surface positions of cerebral structures, meningeal arteries and dural venous sinuses may be approximated via a number of standardized reference lines and planes. The midsagittal nasion–inion line curves around the sagittal plane of the skull from the nasion anteriorly to the inion posteriorly (**Fig. 24.15**). Reid's baseline (Frankfurt plane) passes through the inferior margin of the orbit and the superior margin of the external acoustic meatus (porion). The infraorbitomeatal line passes from the inferior margin of the orbit and through the centre of the external acoustic meatus (auricular point). The preauricular/condylar line passes through the preauricular point/mandibular condyle and sits perpendicular to the infraorbitomeatal line.

Cerebral sulci and lobes

The central sulcus (Rolandic fissure) and lateral sulcus (Sylvian fissure) of the cerebral hemispheres can be landmarked via the cranium using multiple methods, the most common being that developed by Taylor and Haughton (**Fig. 24.16**) (Taylor and Haughton 1900, Taylor et al 1980). Analysis of these methods has shown them to be accurate to within a few millimetres (Reis et al 2011). Using Taylor–Haughton craniometric lines, the lateral sulcus sits on the frontozygomatic (Sylvian) line, which passes from the frontozygomatic suture to a point 75% the way along the nasion–inion midsagittal line. The lateral sulcus extends posteroinferiorly from the Sylvian point, which

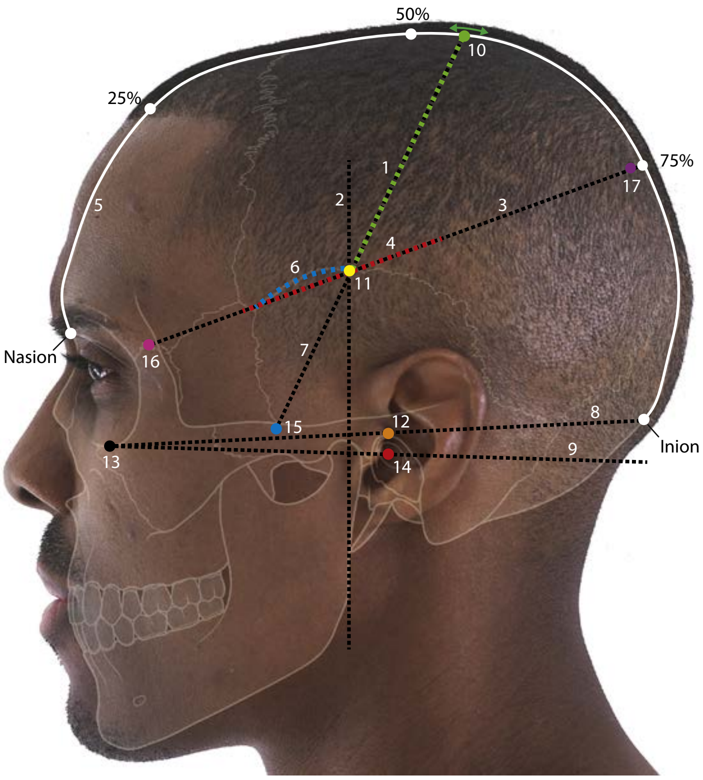

Fig. 24.15 Cranial reference lines, craniometric points and cerebral sulci. Key: 1, Rolandic line/central sulcus (green line); 2, pre-auricular/mandibular condylar line orientated perpendicular to the infra-orbitomeatal line; 3, frontozygomatic/Sylvian line passing from the frontozygomatic suture (16) to a point 75% of the way along the nasion–inion midsagittal line; 4, lateral sulcus/Sylvian fissure (red line); 5, nasion–inion midsagittal line; 6, lateral sulcus/Sylvian fissure alternative location (blue line): aligns anteriorly with the anterior part of the squamosal suture in a zone from 2.5 cm to 4.0 cm anterior to the external acoustic meatus; 7, line from the superior Rolandic point (green dot) to the midpoint of the zygomatic arch (15, blue dot); 8, Reid's baseline/Frankfurt plane; 9, infra-orbitomeatal line; 10 (green dot), superior Rolandic point located 2 ± 1 cm (green arrow) posterior to the midpoint of the nasion–inion line (at the 53–55% point of the nasion–inion line); 11 (yellow dot), inferior Rolandic point; 12 (orange dot), porion; 13 (black dot), lowest point of inferior orbital margin; 14 (red dot), auricular point; 15 (blue dot), midpoint of zygomatic arch; 16 (pink dot), frontozygomatic suture; 17 (purple dot), superior extent of the parieto-occipital sulcus. (Adapted with permission from Drake RL, Vogl AW, Mitchell A et al (eds) Gray's Atlas of Anatomy. Elsevier, Churchill Livingstone. Copyright 2008.)

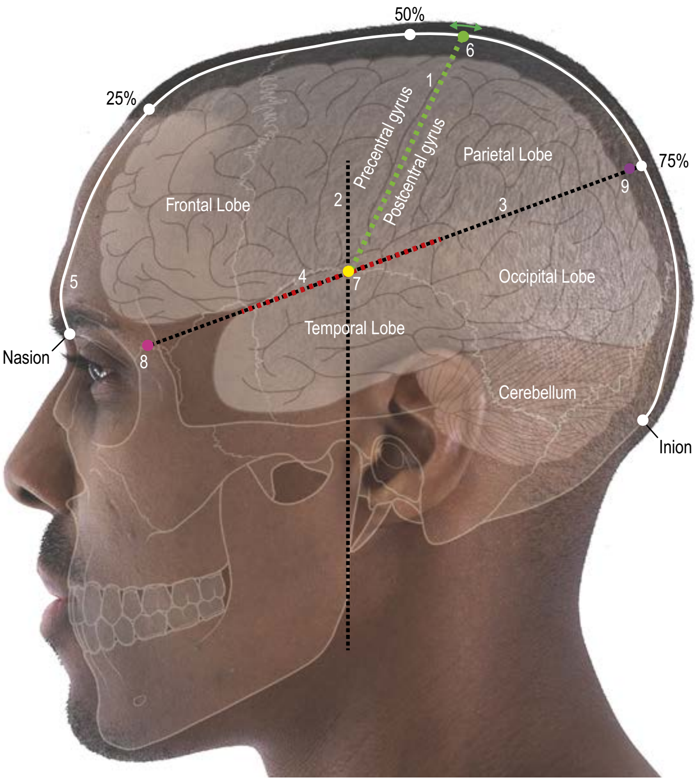

Fig. 24.16 Cerebral sulci, gyri and lobes. Key: 1, Rolandic line/central sulcus (green line); 2, pre-auricular/mandibular condylar line orientated perpendicular to the infra-orbitomeatal line; 3, frontozygomatic/Sylvian line passing from the frontozygomatic suture (8) to a point 75% of the way along the nasion–inion midsagittal line; 4, lateral sulcus/Sylvian fissure (red line); 5, nasion–inion midsagittal line; 6 (green dot), superior Rolandic point located 2 ± 1 cm (green arrow) posterior to the midpoint of the nasion–inion line (at the 53–55% point of the nasion–inion line); 7 (yellow dot), inferior Rolandic point; 8 (pink dot), frontozygomatic suture; 9 (purple dot), superior extent of the parieto-occipital sulcus. (Adapted with permission from Drake RL, Vogl AW, Mitchell A et al (eds) Gray's Atlas of Anatomy. Elsevier, Churchill Livingstone. Copyright 2008.)

is located in the region of the pterion, about 3 cm posterior to the zygomatic process of the frontal bone, to a vertical line passing through the apex (tip) of the mastoid process. The lateral sulcus has also been shown to align with the anterior part of the squamosal suture in a zone located from 2.5 cm to 4.0 cm anterior to the external acoustic meatus (Rahmah et al 2011). The position of the central sulcus is approximated via a line passing from the superior Rolandic point, situated within 2 ± 1 cm posterior to the midpoint of the nasion–inion midsagittal line (Mirjalili et al 2012), to the inferior Rolandic point, situated at the intersection of the frontozygomatic line with the pre-auricular/condylar line. The position of the superior Rolandic point may vary between sides and individuals (Hamasaki et al 2012). Alternatively, the position of the central sulcus can be approximated using a line passing from the superior Rolandic point to the midpoint of the zygomatic arch, with the central sulcus ending at the point of intersection of this line with the frontozygomatic line (Rhoton 2002). The superior extent of the parieto-occipital sulcus sits at the point of intersection of the frontozygomatic line and the 75% point on the nasion–inion line. The approximate positions of the lobes of the brain, and of the precentral and postcentral gyri, can be determined following localization of the central, lateral and parieto-occipital sulci (see Fig. 24.16).

Dural venous sinuses

The superior sagittal sinus passes along the nasion–inion midsagittal line on the inner surface of the calvaria (**Fig. 24.17**) (Reis et al 2015). It may deviate either side of the midsagittal plane/superior sagittal suture by up to 11 mm, but is more commonly to the right (Tubbs et al 2001, Samadian et al 2011, Reis et al 2015). The confluence of the dural venous sinuses sits mainly to the upper right side of the inion on the inner surface of the occipital bone (Sheng et al 2012). The course of the transverse sinus has been shown to vary widely and no single plane or surface marking can be used to predict its route accurately (Sheng et al 2012). The position of the lower border of the proximal transverse sinus is best approximated via the insertion of semispinalis capitis into the cranium (Tubbs et al 2000). The asterion, found at the junction of the lambdoid, occipitomastoid and parietomastoid sutures, sits over the junction between the transverse and sigmoid sinuses in 81% of subjects, inferior to it in 15% and superior to it in 4% (Sheng et al 2012).

Middle meningeal artery

The surface positions of the anterior and posterior branches of the middle meningeal artery can be determined relative to cranial landmarks (see Fig. 33.8A).

Vertebral column, spinal cord and meninges

The surface positions of the termination of the spinal cord and dural sac can be mapped relative to the vertebrae and their spinous processes (see Figs 46.81–46.82).

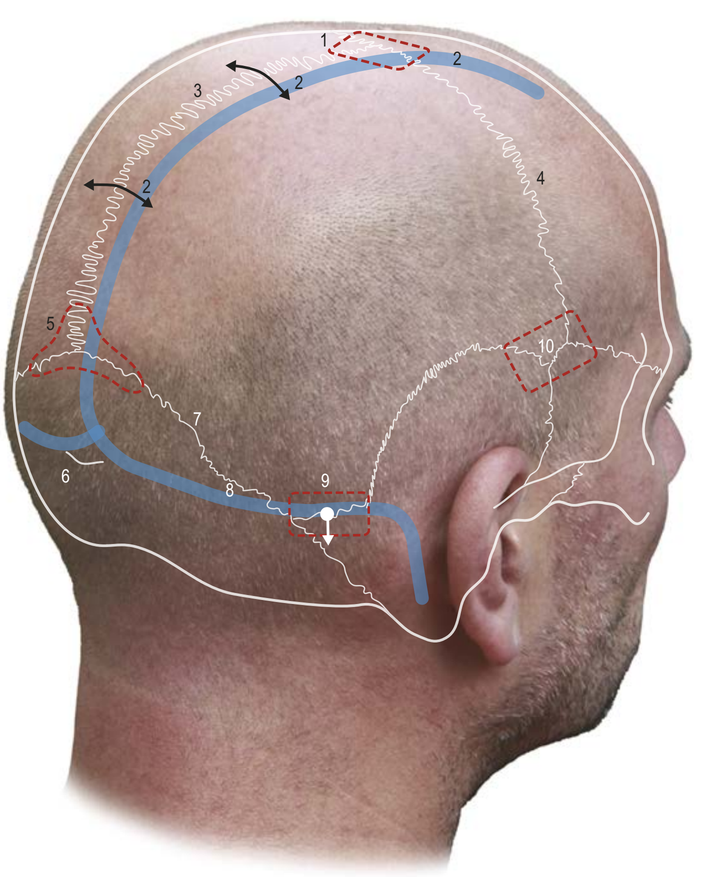

Fig. 24.17 Cranial suture joints, fontanelles and dural venous sinuses. Key: 1, bregma (site of infant anterior fontanelle); 2, superior sagittal sinus: deviates either side of the sagittal suture by up to 11 mm (black arrows), most commonly to the right (as shown); 3, sagittal suture: sits on the nasion–inion midsagittal line; 4, coronal suture; 5, lambda (site of infant posterior fontanelle); 6, inion: normally sits below and to the left of the confluence of the sinuses and just below the level of the internal occipital protruberance; 7, lambdoid suture; 8, transverse sinus; 9, asterion (site of infant posterolateral mastoid fontanelle): commonly sits over (in 81%) or just below (in 15%) the transverse–sigmoid sinus complex (white arrow shows range of positions); 10, pterion (site of infant anterolateral sphenoidal fontanelle). (Adapted with permission from Tunstall R, Shah N Surface Anatomy (Pocket Tutor series) 2012, JP Medical Ltd.)

References

Apok V, Gurusinghe NT, Mitchell JD et al 2011 Dermatomes and dogma. Pract Neurol 11:100–5.

Bielefeldt K, Gebhart GF 2013 Visceral pain: basic mechanisms. In: McMahon SB, Koltzenburg M, Tracey I et al (eds) Wall and Melzack's Textbook of Pain, 6th ed. Philadelphia: Elsevier, Saunders; Ch. 51, pp. 703–17.

Brodal A 1981 Neurological Anatomy in Relation to Clinical Medicine, 3rd ed. Oxford: Oxford University Press.

An unconventional but highly readable text on neuroanatomy with a strong emphasis on clinical relevance. Contains a particularly good account of motor pathways.

Burnstock G 2013 Cotransmission in the autonomic nervous system. Handb Clin Neurol 117:23–35.

Crossman AR, Neary D 2019 Neuroanatomy: An Illustrated Colour Text, 6th ed. Edinburgh: Elsevier, Churchill Livingstone.

Greenberg SA 2003 The history of dermatome mapping. Arch Neurol 60:126–31.

Hamasaki T, Imamura JI, Kawai H et al 2012. A three-dimensional MRI study of variations in central sulcus location in 40 normal subjects. J Clin Neurosci 19:115–20.

Lack EE, Wieneke J 2014 Tumors of the autonomic nervous system, including paraganglia. In: Fletcher CDM (ed) Diagnostic Histopathology of Tumors, 4th ed. Philadelphia: Elsevier, Saunders; Ch. 28, pp. 2064–85.

Ladak A, Tubbs RS, Spinner RJ 2013 Mapping sensory nerve communications between peripheral nerve territories. Clin Anat 27:681–90.

Lee MW, McPhee RW, Stringer MD 2008 An evidence-based approach to human dermatomes. Clin Anat 21:363–73.

Mirjalili SA, Hale SJ, Stringer MD et al 2012 The surface anatomy of the central sulcus. J Clin Neurosci 19:1467.

Poole DP, Furness JB 2012 Enteric nervous system structure and neurochemistry related to function and neuropathology. In: Johnson LR, Ghishan FK, Kaunitz JD et al (eds) Physiology of the Gastrointestinal Tract, 5th ed. Amsterdam: Elsevier, Academic Press; Ch. 19, pp. 557–81.

Rahmah NN, Murata T, Yako T et al 2011 Correlation between squamous suture and Sylvian fissure: Osirix DICOM viewer study. PLOS One 6:e18199.

Reis CV, Gusmao SNS, Elhadi AM 2015 Midline as a landmark for the position of the superior sagittal sinus on the cranial vault: an anatomical and imaging study Surg Neurol Int 6:121

Rhoton AL Jr 2002 The cerebrum. Neurosurgery 51:S1–S51.

Rosai J 2011 Adrenal gland and other paraganglia. In: Rosai and Ackerman's Surgical Pathology, 10th ed. Edinburgh: Elsevier, Mosby; Ch. 16, pp. 1057–100.

Samadian MI, Nazparvar B, Haddadian K et al 2011 The anatomical relation between the superior sagittal sinus and the sagittal suture with surgical considerations. Clin Neurol Neurosurg 113:89–91.

Sheng B, Lv F, Xiao Z et al 2012 Anatomical relationship between cranial surface landmarks and venous sinus in posterior cranial fossa using CT angiography. Surg Radiol Anat 34:701–8.

Taylor EH, Haughton WS 1900 Some recent researches on the topography of the convolutions and fissures of the brain. Trans R Acad Med Ireland 18:511–22.

Taylor AJ, Haughton VM, Syvertsen A et al 1980 Taylor–Haughton line revisited. Am J Neuroradiol 1:55–6.

Tubbs RS, Salter G, Oakes WJ 2000 Superficial surgical landmarks for the transverse sinus and torcular herophili. J Neurosurg 93:279–81.

Tubbs RS, Salter G, Elton S et al 2001 Sagittal suture as an external landmark for the superior sagittal sinus. J Neurosurg 94:985–7.

Xanthos DN, Sandkühler J 2014 Neurogenic neuroinflammation: inflammatory CNS reactions in response to neuronal activity. Nature Rev Neurosci 15:43–53.

CHAPTER

25

Meninges and ventricular system

The meninges consist of three concentric membranes that envelop the brain and spinal cord, supporting and protecting the delicate tissues they surround. The individual layers, from outside to inside, are the dura mater (pachymeninx), arachnoid mater and pia mater. The dura is an opaque, tough, fibrous coat that incompletely divides the cranial cavity into compartments and accommodates the dural venous sinuses. The arachnoid is much thinner than the dura and is mostly translucent. It loosely surrounds the brain, cranial nerves and vessels and spans fissures and sulci. The pia mater is a transparent, microscopically thin membrane that follows the contours of the brain and is closely adherent to its surface.

The dura is separated from the arachnoid by a narrow subdural space. The arachnoid is separated from the pia by the subarachnoid space, which varies greatly in depth; the larger expanses are termed subarachnoid cisterns. The subarachnoid space contains cerebrospinal fluid (CSF) which is secreted by the choroid plexuses of the cerebroventricular system, circulates within the subarachnoid space and is reabsorbed into the venous system through arachnoid villi associated with the dural venous sinuses.

Cranial and spinal meninges are continuous through the foramen magnum. The cranial meninges are described in this section and the spinal meninges are described in Chapter 47.

DURA MATER

The dura mater is largely acellular and consists mainly of densely packed fascicles of collagen fibres arranged in laminae. The fascicles run in different directions in adjacent laminae, producing a lattice-like appearance that is particularly obvious in the tentorium cerebelli and around the defects or perforations that sometimes occur in the anterior portion of the falx cerebri.

The cranial dura differs from the spinal dura mainly in its relationship to the surrounding bones. It lines the cranial cavity and has an inner, meningeal, layer and an outer, endosteal layer. The two membranes are physically joined only at sites where veins pass from the brain into venous sinuses, e.g. the superior sagittal sinus. There is little histological difference between the layers: both contain fibroblasts, and the endosteal layer also contains osteoblasts. Focal calcification may occur in the falx cerebri and near the superior sagittal sinus. As a general rule, the meningeal layer covers neural tissues. It provides tubular sheaths for the cranial nerves as they pass out through the cranial foramina: the sheaths fuse with the epineurium as the nerves emerge from the skull. The dura fuses with the adventitia of major vessels, such as the internal carotid and vertebral arteries, at sites where they pierce it to enter the cranial cavity. The dural sheath of the optic nerve is continuous with the ocular sclera. The endosteal layer of dura adheres to the internal surfaces of the cranial bones, particularly at the sutures and the cranial base, and around the foramen magnum. It is continuous with the pericranium through the cranial sutures and foramina and with the orbital periosteum through the superior orbital fissure. Fibrous bands pass from the dura into the bones, so that it is difficult to remove the dura from the suture lines in young skulls: as the suture lines fuse, the dura becomes separated from them. The meningeal layer of dura is closely applied to the arachnoid mater over the surface of the brain: the layers are united except where they separate to enclose the venous sinuses that drain blood from the brain.

Extradural haematoma

The anatomical organization of the dura, and its relationships to the major venous sinuses, sutures and blood vessels, are clinically important. Separation of the dura from the cranial bones requires significant force, and consequently happens when high-pressure arterial bleeding takes place into the extradural or epidural space: this can result from damage to any meningeal vessel, commonly following skull fracture. The classic site for such injury is along the course of the middle meningeal artery, where a direct blow causing a fracture of the temporal and/or parietal bones can rupture the artery and cause rapid collection of blood into the extradural space. An extradural haematoma therefore acts as a rapidly expanding intracranial mass lesion that causes acute brain compression and displacement: it is a classic medical emergency that requires immediate diagnosis and surgery through a craniotomy for epidural blood clot evacuation and coagulation of the ruptured vessel (**Fig. 25.1**).

Dural partitions

The meningeal layer of the dura is reflected inwards to form four septa, the falx cerebri, falx cerebelli, diaphragma sellae and tentorium cerebelli, that partially divide the cranial cavity into compartments.

Falx cerebri

The falx cerebri is a strong, crescent-shaped sheet that lies in the sagittal plane and occupies the longitudinal fissure between the two cerebral hemispheres (**Fig. 25.2**). The crescent is narrow anteriorly, where the falx is fixed to the crista galli, and broad posteriorly, where it blends with the tentorium cerebelli: the straight sinus runs along this line of attachment to the tentorium (see Fig. 25.2). The anterior part of the falx is thin and may have a number of irregular perforations. Its convex upper margin is attached to the internal cranial surface on each side of the midline, as far posteriorly as the internal occipital protuberance. The superior sagittal sinus runs in a cranial groove within the dura along this margin, and the falx cerebri is attached to the lips of this groove. The lower edge of the falx is free and concave, and contains the inferior sagittal sinus.

Falx cerebelli

The falx cerebelli is a small midline fold of dura mater that lies below the tentorium cerebelli and projects forwards into the posterior cerebellar notch between the cerebellar hemispheres. Its base is directed upwards and is attached to the posterior part of the inferior surface of the tentorium cerebelli in the midline. Its posterior margin contains the occipital sinus and is attached to the internal occipital crest. The lower apex of the falx cerebelli frequently divides into two small folds that disappear at the sides of the foramen magnum.

Diaphragma sellae

The diaphragma sellae is a small, circular, horizontal sheet of dura mater that forms a roof over the sella turcica and covers the pituitary gland (hypophysis). The infundibulum (pituitary stalk) passes into the pituitary fossa through a central opening in the diaphragm: there is wide individual variation in the size of this opening. The diaphragma sellae is an important landmark in pituitary surgery because large pituitary tumours extend above it and may adopt a characteristic dumbbell shape. A trans-sphenoidal approach is currently the preferred option for accessing pituitary tumours, irrespective of whether there is suprasellar extension beyond the diaphragma sellae.

Tentorium cerebelli

The shape of the tentorium cerebelli (see Fig. 25.2B) is reminiscent of a single-poled tent, as its name suggest. It lies between the cerebellum and the occipital lobes of the cerebral hemispheres, and divides the cranial cavity into supratentorial and infratentorial compartments that contain the forebrain and hindbrain, respectively. Its concave anterior edge is free and separated from the dorsum sellae of the sphenoid bone by a large curved hiatus, the tentorial incisure or notch, which is occupied by the midbrain and the anterior part of the superior aspect of the cerebellar vermis. The convex outer limit of the tentorium is attached posteriorly to the lips of the transverse sulci of the occipital bone and

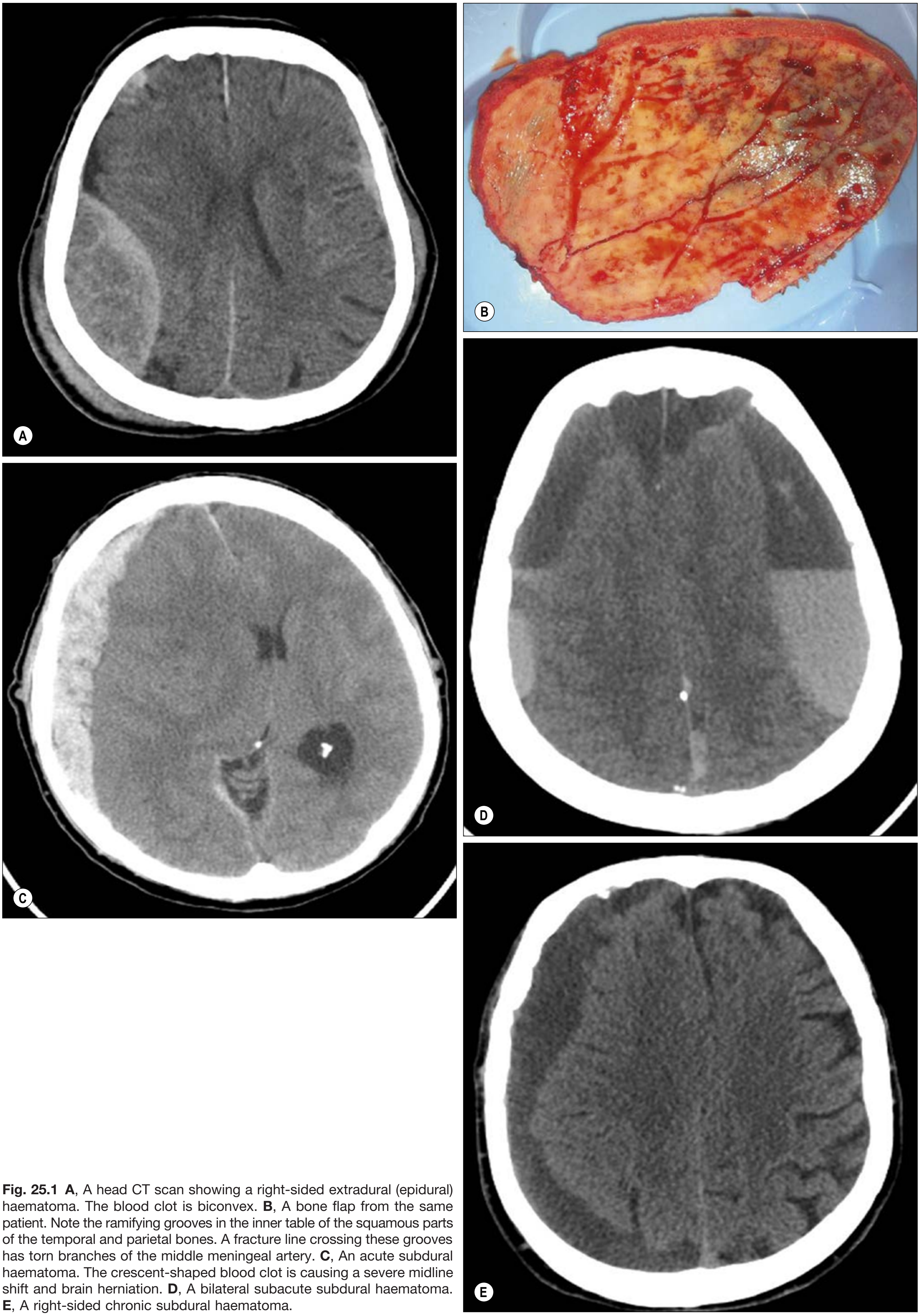

Fig. 25.1 **A**, A head CT scan showing a right-sided extradural (epidural) haematoma. The blood clot is biconvex. **B**, A bone flap from the same patient. Note the ramifying grooves in the inner table of the squamous parts of the temporal and parietal bones. A fracture line crossing these grooves has torn branches of the middle meningeal artery. **C**, An acute subdural haematoma. The crescent-shaped blood clot is causing a severe midline shift and brain herniation. **D**, A bilateral subacute subdural haematoma. **E**, A right-sided chronic subdural haematoma.

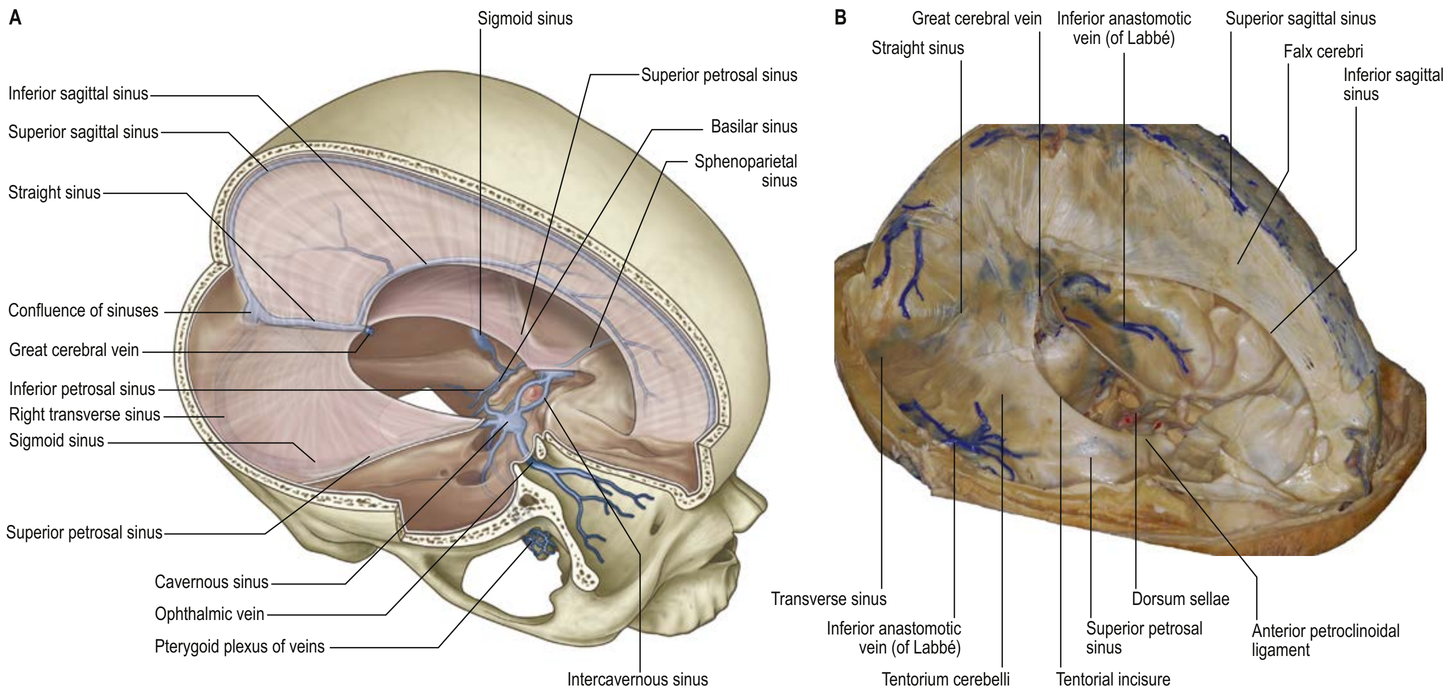

Fig. 25.2 **A**, The cerebral dura mater, its reflections and associated major venous sinuses. **B**, An anatomical dissection of a silicon-injected specimen. (A, Adapted with permission from Drake RL, Vogl AW, Mitchell A (eds) Gray's Anatomy for Students, 2nd ed. Elsevier, Churchill Livingstone. Copyright 2010.)

to the posterior inferior angles of the parietal bones, where it encloses the transverse sinuses. Laterally, it is attached to the superior borders of the petrous parts of the temporal bones, where it contains the superior petrosal sinuses. On each side, near the apex of the petrous temporal bone, the lower layer of the tentorium is evaginated anterolaterally under the superior petrosal sinus to form a recess, Meckel's cave, between the endosteal and meningeal dural layers in the middle cranial fossa. The cave is entered by the posterior root of the trigeminal nerve and contains cerebrospinal fluid and the trigeminal ganglion; the evaginated meningeal layer fuses anteriorly with the anterior part of the ganglion.

The arrangement of the dura mater in the central part of the middle cranial fossa is complex. The tentorium forms the medial part of the floor of the middle cranial fossa. On both sides, the rim of the tentorial incisure is attached to the apex of the petrous temporal bone. It continues forwards as a ridge of dura, the anterior petroclinoidal ligament, that is attached to the anterior clinoid process: this ligament marks the junction of the roof and the lateral wall of the cavernous sinus. The periphery of the tentorium cerebelli (attached to the superior border of the petrous temporal bone), crosses under the free border of the tentorial incisure at the apex of the petrous temporal bone, and continues forwards to the posterior clinoid process as a rounded ridge of dura mater, the posterior petroclinoidal ligament. The dural extension between the anterior and posterior petroclinoidal ligaments forms the roof of the cavernous sinus. On either side, it is pierced superiorly by the oculomotor nerve and posteriorly by the trochlear nerve: both nerves proceed anteroinferiorly into the lateral wall of the cavernous sinus.

In the anteromedial part of the middle cranial fossa, the dura ascends as the lateral wall of the cavernous sinus. It reaches the ridge produced by the anterior petroclinoidal ligament and runs medially as the roof of the cavernous sinus, where it is pierced by the internal carotid artery. The interclinoidal ligament, between the anterior and posterior clinoid processes, forms the medial limit of the roof of the cavernous sinus and continues medially with the diaphragma sellae. At, or just below, the opening in the diaphragma for the pituitary stalk, the dura of the diaphragma and the suprasellar arachnoid blend with each other and with the capsule of the pituitary gland: the subarachnoid space does not extend into the sella turcica.

Transtentorial coning

Normally, the arrangement of dural partitions such as the falx cerebri and tentorium cerebelli may help to stabilize the brain within the cranial cavity. However, when there is focal brain swelling or a focal space-occupying lesion within the brain or cranial cavity, mass effect and raised intracranial pressure may cause the brain to herniate under the falx cerebri or, more significantly, through the tentorial incisure. In this case, the medial temporal lobe, and particularly the uncus, will compress the oculomotor nerve, midbrain and the posterior cerebral arteries. This life-threatening event and neurosurgical emergency, occurring in patients with supratentorial space-occupying lesions, is known as transtentorial uncal herniation. Similarly, space-occupying lesions in the smaller infratentorial compartment may cause upward herniation of the cerebellar vermis through the tentorial hiatus (upward transtentorial herniation) or downward herniation of the cerebellar tonsils through the foramen magnum (tonsillar herniation) (see Fig. 28.23); these neurosurgical emergencies require a suboccipital craniectomy.

Innervation of the cranial dura mater

The cranial dura mater is innervated mainly by branches of the three divisions of the trigeminal nerve, the second and third cervical spinal nerves and the cervical sympathetic trunk (**Fig. 25.3**).

Sensory nerve endings are restricted to the dura mater and cerebral blood vessels, and are not found in either the brain itself, or in the arachnoid or pia mater. Stimulation of these nerve endings causes pain, as evidenced during awake craniotomy procedures, and is the basis of certain forms of headache. The density of dural innervation, particularly around the dural venous sinuses, increases during the later part of gestation, peaking at term and subsequently decreasing during the first year of postnatal life (Davidson et al 2012).

Dural venous sinuses

Dural venous sinuses form a complex network of venous channels that drain blood from the brain and cranial bones (**Fig. 25.4**; see Figs 25.2, 26.10–26.11, 26.13). They lie between the endosteal and meningeal layers of dura mater, are lined by endothelium, lack valves and their walls are devoid of muscular tissue (Kılıç and Akakın 2008). They develop initially as venous plexuses and, to a variable degree, most adult sinuses retain that form. Plexiform arrays of small veins adjoin the superior and inferior sagittal and straight sinuses, and, less frequently, the transverse sinuses. Ridges of 'spongy' venous tissue, venous lacunae, often project into the lumina of the superior sagittal and transverse sinuses (Browder and Kaplan 1976, Kaplan and Browder 1976).

The named sinuses are the superior and inferior sagittal, straight, transverse, sigmoid, occipital, cavernous, intercavernous, superior and inferior petrosal, sphenoparietal, basilar and marginal.

Superior sagittal sinus

The superior sagittal sinus runs in the attached convex margin of the falx cerebri. It grooves the internal surface of the frontal bone, the adjacent margins of the two parietal bones and the squamous part of the occipital bone (**Fig. 25.5**; see Figs 25.2, 26.10, 26.11B,C, 26.13).

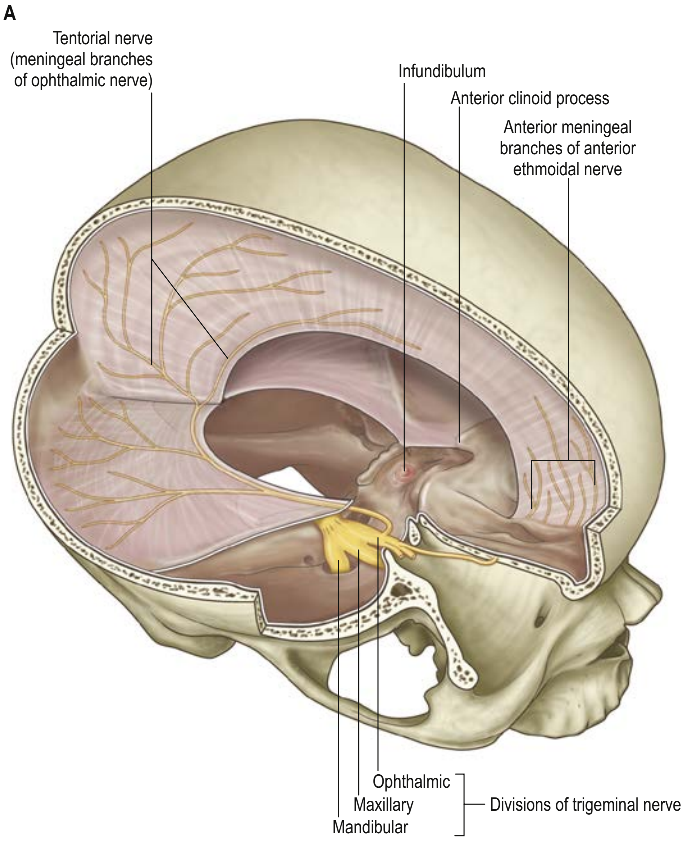
A
Tentorial nerve (meningeal branches of ophthalmic nerve)
Infundibulum
Anterior clinoid process
Anterior meningeal branches of anterior ethmoidal nerve
Ophthalmic
Maxillary
Mandibular
Divisions of trigeminal nerve

Fig. 25.3 The innervation of the cranial meninges. (**B**, *continued online*)

It begins near the crista galli, a few millimetres posterior to the foramen caecum, and receives primary tributaries from the cortical veins draining the superior part of the frontal, parietal and occipital lobes, and the anterior part of the orbital surface of the frontal lobe. The sinus is triangular in cross-section, with the apex directed downwards, and is continuous with the falx cerebri. Its lumen is invaded in its intermediate third by projections from its dural walls that may divide the lumen into superior and inferior channels. It is narrow anteriorly, and widens gradually to approximately 1 cm in diameter as it runs posteriorly to enter the confluence of the sinuses, situated to one side (usually the right) of the internal occipital protuberance (see Fig. 25.4). (The confluence of the sinuses is also known as the torcular Herophili or the torcula, although the term actually describes the bony gutter in which the confluence lies). At the confluence of the sinuses the superior sagittal sinus usually deviates to become continuous with the right transverse sinus, but also usually connects with the occipital and contralateral transverse sinuses. The size and degree of communication of the channels meeting at the confluence are highly variable; any sinus involved may be duplicated, narrowed or widened near the confluence (see Fig. 26.13B).

There are usually two or three lateral venous lacunae on each side of the midline, named frontal (small), parietal (large) and occipital (intermediate) lacunae; they tend to become confluent in the elderly, producing a single elongated lacuna on each side. Fine fibrous bands cross the lacunae, and numerous arachnoid granulations project into them (**Fig. 25.6**; see Fig. 25.5). The lacunae mainly drain diploic and meningeal veins. The cortical veins typically pass beneath the lacunae on their way to the sinus. The superior anastomotic vein (of Trolard), the largest cortical vein that connects the superficial middle cerebral (Sylvian) vein and the superior sagittal sinus, often runs in the precentral, central or postcentral sulci. Near its posterior end, the superior sagittal sinus receives veins from the pericranium that pass through parietal foramina. Acute and complete thrombosis of the superior sagittal sinus is an extremely severe condition causing acute elevation of the intracranial pressure and herniation. Slow and progressive occlusion of

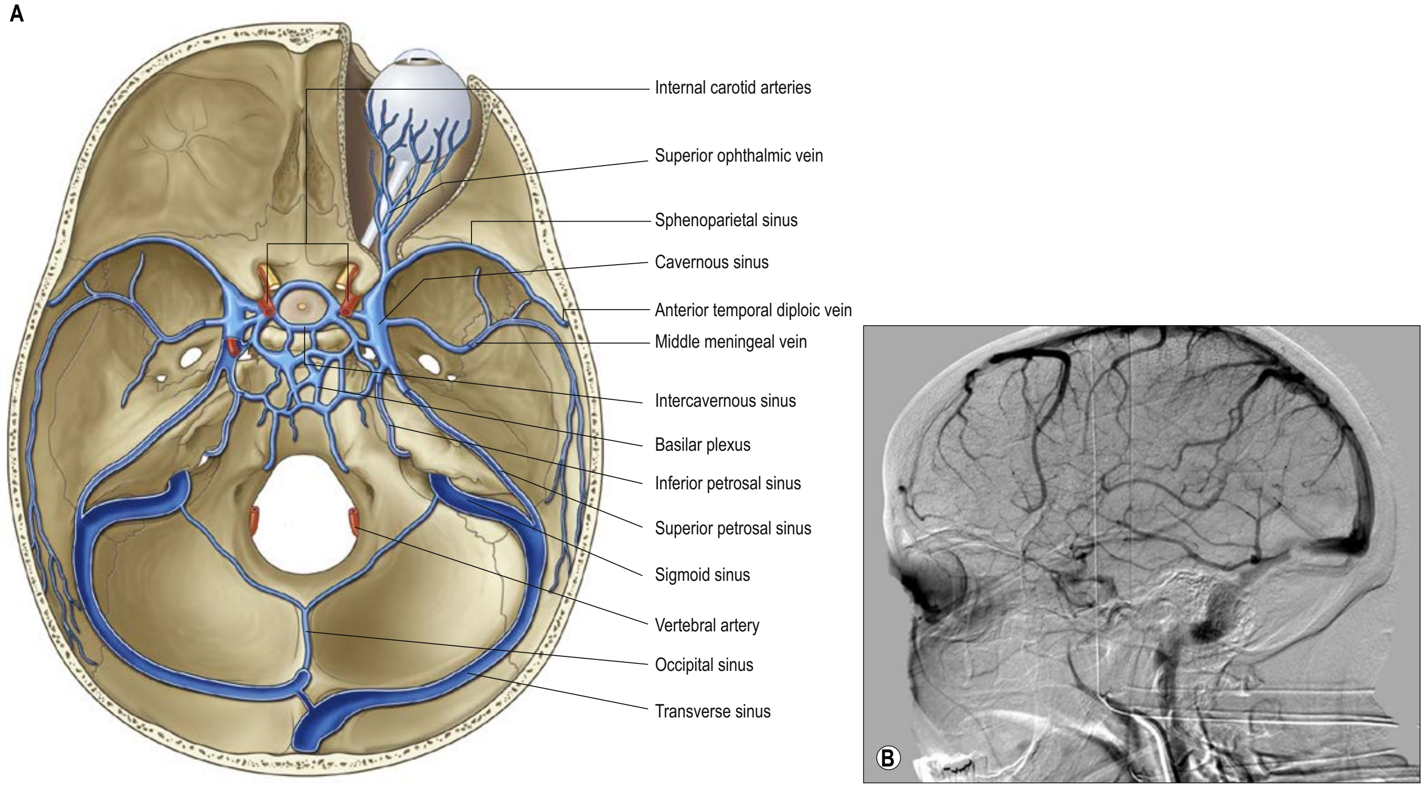
A
Internal carotid arteries
Superior ophthalmic vein
Sphenoparietal sinus
Cavernous sinus
Anterior temporal diploic vein
Middle meningeal vein
Intercavernous sinus
Basilar plexus
Inferior petrosal sinus
Superior petrosal sinus
Sigmoid sinus
Vertebral artery
Occipital sinus
Transverse sinus
B

Fig. 25.4 The major venous sinuses at the base of the skull. **A**, The sinuses coloured dark blue have been opened up. **B**, **C**. Digital subtraction angiography, venous phase. **B**, Sagittal view. (**C**, *continued online*)

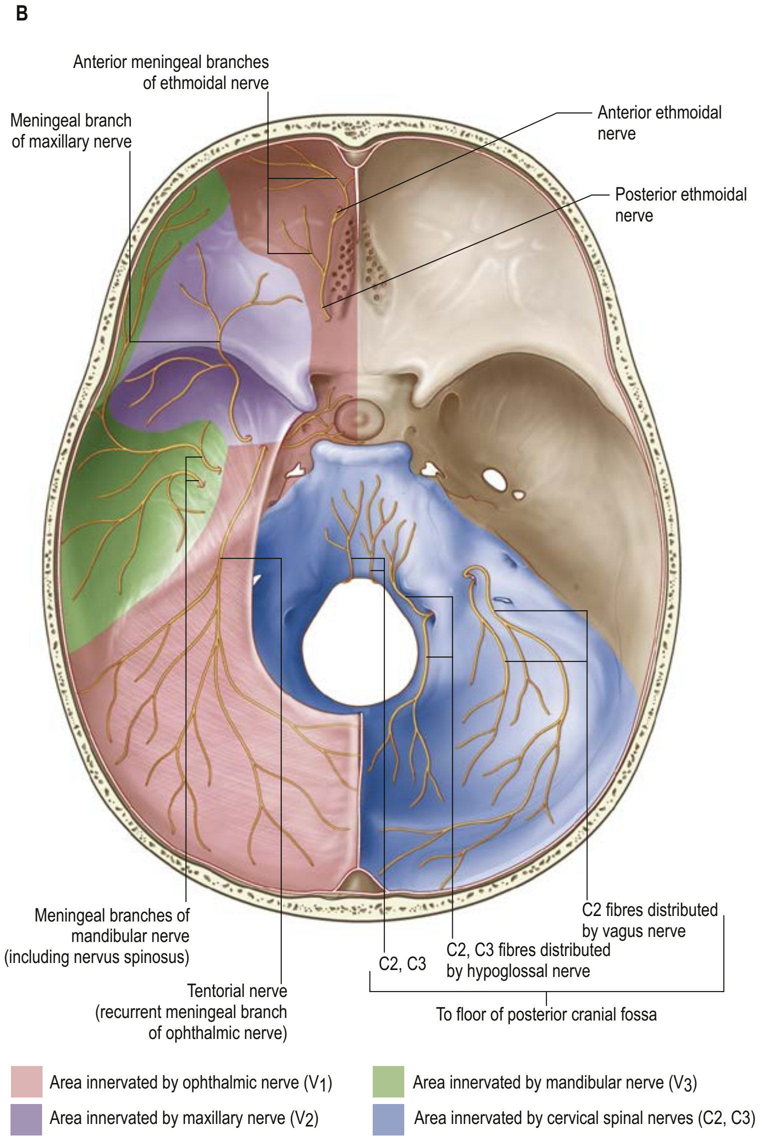
B
Anterior meningeal branches of ethmoidal nerve
Meningeal branch of maxillary nerve
Anterior ethmoidal nerve
Posterior ethmoidal nerve
Meningeal branches of mandibular nerve (including nervus spinosus)
Tentorial nerve (recurrent meningeal branch of ophthalmic nerve)
C2, C3
C2, C3 fibres distributed by hypoglossal nerve
C2 fibres distributed by vagus nerve
To floor of posterior cranial fossa
Area innervated by ophthalmic nerve (V1)
Area innervated by maxillary nerve (V2)
Area innervated by mandibular nerve (V3)
Area innervated by cervical spinal nerves (C2, C3)

Fig. 25.3, cont'd B, The innervation of the cranial meninges.

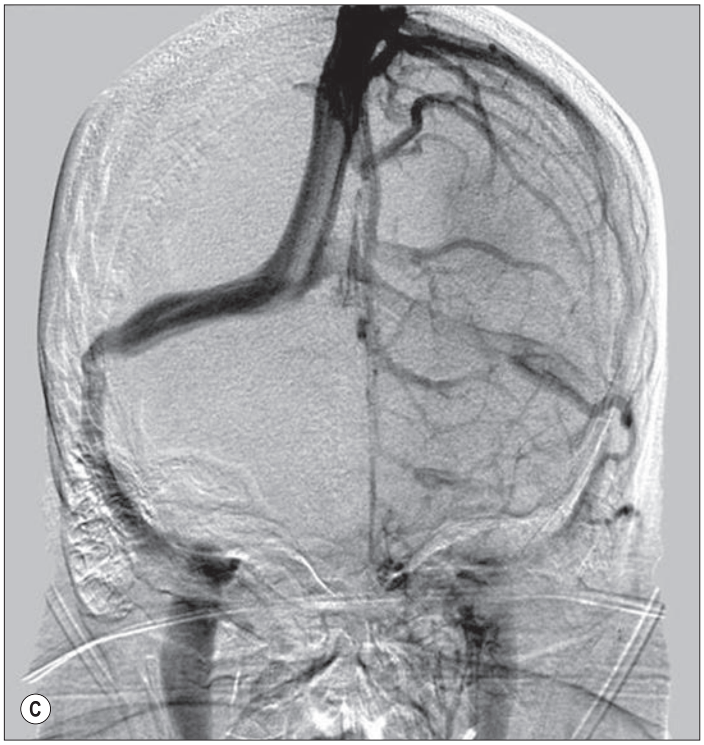

Fig. 25.4, cont'd C, Posterior view; note the asymmetry of the transverse sinuses.

Less well established meningeal branches have been described arising from the vagus and hypoglossal nerves, and possibly from the facial and glossopharyngeal nerves.

In the anterior cranial fossa, the dura is innervated by meningeal branches of the anterior and posterior ethmoidal nerves and anterior filaments of the meningeal rami of the maxillary (nervus meningeus medius) and mandibular (nervus spinosus) divisions of the trigeminal nerve. Nervi meningeus medius and spinosus are largely distributed to the dura of the middle cranial fossa, which also receives filaments from the trigeminal ganglion. The nervus spinosus re-enters the cranium through the foramen spinosum with the middle meningeal artery, and divides into anterior and posterior branches that accompany the main divisions of the artery and supply the dura mater in the middle cranial fossa and, to a lesser extent, the anterior fossa and calvarium. The anterior branch communicates with the meningeal branch of the maxillary nerve. The posterior branch also supplies the mucous lining of the mastoid air cells. The nervus spinosus contains sympathetic postganglionic fibres from the middle meningeal plexus. The nervus tentorii, a recurrent branch of the intracranial portion of the ophthalmic division of the trigeminal nerve, supplies the supratentorial falx cerebri and the tentorium cerebelli. Intraoperative mechanical stimulation of the falx may trigger the trigeminocardiac reflex (Bauer et al 2005). The space between the anterior half of the straight sinus and the medial tentorial notch can be considered a safe surgical area where innervation is scarce, whereas the entire region of the transverse sinus and the posterior half of the straight sinus are densely innervated by the nervus tentorii (Lee et al 2017). The dura in the posterior cranial fossa is innervated by ascending meningeal branches of the upper cervical nerves that enter through the anterior part of the foramen magnum (second and third cervical nerves) and through the hypoglossal canal and jugular foramen (first and second cervical nerves).

Meningeal branches from the vagus nerve apparently originate from the superior vagal ganglion and are distributed to the dura mater in the posterior cranial fossa. Meningeal branches from the hypoglossal nerve leave the nerve in its canal and supply the diploë of the occipital bone, the dural walls of the occipital and inferior petrosal sinuses, and much of the floor and anterior wall of the posterior cranial fossa. These meningeal rami may not contain vagal or hypoglossal fibres but ascending, mixed sensory and sympathetic fibres from the upper cervical nerves and superior cervical sympathetic ganglion. All meningeal nerves contain a postganglionic sympathetic component, either from the superior cervical sympathetic ganglion or by communication with its perivascular intracranial extensions. The role of the autonomic nerve supply of the cranial dura mater is uncertain.

The plexiform nature of the cranial venous sinuses and their wide connections with cerebral and cerebellar veins vary considerably, particularly in earlier years, e.g. in infancy, the falx cerebelli may contain large plexiform channels and venous lacunae that augment the occipital sinus. These variations must be established for each patient by catheter-based angiography, magnetic resonance (MR) venography or computed tomographic (CT) venography, when clinical necessity arises. The existence of arteriovenous shunts has been inferred from the demonstration of a connection between the middle meningeal arteries and the superior sagittal sinus (Browder and Kaplan 1976). Dural arteriovenous fistulae are thought to be acquired lesions that form in an area of thrombosis within a sinus. If the sinus remains completely thrombosed, venous drainage from these lesions takes place through cortical veins: when the sinus remains closed, the elevated pressure within the cortical veins receiving the arterial flow carries the risk of haemorrhage. If the sinus is partially open, venous drainage is usually into the involved sinus.

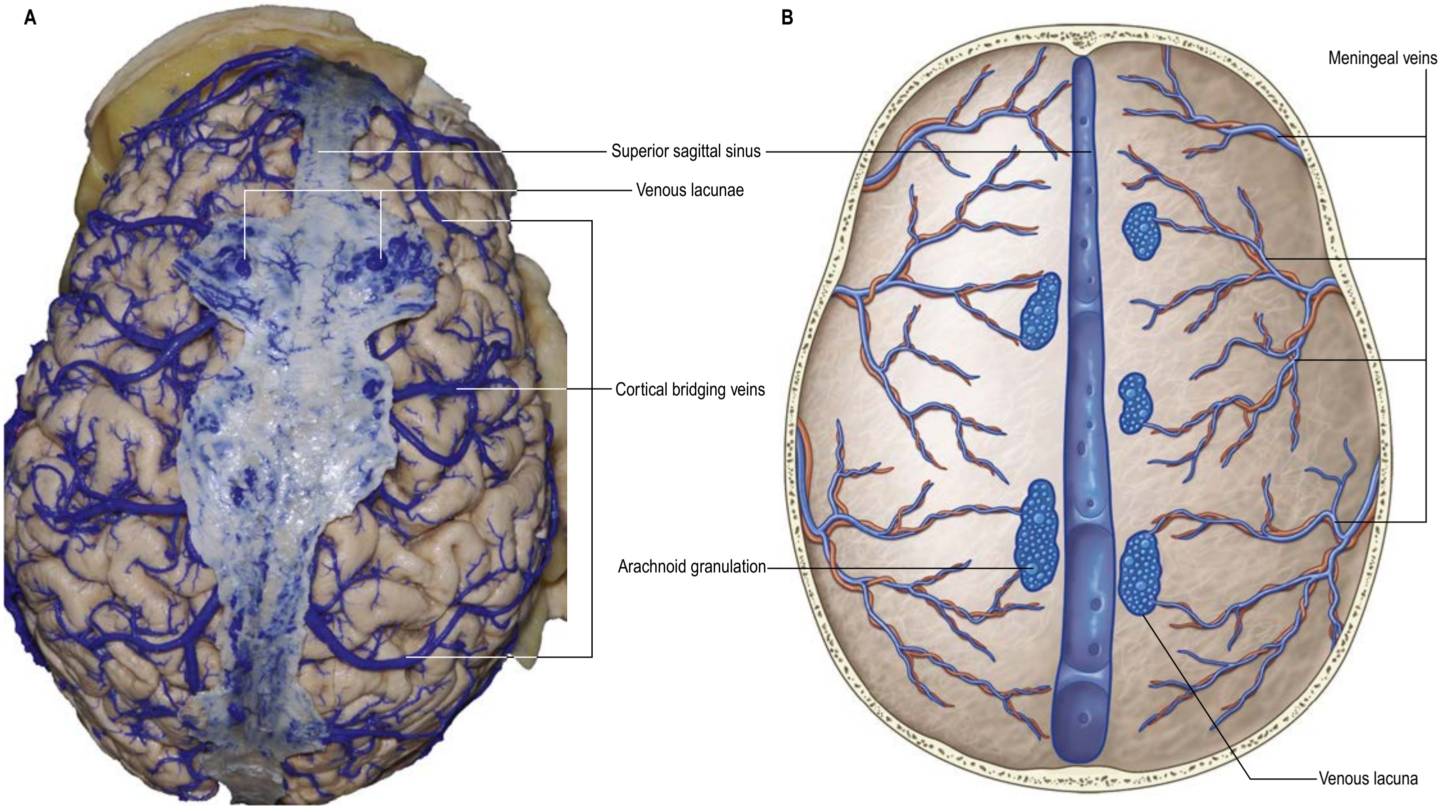
A
B
Superior sagittal sinus
Venous lacunae
Cortical bridging veins
Arachnoid granulation
Meningeal veins
Venous lacuna

Fig. 25.5 The superior sagittal sinus and venous lacunae. **A**, An anatomical dissection of a silicon-injected specimen. **B**, The superior sagittal sinus opened up after removal of the cranial vault. Note the fibrous bands that cross the sinus from two of the venous lacunae. (A, From the Rhoton Collection.)

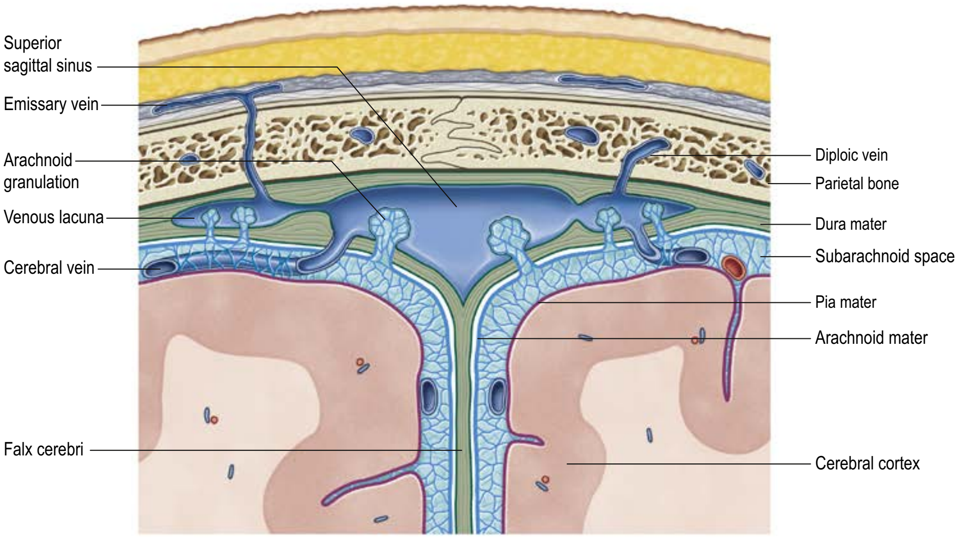
Superior sagittal sinus
Emissary vein
Arachnoid granulation
Venous lacuna
Cerebral vein
Falx cerebri
Diploic vein
Parietal bone
Dura mater
Subarachnoid space
Pia mater
Arachnoid mater
Cerebral cortex

Fig. 25.6 A coronal section through the vertex of the skull to show the relationships between the superior sagittal sinus, meninges and arachnoid granulations. (Adapted with permission from Drake RL, Vogl AW, Mitchell A (eds) Gray's Anatomy for Students, 2nd ed. Elsevier, Churchill Livingstone. Copyright 2010.)

the sinus, as is typical for sagittal meningiomas, may be compensated by the development of collateral venous drainage with no clinical consequences.

Inferior sagittal sinus

The inferior sagittal sinus is located in the posterior half or two-thirds of the free margin of the falx cerebri (see Figs 25.2, 26.11C). It increases in size posteriorly, ends in the straight sinus, and receives veins from the falx and sometimes from the medial surfaces of the cerebral hemispheres (anterior pericallosal veins).

Straight sinus

The straight sinus lies in the junction of the falx cerebri and the tentorium cerebelli (see Figs 25.2, 26.10, 26.11A,C). It runs posteroinferiorly as a continuation of the inferior sagittal sinus and drains into the transverse sinus, most commonly into the left sinus. It is not (or is only tenuously) continuous with the superior sagittal sinus. Its tributaries include the great cerebral vein (of Galen), formed by the convergence of the internal cerebral and basal veins, and some superior cerebellar veins which may drain initially into the medial tentorial sinus (a short sinus within the tentorium).

Transverse sinus

The transverse sinuses are attached to the internal occipital protuberance (see Figs 25.2, 25.4, 26.11, 26.13). They begin at the confluence of the sinuses: one, usually the right, is directly continuous with the superior sagittal sinus, and the other is directly continuous with the straight sinus. The right transverse sinus is typically larger and drains blood from the superficial parts of the brain. The left transverse sinus mainly drains blood from the deep parts of the brain. On each side, the sinuses run in the attached margin of the tentorium cerebelli, first on the squama of the occipital bone, then on the mastoid angle of the parietal bone. Each follows a gentle anterolateral curve, increasing in size as it does so, to the posterolateral part of the petrous temporal bone, where it turns down as a sigmoid sinus that ultimately becomes continuous with the internal jugular vein. The transverse sinuses receive tributaries from the lateral temporal surface and basal surface of the temporal and occipital lobes. The inferior anastomotic vein (of Labbé) is the largest vein that connects the veins of the Sylvian fissure with the transverse sinus. All tributaries of each transverse sinus may drain first into a lateral tentorial sinus. The superior petrosal sinuses drain into the transition between the transverse and sigmoid sinuses on each side (see Figs 25.2, 25.4).

Sigmoid sinus

The sigmoid sinuses are continuations of the transverse sinuses, beginning where these leave the tentorium cerebelli (**Fig. 25.7**; see Figs 25.4, 26.11, 26.13C). Each sigmoid sinus curves inferomedially in a groove on the mastoid process of the temporal bone, crosses the jugular process of the occipital bone and turns forwards to the superior jugular bulb, lying posteriorly in the jugular foramen. Anteriorly, a thin plate of bone separates its upper part from the mastoid antrum and mastoid air cells. The sigmoid sinus is connected with pericranial veins via mastoid and condylar emissary veins. Neurosurgical approaches to the lateral aspect of the posterior fossa (cerebellopontine angle) are classified as retrosigmoid, when the craniectomy is located just behind the sigmoid sinus, and presigmoid, when the mastoid bone in front of the sinus is drilled away to provide a more anterior corridor into the posterior fossa.

Superior petrosal sinus

The superior petrosal sinuses are small, narrow sinuses that drain the cavernous sinus into the transverse sinus on each side (**Figs 25.8–25.9**; see Figs 25.2, 25.4, 26.11A). Each leaves the posterosuperior part of the cavernous sinus and runs posterolaterally in the attached margin of the tentorium cerebelli, crosses superior to the trigeminal nerve to lie in a groove on the superior border of the petrous part of the temporal bone, and ends by joining the transverse sinus at the point where this curves down to become the sigmoid sinus. The superior petrosal sinuses may receive cerebellar and brainstem veins, such as the superior petrosal vein, and, rarely, the inferior cerebral and tympanic veins; they are connected with the inferior petrosal sinuses and the basilar plexus.

Inferior petrosal sinus

The inferior petrosal sinuses drain the cavernous sinus into the internal jugular veins (see Figs 25.4, 26.10, 26.11A). They begin at the posteroinferior aspect of the cavernous sinus and run back in the petroclival fissure (a groove between the petrous part of the temporal bone and the basilar part of the occipital bone). On each side, the inferior petrosal sinus then passes through the anteromedial part of the jugular foramen, accompanied by a meningeal branch of the ascending pharyngeal artery, and descends obliquely backwards to drain into the superior jugular bulb. It sometimes drains via a vein in the hypoglossal canal to the suboccipital vertebral plexus.

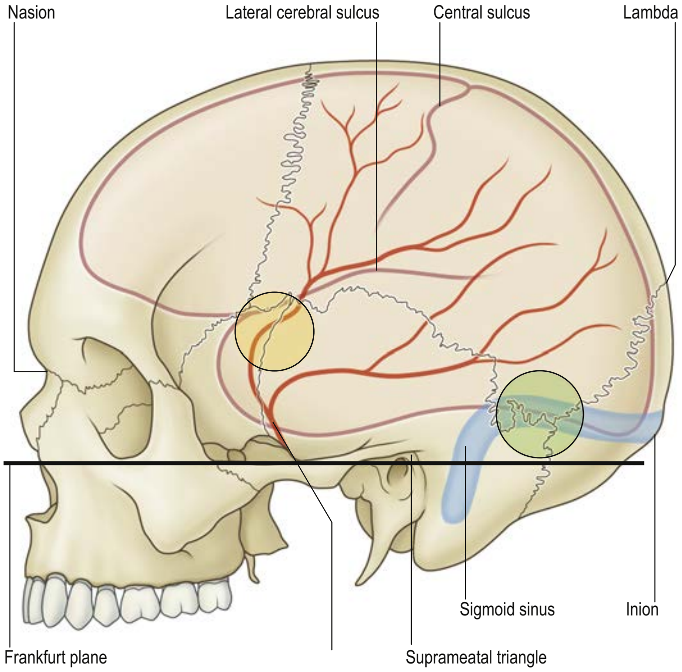
Nasion
Lateral cerebral sulcus
Central sulcus
Lambda
Sigmoid sinus
Inion
Frankfurt plane
Suprameatal triangle

Fig. 25.7 The relations of the brain, the middle meningeal artery and the transverse and sigmoid sinuses to the surface of the skull. The area enclosed in the yellow circle (including the pterion) is used when performing a pterional craniotomy over the frontal branch of the middle meningeal artery and lateral Sylvian fissure; the area enclosed in the green circle is used when performing a retrosigmoid craniotomy extending to the confluence of the transverse and sigmoid sinuses.

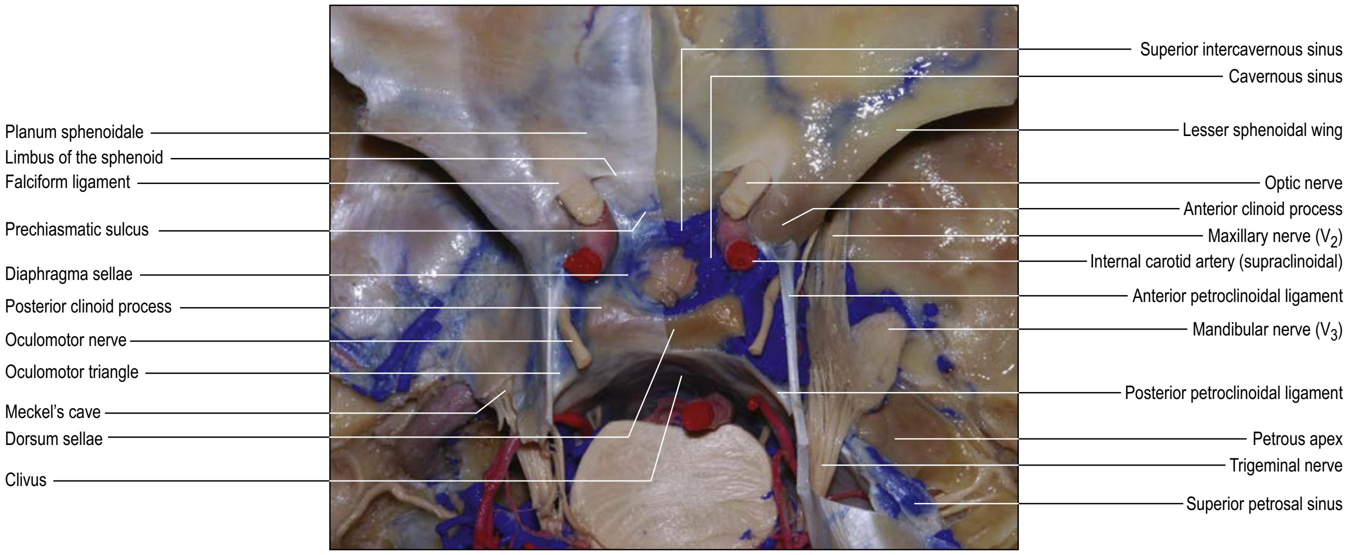
Planum sphenoidale
Limbus of the sphenoid
Falciform ligament
Prechiasmatic sulcus
Diaphragma sellae
Posterior clinoid process
Oculomotor nerve
Oculomotor triangle
Meckel's cave
Dorsum sellae
Clivus
Superior intercavernous sinus
Cavernous sinus
Lesser sphenoidal wing
Optic nerve
Anterior clinoid process
Maxillary nerve (V_2)
Internal carotid artery (supraclinoidal)
Anterior petroclinoidal ligament
Mandibular nerve (V_3)
Posterior petroclinoidal ligament
Petrous apex
Trigeminal nerve
Superior petrosal sinus

Fig. 25.8 The sellar region and adjacent middle and anterior cranial fossae, viewed from above, in a silicon-injected anatomical specimen. The dura has been removed on the right half of the specimen to show the roof of the cavernous sinus (oculomotor triangle), and the maxillary and mandibular nerves running on the floor of the middle fossa.

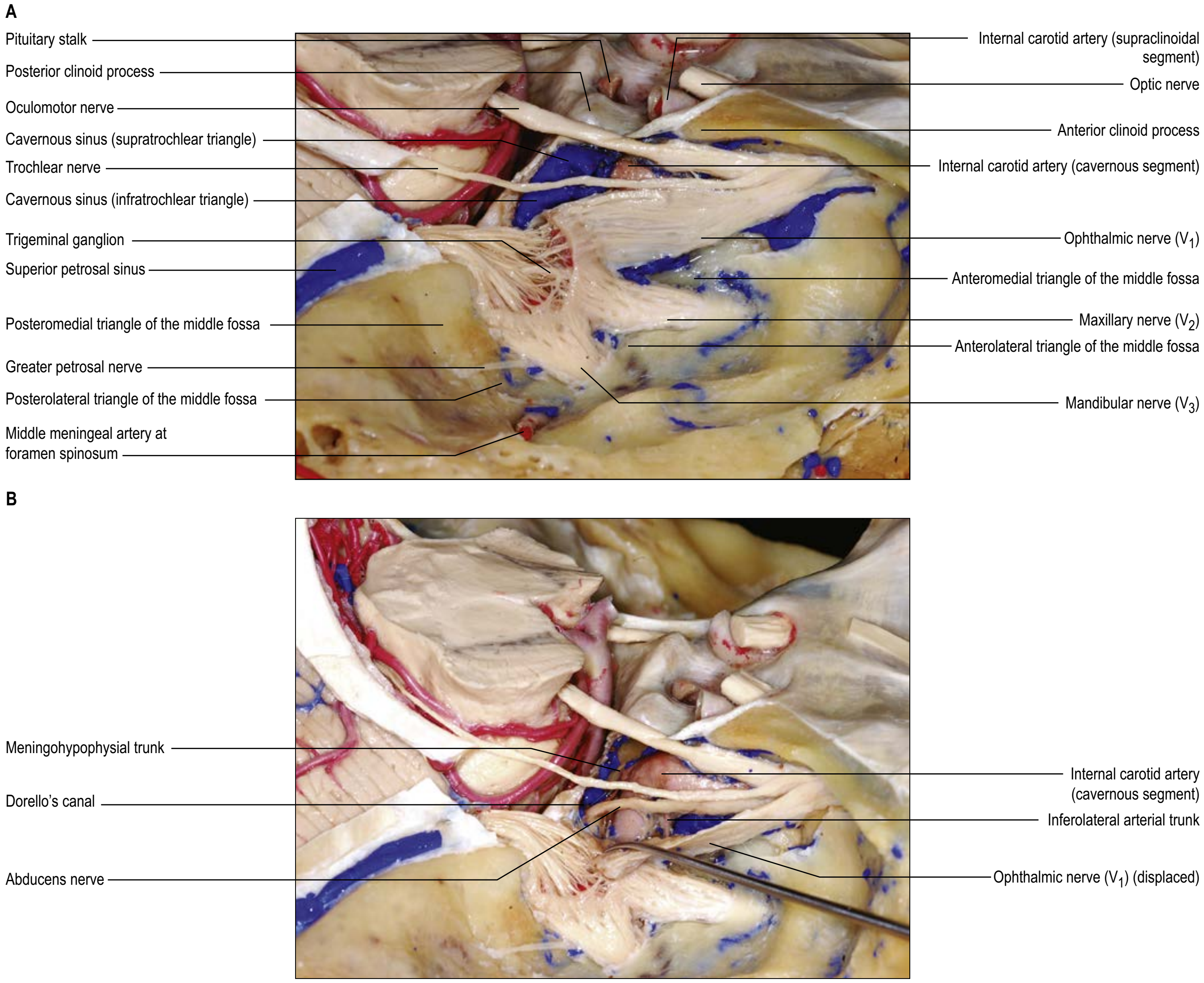
A
Pituitary stalk
Posterior clinoid process
Oculomotor nerve
Cavernous sinus (supratrochlear triangle)
Trochlear nerve
Cavernous sinus (infratrochlear triangle)
Trigeminal ganglion
Superior petrosal sinus
Posteromedial triangle of the middle fossa
Greater petrosal nerve
Posterolateral triangle of the middle fossa
Middle meningeal artery at foramen spinosum
Internal carotid artery (supraclinoidal segment)
Optic nerve
Anterior clinoid process
Internal carotid artery (cavernous segment)
Ophthalmic nerve (V_1)
Anteromedial triangle of the middle fossa
Maxillary nerve (V_2)
Anterolateral triangle of the middle fossa
Mandibular nerve (V_3)
B
Meningohypophysial trunk
Dorello's canal
Abducens nerve
Internal carotid artery (cavernous segment)
Inferolateral arterial trunk
Ophthalmic nerve (V_1) (displaced)

Fig. 25.9 **A**, A lateral view of the right middle cranial fossa and lateral wall of the cavernous sinus in a silicon-injected anatomical specimen. **B**, The ophthalmic nerve has been retracted inferiorly to show the inside of the cavernous sinus (abducens nerve, internal carotid artery and its branches) through the infratrochlear triangle.

Cavernous sinus

The cavernous sinuses are two large venous plexuses that lie on either side of the body of the sphenoid bone (see Figs 25.4, 26.11A). They extend from the superior orbital fissure to the apex of the petrous temporal bone, with an average length of 2 cm and width of 1 cm. The cavity of the cavernous sinus is formed when the two layers of dura that cover the anterior aspect of the pituitary gland separate from each other at the lateral margin of the sella: the outer (endosteal) layer continues laterally to form the anterior (sphenoidal) wall of the cavernous sinus, and the inner (meningeal) layer remains attached to the pituitary gland and runs back towards the dorsum sellae to form the medial (sellar) wall of the cavernous sinus. The posterior dural wall is posterior to the dorsum sellae and upper clivus, and is shared with the basilar plexus. The lateral wall extends from the superior orbital fissure to the petrous apex, and separates the cavernous sinus from Meckel's cave, which is inferior and posterior to the sinus. The roof of the cavernous sinus is formed by the clinoidal triangle (the dura lining the lower margin of the anterior clinoid process anteriorly), and the oculomotor triangle (the patch of dura between the anterior and posterior clinoids and the petrous apex).

Each sinus contains the cavernous segment of the internal carotid artery which is associated with a perivascular sympathetic plexus. From proximal to distal, the cavernous carotid artery has several portions, named short ascending, posterior genu, horizontal and anterior genu. The anterior genu of the cavernous carotid artery continues as the paraclinoidal segment of the carotid artery, which typically protrudes into the cavity of the sphenoidal sinus. The cavernous carotid gives off two major arterial branches: the meningohypophysial and inferolateral trunks (see Fig. 25.9B). The meningohypophysial trunk typically arises from the posterior genu and gives off the inferior hypophysial, tentorial and dorsal meningeal arteries. The inferolateral trunk arises a few millimetres distal to the meningohypophysial and is distributed around the nerves on the lateral wall of the sinus. (For more detailed descriptions of these branches, including their main variations, see Krisht et al (1994), Reisch et al (1996), Tekdemir et al (1998).)

Several cranial nerves run forwards through the cavernous sinus to enter the orbit via the superior orbital fissure (see Fig. 25.9). The oculomotor and trochlear nerves and the ophthalmic division of the trigeminal nerve all lie in the lateral wall of the sinus. The abducens nerve enters the cavernous sinus by passing inferior to the petrosphenoidal ligament within a dural tunnel (Dorello's canal) just posterior to the short ascending portion of the cavernous carotid artery, and then runs on the inferolateral side of the horizontal portion of the cavernous carotid artery, just medial to the ophthalmic nerve. The space between the trochlear and ophthalmic nerves at the lateral wall of the sinus, known as the infratrochlear or Parkinson's triangle, gives access to the horizontal and posterior genu portions of the cavernous carotid and the meningohypophysial trunk, and the abducens nerve. Unlike the ophthalmic division of the trigeminal nerve, the maxillary division of the trigeminal nerve does not run through the cavernous sinus or its lateral wall, but courses beneath the dura of the middle cranial fossa below the level of the cavernous sinus (Abhinav et al 2017).

Caroticocavernous sinus fistula and cavernous sinus thrombosis

Available with the *Gray's Anatomy* e-book

The inferior petrosal sinuses are often plexiform. Each receives labyrinthine veins via the cochlear canaliculus and the vestibular aqueduct, and tributaries from the medulla oblongata, pons and inferior cerebellar surface. The venous spaces in the sphenopetroclival area, which are filled anteriorly by blood from the cavernous sinus, medially by blood from the basilar plexus, and laterally by blood from the superior petrosal sinus, typically drain into the inferior petrosal sinuses (Iaconetta et al 2003).

Several major venous spaces or compartments can be identified within the sinus in relation to the cavernous carotid artery: superior, posterior, inferior and lateral (Fernandez-Miranda et al 2017, modified from Harris and Rhoton 1976). The superior and inferior ophthalmic veins drain into the inferior space; the basilar plexus and inferior petrosal sinus drain into the posterior space; the superior petrosal sinus opens into the superior space; and the superficial middle cerebral vein, the inferior cerebral veins and the sphenoparietal sinus may drain into the lateral compartment. Veins traversing the emissary sphenoidal foramen, foramen ovale and foramen lacerum and, less frequently, the central retinal vein and frontal tributary of the middle meningeal vein, also drain into the cavernous sinus.

Tumours (meningiomas, haemangiomas, schwannomas) can arise within the cavernous sinus or extend into the cavernous sinus from adjacent regions; typically, these are pituitary adenomas that invade the medial wall of the sinus. Transcranial microsurgical approaches enter the cavernous sinus through the lateral wall (infratrochlear triangle) or roof (oculomotor triangle) of the sinus. Recently introduced endoscopic endonasal approaches facilitate access to the cavernous sinus from its anterior (sphenoidal) and medial (sellar) walls and provide access to the posterior clinoids (Fernandez-Miranda et al 2014). (For more detailed descriptions of the microsurgical anatomy of the cavernous sinus, see Dolenc (1987), Umansky et al (1994), Seoane et al (1998), Yasuda et al (2004), Dolenc and Rogers (2009), Fernandez-Miranda et al (2014, 2017).)

Direct communication between the intracavernous portion of the internal carotid artery and the cavernous sinus, creating a caroticocavernous sinus fistula (CCF), may occur as a result of either severe head trauma or aneurysmal vessel disease. The classic signs are ptosis, proptosis (which may be pulsatile), chemosis, periorbital oedema, and extraocular dysmotility causing diplopia secondary to a combination of third, fourth and sixth cranial nerve palsies. Hypo- or hyperaesthesia in the distribution of the ophthalmic division of the trigeminal nerve and a decreased corneal reflex may also be detected. There may be evidence of dilated, tortuous retinal veins and papilloedema. These changes can cause permanent blindness. CCFs are most commonly treated by passing a catheter up the carotid into the fistula, and then occluding it with dilatable balloons or flexible metal coils. Any spreading infection involving the upper nasal cavities, paranasal sinuses, cheek (especially near the medial canthus), upper lip, anterior nares, or even an upper incisor or canine tooth, may very rarely lead to septic thrombosis of the cavernous sinuses; infected thrombi pass from the facial vein or pterygoid venous complex into the sinus via either ophthalmic veins or emissary veins that enter the cranial cavity through the foramen ovale. This is a critical medical emergency with a high risk of disseminated cerebritis and cerebral venous thrombosis.

Intercavernous sinuses

The two cavernous sinuses are connected by superior, inferior and posterior intercavernous sinuses, and the basilar plexus (see Figs 25.4, 25.8, 26.11A). The superior and posterior intercavernous sinuses lie in the anterior and posterior attached borders of the diaphragma sellae and they thus form a complete circular venous sinus. The inferior intercavernous sinuses are irregular and plexiform in nature, and commonly encountered in a surgical transnasal approach to the pituitary gland. Obliteration of any intercavernous sinus has no clinical consequences because all connections are valveless and the direction of flow in them is reversible.

Basilar venous plexus

The basilar sinus and plexus consist of interconnecting channels between the two layers of dura mater on the clivus (see Figs 25.4, 25.8). The basilar venous plexus interconnects the cavernous sinuses and inferior and superior petrosal sinuses, and joins the internal vertebral venous plexus.

Sphenoparietal sinus

The sphenoparietal sinuses are inconstant dural venous channels that lie under the lesser wings of the sphenoid bone, near their posterior edge (see Figs 25.4, 26.11A,C). Each sinus curves medially to open into the anterior part of the cavernous sinus, and receives small veins from the adjacent dura mater and sometimes from the frontal ramus of the middle meningeal vein. In its middle course, each may also receive connecting rami from the superficial middle cerebral vein, temporal lobe veins and the anterior temporal diploic vein. When these connections are well developed, the sphenoparietal sinus is a large channel. It has been suggested that the term sphenoparietal sinus should be abandoned on the basis that it is not an anatomical entity, but an artificial combination of two independent meningeal vessels, namely the parietal portion of the anterior branch of the middle meningeal veins and the sinus of the lesser wing of the sphenoid (Ruíz et al 2004).

Occipital sinus

The occipital sinus is the smallest of the sinuses and is typically larger in children. It lies in the attached margin of the falx cerebelli (see Fig. 25.4) and is occasionally paired. It starts near the foramen magnum in several small channels, one of which joins the end of the sigmoid sinus and connects with the internal vertebral plexuses. It ends in the confluence of the sinuses.

Marginal sinus

The marginal sinus encircles the foramen magnum. It communicates anteriorly with the basilar plexus and posteriorly with the occipital sinus. It typically drains to the sigmoid sinus or jugular bulb by small sinuses and may connect extracranially to the internal vertebral venous plexus or the paravertebral or deep cervical veins in the suboccipital region.

Emissary veins

Emissary veins traverse cranial apertures and connect intracranial venous sinuses and extracranial veins. Some are relatively constant, others may be absent. These connections are of clinical significance in determining the spread of infection from extracranial foci to venous sinuses, e.g. the spread of infection from the mastoid to the venous sinuses or from the paranasal sinuses to the cavernous sinus, and they may provide alternative drainage pathways in cases of venous sinus thrombosis.

Meningeal arteries and veins and diploic veins

Despite their names, the cranial meningeal arteries are predominantly periosteal (**Fig. 25.10A**). Their main targets are bone and haemopoietic marrow, and only some arterial branches are distributed to the cranial dura mater *per se*.

The branches of the meningeal vessels lie mainly in the endosteal layer of dura. In the anterior cranial fossa, the dura is supplied by the anterior meningeal branches of the anterior and posterior ethmoidal and internal carotid arteries and a branch of the middle meningeal artery. In the middle cranial fossa, the dura is supplied by the middle and accessory meningeal branches of the maxillary artery; a branch of the ascending pharyngeal artery (entering via the foramen lacerum); branches of the internal carotid artery; and a recurrent branch of the lacrimal artery. In the posterior fossa, the dura is supplied by meningeal branches of the occipital artery which enter the skull by the jugular and mastoid foramina; the posterior meningeal branches of the vertebral artery; occasional small branches of the ascending pharyngeal artery which enter the skull by the jugular foramen and hypoglossal canal; and dorsal meningeal and tentorial branches from the meningohypophysial trunk. The anatomy of the meningeal arteries explains the vascular supply of tumours arising from the meninges (meningiomas) and the architecture of dural arteriovenous fistulae and malformations. (For detailed information on the surgical anatomy of the meningeal arteries, see Lasjaunias et al (2001), Martins et al (2005).)

Middle meningeal artery

The middle meningeal artery is the largest of the meningeal arteries. It arises from the first part of the maxillary artery in the infratemporal fossa and passes between the roots of the auriculotemporal nerve. It lies lateral to tensor veli palatini, then enters the cranial cavity through the foramen spinosum and runs in an anterolateral groove on the squamous part of the temporal bone, dividing into frontal and parietal branches (see Fig. 25.10A). The larger frontal (anterior) branch crosses the greater wing of the sphenoid and enters a groove or canal in the sphenoidal angle of the parietal bone (the sphenoparietal canal). It divides into branches between the dura mater and cranium, and some branches ascend to the vertex. The parietal (posterior) branch curves back on the squamous temporal bone, reaches the lower border of the parietal bone anterior to its mastoid angle and divides to supply the posterior parts of the dura mater and cranium. These frontal and parietal branches anastomose with their fellows and with the anterior and posterior meningeal arteries.

Ganglionic branches supply the trigeminal ganglion and associated roots. The petrosal branch enters the hiatus for the greater petrosal nerve, supplies the facial nerve, geniculate ganglion and tympanic cavity, and anastomoses with the stylomastoid artery (El Khouly et al 2008). The superior tympanic artery runs in the canal for tensor tympani and supplies the muscle and the mucosa that lines the canal. Temporal branches traverse minute foramina in the greater wing of the sphenoid and anastomose with deep temporal arteries that supply temporalis. An anastomotic branch enters the orbit laterally in the superior orbital fissure, and anastomoses with a recurrent branch of the lacrimal artery; enlargement of this anastomosis is believed to account for the occasional origin of the lacrimal artery from the middle meningeal artery.

Accessory meningeal artery

Available with the *Gray's Anatomy* e-book

Meningeal veins

Meningeal veins begin from plexiform vessels in the dura mater. They drain into efferent vessels in the outer dural layer that connect with lacunae associated with some of the cranial sinuses. They include the middle meningeal and the diploic veins. Intracranial veins also communicate with extracranial vessels via emissary veins.

Middle meningeal vein (sinus)

The frontal (anterior) branch of the middle meningeal vein crosses the floor of the middle cranial fossa, from either the foramen ovale or foramen spinosum, to the pterion, usually in the form of two parallel channels that accompany the middle meningeal artery. The vein subsequently passes cranially along the anterior margin of the parietal squama to empty into the venous lakes of the superior sagittal sinus. As they course under the most lateral aspect of the lesser sphenoidal wing, the anterior branches of the middle meningeal vessels are contained for a short distance within a bony canal, the sphenoparietal canal (of Trolard), which they leave to enter a groove on the internal surface of the parietal squama. The veins lie closer to the bone than the artery, sometimes occupying separate grooves, and are particularly liable to tear in cranial fractures. Before it enters the sphenoparietal canal, the anterior branch of the middle meningeal vein usually connects with the sinus of the lesser sphenoidal wing, which is connected medially with the anterior and superior aspect of the cavernous sinus by a channel that crosses over the superior ophthalmic vein to reach the sinus. The parietal (posterior) trunk of the middle meningeal vein may traverse the foramen spinosum to end in the pterygoid venous plexus. The frontal trunk may also reach this

The following emissary veins have been recognized. A mastoid emissary vein in the mastoid foramen connects the sigmoid sinus with the posterior auricular or occipital veins. A parietal emissary vein in the parietal foramen connects the superior sagittal sinus with the veins of the scalp. The venous plexus of the hypoglossal canal (occasionally a single vein) connects the sigmoid sinus and the internal jugular vein. A supracondylar emissary vein connects the sigmoid sinus and veins in the suboccipital triangle via the posterior condylar canal. A plexus of emissary veins (venous plexus of the foramen ovale) connects the cavernous sinus to the pterygoid plexus via the foramen ovale. Two or three small veins traverse the foramen lacerum and connect the cavernous sinus and the pharyngeal veins and pterygoid plexus. A vein in the emissary sphenoidal foramen (of Vesalius) connects the cavernous sinus with the pharyngeal veins and pterygoid plexus. The internal carotid venous plexus, which passes through the carotid canal, connects the cavernous sinus and the internal jugular vein. A vein may traverse the foramen caecum and connect nasal veins with the superior sagittal sinus. An occipital emissary vein usually connects the confluence of the sinuses with the occipital vein through the occipital protuberance, and also receives the occipital diploic vein. The occipital sinus connects with variably developed veins around the foramen magnum (marginal sinuses) and thus with the vertebral venous plexuses; this pathway provides an alternative venous drainage when the jugular vein is blocked or tied. The ophthalmic veins are potentially emissary because they connect intracranial and extracranial veins. The petrosquamous sinus arises from the dorsolateral portion of the transverse sinus before its confluence with the superior petrosal sinus, courses over the lateral superior surface of the petrous part of the temporal bone, and drains anteroinferiorly into the retromandibular vein and anteromedially into the pterygoid venous plexus. It usually disappears during the development of adult venous patterns in the last three months of prenatal life.

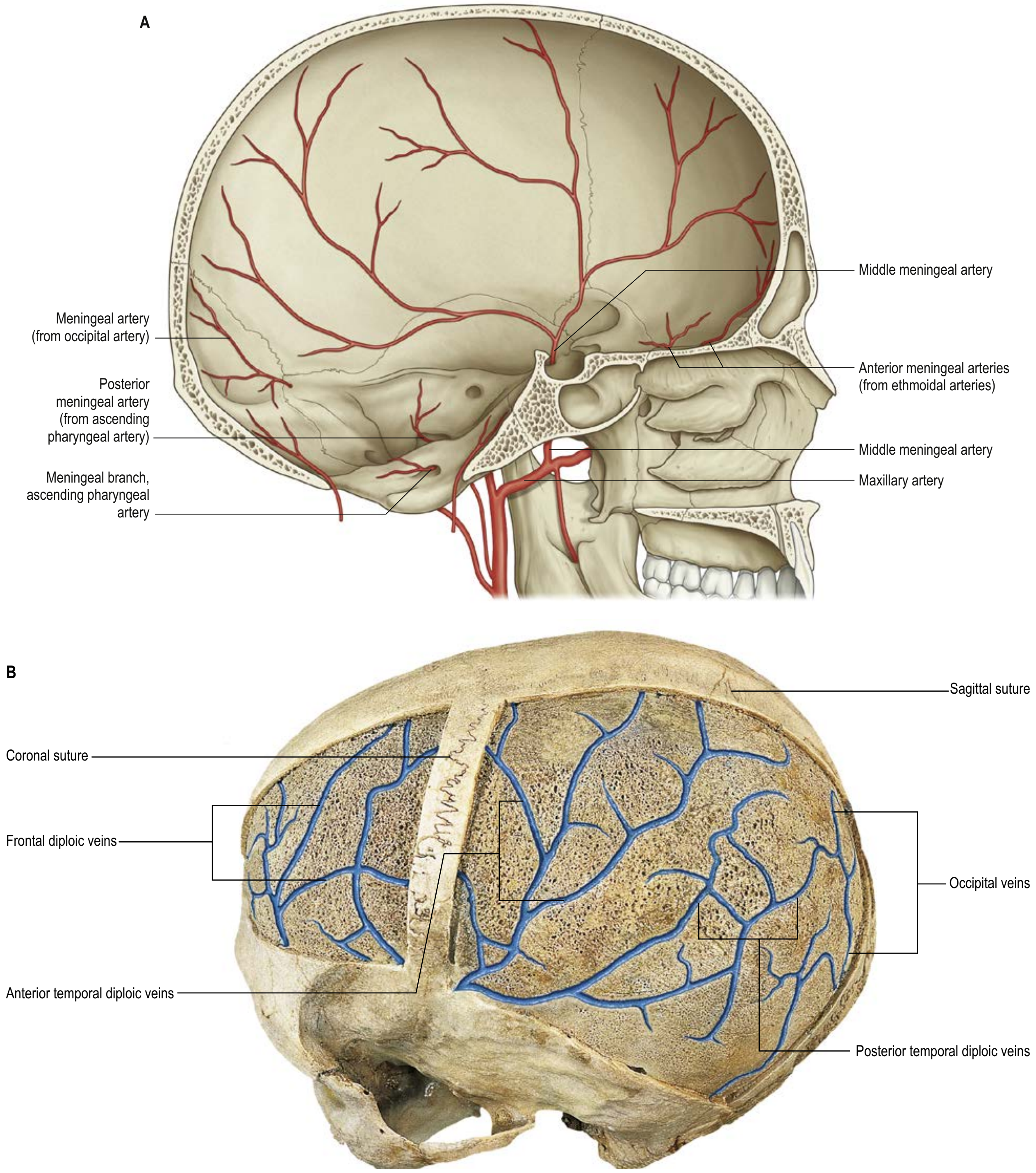
A
Meningeal artery (from occipital artery)
Posterior meningeal artery (from ascending pharyngeal artery)
Meningeal branch, ascending pharyngeal artery
Middle meningeal artery
Anterior meningeal arteries (from ethmoidal arteries)
Middle meningeal artery
Maxillary artery
B
Sagittal suture
Coronal suture
Frontal diploic veins
Occipital veins
Anterior temporal diploic veins
Posterior temporal diploic veins

Fig. 25.10 **A**, The meningeal arteries. **B**, The diploic canals and veins after removal of the external table of the calvaria. (A, Adapted with permission from Drake RL, Vogl AW, Mitchell A (eds) Gray's Anatomy for Students, 2nd ed. Elsevier, Churchill Livingstone. Copyright 2010. B, Sobotta Atlas of Human Anatomy © Elsevier GmbH, Urban & Fischer, Munich.)

plexus via the foramen ovale, or it may end in the sphenoparietal or cavernous sinus (see Fig. 25.4). The middle meningeal vein receives meningeal tributaries and small inferior cerebral veins, and connects with the diploic and superficial middle cerebral veins. It frequently bears arachnoid granulations.

Diploic veins

The diploic veins are large, thin-walled vessels that occupy channels in the diploë of the cranial bones (Fig. 25.10B). Four main trunks are usually described: the frontal, anterior and posterior temporal, and occipital diploic veins. The frontal vein opens into the supraorbital vein and the superior sagittal sinus; the anterior temporal vein is confined mainly to the frontal bone, and opens into the sphenoparietal sinus and one of the deep temporal veins through an aperture in the greater wing of the sphenoid; the posterior temporal vein lies in the parietal bone and empties into the transverse sinus either through an opening at the mastoid angle of the parietal bone or through the mastoid foramen; the occipital vein, the largest of the four, is confined to the occipital bone and may open externally into the occipital vein or internally into either the transverse sinus or the confluence of the sinuses.

Sinus pericranii

Available with the *Gray's Anatomy* e-book

ARACHNOID AND PIA MATER

The arachnoid mater and the pia mater together are sometimes referred to as the leptomeninges. They are separated by the subarachnoid space and joined by trabeculae. The outer layer of the arachnoid, the dura–arachnoid interface, is formed from five or six layers of cells joined by numerous desmosomes and tight junctions and forms a barrier that normally prevents permeation of CSF through the arachnoid into the

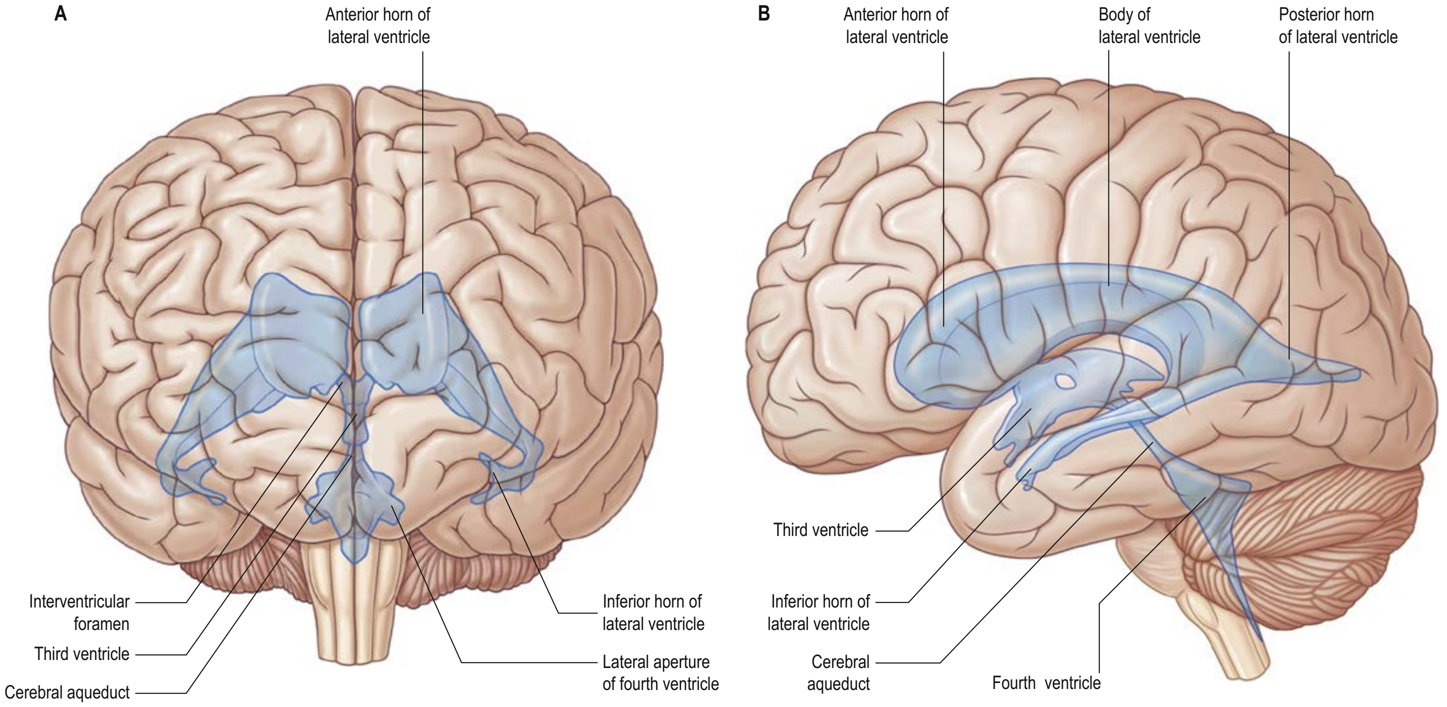
A
Anterior horn of lateral ventricle
Interventricular foramen
Third ventricle
Cerebral aqueduct
Inferior horn of lateral ventricle
Lateral aperture of fourth ventricle
B
Anterior horn of lateral ventricle
Body of lateral ventricle
Posterior horn of lateral ventricle
Third ventricle
Inferior horn of lateral ventricle
Cerebral aqueduct
Fourth ventricle

Fig. 25.11 The ventricular system. **A**, Anterior view. **B**, Left lateral view.

subdural space. The central portion of the arachnoid is closely apposed to the outer layer, and is formed from tightly packed polygonal cells joined by desmosomes and gap junctions. The cells are more loosely packed in the inner layer of the arachnoid, where they intermingle with bundles of collagen continuous with the trabeculae that cross the subarachnoid space. The leptomeningeal cells are not surrounded by basement membrane, except where they are in contact with collagen in the inner layers of the arachnoid and on the deep aspects of the pia mater.

The anatomical relationships of the arachnoid and pia differ to some extent in the cerebral and spinal regions. The cerebral part of the arachnoid mater invests the brain loosely: it does not enter the sulci or fissures, other than the interhemispheric and Sylvian fissures, and it coats the superior surface of the pituitary fossa. The arachnoid is easily separated from the dura over the surface of the brain, but it is adherent to the adventitia of the internal carotid and the vertebral arteries where they enter the subarachnoid space. It is reflected onto the surface of blood vessels and cranial nerves in the subarachnoid space: this is the basis for microsurgical subarachnoid dissection to expose brain vessels and cranial nerves. The subarachnoid cisterns are cavities formed by the wide separation of the pia and arachnoid, which is particularly common on the basal aspect of the brain, where the basal cisterns are located. Knowledge of the neural and vascular contents of each of the basal cisterns is of particular value to the neurosurgeon in the planning and execution of intracranial procedures (Yasargil 1984).

Subdural haematoma

Separation of the arachnoid and dura mater requires little physical force, which means that damage to small bridging veins in the space can result in a subdural haematoma after even relatively mild head trauma. In cases of chronic or subacute subdural haematomas, the accumulation is of relatively low pressure and seldom presents as a medical emergency; even sizeable accumulations may be tolerated on a chronic basis with mild or no symptoms, and can be surgically drained through small openings in the skull (burr-holes). In many cases, there is some predisposing factor, such as cerebral atrophy or an increase in the size of the underlying subarachnoid space. In cases of acute subdural haematoma, typically after severe head trauma, there is rapid accumulation of blood in the subdural space which requires emergency neurosurgical drainage through a large craniotomy or craniectomy. The distinction between subdural and extradural haematoma on a CT scan relies on the anatomical features of the clot. Extradural collections tend to be lentiform in shape, reflecting the pressure required to separate the dura and periosteum: they will not pass deep to any major dural sinus and cannot extend along the falx cerebri or tentorium cerebelli. In contrast, acute subdural haematomas tend to be biconcave in shape and often follow the line of the dura along the falx or tentorium (see Fig. 25.1).

TOPOGRAPHY AND RELATIONSHIPS OF THE VENTRICULAR SYSTEM

The cerebral ventricular system consists of a series of interconnecting spaces and channels within the brain (**Figs 25.11–25.12**), which are derived from the central lumen of the embryonic neural tube and the cerebral vesicles to which it gives rise (Ch. 14). Each cerebral hemisphere contains a large lateral ventricle that communicates near its rostral end with the third ventricle via the interventricular foramen (foramen of Monro). The third ventricle is a midline, slit-like cavity lying between the right and left thalamus and hypothalamus. Caudally, the third ventricle is continuous with the cerebral aqueduct. This narrow tube passes through the midbrain and is continuous with the fourth ventricle, a wide cavity lying between the brainstem and cerebellum. The fourth ventricle communicates with the subarachnoid space of the cisterna magna through the foramen of Magendie, and with the cerebellopontine angles through the foramina of Luschka; caudally it is continuous with the vestigial central canal of the spinal cord.

The ventricular system contains cerebrospinal fluid (CSF), which is mostly secreted by the choroid plexuses located within the lateral, third and fourth ventricles.

Lateral ventricle

Viewed from its lateral aspect, the lateral ventricle has a roughly C-shaped profile (see Figs 25.11–25.12; **Fig. 25.13**). The shape is a consequence of the developmental expansion of the frontal, parietal and occipital regions of the cerebral hemisphere that displaces the temporal lobe inferiorly and anteriorly. Both the caudate nucleus and the fornix, which lie in the wall of the ventricle, have adopted a similar morphology, so that the tail of the caudate nucleus encircles the thalamus in a C shape, and the fornix traces the outline of the ventricle forwards to the interventricular foramen.

The lateral ventricle is divided into five parts: the frontal (anterior), occipital (posterior) and temporal (inferior) horns, the body and the atrium (Rhoton 2002).

The frontal horn lies within the frontal lobe. The posterior aspect of the genu and the rostrum of the corpus callosum bound it anteriorly, forming the floor and anterior wall. Its roof is formed by the anterior part of the body of the corpus callosum. The frontal horns of the two ventricles are separated by the septum pellucidum. The coronal profile of the frontal horn is roughly that of a flattened triangle in which the rounded head of the caudate nucleus forms the lateral wall (**Figs 25.14–25.15**). The frontal horn extends posteriorly as far as the interventricular foramen.

Cavum septum pellucidum (CSP) describes a septum pellucidum that has a separation between its two leaflets (septal laminae). The

The accessory meningeal artery may arise from the maxillary artery or the middle meningeal artery. It enters the cranial cavity through the foramen ovale and supplies the trigeminal ganglion, dura mater and bone. Its main distribution is extracranial, principally to medial pterygoid, lateral pterygoid (upper head), tensor veli palatini, the greater wing and pterygoid processes of the sphenoid bone, the mandibular nerve and the otic ganglion. It is sometimes replaced by separate small arteries.

Sinus pericranii is a rare condition involving congenital or acquired anomalous connections between an extracranial blood-filled nodule and an intracranial dural venous sinus via dilated diploic and/or emissary veins of the skull (Sheu et al 2002).

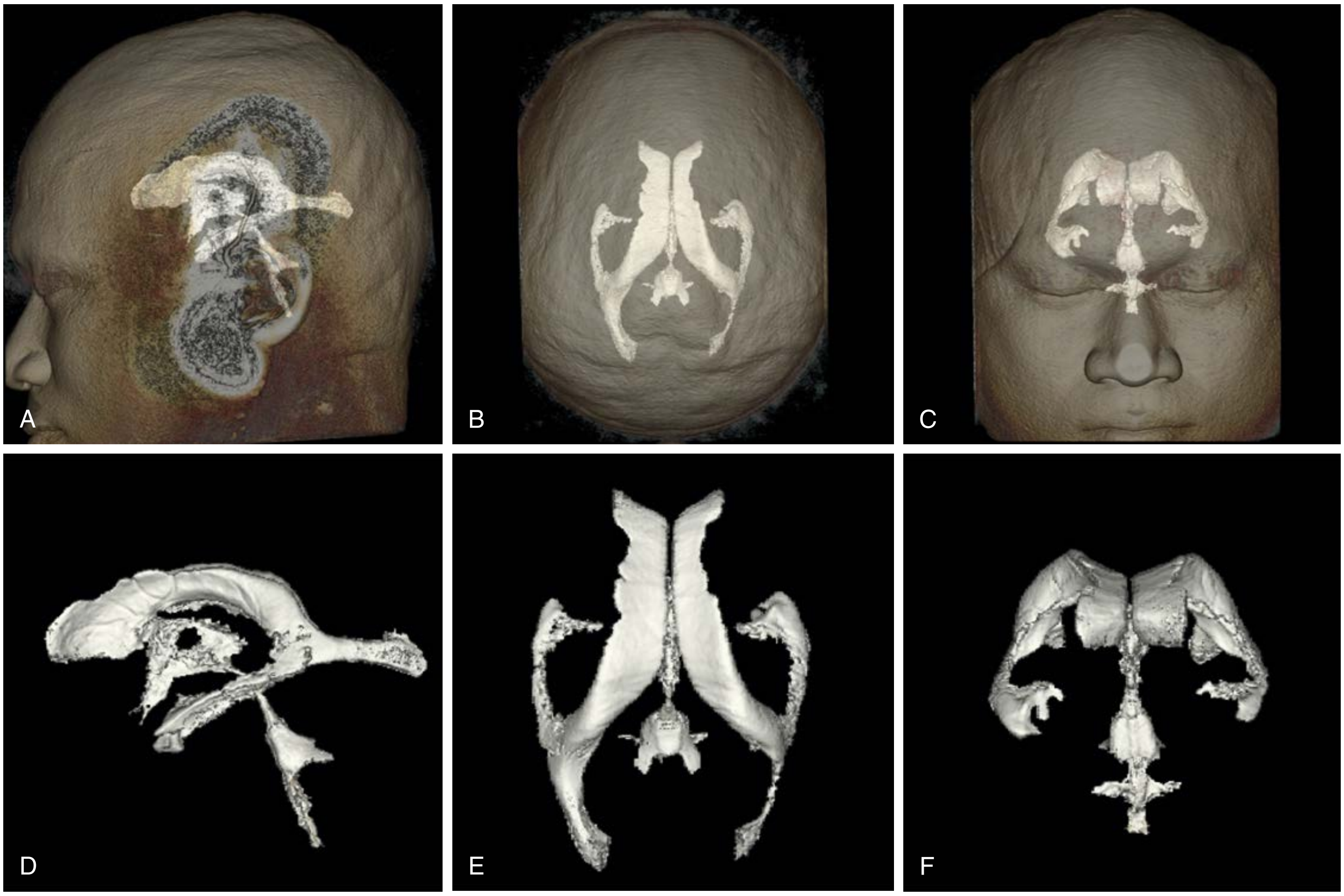

Fig. 25.12 The ventricular system. Three-dimensional computer-reformatted volumetric T2-weighted magnetic resonance images display the ventricles in lateral (**A**, **D**), superior (**B**, **E**) and anterior (**C**, **F**) views. **A–C**, Orientation of the ventricular system within the head, seen through the partially transparent skin surface. **D–F**, Magnified display of the isolated ventricles in the same orientation. (With permission from Rios JC, Galper MW, Naidich TP Ventricles and intracranial subarachnoid spaces. In: Naidich TP, Castillo M, Cha S et al (eds) Imaging of the Brain. Elsevier, Saunders. Copyright 2013.)

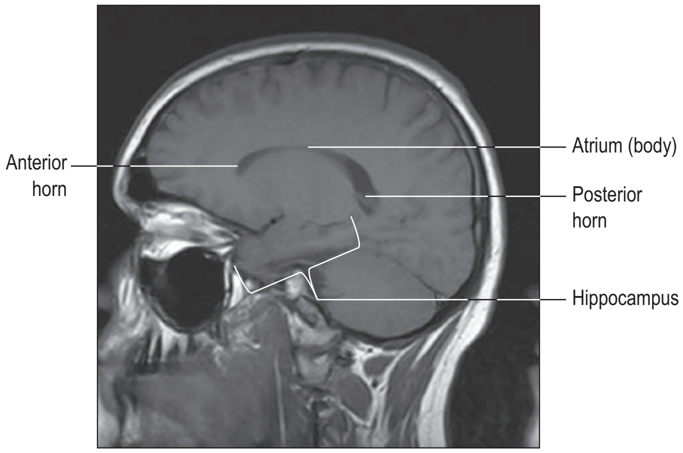

Fig. 25.13 A sagittal T1-weighted MRI, showing the C-shaped profile of the lateral ventricle.

cavity contains cerebrospinal fluid that filters from the ventricles through the septal laminae. The most common type of cavum septum pellucidum is non-communicating, i.e. it is not connected to the ventricular system. Cavum septum pellucidum is present in 100% of fetuses below 36 postmenstrual weeks. Its prevalence gradually decreases with age, being present in approximately 2% of the adult population (Farruggia and Babcock 1981, Nakano et al 1981, Mott et al 1992).

The body of the lateral ventricle lies within the frontal and parietal lobes and extends from the interventricular foramen to the splenium of the corpus callosum, where the septum pellucidum disappears and the corpus callosum and fornix meet. The bodies of the lateral ventricles are separated by the septum pellucidum, which contains the columns of the fornices in its lower edge. The lateral wall of the body of the ventricle is formed by the caudate nucleus superiorly and the thalamus inferiorly. The boundary between the thalamus and caudate nucleus is marked by the thalamostriate sulcus, a groove that is occupied by a fascicle of nerve fibres, the stria terminalis, and by the thalamostriate vein (**Fig. 25.16**; see Fig. 25.14). The inferior limit of the body of the ventricle and its medial wall are formed by the body of the fornix (**Fig. 25.17**; see Fig. 25.14). The fornix is separated from the thalamus by a narrow cleft, the choroidal fissure, along which the choroid plexus in the lateral ventricle is attached. The choroidal fissure extends in a C-shaped arc that starts from the interventricular foramen, runs along the superior, posterior and inferior aspects of the thalamus, and ends at the inferior choroidal point, located in the temporal horn just behind the head of the hippocampus. On either side, the tela choroidea, the membrane in which the choroid plexus arises, is attached to the taeniae (the edges of the thalamus and fornix bordering the choroidal fissure) (Nagata et al 1988).

The body of the lateral ventricle widens posteriorly to become continuous with the occipital and temporal horns at the atrium (collateral trigone). The roof of the atrium is formed by the posterior body and splenium of the corpus callosum. The medial wall is formed by two prominences: an upper prominence, the bulb of the corpus callosum, formed by fibres of the corpus callosum as they sweep posteriorly into the occipital lobe (forceps major); and an inferior prominence, the calcar avis, which overlies the calcarine fissure. The lateral wall is formed by the caudate nucleus as it wraps around the pulvinar of the thalamus and more posteriorly by fibres of the tapetum of the corpus callosum. The anterior wall has a medial part formed by the crus of the fornix, and a lateral part formed by the pulvinar of the thalamus. The floor is formed by the collateral trigone, a bulge that overlies the collateral sulcus. Posteriorly, the atrium is continuous with the occipital horn.

The occipital horn curves posteromedially into the occipital lobe. It is usually diamond-shaped in outline and it varies in size: it can

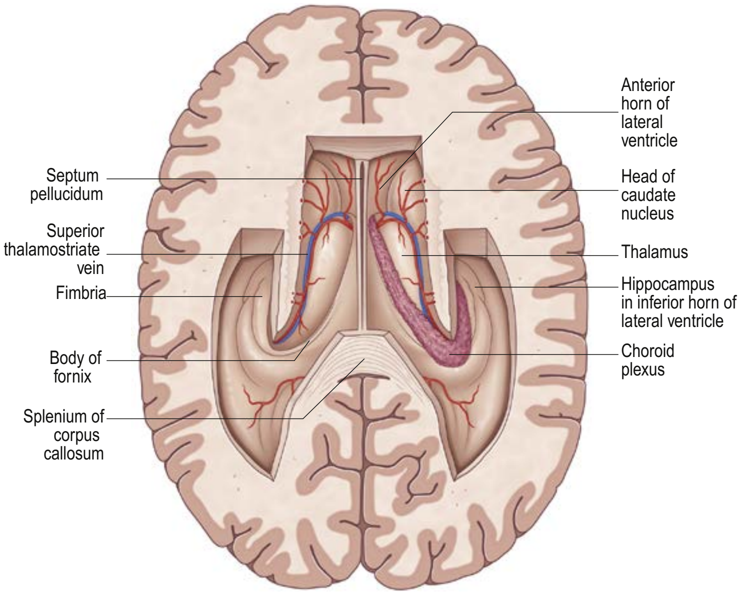
Septum pellucidum
Superior thalamostriate vein
Fimbria
Body of fornix
Splenium of corpus callosum
Anterior horn of lateral ventricle
Head of caudate nucleus
Thalamus
Hippocampus in inferior horn of lateral ventricle
Choroid plexus

Fig. 25.14 A horizontal section of the cerebrum dissected to remove the roofs of the lateral ventricles.

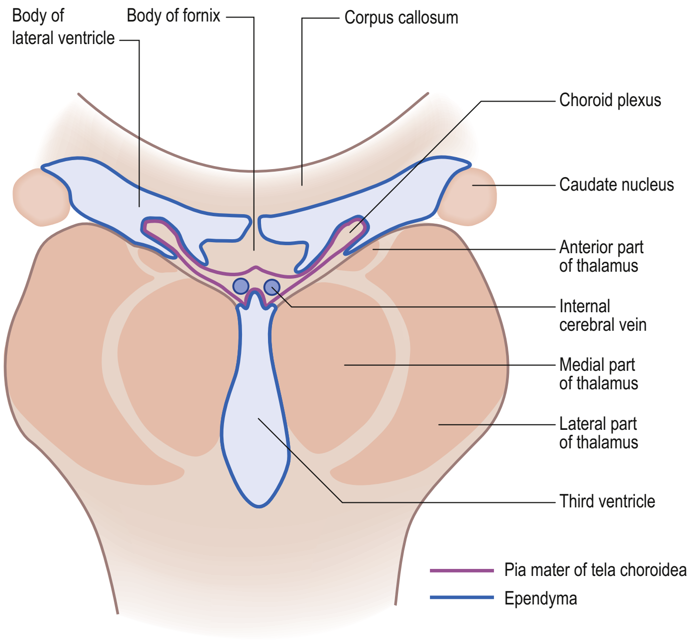
Body of lateral ventricle
Body of fornix
Corpus callosum
Choroid plexus
Caudate nucleus
Anterior part of thalamus
Internal cerebral vein
Medial part of thalamus
Lateral part of thalamus
Third ventricle
Pia mater of tela choroidea
Ependyma

Fig. 25.17 The lateral and third ventricles, coronal section.

Fig. 25.15 Coronal T2-weighted MRI scan, at the level of the frontal (anterior) horn of the lateral ventricle. Note the bifurcation of the right internal carotid artery into the middle and anterior cerebral arteries at the base of the Sylvian fissure.

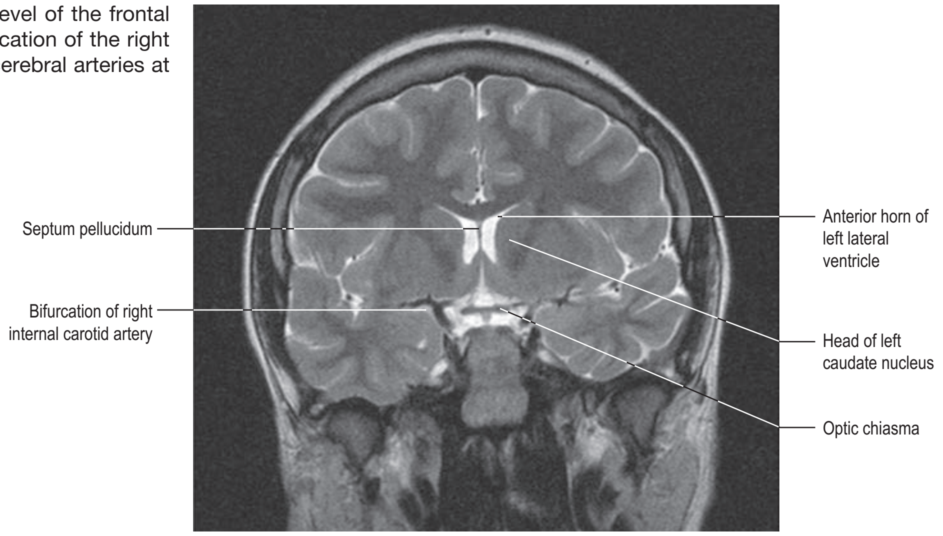
Septum pellucidum
Bifurcation of right internal carotid artery
Anterior horn of left lateral ventricle
Head of left caudate nucleus
Optic chiasma

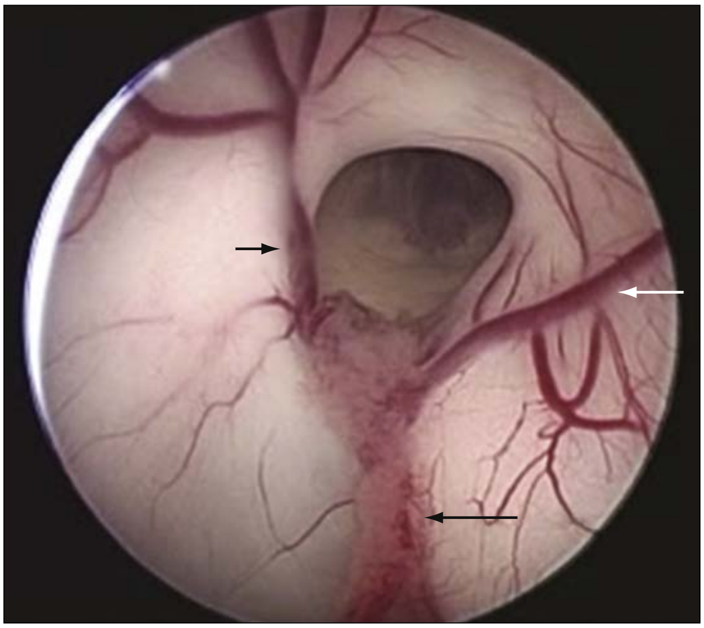

Fig. 25.16 Endoscopic view into the right lateral ventricle. The thalamostriate vein (white arrow) runs along the lateral wall and converges with the anterior septal vein (short black arrow) before converging and entering the foramen of Monro as the internal cerebral vein. The superior choroidal vein (long black arrow) is also seen coursing through the choroid plexus. (With permission from Winn HR (ed) Youmans Neurological Surgery, 6th ed. Elsevier, Saunders. Copyright 2011.)

be almost entirely absent or extend far into the occipital lobe. The two sides are often asymmetric. Fibres of the tapetum of the corpus callosum separate the ventricle from the optic radiation and the inferior fronto-occipital fasciculus, and form the roof and lateral wall of the occipital horn. The medial wall of the occipital horn is formed by fibres of the forceps major superiorly and the calacar avis inferiorly.

The temporal horn extends forwards from the atrium into the temporal lobe. It curves round the posterior aspect of the thalamus (pulvinar), passes downwards and posterolaterally and then curves anteriorly to end behind the amygdala, usually within 2.5 cm of the temporal pole, near the uncus. The roof of the temporal horn is formed by the tapetum of the corpus callosum laterally and by the tail of the caudate nucleus medially (Fig. 25.18). The latter is separated from the inferior surface of the thalamus by the striothalamic sulcus and the stria terminalis, which extend forwards in the roof to terminate in the amygdala at the anterior end of the ventricle. The floor of the temporal horn consists of the hippocampus medially and the collateral eminence, formed by the infolding of the collateral sulcus, laterally. The inferior part of the choroidal fissure, located between the fimbria of the fornix and the inferolateral aspect of the thalamus, lies in the medial wall. The temporal extension of the choroid plexus fills the choroidal fissure, covers the outer surface of the hippocampus and ends at the inferior choroidal point as previously described.

The position of the lateral ventricle relative to the surface of the hemisphere is important in understanding the topographical anatomy of the ventricles (see Fig. 25.11). The frontal horn usually corresponds to the inferior frontal gyrus; the body and atrium project along the precentral and postcentral gyri and inferior parietal lobule; the occipital horn corresponds to the occipital convexity; the temporal horn projects along the superior temporal sulcus.

Third ventricle

The third ventricle is a midline, slit-like cavity derived from the primitive forebrain vesicle (**Figs 25.19–25.20**; see Figs 25.11, 25.17) (Rhoton 2002). The lateral wall of the third ventricle is formed in its upper part by the medial surface of the anterior two-thirds of the thalamus, and in its lower part by the hypothalamus. A faint hypothalamic sulcus extends horizontally on the ventricular wall between the interventricular foramen and the cerebral aqueduct, marking the boundary between the thalamus and hypothalamus. Dorsally, the lateral wall is limited by a ridge covering the stria medullaris thalami. The lateral walls of the third ventricle are commonly joined by an interthalamic adhesion (massa intermedia), a band of grey matter that extends between the two thalami. An interthalamic adhesion is almost always found in humans, more often in females (Orly and Haines 2005). The anterior wall of the third ventricle is formed mainly by the lamina terminalis (see Fig. 25.20). This thin structure stretches from the optic chiasma inferiorly to the rostrum of the corpus callosum superiorly and represents the rostral boundary of the embryonic neural tube. The lamina terminalis forms the roof of a small virtual cavity, the cistern of the lamina terminalis, which lies immediately below the ventricle and is an extension of the interpeduncular cistern. This is clinically important because it contains the anterior communicating artery; aneurysm development and rupture at this site may cause intraventricular haemorrhage through the thin membrane of the lamina terminalis. Superior to the lamina terminalis, the anterior wall of the third ventricle is formed by the diverging columns of the fornices and by the transversely orientated anterior commissure, which crosses the midline. The narrow interventricular foramen is located immediately posterior to the column of the fornix and separates the fornix from the anterior nucleus of the thalamus. A small, angular, optic recess occurs inconsistently at the base of the lamina terminalis just dorsal to, and extending into, the optic chiasma.

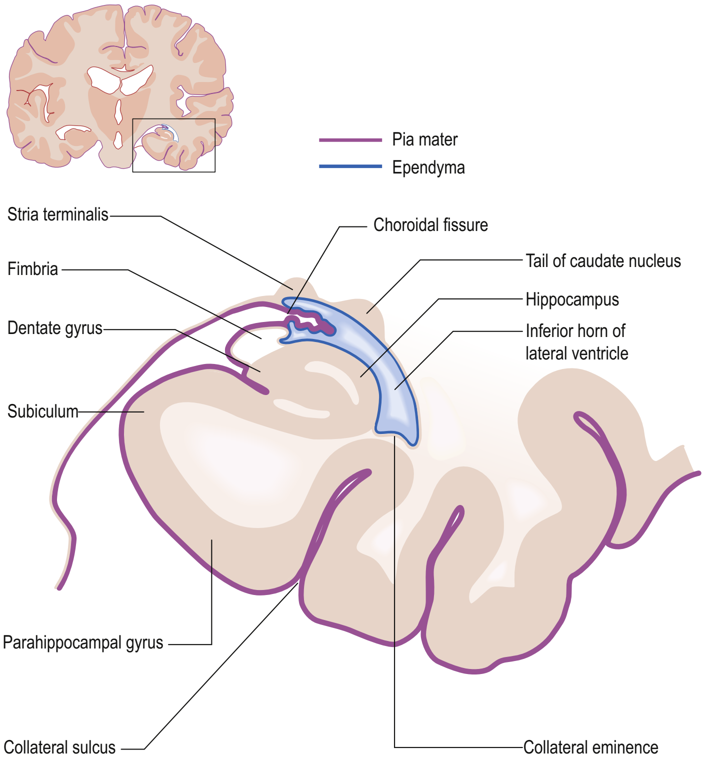

Fig. 25.18 The temporal (inferior) horn of the left lateral ventricle, coronal section.

In its anterior part, the floor of the third ventricle is formed mainly by hypothalamic structures (**Fig. 25.21**). The thin infundibular recess lies immediately posterior to the optic chiasma and extends into the pituitary stalk. Behind this recess, the tuber cinereum and the mammillary bodies complete the floor of the ventricle posteriorly.

The roof of the third ventricle consists of four layers. The most superior layer is formed by the two fornices (bodies anteriorly and crura posteriorly). The tela choroidea, giving rise to the choroid plexus, form two of the three layers located below the fornices. The choroid plexus extends from the floor of the lateral ventricle through the interventricular foramen into the roof of the third ventricle. The final layer in the roof lies between the two layers of tela choroidea and contains the internal cerebral veins and the medal posterior choroidal arteries (see Fig. 25.17).

The posterior wall of the ventricle is marked by a suprapineal recess, the habenular commissure, a pineal (epiphysial) recess that extends into the pineal stalk, and by the posterior commissure. The ventricle is continuous with the cerebral aqueduct of the midbrain inferior to the posterior commissure (see Fig. 25.20).

Cerebral aqueduct

The cerebral aqueduct is a small tube, roughly circular in transverse section and 1–2 mm in diameter. It is commonly described as having a pars anterior, an antrum and a pars posterior, and extends throughout the dorsal quarter of the midbrain in the midline, surrounded by the periaqueductal (central) grey matter (see Fig. 25.20). Rostrally, it commences immediately inferior to the posterior commissure, where it is continuous with the caudal aspect of the third ventricle. Caudally, it is continuous with the lumen of the fourth ventricle at the junction of the midbrain and pons. The superior and inferior colliculi are dorsal to the aqueduct and the midbrain tegmentum is ventral. Primary aqueductal stenosis is a cause of congenital hydrocephalus in newborns.

Fourth ventricle

The fourth ventricle lies between the brainstem and the cerebellum (**Fig. 25.22**; see Figs 25.11, 25.19–25.20, 28.5) (Rhoton 2000). Rostrally, it is continuous with the cerebral aqueduct, and caudally it is continuous with the central canal of the spinal cord. In sagittal section, the fourth ventricle has a characteristic triangular profile; the apex of its tented roof protrudes into the inferior aspect of the cerebellum. The ventricle is at its widest at the level of the pontomedullary junction, where a lateral recess on both sides extends to the lateral border of the brainstem. At this point the lateral apertures of the fourth ventricle (foramina of

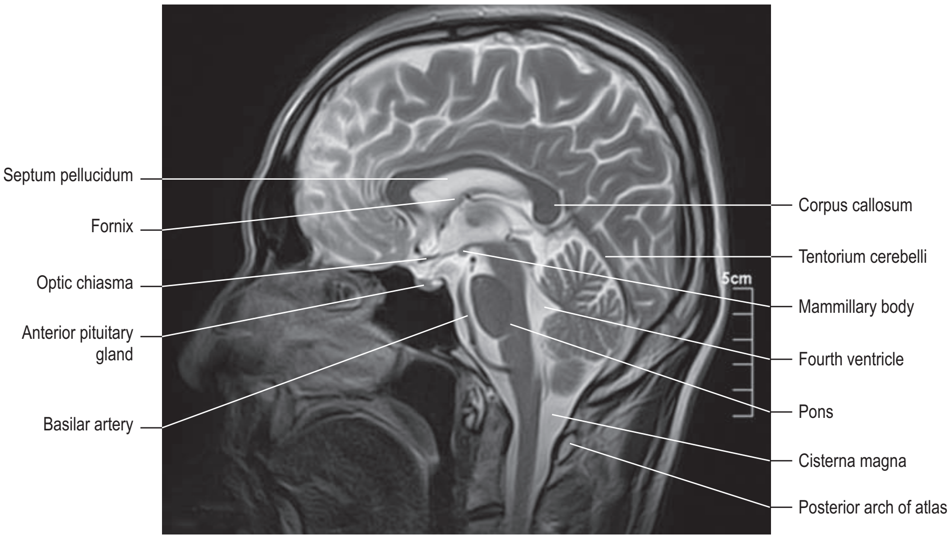

Fig. 25.19 A sagittal T2-weighted MRI scan of the head.

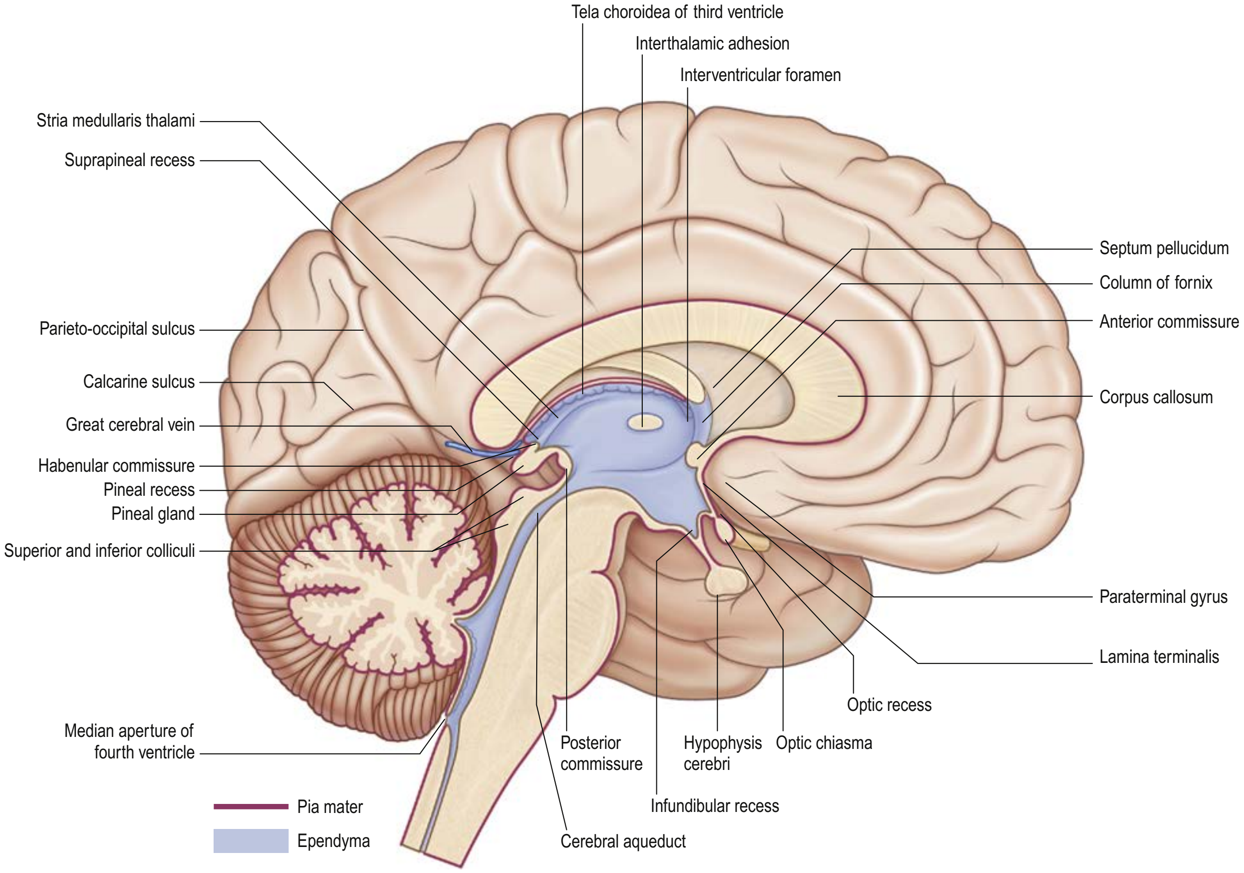
Tela choroidea of third ventricle
Interthalamic adhesion
Interventricular foramen
Stria medullaris thalami
Suprapineal recess
Parieto-occipital sulcus
Calcarine sulcus
Great cerebral vein
Habenular commissure
Pineal recess
Pineal gland
Superior and inferior colliculi
Median aperture of fourth ventricle
Septum pellucidum
Column of fornix
Anterior commissure
Corpus callosum
Paraterminal gyrus
Lamina terminalis
Optic recess
Posterior commissure
Hypophysis cerebri
Optic chiasma
Infundibular recess
Cerebral aqueduct
Pia mater
Ependyma

Fig. 25.20 A sagittal hemisection of the brain, third and fourth ventricles.

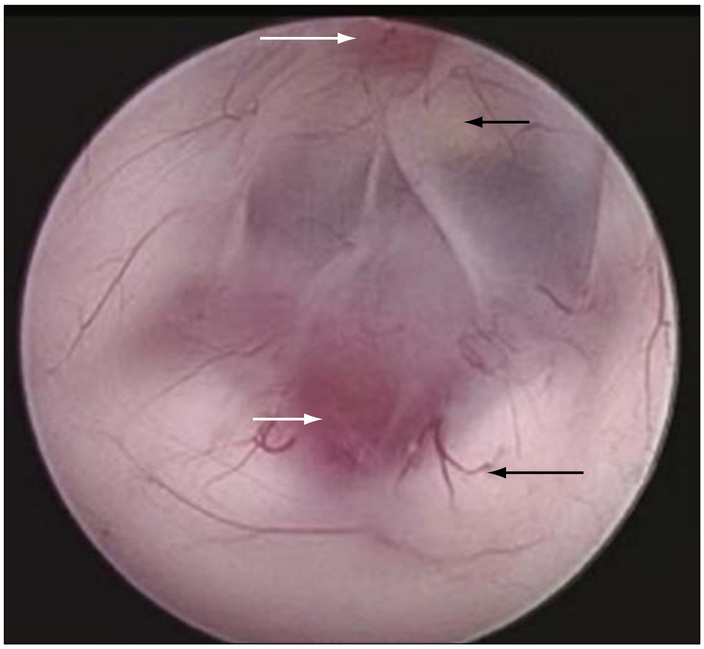

Fig. 25.21 An endoscopic view of the floor of the third ventricle. The ideal spot for fenestration is in the midline, midway between the dorsum sellae (short black arrow) and the basilar artery (short white arrow). The paired mammillary bodies (long black arrow) and the infundibular recess (long white arrow) are also seen. (With permission from Winn HR Youmans Neurological Surgery, 6th ed. Elsevier, Saunders. Copyright 2011.)

Luschka) open into the subarachnoid space at the cerebellopontine angle, behind the upper roots of the glossopharyngeal nerves.

The floor of the fourth ventricle is a shallow diamond-shaped, or rhomboidal, depression (rhomboid fossa) on the dorsal surfaces of the pons and the rostral half of the medulla (see Fig. 25.12). It consists largely of grey matter and contains important cranial nerve nuclei (V–XII). The precise location of some nuclei is discernible from surface features. The floor of the ventricle can be divided into a superior and inferior part: both parts are triangular in shape and are separated by the striae medullares, which have a horizontal course across the floor of the ventricle. The superior triangle is limited laterally by the superior cerebellar peduncles as they converge towards the cerebral aqueduct; its apex is directed superiorly, towards the aqueduct. The inferior triangle is bounded caudally by the gracile and cuneate tubercles, which contain the dorsal column nuclei, and, more rostrally, by the diverging inferior cerebellar peduncles. The apex of the inferior triangle is known as the obex. A longitudinal median sulcus divides the floor of the fourth ventricle into two halves. Each half is itself divided, by an often indistinct sulcus limitans, into a medial region, the medial eminence, and a lateral region, the vestibular area. The vestibular nuclei lie beneath the vestibular area. In the superior part, the medial eminence is represented by the facial colliculus, a small elevation produced by an underlying loop of efferent fibres from the facial nucleus that covers the abducens nucleus. Between the facial colliculus and the vestibular area the sulcus limitans widens into a small depression, the superior fovea. In its upper part, the sulcus limitans constitutes the lateral limit of the floor of the fourth ventricle. Here, a small region of bluish-grey pigmentation denotes the presence of the subjacent locus coeruleus. Caudal to the facial colliculus, at the level of the lateral recess of the ventricle, a variable group of nerve fibre fascicles, the striae medullares, runs transversely across the ventricular floor and passes into the median sulcus. In the inferior part, the medial eminence is represented by the hypoglossal triangle (trigone), which lies over the hypoglossal nucleus. Laterally, the sulcus limitans widens to produce an indistinct inferior fovea. Caudal to the inferior fovea, between the hypoglossal triangle and the vestibular area, the vagal triangle (trigone) covers the dorsal motor nucleus of the vagus. A narrow translucent ridge, the funiculus separans, separated from the gracile tubercle by the small area postrema, crosses below the vagal triangle.

The roof of the fourth ventricle is formed by the superior and inferior medullary veli. The thin superior medullary velum stretches across the ventricle between the converging superior cerebellar peduncles (see Fig. 25.22) and is continuous with the cerebellar white matter. Dorsally, it is covered by the lingula of the superior vermis. The inferior medullary velum is more complex and is mostly composed of a thin sheet, devoid of neural tissue, formed by ventricular ependyma and the pia mater of the tela choroidea. Just inferior to the nodule of the cerebellum, a median aperture, the foramen of Magendie, opens the roof of the fourth ventricle into the cisterna magna. The aperture forms when a membranous structure (Blake's pouch) perforates into the fourth ventricle during early development; persistence of this membrane results in cystic obstruction of the median outlet from the fourth ventricle (Paladini et al 2012).

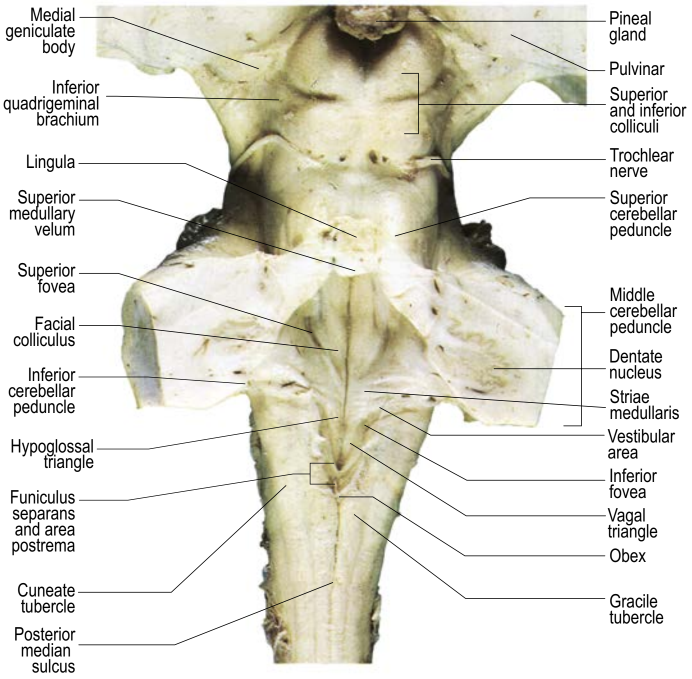

Fig. 25.22 The floor of the fourth ventricle, dorsal aspect of the brainstem.

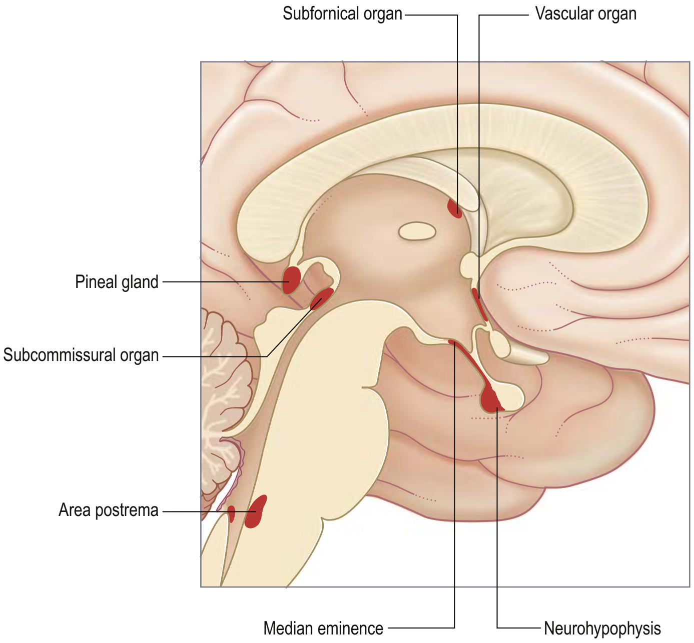

Fig. 25.23 Locations of the circumventricular organs, median sagittal section of the brain.

Circumventricular organs

The walls of the ventricular system are lined with ependymal cells that cover a subependymal layer of glia. At certain midline sites in the ventricular walls, collectively referred to as circumventricular organs, the blood–brain barrier is absent and specialized ependymal cells, tanycytes, are present (Horsburgh and Massoud 2013). The functions of ependyma and tanycytes may include secretion into the CSF; transport of neurochemicals from subjacent neurones, glia or vessels to the CSF; transport of neurochemicals from the CSF to the same subjacent structures; and chemoreception (Rodríguez et al 2005). Adult mammalian neurogenesis occurs in discrete neurogenic sites that are best characterized in the ependymal and subependymal glial cell layers in the subgranular zone of the dentate gyrus and in the subventricular zone (Sanai et al 2004).

The circumventricular organs include the vascular organ (organum vasculosum), subfornical organ, neurohypophysis, median eminence, subcommissural organ, pineal gland and area postrema (Fig. 25.23). The vascular organ lies in the lamina terminalis between the optic chiasma and the anterior commissure. Its external zone contains a richly fenestrated vascular plexus that covers glia and a network of nerve fibres. Its major inputs appear to come from the subfornical organ, locus coeruleus and a number of hypothalamic nuclei, and it projects to the median preoptic and supraoptic nuclei. The vascular organ is involved in the regulation of fluid balance and may also have neuroendocrine functions. The subfornical organ lies at the level of the interventricular foramen. It contains many neurones, glial cells and a dense fenestrated capillary plexus, and is covered by flattened ependyma. It is believed to have widespread hypothalamic interconnections and to function in the regulation of fluid balance and thirst.

The neurohypophysis (posterior pituitary) is the site of termination of neurosecretory projections from the supraoptic and paraventricular nuclei of the hypothalamus. Neurones in these nuclei release vasopressin and oxytocin respectively into the capillary bed of the neurohypophysis, where the hormones gain access to the general circulation.

The median eminence contains the terminations of axons of hypothalamic neurosecretory cells. Peptides released from these axons control the hormonal secretions of the anterior pituitary via the pituitary portal system of vessels.

The subcommissural organ lies ventral to and below the posterior commissure, near the inferior wall of the pineal recess. The pineal gland is a small structure, approximately 8 mm in diameter, situated rostrodorsal to the superior colliculus and behind the stria medullaris. It is part of the epithalamus and produces melatonin, a serotonin-derived hormone implicated in the regulation of sleep–wake patterns in both circadian and seasonal cycles.

The area postrema is a bilaterally-paired structure, located at the caudal limit of the floor of the fourth ventricle. It is an important chemoreceptive area that triggers vomiting in response to the presence of emetic substances in the blood. The area postrema, the nucleus of the solitary tract and the dorsal motor nucleus of the vagus, collectively constitute the dorsal vagal complex, the major termination site of vagal afferent nerve fibres.

CHOROID PLEXUS AND CEREBROSPINAL FLUID

Choroid plexus

The vascular pia mater in the roofs of the third and fourth ventricles and in the medial wall of the lateral ventricle along the line of the choroid fissure, is closely apposed to the ependymal lining of the ventricles. It forms the tela choroidea, which gives rise to the highly vascularized choroid plexuses from which CSF is secreted into the lateral, third and fourth ventricles (see Figs 25.14, 25.17–25.18). The body or stroma of the choroid plexus consists of many capillaries, separated from the ventricles by the pia mater and choroid ependymal cells (Strazielle et al 2000).

In the lateral ventricle, the choroid plexus extends anteriorly as far as the interventricular foramen, through which it is continuous, across the third ventricle, with the plexus of the contralateral lateral ventricle. From the interventricular foramen, the plexus passes posteriorly, in contact with the thalamus, curving round its posterior aspect to enter the temporal horn of the lateral ventricle and reaching the hippocampus at the level of the inferior choroidal point (see above: topographical anatomy of the lateral ventricle). Throughout the body of the ventricle, the choroid fissure lies between the fornix superiorly and the thalamus inferiorly (see Fig. 25.17).

In the lateral ventricle, the tela choroidea, has a triangular shape when seen from above. Its apex lies between the interventricular foramina, often indented by the anterior columns of the fornices. Its lateral edges are delimited by the fornix (taeniae fornicis) and the thalamus is attached to the taeniae on either side (taeniae thalami).

The choroid plexus of the third ventricle is attached to the tela choroidea which contributes to the thin roof of the third ventricle as it develops during fetal life. In coronal sections of the cerebral hemispheres, the choroid plexus of the third and lateral ventricles are seen to be continuous.

The choroid plexus of the fourth ventricle is similar in structure to that of the lateral and third ventricles. The roof of the inferior part of the fourth ventricle develops as a thin sheet in which the pia mater is in direct contact with the ependymal lining of the ventricle. This thin sheet, the tela choroidea of the fourth ventricle, lies between the cerebellum and the inferior part of the roof of the ventricle. The choroid plexus of the fourth ventricle is T-shaped, i.e. it has vertical and horizontal limbs; the precise form varies widely from a single vertical limb to an elongated 'T' that extends out through the foramina of Luschka into the cerebellopontine angle. The vertical (longitudinal) limb is double, flanks the midline and is adherent to the roof of the ventricle. The limbs fuse at the superior margin of the median aperture (foramen of Magendie) and are often prolonged onto the ventral aspect of the cerebellar vermis. The horizontal limbs of the plexus project into the lateral recesses of the ventricle. Small tufts of plexus may pass through the lateral apertures (foramina of Luschka) and emerge, still covered by ependyma, in the subarachnoid space of the cerebellopontine angle. The mean thickness of the choroid plexus in the fourth ventricle in children is 2.5 mm (Madhukar et al 2012).

Fig. 25.24 Relationships between the dura mater, the leptomeninges and the blood vessels that enter and leave the cerebral cortex. The subarachnoid space is divided by trabeculae.

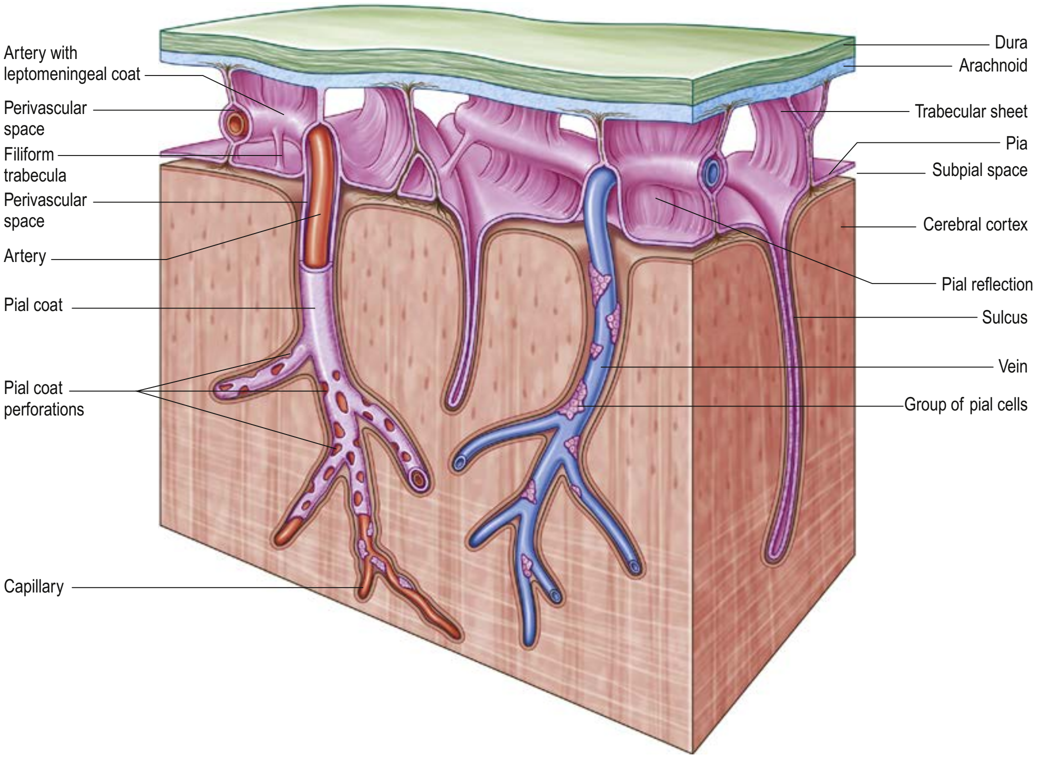
Artery with leptomeningeal coat
Perivascular space
Filiform trabecula
Perivascular space
Artery
Pial coat
Pial coat perforations
Capillary
Dura
Arachnoid
Trabecular sheet
Pia
Subpial space
Cerebral cortex
Pial reflection
Sulcus
Vein
Group of pial cells

The blood supply of the choroid plexus in the tela choroidea of the lateral and third ventricles is usually via a single vessel from the anterior choroidal branch of the internal carotid artery and several choroidal branches of the posterior cerebral artery; the two sets of vessels anastomose to some extent. Capillaries drain into a rich venous plexus served by a single choroidal vein. The blood supply of the choroid plexus of the fourth ventricle is from the inferior cerebellar arteries.

Physiological calcification of the choroid plexus and pineal gland are the most frequently described intracranial calcifications incidentally discovered during head computed tomography (CT) examinations (Doyle and Anderson 2006).

Cerebrospinal fluid

The cerebrospinal fluid (CSF) is a clear, colourless liquid. Normal CSF contains small amounts of protein and differs from blood in its electrolyte content. Different pathologies can be diagnosed by looking at alterations in the composition of the CSF (Deisenhammer et al 2006). CSF is not simply an ultrafiltrate of blood but is actively secreted by the choroid plexuses in the lateral, third and fourth ventricles.

The choroid plexus epithelium constitutes a blood–CSF barrier. Choroid plexus epithelial cells have the characteristics of transport and secretory cells (see Figs 3.19, 3.20); their apical surfaces have microvilli, and their basal surfaces exhibit interdigitations and folding. Tight junctions (occluding junctions, zonulae adherentes) at the apical ends of the cells are permeable to small molecules. Fenestrated capillaries lie just beneath the epithelial cells in the stroma of the choroid plexus. The ependymal lining of the ventricles and the extracellular fluid from the brain parenchyma are additional sources of CSF, but how much each source contributes to CSF production is unclear.

The total volume of CSF in the adult is approximately 150 ml; the volume of the ventricles is about 25 ml. CSF is produced at a rate of 0.3–0.4 ml per minute (20 ml/hour, approximately 500 ml per day), which means that the entire CSF volume is replaced 3–4 times per day.

CSF production in children, as measured by output through external ventricular drainage, increases during infancy, reaching 64% of the output of a 15-year-old child by 2 years of age. There is a logarithmic increase in CSF output with age and body weight (Yasuda et al 2002). Mixing of CSF from different sources within the subarachnoid space is probably assisted by ciliary motion on the ependymal cells lining the ventricles and by arterial pulsations.

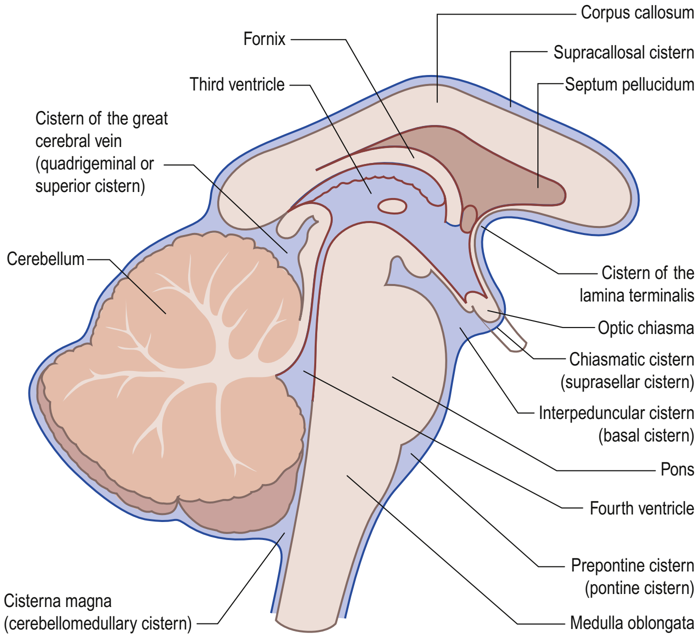
Corpus callosum
Fornix
Supracallosal cistern
Third ventricle
Septum pellucidum
Cistern of the great cerebral vein (quadrigeminal or superior cistern)
Cerebellum
Cistern of the lamina terminalis
Optic chiasma
Chiasmatic cistern (suprasellar cistern)
Interpeduncular cistern (basal cistern)
Pons
Fourth ventricle
Prepontine cistern (pontine cistern)
Cisterna magna (cerebellomedullary cistern)
Medulla oblongata

Fig. 25.25 The principal subarachnoid cisterns, sagittal section.

Subarachnoid space

The subarachnoid space lies between the arachnoid and the pia mater. It is continuous with the lumen of the fourth ventricle via the median aperture (foramen of Magendie) and the paired lateral apertures (foramina of Luschka). The subarachnoid space contains CSF, the larger arteries and veins that traverse the surface of the brain, and the intracranial or intravertebral portions, respectively of the cranial and spinal nerves.

Trabeculae, in the form of sheets or fine filiform structures, each containing a core of collagen, cross the subarachnoid space from the deep layers of the arachnoid mater to the pia mater (Fig. 25.24). The trabeculae are attached to the large blood vessels within the subarachnoid space and may form compartments, particularly in the perivascular regions, thereby possibly facilitating directional flow of CSF through the space. A thin layer of leptomeninges, often only one cell thick, coats the trabeculae, vessels and nerves that cross the subarachnoid space, and fuses with the arachnoid mater at the margins of the exit foramina in the skull and vertebral column.

Arachnoid and pia mater are in close apposition over the convexities of the brain, such as the cortical gyri, whereas concavities are followed by the pia but spanned by the arachnoid. This arrangement produces a subarachnoid space of greatly variable depth that is location-dependent. The more expansive spaces form subarachnoid cisterns (Figs 25.25–25.27), which are continuous with the general subarachnoid space and crossed by long, filamentous trabeculae (Inoue et al 2009).

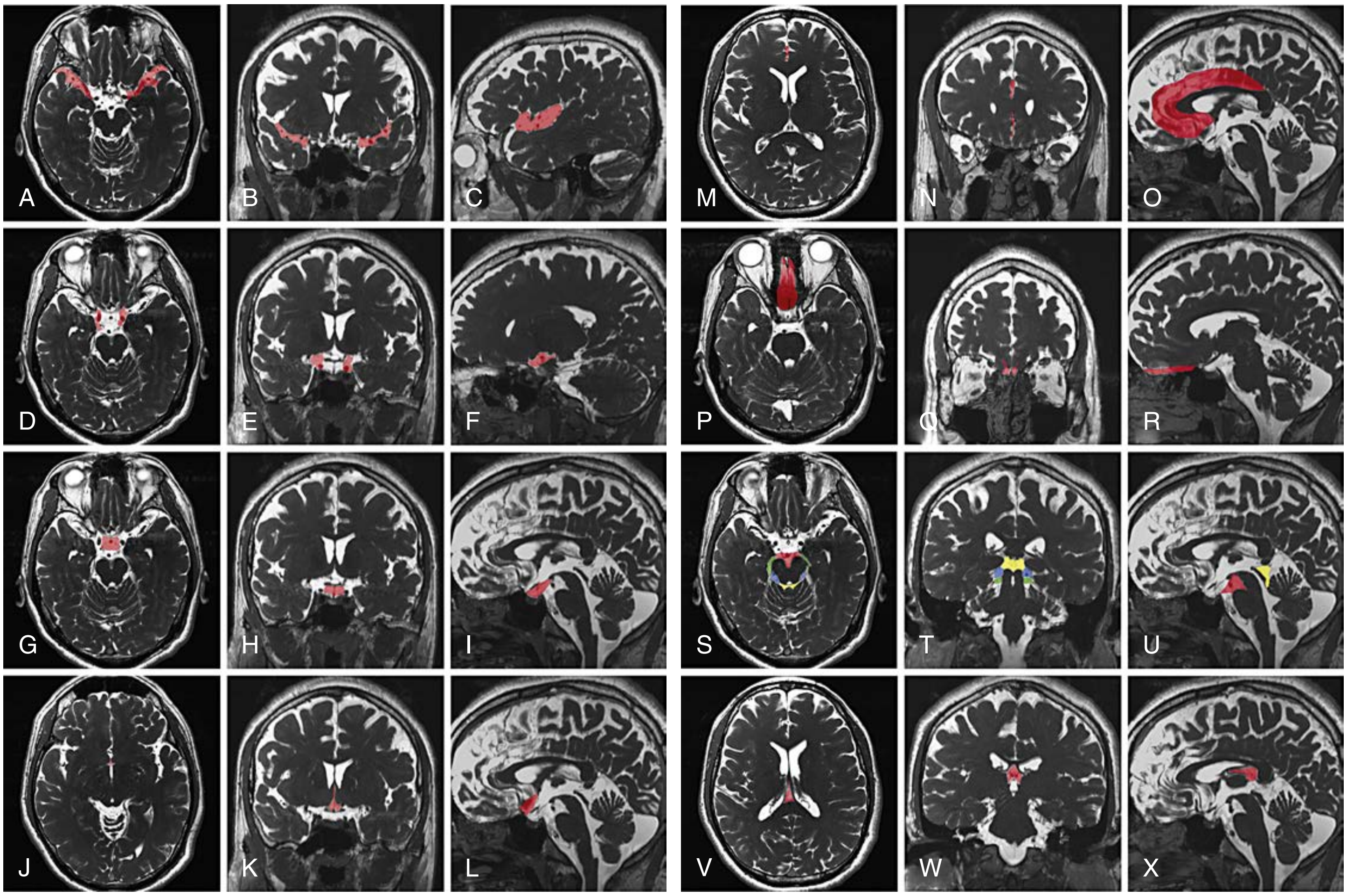

Fig. 25.26 The supratentorial subarachnoid cisterns. FIESTA MR images colour-coded to provide a visual approximation to the borders of the individually named supratentorial cisterns. These images are arrayed so that each row depicts a single cistern, in the axial plane (column 1), coronal plane (column 2) and sagittal plane (column 3). This montage is intended to indicate the general location for each cistern within the 'sea' of multiple confluent CSF spaces around the brain. **A**–**C**, Paired Sylvian cisterns. **D**–**F**, Paired carotid cisterns. **G**–**I**, Midline chiasmatic cistern. **J**–**L**, Midline cistern of the lamina terminalis. **M**–**O**, Midline pericallosal cistern. **P**–**R**, Paired olfactory cisterns. **S**–**U**, Midline perimesencephalic cistern. **V**–**X**, Cistern of the velum interpositum. The perimesencephalic cistern is often considered in four portions (**S–U**): midventral interpeduncular fossa (red), paired anterolateral crural cisterns (green), paired posterolateral ambient cisterns (blue) and mid-dorsal quadrigeminal plate (vein of Galen) cistern (yellow). (With permission from Rios JC, Galper MW, Naidich TP Ventricles and intracranial subarachnoid spaces. In: Naidich TP, Castillo M, Cha S et al (eds) Imaging of the Brain. Elsevier, Saunders; Ch. 13, pp. 245–71. Copyright 2013.)

Magnetic resonance imaging with fluid movement-sensitive sequences performed on normal subjects has shown CSF flow to be pulsating and bidirectional between the compartments of the ventricular system, probably with a net flow in a direction towards the fourth ventricle (Yamada et al 2008). The flow of CSF changes at the age of 2 years from an infantile to a mature pattern. The infantile pattern is characterized by flow directed into the ventricular system, and the mature pattern by flow directed out of the ventricles (Bateman and Brown 2012). The route of CSF through the subarachnoid space is even more complex and less understood, and it is debated whether CSF moves mainly over the cerebral convexities or mainly at the cranial base. It is known that CSF is absorbed into the superior sagittal sinus, but also that this site is insufficient to account for all CSF absorption and that this absorption system may only start to operate when CSF pressure is increased. Therefore one or more additional routes of absorption must exist but their precise location, function and mutual contributions to CSF absorption have yet to be clarified (Pollay 2010). Absorption through pial and subarachnoid vessels, across the ependymal ventricular surfaces and pial surfaces and via extracranial lymphatics may all be involved (Zakharov et al 2004).

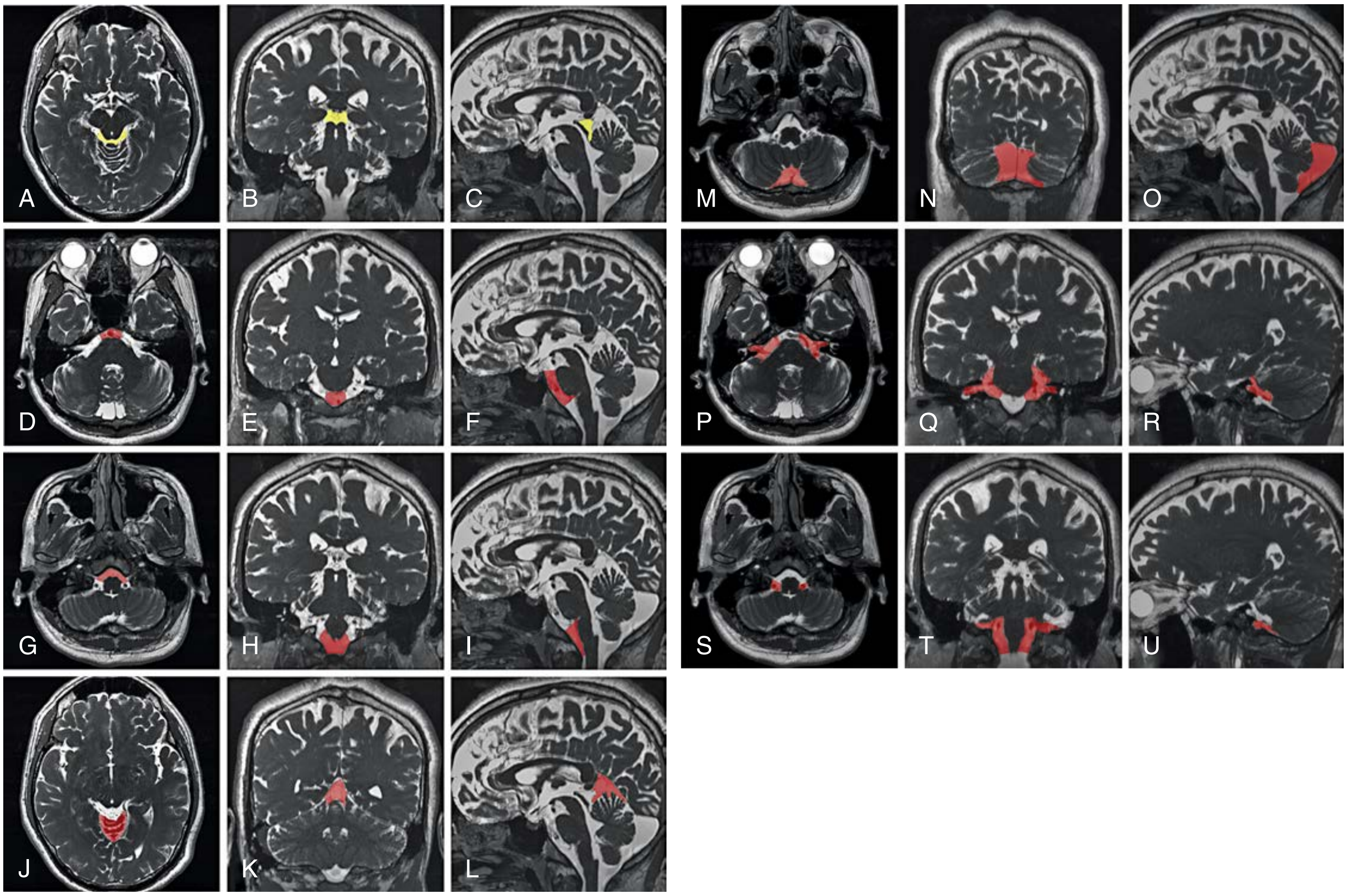

Fig. 25.27 The infratentorial subarachnoid cisterns. FIESTA MR images colour-coded to provide a visual approximation to the borders of the individually named infratentorial cisterns. These images are arrayed so that each row depicts a single cistern, in axial plane (column 1), coronal plane (column 2) and sagittal plane (column 3) images. This montage is intended to indicate the general location for each cistern within the 'sea' of multiple confluent CSF spaces around the brain. **A**–**C**, Midline quadrigeminal plate (vein of Galen) cistern (yellow). **D**–**F**, Midline prepontine cistern. **G**–**I**, Midline premedullary cistern. **J**–**L**, Midline superior vermian cistern. **M**–**O**, Midline cisterna magna. **P**–**R**, Paired cerebellopontine angle cisterns. **S**–**U**, Paired cerebellomedullary cisterns. (With permission from Rios JC, Galper MW, Naidich TP Ventricles and intracranial subarachnoid spaces. In: Naidich TP, Castillo M, Cha S et al (eds) Imaging of the Brain. Elsevier, Saunders; Ch. 13, pp. 245–71. Copyright 2013.)

The largest cistern, the cisterna magna (cerebellomedullary cistern) is formed where the arachnoid bridges the space between the dorsal aspect of the medulla oblongata and the inferior surface of the cerebellum. The cistern is continuous above with the lumen of the fourth ventricle through its median aperture (foramen of Magendie) and below with the spinal subarachnoid space. It contains the vertebral arteries and the origins of the posterior inferior cerebellar arteries, the glossopharyngeal, vagus, accessory and hypoglossal nerves, and the choroid plexus.

On either side, the paired cerebellopontine cisterns (angle cisterns or cerebellopontine angle cisterns) are situated in the lateral angle between the cerebellum and the pons. They are traversed by the trigeminal, facial and vestibulocochlear nerves, the anterior inferior cerebellar arteries and the superior petrosal veins.

The prepontine cistern (pontine cistern) is an extensive space ventral to the pons, which is continuous inferiorly with the spinal subarachnoid space, posteriorly and laterally with the cerebellopontine cisterns, and rostrally with the interpeduncular cistern. The prepontine cistern contains the origin of the abducens nerve and the basilar artery and its two main branches, the anterior inferior cerebellar and superior cerebellar arteries. The quadrigeminal cistern (superior cistern, vein of Galen cistern, peripineal cistern) lies posterior to the brainstem and third ventricle, and occupies the interval between the splenium of the corpus callosum and the superior cerebellar surface. The great cerebral vein, formed by the union of the basal veins (of Rosenthal) and the internal cerebral veins, traverses this cistern and the pineal gland protrudes into it. It also contains the P3 segments of the posterior cerebral arteries and portions of the medial and lateral posterior choroidal arteries.

The paired ambient cisterns are extensions of the quadrigeminal cistern. On each side, they lie between the parahippocampal and dentate gyri of the temporal lobes laterally and the lateral surface of the midbrain behind the cerebral peduncles medially; they therefore extend laterally and anteriorly around the midbrain on either side to the interpeduncular cistern (basal cistern) (see Fig. 25.26). They are divided into supra- and infra-tentorial compartments and contain the basal vein (of Rosenthal), the P2P segment of the posterior cerebral artery, the superior cerebellar artery and the trochlear nerves.

The paired crural cisterns lie between the posterior borders of the unci and the cerebral peduncles on each side and contain the P2A segments of the posterior cerebral artery and the postoptic part of the anterior choroidal artery. The midline interpeduncular cistern (basal cistern) lies between the two crura cerebri, bordered superiorly and inferiorly by the diencephalic and mesencephalic leaves respectively of Liliequist's membrane. It contains the basilar artery, the origins of the posterior cerebral and posterior thalamo-perforating arteries, the proximal portion of the anterior ponto-mesencephalic vein and the proximal portions of the oculomotor nerves. Anteriorly, the interpeduncular cistern extends to the optic chiasma.

The cistern of the lateral sulcus (Sylvian cistern) is formed by the arachnoid as it bridges the lateral sulcus between the frontal, parietal and temporal opercula and it contains the middle cerebral artery and veins.

Several smaller cisterns have been described. They include the chiasmatic cistern (suprasellar cistern), which is related to the optic chiasma, the cistern of the lamina terminalis and the supracallosal cistern, all of which are extensions of the interpeduncular cistern and contain the anterior cerebral arteries. The subarachnoid space extends through the optic foramina into the orbits, where it is bounded by the sheath of the optic nerve. It is for this reason that a raised intracranial pressure is transmitted to the optic nerve and can be visible on direct examination of the fundus as papilloedema. The sheath of the optic nerve is formed by fusion of the arachnoid mater and dura mater, and surrounds the orbital portion of each optic nerve as far as the back of the globe, where the dura fuses with the sclera of the eyeball. For further reading, see Rios et al (2013).

Arachnoid villi and granulations

Arachnoid villi and granulations (Pacchionian bodies) are focal pouches of arachnoid mater and subarachnoid space that protrude through the walls of the dural venous sinuses, very often close to points where veins enter the sinuses. They are found in the superior sagittal, transverse, superior petrosal and straight sinuses in decreasing frequency and are most prominent along the margins of the great longitudinal fissure, commonly in the lateral lacunae of the superior sagittal sinus.

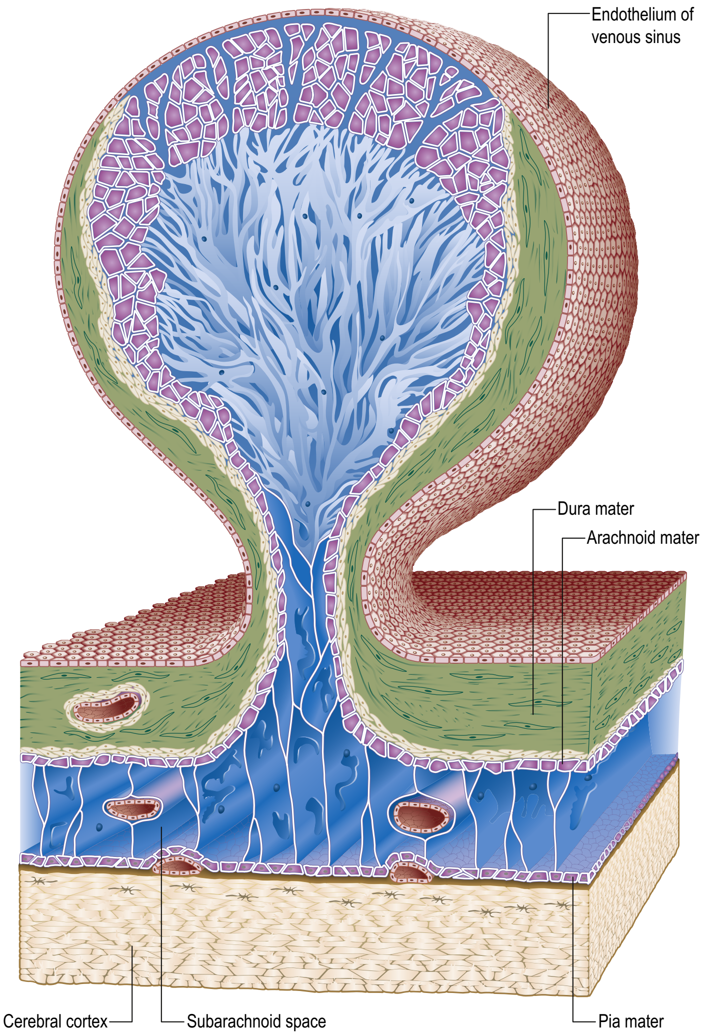

Fig. 25.28 An arachnoid granulation. (Adapted with permission from Kida S, Weller RO 1994 Morphology of CSF drainage pathways in man. In: Raimondi A (ed) Principles of Pediatric Neurosurgery, vol. 4. Berlin: Springer.)

At the base of each arachnoid granulation, a thin neck of arachnoid mater projects through an aperture in the dural covering of a venous sinus and then expands to form a core of collagenous trabeculae and interwoven channels (Fig. 25.28). An apical cap of arachnoid cells, some 150 μm thick, surmounts the core and is attached to the endothelium of the sinus over an area some 300 μm in diameter. The rest of the core of the granulation is separated from the endothelium by a fibrous dural cupula. Channels extend through the cap to reach the subendothelial regions of the granulation. Meningiomas, the most common benign intracranial tumours, arise from arachnoid cap cells.

Arachnoid villi develop during fetal life. At term, the number and complexity of the villi increase. It is generally believed that the fetal and early infantile villi do not fully penetrate the dura, but with maturation they grow in size, achieve penetration through the wall of the venous sinus, and are thereafter referred to as arachnoid granulations. In the elderly, the arachnoid membrane thickens and the arachnoid granulations degenerate and often calcify.

The function of arachnoid granulations is not fully understood, although they are thought to be involved in the reabsorption of CSF. There are observations both to support and to question their role in the absorption of CSF. Their relative paucity in the fetal and early postnatal period strongly suggests the importance of other absorption routes. The degenerative changes in arachnoid granulations in old age could be the substrate for the condition of 'normal pressure hydrocephalus' and for decreased CSF absorption, which could play an important role in degenerative brain diseases of the elderly. An alternative, and not necessarily mutually exclusive, view of arachnoid granulations is that they are involved in dissipating the pressure wave that occurs in the subarachnoid space during arterial systole (caused by the pulsation of the arterial vessels within the space). Since the dural venous sinuses lie within thick, non-compliant dural coverings, pressure changes within them functionally represent the extracranial venous compartment; systolic dilation of the arachnoid granulations would therefore dissipate intracranial pressure changes into the extracranial venous system.

PIA MATER

The pia mater is a delicate membrane that closely invests the surface of the brain and spinal cord, from which it is separated by a microscopic subpial space. It follows the contours of the brain into concavities and the depths of fissures and sulci. In the spinal canal, it contributes to the formation of the dentate ligaments and the filum terminale (Adeeb et al 2013) (see Figs 47.1C, 47.5).

Pia mater is formed from a layer of leptomeningeal cells, often only 1–2 cells thick, in which the cells are joined by desmosomes and gap junctions but few, if any, tight junctions. The cells are continuous with the coating of the subarachnoid trabeculae and separated from the basal lamina of the glia limitans by bundles of collagen, fibroblast-like cells and microscopic vessels that lie in the subpial space (Mercier et al 2002) (see Fig. 25.24).

It was long thought that the subarachnoid space was connected directly with the perivascular spaces (Virchow–Robin spaces) that surround blood vessels in the brain. However, it is now recognized that the pia mater is reflected from the surface of the brain onto the surface of blood vessels in the subarachnoid space, which means that the subarachnoid space is separated by a layer of pia from the subpial and perivascular spaces of the brain (see Fig. 25.24). The pia mater appears to form a regulatory interface between the subarachnoid space and the brain, across which small molecules may diffuse between the interstitial space and the CSF through the perivascular space. This may allow movement of metabolites and could play a role in blood–brain barrier function (Zhang et al 1990).

During development, the pia mater becomes apposed to the ependyma in the roof of the telencephalon and fourth ventricle to form the tela choroidea. It shares a common embryological origin and structural similarity with the arachnoid mater.

Bonus e-book content

Fig. 25.1 **A**, A head CT scan showing a right-sided extradural (epidural) haematoma. **B**, A bone flap from the same patient. **C**, An acute subdural haematoma. **D**, A bilateral subacute subdural haematoma. **E**, A right-sided chronic subdural haematoma.

Fig. 25.3 **B**, The innervation of the cranial meninges.

Fig. 25.4 **C**, Posterior view; note the asymmetry of the transverse sinuses.

Fig. 25.26 The supratentorial subarachnoid cisterns.

Fig. 25.27 The infratentorial subarachnoid cisterns.

Key references

Adeeb N, Mortazavi MM, Deep A et al 2013 The pia mater: a comprehensive review of literature. Childs Nerv Syst 29:1803–10.

A review of the literature relating to the history, embryology, anatomy and function of the pia mater and related structures.

Browder J, Kaplan HA 1976 Cerebral Dural Sinuses and their Tributaries. Springfield, IL: Thomas.

A description of variations in the form of the superior sagittal and other venous sinuses.

Dolenc VV 1987 The Cavernous Sinus. Vienna: Springer.

Professor Dolenc's description of his pioneering studies on the surgical anatomy of the cavernous sinus, which enabled the development of surgical approaches to this region.

Horsburgh A, Massoud TF 2013 The circumventricular organs of the brain: conspicuity on clinical 3T MRI and a review of functional anatomy. Surg Radiol Anat 35:343–9.

A description of the normal appearances and prevalence of contrast enhancement of the circumventricular organs on routine clinical brain MRI and a review of the functional anatomy.

Iaconetta G, Fusco M, Samii M 2003 The sphenopetroclival venous gulf: a microanatomical study. J Neurosurg 99:366–75.

A detailed anatomical study of the abducens nerve, Dorello's canal and the so-called sphenopetroclival venous gulf.

Kida S, Weller RO 1994 Morphology of CSF drainage pathways in man. In: Raimondi A (ed) Principles of Pediatric Neurosurgery, vol 4. Berlin: Springer.

A description of the morphology and relationships of the subarachnoid space, including the structure of arachnoid granulations.

Lasjaunias P, Berenstein A, ter Brugge KG 2001 Surgical Neuroangiography. Berlin: Springer.

A comprehensive angiographic study describing the anatomical variations of the meningeal arteries.

Martins C, Yasuda A, Campero A et al 2005 Microsurgical anatomy of the dural arteries. Neurosurgery 56:211–51.

A detailed anatomical study of the variations of the meningeal arteries and their surgical implications.

Mercier F, Kitasako JT, Hatton GI 2002 Anatomy of the brain neurogenic zones revisited: fractones and the fibroblast/macrophage network. J Comp Neurol 451:170–88.

A description of the structure and ultrastructure of the basal laminae and subependymal layer.

Nagata S, Rhoton AL Jr, Barry M 1988 Microsurgical anatomy of the choroidal fissure. Surg Neurol 30:3–59.

A description of the microsurgical anatomy of the choroidal fissure in cadaveric heads.

Pollay M 2010 The function and structure of the cerebrospinal fluid outflow system. Cerebrospinal Fluid Res 7:9.

A review that traces the development of our understanding of the anatomy and physiological properties of the systems responsible for the drainage of cerebrospinal fluid into the systemic circulation.

Rhoton AL Jr 2000 Cerebellum and fourth ventricle. Neurosurg 47:S7–27.

A comprehensive description of the microsurgical anatomy of the cerebellum and fourth ventricle.

Rhoton AL Jr 2002 The lateral and third ventricles. Neurosurg 51:S207–71.

A comprehensive description of the microsurgical anatomy of the lateral and third ventricles.

Rhoton AL 2007 Cranial Anatomy and Surgical Approaches. Baltimore: Lippincott Williams & Wilkins.

An essential masterpiece in microsurgical neuroanatomy and surgical approaches developed by Professor Rhoton after 40 years devoted to the field.

Strazielle N, Ghersi-Egea JF 2000 Choroid plexus in the central nervous system: biology and physiopathology. J Neuropathol Exp Neurol 59:561–74.

A description of choroid plexus functions in brain development, transfer of neurohumoral information, brain/immune system interactions, brain ageing and cerebral pharmacotoxicology.

Yasargil MG 1984 Microneurosurgery, vol 1. New York: Thieme.

A monumental work in which Professor Yasargil describes the basal cisterns and their implications for microneurosurgery.

Zhang ET, Inman CBE, Weller RO 1990 Interrelationships of the pia mater and the perivascular (Virchow–Robin) spaces in the human cerebrum. J Anat 170:111–23.

A summary of the anatomical relationships between the pia mater and blood vessels in the human cerebrum, and discussion of a possible role for pial cells as an enzymic barrier protecting the brain from exogenous catecholamines.

References

Abhinav K, Panczykowski D, Wang WH et al 2017 Endoscopic endonasal interdural middle fossa approach to the maxillary nerve: anatomical considerations and surgical relevance. Oper Neurosurg (Hagerstown) 13:522–8.

Adeeb N, Mortazavi MM, Deep A et al 2013 The pia mater: a comprehensive review of literature. Childs Nerv Syst 29:1803–10.

A review of the literature relating to the history, embryology, anatomy and function of the pia mater and related structures.

Bateman GA, Brown KM 2012 The measurement of CSF flow through the aqueduct in normal and hydrocephalic children: from where does it come, to where does it go? Childs Nerv Syst 28:55–63.

Bauer DF, Youkilis A, Schenck C et al 2005 The falcine trigeminocardiac reflex: case report and review of the literature. Surg Neurol 63:143–8.

Browder J, Kaplan HA 1976 Cerebral Dural Sinuses and their Tributaries. Springfield, IL: Thomas.

A description of variations in the form of the superior sagittal and other venous sinuses.

Davidson JR, Mack J, Gutnikova A et al 2012 Developmental changes in human dural innervation. Childs Nerv Syst 28:665–71.

Deisenhammer F, Bartos A, Egg R et al; EFNS Task Force 2006 Guidelines on routine cerebrospinal fluid analysis. Report from an EFNS task force. Eur J Neurol. 13:913–22.

Dolenc VV 1987 The Cavernous Sinus. Vienna: Springer.

Professor Dolenc's description of his pioneering studies on the surgical anatomy of the cavernous sinus, which enabled the development of surgical approaches to this region.

Dolenc VV, Rogers L 2009 Cavernous Sinus: Developments and Future Perspectives. Vienna: Springer.

Doyle AJ, Anderson GD 2006 Physiologic calcification of the pineal gland in children on computed tomography: prevalence, observer reliability and association with choroid plexus calcification. Acad Radiol 13:822–6.

El Khouly H, Fernandez-Miranda JC, Rhoton AL Jr 2008 Blood supply of the facial nerve in the middle fossa: the petrosal artery. Neurosurgery 62:ONS297–303.

Farruggia S, Babcock D 1981 The cavum septi pellucidi: its appearance and incidence with cranial ultrasonography in infancy. Radiology 139:147–50.

Fernandez-Miranda JC, Gardner PA, Rastelli MM Jr et al 2014 Endoscopic endonasal transcavernous posterior clinoidectomy with interdural pituitary transposition. J Neurosurg 121:91–9.

Fernandez-Miranda JC, Zwagerman NT, Abhinav K et al 2017 Cavernous sinus compartments from the endonasal endoscopic approach: anatomical considerations and surgical relevance to adenoma surgery. J Neurosurg 1:1–12.

Harris FS, Rhoton AL 1976 Anatomy of the cavernous sinus: a microsurgical study. J Neurosurg 45:169–80.

Horsburgh A, Massoud TF 2013 The circumventricular organs of the brain: conspicuity on clinical 3T MRI and a review of functional anatomy. Surg Radiol Anat 35:343–9.

A description of the normal appearances and prevalence of contrast enhancement of the circumventricular organs on routine clinical brain MRI and a review of the functional anatomy.

Iaconetta G, Fusco M, Samii M 2003 The sphenopetroclival venous gulf: a microanatomical study. J Neurosurg 99:366–75.

A detailed anatomical study of the abducens nerve, Dorello's canal and the so-called sphenopetroclival venous gulf.

Inoue K, Seker A, Alencastro LF et al 2009 Microsurgical and endoscopic anatomy of the supratentorial arachnoid membranes and cisterns. Neurosurg 65:644–64.

Kaplan HA, Browder J 1976 Neurosurgical consideration of some features of the cerebral dural sinuses and their tributaries. Clin Neurosurg 23:155–69.

Kida S, Weller RO 1994 Morphology of CSF drainage pathways in man. In: Raimondi A (ed) Principles of Pediatric Neurosurgery, vol 4. Berlin: Springer.

A description of the morphology and relationships of the subarachnoid space, including the structure of arachnoid granulations.

Kılıç T, Akakın A 2008 Anatomy of cerebral veins and sinuses. In: Caso V, Agnelli G, Paciaroni M (eds) Handbook on Cerebral Venous Thrombosis. Front Neurol Neurosci 23:4–15.

Krisht A, Barnett DW, Barrow DL et al 1994 The blood supply of the intracavernous cranial nerves: an anatomic study. Neurosurgery 34:275–9.

Lasjaunias P, Berenstein A, ter Brugge KG 2001 Surgical Neuroangiography. Berlin: Springer.

A comprehensive angiographic study describing the anatomical variations of the meningeal arteries.

Lee S, Shin K, Koh K et al 2017 Visualization of the tentorial innervation of human dura mater. J Anat 231:683–9.

Madhukar M, Choudhary AK, Boal DK et al 2012 Choroid plexus: normal size criteria on neuroimaging. Surg Radiol Anat 34:887–95.

Martins C, Yasuda A, Campero A et al 2005 Microsurgical anatomy of the dural arteries. Neurosurgery 56:211–51.

A detailed anatomical study of the variations of the meningeal arteries and their surgical implications.

Mercier F, Kitasako JT, Hatton GI 2002 Anatomy of the brain neurogenic zones revisited: fractones and the fibroblast/macrophage network. J Comp Neurol 451:170–88.

A description of the structure and ultrastructure of the basal laminae and subependymal layer.

Mott SH, Bodensteiner JB, Allan WC 1992 The cavum septi pellucidi in term and preterm newborn infants. J Child Neurol 7:35–8.

Nagata S, Rhoton AL Jr, Barry M 1988 Microsurgical anatomy of the choroidal fissure. Surg Neurol 30:3–59.

A description of the microsurgical anatomy of the choroidal fissure in cadaveric heads.

Nakano S, Hojo H, Kataoka K et al 1981 Age related incidence of cavum septi pellucidi and cavum vergae on CT scans of pediatric patients. J Comput Assist Tomogr 5:348–9.

Olry R, Haines DE 2005 Interthalamic adhesion: scruples about calling a spade a spade? J Hist Neurosci 14:116–8.

Paladini D, Quarantelli M, Pastore G et al 2012 Abnormal or delayed development of the posterior membranous area of the brain: anatomy, ultrasound diagnosis, natural history and outcome of Blake's pouch cyst in the fetus. Ultrasound Obstet Gynecol 39:279–87.

Pollay M 2010 The function and structure of the cerebrospinal fluid outflow system. Cerebrospinal Fluid Res 7:9.

A review that traces the development of our understanding of the anatomy and physiological properties of the systems responsible for the drainage of cerebrospinal fluid into the systemic circulation.

Rhoton AL Jr 2000 Cerebellum and fourth ventricle. Neurosurg 47:S7–27.

A comprehensive description of the microsurgical anatomy of the cerebellum and fourth ventricle.

Rhoton AL Jr 2002 The lateral and third ventricles. Neurosurg 51:S207–71.

A comprehensive description of the microsurgical anatomy of the lateral and third ventricles.

Rhoton AL 2007 Cranial Anatomy and Surgical Approaches. Baltimore: Lippincott Williams & Wilkins.

An essential masterpiece in microsurgical neuroanatomy and surgical approaches developed by Professor Rhoton after 40 years devoted to the field.

Rios JC, Galper MW, Naidich TP 2013 Ventricles and intracranial subarachnoid spaces. In: Naidich TP, Castillo M, Cha S et al (eds) Imaging of the Brain. Philadelphia: Elsevier, Saunders; Ch. 13, pp. 245–71.

Rodríguez EM, Blázquez JL, Pastor FE et al 2005 Hypothalamic tanycytes: a key component of brain–endocrine interaction. Int Rev Cytol 247:89–164.

Reisch R, Vutskits L, Patonay L et al 1996 The meningohypophyseal trunk and its blood supply to different intracranial structures. An anatomical study. Minim Invasive Neurosurg 39:78–81.

Ruíz DSM, Fasel JHD, Rüfenacht DA et al 2004 The sphenoparietal sinus of Breschet: does it exist? An anatomic study. Am J Neuroradiol 25:112–20.

Sanai N, Tramontin AD, Quiñones-Hinojosa A et al 2004 Unique astrocyte ribbon in adult human brain contains neural stem cells but lacks chain migration. Nature 427(6976):740–4.

Seoane E, Rhoton AL Jr, de Oliveira E 1998 Microsurgical anatomy of the dural collar (carotid collar) and rings around the clinoid segment of the internal carotid artery. Neurosurgery 42:869–84.

Sheu M, Fauteux G, Chang H et al 2002 Sinus pericranii: dermatologic considerations and literature review. J Am Acad Dermatol 46:934–41.

Strazielle N, Ghersi-Egea JF 2000 Choroid plexus in the central nervous system: biology and physiopathology. J Neuropathol Exp Neurol 59:561–74.

A description of choroid plexus functions in brain development, transfer of neurohumoral information, brain/immune system interactions, brain ageing and cerebral pharmacotoxicology.

Tekdemir I, Tuccar E, Cubuk HE et al 1998 Branches of the intracavernous internal carotid artery and the blood supply of the intracavernous cranial nerves. Ann Anat 180:343–8.

Umansky F, Valarezo A, Elidan J 1994 The superior wall of the cavernous sinus: a microanatomical study. J Neurosurg 81:914–20.

Yamada S, Miyazaki M, Kanazawa H et al 2008 Visualization of cerebrospinal fluid movement with spin labeling at MR imaging: preliminary results in normal and pathophysiologic conditions. Radiology 249:644–52.

Yasargil MG 1984 Microneurosurgery, vol 1. New York: Thieme.

A monumental work in which Professor Yasargil describes the basal cisterns and their implications for microneurosurgery.

Yasuda T, Tomita T, McLone DG et al 2002 Measurement of cerebrospinal fluid output through external ventricular drainage in one hundred infants and children: correlation with cerebrospinal fluid production. Pediatr Neurosurg 36:22–8.

Yasuda A, Campero A, Martins C et al 2004 The medial wall of the cavernous sinus: microsurgical anatomy. Neurosurgery 55:179–89.

Zakharov A, Papaiconomou C, Koh L et al 2004 Integrating the roles of extracranial lymphatics and intracranial veins in cerebrospinal fluid absorption in sheep. Microvasc Res 67:96–104.

Zhang ET, Inman CBE, Weller RO 1990 Interrelationships of the pia mater and the perivascular (Virchow–Robin) spaces in the human cerebrum. J Anat 170:111–23.

A summary of the anatomical relationships between the pia mater and blood vessels in the human cerebrum, and discussion of a possible role for pial cells as an enzymic barrier protecting the brain from exogenous catecholamines.

CHAPTER
26

Vascular supply and drainage of the brain

The brain is a highly vascular organ, its profuse blood supply characterized by a densely branching arterial network (Kaplan and Ford 1966). It has a high metabolic rate that reflects the energy requirements of constant neural activity. It receives about 15% of the cardiac output and utilizes 25% of the total oxygen consumption of the body. The brain is supplied by two internal carotid arteries and two vertebral arteries that form a complex anastomosis (circulus arteriosus cerebri, circle of Willis) on the base of the brain. Vessels diverge from this anastomosis to supply the various cerebral regions. In general, the internal carotid arteries and the vessels arising from them supply the forebrain, with the exception of the occipital lobe of the cerebral hemisphere, and the vertebral arteries and their branches supply the occipital lobe, the brainstem and the cerebellum. Venous blood from the brain drains into sinuses within the dura mater. Acute interruption of the blood supply to the brain for more than a few minutes causes permanent neurological damage. Such ischaemic strokes, along with intracranial haemorrhage, are major contemporary sources of morbidity and mortality.

ARTERIES OF THE BRAIN

The arterial supply of the brain is derived from the internal carotid and vertebral arteries which lie, together with their proximal branches, within the subarachnoid space at the base of the brain.

Internal carotid artery

The internal carotid arteries (Fig. 26.1) and their major branches (the internal carotid system or 'anterior' circulation) supply blood to the majority of the forebrain (**Video 26.1**). Some parts of the occipital and temporal lobes are supplied by branches of the vertebrobasilar system (see Fig. 26.5).

The internal carotid artery arises from the bifurcation of the common carotid artery, approximately at the level of C4, ascends in the neck (cervical segment) and enters the carotid canal of the temporal bone. Its subsequent course is said to have petrous, cavernous and intracranial parts.

Petrous part

The petrous part of the internal carotid artery ascends in the carotid canal, curves anteromedially and then superomedially above the cartilage that fills the foramen lacerum, and enters the cranial cavity. It lies at first anterior to the cochlea and tympanic cavity, and is separated from the latter and the pharyngotympanic tube by a thin, bony lamella that is cribriform in the young and partly absorbed in old age. Further anteriorly, it is separated from the trigeminal ganglion by the thin roof of the carotid canal, although this is often deficient. The artery is surrounded by a venous plexus and by the carotid autonomic plexus, derived from the internal carotid branch of the superior cervical ganglion. The petrous part of the artery gives rise to two branches. The

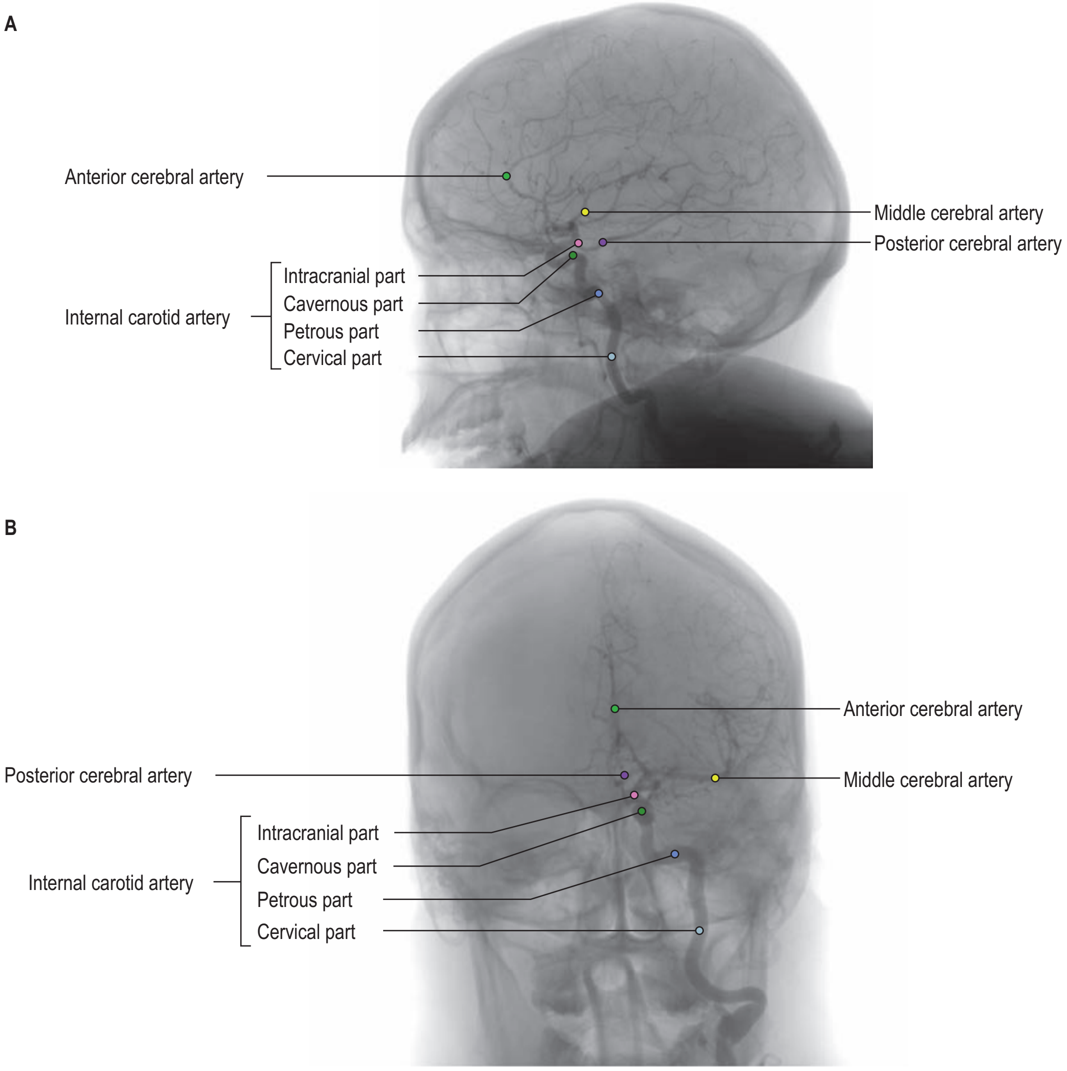

Fig. 26.1 Internal carotid arteriograms (note the perfusion of the posterior cerebral artery due to a fetal posterior communicating artery variant). **A**, Lateral projection. **B**, Towne's projection.

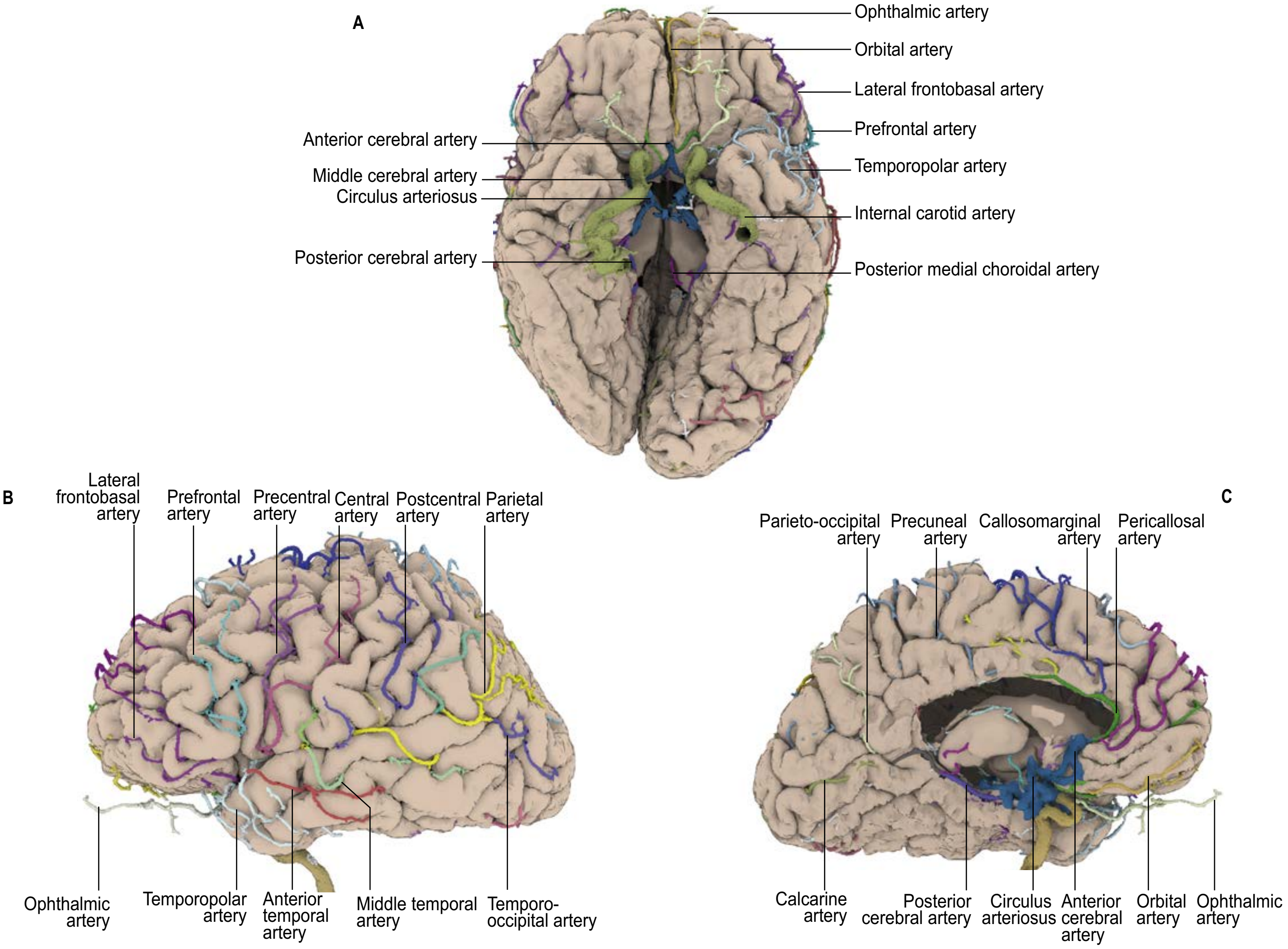
A
Ophthalmic artery
Orbital artery
Lateral frontobasal artery
Anterior cerebral artery
Prefrontal artery
Middle cerebral artery
Circulus arteriosus
Temporopolar artery
Internal carotid artery
Posterior cerebral artery
Posterior medial choroidal artery
B
Lateral frontobasal artery
Prefrontal artery
Precentral artery
Central artery
Postcentral artery
Parietal artery
Ophthalmic artery
Temporopolar artery
Anterior temporal artery
Middle temporal artery
Temporo-occipital artery
C
Parieto-occipital artery
Precuneal artery
Callosomarginal artery
Pericallosal artery
Calcarine artery
Posterior cerebral artery
Circulus arteriosus
Anterior cerebral artery
Orbital artery
Ophthalmic artery

Fig. 26.2 Volumetric reconstruction from real subject data showing the major arteries supplying the basal (**A**), lateral (**B**) and medial (**C**) aspects of the brain.

caroticotympanic artery is a small, occasionally double, vessel that enters the tympanic cavity by a foramen in the carotid canal and anastomoses with the anterior tympanic branch of the maxillary artery and the stylomastoid artery. The pterygoid artery is inconsistent; when present, it enters the pterygoid canal with the nerve of the same name, and anastomoses with a (recurrent) branch of the greater palatine artery.

Cavernous part

The cavernous part of the internal carotid artery ascends to the posterior clinoid process. It turns anteriorly to the side of the body of the sphenoid within the cavernous sinus and then curves superiorly and medial to the anterior clinoid process, to emerge through the dural roof of the sinus. The oculomotor, trochlear, ophthalmic and abducens nerves are lateral to it within the cavernous sinus. The abducens nerve is closely related to the lateral wall of the internal carotid artery, whilst the oculomotor and trochlear nerves are situated in the lateral wall of the cavernous sinus (see Figs 25.8–25.9). This explains the higher risk of abducens nerve injury secondary to pathology such as aneurysms of the cavernous part of the carotid artery. Occasionally, the caroticoclinoid ligament between the anterior and middle clinoid processes becomes ossified, forming a bony ring (caroticoclinoid foramen) around the artery (Ray and Gupta 2006).

The cavernous part of the artery gives off a number of small vessels. Branches supply the trigeminal ganglion, the walls of the cavernous and inferior petrosal sinuses, and the nerves contained therein. A minute meningeal branch passes over the lesser wing of the sphenoid to supply the dura mater and bone in the anterior cranial fossa, and also anastomoses with a meningeal branch of the posterior ethmoidal artery. Numerous small hypophysial branches supply the neurohypophysis, and are of particular importance because they form the pituitary portal system (see Fig. 30.11).

Intracranial part

After piercing the dura mater, the internal carotid artery turns back below the optic nerve to run between it and the oculomotor nerve. It reaches the anterior perforated substance at the medial end of the lateral fissure and terminates by dividing into the anterior and middle cerebral arteries (Fig. 26.2).

Several preterminal vessels leave the cerebral portion of the internal carotid. The ophthalmic artery arises from the anterior part of the internal carotid as it leaves the cavernous sinus, often at the point of piercing the dura, and enters the orbit through the optic canal. The posterior communicating artery (Fig. 26.3) runs back from the internal carotid above the oculomotor nerve, and anastomoses with the posterior cerebral artery (a terminal branch of the basilar artery), thereby contributing to the circulus arteriosus around the interpeduncular fossa. The posterior communicating artery is usually very small. However, sometimes it is so large that the posterior cerebral artery is supplied via the posterior communicating artery rather than from the basilar artery ('fetal posterior communicating artery', Lambert et al 2016); it is often larger on one side only. Small branches from its posterior half pierce the posterior perforated substance together with branches from the posterior cerebral artery. Collectively they supply the medial thalamic surface and the walls of the third ventricle. The anterior choroidal artery leaves the internal carotid just distal to its posterior communicating branch and passes back above the medial part of the uncus. It crosses the optic tract to reach and supply the crus cerebri of the midbrain, then turns laterally, recrosses the optic tract, and gains the lateral side of the lateral geniculate body, which it supplies with several branches. It finally enters the temporal (inferior) horn of the lateral ventricle via the choroidal fissure and ends in the choroid plexus. This small, but important, vessel also contributes to the blood supply of the globus pallidus, caudate nucleus, amygdala, hypothalamus, tuber cinereum, red nucleus, substantia nigra, posterior limb of the internal capsule, optic radiation, optic tract, hippocampus and the fimbria of the fornix.

The combination of the petrous, cavernous and intracranial parts of the internal carotid artery is called the 'carotid siphon' because of its sigmoid course (see Fig. 26.1 and Video 26.1). However, in infants, the parasellar region of the internal carotid artery does not form a siphon but takes a relatively straight course (Weninger and Muller 1999). The cranial and sympathetic nerves therefore have different topographical relationships with the artery in the infant compared with that found in older children and adults.

The initial millimetres of the intracranial part lie between two rings (proximal and distal rings) of dense connective tissue that surround the carotid artery where the ophthalmic artery usually branches. In cases of surgical clipping of ophthalmic artery aneurysms it is of surgical relevance for neurosurgeons to expose this part of the artery by removing the anterior clinoid process and exposing this segment of the carotid, where there is no venous flow (Video 26.1).

Anterior cerebral artery

The anterior cerebral artery is the smaller of the two terminal branches of the internal carotid (see Fig. 26.3).

Surgical nomenclature divides the vessel into three parts: A1, from the termination of the internal carotid artery to the junction with the anterior communicating artery; A2, from the junction with the anterior communicating artery to the origin of the callosomarginal artery; and A3, distal to the origin of the callosomarginal artery. The A3 segment is also known as the pericallosal artery.

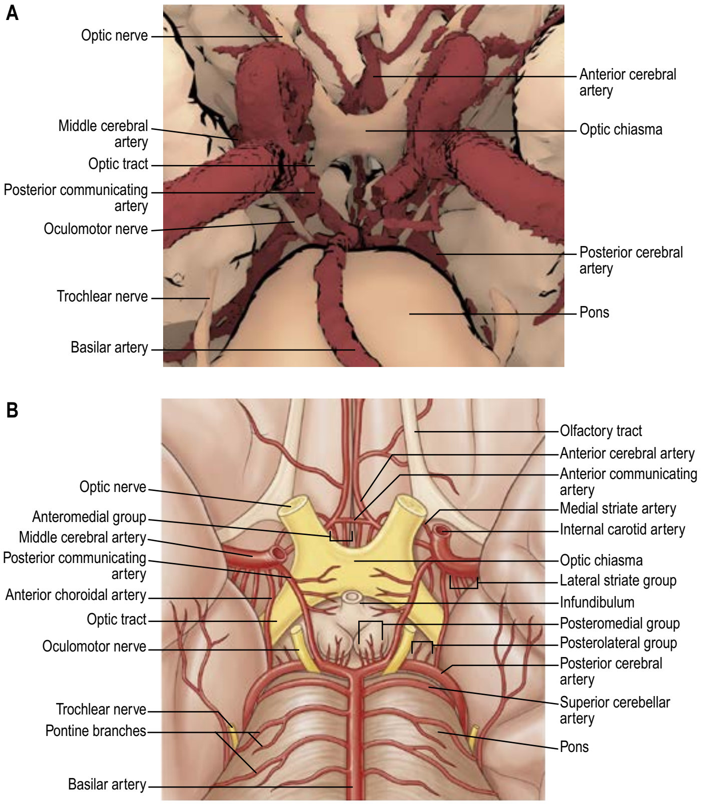
A
Optic nerve
Middle cerebral artery
Optic tract
Posterior communicating artery
Oculomotor nerve
Trochlear nerve
Basilar artery
Anterior cerebral artery
Optic chiasma
Posterior cerebral artery
Pons
B
Optic nerve
Anteromedial group
Middle cerebral artery
Posterior communicating artery
Anterior choroidal artery
Optic tract
Oculomotor nerve
Trochlear nerve
Pontine branches
Basilar artery
Olfactory tract
Anterior cerebral artery
Anterior communicating artery
Medial striate artery
Internal carotid artery
Optic chiasma
Lateral striate group
Infundibulum
Posteromedial group
Posterolateral group
Posterior cerebral artery
Superior cerebellar artery
Pons

Fig. 26.3 The circulus arteriosus on the base of the brain. **A**, Volumetric reconstruction from real subject data showing the anatomical relations of the circulus arteriosus at the base of the brain. **B**, The distribution of central (perforating or ganglionic) branches.

The anterior cerebral artery starts at the medial end of the stem of the lateral fissure. It passes anteromedially above the optic nerve to the great longitudinal fissure where it connects with its contralateral fellow by a short transverse anterior communicating artery. The latter is about 4 mm in length and may be double. It gives off numerous anteromedial central branches that supply the optic chiasma, lamina terminalis, hypothalamus, para-olfactory areas, anterior columns of the fornix and the cingulate gyrus (Fig. 26.2C).

The two anterior cerebral arteries travel together in the great longitudinal fissure. They pass around the curve of the genu of the corpus callosum and then along its upper surface to its posterior end, where they anastomose with posterior cerebral arteries.

The anterior cerebral artery has cortical and central branches. Cortical branches are named according to their distribution. Two or three orbital branches ramify on the orbital surface of the frontal lobe and supply the olfactory cortex, gyrus rectus and medial orbital gyrus. Frontal branches supply the corpus callosum, cingulate gyrus, medial frontal gyrus and paracentral lobule and parietal branches supply the precuneus. The frontal and parietal branches both send twigs over the superomedial border of the hemisphere to supply a strip of territory on the superolateral surface (see Figs 26.2B, 26.4). Cortical branches of the anterior cerebral artery, therefore, supply the areas of the motor and somatosensory cortices that represent the lower limb.

Central branches of the anterior cerebral artery arise from its proximal portion and enter the anterior perforated substance (see Fig. 26.3B) and lamina terminalis. Collectively, they supply the rostrum of the corpus callosum, septum pellucidum, anterior part of the putamen, head of the caudate nucleus and adjacent parts of the internal capsule. Immediately proximal or distal to its junction with the anterior communicating artery, the anterior cerebral artery gives rise to the medial striate artery, which supplies the anterior part of the head of the caudate nucleus and adjacent regions of the putamen and internal capsule (Video 26.1).

Middle cerebral artery

The middle cerebral artery is the larger terminal branch of the internal carotid. Surgical nomenclature divides the vessel into four parts: M1 (sphenoidal), from the termination of the internal carotid artery to the bi/trifurcation; M2 (insular), running in the lateral (Sylvian) fissure; M3 (opercular), coming out of the lateral fissure; M4, cortical portions. The middle cerebral artery runs at first in the lateral fissure, then posterosuperiorly on the insula, and divides into branches distributed to the insula and the adjacent lateral cerebral surface (**Fig. 26.4**, see Fig. 26.2).

The middle cerebral artery has cortical and central branches. Cortical branches send orbital vessels to the inferior frontal gyrus and the lateral orbital surface of the frontal lobe. Frontal branches supply the precentral, middle and inferior frontal gyri. Two parietal branches are

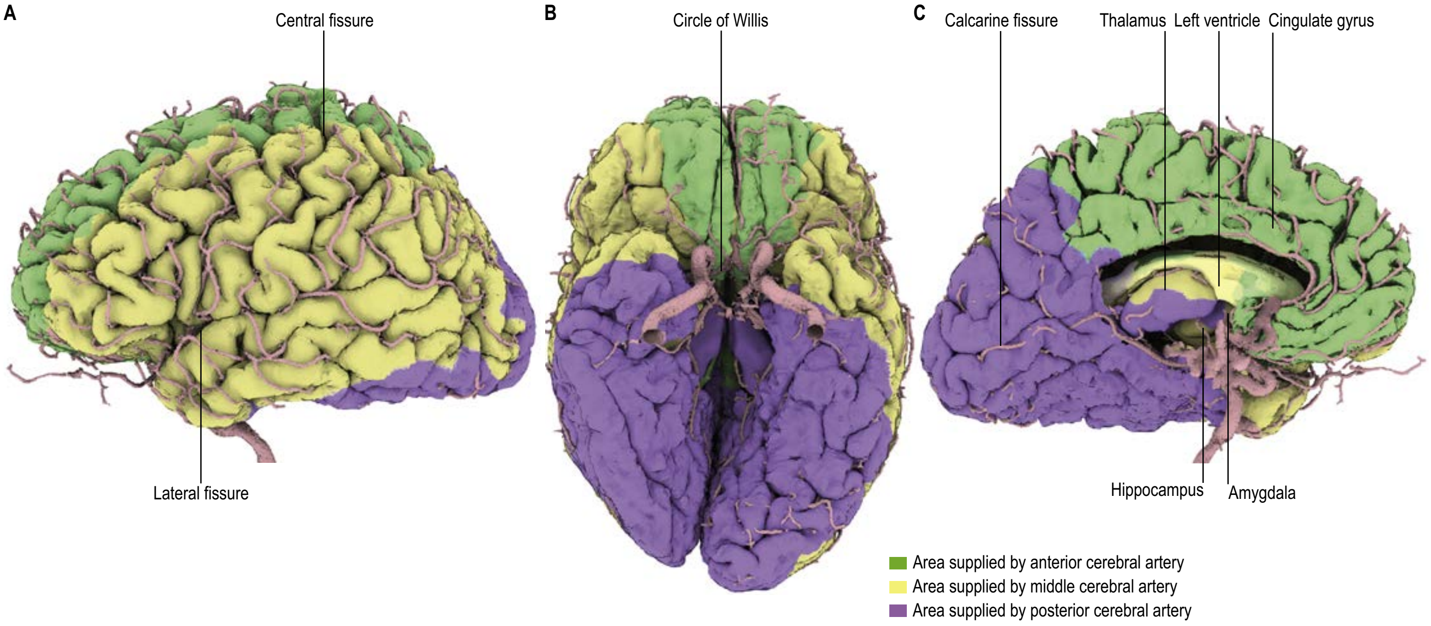
A
Central fissure
Lateral fissure
B
Circle of Willis
C
Calcarine fissure
Thalamus
Left ventricle
Cingulate gyrus
Hippocampus
Amygdala
🟩 Area supplied by anterior cerebral artery
🟨 Area supplied by middle cerebral artery
🟪 Area supplied by posterior cerebral artery

Fig. 26.4 Volumetric reconstruction from real subject data showing the arteries supplying the left cerebral hemisphere. **A**, Lateral surface. **B**, Basal surface. **C**, Medial surface.

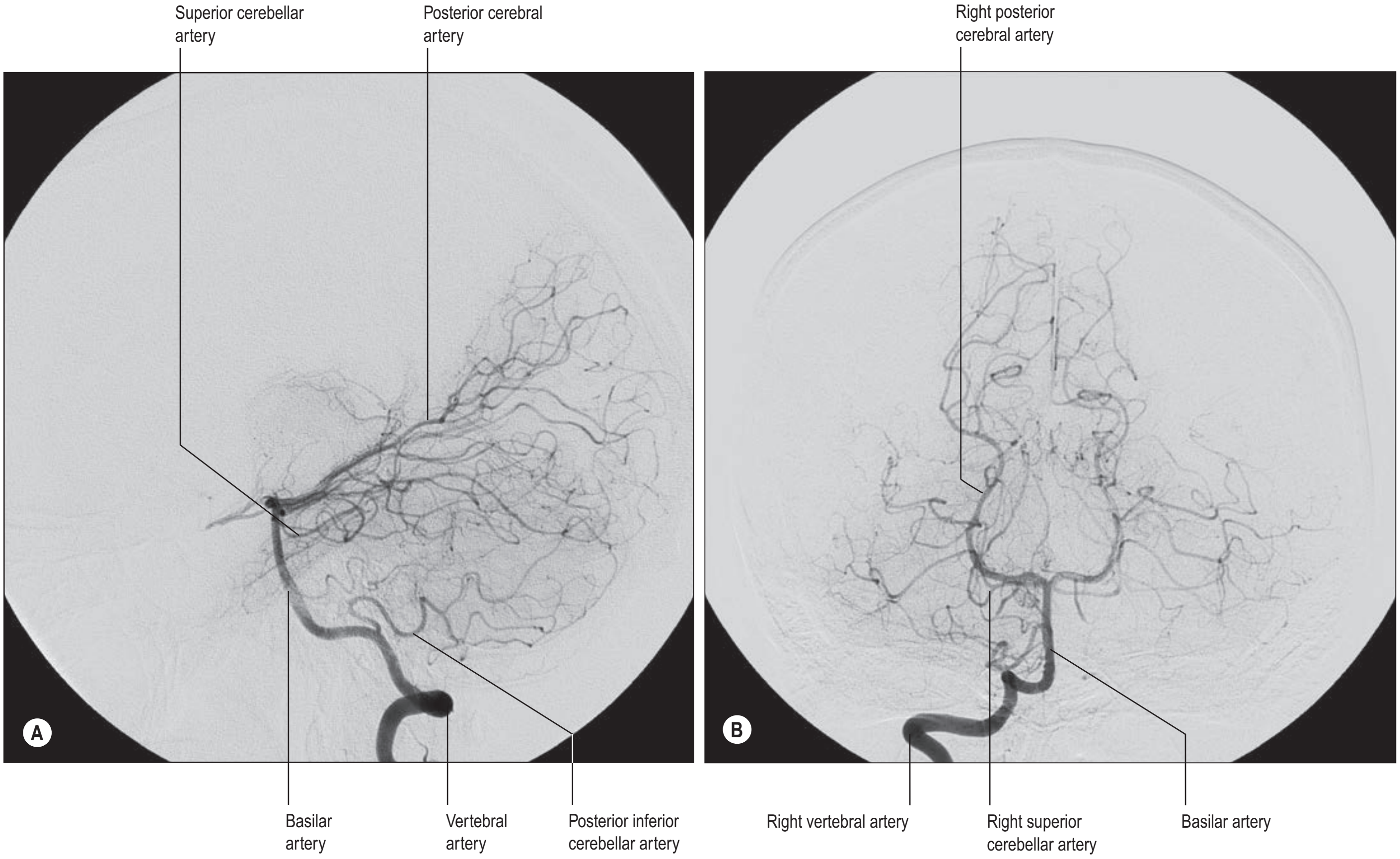
Superior cerebellar artery
Posterior cerebral artery
Right posterior cerebral artery
A
B
Basilar artery
Vertebral artery
Posterior inferior cerebellar artery
Right vertebral artery
Right superior cerebellar artery
Basilar artery

Fig. 26.5 Vertebral arteriograms. **A**, Lateral projection. **B**, Towne's projection.

distributed to the postcentral gyrus, the lower part of the superior parietal lobule and the whole inferior parietal lobule. Two or three temporal branches supply the lateral surface of the temporal lobe. Cortical branches of the middle cerebral artery therefore supply the motor and somatosensory cortices that represent the whole of the body (other than the lower limb), the auditory area and the insula.

Small central branches of the middle cerebral artery, the lateral striate or lenticulostriate arteries, arise at its origin and enter the anterior perforated substance together with the medial striate artery. Lateral striate arteries ascend in the external capsule over the lower lateral aspect of the lentiform complex, then turn medially, traverse the lentiform complex and the internal capsule and extend as far as the caudate nucleus (Video 26.1).

Vertebral artery

The vertebral arteries and their major branches (sometimes referred to as the 'vertebrobasilar system') essentially supply blood to the upper spinal cord, the brainstem and cerebellum, and a significant but variable part of the posterior cerebral hemispheres (**Fig. 26.5**).

The vertebral arteries are derived from the subclavian arteries, ascend through the neck in the foramina transversaria of the upper six cervical vertebrae and enter the cranial cavity through the foramen magnum, close to the anterolateral aspect of the medulla (see Fig. 35.11). They converge medially as they ascend the medulla and unite to form the midline basilar artery at approximately the level of the junction between the medulla and pons.

One or two meningeal branches arise from the vertebral artery near the foramen magnum, ramify between the bone and dura mater in the posterior cranial fossa, and supply bone, diploë and the falx cerebelli. A small anterior spinal artery arises near the end of the vertebral artery, descends anterior to the medulla oblongata and unites with its fellow from the opposite side at mid-medullary level. The common trunk descends on the ventral midline of the spinal cord, and is reinforced sequentially by small spinal rami from the vertebral, ascending cervical, posterior intercostal and first lumbar arteries, which all enter the vertebral canal via intervertebral foramina. Branches from the anterior spinal arteries and the beginning of their common trunk are distributed to the medulla oblongata.

The largest branch of the vertebral artery is the posterior inferior cerebellar artery (see Fig. 26.5A). It arises near the lower end of the olive and then ascends behind the roots of the glossopharyngeal and vagus nerves to reach the inferior border of the pons. Here it curves and descends along the inferolateral border of the fourth ventricle, then turns laterally into the cerebellar vallecula between the hemispheres and divides into medial and lateral branches. The medial branch runs back between the cerebellar hemisphere and inferior vermis, supplying both. The lateral branch supplies the inferior cerebellar surface as far as its lateral border and anastomoses with the anterior inferior and superior cerebellar arteries (branches of the basilar artery). The trunk of the posterior inferior cerebellar artery supplies the medulla oblongata dorsal to the olivary nucleus and lateral to the hypoglossal nucleus and its emerging nerve roots. It also supplies the choroid plexus of the fourth ventricle and sends a branch lateral to the cerebellar tonsil to supply the dentate nucleus. The posterior inferior cerebellar artery is sometimes absent.

A posterior spinal artery usually arises from the posterior inferior cerebellar artery, but may originate directly from the vertebral artery near the medulla oblongata. It passes posteriorly and descends as two branches that lie anterior and posterior to the dorsal roots of the spinal nerves. These are reinforced by spinal twigs from the vertebral, ascending cervical, posterior intercostal and first lumbar arteries, all of which reach the vertebral canal via intervertebral foramina and sustain the posterior spinal arteries to the lower spinal levels.

Very small medullary arteries arise from the vertebral artery and its branches and are distributed widely to the medulla oblongata.

Basilar artery

The basilar artery is a large median vessel formed by the union of the vertebral arteries at the junction of the medulla and pons (see Figs 26.3, 26.5). It lies in the pontine cistern and follows a shallow median groove on the ventral pontine surface, extending to the upper border of the pons. It ends by dividing into two posterior cerebral arteries at a variable level behind the dorsum sellae, usually in the interpeduncular cistern.

Numerous small pontine branches arise from the front and sides of the basilar artery along its course and supply the pons. The long and slender labyrinthine (internal auditory) artery has a variable origin. It usually arises from the anterior inferior cerebellar artery, but may arise from the lower part of the basilar artery, the superior cerebellar artery or, occasionally, the posterior inferior cerebellar artery. The labyrinthine artery accompanies the facial and vestibulocochlear nerves into the internal acoustic meatus and is distributed to the internal ear.

The anterior inferior cerebellar artery is given off from the distal part of the basilar artery and runs posterolaterally, usually ventral to the abducens, facial and vestibulocochlear nerves. It commonly exhibits a loop into the internal acoustic meatus below the nerves; when this occurs, the labyrinthine artery may arise from the loop. The anterior inferior cerebellar artery supplies the inferior cerebellar surface anterolaterally and anastomoses with the posterior inferior cerebellar branch of the vertebral artery. A few branches supply the inferolateral parts of the pons and occasionally also supply the upper medulla oblongata.

The superior cerebellar artery (see Figs 26.3, 26.5) arises near the distal portion of the basilar artery, immediately before the formation of the posterior cerebral arteries. It passes laterally below the oculomotor nerve, which separates it from the posterior cerebral artery, and curves round the cerebral peduncle below the trochlear nerve to gain the superior cerebellar surface. Here it divides into branches that ramify in the pia mater and supply this aspect of the cerebellum, and also anastomose with branches of the inferior cerebellar arteries. The superior cerebellar artery supplies the pons, pineal body, superior medullary velum and tela choroidea of the third ventricle.

Posterior cerebral artery

The paired posterior cerebral arteries are the terminal branches of the basilar artery (see Figs 26.2–26.4). Surgical nomenclature divides the vessel into three parts: P1, from the basilar bifurcation to the junction with the posterior communicating artery; P2, from the junction with the posterior communicating artery to the portion in the perimesencephalic cistern; and P3, the portion that runs in the calcarine fissure.

The posterior cerebral artery is larger than the superior cerebellar artery, from which it is separated near its origin by the oculomotor nerve and, lateral to the midbrain, by the trochlear nerve. It passes laterally, parallel with the superior cerebellar artery, and receives the posterior communicating artery. It then winds round the cerebral peduncle and reaches the tentorial cerebral surface, where it supplies the temporal and occipital lobes.

The posterior cerebral artery has cortical and central branches. Cortical branches are named according to their distribution. Temporal branches, usually two, are distributed to the uncus and parahippocampal, medial occipitotemporal and lateral occipitotemporal gyri. Occipital branches supply the cuneus, lingual gyrus and posterolateral surface of the occipital lobe. Parieto-occipital branches supply the cuneus and precuneus. The posterior cerebral artery supplies the visual areas of the cerebral cortex and other structures in the visual pathway.

The central branches supply subcortical structures. Several small posteromedial central branches arise from the beginning of the posterior cerebral artery (see Fig. 26.3B) and, together with similar branches from the posterior communicating artery, pierce the posterior perforated substance to supply the anterior thalamus, subthalamus, lateral wall of the third ventricle and globus pallidus. One or more posterior choroidal branches pass over the lateral geniculate body and supply it before entering the posterior part of the temporal horn of the lateral ventricle via the lower part of the choroidal fissure. Branches also curl round the posterior end of the thalamus and pass through the transverse fissure, or go to the choroid plexus of the third ventricle, or traverse the upper choroidal fissure: collectively, these branches supply the choroid plexuses of the third and lateral ventricles and the fornix. Small posterolateral central branches arise from the posterior cerebral artery beyond the cerebral peduncle and supply the peduncle and the posterior thalamus, superior and inferior colliculi, pineal gland and medial geniculate body.

Circulus arteriosus cerebri

The circulus arteriosus cerebri (cerebral arterial circle, circle of Willis) is a large arterial anastomosis that unites the internal carotid and vertebrobasilar systems (see Figs 26.3, 26.5B). It lies in the subarachnoid space within the basal cisterns that surround the optic chiasma and infundibulum. The anterior cerebral arteries are derived from the internal carotid arteries and are linked by a small, but functionally important, anterior communicating artery. Posteriorly, the two posterior cerebral arteries, formed by the division of the basilar artery, are joined to the ipsilateral internal carotid artery by a posterior communicating artery.

There is considerable individual variation in the pattern and calibre of vessels that make up the circulus arteriosus (Puchades-Orts et al 1976). Although a complete circular channel almost always exists, one vessel is usually sufficiently narrowed to reduce its role as a collateral route and the circle is rarely functionally complete. Individual cerebral and communicating arteries may be absent, variably hypoplastic, double or even triple. The haemodynamics of the circle are influenced by variations in the calibre of communicating arteries and in the segments of the anterior and posterior cerebral arteries that lie between their origins and their junctions with the corresponding communicating arteries. The greatest variation in calibre occurs in the posterior communicating artery, which is normally very small, so that only limited flow is possible between the anterior and posterior circulations. Commonly, the diameter of the pre-communicating part of the posterior cerebral artery is larger than that of the posterior communicating artery, which means that the blood supply to the occipital lobes is mainly from the vertebrobasilar system. When the diameter of the pre-communicating part of the posterior cerebral artery is smaller than that of the posterior communicating artery, the blood supply to the occipital lobes is mainly from the internal carotid arteries via the posterior communicating arteries. The primary purpose of the vascular circle is to provide anastomotic channels if one vessel is occluded, but a normal-sized posterior communicating artery cannot usually fulfil this role. Agenesis or hypoplasia of the initial segment of the anterior cerebral artery are more frequent than anomalies in the anterior communicating artery and contribute to defective circulation in about one-third of individuals (Video 26.1).

Central or perforating arteries

Numerous small central (perforating or ganglionic) arteries arise from the circulus arteriosus or from vessels near it (see Fig. 26.3), and many enter the brain through the anterior and posterior perforated substances. Central branches supply nearby structures on or near the base of the brain together with the interior of the cerebral hemisphere, including the internal capsule, basal ganglia and thalamus. These branches form four principal groups (antero- and posteromedial and antero- and posterolateral). Arteries in the anteromedial group arise from the anterior cerebral and anterior communicating arteries, and pass through the medial part of the anterior perforated substance. They supply the optic chiasma, lamina terminalis, anterior, preoptic and supraoptic areas of the hypothalamus, septum, para-olfactory areas, anterior columns of the fornix, cingulate gyrus, rostrum of the corpus callosum and the anterior part of the putamen and the head of the caudate nucleus. Arteries in the posteromedial group arise from the entire length of the posterior communicating artery and from the proximal portion of the posterior cerebral artery. Anteriorly, they supply the hypothalamus and pituitary gland, and the anterior and medial parts of the thalamus via thalamoperforating arteries. Caudally, they supply the mammillary bodies, subthalamus, the lateral wall of the third ventricle, including the medial thalamus, and the globus pallidus. Arteries in the anterolateral group are mainly branches from the proximal part of the middle cerebral artery; they are also known as striate, lateral striate or lenticulostriate arteries. They enter the brain through the anterior perforated substance and supply the posterior striatum, lateral globus pallidus and the anterior limb, genu and posterior limb of the internal capsule. The medial striate artery, derived from the middle or anterior cerebral arteries, supplies the rostral part of the caudate nucleus and putamen, and the anterior limb and genu of the internal capsule. Arteries in the posterolateral group arise from the posterior cerebral artery distal to its junction with the posterior communicating artery, and supply the cerebral peduncle, colliculi, pineal gland and, via thalamogeniculate branches, the posterior thalamus and medial geniculate body.

Regional arteries of the brain

Brainstem

The medulla oblongata is supplied by branches of the vertebral, anterior and posterior spinal, posterior inferior cerebellar and basilar arteries, which enter along the ventral median fissure and the dorsal median sulcus. Vessels that supply the central substance enter along the rootlets of the glossopharyngeal, vagus and hypoglossal nerves. There is an additional supply via a pial plexus from the same main arteries. The choroid plexus of the fourth ventricle is supplied by the posterior inferior cerebellar arteries. The pons is supplied by the basilar artery and the anterior inferior and superior cerebellar arteries. Direct branches from the basilar artery enter the pons along the basilar sulcus; other vessels enter along the trigeminal, abducens, facial and vestibulocochlear nerves and from the pial plexus. The midbrain is supplied by the posterior cerebral, superior cerebellar and basilar arteries. The crura cerebri are supplied by vessels that enter on their medial and lateral sides: medial vessels enter the medial side of each crus and also supply the superomedial part of the tegmentum, including the oculomotor nucleus, and lateral vessels supply the lateral part of each crus and the tegmentum. The colliculi are supplied by the posterior cerebral and superior cerebellar arteries. The posterolateral group of central branches of the posterior cerebral artery also supply the crura and the colliculi.

Cerebellum

The cerebellum is supplied by the posterior inferior, anterior inferior and superior cerebellar arteries, which form superficial anastomoses on the cortical surface. Anastomoses between deeper, subcortical, branches have been postulated (Duvernoy et al 1983).

Optic chiasma, tract and radiation

The blood supply to the optic chiasma, tract and radiation is of considerable clinical importance. The chiasma is supplied in part by the anterior cerebral arteries, but its median zone depends upon rami from the internal carotid arteries reaching it via the stalk of the hypophysis. The anterior choroidal and posterior communicating arteries supply the optic tract, and the optic radiation receives blood through deep branches of the middle and posterior cerebral arteries.

Diencephalon

The thalamus is supplied mainly by branches of the posterior communicating, posterior cerebral and basilar arteries (Plets et al 1970). A contribution from the anterior choroidal artery is often noted but this has been disputed. The medial branch of the posterior choroidal artery supplies the posterior commissure, habenular region, pineal gland and medial parts of the thalamus, including the pulvinar. Small central branches, which arise from the circulus arteriosus and its associated vessels, supply the hypothalamus. The pituitary gland is supplied by hypophysial arteries derived from the internal carotid artery, and the anterior cerebral and anterior communicating arteries supply the lamina terminalis. The choroid plexuses of the third and lateral ventricles are supplied by branches of the internal carotid and posterior cerebral arteries.

Basal ganglia

Most of the arterial supply to the basal ganglia comes from the striate arteries, which are branches from the roots of the anterior and middle cerebral arteries that enter the brain through the anterior perforated substance and also supply the internal capsule. The caudate nucleus receives blood additionally from the anterior and posterior choroidal arteries. The posteroinferior part of the lentiform complex is supplied by the thalamostriate branches of the posterior cerebral artery. The anterior choroidal artery, a preterminal branch of the internal carotid artery, contributes to the blood supply of both segments of the globus pallidus and the caudate nucleus. Famously, the ligation of this vessel during a neurosurgical procedure on a patient suffering from Parkinson's disease led to alleviation of the parkinsonian symptoms, presumably as a consequence of infarction of the globus pallidus. This chance observation led to the initiation of pallidal surgery (pallidotomy) for this condition (Ch. 31).

Internal capsule

The internal capsule is supplied by central, or perforating, arteries that arise from the circulus arteriosus and its associated vessels. These include the lateral and medial striate arteries that come from the middle and anterior cerebral arteries and also supply the basal ganglia. The lateral striate arteries supply the anterior limb, genu and much of the posterior limb of the internal capsule and are commonly involved in ischaemic and haemorrhagic stroke; indeed, one of the larger striate branches of the middle cerebral artery is known anachronistically as 'Charcot's artery of cerebral haemorrhage'. The medial striate artery, a branch of the proximal part of either the middle or anterior cerebral arteries, supplies the anterior limb and genu of the internal capsule and the basal ganglia. The anterior choroidal artery also contributes to the supply of the ventral part of the posterior limb and the retrolenticular part of the internal capsule.

Cerebral cortex

The entire blood supply of the cerebral cortex comes from cortical branches of the anterior, middle and posterior cerebral arteries (see Figs 26.2, 26.4, Video 26.1; Duvernoy et al 1981). In general, long branches traverse the cortex and penetrate the subjacent white matter for 3 or 4 cm without communicating. Short branches are confined to the cerebral cortex and form a compact network in the middle zone of the grey matter, whereas the outer and inner zones are sparingly supplied. Although adjacent vessels anastomose on the surface of the brain, they become end arteries as soon as they enter it. In general, superficial anastomoses only occur between microscopic branches of the cerebral arteries, and there is little evidence that they can provide an effective alternative circulation after the occlusion of larger vessels.

The lateral surface of the hemisphere, which includes the territories of the motor and somatosensory cortices (representing the whole of the body apart from the lower limb) and the auditory cortex and language areas, is supplied mainly by the middle cerebral artery. The anterior cerebral artery supplies a strip next to the superomedial border of the hemisphere, as far back as the parieto-occipital sulcus. The occipital lobe and most of the inferior temporal gyrus (excluding the temporal pole) are supplied by the posterior cerebral artery.

Medial and inferior surfaces of the hemisphere are supplied by the anterior, middle and posterior cerebral arteries. The area supplied by the anterior cerebral artery is the largest, extending almost to the parieto-occipital sulcus and including the medial part of the orbital surface. The rest of the orbital surface and the temporal pole are supplied by the middle cerebral artery, and the remaining medial and inferior surfaces are supplied by the posterior cerebral artery.

Near the occipital pole, the junctional zone between the territories of the middle and posterior cerebral arteries corresponds to the visual (striate) cortex, which receives information from the macula. When the posterior cerebral artery is occluded, a phenomenon known as 'macular sparing' may occur, where vision with the central part of the retina is preserved. Collateral circulation of blood from branches of the middle cerebral artery into those of the posterior cerebral artery may account for this phenomenon. In some individuals, the middle cerebral artery may directly supply the macular area.

Cerebral blood flow

The brain is devoid of either glucose stores or a means of storing oxygen and is therefore dependent minute-by-minute on an adequate blood supply. It has a high metabolic rate in comparison to other organs, reflecting the metabolic demands of constant neural activity: the blood supply of grey matter is more copious than that of white matter.

Cerebral blood flow in the human brain is approximately $50\,\mathrm{ml\,g^{-1}\,min^{-1}}$. Global cerebral blood flow is autoregulated, i.e. it remains constant in normal individuals despite variations in mean arterial blood pressure over a range of 8.7–18.7 kPa (65–140 mmHg). If the blood pressure falls below this range, cerebral blood flow decreases, and if the pressure rises above this range, cerebral blood flow may increase. Arterial and arteriolar intraluminal pressure directly control contraction of intramural muscle, e.g. an increase in arterial pressure causes arterial constriction, and blood flow remains constant.

Although autoregulation normally ensures that global cerebral blood flow remains constant, regional blood flow varies in response to the level of neural activity and local metabolic demand. This has been demonstrated for many brain areas, including the motor and sensory cortical regions, areas involved in convulsive activity and cortical areas involved in complex thought processes. The principal local factors affecting regional blood flow are the local hydrogen ion (H^+) or carbon dioxide concentrations, which cause arterial dilation both by a direct action on the endothelium and through indirect mediators, such as nitric oxide.

Not all substances circulating in arterial blood have access to the brain parenchyma: particulate matter, such as bacteria, is excluded. In general, lipophilic molecules and small molecules, such as oxygen and carbon dioxide, can cross the blood–brain barrier but hydrophilic ones (excluding glucose) cannot. The cellular basis for the blood–brain barrier is discussed in Chapter 3.

Ischaemic stroke

Stroke refers to the clinical syndrome of a rapidly developing focal neurological deficit that is not due to seizure activity. If the cause is lack of, or reduced, blood supply to a portion of the brain, then the term ischaemic stroke (**Fig. 26.6**) is used, as opposed to haemorrhagic stroke, e.g. subarachnoid haemorrhage. The lack of blood flow can be due to pathology in the vessel lumen, such as thrombosis or embolus (common); pathology outside the blood vessel, such as occlusion from the mass effect of a tumour or haematoma (rare); or pathology of the vessel wall, such as inflammatory or infective arteritides (rare). The symptoms and signs of ischaemic stroke depend on the location and extent of the arterial infarction (Bogousslavsky and Caplan 2002). In certain locations, even a small volume stroke can have devastating effects. For example, the internal capsule and most of the adjacent basal

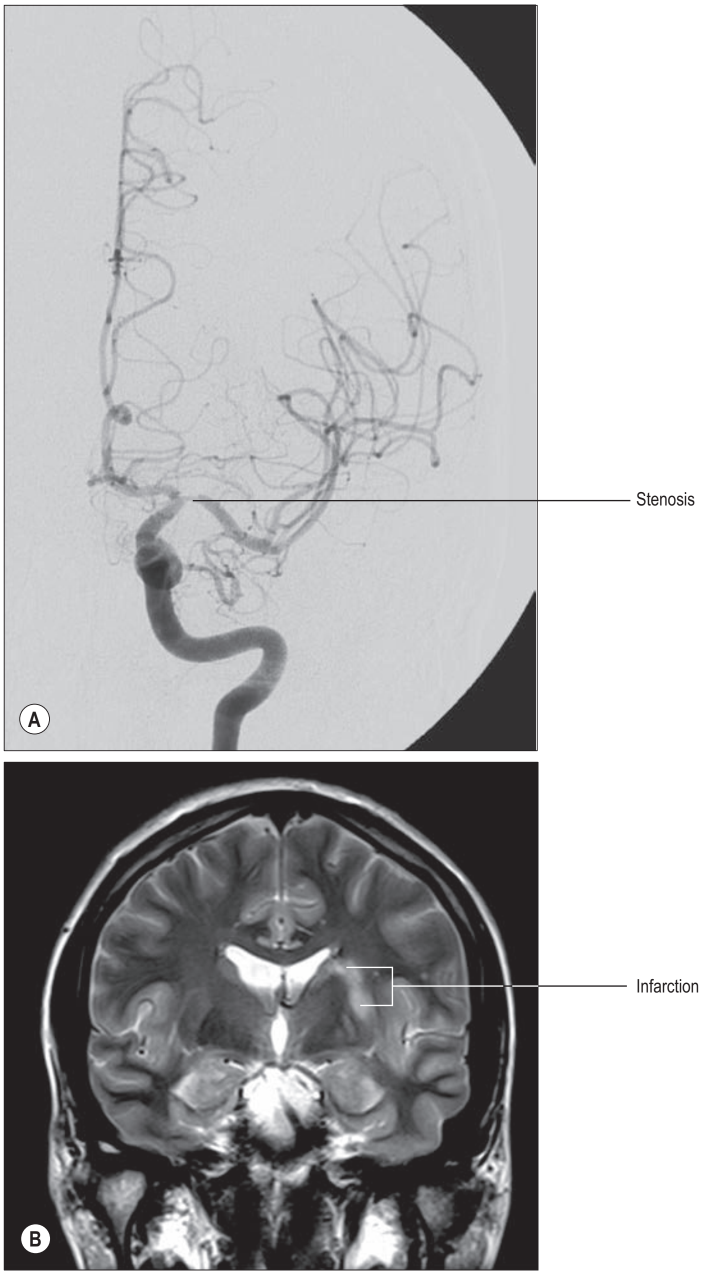

Fig. 26.6 **A**, A frontal projection of a selective catheter angiogram of the left internal carotid artery, showing a focal narrowing at the termination of the left internal carotid artery and the origin of the left middle cerebral artery. **B**, A coronal T2-weighted image of the brain at the level of the basal ganglia. There is an abnormal high signal in the left putamen and adjacent white matter, consistent with infarction. It is likely that the infarction was due to occlusion of small perforating vessels originating in the area of the stenosis and supplying the basal ganglia.

ganglia are supplied by small perforating arteries, common sites for ischaemic stroke. Corticonuclear and corticospinal motor pathways and third-order thalamocortical sensory fibres all pass through the internal capsule, which means that effectively it is the only route connecting the cerebral cortex with other regions of the neuraxis. The neurological deficits that result from stroke in the internal capsule therefore may include contralateral spastic hemiparesis, contralateral hemisensory loss and psychological deficits.

It is possible for a major vessel, such as the internal carotid artery in the neck, to become occluded and for the affected individual to remain asymptomatic, provided that an appropriate flow of blood can be recruited to supply the affected brain region from other sources (collateral supply). The primary role of the circulus arteriosus is to allow for this eventuality by redirecting blood from other sources, such as the contralateral internal carotid artery and vertebrobasilar system. If the circulus arteriosus is complete, two or even three of the four major arteries supplying the brain can be occluded without producing an ischaemic stroke. Unfortunately, the circulus arteriosus is rarely haemodynamically complete and ischaemic stroke often occurs because the collateral supply is inadequate.

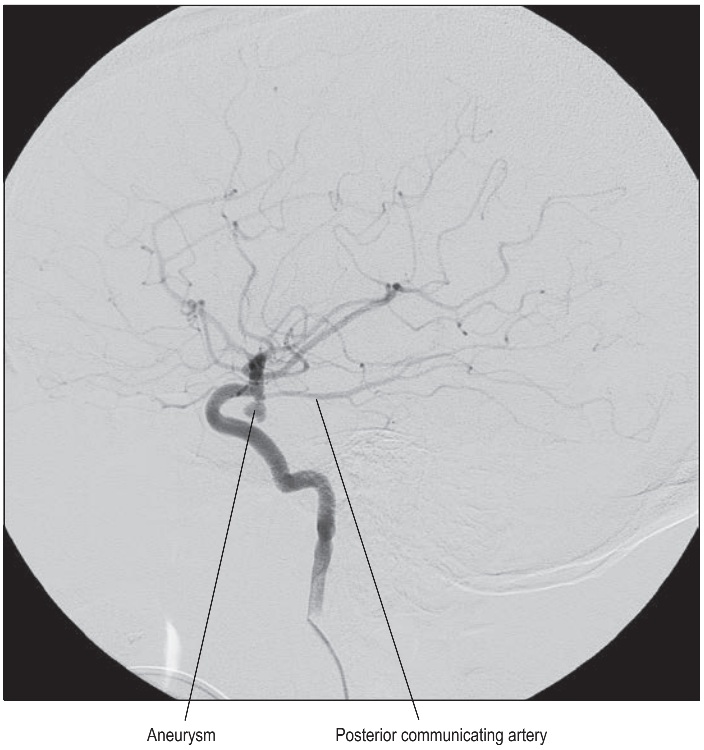

Fig. 26.7 An intra-arterial digital subtraction angiogram of the right internal carotid artery in a patient with a complete right oculomotor nerve palsy, reflecting compression of the nerve by an aneurysm on the posterior communicating artery, lateral projection.

For example, an individual in whom neither anterior nor posterior communicating arteries are patent will suffer an ischaemic stroke if there is occlusion of one internal carotid artery because the proximal anterior and middle cerebral arteries cannot receive collateral flow via the incomplete circulus arteriosus. Some collateral flow may be available from anastomoses between distal branches of the external carotid artery (e.g. middle meningeal artery) but invariably this is not sufficient to supply the whole hemisphere.

Somewhat paradoxically, the more distally an occlusion occurs in the cerebral vasculature, the more likely it is to cause an ischaemic stroke (although the volume of infarcted tissue will be less). This is because the major capacity to form collateralization is proximal, mainly at the circulus arteriosus. For example, an embolus formed in the proximal internal carotid artery may travel to the M1 portion of the ipsilateral middle cerebral artery and occlude the vessel. There is very little scope for collateralization at this site and an ischaemic stroke is unavoidable, unless the embolus can be cleared and flow restored in good time.

Watershed areas Regions of the brain lying at the extreme edges of the major cerebral arterial territories are called watershed areas and are the first to be deprived of sufficient blood flow in the event of cerebral hypoperfusion. Ischaemic infarcts of the cortex and adjacent subcortical white matter in the border zones between these territories are known as watershed, boundary-zone or border-zone infarcts. There is some evidence that a second arterial border zone, the internal arterial border zone, exists within the white matter of the centrum semiovale and corona radiata (between the lenticulostriate perforators and the deep penetrating branches of the distal middle cerebral artery).

Cerebral aneurysms Aneurysms are balloon-like swellings that occur on arteries as a result of defects in the vessel wall. They are most commonly found on the vessels of the circulus arteriosus, particularly at or near the junctions of vessels. Aneurysms on the internal carotid artery near its termination may compress the lateral aspect of the optic chiasma and compromise axons derived from the temporal side of the ipsilateral retina, causing a defect in the nasal visual field. Aneurysms in the vicinity of the oculomotor nerve, e.g. on the posterior communicating artery, superior cerebellar artery or the tip of the basilar artery, can cause damage to the oculomotor nerve by compression (Fig. 26.7).

Subarachnoid haemorrhage Bleeding into the subarachnoid compartment, subarachnoid haemorrhage, is the most common pathology that involves the subarachnoid space (Sengupta and McAllister 1986). There are many causes: in adults, the most common is rupture of an aneurysm of the intracranial vessels that run within the subarachnoid

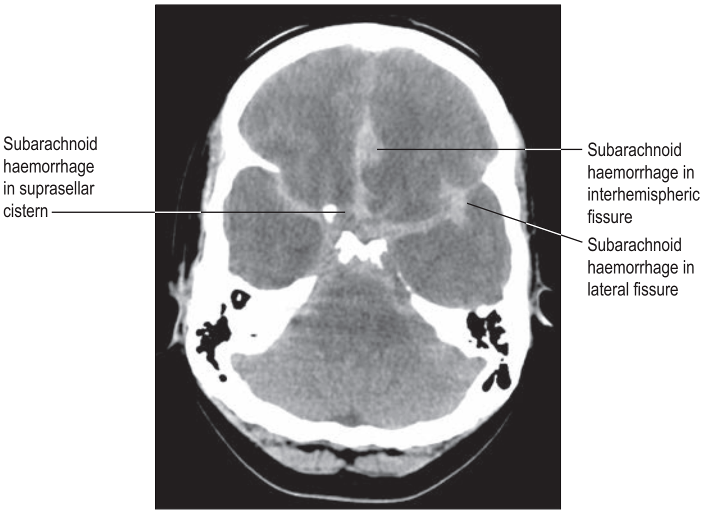
Subarachnoid haemorrhage in suprasellar cistern
Subarachnoid haemorrhage in interhemispheric fissure
Subarachnoid haemorrhage in lateral fissure

Fig. 26.8 An axial CT image (without intravenous contrast agent) at the level of the posterior clinoid processes. There is abnormally high attenuation in the basal cisterns and subarachnoid space of the interhemispheric fissure, indicating an acute subarachnoid haemorrhage, subsequently shown to be due to a ruptured aneurysm on the anterior communicating artery.

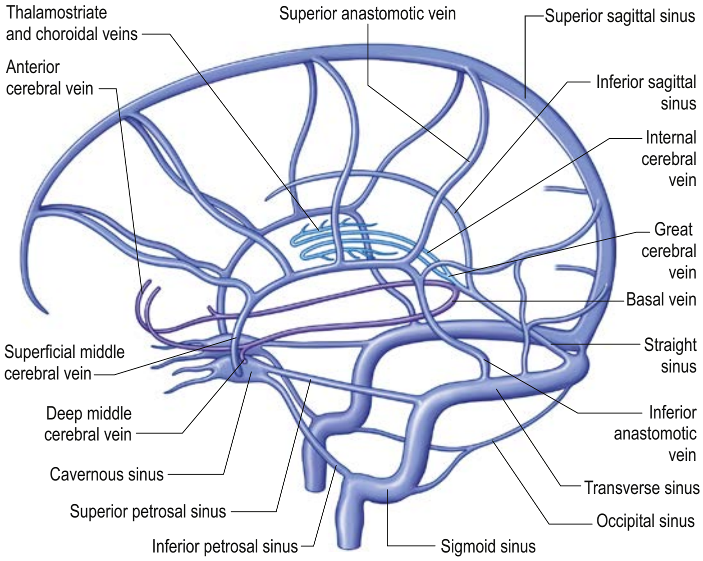

Fig. 26.10 The cerebral venous system showing the principal superficial and deep veins of the brain and their relationship to the dural venous sinuses, viewed from the left side.

space. An individual who has suffered a subarachnoid haemorrhage usually complains of a headache of very sudden onset that is frequently described as being their ‘worst ever headache’ or ‘like being hit on the head with a hammer’. When this is suspected, the first investigation is a CT examination, which has a very high sensitivity for detecting fresh haemorrhage. Blood will be seen in the basal cisterns and entering the depths of the cortical sulci, i.e. delineating the anatomy of the subarachnoid space, a presentation that permits an accurate diagnosis (Fig. 26.8). In marked contrast, the spread of blood in a subdural haemorrhage is limited by the arachnoid mater on its deep surface, and the blood therefore remains on the surface of the brain.

Arteriovenous malformations Arteriovenous malformations (AVMs) of the brain are developmental abnormalities of the blood vessels supplying the brain and are thought to occur in 1–2 per 10,000 people. In the normal brain, blood flows from a cerebral artery into a capillary system and then into a draining vein(s). When an AVM is present, arterial blood passes into a tangle (nidus) of abnormal blood vessels that allows passage into the venous system without passing through normal capillaries (Fig. 26.9).

VEINS OF THE BRAIN

The venous drainage of the brain occurs through a complex system of deep and superficial veins (Andeweg 1996) devoid of valves and with thin walls that lack muscular tissue. They pierce the arachnoid mater and the inner layer of the dura mater to open into the dural venous sinuses.

Veins of the posterior fossa

The veins of the brainstem form a superficial venous plexus deep to the arteries. Veins of the medulla oblongata drain into the veins of the spinal cord or the adjacent dural venous sinuses, or into variable radicular veins that accompany the last four cranial nerves to either the inferior petrosal or occipital sinuses, or to the superior bulb of the jugular vein. Anterior and posterior median medullary veins may run along the ventral median fissure and dorsal median sulcus to become continuous with the spinal veins in corresponding positions. Pontine veins, which may include a median vein and a lateral vein on each side, drain into the basal vein, cerebellar veins, the petrosal or transverse sinuses or the venous plexus of the foramen ovale. Veins of the midbrain join the great cerebral vein (of Galen) or the basal vein.

The veins of the cerebellum drain mainly into sinuses adjacent to them or, from the superior surface, into the great cerebral vein. The cerebellar veins course on the cerebellar surface, and consist of superior and inferior groups. Superior cerebellar veins run either anteromedially across the superior vermis to the straight sinus or great cerebral vein, or they run laterally to the transverse and superior petrosal sinuses. Inferior cerebellar veins include a small median vessel that runs backwards on the inferior vermis to enter the straight or sigmoid sinus. Laterally coursing vessels join the inferior petrosal and occipital sinuses.

Veins of the cerebral hemisphere

Superficial and deep cerebral veins drain the surfaces and interior of the cerebral hemisphere, respectively (**Figs 26.10–26.11**, Video 26.2). The superficial veins may be divided into superior, middle and inferior groups. Between 8 and 12 superior cerebral veins drain the superolateral and medial surfaces of each hemisphere. They mainly follow the sulci, although some pass across gyri. They ascend to the superomedial border of the hemisphere, where they receive small veins from the medial surface, and then open into the superior sagittal sinus. Superior cerebral veins in the anterior part of the hemisphere join the sinus almost at right angles. The larger posterior veins are directed obliquely forwards, against the direction of flow in the sinus, an arrangement that may resist their collapse when intracranial pressure is raised.

The superficial middle cerebral vein drains most of the lateral surface of the hemisphere and follows the lateral fissure to end in the cavernous sinus. A superior anastomotic vein runs posterosuperiorly between the superficial middle cerebral vein and the superior sagittal sinus, connecting the superior sagittal and cavernous sinuses. An inferior anastomotic vein courses over the temporal lobe and connects the superficial middle cerebral vein to the transverse sinus. The deep middle cerebral vein drains the insular region and joins the anterior cerebral and striate veins to form a basal vein. Regions drained by the anterior cerebral and striate veins correspond approximately to those supplied by the anterior cerebral artery and the central branches that enter the anterior perforated substance. The basal veins pass back alongside the interpeduncular fossa and midbrain, receiving tributaries from this vicinity, and join the great cerebral vein.

Inferior cerebral veins on the orbital surface of the frontal lobe join the superior cerebral veins and thus drain to the superior sagittal sinus. Those on the temporal lobe anastomose with basal veins and middle cerebral veins, and drain to the cavernous, superior petrosal and transverse sinuses.

The basal vein is formed at the anterior perforated substance by the union of several vessels: a small anterior cerebral vein, which accompanies the anterior cerebral artery; a deep middle cerebral vein, which receives tributaries from the insula and neighbouring gyri, and runs in the lateral cerebral fissure; and striate veins, which emerge from the anterior perforated substance. The basal vein passes back round the cerebral peduncle to the great cerebral vein and receives tributaries from the interpeduncular fossa, temporal horn of the lateral ventricle, parahippocampal gyrus and midbrain.

The internal cerebral vein drains the deep parts of the hemisphere and the choroid plexuses of the third and lateral ventricles (Fig. 26.12). It is formed behind the column of the fornix, near the interventricular foramen, primarily by union of the thalamostriate and choroidal veins, although numerous smaller veins from surrounding structures also converge here. The thalamostriate vein runs anteriorly, between the caudate nucleus and thalamus, and receives many tributaries from both. The choroidal vein runs a convoluted course along the whole choroid

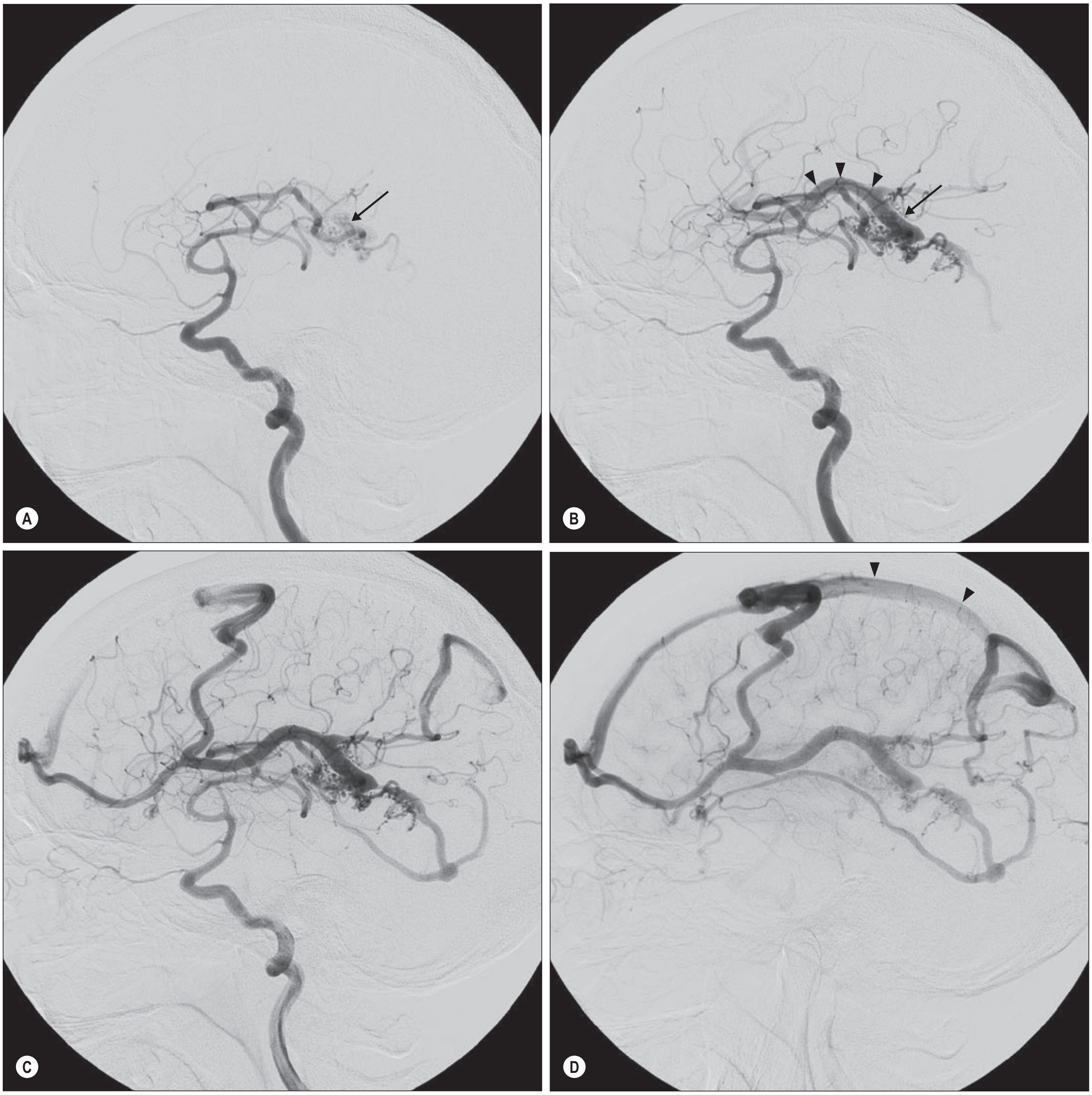

Fig. 26.9 Selective catheter angiograms showing an arteriovenous malformation (AVM) in the left cerebral hemisphere. **A**, Injection of contrast medium into the left internal carotid artery shows the nidus of an AVM being supplied by enlarged posterior branches of the middle cerebral artery (arrow). **B**, An image taken one-third of a second later shows better filling of the nidus (arrow) and early filling of a draining vein (arrowheads). **C**, One second after the original image was taken, abnormally large cortical veins can be seen draining towards the superior sagittal sinus. **D**, Two seconds after the original, the superior sagittal sinus is opacified but the remainder of the dural venous system is not filled with contrast, indicating rapid shunting through the AVM.

As a result, there is often rapid, high-volume blood flow through the nidus, and coupled with abnormal vessel walls, this leads to a high risk of rupture. The resulting haemorrhage from a cerebral AVM is associated with high mortality/morbidity, and recurrent haemorrhages are common in survivors. Not all brain AVMs present with rupture but they may cause headaches, seizures or focal neurological deficits; some brain AVMs are discovered incidentally. There are several treatment options for brain AVMs, including surgical resection, endovascular obliteration and stereotactic radiosurgery. In some circumstances, conservative management is appropriate.

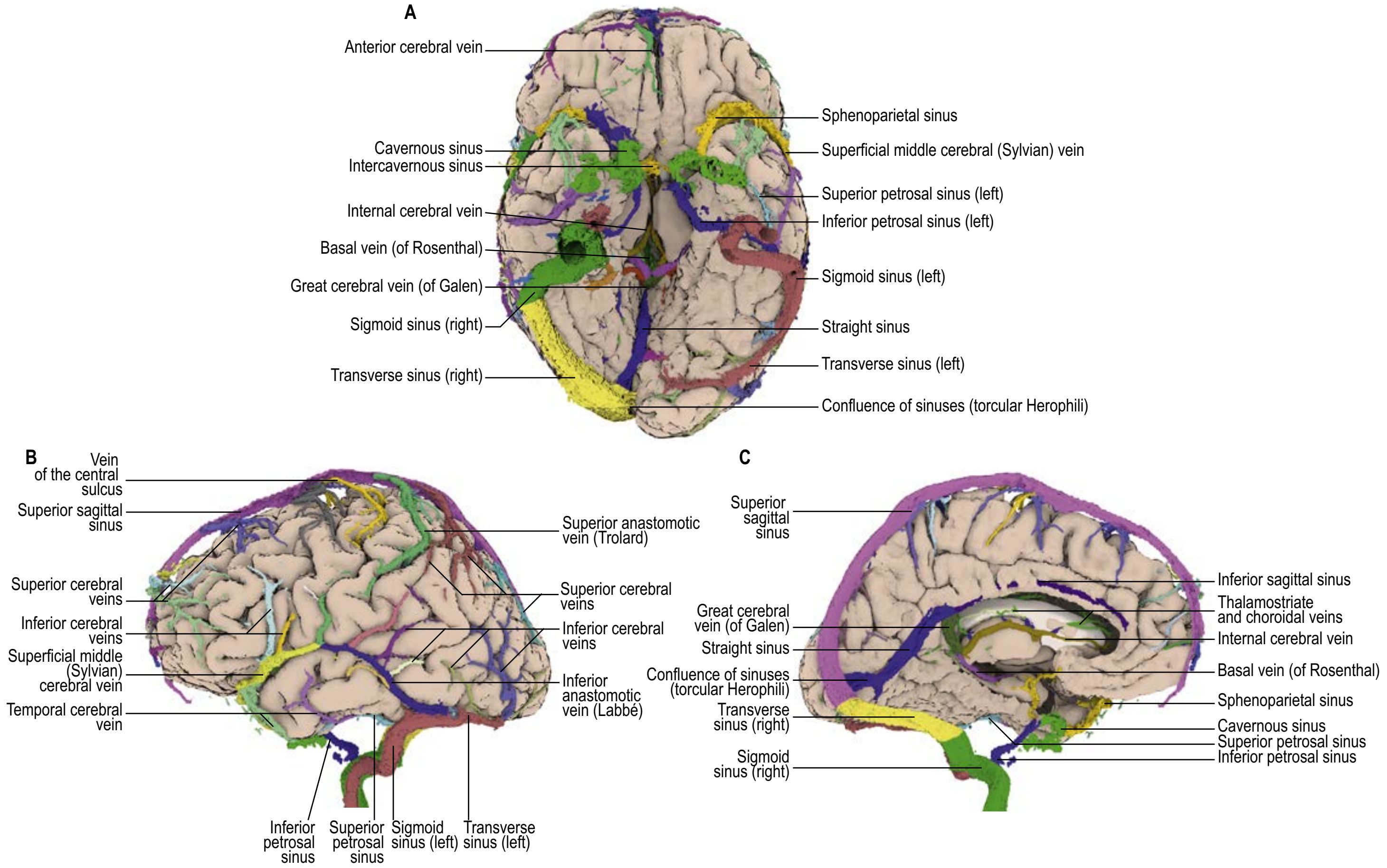
A
Anterior cerebral vein
Cavernous sinus
Intercavernous sinus
Internal cerebral vein
Basal vein (of Rosenthal)
Great cerebral vein (of Galen)
Sigmoid sinus (right)
Transverse sinus (right)
Sphenoparietal sinus
Superficial middle cerebral (Sylvian) vein
Superior petrosal sinus (left)
Inferior petrosal sinus (left)
Sigmoid sinus (left)
Straight sinus
Transverse sinus (left)
Confluence of sinuses (torcular Herophili)
B
Vein of the central sulcus
Superior sagittal sinus
Superior cerebral veins
Inferior cerebral veins
Superficial middle (Sylvian) cerebral vein
Temporal cerebral vein
Superior anastomotic vein (Trolard)
Superior cerebral veins
Inferior cerebral veins
Inferior anastomotic vein (Labbé)
Inferior petrosal sinus
Superior petrosal sinus
Sigmoid sinus (left)
Transverse sinus (left)
C
Superior sagittal sinus
Great cerebral vein (of Galen)
Straight sinus
Confluence of sinuses (torcular Herophili)
Transverse sinus (right)
Sigmoid sinus (right)
Inferior sagittal sinus
Thalamostriate and choroidal veins
Internal cerebral vein
Basal vein (of Rosenthal)
Sphenoparietal sinus
Cavernous sinus
Superior petrosal sinus
Inferior petrosal sinus

Fig. 26.11 Volumetric reconstruction from real subject data showing the veins and sinuses draining the basal (**A**), lateral (**B**) and medial (**C**) aspects of the brain.

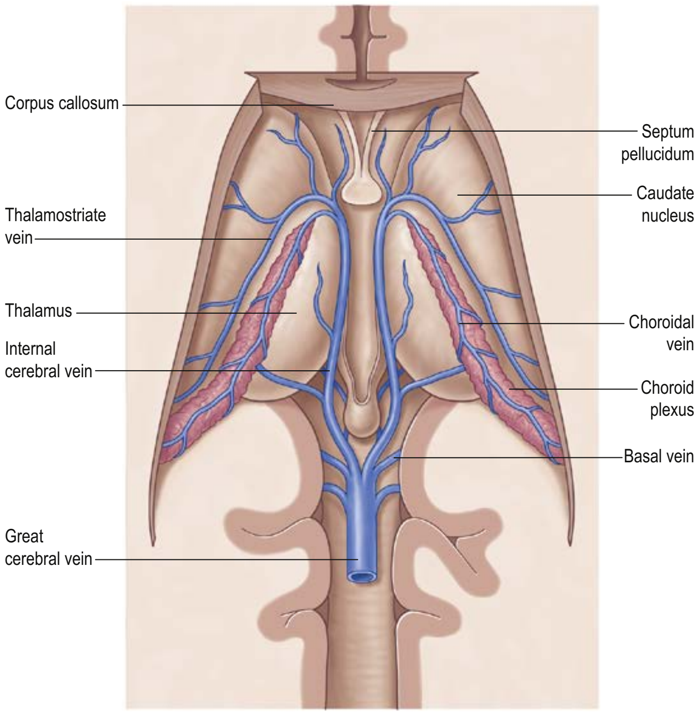
Corpus callosum
Thalamostriate vein
Thalamus
Internal cerebral vein
Great cerebral vein
Septum pellucidum
Caudate nucleus
Choroidal vein
Choroid plexus
Basal vein

Fig. 26.12 The internal (deep) cerebral veins, viewed from above after removal of the central portion of the corpus callosum.

plexus, and receives veins from the hippocampus, fornix, corpus callosum and adjacent structures. After their formation, the two internal cerebral veins travel back parallel to one another beneath the splenium of the corpus callosum, where they unite to form the great cerebral vein (Fig. 26.13). The great cerebral vein is a short median vessel that curves sharply up around the splenium of the corpus callosum and opens into the anterior end of the straight sinus after receiving the right and left basal veins (Video 26.2).

Intracranial venosinus thrombosis One of the most potentially serious pathologies affecting the intracranial venous system is venosinus thrombosis (Fig. 26.14). In this condition, blood clots within the dural sinuses and/or intracranial veins, and the resulting obstruction of venous drainage, may produce life-threatening complications.

In many cases, the cause of the venosinus thrombosis is not found; trauma involving the dural sinuses and infections in the vicinity of the sinuses (e.g. mastoiditis) present significant risk. Conditions that increase the coagulability of the blood, such as the oral contraceptive pill, pregnancy, dehydration and inborn abnormalities of the coagulation pathways, are also risk factors.

Individuals with intracranial venosinus thrombosis at its most severe present moribund, in coma or with major seizure activity, and in these situations the prognosis is poor. The clot within the dural sinuses and/or cortical veins obstructs the drainage of venous blood from the brain and causes venous hypertension. As the pressure in the venous system approaches the arterial pressure, the blood flow perfusing the affected parts of the brain decreases. If it dips below a critical level, the brain tissue will become ischaemic and may die (venous infarction). As the arterial supply to the brain is still present, the infarcted areas of the brain frequently undergo major haemorrhage and this is often the factor that kills the patient.

Clinicians distinguish between thrombosis that affects the 'superficial' and 'deep' venous systems, although they may occur together. Superficial thrombosis usually occurs in the superior sagittal sinus (with or without involvement of the cortical veins). Deep intracranial thrombotic disease usually affects the great cerebral vein and the straight sinus. The parts of the cerebral hemispheres affected are different in the two situations: superficial thrombosis affects the cerebral hemispheres (particularly the white matter) and deep thrombosis affects the thalami and basal ganglia. A common feature is the tendency for bilateral involvement because all of the main draining venous channels are in the midline and accept venous drainage from both hemispheres. If the extent of the intracranial venosinus thrombosis is less severe, or if alternative venous drainage has been accommodated by reasonable collateral channels, the patient may have more modest symptoms such as headaches or visual disturbance. Those symptoms are due to raised intracranial pressure and, if untreated, may become chronic.

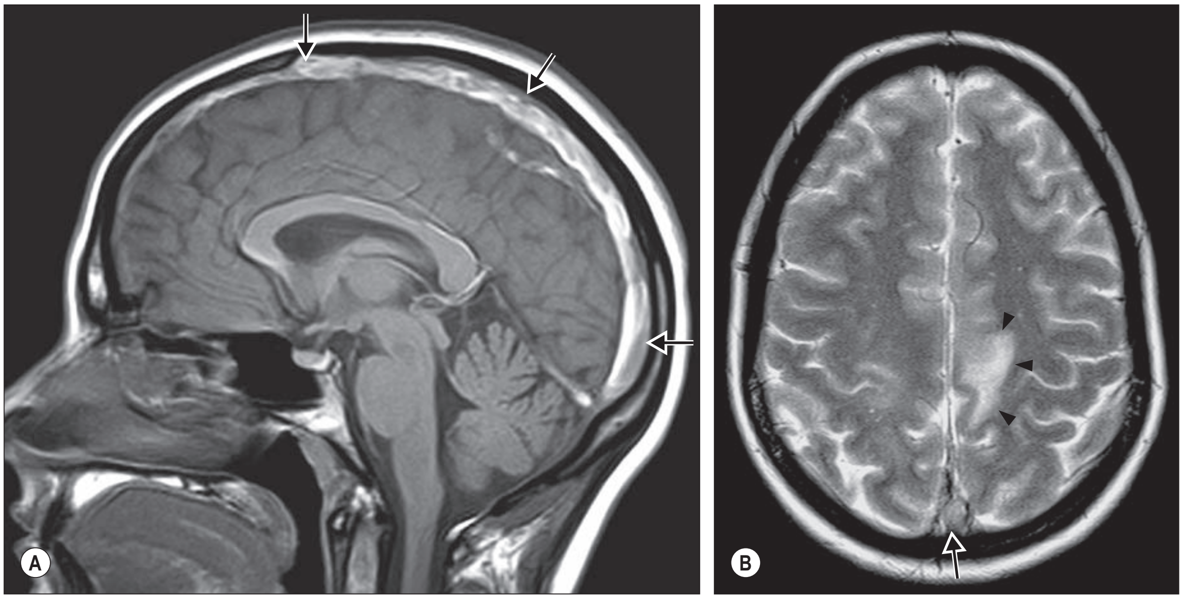

Fig. 26.14 Venosinus thrombosis. Images from a magnetic resonance study in an adult patient with a 6 day history of headache and increasingly severe seizures. **A**, The sagittal T1-weighted image shows abnormal high signal along the course of the superior sagittal sinus (arrows). **B**, The axial T2-weighted image also shows high signal in the enlarged superior sagittal sinus (arrow). This pattern of abnormal signal indicates extensive subacute thrombus in the sinus. There are abnormal high signal changes in the left paracentral lobule (arrowheads), indicating venous infarction, which was shown to be bilateral and haemorrhagic on other images.

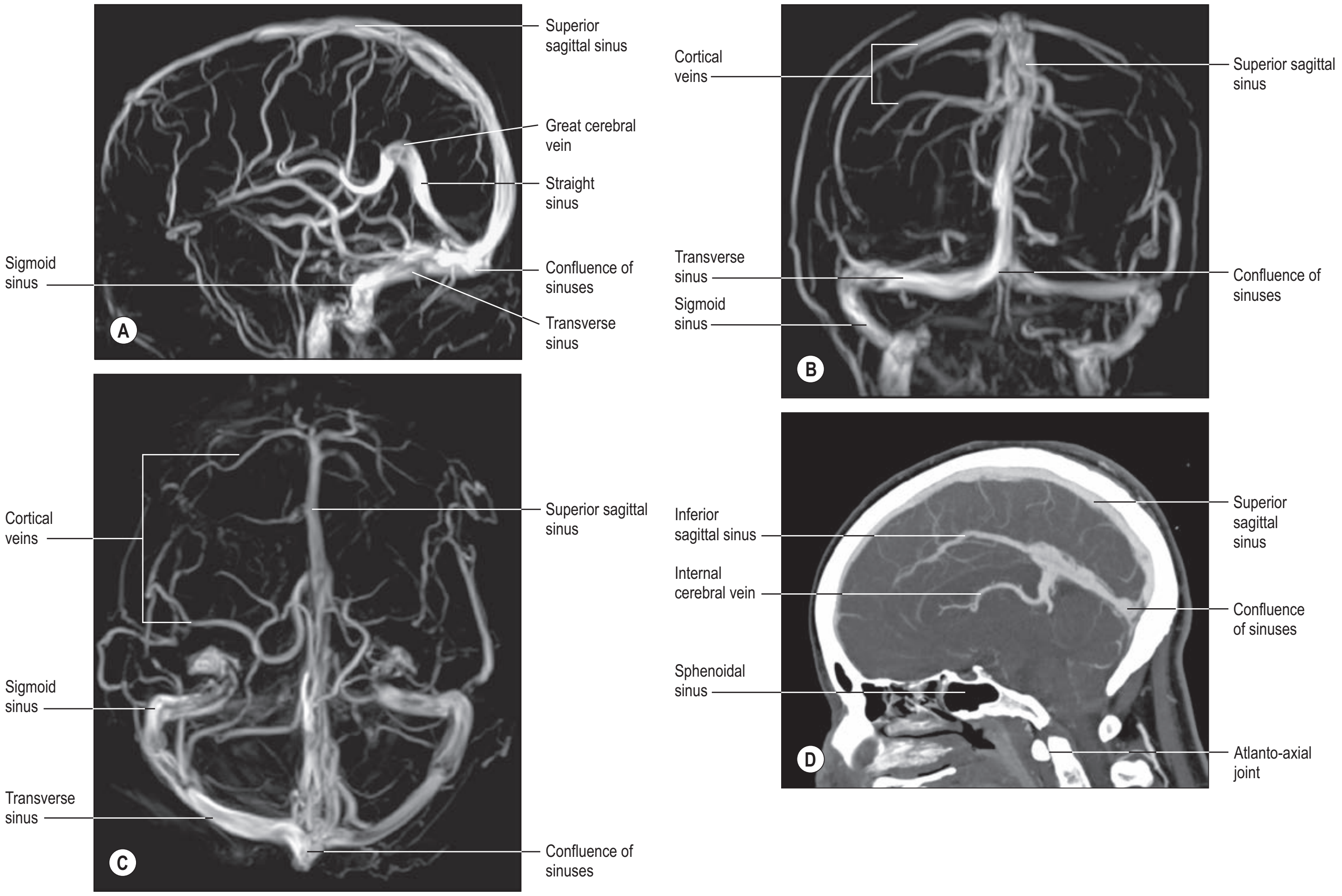
Superior sagittal sinus
Great cerebral vein
Straight sinus
Sigmoid sinus
Confluence of sinuses
Transverse sinus
A
Cortical veins
Superior sagittal sinus
Transverse sinus
Sigmoid sinus
Confluence of sinuses
B
Cortical veins
Superior sagittal sinus
Sigmoid sinus
Transverse sinus
Confluence of sinuses
C
Inferior sagittal sinus
Superior sagittal sinus
Internal cerebral vein
Confluence of sinuses
Sphenoidal sinus
Atlanto-axial joint
D

Fig. 26.13 Phase contrast magnetic resonance venograms taken at 3.0T in lateral (**A**), frontal (**B**) and superior (**C**) projections. **D**, A CT venogram, sagittal section in the midline.

Bonus e-book content

Fig. 26.9 An arteriovenous malformation, left cerebral hemisphere, selected angiograms.

Fig. 26.14 Venosinus thrombosis.

Video 26.1 From angiography to anatomy: the internal carotid artery and its major branches.

Video 26.2 From angiography to anatomy: veins of the cerebral system.

Key references

Andeweg J 1996 The anatomy of collateral venous flow from the brain and its value in aetiological interpretation of intracranial pathology. Neurorad 38:621–8.
A brief historical review is included.

Bogousslavsky J, Caplan L 2002 Stroke Syndromes, 2nd ed. Cambridge: Cambridge University Press.
A classic textbook encompassing all aspects of stroke.

Duvernoy H, Delon S, Vannson JL 1983 The vascularization of the human cerebellar cortex. Brain Res Bull 11:419–80.
A detailed study of pial and intracortical vessels of the cerebral cortex.

Duvernoy HM, Delon S, Vannson JL 1981 Cortical blood vessels of the human brain. Brain Res Bull 7:519–79.
A detailed study of pial and intracortical vessels of the cerebellar cortex.

Kaplan HA, Ford DH 1966 The Brain Vascular System. Amsterdam: Elsevier.

Plets C, De Reuck J, Vander Eecken H et al 1970 The vascularization of the human thalamus. Acta Neurol Belg 70:687–770.

Puchades-Orts A, Nombela-Gomez M, Ortu-o-Pacheco G 1976 Variation in form of the circle of Willis. Some anatomical and embryological considerations. Anat Rec 185:119–23.
A postmortem study of 62 cases.

Sengupta RP, McAllister VL 1986 Subarachnoid Haemorrhage. Berlin: Springer.
Details on variations in the circulus arteriosus cerebri are included.

Weninger WJ, Muller GB 1999 The parasellar region of infants: cavernous sinus topography and surgical approaches. J Neurosurg 90:484–90.
A postmortem study highlighting the differences between the vascular anatomy of infants and adults.

References

Andeweg J 1996 The anatomy of collateral venous flow from the brain and its value in aetiological interpretation of intracranial pathology. Neurorad 38:621–8.

A brief historical review is included.

Bogousslavsky J, Caplan L 2002 Stroke Syndromes, 2nd ed. Cambridge: Cambridge University Press.

A classic textbook encompassing all aspects of stroke.

Duvernoy HM, Delon S, Vannson JL 1981 Cortical blood vessels of the human brain. Brain Res Bull 7:519–79.

A detailed study of pial and intracortical vessels of the cerebellar cortex.

Duvernoy H, Delon S, Vannson JL 1983 The vascularization of the human cerebellar cortex. Brain Res Bull 11:419–80.

A detailed study of pial and intracortical vessels of the cerebral cortex.

Kaplan HA, Ford DH 1966 The Brain Vascular System. Amsterdam: Elsevier.

Lambert SL, Williams FJ, Oganisyan ZZ et al 2016 Fetal-type variants of the posterior cerebral artery and concurrent infarction in the major arterial territories of the cerebral hemisphere. J Investig Med High Impact Case Rep 4:2324709616665409. doi: 10.1177/2324709616665409.

Plets C, De Reuck J, Vander Eecken H et al 1970 The vascularization of the human thalamus. Acta Neurol Belg 70:687–770.

Puchades-Orts A, Nombela-Gomez M, Ortu-o-Pacheco G 1976 Variation in form of the circle of Willis. Some anatomical and embryological considerations. Anat Rec 185:119–23.

A postmortem study of 62 cases.

Ray B, Gupta N 2006 Caroticoclinoid foramen with interclinoid osseous bar. Clin Anat 19:732–3.

Sengupta RP, McAllister VL 1986 Subarachnoid Haemorrhage. Berlin: Springer.

Details on variations in the circulus arteriosus cerebri are included.

Weninger WJ, Muller GB 1999 The parasellar region of infants: cavernous sinus topography and surgical approaches. J Neurosurg 90:484–90.

A postmortem study highlighting the differences between the vascular anatomy of infants and adults.

CHAPTER

27

Spinal cord

The spinal cord provides innervation for the trunk and limbs via spinal nerves and their peripheral ramifications. It receives primary afferent fibres from peripheral receptors located in widespread somatic and visceral structures, and sends motor axons to skeletal muscle. It also contains the cell bodies of all the preganglionic neurones responsible for the sympathetic innervation of cardiac and smooth muscle and secretory glands, and for the parasympathetic innervation of smooth muscle in the distal part of the hindgut, the pelvic viscera and the erectile tissues of the external genitalia. Many bodily functions are regulated at an unconscious level by intraspinal reflex connections between afferent and efferent neurones. Profuse ascending and descending pathways link the spinal cord with the brain, allowing higher centres to monitor and perceive external and internal stimuli and to modulate and control spinal efferent activity.

EXTERNAL FEATURES AND RELATIONS

The topographical anatomy of the spinal cord in relation to other structures within the vertebral canal is described in more detail in Chapter 47. In brief, the cord begins just below the level of the foramen magnum where it is continuous rostrally with the medulla oblongata. It terminates caudally as the conus medullaris, which narrows into the filum terminale, anchored to the dorsum of the coccyx. The cord is ensheathed by spinal meninges that are continuous with the cranial meninges through the foramen magnum. Although it is approximately circular in cross-section, the diameter of the spinal cord varies according to level; it bears two enlargements, cervical and lumbosacral (**Fig. 27.1**).

The spinal cord is essentially a segmental structure, each of the 31 segments giving rise to bilaterally paired spinal nerves: 8 cervical, 12 thoracic, 5 lumbar, 5 sacral and 1 coccygeal (see Fig. 27.1). The spinal nerves attach to the cord as a linear series of small dorsal and ventral nerve rootlets. Dorsal rootlets contain afferent nerve fibres and ventral rootlets contain efferent fibres (see Fig. 27.1). Groups of adjacent rootlets coalesce to form dorsal or ventral nerve roots that cross the subarachnoid space and unite to form functionally mixed spinal nerves as they exit the vertebral canal through the intervertebral foramina. The dorsal roots bear dorsal root ganglia which contain the cell bodies of primary afferent neurones.

INTERNAL ORGANIZATION

In transverse section, the spinal cord is incompletely divided into symmetrical halves by a dorsal (posterior) median sulcus and septum and a ventral (anterior) median fissure (see Fig. 27.1). The cord consists of an outer layer of white matter and an inner core of grey matter, their relative sizes and configuration varying according to the level. The amount of grey matter reflects the number of neuronal cell bodies present; it is proportionately largest in the cervical and lumbosacral enlargements, which contain the neurones that innervate the upper and lower limbs, respectively (see Fig. 27.1). The absolute amount of white matter is greatest at cervical levels, where ascending tracts increasingly accumulate fibres, and decreases progressively at lower levels as descending tracts shed their fibres.

A diminutive central canal, lined by columnar, ciliated epithelium (ependyma) and containing cerebrospinal fluid (CSF), extends the whole length of the spinal cord, lying in the centre of the spinal grey matter (see Fig. 27.1). Rostrally, the central canal extends into the caudal half of the medulla oblongata and then opens into the fourth ventricle.

Spinal grey matter

In transverse section, the spinal grey matter is often described as being ‘butterfly-shaped’ or resembling the letter ‘H’ (see Fig. 27.1). It consists of two dorsal horns, which project dorsolaterally, and two ventral horns, which project ventrolaterally towards the surface. The grey matter that immediately surrounds the central canal and unites the two sides constitutes the dorsal and ventral grey commissures. The dorsal horn is the site of termination of the primary afferent fibres that enter the cord via the dorsal roots of spinal nerves. The tip of the dorsal horn is separated from the dorsolateral surface of the cord by a thin tract (of Lissauer), in which branches of primary afferent fibres ascend and descend for a short distance before terminating in the subjacent grey matter. The ventral horn includes efferent motor neurones; their axons leave the spinal cord in ventral nerve roots. A small lateral or intermediate horn is present at thoracic and upper lumbar levels; it contains the cell bodies of preganglionic sympathetic neurones.

Spinal grey matter (**Fig. 27.2**) is a complex mixture of neuronal cell bodies, their processes and synaptic connections, neuroglia and blood vessels. Neurones in the grey matter are multipolar. They vary in size and features such as the length and the arrangement of their axons and

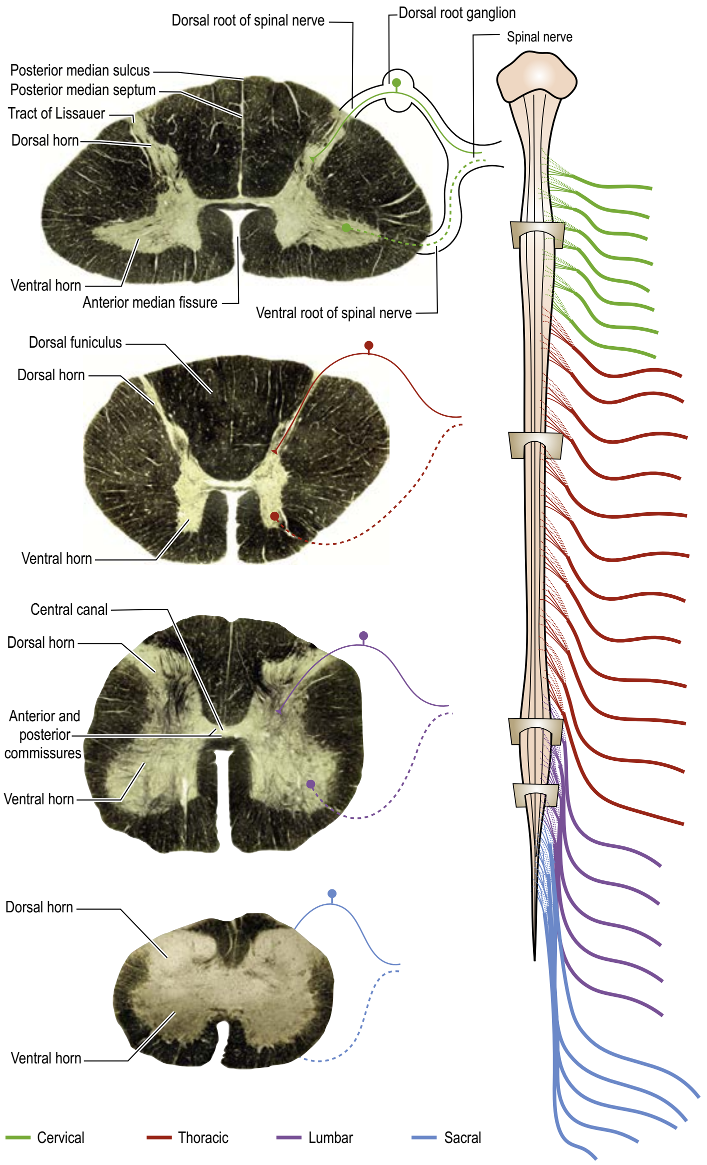

Fig. 27.1 A longitudinal diagram of the human spinal cord, with transverse sections through the spinal cord at representative cervical, thoracic, lumbar and sacral levels. Approximately ×5. (Figure enhanced by B Crossman.)

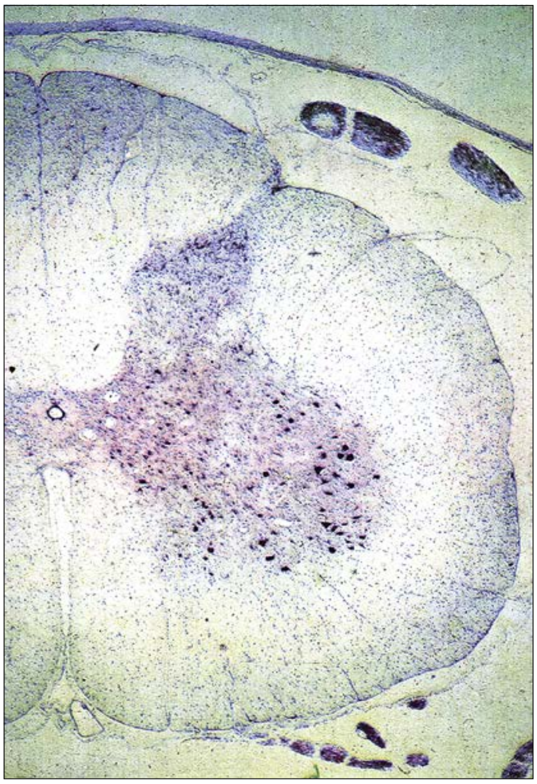

Fig. 27.2 A transverse section of a spinal cord at a mid-lumbar level. Groups of the larger motor neurones in the ventral grey column are prominent. Stained with cresyl fast violet.

dendrites. Neurones may be intrasegmental, i.e. contained within a single segment, or intersegmental, i.e. their ramifications spread through several segments. Research in a number of animal models has demonstrated groups of dorsal and ventral groups of interneurones, each with a characteristic genetic signature, some excitatory and some inhibitory. These different classes of interneurones have been demonstrated to be important for different reflex and locomotor activities (Kiehn 2016).

Neuronal cell groups of the spinal cord

The grey matter of the spinal cord may be divided, on the basis of cytoarchitecture, into nine zones, known as Rexed's laminae, which are numbered sequentially from dorsal to ventral, and an additional area X (**Fig. 27.3B**). The laminae are defined on the basis of neuronal size, shape, cytological features and density. Some of these laminae are equated with cell groupings of particular functional types (see Fig. 27.3B) (Rexed 1952, Mai and Paxinos 2011).

Laminae I–IV correspond to the dorsal part of the dorsal horn, and are the main site of termination of cutaneous primary afferent terminals and their collaterals. Many complex polysynaptic reflex paths (ipsilateral, contralateral, intrasegmental and intersegmental) start from this region, as also do many long ascending tract fibres that pass to higher levels. Lamina I (lamina marginalis) is a very thin layer with an ill-defined boundary at the dorsolateral tip of the dorsal horn. The much larger lamina II consists of densely packed small neurones that are responsible for its dark appearance in Nissl-stained sections. With myelin stains, lamina II is characteristically distinguished from adjacent laminae by the almost total lack of myelinated fibres. Lamina II corresponds approximately to the substantia gelatinosa. Laminae I and II are the primary termination for nociceptive peripheral afferents, and are also targets for descending projections from the cortex, brainstem and hypothalamus involved in modulatory control of these inputs. Lamina III consists of somata that are mostly larger, more variable and less closely packed than those in lamina II: it contains interneurones that transmit tactile and nociceptive afferent inputs to the cells of origin of ascending sensory pathways, including the dorsal columns and spinocervical tract. The ill-defined nucleus proprius of the dorsal horn corresponds to some of the cellular constituents of laminae III and IV. Lamina IV is a thick, loosely packed, heterogeneous zone permeated by fibres. Its neuronal somata vary considerably in size and shape, from small and round, through intermediate and triangular, to very large and stellate (Schoenen and Faull 1990). Laminae IV and V contain projection neurones that give rise to fibres in ascending pathways including the spinocervical and dorsal column pathways.

Laminae V and VI lie at the base of the dorsal horn. They receive most of the terminals of proprioceptive primary afferents, profuse corticospinal projections from the motor and sensory cortices, and input from subcortical levels, suggesting their involvement in the regulation of movement. Lamina V is a thick layer, divisible into a lateral third and medial two-thirds. Both have a mixed cell population but the former contains many prominent somata interlaced by numerous bundles of transverse, dorsoventral and longitudinal fibres. Lamina VI is particularly prominent in the limb enlargements and is mostly concerned with local and propriospinal projections. It has an intensely staining medial third of small, densely packed neurones and a lateral two-thirds containing larger, more loosely packed, triangular or stellate somata.

Lamina VII occupies the region just ventral to lamina VI and extends across the spinal grey matter on each side: this region is known as the intermediate zone throughout the cord. The size of lamina VII varies at different spinal levels. In the cervical and lumbar enlargements, it extends laterally and ventrally throughout the ventral horn, and cell groups of lamina IX neurones are embedded within it. In the thoracic region, lamina VII occupies the intermediate zone and the dorsal part of the ventral horn, and it includes the lateral horn. Lamina VII contains three important nuclear groups: the posterior thoracic nucleus (nucleus thoracis or Clarke's column, **Figs 27.3A,C**), which extends throughout the thoracic and upper lumbar segments and gives rise to the fibres of the dorsal spinocerebellar tract; the intermediolateral nucleus, which is located between T1 and L2 and gives rise to the preganglionic sympathetic fibres; and the intermediomedial nucleus, which extends the full length of the cord and may be involved in the control of visceral motor neurones (see Fig. 27.3).

Lamina VIII spans the base of the ventral horn in the thoracic region but is restricted to the medial aspect of the ventral horn in the cervical and lumbar enlargements. Its neurones display a heterogeneous mixture of sizes and shapes from small to moderately large. Lamina VIII is a mass of propriospinal interneurones. It receives terminals from the adjacent laminae, many commissural fibres from the contralateral lamina VIII, and descending connections from the interstitiospinal, reticulospinal, corticospinal and vestibulospinal tracts and the medial longitudinal fasciculus. The axons from these interneurones influence α motor neurone activity bilaterally, perhaps directly but also by reflex excitation of small γ motor neurones supplying efferent fibres to muscle spindles.

Lamina IX consists of several distinct groups or columns of somatic motor neurones located throughout the ventral horn. In the thoracic cord, these nuclear groups are embedded within lamina VIII, whereas the lamina IX cell groups are embedded within both lamina VII and lamina VIII in the cervical and lumbar enlargements. Lamina IX is a complex array of cells consisting of α and γ motor neurones and many interneurones. The large α motor neurones supply motor end-plates of extrafusal muscle fibres in striated muscle. Recording techniques have demonstrated the existence of tonic and phasic α motor neurones. Tonic α motor neurones have a lower firing rate and lower conduction velocity, and tend to innervate type S muscle units. Phasic α motor neurones have a higher conduction velocity and tend to supply fast twitch motor units, either fast-resistable (FR) or fast-fatigable (FF) types. The smaller γ motor neurones give rise to small-diameter efferent axons (fusimotor fibres), which innervate the intrafusal muscle fibres in muscle spindles. There are several functionally distinct types of γ motor neurone. The 'static' and 'dynamic' responses of muscle spindles have separate controls mediated by static and dynamic fusimotor fibres, which are distributed variously to nuclear chain and nuclear bag fibres (Boyd and Gladden 1985). β-motor neurones innervate both extrafusal and intrafusal fibres which constitute the skeletofusimotor innervation that is particularly prominent in human hand and wrist muscles.

Area X surrounds the central canal and is crossed by the dorsal and ventral grey commissures, which include the axons of commissural interneurones coordinating activity between the two sides of the spinal cord.

The Rexed system provides the classification of neuronal cell groups in the spinal grey matter when considered in transverse section. These cell groups are also organized into longitudinal columns (see Fig. 27.3), some of which have been mentioned already, such as the dorsal (posterior) thoracic nucleus (Clarke's column) and the motor neuronal columns located in different subgroups within lamina IX. There are also columns of neurones in the dorsal horn, including the nucleus proprius. The intermediolateral cell columns in lamina VII provide preganglionic parasympathetic and sympathetic outflows from the cord.

Dorsal horn

The dorsal horn is a major zone of termination of primary afferent fibres that enter the spinal cord through the dorsal roots of spinal nerves. Dorsal

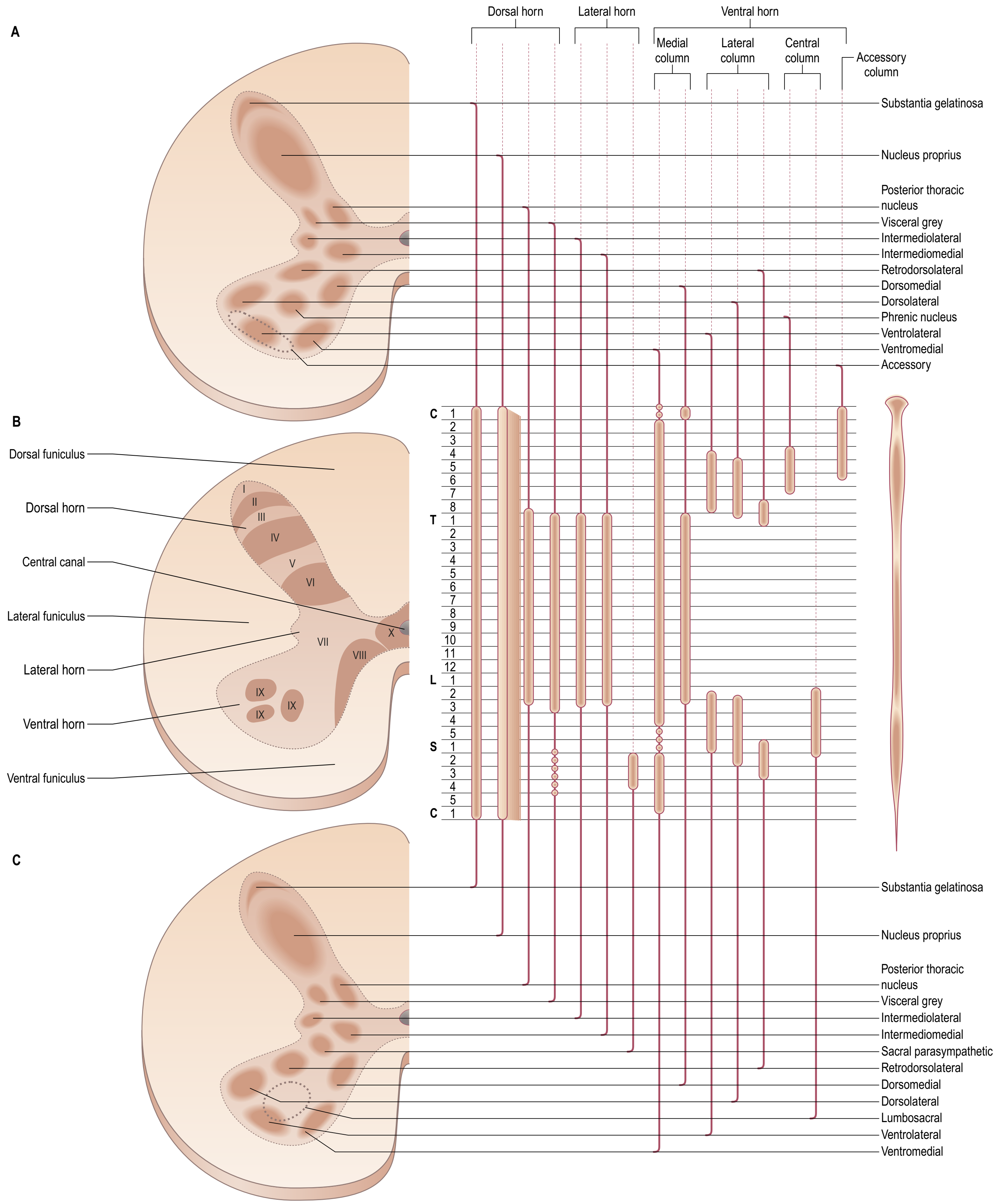
A
Dorsal horn
Lateral horn
Ventral horn
Medial column
Lateral column
Central column
Accessory column
Substantia gelatinosa
Nucleus proprius
Posterior thoracic nucleus
Visceral grey
Intermediolateral
Intermediomedial
Retrodorsolateral
Dorsomedial
Dorsolateral
Phrenic nucleus
Ventrolateral
Ventromedial
Accessory
B
Dorsal funiculus
Dorsal horn
Central canal
Lateral funiculus
Lateral horn
Ventral horn
Ventral funiculus
I
II
III
IV
V
VI
VII
VIII
IX
IX
IX
X
C 1
2
3
4
5
6
7
8
T 1
2
3
4
5
6
7
8
9
10
11
12
L 1
2
3
4
5
S 1
2
3
4
5
C 1
C
Substantia gelatinosa
Nucleus proprius
Posterior thoracic nucleus
Visceral grey
Intermediolateral
Intermediomedial
Sacral parasympathetic
Retrodorsolateral
Dorsomedial
Dorsolateral
Lumbosacral
Ventrolateral
Ventromedial

Fig. 27.3 The groups of nerve cells in the grey columns of the spinal cord. The relative positions of these columnar groups and their extent through spinal segments (C: cervical, T: thoracic, L: lumbar, S sacral, C: coccygeal) are indicated. **A** and **C** show the main cell groupings while **B** shows the system of Rexed laminae I–IX, and the white matter distributed in the dorsal, lateral and ventral funiculi. (From Correlative Anatomy of the Nervous System by E Crosby, T Humphrey, E Lauer. Copyright © 1962 Macmillan Publishing Company; copyright renewed 1990 by Elizabeth C. Crosby. Reprinted with the permission of Scribner, a division of Simon & Schuster, Inc. All rights reserved.)

root fibres contain numerous molecules that are either known, or suspected, to fulfil a neurotransmitter or neuromodulator role. These include glutamic acid, substance P, calcitonin gene-related peptide (CGRP), bombesin, vasoactive intestinal polypeptide (VIP), cholecystokinin (CCK), somatostatin, dynorphin and angiotensin II (Mai and Paxinos 2011). Dorsal root afferents carry exteroceptive, proprioceptive and interoceptive information. Laminae I–IV are the main cutaneous receptive areas; lamina V receives fine afferents from the skin, muscle and viscera; lamina VI receives proprioceptive and some cutaneous afferents. Most, if not all, primary afferent fibres divide into ascending and descending branches on entering the cord that then travel for variable distances in the tract of Lissauer, near the surface of the cord, and send collaterals into the subjacent grey matter.

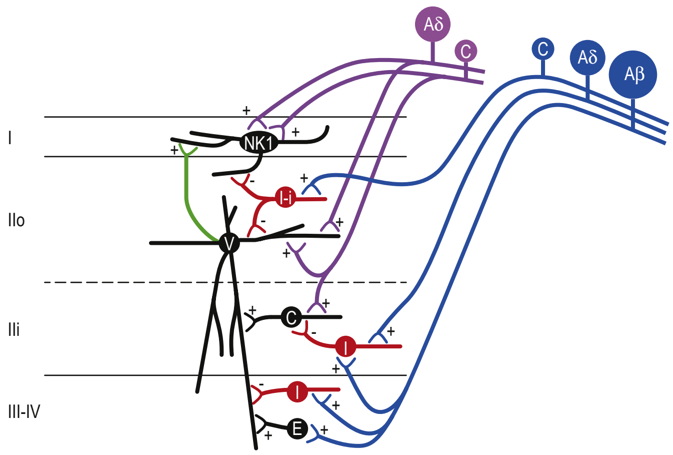

Fig. 27.4 Routes by which noxious (purple) and non-noxious (blue) primary afferent inputs may engage spinothalamic projection neurones in laminae I–IV of the dorsal horn. Nociceptive C and Aδ fibres (purple) activate neurokinin 1 (NK1)-expressing spinothalamic projection neurones of lamina I directly, and through the vertical cells (V) of the outer part of lamina II (IIo) indirectly (green axon). Nociceptive C fibres also activate central cells (C) of lamina II (IIi); the C cells contact, and probably excite, V cells in lamina IIo. Non-nociceptive Aβ fibres (blue) establish monosynaptic connections with local excitatory interneurones (E) of deeper laminae (III–IV), which directly activate V cells. These dorsally directed circuits are the route through which both noxious and non-noxious primary afferent input can engage the projection neurones of lamina I, which results in onward transmission in the spinothalamic tract. The excitatory circuits in the superficial dorsal horn are subject to profound inhibitory control (red), which allows for control of that onward transmission. For example, the majority of the inhibitory neurones (I) in lamina II are islet cells (I-i) and these can be directly engaged by input from low-threshold, mechanoreceptive C fibres (blue). The islet cells in turn establish monosynaptic inhibitory connections with both vertical cells of lamina IIo and NK1 receptor-expressing projection neurones of lamina I. Low-threshold Aδ and Aβ fibres (both in blue) also directly engage inhibitory interneurones in laminae IIi–IV. The latter in turn exert inhibitory control of a variety of excitatory interneurones, including vertical (V) and central (C) cells. According to the gate control theory the Aβ-to-inhibitory cell circuit is presumably responsible for closing the ‘gate’. (Adapted with permission from Braz J, Solorzano C, Wang X et al 2014 Transmitting pain and itch messages: a contemporary view of the spinal cord circuits that generate gate control. Neuron 82:522–36.)

The lamina marginalis (lamina I) is a thin lamina of neurones at the dorsolateral tip of the dorsal horn, deep to the tract of Lissauer. Beneath it lies the substantia gelatinosa (laminae II), which is present at all levels and consists mostly of small neurones, with some larger neurones. The substantia gelatinosa receives afferents via the dorsal roots; its neurones give rise to fibres that form the contralateral spinothalamic tract. The large propriospinal neurones of the nucleus proprius lie ventral to the substantia gelatinosa within laminae III and IV and link segments for the mediation of intraspinal coordination (see Fig. 27.3).

The posterior thoracic nucleus can usually be identified from the eighth cervical to the third or fourth lumbar segments. It lies at the base of the dorsal horn within lamina VII, near the dorsal white funiculus, and may project into it. Neurones of the posterior thoracic nucleus vary in size but most are large, especially in the lower thoracic and lumbar segments; some send axons into the dorsal spinocerebellar tracts and some are interneurones.

Local circuitry mediating pain transmission

The gate control theory (GCT) of pain describes a mechanism by which nociceptive input from the skin is modulated (‘gated’) by local circuits within the dorsal horn and by descending inputs from the brain (Melzack and Wall 1965). According to the GCT, interneurones in the substantia gelatinosa modulate afferent input to spinothalamic tract projection neurones that mediate onward transmission of nociceptive information to the brain. Increased activity in the collaterals of large-calibre non-noxious afferents excite substantia gelatinosa cells, which in turn inhibit the tract cells, i.e. the ‘gate’ is closed. Activity in small-calibre nociceptive afferents have the opposite effect of inhibiting the substantia gelatinosa interneurones and opening the ‘gate’ to nociceptive inputs. The main elements in the circuitry by which noxious and non-noxious primary afferent inputs are thought to influence projection neurones within lamina I of the dorsal horn are shown in Fig. 27.4.

Interneurones in laminae I–IV are morphologically, topographically and neurochemically heterogeneous: islet, central, radial and vertical cells have been identified in experimental animal studies. Islet cells are predominantly GABAergic (transmitting or secreting γ-aminobutyric acid); a subset co-express glycine and are presumed to be exclusively inhibitory. Radial and vertical cells are predominantly glutamatergic and presumed to be excitatory, and central cells include both inhibitory and excitatory subsets. All these interneurones can influence the output from spinothalamic projection neurones in lamina I (NK1 in Fig. 27.4). The input from C fibre nociceptors is concentrated in lamina I and lamina II (see Fig. 27.4). Recent evidence has refocused attention on the concept of ‘labelled lines’ with each sensory modality processed via a fixed path from skin to brain. This applies to noxious heat, cold, noxious mechanical stimulation and pruritogens, at least at the level of the primary afferent input. (For further reading, see Ma (2010), Moayedi and Davis (2013), Todd and Koerber (2013), Zhang et al (2013), Braz et al (2014), Mendell (2014).)

Onward transmission in the lateral spinothalamic tract (see Fig. 27.10) evokes the perception of pain at supraspinal levels, although the activity of spinothalamic tract neurones is modulated by descending projections from the cortex and from a number of brainstem nuclei, which constitute an endogenous analgesic control system. In the mesencephalon, these regions are the periaqueductal grey matter, dorsal raphe nucleus and part of the cuneiform nucleus. Neurones in these sites contain 5-HT (5-hydroxytryptamine, serotonin), GABA, substance P, CCK, neurotensin, enkephalin and dynorphin. The periaqueductal grey matter receives afferents from the frontal, somatosensory and cingulate neocortices, the amygdala, numerous local reticular nuclei and the hypothalamus. Afferents from the latter are separate bundles that carry histamine, luteinizing hormone-releasing hormone (LHRH), vasopressin, oxytocin, adrenocorticotrophic hormone (ACTH), melanocyte-stimulating hormone (γ-MSH), endorphin and angiotensin II. Some fibres descend from the periaqueductal grey matter to nuclei of the brainstem, while others pass directly to the spinal cord.

In the brainstem, the nucleus raphe magnus and the medial reticular column constitute an important multi-neuromodulation system, involving a number of different neurotransmitters and neuromodulators (see p. 454). Neurones in these sites contain 5-HT, substance P, CCK, thyrotrophin-releasing hormone (TRH), enkephalin and dynorphin; some neurones contain and release two or even three neurotransmitters. Descending corticospinal fibres from somatosensory cortex pass to the nucleus of the spinal tract of the trigeminal nerve and its continuation, the substantia gelatinosa. The latter extends throughout the length of the cord and contains populations of neurones that express many different neuromediators, e.g. GABA, substance P, neurotensin, enkephalin and dynorphin. There is abundant physiological and pharmacological evidence that all of these regions are intimately concerned with the control of nociceptive (and probably other modality) inputs.

Stimulation of forebrain sites, including the periventricular grey matter, the ventral posterolateral nucleus of the thalamus, and the primary sensory (S1) and posterior parietal cortices, inhibit spinothalamic tract neurones. In contrast, some spinothalamic tract neurones are excited by stimulation of the medullary reticular formation and the primary motor cortex, the latter effect probably being mediated by the corticospinal tract.

Lateral horn

The lateral horn is a small lateral projection of grey matter located between the dorsal and ventral horns in lamina VII. It is present from the eighth cervical or first thoracic segment to the second or third lumbar segment. It contains the cell bodies of preganglionic sympathetic neurones that develop in the embryonic cord dorsolateral to the central canal and migrate laterally, forming the intermediolateral cell columns. Their axons travel via ventral spinal roots and white rami communicantes to the sympathetic trunk. A similar cell group is found in the second to fourth sacral segments but, unlike the thoracolumbar lateral cell column, it does not form a visible lateral projection. It has long been regarded as the source of the sacral outflow of parasympathetic preganglionic nerve fibres: there is an alternative view that the sacral autonomic flow may be entirely sympathetic (Ch. 3) (Espinosa-Medina et al 2016, 2017, Horn 2018).

Ventral horn

The ventral horn is formed by laminae VII, VIII and IX. Laminae VII and VIII contribute to the intermediate zone, which is a major target for proprioceptive reflex afferents and descending motor pathways. The

Modern neuroimaging and molecular, genetic and behavioural studies confirm that the experience of pain involves a complex network of responsive brain regions. The somatosensory cortices (S1 and S2) and the insula are thought to encode the sensory features of pain, whereas the prefrontal cortex, components of the limbic system (anterior cingulate cortex, amygdala), the nucleus accumbens and the ventral tegmental area mediate the affective and contextual aspects of pain. Mechanisms underlying 'deep' visceral, muscular, neuropathic and persistent, chronic pain remain even less clear than those mediating cutaneous pain (Devor 2013). Patients with chronic pain may have anatomical alterations within the regions involved in the cognitive and emotional modulation of pain, e.g. the dorsolateral and medial prefrontal cortex, anterior cingulate gyrus and insula (Bushnell et al 2013, Denk et al 2014) and dysregulation of the descending pain modulation systems (Ossipov et al 2014).

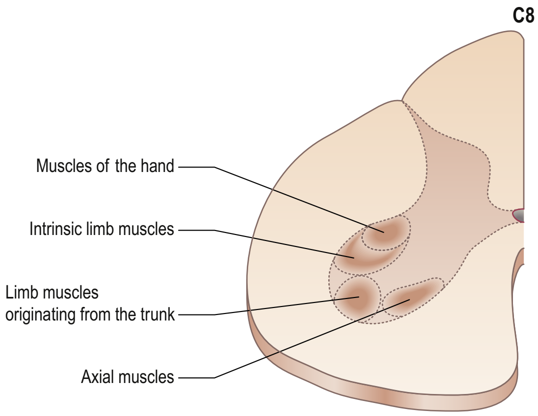

Fig. 27.5 The approximate location of motor neurone groups at the C8 segmental level of the spinal cord.

largest cell bodies in the ventral horn are those of lamina IX α motor neurones, which are multipolar and may range from 25 to 70 µm in diameter. Their axons emerge in ventral roots of spinal nerves to innervate extrafusal fibres in striated skeletal muscles. Large numbers of smaller neurones, 15–25 µm in diameter, are also present: some are γ motor neurones which innervate intrafusal fibres of muscle spindles, and the rest are interneurones. α and γ motor neurones that innervate a given muscle are intermixed and both types utilize acetylcholine as their neurotransmitter.

The motor neurones in lamina IX are organized into two major longitudinal columns, medial and lateral: in transverse section, they form the dorsomedial, ventromedial, dorsolateral and ventrolateral cell groups in the ventral horn (see Fig. 27.3A). The motor neurones of lamina IX are somatotopically organized according to a medial-to-lateral and a dorsal-to-ventral gradient. The basic arrangement is that medial cell groups innervate the axial musculature, and lateral cell groups innervate the muscles of the limbs. Motor neurones innervating flexor muscles are located dorsally and those innervating extensors are located ventrally. The classical work of George Romanes demonstrated further subdivisions of these longitudinally orientated cell groups and the importance of spatial codes in the location of motor neurones innervating particular muscles: motor neurones innervating a specific muscle are located together in longitudinal clusters within the column and have a constant coordinate position within the cord. Clusters of motor neurones innervating synergist muscles form neighbouring groups or 'columels' that conform, in a precise pattern, to the three major rostrocaudal, mediolateral and dorsoventral axes of limb organization. Work in mice suggests that this positional map involves a motor neurone transcriptional network engaging the action of several Hox proteins (Jessel et al 2011).

The medial nuclear group extends throughout the length of the spinal cord. Its neurones innervate epaxial muscle groups and hypaxial muscle groups. Epaxial muscles are extensors of the head and vertebral column and include the erector spinae group: they are innervated by branches of the dorsal primary rami of the spinal nerves. Hypaxial muscles are flexors of the head and vertebral column and include the prevertebral muscles of the neck and the intercostal and anterior abdominal wall muscles: they are innervated by branches of the ventral primary rami. In the medial column, motor neurones supplying epaxial muscles are sited ventral to those that supply hypaxial muscles.

The columns of the lateral nuclear group innervate the rest of the body musculature and their organization presents some segmental variations. In the thoracic region, the lateral group is small and innervates the lateral trunk muscles. In the cervical and lumbosacral enlargements, the lateral nuclear group is greatly enlarged and a number of subgroups may be distinguished, including the ventrolateral (anterolateral), dorsolateral (posterolateral), central and retrodorsolateral (retroposterolateral) groups.

In the cervical and lumbosacral enlargements, the lateral nuclear group innervates muscles of the upper and lower limbs, respectively. The somatotopic organization of the cervical ventral horn includes, clockwise from ventromedial to dorsolateral, α motor neurones to the muscles of the trunk, shoulder girdle, upper arm and lower arm and hand (**Fig. 27.5**). The proximal muscles of the limb are supplied from motor cell groups located more rostrally in the enlargement than those supplying the distal muscles, thus, motor neurones in C5 and C6 innervate shoulder muscles and motor neurones in C8 and T1 innervate the intrinsic muscles of the hand. There is a similar overall arrangement in the lumbosacral cord for motor neurones innervating the muscles in the lower limb (**Fig. 27.6**).

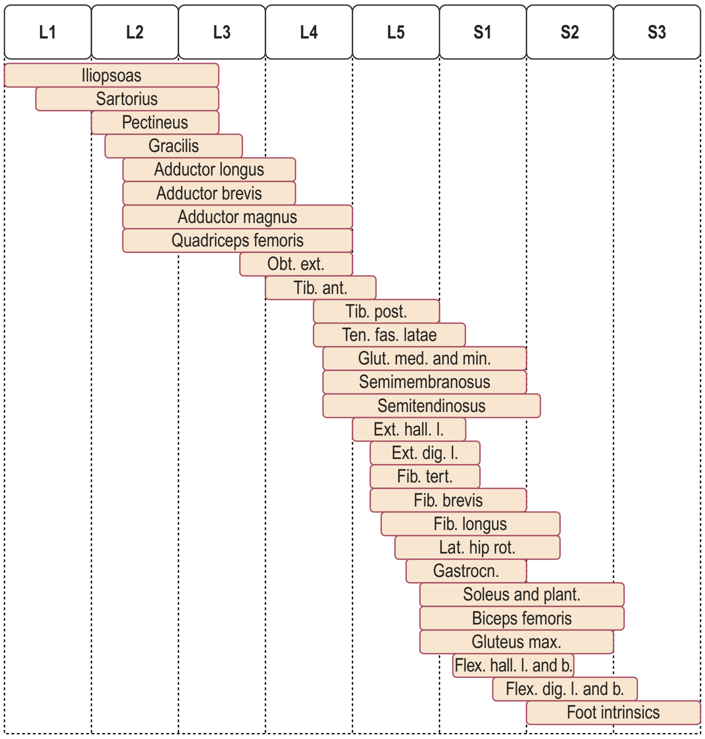

Fig. 27.6 The segmental arrangement of motor neurones innervating muscles of the lower limb. Abbreviations: Obt. ext., obturator externus; Tib. ant., tibialis anterior; Tib. post., tibialis posterior; Ten. fas. latae, tensor fasciae latae; Glut. med. and min., gluteus medius and minimus; Ext. hall. l., extensor hallucis longus; Ext. dig. l., extensor digitorum longus; Fib. tert., fibularis tertius; Fib. brevis, fibularis brevis; Fib. longus, fibularis longus; Lat. hip. rot., lateral hip rotators; Gastrocn., gastrocnemius; Soleus and plant., soleus and plantaris; Gluteus max., gluteus maximus; Flex. hall. l. and b., flexors hallucis longus and brevis; Flex. dig. l. and b., flexors digitorum longus and brevis.

Other groups of neurones form a central column and an accessory column that can be identified at the cervical and lumbar levels. The phrenic nucleus, containing the motor neurones that innervate the respiratory diaphragm, forms the central column at the level of the third to fifth cervical segments. The same position is occupied by the lumbosacral nucleus that extends between the second lumbar and second sacral segment; its axons have an unknown distribution.

The spinal nucleus of the accessory nerve contains motor neurones that innervate sternocleidomastoid and trapezius. Described as a curvilinear band of motor neurones extending within the ventral horn from C1/2 to C5/6 (Orhan et al 2009, Saylam et al 2009) in line rostrally with the nucleus ambiguus of the medulla, the spinal nucleus of the accessory nerve is unusual not only for its position between the medial and lateral columns (Routal and Pal 2000) but also for its rootlets exiting the spinal cord just dorsal to the ligamentum denticulatum (Jenny et al 1988). They subsequently combine to form the intraspinal portion of the accessory nerve, which ascends the vertebral canal to enter the posterior cranial fossa via the foramen magnum. The supranuclear innervation of the spinal nucleus of the accessory nerve is uncertain. The bulk of current evidence favours bilateral hemispheric innervation of motor neurones in the rostral spinal nucleus of the accessory nerve (innervating sternocleidomastoid). Opinion varies as to the extent of the ipsilateral input: supranuclear control of the neurones in the caudal spinal nucleus of the accessory nerve (innervating the upper and middle fibres of trapezius) is thought to be predominantly contralateral. This pattern is analogous to the supranuclear innervation of the facial nerve motor nucleus.

The nucleus of Onuf (see Fig. 73.13), which is thought to innervate the perineal striated and sphincter muscles, is a ventrolateral (anterolateral) group of lamina IX in the first and second sacral segments.

The main afferent connections to motor neurones are direct monosynaptic connections from proprioceptive dorsal root afferents in the same or nearby segments; connections from axonal collaterals of dorsal horn and other interneurones, including Renshaw cells (which provide negative feedback control of α-motor neurones) and last-order excitatory and inhibitory interneurones; and direct monosynaptic connections from the vestibulospinal, reticulospinal and corticospinal tracts.

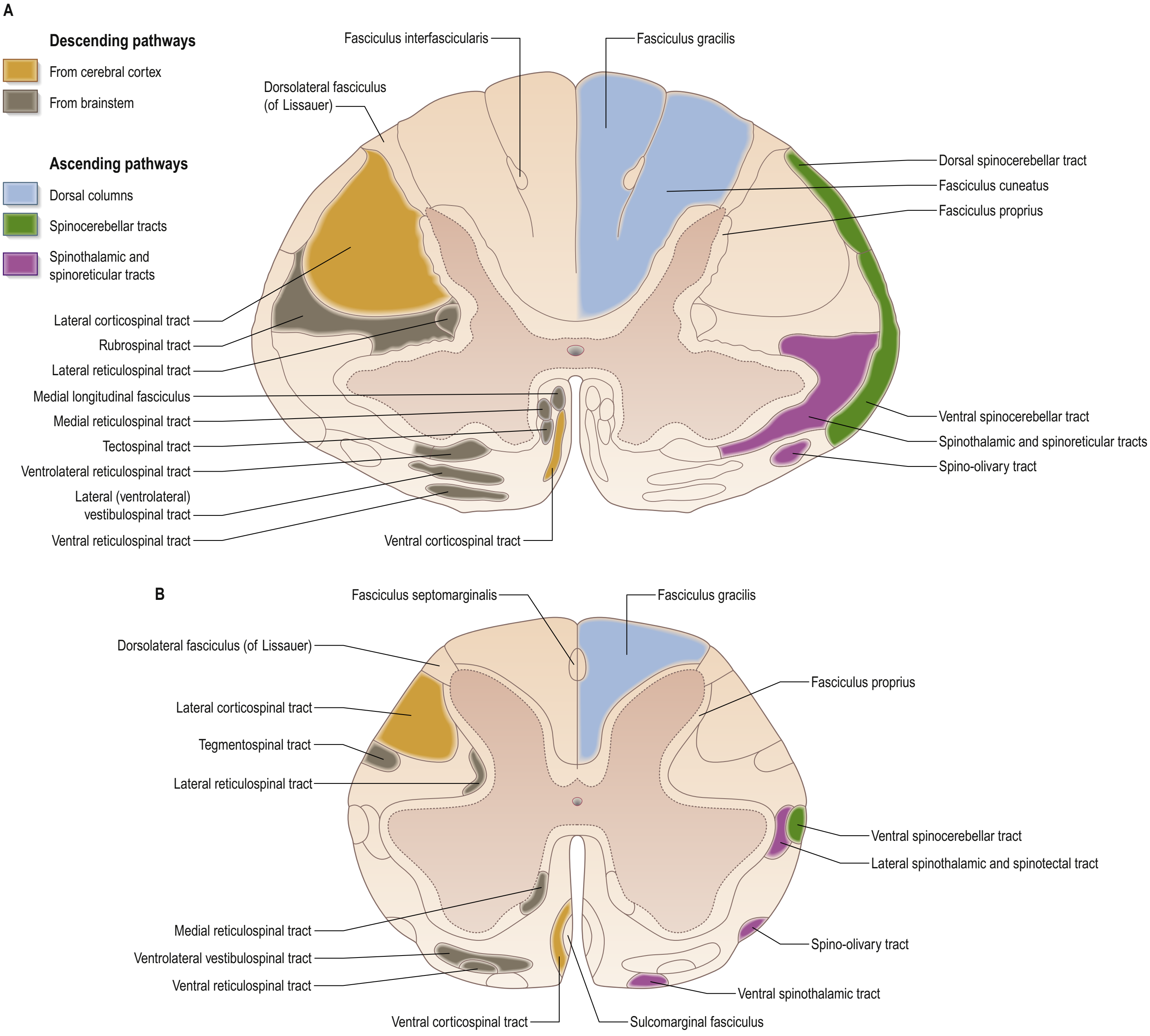
A
Descending pathways
From cerebral cortex
From brainstem
Ascending pathways
Dorsal columns
Spinocerebellar tracts
Spinothalamic and spinoreticular tracts
Fasciculus interfascicularis
Fasciculus gracilis
Dorsolateral fasciculus (of Lissauer)
Dorsal spinocerebellar tract
Fasciculus cuneatus
Fasciculus proprius
Lateral corticospinal tract
Rubrospinal tract
Lateral reticulospinal tract
Medial longitudinal fasciculus
Medial reticulospinal tract
Tectospinal tract
Ventrolateral reticulospinal tract
Lateral (ventrolateral) vestibulospinal tract
Ventral reticulospinal tract
Ventral corticospinal tract
Ventral spinocerebellar tract
Spinothalamic and spinoreticular tracts
Spino-olivary tract
B
Fasciculus septomarginalis
Fasciculus gracilis
Dorsolateral fasciculus (of Lissauer)
Fasciculus proprius
Lateral corticospinal tract
Tegmentospinal tract
Lateral reticulospinal tract
Ventral spinocerebellar tract
Lateral spinothalamic and spinotectal tract
Medial reticulospinal tract
Spino-olivary tract
Ventrolateral vestibulospinal tract
Ventral reticulospinal tract
Ventral spinothalamic tract
Ventral corticospinal tract
Sulcomarginal fasciculus

Fig. 27.7 The approximate positions of ascending and descending tracts in the spinal cord at mid-cervical (**A**) and lumbar (**B**) levels.

Spinal white matter

The spinal white matter surrounds the central core of grey matter and consists primarily of longitudinally running nerve fibres. Fibres subserving related functions, or those with common origins or destinations, are generally grouped together anatomically to form tracts (fasciculi), which may be ascending, descending or propriospinal. Ascending tracts carry afferent impulses to supraspinal levels and consist of either primary afferent fibres, which enter the cord via the dorsal roots of spinal nerves, or fibres derived from intrinsic spinal neurones. Descending tracts contain fibres that originate from cell bodies in the cerebral cortex or brainstem nuclei to control the activity of spinal neurones. Propriospinal tracts connect neurones that are localized entirely to the spinal cord and contain both ascending and descending components, collectively mediating intersegmental coordination.

The spinal white matter is conventionally described as being arranged into three large, bilaterally paired masses, the dorsal, lateral and ventral funiculi, each of which contains a number of specific tracts (see Figs 27.1, 27.3B, 27.7). The dorsal funiculus lies between the dorsal horn and the dorsal median septum. The lateral funiculus lies between the dorsal root entry zone and the site where the ventral roots emerge. The ventral funiculus lies between the ventral median fissure and the site where the ventral roots emerge. Narrow dorsal and ventral white commissures run close to the central canal and unite the two halves of the cord.

Fibres in the spinal white matter vary in calibre. Many are small and are either thinly myelinated or unmyelinated. Most regions contain a wide spectrum of fibre diameters, from 1 μm or less to 10 μm. Some tracts typically contain only small fibres, e.g. the dorsolateral tract, fasciculus gracilis and central part of the lateral funiculus. The fasciculus cuneatus, ventral funiculus and peripheral zone of the lateral funiculus all contain many large diameter fibres. The ascending and descending tracts are, to a large extent, discrete and regularly located (**Fig. 27.7**), but significant overlap between adjacent tracts does occur (Parent and Carpenter 1996).

Ascending pathways

Dorsal columns

The dorsal funiculus consists of two large ascending tracts, the fasciculus gracilis and fasciculus cuneatus (see Fig. 27.7; **Fig. 27.8**), which are also known as the dorsal columns. They are separated by a postero-intermediate septum. The dorsal columns contain a high proportion of myelinated fibres carrying proprioceptive (position sense and kinaesthesia), exteroceptive (touch-pressure) and vibratory sensation to higher levels. These fibres come from several sources: the central branches of primary afferent fibres that enter the cord in the dorsal roots of spinal nerves and ascend to the dorsal column nuclei in the medulla oblongata; shorter primary afferent fibres that project to neurones of the posterior thoracic nucleus and other spinal neurones; and axons of secondary

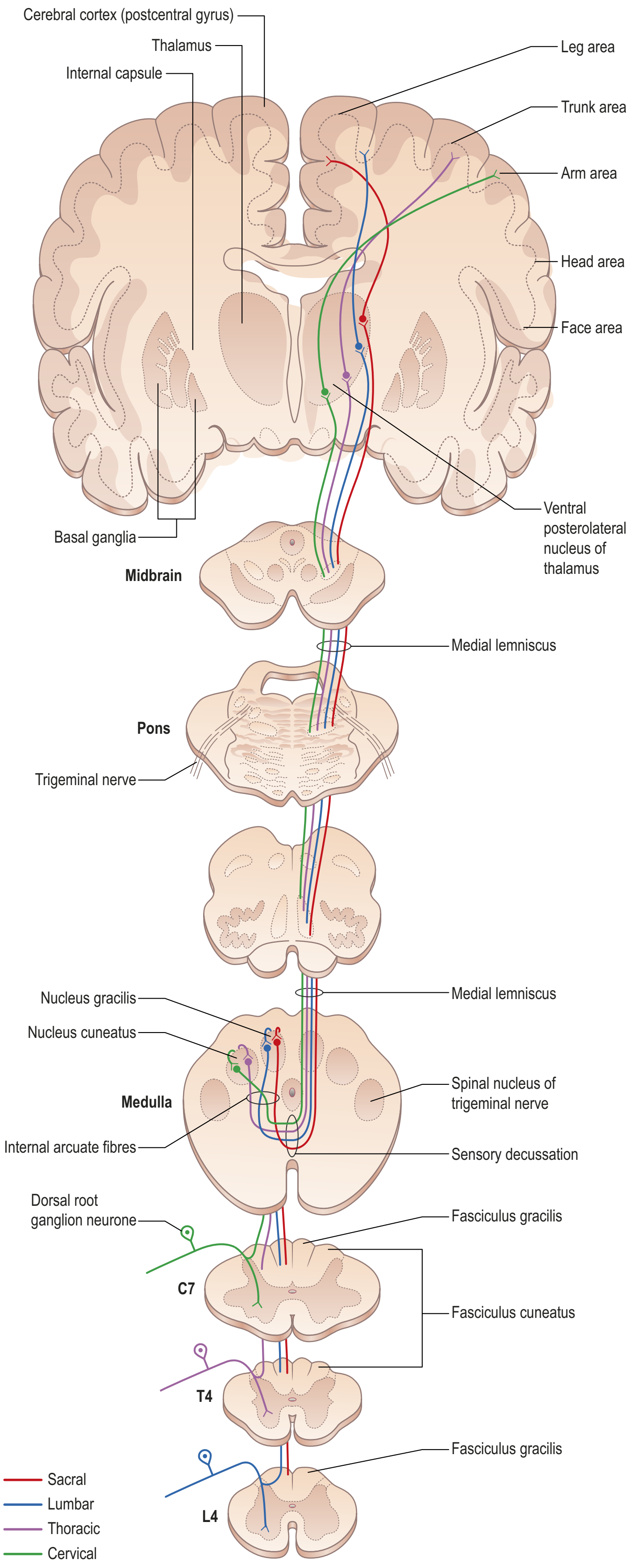

Fig. 27.8 The dorsal columns. Primary afferent fibres from different levels and their associated second- and third-order neurones are depicted in different colours.

neurones of the spinal cord ascending to the dorsal column nuclei. The dorsal columns also contain axons of propriospinal neurones.

The fasciculus gracilis begins at the caudal end of the spinal cord. It contains long ascending branches of primary afferents that enter the cord through ipsilateral dorsal spinal roots and ascending axons of secondary neurones in laminae IV–VI of the ipsilateral dorsal horn. As the fibres ascend, they are joined by axons of successive dorsal roots. Fibres entering in coccygeal and lower sacral regions are shifted medially by successive additions of fibres entering at higher levels.

The fasciculus gracilis lies medial to the fasciculus cuneatus in the upper spinal cord (see Fig. 27.7). At upper cervical levels, the fasciculus gracilis contains a larger proportion of afferents from cutaneous receptors than from deep proprioceptors because many of the latter leave the fasciculus at lower segments to synapse in the posterior thoracic nucleus (Clarke's column). Proprioception from the lower limb mainly reaches the thalamus by relaying in the posterior thoracic nucleus and then again in nucleus Z in the brainstem. Axons of the fasciculus gracilis, from both primary and secondary neurones, terminate in the nucleus gracilis of the dorsal medulla.

The fasciculus cuneatus (see Fig. 27.7) begins at mid-thoracic level and lies lateral to the fasciculus gracilis. It is composed mostly of primary afferent fibres of the upper thoracic and cervical dorsal roots. At upper cervical levels, it contains a large population of afferents from both proprioceptive and cutaneous receptors of the upper limb. Some of its axons arise from secondary neurones in laminae IV–VI of the ipsilateral dorsal horn. Many axons (both primary and secondary) that ascend in the fasciculus cuneatus terminate in the nucleus cuneatus of the dorsal medulla and some also end in the lateral (external or accessory) cuneate nucleus which projects to the cerebellum via the cuneocerebellar pathway.

Many ascending fibres of the fasciculus gracilis and fasciculus cuneatus terminate by synapsing on neurones of the dorsal column nuclei (nucleus gracilis and nucleus cuneatus, respectively) in the medulla oblongata (see Fig. 27.8). (The connections of the dorsal column nuclei are described further with the medulla oblongata in Ch. 28). Axons arising from neurones in the dorsal column nuclei arch ventromedially round the central grey matter of the medulla as internal arcuate fibres (see Fig. 28.7) and decussate in the great sensory decussation to form the medial lemniscus. They ascend to the ventral posterolateral nucleus of the thalamus, from where neurones project to the somatosensory cortex in the postcentral gyrus of the parietal lobe (areas 1, 2 and 3). Some neurones of the dorsal column nuclei form posterior external arcuate fibres that enter the cerebellum.

A high degree of somatotopic organization is preserved as the pathways ascend from the dorsal columns to the primary somatosensory cortex (see Fig. 27.8). The orientation of the somatotopic organization changes at different levels. In the dorsal column nuclei, the lower limb is represented medially in the nucleus gracilis, the upper limb laterally in the nucleus cuneatus, and the trunk in an intermediate position between them. Within the medial lemniscus at the level of the medulla, the lower limb is represented ventral to the trunk and upper limb. This representation rotates at the level of the pons and becomes the reverse of the spinal arrangement. Fibres are also segregated by modality in the dorsal columns: fibres from hair receptors are most superficial, and fibres from tactile and vibratory receptors lie in deeper layers.

Spinocerebellar tracts

The dorsal and ventral spinocerebellar tracts occupy the periphery of the lateral funiculi (see Fig. 27.7; **Fig. 27.9**) and carry proprioceptive and cutaneous information to the cerebellum for the coordination of movement. The dorsal tract has a greater number of large diameter myelinated fibres and more small calibre fibres are present in the ventral tract.

The dorsal spinocerebellar tract lies lateral to the lateral corticospinal tract. Its axons originate ipsilaterally from the larger neurones of the posterior thoracic nucleus located in lamina VII of spinal segments T1–L2. The posterior thoracic nucleus receives input from primary afferents ascending from segments caudal to L2. In the medulla, the dorsal spinocerebellar tract passes through the restiform body and the inferior cerebellar peduncle and terminates ipsilaterally in the rostral and caudal parts of the cerebellar vermis.

The ventral spinocerebellar tract lies lateral to the rubrospinal, spinothalamic and spinoreticular tracts. The cells of origin are in laminae V–VII of the lumbosacral cord and the tract carries proprioceptive information from the lower limb. Unlike the dorsal spinocerebellar tract, most of the axons forming the ventral spinocerebellar tract decussate at their origin and then again before their termination; some remain ipsilateral. The tract begins in the upper lumbar region, ascends through the medulla oblongata to reach the upper pontine level and then descends in the dorsal part of the superior cerebellar peduncle to terminate, mainly contralaterally, in the anterior cerebellar vermis.

The rostral spinocerebellar tract originates from cell groups of the intermediate zone of the contralateral cervical enlargement and is considered to be the upper limb and upper trunk equivalent of the ventral spinocerebellar tract.

Experimental tracing studies in animals have demonstrated a cervicospinocerebellar tract arising from a central cervical nucleus in the upper cervical spinal cord (C1–C4); the central cervical nucleus, possibly Cajal's nucleus intermedius, receives primary afferents from the vestibular labyrinth and muscle afferents from the deep muscles of the neck. A similar pathway may exist in humans where the nucleus intermedius of Cajal receives fibres from only the upper two cervical roots (Marani and Schoen 2005).

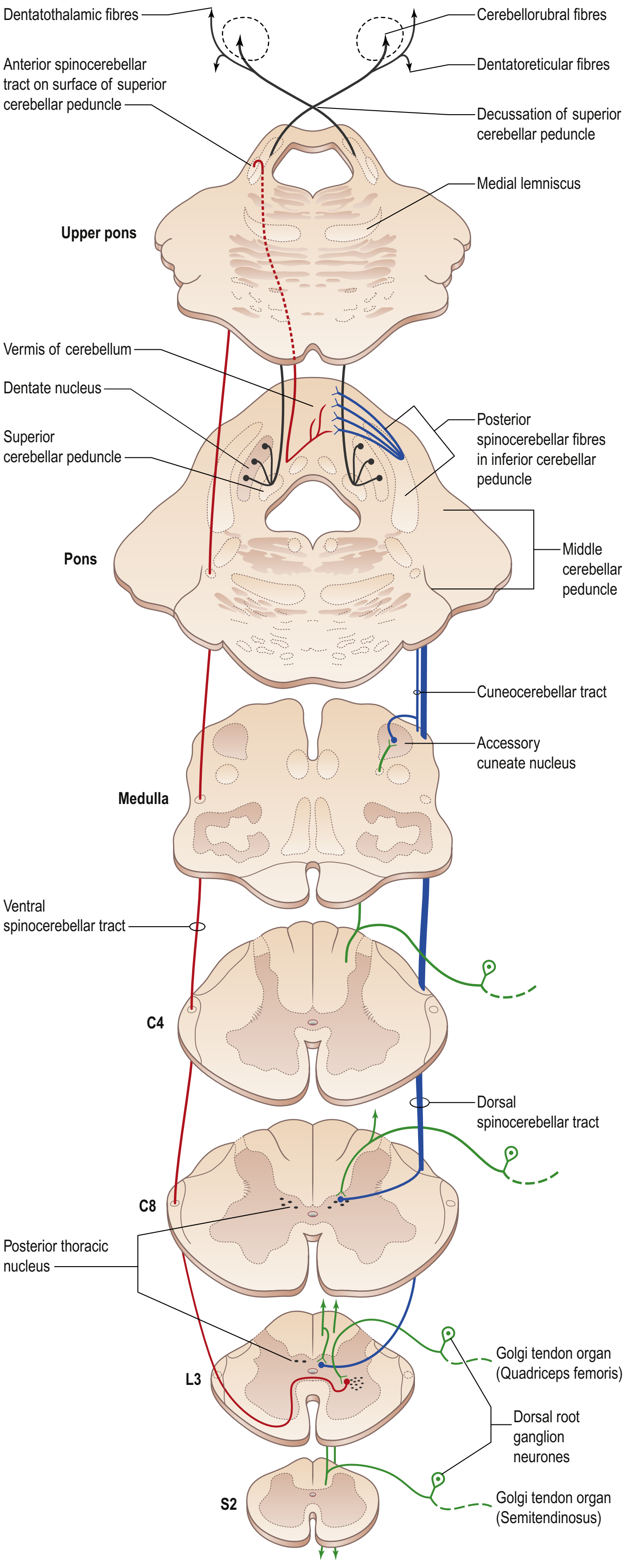
Dentatothalamic fibres
Cerebellorubral fibres
Anterior spinocerebellar tract on surface of superior cerebellar peduncle
Dentatoreticular fibres
Decussation of superior cerebellar peduncle
Medial lemniscus
Upper pons
Vermis of cerebellum
Dentate nucleus
Superior cerebellar peduncle
Posterior spinocerebellar fibres in inferior cerebellar peduncle
Pons
Middle cerebellar peduncle
Cuneocerebellar tract
Accessory cuneate nucleus
Medulla
Ventral spinocerebellar tract
C4
Dorsal spinocerebellar tract
C8
Posterior thoracic nucleus
L3
Golgi tendon organ (Quadriceps femoris)
Dorsal root ganglion neurones
S2
Golgi tendon organ (Semitendinosus)

Fig. 27.9 The spinocerebellar tracts. (Adapted with permission from Carpenter MB 1991 Core Text of Neuroanatomy, 4th ed. Baltimore: Williams and Wilkins.)

The dorsal and ventral spinocerebellar tracts are organized such that fibres from lower spinal segments are most superficial. Both tracts convey proprioceptive and exteroceptive information, but they are functionally different. Neurones of the posterior thoracic nucleus are excited monosynaptically by group Ia and Ib primary afferent fibres (from muscle spindles and tendon organs, respectively) and also by group II muscle afferents and cutaneous touch and pressure afferents. The proprioceptive impulses often arise from a single muscle or from synergistic muscles acting at a common joint. Thus, the dorsal spinocerebellar tract transmits modality-specific and space-specific information that is used in the fine coordination of individual limb muscles. On the other hand, the cells of the ventral tract are activated monosynaptically by Ib afferents and transmit information from large receptive fields that include different segments of a limb. The ventral tract lacks subdivisions for different modalities and transmits information for the coordinated movement and posture of the entire lower limb.

Since the posterior thoracic nucleus diminishes rostrally (see Fig. 27.3) and does not extend above the lowest cervical segment, it follows that the dorsal spinocerebellar tract carries information from the trunk and lower limb. Proprioceptive and exteroceptive information from the upper limb travel in primary afferent fibres of the fasciculus cuneatus. These fibres end somatotopically in the accessory (external or lateral) cuneate nucleus and the adjoining part of the cuneate nucleus situated in the medulla oblongata. Cells of these nuclei give rise to the posterior external arcuate fibres that form the cuneocerebellar tract (see Fig. 27.9), which enters the cerebellum via the ipsilateral inferior cerebellar peduncle. The cells in the accessory cuneate nucleus and the lateral part of the cuneate nucleus are considered to be homologous to the cells in the posterior thoracic nucleus. The cuneocerebellar tract is therefore functionally allied to the dorsal spinocerebellar tract and is its upper limb equivalent.

Axons of all the spinocerebellar tracts and the cuneocerebellar tract form part of the ‘mossy-fibre system’ and end in the cerebellar cortex in a highly somatotopically and functionally organized pattern (Ch. 29).

Spinothalamic tracts

Some authorities describe two spinothalamic tracts (lateral and ventral) with more or less distinct anatomical locations and functions. However, physiological studies in animals suggest that these tracts may be best considered as a structural and functional continuum. The spinothalamic tracts (see Fig. 27.7) consist of second-order neurones that convey pain, temperature, coarse (non-discriminative) touch and pressure information to the thalamus. The cells of origin lie in a wide range of spinal laminae and are found in all segments of the spinal cord. Fibres decussate in the ventral white commissure to reach the contralateral spinothalamic tract. Pain and temperature fibres do so promptly, within about one segment of their origin, whilst fibres carrying other modalities may ascend for several segments before crossing. Spinothalamic fibres mostly ascend in the white matter of the lateral and ventral funiculi.

The lateral spinothalamic tract (**Fig. 27.10**) is sited in the lateral funiculus, lying medial to the ventral spinocerebellar tract. Clinical evidence indicates that it subserves sensations of pain and temperature. The anterior (ventral) spinothalamic tract (see Fig. 27.10) lies in the ventral funiculus medial to the point of exit of the ventral spinal nerve roots and dorsal to the vestibulospinal tract, which it overlaps: on the basis of clinical evidence, it subserves coarse tactile and pressure modalities.

On reaching the lower brainstem, spinothalamic tract axons separate. Axons in the ventral tract join the medial lemniscus and axons in the lateral tract continue as the spinal lemniscus.

It is claimed that a somatotopic organization of the fibres in the spinothalamic tracts exists throughout their extent. Fibres crossing at any cord level join the deep aspect of those that have already crossed. Somatotopy is maintained throughout the medulla oblongata and pons. In the midbrain, fibres in the spinal lemniscus conveying pain and temperature sensation from the lower limb extend dorsally, while those from the trunk and upper limb are more ventrally placed: both lemnisci ascend to end in the thalamus. The major spinothalamic projections in humans are to the ventral posterolateral nucleus and centrolateral intralaminar nucleus.

Neurones of the spinothalamic tracts

The specific localization of spinothalamic tract cell bodies is poorly documented in humans. In animals, about one-third are localized to the upper three cervical segments, about 20% are located in lower cervical segments, 20% in the thoracic region (mostly in segments T1–T3), 20% in the lumbar region and 10% in the sacrococcygeal cord. Cells are located in laminae I and IV–VIII, the greatest concentration being in laminae VI and VII. Cell bodies giving rise to spinothalamic tract axons are predominantly contralateral, although a relatively small number (10%), mostly in the upper three cervical segments, are ipsilateral.

Neurones of the spinothalamic tracts have varied receptive fields. Specificity of separate types of afferents, as exists in the dorsal column nuclei, is absent in the spinothalamic nuclei; convergence of different

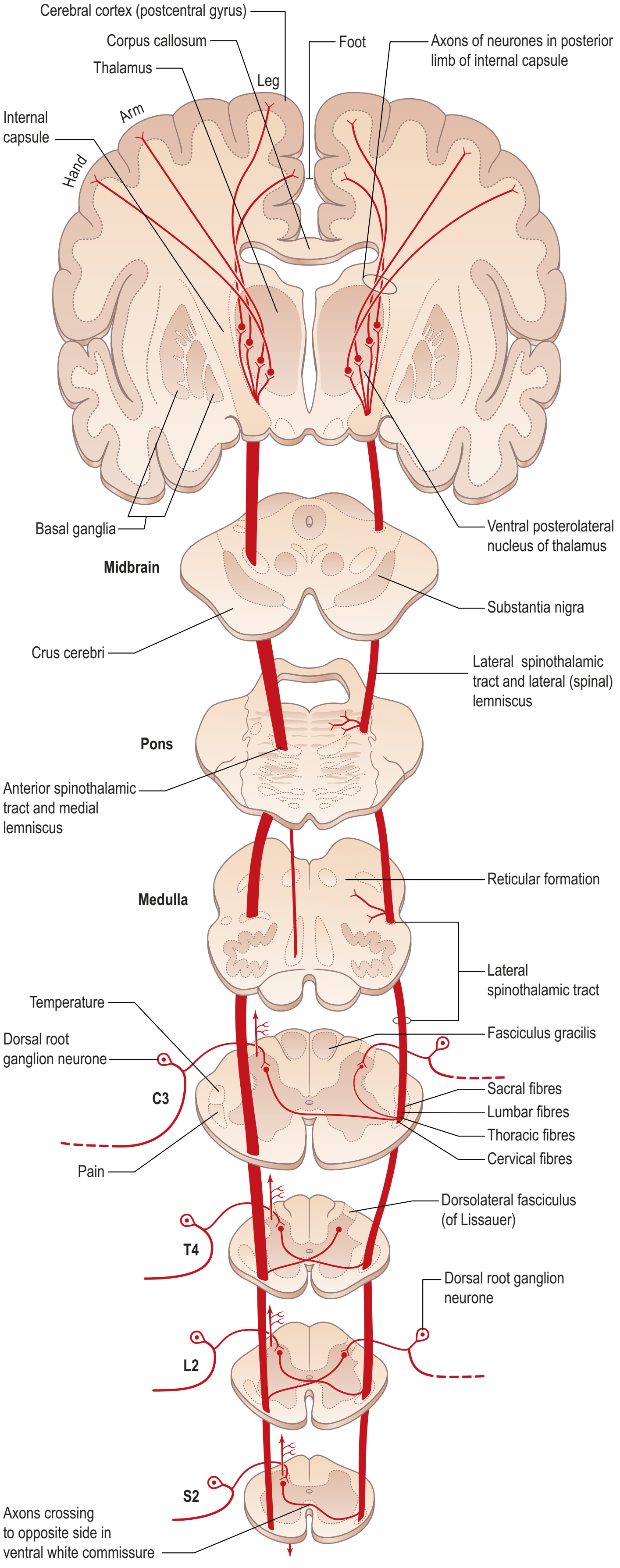
Cerebral cortex (postcentral gyrus)
Corpus callosum
Thalamus
Foot
Axons of neurones in posterior limb of internal capsule
Leg
Internal capsule
Arm
Hand
Basal ganglia
Ventral posterolateral nucleus of thalamus
Midbrain
Substantia nigra
Crus cerebri
Lateral spinothalamic tract and lateral (spinal) lemniscus
Pons
Anterior spinothalamic tract and medial lemniscus
Reticular formation
Medulla
Lateral spinothalamic tract
Temperature
Dorsal root ganglion neurone
Fasciculus gracilis
C3
Sacral fibres
Lumbar fibres
Thoracic fibres
Cervical fibres
Pain
Dorsolateral fasciculus (of Lissauer)
T4
Dorsal root ganglion neurone
L2
S2
Axons crossing to opposite side in ventral white commissure

Fig. 27.10 The lateral and ventral (anterior) spinothalamic tracts. (Adapted with permission from Carpenter MB 1991 Core Text of Neuroanatomy, 4th ed. Baltimore: Williams and Wilkins.)

functional types of afferent fibres onto an individual tract cell is a common feature in the cord. On the basis of laminar site, functional properties, and specific thalamic termination of their axons, spinothalamic tract neurones may be divided into three separate groups: the apical cells of the dorsal horn (lamina I), deep dorsal horn cells (laminae IV–VI), and cells in the ventral horn (laminae VII and VIII). There are species differences and the description above is derived from studies in non-human primates.

Spinoreticular pathway

Spinoreticular fibres are intermingled with those of the spinothalamic tracts and ascend in the ventrolateral quadrant of the spinal cord (see Fig. 27.7, Fig. 27.14). Evidence from animal studies suggests that cells of origin occur at all levels of the spinal cord, particularly in the upper cervical segments. Most neurones are in lamina VII, some are in lamina VIII, and others are in the dorsal horn, especially lamina V. Most axons in the lumbar and cervical enlargements cross the midline; there is a large uncrossed component in cervical regions. Most axons are myelinated. The pattern of anterograde degeneration, in both human postmortem studies and in experimental animals following anterolateral cordotomy, indicates the existence of spinoreticular projections to many nuclei of the medial pontomedullary reticular formation. There is also a projection to the lateral reticular nucleus (a precerebellar relay nucleus). These projections do not appear to be somatotopically organized. Spinoreticular neurones respond to inputs from the skin or deep tissues. Non-noxious cutaneous stimuli may inhibit or excite a particular cell, whereas noxious stimuli are often excitatory. A spino-reticulo-thalamo-cortical pathway has been proposed as an important route serving pain perception: like other ascending pathways, the tract cells are influenced by descending control. For example, electrical stimulation of the periaqueductal grey matter inhibits the responses of certain spinoreticular cells to input from cardiopulmonary afferents. Stimulation of the reticular formation also alters the activity of spinoreticular neurones.

Spinocervicothalamic pathway

In humans, the lateral cervical nucleus is small and lies in the lateral funiculus, ventrolateral to the dorsal horn in the upper two cervical segments. In some human cord specimens it is not distinctly defined and is possibly incorporated into the dorsal horn. The lateral cervical nucleus receives axons from the spinocervical tract that ascends in the dorsolateral funiculus. The tract cells are found in laminae III–V at all levels of the spinal cord, ipsilateral to the nucleus. Most neurones of the nucleus project to the contralateral thalamus via the medial lemniscus, and some project to the contralateral midbrain. Specific thalamic targets include the ventral posterolateral nucleus and part of the posterior complex. Spinocervical tract neurones respond to hair movement, pressure, pinch and thermal stimuli and to high-threshold muscle input; many also respond to noxious stimuli. Like the tract cells of other ascending pathways, they are under tonic descending inhibitory control.

Spinomesencephalic pathway

Available with the *Gray's Anatomy* e-book

Spino-olivary tract

Available with the *Gray's Anatomy* e-book

Descending tracts

Descending pathways to the spinal cord originate primarily from the cerebral cortex and from numerous sites within the brainstem (see Figs 27.11–27.14). They are concerned with the control of movement, muscle tone and posture, the modulation of spinal reflex mechanisms and central pattern generators, and the modulation of transmission of afferent information, including nociceptive input, to higher levels. They also mediate control over spinal autonomic neurones and have long-term trophic functions (Kuypers 1981, Lemon 2008). A generalized scheme of the organization of the descending pathways is given in **Fig. 27.11**.

Corticospinal and corticonuclear tracts

Corticospinal and corticonuclear (corticobulbar) fibres arise from neurones in the cerebral cortex. They project to neurones located in the spinal cord or brainstem, respectively (**Fig. 27.12**). Corticonuclear projections include those to the cells of origin of other descending pathways (such as the reticulospinal tract), to cranial motor nuclei, and to cell groups such as the dorsal column nuclei. The majority of corticospinal and corticonuclear fibres arise from cells situated in the primary motor cortex (area 4), premotor cortex and supplementary motor areas (area 6), and cingulate motor cortex (area 24). A significant contribution comes from cells in the postcentral gyrus (somatosensory cortex; areas 3, 1 and 2) and the adjacent parietal cortex (area 5). In the monkey, 30% of corticospinal fibres arise from area 4, 30% from area

Lamina I cells project to the thalamus. They respond maximally to noxious or thermal cutaneous stimulation and consist mainly of high-threshold but also some wide-dynamic-range units (responding to various different intensities of stimulus). Their receptive fields are usually small, representing a part of a digit or a small area of skin involving several digits. Lamina I spinothalamic tract neurones receive input from Aδ and C fibres, and some respond to convergent input from deep somatic and visceral receptors. Spinothalamic tract cells in the thoracic cord display marked viscero-somatic convergence and so, for example, pain from cardiac disease such as angina or a myocardial infarction is commonly felt as a tightness around the chest wall (referred pain). Lamina I spinothalamic tract neurones project via the lateral spinothalamic tract and terminate preferentially in the ventral posterolateral nucleus of the thalamus, with limited projections to the centrolateral intralaminar and mediodorsal thalamic nuclei. These projections are probably concerned with affective aspects of pain sensation.

The spinothalamic neurones of the deep dorsal horn (laminae IV–VI) are of varied types. In the lumbar cord, for example, 60% are wide-dynamic-range types, 30% are high-threshold and only 10% are low-threshold types. They can accurately code both non-noxious and noxious cutaneous stimuli. Some cells also respond to input from deep somatic and visceral receptors. In the lumbar cord, their receptive fields are small or medium-sized: they are larger than the area of the foot but smaller than the entire leg. In the thoracic cord, the fields of these laminar cells are larger and often include the entire upper limb plus part of the chest. Many of the deep dorsal grey column spinothalamic tract neurones in the thoracic segments receive convergent input from visceral afferent fibres. Spinothalamic axons from laminae IV–VI project via the anterior (ventral) spinothalamic tract either to the ventral posterolateral nucleus or to the centrolateral intralaminar nucleus of the thalamus, and sometimes to both. Units projecting to the ventral posterolateral nucleus receive input from all classes (Aβ, Aδ and C) of cutaneous fibres.

Spinothalamic neurones in the ventral horn (laminae VII and VIII) respond mainly to deep somatic (muscle and joint) stimuli but also to non-noxious and/or noxious cutaneous stimuli. In the thoracic regions of the spinal cord, they also receive convergent input from visceral sources. The majority of these neurones have large, complex receptive fields (often bilateral), which encompass widespread areas of the body. Cells of this group receive input from Aβ, Aδ and C classes of afferent fibres, and many respond to convergent input from receptors of deep structures. This population of neurones contains wide-dynamic-range (25%), high-threshold (63%) and low-threshold (12%) units. Most of the spinothalamic axons from the ventral horn project to the intralaminar nuclei of the thalamus, and these are again related to affective aspects of pain sensation. The wide-dynamic-range type of neurones are particularly effective for discriminating between different intensities of painful stimulation.

The spinomesencephalic pathway consists of a number of tracts ascending from the spinal cord to various regions of the midbrain. It includes the spinotectal tract projecting to the superior colliculus, neurones synapsing in the periaqueductal grey matter, and other spinal cord projections that terminate in the parabrachial nucleus, the pretectal nuclei and the nucleus of Darkschewitsch. Cells of origin are located throughout the length of the spinal cord, particularly in the cervical segments and the lumbosacral enlargement, mostly in lamina I, but they are also present in laminae IV–VIII, where they are concentrated in lamina V. Most are contralateral, but a prominent ipsilateral group is also found at upper cervical levels. Spinomesencephalic fibres are mostly myelinated and ascend in the white matter of the ventrolateral quadrant of the spinal cord, in association with the spinothalamic and spinoreticular tracts.

Spinomesencephalic neurones are of low-threshold, wide-dynamic-range or high-threshold classes. Their receptive fields may be small, or very complex and encompass large surface areas of the body. Many spinomesencephalic cells are nociceptive and are likely to be involved in the motivational–affective component of pain. Electrical stimulation of their site of termination in the periaqueductal grey matter results in severe pain in humans. The cells of the deeper layers of the superior colliculus, where spinotectal fibres synapse, are activated by noxious stimuli.

The spino-olivary tract is described in animals as arising from neurones in the deeper laminae of grey matter. Axons forming the tract cross and then ascend superficially at the junction of the ventral and lateral white funiculi, to end in the dorsal and medial accessory olivary nuclei. The tract carries information from muscle and tendon proprioceptors and from cutaneous receptors. A functionally similar route, the dorsal spino-olivary tract, ascends in the dorsal white funiculi and relays in the dorsal column nuclei to the contralateral inferior olivary nucleus. Information on these tracts in primates is scant, but postmortem evidence following cordotomies in humans has revealed degenerating axonal terminals in the inferior olivary nucleus.

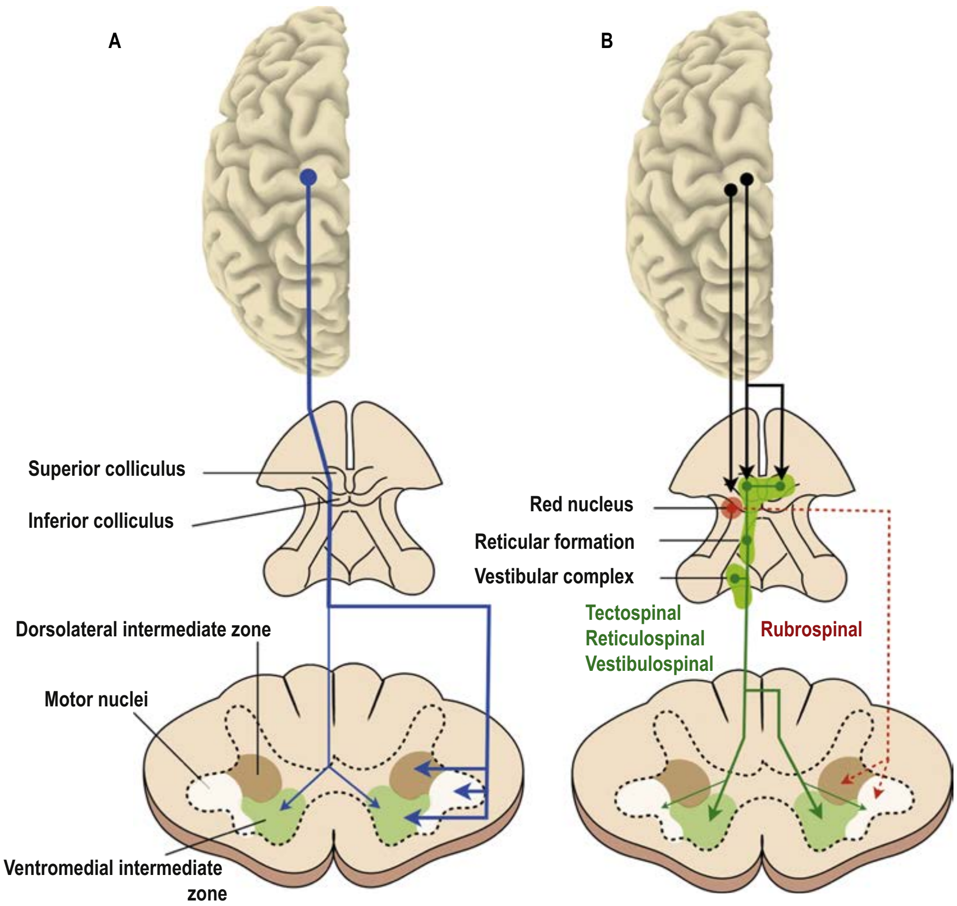

Fig. 27.11 Schematic representation of the main descending pathways. The distribution of fibres belonging to the (**A**) corticospinal system (blue) and (**B**) dorsolateral (red) and ventromedial (green) brainstem pathways, according to the scheme proposed by Kuypers (1981). For simplicity, descending projections from the cortex in **A** and **B** are shown arising from the motor cortex, but in fact they arise from widespread frontal and parietal areas (see text). Some uncrossed fibres in the anterior corticospinal tract terminate bilaterally in the ventromedial intermediate zone (lamina VIII; green shading in spinal sections). The majority of corticospinal fibres decussate and descend in the lateral corticospinal tract, terminating contralaterally in the dorsolateral intermediate zone (lamina VII; brown shading), with some projecting to lamina VIII (green) and many terminating directly on motor neurones innervating the arm and hand (lamina IX; white area). In **B**, ventromedial fibre pathways (reticulospinal, tectospinal, vestibulospinal) are shown in green, arising from the brainstem reticular formation, superior colliculus, and vestibular complex, respectively. These fibres terminate, for the most part, bilaterally in the ventromedial intermediate zone (green shading), but also have direct projections to motor neurones supplying trunk and girdle muscles, and some projections to hand and forearm motor neurones (green arrows extending into lateral lamina IX, white area). The dorsolateral pathways include the rubrospinal tract (red) which arises from the magnocellular red nucleus; its fibres terminate contralaterally in the dorsolateral region of the intermediate zone (brown shading), with some projections to the lateral group of motor nuclei innervating the arm and hand. The existence of a rubrospinal tract in humans has not been established, so the pathway is shown by dashed red lines. All of the nucleii giving rise to brainstem pathways receive significant cortical projections (black). (Adapted with permission from Lemon RN 2008 Descending pathways in motor control Ann Rev Neurosci 31:195–218.)

6 and 40% from the parietal regions. The cells of origin of corticospinal and corticonuclear fibres vary in size according to their cortical origins and are clustered into groups or strips. The largest neurones (giant pyramidal neurones; Betz cells) are located in the primary motor cortex of the precentral gyrus, with most of them located in the leg, and to a lesser extent in the hand/arm area. Each corticospinal neurone has an axon that branches and contacts a number of different target structures at cortical, subcortical and spinal levels.

Corticospinal and corticonuclear fibres descend through the subcortical white matter to enter the genu and posterior limb of the internal capsule. They then pass through the ventral part of the midbrain in the crus cerebri. As they continue caudally through the pons, they are separated from its ventral surface and fragmented into fascicles by transversely running pontocerebellar fibres. Corticopontine fibres, which are far more numerous than corticospinal or other corticonuclear fibres, terminate in the different divisions of the pontine nuclei (see Fig. 29.34). Corticonuclear fibres terminate on cranial nerve and other nuclei of the midbrain, pons and medulla. In the medulla oblongata, the cortical efferent fibres destined for the spinal cord (corticospinal fibres) form a discrete bundle (the pyramid) on the ventral surface of the medulla: the corticospinal tract is therefore also referred to as the pyramidal tract (see Fig. 28.4). Each pyramid contains about a million axons of various diameters: the majority have a diameter of 1–4 μm and are myelinated, approximately 10% have diameters of 5–10 μm and an even smaller number have diameters of 11–22 μm. The largest diameter axons probably arise from the giant pyramidal neurones (Betz cells) of the primary motor cortex. The function of the smallest fibres is unknown.

Just rostral to the spinomedullary junction, approximately 90% of the corticospinal fibres in the pyramid cross the midline in the decussation of the pyramids and continue caudally as the lateral corticospinal tract. About 10% of the fibres continue ipsilaterally as the ventral corticospinal tract and a small fraction descend ipsilaterally in the lateral corticospinal tract. The lateral corticospinal tract (see Fig. 27.12) descends in the lateral funiculus throughout most of the length of the spinal cord until about the fourth sacral segment. It occupies an oval area, ventrolateral to the dorsal horn and medial to the dorsal spinocerebellar tract (see Fig. 27.7). In the lower lumbar and sacral regions, where the dorsal spinocerebellar tract is absent, the lateral corticospinal tract reaches the dorsolateral surface of the cord. Studies in both human and non-human primates show that axons derived from the different cortical areas giving rise to the corticospinal tract (Brodmann's areas 4, 6 etc.) remain separated within the internal capsule, but show increasing overlap as they pass from the crus cerebri to the pyramid and thence into the lateral corticospinal tract where the overlap is complete. As the lateral corticospinal tract descends, approximately 50% of the fibres terminate in the cervical cord, 20% in the thoracic cord and 30% in the lumbosacral cord.

The smaller ventral corticospinal tract descends in the ventral funiculus (see Fig. 27.12). It lies close to the ventral median fissure and is separated from it by the sulcomarginal fasciculus (medial longitudinal fasciculus, medial vestibulospinal tract; see Fig. 27.7). Near their

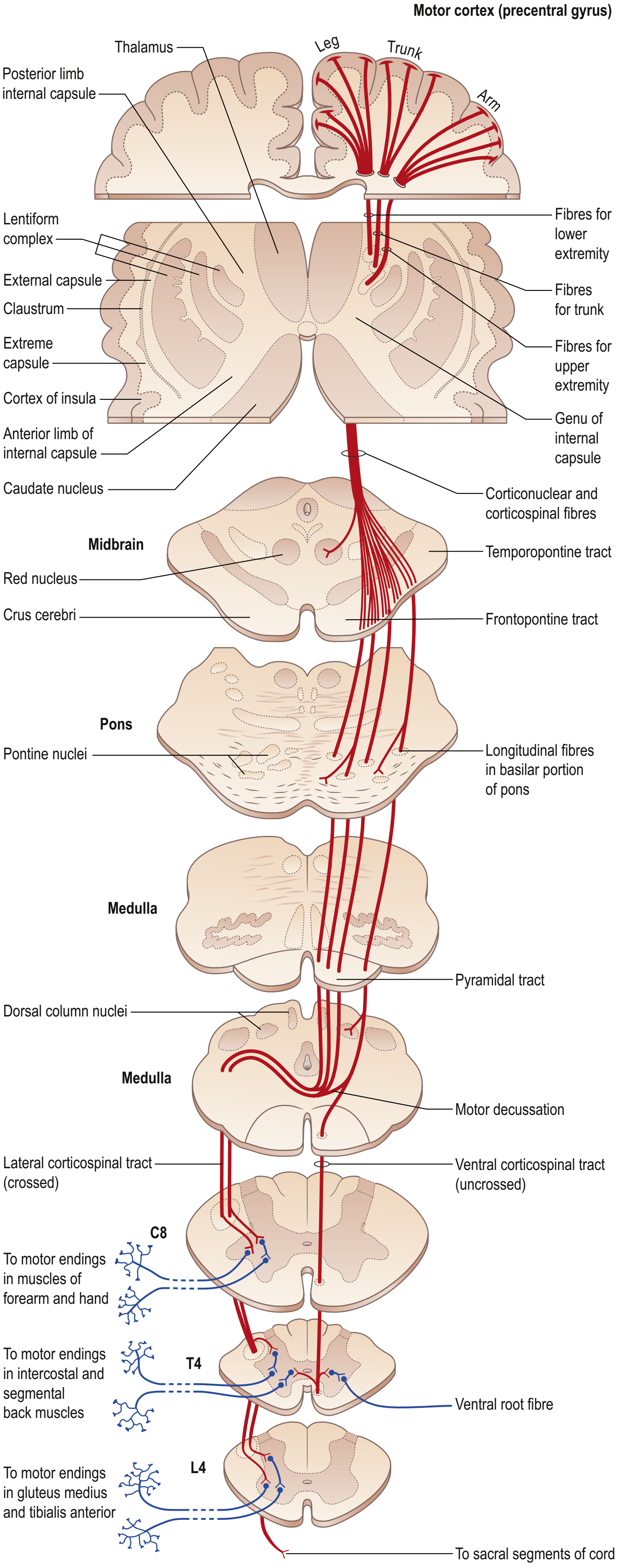
Motor cortex (precentral gyrus)
Leg
Trunk
Arm
Thalamus
Posterior limb internal capsule
Lentiform complex
External capsule
Claustrum
Extreme capsule
Cortex of insula
Anterior limb of internal capsule
Caudate nucleus
Fibres for lower extremity
Fibres for trunk
Fibres for upper extremity
Genu of internal capsule
Corticonuclear and corticospinal fibres
Midbrain
Red nucleus
Crus cerebri
Temporopontine tract
Frontopontine tract
Pons
Pontine nuclei
Longitudinal fibres in basilar portion of pons
Medulla
Pyramidal tract
Dorsal column nuclei
Medulla
Motor decussation
Lateral corticospinal tract (crossed)
Ventral corticospinal tract (uncrossed)
C8
To motor endings in muscles of forearm and hand
T4
To motor endings in intercostal and segmental back muscles
Ventral root fibre
L4
To motor endings in gluteus medius and tibialis anterior
To sacral segments of cord

Fig. 27.12 The corticospinal tracts, also showing some of the corticonuclear projections. (Adapted with permission from Carpenter MB 1991 Core Text of Neuroanatomy, 4th ed. Baltimore: Williams and Wilkins.)

termination, most fibres of the tract cross the midline in the ventral white commissure to synapse on contralateral neurones, which means that the vast majority of corticospinal fibres projecting to the cervical cord, irrespective of the tract in which they descend, terminate in the spinal cord on the side contralateral to their cortical origin. In contrast, some of the corticospinal fibres projecting to the lumbosacral cord have ipsilateral terminations. Corticospinal fibres from the motor areas do not terminate in the dorsal horn.

Modern tractography methods have made it possible to image the course of the human corticospinal tract. Knowledge of the detailed termination of corticospinal fibres is based largely on animal studies, but is supplemented by data from postmortem studies on human brains using anterograde degeneration methods. Corticospinal projections from different cortical areas have different patterns of termination within the spinal grey matter. Most corticospinal fibres projecting to the cervical cord from the motor cortex terminate contralaterally on interneurones in the lateral parts of laminae IV–VI and both lateral and medial parts of lamina VII, which receives the strongest projection (Morecraft et al 2013). Some corticospinal fibres are distributed to lamina VIII bilaterally.

Corticospinal fibres from the motor areas also terminate directly on α motor neurones in lamina IX: these are the cortico-motoneuronal projections (Lemon 2008), which constitute the second largest projection from the motor cortex to the cervical cord (Morecraft et al 2013). The corticospinal tract therefore influences motor neurones both directly and indirectly, via interneurones, and this may involve branches of the same corticospinal axons. As the widespread dendrites of multipolar motor neurones in lamina IX extend into laminae VII and VIII, direct monosynaptic axodendritic contacts can also exist on large α motor neurones in these laminae. Direct terminations on motor neurones are most abundant in the spinal cord enlargements, and particularly in the dorsolateral motor nuclei supplying hand and digit muscles (Schoen 1964, Morecraft et al 2013). There is evidence in both human and monkey cortices for rostral and caudal subdivisions of area 4; most of the direct, cortico-motoneuronal projections originate from the caudal division, referred to as 'new M1' to reflect its more recent evolution (Rathelot and Strick 2009). In contrast, 'old' M1 lacks cortico-motoneuronal projections and its corticospinal fibres influence spinal motor neurones indirectly; it is also the source of major corticonuclear projections to brainstem structures giving rise to descending pathways such as the reticulospinal tract.

Experimental evidence shows that precentral corticospinal neurones influence the activities of both α and γ spinal motor neurones, facilitating flexor muscles and inhibiting extensors, which are the opposite effects to those mediated by lateral vestibulospinal fibres. Evidence from animal studies shows that direct projections from the precentral cortical areas to spinal motor neurones are concerned with highly fractionated, precision movements of the limbs. Accordingly, in primates, precentral corticospinal fibres are mainly distributed to motor neurones supplying the distal limb muscles. Corticospinal projections probably use glutamate or aspartate, often co-localized, as excitatory neurotransmitters.

Corticospinal fibres from parietal sources end mainly in the contralateral dorsal horn, including laminae I–II and the lateral parts of laminae IV–VI, and these fibres are a major source for the presynaptic inhibition of peripheral afferent input. They do not terminate in the ventral horn. Phylogenetically, these fibres may represent the oldest part of the corticospinal system (Kuypers 1981). Axons from the sensory cortex terminate chiefly in laminae IV and V and are concerned with the supraspinal modulation of the transmission of afferent impulses to higher centres, including the motor cortex.

Experimental studies in primates indicate that complete transection of corticospinal fibres at the level of the pyramid (pyramidotomy) results in flaccid paralysis or paresis of the contralateral limbs and loss of independent hand and finger movements. Destruction of human corticospinal fibres at the level of the internal capsule, commonly caused by a cerebral vascular accident or 'stroke', results in a contralateral hemiplegia. The paralysis is initially flaccid but later becomes spastic, and is most marked in the distal muscles of the extremities, especially those concerned with individual movements of the fingers and hand. An abnormally active synergy develops between elbow flexors and shoulder abductors. Associated signs on the paralysed side are: hyperactive deep tendon reflexes; increased tone; the loss of superficial abdominal and cremasteric reflexes; and the appearance of dorsiflexion of the toes (Babinski sign) in response to stroking the sole of the foot. The latter is usually interpreted as pathognomonic of corticospinal damage, but it is not always present in patients with confirmed corticospinal lesions. Moreover, Babinski's sign is normally present in human infants up to about 2 years of age; its subsequent disappearance may reflect the completion of myelination of the corticospinal fibres and/or the establishment of direct cortical connections to lower motor neurones.

It is generally accepted that the sequelae of stroke damage to the internal capsule reflect a combination of negative effects, including weakness and loss of dexterity, and positive effects, in particular hyperreflexia and hypertonia. The latter are probably due to the involvement of other pathways in addition to the corticospinal tract, including descending cortical projections to the cells of origin of the rubrospinal, vestibulospinal and reticulospinal tracts (Baker 2011, Krakauer and Carmichael 2017).

There are very considerable differences across animal species in the organization and function of the corticospinal system, and these differences are useful in understanding the function of the human corticospinal tract (see Commentary 3.1).

Rubrospinal tract

The rubrospinal tract arises from neurones in the caudal, magnocellular part of the red nucleus, situated in the midbrain tegmentum; see p. 451). This part of the nucleus is very small in humans and contains only a few large neurones. The origin, localization, termination and functions of the rubrospinal tract are poorly defined in humans, and the tract is often referred to as rudimentary. Rubrospinal fibres cross in the ventral tegmental decussation and descend in the lateral funiculus of the cord, where they lie ventral to, and intermingled with, fibres of the lateral corticospinal tract (see Fig. 27.7). In humans, the rubrospinal tract appears to project only to the upper three cervical cord segments: fibres are distributed to the lateral parts of laminae V–VI and the dorsal part of lamina VII of the spinal grey matter. The terminal zones of the tract are similar to those of corticospinal fibres from the motor cortex. In animals, the rubrospinal tract is considered to be part of the group of descending pathways that exert their main influence on muscles of the contralateral extremities. In animals, the effects of rubrospinal fibres on α and γ motor neurones are similar to those of corticospinal fibres, with particularly strong effects on upper limb extensor muscles.

Tectospinal tract

The tectospinal tract arises from neurones in the intermediate and deep layers of the superior colliculus of the midbrain. It crosses ventral to the periaqueductal grey matter in the dorsal tegmental decussation and descends in the medial part of the ventral funiculus of the spinal cord (see Fig. 27.7). Fibres of the tract project only to the upper cervical cord segments, ending in laminae VI–VIII. They make polysynaptic connections with motor neurones serving muscles in the neck, facilitating those that innervate contralateral muscles and inhibiting those that innervate ipsilateral ones. In animals, unilateral electrical stimulation of the superior colliculus causes turning of the head to the contralateral side, an effect mainly mediated through the tectospinal tract. It is speculated that the tectospinal tract is concerned with reflex orientation of the head in response to visual stimuli.

Vestibulospinal tracts

The vestibular nuclear complex lies in the lateral part of the floor of the fourth ventricle, at the level of the pontomedullary junction and gives rise to the lateral and medial vestibulospinal tracts, which are functionally and topographically distinct (**Fig. 27.13**).

The lateral vestibulospinal tract (green in Fig. 27.13) arises from small and large neurones of the lateral vestibular nucleus (Deiters' nucleus). It descends ipsilaterally, initially in the periphery of the ventrolateral spinal white matter, but subsequently migrating into the medial part of the ventral funiculus at lower spinal levels. Fibres of this tract are somatotopically organized: fibres projecting to the cervical, thoracic and lumbosacral segments of the cord arise from neurones in the rostroventral, central and dorsocaudal parts, respectively, of the lateral vestibular nucleus. Lateral vestibulospinal fibres end ipsilaterally, mostly in the medial part of the ventral horn in lamina VIII and the medial part of lamina VII.

The medial vestibulospinal tract (red in Fig. 27.13) arises mainly from neurones in the medial vestibular nucleus, and also from neurones in the inferior and lateral vestibular nuclei. It descends in the medial longitudinal fasciculus into the ventral funiculus of the spinal cord, where it lies close to the midline in the sulcomarginal fasciculus (see Fig. 27.7). Unlike the lateral tract, it contains both crossed and uncrossed fibres, and does not extend beyond the mid-thoracic cord level. Fibres of the medial tract project mainly to the cervical cord segments and end in lamina VIII and the adjacent dorsal part of lamina VII.

The vestibular nuclei exert a strong excitatory influence upon the motor neurones that innervate antigravity muscles (including the epaxial muscles of the vertebral column and the extensor muscles of the lower limbs) by way of the medial and lateral vestibulospinal tracts.

Reticulospinal tracts

The reticulospinal tracts pass from the brainstem reticular formation to the spinal cord, and are for the most part uncrossed (**Fig. 27.14**). The pontine reticulospinal tract (red in Fig. 27.14) originates from the pontine tegmentum. The medullary reticulospinal tract (black in Fig. 27.14) arises from the nucleus gigantocellularis, which lies dorsal to the inferior olivary complex. The terminals of reticulospinal fibres are distributed to lamina VIII, and the central and medial parts of lamina VII of the spinal grey matter. The medullary reticulospinal terminals are more widely distributed, ending additionally in the lateral parts of laminae VI and VII, and also directly on motor neurones. In general, terminations of reticulospinal fibres that originate in the medulla are more dorsally placed than those that originate in the pons, although there is considerable overlap.

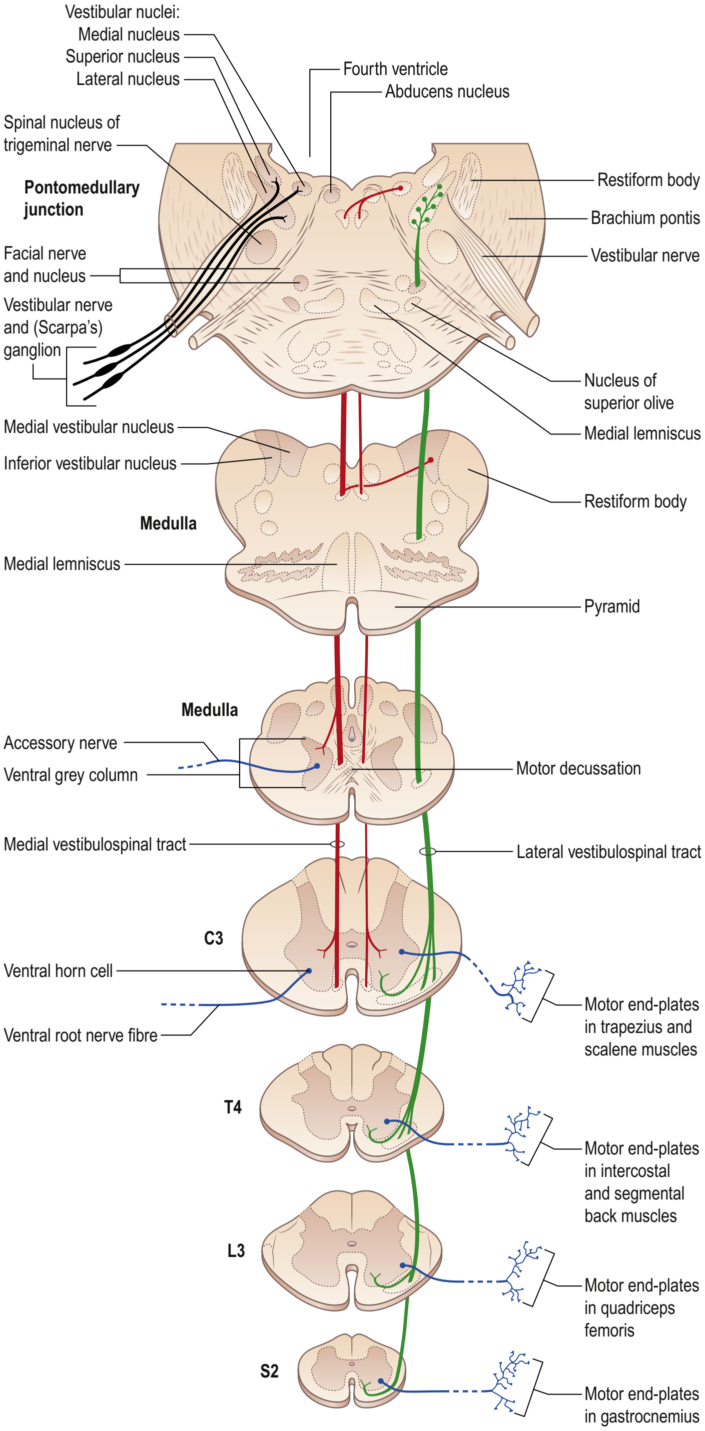
Vestibular nuclei:
Medial nucleus
Superior nucleus
Lateral nucleus
Fourth ventricle
Abducens nucleus
Spinal nucleus of trigeminal nerve
Pontomedullary junction
Restiform body
Brachium pontis
Vestibular nerve
Facial nerve and nucleus
Vestibular nerve and (Scarpa's) ganglion
Nucleus of superior olive
Medial lemniscus
Medial vestibular nucleus
Inferior vestibular nucleus
Restiform body
Medulla
Medial lemniscus
Pyramid
Medulla
Accessory nerve
Ventral grey column
Motor decussation
Medial vestibulospinal tract
Lateral vestibulospinal tract
C3
Ventral horn cell
Ventral root nerve fibre
Motor end-plates in trapezius and scalene muscles
T4
Motor end-plates in intercostal and segmental back muscles
L3
Motor end-plates in quadriceps femoris
S2
Motor end-plates in gastrocnemius

Fig. 27.13 The vestibulospinal tracts. (Adapted with permission from Carpenter MB 1991 Core Text of Neuroanatomy, 4th ed. Baltimore: Williams and Wilkins.)

Some anatomical texts classify the reticulospinal tracts into medial, ventral and ventrolateral tracts, but this is based mainly on studies in animals (see Fig. 27.7). The course and location of the human reticulospinal tracts are poorly defined: fibres do not form well-defined tracts but are typically scattered throughout the ventral and lateral columns (Nathan et al 1996).

Both α and γ motor neurones are influenced by reticulospinal fibres through polysynaptic and monosynaptic connections. There is

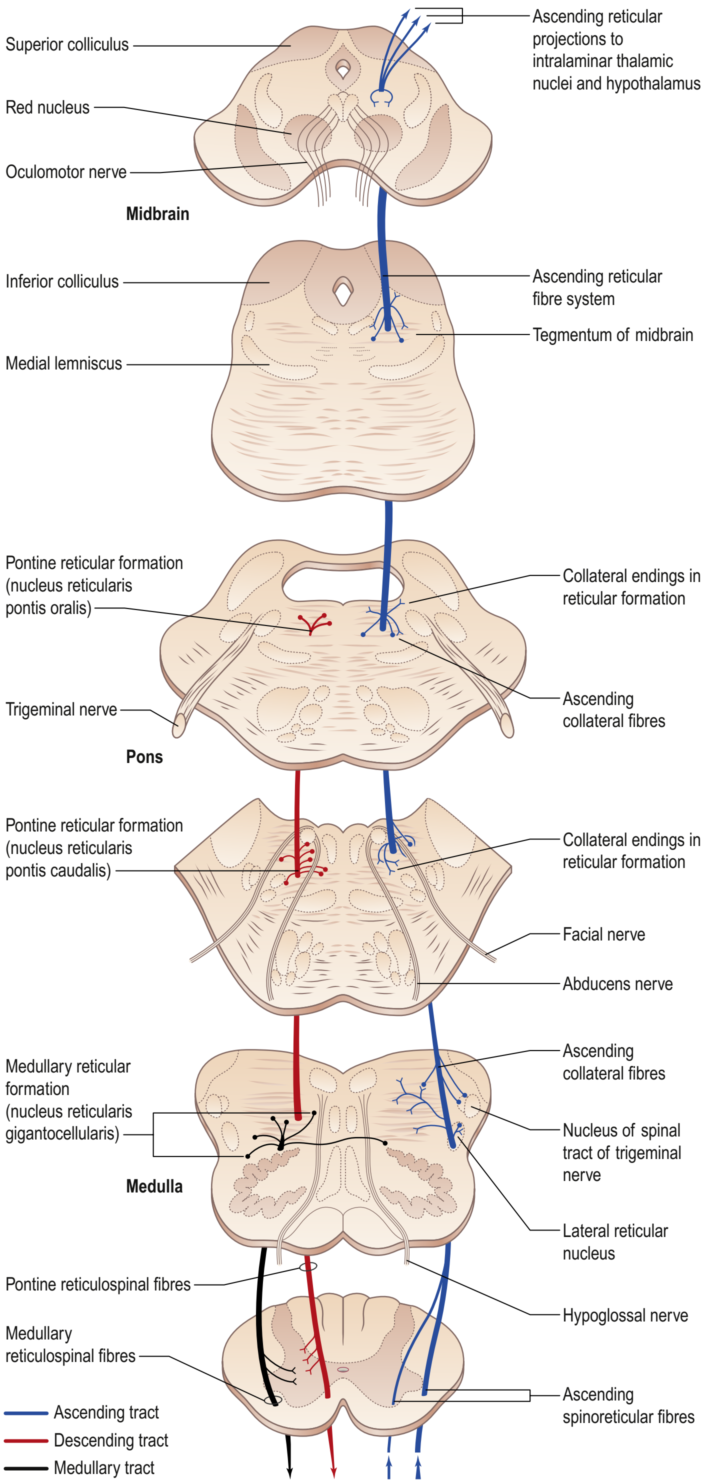
Superior colliculus
Red nucleus
Oculomotor nerve
Midbrain
Ascending reticular projections to intralaminar thalamic nuclei and hypothalamus
Inferior colliculus
Medial lemniscus
Ascending reticular fibre system
Tegmentum of midbrain
Pontine reticular formation (nucleus reticularis pontis oralis)
Trigeminal nerve
Pons
Collateral endings in reticular formation
Ascending collateral fibres
Pontine reticular formation (nucleus reticularis pontis caudalis)
Collateral endings in reticular formation
Facial nerve
Abducens nerve
Medullary reticular formation (nucleus reticularis gigantocellularis)
Medulla
Ascending collateral fibres
Nucleus of spinal tract of trigeminal nerve
Lateral reticular nucleus
Pontine reticulospinal fibres
Hypoglossal nerve
Medullary reticulospinal fibres
Ascending spinoreticular fibres
Ascending tract
Descending tract
Medullary tract

Fig. 27.14 The spinoreticular (blue) and reticulospinal (red, black) tracts. (Adapted with permission from Carpenter MB 1991 Core Text of Neuroanatomy, 4th ed. Baltimore: Williams and Wilkins.)

significant overlap in the termination of reticulospinal and corticospinal projections to segmental interneurones (Lemon 2008, Baker 2011). The pontine reticulospinal tract appears to be tonically active and is excitatory to the antigravity muscles, including the epaxial muscles of the vertebral column and the extensor muscles of the lower limbs. In marked contrast, the medullary reticulospinal tract is inhibitory to antigravity muscles. The cells of origin of the medullary reticulospinal tract receive a dense cortical input from the rostral region of primary motor cortex ('old M1') and premotor cortex. The reticulospinal tracts normally function in a coordinated, balanced fashion to control muscle tone. However, if the descending control from higher centres is lost, such as occurs after a stroke in the internal capsule, then the natural excitability and enhanced connectivity of the ipsilateral pontine reticulospinal tract, combined with the activity of the vestibulospinal tracts, causes the antigravity muscles (upper limb flexors and lower limb extensors) to become hypertonic and hyperreflexic (spasticity), with weakened upper limb extensors (Guyton and Hall 2006, Krakauer and Carmichael 2017). There are also increased excitatory effects on intrinsic hand muscles, probably explaining the crude grasp that persists after corticospinal lesions (Baker 2011).

Interstitiospinal tract

The interstitiospinal tract arises from neurones in the midbrain interstitial nucleus (of Cajal) in the dorsal midbrain and the immediate surrounding area, and descends via the medial longitudinal fasciculus into the ventral funiculus of the spinal cord. Its fibres project, mainly ipsilaterally, as far as lumbosacral levels, and are mostly distributed to the dorsal part of lamina VIII and the dorsally adjoining part of lamina VII. They establish some monosynaptic connections with motor neurones supplying neck muscles, but their main connections are disynaptic with motor neurones supplying limb muscles.

Solitariospinal tract

The solitariospinal tract is a small group of mostly crossed fibres that arises from neurones in the ventrolateral part of the nucleus solitarius of the medulla. Descending in the ventral funiculus and ventral part of the lateral funiculus of the spinal cord, these axons terminate on phrenic motor neurones supplying the respiratory diaphragm and thoracic motor neurones that innervate the intercostal muscles. A pathway with somewhat similar course and terminations to that of the solitariospinal tract originates from the nucleus retroambiguus. Both pathways subserve respiratory activities by driving inspiratory muscles, and some descending axons from the nucleus retroambiguus facilitate expiratory motor neurones. There is clinical evidence that bilateral ventrolateral cordotomy at high cervical levels abolishes rhythmic ventilatory movements.

Hypothalamospinal fibres

Hypothalamospinal fibres exist in animals. They arise from the paraventricular nucleus and other areas of the hypothalamus, and descend ipsilaterally, mainly in the dorsolateral region of the cord, to be distributed to sympathetic and parasympathetic preganglionic neurones in the intermediolateral column. They are also distributed to laminae I and area X in the spinal cord. Descending fibres from the dopaminergic cell group (A11) situated in the caudal hypothalamus innervate sympathetic preganglionic neurones and neurones in the dorsal horn. That similar pathways exist in humans may be inferred from ipsilateral sympathetic deficits (e.g. Horner's syndrome) that follow lesions of the hypothalamus, the lateral tegmental brainstem, or the lateral funiculus of the cord.

Monoaminergic spinal pathways

Monoaminergic cell groups utilize dopamine, adrenaline (epinephrine), noradrenaline (norepinephrine) and 5-HT as neurotransmitters. They are widely and diffusely distributed throughout the brainstem and in the hypothalamus, and do not form well-identified spinal tracts. They project rostrally to many forebrain areas and caudally to the spinal cord, and appear to be concerned with the modulation of sensory transmission and the control of autonomic and somatic motor neuronal activities.

The projections to the spinal cord are highly branched and arise from several sources. Coeruleospinal projections originate from noradrenergic cell groups A4 and A6 in the locus coeruleus complex in the pons and descend via the ventrolateral white matter to innervate all cord segments bilaterally. They end in the dorsal grey matter (laminae IV–VI) and the intermediate zone and ventral horn. They also project extensively to preganglionic parasympathetic neurones in the sacral cord. Descending noradrenergic fibres, which arise from the lateral tegmental cell groups A5 and A7 of the pons, travel in the dorsolateral white matter and are distributed to laminae I–III, particularly to the intermediate zone. Descending fibres from adrenergic cell groups C1 and C3 of the medulla oblongata have been traced into the ventral funiculus of the cord and are extensively distributed to the intermediolateral column. Dopaminergic fibres projecting to the spinal cord travel in the hypothalamospinal pathway.

The raphe nuclei pallidus (B1), obscurus (B2) and magnus (B3) in the brainstem give rise to two serotoninergic descending bundles. The lateral raphe spinal bundle, from B3 neurones, is concerned with the control of nociception. It descends close to the lateral corticospinal tract and ends in the dorsal horn (laminae I, II and V). The ventral bundle, composed mainly of axons from B1 neurones, travels in the medial part of the ventral white column and ends in the ventral horn (laminae VIII and IX). It facilitates extensor and flexor motor neurones. Some descending serotoninergic fibres project to sympathetic preganglionic neurones and are concerned with the central control of cardiovascular function.

Propriospinal pathways

Propriospinal pathways (fasciculi proprii) consist of intrinsic ascending and descending fibres that connect spinal neurones. They contact other neurones within the same segment and/or in more distant segments of the spinal cord and so subserve intrasegmental and intersegmental integration and coordination. The majority of spinal neurones are propriospinal neurones, most of which lie in laminae V–VIII. Propriospinal fibres are mainly concentrated around the margins of the grey matter where they form the fasciculus proprius (see Fig. 27.7), but are also dispersed diffusely in the white matter funiculi.

Tract of Lissauer

The tract of Lissauer (dorsolateral fasciculus) lies between the apex of the dorsal horn and the surface of the spinal cord, where it surrounds the incoming dorsal root fibres (see Fig. 27.7). It is present throughout the spinal cord and is most developed in the upper cervical regions.

The tract consists of small myelinated and unmyelinated axons: many are the branches of primary afferent axons in the lateral bundles of the dorsal roots. These axons bifurcate into ascending and descending branches as they enter the cord. The branches travel in the tract of Lissauer for one or two segments and give off collaterals that terminate on neurones in the dorsal horn. Up to 50% of the tract consists of propriospinal fibres: some are short axons of small substantia gelatinosa neurones which re-enter the dorsal horn and transmit nociceptive information onwards to cells that give rise to sensory ascending pathways.

SPINAL REFLEXES

The intrinsic connections of the spinal cord and brainstem subserve a number of reflexes by which the functions of peripheral structures are modulated in response to afferent information in a relatively automatic and autonomous fashion. The fundamental components of such reflex 'arcs' are an afferent and an efferent neurone, although in all but the simplest of reflexes, interneurones are intercalated between the afferent and efferent components, conferring increased versatility and complexity of reflex responses. Reflexes may be confined to a single cord level (intrasegmental) or involve several cord segments (intersegmental). By their very nature, reflexes are relatively fixed and stereotyped in form, nevertheless, they are strongly influenced and modulated by descending connections. In the case of spinal reflexes, these descending controls come from both the brainstem and the cerebral cortex. Pathology of descending supraspinal pathways is associated with abnormalities of spinal reflex activity that are routinely tested for in neurological examination: reflexes may be absent (areflexia), diminished (hyporeflexia) or exaggerated (hyperreflexia). During development, descending control mechanisms suppress what may be regarded as 'primitive' spinal reflex responses, such as the extensor plantar reflex and the grasp reflex: when the higher control mechanisms become damaged, these reflexes are released and reappear as a sign of central nervous system pathology (e.g. the Babinski reflex).

Muscle stretch reflex

The muscle stretch reflex (also somewhat misleadingly called the tendon reflex or deep tendon reflex) is the mechanism by which stretch applied to a muscle elicits its reflex contraction. It is essential for the maintenance of both muscle tone and an upright stance (via the innervation of the postural muscles of the neck, back and lower limbs). Anatomically it is the simplest of reflexes, mediated by an afferent and an efferent neurone, and it is therefore also known as a monosynaptic stretch reflex or a myotatic reflex. The anulospiral endings of large sensory fibres (group Ia afferents) spiral around the intrafusal muscle fibres of muscle spindles (see Fig. 3.33). The central processes of these afferent axons enter the spinal cord and make excitatory synaptic contact directly onto the α motor neurones that innervate the same muscle (Fig. 27.15). The α motor neurones of antagonistic muscles are simultaneously inhibited via collateral connections to inhibitory interneurones (reciprocal innervation).

Gamma effects on reflex sensitivity

Extrafusal muscle fibres are innervated by α motor neurones. Intrafusal muscle fibres are innervated by γ motor neurones. Activation of different classes of γ motor neurones increases the sensitivity of the intrafusal fibres to either dynamic or static stretch; changes in γ activity have a profound effect on the stretch reflex and on muscle tone. Like α motor neurones, γ motor neurones are under the influence of descending pathways from the brainstem and cerebral cortex. Changes in muscle tone and in the activity of the stretch reflex are commonly found in disorders of the central and peripheral nervous systems.

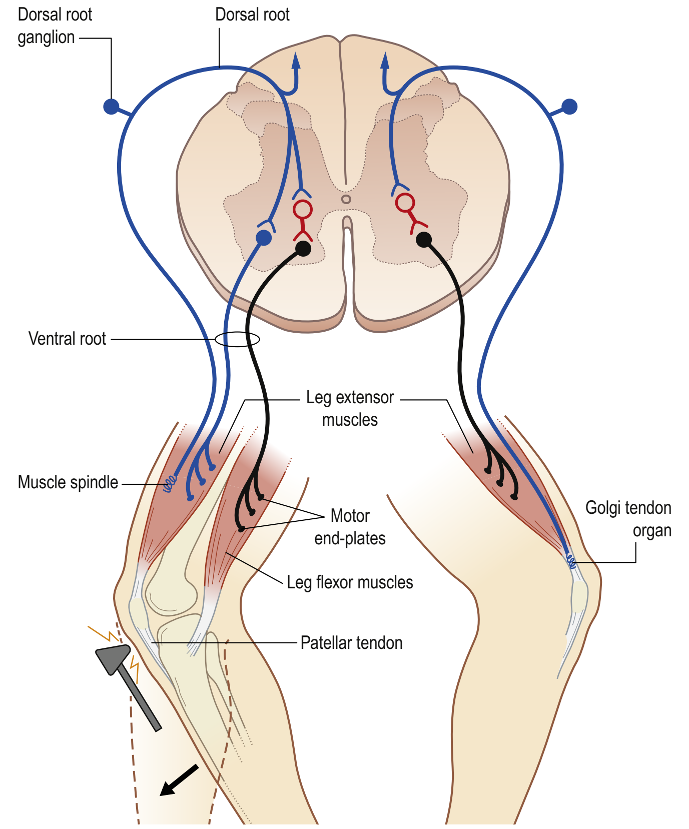

Fig. 27.15 The pathway for the patellar tendon reflex and reciprocal inhibition (left) and autogenic inhibition (right). The inhibitory glycinergic interneurones are represented by the red open cell bodies. (Adapted with permission from Haines D Fundamental Neuroscience for Basic and Clinical Applications, 4th ed. Elsevier, Saunders. Copyright 2013.)

Flexor reflex and crossed extensor reflex

Painful stimulation of the limbs leads to flexion withdrawal, mediated by a polysynaptic reflex in which interneurones link the afferent and efferent neurones (Fig. 27.16). Thus, activation of nociceptive primary afferents indirectly causes activation of limb flexor motor neurones. Collateralization of fibres to nearby spinal segments mediates flexion of a limb at several joints, depending on the intensity of the stimulus. Decussating connections to the contralateral side of the cord activate α motor neurones innervating corresponding extensor muscles, which produces a crossed extensor reflex (Fig. 27.17). In principle, virtually any cutaneous stimulus has the potential to induce a flexor reflex but, other than in the case of noxious stimuli, this response is normally inhibited by descending pathways. When descending influences are lost, even harmless cutaneous stimulation can elicit flexion of the limbs. The Babinski (extensor plantar) reflex, which is generally regarded as pathognomonic of damage to the corticospinal tract, is part of a flexion withdrawal of the lower limb in response to stimulation of the sole of the foot.

Central pattern generators

Available with the *Gray's Anatomy* e-book

SPINAL CORD LESIONS

A sound understanding of spinal cord anatomy is vital in making the correct diagnosis (Boxes 27.1–27.5).

Mechanical compression and secondary ischaemic damage to underlying nervous tissue cause surgically relevant spinal cord disease

Box 27.1 Case history 1: Complete transection of the spinal cord

A 29-year-old male fractured his cervical spine after a road traffic accident, leading to transection of the spinal cord at C5. When examined 6 months later, he had paralysis of all four limbs but shoulder abduction and elbow flexion were spared (i.e. all muscles innervated by nerve fibres arising below C5 were paralysed). Tone was increased in the limbs with brisk reflexes and extensor plantar responses (i.e. the weakness was upper motor neurone or pyramidal weakness). He had complete loss of sensation below C5 and a neurogenic bladder.

Box 27.2 Case history 2: Hemisection of the spinal cord giving rise to the Brown–Séquard syndrome

A 20-year-old female presented with a 4-day history of gradually worsening right leg weakness, burning pain and loss of sensation in the left leg. On examination she had pyramidal pattern weakness of the right leg (i.e. hip and knee flexion and ankle dorsiflexion were mainly affected). Tone was increased in the right leg: there were brisk right leg reflexes and a right extensor plantar response (i.e. right pyramidal weakness). There was impaired proprioception in the right leg and reduced pinprick sensation affecting the left leg and side up to the umbilicus.

This case illustrates a Brown–Séquard syndrome resulting from hemisection of the cord caused by a right-sided cord lesion in the thoracic spine. Involvement of the corticospinal tract caused 'pyramidal' weakness below the level of the lesion on the same side as the lesion (because the pyramidal tract predominantly crosses in the medulla). Involvement of the dorsal columns caused impaired proprioception below the level of the lesion on the same side as the lesion (because the fibres in the dorsal columns also cross in the medulla). Involvement of the spinothalamic tract caused loss of pinprick sensation below the lesion on the contralateral side (because the spinothalamic tract crosses the midline soon after entering the cord). The progression of symptoms over several days suggests an inflammatory problem. Magnetic resonance imaging of the cord showed a right-sided area of cord inflammation (myelitis) at T10. The patient had previously had an episode of inflammation affecting the optic nerve (optic neuritis) and the diagnosis was therefore one of multiple sclerosis.

Box 27.3 Case history 3: Anterior (ventral) cord syndrome

A 75-year-old male with diabetes and hypertension presented with sudden onset of weakness and sensory disturbance in both legs. When examined 6 months later, he had a 'pyramidal' weakness of both legs with increased tone, brisk reflexes and extensor plantar responses, and a complete loss of pinprick sensation below T10. Proprioception was normal.

The acute onset suggested a vascular problem and the diagnosis was of an anterior spinal artery infarction. Proprioception was spared because the anterior spinal artery supplies only the anterior cord, whereas the posterior cord, including the dorsal columns, is supplied by the posterior spinal arteries.

Box 27.4 Case history 4: Posterior (dorsal) cord syndrome

A 73-year-old male presented with a 6-month history of unsteadiness on walking. When examined, he had an unsteady gait, a tendency to fall when asked to stand still with his eyes closed (positive Romberg's test), and impaired proprioception in all four limbs. Spinothalamic sensation (pinprick sensation) was intact and his power was normal.

Investigations revealed signal change in the posterior cervical cord on magnetic resonance imaging and his vitamin B_{12} levels were very low. A diagnosis of posterior cord syndrome secondary to B_{12} deficiency was made. Posterior cord syndromes involve the dorsal columns, leading to impaired proprioception. Although not illustrated in this case, B_{12} deficiency sometimes affects the corticospinal tract, causing weakness in the limbs, and may also sometimes affect the peripheral nerves.

Box 27.5 Case history 5: Central cord syndrome

A 20-year-old female presented with a 4-month history of painless injuries to her hands. For example, after gardening she would sometimes come inside and notice later that there were rose thorns sticking into her hands. Examination showed reduced pinprick sensation (spinothalamic sensation) over the upper limbs.

Magnetic resonance imaging of her cervical spine showed a collection of fluid in the centre of the cervical spinal cord (syringomyelia): a diagnosis of central cord syndrome secondary to syringomyelia was made. As spinothalamic tract fibres cross over from the dorsal horn to run in the contralateral spinothalamic tract, they pass very close to the centre of the cord. Central cord syndromes thus initially damage the spinothalamic tracts, resulting in altered pain sensation at the level of the lesion. As the lesion expands to involve the ventral horns, patients may develop lower motor neurone weakness of the upper limbs. They may subsequently experience upper motor neurone problems in the legs if the lesion expands further to involve the corticospinal tracts.

The propriospinal system plays important roles in spinal functions. Most of the descending pathways end on specific subgroups of propriospinal neurones and these, in turn, relay to motor neurones and other spinal neurones. The system mediates all those automatic functions that continue after transection of the spinal cord, e.g. sudomotor and vasomotor activities, and bowel and bladder functions. Propriospinal effects can be detected indirectly in humans and may be particularly important in the recovery of motor function after spinal cord injury (Pierrot-Deseilligny and Burke 2005).

Some propriospinal axons are very short and span only one segment, while others run the entire length of the cord. The shortest axons lie immediately adjacent to the grey matter and the longer ones are situated more peripherally. Propriospinal neurones can be categorized as long, intermediate or short according to the length of their axons. Axons of long propriospinal neurones are distributed throughout the length of the cord, mainly via the ventral and lateral funiculi; their cell bodies are in lamina VIII and the dorsally adjoining part of lamina VII. Axons from the long propriospinal neurones of the cervical cord descend bilaterally, whereas those from the corresponding lumbosacral neurones ascend mainly contralaterally. Most of the fibres are less than 3 μm in diameter and some are the first spinal tract axons to become myelinated. Intermediate propriospinal neurones occupy the central and medial parts of lamina VII and project mainly ipsilaterally. Short propriospinal neurones are found in the lateral parts of laminae V–VIII and their axons run ipsilaterally in the lateral funiculus.

Propriospinal fibres in the different parts of the white funiculi are distributed preferentially to specific regions of the spinal grey matter. In the spinal enlargements, the propriospinal fibres in the dorsolateral funiculus project to the dorsal and lateral parts of the intermediate zone, and to spinal motor neurones that supply distal limb muscles, especially those of the hand and the foot. The propriospinal fibres in the ventral part of the ventrolateral funiculus are distributed to the central and medial parts of lamina VII and to motor neurones of proximal limb and girdle muscles. Other propriospinal fibres run in the medial part of the ventral funiculus and travel mainly to the ventromedial part of the intermediate zone, which characteristically contains long propriospinal neurones, and to motor neurones that innervate axial and girdle muscles.

Research in animals has demonstrated that the spinal cord contains a number of 'central pattern generators' that can generate the rhythmic movements and patterns required for walking, swimming, breathing, scratching etc. These generators are made of multiple interneuronal cell types that collectively form highly interconnected neural circuits. By definition, a central pattern generator can generate motor patterns or rhythms when completely isolated from both descending supraspinal influences and peripheral afferent input. There is some evidence that a central pattern generator for locomotion exists in the human spinal cord (Minassian et al 2017).

In the mouse, a number of classes of spinal interneurone are thought to constitute the central pattern generator for locomotion. Commissural interneurones that influence contralateral motor neurones play an important role in side-to-side excitation of locomotor muscles. V_0 neurones can be either excitatory or inhibitory and together with the V_3 class of interneurones are responsible for side-to-side alterations in muscle activity. Other classes of interneurones that exert ipsilateral effects include V2a (excitatory) and V1 and V2b (inhibitory) interneurones. Reciprocal inhibition of motor neurones by muscle spindle Ia inputs are all thought to be mediated by either V1 or V2b interneurones (Kiehn 2016).

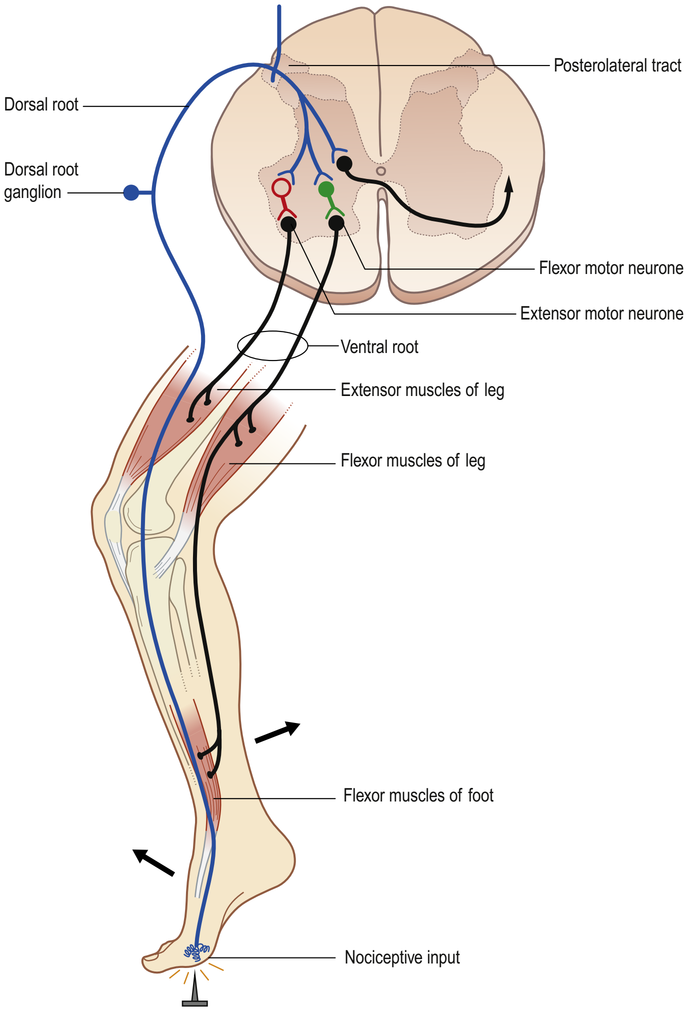

Fig. 27.16 The pathway for the flexor reflex. The inhibitory glycinergic interneurone is represented by the red open cell body and the excitatory glutaminergic interneurone by the green closed cell body. In addition to being involved in reflexes, this nociceptive input is also relayed to higher levels of the neuraxis via the anterolateral system (ascending black fibre). (Adapted with permission from Haines D Fundamental Neuroscience for Basic and Clinical Applications, 4th ed. Elsevier, Saunders. Copyright 2013.)

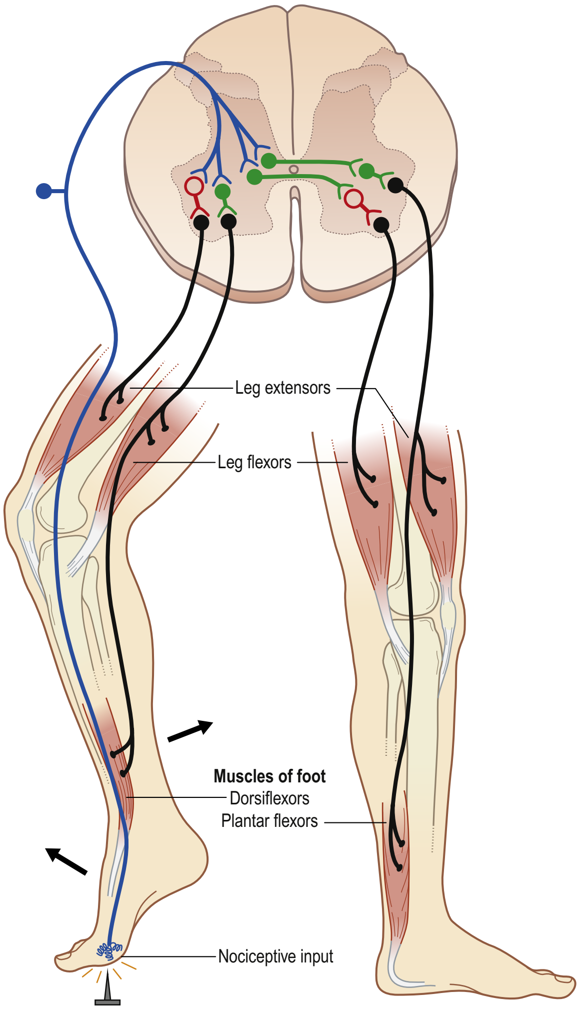

Fig. 27.17 The pathway for the crossed extensor reflex. Glycinergic interneurones (inhibitory) are represented by the open red cell bodies and glutaminergic interneurones (excitatory) by the closed green cell bodies. (Adapted with permission from Haines D, Fundamental Neuroscience for Basic and Clinical Applications, 4th ed. Elsevier, Saunders. Copyright 2013.)

(myelopathy). The site and the level of damage to the cord determine the particular clinical syndrome, e.g. whether the lesion involves the upper or lower cervical, thoracic or lumbosacral spinal cord. At each of these levels, symptoms and signs are determined by direct destruction of segmental tissue (transversely distributed damage) and disconnection of suprasegmental ascending and descending tracts above and below the level of a lesion (longitudinally distributed damage; Fig. 27.18). For example, a lower cervical spinal cord lesion damages the segmental sensory and motor contributions to the nerve roots and to the brachial plexus, causing sensory loss, weakness and wasting of the muscles and loss of tendon reflexes in the upper limbs. Disruption of the ascending sensory pathways in the lateral and dorsal columns of the cervical spinal cord leads to loss of sensation to pain and temperature (lateral spinothalamic tracts) and touch and proprioception (dorsal columns) below the 'sensory level' corresponding to the segment of the spinal cord. Damage to the descending corticospinal tracts in the lateral columns of the spinal cord produces a spastic paraparesis, i.e. increased tone of the muscles, weakness of an upper motor neurone pattern (weakness of extensors more than flexors in the upper limbs; weakness of flexors more than extensors in the lower limbs), exaggerated tendon reflexes and abnormal superficial reflexes, e.g. extensor plantar responses and absent abdominal reflexes. Descending pathways to the bladder are interrupted and this produces a 'neurogenic bladder', characterized by incontinence, frequency, urgency or retention of urine. The same principles apply to lesions at other levels of the spinal cord and these are illustrated in Fig. 27.18.

The time course of spinal cord disease is very important in suggesting the likely cause, as the rate of evolution of a disorder varies depending on the aetiology. Disorders with sudden or rapid onset are usually caused by trauma or by a vascular accident (i.e. stroke). When a condition develops over days it is often due to an inflammatory disorder such as multiple sclerosis. Neoplastic lesions such as a spinal cord meningioma often progress over months. Degenerative problems usually progress over months (such as amyotrophic lateral sclerosis or motor neurone disease) or even years (e.g. hereditary spastic paraparesis).

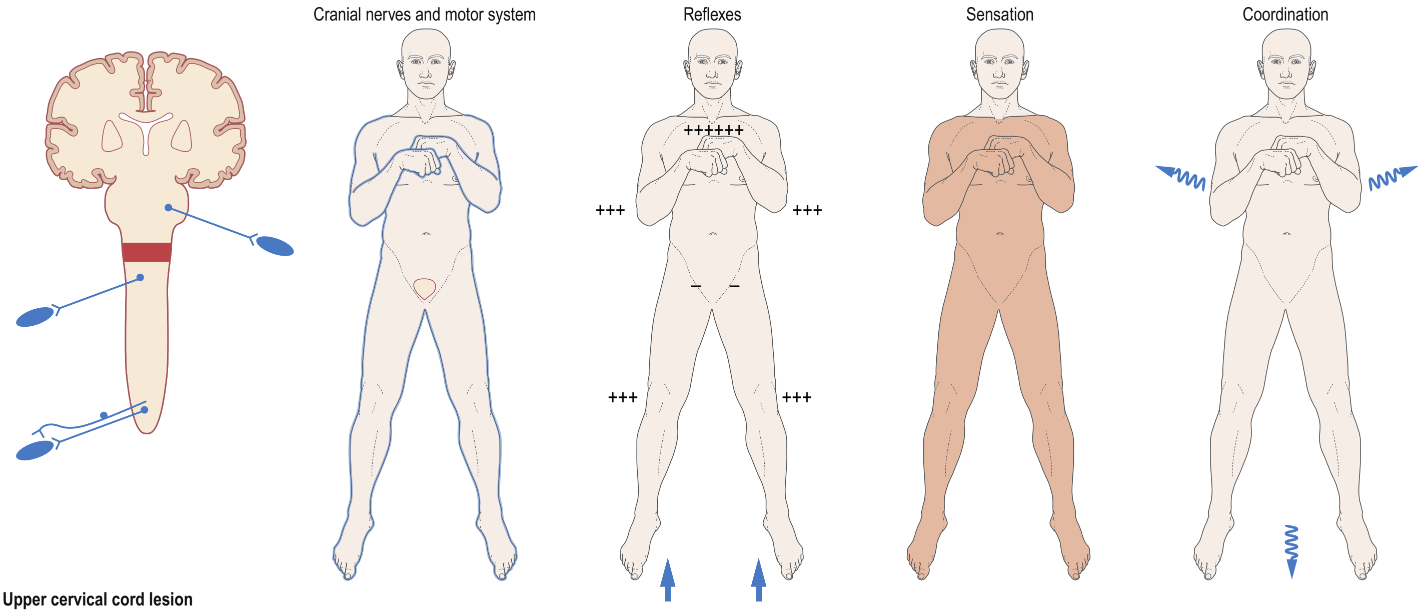
Cranial nerves and motor system
Reflexes
Sensation
Coordination
++++++
+++
+++
+++
+++

Upper cervical cord lesion

A high cervical cord lesion causes spastic tetraplegia with hyperreflexia, extensor plantar responses (upper motor neurone lesion), incontinence, sensory loss below the level of the lesion and 'sensory' ataxia.

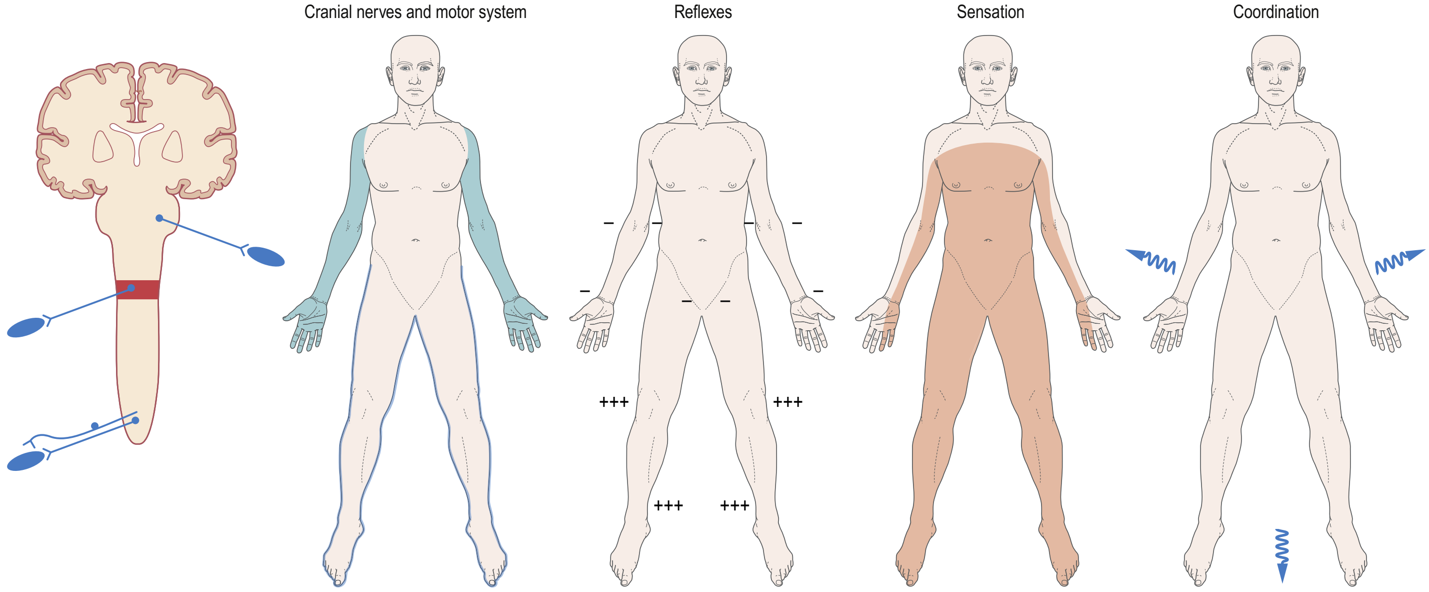
Cranial nerves and motor system
Reflexes
Sensation
Coordination
–
–
–
–
–
–
–
–
+++
+++
+++
+++

Lower cervical cord lesion

A lower cervical cord lesion causes weakness, wasting and fasciculation of muscles and areflexia of the upper limbs (lower motor neurone lesion). In addition, there is spastic paraparesis, hyperreflexia and extensor plantar responses (upper motor neurone lesion) in the lower limbs, incontinence, sensory loss below the level of the lesion and 'sensory' ataxia.

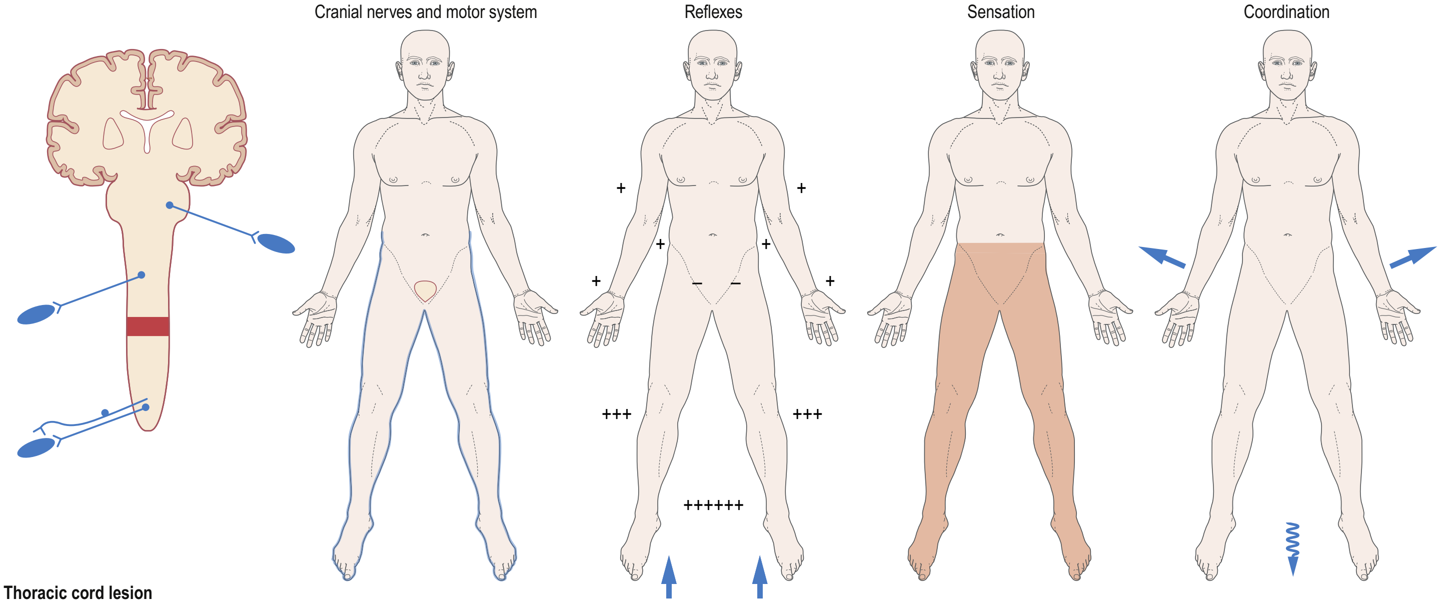
Cranial nerves and motor system
Reflexes
Sensation
Coordination
+
+
+
+
+
+
–
–
+++
+++
++++++

Thoracic cord lesion

A thoracic cord lesion causes a spastic paraparesis, hyperreflexia and extensor plantar responses (upper motor neurone lesion), incontinence, sensory loss below the level of the lesion and 'sensory' ataxia.

Fig. 27.18 Lesions of the spinal cord. (Adapted with permission from Crossman AR, Neary D Neuroanatomy: An Illustrated Colour Text, 4th ed. Elsevier, Churchill Livingstone. Copyright 2010.)

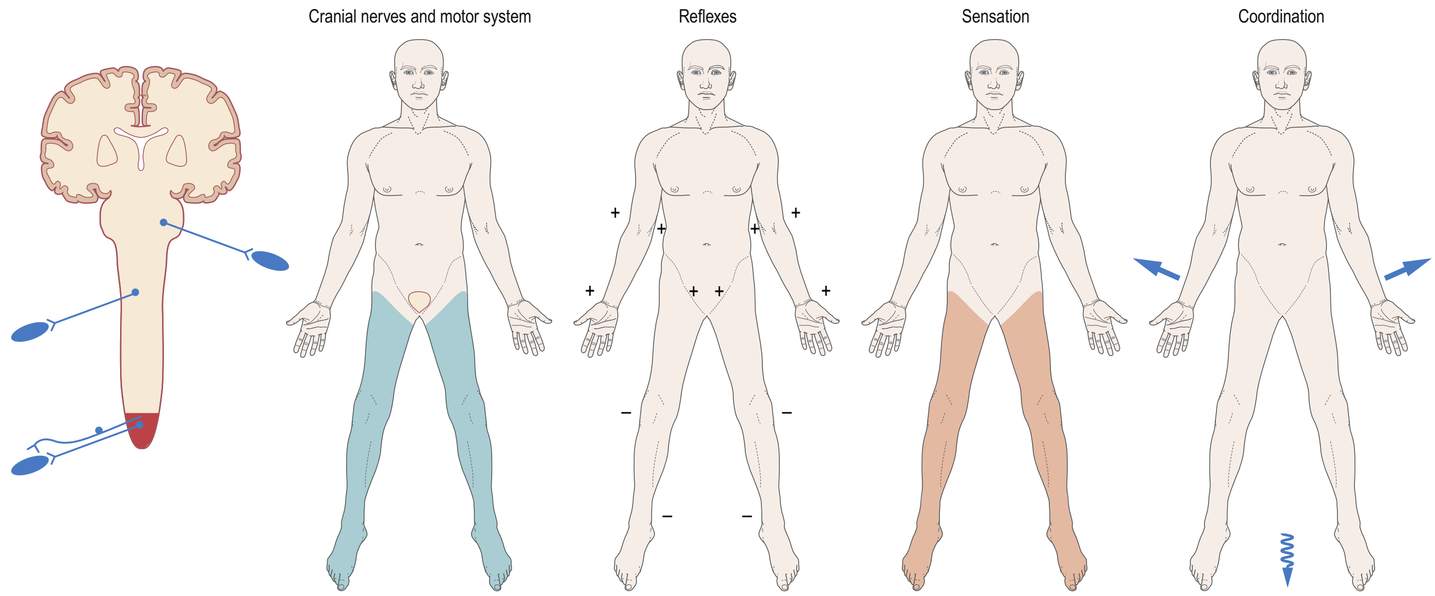

Lumbar cord lesion

A lumbar cord lesion causes weakness, wasting and fasciculation of muscles, areflexia of the lower limbs (lower motor neurone lesion), incontinence, sensory loss below the level of the lesion and 'sensory' ataxia.

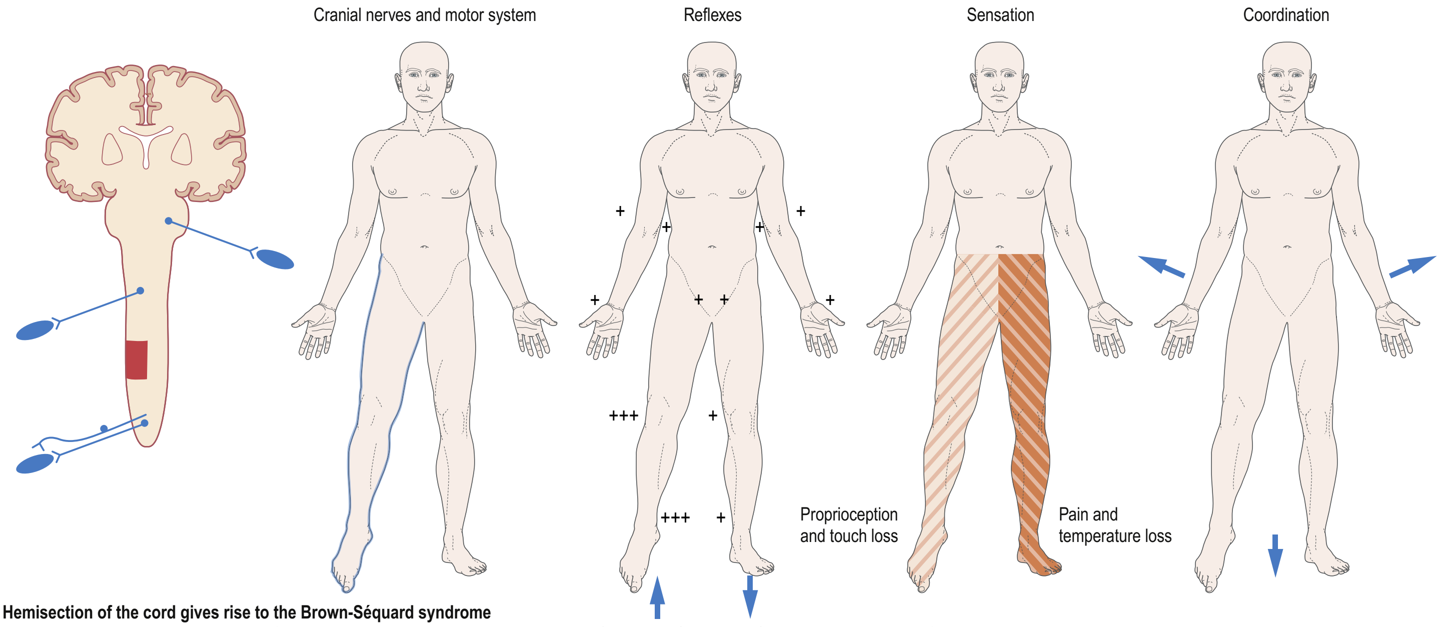
Cranial nerves and motor system
Reflexes
Sensation
Coordination
+
+
+
+
+
+
+ +
+++
+
+++
+
Proprioception and touch loss
Pain and temperature loss

Hemisection of the cord gives rise to the Brown-Séquard syndrome

This is characterized by ipsilateral loss of proprioception and upper motor neurone signs (hemiplegia/monoplegia) plus contralateral loss of pain and temperature sensation.

Fig. 27.18 cont'd—Lesions of the spinal cord. (Adapted with permission from Crossman AR, Neary D Neuroanatomy: An Illustrated Colour Text, 4th ed. Elsevier, Churchill Livingstone. Copyright 2010.)

Bonus e-book content

Boxes 27.1–27.5 Five brief case histories outlining aspects of complete transection of the spinal cord; hemisection of the spinal cord; anterior (ventral) cord syndrome; posterior (dorsal) cord syndrome; central cord syndrome.

Key references

Boyd IA, Gladden MH 1985 The Muscle Spindle. London: Macmillan.

A detailed classic review of the structure and function of muscle spindles.

Denk F, McMahon SB, Tracey I 2014 Pain vulnerability: a neurobiological perspective. Nat Neurosci 17:192–200.

A discussion of the potential mechanisms that have been proposed as underlying vulnerability and resilience towards developing chronic pain.

Guyton A, Hall J 2006 Cortical and brain stem control of motor function. In: Guyton A, Hall J (eds) Textbook of Medical Physiology. Philadelphia: Elsevier, Saunders, pp. 685–97.

A review of the function of the descending motor pathways, including the vestibulospinal and reticulospinal tracts.

Lemon RN 2008 Descending pathways in motor control. Ann Rev Neurosci 31:195–218.

An updated review of the function of the descending pathways.

Melzack R, Wall PD 1965 Pain mechanisms: a new theory. Science 150:971–9.

The original description of the gate theory of pain.

Nathan PW, Smith M, Deacon P 1996 Vestibulospinal, reticulospinal and descending propriospinal nerve fibres in man. Brain 119:1809–33.

An analysis of the vestibulospinal, reticulospinal and propriospinal pathways in humans, illustrating that these pathways are scattered throughout the ventral and lateral columns rather than forming discrete tracts.

Rexed B 1952 The cytoarchitectonic organization of the spinal cord in the cat. J Comp Neurol 96:415–95.

The original description of Rexed's laminae.

Todd A, Koerber R 2013 Neuroanatomical substrates of spinal nociception. In: McMahon S, Koltzenburg M, Tracey I et al (eds) Wall and Melzack's Textbook of Pain. Philadelphia: Elsevier, Saunders, pp. 77–93.

A review of the structure and function of the dorsal horn, with particular emphasis on its role in the modulation of pain.

References

Baker 2011 The primate reticulospinal tract, hand function and functional recovery. J Physiol 589: 5603–12.

Boyd IA, Gladden MH 1985 The Muscle Spindle. London: Macmillan.

A detailed classic review of the structure and function of muscle spindles.

Braz J, Solorzano C, Wang X et al 2014 Transmitting pain and itch messages: a contemporary view of the spinal cord circuits that generate gate control. Neuron 82:522–36.

Bushnell MC, Čeko M, Low LA 2013 Cognitive and emotional control of pain and its disruption in chronic pain. Nat Rev Neurosci 14:502–11.

Denk F, McMahon SB, Tracey I 2014 Pain vulnerability: a neurobiological perspective. Nat Neurosci 17:192–200.

A discussion of the potential mechanisms that have been proposed as underlying vulnerability and resilience towards developing chronic pain.

Devor M 2013 Neuropathic pain: pathophysiological response of nerves to injury. In: McMahon SB, Koltzenburg M, Tracey I et al (eds) Wall and Melzack's Textbook of Pain, 6th ed. Philadelphia: Elsevier, Saunders; Ch. 61, pp. 861–88.

Espinosa-Medina I, Saha O, Boismoreau F et al 2016 The sacral autonomic outflow is sympathetic. Science 354:893–7.

Espinosa-Medina I, Saha O, Boismoreau F et al 2017 The 'sacral parasympathetic': ontogeny and anatomy of a myth. Clin Auton Res 28:13–21.

Guyton A, Hall J 2006 Cortical and brain stem control of motor function. In: Guyton A, Hall J (eds) Textbook of Medical Physiology. Philadelphia: Elsevier, Saunders, pp. 685–97.

A review of the function of the descending motor pathways, including the vestibulospinal and reticulospinal tracts.

Horn JP 2018 The sacral autonomic outflow is parasympathetic: Langley got it right. Clin Auton Res 28:181–5.

Jenny A, Smith J, Decker J 1988 Motor organization of the spinal accessory nerve in the monkey. Brain Res 441:352–6.

Jessel TM, Sürmeli G, Kelly JS 2011 Motor neurons and the sense of place. Neuron 72:419–24.

Kiehn O 2016 Decoding the organisation of spinal circuits that control locomotion. Nature Rev Neurosci 17:224–38.

Krakauer JW, Carmichael ST 2017 Broken Movement. The Neurobiology of Motor Recovery after Stroke. Cambridge, MA: MIT Press.

Kuypers HGJM 1981 Anatomy of descending pathways. In: Brookhart JM, Mountcastle VB, Brooks VB et al (eds) Handbook of Physiology, vol. 2. Motor Control, pt 1. Bethesda, MD: American Physiology Society, pp. 597–666.

Lemon RN 2008 Descending pathways in motor control. Ann Rev Neurosci 31:195–218.

An updated review of the function of the descending pathways.

Ma Q 2010 Labeled lines meet and talk: population coding of somatic sensations. Clin Invest 120:3773–8.

Mai JK, Paxinos G 2011 The Human Nervous System, 3rd ed. Amsterdam: Elsevier, Academic Press.

Marani E, Schoen JHR 2005 A Reappraisal of the Ascending Systems in Man, with Emphasis on the Medial Lemniscus. Advances in Anatomy, Embryology and Cell Biology 179. Berlin: Springer.

Melzack R, Wall PD 1965 Pain mechanisms: a new theory. Science 150:971–9.

The original description of the gate theory of pain.

Mendell LM 2014 Constructing and deconstructing the gate theory of pain. Pain 155:210–16.

Minassian K, Hofstoetter US, Dzeladini F et al 2017 The human central pattern generator for locomotion: does it exist and contribute to walking? Neuroscientist 23:649–63.

Moayedi M, Davis KD 2013 Theories of pain: from specificity to gate control. J Neurophysiol 109:5–12.

Morecraft RJ, Ge J, Stilwell-Morecraft KS et al 2013 Terminal distribution of the corticospinal projection from the hand/arm region of the primary motor cortex to the cervical enlargement in Rhesus monkey. J Comp Neurol 521:4205–35.

A quantitative analysis of labelled corticospinal boutons in the monkey spinal grey matter.

Nathan PW, Smith M, Deacon P 1996 Vestibulospinal, reticulospinal and descending propriospinal nerve fibres in man. Brain 119:1809–33.

An analysis of the vestibulospinal, reticulospinal and propriospinal pathways in humans, illustrating that these pathways are scattered throughout the ventral and lateral columns rather than forming discrete tracts.

Orhan M, Saylam CY, Ikiz ZAA et al 2009 Connections between the accessory nerve and the posterior root of the first cervical nerve. Surg Radiol Anat 31:107–11.

Ossipov MH, Morimura K, Porreca F 2014 Descending pain modulation and chronification of pain. Curr Opin Support Palliat Care 8:143–51.

Parent A, Carpenter M 1996 Carpenter's Human Neuroanatomy. Baltimore: Williams & Wilkins.

Pierrot-Deseilligny E, Burke D 2005 The Circuitry of the Human Spinal Cord. Cambridge: Cambridge University Press.

Rathelot J-A, Strick PL 2009 Subdivisions of primary motor cortex based on cortico-motoneuronal cells. PNAS 106:918–23.

Rexed B 1952 The cytoarchitectonic organization of the spinal cord in the cat. J Comp Neurol 96:415–95.

The original description of Rexed's laminae.

Routal RV, Pal GP 2000 Location of the spinal nucleus of the accessory nerve in the human spinal cord. J Anat 196:263–8.

Saylam CY, Orhan M, Ikiz ZAA et al 2009 Connection types between the spinal root of the accessory nerve and the posterior roots of the C2–C6 spinal nerves. Surg Radiol Anat 31:419–23.

Schoen JHR 1964 Comparative aspects of the descending fibre systems in the spinal cord. Progr Brain Res 11:203–22.

Schoenen J, Faull RLM 1990 Spinal cord: cytoarchitectural, dendroarchitectural and myeloarchitectural organization. In: Paxinos G (ed) The Human Nervous System. San Diego: Academic Press, pp. 19–53.

Todd A, Koerber R 2013 Neuroanatomical substrates of spinal nociception. In: McMahon S, Koltzenburg M, Tracey I et al (eds) Wall and Melzack's Textbook of Pain. Philadelphia: Elsevier, Saunders, pp. 77–93.

A review of the structure and function of the dorsal horn, with particular emphasis on its role in the modulation of pain.

Zhang J, Cavanaugh DJ, Nemenov MI et al 2013 The modality-specific contribution of peptidergic and non-peptidergic nociceptors is manifest at the level of dorsal horn nociresponsive neurons. J Physiol 591:1097–110.

CHAPTER
28
Brainstem

The brainstem is situated in the posterior cranial fossa, where it faces the clivus and dorsum sellae ventrally and the cisterna magna, fourth ventricle and cerebellum dorsally (**Fig. 28.1**). It is approximately 6–7.5 cm in length and 3–4 cm in width at its widest portion. Its caudal border corresponds to the transverse plane immediately above the exit of the first cervical nerve roots. Its cephalic border is defined by the plane cutting through the caudal edge of the mammillary bodies, optic tracts and the posterior commissure. From caudal to cranial, the brainstem is divided into the medulla oblongata (myelencephalon), pons and midbrain (mesencephalon). The medulla oblongata, pons and midbrain each have a ventral portion (basis) and a dorsal portion (tegmentum): only the midbrain has a third portion, the tectum, dorsal to the tegmentum (**Fig. 28.2**) (Riley 1943, Mai and Paxinos 2012).

The brainstem contains numerous intrinsic neuronal cell bodies and their processes, some of which are the brainstem homologues of spinal cell groups. Some brainstem cell groups are the nuclei of cranial nerves and are concerned with the sensory, motor and autonomic innervation of the head and neck. Others give rise to autonomic (visceromotor) fibres that are distributed widely within the thorax and abdomen via branches of the vagus nerve. The brainstem also contains the reticular formation, a complex and sometimes ill-defined network of neurones that extends throughout its length, and is continuous caudally with its spinal counterpart (Olszewski and Baxter 1954, Haines and Mihailo 2018). Some reticular nuclei are referred to as vital centres because they are concerned with regulation of cardiac and respiratory activities; other parts of the reticular formation are essential for cerebral cortical arousal and the maintenance of consciousness, or are involved in the regulation of muscle tone, posture and reflex activities. The brainstem is the site of origin and/or termination of numerous ascending and descending fibres and is traversed by many others. The anterolateral system (spinal lemniscus), medial lemniscus and the trigeminothalamic tracts all ascend through the brainstem to reach the thalamus. Prominent corticospinal projections descend through the brainstem and corticonuclear projections end within it.

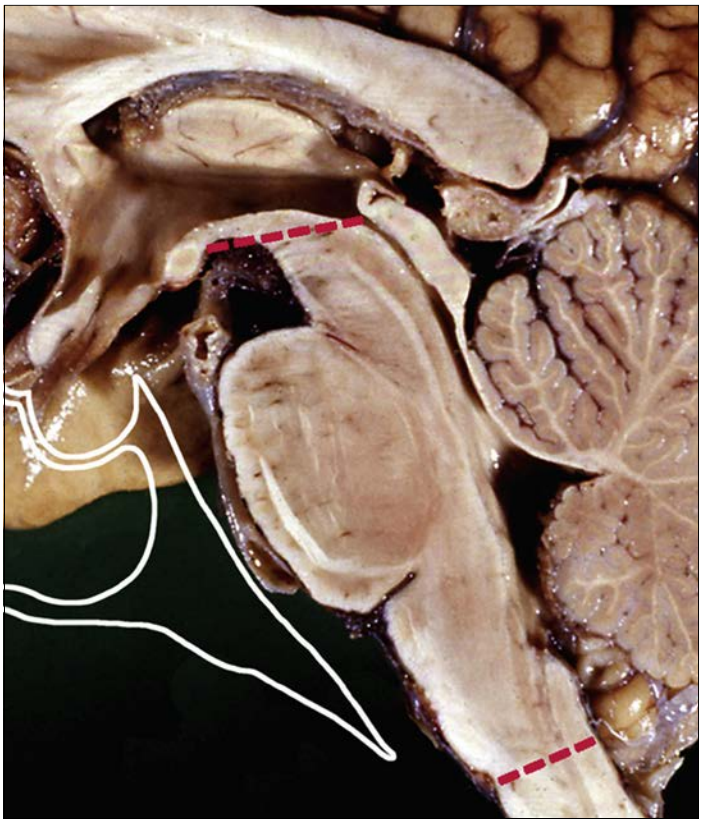

Fig. 28.1 A midline sagittal section through the brainstem delineating the lower and upper borders of the brainstem (dashed red lines) and the relative proportions of the medulla, pons and midbrain. The bony clivus, pituitary fossa and sphenoidal sinus are diagrammed in white.

Because the brainstem is so compact, structurally and functionally, even small lesions can destroy vital centres, disconnect forebrain motor areas from motor neurones in the brainstem and spinal cord, and sever incoming sensory fibres from higher centres of consciousness, perception and cognition. Clinically, irreversible cardiac and respiratory arrest often follows complete destruction of the respiratory and cardiac centres in the medulla. Damage to substantial portions of the reticular system bilaterally may cause coma. Damage to the ventral pons bilaterally may cause the ‘locked in’ syndrome, where interruption of motor function causes total paralysis and inability to speak, despite maintenance of consciousness. Accurate anatomical knowledge of brainstem anatomy is essential to reach a correct diagnosis and determine proper patient management.

OVERVIEW OF CRANIAL NERVES AND THEIR NUCLEI

The cranial nerves are the routes by which the brain receives information directly from, and controls the functions of, structures that are located mainly, although not exclusively, within the head and neck. All but three of the 12 pairs of cranial nerves are regarded as being attached to the brainstem, the exceptions being the olfactory, optic and accessory nerves.

The 12 pairs of cranial nerves are individually named and are numbered (using Roman numerals) from rostral to caudal, reflecting the order in which they emerge from the brain (see Table 24.1). The olfactory nerve (I) arises from the olfactory epithelium in the nasal cavity (see Fig. 39.13) and terminates directly in cortical and subcortical areas of the frontal and temporal lobes; it is closely associated functionally with the limbic system and is described in that context. The axons of the optic nerve (II) pass into the optic chiasma, where medially positioned axons decussate; all of the axons emerge as the optic tract, which terminates in the lateral geniculate nucleus of the thalamus (the visual pathways are discussed in Chapter 45). The oculomotor (III) and trochlear (IV) nerves arise in, and emerge from the midbrain. The trigeminal nerve (V) emerges from the pons, medial to the middle cerebellar peduncle. The abducens (VI), facial (VII) and vestibulocochlear (VIII) nerves emerge from the brainstem at, or close to, the pontomedullary junction. The glossopharyngeal (IX), vagus (X), cranial accessory (XI_{cr}) and hypoglossal (XII) nerves all emerge from the medulla. The spinal accessory nerve (XI_{sp}) arises from cervical levels C1–C5/C6.

Cranial nerves III–X, XI_{cr} and XII are associated with brainstem cell groupings referred to collectively as the cranial nerve nuclei (**Fig. 28.3**). The latter are either the origin of efferent cranial nerve fibres or the site of termination of cranial nerve or descending cerebral cortical afferents. They are considered to be organized into discontinuous longitudinal cell columns corresponding to columns that may be identified in the embryo.

MEDULLA OBLONGATA

The medulla oblongata (myelencephalon or bulb) is the most caudal part of the brainstem and is demarcated from the pons by a transverse plane that cuts through the transverse pontine sulcus ventrally and the striae medullares on the floor of the fourth ventricle dorsally. It is approximately 2.5–3.5 cm in length, about 1.5 cm wide at the level of the olives, and 2–2.5 cm wide at the greatest expanse of the inferior cerebellar peduncles. The medulla oblongata occupies the anterior space of the low posterior fossa and the foramen magnum: its ventral

The accessory nerve is conventionally described as having a cranial root composed of a variable number of small rootlets that emerge from the postolivary groove of the dorsolateral medulla, caudal to the rootlets of the vagus, and a spinal root composed of fibres derived from the cervical segments of the spinal cord. The cranial rootlets carry axons of motor neurones located in the caudal part of the nucleus ambiguus, and the spinal rootlets carry axons of motor neurones located in a nucleus in the ventral horn of the cervical spinal cord in line with the nucleus ambiguus. The spinal root ascends the vertebral canal and enters the skull via the foramen magnum. The cranial and spinal roots join, either before or within the jugular foramen, and the bundle so formed then divides into internal and external branches on leaving the jugular foramen. The internal branch joins the vagus nerve and its fibres innervate branchiomeric muscles via the pharyngeal and laryngeal branches of the vagus nerve. The external branch descends into the neck to innervate sternocleidomastoid and the upper and middle fibres of trapezius. There is an alternative view that the cranial root is anatomically and functionally part of the vagus nerve, and that the spinal root is the *de facto* accessory nerve. Paradoxically, meticulous cadaveric dissection studies, often undertaken stereomicroscopically, have failed to reach a consensus, finding either no connections between rootlets arising from the dorsolateral medulla and the spinal root of the accessory nerve because the cranial root was absent, or significant variations in the arrangement and size of plexiform connections between the cranial rootlets and the spinal root. Plexiform interconnections between neighbouring cranial nerves are not uncommon and are certainly not confined to the accessory and vagus nerves (Shoja et al 2014); their functional significance is often uncertain. (For further reading, see Krammer et al (1987), Lachman et al (2002), Ryan et al (2007), Wiles et al (2007), Benninger and McNeil (2010), Skinner (2011), Liu et al (2014), Tubbs et al (2014).)

The three columns that are derived from the basal plate of the neural tube are motor in function and include, from ventromedial to dorsolateral, general somatic efferent (GSE), special visceral efferent (SVE) and general visceral efferent (GVE) columns. The four columns derived from the alar plate of the neural tube are sensory in function and include, from ventral to dorsal, general visceral afferent (GVA), special visceral afferent (SVA), general somatic afferent (GSA) and special somatic afferent (SSA) (see Table 24.1 and Ch. 14). In humans, the general and special visceral afferent columns are united into the single nucleus of the solitary tract (Nieuwenhuys et al 2008).

The sensory nucleus of the trigeminal nerve, which extends throughout the length of the brainstem and into the cervical spinal cord, represents a general somatic afferent (GSA) cell column (Olszewski 1950, Haines 2015, Haines and Mihailo 2018). Its principal afferents are carried in the trigeminal nerve. General visceral afferents (GVA) carried by the facial, glossopharyngeal and vagus nerves end in the nucleus solitarius of the medulla. The special somatic afferent (SSA) column corresponds to the vestibular and cochlear nuclei, which are located beneath the vestibular area of the floor of the fourth ventricle.

The general somatic efferent (GSE) cell column consists of four nuclei that lie near the midline and give rise to motor fibres that run in nerves of the same name. From rostral to caudal, these are the oculomotor, trochlear and abducens nuclei, which innervate the extraocular muscles, and the hypoglossal nucleus, which innervates all but one of the muscles of the tongue. The general visceral efferent, or parasympathetic, (GVE) cell column is made up of the Edinger–Westphal preganglionic nucleus of the midbrain, the salivatory nuclei of the pons and the vagal nucleus of the medulla. Cells in the special visceral efferent (SVE) column innervate muscles derived from the branchial arches and lie in the trigeminal motor nucleus, the facial nucleus and the nucleus ambiguus.

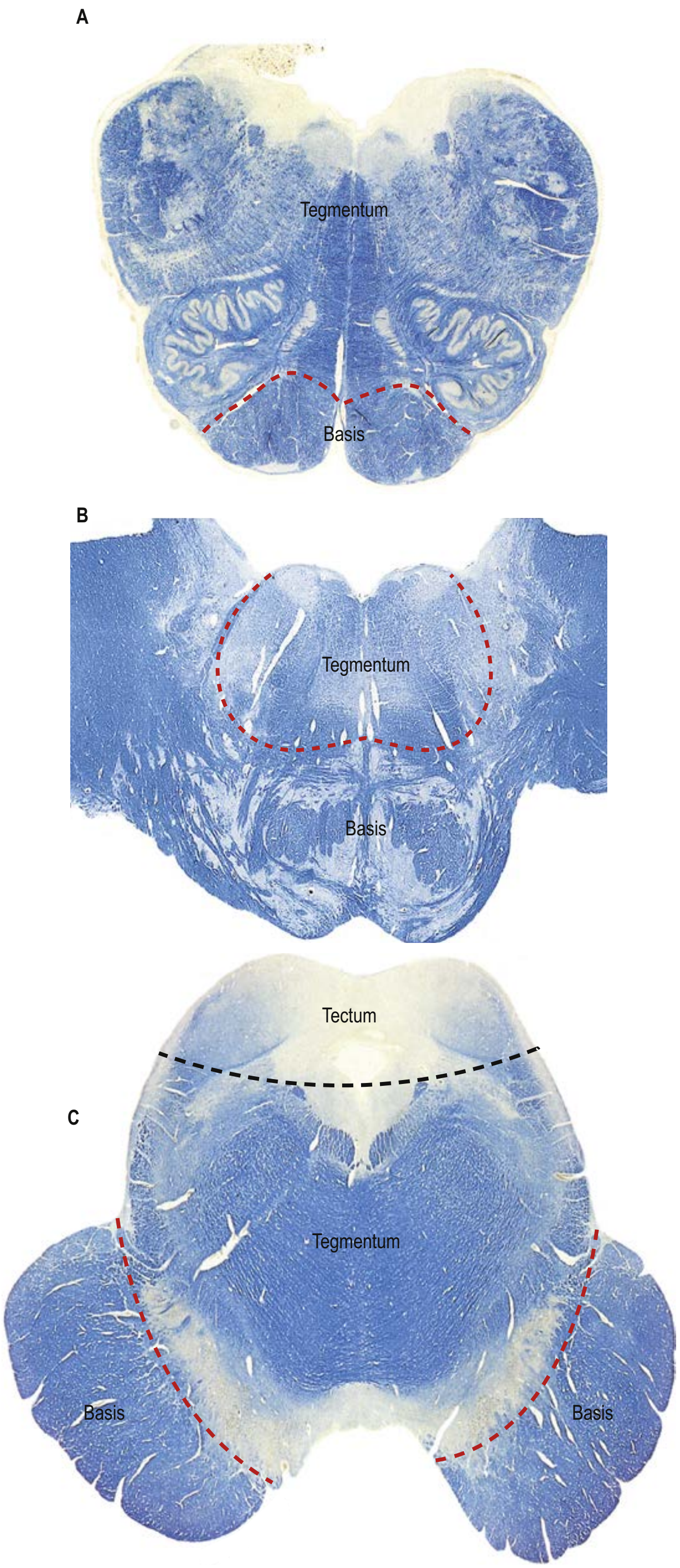

Fig. 28.2 The three ventrodorsal tiers of the brainstem, transverse histological sections prepared using Luxol fast blue stain for myelinated nerve fibres (blue). **A**, Medulla. **B**, Pons. **C**, Midbrain. The demarcation (dashed red lines) between the basis and the tegmentum lies along the dorsal surface of the pyramids in the medulla (**A**), along the ventral surface of the medial lemnisci in the pons (**B**) and along the ventral surface of the substantia nigra in the midbrain (**C**).

surface is separated from the inferior clivus (basilar part of the occipital bone) and apex of the dens by the meninges and occipito-axial ligaments. Dorsally and laterally, the inferior half of the medulla faces the overlying cerebellum and the CSF within the cisterna magna (a subarachnoid cistern between the cerebellar hemispheres). The superior medulla forms the caudal part of the floor of the fourth ventricle. The glossopharyngeal, vagus, (cranial) accessory and hypoglossal nerves either emerge from or enter the medulla.

External features and relations

The ventral and dorsal surfaces of the medulla (Figs 28.4–28.5) possess a longitudinal median fissure and sulcus respectively, which are continuous with their spinal counterparts. Caudally, the ventral (anterior) median fissure is interrupted by the obliquely crossing fascicles of the motor decussation (pyramidal decussation). Rostrally, the fissure ends at the pontine border in a diminutive depression, the foramen caecum. A prominent elongated ridge, the pyramid, which contains descending corticospinal axons, lies immediately lateral to the ventral median fissure. The lateral margin of the pyramid is indicated by a shallow ventrolateral sulcus: the rootlets of the hypoglossal nerve emerge from this sulcus in line with the ventral spinal nerve roots. The abducens nerve emerges at the caudal border of the pons generally in line with the rootlets of the hypoglossal nerve. Caudally, most fibres of the pyramid taper, decussate and enter the lateral funiculus of the spinal cord. The olive forms an oval prominence lateral to the pyramid and the ventrolateral sulcus: it contains the inferior olivary nuclear complex (see Fig. 28.4). Lateral to the olive, the glossopharyngeal and vagus nerves emerge from the brainstem along the posterolateral sulcus, in line with the dorsal spinal nerve roots.

The spinal central canal extends into the caudal half of the medulla, migrating progressively more dorsally until it opens out into the lumen of the fourth ventricle at the obex. This divides the medulla into a caudal closed part, in which the central canal is surrounded by neural tissue, and a rostral open part, in which the central canal opens into the caudal floor or medullary triangle of the fourth ventricle (see Fig. 28.5). The inferior cerebellar peduncles form the lateral walls of the medullary triangle and the striae medullares mark its upper end.

In the closed part of the medulla, a shallow dorsal intermediate sulcus on either side of the dorsal median sulcus that is continuous with its cervical spinal counterpart, indicates the location of the dorsal columns (fasciculi gracilis and cuneatus). The fasciculus gracilis terminates superiorly in the gracile tubercle and the fasciculus cuneatus terminates superiorly in the cuneate tubercle. The restiform body lies dorsolaterally in the medulla, forming a rounded ridge between the caudal part of the fourth ventricle and the glossopharyngeal and vagal rootlets on each side. It contains a wide variety of fibres (dorsal spinocerebellar, cuneocerebellar, olivocerebellar, reticulocerebellar and other cerebellar afferents). The restiform bodies on the two sides diverge and incline to enter the cerebellar hemispheres as the major component of the inferior cerebellar peduncles. Rostrally, in the open portion of the medulla, the dorsal surface of the medulla is demarcated from medial to lateral by the hypoglossal trigone, the sulcus limitans, the vagal trigone, the medullary vestibular area containing portions of the medial and inferior vestibular nuclei, and the dorsal aspect of the inferior cerebellar peduncle. The area postrema lies just inferior to the vagal trigone. The lateral recess of the fourth ventricle opens into the cerebellopontine angle cistern through the lateral aperture of Luschka and conveys a tuft of choroid plexus into the cistern. Inferiorly, the peduncles converge to form a deep 'V', the most caudal point of which, the obex, marks the transition from the fourth ventricle to the central canal of the lower medulla.

Internal organization

Transverse section of the medulla at the level of the motor (pyramidal) decussation

In the inferior medulla, the anatomical configuration typical of the spinal cord is modified to accommodate the intrinsic nuclei and fibres of the brainstem. The continuity between the ventral grey column and central grey matter that is maintained throughout the spinal cord is disturbed by corticospinal fibres crossing in the motor (pyramidal) decussation to reach the contralateral lateral funiculi (Fig. 28.6). As corticospinal fibres leave the anterior funiculi to enter the decussation, the pyramids progressively reduce in volume. At this level, the ventral grey column is subdivided into the supraspinal nucleus (the efferent source of the first cervical nerve and continuous rostrally with the nucleus of the hypoglossal nerve), and the nucleus of the accessory nerve (in line rostrally with the nucleus ambiguus). These nuclei are surrounded by the ventral corticospinal tract medioventrally and the ventral and dorsal spinocerebellar tracts dorsolaterally.

The dorsal grey column is also modified at this level as the nucleus gracilis appears in the ventral part of the fasciculus gracilis. The nucleus gracilis begins caudal to the nucleus cuneatus and both nuclei lie ventral to their corresponding fasciculi. The spinal nucleus and tract of the trigeminal nerve are visible lateral to the dorsal grey

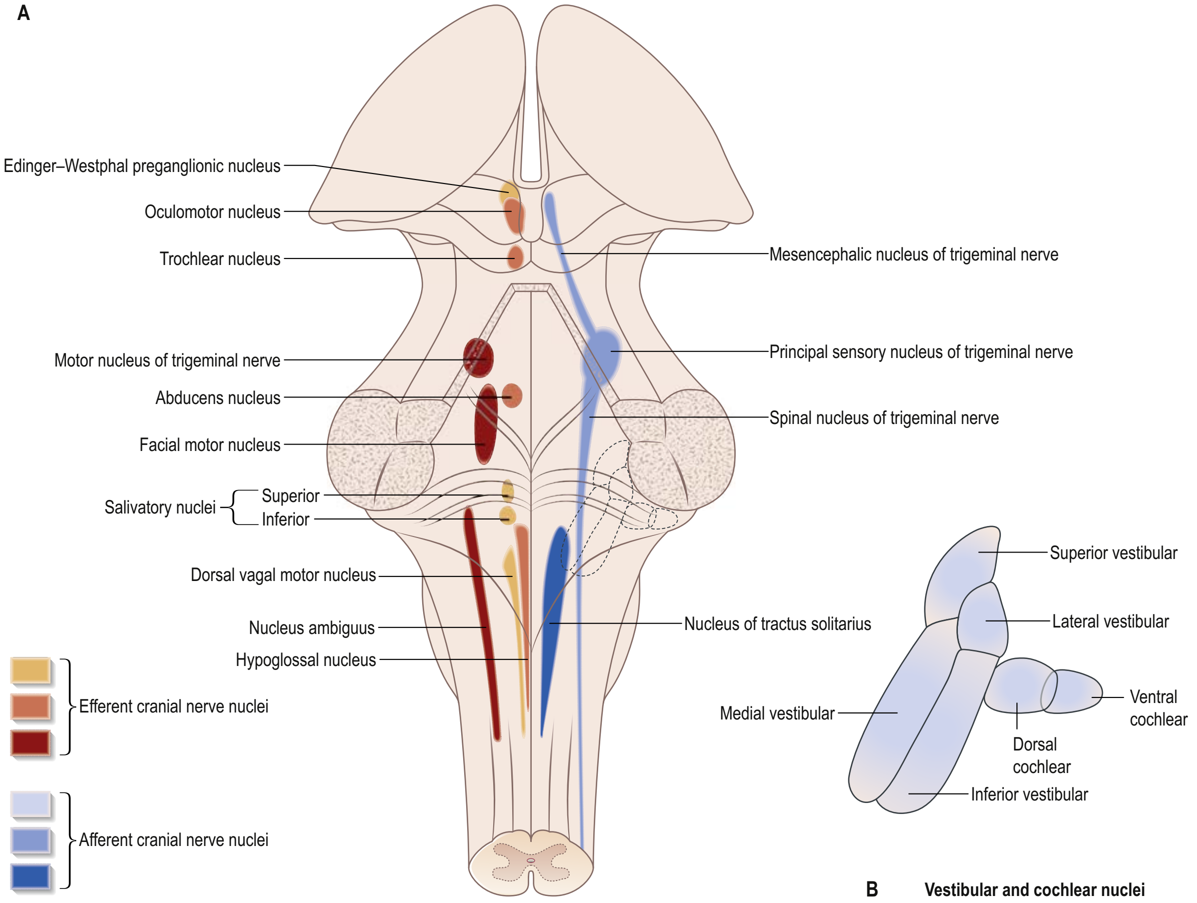
A
Edinger–Westphal preganglionic nucleus
Oculomotor nucleus
Trochlear nucleus
Motor nucleus of trigeminal nerve
Abducens nucleus
Facial motor nucleus
Salivatory nuclei
Superior
Inferior
Dorsal vagal motor nucleus
Nucleus ambiguus
Hypoglossal nucleus
Efferent cranial nerve nuclei
Afferent cranial nerve nuclei
Mesencephalic nucleus of trigeminal nerve
Principal sensory nucleus of trigeminal nerve
Spinal nucleus of trigeminal nerve
Nucleus of tractus solitarius
Superior vestibular
Lateral vestibular
Medial vestibular
Ventral cochlear
Dorsal cochlear
Inferior vestibular
B Vestibular and cochlear nuclei

Fig. 28.3 **A**, The cranial nerve nuclei. The components of the vestibular and cochlear nuclei are indicated by the dotted lines. **B**, The components of the vestibular and cochlear nuclei shown in more detail.

columns and are continuous with the substantia gelatinosa and tract of Lissauer of the spinal cord, respectively.

Transverse section of the closed medulla at the level of the sensory decussation of the dorsal column–medial lemniscus system

A transverse section of the closed medulla at the level of the sensory decussation (Fig. 28.7) again displays the dorsal median sulcus, the fasciculus and nucleus gracilis, the dorsal intermediate sulci, and the fasciculus and nucleus cuneatus. First-order afferent fibres contained within the fasciculi gracilis and cuneatus synapse on neurones in their respective nuclei (Millar and Basbaum 1975). Second-order axons emerge from these nuclei as internal arcuate fibres that curve ventrally around the central grey matter toward the midline. Ventral to the central canal, the internal arcuate fibres cross the midline as the sensory decussation and aggregate into the medial lemniscus that ascends from the sensory decussation as a flattened tract near the median raphe. At this level the medial lemniscus lies near the midline, just dorsal to the medial aspect of the pyramid. The inferior olivary complex is just becoming visible lateral to the medial lemniscus and dorsal to the pyramid. The internal arcuate fibres separate the spinal nucleus and tract of the trigeminal nerve from the central grey matter, which is gradually replaced by the inferior tips of the hypoglossal nucleus and the dorsal motor nucleus of the vagus. The fibres of the dorsal spinocerebellar tract now cover over the spinal tract of the trigeminal nerve as they move dorsally. The ventral spinocerebellar tract ascends along the anterolateral surface of the medulla. The reticular formation lies ventromedial to the spinal trigeminal nuclei. The corticospinal tract lies ventrally, and the medial longitudinal fasciculus and the tectospinal tract lie dorsally.

Transverse sections of the medulla at the level of the caudal end of the fourth ventricle and at the level of the striae medullares

The total area of grey matter in the transverse sections through the upper medulla and fourth ventricle is increased by the presence of the nuclei of the vestibulocochlear, glossopharyngeal and vagus nerves dorsally and by the appearance of the inferior olivary nuclear complex, composed of the principal olivary nucleus and the smaller dorsal and medial accessory olivary nuclei (Figs 28.8–28.9). The central canal merges into the fourth ventricle. At this level, the central grey matter forms the floor of the ventricle: from medial to lateral, it contains the hypoglossal nucleus covered by the myelinated dorsal longitudinal fasciculus, the dorsal motor nucleus of the vagus, the salivatory nuclei, the nucleus and tractus solitarius and the caudal ends of the inferior and medial vestibular nuclei. The dorsal and ventral cochlear nuclei lie along the dorsal and lateral contour of the dorsal medulla. The dorsal lateral border is formed by the restiform body that conveys afferent fibres, including the dorsal spinocerebellar and olivocerebellar tracts, to the cerebellum. The spinal trigeminal nucleus and tract, the nucleus ambiguus and the reticular formation lie ventromedial to the restiform body. Further ventrally, the ventral spinocerebellar, lateral spinothalamic and rubrospinal tracts lie along the anterolateral border of the medulla, dorsal to the olivary complex and the pyramid (Nathan and Smith 1982).

The bulge of the olive on the ventrolateral aspect of the medulla is formed by the principal olivary nucleus which receives the descending fibres of the central tegmental tract. The olive is delimited by the pre-olivary sulcus ventrally and retro-olivary sulcus dorsally. The principal olivary nucleus appears as an irregularly crenated ‘C-shaped’ mass of grey matter with a medially directed hilum. Olivocerebellar fibres emerge from the hilum, course across the full transverse extent of the medulla as olivocerebellar fibres, and aggregate into the major component of the contralateral restiform body (Fig. 28.10). The rootlets of the vestibular nerve emerge inferior to the inferior cerebellar peduncle; the rootlets of the glossopharyngeal, vagus and accessory nerves emerge at the retro-olivary sulcus; the rootlets of the hypoglossal nerve run ventrally between the medial accessory and principal olivary nuclei to emerge at the pre-olivary sulcus, between the olive and the pyramid.

Pathways and nuclei of the medulla

Corticospinal and corticonuclear tracts

The corticospinal and corticonuclear tracts arise in the cerebral hemispheres, traverse the corona radiata and pass through the posterior limb and genu, respectively, of the internal capsule. At the level of the

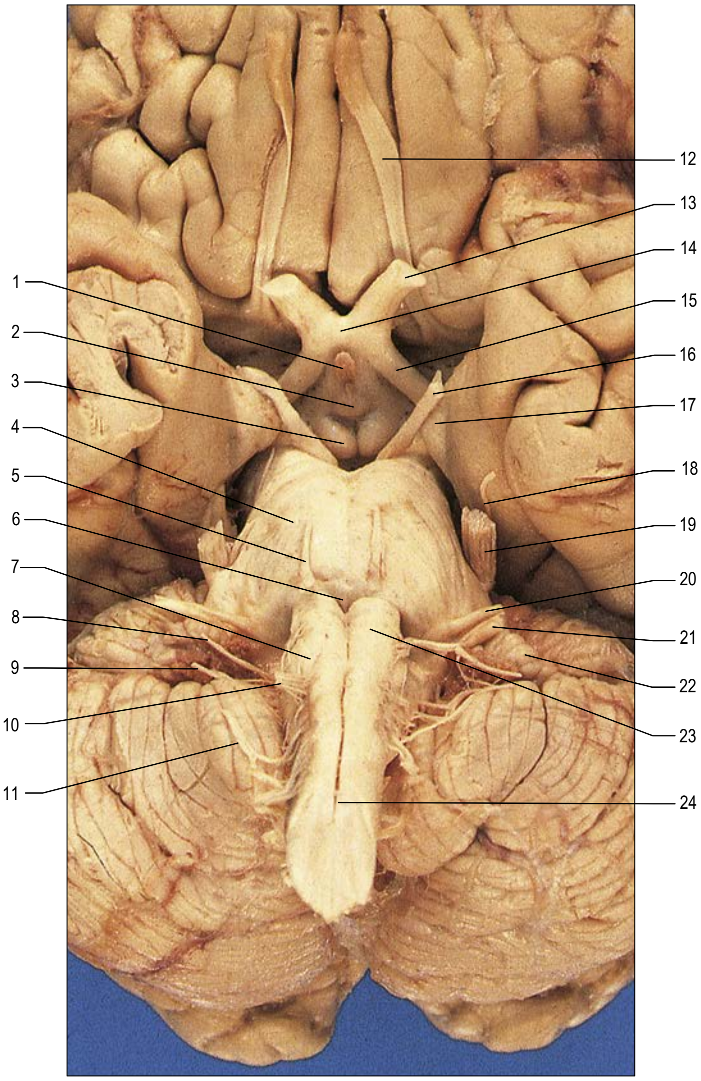

Fig. 28.4 The ventral aspect of the brainstem. Key: 1, infundibulum; 2, tuber cinereum; 3, mammillary body; 4, basilar pons; 5, abducens nerve; 6, foramen caecum; 7, olive; 8, glossopharyngeal nerve; 9, vagus nerve; 10, rootlets of hypoglossal nerve; 11, accessory nerve; 12, olfactory tract; 13, optic nerve; 14, optic chiasma; 15, optic tract; 16, oculomotor nerve; 17, uncus; 18, trochlear nerve; 19, trigeminal nerve; 20, facial nerve; 21, vestibulocochlear nerve; 22, flocculus; 23, pyramid; 24, motor decussation (decussation of pyramids).

cerebral peduncles these fibres assemble into compact tracts that descend through the midbrain, pons and medulla. Corticonuclear fibres terminate within the motor nuclei of the brainstem. In the medulla, the corticonuclear (corticobulbar) fibres project to the nucleus ambiguus and the hypoglossal nucleus: these projections are predominantly contralateral.

The corticospinal tract displays somatotopy at almost all levels of the brainstem: fibres representing the hand descend ventromedially and those representing the foot descend dorsolaterally. Corticospinal fibres continue caudally through the pyramids. Most decussate at this level and pass into the contralateral lateral column of the spinal cord as the crossed lateral corticospinal tract (Nathan et al 1990) (Ch. 27). The majority of corticospinal fibres cross the midline between the central grey matter and the ventral median fissure as the motor (pyramidal) decussation (see Fig. 28.6). Fibres to cervical levels cross first in the rostral part of the decussation, and fibres to lumbosacral levels cross more caudally. The corticospinal fibres that do not decussate here continue caudally into the ipsilateral anterior column of the spinal cord as the ventral corticospinal tract, lying just lateral to the ventral median fissure. Most of these fibres ultimately decussate within each cord segment and cross the ventral white commissure to reach the contralateral ventral horn: a small proportion of corticospinal fibres do not decussate at any level and terminate ipsilaterally.

Dorsal column nuclei and medial lemniscus system

The nuclei gracilis and cuneatus are part of the dorsal column–medial lemniscus pathway that is the major route for discriminative aspects of tactile and proprioceptive sensation (Millar and Basbaum 1975, Haines 2015). Sensory input concerning deformation of skin, movement of hairs, joint movement and vibration is conveyed by the ipsilateral fasciculi gracilis and cuneatus to the secondary neurones of their respective nuclei in the medulla. Afferents from the body inferior to approximately T6 ascend in the fasciculus gracilis to synapse in the nucleus gracilis; afferents from the body rostral to T6 ascend in the fasciculus cuneatus to synapse in the nucleus cuneatus (Miller and Burack 1982). The fibres display a somatotopic organization in the transverse plane: the sacral regions are represented dorsomedially in the nucleus gracilis and cervical regions are represented ventrolaterally in the nucleus cuneatus. The afferent fibres terminate somatotopically in the dorsal column nuclei. Caudal regions of the nuclei receive afferents from the most caudal dorsal root ganglia (i.e. nucleus gracilis from sacral and nucleus cuneatus from mid-thoracic ganglia) and rostral regions receive afferents from the most rostral dorsal root ganglia (i.e. nucleus gracilis from lower thoracic and nucleus cuneatus from cervical ganglia) (Ferraro and Barrera 1935).

A variety of control mechanisms can modulate the transmission of impulses through the dorsal column–medial lemniscus pathway. Descending afferents from the somatosensory cortex reach the nuclei through the corticonuclear tracts, and appear to be restricted to the upper reticular zones. These afferents modulate the transmission of impulses by both pre- and postsynaptic inhibitory mechanisms, and sometimes by facilitation. The reticular zones also receive modulatory afferents from the reticular formation and raphe nuclei.

Inferior cerebellar peduncle, restiform body and olivary complex

The inferior cerebellar peduncle forms the lateral wall of the medullary triangle of the fourth ventricle and the anterior rostral margin of the lateral recess of the fourth ventricle. The dorsal and ventral cochlear nuclei lie along the outer margin of the peduncle. The intramedullary portion of the inferior cerebellar peduncle is composed of the small juxtarestiform body medially and the larger restiform body laterally (see **Fig. 28.11**). The juxtarestiform body carries fibres to and from the vestibular nuclei. The lateral vestibular nucleus (of Deiter) lies within the juxtarestiform body. The restiform body carries afferent fibres to the cerebellum, including ascending fibres from the accessory cuneate nucleus in the cuneocerebellar tract; ascending fibres from the spinal cord in the dorsal spinocerebellar tract; crossed fibres from the contralateral inferior olivary system in the olivocerebellar tract; both crossed and uncrossed anterior external arcuate fibres in the anterior arcuatocerebellar tract; and fibres from the reticular nuclei of the lateral and anterior funiculi in the reticulocerebellar tract. The restiform body ascends medial to the middle cerebellar peduncle to enter the cerebellum further rostrally in the pons.

The cuneocerebellar tract is composed of posterior external arcuate fibres from the accessory cuneate nucleus situated dorsolateral to the cuneate nucleus. It is part of the spinocerebellar system of precerebellar relay nuclei and functions as the upper extremity counterpart of the posterior thoracic nucleus (nucleus thoracis, Clarke's column) (see Fig. 28.10). Proprioceptive impulses from muscle stretch receptors and cutaneous touch receptors in the upper limb that enter the spinal cord rostral to the posterior thoracic nucleus ascend through the lateral fibres of the fasciculus cuneatus to synapse in a somatotopic pattern on large neurones in the accessory cuneate nucleus. From there, fibres form the cuneocerebellar fasciculus that ascends through the ipsilateral restiform body to reach the cerebellum. A smaller number of accessory cuneate efferents cross the midline and ascend within the contralateral medial lemniscus to reach the thalamus (Nieuwenhuys et al 2008).

The dorsal (posterior) spinocerebellar tract carries proprioceptive impulses from muscle stretch receptors and cutaneous touch receptors for the lower extremities and trunk. Tract fibres originate from the ipsilateral posterior thoracic nucleus situated in the intermediate grey matter of the spinal cord (Rexed lamina VII). Sensory inputs entering from segments caudal to L3 first ascend in the fasciculus gracilis and then pass to the caudal end of the posterior thoracic nucleus where they synapse. Sensory information from more rostral segments, L3 to C8, enter with the segmental dorsal roots and pass directly to the posterior thoracic nucleus. Second-order afferent fibres originating from the posterior thoracic nucleus form the dorsal spinocerebellar tract which ascends ipsilaterally to the brainstem (see Fig. 28.10). Within the brainstem, the dorsal spinocerebellar tract ascends along the lateral surface of the caudal medulla, just ventral to the spinal trigeminal tract. It then passes dorsally and superiorly, external to and covering over, the spinal trigeminal tract, to enter the ipsilateral restiform body of the inferior cerebellar peduncle.

The extent and symmetry of decussation of the pyramids vary. In some adults, up to 30% of corticospinal fibres descend as uncrossed fibres that pass into the ipsilateral anterior (ventral) funiculus of the spinal cord (Nathan et al 1990). In human fetuses, the anterior tract was found to be highly variable in size, often asymmetric and even absent, unilaterally or bilaterally (Jin et al 2016). In three-quarters of corticospinal decussations, the fibres crossing from left to right decussated at a more rostral level than fibres decussating from right to left: fewer fibres descended uncrossed in the left anterior column (Nathan et al 1990). This asymmetry does not appear to correlate with handedness (Kertesz and Geschwind 1971).

The upper regions of both nuclei are reticular and contain small and large multipolar neurones with long dendrites. The lower regions contain clusters of large, round neurones with short and profusely branching dendrites. Upper and lower zones differ in their connections but both receive terminals from the dorsal spinal roots at all levels. Dorsal funicular fibres from neurones in the spinal grey matter are components of the postsynaptic dorsal column system and terminate only in the superior, reticular zone. Variable ordering and overlap of terminals, on the basis of spinal root levels, occur in both zones. The lower extremity is represented medially, the trunk ventrally and the digits dorsally. There is modal specificity, i.e. lower levels respond to low-threshold cutaneous stimuli, and upper reticular levels to inputs from fibres serving receptors in the skin, joints and muscles. The nucleus cuneatus is divided into several zones. Its middle zone contains a large pars rotunda, in which rostrocaudally elongated, medium-sized neurones are clustered between bundles of densely myelinated fibres. The reticular poles of its rostral and caudal zones contain scattered, but evenly distributed, neurones of various sizes. The pars triangularis is smaller and laterally placed.

The pattern of termination of cutaneous afferents is apparently somtatotopically organized for the pars rotunda and more diffuse in the reticular poles. Unit recording of the neurones in the dorsal column nuclei shows that their tactile receptive fields (i.e. the skin area in which a response can be elicited) vary in size. Especially small receptive fields appear to account for the great sensitivity found in the digits, the face and the lips. Some fields have excitatory centres and inhibitory surrounds, which means that stimulation just outside its excitatory field inhibits the neurone. In general, sensory modal specificity is high. Many cells receive input from one or a few specific receptor types, e.g. hair, type I and II slowly adapting receptors, and Pacinian corpuscles. Some cells respond to Ia muscle spindle input, or receive convergent input from tactile pressure and hair follicle receptors. Primary spinal afferents synapse directly onto multipolar neurones in nuclei that provide the major nuclear efferent projections. The nuclei also contain interneurones, many of which are inhibitory.

A group of neurones, designated nucleus Z, has been identified in animals between the upper pole of the nucleus gracilis and the inferior vestibular nucleus. This nucleus is said to be present in the human medulla. Collaterals of the dorsal spinocerebellar tract convey proprioceptive input from both lower extremities to Group Z neurones (Nieuwenhuys et al 2008). These neurones project efferents through internal arcuate fibres to the contralateral medial lemniscus.

The external surface of the pyramids displays a layer of neurones that are considered to be displaced pontine neurones and are designated collectively as the arcuate nucleus. These neurones give rise to anterior external arcuate (arcuatocerebellar) fibres that spread around the medulla, above and below the olivary eminence, enter the restiform body, traverse the inferior cerebellar peduncle and project mainly to the contralateral cerebellum (see Figs 28.7, 28.10). The arcuate nucleus also gives rise to the anterior internal arcuate fibres that course through the midline, decussate near the floor of the fourth ventricle, then turn laterally under the ependyma and enter the contralateral cerebellum as striae medullares of the fourth ventricle.

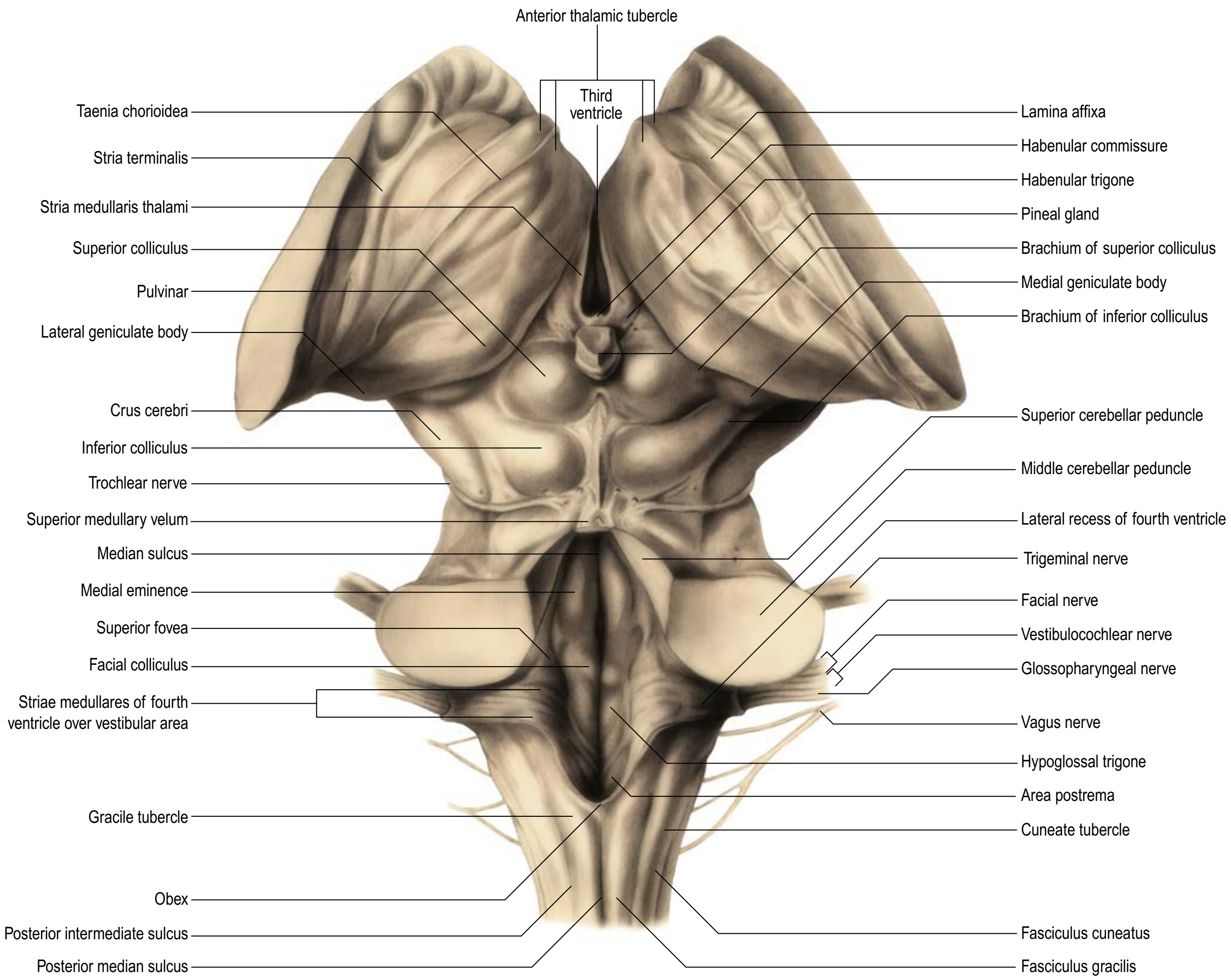
Anterior thalamic tubercle
Third ventricle
Taenia chorioidea
Stria terminalis
Stria medullaris thalami
Superior colliculus
Pulvinar
Lateral geniculate body
Crus cerebri
Inferior colliculus
Trochlear nerve
Superior medullary velum
Median sulcus
Medial eminence
Superior fovea
Facial colliculus
Striae medullares of fourth ventricle over vestibular area
Gracile tubercle
Obex
Posterior intermediate sulcus
Posterior median sulcus
Lamina affixa
Habenular commissure
Habenular trigone
Pineal gland
Brachium of superior colliculus
Medial geniculate body
Brachium of inferior colliculus
Superior cerebellar peduncle
Middle cerebellar peduncle
Lateral recess of fourth ventricle
Trigeminal nerve
Facial nerve
Vestibulocochlear nerve
Glossopharyngeal nerve
Vagus nerve
Hypoglossal trigone
Area postrema
Cuneate tubercle
Fasciculus cuneatus
Fasciculus gracilis

Fig. 28.5 The dorsal aspect of the brainstem: the floor of the fourth ventricle has been exposed by cutting the cerebellar peduncles and removing the cerebellum. (With permission from Neuroanatomy by FA Mettler (1948) 2nd edn; St Louis: The CV Mosby Company.)

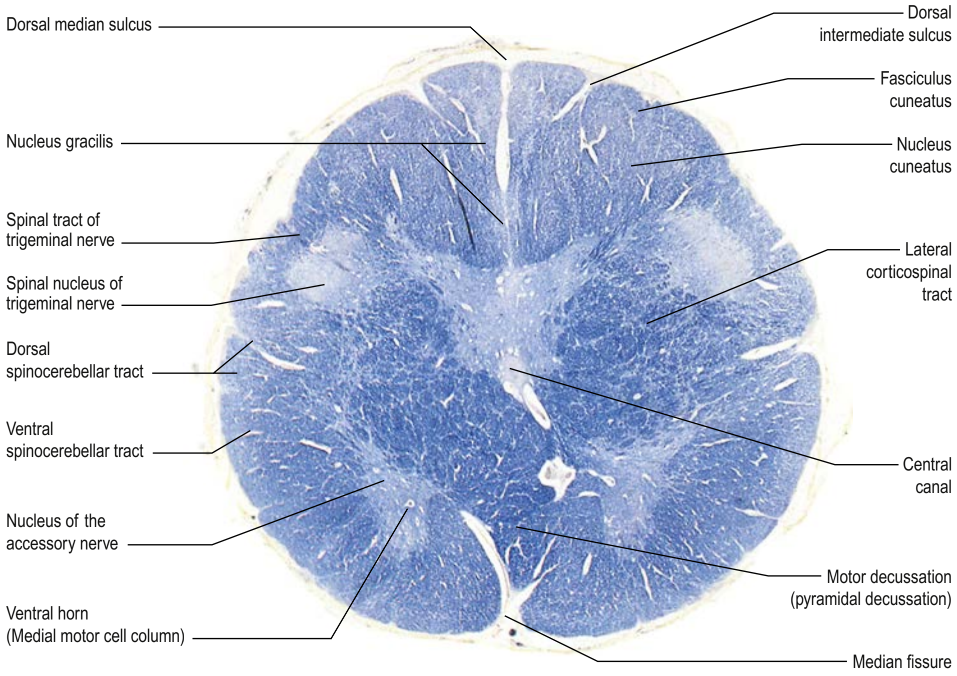
Dorsal median sulcus
Nucleus gracilis
Spinal tract of trigeminal nerve
Spinal nucleus of trigeminal nerve
Dorsal spinocerebellar tract
Ventral spinocerebellar tract
Nucleus of the accessory nerve
Ventral horn (Medial motor cell column)
Dorsal intermediate sulcus
Fasciculus cuneatus
Nucleus cuneatus
Lateral corticospinal tract
Central canal
Motor decussation (pyramidal decussation)
Median fissure

Fig. 28.6 A transverse section through the medulla oblongata at the level of the motor decussation, prepared using Luxol fast blue stain for myelinated nerve fibres (blue).

Inferior olivary complex

The inferior olivary complex is situated in the lateral portion of the ventral medulla at the level of the caudal end of the fourth ventricle. It consists of the large principal olivary nucleus and the smaller medial and dorsal accessory olivary nuclei (see Figs 28.7–28.9). They are also precerebellar nuclei, a group that includes the pontine, arcuate, vestibular, reticulocerebellar and spinocerebellar nuclei, all of which receive afferents from specific sources and project to the cerebellum. The principal olivary nucleus is an irregularly crenated cup of grey matter with

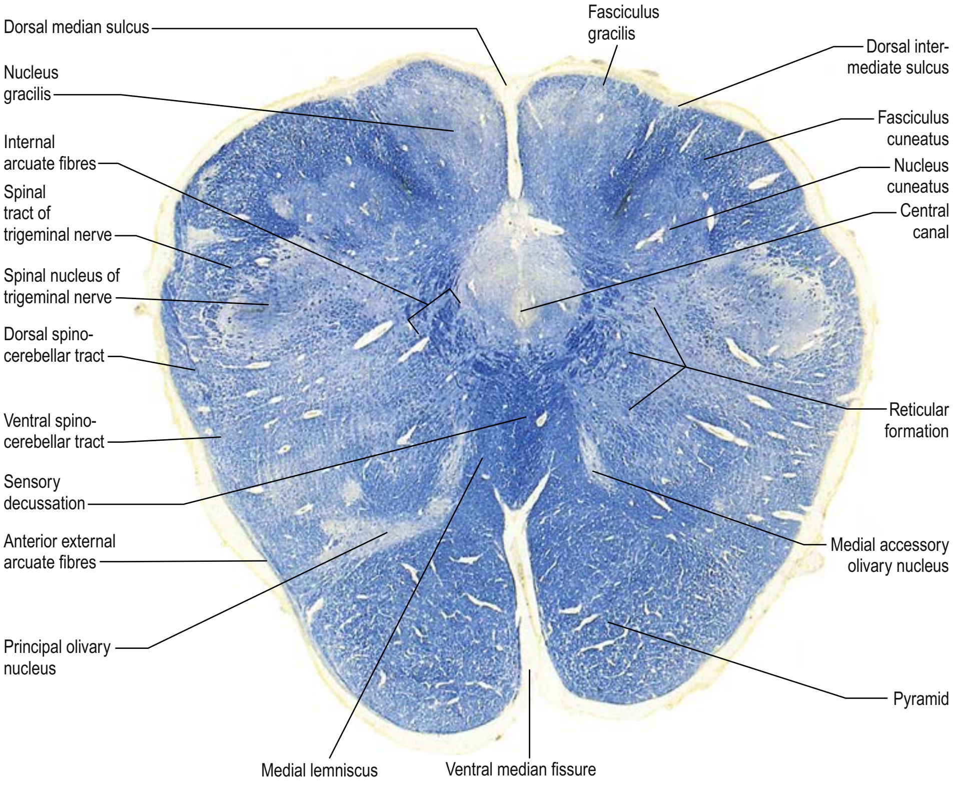
Dorsal median sulcus
Fasciculus gracilis
Nucleus gracilis
Dorsal inter-mediate sulcus
Internal arcuate fibres
Fasciculus cuneatus
Spinal tract of trigeminal nerve
Nucleus cuneatus
Central canal
Spinal nucleus of trigeminal nerve
Dorsal spino-cerebellar tract
Reticular formation
Ventral spino-cerebellar tract
Sensory decussation
Medial accessory olivary nucleus
Anterior external arcuate fibres
Principal olivary nucleus
Pyramid
Medial lemniscus
Ventral median fissure

Fig. 28.7 A transverse section through the medulla oblongata at the level of the sensory decussation, prepared using Luxol fast blue stain for myelinated nerve fibres (blue).

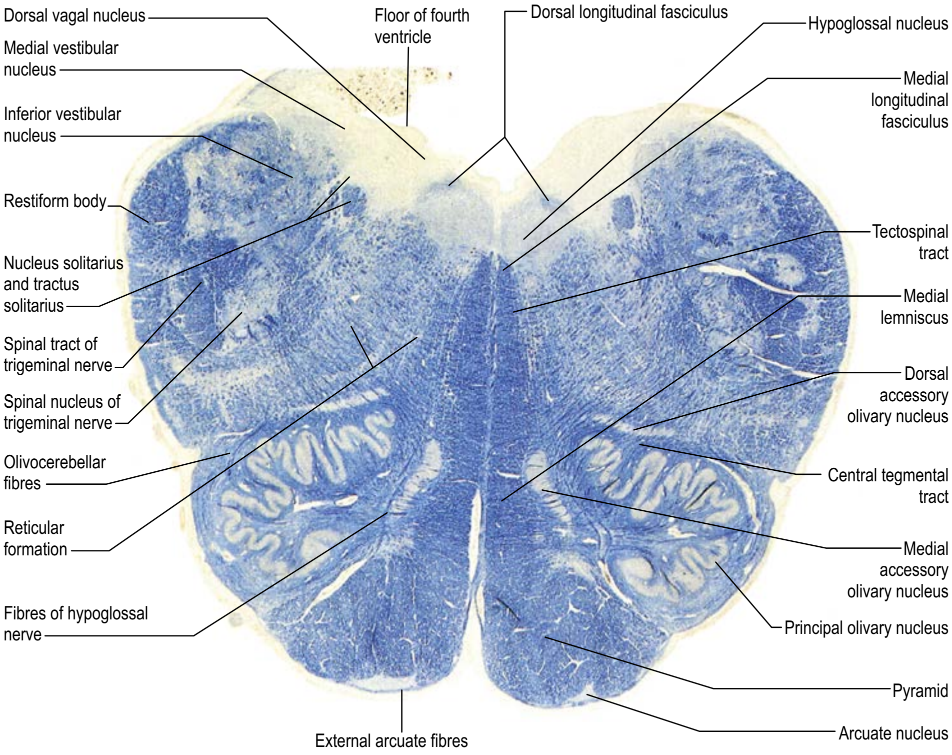
Dorsal vagal nucleus
Floor of fourth ventricle
Dorsal longitudinal fasciculus
Hypoglossal nucleus
Medial vestibular nucleus
Medial longitudinal fasciculus
Inferior vestibular nucleus
Restiform body
Tectospinal tract
Nucleus solitarius and tractus solitarius
Medial lemniscus
Spinal tract of trigeminal nerve
Dorsal accessory olivary nucleus
Spinal nucleus of trigeminal nerve
Olivocerebellar fibres
Central tegmental tract
Reticular formation
Medial accessory olivary nucleus
Fibres of hypoglossal nerve
Principal olivary nucleus
Pyramid
Arcuate nucleus
External arcuate fibres

Fig. 28.8 A transverse section through the medulla oblongata at the caudal end of the fourth ventricle, prepared using Luxol fast blue stain for myelinated nerve fibres (blue).

a medially directed hilum, through which numerous fibres enter and leave the nucleus.

The inferior olivary nuclei receive both ascending and descending afferent fibres. Ascending fibres, mainly crossed, arrive from all spinal levels via the spino-olivary tracts and via the dorsal columns. Descending ipsilateral afferents arrive from the cerebral cortex, cerebellar nuclei, thalamus, red nucleus and central grey matter of the midbrain. The afferent fibres from the red nucleus and the central mesencephalic grey matter are major components of the central tegmental tract.

Efferent fibres arise from small neurones of the principal olivary nucleus, most of which form the olivocerebellar tract. The olivocerebellar tract emerges primarily from the hilum of the olive and then sweeps medially across the medulla to enter the contralateral restiform body of the inferior cerebellar peduncle. In this course, the olivocerebellar fibres first cross through the medial lemniscus (see Fig. 28.8), then cross the midline, and pass dorsal to, or right through, the opposite olivary nuclei. They intersect the lateral spinothalamic and rubrospinal tracts and the spinal nucleus of the trigeminal nerve, and enter the contralateral restiform body (and eventually the inferior cerebellar peduncle), where they constitute its major component. Fibres from the contralateral inferior olivary complex terminate on Purkinje cells in the cerebellum as climbing fibres; there is a one-to-one relationship between Purkinje cells and neurones in the complex (Nieuwenhuys et al 2008).

Anterolateral system, including spinothalamic and spinoreticular tracts (spinal lemnisci)

The anterolateral fasciculus (anterolateral system) is a diffuse, composite pathway arising from different laminae of the spinal grey matter. Most of its fibres decussate in the anterior white commissure and ascend

The medial accessory olivary nucleus is a long curved lamina of grey matter, concave laterally, that is situated between the medial lemniscus and pyramid medially and the ventromedial aspect of the olivary nucleus laterally (see **Fig. 28.8**). In axial sections, the medial accessory olivary nuclei take the form of a right-angle, with a dorsal leg that is orientated sagittally and a ventral leg that is orientated transversely. The dorsal accessory olivary nucleus is a similar lamina, situated dorsomedial to the principal olivary nucleus. Both accessory nuclei are phylogenetically older than the principal olivary nucleus, and are connected with the paleocerebellum. In all connections, cerebral, spinal and cerebellar, the olivary nuclei display specific topographical organization (Ch. 29).

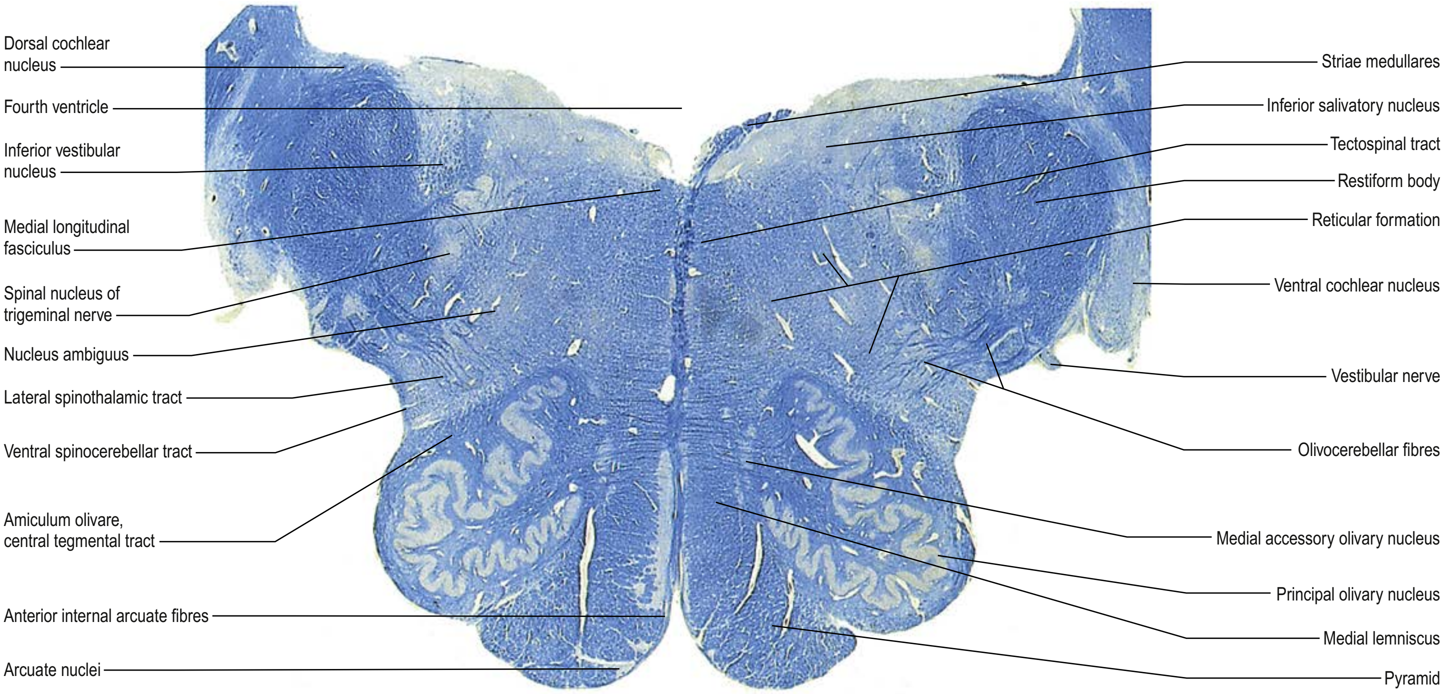
Dorsal cochlear nucleus
Fourth ventricle
Inferior vestibular nucleus
Medial longitudinal fasciculus
Spinal nucleus of trigeminal nerve
Nucleus ambiguus
Lateral spinothalamic tract
Ventral spinocerebellar tract
Amiculum olivare, central tegmental tract
Anterior internal arcuate fibres
Arcuate nuclei
Striae medullares
Inferior salivatory nucleus
Tectospinal tract
Restiform body
Reticular formation
Ventral cochlear nucleus
Vestibular nerve
Olivocerebellar fibres
Medial accessory olivary nucleus
Principal olivary nucleus
Medial lemniscus
Pyramid

Fig. 28.9 A transverse section through the superior half of the medulla oblongata at the level of the inferior olivary nucleus prepared using Luxol fast blue stain for myelinated nerve fibres (blue).

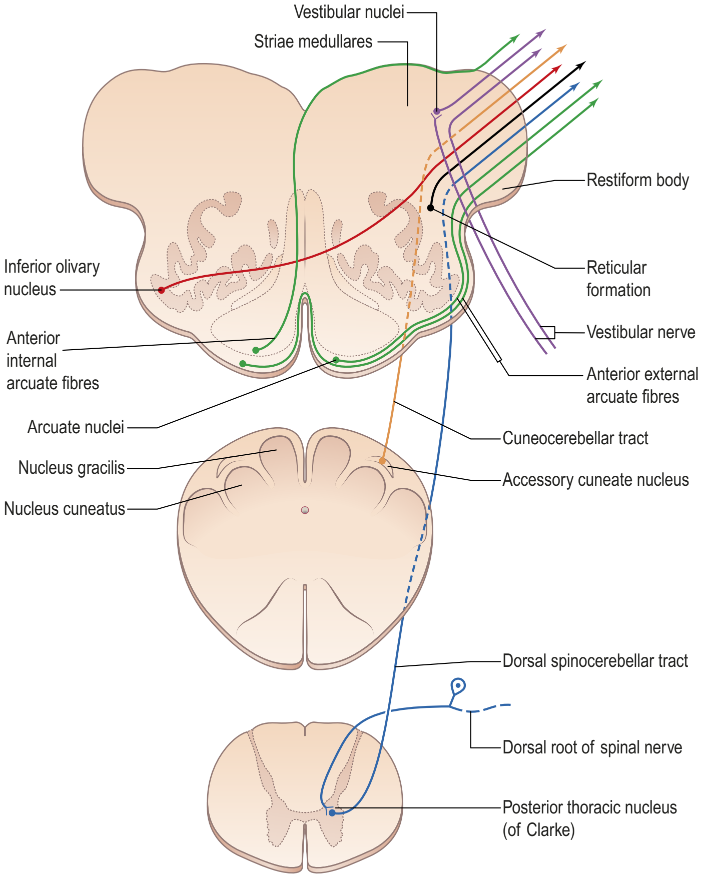
Vestibular nuclei
Striae medullares
Restiform body
Inferior olivary nucleus
Reticular formation
Vestibular nerve
Anterior internal arcuate fibres
Anterior external arcuate fibres
Arcuate nuclei
Cuneocerebellar tract
Nucleus gracilis
Accessory cuneate nucleus
Nucleus cuneatus
Dorsal spinocerebellar tract
Dorsal root of spinal nerve
Posterior thoracic nucleus (of Clarke)

Fig. 28.10 The components of the restiform body that are afferent to the cerebellum. Fibres that are efferent from the cerebellum have been omitted.

in the contralateral anterolateral funiculus to terminate at multiple sites in the brainstem, diencephalon and basal telencephalon. The spinothalamic and spinoreticular tracts are the major components of this system; other tracts running in parallel include the spinotectal, vestibulospinal, rubrospinal and ventral spinocerebellar tracts (Nathan and Smith 1982). In the medulla, these tracts are limited dorsally by the spinal tract and nucleus of the trigeminal nerve, and ventrally by the pyramid.

The spinothalamic and spinoreticular tracts are a longitudinal system of ascending fibres that convey pain, itch, temperature, tactile and proprioceptive information from the contralateral side of the body to the brain. Similar sensory input from the face passes to the trigeminal sensory system. The neuronal cell bodies that mediate noxious stimuli are found in the dorsal root ganglia at all levels of the spinal cord (Gilman and Newman 2003). Their central fibres synapse within the ipsilateral spinal cord. Most secondary relay fibres then cross the midline in the ventral white commissure; a few remain ipsilateral. On both sides, the spinothalamic tracts ascend along the anterolateral margins of the spinal cord to reach the brainstem. They continue upward along the anterolateral aspect of the medulla and pons and ascend posterolateral to the medial lemniscus in the low midbrain. The spinothalamic tracts then ascend through the midbrain deep to the brachium of the inferior colliculus and medial geniculate body to reach the ventroposterolateral nucleus of the thalamus (Haines and Mihailo 2018). Ascending fibres also reach the superior colliculus. In humans, few of the ascending spinothalamic fibres are thought to reach the thalamus directly: the spinothalamic relay system is predominantly a polysynaptic system in which most ascending fibres synapse in the reticular formation of the brainstem as the spinoreticular system (Nieuwenhuys et al 2008).

The ventral (anterior) spinocerebellar tract runs in parallel with its dorsal counterpart in the lower medulla but the two separate as they approach the restiform body. Somatosensory fibres for proprioception, pain and pressure from the lumbar and some sacral levels enter the dorsal horns of the spinal cord to synapse with neurones in the intermediate grey matter and base of the dorsal horns (Rexed's laminae V–VII). Most relay fibres then cross the midline via the ventral white commissure and ascend to the brainstem as the ventral spinocerebellar tract (see **Figs 28.6–28.7**). A few remain uncrossed and ascend ipsilaterally (Carpenter and Sutin 1983). Within the medulla, the tract ascends along the anterolateral border of the medulla, with the spinothalamic tract. Further rostrally, the ventral spinocerebellar tract curves posterolaterally and spreads out into a thin lamina that ascends along the external surface of the superior cerebellar peduncle of the midbrain. At the upper border of the superior cerebellar peduncle, these fibres recurve ventrally and medially over the top of the peduncle and enter the superior cerebellum. Most anterior spinocerebellar fibres then recross the midline to terminate in the contralateral cerebellum (i.e. ipsilateral to their cells of origin). About 15% of ventral spinocerebellar fibres terminate bilaterally (Carpenter and Sutin 1983).

Hypoglossal nucleus

The hypoglossal nucleus lies near the midline in the dorsal medullary grey matter. It is approximately 2 cm long and extends from the hypoglossal trigone in the floor of the fourth ventricle into the closed part of the medulla (see **Figs 28.3**, **28.5**, **28.8**). It consists of large motor neurones interspersed with myelinated fibres and is organized into dorsal and ventral nuclear tiers, each divisible into medial and lateral subnuclei. A musculotopic organization of motor neurones within the nuclei corresponds to the structural and functional divisions of tongue musculature. Motor neurones innervating tongue retrusor muscles are located in dorsal/dorsolateral subnuclei, and those innervating the main tongue protrusor muscle are located in ventral/ventromedial regions of the nucleus.

The hypoglossal nucleus receives corticonuclear fibres from the precentral gyrus and adjacent areas, predominately from the contralateral hemisphere. The corticonuclear fibres synapse either on motor neurones of the nucleus directly or on interneurones. Most medial hypoglossal subnuclei receive projections from both cerebral hemispheres. The hypoglossal nucleus may connect with the cerebellum via the adjacent perihypoglossal nucleus, and perhaps also with the medullary reticular formation, the trigeminal sensory nucleus and the nucleus solitarius (Holstein 2012).

Hypoglossal fibres emerge from the ventral aspect of the nucleus and traverse the reticular formation lateral to both the medial lemniscus and the medial accessory olivary nucleus. They continue ventrally, between the medial accessory and the principal inferior olivary nuclei, and then curve laterally to emerge from the brainstem as a series of 10–15 rootlets arranged linearly along the preolivary sulcus (see **Figs 28.4**, **28.8**) (Yousry et al 2002b). These rootlets coalesce into two bundles that exit separately through the hypoglossal canal and unite extradurally.

Perihypoglossal nuclei

Available with the *Gray's Anatomy* e-book

Dorsal motor nucleus of the vagus

The dorsal motor nucleus of the vagus lies slightly dorsolateral to the hypoglossal nucleus, from which it is separated by the nucleus intercalatus (see **Fig. 28.8**). The vagal nucleus extends caudally to the first cervical spinal segment and rostrally to the open portion of the medulla subjacent to the vagal trigone of the fourth ventricle. It is a general visceral efferent nucleus and is the largest parasympathetic nucleus in the brainstem. Most (80%) of its neurones give rise to the preganglionic parasympathetic fibres that pass into the vagus nerve. The remainder are interneurones or neurones that project centrally. The nucleus innervates the cardiac and smooth muscle of the thoracic viscera (heart, bronchi, lungs, oesophagus) and abdomen (stomach, liver, pancreas, spleen, small intestine and proximal part of the colon), and glandular epithelium. Sparse sensory afferents from the nodose ganglion project directly to the dorsal and lateral edges of the dorsal vagal nucleus, and possibly beyond it into the nucleus of the solitary tract (Holstein 2012).

Neurones within the nucleus are heterogeneous and can be classified into nine subnuclei, grouped into rostral, intermediate and caudal divisions. Topographic maps of visceral representation in animals suggest that the heart and lungs are represented in the caudal and lateral parts of the nucleus; the stomach and pancreas in intermediate regions; and the remaining abdominal organs in the rostral and medial parts of the nucleus.

Nucleus ambiguus

The nucleus ambiguus is a complex group of large motor neurones that are situated deep in the medullary reticular formation (see **Figs 28.3**, **28.9**). Rostrally, it extends as far as the rostral end of the vagal nucleus. Caudally, the nucleus is in line with, but not continuous with, the nucleus of the accessory nerve. A small retrofacial nucleus separates the upper end of the nucleus ambiguus from the facial nucleus. The nucleus ambiguus contains cellular subgroups that exhibit some topographical representation. Relatively discrete groups of cells in the caudal region innervate individual laryngeal muscles. Neurones in the intermediate area innervate the pharynx and neurones in the rostral area innervate the oesophagus and soft palate.

The nucleus ambiguus contributes special visceral efferent fibres to the glossopharyngeal nerve and may give general visceral efferent fibres to the vagus nerve. Fibres emerging from the nucleus ambiguus pass dorsomedially, then curve laterally. Rostral fibres join the glossopharyngeal nerve. Caudal fibres join the vagus and are distributed to the pharyngeal constrictors, intrinsic laryngeal muscles and striated muscles of the palate and upper oesophagus. A specific caudal pool of laryngeal motor neurones gives rise to the recurrent laryngeal nerve.

Traditionally, the nucleus ambiguus has been considered to give rise to visceral efferent fibres that join fibres derived from ventral (anterior) horn neurones in the upper five cervical cord segments (Gilman and Newman 2003). After travelling together for a short time, the medullary and spinal roots separate; the medullary fibres join the vagus nerve and the spinal fibres traverse the jugular foramen and ultimately innervate sternocleidomastoid and trapezius (Ch. 35). The nucleus ambiguus receives corticonuclear fibres from both hemispheres with a contralateral preponderance and is reciprocally connected to many brainstem nuclei.

Nucleus solitarius

The nucleus solitarius (solitary nucleus; nucleus of the solitary tract) lies within the dorsal tegmentum of the medulla, mostly medial to the tractus solitarius (solitary tract) from which it receives its main afferents (see **Figs 28.3**, **28.8**) (Paxinos et al 2012). This heavily myelinated tract descends through the medulla lateral or ventrolateral to the vagal nucleus and carries afferent fibres from the facial, glossopharyngeal and vagus nerves to the nucleus solitarius (Ciriello 1983, Hamilton and Norgren 1984, Haines and Mihailo 2018). Termination of special visceral afferents (taste) within the nucleus shows a viscerotopic pattern, predominantly in the rostral region (the gustatory nucleus). Experimental evidence suggests that fibres from the anterior two-thirds of the tongue and the roof of the oral cavity (which travel via the chorda tympani and greater petrosal branches of the facial nerve) terminate in the most rostral part of the solitary complex. Those from the circumvallate and foliate papillae of the posterior third of the tongue, tonsils, palate and pharynx (which travel via the lingual branch of the glossopharyngeal nerve) are distributed diffusely throughout the rostrocaudal extent of the nucleus, predominantly rostral to the obex. Afferents from the larynx and epiglottis (which travel via the superior laryngeal branch of the vagus) have a more caudal and lateral distribution.

Gastrointestinal afferents appear to terminate predominantly in medial and commissural subnuclei in the caudal part of the nucleus. Ventral and interstitial subnuclei probably receive tracheal, laryngeal and pulmonary afferents and play an important role in respiratory control and possibly rhythm generation. The carotid sinus and aortic body nerves terminate in the dorsal and dorsolateral region of the nucleus solitarius, which may be involved in cardiovascular regulation. Connections with the reticular formation underlie the reflex control of cardiovascular, respiratory and cardiac functions (Ciriello 1983). For these reasons, the caudal portion of the nucleus solitarius is also known as the cardiorespiratory nucleus.

Many secondary gustatory axons from the solitary nucleus cross the midline and ascend with the medial lemniscus to synapse on the most medial neurones of the ventral posteromedial thalamic nucleus in a region sometimes termed the accessory arcuate nucleus. From there, axons radiate to the anteroinferior portion of the sensory cortex and to the insula. Other ascending paths may end in hypothalamic nuclei that mediate the flow of gustatory information to the limbic system to facilitate appropriate autonomic responses. The nucleus solitarius also projects extensively to many areas of the reticular formation (Paxinos et al 2012) and it may project to the upper levels of the spinal cord through a solitariospinal tract (Hamilton and Norgren 1984).

Spinal trigeminal nucleus

The sensory nuclei of the trigeminal nerve form a longitudinal column that extends from the midbrain to the cervical spinal cord and consists of the spinal trigeminal nucleus (nucleus of the spinal tract of the trigeminal nerve) in the dorsal spinal cord and medulla oblongata, the principal sensory nucleus in the pons, and the mesencephalic nucleus in the midbrain (see **Figs 28.3**, **28.14**, **28.15**) (Olszewski 1950, Nieuwenhuys et al 2008). The term trigeminal sensory nuclear complex refers to the spinal sensory and principal sensory nuclei (Henssen et al 2016). The mesencephalic nucleus of the trigeminal nerve is regarded separately as group of ectopic primary afferent cell bodies.

The spinal nucleus of the trigeminal nerve has three parts: the pars oralis, which adjoins the principal sensory nucleus, the pars interpolaris, and the pars caudalis, which is directly continuous with the dorsal horn of the spinal cord (see **Figs 28.7–28.9**). Afferent fibres that convey pain, temperature and light touch from the orofacial region enter the brainstem at the pons and course dorsomedially towards the principal sensory nucleus: before reaching the nucleus, approximately 50% of the fibres divide into ascending and descending branches, and the remainder ascend or descend without division. The descending trigeminal fibres form the spinal tract of the trigeminal nerve, which courses along the lateral border of the spinal nucleus from the midpons to the C2 level, where it becomes continuous with the the dorsal tract of Lissauer (Waite and Ashwell 2012).

The great majority of the fibres are less than 4 μm in diameter. There is a precise somatotopic organization within the tract. Fibres from the ophthalmic division of the trigeminal nerve lie ventrally, those from the

Experimental evidence suggests that motor neurones of the medial division of the hypoglossal nucleus innervate tongue muscles that are orientated in planes transverse to the long axis of the tongue (transverse and vertical intrinsics and genioglossus), whereas motor neurones of the lateral division innervate tongue muscles that are orientated parallel to this axis (styloglossus, hyoglossus, superior and inferior longitudinal).

Several small groups of cells lie near the hypoglossal nucleus, including the nucleus intercalatus, sublingual nucleus, nucleus prepositus hypoglossi and nucleus paramedianus dorsalis (reticularis). Despite their name, none of these nuclei is presently known to be connected with the hypoglossal nerve or nucleus. The nucleus prepositus hypoglossi subserves vestibular and oculogyric functions and is discussed with those systems. The nucleus intercalatus extends from below the obex up to the rostral pole of the hypoglossal nucleus, where it gives way to the nucleus prepositus hypoglossi. It starts as a narrow wedge between the hypoglossal and the dorsal vagal nuclei, but expands rostrally as the vagal nucleus migrates laterally (Paxinos et al 2012); gustatory and visceral connections are attributed to the nucleus intercalatus.

mandibular division lie dorsally, and fibres from the maxillary division lie between. The tract is completed on its dorsal rim by fibres from the sensory roots of the facial, glossopharyngeal and vagus nerves. All of these fibres synapse in the pars caudalis of the spinal nucleus of the trigeminal nerve.

Other afferents to the spinal nucleus arise from the dorsal roots of the upper cervical nerves. All of these fibres synapse in the pars caudalis of the spinal nucleus of the trigeminal nerve, although the ophthalmic division may not project fibres as far.

Efferent fibres from the pars oralis and interpolaris of the spinal nucleus ascend through the ventral pontine tegmentum, decussate and ascend along the dorsomedial side of the contralateral medial lemniscus as the ventral trigeminothalamic tract (trigeminal lemniscus) (Waite and Ashwell 2012). These fibres end in the ventral posteromedial nucleus of the thalamus contralateral to the spinal trigeminal nucleus of origin. Fibres from the pars caudalis ascend in both ventral and dorsal trigeminothalamic tracts to terminate in the ventral posteromedial nucleus as well as in the mediodorsal and intralaminar thalamic nuclei (Waite and Ashwell 2012, Henssen et al 2016). From the thalami, third-order neurones project to the cortical postcentral gyrus (Brodmann areas 3, 1, 2). Other afferent fibres from the pars caudalis, especially from laminae I, V and VI, project to the rostral trigeminal nuclei, cerebellum, periaqueductal grey of the midbrain, parabrachial area of the pons, the brainstem reticular formation and the spinal cord.

There are conflicting opinions on the pattern of termination of the fibres in the spinal nucleus. It has long been held that fibres are organized rostrocaudally within the tract. According to this view, ophthalmic fibres are ventral and descend to the lower limit of the first cervical spinal segment, maxillary fibres are central and do not extend below the medulla oblongata, whilst mandibular fibres are dorsal and do not extend much below the mid-medullary level. The results of section of the spinal tract in cases of severe trigeminal neuralgia support this distribution. It was found that a section 4 mm below the obex rendered the ophthalmic and maxillary areas analgesic but tactile sensibility, apart from the abolition of 'tickle', was much less affected. To include the mandibular area it was necessary to section at the level of the obex.

Medullary reflexes

Swallowing and gag reflexes

Available with the *Gray's Anatomy* e-book

Cough reflex

Available with the *Gray's Anatomy* e-book

Sneeze reflex

Available with the *Gray's Anatomy* e-book

PONS

The pons (metencephalon) is the middle segment of the brainstem. It is approximately 2.5–3 cm in length and 3–4 cm wide at the root entry zones of the trigeminal nerves. It occupies the anterior portion of the mid posterior fossa behind the clivus. The ventral surface of the pons is separated from the upper clivus by the meninges and prepontine cistern. The dorsal surface of the pons faces the cerebrospinal fluid within the fourth ventricle and is covered over by the cerebellum. The lower border of the pons is marked by the transverse pontomedullary sulcus ventrally and the striae medullares of the fourth ventricle dorsally. The upper border of the pons is the upper margin of the pontine curvature ventrally and the decussation of the trochlear nerve in the superior medullary velum dorsally. The ventral edges of the medial lemnisci separate the basal pons (ventrally) from the pontine tegmentum (dorsally). The decussation of the superior cerebellar peduncle marks the transition from the pontine tegmentum to the midbrain tegmentum.

External features and relations

From medial to lateral, the ventral surface of the pons is marked by the shallow basilar sulcus, transverse ridges formed by underlying nerve fibre fascicles and the ventral aspect of the middle cerebellar peduncle (brachium pontis) (see Fig. 28.4). The abducens nerve emerges from the medullopontine sulcus 1–2 cm lateral to the midline. The facial nerve, vestibulocochlear nerve and the nervus intermedius emerge from the supraolivary fossette just inferior to the brachium pontis. The trigeminal nerve emerges from the lateral-most edge of the midpons, and marks the transition from the pons ventrally to the middle cerebellar peduncle dorsally. Typically, a single small motor root of the trigeminal nerve (portio minor) emerges dorsomedial to the larger sensory root (portio major). On occasion, the motor root appears as two separate superior and inferior divisions, rather than a single fascicle (Yousry et al 2004).

The dorsal surface of the pons is the upper portion of the floor of the fourth ventricle rostral to the striae medullares (pontine triangle) (see Fig. 28.5). From medial to lateral, the dorsal surface of the pons is marked by a median sulcus, a median eminence and paramedian sulcus limitans. Caudal to the median eminence, the facial colliculus marks the site where the fibres of the facial nerve curve over the abducens nucleus. The inferior fovea separates the facial colliculus from the hypoglossal trigone. Superolaterally, a small depression in the floor of the fourth ventricle, the superior (trigeminal) fovea, marks the site of the underlying principal sensory and motor nuclei of the trigeminal nerve. The pontine vestibular area lies far laterally, at the lateral angle of the fourth ventricle. Lateral to the fourth ventricle, a groove (lateral recess) separates the middle from the superior cerebellar peduncles.

Internal organization

Transverse section through the pons at the level of the facial colliculus

A transverse section through the lower pons at the level of the facial colliculus cuts through the upper half of the fourth ventricle just above the striae medullares (Fig. 28.11). Dorsally, the medial longitudinal fasciculus lies beneath the floor of the fourth ventricle just lateral to the median sulcus. Lateral to this, the ovoid abducens nucleus gives rise to the nerve fibres that emerge from the ventromedial aspect of the nucleus and course ventrolaterally and caudally across the pons. The facial nerve nucleus lies ventral, lateral and caudal to the abducens nucleus in the low lateral pontine tegmentum. The fibres of the facial nerve ascend to the medial aspect of the abducens nucleus, curve dorsally and laterally as the genu of the facial nerve, and pass over the dome of the abducens nucleus, forming the facial collicus (Fig. 28.12). The facial fibres then recurve ventrally, and descend between the facial nucleus and the spinal trigeminal nucleus and tract to emerge from the brainstem below the middle cerebellar peduncle. Dorsolaterally, the restiform and juxtarestiform bodies of the inferior cerebellar peduncle lie superolateral to the superior and lateral vestibular nuclei. The vestibulocerebellar fibres emerge lateral to the vestibular nuclei while the vestibular nerve emerges ventrally. At this level, the ascending fibres of the medial lemniscus assemble into an ovoid bundle in the ventral pontine tegmentum. The transverse fibres of the trapezoid body and the trapezoid nuclei cross the midline in the ventral tegmentum, along the medial lemnisci. The central tegmental tract courses longitudinally through the mid pontine tegmentum. Within the basal part of the pons, myriad pontine nuclei give rise to the transverse fibres of the pons (pontocerebellar fibres) that cross the midline to form the contralateral middle cerebellar peduncle. The descending frontopontine, corticospinal and parieto-temporo-occipito-pontine fibres course longitudinally through the central portion of the basal pons, and partially separate the transverse fibres of the pons into prominent ventral and dorsal bundles.

Transverse section through the pons at the level of the principal sensory and motor nuclei of the trigeminal nerve

At this level, the superior cerebellar peduncle forms the upper lateral wall of the fourth ventricle and the superior medullary velum forms its roof (Fig. 28.13). The lateral margin of the fourth ventricle contains the superior fovea that overlies, from medial to lateral, the motor nucleus and the principal sensory nucleus of the trigeminal nerve and the intervening fibres of the sensory root of the trigeminal nerve. The mesencephalic tract of the trigeminal nerve courses longitudinally in the adjacent dorsolateral tegmentum. The medial lemniscus and lateral lemniscus form a ventrally convex 'lemniscal arch' that delimits the tegmentum from the basal pons. The transverse fibres of the trapezoid body and contained trapezoid nuclei curve across the midline in the ventral tegmentum. Further dorsally the central tegmental tract courses longitudinally through the central pontine tegmentum.

The structure of the pars caudalis is analogous to that of the dorsal horn of the spinal cord, with a similar arrangement of cell laminae (subnuclei zonalis, gelatinosus and magnocellularis). Cutaneous nociceptive afferents and small-diameter muscle afferents terminate in layers I, II, V and VI of the pars caudalis. Low-threshold mechanosensitive afferents of Aβ neurones terminate in layers III and IV of the pars caudalis and in the rostral (interpolaris, oralis, principal sensory) nuclei. Many of the neurones in the pars caudalis that respond to cutaneous or tooth-pulp stimulation are also excited by stimulation of jaw or tongue muscles, indicating convergence of superficial and deep afferent inputs via wide-dynamic-range or nociceptive-specific neurones. Similar convergence of superficial and deep inputs occurs in the rostral parts of the trigeminal nucleus, which may account for the poor localization of trigeminal pain, and for the spread of pain, which often makes diagnosis difficult.

Cells in lamina II of the pars caudalis also receive afferents from the sensorimotor cortex, the periaqueductal grey matter, the nucleus raphe magnus and the reticular formation. The nucleus raphe magnus projects directly to the pars caudalis, probably via enkephalin, noradrenaline (norepinephrine) and 5-HT (5-hydroxytryptamine, serotonin)-containing terminals. These fibres directly, or indirectly through local interneurones, influence pain perception. Stimulation of periaqueductal grey matter or nucleus raphe magnus inhibits the jaw-opening reflex to nociception, and may induce primary afferent depolarization in tooth-pulp afferents and other nociceptive facial afferents. Neurones in the pars caudalis can be suppressed by stimuli applied outside their receptive field, particularly by noxious stimuli. The pars caudalis is an important site for relay of nociceptive input and functions as part of the pain 'gate control'. However, rostral nuclei may also have a nociceptive role as tooth-pulp afferents via wide-dynamic-range and nociceptive-specific neurones terminate in rostral nuclei, which all project to the subnucleus caudalis.

The separation of the entering fibres can give rise to a segmental (cross-divisional) sensory loss when focal medullary pathology such as syringobulbia occurs at a strategic site. Tractotomy of the spinal tract performed at a lower level can spare the perioral region, a finding that would accord with the classical 'onion-skin' pattern of loss of pain sensation. However, in clinical practice, the progression of anaesthesia on the face is commonly 'divisional' rather than strictly 'onion-skin' in distribution. GSA fibres subserving common sensation enter the dorsal region of the spinal tract of the trigeminal nerve from the glossopharyngeal, vagus and facial nerves (nervus intermedius) and synapse with cells in the caudal part of the spinal nucleus. Consequently, operative section of the dorsal part of the spinal tract results in analgesia that extends to the mucosa of the tonsillar sinus, the posterior third of the tongue and adjoining parts of the pharyngeal wall (supplied by the glossopharyngeal nerve), and the cutaneous areas of the ear (supplied by the auricular branch of the vagus).

During the normal processes of eating and drinking, the passage of food or liquid to the rear of the mouth stimulates branches of the glossopharyngeal nerve in the oropharynx and swallowing is initiated. The nasopharynx is closed off from the oropharynx by elevation of the soft palate, the larynx is raised, its entrance narrowed, the glottis is closed and peristaltic activity down the oesophagus to the stomach is mediated through the pharyngeal plexus.

The patterning and timing of striated muscle contraction that occur during swallowing are generated in the brainstem by a network of neural circuits involving the nucleus solitarius (afferent limb) and the nucleus ambiguus (efferent limb).

If stimulation of the oropharynx occurs other than during swallowing, the gag reflex may be initiated: a reflex contraction of the muscles of the pharynx, soft palate and fauces occurs that, if extreme, can result in retching and vomiting.

The cough reflex is normally initiated by irritation of tracheal or laryngeal mucosae: there is evidence of both mechanosensing and chemosensing cough receptors (McGarvey 2014). Coughing involves a sequence of coordinated events that produce the profound change in breathing pattern needed to expel an irritant from the lower airway. Rapid inspiration is followed by an expiratory effort against a closed glottis, the rapid generation of intrapulmonary pressure and the sudden opening of the glottis and contraction of intercostal and abdominal wall muscles, collectively producing a high-velocity flow of expired air that sweeps irritant material up towards the pharynx in a forceful exhalation (cough). Laryngeal branches of the vagus nerve carrying general visceral afferent information (with cell bodies in the inferior vagal ganglion) terminate in the nucleus of the solitary tract. Second-order neurones project to medullary respiratory centres (including a putative cough centre) and to the nucleus ambiguus, recruiting motor neurones innervating pharyngeal, laryngeal, diaphragmatic, intercostal and abdominal muscles.

The sneeze reflex arises from stimulation of the nasal mucosa by physical or chemical irritants. Afferent impulses travel via the ethmoidal and maxillary nerves to the spinal nucleus of the trigeminal nerve. Interneurones project to the nucleus ambiguus and a putative 'sneezing centre' in the rostral dorsolateral medulla (Seijo-Martínez et al 2006). Recruitment of a critical number of inspiratory and expiratory neurones initiates a sneeze, which involves eye closing and deep inspiration, followed by explosive exhalation as described above. If the oropharyngeal isthmus is closed by the action of palatoglossus, the air flow is diverted through the nasal cavity, otherwise the stream of expelled air flows through both oral and nasal cavities.

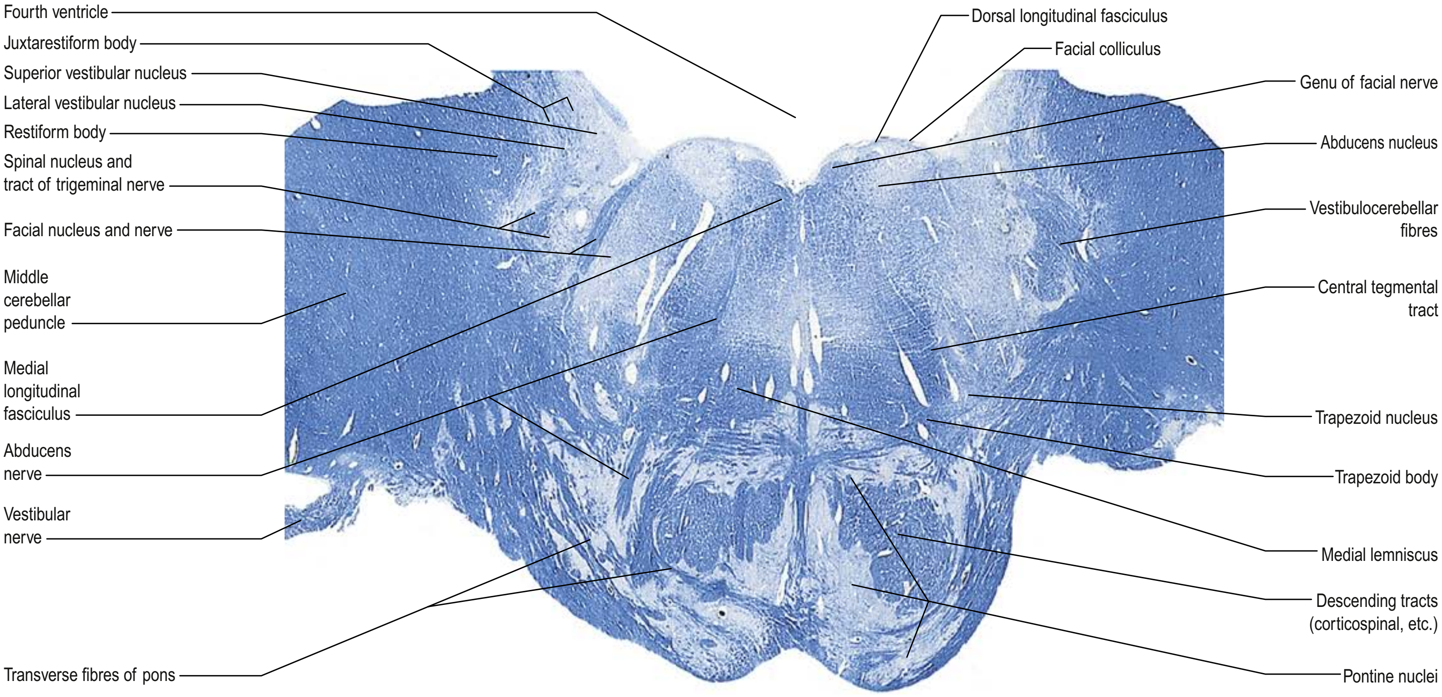
Fourth ventricle
Juxtarestiform body
Superior vestibular nucleus
Lateral vestibular nucleus
Restiform body
Spinal nucleus and tract of trigeminal nerve
Facial nucleus and nerve
Middle cerebellar peduncle
Medial longitudinal fasciculus
Abducens nerve
Vestibular nerve
Transverse fibres of pons
Dorsal longitudinal fasciculus
Facial colliculus
Genu of facial nerve
Abducens nucleus
Vestibulocerebellar fibres
Central tegmental tract
Trapezoid nucleus
Trapezoid body
Medial lemniscus
Descending tracts (corticospinal, etc.)
Pontine nuclei

Fig. 28.11 A transverse section through the pons at the level of the facial colliculus, prepared using Luxol fast blue stain for myelinated nerve fibres (blue).

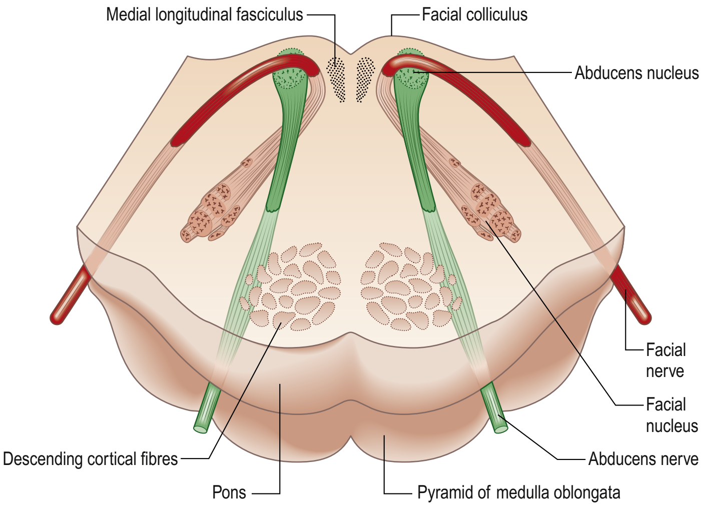
Medial longitudinal fasciculus
Facial colliculus
Abducens nucleus
Facial nerve
Facial nucleus
Abducens nerve
Descending cortical fibres
Pons
Pyramid of medulla oblongata

Fig. 28.12 A transverse section of the pons, viewed from the rostral aspect, showing the central course of fibres of the facial nerve.

Pathways and nuclei of the pons

Medial longitudinal fasciculus

The medial longitudinal fasciculus is the main intersegmental tract in the brainstem (see Figs 28.8–28.9, **28.11–28.13**, **28.15**). It is a small paramedian tract that courses through the dorsal tegmentum of the brainstem from the upper cervical spinal cord through the medulla, pons and midbrain to the interstitial nucleus of Cajal in the lateral wall of the third ventricle. It passes immediately ventral to the abducens nucleus in the pons and immediately ventral to the trochlear and oculomotor nuclei in the midbrain. It interconnects the oculomotor, trochlear, abducens, Edinger–Westphal, vestibular, reticular and spinal accessory nuclei, coordinating conjugate eye movements with associated movements of the head and neck. Ascending fibres in the fasciculus arise from all four vestibular nuclei. Those from the superior vestibular nucleus remain uncrossed, while the others are partly crossed. Some fibres reach the interstitial and posterior commissural nuclei, and some decussate to the contralateral nuclei. Some ascending fibres may reach the thalamus. Descending axons from the medial vestibular nucleus, and perhaps the lateral and inferior vestibular nuclei, partially decussate and descend in the medial longitudinal fasciculus as the medial vestibulospinal tract that passes into the ventral funiculus of the spinal cord. Fibres join the medial longitudinal fasciculus from the dorsal trapezoid, lateral lemniscal and posterior commissural nuclei, which means that both the cochlear and vestibular components of the vestibulocochlear nerve can influence movements of the eyes and head via the medial longitudinal fasciculus. The descending and ascending connections through the medial longitudinal fasciculus enable conjugate eye movements (Frohman et al 2008, Aw et al 2017). Lesions affecting the medial longitudinal fasciculus cause internuclear ophthalmoplegia.

Central tegmental tract

The central tegmental tract is a longitudinal fibre bundle situated in the central portion of the reticular formation (Nathan and Smith 1982) (see Figs 28.11, **28.13**, **28.15–28.16**). It contains descending and ascending fibres. The major descending fibres are rubro-olivary, which arise from the rostral parvocellular portion of the red nucleus and descend ipsilaterally through the superior cerebellar peduncle and the central portion of the tegmentum to terminate in the amiculum (capsule) of the principal inferior olivary nucleus. These descending fibres form one leg of the triangle of Guillain-Mollaret (see p. 458.e2). Ascending fibres in the central tegmental tract include taste fibres from the rostral gustatory portion of the solitary nucleus travelling to the ventral posteromedial nucleus of the thalamus, and projections from the reticular formation to the thalamus and hypothalamus.

Dorsal longitudinal fasciculus

The dorsal longitudinal fasciculus of Schütz (periventricular system) is a periventricular longitudinal fibre bundle that courses from the posterior hypothalamus to the lower medulla. It contains thin ascending and descending fibres that connect the forebrain with visceral autonomic centres in the lower brainstem.

Pontine nuclei

The pontine nuclei include all of the neurones that are dispersed throughout the basilar pons: in humans, these number some 20 million neurones (Brodal and Bjaalie 1992) (see Figs 28.11, 28.13). They are probably all glutamatergic, and most project to the contralateral cerebellar cortex, with collaterals to the cerebellar nuclei.

Corticopontine fibres arise mainly from neurones in layer V of the premotor, somatosensory, posterior parietal, extrastriate visual and cingulate neocortices. Projections from prefrontal, temporal and striate cortices are sparse. Frontopontine fibres end rostral to the level of the trigeminal nerve, and connect with pontine neurones that project to the contralateral cerebellum through the more rostral transverse pontine fibres. The terminal fields, although divergent, form topographically segmented patterns resembling overlapping columns, slabs or lamellae within the pons.

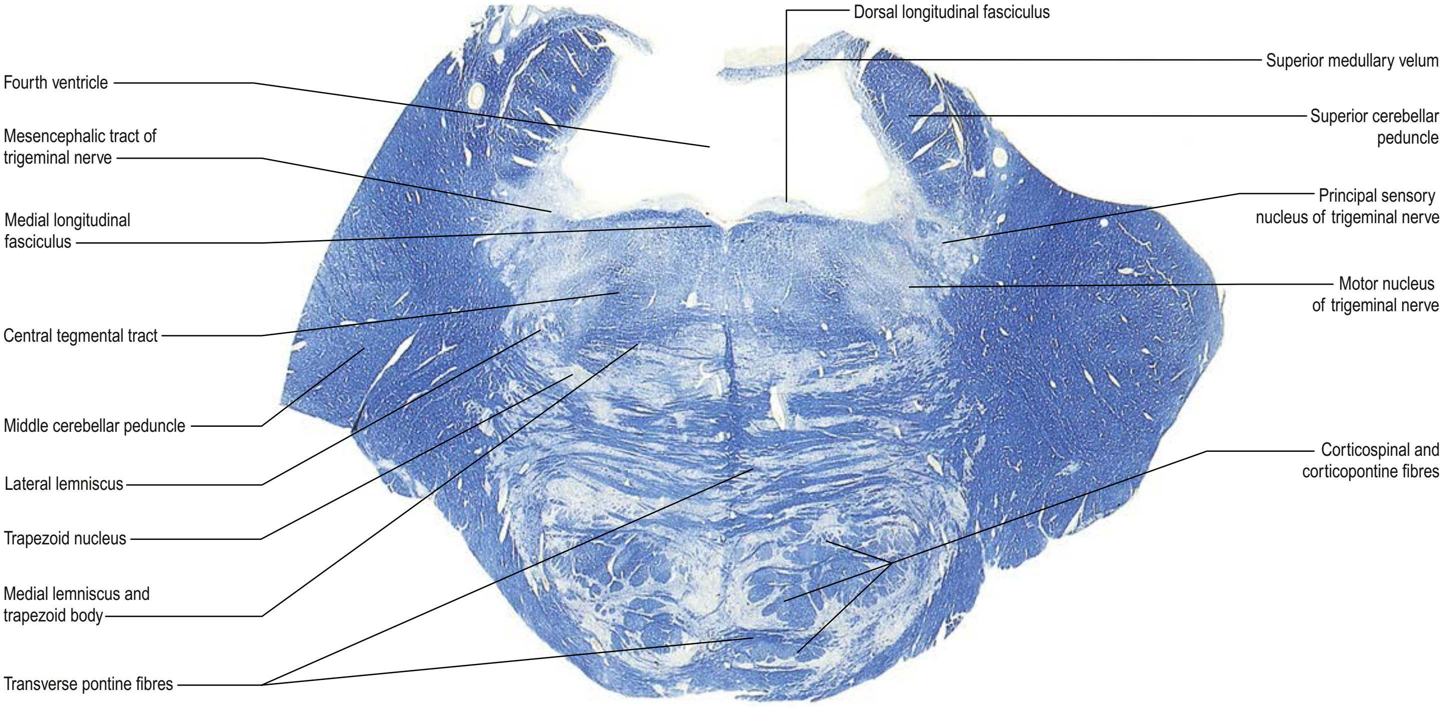
Dorsal longitudinal fasciculus
Superior medullary velum
Fourth ventricle
Superior cerebellar peduncle
Mesencephalic tract of trigeminal nerve
Principal sensory nucleus of trigeminal nerve
Medial longitudinal fasciculus
Motor nucleus of trigeminal nerve
Central tegmental tract
Middle cerebellar peduncle
Corticospinal and corticopontine fibres
Lateral lemniscus
Trapezoid nucleus
Medial lemniscus and trapezoid body
Transverse pontine fibres

Fig. 28.13 A transverse section of the pons at the level of the principal sensory and motor nuclei of the trigeminal nerve, prepared using Luxol fast blue stain for myelinated nerve fibres (blue).

Subcortical projections to the pontine nuclei include those from the superior colliculus to the dorsolateral pons, and from the medial mammillary nucleus to the rostromedial pons and pretectal nuclei. Afferents that arise from the lateral geniculate nucleus, dorsal column nuclei, trigeminal nuclei, hypothalamus and cerebellar nuclei project to restricted neurones of the pons. Functionally related subcortical and cerebrocortical afferents converge, e.g. those from the somatosensory cortex and dorsal column nuclei. There is non-specific input from the reticular formation, raphe nuclei, locus coeruleus and periaqueductal grey matter. Efferent axons from the pontine nuclei constitute the transverse pontine (pontocerebellar) fibres, most of which cross the midline and continue into the cerebellum as the major constituent of the contralateral middle cerebellar peduncle. All pontocerebellar fibres end as mossy fibres in the cerebellar cortex. A degree of somatotopy is maintained in these connections.

Cranial nerve nuclei and related tracts

Cochlear nuclei

The primary afferents of the auditory pathway are the central processes of type I and II sensory neurones in the spiral ganglion in the cochlea (Ch. 43). They travel in the cochlear division of the vestibulocochlear nerve and enter the brainstem just caudal to the vestibular division of the vestibulocochlear nerve at the cerebellopontine angle. The axons bifurcate and terminate in the dorsal (posterior) and ventral (anterior) cochlear nuclei lying along the lateral surface of the restiform body. The dorsal cochlear nucleus forms a bulge, the auditory tubercle (auditory eminence), on the posterior surface of the restiform body and also forms the floor of the lateral recess of the fourth ventricle; it is continuous medially with the vestibular area in the floor of the fourth ventricle. The ventral cochlear nucleus lies between the cochlear and vestibular fibres of the vestibulocochlear nerve. The dorsal and ventral cochlear nuclei are separated only by a thin stratum of nerve cell bodies and fibres.

The axons that emerge from the cochlear nuclei are aggregated into three, mostly transverse, fibre bundles, the dorsal and intermediate acoustic striae and the trapezoid body. These axons pursue a complex, often crossed, course as they ascend through the acoustic striae, the superior olivary complex, and the lateral lemniscus to reach the inferior colliculus. The dorsal cochlear nucleus projects via the dorsal acoustic stria to the contralateral inferior colliculus. The dorsal acoustic stria curve dorsally and medially, dorsal to the restiform body, traverse the reticular formation ventral to the striae medullares, cross the midline, pass to the contralateral superior olivary complex, and ascend in the contralateral lateral lemniscus. The ventral cochlear nucleus projects via the trapezoid body or the intermediate acoustic stria to relay centres in either the superior olivary complex, the nuclei of the lateral lemniscus, or the inferior colliculus. Initially, the intermediate acoustic stria accompanies the dorsal acoustic stria as they pass medially, immediately dorsal to the restiform body, but it then separates from the dorsal acoustic stria, angles sharply ventrally in the ipsilateral tegmentum, passes through the spinal trigeminal nucleus, joins the trapezoid body and crosses the midline to join and ascend with the contralateral lateral lemniscus.

The cochlear nerve also conveys efferent fibres that pass outward from the brainstem to terminate on the hair cells and on the cells of the spiral ganglion.

The trapezoid body is a large, complex, transversely orientated fibre bundle that extends across the midline at the level of the pontomedullary junction (see Fig. 28.11). It is formed by the fibres of the intermediate acoustic stria, and secondary fibres that arise from the superior olivary complex. The fibres pass either through or ventral to the medial lemniscal fibres, decussate with the contralateral fibres in the median raphe, and relay onward in the contralateral nuclei of the superior olivary complex. The trapezoid fibres from both sides then pass below the emerging axons of the facial nerve, and turn upward abruptly to enter the lateral lemnisci. By this route, secondary auditory fibres from the cochlear and related nuclei pass to the lateral lemnisci bilaterally. A few auditory fibres do not cross the midline and synapse in the ipsilateral superior olivary nuclei. A further few fibres cross the midline but relay more distally in the nuclei of the lateral lemniscus. Some trapezoid axons may enter the medial longitudinal fasciculus and ascend to end in the trigeminal motor, facial, oculomotor, trochlear and abducens nuclei, where they mediate reflexes involving tensor tympani, stapedius and oculogyric muscles, respectively.

Superior olivary complex

The superior olivary complex is a major link in the ascending and descending auditory pathways (see Fig. 43.20). The nuclei of the superior olivary complex include the medial and lateral superior olivary nuclei, the medial nucleus of the trapezoid body, the periolivary nuclei and many unnamed cell clusters (Paxinos et al 2012). These nuclei lie rostral and ventral to the nuclei of the facial nerve, partially overlapping with the trapezoid body. The lateral superior olive appears to analyze differences in sound frequency and sound intensity between the two ears (Nieuwenhuys et al 2008).

Lateral lemniscal nuclei

The lateral lemniscus ascends along the dorsolateral border of the pons and caudal midbrain superficial to (external to) the superior cerebellar peduncle to reach the inferior colliculus (see Fig. 28.15). Most of the lemniscal fibres are crossed fibres that ascend from the contralateral auditory apparatus to synapse in the inferior colliculus: they include fibres relayed from the superior olivary nucleus and trapezoid body (see Fig. 43.20). Some lateral lemniscal fibres carry information from the ipsilateral cochlea that has passed through the ipsilateral superior olivary nucleus.

Vestibular nuclear complex

The vestibular nuclear complex is situated beneath the floor of the fourth ventricle. It has traditionally been divided into four cellular masses, the

The axons of type 1 spiral ganglion cells enter the ventral cochlear nucleus and bifurcate within its centre, dividing it into anterior and posterior ventral subnuclei. The fibres are organized into dorsoventrally orientated sheets: fibres conveying low frequency sounds from apical spiral ganglion cells terminate ventrally and fibres conveying high frequency sounds from the basal turn of the spiral ganglion terminate dorsally. Posterior processes of type 1 ganglion cells pass to the caudal pole of the ventral nucleus, from which they enter the dorsal cochlear nucleus. Thin unmyelinated axons of type 2 spiral ganglion cells contact clusters of small interneurones scattered through the cochlear nuclei.

The dorsal, ventral and intermediate lemniscal nuclei are longitudinal columns of cells embedded among the most medial fibres of the lateral lemniscus. They receive afferent axons from both cochlear nuclei, are tonotopically organized and serve as links in the auditory pathways that ascend and descend through the superior olivary complex and cochlear nuclei. Among other functions, the dorsal nucleus relays afferent data from the superior olives by GABAergic projections to both inferior colliculi. The ventral nucleus serves as an important interconnection between the cochlear nuclei and the central nucleus of the inferior colliculus.

lateral nucleus (of Deiter), medial nucleus (of Schwalbe), superior nucleus (of Bechterew) and inferior (spinal, descending) vestibular nucleus (see **Figs 28.3B, 28.8, 28.11**) (Haines and Mihailo 2018). The nucleus prepositus hypoglossi, located medial to the medial vestibular nucleus, may also be regarded as a vestibular nucleus. Cell groups X and Y have been identified as accessory nuclei of the vestibular complex.

The medial vestibular nucleus is the largest of the vestibular nuclei. It lies lateral and superior to the visceromotor nuclei of the glossopharyngeal and vagus nerves, is crossed dorsally by the striae medullares of the fourth ventricle and is continuous with the nucleus intercalatus below. The superior vestibular nucleus is small and lies above the medial and lateral nuclei. It extends higher into the pons than do the other subdivisions, to occupy the upper part of the vestibular area. The inferior vestibular nucleus is the smallest of the group. It lies between the medial vestibular nucleus and the restiform body, from the level of the upper end of the nucleus gracilis to the pontomedullary junction, and is traversed by descending fibres of the vestibular nerve, from the cerebellum and the vestibulospinal tract. The lateral vestibular nucleus lies ventrolateral to the upper portion of the medial nucleus, just above the inferior nucleus and ascends almost to the level of the abducens nucleus. Its rostral end is continuous with the caudal end of the superior nucleus. It projects to the spinal cord through the lateral vestibulospinal tract (Voogd 2016). The lateral vestibular nucleus can be subdivided into dorsal and ventral components. The dorsal portion contains giant cells and is located within the juxtarestiform body: it receives no direct vestibular afferents, but receives Purkinje cell axons from the anterior vermis, and extends efferent connections to the cerebellum. The ventral portion contains cells of various sizes and is located medial to the juxtarestiform body

Vestibulocerebellar fibres (primary and secondary) travel via the juxtarestiform body mainly to the flocculus and nodule. Cerebellovestibular fibres pass to the nuclei, also via the juxtarestiform body. They arise mainly in the flocculus and nodule (posterior lobe), but some fibres are derived from the anterior lobe and the fastigial nucleus. A few vestibular fibres enter the cerebellum directly through the juxtarestiform body and end in the fastigial nucleus, flocculonodular lobe and uvula.

The vestibular nuclei receive afferent fibres from multiple sources, including the vestibular portion of the vestibulocochlear nerve, cerebellum, brainstem reticular formation and spinal cord. Myelinated fibres of the vestibular nerve enter the medulla between the restiform body and the spinal tract of the trigeminal nerve and bifurcate into ascending and descending branches. Most ascending vestibular fibres end in the superior vestibular nucleus. Descending vestibular fibres traverse the juxtarestiform body and give off extensive transverse collaterals to the inferior and medial (but not the lateral) vestibular nuclei. Additional afferent fibres descend from the cerebral cortex to innervate the vestibular nuclei bilaterally.

The vestibular nuclei project extensively to the cerebellum and also receive fibres from the cerebellar cortex and the fastigial nuclei. Vestibulocerebellar fibres pass through the juxtarestiform body to the cerebellum (Carpenter and Sutin 1983). A few vestibular nerve fibres bypass the vestibular nuclei and traverse the juxtarestiform body to terminate directly in the fastigial nucleus, the flocculonodular lobe and uvula. Evidence suggests that the vestibular apparatus is spatially represented in these nuclei. Efferents from the lateral vestibular nucleus descend to the spinal cord through the ipsilateral lateral vestibulospinal tract and extend along the full length of the spinal cord to exert a facilitatory influence on spinal reflex activity and on extensor muscle tone. Vestibular nuclear efferents form a major part of the medial longitudinal fasciculus. Through this, interconnections between the vestibular and oculogyric nuclei and the pontine reticular formation provide for conjugate eye movements that compensate for head movements perceived by the labyrinths. The reflex arcs stabilize visual fixation despite changing head position. Vestibular efferents project to the thalamus (probably via the posterior portions of the ventroposterior complex and the medial pulvinar) which in turn project to the primary vestibular cortex in the parietal lobe at the junction of the intraparietal and postcentral sulci, adjacent to the head portion of the postcentral gyrus. There may be additional representation of the vestibular system in the superior temporal gyrus near to the auditory cortex.

Facial nucleus

The facial (motor) nucleus is situated caudal, ventral and lateral to the abducens nucleus. It lies within the caudal pontine reticular formation, ventromedial to the spinal tract and nucleus of the trigeminal nerve (see **Fig. 28.11**) (Haines and Mihailo 2018). Groups of facial nucleus neurones form columns, which innervate individual muscles or which correspond to branches of the facial nerve. Within the nucleus, neurones that innervate the muscles of the scalp and upper face lie dorsal to the neurones that supply the muscles of the lower face.

The facial nucleus receives corticonuclear fibres for volitional control of the facial musculature. Neurones that innervate the muscles in the scalp and upper face receive bilateral corticonuclear fibres, while neurones that innervate the muscles of the lower face receive a predominately contralateral innervation. Clinically, therefore, upper and lower motor neurone lesions affecting the facial nerve can be differentiated: upper motor neurone lesions cause paralysis that is confined to the contralateral lower face (supranuclear facial palsy), whilst lower motor neurone lesions cause complete ipsilateral facial paralysis (Bell's palsy). The facial nucleus also receives ipsilateral afferents from the nucleus solitarius and from the sensory nucleus of the trigeminal nerve, establishing important reflex connections.

Efferent fibres that arise from large motor neurones of the facial nucleus form the motor root of the facial nerve. At first, the facial fibres course dorsomedially towards the floor of the fourth ventricle as a more-or-less diffuse spread of fibres. These fibres pass dorsal and medial to the abducens nucleus, and then coalesce into a defined fibre bundle that recurves dorsally and laterally, over the rostral pole of the abducens nucleus, creating the bulge in the floor of the fourth ventricle, referred to as the facial colliculus (see **Fig. 28.12**). The fibres then descend ventrolaterally through the reticular formation and pass between their nucleus of origin medially and the nucleus of the spinal tract of the trigeminal nerve laterally. The facial nerve emerges from the brainstem at the supraolivary fossette, between the olive and restiform body, and passes laterally through the cerebellopontine angle cistern to the internal acoustic meatus (internal auditory canal).

General visceral efferent (GVE) fibres of the facial nerve arise from preganglionic parasympathetic neurones in the superior salivatory nucleus. These fibres run in the nervus intermedius and pass via the chorda tympani to the submandibular ganglion and via the greater petrosal nerve and the nerve of the pterygoid canal to the pterygopalatine ganglion.

Abducens nucleus

The abducens nucleus lies in the floor of the fourth ventricle, just lateral to the midline, immediately subjacent to the facial colliculus and slightly lateral to the medial longitudinal fasciculus (see **Fig. 28.11**). The abducens nucleus is composed of approximately 6500 neurones that align with the trochlear, oculomotor and hypoglossal nuclei to form the somatic motor column (GSE). Within the nucleus, large motor neurones are intermixed with small multipolar interneurones; the interneurones are most heavily concentrated in the lateral and ventral aspects of the nucleus.

The abducens nucleus receives afferent connections from multiple sources. These include corticonuclear fibres (which are principally contralateral, some of the fibres being aberrant corticospinal fibres that descend from the midbrain to this level in the medial lemniscus); the medial longitudinal fasciculus (by which the abducens nucleus is connected to oculomotor, trochlear and vestibular nuclei); the tectobulbar tract (from the deep layers of the superior colliculus); the paramedian pontine reticular formation (which lies rostral and caudal to the nucleus); the nucleus prepositus hypoglossi; and the contralateral medullary reticular formation.

The motor fibres of the abducens nucleus arise as a diffuse spread of fibres from the ventromedial aspect of the nucleus. Fifteen to twenty fascicles of the nerve pass ventrally, laterally and caudally, directly through the intervening reticular formation, trapezoid body, medial lemniscus, pontocerebellar fibres, pontine nuclei and descending corticospinal tracts to emerge from the brainstem at the pontomedullary sulcus about 1–2 cm lateral to the midline. In their course, the rootlets typically coalesce to emerge from the brainstem as a compact bundle of fibres. Occasionally all or some of the rootlets may emerge anomalously, rostral to the pontomedullary sulcus. The abducens nerve passes anteriorly, rostrally and slightly laterally across the prepontine cistern, penetrates the clivus through Dorello's canal, and enters the cavernous sinus lateral to the cavernous segment of the internal carotid artery. The abducens innervates the ipsilateral lateral rectus. Abducens interneurones give rise to fibres that cross the midline at the level of the nucleus and then ascend in the contralateral medial longitudinal fasciculus to all three medial rectus subnuclei of the oculomotor nucleus.

Trigeminal sensory nuclei

The sensory neurones of the trigeminal ganglion lie within the trigeminal (Gasserian, semilunar) ganglion situated in Meckel's cave. Their peripheral processes pass to sensory receptors in the head via the ophthalmic (V_1), maxillary (V_2) and mandibular (V_3) divisions of the trigeminal nerve (**Fig. 28.14**). Their central processes exit Meckel's cave

Afferent fibres arising from the interstitial nucleus of Cajal descend through the medial longitudinal fasciculus to synapse in the ipsilateral superior and medial vestibular nuclei and the nucleus prepositus hypoglossi. Afferent fibres from the Edinger–Westphal nucleus project to the medial and inferior vestibular nuclei, which also receive root fibres from the upper cervical nerve roots (C2, C3). The lateral vestibular nucleus and inferior portions of the medial and inferior vestibular nuclei receive ipsilateral spinovestibular fibres that ascend from lower spinal levels through the dorsospinocerebellar tract.

The nucleus prepositus hypoglossi is located in the upper medulla and lower pons, rostral to the hypoglossal nucleus, caudal to the abducens nucleus and medial to the medial vestibular nucleus. The nucleus prepositus does not receive primary vestibular afferents, but does receive bilateral input from the medial and dorsal vestibular nuclei (Holstein 2012). The nucleus prepositus has reciprocal connections with the medial vestibular nucleus, and extends efferents to most of the other vestibular nuclei. It also has reciprocal connections with the vestibulocerebellum. The nucleus prepositus receives input from the frontal eye fields and has extensive connections to the oculomotor system, including the oculomotor (Holstein 2012) and abducens nuclei and the paramedian pontine reticular formation (Talman and Robertson 1991). It is connected to the superior colliculus by the predorsal fasciculus. By these connections, the nucleus prepositus plays a key role in the integration of velocity signals with position signals for horizontal eye movements, so that the eyes can be held steady in eccentric positions in the orbit (Kim et al 2016). The reciprocal connections between the nucleus prepositus hypoglossi and the serotoninergic raphe system may have a role in regulating blood pressure (Talman and Robertson 1991).

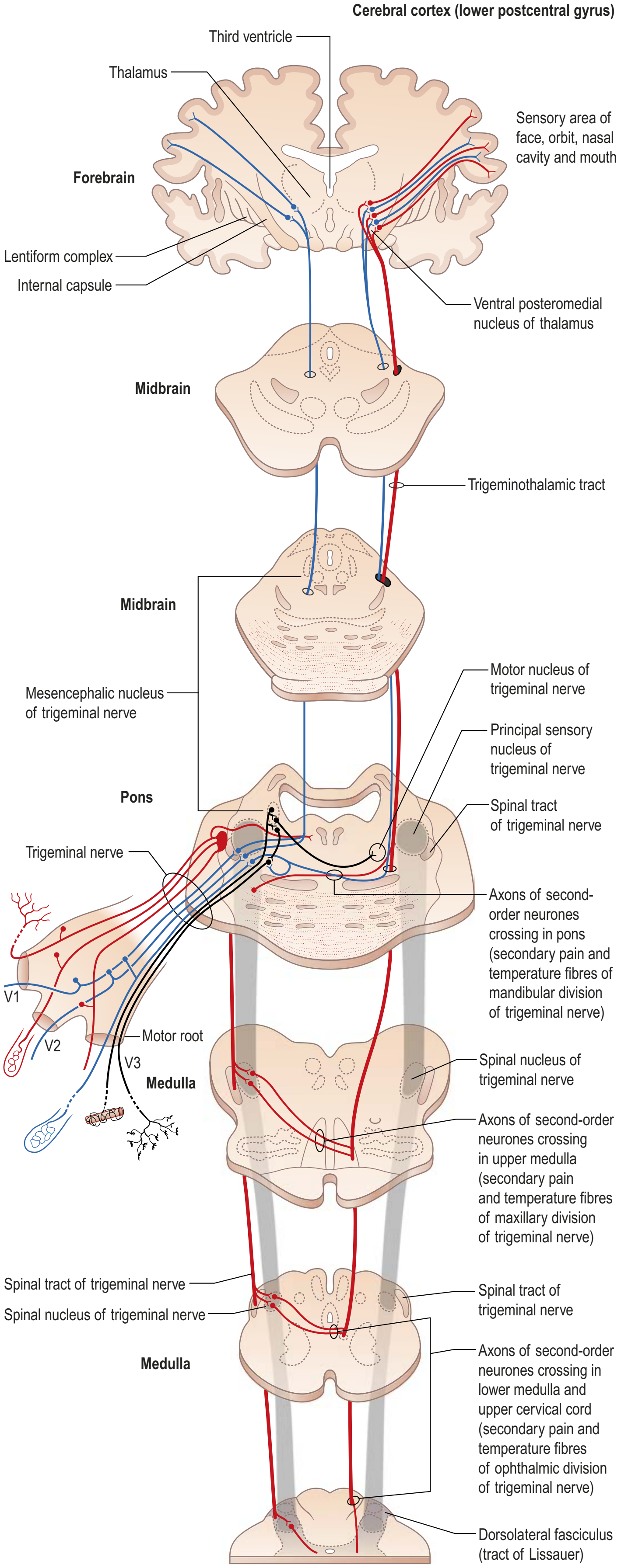
Cerebral cortex (lower postcentral gyrus)
Third ventricle
Thalamus
Sensory area of face, orbit, nasal cavity and mouth
Forebrain
Lentiform complex
Internal capsule
Ventral posteromedial nucleus of thalamus
Midbrain
Trigeminothalamic tract
Midbrain
Mesencephalic nucleus of trigeminal nerve
Motor nucleus of trigeminal nerve
Principal sensory nucleus of trigeminal nerve
Pons
Spinal tract of trigeminal nerve
Trigeminal nerve
Axons of second-order neurones crossing in pons (secondary pain and temperature fibres of mandibular division of trigeminal nerve)
V1
V2
Motor root
V3
Medulla
Spinal nucleus of trigeminal nerve
Axons of second-order neurones crossing in upper medulla (secondary pain and temperature fibres of maxillary division of trigeminal nerve)
Spinal tract of trigeminal nerve
Spinal nucleus of trigeminal nerve
Spinal tract of trigeminal nerve
Medulla
Axons of second-order neurones crossing in lower medulla and upper cervical cord (secondary pain and temperature fibres of ophthalmic division of trigeminal nerve)
Dorsolateral fasciculus (tract of Lissauer)

Fig. 28.14 The trigeminal nerve and its central connections.

posteriorly, aggregate into the primary sensory nerve (portio major) of the trigeminal nerve, and pass posteriorly through the upper cerebellopontine angle cistern to enter the lateral aspect of the pons. On entering the pons, the fibres of the sensory root of the trigeminal nerve course dorsomedially towards the principal sensory nucleus (see **Fig. 28.3**). About 50% of the fibres divide into ascending and descending branches and the remainder ascend or descend without division. The descending fibres form the spinal tract of the trigeminal nerve that terminates in the medially adjacent nucleus of the spinal tract of the trigeminal nerve. Some of these fibres provide short ascending collaterals to the principal sensory nucleus (Waite and Ashwell 2012).

The principal sensory nucleus lies in the lateral pontine tegmentum medial to the middle cerebellar peduncle and lateral to both the trigeminal motor nucleus and the incoming trigeminal root fibres. It is continuous inferiorly with the spinal nucleus of the trigeminal nerve. The principal nucleus may be divided into dorsal and ventral subnuclei: the sizes and shapes of the neurones appear similar in the two portions but they have differing connections (Henssen et al 2016).

The principal sensory nucleus receives afferent fibres from mechanoreceptors and is mainly concerned with tactile discrimination. As with the fibres entering the spinal trigeminal tract, the incoming sensory fibres segregate ventrodorsally, with the fibres from V_1 most anterior, those from V_2 in the middle, and those from V_3 most dorsal. Some ascending trigeminal fibres, many of them heavily myelinated, synapse around the small neurones in the principal sensory nucleus.

Efferent fibres from the ventral portion of the principal sensory nucleus traverse the ventral trigeminothalamic tract (trigeminal lemniscus), cross the midline and ascend with the contralateral medial lemniscus to the ventral posteromedial nucleus (VPM) of the thalamus (Waite and Ashwell 2012). Efferent fibres arising from the dorsomedial portion of the principal sensory nucleus traverse the ipsilateral dorsal trigeminothalamic tract to the VPM of the ipsilateral thalamus (Waite and Ashwell 2012). From there, thalamic efferents project to the postcentral gyrus (areas 3, 1, 2). Thus both principal sensory nuclei project bilaterally to both VPM nuclei.

Tactile and nociceptive pain and temperature data from the orofacial region is received in the trigeminal sensory nuclei and projected to the rest of the brain mainly by the ventral and dorsal trigeminothalamic tracts.

The mesencephalic nucleus of the trigeminal nerve is a column of large, round unipolar cells that extend from the sensory nucleus of the trigeminal nerve in the pons into the lateral margins of the periaqueductal grey matter in the midbrain (**Fig. 28.15**; see **Figs 28.3, 28.14**). Within the cell column, the neurones are arranged in many small groups and are most numerous caudally. The mesencephalic nucleus contains the only primary sensory unipolar neuronal somata within the CNS rather than in a senory ganglion. The neurones of the mesencephalic nucleus extend axons caudally within the mesencephalic tract of the trigeminal nerve. There, the axons bifurcate into central and peripheral branches. The central processes terminate on trigeminal motor neurones. The peripheral processes extend between the motor and principal sensory nuclei of the trigeminal nerve, leave the brainstem with the trigeminal motor fibres in the portio minor, and pass into the mandibular division of the trigeminal nerve: they convey Ia afferent fibres from the masticatory muscles. This arrangement establishes the only significant supraspinal monosynaptic reflex and is the basis for the 'jaw jerk'. The peripheral processes may also convey proprioceptive impulses from the teeth, the facial and oculogyric muscles (Waite and Ashwell 2012). Nerve fibres that ascend to the mesencephalic nucleus may also give collaterals to the motor nucleus of the trigeminal nerve and to the cerebellum. Projections from the mesencephalic nucleus to the principal sensory nucleus may relay proprioceptive sensation to the thalamus (Waite and Ashwell 2012).

Trigeminal motor nucleus

The motor nucleus of the trigeminal nerve is an ovoid cell mass that lies in the upper pontine tegmentum, beneath the fovea trigeminalis, and medial to the principal sensory nucleus, from which it is separated by fibres of the trigeminal nerve (see **Figs 28.3, 28.13**). It forms the rostral part of the pharyngeal efferent column (SVE).

The motor nucleus contains characteristic large multipolar neurones interspersed with smaller multipolar cells. The neurones are organized into a number of relatively discrete subnuclei, the axons from which innervate individual muscles. It receives afferent input from the motor cortices of both cerebral hemispheres (Gilman and Newman 2003, Paxinos et al 2012). These fibres leave the corticonuclear tract at the level of the trigeminal motor nucleus (or higher in the pons as aberrant corticospinal fibres), and may end on motor neurones or interneurones. The motor nucleus of each side also receives afferents from the sensory nuclei of the trigeminal nerve (possibly including some from the mesencephalic nucleus, which form monosynaptic reflex arcs for proprioceptive control of the masticatory muscles), as well as from the reticular formation, the red nucleus and tectum, the medial longitudinal fasciculus and possibly from the locus coeruleus. Collectively, these represent pathways by which salivary secretion and mastication may be coordinated.

Secondary relay fibres originating from the ventral portion of the principal sensory nucleus and from the rostral and interpolar portions of the spinal trigeminal nucleus form the ventral trigeminothalamic tract (thalamic lemniscus). This tract courses upward and medially through the pontine tegmentum, crosses the midline and ascends along the dorsomedial side of the contralateral medial lemniscus to terminate mainly within the VPM of the thalamus. Secondary relay fibres arising from the dorsomedial portion of the principal sensory nucleus traverse the ipsilateral dorsal trigeminothalamic tract to the ipsilateral thalamus. Secondary relay fibres from different regions of the caudal portion of the spinal trigeminal nucleus also traverse the dorsal trigeminothalamic tracts, but pass, variably, to the ipsilateral or the contralateral thalamus (Waite and Ashwell 2012, Henssen et al 2016). The dorsal trigeminothalamic tract ascends within the dorsal tegmentum of the pons and lower midbrain, passes ventral and lateral to the periaqueductal grey matter, curves laterally and enters the dorsomedial portion of the ipsilateral VPM of the thalamus. Henssen et al (2016) discuss a third intranuclear efferent pathway by which secondary relay fibres arising from the interpolar and caudal portions of the spinal trigeminal nucleus pass toward or into the periaqueductal grey matter.

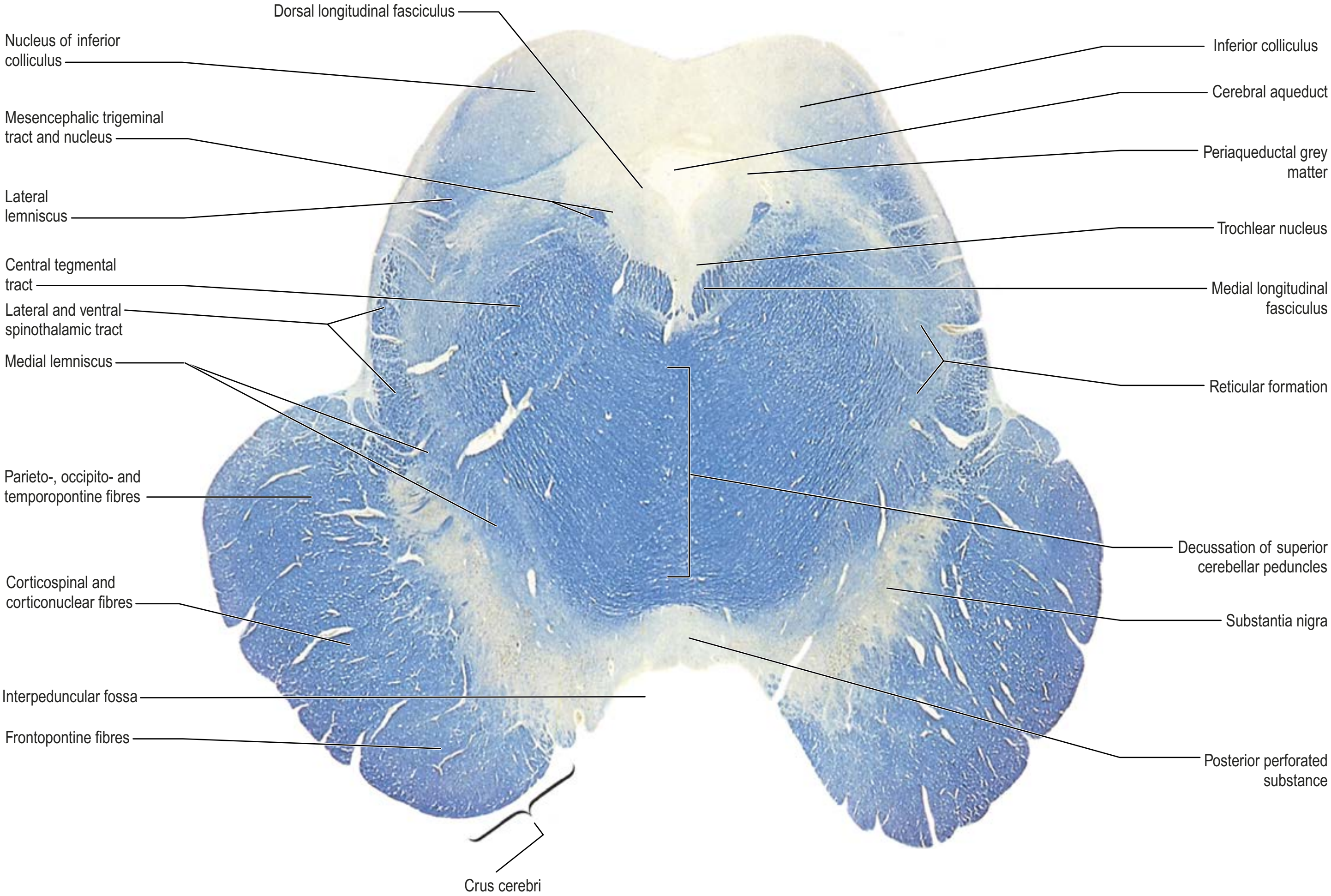
Dorsal longitudinal fasciculus
Nucleus of inferior colliculus
Mesencephalic trigeminal tract and nucleus
Lateral lemniscus
Central tegmental tract
Lateral and ventral spinothalamic tract
Medial lemniscus
Parieto-, occipito- and temporopontine fibres
Corticospinal and corticonuclear fibres
Interpeduncular fossa
Frontopontine fibres
Crus cerebri
Inferior colliculus
Cerebral aqueduct
Periaqueductal grey matter
Trochlear nucleus
Medial longitudinal fasciculus
Reticular formation
Decussation of superior cerebellar peduncles
Substantia nigra
Posterior perforated substance

Fig. 28.15 A transverse section of the midbrain at the level of the inferior colliculi, prepared using Luxol fast blue stain for myelinated nerve fibres (blue).

Axons from the motor nucleus form the motor root of the trigeminal nerve, which courses outward in tandem with the sensory root to reach Meckel's cave and then descends with the mandibular division (V_3) to innervate the major muscles of mastication (temporalis, masseter, medial and lateral pterygoid), and tensor typmpani, tensor veli palatini, mylohyoid and anterior belly of the digastric.

Salivatory nuclei

The preganglionic parasympathetic neurones controlling salivation are found in the caudal pons, dorsal and lateral to the facial nucleus, with additional cells distributed more dorsally along the intramedullary course of the seventh nerve (see Fig. 28.3) (Blessing and Benarroch 2012). These neurones supply axons to the facial (nervus intermedius) and glossopharyngeal nerves for secretomotor control of the salivatory and lacrimal glands. Although these cells have traditionally been divided into a superior salivatory nucleus that supplies fibres to the nervus intermedius and an inferior salivatory nucleus that supplies fibres to the glossopharyngeal nerves, the brainstem distributions of the neurones innervating the two nerves is reported to be nearly indistinguishable (Blessing and Benarroch 2012). 'Salivatory neurones' may also play a significant part in the parasympathetic regulation of extracranial and intracranial vasculature (Blessing and Benarroch 2012).

Superior cerebellar peduncle

The superior cerebellar peduncle (brachium conjunctivum) is the main ascending efferent pathway from the cerebellum. It lies within the lateral wall of the fourth ventricle, medial to the restiform body (see **Fig. 28.13**) (Nieuwenhuys et al 2008). Numerous fibres that enter the mesencephalic tegmentum arise from the cerebellar nuclei, pass ventromedially and cross the midline via the decussation of the superior cerebellar peduncles at the border between the pons and midbrain. The ventral-most fibres from the dorsomedial portion of the peduncle decussate first, crossing immediately dorsal to the interpedunular nucleus. The midportion of the superior cerebellar peduncle decussates further rostrally. Rostral to the decussation, the ascending fibres laterally encapsulate and penetrate the red nucleus, in which some fibres, or their collaterals, terminate. However, the majority of the superior cerebellar fibres ascend to terminate in the ventral lateral nucleus of the thalamus. A relatively small number of uncrossed fibres are believed to end in the periaqueductal grey matter and reticular formation, the interstitial nucleus and the nucleus of the posterior commissure. Descending crossed fibres from the decussation of the superior cerebellar peduncle also end in the pontine nuclei, the medullary reticular formation and the nuclei of the inferior olivary complex.

Pontine reflexes

Corneal and blink reflexes

Touching the cornea of one eye elicits reflex closure of both eyes via the corneal reflex. The afferent limb of this pathway involves mainly nasociliary branches of the ophthalmic division of the trigeminal nerve, with cell bodies in the trigeminal ganglion and central processes synapsing on second-order neurones in the ipsilateral spinal tract and principal sensory nuclei of the trigeminal nerve. These neurones drive a polysynaptic chain of interneurones in the lateral reticular formation of the pons and medulla which, in turn, activate neurones innervating the palpebral components of orbicularis oculi in the facial motor nuclei bilaterally: the stimulated muscles then contract to produce a bilateral blink. The sweep of the eyelids carries lacrimal secretions across the eye, helping to remove any irritating particles. Shining a bright light into one eye elicits a similar reflex closure of both eyes via the blink reflex; the afferent limb of this reflex involves stimulation of the retina and optic pathway.

Jaw jerk reflex

Rapid stretching of the muscles that close the jaw (masseter, temporalis, medial pterygoid) activates muscle spindle afferents, which travel via the mandibular division of the trigeminal nerve to the brainstem. The cell bodies of these primary afferent neurones are located in the mesencephalic trigeminal nucleus. Collaterals project monosynaptically to the motor nucleus of the trigeminal nerve in the pons. Axons arising in the motor nucleus travel via the mandibular nerve to innervate the muscles that act on the temporomandibular joint and close the jaw (Ch. 38).

Tensor tympani and stapedius reflexes

Loud sounds elicit reflex contraction of the tensor tympani and stapedius to dampen excess excursion of the tympanic membrane and middle ear ossicles. Afferent impulses travel in the cochlear nerve to the cochlear nuclei in the brainstem. Efferent fibres to the tensor tympani arise in the motor nucleus of the trigeminal nerve and travel in the mandibular division of the nerve. Efferent fibres to the stapedius originate in the facial nucleus and travel in the facial nerve.

MIDBRAIN

The midbrain (mesencephalon) is the most rostral and the shortest of the three brainstem segments. It is usually less than 2 cm in length and about 2–2.5 cm wide at the greatest expanse of the crura cerebri: much of it lies in the posterior cranial fossa. It courses through the tentorial incisura from the infratentorial to the supratentorial compartment. The midventral surface of the midbrain is related to the dorsum sellae, the proximal basilar artery and its branches, and the undersurface of the hypothalamus. Laterally, the ventral surface abuts the optic tracts and the medial temporal lobes. Dorsally, the midbrain is related to the habenular nuclei and pineal gland of the epithalamus, the great cerebral vein, and the anterior face of the cerebellum. The midbrain contains the nuclei of the trochlear and oculomotor nerves.

External features and relations

The caudal border of the midbrain is the rostral edge of the pons ventrally and the decussation of the trochlear nerve in the superior medullary velum dorsally. The rostral border is the caudal edge of the mammillary bodies ventrally, the lower edge of the optic tracts laterally and the lower edge of the posterior commissure dorsally. A curved line drawn along the anterior borders of the substantiae nigrae demarcates the base of the midbrain from the tegmentum. A curved line drawn in relation to the anterior surface of the aqueduct demarcates the tegmentum from the tectum. The decussation of the superior cerebellar peduncle marks the transition of the tegmentum pontis into the tegmentum mesencephali.

The ventral surface of the midbrain is marked by the crus cerebri, flanking the interpeduncular fossa. The medial mesencephalic sulci delimit the crura cerebri from the hypothalamus medially (Naidich et al 2009). At the level of the tentorial incisure, the basilar artery divides in the interpeduncular fossa into the right and left P1 segments of the posterior cerebral arteries. On each side, 1–3 superior cerebellar arteries branch from the basilar artery immediately before this bifurcation. The posterior cerebral and superior cerebellar arteries both run laterally around the ventral surface of the crus, the former passing above the tentorium cerebelli, the latter passing below. On each side, multiple rootlets of the oculomotor nerve emerge into the interpeduncular fossa through the medial walls of the crura cerebri and aggregate into a single fascicle that then passes forward between the uppermost superior cerebellar artery and the P1 segment of the posterior cerebral artery, traverses the suprasellar cistern, and penetrates the superior surface of the lateral wall of the cavernous sinus. The posterior communicating artery joins the posterior cerebral artery on the medial surface of the peduncle in the interpeduncular fossa. Numerous small openings in the interpeduncular fossa constitute the posterior perforated substance, which is pierced by central branches of the basilar and posterior cerebral arteries. The optic tract is located at the point where the crus emerges from the cerebral hemispheres.

The dorsal surface of the midbrain is marked by the superior and inferior colliculi. The superior colliculi are broader and extend further laterally than the inferior colliculi. The infracollicular sulcus defines the inferior borders of the inferior colliculi. Below the inferior colliculi, the midline frenulum veli helps to suspend the superior medullary velum over the fourth ventricle. The trochlear nerve emerges from the dorsal surface of the midbrain just caudal to the inferior colliculus and courses laterally and ventrally around the midbrain. Laterally, on each side, the brachium of the inferior colliculus ascends to the medial geniculate body. The brachium of the superior colliculus ascends over the medial geniculate body to reach the lateral geniculate body. The pretectum, the pineal gland, the habenular trigone and the striae medullares thalami all lie superior to the superior colliculus.

Internal organization

Lower midbrain: Transverse section at the level of the inferior colliculi

From dorsal to ventral, a transverse (axial) section through the midbrain at the level of the inferior colliculi contains the inferior colliculus, lateral lemniscus, cerebral aqueduct and periaqueductal grey matter, superior cerebellar peduncle and its midline decussation, posterior perforated substance just dorsal to interpeduncular fossa, and the crus cerebri (see Fig. 28.15). The crus cerebri contains, from medial to lateral, the descending frontopontine, corticonuclear, corticospinal, and parieto-, occipito- and temporopontine fibres. The substantia nigra lies dorsal to the crus cerebri and consists of a ventral pars reticulata (SNr) and a dorsal pars compacta (SNc). The medial and lateral lemnisci form a prominent lemniscal arc of white matter dorsolateral to the decussation of the superior cerebellar peduncles. Dorsally, the trochlear nucleus lies at the ventral aspect of the periaqueductal grey matter, enveloped by the medial longitudinal fasciculus. The fibres of the trochlear nerve course dorsolaterally and caudally, just within the perimeter of the periaqueductal grey matter, toward their decussation in the superior medullary velum. The central tegmental tract and the reticular formation lie within the tegmentum.

Upper midbrain: Transverse section at the level of the superior colliculi

A transverse (axial) section through the upper midbrain and mesencephalic–diencephalic junction at the level of the superior colliculi contains the superior colliculi, the cerebral aqueduct (of Sylvius) and the periaqueductal grey matter (**Fig. 28.16**). Depending on precise section angulation, this section may also display the inferior pole of the medial geniculate nucleus rostrally. Just dorsal to the substantia nigra, the red nuclei replace the decussation of the superior cerebellar peduncles. Crossed fibres from the contralateral superior cerebellar peduncle pass through and around the red nuclei en route to the thalamus. The ascending fibres of the medial lemniscus and the spinothalamic tract converge dorsolateral to the red nuclei as they approach the ventral posteromedial and ventral posterolateral nuclei of the thalamus. The structures of the lemniscal arc no longer include the lateral lemniscus, because this tract terminates in the inferior colliculus. The oculomotor nuclear complex lies at the ventral aspect of the periaqueductal grey matter, partly enclosed on the ventral border by the fibres of the medial longitudinal fasciculus. The fibres of the oculomotor nerve emerge from the ventrolateral aspect of the nucleus and curve though the tegmentum, the red nucleus and the medial part of the substantia nigra to emerge into the interpeduncular fossa through the medial wall of the crus cerebri. The parasympathetic Edinger–Westphal nucleus is a paramedian structure situated dorsal to the oculomotor nucleus. The posterior perforated substance lies along the dorsomedial margin of the interpeduncular fossa. The central tegmental tract runs within the pontine and medullary tegmentum from the dorsomedial aspect of the red nucleus down to the inferior olivary nuclei of the medulla. The reticular formation occupies the dorsal tegmentum.

Pathways and nuclei of the midbrain

Tectum

The tectum consists of the superior and inferior colliculi with their brachia and commissural connections, the ascending spinal and lateral lemnisci, and the descending tectobulbar and tectospinal tracts.

Inferior colliculus

The inferior colliculus is a key part of the ascending auditory pathway and is the principal site of termination of the lateral lemniscus (see Fig. 28.15). Its core, the central nucleus, is surrounded by afferent fibres from the lateral lemniscus. A group of smaller paracentral nuclei include the external and pericentral nuclei.

The inferior colliculus receives ascending fibres from the cochlear nuclei via the lateral lemniscus. Many of these fibres synapse within the central nucleus for relay to the anterior division of the medial geniculate nucleus. Other fibres pass through the inferior colliculus directly to the medial geniculate nucleus, without relay. Descending projections from the auditory cortex reach the inferior colliculus directly or via the medial geniculate nucleus. The two inferior colliculi are reciprocally interconnected by the commissure of the inferior colliculi, which crosses the midline dorsal to the cerebral aqueduct.

The central nucleus is composed of four cortical layers: layer I contains small neurones with flattened radial dendritic fields; layer II contains medium-sized neurones with ovoid dendritic fields aligned parallel with the collicular surface; layer III contains medium-sized neurones with spherical dendritic fields; and layer IV contains large neurones with variably shaped dendritic fields. Bands of cells with disc-shaped or stellate dendritic fields orthogonally span the fibre layers in which the terminals of lateral lemniscal fibres ramify. Experimental studies have found cells driven by low frequencies in the dorsal laminae, and cells driven by high frequencies in the ventral laminae. Neurones are broadly frequency-tuned in the dorsal cortex and lateral nucleus. Lesions of either the inferior colliculus or its brachium produce severe defects in tonal discrimination, sound localization and auditory reflexes.

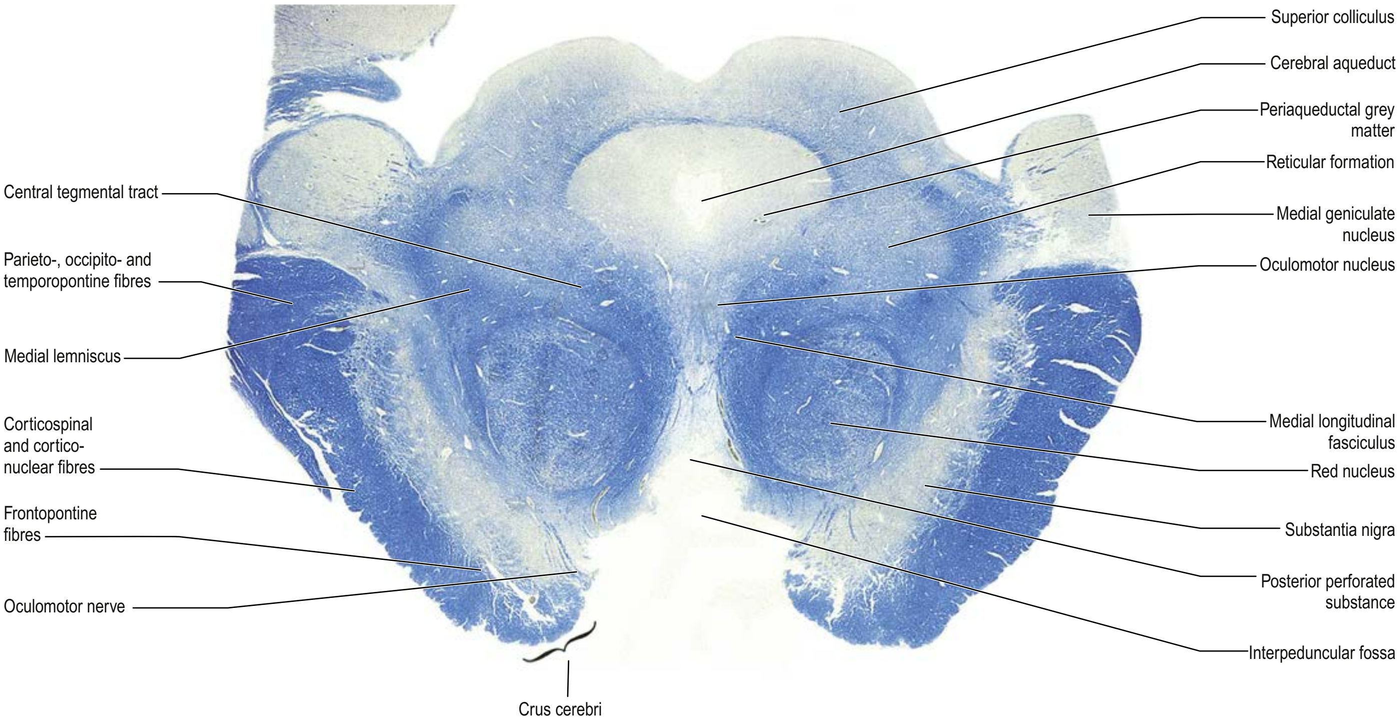

Fig. 28.16 A transverse section of the midbrain at the level of the superior colliculi, prepared using Luxol fast blue stain for myelinated nerve fibres (blue).

Most efferent fibres from the inferior colliculus ascend through the brachium of the inferior colliculus to reach the ipsilateral medial geniculate nucleus. In humans, the ventral division of the medial geniculate nucleus receives a topographic projection from the central nucleus of the inferior colliculus. The dorsal division of the medial geniculate receives a similar projection from the dorsal cortex. From the medial geniculate body impulses are relayed on to the primary auditory cortex through the auditory radiations. Other efferents from the inferior colliculus pass through the medial geniculate nucleus without relay and continue on to the auditory cerebral cortex. Caudally directed projections of the inferior colliculus to the brainstem and spinal cord form part of the tectospinal and tectotegmental tracts. These projections are relatively small and probably mediate reflex turning of the head and eyes in response to sounds. For further reading on the auditory pathways, see Chapter 43.

Superior colliculus

The superior colliculus (see Fig. 28.16) is composed of multiple layers of neuronal somata alternating with their white matter processes (May 2005). At successive depths from the external surface, it may be divided into seven layers: zonal, superficial grey (stratum cinereum), optic, intermediate grey, deep grey, deep white and periventricular strata, composed alternately of neuronal somata or their processes (Crosby et al 1962). The zonal layer consists chiefly of myelinated and non-myelinated fibres from the occipital cortex (areas 17, 18 and 19), which arrive as the external corticotectal tract. It also contains a few small neurones, which are horizontally arrayed. The superficial grey layer forms a crescentic lamina over the deeper layers and contains many small multipolar interneurones, on which cortical fibres synapse. The optic layer consists partly of fibres from the optic tract that permeate the entire anterior–posterior extent of the superficial layers with numerous collateral branches as they terminate. This arrangement provides a retinotopic map of the contralateral visual field, in which the fovea is represented anterolaterally. Retinal axons terminate in clusters from specific retinotectal neurones and as collaterals of retinogeniculate fibres. The layer also contains some large multipolar neurones. Efferent fibres to the retina are said to start in this layer.

The seven layers can be grouped into a superficial division consisting of the zonal, superficial grey and optic layers; an intermediate division consisting of the intermediate grey and white layers, and a deep division consisting of the deep grey and white layers. The deep grey and deep white layers adjacent to the periaqueductal grey matter are collectively called the parabigeminal nucleus. The intermediate grey and white layers collectively constitute the main receptive zone. The main afferent input is via the medial corticotectal path from layer V neurones of the ipsilateral occipital cortex (Brodmann area 18), and from other neocortical areas that are concerned with eye pursuit movements.

The extensive connections of the superior colliculus make it a major centre for initiating eye movements and coordinating them with movements of the head and neck. The superficial layers of the superior colliculus contain a retinotopic map of the environment and the deeper layers contain premotor neurones with conections to networks that generate saccades and head movements. The auditory, somatosensory and visual signals that converge on the superior colliculus move the eyes, head and body to direct the line of sight towards objects of interest for orienting behaviour. These interconnections are discussed in detail in Chapters 29 and 44.

The superficial layers of the superior colliculus give rise to ascending connections to the visual centres such as the pretectum and the visual thalamic nuclei. Fibres passing from the pulvinar are relayed to primary and secondary visual cortices and form an extrageniculate retinocortical pathway for visual orientation and attention. The intermediate layers of the superior colliculus give rise to the coarse fibres of the tectospinal tract. After crossing the midline in the dorsal tegmental decussation these fibres descend in the pons and become incorporated into the medial longitudinal fasciculus and the ventral funiculus of the cervical spinal cord. The tectonuclear tract, mainly crossed, descends near the tectospinal tract, and ends in the pontine nuclei and motor nuclei of the cranial nerves, particularly those innervating the oculogyric muscles. It subserves reflex ocular movements. The deep layers of the superior colliculus extend widely to thalamic, reticular and precerebellar nuclei and to the spinal cord.

Tegmentum

Trochlear nucleus

The trochlear nucleus is a small ovoid mass of grey matter just to the side of the midline (see Fig. 28.15). The trochlear nucleus is bounded by the periaqueductal grey matter dorsally and is enveloped by the fibres of the longitudinal fasciculi ventrally and laterally (Naidich et al 2009). The nucleus is part of the somatic efferent column in line with the oculomotor, abducens and hypoglossal nuclei more caudally.

Afferent inputs to the trochlear nucleus include fibres from the rostral intermediate nucleus of the medial longitudinal fasciculus and from the interstitial nucleus of Cajal, both of which are involved in the control of vertical and torsional gaze. Other inputs come from the vestibular, abducens and oculomotor nuclei and, directly or indirectly, from the nuclei of the posterior commissure (nuclei of Darkschewitsch and of Cajal) and, via these nuclei, from the superior colliculus, frontal eye fields and other cortical areas. Other afferents arrive from the nucleus prepositus hypoglossi.

Efferent trochlear fibres first course dorsally and caudally, just deep to the outer perimeter of the periaqueductal grey matter and medial to the mesencephalic trigeminal nucleus. The trochlear nerves then

Other afferent fibres to the inferior colliculi originate from the contralateral spinal cord (via spinotectal fibres in the anterolateral system), the inferior colliculus, the noradrenergic locus coeruleus and the serotoninergic raphe nuclei. The cholinergic parabigeminal nucleus contains neurones whose dendrites extend into the optic layer, and whose axons form many of the collicular efferents.

The deep collicular laminae give rise to a tecto-olivary projection to the contralateral upper third of the medial accessory olivary nucleus. Tectotegmental fibres reach various tegmental reticular nuclei in the ipsilateral mesencephalic and contralateral pontomedullary reticular formation (gigantocellular reticular, caudal pontine reticular, oral pontine reticular nuclei), and the substantia nigra and red nucleus. Tectopontine fibres, which probably descend with the tectospinal tract, terminate in dorsolateral pontine nuclei, with a relay to the cerebellum.

decussate within the superior medullary velum of the fourth ventricle. The fully decussated nerves emerge from the dorsal surface of the brainstem just caudal to the inferior colliculus and just to each side of the frenulum veli. The trochlear nerve is the only cranial nerve to emerge on the dorsal surface of the brainstem. At the point of emergence, a variable number of rootlets, usually two, unite to form the nerve trunk. The trochlear fibres then curve ventrally through the perimesencephalic cistern, between the superior cerebellar arteries below and the posterior cerebral arteries above, to enter the lateral dural wall of the cavernous sinus (Yousry et al 2002a, Naidich et al 2009, Naidich et al 2013). A few fibres may remain ipsilateral.

Oculomotor nuclear complex

The nuclear complex from which the oculomotor nerve arises consists of several groups of large motor neurones that are collectively designated the oculomotor nucleus, and the smaller preganglionic parasympathetic Edinger–Westphal nucleus (see Figs 28.3, 28.16). The nuclear complex lies at the ventromedial aspect of the periaqueductal grey matter, superior to the trochlear nuclei and is partially enclosed by the fibres of the median longitudinal fasciculi. The oculomotor complex is approximately 5 mm long and is divisible into neuronal groups that correlate with the distribution of motor fibres within the oculomotor nerve.

Afferent inputs to the oculomotor nuclear complex include fibres from the rostral interstitial nucleus of the medial longitudinal fasciculus and the interstitial nucleus of Cajal, both of which are involved in the control of vertical and torsional gaze. Other inputs come, directly or indirectly, from the nuclei of the posterior commissure and, via these nuclei, from the frontal eye fields, the superior colliculus, the dentate nucleus and cortical areas. The medial longitudinal fasciculus carries afferent connections from the trochlear, abducens and vestibular nuclei. The fibres from the medial vestibular nucleus project to the medial rectus subnucleus.

In order from dorsal to ventral, the oculomotor neurone groups innervate the ipsilateral inferior rectus, inferior oblique and medial rectus. A medially placed column of cells innervates the contralateral superior rectus through axons that decussate in the caudal part of this subnucleus. A median subnucleus of large neurones, designated the caudal central nucleus, lies at the caudal pole of the oculomotor nucleus adjacent to the superior rectus and medial rectus subnuclei.

Fascicles of axons from these subnuclei course forwards in the midbrain, through the tegmentum, red nucleus and medial substantia nigra, to emerge as the oculomotor nerve in the interpeduncular fossa. The fascicles are most probably arranged from medial to lateral subserving the pupil, inferior rectus, medial rectus, levator palpebrae superioris and superior rectus, and inferior oblique.

Edinger–Westphal nucleus

The Edinger–Westphal nucleus lies dorsal to the main oculomotor nucleus. It is composed of small, multipolar, preganglionic parasympathetic (general visceral efferent, GVE) neurones. Afferent inputs to the nucleus come primarily from the pretectal nuclei bilaterally, mediating the pupillary light reflex, and from the visual cortex, mediating accommodation. Efferent fibres from the nucleus travel in the oculomotor nerve to synapse with postganglionic neurones in the ciliary ganglion (Kozicz et al 2011). Efferents from the Edinger–Westphal nucleus also descend through the medial longitudinal fasciculus to innervate the medial and descending vestibular nuclei (Nieuwenhuys et al 2008).

Pretectal nuclei

Available with the *Gray's Anatomy* e-book

Premotor neurones for vertical gaze

Available with the *Gray's Anatomy* e-book

Interstitial nucleus of Cajal

Available with the *Gray's Anatomy* e-book

Rostral interstitial nucleus of the medial longitudinal fasciculus

Available with the *Gray's Anatomy* e-book

Periaqueductal grey matter

The periaqueductal grey matter (PAG) is a zone of small, closely packed cells that lies in the dorsal tegmentum surrounding and ventral to the cerebral aqueduct (see Figs 28.15–28.16). It is continuous with the grey matter of the hypothalamus rostrally and with the floor of the fourth ventricle caudally.

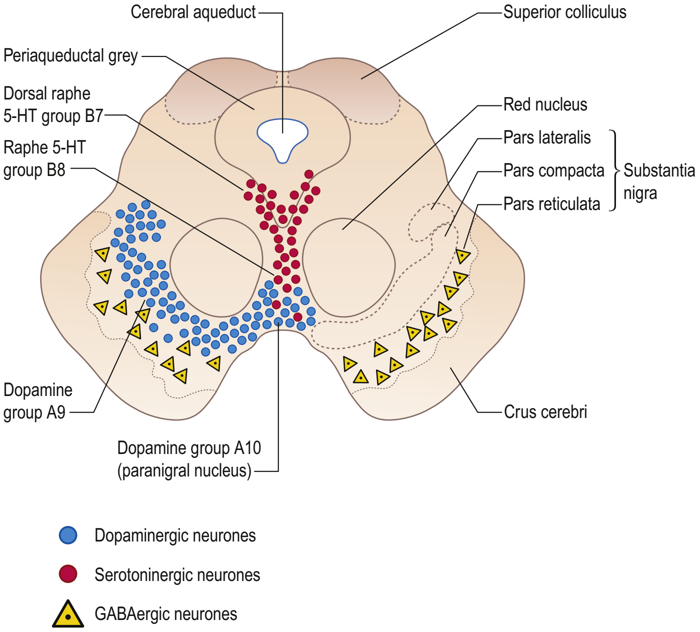

Fig. 28.17 Transverse section through the midbrain to show the arrangement of dopaminergic cell groups A9 and A10 in the substantia nigra (left) and serotoninergic cell groups B7 and B8 in the raphe.

The PAG receives afferents from the hypothalamus and amygdala and projects to the intermediate reticular zone. In animals, a complex of cell groups collectively designated the hypothalamic defensive complex project to the PAG via the dorsal longitudinal fasciculus (of Schütz). A somatosensory homunculus has been suggested for the periaqueductal grey matter, with the lower limbs represented rostrally, the head caudally and the trunk and upper limbs in the intermediate position. This somatosensory representation is contralateral, except for the forehead and scalp (Paxinos et al 2012).

The nucleus of Darkschewitsch

Available with the *Gray's Anatomy* e-book

Red nucleus

The red nucleus is an ovoid group of neurones within the upper midbrain, approximately 5 mm in diameter, situated dorsomedial to the substantia nigra and rostral to the decussation of the superior cerebellar peduncles (**Fig. 28.17**; see Fig. 28.16). It appears pink in fresh gross sections – hence its name. The red nucleus consists of two subnuclei: the caudal magnocellular portion containing about 150–200 giant to large-sized neurones and the rostral parvocellular portion that is considered to be phylogenetically more recent. The parvocellular subnucleus is larger and better defined in primates than in lower mammals. There is an increasing, age-dependent deposition of iron within the nucleus (**Fig. 28.18**).

Most of the ascending fibres of the superior cerebellar peduncle give off collaterals that synapse on cells within the red nucleus. There are bilateral, probably reciprocal, connections between the red nucleus and the superior colliculi. The magnocellular portion receives afferent input from the primary motor cortex via collateral projections of the corticospinal (pyramidal) tract. The parvocellular red nucleus receives direct input from layer V pyramidal neurones in the motor, premotor, supplementary motor and cingulate motor cortices and from the frontal and supplementary eye fields. The motor and supplementary motor projections to the parvocellular red nucleus are organized somatotopically.

The largest group of efferents arise from the rostral parvocellular portion of the red nucleus and descend in the ipsilateral central tegmental tract to the ipsilateral principal olivary nucleus. Some tract fibres terminate in the brainstem reticular nuclei. In humans, the rubrospinal tract is very small; it runs ventral to the lateral corticospinal tract and is generally believed to terminate in the contralateral upper cervical segments of the spinal cord.

Substantia nigra

The substantia nigra (see Figs 28.15–28.18) is a crescent-shaped zone of grey matter that extends through the length of the midbrain just

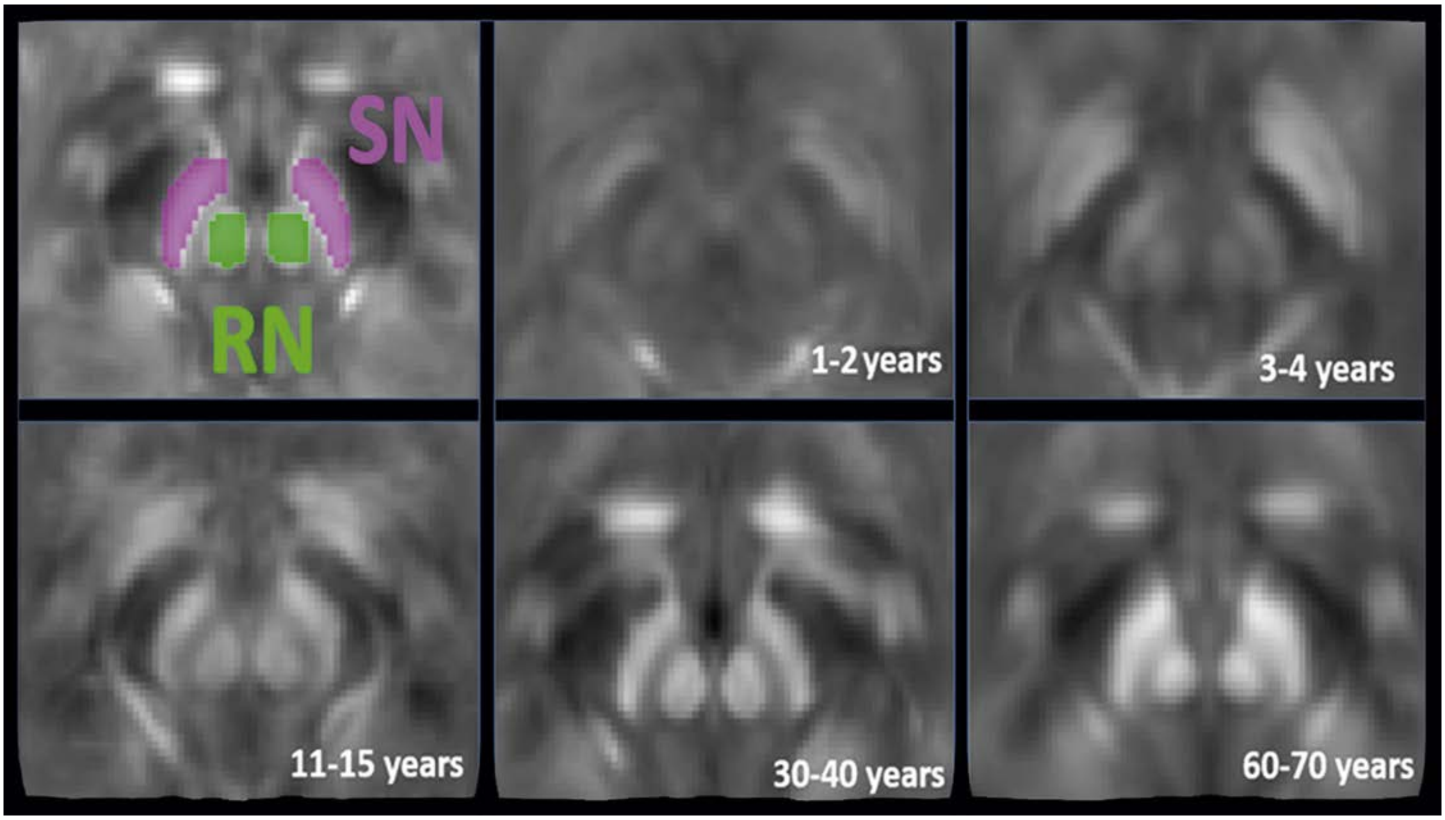

Fig. 28.18 Increasingly bright signal indicates progressive deposition of iron within the substantia nigra (SN) and red nuclei (RN) with age. (Adapted with permission from Zhang et al 2018 Longitudinal data for magnetic susceptibility of normative human brain development and aging over the lifespan. Data in Brief 2018; 20:623–31 (Fig. 3).)

The medial rectus subnucleus consists of three anatomically distinct subpopulations. The ventral portion contains the largest number of motor neurones and occupies the rostral two-thirds of the nucleus. A population of smaller motor neurones lies dorsally throughout the rostral two-thirds of the nucleus and innervates the small orbital fibres of medial rectus and a third subpopulation lies dorsolaterally in the caudal two-thirds of the nucleus.

The pretectal nuclei are a poorly defined group of neurones situated at the junction of the mesencephalon and diencephalon. They extend caudally from a position dorsolateral to the posterior commissure towards the superior colliculus, with which they are partly continuous. They include the olivary pretectal nucleus. Afferent fibres to the pretectal nuclei arrive from the visual cortex via the brachium of the superior colliculus, from the retina via the lateral root of the optic tract and from the superior colliculus. The pretectal nuclei send efferent fibres to the Edinger–Westphal preganglionic nuclei bilaterally. Those efferent fibres that decussate pass ventral to the aqueduct or through the posterior commissure. In this way, the sphincter pupillae contract in both eyes in response to impulses from either eye. This bilateral light reflex may not be the sole activity of the pretectal nucleus. Some efferent fibres from the pretectum project to the pulvinar and deep laminae of the superior colliculus, and provide an additional extrageniculate path to the cerebral cortex.

Premotor neurones for vertical gaze are located in the reticular formation of the midbrain, including the interstitial nucleus of Cajal and the rostral intermediate nucleus of the medial longitudinal fasciculus. These nuclei lie adjacent to each other between the periaqueductal grey matter and the red nucleus. The interstitial nucleus of Cajal acts to integrate eye-velocity signals with eye-position signals. The rostral intermediate nucleus of the medial longitudinal fasciculus (MLF) contains medium-lead burst neurones.

The interstitial nucleus of Cajal is an aggregate of widely spaced, medium-sized, parvalbumin-positive neurones in the dorsomedial region of the upper mesencephalic tegmentum. The cells of the nucleus are interspersed among and lateral to the fibres of the MLF and lie immediately lateral to the nucleus of Darkschewitsch. The interstitial nucleus of Cajal is classified with the accessory oculomotor (pre-oculomotor) nuclei. It acts to integrate eye-velocity signals with eye-position signals to coordinate movements of the head with movements of the eyes, particularly for vertical and oblique movements of the eyes. The interstitial nucleus has reciprocal connections with the vestibular nuclei and with the nucleus prepositus hypoglossi. Afferent fibres ascend to the interstitial nucleus of Cajal from the vestibular nuclei through the median longitudinal fasciculus and from the spinal cord via the spinomesencephalic tract (Sengul and Watson 2012). In turn, the interstitial nucleus of Cajal sends efferent fibres down the MLF to the ipsilateral superior and medial vestibular nuclei, the nucleus prepositus hypoglossi and the reticular formation. Major efferent fibres from the interstitial nucleus project to the oculomotor and trochlear nuclei bilaterally. Projections to all levels of the spinal cord descend as the interstitiospinal tract within the MLF.

The rostral interstitial nucleus of the medial longitudinal fasciculus (riMLF) represents the vertical gaze centre. It is a wing-shaped nucleus located dorsal to the rostral pole of the red nucleus, rostral to the fasciculus retroflexus and rostral to the interstitial nucleus of Cajal. It has predominantly ipsilateral connections to the oculomotor and trochlear nuclei for conjugated vertical eye movements. It has unilateral connections to the interstitial nucleus of Cajal and bilateral connections to the vestibular nuclei and the reticular formation. In humans the cells of this nucleus can be distinguished by their high content of parvalbumin. Burst neurones for motoneurones of the oculomotor and trochlear nerves lie in the riMLF (Horn and Büttner-Ennever 1998).

The PAG is organized into four longitudinal compartments, designated lateral, ventrolateral, dorsomedial and dorsolateral columns.

Stimulation of the lateral column leads to defensive behaviour with increased heart rate, blood pressure and respiration, and a shift of the blood from the viscera to the lower limb muscles. Stimulation of the ventrolateral column leads to immobility (freezing) with decreased blood pressure and decreased heart rate. Efferents from these columns pass to somatic and autonomic premotor neurones in the lower brainstem and spinal cord. The periaqueductal grey matter also contributes significantly to pathways for micturition, for control of ejaculation and for control of pain. A region in the caudal PAG plays a central role in vocalization, giving excitatory projections to the nucleus ambiguus, and a strong projection to the retroambiguus nucleus that sends motoneurones to the larynx, abdominal and other muscles involved in vocalization. There is also a strong projection to the region of a cell group designated VOC that has been identified as a vocal pattern generator.

The nucleus of Darkschewitsch is found in the ventrolateral portion of the periaqueductal grey matter, dorsomedial to the interstitial nucleus of Cajal, the medial longitudinal fasciculus and the red nucleus at a level posterior to the fasciculus retroflexus. It gives rise to the medial tegmental tract that contributes innervation to the rostral medial accessory olive, and via the olive, to the cerebellum. A proposed connection of the nucleus of Darkschewitsch with the oculomotor nerve and the posterior commissure has not been confirmed.

The central tegmental tract initially lies ventrolateral to the medial longitudinal fasciculus and dorsolateral to both the red nucleus and the decussation of the superior cerebellar peduncles. It traverses the superior cerebellar peduncle and occupies a central position in the reticular formation of the pontine tegmentum as it descends to the inferior olivary complex. Efferents from the caudal magnocellular red nucleus form the descending rubrobulbar tracts. These tracts cross the midline in the ventral tegmental decussation and pass caudally to innervate contralateral structures, including the motor neurones of the facial nucleus, interneurones in the lateral tegmental field and the nucleus of the lateral funiculus in the caudal medulla.

The Guillain–Mollaret triangle, otherwise known as the dentatorubro-olivary pathway, has three corners, the red nucleus in the midbrain, the ipsilateral inferior olive in the medulla and the contralateral dentate nucleus in the cerebellum (see Chapter 29). Rubro-olivary fibres descend from the parvocellular division of each red nucleus along the central tegmental tracts to enter the capsule (amiculum) of the ipsilateral inferior olivary nucleus and pass into the nucleus. Olivocerebellar fibres emerge from the hilum of that olive, pass across the midline, traverse the contralateral inferior cerebellar peduncle, and, by a complex route, reach the cerebellar cortex and dentate nucleus contralateral to the side of the original red nucleus. The dentate nucleus gives rise to dentatorubral fibres that ascend through the superior cerebellar peduncle, cross the midline in the decussation of the superior cerebellar peduncles, and "return" to the original red nucleus, completing the triangle of Guillain-Mollaret. Interruption of this triangle can result in palatal myoclonus and a dentatorubral upper limb tremor (Holmes tremor). These interruptions are most commonly due to ischaemic infarction, haemorrhage or plaques of multiple sclerosis that disrupt the central tegmental tract.

dorsomedial to the crus cerebri on each side. It is subdivided into a pars reticulata (SNr) ventrolaterally, a pars compacta (SNc) dorsomedially and a small pars lateralis laterally.

The SNr extends through the whole of the ventral midbrain and rostrally as far as the subthalamic region. It consists of clusters of large, non-pigmented, multipolar neurones, many of which intermingle with fibres of the crus cerebri. These neurones contain iron and show increasing iron concentration with age (see Fig. 28.18). In Parkinson's disease and related disorders, disproportionate increase in iron accumulation correlates with the clinical stage of disease and disease progression (An et al 2018, Xuan et al 2017). Most pars reticulata neurones are inhibitory GABAergic cells. They are highly similar in form and connectivity to those of the internal segment of the globus pallidus, with similar disc-like dendritic trees that are orientated at right-angles to afferents from the striatum, probably making *en passant* contacts. Functionally, the SNr is a homologue of the internal segment of the globus pallidus, which means that the two may be considered together as a single major output nucleus for the basal ganglia.

There are reciprocal connections between the substantia nigra and the basal ganglia and these are discussed in Chapter 31. Briefly, topographically organized striatonigral axons, some of which may be collaterals of striatopallidal axons, originate from the caudate nucleus and putamen and project to the pars reticulata. They utilize GABA and substance P or enkephalin as their neurotransmitters, and are distributed differentially in the pars reticulata: enkephalinergic axons terminate in the medial part, whereas substance P axons terminate throughout. The head of the caudate nucleus projects to the rostral third of the substantia nigra, while the putamen projects to all parts. The fibres end in axodendritic synapses. A small number of GABAergic pallidonigral fibres from the external segment of the globus pallidus end mostly in the pars reticulata. The subthalamic nucleus sends an important glutamatergic projection to the pars reticulata and to the globus pallidus. Some, predominantly glutamatergic, corticonigral fibres appear to exist, passing from precentral and postcentral gyri to neurones in the pars reticulata.

Fibres from the SNr project rostrally to the ventral anterior and dorsomedial thalamic nuclei and to the deep (polysensory) layers of the superior colliculus. They project caudally to the pedunculopontine nucleus and brainstem reticular formation, from where impulses are relayed to neurones in the ventral horn of the spinal cord. A major connection from the striatum to the superior colliculus, via the pars reticulata, is thought to function in the control of gaze in a manner analogous to the pathway that initiates general body movement via the pallidum, thalamus and supplementary motor cortex. The uncontrolled or fixed-gaze disturbances of advanced Parkinson's disease, progressive supranuclear palsy and Huntington's disease tend to support this.

The SNc consists of closely packed, darkly pigmented neurones, which contain neuromelanin granules. Their arrangement is irregular and they partially penetrate the subjacent SNr. The pigmented neurones synthesize dopamine as their neurotransmitter and correspond to the dopaminergic cell group A9 (see Fig. 28.17). The dopamine-containing neurones are acetylcholinesterase-positive but are not cholinergic (Paxinos et al 2012). The pigment is most abundant in primates, maximal in humans and present even in albinos. The cells of the SNc are reciprocally connected with the striatum. They project predominantly to the caudate nucleus and putamen in a topographically organized fashion, but also project to the globus pallidus and subthalamic nucleus. Together with the retrorubral nucleus (A8) and the ventral tegmental area (A10), they comprise most of the dopaminergic neuronal population of the midbrain. The pars lateralis projects to the ipsilateral superior colliculus and may be involved in the control of saccadic eye movements.

Ventral tegmental area

The ventral tegmental area (VTA) lies in the midline between the cerebral peduncles and at the depth of the interpeduncular fossa. It is continuous with the pars compacta of the substantia nigra to each side and with the lateral hypothalamus rostrally. The VTA contains cell group A10 (paranigral nucleus) and is the source of the mesolimbic dopamine system that supplies the ventral striatum, neighbouring parts of the dorsal striatum, the nucleus accumbens, the amygdala, the prefrontal cortex and the anterior cingulate cortex (Nieuwenhuys et al 2008). The dopaminergic neurones of the VTA also contain cholecystokinin (CCK) or somatostatin. The ventral tegmental system acts as an integrative centre for adaptive behaviour. It receives afferent input from a wide variety of sources including the habenular nuclei and the rostromedial tegmental nucleus (Matsumoto and Hikosaka 2007, Hikosaka 2008, Hikosaka 2010). The VTA projects ascending fibres into the ipsilateral medial forebrain bundle, a composite tract that includes a mesodiencephalic system that terminates in thalamic and hypothalamic nuclei; mesostriatal projections to the caudate nucleus and putamen; a mesolimbic pathway to the nucleus accumbens, olfactory tubercle, lateral septum, interstitial nucleus of the stria terminalis, amygdala and entorhinal cortex; and mesocortical fibres to prefrontal, orbitofrontal and cingulate cortices.

Habenular control of dopamine release is a major contributor to reward-based motivation and action. The habenular nuclei, which are part of the diencephalon (Ch. 30) receive input from the limbic system and the striatum and project to the dopaminergic and serotoninergic centres of the brainstem via the habenulointerpeduncular tract (fasciculus retroflexus of Meynert).

In humans, the core of the fasciculus retroflexus is acetylcholine esterase-dense, while the surround is acetylcholine esterase-negative (Paxinos et al 2012). The medial habenular nuclei receive input mainly from the limbic system and project to the interpeduncular nucleus, which then projects to the serotoninergic nuclei of the raphe. The lateral habenular nuclei receive input mainly from the basal ganglia and project to the dopaminergic and serotoninergic centres partly through the rostromedial tegmental nucleus. Actual or anticipated negative reward activates the GABAergic rostromedial tegmental nucleus that then represses the dopaminergic centres of the ventral tegmental area and the substantia nigra in order to minimize energy expenditure or avoid harm (Hikosaka 2010).

Reticular formation

The tegmentum of the brainstem contains myriad islets of grey matter containing cells of different types and sizes interspersed among nerve fibres that run in all directions: collectively they form the reticular formation that extends from the spinal cord through the full length of the brainstem into the diencephalon (Olszewski and Baxter 1954, Haines and Mihailo 2018). Caudally, the reticular formation of the brainstem is continuous with the reticular intermediate grey matter of the spinal cord. Rostrally, it merges into the reticular and interlaminar nuclei of the thalamus and restricted regions of the subthalamus.

The reticular regions are often regarded as phylogenetically ancient, representing a primitive nerve network on which more anatomically organized, functionally selective connections have developed during evolution. Reticular regions tend to be ill-defined collections of neurones with diffuse connections. The neurones have long dendrites that spread transversely or longitudinally within the brainstem: axons may ascend or descend, bifurcate in both directions, be crossed, uncrossed or even bilateral, and often travel far, some through the whole brainstem and beyond. For these reasons, conduction paths through the reticular formation are difficult to define, often complex and polysynaptic.

Despite these complexities, on the basis of cytoarchitectonic, chemoarchitectonic and functional criteria, the reticular formation is divided into three longitudinal columns – median; medial, containing mostly large reticular neurones; and lateral, containing mostly small to intermediate neurones (**Fig. 28.19**). Within these columns, specific portions of the reticular regions may be classified into groups on the basis of their connections and their predominant neurotransmitters, namely, dopaminergic and noradrenergic neurones (group A), serotoninergic neurones (group B), adrenergic neurones (group C) and cholinergic neurones (group Ch) (Dahlström and Fuxe 1964, Dahlström and Fuxe 1965, Nieuwenhuys 1985, Siegel et al 1999).

Median column of reticular nuclei

The median column of reticular nuclei extends throughout the medulla, pons and midbrain and contains neurones that are largely aggregated in bilateral, vertical sheets, located immediately adjacent to the midline and occupying the paramedian zones. Collectively they are called the nuclei of the raphe, or raphe nuclei. Many neurones in raphe nuclei are serotoninergic and are grouped into nine clusters (**Fig. 28.20**) (Dahlström and Fuxe 1964, Dahlström and Fuxe 1965, Nieuwenhuys 1985, Hornung 2003). The serotonergic neurone clusters may be allocated, on the basis of their distribution and main projections, into rostral and caudal groups. The rostral group is confined to the mesencephalon and rostral pons and has major projections to the forebrain. It includes the median (superior) raphe nucleus (B6), the dorsal (rostral) raphe nucleus (B7) and linear raphe nucleus (B8). Neurones in the caudal group in the caudal pons and medulla oblongata project to brainstem nuclei and to the spinal cord (Hornung 2003). The caudal group includes the raphe pallidus nucleus (B1) and associated raphe obscurus nucleus (B2), which lie in the upper two-thirds of the medulla and cross the pontomedullary junction. The raphe magnus nucleus (B3) minimally overlaps B1 and B2 and ascends into the caudal pons; it is caudal to the pontine raphe nucleus (B5). The serotoninergic cells

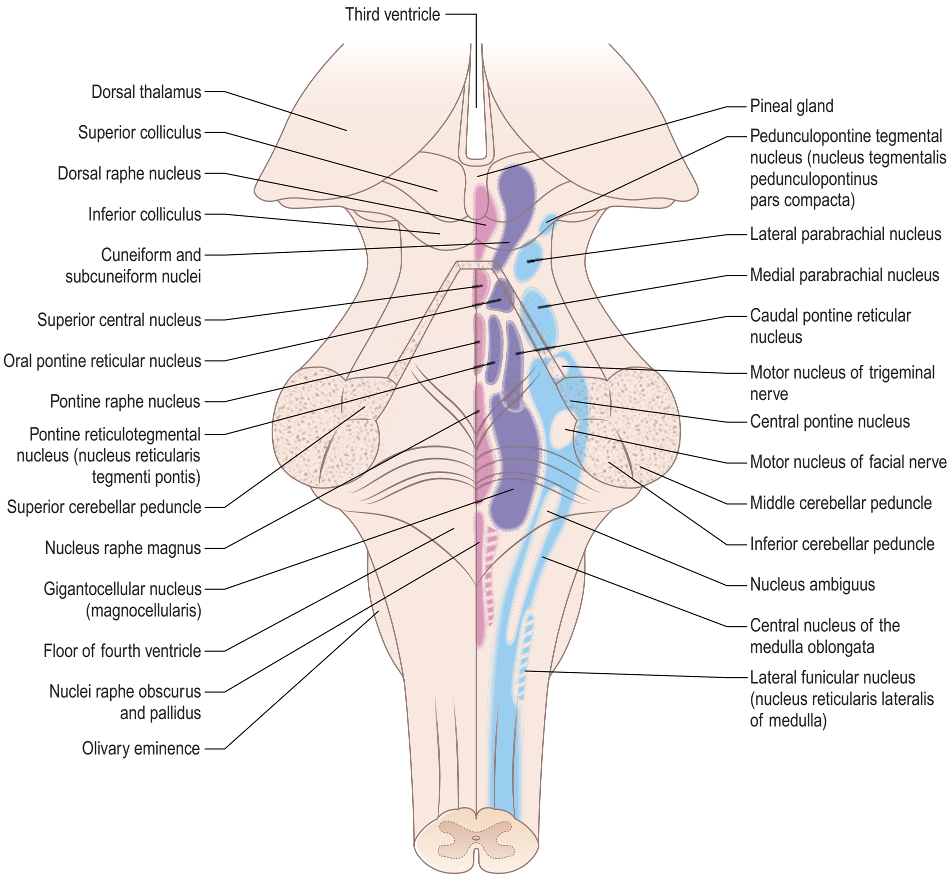
Third ventricle
Dorsal thalamus
Superior colliculus
Dorsal raphe nucleus
Inferior colliculus
Cuneiform and subcuneiform nuclei
Superior central nucleus
Oral pontine reticular nucleus
Pontine raphe nucleus
Pontine reticulotegmental nucleus (nucleus reticularis tegmenti pontis)
Superior cerebellar peduncle
Nucleus raphe magnus
Gigantocellular nucleus (magnocellularis)
Floor of fourth ventricle
Nuclei raphe obscurus and pallidus
Olivary eminence
Pineal gland
Pedunculopontine tegmental nucleus (nucleus tegmentalis pedunculopontinus pars compacta)
Lateral parabrachial nucleus
Medial parabrachial nucleus
Caudal pontine reticular nucleus
Motor nucleus of trigeminal nerve
Central pontine nucleus
Motor nucleus of facial nerve
Middle cerebellar peduncle
Inferior cerebellar peduncle
Nucleus ambiguus
Central nucleus of the medulla oblongata
Lateral funicular nucleus (nucleus reticularis lateralis of medulla)

Fig. 28.19 Dorsal aspect of the brainstem showing the approximate location of nuclei of the reticular formation. Nuclei of the median and paramedian nuclear column, pink; medial column nuclei, purple; lateral column nuclei, blue.

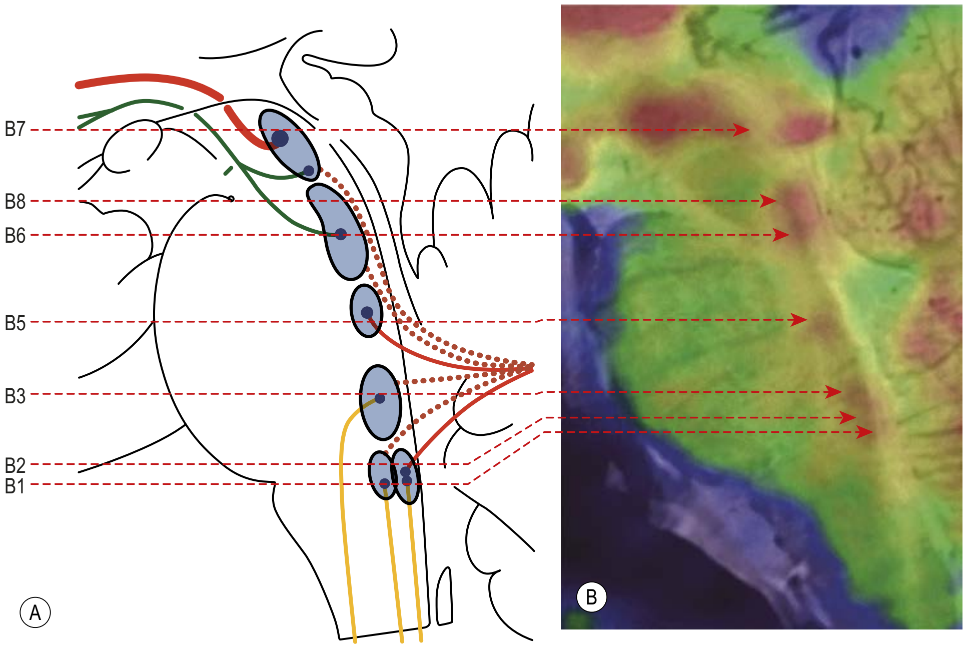
B7
B8
B6
B5
B3
B2
B1
A
B

Fig. 28.20 Sagittal display of the serotoninergic raphe nuclei B1–B8. **A**, Diagram of the known positions of the serotoninergic raphe nuclei. **B**, *In vivo* display of these nuclei obtained by overlaying 18F-FDG PET (18F-fluorodeoxyglucose positron emission tomography) scans onto 7 Tesla T2* (susceptibility-weighted) MRI in the same patient. (Courtesy of Dr Z-H Cho, Seoul, South Korea. Adapted with permission from Cho ZH, Son YD, Choi EJ et al 2013 In-vivo human brain molecular imaging with a brain-dedicated PET/MRI system. Magn Reson Mater Phys 26:71–9.)

of vestibular area (B4) and group B9 are small cell groups located in the medulla and midbrain, respectively.

Connections of the serotoninergic raphe neurones are multiple and complex. Principally, the rostral serotoninergic group is reciprocally interconnected rostrally with the limbic system, septum, prefrontal cortex and hypothalamus. Efferents ascend and form a large ventral and a diminutive dorsal pathway. The fibres of the ventral ascending serotoninergic pathway exit the ventral aspect of the mesencephalic raphe nuclei, and then course rostrally through the ventral tegmentum from where fibres pass to the ventral tegmental area, substantia nigra and interpeduncular nucleus. A large number of fibres then enter the fasciculus retroflexus (habenulo-interpeduncular tract) and run rostrally to innervate the habenular nucleus, intralaminar, midline, anterior, ventral and lateral dorsal thalamic nuclei, and the lateral geniculate body. The ventral ascending serotoninergic pathway enters the medial forebrain bundle in the lateral hypothalamic area and splits to pass medially and laterally. The fibres in the medial tract terminate in the mammillary body, dorsomedial, ventromedial, infundibular, anterior and lateral hypothalamic, medial and lateral preoptic, and suprachiasmatic nuclei. Those in the lateral tract take the ansa peduncularis–ventral amygdalofugal path to the amygdala, striatum and neocortex. The medial forebrain bundle carries the remaining ventral ascending serotoninergic axons into the medullary stria, stria terminalis, fornix, diagonal band, external capsule, cingulate fasciculus and medial olfactory stria, to terminate in all the structures that these systems interconnect. The ventral and dorsal pathways both originate from neurones in the dorsal and central superior raphe nuclei. The smaller dorsal ascending serotoninergic pathway is initially incorporated into the dorsal longitudinal fasciculus (of Schütz). A few fibres terminate in the central mesencephalic grey matter and posterior hypothalamus, but most continue into the medial forebrain bundle and merge with the axons of the ventral pathway, which are distributed to the same targets.

Major afferents to the mesencephalic raphe nuclei include those from the interpeduncular nucleus (linking the limbic and serotoninergic systems); from the lateral habenular nucleus (linking the septum, preoptic hypothalamus and prefrontal cortex via the fasciculus retroflexus and the medial forebrain bundle); and from the pontine central grey matter. The ascending raphe system probably functions to moderate forebrain activities, particularly limbic, septal and hypothalamic activities. A degree of region-specific connectivity suggests that it exerts precise, as well as tonal, control.

The caudal group projects as ventral, dorsal and intermediate spinal tracts in the ventral and lateral funiculi. These terminate respectively in the ventral horns and laminae I, II and V of the dorsal horns of all segments, and in the thoracolumbar intermediolateral sympathetic and sacral parasympathetic preganglionic cell columns. The dorsal raphe nucleus also projects to the locus coeruleus, the dorsal tegmental nucleus and most of the rhombencephalic reticular formation. Its spinal projections function as a pain control pathway that descends from a mesencephalic pain control centre located in the periaqueductal grey matter, dorsal raphe and cuneiform nuclei. The intermediate raphe–spinal projection is inhibitory and, in part, modulates central sympathetic control of cardiovascular function. The ventral raphe–spinal system excites ventral horn cells and could function to enhance motor responses to nociceptive stimuli.

Medial column of reticular nuclei

The medial column of reticular nuclei is composed predominantly of neurones of medium size, although very large neurones are found in some regions, and most have processes orientated in the transverse plane. In the lower medulla the column is indistinct, and is perhaps represented by a thin lamina lateral to the raphe nuclei. However, in the upper medulla the medial column expands into the medullary gigantocellular (magnocellular) nucleus, which lies ventrolateral to the hypoglossal nucleus, ventral to the vagal nuclei and dorsal to the inferior olivary complex (see **Fig. 28.19**). Ascending further, the column continues as the pontine gigantocellular nucleus, which lies medially in the tegmentum. Its neurones suddenly diminish in size to form, in rostral order, the almost co-extensive caudal and oral pontine tegmental reticular nuclei. It then expands into the cuneiform nucleus and subcuneiform nucleus, before fading away in the midbrain tegmentum (Haines and Mihailo 2018).

The connections of the medial reticular formation suggest that the medial column is integrated into both sensory and motor pathways (Nieuwenhuys et al 2008). Retinotectal and tectoreticular fibres relay visual information and the medial forebrain bundle transmits olfactory impulses. Within the medial column, the region above and below the abducens nucleus is designated the paramedian pontine reticular formation and corresponds to the horizontal gaze centre. Afferent inputs to the medial reticular nuclear column include the spinoreticular projections and collaterals of centrally projecting spinal trigeminal, vestibular and cochlear fibres. Spinoreticular fibres, part of the anterolateral system, arise from neurones in the intermediate grey matter of the spinal cord. They decussate in the ventral white commissure, ascend in the ventrolateral funiculus, and terminate not only at all levels of the medial column of reticular nuclei but also in the intralaminar nuclei of the thalamus: the latter project directly to the striatum and neocortex.

Efferent axons of medial reticular column neurones form a multisynaptic ascending and descending system within the column and ultimately enter the spinal cord and diencephalon.

Descending fibres form pontine (medial) and medullary (lateral) reticulospinal tracts. Pontine reticulospinal axons arise from neurones in the caudal and oral parts of the pontine reticular nucleus, descend largely uncrossed in the ventral spinal funiculus, and terminate in spinal cord laminae VII, VIII and IX. Medullary reticulospinal axons descend bilaterally, but with an ipsilateral preponderance, to end in laminae VII, VIII, IX and X, and descend ipsilaterally to end in laminae IV, V and VI. This system modulates spinal motor function and segmental nociceptive input.

Lateral column of reticular nuclei

The lateral column of reticular nuclei contains six nuclear groups (see Fig. 28.19). These are the parvocellular reticular area, superficial ventrolateral reticular area, lateral pontine tegmental noradrenergic cell groups A1, A2, A4–A7 (A3 is absent in primates), adrenergic cell groups C1–C3 and cholinergic cell groups Ch5–Ch6 (Nieuwenhuys 1985, Siegel et al 1999). Cell groups Ch1–Ch4 are located in the basal forebrain. The column descends through the lower two-thirds of the lateral pontine tegmentum and upper medulla, where it lies between the gigantocellular nucleus medially, and the sensory nuclei of the trigeminal nerve laterally. It continues caudally and expands to form most of the reticular formation lateral to the raphe nuclei. It abuts the superficial ventrolateral reticular area, nucleus solitarius, nucleus ambiguus and vagal nucleus, and there contains the adrenergic cell group C2 and the noradrenergic group A2.

The lateral paragigantocellular nucleus lies at the rostral pole of the diffuse superficial ventrolateral reticular area (at the level of the facial nucleus). The zone extends caudally as the nucleus retroambiguus and descends into the spinal cord. It contains noradrenergic cell groups A1, A2, A4 and A5, and the adrenergic cell group C1. The ventrolateral reticular area is involved in cardiovascular, respiratory, vasoreceptor and chemoreceptor reflexes, and in the modulation of nociception. The A2 or noradrenergic dorsal medullary cell group lies in the nucleus of the tractus solitarius, vagal nucleus and adjoining parvocellular reticular area. Adrenergic group C1 lies rostral to the A2 cell group. Noradrenergic cell group A4 extends into the lateral pontine tegmentum, along the subependymal surface of the superior cerebellar peduncle. Noradrenergic group A5 forms part of the paragigantocellular nucleus in the caudolateral pontine tegmentum. Noradrenergic cell group A5 and adrenergic cell group C1 probably function as centres of vasomotor control. The entire region is subdivided into functional areas on the basis of experiments in animals, in which vasoconstrictor, cardioaccelerator, depressor, inspiratory, expiratory and sudomotor responses have been elicited.

The lateral pontine tegmental reticular grey matter is related to the superior cerebellar peduncle and forms the medial and lateral parabrachial nuclei and the ventral Kölliker–Fuse nucleus, part of the brainstem respiratory control network. There is experimental animal evidence that the Kölliker-Fuse nucleus provides some of the densest projections to the entire lateral pontomedullary column of respiratory neurones and to respiratory-related neurones in the medulla and cervical spinal cord, including phrenic motor neurones. The locus coeruleus (noradrenergic cell group A6), area subcoeruleus, noradrenergic cell group A7 and cholinergic group Ch5 in the pedunculopontine tegmental nucleus (nucleus tegmentalis pedunculopontinus) are all located in the lateral pontine and mesencephalic tegmental reticular zones. A4 is sometimes considered part of the coeruleus complex. The mesencephalic group Ch5 is continuous caudally with cell group Ch6 in the pontine central grey matter.

Cell group A6 (also parts of A4) contains all the noradrenergic cells in the central region of the locus coeruleus (**Fig. 28.21**). Group A6 has ventral (nucleus subcoeruleus, A6sc), rostral and caudolateral extensions (A6cg), the latter merging with the A4 group. The locus coeruleus probably functions as an attention centre, focusing neural functions to prevailing needs. The noradrenergic A7 group occupies the rostroventral part of the pontine tegmentum and is continuous with groups A5 and A1 through the lateral rhombencephalic tegmentum. The A7, A5, A1 complex is also connected by noradrenergic cell clusters with group A2, caudally, and group A6, rostrally. The A5 and A7 groups lie mainly within the medial parabrachial and Kölliker–Fuse nuclei. Reticular neurones in the lateral pontine tegmental reticular area, like those of the ventrolateral zone, function to regulate respiratory, cardiovascular and gastrointestinal activity. Two micturition centres are located in the dorsomedial and ventrolateral parts of the lateral pontine tegmentum.

The connections of the lateral column reticular nuclei are complex. The short ascending and descending axons of the parvocellular reticular area constitute medullary reflex pathways, which connect all branchiomotor nuclei and the hypoglossal nucleus with central afferent cranial nerve complexes through a propriobulbar system. This area also receives descending afferents from the contralateral motor cortex via the corticotegmental tract, and from the contralateral red nucleus via the rubrospinal tract. The longitudinal catecholamine bundle passes through the parvocellular reticular formation.

The superficial ventrolateral reticular area receives its input from the nucleus solitarius, and subserves cardiovascular, baroreceptor, chemoreceptor and respiratory reflexes; it also receives some input from the spinal cord, insular cortex and amygdala. Reticulospinal fibres from this region terminate bilaterally on sympathetic preganglionic neurones in the thoracic spinal cord.

Reticulospinal fibres descend from the lateral pontine tegmentum. A mainly ipsilateral subcoeruleospinal pathway is distributed to all spinal segments of the cord through the lateral spinal funiculus. Crossed pontine reticulospinal fibres descend from the ventrolateral pontine tegmentum, decussate in the rostral pons and occupy the contralateral dorsolateral spinal funiculus. They terminate in laminae I, II, V and VI of all segments of the spinal cord.

Bilateral projections from the micturition centres travel in the lateral spinal funiculus. They terminate on preganglionic parasympathetic neurones in the sacral cord (which innervate the detrusor muscle in the urinary bladder), and on neurones in the nucleus of Onuf (which innervate the musculature of the pelvic floor and the anal and urethral sphincters) (Ch. 73).

Descending fibres of the A6 noradrenergic neurones of the locus coeruleus project into the longitudinal dorsal fasciculus (as the caudal

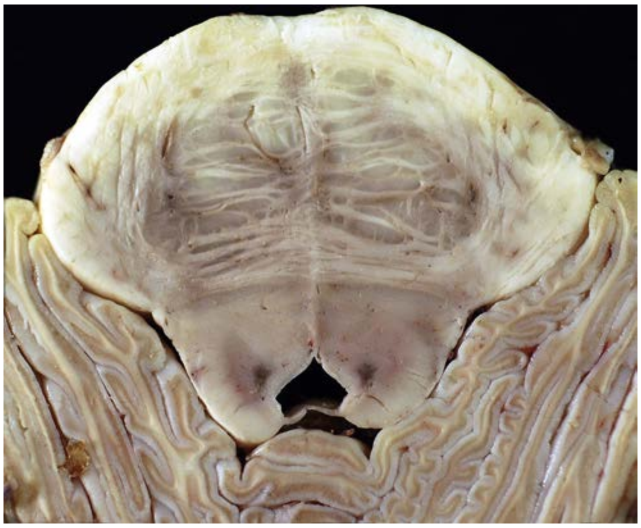

Fig. 28.21 Locus coeruleus. Gross axial section through the basis and tegmentum of the upper pons. The paired dark round foci of neuromelanin identify the locus coeruleus on each side of the upper fourth ventricle.

The superficial ventrolateral area is also the seat of the 'visceral alerting response'. Fibres from the hypothalamus, periaqueductal grey matter and midbrain tegmentum mediate increased respiratory activity, raised blood pressure, tachycardia, vasodilation in skeletal muscle and renal and gastrointestinal vasoconstriction. Ascending efferents from the superficial ventrolateral area synapse on neurones of the supraoptic and paraventricular hypothalamic nuclei. Excitation of these neurones causes release of vasopressin from the neurohypophysis. Medullary noradrenergic cell groups A1 and A2 also innervate (directly and indirectly) the median eminence and control the release of growth hormone, luteinizing hormone and adrenocorticotrophic hormone.

The lateral pontine tegmentum, particularly the parabrachial region, is reciprocally connected to the insular cortex. It shares reciprocal projections with the amygdala through the ventral amygdalofugal pathway, medial forebrain bundle and central tegmental tract, and with hypothalamic, median preoptic and paraventricular nuclei, which preferentially project to the lateral parabrachial nucleus and the micturition centres. It also shares reciprocal bulbar projections, many from the brainstem respiratory control network, with the nucleus solitarius and superficial ventrolateral reticular area.

Other axons that contribute to the longitudinal catecholamine bundle originate from cell groups C1, A1, A2, A5 and A7. The main projection is a descending one from cell groups C1 and A5, which are sudomotor neural control centres and innervate preganglionic sympathetic neurones

Fibres from the locus coeruleus that travel in the rostral limb of the dorsal periventricular pathway ascend in the ventromedial periaqueductal grey matter adjacent to the longitudinal dorsal fasciculus and terminate in the parvocellular part of the paraventricular nucleus in the hypothalamus. The A1, A2, A5 and A7 noradrenergic cell groups project rostrally, mainly through the central tegmental tract. Their axons constitute a major longitudinal catecholamine pathway that continues through the medial forebrain bundle and ends in the amygdala, lateral septal nucleus, bed nucleus of the stria terminalis, nucleus of the diagonal band and the hypothalamus. The ascending dorsal periventricular pathway contains a few non-coerulean noradrenergic fibres, which terminate in the periventricular region of the thalamus.

Projections arising in the rhombencephalon receive contributions from the diffusely organized dorsal medullary and lateral tegmental noradrenergic cell groups. These interconnect cranial nerve nuclei and other reticular cell groups, particularly those of the vagus, facial and trigeminal nerves, and the rhombencephalic raphe and parabrachial nuclei.

Precerebellar nuclei are those that send axons to the cerebellar cortex and nuclei. Three precerebellar nuclei related to the reticular formation are the lateral and paramedian reticular nuclei, and the reticulotegmental nucleus. These three help relay spinal information primarily into the vermis and paravermal regions of the ipsilateral cerebellar hemisphere. They receive inputs from the contralateral primary motor and sensory neocortices, and the ipsilateral cerebellar and vestibular nuclei and spinal cord (the latter through the ascending spinoreticular pathway). This system augments the dorsal and ventral spinocerebellar, cuneocerebellar, accessory cuneocerebellar and trigeminocerebellar tracts. The locus coeruleus may function to control the level of attentiveness and the wake–sleep cycle, and regulate blood flow.

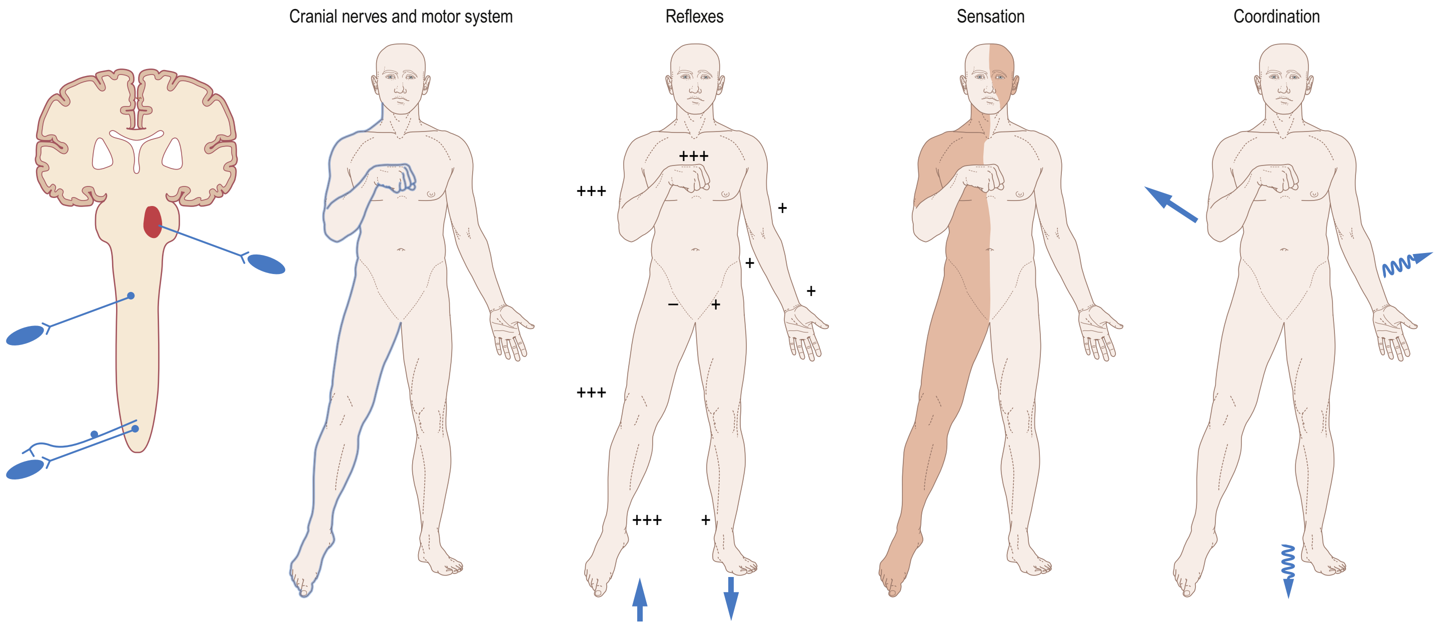

Fig. 28.22 Brainstem lesions. (Adapted with permission from Crossman AR, Neary D 2019 Neuroanatomy: An Illustrated Colour Text, 6th ed. Elsevier, Churchill Livingstone. Copyright 2019.)

limb of the dorsal periventricular pathway), and into the caudal limb of the dorsal noradrenergic bundle (as part of the longitudinal catecholamine bundle). In this way they innervate, mainly ipsilaterally, all other rhombencephalic reticular areas, and the spinal nuclei of the trigeminal nerve, pontine nuclei, cochlear nuclei, nuclei of the lateral lemniscus, and bilaterally, all spinal preganglionic autonomic neurones and the ventral region of the dorsal horn in all segments of the spinal cord.

Most ascending fibres from the locus coeruleus pass in the dorsal noradrenergic (or tegmental) bundle; others run either in the rostral limb of the dorsal periventricular pathway or in the superior cerebellar peduncle. The latter fibres terminate on the cerebellar nuclei. The dorsal noradrenergic bundle is large and runs through the ventrolateral periaqueductal grey matter to join the medial forebrain bundle in the hypothalamus, from where fibres continue forwards to innervate all rostral areas of the brain. The pathway contains efferent and afferent axons that reciprocally connect the locus coeruleus with adjacent structures along its course, e.g. central mesencephalic grey matter, dorsal raphe nucleus, superior and inferior colliculi, interpeduncular nucleus, epithalamus, dorsal thalamus, habenular nuclei, amygdala, septum, olfactory bulb and anterior olfactory nucleus, the entire hippocampal formation and neocortex.

Pedunculopontine nucleus

The pedunculopontine nucleus (nucleus tegmenti pedunculopontinus; PPN) lies in the dorsolateral part of the pontomesencephalic tegmentum. Despite some terminological confusion, most authors agree that the pedunculopontine nucleus is bounded laterally by the medial lemniscus, medially by the superior cerebellar peduncle and its decussation, dorsally by the pontine cuneiform and subcuneiform nuclei and ventrally by the pontine reticular formation. Rostrally, its ventral border contacts the dorsomedial aspect of the substantia nigra and it is separated from the subthalamic nucleus by the retrorubral field. Its most caudal pole is adjacent to the locus coeruleus (Pahapill and Lozano 2000).

On the basis of their cytoarchitectonic and neurochemical characteristics, the pedunculopontine nucleus has been subdivided into a caudal pars compacta consisting mainly of cholinergic neurones, and a rostral pars dissipata consisting of approximately equal numbers of cholinergic and glutamatergic neurones scattered from the mid-mesencephalic to mid-pontine levels (Hamani et al 2007). The pedunculopontine nucleus is encircled by the mesencephalic locomotor region (MLR), a region that also includes the cuneiform and subcuneiform nuclei. Based on experimental studies in animals, where stimulation of the mesencephalic locomotor region elicits locomotion, the pedunculopontine nucleus has been implicated in the initiation and modulation of gait and other stereotyped movements. Functionally, the pedunculopontine nucleus is associated with the reticular activating system via its cholinergic and glutaminergic connections with intralaminar thalamic nuclei. However, its most important and complex connections are reciprocal pathways with the basal ganglia, especially the internal globus pallidus and the substantia nigra; these pathways are described in detail in Chapter 31.

BRAINSTEM LESIONS

General concepts

Brainstem lesions (Fig. 28.22) may arise as a result of extrinsic compression of the brainstem by space-occupying tumours (e.g. meningioma, vestibular schwannoma, metastatic carcinoma) or may be caused by intrinsic disease (e.g. glioma, demyelination, stroke). The clinical syndrome is generally characterized by ipsilateral cranial nerve deficits and contralateral hemiplegia (from corticospinal involvement) and/or contralateral hemianaesthesia (from anterolateral system, dorsal column–medial lemniscus). Brainstem lesions may also result in cerebellar signs (damage to cerebellar afferents or efferents) or in symptoms reflecting small defects (nystagmus, internuclear ophthalmoplegia) (Haines and Mihailo 2018).

The cranial nerve deficit is the best localizing sign because it specifies the side of the lesion and the level within the brainstem. Midbrain lesions (involving the oculomotor and/or trochlear nerves) cause ophthalmoplegia, pupillary dilation and ptosis (oculomotor nerve palsy), and impaired upward gaze (e.g. due to a pinealoma). Mid-pontine lesions (involving the trigeminal nerve) may result in a loss of sensation on the face and in the oral cavity and weakness of the masticatory muscles. Tumours or lesions at the level of the pontomedullary junction (involing the abducens, facial and/or vestibulocochlear nerves) may produce weakness of lateral rectus, a loss of facial sensation and deafness, vertigo or tinnitus. Medullary lesions (involving the glossopharyngeal, vagus and hypoglossal nerves and traversing fibres of the accessory nerve) may cause a 'bulbar palsy': dysarthria, dysphagia and dysphonia, with wasting of the hemitongue, and deviation, weakness and wasting of sternocleidomastoid and trapezius. All these deficits are usually accompanied by signs or symptoms of long tract involvement (motor, sensory or both).

Herniation syndromes

Damage to the brainstem results in characteristic deficits that form part of the so-called herniation syndromes. The falx cerebri and tentorium cerebelli incompletely partition the intracranial volume into partially communicating compartments. The tentorium cerebelli incompletely separates the intracranial volume into the supratentorial space (above) and the infratentorial space (below). The supratentorial space is partially partitioned into left and right halves by the falx cerebri. The supra- and infratentorial spaces communicate through a narrow opening in the tentorium, the tentorial notch or incisura. The infratentorial compartment is continuous inferiorly with the intraspinal compartment through the small foramen magnum. A significant increase in the intracranial pressure within one compartment (due to tumour, haemorrhage, abscess, metabolic disturbance, and signalled by headache, nausea and papilloedema) may cause brain tissue to be displaced (herniated) into an adjacent compartment.

Left–right displacement of brain tissue under the falx is subfalcial herniation (Fig. 28.23, A). Superior–inferior displacement through the incisura is designated transincisural (transtentorial) herniation and is subclassified as upward or downward transincisural herniation. Herniation of posterior fossa tissue into the upper spinal canal typically displaces the cerebellar tonsils into the foramen magnum and the bony ring of the atlas (C1), and is typically designated as downward tonsillar herniation. All herniation syndromes, directly or indirectly, will compromise brainstem viability (Haines 2015).

An expanding lesion in parietofrontal areas, a supratentorial position, may result in herniation of structures such as the cingulate gyrus underneath the edge of the falx cerebri (see Fig. 28.23A). This may initially be a 'silent' event (i.e. no signs or symptoms) or may present as weakness of the lower extremities related to compression of the anterior cerebral artery (ipsilateral, contralateral or bilateral) and decreased levels of consciousness.

Hemisphere lesions may enlarge, impinge into the opposite side of the brain, and produce a characteristic series of deficits (Fig. 28.23B). These include decrease in consciousness indicating damage to the thalamic relays of the reticular activating system, generally increased muscle tone, a change in respiratory patterns, and altered pupils and eye movements. These patients may become decorticate with extended lower extremities and flexed, upper extremities.

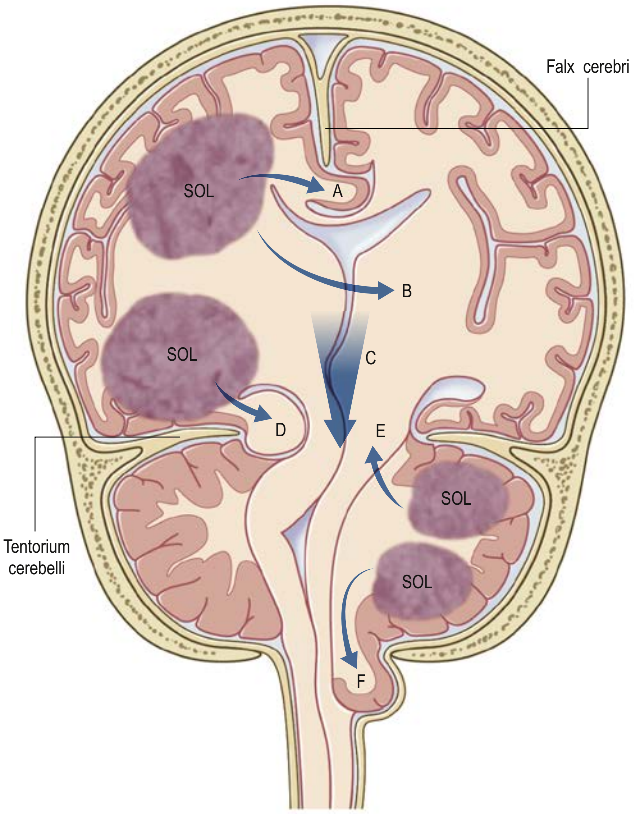

A Cingulate herniation under falx, potential anterior cerebral artery damage
B Herniation into opposite hemisphere, potential decorticate posturing
C Transtentorial or central herniation, potential decerebrate posturing, somnolence
D Uncal/parahippocampal gyrus herniation, pupillary signs, hemiparesis, somnolence, stupor
E Upward cerebellar herniation, increased intracranial pressure, hydrocephalus, impaired upward gaze
F Tonsillar herniation, potential cardiac and respiratory arrest

Fig. 28.23 Effects of space-occupying lesions (SOL).

As a cerebral mass compromises the available supratentorial space and the clinical picture deteriorates, the herniation traverses the tentorial notch as a downward transtentorial (or central) herniation (Fig. 28.23C). These patients have a significantly decreased level of consciousness (some may be stuporous or in coma); breathing patterns are irregular (tachypnoea, Cheyne–Stokes); and eye movements are compromised such that the pupils are dilated and may be fixed. A state of decortication may convert to decerebrate rigidity, when all extremities are extended.

Lesions located in the temporal lobe may expand medially, forcing the uncus and possibly the parahippocampal gyrus over the edge of the tentorium cerebelli with impingement on the midbrain (Fig. 28.23D). This is uncal herniation and may present in two forms. The midbrain injury involves structures on the side of the herniation with predictable deficits: ipsilateral pupil dilation and ophthalmoplegia, contralateral weakness of upper and lower extremities, an altered level of consciousness and hyperactive reflexes. Alternatively, the herniation may shift the midbrain to the side opposite the herniation (e.g. with herniation on the right, the midbrain shifts to the left) and it is compressed against the edge of the tentorium. In this case the dilated pupil and third nerve ophthalmoplegia are on the right, and the crus cerebri damage on the left results in a right hemiplegia; both motor deficits are on the right side. The corticospinal deficit, in this case, is a false localizing sign.

Pressure increase in the posterior fossa, an infratentorial location, may result in herniation upwards through the tentorial notch or downwards into the foramen magnum. Upward cerebellar herniation (Fig. 28.23E) displaces the brainstem against the tentorium and into the notch with resultant symptoms of increased intracranial pressure, paralysis of upward gaze, motor deficits and altered consciousness. Extrusion of the cerebellar tonsils (Fig. 28.23F) downwards into the foramen magnum may result in damage to medullary cardiac and respiratory centres, with resultant changes in heart and respiratory rates. Both of these syndromes may constitute a medical emergency, the former due to rapidly developing hydrocephalus, the latter due to compromise of cardiac and respiratory centres.

VIEW TO THE FUTURE

With increasing sophistication of anatomical and imaging techniques, clinician-scientists will be able to depict the anatomy of the brainstem with increasing resolution, potentially opening avenues to increased understanding of the circuitry that underlies function (**Fig. 28.24**).

And beyond: refining traditional anatomical descriptions

Available with the *Gray's Anatomy* e-book

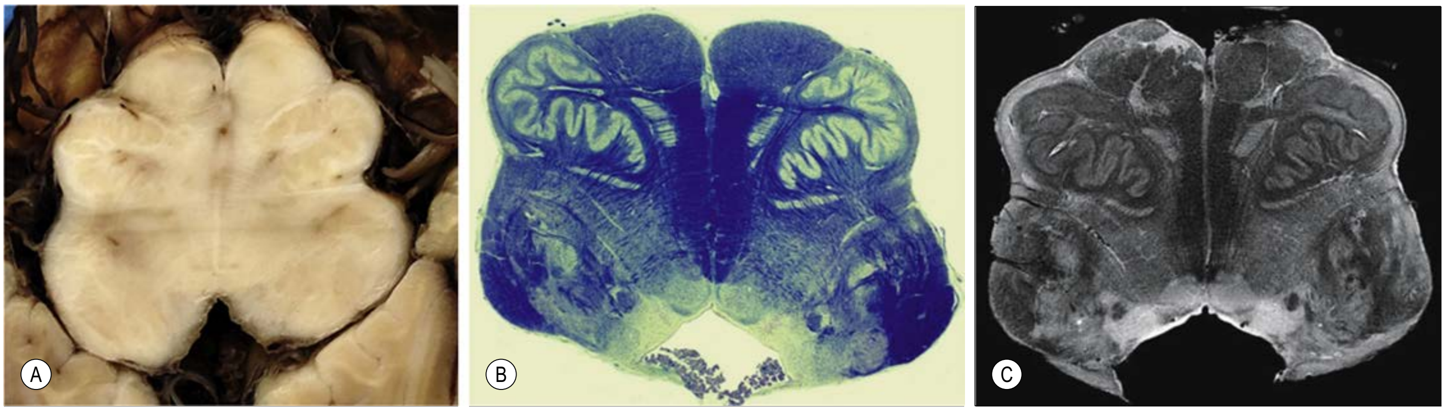

Fig. 28.24 Image comparison. Display of the medulla oblongata at the level of the principal olivary nuclei as revealed by (**A**) gross anatomy, (**B**) myelin staining and (**C**) postmortem 9.4 Tesla proton density MRI. The images in **A** and **B** have been rotated through 180° from the conventional anatomical orientation to allow their direct comparisons with the axial MRI view.

The human brain is composed of segments designated neuromeres that create the final brain structure. Traditional anatomical descriptions have been based on the gross anatomical appearance of the structures observed. Increasingly, however, molecular studies of embryogenesis are now revealing the key signalling molecules and pathways that initiate segment formation, establish segment boundaries, and define final segment identity and function (Fig. 28.25) (Watson et al 2019). This deeper, molecular understanding of segment architecture provides the opportunity to update traditional definitions to reflect newly discovered commonalities and differences among structures that were previously considered to be single or separate units. The changes now proposed are new boundaries for the midbrain, new definitions of the pons, and a new definition of the caudal medulla that reassigns the pyramidal decussation to the C1 segment. The new parcellation of the brainstem also extends to the reticular formation. A diagrammatic representation of the rhombomeres of the stem (Fig. 28.26, see Fig. 14.17) and Table 28.1 introduce some of these proposed revisions.

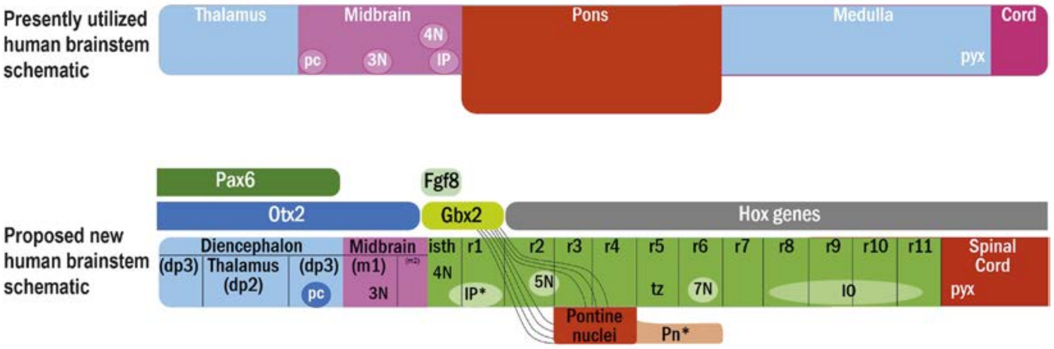

Fig. 28.25 Diagrammatic representation comparing the traditional nomenclature of the brainstem (upper portion) with the proposed new nomenclature based upon the patterns of developmental gene expression (lower portion). **Upper portion**: In the traditional nomenclature, the brainstem is divided into the midbrain, pons and medulla. The oculomotor (3N), trochlear (4N) and interpeduncular (IP) nuclei are allocated to the midbrain. The decussation of the pyramids (pyx) marks the caudal end of the medulla. **Lower portion**: In the proposed new nomenclature, the same tissue is re-apportioned to accord with the patterns of expression of developmental genes. The midbrain consists of two mesomeres (m1, m2). The hindbrain consists of 12 neuromeres designated r0 through r11, and is subdivided into a rostral hindbrain (r0–r6) and a caudal hindbrain (r7–r11). The oculomotor nerve (3N) lies within m1. The abducens nerve (4N) lies within r0 (isth., isthmus), and the interpeduncular nucleus lies within r1. The pontine region comprises r3 and r4, but, by overgrowth, the pons bulges over the ventral aspect of r2 rostrally and overhangs the ventral aspect of r5 and r6 caudally, obscuring them from view. The motor nucleus of the trigeminal nerve (5N) lies within r2 and r3. The trapezoid body (tz) and abducens nucleus (not shown) lie within r5, and the motor nucleus of the facial nerve (7N) lies within r6. The inferior olive (IO) lies within r8–r11. The decussation of the pyramids is reassigned to an expanded C1 segment. The segments over which the developmental genes act is given just above the lower portion. In broad terms, the Hox genes define the range of r2–r11 (and also act caudally for the full length of the spinal cord). Gbx2 is expressed in the rostral hindbrain (r0, r1) but not in the midbrain. *Fgf8* is selectively expressed in the isthmus. *Otx2* distinguishes the midbrain and forebrain from the hindbrain, and Pax6 identifies the diencephalon. (Reproduced with permission from Watson C, Bartholomaeus C, Puelles L 2019 Time for radical changes in brain stem nomenclature – applying the lessons from developmental gene patterns. Front Neuroanat 13:10.)

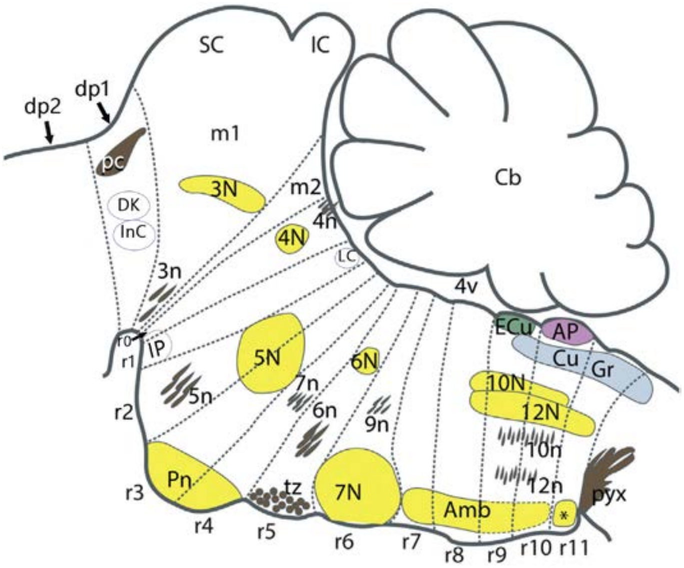

Fig. 28.26 Nuclei and nerve fibres within the neuromere segments of the brainstem. The diencephalon, cerebellum (Cb) and fourth ventricle (4V) are also labeled for orientation. Note: the diencephalic segments are numbered progressively from caudal to cranial, whereas the midbrain and hindbrain segments are numbered progressively from cranial to caudal. Cranial nerve nuclei are coloured yellow. Cranial nerves are indicated by "vertical" black lines and the decussating trapezoid fibres by dots. **Diencephalon:** Diencephalic prosomere 1 (dp1) contains the pretectal posterior commissure (pc). Dp 1 also contains the nucleus of Darkschewitsch (DK) and the interstitial nucleus of Cajal (InC). **Midbrain:** Mesomere 1 (m1) contains the oculomotor nucleus (3N), the emerging oculomotor nerve (3n), the superior colliculus (SC) and inferior colliculus (IC). Mesomere 2 (m2) is a thin band separating m1 from the isthmus (r0). **Hindbrain**: From rostral to caudal, the 12 hindbrain segments, r0 (isthmus) to r11, contain: **r0,** trochlear nucleus (4N) and dorsally emerging trochlear nerve (4n); **r1,** interpeduncular nucleus (IP) ventrally and locus coeruleus (LC) dorsally; **r2,** rostral part of the motor trigeminal nucleus (5N) and the emerging motor trigeminal nerve (5n); **r3,** caudal part of the motor trigeminal nucleus (5N) and the rostral pontine nuclei (Pn); **r4,** caudal pontine nuclei (Pn) and the emerging facial nerve (7n); **r5,** abducens nucleus (6N), emerging abducens nerve (6n), and decussation of the trapezoid body (tz); **r6,** migrated facial nucleus (7N) and emerging glossopharyngeal nerve (9n); **r7 and r8,** the rostral ambiguus nucleus (Amb), and rostral portions of the dorsal motor nucleus of the vagus (10N) and the hypoglossal nucleus (12N); **r9 and r10,** the caudal portions of the ambiguus nucleus (Amb) and the vagal nucleus (10N), much of the hypoglossal nucleus (12N) and the emerging fibres of the vagus (10n) and hypoglossal (12n) nerves; **r11,** remainder of the hypoglossal nucleus (12N) and the noncholinergic caudal extension of the ambiguus nucleus, called retroambiguus (asterisk). **Cervical cord:** The pyramidal decussation (pyx) is proposed to lie in the uppermost portion of the cervical spinal cord.The rostral–caudal positions of the external (accessory) cuneate nucleus (ECu), cuneate nucleus (Cu), gracile nucleus (Gr), and area postrema (AP) are also shown. (Modified with permission from Watson C, Kirkcaldie M, Puelles L 2017 Developmental gene expression redefines the mammalian brain stem. In: Kass JH (ed) Evolution of Nervous Systems, 2nd ed. Elsevier; pp. 467–75.)

TABLE 28.1 Neuromeric organization of the brainstem

Portion of brain	Neuromere	Structures included
Diencephalon		
	Prosomere 1 (dp1)	Posterior commissure Pretectal nuclei Nucleus of Darkschewitsch Interstitial nucleus of Cajal Red nucleus (parvocellular part)
Midbrain		
	Mesomere 1 (m1)	Superior colliculus Inferior colliculus Oculomotor nucleus (III) Emerging oculomotor nerve Red nucleus (magnocellular part)
	Mesomere 2 (m2)	Sagulum nucleus Retrorubral field (DA8) Subbrachial nucleus
Hindbrain		
Isthmocerebellar region (i.e. prepontine region)	Isthmus (r0)	Trochlear nucleus Emerging trochlear nerve Parabigeminal nucleus Microcellular tegmental nucleus
	Rhombomere 1 (r1)	Locus coeruleus Rostral interpeduncular nucleus Caudal interpeduncular nucleus Parabrachial nuclei
Pontine region	Rhombomere 2 (r2)	Rostral motor trigeminal nucleus Emerging motor trigeminal nerve
	Rhombomere 3 (r3)	Caudal motor trigeminal nucleus Rostral pontine nuclei
	Rhombomere 4 (r4)	Emerging facial nerve Caudal pontine nuclei
Retropontine region	Rhombomere 5 (r5)	Abducens nucleus Emerging abducens nerves Superior olive and trapezoid body
	Rhombomere 6 (r6)	Facial nucleus (migrated) Emerging glossopharyngeal nerve
Medulla oblongata	Rhombomere 7 (r7)	Compact ambiguus nucleus
	Rhombomere 8 (r8)	Compact ambiguus nucleus Rostral inferior olive
	Rhombomere 9 (r9)	Semicompact ambiguus nucleus Middle inferior olive
	Rhombomere 10 (r10)	Loose ambiguus nucleus Caudal inferior olive Area postrema
	Rhombomere 11 (r11)	Retroambiguus nucleus
Rostral Spinal Cord		
Cervical spinal cord	C1 segment (C1)	Pyramidal decussation

Modified with permission from Watson C, Bartholomaeus C, Puelles L 2019 Time for radical changes in brain stem nomenclature – applying the lessons from developmental gene patterns. Front Neuroanat 13:10.

Acknowledgements

I would like to formally acknowledge my gratitude to the following people for their assistance in the preparation of this chapter. Their efforts have improved the work: Ms Elba Colman, Ms Etty Cortes, Dr John F Crary, Dr Howard Dai, Dr Bradley N Delman, Dr Mary Fowkes, Dr James C Iatridis, Mr Calvin Keys, Mr Damien Laudier, and Dr Karl Zilles.

Bonus e-book content

Fig. 28.18 Deposition of iron within the substantia nigra (SN) and red nuclei (RN) with age.

Fig. 28.21 Locus coeruleus.

Fig. 28.25 Diagrammatic representation comparing the traditional nomenclature of the brainstem (upper portion) with the proposed new nomenclature based upon the patterns of developmental gene expression (lower portion).

Fig. 28.26 Nuclei and nerve fibres within the neuromere segments of the brainstem.

Table 28.1 Neuromeric organization of the brainstem.

Key references

Dahlström A, Fuxe K 1964 Evidence for the existence of monamine-containing neurones in the central nervous system. Acta Physiol Scand Suppl 232:1–55.

A historically significant paper elucidating the organization of monamine-containing cells within the brain; a particularly useful source of information.

Drayer B, Burger P, Darwin R et al 1986 Magnetic resonance imaging of brain iron. Am J Neuroradiol 7:373–380.

The seminal report of detection and demonstration of brain iron by MRI.

Haines DE 2015 Neuroanatomy in Clinical Context: An Atlas of Structures, Sections, Systems, and Syndromes, 9th ed. Baltimore: Wolters Kluwer/Lippincott Williams & Wilkins.

A very useful source of information on brainstem anatomy, vasculature and selected clinical syndromes that are seen following injury to the brainstem, whether these are vascular lesions or otherwise. There is a particular emphasis on the nuclei and pathways of the brainstem.

Haines DE, Mihailo GA 2018 Fundamental Neuroscience for Basic and Clinical Applications, 5th ed. Philadelphia: Elsevier, Saunders.

A comprehensive treatment of the brainstem that includes development, external and internal anatomy, with a particular emphasis on cranial nerves and detailed treatment of vasculature territories. This source also contains comprehensive coverage of clinical syndromes affecting the brainstem.

Kozicz, T, Bittencourt JC, May PJ et al 2011 The Edinger–Westphal nucleus: a historical, structural, and functional perspective on a dichotomous terminology. J Comp Neurol 519:1413–34.

A pivotal reference clearly explaining that the Edinger–Westphal complex (nucleus) is actually comprised of two parts: a centrally projecting nucleus that projects to a variety of central targets that do not communicate with the ciliary pathways, and a preganglionic nucleus that projects only to the ciliary ganglion.

Mai JK, Paxinos G (eds) 2012 The Human Nervous System, 3rd ed. Amsterdam: Elsevier, Academic Press.

A beautiful, advanced, highly detailed evaluation of the gross anatomy, cytoarchitecture and chemoarchitecture of the brain and brainstem.

Naidich TP, Duvernoy HM, Delman BN et al 2009 Duvernoy's Atlas of the Human Brain Stem and Cerebellum. High-Field MRI: Surface Anatomy, Internal Structure, Vascularization and 3D Sectional Anatomy. Heidelberg: Springer Verlag.

A detailed review of the gross anatomy, nuclei, tracts and vasculature of the brainstem as shown by microvascular injection for the capillary bed and extremely high resolution MR for display of internal structure of the stem in axial, sagittal and coronal planes.

Nieuwenhuys R 1985 Chemoarchitecture of the Brain. Berlin: Springer.

A particularly useful and well organized source of information on the locations of cell bodies containing particular neurotransmitter substances, their trajectory and termination sites.

Nieuwenhuys R, Voogd J, van Huijzen C 2008 The Human Central Nervous System, 4th ed. Berlin: Heidelberg Springer.

A beautifully illustrated, highly detailed review of the neuroanatomy at a very advanced level.

Olszewski J, Baxter D 1954 Cytoarchitecture of the Human Brainstem, 2nd ed. Basel: Karger.

A classic, detailed source of information on the organization of the nuclei of the human brainstem.

Riley HA 1943 An Atlas of the Basal Ganglia, Brain Stem and Spinal Cord. Baltimore, MD: Williams & Wilkins.

A wonderful atlas displaying the myelin-stained sections of the brainstem and related structures in three orthogonal planes with overview sections, highly detailed magnified views and very extensive labelling of the nuclei and tracts.

References

An H, Zeng X, Niu T et al 2018 Quantifying iron deposition within the substanta nigra of Parkinson's disease by quantitative susceptibility mapping. J Neurolog Sci 386:46–52.

Aw ST, Chen L, Todd MJ et al 2017 Vestibulo-ocular reflex deficits with medial longitudinal fasciculus lesions. J Neurol 264:2119–129.

Benninger B, McNeil J 2010 Transitional nerve: a new and original classification of a peripheral nerve supported by the nature of the accessory nerve (CN XI). Neurol Res Int 2010(2):476018:1–15.

Blessing WW, Benarroch EE 2012 Lower brainstem regulation of visceral, cardiovascular, and respiratory function In: Mai JK, Paxinos G (eds) The Human Nervous System, 3rd ed. Amsterdam: Academic Press, Elsevier; Ch. 29, pp. 1058–73.

Brodal P, Bjaalie JG 1992 Organization of the pontine nuclei. Neurosci Res 13:83–118.

Carpenter MB, Sutin J 1983 Human Neuroanatomy, 8th ed. Baltimore, MD: Williams & Wilkins.

Cho Z-H, Son YD, Choi EJ et al 2013 In-vivo human brain molecular imaging with a brain-dedicated PET/MRI system. Magn Reson Mater Phys 26:71–9.

Ciriello J 1983 Brainstem projections of aortic baroreceptor afferent fibres in the rat. Neurosci Lett 36:37–42.

Crosby EC, Humphrey T, Lauer EW 1962 Correlative Anatomy of the Nervous System. New York: Macmillan.

Dahlström A, Fuxe K 1964 Evidence for the existence of monamine-containing neurones in the central nervous system. Acta Physiol Scand Suppl 232:1–55.

A historically significant paper elucidating the organization of monamine-containing cells within the brain; a particularly useful source of information.

Dahlström A, Fuxe K 1965 Evidence for the existence of monoamine neurones in the central nervous system. II. Experimentally induced changes in the intraneuronal amine levels of bulbospinal neurone systems. Acta Physiol Scand Suppl 247:1–36.

Drayer B, Burger P, Darwin R et al 1986 Magnetic resonance imaging of brain iron. Am J Neuroradiol 7:373–380.

The seminal report of detection and demonstration of brain iron by MRI.

Ferraro A, Barrera SE 1935 Posterior column fibers and their termination in Macacus rhesus. J Comp Neurol 62:507–30.

Frohman TC, Galetta S, Fox R et al 2008 Pearls & Oy-sters: the medial longitudinal fasciculus in ocular motor physiology. Neurology 70:e57-e67.

Gilman S, Newman SW (eds) 2003 Manter and Gatz's Essentials of Clinical Neuroanatomy and Neurophysiology, 10th ed. Philadelphia: F.A. Davis.

Haines DE 2015 Neuroanatomy in Clinical Context: An Atlas of Structures, Sections, Systems, and Syndromes, 9th ed. Baltimore: Wolters Kluwer/ Lippincott Williams & Wilkins.

A very useful source of information on brainstem anatomy, vasculature and selected clinical syndromes that are seen following injury to the brainstem, whether these are vascular lesions or otherwise. There is a particular emphasis on the nuclei and pathways of the brainstem.

Haines D, Mihailo GA 2018 Fundamental Neuroscience for Basic and Clinical Applications, 5th ed. Philadelphia, Elsevier, Saunders.

A comprehensive treatment of the brainstem that includes development, external and internal anatomy, with a particular emphasis on cranial nerves and detailed treatment of vasculature territories. This source also contains comprehensive coverage of clinical syndromes affecting the brainstem.

Hamani C, Stone S, Laxton A et al 2007 The pedunculopontine nucleus and movement disorders: anatomy and the role for deep brain stimulation. Parkinsonism Relat Disord 13:S276–S280.

Hamilton RB, Norgren R 1984 Central projections of gustatory nerves in the rat. J Comp Neurol 222:560–77.

Henssen DJHA, Kurt E, Kozicz T et al 2016 New insights in trigeminal anatomy: a double orofacial tract for nociceptive input. Front Neuroanat 10 May Article 53. doi: 10.3389/fnana.2016.00053.

Hikosaka O 2008 Habenula. J Neurosci 28:11825–9.

Hikosaka O 2010 The habenula: from stress evasion to value-based decision-making. Nat Rev Neurosci 11(7):503–13.

Holstein GR 2012 The Vestibular System. In: Mai JK, Paxinos G (eds) The Human Nervous System, 3rd ed. Amsterdam: Elsevier, Academic Press; Ch. 35, pp. 1239–69.

Horn AKE, Büttner-Ennever J 1998 Premotor neurones for vertical eye movements in the rostral mesencephalon of monkey and human: histologic identification by parvalbumin immunostaining. J Comp Neurol 392:413–27.

Hornung JP 2003 The human raphe nuclei and the serotonergic system. J Chem Neuroanat 26:331–43.

Jin ZW, Cho KH, Jang HS 2016 Anterior corticospinal tract revisited: a study using human fetuses. Pediatr Neurosurg 51:121–6.

Kertesz A, Geschwind N 1971 Patterns of pyramidal decussation and their relationship to handedness. Arch Neurol 24:326–32.

Kim S-H, Zee DS, du Lac S 2016 Nucleus prepositus hypoglossi lesions produce a unique ocular motor syndrome. Neurology 87:2026–33.

Kozicz T, Bittencourt JC, May PJ et al 2011 The Edinger–Westphal nucleus: a historical, structural, and functional perspective on a dichotomous terminology. J Comp Neurol 519:1413–34.

A pivotal reference clearly explaining that the Edinger–Westphal complex (nucleus) is actually comprised of two parts: a centrally projecting nucleus that projects to a variety of central targets that do not communicate with the ciliary pathways, and a preganglionic nucleus that projects only to the ciliary ganglion.

Krammer EB, Lischka MF, Egger TP et al 1987 The motoneuronal organization of the spinal accessory nuclear complex. Advances in Anatomy Embryology and Cell Biology 103. Berlin: Springer.

Lachman N, Acland RD, Rosse C 2002 Anatomical evidence for the absence of a morphologically distinct cranial root of the accessory nerve in man. Clin Anat 15:4–10.

A citation that offers details of the view that the accessory nerve may receive little or no contribution from the brainstem. Rather, this cranial nerve is composed of axons that arise predominately from upper cervical levels.

Liu HF, Won HS, Chung IH et al 2014 Variable composition of the internal and external branches of the accessory nerve. Clin Anat 27:97–101.

Mai JK, Paxinos G (eds) 2012 The Human Nervous System, 3rd ed. Amsterdam: Elsevier, Academic Press.

A beautiful, advanced, highly detailed evaluation of the gross anatomy, cytoarchitecture and chemoarchitecture of the brain and brainstem.

Matsumoto M, Hikosaka O 2007 Lateral habenula as a source of negative reward signals in dopamine neurones. Nature 447:1111–15.

A beautiful, advanced, highly detailed evaluation of the gross anatomy, cytoarchitecture and chemoarchitecture of the brain and brainstem.

May PJ 2005 The mammalian superior colliculus: laminar structure and connections. Progr Brain Res 151:321–78.

McGarvey L 2014 Update: The search for the human cough receptor. Lung 192:459–65.

Millar J, Basbaum AI 1975 Topography of the projection of the body surface of the cat to cuneate and gracile nuclei. Exp Neurol 49:281–90.

Miller RA, Burack E 1982 Atlas of the Central Nervous System in Man, 3rd ed. Baltimore, MD: Williams & Wilkins.

Naidich TP, Duvernoy HM, Delman BN et al 2009 Duvernoy's Atlas of the Human Brain Stem and Cerebellum. High-Field MRI: Surface Anatomy, Internal Structure, Vascularization and 3D Sectional Anatomy. Heidelberg: Springer Verlag.

A detailed review of the gross anatomy, nuclei, tracts and vasculature of the brainstem as shown by microvascular injection for the capillary bed and extremely high resolution MR for display of internal structure of the stem in axial, sagittal and coronal planes.

Naidich TP, Castillo M, Cha S et al 2013 Imaging of the Brain. Philadelphia: Saunders, Elsevier.

Nathan PW, Smith MC 1982 The rubrospinal and central tegmental tracts in man. Brain 105:223–69.

A historically important source of information on the arrangement of select brainstem pathways in the human brainstem.

Nathan PW, Smith MC, Deacon P 1990 The corticospinal tracts in man. Course and location of fibres at different segmental levels. Brain 113 (Pt 2):303–24.

Nieuwenhuys R 1985 Chemoarchitecture of the Brain. Berlin: Springer.

A particularly useful and well organized source of information on the locations of cell bodies containing particular neurotransmitter substances, their trajectory and termination sites.

Nieuwenhuys R, Voogd J, van Huijzen C 2008 The Human Central Nervous System, 4th ed. Berlin: Heidelberg Springer.

A beautifully illustrated, highly detailed review of the neuroanatomy at a very advanced level.

Olszewski J 1950 On the anatomical and functional organization of the spinal trigeminal nucleus. J Comp Neurol 92:401–9.

Olszewski J, Baxter D 1954 Cytoarchitecture of the Human Brainstem, 2nd ed. Basel: Karger.

A classic, detailed source of information on the organization of the nuclei of the human brainstem.

Pahapill PA, Lozano AM 2000 The pedunculopontine nucleus and Parkinson's disease. Brain 123:1767–83.

Paxinos G, Xu-Feng H, Sengul G et al 2012 Organization of brainstem nuclei. In: Mai JK, Paxinos G (eds) The Human Nervous System, 3rd ed. Amsterdam: Elsevier, Academic Press; Ch. 8, pp. 260–327.

Riley HA 1943 An Atlas of the Basal Ganglia, Brain Stem and Spinal Cord. Baltimore, MD: Williams & Wilkins.

A wonderful atlas displaying the myelin-stained sections of the brainstem and related structures in three orthogonal planes with overview sections, highly detailed magnified views and very extensive labelling of the nuclei and tracts.

Ryan S, Blyth P, Duggan N et al 2007 Is the cranial accessory nerve really a portion of the accessory nerve? Anatomy of the cranial nerves in the jugular foramen. Anat Sci Int 82:1–7.

A consideration of the issue of whether or not the accessory nerve receives contributions from the medulla, concluding that such connections are rare.

Seijo-Martínez M, Varela-Freijanes A, Grandes J et al 2006 Sneeze-related area in the medulla: localisation of the human sneezing centre? Neurol Neurosurg Psychiatry 77:559–61.

Sengul G, Watson C 2012 Spinal cord: connections. In: Mai JK, Paxinos G (eds) The Human Nervous System, 3rd ed. Amsterdam: Elsevier, Academic Press; Ch. 7, pp. 233–58.

Shoja MM, Oyesiku NM, Shokouhi G et al 2014 A comprehensive review with potential significance during skull base and neck operations, Part II: Glossopharyngeal, vagus, accessory, and hypoglossal nerves and cervical spinal nerves 1–4. Clin Anat 27:131–44.

Siegel GA, Agranoff BW, Albers AW et al 1999 Basic Neurochemistry: Molecular, Cellular and Medical Aspects, 6th ed. Philadelphia: Lippincott–Raven.

Skinner SA 2011 Neurophysiologic monitoring of the spinal accessory nerve, hypoglossal nerve, and the spinomedullary region. J Clin Neurophysiol 28:587–98.

Talman WT, Robertson SC 1991 Nucleus prepositus hypoglossi: a medullary pressor region. Hypertension 17(6 Pt 2):1173–6.

Tubbs RS, Benninger B, Loukas M et al 2014 Cranial roots of the accessory nerve exist in the majority of adult humans. Clin Anat 27:102–7.

Voogd J 2016 Deiters' nucleus: its role in cerebellar ideogenesis: The Ferdinando Rossi Memorial Lecture. Cerebellum 15:54–66.

Waite PME, Ashwell KWS 2012 Trigeminal sensory system. In: Mai JK, Paxinos G (eds) The Human Nervous System, 3rd ed. Amsterdam: Elsevier, Academic Press; Ch. 31, pp. 1110–43.

Watson C, Bartholomaeus C, Puelles L 2019 Time for radical changes in brain stem nomenclature – applying the lessons from developmental gene patterns. Front Neuroanat 13:10.

Wiles CC, Wrigley B, Greene JR 2007 Re-examination of the medullary rootlets of the accessory and vagus nerves. Clin Anat 20:19–22.

Xuan M, Guan X, Gu Q et al 2017 Different iron deposition patterns in early- and middle-late-onset Parkinson's disease. Parkinsonism Relat Disord 44:23–27.

Yousry I, Moriggl B, Naidich TP et al 2002a MR anatomy of the proximal cisternal segment of the trochlear nerve. Neurovascular relationships and landmarks. Radiology 223:31–8.

Yousry I, Morrigl B, Schmid UD et al 2002b Detailed anatomy of the hypoglossal nerve: neurovascular relationships and landmarks on magnetic resonance imaging sequences J Neurosurg 96:1113–22.

Yousry I, Moriggl B, Holtmannspoetter M et al 2004 Detailed anatomy of the motor and sensory roots of the trigeminal nerve and their neurovascular relationships: a magnetic resonance imaging study. J Neurosurgery 101:427–34.

Zhang Y, Wei H, Cronin MJ et al 2018 Longitudinal data for magnetic susceptibility of normative human brain development and aging over the lifespan. Data in Brief 20:623–31.

CHAPTER

29

Cerebellum

The cerebellum is the largest part of the hindbrain, recognized as a distinct division of the brain from the time of Herophilus (335–280 BC) and Galen (AD 131–200). It is situated in the posterior cranial fossa, beneath the tentorium cerebelli, the medial extension of the falx cerebri and the overlying occipital lobe and lies behind the pons and medulla, from which it is separated by the fourth ventricle (**Figs 29.1–29.2**). It is joined to the brainstem by three bilaterally paired major fibre tracts, the inferior, middle and superior cerebellar peduncles, through which it communicates with the remainder of the central nervous system. In adults, the ratio of the weight of the cerebellum to the cerebrum is about 1 to 10, in infants about 1 to 20. The adult human cerebellum has a volume of approximately 145 ml and weighs 150 grams, but its surface area is 40% that of the cerebral cortex. The great majority of cerebellar neurones are small granule cells, which are so densely packed that the cerebellar cortex contains approximately 70% of the 100 billion neurones in the central nervous system (Andersen et al 2012).

The basic internal organization of the cerebellum is of a superficial cortex overlying a core of white matter and deep cerebellar nuclei. The cortex is characteristically highly convoluted by numerous transverse furrows of varying depths that separate its surface into lobes, lobules and folia (leaflets). Aggregations of neuronal cell bodies embedded within the white matter form the fastigial (medial), globose (posterior interposed), emboliform (anterior interposed) and dentate (lateral) nuclei, collectively known as the deep cerebellar nuclei.

An earlier schema of the cerebellum regarded the cerebellum as being divided into three zones of connectional and functional organization (Jansen and Brodal 1940, Chambers and Sprague 1955a, 1955b). In this approach, the archicerebellum (vestibulocerebellum/flocculonodular lobe) has reciprocal links to vestibular nuclei either directly or indirectly and is concerned with eye movements and equilibrium. The paleocerebellum (spinocerebellum) in the vermis and paravermal regions receive cutaneous and kinaesthetic afferents from the spinal cord. The vermis is linked with the fastigial nucleus and influences the medial motor system through brainstem vestibular and reticular nuclei that send descending projections to the spinal cord, and is important for balance and equilibrium; the paravermal area is linked with the interpositus nuclei that project to the red nucleus and primary motor cortex and influences the lateral motor system which is important for the control of distal limb movements. The neocerebellum (pontocerebellum) is regarded as the lateral part of the cerebellum, receiving descending input from the cerebral cortex, projecting through the dentate nucleus back to thalamic areas that mostly project to motor and premotor cortices, and is important for fine motor control and perhaps motor planning and motor learning. These concepts retain some overall validity, but they have limitations in the light of evolving knowledge. The most salient are that the parasagittal organization of the cerebellum is exponentially more complex than this tripartite division; the anterior lobe–posterior lobe dichotomy of cerebellar function is a major organizing feature; pontine projections are not confined to the cerebellar hemispheres; the cerebellar incorporation into brainstem, diencephalic and cerebrocerebellar circuits extends considerably beyond the sensorimotor domains into the association areas and paralimbic cortices; and there are multiple representations of unimodal, multimodal and transmodal forms of sensorimotor, cognitive and affective systems within the human cerebellum.

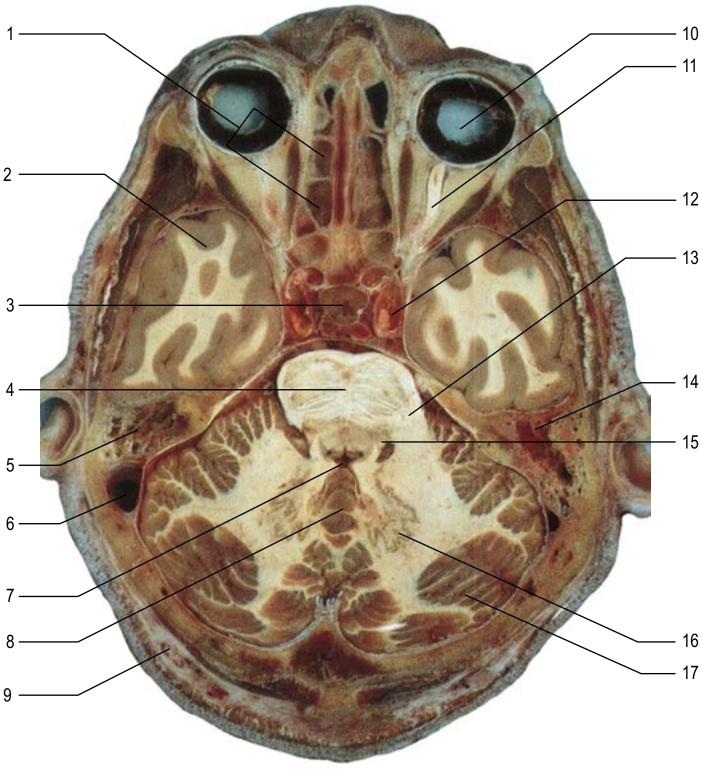

Fig. 29.1 A horizontal section through the cerebellum and brainstem. Key: 1, ethmoidal air cells; 2, temporal lobe of brain; 3, hypophysis; 4, pons; 5, cochlea; 6, sigmoid sinus; 7, fourth ventricle; 8, vermis; 9, diploë of occipital bone; 10, eyeball; 11, optic nerve; 12, internal carotid artery; 13, middle cerebellar peduncle; 14, petrous temporal bone; 15, superior cerebellar peduncle; 16, dentate nucleus; 17, folia of cerebellar cortex. (Courtesy of Dr GJA Maart.)

The cerebellum is subdivided into modules, each consisting of a longitudinal cortical zone, a cerebellar or vestibular target nucleus, and a supporting olivocerebellar climbing fibre system. The longitudinal cortical zones are characterized by their connections as well as their immunohistochemical properties. The cerebellum receives topographically highly arranged input from peripheral receptors, spinal cord and brainstem, and from most of the cerebral cortex through two different afferent systems: mossy fibres and climbing fibres. It now appears that a fundamental role of the cerebellum is to enhance function in almost all domains, modulating behaviour, both motor and nonmotor, to optimize performance in a context-dependent manner.

Ideas on the involvement of the cerebellum in motor functions were derived mainly from movement disorders seen in experimental studies dating back to Rolando and Flourens (1824) (summarized by Luciani 1891), and in observations of patients with acquired cerebellar lesions or degeneration (Brown 1892, Marie 1893, Babinski 1899, Holmes 1939), who displayed characteristic gait ataxia (unstable balance and walking), dysmetria (disordered control) of the limbs, dysarthria (impaired articulatory clarity), and abnormal oculomotor control. The more recent observation that lesions of the cerebellar posterior lobes produce the cerebellar cognitive-affective syndrome in adults (Schmahmann and Sherman 1998) prompted the suggestion that the human cerebellum is also concerned with non-motor functions, which, together with the vestibulocerebellar and motor disorders, comprise the modern triad of clinical cerebellar ataxiology (Manto and Mariën 2015).

EXTERNAL FEATURES AND RELATIONS

The cerebellum consists of two large, laterally located hemispheres united by a midline vermis (**Fig. 29.3**). It is a multiply folded structure; when viewed from the external surface, the fissures (the cerebellar equivalent of cerebral sulci) run horizontally and follow the curve of the cerebellar external surface. The cerebellum has three surfaces. The superior surface adjoins the tentorium cerebelli and projects beyond its free edge: the distinction between the vermis and hemispheres on the superior surface is indistinct, with shallow paramedian kinks in the transverse fissures likely reflecting indentations of the superior cerebellar

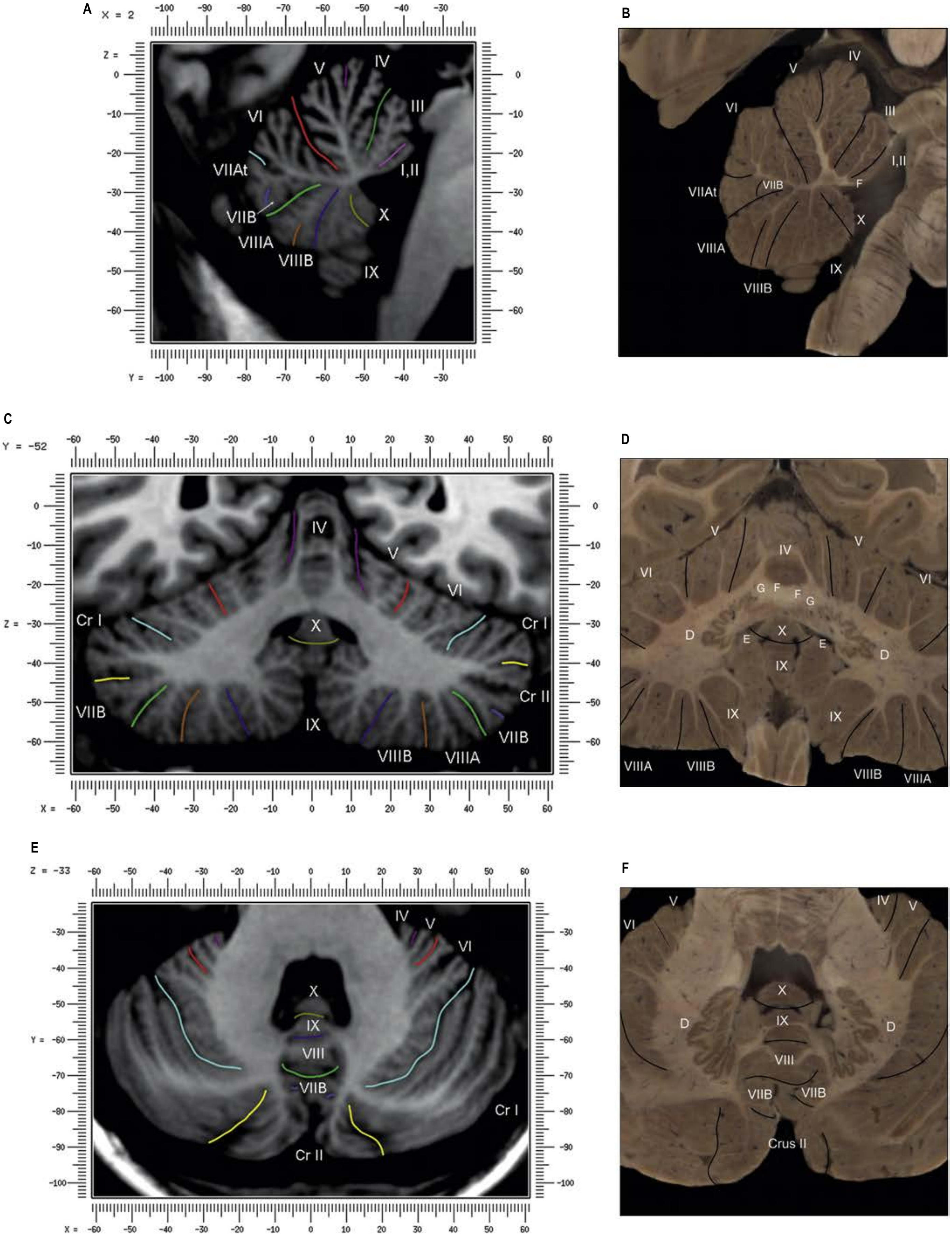
A
X = 2
Z =
Y =
V
IV
III
VI
I,II
VIIAt
VIIB
X
VIIIA
VIIIB
IX
B
IV
V
VI
III
I,II
VIIAt
VIIB
F
X
VIIIA
IX
VIIIB
C
Y = -52
Z = -30
X =
IV
V
VI
Cr I
X
Cr I
VIIB
Cr II
IX
VIIB
VIIIB
VIIIA
D
V
IV
V
VI
VI
G
F
F
G
X
D
E
E
D
IX
IX
IX
VIIIA
VIIIB
VIIIB
VIIIA
E
Z = -33
Y = -60
X =
IV
V
VI
X
IX
VIII
VIIB
Cr I
Cr II
F
V
IV
V
VI
X
D
IX
D
VIII
VIIB
VIIB
Crus II

Fig. 29.2 The appearance of a human cerebellum on magnetic resonance imaging (MRI) images (left panel) and on cryosection images taken post-mortem from another cerebellum (right panel). The cerebellum is sectioned in the sagittal plane 2 mm to the right of midline in **A** and **B**; in the coronal plane 52 mm behind the anterior commissure–posterior commissure (AC–PC) line in **C** and **D**; and in the transverse plane 33 mm below the AC–PC line in **E** and **F**. Fissures are colour-coded according to the convention used in Figs 29.3 and 29.5, and the lobules are designated. Deep cerebellar nuclei are identified in the cryosection brain. Abbreviations: D, dentate nucleus; E, emboliform nucleus; F, fastigial nucleus; G, globose nucleus. (With permission from Schmahmann JD, Doyon J, Toga A et al 2000 MRI Atlas of the Human Cerebellum. San Diego: Academic Press.)

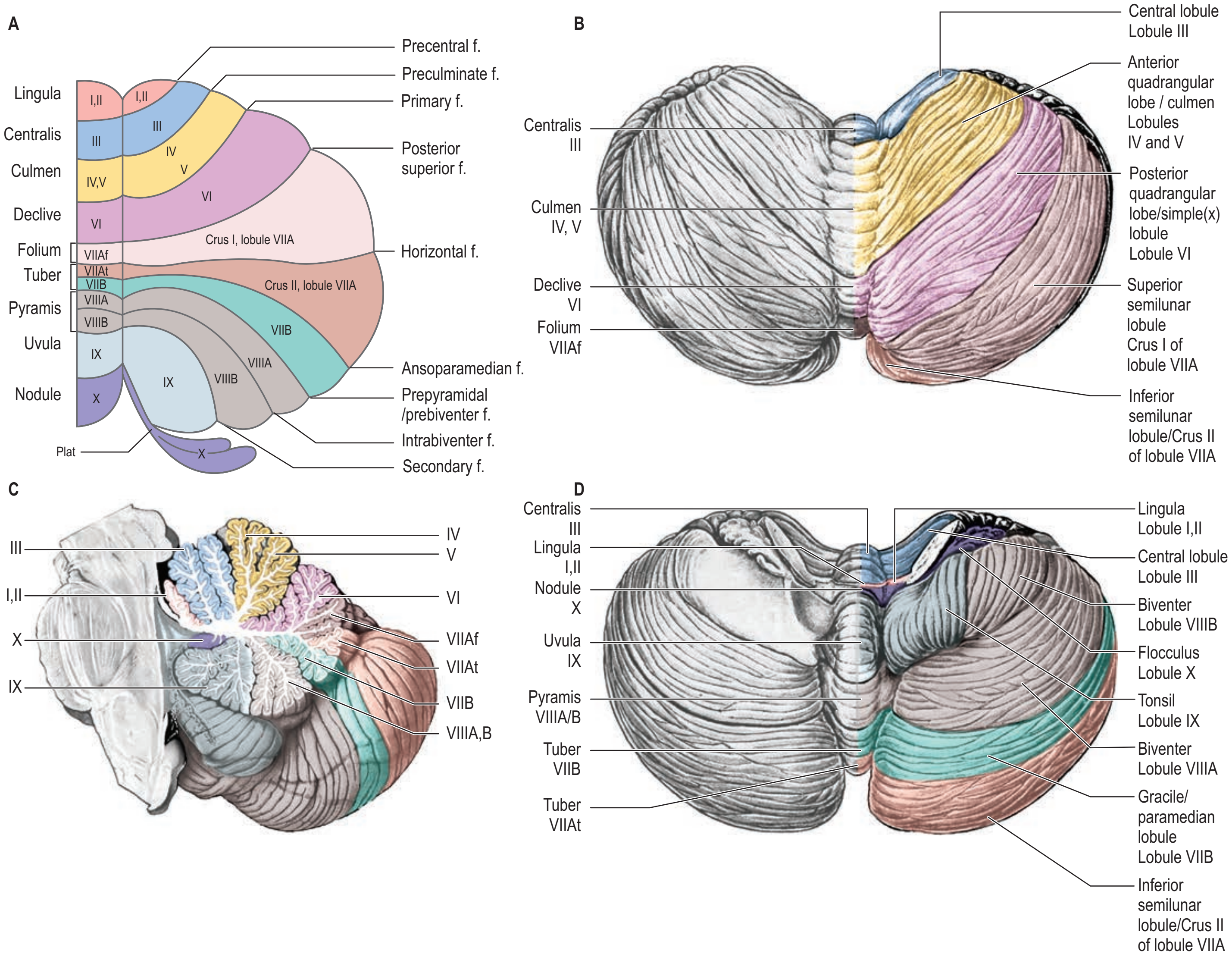
A
Lingula
Centralis
Culmen
Declive
Folium
Tuber
Pyramis
Uvula
Nodule
Plat
I,II
I,II
III
III
IV
IV,V
V
VI
VI
Crus I, lobule VIIA
VIIAf
VIIAt
VIIB
Crus II, lobule VIIA
VIIIA
VIIIB
VIIB
IX
IX
VIIIA
VIIIB
X
X
Precentral f.
Preculminate f.
Primary f.
Posterior superior f.
Horizontal f.
Ansoparamedian f.
Prepyramidal /prebiventer f.
Intrabiventer f.
Secondary f.
B
Centralis III
Culmen IV, V
Declive VI
Folium VIIAf
Central lobule Lobule III
Anterior quadrangular lobe / culmen Lobules IV and V
Posterior quadrangular lobe/simple(x) lobule Lobule VI
Superior semilunar lobule Crus I of lobule VIIA
Inferior semilunar lobule/Crus II of lobule VIIA
C
III
I,II
X
IX
IV
V
VI
VIIAf
VIIAt
VIIB
VIIIA,B
D
Centralis III
Lingula I,II
Nodule X
Uvula IX
Pyramis VIIIA/B
Tuber VIIB
Tuber VIIAt
Lingula Lobule I,II
Central lobule Lobule III
Biventer Lobule VIIIB
Flocculus Lobule X
Tonsil Lobule IX
Biventer Lobule VIIIA
Gracile/ paramedian lobule Lobule VIIB
Inferior semilunar lobule/Crus II of lobule VIIA

Fig. 29.3 Terminology of the cerebellar lobules and fissures at the vermis and hemispheres. **A**, Schematic unrolled diagram of the cerebellar cortex. The vermal and hemisphere lobules are labelled according to the elaboration by Schmahmann et al (1999, 2000) of the nomenclature of Larsell (Larsell and Jansen 1972) and Bolk (1906), as well as the classical nomenclature of the vermal lobules, and the named cerebellar fissures. **B**, The cerebellum viewed from above. **C**, Midline sagittal section of the cerebellum. **D**, The cerebellum viewed from below. Abbreviations: f, fissure.

artery. The superior surface slopes gently laterally and posteriorly as it reaches its margins. The transverse sinus borders the cerebellum at the point where the superior and inferior surfaces meet. The inferior surface of the cerebellum is characterized by a massive enlargement of the cerebellar hemispheres, separated from each other medially by a deep groove, or vallecula, which contains the dural falx cerebelli. The posterior vermis is a well-defined anatomical structure when viewed from posterior and inferior, named for its worm-like appearance by Vincenzo Malacarne (1744–1816) (Malacarne 1776), who also named the uvula and tonsils because of their resemblance to structures in the oral cavity. The posterior vermis is demarcated from the cerebellar hemispheres by deep paramedian sulci, although the hemispheres may extend medially and overlie the vermis. The inferior cerebellar surface lies against the occipital squama. The shape of the anterior cerebellar surface facing the brainstem is irregular, forming the roof of the fourth ventricle and the lateral recesses on each side. The cerebellar peduncles define the diamond shape of the ventricle when viewed from behind. Anterolaterally, the cerebellum lies against the posterior surface of the petrous part of the temporal bone.

Cerebellar fissures and lobules

The cerebellar surface is divided by numerous curved transverse fissures which separate its folia (the cerebellar equivalent of cerebral gyri) and give it a laminated appearance. The individual cerebellar folia group together as 10 lobules, arising usually from a common ray of medullary white matter. The lobules are continuous across the midline from one hemisphere to the other. They are distinguished from each other by named fissures, and they are grouped into three lobes: the anterior lobe (lobules I–V), posterior lobe (lobules VI to IX) and the flocculonodular lobe (lobule X) (**Fig. 29.4**; see Fig. 29.3). Because the cerebellar cortex has a roughly spherical shape, the true relations between its parts can sometimes be obscure. Thus, the most anterior lobules I/II of the cerebellar vermis lie very close to the most posterior vermal lobule X. The Roman numerals and subdivisions adopted by Schmahmann et al (1999, 2000) in the *MRI Atlas of the Human Cerebellum* (**Fig. 29.5**; see Fig. 29.2) and used here to designate the lobules are according to Larsell and Jansen (1972) and Bolk (1906) (**Fig. 29.6**) and replace earlier nomenclatures that were often conflicting or contradictory. The *MRI Atlas* enabled the development of probabilistic MR atlases of the human cerebellum and cerebellar nuclei (Diedrichsen et al 2009, 2011) used in functional imaging studies to correlate structure with function in health and disease.

Cerebellar peduncles

Three pairs of peduncles connect the cerebellum with the brainstem (**Fig. 29.7**). The inferior cerebellar peduncle runs parallel to the major axis of the brainstem, medial to the middle cerebellar peduncle. It consists of an outer, compact fibre tract, the restiform body, and a medial, juxtarestiform body. The restiform body is a purely afferent system conveying fibres from the dorsal spinocerebellar tract and trigeminocerebellar, cuneocerebellar, reticulocerebellar and olivocerebellar tracts (see Fig. 29.24). The juxtarestiform body is mainly an efferent system, made up almost entirely of Purkinje cell axons destined for the vestibular nuclei and uncrossed fibres from the fastigial nucleus. It also contains primary afferent mossy fibres from the vestibular nerve and secondary afferent fibres from the vestibular nuclei. The crossed fibres

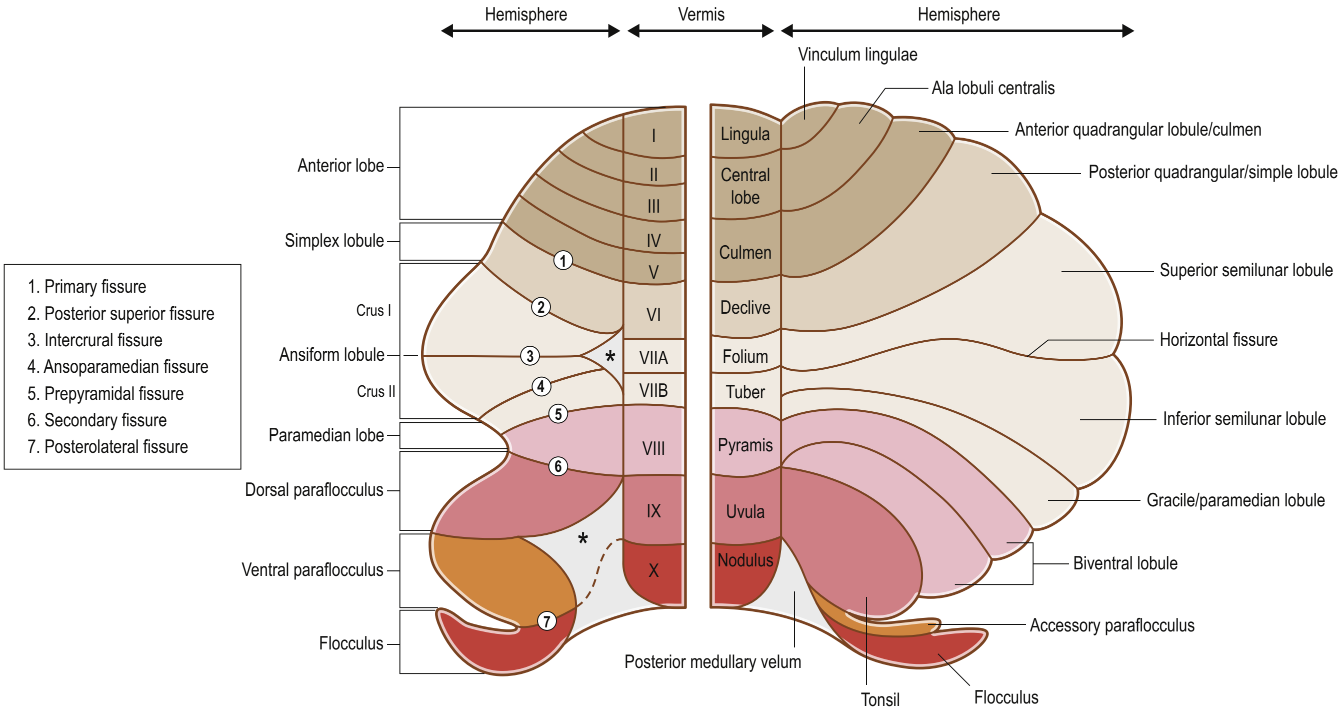
Hemisphere
Vermis
Hemisphere
Vinculum lingulae
Ala lobuli centralis
Anterior quadrangular lobule/culmen
Posterior quadrangular/simple lobule
Superior semilunar lobule
Horizontal fissure
Inferior semilunar lobule
Gracile/paramedian lobule
Biventral lobule
Accessory paraflocculus
Flocculus
Tonsil
Posterior medullary velum
Anterior lobe
Simplex lobule
Crus I
Ansiform lobule
Crus II
Paramedian lobe
Dorsal paraflocculus
Ventral paraflocculus
Flocculus
1. Primary fissure
2. Posterior superior fissure
3. Intercrural fissure
4. Ansoparamedian fissure
5. Prepyramidal fissure
6. Secondary fissure
7. Posterolateral fissure
I
II
III
IV
V
VI
VIIA
VIIB
VIII
IX
X
Lingula
Central lobe
Culmen
Declive
Folium
Tuber
Pyramis
Uvula
Nodulus
①
②
③
④
⑤
⑥
⑦
*
*

Fig. 29.4 Cerebellar nomenclature. The left-hand panel illustrates the comparative anatomical nomenclature for the hemisphere and Larsell's numbering system for the lobules of the vermis (Larsell and Jansen 1972). The right-hand panel shows the more commonly used classical nomenclatures according to different investigators over the past 140 years (Schmahmann et al 2000). The homology of these lobules is indicated using the same colour. Asterisks denote areas devoid of cortex in the centre of the folial rosettes of the ansiform lobule and the paraflocculus.

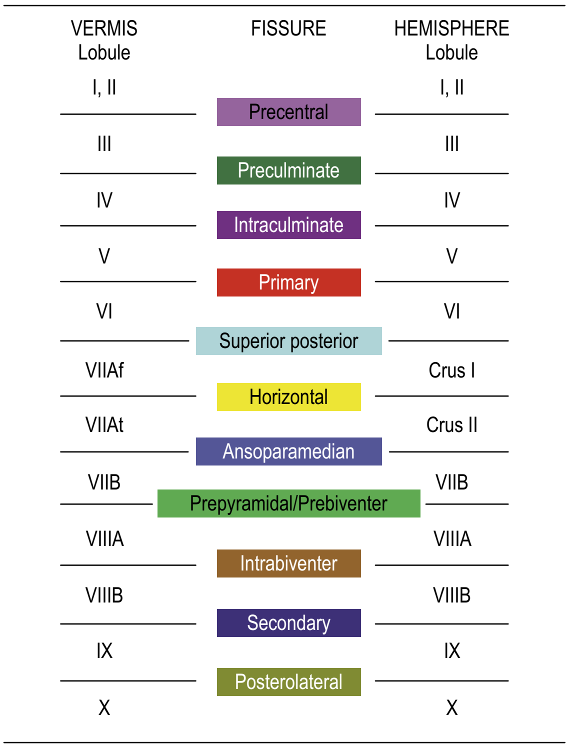

VERMIS Lobule	FISSURE	HEMISPHERE Lobule
I, II		I, II
	Precentral	
III		III
	Preculminate	
IV		IV
	Intraculminate	
V		V
	Primary	
VI		VI
	Superior posterior	
VIIAf		Crus I
	Horizontal	
VIIAt		Crus II
	Ansoparamedian	
VIIB		VIIB
	Prepyramidal/Prebiventer	
VIIIA		VIIIA
	Intrabiventer	
VIIIB		VIIIB
	Secondary	
IX		IX
	Posterolateral	
X		X

Fig. 29.5 The relationship of the named cerebellar fissures to the lobules in the vermis and hemispheres. (With permission from Schmahmann JD, Doyon J, McDonald D et al 1999 Three-dimensional MRI atlas of the human cerebellum in proportional stereotaxic space. Neuroimage 10:233–60; and Schmahmann JD, Doyon J, Toga A et al 2000 MRI Atlas of the Human Cerebellum. San Diego: Academic Press.)

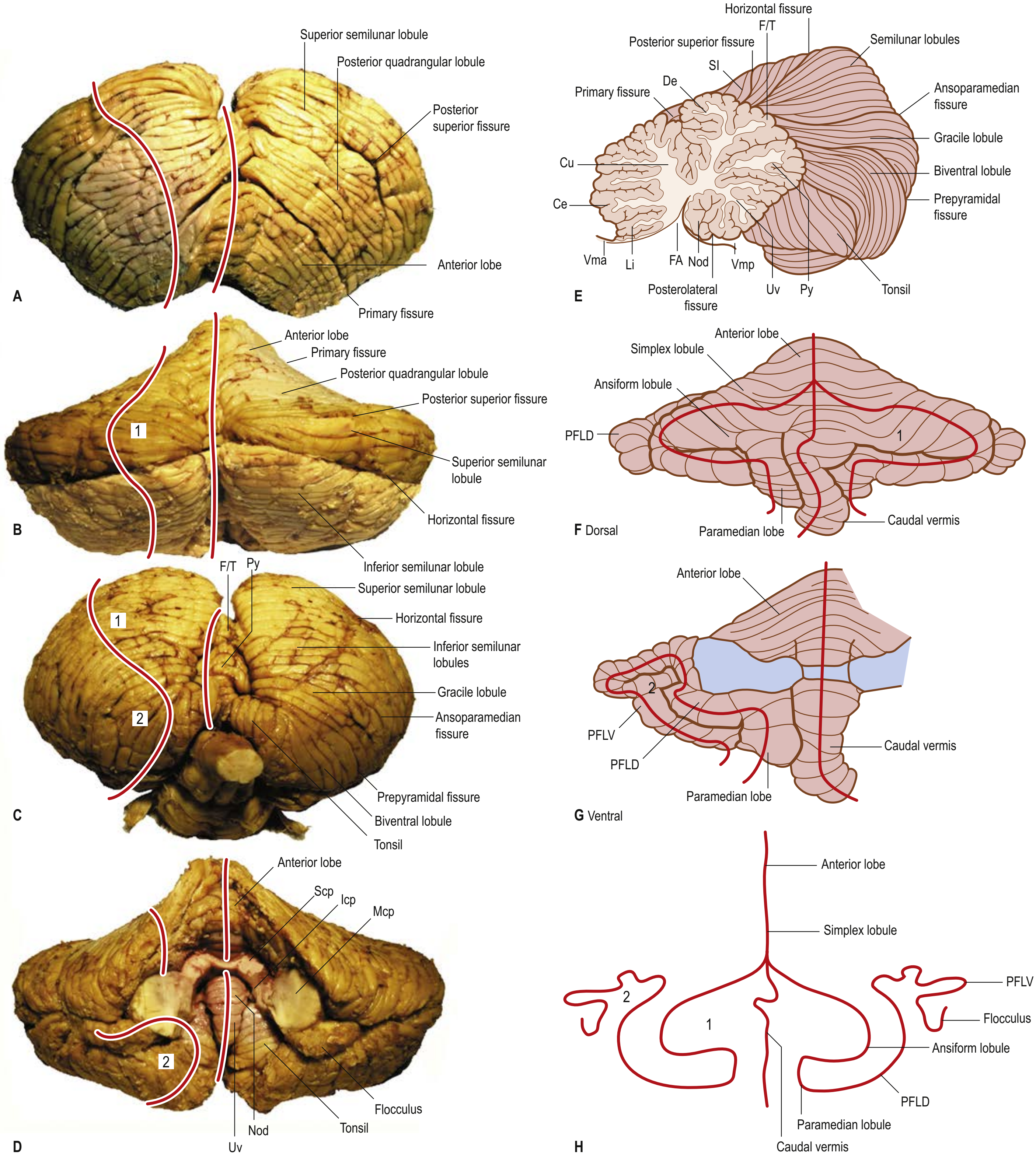
Superior semilunar lobule
Posterior quadrangular lobule
Posterior superior fissure
Anterior lobe
Primary fissure
A
Horizontal fissure
F/T
Posterior superior fissure
SI
De
Primary fissure
Semilunar lobules
Ansoparamedian fissure
Gracile lobule
Biventral lobule
Prepyramidal fissure
Cu
Ce
Vma
Li
FA
Nod
Vmp
Posterolateral fissure
Uv
Py
Tonsil
E
Anterior lobe
Primary fissure
Posterior quadrangular lobule
Posterior superior fissure
1
Superior semilunar lobule
Horizontal fissure
Inferior semilunar lobule
B
Anterior lobe
Simplex lobule
Ansiform lobule
PFLD
1
Paramedian lobe
Caudal vermis
F Dorsal
F/T
Py
Superior semilunar lobule
1
Horizontal fissure
Inferior semilunar lobules
2
Gracile lobule
Ansoparamedian fissure
Prepyramidal fissure
Biventral lobule
Tonsil
C
Anterior lobe
2
PFLV
PFLD
Paramedian lobe
Caudal vermis
G Ventral
Anterior lobe
Scp
Icp
Mcp
2
Flocculus
Nod
Tonsil
Uv
D
Anterior lobe
Simplex lobule
PFLV
2
1
Flocculus
Ansiform lobule
PFLD
Paramedian lobule
Caudal vermis
H

Fig. 29.6 Historically relevant figure that depicts Bolk's (1906) prototype for his ground plan of the mammalian cerebellum. **A–D**, Anterior, dorsal, posterior and ventral views of the human cerebellum. **E**, A sagittal section of the human cerebellum. **F–G**, Dorsal and ventral views of the cerebellum of *Eulemur albifrons* (white-headed lemur). Two loops are present in the folial chain of the hemisphere: (1) as the ansiform lobule, (2) as the paraflocculus. The course of the folial chains of the vermis and hemisphere in **A–D** and **F–G** is indicated with red lines. **H**, Bolk's stick diagram of the folial chains of the vermis and hemisphere. Key and abbreviations: 1, 2, ansiform and parafloccular loops of the folial chain of the hemisphere; Ce, central lobule; Cu, culmen; De, declive; FA, fastigium; F/T, folium and tuber; Icp, inferior cerebellar peduncle; Li, lingula; Mcp, middle cerebellar peduncle; Nod, nodulus; PFLD, dorsal paraflocculus; PFLV, ventral paraflocculus; Py, pyramis; Scp, superior cerebellar peduncle; SI, simplex (posterior quadrangular) lobule; Uv, uvula; Vma, anterior (superior) medullary velum; Vmp, posterior medullary velum.

Vermal lobules I and II constitute a single lamina of four or five shallow folia; their white core is continuous with the anterior (or superior) medullary velum lying anterior and inferior to the vermis. Lobule I is distinct from lobule II in some human cerebella and in lower primates. The vermal and hemispheric components of lobule I/II together were termed the lingula. The precentral fissure separates lobules I/II from lobule III (centralis) both in the vermis and the hemispheres. Lobule III is partially obscured by lobule IV when viewed from the superior aspect, but it is sizeable, and has a semilunar form with its wing (ala, in prior terminology) extending into the hemispheres on each side. Lobule III is the first distinct folium that is not attached to the anterior medullary velum. The preculminate fissure separates lobule III from lobule IV. The use of the term culmen (including both the vermis and the hemisphere) obscures the fact of the division of the culmen into lobules IV and V by the intraculminate fissure. This fissure is readily discernible on the hemisphere, but at the midline is continuous with a small fissure situated between the branches of a folium. Lobule IV usually contains one folium, and lobule V contains two. The deepest fissure in the vermis that is visible in mid-sagittal section is the primary fissure, which curves ventrolaterally around the superior surface of the cerebellum. It appears early in embryological development and marks the boundary between the anterior lobe (lobules I to V) and the posterior lobe (lobules VI to IX). Specifically, it separates lobule V from lobule VI in the vermis and in the hemisphere. The primary fissure, like other fissures within the anterior lobe, is progressively more difficult to discern on parasagittal sections as one moves laterally, becoming continuous with an undistinguished small fissure in the intermediate sectors of the hemispheres.

Lobule VI is sizeable and contains two large folia with medullary rays that take their origin off the medullary core. The vermal and hemispheric components of lobule VI have previously received different names: in the vermis, lobule VI was called the declive, and in the hemisphere it was called the lobulus simplex, among others.

The superior posterior fissure appears early in development and is visible on the superior surface of the cerebellum separating lobule VI from lobule VII. Vermal lobule VII is complex; its lateral extension in the hemispheres into what Lodewjck Bolk (1866–1930) called the ansiform lobule, forms a large part of the hemisphere in the human cerebellum. The massive expansion through evolution of the human cerebellum is a reflection in large part of the expansions of lobules VI and VII. The terms folium and tuber have been used to denote vermis lobule VII, but this fails to convey the complexity of their equivalent hemispheric extensions, as below.

The horizontal fissure appears relatively late in embryological development. It is prominent in the hemisphere, extending around the dorsolateral border of each hemisphere from the middle cerebellar peduncle to the vallecula, separating the superior and inferior surfaces. The horizontal fissure divides lobule VII into two sectors, with important differences in their hemispheric extensions. Vermal lobule VIIAf (identical to the folium) expands laterally to form crus I (of Bolk's ansiform lobule, formerly known as the superior semilunar lobule). Vermal lobule VIIAt (formerly called the rostral half of the tuber of the vermis) is continuous in the hemispheres with crus II (of Bolk's ansiform lobule, formerly known as the inferior semilunar lobule). The horizontal fissure therefore separates lobule VIIAf from VIIAt in the vermis, and crus I from crus II in the hemisphere. In some brains, lobule VIIAf may not be discernible at the midline, in which case the superior posterior fissure is bounded caudally by the ansoparamedian and not the horizontal fissure.

The ansoparamedian fissure can be traced across the midline separating lobule VIIAt and crus II from vermal and hemispheric lobule VIIB (previously termed the paramedian, or gracile lobule). The ansoparamedian fissure is not symmetrical in the hemispheres in all brains. The horizontal and ansoparamedian fissures sometimes meet on the posterior inferior cerebellar surface, so that crus II appears as a triangular lobe situated on the superior and posterior aspects of the posterior lobe, and on lateral parasagittal sections, crus I is adjacent to lobule VIIB. When the horizontal and ansoparamedian fissures do not meet, crus II continues laterally and forward onto the anterior surface of the cerebellum, and on lateral parasagittal sections crus II is adjacent to VIIB. These details are relevant for precise mapping of the human brain and can affect intra-and inter-individual functional mapping studies. Even when the folia at the lateral inferior cerebellar surface are asymmetric across the two hemispheres, they can be seen to be derived from medullary rays that are morphologically similar.

Lobule VIIIA and VIIIB in the vermis were formerly known as the pyramis, and in the hemispheres as the biventer. Thus, the prepyramidal/prebiventer fissure separates lobule VIIB from VIIIA and is named according to whether the lobule VIIB/VIIIA distinction is in the vermis (prepyramidal fissure) or hemisphere (prebiventer fissure). The intrapyramidal/intrabiventer fissure separates lobule VIIIA from VIIIB. The secondary fissure is interposed both at the vermis and in the hemispheres between lobules VIIIB and IX. In earlier terminology, vermal lobule IX is referred to as the uvula, and hemisphere lobule IX as the tonsil, and subsequently as the ventral paraflocculus (equivalent to the dorsal paraflocculus in monkeys). In the human, the folial loop of lobule IX is directed medially, contrary to the situation in most mammals, where the paraflocculus arches laterally. Note that the term cerebellar tonsil refers to a grossly visible anatomical structure at the inferior and medial cerebellum which is of great relevance in clinical neurology and neurosurgery (tonsillar herniation, Chiari malformation). Although the tonsil was previously equated with lobule IX, it also incorporates folia within lobule VIIIB, which means that the term is anatomically imprecise.

The posterolateral fissure separates lobules IX from X, and forms the boundary between the posterior lobe of the cerebellum and the flocculonodular lobe. Vermal lobule X (nodulus) is the last of the vermis divisions. Where its cortex ends it forms the attachment (taenia) of the ependymal roof of the fourth ventricle. Hemispheric lobule X (flocculus) is a small cerebellar lobule adjacent to the caudal surface of the middle cerebellar peduncle. It is located in the roof of the lateral recess of the fourth ventricle, and dorsal to the cochlear nuclei and the vestibulocochlear nerve which are ventral to the recess. Hemispheric lobule X appears as a double folial rosette; its dorsal leaf is known as the accessory paraflocculus of Henle (the ventral paraflocculus in monkeys), its ventral leaf represents the true flocculus. Between vermal lobule X (nodulus) and hemispheric lobule X (flocculus and accessory paraflocculus), the cortex is absent and the tissue is stretched out as the posterior medullary velum (inferior medullary velum) which forms the infero-posterior part of the fourth ventricle. The internal surface of the posterior medullary velum is the ventricular ependyma; its outer surface is covered by pia mater.

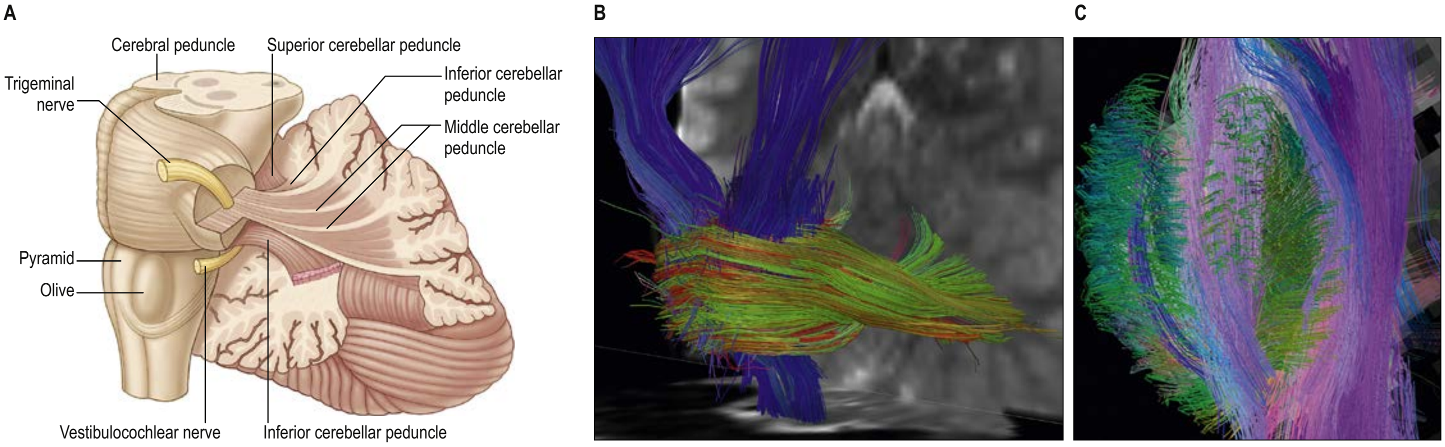
A
Cerebral peduncle
Superior cerebellar peduncle
Trigeminal nerve
Inferior cerebellar peduncle
Middle cerebellar peduncle
Pyramid
Olive
Vestibulocochlear nerve
Inferior cerebellar peduncle
B
C

Fig. 29.7 **A**, Dissection of the left cerebellar hemisphere and its peduncles. **B**, Diffusion spectrum tractography (DSI) image *in vivo* showing descending corticofugal fibres to the pons and spinal cord (blue). Fibres from the rostral pons course in the middle cerebellar peduncle to cerebellar posterior lobe; fibres from caudal pons are directed more to the cerebellar anterior lobe and superior cerebellum. **C**, *Ex vivo* image of pontocerebellar fibres coursing through the middle cerebellar peduncle, between and around the descending fibres of the corticopontine and corticospinal tracts. (B and C, Courtesy of JD Schmahmann and VJ Wedeen, Departments of Neurology, Radiology, and Athinoula A. Martinos Center for Biomedical Imaging, Massachusetts General Hospital.)

from the fastigial nucleus pass dorsal to the superior cerebellar peduncle as the uncinate tract (the hook bundle of Russell) and enter the brainstem at the border of the juxtarestiform and restiform bodies.

The middle cerebellar peduncle (see Figs 29.7B–C) is the most lateral and by far the largest of the three. It passes obliquely from the basal pons to the cerebellum and contains the massive pontocerebellar mossy fibre pathway, composed almost entirely of fibres that arise from the contralateral basal pontine nuclei, with a small addition from nuclei in the pontine tegmentum.

The superior cerebellar peduncle (brachium conjunctivum) contains all the efferent fibres from the dentate, emboliform and globose nuclei, and a small fascicle from the fastigial nucleus. Fibres from the globose nucleus occupy a medial position; those from the emboliform and dentate nucleus are successively more lateral. Axons in the extreme ventrolateral portion of the peduncle arise from the superior vestibular nucleus and relay excitation from the anterior semicircular canal to the oculomotor nucleus (the excitatory vestibulo-ocular relay). Nucleo-olivary fibres of the interposed and dentate nuclei are located in a separate bundle, ventral to the peduncle. The superior cerebellar peduncle, including its nucleo-olivary component, decussates in the caudal mesencephalon (the decussation of the brachium conjunctivum). The decussation consists of dorsal and ventral portions. The dorsal portion contains fibres that occupy the medial two-thirds of the peduncle and start to cross the midline at the level of the inferior colliculus, ventral to the medial longitudinal fasciculus. The ventral portion contains fibres that occupy the lateral third of the peduncle, and decussate in the ventral tegmentum, immediately dorsal to the interpeduncular nucleus. Rostrally, at the level of the caudal red nucleus, the ventral and dorsal portions of the decussation merge and the entire decussation is displaced ventrally by the dorsal tegmental (tectospinal) decussation. After its decussation the peduncle divides into descending and ascending branches. The descending branch terminates in the medial reticular formation of the pons and the medulla and in the reticulotegmental nucleus (nucleus reticularis tegmenti pontis, NRTP). The nucleo-olivary fibres join the descending branch to terminate in the inferior olive in a strict orderly manner (see below). The much larger ascending branch distributes to the mesencephalon and the diencephalon; the red nucleus and the thalamus are its main targets. The fibres of the superior cerebellar peduncle always decussate to the opposite hemisphere, except in rare developmental disorders of axonal guidance (Spampinato et al 2008).

The superior cerebellar peduncle also conveys afferents to the cerebellum that arise in the spinal cord and course in the ventral spinocerebellar tract. These fibres reach the upper part of the pontine tegmentum, loop around the entrance of the trigeminal nerve and join the peduncle, uniting with the dorsal spinocerebellar fibres entering through the restiform body.

INTERNAL ORGANIZATION

White matter

On its cut surface, the characteristic appearance of the cerebellum is a central white matter core surrounded by multiple, deeply folded folia. The white matter core branches into the diverging medullary laminae, which occupy the central part of the lobules and then further branch out into their folia and subfolia. On sagittal section, the highly branched pattern of medullary laminae gave rise to the name arbor vitae, for its resemblance to the leaf of the coniferous arbor vitae or cedar tree (see Fig. 29.2). The white matter of the medullary rays contains the afferents to the cerebellar cortex, and the Purkinje cell axonal efferents from the cortex to the deep nuclei.

Fibres crossing the midline in the anterior medullary velum and the white matter core of the cerebellum constitute the cerebellar commissure, which contains the decussating afferent fibres of the inferior and middle cerebellar peduncles, and decussating efferent fibres from the fastigial nucleus. Note that the term commissure here denotes the crossing of the midline by cerebellar afferent and efferent fibres; there are no cerebellar cortico-cortical connections either ipsilaterally or between the two hemispheres.

Deep cerebellar nuclei

The medullary core contains the four deep cerebellar nuclei (**Fig. 29.8**). These were first described by Stilling (1864) as comprising, from medial to lateral, the fastigial, globose, emboliform and dentate nuclei. In rodent, cat and monkey brains the anterior and posterior interposed nuclei are equivalent in humans to the emboliform and globose nuclei respectively. The nuclei form two interconnected groups. The caudomedial group includes the fastigial nucleus located next to the midline and bordering on the fastigium (roof) of the fourth ventricle, and the closely adjacent globose nucleus. The rostrolateral group consists of the emboliform nucleus which is medially adjacent to the dentate nucleus.

The dentate is the largest of the deep cerebellar nuclei and has expanded most in evolution. It is an irregularly folded sheet of neurones, resembling a crumpled leather purse with a medially directed opening. The convolutions of the dentate nucleus are narrow rostromedially (microgyric) and contain large neurones, whereas the much wider ventrocaudal (macrogyric) part contains smaller neurones. This is important from the perspective of anthropology as well as cognitive neuroscience and behavioural neurology (see below). The dentate nucleus surrounds the hilum, a mass of efferent fibres arising from dentate neurones that forms the bulk of the superior cerebellar peduncle.

The cerebellar nuclei contain three types of neurones. Multipolar neurones have different sizes, with long ramifying dendrites and an axon that leaves the cerebellum through the superior cerebellar peduncle, the uncinate tract or the juxtarestiform body. These provide glutamatergic, excitatory input to the brainstem, thalamus and spinal cord. Some collaterals of these efferent axons enter the cerebellar cortex, where they terminate sparsely as mossy fibres. A population of small, inhibitory neurones gives rise to the pathway terminating in the contralateral inferior olive, the nucleo-olivary projection (Nelson et al 1989), travelling mostly in the superior cerebellar peduncle. These contain immunoreactivity for GAD (glutamic acid decarboxylase), the endogenous marker enzyme for GABAergic neurones, as well as CGRP- (calcitonin gene-related

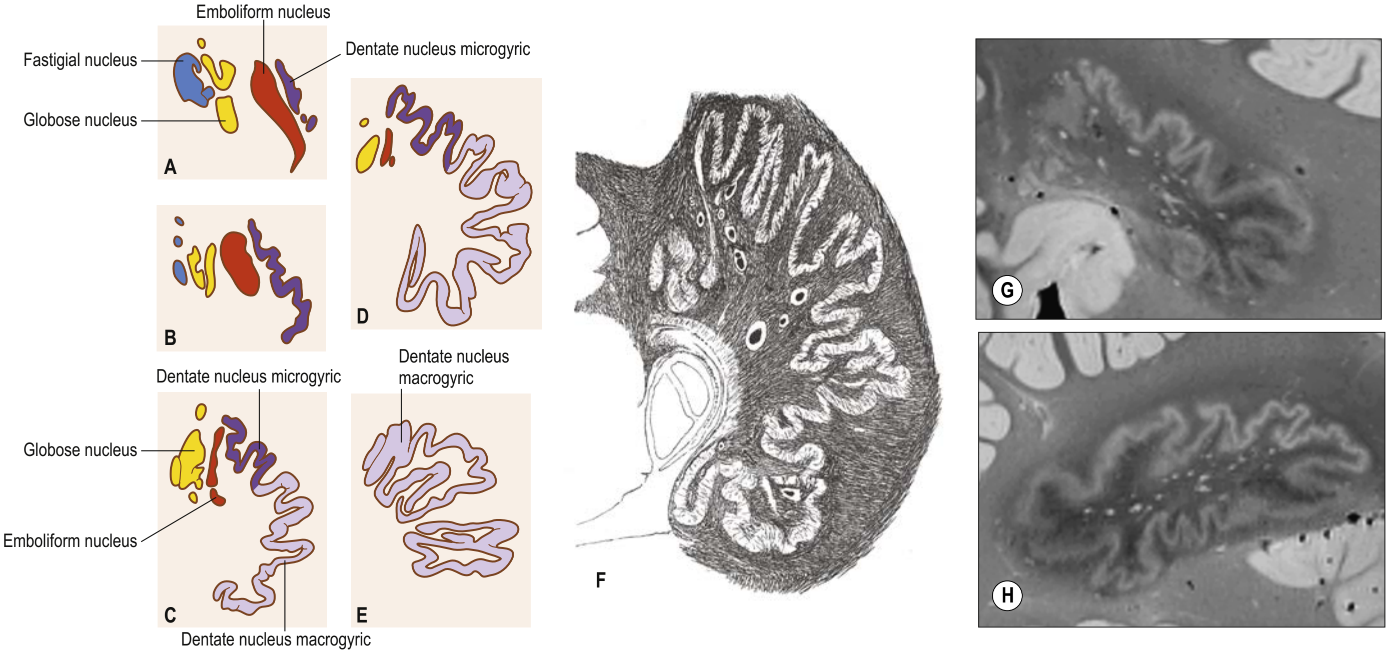

Fig. 29.8 The human cerebellar nuclei. **A–E**, Transverse sections through the cerebellar nuclei, **A** being the most rostral level. The dentate nucleus can be subdivided into dorsomedial microgyric and ventrocaudal macrogyric parts. **F**, A Weigert-stained section through the dentate nucleus, showing its subdivision into micro- and macrogyric parts. **G**, Coronal view, and **H**, sagittal view, postmortem 7T MRI through the dentate nucleus of human brain. (A–E, Adapted with permission from Larsell O, Jansen J 1972 The comparative anatomy and histology of the cerebellum. III. The human cerebellum, cerebellar connections, and cerebellar cortex. Minneapolis, University of Minnesota Press. F, With permission from Winkler C 1926 De bouw van het zenuwstelsel. Haarlem, de erven Bohn. G, H, Courtesy of Drs Bruce Fischl and Andre van der Kouwe, Laboratory for Computational Neuroimaging, Athinoula A. Martinos Center for Biomedical Imaging, Massachusetts General Hospital.)

peptide)-like immunoreactivity. Local inhibitory interneurones in the cerebellar nuclei contain glycine, often colocalized with GABA (γ-aminobutyric acid). Purkinje cell axons are the main input to the neurones of the cerebellar nuclei: there are GABAergic inhibitory synapses on both dendrites and somata. Collaterals of climbing and mossy fibres terminate on proximal and distal dendrites and provide the cerebellar nuclei with glutamatergic excitatory input.

A collection of small, cholinergic neurones extends from the flocculus to the nodulus (hemispheric and vermal lobule X) in the roof of the fourth ventricle, invading the spaces between the nuclei. These form the basal interstitial nucleus (Langer 1985).

Cerebellar cortex

The cerebellar cortex is characterized by its regular, repeating, lattice-like histological structure (Figs 29.9–29.11). In contrast to the cerebral cortex, obvious local differences and architectonic heterogeneity do not occur and, with a few exceptions, different areas of the cerebellar cortex are largely indistinguishable. The same homogeneity is present throughout all mammals and, with only minor differences, throughout the vertebrates. The cerebellar cortex has three main layers, a Purkinje cell layer interleaved between the overlying molecular layer and the granule cell layer beneath. The three layers are interconnected by a complex circuitry with an architecture that is essentially invariant throughout. Cerebellar functional topography is entirely explained by the arrangement of the fibres that connect the cerebellum to other regions of the central nervous system. (For further reading, see Jansen and Brodal (1954), Braitenberg and Atwood (1958), Dow and Moruzzi (1958), Eccles et al (1967), Fox and Snider (1967), Llinas and Sotelo (1992), Larsell and Jansen (1972), Palay and Chan-Palay (1974), Ito (1984), Glickstein et al (1987), Strata (1989), Manto et al (2013).)

Purkinje cell layer

This layer is characterized by the presence of Purkinje cells (PC), one of the largest cells in the nervous system (Fig. 29.12) (Purkinje 1837). Smaller somata of epithelial (Bergmann) glial cells are located at this level. Clumps of granule cells and occasional Golgi cells penetrate between the Purkinje cell somata. There are estimated to be 25 million Purkinje cells in the human cerebellum (Andersen et al 2012), each with a pear-shaped soma, 30–35 μm in diameter and 50–70 μm in length. Individual Purkinje cells are separated by about 50 μm transversely and 50–100 μm longitudinally. This geometry occurs in its typical form in all vertebrate classes. The entire Purkinje cell soma, its dendrites and axonal initial segment, are covered with a neuroglial sheath, and the axon is myelinated. Axo-somatic contacts on the Purkinje cells penetrate this sheath, and the dendritic spines protrude through the sheath to contact the parallel and climbing fibres.

One or sometimes two large primary proximal dendrites arise from the apical pole (superficial pole, neck) of each Purkinje cell soma. They divide, usually into two major dendrites, from which an abundant arborization arises, with several orders of subdivision, that extends towards the surface, forming a flattened plate orientated perpendicular to the long axis of the folium. The fan-like appearance of the Purkinje cell dendritic tree is a defining feature. It measures 300–400 μm in the sagittal plane, but only 15–20 μm in the transverse plane. Approximately 90% of the Purkinje cell dendritic tree consists of terminal branches containing about 180,000 spines (Fox and Barnard 1957). They are not uniformly distributed: proximal first and second order dendrites have smooth surfaces with short, stubby spines which are contacted by climbing fibres, whereas distal branches have a dense array of short-necked dendritic spines on which the terminals of parallel fibres synapse. This differential proximal vs distal Purkinje cell spine density is under dual control: an intrinsic mechanism that promotes spine growth over the entire dendritic tree, and activity-dependent spine pruning by the climbing fibre at the proximal dendrite.

The subcellular structure of a Purkinje cell is essentially similar to that of other neurones. A distinguishing feature is the presence of subsurface cisterns below the plasmalemma of the soma and dendrites; these may penetrate into the spines and are often associated with a mitochondrion. The cisterns represent intracellular calcium stores which are important links in the second messenger systems of the cell. Excitatory (asymmetrical) synapses of the climbing fibres contact the proximal spines of the spiny branchlets; parallel fibres contact the distal spines of the spiny branchlets. Excitatory synapses are rare on the soma of a Purkinje cell. Inhibitory (symmetrical) synapses from basket cell axons and stellate cells and recurrent collaterals of the Purkinje cell axon contact the shafts of the proximal dendrites. The non-synaptic area of the surface of the soma and dendrites of a Purkinje cell is covered by lamellar protrusions of the Bergmann glial fibres.

The Purkinje cell axon arises from the pole opposite the dendrites and traverses the granular layer into the subjacent white matter. Its initial portion is narrow, unmyelinated and has the typical features of an initial axon segment. It is surrounded by the distal branches of the basket cell axons as the pinceau (paintbrush). Beyond the initial

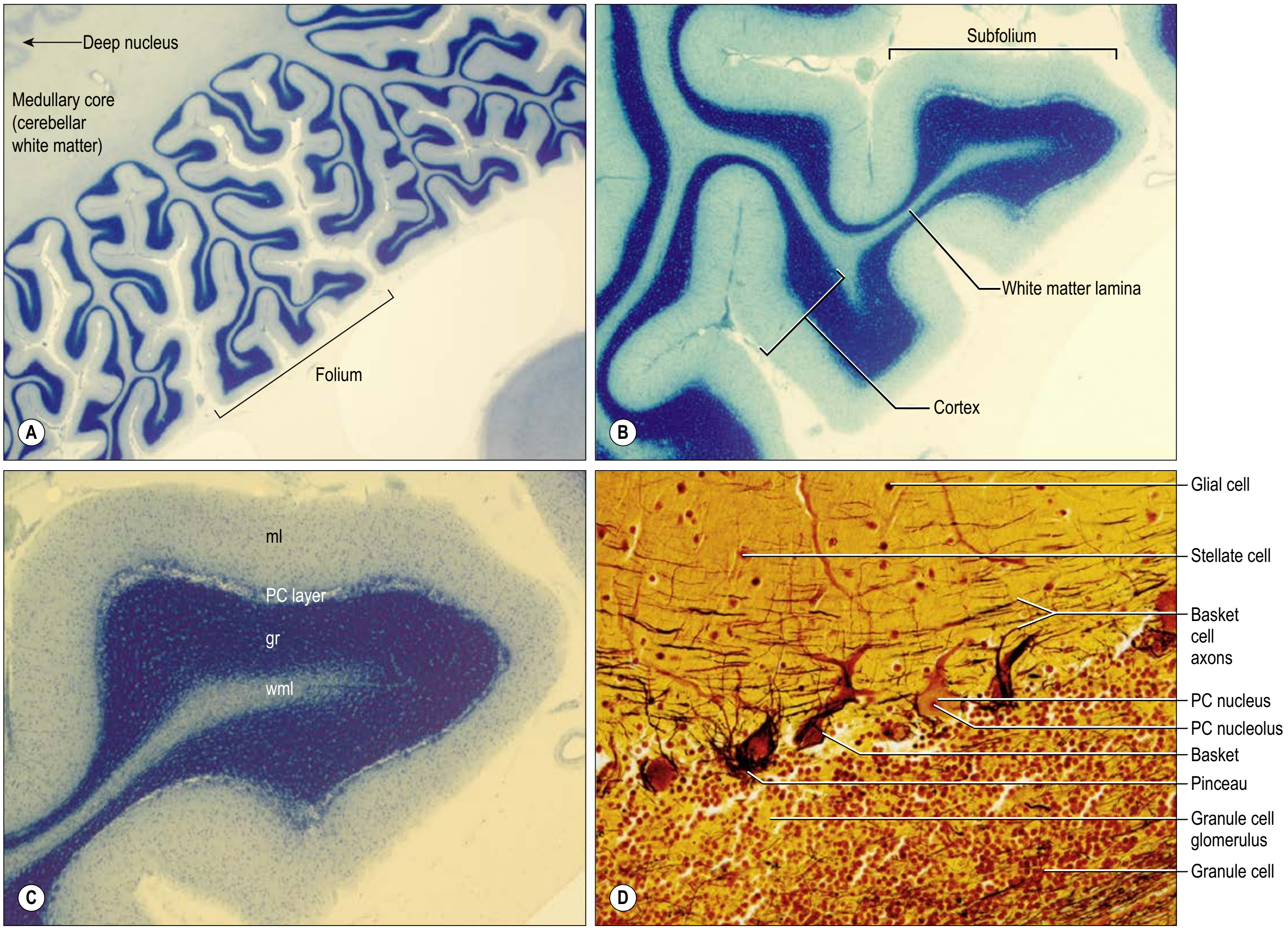

Fig. 29.9 Histologic sections of human cerebellar cortex at progressively higher levels of magnification. Stain for Nissl substance in **A**–**C**, and Bielschowsky silver stain in **D**. Abbreviations: gr, granule cell layer; ml, molecular layer; PC, Purkinje cell; wml, white matter lamina. Magnification: A ×0.5, B ×2, C ×4, D ×20. (A–C, Courtesy of JD Schmahmann, Department of Neurology, Massachusetts General Hospital. D, Courtesy of Dr Matthew Frosch, Department of Neuropathology, Massachusetts General Hospital.)

segment, about 50 µm beneath the Purkinje cell soma, the axon suddenly enlarges, acquires a myelin sheath and gives off collateral branches. The main axon descends into the white matter and forms a plexus in the deep cerebellar nuclei and, in the case of lobule X, the vestibular nuclei. Recurrent collateral branches of Purkinje axons form plexuses above and below their somata. These collaterals are orientated in the same plane as the Purkinje cell dendritic tree and the inhibitory synapses from basket and stellate cells. Purkinje cell axon recurrent collaterals terminate on neighbouring Purkinje neurones and on basket and Golgi neurones. Purkinje cells are inhibitory and use GABA as their main neurotransmitter, as well as the neuropeptides motilin, cerebellin and CGRP. They are the only efferent neurone of the cerebellar cortex and project to the deep cerebellar or vestibular nuclei.

Molecular layer

The molecular layer is about 300–400 µm thick. By ordinary histological technique it is almost featureless, contrasting with the immense cellular population of the granule cell layer. It is composed of dendritic arborizations of the Purkinje and Golgi cells, axons and parallel fibres of the granule cells, climbing fibres, radial fibres of the Bergmann neuroglial cells, and sparse basket and stellate interneurones. Purkinje cell dendritic trees extend towards the surface and spread out in a plane perpendicular to the long axis of the cerebellar folia. Dendritic trees of Golgi neurones lying in the superficial part of the granular layer reach towards the cerebellar surface. Unlike the flattened dendritic tree of the Purkinje cells, Golgi cell dendrites have the shape of a goblet and span the territory of many Purkinje neurones longitudinally as well as transversely. These dendrites receive synapses from parallel fibres. Some Golgi cell dendrites enter the granular layer where they are contacted by mossy fibre terminals.

The granule cell axon ascends into the molecular layer and bifurcates into the parallel fibre, one of the thinnest known vertebrate axons. Parallel fibres extend in opposite directions along the long axis of the folium and terminate on the dendrites of the Purkinje cells and Golgi cells that they encounter, and on the basket and stellate cells of the molecular layer. Climbing fibres are the terminals of olivocerebellar fibres which ascend through the granular layer to contact Purkinje dendrites in the molecular layer. Radiating branches of the large Bergmann glial cells give off processes that surround all neuronal elements except at the synapses; at the cortical surface their expansions join to form an external limiting membrane.

The cerebellar cortical interneurones were described by Ramón y Cajal (1909–10) (see Fig. 29.10). Basket and stellate cells are the inhibitory GABAergic interneurones of the molecular layer. They receive excitatory (asymmetrical) synapses from parallel fibres as they pass through their dendritic trees: their sparsely branched dendritic trees and the ramifications of their axons are located in a plane perpendicular to the long axis of a folium, i.e. in the same plane as the Purkinje cell dendritic tree and the ramifications of the Purkinje cell recurrent collaterals.

The basket cell has a pyramidal or oval shape, measures about 15 µm in length, and lies in the lower third of the molecular layer just above the Purkinje cells (**Fig. 29.13A–B**). Its dendrites extend up throughout the molecular layer in a fan-shaped field of 30 µm in the parasagittal plane, giving off relatively few branches, interdigitating with the dendritic fields of the Purkinje cells, and contacted by the parallel fibres. The complex axon of the basket cell has a horizontal course deep in the molecular layer just above the Purkinje cells, lying in the parasagittal plane perpendicular to the long axis of a folium (that is, perpendicular to the orientation of the parallel fibres and in the same plane as the flattened plate of the Purkinje cell dendritic tree).

The axon of each basket cell is about 1 mm in length and contacts approximately 9–12 Purkinje cells. As it moves away from its soma, the axon increases in size, giving off a succession of descending branches

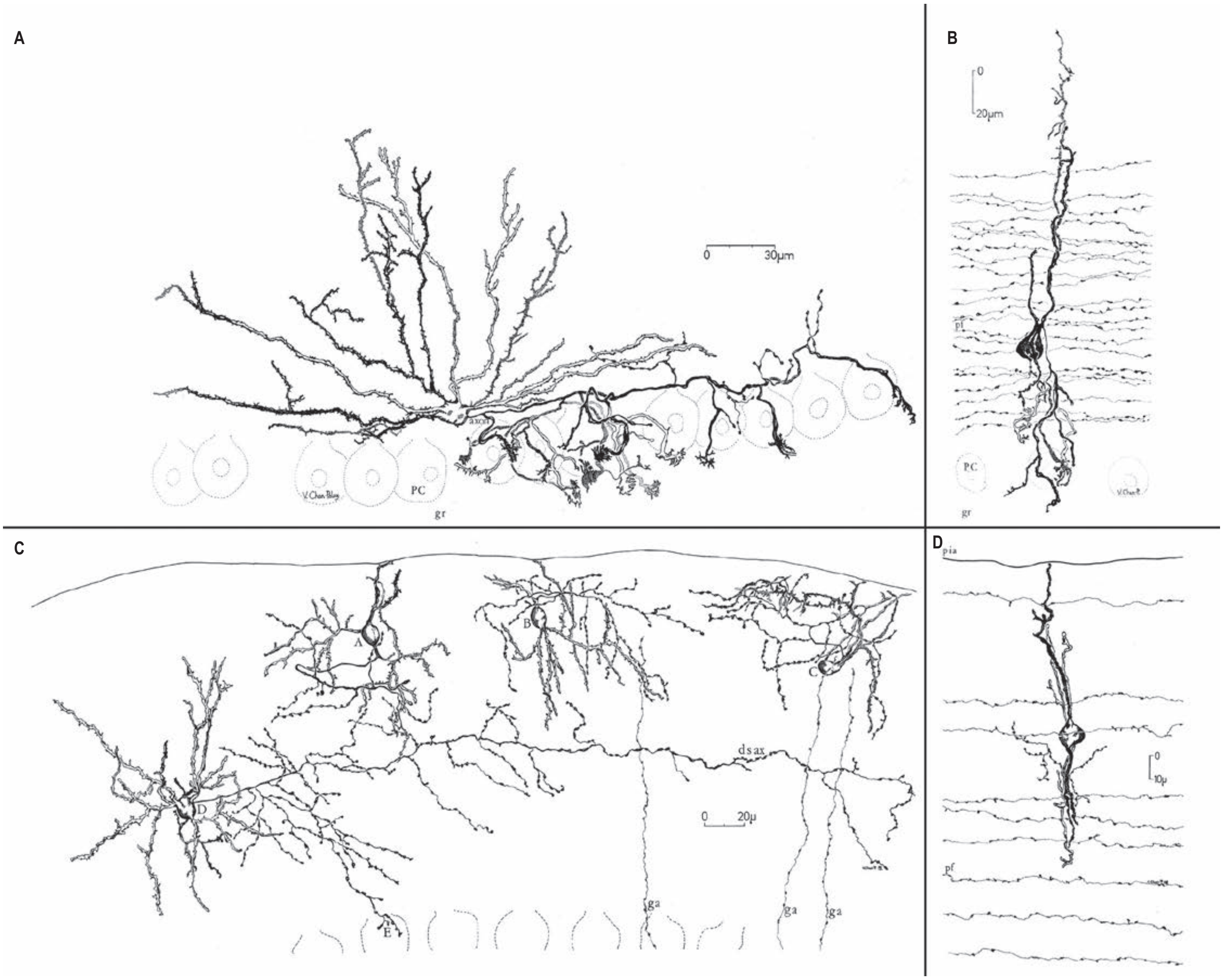

Fig. 29.13 Camera lucida drawings of Golgi-impregnated molecular layer interneurones. **A**, Basket cell with spine-laden dendrites radiating in the molecular layer. An axon is shown travelling horizontally across the folium giving off descending collaterals that form the pericellular basket and pinceau around the Purkinje cell (PC) cell body and initial segment of the axon as it enters the granular layer (gr). Some ascending collaterals are noted. **B**, The basket cell processes are orientated in the same plane as the PCs, i.e. perpendicular to the long axis of the folium and the direction of the parallel fibres (pf). **C**, Three superficial stellate cells (A–C) have dendrites that reach the pial surface, and axonal arborizations distributed in a tangle of beaded threads around the dendrites. Ascending granule cell axons (ga) contact their dendrites and somata. The deep stellate cell (D) has an axonal plexus proximally that gives way to a long axon coursing across the folium. **D**, View of the stellate cell to show its processes orientated in the same plane as the PCs. Parallel fibres (pf) contact the stellate cell dendrites and soma. (With permission from Palay S, Chan-Palay V 1974 Cerebellar Cortex: Cytology and Organization. New York: Springer-Verlag.)

that envelope the Purkinje cell soma in an axonal sheath with numerous synaptic contacts over its entire surface, forming pericellular networks, or baskets. The terminal branches of the basket cell axons descend to surround the initial segment of the Purkinje cell axon in a dense plexus of convoluted and branching fibres measuring 15–20 µm across, with the appearance of a paintbrush or 'pinceau' (see Fig. 29.9D). This axo-axonic complex is unique in the mammalian nervous system. According to Palay and Chan Palay (1974) the pinceau is historically significant because it led Cajal to the view that nerve cells are in contact but not continuity with each other, and that impulses are directed from an axon to a cell body, essential tenets of the neurone doctrine. In addition to the descending collaterals, there are sparser ascending collaterals from the basket cell that synapse on the secondary and tertiary Purkinje cell dendrites. Branches from each basket cell axon also extend in the direction of the long axis of a folium to a further 3–6 rows of Purkinje neurones flanking the axon. Hence an estimated 72 Purkinje cell neurones may receive inhibitory synapses from a single basket cell.

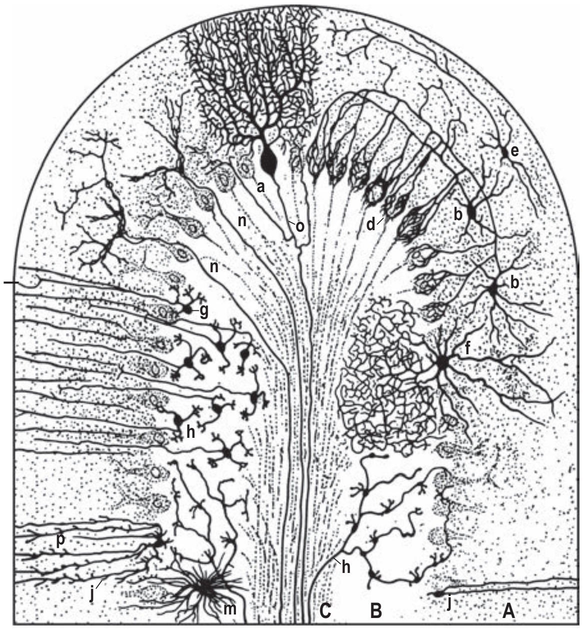

Fig. 29.10 Santiago Ramón y Cajal's (1909) diagram of the neurones in the cerebellar cortex orientated perpendicular to the long axis of the folium, as well as fibres and glial cells. Abbreviations: A, molecular layer; a, Purkinje cell; B, granular layer; b, basket cell; C, white matter of the folium; d, pericellular baskets around the Purkinje cell soma formed by the basket cell axon; e, superficial stellate cell; f, Golgi cell; g, granule cell; h, mossy fibre; i, ascending axon of granule cell; j, Bergmann glial cell; m, astroglial cell; n, climbing fibre; o, recurrent collateral branches of a Purkinje cell. (With permission from Ramón y Cajal S 1909–1910 Histologie du système nerveux de l'homme et des vertébrés. Translated into French by L. Azoulay. Paris: Maloine. Translated into English by Swanson N, Swanson LW 1995 Histology of the nervous system of man and vertebrates. New York, Oxford University Press.)

Stellate cells have small cell bodies 5–10 µm in diameter (**Fig. 29.13C–D**). Their dendrites are contacted by parallel fibres and their axons terminate on the Purkinje cell dendrites. Superficial stellate cells in the upper reaches of the molecular layer generally have short, profusely branching dendrites. Their short axons lie within a narrow parasagittal plane perpendicular to the long axis of a folium, the same as that of the Purkinje cell dendritic tree. The deep, long-axon stellate cells in the middle part of the molecular layer have dendritic trees similar to their superficial counterparts. However, the axon is quite different because it can extend for a considerable distance in the parasagittal plane, up to 450 µm, and it provides ascending and descending collaterals early in its course. Unlike the basket cell axon that also has a long course in the plane of the Purkinje cells, the axon of the deep stellate cell only rarely enters the pericellular Purkinje cells plexus and does not participate in the pinceau.

Granule cell layer

The granule cell layer is 200–300 µm thick on folial summits and about 100 µm thick in the depths of the fissures. It contains granule cells, Golgi cells, Lugaro cells, unipolar brush cells and neuroglial cells. The granule cell is among the smallest neurones in the brain, with a spherical nucleus 5–8 µm in diameter, and a shell of cytoplasm containing a few small mitochondria, ribosomes and a diminutive Golgi complex (**Fig. 29.14A**). There are about 2.4 million per mm^3 in the simian cerebellar cortex and 2–7 million per mm^3 in the human cortex (Fox and Barnard 1957, Braitenberg and Atwood 1958). The number of granule cells in the human cerebellum has been estimated to be from 4.3×10^{10} (Zagon et al 1977) to about 7×10^{10} (Andersen et al 2012), making it the most numerous single neuronal element in the nervous system. There are about 3000 granule cells for each Purkinje cell (Lange 1975). Granule cells usually give rise to 3–5 dendrites, each about 10–30 µm in length, ending in claw-like terminal expansions that synapse with the terminals of mossy fibres and Golgi cell axons in the cerebellar glomeruli, visible by light microscopy in the intervals between groups of granular neurones. Cerebellar glomeruli are synaptic complexes wherein a central mossy fibre terminal synapses with the dendrites of granule cells and Golgi cells, and the granule cell dendrites receive synaptic contacts from Golgi terminals. The fine axons of granule cells pass from their superficial aspect into the molecular layer and branch at a T-junction to form the parallel fibres.

Golgi cells (**Fig. 29.14B**) are irregularly rounded or polygonal GABAergic, inhibitory interneurones: they number approximately 1 per 1.5 Purkinje cells in the human brain. Golgi cells contain the inhibitory amino acid glycine, as well as acetylcholine and leucine-5-enkephalin.

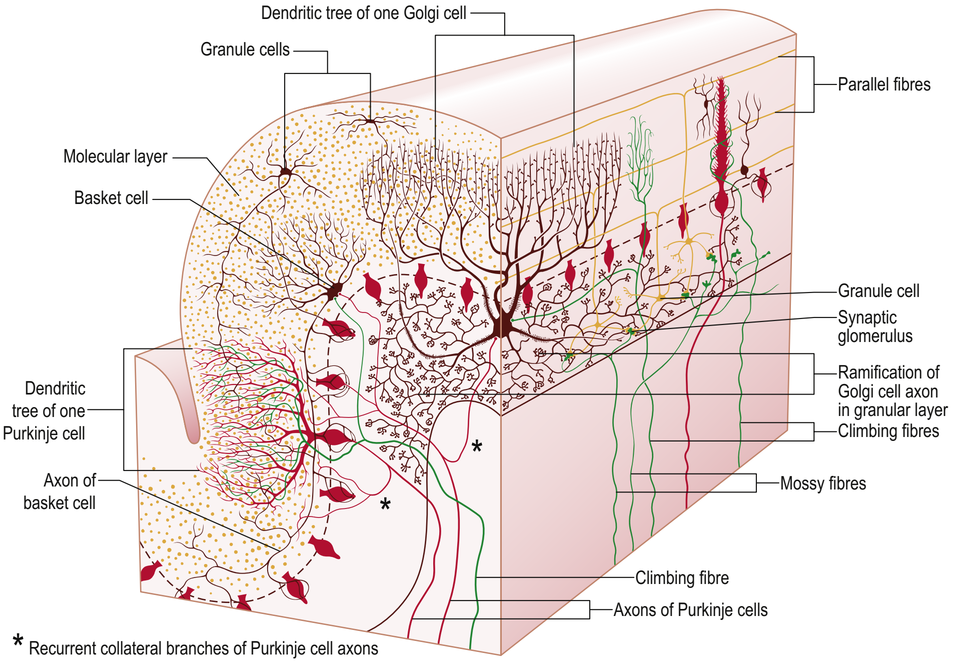
Dendritic tree of one Golgi cell
Granule cells
Parallel fibres
Molecular layer
Basket cell
Granule cell
Synaptic glomerulus
Ramification of Golgi cell axon in granular layer
Climbing fibres
Dendritic tree of one Purkinje cell
Mossy fibres
Axon of basket cell
*
*
Climbing fibre
Axons of Purkinje cells
* Recurrent collateral branches of Purkinje cell axons

Fig. 29.11 The general organization of the cerebellar cortex; a single cerebellar folium has been sectioned vertically, both in its longitudinal axis (right part of the diagram) and transversely (on the left). Red, Purkinje cells; brown, inhibitory interneurones, including outer stellate, basket and Golgi cells; yellow, granule cells and their ascending axons which bifurcate into longitudinally disposed horizontal fibres; green, climbing fibres and mossy afferents. Note also the synaptic glomeruli formed between the terminals of the mossy afferent fibres, the complex dendrite tips of the granule cells and the ramifications of the Golgi cell axon. Lugaro and unipolar brush cells are not shown. (Adapted from Eccles J, Ito M, Szentagothai J 1967 The Cerebellum as a Neuronal Machine. New York and Heidelberg: Springer-Verlag, with permission of the authors and publishers.)

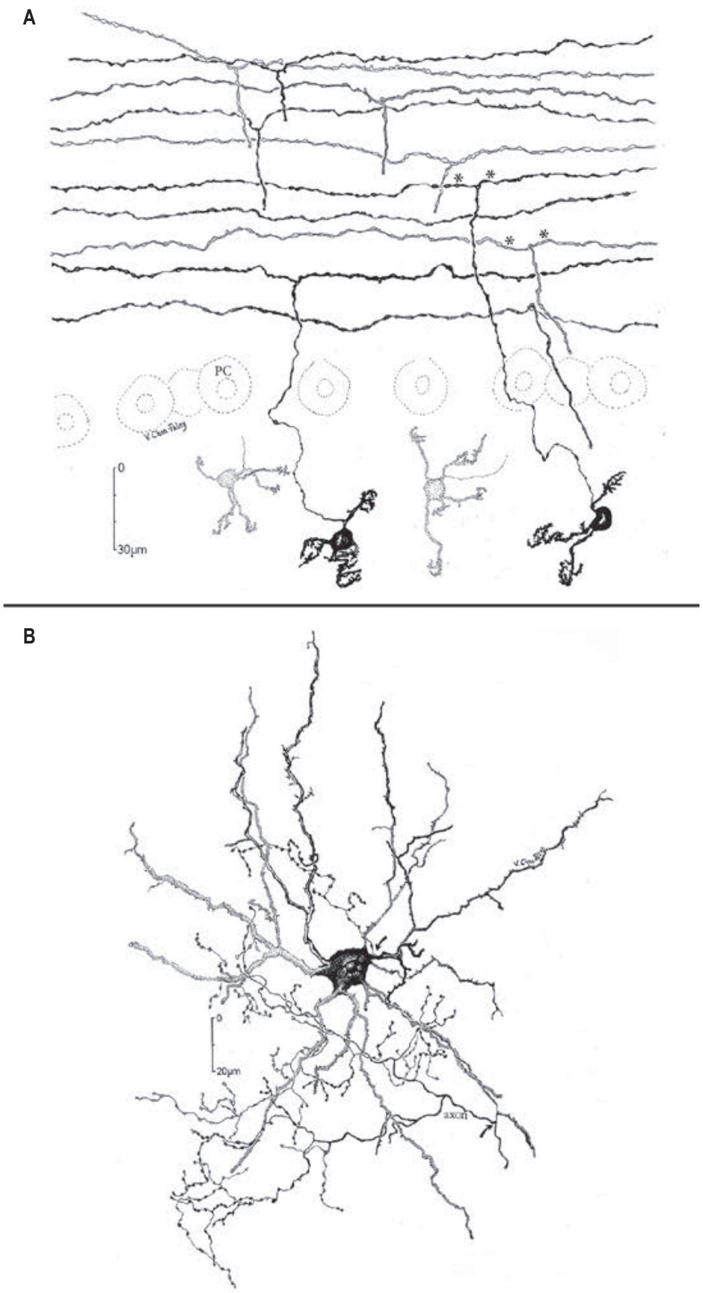

Fig. 29.14 Camera lucida drawings of Golgi-impregnated neurones in the granular layer. **A**, Granule cells with dendritic claws, and axons ascending with a tortuous course to the molecular layer where they bifurcate (asterisks) to form parallel fibres. **B**, A horizontal view of a large Golgi cell with dendrites that radiate up in the granular layer, and axons that arise like thin threads from the dendrites (arrows) that emit multiple fine, beaded collaterals. (With permission from Palay S, Chan-Palay V 1974 Cerebellar Cortex: Cytology and Organization. New York: Springer-Verlag.)

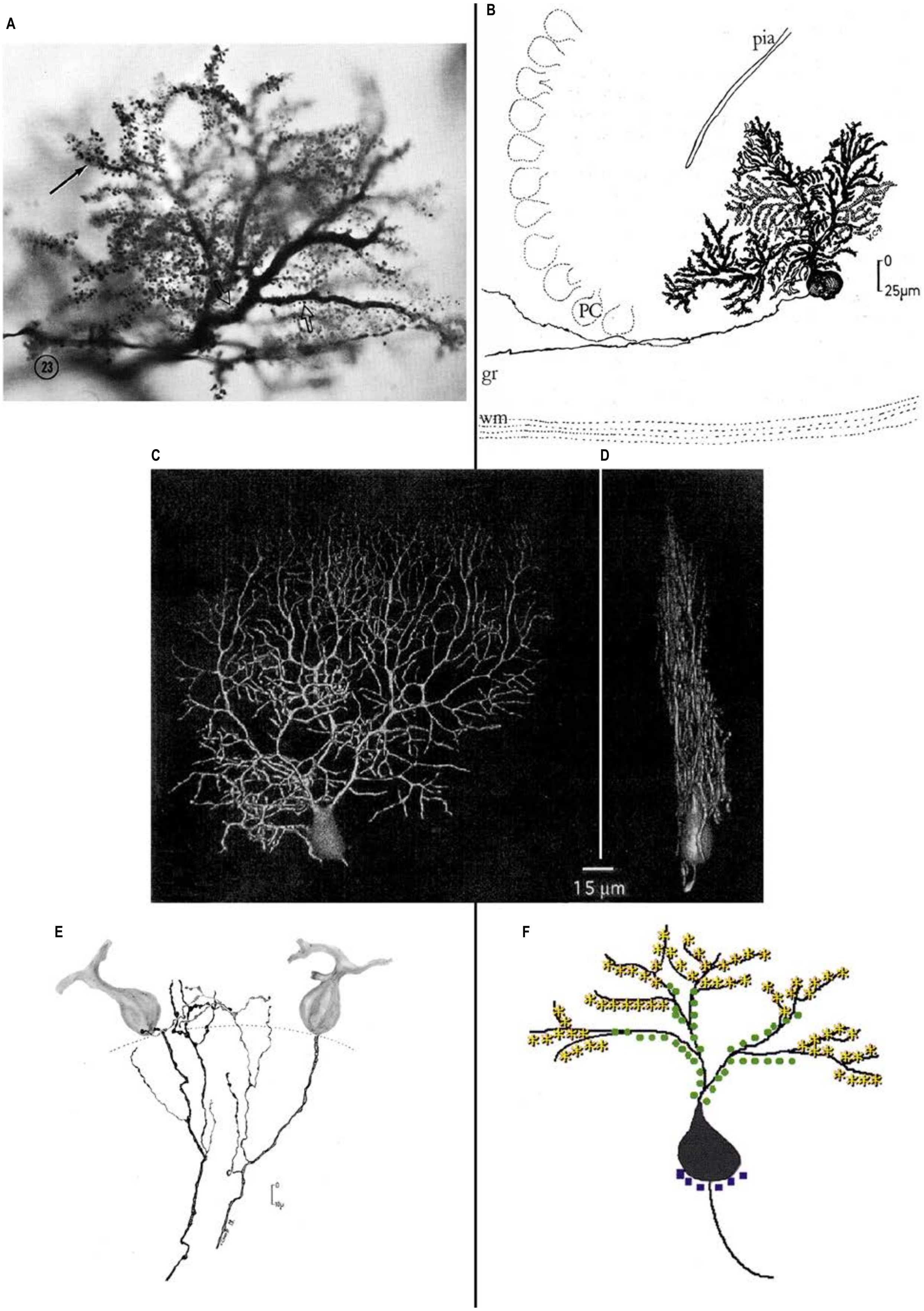

Fig. 29.12 Images of the Purkinje neurone of the cerebellar cortex. **A**, Photomicrograph of a Golgi-impregnated Purkinje cell (PC) showing high density of spines on distal dendrites (black arrow) and low density of spines on proximal dendrites (open arrows). **B**, Camera lucida drawing of a Golgi-impregnated PC with its axon at the base of a folium. The PC axon courses through the granule cell layer (gr) to the white matter (wm), giving of a collateral branch. Three-dimensional reconstruction of Lucifer yellow-filled PC viewed in a plane perpendicular to (**C**) and parallel to (**D**) the long axis of the folium. **E**, Camera lucida drawing of Golgi-impregnated PCs showing the recurrent collateral plexuses of two PCs. The recurrent collaterals ramify and terminate in the granular layer, and in the vicinity of the PC soma as the more profuse infraganglionic plexus, or at the apical pole of the PC as the sparse supraganglionic plexus. **F**, Schematic view of the PC illustrating the segregation of afferents. Parallel fibres synapse on dendritic spines on intermediate and distal dendrites (yellow), climbing fibres synapse on more sparsely distributed spines on proximal dendrites (green). Basket cell axons synapse on the PC soma and proximal segment of the PC axon (purple). (A, B, E, With permission from Palay S, Chan-Palay V 1974 Cerebellar Cortex: Cytology and Organization. New York: Springer-Verlag. C and D, With permission from Rossi DJ, Alford S, Mugnaini E, Slater NT 1995. Properties of transmission at a giant glutamatergic synapse in cerebellum: the mossy fibre-unipolar brush cell synapse. J Neurophysiol 74:24–42. F, Adapted with permission from Oberdick J, Baader SL, Schilling K 1998 From zebra stripes to postal zones: deciphering patterns of gene expression in the cerebellum. Trends Neurosci 21:383–90.)

Larger Golgi cells are 10–24 µm in diameter, and most lie in the upper half of the granular layer, below the level of the Lugaro cell and the infraganglionic plexus. Smaller Golgi cells are 9–18 µm in diameter and are generally located in the depths of the granular layer. Dendrites either radiate out from the soma or arise as one or two main trunks that give off subsidiary branches as they ascend to the outer zone of the molecular layer, predominantly at right-angles to the surface. Larger Golgi cells have either dendritic morphology, whereas smaller Golgi cells tend to have the radiating dendritic pattern. The Golgi dendritic tree is unlike that of the Purkinje, basket or stellate cell, which is flattened and confined to a single plane, but instead has a three-dimensional configuration, appearing much the same in transverse and longitudinal foliar sections. In both planes, the Golgi dendritic tree overlaps the territories of several Purkinje cells and neighbouring Golgi cells. Some Golgi dendrites do not enter the molecular layer, but divide in the granular layer to join the cerebellar glomeruli. The Golgi cell axon arises from the base of the soma or from a central dendrite, immediately dividing into a profuse arborization that extends through the entire thickness of the granular layer. The territory occupied by the axonal ramifications has a volume corresponding approximately to its dendritic tree in the molecular layer, overlapping with the axonal arborizations of adjacent Golgi cells. The main synaptic input to Golgi cell dendrites is from parallel fibres in the molecular layer. Purkinje cell recurrent collaterals and mossy and climbing fibres also terminate on their proximal dendrites and, more sparsely, on their somata. Golgi neurones are the principal inhibitory interneurones at the input stage of the cerebellum, providing feedforward inhibition through their axonal synapses with mossy fibres at the granule cell glomeruli and feedback inhibition at their dendritic synapses with parallel fibres.

The Lugaro cell is a fusiform cell measuring about 10 µm across and 25–30 µm in length (**Fig. 29.15A**) (Lugaro 1894a, 1894b). It is an inhibitory interneurone using both GABA and glycine as neurotransmitters. Its major axis lies parallel to the pial surface, horizontally or obliquely in the outermost third of the granular layer, sometimes alongside the somata of Purkinje cells or immediately above them. Its dendrites originate from the gradually tapering extremities at the two poles and extend horizontally for a considerable distance (up to 600 µm) at the level of the Purkinje cell bodies, mostly in the infraganglionic plexus formed by the recurrent axon collaterals of the Purkinje cells. Lugaro cell axons arise from the soma or a large proximal dendrite and form two types of axonal plexuses: a parasagittal axon ascends to the molecular layer and contacts the somata and dendrites of stellate and basket cells, alternatively, an axon lies in the transverse plane in the granule cell layer and contacts Golgi cells (Lugaro 1894a, 1894b, Palay and Chan Palay 1974, Lainé and Axelrad 1996, Berlucchi 2002). Excitatory input to Lugaro cells is from granule cell axons. The Lugaro cell is the major recipient in the cerebellum of serotoninergic input through volume transmission. Serotonin-induced activation of Lugaro cells causes synchronization of the activities of Golgi and granule cells over extended longitudinal domains, and of the simple-spike activity of Purkinje cells, thereby influencing the processing of mossy fibre information by the cerebellar cortex and modulation of the deep cerebellar nuclei (Dieudonné 2001, Berlucchi 2002).

The unipolar brush cell is the only known glutamatergic excitatory interneurone in the cerebellum, found particularly in vestibular regions in lobule X and the vermis, as well as in the dorsal cochlear nucleus (Altman and Bayer 1977, Braak and Braak 1993, Mugnaini and Floris 1994, Mugnaini et al 1997, 2011). It has a soma 9–12 µm in diameter and a single short dendrite ending in a tight brush-like tip of dendrioles that have extensive synaptic contact with mossy fibre rosettes (**Fig. 29.15B**). Its thin axon branches locally and synapses on granule and Golgi cells. The unipolar brush cell is thought to amplify vestibular mossy fibre input and provide feedforward excitation to granule cells.

Synaptic contacts between climbing fibres and the dendrites or cell bodies of cerebellar interneurones in the molecular or granular layers have not been observed. However, interneurones of the molecular layer can be activated by 'spillover' of glutamate from the climbing fibres (Szapiro and Barbour 2007, Galliano et al 2013). Golgi cells, therefore, provide feedback inhibition to the granule cells. Interneurones of the molecular layer provide feedforward inhibition to the Purkinje cells. Stellate cells (Mann-Metzer and Yarom 2000) and Golgi cells (Dugué et al 2009) are electrotonically coupled, although the extent of this coupling is not known. It may be restricted to the sagittal compartments that are one of the main features of the connectivity of the cerebellum, discussed below.

Neuroglial cells in the cerebellar cortex are specialized forms of protoplasmic astrocytes that envelop the somata of the Purkinje cells in a neuroglial sheath. Bergmann glial cells in the Purkinje cell layer give rise to two or more processes that branch in the parasagittal plane with up to five polarized main processes, the Bergmann fibres, giving the appearance of a candelabra (**Fig. 29.16**). These radial fibres ascend vertically over the full depth of the molecular layer, overlapping with fibres of neighbouring cells to form palisades and giving rise to small convoluted side branches that form sites of putative neuronal–glial interaction. The Bergmann glial fibres terminate beneath the pia as the external glial limiting membrane of the cortex. Bergmann glial cells are intricately involved in migration and development of the cerebellar cortex (Rakic 1971) (Ch. 3). In the mature cerebellum they regulate glutamatergic neural transmission and are important for extracellular ion homeostasis, synapse stability, plasticity, metabolic function and neuroprotection. They also contribute to information processing in the cerebellum (see De Zeeuw and Hoogland 2015 for review).

Fañanas cells are glial cells in the deeper molecular layer. Velate astrocytes have intersecting diaphanous veils that compartmentalize the granular layer. Rare smooth protoplasmic astrocytes are present in the molecular as well as the granular layers (Palay and Chan-Palay 1974). Oligodendroglia are seen mostly in the granular layer where there are more myelinated fibres, and in the cerebellar white matter. Glial cells play a role in supporting neuronal metabolism, controlling the extracellular potassium ion concentration, and clearing neurotransmitters from the extracellular space.

Cerebellar inputs

The neurones of the cerebellar cortex and nuclei are linked together in multiple repeating anatomical microcircuits (corticonuclear microcomplexes) that subserve the distinctive functional characteristics of the cerebellum. There are two major cerebellar inputs, the climbing fibre and mossy fibre systems. Monoaminergic fibres are a third contingent of afferent fibres, but they are less influential in determining the organization of the intracortical and corticonuclear connectivity.

Mossy fibres

The thick, heavily myelinated mossy fibres were so named by Ramon y Cajal because the 'thickened ends of the mossy fibres are indented, or, more accurately, bristle with thick, short, divergent, varicose branches that are themselves modestly ramified. The ending as a whole resembles a piece of moss' (Ramon y Cajal 1909–10/1995, **Fig. 29.17**). Mossy fibres enter through the three cerebellar peduncles depending on their site of origin. Most (up to 70%) run a transverse course to decussate in the cerebellar commissure, terminating bilaterally in the cerebellum. Like the climbing fibres, mossy fibres branch profusely, emitting 20–30 thin collateral branches that enter the white matter of the lobules and terminate in multiple, longitudinally orientated and symmetrically distributed aggregates of mossy fibre terminals in the granular layer (Wu et al 1999).

The terminal or synaptic arborizations of the mossy fibres, termed rosettes, are located along the course of the fibre in the granular layer, at the branch points, and at their sites of termination (**Fig. 29.18**). There are three kinds of mossy fibre rosettes. The most common type is an elongated one that expands, emitting tubular and filamentous processes, and is found at the mossy fibre terminal in the outer third of the granular layer just beneath the Purkinje cell layer. Simple fusiform enlargements have globular contours and a few short, finger-like projections. Terminations with more complex shape have a massive central expansion out of which several appendages project.

Mossy fibres provide excitatory, glutamatergic afferents to the cerebellar cortex from most non-olivary sources. Their excitatory input is not to the Purkinje cell directly, but to the granule cells that provide excitatory input to the Purkinje cell dendrites. Mossy fibres activate α-amino-3-hydroxy-5-methyl-4-isoxazoleproprionate (AMPA), N-methyl-D-aspartate (NMDA) and metabotropic glutamate receptors (mGluRs) on granule cells. The mossy fibre rosette is the central component of the granule cell glomerulus. Seen on light microscopy as pale islands between the granule cells, the glomerulus is a complex articulation between mossy fibre rosettes, the claw-like dendrites of the granule cells and Golgi cell axons. Each mossy fibre rosette makes excitatory synaptic contact with 50–100 dendritic terminals from up to 20 granule cells, while receiving inhibitory feedback from the descending axons of Golgi cells. Each mossy fibre branch synapses with 400 or more granule cells in one folium. If branches to adjacent folia are included, the number is probably several thousand. Conversely, each granule cell receives synapses from four or five different mossy fibre terminals.

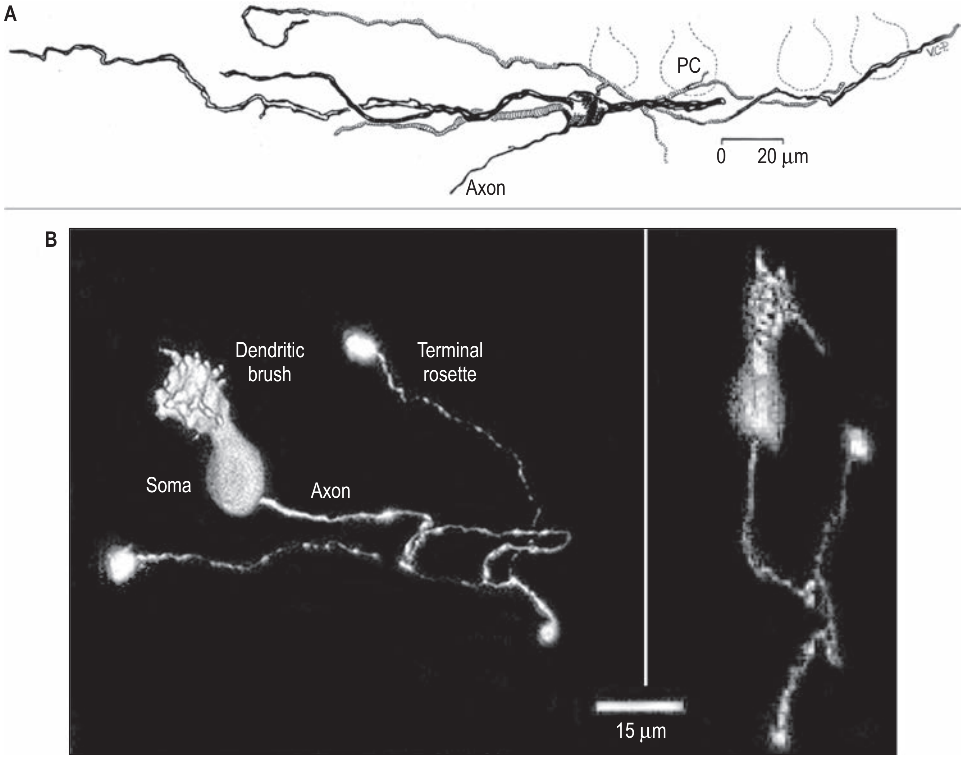

Fig. 29.15 **A**, A camera lucida drawing of a Golgi-impregnated Lugaro cell with its dendrite that courses in the sagittal plane at the level of the Purkinje cell (PC), and the axon that descends into the granular layer. **B**, A confocal microscopic image of a Lucifer yellow-filled unipolar brush cell (UBC) with its axon and terminal rosettes identified. The UBC, like the PC, has a parasagittal orientation and is seen perpendicular to (left) and parallel to (right) the long axis of the folium. (A, With permission from Palay S, Chan-Palay V 1974 Cerebellar Cortex: Cytology and Organization. New York: Springer-Verlag. B, With permission from Rossi DJ, Alford S, Mugnaini E et al 1995. Properties of transmission at a giant glutamatergic synapse in cerebellum: the mossy fibre-unipolar brush cell synapse. J Neurophysiol 74:24–42.)

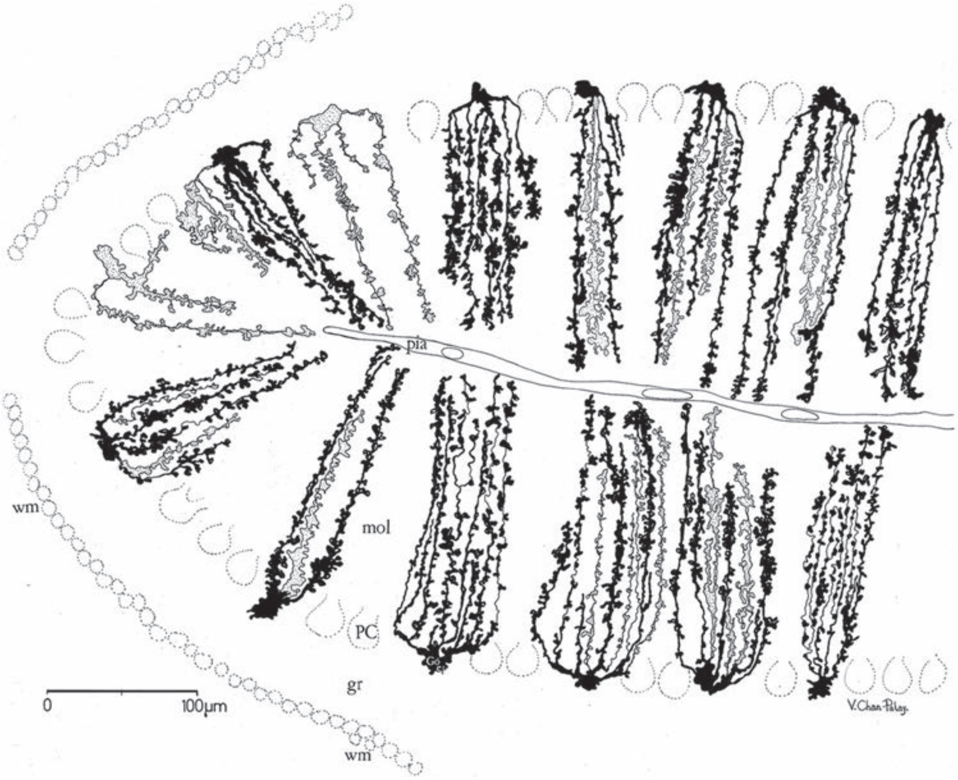

Fig. 29.16 A camera lucida drawing of Golgi-impregnated epithelial cells (Go ep) in a folium. 'Each cell, like a candelabrum, has processes [Bergmann glia] with warty excrescences that rise, like corroded wires, to the pial surface (pia).' The locations of the Purkinje cells (PC), molecular layer (mol), granule cells (gr) and white matter (wm) are indicated. (With permission from Palay S, Chan-Palay V 1974 Cerebellar Cortex: Cytology and Organization. New York: Springer-Verlag, pp. 288–9.)

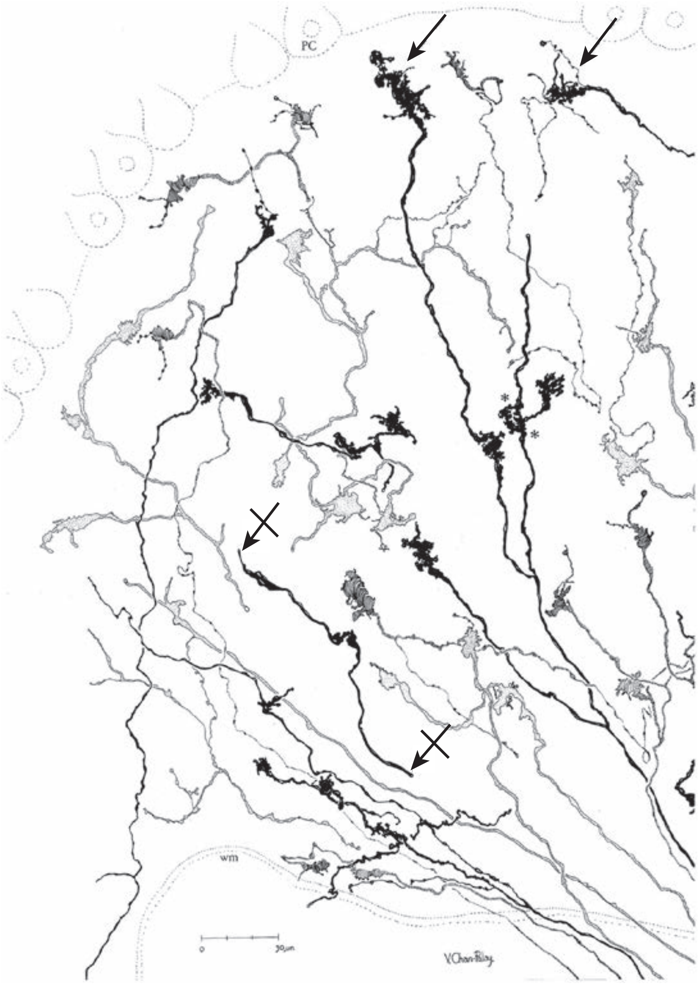

Fig. 29.17 A camera lucida drawing of Golgi-impregnated complex mossy fibres of the cerebellum showing complex varicosities at the bifurcation points (asterisks) and terminal rosettes (arrows) of the mossy fibres and at the terminations. A simple mossy fibre is seen at lower left (crossed arrows). Abbreviations: PC, Purkinje cell; wm, white matter. (With permission from Palay S, Chan-Palay V 1974 Cerebellar Cortex: Cytology and Organization. New York: Springer-Verlag.)

Collaterals to the deep cerebellar nuclei are derived from mossy fibres arising in the reticulotegmental nucleus, lateral reticular nucleus (LRN), and the spinocerebellar and vestibulocerebellar projections.

Cholecystokinin (CCK), calcitonin gene-related peptide (CGRP), corticotropin releasing factor (CRF) and leucine-5-enkephalin neuropeptides co-exist in many mossy fibres and some, mainly vestibulocerebellar mossy fibres, use acetylcholine as their neurotransmitter.

Climbing fibres

Climbing fibres arise exclusively from neurones of the inferior olive in the medulla oblongata and course to the cerebellum through the contralateral inferior cerebellar peduncle. Most olivocerebellar projections are contralateral, although a few axons project bilaterally by crossing the midline within the cerebellum. The parent climbing fibre splits into 7–10 thick branches in the cerebellar white matter, emitting thin collaterals to the deep cerebellar nuclei, before passing through the granular layer on their way to the molecular layer (**Fig. 29.19**). In the lower two-thirds of the molecular layer each branch of a climbing fibre lies closely opposed to the trunk and major branches of the dendritic tree of its target Purkinje cell, providing extensive direct excitatory glutamatergic synaptic contact with the stubby spines on the proximal dendrites of a single Purkinje cell in a one-to-one relationship (**Fig. 29.20**; see Fig. 29.12F). Each varicosity of the climbing fibre synapses with several dendritic spines, enabling 1000–1500 synaptic contacts between a climbing fibre and its Purkinje cell. The fine tendrils that branch off from the climbing fibres in the molecular layer make non-synaptic contact with ascending branches of the basket cell axons that enter the molecular layer, and with the dendritic trees of the stellate cells and the dendrites and somata of Golgi cells (Palay and Chan-Palay 1974, Sugihara et al 1999). Electrotonic coupling through gap junctions between the neurones of the inferior olive generates synchronous subthreshold oscillations (e.g. Leznik and Llinas 2005). Climbing fibres thus exert control over inhibition at both the input and output layers of the cerebellar cortex, regulating Golgi cell and stellate cell activity by releasing glutamate and activating ionotropic and metabotropic receptors through spillover-mediated transmission (Szapiro and Barbour 2007, Nietz et al 2017).

Climbing fibres use glutamate as their principal neurotransmitter, but there is chemical heterogeneity in the climbing fibre system: CCK is expressed in vermal lobules IV, VII and VIII, and in axons arising in the caudal part of the medial accessory olive. Enkephalin reactivity is present in the vermis, paramedian lobule and flocculus.

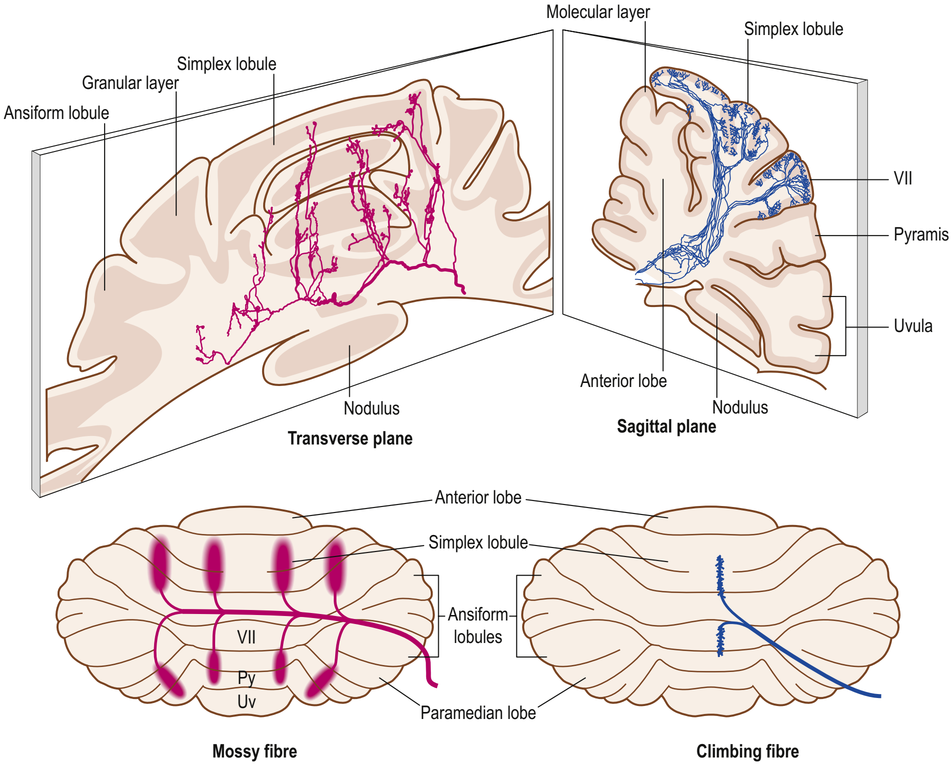

Fig. 29.18 The orientation and branching pattern of mossy and climbing fibres. Left-hand panels: mossy fibres are orientated transversely. They distribute bilaterally and emit collaterals at specific, symmetrical locations. These collaterals terminate as sagittally orientated aggregates of mossy fibre terminals. Right-hand panels: olivocerebellar fibres branch in the sagittal plane. Each branch provides a Purkinje cell with a single climbing fibre. These climbing fibres form narrow, longitudinally orientated strips that may correspond to the microzones; strips of Purkinje cells that share the same climbing fibre receptive fields. Abbreviations: Py, pyramis; Uv, uvula. (With permission from Nieuwenhuys R, Voogd J, van Huijzen 2008 The Human Nervous System, 4th ed. Berlin: Springer-Verlag.)

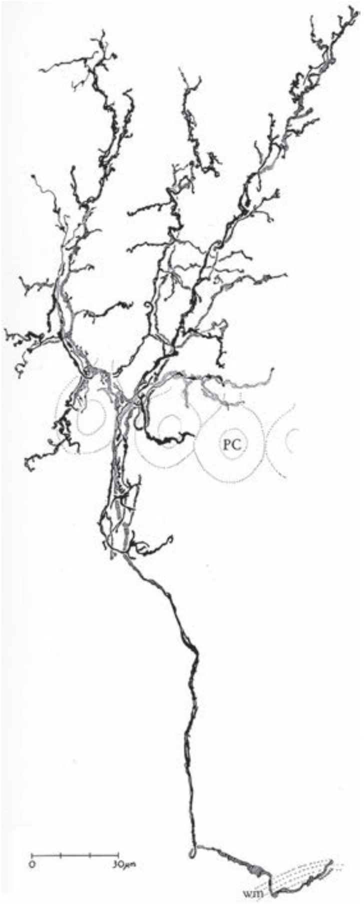

Fig. 29.20 A camera lucida drawing of a Golgi-impregnated climbing fibre entering the white matter (wm) as an unbranched twisted stalk and coursing through the granular layer. In the upper third of the granular layer a branching collateral plexus of beaded tendrils diverges from the parent fibre. At the level of the Purkinje cell (PC) body the axon breaks into its terminal arborization to climb upon the dendrites of a PC. (With permission from Palay S, Chan-Palay V 1974 Cerebellar Cortex: Cytology and Organization. New York: Springer-Verlag.)

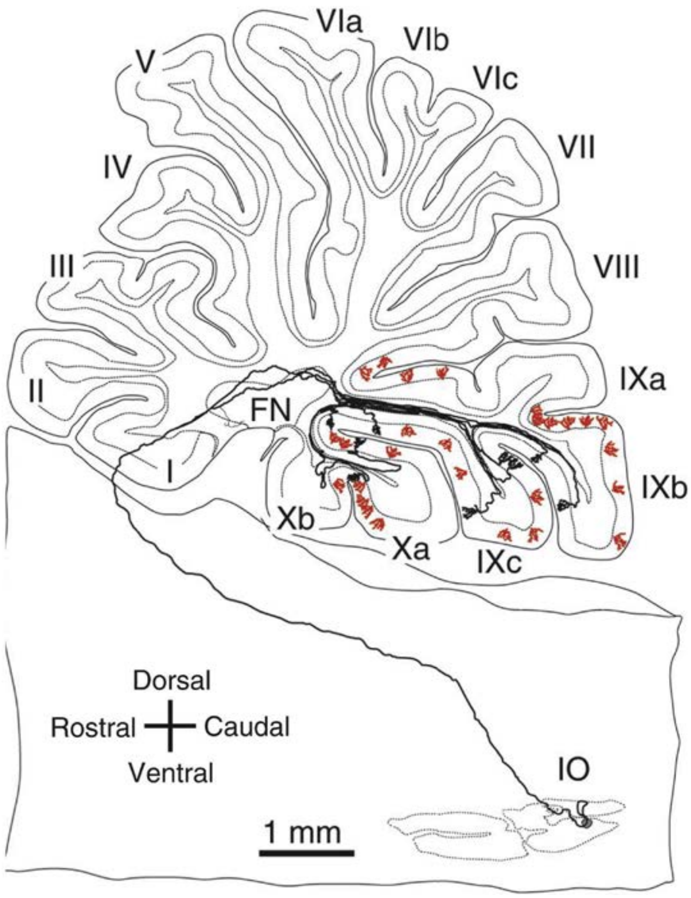

Fig. 29.19 Projection patterns of olivary axons in the cerebellum. Entire trajectory of a single olivocerebellar axon labelled after a small injection of biotinylated dextran amine (BDA) into the mediocaudal portion of the medial accessory olive (reconstructed from 77 serial parasagittal sections). This axon gave rise to nine climbing fibres terminating in the uvula (lobule IXb–c) and the nodule (lobule Xa), and thin collaterals terminating in the fastigial nucleus and the granular layer. The terminations of all other climbing fibres (n = 28) labelled by the tracer injection are shown in red. All climbing fibres were distributed from caudal lobule VIII to lobule X. Abbreviations: I–X, lobules I–X; a–c, sublobules a–c; FN, fastigial nucleus; IO, inferior olive. (With permission from Sugihara I, Wu H-S, Shinoda Y 2001 The entire trajectories of single olivocerebellar axons in the cerebellar cortex and their contribution to cerebellar compartmentalization. J Neuroscience 21:7715–23.)

The olivocerebellar projection has a strict medio-lateral parasagittal zonal organization. The branches of a single olivocerebellar fibre innervate one or more sagittally orientated strips of Purkinje cells (Sugihara et al 2001) (**Fig. 29.21**; see Fig. 29.19). These strips correspond to microzones consisting of a narrow strip of Purkinje cells innervated by climbing fibres that share the same receptive field. Microzones with their Purkinje cells are considered to be the basic structural and functional unit of the cerebellar cortex (Andersson and Oscarsson 1978).

Monoaminergic inputs

Monoaminergic afferents to the cerebellum modulate the release of other neurotransmitters. Noradrenergic innervation arises from neurones in the caudal portion of the locus coeruleus as axonal collaterals of projections to the forebrain. These fibres synapse on granule cell dendrites and run adjacent to the parallel fibres to terminate on the Purkinje cell dendrites. Serotoninergic afferents to the cerebellum arise from the raphe nuclei and are present throughout all regions of the cerebellum. Histaminergic fibres arise from neurones in the tuberomammillary nucleus of the posterior hypothalamus and innervate most regions of the cerebellum. Dopaminergic inputs arise from the neurones of the midbrain including the ventral tegmental area. Cholinergic projections are present diffusely, particularly in the flocculonodular lobe and in lobules I and II, terminating on excitatory unipolar brush cells and on inhibitory interneurones.

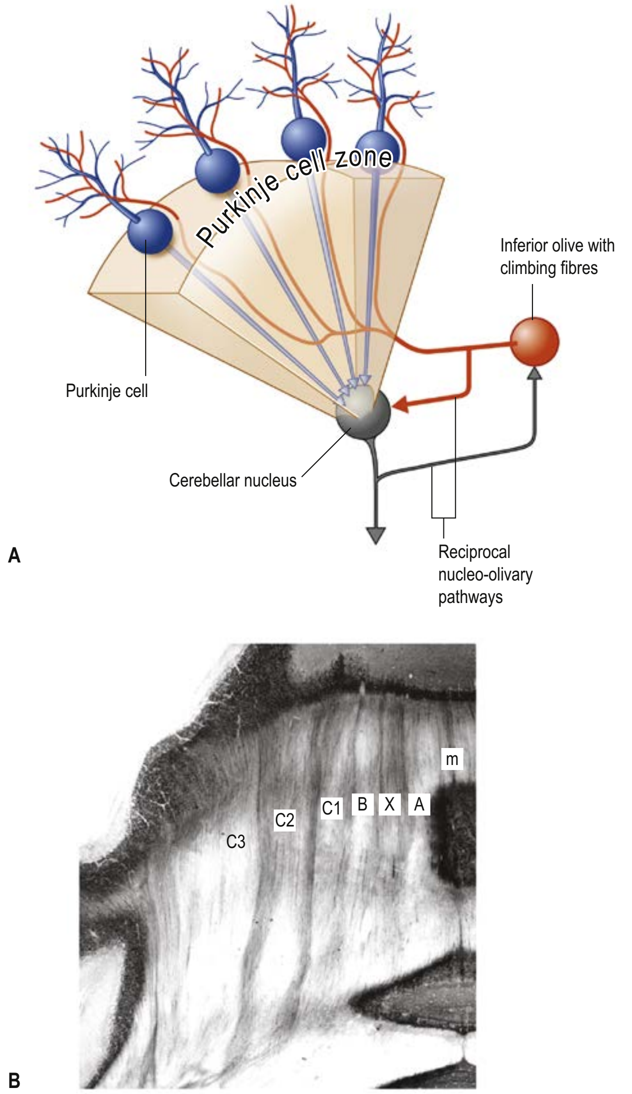
Purkinje cell zone
Inferior olive with climbing fibres
Purkinje cell
Cerebellar nucleus
Reciprocal nucleo-olivary pathways
A
m
C1
B
X
A
C2
C3
B

Fig. 29.21 **A**, A cerebellar module. Purkinje cell axons and climbing fibres are located in a white matter compartment, shown as a transparent structure in this diagram. **B**, An acetylcholinesterase-stained section through the anterior lobe (*Macaca mulatta*). There is heavy staining of the borders between the white matter compartments of the modules A, X, B, C1, C2 and C3. Abbreviation: m, midline.

Overview of cortical circuitry

The granule cell axon ascends in the cerebellar cortex through the dense granule cell layer and splits into two branches that travel in opposite directions along the long axis of a cerebellar folium, perpendicular to the ascending axon, and form the parallel fibres. The length of each parallel fibre branch is between 1 and 3 mm in the rat and cat, longer in nonhuman primates (6–8 mm) and probably no more than 10 mm in humans. Terminals located along the parallel fibre give it a beaded or varicose appearance; these terminals are the sites of synapses between the parallel fibres and the distal dendritic trees of Purkinje cells and the dendrites and somata of the stellate, basket and Golgi cells that they encounter along their course (**Fig. 29.22**). There is enormous convergence of mossy fibre inputs to individual Purkinje neurones; a dendritic tree of one Purkinje cell receives an estimated total of 175,000 synapses from different parallel fibres in the rat (Napper and Harvey 1988), although every parallel fibre may not synapse with the dendritic tree which it crosses. On its way to the distal arbors of a Purkinje cell dendritic tree, and before dividing to form the parallel fibres, the ascending axon of a granule cell makes synaptic contact first with dendrites of Golgi cells in the granular layer, and then with the spines of the proximal dendrites of Purkinje cells. Approximately 20% of the granule cell synapses on a Purkinje cell are made by the ascending segment of the granule cell axon, facilitating a more restricted influence on a single Purkinje cell than the parallel fibre–Purkinje cell synapses would allow.

A Purkinje cell generates two very different classes of action potentials mediated by its two principal afferents. Climbing fibre input to a Purkinje cell induces a complex spike with a very low frequency of 0.5

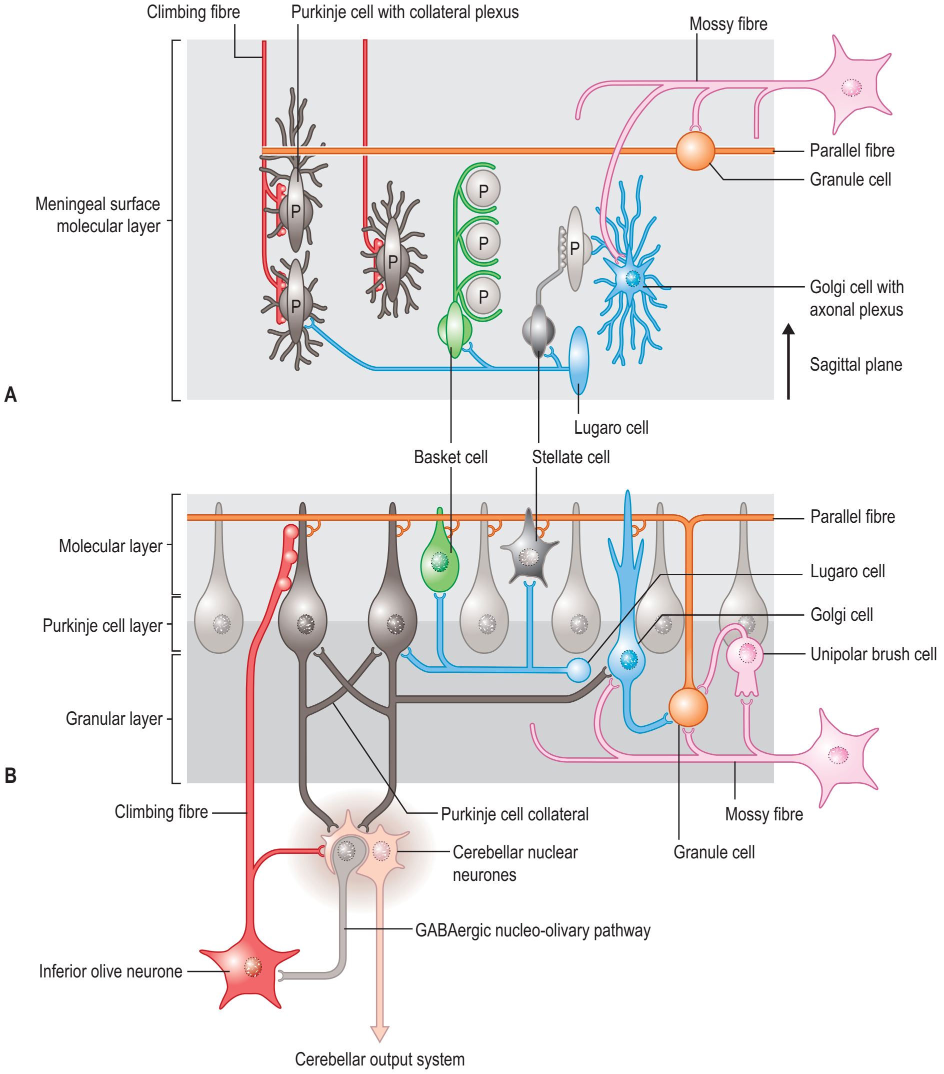

Fig. 29.22 The circuitry of the cerebellar cortex. Glutamatergic neurones are shown in dark grey, GABAergic neurones in red and glycinergic elements in blue. **A**, A transparent dorsal view of the cortex showing the orientation of its major elements. Dendrites of Purkinje, stellate and basket cells, the collateral plexus of Purkinje cells, the cell bodies of the Lugaro cells, and the climbing fibres and the axonal plexus of the Golgi cells are orientated in the sagittal plane. **B**, A transverse section. Parallel fibres and the axons of the Lugaro cells are the only elements with a transverse orientation.

to 2 spikes per second, which is the same rate of firing as the olivary neurones from which the climbing fibre originates. The climbing fibre input to a Purkinje cell is thought to signal the occurrence of errors. In contrast, the mossy fibre input to a Purkinje cell induces a repetitive simple spike with a frequency between 50 and 150 spikes per second. The parallel fibre input is thought to provide information about incoming signals, such as direction and speed of limb movement: in the cognitive domain, this input may provide a Purkinje cell with the context in which specific behaviours occur.

These circuits are relevant to synaptic plasticity involved in learning and memory. Long-term depression (LTD) is characterized by the persistent depression of synaptic transmission from parallel fibres to the Purkinje cell that occurs when the parallel fibres are activated concurrently with the activation of climbing fibres to the same Purkinje cell. Long-term depression has also been noted in the climbing fibre–Purkinje cell synapse. Long-term potentiation (LTP) occurs in the mossy fibre–granule cell interaction (D'Angelo et al 2005) and at the parallel fibre–Purkinje cell synapse (Hansel et al 2001).

Purkinje cells receive inhibitory feedback from cortical interneurones (stellate, basket and Lugaro cells), all of which receive afferents from the parallel fibres and the recurrent collaterals of a Purkinje cell axon. The output from the cerebellar cortex is derived exclusively from the Purkinje cells, precisely organized, and directed towards the deep cerebellar nuclei and precerebellar nuclei. Purkinje cells in each lobule project to that part of the deep cerebellar nuclei that is closest to them. Thus, the vermis projects to the fastigial nucleus, the intermediate cortex to the globose and emboliform nuclei, and much of the lateral hemisphere projects to the dentate nucleus.

Climbing fibre microzones and the subjacent mossy fibre aggregates share the same receptive fields in regions of the cerebellum that receive somatosensory information from the periphery (Ekerot and Larson 1980, Ekerot and Jörntell 2003). A similar topographical relationship between microzones and mossy fibre terminal aggregates exists in other parts of the cerebellar cortex (Pijpers et al 2006). Parallel fibres disperse a localized mossy fibre input over a wide, mediolateral region of the molecular layer, and the localized functional topography is thought to be related, at least in part, to the more topographically focal synaptic inputs of the ascending axon of the granule cell (Cohen and Yarom 1998).

CEREBELLAR FUNCTIONAL TOPOGRAPHY AND CONNECTIVITY

Whereas cerebellar cortical architecture is essentially invariant throughout, the topographically arranged circuits that link the cerebellum with the spinal cord, brainstem and cerebral hemispheres enable the cerebellum to contribute to the many different aspects of nervous system function. This arrangement is fundamental to the idea that the architecture of a brain region determines the nature of the information processing that takes place in that region (Schmahmann and Pandya 2008), and the principle expressed in the notion of the universal cerebellar transform (UCT) (Schmahmann 2000), which is that the cerebellum performs the same computation for sensorimotor processing as it does for cognition, emotion, autonomic and vestibular functions. Superimposed upon this principle is the presence of highly organized and functionally specific heterogeneity of cerebellar connections with the spinal cord, brainstem and cerebral cortex (Brodal 1981, Ito 1984, Schmahmann 1996, 1997, 2000, 2001, Schmahmann and Pandya 1997a, Voogd and Glickstein 1998, Voogd 2004).

On a large scale, cerebellar functional topography distinguishes anterior and posterior cerebellar lobes. The cerebellar anterior lobe (lobules I to V) and parts of lobule VI, together with lobule VIII receive spinal afferents through the spinocerebellar tracts (Oscarsson 1965). They are also reciprocally interconnected with the motor cortices via the feedforward motor corticopontine projections (Brodal 1978, Hartmann-von Monakow et al 1981, Schmahmann et al 2004a) and through feedback to motor regions from cerebellar nuclei via the thalamus (Thach 1987, Kelly and Strick 2003). These cerebellar regions (i.e. anterior lobe, adjacent parts of lobule VI and lobule VIII) are also reciprocally linked with the medial and dorsal accessory nuclei of the inferior olivary complex, which in turn receive afferents from the spinal cord (Brodal 1981, Voogd 2004). The deep cerebellar nuclei that are linked with these cerebellar cortical areas are the anterior and posterior interpositus in the monkey (equivalent to the emboliform and globose nuclei in humans) and the dorsal part of the dentate nucleus. The cerebellar vermis and fastigial nucleus are interconnected with the vestibular and other brainstem nuclei engaged in midline body control, gait and equilibrium, as well as with brainstem nuclei linked with limbic and paralimbic cortical and subcortical regions (Schmahmann 2001).

In contrast to the connections of the anterior lobe and lobule VIII, the great expansion of the human cerebellum, i.e. the remainder of lobule VI, all of lobule VII (that includes lobule VIIA in the vermis and crus I and crus II in the hemispheres, lobule VIIB and most of lobule IX) has no connections with the cerebral cortical sensorimotor areas, and no spinal cord inputs from the spinocerebellar tracts (Brodal 1981, Voogd 2004). These areas are linked instead in a reciprocal feedforward and feedback manner with the association areas of the cerebral cortex concerned with higher order behaviour, namely, the prefrontal cortex, posterior parietal cortex, superior temporal polymodal regions, cingulate gyrus and posterior parahippocampal area (Schmahmann 1991, 1996, Schmahmann and Pandya 1989, 1991, 1992, 1993, 1997a, 1997b, Kelly and Strick 2003). The dentate nucleus of the cerebellum conveys the cerebellar posterior lobe efferents to these higher order regions of the cerebral cortex (Middleton and Strick 1994). The ventral and lateral parts of the dentate nucleus most involved in these projections (Dum and Strick 2003) have expanded through evolution together with the cerebellar posterior lobe and the cerebral cortical association areas (Dow 1974, Leiner et al 1986, Whiting and Barton 2003). The reciprocal interconnections between the inferior olivary nucleus and the cerebellar posterior lobe are distinct from those with the cerebellar motor regions, which are derived from the principal olivary nucleus, which has minimal or no spinal cord input (Sugihara and Shinoda 2004).

These anatomical connections set up a dichotomy of cerebellar linkage with the cerebral cortex, brainstem and spinal cord, and portray a complex connectional and functional heterogeneity. The sensorimotor cerebellum mostly in the anterior lobe, adjacent parts of lobule VI, and lobule VIII, appears to be an integral part of the distributed neural circuits that subserve the motor system, whereas the cognitive cerebellum in the posterior lobe, and the limbic cerebellum (likely represented principally in the vermis), are incorporated into the distributed neural circuits necessary for cognition and emotion.

On a smaller scale, the cerebellum is organized as a series of parallel, sagittally orientated modules (Voogd and Bigaré 1980, Voogd and Ruigrok 2012), each consisting of one or more Purkinje cell zones. From medial to lateral, zones A, B, X, C1, C2, C3, D1, D2 and Y can be distinguished. Climbing fibres from a subdivision of the contralateral inferior olive terminate on the Purkinje cells of a particular zone and also send a collateral innervation to the corresponding deep cerebellar nucleus (Groenewegen et al 1979). This collateral innervation is reciprocated by the, mainly crossed, nucleo-olivary pathway that originates from the small GABAergic neurones of the cerebellar nuclei (see Figs 29.19, 29.21). The outflow from the cerebellar cortex is directed to similarly topographically arranged regions in the fastigial, globose, emboliform and dentate nuclei. Efferents from the cerebellum to extracerebellar structures are conveyed exclusively through these nuclei, with the single exception of the cortex of the vestibulocerebellum (lobule X – flocculus and nodulus, and the vermal part of lobule IX – uvula), which projects directly to the vestibular nuclei. Cerebellar corticonuclear circuitry and feedback to the spinal cord, brainstem and cerebral hemispheres are thus arranged in a topographically precise manner respecting the zonal organization of the cerebellar cortex and its related deep cerebellar nuclei and inferior olivary complex.

The modular organization of the cerebellum appears very early during its development, before the emergence of its transverse fissures. Purkinje cells, born in the ventricular matrix of the cerebellar anlage, migrate to the meningeal surface, where they form a series of mediolaterally arranged clusters (Korneliussen 1968). During the later expansion of the cerebellar surface in the rostrocaudal dimension, reflecting the proliferation of millions of granule cells in the transient external matrix (the external granular layer), the Purkinje cell clusters increase in length and transform into Purkinje cell zones. The Purkinje cells become located in a monolayer and the original borders between the clusters are no longer visible. Purkinje cell clustering in the human brain does not differ from that in other species, with the exception of the immense size of the most lateral cluster, which is related to the anlage of the dentate nucleus (**Fig. 29.23**). This cluster develops into the D2 zone, the most lateral Purkinje cell zone, and is responsible for the large size of the human cerebellar hemisphere.

Afferent cerebellar fibres

Mossy fibre inputs to the cerebellum

Mossy fibre systems take their origin from multiple sites in the spinal cord and the brainstem, distribute bilaterally in the cerebellum and give off collaterals distributed in the mediolateral dimension that terminate as longitudinal aggregates of mossy fibre rosettes (see Fig. 29.18; **Fig. 29.24A**). These bands of rosettes are not continuous but are often restricted to either the apices or the bases of the folia. Exteroceptive components of mossy fibre systems terminate superficially, whereas proprioceptive systems terminate in the bases of the folia (Ekerot and Larson 1972) (**Fig. 29.24B**). The mossy fibre aggregates are not as distinct as the climbing fibre zones and often merge in the bases of the fissures. Mossy fibre aggregates of different systems interdigitate or overlap.

Spinal and trigeminocerebellar mossy fibre afferents

The spinal cord is connected with the cerebellum through spino-cerebellar tracts and through indirect mossy fibre pathways relayed by the lateral reticular nucleus. The spinocerebellar tracts are classified on the basis of their origin, their decussation within the spinal cord, their position in the lateral funiculus, their entrance route into the cerebellum and their lobular and zonal distribution.

The termination of the spinocerebellar, reticulocerebellar, cuneocerebellar and trigeminocerebellar tracts is restricted to the anterior and posterior motor regions of the cerebellum, i.e. to lobules III–V in the anterior lobe, lobule VI, parts of lobule VIIB and lobule VIII. These lobules also receive primary and secondary vestibulocerebellar inputs and pontocerebellar mossy fibres relaying information from cortical motor areas. Many of these mossy fibre systems terminate according to a somatotopical pattern (**Fig. 29.24C**). A very similar somatotopical organization occurs in the C1, C3 and Y climbing fibre zones that are restricted to the hemisphere of the same lobules (see Fig. 29.24).

The dorsal spinocerebellar tract transmits information from the ipsilateral lower limb. It contains proprioceptive fibres that arise from neurones in the posterior thoracic nucleus (Clarke's column) in the thoracic and upper lumbar spinal cord, and exteroceptive fibres from the thoracic and lumbar dorsal horns. It enters the cerebellum in the inferior cerebellar peduncle and terminates mainly ipsilaterally in the vermis and hemisphere of the anterior and posterior lower limb regions.

The cuneocerebellar tract is the upper limb equivalent of the dorsal spinocerebellar tract. It takes its origin from the dorsal column nuclei, the proprioceptive component from the external cuneate nucleus, and the exteroceptive component from the internal cuneate and gracile nuclei. Both components terminate in the anterior and posterior upper limb regions, the proprioceptive component bilaterally in the bases of the fissures and the exteroceptive component ipsilaterally in the apices of the lobules of the hemisphere. The exteroceptive component has been shown to terminate in multiple longitudinal zones that are congruent with the climbing fibre zones of this region; these zones share the same detailed somatotopical organization as the C1, C3 and the Y climbing fibre zones (Ekerot and Larson 1980).

The ventral spinocerebellar tract is a composite pathway that informs the cerebellum about the state of activity of spinal reflex arcs related to the lower limb and lower trunk. Its fibres originate in the intermediate grey matter and the spinal border cells of the lumbar and sacral segments of the spinal cord, cross near their origin, and ascend close to the surface as far as the lower midbrain before looping around the emergent fibres of the trigeminal nerve to join the superior cerebellar peduncle. Most of these fibres cross again in the cerebellar white matter.

The rostral spinocerebellar tract originates from cell groups of the intermediate zone and horn of the contralateral cervical enlargement. It is considered to be the upper limb and upper trunk equivalent of the ventral spinocerebellar tract, but unlike its ventral counterpart, most of its fibres remain ipsilateral throughout their course and enter the cerebellum through both the superior and the inferior cerebellar peduncles terminating in the anterior and posterior vermis.

The central cervical spinocerebellar tract originates from a central cervical nucleus at high cervical levels (C1–C4). The tract terminates bilaterally in the bases of the fissures of the entire cerebellum, lacks a somatotopical organization and conveys labyrinthine information and proprioception from neck muscles (Matsushita and Tanami 1987).

Trigeminocerebellar mossy fibres originate from the ipsilateral principal sensory nucleus and nucleus of the spinal tract of the trigeminal nerve and terminate in the hemisphere in the anterior and posterior face regions in lobules VI and VIIB.

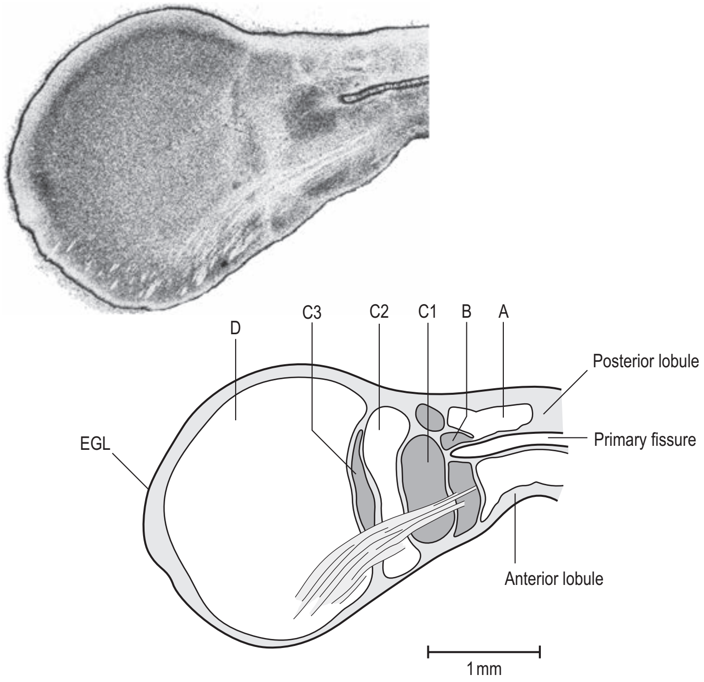

Fig. 29.23 A transverse section through the cerebellum of a 65 mm human fetus, showing the Purkinje cell clusters that will develop into the A, B, C1–C3 and D Purkinje cell zones. Note the large size of the D cluster. Abbreviations: EGL, external granular layer. (Courtesy of the Schenk collection of the Department of Pathology of the Erasmus Medical Center, Rotterdam.)

Cerebellar modules can be visualized because their Purkinje cell axons and climbing fibre afferents collect in compartments in the cerebellar white matter and are visible when stained for acetylcholine esterase (AChE) (see Fig. 29.21B). Some of the Purkinje cell zones are restricted to certain lobules; others span the entire rostrocaudal length of the cerebellum. Eight or nine of the modules can be recognized in the cerebellum of nonhuman primates and lower mammals (see Fig. 29.36). Purkinje cell zones differ in their climbing fibre afferents and cerebellar or vestibular target nucleus. Purkinje cells of the different zones also differ in their immunohistochemical properties (Voogd and Ruigrok 2012). A Purkinje cell-specific antibody, known as zebrin 2, is distributed in a pattern of zebrin-positive and zebrin-negative Purkinje cell zones (see Fig. 29.36D–E). This pattern has been shown to be congruent with the olivocerebellar and corticonuclear projection zones (Voogd et al 2003, Sugihara and Shinoda 2004). Many substances, such as the enzymes aldolase C, 5′ nucleotidase, protein kinase C and the metabotropic glutamate transporter 1A, colocalize with zebrin 2. Neurotransmission in different Purkinje cell zones may therefore differ: zebrin-positive Purkinje cells fire at a slower rate than the zebrin-negative cells (Zhou et al 2014). Apart from the parallel fibres, which may cross several Purkinje cell zones or microzones as they course through the molecular layer, there is no crosstalk between the modules. Parallel fibres are a key element in the integrative function of the cerebellum, but the relative independence of the cerebellar modules is an important difference between the cerebellum and the cerebral cortex, where different functional areas are interconnected through association fibres.

The distinct somatotopic organization of the anterior and posterior motor regions of the hemispheres is reflected in the termination of the exteroceptive components of the dorsal spinocerebellar, cuneocerebellar and trigeminocerebellar tracts. The organization is much less distinct for proprioceptive systems such as the central cervical spinocerebellar tract.

Reticulocerebellar mossy fibre afferents

In the reticular formation, the paramedian reticular nucleus, the lateral reticular nucleus and the reticulotegmental nucleus (nucleus reticularis tegmenti pontis, NRTP) all give rise to mossy fibres. Major collateral projections to the cerebellar nuclei arise from the lateral reticular nucleus and the reticulotegmental nucleus.

The paramedian reticular nucleus consists of cell groups at the lateral border of the medial longitudinal fasciculus in the caudal medulla. It receives fibres from the vestibular nuclei, the interstitiospinal and tectospinal tracts that descend in the medial longitudinal fasciculus, and from the spinal cord and the cerebral cortex, and projects to the entire cerebellum, with the possible exception of the paraflocculus.

The lateral reticular nucleus is in the lateral funiculus of the caudal medulla, surrounded by the ascending fibre systems of the lateral funiculus and the rubrospinal and lateral vestibulospinal tracts. It receives spinoreticular fibres that terminate in a somatotopic pattern within the entire lateral reticular nucleus, and descending fibres from the cerebral cortex. The dorsal part of the lateral reticular nucleus receives collaterals from the rubrospinal tract and projects to the ipsilateral cerebellar hemisphere. The ventral part of the lateral reticular nucleus receives a collateral projection from the lateral vestibulospinal tract and projects bilaterally, mainly to the vermis. The lateral reticular nucleus has strong projections as axon collaterals to the rostral part of the fastigial and emboliform nuclei and the medial pole of the globose nucleus (Wu et al 1999).

The reticulotegmental nucleus is a butterfly-shaped nucleus in the caudal half of the pontine tegmentum, next to the midline and dorsal to the pontine nuclei. It receives inputs from the cerebral cortex, tectum, nucleus of the optic tract and cerebellar nuclei via the crossed descending branch of the superior cerebellar peduncle and it projects to the cerebellum via the middle cerebellar peduncle. The medial visuomotor division of this nucleus receives visuomotor afferents from the frontal eye fields, the contralateral superior colliculus (through the tectopontine tract) and other visuomotor centres in the brainstem, and targets the visual vermis in lobule VII, crus I, the flocculus and the adjacent ventral paraflocculus. The bilateral projection of its lateral, motor portion overlaps similar motor projections from the pontine nuclei in the anterior lobe, lobule VI and lobule VIII. Mossy fibres from the reticular nucleus of the pontine tegmentum provide the cerebellar nuclei with a collateral innervation complementary to that of the lateral reticular nucleus. An uncrossed component of the tectopontine tract terminates in the dorsolateral corner of the pontine nuclei, where it overlaps with extrastriatal visual afferents.

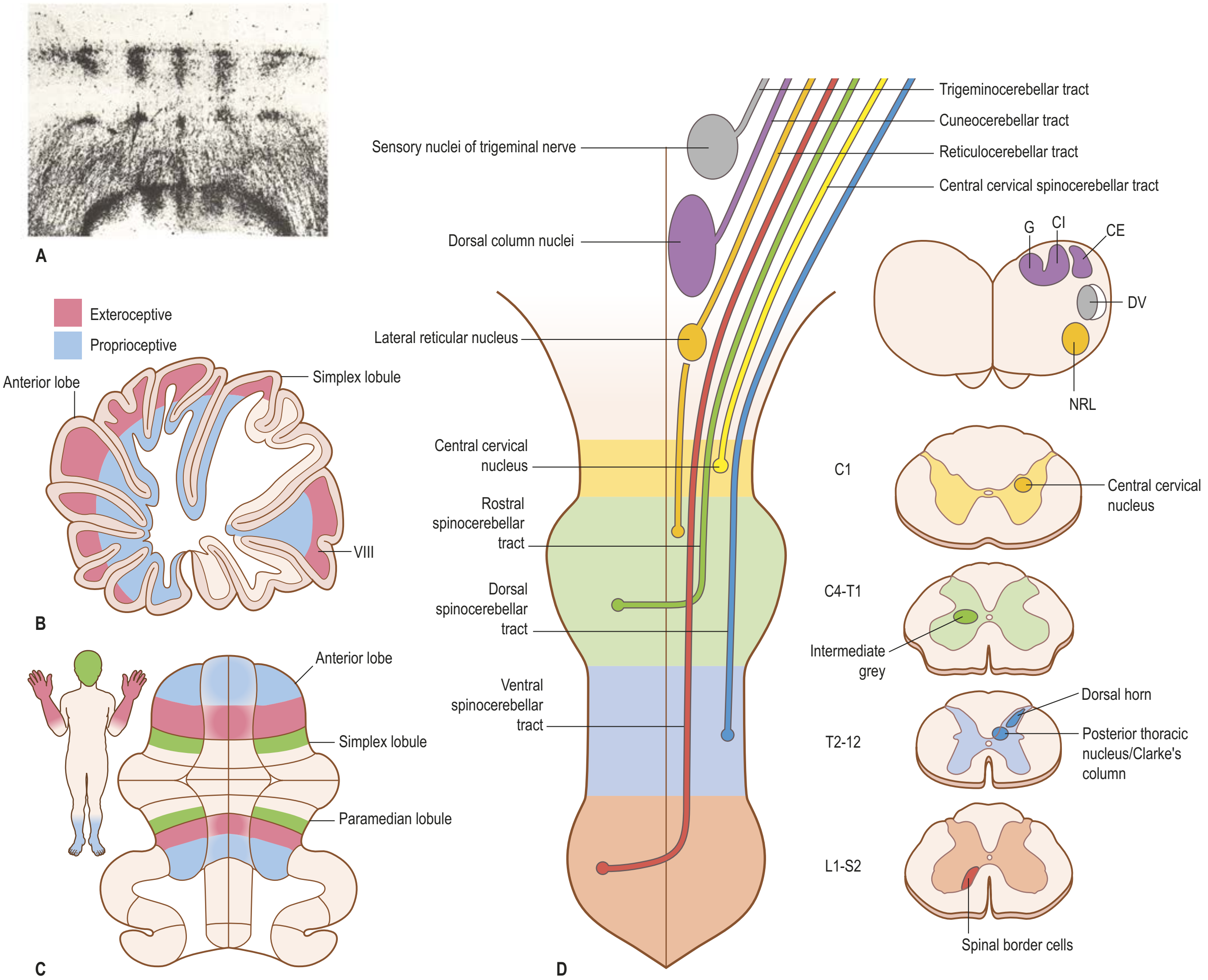
A
Exteroceptive
Proprioceptive
Anterior lobe
Simplex lobule
VIII
B
Anterior lobe
Simplex lobule
Paramedian lobule
C
Sensory nuclei of trigeminal nerve
Dorsal column nuclei
Lateral reticular nucleus
Central cervical nucleus
Rostral spinocerebellar tract
Dorsal spinocerebellar tract
Ventral spinocerebellar tract
D
Trigeminocerebellar tract
Cuneocerebellar tract
Reticulocerebellar tract
Central cervical spinocerebellar tract
G
CI
CE
DV
NRL
C1
Central cervical nucleus
C4-T1
Intermediate grey
Dorsal horn
T2-12
Posterior thoracic nucleus/Clarke's column
L1-S2
Spinal border cells

Fig. 29.24 **A**, The termination of spinocerebellar fibres as multiple sagittal bands in the anterior lobe of *Tupaia glis* (the common tree shrew). **B**, A sagittal section through the cerebellum showing the termination of exteroceptive mossy fibre systems in the apices of the lobules of the anterior lobe, the simplex lobule and lobule VIII (pyramis), and of proprioceptive systems in the bases of the fissures. **C**, The somatotopic organization of the termination of the exteroceptive components of the spinocerebellar, cuneocerebellar and trigeminocerebellar tracts in the hemisphere of the anterior lobe, the simplex lobule (lobule VI) and the paramedian/biventral lobule (lobule VIII). **D**, The origin of the spinocerebellar, cuneocerebellar and reticulocerebellar tracts. Abbreviations: CE, external cuneate nucleus; CI, internal cuneate nucleus; DV, nucleus of the spinal tract of the trigeminal nerve; G, gracile nucleus; NRL, lateral reticular nucleus.

Primary and secondary vestibulocerebellar mossy fibres

Primary vestibulocerebellar mossy fibres to the cerebellum are derived from vestibular ganglion cells that travel in the ascending branch of the vestibular nerve. They pass through the superior vestibular nucleus and the juxtarestiform body before entering the cerebellum and project directly to the ipsilateral vermis in the ventral part of lobule IX (uvula) and lobule X (nodulus) and to the ventral part of the anterior lobe and bases of the deep fissures of the vermis (Fig. 29.25). The flocculus (hemisphere lobule X) receives few, if any, vestibular fibres. Secondary vestibulocerebellar mossy fibres arise from the superior vestibular nucleus, the caudal portions of the medial and inferior vestibular nuclei, and the group X neurones, and terminate bilaterally in the same regions that receive primary vestibulocerebellar fibres with the exception of vermal lobule X (nodulus), and in hemisphere X (flocculus) and the adjacent ventral paraflocculus (the accessory paraflocculus of the human cerebellum) that lack a primary vestibulocerebellar projection. Some of the mossy fibres from the medial and inferior vestibular nuclei are cholinergic.

Corticopontocerebellar projections

The cerebral cortex is linked with the cerebellum in a two-stage feed-forward limb of cerebral cortical projections to the nuclei of the basis pontis (corticopontine projection), and the mossy fibre projection from the pontine nuclei through the middle cerebellar peduncle to the contralateral cerebellum (pontocerebellar projection). The reciprocal feedback pathway from the cerebellum to the cortex is mediated by the thalamus via cerebellothalamic and thalamocortical projections.

All corticopontine axons arise from lamina V pyramidal cells (Figs 29.26–29.27). Some corticopontine fibres are collaterals of axons that project to other targets in the brain or spinal cord: in the motor system it is likely that corticospinal fibres give off collaterals to the pontine nuclei (Ugolini and Kuypers 1986).

The nuclei of the basis pontis pons receive prominent projections from unimodal and multimodal cerebral cortical association areas (Fig. 29.31). These occupy largely separate areas of the basis pontis in the rostrocaudal and transverse dimensions. The enlargement of the basis pontis along with the lateral cerebellar hemispheres and the ventrolateral dentate nucleus is in accord with the view that the major expansion in the cerebrocerebellar pathways reflect cerebellar linkage with the cerebral association areas rather than with the motor system.

In monkeys, prefrontal projections to the pons arise mostly in dorsolateral and dorsomedial prefrontal cortices and terminate in the rostral third of the medial pons. Posterior parietal projections arise from both gyral and sulcal cortices, including the multimodal caudal regions. Inferior parietal lobule projections to the pons are predominantly rostral, whereas those from the superior parietal lobule are seen throughout the rostrocaudal extent of the pons. These parietal projections are mostly in the intermediate and lateral sectors of the pons, with a degree of topographical organization determined by their site of origin. Temporal lobe projections arise from the multimodal regions of the cortex of the upper bank of the superior temporal sulcus, as well as from the superior temporal gyrus and supratemporal plane, and terminate in the lateral and dorsolateral pontine regions. Parastriate cortices at the dorsomedial and dorsolateral convexity, as well as the posterior parahippocampal gyrus, project to the lateral and dorsolateral pontine regions in a pattern that interdigitates with the other terminations in this area. The rostral cingulate cortex projects to medial pontine nuclei and the caudal cingulate cortex projects to more lateral regions. Pontine projections have also been shown in experimental retrograde studies to arise from the anterior insular cortex.

These connections provide the cerebellum with access to higher order information, enabling it to modulate cognitive and emotional processing.

Apart from the cortical projection to the basis pontis, there are also pontine inputs from the superior colliculus to the dorsolateral pons and to the reticular nucleus of the pontine tegmentum. The tectocerebellar pathway thus uses the pontine nuclei and the reticular nucleus of the pontine tegmentum as the link in its projection to the vermal visual area. Pontine inputs are also derived from the medial mammillary bodies.

The pontocerebellar projection is almost completely crossed. Projection fibres arise from the pontine neurones, course horizontally toward the midline in a focused aggregate, and fan out in multiple directions to course in the transverse pontocerebellar fibre bundles

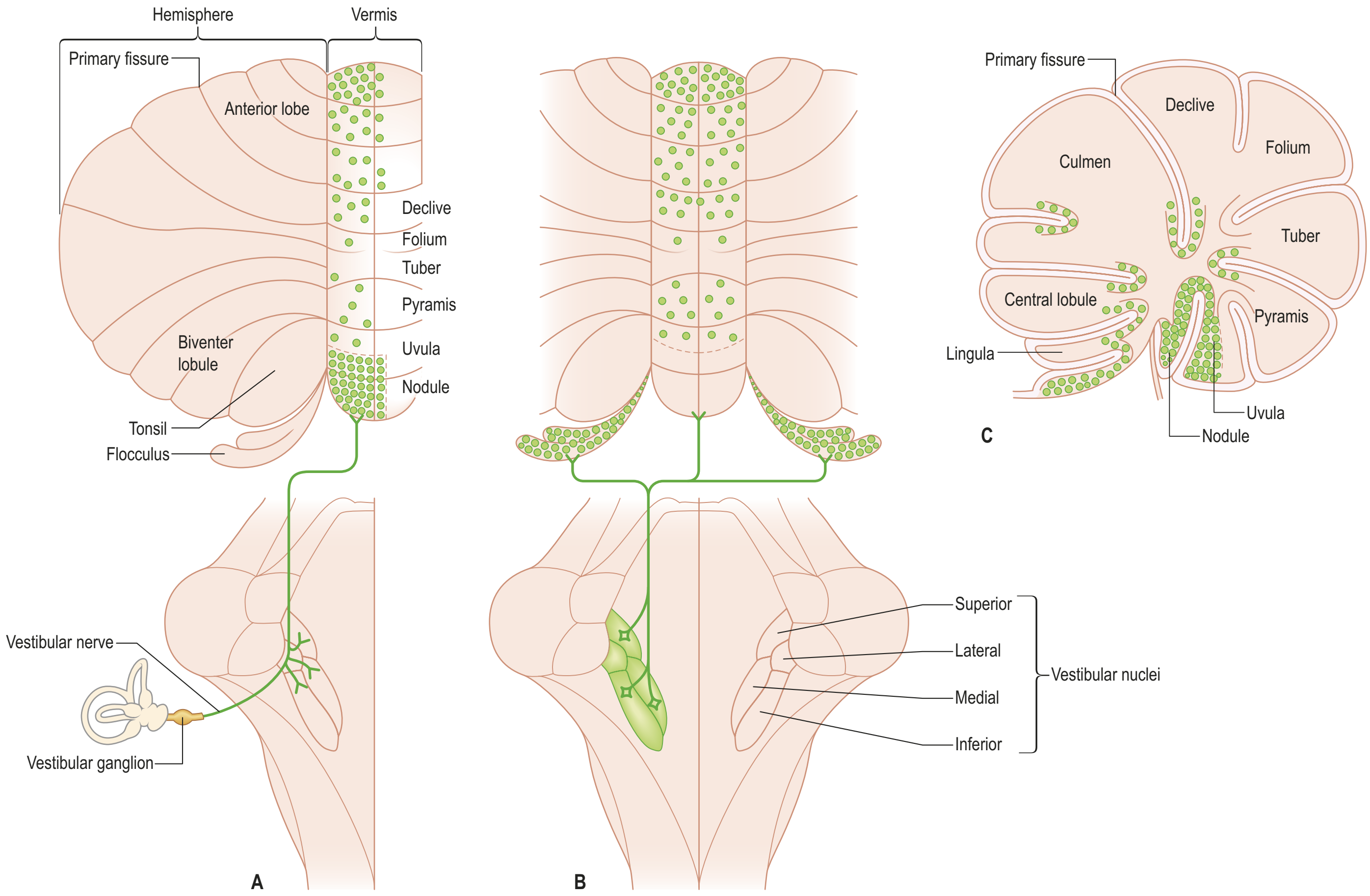

Fig. 29.25 Vestibulocerebellar mossy fibre projections. **A**, Primary vestibulocerebellar projections from the bipolar neurones of the vestibular ganglion. **B**, Secondary vestibulocerebellar projections from the vestibular nuclei. **C**, A sagittal section showing the distribution of both sets of afferents.

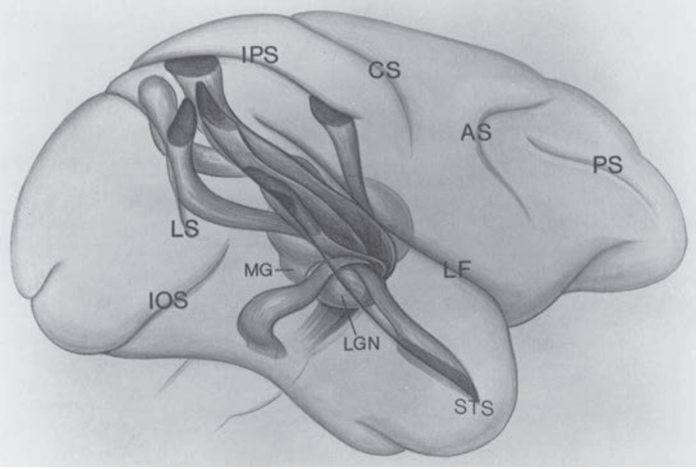

Fig. 29.26 Composite summary diagram showing an artist's representation of the trajectory and organization of fibres from the parietal, temporal and occipital association areas as they course toward the critical point in the white matter above and medial to the midportion of the lateral geniculate nucleus before descending into the cerebral peduncle. Abbreviations: AS, arcuate sulcus; CS, central sulcus; IOS, inferior occipital sulcus; IPS, intraparietal sulcus; LF, lateral fissure; LGN, lateral geniculate nucleus; LS, lunate sulcus; MG, medial geniculate; PS, principalis sulcus; STS, superior temporal sulcus. (With permission from Schmahmann JD, Pandya DN 1992 Course of the fiber pathways to pons from parasensory association areas in the rhesus monkey. J Comp Neurol 326:159–79.)

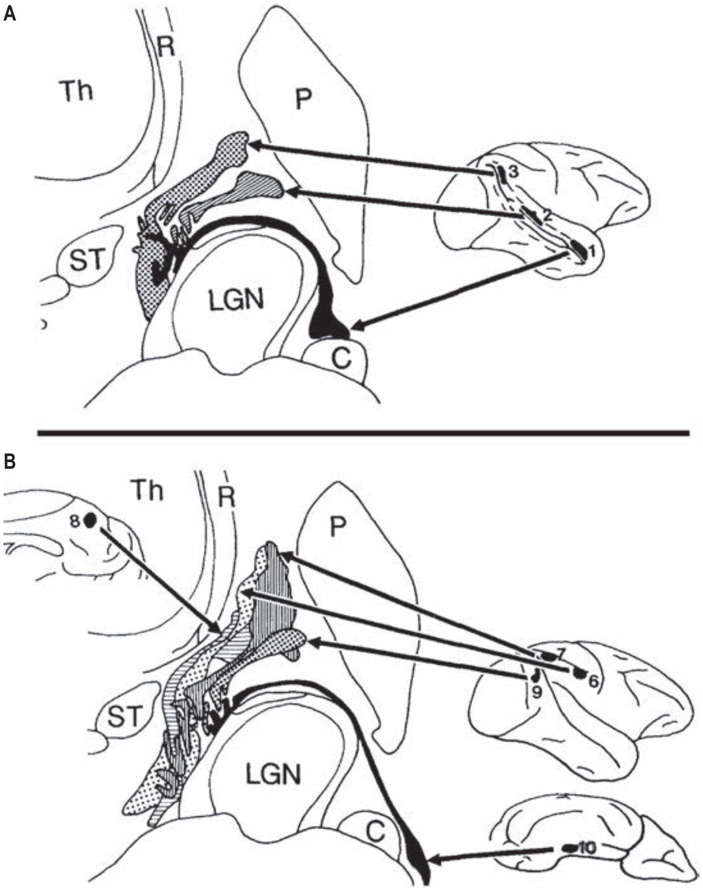

Fig. 29.27 Composite summary diagrams to show the topographic organization of (**A**) the superior temporal sulcus to pontine fibre system and (**B**) the parietal, occipital and posterior parahippocampal corticopontine fibre systems as they descend from the posterior aspect of the internal capsule above the midpoint of the lateral geniculate nucleus into the rostral part of the cerebral peduncle. Abbreviations: C, caudate nucleus; LGN, lateral geniculate nucleus; P, putamen; R, reticular nucleus of thalamus; ST, subthalamic nucleus; Th, thalamus. (With permission from Schmahmann JD, Pandya DN 1992 Course of the fiber pathways to pons from parasensory association areas in the rhesus monkey. J Comp Neurol 326:159–79.)

Tract tracing studies of white matter pathways in the monkey reveal that axons destined for the pons emanate from a given cortical area in a cord of fibres together with commissural fibres before separating as a distinct subcortical bundle. This subcortical bundle courses in the anterior limb of the internal capsule from prefrontal regions, or the sagittal stratum and/or posterior limb of the internal capsule from posterior regions (see Fig. 29.26). As thalamic fibres separate off from the subcortical bundle, the pontine fibres continue towards the cerebral peduncle. There is a common region through which the corticopontine fibres lead to the basis pontis, that is situated initially in the white matter above the mid-point of the lateral geniculate nucleus and then at the medial aspect of the lateral geniculate nucleus (see Fig. 29.27). These descending fibres demonstrate a certain degree of topographical organization, indicating that the corticopontine system consists of segregated and partially overlapping pathways that are, to some extent, distinguishable anatomically at each stage of their trajectory from origin to destination.

As the corticopontine fibres descend in the cerebral peduncle, they are topographically arranged such that those from prefrontal regions are situated most medially; those from premotor and then motor cortices occupy the middle third of the peduncle, and fibres from the parietal, temporal and occipital regions that are destined for the pons are in the lateral third of the cerebral peduncle. The relative area of the cerebral peduncle that contains fibres derived from the association cortices is larger in humans than in monkeys (as evidenced in comparative anatomy and tractography studies for the prefrontal cortex in particular (Ramnani et al 2006)) (Fig. 29.28), which appears to reflect the phenomenon of evolutionary pressure on interrelated cerebrocerebellar systems.

Within the pons, a given cortical area projects to multiple patches of pontine neurones distributed within both transverse and rostrocaudal dimensions. Some projections are arranged in rostrocaudal columns that further branch and coalesce. Each cerebral area commits fibres to a predictable trajectory in the cerebral white matter and cerebral peduncle, which leads to a unique mosaic of patches of terminations in precisely arranged regions of the basilar pons.

The motor projections are topographically organized, preferentially in the caudal half of the pons, lying close to the traversing corticofugal fibres (**Fig. 29.29**). In nuclei that receive multiple inputs, the terminations appear to interdigitate. Projections from the face region of the supplementary motor area (SMA) are most medial and include the median pontine nucleus. Projections from the ventral precentral gyrus (M1 face representation) are also medial, but lateral to those from SMA-face. M1 hand projections are in medially placed curved lamellae in the mid and caudal pons. Dorsal trunk projections are in medial and ventral locations, ventral trunk/hip projections encircle the peduncle in the caudal pons, and projections from the foot are heaviest caudally in laterally placed curved lamellae (Schmahmann et al 2004a).

Motor topography is also apparent in the human pons (**Fig. 29.30**). A topographical map in the human as determined by structure–function correlations in patients with stroke reveals that facial movement and articulation are localized to the rostral and medial basilar pons; hand coordination and dexterity are medial and ventral in rostral and midpons; arm coordination is represented ventral and lateral to the hand; leg coordination is in the caudal half of the pons, with lateral predominance. Gait is represented in medial and lateral locations throughout the rostral–caudal extent of the pons (Schmahmann et al 2004b).

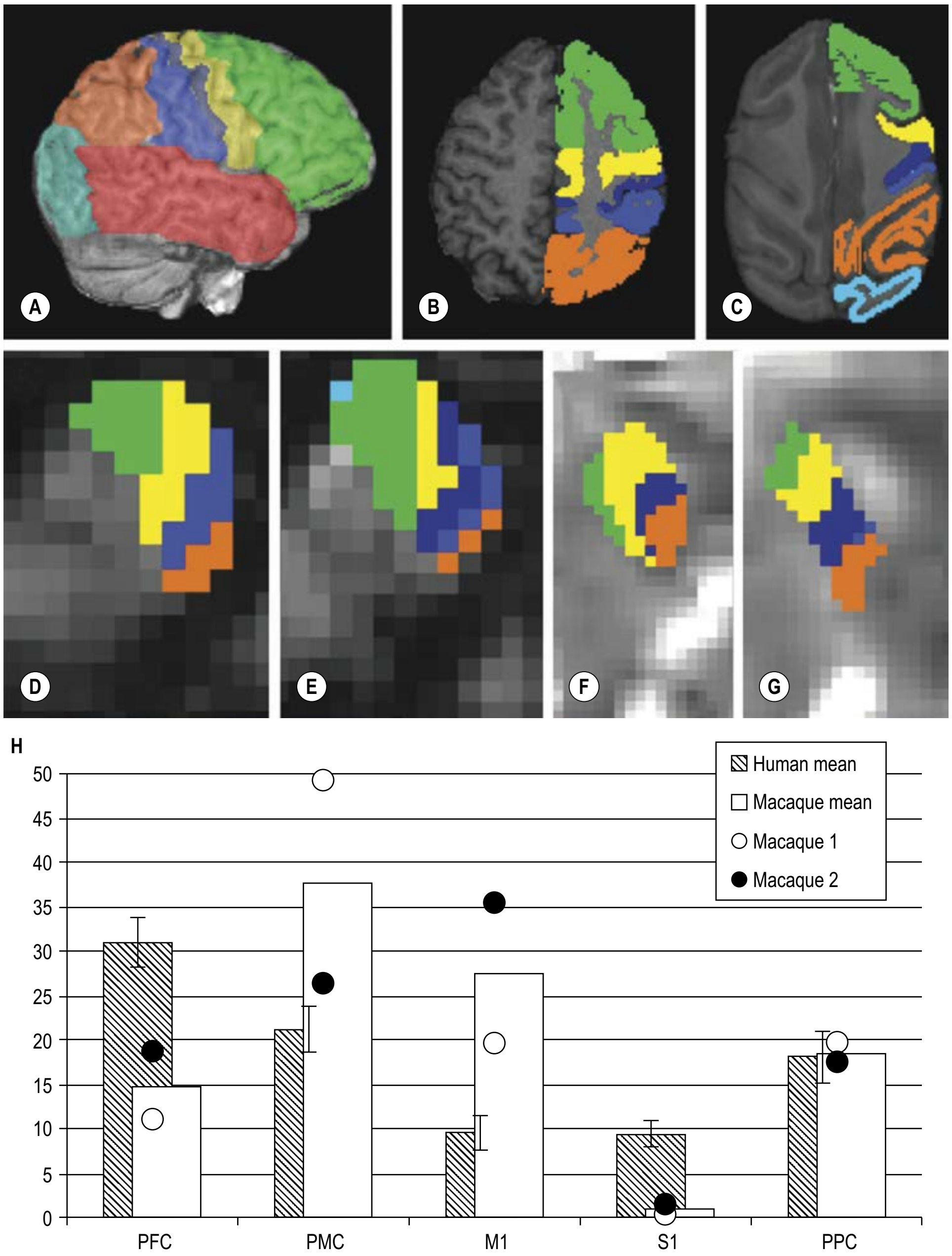

Fig. 29.28 Cerebral cortical origins of cerebral peduncle fibres in human and monkey revealed by diffusion tractography MRI. A schematic illustration of cortical areas used for delineation of projections from the cerebral peduncle in the human brain (3D rendering) (**A**), in axial section (**B**) and in *Macacca mulatta* (**C**; axial section). Anterior–posterior: green, prefrontal cortex (PFC); yellow, premotor cortex (PMC); dark blue, primary motor cortex (M1); light blue, somatosensory cortex (S1 and S2); orange, posterior parietal cortex (PPC); cyan, visual cortex; red, temporal lobe. Parcellation of the right cerebral peduncle using DT-MRI in two representative human cases (**D**, **E**) and two monkey cases (**F**, **G**) showing hard segmentations (coloured according to **A** and **B**) of fibres from cortical areas overlaid on the cerebral peduncles (grey). **H**, The percentage of the cerebral peduncle area occupied by segments of fibres from different cortical areas (y-axis): hatched bars, human cases (left and right averaged); white bars, averaged monkey cases (right hemisphere). Temporal lobe and visual cortex representations were negligible and were not included in the graphs. (With permission from Ramnani N, Behrens TE, Johansen-Berg H et al 2006 The evolution of prefrontal inputs to the cortico-pontine system: diffusion imaging evidence from macaque monkeys and humans. Cereb Cortex 16:811–18.)

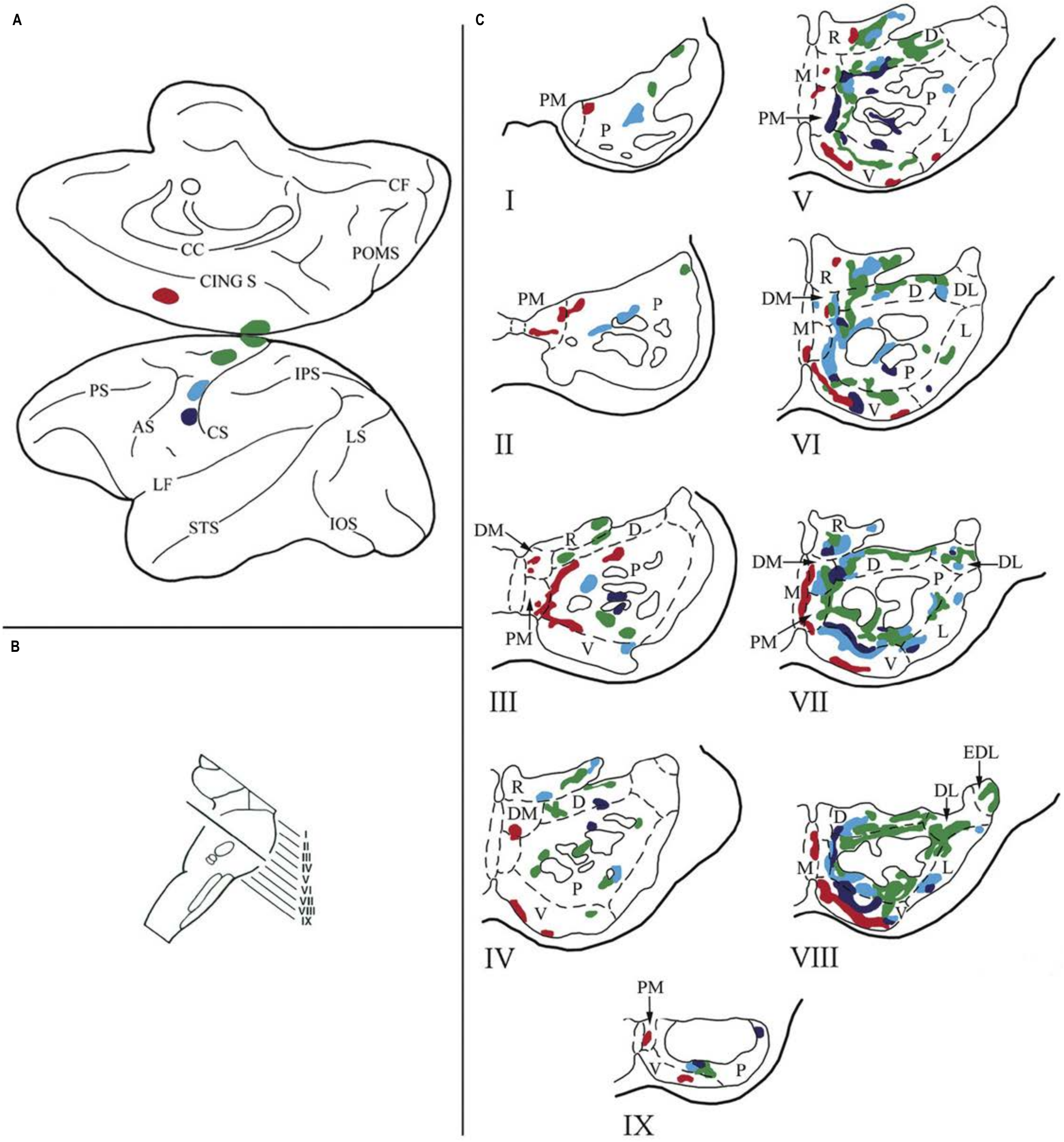

Fig. 29.29 A composite colour-coded summary diagram of projections to the basis pontis from motor and supplementary motor cortices in the rhesus monkey. **A**, Injection sites in the cerebral cortex (filled areas) are colour-coded as below. **B**, Brainstem view of the nine rostrocaudal levels of the pons from which the sections in **C** are taken to show the termination patterns. Supplementary motor area (SMA), red; trunk and leg, green; hand, light blue; face–hand overlapping area, dark blue. The terminations are predominantly in the caudal half of the pons, each cortical area projecting to unique subpopulations of neurones within the pons. The SMA projections are most medial, and the face, hand and leg projections are progressively more laterally situated. Abbreviations: Cerebral cortex: AS, arcuate sulcus; CC, corpus callosum; CF, calcarine fissure; CING S, cingulate sulcus; CS, central sulcus; IOS, inferior occipital sulcus; IPS, intraparietal sulcus; LF, lateral (Sylvian) fissure; LS, lunate sulcus; POMS, parieto-occipital medial sulcus; PS, principal sulcus; STS, superior temporal sulcus. Pons: D, dorsal pontine nucleus; DL, dorsolateral pontine nucleus; DM, dorsomedial pontine nucleus; EDL, extreme dorsolateral pontine nucleus; L, lateral pontine nucleus; M, median pontine nucleus; P, peduncular nucleus (peripeduncular vs. intrapeduncular not differentiated in the diagrams); PM, paramedian pontine nucleus; R, reticulotegmental nucleus (nucleus reticularis tegmenti pontis); V, ventral pontine nucleus. (Pontine nuclei according to Nyby and Jansen (1951) modified by Schmahmann and Pandya (1989). With permission from Schmahmann JD, Rosene DL, Pandya DN 2004 Motor projections to the basis pontis in rhesus monkey. J Comp Neurol 478:248–68.)

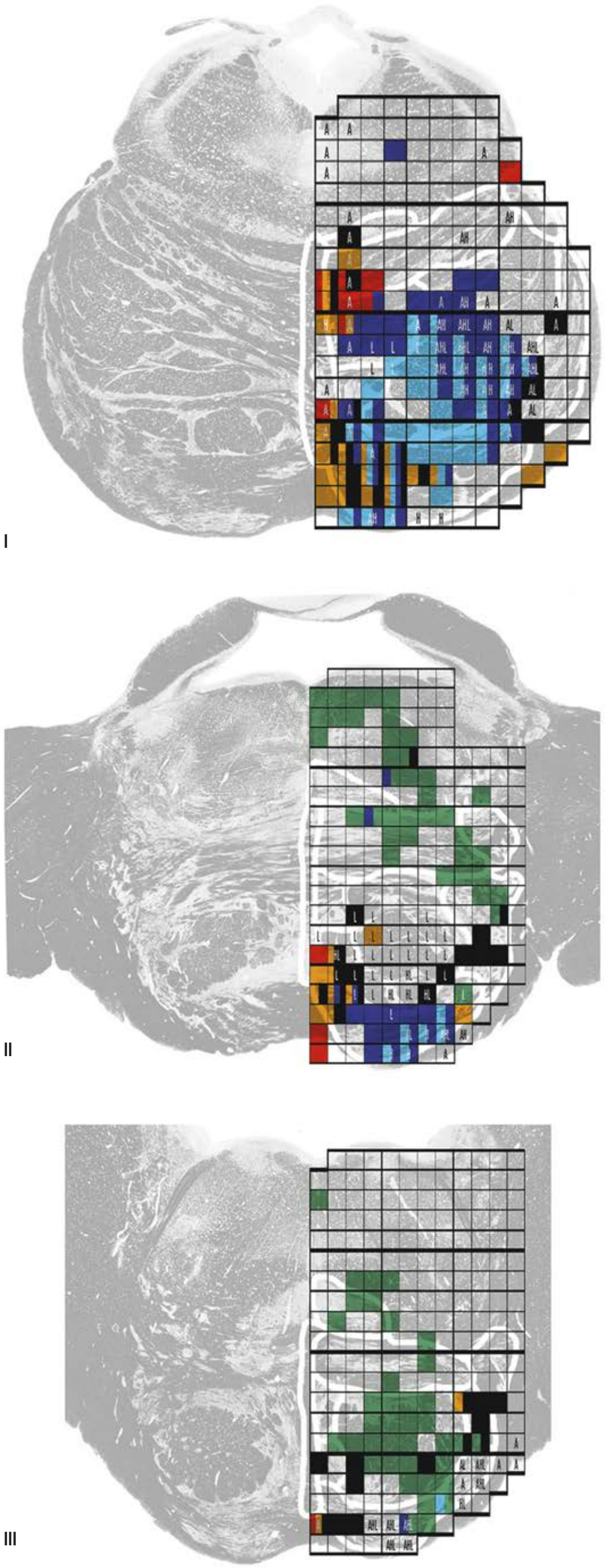

Fig. 29.30 A topographic map of motor representations in the human basis pontis. Colour-coded composite summary diagram to illustrate topography in the human pons in three rostral to caudal levels (I, II, III) in the transverse plane as determined by structure–function correlation in patients with lacunar pontine stroke. Face movement, red; speech, orange; hand dexterity, dark blue; arm dysmetria, light blue; leg dysmetria, green; gait, black. A = arm strength, H = hand strength, L = leg strength. (With permission from Schmahmann JD, Ko R, MacMore J 2004 The human basis pontis: motor syndromes and topographic organization. Brain 127:1269–91.)

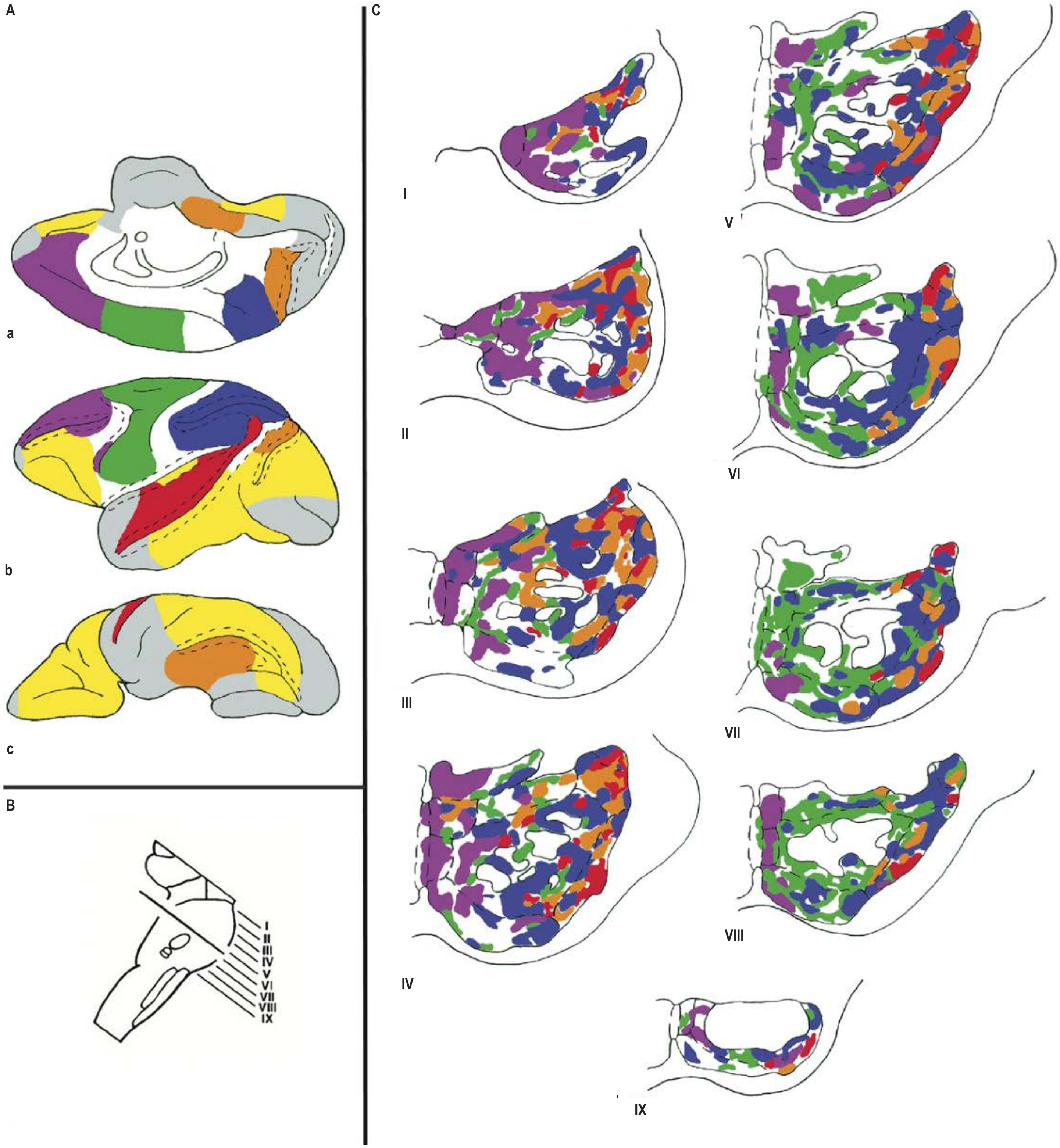

Fig. 29.31 Composite colour-coded summary diagram illustrating the distribution within the basis pontis of the rhesus monkey of projections derived from association and paralimbic cortices in the prefrontal (purple), posterior parietal (blue), superior temporal (red), and parastriate and parahippocampal regions (orange), and from motor, premotor and supplementary motor areas (green). **A**, Medial (a), lateral (b) and orbital (c) views of the cerebral hemisphere from which the projections are derived. **B**, Plane of section through the pons from which the rostrocaudal levels of the pons I through IX are taken. **C**, Patterns of termination within the nuclei of the basis pontis. Other cerebral areas known to project to the pons are depicted in white. Cortical areas with no pontine projections are shown in yellow (from anterograde and retrograde studies) or grey (from retrograde studies). Dashed lines in the hemisphere diagrams represent sulcal cortices. Dashed lines in the pons diagrams represent pontine nuclei; solid lines depict corticofugal fibres. (With permission from Schmahmann JD 1996 From movement to thought: anatomic substrates of the cerebellar contribution to cognitive processing. Human Brain Mapping 4:174–98 and Schmahmann JD, Pandya DN 1997a The cerebrocerebellar system. In: Schmahmann JD (ed) The cerebellum and cognition. Int Rev Neurobiol 41:31–60.)

There is a dichotomy in the pattern of corticopontine projections according to the dorsal ('where' pathway) versus ventral streams ('what' pathway) of cognitive processing. Dorsal stream areas concerned with visual motion and the peripheral visual field (the dorsal part of the prelunate gyrus, caudal lower bank of the cortex in the superior temporal sulcus, polymodal convergence zones in the lower bank of the cortex in the intraparietal sulcus, and paralimbic parts of the caudal inferior parietal lobule, as well as dorsolateral and dorsomedial prefrontal cortices concerned with spatial features of working memory) have projections to the pons. In contrast, in anatomical studies in monkeys, ventral stream cortices concerned with visual feature discrimination and the central visual field (ventral prelunate gyrus, rostral lower bank of the superior temporal sulcus, middle and inferior temporal gyri, lateral aspects of the posterior parahippocampal gyrus, and ventral prefrontal and orbitofrontal cortices with which these areas are interconnected) do not send projections into the basis pontis. These connections in monkeys suggested that the cerebellum plays a role in spatial awareness, and in attentional, auditory and linguistic functions subserved by the dorsal stream of cognitive processing. However, human imaging studies point to connections with medial and orbital prefrontal cortices, so there may be species differences in the corticopontocerebellar linkage and cerebellar engagement in functions subserved by the ventral stream.

dispersed throughout much of the contralateral hemipons at the same rostrocaudal level as the site of origin. They then regroup to form a concentrated collection before coursing in the middle cerebellar peduncle to enter the cerebellum (Schmahmann et al 2004c) (**Fig. 29.32**).

The general principle of the rostrocaudal reversal in the pontocerebellar projection through the middle cerebellar peduncle was established by von Bechterew (1885) based on myelin stains in developing brain. The caudal pons (more heavily motor) is linked with cerebellar anterior and medial areas, whereas the rostral pons (more heavily associative) is linked with the lateral and caudal cerebellum (see Fig. 29.7B). Divergence and convergence in the corticopontine projection is further complicated by a similar arrangement in the pontocerebellar pathways. Pontine regions project to multiple cerebellar cortical areas; cerebellar areas receive input from a unique complement of neurones distributed throughout multiple pontine nuclei (**Fig. 29.33**). Cerebellar hemispheres receive a relatively greater pontine input than the vermis.

In monkeys, medial parts of the caudal pons project mainly to lobule V in the anterior lobe. The intrapeduncular nucleus projects to vermal lobule VIIIB, the paramedian lobule. These cerebellar regions contain sensorimotor representations of the upper and lower extremities. The dorsolateral pontine region and the reticular nucleus of the pontine tegmentum project to the dorsal paraflocculus, uvula and the vermal visual area. Neurones in the dorsomedial nucleus also project to the vermal visual area. Medial parts of the rostral pons project to crus I, and neurones in the medial, ventral and lateral pons send their axons to crus II.

Anatomical and physiological techniques in experimental animal models provide insights into the destination of cerebral cortical afferents in the cerebellum. The anterior lobe (particularly lobules IV and V) and the paramedian lobule (lobule VIII) receive afferents from pericentral motor and sensory cortices; crus I of the ansiform lobule receives inputs from premotor and prefrontal cortices; and crus II is linked with posterior parietal areas. One region of the cerebral cortex is distributed to numerous discrete sites in the cerebellar cortex, and conversely, multiple cerebral cortical areas contribute converging projections to common cerebellar areas. There are reciprocal loops of information processing between cerebral cortex and cerebellum: cerebral areas that project to discrete regions of cerebellum receive information back from those cerebellar areas (see Nieuwenhuys et al 2008, Voogd and Ruigrok 2012, Strick et al 2009, Schmahmann et al 2019 for reviews). See Fig. 29.34 for a simplified version of this projection (Glickstein et al 1985).

Climbing fibre afferents from the inferior olive

The subdivisions of the inferior olive, the sole source of climbing fibres, are summarized in **Fig. 29.35**. The three major nuclei are the principal olive and the medial and dorsal accessory olivary nuclei. The principal olive has a dorsal lamina, a bend and a ventral lamina with ventrolateral and ventromedial parts. The medial accessory olivary nucleus has rostral and caudal parts: its subnuclei, located dorsomedially, are the group beta (continuous medially with the dorsomedial cell column) and the dorsal cap of Kooy (continuous rostrally with the ventrolateral outgrowth and the ventral lamina of the principal olive). An intermediate portion of the medial accessory olivary nucleus is present in rat and monkey brains. The dorsal accessory olivary nucleus has rostral and caudal parts.

Connectional data for the inferior olivary nuclei, derived from experimental studies in the cat, rat and nonhuman primates, has defined

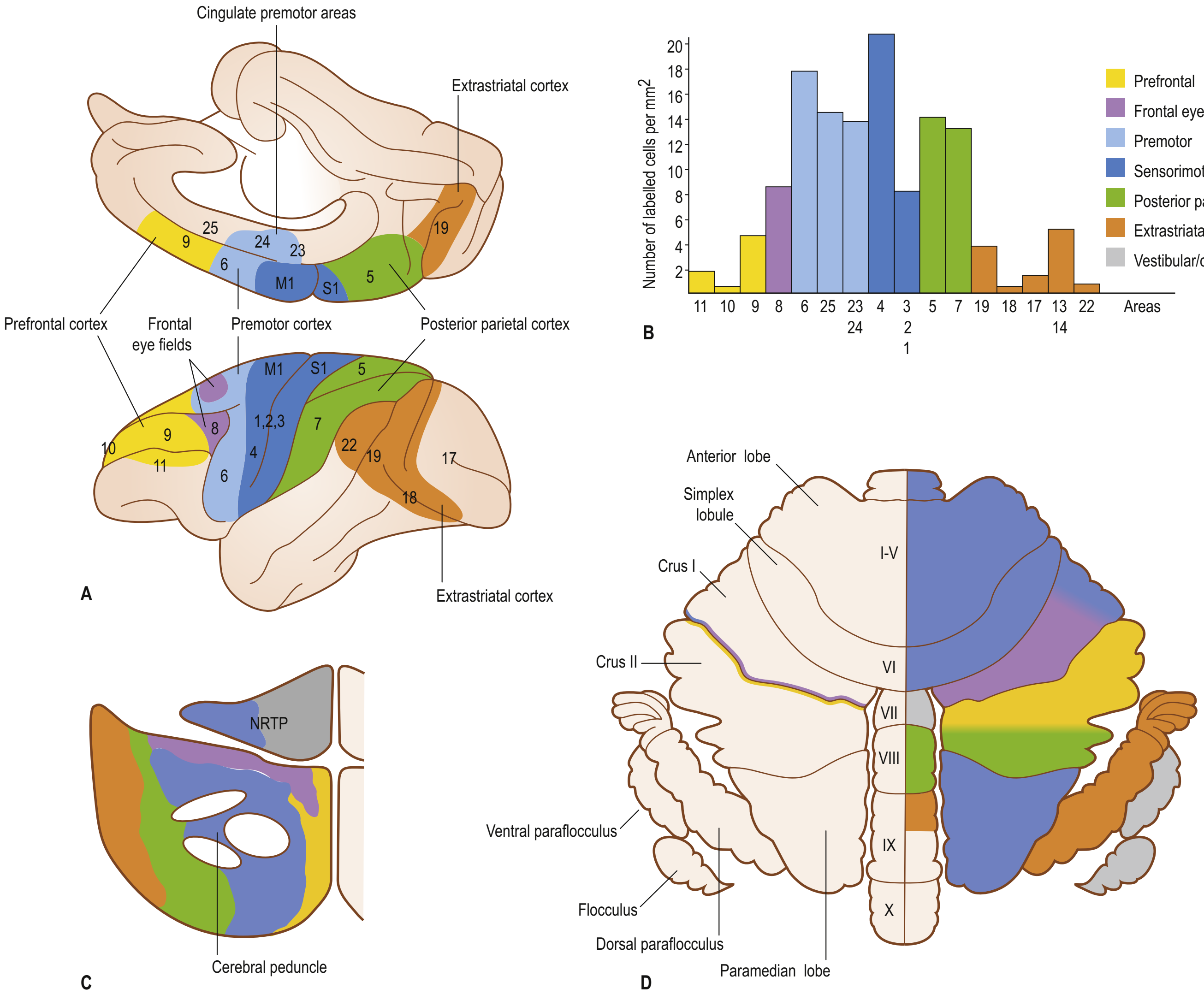
Cingulate premotor areas
Extrastriatal cortex
25
9
24
23
6
M1
S1
5
19
Prefrontal cortex
Frontal eye fields
Premotor cortex
Posterior parietal cortex
M1
S1
5
9
8
1,2,3
7
10
11
4
6
22
19
17
18
Extrastriatal cortex
A
Number of labelled cells per mm2
20
18
16
14
12
10
8
6
4
2
11
10
9
8
6
25
23
24
4
3
2
1
5
7
19
18
17
13
14
22
Areas
B
Prefrontal
Frontal eye fields
Premotor
Sensorimotor
Posterior parietal
Extrastriatal
Vestibular/optokinetic
NRTP
Cerebral peduncle
C
Anterior lobe
Simplex lobule
Crus I
I-V
Crus II
VI
VII
VIII
Ventral paraflocculus
IX
Flocculus
X
Dorsal paraflocculus
Paramedian lobe
D

Fig. 29.34 The corticopontocerebellar system. **A**, The origin of corticopontine fibres from the cerebral cortex in the monkey (macaque). **B**, The relative proportions of corticopontine neurones in different areas of the cerebral cortex of the monkey, indicated in panel **A**. **C**, A transverse section through the pons showing the distribution of corticopontine fibres in the pontine nuclei and the reticulotegmental nucleus (nucleus reticularis tegmenti pontis, NRTP). **D**, The flattened cortex of the monkey cerebellum showing the distribution of pontocerebellar mossy fibres. (B, Adapted with permission from Glickstein M, May JG, 3rd, Mercier BE 1985 Corticopontine projection in the macaque: the distribution of labelled cortical cells after large injections of horseradish peroxidase in the pontine nuclei. J Comp Neurol 235:343–59.)

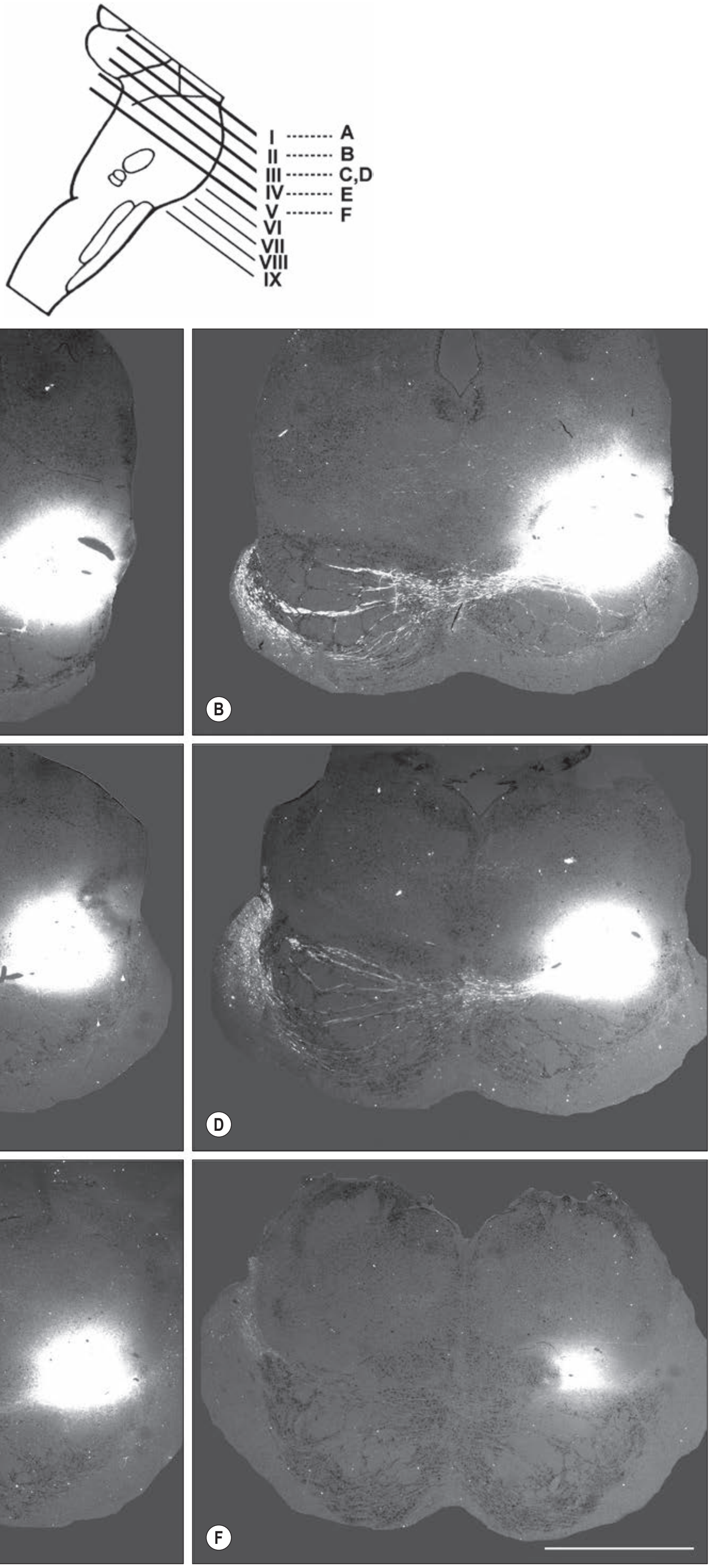

Fig. 29.32 Intrapontine course of pontocerebellar fibres in a rhesus monkey. Dark-field photomicrographs with partial light-field illumination of pontine levels I through V (of nine possible transverse levels according to Nyby and Jansen (1951) and Schmahmann and Pandya (1989)). A schematic view of the lateral aspect of the pons (top) illustrates the levels from which the pontine sections below are derived. The injection site of radiolabelled amino acids is seen in the dorsolateral parts of the peripeduncular nucleus and the dorsolateral nucleus of the basis pontis of *Macaca mulatta*. Pontocerebellar fibres emanate from the injection site and fan out in the contralateral hemipons as they course toward the middle cerebellar peduncle, and into the posterior lobe of the cerebellum (not shown). Pontine level I is seen in **A**, II in **B**, adjacent sections of level III in **C** and **D**, level IV in **E**, and level V in **F**. Magnification ×0.5; bar ×5.0 mm. (With permission from Schmahmann JD, Rosene DL, Pandya DN 2004 Ataxia after pontine stroke: insights from pontocerebellar fibres in monkey. Ann Neurol 55:585–9.)

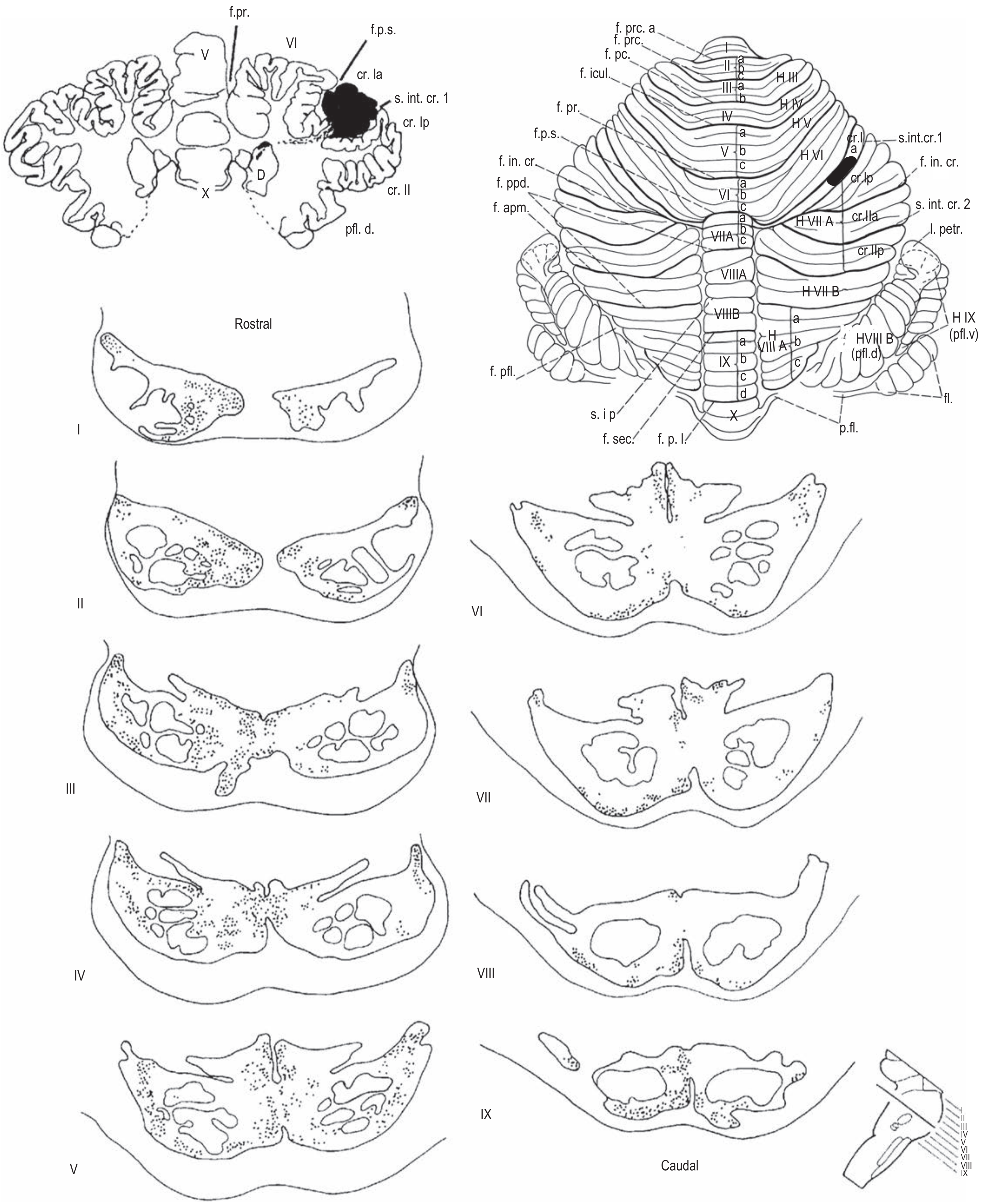
f.pr.
f.p.s.
V
VI
cr. la
s. int. cr. 1
cr. lp
D
X
cr. II
pfl. d.
f. prc. a
f. prc.
f. pc.
f. icul.
f. pr.
f.p.s.
f. in. cr.
f. ppd.
f. apm.
I
II
III
IV
V
VI
VIIA
VIIIA
VIIIB
IX
X
a
b
c
d
H III
H IV
H V
H VI
cr.l
s.int.cr.1
f. in. cr.
cr.lp
s. int. cr. 2
H VII A
cr.IIa
l. petr.
cr.IIp
H VII B
H IX
(pfl.v)
H
VIII A
HVIII B
(pfl.d)
fl.
f. pfl.
s. i p
f. sec.
f. p. l.
p.fl.
Rostral
I
II
III
IV
V
VI
VII
VIII
IX
Caudal
I
II
III
IV
V
VI
VII
VIII
IX

Fig. 29.33 The distribution of labelled neurones (shown as black dots) in the basilar pons following injection of a tracer substance (wheatgerm agglutinin–horseradish peroxidase (WGA–HRP) shown here in black shading) into crus I anterior of hemisphere lobule VIIA of a rhesus monkey cerebellum. The plane of the transverse section of the cerebellum (top left) showing the injection site is marked on the flattened map of the cerebellum (top right) according to Larsell (1970). The plane of section of the rostrocaudal levels of the pons from I to IX is depicted in the diagram at lower right. Pontine nuclear subdivisions are not shown. Labelled neurones are seen bilaterally in the pons, but with a contralateral predominance. Neurones are distributed in multiple but distinct regions of the basilar pons following the injection in this single folium. This arrangement seems to allow for multiple cerebral cortical areas to communicate with the cerebellar folium via the distributed pontine neurones. Pontine projections to subdivisions of each cerebellar folium are likely to be more restricted. Incidentally noted is anterograde transport of label from the injection site to a restricted site within the dentate nucleus of the ipsilateral cerebellum. Abbreviations: cr. Ia, crus I anterior; cr. Ip, crus I posterior; cr. II, crus II; cr. IIa, crus II anterior; cr. IIp, crus II posterior; D, dentate nucleus; f. apm., ansoparamedian fissure; fl., flocculus; f. icul., intraculminate fissure; f. in. cr., intercrural fissure; f. pc., preculminate fissure; f. pfl., parafloccular fissure; f. p.l., posterolateral fissure; f. ppd., prepyramidal fissure; f. pr., primary fissure; f. prc., precentral fissure; f. prc.a, precentral fissure a; f. p.s., posterior superior fissure; f. sec., secondary fissure; H, hemisphere; l. petr., petrosal lobule; p.fl, paraflocculus; pfl. d., dorsal paraflocculus; pfl.v, ventral paraflocculus; s. int. cr. 1, intracrural sulcus of crus I; s. int. cr. 2, intracrural sulcus of crus II; s. ip., intrapyramidal sulcus. Top left: Roman numerals V, VI and X designate cerebellar lobules. Top right: Roman numerals I to X designate vermal lobules; Roman numerals H III to H IX designate hemispheric lobules; Arabic letters a to d shown in the vermis and lobule H VIIA designate folia of the different lobules. Abbreviations for top left: cr. Ia, crus I anterior; cr. Ip, crus I posterior; cr. II, crus II; D, dentate nucleus; f.pr., primary fissure; f.p.s., superior posterior fissure; s.int.cr. I , internal sulcus of crus I. Roman numerals V, VI and X refer to cerebellar lobules according to Larsell (1970). (With permission from Schmahmann JD 1996 From movement to thought: anatomic substrates of the cerebellar contribution to cognitive processing. Human Brain Mapping 4:174–98.)

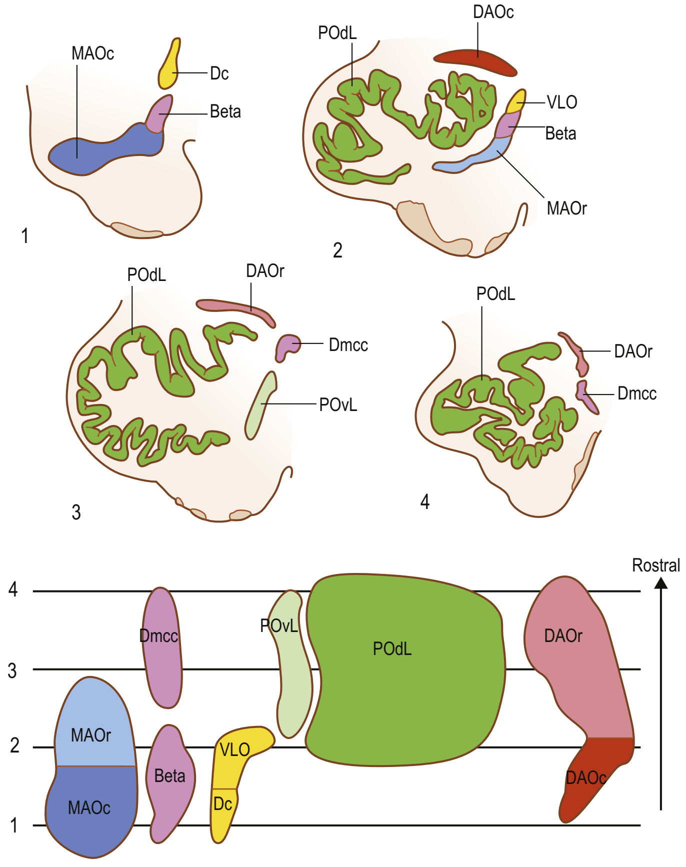

Fig. 29.35 Transverse sections through the human inferior olive, section 1 being the most rostral. Lower panel: the flattened inferior olive showing the levels of sections 1–4 in the upper panel. Note the large size of the convoluted dorsal lamina of the principal olive (POdL), and the small ventral lamina (POvL). Other abbreviations: Beta, group beta; DAOc/r, caudal/rostral dorsal accessory olive; Dc, dorsal cap; Dmcc, dorsomedial cell column; MAOc/r, caudal/rostral medial accessory olive; VLO, ventrolateral outgrowth.

different cerebellar zones (see Courville et al 1980, reviewed in Voogd and Ruigrok 2012). The A zone of the cerebellum is located next to the midline and extends over the entire vermis (**Fig. 29.36A**). It is composed of several zebrin-positive and zebrin-negative subzones that may be present over limited segments. Its climbing fibres are derived from the caudal medial accessory olive and it projects to the fastigial and vestibular nuclei. The X and B zones are restricted to the vermis of the anterior lobe and lobules VI and VIII. The X zone is narrow and separates the A zone from the B zone, which occupies the lateral vermis of these lobules. The X zone receives climbing fibres from the intermediate region of the medial accessory olive and projects to the interstitial cell groups located between the fastigial and posterior interposed nuclei. The B zone is innervated by climbing fibres from the caudal part of the dorsal accessory olive and projects to the lateral vestibular nucleus (Deiters' nucleus). The dorsal accessory olive, the B zone and the lateral vestibular nucleus are somatotopically organized. In the B zone, the hindlimb is represented laterally and the forelimb is represented medially (Andersson and Oscarsson 1978). In rodents, Purkinje cells of the X and B zones are zebrin-negative.

The cerebellar hemisphere is composed of the C1–C3 and the D1, Y and D2 zones (see Fig. 29.36). Like the X and B zones, C1, C3 and the Y zone are restricted to the anterior lobe, the simplex lobule (HVI) and the paramedian lobule (HVIIB, the gracile lobule and HVIII, the biventral lobule). The Purkinje cells of these zones are zebrin-negative and thus appear as blank spaces in suitably immunostained histological sections of the anterior and posterior cerebellum (see Fig. 29.36E). The C1, C3 and Y zones project to the emboliform nucleus and receive their climbing fibre input from the rostral dorsal accessory olive. This subnucleus receives input from peripheral receptors through dorsal column and trigeminal pathways. The climbing fibre projections of the rostral dorsal accessory olive to the C1, C3 and Y zones and the emboliform nucleus are somatotopically organized. In each of the zones, the hindlimb is represented rostrally in the anterior cerebellum and caudally in the posterior lobe; the forelimb and face occupy more central areas (Ekerot and Larson 1979a, 1979b) (**Fig. 29.37**). This rostrocaudal distribution clearly differs from the mediolateral somatotopy in the vermal B zone. The somatotopical localization is extremely detailed, repeated in each of the zones. The C1, C3 and Y zones connect with motor centres in the brainstem and the cerebral cortex. The hemisphere of the anterior lobe, adjacent part of lobule VI, and lobule VIII are considered as the motor regions of the cerebellum. The C2, D1 and D2 zones extend beyond the anterior and posterior motor regions, where they interdigitate with the C1, C3 and Y zones over most of the rostrocaudal length of the cerebellum. In rodents, these zones are zebrin-positive.

The C2 zone receives its climbing fibre input from the rostral medial accessory olive and projects to the posterior interposed nucleus (**Fig. 29.38**). Somatotopical organization is lacking in the C2 zone. The D1 zone receives its climbing fibres from the ventral lamina of the principal olive and projects to the caudal dentate; the D2 zone receives its climbing fibres from the dorsal lamina of the principal olive and projects to the rostral dentate. The main connections of the C2 and the D zones are with the cerebral cortex. Sections of the C2 zone and the somatotopically organized part of the D2 zone located in the anterior and posterior motor regions of the cerebellar hemisphere are connected with motor, premotor and parietal cortical areas. Sections of the C2 and the D zones located in hemispheric lobules VII (lobule VIIA crus I, lobule VIIA crus II, and lobule VIIB) and lobule IX subserve visuomotor and a wide range of cognitive functions.

The modular organization of the vestibulocerebellum includes multiple Purkinje cell zones, innervated by climbing fibres from subnuclei in the inferior olive that transmit optokinetic and vestibular information. There are five Purkinje cell zones in the cortex of the flocculus and the adjacent ventral paraflocculus (**Fig. 29.39**; see Fig. 29.23).

Efferent connections of the cerebellar nuclei

The connections of the cerebellar nuclei with the brainstem, thalamus and spinal cord determine the sphere of influence of the cerebellar modules. The A, X, B and D zones project to the fastigial nucleus, the interstitial cell groups, the lateral vestibular nucleus and dentate nucleus respectively (see Fig. 29.36).

Fastigial nucleus

The uncinate tract is the major efferent pathway from the caudal part of the fastigial nucleus (see Fig. 29.39). Its fibres cross in the rostral part of the cerebellar commissure, pass dorsal to the superior cerebellar peduncle, enter the contralateral medial, superior and inferior vestibular nuclei laterally, traverse the nuclei and terminate in the medial reticular formation. Direct, uncrossed, fastigiobulbar fibres from the rostral part of the fastigial nucleus enter the vestibular nuclei medially via the juxtarestiform body (which passes along the lateral margin of the fourth ventricle); their termination in the reticular formation mirrors the termination of the uncinate tract (Batton et al 1977). The distribution of the fibres of the uncinate tract and the direct fastigiobulbar fibres is bilateral, but with a contralateral preponderance. Some crossed fibres can be traced caudally into the spinal cord.

The fastigial nucleus projects bilaterally to several subcortical motor centres from which descending brainstem pathways arise. This enables each hemivermis to influence different functional systems, including the medial and spinal vestibular nuclei and the medial bulbar reticular formation (which gives rise to the bilaterally descending medial reticulospinal tracts). Through these pathways the A zone of the vermis exerts a bilateral influence on ventromedially located spinal interneurones and motor neurones that innervate axial, truncal and proximal limb muscles (Kuypers' medial motor system) (Lawrence and Kuypers 1968a, 1968b, Lemon et al 2012). Fibres of the uncinate tract that descend as far as the cervical cord terminate on the same neurones. The termination in the ventrolateral spinal nucleus is medial with respect to the projections of the dentate and interposed nuclei. The fastigial nucleus therefore influences motor centres in the brainstem that exert control bilaterally over the medial motor system of the spinal cord.

The caudal pole of the fastigial nucleus receives its Purkinje cell afferents from vermal visual areas in lobule VII that are involved in the long-term adaptation of saccades. Fastigial oculomotor projections are crossed and terminate in the rostral mesencephalic and pontine reticular formation that contains the horizontal gaze centre (paramedian pontine reticular formation), the vertical gaze centre (rostral interstitial nucleus of the medial longitudinal fasciculus), deep layers of the superior colliculus (bilaterally) and thalamic nuclei that probably include the frontal and parietal eye fields as their targets (Noda et al 1990).

Cerebellar influences on visceromotor systems are mediated by the projections of the fastigial nucleus to the parasolitary nucleus, a region bordering on the viscerosensory nuclei of the solitary tract; the dorsal visceromotor nucleus of the vagus nerve; central grey, serotoninergic raphe nuclei; and the noradrenergic nucleus of the locus coeruleus. The

In addition to the C2 zone located most medially in the flocculus and adjacent ventral paraflocculus, two pairs of zones occupy its lateral portion. Zones F1 and F3 connect with the oculomotor neurones in the vestibular nuclei that subserve the anterior canal vestibulo-ocular reflex (**Fig. 29.40**). The F2 and F4 zones connect with oculomotor neurones that subserve the horizontal canal vestibulo-ocular reflex. The flocculus and ventral paraflocculus receive vestibular mossy fibre input, relaying an efferent copy of the output of the vestibulo-oculomotor neurones. They also receive climbing fibre input, signalling retinal slip that occurs when the stabilization of the retina by the vestibulo-ocular reflex is incomplete. Retinal slip is perceived by two groups of neurones in the mesencephalon. In the horizontal plane, it is relayed by the nucleus of the optic tract. This nucleus, located in the pretectum, receives fibres of the contralateral optic nerve via the optic tract and projects to the dorsal cap of the inferior olive, located dorsomedial to the caudal medial accessory olive (see Fig. 29.35). The dorsal cap provides the F2 and F4 zones with climbing fibres. Retinal slip in the plane of the anterior canal is conveyed by the lateral and medial nuclei of the accessory system, part of a group of nuclei located on the periphery of the rostral mesencephalon that receive optic nerve fibres from the accessory optic tract (an offshoot of the optic nerve). These nuclei project to the ventrolateral outgrowth of the inferior olive, located immediately rostral to the dorsal cap (see Fig. 29.35). The ventrolateral outgrowth innervates the F1 and F3 zones. Repeated simultaneous activation of the vestibular mossy fibre-parallel fibre input and the climbing fibres, relaying retinal slip, induces plastic changes in the Purkinje cell output that compensates for the retinal slip. Combinations of the horizontal and anterior canal systems ensure compensation of retinal slip in all possible planes. Knowledge of this system has been instrumental in the concept that climbing fibres are carriers of error signals used in cerebellar learning (Marr 1969, Ito 1982).

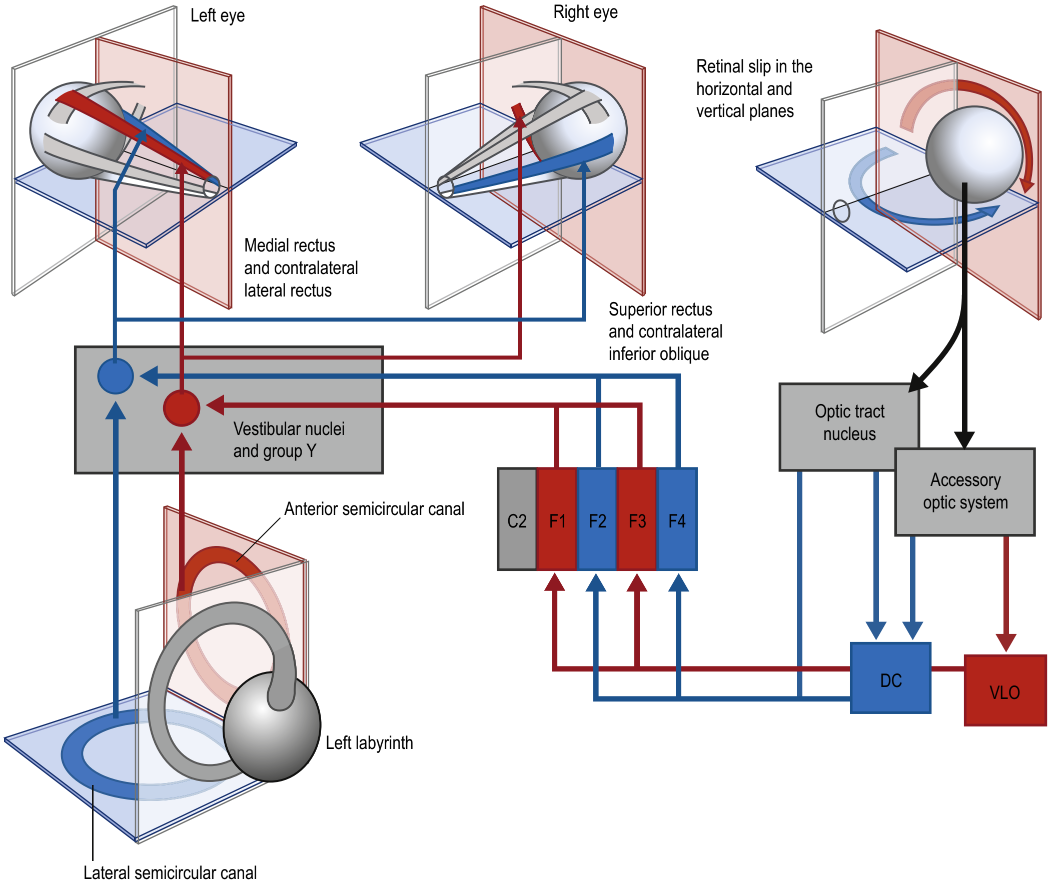
Left eye
Right eye
Retinal slip in the horizontal and vertical planes
Medial rectus and contralateral lateral rectus
Superior rectus and contralateral inferior oblique
Vestibular nuclei and group Y
Optic tract nucleus
Accessory optic system
Anterior semicircular canal
C2
F1
F2
F3
F4
DC
VLO
Left labyrinth
Lateral semicircular canal

Fig. 29.40 The circuitry used by the flocculus in long-term adaptation of the vestibulo-ocular reflex (VOR). The system is organized in the planes of the semicircular canals. For an explanation, see the text. Abbreviations: C2, C2 Purkinje cell zone; DC, dorsal cap; F1–F4, floccular Purkinje cell zones F1–F4; VLO, ventrolateral outgrowth. (Adapted with permission from Voogd J et al 2012 Visuomotor cerebellum in human and nonhuman primates. Cerebellum 11:392–410.)

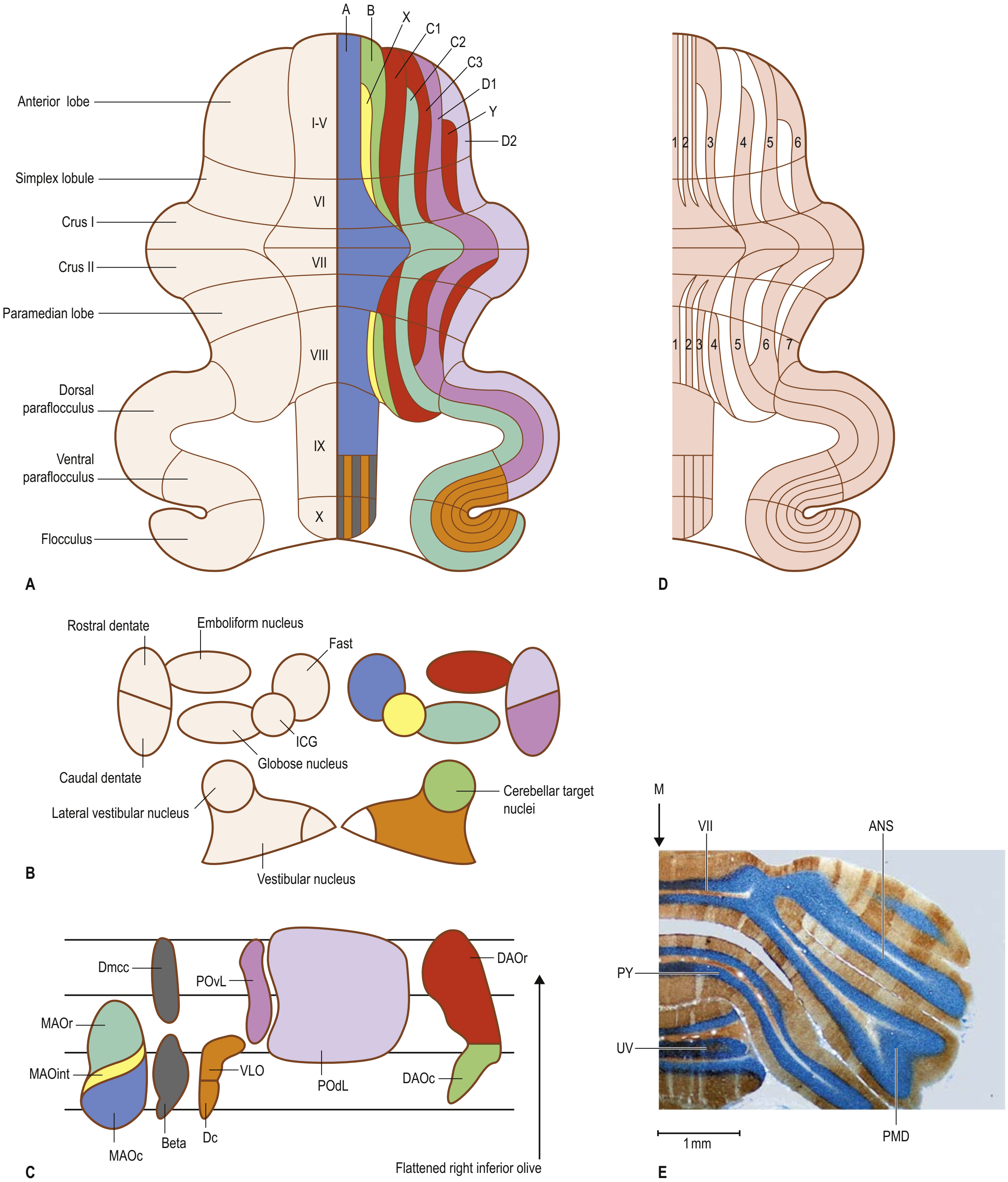
A
B
X
C1
C2
C3
D1
Y
D2
Anterior lobe
Simplex lobule
Crus I
Crus II
Paramedian lobe
Dorsal paraflocculus
Ventral paraflocculus
Flocculus
I-V
VI
VII
VIII
IX
X
A
1 2 3 4 5 6
1 2 3 4 5 6 7
D
Rostral dentate
Emboliform nucleus
Fast
ICG
Globose nucleus
Caudal dentate
Lateral vestibular nucleus
Vestibular nucleus
Cerebellar target nuclei
B
Dmcc
POvL
DAOr
MAOr
MAOint
VLO
POdL
DAOc
MAOc
Beta
Dc
Flattened right inferior olive
C
M
VII
ANS
PY
UV
1 mm
PMD
E

Fig. 29.36 The connections of the Purkinje cell zones of the mammalian cerebellum. **A**, The flattened cerebellar cortex. **B**, Target nuclei of Purkinje cells. **C**, Sources of climbing fibres associated with Purkinje cells, shown in the flattened contralateral inferior olive (see Fig. 29.35) and indicated in the same colour. **D**, Zebrin-positive and zebrin-negative Purkinje cell bands. The zebrin-positive bands are numbered from 1 to 7. A comparison with panel **A** shows that the A zone is a composite of zebrin-positive and zebrin-negative subzones; the X, B, C1, C3 and Y zones consist of zebrin-negative Purkinje cells. **E**, The zebrin-positive and zebrin-negative bands of the cerebellum of a rat. Abbreviations: A–D2, Purkinje cell zones A–D2; ANS, ansiform lobule; Beta, group beta; DAOc/r, caudal/rostral dorsal accessory olive; Dc, dorsal cap; Dmcc, dorsomedial cell column; Fast, fastigial nucleus; ICG, interstitial cell groups; M, midline; MAOc/int/r, caudal/intermediate/rostral medial accessory olive; PMD, paramedian lobule; POdL, dorsal lamina of the principal olive; POvL, ventral lamina of the inferior olive; PY, pyramis (lobule VIII); UV, uvula (lobule IX); VII, vermal lobule VII; VLO, ventrolateral outgrowth.

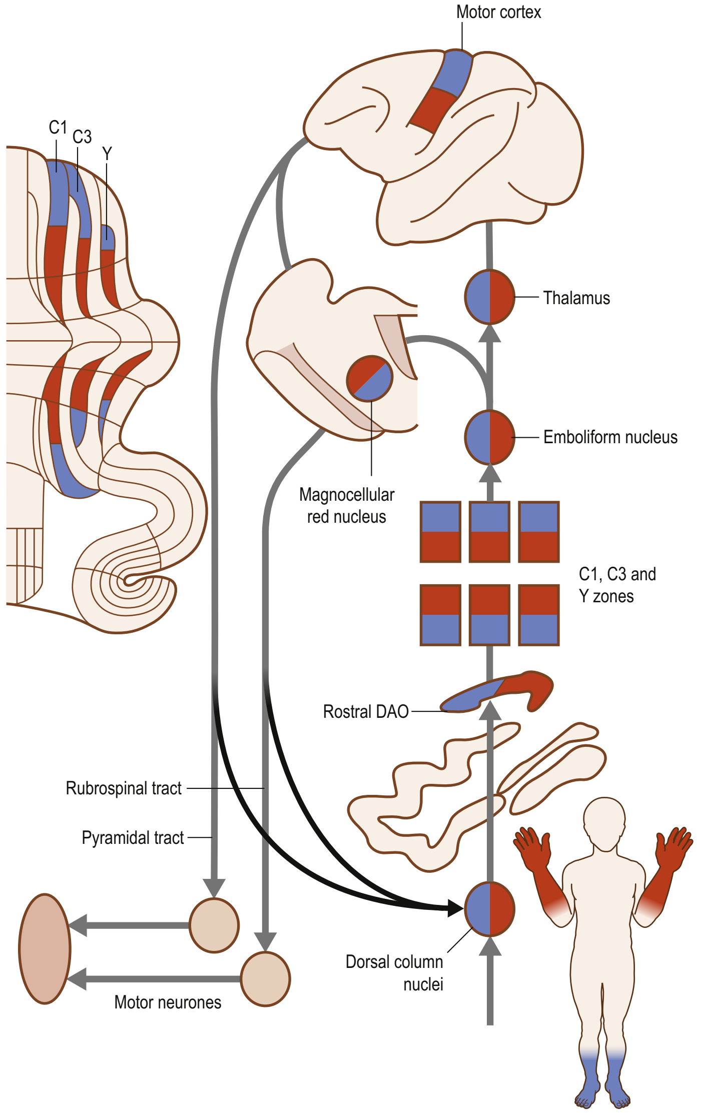

Fig. 29.37 The connections of the emboliform (anterior interposed) nucleus. The entire system is somatotopically organized: this organization is more detailed than indicated in the diagram. Abbreviations: DAO, dorsal accessory olive.

fastigial nucleus also influences visceromotor systems via projections of the vestibular nuclei and connections with the catecholaminergic nuclei of the brainstem and the hypothalamus (Zhu et al 2006).

Some fastigial nuclear fibres ascend along the superior cerebellar peduncle, separate from the peduncle at its decussation, and are distributed to the dorsal tegmentum, including the deep and intermediate layers of the nucleus of the tractus solitarius, the parabrachial nucleus, deep layers of the superior colliculus and intercollicular region, pretectal area, periaqueductal grey, interpeduncular nucleus and nuclei of the posterior commissure. The fastigial nucleus also projects to the ventral tegmental area, which sends a widespread dopaminergic innervation to the cerebral hemispheres: this fastigial projection has been shown to influence social cognition in a rodent model (Carta et al 2019). In the thalamus, fibres terminate in the contralateral internal medullary lamina, the intralaminar nuclei (paraventricular, paracentral, centromedian, parafascicular and central lateral), medial dorsal, ventrolateral and ventromedial thalamic nuclei. Ipsilateral projections recross in the commissure of the superior colliculus, the posterior commissure and the massa intermedia. The contralateral hypothalamus receives fastigial projections in the lateral, posterior and dorsal hypothalamic areas and the dorsomedial and paraventricular nuclei. These fastigial influences on autonomic and limbic circuits in the hypothalamus and thalamus are relevant when considering the cerebellar vermis and fastigial nucleus as nodes in limbic circuitry (Haines et al 1997, Schmahmann 1991, 2000).

Recurrent circuits involving the fastigial nucleus include excitatory efferents to the reticulotegmental nucleus and the GABAergic nucleo-olivary projection to the contralateral caudal medial accessory olive. The direct fastigiobulbar tract is an inhibitory, glycinergic system (Bagnall et al 2009).

Interstitial cell groups

The projections of the interstitial cell groups located between the fastigial and posterior interposed nuclei, the target nucleus of the X module, are directed to the vestibular nuclei, reticular formation, red nucleus and thalamus. They provide collaterals also to the spinal cord and superior colliculus (Bentivoglio and Kuypers 1982).

Lateral vestibular nucleus (Deiters' nucleus)

The lateral vestibular nucleus (Deiters' nucleus) is the target nucleus of the lateral vermal B zone. Despite its location outside the cerebellum, it might be better considered as one of the cerebellar nuclei because, unlike the other vestibular nuclei, it does not receive primary inputs from the labyrinth, but, like the deep cerebellar nuclei, it receives collateral innervation from the climbing fibres that innervate the B zone and it sends nucleo-olivary projections to the caudal dorsal accessory olive. The lateral vestibular nucleus gives rise to the lateral vestibulospinal tract. Through its projection to the lateral vestibular nucleus, the B zone, like the A zone, exerts an influence on ipsilateral interneurones and motor neurones in the anterior horn of the spinal cord that innervate axial, truncal and proximal limb muscles (Kuypers' medial motor system).

The zones of the cerebellar vermis affect neurotransmission in the vestibulospinal and reticulospinal systems, controlling bilateral postural and vestibular reflexes of the axial and proximal musculature, and the oculomotor centres in the brainstem. The skeletomotor functions are located in the anterior vermis and posterior lobule VIII (the X and B zones are restricted to these lobules), and oculomotor functions are in lobule VII. Most caudally, lobule X (nodulus) belongs to the vestibulocerebellum and is considered below. Other functions, such as vegetative regulation, are subserved by the vermis but have not been studied in detail.

Emboliform (anterior interposed) nucleus

Climbing fibres innervating the C1, C3 and Y zones and the emboliform (anterior interposed) nucleus originate in the rostral half of the dorsal accessory olive. The latter receives somatotopically organized cutaneous input mainly through the dorsal column and trigeminal nuclei and contains a refined cutaneous map of the entire contralateral body surface (Gellman et al 1983). The corticospinal and rubrospinal tracts provide the dorsal column nuclei with collateral innervation.

The emboliform nucleus is the target of the C1, C3 and Y zones. The detailed somatotopic organization of these Purkinje cell zones is maintained in the nucleus, where Purkinje cells of different zones, but with the same climbing fibre input from a particular region of the body, project to a common set of neurones (see Fig. 29.37). Ascending axons from the anterior interposed nucleus enter the brachium conjunctivum, which decussates at the border of the pons and the mesencephalon. The ascending branch enters and surrounds the caudal half of the magnocellular red nucleus, then proceeds to terminate in the ventrolateral and ventral anterior nuclei of thalamus, which are linked with the contralateral primary motor and premotor cortices. The descending branch of the brachium conjunctivum terminates in the reticulotegmental nucleus. The entire system, including the magnocellular red nucleus and the primary motor cortex and their efferent tracts, is somatotopically organized. The reciprocal nucleo-olivary pathway from the emboliform nucleus terminates in the rostral half of the dorsal accessory olive: the emboliform nucleus does not participate in the recurrent cerebello–mesencephalon–olivary circuits.

The motor cortex and the caudal, magnocellular part of the red nucleus give rise to the two main descending motor systems: the corticospinal (pyramidal) tract that crosses the midline in the caudal medulla at the bulbospinal junction, and the rubrospinal tract that crosses the midline at its level of origin in the midbrain. The corticospinal tract provides the magnocellular red nucleus with collateral innervation. Both tracts terminate on laterally located spinal interneurones and motor neurones that innervate distal limb muscles. Control of the ipsilateral limbs by the pars intermedia of the spinal cord grey is therefore effected by the emboliform nucleus through two different pathways, the rubrospinal and the corticospinal tracts, which converge upon the same interneurones and motor neurones. During primate evolution, the corticospinal system increases in prominence at the cost of the rubrospinal system, which comes to occupy a subsidiary position in the human brain.

The role of the cerebellum in the motor system is closely allied to the circuitry of the C1, C3 and Y zones, and to the emboliform nucleus and its output systems. The double decussation of the brachium conjunctivum and the rubrospinal and corticospinal tracts is responsible for the clinical observation that lesions of the cerebellum affect the ipsilateral half of the body.

Globose (posterior interposed) nucleus

The globose (posterior interposed) nucleus is reciprocally interconnected with the contralateral rostral medial accessory olive. Its projections ascend and decussate in the superior cerebellar peduncle and terminate in a group of nuclei at the meso-diencephalic junction that includes the parvocellular red nucleus and the nucleus of Darkschewitsch in the central grey, the superior colliculus and thalamic nuclei that project to motor and premotor cortical areas (see Fig. 29.38). The nuclei at the meso-diencephalic junction give rise to ipsilaterally descending tegmental tracts that also terminate in the rostral half of the medial accessory olive, forming reciprocally organized loops.

The nucleus of Darkschewitsch is in a reciprocal loop by way of its fibres descending through the medial tegmental tract to the rostral medial accessory olive, which sends climbing fibres to the C2 zone and the globose nucleus. Motor and visual divisions can be distinguished in this system: the segments of the C2 zone located in the anterior and

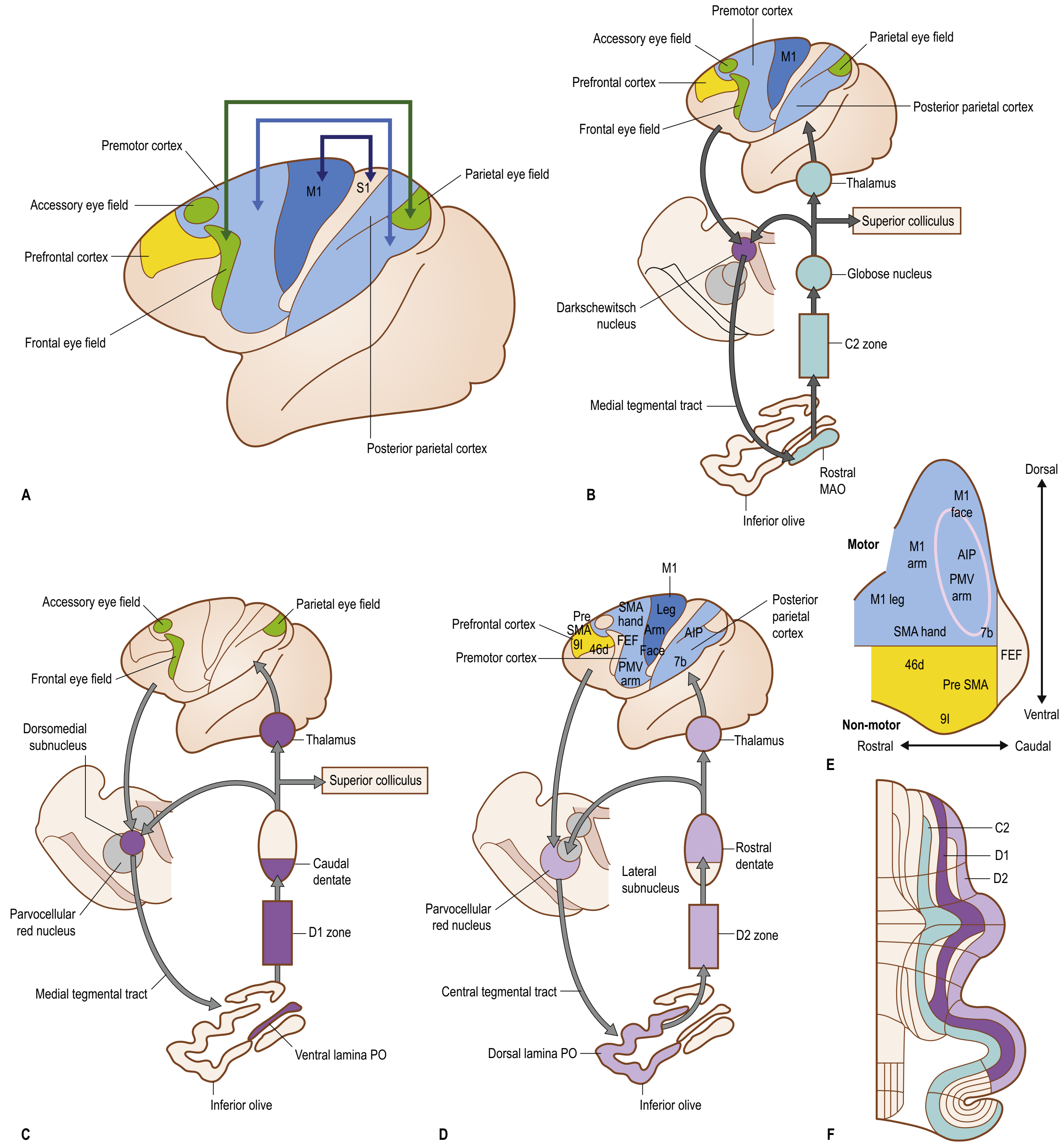
Premotor cortex
Accessory eye field
Prefrontal cortex
Frontal eye field
M1
S1
Parietal eye field
Posterior parietal cortex
A
Premotor cortex
Accessory eye field
Parietal eye field
M1
Prefrontal cortex
Posterior parietal cortex
Frontal eye field
Thalamus
Superior colliculus
Globose nucleus
Darkschewitsch nucleus
C2 zone
Medial tegmental tract
Rostral MAO
Inferior olive
B
Dorsal
M1 face
Motor
M1 arm
AIP
PMV arm
M1 leg
SMA hand
7b
FEF
46d
Pre SMA
9l
Non-motor
Ventral
Rostral
Caudal
E
Accessory eye field
Parietal eye field
Frontal eye field
Dorsomedial subnucleus
Thalamus
Superior colliculus
Caudal dentate
Parvocellular red nucleus
D1 zone
Medial tegmental tract
Ventral lamina PO
Inferior olive
C
M1
Prefrontal cortex
Pre SMA
SMA hand
Leg
Arm
AIP
Face
FEF
9l
46d
PMV arm
7b
Premotor cortex
Posterior parietal cortex
Thalamus
Rostral dentate
Lateral subnucleus
Parvocellular red nucleus
D2 zone
Central tegmental tract
Dorsal lamina PO
Inferior olive
D
C2
D1
D2
F

Fig. 29.38 **A**, Cortical areas targeted by the cerebellothalamic pathways of the posterior interposed and dentate nuclei. The primary motor area (M1) with the primary sensory area (S1), the premotor cortex with the posterior parietal areas and the frontal and parietal eye fields constitute interconnected networks. **B**, The connections of the globose (posterior interposed) nucleus. **C**, The connections of the caudal pole of the dentate nucleus. **D**, The connections of the rostral dentate nucleus. **E**, The subdivision of the rostral dentate into rostral motor and caudal non-motor divisions, showing the location of neurones retrogradely labelled from injection sites indicated in the diagram of the cerebral cortex in **D**. **F**, The flattened cerebellar cortex showing localization of the C2, D1 and D2 zones. Abbreviations: AIP, anterior intraparietal area; FEF, frontal eye field; PMV, ventral premotor cortex; PO, principal olive; rostral MAO, rostral medial accessory olive; SMA, supplementary motor area; 7b, 46d, 9l, cortical areas. (D, Adapted with with permission from Strick PL, Dum RP, Fiez JA 2009 Cerebellum and nonmotor function. Annu Rev Neurosci 32:413–434.)

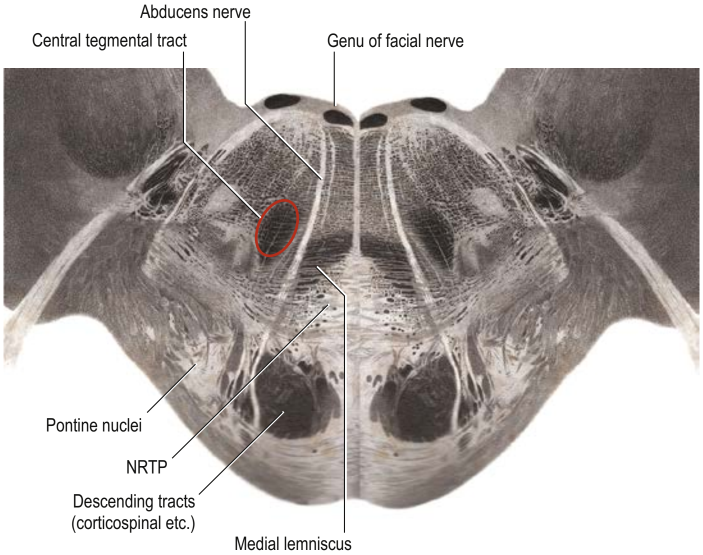

Fig. 29.41 A lithograph of a transverse section through the pons, showing the localization of the central tegmental tract in the pontine tegmentum. Abbreviation: NRTP, nucleus reticularis tegmenti pontis (reticulotegmental nucleus). (Reproduced from Stilling B 1846 Untersuchungen über den Bau und die Verrichtungen des Gehirns. I. Über den Bau des Hirnknotens oder der Varolischen Brücke. Jena, Druck und Verlag von Friedrich Make.)

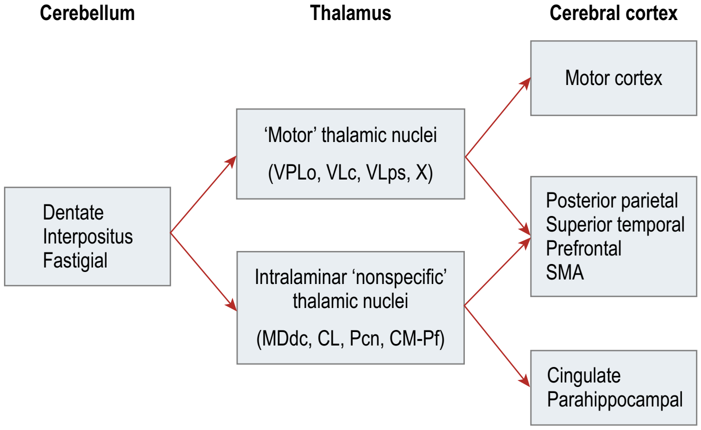

Fig. 29.42 Diagram of the cerebello-thalamo-cortical pathways. Traditionally motor cerebellar-recipient thalamic nuclei (VPLo, VLc, VLps and X) project to motor and premotor cortex, as well as to supplementary motor area (SMA), prefrontal (areas 8 and 46), posterior parietal (superior and inferior parietal lobules) and multimodal temporal regions (area TPO in the upper bank of the superior temporal sulcus). Intralaminar (CL, Pcn, CM-Pf) and medial dorsal (MDdc) thalamic nuclei that receive cerebellar input project in turn to association, limbic and motor cortices. Abbreviations of thalamic nuclei: CL, centralis lateralis; CM, centromedian; MDdc, medial dorsal nucelus, pars densocellularis; Pcn, paracentralis; Pf, parafascicularis; VLc, ventral lateral, pars caudalis; VPLo, ventral lateral, pars oralis; VLps, ventral lateral, pars postrema; X, nucleus. (Thalamic nuclei according to Olszewski 1952. With permission from Schmahmann JD 1996 From movement to thought: anatomic substrates of the cerebellar contribution to cognitive processing. Human Brain Mapping 4:174–98.)

The cerebral cortical projections of the classic cerebellar recipient motor thalamic nuclei (pars oralis of the ventral posterolateral nucleus, VPLo, the caudal and pars postrema aspects of the ventrolateral nucleus, VLc and VLps, and nucleus X) are not confined to the motor region (**Fig. 29.42**). The upper bank of the superior temporal sulcus receives projections from the VLc and VLps nuclei; widespread regions of the posterior parietal cortex receives projections from the VLps nucleus, and the VLc projections to the parietal lobe are similar although less intense; nucleus X projects to both the upper and lower banks of the intraparietal sulcus; VPLo projects to both the gyral and sulcal cortices of the superior parietal lobule at the lateral convexity of the hemisphere. Further, in the frontal lobe, the prefrontal periarcuate areas are reciprocally interconnected with nucleus X, and with the VLc, and VPLo nuclei.

The cerebellar outflow is also directed to the medial dorsal thalamic nucleus in its paralaminar parts, the laterally situated pars multiformis and the more caudal pars densocellularis. These nuclei have reciprocal connections with the prefrontal cortex in area 8, area 46 at both banks of the principal sulcus, and area 9, as well as with the cingulate gyrus, posterior parietal cortex, and multimodal parts of the superior temporal sulcus. In addition, nonmotor thalamic nuclei, including the intralaminar nuclei, receive major cerebellar projections, particularly centralis lateralis (CL), as well as the paracentralis (Pcn) and centromedian-parafascicular (CM-Pf) complex. The CL nucleus, like other intralaminar nuclei, has widespread cortical connections including the posterior parietal cortex, the multimodal regions of the upper bank of the superior temporal sulcus, the prefrontal cortex, the cingulate gyrus, and the primary motor cortex. Pcn nucleus projections include the parahippocampal gyrus. These thalamic projections to higher order association areas originate not only in the dentate nucleus but also from parts of the interposed and fastigial nuclei (see Schmahmann 1996).

The understanding of the zonal organization of the connections of the inferior olive and the cerebellar nuclei is derived from studies in lower mammals, but knowledge of the connections of the cerebellar hemispheres that account for the bulk of the cerebellar cortex in the great apes and human remains incomplete. The demonstration by Fujita et al (2010) of the presence of D1 and D2 zones in the marmoset hemisphere supports the idea that the construction of the primate hemisphere is similar to that in rodents and carnivores, but the relative proportions of the marmoset hemisphere are not very different from rodents. The source of the climbing fibre projection to the D1 zone in rodents and primates is the ventral, non-convoluted lamina of the principal olive. Although the ventral lamina of the principal olive is prominent in lower mammals, if this subdivision is represented in the human inferior olive by its medial lamina, the contribution of the human D1 zone to the hemisphere would be very small (see **Fig. 29.35**). Its major output would be represented by the D2 zone, and projections to the convoluted dentate nucleus.

Explanations for the evolutionary increase in size of the dentate nucleus and its connections include the increasing complexity of the cortical motor system, which is a major target of the dentate nucleus, as multiple, interconnected premotor and posterior parietal areas involved in the preparation of movement converge on the primary motor cortex. However, converging lines of evidence from numerous avenues of investigation suggest that the increased size of the dentate nucleus and its interconnected cerebellar posterior lobe lateral hemispheres reflect increased connectivity with cerebral association and paralimbic areas that subserve non-motor functions, enabling a cerebellar role in the modulation of intellect and emotion (Leiner et al 1986, Schmahmann 1991, 1996, 1997, Middleton and Strick 1994, Stoodley and Schmahmann 2009a, 2010, Strick et al 2009, Schmahmann et al 2019). Trans-synaptic viral tracer studies in monkeys further reveal that cerebellar circuits have disynaptic linkage with the subthalamic nucleus, providing evidence for cerebellar-basal ganglia communication in both the motor and nonmotor domains (Hoshi et al 2005).

Geographically distant areas of the cerebral cortex that are functionally coupled form intrinsic connectivity networks that subserve specific functions and can be studied with resting state functional connectivity MRI (rsfcMRI) (Habas et al 2009, Krienen and Buckner 2009, O'Reilly et al 2010, Buckner et al 2011). These cerebral networks map onto the cerebellum with topographic specificity and some degree of inter-individual variability. The motor networks map onto sensorimotor parts of the cerebellum in the anterior lobe and lobule VIII. The dorsal attention, ventral attention, frontoparietal, default mode and salience networks map onto focal areas within the posterior lobe of the cerebellum (**Fig. 29.43**). Among all the networks, the frontoparietal network for adaptive control is overrepresented in the cerebellum compared to the cerebral cortex (Marek et al 2018).

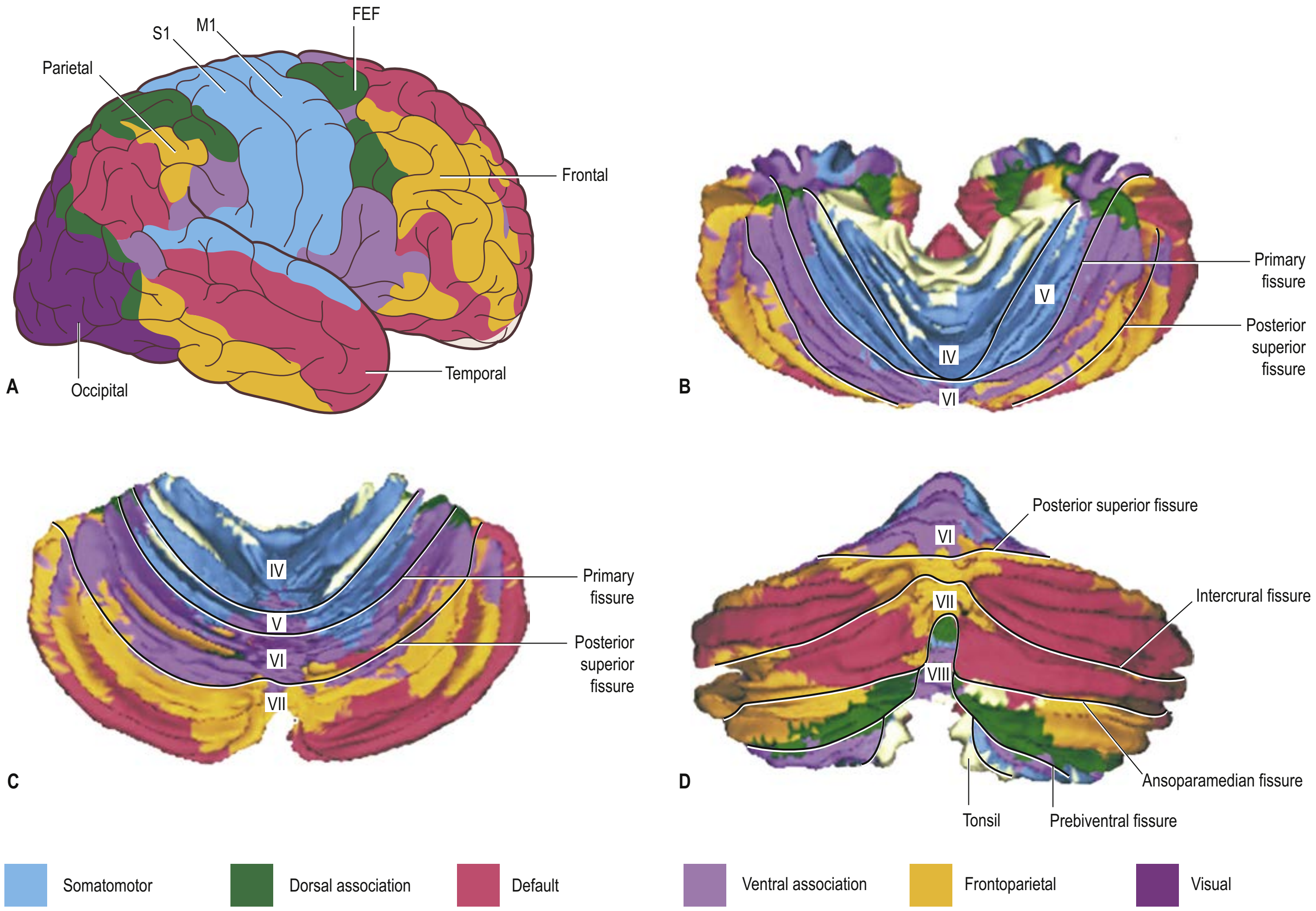
S1
M1
FEF
Parietal
Frontal
Temporal
Occipital
A
Primary fissure
Posterior superior fissure
V
IV
VI
B
IV
V
VI
VII
Primary fissure
Posterior superior fissure
C
Posterior superior fissure
VI
VII
Intercrural fissure
VIII
Ansoparamedian fissure
Tonsil
Prebiventral fissure
D
Somatomotor
Dorsal association
Default
Ventral association
Frontoparietal
Visual

Fig. 29.43 A map of the topographical correlations between remote, functionally coupled regions in the human cerebral cortex and the cerebellum using resting state functional connectivity fMRI. **A**, Networks distinguished in the cerebral cortex. **B**, An anterior superior oblique view of the human cerebellum showing regions that are functionally coupled to the different cerebral networks. **C**, A dorsal view of the human cerebellum. **D**, A caudal view of the human cerebellum. Abbreviation: FEF, frontal eye field. (A, Adapted with permission from Yeo BTT, Krienen FM, Sepulcre J et al 2011 The organization of the human cerebral cortex estimated by intrinsic functional connectivity. J Neurophysiol 106:1125–65; B–D, Reconstructions based on the transverse sections illustrated in Buckner RJ, Krienen FM, Castellanos A et al 2011 The organization of the human cerebellum estimated by functional connectivity. J Neurophysiol 106:2322–45.)

posterior motor regions of the cerebellum and the rostromedial globose nucleus receive input from the motor cortex, whereas visual and prefrontal input dominates in segments located in hemispheric lobules VII, IX (paraflocculus) and X (flocculus).

Dentate (lateral) nucleus

The shape of the dentate nucleus and the principal olivary nucleus change through evolution from compact nuclei to intricately folded sheets. In humans, the dentate nucleus has a rostromedial, microgyric, large-celled region, and a ventrocaudal, macrogyric, small-celled region (Dow 1974) (see Fig. 29.8). This corresponds to similar observations in monkeys, where the dentate consists of a rostromedial sector that is motor related, and a ventrocaudal component linked with nonmotor brain areas (Strick et al 2009) (see Fig. 29.38). The main projections from the dentate nucleus include the contralateral parvocellular red nucleus and thalamus. Group Y, a cell group located ventral to the dentate nucleus located within the floccular peduncle, projects to the contralateral oculomotor nucleus

The rostral dentate in lower mammals is the target of the D2 zone. Its dentate-olivary connections are with the dorsal lamina of the principal olivary nucleus. The rostral dentate receives projections from motor regions of the cerebellum and is somatotopically organized: the hindlimb is represented rostrally, then the arm and the face more caudally. It projects to the ventral, central and dorsolateral parts of the parvocellular red nucleus**.** Its thalamic targets are in the ventral intermediate and ventrolateral thalamic nuclei, which are reciprocally connected with the motor and premotor cortices (see Fig. 29.38D–E). Retrograde and transneuronal labelling reveals that the rostrodorsal dentate sends its efferents via the thalamus to the primary motor cortex (Wiesendanger and Wiesendanger 1985, Orioli and Strick 1989, Hoover and Strick 1999, Lu et al 2007), ventral premotor area (Orioli and Strick 1989), caudal part of the dorsal premotor area (Hashimoto et al 2010) and supplementary motor area (SMA proper) (Sakai et al 1999, Akkal et al 2007). Anterior and medial parietal areas also receive projections via the thalamus from the rostromedial dentate nucleus. The rostral dentate nucleus sends descending projections via the brachium conjunctivum to the reticulotegmental nucleus.

The caudal dentate is the target nucleus of the D1 zone, and its projections terminate in the ventral lamina of the principal olive. It receives its corticonuclear projections from lobule VII (hemispheric extensions of lobule VIIA as crus I and crus II, as well as lobule VIIB) and from lobule IX (paraflocculus/tonsil). The ventrocaudal dentate projects to the dorsomedial part of the parvocellular red nucleus. In the thalamus, it targets the medial parts of the ventrolateral thalamic nucleus, area X (Chan-Palay 1977), the parvo- and magnocellular anterior nucleus, and the lateral rim of the mediodorsal nucleus (Middleton and Strick 2001). These thalamic nuclei convey the projections to the cerebral cortical areas in the preSMA at the rostral part of the dorsal premotor area, prefrontal cortex in areas 46d and 9l (Middleton and Strick 1997, 2001), the frontal and supplementary eye fields (Lynch et al 1994, Lynch and Tian 2006) and the inferior parietal lobule area 7b (Clower et al 2001).

The recurrent pathways that link the parvocellular red nucleus by way of the central tegmental tract with the inferior olive, and via the olivocerebellar projection to the dentate nucleus, form the Guillain–Mollaret triangle. Projections from the rostrolateral and caudal parvocellular red nucleus course in the central tegmental tract to the dorsal lamina and bend of the principal olive, which provide climbing fibres to the caudal dentate and the cerebellar D2 zone. The dorsomedial parvocellular red nucleus sends its projections in the medial tegmental tract to the ventral lamina of the principal olive, which provides climbing fibres to the rostral dentate and the cerebellar D1 zone. The first published lithograph of a section through the pontine tegmentum (Stilling 1846), shows the central tegmental tract linking the dentate and recipient parvocellular red nucleus with the inferior olive to be one of the largest fibre systems in the brainstem (**Fig. 29.41**).

Single axon tracing studies of cerebellothalamic projections and thalamocortical pathways in monkeys demonstrated that there is considerable feedback from the cerebellum to cerebral association areas (see Fig. 29.41). This is consistent with the demonstration of associative projections into the cerebellum through the feedforward limb via the corticopontine pathways, and with the concept that regions of the cerebellum and cerebral cortex are reciprocally interconnected in circuits, or loops.

Trans-synaptic tract tracing studies using attenuated viral tracers further defined the feedback limb, showing that the morphological distinction between the phylogenetically older, dorsal magnocellular part of the dentate nucleus, and the more recently evolved ventral small-celled region have connectional and functional relevance. The primary motor cortex receives projections via the thalamus from dorsal portions of the dentate nucleus at mid-rostrocaudal levels and in the caudal portions of the emboliform nucleus where neuronal activity related to arm movement has been recorded (see Fig. 29.35). About 25–30% of the dentate nucleus projects to the primary motor cortex. In flattened maps of the dentate nucleus, neurones projecting to the arm representation of M1 are situated in a cluster in the dorsal portion of the dentate at mid-rostrocaudal levels; those to the leg representation are in the rostral pole of the dorsal dentate; and those projecting to the face representation are in caudal levels of the dorsal dentate (Strick et al 2009). Each M1 cortical area thus receives input from a spatially separate set of neurones in the dorsal part of the dentate nucleus. The premotor cortex receives input from the mid-rostrocaudal part of the dentate, ventral to the M1 projecting neurones. Frontal eye field projecting neurones are in the caudal third of the dentate which is correlated with saccadic eye movements. The prefrontal cortex (areas 46 and 9) receives projections from the ventral part of the dentate, mostly in its middle third rostrocaudally. Projections to the posterior parietal cortex, including the lower bank of the intraparietal sulcus, arise from neurones located ventrally in the caudal pole of the dentate. Projections to the anterior intraparietal area arise from neurones located dorsally in the dentate at mid-rostrocaudal levels (Clower et al 2001, Ugolini et al 2006, Strick et al 2009).

In humans, the D2 zone accounts for most of the cerebellar hemisphere, exemplified by its development (see Fig. 29.23) and by the size of the different components of its circuitry. The subdivision of the human dentate in rostrodorsal microgyric and caudolateral macrogyric portions would correspond with two major subdivisions of the D2 zone. Projections from the dorsal lamina of the principal olive to the D2 zone would be topographically arranged such that motor inputs are transmitted to the rostrodorsal microgyric dentate and segments of the D2 zone located in the motor regions of the cerebellum, and nonmotor inputs are directed to the caudolateral macrogyric dentate nucleus and segments of the D2 zone in hemispheric lobules VII and IX. This is in agreement with the clinical-anatomical observations of crossed cerebro-cerebellar atrophy in patients by Demolé (1927a, 1927b) and by Verhaart and Wieringen-Rauws (1950) that degeneration of the rostrodorsal, microgyric dentate occurred with large, chronic lesions involving the pre- and postcentral gyri, whereas lesions of more posterior parts of the hemisphere, involving parietal, occipital and temporal areas, resulted in atrophy of the ventrocaudal macrogyric dentate.

NEUROIMAGING OF HUMAN CEREBELLAR STRUCTURE AND FUNCTION

Task-based functional MRI within single subjects and at the group level provides independent confirmation of the cerebellar sensorimotor-cognitive dichotomy (Stoodley and Schmahmann 2009a, Stoodley et al 2010, 2012) (**Fig. 29.44A**). Tasks such as moving the arm or leg activate the primary sensorimotor cerebellum – anterior lobe and adjacent parts of lobule VI, as well as lobule VIII which is regarded (in the conceptualizing of Woolsey 1952) as the second sensorimotor area in the cerebellum. Cognitive paradigms activate topographically distinct regions within the cerebellar posterior lobe. Lobules VI and crus I are engaged in language and verbal working memory; lobule VI in spatial tasks; lobules VI, crus I and VIIB are activated by executive functions such as working memory, planning, organizing and strategy formation; and vermal lobules VI and VII are involved in emotional processing. Language is heavily right lateralized and spatial functions left-lateralized, reflecting crossed cerebro-cerebellar projections. Hemispheric lobules VI, crus I and VIIB appear to be involved in encoding generalized aversive processing. Threatening stimuli such as noxious heat and viewing unpleasant pictures activate these cerebellar regions together with limbic system structures – the anterior hypothalamus, subgenual anterior cingulate cortex and parahippocampal gyrus (Moulton et al 2011). There are fine-scale gradients within different cognitive networks, exemplified by the dorsal attention system. Visual working memory is encoded in hemisphere lobule VIIB, with spatial encoding (location of the stimulus) represented in medial portions of the lobule whereas memory load (number of stimuli) is encoded more laterally (Brissenden et al 2018) (**Fig. 29.44B**). This pattern is reflected also within the intraparietal sulcus with which cerebellum is interconnected (Schmahmann and Pandya 1989), with

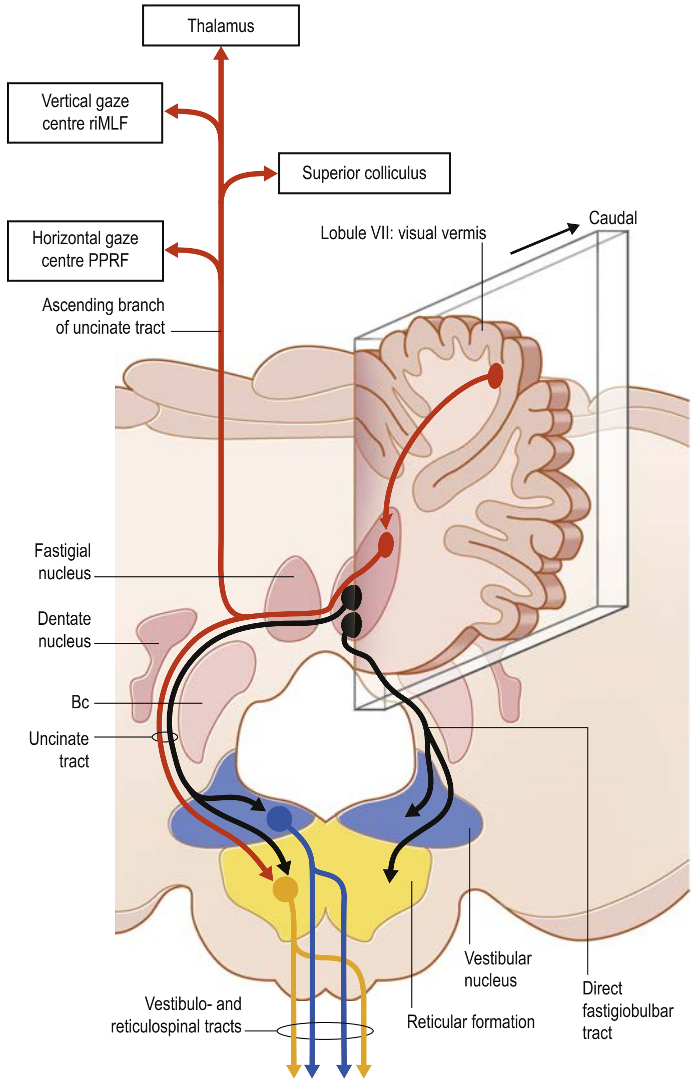
Thalamus
Vertical gaze centre riMLF
Superior colliculus
Horizontal gaze centre PPRF
Lobule VII: visual vermis
Caudal
Ascending branch of uncinate tract
Fastigial nucleus
Dentate nucleus
Bc
Uncinate tract
Vestibular nucleus
Direct fastigiobulbar tract
Vestibulo- and reticulospinal tracts
Reticular formation

Fig. 29.39 A transverse section through the cerebellum and medulla oblongata, showing the symmetrical distribution of the crossed and uncrossed connections of the fastigial nucleus. The inset depicts a sagittal section, showing the connections of the visual vermis (lobule VII) with the caudal pole of the fastigial nucleus and its efferent pathways in red. Abbreviations: Bc, brachium conjunctivum; PPRF, paramedian pontine reticular formation; riMLF, rostral interstitial nucleus of the medial longitudinal fasciculus.

more posterior parietal regions representing location and anterior regions representing load.

Voxel-based lesion symptom mapping following cerebellar stroke shows motor topography in the nuclei and in cerebellar cortex confined to lobules II through VI (Schoch et al 2006). The study of Stoodley et al (2016) confirmed the dichotomy of motor ataxia arising from damage to lobules IV through VI, whereas the cerebellar cognitive affective syndrome, but not motor ataxia, occurred following stroke in lobules crus II through lobule IX (crus I was largely spared in patients in this study) (**Fig. 29.44C**).

Task-based and rsfc-MRI studies using a large dataset accumulated in the Human Connectome Project (HCP) confirm the double motor representation in the anterior lobe and lobule VIII (Guell et al 2018a). They also confirm and extend the demonstration with rsfc-MRI (Buckner et al 2011) of a triple representation of cognitive domains in the cerebellar posterior lobe. These three representations are in (i) lobules VI-crus I, (ii) crus II-VIIB, and (iii) lobule IX (**Fig. 29.44D**). Studies of intrinsic cerebellar functional connectivity (Guell et al 2018b) further reveal that the cerebellum demonstrates the same kind of sensorimotor-to-cognition hierarchical gradient pattern (**Fig. 29.45**) that has previously been identified in the cerebral cortex (Mesulam 2000). These fundamental organizing principles of cerebellar structure and function dovetail with the deeper understanding of cerebellar clinical neurology and neuropsychiatry (Schmahmann et al 2019).

Modulating cerebellar circuits alters cerebral cortical connections and physiology

The cerebellar areas that are incorporated into neural circuits subserving higher order functions and emotion are functionally relevant. By stimulating the cerebellum non-invasively using transcranial magnetic stimulation (TMS) it is possible to demonstrate that cerebellar modulation of cerebral–cortical circuits is anatomically and functionally specific.

THE TRIAD OF CLINICAL ATAXIOLOGY IN RELATION TO NEUROANATOMY

Three major clinical syndromes can be identified following cerebellar lesions. They are the cerebellar motor syndrome (Holmes 1939), the vestibulocerebellar syndrome (Ito 1984, Barmack and Yakhnitsa 2013) and the cerebellar cognitive affective syndrome (Schmahmann and Sherman 1998), each of which has its own distinct anatomical signature in the cerebellum. These may occur individually or together depending on the location of the injury. The timing of the onset and progression of the underlying disorder also influence the nature and severity of the presentation.

Cerebellar motor syndrome

Available with the *Gray's Anatomy* e-book

Cerebellar vestibular syndrome and the oculomotor cerebellum

Available with the *Gray's Anatomy* e-book

Cerebellar cognitive affective syndrome

Available with the *Gray's Anatomy* e-book

Acknowledgements

Supported in part by NIH 1U01NS104326-01 and 1R01NS080816-01A1, the National Ataxia Foundation, Ataxia Telangiectasia Children's Project and the MINDlink Foundation.

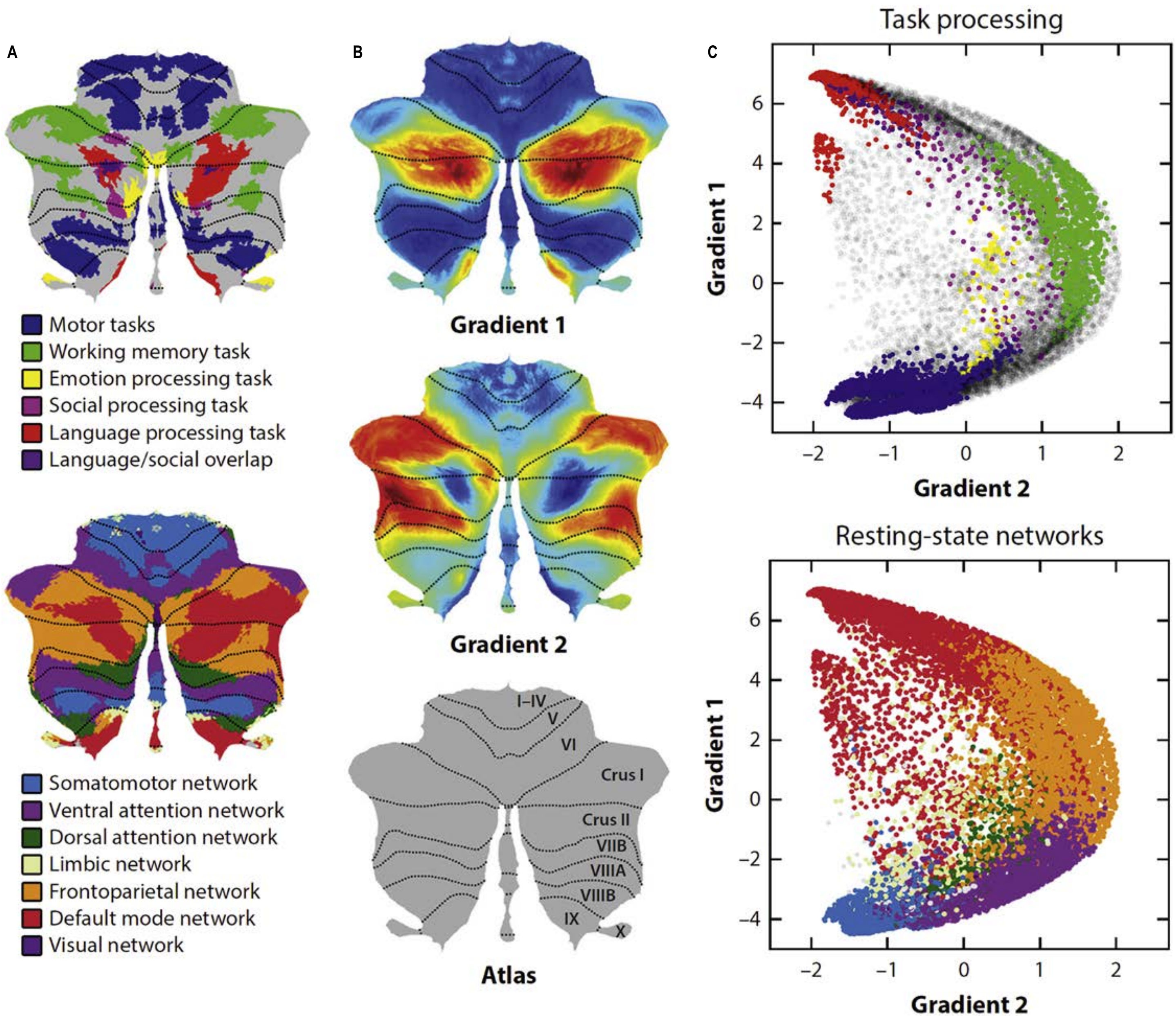

Fig. 29.45 Functional gradients of the human cerebellum. **A**, Discrete task activity maps and resting-state maps. **B**, Cerebellar gradients 1 and 2 and the cerebellum flatmap atlas. **C**, Voxel map along gradients 1 and 2. Gradient 1 extends from the language task/default mode network to motor regions, and gradient 2 isolates working memory/frontoparietal network areas. Each dot corresponds to a cerebellar voxel. The position of each dot along the x- and y-axes corresponds to the position along gradient 1 and gradient 2 for that cerebellar voxel. The colour of the dot corresponds to the task activity (top) or resting-state network (bottom) associated with that voxel. (A, Discrete task activity maps adapted from Guell et al 2018a, resting-state maps adapted from Buckner et al 2011; C, adapted from Guell et al 2018b. Reproduced with permission from Schmahmann JD, Guell XP, Stoodley CJ et al 2019 The theory and neuroscience of cerebellar cognition. Annu Rev Neurosci 42:337–64.)

Intermittent theta-burst TMS, which produces excitation, applied to vermal lobule VII results in increased connectivity within the dorsal attention network, but when applied to lateral parts of crus I/II it leads to increased connectivity in the default network (Halko et al 2014) (see Fig. 29.4). Inhibition-inducing continuous theta-burst TMS applied to lateral cerebellar hemisphere produces decreased functional connectivity with frontal and parietal cognitive regions, but connectivity with motor regions remains unaltered (Rastogi et al 2017). Cerebellar stimulation with intermittent theta-burst TMS has the shared physiological effect of increasing the temporal complexity of the cerebral cortical EEG pattern, but in a network-specific manner: vermal stimulation impacts high-beta/low-gamma-range oscillations, whereas lateral stimulation impacts low-theta and high-gamma-range oscillations (Farzan et al 2016). These TMS studies provide experimental evidence for the dysmetria of thought and universal cerebellar transform theories (Schmahmann 1991, 2000) that different subregions of the cerebellum modulate different cerebral cortical networks, and that the underlying nature of the cerebellar physiological effects on these different networks is similar.

The cerebellar motor syndrome, previously regarded as the sole manifestation of cerebellar disruption, is characterized by disturbed initiation, rate, rhythm and force of voluntary movements, the underlying basis of the incoordination (or ataxia, Greek, lack of order). Cerebellar lesions do not produce weakness but resting motor tone in pure cerebellar disease is decreased (hypotonic).

The somatotopy identified in experimental animal models and in functional imaging studies in healthy humans is reflected in structure–function correlation studies using voxel-based morphometry and lesion symptom mapping in patients with focal cerebellar lesions. Patients with lesions to the anterior cerebellar lobe and vermis often present with ataxia that may affect speech and deglutition, core muscles of the trunk and movement of their upper and lower limbs.

Speech is slurred, syllables are poorly articulated, cadence is slow and irregular, and rapid alternating buccal, palatal and lingual consonants are degraded. Dysarthria is compounded by impaired volume control, which is inconstant and not well modulated. Scanning speech was an older term to describe cerebellar dysarthria, but it does not fully capture the range of the characteristic deficits. Dysarthria in cerebellar developmental disorders differs in quality from that of the acquired and neurodegenerative ataxias, with a persistent childlike quality, as well as impaired prosody (the use of vocal intonation, stress and cadence). Cerebellar disorders affect the control of breathing, and ataxic respiration further degrades the quality of speech. Impaired control of the muscles of deglutition predisposes to dysphagia (impaired swallowing), causing choking on liquids and solids and the risk of aspiration pneumonia.

Truncal ataxia occurs with midline lesions, including titubation, or oscillation of the head and trunk. The patient with cerebellar ataxia has a widened stance and difficulty standing. In mild instances there is inability to stand in the tandem position, and in progressively more severe ataxia, inability to stand with the feet in parallel, or in the natural position, eventually needing to hold on to stationary objects or another person in order to stand. The cerebellar ataxic gait is staggering, uneven, irregular, and veers from side to side. Unilateral lesions cause stumbling towards the affected side.

Dysmetria (Greek, disordered timing or measurement) refers to the impaired ability to judge, regulate and control behaviour. It applies to both the motor and cognitive domains. Upper limb dysmetria is identified with tests such as the finger to nose test, or rapid finger following/mirror test, rapid alternating movements, and tests of finger dexterity such as tapping the index finger on the crease of the thumb. These reveal inaccurate and clumsy movements, jerking trajectory, overshooting (hypermetria) and undershooting the target (hypometria), oscillation at the fingers and wrists as well as more proximally at the elbows and shoulders when more severe, as well as overshoot, rebound and dysdiadochokinesis (dysrhythmic attempts at rapid alternating movements). Finger and hand dexterity for compound movements involving more than one joint are particularly affected. Lower limb dysmetria tested with the heel-to-shin test, reveals proximal overshoot as the heel is placed on the opposite knee, tremor of the heel on the knee, and slowing, jerking, or side-to-side movements as the heel moves down the shin. The attempt to draw a circle in the air with the legs is degraded by decomposition manifested as irregular or chaotic motions.

Postural tremor may be present in the arms, usually with activation. Cerebellar tremor is large amplitude, 2–3 Hz, and may involve many body parts. Rubral tremor from red nucleus lesions and its connections involves multiple joints, change directions and is frequently rotatory. Palatal tremor is slow and semi-rhythmic, resulting from lesions affecting the Guillain–Mollaret triangle (red nucleus – inferior olivary nucleus – deep cerebellar nuclei).

Ataxia rating scales assess and measure these areas of impairment, i.e. stance, gait, upper and lower limb control, and speech. Oculomotor deficits reflecting involvement of the vestibulocerebellum are also measured. The scales commonly in use are the International Cooperative Ataxia Rating Scale (ICARS: Trouillas et al 1997), the Friedreich's Ataxia Rating Scale (FARS: Subramony et al 2005), the Scale for Assessment and Rating of Ataxia (SARA: Schmitz-Hübsch et al 2006), and the Brief Ataxia Rating Scale (BARS: Schmahmann et al 2009).

The flocculus and the nodulus are known as the vestibulocerebellum because they maintain afferent and efferent connections with the vestibular system. They also belong to the functionally more comprehensive oculomotor division of the cerebellum, which includes lobule VII (visual vermis), uvula (dorsal vermal lobule IX), the ventral paraflocculus (the human accessory paraflocculus) and the dorsal paraflocculus (the human tonsil, particularly hemispheric lobule IX). The mossy fibre projection of the nucleus prepositus hypoglossi, a key element in the saccade-producing system, outlines the entire oculomotor cerebellum, with the exception of the dorsal paraflocculus (Belknap and McCrea 1988) (**Fig. 29.46**). The functions of the nodulus (vermal lobule X) are not exclusively oculomotor: it also influences labyrinthine and postural reflexes and vegetative systems.

The oculomotor cerebellum is involved in long-term adaptation of saccades, ocular stabilization reflexes and smooth pursuit (reviewed in Voogd et al (2012)) that permit bringing and maintaining images of objects of interest on the fovea. The flocculus/paraflocculus supports brief, high-frequency vestibular responses, sustained pursuit eye movements and gaze holding. The nodulus/ventral uvula enables sustained, low-frequency vestibular responses. The dorsal oculomotor vermis and its target in the posterior portion of the fastigial nucleus (the fastigial oculomotor region) are essential for saccades and the initiation of pursuit eye movements (Kheradmand and Zee 2011).

The vestibulo-ocular reflex (VOR) is an ancient reflex, present in both fishes and agnatha (jawless fish). It stabilizes the position of the retina in space during movements of the head by rotating the eyeball in the opposite direction. It is an open reflex, meaning that there is no time for a feedback connection that would compensate for inaccuracies in the execution of the reflex. This function is undertaken by the long-term adaptation of the reflex by the flocculus. The circuitry of the flocculus, similar to the vestibuloocular reflex, is organized on the coordinate system of the semicircular canals (Simpson and Graf 1981, Barmack and Yakhnitsa 2013). The vestibulo-ocular reflex consists of different components. One component connects the lateral (horizontal) semicircular canal, via oculomotor neurones in the vestibular nuclei, with the oculogyric muscles that move the eyes in a plane colinear with the plane of the lateral canal (see Fig. 29.40). The anterior semicircular canal influences the ipsilateral superior oblique and the contralateral inferior oblique muscles that move the eye in the plane of this canal.

Stroke in the territory of the posterior inferior cerebellar artery results in infarction of the vestibulocerebellum–flocculonodular region and lobule IX, producing abrupt-onset severe vertigo (sensation of movement in the absence of stimulus), almost always with nausea and vomiting. The vertigo makes it impossible to walk at the time of the acute event, but if the cerebellar motor areas are not damaged, there is no dysmetria of the limbs or dysarthria. Oculomotor abnormalities from cerebellar lesions produce visual disturbances including diplopia, oscillopsia and a sense of dysequilibrium. The range, complexity and varying combinations of oculomotor abnormalities on examination include deficits in gaze holding, reflex pursuit eye movements, voluntary initiation and direction of saccadic eye movements, and spontaneous or gaze-evoked nystagmus. The condition of isolated downbeat nystagmus, linked to a potassium channelopathy of the flocculonodular system, produces a cautious and unstable gait, likely a result of mismatched visual–vestibular interaction. Opsoclonus myoclonus syndrome is a dramatic impairment of oculomotor control with chaotic eye movements in horizontal and vertical directions in primary position, a heralding sign of a paraneoplastic syndrome that may be observed in neoplasms such as hypernephroma of the kidney in children, and the anti-Yo antibody syndrome directed at Purkinje cells in Hodgkin's lymphoma and breast, ovarian and lung carcinomas.

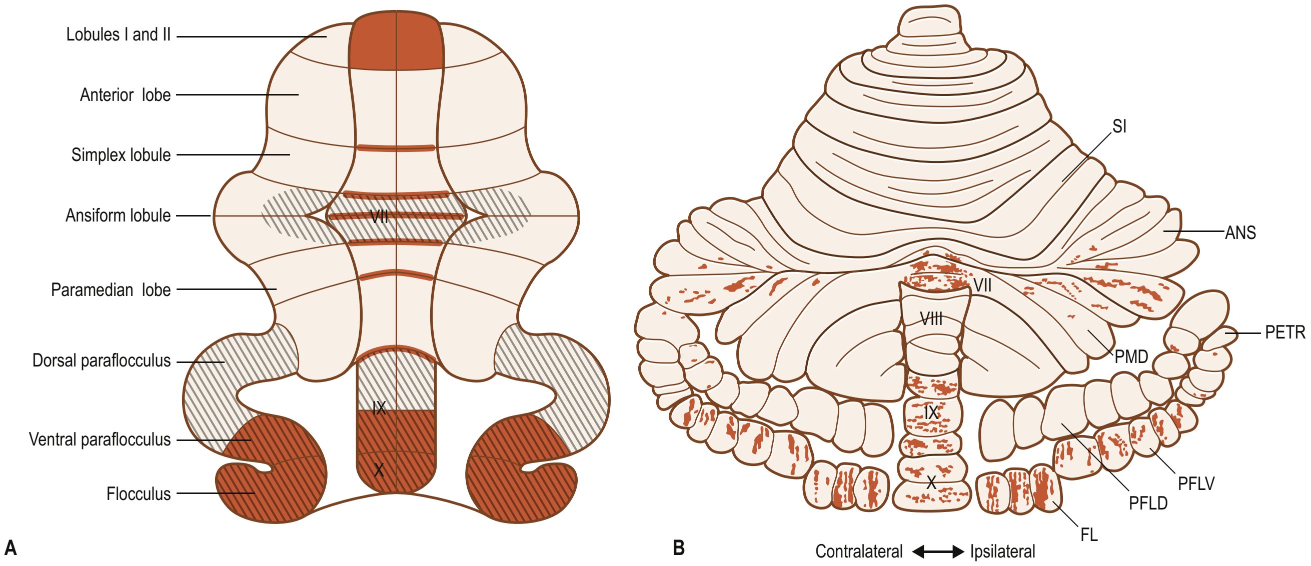

Fig. 29.46 **A**, A flattened map of the cerebellar cortex of the mammalian cerebellum showing the distribution of vestibulocerebellar mossy fibres in orange. The hatched lobules belong to the oculomotor cerebellum. **B**, The distribution of mossy fibres originating from the nucleus prepositus hypoglossi outlines the oculomotor cerebellum of the squirrel monkey, with the exception of the dorsal paraflocculus (PFLD). Other abbreviations: ANS, ansiform lobule; FL, flocculus; PETR, petrosal lobule; PFLV, ventral paraflocculus; PMD, paramedian lobule; SI, simplex lobule; VII–X, lobules VII–X. (With permission from Belknap DB, McCrea RA 1988 Anatomical connections of the prepositus and abducens nuclei in the squirrel monkey. J Comp Neurol 268:13–28.)

The cerebellar cognitive affective syndrome (CCAS) is characterized by impairments in executive function (planning, set-shifting, abstract reasoning, verbal fluency, working memory), often with perseveration, distractibility or inattention; visual–spatial disorganization and impaired visual–spatial memory; difficulties with language production including dysprosodia, agrammatism and mild anomia (Schmahmann and Sherman 1998). Language problems also include decreased verbal fluency (Molinari et al 1997), inability to detect one's own errors in tasks such as the verb-for-noun generation paradigm (Fiez et al 1992, Stoodley and Schmahmann 2009b), and impaired metalinguistics, the use of language for the purpose of social communication (Mariën et al 2014, Guell et al 2015). Personality changes include blunting of affect or disinhibited and inappropriate behaviour, particularly following lesions of the vermis (the putative limbic cerebellum). The affective symptoms include impaired emotional and attentional control, and abnormal social skills that resemble symptoms typical of autism spectrum disorder and psychosis (Schmahmann et al 2007). The net effect of these disturbances in cognitive abilities is a general lowering of intellectual function. The CCAS arises from damage to the cognitive cerebellum in the cerebellar posterior lobe (lobules VI, VII, probably lobule IX), and is postulated to reflect dysmetria of thought analogous to the dysmetria of motor control from damage to the sensorimotor cerebellum (Schmahmann 1991, 1996, 2010, Schmahmann and Sherman 1998, Stoodley and Schmahmann 2009a, 2010, Stoodley et al 2012, 2016). The CCAS may occur separately or together with the cerebellar motor syndrome and the vestibular syndrome. It has been regarded as the third cornerstone of clinical ataxiology and eponymously named Schmahmann's syndrome (Manto and Mariën 2015, Argyropoulos et al 2020). The defining features of the CCAS occur across disease types and in children as well as adults; a developmental form of the CCAS is present in children with hereditary or congenital disorders. The syndrome of paediatric postoperative cerebellar mutism, likely a profound apraxia of speech, may occur together with the CCAS as a consequence of accidental damage to cerebellar outflow pathways (the deep nuclei and the superior cerebellar peduncle) during surgery to remove posterior fossa tumours (Wisoff and Epstein 1984, Rekate et al 1985, Gudrunardottir et al 2016, Albazron et al 2019, Schmahmann 2020).

The affective component of the CCAS has been conceptualized as an acquired impairment of those functions commonly affected in neurodevelopmental disorders such as autism spectrum and schizophrenia (Schmahmann et al 2007, Van Overwalle et al 2015). Conversely, cerebellar abnormalities are increasingly reported in neuropsychiatric conditions including schizophrenia, autism and depression (Schmahmann 1991, Fatemi et al 2012, Baumann et al 2015). The maturing field of the cognitive neuroscience of the cerebellum is addressing these possibilities in studies of complex behavioural repertoires that are far removed from sensorimotor domains, demonstrating, for example, granule cell activation during conditions of reward (Wagner et al 2017) and social cognition (Carta et al 2019), and elucidating the role of the cerebellum in learning and memory (Thompson 1983, Freeman 2015), fear conditioning (Supple and Leaton 1990) and empathy (Schmahmann et al 2007, Koziol et al 2013).

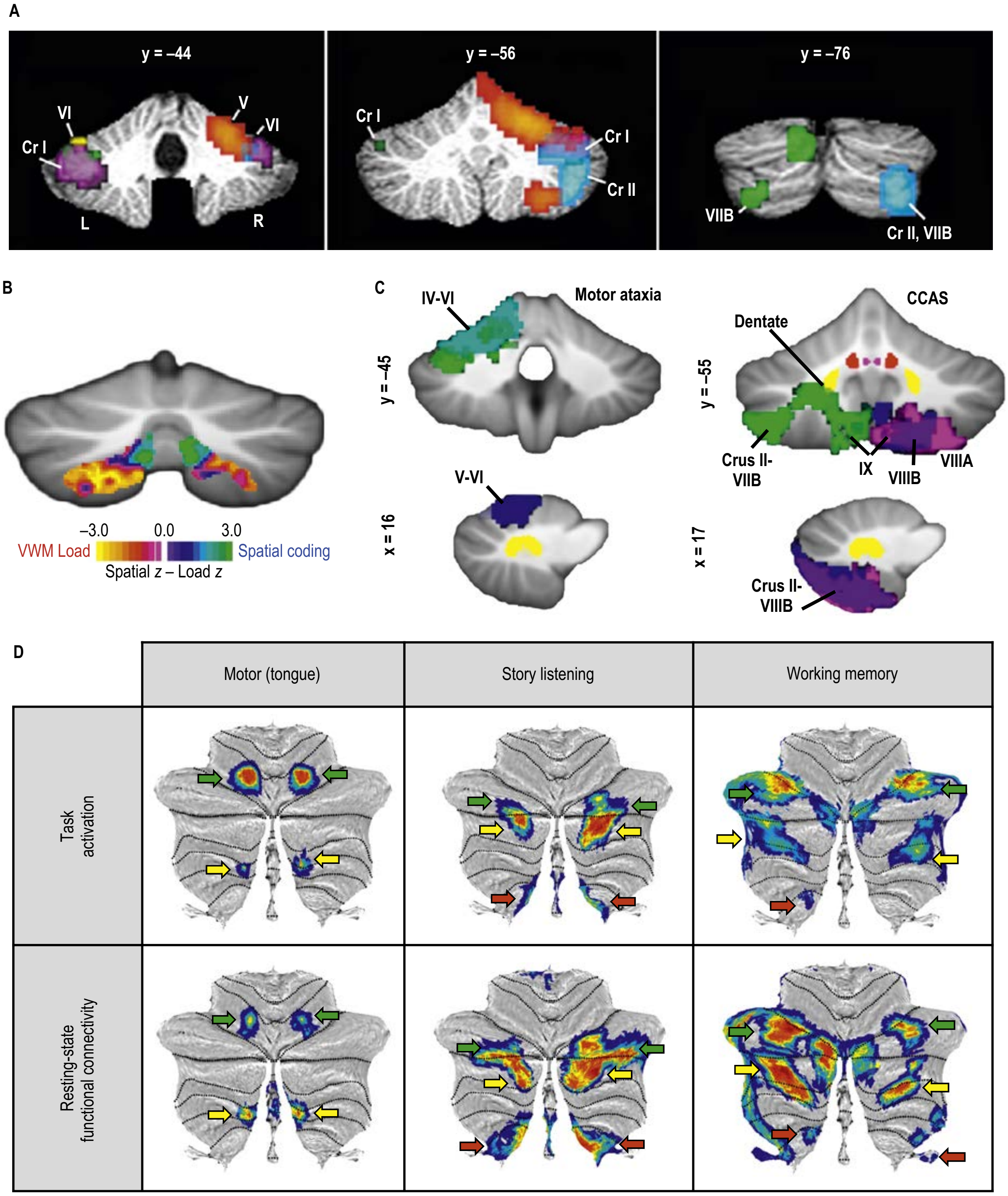
A
y = –44
VI
V
VI
Cr I
L
R
y = –56
Cr I
Cr I
Cr II
y = –76
VIIB
Cr II, VIIB
B
–3.0
0.0
3.0
VWM Load
Spatial coding
Spatial z – Load z
C
IV-VI
Motor ataxia
y = –45
V-VI
x = 16
CCAS
Dentate
y = –55
Crus II-VIIB
IX
VIIIB
VIIIA
x = 17
Crus II-VIIIB
D
Motor (tongue)
Story listening
Working memory
Task activation
Resting-state functional connectivity

Fig. 29.44 Functional topography of the human cerebellum. **A**, Intraindividual topography of task-based activations in the cerebellum for finger tapping (red), working memory (purple), verb generation (blue) and mental rotation (green) (Stoodley et al 2010). **B**, Spatial gradients within the dorsal attention network in lobule VIIB on a working memory task. The locus of spatial attention encoding is medially situated; attentional load content is more lateral. This gradient of activity also exists within the cortical dorsal attention network (not shown). **C**, In patients with stroke, lesions of lobules IV–V of the anterior lobe extending into adjacent lobule VI produce the cerebellar motor syndrome of ataxia. Lesions confined to posterior lobe lobules crus II through lobule IX produce the cerebellar cognitive affective/Schmahmann syndrome but no motor ataxia. **D**, Task and resting-state activation topography in motor and nonmotor domains. Task activation (top row) reveals a pattern of two motor (first column) and three nonmotor representations (second and third columns). An overlapping pattern was observed when calculating resting-state functional connectivity from cerebral cortical activation peaks for each corresponding task activity contrast (bottom row). First motor (lobules I–VI) or first nonmotor representation (VI/crus I) (green arrows), second motor (VIII) or second nonmotor representation (crus II/lobule VIIB) (yellow arrows), and third nonmotor representation (IX/X) (red arrows) are shown. First and second nonmotor representations can be contiguous (as in story listening) or separate (as in working memory). Abbreviations: CCAS, cerebellar cognitive affective syndrome; Cr, crus; L, left; R, right; VWM, verbal working memory. (B, Adapted from Brissenden et al (2018); C, adapted from Stoodley et al (2016); D, adapted from Guell et al (2018a, reproduced with permission from Schmahmann JD, Guell XP, Stoodley CJ et al 2019 The theory and neuroscience of cerebellar cognition. Annu Rev Neurosci 42:337–64)

Bonus e-book content

Fig. 29.4 Cerebellar nomenclature.

Fig. 29.5 The relationship of the named cerebellar fissures to the lobules in the vermis and hemispheres.

Fig. 29.6 Historically relevant figure that depicts Bolk's (1906) prototype for his ground plan of the mammalian cerebellum.

Fig. 29.13 Camera lucida drawings: Golgi-impregnated molecular layer interneurones.

Fig. 29.14 Camera lucida drawings: Golgi-impregnated neurones in the granular layer.

Fig. 29.15 Camera lucida drawing: a Golgi-impregnated Lugaro cell. Confocal microscopic image: a Lucifer yellow-filled unipolar brush cell.

Fig. 29.16 Camera lucida drawing: Golgi-impregnated epithelial cells.

Fig. 29.20 Camera lucida drawing: a Golgi-impregnated climbing fibre entering the white matter.

Fig. 29.23 A transverse section through the cerebellum of a 65 mm human fetus, showing the Purkinje cell clusters that will develop into the A, B, C1–C3 and D Purkinje cell zones.

Fig. 29.26 Trajectory and organization of fibres from the parietal, temporal and occipital association areas coursing toward the white matter above and medial to the midportion of the lateral geniculate nucleus before descending into the cerebral peduncle.

Fig. 29.27 Composite summary diagrams: topographic organization of the superior temporal, parietal, occipital, and posterior parahippocampal corticopontine fibre systems as they descend from the posterior aspect of the internal capsule above the midpoint of the lateral geniculate nucleus into the rostral part of the cerebral peduncle.

Fig. 29.28 Cerebral cortical origins of cerebral peduncle fibres in human and monkey revealed by diffusion tractography MRI.

Fig. 29.29 Composite colour-coded summary diagram: projections to the basis pontis from motor and supplementary motor cortices in the rhesus monkey.

Fig. 29.30 Topographic map: motor representations in the human basis pontis.

Fig. 29.31 Composite colour-coded summary diagram: distribution in the basis pontis of the rhesus monkey of projections derived from association and paralimbic cortices in the prefrontal, posterior parietal, superior temporal and parastriate and parahippocampal regions, and from motor, premotor and supplementary motor areas.

Fig. 29.32 Intrapontine course of pontocerebellar fibres in *Macaca mulatta*.

Fig. 29.33 Distribution of labelled neurones in the basilar pons following injection of a tracer substance (wheatgerm agglutinin–horseradish peroxidase (WGA–HRP)) into crus I anterior of hemisphere lobule VIIA of a rhesus monkey cerebellum.

Fig. 29.40 The circuitry used by the flocculus in long-term adaptation of the vestibulo-ocular reflex.

Fig. 29.41 The localization of the central tegmental tract in the pontine tegmentum.

Fig. 29.42 The cerebello-thalamo-cortical pathways.

Fig. 29.43 Map of the topographical correlations between remote, functionally coupled regions in the human cerebral cortex and the cerebellum using resting state functional connectivity fMRI.

Fig. 29.45 Functional gradients of the human cerebellum.

Fig. 29.46 **A**, A flattened map of the mammalian cerebellar cortex showing the distribution of vestibulocerebellar mossy fibres. **B**, The distribution of mossy fibres originating from the nucleus prepositus hypoglossi outlines the oculomotor cerebellum of the squirrel monkey, with the exception of the dorsal paraflocculus.

Key references

Courville J, de Montigny C, Lamarre Y (eds) 1980 The Inferior Olivary Nucleus: Anatomy and Physiology. New York, Raven Press.
An edited volume of authoritative studies on the inferior olivary nucleus.

Dow RS, Moruzzi G 1958 The Physiology and Pathology of the Cerebellum. Minneapolis: University of Minnesota Press.
A major earlier reference work on cerebellar anatomy, physiology and pathology.

Holmes G 1939 The cerebellum of man (Hughlings Jackson memorial lecture). Brain 62:1–30.
The understanding of clinical motor ataxiology derives in large part from these landmark observations and contributions.

Ito M 1984 The Cerebellum and Neural Control. New York: Raven Press.
An authoritative and influential monograph on cerebellar anatomy and physiology.

Larsell O, Jansen J 1972 The Comparative Anatomy and Histology of the Cerebellum. The Human Cerebellum, Cerebellar Connections, and Cerebellar Cortex. Minneapolis: University of Minnesota Press.
The definitive work on comparative anatomy of the cerebellum. It builds on earlier work (Larsell 1970) on lower vertebrates through the great apes.

Manto M, Gruol DL, Schmahmann JD et al (eds) 2013 Handbook of the Cerebellum and Cerebellar Disorders. New York: Springer-Verlag.
The most comprehensive (4-volume) text currently available covering all aspects of cerebellar neuroscience and clinical neurology.

Palay S, Chan-Palay V 1974 Cerebellar Cortex: Cytology and Organization. New York: Springer-Verlag.
A monograph that details the organization and cytoarchitecture of the cerebellar cortex and its neuronal elements.

Schmahmann JD (ed) 1997 The Cerebellum and Cognition. Int Rev Neurobiol Vol. 41. San Diego: Academic Press.
The anatomical, theoretical and clinical foundations of the cerebellar contribution to cognition and emotion. More recent review papers are in the literature.

Schmahmann JD, Doyon J, Toga A et al 2000 MRI Atlas of the Human Cerebellum. San Diego: Academic Press.
The MRI Atlas identifies cerebellar lobules and fissures in stereotaxic coordinate space, and harmonizes earlier nomenclatures with the current modified Larsell terminology.

Voogd J 2004 Cerebellum and precerebellar nuclei. In: Paxinos G, Mai JK (eds) The Human Nervous System. Amsterdam: Elsevier, Academic Press, pp. 321–92.
The detailed elucidation of the zonal organization of the cerebellum and cerebellar corticonuclear relations is well laid out in this chapter by a contemporary pioneer in cerebellar anatomy.

References

Akkal D, Dum RP, Strick PL 2007 Supplementary motor area and presupplementary motor area: targets of basal ganglia and cerebellar output. J Neurosci 27:10659–73.

Albazron FM, Bruss J, Jones RM et al 2019 Pediatric postoperative cerebellar cognitive affective syndrome follows outflow pathway lesions. Neurology 93:e1561–71.

Altman J, Bayer SA 1977 Time of origin and distribution of a new cell type in the rat cerebellar cortex. Exp Brain Res 29:265–74.

Andersen K, Andersen BB, Pakkenberg B 2012 Stereological quantification of the cerebellum in patients with Alzheimer's disease. Neurobiol Aging 33:197.

Andersson G, Oscarsson O 1978 Climbing fibre microzones in cerebellar vermis and their projection to different groups of cells in the lateral vestibular nucleus. Exp Brain Res 32:565–79.

Argyropoulos GPD, van Dun K, Adamaszek M et al 2020 The Cerebellar Cognitive Affective/Schmahmann Syndrome: a Task Force Paper. Cerebellum 19:102–25.

Babinski J 1899 De l'asynergie cérébelleuse. Revue Neurologique 7:806–16.

Bagnall MW, Zingg B, Sakatos A et al 2009 Glycinergic projection neurones of the cerebellum. J Neurosci 29:10104–10.

Barmack NH, Yakhnitsa V 2013 Vestibulocerebellar connections. In: Manto M, Gruol DL, Schmahmann JD et al (eds) Handbook of the Cerebellum and Cerebellar Disorders. New York: Springer-Verlag, pp. 357–75.

Batton RR 3rd, Jayaraman A, Ruggiero D et al 1977 Fastigial efferent projections in the monkey: an autoradiographic study. J Comp Neurol 174:281–305.

Baumann O, Borra RJ, Bower JM et al 2015 Consensus paper: the role of the cerebellum in perceptual processes. Cerebellum 14(2):197–220.

Belknap DB, McCrea RA 1988 Anatomical connections of the prepositus and abducens nuclei in the squirrel monkey. J Comp Neurol 268:13–28.

Bentivoglio M, Kuypers HG 1982 Divergent axon collaterals from rat cerebellar nuclei to diencephalon, mesencephalon, medulla oblongata and cervical cord. A fluorescent double retrograde labeling study. Exp Brain Res 46:339–56.

Berlucchi G 2002 The origin of the term plasticity in the neurosciences: Ernesto Lugaro and chemical synaptic transmission. J Hist Neurosci 11:305–9.

Bolk L 1906 Das Cerebellum der Säugetiere. Haarlem: Fischer.
A classic text on the subdivision and the comparative anatomy of the mammalian cerebellum.

Braak E, Braak H 1993 The new monodendritic neuronal type within the adult human cerebellar granule cell layer shows calretinin-immunoreactivity. Neurosci Lett 154:199–202.

Braitenberg V, Atwood RP 1958 Morphological observations on the cerebellar cortex. J Comp Neurol 109:1–33.

Brissenden JA, Tobyne SM, Osher DE et al 2018 Topographic cortico-cerebellar networks revealed by visual attention and working memory. Curr Biol 28:3364–672 e5.

Brodal P 1978 The corticopontine projection in the rhesus monkey. Origin and principles of organization. Brain 101:251–83.

Brodal A 1981 Neurological anatomy in relation to clinical medicine. New York: Oxford University Press.

Brown S 1892 On hereditary ataxia, with a series of twenty-one cases. Brain 15:250–82.

Buckner RL, Krienen FM, Castellanos A et al 2011 The organization of the human cerebellum estimated by intrinsic functional connectivity. J Neurophysiol 106:2322–45.

Carta I, Chen CH, Schott AL et al 2019 Cerebellar modulation of the reward circuitry and social behavior. Science 363(6424):eaav0581. doi: 10.1126/science.aav0581.

Chambers WW, Sprague JM 1955a Functional localization in the cerebellum. I. Organization in longitudinal cortico-nuclear zones and their contribution to the control of posture, both extrapyramidal and pyramidal. J Comp Neurol 103:105–29.

Chambers WW, Sprague JM 1955b Functional localization in the cerebellum. II. Somatotopic organization in cortex and nuclei. AMA Arch Neurol Psychiatry 74:653–80.

Chan-Palay V 1977 Cerebellar dentate nucleus: organization, cytology and transmitters. Berlin: Springer-Verlag.

Clower DM, West RA, Lynch JC et al 2001 The inferior parietal lobule is the target of output from the superior colliculus, hippocampus, and cerebellum. J Neurosci 21:6283–91.

Cohen D, Yarom Y 1998 Patches of synchronized activity in the cerebellar cortex evoked by mossy-fibre stimulation: questioning the role of parallel fibres. Proc Natl Acad Sci USA 95:15032–6.

Courville J, de Montigny C, Lamarre Y (eds) 1980 The Inferior Olivary Nucleus: Anatomy and Physiology. New York, Raven Press.
An edited volume of authoritative studies on the inferior olivary nucleus.

D'Angelo E, Rossi P, Gall D et al 2005 Long-term potentiation of synaptic transmission at the mossy fibre-granule cell relay of cerebellum. Prog Brain Res 148:69-80.

Demolé V 1927a Structure et connexions des noyeaux dentelés du cervelet. I. Schweiz Arch Psychiat Neurol 20:271–94.

Demolé V 1927b Structure et connexions des noyeaux dentelés du cervelet. II. Schweiz Arch Psychiat Neurol 21:73–110.

De Zeeuw CI, Hoogland TM 2015 Reappraisal of Bergmann glial cells as modulators of cerebellar circuit function. Front Cell Neurosci 9:246.

Diedrichsen J, Balsters JH, Flavell J et al 2009 A probabilistic MR atlas of the human cerebellum. Neuroimage 46:39–46.

Diedrichsen J, Maderwald S, Küper M et al 2011 Imaging the deep cerebellar nuclei: a probabilistic atlas and normalization procedure. Neuroimage 54:1786–94.

Dieudonné S 2001 Serotonergic neuromodulation in the cerebellar cortex: cellular, synaptic, and molecular basis. Neuroscientist 7:207–19.

Dow RS 1974 Some novel concepts of cerebellar physiology. Mt Sinai J Med 41:103–19.

Dow RS, Moruzzi G 1958 The Physiology and Pathology of the Cerebellum. Minneapolis: University of Minnesota Press.
A major earlier reference work on cerebellar anatomy, physiology and pathology.

Dugué GP, Brunel N, Hakim V et al 2009 Electrical coupling mediates tunable low-frequency oscillations and resonance in the cerebellar Golgi cell network. Neurone 61:126-39.

Dum RP, Strick PL 2003 An unfolded map of the cerebellar dentate nucleus and its projections to the cerebral cortex. J Neurophysiol 89:634–9.

Eccles J, Ito M, Szentagothai J 1967 The Cerebellum as a Neuronal Machine. New York and Heidelberg: Springer-Verlag.

Ekerot CF, Jörntell H 2003 Parallel fibre receptive fields: a key to understanding cerebellar operation and learning. Cerebellum 2:101–9.

Ekerot CF, Larson B 1972 Differential termination of the exteroceptive and proprioceptive components of the cuneocerebellar tract. Brain Res 36:420–4.

Ekerot CF, Larson B 1979a The dorsal spino-olivocerebellar system in the cat. I. Functional organization and termination in the anterior lobe. Exp Brain Res 36:201–17.

Ekerot CF, Larson B 1979b The dorsal spino-olivocerebellar system in the cat. II. Somatotopical organization. Exp Brain Res 36:219–32.

Ekerot CF, Larson B 1980 Termination in overlapping sagittal zones in cerebellar anterior lobe of mossy and climbing fibre paths activated from dorsal funiculus. Exp Brain Res 38:163–72.

Farzan F, Vernet M, Shafi MM et al 2016 Characterizing and modulating brain circuitry through transcranial magnetic stimulation combined with electroencephalography. Front Neural Circuits 10:73.

Fatemi SH, Aldinger KA, Ashwood P et al 2012 Consensus paper: pathological role of the cerebellum in autism. Cerebellum 11(3):777–807.

Fiez JA, Petersen SE, Cheney MK et al 1992 Impaired non-motor learning and error detection associated with cerebellar damage. A single case study. Brain 115 Pt 1:155–78.

Flourens P 1824 Recherches expérimentales sur les propriétés et les fonctions du système nerveux, dans les animaux vertébrés. Paris: Crevot.

Fox CA, Barnard JW 1957 A quantitative study of the Purkinje cell dendritic branchlets and their relationship to afferent fibres. J Anat 91:299–313.

Fox CA, Snider RS (eds) 1967 The Cerebellum. Progress in Brain Research, vol. 25. Amsterdam: Elsevier.

Freeman JH 2015 Cerebellar learning mechanisms. Brain Res 1621:260–9.

Fujita H, Oh-Nishi A, Obayashi S et al 2010 Organization of the marmoset cerebellum in three-dimensional space: lobulation, aldolase C compartmentalization and axonal projection. J Comp Neurol 518:1764–91.

Galliano E, Baratella M, Sgritta M et al 2013 Anatomical investigation of potential contacts between climbing fibres and cerebellar Golgi cells in the mouse. Front Neural Circuits 7:59.

Gellman R, Houk JC, Gibson AR 1983 Somatosensory properties of the inferior olive of the cat. J Comp Neurol 215:228–43.

Glickstein M, May JG 3rd, Mercier BE 1985 Corticopontine projection in the macaque: the distribution of labelled cortical cells after large injections of horseradish peroxidase in the pontine nuclei. J Comp Neurol 235:343–59.

Glickstein M, Yeo C, Stein J (Eds.) 1987 Cerebellum and Neuronal Plasticity. New York: Plenum Press.

Groenewegen HJ, Voogd J, Freedman SL 1979 The parasagittal zonation within the olivocerebellar projection. II. Climbing fibre distribution in the intermediate and hemispheric parts of cat cerebellum. J Comp Neurol 183:551–601.

Gudrunardottir T, Morgan AT, Lux AL, et al 2016 Consensus paper on post-operative pediatric cerebellar mutism syndrome: the Iceland Delphi results. Childs Nerv Syst 32:1195–203.

Guell X, Hoche F, Schmahmann JD 2015 Metalinguistic deficits in patients with cerebellar dysfunction: empirical support for the dysmetria of thought theory. Cerebellum 14:50–8.

Guell X, Gabrieli JDE, Schmahmann JD 2018a Triple representation of language, working memory, social and emotion processing in the cerebellum: convergent evidence from task and seed-based resting-state fMRI analyses in a single large cohort. Neuroimage 172:437–49.

Guell X, Schmahmann JD, Gabrieli JDE et al 2018b Functional gradients of the cerebellum: a fundamental movement-to-thought principle. eLife 7. pii: e36652. doi: 10.7554/eLife.36652.

Habas C, Kamdar N, Nguyen D et al 2009 Distinct cerebellar contributions to intrinsic connectivity networks. J Neurosci 29:8586–94.

Haines DE, Dietrichs E, Mihailoff GA et al 1997 The cerebellar-hypothalamic axis: basic circuits and clinical observations. Int Rev Neurobiol 41:83–107.

Halko M, Farzan F, Eldaief M 2014 Intermittent theta-burst stimulation of the lateral cerebellum increases functional connectivity of the default network. J Neurosci 34:12049–56.

Hansel C, Linden DJ, D'Angelo E 2001 Beyond parallel fibre LTD: the diversity of synaptic and non-synaptic plasticity in the cerebellum. Nat Neurosci 4:467–75.

Hartmann-von Monakow K, Akert K, Kunzle H 1981 Projection of precentral, premotor and prefrontal cortex to the basilar pontine grey and to nucleus reticularis tegmenti pontis in the monkey (*Macaca fascicularis*). Schweiz Arch Neurol Neurochir Psychiatr 129:189–208.

Hashimoto M, Takahara D, Hirata Y et al 2010 Motor and non-motor projections from the cerebellum to rostrocaudally distinct sectors of the dorsal premotor cortex in macaques. Eur J Neurosci 31:1402–13.

Holmes G 1939 The cerebellum of man (Hughlings Jackson memorial lecture). Brain 62:1–30.

The understanding of clinical motor ataxiology derives in large part from these landmark observations and contributions.

Hoover JE, Strick PL 1999 The organization of cerebellar and basal ganglia outputs to primary motor cortex as revealed by retrograde transneuronal transport of herpes simplex virus type 1. J Neurosci 19:1446–63.

Hoshi E, Tremblay L, Féger J et al 2005 The cerebellum communicates with the basal ganglia. Nat Neurosci 8:1491–3.

Ito M 1982 Questions in modeling the cerebellum. J Theor Biol 99:81–6.

Ito M 1984 The Cerebellum and Neural Control. New York: Raven Press.

An authoritative and influential monograph on cerebellar anatomy and physiology.

Jansen A, Brodal A (eds) 1954 Aspects of cerebellar anatomy. Oslo: Johan Grundt Tanum Vorlag.

Jansen J, Brodal A 1940 Experimental studies on the intrinsic fibres of the cerebellum. II. The cortico-nuclear projection. J Comp Neurol 73:267–321.

Kelly RM, Strick PL 2003 Cerebellar loops with motor cortex and prefrontal cortex of a nonhuman primate. J Neurosci 23:8432–44.

Kheradmand A, Zee DS 2011 Cerebellum and ocular motor control. Front Neurol 2:53.

Korneliussen HK 1968 On the ontogenetic development of the cerebellum (nuclei, fissures, and cortex) of the rat, with special reference to regional variations in corticogenesis. J Hirnforsch 10:379–412.

Koziol LF, Budding D, Andreasen N et al 2013 Consensus paper: the cerebellum's role in movement and cognition. Cerebellum 13:151–77.

Krienen FM, Buckner RL 2009 Segregated fronto-cerebellar circuits revealed by intrinsic functional connectivity. Cereb Cortex 19: 2485–97.

Lainé J, Axelrad H 1996 Morphology of the Golgi-impregnated Lugaro cell in the rat cerebellar cortex: a reappraisal with a description of its axon. J Comp Neurol 375:618–40.

Lange W 1975 Cell number and cell density in the cerebellar cortex of man and some other mammals. Cell Tissue Res 157:115–24.

Langer TP 1985 Basal interstitial nucleus of the cerebellum: cerebellar nucleus related to the flocculus. J Comp Neurol 235:38–47.

Larsell O 1970 The Comparative Anatomy and Histology of the Cerebellum from Monotremes through Apes. Minneapolis: University of Minnesota.

Larsell O, Jansen J 1972 The Comparative Anatomy and Histology of the Cerebellum. The Human Cerebellum, Cerebellar Connections, and Cerebellar Cortex. Minneapolis: University of Minnesota Press.

The definitive work on comparative anatomy of the cerebellum. It builds on earlier work (Larsell 1970) on lower vertebrates through the great apes.

Lawrence DG, Kuypers HG 1968a The functional organization of the motor system in the monkey. I. The effects of bilateral pyramidal lesions. Brain 91:1–14.

Lawrence DG, Kuypers HG 1968b The functional organization of the motor system in the monkey. II. The effects of lesions of the descending brain-stem pathways. Brain 91:15–36.

Leiner HC, Leiner AL, Dow RS 1986 Does the cerebellum contribute to mental skills? Behav Neurosci 100:443–54.

Lemon RN, Landau W, Tutssel D et al 2012 Lawrence and Kuypers (1968a,b) revisited: copies of the original filmed material from their classic papers in Brain. Brain 135(Pt 7):2290–5.

Leznik E, Llinás R 2005 Role of gap junctions in synchronized neuronal oscillations in the inferior olive. J Neurophysiol 94(4):2447–56.

Llinas R, Sotelo C (eds) 1992 The Cerebellum Revisited. New York: Springer-Verlag.

Lu X, Miyachi S, Ito Y et al 2007 Topographic distribution of output neurones in cerebellar nuclei and cortex to somatotopic map of primary motor cortex. Eur J Neurosci 25:2374–82.

Luciani L 1891 Il cervelletto: nuovi studi Difisiologia normale e patologica. Florence: Le Monnier. Translated Brain (1982)15:283–99.

Lugaro E 1894a Sulle connessioni tra gli elementi nervosi della corteccia cerebellare con considerazioni generali sul significato fisiologico dei rapporti tra gli elementi nervosa. Riv Sper Fren Med Leg 20:297–331.

Lugaro E 1894b Ueber die Histogenese der Körner der Kleinhirnrinde. Anat Anz 9:710–13.

Lynch JC, Tian JR 2006 Cortico-cortical networks and cortico-subcortical loops for the higher control of eye movements. Prog Brain Res 151:461–501.

Lynch JC, Hoover JE, Strick PL 1994 Input to the primate frontal eye field from the substantia nigra, superior colliculus, and dentate nucleus demonstrated by transneuronal transport. Exp Brain Res 100:181–6.

Malacarne MVG 1776 Nuova Esposizione della Vera Struttura del Cervelletto Umano. Turin: Briolo.

Mann-Metzer P, Yarom Y 2000 Electrotonic coupling synchronizes interneurone activity in the cerebellar cortex. Prog Brain Res 124:115–22.

Manto M, Mariën P 2015 Schmahmann's syndrome – identification of the third cornerstone of clinical ataxiology. Cerebellum Ataxias 2:2.

Manto M, Gruol DL, Schmahmann JD (eds) 2013 Handbook of the Cerebellum and Cerebellar Disorders. New York: Springer-Verlag.

The most comprehensive (4-volume) text currently available covering all aspects of cerebellar neuroscience and clinical neurology.

Marek S, Siegel JS, Gordon EM et al 2018 Spatial and temporal organization of the individual human cerebellum. Neurone 100:1–17.

Marie P 1893 Sur l'hérédo-ataxie cérébelleuse. Sem Méd 13:444–7.

Mariën P, Ackermann H, Adamaszek M et al 2014 Consensus paper: Language and the cerebellum: an ongoing enigma. Cerebellum 13:386–410.

Marr D 1969 A theory of cerebellar cortex. J Physiol 202:437–70.

Matsushita M, Tanami T 1987 Spinocerebellar projections from the central cervical nucleus in the cat, as studied by anterograde transport of wheatgerm agglutinin–horseradish peroxidase. J Comp Neurol 266:376–97.

Mesulam M 2000 Principles of Behavior Neurology, 2nd ed. New York: Oxford University Press.

Middleton FA, Strick PL 1994 Anatomical evidence for cerebellar and basal ganglia involvement in higher cognitive function. Science 266(5184):458–61.

Middleton FA, Strick PL 1997 Cerebellar output channels. Int Rev Neurobiol 41:61–82.

Middleton FA, Strick PL 2001 Cerebellar projections to the prefrontal cortex of the primate. J Neurosci 21:700–12.

Molinari M, Leggio MG, Solida A et al 1997 Cerebellum and procedural learning: evidence from focal cerebellar lesions. Brain 120(Pt 10):1753–62.

Moulton EA, Elman I, Pendse G et al 2011 Aversion-related circuitry in the cerebellum: responses to noxious heat and unpleasant images. J Neurosci 31:3795–804.

Mugnaini E, Floris A 1994 The unipolar brush cell: a neglected neurone of the mammalian cerebellar cortex. J Comp Neurol 339:174–80.

Mugnaini E, Dino MR, Jaarsma D 1997 The unipolar brush cells of the mammalian cerebellum and cochlear nucleus: cytology and microcircuitry. Prog Brain Res 114:131–50.

Mugnaini E, Sekerkova G, Martina M 2011 The unipolar brush cell: a remarkable neurone finally receiving deserved attention. Brain Res Rev 66:220–45.

Napper RM, Harvey RJ 1988 Number of parallel fibre synapses on an individual Purkinje cell in the cerebellum of the rat. J Comp Neurol 274:168–77.

Nelson BJ, Adams JC, Barmack NH et al 1989 Comparative study of glutamate decarboxylase immunoreactive boutons in the mammalian inferior olive. J Comp Neurol 286:514–39.

Nietz AK, Vaden JH, Coddington LT et al 2017 Non-synaptic signaling from cerebellar climbing fibres modulates Golgi cell activity. eLife 6. pii: e29215. doi: 10.7554/eLife.29215.

Nieuwenhuys R, Voogd J, van Huijzen C 2008 The Human Nervous System, 4th ed. Berlin: Springer-Verlag.

Noda H, Sugita S, Ikeda Y 1990 Afferent and efferent connections of the oculomotor region of the fastigial nucleus in the macaque monkey. J Comp Neurol 302:330–48.

Nyby O, Jansen J 1951 An experimental investigation of the corticopontine projection in *Macaca mulatta*. Skrifter utgitt av det Norske Vedenskapsakademie: Oslo; 1. Mat Naturv Klasse 3:1–47.

Olszewski J 1952 The Thalamus of the *Macaca mulatta*. Basel: S. Karger.

O'Reilly JX, Beckmann CF, Tomassini V et al 2010 Distinct and overlapping functional zones in the cerebellum defined by resting state functional connectivity. Cereb Cortex 20:953–65.

Orioli PJ, Strick PL 1989 Cerebellar connections with the motor cortex and the arcuate premotor area: an analysis employing retrograde transneuronal transport of WGA-HRP. J Comp Neurol 288:612–26.

Oscarsson O 1965 Functional Organization of the Spino- and Cuneocerebellar Tracts. Physiol Rev 45:495–522.

Palay S, Chan-Palay V 1974 Cerebellar Cortex: Cytology and Organization. New York: Springer-Verlag.

A monograph that details the organization and cytoarchitecture of the cerebellar cortex and its neuronal elements.

Pijpers A, Apps R, Pardoe J et al 2006 Precise spatial relationships between mossy fibres and climbing fibres in rat cerebellar cortical zones. J Neurosci 26:12067–80.

Purkinje J 1837–1838 Die XV Versammlung deutscher Naturforscher und Aerzte zu Prag im September 1837. Sitzungen der Fachabtheilungen. V. Anatomie Ueber die scheinbar kanalikolöse Beschaffenheit der elementaren Nervencylinder. pp. 582–3.

Rakic P 1971 Neuron–glia relationship during granule cell migration in developing cerebellar cortex. A Golgi and electron microscopic study in Macacus rhesus. J Comp Neurol 141:283–312.

Ramnani N, Behrens TE, Johansen-Berg H et al 2006 The evolution of prefrontal inputs to the cortico-pontine system: diffusion imaging evidence from macaque monkeys and humans. Cereb Cortex 16:811–18.

Ramón y Cajal S 1909–1910 Histologie du système nerveux de l'homme et des vertébrés. Translated into French by L. Azoulay. Paris: Maloine. Translated into English by Swanson N, Swanson LW 1995 Histology of the nervous system of man and vertebrates. New York: Oxford University Press.

Rastogi A, Cash R, Dunlop K et al 2017 Modulation of cognitive cerebello-cerebral functional connectivity by lateral cerebellar continuous theta burst stimulation. Neuroimage 158:48–57.

Rekate HL, Grubb RL, Aram DM et al 1985 Muteness of cerebellar origin. Arch Neurol 42(7):697–8.

Sakai ST, Inase M, Tanji J 1999 Pallidal and cerebellar inputs to thalamocortical neurones projecting to the supplementary motor area in *Macaca fuscata*: a triple-labeling light microscopic study. Anat Embryol (Berl) 199(1):9–19.

Schmahmann JD 1991 An emerging concept. The cerebellar contribution to higher function. Arch Neurol 48:1178–87.

Schmahmann JD 1996 From movement to thought: anatomic substrates of the cerebellar contribution to cognitive processing. Human Brain Mapping 4:174–98.

Schmahmann JD (ed) 1997 The Cerebellum and Cognition. Int Rev Neurobiol. Vol 41. San Diego: Academic Press.

The anatomical, theoretical and clinical foundations of the cerebellar contribution to cognition and emotion. More recent review papers are in the literature.

Schmahmann JD 2000 The role of the cerebellum in affect and psychosis. J Neurolinguistics 13:189–214.

Schmahmann JD 2001 The cerebrocerebellar system: anatomic substrates of the cerebellar contribution to cognition and emotion. Int Rev Psychiatry 13:247–60.

Schmahmann JD 2010 The role of the cerebellum in cognition and emotion: personal reflections since 1982 on the dysmetria of thought hypothesis, and its historical evolution from theory to therapy. Neuropsychol Rev 20:236–60.

Schmahmann JD 2020 Pediatric post-operative cerebellar mutism syndrome, cerebellar cognitive affective syndrome, and posterior fossa syndrome: Historical review and proposed resolution to guide future study. Child's Nervous System 36:1205–14.

Schmahmann JD, Pandya DN 1989 Anatomical investigation of projections to the basis pontis from posterior parietal association cortices in rhesus monkey. J Comp Neurol 289:53–73.

Schmahmann JD, Pandya DN 1991 Projections to the basis pontis from the superior temporal sulcus and superior temporal region in the rhesus monkey. J Comp Neurol 308:224–48.

Schmahmann JD, Pandya DN 1992 Course of the fibre pathways to pons from parasensory association areas in the rhesus monkey. J Comp Neurol 326:159–79.

Schmahmann JD, Pandya DN 1993 Prelunate, occipitotemporal, and parahippocampal projections to the basis pontis in rhesus monkey. J Comp Neurol 337:94–112.

Schmahmann JD, Pandya DN 1997a The cerebrocerebellar system. In: Schmahmann JD (ed) The cerebellum and cognition. Int Rev Neurobiol 41:31–60.

Schmahmann JD, Pandya DN 1997b Anatomic organization of the basilar pontine projections from prefrontal cortices in rhesus monkey. J Neurosci 17:438–58.

Schmahmann JD, Pandya DN 2008 Disconnection syndromes of basal ganglia, thalamus, and cerebrocerebellar systems. Cortex 44:1037–66.

Schmahmann JD, Sherman JC 1998 The cerebellar cognitive affective syndrome. Brain 121(Pt 4):561–79.

Schmahmann JD, Doyon J, McDonald D et al 1999 Three-dimensional MRI atlas of the human cerebellum in proportional stereotaxic space. Neuroimage 10:233–60.

Schmahmann JD, Doyon J, Toga A et al 2000 MRI Atlas of the Human Cerebellum. San Diego: Academic Press.

The MRI Atlas identifies cerebellar lobules and fissures in stereotaxic coordinate space, and harmonizes earlier nomenclatures with the current modified Larsell terminology.

Schmahmann JD, Rosene DL, Pandya DN 2004a Motor projections to the basis pontis in rhesus monkey. J Comp Neurol 478:248–68.

Schmahmann JD, Ko R, MacMore J 2004b The human basis pontis: motor syndromes and topographic organization. Brain 127:1269–91.

Schmahmann JD, Rosene DL, Pandya DN 2004c Ataxia after pontine stroke: insights from pontocerebellar fibres in monkey. Ann Neurol 55:585–9.

Schmahmann JD, Pandya DN, Wang R et al 2007 Association fibre pathways of the brain: parallel observations from diffusion spectrum imaging and autoradiography. Brain 130:630–53.

Schmahmann JD, Gardner R, MacMore J et al 2009 Development of a brief ataxia rating scale (BARS) based on a modified form of the ICARS. Mov Disord 24:1820–28.

Schmahmann JD, Guell XP, Stoodley CJ et al 2019 The theory and neuroscience of cerebellar cognition. Annu Rev Neurosci Apr 2. doi: 10.1146/annurev-neuro-070918-050258.

Schmitz-Hübsch T, du Montcel ST, Baliko L et al 2006 Scale for the assessment and rating of ataxia: development of a new clinical scale. Neurology 66:1717–20.

Schoch B, Dimitrova A, Gizewski ER et al 2006 Functional localization in the human cerebellum based on voxelwise statistical analysis: a study of 90 patients. Neuroimage 30:36–51.

Simpson JI, Graf W 1981 Eye-muscle geometry and compensatory eye movements in lateral-eyed and frontal-eyed animals. Ann N Y Acad Sci 374:20–30.

Spampinato MV, Kraas J, Maria BL et al 2008 Absence of decussation of the superior cerebellar peduncles in patients with Joubert syndrome. Am J Med Genet A 46A:1389–94.

Stilling B 1846 Untersuchungen über den Bau und die Verrichtungen des Gehirns. I. Uber den Bau des Hirnknotens oder Varoli'schen Brucke. Jena: Druck und Verlag von Friedrich Mauke.

Stilling B 1864 Untersuchungen über den Bau des kleinen Gehirns des Menschen. Kassel: T. Fischer.

Stoodley CJ, Schmahmann JD 2009a Functional topography in the human cerebellum: a meta-analysis of neuroimaging studies. Neuroimage 44:489–501.

Stoodley CJ, Schmahmann JD 2009b The cerebellum and language: evidence from patients with cerebellar degeneration. Brain Lang 110:149–53.

Stoodley CJ, Schmahmann JD 2010 Functional topography in the human cerebellum: Evidence for an anterior–posterior dichotomy for motor control versus cognitive/emotional processing. Cortex 46:831–44.

Stoodley CJ, Valera EM, Schmahmann JD 2010 An fMRI study of intra-individual functional topography in the human cerebellum. Behav Neurol 23:65–79.

Stoodley CJ, Valera EM, Schmahmann JD 2012 Functional topography of the cerebellum for motor and cognitive tasks: an fMRI study. Neuroimage 59:1560–70.

Stoodley CJ, MacMore JP, Makris N et al 2016 Location of lesion determines motor vs. cognitive consequences in patients with cerebellar stroke. Neuroimage Clin 12:765–75.

Strata P 1989 The Olivocerebellar System in Motor Control. Experimental Brain Research Series 17. Berlin: Springer-Verlag

Strick PL, Dum RP, Fiez JA 2009 Cerebellum and nonmotor function. Annu Rev Neurosci 32:413–34.

Subramony SH, May W, Lynch D et al 2005 Measuring Friedreich ataxia: interrater reliability of a neurologic rating scale. Neurology 64:1261–2.

Sugihara I, Shinoda Y 2004 Molecular, topographic, and functional organization of the cerebellar cortex: a study with combined aldolase C and olivocerebellar labeling. J Neurosci 24:8771–85.

Sugihara I, Wu H, Shinoda Y 1999 Morphology of single olivocerebellar axons labeled with biotinylated dextran amine in the rat. J Comp Neurol 414(2):131–48.

Sugihara I, Wu H-S, Shinoda Y 2001 The entire trajectories of single olivocerebellar axons in the cerebellar cortex and their contribution to cerebellar compartmentalization. J Neurosci 21(19):7715–23.

Supple WF, Leaton RN 1990 Cerebellar vermis: essential for classically conditioned bradycardia in the rat. Brain Res 409:17–23.

Szapiro G, Barbour B 2007 Multiple climbing fibres signal to molecular layer interneurones exclusively via glutamate spillover. Nat Neurosci 10:735–42.

Thach WT 1987 Cerebellar inputs to motor cortex. Ciba Found Symp 132:201–20.

Thompson RF 1983 Neuronal substrate of simple associative learning. Classical conditioning. Trends Neurosci 6:270–5.

Trouillas P, Takayanagi T, Hallett M et al 1997 International Cooperative Ataxia Rating Scale for pharmacological assessment of the cerebellar syndrome. The Ataxia Neuropharmacology Committee of the World Federation of Neurology. J Neurol Sci 145:205–11.

Ugolini G, Kuypers HG 1986 Collaterals of corticospinal and pyramidal fibres to the pontine grey demonstrated by a new application of the fluorescent fibre labelling technique. Brain Res 365:211–27.

Ugolini G, Klam F, Doldan Dans M et al 2006 Horizontal eye movement networks in primates as revealed by retrograde transneuronal transfer of rabies virus: differences in monosynaptic input to 'slow' and 'fast' abducens motoneurones. J Comp Neurol 498:762–85.

Van Overwalle F, Baetens K, Mariën P et al 2015 Cerebellar areas dedicated to social cognition? A comparison of meta-analytic and connectivity results. Soc Neurosci 10:337–44.

Verhaart WJ, van Wieringen-Rauws G 1950 On cerebro-cerebellar atrophy. Folia Psychiatr Neurol Neurochir Neerl 53:481–501.

Voogd J 2004 Cerebellum and precerebellar nuclei. In: Paxinos G and Mai JK (eds) The Human Nervous System. Amsterdam: Elsevier, Academic Press, pp. 321–92.

The detailed elucidation of the zonal organization of the cerebellum and cerebellar corticonuclear relations is well laid out in this chapter by a contemporary pioneer in cerebellar anatomy.

Voogd J, Bigaré F 1980 Topographical distribution of olivary and corticonuclear fibres in the cerebellum: a review. In: Courville J (ed.) The Olivary Nucleus. Anatomy and Physiology. New York: Raven, pp. 207–34.

Voogd J, Glickstein M 1998 The anatomy of the cerebellum. Trends Neurosci 21:370–5.

Voogd J, Ruigrok TJH 2012 Cerebellum and precerebellar nuclei. In: May J, Paxinos G (eds) The Human Nervous System. Amsterdam: Elsevier, pp. 471–547.

Voogd J, Pardoe J, Ruigrok TJ et al 2003 The distribution of climbing and mossy fibre collateral branches from the copula pyramidis and the paramedian lobule: congruence of climbing fibre cortical zones and the pattern of zebrin banding within the rat cerebellum. J Neurosci 23:4645–56.

Voogd J, Schraa-Tam CK, van der Geest JN et al 2012 Visuomotor cerebellum in human and nonhuman primates. Cerebellum 11:392–410.

von Bechterew W 1885 Zur Anatomie der Schenkel des Kleinhirns, insbesondere der Brückenarme. Neurologisches Centralblatt 4:121–5.

Wagner MJ, Kim TH, Savall J et al 2017 Cerebellar granule cells encode the expectation of reward. Nature 544:96–100.

Whiting BA, Barton RA 2003 The evolution of the cortico-cerebellar complex in primates: anatomical connections predict patterns of correlated evolution. J Hum Evol 44:3–10.

Wiesendanger R, Wiesendanger M 1985 Cerebello-cortical linkage in the monkey as revealed by transcellular labeling with the lectin wheat germ agglutinin conjugated to the marker horseradish peroxidase. Exp Brain Res 59:105–17.

Wisoff JH, Epstein FJ 1984 Pseudobulbar palsy after posterior fossa operation in children. Neurosurgery 15:707–9.

Woolsey C 1952 Summary of the papers on the cerebellum. Res Publ Assoc Res Nerv Ment Dis 30:334–6

Wu HS, Sugihara I, Shinoda Y 1999 Projection patterns of single mossy fibres originating from the lateral reticular nucleus in the rat cerebellar cortex and nuclei. J Comp Neurol 411:97–118.

Zagon IS, McLaughlin PJ, Smith S 1977 Neural populations in the human cerebellum: estimations from isolated cell nuclei. Brain Res 127:279–82.

Zhou H, Lin Z, Voges K, et al 2014 Cerebellar modules operate at different frequencies. eLife 3:e02536.

Zhu JN, Yung WH, Kwok-Chong Chow B et al 2006 The cerebellar–hypothalamic circuits: potential pathways underlying cerebellar involvement in somatic–visceral integration. Brain Res Rev 52:93–106.

CHAPTER
30

Diencephalon

The diencephalon is part of the prosencephalon (forebrain), which develops from the most rostral primary cerebral vesicle that differentiates into the caudal diencephalon and the rostral telencephalon. The cerebral hemispheres, containing the lateral ventricles, develop from the telencephalon. The sites of evagination of the telencephalon become the interventricular foramina, through which the two lateral ventricles and the midline third ventricle communicate. The diencephalon corresponds largely to the structures that develop lateral to the third ventricle. The lateral walls of the diencephalon form the epithalamus most superiorly, the thalamus centrally, and the subthalamus and hypothalamus inferiorly.

THALAMUS

The thalamus plays a crucial role in many brain functions, serving as a processing and distribution centre, relaying and regulating information from the outside world and the internal milieu to the cerebral cortex and sustaining cortico-thalamo-cortical communication. It is involved in multiple activities, including consciousness, sleep, attention, memory and sensory and motor functions. Our increasing understanding of the role of the thalamus is providing insights into pathological disorders of the brain and is opening up the possibility of targeting its various constituent nuclei to treat a variety of disorders, including epilepsy, Parkinson's disease, pain and psychiatric disorders (**Table 30.1**; see Fig. 30.5). (For review, see Lozano et al 2019.)

Morphologically, the thalamus is a large ovoid nuclear mass, about 4 cm long, which borders the dorsal part of the third ventricle (**Figs 30.1–30.2**). Its narrow anterior pole lies close to the midline and forms the posterior boundary of the interventricular foramen. Posteriorly, an expansion, the pulvinar, extends beyond the third ventricle to overhang the superior colliculus (see Fig. 28.5). The brachium of the superior colliculus (superior quadrigeminal brachium) separates the pulvinar superiorly from the medial geniculate body inferiorly. A small oval elevation, the lateral geniculate body, lies lateral to the medial geniculate body.

The superior (dorsal) surface of the thalamus is covered by a thin layer of white matter, the stratum zonale. This curved surface is separated from the overlying body of the fornix by the choroid fissure containing the tela choroidea. More laterally, it forms part of the floor of the lateral ventricle. The lateral border of the superior surface of the thalamus is marked by the stria terminalis and overlying thalamostriate vein, which separate the thalamus from the body of the caudate nucleus. Laterally, a slender sheet of white matter, the external medullary lamina, separates the main body of the thalamus (dorsal thalamus), from the reticular nucleus (prethalamus). The dorsal thalamus and the reticular nucleus differ in their ontogeny and connections. Lateral to the reticular nucleus, the thick posterior limb of the internal capsule lies between the thalamus and the lentiform complex.

The medial surface of the thalamus is the superior (dorsal) part of the lateral wall of the third ventricle and is usually connected to the contralateral thalamus by an interthalamic adhesion (see Fig. 25.20). The boundary with the hypothalamus is marked by a faint hypothalamic sulcus, which curves from the upper end of the cerebral aqueduct to the interventricular foramen. The thalamus is continuous with the midbrain tegmentum, the subthalamus and the hypothalamus.

Internally, the dorsal thalamus is divided into anterior, medial and lateral nuclear groups by the internal medullary lamina, a vertical Y-shaped sheet of white matter (**Figs 30.3–30.4**; **Table 30.2**). Intralaminar nuclei are embedded within the internal medullary lamina. Midline nuclei abut the lateral walls of the third ventricle. The reticular nucleus forms a shell-like lateral covering to the main nuclear mass, from which it is separated by an external medullary lamina of nerve fibres.

The thalamus is connected with virtually all of the cerebral hemisphere. In general, thalamic nuclei both project to and receive fibres from the cerebral cortex (Jones 2007, Sherman 2016) (see Fig. 30.4). The thalamus is the major route by which subcortical neuronal activity influences the cerebral cortex, and the greatest input to most thalamic nuclei comes from the cerebral cortex. Some thalamic nuclei are connected with the basal ganglia and the amygdala.

The connections between the dorsal thalamus and the cerebral cortex are reciprocal; each cortical area projects in a topographically organized manner to all sites in the thalamus from which it receives an input (see Table 30.2). Thalamocortical fibres terminate predominantly in layer IV of the cortex. Corticothalamic fibres arise mostly from modified pyramidal cells of layer VI. In addition, some thalamic nuclei, the 'high-order' or 'association' nuclei, receive corticothalamic fibres from layer V pyramidal neurones; these fibres are collaterals of axons projecting to other subcortical nuclei. The reticular nucleus is connected reciprocally to all thalamic nuclei and receives input from corticothalamic fibres arising in layer VI but it does not project to the cortex.

The dorsal thalamic nuclei contain projection neurones (approximately 70%), and local circuit interneurones (30%). They are divided into 'relay' or 'first-order' nuclei that mediate finely organized and precisely transmitted sensory and motor information to discrete cortical sensory and motor areas, and 'association' or 'high-order' nuclei that have more complex integrative functions (Rovó et al 2012, Sherman 2016). Relay nuclei receive their main or 'driver' input from a major subcortical pathway, and process and transfer information from

TABLE 30.1 Thalamic deep brain stimulation targets

Indication	Target	References
Pain	VPI/VPm, PVG	Boccard et al 2013
Tremor	VL (Vim)	Benabid et al 1991, Hubble et al 1996
Epilepsy	Anterior thalamus	Hodaie et al 2002
Obsessive–compulsive disorder	Inferior thalamic peduncle	Jiménez et al 2013
Minimally conscious state	CM (central thalamus)	Giacino et al 2012
Tourette's syndrome	CM	Piedad et al 2012
Dystonia	VL (Voa/Vop), VL (Vim)	Cooper 1976, Tasker et al 1988
Myoclonus–dystonia	Vim	Gruber et al 2010

Abbreviations: CM, centromedian nucleus of thalamus; PVG, periventricular grey; Vim, ventral intermediate nucleus of thalamus (nucleus ventrointermedius); VL, ventral lateral thalamic nucleus (nucleus ventrolateralis); Voa, nucleus ventro-oralis anterior; Vop, nucleus ventro-oralis posterior; VPl, ventral posterolateral nucleus; VPm, ventral posteromedial nucleus.

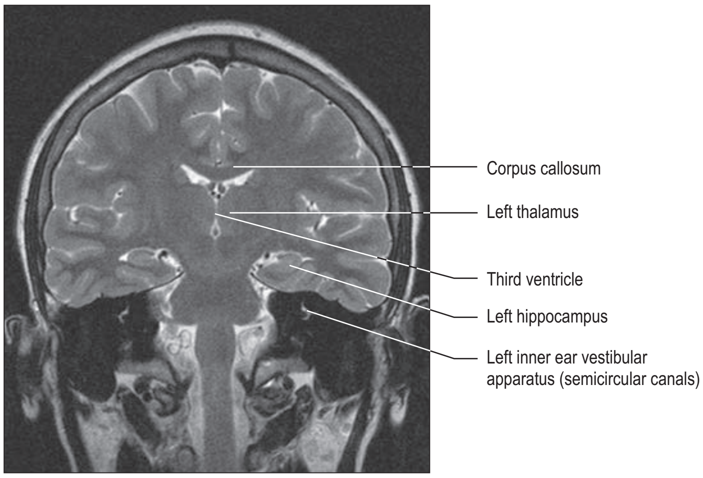

Fig. 30.1 A coronal T2-weighted magnetic resonance image at the level of the thalamus and third ventricle. (Courtesy of Professor Alan Jackson, Wolfson Molecular Imaging Centre, The University of Manchester, UK.)

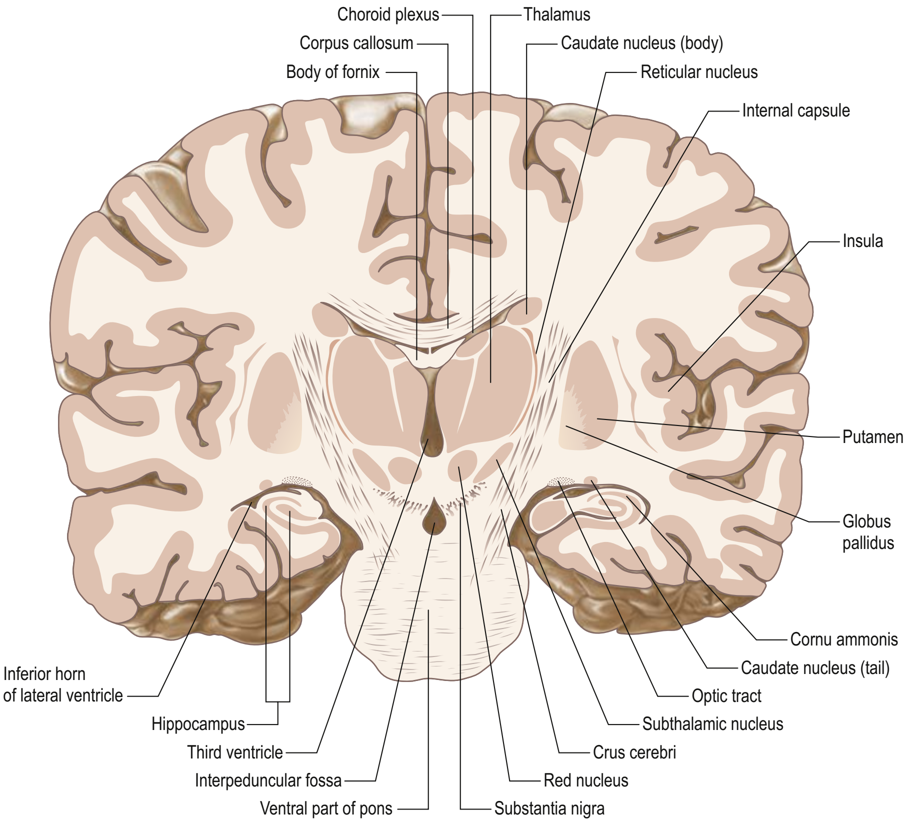

Fig. 30.2 The principal parts of the diencephalon and basal ganglia, coronal section.

subcortical nuclei to the cerebral cortex. Association nuclei receive their 'driver' input from layer V pyramidal neurones in association cortical areas and participate in cortico-thalamo-cortical transmission. Both relay and association nuclei receive 'modulatory' input from layer VI pyramidal neurones of the cerebral cortex. All thalamic nuclei receive 'non-specific' subcortical input from cholinergic and aminergic (serotoninergic, histaminergic, dopaminergic, noradrenergic, adrenergic) axons arising in the brainstem and basal telencephalon.

Anterior thalamic nuclei

The anterior thalamic nuclei are relay or first-order nuclei, believed to be involved in the regulation of alertness and attention and in the acquisition of memory. They lie between the arms of the Y-shaped internal medullary lamina, and underlie the anterior thalamic tubercle (see Figs 28.5, 30.4). Three subdivisions are recognized: the largest is the anteroventral nucleus, the others are the anteromedial and anterodorsal nuclei. These nuclei are the principal recipients of the mammillothalamic tract, which arises from the mammillary nuclei of the hypothalamus. (The mammillary nuclei receive fibres from the hippocampal formation via the fornix). The medial mammillary nucleus projects to the anteroventral and anteromedial thalamic nuclei, and the lateral mammillary nucleus projects to the anterodorsal nucleus. The nuclei of the anterior group also receive a prominent cholinergic input from the basal forebrain and the brainstem. The cortical targets of efferent fibres from the anterior nuclei of the thalamus lie largely on the medial surface of the hemisphere. They include the anterior limbic area (anterior and inferior to the corpus callosum), the cingulate gyrus and the parahippocampal gyrus (including the medial entorhinal cortex, presubiculum and parasubiculum). There also appear to be minor connections between the anterior nuclei and the dorsolateral prefrontal and posterior areas of neocortex.

Medial thalamic nuclei

The single component of this thalamic region is the mediodorsal (dorsomedial) nucleus, an association nucleus, which is particularly large in humans. Laterally, it is limited by the internal medullary lamina and intralaminar nuclei. Medially, it abuts the midline parataenial and reuniens (medioventral) nuclei. It consists of a smaller, anteromedial magnocellular division and a larger, posterolateral parvocellular division.

The anteromedial magnocellular division receives olfactory input from the piriform and adjacent cortex, the ventral pallidum and the amygdala. The mediobasal amygdaloid nucleus projects to the dorsal part of the anteromedial magnocellular nucleus, and the lateral nuclei project to the more central and anteroventral regions. The magnocellular division projects to the orbital and medial prefrontal cortex, notably to the lateral posterior and central posterior olfactory areas on the orbital surface of the frontal lobe. Fibres also pass to the ventromedial cingulate cortex and to the inferior parietal cortex and anterior insula. These cortical connections are reciprocal.

The posterolateral parvocellular division is connected reciprocally with the dorsolateral and dorsomedial prefrontal cortex, the anterior cingulate gyrus and the supplementary motor area. Efferent fibres also pass to the posterior parietal cortex.

The mediodorsal nucleus appears to be involved in a wide variety of higher functions. Damage may lead to a decrease in anxiety, tension, aggression or obsessive thinking. There may also be transient amnesia, with confusion developing particularly over the passage of time. Much of the neuropsychology of medial nuclear damage reflects defects in functions similar to those performed by the prefrontal cortex, with which it is closely linked, and the effects of ablation of the mediodorsal nuclei parallel, in part, the results of prefrontal lobotomy.

Lateral thalamic nuclei

The lateral nuclear complex, lying lateral to the internal medullary lamina, is the largest division of the thalamus and is divided into dorsal and ventral tiers of nuclei. The lateral dorsal nucleus, lateral posterior nucleus and the pulvinar all lie dorsally. The lateral and medial geniculate nuclei lie inferior to the pulvinar near the posterior pole of the thalamus. The ventral tier nuclei are the ventral anterior, ventral lateral and ventral posterior nuclei.

Ventral anterior nucleus

The ventral anterior (VA) nuclear complex lies at the anterior pole of the ventral nuclear group. It is limited anteriorly by the reticular nucleus and posteriorly by the ventral lateral nucleus, and lies between the external and internal medullary laminae. It consists of a principal part (VApc) and a magnocellular part (VAmc). The subcortical connections to this region are largely ipsilateral from the medial (internal) globus pallidus and the pars reticulata of the substantia nigra. These afferents use γ-aminobutyric acid (GABA) as a neurotransmitter: they are inhibitory and therefore unusual among the 'driver' inputs to relay nuclei which are typically glutamatergic

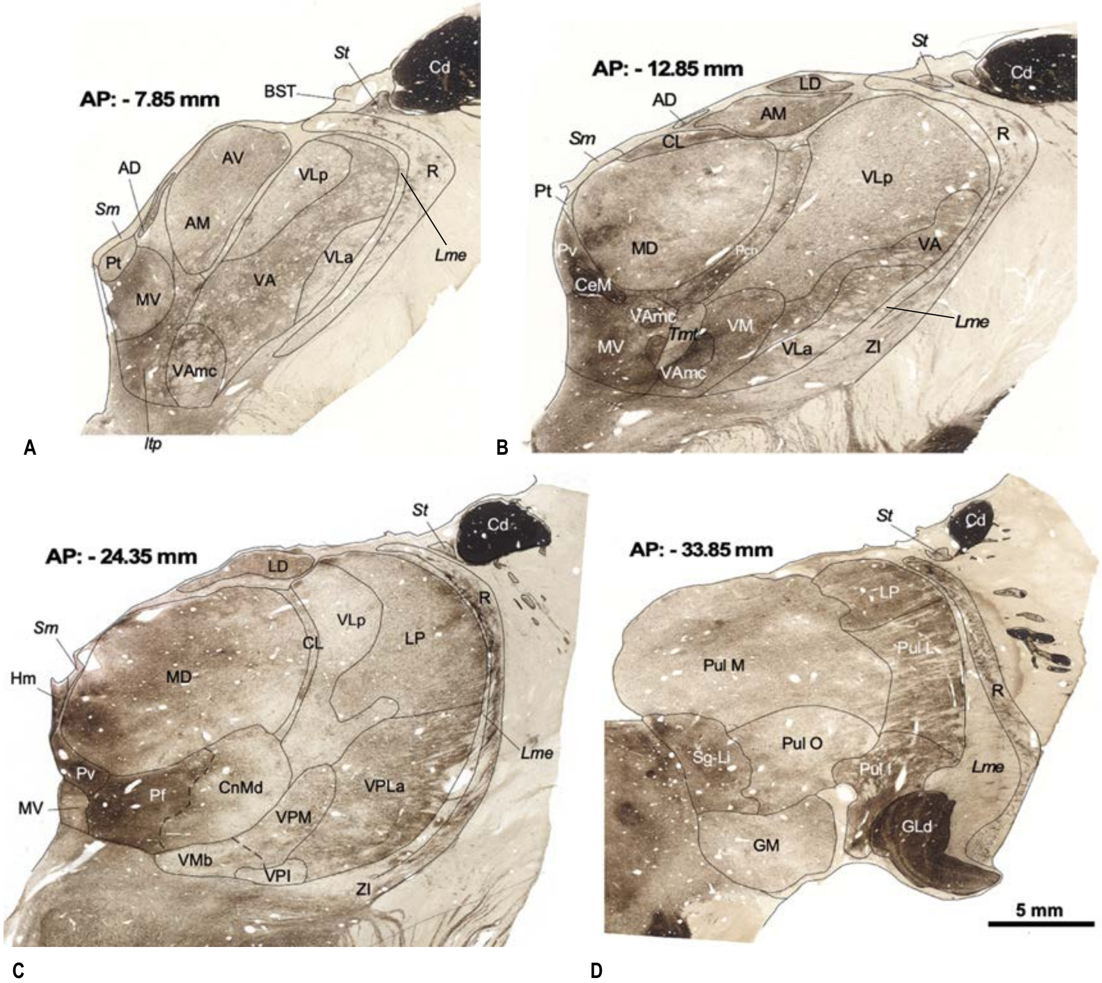

Fig. 30.3 A series of coronal sections from a human hemithalamus stained for acetylcholinesterase histochemistry. The midline is to the left. The stereotaxic anteroposterior level is given next to each section (stereotaxic brain sectioning followed Talairach and Tournoux (1988) criteria). Abbreviations: AD, anterodorsal nucleus; AM, anteromedial nucleus; AV, anteroventral nucleus; BST, bed nucleus of the stria terminalis; Cd, caudate nucleus; CeM, central medial nucleus; CL, central lateral nucleus; CnMd, centromedian nucleus; GLd, dorsal lateral geniculate nucleus; GM, medial geniculate nucleus; Hm, medial habenular nucleus; Itp, inferior thalamic peduncle; LD, lateral dorsal nucleus; Li, limitans nucleus; Lme, external medullary lamina; LP, lateral posterior nucleus; MD, mediodorsal nucleus; MV, medioventral nucleus; Pcn, paracentral nucleus; Pf, parafascicular nucleus; Pt, parataenial nucleus; Pul I, inferior pulvinar nucleus; Pul L, lateral pulvinar nucleus; Pul M, medial pulvinar nucleus; Pul O, oral pulvinar nucleus; Pv, paraventricular nucleus; R, reticular nucleus; Sg, suprageniculate nucleus; Sm, stria medullaris; St, stria terminalis; Tmt, mamillothalamic tract; VA, ventral anterior nucleus; VAmc, ventral anterior nucleus-magnocellular part; VLa, ventral lateral nucleus-anterior part; VLp, ventral lateral nucleus-posterior part; VM, ventral medial nucleus; VMb, basal ventral medial nucleus; VPI, ventral posterior inferior nucleus; VPLa, ventral posterior lateral nucleus-anterior part; VPM, ventral posterior medial nucleus; ZI, zona incerta.

and excitatory. The pallidal and nigral terminal fields do not overlap in the ventral anterior nuclear complex: fibres from the globus pallidus end in the principal part of the nuclear complex and the substantia nigra pars reticulata, projects to the magnocellular part of the nuclear complex. Corticothalamic fibres from the premotor cortex (area 6) terminate in the principal part and fibres from the frontal eye field (area 8) terminate in the magnocellular part. The efferent projections from the ventral anterior nuclear complex are incompletely known; it projects to widespread regions of the frontal lobe and to the parietal cortex. Their functions are also unclear: the ventral anterior thalamus appears to play a central role in the transmission of the cortical 'recruiting response', a phenomenon in which stimulation of the thalamus can initiate long-lasting, high-voltage, repetitive negative electrical waves over much of the cerebral cortex.

Ventral lateral nucleus

The ventral lateral (VL) nucleus may be considered a motor relay nucleus: it consists of two major divisions with distinctly different connections and functions. The anterior division, or pars oralis (VLo), receives topographically organized fibres from the ipsilateral medial globus pallidus. The posterior division, or pars caudalis (VLc), receives topographically organized fibres from the contralateral deep cerebellar nuclei. Additional subcortical projections have been reported from the spinothalamic tract and the vestibular nuclei. Numerous cortical afferents to both the pars oralis and the pars caudalis originate from precentral motor cortical areas, including both area 4 and area 6.

The pars oralis of the ventral lateral nucleus sends efferent fibres mostly to the supplementary motor cortex on the medial surface of the hemisphere and to the lateral premotor cortex. The pars caudalis of the ventral lateral nucleus projects efferent fibres mostly to the primary motor cortex, where they end in a topographically arranged fashion. The head region of area 4 receives fibres from the medial part of pars caudalis, and the leg region receives fibres from the lateral pars caudalis.

Responses can be recorded in ventral lateral thalamic neurones during both passive and active movement of the contralateral body. The topography of its connections, and recordings made within the nucleus, suggest that the pars caudalis contains a body representation comparable to that in the ventral posterior nucleus. In patients with tremor, clusters of ventral lateral neurones fire in bursts that are synchronous with peripheral tremor: so-called 'tremor cells'.

Stereotaxic surgery of the ventral lateral nucleus is sometimes used in the treatment of essential tremor (see Table 30.1; **Fig. 30.5**). In the past, thalamotomy was used extensively for the treatment of Parkinson's disease: the medial globus pallidus and the subthalamic nucleus are now the preferred neurosurgical targets for Parkinson's disease.

Ventral posterior nucleus

The ventral posterior (VP) nucleus is the principal thalamic relay for the somatosensory pathways. It consists of two major divisions, the ventral posterolateral (VPl) and ventral posteromedial (VPm) nuclei.

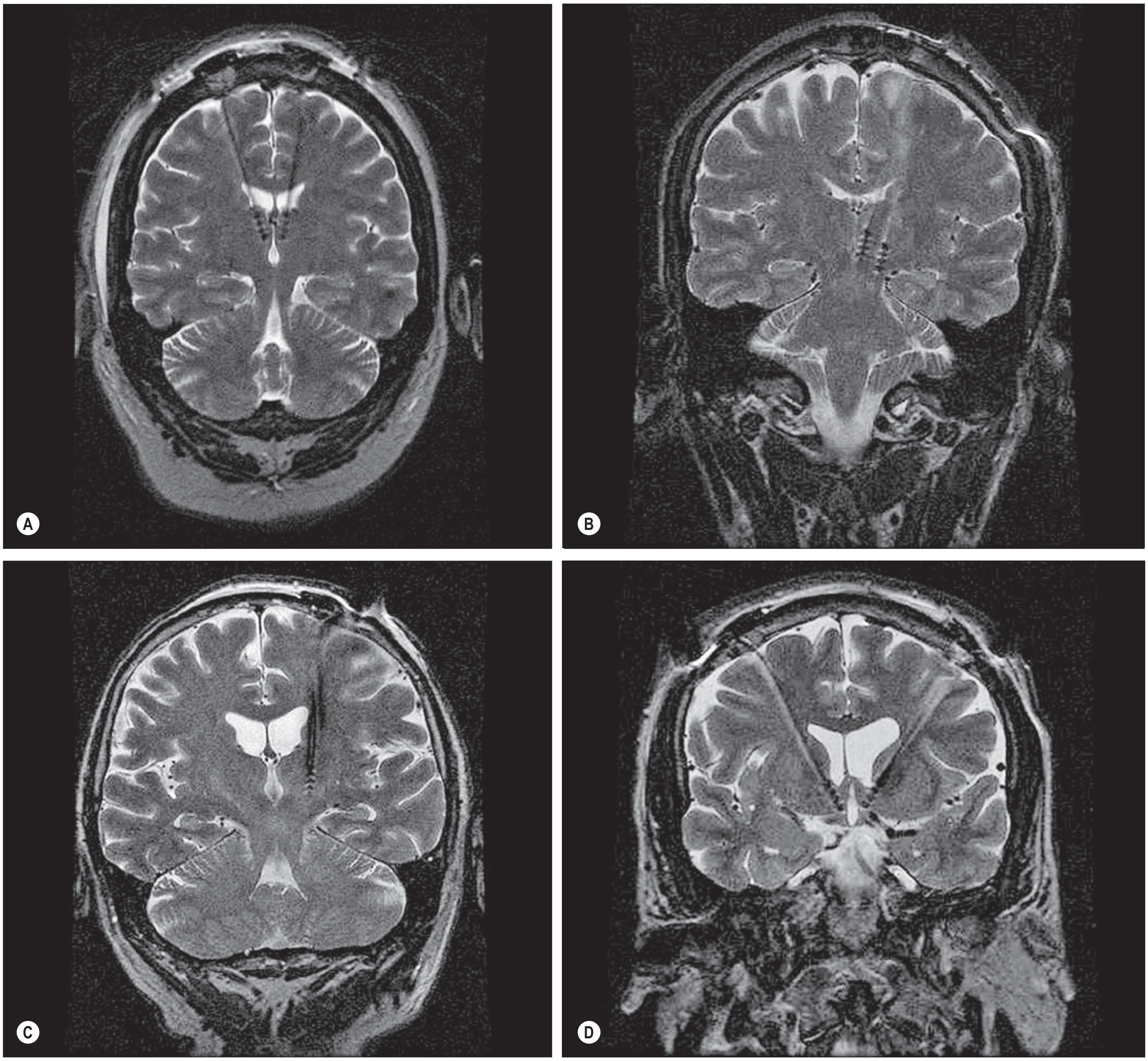

Fig. 30.5 Magnetic resonance images from four different patients with neurological or psychiatric disorders, showing the position of deep brain stimulation (DBS) electrodes. **A**, Bilateral anterior thalamic DBS for epilepsy. **B**, Left thalamic DBS for pain, with electrodes in the sensory relay nucleus (ventral posterior nucleus of the thalamus) laterally and the periventricular grey medially. **C**, DBS electrode in the ventral intermediate nucleus of the thalamus in a patient with essential tremor. **D**, Bilateral inferior thalamic peduncle DBS electrodes in a patient with obsessive–compulsive disorder.

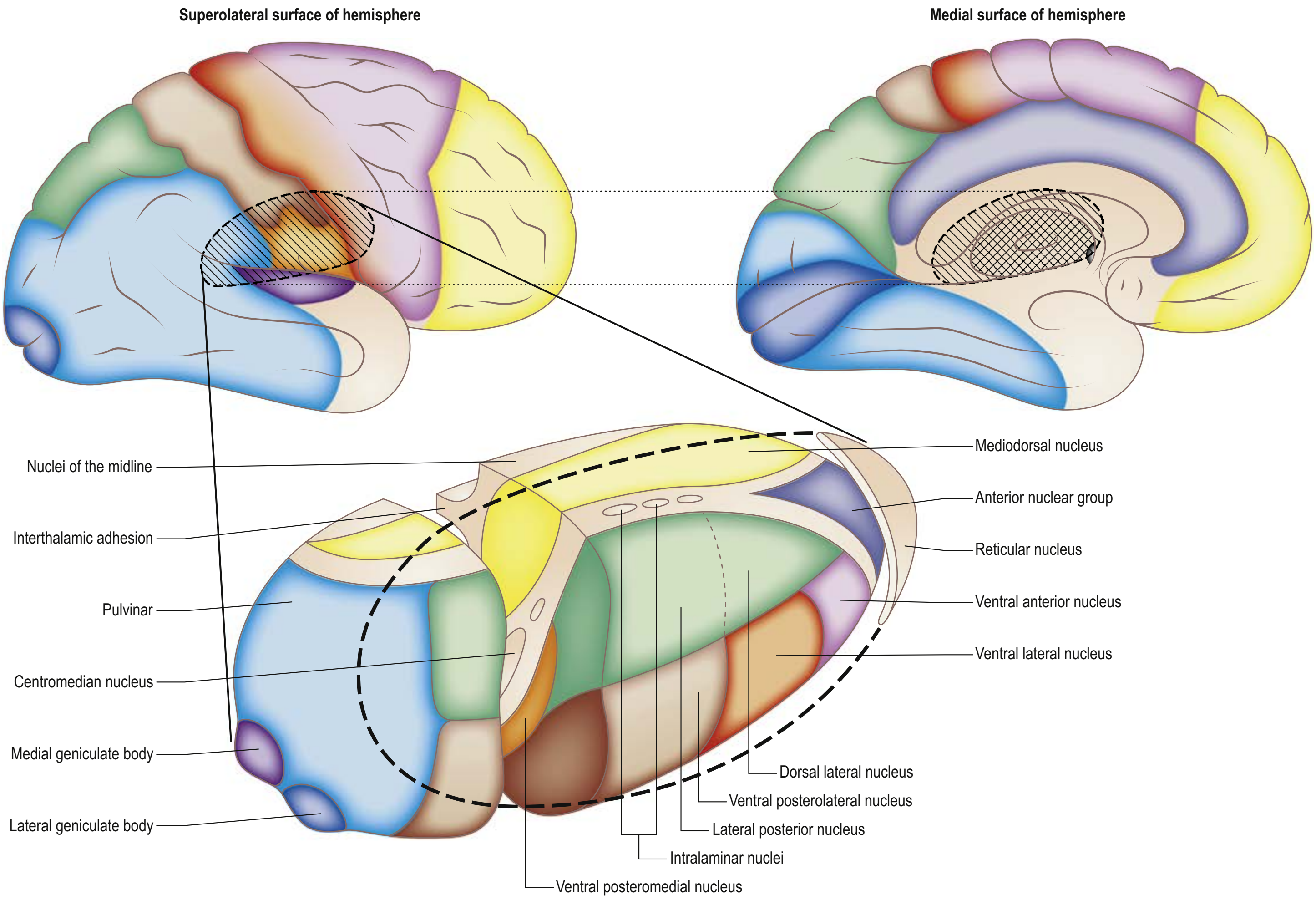

Fig. 30.4 The main nuclear masses of the thalamus (viewed from the lateral aspect in the lower illustration), colour-coded to indicate the areas of cerebral neocortex with which they are interconnected. The pale colour in the centromedian, intralaminar and reticular nuclei and in areas of the frontal and temporal lobes is not related to the colour code. The reticular nucleus lies lateral to the main mass of the thalamus. Only the anterior pole of the reticular nucleus is shown, its posterior extent is depicted by the heavy dashed line.

TABLE 30.2 Main thalamic nuclei and their major afferent and efferent connections

Group	Nucleus	Major subcortical connection	Major cortical connections	System
Anterior	Anterior	Mammillary bodies (MTT)	Cingulate and parahippocampal gyrus	Relay limbic
Medial	Dorsomedial	Amygdala, thalamic nuclei	Prefrontal cortex	Association
Lateral				
Ventral	VA	GPm, SNr	Premotor cortex	Relay motor
	VL	Ipsilateral GPm, contralateral cerebellum	Supplementary and primary motor cortex	Relay motor
	VPl, VPm	STT to VPl, TTT to VPm, MLT to anterior surface	Somatosensory cortex, insula	Relay somato-sensory
	LGB	Optic tract	Visual cortex	Relay visual
	MGB	Auditory pathway (inferior brachium)	Auditory cortex	Relay auditory
Dorsal	Pulvinar – LP	Superior colliculus	Parieto-occipito-temporal	Association
	LD	Pretectum and superior colliculus	Cingulate, parahippocampus	
Intralaminar	CM	GPm, cerebellum	Striatum, motor cortex	
Reticular		Widespread connections	Widespread connections (afferent only)	

Abbreviations: CM, centromedian nucleus of thalamus; GPm, medial (internal) segment of globus pallidus; LD, lateral dorsal nucleus of thalamus; LGB, lateral geniculate body; LP, lateral posterior nucleus of thalamus; MGB, medial geniculate body; MLT, medial lemniscal tract; MTT, mammillothalamic tract; SNr, substantia nigra pars reticulata; STT, spinothalamic tract; TTT, trigeminothalamic tract; VA, ventral anterior nucleus; VL, ventral lateral nucleus; VPl, ventral posterolateral nucleus; VPm, ventral posteromedial nucleus.

The ventral posterolateral nucleus receives its driver input from the medial lemniscal and spinothalamic pathways, and the ventral posteromedial nucleus receives its driver input from the trigeminothalamic pathway. Connections from the vestibular nuclei terminate along the ventral surface of the ventral posterior nucleus.

There is a well-ordered topographic representation of the body in the ventral posterior nucleus. The ventral posterolateral nucleus is organized so that sacral segments are represented laterally and cervical segments medially. The latter abut the face area of representation (trigeminal territory) in the ventral posteromedial nucleus. Taste fibres synapse most anteriorly and ventromedially within the ventral posterolateral nucleus.

At a more detailed level, single body regions are represented as curved lamellae of neurones, parallel to the lateral border of the ventral posterior nucleus, such that there is a continuous overlapping progression of adjacent receptive fields from dorsolateral to ventromedial. Considerably less change in location of receptive field on the body is seen when passing anteroposteriorly through the nucleus. While not precisely dermatomal in nature, these curvilinear lamellae of cells are probably derived from afferents related to a few adjacent spinal segments. There is considerable distortion of the body map within the nucleus, reflecting the differences in the density of peripheral innervation that occur in different body regions, e.g. many more neurones respond to stimulation of the hand than of the trunk. Within a single lamella, neurones in the anterodorsal part of the nucleus respond to deep stimuli, including movement of joints, tendon stretch and manipulation of muscles. Most ventrally, neurones once again respond to deep stimuli, particularly tapping. Intervening cells within a single lamella respond only to cutaneous stimuli. This organization has been confirmed by recordings made in the human ventral posterior nucleus.

The ventral posterior nucleus projects to the primary somatic sensory cortex (SI) of the postcentral gyrus and to the second somatic sensory area (SII) in the parietal operculum. The posterior part of the ventral posteromedial nucleus projects to the insular cortex. Within the primary

Single lemniscal axons have an extended anteroposterior terminal zone within the nucleus. Rods of cells running the length of the anteroposterior, dorsoventrally orientated lamellae respond with closely similar receptive field properties and locations, derived from a small bundle of lemniscal afferents. It appears, therefore, that each lamella contains the complete representation of a single body part, e.g. a finger. Lamellae consist of multiple narrow rods of neurones, orientated anteroposteriorly, each of which receives input from the same small region of the body that is represented within the lamella, and from the same type of receptors. These thalamic 'rods' form the basis for both place- and modality-specific input to columns of cells in the somatic sensory cortex. Spinothalamic tract afferents to the ventral posterolateral nucleus terminate throughout the nucleus. The neurones from which these axons originate appear to be mainly of the 'wide-dynamic-range' class, responding to both low-threshold mechanoreceptors and high-threshold nociceptors; a smaller proportion of neurones respond exclusively to high-threshold nociceptors. Some neurones respond to temperature changes. There is evidence that spinothalamic tract neurones carrying nociceptive and thermal information terminate in a distinct nuclear area, identified as the posterior part of the ventral medial nucleus (VMpo).

sensory cortex, the central cutaneous core of the ventral posterior nucleus projects solely to area 3b; dorsal and ventral to this, a narrow band of cells projects to both area 3b and area 1. The most dorsal and ventral deep stimulus receptive cells project to areas 3a and 2. The whole nucleus projects to the second somatic sensory area.

Medial geniculate nucleus

The medial geniculate nucleus is the relay nucleus of the auditory pathway. It is located within the medial geniculate body, a rounded elevation situated posteriorly on the ventrolateral surface of the thalamus, separated from the pulvinar by the brachium of the superior colliculus. It receives fibres travelling in the brachium of the inferior colliculus. The medial geniculate nucleus contains three major subnuclei, medial (magnocellular), ventral and dorsal. The inferior brachium separates the medial nucleus, which consists of sparse, deeply staining neurones, from the lateral region, which consists of medium-sized, densely packed and darkly staining neurones. In the lateral region, the dorsal nucleus overlies the ventral nucleus and expands posteriorly; it is sometimes known as the posterior nucleus of the medial geniculate. It contains small- to medium-sized, pale-staining neurones that are less densely packed than those of the ventral nucleus.

The dorsal nucleus receives afferents from the pericentral nucleus of the inferior colliculus and from other brainstem nuclei of the auditory pathway and projects to auditory areas surrounding the primary auditory cortex. Neurones within the dorsal nucleus respond to a broad range of frequencies and a tonotopic representation has not been described in this subdivision. The ventral nucleus receives fibres from the central nucleus of the ipsilateral inferior colliculus via the brachium of the inferior colliculus and from the contralateral inferior colliculus and projects primarily to the primary auditory cortex. It contains a complete tonotopic representation: low-pitched sounds are represented laterally, and progressively higher-pitched sounds are encountered as the nucleus is traversed from lateral to medial. The magnocellular medial nucleus receives fibres from the inferior colliculus and from the deep layers of the superior colliculus and projects diffusely to auditory areas of the cortex and to adjacent insular and opercular fields.

Neurones within the magnocellular subdivision may respond to modalities other than sound, but many cells respond to auditory stimuli, usually to a wider range of frequencies than neurones in the ventral nucleus. Many units show evidence of binaural interaction, with the leading effect arising from stimuli in the contralateral cochlea.

Lateral geniculate nucleus

The lateral geniculate body holds the thalamic relay of the visual pathway. It is a small, ovoid, ventral projection from the posterior thalamus (see Figs 28.5, 30.4). The brachium of the superior colliculus enters the posteromedial part of the lateral geniculate body dorsally, lying between the medial geniculate body and the pulvinar.

The lateral geniculate nucleus is an inverted, somewhat flattened, U-shaped nucleus and is laminated (**Fig. 30.6A**). Its internal organization is usually described on the basis of six laminae, although seven or eight may be present. The laminae are numbered 1–6, from the innermost ventral to the outermost dorsal (**Fig. 30.6B–C**). Laminae 1 and 2 consist of large cells, the magnocellular layers, whereas layers 4–6 have smaller neurones, the parvocellular laminae. The apparent gaps between laminae are the interlaminar zones. Most ventrally, an additional superficial, or S, lamina is recognized.

The lateral geniculate nucleus receives its driver input from the retina. The contralateral nasal hemiretina projects to laminae 1, 4 and 6, whereas the ipsilateral temporal hemiretina projects to laminae 2, 3 and 5. The parvocellular laminae receive axons predominantly of parvocellular (X-type) retinal ganglion cells, i.e. more slowly conducting cells with sustained responses to visual stimuli. The faster-conducting, rapidly adapting magnocellular (Y-type) retinal ganglion cells project mainly to the magnocellular laminae 1 and 2, and give off axonal branches to the superior colliculus. A third type of retinal ganglion cell, the W cells, which have large receptive fields and slow responses, project to both the superior colliculus and the lateral geniculate nucleus, where they terminate particularly in the interlaminar zones and in the S lamina.

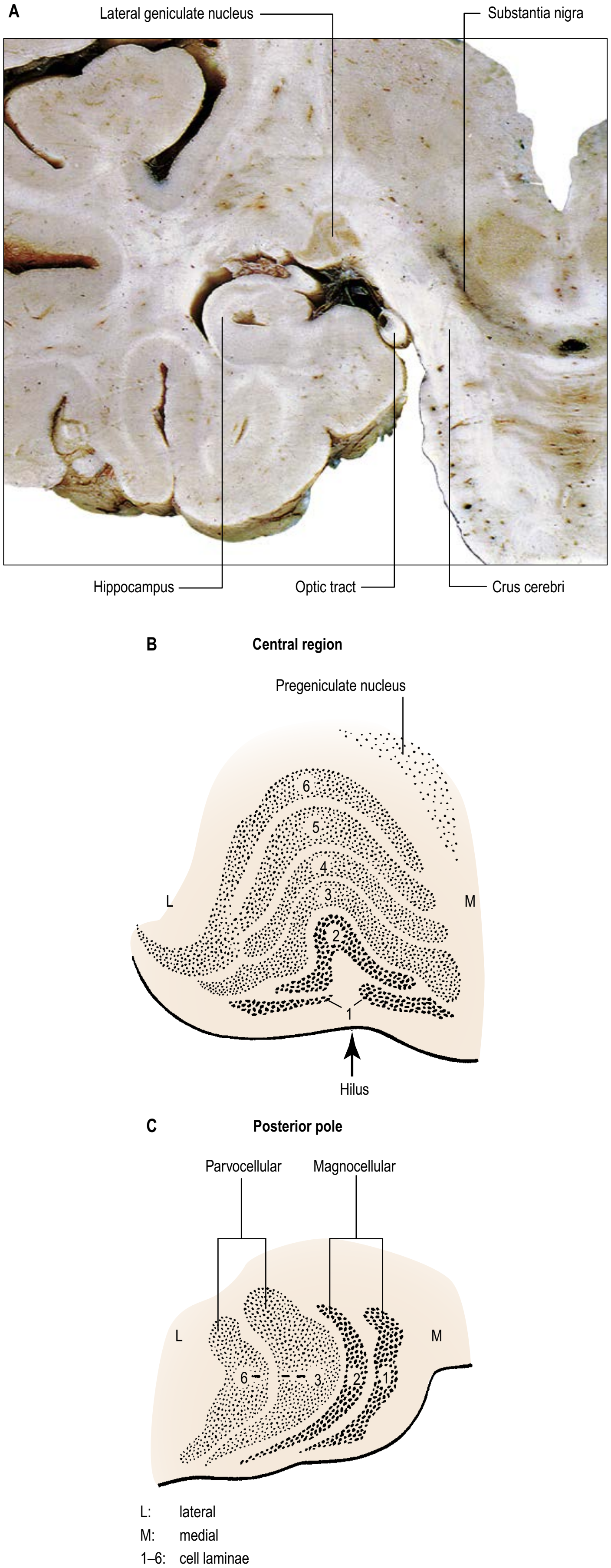

Fig. 30.6 **A**, A coronal section that includes the lateral geniculate nucleus. **B–C**, Coronal sections through the lateral geniculate nucleus illustrating the laminar arrangement of neurones near its central region (**B**) and near its posterior pole (**C**). (A, Photograph by Kevin Fitzpatrick, London.)

The lateral geniculate nucleus is organized in a visuotopic manner and contains a precise map of the contralateral visual field. The vertical meridian is represented posteriorly, the peripheral field anteriorly, the upper field laterally, and the lower field medially. Similar precise, point-to-point representation is also found in the projection of the lateral geniculate nucleus to the visual cortex. Radially arranged neurones in all laminae respond to a single small area of the contralateral visual field and project to a circumscribed area of cortex. The termination of geniculocortical axons in the visual cortex is considered in detail in Chapter 32.

The efferent fibres of the lateral geniculate nucleus pass principally to the primary visual cortex (area 17) in the banks of the calcarine

The axons of a major corticothalamic projection ramify densely in the interlaminar zones. Most of this projection arises from the primary visual cortex, Brodmann's area 17, but smaller projections from extrastriate visual areas pass to the magnocellular and S laminae. Other afferents include fibres from the superficial layer of the superior colliculus (that terminate in the interlaminar zones between laminae 1 and 2, and 2 and 3, and around lamina S); noradrenergic fibres from the locus coeruleus; serotoninergic afferents from the midbrain raphe nuclei; and cholinergic fibres from the pontine and mesencephalic cholinergic nuclei.

sulcus. It is possible that additional small projections pass to extrastriate visual areas in the occipital lobe, possibly arising primarily in the interlaminar zones. For further reading on processing in the lateral geniculate nucleus, see Casagrande and Ichida (2011).

Lateral dorsal nucleus

The lateral dorsal nucleus is the most anterior of the dorsal tier of lateral nuclei and is connected with the cingulate, retrosplenial and posterior parahippocampal cortices, the presubiculum of the hippocampal formation, and the parietal cortex. Its anterior pole lies within a splitting of the internal medullary lamina, and is thus continuous with the anterior nuclei; posteriorly it merges with the lateral posterior nucleus. Subcortical afferents to the lateral dorsal nucleus are from the pretectum and superior colliculus.

Lateral posterior nucleus

The lateral posterior nucleus, which lies dorsal to the ventral posterior nucleus, receives its subcortical afferents from the superior colliculus. It is reciprocally connected with the superior parietal lobe. Additional connections have been reported with the inferior parietal, cingulate and medial parahippocampal cortices.

Pulvinar

The pulvinar corresponds to the posterior expansion of the thalamus and overhangs the superior colliculus (see Fig. 28.5). It is a typical association nucleus that is greatly expanded in humans. It has four major subdivisions, the anterior, medial, lateral and inferior pulvinar nuclei. The anterior pulvinar is posterior to the ventral posteromedial nucleus and lateral to the posterior intralaminar nuclei. The medial pulvinar nucleus is dorsomedial and consists of compact, evenly spaced neurones. The lateral pulvinar nucleus lies laterally, and is traversed by bundles of axons in the mediolateral plane, an arrangement that confers a fragmented appearance of horizontal cords or sheets of cells separated by bundles of fibres. The inferior pulvinar nucleus lies most inferiorly and laterally.

The subcortical afferents to the pulvinar are uncertain. Medial and lateral pulvinar nuclei may receive fibres from the superior colliculus. It has been suggested that the inferior pulvinar nucleus receives fibres both from the superior colliculus and directly from the retina, and that it contains a complete retinotopic representation.

The cortical targets of efferent fibres from the pulvinar are widespread. In essence, the anterior pulvinar nucleus projects to posterior parietal somatosensory association areas and to the insula; the medial pulvinar nucleus projects to association areas of the frontoparietotemporal cortex; and the lateral and inferior pulvinar nuclei project to visual areas in the occipitoparietotemporal cortex. Thus, the inferior pulvinar nucleus connects with the striate and extrastriate cortex in the occipital lobe, and with visual association areas in the posterior part of the temporal lobe. The lateral pulvinar nucleus connects with extrastriate areas of the occipital cortex, with posterior parts of the temporal association cortex and with the parietal cortex. The medial pulvinar nucleus connects with the inferior parietal cortex, with the posterior cingulate gyrus and with widespread areas of the temporal lobe, including the posterior parahippocampal gyrus and perirhinal and entorhinal cortex, and also has extensive connections with prefrontal and orbitofrontal cortices.

Little is known of the functions of the pulvinar. The inferior pulvinar nucleus contains a complete retinotopic representation, and lateral and medial pulvinar nuclei also contain visually responsive cells. However, the latter nucleus, at least, is not purely visual: other modality responses can be recorded and some cells may be polysensory. Given the complexity of functions of the association areas to which they project, particularly in the temporal lobe (e.g. perception, cognition and memory), it is likely that the role of the pulvinar in modulating these functions is equally complex.

Anteriorly, the major subdivisions of the pulvinar blend into a poorly differentiated region, within which several nuclear components have been recognized, including the suprageniculate limitans nucleus and the posterior nuclei. The connectivity of this complex is also not well understood. It is recognized that different components receive subcortical afferents from the spinothalamic tract and the superior and inferior colliculi. Cortical connections centre primarily on the insula and adjacent parts of the parietal operculum posteriorly. Stimulation of this region has been reported to elicit pain, and large lesions may alleviate painful conditions. Similarly, excision of its cortical target in the parietal operculum, or small infarcts in this cortical region, may result in hypoalgesia.

Intralaminar nuclei

The term intralaminar nuclei refers to collections of neurones within the internal medullary lamina of the thalamus (see Fig. 30.4). Two groups of nuclei are recognized. The anterior (rostral) group is subdivided into central medial, paracentral and central lateral nuclei. The posterior (caudal) intralaminar group consists of the centromedian and parafascicular nuclei. The designations central medial and centromedian are open to confusion but they are an accepted part of the terminology of thalamic nuclei that is in common usage. The centromedian nucleus is much larger, is considerably expanded in humans in comparison with other species, and is importantly related to the globus pallidus, striatum, deep cerebellar nuclei and motor cortex. Anteriorly, the internal medullary lamina separates the mediodorsal nucleus from the ventral lateral complex. It is occupied by the paracentral nucleus laterally, and the central medial nucleus ventromedially, as the two laminae converge towards the midline. A little more posteriorly, the central lateral nucleus appears dorsally in the lamina as the latter splits to enclose the lateral dorsal nucleus. More posteriorly, at the level of the ventral posterior nucleus, the lamina splits to enclose the ovoid centromedian nucleus. The smaller parafascicular nucleus lies more medially.

The anterior intralaminar nuclei, i.e. central medial, paracentral and central lateral, have reciprocal connections with widespread cortical areas. There is some evidence of regional specificity: the central lateral nucleus projects mainly to parietal and temporal association areas; the paracentral nucleus to occipitotemporal and prefrontal cortex; and the central medial nucleus to orbitofrontal and prefrontal cortex and to the cortex on the medial surface. In contrast, the posterior nuclei, i.e. centromedian and parafascicular nuclei, have more restricted connections, principally with the motor, premotor and supplementary motor areas. Both anterior and posterior intralaminar nuclei also project to the striatum. Many cells throughout the anterior nuclei have branched axons that pass to both the cortex and the striatum. Dual projections are less frequent in the posterior nuclei. The thalamostriate projection is topographically organized. The posterior intralaminar nuclei receive a major input from the internal pallidum. Additional afferents come from the pars reticulata of the substantia nigra, the deep cerebellar nuclei, the pedunculopontine nucleus of the caudal midbrain, and possibly the spinothalamic tract. The anterior nuclei have widespread subcortical afferents. The central lateral nucleus receives afferents from the spinothalamic tract, and all component nuclei receive fibres from the brainstem reticular formation, the superior colliculus and several pretectal nuclei. Afferents to all intralaminar nuclei from the brainstem include a prominent cholinergic pathway.

The precise functional role of the intralaminar nuclei is unclear. They appear to mediate cortical activation from the brainstem reticular formation and to play a part in sensory–motor integration. Damage to the intralaminar nuclei may contribute to thalamic neglect, i.e. the unilateral neglect of stimuli originating from the contralateral body or extrapersonal space. This may arise particularly from unilateral damage to the centromedian–parafascicular complex. The latter has been targeted in humans for the neurosurgical control of pain and epilepsy. Bilateral injury to the posterior intralaminar nuclei leads to a kinetic mutism with apathy and loss of motivation. A second syndrome associated with damage involving the intralaminar nuclei is that of unilateral motor neglect, in which there is contralateral paucity of spontaneous movement and motor activity.

Midline nuclei

There is considerable divergence between different authorities as to which elements of the medial diencephalon constitute the nuclei of the midline thalamic group. Here, the midline group of nuclei is taken to include those medial thalamic structures ventral to the central medial nucleus, i.e. the rhomboid and reuniens nuclei, and the parataenial nuclei more dorsolaterally.

The midline nuclei receive subcortical afferent fibres from the hypothalamus, the periaqueductal grey matter of the midbrain, the spinothalamic tract and the medullary and pontine reticular formation. They are the major thalamic target of ascending dopaminergic, noradrenergic and serotoninergic axons from the midbrain and pons, locus coeruleus and raphe nuclei, respectively, and they also receive a cholinergic input from the midbrain. Efferents from the midline nuclei pass to the hippocampal formation, the amygdala and the nucleus accumbens. Additional thalamocortical axons reach the cingulate, and possibly the orbitofrontal, cortex. The dual cortical and basal nuclear relationship of these nuclei has often led to their being considered a part of the intralaminar system. The cortical projections are reciprocal. The relationships of the midline nuclei clearly identify them as part of the

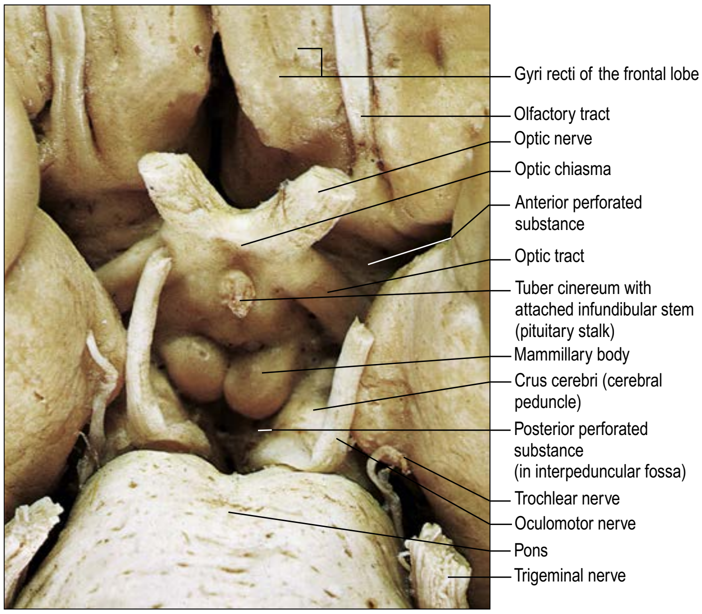
Gyri recti of the frontal lobe
Olfactory tract
Optic nerve
Optic chiasma
Anterior perforated substance
Optic tract
Tuber cinereum with attached infundibular stem (pituitary stalk)
Mammillary body
Crus cerebri (cerebral peduncle)
Posterior perforated substance (in interpeduncular fossa)
Trochlear nerve
Oculomotor nerve
Pons
Trigeminal nerve

Fig. 30.7 The inferior aspect of the hypothalamus and surrounding structures. The cut end of the trochlear nerve on the left side has folded during processing. (Photograph by Kevin Fitzpatrick, London.)

limbic system. There is some evidence that they may play a role in memory and arousal and, pathologically, may be important in the regulation of seizure activity.

Reticular nucleus

The reticular nucleus is believed to function in gating information relayed through the thalamus. It is a curved lamella of large, deeply staining fusiform neurones that wraps around the lateral margin of the thalamus, separated from it by the external medullary lamina. Anteriorly, it curves around the rostral pole of the thalamus. The nucleus is so named because it is criss-crossed by bundles of fibres that, as they pass between thalamus and cortex, produce a reticular appearance.

The reticular nucleus receives collateral branches of corticothalamic, thalamocortical and probably thalamostriatal and pallidothalamic fibres as they traverse it. It receives additional cholinergic, dopaminergic, noradrenergic and serotoninergic afferents. Broadly speaking, the afferents from the cortex and thalamus are topographically arranged. The reticular nucleus contains visual, somatic and auditory regions, each with a crude topographic representation of each sensorium. Cells within these regions respond to visual, somatic or auditory stimuli with a latency, suggesting that these properties arise from activation by thalamocortical axon collaterals. Cells only show modality convergence in areas where representations abut.

The efferent fibres from the reticular nucleus pass into the body of the thalamus and are GABAergic. The projections into the main thalamic nuclei broadly, but not entirely, reciprocate the thalamoreticular connections. There may also be projections to the contralateral dorsal thalamus.

HYPOTHALAMUS

The hypothalamus consists of only 4 cm^3 of neural tissue, or 0.3% of the total brain. Nevertheless, it contains the integrative systems that, via the autonomic and endocrine systems, control fluid and electrolyte balance, food intake and energy balance, reproduction, thermoregulation, and immune and many emotional responses.

The hypothalamus extends rostrocaudally from the lamina terminalis to a vertical plane caudal to the mammillary bodies, and dorsoventrally from the hypothalamic sulcus to the base of the brain inferior to the third ventricle. It lies beneath the thalamus (see Fig. 24.6) and anterior to the tegmental part of the subthalamus and the mesencephalic tegmentum. Laterally, it is bordered by the anterior part of the subthalamus, internal capsule and optic tract. Structures in the floor of the third ventricle reach the pial surface in the interpeduncular fossa. From anterior to posterior they are the optic chiasma, the tuber cinereum, the median eminence and the infundibular stalk, the mammillary bodies and the posterior perforated substance (Fig. 30.7). The latter lies in the interval between the diverging crura cerebri, and is pierced by small central branches of the posterior cerebral arteries. It contains the small interpeduncular nucleus, which receives terminals of the fasciculus retroflexus (habenulo-interpeduncular tract) of both sides, and has other connections with the mesencephalic reticular formation and mammillary bodies.

The mammillary bodies are smooth, hemispherical, pea-sized eminences, lying side by side, anterior to the posterior perforated substance, each with nuclei enclosed in fascicles of fibres derived largely from the fornix. The tuber cinereum, between the mammillary bodies and the optic chiasma, is a convex mass of grey matter from which the median, conical, hollow infundibulum becomes continuous ventrally with the posterior lobe of the hypophysis (neurohypophysis). Around the base of the infundibulum, the median eminence is demarcated by a shallow tubero-infundibular sulcus.

Hypothalamic lesions have long been linked with widespread and bizarre endocrine syndromes and with metabolic, visceral, motor and emotional disturbances. The hypothalamus has major interactions with the neuroendocrine system and the autonomic nervous system, integrating responses to both internal and external afferent stimuli with the complex analysis of the world provided by the cerebral cortex.

The hypothalamus controls the endocrine system in a variety of ways: via magnocellular neurosecretory projections to the neurohypophysis; via parvocellular neurosecretory projections to the median eminence (these control the endocrine output of the anterior hypophysis and thereby the peripheral endocrine organs); and via the autonomic nervous system (Nieuwenhuys 1985). The posterior hypophysial neurohormones, vasopressin and oxytocin, are primarily involved in the control of osmotic homeostasis and various aspects of reproductive function, respectively. Through its effects on the anterior hypophysis, the hypothalamus influences the thyroid gland (thyroid-stimulating hormone, TSH); suprarenal cortex (adrenocorticotrophic hormone, ACTH); gonads (luteinizing hormone, LH; follicle-stimulating hormone, FSH; prolactin); mammary gland (prolactin); and the processes of growth and metabolic homeostasis (growth hormone, GH).

The hypothalamus influences both parasympathetic and sympathetic divisions of the autonomic nervous system. Broadly speaking, parasympathetic effects predominate when the anterior hypothalamus is stimulated and sympathetic effects depend more on the posterior hypothalamus.

Stimulation of the anterior hypothalamus and paraventricular nucleus can cause decreased blood pressure and decreased heart rate. Stimulation in the anterior hypothalamus induces sweating and vasodilation (and thus heat loss) via projections that pass through the medial forebrain bundle to autonomic centres in the brainstem and spinal cord. Damage to the anterior hypothalamus, e.g. during surgery for suprasellar extensions of pituitary tumours, can result in an uncontrollable rise in body temperature. The ventromedial hypothalamus regulates food intake; damage to this nucleus during surgery for hypothalamic lesions (e.g. craniopharyngioma) can result in uncontrolled eating and consequent obesity. Stimulation in the posterior part of the hypothalamus induces sympathetic arousal, producing vasoconstriction, piloerection, shivering and increased metabolic heat production. Circuitry mediating shivering is located in the dorsomedial posterior hypothalamus. This does not, however, imply the existence of discrete parasympathetic and sympathetic 'centres'. Stimuli in many different parts of the hypothalamus can cause profound changes in heart rate, cardiac output, vasomotor tone, peripheral resistance, differential blood flow in organs and limbs, the frequency and depth of respiration, motility and secretion in the alimentary tract, erection and ejaculation.

Hypothalamic zones and nuclei

The hypothalamus contains a number of neuronal groups that have been classified on phylogenetic, developmental, cytoarchitectonic, synaptic and histochemical grounds into named nuclei, many of which are not very clearly delimited, especially in the adult. While the hypothalamus contains a few large myelinated tracts, many of the connections are diffuse and unmyelinated, and the precise paths of many afferent, efferent and intrinsic connections are uncertain.

The hypothalamus can be divided anteroposteriorly into chiasmatic (supraoptic), tuberal (infundibulotuberal) and posterior (mammillary) regions, and mediolaterally into periventricular, intermediate (medial) and lateral zones. Between the intermediate and lateral zones is a paramedian plane that contains the prominent myelinated fibres of the fornix, the mammillothalamic tract and the fasciculus retroflexus. For this reason, some authorities group the periventricular and intermediate zones as a single medial zone. These divisions are artificial and functional systems cross them. The hypothalamic zones, main nuclear groups and myelinated tracts are illustrated in Figs 30.8–30.9 and are summarized in Table 30.3.

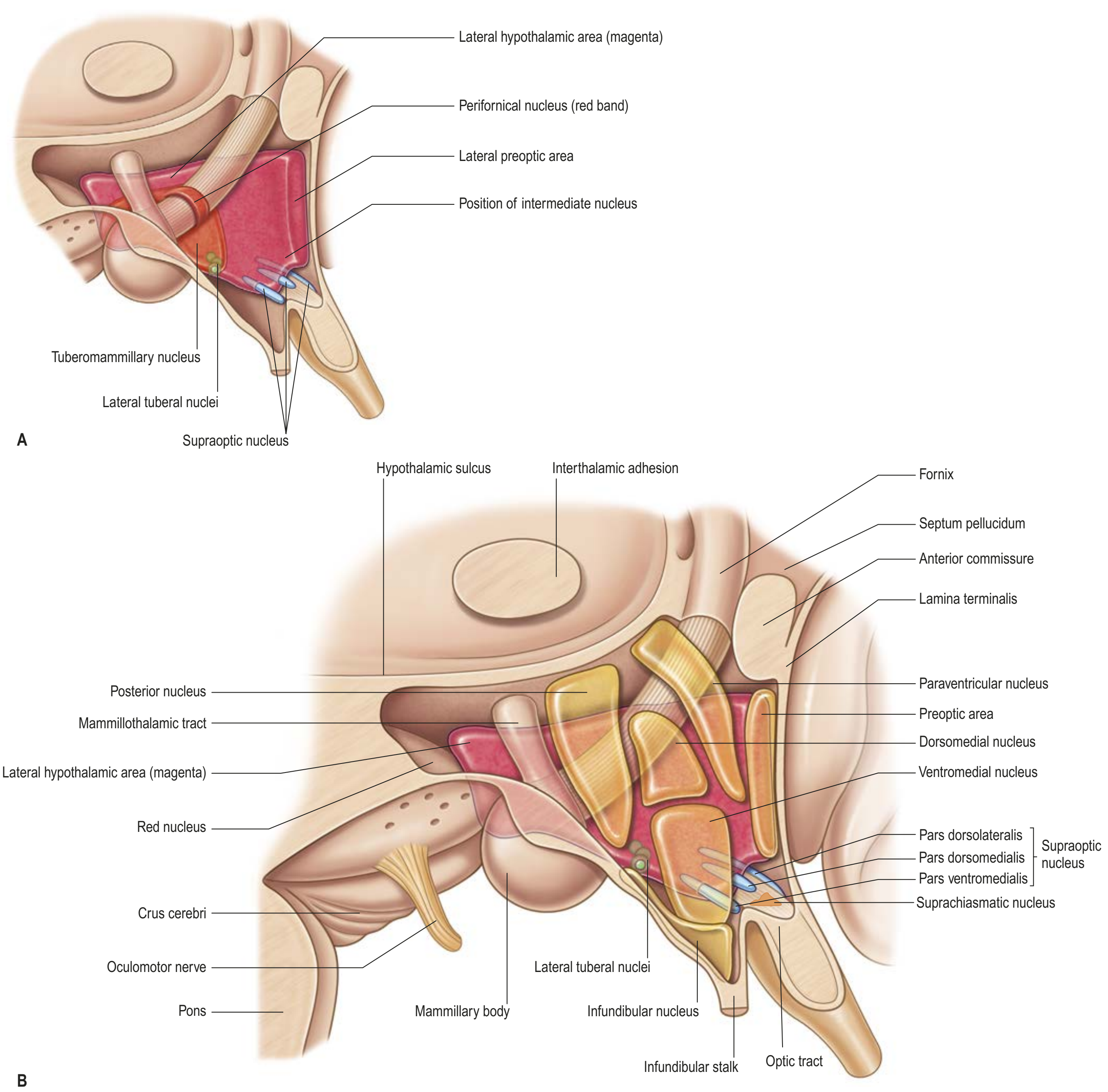
Lateral hypothalamic area (magenta)
Perifornical nucleus (red band)
Lateral preoptic area
Position of intermediate nucleus
Tuberomammillary nucleus
Lateral tuberal nuclei
Supraoptic nucleus
A
Hypothalamic sulcus
Interthalamic adhesion
Fornix
Septum pellucidum
Anterior commissure
Lamina terminalis
Posterior nucleus
Mammillothalamic tract
Lateral hypothalamic area (magenta)
Red nucleus
Paraventricular nucleus
Preoptic area
Dorsomedial nucleus
Ventromedial nucleus
Pars dorsolateralis
Pars dorsomedialis
Pars ventromedialis
Supraoptic nucleus
Suprachiasmatic nucleus
Crus cerebri
Oculomotor nerve
Pons
Mammillary body
Lateral tuberal nuclei
Infundibular nucleus
Infundibular stalk
Optic tract
B

Fig. 30.8 The hypothalamic region of the left cerebral hemisphere viewed from the medial aspect and dissected to display the major hypothalamic nuclei. **A**, The medially placed nuclear groups have been removed. **B**, Both lateral and medial groups are included. Lateral to the fornix and the mammillothalamic tract is the lateral hypothalamic region (magenta), in which the tuberomammillary nucleus is situated posteriorly and the lateral preoptic nucleus rostrally. Surrounding the fornix is the perifornical nucleus, which joins the lateral hypothalamic area with the posterior hypothalamic nucleus. The medially placed nuclei (yellow) fill in much of the region between the mammillothalamic tract and the lamina terminalis, but also project caudal to the tract. The lateral tuberal nuclei are situated ventrally, mainly in the lateral hypothalamic area. The supraoptic nucleus may form three rather separate parts. The intermediate nuclei form three groups between the supraoptic and paraventricular nuclei. (Adapted from Nauta WJH, Haymaker W 1969 Hypothalamic nuclei and fibre connections. In: Haymaker W, Anderson E, Nauta WJH (eds) The Hypothalamus, by permission of Charles C Thomas Publisher, Ltd, Springfield, Illinois.)

The periventricular zone of the hypothalamus borders the third ventricle. The anterior wall of the ventricle contains the vascular organ of the lamina terminalis (OVLT, organum vasculosum), which is continuous dorsally with the medial preoptic nucleus and subfornical organ. The chiasmatic region contains part of the sexually dimorphic medial preoptic nucleus, the suprachiasmatic and supraoptic nuclei, and periventricular neurones that are medial to, and blend with, the paraventricular nucleus. In the tuberal region, the periventricular cell group expands around the base of the third ventricle to form the arcuate nucleus, which overlies the median eminence. The ventromedial and dorsomedial nuclei are located more dorsally in the tuberal region. The posterior region contains the mammillary bodies; more dorsally, the narrow periventricular zone is continuous laterally with the posterior hypothalamic area and behind that with midbrain periaqueductal grey matter. The periventricular zone also contains a prominent periventricular fibre system.

Suprachiasmatic nucleus

Although it contains only a few thousand neurones, the suprachiasmatic nucleus is a remarkable structure (see Fig. 30.8B). Sometimes called the master circadian pacemaker in mammals, it appears to be the neural substrate for day–night cycles in motor activity, body temperature, plasma concentration of many hormones, renal secretion, sleeping and waking, and numerous other variables. Lesions of the suprachiasmatic region lead to a disordered sleep–wake cycle. (For further reading, see Mohawk and Takahashi (2011).)

The suprachiasmatic nucleus has two principal subdivisions: ventrolateral and dorsomedial. Retinal fibres terminate in the ventrolateral subdivision, characterized by neurones that are immunoreactive for vasoactive intestinal polypeptide (VIP). This appears to be a general input zone that also receives afferents from the midbrain raphe and parts

The suprachiasmatic nucleus also influences the activity of preganglionic sympathetic neurones in the upper part of the thoracolumbar outflow. These neurones project to neurones in the superior cervical ganglion, which project to the pineal gland. Circadian variation in this postganglionic sympathetic input causes parallel variation in pineal *N*-acetyltransferase activity and thus pineal melatonin production. The role of the pineal gland in humans is uncertain: pineal tumours can influence reproductive development, and administration of melatonin has been advocated to alleviate jet-lag.

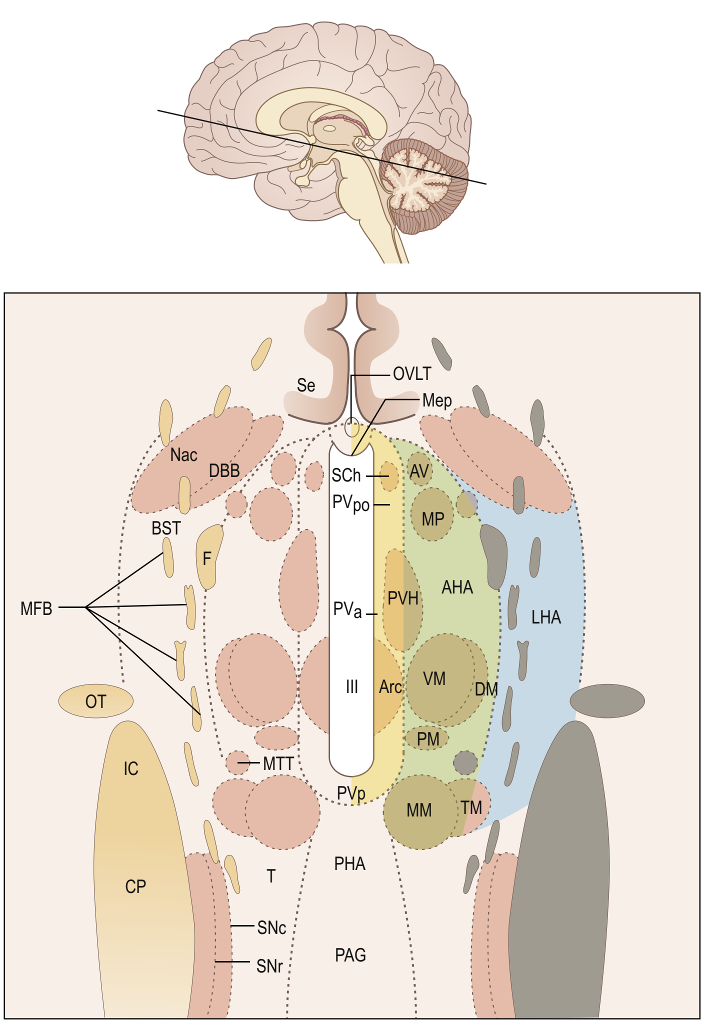

Fig. 30.9 Horizontal section showing the major cell groups and tracts in and around the hypothalamus. The yellow, green and blue areas on the right side represent the periventricular, intermediate and lateral hypothalamic zones, respectively. Abbreviations: III, third ventricle; AHA, anterior hypothalamic area; Arc, arcuate nucleus; AV, anteroventral preoptic nucleus; BST, bed nucleus of stria terminalis; DBB, nucleus of diagonal band; DM, dorsomedial nucleus; LHA, lateral hypothalamic area; MeP, median preoptic nucleus; MM, mammillary body (mainly medial mammillary nucleus); MP, medial preoptic nucleus; Nac, nucleus accumbens; OVLT, vascular organ of the lamina terminalis; PAG, periaqueductal grey matter; PHA, posterior hypothalamic area; PM, posteromedial nucleus in the tuberal region of the hypothalamus; PV, periventricular nucleus (PVa, anterior part; PVp, posterior part; PVpo, preoptic part); PVH, paraventricular (hypothalamic) nucleus; SCh, suprachiasmatic nucleus; Se, septal cortex; SNc, substantia nigra pars compacta; SNr, substantia nigra pars reticulata; T, midbrain tegmentum; TM, tuberomammillary nucleus; VM, ventromedial nucleus. Fibre tracts: CP, cerebral peduncle; F, fornix; IC, internal capsule; MFB, medial forebrain bundle; MTT, mammillothalamic tract; OT, optic tract. (Adapted with permission from Swanson LW, Biochemical switching in hypothalamic circuits mediating responses to stress. Progress in Brain Research, vol. 87, pp. 181–200. Elsevier. Copyright 1991.)

TABLE 30.3 Main hypothalamic nuclei and their functions

Region		Nucleus	Hormone secreted	Function
Chiasmatic	Medial	Median preoptic	GnRH	
		Periventricular	GnRH, somatostatin, CRH, TRH	
		Suprachiasmatic		'Master' clock
	Intermediate	Supraoptic	Vasopressin	
		Paraventricular	Vasopressin, oxytocin	
Tuberal	Medial	Dorsomedial	TRH, ANP	
		Ventromedial	TRH	'Satiety centre'
		Arcuate	GHRH, dopamine	Secrete to portal system
	Lateral	Lateral		'Feeding centre'
Posterior	Medial	Mammillary body		Memory

Abbreviations: ANP, atrial natriuretic peptide; CRH, corticotrophin-releasing hormone; GHRH, growth hormone-releasing hormone; GnRH, gonadotrophin-releasing hormone; TRH, thyrotrophin-releasing hormone.

of the lateral geniculate nucleus of the thalamus. The dorsomedial subdivision has a relatively sparse afferent innervation, and characteristically contains parvocellular neurones that are immunoreactive for arginine vasopressin (AVP). Neurones within the suprachiasmatic nuclei that receive a direct retinal input do not respond to pattern, movement or colour, but operate as luminance detectors, responding to the onset and offset of light: their firing rates vary in proportion to light intensity, thereby synchronizing to the light–dark cycle.

The suprachiasmatic nucleus receives glutamatergic afferents from melanopsin-containing retinal ganglion cells that entrain the rhythm to the light–dark cycle. The rhythm persists in blind patients suffering from retinitis pigmentosa or other conditions that affect the retinal photoreceptors because the melanopsin-containing retinal ganglion cells are intrinsically sensitive to light (i.e. they do not depend on photoreceptor inputs). The suprachiasmatic nucleus contains many different neurotransmitters, including vasopressin, VIP, neuropeptide Y (NPY) and neurotensin. Axons from the suprachiasmatic nucleus pass to numerous other hypothalamic nuclei, including the paraventricular, ventromedial, dorsomedial and arcuate nuclei.

Supraoptic and paraventricular nuclei

The supraoptic nucleus curves over the lateral part of the optic chiasma. It contains a uniform population of large neurones that synthesize vasopressin and oxytocin and project to the neurohypophysis. The magnocellular vasopressin neurones detect as little as 1% increase in the osmotic pressure of the blood and stimulate release of vasopressin from the neurohypophysis: a fall in blood volume or blood pressure greater than 5–10% similarly stimulates the release of vasopressin and the urge to drink. These responses are mediated via volume receptors in the walls of the great veins and atria and baroreceptors in the carotid sinus that all project via the vagus and glossopharyngeal nerves to the nucleus tractus solitarius and thence to the magnocellular nuclei. A biochemical defect in vasopressin production, or interruption of the hypothalamo-hypophysial pathway (e.g. due to a head injury), can cause cranial diabetes insipidus.

The paraventricular nucleus extends from the hypothalamic sulcus downwards across the medial aspect of the column of the fornix, its ventrolateral angle reaching towards the supraoptic nucleus. Its neurones are more diverse than those of the supraoptic nucleus. Magnocellular neurones project to the neurohypophysis and tend to lie laterally; parvocellular neurones project to the median eminence and infundibulum and lie more medially; intermediate-sized neurones may project caudally and lie posteriorly. The axons of paraventricular magnocellular neurones pass towards the supraoptic nucleus, where they join the axons of supraoptic neurones and form a hypothalamo-hypophysial tract that runs down the infundibulum, superficially, into the posterior hypophysis. Here, the axons are distended and branch repeatedly around the capillaries. Vasopressin and oxytocin are produced by separate neurones: those secreting vasopressin tend to cluster in the ventrolateral part of the paraventricular nucleus and neurones secreting oxytocin lie around them.

Periventricular zone and arcuate nucleus

Parvocellular neurosecretory neurones lie principally within the periventricular zone, some in the medial parvocellular part of the paraventricular nucleus and most in the arcuate nucleus. The axons of parvocellular neurones converge on the infundibulum, forming the tubero-infundibular tract that ends on the capillary loops forming the hypophysial portal vessels.

Neurones producing growth hormone-releasing hormone (GHRH) are largely restricted to the arcuate nucleus. Some extend dorsally into the periventricular nucleus and laterally into the retrochiasmatic area. Their fibres run through the periventricular region to the neurovascular zone of the median eminence. The neurones receive afferent information from glucose receptors in the ventromedial nucleus. Inputs from the hippocampal–amygdala–septal complex could explain the release of GH during stress. In humans, midline defects such as septo-optic dysplasia are associated with defective GH secretion. Dopamine has a stimulatory effect.

Neurones producing somatostatin (growth hormone release-inhibiting hormone) are located in the periventricular zone. GHRH and somatostatin are secreted in intermittent (3–5-hour) reciprocal pulses: the origin of the pulses is unclear. A large pulse of GH is secreted at the onset of slow-wave sleep. Somatostatin also inhibits release of TSH in the adenohypophysis.

Neurones producing gonadotrophin-releasing hormone (GnRH) that project to the median eminence are located in the periventricular

The arcuate nucleus is median in the post-infundibular part of the tuber cinereum. It extends forwards into the median eminence and almost encircles the infundibular base, but does not meet anteriorly, where the infundibulum adjoins the median part of the optic chiasma. Its numerous neurones are all small and round in coronal section, and oval or fusiform in sagittal section. No glial layer intervenes between the nucleus and the ependymal tanycytes that line the infundibular recess of the third ventricle. Circadian variation in the secretion of all anterior pituitary hormones suggests that projections from the suprachiasmatic nucleus must reach parvocellular neurosecretory neurones. Afferents from the limbic system probably mediate the widespread effects of stress, and 5-HT (5-hydroxytryptamine, serotonin) and noradrenaline (norepinephrine) from the brainstem influence the output of most anterior pituitary hormones.

The hypothalamus is essential for the control of oxytocin, gonadotrophin and prolactin secretion. The release of oxytocin from neurosecretory nerve terminals in the neurohypophysis induces contraction of the uterus and of the myoepithelial cells that surround the mammary gland alveoli. Two neuroendocrine reflexes are involved. Stretching of the cervix of the uterus during childbirth stimulates a multisynaptic afferent pathway that passes via the pelvic plexus, anterolateral column and brainstem to the magnocellular oxytocin neurones (the Ferguson reflex). This is a positive feedback mechanism, which is terminated by the birth of the baby. The milk ejection reflex is evoked by suckling: mechanical stimulation of the nipple activates a multisynaptic afferent connection to the hypothalamus via the anterior and lateral cutaneous branches of T4 (range T3–T5), the anterolateral column and brainstem. The reflex can be both conditioned to a baby's cry and inhibited by stress.

zone and arcuate nucleus. Other GnRH neurones are found in the median preoptic area, but they appear to project to the vascular organ of the lamina terminalis. LH and FSH are secreted by the adenohypophysis in circhoral (hourly) pulses: secretion is stimulated by GnRH, and influenced by central monoamines and GABA; by oestrogen and progesterone acting indirectly through other neurones; by corticotrophin-releasing factor; and by endogenous opioids. Gonadotrophin-inhibitory hormone (GnIH) is produced by neurones located in the dorsomedial hypothalamic area that project to the median eminence. GnIH inhibits gonadotrophin synthesis and release by decreasing the activity of GnRH neurones and also by acting directly on adenohypophysial gonadotropes.

Corticotrophin-releasing hormone (CRH) is located primarily in parvocellular periventricular neurones. These neurones are profoundly stimulated by neurogenic and hypoglycaemic stress, mediated by limbic input and the ventromedial nucleus, respectively, and are also controlled, via negative feedback, by cortisol levels.

Thyrotrophin-releasing hormone (TRH) neurones are rather more widely distributed in the periventricular, ventromedial and dorsomedial nuclei. TRH release is influenced by core temperature, sensed in the anterior hypothalamus, and by thyroid hormone levels, via negative feedback. It stimulates release of pituitary TSH and also acts to excite cold-sensitive neurones in the preoptic area and to inhibit warm-sensitive ones.

Other tubero-infundibular arcuate neurones contain NPY and neurotensin. Arcuate neurones, containing pro-opiomelanocortin peptides, project to the periventricular nucleus rather than the median eminence.

In addition to these peptide-containing cells, dopamine neurones in the arcuate nucleus (A12 group) have terminals in the median eminence and infundibulum. Dopamine acts as the principal prolactin release-inhibiting hormone, and also inhibits secretion of TSH (likewise, TSH acts as a prolactin-releasing hormone). Noradrenergic terminals are found in the median eminence, where they may act largely in a paracrine manner.

Ventromedial and dorsomedial nuclei

At the tuberal level, the ventromedial nucleus is well-defined by a surrounding neurone-poor zone but the dorsomedial nucleus above it is much less distinct. The ventromedial nucleus contains neurones receptive to plasma levels of glucose and other nutrients, and receives visceral somatic afferents via the nucleus tractus solitarius. The lateral hypothalamus receives olfactory afferents that convey important food signals. Both areas receive extensive inputs from limbic structures.

Bilateral electrolytic lesioning experiments in rats in the 1940s established the involvement of the hypothalamus in regulating food intake and body weight. The ventromedial nucleus was thought to serve as a 'satiety centre', while the lateral hypothalamic acted as a 'feeding centre'. Although the validity of this dual centre model was challenged on methodological grounds (the lesions were imprecise and damaged other cells and tracts), more recent work supports the key role of the ventromedial nucleus in the complex pathways involved in the neuronal regulation of feeding (Ahima and Antwi 2008).

The dorsomedial hypothalamic nucleus is involved in the expression of emotion: its stimulation results in aggressive behaviour that stops when the stimulation ceases.

Mammillary bodies

The prominent medial mammillary nuclei, from which the mammillothalamic and mammillotegmental tracts arise, form the bulk of the mammillary bodies. A group of larger cells occurs along the lateral border of the medial mammillary nucleus, but the existence of a distinct lateral mammillary nucleus is controversial. The tuberomammillary nucleus is lateral to this group.

Lateral zone of the hypothalamus

The lateral zone of the hypothalamus forms a continuum that runs from the preoptic nucleus through the lateral hypothalamic area to the posterior hypothalamus. It contains the lateral hypothalamic nucleus, the perifornical nuclei and the tuberomammillary nucleus. The perifornical nuclei contain neurones that synthetize peptides known as orexins (hypocretins) that are important to maintain wakefulness: their damage results in narcolepsy. They may be also involved in regulating food intake and energy balance. The tuberomammillary nucleus contains histaminergic neurones that diffusely innervate the entire cerebral cortex, hypothalamus, thalamus and brainstem.

Connections of the hypothalamus

The hypothalamus has reciprocal interaction with the rest of the body via two (possibly three) routes: neural connections, the blood stream and (possibly) the cerebrospinal fluid.

Some hypothalamic neurones have specific receptors that sense the temperature, osmolarity, glucose, free fatty acid and hormone content of the blood. Neurosecretory neurones secrete neurohormones into the blood. These control the anterior hypophysis and act on organs such as the kidney, breast, uterus and blood vessels. Some of the neural connections, especially those to the mammillary bodies, form discrete myelinated fascicles, but most are diffuse and unmyelinated, and their origin and termination are uncertain. Most pathways are multisynaptic and many of the synapses on hypothalamic neurones are derived from intrinsic interneurones.

Broadly, neural inputs to the hypothalamus are derived from the ascending visceral and somatic sensory systems, the visual and olfactory systems, and numerous tracts from the brainstem, thalamus, 'limbic' structures and neocortex. Efferent neural projections are reciprocal to most of these and, in particular, they impinge on and control the central origins of autonomic nerve fibres. The hypothalamus, therefore, exerts control via the autonomic and endocrine systems and through its connections to the telencephalon.

Afferent connections

The hypothalamus receives visceral, gustatory and somatic sensory information from the spinal cord and brainstem. It receives largely polysynaptic projections from the nucleus tractus solitarius, probably directly and indirectly via the parabrachial nucleus and medullary noradrenergic cell groups (ventral noradrenergic bundle); collaterals of spinothalamic and lemniscal somatic afferents (to the lateral hypothalamus); and projections from the reticular formation. Many enter via the medial forebrain bundle (see Fig. 30.9) and periventricular fibre system. Others converge in the midbrain tegmentum, forming the mammillary peduncle to the mammillary body.

The major forebrain inputs to the hypothalamus are derived from structures in the limbic system, including the hippocampal formation, amygdala and septum, and from the piriform cortex and adjacent neocortex. These connections, which are reciprocal, form prominent fibre systems, i.e. the fornix, stria terminalis and ventral amygdalofugal tracts.

The hippocampal formation, and the subiculum in particular, is reciprocally connected to the hypothalamus by the fornix, a complex tract that also contains commissural connections. As the fornix curves ventrally towards the anterior commissure, it is joined by fascicles from the cingulate gyrus, indusium griseum and the septal area. It divides around the anterior commissure into pre- and postcommissural parts. The precommissural fornix is distributed to the orbital and medial frontal cortex, and to the septum and preoptic hypothalamus; the septum sends numerous fibres to the hypothalamus. The postcommissural fornix passes ventrally and posteriorly through the hypothalamus to the medial mammillary nucleus, giving off many fibres to the medial and lateral hypothalamic nuclei in its course.

The amygdala innervates most hypothalamic nuclei anterior to the mammillary bodies. Its corticomedial nucleus innervates preoptic and anterior hypothalamic areas and the ventromedial nucleus. The central nuclei project to the lateral hypothalamus, their fibres reaching the hypothalamus by two routes. The short ventral amygdalofugal path passes medially over the optic tract, beneath the lentiform complex, to reach the hypothalamus. The long, curved stria terminalis runs parallel to the fornix, separated from it by the lateral ventricle, passes through the bed nucleus of the stria terminalis and is distributed to the anterior hypothalamus via the medial forebrain bundle.

Olfactory afferents reach the hypothalamus largely via the nucleus accumbens and septal nuclei, and most terminate in the lateral hypothalamus. Visual afferents leave the optic chiasma and pass dorsally into the suprachiasmatic nucleus. No auditory connections have been identified, though it is clear that such stimuli influence hypothalamic activity. However, many hypothalamic neurones respond best to complex sensory stimuli, suggesting that sensory information reaching the neocortex has converged and been processed by the amygdala, hippocampus and neocortex. Neocortical corticohypothalamic projections arise from frontal and insular cortices and end in lateral, chiasmatic, tuberal and posterior hypothalamic nuclei.

Like the rest of the forebrain, the hypothalamus receives diffuse aminergic inputs from the locus coeruleus, dopaminergic nuclei and raphe nuclei. It also receives input from ascending cholinergic fibres. A noradrenergic input reaches the dorsomedial, periventricular, The ventromedial nucleus, lateral hypothalamic area and paraventricular nucleus also influence intermediate metabolism through the autonomic and endocrine systems. These appear to complement the effects on feeding behaviour. Thus, ventromedial stimulation facilitates glucagon release and increases glycogenolysis, gluconeogenesis and lipolysis, whereas lateral hypothalamic stimulation causes insulin release and the opposite metabolic effects. Lesions of the ventromedial nucleus also cause increased vagal and decreased sympathetic tone.

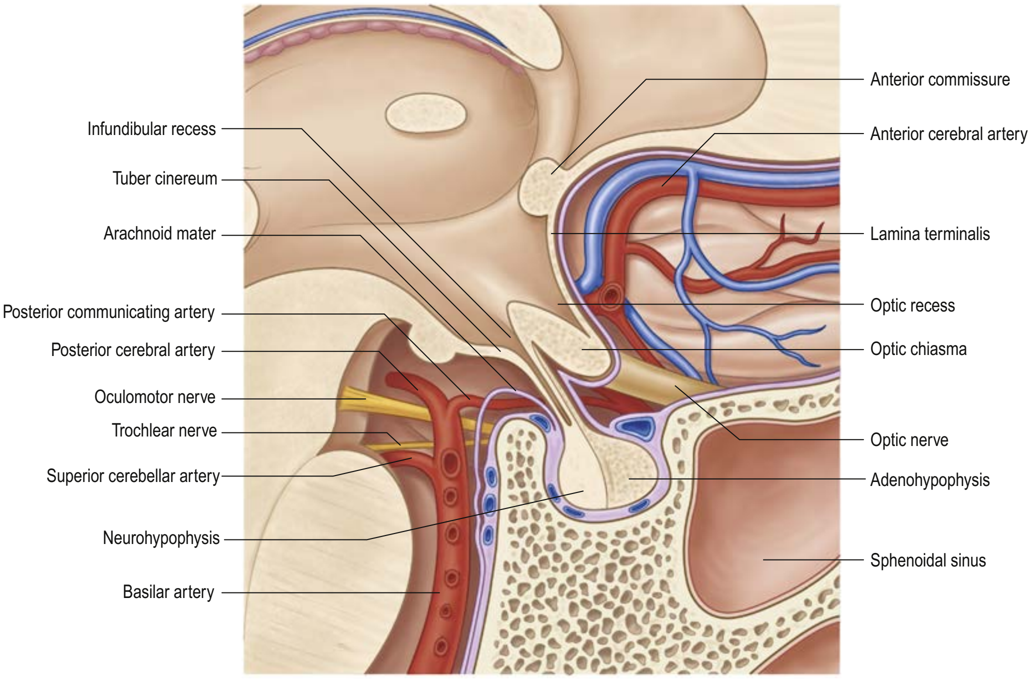

Fig. 30.10 Median section through the pituitary gland.

paraventricular, supraoptic and lateral hypothalamic nuclei. The periaqueductal dopaminergic group A11 innervates the medial hypothalamic nuclei, and hypothalamic dopaminergic groups A13 and A14 innervate the dorsal and rostral hypothalamic nuclei. Many of these fibres also run in the medial forebrain bundle.

The medial forebrain bundle is a loose grouping of fibre pathways that run longitudinally through the lateral hypothalamus (see Fig. 30.9). It connects forebrain autonomic and limbic structures with the hypothalamus and brainstem, receiving and giving off small fascicles throughout its course. It contains descending hypothalamic afferents from the septal area and orbitofrontal cortex, ascending afferents from the brainstem, and efferents from the hypothalamus.

Efferent connections

Hypothalamic efferents include reciprocal paths to the limbic system, descending polysynaptic paths to autonomic and somatic motor neurones, and neural and neurovascular links with the pituitary gland (hypophysis).

Septal areas and the amygdaloid complex have reciprocal hypothalamic connections along the paths described above. The medial preoptic and anterior hypothalamic areas give short projections to nearby hypothalamic groups. The ventromedial nucleus has more extensive projections that pass via the medial forebrain bundle to the bed nucleus of the stria terminalis, nucleus basalis (basal nucleus of Meynert), central nucleus of the amygdala, and midbrain reticular formation. The posterior hypothalamus projects largely to the midbrain central grey matter. Some tuberal and posterior lateral hypothalamic neurones project directly to the entire neocortex and appear to be essential for maintaining cortical arousal.

Hypothalamic neurones projecting to autonomic neurones are found in the paraventricular nucleus (oxytocin and vasopressin neurones), perifornical and dorsomedial nuclei (atrial natriuretic peptide neurones), lateral hypothalamic area (α-melanocyte-stimulating hormone; α-MSH neurones) and zona incerta (dopamine neurones). These fibres run through the medial forebrain bundle into the tegmentum, ventrolateral medulla and dorsal lateral funiculus of the spinal cord. In the brainstem, fibres innervate the parabrachial nucleus, nucleus ambiguus, nucleus tractus solitarius and dorsal motor nucleus of the vagus. In the spinal cord, they terminate on sympathetic and parasympathetic preganglionic neurones in the intermediolateral column. Both oxytocin- and vasopressin-containing fibres can be traced to the most caudal spinal autonomic neurones.

The medial mammillary nucleus gives rise to a large ascending fibre bundle that diverges into the mammillothalamic and mammillotegmental tracts (see Fig. 30.9). The mammillothalamic tract ascends through the lateral hypothalamus to reach the anterior thalamic nuclei, from which massive projections radiate to the cingulate gyrus. The mammillotegmental tract curves inferiorly into the midbrain ventral to the medial longitudinal fasciculus and is distributed to tegmental reticular nuclei.

PITUITARY GLAND (HYPOPHYSIS)

The pituitary gland (hypophysis) is a reddish-grey, ovoid body, about 12 mm in transverse and 8 mm in anteroposterior diameter, and with an average adult weight of 500 mg (**Fig. 30.10**; see Fig. 25.20). It is continuous with the infundibulum, a hollow, conical, inferior process from the tuber cinereum of the hypothalamus, and lies within the pituitary (hypophysial) fossa of the sphenoid bone, where it is covered superiorly by a circular diaphragma sellae of dura mater. The latter is pierced centrally by an aperture for the infundibulum and separates the anterosuperior aspect of the pituitary gland from the optic chiasma. Inferiorly, the gland is separated from the floor of the fossa by a venous sinus that communicates with the circular sinus. The meninges blend with the capsule of the pituitary gland and are not separate layers.

The pituitary gland has two major parts, the neurohypophysis, which is posterior, and the adenohypophysis, which is anterior (Sam and Frohman 2008). They differ in their origin, structure and function. The neurohypophysis is a diencephalic downgrowth connected with the hypothalamus and the adenohypophysis is an ectodermal derivative of the stomatodeum (Ch. 14).

Both the neurohypophysis and the adenohypophysis include parts of the infundibulum (whereas the older descriptive terms, 'anterior lobe' and 'posterior lobe', do not). The infundibulum has a central infundibular stem that contains neural hypophysial connections and is continuous with the median eminence of the tuber cinereum. The neurohypophysis includes the pars posterior (pars nervosa, posterior or neural lobe), infundibular stem and median eminence. The adenohypophysis includes the pars anterior (pars distalis or glandularis), pars intermedia and pars tuberalis. The latter surrounds the infundibular stem.

Neurohypophysis

Axons arising from groups of hypothalamic neurones (e.g. the magnocellular neurones of the supraoptic and paraventricular nuclei) terminate in the neurohypophysis. The long magnocellular axons pass to the main mass of the neurohypophysis: they form the neurosecretory hypothalamohypophysial tract and terminate near the sinusoids of the posterior lobe. The neurohormones stored in the main part of the neurohypophysis are vasopressin (antidiuretic hormone; ADH), which controls reabsorption of water by renal tubules, and oxytocin, which promotes the contraction of uterine smooth muscle in childbirth and the ejection of milk from the breast during lactation (pituitary hormones are summarized in **Table 30.4**). Storage granules containing active hormone polypeptides bound to a transport glycoprotein, neurophysin, pass down axons from their site of synthesis in the neuronal somata (**Fig. 30.11**).

Adenohypophysis

The adenohypophysis is highly vascular. It consists of epithelial cells of varying size and shape arranged in cords or irregular follicles, between

The unmyelinated axons of the neurohypophysis are ensheathed by typical astrocytes in the infundibulum. Near the posterior lobe, astrocytes are replaced by pituicytes, dendritic neuroglial cells of variable appearance, often with long processes running parallel to adjacent axons and that constitute most of the non-excitable tissue in the neurohypophysis. Typically, their cytoplasmic processes end on the walls of capillaries and sinusoids between nerve terminals. Axons also end in perivascular spaces, lying close to the walls of the sinusoids but separated from them by two basal laminae, one around the nerve endings and the other underlying the fenestrated endothelial cells. The spaces between the basal laminae are occupied by fine collagen fibrils.

The trabecula is a compact band of connective tissue and blood vessels lying within the pars distalis on either side of the midline; it forms a prominent fibrovascular tuft close to the junction of the central and lateral parts of the pars distalis (Xuereb et al 1954).

which lie thin-walled vascular sinusoids supported by a delicate reticular connective tissue (**Fig. 30.12**). Most of the hormones synthesized by the adenohypophysis are trophic (see Table 30.4). They include GH, involved in the control of body growth, and prolactin, which stimulates growth of breast tissue and milk secretion; TSH, which stimulates thyroid follicular cells to release thyroxine (T4) and triiodothyronine (T3); FSH, which stimulates growth and secretion of oestrogens in ovarian follicles and spermatogenesis in the testis; and LH, which induces progesterone secretion by the corpus luteum and testosterone synthesis by Leydig cells in the testis. The pro-hormone pro-opiomelanocortin (POMC), synthesized in the adenohypophysis and in the arcuate nucleus of the hypothalamus, is post-translationally cleaved into a number of peptide hormones including adrenocorticotropin (ACTH), α-, β- and γ-melanocyte stimulating hormone (MSH) and β-lipotropin in the corticotrophs of the adenohypophysis, and β-endorphin in the melanotrophs of the pars intermedia (Cawley et al 2016, Navarro et al 2016, Toda et al 2017).

Neurones that secrete the peptides and amines that control the adenohypophysis are widely distributed within the hypothalamus, mainly in the periventricular zone, arcuate nucleus and medial parvocellular part of the paraventricular nucleus.

TABLE 30.4 Pituitary hormones

Hormone	Cell type	Function/effector site	Releasing factor	Inhibitor
ACTH	Corticotrophs (basophils)	Suprarenal cortex	CRH	
TSH	Thyrotrophs (basophils)	Thyroid gland	TRH	Somatostatin
LH, FSH	Gonadotrophs (basophils)	Gonads	GnRH (pulsatile)	GnIH
GH	Somatotrophs (acidophils)	Body growth and metabolism	GHRH	Somatostatin
Prolactin	Lactotrophs (acidophils)	Mammary gland		Dopamine
Vasopressin (ADH)	Magnocellular hypothalamic neurones	Water absorption in distal renal tubule		
Oxytocin	Magnocellular hypothalamic neurones	Contraction of uterine smooth muscle and ejection of breast milk		

Abbreviations: ACTH, adrenocorticotrophic hormone; ADH, antidiuretic hormone; CRH, corticotrophin-releasing hormone; FSH, follicle-stimulating hormone; GH, growth hormone; GHRH, growth hormone-releasing hormone; GnIH, gonadotrophin-inhibitory hormone; GnRH, gonadotrophin-releasing hormone; LH, luteinizing hormone; TRH, thyrotrophin-releasing hormone; TSH, thyroid-stimulating hormone.

Arteries and veins of the pituitary gland

The arteries of the pituitary arise from the internal carotid arteries via a single inferior and several superior hypophysial arteries on each side (Page 1982). The former come from the cavernous part of the internal carotid artery, the latter from its supraclinoid part and from the anterior and posterior cerebral arteries. The inferior hypophysial arteries divide into medial and lateral branches, which anastomose across the midline and form an arterial ring around the infundibulum. Fine branches from this circular anastomosis enter the neurohypophysis to supply its capillary bed. The superior hypophysial arteries supply the median eminence, upper infundibulum and the lower infundibulum. A confluent capillary net, extending through the neurohypophysis, is supplied by both sets of hypophysial vessels. Reversal of flow can occur in cerebral capillary beds lying between the two supplies.

The arteries of the median eminence and infundibulum end in characteristic sprays of capillaries, which are most complex in the

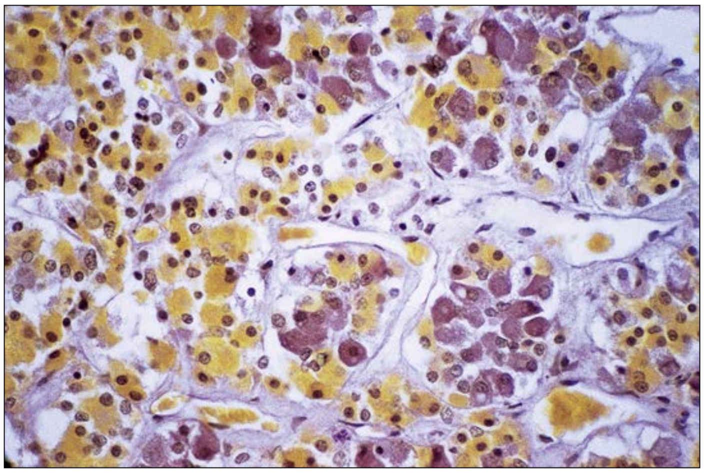

Fig. 30.12 The endocrine cells of the adenohypophysis (trichrome-stained). Chromophils can be distinguished as acidophils (yellow) and basophils (pink), whereas chromophobes are pale-staining cells. A network of sinusoids is seen between clusters of secretory cells.

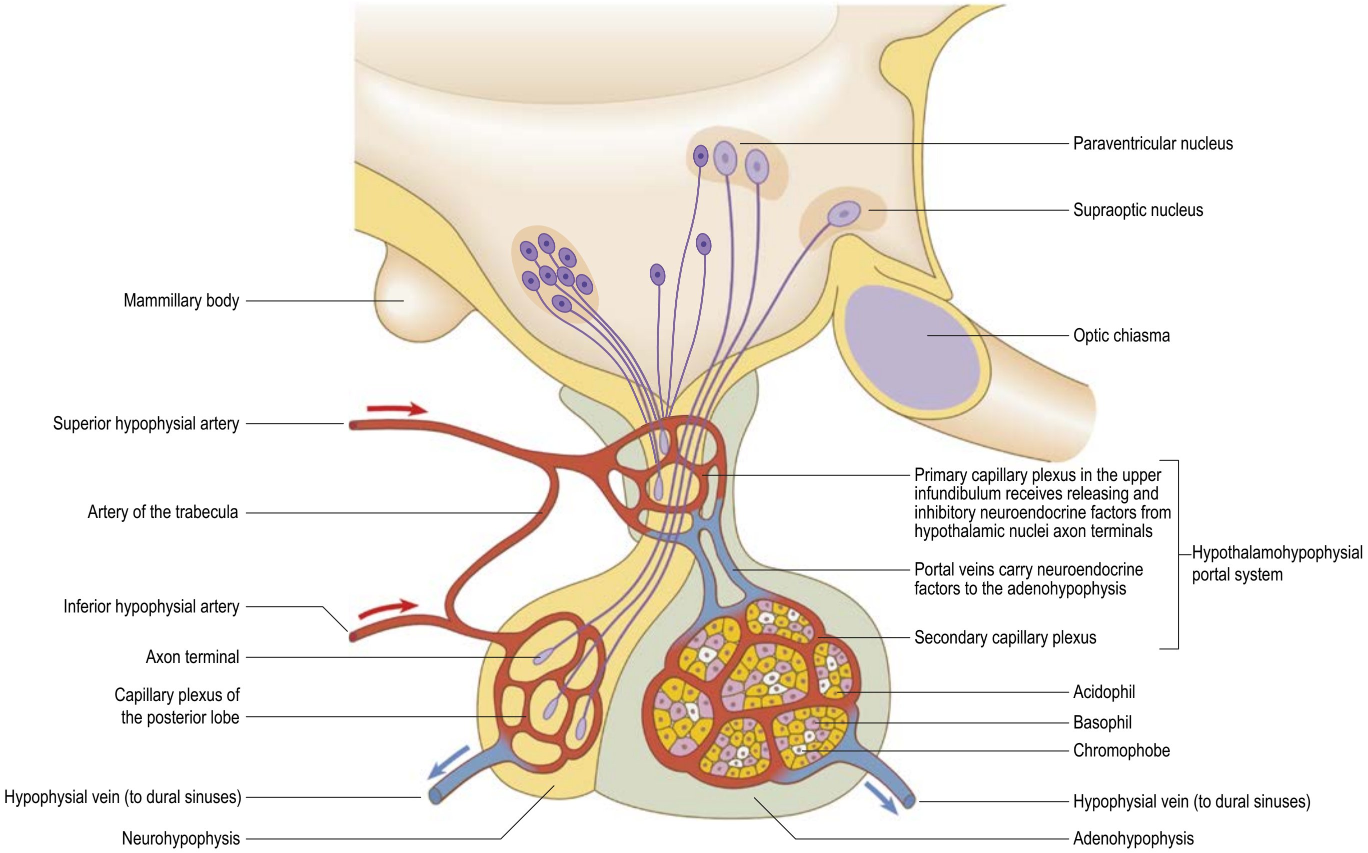
Paraventricular nucleus
Supraoptic nucleus
Mammillary body
Optic chiasma
Superior hypophysial artery
Artery of the trabecula
Primary capillary plexus in the upper infundibulum receives releasing and inhibitory neuroendocrine factors from hypothalamic nuclei axon terminals
Portal veins carry neuroendocrine factors to the adenohypophysis
Hypothalamohypophysial portal system
Inferior hypophysial artery
Secondary capillary plexus
Axon terminal
Acidophil
Capillary plexus of the posterior lobe
Basophil
Chromophobe
Hypophysial vein (to dural sinuses)
Hypophysial vein (to dural sinuses)
Neurohypophysis
Adenohypophysis

Fig. 30.11 The main systems controlling the endocrine secretory activities of the pituitary gland.

upper infundibulum. In the median eminence, these form an external or 'mantle' plexus and an internal or 'deep' plexus. The external plexus, fed by the superior hypophysial arteries, is continuous with the infundibular plexus and is drained by long portal vessels that descend to the pars anterior. The internal plexus lies within and is supplied by the external plexus. It is continuous posteriorly with the infundibular capillary bed and, like the external plexus, is drained by long portal vessels. Short portal vessels run from the lower infundibulum to the pars anterior. Both types of portal vessel open into vascular sinusoids, which lie between the secretory cords in the adenohypophysis and provide most of its blood. There is no direct arterial supply to the adenohypophysis. The portal system carries hormone-releasing and hormone-inhibiting hormones synthesized in parvocellular hypothalamic neurones, and these control the secretory cycles of cells in the adenohypophysis.

There are three possible routes for venous drainage of the neurohypophysis: via long and short portal vessels to the adenohypophysis; via the large inferior hypophysial veins into the dural venous sinuses; via capillaries passing to the median eminence to the hypothalamus. The venous drainage carries hypophysial hormones from the gland to their targets and also facilitates feedback control of secretion. The venous drainage of the adenohypophysis appears more restricted because few vessels connect it directly to the systemic veins.

SUBTHALAMUS

The subthalamus is a complex region of nuclear groups and fibre tracts. The main nuclear groups are the subthalamic nucleus, the reticular nucleus, the zona incerta, the fields of Forel and the pregeniculate nucleus tracts (see Fig. 31.11). The rostral poles of the red nucleus and substantia nigra also extend into this area. The main subthalamic tracts are the upper parts of the medial, spinal and trigeminal lemnisci and the solitariothalamic tract, which all approach their terminations in the thalamic nuclei; the dentatothalamic tract from the contralateral superior cerebellar peduncle; the fasciculi lenticularis, retroflexus and subthalamicus; the ansa lenticularis; fascicles from the prerubral field (H field of Forel); the continuation of the fasciculus lenticularis (in the H_2 field of Forel); and the fasciculus thalamicus (the H_1 field of Forel).

Subthalamic nucleus

The subthalamic nucleus is structurally and functionally related to the basal ganglia and is therefore considered with them in Chapter 31.

Zona incerta and fields of Forel

The zona incerta is an aggregation of small cells that lies between the ventral part of the external medullary lamina of the thalamus and the cerebral peduncle. It extends from the rostral pole of the thalamus, level with the caudal pole of the hypothalamic paraventricular nucleus, to the rostral pole of the medial geniculate nucleus. The central portion of the zona incerta (dorsal zona incerta) lies between the subthalamic nucleus (ventrolaterally), the ventrolateral and ventromedial thalamic nuclei (dorsally) and the superior cerebellar peduncle medially. Caudally, the zona incerta lies between the base of the cerebral peduncle and the substantia nigra ventrolaterally, the thalamic fasciculus (H_1 field of Forel) and ventroposterior thalamic nucleus dorsally, the subthalamic nucleus anteriorly, and the lateral and medial lemnisci posteriorly (Watson et al 2014).

The zona incerta receives fibres from the sensorimotor cortex, the pregeniculate nucleus, the deep cerebellar nuclei, the trigeminal nuclear complex and the spinal cord. It contains neurones that project to the cerebral cortex, superior colliculus, pretectal region and basilar pons.

The H fields of Forel lie within the posterior subthalamus: they consist of a scattered group of cells in a dense matrix of fibres that include corticofugal, pallidothalamic and cerebellothalamic projections (Neudorfer and Maarouf 2018) (Ch. 31). Field H_1 of Forel consists of the thalamic fasciculus, which lies dorsal to the zona incerta. Field H_2 of Forel contains the fasciculus lenticularis and lies ventrally, between the zona incerta and the subthalamic nucleus (see Fig. 31.11).The scattered neurones of the H field of Forel (prerubral area) receive afferents from the spinal cord (fibres of the medial and trigeminal lemniscus and spinothalamic tract), the reticular formation of the brainstem and, possibly, the internal pallidum.

In addition to terminal parts of the lemniscal and dentatothalamic tracts, the subthalamus contains massive fibre tracts derived from the globus pallidus. The fasciculus lenticularis is the dorsal component of pallidofugal fibres that traverse the internal capsule. It turns medially near the medial aspect of the capsule, partly intermingled with the dorsal zone of the subthalamic nucleus and the ventral part of the zona incerta, where the fasciculus traverses the H_2 field of Forel. Reaching the medial border of the zona incerta, the fasciculus intermingles with fibres of the ansa lenticularis, scattered elements of the prerubral nucleus, and dentatothalamic fibres.

The ansa lenticularis has a complex origin from both parts of the globus pallidus and possibly other adjacent structures. It curves medially round the ventral border of the internal capsule and continues dorsomedially to mingle with other fibres in the prerubral field. Some of the fibres in the fasciculus lenticularis and ansa lenticularis synapse in the subthalamic nucleus, prerubral field and zona incerta. The remainder continue medially, with other fascicles, into the thalamic nuclei, particularly the ventral anterior, ventral lateral and centromedian nuclei.

The thalamic fasciculus extends from the prerubral field; its territory is termed the H_1 field of Forel. It lies dorsal to, and also partly traverses, the zona incerta, and is related dorsally to the ventral thalamic nuclei. It contains continuations of the fasciculus lenticularis and ansa lenticularis, dentatothalamic and thalamostriate fibres.

The subthalamic fasciculus connects the subthalamic nucleus with the globus pallidus. It contains an abundant two-way array of fibres that traverse the internal capsule, interweaving with it at right-angles.

EPITHALAMUS

The epithalamus consists of the anterior and posterior paraventricular nuclei, the medial and lateral habenular nuclei, the stria medullaris thalami, the posterior commissure and the pineal body.

Habenular nuclei and stria medullaris thalami

The habenular nuclei lie posteriorly at the dorsomedial aspect of the thalamus, immediately deep to the ependyma of the third ventricle; the stria medullaris thalami are superior and lateral (see Fig. 30.3). Each nucleus is divided into medial and lateral parts, connected by the habenular commissure. Experimental evidence from electrophysiological studies in monkeys, optogenetic studies in rodents and genetic studies in fish have revealed that habenular neurones are predominantly glutamatergic, but neurones in the ventral medial habenula co-release acetylcholine and those in the dorsal medial habenula co-release the neuropeptide substance P (Namboodiri et al 2016).

The fasciculus retroflexus (habenulo-interpeduncular tract) emerges from the ventral margin of the nuclei and courses ventrally, skirts the inferior zone of the thalamic mediodorsal nucleus, and traverses the parafascicular thalamic nucleus and the superomedial region of the red nucleus to reach the interpeduncular nucleus. The habenular nuclear complex is limited laterally by a fibrous lamina that enters the fasciculus retroflexus. Posteriorly, the nuclei of the two sides and the internal medullary laminae are linked across the midline by the habenular commissure. The tela choroidea of the third ventricle usually arises from the ependyma at the superolateral corner of the medial habenular nucleus.

Afferent fibres to the habenular nuclei travel in the stria medullaris from the prepiriform cortex bilaterally, the nucleus basalis (of Meynert) and the hypothalamus. Afferents from the internal pallidum ascend through the thalamus and may be collaterals of pallidothalamic axons. Additional inputs come from the pars compacta of the substantia nigra, the midbrain raphe nuclei and the lateral dorsal tegmental nucleus. The afferent pathways mostly end in the lateral habenular nucleus; the only identified afferent fibres to the medial habenular nucleus come from the septofimbrial nucleus.

The medial habenular nucleus sends efferent fibres to the interpeduncular nucleus of the midbrain. The lateral habenular nucleus sends fibres to the raphe nuclei and the adjacent reticular formation of the midbrain, the pars compacta of the substantia nigra and the ventral tegmental area, and the hypothalamus and basal forebrain. Collectively, the main habenular outflow reaches the interpeduncular nucleus, mediodorsal thalamic nucleus, mesencephalic tectum and reticular formation: the largest component constitutes the fasciculus retroflexus to the interpeduncular nucleus. The latter provides relays to the midbrain reticular formation, from which tecto-tegmento-spinal tracts and dorsal longitudinal fasciculi connect with autonomic preganglionic neurones controlling salivation, gastric and intestinal secretory activity and motility, and motor nuclei for mastication and deglutition.

The stria medullaris crosses the superomedial thalamic aspect, skirts medial to the habenular trigone and sends many fibres into the ipsilateral habenula. Other fibres decussate, as the habenular commissure, to reach the contralateral habenula. Some fibres are really commissural and interconnect the amygdaloid complexes and hippocampal cortices. They are accompanied by crossed tectohabenular fibres. Serotonin-containing fibres from the ventral ascending tegmental serotoninergic bundle, which join the fasciculus retroflexus to reach the nuclei, may control neurones of the habenulopineal tract, and thus influence innervation of pinealocytes. Similarly, habenular nuclear afferents from the dorsal ascending tegmental noradrenergic bundle may influence pinealocytes.

What little is known about the physiological functions of the habenular nuclei in humans is based very largely on research in non-human primates and rats (Boulos et al 2017). Together with the stria medullaris and fasciculus retroflexus, the habenula is considered to be part of the dorsal diencephalic conduction system that is thought to play crucial roles in the modulation of reward and goal-directed behaviours (Fakhoury 2018) and has also been implicated in regulation of sleep homeostasis, anxiety, pain and analgesia.

Posterior commissure

The posterior commissure is a small fasciculus that decussates in the inferior pineal lamina. Various small nuclei are associated with it, including the interstitial nuclei of the posterior commissure; the nucleus of Darkschewitsch in the periaqueductal grey matter; and the interstitial nucleus of Cajal near the upper end of the oculomotor complex, closely linked with the medial longitudinal fasciculus. Fibres from all these nuclei and the medial longitudinal fasciculus cross in the posterior commissure. It also contains fibres from thalamic and pretectal nuclei and the superior colliculi, and fibres that connect the tectal and habenular nuclei. The destinations and functions of many of these fibres are obscure.

Pineal gland

The pineal gland or epiphysis cerebri (see Fig. 25.20) is a small, reddish-grey organ, occupying a depression between the superior colliculi. It is inferior to the splenium of the corpus callosum, from which it is separated by the tela choroidea of the third ventricle and the contained cerebral veins: it is enveloped by the lower layer of the tela, which is reflected from the gland to the tectum. The pineal is about 8 mm long. Its base, directed anteriorly, is attached by a peduncle, which divides into inferior and superior laminae that are separated by the pineal recess of the third ventricle and contain the posterior and habenular commissures, respectively. Aberrant commissural fibres may invade the gland but do not terminate near parenchymal cells.

Septa extend into the pineal gland from the surrounding pia mater. They divide the gland into lobules and carry blood vessels and sympathetic axons. The pineal gland has a rich blood supply: pineal arteries are branches of the medial posterior choroidal arteries, which are themselves branches of the posterior cerebral artery. Within the gland, branches of the arteries supply fenestrated capillaries where the endothelial cells rest on a tenuous and sometimes incomplete basal lamina. The capillaries drain into numerous pineal veins that open into the internal cerebral veins and/or into the great cerebral vein. Unmyelinated postganglionic adrenergic sympathetic axons (derived from neurones in the superior cervical ganglion) enter the dorsolateral aspect of the pineal gland from the region of the tentorium cerebelli as the nervus conarii, which may be single or paired. The nerve lies deep to the endothelium of the wall of the straight sinus and is associated with intraglandular blood vessels and parenchymal cells.

The pineal gland contains cords and clusters of pinealocytes, associated with astrocyte-like neuroglia, which are the main cellular component of the pineal stalk. Pinealocytes are highly modified neurones. They contain multiple synaptic ribbons, randomly distributed between adjacent cells, and are coupled by gap junctions. Two or more processes extend from each cell body and end in bulbous expansions near capillaries or, less frequently, on the ependymal cells of the pineal recess. These terminal expansions contain rough endoplasmic reticulum, mitochondria and dense-cored vesicles that store melatonin. Melatonin, and its precursor 5-HT (serotonin), are synthesized from tryptophan by the pinealocytes, and secreted into the surrounding network of fenestrated capillaries.

The pineal gland is an endocrine gland of major regulatory importance (Macchi and Bruce 2004). It modifies the activity of the adenohypophysis, neurohypophysis, endocrine pancreas, parathyroids, suprarenal cortex, suprarenal medulla and gonads. Its effects are largely inhibitory. Indoleamine and polypeptide hormones secreted by pinealocytes are believed to reduce the synthesis and release of hormones by the pars anterior, either by direct action on its secretory cells or indirectly by inhibiting production of hypothalamic releasing factors. Pineal secretions may reach their target cells via the cerebrospinal fluid or the blood stream. Some pineal indoleamines, including melatonin and enzymes for their biosynthesis (e.g. 5-HT, *N*-acetyltransferase), show circadian rhythms in concentration. The levels rise during darkness and fall during the day, when secretion may be inhibited by sympathetic activity. The intrinsic rhythmicity of an endogenous circadian oscillator in the suprachiasmatic nucleus of the hypothalamus apparently governs cyclical pineal behaviour (see above).

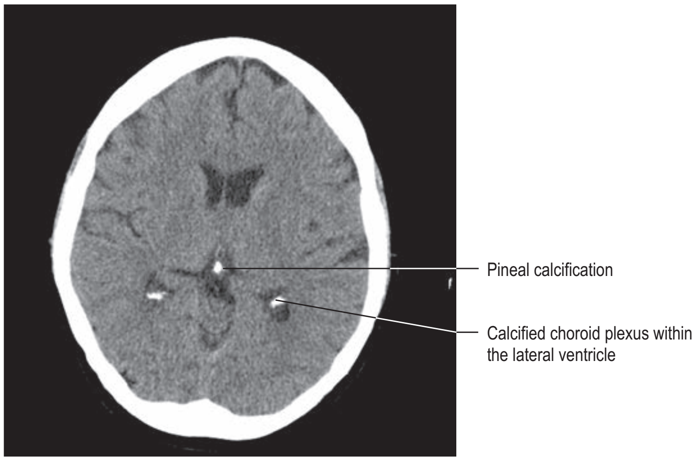

Fig. 30.13 An axial CT image showing calcification of the pineal gland and choroid plexus.

From the second decade, calcareous deposits accumulate in pineal extracellular matrix, where they are deposited concentrically as corpora arenacea or 'brain sand' (Fig. 30.13). Pineal gland and choroid plexus calcifications are the most frequent sites of intracranial calcifications that are incidentally discovered among head CT scans; calcification can provide a useful indicator of a space-occupying lesion if the gland is significantly displaced from the midline.

Bonus e-book content

Fig. 30.5 Magnetic resonance images from four different patients with neurological or psychiatric disorders, showing the position of deep brain stimulation electrodes.

Key references

Benabid AL, Pollak P, Gervason C et al 1991 Long-term suppression of tremor by chronic stimulation of the ventral intermediate thalamic nucleus. Lancet 337:403–6.

The first description of deep brain stimulation of the ventral intermediate (Vim) nucleus of the thalamus for tremor reduction.

Hodaie M, Wennberg RA, Dostrovsky JO et al 2002 Chronic anterior thalamus stimulation for intractable epilepsy. Epilepsia 43:603–8.

A description of the use of deep brain stimulation for seizure reduction in intractable epilepsy.

Jones EG 2007 The Thalamus, 2nd ed. Cambridge: Cambridge University Press.

A description of the nomenclature and connections of thalamic nuclei.

Macchi MM, Bruce JN 2004 Human pineal physiology and functional significance of melatonin. Front Neuroendocrinol 25:177–95.

A review of the neuroanatomy and physiology of the pineal gland, including its rhythmic output functions, particularly the regulation of melatonin synthesis.

Nieuwenhuys R 1985 Chemoarchitecture of the brain. Berlin: Springer.

A description of the connections and neurochemistry of the hypothalamus.

Page RB 1982 Pituitary blood flow. Am J Physiol 243:E427–42.

A detailed description of the pituitary portal system.

Sam S, Frohman LA 2008 Normal physiology of hypothalamic pituitary regulation. Endocrinol Metab Clin North Am 37:1–22, vii.

A description of the normal physiology of the hypothalamic–pituitary axis.

Tasker RR, Doorly T, Yamashiro K 1988 Thalamotomy in generalized dystonia. Adv Neurol 50:615–31.

A description of the effect of thalamotomy on different aspects of dystonia.

References

Ahima RS, Antwi DA 2008 Brain regulation of appetite and satiety. Endocrinol Metab Clin North Am 37:811–23.

Benabid AL, Pollak P, Gervason C et al 1991 Long-term suppression of tremor by chronic stimulation of the ventral intermediate thalamic nucleus. Lancet 337:403–6.

The first description of deep brain stimulation of the ventral intermediate (Vim) nucleus of the thalamus for tremor reduction.

Boccard SG, Pereira EA, Moir L et al 2013 Long-term outcomes of deep brain stimulation for neuropathic pain. Neurosurgery 72:221–30.

Boulos LJ, Darcq E, Kieffer BL 2017 Translating the habenula – from rodents to humans. Biol Psychiatry 81:296–305.

Casagrande V, Ichida J 2011 Processing in the lateral geniculate nucleus (LGN). In: Levin LA, Nilsson SFE, Ver Hoeve J et al (eds) Adler's Physiology of the Eye, 11th ed. Philadelphia: Elsevier, Saunders; Ch. 29, pp. 574–85.

Cawley NX, Li Z, Loh YP 2016 60 years of POMC: biosynthesis, trafficking, and secretion of pro-opiomelanocortin-derived peptides. J Mol Endocrinol 56:T77–T97.

Cooper IS 1976 20-year followup study of the neurosurgical treatment of dystonia musculorum deformans. Adv Neurol 14:423–52.

Fakhoury M 2018 The dorsal diencephalic conduction system in reward processing: spotlight on the anatomy and functions of the habenular complex. Behav Brain Res 348:115–26.

Giacino J, Fins JJ, Machado A et al 2012 Central thalamic deep brain stimulation to promote recovery from chronic posttraumatic minimally conscious state: challenges and opportunities. Neuromodulation 15:339–49.

Gruber D, Kühn AA, Schoenecker T et al 2010 Pallidal and thalamic deep brain stimulation in myoclonus-dystonia. Mov Disord 25:1733–43.

Hodaie M, Wennberg RA, Dostrovsky JO et al 2002 Chronic anterior thalamus stimulation for intractable epilepsy. Epilepsia 43:603–8.

A description of the use of deep brain stimulation for seizure reduction in intractable epilepsy.

Hubble JP, Busenbark KL, Wilkinson S et al 1996 Deep brain stimulation for essential tremor. Neurology 46:1150–3.

Jiménez F, Nicolini H, Lozano AM et al 2013 Electrical stimulation of the inferior thalamic peduncle in the treatment of major depression and obsessive compulsive disorders. World Neurosurg 80:S30.e17–25.

Jones EG 2007 The Thalamus, 2nd ed. Cambridge: Cambridge University Press.

A description of the nomenclature and connections of thalamic nuclei.

Lozano AM, Lipsman N, Bergman H et al 2019 Deep brain stimulation: current challenges and future directions. Nat Rev Neurol 15:148–60.

Macchi MM, Bruce JN 2004 Human pineal physiology and functional significance of melatonin. Front Neuroendocrinol 25:177–95.

A review of the neuroanatomy and physiology of the pineal gland, including its rhythmic output functions, particularly the regulation of melatonin synthesis.

Mohawk JA, Takahashi JS 2011 Cell autonomy and synchrony of suprachiasmatic nucleus circadian oscillators. Trends Neurosci 34:349–58.

Namboodiri VMK, Rodriguez-Romaguera J, Stuber GD 2016 The habenula. Current Biol 26:R865–R881.

Navarro S, Soletto L, Puchol S et al 2016 60 years of POMC: an evolutionary perspective. J Mol Endocrinol 56:T113–8.

Neudorfer C, Maarouf M 2018 Neuroanatomical background and functional considerations for stereotactic interventions in the H fields of Forel. Brain Struct Function 223:17–30.

Nieuwenhuys R 1985 Chemoarchitecture of the brain. Berlin: Springer.

A description of the connections and neurochemistry of the hypothalamus.

Page RB 1982 Pituitary blood flow. Am J Physiol 243:E427–42.

A detailed description of the pituitary portal system.

Piedad JCP, Rickards HE, Cavanna AE 2012 What patients with Gilles de la Tourette syndrome should be treated with deep brain stimulation and what is the best target? Neurosurgery 71:173–92.

Rovó Z, Ulbert I, Acsády L 2012 Drivers of the primate thalamus. J Neurosci 32:17894–908.

Sam S, Frohman LA 2008 Normal physiology of hypothalamic pituitary regulation. Endocrinol Metab Clin North Am 37:1–22, vii.

A description of the normal physiology of the hypothalamic–pituitary axis.

Sherman SM 2016 Thalamus plays a central role in ongoing cortical functioning. Nat Neurosci 19:533–41.

Talairach J, Tournoux P 1988 Co-planar Stereotaxic Atlas of the Human Brain. New York: Thieme.

Tasker RR, Doorly T, Yamashiro K 1988 Thalamotomy in generalized dystonia. Adv Neurol 50:615–31.

A description of the effect of thalamotomy on different aspects of dystonia.

Toda C, Santoro A, Kim JD et al 2017 POMC neurons: from birth to death. Annu Rev Physiol 79:209–36.

Watson C, Lind CR, Thomas MG 2014 The anatomy of the caudal zona incerta in rodents and primates. J Anat 224:95–107.

Xuereb GP, Prichard MM, Daniel PM 1954 The arterial supply and venous drainage of the human hypophysis cerebri. Q J Exp Physiol Cogn Med Sci 39:199–217.

CHAPTER 31

Basal ganglia

The term basal ganglia is used to denote a number of subcortical nuclear masses that lie in the inferior part of the cerebral hemisphere, in close relationship with the internal capsule (**Fig. 31.1**). The traditional definition of the basal ganglia included the corpus striatum, claustrum and amygdaloid complex. The term has now been restricted to the corpus striatum and, according to some authorities, other nuclei in the diencephalon and midbrain (principally the subthalamic nucleus and substantia nigra) that collectively form a functional complex involved in the control of movement and motivational aspects of behaviour (Jankovic 2012). The function of the claustrum is unknown; the amygdala is more closely related to the limbic system and is, therefore, described in that context.

Disorders of the basal ganglia are principally characterized by abnormalities of movement, muscle tone and posture. There is a wide spectrum of clinical presentations ranging from poverty of movement and hypertonia at one extreme (typified by Parkinson's disease) to abnormal involuntary movements (dyskinesias) at the other. The underlying pathophysiological mechanisms that mediate these disorders have been much studied in recent years and are better understood than for any other type of complex neurological dysfunction (Penney and Young 1986, Jankovic 2012). This improved understanding has led to the introduction of new rational therapeutic strategies for both medical and neurosurgical treatments of movement disorders.

CORPUS STRIATUM

The corpus striatum consists of the caudate nucleus, putamen and globus pallidus (**Fig. 31.2**). Because of their close proximity, the putamen and globus pallidus were once considered as a single entity, the lentiform (lenticular) complex or nucleus. However, although the name has been retained in gross anatomical terminology and in some compound names (e.g. sublenticular, retrolenticular thalamic projections), the putamen and globus pallidus have quite different connections and functions. Rather, it is now known that the putamen and caudate nucleus share a common chemocytoarchitecture and connections, and they are referred to jointly as the neostriatum, or simply the striatum.

The striatum is considered to be the principal 'input' structure of the basal ganglia since it receives the majority of afferents from other parts of the neuraxis. Its principal efferent connections are to the globus pallidus and the substantia nigra, pars reticulata. The globus pallidus and, more particularly, its medial (internal) segment, together with the pars reticulata of the substantia nigra, is regarded as the main 'output' structure because it is the source of basal ganglia efferent fibre projections, mostly directed to the thalamus.

Lentiform complex

The lentiform complex (see Fig. 31.1; **Fig. 31.3**) lies deep to the insular cortex, with which it is roughly coextensive, although they are separated by a thin layer of white matter and by the claustrum. The latter splits the insular subcortical white matter to create the extreme and external capsules. The external capsule separates the claustrum from the putamen and the internal capsule separates the lentiform complex from the caudate nucleus.

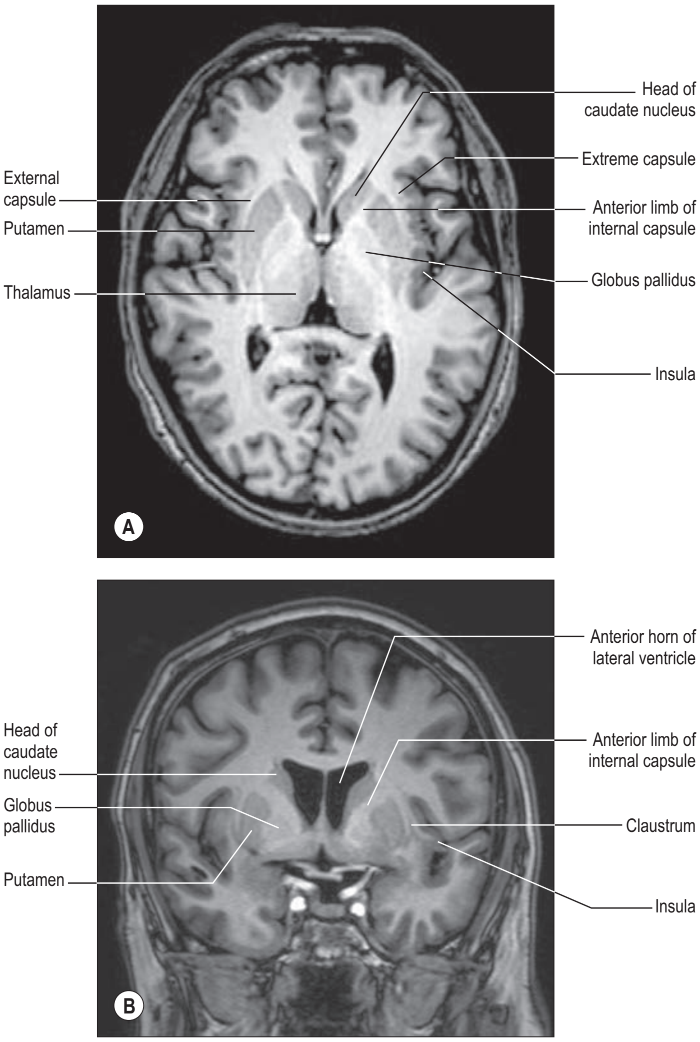
Head of caudate nucleus
Extreme capsule
External capsule
Anterior limb of internal capsule
Putamen
Globus pallidus
Thalamus
Insula
A
Anterior horn of lateral ventricle
Head of caudate nucleus
Anterior limb of internal capsule
Globus pallidus
Claustrum
Putamen
Insula
B

Fig. 31.1 Axial (**A**) and coronal (**B**) magnetic resonance images of the brain showing the basal ganglia, thalamus and internal capsule. (Courtesy of Alan Jackson.)

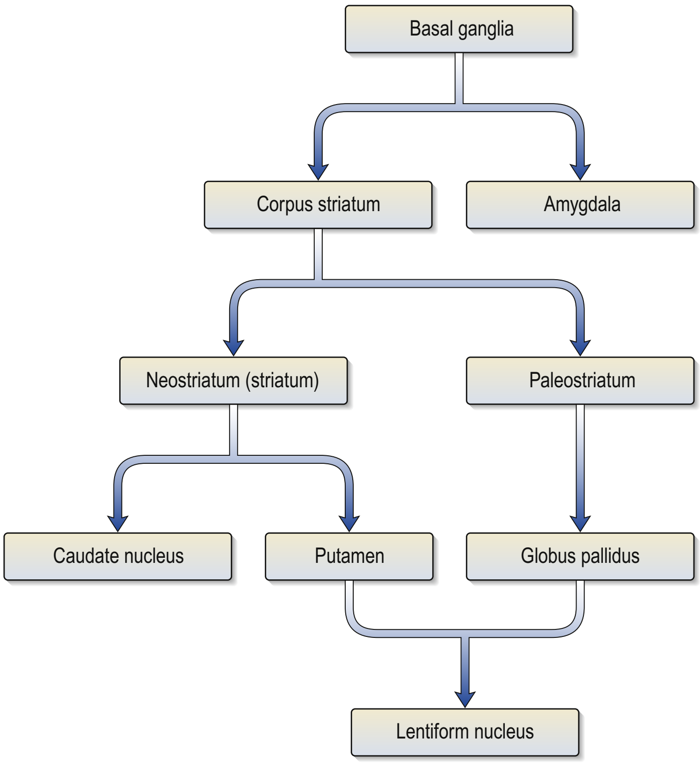
Basal ganglia
Corpus striatum
Amygdala
Neostriatum (striatum)
Paleostriatum
Caudate nucleus
Putamen
Globus pallidus
Lentiform nucleus

Fig. 31.2 Terminology and relationships of structures forming the basal ganglia.

The lentiform complex consists of the laterally placed putamen and the more medially placed globus pallidus (pallidum), separated by a thin layer of fibres, the external medullary lamina. The globus pallidus is itself divided into two segments, a lateral (external) segment and a medial (internal) segment, separated by an internal medullary lamina. The two segments have distinct afferent and efferent connections. Inferiorly, a little behind the fundus striati, the lentiform complex is grooved by the anterior commissure that connects inferior parts of the temporal lobes and the anterior olfactory cortex of the two sides (see Fig. 31.6). The area above the commissure is referred to as the dorsal pallidum, and that below it as the ventral pallidum.

STRIATUM

The striatum consists of the caudate nucleus, putamen and ventral striatum, which are all highly cellular and well-vascularized. The vast bulk of the caudate nucleus and putamen are often referred to as the dorsal striatum. A smaller inferomedial part of the rostral striatum, referred to as the ventral striatum, includes the nucleus accumbens. The caudate and putamen are traversed by the anterior thalamic projections and by numerous small bundles of thinly myelinated, or unmyelinated, small-diameter axons, which are mostly striatal afferents and efferents. They radiate through the striatal tissue as though converging on, or radiating from, the globus pallidus. These bundles are occasionally referred to by the archaic term 'Wilson's pencils' and they account for the striated appearance of the corpus striatum.

Caudate nucleus

The caudate nucleus is a curved, tadpole-shaped mass. It has a large anterior head that tapers to a body, and a down-curving tail (Fig. 31.4). The head is covered with ependyma and lies in the floor and lateral wall of the frontal (anterior) horn of the lateral ventricle, anterior to the interventricular foramen. The tapering body is in the floor of the body of the ventricle, and the narrow tail follows the curve of the temporal (inferior) horn, and so lies in the ventricular roof, in the temporal lobe. Medially, the greater part of the caudate nucleus abuts the thalamus, along a junction that is marked by a groove, the sulcus terminalis. The sulcus contains the stria terminalis, lying deep to the ependyma (Fig. 31.5). The sulcus terminalis is especially prominent anterosuperiorly (because of the large size of the head and body of the caudate nucleus relative to the tail), and here the stria terminalis is accompanied by the thalamostriate vein.

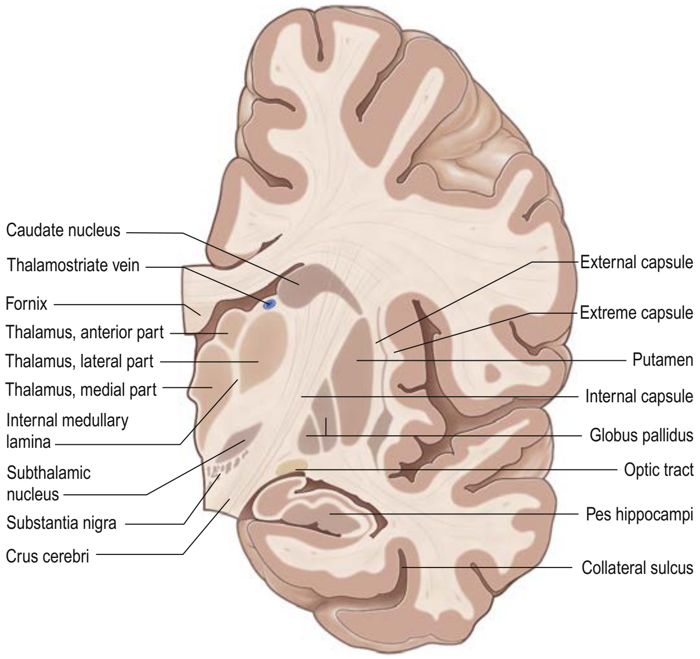
Caudate nucleus
Thalamostriate vein
Fornix
Thalamus, anterior part
Thalamus, lateral part
Thalamus, medial part
Internal medullary lamina
Subthalamic nucleus
Substantia nigra
Crus cerebri
External capsule
Extreme capsule
Putamen
Internal capsule
Globus pallidus
Optic tract
Pes hippocampi
Collateral sulcus

Fig. 31.3 Anterior aspect of a coronal section through the left cerebral hemisphere.

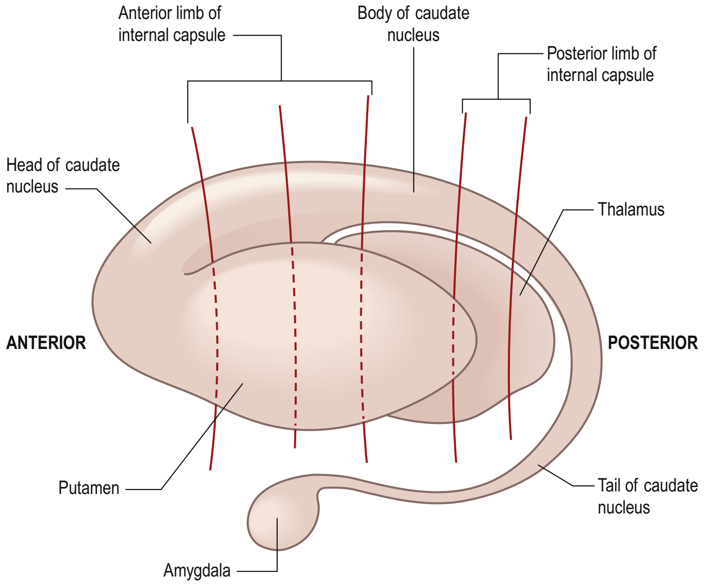
Anterior limb of internal capsule
Body of caudate nucleus
Posterior limb of internal capsule
Head of caudate nucleus
Thalamus
ANTERIOR
POSTERIOR
Putamen
Tail of caudate nucleus
Amygdala

Fig. 31.4 The striatum within the left cerebral hemisphere. (With permission from Crossman AR, Neary D Neuroanatomy: An Illustrated Colour Text, 6th ed. Elsevier, Churchill Livingstone. Copyright 2019.)

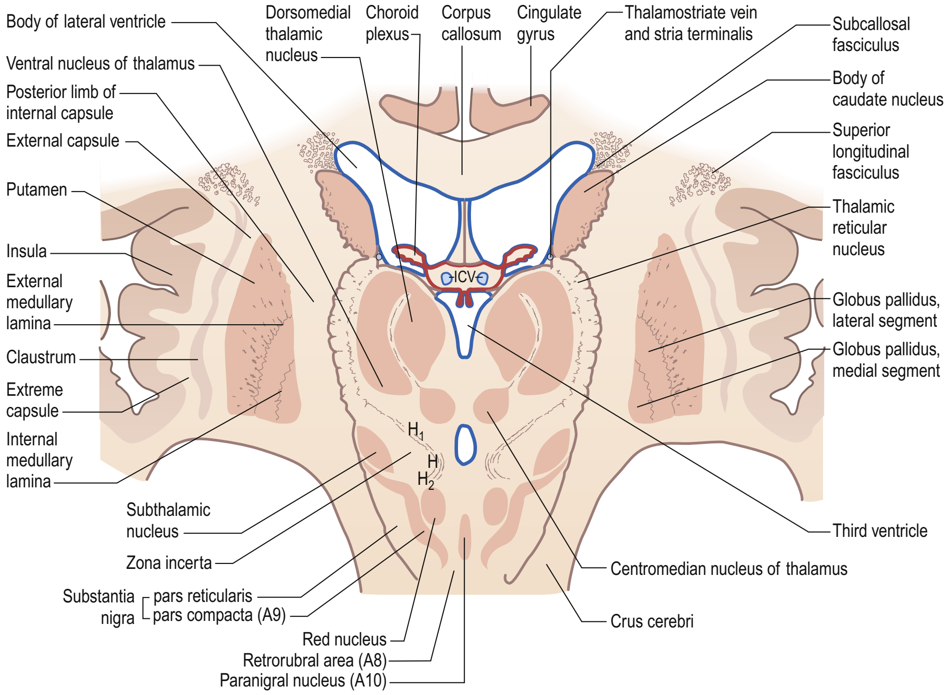
Body of lateral ventricle
Ventral nucleus of thalamus
Posterior limb of internal capsule
External capsule
Putamen
Insula
External medullary lamina
Claustrum
Extreme capsule
Internal medullary lamina
Subthalamic nucleus
Zona incerta
Substantia nigra pars reticularis
pars compacta (A9)
Red nucleus
Retrorubral area (A8)
Paranigral nucleus (A10)
Dorsomedial thalamic nucleus
Choroid plexus
Corpus callosum
Cingulate gyrus
Thalamostriate vein and stria terminalis
Subcallosal fasciculus
Body of caudate nucleus
Superior longitudinal fasciculus
Thalamic reticular nucleus
Globus pallidus, lateral segment
Globus pallidus, medial segment
ICV
H_1
H
H_2
Third ventricle
Centromedian nucleus of thalamus
Crus cerebri

Fig. 31.5 Oblique section through the diencephalon and basal ganglia. Abbreviations: ICV, internal cerebral veins; H, H_1, H_2, subthalamic fields of Forel.

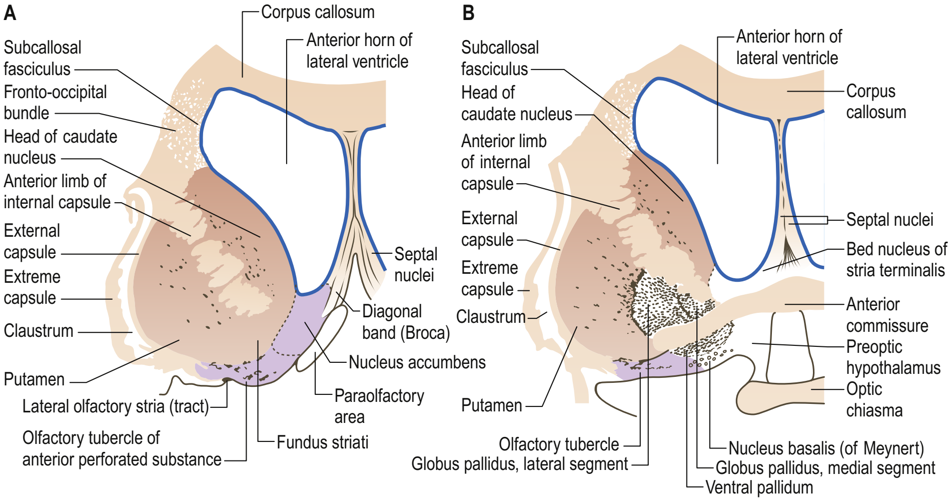
A
Corpus callosum
Anterior horn of lateral ventricle
Subcallosal fasciculus
Fronto-occipital bundle
Head of caudate nucleus
Anterior limb of internal capsule
External capsule
Extreme capsule
Claustrum
Putamen
Lateral olfactory stria (tract)
Olfactory tubercle of anterior perforated substance
Septal nuclei
Diagonal band (Broca)
Nucleus accumbens
Paraolfactory area
Fundus striati
B
Subcallosal fasciculus
Head of caudate nucleus
Anterior limb of internal capsule
External capsule
Extreme capsule
Claustrum
Putamen
Olfactory tubercle
Globus pallidus, lateral segment
Anterior horn of lateral ventricle
Corpus callosum
Septal nuclei
Bed nucleus of stria terminalis
Anterior commissure
Preoptic hypothalamus
Optic chiasma
Nucleus basalis (of Meynert)
Globus pallidus, medial segment
Ventral pallidum

Fig. 31.6 Coronal sections through the corpus striatum and anterior perforated substance. **A** is anterior to **B**.

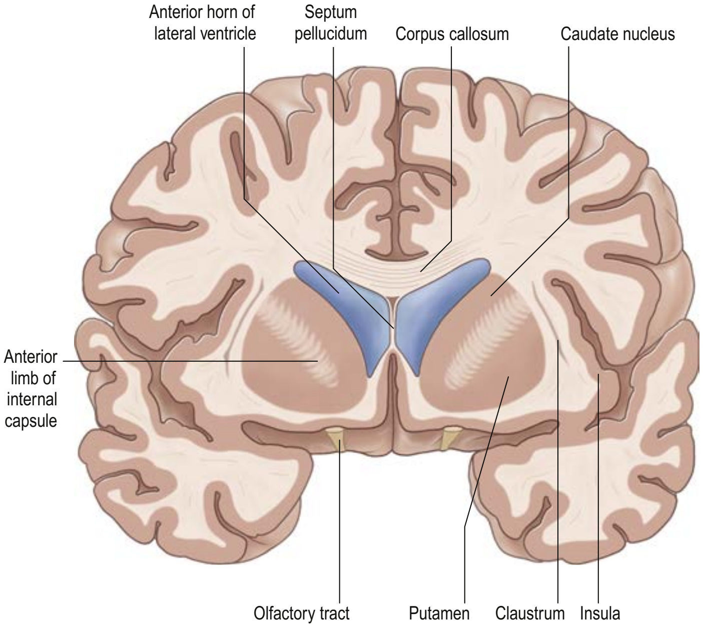
Anterior horn of lateral ventricle
Septum pellucidum
Corpus callosum
Caudate nucleus
Anterior limb of internal capsule
Olfactory tract
Putamen
Claustrum
Insula

Fig. 31.7 Posterior aspect of a coronal section through the frontal (anterior) horn of the lateral ventricles.

The corpus callosum is superior to the head and body of the caudate nucleus. The two are separated by the fronto-occipital fasciculus laterally and by the subcallosal fasciculus, which caps the nucleus, medially (see Fig. 31.5). The caudate nucleus is largely separated from the lentiform complex by the anterior limb of the internal capsule (**Figs 31.6–31.7**). The inferior part of the head of the caudate becomes continuous with the most inferior part of the putamen immediately above the anterior perforated substance; this junctional region is sometimes known as the fundus striati (see Fig. 31.6A). Variable bridges of cells connect the putamen to the caudate nucleus for most of its length. They are most prominent anteriorly, in the region of the fundus striati and the head and body of the caudate nucleus, where they penetrate the anterior limb of the internal capsule (see Fig. 31.7). In the temporal lobe, the anterior part of the tail of the caudate nucleus becomes continuous with the posteroinferior part of the putamen.

Ventral striatum

The ventral striatum consists of the nucleus accumbens and the olfactory tubercle. Anterior to the anterior commissure, much of the grey matter of the anterior perforated substance, and especially the olfactory tubercle, is indistinguishable from, and continuous with, the fundus striati, in terms of cellular composition, histochemistry and interconnections. The caudate nucleus is continuous medially with the nucleus accumbens (see Fig. 31.6A), which abuts the nuclei of the septum, close by the para-olfactory area, diagonal band of Broca and the fornix.

The nucleus accumbens receives a dopaminergic innervation from the midbrain ventral tegmental area (cell group A10). It is believed to represent the neural substrate for the rewarding effects of several classes of drugs and is, therefore, a major determinant of their addictive potential. The experimental observation that the locomotor activating effects of psychomotor stimulant drugs such as amphetamine and cocaine (which act presynaptically on dopaminergic neurones to either enhance dopamine release or block its reuptake) are dependent on dopamine transmission in the nucleus accumbens, led to the hypothesis that the reinforcing or rewarding properties of these drugs are mediated by the mesolimbic dopamine system.

Striatal connectivity

Neurones of both dorsal and ventral striatum are mainly medium-sized multipolar cells. They have round, triangular or fusiform cell bodies, mixed with a smaller number of large multipolar cells. The ratio of medium to large cells is at least 20:1. The large neurones have extensive spherical or ovoid dendritic trees up to 60 μm across. The medium-sized neurones also have spherical dendritic trees, approximately 20 μm across, which receive the synaptic terminals of many striatal afferents. The dendrites of both medium and large striatal cells may be either spiny or non-spiny. The most common neurone (approximately 75% of the total) is a medium-sized cell with spiny dendrites (so-called medium spiny neurones). These cells utilize γ-aminobutyric acid (GABA) as their transmitter and also express the genes coding for either enkephalin or substance P/dynorphin, depending on their efferent connections. Enkephalinergic neurones express D2 dopamine receptors. Substance P/dynorphin neurones express D1 receptors. These neurones are the major, and perhaps exclusive, source of striatal efferents to the pallidum and substantia nigra pars reticulata. The other medium-sized striatal neurones are aspiny, and are intrinsic cells that contain acetylcholinesterase (AChE), choline acetyltransferase (CAT) and somatostatin. Large neurones with spiny dendrites contain AChE and CAT; most, perhaps all, are intrinsic neurones. Aspiny large neurones are all intrinsic neurones.

Intrinsic synapses are probably largely asymmetric (type II), while those derived from external sources are symmetric (type I). The aminergic afferents from the substantia nigra, raphe and locus coeruleus all end as profusely branching axons with varicosities that contain dense-core vesicles (the presumed store of amine transmitters). Many of these varicosities have no conventional synaptic membrane specializations, and may release transmitter in a way analogous to that found in peripheral postsynaptic sympathetic axons.

Neuroactive chemicals, whether intrinsic or derived from afferents, are not distributed uniformly in the striatum. For example, 5-HT (5-hydroxytryptamine, serotonin) and glutamic acid decarboxylase (GAD) concentrations are highest caudally, while substance P, acetylcholine (ACh) and dopamine are highest rostrally. However, there is a finer-grain neurochemical organization showing that the striatum consists of a mosaic of islands or striosomes (sometimes referred to as patches), each 0.5–1.5 mm across, packed into a background matrix. Striosomes contain substance P and enkephalin. During development, the first dopamine terminals from the substantia nigra are found in striosomes: although this exclusivity does not persist after birth, striosomes in the adult caudate nucleus still contain a higher concentration of dopamine than the matrix. The latter contains ACh and somatostatin, and is the target of thalamostriatal axons. Receptors for at least some neurotransmitters are also differentially distributed. For example, opiate receptors

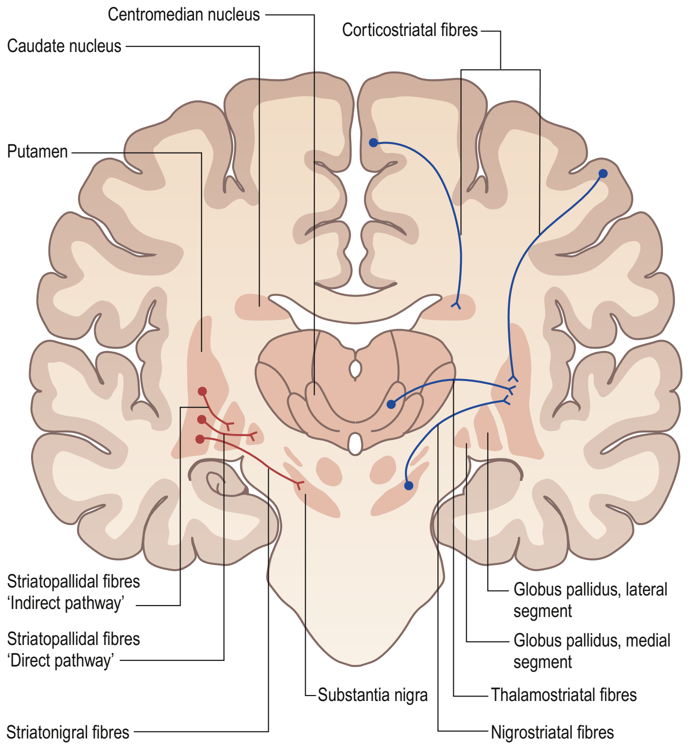

Fig. 31.8 Connections of the striatum. The major afferent projections to the striatum are shown on the right and major efferent projections from the striatum on the left.

are found almost exclusively within striosomes, and muscarinic receptors predominantly so. Moreover, the distribution of neuroactive substances within the striosomes is not uniform. In humans, the striosome/matrix patchwork is more evident in the caudate than the putamen, the latter consisting predominantly of matrix.

All afferents to the striatum terminate in a mosaic manner. The size of a cluster of terminals is usually 100–200 µm across. Some afferent terminal clusters are not arranged in register with the clear striosome/matrix distributions seen in nigrostriatal and thalamostriatal axons. In general, afferents from the neocortex end in striatal matrix and those from the allocortex end in striosomes. However, the distinction is not absolute: although afferents from the neocortex arise in layers V and VI, those from the superficial part of layer V end predominantly in striatal matrix, whereas those from deeper neocortex project to striosomes. Striatal cell bodies that are the sources of efferents also form clusters but, again, are not uniformly related to striosomes. For example, the cell bodies of some striatopallidal and striatonigral axons lie clustered within striosomes, but others lie outside them, still in clusters. The neurones and neuropil of the ventral striatum are essentially similar to those of the dorsal striatum, but the striosomal/matrix organization is less well-defined and seems to consist predominantly of striosomes.

The major connections of the striatum are summarized in Fig. 31.8. The connections of the dorsal and ventral divisions overlap, however, the generalization can be made that the dorsal striatum is predominantly connected with motor and associative areas of the cerebral cortex, whilst the ventral striatum is connected with the limbic system and orbitofrontal and temporal cortices. For both dorsal and ventral striatum, the pallidum and substantia nigra pars reticulata are key efferent structures. The fundamental arrangement is the same for both divisions. The cerebral cortex projects to the striatum, which in turn projects to the pallidum and substantia nigra pars reticulata. Efferents from the pallidum and substantia nigra pars reticulata influence the cerebral cortex (either the supplementary motor area or prefrontal and cingulate cortices via the thalamus) and the superior colliculus (see below).

The entire neocortex sends glutamatergic axons to the ipsilateral striatum. Previously, these axons were thought to be collaterals of cortical efferents to other regions, but it is now known that they arise exclusively from small pyramidal cells in layers V and VI. It has also been suggested that some of the cells of origin lie in the supragranular 'cortical association' layers II and III. The projection is organized topographically. The greater part of the input from the cerebral cortex to the dorsal striatum is derived from the frontal and parietal lobes; the input from the occipitotemporal cortex is relatively small. The orbitofrontal association cortex projects to the inferior part of the head of the caudate nucleus, which lies next to the ventral striatum. The dorsolateral frontal association cortex and frontal eye fields project to the rest of the head of the caudate nucleus, and much of the parietal lobe projects to the body of the nucleus. The somatosensory and motor cortices project predominantly to the putamen: their terminals establish a somatotopic pattern, in which the lower body is represented laterally and the upper body is represented medially. The motor cortex is unique in also sending axons through the corpus callosum to the opposite putamen, where they end with the same spatial ordering. The occipital and temporal cortices project to the tail of the caudate nucleus and to the inferior putamen.

The striatum receives afferents from the polysensory intralaminar thalamus and these are more crudely organized spatially. The nucleus centralis lateralis, which receives a cerebellar input, projects to the anterior striatum (especially the caudate nucleus), while the centromedian nucleus, which receives input from both the cerebellum and medial globus pallidus, projects to the putamen.

The aminergic inputs to the caudate and putamen are derived from the substantia nigra pars compacta (dopaminergic group A9; see Fig. 28.17), the retrorubral nucleus (dopaminergic group A8), the dorsal raphe nucleus (serotoninergic group B7) and the locus coeruleus (noradrenergic group A6). The nigrostriatal input is sometimes referred to as the 'mesostriatal' dopamine pathway; it reaches the striatum by traversing the H fields (of Forel) in the subthalamus and running in the medial forebrain bundle. These aminergic inputs appear to modulate the responses of the striatum to cortical and thalamic afferent influences.

Efferents from the striatum pass to both segments of the globus pallidus and to the substantia nigra pars reticulata, where they end in a topically ordered fashion. Fibres ending in either the lateral or medial pallidum originate from different striatal cells (see Fig. 31.8). Those projecting to the lateral pallidum are axons of neurones that co-localize GABA and enkephalin, and give rise to the so-called 'indirect pathway'. This name refers to the fact that these striatal neurones influence the activity of basal ganglia output neurones in the medial pallidum via the intermediary of the subthalamic nucleus. Other striatal neurones, which co-localize GABA and substance P/dynorphin, project directly to the medial pallidum and are, therefore, described as the 'direct pathway'.

The striatal projection to the pars reticulata of the substantia nigra also has both direct and indirect components, via the lateral pallidum and subthalamic nucleus (**Figs 31.9–31.10**). The axons of the direct striatonigral projection constitute the laterally placed 'comb' system, which is spatially quite distinct from the ascending dopaminergic nigrostriatal pathway. Striatonigral fibres end in a spatially ordered way in the pars reticulata.

The ventral striatum is the primary target of fibres from limbic cortices, including allocortex, and from limbic associated regions (see Fig. 31.9). Thus, the hippocampus (through the fornix) and orbitofrontal cortex (through the internal capsule) project to the nucleus accumbens, and the olfactory, entorhinal, anterior cingulate and temporal visual cortices project to both the nucleus accumbens and olfactory tubercle. The olfactory tubercle also receives afferents from the amygdala. The contiguity of the cortical areas that project to the ventral striatum and neighbouring dorsal striatum emphasizes the imprecise nature of the boundaries between these two divisions. All the cortical regions abut and overlap with neighbouring areas and they project to neighbouring parts of the dorsal striatum as well as to the ventral striatum. The fundus striati and ventromedial caudate nucleus abut the olfactory tubercle and nucleus accumbens (see Fig. 31.6A) and receive connections from the orbitofrontal cortex and, to a lesser extent, from the lateral prefrontal and anterior cingulate cortices (which also project to the head of the caudate nucleus).

This continuity of the ventral and dorsal striata, as revealed by the arrangements of corticostriatal projections, is reinforced by consideration of the aminergic inputs to the ventral striatum. These are derived from the dorsal raphe (serotoninergic group B7), the locus coeruleus (noradrenergic group A6) and the ventral tegmental area (dopamine group A10), as well as the most medial part of the substantia nigra, pars compacta (A9) (see Fig. 28.17). The dopamine projections constitute the so-called mesolimbic dopamine pathway, which also projects to the septal nuclei, hippocampus and amygdala, and the prefrontal and cingulate cortices through the medial forebrain bundle. The lateromedial continuity of cell groups A9 and A10 is reflected in the relative positions of their ascending fibres in the subthalamus and hypothalamus (the H fields and medial forebrain bundle, respectively), as well as in the lateromedial topography of the dorsal and ventral striata, which in turn have contiguous and overlapping sources of cortical afferents.

As with the dorsal striatum, efferents from the ventral striatum project to the pallidum (in this case, the ventral pallidum) and the

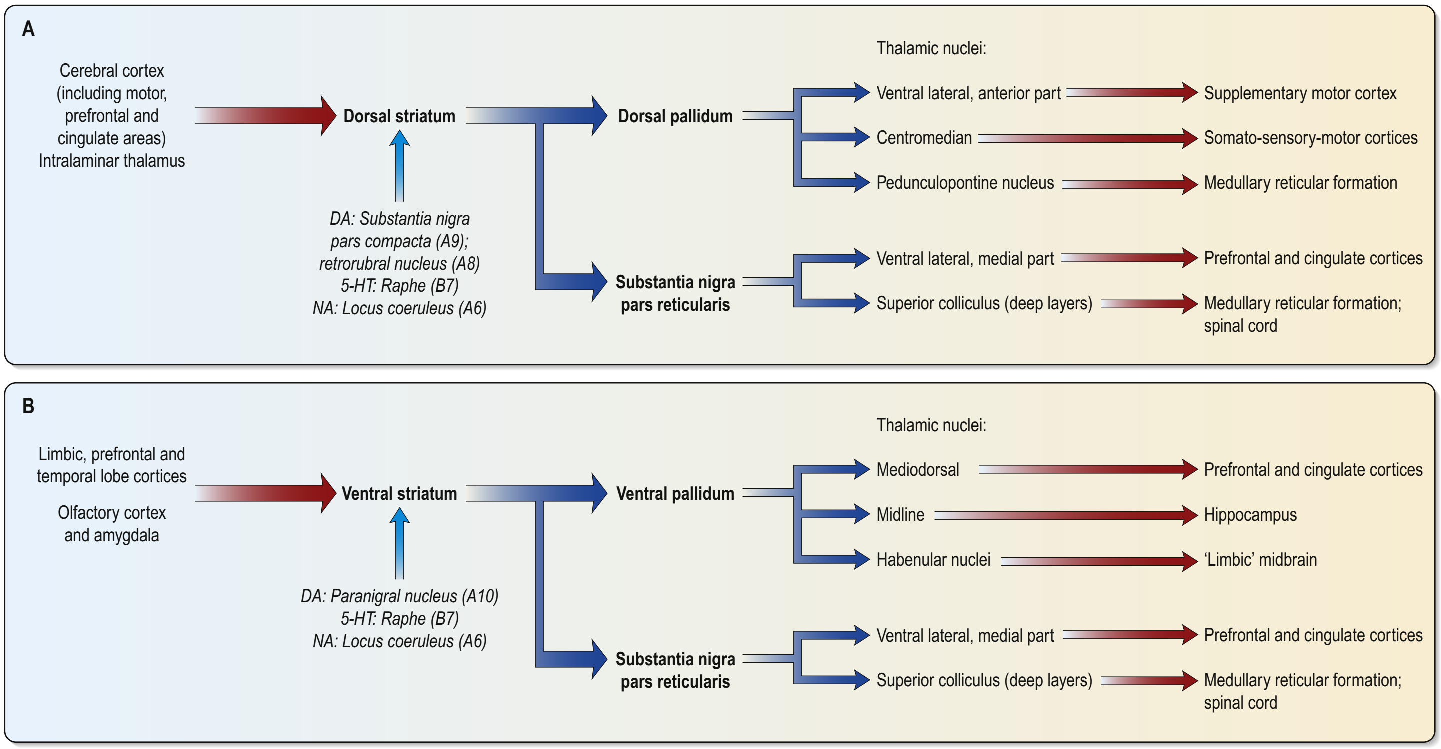
A
Cerebral cortex (including motor, prefrontal and cingulate areas) Intralaminar thalamus
Dorsal striatum
DA: Substantia nigra pars compacta (A9); retrorubral nucleus (A8)
5-HT: Raphe (B7)
NA: Locus coeruleus (A6)
Dorsal pallidum
Substantia nigra pars reticularis
Thalamic nuclei:
Ventral lateral, anterior part
Centromedian
Pedunculopontine nucleus
Ventral lateral, medial part
Superior colliculus (deep layers)
Supplementary motor cortex
Somato-sensory-motor cortices
Medullary reticular formation
Prefrontal and cingulate cortices
Medullary reticular formation; spinal cord
B
Limbic, prefrontal and temporal lobe cortices
Olfactory cortex and amygdala
Ventral striatum
DA: Paranigral nucleus (A10)
5-HT: Raphe (B7)
NA: Locus coeruleus (A6)
Ventral pallidum
Substantia nigra pars reticularis
Thalamic nuclei:
Mediodorsal
Midline
Habenular nuclei
Ventral lateral, medial part
Superior colliculus (deep layers)
Prefrontal and cingulate cortices
Hippocampus
'Limbic' midbrain
Prefrontal and cingulate cortices
Medullary reticular formation; spinal cord

Fig. 31.9 Principal output connections of the basal ganglia derived from dorsal (**A**) and ventral (**B**) divisions of the striatum. In each case, pathways established through the pallidum are distinguished from those passing through the substantia nigra pars reticularis. Abbreviations: DA, dopamine; NA, noradrenaline (norepinephrine); 5-HT, 5-hydroxytryptamine (serotonin).

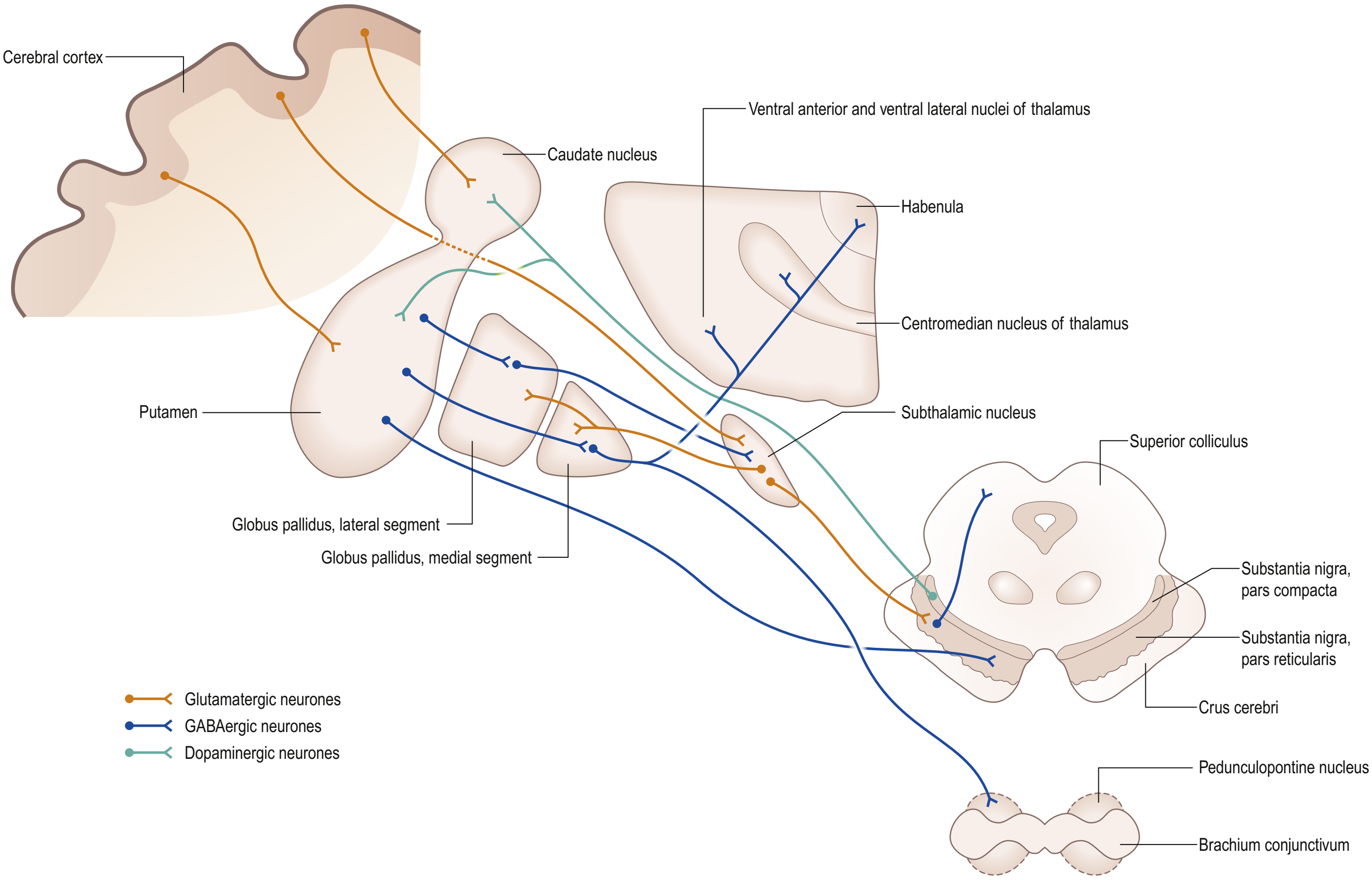
Cerebral cortex
Caudate nucleus
Ventral anterior and ventral lateral nuclei of thalamus
Habenula
Centromedian nucleus of thalamus
Putamen
Subthalamic nucleus
Superior colliculus
Globus pallidus, lateral segment
Globus pallidus, medial segment
Substantia nigra, pars compacta
Substantia nigra, pars reticularis
Crus cerebri
Glutamatergic neurones
GABAergic neurones
Dopaminergic neurones
Pedunculopontine nucleus
Brachium conjunctivum

Fig. 31.10 Principal connections of the basal ganglia with the diencephalon and brainstem.

substantia nigra pars reticulata (see Figs 31.9–31.10). The connection with the substantia nigra is both direct and indirect, via the subthalamic nucleus. The projections from the pars reticulata are as described for the dorsal system, but axons from the ventral pallidum reach the thalamic mediodorsal nucleus (which projects to prefrontal association and cingulate cortices) and midline nuclei (which project to the hippocampus). Ventral pallidal axons also reach the habenular complex of the limbic system.

The brain areas beyond the basal ganglia, substantia nigra and subthalamic nucleus to which both ventral and dorsal systems appear to project are the prefrontal association and cingulate cortices and the deep superior colliculus.

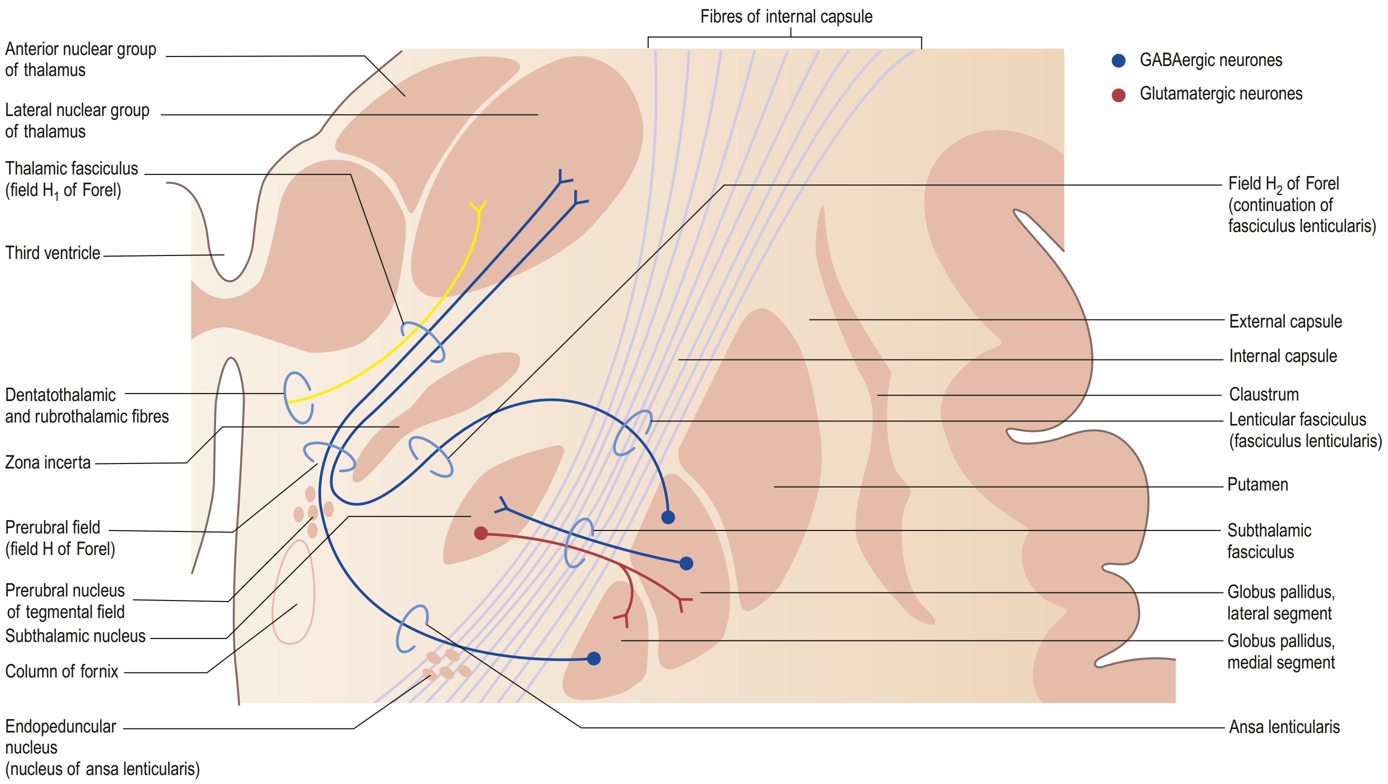
Fibres of internal capsule
Anterior nuclear group of thalamus
Lateral nuclear group of thalamus
Thalamic fasciculus (field H_1 of Forel)
Third ventricle
Dentatothalamic and rubrothalamic fibres
Zona incerta
Prerubral field (field H of Forel)
Prerubral nucleus of tegmental field
Subthalamic nucleus
Column of fornix
Endopeduncular nucleus (nucleus of ansa lenticularis)
● GABAergic neurones
● Glutamatergic neurones
Field H_2 of Forel (continuation of fasciculus lenticularis)
External capsule
Internal capsule
Claustrum
Lenticular fasciculus (fasciculus lenticularis)
Putamen
Subthalamic fasciculus
Globus pallidus, lateral segment
Globus pallidus, medial segment
Ansa lenticularis

Fig. 31.11 Coronal section of the brain showing the major connections of the basal ganglia with the diencephalon.

GLOBUS PALLIDUS

The globus pallidus (pallidum) lies medial to the putamen and lateral to the internal capsule. It consists of lateral (external) and medial (internal) segments separated by an internal medullary lamina. Both segments receive large numbers of fibres from the striatum and subthalamic nucleus, but they have substantially different connections. The lateral segment projects to the subthalamic nucleus as part of the 'indirect pathway'. The medial segment is considered to be a homologue of the pars reticulata of the substantia nigra, with which it shares similar cellular and connectional properties. Together, the segments constitute the main output of the basal ganglia to other levels of the neuraxis, principally to the thalamus.

The cell density of the globus pallidus is less than one-twentieth that of the striatum. The morphology of the majority of cells is identical in the two segments, i.e. large multipolar GABAergic neurones which closely resemble the neurones in the substantia nigra pars reticulata. Their dendritic fields are discoid, with planes at right-angles to incoming striatopallidal axons, each of which, therefore, potentially contacts many pallidal dendrites *en passant*. This arrangement, coupled with the diameters of the dendritic fields (500 µm), suggests that a precise topographical organization is unlikely within the pallidum.

Striatopallidal fibres are of two main types. They project to either the lateral or the medial pallidum. Those projecting to the lateral segment constitute the beginning of the 'indirect pathway'. They utilize GABA as their primary transmitter and also contain enkephalin. Efferent axons from neurones in the lateral segment pass through the internal capsule in the subthalamic fasciculus and travel to the subthalamic nucleus (**Fig. 31.11**).

Striatopallidal axons destined for the medial pallidum constitute the 'direct pathway'. Like the indirect projection, these utilize GABA as their primary transmitter but they also contain substance P and dynorphin. Efferent axons from the medial pallidum project through the ansa lenticularis and fasciculus lenticularis (see Fig. 31.11). The former runs round the anterior border of the internal capsule and the latter penetrates the capsule directly. Having traversed the internal capsule, both pathways unite in the subthalamic region, where they follow a horizontal hairpin trajectory, and turn upwards to enter the thalamus as the thalamic fasciculus. The trajectory circumnavigates the zona incerta and creates the so-called 'H' fields of Forel (see Figs 31.5, 31.11). Within the thalamus, pallidothalamic fibres end in the ventral anterior and ventral lateral nuclei and in the intralaminar centromedian nucleus. These in turn project excitatory (presumed glutamatergic) fibres primarily to the frontal cortex, including the primary and supplementary motor areas. The medial pallidum also projects fibres caudally to the pedunculopontine nucleus, as described below (see Fig. 31.10).

SUBTHALAMIC NUCLEUS

The subthalamic nucleus is a biconvex, lens-shaped nucleus in the subthalamus of the diencephalon. It lies medial to the internal capsule, immediately rostral to the level at which the latter becomes continuous with the crus cerebri of the midbrain (see Figs 31.3, 31.5). Within the nucleus, small interneurones intermingle with large multipolar cells with dendrites that extend for about one-tenth the diameter of the nucleus. Dorsally, the nucleus is encapsulated by axons, many of which are derived from the subthalamic fasciculus and carry a major GABAergic projection from the lateral segment of the globus pallidus as part of the indirect pathway. The nucleus also receives afferents from the cerebral cortex. It is unique in the intrinsic circuitry of the basal ganglia in that its cells are glutamatergic and project excitatory axons to both the globus pallidus and substantia nigra pars reticulata. Within the pallidum, subthalamic efferent fibres end predominantly in the medial segment but many also end in the lateral segment.

The subthalamic nucleus plays a central role in the normal function of the basal ganglia and in the pathophysiology of basal ganglia-related disorders. Destruction of the nucleus, which occurs rarely as a result of stroke, results in the appearance of violent, uncontrolled involuntary movements of the contralateral side of the body, known as ballism (hemiballismus). The subthalamic nucleus is crucially involved in the pathophysiology of Parkinson's disease (Mitchell et al 1989) and is a target for functional neurosurgical therapy of the condition. (For a detailed description of the anatomical structure and variability of the subthalamic nucleus seen using high-field magnetic resonance imaging (MRI) with histological validation, see Massey et al (2012) and Massey and Yousry (2010).)

SUBSTANTIA NIGRA

The substantia nigra is a nuclear complex deep to the crus cerebri of the midbrain (see Fig. 28.16); its cytoarchitecture and connections are described in Chapter 28. Briefly, it consists of a pars compacta, a pars reticulata and a smaller pars lateralis. The pars compacta and pars lateralis correspond to the dopaminergic cell group A9. The pars compacta projects heavily to the caudate nucleus and putamen; smaller projections end in the globus pallidus and the subthalamic nucleus. The neurones of the pars reticulata and the medial pallidum collectively constitute the output neurones of the basal ganglia system. In Parkinson's disease, the levels of dopamine in the substantia nigra and striatum decrease dramatically as a result of the degeneration of pars compacta neurones and their terminals in the neostriatum.

PEDUNCULOPONTINE NUCLEUS

The pedunculopontine nucleus (nucleus tegmenti pedunculopontinus) lies in the dorsolateral part of the pontomesencephalic tegmentum (Hamani et al 2007). Anterograde tract-tracing studies in non-human primates and rodents have revealed multiple afferent and efferent connections between the pedunculopontine nucleus and the basal ganglia, cerebellum, substantia nigra, thalamus, cerebral cortex and spinal cord. The nucleus receives GABAergic efferent fibres from the globus pallidus and substantia nigra. In animal models of Parkinson's disease, these projections are overactive and the pedunculopontine nucleus is inhibited. Taken in conjunction with other experimental evidence, this suggests that the pedunculopontine nucleus is involved in the pathophysiology of disturbances of locomotion, gait and posture in Parkinson's disease (Mena-Segovia et al 2004). That said, the variation in nuclear connectivity between quadripedal and bipedal animals must be considered when evaluating evidence from any non-primate animal model (Alam et al 2011, Stein and Aziz 2012).

PATHOPHYSIOLOGY OF BASAL GANGLIA DISORDERS

The basal ganglia might be said to guide intention into action. As far as their role in movement control is concerned, they appear to promote and support patterns of behaviour that are appropriate in the prevailing circumstances and to inhibit unwanted or inappropriate movements. This is exemplified by disorders of the basal ganglia, which are characterized, depending on the underlying pathology, by either an inability to initiate and execute wanted movements (as in Parkinson's disease) or an inability to prevent unwanted movements (as in Huntington's disease).

Parkinson's disease is the most common pathological condition affecting the basal ganglia. It is characterized by akinesia, muscular rigidity and tremor due to degeneration of the dopaminergic neurones of the substantia nigra pars compacta (which project to the striatum in the nigrostriatal pathway). As a consequence, dopamine terminals are lost in the striatum and dopamine levels are severely depleted: dopamine receptors located on medium spiny neurones, which are the target of the nigrostriatal pathway, are spared.

Dopamine appears to have a dual action on medium spiny striatal neurones. It inhibits those of the indirect pathway and excites those of the direct pathway: when dopamine is lost from the striatum, the indirect pathway therefore becomes overactive and the direct pathway becomes underactive (**Fig. 31.12**). Overactivity of the striatal projection to the lateral pallidum results in inhibition of pallidosubthalamic neurones and, consequently, overactivity of the subthalamic nucleus. Subthalamic efferents mediate excessive excitatory drive to the medial globus pallidus and substantia nigra pars reticulata. This is exacerbated by underactivity of the GABAergic, inhibitory direct pathway. Overactivity of basal ganglia output then inhibits the motor thalamus and its excitatory thalamocortical connections. While this description is little more than a first approximation of the underlying pathophysiology, this model of the basis of parkinsonian symptoms has led to the introduction of new neurosurgical approaches to the treatment of Parkinson's disease, based upon lesioning and deep brain stimulation of the medial globus pallidus and subthalamic nucleus (see below).

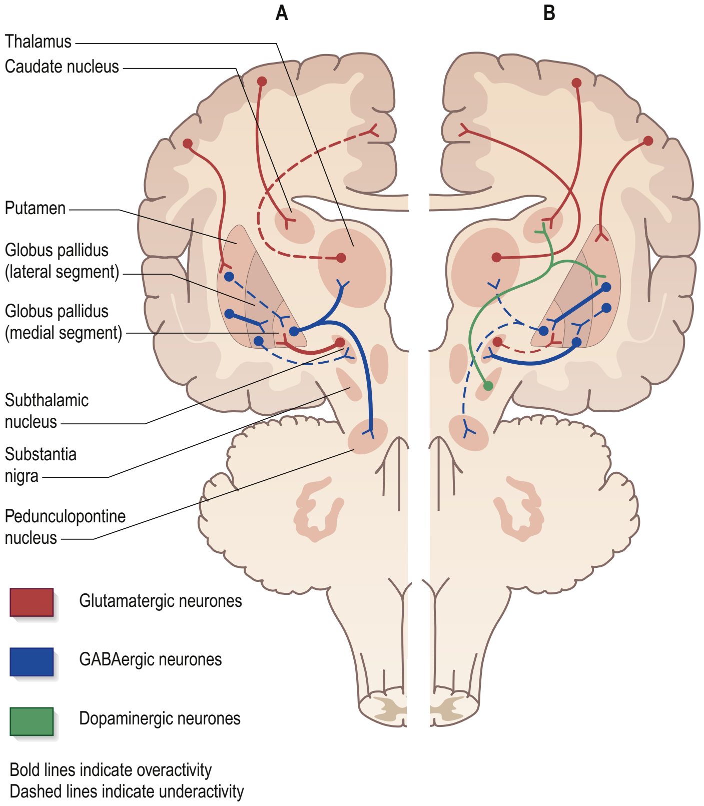

Fig. 31.12 The pathophysiology of Parkinson's disease (**A**) and dyskinesias (**B**). (Adapted with permission from Crossman AR, Neary D Neuroanatomy: An Illustrated Colour Text, 6th ed. Elsevier, Churchill Livingstone. Copyright 2019.)

The current medical treatment for Parkinson's disease largely relies on levodopa (L-DOPA; L-dihydroxyphenylalanine), the immediate metabolic precursor of dopamine, or on dopamine agonists. Whilst these usually provide good symptomatic relief for many years, eventually they lead to the development of side-effects, including dyskinesias. The involuntary movements that occur as a consequence of long-term treatment of Parkinson's disease resemble those seen in Huntington's disease, i.e. tardive dyskinesia and ballism. Experimental evidence suggests that these may share a common neural mechanism (Mitchell et al 1985, Mitchell et al 1992) (see Fig. 31.12). Thus, the indirect pathway becomes underactive, e.g. due to the effects of dopaminergic drugs in Parkinson's disease, or the degeneration of the striatopallidal projection to the lateral pallidum in Huntington's disease. This leads to physiological inhibition of the subthalamic nucleus by overactive pallidosubthalamic neurones. The involvement of the subthalamic nucleus explains why the dyskinetic movements of levodopa-induced dyskinesia and Huntington's disease resemble those of ballism produced by a lesion of the subthalamic nucleus. Underactivity of the subthalamic nucleus removes the excitatory drive from medial pallidal neurones, which are known to be underactive in dyskinesias (Crossman 1990). Once again, this anatomical model of basal ganglia function is an oversimplification. Whilst it is true that underactivity of the medial globus pallidus is associated with dyskinesias, it is also known that lesions of the globus pallidus alleviate them. This so-called 'pallidotomy paradox' suggests that the dynamic aspects of pallidal and nigral efferent activity are important factors in the generation of dyskinesia (Marsden and Obeso 1994). A more recent 'rate model' of basal ganglia function hypothesizes that specific components oscillate in neuronal synchrony at different frequencies to select specific voluntary motor patterns (Little and Brown 2014). Both rodent electrophysiology and recording from deep brain electrodes implanted in patients with Parkinson's disease suggest that neuronal activity suppression in the 8–30 Hz beta frequency band correlates with relief of parkinsonian akinesia and rigidity by both dopamine and subthalamic nucleus deep brain stimulation.

There is evidence that dysfunction of the basal ganglia is also involved in other complex, less well understood, behavioural disorders. In animal experiments, lesions of the basal ganglia, especially of the caudate nucleus, induce uncontrollable hyperactivity (e.g. obstinate progression, incessant pacing and other constantly repeated behaviours). This and other evidence has led to the notion that the corpus striatum enables an individual to make motor choices and avoid 'stimulus-bound' behaviour. Positron emission tomography (PET) studies in humans have shown that sufferers from obsessive–compulsive disorder (OCD), which is characterized by repeated ritualistic motor behaviour and intrusive thoughts, exhibit abnormal activity in the prefrontal cortex and caudate nuclei. There are similar suggestive observations in childhood attention deficit hyperactivity disorder (ADHD), Huntington's disease and Tourette's syndrome. In this respect, it may be significant that the basal ganglia, besides receiving connections from the frontal lobe and limbic cortices, also have an ascending influence on the prefrontal and cingulate cortices through the substantia nigra pars reticulata and dorsomedial and ventromedial thalamus in parallel, functionally segregated, cortico-striato-thalamic circuits that subserve locomotor, oculomotor, cognitive and affective behaviour (Alexander et al 1986; see Fig. 31.9).

Before the advent of levodopa therapy, neurosurgery for Parkinson's disease was commonplace. The medial globus pallidus and thalamus were favoured targets for chemical or thermal lesions. Pallidotomy and thalamotomy often improved rigidity and tremor, but they produced little consistent beneficial effect on akinesia. With the arrival of levodopa

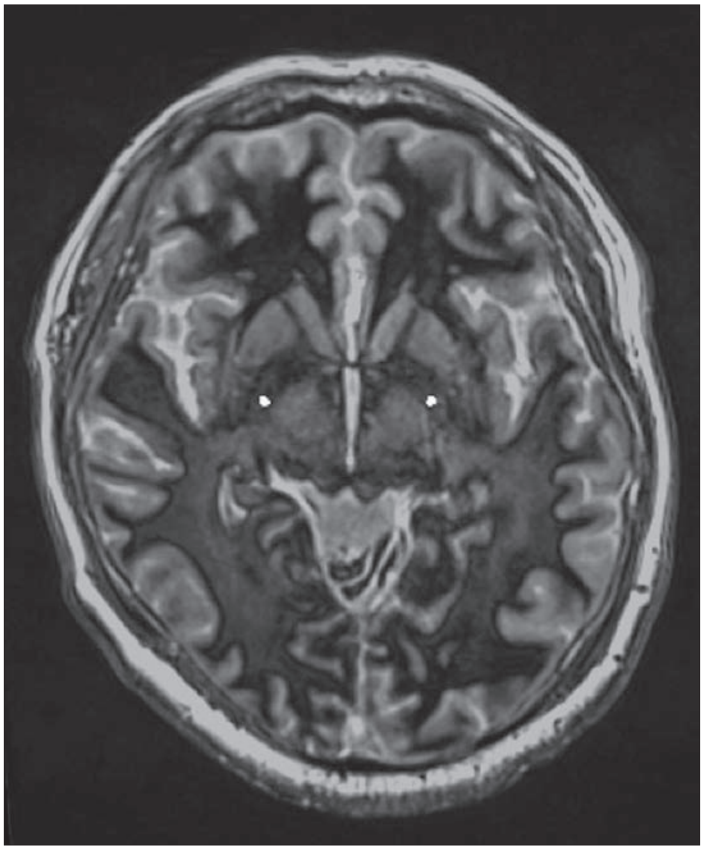

Fig. 31.13 Magnetic resonance image with CT overlaid showing the placement of deep brain stimulation electrodes (white dots) bilaterally in the globus pallidus of a patient with dystonia (Courtesy of Mr E Pereira, St George's, University of London.)

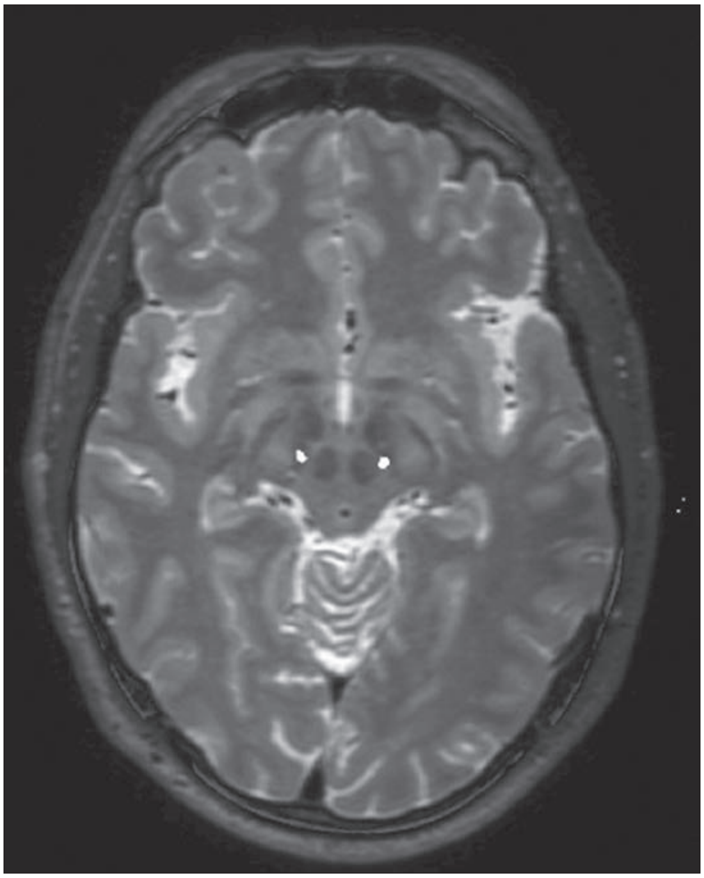

Fig. 31.14 Magnetic resonance image with CT overlaid showing the placement of deep brain stimulation electrodes (white dots) bilaterally in the subthalamic nucleus of a patient with Parkinson's disease. (Courtesy of Mr E Pereira, St George's, University of London.)

therapy, which very effectively alleviates akinesia, the surgical treatment of Parkinson's disease underwent a progressive decline. It soon became clear, however, that long-term use of levodopa was associated with a number of side-effects such as dyskinesias, 'wearing-off' and the 'on–off' phenomenon. More recent advances in understanding the pathophysiology of movement disorders, and of Parkinson's disease in particular, have stimulated a renaissance in the use of neurosurgery to treat movement disorders.

Lesioning the subthalamic nucleus in experimental primates made parkinsonian with the neurotoxin MPTP dramatically alleviated the parkinsonian symptoms, suggesting that the subthalamic nucleus might be an appropriate clinical target (Pereira and Aziz 2006). While therapeutic surgical lesions of the subthalamic nucleus can alleviate tremor, rigidity and bradykinesia in patients with Parkinson's disease, the risk of side-effects is not trivial: the subthalamic nucleus is a small structure wrapped by fibres of passage and close to the hypothalamus and internal capsule.

In 1992, Laitinen et al reintroduced pallidotomy for the treatment of end-stage Parkinson's disease, but confined the lesions to the posteroventral part of the medial pallidum. These lesions were found to be extremely reliable in abolishing contralateral rigidity and drug-induced dyskinesias, with slightly less efficacy on tremor and bradykinesia (Laitinen et al 1992).

Implantation of deep brain electrodes, through which high-frequency pulses generated by a pacemaker could inhibit cells in the vicinity, has been a concept since the early 1970s. It did not become a widespread reality until the late 1980s, when it was facilitated by technological advances. The introduction of the technique of deep brain stimulation (DBS), which avoids making permanent lesions, made bilateral surgery safer. There have been numerous reports of the effectiveness of both bilateral pallidal and subthalamic nucleus stimulation in Parkinson's disease (Rodriguez-Oroz et al 2012; **Figs 31.13–31.14**). Subthalamic nucleus stimulation is largely favoured for relieving akinesia and rigidity, with pallidal stimulation considered to ameliorate dyskinesias if cognition and speech are at risk. Subthalamic stimulation is more effective than pallidal stimulation in allowing patients to reduce their anti-parkinson medication. Isolated tremor syndromes are best relieved by stimulation of either the contralateral ventral intermediate thalamic nucleus or the zona incerta.

Another manifestation of basal ganglia dysfunction is dystonia, which is characterized by increased muscle tone and abnormal postures. Dystonia may occur as a consequence of levodopa treatment in Parkinson's disease or inherited disease (e.g. early-onset torsion, or Oppenheim's dystonia, an autosomal dominant disorder most commonly associated with a mutation in the *DYT1* gene that encodes torsin A). Although the pathophysiological basis of dystonia is unclear (Hallett 2006), it is probably caused by underactivity of basal ganglia output. The observation that painful dystonic posturing of the limbs in parkinsonian patients responds dramatically to bilateral pallidal stimulation led to the development of bilateral pallidal stimulation for dystonia. Intriguingly, in dystonia the pallidal neurones are believed to fire at rates below normal, and so it is open to question how this stimulation works. Moreover, while the effect of stimulation is immediate in the case of Parkinson's disease, in dystonia the improvement may take weeks to emerge, suggesting that the neural mechanism underlying the therapeutic effect of stimulation for this condition is different and implicating a role for neuroplasticity in dystonia. Targeting of the subthalamic nucleus and ventral intermediate thalamus for both phasic and tonic components of craniocervical dystonia has an immediate effect and shows great promise.

Another recent neurosurgical development in the therapy of Parkinson's disease has involved targeting the pedunculopontine nucleus, which both receives fibres from and sends fibres to basal ganglia and related nuclei. Recently, DBS of the pedunculopontine nucleus through implanted electrodes has been applied in drug-resistant akinetic parkinsonian patients. Low-frequency stimulation sometimes alleviates postural instability and on-medication gait freezing and falling, symptoms that conventional medication and surgery fail to improve (Garcia-Rill et al 2019).

The advent of novel DBS electrodes of longer contact span enabling dual targeting, for example of the ventral intermediate thalamus and either the subthalamic nucleus or zona incerta, has opened up increased treatment possibilities in movement disorders. Additionally, segmented directional electrodes enable current steering to reduce capsular or other side-effects from subthalamic or thalamic stimulation and increase the therapeutic window of stimulation. Future directions include miniaturization and 'closed loop' stimulation where neuronal oscillations are recorded from the deep brain electrodes and responded to, either for more effective stimulation in Parkinson's disease or for motor control via brain/computer interfaces in spinal cord injury or motor neurone disease (Lozano et al 2019).

Key references

Alexander GE, DeLong MR, Strick PL 1986 Parallel organization of functionally segregated circuits linking basal ganglia and cortex. Ann Rev Neurosci 9:357–82.

A landmark publication setting out a conceptual framework for the way in which the basal ganglia and cerebral cortex process different types of information through largely distinct parallel circuits based on known anatomical connectivity.

Crossman AR 1990 A hypothesis on the pathophysiological mechanisms that underlie levodopa- or dopamine agonist-induced dyskinesia in Parkinson's disease: implications for future strategies in treatment. Mov Disord 5:100–8.

A seminal paper outlining the limitations of dopaminergic treatments of Parkinson's disease and translating an anatomical model of basal ganglia function into potential neurosurgical treatment targets.

Hallett M 2006 Pathophysiology of dystonia. Neural Transm Suppl 70:485–8.

An explanation of the abnormalities in basal ganglia function involved in dystonia.

Laitinen LV, Bergenheim AT, Hariz MI 1992 Ventroposterolateral pallidotomy can abolish all Parkinsonian symptoms. Stereotact Funct Neurosurg 58:14–21.

A key paper that ignited widespread interest in functional neurosurgery for Parkinson's disease.

Lozano AM, Lipsman N, Bergman H et al 2019. Deep brain stimulation: current challenges and future directions. Nat Rev Neurol 5(3):148–60.

Review of current and future technologies in deep brain stimulation including directional electrodes and closed loop stimulation.

Marsden CD, Obeso JA 1994 The functions of the basal ganglia and the paradox of stereotaxic surgery in Parkinson's disease. Brain 117:877–97.

A review that highlights some limitations of the anatomical model of basal ganglia function.

Mena-Segovia J, Bolam JP, Magill PJ 2004 Pedunculopontine nucleus and basal ganglia: distant relatives or part of the same family? Trends Neurosci 27:585–8.

A review presenting a persuasive argument for functional similarities and intimate reciprocal connections between pedunculopontine nucleus and other basal ganglia structures.

Penney JB Jr, Young AB 1986 Striatal inhomogeneities and basal ganglia function. Mov Disord 1:3–15.

A landmark publication, introducing some of the basic concepts behind current models of the pathophysiology of Parkinson's disease and Huntington's disease.

Pereira EA, Aziz TZ 2006 Parkinson's disease and primate research: past, present, and future. Postgrad Med J 82:293–9.

A review of the non-human primate experiments that led to contemporary functional neurosurgery for Parkinson's disease that discusses the anatomical model of basal ganglia function.

Rodriguez-Oroz MC, Moro E, Krack P 2012 Long-term outcomes of surgical therapies for Parkinson's disease. Mov Disord 27:1718–28.

A contemporary review and results of five-year, long-term follow-up of patients receiving deep brain stimulation for Parkinson's disease.

References

Alam M, Schwabe K, Krauss J 2011 The pedunculopontine nucleus area: critical evaluation of interspecies differences relevant for its use as a target for deep brain stimulation. Brain 134:11–23.

Alexander GE, DeLong MR, Strick PL 1986 Parallel organization of functionally segregated circuits linking basal ganglia and cortex. Ann Rev Neurosci 9:357–82.

A landmark publication setting out a conceptual framework for the way in which the basal ganglia and cerebral cortex process different types of information through largely distinct parallel circuits based on known anatomical connectivity.

Crossman AR 1990 A hypothesis on the pathophysiological mechanisms that underlie levodopa- or dopamine agonist-induced dyskinesia in Parkinson's disease: implications for future strategies in treatment. Mov Disord 5:100–8.

A seminal paper outlining the limitations of dopaminergic treatments of Parkinson's disease and translating an anatomical model of basal ganglia function into potential neurosurgical treatment targets.

Garcia-Rill E, Tackett AJ, Byrum SD et al 2019 Local and relayed effects of deep brain stimulation of the pedunculopontine nucleus. Brain Sci 9(3):64.

Hallett M 2006 Pathophysiology of dystonia. Neural Transm Suppl 70:485–8.

An explanation of the abnormalities in basal ganglia function involved in dystonia.

Hamani C, Stone S, Laxton A et al 2007 The pedunculopontine nucleus and movement disorders: anatomy and the role for deep brain stimulation. Parkinsonism Relat Disord 13:S276–S280.

Jankovic J 2012 Movement disorders. In: Daroff RB, Fenichel GM, Jankovic J et al (eds) Bradley's Neurology in Clinical Practice, 6th ed. Philadelphia: Elsevier, Saunders; Ch.71, pp. 1762–1801.

Laitinen LV, Bergenheim AT, Hariz MI 1992 Ventroposterolateral pallidotomy can abolish all Parkinsonian symptoms. Stereotact Funct Neurosurg 58:14–21.

A key paper that ignited widespread interest in functional neurosurgery for Parkinson's disease.

Little S, Brown P 2014 The functional role of beta oscillations in Parkinson's disease. Parkinsonism Relat Disord 20(Suppl 1):S44–S48.

Lozano AM, Lipsman N, Bergman H et al 2019. Deep brain stimulation: current challenges and future directions. Nat Rev Neurol 5(3):148–60.

Review of current and future technologies in deep brain stimulation including directional electrodes and closed loop stimulation.

Marsden CD, Obeso JA 1994 The functions of the basal ganglia and the paradox of stereotaxic surgery in Parkinson's disease. Brain 117:877–97.

A review that highlights some limitations of the anatomical model of basal ganglia function.

Massey LA, Miranda MA, Zrinzo L et al 2012 High resolution MR anatomy of the subthalamic nucleus: imaging at 9.4 T with histological validation. Neuroimage 59:2035–44.

Massey LA, Yousry TA 2010 Anatomy of the substantia nigra and subthalamic nucleus on MR imaging. Neuroimaging Clin North Am 20:7–27.

Mena-Segovia J, Bolam JP, Magill PJ 2004 Pedunculopontine nucleus and basal ganglia: distant relatives or part of the same family? Trends Neurosci 27:585–8.

A review presenting a persuasive argument for functional similarities and intimate reciprocal connections between pedunculopontine nucleus and other basal ganglia structures.

Mitchell IJ, Jackson A, Sambrook MA et al 1985 Common neural mechanisms in experimental chorea and hemiballismus in the monkey. Evidence from 2-deoxyglucose autoradiography. Brain Res 339:346-50.

Mitchell IJ, Clarke CE, Boyce S et al 1989 Neural mechanisms underlying parkinsonian symptoms based upon regional uptake of 2-deoxyglucose in monkeys exposed to 1-methyl-4-phenyl-1,2,3,6-tetrahydropyridine. Neuroscience 32:213–26.

Mitchell IJ, Crossman AR, Liminga U et al 1992 Regional changes in 2-deoxyglucose uptake associated with neuroleptic-induced tardive dyskinesia in the Cebus monkey. Mov Disord 7:32–7.

Penney JB Jr, Young AB 1986 Striatal inhomogeneities and basal ganglia function. Mov Disord 1:3–15.

A landmark publication, introducing some of the basic concepts behind current models of the pathophysiology of Parkinson's disease and Huntington's disease.

Pereira EA, Aziz TZ 2006 Parkinson's disease and primate research: past, present, and future. Postgrad Med J 82:293–9.

A review of the non-human primate experiments that led to contemporary functional neurosurgery for Parkinson's disease that discusses the anatomical model of basal ganglia function.

Rodriguez-Oroz MC, Moro E, Krack P 2012 Long-term outcomes of surgical therapies for Parkinson's disease. Mov Disord 27:1718–28.

A contemporary review and results of five-year, long-term follow-up of patients receiving deep-brain stimulation for Parkinson's disease.

Stein JF, Aziz TZ 2012 Basal ganglia output to the PPN, a commentary. Exp Neurol 233:745–6.

CHAPTER
32

Cerebral hemispheres

The cerebral hemispheres are the largest part of the human brain: they consist of the telencephalon (cerebral cortex and underlying white matter), basal ganglia and diencephalon. Both hemispheres are interconnected by the corpus callosum and the anterior commissure. The cerebral cortex contains the motor and premotor regions, the highest level at which motor activities are controlled, and the primary sensory regions, which provide the first cortical level for the conscious experience of sensory stimuli and to which sensory organs project either directly (olfactory stimuli) or via specific thalamic nuclei. Cortical areas of higher levels are either modality-specific (higher unimodal cortices) or multimodal (association cortex), enabling complex analyses of the internal and external environments. The cortical part of the limbic system (hippocampal formation, amygdala, cingulate and retrosplenial cortex) is a multimodal region that is particularly concerned with memory and the emotional aspects of sensory experience and behaviour. It is also connected with subcortical areas such as the hypothalamus in integrating widespread physiological activities that include endocrine and vegetative reactions. Other association regions within the frontal, temporal and parietal lobes are concerned with the highest aspects of cognitive function, such as social communication, language and visuospatial attention. Anterior association regions of the frontal lobe contribute to personality, judgement, foresight and planning.

The white matter contains association fibres limited to each hemisphere; commissural fibres linking corresponding areas of both hemispheres; and projection fibres connecting the cerebral cortex with subcortical, brainstem and spinal cord nuclei. Some of these bundles (tracts, fasciculi) are relatively well defined and compact, while others fan out and are less easy to identify. A detailed knowledge of the three-dimensional anatomical interrelationships of white matter tracts is a requisite for the planning, intraoperative monitoring and execution of neurosurgical procedures for tumour surgery, resection of epileptic foci and deep brain stimulation. Current understanding of the fibre tracts owes much to the introduction of diffusion-weighted magnetic resonance imaging (dMRI), which enables both postmortem and *in vivo* visualization of the trajectory of the white matter tracts that connect distant regions (structural connectivity). Functional MRI (fMRI) defines the role of cortical areas by task-driven activation or resting state analyses of cortical networks, and thus allows the study of functional connectivity. Stereotaxic atlases in which data are registered to a reference brain are used to integrate different multimodal imaging findings and bridge between data acquired at different scales, from macroscopical *in vivo* MRI to microscopical postmortem anatomy (Eickhoff et al 2005, Van Essen 2005, Zilles and Amunts 2010, Catani and Thiebaut de Schotten 2012).

CEREBRAL HEMISPHERE SURFACES, SULCI AND GYRI

The external surface of each hemisphere is highly convoluted into a series of gyri, separated by sulci that represent extensions of the subarachnoid space (**Figs 32.1–32.3**). The term fissure is used for the deepest sulci, whereas incisures or notches are short, shallow indentations. The main sulci have depths of 1–3 cm, and may harbour small annectant gyri connecting the walls of two adjacent gyri. Most sulci are orientated towards the nearest ventricular cavity and for this reason the sulcal floor is often used by neurosurgeons as point of entry into the underlying ventricle. The sulci of the adult brain are highly variable between subjects, and can be long or short, branching, continuous or interrupted by short transitional gyri (Ono et al 1990, Ribas 2010, Catani and Thiebaut de Schotten 2012, Naidich et al 2012). All long primary sulci can be consistently identified in most human brains (e.g. lateral fissure, central, precentral, postcentral, calcarine, parieto-occipital, collateral, cingulate and callosal sulci). Among the short sulci, primary sulci such as the rhinal, olfactory, lateral and occipital sulci are consistently found in all brains, whereas other short sulci are highly variable and composed of several branches (e.g. orbital and subparietal sulci), or are sometimes absent and therefore indicated as supplementary (e.g. middle frontal sulcus).

Each gyrus is composed of two lateral walls, and a crown that is visible on the external surface. It is estimated that about two-thirds of the cerebral cortex lies along the gyral walls and is therefore buried in the depths of the sulci (Henneberg 1910, Zilles et al 1988). The majority of the sulci appear during postmenstrual weeks 18–21: cortical folding (gyrification) accelerates conspicuously from postmenstrual week 28 and reaches a transient maximum between the 7th and 13th months

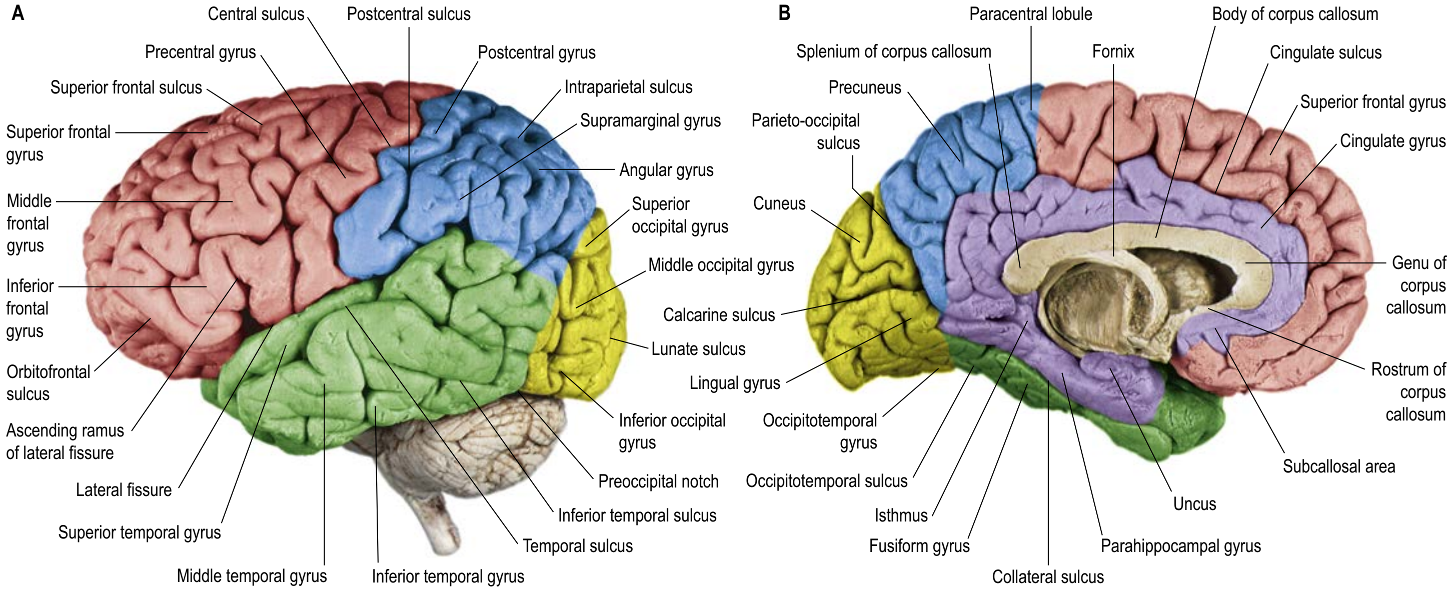
A
Central sulcus
Postcentral sulcus
Precentral gyrus
Postcentral gyrus
Superior frontal sulcus
Intraparietal sulcus
Supramarginal gyrus
Superior frontal gyrus
Angular gyrus
Middle frontal gyrus
Superior occipital gyrus
Middle occipital gyrus
Inferior frontal gyrus
Calcarine sulcus
Lunate sulcus
Orbitofrontal sulcus
Ascending ramus of lateral fissure
Inferior occipital gyrus
Preoccipital notch
Lateral fissure
Inferior temporal sulcus
Superior temporal gyrus
Temporal sulcus
Middle temporal gyrus
Inferior temporal gyrus
B
Paracentral lobule
Body of corpus callosum
Splenium of corpus callosum
Fornix
Cingulate sulcus
Precuneus
Superior frontal gyrus
Parieto-occipital sulcus
Cingulate gyrus
Cuneus
Genu of corpus callosum
Lingual gyrus
Rostrum of corpus callosum
Occipitotemporal gyrus
Subcallosal area
Occipitotemporal sulcus
Uncus
Isthmus
Fusiform gyrus
Parahippocampal gyrus
Collateral sulcus

Fig. 32.1 Lateral (**A**) and medial (**B**) aspect of the left cerebral hemisphere, indicating the major gyri and sulci. The colours indicate the lobes: frontal (red), parietal (blue), temporal (green), occipital (yellow) and limbic (purple). (Dissected by EL Rees, photograph by Kevin Fitzpatrick on behalf of GKT School of Medicine, London; enhanced and labelled by M Catani and B Crossman.)

The process of fetal cortical development includes sequential neural cell proliferation at the ventricular zone, ventriculofugal migration of neuronal progeny to form the most recent outer layer of the cortex, and increases in cortical thickness and expansion of the cortical surface area (Ch. 14). The description of the external appearance of this process as a measurement of cerebral hemisphere growth and fetal age, i.e. the visualization of early surface ridges adjacent to neighbouring depressions, is fraught with limitations similar to those noted when describing the pre- and postnatal growth of individuals. Techniques to study hemispheric growth include examination of postmortem brains that have been fixed and removed from the cranium after spontaneous fetal death (Nishkuni and Ribas 2013); MR imaging of brains within the calvaria (Zhang et al 2013); and ultrasound examination of routine second and third trimester scans of live fetuses (Chen et al 2017, Husen et al 2019). These studies have noted different ages at which sulci first appear, reflecting the heterogeneous ethnic, gender and nutritional status of the fetuses: in the case of postmortem studies, there is also the possibility that underlying pathology might have affected cerebral growth.

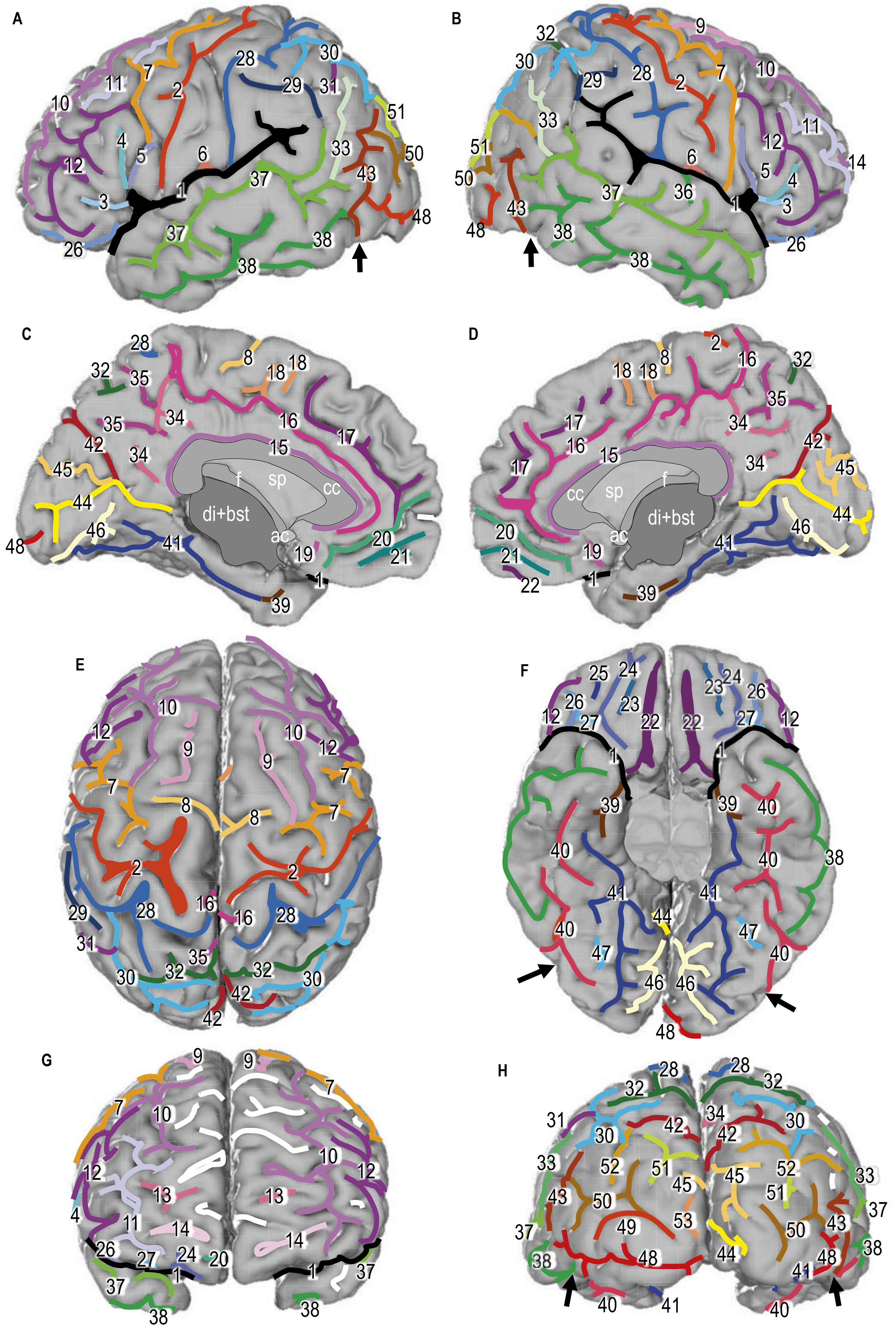
A
10
11
7
2
28
30
29
31
51
12
4
5
6
33
50
43
3
1
37
48
26
37
38
38
B
32
9
30
29
28
2
7
10
33
11
51
12
14
50
6
5
4
37
36
1
3
43
48
38
26
38
C
28
8
18
18
32
35
35
34
16
17
42
15
34
45
f
sp
cc
44
di+bst
46
ac
20
48
41
19
21
1
39
D
2
8
18
18
16
32
35
17
34
16
15
42
17
34
45
f
cc
sp
di+bst
44
46
20
ac
41
21
19
1
22
39
E
10
12
10
9
12
9
7
7
8
8
7
2
2
29
28
16
16
28
31
35
30
32
32
30
42
42
F
25
24
24
23
26
26
12
27
23
22
22
27
12
1
1
39
39
40
40
38
40
41
41
44
40
47
47
40
46
46
48
G
9
9
7
7
10
10
12
12
13
13
4
11
14
14
26
27
24
20
1
1
37
37
38
38
H
28
28
32
32
31
34
30
42
30
42
33
52
51
52
33
45
45
51
37
43
50
53
50
43
37
49
44
48
48
38
38
41
40
41
40

Fig. 32.2 A–H, Lateral (**A–B**), medial (**C–D**), dorsal (**E**), basal (**F**), frontal (**G**) and caudal views (**H**) of the Montreal Neurological Institute (MNI) single subject template. Key and abbreviations: 1, Sylvian fissure; 2, central sulcus; 3, horizontal ramus of the Sylvian fissure; 4, ascending ramus of the Sylvian fissure; 5, diagonal sulcus; 6, posterior subcentral sulcus; 7, precentral sulcus; 8, medial precentral sulcus; 9, medial frontal sulcus (superior frontal paramidline sulcus); 10, superior frontal sulcus; 11, intermediate sulcus; 12, inferior frontal sulcus; 13, frontal polar sulcus; 14, frontomarginal sulcus; 15, callosal sulcus; 16, cingulate sulcus; 17, paracingulate sulcus; 18, paracentral sulci; 19, anterior parolfactory sulcus; 20, superior rostral sulcus; 21, inferior rostral sulcus; 22, olfactory sulcus; 23, sulcus fragmentosus; 24, medial orbital sulcus; 25, intermediate orbital sulcus; 26, lateral orbital sulcus; 27, transverse orbital sulcus; 28, postcentral sulcus; 29, supramarginal sulcus; 30, intraparietal sulcus; 31, Jensen sulcus (primary intermediate sulcus); 32, superior parietal sulcus; 33, angular sulcus; 34, subparietal sulcus; 35, precuneal sulcus; 36, transverse temporal sulcus (Heschl's sulcus); 37, superior temporal sulcus; 38, inferior temporal sulcus; 39, rhinal sulcus; 40, occipitotemporal sulcus; 41, collateral sulcus; 42, parieto-occipital sulcus; 43, anterior occipital sulcus; 44, calcarine sulcus; 45, cuneal sulcus (paracalcarine sulcus); 46, lingual sulcus; 47, mid-fusiform sulcus; 48, inferior occipital sulcus; 49, inferior lateral occipital sulcus; 50, superior lateral occipital sulcus; 51, superior occipital sulcus; 52, transverse occipital sulcus; 53, accessory sulcus; ac, anterior commissure; bst, brainstem; cc, corpus callosum; di, diencephalon; f, fornix; sp, septum pellucidum. Arrows indicate position of the occipitotemporal incisure. For general aspects concerning anatomical variability, see Ono et al (1990). For more detailed information concerning sulci, see Amunts et al (1999), Caspers et al (2006), Duvernoy (1999), Malikovic et al (2012), Tzourio-Mazoyer et al (2002), Öngür et al (2003), Petrides and Pandya (2012), Vogt et al (1995) and Weiner et al (2014). (With permission from Zilles K, Palomero-Gallagher N 2015 Gyrification in the human brain. In: Toga AW (ed) Brain Mapping: An Encyclopedic Reference. Anatomy and Physiology. Elsevier, Academic Press. Copyright 2015.)

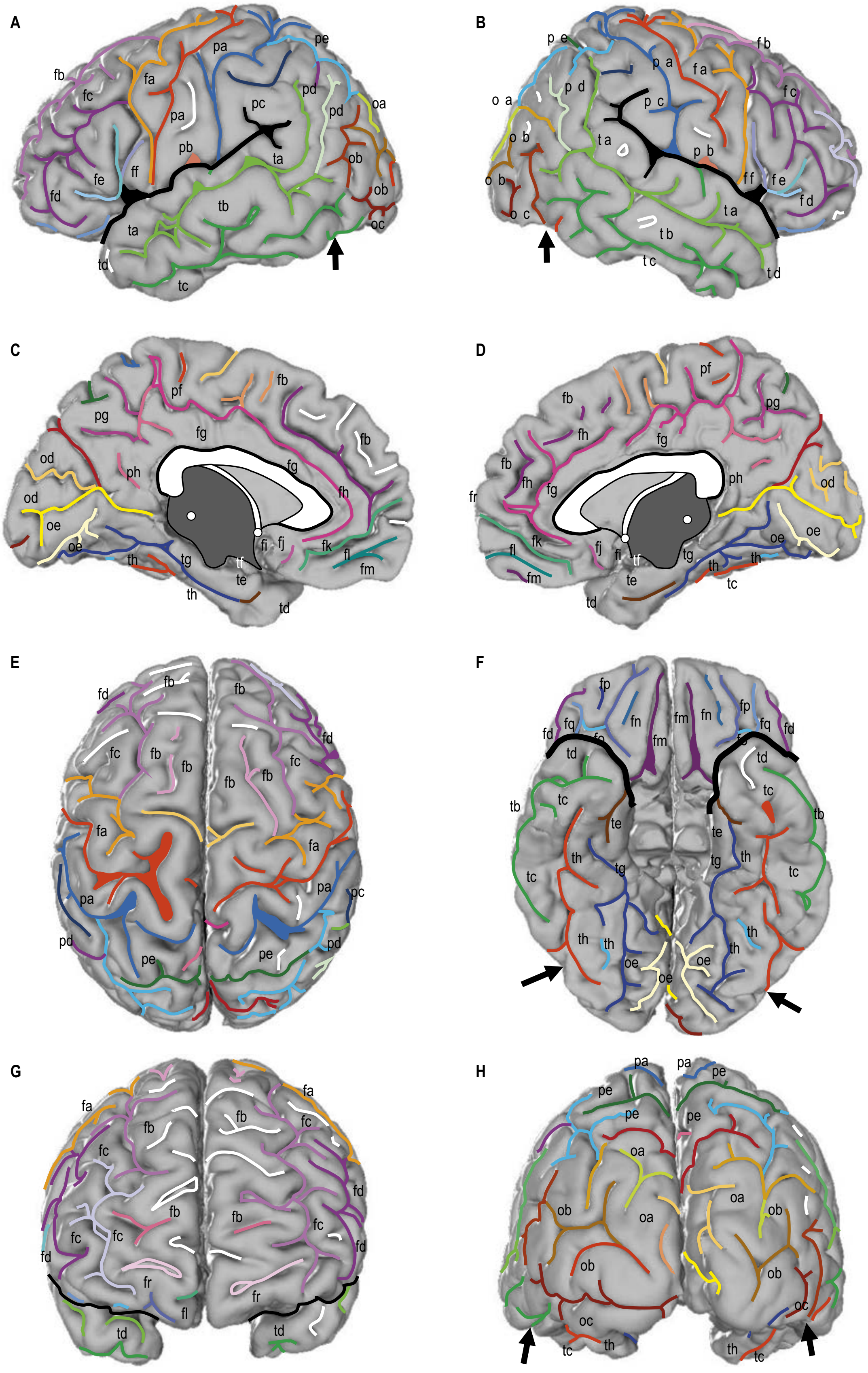
A
fb
fc
fa
pa
pe
pa
pc
pd
pd
oa
pb
ta
ob
ff
fe
fd
tb
oc
ta
td
tc
B
pe
pa
fa
fb
oa
pd
pc
fc
ob
ta
pb
ob
ff
fe
fd
oc
ta
tb
tc
td
C
fb
pf
pg
fg
fb
od
ph
fg
od
fh
oe
oe
fi
fj
fk
th
tg
tf
fl
te
fm
th
td
D
pf
fb
pg
fh
fg
fb
fh
fg
ph
od
fr
oe
oe
fk
fl
fj
fi
tf
tg
th
th
fm
te
tc
td
E
fb
fd
fb
fd
fc
fb
fb
fc
fb
fb
fa
fa
pa
pc
pa
pd
pe
pe
pd
F
fp
fn
fm
fn
fp
fq
fd
fq
fd
fo
fm
fo
td
td
tb
tc
tc
tb
te
te
th
tg
tg
th
tc
tc
th
th
th
oe
oe
oe
th
G
fa
fa
fb
fb
fc
fc
fd
fb
fb
fc
fc
fc
fd
fd
fr
fr
fl
td
td
H
pa
pa
pe
pe
pe
pe
oa
oa
oa
ob
ob
ob
ob
oc
oc
tc
th
th
tc

Fig. 32.3 A-H, Lateral (**A–B**), medial (**C–D**), dorsal (**E**), basal (**F**), frontal (**G**) and caudal views (**H**) of the MNI single subject template, on which gyri have been identified. Sulci are colour-coded as in Fig. 32.2. Abbreviations: fa, precentral gyrus; fb, superior frontal gyrus; fc, medial frontal gyrus; fd, inferior frontal gyrus; fe, pars triangularis; ff, pars opercularis; fg, cingulate gyrus; fh, superior cingulate gyrus; fi, paraterminal gyrus; fj, subcallosal gyrus; fk, superior rostral gyrus; fl, inferior rostral gyrus; fm, gyrus rectus; fn, medial orbital gyrus; fo, posterior orbital gyrus; fp, anterior orbital gyrus; fq, lateral orbital gyrus; fr, frontomarginal gyrus; pa, postcentral gyrus; pb, subcentral gyrus; pc, supramarginal gyrus; pd, angular gyrus; pe, superior parietal lobule; pf, paracentral lobule; pg, precuneus; ph, cingulate gyrus, parietal part; ta, superior temporal gyrus; tb, intermediate temporal gyrus; tc, inferior temporal gyrus; td, temporal pole; te, gyrus ambiens; tf, gyrus semilunaris; tg, parahippocampal gyrus; th, fusiform gyrus (lateral occipito-temporal gyrus); oa, superior occipital gyrus; ob, middle occipital gyrus; oc, inferior occipital gyrus; od, cuneus; oe, lingual gyrus (medial occipito-temporal gyrus). (With permission from Zilles K, Palomero-Gallagher N 2015 Gyrification in the human brain. In: Toga AW (ed) Brain Mapping: An Encyclopedic Reference. Anatomy and Physiology. Elsevier, Academic Press. Copyright 2015.)

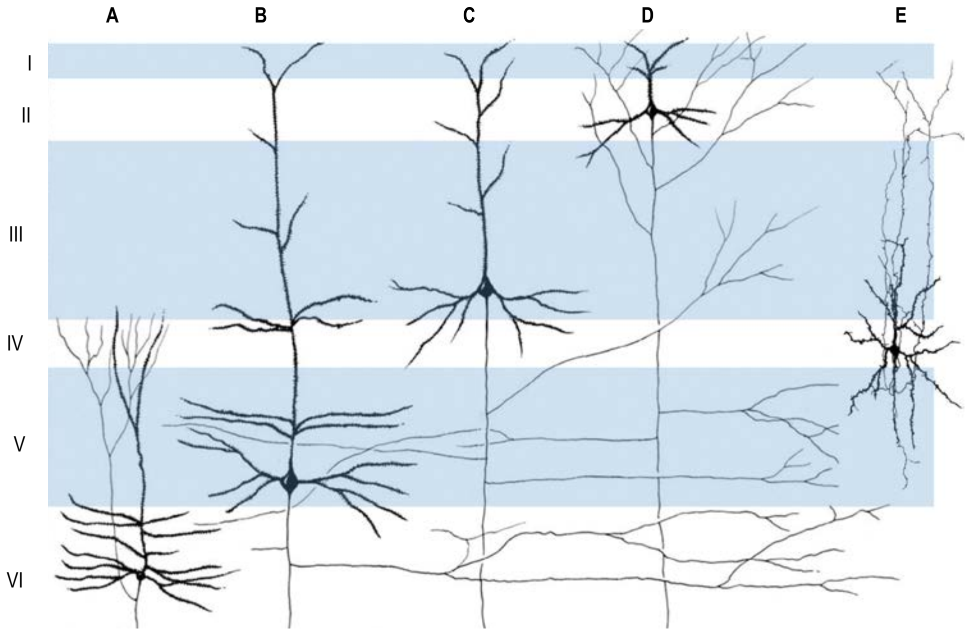

Fig. 32.4 Pyramidal and spiny stellate cells with their dendritic (thick) and axonal (thin) processes in different layers of the isocortex. **A**, Cortico-thalamic and cortico-claustral projection neurones. **B**, Cortico-striate, cortico-pontine, cortico-bulbar and cortico-spinal projection neurones. **C**, Cortico-cortical and commissural projection neurones. **D**, Cortico-cortical projection neurones. **E**, Spiny stellate cell.

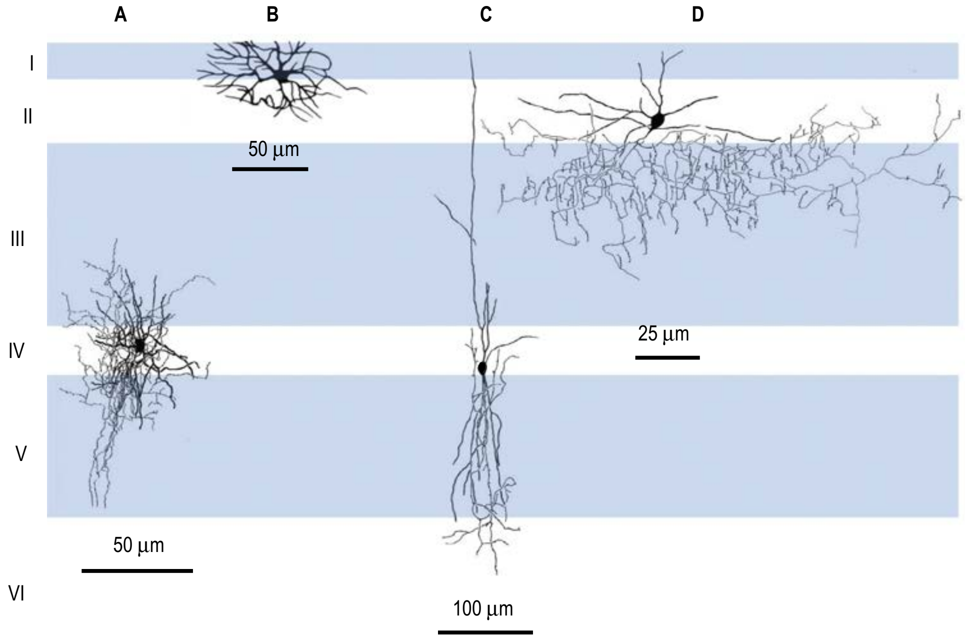

Fig. 32.5 A–D, Interneurones with axons (thin) and dendrites (thick) in the cerebral cortex. **A**, Neurogliaform cell in layer IV of the squirrel monkey S1. **B**, Cajal–Retzius cell in layer I of the human primary motor cortex. **C**, Bipolar cell in layer IV of the macaque primary visual cortex. **D**, Chandelier cell in layer II of the rat primary auditory cortex. (A, With permission from Jones EG 1975 Varieties and distribution of non-pyramidal cells in the somatic sensory cortex of the squirrel monkey. J Comp Neurol 160:205–68; B, with permission from Marin-Padilla M, Marin-Padilla MT 1982 Origin, prenatal development and structural organization of layer I of the human cerebral (motor) cortex: a Golgi study. Anat Embryol 164:161–206; C, D, with permission from Peters A, Jones EG (eds) 1984 Cerebral Cortex, Vol. 1. New York: Plenum Press.)

postnatally. From this time on, the degree of folding declines by 18% until the adult value will be reached at an age of approximately 23 years (Armstrong et al 1995).

The main cerebral sulci divide the hemispheres into frontal, parietal, occipital, temporal, insular and limbic lobes (Fig. 32.1A,B). In the adult brain, the limbic lobe is visible on the medial surface of each hemisphere. Parts of the frontal, parietal and temporal lobes cover the insular lobe, which is present in the depth of the lateral fissure (opercularization). Each hemisphere has superolateral, medial and inferior (basal) surfaces and a frontal, temporal and occipital pole (see Fig. 32.1A,B).

The superolateral surface is convex and lies beneath the bones of the calvaria: the frontal, parietal, temporal and occipital lobes correspond approximately in surface extent to the overlying bones from which they take their names. The frontal and parietal lobes are separated by the central (Rolandic) sulcus and both are separated from the temporal lobe by the prominent lateral (Sylvian) fissure. Frontal and temporal regions are each composed of three horizontal gyri, the superior, middle and inferior frontal and temporal gyri, respectively. The central region is composed of two slightly oblique gyri, the frontal precentral gyrus and the parietal postcentral gyrus, that are separated by the central sulcus. The deep intraparietal sulcus divides the superior parietal lobule from the inferior parietal lobule (which is subdivided into supramarginal and angular gyri). The occipital region is composed of three horizontal gyri (superior, middle and inferior occipital gyri), which are highly variable between subjects. The insula lies deep in the floor of the lateral fissure and consists of 4–5 diagonal gyri, separated by the central insular sulcus into anterior short and posterior long insular gyri.

The inferior surface has a smaller anterior frontal orbital part and a larger posterior tentorial part that belongs to the temporal and occipital lobes. The orbital part rests on the floor of the anterior cranial fossa, and the posterior part rests on the floor of the middle cranial fossa and the upper surface of the tentorium cerebelli. The orbital part of the inferior surface is made up of the orbital gyri and the gyrus rectus. The tentorial part of the inferior surface is covered by the basal aspects of the inferior temporal, inferior occipital and lingual gyri, and the fusiform gyrus.

The medial surface is flat and vertical, and is separated from the contralateral hemisphere by the longitudinal fissure and the falx cerebri. The medial surface of the hemisphere includes a C-shaped inner ring composed of two continuous gyri (the cingulate and parahippocampal gyri), surrounded by the gyrus rectus, superior frontal gyrus, paracentral lobule, precuneus, cuneus and lingual gyrus. Some details of the anatomy of the gyri and sulci of each lobe are illustrated in Figs 32.2–32.3.

NEURONAL TYPES IN THE CEREBRAL CORTEX

The cerebral cortex is an intricate complex of neuronal somata and fibres, neuroglia and blood vessels. The neocortex contains two major neuronal cell types: excitatory pyramidal cells with long axons (projection neurones) and stellate cells (**Fig. 32.4**). Pyramidal cells are the most abundant type and represent about 75% of the cortical neurones. Stellate cells have been subdivided into spiny stellate cells that express glutamate as neurotransmitter, and GABA-containing inhibitory aspinous interneurones with relatively short, locally terminating axons (Fig. 32.5). All types have been further divided on the basis of their size and shape, connectivity, neurotransmitter and gene expression, and electrophysiological characteristics.

Laminar organization

The most obvious microscopic feature of the cortex is its horizontal organization in layers or laminae that are visible to the naked eye or under the microscope after cell body or myelin staining. The isocortex has six layers in histological sections stained to show the somata (Nissl stain) (**Fig. 32.9**). The laminar pattern of the allocortex is heterogeneous, showing less or more layers depending on the allocortical region. The most important features of myeloarchitectonic lamination are given in **Table 32.2**.

The molecular layer I of the adult brain is cell-sparse and contains few scattered neurones. It consists mainly of the apical dendritic tufts of pyramidal neurones and horizontally orientated axons, as well as glial cells. Some spiny stellate, neurogliaform, horizontal and a few scattered Cajal–Retzius cells are found in this layer. Inputs to the apical tufts are thought to be of cortico-cortical origin, but thalamo-cortical axonal terminals also occur. There are several subtypes of Cajal–Retzius cells; they are numerous in the fetal brain, but most are eliminated during early postnatal stages. They release the neurotransmitter glutamate, but their precise function is not clear. They control the laminar organization of the developing cortex by releasing the glycoprotein Reelin which acts like a stop signal for the outwardly migrating neurones. A lack of Reelin or other molecules in its signalling pathway results in a severe impairment of laminar organization. Decreased Reelin has been associated with lissencephaly and major psychiatric disorders in the human brain. The horizontally running dendrites of Cajal–Retzius cells are embedded in a mass of tangentially running myelinated and unmyelinated axons and dendrites. These tangential fibres consist of afferent fibres that arise from outside the actual cortical area, fibres from cortical interneurones, and the apical dendritic arborizations of virtually all pyramidal neurones of layers III and V. In myelin stained sections, a narrow band of tangential fibres, the Cajal–Retzius stripe, is visible in the centre of layer I (see Fig. 32.9).

The external granular lamina II is dominated by the somata of small pyramidal and non-pyramidal cells ('granular' cells). Myelin staining shows mainly vertically orientated fibres traversing the layer. In many brain regions, tangentially orientated myelinated fibres are found in higher density at the border between layers II and III, the horizontal Exner stripe (see Fig. 32.9). This border is difficult to determine in those cortical regions where the neuronal density of layer II is low.

The external pyramidal layer III predominantly contains small and medium-size pyramidal cells, as well as non-pyramidal neurones with vertically orientated intracortical axons. Together with layers I and II, layer III is the main target of interhemispheric (callosal) cortico-cortical afferents, and the principal source of cortico-cortical efferents. Scattered interneurones are also found in this layer. The pyramidal cells are smallest in the most superficial part of the layer and their size increases towards its deeper part. Layer III can frequently be subdivided into IIIa, IIIb and IIIc, where IIIa is most superficial and IIIc is the deepest. As in layer II, myelin stains reveal a mostly vertical organization of fibres; a band of horizontally running and myelinated fibres, the outer Baillarger stripe, can be seen at the border between layer IIIc and IV in many isocortical regions (see Fig. 32.9).

The width of the internal granular layer IV varies according to area. In Nissl-stained preparations it is seen to consist mainly of small round granular cells, which are different types of spiny stellate and pyramidal neurones and various types of aspiny interneurones. Layer IV is the main target of thalamo-cortical afferents and intra-hemispheric cortico-cortical afferents. In myelin-stained sections, the outer band of Baillarger is seen in layer IV of the primary visual cortex. The band is so obvious in this cortical area that it can be detected with the naked eye in histological sections of unstained fresh or frozen brains. It was first observed by Francesco Gennari in the year 1776, and independently 10 years later, by Félix Vicq d'Azyr: the horizontal, myelin-rich band is, therefore, often named the stripe of Gennari or of Vicq d'Azyr. It subdivides layer IV of the primary visual cortex into three sublayers: IVa, IVb (where the stripe is found) and IVc.

The internal pyramidal layer V often contains the largest pyramidal cells of any cortical layer. However, actual sizes vary considerably from area to area; in some association areas, layer III pyramidal cells are larger than those of layer V (externopyramidization). Layer V pyramidal neurones give rise to axons that leave the cortex and run down to subcortical structures. Scattered non-pyramidal cells are also present in layer V. In many cortical areas, layer V can be subdivided into sublayers Va, Vb and

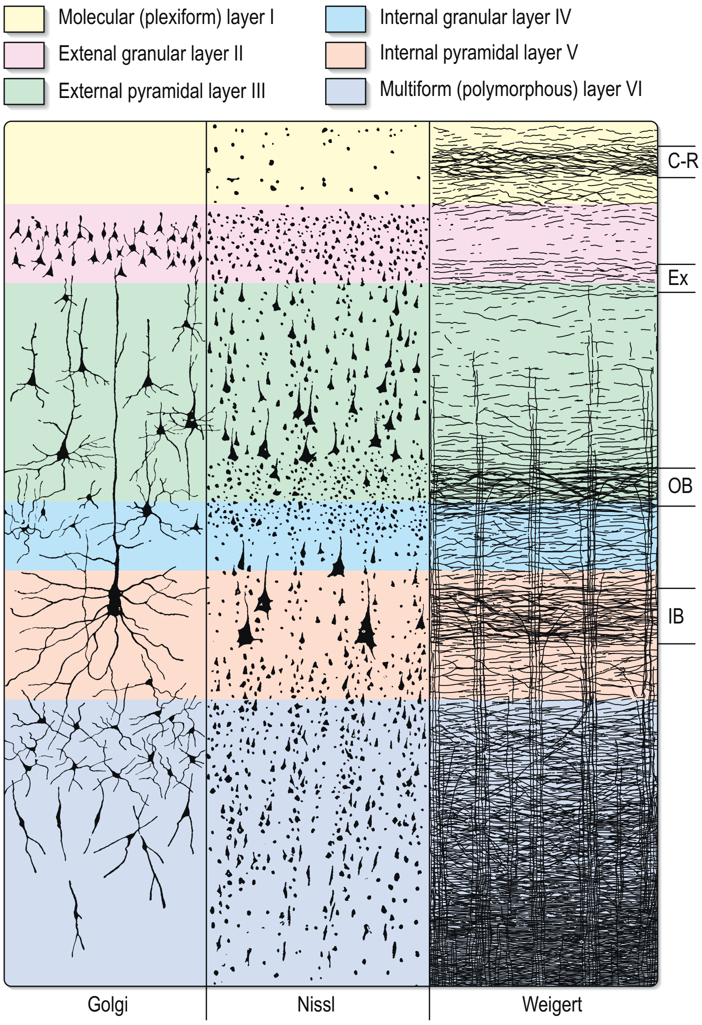
Molecular (plexiform) layer I
Extenal granular layer II
External pyramidal layer III
Internal granular layer IV
Internal pyramidal layer V
Multiform (polymorphous) layer VI
C-R
Ex
OB
IB
Golgi
Nissl
Weigert

Fig. 32.9 The layers of the isocortex. The three vertical columns represent the distribution of cellular elements, as revealed by the techniques of Golgi (impregnating some complete neurones), Nissl (staining cell bodies) and Weigert (staining myelinated fibres). Horizontally running and densely packed myelinated fibres represent the Cajal–Retzius stripe (C–R) in layer I, the Exner stripe (Ex) at the layer II/III border, the outer band of Baillarger (OB) in deeper layer III or layer IVb of the primary visual cortex, and the inner band of Baillarger (IB) in layer V.

Pyramidal cells have a flask-shaped or triangular soma that ranges from 10 to 80 μm in diameter and gives rise to a single thick apical dendrite and multiple basal dendrites. The apical dendrite ascends towards the cortical surface, tapering and branching (see Fig. 32.4). Some dendrites end in the most superficial lamina, the molecular layer (layer I), others end at the level of the outer granular (layer II) or outer pyramidal layer (layer III). From the basal surface of the soma, dendrites spread horizontally or obliquely for distances up to 1 mm, depending on the size of the soma. Like apical dendrites, the basal dendrites branch profusely along their length. All pyramidal cell dendrites are studded with dendritic spines that become more numerous as the distance from the cell soma increases. A single slender axon arises from the axon hillock, which is usually situated centrally on the basal surface of a pyramidal neurone. For the vast majority, if not in all, pyramidal neurones, the axon leaves the cortical grey matter to enter the white matter. Before an axon reaches the white matter, it gives rise to a recurrent branch that terminates in the cortical region of origin of the parent axon. Pyramidal cells use an excitatory amino acid, either glutamate or aspartate, as neurotransmitter. Various types of pyramidal cells can be identified by their connectivity (e.g. axonal projections to the ipsi- or contralateral hemisphere, cortico-striate, cortico-thalamic, cortico-pontine and cortico-spinal projections), electrophysiological (e.g. regular fast or slow spiking, or intrinsically bursting types) and genetic characteristics. The giant Betz cells and the solitary Meynert cells are very large pyramidal cells with special morphological features.

The volume of the somata of Betz cells, located in lamina V of the primary motor cortex, is ten times larger than that of common layer V pyramidal cells. A Betz cell gives rise to a 10 μm thick myelinated axon that terminates on motor neurones in the brainstem and anterior horn of the spinal cord via the cortico-nuclear and cortico-spinal tracts, respectively. In contrast to common pyramidal cells, which have a single apical dendrite and dendritic arbors that exit the soma from basal angles, Betz cells have many dendrites that arise directly from the entire circumference of the soma. Meynert cells are located at the border between layers V and VI of the primary visual cortex; their somata are three times larger than those of common layer V pyramidal cells. In contrast to other pyramidal cells, most of their spines are found on the extensively arborized basal dendrites in layers V and VI, which extend below several blobs and interblobs (see below). Meynert cells are involved in motion detection, mediated via their connections with area MT/V5, and with the superior colliculus via axon collaterals. The von Economo neurone (spindle neurone) is a subtype of projection neurone that occurs preferentially in the deeper layer V of fronto-insular and anterior cingulate regions and has also been described in the entorhinal cortex, the hippocampal formation, and the dorsomedial Brodmann's area 9 (BA9). These neurones are characterized by a single apical dendrite, a single basal dendrite and a long projection axon and are probably glutamatergic: their selective degeneration is found in early stages of fronto-temporal dementia.

Spiny stellate cells (see Fig. 32.4) are the second most numerous cell type in the neocortex. They are found preferentially in lamina IV and are the major target of thalamo-cortical input. Their relatively small multipolar somata commonly measure 6–10 μm in diameter. Several primary dendrites, profusely covered in spines, radiate for variable distances from each soma. The axons ramify within the grey matter, predominantly in the vertical plane. Spiny stellate cells use glutamate as neurotransmitter. These morphological and chemical characteristics led some authors to classify spiny stellates as a variant pyramidal cell, but their locally terminating axons also argues for a classification as interneurone.

All aspiny or sparsely spinous stellate cells are GABAergic (γ-aminobutyric acid) inhibitory interneurones (see Fig. 32.6). Their axons are confined to grey matter and terminate on other interneurones and pyramidal cells. Interneurones form inhibitory synapses with pyramidal neurones, and can also receive inhibitory synapses from other interneurones, but such connections are sparse: most synapses on interneurones are excitatory. There are many different subtypes of interneurones, including basket, horizontal, chandelier, double bouquet, bipolar/fusiform, bitufted, neurogliaform and Martinotti cells, and layer I interneurones (see Fig. 32.5; **Fig. 32.6**). Each morphological interneurone type can display widely varying electrophysiological or molecular properties. GABAergic interneurones often co-express neuropeptides (neuropeptide Y (NPY), somatostatin (SOM), cholecystokinin (CCK), vasoactive intestinal polypeptide (VIP)) and/or calcium binding proteins (parvalbumin (PV), calbindin (CB), calretinin (CR)) in a cell-type specific manner. GABAergic interneurones can be subdivided into several non-overlapping types according to differences in their developmental origin, target cells, and molecular markers. The embryonic medial and caudal ganglionic eminences are the origin of three GABAergic interneuronal types that co-express PV, SOM, and the serotonin receptor 5-HT$_{3A}$. The PV type includes basket and chandelier cells: axons of PV basket cells terminate mainly in the perisomatic region, and chandelier cells co-express PV and CCK and terminate on the axon initial segment of pyramidal cells. The SOM type includes Martinotti cells that project to distal dendrites. The 5-HT$_{3A}$ type includes bipolar cells that co-express VIP and can lead to disinhibition (interneurone-selective disinhibitory cells, **Fig. 32.7**); Reelin cells (including Cajal–Retzius cells; see Fig. 32.5 and Martínez-Cerdeño and Noctor 2014); and CCK-expressing small basket cells. Neuronal nitric oxide synthase (nNOS) is constitutively expressed in 2% of cortical interneurones and is co-localized with SOM or NPY: these interneurones have high numbers of glutamate receptors that mediate the glutamate-induced hyperexcitation that follows cerebral impairment.

The common PV basket cells (see Fig. 32.6) are found in layers II–VI. They never express Reelin. Small basket cells express SOM, CCK and VIP. All basket cells show a mostly multipolar dendritic arbor, and a short, vertical axon that rapidly divides into horizontal collaterals that typically end in large terminal sprays on the somata and proximal dendrites of pyramidal cells, and rarely on other PV-expressing interneurones. The synaptic outputs of the fast-spiking (common) basket cells are strongly depressing.

The cell bodies of horizontal cells (see Fig. 32.6) lie mainly at the border between layers I and II, occasionally deep in lamina I (molecular layer). They are small and fusiform, and their dendrites spread short distances in layer I in two opposite directions. Their axons often stem from a dendrite, then divide into two branches that travel away from each other for great distances in the same layer. The morphological subtype of horizontal cells is heterogeneous with respect to the co-expression of PV, Reelin, SOM, VIP and NPY. Layer I horizontal cells express PV and Reelin, which is particularly important for the development of the regular lamination of the cortex during development. Other horizontal cells also express VIP, NPY and SOM.

Chandelier cells (see Fig. 32.5) are frequently found at the border between layers I/II and layer VI. Some, but not all, express PV. They have a variable morphology, although most somata are ovoid. Their dendrites arise from the upper and lower poles of the cell body and the axon emerges from either the cell body or a proximal dendrite. The ascending or descending axons ramify close to the cell body and terminate in numerous vertically orientated strings that run alongside the axon initial segment of pyramidal cells, where they build very effective inhibitory synapses.

Double bouquet cells (see Fig. 32.6) are found in laminae II and III and their axonal arborization is predominantly perpendicular to the pial surface, traversing layers II and V. Generally, these neurones have two or three main dendrites that terminate in a superficial and deep dendritic tuft. A single axon arises usually from the oval or spindle-shaped soma and rapidly divides into ascending and descending branches that collateralize extensively; the axonal arbor is confined to a perpendicularly extended, but horizontally confined, cylinder.

The bipolar cell (see Figs 32.5–32.6) has a very small, ovoid soma with a single ascending and a single descending dendrite that arise from the upper and lower poles, respectively of the soma. Sixty per cent of these cells are located in layers II and III. They co-express VIP, PV, CCK and acetycholine. They receive GABAergic input from basket cells on their somata, and from layer V pyramidal cells on their proximal dendrites. The dendrites branch sparsely and run vertically to produce a narrow dendritic tree that may extend through most of the cortical layers. Commonly, the axon originates from one of the primary dendrites and branches into a vertically elongated and horizontally confined axonal arbor that closely parallels the dendritic tree. Since pyramidal cells represent a major target for the GABA/PV/VIP synapses, the activation of these synapses may lead to coherent oscillations that provide the necessary signal to synchronize pyramidal cell discharges across and within cortical columns.

Bitufted cells (see Fig. 32.6) have two tufts of dendrites that originate directly from the soma and extend in vertical directions through all layers. The somata of these interneurones are most frequently located in layers II–IV and express Reelin. Some bitufted cells also express SOM. Layer II–III bitufted interneurones receive excitatory input from pyramidal cells in the same layers. Depression can be observed at these excitatory synapses: it may be caused by exocytotic GABA release from dendrites (since GABA-activated presynaptic GABA$_B$ receptors are found on the glutamatergic terminals), causing a reduction of glutamate release, i.e. conditioning. The axons of bitufted cells generate inhibitory synapses with pyramidal cells of the same cortical column (feedback inhibition). Since the elongated dendritic arbors span the entire cortex, bitufted interneurones receive input from all cortical layers, which means that bitufted cells can control the excitability of cortical columns.

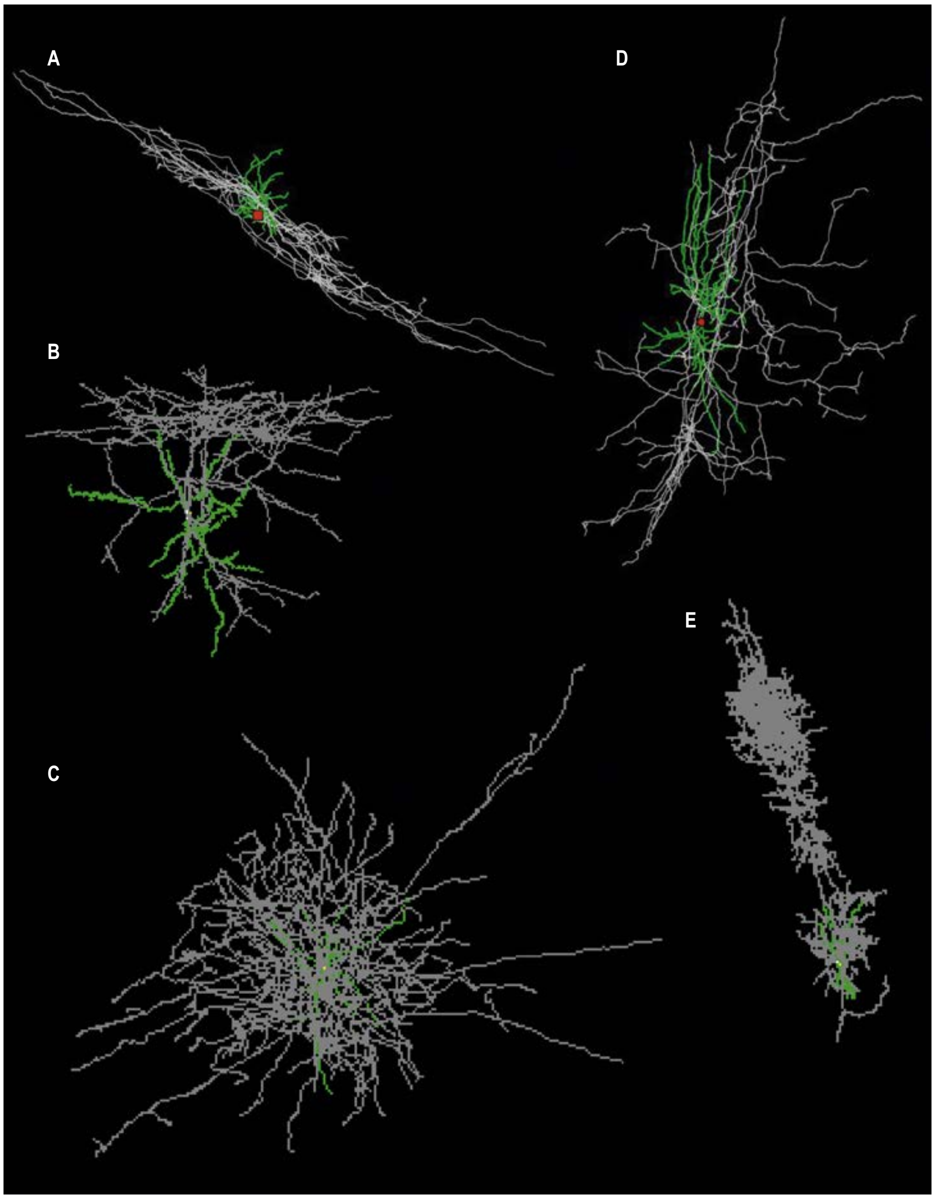

Fig. 32.6 **A–E**, Interneurones of the cerebral cortex. Grey, dendrites; green, axons; red, incomplete soma. **A**, Biocytin-stained horizontal cell in layer I of the primary somatosensory cortex (NMO_37241). **B**, Biocytin-stained Martinotti cell in layers II–III of the rat motor cortex (NMO_07436). **C**, Neurobiotin-stained basket cell in layers II–III of the macaque prefrontal cortex (NMO_01863). **D**, Biocytin-stained bitufted neurone in layer IV of the human temporal isocortex (NMO_97192). **E**, Neurobiotin-stained double bouquet cell in layers II–III of the macaque prefrontal cortex (NMO_01870). (All images are from NeuroMorpho.Org (Ascoli et al 2007), a central open resource for neuronal morphologies.)

The neurogliaform or spiderweb cell (see Fig. 32.5) is a small spherical cell found in layers I–IV. Most cells in layer I are neurogliaform cells that co-express PV, Reelin, NPY and VIP. Those in deeper layers also contain nNOS. Numerous short dendrites typically radiate out from their somata. The axon arises from the soma or a proximal dendrite and forms a wider, very dense axonal plexus composed of fine branches.

Most of the Martinotti cells (see Fig. 32.6) are located in supragranular layers II and III. They are more sparsely distributed throughout granular and infragranular layers. All express SOM and Reelin, but not all SOM-positive cells are Martinotti cells. They can also express CB, CR, CCK, VIP and NPY. The most striking feature of Martinotti cells in layers V–VI is their characteristic long ascending axon that spreads horizontally and arborizes extensively in layer I. Their bipolar or multipolar dendrites branch locally or down to deeper layers. **Table 32.1** provides a summary of GABAergic interneurones, main targets and anatomical signatures.

These interneurones build the microcircuitry of the cerebral cortex with other interneurones and pyramidal (projection neurones) cells (see Fig. 32.7). They synaptically connect neurones of the same and/or different layers. Various sequences of direct or indirect synaptic connections between inhibitory interneurones and excitatory pyramidal cells are the basis of the complex modulatory mechanism of cortical microcircuitry. If GABAergic interneurones receive an excitatory input, they will inhibit the excitatory output of those cells by a direct synaptic connection with pyramidal cells (feedforward inhibition; **Fig. 32.8**). However, they will excite pyramidal cells if they are indirectly connected with them via an interposed inhibitory GABAergic cell that contacts the pyramidal cell (disinhibition). A third principal type of connectivity in microcircuits occurs if GABAergic interneurones receive an excitatory input from a pyramidal cell and send back an inhibitory output to the pyramidal cell (feedback inhibition). Impaired microcircuitry can lead to synchronized excitatory activity in cases of epilepsy.

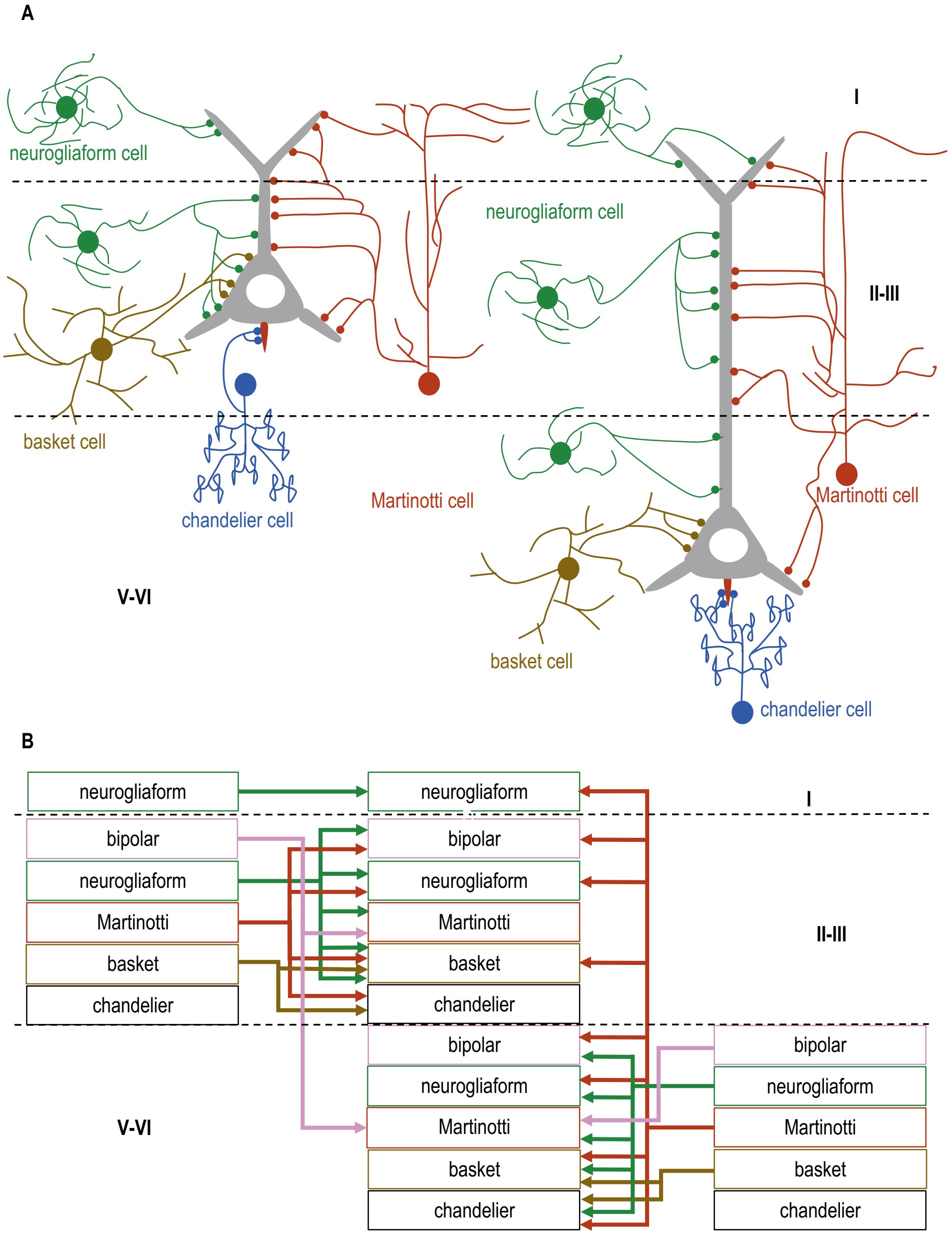
A
neurogliaform cell
I
neurogliaform cell
II-III
basket cell
chandelier cell
Martinotti cell
Martinotti cell
V-VI
basket cell
chandelier cell
B
neurogliaform
neurogliaform
I
bipolar
bipolar
neurogliaform
neurogliaform
Martinotti
Martinotti
II-III
basket
basket
chandelier
chandelier
bipolar
bipolar
neurogliaform
neurogliaform
V-VI
Martinotti
Martinotti
basket
basket
chandelier
chandelier

Fig. 32.7 **A**, Connections between GABAergic interneurones (examples are neurogliaform, basket, chandelier and Martinotti cells) and pyramidal cells of layers III and V. The neurogliaform cells of layer I contact the dendritic tufts in the same layer. The soma and the proximal dendrites of pyramidal cells of layers III and V receive input from neurogliaform cells of the respective layer, and from cholecystokinin- and parvalbumin-expressing basket cells. The chandelier cells contact the initial axon segment of pyramidal cells. Martinotti cells of layers III and V have axon terminals on basal, proximal, apical and dendritic tufts of pyramidal cells. **B**, Connections between different types of GABAergic interneurones in layers I–VI of the isocortex. (Adapted with permission from Tremblay R, Lee S, Rudy B 2016 GABAergic interneurones in the neocortex: from cellular properties to circuits. Neuron 20:260–92.)

TABLE 32.1 Isocortical GABAergic interneurones classified by their co-localization of parvalbumin, somatostatin and serotonin 5-HT$_{3A}$ receptors, morphological types, main targets and anatomical signatures

Main marker	Parvalbumin		Somatostatin		5-HT$_{3A}$					
% interneurones	40%		30%		30%					
Morphological type	Basket cell	Chandelier cell	Martinotti cell	Non-Martinotti cell	VIP cell			Non-VIP cell		
					40% of 5-HT$_{3A}$			60% of 5-HT$_{3A}$		
					Bipolar	CCK small basket	Multi polar	Small basket	CCK large basket	Neurogliaform cell
Main target	Soma and proximal dendrite	Only pyramidal cells; axon initial segment	Dendrites		Interneurones			Synaptic and volume transmission		
Anatomical signature	• Present in layers II–VI • Most prominent in layers IV–V • Multipolar dendritic arbor • Axonal arbor within and between layers and columns • Extensive connectivity with pyramidal cells and parvalbumin + interneurones	• Most frequent in layers II–VI • Multipolar dendritic arbor • Local axonal arbor	• Present in layers II–VI • Most prominent in layer V • Multipolar or bitufted dendritic arbor • Local axonal but transcolumnar arbor • No connections to other somatostatin neurones	• Present in layers IV–V • Multipolar or bitufted dendritic arbor • No axonal plexus in layer I	• Most frequent in layers II–III • Intracolumnar but interlayer vertical dendrites • Intracolumnar axonal arbor			• Present in layer I • Multipolar dendritic arbor • Short translaminar axon		• Present in layers I–VI • Small multipolar dendritic arbor • Dense axonal arbor

Adapted from Tremblay et al 2016.

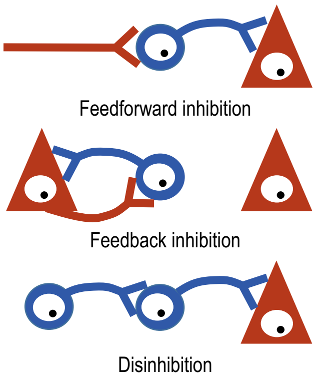

Fig. 32.8 Circuit motifs between excitatory glutamatergic pyramidal cells and inhibitory GABAergic interneurones. Feedforward inhibition is based on the excitation of an interneurone by an external input (e.g. thalamo-cortical input): the interneurone inhibits a cortical pyramidal cell. Feedback inhibition is based on the excitation of an interneurone by a cortical pyramidal cell and the recurrent inhibition of the pyramidal cell by an interneurone. Disinhibition occurs when an interneurone is excited and this interneurone gives rise to an inhibitory connection with another interneurone: in this case, the inhibition of the second interneurone leads to a decrease of its inhibitory action on a pyramidal cell. (Adapted with permission from Tremblay R, Lee S, Rudy B 2016 GABAergic interneurones in the neocortex: from cellular properties to circuits. Neuron 20:260–92.)

TABLE 32.2 **Most important criteria for myeloarchitectonic descriptions (Vogt 1910, Vogt and Vogt 1919)**

Presence of Baillarger (layers 4 and 5b) stripes		
	Astriate	Baillarger stripes cannot be delineated due to the very high fibre density in layers 5a and 6a[1] Occurrence: large parts of the precentral gyrus
	Propeastriate	A modification of the astriate type, because of a slight decrease of the fibre density in layers 5a and 6a,[1] i.e. the cortex is nearly astriate Occurrence: parts of the precentral gyrus, inferior parietal lobule, parts of the superior temporal gyrus
	Propeunistriate	The outer Baillarger stripe is well demarcated, the inner stripe is less obvious, but better visible than in the unistriate type, since layer 6a is less dense than 5b. Fibre density in layer 5a is slightly lower than in the propeastriate type Occurrence: dorsal part of the medial frontal gyrus, parts of transverse and superior temporal gyri
	Bistriate	Both Baillarger stripes clearly detectable because of lower fibre densities in layers 5b and 6a[1] Occurrence: frontal pole, medial frontal gyrus, parts of the transverse temporal gyrus, postcentral gyrus, superior parietal lobule, parts of extrastriate visual cortex
	Unistriate	A distinct outer Baillarger stripe is visible, but the inner stripe cannot be delineated from layer 6 due to high fibre density in sublayer 6a[1] Occurrence: superior frontal gyrus, parts of precentral gyrus, medial orbital region, anterior cingulate cortex, inferior temporal gyrus
	Unitostriate (conjunctostriate)	Both Baillarger stripes appear to be fused to a broad band, due to an increased fibre density in layer 5a (accompanied by a more or less prominent thinning of this layer) and a lightly stained layer 6a Occurrence: lateral orbital region, posterior part of the inferior frontal gyrus, parts of extrastriate visual cortex
	Singulostriate	The inner Baillarger stripe is lacking Occurrence: temporopolar region, primary visual cortex
Myelin density in Baillarger stripes		
	Equodensus	Both Baillarger stripes are equally dense
	Externodensior	Outer Baillarger stripe denser than inner stripe
	Internodensior	Inner Baillarger stripe denser than outer stripe
Intrusion depth of radiate bundles into the cortical ribbon		
	Euradiate	Radiate bundles reach upper border of layer 3b
	Infraradiate	Radiate bundles reach upper border of layer 5b
	Supraradiate	Radiate bundles extend into layers 1–2

From Zilles et al 2015c, modified

Vc. In myelin stained sections, the lamina is seen to be traversed by ascending and descending vertical fibres and to contain another prominent band of horizontal fibres, the inner band of Baillarger (see Fig. 32.9).

The multiform layer VI consists of excitatory cells (pyramidal neurones with dendrites and axons that branch and terminate in layers IV to V, spiny stellate cells with local dendritic branches and axons that terminate in layer VI, inverted pyramidal neurones, and bipolar/fusiform and other odd-shaped cells), and inhibitory interneurones. The upper part of this layer (layer VIa) has a higher cell density than its lower part (layer VIb), which blends gradually with the underlying white matter. A clear demarcation of layer VIb from the white matter is difficult in most brain regions. In some regions the cells of layer VIb can cover an area several times thicker than the cortex.

Cortical layers and their connections

Non-thalamic subcortical afferents to the neocortex from the basal forebrain (Ch1–4, cholinergic), pedunculopontine (Ch5, cholinergic) and laterodorsal tegmental (Ch6, cholinergic) nuclei, ventral tegmental area (A10, dopaminergic), raphe nuclei (B1–9, serotoninergic), and nucleus coeruleus (A6, noradrenergic), terminate throughout all cortical layers; the laminar pattern of the density of their endings varies considerably from area to area.

Thalamo-cortical afferent fibres are found particularly in layers III–IV, and to a lesser extent also in layers I–II. Cortico-cortical input projects as long-distance feedback input mainly to layers II–IIIa, and as short-distance feedforward connections to layers IIIb and IV. Cortico-cortical input from the contralateral hemisphere (callosal afferents) mainly ends in layer III. In general, the largest input to a cortical area tends to terminate mainly in layer IV. This pattern of termination is best seen in the major thalamic input to primary visual, auditory and somatic sensory areas (Fig. 32.10).

Supragranular pyramidal cells, predominantly layer III but also lamina II, give rise to both association and commissural cortico-cortical efferents. Generally, short cortico-cortical fibres arise more superficially, and long cortico-cortical (both association and commissural) axons come from cells in the deeper parts of layer III. The cortico-cortical long-distance feedforward fibres originate in layers II–III, and the long-distance feedback fibres from layers V and VI. Layer V also gives rise to cortico-striate (to the basal ganglia), cortico-thalamic, cortico-tectal, cortico-bulbar/nuclear (including cortico-pontine) and cortico-spinal fibres. Layer VI is the major source of cortico-thalamic and cortico-claustral fibres (see Fig. 32.10).

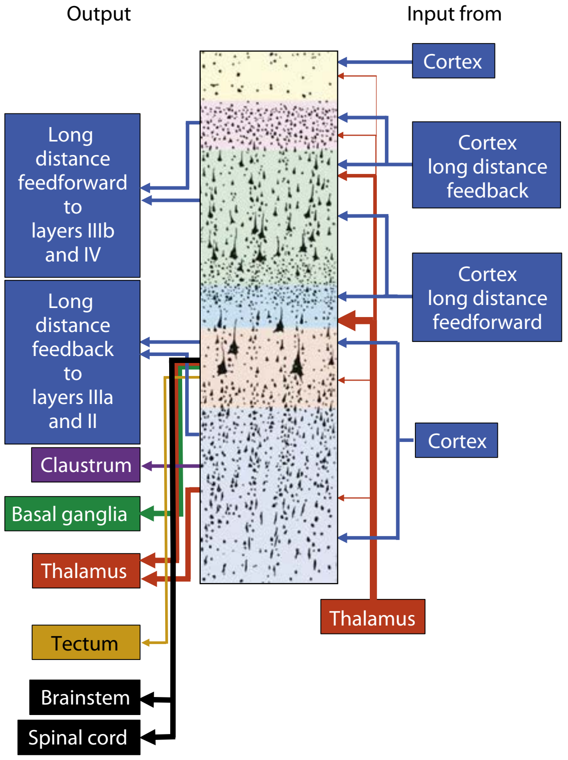
Output
Input from
Cortex
Long distance feedforward to layers IIIb and IV
Cortex long distance feedback
Cortex long distance feedforward
Long distance feedback to layers IIIa and II
Cortex
Claustrum
Basal ganglia
Thalamus
Thalamus
Tectum
Brainstem
Spinal cord

Fig. 32.10 Major afferent and efferent connections of the isocortical layers. Long-distance feedforward cortico-cortical output originates from supragranular layers; progressively more infragranular layers are recruited on approaching the target site and terminate in layers IV and IIIb. Long-distance feedback cortico-cortical output originates from the infragranular layers; progressively more supragranular layers are recruited on approaching the target site and terminate in layers IIIa and II.

Columns and modules

Experimental physiological and connectional studies have demonstrated an internal organization of the cortex that is at right-angles to the pial surface and the underlying layers, with vertical columns or modules running through the depth of the cortex (Fig. 32.11). The term ‘column’ refers to the observation that all cells encountered by a microelectrode penetrating and passing perpendicularly through the cortex respond to a single peripheral stimulus, a phenomenon first identified in the somatosensory and visual cortices (Mountcastle 1957, Hubel and Wiesel 1959, 1972). In the visual cortex, narrow (50 µm) vertical strips of neurones respond to a bar stimulus of the same orientation (orientation columns), and wider strips (500 µm) respond preferentially to stimuli detected by one eye (ocular dominance columns; see p. 531). Adjacent orientation columns aggregate within an ocular dominance column to form a hypercolumn, responding to all orientations of stimulus for both eyes for one point in the visual field. Similar functional columnar organization has been described in widespread areas of neocortex, including motor cortex and association areas.

MAPS OF THE HUMAN CEREBRAL CORTEX

The systematic study of variations in cortical layering across the cerebral mantle has produced several maps of the human and non-human brain. Currently, the most widely used map is the cytoarchitectonic map of Brodmann (1910) which segregates the human iso- and allocortex into approximately 50 areas or fields (Fig. 32.12). Brodmann’s map lacks data on the areas buried within the intrasulcal surface and on interindividual variability in the extent and location of the areas. The Brodmann–Jülich map is shown in Fig. 32.13 (with some examples of probabilistic maps in Fig. 32.14): functional specialization will be discussed in this chapter in the context of the cytoarchitectonic divisions of the cerebral lobes.

TRANSMITTERS IN THE HUMAN CEREBRAL CORTEX

Available with the *Gray’s Anatomy* e-book

Glutamate

Glutamate is the ubiquitous major excitatory transmitter in the human cerebral cortex, found in pyramidal neurones and astrocytes. The latter rapidly take up synaptically released glutamate via specific transporter molecules and metabolize it into glutamine and water. Glutamine is discharged from astrocytes by transporters, enters nerve terminals by electrogenic transporters, and is converted back into glutamate which is used again for neuronal transmission or is assimilated into the neuronal Krebs cycle. This glutamate–glutamine shuttle is crucial for the function of glutamate: excessive activation by high glutamate concentrations leads to pathological conditions and cell death.

GABA

Available with the *Gray’s Anatomy* e-book

Monoaminergic neurotransmitters

Available with the *Gray’s Anatomy* e-book

Neuropeptides

Available with the *Gray’s Anatomy* e-book

Transmitter receptors in the human cerebral cortex

Available with the *Gray’s Anatomy* e-book

The minicolumn is a distinctive module in the neocortex (Buxhoveden and Casanova 2002). It is a highly repetitive cortical unit consisting of horizontal and vertical components. Minicolumns display a considerable structural and functional heterogeneity between areas. The potential impact of the minicolumn concept seems to be important for comparative neuroanatomy and brain pathology (Buxhoveden et al 2006).

Apical dendrites of layer V pyramidal cells form columnar structures called dendritic bundles (Fleischhauer et al 1972). Each bundle consists of several apical dendrites and extends through layer IV into layer III/II where the dendrites begin to ramify (see Fig. 32.11B). Within the bundle, some dendrites approach each other so closely as to be separated only by the extracellular space. Dendritic bundles and minicolumns of neuronal somata are spatially closely related. The dendritic bundles lie between the columns of cell bodies. The transverse diameter of both (about 50 μm) is roughly the same in the entire isocortex. Neurones in a minicolumn can send their apical dendrite to different bundles, some of them through bifurcating apical dendrites; neurones in separate minicolumns can send their dendrites to the same bundle. They might correspond to narrower assemblies of neurones with radially invariant activation/response to motion in the visual, motor and auditory areas. Electrophysiological studies suggest that the vertical bundles of dendrites are the morphological substrate of vertical functional units. Myelinated axons entering or leaving the cerebral cortex are also not distributed at random but are organized in axonal bundles (see Fig. 32.11B).

Similar criticisms apply to the more elaborate cytoarchitectonic map produced by von Economo and Koskinas (1925) (**Fig. 32.15**): **Tables 32.3–32.4** compare the parcellation in the maps of Brodmann (1909) and von Economo and Koskinas (1925). Ongoing work on a cytoarchitectonic map of the entire human cerebral cortex based on a quantitative, statistically testable parcellation method, and information on intersubject variability and the cortical areas within the intrasulcal surface, is presented here (see Fig. 32.14) in a map that is three-dimensional; the brain with the map can be tilted by the user into any direction of view.

Maps of cortical segregation using myeloarchitectonic criteria contained over 100 myeloarchitectonic areas (**Figs 32.16–32.18**) (Vogt and Vogt 1919, Hopf 1954) (**Fig. 32.19**; see Table 32.2). The various cyto- and myelo-architectonic maps that were produced using different staining methods were roughly comparable: one of Brodmann's areas (Brodmann 1910) contains several subdivisions represented in the maps of von Economo and Koskinas (1925) and of Vogt and Vogt (1919) and in the probability maps (Tables 32.3–32.4). However, some of the areas in Brodmann's map (e.g. BA19, BA37), particularly in the higher eulaminate regions, could not be corroborated using more observer-independent methods and comparison with functional observations (Zilles and Amunts 2010).

The development of *in vitro* tissue slice binding techniques and quantitative autoradiography has enabled the visualization and quantification of neurotransmitters and their receptors within individual cortical fields. Although a single receptor type can characterize the borders of functionally and cytoarchitectonically defined cortical regions, in most cases only the characterization of the expression patterns of multiple receptors in the same cortical region can provide the criteria for a multimodal parcellation. These multi-receptor expression patterns are the characteristic fingerprints of each cortical area (**Figs 32.20–32.22**). They facilitate detailed mapping of the human cerebral cortex and provide insight into the hierarchical relationships of these areas and the principles of their organization into structurally and functionally defined networks (Palomero-Gallagher and Zilles 2009, Palomero-Gallagher et al 2015, Zilles and Amunts 2010, Amunts and Zilles 2015, Zilles and Palomero-Gallagher 2017). Maps of cortical neurotransmitters are important for understanding the neuropathological signatures of neurological and psychiatric disorders and the development of new molecules that can selectively modulate the activity of individual areas.

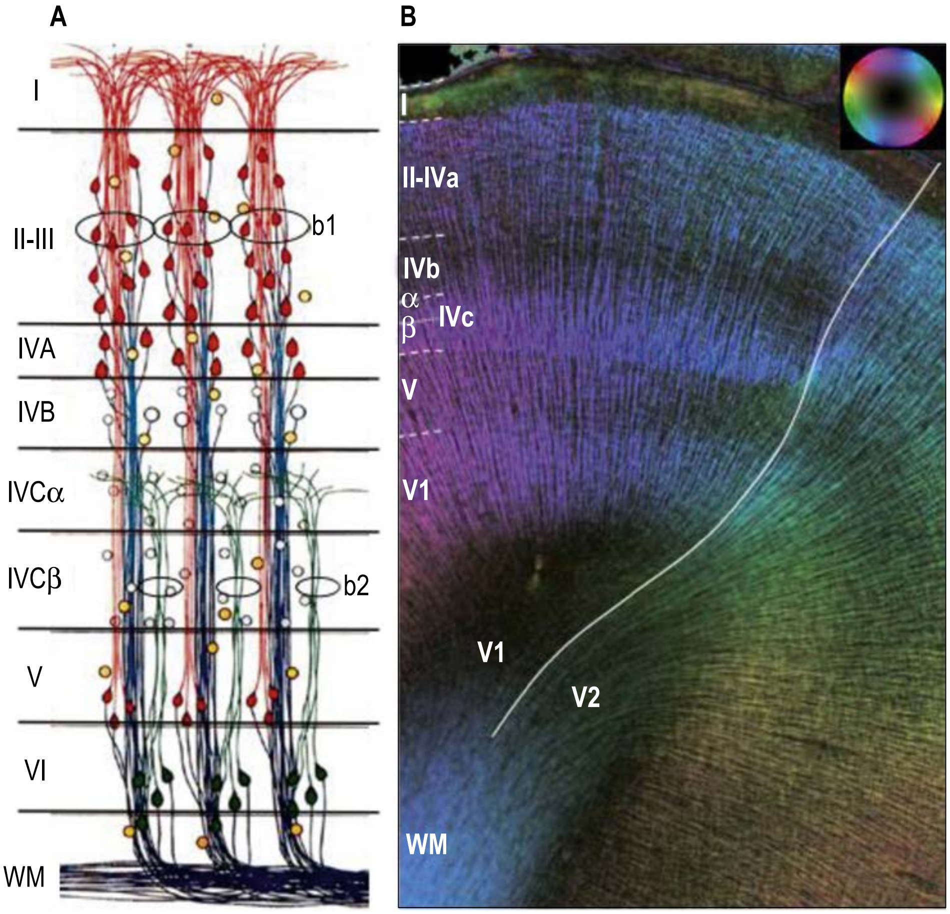

Fig. 32.11 A–B, Columns of dendritic bundles originating in layer V (b1) and layer VI (b2) pyramidal cells (modified after Mountcastle 1957). Dendritic bundles originating in layer V terminate in layer I (red fibres), those originating in layer VI terminate in layer IV (green fibres). **B**, Bundles of vertically orientated myelinated axons in the primary (V1) and secondary (V2) visual cortex. The myelinated fibers can be visualized with polarized light imaging because myelin is birefringent. The colour of fibres encodes for their spatial orientation according to the colour sphere (top right). Fibres running vertical to the image plane are hidden in the black regions. Roman numerals indicate cortical layers; V1, primary visual cortex (BA17); V2, secondary visual cortex (BA18); WM, white matter.

Fig. 32.12 Cytoarchitectonic parcellation of the cerebral cortex by Brodmann (1910). BA (Brodmann area) 3, represents the primary somatosensory cortex; BA17, primary visual cortex; BA41, primary auditory cortex. BA1 and BA2 are probably secondary somatosensory areas. BA18, secondary visual area; BA42, secondary auditory area; BA4, primary motor cortex; BA6, entire premotor cortex. BA8–BA12 represent the prefrontal; BA5, BA7, BA39 and BA40 the posterior parietal; and BA20, BA21, BA22 and BA38 the temporal association cortices. The Broca region consists of BA44, BA45 and probably BA47. BA23–BA25 and BA31–BA33 are parts of the cingulate cortex, whereas BA26, BA29 and BA30 are listed by Brodmann (1909) as retrosplenial cortex. BA27, presubiculum; BA28 and BA34, entorhinal cortex; BA35, perirhinal cortex, are parts of the hippocampal region: Brodmann did not completely map this region, because the subiculum, cornu Ammonis and dentate gyrus are not identified. **A**, lateral view, left side; **B**, medial view, right side. (Adapted from Brodmann 1910.)

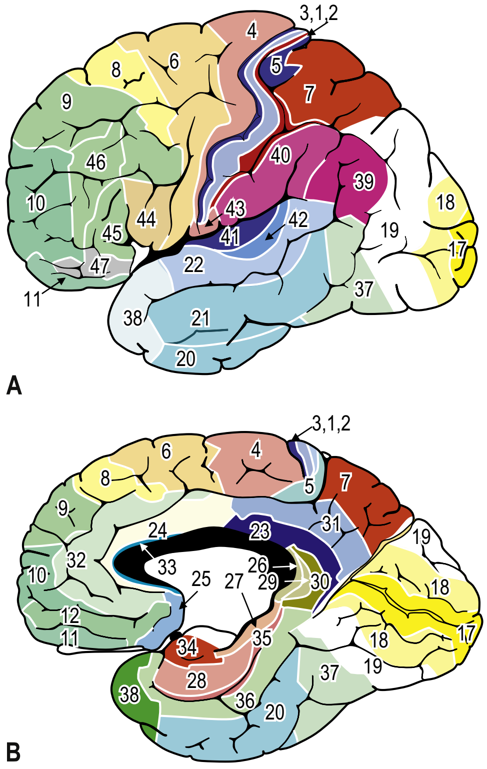
3,1,2
4
5
6
8
7
9
46
40
39
10
18
43
44
45
41
42
19
17
47
22
11
37
38
21
20
A
3,1,2
6
4
8
5
7
9
24
23
31
19
32
33
26
25
27
29
30
18
10
12
11
34
35
18
17
37
19
28
38
36
20
B

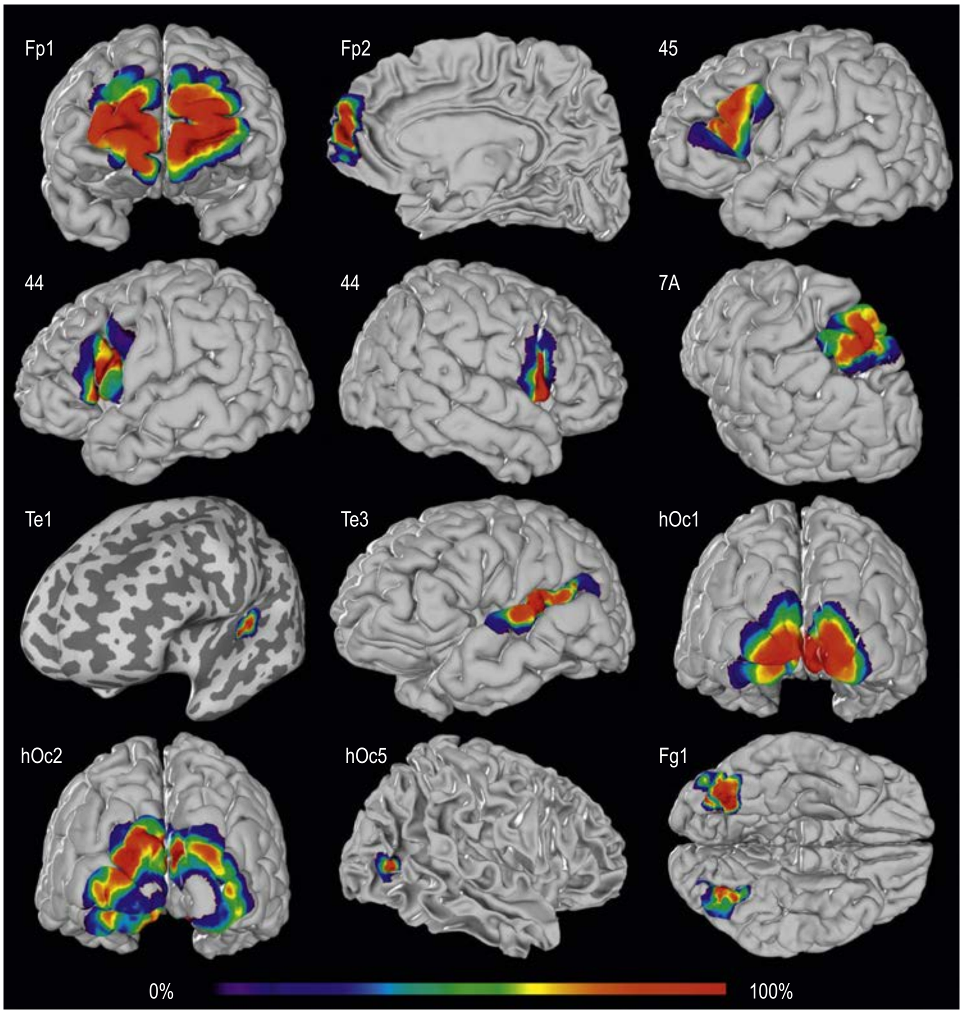
Fp1
Fp2
45
44
44
7A
Te1
Te3
hOc1
hOc2
hOc5
Fg1
0%
100%

Fig. 32.14 Continuous probability maps provided by the Jülich/Düsseldorf group and publicly available under https://interactive-viewer.apps.hbp.eu. The probabilities from low (blue) to high (red) for each area are visualized separately. (From https://tinyurl.com/ydncaz7q.)

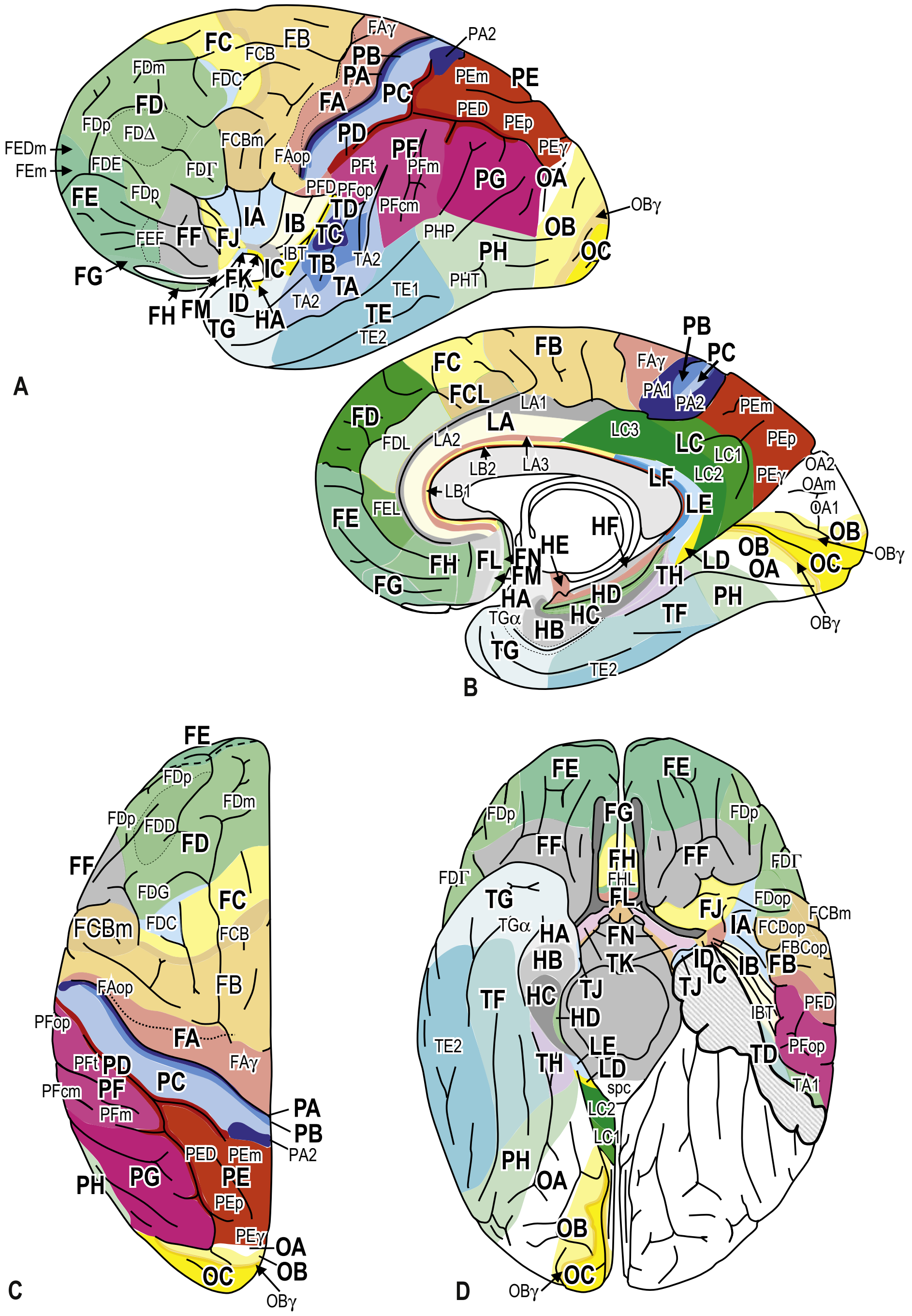
A
FC
FB
FAγ
PA2
FCB
PB
FDm
PA
PEm
PE
FDC
PC
FD
FA
PED
FDp
FDΔ
PEp
FCBm
PD
FEDm
FAop
PF
PEγ
FEm
FDE
FDΓ
PFt
PFm
PG
OA
PFD
PFop
FE
FDp
OBγ
IA
TD
PFcm
IB
TC
OB
FEF
FF
FJ
PHP
IBT
PH
OC
IC
TB
TA2
FG
FK
TA
PHT
ID
TE1
FH
FM
HA
TA2
TE
TG
TE2
B
PB
PC
FC
FB
FAγ
FCL
LA1
PA1
PA2
PEm
FD
LA
LC3
FDL
LA2
LC
PEp
LB2
LA3
LC1
OA2
LF
LC2
PEγ
OAm
LB1
FEL
LE
OA1
FE
HF
OB
HE
OB
FH
FL
FN
LD
OA
OC
OBγ
FM
TH
FG
HA
PH
HD
OBγ
TGα
HC
TF
HB
TG
TE2
B
FE
FDp
FDm
FDp
FDD
FD
FF
FDG
FC
FCBm
FDC
FCB
FAop
FB
PFop
FA
FAγ
PFt
PD
PC
PFcm
PF
PA
PFm
PB
PED
PEm
PA2
PH
PG
PE
PEp
PEγ
OA
OC
OB
C
OBγ
FE
FE
FG
FDp
FDp
FF
FH
FF
FDΓ
FDΓ
FHL
FDop
TG
FL
FCBm
FJ
TGα
HA
FN
IA
FCDop
HB
TK
FBCop
ID
IB
FB
TJ
TJ
IC
HC
TF
IBT
PFD
HD
TE2
LE
TD
PFop
TH
LD
TA1
spc
LC2
LC1
PH
OA
OB
OBγ
OC
D

Fig. 32.15 Cytoarchitectonic parcellation of the cerebral cortex by von Economo and Koskinas (1925). Brodmann's (1910) map and this map have been compared and putative matches between both maps are given in Table 32.4, as well as by the same colour coding of comparable cortical areas in Fig. 32.12 (Brodmann's map) and this figure. **A**, lateral view, left side; **B**, medial view, right side; **C**, dorsal view; **D**, ventral view. (Modified after von Economo and Koskinas 1925.)

TABLE 32.3 Comparison between the map and nomenclature system used by Brodmann (1909, 1914) and those of Vogt (1910), Vogt and Vogt (1919) and the Jülich/Düsseldorf group (modified after Zilles et al 2015c)

	Brodmann (1909, 1914)	Vogt (1910), Vogt and Vogt (1919)	Jülich/Düsseldorf Group
Frontal lobe			
	BA4	V42, V43	4a, 4p
	BA6	V36–V41	6 (preliminary delineation)
	BA8	Comparability not clear	n.d.
	BA9	Comparability not clear	n.d.
	BA10	V50, V51	Fp1, Fp2
	BA11, BA12	V1, V4-V9, V10-V12 (ventral parts)	n.d.
	BA24	Subregio typica (V17–V24, dorsal part of V12)	s24, p24a, p24b, pv24c, pd24cv, pd24cd
		Subregio medioradiata (V25–V32)	a24a′, a24b′, 24c′v 24c′d, p24a′, p24b′, p24dv, p24dd
	BA25	V13, V14	25a, 25p
	BA32	V3, V10–V11 (dorsal parts), V33–V35	s32, p32, 32′
	BA33	Subregio extrema (V15, V16)	33
	BA44	V56, V57	44d, 44v
	BA45	V58, V59 (dorsal part)	45a, 45p
	BA46	V53, V54	n.d.
	BA47	V59 (ventral part)	n.d.
Parietal lobe			
	BA1	V70	1
	BA2	V71, V72 (?)	2
	BA3	V67	3a
		V69	3b
	BA5	V75	5L, 5M, 5Ci
	BA7	V83, V85, V86, V87 (?)	7A, 7P, 7PC, hIP3
	BA23	V77–V80,V 91–V96	23d, 23c, d23, v23
	BA26	Vλ areas except Vλ3	n.d.
	BA29	Vλ3	29l, 29m
	BA30	Vλ areas except Vλ3	30
	BA31	V76, V81, V82, V84	31
	BA39	V90	PGa, PGp
	BA40	V73-V74 (parts), V88, V89	OP 1, OP2, PFop, PFt, PFcm, PF, PFm
	BA43	V68, V72 (?), V73-V74 (parts)	OP 3, OP 4
Occipital lobe			
	BA17	Area striata	hOc1
	BA18	Area occipitalis	hOc2
	BA19	Area praeoccipitalis	hOc3d, hOc3v, hOc4d, hOc4v, hOc5 (areas located within the region of BA19 and lateral BA37) and other areas. Note that a homogeneous cytoarchitectonic or functional area 19 does not exist
Temporal lobe			
	BA20	n.d.	n.d.
	BA21	n.d.	n.d.
	BA22	n.d.	Te3, Te4 (areas within BA22)
	BA38	V38	n.d.
	BA41	Area temporalis transversa interna	Te1 (Te1.0, Te1.1, Te1.2)
	BA42	Area temporalis transversa externa	Te2 (Te2.1, Te2.2)
	BA37	n.d.	Fg1, Fg2 (on the fusiform gyrus as parts of medial PH)
Insular lobe			
	Regio insularis anterior and posterior	Vi^1–Vi^6, Vai^1–Vai^4, Vai^6, Vai^7	Ig1 and Ig2 (dorsal part of Vi^5), Id1 (Vai^6). Most of the dysgranular and agranular areas have not yet been parcellated
	n.d.	VTb^1, VTb^2	n.d.

Abbbreviation: n.d., not determined.

The Vogt map is mainly based on myeloarchitectonic observations, but also includes comparisons with cytoarchitecture. The other maps are based on cytoarchitectonic observations.

The Düsseldorf/Jülich map is based on the following publications: Amunts et al 1999, Amunts et al 2010, Amunts et al 2012, Bludau et al 2014, Caspers et al 2013b, Caspers et al 2006, Eickhoff, Amunts et al 2006, Geyer et al 1996, Geyer et al 1999, Grefkes et al 2001, Kujovic et al 2013, Kurth, Eickhoff et al 2010, Malikovic et al 2007, Palomero-Gallagher 2008, Palomero-Gallagher et al 2013, Rottschy et al 2007, Scheperjans, Eickhoff et al 2008, Scheperjans, Hermann et al 2008.

Maps of the Jülich/Düsseldorf group are shown in the JuBrain Cytoarchitectonic Atlas Viewer atlas and the SPM Anatomy Toolbox.

TABLE 32.4 List of cytoarchitectonic areas according to (1) von Economo and Koskinas (1925), (2) Brodmann (1909) and (3) JuBrain (Amunts and Zilles 2015). The areas listed under Brodmann and JuBrain overlap completely or partially with those of von Economo and Koskinas. In (1), main areas (bold font) are distinguished from their subdivisions (normal font) as originally proposed by von Economo and Koskinas.

	1	Area name after von Economo and Koskinas	2	3
Frontal lobe (F)				
Prerolandic region				
1	**FA**	Precentral area	4	4a, 4p
2	FAγ	Giant pyramidal precentral area	4	4a, 4p
3	FAop	Opercular precentral area	4	4a, 4p
4	**FB**	Agranular frontal area	6	6
5	FBop	Opercular agranular frontal area	6	6
6	**FC**	Intermediate frontal area	8	n.d.
7	FCL	Limbic intermediate frontal area	32	n.d.
8	FCBm	Magnocellular agranular intermediate frontal (Broca's) area	44	44
9	FCI	Intermediate frontal area at beginning of insula	n.d.	n.d.
10	FCDop	Opercular intermediate granular frontal area	n.d.	n.d
Anterior frontal (prefrontal) region				
11	**FD**	Granular frontal area	9, 46	n.d.
12	FDm	Magnocellular granular frontal area	9	n.d.
13	FDp	Parvocellular granular frontal area	9	n.d.
14	FDop	Opercular granular frontal area	46	n.d.
15	FDL	Limbic granular frontal area	32	p32
16	FDΔ	Middle granular frontal area	46	n.d.
17	FDΓ	Triangular granular frontal area	45	45
18	**FE**	Frontopolar area	10	Fp1, Fp2
19	FEL	Limbic frontopolar area	32	p32
Orbital (orbitomedial) region				
20	**FF**	Granular orbital area	47	Fo3
21	FFα	Agranular orbital area	47	Fo3
22	FFΦ	Pretriangular orbital area	47	n.d.
23	**FG**	Area of straight gyrus (area recta)	11	Fo1
24	FGi	Internal area of straight gyrus	11	Fo1
25	**FH**	Prefrontal area	11, 12, 32	Fo2, n.d., s32
26	FHL	Parolfactory prefrontal area	11	
27	FH*L*	Limbic prefrontal area	32	s32
28	**FJ**	Frontoinsular area	n.d.	n.d.
29	**FK**	Frontal piriform area	n.d.	n.d.
30	FL1	Primary parolfactory area	25	25
31	FL2	Secondary parolfactory area	25	25
32	FL3	Tertiary parolfactory area	25	25
33	**FM**	Geniculate area	25	25
34	FMt	Geniculate area of olfactory triangle	n.d.	n.d.
35	**FN**	Precommissural area	n.d.	n.d.
Superior limbic lobe (L)				
Anterior superior limbic region				
36	LA1	Precingulate agranular anterior limbic area	24	p24c
37	LA2	Anterior cingulate agranular anterior limbic area	24	s24b, p24b
38	LA3	Cingulate agranular anterior limbic area limitans	24	s24a, p24a
39	LB1	Anterior ultracingulate area	33	33
40	LB2	Area of indusium griseum	Indusium griseum	n.d.
Posterior superior limbic region				
41	LC1	Dorsal posterior cingulate area	31	n.d.
42	LC2	Ventral posterior cingulate area	23	n.d.
43	LC3	Posterior cingulate area limitans	23	n.d.
Retrosplenial subregion				
44	**LD**	Agranular retrosplenial area	30	n.d.
45	LE1	Superior retrosplenial area granulosa	29	n.d.
46	LE2	Inferior retrosplenial area granulosa	29	n.d.
47	LF1	Posterior ultracingulate area	26	n.d.
48	LF2	Ultracingulate area obtecta	26	n.d.

(Continued)

TABLE 32.4 List of cytoarchitectonic areas according to (1) von Economo and Koskinas (1925), (2) Brodmann (1909) and (3) JuBrain (Amunts and Zilles 2015). The areas listed under Brodmann and JuBrain overlap completely or partially with those of von Economo and Koskinas. In (1), main areas (bold font) are distinguished from their subdivisions (normal font) as originally proposed by von Economo and Koskinas.—cont'd

	1	Area name after von Economo and Koskinas	2	3
Insular lobe (I)				
49	IA1	Dorsal precentral insular area	n.d.	n.d.
50	IA2	Ventral precentral insular area	n.d.	n.d.
51	**IB**	Postcentral insular area	n.d.	Ig1, Ig2, Id1
52	IBT	Postcentral insular area at temporal entrance	n.d.	n.d.
53	**IC**	Orbito-insular area	n.d.	n.d.
54	**ID**	Piriform insular area	n.d.	n.d.
Parietal lobe (P)				
Postcentral (anterior parietal) region				
55	PA1	Giant pyramidal postcentral area	3	3a
56	PA2	Giant pyramidal postparacentral area	5	5l
57	PB2	Oral postcentral area simplex	3	3b
58	PB1	Oral postcentral area granulosa	3	3b
59	PC	Intermediate postcentral area	1	1
60	PD	Caudal postcentral area	2	2
Superior parietal region				
61	PE(D)	Superior parietal area (transition postcentral)		
62	PEm	Magnocellular superior parietal area	7	
63	PEp	Parvocellular superior parietal area	7	
64	PEγ	Giant pyramidal posterior superior parietal area	7	
Inferior parietal region				
65	**PF**	Supramarginal area	40	
66	PFt	Tenuicortical supramarginal area	40	PFt
67	PFop	Opercular supramarginal area		PFop
68	PFcm	Magnocellular (posterior) supramarginal area		PFcm
69	**PG**	Angular area	39	PGa, PGp
Basal parietal region				
70	PHP	Basal (temporo-occipital) parietal area at parietal entrance	37	
71	PHT	Basal (temporo-occipital) parietal area at temporal entrance	37	
72	PHO	Basal (temporo-occipital) parietal area at occipital entrance	37	
Occipital lobe (O)				
73	OA2	Anterior peristriate area	19	
74	OA1	Posterior peristriate area	19	
75	OAm	Magnocellular peristriate area	19	
76	**OB**	Parastriate area	18	hOC2
77	OBγ	Giant pyramidal parastriate boundary of parastriate area	17/18 border	
78	OBΩ	Maculae granulosae of parastriate area	18	
79	**OC**	Striate area (granulosa)	17	hOC1
Temporal lobe (T)				
Supratemporal region				
80	TA1	Posterior superior temporal area	22	
81	TA2	Anterior superior temporal area	22	
82	**TB**	Magnocellular supratemporal area simplex	42	Te2
83	**TC**	Supratemporal area granulosa	41	Te1
84	**TD**	Intercalated supratemporal area		
Temporal region proper				
85	TE1	Middle temporal area proper	21	
86	TE2	Inferior temporal area proper	21	
Fusiform region				
87	**TF**	Fusiform area		
88	**TH**	Hippocampo-temporal area	36	
89	THα	Agranular hippocampo-temporal area	35	
Temporopolar region				
90	**TG**	Temporopolar area	38	
91	TGα	Agranular temporopolar area	38	

TABLE 32.4 List of cytoarchitectonic areas according to (1) von Economo and Koskinas (1925), (2) Brodmann (1909) and (3) JuBrain (Amunts and Zilles 2015). The areas listed under Brodmann and JuBrain overlap completely or partially with those of von Economo and Koskinas. In (1), main areas (bold font) are distinguished from their subdivisions (normal font) as originally proposed by von Economo and Koskinas.—cont'd

	1	Area name after von Economo and Koskinas	2	3
92	**TJ**	Temporal piriform area		
93	**TK**	Area of substantia perforata		
Hippocampal (inferior limbic) lobe (H)				
94	HA1	Primary uncinate area	34	
95	HA2	Secondary uncinate area	34	
96	HA3	Tertiary uncinate area	34	
97	HB1	Primary para-uncinate area	28	
98	HB2	Secondary para-uncinate area	28	
99	**HC**	Rhinal area limitans	28	
100	HD1	Presubicular area granulosa limitans	27	
101	HD2	Middle presubicular area granulosa	27	
102	HD3	Glomerular presubicular area granulosa	27	
103	HE1α	Subicular glomerular pyramidal area		
104	HE1β	Subicular pyramidal area simplex		
105	HE2	Pyramidal area of Ammon's horn		
106	HE3	Pyramidal area of digitate gyrus of uncus		
107	**HF**	Dentate area		

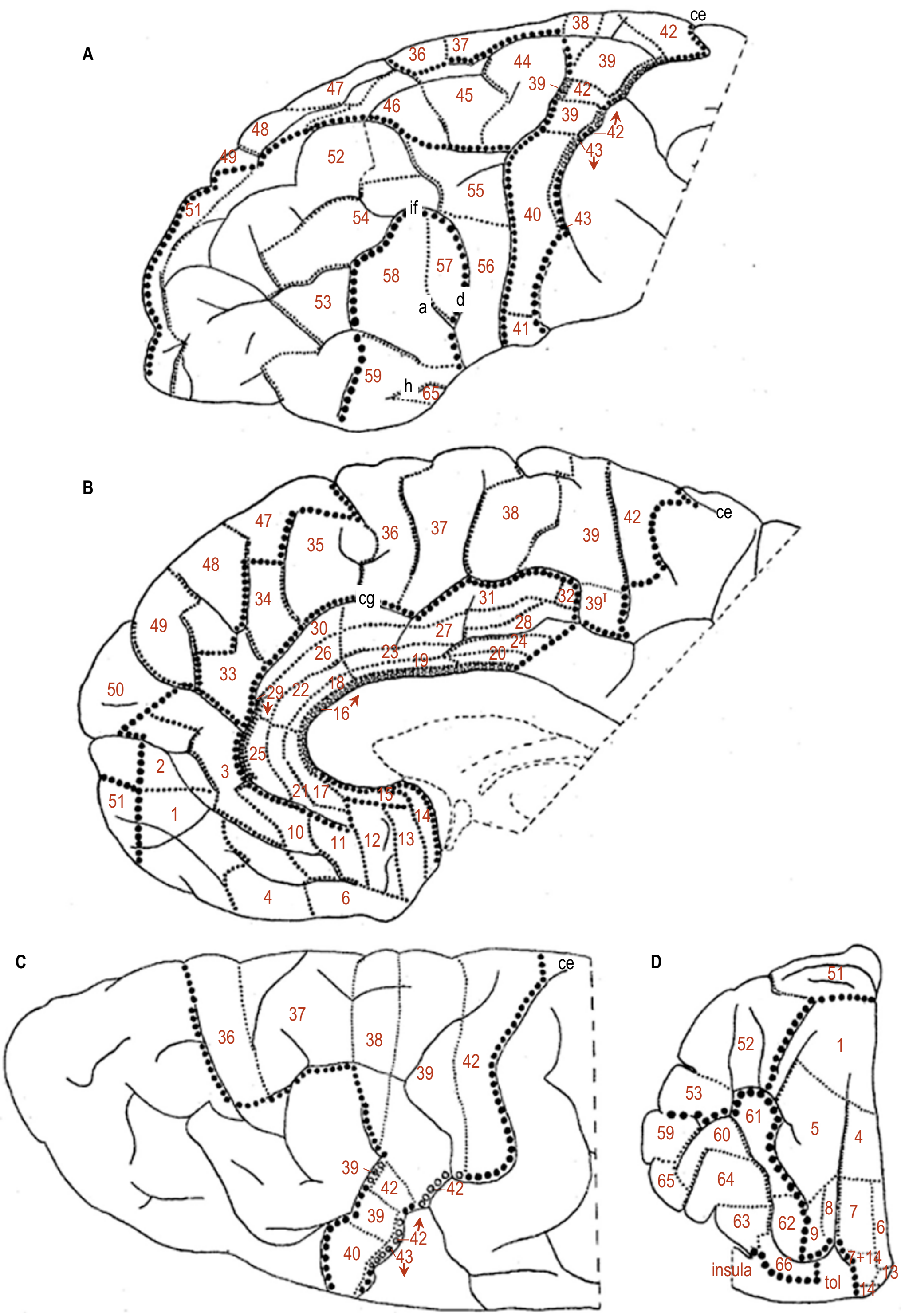
A
ce
38
42
36
37
44
39
47
46
45
39
42
39
48
42
49
43
52
55
51
54
if
40
43
57
56
58
a
d
53
41
59
h
65
B
47
36
37
38
42
ce
35
39
48
cg
34
31
32
39'
49
30
27
28
26
23
24
20
19
33
50
29
22
18
16
25
2
3
51
21
17
15
1
14
10
11
12
13
4
6
C
ce
37
36
38
39
42
39
42
42
39
42
40
43
D
51
52
1
53
61
5
59
60
4
65
64
8
7
63
62
9
6
insula
66
7+14
tol
13
14

Fig. 32.16 A myeloarchitectonic map of the human frontal lobe after Vogt (1910). **A**, lateral view; **B**, medial view; **C**, dorsal view; **D**, ventral view. Prefrontal areas rostral to areas V36, V39 and V40 are not shown in the dorsal view. Arabic numbers indicate Vogt's myeloarchitectonically defined areas. Abbreviations: a, ascending branch of the lateral fissure; ce, central sulcus; cg, cingulate sulcus; d, diagonal sulcus; h, horizontal branch of the lateral fissure; if, inferior frontal sulcus; tol, olfactory tuberculum. (With permission from Zilles K, Palomero-Gallagher N, Bludau S Cytoarchitecture and maps of the human cerebral cortex. In: Toga AW (ed) Brain Mapping: An Encyclopedic Reference. Anatomy and Physiology. Elsevier, Academic Press. Copyright 2015.)

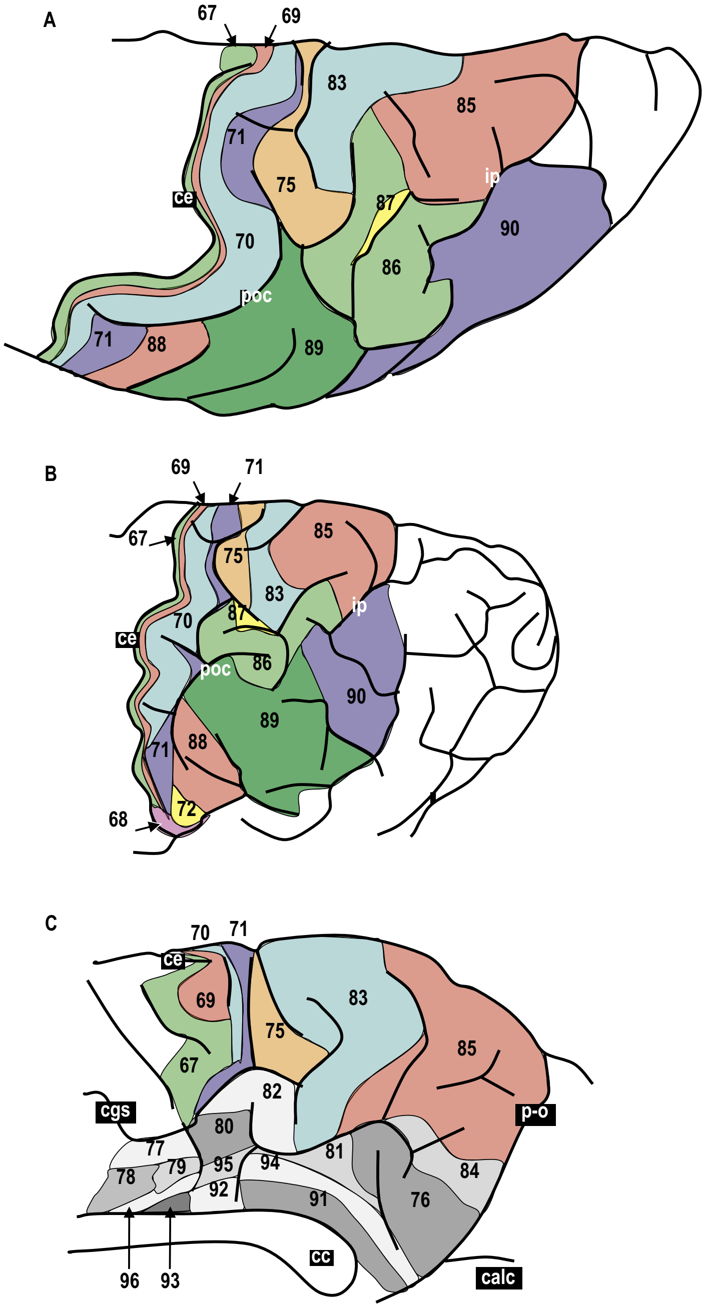
A
67
69
83
85
71
75
ce
ip
87
90
70
86
poc
71
88
89
B
69
71
85
67
75
83
70
87
ip
ce
poc
86
90
89
71
88
72
68
C
70
71
ce
69
83
75
85
67
82
cgs
p-o
80
77
81
79
95
94
84
78
92
91
76
cc
calc
96
93

Fig. 32.17 Myeloarchitectonic maps of the human parietal cortex after Vogt (1911): **A**, dorsal view; **B**, lateral view; **C**, medial view. Arabic numerals indicate myeloarchitectonic areas. Abbreviations: calc, calcarine sulcus; cc, corpus callosum; ce, central sulcus; cgs, cingulate sulcus; ip, intraparietal sulcus; p-o, parieto-occipital sulcus; poc, postcentral sulcus. (With permission from Zilles K, Palomero-Gallagher N, Bludau S Cytoarchitecture and maps of the human cerebral cortex. In: Toga AW (ed) Brain Mapping: An Encyclopedic Reference. Anatomy and Physiology. Elsevier, Academic Press. Copyright 2015.)

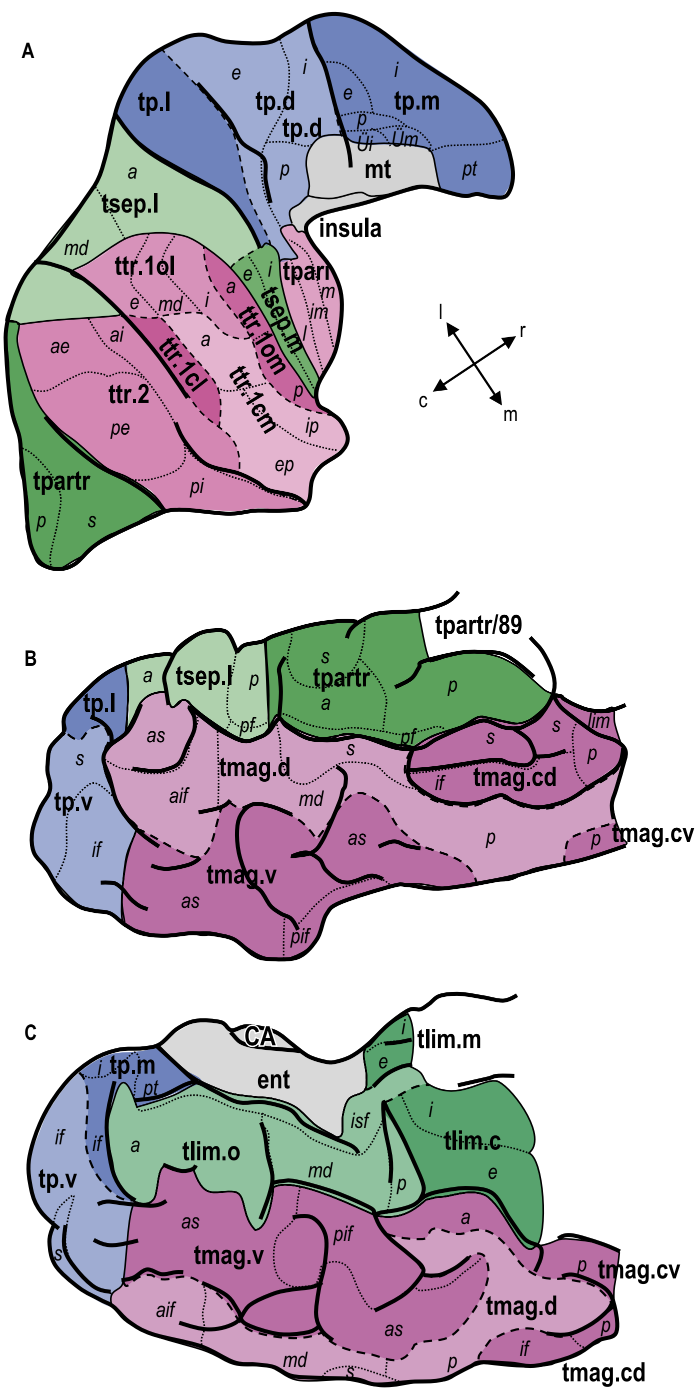
A
tp.l
e
i
i
tp.d
tp.d
e
tp.m
p
Ül
Üm
p
mt
pt
insula
a
tsep.l
md
ttr.1ol
e
i
tpari
a
e
md
i
tsep.m
m
im
ae
ai
a
ttr.1om
ttr.1cl
ttr.2
p
ttr.1cm
pe
ip
ep
tpartr
pi
p
s
l
r
c
m
B
tpartr/89
a
tsep.l
p
s
tpartr
a
p
tp.l
pf
as
pf
s
lim
s
s
p
tmag.d
if
tmag.cd
tp.v
aif
md
as
p
p
tmag.cv
if
tmag.v
as
pif
C
CA
i
tlim.m
i
tp.m
ent
e
pt
isf
i
if
if
a
tlim.o
tlim.c
md
e
tp.v
p
as
pif
a
tmag.v
p
tmag.cv
s
aif
tmag.d
as
p
if
md
s
p
tmag.cd

Fig. 32.18 A–C, A myeloarchitectonic map of the human temporal lobe: **A**, dorsal view; **B**, lateral view; **C**, medial view (modified from Hopf 1954). Bold letters are code names of regions and subregions, italics are code names of areas. Continuous lines surround the regions, dashed lines indicate subregional borders, and dotted lines areal borders. Orientations of the map in **A** are indicated. Abbreviations: c, caudal direction; m, medial direction; l, lateral direction; r, rostral direction; CA, cornu Ammonis region of the hippocampus; ent, entorhinal area; mt, mesocortex. The regio temporalis limitans (tlim) is subdivided into caudal (c), medial (m) and oral (o) subregions; tlim.c contains two areas (e, i), tlim.m two areas (e, i) and tlim.o four areas (a, isf, md, p). The regio temporalis magna (tmag) is subdivided into the caudodorsal (cd), caudoventral (cv), dorsal (d) and ventral (v) subregions. tmag.cd consists of four areas (lim, if, p, s), tmag.cv of two areas (a, p), tmag.d of five areas (aif, as, md, p, s), and tmag.v of two areas (as, pif). The regio temporopolaris (tp) is subdivided into the dorsal (d), lateral (l), medial (m) and ventral (v) subregions. tp.d consists of three areas (e, I, p), tp.l is not further subdivided, tp.m has seven areas (e, i, if, p, pt, Ül, Üm), and tp.v two areas (if, s). The regio temporalis parainsularis (tpari) contains three areas (im, l, m). The regio temporalis paratransversa (tpartr) contains four areas (a, p, pf, s). The regio temporalis separans (tsep) is subdivided into the lateral (l) and medial (m) subregions. tsep.l contains four areas (a, md, p, pf) and tsep.m two areas (e, i). The regio temporalis transversa (ttr) is subdivided into the prima caudolateralis (1cl), prima caudomedialis (1cm), prima orolateralis (1ol), prima oromedialis (1om) and secunda (2) subregions. ttr.1cl is not further subdivided, ttr.1cm has three areas (a, ep, ip), ttr.1ol three areas (e, I, md), ttr.1om two areas (a, p) and ttr.2 four areas (ae, ai, pe, pi). (C, Adapted from Hopf 1954, reproduced with permission from Zilles K, Palomero-Gallagher N, Bludau S Cytoarchitecture and maps of the human cerebral cortex. In: Toga AW (ed) Brain Mapping: An Encyclopedic Reference. Anatomy and Physiology. Elsevier, Academic Press. Copyright 2015.)

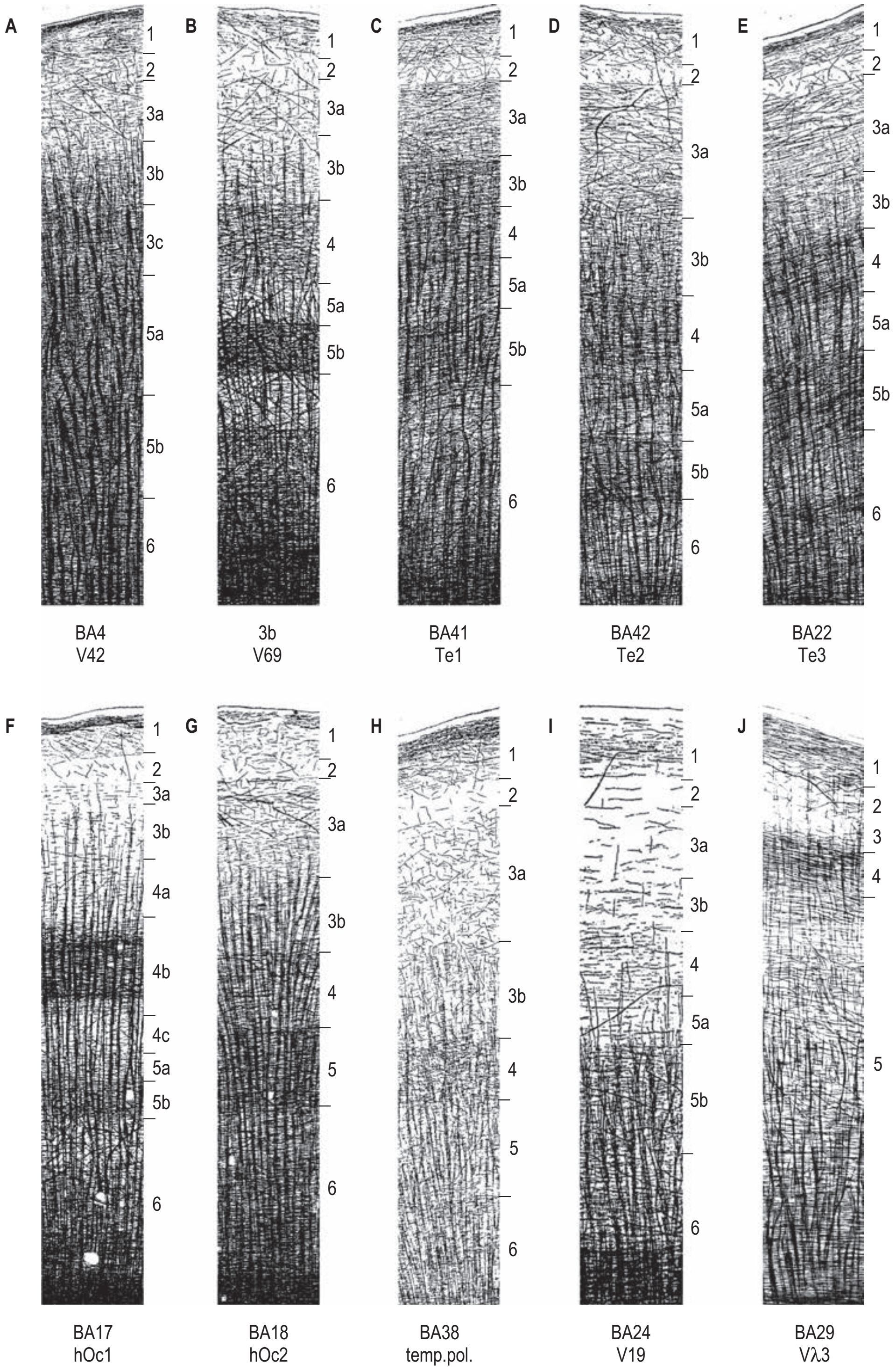
A
1
2
3a
3b
3c
5a
5b
6
BA4
V42
B
1
2
3a
3b
4
5a
5b
6
3b
V69
C
1
2
3a
3b
4
5a
5b
6
BA41
Te1
D
1
2
3a
3b
4
5a
5b
6
BA42
Te2
E
1
2
3a
3b
4
5a
5b
6
BA22
Te3
F
1
2
3a
3b
4a
4b
4c
5a
5b
6
BA17
hOc1
G
1
2
3a
3b
4
5
6
BA18
hOc2
H
1
2
3a
3b
4
5
6
BA38
temp.pol.
I
1
2
3a
3b
4
5a
5b
6
BA24
V19
J
1
2
3
4
5
BA29
Vλ3

Fig. 32.19 Myelinated fibres and their lamination pattern in representative iso- and periallocortical areas. The cortical thickness of the different areas has been normalized. Arabic numerals indicate myeloarchitectonic layers. **A**, Primary motor cortex (BA4/V42). **B**, Primary somatosensory cortex (area 3b/V69). **C**, Primary auditory cortex (BA41/Te1). **D**, Secondary auditory cortex (BA42/Te2). **E**, Superior temporal gyrus (BA22/Te3). **F**, Primary visual cortex (BA17/hOc1). **G**, Secondary visual cortex (BA18/hOc2). **H**, Temporal pole (BA38/temp.pol.). **I**, Anterior cingulate cortex (BA24/V19). **J**, Retrosplenial cortex (BA29/Vλ3). Abbreviations: BA, Brodmann areas (Brodmann 1909); hOc1 and hOc2, cytoarchitectonically defined primary and secondary visual cortex as reported by Amunts et al (2000); Te1 and Te2, cytoarchitectonically defined primary and secondary auditory areas as reported by Morosan et al (2001); Te3, higher auditory area (part of BA22) as reported by Morosan et al (2005); V, Vogt areas (Vogt and Vogt 1919). (With permission from Zilles K, Palomero-Gallagher N, Amunts K Myeloarchitecture and maps of the cerebral cortex. In: Toga AW (ed) Brain Mapping: An Encyclopedic Reference. Anatomy and Physiology. Elsevier, Academic Press. Copyright 2015.)

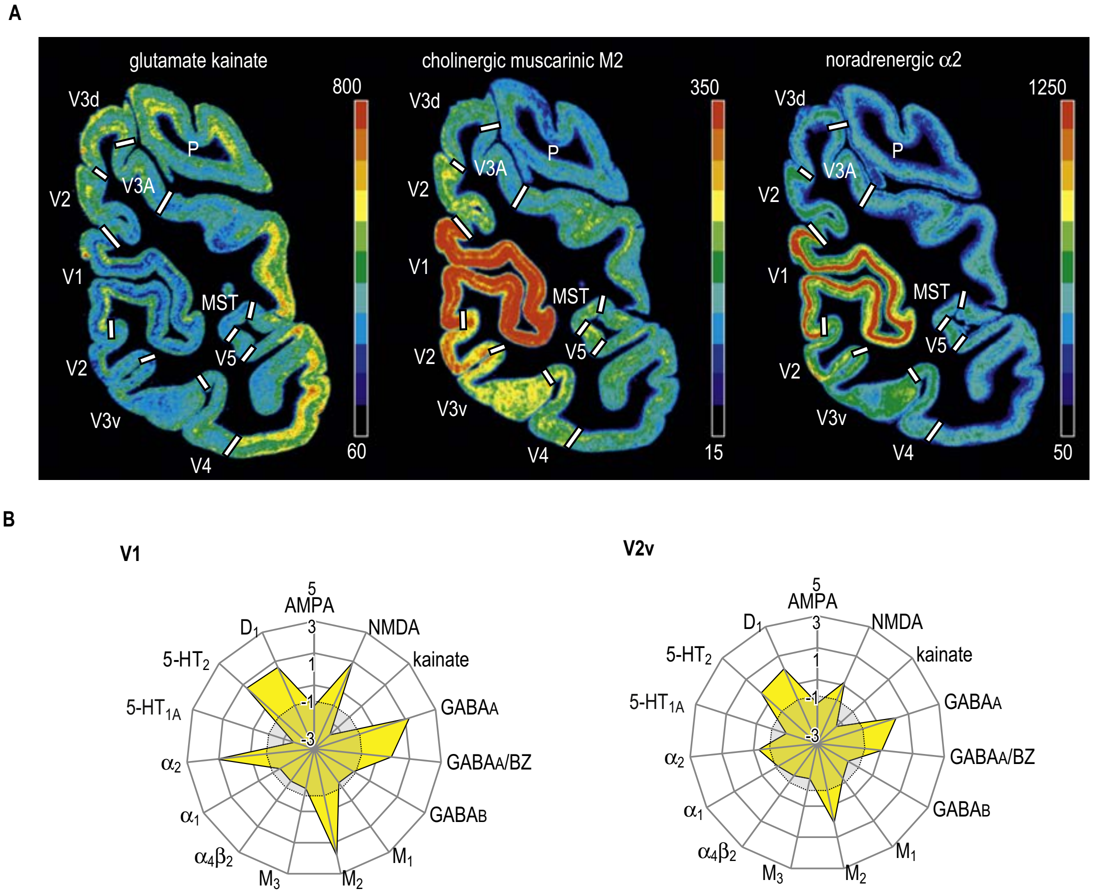
A
glutamate kainate
800
60
cholinergic muscarinic M2
350
15
noradrenergic α2
1250
50
V3d
P
V3A
V2
V1
MST
V5
V3v
V4
B
V1
V2v
5
3
1
-1
-3
AMPA
NMDA
kainate
GABAA
GABAA/BZ
GABAB
M1
M2
M3
α4β2
α1
α2
5-HT1A
5-HT2
D1

Fig. 32.20 Receptor analysis of the occipital areas. **A**, Distribution of three receptors in a coronal slice of the occipital cortex. **B**, Receptor fingerprints of areas V1 and V2. (Modified from Zilles and Palomero-Gallagher (2017).)

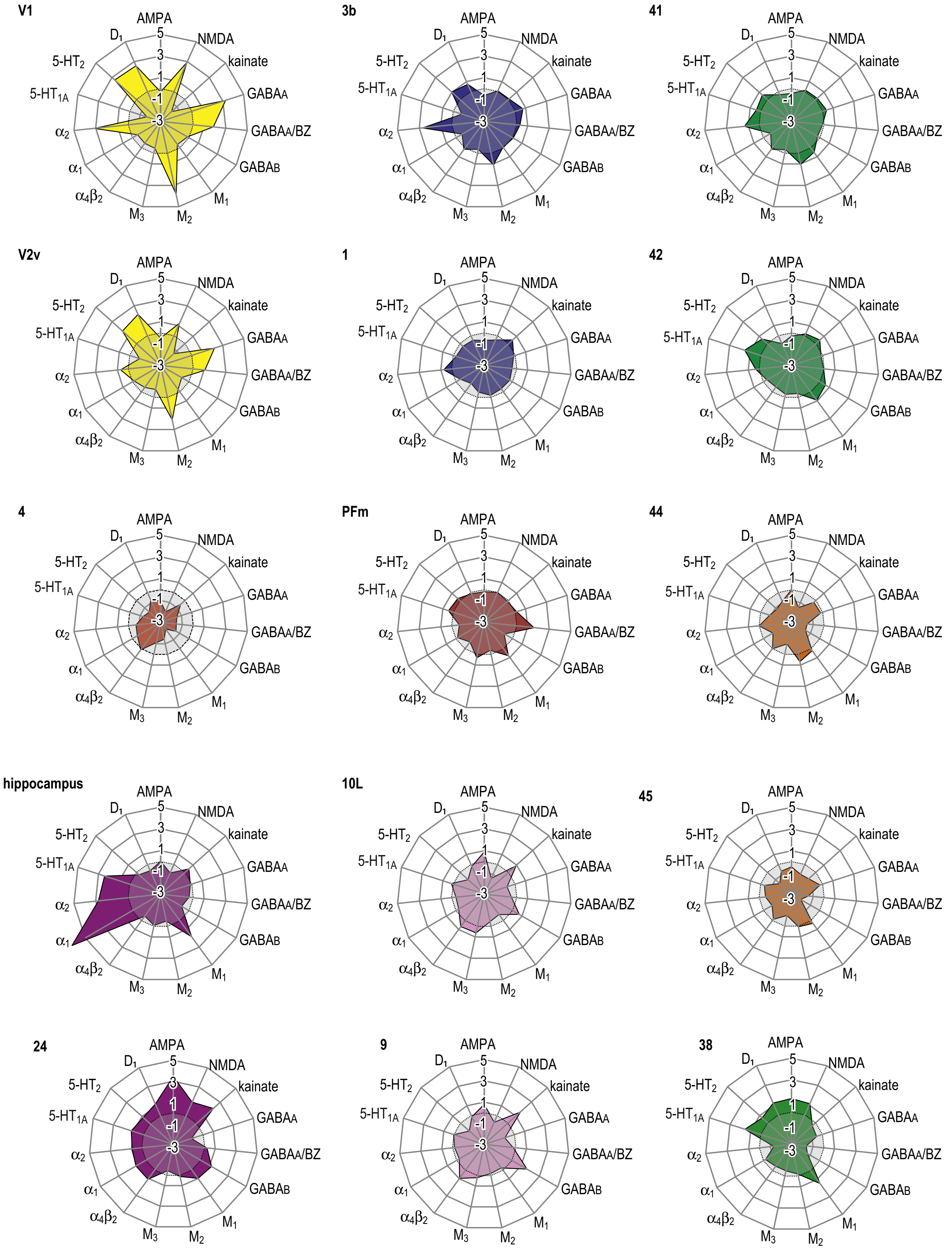

Fig. 32.21 Multi-receptor fingerprints of cortical areas of the human brain. V1, primary visual cortex; V2v, ventral part of the secondary visual cortex; 1, somatosensory system; 3b, BA1 and BA2 areas of the primary somatosensory cortex; 41 and 42, primary and secondary auditory cortex; 4, primary motor cortex; 44 and 45, areas of Broca's region; PFm, inferior parietal area; 10L, frontopolar area; 9, BA9; 24, BA24; 38, BA38. (Courtesy of Karl Zilles, unpublished data.)

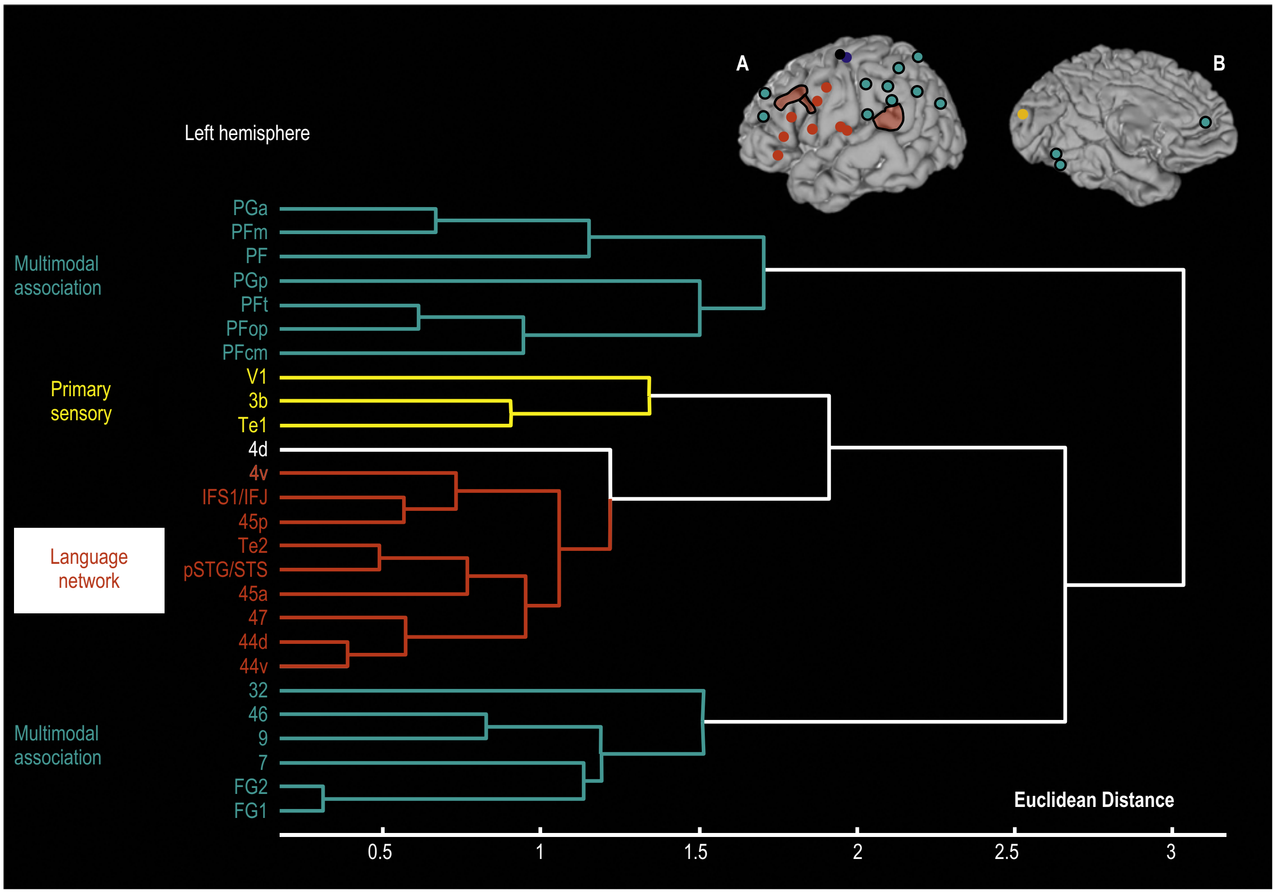

Fig. 32.22 Hierarchical Cluster Analysis of receptor fingerprints in the left (**A**) and right (**B**) hemispheres. (Adapted with permission from Zilles K, Bacha-Trams M, Palomero-Gallagher N et al 2015 Common molecular basis of the sentence comprehension network revealed by neurotransmitter receptor fingerprints. Cortex 63:79–89.)

A single receptor type can characterize the borders of functionally and cytoarchitectonically defined cortical regions. Prominent examples are the M_2 receptor and the delineation of BA17, area 3 and BA41 from surrounding cortical areas, or the identification of mossy fibre terminations on kainate receptors in the hippocampus. However, in many cases only the comparative evaluation of the expression patterns of multiple receptors in the same cortical region provides the criteria for a multimodal parcellation, which cannot be achieved by a single receptor type analysis. These multireceptor expression patterns, the characteristic fingerprints of each cortical area (see **Figs 32.20–32.22**), allow a detailed mapping of the human cerebral cortex and the identification of cortical networks. The analysis of receptor fingerprints reveals cortical regions that belong to the same functional network. For example, analysis of receptor fingerprints in the cingulate cortex has revealed four regions that are differentially involved in emotional processing, mediation of motor and cognitive processes via premotor planning with motivational characteristics, spatial orientation, memory and visuospatial functions (Palomero-Gallagher et al 2009).

The fingerprints of BA44 and BA45 are more similar to each other than they are to those of the ventral premotor cortex or the ventrally adjacent BA47, often interpreted as part of Broca's region. Subsequent analysis of many functionally identified language and non-language regions revealed that the receptor fingerprints of BA44 and BA45 belong to a complex system of language-related areas in the left hemisphere that consists of the subdivisions of BA44 and BA45, BA47, the secondary auditory area BA42, and a region in the posterior part of the superior temporal gyrus and sulcus within Wernick's area (Amunts et al 2010, Zilles et al 2015b; see Fig. 32.22). The fingerprints of the areas in this functional system clearly differ from those of primary sensory cortical areas, multimodal areas of the inferior and superior parietal lobules, higher extrastriate visual areas, BA32 and the primary motor cortex. A separate analysis of the fingerprints of the right and left hemispheres revealed a notable interhemispheric difference that underlines the lateralized language function.

Fingerprint analysis of the different areas of the inferior parietal lobule demonstrated a very close relation between BA39 and the extrastriate area V3v (Caspers et al 2013b), supporting the notion that at least the posterior part of BA39 is a hub in the ventrodorsal visual stream (Pisella et al 2006). Hierarchical cluster analysis of the receptor fingerprints of fusiform areas FG1 and FG2 argues for their position between the ventral visual stream and multimodal association areas of the inferior parietal lobule (Caspers et al 2013a). FG1 and FG2 differ from the early visual areas of the ventral stream: a principal component analysis found that all visual areas were separated from nearly all other cortical areas studied, but FG1 and FG2 were segregated from early visual areas, indicating their close association with multimodal association areas of the inferior parietal lobule (Caspers et al 2013b).

Numerous glutamatergic pathways can be identified in the forebrain (see Fig. 32.7; **Figs 32.23–32.24**). Axons of glutamatergic pyramidal neurones in layers II and III project to cortical neurones of layers IV (short distance cortico-cortical feedforward projections) and V–VI (long distance cortico-cortical feedforward projections), and reciprocally from layers V and VI to layer II and superficial part of layer III (feedback projections): these are cortico-cortical pathways. Axons in layer VI project to the claustrum (cortico-claustral pathway). Axons in layer V excite GABAergic medium-spiny neurones (principal neurones) in the caudate nucleus and putamen via asymmetric synapses on their dendritic spines (cortico-striatal pathway). Axons in layers V and VI are connected via the internal capsule with neurones in the thalamus (cortico-thalamic pathway). Axons of neurones in thalamic nuclei mainly terminate on neurones in layer IV (thalamo-cortical pathway) and can extend to various degrees into layer III. Axons in layer V terminate on dopaminergic and GABAergic neurones in the substantia nigra (SN)/ventral tegmental area (VTA) (cortico-nigral/VTA pathway). Axons in layer V descend via the internal capsule and crus cerebri to multipolar cells of the pontine nuclei (cortico-pontine pathway), which in turn project as mossy fibres to the cerebellar cortex. Axons in layer V terminate via the internal capsule and crus cerebri on multipolar cells of the motor nuclei of the brainstem and tectum (cortico-nuclear and cortico-tectal pathways). Axons in layer V terminate via capsula interna, crus cerebri and pyramidal tract on motoneurones of the anterior horn of the spinal cord (cortico-spinal pathway). Axons in layer III terminate as commissural fibres via the corpus callosum on neurones of homologous or heterologous cortical areas of the contralateral hemisphere (callosal pathway).

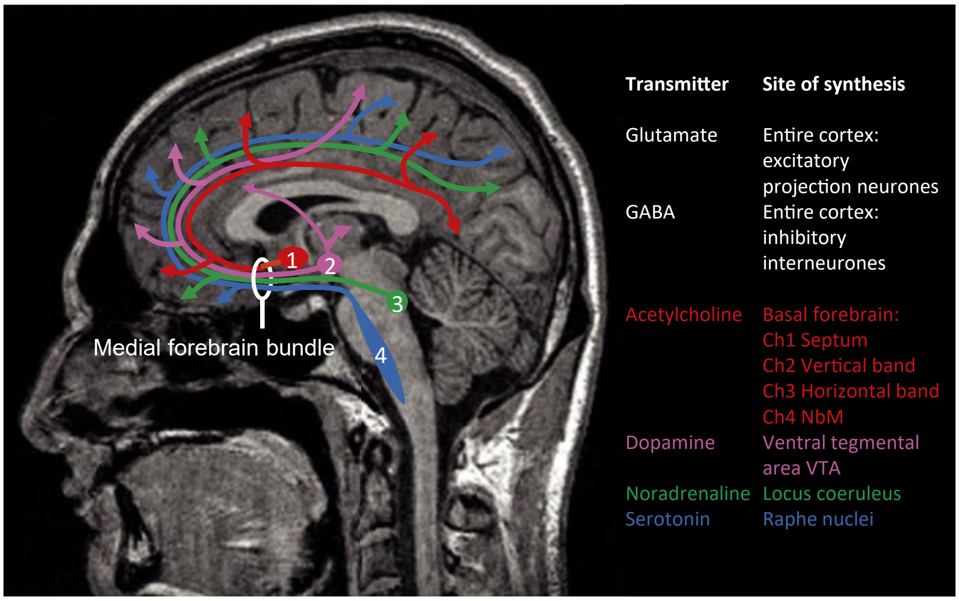
1
2
3
4
Medial forebrain bundle
Transmitter
Site of synthesis
Glutamate
Entire cortex: excitatory projection neurones
GABA
Entire cortex: inhibitory interneurones
Acetylcholine
Basal forebrain: Ch1 Septum Ch2 Vertical band Ch3 Horizontal band Ch4 NbM
Dopamine
Ventral tegmental area VTA
Noradrenaline
Locus coeruleus
Serotonin
Raphe nuclei

Fig. 32.23 Transmitter systems in the cerebral cortex and sites of transmitter synthesis. Key: 1, basal forebrain; 2, ventral tegmental area; 3, locus coeruleus; 4, raphe nuclei. Abbreviation: NbM, nucleus basalis Meynert.

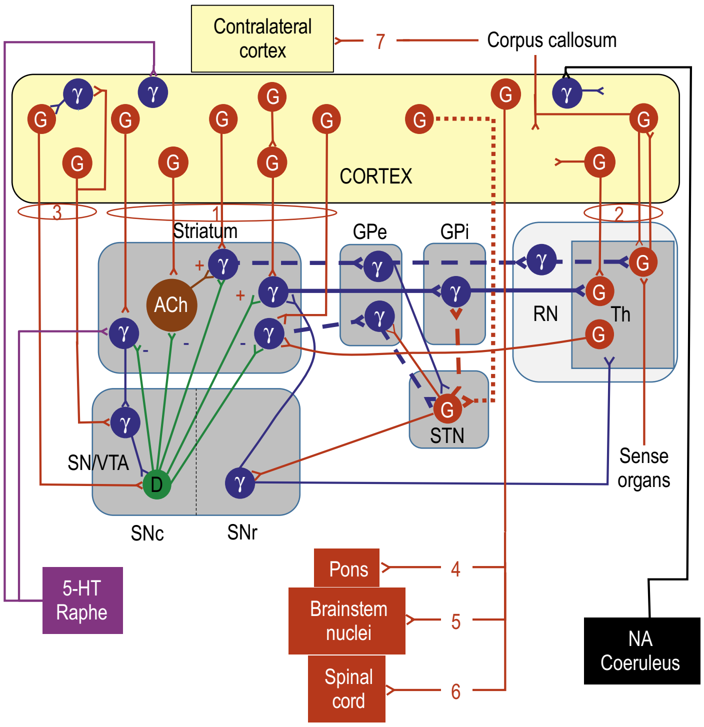
Contralateral cortex
7
Corpus callosum
CORTEX
G
γ
1
2
3
Striatum
GPe
GPi
ACh
RN
Th
STN
SN/VTA
D
SNc
SNr
Sense organs
5-HT Raphe
Pons
4
Brainstem nuclei
5
Spinal cord
6
NA Coeruleus

Fig. 32.24 Efferent and afferent pathways of the cerebral cortex and their transmitters. Dashed thick blue lines label the indirect pathway, continuous thick lines label the direct pathway and the pointed line indicates the hyperdirect pathway. Key: 1, cortico-striatal pathway; 2, cortico-thalamic and thalamo-cortical pathways; 3, cortico-nigral pathway; 4, cortico-pontine pathway; 5, cortico-nuclear pathway; 6, cortico-spinal pathway; 7, callosal connections. Afferent fibres from the raphe nuclei (serotonin, 5-HT) and from the locus coeruleus (noradrenaline, NA) run in the medial forebrain bundle. ACh, cholinergic neurones; D, dopaminergic neurones; G, glutamatergic neurones; γ, GABAergic neurones; GPe, lateral (external) part of the globus pallidus; GPi, medial (internal) part of the globus pallidus; NA, noradrenaline (norepinephrine); RN, reticular nucleus; SNc, substantia nigra pars compacta; SNr, substantia nigra pars reticulata; SN/VTA, substantia nigra/ventral tegmental area; STN, subthalamic nucleus; Th, thalamus.

GABA is the ubiquitous major inhibitory neurotransmitter in the human cerebral cortex. However, it can also have an excitatory effect under certain conditions. GABA-induced depolarization occurs in the developing cortex, and in mature cortical neurones following dendritic $GABA_A$ receptor activation. All cortical interneurones, with the notable exception of the spiny stellate cells, are GABAergic. Ninety-five per cent of cortical interneurones co-express GABA and calcium-binding proteins (CBPs): parvalbumin (PV), calbindin (CB), and calretinin (CR). Most of these cells are located in layers II–III. In the primary visual cortex of the macaque monkey, the majority of interneurones (97%) express only one of the three CBPs (**Fig. 32.25**): about half of the cells are positive for PV, nearly one-third for CB and the rest are positive for CR. The three interneuronal subtypes also differentially express glutamate receptors (Kooijmans et al 2014). The fast-spiking PV cells show high expression of the GluA2 and GluA3 subunits, whereas the intermediate spiking CB and CR cells show high expression of the GluA1 and GluA4 glutamatergic AMPA (alpha-amino-3-hydroxy-5-methyl-4-isoxazole propionic acid) receptor subunits (Kooijmans 2016). Interneurones can be categorized according to their co-expression of the GluN2 subunits of the glutamatergic NMDA (N-methyl-D-aspartate) receptor. PV-IR cells show a low expression of the receptor, largely confined to their somata, whereas CB and CR expressing cells also express high levels of GluN2 subunits, both on their somata and in their dendrites (Kooijmans 2016).

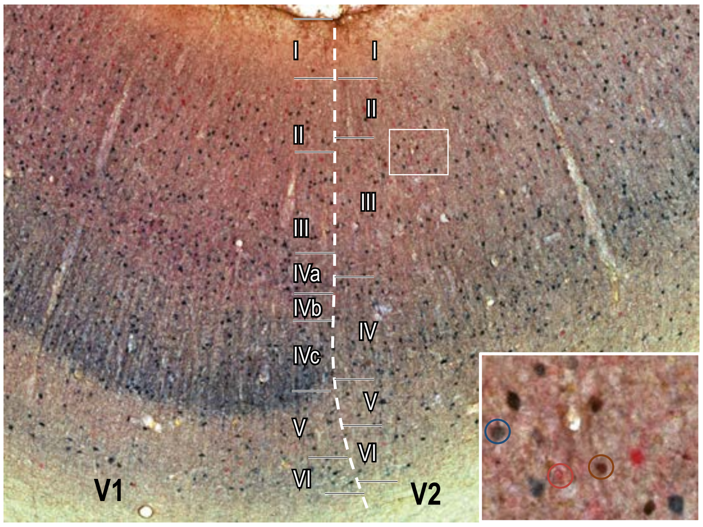

Fig. 32.25 Neurones expressing calcium-binding proteins at the border (dashed line) between human V1 and V2. Parvalbumin in blue, calbindin in magenta and calretinin in brown (see inset). Roman numerals indicate cortical layers. (Courtesy of Dr RN Kooijmans, NIN/KNAW Amsterdam.)

The neuromodulatory transmitters of the cortex are acetylcholine, dopamine, noradrenaline and serotonin. Neurones that synthesize these neuromodulators are all located in subcortical regions and send long projection axons to the cerebral cortex. These transmitters can positively or negatively modulate the excitability of cortical neurones by binding to numerous different receptor subtypes linked to multiple signal transduction mechanisms: they enhance the signal-to-noise ratio of cortical responses and modify the threshold for activity-dependent synaptic modifications.

Acetylcholine is synthesized in large multipolar neurones in various regions of the basal forebrain (Ch1–Ch4) (**Fig. 32.26**). Their axons reach the entire cortex: cholinergic synapses are found on dendritic shafts, apical dendrites, the somata of pyramidal cell dendrites and of non-pyramidal cells. The density and laminar distribution pattern of cholinergic fibres differ significantly between different cytoarchitectonic areas. In the primary visual cortex, cholinergic fibres are particularly dense in layers I–IIIa, followed by layer IIIb, layers IVA and IVB, and alternating patches in layer IVC display a higher density of cholinergic fibres than layers IVB and V. Most but not all cholinergic synapses are symmetric.

Dopamine-containing neurones located in the dorsal parts of the substantia nigra (A9), ventral tegmental area (A10) and the retrorubral area (A8) send axons to the entire cortex (see Fig. 32.23). The whole frontal lobe receives dopaminergic afferents from these three sites (Björklund and Dunnet 2007). Dopamine interneurones (A16) are present in the glomerular layer of the olfactory bulb. The densities and laminar distribution patterns of dopaminergic terminals differ between cortical areas: the primary motor cortex is densely innervated, the primary sensory cortices are sparsely innervated. In the motor cortex, dopaminergic fibres are evenly distributed throughout the different layers, other cortical regions show higher densities in layers I–IIIa and V–VI than in the middle layers. Dopaminergic terminals form symmetric synapses with dendritic shafts and spines, somata and axons. Direct local dopaminergic modulation of the excitability of cortical neurones is thought to be mediated via asymmetric membrane specializations of dopaminergic afferents on dendrites and dendritic spines, i.e. via the postsynaptic targets of both dopaminergic and excitatory input (synaptic triads) (Jacob and Nienborg 2018).

Noradrenaline (norepinephrine) is synthesized in the locus coeruleus (see Fig. 32.23): the efferent projections reach the entire cortex via the medial forebrain bundle. Noradrenaline-containing axons are found in all cortical areas. There are differing regional and laminar densities, for example, in the human primary visual cortex, axon terminals are most dense in layer V, followed by layer VI, and relatively sparse in other layers. Noradrenaline is particularly important for the developmental plasticity of the cortex: it facilitates activity-dependent synaptic modifications in the cortex. Noradrenaline-containing varicosities form either symmetric or asymmetric synapses mainly on spines and dendritic shafts. Axosomatic synapses on pyramidal and non-pyramidal neurones are rare.

Serotonin (5-hydroxytryptamine, 5-HT) innervation of the entire cortex originates from either the dorsal raphe nucleus (see Fig. 32.23), via thin fibres with small varicosities, or the median raphe nucleus, via thick fibres with large spherical varicosities: the efferent projections from both raphe nuclei reach the entire cortex via the medial forebrain bundle. 5-HT axon terminals are present in all cortical areas and layers. 5-HT fibres synapse with pyramidal neurones and GABAergic interneurones, preferentially on spines and dendritic shafts, but also on somata.

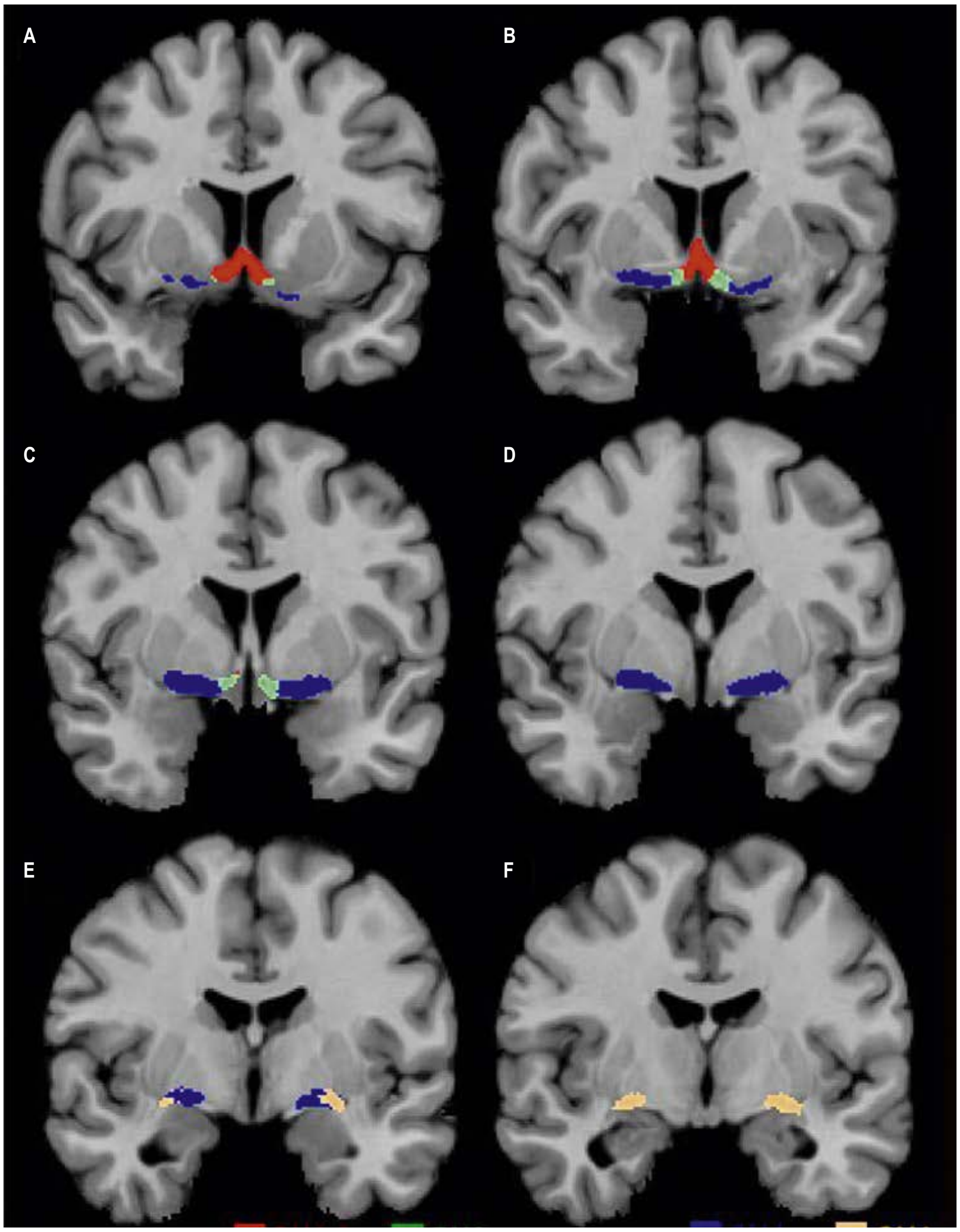

Fig. 32.26 A–F, Magnocellular cholinergic cell groups Ch1 to Ch4 in the basal forebrain and their maximum probability maps in the anatomical MNI space in rostral to caudal coronal planes (A, rostral; F, caudal). In the MPM each voxel is assigned to the cytoarchitectonic compartment that showed the greatest overlap among ten brains. Red, Ch1–2 cell groups (septum + vertical limb of Broca); green, Ch3 (horizontal limb of Broca); blue, Ch4 (Ncl. basalis Meynert); beige, Ch4p.

Neuropeptides are small proteins or polypeptides that are synthesized by neurones and serve as modulatory neurotransmitters. They act in or out of the central nervous system via G protein and second messenger systems, and increase or decrease the functional impact of co-released neurotransmitters in the brain. More than 100 different neuropeptides have been identified, and only a selection of the most abundant types can be described here. Vasoactive intestinal polypeptide (VIP), neuropeptide Y (NPY), somatostatin (SOM), substance P (SP) and cholecystokinin (CCK) are among the frequently occurring neuropeptides in the human cerebral cortex. Many of the neuropeptide-containing neurones are interneurones. VIP is synthesized in bipolar interneurones and plays an important role in the local regulation of metabolism in the cerebral cortex by stimulating glycogenolysis and altering cortical blood flow. VIP inhibitory cells receive long range projections and inhibit SOM inhibitory interneurones. Dendrites of VIP cells most extensively branch in layers I and deep IV to superficial V. The density of their axons is highest in layers II–IV. NPY can be co-released with GABA and glutamate, reduces pain perception and voluntary alcohol intake, and controls epileptic seizures. Impairment of NPY functions also seems to play a role in obesity, anxiety, and neurodegenerative disorders. All SOM-expressing neurones of the cortex are a subset of GABAergic inhibitory interneurones (Martinotti cells, bitufted interneurones and basket cells). Basket cells are particularly abundant in the frontal or entorhinal cortices. SOM, NPY, SP and calbindin are often co-expressed in the same cell. The somata of such neurones occur mainly in the infragranular layers, or in the subcortical white matter. The activity of SOM cells is regulated by changes in brain state, during learning and reward: they undergo long-lasting structural and functional changes during experience-dependent plasticity of the cortical network. SOM cells play a role in schizophrenia and epilepsy. Only a few pyramidal cells of the isocortex contain SP, which is often co-localized with serotonin or noradrenaline. CCK can be co-localized with glutamatergic, GABAergic, dopaminergic and serotoninergic neurones that project to the cortex: it plays a role in regulating satiety and appetite, thermoregulation, sexual behaviour and memory. The cell bodies of CCK-containing neurones are frequently observed in the supragranular layers. Cell bodies of SP- and SOM-containing neurones prevail in the temporal lobe, those of CCK- and NPY-containing neurones in the frontal lobe. Axons containing NPY, SOM and SP are present in all cortical layers, particularly as horizontally orientated fibres in layer I, and randomly orientated fibres in the supra- and infragranular layers, but they are sparse in the inner granular layer IV.

Transmitter receptors are key molecules of signal processing in the nervous system. The functional receptors are homomeric or heteromeric proteins in the cell membrane of neurones or glial cells (Table 32.5). The effects of transmitters are defined by the receptors to which they bind after release from the presynaptic neurone. One transmitter can bind to multiple receptor types. This non-covalent binding leads to local changes of the membrane potential that may be fast (via ionotropic receptors, which are ligand-controlled ion channels) or slow (via metabotropic receptors, coupled to G-proteins that control the activation of second messengers). These changes are either excitatory or inhibitory depending on the actual receptor type. Receptors are located postsynaptically or presynaptically as heteroreceptors, i.e. receptors that regulate the synthesis and/or the release of transmitters other than their own transmitter, or as autoreceptors, i.e. receptors located on the terminal of a presynaptic cell. Autoreceptors are usually G protein-coupled receptors and only respond to the same transmitter released by the presynaptic neurone: they are located in the dendrites, soma, axon, or axon terminals, and act as part of a negative feedback loop in signal transduction.

The heterogeneous regional and laminar expression patterns of each receptor type indicate a parcellation of the cerebral cortex on a molecular basis. The regional segregation of transmitter receptors (**Fig. 32.27**) can be demonstrated *in vivo* by positron emission tomography (PET) or single photon emission tomography (SPECT). Both methods are clinically important, but their spatial resolution does not enable an analysis of the laminar or cellular localization of receptors. *In vitro* demonstration of receptors at high spatial resolution and receptor type specificity is possible with immunohistochemistry, in situ hybridization or quantitative receptor autoradiography (see Fig. 32.27).

TABLE 32.5 Receptor subtypes of the cerebral cortex and their subunit composition, genes, ion effects and function

Transmitter and receptor type	Subunits	Genes	Ion	Function
Glutamate				
Subtypes				
Ionotropic AMPA receptor	GluA1-GluA4	*GRIA1-GRIA4*	Ca^{2+}	Fast excitation
Ionotropic NMDA receptor	GluN1	*GRIN1*	Na^{+} and Ca^{2+}	Slow excitation
	GluN2A-D	*GRIN2A-D*		-
	GluN3A-B	*GRIN3A-B*	K^{+} (out)	
Ionotropic kainate receptor	GluR5-GluR7	*GRIK1-GRIK3*	Na^{+} and Ca^{2+}	Excitation (postsynaptic)
	KA1, KA2	*GRIK4-GRIK5*	K^{+} (out)	Inhibition (presynaptic)
Metabotropic GluR2/3 receptor		*GRM2, GRM3*	K^{+} activation	Inhibit release of glutamate, GABA
G-protein-coupled receptor			Ca^{2+} inactivation	Noradrenaline, dopamine; pre-, post-, and extrasynaptic inhibition via cAMP inhibition
GABA				
Subtypes				
Ionotropic GABA$_A$ receptor	α_1–α_6, β_1–β_3	*GABRA1-6*	Cl^{-} (in)	Fast inhibition
	γ_1–γ_3, δ, ε, π,	*GABPB1–3*		$\alpha + \gamma$ provide benzodiazepine binding sites
	θ	*GABRC1-3*		
Metabotropic GABA$_B$		*GABBR1-2*	K^{+}	Slow inhibition G-protein-coupled receptor pre-, post-, and extrasynaptic
Acetylcholinesterase				
Subtypes				
Ionotropic nicotinic $\alpha_4\beta_2$ receptor				Post- and presynaptic excitation
Metabotropic muscarinic M$_1$ receptor				Excitation
Metabotropic muscarinic M$_2$ receptor				Inhibition
Metabotropic muscarinic M$_3$ receptor				?
Dopamine				
Subtypes				
Metabotropic D$_1$ receptor				Excitation
Metabotropic D$_2$ receptor				Inhibition
Noradrenaline (Norepinephrine)				
Subtypes				
Metabotropic α_1 receptor				Excitation
Metabotropic α_2 receptor				Inhibition
Serotonin (5-hydroxytryptamine)				
Subtypes				
Metabotropic 5-HT$_{1A}$ receptor				Inhibition
Metabotropic 5-HT$_{2A}$ receptor				Excitation/Inhibition

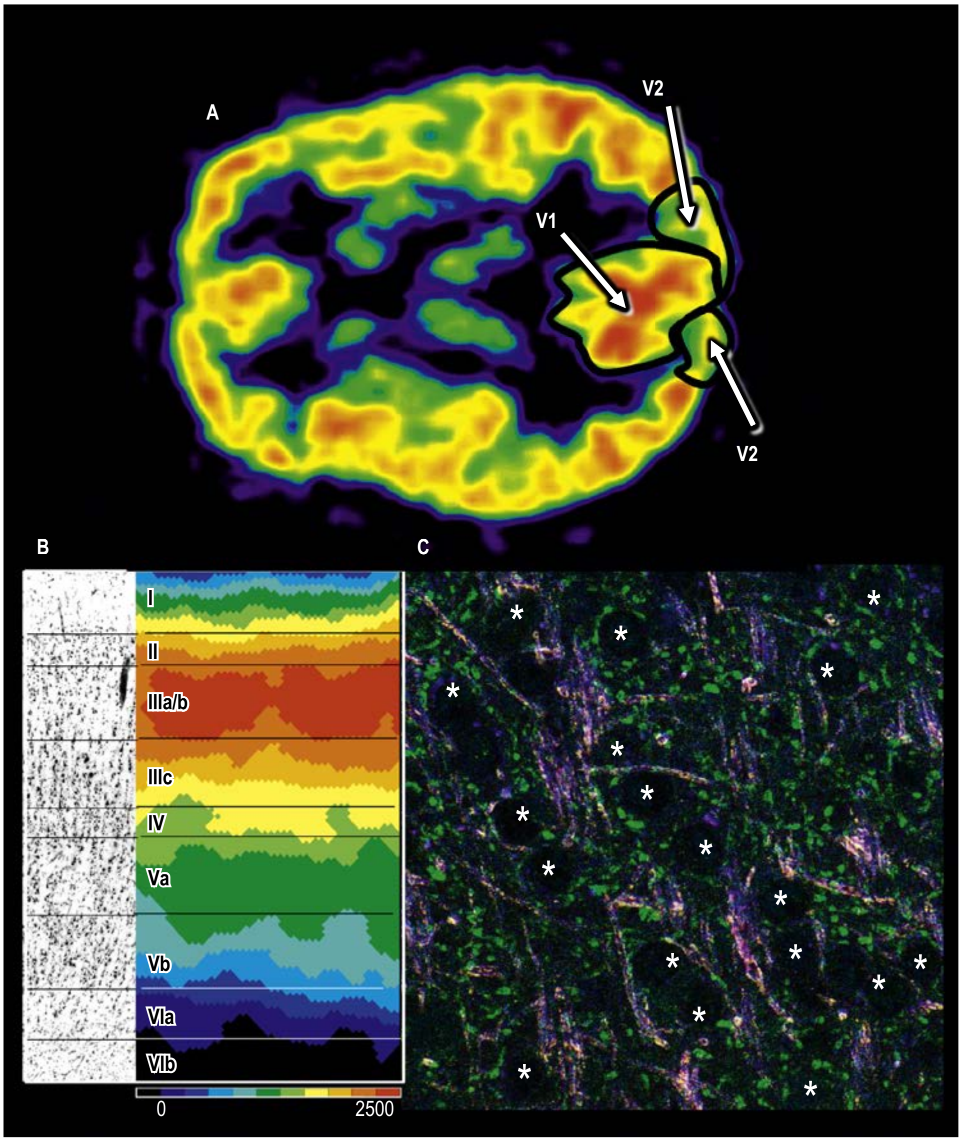

Fig. 32.27 **A**, Visualization of the regional distribution of serotonin 5-HT_2 receptors with PET in a horizontal section through the human brain. **B**, Laminar distribution of the density (colour scale in fmol/mg protein) inhibitory $GABA_A$ receptor in the human superior parietal cortex (area 7a) visualized with quantitative *in vitro* receptor autoradiography. **C**, Cellular (macaque cortex, immunohistochemistry) distributions of transmitter receptors in the cerebral cortex. Green, vesicular glutamate transporter (VGluT2, thalamo-cortical glutamatergic boutons); red, NMDA glutamate receptor subunit (GluN2A); blue, NLGN 1 (neuroligin 1, postsynaptic partner of transsynaptic scaffolding complex). Asterisks = cell bodies. (Courtesy of Dr RN Kooijmans, NIN/KNAW Amsterdam.)

Glutamate receptors are either ionotropic receptors (AMPA, alpha-amino-3-hydroxy-5-methyl-4-isoxazole-propionic acid; NMDA, N-methyl-D-aspartate; and kainate receptors), which control ion channels, or metabotropic receptors which act through second messenger systems. All glutamate receptor types are expressed by neurones and astrocytes. Activated AMPA and kainate receptors lead to fast excitatory synaptic signal transmission.

The highest densities of the ionotropic glutamate AMPA receptor (**Figs 32.28–32.29**) are found in the orbitofrontal (BA11) and lateral prefrontal (BA8–10, 46, 47), temporal (BA20, 21, 36, 38), early and higher visual (V3A, FG1, FG2) and part of the insular cortical areas. Lowest densities are found in the motor (BA4, 6), somatosensory (BA1, area 3b), parietal (BA5, PGa, PGp), early visual (V2, V4v), and anterior and posterior cingulate (BA23, 31, 32) cortices. Preferential cellular localizations are the dendritic spines of pyramidal cells in the supragranular layers.

The ionotropic glutamate NMDA receptor (Figs 32.28–32.29) is a heterotetrameric protein complex consisting of subunits NR1–NR3. It has a cation channel that enables sodium and calcium ions to move from extracellular space into a neurone after binding of glutamate and glycine. The current through the channel is voltage-dependent, since magnesium ions block the channel for the influx of sodium and calcium

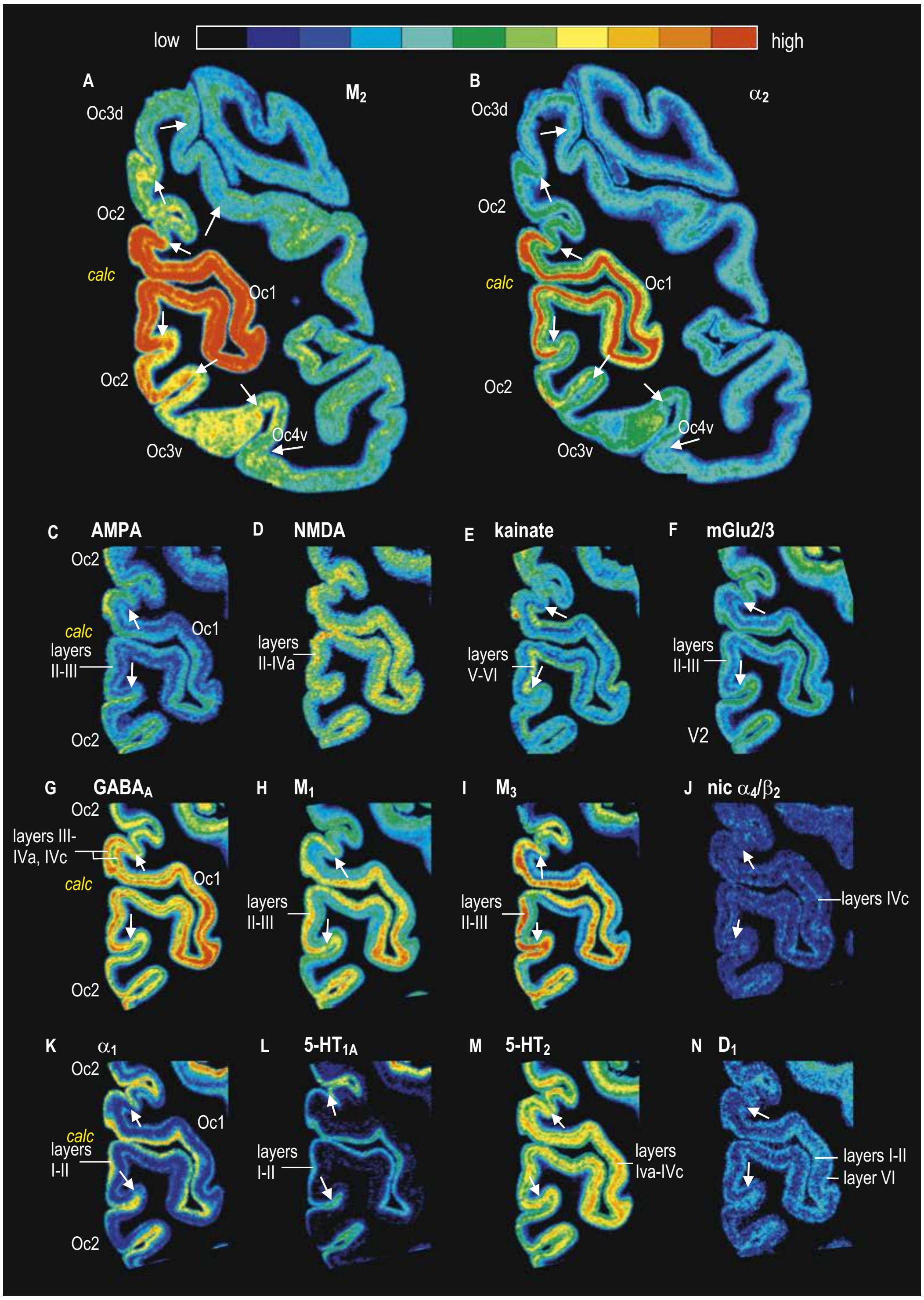
low
high
A
M$_2$
Oc3d
Oc2
calc
Oc1
Oc2
Oc3v
Oc4v
B
α_2
Oc3d
Oc2
calc
Oc1
Oc2
Oc3v
Oc4v
C AMPA
Oc2
calc
layers II-III
Oc1
Oc2
D NMDA
layers II-IVa
E kainate
layers V-VI
F mGlu2/3
layers II-III
V2
G GABA$_A$
Oc2
layers III-IVa, IVc
calc
Oc1
Oc2
H M$_1$
layers II-III
I M$_3$
layers II-III
J nic α_4/β_2
layers IVc
K α_1
Oc2
calc
layers I-II
Oc1
Oc2
L 5-HT$_{1A}$
layers I-II
M 5-HT$_2$
layers Iva-IVc
N D$_1$
layers I-II
layer VI

Fig. 32.28 A–B, Regional and laminar distribution of acetylcholine muscarinic M$_2$ (**A**), and adrenergic α_2 (**B**) receptors in coronal section through the occipital lobe of a human brain. M$_2$ and α_2 receptors delineate the primary visual area Oc1 by their distinctly higher densities compared to the secondary visual area Oc2 (BA18, V2). The borders of the early visual areas Oc3v (V3v), Oc4v (V4v) and Oc3d (V3d) are also visible by differences in their higher or lower regional and laminar receptor densities (arrows). **C–N**, The layer-specific localization of low or high densities of glutamate (**C**, glutamate AMPA; **D**, glutamate NMDA; **E**, glutamate kainate; **F**, glutamate mGluR 2/3; **G**, GABA$_A$; **H**, acetylcholine muscarinic M$_1$; **I**, acetylcholine muscarinic M$_3$; **J**, acetylcholine nicotinic $\alpha_4\beta_2$; **K**, noradrenaline α_1; **L**, serotonin 5-HT$_{1A}$; **M**, serotonin 5-HT$_2$; **N**, dopamine D1). Arrows indicate the border between Oc1 (BA17, V1) and Oc2 (BA18, V2). Colour scale indicates relative density of each receptor.

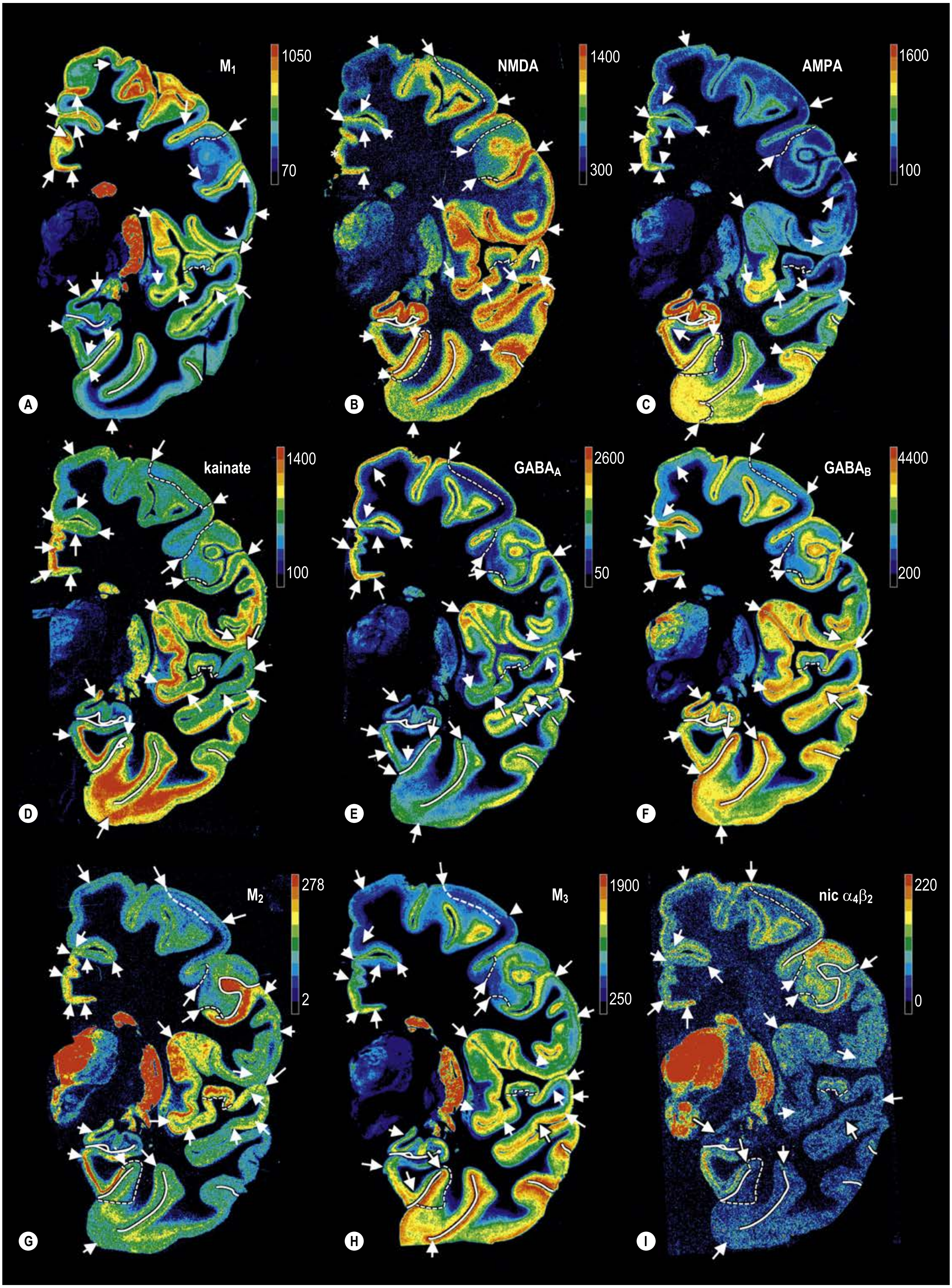
M$_1$
1050
70
A
NMDA
1400
300
B
AMPA
1600
100
C
kainate
1400
100
D
GABA$_A$
2600
50
E
GABA$_B$
4400
200
F
M$_2$
278
2
G
M$_3$
1900
250
H
nic $\alpha_4\beta_2$
220
0
I

Fig. 32.29 A–R, Regional and laminar distribution of various neurotransmitter receptors of the human brain visualized with colour-coded quantitative receptor autoradiography. Each image, obtained from nine contiguous coronal slices at the level of the central sulcus, shows the distribution of the following receptors: **A**, Acetylcholine muscarinic M$_1$ receptor; **B**, glutamate NMDA receptor; **C**, glutamate AMPA receptor; **D**, glutamate kainate receptor; **E**, GABA$_A$ receptor; **F**, GABA$_B$ receptor; **G**, acetylcholine muscarinic M$_2$ receptor; **H**, acetylcholine muscarinic M3 receptor; **I**, acetylcholine nicotinic $\alpha_4\beta_2$ receptor;

(Continued)

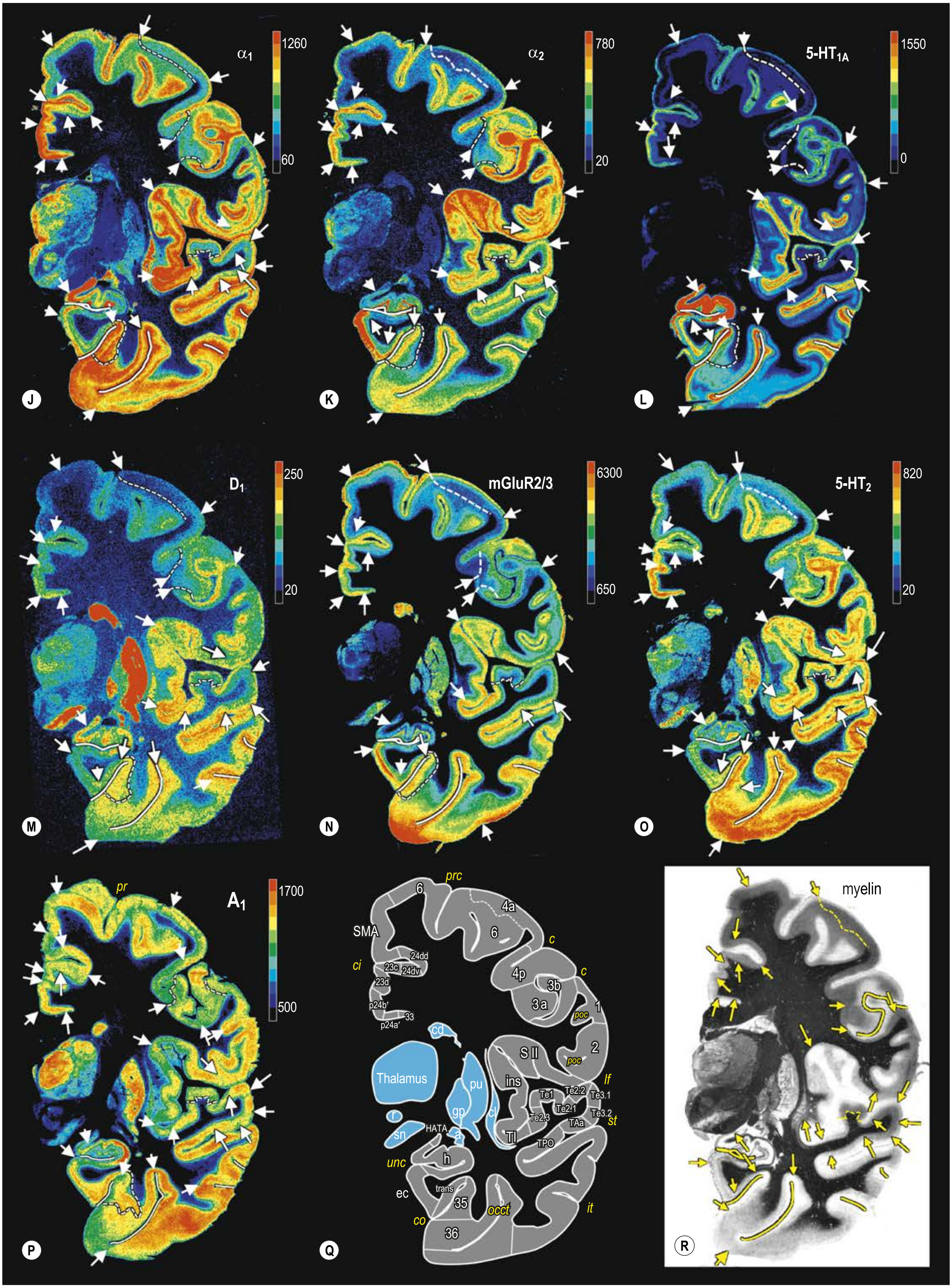
α1
1260
60
J
α2
780
20
K
5-HT1A
1550
0
L
D1
250
20
M
mGluR2/3
6300
650
N
5-HT2
820
20
O
pr
A1
1700
500
P
prc
6
4a
SMA
6
c
ci
24dd
23c
24dv
23d
4p
3b
c
3a
1
p24b′
33
poc
p24a′
cd
2
S II
poc
Thalamus
pu
ins
lf
Te1
Te2.2
Te3.1
gp
cl
Te2.1
Te2.3
Te3.2
r
TAa
st
HATA
sn
a
TI
TPO
unc
h
ec
trans
35
occt
it
co
36
Q
myelin
R

Fig. 32.29, cont'd J, noradrenaline α_1 receptor; **K**, noradrenaline α2 receptor; **L**, serotonin 5-HT$_{1A}$ receptor; **M**, dopamine D$_1$ receptor; **N**, glutamate metabotropic mGluR2/3 receptor; **O**, serotonin 5-HT$_2$ receptor; **P**, adenosine A$_1$ receptor; **Q**, map of the respective cortical areas; **R**, myelin-stained alternate section. Key and abbreviations: 1, area 1 (part of primary somatosensory cortex); 2, area 2 (part of primary somatosensory cortex); 3a, area 3a (part of primary somatosensory cortex); 3b, area 3b (part of primary somatosensory cortex); 4a, area 4a (part of primary motor cortex); 4p, area 4p (part of primary motor cortex); 6, area 6 (lateral premotor cortex); 23c, area 23c (posterior cingulate cortex); 23d, area 23d (posterior cingulate cortex); 24dd, area 24dd (midcingulate cortex); 24dv, area 24dv (midcingulate cortex); 33, area 33 (cingulate cortex); 35, area 35 (perirhinal cortex); 36, area 36 (ectorhinal cortex); a, amygdala; c, central sulcus; cd, caudate nucleus; ci, cingulate sulcus; cl, claustrum; co, colateral sulcus; ec, entorhinal cortex; gp, globus pallidus; h, hippocampal formation; HATA, hippocampo-amygdaloid transition area; ins, insula; it, inferior temporal sulcus; lf, lateral fissure; occt, occipito-temporal sulcus; p24a′, area p24a′; p24b′, area p24b′; poc, postcentral cortex; prc, precentral sulcus; pu, putamen; r, nucleus ruber; S II, secondary somatosensory cortex (parietal opercular cortex); SMA, supplementary motor cortex; sn, substantia nigra; st, superior temporal sulcus; unc, uncinate sulcus; Te1, area Te1 (primary auditory cortex); Te2.1, area Te2.1 (secondary auditory cortex); Te2.2, area Te2.2 (secondary auditory cortex); Te2.3, area Te2.3 (secondary auditory cortex); Te3.1, area Te3.1; Te3.2, area Te3.2; TI, temporo-insular area; TPO, temporo-parieto-occipital cortex; trans, transentorhinal area. Arrows label boundaries of cortical areas. Colour scales indicate densities of receptors in fmol/mg protein.

ions at resting membrane potential, i.e. the cell must be depolarized to remove magnesium ions from the channel before the influx of sodium and calcium ions can occur. Calcium ions are important for synaptic plasticity (long-term potentiation, LTP), a cellular mechanism for learning and memory. Since the effects of those synapses are potentiated, because the postsynaptic part is already depolarized by another channel, i.e. by AMPA receptors, the NMDA receptor is the molecular basis of Hebb synapses. Whereas LTP is caused by synaptic NMDA receptors, long-term depression (LTD) seems to be linked to extrasynaptic NMDA receptors. Excessive influx of calcium ions mainly via extrasynaptic NMDA receptors leads to excitotoxicity, found in Alzheimer's, Parkinson's and Huntington's diseases, amyotrophic lateral sclerosis (ALS), stroke and epilepsy. Blocking of NMDA receptors by antagonists (e.g. memantine) is thought to be potentially helpful in the therapy of Alzheimer's disease. Most NMDA receptors are preferentially expressed by pyramidal neurones and are localized postsynaptically on dendrites and dendritic spines in the supragranular layers II–III of the isocortex: their distribution is much sparser in layer IV. The glutamatergic thalamo-cortical input, which largely terminates in layer IV, is largely mediated by non-NMDA receptors. Relatively few NMDA receptors are presynaptic auto- and heteroreceptors. The highest NMDA receptor densities are found in parts of the insular, temporal (BA21, 36, 38), occipito-temporal (BA37), visual (V1, V2, V3v, V3A, V3d, FG1, FG2) and anterior cingulate (BA24, 32) cortices and the lowest densities are found in the motor (BA4, 6), part of the lateral prefrontal (BA9, 10, 46, 47), Broca's (BA44, 45), parietal (BA5, PFt) and posterior cingulate (BA23) cortices.

The ionotropic kainate receptors (see Figs 32.28–32.29) are preferentially found in the anterior cingulate (BA24, 32), orbitofrontal (BA11), lateral prefrontal (BA8–10), somatosensory (BA2) and temporal (BA42, 20–22, 36) regions, and the lowest densities are found in the motor (BA4, 6), part of Broca's region (BA45), superior parietal (BA5), occipito-temporal (BA37) and visual (V1, V2, V3A, Vd, V4v, FG1, FG) cortices. In the isocortex, kainate receptors are found with highest densities in the infragranular layers.

The metabotropic mGluR2/3 receptor (see Figs 32.28–32.29) reaches higher densities than any of the ionotropic glutamate receptors. The highest densities occur in the inferior temporal, anterior cingulate and entorhinal cortices. The vast majority of mGluR2/3 receptors occur as presynaptic autoreceptors in axonal terminals. The metabotropic mGluR1 receptor occurs only at very low concentrations in the cerebral cortex. The metabotropic mGluR5 receptor reaches highest densities in the cingulate and insular cortices.

GABA receptors are either ionotropic or metabotropic. The highest densities of the inhibitory ionotropic GABA$_A$ receptor (see Figs 32.28–32.29) occur on somata and initial axonal segments in the supragranular layers of the primary and early visual cortex (V1, V2, V3v, V4v, V3d, V3A) followed by the primary somatosensory (area 3b), inferior parietal (PFm, PGp, PGp), posterior cingulate (BA31) and primary auditory (BA41) cortices. The lowest densities occur in the motor (BA4, 6), lateral prefrontal (BA8–10), anterior cingulate (BA24, 32), inferior parietal (PFt) and ectorhinal (BA36) areas, as well as part of Broca's region (BA44).

The metabotropic GABA$_B$ receptor (see Figs 32.28–32.29) reaches generally higher densities than the GABA$_A$ receptor in the cerebral cortex. The highest densities are found in the orbitofrontal (BA11), lateral prefrontal (BA8–10, 47), primary somatosensory (BA2), superior parietal (BA5), anterior cingulate (BA24, 32), ectorhinal (BA36), insular and temporal (BA20, 21, 42) regions, and the lowest densities in the motor (BA4, 6) cortex, Broca's region (BA44, 45), inferior parietal (PFm, PGa), temporo-polar (BA38), early visual (V2, V3d, V3A, V4v) and posterior cingulate (BA23) regions.

Acetylcholine receptors are either ionotropic or metabotropic. The metabotropic muscarinic receptors (mAChRs) occur at considerably higher densities than the ionotropic nicotinic receptors (nAChRs). Five subtypes of mAChRs have been identified (M$_1$–M$_5$). The excitatory M$_1$, M$_3$ and M$_5$ receptors are coupled to Gq proteins which activate phospholipase C leading to influx of calcium ions and activation of intracellular signalling cascades. The inhibitory M$_2$ and M$_4$ receptors are coupled to G$_{i/o}$ proteins that inhibit the enzyme adenylyl cyclase and so reduce the production of cAMP.

The metabotropic excitatory M$_1$ receptor has seven transmembrane domains and suppresses potassium ion channels through G$_q$ protein coupling. The receptor mediates slow excitation. It reaches generally higher densities than the M$_2$, but lower densities than the M$_3$ receptor (see Figs 32.28–32.29). The M$_1$ receptor plays a major role in learning and attention and the pathogenesis of amyloid plaques in Alzheimer's disease: high receptor densities favour the non-amyloidogenic pathway in the metabolism of the amyloid precursor protein, whereas low expression of this receptor seems to favour the amyloidogenic pathway. Highest densities of M$_1$ receptors are found in the lateral prefrontal (BA46, 47), occipito-temporal (BA37), primary and secondary auditory (BA41, 42), temporal (BA21, 22), temporo-polar (BA38), ectorhinal (BA36), inferior parietal (PFm, PFt) and cingulate (BA24, 31) regions: nearly all of these regions are found in the default mode network. Motor (BA4, 6), lateral prefrontal (BA10), orbitofrontal (BA11), somatosensory (area 3a), early and higher visual (V2, V3A, V3d, V3v, FG1, FG2) and superior parietal (BA5) regions have the lowest densities.

The inhibitory M$_2$ and M$_4$ receptors have seven transmembrane domains, which act via G$_{i/o}$ proteins that lead finally to opening of potassium ion and closing of calcium ion channels. The M$_2$ receptor (see Figs 32.28–32.29) is located pre- and postsynaptically. Highest densities are found in layers III and IV of the primary sensory cortices, i.e. area 3b as part of the primary somatosensory cortex, BA41 (primary auditory cortex) and BA17 (primary visual cortex), where it improves the signal-to-noise ratio. Early visual areas (V2, V3v, V4v, V3d), Broca's region (BA44, 45), lateral prefrontal (BA46), inferior parietal (PGa, PGp) and anterior cingulate (BA24, 32) areas also show high receptor densities, whereas the primary sensory areas of the isocortex, the motor cortex (BA4, 6), orbitofrontal (BA11), somatosensory (BA2), parietal (BA5, PFt), temporal (BA20–22), ectorhinal (BA36), occipito-temporal (BA37) and hippocampal areas show a distinctly lower M$_2$ receptor density.

The cholinergic excitatory metabotropic M$_3$ receptor also has seven transmembrane domains and acts via G$_q$ proteins. They upregulate phospholipase C and, therefore, inositol trisphosphate and intracellular calcium as a signalling pathway. Highest densities of this receptor (see Figs 32.28–32.29) are found in the supragranular layers of superior and inferior parietal (BA5, PGa, PGp, P, Pft), medial temporal (BA21), occipito-temporal (BA37), posterior cingulate (BA31), fronto-polar (BA10), lateral prefrontal (BA9, 46) and orbitofrontal (BA11) regions and lowest densities are seen in Broca's region (BA44, 45), motor (BA4, 6), somatosensory (area 3a, BA1), temporo-polar (BA38), anterior cingulate (BA32) and visual (V2, V3A, V3d, V3v, V4v) cortices.

The neuronal nicotinic acetylcholine receptors consist of five subunits, of which each has four tansmembrane domains. The subunits are symmetrically arranged around the cation channel. Cations cause a depolarization: calcium ions act on different intracellular signal cascades that can lead to the gene regulation or release of transmitters. The nicotinic receptors are either homomeric or heteromeric (at least one α and one β subunit) combinations of 12 different subunits (α2–α10 and β2–β4). The excitatory nicotinic $\alpha_4\beta_2$ acetylcholine receptor (see Figs 32.28–32.29) reaches highest densities in the layer IV of the primary visual (V1), auditory (BA41) and somatosensory (areas 3a and 3b) cortices and layer III of the primary motor cortex (BA4). Relatively high densities are also found in the supragranular layers of the frontopolar (BA10), orbitofrontal (BA11), lateral prefrontal (BA8, 9, 46, 47), cingulate (BA24, 23, 32), higher visual (FG1) and entorhinal (BA28) cortices. Lowest densities occur in the premotor (BA6), somatosensory (BA1, 2), inferior parietal (PFm, PFt), temporal (BA20–22), occipitotemporal (BA37), early visual (V2, V3d) and ectorhinal (BA36) areas.

Noradrenaline (norepinephrine) improves the signal-to-noise ratio in the processing of sensory stimuli and enhances consolidation of long-term memory. It is also important for regulating the working memory and attention functions of the prefrontal cortex. Moderate levels of noradrenaline enhance prefrontal cortical functions via postsynaptic α_2 adrenoceptors under normal conditions; high levels of noradrenaline during stress impair prefrontal cortical functions via α_1 receptors.

The excitatory metabotropic α_1 adrenoceptor (see Figs 32.28–32.29) is coupled to the G_q protein, which causes an increase of intracellular calcium ions (via second messenger pathways), followed by a slow depolarization. Highest α_1 receptor densities are found in the supragranular layers of the cingulate (BA24, 31, 32), premotor (BA6), orbitofrontal (BA11), lateral prefrontal (BA8), somatosensory (BA2), inferior parietal (PFm), temporal (BA20–22), secondary visual (V2) and ectorhinal (BA 36) areas, whereas lowest values are found in the Broca region (BA44, 45) and the primary motor (BA4), somatosensory (area 3b, BA1), auditory (A41)and visual (V1) cortices. Low densities are also seen in posterior cingulate (BA23), inferior parietal (PFt) and early as well as higher visual areas (V3d, V3A, V4v, FG1, FG2).

Inhibitory metabotropic α_2 adrenoceptors (see Figs 32.28–32.29) is coupled to the G_i protein. This causes a low cAMP level. The α_2 adrenoceptors are generally rarer than the α_1 adrenoceptors in the cerebral cortex. The α_2 adrenoceptors are found post- and presynaptically with highest densities in the supraganular layers. The presynaptic α_2 subtype occur as autoreceptors on noradrenaline-containing neurones and terminals and cause negative feedback on noradrenaline release, while both α subtypes are found post-synaptically. Like the cholinergic muscarinic M_2 receptor, by far the highest densities of the α_2 receptors are found in the primary sensory areas (V1, area 3a, 3b, 1, 2, BA41). This is in sharp contrast to the low densities of the expression of the α_1 receptor in these regions. High densities are also present in lateral prefrontal (BA8), anterior cingulate (BA24, 32), and early visual areas (V2, V3d, V3A, V3v). Lowest densities are found in the motor (BA4, 6), superior (BA5) and inferior (PFm, PFt, PGa) parietal, temporo-polar (BA38), occipito-temporal (BA37), higher visual (FG1, FG2), and posterior cingulate (BA23, 31) areas.

The excitatory metabotropic β_1 and β_2 adrenoceptors occur at lower densities than the α subtypes in the isocortex. They are coupled to a G protein, which causes high cAMP levels. Highest β adrenoceptor densities are found in the motor and layers III and IV of the temporal cortex, whereas lowest concentrations are located in the occipital pole.

Serotonin (5-hydroxytryptamine, 5-HT) modulates the excitability of cortical neurones by binding to 14 different receptor subtypes, mainly the 5-HT_{1A}, 5-HT_{1B} and 5-HT_2 subtypes. Serotonin influences sleep and arousal processes, executive functions of the prefrontal cortex, affective behaviour, aggression, learning and memory, and modulation of pain. 5-HT receptors are localized on GABAergic interneurones or projection neurones, and on axon terminals, dendrites and the somata of glutamatergic neurones as well as on cells that modulate noradrenergic, dopaminergic and cholinergic neurones.

The inhibitory metabotropic 5-HT_{1A} receptor (see Figs 32.28–32.29) binds to G_i proteins and thus inhibits adenylate cyclase, opens potassium channels, closes calcium channels and inhibits phosphatidylinositol (PI) turnover. This receptor is a somatodendritic autoreceptor on serotoninergic neurones of the raphe nuclei throughout the brainstem and modulates the pacemaker role of these neurones in a negative feedback loop. 5-HT_{1A} receptors are predominantly found in layers I to upper III of the isocortex, localized mainly in somata and dendrites of pyramidal cells in the most superficial layers, and at a much lower level on the initial axonal segment of layer V and VI pyramidal cells. The highest densities of these receptors are seen in the most posterior part of lateral prefrontal (BA46, 47), orbitofrontal (BA11), somatosensory (BA2), inferior parietal (PFt), secondary auditory (BA42, auditory belt), temporal (BA20–22), temporo-polar (BA38), occipito-temporal (BA37), anterior cingulate (BA24), ecto- (BA36) and entorhinal (BA28) cortices. The lowest densities are found in motor (BA4, 6), primary somatosensory (area 3b) and visual (V1) regions, as well as the BA44 in the Broca region, PGa in the inferior parietal, early and higher visual (V2, V3d, V3A, V3v, FG1, FG2), and posterior cingulate (BA 23) areas.

The inhibitory metabotropic 5-HT_{1B} receptor is almost always postsynaptically localized. It is found at high density in the primary visual cortex.

The excitatory metabotropic 5-HT_2 receptors are coupled to Gq proteins; their activiation ultimately leads to an increase in the concentration of intracellular calcium ions and PI hydrolysis. The highest densities of the 5-HT_2 receptor (see Figs 32.28–32.29) are found in layers III and IV of primary sensory areas (area 3b, BA2, BA17, BA41), posterior parietal (BA5, PGa), secondary auditory (BA42), early visual (V2, V3v), middle temporal (BA21), temporo-polar (BA38), early visual (V3v), and anterior and posterior cingulate (BA24, 23, 31) regions. The lowest concentrations have been reported in the motor cortex (BA4, 6), Broca's region (BA44, 45), lateral prefrontal (BA8–10), somatosensory (BA1), inferior parietal (PGp), occipito-temporal (BA37) and higher visual (FG1 and FG2) regions. 5-HT_{2A} receptors play a major role in the psychotomimetic effects of serotoninergic hallucinogens, e.g. LSD; they are localized postsynaptically on layer II, III and V pyramidal cells, GABAergic interneurones and glial cells.

5-HT_3, 5-HT_4 and 5-HT_7 receptors are present at very low densities in the cerebral cortex. The 5-HT_3 receptor, the only ionotropic 5-HT receptor, is a ligand-gated sodium channel, found in calbindin-, calretinin- and CCK-containing interneurones. The excitatory metabotropic 5-HT_4 and 5-HT_7 receptors are coupled to G_s proteins and activate adenylate cyclase. In the isocortex, the 5-HT_4 receptor occurs at low levels and the highest densities of the 5-HT_7 receptor occur in the infragranular layers.

Dopamine receptors are represented by five metabotropic receptor subtypes each with seven transmembrane domains. The two D1-like receptor subtypes (D_1 and D_5) are coupled to the adenylate cyclase-activating G_s protein, and the three D2-like receptors (D_2, D_3, and D_4) are G_i protein-coupled receptors that inhibit adenylyl cyclase and activate potassium channels. Dopamine receptors are involved in locomotion, cognition, emotion and affect as well as neuroendocrine secretion. Both D1-like receptor subtypes are expressed in layer V pyramidal neurones of the prefrontal, premotor, cingulate and entorhinal cortex, and are localized pre- and postsynaptically on dendritic spines and shafts. Highest densities of the excitatory D_1 receptor (see Figs 32.28–32.29) are present in the primary somatosensory (area 3b, BA2), fronto-orbital (BA11), inferior parietal (PGp), occipito-temporal (BA37), primary visual (V1), early visual (V2, V3v, V3d, V3A, V4v), temporopolar (BA38) and anterior cingulate (BA24) regions. Lowest densities are found in the motor cortex (BA4, 6), Broca's region (BA44, 45), somatosensory (area 3a), inferior parietal (PGa), temporal (BA20–22, 42), ectorhinal (BA36) and higher visual (FG 1, FG2) regions.

D_2 receptors are present at very low density in the deeper layers of the entire iso- and allocortex. The relatively highest D_2 densities are found in the prefrontal and temporal regions, and the glomerular and internal plexiform layers of the olfactory bulb, hippocampus and amygdala.

D_4 receptors are present in the hippocampus and isocortical regions in pyramidal cells and GABAergic interneurones.

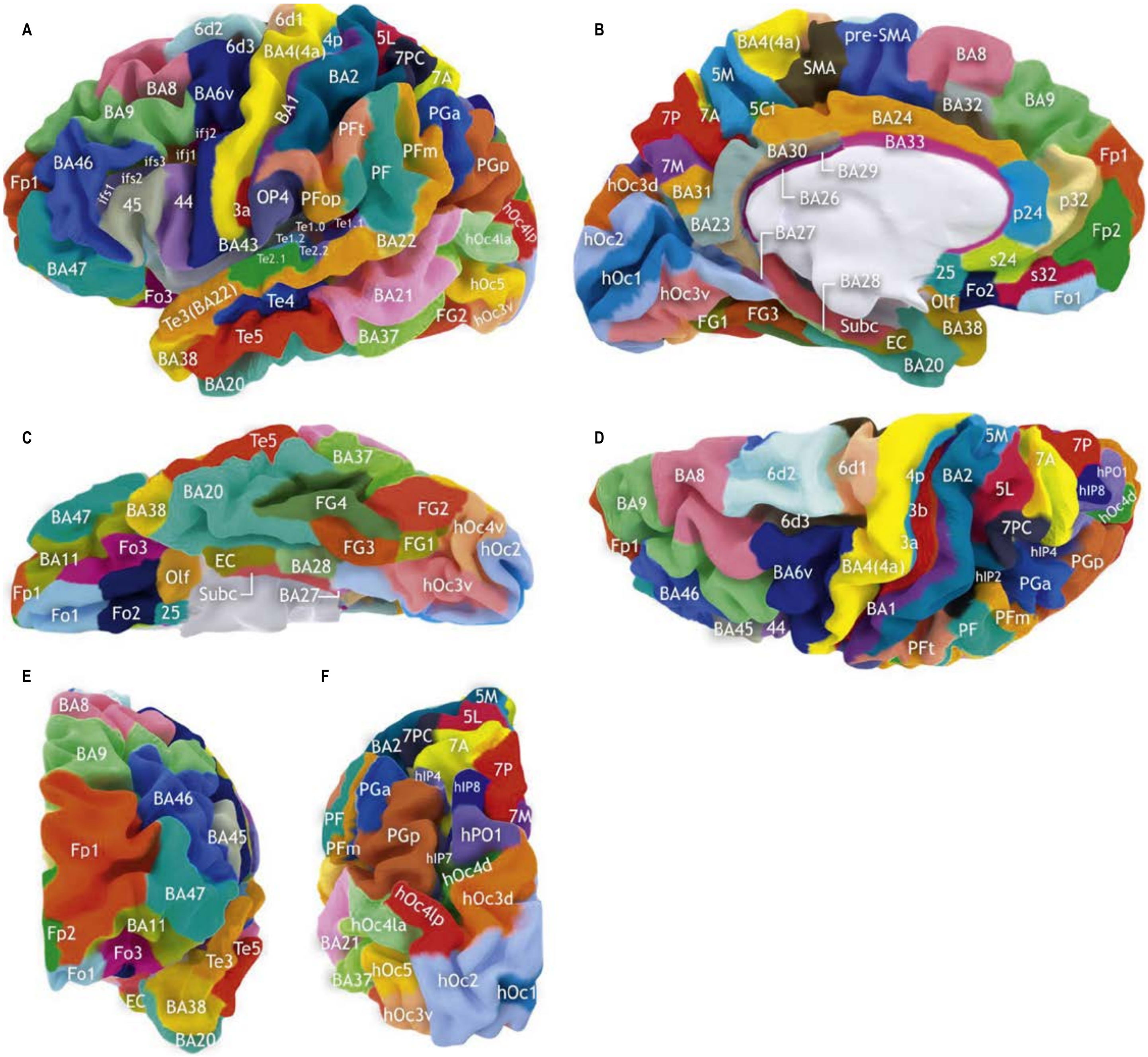
A
6d2
6d1
6d3
BA4(4a)
4p
5L
7PC
BA8
BA6v
BA2
7A
BA9
BA1
PGa
ifj2
PFt
PFm
BA46
ifs3
ifj1
PF
PGp
Fp1
ifs2
ifs1
45
44
3a
OP4
PFop
hOc4lp
Te1.0
Te1.1
Te1.2
Te2.1
Te2.2
BA43
BA22
hOc4la
BA47
hOc5
Fo3
Te3(BA22)
Te4
BA21
FG2
hOc3v
Te5
BA37
BA38
BA20
B
BA4(4a)
pre-SMA
SMA
BA8
5M
5Ci
BA32
BA9
7P
7A
BA24
BA33
BA30
Fp1
7M
BA29
hOc3d
BA31
BA26
p32
p24
Fp2
BA23
BA27
hOc2
s24
hOc1
BA28
25
s32
hOc3v
Olf
Fo2
Fo1
FG1
FG3
Subc
BA38
EC
BA20
C
Te5
BA37
BA20
FG4
BA47
BA38
FG2
hOc4v
BA11
Fo3
FG3
FG1
hOc2
EC
BA28
Olf
Fp1
Subc
BA27
hOc3v
Fo1
Fo2
25
D
5M
7P
6d1
7A
BA8
6d2
4p
BA2
hPO1
hIP8
5L
BA9
3b
hOc4d
6d3
7PC
3a
Fp1
hIP4
PGp
BA6v
BA4(4a)
hIP2
PGa
BA46
BA1
PF
PFm
BA45
44
PFt
E
BA8
BA9
BA46
BA45
Fp1
BA47
Fp2
BA11
Fo3
Te5
Te3
Fo1
EC
BA38
BA20
F
5M
5L
BA2
7PC
7A
hIP4
7P
PGa
hIP8
PF
7M
PGp
hPO1
PFm
hIP7
hOc4d
hOc3d
hOc4lp
hOc4la
BA21
BA37
hOc5
hOc2
hOc1
hOc3v

Fig. 32.13 A map of cytoarchitectonic parcellation of the cerebral cortex by Brodmann (1910) and the Jülich/Düsseldorf group. Brodmann areas are indicated with BA. Areas ifs1, ifs2, ifj1 and ifj2 are subdivisions of the inferior frontal sulcus cortex. EC, entorhinal cortex; Subc, subiculum; Olf, olfactory area. (Figure created by Daniele Cancemi, Karl Zilles and Marco Catani.)

Glutamate receptors

Available with the *Gray's Anatomy* e-book

GABA receptors

Available with the *Gray's Anatomy* e-book

Monoaminergic receptors

Available with the *Gray's Anatomy* e-book

FUNDAMENTAL SEGREGATION OF CORTICAL STRUCTURES

The two major architectonic types in the cerebral cortex are the isocortex and the allocortex. Isocortex is also called neocortex because it developed late during brain evolution, coinciding with the appearance of the first mammalian species. All areas of isocortex have a six-layered structure that emerges during the late fetal period. Isocortex forms the largest part of the human cortex (Fig. 32.30). It is described as homogenetic because of its uniform pattern of lamination (Brodmann 1909): adult isocortex is either homotypical (eulaminate) or heterotypical (koniocortical or dysgranular/agranular). Allocortex is heterogenetic (Brodmann 1909) and is distinguished developmentally by the fact that it does not develop through the cortical plate. In general, allocortex is composed of fewer layers than the isocortex (e.g. in the hippocampus and olfactory cortex), although the entorhinal cortex has more than six layers. Allocortex is subdivided into paleocortex and archicortex (hippocampus and part of the cingulate cortex). Transition zones, where the number and thickness of cortical layers vary, occur between the allo- and isocortex and are called peripaleo-, periarchi- and proisocortex, depending on the adjoining parts of allo- and isocortex (Fig. 32.31).

Eulaminate isocortex retains the six-layered structure with a well-defined layer IV and is found in most of the prefrontal, parietal, temporal and occipital cortices. Heterotypical koniocortical cortex is found in the primary somatosensory (area 3b), visual (BA17) and auditory (BA41) areas that are characterized by the presence of layer IV granule cells in the more superficial layers (granularization). Heterotypical dysgranular/agranular cortex is observed in cortical

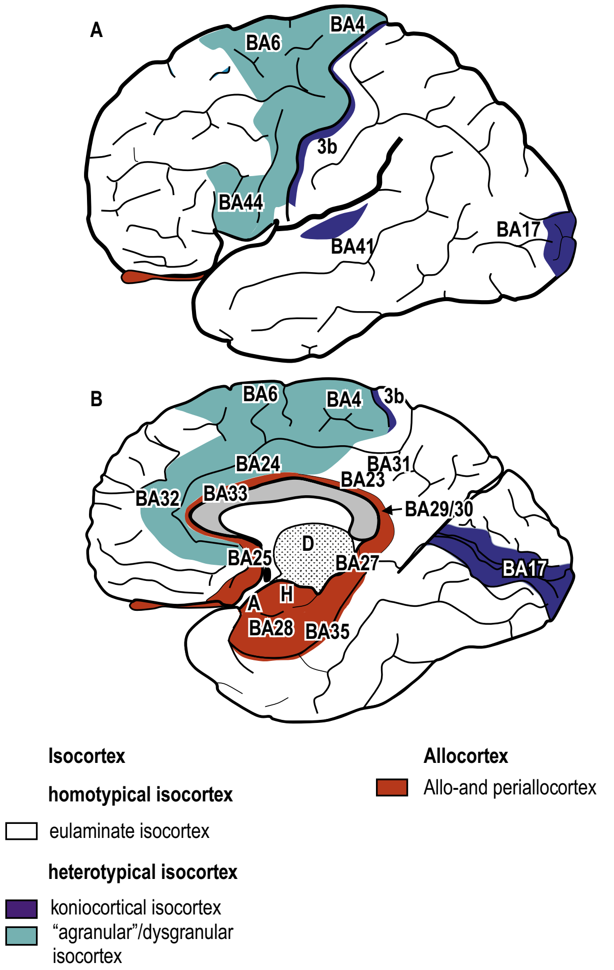

Fig. 32.30 The principal cortical types in lateral (**A**) and medial (**B**) views of the human brain. The eulaminate (white, most areas of the isocortex), koniocortical (blue, areas 3b, BA17, BA41) and 'agranular'/dysgranular regions (turquoise, BA4, BA6, BA44, BA32) of the iso- and proisocortex, as well as the allo- and periallocortex (orange) are shown. Abbreviations: A, amygdala; D, diencephalon, H, hippocampus retrocommissuralis.

areas where layer IV appears to be invaded by pyramidal cells from layers III and V to varying degrees, so that layer IV appears very thin and sometimes interrupted (dysgranular) or is not visible as a distinct layer (agranular) in Nissl-stained sections. The motor cortex (BA4 and BA6), prefrontal area BA8, anterior part of the insular lobe, posterior part of Broca's language region (BA44), and the rostral area 32 of the anterior cingulate cortex have a dysgranular or agranular cytoarchitectonic appearance.

Paleo- and peripaleocortex

The paleocortex consists of the olfactory bulb, the area retrobulbaris (anterior olfactory nucleus), the tuberculum olfactorium and the area prepiriformis. The peripaleocortex is found in the most anterior part of the insular cortex adjacent to the paleocortex (Fig. 32.31).

The olfactory nerves arise from olfactory receptor neurones in the olfactory mucosa. The axons collect into numerous small bundles ensheathed by glia and surrounded by layers of meninges and enter the anterior cranial fossa by passing through the foramina in the cribriform plate of the ethmoid bone. They are attached to the inferior surface of the olfactory bulb lying at the anterior end of the olfactory sulcus on the orbital surface of the frontal lobe, and terminate in the olfactory bulb.

Olfactory bulb

The olfactory bulb is continuous posteriorly with the olfactory tract, through which the output of the bulb projects directly to the ipsilateral retrobulbar area (anterior olfactory nucleus), olfactory tubercle, prepiriform area, amygdala and rostral entorhinal cortex. There is a clear laminar structure in the olfactory bulb (**Fig. 32.32A**). From the surface inwards, the laminae are the olfactory nerve layer, glomerular layer, external plexiform layer, mitral cell layer, internal plexiform layer and granule cell layer (**Fig. 32.32B**). The olfactory nerve layer is formed by the unmyelinated axons of the olfactory receptor neurones. These axons divide and synapse on terminal dendrites of secondary olfactory neurones (mitral, tufted and periglomerular cells) forming glomeruli. The external plexiform layer contains the principal and secondary dendrites of the mitral and tufted cells. The mitral cell layer is a thin sheet composed of the cell bodies of mitral cells, each of which sends a single principal dendrite to a glomerulus, secondary dendrites to the external plexiform layer and a single axon to the olfactory tract. It also contains a few granule cell bodies. The internal plexiform layer contains recurrent and deep axon collaterals of mitral and tufted cells and granule cell somata. The granule cell layer contains the majority of the granule cells and their superficial and deep processes; numerous centripetal and centrifugal fibres pass through the layer.

Different odour molecules are represented by different patterns of spatial activity in the olfactory bulb (Shepherd 2006). The axons of the principal neurones in the olfactory bulb (the mitral and tufted cells) form its output via the olfactory tract. These cells are morphologically similar and probably use glutamate or aspartate as their neurotransmitter. Mitral cells span the layers of the bulb and receive the sensory input at their glomerular tufts. The axons of mitral and tufted cells are parallel output pathways from the olfactory bulb. Periglomerular and granule cells are the main types of interneurones in the olfactory bulb. The majority of periglomerular cells are dopaminergic (cell group A15), but some are GABAergic. Granule cells are similar in size to periglomerular cells; they lack an axon and therefore resemble amacrine cells in the retina. Granule cells are GABAergic and have two principal spine-bearing dendrites that pass radially in the bulb. They are likely to be a powerful inhibitory influence on the output neurones of the olfactory bulb. D_1 receptors are present mainly in the internal granular and plexiform layers. The highest densities of D_2 receptors are found in the glomerular and internal plexiform layers of the olfactory bulb.

Neurones of the retrobulbar area and collaterals of pyramidal neurones in the olfactory cortex project to the granule cells of the olfactory bulb. Cholinergic neurones in the horizontal limb nucleus of the diagonal band of Broca, which is part of the basal forebrain cholinergic system, project to the granule cell layer and to the glomerular layer. Other afferents to the granule cell layer and the glomeruli arise from the noradrenergic pontine locus coeruleus and the serotonergic mesencephalic raphe nucleus.

Retrobulbar area

The granule cell layer of the olfactory bulb extends into the olfactory tract with scattered medium-sized multipolar neurones that constitute the retrobulbar area (see Fig. 32.31; **32.32C**). This area extends from the caudal part of the olfactory bulb to the point where the olfactory peduncle joins the cortex of the frontal lobe. Many centripetal axons from mitral and tufted cells relay to this area, and axons from the retrobulbar area join the remaining direct fibres from the bulb and continue into the olfactory tract.

As the olfactory tract approaches the anterior perforated substance, it flattens and splays out as the olfactory trigone. Fibres of the tract continue from the caudal angles of the trigone as diverging medial and lateral olfactory tracts that border the anterior perforated substance (see Fig. 32.31). The lateral olfactory tract follows the anterolateral margin of the anterior perforated substance to the insula, where it bends posteromedially to merge with an elevated region, the gyrus semilunaris, at the rostral margin of the uncus in the temporal lobe. The tenuous grey layer that covers the lateral olfactory tract merges laterally with the gyrus ambiens. The grey layer over the lateral olfactory tract and the gyrus ambiens form the prepiriform area, which extends caudally into the entorhinal area of the parahippocampal gyrus. The prepiriform area, periamygdaloid regions and the entorhinal area (BA28) together make up the piriform cortex. The anterior perforated substance is continuous laterally with the peduncle of the temporal stem and the amygdaloid complex, and medially with the septal region.

The main targets of the lateral olfactory tract are the prepiriform area, amygdala and rostral entorhinal cortex. Neurones in the prepiriform area project to targets that include the orbitofrontal and agranular insular cortex, thalamus (especially the medial dorsal thalamic nucleus), hypothalamus, amygdala and hippocampal formation.

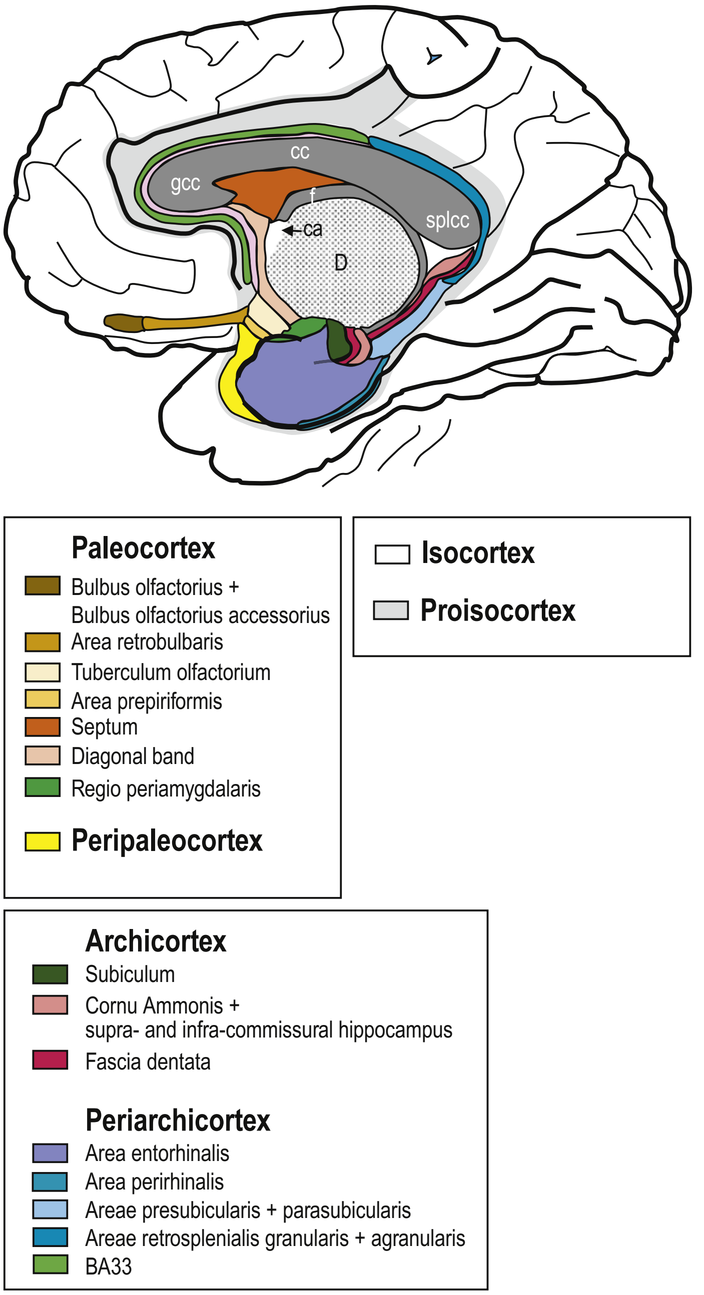

Fig. 32.31 The paleo-, peripaleo-, archi-, periarchi-, proiso- and isocortical regions of the human brain. Abbreviations: Ca, anterior commissure; cc, corpus callosum; D, diencephalon; f, fornix; gcc, genu of the corpus callosum; splcc, splenium corporis callosi of the corpus callosum.

Prepiriform area

The prepiriform area (BA51, primary olfactory cortex) is the largest olfactory cortical area and extends from the lateral olfactory tract to the limen insulae and temporal cortex (**Fig. 32.33**). This paleocortical area can be subdivided into a frontal portion at the base of the frontal lobe, and a temporal portion in the region between the frontal and temporal lobes. It is partly underlain by a ventral extension of the claustrum (endopiriform nucleus) and shows the prototypical three-layered structure of the paleocortex, i.e. a superficial molecular layer, thin intermediate densocellular layer and a deep multiform layer. The superficial molecular layer is differentiated into three sublayers: an outermost, cell-poor sublayer (a), an intermediate sublayer (b) which contains many glial cells and the fibres of the lateral olfactory tract; and the deepest sublayer (c) which has a lower cell density. The intermediate densocellular layer varies in thickness and appears to be interrupted; it contains pyramidal and polymorphic cells with dendrites that extend in the first layer. The deep multiform layer consists of the largest cells in the prepiriform area with an intermediate packing density. A very thin, nearly cell-free sheet (external capsule) separates the multiform layer from the underlying claustrum.

The prepiriform area receives afferents from the olfactory bulb, retrobulbar area, olfactory tubercle, septum, amygdala, orbitofrontal cortex, and the contralateral prepiriform area (via the anterior commissure). Efferent reciprocal connections are found in all these areas, and in the anterior insular and hippocampal cortices, claustrum and ventral putamen.

Neuroimaging studies in humans demonstrate activity in the prepiriform cortex during olfactory learning and memory tasks as well as in olfactory-induced motivational and cognitive states: olfactory dysfunction is a major finding in anhedonia.

Olfactory tubercle

The olfactory tubercle is located caudal to the retrobulbar area and medial to the prepiriform area in the anterior perforated substance. Its three-layered structure is poorly differentiated in the human brain (see Figs 32.31, 32.33C). Numerous islands of Calleja, consisting of very small and densely packed granule cell neurones, are found in all layers of the tubercle and between the tubercle and the ventral striatum. The olfactory tubercle receives input from the olfactory part of the amygdala and from the olfactory bulb via the lateral olfactory tract and sends efferents to the ventral pallidum. Medium spiny cells are the dominant cell type; they resemble neurones in the striatum.

Periamygdaloid cortex

The periamygdaloid cortex (see Figs 32.31, 32.33) is located ventral to the prepiriform area and medial to the entorhinal area. It is a cytoarchitectonically heterogeneous region with several subdivisions, all of which receive olfactory input from the olfactory bulb and other paleocortical regions. The periamygdaloid cortex is therefore considered part of the olfactory cortex.

Between the piriform cortex and the laterally adjoining insular cortex, a peripaleocortical transition zone (BA16, Brodmann 1905) (see Fig. 32.31) can be demonstrated in non-human primate brains that has been called the peripaleocortical claustral region by Stephan (1975), because of its close topographical relation to the claustrum. BA16 is the least differentiated area in the insular cortex and shows an agranular architecture. It seems to be comparable with the areas ID and TI of von Economo and Koskinas (1925) and shows a four-layered type (for details see Stephan 1975).

Connections of the peripaleocortical claustral region with the prepiriform cortex, amygdala, adjoining isocortex, claustrum and contralateral BA16 have been described in primates. The strong connections with the piriform cortex make an olfactory function of the peripaleocortical insular cortex probable, but a definite statement about the function of area 16 in the human brain is presently not possible.

Amygdala

The amygdala is located in the rostral part of the temporal lobe at the transition between the piriform cortex, ventral striatum and claustrum dorsally, the entorhinal cortex ventrally and the hippocampus posteriorly (**Fig. 32.34**). It forms the ventral, superior and medial walls of the tip of the temporal (inferior) horn of the lateral ventricle, and neighbours the inferomedial margin of the claustrum. Fibres of the external capsule and basal forebrain, including the cholinergic magnocellular nucleus basalis of Meynert, partially separate the amygdala from the putamen and globus pallidus. Laterally, the amygdala lies close to the optic tract. The rostral portions of the amygdala are bordered medially by the piriform cortex. The amygdala reaches the medial surface of the temporal lobe by forming the semilunar gyrus, which is separated from the ventrally located entorhinal cortex by the semi-anular sulcus. At a caudal level, the amygdala is surrounded laterally by the temporal horn of the lateral ventricle. The head of the hippocampus is interposed between the amygdala and entorhinal cortex. Transition zones are present between the amygdala and the surrounding structures.

The amygdala is composed of numerous nuclei that have different cyto-, myelo- and receptor architectonics: they can be assigned to three major groups named superficial, basolateral and centromedial (Heimer et al 1999).

The superficial (cortex-like) group consists of the anterior amygdaloid area, amygdalopiriform transition area, amygdalohippocampal transition area, posterior cortical nucleus and ventral cortical nucleus. All parts of this group have a superficial molecular layer, which is characteristic of the cerebral cortex, overlying a densely packed cellular layer, and so resemble a two-layered cortex (cortex-like nuclei). The term

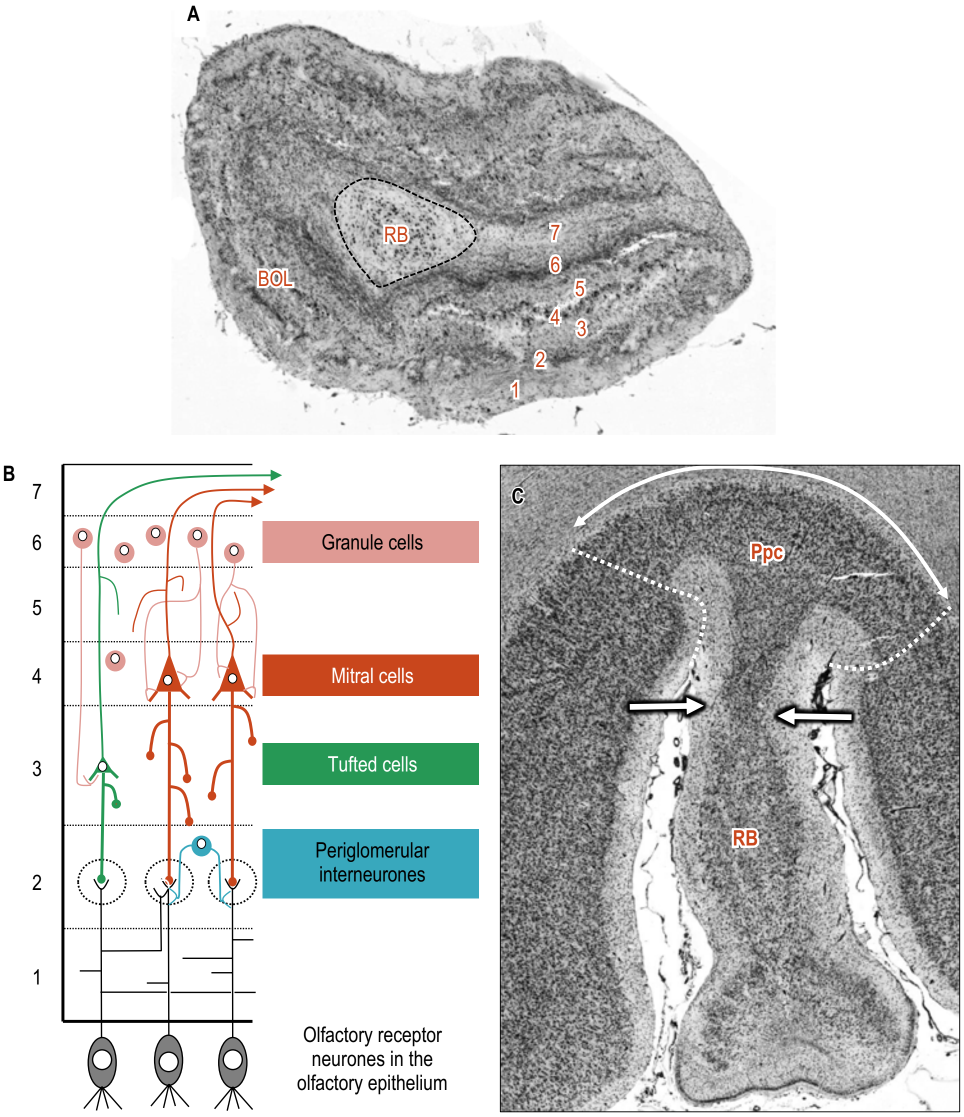
A
RB
BOL
7
6
5
4
3
2
1
B
7
6
5
4
3
2
1
Granule cells
Mitral cells
Tufted cells
Periglomerular interneurones
Olfactory receptor neurones in the olfactory epithelium
C
Ppc
RB

Fig. 32.32 The paleocortical areas of the human brain. **A**, Olfactory bulb (bulbus olfactorius, BOL) with the most rostral part of the retrobulbar area (area retrobulbaris, RB). **B**, Major cell types and connections in the olfactory bulb. **C**, Retrobulbar area (area retrobulbaris, RB) and peripaleocortex (Ppc). Layers of the olfactory bulb: 1, stratum fibrosum externum (olfactory nerve layer); 2, stratum glomerulosum; 3, stratum plexiforme externum; 4, stratum mitrale; 5, stratum plexiforme internum; 6, stratum granulosum internum; 7, tractus olfactorius.

nucleus is therefore misleading, because these nuclei possess a cortical architecture. However, this group develops in an outside-in manner typical of non-cortical structures, whereas isocortex develops in a characteristic inside-out manner. Comparative anatomical studies suggest that this part of the amygdala should be classified as paleocortex. The anterior amygdaloid area is found in the dorsal lip of the entorhinal sulcus (see Fig. 32.34). Most of the loosely packed neurones of this area are small and spindle-shaped. Magnocellular neurones of the basal nucleus of Meynert are visible adjacent to the anterior amygdaloid area and the central and medial nuclei. The amygdalopiriform transition area, which borders the entorhinal area dorsally and the prepiriform cortex ventrally, contains cell clusters (medial) and loosely packed neurones (lateral) of varying shapes. The amygdalohippocampal transition area contains darkly stained and densely packed neurones. The ventral cortical nucleus consists of fork-shaped neurones (dorsal) and radially arranged and densely packed neurones (ventral).

The basolateral group consists of lateral, basolateral, basomedial and paralaminar nuclei. This group contains a high density of neurones of variable size. The lateral nucleus has dorsomedial and ventrolateral subnuclei. The basolateral nucleus contains the largest cells of the amygdala: it is commonly divided into dorsal magnocellular and intermediate parvocellular basal nuclei and a ventral band of darkly staining and densely packed cells, the paralaminar nucleus, which borders the basolateral and lateral nuclei. It has been suggested that the basolateral nuclear complex should be considered as a quasicortical structure because it shares several characteristics with the cortex. Although it lacks a laminar structure, it has direct, often reciprocal, connections with adjacent temporal and other areas of cortex, and it projects to the motor or premotor cortex. It receives direct cholinergic and non-cholinergic inputs from the magnocellular system in the basal forebrain and has reciprocal connections with the mediodorsal thalamus. The distribution of small peptidergic neurones in the basolateral nuclear group, e.g. those containing neuropeptide Y (NPY), somatostatin (SOM) and cholecystokinin (CCK), are also similar in form and density to those found in the adjacent cortex of the temporal lobe. Projection neurones from this part of the amygdala appear to utilize, at least in part, the excitatory amino acids glutamate or aspartate as transmitters. Moreover, they project to the ventral striatum rather than to hypothalamic and brainstem sites. Thus, it may be appropriate to consider this part of the amygdaloid complex as a polymodal cortex-like area, separated from the cerebral cortex by fibres of the external capsule. The vast majority of projection neurones in the basolateral group are excitatory spiny pyramidal and modified pyramidal neurones, intermingled with nonpyramidal interneurones. Nonpyramidal projection neurones in the basolateral group that target the mediodorsal nucleus of the thalamus also point to a position of the basolateral group between the cerebral cortex and noncortex-like deeper nuclei.

The neocortex-like centromedial group consists of medial and central nuclei. The basal nucleus of Meynert is a dorsal neighbour. The centromedial group contains mainly GABAergic and peptidergic projection neurones: small neurones are densely packed in the medial nucleus and sparse in the central nucleus. The bed nucleus of the stria terminalis at the frontal (anterior) horn of the lateral ventricle is surrounded medially by the lateral septum and fornix, and medially by the striatum. It is connected with the central and medial nuclei of the amygdala by the sublenticular extended amygdala (heterogeneous cell groups in the substantia innominata) that is often referred to as the anterior amygdaloid area. Whereas the central nucleus projects to areas that are involved in fear and stress responses, the medial nucleus mainly modulates food intake and sexual behaviour: both nuclei play a major role in endocrine homeostasis.

A consistent feature of the intrinsic connections among amygdaloid nuclei is that they arise primarily in the lateral and basal nuclei, and terminate in the central and medial nuclei, suggesting a largely unidirectional flow of information. The lateral nucleus projects to all divisions of the basal nucleus, accessory basal nucleus, paralaminar and anterior cortical nuclei, and less heavily to the central nucleus; it receives few afferents from other nuclei. The magnocellular, parvocellular and intermediate

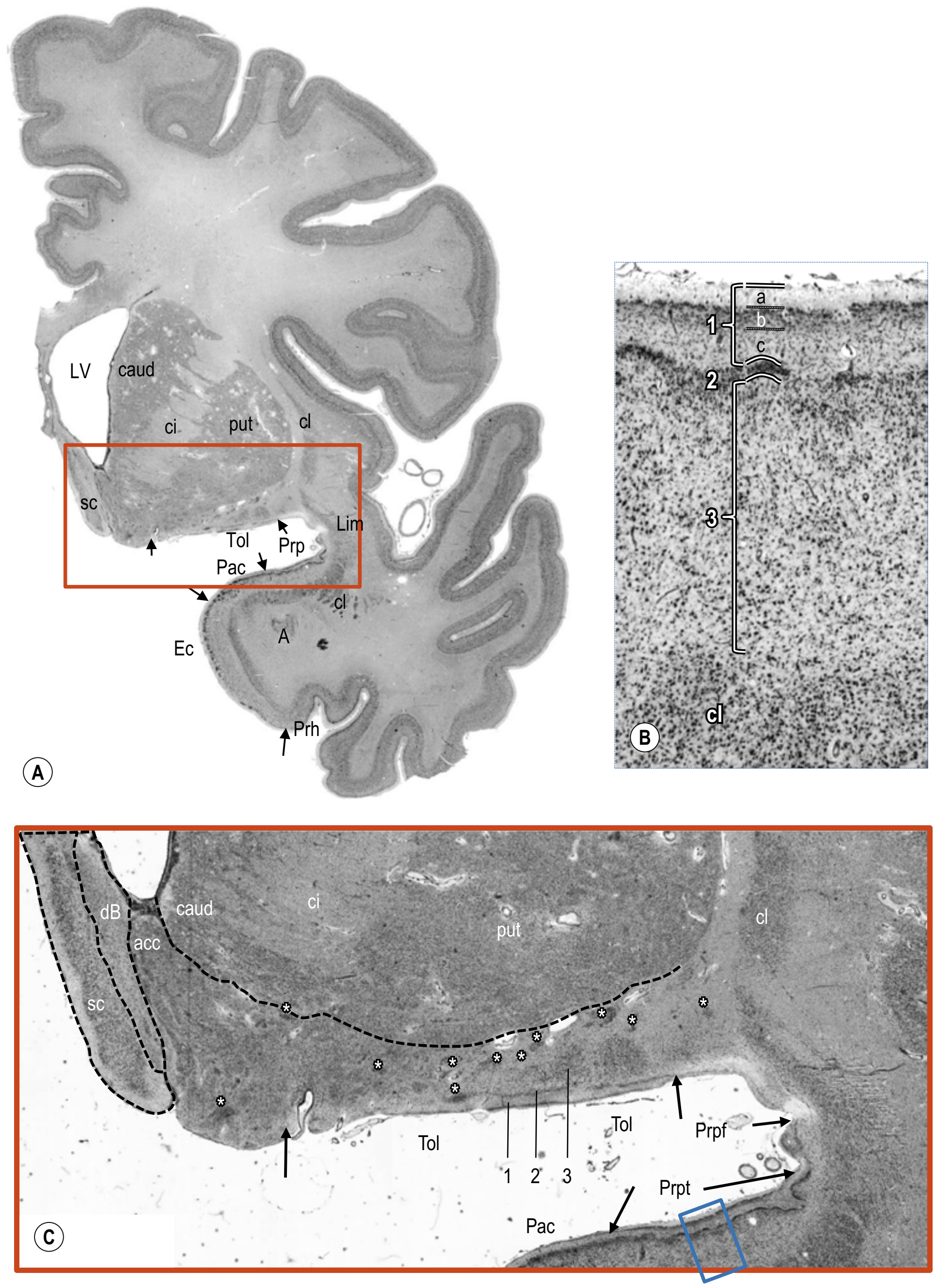

Fig. 32.33 A–B, The paleocortical areas of the human brain. **A**, Frontal section through a right hemisphere. **B**, Area prepiriformis temporalis. Layers of the prepiriform area: 1, stratum moleculare; 1a, non-myelinated outer zone; 1b, cell-rich intermediate zone; 1c, myelinated inner zone (lateral olfactory tract); 2, stratum densocellulare; 3, stratum multiforme. **C**, Tuberculum olfactorium. Layers of the olfactory tubercle: 1, stratum moleculare; 2, stratum densocellulare; 3, stratum multiforme. Asterisks highlight islands of Calleja. Abbreviations: A, amygdala; acc, nucleus accumbens; caud, caudate nucleus; ci, internal capsule; cl, claustrum; dB, diagonal band of Broca; Ec, entorhinal cortex; Lim, limen insulae (temporal stem); LV, lateral ventricle; Pac, periamygdaloid cortex; Prh, perirhinal cortex; Prp, prepiriform cortex; Prpf, frontal prepiriform area; Prpt, temporal prepiriform area; put, putamen; sc, subcallosal gyrus; Tol, olfactory tubercle.

parts of the basal nucleus project to the accessory basal, central (especially the medial part) and medial nuclei, as well as to the periamygdaloid cortex and the amygdalohippocampal area. The accessory basal nucleus projects densely to the central nucleus, especially its medial division, as well as to the medial and cortical nuclei. Its major intra-amygdaloid afferents arise from the lateral nucleus. The medial nucleus projects to the accessory basal, anterior cortical and central nuclei, as well as to the periamygdaloid cortex and amygdalohippocampal area, while afferents arise especially from the lateral nucleus. The intrinsic connections of the cortical nucleus are not well understood. The posterior part of the cortical nucleus projects to the medial nucleus but it has been difficult to differentiate this projection from that arising in the amygdalohippocampal area. The central nucleus projects to the anterior cortical nucleus and the various cortical transition zones and forms an important relay for afferents from many of the amygdaloid nuclei, especially the basal and accessory basal nuclei; it has major extrinsic connections.

The amygdala is connected with both cortical areas of the telencephalon and subcortical structures. Bidirectional amygdalo-cortical connections are established with the iso- and pro-isocortex of the temporal, prefrontal, cingulate and insular areas. They run in the external capsule, whereas the allocortical connections with the entorhinal cortex, posterior parahippocampal gyrus, Ammon's horn and subiculum are located in the white matter between the entorhinal cortex and amygdala. The subcortical connections of the amygdala are mediated by the stria terminalis, the ventral amygdalofugal pathway and the medial forebrain bundle. The stria terminalis runs parallel to the fornix and medial to the body and tail of the caudate nucleus; it connects the caudal medial regions of the amygdala to the bed nucleus of the stria terminalis, hypothalamus and nucleus accumbens. Some projections of the stria terminals terminate in the olfactory cortex. The ventral amygdalafugal pathway is a shorter pathway running parallel and inferior to the anterior commissure and connecting the amygdala to the hypothalamus.

The medial forebrain bundle contains many fibres that connect the amygdala to the brainstem. Noradrenergic fibres arise primarily from the locus coeruleus; serotoninergic fibres arise from the dorsal and, to some extent the median, raphe nuclei; dopaminergic fibres arise primarily in the midbrain ventral tegmental area (A10). The basal and parvocellular accessory basal nuclei, the amygdalohippocampal area and nucleus of the lateral olfactory tract receive a very dense cholinergic innervation that arises from the magnocellular nucleus basalis of Meynert.

The amygdala plays a role in a variety of functions, including arousal and attention, goal-directed behaviour, fear responses, adaptation to stress, social behaviour, olfaction, food intake and sexual behaviour (see also the limbic system). Damage to the amygdala is often due to neurodegenerative disorders including Alzheimer's, Parkinson's and Huntington's disease, encephalitis, temporal lobe epilepsy and autism. The anatomical basis for these functions and dysfunctions is the multimodal input converging from many cortical and subcortical regions to the amygdala. Functional analyses using imaging also show an activation of the amygdala by faces and emotional stimuli. Bilateral complete calcification of the amygdala is characteristic of the rare Urbach–Wiethe syndrome (Fig. 32.36), which is associated with impaired emotional processing of both negative and positive stimuli.

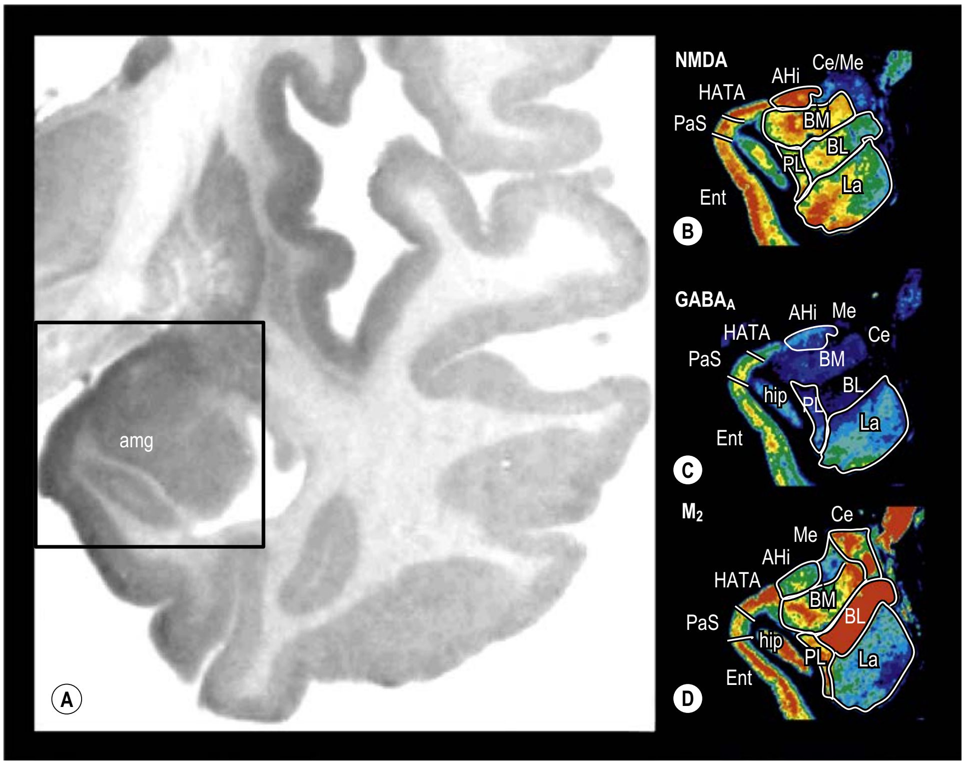

Fig. 32.35 The distribution of receptors in the human amygdala. **A**, Magnetic resonance image (4 Tesla, spatial resolution 350 mm isotropic). **B**, Glutamate NMDA receptor. **C**, GABA$_A$ receptor. **D**, Acetylcholine muscarinic M$_2$ receptor. Abbreviations: Ahi, amygdalo-hippocampal transition area; amg, amygdala; BL, basolateral nucleus; BM, basomedial nucleus; Ce, central nucleus; Ent, entorhinal cortex; HATA, hippocampal–amygdaloid transition area; hip, hippocampus; La, nucleus lateralis; Me, medial nucleus; PaS, parasubiculum; PL, paralaminar nucleus.

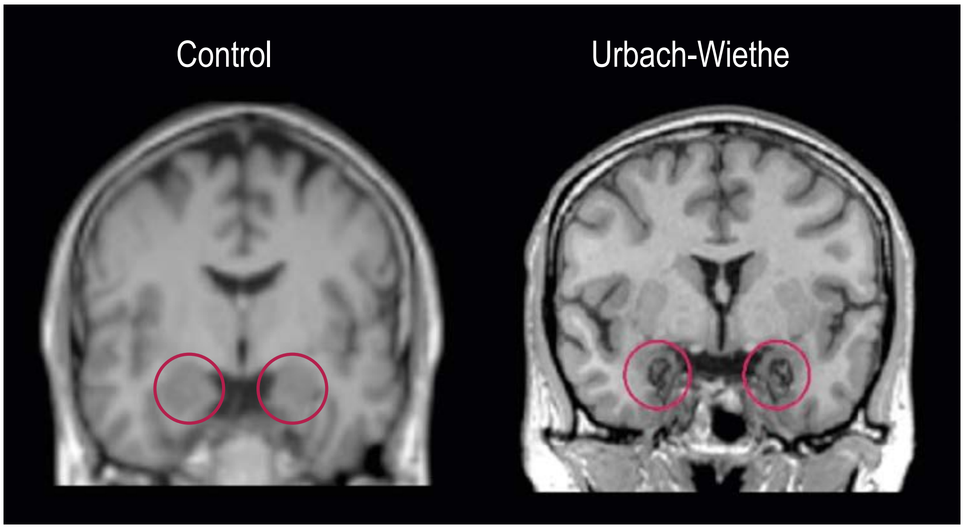

Fig. 32.36 Magnetic resonance imaging of the amygdala in a healthy control subject (left) and the Urbach–Wiethe syndrome (right). (Adapted with permission from Hurlemann R, Schlaepfer T, Matusch A et al 2009 Reduced 5-HT$_{2A}$ receptor signaling following selective bilateral amygdala damage. Social Cogn Affect Neurosci 4:79–84.)

Differences in transmitter receptor densities support the cytoarchitectonic subdivision of the amygdala and its functional specializations (Fig. 32.35). The amygdalohippocampal transition area shows the highest α_1 and α_2 adrenoceptor densities in the amygdala. The amygdalopiriform transition area has the highest serotoninergic 5-HT$_{1A}$ receptor density. The border of the ventral cortical nucleus with the medial nucleus is marked by higher densities of cholinergic (except for M$_2$), glutamatergic, serotoninergic and GABAergic receptors when compared to its neighbours. Densities of α_1 and 5-HT$_{1A}$ receptors are higher in the ventral cortical nucleus than in the adjacent basomedial nucleus. There are higher densities of muscarinic M$_2$, nicotinic $\alpha_4\beta_2$, α_1 and α_2 receptors in the anterior amygdaloid area than in the neighbouring basomedial nucleus. The central nucleus has the highest kainate receptor densities. The medial nucleus has relatively low receptor densities, but its border with the anterior amygdaloid area is highlighted by higher densities of benzodiazepine binding sites and GABA$_B$ receptors in the medial nucleus. Lower M$_1$, M$_3$ and higher α_1 receptor densities in the medial nucleus mark its border with the central nucleus. The lateral nucleus displays the highest GABA$_A$ receptor density in the amygdala. The basolateral nucleus has higher M$_2$ and lower GABA$_A$ receptor and benzodiazepine binding site densities as compared to the lateral nucleus. The basomedial nucleus has higher α_1 receptor densities than the basolateral nucleus. The paralaminar nucleus is demarcated by the highest density of M$_1$ receptors in the amygdala and also has higher 5-HT$_{1A}$ receptor densities than the dorsally adjacent nuclei. Its border with the basolateral nucleus is clearly delineated by the higher AMPA, kainate, M$_1$, M$_3$ receptor and benzodiazepine binding site densities in the paralaminar nucleus.

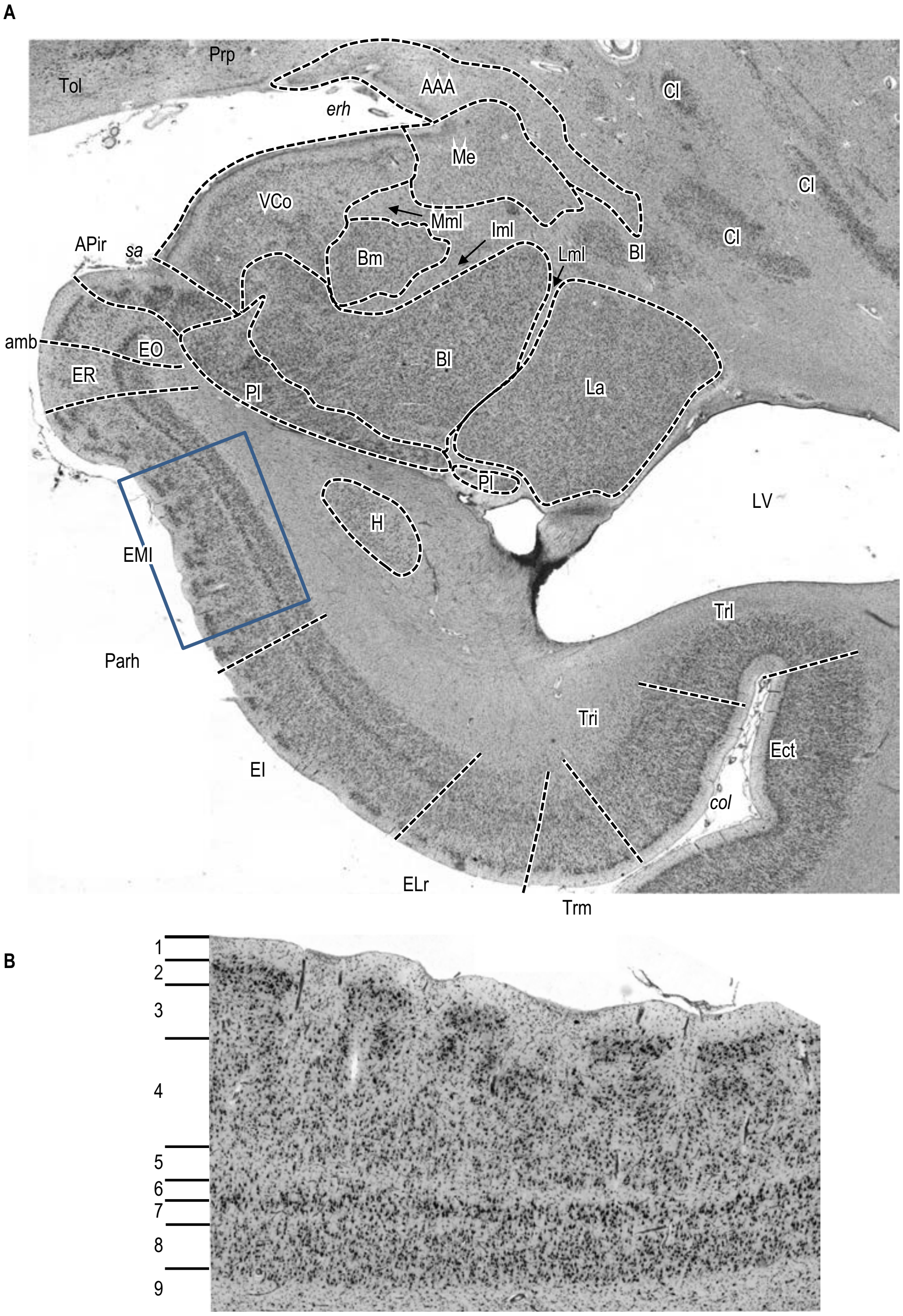

Fig. 32.34 **A**, A frontal section through the amygdala, entorhinal (BA28), perirhinal (transentorhinal, BA35) and ectorhinal (BA36) cortex (Nissl stain). Abbreviations: AAA, anterior amygdaloid area; amb, Gyrus ambiens; APir, amygdalopiriform transition area; Bl, Ncl. basolateralis; Bm, Ncl. basomedialis; Cl, claustrum; col, sulcus collateralis; Ect, area ectorhinalis (BA36); El, intermediate subfield of the entorhinal area (part of BA28); ELr, lateral rostral subfield of the entorhinal area (part of BA28); EMl, medial intermediate subfield of the entorhinal area (part of BA28); EO, olfactory subfield of the entorhinal area (part of BA28); ER, rostral subfield of the entorhinal area (part of BA28); erh, sulcus entorhinalis; H, hippocampus; Iml, intermediate medullary lamina; Lml, lateral medullary lamina; La, nucleus lateralis; LV, lateral ventricle; Mml, medial medullary lamina; Me, nucleus medialis; Parh, gyrus parahippocampalis; Pl, nucleus paralaminaris; Prp, prepiriform cortex; sa, semianular sulcus; Tol, tuberculum olfactorium; Tri, intermediate transentorhinal area (part of BA35); Trl, lateral transentorhinal area (part of BA35); Trm, medial transentorhinal area (part of BA35); VCo, ventralis corticalis. **B**, The layers of the entorhinal area (higher magnification of area within blue rectangle): 1, molecular layer; 2, pre-alpha layer; 3, pre-beta layer; 4, pre-gamma layer; 5, dissecans layer; 6, pri-alpha layer; 7, pri-beta layer; 8, pri-gamma layer; 9, white matter.

Archi- and peri-archicortex and the concept of the limbic system

The limbic system is composed of interconnected cortical and subcortical regions (**Fig. 32.37**) dedicated to memory, and linking visceral states and emotion to cognition and behaviour (Mesulam 2000; Heimer and Van Hoesen 2006). The Latin term *limbus* means border and was originally used by Thomas Willis (1664) to describe the parahippocampal and cingulate gyri encircling the thalamus. Paul Broca suggested that the limbic structures might be associated mainly with olfaction and for many years the term *rhinencephalon* ('olfactory brain') was used synonymously with limbic lobe. With the identification of extensive connections between limbic cortical regions and subcortical structures in the diencephalon (mammillary bodies, anterior thalamic nuclei) and the clinical description of syndromes associated with damage to its single constituents, the functions of the limbic system were extended to social interactions and behaviour (Brown and Schäfer 1888), consolidating memories (Bechterew 1900) and forming emotions (Cannon 1927) (for a review see Catani et al 2013). Currently the limbic system includes two divisions (**Fig. 32.37A–B**): a network including the amygdala and orbitofrontal cortex connected by the uncinate fasciculus (Yakovlev's circuit) involved in emotion, reward and social behaviour; and a network including the hippocampus, parahippocampal cortex, mammillary bodies, anterior thalamus, ventromedial frontal and cingulate cortices, connected by the fornix, mammillo-thalamic tract and anterior thalamic projections involved in episodic memory. This second network is commonly referred to as the Papez circuit (1937), although its constituents were already anatomically defined by early anatomists, including Bechterew (1900) and Jakob (1906). Both divisions are extensively connected to the cingulate cortex and nuclei of the septum, hypothalamus, striatum (nucleus accumbens) and midbrain (ventral tegmental area) (Mesulam 2000).

The cortical components of the limbic system include the archicortex of the hippocampus proper, and the periarchicortex of the parahippocampal gyrus, retrosplenial region and cingulate gyrus (**Fig. 32.37C**). The parahippocampal and cingulate gyri contact each other in the region behind the splenium of the corpus callosum (retrosplenial cortex) and form the so-called great limbic lobe of Broca. These two gyri are outwardly delimited by the subcallosal, cingulate, subparietal, anterior calcarine, collateral and rhinal sulci which are collectively considered to form the limbic fissure.

At its anterior end, the parahippocampal gyrus folds back on itself to form the uncus, which is bordered superiorly by the most lateral aspect of the frontobasal region via a peduncle anterior to the temporal horn of the lateral ventricle. The anteromedial surface of the uncus region faces the carotid cistern and its posteromedial surface borders the crural cistern and the cerebral peduncle. The semilunar gyrus, a lateral extension of the lateral olfactory stria, and the ambient gyrus form two small prominences on its medial and anterior surface (see Fig. 32.37C). Both gyri cover the amygdala and are separated by the semi-anular sulcus, which harbours the anterior choroidal artery. The most rostral and anterior aspects of the uncus correspond to the entorhinal cortex (see Fig. 32.37C). The

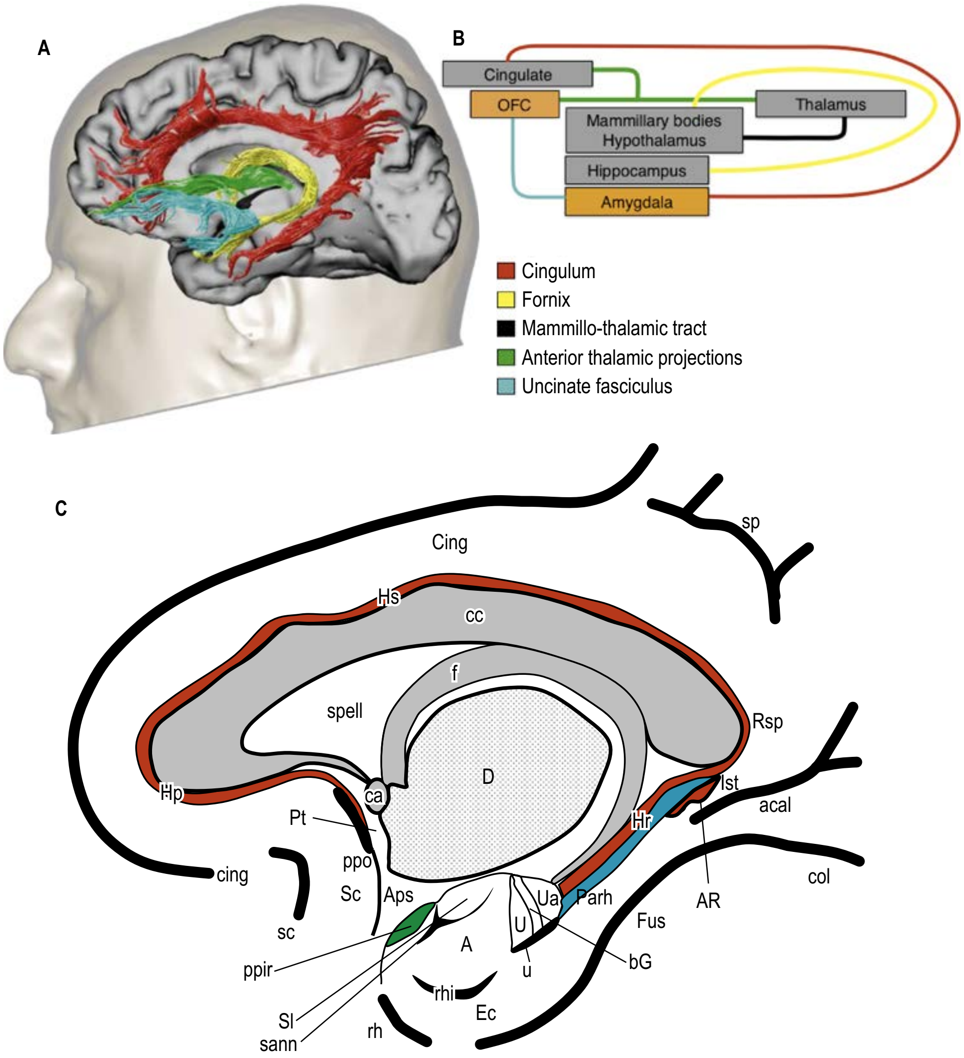

Fig. 32.37 The limbic system. **A**, Tractography reconstruction of the major limbic pathways. **B**, Diagram of the main limbic areas, subcortical structures and their reciprocal connections. **C**, Sagittal view of the right hemisphere indicating the hippocampus, gyri and sulci in a human brain. Abbreviations: A, ambiens gyrus; acal, anterior calcarine sulcus; Aps, anterior perforate substance; AR, gyri of Andreas Retzius; bG, bandaletta Giacomini; ca, commissura anterior; cc, corpus callosum; cing, cingulate sulcus; Cing, cingulate gyrus; col, collateral sulcus; D, diencephalon; Ec, entorhinal cortex; f, fornix; Fus, fusiform gyrus; Hp, hippocampus precommissuralis; Hr, hippocampus retrocommissuralis (cornu Ammonis red, dentate gyrus blue); Hs, hippocampus supracommissuralis; Ist, isthmus; OFC, orbitofrontal cortex; Parh, parahippocampal gyrus; ppir, area prepiriformis; ppo, posterior parolfactory sulcus; Pt, paraterminal gyrus; rh, rhinal sulcus; rhi, intrarhinal sulcus; Rsp, retrosplenial region; sann, semiannular sulcus; sc, subcallosal sulcus (anterior parolfactory sulcus); Sc, subcallosal gyrus; Sl, semilunar gyrus; sp, subparietal sulcus; spell, septum pellucidum; u, uncal sulcus; U, uncinate gyrus; Ua, uncinate apex. (A, B, With permission from Catani M, Thiebaut de Schotten M 2012 Atlas of Human Brain Connections. Oxford: Oxford University Press; C, with permission from Duvernoy HM 1998 The Human Hippocampus. Functional Anatomy, Vascularization and Serial Sections with MRI. Berlin: Springer.)

posterior half of the uncus contains the head of the hippocampus and is separated inferiorly from the parahippocampal gyrus by the uncal sulcus. Its inferior surface is hidden inside the uncal sulcus, in which the posterior half of the uncus region harbours the uncinate gyrus anteriorly and the uncal apex (intralimbic gyrus, hippocampus inversus) posteriorly, separated by the band of Giacomini (see Fig. 32.37C). Collectively, these structures correspond to the extraventricular part of the head of the hippocampus. The band of Giacomini corresponds to the tail of the dentate gyrus, which vanishes on the medial aspect of the uncus.

On its lateral aspect, the parahippocampal gyrus is delimited by the collateral sulcus that separates it from the fusiform gyrus, and more anteriorly by the rhinal sulcus, which is occasionally continuous with the collateral sulcus. The latter is a long, deep sulcus that extends along the basal temporal and occipital surface, with multiple side branches (see Figs 32.3C,D,F, 32.37C). Its temporal segment bulges into the ventricular floor as the collateral eminence, located lateral to the hippocampus. Its occipital segment corresponds to the collateral trigone that forms the triangular, flat surface of the ventricular atrium and occipital (posterior) horn. The rhinal sulcus, which is not always readily identifiable, separates the uncus from the rest of the temporal pole. Medially, it lies under the thalamus along the choroidal fissure. Superiorly, it is attached along the inferior aspect of the insular lobe via fibres that cover the inferior horn. The choroidal fissure extends between the entire fornix and thalamus, from the head and the body of the hippocampus to the interventricular foramen. Anteriorly, the anterior and mesial parts of the temporal lobe and the parahippocampal gyrus merge with the basal and lateral aspect of the frontal lobe through a neural peduncle that constitutes the so-called temporal stem (limen insulae). Posteriorly, the choroidal fissure lies within the inferior horn between the fimbria of the fornix and the inferior aspect of the thalamus, along the parapeduncular space that harbours the ambient cistern. More superiorly and anteriorly, the choroidal fissure lies between the body of the fornix and the superior surface of the thalamus.

The hippocampal gyrus folds medially where it harbours the hippocampus proper. The latter encircles the corpus callosum and is divided into precommissural, supracommissural and retrocommissural parts, according to its relation to the anterior commissure (see Fig. 32.37C). The retrocommissural hippocampus is a major part of the limbic lobe, and is separated from the parahippocampal gyrus by the hippocampal fissure. The parahippocampal gyrus includes Brodmann's periarchicortical areas BA27 (presubiculum), BA28 (entorhinal cortex) and BA35 (perirhinal cortex). In primates, areas of the parahippocampal gyrus project to virtually all multimodal association areas of the cortex, and it also provides the major funnel through which multimodal inputs converge on the hippocampus.

Posteriorly, the parahippocampal gyrus is continuous with the lingual gyrus and the cingulate gyrus along its isthmus. Buried within the posterior wall of the callosal sulcus, the retrosplenial cortex occupies the anterior region of the isthmus cinguli. The retrosplenial cortex is microstructurally different from the cingulate cortex and functionally is closer to the posterior parahippocampal place area (see below). At its rostral extension, the cingulate gyrus ends in the subcallosal gyrus below the genu of the corpus callosum (see Figs 32.1, 32.3C–D). The anterior and posterior paraolfactory gyri lie anterior to the paraterminal gyrus, separated by the anterior para-olfactory sulcus (see Figs 32.1, 32.2C–D). Anteriorly, a fold connects the most basal portion of the cingulate gyrus with the gyrus rectus, encircling the posterior end of the superior rostral sulcus (the cingulate pole). The paraterminal gyrus lies on the medial wall of the cerebral hemisphere posterior to the paraolfactory gyri, immediately facing the lamina terminalis, and delineated anteriorly by the short, vertical posterior olfactory sulcus. Inferiorly, the paraterminal gyrus extends along the diagonal band of Broca and the lateral olfactory stria. The cingulate gyrus includes Brodmann's periarchicortical areas BA26 (area ectosplenialis; hidden in the callosal sulcus at the level of splenium), BA25 (area subgenualis or preterminalis), BA29 (granular retrosplenial cortex), BA30 (agranular retrosplenial cortex), BA33 (area pregenualis) as well as the proisocortical areas BA23 (area cingularis posterior) and BA24 (area cingularis anterior). Area 24 is surrounded by the isocortical BA32, and BA23 is bordered by the isocortical BA31.

Hippocampal formation

The hippocampal formation consists of the archicortical hippocampus proper (cornu Ammonis, dentate gyrus and subiculum) and the periarchicortical presubiculum (BA27) and parasubiculum (BA26), as well as the entorhinal (BA28) and perirhinal (BA35) cortices (Table 32.6). The

TABLE 32.6 **Hippocampal formation and its archi- and periarchicortical parts**

Hippocampal formation			
	Hippocampus retrocommissuralis (HR)		
		Cornu Ammonis (CA)	
			CA1
			CA2
			CA3
		Dentate gyrus (DG)	
			Fascia dentata (FD)
			Hilus
			CA4
		Subiculum (Sub)	
	Presubiculum (Prs, BA27)		
	Parasubiculum (ParS, BA26)		
	Hippocampus precommissuralis (HP)		
	Hippocampus supracommissuralis (HS)		
	Entorhinal cortex (BA28)		
	Perirhinal cortex (BA35)		

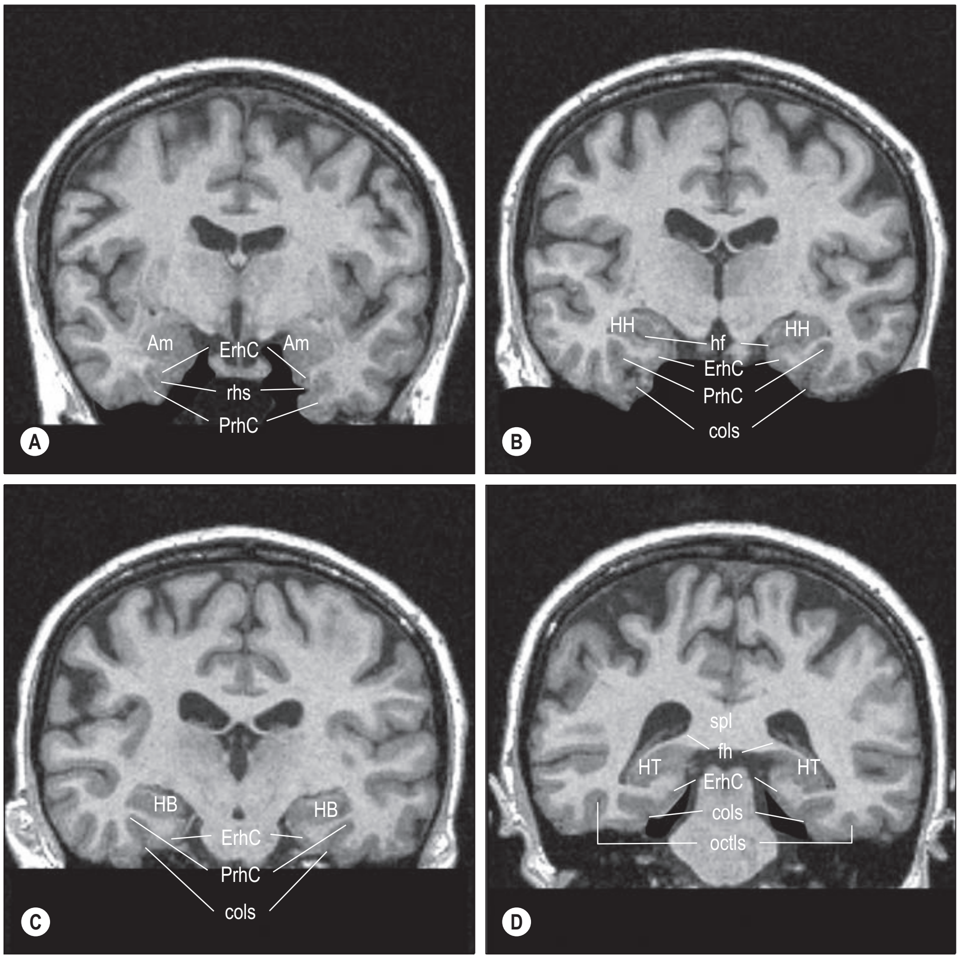

Fig. 32.38 Rostral (**A**), intermediate (**B–C**) and caudal (**D**) sections through the hippocampal formation with MRI. Abbreviations: Am, amygdala; cols, collateral sulcus; ErhC, entorhinal cortex; fh, fimbria hippocampi; HB, hippocampal body; hf, hippocampal sulcus; HH, hippocampal head; HT, hippocampal tail; octls, occipito-temporal sulcus; PrhC, perirhinal cortex; rhs, rhinal sulcus; spl, splenium.

entorhinal cortex is laterally confined by the collateral sulcus, in which most of the perirhinal cortex is buried. Except for the most rostral parts of BA28 and BA35 in the gyrus ambiens, the periarchicortical cortex of the hippocampal formation is located in the parahippocampal gyrus.

Hippocampus proper

The retrocommissural part of the hippocampus proper is a convex elevation, approximately 5 cm long, within the parahippocampal gyrus and neighbouring the temporal (inferior) horn of the lateral ventricle. It can be macroscopically divided into a head, a body and a tail (**Fig. 32.38**). The surface of the hippocampus, the alveus, is covered by ependyma inside the ventricular cavity. On the surface of the dentate gyrus, small cortical prominences form a chain along the medial aspect of the hippocampus. Along its medial margin, the hippocampus is separated from the subiculum of the parahippocampal gyrus by the shallow hippocampal sulcus that usually terminates anteriorly within the uncus. The dentate gyrus is separated from the fimbria of the fornix by the fimbriodentate sulcus which lies parallel with the hippocampal sulcus (**Fig. 32.39**).

The large retrocommissural part of the hippocampus proper is a three-layered archicortical structure (**Figs 32.40–32.41**) that continues as the supracommissural hippocampus, lying as the indusium griseum on the corpus callosum, and a thin vertical structure rostral to the septum and the genu of the corpus callosum. The indusium griseum is a thin layer of grey matter lying over the whole length of the dorsal surface of the corpus callosum, and covered by medial and lateral longitudinal striae that run within the callosal sulcus beneath each cingulate gyrus. Anteriorly, the indusium griseum is connected to the paraterminal gyrus; posteriorly, it circles the splenium of the corpus callosum and runs along the fasciolar gyrus on each side. The retrocommissural hippocampus (hippocampus proper) consists of Ammon's horn (cornu Ammonis), the fascia dentata and the subiculum. Ammon's horn and the fascia dentata are distinguished on the basis of their principal excitatory neurones, which are pyramidal and granule cells, respectively.

The archicortical fascia dentata is located in the dentate gyrus and consists of three layers: a superficial molecular layer containing the dendrites of the granule cells, an intermediate granular layer with densely packed somata of the granule cells, and an internal, relatively cell-sparse multiform layer surrounding a continuation of the cornu Ammonis, the CA4 region of the hilus. The multiform layer contains cells that give rise primarily to ipsilateral association fibres that remain within the dentate gyrus and do not extend into other hippocampal fields. The hilus and fascia dentata together form the dentate gyrus. The cortex of the dentate gyrus is the least complex of the hippocampal formation (see Figs 32.40–32.41). The outer two-thirds of its molecular layer receive most of the afferent projections to the dentate gyrus, primarily from the entorhinal cortex via the perforant path, whereas the inner third is a termination field for commissural and associational projections.

The cornu Ammonis can be subdivided into four regions, CA1–CA4 (see Fig. 32.40). CA1 is the largest region in the hippocampus proper, and is the most complex of the hippocampal subdivisions: its appearance varies along its extent. CA1 is bordered laterally by the prosubiculum, which is a subfield of the subiculum, and medially by CA2. The most caudal portion of CA1 is located on Retzius's gyrus beneath the splenium of the corpus callosum. Approximately 10% of neurones in CA1 are interneurones, and 90% are glutamatergic projection neurones (pyramidal cells). CA2 has the most compact layer of pyramidal cells. Like CA1, it lacks a mossy fibre input from dentate granule cells and receives a major input from the supramammillary region of the hypothalamus. CA3 borders the hilus of the dentate gyrus at one end, and CA2 at the other. CA3 pyramidal cells are the largest in the hippocampus and receive a mossy fibre input from dentate granule cells on their proximal dendrites. The whole pyramidal cell layer in this field is about 10 cells thick. CA4 is not universally accepted as a distinct region but considered to be a mere continuation of CA3 within the hilus of the dentate gyrus: it merges with the multiform layer of the fascia dentata. The cornu Ammonis (see Fig. 32.41) consists of three layers: the thin, cell-sparse stratum oriens contains intrahippocampal association fibres, the basal dendrites and axons of pyramidal neurones and some interneurones; the pyramidal layer contains the somata of pyramidal cells and interneurones; and a wide, cell-sparse layer, the stratum radiatum-lacunosum-moleculare, contains the apical dendrites of the pyramidal cells and the perforant path, Schaffer collaterals, septal and commissural fibres. CA3 and CA2 cells in the stratum radiatum and stratum oriens receive associational connections from other rostrocaudal levels of the hippocampus, and afferents from subcortical structures such as the septal nuclei and supramammillary region. Schaffer collaterals, the projections from pyramidal cells in CA3 and CA2 to CA1, terminate in the stratum radiatum and stratum oriens. The projections from the entorhinal cortex to

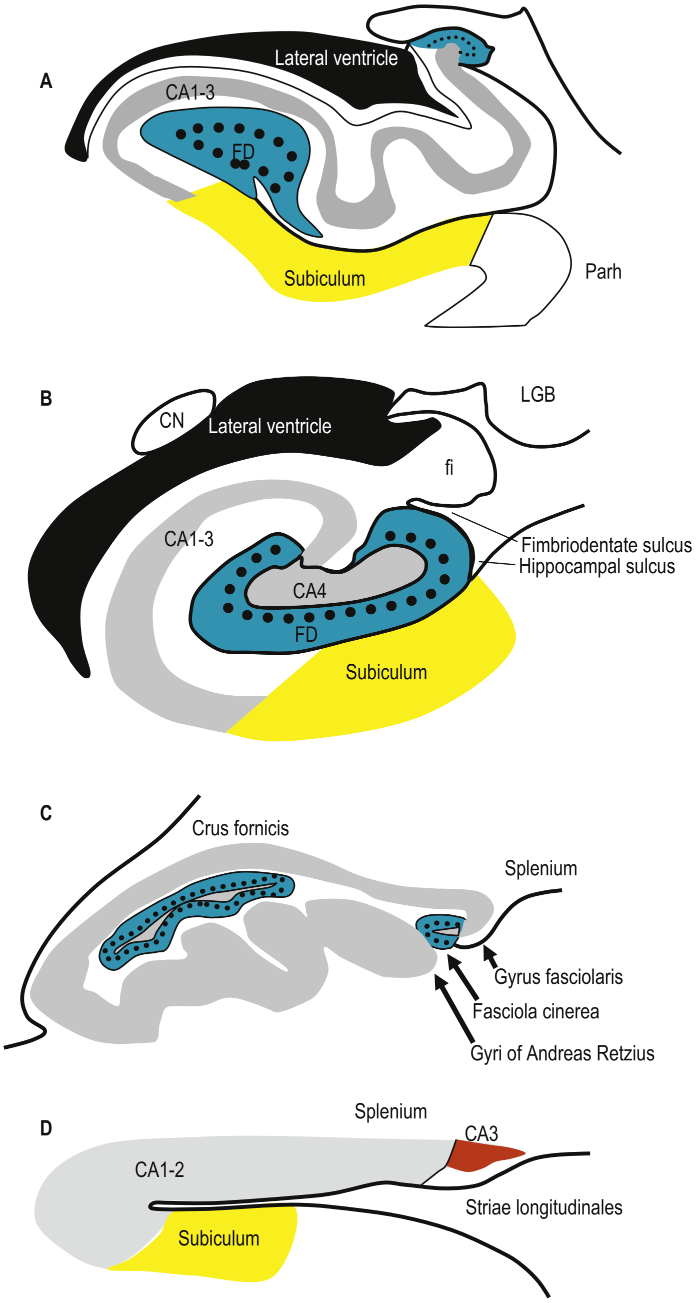
A
Lateral ventricle
CA1-3
FD
Subiculum
Parh
B
CN
Lateral ventricle
LGB
fi
CA1-3
CA4
FD
Fimbriodentate sulcus
Hippocampal sulcus
Subiculum
C
Crus fornicis
Splenium
Gyrus fasciolaris
Fasciola cinerea
Gyri of Andreas Retzius
D
Splenium
CA3
CA1-2
Striae longitudinales
Subiculum

Fig. 32.39 Frontal sections through the hippocampal head (**A**), body (**B**) and tail (**C–D**). Abbreviations: CA, cornu Ammonis; CN, caudate nucleus; FD, fascia dentata; fi, fimbria fornicis; LGB, lateral geniculate body; Parh, parahippocampal gyrus. (Adapted with permission from Duvernoy HM 1998 The Human Hippocampus. Functional Anatomy, Vascularization and Serial Sections with MRI. Berlin: Springer.)

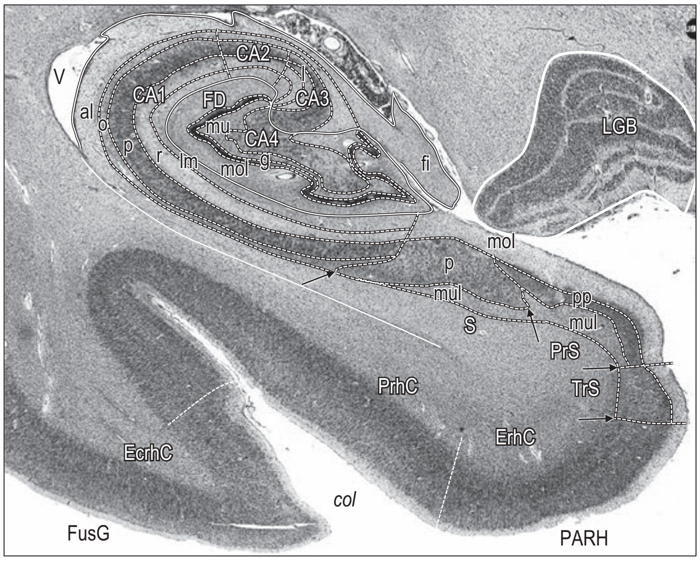
V
al
o
CA1
p
r
lm
FD
mu
CA2
l
CA3
CA4
g
mol
fi
LGB
mol
p
mul
S
pp
mul
PrS
TrS
PrhC
ErhC
EcrhC
col
FusG
PARH

Fig. 32.40 A frontal section through the medial temporal lobe, consisting of the archicortical hippocampus proper (cornu Ammonis + fascia dentata + subiculum), the periarchicortical presubiculum (BA27) and trans-/parasubiculum. The neighbouring areas are the isocortical parahippocampal cortex. Nissl staining. Abbreviations: al, alveus; CA1–CA4 regions of the cornu Ammonis; col, sulcus collateralis; EcrhC, ectorhinal cortex; ErhC, entorhinal cortex; FD, fascia dentata; fi, fimbria hippocampi; FusG, fusiform gyrus; g, stratum granulosum; l, stratum lucidum; LGB, lateral geniculate body; lm, stratum lacunosum-moleculare; mol, stratum moleculare; mu, stratum multiforme; o, stratum oriens; p, stratum pyramidale; PARH, gyrus parahippocampalis; pp, stratum parvopyramidale; PrhC, perirhinal cortex; PrS, presubiculum; r, stratum radiatum; S, subiculum; TrS, transsubiculum; V, ventricle.

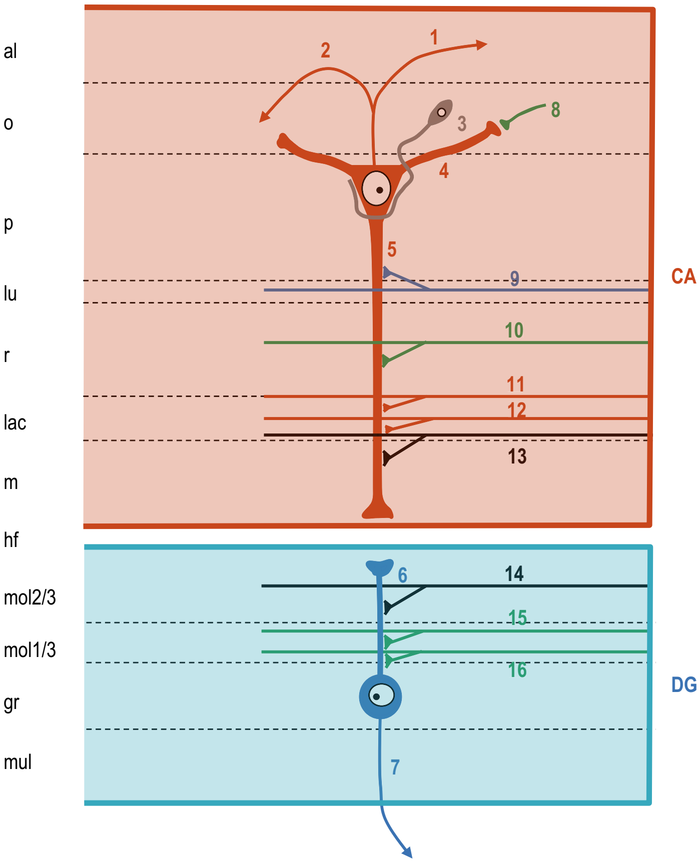
al
o
p
lu
r
lac
m
hf
mol2/3
mol1/3
gr
mul
1
2
3
4
5
6
7
8
9
10
11
12
13
14
15
16
CA
DG

Fig. 32.41 The hippocampal layers and their major connections. Abbreviations and key: al, alveus; CA, cornu Ammonis; DG, dentate gyrus; gr, stratum granulosum; hf, hippocampal sulcus; lac, stratum lacunosum; lu, stratum lucidum; m, stratum moleculare of CA; mol1/3, stratum moleculare inner third; mol2/3, stratum moleculare outer two-thirds; mul, stratum multiforme; o, stratum oriens; p, stratum pyramidale; r, stratum radiatum; 1, axon of pyramidal cell; 2, Schaffer collateral; 3, basket cell; 4, basal dendrite; 5, apical dendrite; 6, apical dendrite; 7, mossy fibre; 8, basal dendrite connection with septal and commissural fibres; 9, mossy fibre in stratum lucidum of CA3; 10, septal and commissural fibres; 11, Schaffer collateral; 12, Schaffer collateral; 13, perforant path from entorhinal cortex; 14, perforant path from entorhinal cortex; 15, commissural fibre; 16, septal fibre.

the dentate gyrus (perforant path) travel in the stratum lacunosum-moleculare, where they make synaptic contact *en passant* with the distal apical dendrites of hippocampal pyramidal cells. The stratum lucidum between the pyramidal and radiatum layers contains the terminals of mossy fibres that make contact with the proximal dendrites of pyramidal cells in CA: it is not present in CA1 and CA2. The alveus between the stratum oriens and the ventricular surface consists of subicular and hippocampal pyramidal cell axons converging on the fimbria of the fornix

The archicortical subiculum is located between CA1 and the periarchicortical presubiculum (see Figs 32.39–32.40). It can be subdivided into the prosubiculum medially and the subiculum proper laterally. In addition to the molecular and pyramidal layers of the cornu Ammonis, a variable number of layers from surrounding fields are found in the subiculum, producing an intricate lamination pattern. The subiculum consists of a superficial molecular layer containing apical dendrites of subicular pyramidal cells, a pyramidal cell layer and a deep polymorphic layer. The stratum radiatum of CA1 stops abruptly at the border with the prosubiculum, where pyramidal neurones build a denser outer stripe, a less dense intermediate stripe and a denser inner stripe in the subiculum. The border between the prosubiculum and subiculum proper is difficult to identify. Compared with the prosubiculum, the cell packing density of the pyramidal layer is lower in the outer stripe but higher in the inner stripe of the subiculum. The major subcortical projections of the hippocampal formation to the septum, mammillary nuclei, nucleus accumbens, anterior thalamus and entorhinal cortex, all arise from pyramidal neurones of the subicular complex. The subiculum receives numerous direct cortical inputs, e.g. from the temporal polar and perirhinal cortices and the parahippocampal and superior temporal gyri.

The border between the archicortical subiculum and the periarchicortical presubiculum is characterized by particularly small neurones in the prosubiculum that form a parvocellular layer (see Figs 32.39–32.40). The pyramidal and multiform layers of the subiculum continue into the pyramidal-multiform layer of the presubiculum, where a plexiform layer is interleaved between the pyramidal-multiform and parvocellular layers. The presubiculum projects to the anterior thalamic nuclear complex (anteromedial, anteroventral and laterodorsal nuclei).

The parasubiculum (see Figs 32.39–32.40) can be delineated from the presubiculum by the abrupt appearance of large, loosely packed cells in the parvopyramidal layer, and by large, densely packed cells in the pyramidal-multiform layer of the parasubiculum. Its lateral border is formed by the entorhinal cortex. The parasubiculum is always present in the hippocampal head; it extends into the hippocampal tail in only 20% of human brains. The border between the parasubiculum and the entorhinal cortex is delineated by the increase in the number of cortical layers from four (parasubiculum) to eight (entorhinal cortex).

The hippocampal formation and its connections via the fornix are thought to be responsible for the formation of autobiographical (episodic) memory. Bilateral damage to the hippocampal formation as a result of neurodegeneration (Alzheimer's disease), infection (encephalitis), or bilateral removal of larger parts of the mesial temporal cortex because of epilepsy, is associated with an inability to learn new information (anterograde amnesia) or remember experiences in the relatively recent past (retrograde amnesia).

Neurotransmitters of the hippocampal formation

Available with the *Gray's Anatomy* e-book

Entorhinal cortex

The entorhinal cortex extends rostrally to the anterior limit of the amygdala and caudally overlaps a portion of the hippocampal fields. It can be subdivided into various subfields on the basis of differences in cyto- and myeloarchitecture (see Figs 32.34, 32.42). It receives input from the olfactory, piriform and periamygdaloid cortices; more caudal portions of entorhinal cortex do not generally receive olfactory inputs, but collect input from numerous neocortical regions. The entorhinal cortex provides the main input to the hippocampal formation via the perforant path.

The entorhinal cortex consists of eight layers (see Fig. 32.34B) which are quite distinct from those of the neocortex. Molecular layer 1 is nearly devoid of cell bodies. Layer 2 (pre-α) is a narrow cellular layer consisting of islands of densely packed large pyramidal and stellate cells. These islands are a hallmark feature of entorhinal cortex. They form small bumps (verrucae entorhinalis, previously called verrucae hippocampi) on the surface of the brain that can be seen by the naked eye or in magnetic resonance images, where they indicate the entorhinal cortex (Augustinack et al 2012). Notably, these verrucae disappear in Alzheimer's disease, and are signs of a general reduction of this area caused by the disease. Layer 3 (pre-β) consists of medium-sized pyramidal cells and continues into layer 4 (pre-γ) with a somewhat higher cell packing density. There is no internal granular layer; in its place, there is an acellular region of dense fibres called the lamina dissecans (a distinctive feature of entorhinal cortex), or layer 5. Layers 4 and 6 (pri-α) are apposed in regions where the lamina dissecans is less obvious. Layer 6 consists of large pyramidal cells five or six rows deep. Layer 7 (pri-β) is a cell sparse cleft and only distinguishable from layer 6 close to the border with the perirhinal cortex. Layer 8 (pri-γ) consists of large cells that are relatively densely packed and continue around the angular bundle (subcortical white matter deep to the subicular complex made up largely of perforant path axons) to lie beneath the pre- and parasubiculum.

The entorhinal cortex has reciprocal connections with the hippocampus and numerous neocortical regions. It receives afferents from many areas, including other areas of the parahippocampal gyrus and dorsal bank of the anterior portion of the superior temporal gyrus, as well as from the perirhinal (BA35), temporal polar, agranular insular, posterior orbitofrontal, dorsolateral prefrontal (BA9, BA10, BA46), medial frontal (BA25, BA32), cingulate (BA23, BA24) and retrosplenial cortices. It projects to the perirhinal and temporal polar cortices and the caudal parahippocampal and cingulate gyri. Evidence from clinical and experimental animal studies suggests that the reduction of the entorhinal cortex plays an important role in Alzheimer's disease because it is involved in the frontotemporal cortical memory network.

Septum

The septum is a midline and paramedian structure. It is listed here as part of the periarchicortex, which is much more differentiated in lower primates and insectivores: comparative neuroanatomical studies argue for this classification (Stephan 1975). The septum must not be confused with the septum pellucidum, which separates the lateral ventricles. The septal complex is composed of different nuclei (**Fig. 32.43**). Four main groups, dorsal, ventral, medial and caudal, have been identified. The dorsal group is the dorsal septal nucleus, the ventral group consists of the lateral septal nucleus, the medial group encompasses the medial septal nucleus and the vertical part of the diagonal band of Broca and the caudal group contains the fimbrial and triangular septal nuclei.

The major input to the septum terminates primarily in the lateral septal nuclei. It includes fibres of the fornix that arise from CA3 and CA1, the subiculum and afferent fibres arising from the preoptic area, anterior, paraventricular and ventromedial hypothalamic nuclei, and the lateral hypothalamic area. The lateral septum also receives a rich monoaminergic innervation, including a noradrenergic input from the locus coeruleus and the medullary cell groups (A1, A2), a serotoninergic input from the midbrain raphe nuclei, and a dopaminergic input from the ventral tegmental area (A10).

The output of the lateral septum reaches the medial and lateral preoptic areas, anterior hypothalamus, supramammillary and midbrain ventral tegmental area via the medial forebrain bundle, and the medial habenular nucleus and midline thalamic nuclei via the stria medullaris thalami. Efferent fibres from the medial septal and vertical limb nuclei of the diagonal band travel dorsally via the fornix, fimbria, striae longitudinales, and ventrally via the amygdaloid complex. While these projections reach all hippocampal fields, the most prominent terminations are in the dentate gyrus, CA3, presubiculum, parasubiculum and entorhinal cortex. Many are GABAergic or cholinergic.

Retrosplenial region

The retrosplenial region consists of the periarchicortical areas B26, BA29 and BA30. In the human brain, most of this small region is hidden in the callosal sulcus behind the splenium. Only a part of area 30 reaches the medial surface of the hemispheres on the posterior cingulate sulcus (**Fig. 32.44**; see Fig. 32.13). The retrosplenial cortex is implicated in working and long-term memory and visuospatial functions. This region is part of a network that mediates topokinetic navigation and memory, i.e. the retrosplenial cortex is activated when memory for previously learned routes is required for movement in space.

Area 26 and the posterior part of area 33 are located in the callosal sulcus. Area 26 extends rostrally above the splenium and reaches the level of the midcingulate cortex. Both areas have a poorly differentiated cortical structure with an external granular layer and almost no deep pyramidal layers. Area 29 follows area 26 medially and can be divided into medial and lateral subfields. It is characterized by a second layer of densely packed small neurones that look like granular cells, below the molecular layer, particularly at its rostral levels (granular retrosplenial cortex). Pyramidal and multiform layers follow. The stream of gradually increasing laminar differentiation (see Fig. 32.44L) from the poorly laminated area 33 to area 26, followed by area 29, is continued

Glutamate is the major excitatory transmitter of the hippocampal pyramidal cells and of their connections, namely, the perforant pathway that arises in the entorhinal cortex and terminates in the dentate gyrus and the CA1 region; mossy fibres that run from the dentate granule cells to the pyramidal cells of the CA3 field; and Schaffer collaterals that arise as axonal collaterals of CA3 pyramidal cells and terminate on CA1 pyramidal cells. In addition to the principal pyramidal neurones, various inhibitory, mostly GABAergic, interneurones are found in the CA regions and the fascia dentata. They often co-localize CCK, SOM, VIP and other neuropeptides. For example, the axon terminals of GABAergic chandelier cells in the granule cell layer of the fascia dentata and the pyramidal layer of the CA region end on proximal axonal segments of pyramidal cells. GABAergic basket cells are found mainly in the granule cell layer of the dentate gyrus, but also in the hilar region. Both cell types receive local, commissural and entorhinal afferents. Basket cells are present in the pyramidal and oriens layers of the CA region, and occasionally in the stratum radiatum-lacunosum-moleculare. Most of the neocortical interneurones are also found in the hippocampal formation (for details see Freund and Buzsáki 1996).

There are many peptide-containing neurones in the hippocampal formation. Granule cells in the dentate gyrus contain the opioid peptide dynorphin, which is also present in mossy fibres. Enkephalin, or a related peptide, may be present in fibres arising in the entorhinal cortex. There is a dense plexus of somatostatin-immunoreactive fibres in the molecular layer of the fascia dentata and in the stratum lacunosum-moleculare of the CA regions. Somatostatin-immunoreactive interneurones are found in the multiform layer of the fascia dentata, the stratum oriens of the CA regions, and the deep layers of the entorhinal cortex. VIP-immunoreactive interneurones are numerous in many hippocampal fields. CCK-immunoreactive cells are found in the hilar region of the dentate gyrus, in all strata of the CA regions, particularly in the pyramidal cell layer, and also throughout the subicular complex and entorhinal cortex. There are substantial plexuses of CCK-immunoreactive fibres in the stratum lacunosum-moleculare, and the subiculum. CCK-immunoreactive cells may give rise to extrinsic projections, e.g. to the lateral septum and medial mammillary nucleus, because CCK-immunoreactive fibres are found in the fimbria/fornix.

The medial septal complex and the supramammillary area of the posterior hypothalamus are two major sources of subcortical afferents to the hippocampal formation. There are also projections from the amygdaloid complex and claustrum (to the subicular complex and entorhinal cortex), as well as monoaminergic projections from the ventral tegmental area, the mesencephalic raphe nuclei and the locus coeruleus. Noradrenergic and serotoninergic projections reach all hippocampal fields. Neurones in the supramammillary area project to the hippocampal formation via the fornix and terminate most heavily in the dentate gyrus and fields CA2 and CA3 of the cornu Ammonis. All divisions of the anterior thalamic nuclear complex and associated lateral dorsal nucleus project to the hippocampal formation, predominantly to the subicular complex. Some midline thalamic nuclei, particularly the parataenial, central medial and reuniens nuclei, project especially to the entorhinal cortex.

The highest density of glutamate AMPA receptors are found in the molecular and pyramidal strata of the hippocampus proper and the prosubiculum (**Fig. 32.42A**). NMDA receptors are mainly concentrated in the pyramidal layer of CA1 and the prosubiculum, as well as in the molecular layer and hilus of the dentate gyrus (**Fig. 32.42B**). Kainate receptors show a particular distribution pattern: they are very densely packed in the stratum lucidum of CA3 and the hilus (**Fig. 32.42C**). The highest concentration of $GABA_A$ receptors is found in the molecular layer of the fascia dentata and the pyramidal layer of the CA regions (**Fig. 32.42D**). In the human hippocampus, about 60% of the cholinergic muscarinic receptors are of the M_1, 20% of the M_2, 15% of the M_4 and roughly 5% of the M_3 subtypes. M_1 receptors are widely distributed within the hippocampus (**Fig. 32.42E**) and expressed in somata and dendrites of pyramidal and granule cells: they show a similar distribution to that of the AMPA receptors and are mainly responsible for the modulation of pyramidal cell excitability. The M_2 receptor is restricted to interneurones. M_4 receptors are mainly located in glutamatergic terminals and mediate cholinergic presynaptic inhibition of Schaffer collaterals. The predominant cholinergic nicotinic receptor (nAChR) subtype in the CA and dentate gyrus (DG) is the homomeric α_7 receptor; there are also heteromeric $\alpha_4\beta_2$ and $\alpha_3\beta_4$ receptor subtypes. nAChRs are found in granular cells of the dentate gyrus and pyramidal cells of the CA regions: in CA3, they can enhance the release of glutamate from mossy fibres via activation of protein kinase A. An impaired cholinergic function is a characteristic marker of Alzheimer's disease. These alterations not only pertain to concentrations of the neurotransmitter; cholinergic nicotinic receptors of granule cells of the dentate gyrus, presubiculum and parahippocampal gyrus are also reduced by 30% in Azheimer's patients relative to age-matched control subjects. The noradrenergic α_1 receptors are highly concentrated in all layers of the dentate gyrus and in the stratum lucidum (**Fig. 32.42F**). The α_2-adrenoceptors display a highly restricted maximal density in the radiatum-lacunosum layer of CA1 (**Fig. 32.42G**). β-adrenergic receptors are expressed by hippocampal neurones and play important roles in gating long term depression (LTD). Their density is higher in the fascia dentata than in the CA regions. The serotoninergic 5-HT_{1A} receptor, which hyperpolarizes CA1 and CA3 pyramidal cells, is most densely distributed in the pyramidal and lacunosum strata of CA1 (**Fig. 32.42H**): the hyperpolarizing effects parallel the depolarizing effects induced by 5-HT_{2A} receptors. The 5-HT_3 receptor is present at high densities in interneurones of the lacunosum-molecular layer of the CA1 region, as well as in entorhinal, piriform and cingulate areas. The 5-HT_4 receptor occurs at highest levels in the hippocampus and potentiates the excitation on dendrites of CA1 pyramidal cells in the stratum radiatum by stimulating Schaffer collaterals. The density of post synaptic excitatory 5-HT_7 receptors is highest in the hippocampus and anterior cingulate cortex, increasing the excitability of CA3 pyramidal cells and suppressing the perforant path input to CA1 pyramidal cells. Dopamine D_1/D_5 receptors support long-lasting and learning-related forms of synaptic plasticity at the mossy fibre synapses in CA3 and provide evidence for a neuromodulatory role of this receptor in experience-dependent synaptic encoding in the hippocampal subfield CA3.

The regional and laminar distribution of transmitter receptors in the retrosplenial cortex is inhomogeneous and supports its cytoarchitectonic parcellation (see Fig. 32.44A–J). The densities (averaged over all cortical layers) of glutamate AMPA, kainate and to a lesser degree, of NMDA receptors as well as those of the noradrenergic α_1 and α_2 receptors, increase from area 26 to area 23 of the posterior cingulate cortex and thus parallel the direction of cytoarchitectonic differentiation. The densities of $GABA_A$ and $GABA_B$ receptors in the deeper layers of retrosplenial areas 29 and 30 are lower than those in area 23. The distribution of $GABA_B$ receptors also confirms the subdivision of area 29 into lateral 29l and medial 29m parts: $GABA_A$ receptor densities are lower in the upper layers of the lateral part than they are in the medial subdivision. Area 30 has the highest M_3 receptor densities of the cingulate cortex. Area 29 contains higher densities of muscarinic M_1 and nicotinic $\alpha_4\beta_2$ receptors than area 30. The concentration of 5-HT_{1A} receptors is slightly higher in area 29 than in area 30.

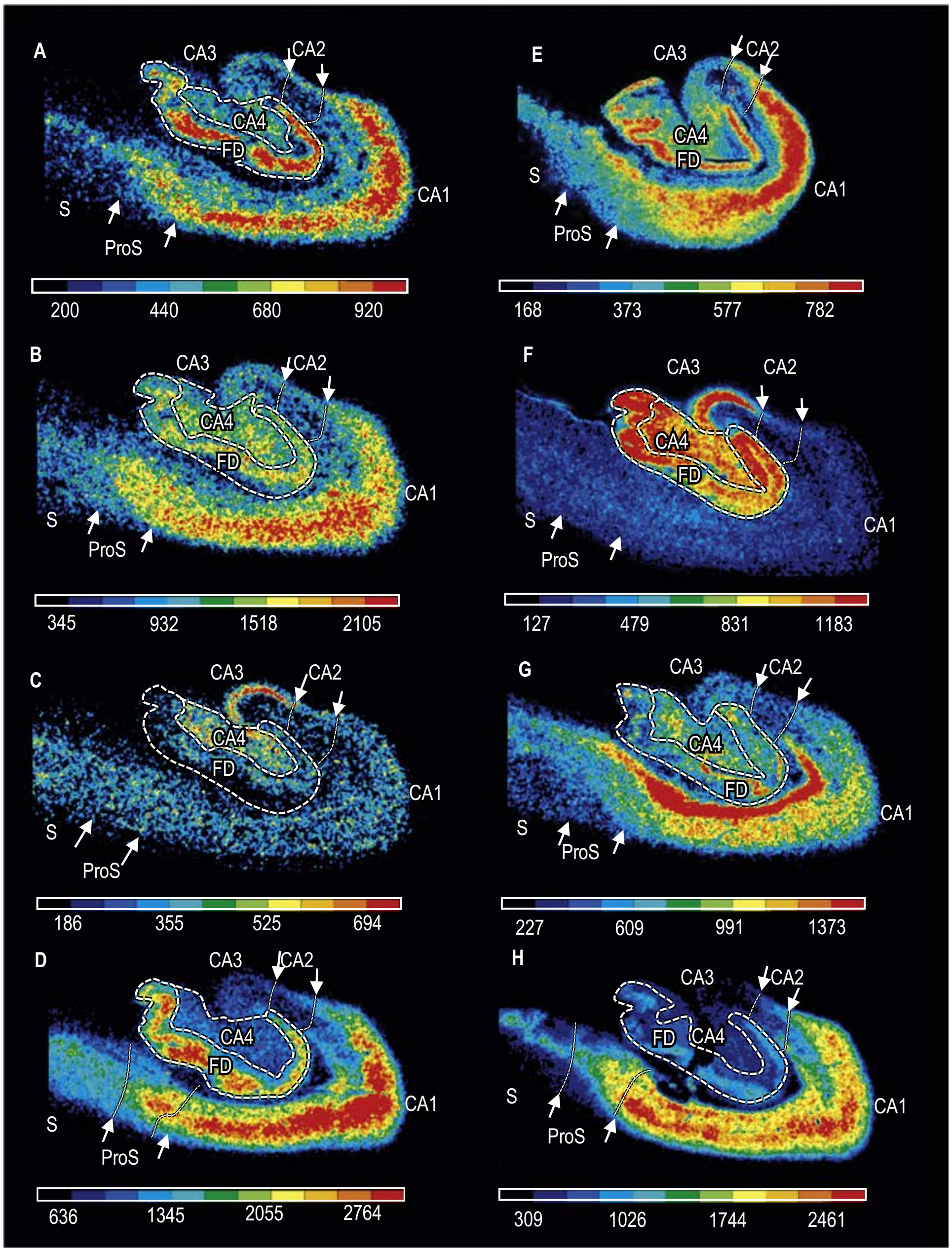
A
CA3
CA2
CA4
FD
CA1
S
ProS
200
440
680
920
E
CA3
CA2
CA4
FD
CA1
S
ProS
168
373
577
782
B
CA3
CA2
CA4
FD
CA1
S
ProS
345
932
1518
2105
F
CA3
CA2
CA4
FD
CA1
S
ProS
127
479
831
1183
C
CA3
CA2
CA4
FD
CA1
S
ProS
186
355
525
694
G
CA3
CA2
CA4
FD
CA1
S
ProS
227
609
991
1373
D
CA3
CA2
CA4
FD
CA1
S
ProS
636
1345
2055
2764
H
CA3
CA2
FD
CA4
CA1
S
ProS
309
1026
1744
2461

Fig. 32.42 The distribution of transmitter receptors in the human hippocampus. **A**, Glutamate AMPA receptor; **B**, glutamate NMDA receptor; **C**, glutamate kainate receptor; **D**, GABA_A receptor; **E**, acetylcholine muscarinic M_1 receptor; **F**, noradrenaline α_1 receptor; **G**, noradrenaline α_2 receptor; **H**, serotonin 5-HT_{1A} receptor. Abbreviations: CA1–CA4, regions of cornu Ammonis FD, fascia dentata; ProS, prosubiculum; S, subiculum. Arrows and dashed lines label boundaries of hippocampal subdivisions. Colour scales indicate densities of receptors in fmol/mg protein.

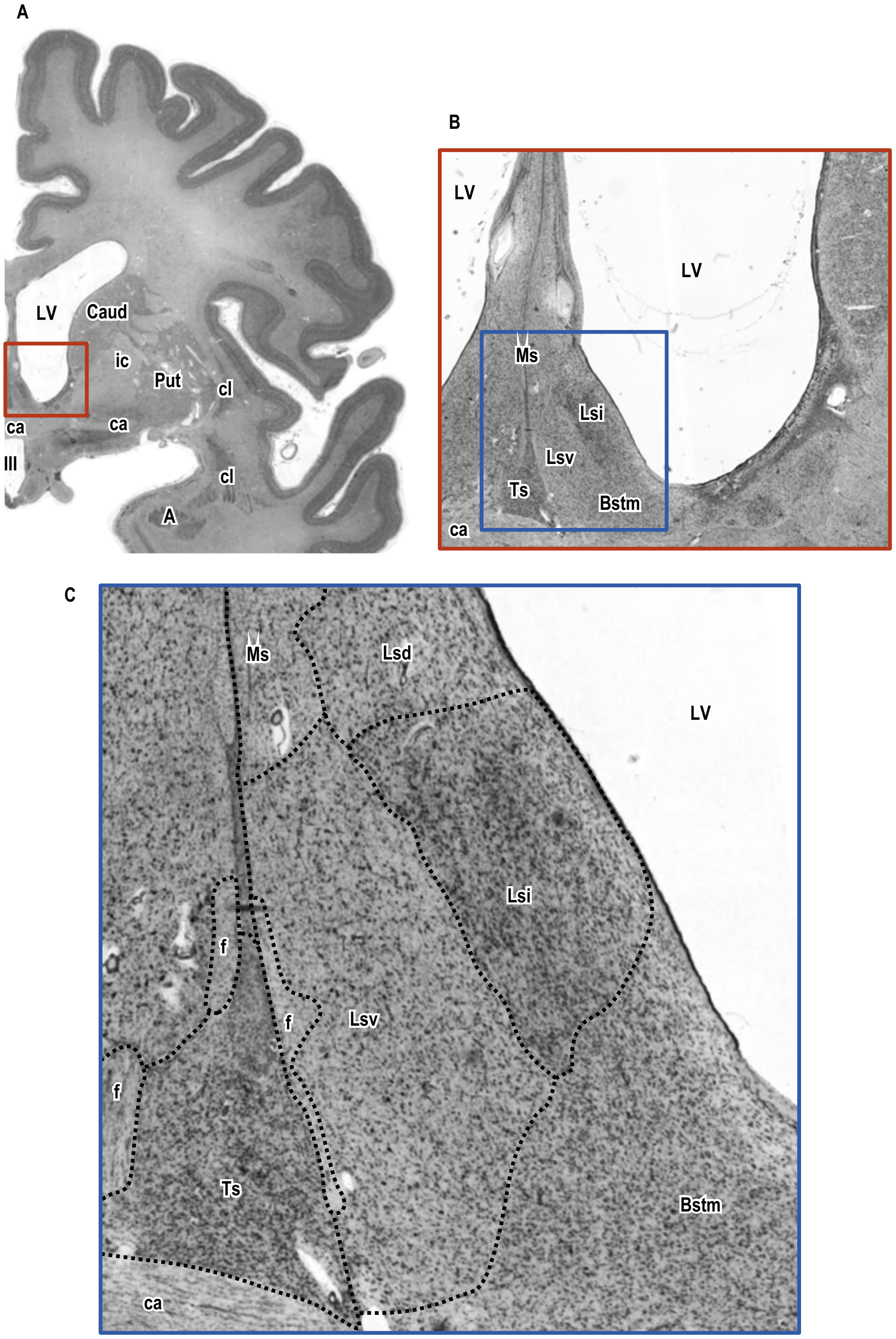
A
LV
Caud
ic
Put
cl
ca
ca
III
cl
A
B
LV
LV
Ms
Lsi
Lsv
Ts
Bstm
ca
C
Ms
Lsd
LV
Lsi
f
f
Lsv
f
Ts
Bstm
ca

Fig. 32.43 The septal complex. **A**, Coronal Nissl stained section through a human hemisphere at low magnification. **B**, Detail as indicated by the orange frame in **A**. **C**, Septal nuclei at higher magnification. Abbreviations: A, amygdala; Bstm, medial division of the bed nucleus of the stria terminalis; ca, anterior commissure; Caud, caudate nucleus; cl, claustrum; f, fornix; ic, internal capsule; Lsd, dorsolateral septal nucleus; Lsi, intermediolateral septal nucleus; Lsv, ventrolateral septal nucleus; LV, lateral ventricle; Ms, medial septal nucleus; Put, putamen; Ts, triangular septal nucleus; III, third ventricle.

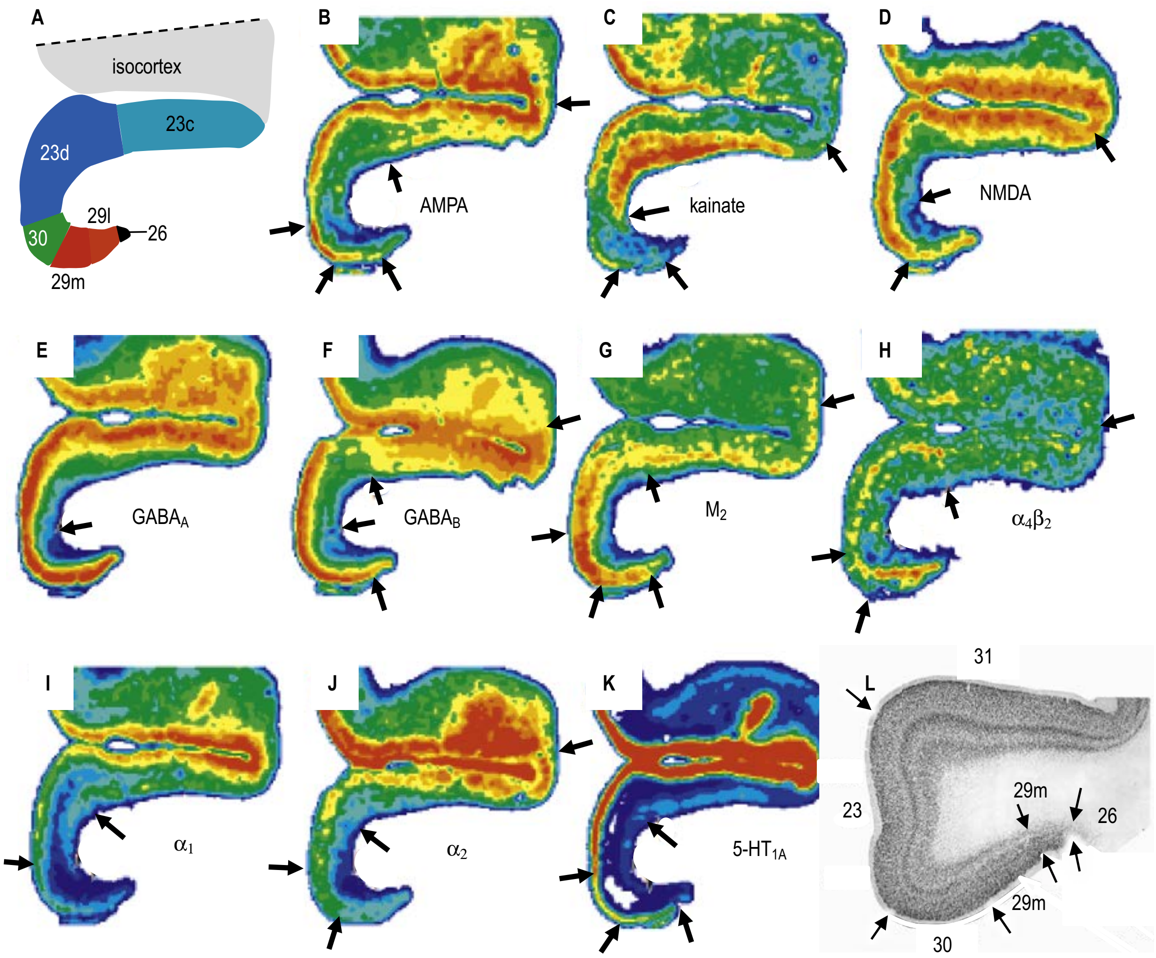

Fig. 32.44 Coronal sections through the retrosplenial region (areas 29l, 29m, 30) and posterior cingulate region (areas 23c and 23d). **A**, Scheme of the areal parcellation. **B–K**, Regional and laminar distribution of glutamatergic (**B–D**), GABAergic (**E–F**), cholinergic (**G–H**), adrenergic (**I–J**) and serotoninergic (**K**) receptors. **L**, Cytoarchitecture of the retrosplenial and posterior cingulate regions. (A–K, Adapted with permission from Palomero-Gallagher N, Zilles K 2009 Transmitter receptor systems in cingulate regions and areas. In: Vogt BA (ed) Cingulate Neurobiology and Disease. New York: Oxford University Press; L, adapted with permission from Vogt BA, Palomero-Gallagher N Cingulate cortex. In: Mai JK, Paxinos G (eds) The Human Nervous System. Elsevier, Academic Press. Copyright 2012.)

medially in area 30. This latter area shows a more differentiated laminar pattern with molecular (I), outer granular (II) and pyramidal (III) layers, followed by an inconspicuous and fragmented inner granular layer (IV), an inner pyramidal (V) and a multiform (VI) layer. Because the inner granular layer is barely visible, area 30 is often designated as agranular retrosplenial cortex.

Cingulate cortex

Within the inner aspect of the medial surface of each cerebral hemisphere, the cingulate gyrus wraps around the corpus callosum. Lying above the callosal sulcus and below the cingulate sulcus, the cingulate gyrus starts anteriorly within the subcallosal area below the rostrum of the corpus callosum and ascends around the genu of the corpus callosum. It borders the medial aspect of the superior frontal gyrus, the paracentral lobule, and more posteriorly the precuneus and the anterior cuneus. Anteriorly and basally, the cingulate sulcus may be continuous with the anterior para-olfactory sulcus under the rostrum of the corpus callosum and the subcallosal gyri. It may be double and parallel, the additional superior sulcus being the paracingulate sulcus. Architectonically, the cingulate cortex is a transition region between allocortex and isocortex and therefore includes periarchi-, proiso- and isocortical areas organized into four major divisions.

The original Brodmann's (1909) division of the cingulate cortex into anterior (BA24, BA25, BA32, BA33) and posterior (BA23 and BA31) regions has been replaced by a four region model that encompasses the anterior cingulate, midcingulate, posterior cingulate and retrosplenial cortices (**Fig. 32.45**) (Palomero-Gallagher et al 2009). These regions can be further subdivided using a multimodal approach informed by cyto- and receptor-architectonical, connectional and functional analyses.

The anterior cingulate cortex includes subgenual (areas 25, s24, s32, 33) and pregenual areas (p24, p32). The periarchicortical areas 25 and 33 display a laminar differentiation that is reduced compared to pro-isocortical agranular areas s24 and p24, and dysgranular isocortical areas s32 and p32 (see Fig. 32.45). Area 33 has the least differentiated lamination, whereas areas s32 and p32 are the most evolved and five layers can be recognized. Layers II–III as well as V–VI cannot be separated from each other in some of the anterior cingulate cortex areas, particularly in area 33.

Area 25 is of particular interest because of its projections to autonomic brainstem nuclei and its role in the regulation of visceromotor functions.

The most rostral portion of area 24 in the cingulate sulcus (subfield 24c) contains the face region of the rostral cingulate premotor area (Morecraft et al 2007). Von Economo and Koskinas (1929) first described a unique neuronal type, the spindle cell of Von Economo, in the anterior cingulate cortex (ACC), anterior insula and orbitofrontal cortices. These neurones have fusiform somata and vertically orientated cell processes and occur mainly in layer V (Nimchinsky et al 1995).

The midcingulate cortex (MCC) is divided into anterior (a24′, 24c′ and 32′) and posterior (p24′ and 24d) parts (see Fig. 32.45). Response selection, including the possibility of generating coordinated and context-dependent movements, is a characteristic function of the midcingulate cortex. Gyral and intrasulcal portions of midcingulate cortex differ in their cytoarchitecture, for example, layer V of the intrasulcal areas contain large pyramidal cells. The gyral cortex of the midcingulate cortex is thicker and has much broader layers than its intrasulcal part. Area 24c′ and ACC area p24c contain large pyramidal cells that represent the functionally defined rostral cingulate premotor area (see Fig. 32.45; Vogt 2016). In area 24d, the gigantopyramidal field of Braak (Braak 1976) contains extremely large pyramidal cells resembling Betz cells. The intrasulcal areas 24d and 23c of the posterior cingulate cortex (PCC) represent the functionally defined caudal cingulate premotor area (see Fig. 32.45; Vogt 2016). The latency of the onset of movements in the caudal cingulate premotor area, which codes for direction, force, target acquisition and orienting movements in space, is shorter than

The layer below lamina I (molecular layer) is broad and fused with layer III and contains scattered aggregations of evenly distributed pyramidal cells. Anterior and posterior divisions of area 25 have been described (Palomero-Gallagher et al 2008). There are cytoarchitectonic differences between the subgenual and pregenual components of area 24 as follows: layer II of area s24 is thinner and less cell dense than that of p24, and the neurones form aggregates only in s24; layer III of area s24 contains pyramidal cells that are larger in its upper than its lower portion, and it is thinner than in p24a; layer V is thinner in area s24 than p24, and layer VI is thinner and more cell sparse in area s24 than in p24.

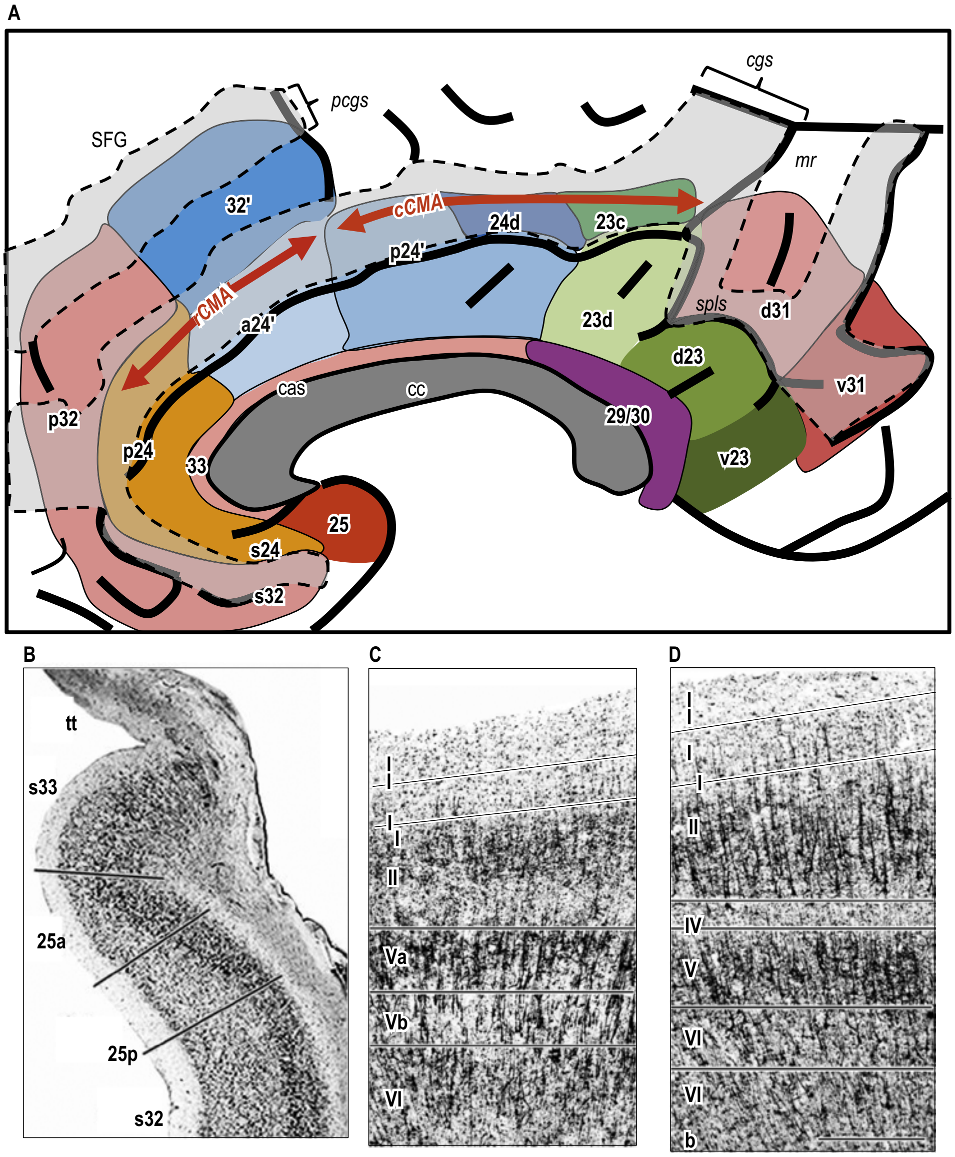

Fig. 32.45 The cytoarchitecture of anterior cingulate areas. **A**, The anterior cingulate cortex comprises areas s24, p24, 25, p32, s32, and the most anterior portion of area 33. The midcingulate cortex encompasses areas a24′, p24′, 24d, 32′ and the underlying portion of area 33. The posterior cingulate cortex contains areas 23c, 23d, d23, v23, d31 and v31. The retrosplenial region is represented by areas 29 and 30. Abbreviations: cas, callosal sulcus; cc, corpus callosum; cCMA, caudal cingulate premotor area; cgs, intrasulcal part of the cortex in the cingulate sulcus; mr, marginal ramus of the cingulate sulcus; pcgs, intrasulcal part of the cortex in the paracingulate sulcus; rCMA, rostral cingulate premotor area; SFG, superior frontal gyrus; spls, splenial sulcus. **B**, Coronal section through areas tt (taenia tecti), s33, anterior part of area 25 (25a), posterior part of area 25 (25p), subgenual part of area 32 (s32). Cell body stain. **C**, Laminar differentiation of area p24. SMI-32 ir stain. **D**, Laminar differentiation of area p32. SMI-32 ir stain. (A, Adapted with permission from Vogt BA, Palomero-Gallagher N Cingulate cortex. In: Mai JK, Paxinos G (eds) The Human Nervous System. Elsevier, Academic Press. Copyright 2012; D, adapted with permission from Palomero-Gallagher N, Mohlberg H, Zilles K et al 2008 Cytology and receptor architecture of human anterior cingulate cortex. J Comp Neurol 508:906–26.)

that of the rostral cingulate premotor area, which is involved in self-initiated movements. The characteristic gigantopyramidal cells of area 24d may indicate its involvement in skeletomotor functions. It mainly regulates the motor activity of the fore- and hindlimbs and that of the trunk. Isocortical area 32′ is also a transitional dysgranular region to the granular isocortical area BA9 and the premotor area 6aβ.

The posterior cingulate cortex consists of isocortical areas 23c, 23d, d23, v23, d31 and v31 (see Fig. 32.45). Area 23d is dysgranular and the remaining subdivisions of BA23 and BA31 are granular. An increasing packing density of granular cells in layer IV can be observed along a gradient from area 23d (low density) to areas v23 and 31 (high density).

The amygdala has reciprocal connections with the cingulate cortex that define the borders of emotion-specific cingulate areas. The basolateral and accessory basal nuclei of the amygdala are preferentially connected with area a24′ (part of the midcingulate region), which is specifically involved in emotion, emotional awareness and facial expressions associated with fear. In contrast, the posterior part of the midcingulate, the posterior cingulate and the retrosplenial cortices and retrosplenial cortices have no direct connections with the amygdala. Their involvement in emotion is related to selecting input from various sensory cortices (Vogt et al 2006). Areas BA25 and BA32, but not a24′ of the midcingulate cortex, are connected with autonomic regulatory nuclei of the brainstem: for example, they regulate gastric motility. These autonomic connections include major projections to the central nucleus of the amygdala, lateral hypothalamus, periaqueductal grey, and parabrachial nucleus. There are additional, though smaller, projections to the nucleus of the solitary tract and the dorsal motor nucleus of the vagus. BA25 also has reciprocal connections with the entorhinal cortex and the anterior cingulate area. Dense reciprocal connections between the posterior cingulate and inferior parietal cortices determine the posterior border of the anterior cingulate cortex (there are fewer connections with the midcingulate cortex and no connections with the anterior cingulate cortex). The cingulospinal projection system originates mainly in areas 24d (the gigantopyramidal caudal cingulate motor area (Braak 1976), which is buried in the cingulate sulcus) and a24′ of the midcingulate cortex, but not in areas 24, 25 or 32 of the anterior cingulate cortex (Dum and Strick 1991).

Chemoarchitecture of the cingulate cortex

Available with the *Gray's Anatomy* e-book

Isocortex

The isocortex and its parcellation into cortical areas will be separately described for each lobe in terms of its external sulci and gyri, internal cortical structure, connectivity and function. The subdivisions of the cerebral cortex as described in the different lobes is mainly based on the cytoarchitectonic parcellation schemes of Brodmann (1909) and von Economo and Koskinas (1925), and recent observer-independent cytoarchitectonic and multimodal parcellation methods (Schleicher et al 1999, Amunts et al 2007, 2014, Zilles and Amunts 2010, 2012, Amunts and Zilles 2015, Palomero-Gallagher et al 2015, Zilles et al 2015c, Palomero-Gallagher and Zilles 2018). Myeloarchitectonic findings will be included as appropriate (for review, see Zilles et al 2015a).

Frontal lobe

The frontal lobe contains numerous cortical areas for motor and cognitive functions, and is the largest lobe of the human forebrain. Its prefrontal cortex developed during the evolution of the brain to an absolute and relative size that is not attained by other primates.

NMDA receptors have the highest densities of the three ionotropic glutamate receptor subtypes in the cingulate cortex (Fig. 32.46). The balance between different glutamate receptor subtypes differs between the ACC and PCC. AMPA and kainate receptors have the second highest density in the ACC and PCC, respectively. They also present a rostro-caudal density gradient, the highest concentrations of both receptor types are in the ACC, and the lowest densities are in the PCC, suggesting that the ACC may work on a higher glutamatergic excitation level via AMPA and kainate receptors than MCC and PCC areas. Additionally, the ACC may be more susceptible to pathological processes that are characterized by increased glutamate levels and hyperexcitation. AMPA receptor densities are lower in area 25 than in the isocortical area 32. Conversely, the lowest NMDA receptor densities occur in the ACC, with the exception of area 25, which contains the highest NMDA receptor densities measured in the entire cingulate cortex. The lower kainate receptor density in s33 demarcates this area from s24. Area 24d, which projects to the spinal cord, contains very low kainate receptor densities. AMPA and NMDA receptors are characterized by higher concentrations in the supragranular than in the infragranular layers, whereas the opposite holds true for the kainate receptors.

The expression of GABA receptor subtypes varies along the rostro-caudal extension of the cingulate cortex. PCC shows higher densities of the inhibitory GABA$_A$ receptors and their benzodiazepine binding sites (BZ) than ACC and MCC. Very low levels of BZ densities occur in panic disorder and suggest a lower GABAergic inhibition of PCC under pathological conditions. PCC also contains higher GABA$_B$ receptor densities than MCC, from which is appears that PCC works on a higher GABAergic inhibition level than ACC and MCC: activation mediated by the glutamate receptors may be counterbalanced by fast inhibition via GABA$_A$ receptors in the PCC rather than in the ACC.

Choline acetyltransferase is synthesized by cholinergic neurones of the basal forebrain and is the most specific marker of cholinergic innervation. Axons of these neurones terminate throughout the cerebral cortex. Mapping of choline acetyltransferase reveals comparable densities of this enzyme in the ACC and PCC. Receptor analysis provides a more nuanced image. Lower nicotinic $\alpha_4\beta_2$, muscarinic M$_1$, M$_2$ and M$_3$ receptor densities are found in ACC than in PCC. This gradual increase in cholinergic receptors along the rostral-to-caudal extension of cingulate areas matches that of GABA receptors, and is the opposite of the observed decrease of the glutamate AMPA and kainate receptor densities. Thus, excitatory neurotransmission in the PCC is not only more strongly countered by GABA inhibition than in the ACC, but it is also subject to a stronger modulation via the cholinergic system. The densities of nicotinic $\alpha_4\beta_2$ receptors are lowest in the ACC and highest in the PCC and the retrosplenial cortex.

The α_1 adrenoceptor is the prevailing α receptor subtype in the cingulate cortex. The density of 5-HT$_{1A}$ receptors is highest in area 25, and it is the prevailing serotonin receptor subtype in ACC. The proiso- and isocortical cingulate areas 23, 24, 31 and 32 contain higher 5-HT$_{1A}$ receptor densities than the periallocortical areas. The 5-HT$_2$ receptor shows higher densities in the PCC than in the ACC.

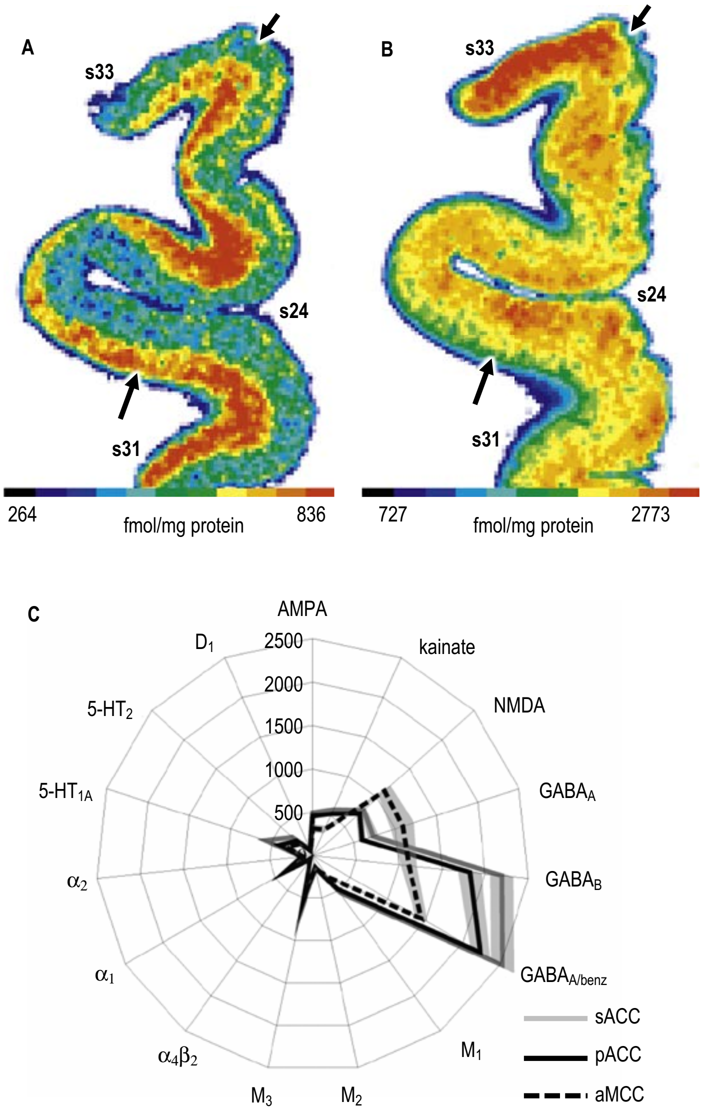

Fig. 32.46 Transmitter receptors in the human cingulate cortex. Coronal sections showing colour-coded regional and laminar densities of various receptors. **A**, Kainate receptors in areas of ACC. **B**, GABA$_B$ receptors in areas of ACC. **C**, Receptor fingerprint (glutamate: AMPA, kainate, NMDA subtypes; GABA: GABA$_A$, GABA$_B$ subtypes and GABA$_A$ benzodiazepine binding site; acetylcholine: muscarinic M$_1$, M$_2$, M$_3$ subtypes and nicotinic $\alpha_4\beta_2$ subtype; noradrenaline: α_1 and α_2 subtypes; serotonin: 5-HT$_{1A}$ and 5-HT$_2$ subtypes; dopamine: D1 subtype) of the entire anterior cingulate cortex. Densities correspond to the average of each receptor over all areas for a given region. sACC encompasses areas 25a, 25p, s33, s24a, s24b, and s32; pACC includes areas p33, p24a, p24b, pv24c, pd24c; aMCC encompasses areas 33, a24a′, a24b′, a24c′ and 32′. Receptor densities range from 0 to 2500 fmol/mg protein. (Adapted with permission from Palomero-Gallagher N, Mohlberg H, Zilles K et al 2008 Cytology and receptor architecture of human anterior cingulate cortex. J Comp Neurol 508:906–26.)

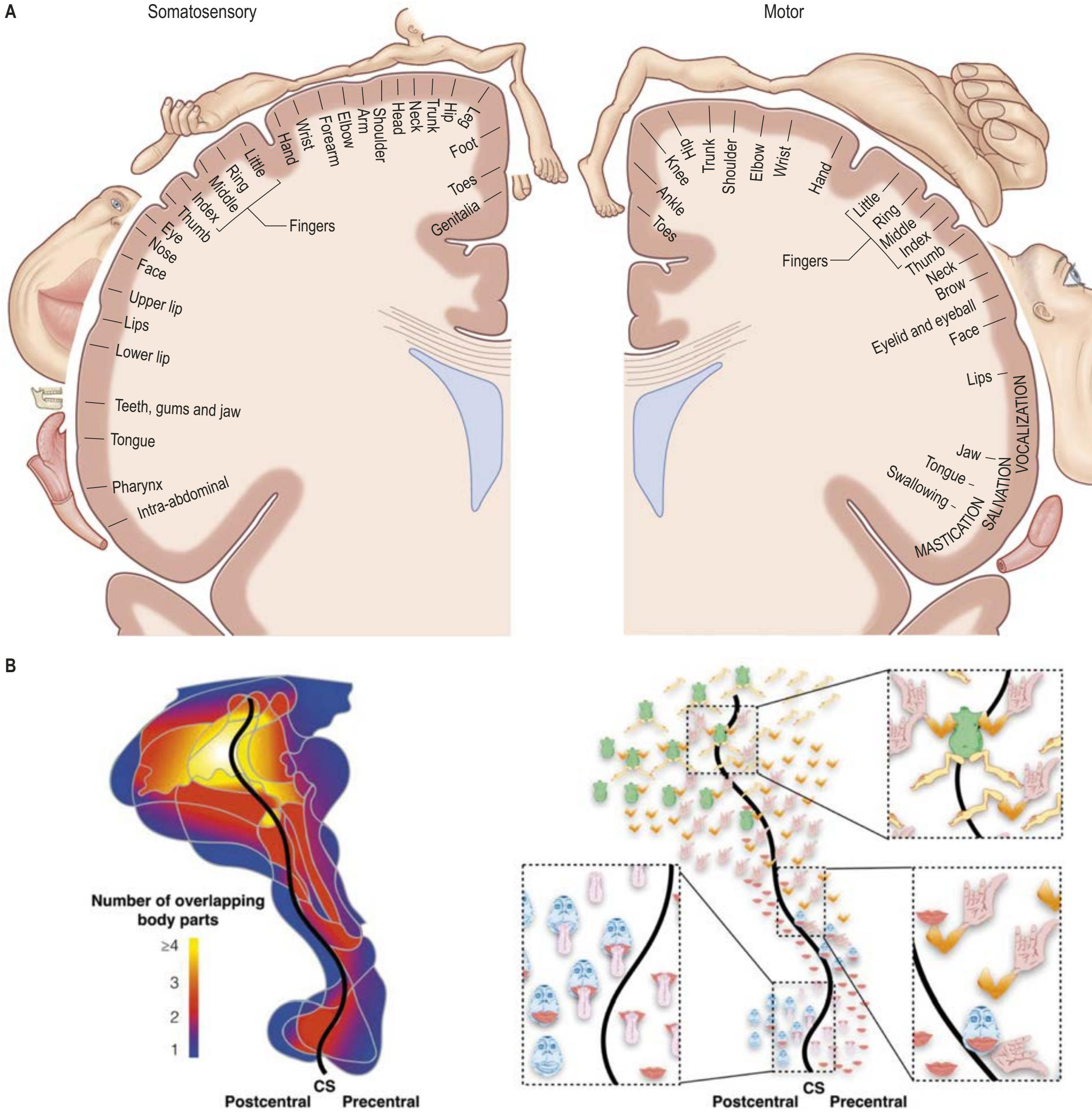
A
Somatosensory
Leg
Hip
Trunk
Neck
Head
Shoulder
Arm
Elbow
Forearm
Wrist
Hand
Little
Ring
Middle
Index
Thumb
Fingers
Eye
Nose
Face
Upper lip
Lips
Lower lip
Teeth, gums and jaw
Tongue
Pharynx
Intra-abdominal
Foot
Toes
Genitalia
Motor
Hip
Knee
Ankle
Toes
Trunk
Shoulder
Elbow
Wrist
Hand
Little
Ring
Middle
Index
Thumb
Fingers
Neck
Brow
Eyelid and eyeball
Face
Lips
Jaw
Tongue
Swallowing
MASTICATION
SALIVATION
VOCALIZATION
B
Number of overlapping body parts
≥4
3
2
1
CS
Postcentral
Precentral
CS
Postcentral
Precentral

Fig. 32.49 The homunculus in the human brain. **A**, Diagram of the somatosensory (left) and motor (right) homunculi of the postcentral and precentral gyri, respectively. The homunuclus was originally created by Penfield and Boldrey (1937) to indicate two fundamental aspects of the organization of the pericentral cortex: the topographical order of body part representations and their altered proportions, reflecting the amount of cortex dedicated to a particular function. **B**, A modern appraisal of the homunculus indicates an overlap between different body parts. Left: Heat map of the degree of overlap ranging from blue (one body part) to yellow (four or more body parts). Right: Map indicating the overlapping body parts of the homunculus. Note that the overlap is between body parts that cooperate for specific functions, such as neurones of the central area that control the mouth, arm and hand for feeding. Abbreviation: CS, central sulcus. (B, Adapted with permission from Catani M 2017 A little man of some importance. Brain 140:3055–61.)

The frontal lobe is delimited posteriorly by the central sulcus, medially by the cingulate sulcus and inferolaterally by the lateral fissure. The precentral gyrus is delimited by the central sulcus posteriorly and the precentral sulcus anteriorly. Anterior to the precentral gyrus the superior, middle and inferior frontal gyri converge anteriorly where they form the frontal pole. Its dorsal surface is covered by the frontal bone, and its ventral surface lies over the orbital part of the frontal bone and the cribriform plate of the ethmoid bone, and displays the orbital and rectus gyri. Its medial surface faces the falx cerebri.

The frontal lobe contains the primary motor area (BA4) in the anterior wall of the central sulcus; the supplementary motor area (SMA) and pre-supplementary motor area (pre-SMA) on its dorsomedial surface (medial part of BA6); premotor areas (lateral part of BA6) on its dorsolateral surface; the medial prefrontal (BA32) and lateral prefrontal (BA8–BA10 and BA44–BA47) cortex rostral to the precentral gyrus; and the fronto-orbital region (BA11–BA12) on its baso-rostral surface (see Fig. 32.13).

Frontal lobe sulci and gyri

Available with the *Gray's Anatomy* e-book

Frontal lobe internal structure and connectivity

The primary motor cortex (BA4) corresponds to a largely intrasulcal part of the precentral gyrus and is visible on the cortical surface only at its most superior level. BA4 has the lowest threshold for eliciting contralateral muscle contraction by electrical stimulation. It contains a topographically organized map ('motor homunculus') of the opposite body half, where the head is represented most laterally and inferiorly, the hand is represented in the central region, and the leg and foot are represented on the medial surface of the hemisphere in the paracentral lobule (Fig. 32.49). A striking feature of this map is the disproportionate representation of body parts in relation to their physical size: large areas represent the muscles of the face and hand, which are capable of finely controlled or fractionated movements (Penfield and Boldrey 1937; for a recent review of the homunculus, see Catani 2017).

In the adult stage, layer IV of BA4 and BA6 is difficult to identify in Nissl-stained sections (Fig. 32.50A), and both areas were traditionally classified as agranular cortex. A distinct inner granular layer IV is visible in fetal brains, but disappears during the first year of life (Amunts et al 1995). The typical small cells of layer IV have been demonstrated at the

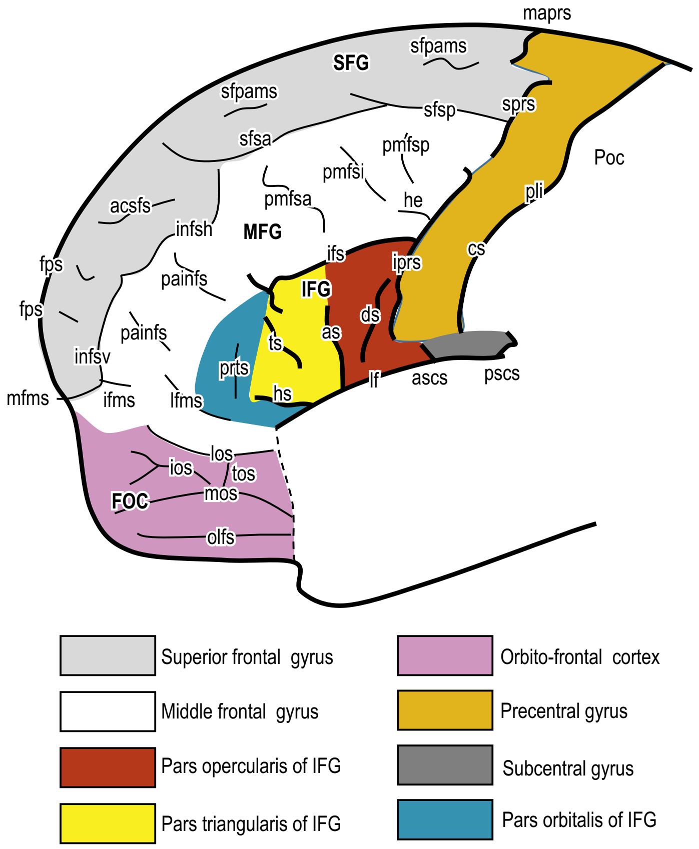

Fig. 32.47 Sulcal and gyral patterns of the frontal lobe. Abbreviations: acsfs, accessory superior frontal sulcus; as, ascending ramus of the lateral fissure; ascs, anterior subcentral sulcus; cs, central sulcus; ds, diagonal sulcus; FOC, fronto-orbital cortex; fps, frontopolar sulcus; he, horizontal extension of the inferior precentral sulcus; hs, horizontal ramus of the lateral fissure; IFG, inferior frontal gyrus; ifms, intermediate frontomarginal sulcus; ifs, inferior frontal sulcus; infsh, horizontal part of the intermediate frontal sulcus; infsv, vertical part of the intermediate frontal sulcus; ios, intermediate orbital frontal sulcus; iprs, inferior precentral sulcus; lf, lateral fissure; lfms, lateral frontomarginal sulcus; los, lateral orbital frontal sulcus; maprs, marginal precentral sulcus; MFG, medial frontal gyrus; mfms, medial frontomarginal sulcus; mos, medial orbital sulcus; olfs, olfactory frontal sulcus; painfs, paraintermediate frontal sulcus; pli, *pli de passage moyen* of Broca; pmfsa, antero-posterior middle frontal sulcus; pmfsi, intermediate posterior-frontal sulcus; pmfsp, postero-medial frontal sulcus; Poc, postcentral gyrus; prts, pretriangular sulcus; pscs, posterior subcentral sulcus; SFG, superior frontal gyrus; sfpams, superior frontal paramidline sulcus; sfsa, anterior branch of the superior frontal sulcus; sfsp, posterior branch of the superior frontal sulcus; sprs, superior precentral sulcus; tos, transverse orbital sulcus; ts, triangular sulcus. (Adapted with permission from Petrides M, Pandya DN 2012 The frontal cortex. In: Mai JK, Paxinos G (eds) The Human Nervous System. Elsevier, Academic Press. Copyright 2010.)

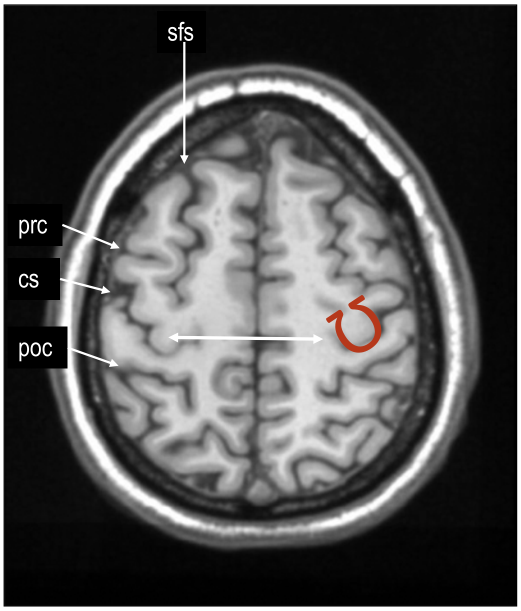

Fig. 32.48 Representation of the hand in the precentral gyrus. Abbreviations: cs, central sulcus; poc, postcentral sulcus; prc, precentral sulcus; sfs, superior frontal sulcus. Ω, hand-knob of the precentral gyrus. (Adapted with permission from Yousry TA, Schmid UD, Alkadhi H et al 1997 Localization of the motor hand area to a knob on the precentral gyrus: a new landmark. Brain 120:141–57.)

The central sulcus demarcates the primary motor (BA4) and somatosensory (BA1–BA3) cortical areas located in the precentral and postcentral gyri, respectively. The central sulcus starts in or near the interhemispheric fissure, a little behind the midpoint between the frontal and occipital poles, and runs in a letter S shape ventrally and rostrally, to end usually shortly above the lateral sulcus: it is mostly continuous in both hemispheres (Fig. 32.47).

The precentral gyrus lies over the dorsolateral and lateral surface of the cerebral hemisphere, its upper aspect extending onto the medial surface. It is continuous medially and inferiorly with the postcentral gyrus along connections that encircle both extremities of the central sulcus. The inferior connection corresponds to the subcentral gyrus, delineated anteriorly and posteriorly by the anterior and posterior subcentral rami of the lateral fissure. They can be situated either completely over the lateral fissure, or in part internal to the fissure. The superior connection corresponds to the paracentral lobule that is located on the medial surface of the hemisphere inside the interhemispheric fissure, and delineated anteriorly by the paracentral sulcus and posteriorly by the ascending marginal ramus of the cingulate sulcus. Some brains show a middle connection between the pre- and postcentral gyri (*pli de passage moyen* of Broca), which is usually hidden within the central sulcus: when this middle connection reaches the brain surface, it interrupts the central sulcus. The motor hand area has been localized by fMRI to an Ω-like protrusion of the precentral gyrus directed to the postcentral gyrus (Fig. 32.48) that is found at the level of the middle genu of the central sulcus (Yousry et al 1997). The precentral gyrus is delimited anteriorly by the precentral sulcus, itself divided into superior and inferior precentral sulci by a connection between the middle frontal gyrus and the precentral gyrus. The superior part of the precentral sulcus is very often interrupted superiorly by a connection between the superior frontal and precentral gyri, producing a more medial segment, the medial precentral sulcus. More dorsally, within the precentral region, the marginal precentral sulcus (see Fig. 32.47) may merge with the superior precentral or central sulci.

The superior frontal gyrus is continuous anteriorly and inferiorly with the rectus gyrus, and may also be connected to the orbital gyri and the middle frontal gyrus. Posteriorly, it is connected to the precentral gyrus (see Fig. 32.47). Usually the superior frontal gyrus is subdivided by an intermediate frontal sulcus into a lateral and a medial portion. The middle frontal gyrus is usually the largest of the frontal gyri, and is frequently connected posteriorly to the precentral gyrus. It harbours a complex of multiple shallow sulcal segments known collectively as the middle or intermediate frontal sulcus (Petrides and Pandya 2012).

The inferior frontal gyrus is subdivided by small sulci into a posterior pars opercularis, an intermediate pars triangularis and an anterior pars orbitalis (see Fig. 32.47). The opercular part is rostrally bordered by the ascending ramus of the lateral fissure, and posteriorly by the precentral sulcus. A diagonal sulcus is occasionally visible in the pars triangularis. The triangular part extends between the ascending and horizontal rami of the lateral fissure, and continues with the lateral orbital part. The frontomarginal sulcus is often a short branching sulcus that separates the frontal pole into different portions.

The olfactory sulcus lies longitudinally in a paramedian position on the frontobasal (orbital) surface of the frontal lobe (see Fig. 32.47). It underlies the olfactory tract and bulb. Posteriorly, the olfactory tract is divided into medial and lateral striae that delineate the most anterior aspect of the anterior perforated substance. The narrow gyrus rectus, medial to the olfactory sulcus, is considered to be the most anatomically constant of the cerebral gyri. The orbital gyri, lateral to the olfactory sulcus, account for the greatest proportion of the frontobasal region. The orbital gyri are delineated by the lateral, medial and transverse orbital sulci that together form a characteristic H shape. The posterior orbital gyrus lies anterior to the anterior perforated substance and typically presents a configuration similar to a tricorn hat, a feature that may facilitate its identification in anatomical specimens where the H-shaped orbital sulcus is less obvious.

On its medial surface, the frontal lobe is limited inferiorly by the cingulate sulcus, which starts within the subcallosal region and extends over the cingulate gyrus. The cingulate sulcus may occasionally be

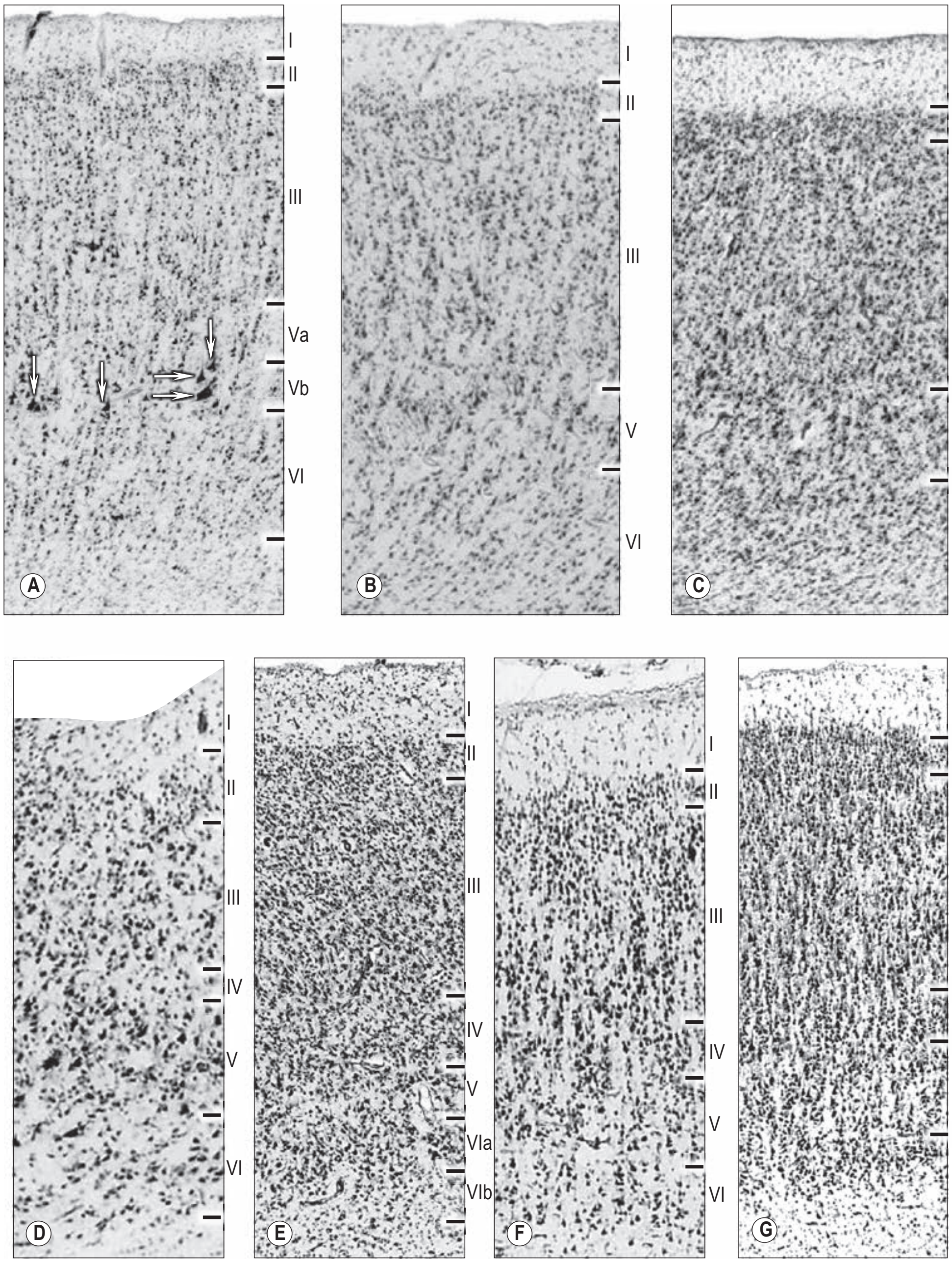

Fig. 32.50 A–C, Nissl stained sections through the human motor and somatosensory cortex. **A**, Primary motor cortex (BA4); arrows indicate Betz cells in layer Vb. **B**, Premotor cortex, area PMdc (dorso-caudal part of BA6). **C**, Premotor cortex, area PMdr (dorso-rostral part of BA6). **D–G**, Nissl staining of the human anterior parietal cortex. **D**, Area 3a (transition area between the primary motor and primary somatosensory cortex). **E**, Primary somatosensory cortex (area 3b). **F**, Primary somatosensory area 1 (BA1), and **G** primary somatosensory area 2 (BA2).

double in its anterior portion, when the more rostrally and dorsally situated sulcus is called the paracingulate sulcus (see Fig. 32.2).

The paracentral lobule contains the distal part of the central sulcus and, inferior to it, the paracentral fossa (see Fig. 32.2). The gyrus rectus is bounded superiorly by the superior rostral sulcus and accommodates the shallower inferior rostral sulcus along its medial surface.

border region between layers III and V in the adult stage (Barbas and Garcia-Cabezas 2015). The most characteristic feature of BA4 are the somata of extremely large pyramidal cells (Betz cells) in lamina V (**Fig. 32.50**). These cells are 80–100 µm in diameter, and their axons form the corticospinal and corticonuclear tracts. BA4 contains a very high density of myelinated axons in the lower half of its cortical depth. It also has the lowest concentration of most transmitter receptor types across all cortical areas (**Fig. 32.51**), presumably because most receptors are found pre- and post-synaptically and myelin sheaths prevent the building of synapses.

The major thalamic connections of BA4 are with the posterior part of the ventral lateral nucleus, which receives afferents from the deep cerebellar nuclei and contains a topographic representation of the contralateral half of the body that is preserved in its projection to BA4. The anterior part of the ventral lateral nucleus projects to the premotor and supplementary motor areas of the cortex. Other thalamic connections of BA4 are with the centromedian and parafascicular thalamic nuclei. Apart from the corticospinal tract and thalamic projections, the motor cortex has extensive subcortical connections with the striatum, subthalamic nucleus, pontine nuclei and all the somatomotor nuclei in the brainstem (oculogyric, facial and hypoglossal nuclei).

BA4 is the origin of polysynaptic descending pathways to the spinal cord that relay in the reticular formation, red nucleus, superior colliculus, vestibular nuclei and inferior olivary nucleus. BA4 is also connected with the ipsilateral somatosensory cortex through short U-fibres, which are topographically organized according to the homuncular principle, i.e. the largest projections are observed for the hand and there are progressively smaller projections for the tongue/mouth and foot areas (Catani et al 2012). These projections to the motor cortex arise mainly in BA1 and BA2, with minor contribution from area 3b. Fibres from the somatosensory cortex terminate in layers II and III of BA4: neurones in the motor cortex that can be activated from the somatosensory cortex tend to have a late onset of activity, mainly during the execution of movement. Connections between motor and somatosensory homunculi may play a role in precision grasping and motor learning. Additional ipsilateral corticocortical fibres to BA4 posterior to the central sulcus come from the opercular part of the somatosensory area (SII). Neurones in BA4 are responsive to peripheral stimuli and have receptive fields similar to those in the primary somatosensory cortex. Cells located posteriorly in the motor cortex (area 4p) have cutaneous receptive fields, whereas more anteriorly situated neurones (in area 4a) respond to stimulation of deeper tissues (Geyer et al 1996).

The motor cortex receives inputs from the lateral premotor cortex, supplementary motor area and insula. Most of these connections are short U-shapes that modulate motor cortical activity in relation to the preparation, guidance and temporal organization of movements. BA4 sends fibres to, and receives fibres from, its contralateral counterpart, and also projects to the contralateral supplementary motor cortex.

Brodmann's 'agranular' area 6 (see Fig. 32.13) lies immediately in front of the primary motor cortex on the precentral gyrus and extends superiorly into the lateral and medial portions of the superior frontal gyrus (Geyer et al 2012). BA6 is subdivided into the lateral premotor cortex and the supplementary motor (SMA proper) and presupplementary motor (pre-SMA) cortices on the medial hemispheric surface (**Fig. 32.52**). The lateral premotor cortex is segregated into a dorsal and a ventral area on cytoarchitectonical, connectional and functional grounds; both dorsal and ventral areas contribute to the corticospinal tract. Further anterior and posterior subdivisions of the dorsal and ventral lateral premotor cortex can be identified (see Fig. 32.50B–C).

The major thalamic connections of the premotor cortex are with the anterior division of the ventrolateral nucleus and with the centromedian, parafascicular and centrolateral components of the intralaminar thalamic nuclei. Subcortical projections to the striatum and pontine nuclei are prominent, and it projects to the superior colliculus and the reticular formation. Commissural connections are with the contralateral premotor, primary motor and superior parietal (BA5) cortices. Ipsilateral corticocortical connections with BA5 are common to both dorsal and ventral subdivisions of the premotor cortex, and both send a major projection to the primary motor cortex. The dorsal premotor area receives fibres from the posterior superior temporal cortex and projects to the supplementary motor cortex. The dorsal subdivision of the lateral premotor area receives projections from the frontal eye field. Perhaps the greatest functionally significant difference in connectivity between the dorsal and ventral subdivisions of the lateral premotor area is that the dorsal premotor area receives fibres from the dorsolateral prefrontal cortex, whereas the ventral subdivision receives fibres from the ventrolateral prefrontal cortex. All of these association connections are reciprocal.

Direction selectivity for movement is a common feature of many premotor neurones. Neurones in the dorsal premotor cortex show anticipatory activity and task-related discharge as well as direction selectivity, but little or no direct stimulus-related activity. Together with the posterior parietal cortex, the dorsal premotor cortex is important in establishing a motor programme or intention, thus contributing to motor preparation in relation to internally guided movement. In contrast, the ventral premotor cortex is related more to the execution of externally guided movements in relation to a specific stimulus, especially visually guided movements.

The supplementary motor area (SMA proper) is found within the medial portion of BA6 (see Fig. 32.52A). An additional functional subdivision, the pre-supplementary motor area (pre-SMA), lies anterior to the supplementary motor area on the medial surface of the cortex. The portion of area 24 buried in the cingulate sulcus and adjacent to BA6 contains two motor areas, the anterior and posterior cingulate motor areas (see Fig. 32.52). SMA proper and pre-SMA are 'agranular' cortices, because a layer IV is not clearly definable in Nissl stained sections of this area (see Fig. 32.52B).

SMA receives its major thalamic input from the anterior part of the ventral lateral thalamic nucleus, which in turn is the major recipient of input from the internal segment of the globus pallidus. Additional thalamic afferents are from the ventral anterior nucleus, intralaminar nuclei (notably the centrolateral and centromedial nuclei) and the mediodorsal nucleus. The connections with the thalamus are reciprocal. SMA makes a substantial contribution to the corticospinal tract. It contains a homuncular representation of the body in which the leg is posterior, the face anterior and the upper limb is represented between them. Its role in the control of movement is primarily in complex tasks that require temporal organization of sequential movements and in the retrieval of motor memory. Stimulation of SMA elicits the sensation of an urge to move, or of anticipation that a movement is about to occur.

Pre-SMA receives connections from widespread regions of the ipsilateral frontal lobe, including the primary motor cortex, dorsal premotor area, dorsolateral and ventrolateral prefrontal, medial prefrontal, fronto-orbital cortices and the frontal eye field. These connections are reciprocal, but the major ipsilateral efferent pathway is to the motor cortex. Parietal lobe connections of pre-SMA are with the superior parietal area BA5 and inferior parietal lobule. Contralateral connections are with SMA and contralateral premotor cortices. Further subcortical connections pass to the striatum, subthalamic and pontine nuclei, the brainstem reticular formation and the inferior olivary nucleus.

The frontal eye field (FEF) is an important area for the control of eye movements. It is located near the junction of the middle frontal and precentral sulci: activation studies in humans indicate a more posterior localization (BA6) compared to monkeys (BA8). It receives its major thalamic projection from the parvocellular mediodorsal nucleus, with additional afferents from the medial pulvinar, ventral anterior nucleus, suprageniculate–limitans complex and the paracentral nucleus of the intralaminar group. The thalamocortical pathways to FEF are part of pathways from the superior colliculus, substantia nigra and the dentate nucleus of the cerebellum. The FEF has extensive ipsilateral corticocortical connections, and receives input from several visual areas in the occipital, parietal and temporal lobes, including the middle temporal area (V5). There are also projections from the auditory superior temporal gyrus and the ventrolateral and dorsolateral prefrontal cortices. The FEF projects to the dorsal and ventral premotor cortices and to a medial motor area, probably the supplementary eye field adjacent to the supplementary motor area proper. The FEF projects prominently to the superior colliculus, the pontine gaze centre within the pontine reticular formation, and oculogyric-related nuclei in the brainstem.

The prefrontal cortex on the dorsolateral surface of the hemisphere consists predominantly of Brodmann's areas 8, 9, 10, 46, 47 and language areas 44 and 45. All prefrontal areas except area 44 have a layer IV, and thus are granular cortices; area 44 is dysgranular (**Fig. 32.53C–D**). These areas receive their major thalamic afferents from the mediodorsal nucleus, with additional contributions from the medial pulvinar and ventral anterior and paracentral nuclei of the anterior intralaminar group. The dorsolateral region receives long association fibres from the posterior and middle superior temporal gyri (including auditory association areas) and from the posterior parietal and much of the middle temporal cortices. It also receives projections from the frontal pole (BA10), and from the medial prefrontal cortex (BA32). It projects to SMA, the dorsal premotor cortex and the frontal eye field. All these thalamic and corticocortical connections are reciprocal. Commissural connections are with the homologous areas and with the contralateral inferior parietal cortex. The ventrolateral prefrontal region receives long association fibres from the inferior parietal lobule, auditory association

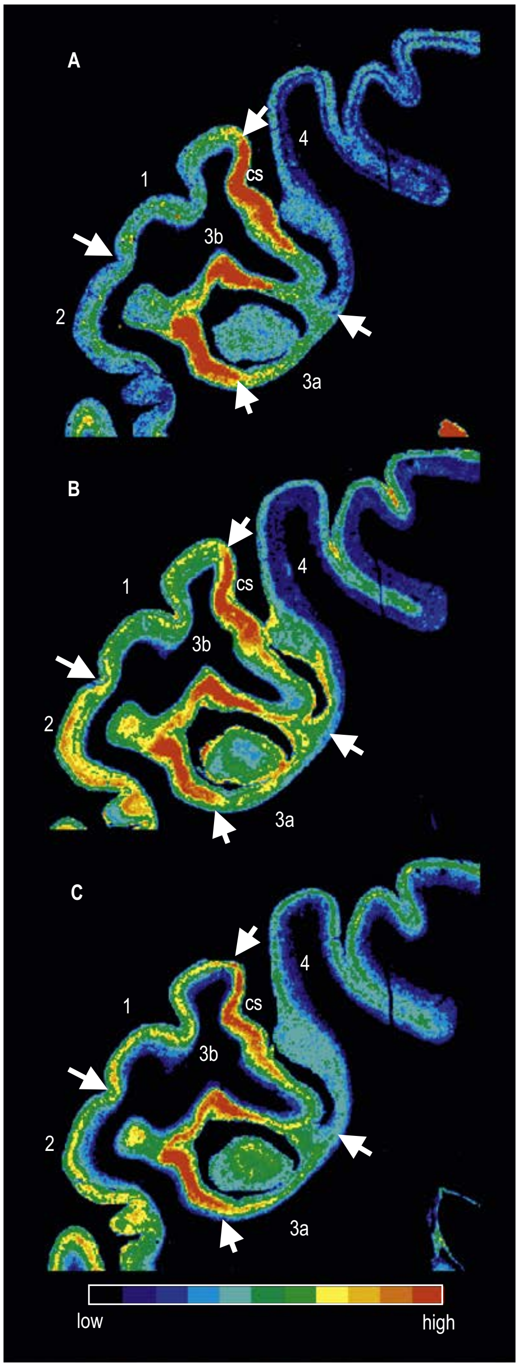

Fig. 32.51 Expression of transmitter receptors in the human primary motor and somatosensory cortices (coronal sections). **A**, Cholinergic muscarinic M_2 receptor. **B**, Noradrenergic α_2 receptor. **C**, Serotoninergic 5-HT_2 receptor. Key: 1, BA1 (primary somatosensory cortex); 2, BA2 (primary somatosensory cortex); 3a, area 3a (transition area between the primary motor and primary somatosensory cortices); 3b, area 3b (primary somatosensory cortex); 4, BA4. Abbreviation: cs, central sulcus. Arrows indicate borders between areas. (Adapted with permission from Zilles K, Palomero-Gallagher N Comparative analysis of receptor subtypes that identify primary cortical sensory areas. In: Kaas J, Striedter G, Krubitzer L (eds) Evolution of the Nervous Systems, 2nd ed, Vol. 2. Elsevier, Academic Press. Copyright 2017.)

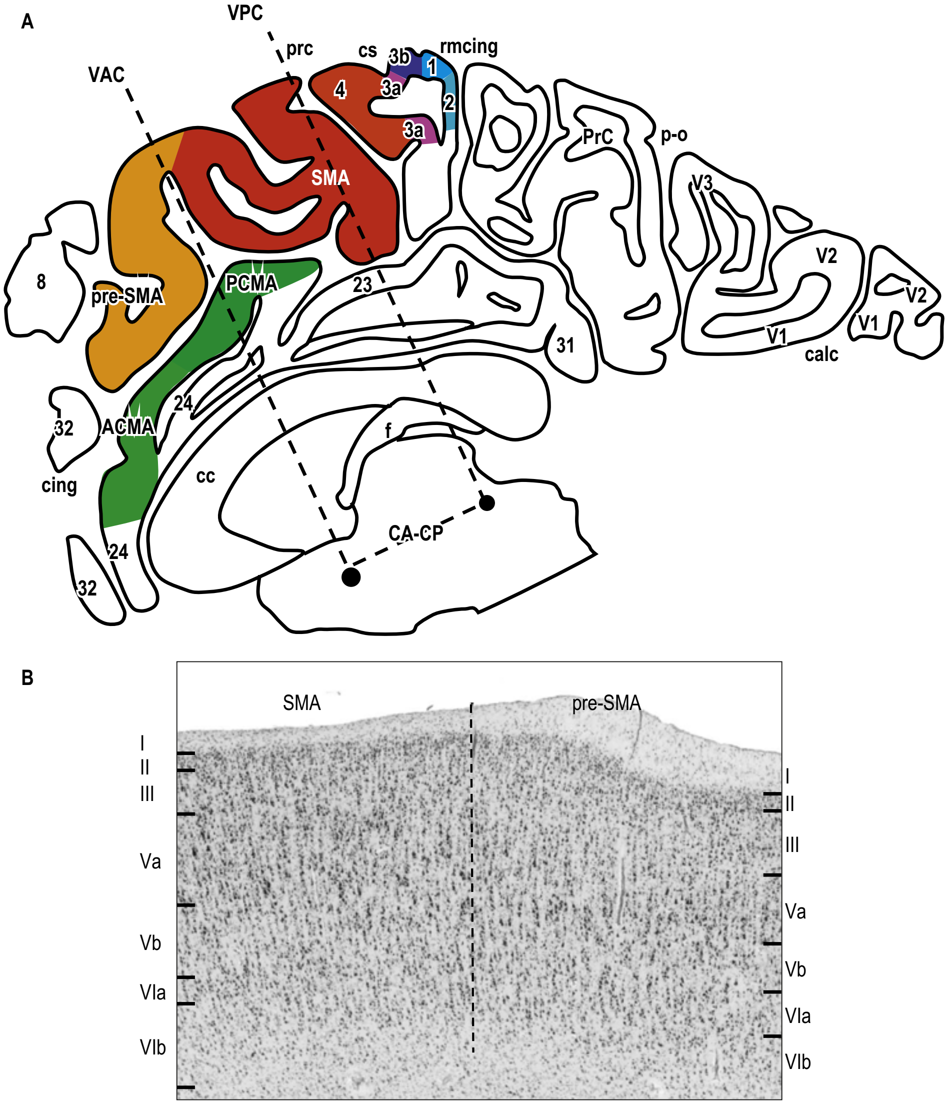
A
VPC
VAC
prc
cs
3b
rmcing
1
4
3a
2
3a
PrC
p-o
SMA
V3
8
pre-SMA
PCMA
23
V2
V2
V1
V1
calc
31
24
32
ACMA
f
cc
cing
CA-CP
24
32
B
SMA
pre-SMA
I
II
III
Va
Vb
VIa
VIb
I
II
III
Va
Vb
VIa
VIb

Fig. 32.52 **A**, A sagittal section through a human cerebral hemisphere indicating the position of the supplementary motor area (SMA), pre-supplementary motor area (pre-SMA), anterior cingulate motor (ACMA) and posterior cingulate motor (PCMA) areas. Key: Arabic numbers show the surrounding Brodmann areas BA1, BA2, BA4, BA8, BA23, BA24, BA31 and BA32; 3a, transition area between BA4 and area 3b (part of the somatosensory cortex); 3b, primary somatosensory area; V1, primary visual area; V2, secondary visual area; V3, tertiary visual area. Abbreviations: CA–CP line through the anterior and posterior commissures; calc, calcarine sulcus; cc, corpus callosum; cing, cingulate sulcus; cs, central sulcus; f, fornix; p-o, parieto-occipital sulcus; prc, precentral sulcus; PrC, precuneus; rmcing, ramus ascendens of the cingulate sulcus; VAC, vertical line through the anterior commissure and the CA–CP line; VPC, vertical line through the posterior commissure and the CA–CP line. **B**, A horizontal section through human SMA and pre-SMA, silver staining of neuronal cell bodies. Dashed line indicates the position of the border between both areas. Laminar differentiation is indicated by Roman numerals.

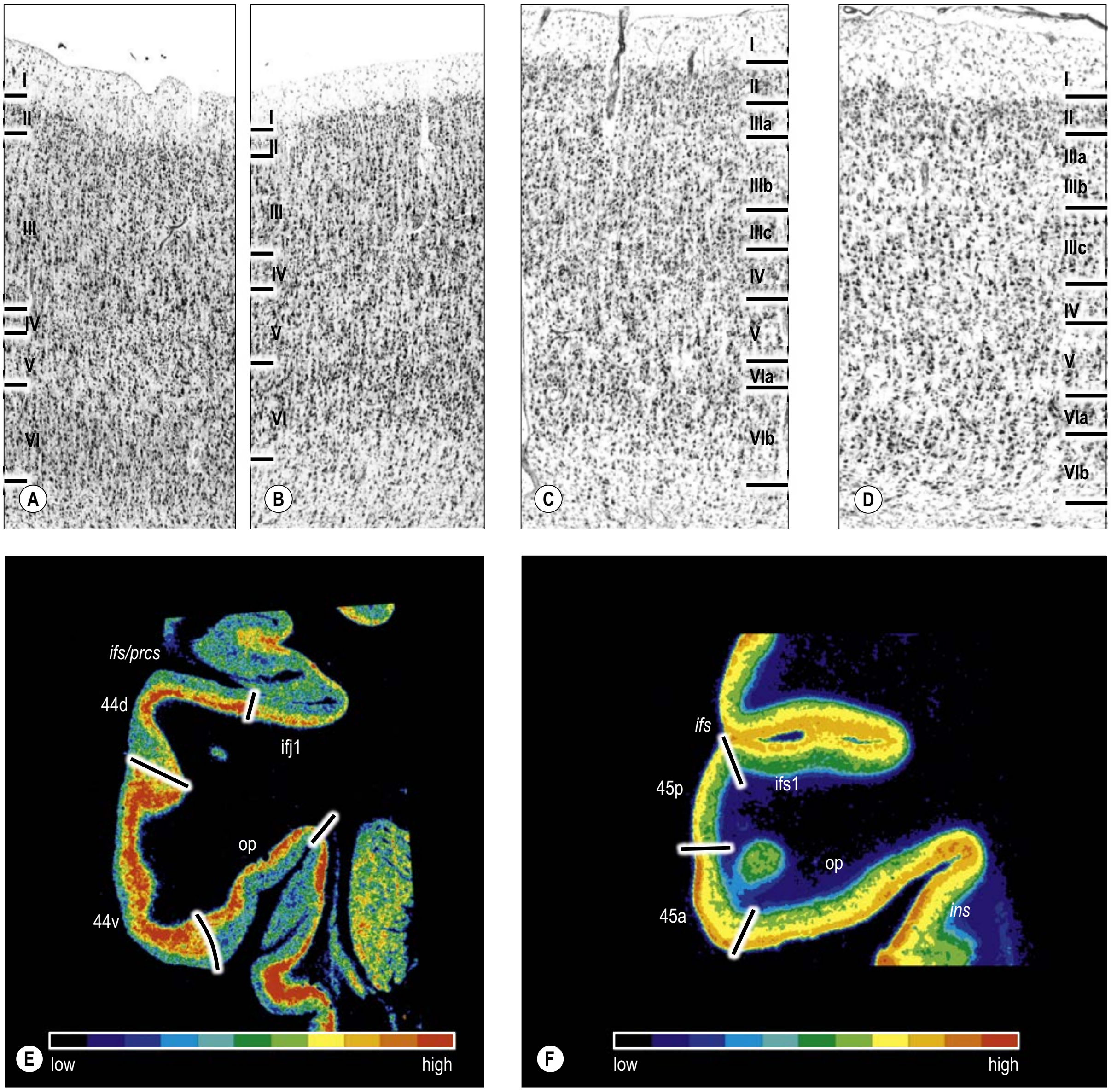
I
II
III
IV
V
VI
A
I
II
III
IV
V
VI
B
I
II
IIIa
IIIb
IIIc
IV
V
VIa
VIb
C
I
II
IIIa
IIIb
IIIc
IV
V
VIa
VIb
D
ifs/prcs
44d
ifj1
op
44v
E
low
high
ifs
45p
ifs1
op
45a
ins
F
low
high

Fig. 32.53 **A–F**, The cytoarchitecture of Broca areas BA44 (**A**), BA45 (**B**), and the frontopolar areas Fp1 (**C**, BA10 lateral) and Fp2 (**D**, BA10 medial). Roman numerals indicate cortical layers. **E–F**, Distribution of glutamate kainate (**E**) and GABA_B (**F**) receptors in Broca areas BA44 and BA45. Abbreviations: ifj1, area in the inferior frontal sulcus (ifs) at the junction with the precentral sulcus (prcs); ifs1, area in the inferior frontal sulcus; ins, insular cortex; op, frontal opercular region. The colour scales indicate low and high receptor densities.

areas of the temporal operculum, the insula and the anterior part of the ventral bank of the superior temporal sulcus. It also receives input from the anterior fronto-orbital cortex and projects to the frontal eye field and the ventral premotor cortex. It is reciprocally connected with the contralateral homologous area via the corpus callosum.

The granular cortex of the frontal pole (BA10) has greatly expanded in humans compared to other species. It receives thalamic inputs from the mediodorsal nucleus, medial pulvinar and paracentral nucleus and is reciprocally connected with the cortex of the temporal pole, the anterior fronto-orbital cortex and the dorsolateral prefrontal cortex. Within the frontal lobe, BA10 has connections with BA32, the ventrolateral prefrontal cortex, and premotor areas on the medial surface of the hemisphere. Commissural connections to the homologous area of the contralateral hemisphere are extensive. BA10 is segregated into lateral (Fp1) and medial (Fp2) areas on cytoarchitectonic, genetic and functional grounds (see Figs 32.13, 32.53C–D) (Bludau et al 2014, 2018). The lateral area is involved in working memory, episodic memory retrieval and attending environmental stimuli, whereas the medial frontal pole region is engaged in self-generated stimuli (i.e. the 'thoughts in our head'). The interaction between the two areas mediated by the fronto-marginal tract determine whether signals from the internal (mental) or external (sensory) world dominate ongoing behaviour and cognition (Burgess et al 2011, Catani et al 2012).

The fronto-orbital cortex is connected with the mediodorsal, anteromedial, ventral anterior, medial pulvinar, paracentral and midline nuclei of the thalamus. Three areas are cytoarchitectonically identified in the fronto-orbital cortex (**Fig. 32.54A**): the granular area Fo1, mainly on the rostral gyrus rectus and medial of the olfactory sulcus; the granular to dysgranular area Fo2, mainly on the posterior part of the ventromedial gyrus rectus and the medial and lateral banks of the olfactory sulcus; and the granular area Fo3 between the olfactory and medial or intermediate orbital sulci. Fo3 is bordered medially by Fo1 and Fo2. The posterior part of the fronto-orbital cortex extends to the olfactory and insular cortices and is partly covered by the temporal lobe. The parolfactory sulcus often marks the border between the medial part of the fronto-orbital cortex and BA25. The medial fronto-orbital cortex has reciprocal connections with various limbic structures including the anterior cingulate, insula, amygdala and entorhinal cortices, hippocampus, diagonal band of Broca, midline thalamic nuclei and the magnocellular sector of the mediodorsal thalamic nucleus. The fronto-orbital cortex is involved in a variety of functions associated with pleasant as well as painful perceptions and reward processing (see limbic lobe). Olfactory and gustatory stimuli elicit activations in the fronto-orbital cortex that are often associated with hedonistic aspects, and is also involved in touch and pain processing.

The language area of Broca consists of BA44 and BA45 in the opercular and triangular parts of the inferior frontal gyrus, respectively. BA44 is found immediately anterior to the most inferior aspect of the precentral gyrus (**Fig. 32.54B**). Both areas are involved in speech production and show considerable inter-individual variability in size and relationship to gyri. Volumes of left BA44 are always larger than those of the right hemisphere. Thus, interhemispheric differences in the volume of BA44 may be interpreted as anatomical correlates of language dominance. Volumes of BA45 do not differ significantly between the hemispheres. BA44 is involved more in syntactic processes, and BA45 more in semantic processes. The borders between these areas are not consistently defined by sulcal landmarks (Amunts et al 1999). BA47, or at least its most posterior part, should also be considered as part of the Broca region for functional reasons. The cytoarchitecture of BA44 and BA45 is characterized by very large pyramidal cells, sometimes clustered, in deeper layer III, and large pyramidal cells in upper layer V (**Fig. 32.53A–B**). The size of cells in layer III increases from its border with layer II to the layer III/IV border. The most important difference between BA44 and BA45 is found in layer IV, which is dysgranular and invaded by pyramidal cells of layers III and V in BA44. In contrast, layer IV of BA45 is seldom invaded by layer III or layer V pyramidal cells, i.e. BA45 is a granular cortical area. Both areas can be further subdivided on the basis of regional and laminar densities of multiple receptors (**Fig. 32.53E–F**).

Parietal lobe

The parietal lobe lies posterior to the central sulcus on the superolateral and medial surfaces of the cerebral hemisphere. The anterior part of the human parietal cortex comprises somatosensory areas 3a, 3b, BA1 and BA2 in the postcentral gyrus, and the parietal operculum (OP1–OP4). The posterior parietal cortex contains multimodal areas in both the superior (BA5, BA7) and inferior (BA40, BA39) parietal lobules, as well as areas in the intraparietal sulcus that were not described by Brodmann (see Fig. 32.13). The posterior parietal cortex is a key node in networks connecting visual occipital and auditory temporal areas with premotor and prefrontal cortices. The superior parietal lobule (SPL) encompasses parts of the lateral as well as the medial surface, the latter including the precuneus.

Parietal lobe sulci and gyri

Available with the *Gray's Anatomy* e-book

Parietal lobe internal structure and connectivity

All parietal areas have a six-layered eulaminate cortex, with the exception of areas 3a and 3b of the primary somatosensory cortex. The molecular layer (layer I) does not differ between the various areas, but differences in layers II to VI help to parcellate the parietal cortex. The basic myeloarchitectonic organization of the isocortex, with radiate fibre bundles reaching the superficial parts of cortical layer III, can be found in all parietal areas, although the preponderance and extent of the inner and outer stripes of Baillarger differ.

The primary somatosensory cortex (SI) located in the postcentral gyrus includes areas 3a, 3b, BA1 and BA2. Area 3a lies in the depth of the central sulcus and is contiguous to area 4p whereas area 3b is in the posterior wall of the central sulcus. BA1 is on the crown of the postcentral gyrus, and BA2 occupies its posterior cortex (see Fig. 32.13). Area 3a has a low cell packing density, with a few larger pyramidal cells in deep layer III, and an incipient layer IV (see Fig. 32.50D). In contrast, area 3b has a very high cell packing density in the supragranular layers, particularly layer IV, and the cells in layer III are homogeneously distributed: this led to the classification of area 3b as koniocortical (see Fig. 32.50E). BA1 is characterized by an obvious layer IV, and a pronounced columnar arrangement of typically large and numerous pyramidal cells in layers III and V, with a marked superficial-to-deep increase in cell size across layer III (see Fig. 32.50F). BA2 also has an obvious layer IV, fewer pyramidal cells in layer III, large pyramidal cells only appearing deep in layer III and a sharp layer VI–white matter border (see Fig. 32.50G).

The primary somatosensory cortex contains a topographical map of the contralateral half of the body. The face, tongue and lips are represented inferiorly, the trunk and upper limb are represented on the superolateral aspect, and the lower limb is represented on the medial aspect of the hemisphere. The function of SI depends on its thalamic input from the ventral posterior nucleus. This nucleus is divided into a ventral posterolateral part, which receives information from the trunk and limbs, and a ventral posteromedial part, in which the head is represented. Within the ventral posterior nucleus, neurones in the central core respond to cutaneous stimuli and those in the most dorsal anterior and posterior parts, which arch as a 'shell' over the central core, respond to deep stimuli. This is reflected in their differential projections to the cortex: the cutaneous central core projects to 3b, the deep tissue-responsive neurones send fibres to areas 3a and 2, and an intervening zone projects to area 1. Within the ventral posterior nucleus, anteroposterior rods of cells respond with similar modality and somatotopic properties. They appear to project to restricted focal patches in the primary somatosensory cortex of approximately 0.5 mm width. The laminar termination of thalamocortical axons from the ventral posterior nucleus is different for the separate cytoarchitectonic subdivisions of the primary somatosensory cortex. In 3a and 3b, these axons terminate mainly in layer IV and the adjacent deep part of layer III, whereas in BA1 and BA2 they end in the deeper half of layer III, avoiding layer IV. Additional thalamocortical fibres to primary somatosensory cortex arise from the intralaminar system, notably the centrolateral nucleus.

There is a complex internal local connectivity among the primary somatosensory areas with a stepwise hierarchical progression of information from area 3b through BA1 to BA2. Short U-fibres connect the primary somatosensory areas with ipsilateral BA4 and parietal areas in the superior and inferior parietal lobule, and the parietal operculum. The primary somatosensory cortex has reciprocal commissural connections with its contralateral homologue, except that the cortices containing the representation of the distal extremities are relatively devoid of such connections. Callosal fibres in the primary somatosensory areas arise mainly from the deep part of layer III and terminate in layers I–IV. Pyramidal cells contributing callosal projections receive monosynaptic thalamic and commissural connections.

The primary somatosensory area has reciprocal connections with subcortical structures that include the claustrum (which in turn receives afferents from the nucleus basalis of Meynert), the locus coeruleus and the midbrain raphe. Corticostriatal fibres originating in layer V project mainly to the ipsilateral putamen. Other projections from layer V of the primary somatosensory cortex terminate in the main pontine nuclei, the nucleus reticularis tegmenti pontis (pontine tegmental reticular nucleus) and the spinal cord. The topographical representation in the cortex is preserved in terms of the spinal segments to which different

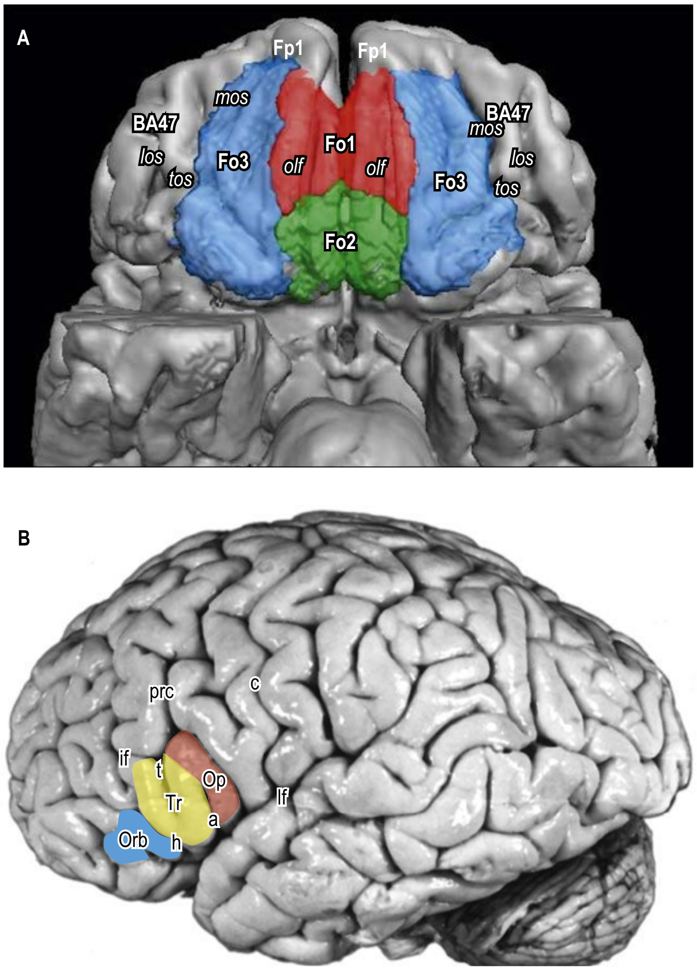

Fig. 32.54 **A**, A cytoarchitectonical map of the fronto-orbital cortex showing areas Fo1–Fo3. Abbreviations: los, lateral orbital sulcus; mos, medial orbital sulcus; olf, olfactory sulcus; tos, transverse orbital sulcus. **B**, Broca's language region areas BA44 on the opercular part, BA45 on the triangular and area 47 on the orbital part of the inferior frontal gyrus. Abbreviations: a, ramus ascendens of the lateral fissure; c, central sulcus; h, ramus horizontalis of the lateral fissure; if, inferior frontal sulcus; lf, lateral fissure; Op, opercular part of the inferior frontal gyrus; Orb, orbital part of the inferior frontal gyrus; prc, precentral sulcus; t, triangular sulcus; Tr, triangular part of the inferior frontal gyrus.

Anteriorly, the parietal lobe is delimited by the central sulcus. Posteriorly, it is well delineated on the medial aspect by the parieto-occipital sulcus, and on the dorso-lateral aspect by a line that can be drawn running from the point where the parieto-occipital sulcus reaches its most superior extremity at the edge of the hemisphere to the occipito-temporal incisure. The inferior boundary is defined by the lateral fissure and its imaginary prolongation to the line connecting the parieto-occipital sulcus and the occipito-temporal incisure.

The lateral aspect of the parietal lobe is divided into three regions by the postcentral and intraparietal sulci. The intraparietal sulcus, which originates from around the midpoint of the postcentral sulcus, is prominent on the superolateral surface of the parietal lobe, running parallel with the superior margin of the hemisphere (see Figs 32.2, 32.3). Anteriorly, the intraparietal sulcus is usually continuous with the inferior portion of the postcentral sulcus and posteriorly it passes into the occipital lobe as the superior occipital sulcus, which continues posteriorly into the transverse occipital sulcus. The intraparietal sulcus delineates the superior parietal lobule, continuous medially with the precuneus, and the inferior parietal lobule, made up of the supramarginal and angular gyri and a more posterior convolution continuous with the occipital lobe. The superior vertical branch of the intraparietal sulcus (transverse parietal sulcus) divides the SPL into an anterior and posterior portion, whereas the inferior vertical branch (intermediate sulcus of Jensen) separates the supramarginal gyrus anteriorly from the angular gyrus posteriorly. The inferior aspect of the supramarginal gyrus within the inferior parietal lobule of the dominant hemisphere corresponds to Wernicke's area, which extends along the posterior aspect of the superior temporal gyrus.

The postcentral gyrus is usually narrower than the precentral gyrus. Both gyri are located obliquely on the superolateral surface of the hemisphere, just superior to the lateral fissure. The superior portions of the pre- and postcentral gyri, which constitute the paracentral lobule on the medial surface of the cerebral hemisphere, are topographically related to the ventricular atrium, situated posterior to the thalamus. The inferior portions of both gyri cover the posterior half of the insula and are topographically related to the body of the lateral ventricle, situated superior to the thalamus. The portion of the subcentral gyrus corresponding to the base of the postcentral gyrus consistently lies over the transverse gyri of Heschl, situated on the opercular surface of the temporal lobe.

The supramarginal gyrus surrounds the distal portion of the lateral fissure (its posterior ascending branch) and becomes continuous with the posterior portion of the superior temporal gyrus. Above the distal end of the lateral fissure, the supramarginal gyrus is connected anteriorly to the postcentral gyrus through a fold that runs underneath the inferior aspect of the postcentral sulcus. Posteriorly, it occasionally rounds the inferior extremity of the intermediate sulcus and connects to the angular gyrus. The angular gyrus is a curved gyrus and always surrounds one of the distal segments of the superior temporal sulcus, usually the middle one (angular sulcus or t2 in Fig. 32.2H); its most inferior portion is continuous with the middle temporal gyrus. The configuration of the angular gyrus is defined by the distal branching of the superior temporal sulcus, which typically ends as three continuous or interrupted caudal branches.

The most superior distal branch of the superior temporal sulcus has an ascending course; it may either penetrate the supramarginal gyrus or coincide with the intermediate sulcus of Jensen separating the supramarginal and angular gyri. The second branch (t2) is usually more horizontal and enters the angular gyrus as the angular sulcus. The most inferior caudal branch (t3) of the superior temporal sulcus is less evident and less constant. It courses underneath a posterior fold that frequently connects the angular gyrus and the most lateral aspect of the occipital lobe, and is usually continuous with the anterior occipital sulcus, lying predominantly vertically along the anterior edge of the middle occipital gyrus.

On the medial surface of each hemisphere, the precuneus lies posterior to the paracentral lobule as a medial extension of the superior parietal lobule. The precuneus is quadrangular, delineated anteriorly by the marginal branch of the cingulate sulcus, posteriorly by the parieto-occipital sulcus and inferiorly by the subparietal sulcus. Inferior to the subparietal sulcus, the precuneus is connected to the isthmus of the cingulate gyrus, which is continuous with the parahippocampal gyrus. The parieto-occipital sulcus separating the precuneus from the cuneus is deep and contains many small sulci and gyri.

parts of the postcentral gyrus project. Thus, the arm representation projects to the cervical enlargement, the leg representation to the lumbosacral enlargement, and so on. Within the grey matter of the spinal cord, fibres from the somatosensory cortex terminate in the dorsal horn, in Rexed's laminae 3–5; fibres from 3b and BA1 end more dorsally, and those from BA2 more ventrally.

The rostral part of the parietal operculum can be subdivided into four areas, i.e. areas OP1–OP4 (Eickhoff, Schleicher et al 2006), which reflect the subdivision of this region into a secondary somatosensory region (SII; OP1, 3, 4) and a putative vestibular cortex (OP2). The parietal opercular areas are characterized by a columnar arrangement. While OP1 has a pronounced superficial-to-deep increase in cell size in layer III, area OP2 appears more homogeneous, but with additional very large pyramidal cells in deep layer III. In area OP3, layer III, V and VI have considerably lower cell packing densities. Area OP4 is characterized by smaller cells throughout, with only medium-sized pyramids in deep layer III, and layer IV is difficult to visualize. The secondary somatosensory region lies along the upper bank of the lateral fissure, posterior to the central sulcus. It contains a somatotopic representation of the body, with the head and face most anterior, adjacent to SI, and the sacral regions most posterior. The secondary somatosensory region is reciprocally connected with the ventral posterior nucleus of the thalamus in a topographically organized fashion. Some thalamic neurones probably project to both primary and secondary somatosensory regions via axon collaterals. Other thalamic connections of the secondary somatosensory region are with the posterior group of nuclei and with the intralaminar central lateral nucleus. The secondary somatosensory region also projects to laminae IV–VII of the dorsal horn of the cervical and thoracic spinal cord, the dorsal column nuclei, the principal trigeminal nucleus and the periaqueductal grey matter of the midbrain. Within the cortex, SII is reciprocally connected with SI in a topographically organized manner and projects to the primary motor cortex. SII also projects in a topographically organized way to the lateral part of PPC, and makes connections with PCC. Both right and left SII areas are interconnected across the corpus callosum, although distal limb representations are probably excluded. Neurones in SII respond particularly to transient cutaneous stimuli, e.g. brush strokes or tapping, which are characteristic of the responses of Pacinian corpuscles in the periphery: they show little response to maintained stimuli.

The superior and inferior parietal lobules are each composed of seven cytoarchitectonically distinct areas (**Fig. 32.55**). The major difference in cytoarchitecture between the areas of the two lobules is that the pyramidal cells in layers IIIc and V are larger in the superior parietal lobule. Using modern quantitative cyto- and receptorarchitectonic methods, BA5 and BA7 in the superior lobule have been subdivided into areas 5L, 5M and 5Ci, and areas 7A, 7P, 7M and 7PC, respectively (Scheperjans et al 2005, Scheperjans, Hermann et al 2008). Using the same methodological approach for the inferior parietal lobule, areas PFop, PFcm, PFt, PF and PFm were identified within BA40, and areas PGa and PGp within BA39 (Caspers and Zilles 2018) (**Fig. 32.56**).

BA5 receives a dense feed-forward projection from all cytoarchitectonic areas of primary somatosensory cortex in a topographically organized manner. The thalamic afferents to this area come from the lateral posterior nucleus and from the central lateral nucleus of the intralaminar group. Ipsilateral corticocortical fibres from BA5 go to BA7, the premotor and supplementary motor cortices, the posterior cingulate gyrus and the insular granular cortex. Commissural connections between BA5 on both sides tend to avoid the areas of representation of the distal limbs. The response properties of cells in BA5 are more complex than in SI, with larger receptive fields and evidence of submodality convergence. BA5 also contributes to the corticospinal tract.

The areas of the inferior parietal lobule are reciprocally connected to adjacent areas in the intraparietal sulcus, the superior parietal lobule, the ventrolateral premotor and prefrontal cortex as well as posterior temporal and occipital areas. These connections are mediated by short U-fibres (Catani et al 2017) and long association fibres of the arcuate fasciculus, and superior and middle longitudinal fasciculi.

Functional anatomy of the superior and inferior parietal lobules

Available with the *Gray's Anatomy* e-book

Occipital lobe

On the superolateral cerebral surface, the occipital lobe is situated posterior to a virtual line connecting the point of emergence of the parieto-occipital fissure on the superomedial border of the cerebral hemisphere with the incisura occipito-temporalis. On the medial surface, the occipital lobe is limited anteriorly by the parieto-occipital sulcus and by its prolongation towards the tentorium cerebelli. Along the inferior cerebral surface, the base of the occipital lobe is continuous with the base of the temporal lobe. The sulci and gyri of the occipital lobe, especially of its superolateral surface, exhibit a greater degree of anatomical variation than is seen in the other lobes. Regarding the major named sulci, there appears to be reasonable consensus that the parieto-occipital, calcarine, paracalcarine, lingual, transverse occipital, inferior lateral occipital and anterior occipital sulci, together with the occipital parts of the collateral and lateral occipitotemporal sulci, are constant features of the surface of the occipital lobe, whereas the superior occipital, superior lateral occipital, inferior occipital, lunate and occipitopolar sulci are less constant.

Occipital lobe sulci and gyri

Available with the *Gray's Anatomy* e-book

Occipital lobe internal structure and connectivity

The occipital lobe is composed of Brodmann's areas BA17, BA18 and BA19 and part of BA37. However, Brodmann's delineation of BA19 and BA37 has not been replicated using modern quantitative approaches and the whole region covered by these two areas has been re-defined (see Fig. 32.13).

BA17, the striate cortex, is the primary visual cortex (V1) and is located mostly on the medial aspect of the occipital lobe: it occupies the upper and lower lips and depths of the calcarine sulcus and extends onto the cuneus and lingual gyrus. V1 receives visual afferent fibres from the lateral geniculate nucleus via the optic radiations. The retina of each eye can be divided into a nasal (medial) and temporal (lateral) half, and the left and right visual fields of each eye are composed of a lateral and medial half, the latter partially overlapping in the midline. Each lateral visual field is perceived by the ipsilateral nasal retina and each medial visual field is perceived by the ipsilateral temporal retina. The fibres from the nasal retinae form the medial half of the optic nerve and decussate in the optic chiasma to form the optic tract with the temporal fibres of the contralateral retina. Projections of the ipsilateral and contralateral retinae reach the lateral geniculate nucleus where representations of the visual hemifields remain segregated in the magnocellular (layers 1–2) and parvocellular layers (layers 3–6). The fibres of the optic radiations originating from the lateral geniculate nucleus terminate in strict retinotopic fashion in the ipsilateral striate area. The cortex of each hemisphere receives impulses from two hemi-retinae, which represent the contralateral half of the binocular visual field. Superior and inferior retinal quadrants are connected with corresponding areas of the striate cortex. According to Elze (1928), Flechsig, in 1896, called attention to the peculiar course of the ventral fibres of the optic radiations, and named the sharp turn made by these fibres the 'temporal knee' (later referred to as Meyer's loop). The superior retinal quadrants (representing the inferior half of the visual field) are connected with V1 above the calcarine sulcus, and the inferior retinal quadrants (representing the upper half of the visual field) are connected through the Meyer's loop with the V1 below the calcarine sulcus. The peripheral nasal parts of the retinae (monocular periphery of the visual field) projects on the most anterior parts in the visual cortex near to the splenium of the corpus callosum: this is the small monocular part of V1. The fovea of the retina concerned with central vision impinges on a disproportionately large posterior part (binocular part of V1) around the occipital pole.

Area V1 is koniocortical (**Fig. 32.57**): in contrast to most of the isocortical areas where layer III is dominated by pyramidal cells, layers II/III of V1 is populated by small, densely packed granule cells. Layers II/III consist of excitatory pyramidal cells and receive massive inputs from layer IVc neurones but only a few thalamic inputs. They are also connected through reciprocal projections with layer V neurones. The neurones of layers II/III have cortico-cortical projections to the extrastriate regions V2, V3, V4 and V5. About 20% of the cells in layers II/III are GABAergic inhibitory interneurones. Layer IV of V1 is divided into three sublayers: IVa, IVb (which harbours the heavily myelinated stria of Gennari and contains a few cells, mainly interneurones), and IVc (**Fig. 32.57B**). Layer IV plays a major role in the M-pathway that originates from magnocellular (M) cells of the lateral geniculate nucleus. After receiving information through the M-pathway in layer IVcα, IVB projects to cytochrome oxidase-positive blobs (see below) in layers II/III, to areas V3 and V5/MT and the superior colliculus. The densely cellular IVc is further subdivided into a superficial IVcα and a deep IVcβ. The input to area 17 from the lateral geniculate nucleus terminates predominantly in layers IVa and IVc. Other thalamic afferents, from the inferior pulvinar nucleus and the intralaminar group, terminate in layers I and VI. Layer V neurones project primarily to III, provide strong feedback to layer VI neurones, and receive feedback via projections from

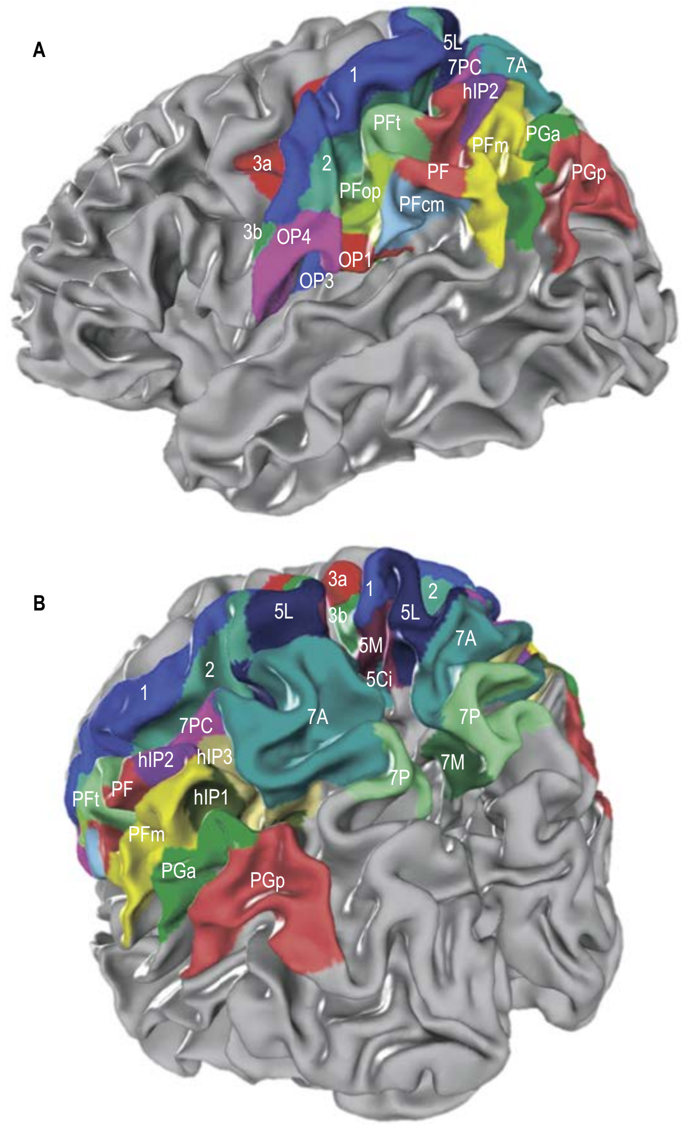

Fig. 32.55 **A**, Lateral view, left hemisphere, showing maximum probability maps of the parietal cortical areas. **B**, Oblique dorsal view on both hemispheres with maximum probability maps of the parietal cortical areas. (Adapted with permission from Caspers S, Zilles K Microarchitecture and connectivity of the parietal lobe. In: Vallar G, Coslett HB (eds) The Parietal Lobe. Handbook of Clinical Neurology, Vol. 151. Elsevier. Copyright 2018.)

Studies of the regional and laminar distribution patterns of multiple neurotransmitter receptors supported the parcellations found by quantitative cytoarchitectonic observations. In SI, area 3b had the highest densities of GABAergic GABA$_A$, cholinergic muscarinic M$_2$, noradrenergic α_2, and serotoninergic 5-HT$_2$ receptors than BA1 and BA2 (see Fig. 32.51). Additionally, areas 3b and BA2 had higher concentrations of cholinergic muscarinic M$_1$ receptors than areas 3a and BA1. In both the IPL and SPL, decreasing concentrations of glutamatergic AMPA receptors and increasing concentrations of serotonergic 5-HT$_{1A}$ and 5-HT$_2$ receptors were observed along caudal-to-rostral gradients, respectively. Caudal as compared to rostral and middle areas of IPL were additionally characterized by higher concentrations of GABAergic GABA$_A$ and GABA$_B$ receptors and lower concentrations of benzodiazepine binding sites of the GABA$_A$ receptor, while middle areas as compared to rostral and caudal areas had higher concentrations of glutamatergic kainate and cholinergic nicotinic receptors (Caspers et al 2013a). In the SPL, rostral as compared to caudal areas additionally expressed higher concentrations of adrenergic α_2 receptors and lower concentrations of cholinergic nicotinic receptors (Scheperjans et al 2005).

There are two or three gyri (superior, middle and inferior) on the superolateral cerebral surface of the occipital lobe that converge posteriorly to form the occipital pole (see Figs 32.2–32.3). The superior occipital gyrus is always well defined, and is continuous along the superomedial margin of the hemisphere with the cuneus. Superiorly, it is delimited by the depth of the parieto-occipital fissure on the superolateral hemispheric surface. It is continuous with the SPL through the parieto-occipital 'pli de passage' of Gratiolet. Laterally, the superior occipital gyrus may be delimited by either the intra-occipital, transverse occipital or superior occipital sulci. The inferior occipital gyrus lies horizontally along the inferolateral margin of the hemisphere. Anteriorly, it is usually continuous with the inferior temporal gyrus; posteriorly, it can extend medially around the occipital pole, becoming continuous with the lingual gyrus on the medial surface of the hemisphere; superiorly, it is delimited by the lateral or inferior occipital sulcus. The superior lateral occipital sulcus is a horizontal sulcus. Anteriorly, it is frequently connected to the inferior temporal sulcus; inferiorly, it may be accompanied by a shorter inferior lateral occipital sulcus. Both of these sulci may be connected with a sulcal complex known as the anterior occipital sulcus, which, when present, lies along the anterior aspect of the middle occipital gyrus.

The intraparietal sulcus extends longitudinally and inferiorly into the occipital lobe, where it becomes the intra-occipital sulcus. The latter may occasionally descend to the occipital pole but it usually terminates on reaching the transverse occipital sulcus, dividing it into lateral and medial parts that penetrate the superior occipital gyrus. The lunate sulcus, although conspicuous in monkeys and apes, is only sometimes identifiable in human brains, when it appears as a well-defined vertical and backward-curved sulcus anterior to the occipital pole.

Despite significant anatomical variation, the superolateral occipital convolutions are connected to the parietal and temporal convolutions by consistent cortical folds. Four folds connect the parietal and temporal lobes with the occipital lobe: the superior parieto-occipital fold (parieto-occipital arcus) connects the SPL with the superior occipital gyrus; the inferior parieto-occipital fold, a posterior extension of the angular gyrus, connects with the middle occipital gyrus and occasionally also with the superior occipital gyrus; the first temporo-occipital fold is the continuation of the middle temporal gyrus with the inferior occipital gyrus; and the second temporo-occipital fold is the continuation of the inferior temporal gyrus with the inferior occipital gyrus.

The medial surface of the occipital lobe is separated from the parietal lobe by the parieto-occipital sulcus and dominated by the calcarine sulcus. The dorsal part of this region, above the calcarine sulcus and posterior to the parieto-occipital sulcus, is the cuneus. The ventral part of this region, lying below the calcarine sulcus and extending as far as the occipital extension of the collateral fissure, is the lingual gyrus. The calcarine sulcus starts anteriorly beneath the splenium of the corpus callosum, delineating the inferior aspect of the isthmus of the cingulate gyrus, and runs posteriorly just above the inferomedial margin of the hemisphere. The parieto-occipital sulcus separates the cuneus from the precuneus, and divides the calcarine sulcus into an anterior and a posterior part. The parieto-occipital and calcarine sulci appear continuous on the surface, but when their borders are retracted it becomes obvious that they are separated by one or more small gyri. The anterior part of the calcarine sulcus is classified as a complete sulcus because its depth creates an elevation (calcar avis) in the medial wall of the occipital horn of the lateral ventricle. The posterior part of the calcarine sulcus is considered an axial sulcus, given that its axis runs along the visual cortex. Only the posterior part includes the primary visual cortical areas, which are located on its superior (cuneal) and inferior (lingual) surfaces: this part of the calcarine sulcus frequently harbours the cuneolingual gyrus that links both gyri.

At the level of the occipital pole, the calcarine sulcus usually branches in a T or Y shape as the retrocalcarine sulcus. The gyrus descendens of Ecker lies posterior to and along the retrocalcarine sulcus and is occasionally bounded posteriorly by the occipitopolar sulcus. The retrocalcarine sulcus and its variations are sometimes referred to as external calcarine sulci.

Given the anatomical constancy of the calcarine and parieto-occipital sulci on the medial occipital surface, the cuneus is always a well-defined wedge-like convolution. The real anterior border of the cuneus is the cuneal limiting sulcus within the parieto-occipital fissure. Posteriorly, the cuneus rests over the posterior part of the calcarine sulcus and over the posterior aspect of the lingual gyrus. Superior to the posterior part of the calcarine sulcus, the cuneus harbours the paracalcarine or cuneal sulcus (the inferior sagittal sulcus of the cuneus of Retzius) and, further dorsally, the occipital paramedial sulcus (the paramesial sulcus of Elliot Smith or superior sagittal sulcus of Retzius). The basal or inferior surface of the occipital lobe is continuous with the basal surface of the temporal lobe. It is formed, from medial to lateral, by the lingual (also known as the medial occipito-temporal gyrus), fusiform (also known as the lateral occipito-temporal gyrus), and inferior occipital gyri respectively. The lingual gyrus lies inferiorly along the entire length of the calcarine sulcus, forming the mediobasal portion of the occipital lobe. It is continuous anteriorly with the parahippocampal gyrus and its basal surface rests on the tentorium cerebelli. Posteriorly, it is frequently divided into a superior and inferior part by an intralingual sulcus, which may be a posteromedial ramus of the collateral sulcus.

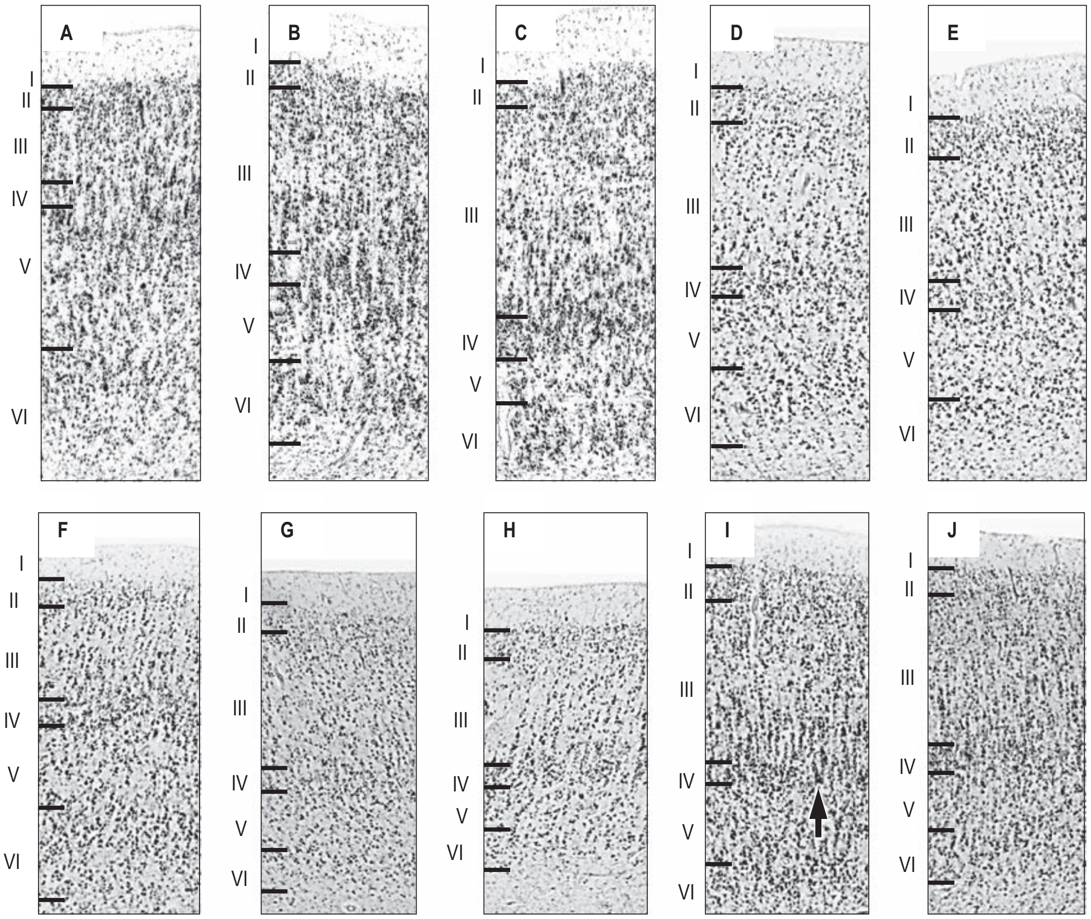

Fig. 32.56 A–J, The cytoarchitecture of cortical areas in the superior (**A–C**) and inferior (**D–J**) parietal lobules. Areas 5L (**A**), 7A (**B**), 7P (**C**) are parts of the superior parietal lobe. Areas PGa (**D**), PGp (**E**) are parts of BA39. Areas PFop (**F**), PFt (**G**), PFcm (**H**), PF (**I**) and PFm (**J**) are parts of BA40. Roman numerals indicate cortical layers.

The fusiform gyrus lies along the temporo-occipital transition. Its posterior or occipital part is bounded medially by the collateral sulcus and laterally by the occipito-temporal sulcus; hence it lies between the lingual gyrus medially and the inferior occipital gyrus laterally. The occipital part of the fusiform gyrus lies over the tentorium cerebelli just posterior to the petrous part of the temporal bone. Topographically, it corresponds to the floor of the ventricular atrium; the temporal part of the gyrus lies beneath the temporal horn of the lateral ventricle. The posterior portion of the fusiform gyrus contains the midfusiform sulcus lying between the collateral and occipito-temporal sulci (Weiner and Zilles 2016). The midfusiform sulcus is of functional importance, because it points to cortical areas involved in object recognition, face perception and reading.

The occipitotemporal sulcus rarely extends posteriorly as far as the occipital pole; both the collateral and occipitotemporal sulci frequently have secondary side branches and merge anteriorly. The inferior or basal aspect of the inferior occipital gyrus lies lateral to the fusiform gyrus and constitutes the most inferior portion of the lateral aspect of the occipital lobe. Along the inferolateral border of the hemisphere, the inferior temporal gyrus is continuous with the inferior occipital gyrus over the occipito-temporal incisure (preoccipital notch), and the inferior occipital gyrus is continuous with the lingual gyrus along the occipital pole. Along the parietal and occipital aspects of the superomedial border of the hemisphere, the superior parietal lobule is continuous with the precuneus, and the superior occipital gyrus is continuous with the cuneus above the calcarine sulcus and with the lingual gyrus below the calcarine sulcus.

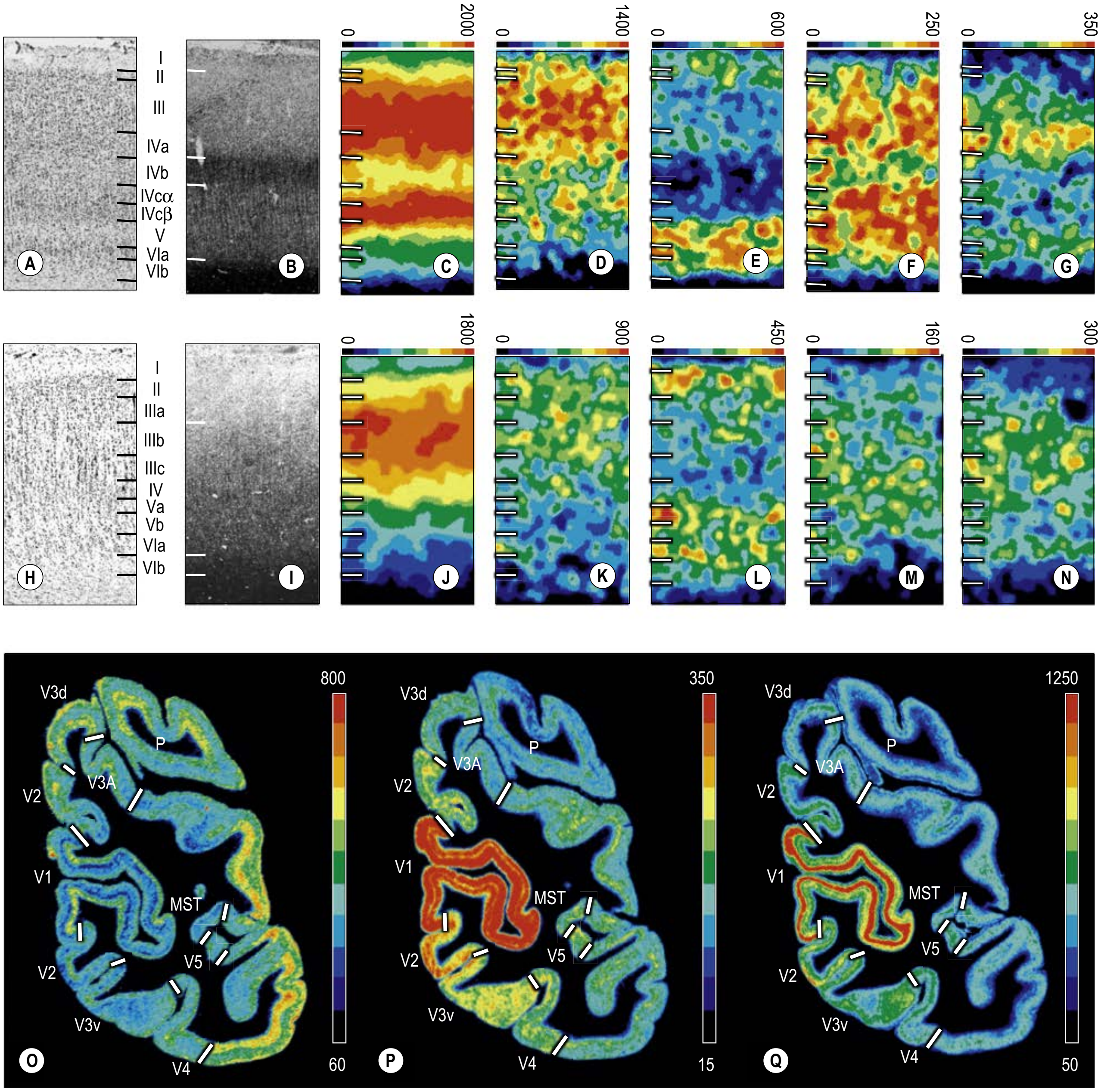
I
II
III
IVa
IVb
IVcα
IVcβ
V
VIa
VIb
A
B
C
D
E
F
G
0
2000
0
1400
0
600
0
250
0
350
I
II
IIIa
IIIb
IIIc
IV
Va
Vb
VIa
VIb
H
I
J
K
L
M
N
0
1800
0
900
0
450
0
160
0
300
V3d
P
V2
V3A
V1
MST
V5
V2
V3v
V4
800
60
350
15
1250
50
O
P
Q

Fig. 32.57 A–Q, Cyto-, myelo- and receptorarchitecture of the human visual cortex in coronal sections. **A-G**, Primary visual cortex (BA17); **H–N**, secondary visual cortex (BA18); **O–Q**, subdivisions of the visual cortex based on three different receptors. **A**, Neuronal cell body-stained BA17; **B**, myelin-stained BA17; **C**, laminar distribution of GABA$_A$ receptors in BA17; **D**, laminar distribution of glutamate NMDA receptors in BA17; **E**, laminar distribution of glutamate kainate receptors in BA17; **F**, laminar distribution of cholinergic muscarinic M$_2$ receptors in BA17; **G**, laminar distribution of noradrenergic α_2 receptors in BA17; **H**, cell body-stained BA18; **I**, myelin-stained BA18; **J**, laminar distribution of GABA$_A$ receptors in BA18; **K**, laminar distribution of glutamate NMDA receptors in BA18; **L**, laminar distribution of glutamate kainate receptors in BA18; **M**, laminar distribution of cholinergic muscarinic M$_2$ receptors in BA18; **N**, laminar distribution of noradrenergic α_2 receptors in BA18; **O**, distribution of glutamate kainate receptors in the visual cortex; **P**, distribution of cholinergic muscarinic M$_2$ receptors in the visual cortex; **Q**, distribution of noradrenergic α_2 receptors in the visual cortex. Abbreviations: MST visual area MST; P, parietal cortex; V1, primary visual cortex (BA17); V2, secondary visual cortex (BA18); V3A, dorsal visual area V3A; V3d, dorsal visual area V3; V3v, ventral visual area V3; V4, visual area V4; V5, visual area V5. Scales indicate absolute receptor densities in fmol/mg protein. Roman numerals indicate cortical layers.

II/III neurones. Very large pyramidal cells, Meynert cells, found at the V/VI border and within layer VI, project to both area MT and the superior colliculus.

The projections of the right and left retinae remain segregated in the lateral geniculate nucleus, where layers 2, 3 and 5 receive information from the ipsilateral eye, and layers 1, 4 and 6 from the contralateral eye. The magnocellular layers 1 and 2 of the lateral geniculate nucleus are important relay stations of the M-pathway from the retina to the visual cortex, whereas the parvocellular layers 3–6 are a relay station in the parallel P-pathway. The M-pathway mainly conveys motion information, the P-pathway information on shape and colour. The optic radiation consists of the geniculo-cortical projections to layer IV of V1, which terminate in alternating cell strips for each eye separately. Thus, the neurones within layer IV are monocularly driven. This horizontal, strip-like segregation is the anatomical basis of ocular dominance columns (Hubel and Wiesel 1977) (**Fig. 32.58**). Neurones encountered in vertical strips from pia to white matter exhibit a preference for stimulation of one or other eye, although binocularly driven neurones are found in the other layers of V1. In the human V1, ocular dominance columns are orientated vertical to the V1/V2 boundary and are about 0.5 mm wide with quite distinct functional borders.

Orientation columns in V1 are based on the finding that all neurones orientated in a column extending from pia to white matter and vertical to the cortical surface, respond preferentially to either a stationary or a moving line of a given orientation (see Fig. 32.58). Cells with simple, complex and hypercomplex receptive fields are found in V1. Simple cells are mainly in layer IV and respond optimally to lines in a narrowly defined position. Complex cells occur in layers II and III or layers V and VI, and respond to stimuli within a receptive field, but with a specific orientation. Hypercomplex cells are also found in layers II and III or layers V and VI: their response is similar to that of complex cells, but the length of a line is critical. The borders of orientation and ocular dominance columns intersect at right-angles.

Cytochrome oxidase (CO) blobs are found in V1 (see Fig. 32.58). They are regions of high staining for the metabolic enzyme cytochrome oxidase (Wong-Riley 1989) in layers II/III and V/VI. Interleaved 'interblob' regions form discrete structures between CO blobs. Layer II/III neurones in the CO blob region receive direct affrents from the interlaminar cells of LGN (I-pathway). Although CO blobs have often been associated with colour vision, their function remains elusive. Direct connections from the blob areas of V1 pass to V4. Output from V1 terminates in the claustrum, lateral geniculate nucleus, superior colliculus, pretectum and parts of the brainstem reticular formation; efferents to the striatum and pontine nuclei are sparse.

The human extrastriate visual cortex covers the remainder of the occipital lobe and extends into the temporal and parietal lobes, which means that about 20% of the entire cerebral cortex is covered by the visual system.

Area V2, which overlaps in part with BA18, contains a complete retinotopic representation of the visual hemifield, which is a mirror image of that in V1, with the vertical meridian along the border between areas V1 and V2. Within area V2 (**Fig. 32.57H–N**), functional modules called thin stripes, thick stripes, and interstripes are present. The blob areas of V1 project to the colour-sensitive neurones of the thin stripes, and those of the interblob regions of V1 terminate in the interstripe regions of V2. The thin stripes of V2 project to V4. The thick stripes of V2 receive input from layer IVb of V1. The neurones in the thick stripes are orientation- and direction-selective, and are also sensitive to binocular disparity, which allows them to code depth information. Reciprocal projections from V2 pass to several other visual areas, including V3 and its subdivisions (V3/V3d, VP/V3v, V3a; see Fig. 32.57O–Q), V4, V5 and areas in the temporal and parietal association cortices and frontal eye field. Afferents to V2 arrive from the lateral geniculate nucleus, inferior and lateral pulvinar nuclei and parts of the intralaminar thalamic nuclei. Subcortical efferents of V2 arise in layers V and VI and pass to the striatum, thalamus, claustrum, superior colliculus, pretectum, brainstem reticular formation, and pons. The reciprocal callosal connections of V2 are restricted to regions with the representation of the vertical meridian.

Area V3 (see Fig. 32.57O–Q) is a narrow strip adjoining the anterior margin of V2 and has been subdivided into two dorsal (V3/V3d; V3A) and a ventral (VP/V3v) regions on the basis of its afferents from area V1, myelo- and receptor architecture, and callosal and receptive field properties. V3d receives input from V1, whereas V3v does not. V3d shows less colour selectivity and greater directional selectivity than V3v. Both areas receive projections from V2 and are interconnected. A further visual area, area V3a, lies anterior to V3d and receives afferents from V1, V2, V3d and V3v. All V3 subdivisions project to diverse visual areas in the parietal, occipital and temporal cortices, and to the frontal eye field.

Area V4 lies within BA19 anterior to V3 (see Fig. 32.57O–Q). It receives afferents from V2, and is colour- and orientation-selective. Bilateral damage, e.g. caused by localized ischaemia, leads to achromatopsia. V4 is also involved in orientation, form and movement selectivity. It projects reciprocally to the inferior temporal cortex and also connects with other visual areas in the temporal and parietal lobes and with the pulvinar and intralaminar thalamic nuclei. Visual processing in the inferior temporal and temporoparietal lobes is realized via the dorsal and ventral visual streams that emanate from the occipital lobe. The dorsal pathway, concerned primarily with visuospatial discrimination, projects from V1 and V2 to the temporal and parietal cortices and enables sensory-motor transformations for visually guided actions directed at an object. V4 is an important relay station for the ventral stream, which is related to the perceptual identification of various classes of objects (see below). It is connected along the inferior temporal gyrus with the posterior, intermediate and anterior parts of the inferior temporal cortex, which feed into the temporal polar and medial temporal areas of the language and limbic networks.

The motion-selective area V5 (also called hMT+) (see Fig. 32.57O–Q) is located close to the junction of the occipital, temporal and parietal lobes and can be identified by its intense myelination. It receives input from layer IVb of V1 and the thick stripes of V2, forming a further M-pathway. Its cells are direction- and motion-sensitive. It is surrounded by the areas MST and FST that process higher-order aspects of stimulus motion. Bilateral lesions of V5 cause akinetopsia, a severe impairment in detecting the movements of objects.

Higher-order visual areas, selective for specific objects such as faces, words or buildings, are localized lateral to the collateral sulcus in the fusiform gyrus around the midfusiform sulcus. Best known is the posterior face recognition area. Lesions of this area cause prosopagnosia, the inability to recognize faces. Recognition of faces, numbers and words are associated with a central visual field bias, whereas the recognition of buildings depends on peripheral vision. Several cyto- and receptor architectonic areas (FG1–FG4) of the fusiform gyrus have been identified (Caspers et al 2013b, Lorenz et al 2017). FG1 and FG3 are medial to the midfusiform sulcus, and FG2 and FG4 are lateral to this sulcus on the fusiform gyrus (**Fig. 32.59**). Combined functional and cytoarchitectonic studies have shown that these areas subserve face, word form (characters), place and object (body) recognition (Weiner et al 2017). FG1 corresponds to the face-selective area in the posterior fusiform gyrus (area pFus-faces); FG2 to the posterior visual word form area (VWFA-1); FG3 to the parahippocampal place area (PPA); and FG4 to the medial face-selective area (mFus-faces), fusiform body area (FBA) and anterior visual word form area (VWFA-2).

Temporal lobe

The lateral surface of the temporal lobe is inferior to the lateral fissure and lies beneath the squamous portion of the temporal bone. The basal surface lies over the floor of the middle cranial fossa posterior to the greater wing of the sphenoid bone. The opercular surface lies inside the lateral fissure. (For the definition of the posterior limit of the temporal lobe, see the occipital lobe). The isocortical part of the temporal lobe is related with auditory functions and, in the dominant hemisphere, mostly with language. It also comprises parts of the visual system in the inferior temporal region (higher visual areas). The medial side of the temporal lobe belongs to the limbic system (see archicortex and periarchicortex).

Temporal lobe sulci and gyri

Available with the *Gray's Anatomy* e-book

Temporal lobe internal structure and connectivity

The superior, middle and inferior temporal gyri correspond to BA22, BA21 and BA20, respectively, and the temporal pole corresponds to BA38 (see Fig. 32.13).

The primary auditory cortex (BA41 or A1) covers a major part of Heschl's gyrus/gyri, and is surrounded by the secondary auditory cortex (BA42). BA41 corresponds to the functionally and connectionally defined core region of the primary auditory cortex, and BA42 to the belt region. BA41 is reciprocally connected with the medial geniculate nucleus via the acoustic radiation. The ventral division of the medial geniculate nucleus mainly projects to BA41, which receives additional projections from the medial pulvinar. The architectonically defined primary auditory cortex does not extend medially into the insular cortex, and does not reach the lateral bulge of the superior temporal gyrus. Posteriorly, it never extends beyond the second transverse temporal gyrus although Heschl's sulcus does not indicate precisely the border between BA41 and BA42.

The lateral surface is composed of the superior, middle and inferior temporal gyri, separated by the superior and inferior temporal sulci, all lying parallel to the lateral fissure. Anteriorly, the middle temporal gyrus is generally shorter, and the superior and inferior gyri fuse to form the temporal pole (see Figs 32.2–32.3).

The superior temporal sulcus terminates within the inferior parietal lobule, posterior to the end of the lateral fissure, by branching into an ascending sulcal segment and an inferior branch that runs towards the occipital lobe. The superior temporal gyrus continues posteriorly to the supramarginal gyrus encircling the terminal portion of the lateral fissure. The middle temporal gyrus is connected to the angular gyrus beneath the distal and horizontal portion of the superior temporal sulcus. The inferior temporal gyrus is continuous posteriorly with the inferior occipital gyrus over the preoccipital notch (occipito-temporal incisure). Both superior and inferior temporal sulci start at the most anterior aspect of the temporal pole and end posterior to the arbitrary border of the temporal lobe, and both have their depths directed towards the temporal horn of the lateral ventricle. Topographically, the depth of the posterior part of the superior temporal sulcus is particularly related to the ventricular atrium.

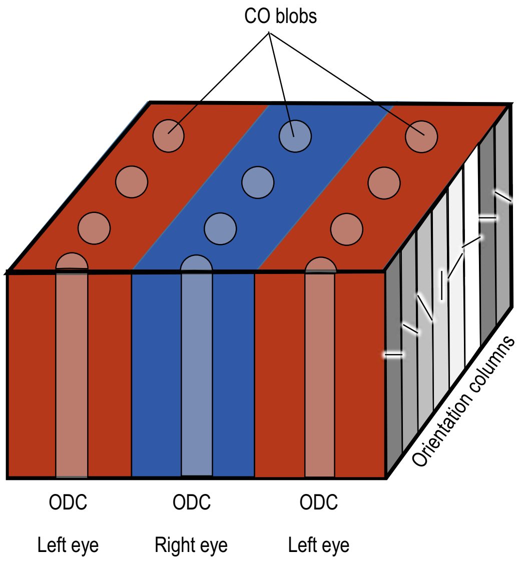

Fig. 32.58 Functional modules in V1. Abbreviation: CO blobs, cytochrome oxidase blobs; ODC, ocular dominance column.

The basal surface of the temporal lobe is composed laterally by the inferior surface of the inferior temporal gyrus and medially by the anterior or temporal portion of the fusiform or lateral temporo-occipital gyrus; the gyri are separated by the temporo-occipital sulcus. Medially, the fusiform gyrus is delimited by the collateral sulcus, which separates it from the parahippocampal gyrus. Although not extensive, the fusiform gyrus has an anterior or temporal part between the inferior temporal and parahippocampal gyri, and a posterior or occipital part between the inferior occipital and lingual gyri. The anterior part of the fusiform gyrus is typically curved or pointed, resembling an arrow; its anterior border usually lies close to the level of the cerebral peduncle. The temporal portion of the fusiform gyrus lies over the posterior aspect of the floor of the middle fossa and the upper surface of the petrous part of the temporal bone. The occipital part of the fusiform gyrus lies underneath the ventricular atrium.

Anterior to the fusiform gyrus, the collateral sulcus may be continuous with the rhinal sulcus. More frequently, these sulci are separated by the so-called temporolimbic passage. The rhinal sulcus separates the entorhinal cortex of the uncus medially from the isocortex of the temporal pole laterally.

The superior or opercular surface of the temporal lobe is formed by the superior surface of the superior temporal gyrus, which lies within the lateral fissure and is composed of multiple transverse gyri, one or two of which are the transverse gyrus/gyri of Heschl. The opercular surface originates around the midpoint of the superior temporal gyrus and is orientated diagonally towards the posterior vertex of the floor of the lateral fissure, with its longest axis orientated towards the ventricular atrium. Heschl's gyrus/gyri is/are bounded anteriorly by the first transverse sulcus and posteriorly by the second transverse sulcus (sulcus of Heschl), and divide the temporal

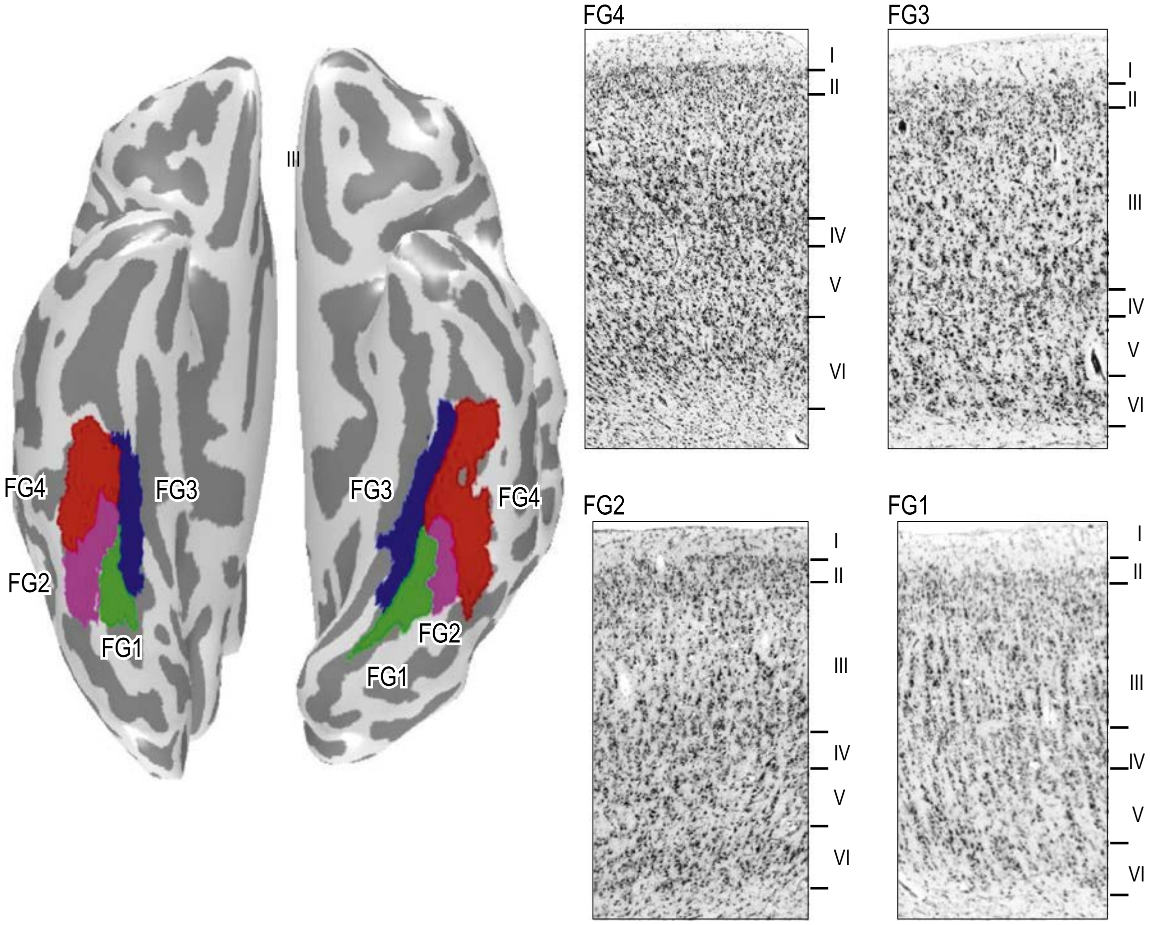

Fig. 32.59 Localization and cytoarchitectonic organization of higher visual areas in the ventral occipito-temporal cortex. (Adapted with permission from Weiner KS, Barnett MA, Lorenz S et al 2017 The cytoarchitecture of domain-specific regions in human high-level visual cortex. Cereb Cortex 27:146–61.)

opercular surface into an anterior polar plane, and a posterior temporal plane.

The surface of the polar plane shows several small transverse gyri directed obliquely towards the inferior part of the insular circular sulcus (inferior limiting sulcus) (see Fig. 32.2). The temporal plane is flat and triangular in shape and is usually larger in the dominant hemisphere, supposedly reflecting its association with language functions. Heschl's gyrus underlies the opercular surface of the postcentral gyrus, and the flat surface of the temporal plane underlies the opercular surface of the supramarginal gyrus.

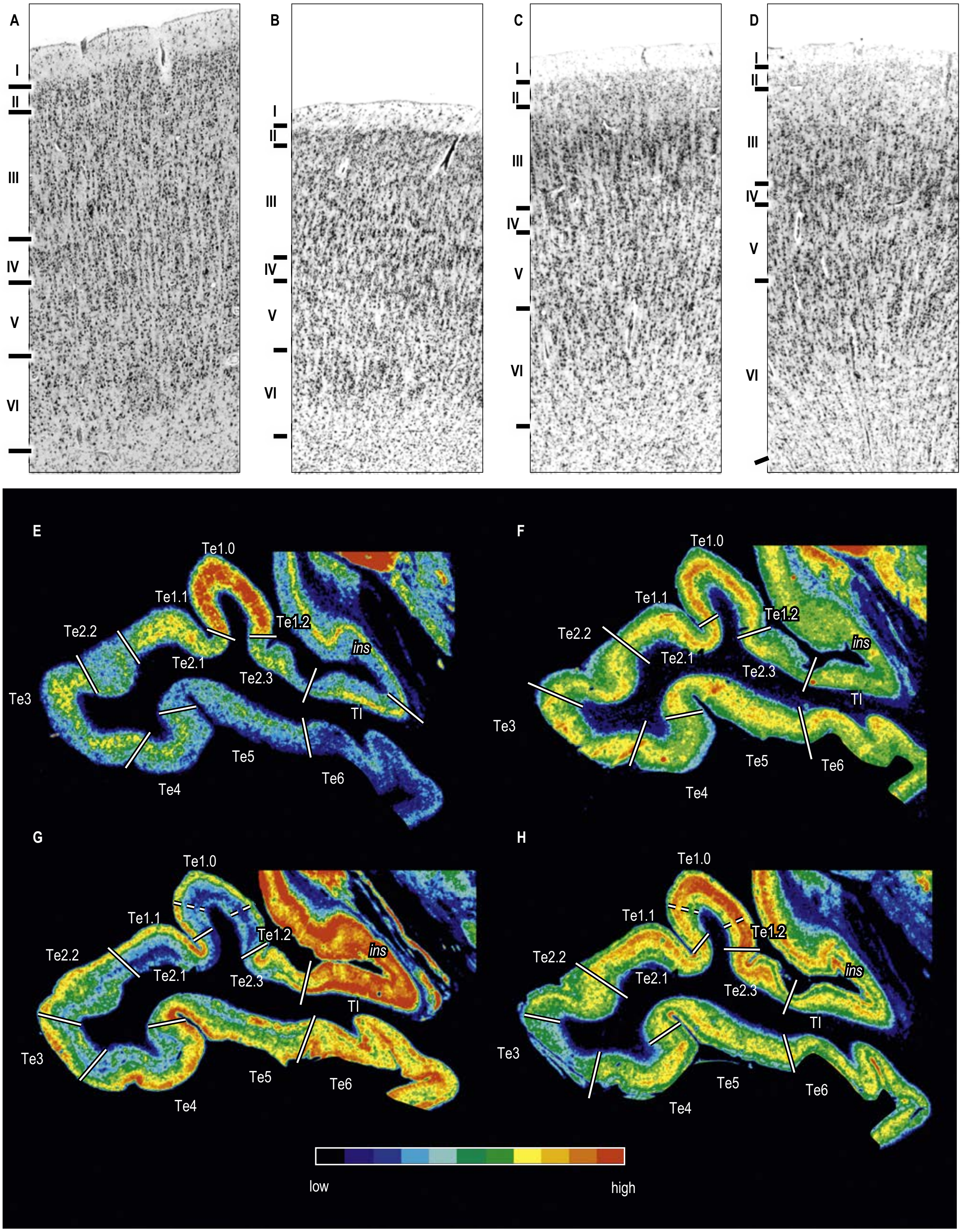

Fig. 32.61 A–D, The cytoarchitecture of the temporal cortical areas: **A**, Te1.0–Te1.2, primary auditory cortex (BA41); **B**, Te2.1–Te2.3, secondary auditory cortex (BA42); **C**, area Te3 (part of BA22 on the superficially exposed part of the superior temporal gyrus); **D**, BA21 on the middle temporal gyrus. **E–F**, Receptor distribution in the superior temporal gyrus (coronal sections): **E**, cholinergic muscarinic M_2 receptor; **F**, serotoninergic 5-HT_2 receptor; **G**, noradrenergic α_1 receptor; **H**, noradrenergic α_2 receptor. Lines indicate the positions of borders between areas. Laminar differentiation is indicated by Roman numerals. Te1, primary auditory cortex; Te2.1, Te2.2 and Te2.3 are subdivisions of the auditory belt region (comparable to BA42); Te3, Te4, Te5 and Te6 are parts of BA22 and belong at least partly to the auditory parabelt. TI is the transition area to the adjacent insular cortex (ins), which can be subdivided by Va2 receptors into TI1 and TI2.

The primary auditory cortex is koniocortical, like parietal area 3b and occipital area V1 (Fig. 32.60). Layer III mainly contains small to medium-sized pyramidal cells arranged in radial columns that extend partially into the neighbouring layers: this arrangement is known as the 'rain shower formation' of the primary auditory cortex (von Economo and Koskinas 1925). The geniculocortical fibres from the medial geniculate nucleus terminate densely in layer IV (Fig. 32.61). Te1 is also characterized by a very high density of cholinergic muscarinic M_2, GABAergic $GABA_A$, and noradrenergic α_2 receptors. The serotoninergic 5-HT_2 receptor has a slightly higher density in Te1. A high density of these receptors also occurs in the primary somatosensory (area 3b) and primary visual (BA17) areas, whereas the noradrenergic α_1 receptor has

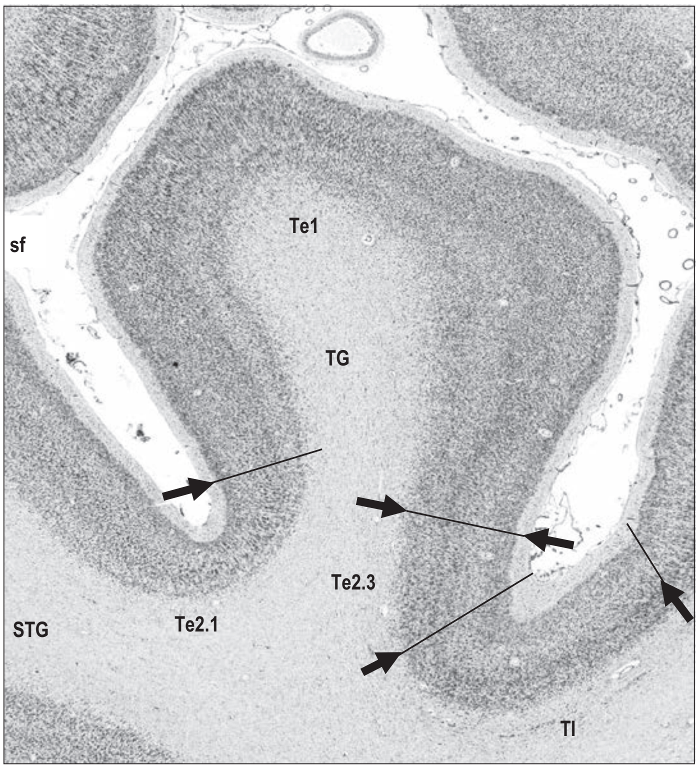

Fig. 32.60 Primary and secondary auditory cortical areas. Te1, primary auditory cortex (BA41); Te2.1 and Te2.3, lateral and medial parts of the secondary auditory cortex; TI is a transition area to the adjacent insular cortex and probably resembles Brodmann's BA52. Abbreviations: sf, Sylvian fissure; STG, superior temporal gyrus; TG, transverse gyrus of Heschl. Arrows indicate major areal borders.

a distinctly low density in the deeper layers of Te1 (see Fig. 32.61E–H). Dense myelination and strong expression of acetylcholine esterase and cytochrome oxidase are further characteristics of the primary auditory cortex. The neurones within the primary auditory cortex are spatially organized according to their response to sounds of different frequency (tonotopy) or intensity (ampliotopy) (Talavage et al 2004, Schreiner and Malone 2015). Using observer-independent cytoarchitectonic and multimodal parcellation methods, the primary auditory cortex (indicated as Te1) can be further subdivided into areas Te1.0, Te1.1 and Te1.2. Whether and how tonotopic fields relate to the architectonic subdivisions of Te1 is not known.

The secondary auditory area Te2 (BA42) is found anteriorly, laterally and caudally to Te1, and occupies the largest portion (>90%) of the temporal plane. Te2 does not extend onto the insular cortex medially nor does it extend on the convexity of the superior temporal gyrus laterally. The medial and the lateral borders are not precisely associated with sulcal landmarks. The koniocortical structure of Te1 disappears in Te2. The packing density of neurones in layer V increases from Heschl's gyrus through the planum temporale to the superior temporal gyrus. The pyramidal cells in layer III of Te2 are also arranged in vertical columns, referred to by von Economo and Koskinas (1925) as the 'organ pipe formation'. $GABA_B$, α_1 and $5\text{-}HT_{1A}$ receptors show higher densities in Te2 than in Te1.

The temporo-insular area TI differs from Te2: it has prominent and cell-dense infragranular layers, and there are differences in the regional and laminar receptor densities (see Fig. 32.61E–H). The border between the transitional area TI and the insular cortex can be defined on the basis of cytoarchitectonic differences and the distribution of cholinergic muscarinic M_2 receptor.

The auditory area Te3 occupies approximately the posterior two-thirds of the free surface of the superior temporal gyrus. Thus, Te3 corresponds to large parts of BA22, and is part of the auditory belt. It has a high density of IIIc pyramidal cells of prominent size and a rather cell-dense layer V. The layer VI/white matter boundary is less sharp than in Te2. Compared to Te2, Te3 has lower densities of M_2, and also slightly lower densities of M_1, NMDA and $GABA_A$ receptors. Compared to the areas (Te4 and Te5; see Fig. 32.61) located ventrally in the upper bank of the superior temporal sulcus, Te3 has lower densities of α_1, $5\text{-}HT_{1A}$, and AMPA receptors, particularly in the infragranular layers. The secondary and higher areas of the auditory cortex are involved in the perception of complex sounds, including frequency-modulated tones, harmonic complexes, amplitude modulations, spectrally dynamic sounds and sound sequences.

Direct corticofugal projections link the auditory cortex with the medial geniculate nucleus and the inferior colliculus. The auditory cortex interconnects with the prefrontal cortex, and posterior parts of the operculum project to areas 8 and 9. Central parts project to areas 8, 9 and 46. More anterior regions project to areas 9 and 46, to area 12 on the latero-orbital surface of the hemisphere, and to the anterior cingulate gyrus on the medial surface. Callosal connections are with the same and adjacent regions in the other hemisphere.

The functionally defined Wernicke's area is not clearly delineated anatomically, but corresponds to BA22 in the middle and posterior third of the superior temporal gyrus. It has a prominent role in comprehension of language, in particular sentences, syntactic processing and auditory working memory.

Temporal lobe areas connect via a 'dorsal' or a 'ventral' pathway with separate regions of the frontal lobe. The 'dorsal' pathway connects posterior temporal areas with the posterior dorsolateral prefrontal cortex; the 'ventral' pathway terminates in the anterior prefrontal cortex. In this context, the arcuate fascicle and the extreme capsule are particularly important for the impairment in Wernicke's aphasia. Considering that the dorsal and ventral prefrontal regions are characterized by spatial and non-spatial functional domains, it has been proposed that auditory information is channelled into at least two parallel processing streams: a dorsal or 'where' stream that subserves spatial localization, and a ventral or 'what' stream that subserves auditory object or pattern recognition. It has been shown that the anterior belt is responsive to the spectrotemporal features of a sound that code object identity, whereas neurones in the caudal belt are more sensitive to the spatial properties of a sound. It thus appears that object and spatial information is transmitted in different pathways beyond the auditory cortex.

BA21 on the middle temporal cortex is multimodal. It establishes reciprocal connections with early auditory, somatosensory and visual areas and connects to frontal areas according to an anterior–posterior gradient: posterior BA21 with BA8 and BA9, intermediate BA21 with BA9 and BA46, and anterior BA21 with BA10, BA46 and fronto-orbital areas. BA21 also projects to the temporal pole and the entorhinal cortex. Thalamic connections are with the pulvinar nuclei and the intralaminar group. Other subcortical connections with the ventral tegmental area, locus coeruleus and raphe nuclei follow the general pattern for all cortical areas.

The inferior temporal cortex, area 20, is, to a large extent, a higher visual association area. The posterior inferior temporal cortex receives major ipsilateral corticocortical fibres from V4. It contains a coarse retinotopic representation of the contralateral visual field and sends a major feed-forward pathway to the anterior part of the inferior temporal cortex. The anterior part of BA20 projects onto the temporal pole and the medial surface of the temporal lobe. Additional ipsilateral connections are with the parieto-temporal region. BA20 is also connected to BA46, the fronto-orbital cortex and the frontal eye field. Reciprocal thalamic connections are with the pulvinar and the intralaminar nuclei. Callosal connections are between corresponding areas and the adjacent higher visual areas of each hemisphere.

The cortex of the temporal pole receives feed-forward projections from widespread areas of temporal association cortex that are immediately posterior to it. The dorsal part receives predominantly auditory input from the anterior part of the superior temporal gyrus. The inferior part receives visual input from the anterior area of the inferior temporal cortex. Other ipsilateral connections are with the anterior insular, posterior and medial orbitofrontal, and medial prefrontal cortices. The temporal pole projects onwards into limbic and paralimbic areas. Thalamic connections are mainly with the medial pulvinar and with intralaminar and midline nuclei. Physiological responses of cells in this and more medial temporal cortex correspond particularly to behavioural performance and to the recognition of high-level aspects of social stimuli. Bilateral lesions of the temporopolar cortex cause retrograde amnesia (loss of all remote memories, but sparing learning and recent memory). Patients with these lesions suffer from a loss of autobiographical memories and the ability to recognize faces and names. The awareness of consolidated recognition of objects thus seems to occur in the temporo-polar cortex.

Insular lobe

The roughly triangular-shaped insular lobe (island of Reil) forms the base of the Sylvian cistern and lies between the frontal and temporal lobes (see Fig. 32.1). It is hidden in the depths of the lateral sulcus and covered by the opercular parts of the frontal, parietal and temporal lobes in the adult human brain.

The insular cortex subserves an extremely wide array of functions. It comprises such diverse functions such as olfaction, gustation, interoception, vestibular functions, general somatosensation, pain, cognition, attention, working memory, emotion including empathy, willed action, addictive behaviour and language. The insula seems to play a major role as a convergence zone and is implicated in the coordination between internal and external information through emotional subjective awareness. If the various functions are classified as larger functional domains, the sensorimotor domain is in the midposterior insula and forms the region posterior to the most posterior gyri breves; the cognitive domain is in the anterior-dorsal part of anterior and middle short gyri; the olfacto-gustatory domain is on the right middle insular gyrus; and the emotional domain is in the anterior-ventral part around the insular pole (**Fig. 32.62**).

Insular lobe sulci and gyri

Available with the *Gray's Anatomy* e-book

Insular lobe internal structure and connectivity

Cytoarchitectonically, four major zones are recognized within the insula. Starting from an allocortical small centre, a peri- to pro-isocortical semicircular zone is surrounded by a dysgranular to eulaminate isocortical zone. Most posteriorly, a relatively small granular isocortical zone follows to the caudal limit of the insula (see Fig. 32.62).

Thalamic afferents to the insula come from subdivisions of the ventral posterior nucleus and of the medial geniculate nucleus, from the oral and medial parts of the pulvinar, the suprageniculate/nucleus limitans complex, the mediodorsal nucleus and the nuclei of the intralaminar and midline groups. It appears that the anterior (agranular) cortex is connected predominantly with the mediodorsal and ventroposterior nuclei, while the posterior (granular) cortex is connected predominantly with the pulvinar and the ventral posterior nuclei.

Ipsilateral cortical connections of the insula are diverse. There are somatosensory connections with S1, S2 and surrounding areas, and the anterior part of the superior parietal lobule. The insular cortex also has connections with the orbitofrontal cortex, and several auditory regions

The insular surface is delineated peripherally by the circular sulcus of Reil, which is interrupted by the transverse insular gyrus running across the limen insulae. The anterior surface of the insula is covered by the fronto-orbital operculum (the posterior portion of the posterior orbital gyrus and the orbital part of the inferior frontal gyrus). Its lateral surface is covered superiorly by the frontoparietal operculum (triangular and opercular parts of the inferior frontal gyrus, subcentral gyrus, and anterior and basal part of the supramarginal gyrus) and inferiorly by the temporal operculum (polar plane of the superior temporal gyrus). Its anteroinferior vertex is the limen insulae, a narrow strip of olfactory cortex that extends along the lateral aspect of the lateral olfactory stria, conjoining the insular cortex and anterior perforate substance. The surface of the insula is divided into anterior and posterior parts by a deep central insular sulcus that courses obliquely from the limen insulae towards the central sulcus between frontal and parietal lobes. The anterior part of the insular surface is composed of short insular gyri (anterior, middle and posterior short insular gyri). The transverse insular gyrus runs along the limen insulae, connecting the anterior insula with the posteromedial part of the fronto-polar cortex. The latter is the connection between the posterior portion of the medial orbital gyrus and the posterior orbital gyrus, and is located anterior to and along the lateral olfactory stria. The accessory gyrus extends from the anterior portion of the anterior short gyrus superiorly to the transverse insular gyrus, beneath the fronto-orbital operculum. Both gyri constitute the insular pole within the anterior aspect of the insula. The posterior part of the insula is located behind its central sulcus and is composed of anterior and posterior insular long gyri. Both of these gyri are separated by the postcentral insular sulcus; the anterior long gyrus is usually larger, and may be single or divided at its upper end (see Fig. 32.62).

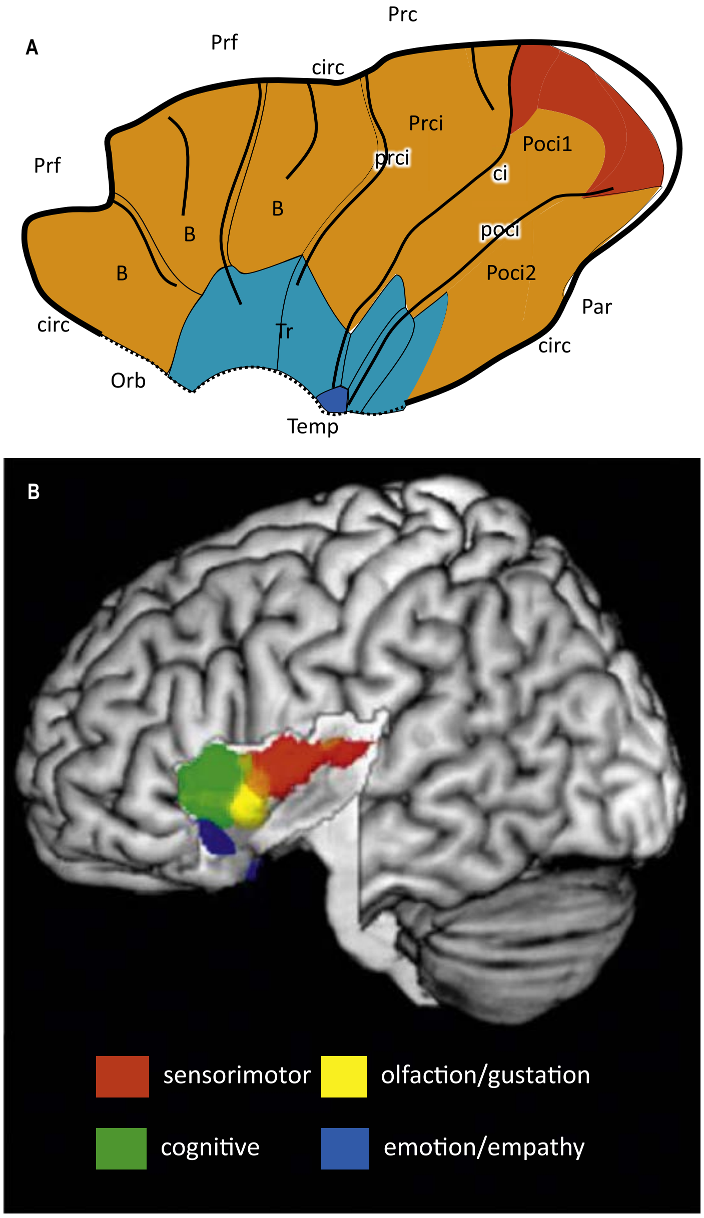

Fig. 32.62 Cortical regions and types (**A**) and functional domains (**B**) in the human insula. **A**, A cytoarchitectonic map of the insular cortex modified after Brockhaus (1940). Red, granular isocortical areas; orange, eulaminate to dysgranular isocortical areas; light blue, proiso- and periallocortical areas; dark blue, allocortical areas. **B**, Maps of functional domains. Abbreviations: B, short insular gyri; ci, central insular sulcus; circ, circular sulcus of the insula; Orb, adjoining fronto-orbital cortex; Par, adjoining parietal cortex; Poci1, first postcentral insular gyrus; Poci2, second postcentral insular gyrus; poci, postcentral sulcus of the insula; Prc, adjoining precentral cortex; Prci, precentral insular gyrus; prci, precentral sulcus of the insula; Prf, adjoining prefrontal cortex; Temp adjoining temporal cortex; Tr transverse orbital gyrus. (B, Adapted with permission from Kurth F, Zilles K, Fox PT et al 2010 A link between the systems: functional differentiation and integration within the human insula revealed by meta-analysis. Brain Struct Funct 214:519–34.)

in the temporal lobe interconnect with the posterior granular and dysgranular insular cortex. Connections with visual areas are virtually absent. The periallo- and allocortical insula has connections primarily with olfactory, limbic and paralimbic structures, including, most prominently, the amygdala.

WHITE MATTER OF THE CEREBRAL HEMISPHERES

The white matter of the cerebral hemispheres is composed of long myelinated axons grouped into larger white matter tracts (fasciculi). According to their origin, course and termination, white matter tracts can be classified into association, commissural or projection pathways (**Fig. 32.63**). The course of the large white matter tracts of the human brain can be studied using postmortem blunt dissections of brains prepared using Klingler's technique or *in vivo* with diffusion imaging tractography (**Video 32.1**).

Association tracts

Association tracts connect cortical areas in the same hemisphere and can be divided into short U-fibres linking adjacent gyri and long association tracts connecting distant gyri (**Fig. 32.64**). Most of the U-shaped fibres connect gyri within the same lobe (intralobar) whereas most of the long association fibres connect gyri of different lobes (interlobar). There is a relationship between the length of the fibres and the depth of their course within the white matter of the cerebral hemispheres: short U-fibres run more superficially, closer to the cortex of the gyri and sulci, whereas longer fibres group together deeper in the white matter of each gyrus and in the centrum semiovale. Association tracts are composed of both feed-forward and feed-back fibres that enable rapid feed-forward propagation of sensory input and top-down modulation of sensory processing.

Most of the intralobar tracts have been recently described and classified for the first time in humans with diffusion tractography.

In the frontal lobe, the frontal aslant tract is a short intralobar connection between the regions of the superior medial frontal lobe (supplementary and presupplementary motor areas, medial prefrontal cortex) and Broca's region (see Fig. 32.64; **Fig. 32.65**). The fronto-orbitopolar tract connects the posterior orbitofrontal, olfactory cortex and nucleus accumbens with the anterior orbitofrontal cortex and inferior frontal pole regions (see Fig. 32.64; **Fig. 32.66**). The superior and inferior frontal longitudinal fasciculi run underneath the superior and inferior frontal sulci, respectively and connect the posterior premotor cortex to the anterior prefrontal cortex (**Fig. 32.67**) (Catani et al 2012). The hand-knob region in the precentral gyrus is particularly rich in short U-fibres that are concentrically arranged around the origin of the corticospinal projections that are directed to the cervical spinal cord controlling finger movements (**Fig. 32.68**). The frontomarginal tract runs underneath the frontomarginal sulcus and connects medial and lateral frontal pole regions (see Fig. 32.66). The fronto-insular tracts are U-fibres connecting different areas of the inferior frontal and precentral gyri to the anterior gyri of the insula (**Fig. 32.69**). In the parietal lobe, short intralobar tracts connect the superior and inferior parietal lobules (intraparietal tract) and the post-central gyrus to the inferior parietal lobule (**Fig. 32.70**) (Catani et al 2017). In the temporal lobe, the temporal longitudinal fasciculus runs along the white matter of the superior, middle and inferior temporal gyri and connects anterior to middle and posterior temporal regions (**Fig. 32.71**). In the occipital lobe, the vertical occipital bundle of Wernicke links the regions of the superior, middle and inferior occipital gyri whereas the medial occipital longitudinal tract connects early visual areas to the parahippocampal place area (**Figs 32.72–32.73**).

Long interlobar association tracts have been originally described using postmortem blunt dissections in humans and axonal tracing studies in non-human primates. They include the arcuate fasciculus, superior, middle and inferior longitudinal fasciculi, inferior fronto-occipital fasciculus, uncinate fasciculus and cingulum. Individual variability in both the three-dimensional topography and size of these tracts has been reported in the healthy population, especially between hemispheres (interhemispheric asymmetry) or between male and female brains. The terminology used to indicate the association tracts often refers to their shape (e.g. the uncinate from the Latin *uncinatus* meaning 'hook-like'), their origin and termination (e.g. inferior fronto-occipital fasciculus), or their course, location and orientation within the cerebral hemispheres (e.g. inferior longitudinal fasciculus).

Arcuate fasciculus

The arcuate fasciculus is a dorsal association tract connecting perisylvian regions of the frontal, parietal and temporal lobe (see Fig. 32.64). In humans, two parallel pathways have been distinguished within the arcuate fasciculus (Catani et al 2005) (**Fig. 32.74**). The medial direct pathway (i.e. the arcuate fasciculus *sensu strictu* or direct long segment) connects Wernicke's region in the temporal lobe (BA41, 42, 22, 37) with Broca's region in the frontal lobe (BA6, 44, 45). The indirect pathway runs more laterally compared to the direct pathway and is composed of two separate segments: the anterior segment links Broca's region in the frontal lobe to Geschwind's region in the inferior parietal lobule (BA39, 40); the posterior segment links Geschwind's to Wernicke's region (Catani et al 2005). The direct long segment of the arcuate fasciculus is larger on the left hemisphere compared to the right in about 80% of the population; the remaining 20% shows a bilateral distribution

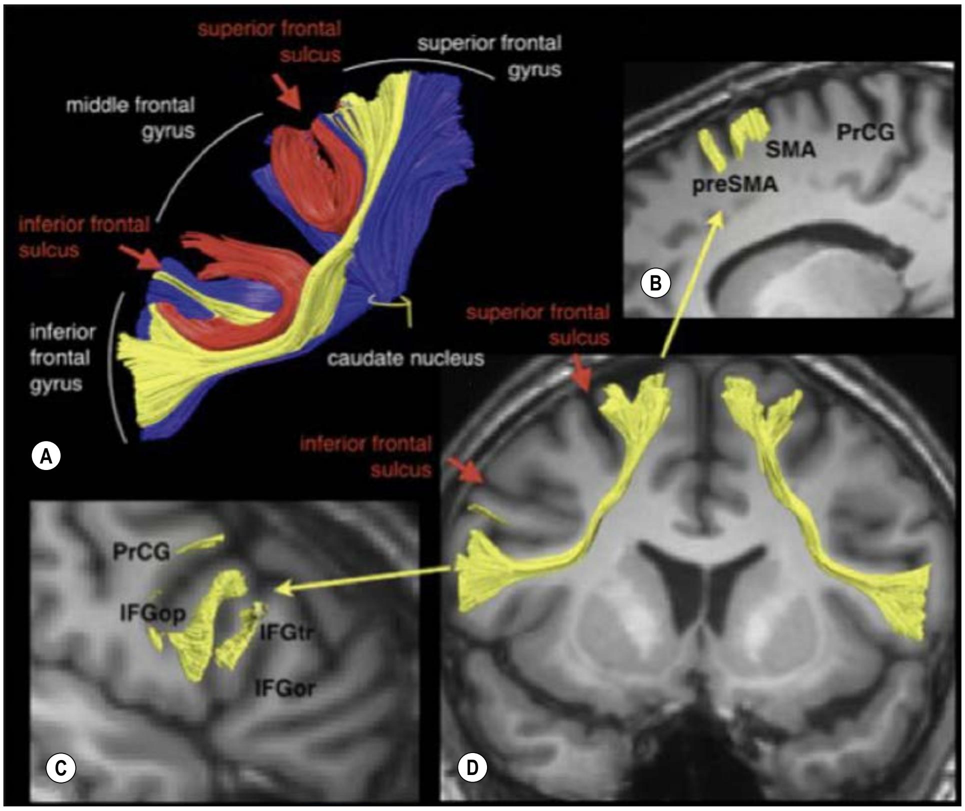
superior frontal sulcus
superior frontal gyrus
middle frontal gyrus
inferior frontal sulcus
inferior frontal gyrus
caudate nucleus
A
SMA
PrCG
preSMA
B
superior frontal sulcus
inferior frontal sulcus
PrCG
IFGop
IFGtr
IFGor
C
D

Fig. 32.65 Intralobar associative connections and projection fibres of the prefrontal cortex. **A**, The frontal aslant tract (yellow) connects superior and inferior regions of the posterior frontal lobe. It is medial to the short U-fibres (red) connecting superior, middle and inferior frontal gyri, and crosses fronto-striatal fibres (blue) projecting to the caudate nucleus and putamen. **B**, Medial cortical projections of the frontal aslant tract terminating in the supplementary motor area (SMA) and preSMA. **C**, Lateral cortical projections of the frontal aslant tract terminating in the precentral gyrus (PrCG) and pars opercularis (IFGop) and triangularis (IFGtr) of the inferior frontal gyrus. Other abbreviation: IFGor, inferior frontal gyrus, pars orbitalis. (Adapted with permission from Catani M et al 2012 Short frontal lobe connections of the human brain. Cortex 48: 273–91.)

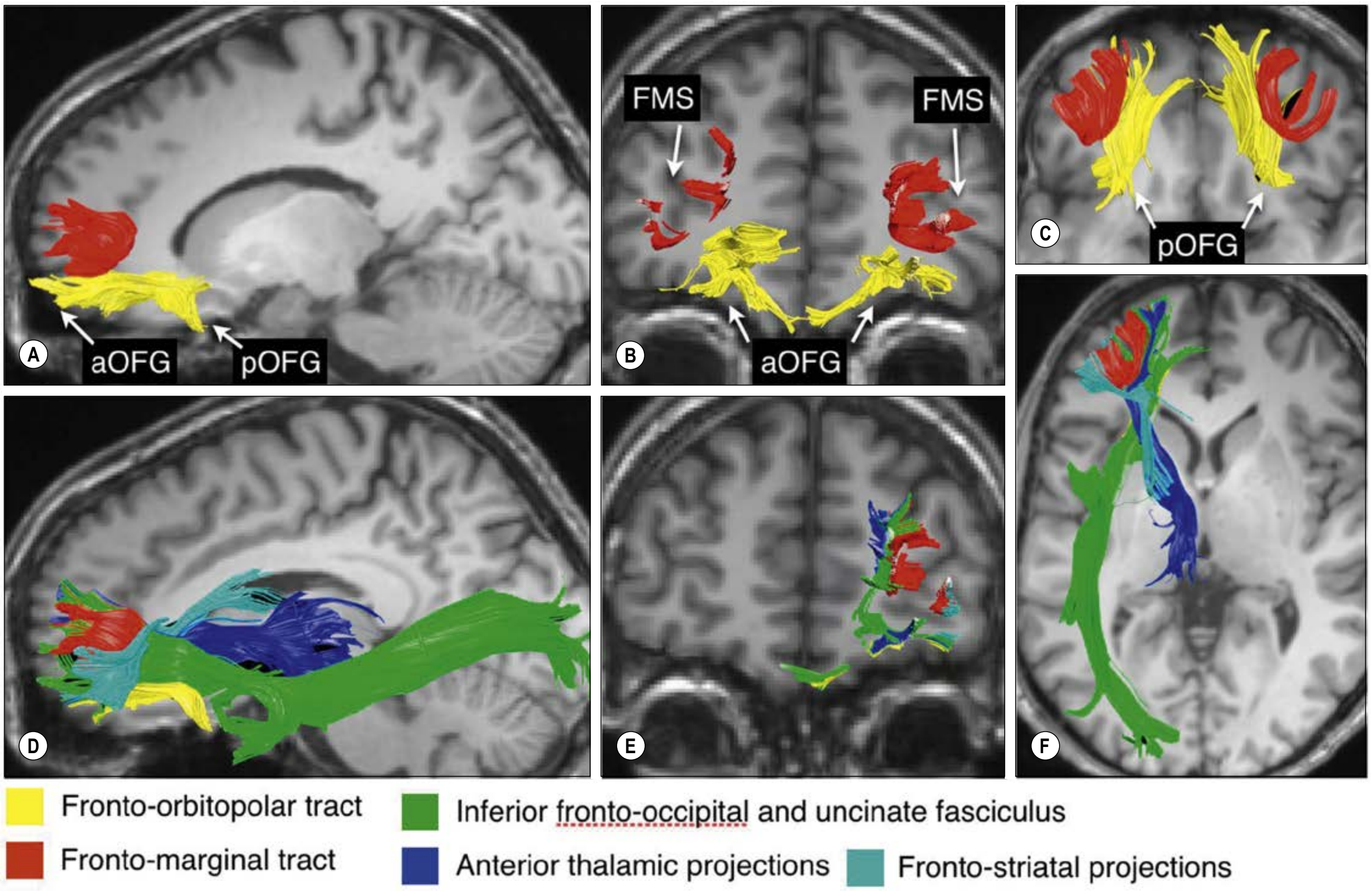
A
aOFG
pOFG
FMS
FMS
B
aOFG
C
pOFG
D
E
F
Fronto-orbitopolar tract
Fronto-marginal tract
Inferior fronto-occipital and uncinate fasciculus
Anterior thalamic projections
Fronto-striatal projections

Fig. 32.66 Intralobar connections and long association and projection tracts of the orbitofrontal and frontal polar region from a lateral **(A, D)**, anterior **(B, E)** and superior **(C, F)** view. Abbreviations: aOFG, anterior orbitofrontal gyrus; FMS, fronto-marginal sulcus; pOFG, posterior orbitofrontal gyrus. (Adapted with permission from Catani M et al 2012 Short frontal lobe connections of the human brain. Cortex 48: 273–91.)

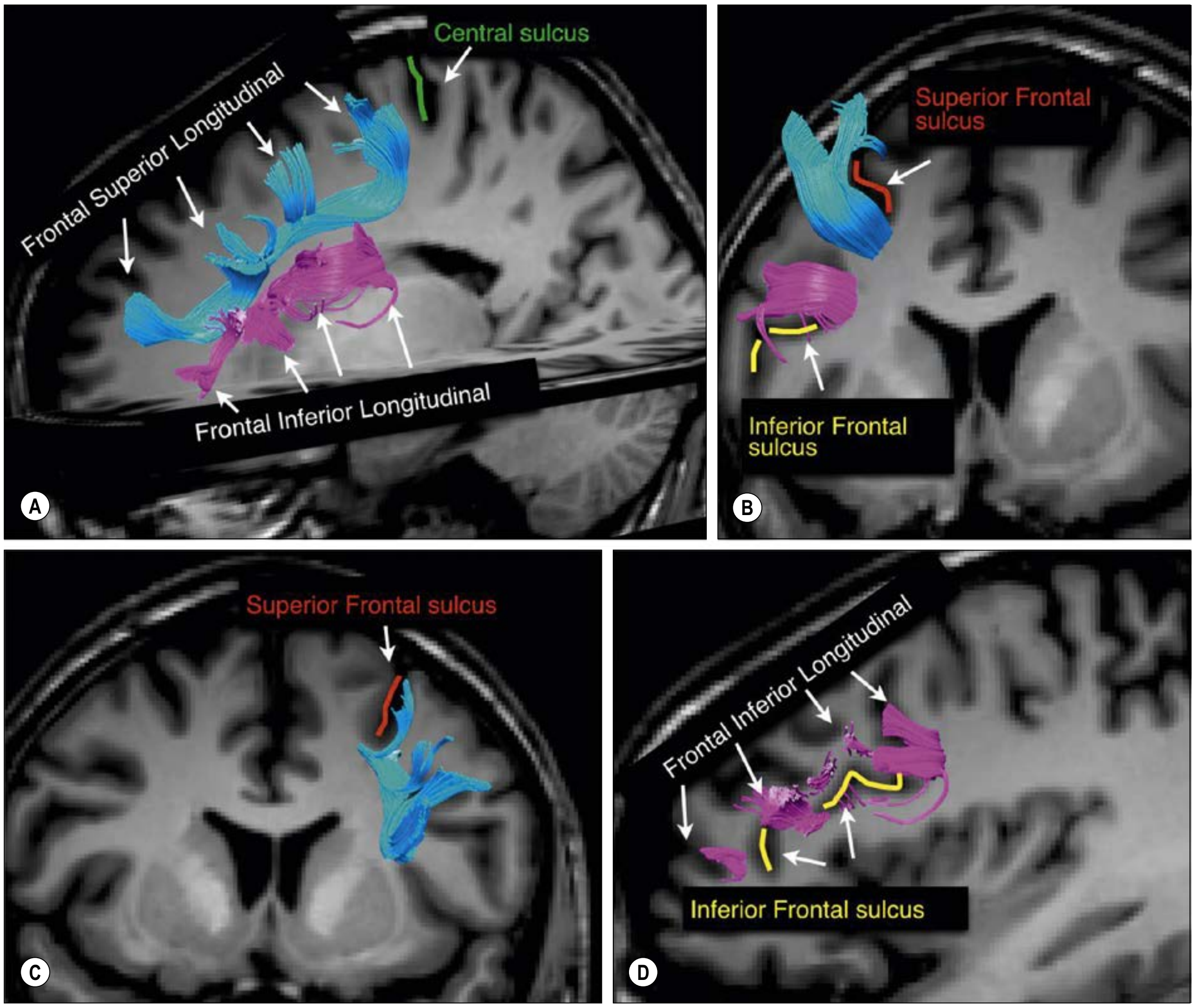
Central sulcus
Frontal Superior Longitudinal
Frontal Inferior Longitudinal
A
Superior Frontal sulcus
Inferior Frontal sulcus
B
Superior Frontal sulcus
C
Frontal Inferior Longitudinal
Inferior Frontal sulcus
D

Fig. 32.67 Frontal longitudinal systems from a lateral **(A, D),** posterior **(B),** and anterior **(C)** view. (Adapted with permission from Catani M et al 2012 Short frontal lobe connections of the human brain. Cortex 48:273–91.)

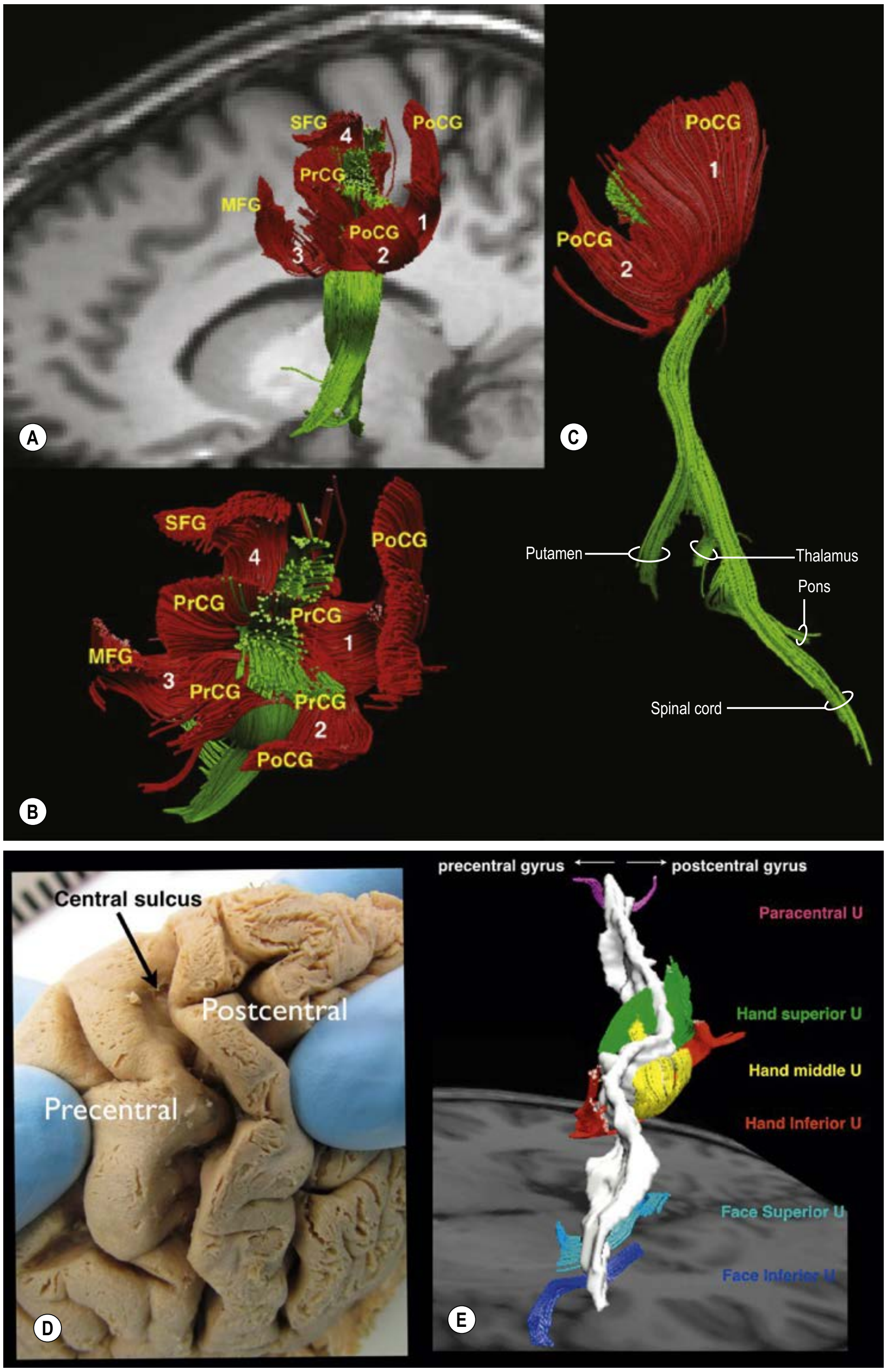
SFG
4
PoCG
PrCG
MFG
PoCG
1
3
2
A
PoCG
1
PoCG
2
C
Putamen
Thalamus
Pons
Spinal cord
SFG
PoCG
4
PrCG
PrCG
1
MFG
3
PrCG
PrCG
2
PoCG
B
Central sulcus
Postcentral
Precentral
D
precentral gyrus
postcentral gyrus
Paracentral U
Hand superior U
Hand middle U
Hand Inferior U
Face Superior U
Face Inferior U
E

Fig. 32.68 Upper panel: A reconstruction of the short U-shaped (red) and long projection (green) tracts of the hand-knob motor region in the left hemisphere. **A**, Left lateral view. **B**, Top view. **C**, Posterior view. The connections of the hand region resemble a 'poppy flower' with a green stem and four red 'petals' (1, posterior; 2, inferior; 3, anterior; 4, superior). The posterior (1) and inferior (2) petals correspond to the frontoparietal U-tracts between the precentral (PrCG) and postcentral (PoCG) gyri (hand superior and hand middle, respectively). The anterior (3) and superior (4) petals correspond to the U-shaped connections between the precentral gyrus and the middle frontal gyrus (MFG), and the middle frontal gyrus and superior frontal (SFG) gyrus, respectively. The 'green stem' is formed by ascending thalamocortical projection fibres and descending projections to the putamen (corticostriatal), pons (corticopontine) and spinal cord (corticospinal). Lower panel: Short U-fibres of the central sulcus connecting different body parts of the motor (precentral) and somatosensory (postcentral) homunculus. (Upper panel with permission from Catani M, Dell'acqua F, Vergani F et al 2012 Short frontal lobe connections of the human brain. Cortex 48(2):273–91.)

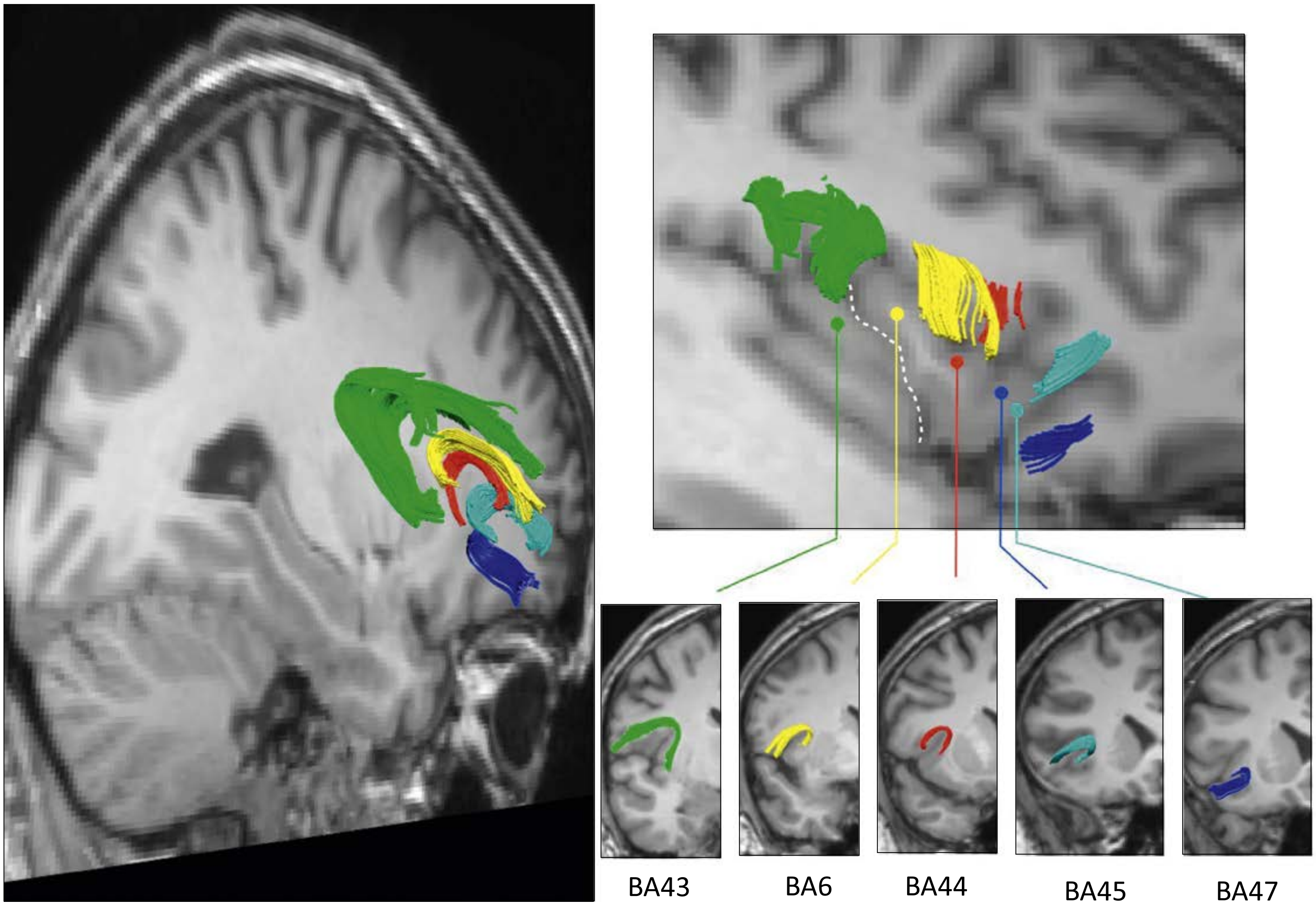

Fig. 32.69 Fronto-insular U-tracts connecting opercular areas of the frontal lobe (BA43, BA6, BA44, BA45, BA47) with the anterior insula. (Adapted with permission from Catani M et al 2012 Short frontal lobe connections of the human brain. Cortex 48: 273–91.)

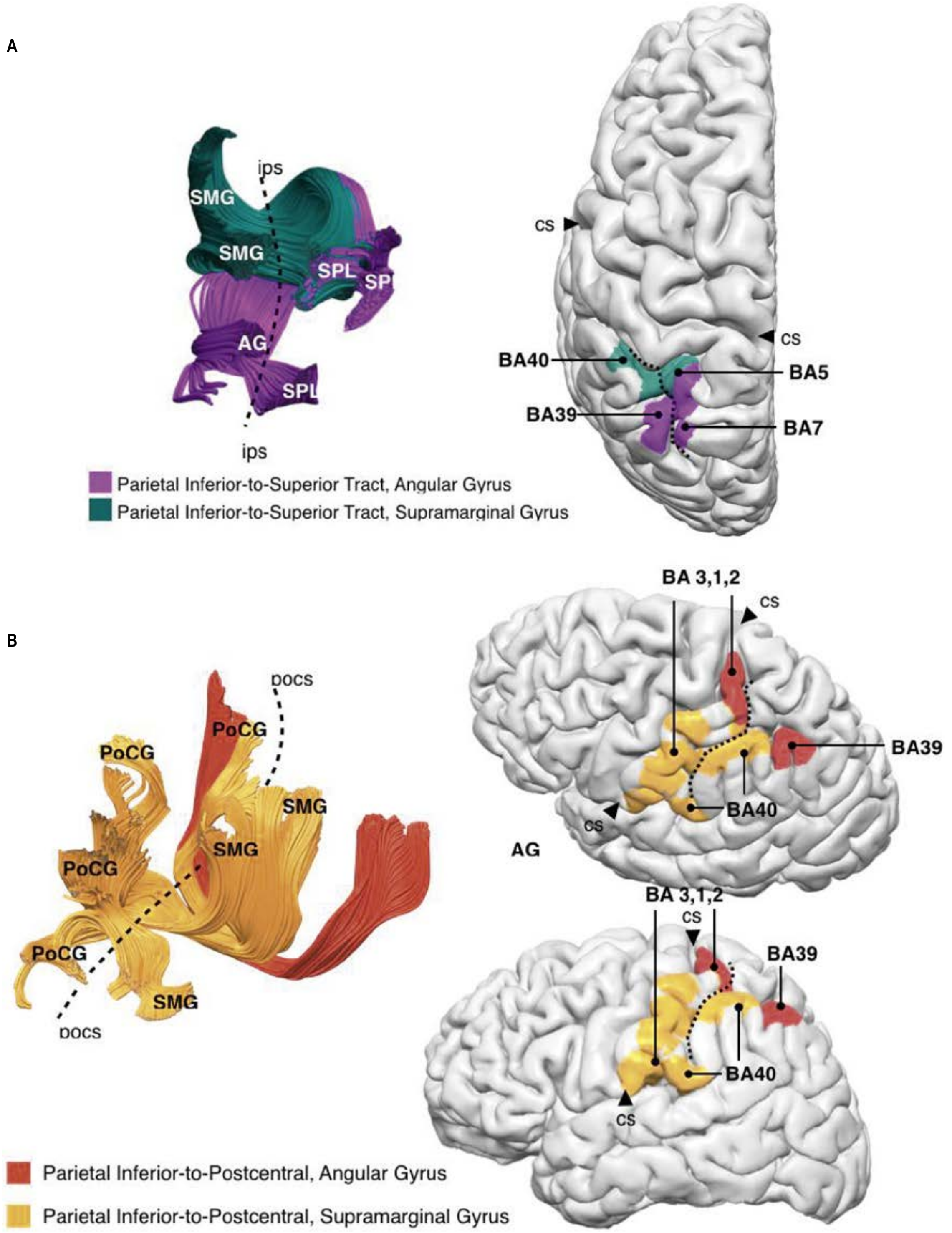
A
ips
SMG
SMG
SPL
SPL
AG
SPL
ips
▨ Parietal Inferior-to-Superior Tract, Angular Gyrus
▨ Parietal Inferior-to-Superior Tract, Supramarginal Gyrus
cs
cs
BA40
BA5
BA39
BA7
B
pocs
PoCG
PoCG
SMG
SMG
PoCG
PoCG
SMG
pocs
BA 3,1,2
cs
BA39
cs
BA40
AG
BA 3,1,2
cs
BA39
BA40
cs
▨ Parietal Inferior-to-Postcentral, Angular Gyrus
▨ Parietal Inferior-to-Postcentral, Supramarginal Gyrus

Fig. 32.70 Major intralobar tracts of the parietal lobe. **A**, U-fibres connecting superior and inferior parietal lobules. **B**, U-fibres connecting the inferior parietal lobule with the postcentral gyrus. (Adapted with permission from Catani M et al 2017 Short parietal lobe connections of the human and monkey brain. Cortex 97:339–357.)

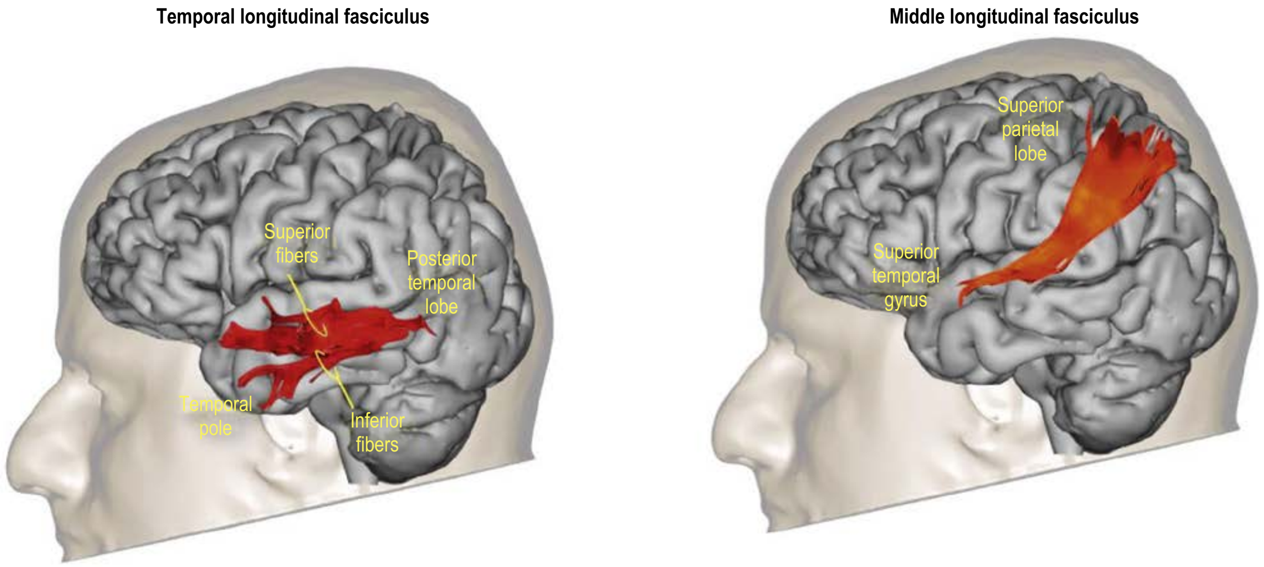
Temporal longitudinal fasciculus
Superior fibers
Posterior temporal lobe
Temporal pole
Inferior fibers
Middle longitudinal fasciculus
Superior parietal lobe
Superior temporal gyrus

Fig. 32.71 Left: the temporal longitudinal fasciculus (TLF) is a long intralobar tract of the temporal lobe connecting posterior, mid- and anterior areas of the temporal gyri. It can be devided into superior (TLF I) and inferior (TLF II) branches. Right: the middle longitudinal fasciculus is a long interlobar tract connecting the superior temporal area to the posterior parietal lobe running medial to the long segment of the arcuate fasciculus.

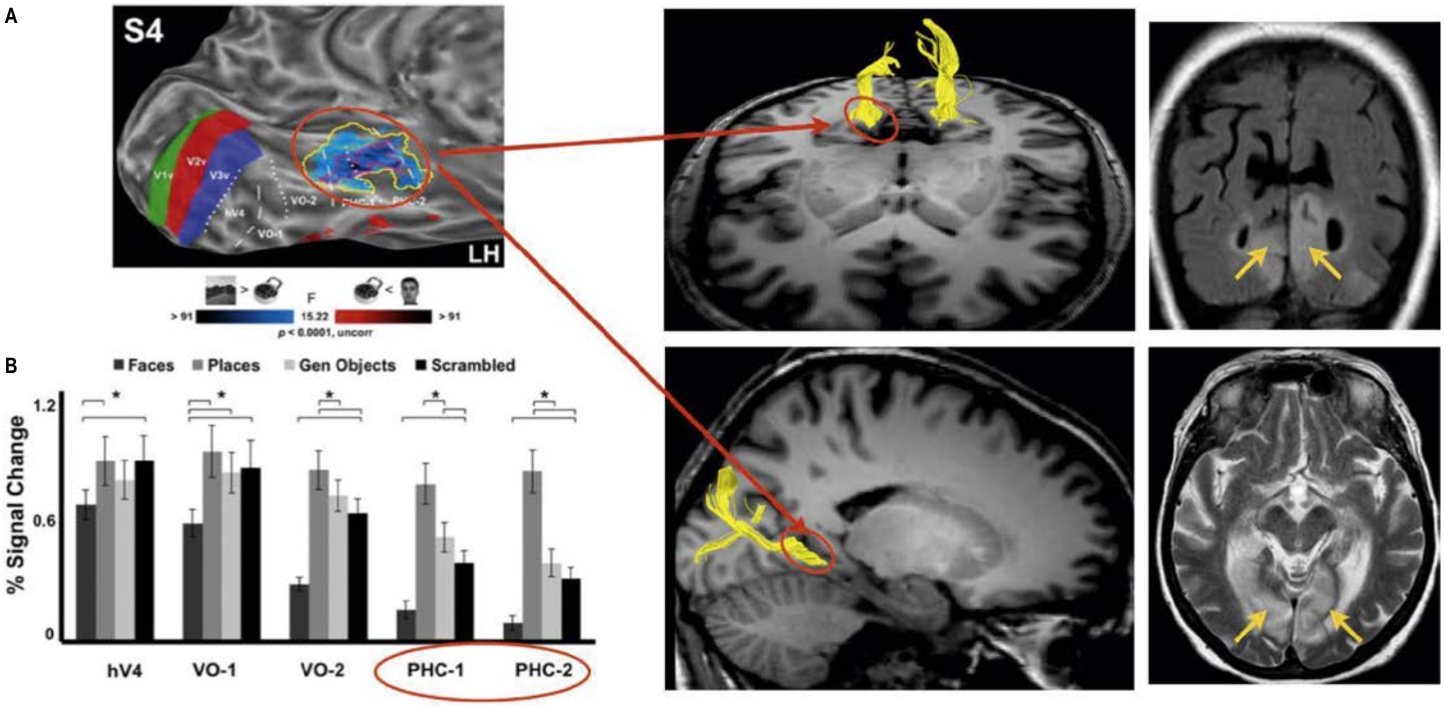
A
S4
V1v
V2v
V3v
hV4
VO-1
VO-2
PHC-1
PHC-2
LH
F
> 91
15.22
> 91
p < 0.0001, uncorr
B
Faces
Places
Gen Objects
Scrambled
% Signal Change
1.2
0.6
0
*
hV4
VO-1
VO-2
PHC-1
PHC-2

Fig. 32.72 The medial occipital longitudinal tract (MOLT, yellow tract) connects early visual areas (V1, V2, V3) of the cuneus and lingual gyrus with the posterior parahippocampal area (PPA, indicated by orange arrows and orange circles). The PPA includes the posterior (PHC-1) and anterior parahippocampal cortex (PHC-2) and is a region that responds selectively to images of scenes, places and buildings compared to other association areas (hV4, VO-1, VO-2) (Arcaro et al 2009). Damage to the MOLT or its cortical projections (indicated by yellow arrows) manifests with deficits in spatial navigation and memory for configurations (Lazzarino et al 2014).

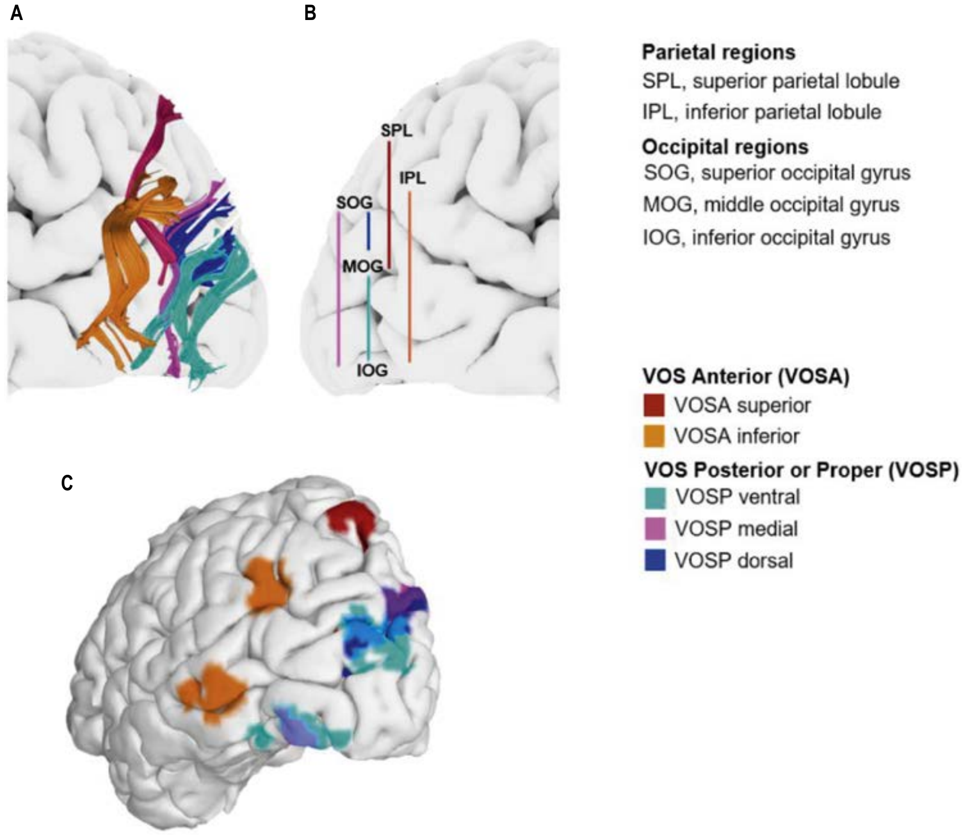
A
B
C
SPL
IPL
SOG
MOG
IOG
Parietal regions
SPL, superior parietal lobule
IPL, inferior parietal lobule
Occipital regions
SOG, superior occipital gyrus
MOG, middle occipital gyrus
IOG, inferior occipital gyrus
VOS Anterior (VOSA)
VOSA superior
VOSA inferior
VOS Posterior or Proper (VOSP)
VOSP ventral
VOSP medial
VOSP dorsal

Fig. 32.73 The vertical occipital tract (VOS) of Wernicke is a system of short and long connections between superior, middle and inferior occipital regions. This tract can be divided into an anterior network (VOSA) composed of superior and inferior fibres, and a posterior network (VOSP) composed of ventral, medial and dorsal fibres. VOSA connects to the posterior parietal cortex. (Courtesy of Marco Catani and Ahmad Beyh, Natbrainlab.)

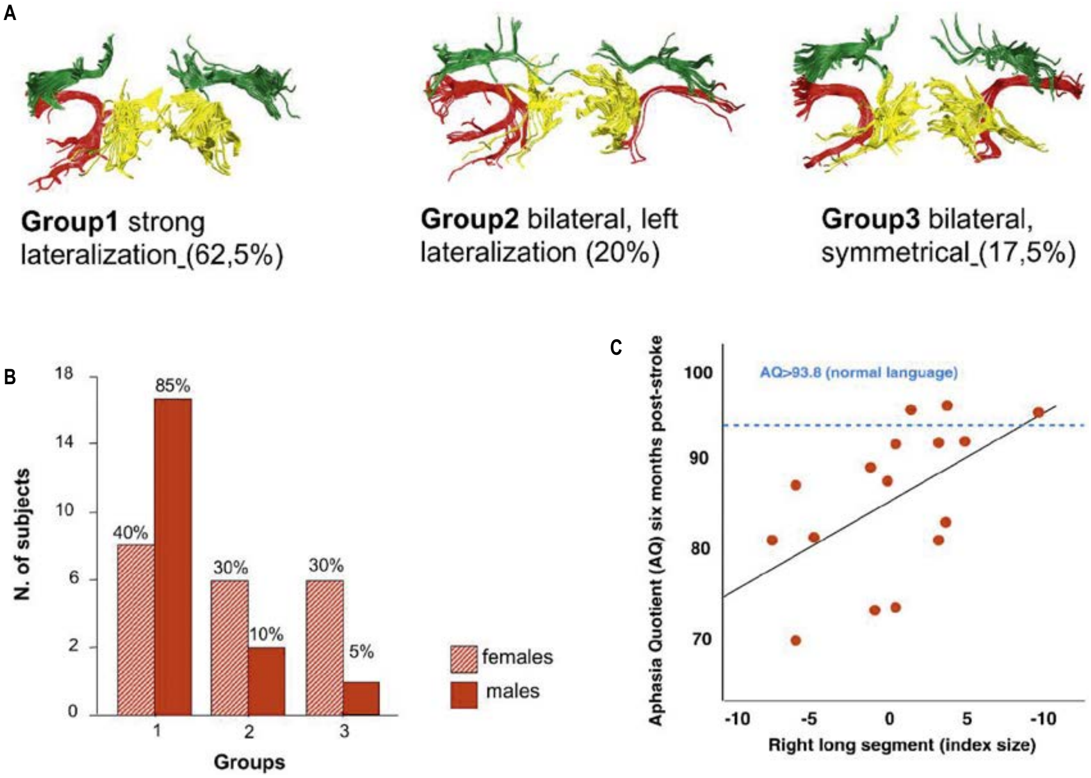

Fig. 32.75 Distribution of the pattern of lateralization of the arcuate long segment (red) in the healthy adult population (**A**) and according to sex (**B**). **C**, Recovery of language after left hemisphere stroke is higher in patients with a larger long segment in the right hemisphere. (With permission from Catani M, Allin MPG, Husain M et al 2007 Symmetries in human brain language pathways correlate with verbal recall. PNAS 104:17163–8; and Forkel SJ, Thiebaut de Schotten M, Dell'Acqua F et al 2014 Anatomical predictors of aphasia recovery: a tractography study of bilateral perisylvian language networks. Brain 137:2027–39.)

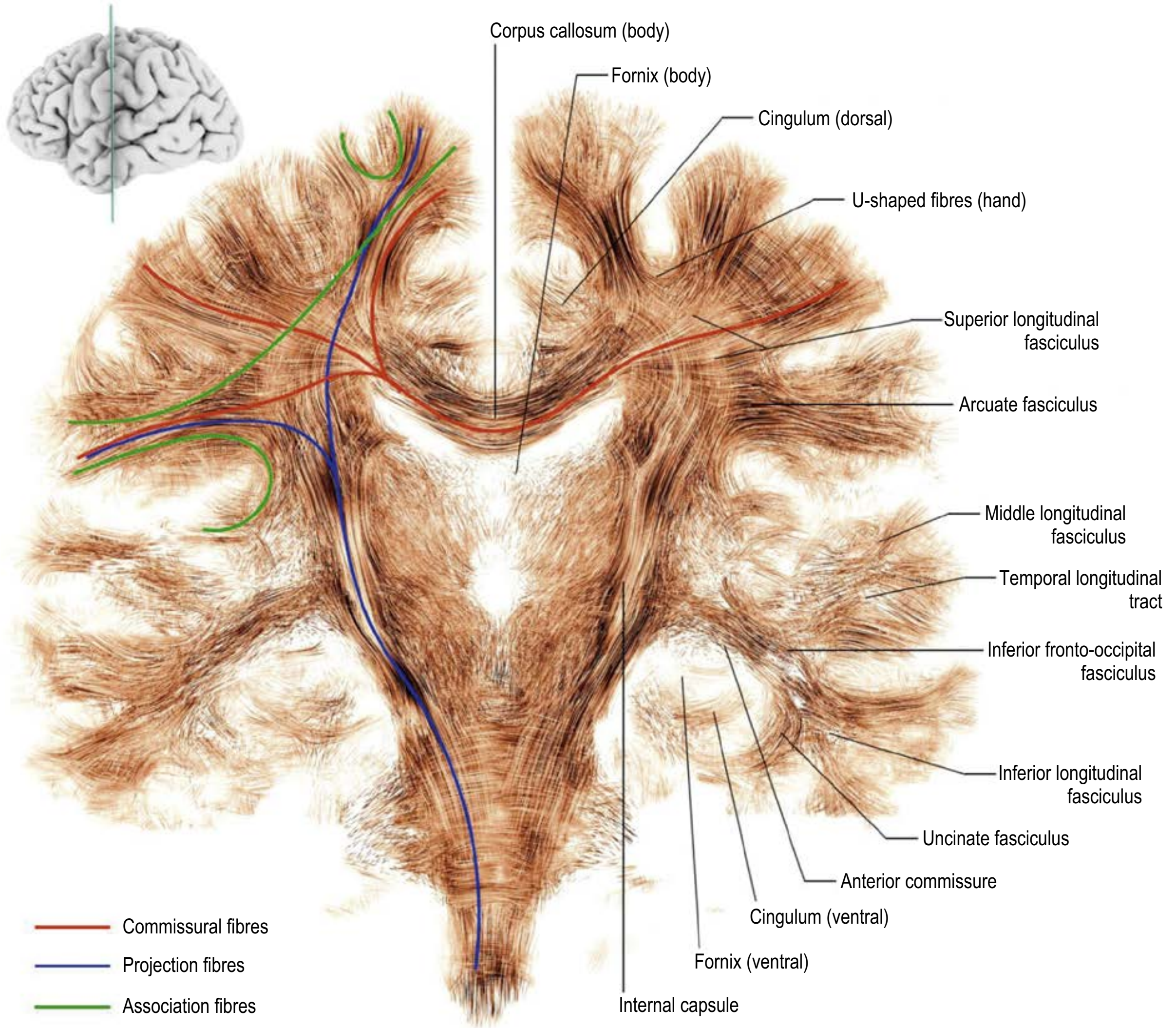

Fig. 32.63 Classification of white matter fibres and location of the major tracts of the cerebral hemispheres passing through a coronal section of the frontoparietal and temporal lobes. The background image was created using diffusion imaging tractography. (Courtesy of Flavio Dell'Acqua and Marco Catani, Natbrainlab.)

(Catani et al 2007) that is more prevalent in the female population and it has been associated with better recovery of language after a left hemisphere stroke (**Fig. 32.75**) (Forkel et al 2014). The arcuate fasciculus is important for language, social communication, working memory and complex limb motor coordination (praxis).

Superior longitudinal fasciculus

The superior longitudinal fasciculus (SLF) has three distinct branches as originally described in the monkey brain using axonal tracing methods (Petrides and Pandya 1984). In humans (see Fig. 32.64) (Thiebaut de Schotten et al 2011), the first branch of the superior longitudinal fasciculus (SLF I) connects the superior parietal lobule and precuneus (BA5 and 7) to the superior frontal (BA8, 9, 32) and perhaps to some anterior cingulate areas (BA24). The SLF I processes the spatial coordinates of trunk and lower limbs and contributes to the preparatory stages of movement planning (e.g. anticipation) (Leiguarda and Marsden 2000), oculomotor coordination (Anderson et al 2012), visual reaching (Johnson et al 1996), and voluntary orientation of attention (Corbetta and Shulman 2002). The SLF I is bilateral and there are lateralization differences between left- and right-handers (rightward lateralized in left-handers) (Howells et al 2018).

The second branch of the superior longitudinal fasciculus (SLF II) projects to the posterior region of the inferior parietal lobule (including the cortex buried in the intraparietal sulcus) and the lateral aspect of the superior (i.e. frontal eye field) and middle frontal gyri (BA6, 8, 9). The SLF II is involved in processing the spatial coordinates of the upper limbs, including the hand for reaching and grasping movements (Leiguarda and Marsden 2000, Goldenberg and Spatt 2009), and contributes to tasks requiring attention, visuospatial and spatial working memory (Levy and Goldman-Rakic 2000, Corbetta and Shulman 2002, Thiebaut de Schotten et al 2005). In humans the SLF II is right lateralized in most, but not all, subjects (about 70%) and the degree of lateralization is correlated with asymmetry in behavioural performances for visuospatial tasks (Thiebaut de Schotten et al 2011). This finding indicates that a right hemispheric specialization for visuospatial attention could be related to an unbalanced speed of signal processing along the SLF II of the two hemispheres.

The most ventral branch of the superior longitudinal fasciculus (SLF III) projects to the inferior parietal lobule (supramarginal and anterior angular gyri) and the posterior region of the inferior frontal gyrus and corresponds to the anterior segment of the arcuate fasciculus. In humans, this branch is almost always right lateralized.

Inferior longitudinal fasciculus

The inferior longitudinal fasciculus (ILF) is an occipito-temporal tract that connects early extrastriate visual cortex with the amygdala, parahippocampal gyrus and temporal pole (see Fig. 32.64). Its fibres run lateral to the optic radiations and inferior to the temporal horn. The inferior longitudinal fasciculus carries visual information from occipital areas to the temporal lobe and plays an important role in visual object and face recognition, language, semantic processing and reading (Epelbaum et al 2008, Fox et al 2008, Ffytche et al 2010).

Inferior fronto-occipital fasciculus

The inferior fronto-occipital fasciculus is a bow-tie-shaped bundle connecting medial occipital regions to the prefrontal regions and orbitofrontal cortex. The fibres of the inferior fronto-occipital fasciculus compact in the anterior floor of the external/extreme capsule where they run parallel to the more inferior fibres of the uncinate fasciculus (see Fig. 32.64) (Forkel et al 2014). Within the temporal lobe, the inferior fronto-occipital fasciculus contributes to the temporal stem and covers the temporal horn of the lateral ventricle and the ventricular atrium superiorly and laterally (Türe et al 2000). The functions of the inferior

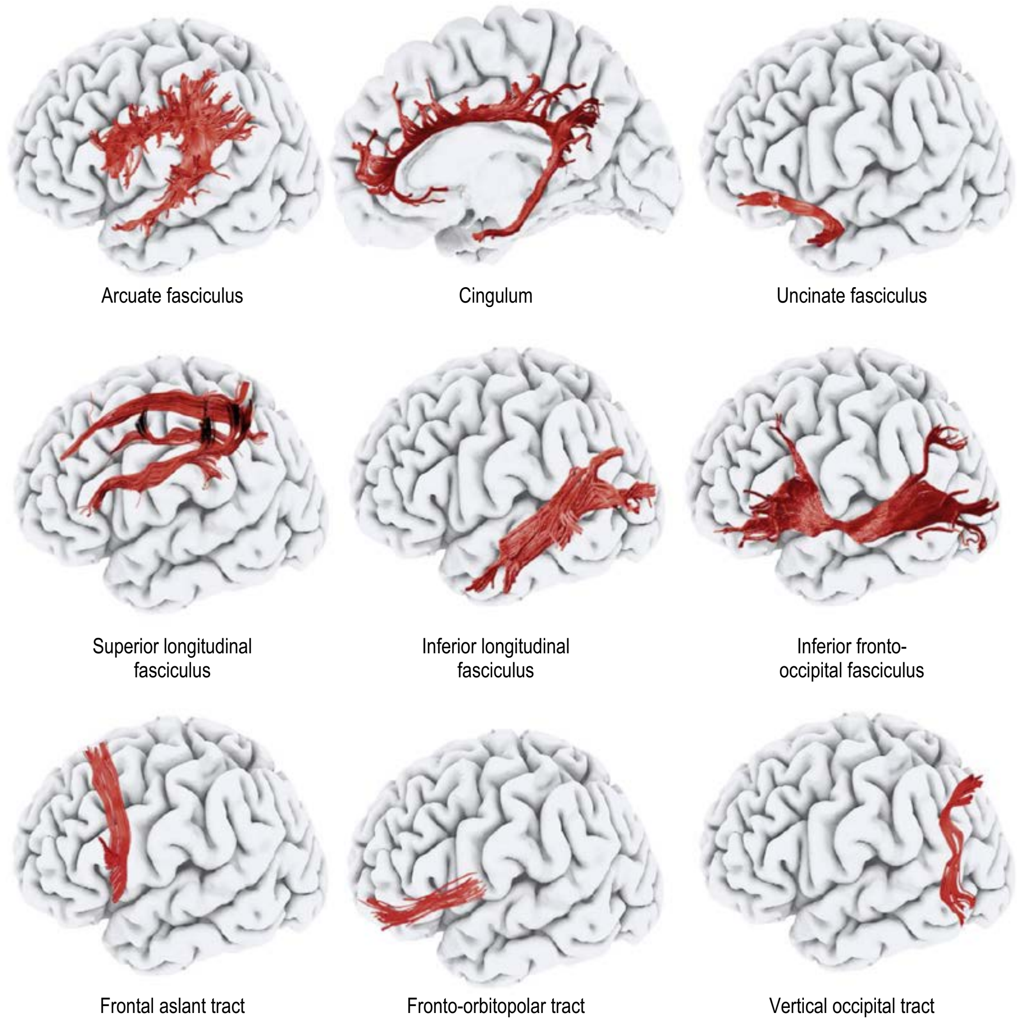
Arcuate fasciculus
Cingulum
Uncinate fasciculus
Superior longitudinal fasciculus
Inferior longitudinal fasciculus
Inferior fronto-occipital fasciculus
Frontal aslant tract
Fronto-orbitopolar tract
Vertical occipital tract

Fig. 32.64 Major interlobar (first and second row) and intralobar association tracts. (Figure kindly provided by Marco Catani, Natbrainlab.)

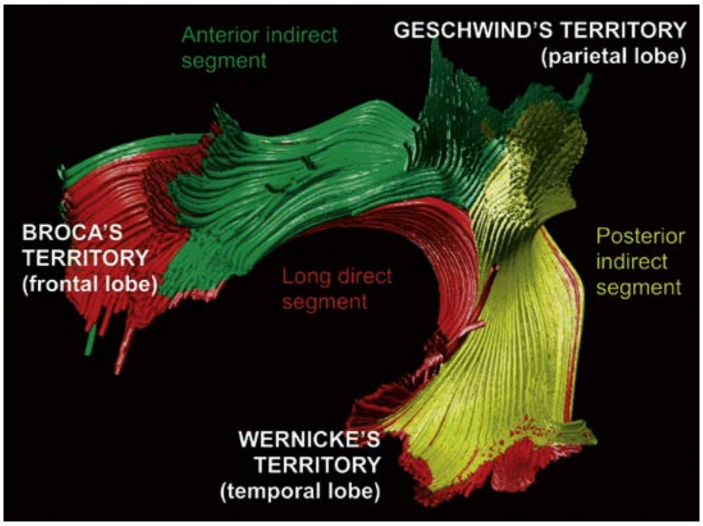
Anterior indirect segment
GESCHWIND'S TERRITORY (parietal lobe)
BROCA'S TERRITORY (frontal lobe)
Long direct segment
Posterior indirect segment
WERNICKE'S TERRITORY (temporal lobe)

Fig. 32.74 The three segments of the arcuate fasciculus. (Adapted with permission from Catani M, Jones DK, Ffytche DH 2005 Perisylvian language networks of the human brain. Ann Neurol 57:8–16.)

fronto-occipital fasciculus remain largely unknown. The occipital areas connected by the inferior fronto-occipital fasciculus include the lingual gyrus and cuneus, which engage in tasks requiring retrieving information from visual memory, spatial attention and recognition of colours, letters and faces. The anterior projections of the inferior fronto-occipital fasciculus terminate in the medial and lateral orbitofrontal cortex, which activates in tasks requiring top-down modulation (either activation or inhibition) of visual perception and short-term memory. These frontal regions seem especially important in guiding decision-making and social behaviour in relation to the emotional value of external sensory stimuli (Rudrauf et al 2008).

Uncinate fasciculus

The uncinate fasciculus is a hook-shaped bundle that connects the anterior temporal lobe, including the amygdala, with the orbitofrontal region and inferior frontal gyrus (see Fig. 32.64). From the temporal lobe, the uncinate fasciculus enters the anterior floor of the external/extreme capsule between the insula and the putamen. Here, it runs inferiorly to the fronto-occipital fasciculus before splitting into a lateral branch which terminates in the lateral orbito-frontal cortex and inferior frontal gyrus (BA11 and 47), and a medial branch which projects to the medial orbitofrontal cortex, gyrus rectus and subcallosal area (Crosby et al 1962). The uncinate fasciculus plays an important role in lexical retrieval, semantic association, naming and social cognition (Craig et al 2009, Papagno et al 2011, Wilson et al 2011, Catani et al 2013). In addition to language and memory, it is also involved in several aspects of behaviour, including response inhibition, outcome monitoring, object–reward association learning and multimodal sensory integration, especially for olfactory–gustatory–visceral functions (Catani et al 2013). Damage to this tract has been correlated with the severity of antisocial traits in psychopaths (Craig et al 2009) and behavioural symptoms in frontotemporal dementia (D'Anna et al 2016) and traumatic brain injury (Zappalà et al 2012).

Middle longitudinal fasciculus

The middle longitudinal fasciculus runs in the white matter within the superior temporal gyrus, connecting the angular gyrus (area 39) with the superior temporal gyrus (area 22) up to the temporal pole (area 38) (see Fig. 32.71) (Makris and Pandya 2009). It lies medial and ventral to branch II of the superior longitudinal fasciculus and the arcuate fasciculus; lateral and superior to the inferior fronto-occipital fasciculus; and dorsal to the inferior longitudinal fasciculus. Its function is still unknown.

Cingulum

The cingulum lies within the depth of the cingulate and parahippocampal gyri, starting below the rostrum of the corpus callosum within the paraolfactory gyri (see Fig. 32.64). It contains fibres of different length; the longest run from the amygdala, uncus (BA35) and parahippocampal cortex (BA36 and 30) to sub-genual areas of the orbito-frontal lobe (BA25 and 11) (Crosby et al 1962, Nieuwenhuys et al 2008, Catani, Dell'acqua et al 2013). Shorter fibres, that join and leave the cingulum along its length, connect to adjacent areas of the cingulate cortex (BA23 and 24), superior medial frontal gyrus (BA32, 6, 8 and 9), paracentral lobule (BA4), precuneus (BA7), cuneus (BA19), lingual (BA18 and 19), and fusiform gyri (BA19 and 37). The cingulum can be divided into a dorsal and a ventral component (Catani and Thiebaut de Schotten 2012, Jones et al 2013). The dorsal component connects those areas in the anterior cingulate/medial frontal cortex and posterior cingulate/precuneus that form the dorsomedial default-mode network (Raichle et al 2001, Raichle and Snyder 2007, Raichle 2015). The activity of these regions decreases in the transition between a 'resting state' and the execution of goal-directed tasks, irrespective of the nature of the task. The default-mode network has been linked to a number of functions including working memory, focusing attention to sensory-driven activities, understanding other people's intention (mentalizing or theory of mind), prospective thinking (envisioning the future) and memory for personal events (autobiographic memory) (see cingulate cortex). The ventral cingulum connects the amygdala and anterior parahippocampal cortex to retrosplenial regions and posterior parahippocampal areas and forms a network dedicated to spatial orientation and memory for navigation (Aggleton 2008, Vann et al 2009).

Commissural fibres

Commissural fibres originate in one hemisphere, cross the midline and project to the contralateral hemisphere. Homotopic fibres interconnect corresponding cortical areas in the two hemispheres and represent the most prevalent type of commissural connections. Heterotopic commissural fibres connect a cortical area with non-corresponding areas in the contralateral hemisphere. The largest commissural tracts of the human brain are the corpus callosum and the anterior commissure.

Corpus callosum

The corpus callosum contains 150–200 million fibres and is the largest fibre pathway of the human brain. On a midsagittal section, it forms an anteroposterior midline arch approximately 10 cm long that early anatomists subdivided into rostrum, genu, trunk (or body), isthmus and splenium. Each division of the corpus callosum contains fibres that project to specific cortical regions (**Fig. 32.76**).

The rostrum corresponds to the floor of the lateral ventricle and its fibres connect the orbitofrontal cortex. The genu is the most anterior portion of the corpus callosum and forms the anterior wall of the frontal horn of the lateral ventricle. Fibres in the genu curve forwards, as the forceps minor, to connect the areas of the prefrontal cortex. The body forms the roof and lateral wall of the lateral ventricles. Its fibres pass laterally, intersecting with the projection fibres of the corona radiata (see Fig. 32.76B, Video 32.1) to connect premotor and motor areas of the frontal lobe and most areas of the parietal lobe. The isthmus corresponds to a narrow portion of the corpus callosum between the body and the splenium. The fibres of the isthmus connect auditory temporal cortices.

The splenium of the corpus callosum overhangs the posterior ends of the thalami, the fornix, the pineal gland and tectum. A superior and an inferior layer of tela choroidea advance below the splenium through the transverse fissure, forming the velum interpositum cistern within the roof of the third ventricle and between the thalami, just below the bodies of the fornices; it contains the distal branches of the medial posterior choroidal arteries and the internal cerebral veins. The majority of the fibres of the splenium curve back into the occipital lobes as the forceps major. Some fibres of the splenium and isthmus arch forwards along the lateral wall of the inferior horn of the lateral ventricle, and constitute the tapetum. Acquired callosal lesions may manifest with disconnection syndromes characterized by the inability to transfer information or competences from one hemisphere to the other. The technique of severing commissural fibres in epileptic patients (split-brain) was introduced in the 1930s to control the spread of ictal discharge from one hemisphere to the other. Split-brain patients provided an opportunity to understand the functions of the corpus callosum and lateralization of cerebral functions (i.e. left cerebral dominance for language and right dominance for visuospatial functions).

Anterior commissure

The anterior commissure runs within the basal forebrain and fans out laterally within the temporal lobe (**Fig. 32.77**). It is believed to connect areas that include the olfactory bulb and anterior olfactory nucleus; the anterior perforated substance, olfactory tubercle and diagonal band of Broca; the prepiriform cortex; the entorhinal area and adjacent parts of the parahippocampal gyrus; part of the amygdaloid complex (especially the nucleus of the lateral olfactory stria); the bed nucleus of the stria terminalis and the nucleus accumbens; and inferior regions of the temporal and occipital lobes.

The anterior commissure has the shape of a classic bicycle handlebar. It crosses the midline just ventral to the supraoptic recess of the third ventricle, immediately anterior to the major component of the column of the fornix that projects to the mammillary body, and posterior to the smaller components of the fornix that project to the septal nuclei (see Fig. 32.77B). At this point, the anterior commissure bulges inside the third ventricle, just underneath the interventricular foramen. The lamina terminalis is attached superiorly to the midline segment of the anterior commissure and inferiorly to the upper surface of the optic chiasma; the optic recess of the third ventricle is the cleft between the lamina terminalis and the midportion of the superior surface of the chiasma.

Each side of the anterior commissure is composed of a well-defined posterolateral bundle (the hemispheric part) and a smaller, anterior component (the olfactory part) (Déjérine and Déjerine-Klumke 1895). The anterior component curves forwards and vertically through the anterior perforated substance towards each olfactory tubercle. The hemispheric component curves posterolaterally, passing through a deep groove on the anteroinferior aspect of the globus pallidus, and fanning out mostly to the anterior part of the temporal lobe, including the parahippocampal gyrus, but also reaching the occipital lobe posteriorly. This component of the anterior commissure runs parallel to the amygdolofugal peduncles which carry information from the amygdala to the hypothalamic nuclei (Fig. 32.77B).

When passing under the inferior limiting sulcus of the insula, superior to the temporal horn of the lateral ventricle, the fibres of the anterior commissure join the temporal stem, merging with the fibres of the uncinate and inferior fronto-occipital fasciculi. They pass posteriorly as the sagittal stratum, together with the inferior fronto-occipital fasciculus and the fibres of the optic radiation, over the lateral aspect of the temporal horn and ventricular atrium. Within the temporal stem, the fibres of the anterior commissure are mostly medial to the uncinate fasciculus; both are inferior to the inferior fronto-occipital fasciculus. Within the sagittal stratum, they intermingle but run predominantly below the inferior fronto-occipital fasciculus, superior to the fibres of the optic radiation. The line between the anterior and posterior commissures, the AC–PC line, is a very important landmark in stereotactic atlases, used when localizing neuroanatomical targets for stereotactic neurosurgical procedures.

Hippocampal commissure

The hippocampal commissure (commissure of the fornix) is a thin triangular sheet of fibres that lies between the crura of the fornices, connecting the hippocampi (**Fig. 32.78**). It is situated underneath and attached to the splenium, overhanging the pineal region.

Projection fibres

Projection fibres connect the cerebral cortex with the subcortical grey matter of the cerebral hemispheres, brainstem and spinal cord. They include large numbers of both corticofugal (descending) and corticopetal (ascending) fibres. Most of the projection fibres originating in the frontal, parietal and occipital lobes converge in the corona radiata and from here pass through the internal capsule to reach their subcortical targets. The projections forming the internal capsule are termed capsular projections and are separated from the non-capsular projections. The extracapsular fibres include the cortico-striatal projections directed to the most external putamen and projections to the claustrum course through the external capsule. The largest limbic projection tracts (fornix, ansa peduncularis, extracapsular thalamic peduncle, ansa and stria terminalis) also have an extracapsular course and do not contribute to the corona radiata. Except for the fornix and cingulum, most of the temporal projection tracts pass through the temporal stem which can be considered as the posterior extension of the external/extreme capsule. The term temporal stem is derived from its appearance in coronal sections of the temporal lobe, where the region resembles a small cauliflower composed of a single short stem and small florets that correspond to the five longitudinal temporal gyri. The stem originates from the floor

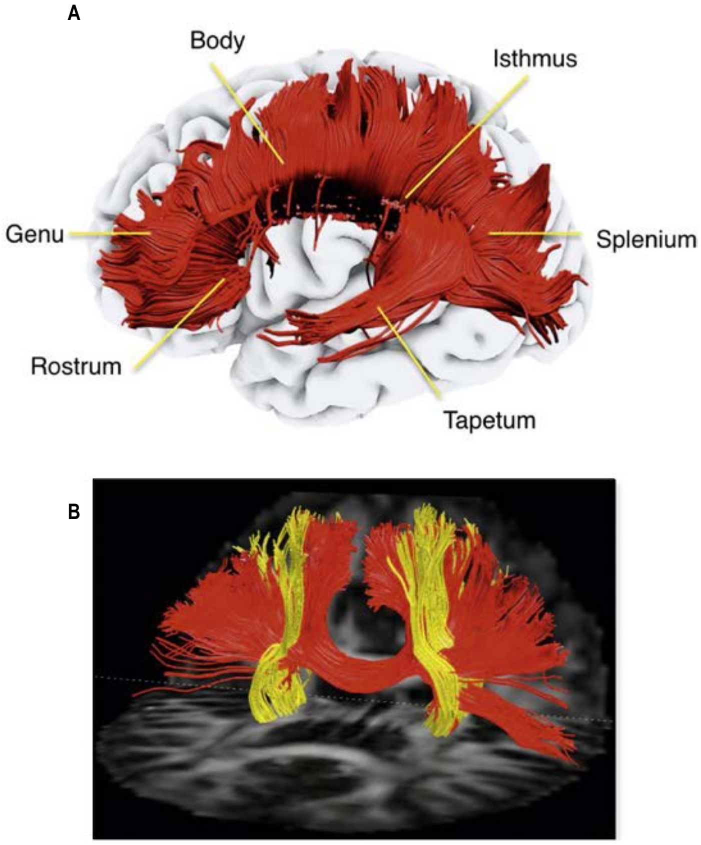
A
Body
Isthmus
Genu
Splenium
Rostrum
Tapetum
B

Fig. 32.76 **A**, A lateral view of fibres of the corpus callosum. **B**, An anterior view of the callosal fibres of the body (red) crossing the projection fibres of the internal capsule (yellow).

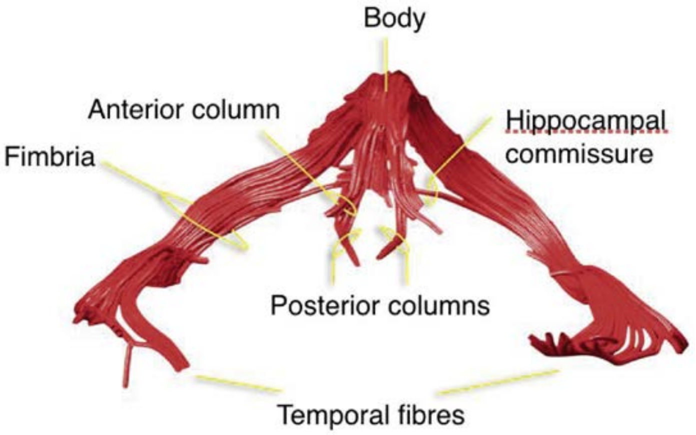
Body
Anterior column
Fimbria
Hippocampal commissure
Posterior columns
Temporal fibres

Fig. 32.78 An anterior view of the fornix. (Adapted with permission from Catani M, Thiebaut de Schotten M 2012 Atlas of Human Brain Connections. Oxford: Oxford University Press.)

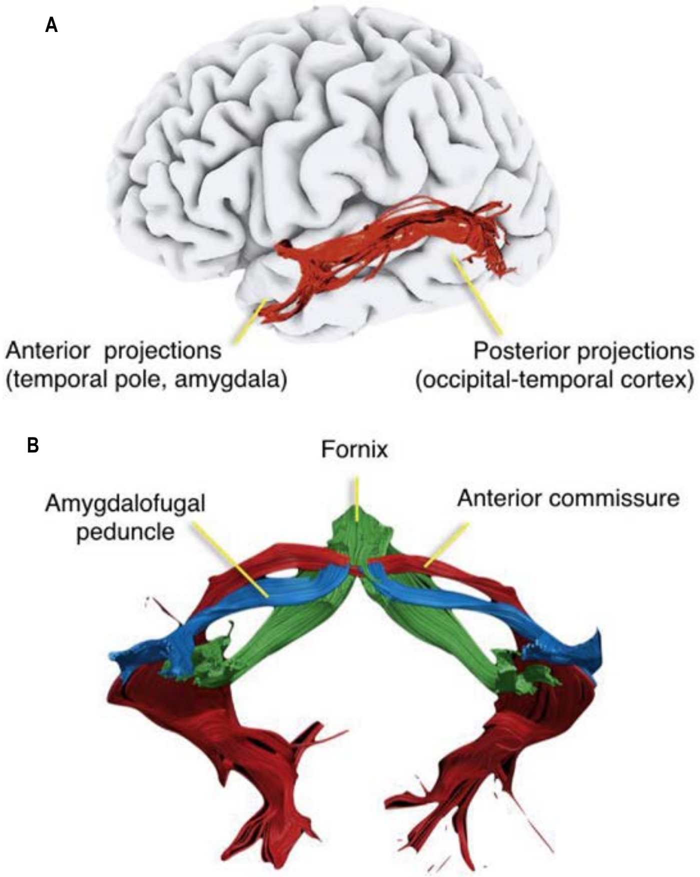
A
Anterior projections
(temporal pole, amygdala)
Posterior projections
(occipital-temporal cortex)
B
Fornix
Amygdalofugal
peduncle
Anterior commissure

Fig. 32.77 **A**, A lateral view of the anterior commissure showing its anterior and posterior projections. **B**, Relationship between the anterior commissure (red), fornix (green) and amygdalofugal peduncle (blue). (Courtesy of Marco Catani, Natbrainlab.)

of the external/extreme capsule; in its narrowest portion it is contained within a space delimited medially by the lateral ventricle and laterally by the inferior branch of the peri-insular sulcus. Within the posterior temporal stem, these fibres run parallel to the lateral ventricle before spreading outward into the temporal gyri to reach their cortical targets.

Internal capsule

The internal capsule has the shape of a V in horizontal section (axial images), with its vertex (genu) located medially between the head of the caudate nucleus and the thalamus (**Fig. 32.79**). For descriptive purposes, the internal capsule is arbitrarily divided into five parts: anterior limb, located between the putamen and the head of the caudate nucleus; genu, lying laterally and adjacent to the interventricular foramen (of Monro); posterior limb, located between the putamen and the thalamus; retrolenticular or retrolentiform portion, located posterior to the putamen; and sublenticular (or sublentiform) portion, located inferior to the putamen (see Fig. 32.79). The internal capsule contains thalamo-cortical fibres that form the thalamic peduncles, the majority of the cortico-striatal fibres, cortico-nuclear and cortico-spinal tracts that course through the cerebral peduncles, and projections to other nuclei of the brainstem.

Corticospinal and corticonuclear tracts

The corticospinal tract provides direct control by the cerebral cortex over motor centres in the contralateral spinal cord. The corticonuclear tract fulfils a similar function in relation to the motor nuclei of the brainstem that give origin to cranial nerves.

About 20–30% of corticospinal fibres arise from the pyramidal cells in layer V of BA4. The remaining corticospinal fibres originate from the premotor cortex and parietal areas of the postcentral gyrus, superior parietal lobule and operculum. Many axons from BA4 terminate in the ventral horn of the spinal cord: a small percentage establish direct monosynaptic connections with α-motoneurones. Between 40% and 60% of pyramidal tract axons arise from parietal areas, including area 3a, area 5 of the superior part of the parietal lobe and secondary somatosensory areas in the parietal operculum. The majority of parietal fibres to the spinal cord terminate in the deeper layers of the dorsal horn. Motor cortical neurones are active in relation to the force of contraction of agonist muscles; their relation to the amplitude of movement is less clear. Their activity precedes the onset of electromyographic activity by 50–100 milliseconds, suggesting a role for cortical activation in generating rather than monitoring movement.

The corticospinal and corticonuclear fibres that arise within the precentral gyrus are disposed as a fan on a coronal plane throughout the corona radiata. They cross the corpus callosum before entering the genu and posterior limb of the internal capsule (see Fig. 32.76, Video 32.1). To join the internal capsule, the corticospinal and corticonuclear fibres not only converge but also undergo an internal rotation of approximately 90 degrees, because the main axes of the precentral gyrus and of the internal capsule genu and posterior limb are almost perpendicular. Throughout their course the fibres retain their somatotopical motor arrangement, organized according to the homuncular cortical representation, adopting an anterior–cranial to a posterior–caudal disposal along the genu (corticonuclear tract) and the posterior limb (corticospinal tract) of the internal capsule. Within the posterior limb of the internal capsule the fibres concerned with the upper limb are anterior to the fibres representing the trunk and lower limbs. From the internal capsule the fibres converge further into the cerebral peduncles, where the corticospinal and corticonuclear fibres are located in the middle half of the crus between frontopontine fibres (medially) and corticopontine fibres from temporal, parietal and occipital cortices (laterally).

Other descending axons include frontopontine fibres (Arnold's bundle), particularly from areas 4 and 6, and corticorubral fibres, coursing through the anterior limb of the internal capsule. The retrolenticular part of the internal capsule contains parietopontine, occipitopontine and occipitotectal fibres and the sublenticular part contains temporopontine and some parietopontine fibres. All corticopontine fibres that originate from parietal, occipital and temporal lobes collectively form the bundle of Türk.

Thalamic radiations

The thalamic radiations originate from the thalamic nuclei. After a short course through the internal capsule they enter the corona radiata and terminate in the cortex of the ipsilateral hemisphere (**Fig. 32.80**). The thalamic radiations from the anterior and medio-dorsal thalamic nuclei enter the anterior limb of the internal capsule and form the anterior thalamic peduncle that projects to all prefrontal and orbitofrontal cortices. The thalamic nuclei of the ventral group and in part those of the lateral group give origin to the superior thalamic peduncle, which courses through both anterior and posterior limbs of the internal capsule, terminating in the posterior frontal cortex (from ventral anterior and ventral lateral thalamic nuclei) and parietal cortex (from ventral posterior and lateral posterior thalamic nuclei), respectively.

The retrolenticular part of the internal capsule includes the optic radiation and the posterior thalamic radiation originating from the pulvinar and directed to the posterior cortex of the parietal and temporal lobes and the occipital cortex.

The fibres of the optic radiation arise from the lateral geniculate body and the pulvinar, join the retrolenticular and the sublenticular parts of the internal capsule, run within the sagittal stratum over the temporal horn and ventricular atrium, and project posteriorly, passing superiorly and inferiorly to the occipital horn as part of the posterior thalamic peduncle to reach both the superior and inferior lips of the calcarine sulcus. Within the temporal lobe, the fibres of the optic radiation are located along the depths of the superior and middle temporal gyri about 2 cm from the brain surface, medial to the arcuate and inferior fronto-occipital fasciculi and inferior to the auditory radiations. Its fibres are divided into anterior (Flechsig's temporal knee or Meyer's loop), central and posterior bundles. On sagittal sections, the occipital fibres are concentrically distributed around the occipital horn of the lateral ventricle in the following order: callosal fibres (the most internal layer); optic radiations and extrastriate thalamocortical projections (internal sagittal stratum of Sachs); association fibres of the inferior longitudinal fasciculus and inferior fronto-occipital fasciculus (external sagittal stratum of Sachs).

The sublenticular part of the internal capsule contains the auditory radiation from the medial geniculate body and direct fibres from the inferior colliculus, that together project to the superior temporal and transverse temporal gyri (areas 41 and 42). Thalamic fibres from the pulvinar to the temporal cortex and insula are also contained within the sublenticular part of the internal capsule. Fibres of the auditory radiation sweep anterolaterally below and behind the lentiform complex and superiorly to the temporal horn, ventricular atrium and optic radiation. As they enter the temporal stem, the auditory radiations fan out and split into two branches. The superior branch continues laterally towards Heschl's gyrus and the surrounding cortex, where it finally projects to early auditory areas. The inferior branch continues anteriorly along the temporal stem in a space delimited by the inferior border of the putamen, the lateral ventricle and the inferior insula. It is directed towards the anterior temporal lobe and sends many projections to the amygdala and most anterior temporal cortex of the superior, middle and inferior temporal gyri. The acoustic radiations also contain fibres that run in the reverse direction from the temporal cortex and amygdala to the medial geniculate nucleus and inferior colliculus (Pickles 2015). This centrifugal system mediates the top-down modulatory effect by which the temporal cortex and amygdala enhance the response of subcortical nuclei to stimuli of significance.

Fornix

The fornix is the fibre bundle of the hippocampus. It wraps round the thalamus, from which it is separated by the choroidal fissure and the choroid plexus. The fornix consists of the fimbria, crus, body and columns or pillars. The fibres of the alveus converge to form the fimbria fornicis (see Fig. 32.78) along the medial portion of the floor of the inferior horn of the lateral ventricle. At a point beneath the splenium of the corpus callosum, the white matter of the fimbria separates from the hippocampus to become the crus fornicis. The two crura pass upwards and forwards beneath the corpus callosum, joined via fibres that cross in the commissure of the fornix (hippocampal commissure). Beyond this point, the crura merge to become the body of the fornix, which continues anteriorly within the roof of the third ventricle, below the lower border of the septum pellucidum and near the midline. At the level of the interventricular foramen (foramen of Monro) and the anterior commissure, the body splits into two anterior (precommissural) and two posterior (postcommissural) columns: the smaller anterior columns terminate in the hypothalamic nuclei whereas the larger posterior columns project to the mammillary bodies. As they separate from the underlying thalamus, the posterior columns of the fornix form the anterior margins of the interventricular foramen.

A smaller number of fornical fibres project to the anterior thalamic nuclei (anterior medial, anterior ventral and anterior dorsal thalamic nuclei), ventral striatum, medial septum and nucleus reuniens; some are exclusively afferent to the hippocampus, e.g. from the supramammillary and raphe nuclei and the locus coeruleus (Aggleton et al 2010, Jang and Kwon 2013, Jang and Kwon 2014). As a midline white matter tract, the fornix is particularly susceptible to involvement by tumours that favour this route of spread, e.g. glioblastoma multiforme, and to rotational shearing injuries responsible for diffuse axonal injury (Thomas et al 2011).

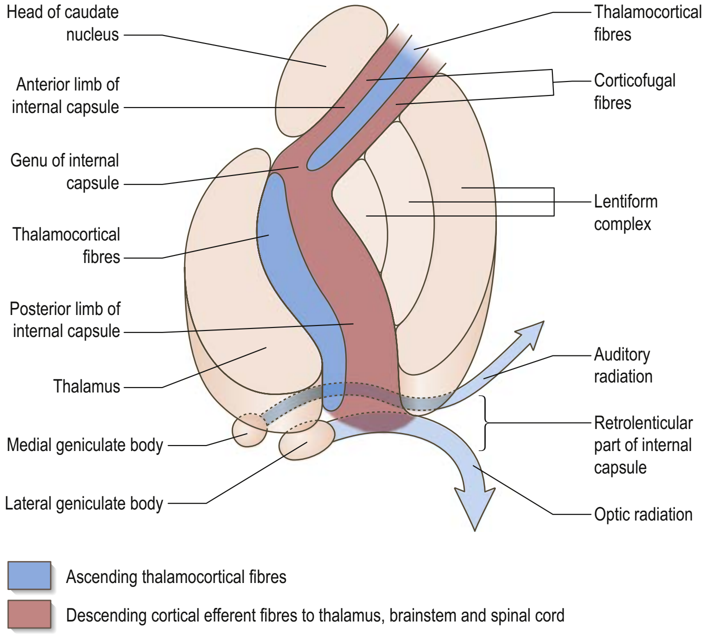
Head of caudate nucleus
Anterior limb of internal capsule
Genu of internal capsule
Thalamocortical fibres
Posterior limb of internal capsule
Thalamus
Medial geniculate body
Lateral geniculate body
Thalamocortical fibres
Corticofugal fibres
Lentiform complex
Auditory radiation
Retrolenticular part of internal capsule
Optic radiation
🟦 Ascending thalamocortical fibres
🟥 Descending cortical efferent fibres to thalamus, brainstem and spinal cord

Fig. 32.79 A horizontal section through the internal capsule illustrating its main components.

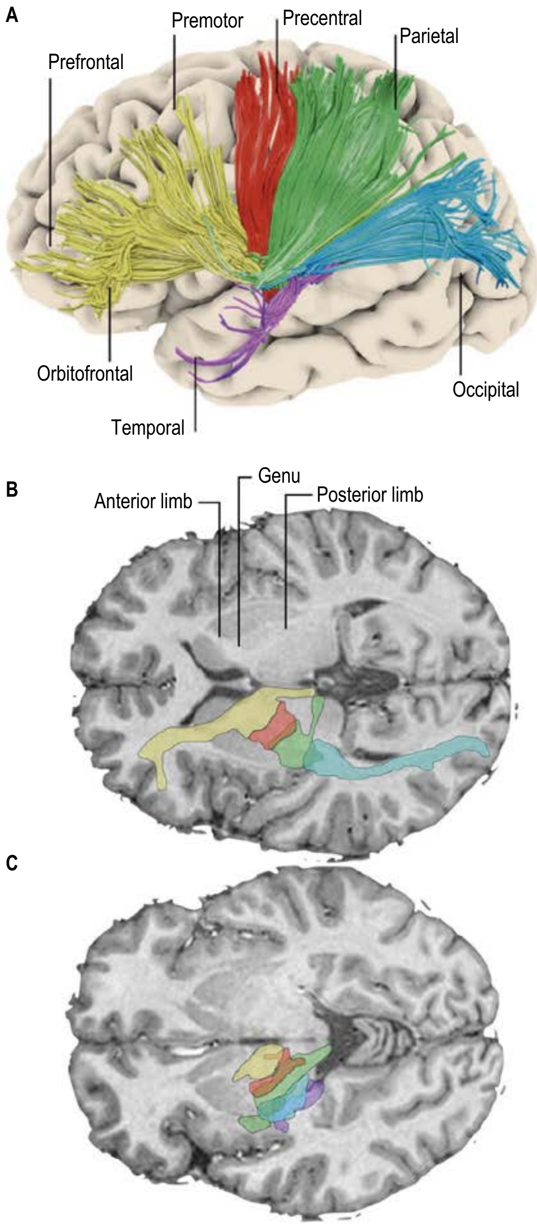
A
Premotor
Precentral
Parietal
Prefrontal
Orbitofrontal
Temporal
Occipital
B
Anterior limb
Genu
Posterior limb
C

Fig. 32.80 Tractography reconstruction of the thalamic projections (**A**) and their course at different levels of the internal capsule (**B**, retrolenticular; **C**, sublenticular). The colours indicate the different thalamic peduncles: anterior (yellow), superior (red and green), posterior (blue) and sublenticular (purple). (Adapted from Catani M, Thiebaut de Schotten M 2012 Atlas of Human Brain Connections. Oxford: Oxford University Press.)

Bonus e-book content

Fig. 32.2 Lateral, medial, dorsal, basal, frontal and caudal views of the Montreal Neurological Institute (MNI) single subject template.

Fig. 32.3 Lateral, medial, dorsal, basal, frontal and caudal views of the MNI single subject template on which gyri have been identified.

Fig. 32.6 Interneurones of the cerebral cortex.

Fig. 32.7 Connections between GABAergic interneurones.

Fig. 32.8 Circuit motifs between excitatory glutamatergic pyramidal cells and inhibitory GABAergic interneurones.

Fig. 32.11 Columns of dendritic bundles originating in layer V (b1) and layer VI (b2) pyramidal cells (modified after Mountcastle 1957).

Fig. 32.12 Cytoarchitectonic parcellation of the cerebral cortex by Brodmann (1910).

Fig. 32.14 Continuous probability maps provided by the Jülich/Düsseldorf group.

Fig. 32.15 Cytoarchitectonic parcellation of the cerebral cortex by von Economo and Koskinas (1925).

Figs 32.16–32.18 Myeloarchitectonic maps of the human frontal, temporal and parietal lobes.

Fig. 32.19 Myelinated fibres and their lamination pattern in representative iso- and periallocortical areas.

Fig. 32.20 Receptor analysis of the occipital areas.

Fig. 32.21 Multi-receptor fingerprints of cortical areas of the human brain.

Fig. 32.22 Hierarchical Cluster Analysis of receptor fingerprints.

Fig. 32.23 Transmitter systems in the cerebral cortex and sites of transmitter synthesis.

Fig. 32.24 Efferent and afferent pathways of the cerebral cortex and their transmitters.

Fig. 32.25 Neurones expressing calcium binding proteins at the border between human V1 and V2.

Fig. 32.26 Magnocellular cholinergic cell groups Ch1 to Ch4 in the basal forebrain and their maximum probability maps in the anatomical MNI space.

Fig. 32.27 Visualization of the regional distribution of serotonin 5-HT$_2$ receptors with PET in a horizontal section through the human brain.

Fig. 32.28 Regional and laminar distribution of muscarinic M$_2$ and adrenergic α_2 receptors in coronal section through the occipital lobe of a human brain, and the layer-specific localization of low or high densities of glutamate.

Fig. 32.29 Regional and laminar distribution of various neurotransmitter receptors on coronal sections at the level of the central sulcus (colour-coded quantitative receptor autoradiography).

Fig. 32.35 Distribution of receptors in the human amygdala.

Fig. 32.36 Magnetic resonance imaging of the amygdala in a healthy control subject and the Urbach-Wiethe syndrome.

Fig. 32.39 Frontal sections through the hippocampal head, body and tail.

Fig. 32.40 Frontal section through the medial temporal lobe.

Fig. 32.41 Hippocampal layers and their major connections.

Fig. 32.42 Distribution of transmitter receptors in the human hippocampus.

Fig. 32.43 The septal complex.

Fig. 32.46 Transmitter receptors in the human cingulate cortex.

Fig. 32.47 Sulcal and gyral patterns of the frontal lobe.

Fig. 32.48 Representation of the hand in the precentral gyrus.

Fig. 32.50 Nissl staining of sections through the human motor and somatosensory cortex.

Fig. 32.51 Transmitter receptors in the human primary motor and somatosensory cortices.

Fig. 32.52 **A**, Sagittal section through a human cerebral hemisphere indicating the position of the SMA, pre-SMA, ACMA and PCMA areas. **B**, A horizontal section through the human SMA and pre-SMA, indicating the position of the border between both areas.

Fig. 32.53 Cytoarchitecture of Broca areas BA44, BA45, and the frontopolar areas Fp1 and Fp2.

Fig. 32.54 Cytoarchitectonical map of the fronto-orbital cortex and Broca's language region areas of the inferior frontal gyrus.

Fig. 32.55 Maximum probability maps of the parietal cortical areas.

Fig. 32.56 Cytoarchitecture of cortical areas in the superior and inferior parietal lobules.

Fig. 32.57 Cyto-, myelo- and receptorarchitecture of the human visual cortex in coronal sections.

Fig. 32.58 Functional modules in V1.

Fig. 32.59 Localization and cytoarchitectonic organization of higher visual areas in the ventral occipito-temporal cortex.

Fig. 32.60 Primary and secondary auditory cortical areas.

Fig. 32.65 Intralobar associative connections and projection fibres of the prefrontal cortex.

Fig. 32.66 Intralobar connections of the orbitofrontal and frontal polar region.

Fig. 32.67 Frontal longitudinal systems.

Fig. 32.68 Connections of the precentral hand-knob area and central sulcus visualized with diffusion tractography.

Fig. 32.69 Fronto-insular U-tracts connecting opercular areas of the frontal lobe with the anterior insula.

Fig. 32.70 Major intralobar tracts of the parietal lobe.

Fig. 32.71 The temporal and middle longitudinal fasciculi.

Fig. 32.72 The medial occipital longitudinal tract.

Fig. 32.73 The vertical occipital tract of Wernicke.

Fig. 32.75 The pattern of lateralization of the arcuate long segment.

Fig. 32.76 The corpus callosum.

Fig. 32.77 The anterior commissure.

Fig. 32.78 The fornix, anterior view.

Fig. 32.79 A horizontal section through the internal capsule illustrating its main components.

Fig. 32.80 Tractography reconstruction of the thalamic projections and their course at different levels of the internal capsule.

Table 32.1 Isocortical GABAergic interneurones classified by their co-localization of parvalbumin, somatostatin and serotonin 5-HT$_{3A}$ receptors, morphological types, main targets and anatomical signatures.

Table 32.2 The most important criteria for myeloarchitectonic descriptions.

Table 32.3 Comparison between the map and nomenclature system used by Brodmann, Vogt and Vogt and the Jülich/Düsseldorf group.

Table 32.4 The maps of von Economo and Koskinas, Brodmann and JuBrain.

Table 32.5 Receptor subtypes of the cerebral cortex and their subunit composition, genes, ion effects and function.

Table 32.6 Hippocampal formation and its archi- and periarchicortical parts.

Video 32.1 Tractography reconstruction of the corpus callosum (yellow) and corticofugal pathways (red) using spherical deconvolution tractography.

Key references

Amunts K, Zilles K 2015 Architectonic mapping of the human brain beyond Brodmann. Neuron 88:1086–107.

Demonstrates the importance of modern multimodal and quantitative architectonic studies to deepen our understanding of cortical segregation.

Broca P 1878 Anatomie comparée des circonvolutions cérébrales: le grande lobe limbique et la scissure limbique dans la série des mammifères. Rev d'Anthropol 1:385–498.

The first description of the limbic system.

Brodmann K 1909 Vergleichende Lokalisationslehre der Großhirnrinde in ihren Prinzipien dargestellt auf Grund des Zellbaues. Leipzig: Barth.

A classic cytoarchitectonic map of cortical areas.

Catani M, Thiebaut de Schotten M 2012 Surface neuroanatomy. In: Atlas of Human Brain Connections. New York: Oxford University Press.

An atlas with detailed anatomical description and anatomical–radiological relationships of the cerebral sulci, gyri and white matter fibres.

Ono M, Kubik S, Abernathey CD 1990 Atlas of Cerebral Sulci. Stuttgart: Thieme.

A classic atlas providing an extensive and detailed study of the cerebral sulci.

Palomero-Gallagher N, Amunts K, Zilles K 2015 Transmitter receptor distribution in the human brain. In: Toga AW (ed) Brain Mapping: An Encyclopedic Reference. Anatomy and Physiology (Section eds Zilles K, Amunts K). San Diego: Elsevier; Ch. 221, pp. 261–75.

An overview of transmitter receptor distribution in the human cerebral cortex.

Ribas GC 2010 The cerebral sulci and gyri. Neurosurg Focus 28: E21–28.

An extensive review of historical and morphological literature relating to the sulci and gyri of the cerebral hemispheres.

Zilles K, Palomero-Gallagher N, Bludau S et al 2015c Cytoarchitecture and maps of the human cerebral cortex. In: Toga AW (ed) Brain Mapping: An Encyclopedic Reference. Anatomy and Physiology (Section eds Zilles K, Amunts K). San Diego: Elsevier; Ch. 207, pp. 115–35.

References

Aggleton JP 2008 Understanding anterograde amnesia: disconnections and hidden lesions. QJ Exp Psychol 61:1441–171.

Aggleton JP, O'Mara SM, Vann SD et al 2010 Hippocampal-anterior thalamic pathways for memory: uncovering a network of direct and indirect actions. Eur J Neurosci 31:2292–307.

Amunts K, Zilles K 2015 Architectonic mapping of the human brain beyond Brodmann. Neuron 88:1086–107.

Demonstrates the importance of modern multimodal and quantitative architectonic studies to deepen our understanding of cortical segregation.

Amunts K, Istomin V, Schleicher A et al 1995 Postnatal development of the human primary motor cortex: a quantitative cytoarchitectonic analysis. Anat Embryol 192:557–71.

Amunts K, Schleicher A, Bürgel U et al 1999 Broca's region revisited: cytoarchitecture and intersubject variability. J Comp Neurol 412:319–41.

Amunts K, Malikovic A, Mohlberg H et al 2000 Brodmann's areas 17 and 18 brought into stereotaxic space – where and how variable? Neuroimage 11:66–84.

Amunts K, Schleicher A, Zilles K 2007 Cytoarchitecture of the cerebral cortex – more than localization. Neuroimage 37:1061–5.

Amunts K, Lenzen M, Friederici AD et al 2010 Broca's region: novel organizational principles and multiple receptor mapping. PLoS Biol 8:e1000489.

Amunts K, Hawrylycz MJ, Van Essen DC et al 2014 Interoperable atlases of the human brain. Neuroimage 99:525–32.

Anderson EJ, Jones DK, O'Gorman RL et al 2012 Cortical network for gaze control in humans revealed using multimodal MRI. Cereb Cortex 22: 765–75.

Arcaro MJ, McMains SA, Singer BD et al 2009 Retinotopic organization of human ventral visual cortex. J Neurosci 29:10638–52.

Armstrong E, Zilles K, Omran H et al 1995 The ontogeny of human gyrification. Cerebral Cortex 5:56–63.

Ascoli GA, Donohue DE, Halavi M 2007 NeuroMorpho.Org: a central resource for neuronal morphologies. J Neurosci 27:9247–51.

Augustinack JC, Huber KE, Postelnicu GM et al 2012 Entorhinal verrucae geometry is coincident and correlates with Alzheimer's lesions: a combined neuropathology and high resolution ex vivo MRI analysis. Acta Neuropathol 123:85–96.

Barbas H, Garcia-Cabezas MA 2015 Motor cortex layer 4: less is more. Trends Neurosci 38(5):259–61.

Bechterew W 1900 Demonstration eines gehirns mit Zestörung der vorderen und inneren Theile der Hirnrinde beider Schläfenlappen. Neurol Centralbl 20:990–1.

Björklund A, Dunnett SB 2007 Dopamine neuron systems in the brain: an update. TINS 30:194–202.

Bludau S, Eickhoff SB, Mohlberg H et al 2014 Cytoarchitecture, probability maps and functions of the human frontal pole. Neuroimage 93:260–75.

Bludau S, Mühleisen TW, Eickhoff SB et al 2018 Integration of transcriptomic and cytoarchitectonic data implicates a role for MAOA and TAC1 in the limbic-cortical network. Brain Struct Funct 223:233–42.

Braak H 1976 A primitive gigantopyramidal field buried in the depth of the cingulate sulcus of the human brain. Brain Res 109:219–33.

Broca P 1878 Anatomie comparée des circonvolutions cérébrales: le grande lobe limbique et la scissure limbique dans la série des mammifères. Rev d'Anthropol 1:385–498.

The first description of the limbic system.

Brockhaus H 1940 Die Cyto- und Myeloarchitektonik des Cortex claustralis und des Claustrum beim Menschen. J Psychol Neurol 49:249–348.

Brodmann K 1905 Beiträge zur histologischen Lokalisation der Grosshirnrinde. III. Die Rindenfelder der niederen Affen. J Psychol Neurol 4:177–226.

Brodmann K 1909 Vergleichende Lokalisationslehre der Großhirnrinde in ihren Prinzipien dargestellt auf Grund des Zellbaues. Leipzig: Barth.

A classic cytoarchitectonic map of cortical areas.

Brodmann K 1910 Feinere Anatomie des Großhirns. In: Lewandowsky M (ed) Handbuch der Neurologie, Erster Band, Allgemeine Neurologie. Berlin: Springer, pp. 206–307.

Brodmann K 1914 Physiologie des Gehirns. In: Von Bruns P (ed) Neue deutsche Chirurgie, vol 11 Pt. 1. Enke, Stuttgart, pp 85–426.

Brown S, Schäfer E 1888 An investigation into the functions of the occipital and temporal lobes of the monkey's brain. Phil Trans R Soc B 179:303–327 (plus plates).

Burgess PW, Gonen-Yaacovi G, Volle E 2011 Functional neuroimaging studies of prospective memory: what have we learnt so far? Neuropsychologia 49:2246–57.

Buxhoeveden DP, Casanova MF 2002 The minicolumn hypothesis in neuroscience. Brain 125:935–51.

Buxhoeveden DP, Semendeferi K, Buckwalter J et al 2006 Reduced minicolumns in the frontal cortex of patients with autism. Neuropathol Appl Neurobiol 32:483–91.

Cannon WB 1927 The James–Lange theory of emotions: a critical examination and an alternative theory. Am J Psychol 39:106–24.

Caspers S, Zilles K 2018 Microarchitecture and connectivity of the parietal lobe. In: Vallar G, Coslett HB (eds) The Parietal Lobe. Handbook of Clinical Neurology, vol. 151. Amsterdam: Elsevier, pp. 53–72.

Caspers S, Schleicher A, Bacha-Trams M et al 2013a Organization of the human inferior parietal lobule based on receptor architectonics. Cereb Cortex 23:615–28.

Caspers J, Zilles K, Eickhoff SB et al 2013b Cytoarchitectonical analysis and probabilistic mapping of two extrastriate areas of the human posterior fusiform gyrus. Brain Struct Funct 218:511–26.

Caspers S, Geyer S, Schleicher A et al 2006 The human inferior parietal cortex: cytoarchitectonic parcellation and interindividual variability. Neuroimage 33:430–448.

Catani M 2017 A little man of some importance. Brain 140:3055–61.

Catani M, Thiebaut de Schotten M 2012 Atlas of Human Brain Connections. Oxford: Oxford University Press.

An atlas with detailed anatomical description and anatomical–radiological relationships of the cerebral sulci, gyri and white matter fibres.

Catani M, Jones DK, Ffytche DH 2005 Perisylvian language networks of the human brain. Ann Neurol 57:8–16.

Catani M, Allin MPG, Husain M et al 2007 Symmetries in human brain language pathways correlate with verbal recall. PNAS 104:17163–8.

Catani M, Dell'acqua F, Vergani F et al 2012 Short frontal lobe connections of the human brain. Cortex 48:273–91.

Catani M, Dell'Acqua F, Thiebaut de Schotten M 2013 A revised limbic system model for memory, emotion and behaviour. Neurosci Biobehav Revs 37:1724–37.

Catani M, Robertsson N, Beyh A et al 2017 Short parietal lobe connections of the human and monkey brain. Cortex 97:339–57.

Chen X, Li SL, Luo GY et al 2017 Ultrasonographic characteristics of cortical sulcus development in the human fetus between 18 and 41 weeks of gestation. Chin Med J (Engl) 130: 920–8.

Corbetta M, Shulman GL 2002 Control of goal-directed and stimulus-driven attention in the brain. Nat Rev Neurosci 3:201–15.

Craig MC, Catani M, Deeley Q et al 2009 Altered connections on the road to psychopathy. Mol Psychiatry 14:946–53.

Crosby EC Humphrey T, Lauer EW 1962 Correlative Anatomy of the Nervous System. New York: Macmillan.

D'Anna L, Mesulam MM, Thiebaut de Schotten M 2016 Frontotemporal networks and behavioral symptoms in primary progressive aphasia. Neurology 86:1393–9.

Déjérine JJ, Déjérine-Klumke A 1895 Anatomie des centres nerveux. Vol 1. Paris: Rueff.

Dum RP, Strick PL 1991 The origin of corticospinal projections from the premotor areas in the frontal lobe. J Neurosci 11:667–89.

Duvernoy HM 1998 The Human Hippocampus. Functional Anatomy, Vascularization and Serial Sections with MRI. Berlin: Springer.

Duvernoy HM 1999 The Human Brain: Surface, Three-Dimensional Sectional Anatomy with MRI, and Blood Supply. Vienna: Springer.

Eickhoff S, Stephan KE, Mohlberg H et al 2005 A new SPM toolbox for combining probabilistic cytoarchitectonic maps and functional imaging data. NeuroImage 25:1325–35.

Eickhoff SB, Amunts K, Mohlberg H et al 2006 The human parietal operculum. II. Stereotaxic maps and correlation with functional imaging results. Cerebral Cortex 16:268–79.

Eickhoff SB, Schleicher A, Zilles K et al 2006 The human parietal operculum. I. Cytoarchitectonic mapping of subdivisions. Cereb Cortex 16:254–67.

Elze C 1928 Einige fasersysteme des mensnschlichen großhirnes mit der abfaserungsmethode untersuchts. Z Anat 88:166–78.

Epelbaum S, Pinel P, Gaillard R et al 2008 Pure alexia as a disconnection syndrome: new diffusion imaging evidence for an old concept. Cortex 44:962–74.

Ffytche DH, Blom JD, Catani M 2010 Disorders of visual perception. J Neurol Neurosurg Psychiatry 81:1280–7.

Fleischhauer K, Petsche H, Wittkowski W 1972 Vertical bundles of dendrites in the neocortex. Z Anat Entwickl-Gesch 136:213–23.

Forkel SJ, Thiebaut de Schotten M, Dell'Acqua F et al 2014 Anatomical predictors of aphasia recovery: a tractography study of bilateral perisylvian language networks. Brain 137:2027–39.

Fox CJ, Iaria G, Barton JJ 2008 Disconnection in prosopagnosia and face processing. Cortex 44:996–1009.

Freund TF, Buzsáki G 1996 Interneurones of the hippocampus. Hippocampus 6:347–470.

Geyer S, Ledberg A, Schleicher A et al 1996 Two different areas within the primary motor cortex of man. Nature 382:805–7.

Geyer S, Schleicher A, Zilles K 1999 Areas 3a, 3b, and 1 of human primary somatosensory cortex. 1. Microstructural organization and interindividual variability. NeuroImage 10:63–83.

Geyer S, Luppino G, Rozzi S 2012 Motor cortex. In Mai JK, Paxinos G (eds) The Human Nervous System. London: Elsevier, Academic Press, pp. 1012–35.

Goldenberg G, Spatt J 2009 The neural basis of tool use. Brain 132:1645–55.

Grefkes C, Geyer S, Schormann T et al 2001 Human somatosensory area 2: observer-independent cytoarchitectonic mapping, interindividual variability, and population map. Neuroimage 14:617–31.

Heimer L, Van Hoesen WG 2006 The limbic lobe and its output channels: implications for emotional functions and adaptive behavior. Neurosci Biobehav Rev 30:126–47.

Heimer L, de Olmos JS, Alheid GF et al 1999 The basal forebrain. Part II. In: Bloom FE, Björklund A, Hökfelt T (eds) Primate Nervous System. Part III. Amsterdam: Elsevier, pp. 57–226.

Henneberg R 1910 Messung der Oberflächenausdehnung der Großhirnrinde. J Psychol Neurol 17:144–58.

Hopf A 1954 Die Myeloarchitektonik des Isocortex temporalis beim Menschen. J Hirnforsch 1:208–79.

Howells H, Thiebaut de Schotten M, Dell'Acqua F, et al 2018 Frontoparietal tracts linked to lateralized hand preference and manual specialization. Cereb Cortex 28: 2482–94.

Hubel D, Wiesel T 1959 Receptive fields of single neurones in the cat's striate cortex. J Physiol 148:574–91.

Hubel D, Wiesel T 1972 Laminar and columnar distribution of geniculo-cortical fibres in the macaque monkey. J Comp Neurol 146:421–43.

Hubel DH, Wiesel TN 1977 Functional architecture of macaque monkey visual cortex. Proc R Soc Lond B Biol Sci 198:1–59.

Hurlemann R, Schlaepfer T, Matusch A et al 2009 Reduced 5-HT2A receptor signaling following selective bilateral amygdala damage. Social Cogn Affect Neurosci 4:79–84.

Husen SC, Koning IV, Go ATJI et al 2019 Three dimensional ultrasound imaging of fetal brain fissures in the growth restricted fetus. PloS One e0217538. doi: 10.1371/journal.pone.0217538. eCollection 2019.

Jacob SN, Nienborg H 2018 Monoaminergic neuromodulation of sensory processing. Front Neural Circuits 12:51. doi: 10.3389/fncir.2018.00051.

Jakob C 1906 Nueva contribución á la fisiopatología de los lóbulos frontales. LaSemana Médica 13:1325–9.

Jang SH, Kwon HG 2013 Neural connectivity of the posterior body of the fornix in the human brain: diffusion tensor imaging study. Neurosci Lett 549:116–9.

Jang SH, Kwon HG 2014 Neural connectivity of the anterior body of the fornix in the human brain: diffusion tensor imaging study. Neurosci Lett 559:72–5.

Johnson PB, Ferraina S, Bianchi L et al 1996 Cortical networks for visual reaching: physiological and anatomical organization of frontal and parietal lobe arm regions. Cereb Cortex 6:102–19.

Jones DK, Christiansen KF, Chapman RJ et al 2013 Distinct subdivisions of the cingulum bundle revealed by diffusion MRI fibre tracking: implications for neuropsychological investigations. Neuropsychologia 51:67–78.

Jones EG 1975 Varieties and distribution of non-pyramidal cells in the somatic sensory cortex of the squirrel monkey. J Comp Neurol 160:205–68.

Kooijmans RN 2016 Inhibitory interneurones of macaque primary visual cortex. PhD Thesis, Amsterdam. http://hdl.handle.net/1871/54840.

Kooijmans RN, Self MW, Wouterlood FG et al 2014 Inhibitory interneuron classes express complementary AMPA-receptor patterns in macaque primary visual cortex. J Neurosci 34:6303–15.

Kujovic M, Zilles K, Malikovic A et al 2013 Cytoarchitectonic mapping of the human dorsal extrastriate cortex. Brain Struct Funct 218:157–72.

Kurth F, Eickhoff SB, Schleicher A et al 2010 Cytoarchitecture and probabilistic maps of the human posterior insular cortex. Cerebral Cortex 20:1448–61.

Kurth F, Zilles K, Fox PT et al 2010 A link between the systems: functional differentiation and integration within the human insula revealed by meta-analysis. Brain Struct Funct 214:519–34.

Lazzarino De Lorenzo LG, ffytche DH, Di Camillo E, et al 2014 The Dide-Botcazo syndrome: forgotten and misunderstood. Cortex 56:182–90.

Leiguarda RC, Marsden CD 2000 Limb apraxias: higher-order disorders of sensorimotor integration. Brain 123:860–79.

Levy R, Goldman-Rakic PS 2000 Segregation of working memory functions within the dorsolateral prefrontal cortex. Exp Brain Res. 133:23–32.

Lorenz S, Weiner KS, Caspers J 2017 Two new cytoarchitectonic areas on the human mid-fusiform gyrus. Cereb Cortex 27:373–85.

Makris N, Pandya DN 2009 The extreme capsule in humans and rethinking of the language circuitry. Brain Struct Funct 213:343–58.

Malikovic A, Amunts K, Schleicher A et al 2007 Cytoarchitectonic analysis of the human extrastriate cortex in the region of V5/MT+: a probabilistic, stereotaxic map of Area hOc5. Cerebr Cortex 17:562–74.

Malikovic A, Vucetic B, Milisavljevic M et al 2012 Occipital sulci of the human brain: variability and morphometry. Anat Sci Int 87:61–70.

Marin-Padilla M, Marin-Padilla MT 1982 Origin, prenatal development and structural organization of layer I of the human cerebral (motor) cortex: a Golgi study. Anat Embryol 164:161–206.

Martínez-Cerdeño V, Noctor SC 2014 Cajal, Retzius, and Caja–Retzius cells. Front Neuroanat 8:48.

Mesulam M-M 2000 Behavioral neuroanatomy: large-scale networks, association cortex, frontal syndromes, the limbic system and hemispheric specialization. In: Mesulam M-M, ed. Principles of Behavioral and Cognitive Neurology. New York: Oxford University Press, pp. 1–120.

Morecraft RJ, McNeal DW, Stilwell-Morecraft KS et al 2007 Amygdala interconnections with the cingulate motor cortex in the rhesus monkey. J Comp Neurol 500:134–65.

Morosan P, Rademacher J, Schleicher A et al 2001 Human primary auditory cortex: cytoarchitectonic subdivisions and mapping into a spatial reference system. Neuroimage 13:684–701.

Morosan P, Schleicher A, Amunts K et al 2005 Multimodal architectonic mapping of human superior temporal gyrus. Anat Embryol 210:401–6.

Mountcastle VB 1957 Modality and topographic properties of single neurones of cat's somatic sensory cortex. J Neurophysiol 20:408–34.

Naidich TP, Castillo M, Cha S et al 2012 Imaging of the Brain: Expert Radiology Series. Philadelphia: Elsevier.

Nieuwenhuys R, Voog J, Huijzen C van 2008 The Human Central Nervous System: A Synopsis and Atlas. Berlin: Springer.

Nimchinsky EA, Vogt BA, Morrison JH et al 1995 Spindle neurones of the human anterior cingulate cortex. J Comp Neurol 355:27–37.

Nishikuni K, Ribas GC 2013 Study of fetal and postnatal morphological development of the brain sulci. J Neurosurg Pediatr 11:1–11.

Öngür D, Ferry AT, Price JL 2003 Architectonic subdivision of the human orbital and medial prefrontal cortex. J Comp Neurol 460:425–49.

Ono M, Kubik S, Abernathey CD 1990 Atlas of the Cerebral Sulci. Stuttgart: Thieme.
A classic atlas providing an extensive and detailed study of the cerebral sulci.

Palomero-Gallagher N, Zilles K 2009 Transmitter receptor systems in cingulate regions and areas. In: Vogt BA (ed) Cingulate Neurobiology and Disease. New York: Oxford University Press, pp. 31–63.

Palomero-Gallagher N, Zilles K 2018 Cyto- and receptorarchitectonic mapping of the human brain. In: Huitinga I, Webster MJ (eds), Brain Banking. San Diego: Elsevier, pp. 355–88.

Palomero-Gallagher N, Mohlberg H, Zilles K et al 2008 Cytology and receptor architecture of human anterior cingulate cortex. J Comp Neurol 508:906–26.

Palomero-Gallagher N, Vogt BA, Schleicher A et al 2009 Receptor architecture of human cingulate cortex: evaluation of the four-region neurobiological model. Hum Brain Mapp 30:2336–55.

Palomero-Gallagher N, Zilles K, Schleicher A et al 2013 Cyto- and receptor architecture of area 32 in human and macaque brains. J Comp Neurol 521:3272–86.

Palomero-Gallagher N, Amunts K, Zilles K 2015 Transmitter receptor distribution in the human brain. In: Toga AW (ed) Brain Mapping: An Encyclopedic Reference. Anatomy and Physiology (Section eds Zilles K, Amunts K). San Diego:Elsevier; Ch. 221, pp. 261–75.
An overview of transmitter receptor distribution in the human cerebral cortex.

Papagno C, Miracapillo C, Casarotti A et al 2011 What is the role of the uncinate fasciculus? Surgical removal and proper name retrieval. Brain 134: 405–14.

Papez JW 1937 A proposed mechanism of emotion. Arch Neurol Psychiat 38:725–43.

Penfield W, Boldrey E 1937 Somatic motor and sensory representation in the cerebral cortex of man as studied by electrical stimulation. Brain 60: 389–440.

Peters A 1983a Bipolar cells. In: Peters A, Jones EG (eds) Cerebral Cortex, vol. 1. New York: Plenum Press, pp. 381–407.

Peters A 1983b Chandelier cells. In: Peters A, Jones EG (eds) Cerebral Cortex, vol. 1. New York: Plenum Press, pp. 361–80.

Petrides M, Pandya DN 1984 Projections to the frontal cortex from the posterior parietal region in the rhesus monkey. J Comp Neurol 228:105–16.

Petrides M, Pandya DN 2012 The frontal cortex. In: Mai JK, Paxinos G (eds) The Human Nervous System. London: Elsevier, Academic Press, pp. 988–1011.

Pickles JO 2015 Auditory pathways: anatomy and physiology. Handb Clin Neurol 129:3–25.

Pisella L, Binkofski F, Lasek K et al 2006 No double-dissociation between optic ataxia and visual agnosia: multiple sub-streams for multiple visuo-manual integrations. Neuropsychologia 44:2734–48.

Raichle ME 2015 The brain's default mode network. Annu Rev Neurosci 38:433–47.

Raichle ME, Snyder AZ 2007 A default mode of brain function: a brief history of an evolving idea. Neuroimage 37:1083–90.

Raichle ME, MacLeod AM, Snyder AZ et al 2001 A default mode of brain function. Proc Natl Acad Sci USA 98:676–82.

Ribas GC 2010 The cerebral sulci and gyri. Neurosurg Focus 28: E21–28. *An extensive review of historical and morphological literature relating to the sulci and gyri of the cerebral hemispheres.*

Rottschy C, Eickhoff SB, Schleicher A et al 2007 Ventral visual cortex in humans: cytoarchitectonic mapping of two extrastriate areas. Hum Brain Mapp 28:1045–59.

Rudrauf D, David O, Lachaux J-P et al 2008 Rapid interactions between the ventral visual stream and emotion-related structures rely on a two-pathway architecture. J Neurosci 28:2793–803.

Scheperjans F, Palomero-Gallagher N, Grefkes C et al 2005 Transmitter receptors reveal segregation of cortical areas in the human superior parietal cortex: relations to visual and somatosensory regions. Neuroimage 28:362–79.

Scheperjans F, Eickhoff SB, Hömke L et al 2008 Probabilistic maps, morphometry, and variability of cytoarchitectonic areas in the human superior parietal cortex. Cerebr Cortex 18:2141–57.

Scheperjans F, Hermann K, Eickhoff SB et al 2008 Observer-independent cytoarchitectonic mapping of the human superior parietal cortex. Cereb Cortex 18:846–67.

Schleicher A, Amunts K, Geyer S et al 1999 Observer-independent method for microstructural parcellation of cerebral cortex: a quantitative approach to cytoarchitectonics. Neuroimage 9:165–177.

Schreiner CE, Malone BJ 2015 Representation of loudness in the auditory cortex. Handb Clin Neurol 129:73–84.

Shepherd G 2006 Smells, brains and hormones. Nature 439:149–51.

Stephan H 1975 Allocortex. Handbuch der mikroskopischen Anatomie des Menschen. Volume IV/9. Heidelberg: Springer.

Talavage TM, Sereno MI, Melcher JR et al 2004 Tonotopic organization in human auditory cortex revealed by progressions of frequency sensitivity. J Neurophysiol 91:1282–96.

Thiebaut de Schotten M, Urbanski M, Duffau H et al 2005 Direct evidence for a parietal-frontal pathway subserving spatial awareness in humans. Science. 309: 2226-8.

Thiebaut de Schotten M, Dell'Acqua F, Forkel SJ et al 2011 A lateralized brain network for visuospatial attention. Nat Neurosci 14:1245–6.

Thomas AG, Koumellis P, Dineen RA 2011 The fornix in health and disease: an imaging review. Radiographics 31:1107–21.

Tremblay R, Lee S, Rudy B 2016 GABAergic interneurones in the neocortex: from cellular properties to circuits. Neuron 20:260–92.

Türe U, Yaşargil MG, Friedman AH et al 2000 Fiber dissection technique: lateral aspect of the brain. Neurosurgery 47:417–26.

Tzourio-Mazoyer N, Landeau B, Papathanassiou D et al 2002 Automated anatomical labeling of activations in SPM using a macroscopic anatomical parcellation of the MNI MRI single-subject brain. Neuroimage 15:273–89.

Van Essen DC 2005 A population-average, landmark- and surface-based (PALS) atlas of human cerebral cortex. NeuroImage 28:635–62.

Vann SD, Aggleton JP, Maguire EA 2009 What does the retrosplenial cortex do? Nat Rev Neurosci 10:792–802.

Vogt O 1910 Die myeloarchitektonische Felderung des menschlichen Stirnhirns. J Psychol Neurol 15:221–32.

Vogt O 1911 Die Myeloarchitektonik des Isocortex parietalis. J Psychol Neurol 18:379–90.

Vogt BA 2016 Midcingulate cortex: structure, connections, homologies, functions and diseases. J Chem Neuroanat 74:28–46.

Vogt BA, Nimchinsky EA, Vogt LJ et al 1995 Human cingulate cortex: surface features, flat maps, and cytoarchitecture. J Comp Neurol 359:490–506.

Vogt BA, Vogt L, Laureys S 2006 Cytology and functionally correlated circuits of human posterior cingulate areas. NeuroImage 29:452–66.

Vogt C, Vogt O 1919 Allgemeinere Ergebnisse unserer Hirnforschung. J Psychol Neurol 25:279–462.

von Economo C, Koskinas GN 1925 Die Cytoarchitektonik der Hirnrinde des erwachsenen Menschen. Berlin: Springer.

von Economo C, Koskinas GN 1929 The Cytoarchitectonics of the Human Cerebral Cortex. London: Oxford University Press.

Weiner KS, Zilles K 2016 The anatomical and functional specialization of the fusiform gyrus. Neuropsychologia 83:48–62.

Weiner KS, Golarai G, Caspers J et al 2014 The mid-fusiform sulcus: a landmark identifying both cytoarchitectonic and functional divisions of human ventral temporal cortex. Neuroimage 84:453–65.

Weiner KS, Barnett MA, Lorenz S et al 2017 The cytoarchitecture of domain-specific regions in human high-level visual cortex. Cereb Cortex 27:146–61.

Wilson SM, Galantucci S, Tartaglia MC et al 2011 Syntactic processing depends on dorsal language tracts. Neuron 72:397–403.

Wong-Riley MT 1989 Cytochrome oxidase: an endogenous metabolic marker for neuronal activity. Trends Neurosci 12:94–101.

Yousry TA, Schmid UD, Alkadhi H et al 1997 Localization of the motor hand area to a knob on the precentral gyrus: a new landmark. Brain 120:141–57.

Zappalà G, Thiebaut de Schotten M, Eslinger PJ 2012 Traumatic brain injury and the frontal lobes: what can we gain with diffusion tensor imaging? Cortex 48:156–65.

Zhang Z, Hou A, Lin X et al 2013 Development of the fetal cerebral cortex in the second trimester: assessment with 7T postmortem MR imaging. AJNR Am J Neuroradiol 34:1462–7.

Zilles K, Amunts K 2010 Centenary of Brodmann's map – conception and fate. Nature Rev Neurosci 11:139–45.

Zilles K, Amunts K 2012 Architecture of the human cerebral cortex: maps, regional and laminar organization. In: JK Mai, G Paxinos (eds), The Human Nervous System, 3rd ed. San Diego: Elsevier, pp. 836–95.

Zilles K, Palomero-Gallagher N 2017 Comparative analysis of receptor subtypes that identify primary cortical sensory areas. In: Kaas J, Striedter G, Krubitzer L (eds) Evolution of the Nervous Systems, 2nd ed. Vol. 2, The Nervous Systems of Early Mammals and their Evolution. London: Elsevier, Academic Press, pp. 225–45.

Zilles K, Armstrong E, Schleicher A et al 1988 The human pattern of gyrification in the cerebral cortex. Anat Embryol 179:173–9

Zilles K, Palomero-Gallagher N, Amunts K 2015a Myeloarchitecture and maps of the cerebral cortex. In: Toga AW (ed) Brain Mapping: An Encyclopedic Reference. Anatomy and Physiology (Section eds Zilles K, Amunts K). San Diego: Elsevier; Ch. 209, pp. 137–56.

Zilles K, Bacha-Trams M, Palomero-Gallagher N et al 2015b Common molecular basis of the sentence comprehension network revealed by neurotransmitter receptor fingerprints. Cortex 63:79–89.

Zilles K, Palomero-Gallagher N, Bludau S 2015c Cytoarchitecture and maps of the human cerebral cortex. In: Toga AW (ed) Brain Mapping: An Encyclopedic Reference. Anatomy and Physiology (Section eds Zilles K, Amunts K). San Diego: Elsevier; Ch. 207, pp. 115–35.

COMMENTARY
3.1

Comparative anatomy of the corticospinal system

Roger Lemon

The comparative anatomy of the long, corticofugal pathways from cortex to subcortical structures is important because we can interpret the key features of these pathways in humans on the basis of their similarities and differences when compared with other animals. This is particularly true of the corticospinal system. All mammals have a corticospinal tract, which originates from a number of parietal and frontal cortical areas, and which projects to different regions of the spinal cord. However, in functional terms, the different components of the corticospinal projection show large species-specific contrasts. There are also marked variations in other anatomical features, such as range of fibre sizes, spinal trajectory, pattern of termination within the spinal grey matter, and extent of the tract along the length of the spinal cord.

CORTICAL ORIGIN

There is a basic pattern across all mammals for the cortical areas that give rise to the corticospinal tract. There are more areas in primates than in non-primates. In the former they include primary motor (M1) and somatosensory (S1) cortex, parietal area 5, S2, and frontal areas including dorsal and ventral premotor cortex and the supplementary motor area (all area 6) and a family of cingulate motor areas in the cingulate cortex on the medial surface of the hemisphere. In all of these areas, corticospinal fibres arise only from lamina V, which of course is very thick in motor cortex. In humans, all of these areas probably give rise to corticospinal fibres. Classical studies suggested that 60% of these fibres come from the frontal areas and 40% from parietal.

Number and size of axons

The number of fibres in the mammalian corticospinal (pyramidal) tract varies from around 30,000 from each cortical hemisphere in the mouse, up to around 1 million fibres in humans. There is a close relationship between fibre number, overall body weight and brain size. In all mammals the great majority of the fibres are of small diameter ($<3\,\mu m$). In some large-bodied primates, there are larger fibres ($>8\,\mu m$) and the largest are in humans ($22\,\mu m$), but large fibres make up only a few per cent of all fibres in the tract.

Spinal trajectory

The course taken by corticospinal fibres within the spinal cord shows great variation. In rodents, rabbits and opossums most of the fibres are located at the base of the dorsal columns, whereas in elephants and hedgehogs, they are exclusively in the ventral funiculus. In carnivores and primates, most of the fibres are in the dorsolateral funiculus, with a smaller number of uncrossed fibres travelling in the ventral funiculus. A few fibres may also be scattered in the dorsal columns. In humans, fibres making up the lateral corticospinal tract are found throughout the dorsolateral funiculus (**Fig. 3.1.1**), although they are considered to lie slightly medial to the ascending dorsocerebellar tract fibres, which occupy the most lateral part of the dorsolateral funiculus. There is no obvious somatotopic organization within the various corticospinal tracts: fibres from different subdivisions (arm, leg) of M1, for example, are intermingled, as are projections from different cortical areas.

Extent of termination

In primates, including humans, the corticospinal tract extends for the full length of the spinal cord to the most caudal segments of the sacral cord. This is also the case in carnivores and rodents. Thus the tract can influence spinal mechanisms concerned with all four limbs (and tail when present). In some species, such as elephants, and ungulates such as goats, the tract does not extend beyond the upper cervical cord. Indeed, in the elephant the heaviest motor projection is to the facial nucleus, supplying the muscles of its trunk. In rodents, the heaviest motor projection from the cortex is again to the facial nucleus, with direct projections involved in the whisker movements, so important for the rodent's exploration of space.

Pattern of spinal termination

Kuypers (1981) reviewed the pattern of corticospinal termination in the spinal grey matter across different species (see Fig. 3.1.1). He recognized that from rodents to carnivores and New World monkeys and from Old World monkeys to chimpanzees and humans there was a distinctive ventral shift in the pattern of terminations.

Projections to the dorsal horn

Kuypers stressed that in rodents and more primitive mammals, the major termination of the tract was in the dorsal horn, and this has been confirmed repeatedly for mouse and rat (**Fig. 3.1.2**). This suggests that at least one function of the tract, probably shared across all mammals and including humans, is the descending control of afferent input, including nociceptive input. This descending control may be very important for sensorimotor control, and in particular for the rapid recognition of predictable patterns of somatosensory input resulting from planned movements. Descending corticospinal signals can alter pain thresholds. In primates, most of the projections to the dorsal horn probably come from S1 (see Fig. 3.1.2), and there is only a weak projection to the dorsal horn from frontal motor areas.

Intermediate zone

In primates, and some non-primates such as cat, racoon, etc., the motor areas project to the intermediate zone, influencing spinal reflex pathways. In macaques the greatest number of corticospinal boutons are found in lamina VII (**Fig. 3.1.3**), which is the source short propriospinal pathways to motor neurones innervating the distal extremity.

Ventral horn

Direct projections (cortico-motoneuronal (CM) projections) to motor neurones of lamina IX are found only in some primate species, and these are best developed in great apes, such as chimpanzee and in humans (see Fig. 3.1.1). In macaques, quantitative analysis of terminal boutons, labelled after injections of tracer material in the M1 hand/arm region, shows that the number of boutons within lamina IX is second only to those in lamina VII (see Fig. 3.1.3).

Retrograde transneuronal virus labelling from different upper limb muscles in macaques suggests that only two areas give rise to significant numbers of CM projections: the caudal part of M1 ('new' M1) and area 3a.

The functional implications of this conspicuous ventral shift in termination pattern are still being researched, but there are some important clues in terms of the comparative anatomy. The long-standing idea that the presence of direct CM projections contributes to the capacity for skilled control of the hand is supported by the fact that CM projections are only well developed in those primates that are tool users/tool manufacturers. These include the New World capuchin monkey and Old World macaque monkey, baboon and the great apes. There is a well-established correlation between the strength of this projection, the size of postsynaptic excitation in hand and digit motor neurones and the measure of digital dexterity (**Fig. 3.1.4**).

Laterality of projections

It is estimated that in humans around 90% of the fibres in the corticospinal tract decussate to the opposite side and most descend in the lateral corticospinal tract. The remaining 10% descend ipsilaterally, mostly in the ventral corticospinal tract. The functions of these two components of the tract is still being investigated. The classical story is that the crossed fibres are mostly involved in control of the contralateral extremity, via their terminations in lamina VII and the lateral motor neurone pools, while ipsilateral fibres make bilateral terminations in lamina VIII and the medial motor neurone pools, innervating axial and girdle muscles.

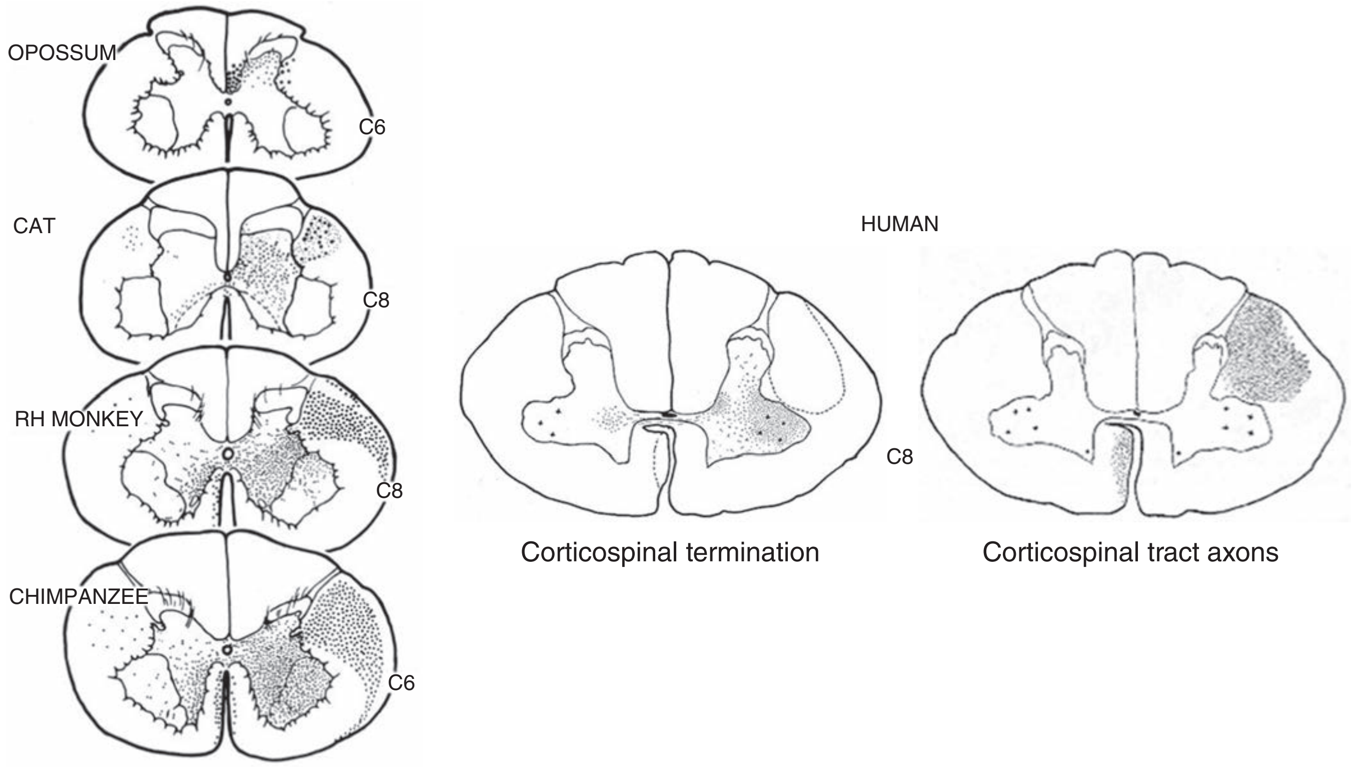

Fig. 3.1.1 Pattern of corticospinal projections from motor cortex in five different species. The black dots in the white matter funiculi indicate the trajectory of crossed corticospinal fibres, which are found in the dorsal columns in the opossum, but mostly in the dorsolateral funiculus in the other species shown. Uncrossed fibres are shown travelling in the ventral funiculus. The black dots in the spinal grey matter indicate the termination of corticospinal fibres, as determined from visualization of degenerating terminals. The diagrams illustrate the ventral shift of terminations from opossum, where most fibres terminate in the contralateral dorsal horn; to cat, where fibres terminate in the contralateral intermediate zone; to the rhesus monkey, chimpanzee and human, which show progressively greater numbers of terminals in the lateral motor neurone pools of the ventral horn. Terminations in ipsilateral lamina VIII are also shown. (Based on Kuypers HGJM 1981 Anatomy of descending pathways. In: Brookhart JM, Mountcastle VB, Brooks VB et al (eds) Handbook of Physiology, vol. 2: Motor Control, pt 1. American Physiological Society, pp. 597–666; and Schoen JHR 1964 Comparative aspects of the descending fibre systems in the spinal cord. Progr Brain Res 11:203-22.)

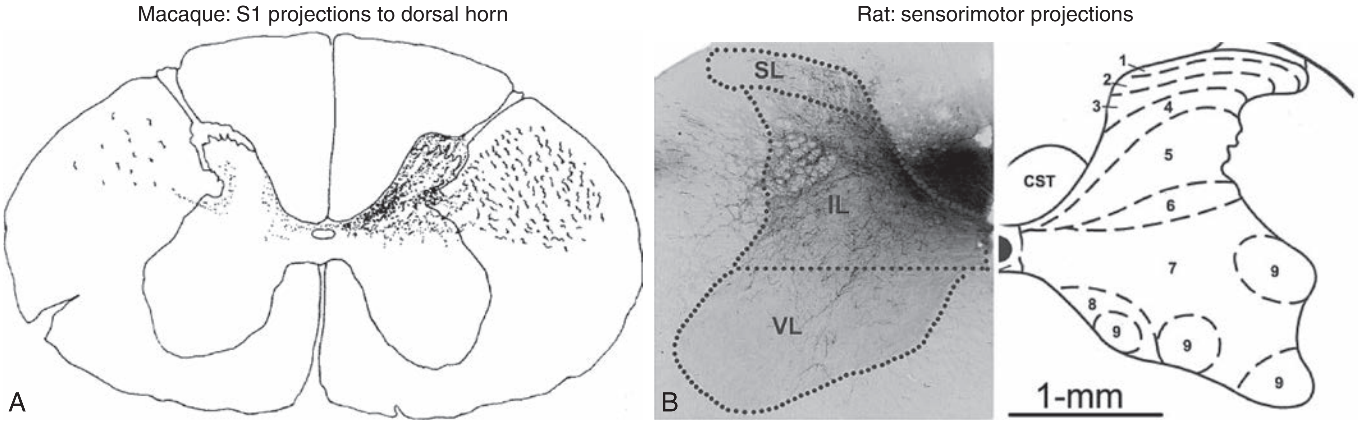
Macaque: S1 projections to dorsal horn
Rat: sensorimotor projections
A
B
SL
IL
VL
CST
1
2
3
4
5
6
7
8
9
9
9
9
1-mm

Fig. 3.1.2 Corticospinal projections to the dorsal horn in macaque and rat: **A** shows the labelling of corticospinal terminals in the dorsal horn of the macaque cord after injection of anterograde (H^3 leucine) tracer in the contralateral somatosensory cortex (S1). Most of the terminals are in the dorsal horn, including the most superficial laminae. **B** shows labelling of the corticospinal projection in the rat after injection of anterograde dextran amine tracer in the sensorimotor cortex (S1 + M1). Note that the corticospinal fibres travel mostly at the base of the dorsal columns, and terminate heavily in the dorsal horn, with little or no labelling in the ventral horn (A, With permission from Ralston DD, Ralston HJ 1985 The terminations of corticospinal tract axons in the macaque monkey. J Comp Neurol 242:325–37; B, with permission from Raineteau O, Fouad K, Bareyre FM et al 2002 Reorganization of descending motor tracts in the rat spinal cord. Eur J Neurosci 16:1761–71.)

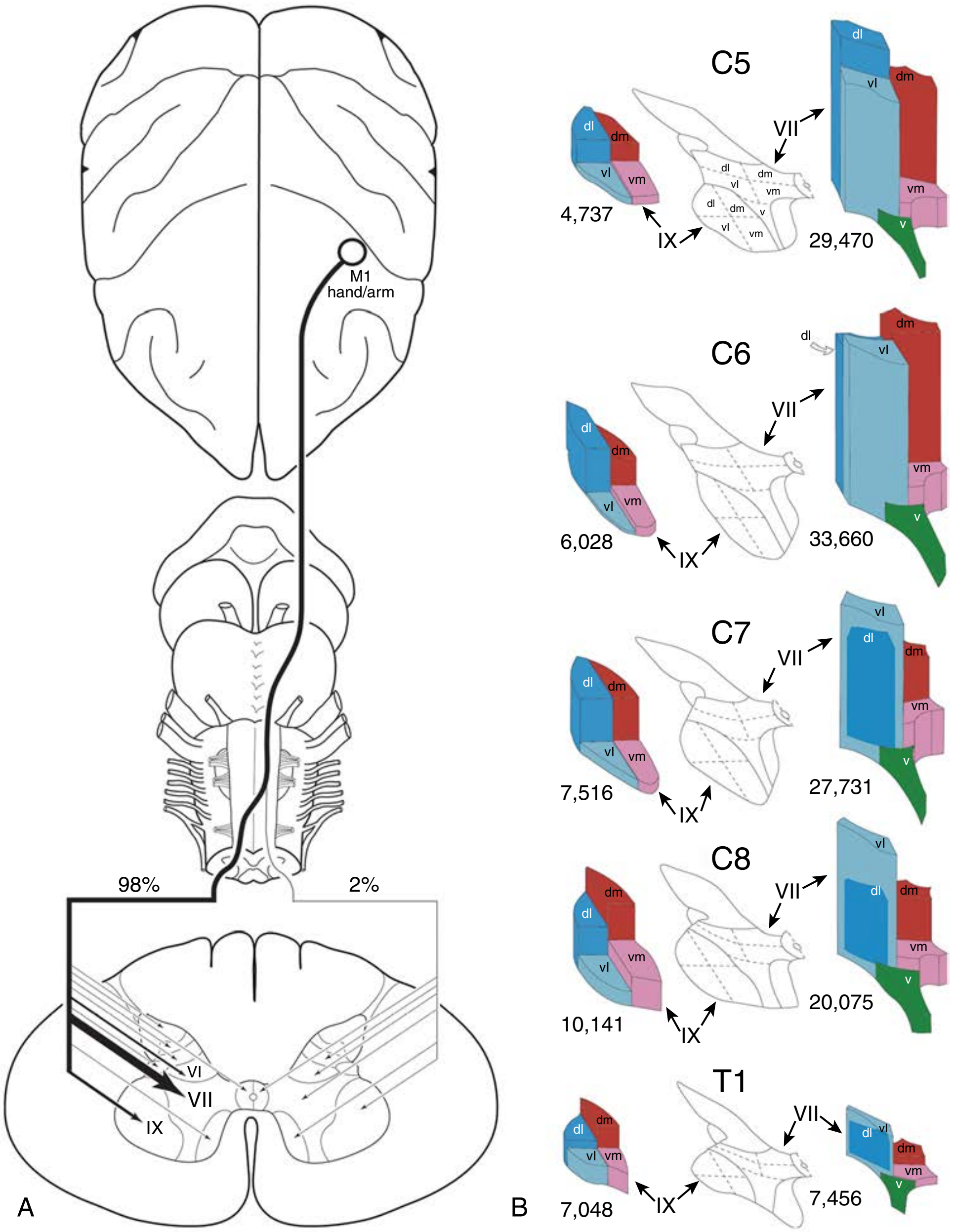

Fig. 3.1.3 Quantification of the M1 corticospinal terminations in the macaque cervical spinal cord. **A**, The overall corticospinal projection from the hand/arm region of the M1. The relative intensity of the projection to spinal cord laminae is indicated by line thickness and arrow head size. The strongest projections are to laminae VI, VII and IX. Note that there is only a weak projection to the dorsal horn. **B**, The relative strength of the contralateral projection to laminae VII and IX at each segmental level illustrated in 3D format. The relative height of each column corresponds to the relative number of estimated boutons labelled after injection of anterograde dextran amine tracers in the arm/hand area of M1, and counted in different quadrants of lamina VII (on the right) and lamina IX (motor nuclei, on the left). The mean number of labelled boutons obtained from three different cases is shown at each cervical level. Note the gradual decrease in the lamina VII projection from rostral to caudal spinal levels and the gradual increase in the lamina IX projection. The lamina IX projection was preferentially distributed to the dorsal quadrants at C5–C7 but was more widely dispersed among the quadrants at C8 and T1 (With permission from Morecraft RJ, Ge J, Stilwell-Morecraft KS et al 2013 Terminal distribution of the corticospinal projection from the hand/arm region of the primary motor cortex to the cervical enlargement in rhesus monkey. J Comp Neurol 521(18):4205–35.)

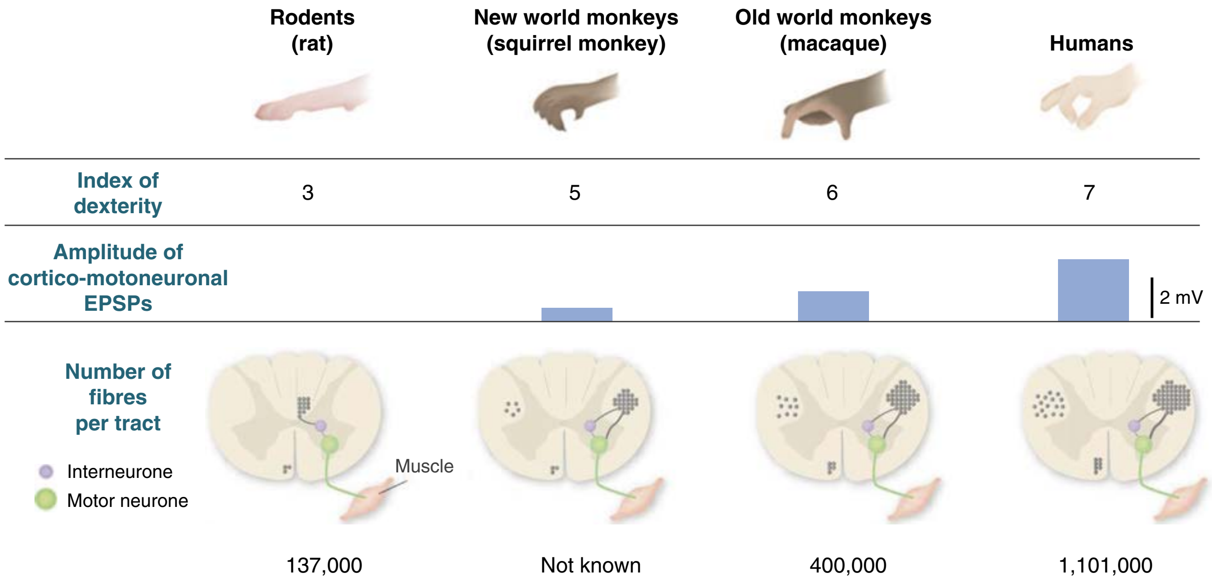
Rodents (rat)
New world monkeys (squirrel monkey)
Old world monkeys (macaque)
Humans
Index of dexterity
3
5
6
7
Amplitude of cortico-motoneuronal EPSPs
2 mV
Number of fibres per tract
Interneurone
Motor neurone
Muscle
137,000
Not known
400,000
1,101,000

Fig. 3.1.4 Species variation in corticospinal organization and contribution to skilled upper limb movement. Relationship between the organization of corticospinal projections and fine motor skills involving the hand/paw. In rodents, there are no direct cortico-motoneuronal (CM) connections between corticospinal neurones and the cervical motor neurones which innervate forelimb muscles. In these species brainstem pathways and spinal interneurones relay cortical input to motor neurones. In non-human primates and humans, direct CM connections with motor neurones have evolved, together with an increase in the size and number of corticospinal fibres. This is reflected in an increase in the size of the excitatory postsynaptic potential (EPSP) elicited by the corticospinal tract in hand motor neurones. CM EPSP amplitudes were assessed in hand motor neurones either by direct recording (monkeys) or inferred from analysis of hand muscle responses to non-invasive cortical stimulation (humans). These changes in the organization of the corticospinal system correlate with the improvement in the index of dexterity. (With permission from Lemon RN 2008 Descending pathways in motor control. Ann Rev Neurosci 31:195–218.)

This account will need to be revised in the light of research in macaques which points to the fact that the balance between contralateral versus ipsilateral terminations (i.e. where the fibres exert their synaptic actions, as opposed to their trajectory within the cord) may vary substantially between cortical areas and for cervical versus lumbosacral enlargement. Projections from the arm/hand region of macaque M1 terminate almost entirely in the contralateral grey matter of C5–T1 (see Fig. 3.1.3A), suggesting that even those fibres that descend ipsilaterally from the M1 arm/hand area cross at the segmental level and terminate contralaterally. In contrast to the arm/hand region, projections from M1 leg area are bilateral and exert bilateral effects on the lumbosacral cord, and this may reflect the involvement of leg motor cortex in skilled forms of locomotion such as skiing, dancing, etc. Secondary motor areas such as the SMA and the dorsal and ventral premotor areas generally give to a greater degree of bilateral projections to the cervical cord.

Bibliography

Dum RP, Strick PL 1991 The origin of corticospinal projections from the premotor areas in the frontal lobe. J Neurosci 11:667–89.

Firmin L, Field P, Maier MA et al 2014 Axon diameters and conduction velocities in the macaque pyramidal tract. J Neurophysiol 112:1229–40.

Kuypers HGJM 1981 Anatomy of descending pathways. In: Brookhart JM, Mountcastle VB, Brooks VB et al (eds) Handbook of Physiology, vol. 2: Motor Control, pt 1. Bethesda, MD: American Physiological Society, pp. 597–666.

Lemon RN 2008 Descending pathways in motor control. Ann Rev Neurosci 31:195–218.

Liu Y, Latremoliere A et al 2018 Touch and tactile neuropathic pain sensitivity are set by corticospinal projections. Nature 561:547–50.

Porter R, Lemon RN 1993 Corticospinal function and voluntary movement. Oxford: Clarendon Press.

Rathelot J-A, Strick PL 2009 Subdivisions of primary motor cortex based on cortico-motoneuronal cells. PNAS 106:918–23.

CHAPTER
33

Head and neck: overview and surface anatomy

SKIN AND FASCIA

Face and scalp

The superficial fascia of the scalp is firm, dense, fibroadipose, and closely adherent to the skin and to the underlying muscle, epicranius and the epicranial aponeurosis. Posteriorly, the fascia is continuous with the superficial fascia of the back of the neck, and laterally it is prolonged into the temporal region, where it is looser in texture. Three fascial layers (a subcutaneous fibroadipose tissue, a superficial musculo-aponeurotic system (SMAS) and the parotid–masseteric fascia) are recognized on the face superficial to the plane of the facial nerve and its branches. On the lateral side of the head, above the zygomatic arch, the temporoparietal fascia lies in the same plane as, but does not blend with, the superficial musculo-aponeurotic system. It is superficial to the temporal fascia and blends superiorly with the epicranial aponeurosis. The parotid gland is surrounded by a fibrous capsule derived from the deep cervical fascia.

Neck

The superficial cervical fascia is a zone of loose connective tissue between dermis and deep fascia and is joined to both. It contains a variable amount of adipose tissue and platysma but is hardly demonstrable as a separate layer. The deep cervical fascia is conventionally subdivided into three sheets (superficial investing, middle and deep layers) that surround the muscles and viscera of the neck to varying degrees, and the carotid sheath, a condensation of deep fascia around the common and internal carotid arteries, internal jugular vein, vagus and ansa cervicalis. The fascial layers of the neck define a number of potential tissue 'spaces' above and below the hyoid bone (Ch. 37). In health, the tissues within these spaces are either closely applied to each other or are filled with relatively loose connective tissue. However, they offer potential routes by which infection may spread within the head and neck, and between the tissue spaces of the face and the mediastinum. They also offer convenient planes for almost bloodless dissection during surgery.

BONES AND JOINTS

Skull and mandible

The skull is composed of 28 separate bones, most of them paired (Ch. 34). It can be divided into the cranium, consisting of the calvaria (brain box) and basicranium, which together surround and protect the brain; a delicate facial skeleton composed mainly of thin-walled bones, some of which contain air-filled cavities that are known collectively as the paranasal sinuses; and the mandible. The cranial cavity contains the brain and the intracranial portions of the cranial nerves; the blood vessels that supply and drain the brain and the haemopoietic marrow of the overlying bones; the meninges (dura, arachnoid and pia mater); and the cerebrospinal fluid in the subarachnoid space. The cavity is incompletely divided by dural partitions, notably the falx cerebri, lying between the cerebral hemispheres, and the tentorium cerebelli, lying between the cerebellum and occipital lobes. Almost all of the venous blood from the brain and cranial bones drains via sinuses lying between the endosteal and meningeal layers of the dura mater into the internal jugular vein. Internally, the cranial base is divided into anterior, middle and posterior cranial fossae, which contain the frontal and temporal lobes of the cerebral hemispheres and the cerebellum, respectively. Foramina in the bones of the skull base and facial skeleton transmit neurovascular bundles that may be compromised at these sites by pathology or trauma.

The bony orbits contain the eyeballs, oculogyric muscles and lacrimal glands with their associated neurovascular supplies (Chs 44 and 45). The temporal bones contain the inner, middle and external ears (Chs 42 and 43). The maxillae are the largest of the pneumatized bones of the midface; they contain the maxillary air sinuses and bear the upper teeth. The mandible bears the lower teeth and articulates with the temporal bones at the temporomandibular joints. The skull articulates with the first cervical vertebra (atlas); movements of the skull on the cervical vertebrae occur at the atlanto-occipital joints.

The skull provides attachments for many muscles, including all the craniofacial muscles, the oculogyric muscles, the muscles that act on the temporomandibular joint, the superior constrictor of the pharynx, the muscles of the soft palate, all but one of the extrinsic muscles of the tongue, the muscles of the suboccipital region, and the cranial attachments of trapezius and sternocleidomastoid.

Cervical vertebrae

There are seven cervical vertebrae. They are the smallest of the movable vertebrae and are characterized by a disproportionately large vertebral canal. All but the seventh are also characterized by a foramen in each transverse process, the foramen transversarium (these foramina may be absent or sometimes duplicated in the seventh cervical vertebra). The first (atlas), second (axis) and seventh (vertebra prominens) cervical vertebrae are atypical.

Hyoid bone and laryngeal cartilages

The hyoid bone lies in the midline at the front of the neck at the level of the fourth cervical vertebra (Badshah et al 2017). It is suspended from the styloid processes by the stylohyoid ligaments and gives attachment to the suprahyoid and infrahyoid groups of muscles. The skeletal framework of the larynx is formed by a series of cartilages interconnected by ligaments and fibrous membranes and moved by a number of muscles (Ch. 41). The laryngeal cartilages are the single cricoid, thyroid and epiglottic cartilages, and the paired arytenoid, cuneiform, corniculate and tritiate cartilages.

MUSCLES

The striated muscles of the head and neck produce the movements of the facial soft tissues that animate so many aspects of communication; the movements at the temporomandibular joint that happen during mastication and speech (Ch. 38); the conjugate movements of the eyeballs; and the coordinated movements that occur during activities such as swallowing, speaking and turning the head in response to visual and/or auditory stimuli. The 'extrinsic' muscles that run between the axial skeleton and upper limb act on the scapula and humerus (Ch. 49).

The superior tarsal muscle, sphincter and dilator pupillae and the ciliary muscle are composed of smooth muscle (Chs 44 and 45).

VASCULAR SUPPLY AND LYMPHATIC DRAINAGE

Arteries

The main arterial supply of the head and neck is derived from branches of the carotid and subclavian arteries (**Figs 33.1–33.2**). Branches of the internal carotid and vertebral arteries anastomose in the circle of Willis within the interpeduncular cistern on the ventral aspect of the brain (Ch. 26).

Carotid system

The cervical portion of the common carotid artery is similar on both sides. Each lies within the carotid sheath of deep cervical fascia, together with the internal jugular vein and vagus nerve. In the lower part of the

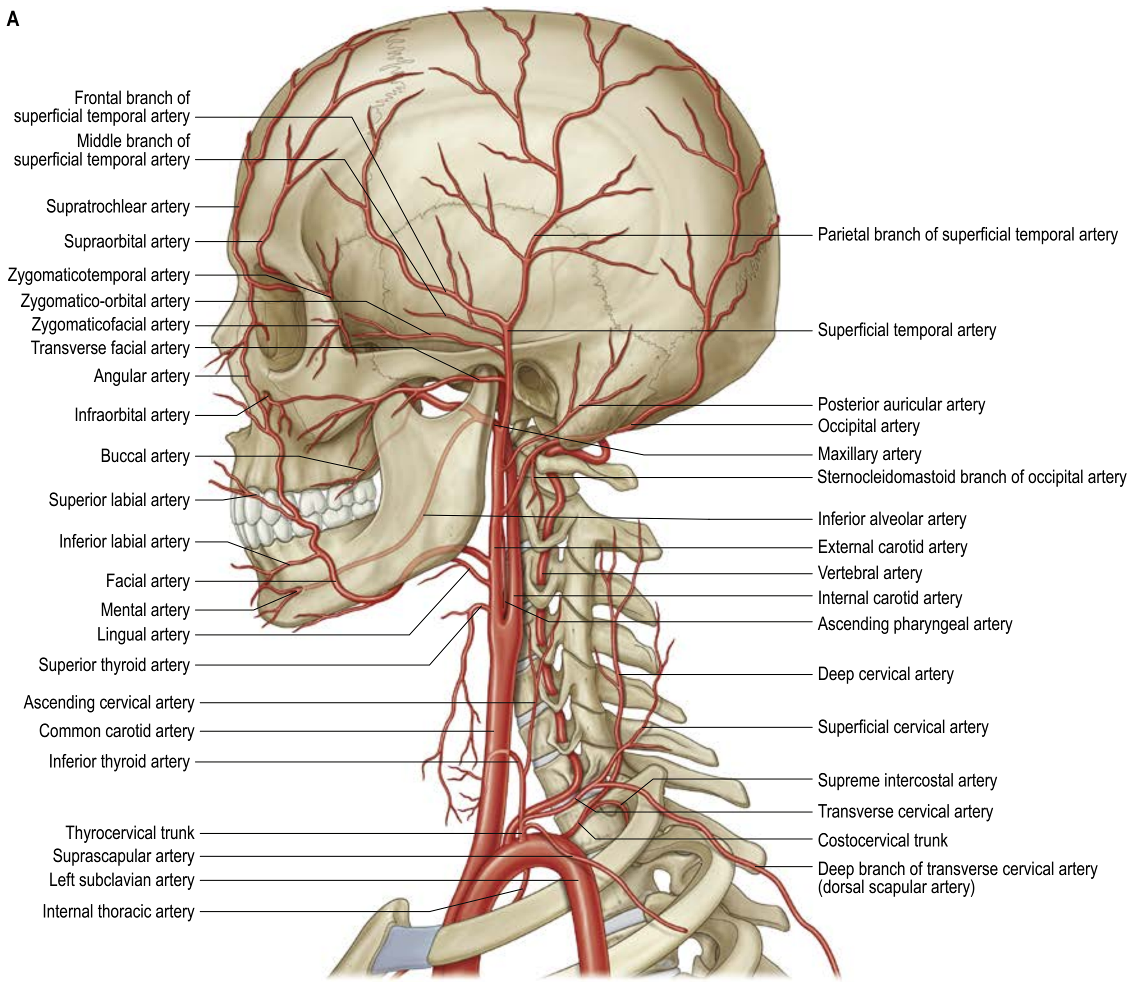
A
Frontal branch of superficial temporal artery
Middle branch of superficial temporal artery
Supratrochlear artery
Supraorbital artery
Zygomaticotemporal artery
Zygomatico-orbital artery
Zygomaticofacial artery
Transverse facial artery
Angular artery
Infraorbital artery
Buccal artery
Superior labial artery
Inferior labial artery
Facial artery
Mental artery
Lingual artery
Superior thyroid artery
Ascending cervical artery
Common carotid artery
Inferior thyroid artery
Thyrocervical trunk
Suprascapular artery
Left subclavian artery
Internal thoracic artery
Parietal branch of superficial temporal artery
Superficial temporal artery
Posterior auricular artery
Occipital artery
Maxillary artery
Sternocleidomastoid branch of occipital artery
Inferior alveolar artery
External carotid artery
Vertebral artery
Internal carotid artery
Ascending pharyngeal artery
Deep cervical artery
Superficial cervical artery
Supreme intercostal artery
Transverse cervical artery
Costocervical trunk
Deep branch of transverse cervical artery (dorsal scapular artery)

Fig. 33.1 A, An overview of the superficial arteries of the head and neck. (B, C, *continued online*)

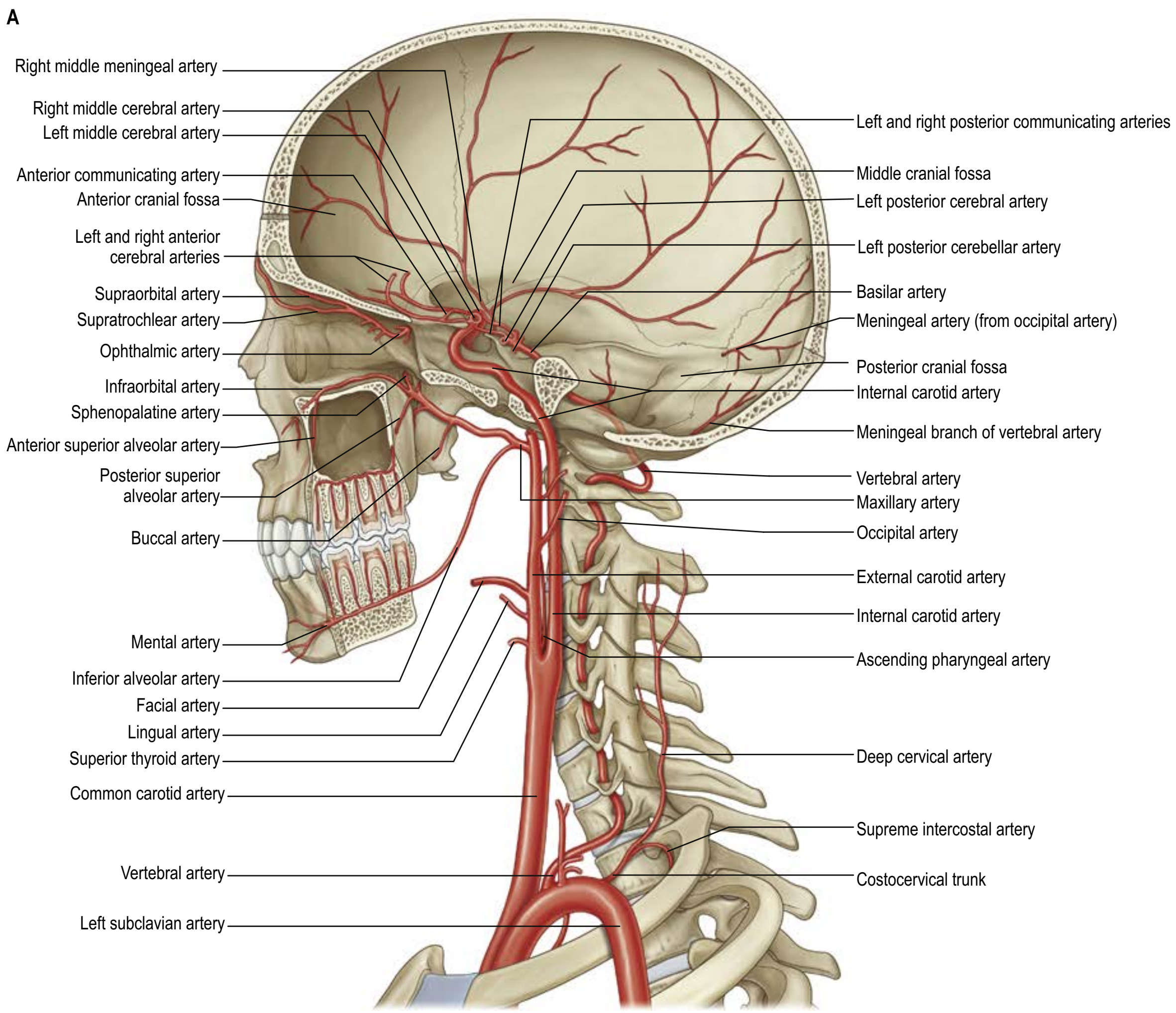
A
Right middle meningeal artery
Right middle cerebral artery
Left middle cerebral artery
Anterior communicating artery
Anterior cranial fossa
Left and right anterior cerebral arteries
Supraorbital artery
Supratrochlear artery
Ophthalmic artery
Infraorbital artery
Sphenopalatine artery
Anterior superior alveolar artery
Posterior superior alveolar artery
Buccal artery
Mental artery
Inferior alveolar artery
Facial artery
Lingual artery
Superior thyroid artery
Common carotid artery
Vertebral artery
Left subclavian artery
Left and right posterior communicating arteries
Middle cranial fossa
Left posterior cerebral artery
Left posterior cerebellar artery
Basilar artery
Meningeal artery (from occipital artery)
Posterior cranial fossa
Internal carotid artery
Meningeal branch of vertebral artery
Vertebral artery
Maxillary artery
Occipital artery
External carotid artery
Internal carotid artery
Ascending pharyngeal artery
Deep cervical artery
Supreme intercostal artery
Costocervical trunk

Fig. 33.2 A, An overview of the deep arteries of the head and neck. (B, *continued online*)

CHAPTER 33

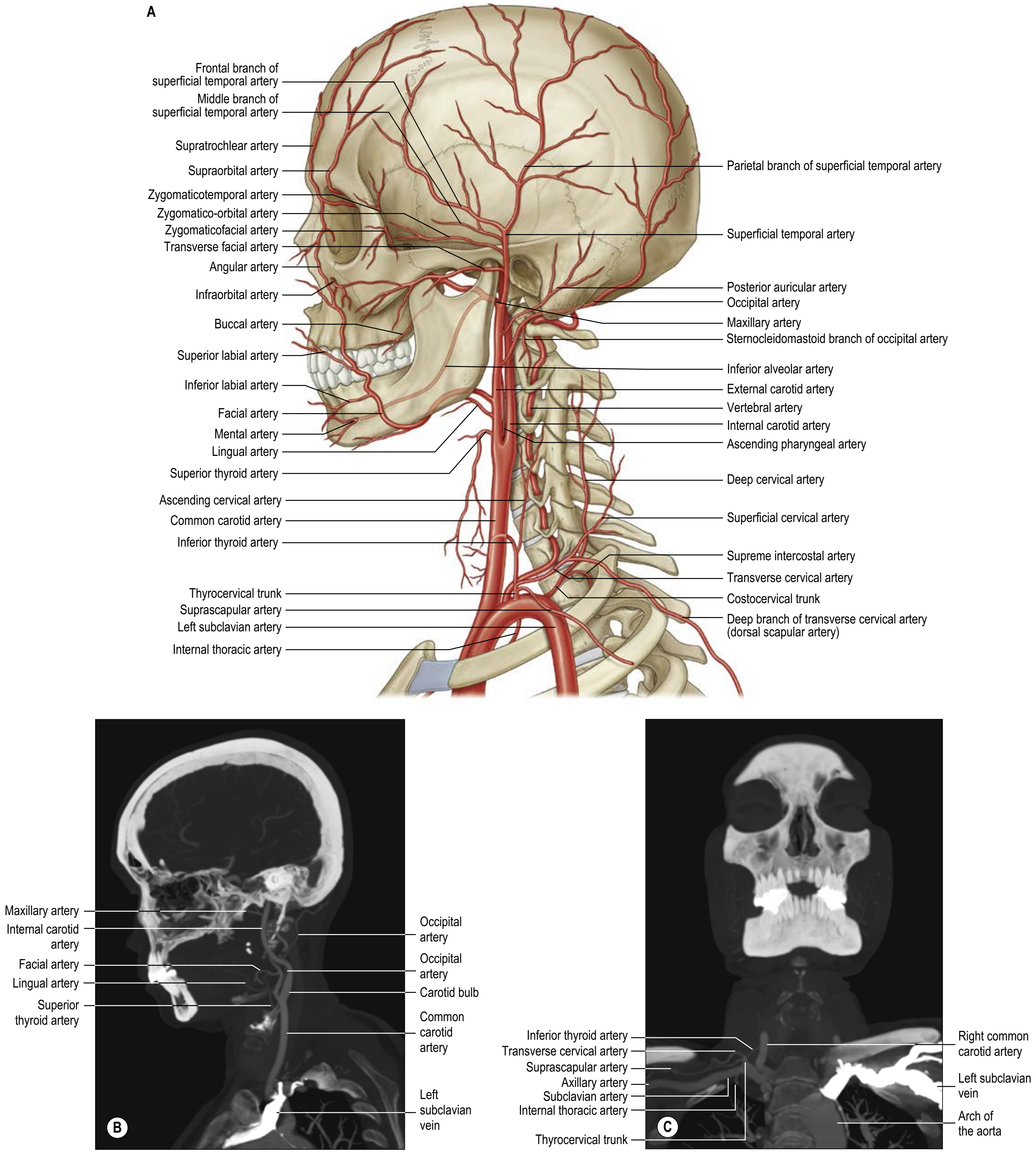
A
Frontal branch of superficial temporal artery
Middle branch of superficial temporal artery
Supratrochlear artery
Supraorbital artery
Zygomaticotemporal artery
Zygomatico-orbital artery
Zygomaticofacial artery
Transverse facial artery
Angular artery
Infraorbital artery
Buccal artery
Superior labial artery
Inferior labial artery
Facial artery
Mental artery
Lingual artery
Superior thyroid artery
Ascending cervical artery
Common carotid artery
Inferior thyroid artery
Thyrocervical trunk
Suprascapular artery
Left subclavian artery
Internal thoracic artery
Parietal branch of superficial temporal artery
Superficial temporal artery
Posterior auricular artery
Occipital artery
Maxillary artery
Sternocleidomastoid branch of occipital artery
Inferior alveolar artery
External carotid artery
Vertebral artery
Internal carotid artery
Ascending pharyngeal artery
Deep cervical artery
Superficial cervical artery
Supreme intercostal artery
Transverse cervical artery
Costocervical trunk
Deep branch of transverse cervical artery (dorsal scapular artery)
Maxillary artery
Internal carotid artery
Facial artery
Lingual artery
Superior thyroid artery
Occipital artery
Occipital artery
Carotid bulb
Common carotid artery
Left subclavian vein
B
Inferior thyroid artery
Transverse cervical artery
Suprascapular artery
Axillary artery
Subclavian artery
Internal thoracic artery
Thyrocervical trunk
Right common carotid artery
Left subclavian vein
Arch of the aorta
C

Fig. 33.1 **A**, An overview of the superficial arteries of the head and neck. **B**, Sagittal oblique maximum intensity projection (MIP) slab view of the left external carotid artery and some of its branches reconstructed from a CT carotid angiogram; note that the occipital artery arises earlier than usual. **C**, Coronal oblique MIP view of the right thyrocervical trunk reconstructed from a CT carotid angiogram. Contrast medium has been injected via the left arm, and loses attenuation as it passes through to the arterial system and is diluted by admixture with blood from the neck, right arm and inferior vena cava.

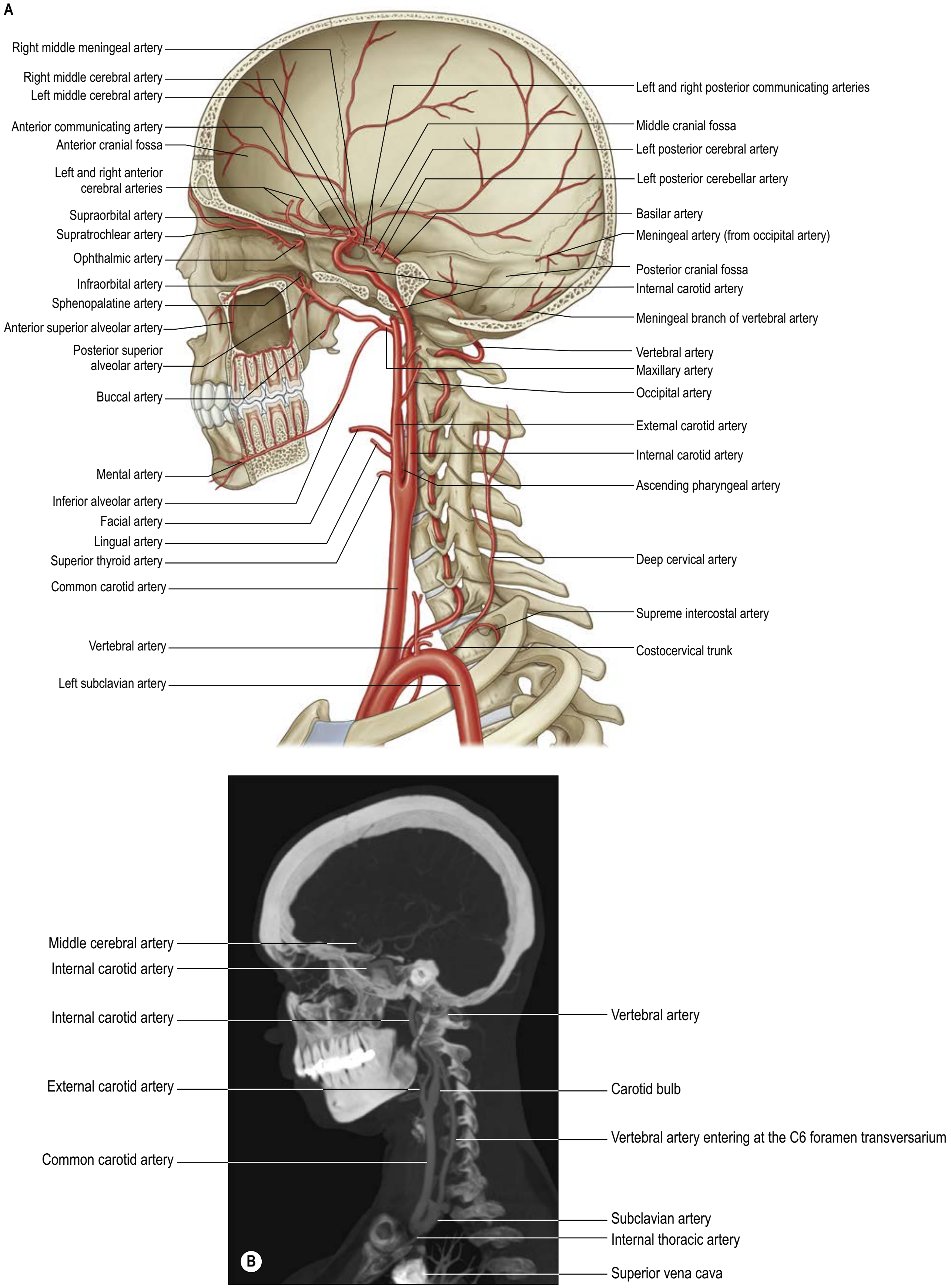
A
Right middle meningeal artery
Right middle cerebral artery
Left middle cerebral artery
Anterior communicating artery
Anterior cranial fossa
Left and right anterior cerebral arteries
Supraorbital artery
Supratrochlear artery
Ophthalmic artery
Infraorbital artery
Sphenopalatine artery
Anterior superior alveolar artery
Posterior superior alveolar artery
Buccal artery
Mental artery
Inferior alveolar artery
Facial artery
Lingual artery
Superior thyroid artery
Common carotid artery
Vertebral artery
Left subclavian artery
Left and right posterior communicating arteries
Middle cranial fossa
Left posterior cerebral artery
Left posterior cerebellar artery
Basilar artery
Meningeal artery (from occipital artery)
Posterior cranial fossa
Internal carotid artery
Meningeal branch of vertebral artery
Vertebral artery
Maxillary artery
Occipital artery
External carotid artery
Internal carotid artery
Ascending pharyngeal artery
Deep cervical artery
Supreme intercostal artery
Costocervical trunk
Middle cerebral artery
Internal carotid artery
Internal carotid artery
External carotid artery
Common carotid artery
Vertebral artery
Carotid bulb
Vertebral artery entering at the C6 foramen transversarium
Subclavian artery
Internal thoracic artery
Superior vena cava
B

Fig. 33.2 **A**, An overview of the deep arteries of the head and neck. **B**, Sagittal oblique maximum intensity projection view of the right vertebral artery reconstructed from a CT carotid angiogram.

neck, the arteries are separated by a narrow gap that contains the trachea, and higher up they are separated by the thyroid gland, larynx and pharynx. At the level of the upper border of the thyroid cartilage (C4), the common carotid artery bifurcates into external and internal carotid arteries: there can be significant variation on one or both sides of the neck. The external carotid artery passes upwards on either side of the neck, inclined at first slightly forwards and then backwards and a little laterally. It usually gives off the ascending pharyngeal, superior thyroid, lingual, facial, occipital and posterior auricular arteries, and then enters the parotid salivary gland where it divides into its terminal branches, the superficial temporal and maxillary arteries. The branches of the external carotid artery supply the face, scalp, tongue, upper and lower teeth and gingivae, palatine tonsil, paranasal sinuses and nasopharyngeal tube, external and middle ears, pharynx, larynx and superior pole of the thyroid gland. They also anastomose with branches of the internal carotid arteries on the scalp, forehead and face, in the orbit, nasopharynx and nasal cavity, and with branches of the subclavian artery in the pharynx, larynx and thyroid glands.

The internal carotid artery supplies most of the ipsilateral cerebral hemisphere, the eye and accessory organs, the forehead and, in part, the external nose, nasal cavity and paranasal sinuses. It passes up the neck anterior to the transverse processes of the upper three cervical vertebrae and enters the cranial cavity via the carotid canal in the petrous part of the temporal bone. The artery has no branches in the neck and so is easily distinguishable from the external carotid artery, should the latter require ligation, e.g. to control haemorrhage from a penetrating injury to the neck (Nowinski et al 2013, 2015).

Subclavian artery

The subclavian arteries give off several branches that supply structures in the head and neck. The vertebral arteries supply the upper spinal cord, brainstem, cerebellum and occipital lobe of the cerebrum. They pass through the foramina transversaria of the first six cervical vertebrae, enter the cranial cavity through the foramen magnum and unite at the lower border of the pons to form the basilar artery (hence this system is often called the vertebrobasilar system). Branches from the thyrocervical trunk supply the inferior poles of the thyroid gland and the parathyroid glands, the larynx and the pharynx, and branches from the costocervical trunks supply deep cervical muscles.

Veins

The veins of the neck lie superficial or deep to the deep investing fascia. Superficial veins ultimately drain into either the external, anterior or posterior external jugular veins; they drain a much smaller volume of tissue than the deep veins. Deep veins tend to drain into either the internal jugular vein or the subclavian vein. The internal jugular vein drains blood from the skull, brain, superficial face and much of the neck. It descends in the neck within the carotid sheath and unites with the subclavian vein behind the sternal end of the clavicle to form the brachiocephalic vein (**Figs 33.3–33.4**). At its junction with the internal jugular vein, the left subclavian vein usually receives the thoracic duct, and the right subclavian vein receives the right lymphatic duct.

Lymphatic drainage

Lymph nodes in the head and neck are arranged in two horizontal rings and two vertical chains on either side of the neck (**Fig. 33.5**). The outer, superficial, ring consists of the occipital, preauricular (parotid), submandibular and submental nodes, and the inner, deep, ring is formed by clumps of mucosa-associated lymphoid tissue (MALT) located primarily in the nasopharynx and oropharynx (Waldeyer's ring). The vertical chain consists of superior and inferior groups of nodes related to the carotid sheath. All lymph vessels of the head and neck drain into the deep cervical nodes, either directly from the tissues or indirectly via nodes in outlying groups (Ch. 17). Lymph is returned to the systemic venous circulation via either the right lymphatic duct or the thoracic duct.

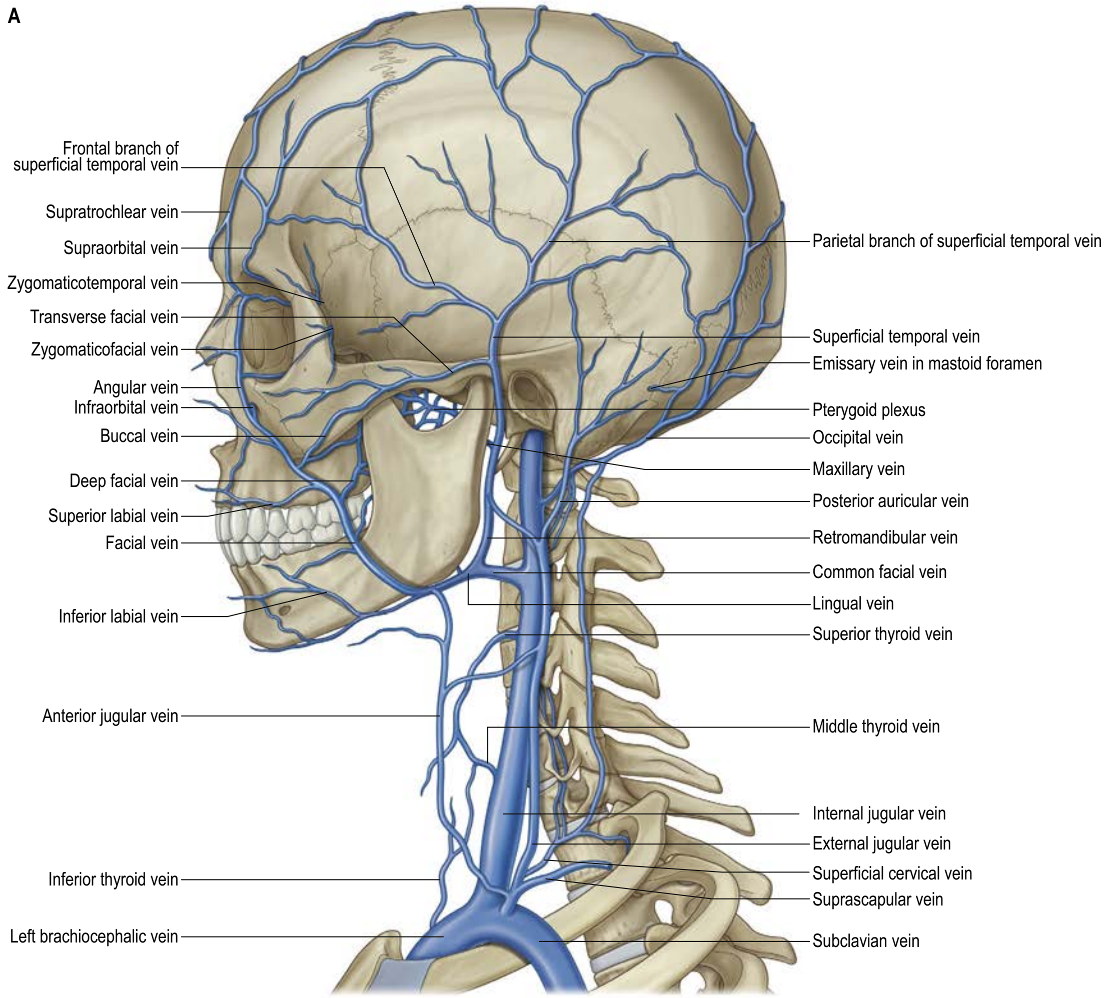
A
Frontal branch of superficial temporal vein
Supratrochlear vein
Supraorbital vein
Zygomaticotemporal vein
Transverse facial vein
Zygomaticofacial vein
Angular vein
Infraorbital vein
Buccal vein
Deep facial vein
Superior labial vein
Facial vein
Inferior labial vein
Anterior jugular vein
Inferior thyroid vein
Left brachiocephalic vein
Parietal branch of superficial temporal vein
Superficial temporal vein
Emissary vein in mastoid foramen
Pterygoid plexus
Occipital vein
Maxillary vein
Posterior auricular vein
Retromandibular vein
Common facial vein
Lingual vein
Superior thyroid vein
Middle thyroid vein
Internal jugular vein
External jugular vein
Superficial cervical vein
Suprascapular vein
Subclavian vein

Fig. 33.3 **A**, An overview of the superficial veins of the head and neck. (**B**, *continued online*)

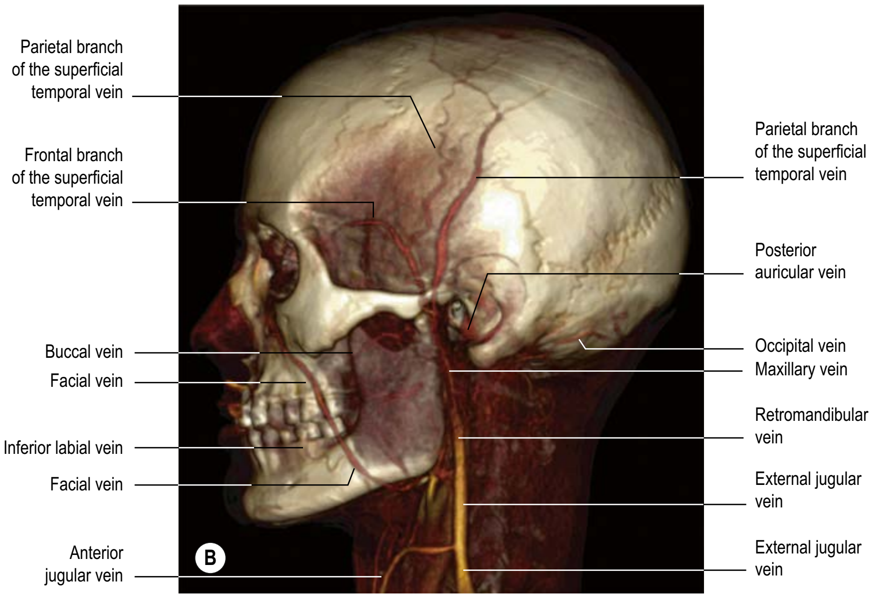
Parietal branch of the superficial temporal vein
Frontal branch of the superficial temporal vein
Buccal vein
Facial vein
Inferior labial vein
Facial vein
Anterior jugular vein
B
Parietal branch of the superficial temporal vein
Posterior auricular vein
Occipital vein
Maxillary vein
Retromandibular vein
External jugular vein
External jugular vein

Fig. 33.3, cont'd B, A volume rendered CT of the head and neck with intravenous contrast medium showing the superficial veins.

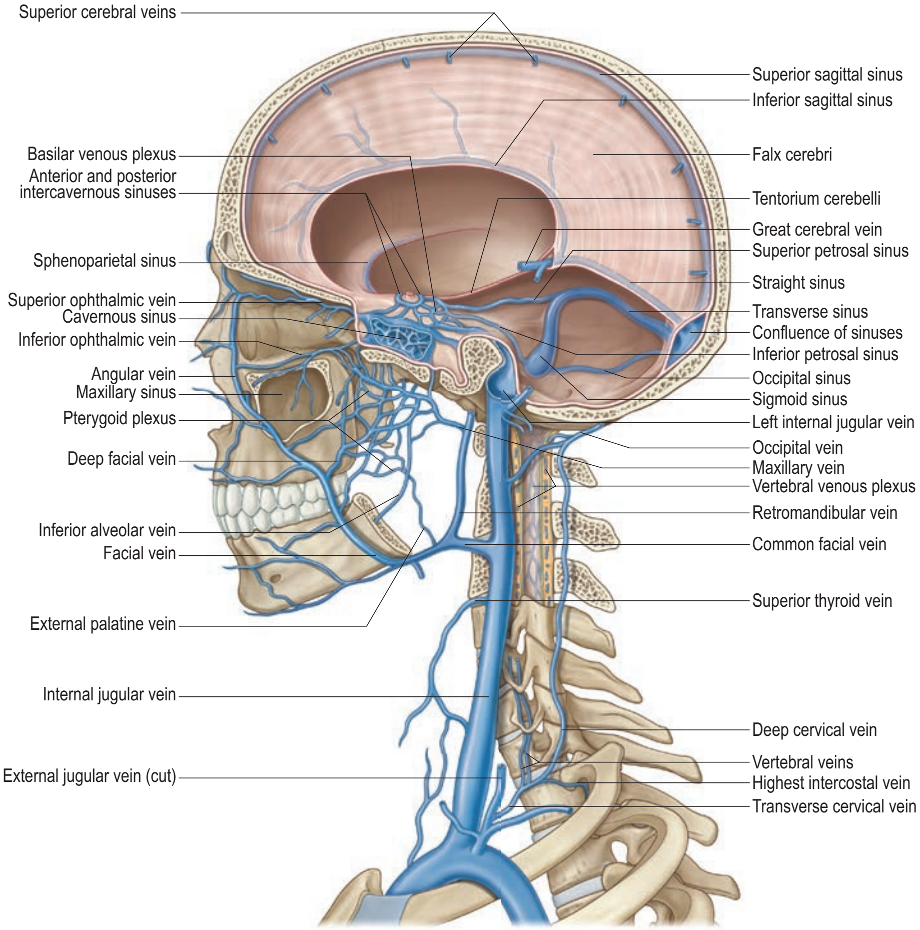
Superior cerebral veins
Basilar venous plexus
Anterior and posterior intercavernous sinuses
Sphenoparietal sinus
Superior ophthalmic vein
Cavernous sinus
Inferior ophthalmic vein
Angular vein
Maxillary sinus
Pterygoid plexus
Deep facial vein
Inferior alveolar vein
Facial vein
External palatine vein
Internal jugular vein
External jugular vein (cut)
Superior sagittal sinus
Inferior sagittal sinus
Falx cerebri
Tentorium cerebelli
Great cerebral vein
Superior petrosal sinus
Straight sinus
Transverse sinus
Confluence of sinuses
Inferior petrosal sinus
Occipital sinus
Sigmoid sinus
Left internal jugular vein
Occipital vein
Maxillary vein
Vertebral venous plexus
Retromandibular vein
Common facial vein
Superior thyroid vein
Deep cervical vein
Vertebral veins
Highest intercostal vein
Transverse cervical vein

Fig. 33.4 An overview of the deep veins of the head and neck.

INNERVATION

Cranial nerves

There are 12 pairs of cranial nerves. They are individually named and numbered (using Roman numerals) in a rostrocaudal sequence (see Table 24.1). Some are functionally mixed, others are either purely motor or purely sensory, and some also carry pre- or postganglionic parasympathetic fibres that are secretomotor to the salivary and lacrimal glands or motor to the smooth muscle within the eyeball and orbit. Branches of the oculomotor, trochlear, trigeminal, abducens, facial, glossopharyngeal, vagus, accessory and hypoglossal nerves supply muscle groups within the eyeball, face, neck, pharynx, larynx and tongue. Branches of the trigeminal, glossopharyngeal and vagus nerves transmit general sensory information from the skin of the face and part of the scalp; the epithelium lining the oral and nasal cavities, the paranasal sinuses, middle ear, pharynx and larynx, and the dorsal surface of the tongue and the cornea; the intracranial meninges; and the periosteum and bones of the skull. Branches of the trigeminal nerve innervate the temporomandibular joint. The olfactory, optic, trigeminal, facial, vestibulocochlear and vagus nerves contain axons that transmit the special sensations of olfaction, vision, hearing, balance and taste. The olfactory nerve is the only sensory cranial nerve that projects directly to the cerebral cortex rather than indirectly via the thalamus (Ch. 32). The optic nerve terminates in the thalamus (Ch. 30). The other ten pairs of cranial nerves are attached to the brainstem or, in the case of the (spinal) accessory nerve, to the upper cervical spinal cord; their component fibres arise from or terminate in named cranial nerve nuclei. The cranial nerves pass through named foramina in the skull, often with named vessels.

With one exception, all the cranial nerves are confined to the head and neck. The exception is the vagus, which travels through the neck and thorax, and enters the abdominal cavity by passing through the respiratory diaphragm with the oesophagus.

Reflexes

A number of reflexes involving structures in the head and neck are mediated by sensory and motor branches of the cranial nerves, coordinated via appropriate nuclei in the brainstem. They include swallowing, gagging, retching and vomiting, sneezing and coughing; lacrimation; jaw jerk; visual reflexes (pupillary light reflex and accommodation); and the corneal ‘blink’ reflex and the cochlear and vestibular reflexes (the stapedial reflex and caloric response of the labyrinth). Reflexes that involve energetic exhalation, e.g. sneezing and coughing, also involve the recruitment of cervical and thoracic spinal neurones to mediate the coordinated contraction of intercostal and abdominal wall muscles that this activity requires.

Spinal nerves

There are eight pairs of cervical spinal nerves (Fig. 33.6). Cutaneous branches of the dorsal rami of the second, third, fourth and fifth cervical nerves innervate the scalp and the skin over the back of the neck, and motor branches of all the cervical dorsal rami supply cervical postvertebral muscles. All the cervical ventral rami supply anterior and lateral groups of prevertebral muscles. The upper four cervical ventral rami form the cervical plexus, whose branches collectively innervate the infrahyoid strap muscles and the respiratory diaphragm, and the skin covering the lateral and anterior parts of the neck, and the angle of the mandible. The lower four cervical ventral rami, together with most of the first thoracic ventral ramus, form the brachial plexus.

Parasympathetic nerves

In the head and neck, the parasympathetic system innervates the salivary and lacrimal glands, the mucous glands of the oral and

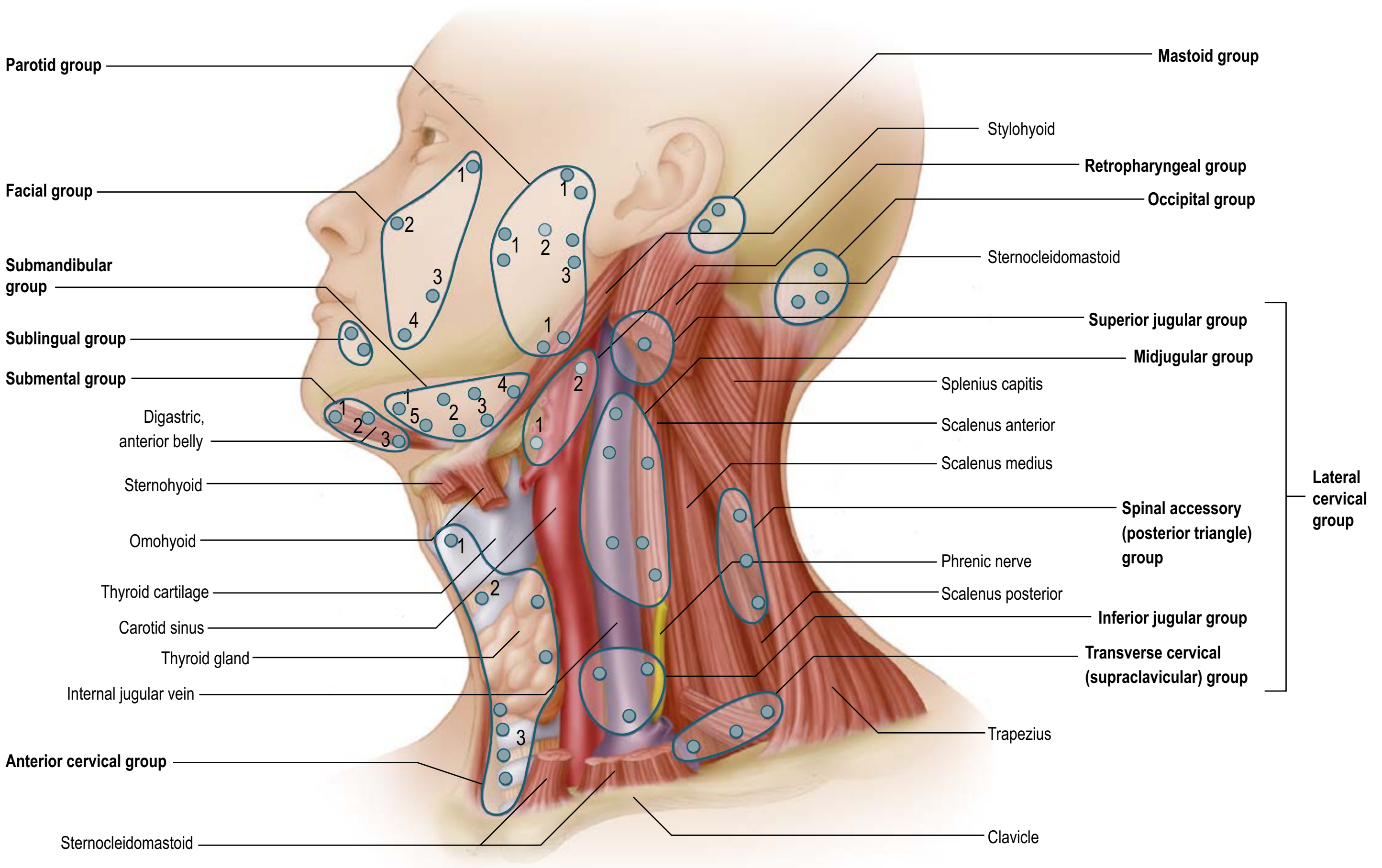
Parotid group
Facial group
Submandibular group
Sublingual group
Submental group
Digastric, anterior belly
Sternohyoid
Omohyoid
Thyroid cartilage
Carotid sinus
Thyroid gland
Internal jugular vein
Anterior cervical group
Sternocleidomastoid
Mastoid group
Stylohyoid
Retropharyngeal group
Occipital group
Sternocleidomastoid
Superior jugular group
Midjugular group
Splenius capitis
Scalenus anterior
Scalenus medius
Spinal accessory (posterior triangle) group
Lateral cervical group
Phrenic nerve
Scalenus posterior
Inferior jugular group
Transverse cervical (supraclavicular) group
Trapezius
Clavicle
1
2
3
4
5

Facial group	1. Malar 2. Infraorbital 3. Buccinator 4. Inferior maxillary	**Submandibular group**	1. Preglandular 2. Prevascular 3. Retrovascular 4. Retroglandular 5. Intracapsular	**Retropharyngeal group**	1. Lateral 2. Medial
Parotid group	1. Subfacial, extraglandular 2. Deep intraglandular 3. Suprafacial	**Submental group**	1. Anterior 2. Middle 3. Posterior	**Anterior cervical group**	1. Superficial anterior jugular chain 2. Prelaryngeal 3. Pretracheal

Fig. 33.5 An overview of the lymph nodes of the head and neck.

nasal cavities and paranasal sinuses, and the sphincter pupillae and ciliary muscles in the eyeball. Many thousands of preganglionic parasympathetic axons travel in the vagus from cell bodies in the dorsal motor nucleus of the vagus in the medulla oblongata. Although they travel through the neck in the right and left vagi, they are destined for pulmonary, cardiac, oesophageal, gastric and intestinal targets; they synapse in minute ganglia in the walls of the viscera and do not innervate structures in the head and neck.

There are four pairs of parasympathetic ganglia in the head, named ciliary, pterygopalatine, otic and submandibular (Fig. 33.7).

Ciliary ganglion

Preganglionic axons originate in the preganglionic nucleus of the midbrain (Edinger–Westphal nucleus) (Ch. 28). They travel via a branch of the oculomotor nerve (nerve to the inferior oblique) to the ciliary ganglion, where they synapse. Postganglionic fibres travel in the short ciliary nerves, which pierce the scleral coat of the eyeball and run forwards in the perichoroidal space to enter the ciliary muscle and sphincter pupillae. Their activation mediates accommodation of the eye to near objects and pupillary constriction.

Submandibular ganglion

Preganglionic axons originate in the superior salivatory nucleus. They emerge from the brainstem in the nervus intermedius and leave the main facial nerve trunk in the middle ear to join the chorda tympani, which subsequently joins the lingual nerve. In this way, they reach the submandibular ganglion, where they synapse. Postganglionic fibres innervate the submandibular, sublingual and lingual salivary glands; some axons presumably re-enter the lingual nerve to access the lingual glands, while others pass directly along blood vessels to enter the submandibular and sublingual glands.

Some preganglionic fibres may synapse around cells in the hilum of the submandibular gland. Stimulation of the chorda tympani dilates the arterioles in both glands, as well as having a direct secretomotor effect.

Pterygopalatine ganglion

Preganglionic axons travel in the greater petrosal branch of the facial nerve and the nerve of the pterygoid canal, and relay in the pterygopalatine ganglion. Postganglionic secretomotor axons innervate secretory acini and blood vessels in the palatine, pharyngeal and nasal

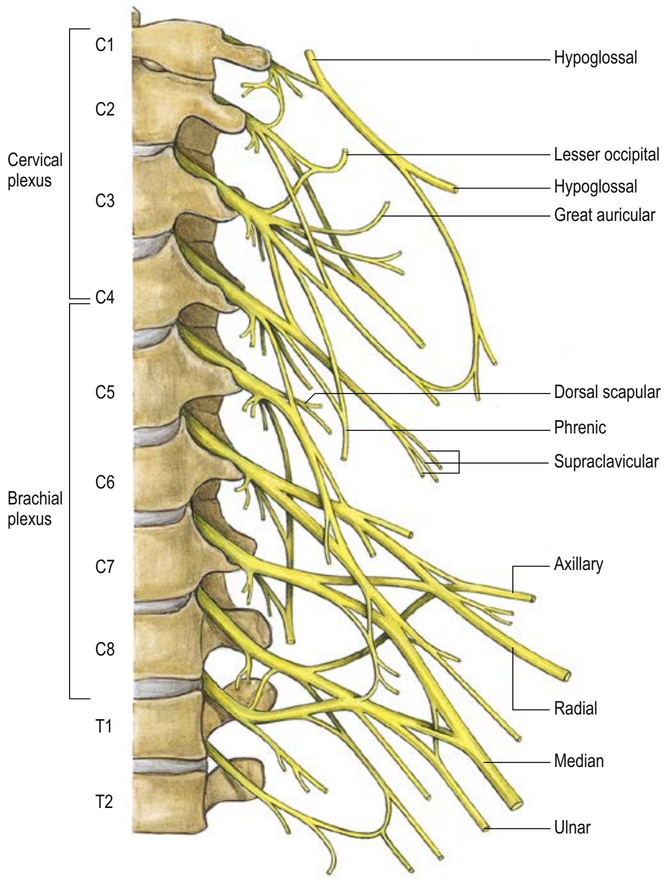
C1
C2
Cervical plexus
C3
C4
C5
Brachial plexus
C6
C7
C8
T1
T2
Hypoglossal
Lesser occipital
Hypoglossal
Great auricular
Dorsal scapular
Phrenic
Supraclavicular
Axillary
Radial
Median
Ulnar

Fig. 33.6 An overview of the nerves forming the cervical and brachial plexuses. (Sobotta Atlas of Human Anatomy © Elsevier GmbH, Urban & Fischer, Munich.)

mucosa via the palatine and nasal nerves: whether they also innervate the lacrimal gland via the zygomatic and zygomaticotemporal branches of the maxillary nerve, as was once thought, is less certain. It is likely that postganglionic orbital branches, carrying a mixture of postganglionic parasympathetic and somatic sensory axons, pass through the inferior orbital fissure and innervate the lacrimal gland and ophthalmic artery directly. Some axons pass into the cranial cavity via the ethmoidal vessels to innervate the choroid; the pterygopalatine ganglion is believed to be the main source of parasympathetic input to the choroid.

Otic ganglion

Preganglionic axons originate in the inferior salivatory nucleus and travel in the glossopharyngeal nerve and its tympanic branch. They traverse the tympanic plexus and lesser petrosal nerve, and pass through the foramen ovale to reach the otic ganglion, where they synapse. Postganglionic fibres pass by communicating branches to the auriculotemporal nerve, which conveys them to the parotid gland. Stimulation of the lesser petrosal nerve produces vasodilator and secretomotor effects.

Sympathetic nerves

In the neck, the sympathetic trunk lies behind and medial to the carotid sheath and anterior to the transverse processes of the cervical vertebrae and the prevertebral muscles. There are usually three cervical ganglia on each side, superior, middle and inferior (cervicothoracic): they may be connected by a solid trunk or by two or three fibrous strands. The ganglia receive preganglionic fibres from neurones whose cell bodies lie in the intermediolateral column of the upper thoracic spinal cord; there is no preganglionic output from the cervical spinal cord. Postganglionic fibres reach their target tissues in the head and neck via the cervical spinal nerves and perivascular nerve plexuses distributed along the carotid and vertebral arteries (see Fig. 33.7).

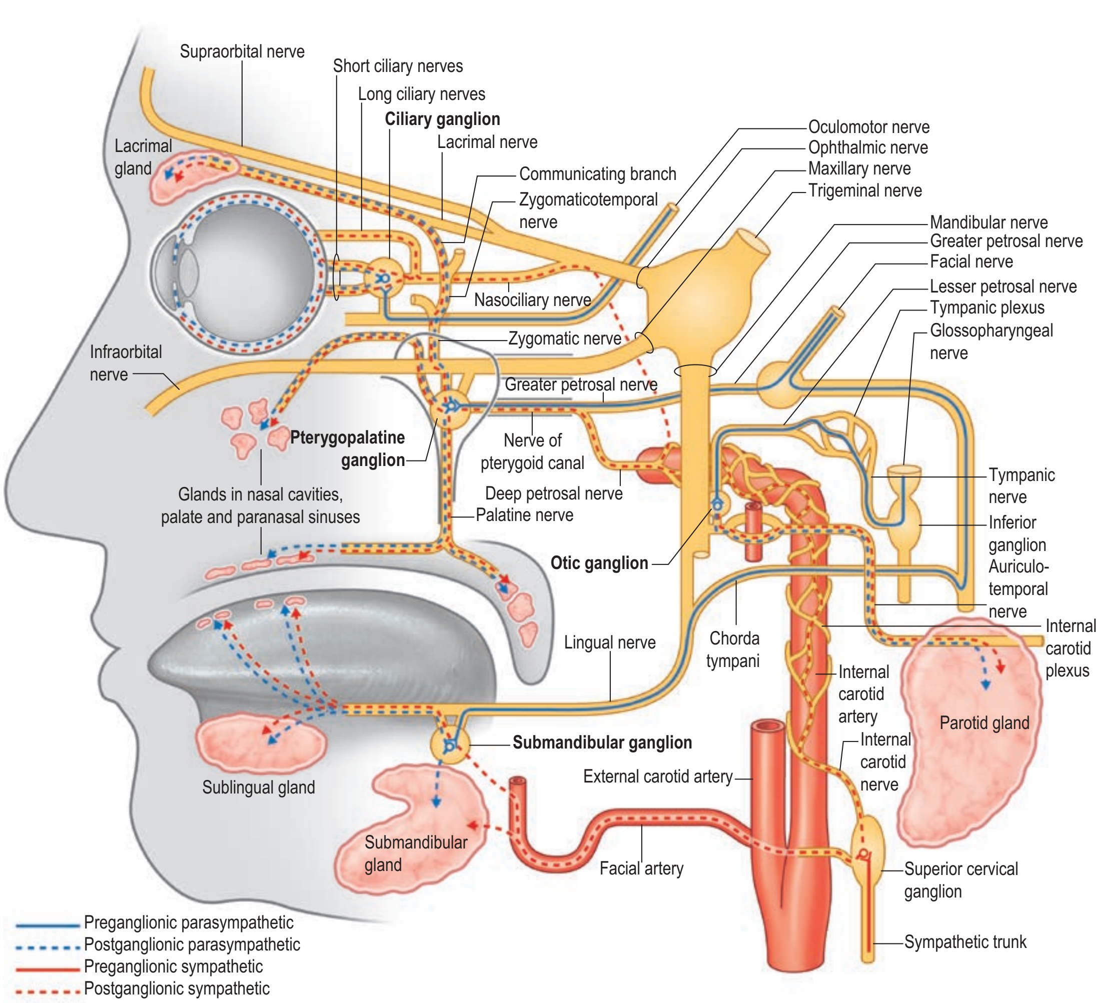
Supraorbital nerve
Short ciliary nerves
Long ciliary nerves
Ciliary ganglion
Lacrimal nerve
Lacrimal gland
Communicating branch
Zygomaticotemporal nerve
Oculomotor nerve
Ophthalmic nerve
Maxillary nerve
Trigeminal nerve
Mandibular nerve
Greater petrosal nerve
Facial nerve
Lesser petrosal nerve
Tympanic plexus
Glossopharyngeal nerve
Nasociliary nerve
Zygomatic nerve
Infraorbital nerve
Greater petrosal nerve
Pterygopalatine ganglion
Nerve of pterygoid canal
Glands in nasal cavities, palate and paranasal sinuses
Deep petrosal nerve
Palatine nerve
Tympanic nerve
Inferior ganglion
Auriculo-temporal nerve
Otic ganglion
Internal carotid plexus
Lingual nerve
Chorda tympani
Internal carotid artery
Parotid gland
Submandibular ganglion
Internal carotid nerve
Sublingual gland
External carotid artery
Submandibular gland
Facial artery
Superior cervical ganglion
Sympathetic trunk
Preganglionic parasympathetic
Postganglionic parasympathetic
Preganglionic sympathetic
Postganglionic sympathetic

Fig. 33.7 An overview of the visceral efferent pathways in the head. (Adapted with permission from Drake RL, Vogl AW, Mitchell A (eds) Gray's Anatomy for Students, 2nd ed. Elsevier, Churchill Livingstone. Copyright 2010.)

SURFACE ANATOMY

Surface anatomy of the head

Skeletal landmarks

The palpable bony landmarks of the head can be examined from the back, sides and front (Figs 33.8–33.9). The pericraniocervical line, which demarcates the head from the neck, runs from the midpoint of the chin anteriorly to the external occipital protuberance posteriorly.

Calvaria

Most of the superficial aspect of the calvaria is covered by skin, subcutaneous tissue and thin muscles; many bony prominences and surfaces are therefore palpable through the hair and are visible in bald people. Suture lines can be palpated as irregular ridges. The anterior fontanelle, at the junction of the coronal and sagittal sutures, may be palpated up to 24 months after birth. The mastoid process is palpable medial to the lobule of the auricle (pinna). Deep palpation immediately anteroinferior to the mastoid tip reveals the relatively indistinct resistance offered by the styloid process and associated soft tissues. When elongated, the tip of the styloid may be palpated in the tonsillar fossa. Palpation posteroinferiorly to the mastoid tip reveals the firm mass of the transverse process of the atlas (C1). The external occipital protuberance (inion) is a palpable bony protuberance located on the posterior midline of the occipital bone. The point of confluence of the dural venous sinuses is commonly located to the upper right side of the inion (Sheng et al 2012). The superior nuchal lines are palpable passing laterally from the inion. The asterion marks the junction of the occipitomastoid, parietomastoid and occipitoparietal sutures. It may be utilised to define the location of the transverse–sigmoid sinus complex, although it does not always do so (Day and Tschabitscher 1998; Sheng et al 2012). The point at which the transverse sinus becomes the sigmoid sinus and is joined by the superior petrosal sinus may sit deep to the asterion (Sheng et al 2012), although it is often located more anteriorly at a point marked by a palpable shallow depression 1–2 cm posterior to the auricle at a level approximately at the junction of the upper third and lower two-thirds of the auricle.

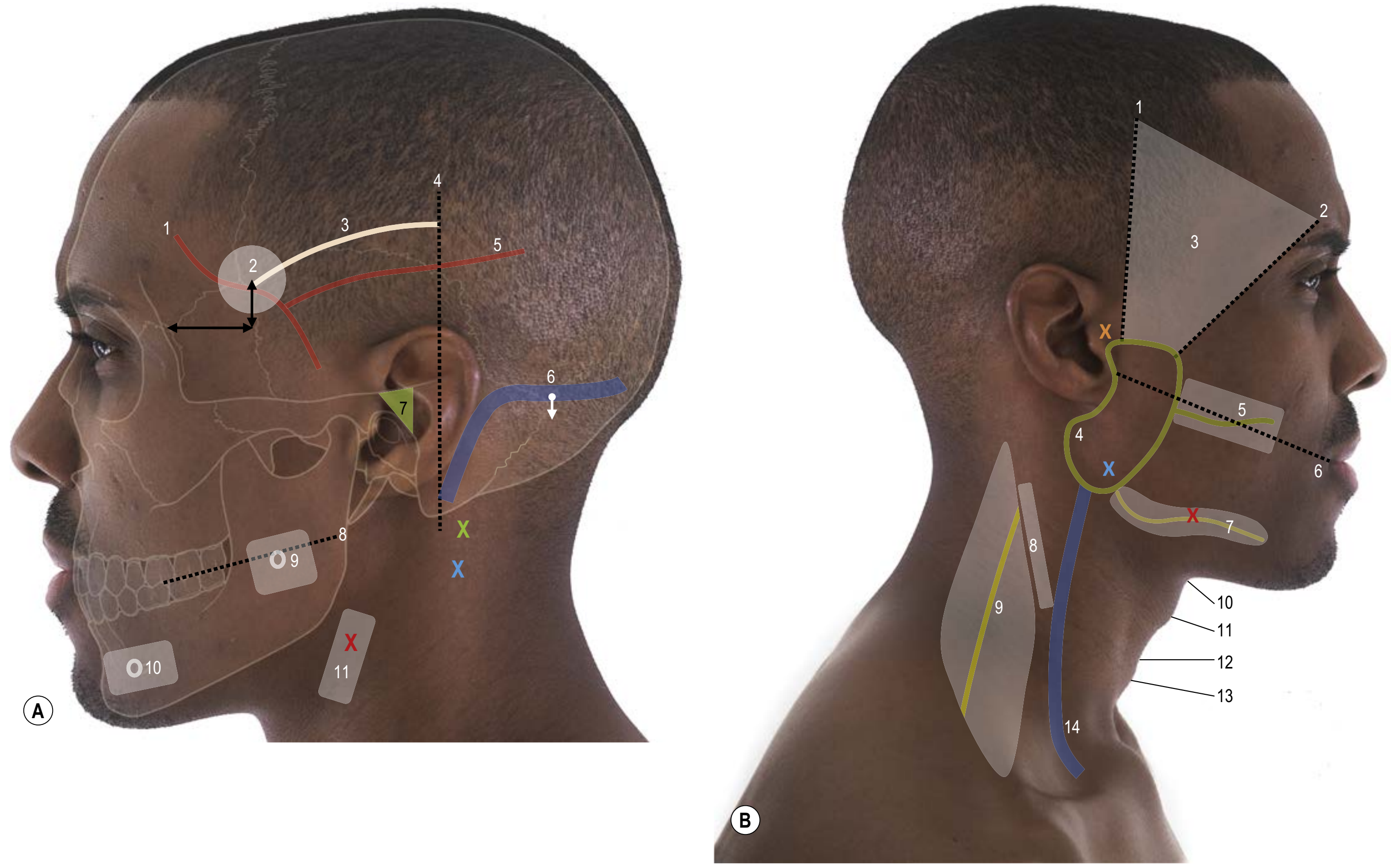

Fig. 33.8 The lateral aspect of the head and neck. **A**, Pterion, meningeal arteries, carotid bifurcation, mental and mandibular foramen. Key: 1, anterior branch of the middle meningeal artery: sits deep to the pterion in over half of subjects; 2, zone of location of the pterion: in a 1 cm diameter circle centred 2.5 cm posterior and 1.5 cm superior (black arrows) to the frontozygomatic suture; 3, lateral (Sylvian) fissure: aligns anteriorly with the anterior part of the squamosal suture in a zone 2.5–4.0 cm anterior to the external acoustic meatus; 4, mastoid line; 5, posterior branch of the middle meningeal artery: runs parallel to the zygomatic arch and sits level with the supraorbital margin on the mastoid line; 6, asterion: commonly sits over or just below (white arrow) the transverse–sigmoid sinus complex; 7, suprameatal triangle; 8, occlusal plane; 9, zone of location (white) of the mandibular foramen: in the majority of cases, the foramen sits level with or below the occlusal plane (8), an average of 2 cm posterior to tooth 8; 10, zone of location (white) of the mental foramen: the foramen commonly sits between the roots of teeth 4 and 5 (range 3–6), usually level with or inferior to the tooth root apex; X (green), transverse process of C1 (atlas); X (blue), transverse process of C2 (axis); 11, zone of location (white) of the bifurcation of the common carotid artery: approximately 0.5–3.0 cm above the level of the thyroid cartilage lamina; X (red), most common level of common carotid bifurcation (vertebral body of C3). **B**, Parotid gland and duct, CN VII and XI, cutaneous branches of cervical plexus and internal jugular vein. Key: 1, porion line; 2, zygomatic sutural line; 3, zone of location of the temporal branches of the facial nerve; 4, parotid gland; 5, zone of location (white) of the parotid duct (green line): sits within 1.5 cm of the middle half of a line passing from the lower tragus to the ipsilateral labial commissure; 6, lower tragus–labial commissure line; 7, zone of location of the marginal mandibular nerve (1.2 cm (range 0.9–1.75 cm) inferior to the mandible when posterior to the facial artery); 8, zone of emergence of the cutaneous branches of the cervical plexus (white), posterior to the middle third of sternocleidomastoid; 9, zone of location of the accessory nerve (white), from 3–10 cm below the tip of the mastoid process to 1–10 cm above the insertion of trapezius into the clavicle; 10, hyoid bone (body); 11, thyroid cartilage (laryngeal prominence); 12, cricothyroid ligament/membrane; 13, cricoid cartilage; 14, external jugular vein; X (blue), angle of the mandible; X (red), facial artery and anterior border of masseter crossing the lower border of the mandible; X (orange), superficial temporal artery. (Adapted with permission from Drake RL, Vogl AW, Mitchell A et al (eds) Gray's Atlas of Anatomy. Elsevier, Churchill Livingstone. Copyright 2008.)

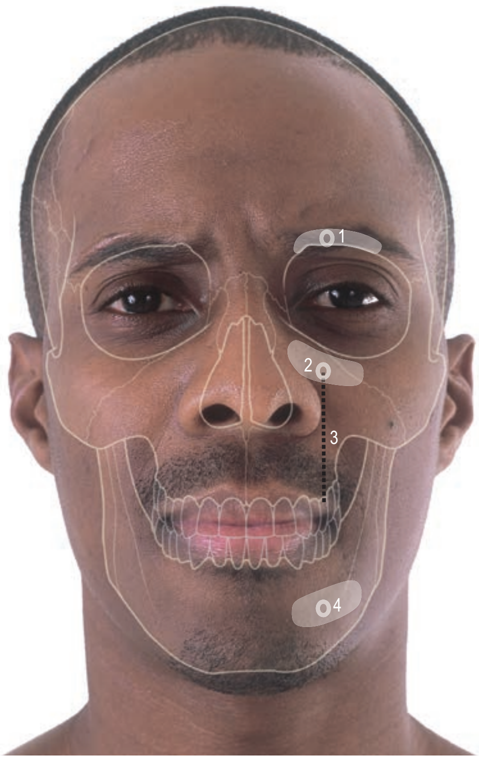

Fig. 33.9 The anterior aspect of the face. Key: 1, zone of location of the supraorbital foramen and neurovascular bundle (white) approximately 3 cm (range 1.8–4.3 cm) from the midline of the face; 2, zone of location of the infraorbital foramen and neurovascular bundle (white), approximately 2.5 cm (range 1.8–3.3 cm) from the midline of the face: aligns with a vertical axis passing through maxillary tooth 5; 3, vertical axis through maxillary tooth 5; 4, zone of location of the mental foramen and neurovascular bundle (white), approximately 2.5 cm from the midline of the face between the root apices of teeth 4 and 5 (range teeth 3–6). (Adapted with permission from Drake RL, Vogl AW, Mitchell A et al (eds) Gray's Atlas of Anatomy. Elsevier, Churchill Livingstone. Copyright 2008.)

Mandible

The mental tubercles are palpable on the anterior chin, and the mandibular body, alveolar processes and teeth are palpable through the cheek. The lower border of the mandible can be traced to the angle, which marks the level of the C2–C3 intervertebral disc (Auerbach et al 2009, Liu, Chen et al 2017). The mental foramen, which transmits the mental nerve and vessels, gradually migrates posteriorly after birth and through childhood (Balcioglu et al 2011). In adults, it lies an average of 2.5 cm (range 2–3 cm) from the midline of the face (Udhaya et al 2013), between the apices of the roots of mandibular teeth 4 and 5 (range teeth 3–6) (Fishel et al 1976, von Arx et al 2013, Udhaya et al 2013). Most foramina usually lie either level with or inferior to the apex of the root of the tooth (Fishel et al 1976). Accessory mental foramina, if present, are mainly situated posterior or inferior to the main mental foramen (Katakami et al 2008). The mandibular foramen lies on the medial surface of the ramus an average of 1.9 cm posterior to the third molar tooth (Nicholson 1985): a 21 mm needle is therefore sufficient to reach the foramen for dental anaesthesia (Menke and Gowgiel 1979). The foramina commonly (Mbajiorgu and Ekanem 2000, Nicholson 1985) lie level with or below the occlusal plane, the remainder sitting above.

The mandibular ramus is largely covered by masseter and the parotid gland. Its posterior border is palpable through the parotid up to the neck of the mandibular condylar process, which lies anterior to the lower tragus or the intertragal notch of the auricle. Movement of the condylar head at the temporomandibular joint is palpable anterior to the tragus during mouth opening/closing. The coronoid process is palpable anterior to the condylar process through the buccal mucosa.

Face

The lateral aspect of the face, from above downwards, consists of the temporal region, cheek and mandible (Ch. 36). The temporal region lies in front of the external ear and above the zygomatic arch. It is demarcated superiorly and posteriorly by the palpable superior temporal line, anteriorly by the frontal process of the zygoma, and inferiorly by the zygomatic arch. The palpable zygomatic arch is formed by the zygomatic process of the temporal bone posteriorly and the temporal process of the zygomatic bone anteriorly, both of which articulate via the palpable temporozygomatic suture. The variable prominence of the 'cheekbone' (zygoma) is largely attributable to the shape of the body of the underlying zygomatic bone. The sharp posterior margin of the frontal process of the zygomatic bone can be palpated superiorly to its articulation with the zygomatic process of the frontal bone at the palpable frontozygomatic suture; the marginal tubercle (Whitnall's tubercle) is palpable just below the suture within the lateral margin of the orbit. From here, the superior temporal line can be palpated passing posteriorly in the line of a gentle curve. The inferior temporal line terminates by curving downwards and forwards to end just above the root of the mastoid process as the supramastoid crest on the squamous part of the temporal bone. The suprameatal triangle overlies the lateral wall of the mastoid (tympanic) antrum and is demarcated superiorly by the palpable supramastoid crest (a palpable ridge of bone posterior to the upper auricle), anteroinferiorly by the posterosuperior margin of the external acoustic meatus, and posteriorly by a vertical line through the posterior border of the external acoustic meatus. The lateral/Sylvian fissure of the brain aligns with the anterior part of squamosal suture in a zone 2.5–4.0 cm anterior to the external acoustic meatus (Rahmah et al 2011). The pterion represents the sutural junction of the frontal, sphenoid, parietal and temporal bones within the temporal fossa. It can be located either within a 1 cm diameter circle centred approximately 2.6 cm posterior and 1.3 cm superior to the posterolateral margin of the frontozygomatic suture (Ma et al 2012), or approximately 4 cm above the midpoint of the zygomatic arch (Ukoha et al 2013). It commonly marks the position of the anterior (frontal) branch of the middle meningeal artery (Ma et al 2012). Knowledge of the surface anatomy of the middle meningeal artery is important for accurate positioning of burrholes to evacuate extradural haematomas: the posterior (parietal) arterial branch runs backwards and parallel with the upper border of the zygomatic arch and is usually exposed vertically above the mastoid process on a level horizontal with the supraorbital margin. The asterion is a craniometric point at the site of the posterolateral (mastoid) fontanelle. It is found at the junction of the lambdoid, occipitomastoid and parietomastoid sutures, and has been used as a landmark in lateral approaches to the posterior cranial fossa because it defines the superior limit of bone removal for the craniectomy. It should be noted that the asterion commonly sits over, or in the region of, the transverse–sigmoid sinus complex (Sheng et al 2012).

The forehead extends from the hair margin of the scalp to the eyebrows. The rounded frontal tuberosity may be felt approximately 3 cm above the midpoint of each supraorbital margin. The superciliary arch is usually palpable above the orbit and is better marked in the male than the female. The glabella, a small horizontal ridge, is easily palpable between the superciliary arches. Below the glabella, the nasal bones articulate with the frontal bone in a small depression, the nasion, at the root of the nose. With a little finger inserted into the nostril, the bony margins of the anterior nasal aperture can be felt; they are formed by the inferior border of the nasal bone, the sharp margins of the nasal notch of the maxilla, and the co-apted nasal spines of the maxillae (Ch. 39).

The orbital opening is relatively quadrangular and its margins are palpable. The supraorbital margin is formed entirely by the frontal bone. The supraorbital foramen/notch can be palpated along the superomedial orbital margin and lies an average of 2.7 cm (range 1.8–4.3 cm) from the midline of the face, although this position is variable (Chrcanovic et al 2011, Tomaszewska et al 2012). The notch/foramen transmits the supraorbital nerve and vessels, and pressure exerted here with the fingertip can be painful. An additional notch that transmits the supratrochlear neurovascular bundle may be found in the orbital margin more medially, towards the bridge of the nose.

The lateral margin of the orbit consists of the frontal process of the zygomatic bone and the zygomatic process of the frontal bone. The frontozygomatic suture between them may be palpated as a depression. Approximately 1 cm below the suture, the marginal tubercle (Whitnall's) can be palpated on the zygomatic bone, within the lateral orbital margin: the lateral palpebral ligament and the check ligament of lateral rectus are attached to the tubercle. The inferior border of the orbit is formed by the zygomatic bone laterally and the maxilla medially. It blends into the medial margin, which is less obvious, and is formed above by the frontal bone and below by the lacrimal crest of the frontal process of the maxilla. A shallow fossa behind the lower part of the medial wall houses the lacrimal sac. The anterior lacrimal crest is a guide to the location of the anterior ethmoidal artery, which may occasionally require ligation to control severe epistaxis; the artery lies approximately 2.4 cm posterior to the crest. The optic canal lies approximately 4.5 cm posterior to the infraorbital margin (approximately 4.2 cm from the anterior lacrimal crest); these distances are important in orbital floor exploration in order to avoid optic nerve injury. The inferior orbital fissure lies approximately 2 cm posterolateral to the infraorbital margin; it does not contain any important structures and therefore surgery can be performed safely in this region. The infraorbital foramen, which transmits the infraorbital nerve and vessels, lies below the middle of the infraorbital margin. It is commonly aligned with a vertical axis passing through maxillary tooth 5 (Raschke et al 2013) and lies an average of 2.5 cm (range 1.8–3.3 cm) from the midline of the face and 6.4 mm (range 3.2–12.1 mm) below the inferior orbital margin (Chrcanovic et al 2011, Raschke et al 2013). In neonates, the infraorbital nerve is located approximately half-way along a line drawn from the angle of the mouth to the midpoint of the palpebral fissure (Bosenberg and Kimble 1995).

The anterior surface of the maxilla is extensive and may be palpated between the infraorbital margin and the alveolar processes that bear the upper (maxillary) teeth. The canine eminence overlies the root of the canine tooth and separates the incisive fossa anteriorly from the deeper canine fossa posteriorly. The bone of the canine fossa is thin and may be removed easily to access the maxillary sinus via an intraoral approach as part of a Caldwell–Luc procedure. The palatine process of the maxilla and the horizontal plate of the palatine bone form the roof of the mouth and are palpable. The incisive (nasopalatine) foramen sits in the midline of the palate, immediately posterior to the incisive papilla, approximately 7.4 mm from the labial surface of the alveolar ridge (Mraiwa et al 2004), and transmits the sphenopalatine artery and nasopalatine nerve. The greater palatine foramen transmits the greater palatine artery and nerve and is commonly located in the region medial to maxillary tooth 8 (range from level with tooth 7 to posterior to tooth 8 (Sujatha et al 2005, Jaffar and Hamadah 2003)), approximately 16 mm from the midline (Wang et al 1988).

Soft tissues and viscera

The muscular, fatty and cutaneous features that so clearly differentiate individuals are readily apparent on inspection. The external features of the eyelids and eyebrows are described in Chapters 44 and 36, respectively. The tympanic membrane may be examined under direct vision using an auroscope and is described in Chapter 42. The retinal vascular supply may be examined directly by ophthalmoscopy (Ch. 45).

The temporalis muscle is palpable if the palmar surface of the hand is placed over the temporal region and the jaw is clenched and relaxed. The anterior border of masseter is palpable and prominent when the jaw is clenched. The masseter is thicker in boys than in girls in both the relaxed and contracted state (Charalampidou et al 2008). With the mouth open, it is possible to examine the teeth, gingivae, tongue and the palatine tonsils lying between the anterior and posterior faucial arches (palatoglossal and palatopharyngeal arches) formed by palatoglossus (anterolaterally) and palatopharyngeus (posteromedially), respectively. Peritonsillar abscess (quinsy) can cause ipsilateral tonsillar enlargement with contralateral displacement of the uvula; parapharyngeal tumours displace the ipsilateral tonsil and palate medially. The openings of the ducts of the submandibular glands can be seen on either side of the lingual frenulum at its point of intersection with the sublingual mucosal folds. The lingual nerve often passes close (2–3 mm) to the lingual side of the alveolar process housing the root of mandibular tooth 8; some lingual nerves can contact the mandibular bone directly or pass across the retromolar triangle (Behnia et al 2000).

Parotid gland

The parotid gland is soft and indistinct to palpation. The superior border sits inferior to the zygomatic arch, passing from the mandibular condyle towards masseter. The anterior border passes inferiorly along the posterior border of masseter, often overlying its lateral surface, then over the mandibular angle to meet the anterior border of sternocleidomastoid, approximately 2 cm posteroinferior to the mandibular angle. The inferior border lies at the level of the C3 vertebral body. The posterior border corresponds to a curve traced from the mandibular condyle to the mastoid process. The deep part of the gland lies within the prestyloid part of the parapharyngeal space. Tumours arising in this region present with medial displacement of the soft palate and palatine tonsil. The parotid duct arises from the anterior border of the gland and can be palpated on the anterior border of a clenched masseter. The duct often follows a curved trajectory and passes along, or within 1.5 cm of, the middle half of a line drawn from the lower border of the tragus to the ipsilateral labial commissure (Stringer et al 2012, Toure et al 2015) (**Fig. 33.8B**). The duct runs over masseter as far as the anterior border of the muscle, and then bends sharply, pierces the underlying buccinator and buccal mucosa and opens into the mouth opposite maxillary tooth 7: the orifice of the duct is visible and palpable. Duct cannulation is required for sialography, ductal dilation and basket retrieval of ductal stones (sialoliths).

Pulses

The facial artery can be palpated in two places; as it crosses the lower border of the mandible immediately anterior to masseter and also on the face, approximately 1 cm lateral to labial commissure. The superficial temporal artery is palpable immediately anterior to the tragus of the auricle. The artery divides into frontal and parietal branches approximately 2.5 cm above the zygomatic arch; both branches are palpable.

Facial nerve

The facial nerve may be injured in its extracranial course as a result of facial trauma and laceration, or iatrogenically during surgery involving the parotid or submandibular glands or the temporomandibular joint, or during facelift procedures. Knowledge of the topographical and surgical landmarks is therefore essential if the nerve is to be preserved during surgery.

The nerve exits the skull at the stylomastoid foramen and so is initially deep to the posterior margin of the external acoustic meatus; the nerve trunk lies approximately 9 mm from the tip of the mastoid process and 14 mm from the transverse process of C1 (Greyling et al 2007). It usually divides within the parotid gland into five main branches that radiate across the face (**Fig. 33.10**; see Fig. 36.24). Cadaveric and intraoperative microdissection studies have revealed that the course of its branches is highly variable and therefore surface coordinates only approximate their trajectory or zone of location. The temporal branches emerge from the superior surface of the parotid and cross the zygomatic arch approximately 1 cm anterior to the superficial temporal artery as that vessel also crosses the zygomatic arch, both nerve and vessel travelling towards the pterion and the superolateral brow. The majority lie in the zone between two lines: line 1 (porion line) joins two points each situated 12 mm from the porion on both the supraorbitomeatal line and the infraorbitomeatal line; and line 2 (zygomatic sutural line) is a line joining the temporozygomatic and frontozygomatic sutures (Davies et al 2012). These branches may be injured in facial rhytidectomy, coronal or endoscopic brow lifting, and temporal craniotomy. The buccal branches run both above and below the parotid duct. The marginal mandibular nerve emerges from the anteroinferior parotid gland and passes anteriorly. When posterior to the facial artery, the nerve almost always lies inferior to the lower border of the mandible by approximately 1.2 cm (range 0.9–1.75 cm) (Batra et al 2010), although some branches can lie as much as 3.6 cm inferiorly (Davies et al 2016). The nerve re-enters the face by crossing the lower border of the mandible near the anterior border of masseter, where it passes superficial to the facial artery and vein. Regional incisions should be made at least two fingers' breadth or 4 cm below the lower border of the mandible to avoid injuring the nerve (Chowdhry et al 2010, Davies et al 2016), and the resultant upturned ipsilateral mouth caused by paralysis of depressor anguli oris and depressor labii inferioris. During surgery, lateral flexion and axial rotation of the head away from the side of the incision may help to move the marginal mandibular nerve superiorly.

Dermatomes

The delineation of individual dermatome position is based on clinical evidence. The dermatomes of the face are determined mainly by the distribution of the cutaneous branches of the three major divisions of the trigeminal nerve. The skin covering the anterolateral neck, the angle of the mandible, lateral scalp and posterior aspect of the auricle is innervated by branches of the cervical plexus (C2–C4), and the skin covering the back of the head is innervated by the greater occipital nerve (C2, posterior primary ramus).

Surface anatomy of the neck

Skeletal and cartilaginous landmarks

The neck extends from the pericraniocervical line superiorly to the level of the clavicle, scapula, first rib and superior manubrium inferiorly. Posteriorly, the spinous processes of C2 and C7 are the most prominent and may be palpated in the midline (the former via deep palpation). The remaining cervical spines are indistinct because they are covered by the ligamentum nuchae, on either side of which lie the masses of the postvertebral musculature. On either side, the transverse process of C1 is palpable in the hollow region posteroinferior to the mastoid process tip; deep palpation inferiorly may reveal the transverse process of C2.

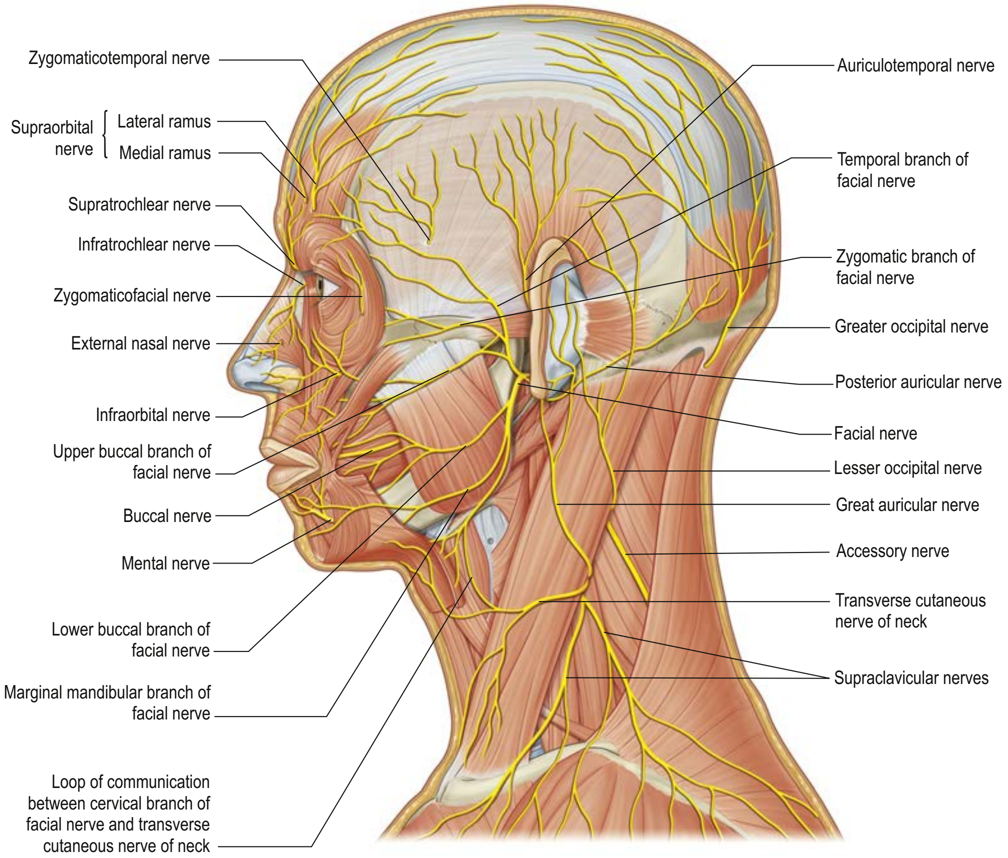
Zygomaticotemporal nerve
Supraorbital nerve
Lateral ramus
Medial ramus
Supratrochlear nerve
Infratrochlear nerve
Zygomaticofacial nerve
External nasal nerve
Infraorbital nerve
Upper buccal branch of facial nerve
Buccal nerve
Mental nerve
Lower buccal branch of facial nerve
Marginal mandibular branch of facial nerve
Loop of communication between cervical branch of facial nerve and transverse cutaneous nerve of neck
Auriculotemporal nerve
Temporal branch of facial nerve
Zygomatic branch of facial nerve
Greater occipital nerve
Posterior auricular nerve
Facial nerve
Lesser occipital nerve
Great auricular nerve
Accessory nerve
Transverse cutaneous nerve of neck
Supraclavicular nerves

Fig. 33.10 The distribution of the cutaneous branches of the trigeminal nerve and of the cervical plexus, and the motor branches of the facial nerve in the face and neck.

The body of the hyoid bone can be felt in the midline neck a few centimetres below and behind the chin, at the junction of the skin covering the anterior neck and the floor of the mouth. It sits level with the vertebral body of C4 (range vertebral body of C3 to the C5–C6 intervertebral disc) (Mirjalili et al 2012b, Badshah et al 2017, Shen et al 2017), and is higher in neonates and children. The left and right greater horns of the hyoid pass posterosuperiorly from the body, and can be palpated between the finger and thumb of one hand. The laryngeal prominence (Adam's apple) of the thyroid cartilage is palpable in the midline of the neck; the thyroid laminae can be felt passing posterolaterally. The prominence is usually visible in postpubertal males, whereas it is not usually apparent in females. The curved upper border of the thyroid cartilage, the midline superior thyroid notch and the superiorly located depression of the thyrohyoid membrane/ligament are easily palpable. The superior border of the thyroid cartilage lamina commonly sits level with the vertebral body of C4 in females and the vertebral body of C5 in males, but there is considerable variation (range upper half of the vertebral body of C3 to the lower half of the vertebral body of C6) (Mirjalili et al 2012b, Shen et al 2017). The firm, smooth anterior arch of the cricoid cartilage is palpable below the inferior border of the thyroid cartilage. The inferior border of the cricoid cartilage commonly sits level with the vertebral body of C6 in females and the vertebral body of C7 in males (range lower half of the vertebral body of C5 to the lower half of the vertebral body of T1). The indentation between the thyroid and cricoid cartilages is covered by the anterior/median cricothyroid ligament, and is a useful site for emergency access to the airway in cases of obstruction at or above the vocal cords (cricothyroidotomy). In the neonate, the dimensions of the cricothyroid membrane are too small to allow safe passage of an airway (Navsa et al 2005). Confirmation of the surface anatomy of the hyoid bone, thyroid and cricoid cartilages, and jugular (suprasternal) notch is essential prior to performing a tracheostomy (Ellis et al 2004).

The use of palpable anatomical landmarks in the neck to predict vertebral levels is not infallible, especially when the neck is extended for surgery on the cervical spine. There can be a difference of at least one vertebral level: on-table radiographic confirmation of vertebral level is therefore prudent to avoid removal of the wrong intervertebral disc (Liu, Du et al 2017).

The clavicle is a sigmoid-shaped bone that is normally palpable and is easily visible in individuals of lower body mass. Its medial two-thirds are rounded and convex anteriorly and the lateral third is flat and concave anteriorly. For much of its length, the clavicle may be almost encircled by two fingers, but medially its ligamentous attachments make definition more difficult. The jugular notch on the superior surface of the sternal manubrium lies between the expanded medial ends of the clavicles. The posterior end of the first rib may be felt indistinctly within the floor of the posterior triangle of the neck.

Soft tissues and viscera

Triangles and root of the neck

The neck is divided into anterior and posterior triangles by sternocleidomastoid (**Fig. 33.11**). The anterior triangle may be further subdivided into submental, muscular, carotid and digastric triangles, and the posterior triangle may be divided into occipital and supraclavicular triangles. Above the hyoid bone, the musculature runs in a predominantly horizontal or oblique direction, and below the hyoid it runs in a vertical direction. The muscles forming the boundaries of the subtriangles of the neck are not readily palpable or visible, although they may be landmarked according to their attachment points, e.g. the two bellies of digastric lie along a line from the anterior midline of the chin to the lateral aspect of the hyoid body and then towards the medial surface of the mastoid process.

The root of the neck is the transitional zone between the neck, thorax and upper limbs. Communication with the thorax via the superior thoracic aperture (thoracic inlet) is marked anteriorly by the superior surface of the manubrium. The trachea is palpable in the midline superior to the jugular notch, a region that may also contain the left brachiocephalic vein, especially in the very young and elderly adults. The apices of the lungs are located posterior to the medial third of the clavicle (Mirjalili, Hale et al 2012).

Anterior triangle

The base of the anterior triangle is formed by the inferior border of the mandible and a line from its angle to the mastoid process. The sides are formed by the midline anteriorly and by the anterior border of sternocleidomastoid laterally. By using these borders, several major vessels and lymphatic node groups situated deep to the sternocleidomastoid muscle are not currently located within a triangle of the neck. It would be preferable, therefore, for the posterior border of sternocleidomastoid to form the lateral boundary of the anterior triangle (Ch. 35), especially since the neck triangles are used in the diagnosis and management of regional masses or lumps. The triangle is best palpated bimanually with the examiner standing behind the subject and using both hands to examine the structures within. Inspection reveals the rounded tendinous sternal head of sternocleidomastoid, which arises from the superior part of the anterior surface of the manubrium, and the broader, more vertical clavicular head, which arises from the upper surface of the medial third of the clavicle. The indentation of the lesser supraclavicular fossa sits between the two heads: the fossa contains the internal jugular vein before it joins the subclavian vein posterior to the sternoclavicular joint and therefore represents an access point for central venous cannulation.

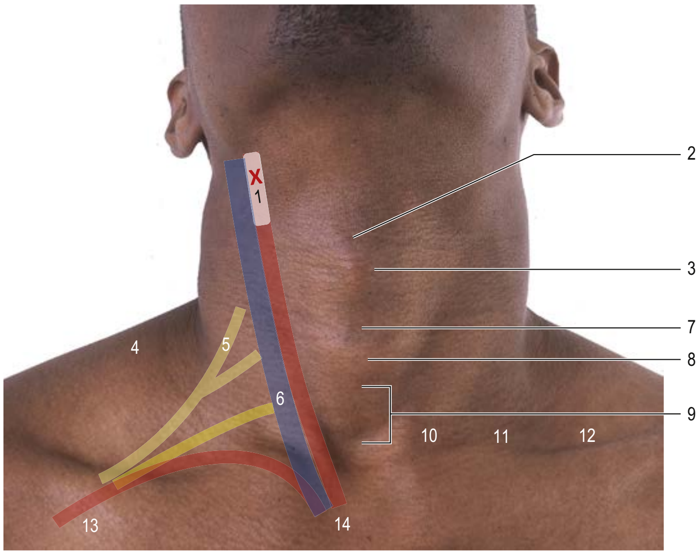

Fig. 33.11 The anterior and posterior triangles of the neck. Key: 1, zone of carotid artery bifurcation (white): usually 0.5–3.0 cm above the level of the thyroid lamina; 2, thyroid notch with thyrohyoid ligament (indented region) above; 3, laryngeal prominence; 4, trapezius; 5, course of brachial plexus (C5 root leading to upper trunk); 6, lesser supraclavicular fossa overlying the internal jugular vein; 7, median cricothyroid ligament; 8, cricoid cartilage; 9, isthmus of thyroid gland; 10, sternal head of sternocleidomastoid; 11, clavicular head of sternocleidomastoid; 12, greater supraclavicular fossa (of posterior triangle); 13, right subclavian artery; 14, right common carotid artery; X (red) carotid bifurcation at the vertebral body of C3. (Adapted with permission from Drake RL, Vogl AW, Mitchell A et al (eds) Gray's Atlas of Anatomy. Elsevier, Churchill Livingstone. Copyright 2008.)

The trachea and its cartilaginous 'rings' may be palpated in the midline inferior to the cricoid cartilage and above the jugular notch. It may be deviated laterally by thyroid masses/growth, atelectasis or tension pneumothorax. The thyroid gland consists of two soft, palpable lobes lying on either side of the lower half of the laminae of the thyroid cartilage and upper part of the trachea, their lower borders extending towards the sternal end of the clavicle on each side. Swallowing may assist palpation of the gland. The lobes are joined by the isthmus (approximately 2 cm wide), which usually sits anterior to the second and third tracheal cartilages; these cartilages may therefore be impalpable.

As a rule, most head and neck lymph node groups are only clinically palpable when enlarged. Lymph nodes above the hyoid bone tend to be distributed in a horizontal plane either on or below the pericraniocervical line, and anterior and posterior to the auricle, whereas the deep cervical nodes run relatively vertically and are related to the internal jugular vein. Enlarged jugulodigastric nodes are palpable in the indented region posterior to the mandibular angle and anterior to sternocleidomastoid. Palpation medial and deep to the inferior border of the mandible can reveal enlarged nodes within the submental and submandibular triangles. Superficial cervical nodes lie adjacent to the external and anterior jugular veins and are landmarked with them.

The submandibular gland is palpable within the submandibular triangle. It extends approximately 2 cm inferior to the inferior border of the posterior part of the body of the mandible and may reach the greater horn of the hyoid bone. Its posterior border is level with the angle of the mandible, from where it extends anteriorly for approximately 4 cm.

Posterior triangle

The posterior triangle is bounded by the posterior border of sternocleidomastoid, the middle third of the superior surface of the clavicle (the base of the triangle), and the anterior margin of trapezius. Its apex is the point where sternocleidomastoid and trapezius approximate at the superior nuchal line. The lower portion of the posterior triangle forms the greater supraclavicular fossa, an important clinical area that lies just above and behind the clavicle at the confluence of the superior thoracic aperture and the opening (aditus) to the axilla and arm. It is best inspected from in front and palpated from behind. Scalenus anterior and medius are palpable as firm masses in the floor of the triangle, posterior to the lower part of sternocleidomastoid. The near-vertical interscalene groove is palpable between them, at or near the level of the vertebral body of C6; it serves as a landmark for the upper trunk of the brachial plexus.

When the greater supraclavicular fossa is inspected, the pulsation of the great veins may be seen if the central venous pressure is raised. The fossa is also a common site in which to feel pathologically enlarged supraclavicular lymph nodes. In particular, cancers of the lung can spread to left- and right-sided nodes, and cancers of the upper gastrointestinal tract can spread to left-sided nodes. The subclavian artery may be felt pulsating as it crosses the first rib, posterior to the medial end of the clavicle, and the upper and middle trunks of the brachial plexus may be felt superior and posterior to the artery. The posterior end of the first rib may be felt as a fullness in the posterior aspect of the fossa. A point approximately 2.5 cm above the middle of the medial third of the clavicle marks the level of the neck of the first rib and is thus the surface marking for the apex of the dome of the cervical pleura and apex of the lung covered by the suprapleural membrane (Sibson's fascia). Any penetrating injury (iatrogenic or otherwise) in this region will run the risk of creating a pneumothorax.

Course of vessels

Carotid arteries

In the neck, the common carotid artery and the internal carotid artery may be represented by an almost straight line passing from the sternoclavicular joint to a point just posterior to the mandibular condyle. The level at which the common carotid artery bifurcates into internal and external carotid arteries is variable (Lo et al 2006). It occurs most commonly level with the vertebral body of C3, but ranges from the level of the vertebral body of C1 to the vertebral body of C5 (Furukawa et al 2012, Mirjalili et al 2012b, Shen et al 2017). Relative to the thyroid cartilage, the bifurcation most commonly sits above the upper border of the lamina by an average of 1.8 cm (Mirjalili et al 2012b, Shen et al 2017). The common carotid artery may be compressed against the prominent transverse process of C6 (the carotid tubercle or Chassaignac's tubercle), which commonly sits lateral to the cricoid cartilage in females and just above this level in males. Above this level, the artery is superficial and its pulsation may be readily felt beneath the anterior border of sternocleidomastoid.

Subclavian artery

The subclavian artery enters the root of the neck behind the sternoclavicular joint. It passes through the inferior part of the palpable interscalene groove and arches upwards to reach a point approximately 2 cm above the clavicle deep to the posterior border of sternocleidomastoid, before passing across the upper surface of the first rib posterior to the midpoint of the clavicle. The subclavian pulse may be palpated posterior to the clavicle at either the lateral border of sternocleidomastoid or where the artery crosses the first rib.

Subclavian and brachiocephalic veins

The subclavian vein sits anterior to the subclavian artery and follows a similar course by passing over the first rib into the root of the neck (inferior neck). It lies closest to the clavicle at the junction of its middle and medial thirds, approximately 7 cm from the midline (Hale et al 2010). The subclavian vein typically joins the internal jugular vein to form the brachiocephalic vein posterior to the sternoclavicular joint (Mirjalili, Hale et al 2012, Pak et al 2017), but other configurations have been described (Keough et al 2016, Shen et al 2016). Subclavian vein cannulation is described in Chapter 35.

Anterior jugular vein

The anterior jugular vein runs downwards from beneath the chin, approximately a finger's breadth from the midline. It turns laterally approximately 2.5 cm from the sternal end of the clavicle and passes beneath sternocleidomastoid to drain into the external jugular vein. The veins of each side join to form the jugular venous arch just above the jugular notch. The anterior jugular vein may be encountered if the operator drifts laterally while creating a surgical airway.

External jugular vein

The external jugular vein lies superficial to sternocleidomastoid and may be represented by a line that starts just below and behind the angle of the mandible and runs to a point close to the lateral extent of the junction of sternocleidomastoid with the clavicle. It drains into the subclavian vein after penetrating the investing layer of deep cervichal fascia and may be kinked at this point. If the proximal part of the vein is damaged, it may be held open by the surrounding fascia, and air may then be sucked in during breathing, resulting in an air embolus. The external jugular vein can be distended if venous pressure is raised, e.g. by performing a Valsalva manoeuvre (forced expiration against a closed glottis and mouth, and blocked nostrils), by supraclavicular digital pressure or if the vessel is kinked.

Internal jugular vein

The internal jugular vein runs in the carotid sheath, lying just lateral or anterolateral to the pulsating carotid arteries. It therefore has similar surface markings to those described for the common and internal carotid arteries and is represented by a broad band passing from just medial to the mastoid process to the sternoclavicular joint, where it joins the subclavian vein (Mirjalili et al 2012a). The inferior bulb of the internal jugular vein lies in the lesser supraclavicular fossa (the depression between the sternal and clavicular heads of sternocleidomastoid), where it may be accessed for central vein cannulation. In children under the age of 5 years, the vein is less than 1 cm deep to skin (Roth et al 2008). The jugular venous pulse reflects the jugular venous pressure (central venous pressure) and may be used as a measure of cardiac function. Pulsation of the great veins may be seen in this region if the central venous pressure is raised (e.g. right-sided heart failure). Internal jugular vein cannulation is described in Chapter 35.

Course of nerves

Accessory nerve

The approximate course of the (spinal) accessory nerve can be mapped by dividing sternocleidomastoid into thirds and drawing a line from the junction of the upper and middle thirds to a point on the anterior border of trapezius about 5 cm above the clavicle: both points vary considerably. The nerve emerges from the posterior border of sternocleidomastoid approximately 6.5 cm (range 3–10 cm) below the tip of the mastoid process. It commonly sits 1.5 cm (range 0–3.8 cm) above the point at which the great auricular nerve passes around the posterior border of the muscle (Salgarelli et al 2009). It crosses the posterior triangle and penetrates the anterior border of trapezius approximately 4.5 cm (range 1–10 cm) above the clavicular insertion of trapezius (Symes and Ellis 2005, Mirjalili et al 2012c). Accessory nerves usually divide into 2–4 branches prior to trapezius.

Cervical plexus

The cutaneous branches of the cervical plexus emerge from behind the posterior border of the middle third of sternocleidomastoid, commonly up to 2 cm inferior to the accessory nerve (Mirjalili et al 2012c) (see Figs 33.8B, 33.10). The greater auricular point (emergence of the greater auricular nerve from the posterior border of sternocleidomastoid) usually sits above the midpoint of sternocleidomastoid, around 6.0 ± 1.4 cm from the mastoid process tip (Raikos et al 2017). The great auricular nerve can be damaged during rhytidectomy. It passes towards the lobule of the auricle and the angle of the mandible, crossing superficial to sternocleidomastoid approximately 6.5 cm below the lower border of the external acoustic meatus; the external jugular vein sits approximately 0.5 cm anteriorly at this position (McKinney and Katrana 1980).

Brachial plexus

The roots and trunks of the brachial plexus can be represented by a line passing between the midpoint of the posterior border of sternocleidomastoid and the midpoint of the clavicle. In thin individuals, the scalene muscles are visible when the head is laterally flexed to the contralateral side; the roots/upper trunk are palpable in the almost vertical interscalene groove, which is located posterior to scalenus anterior. The trunks lie in the lower part of the posterior triangle of the neck, and the divisions lie behind the clavicle near the lateral border of the first rib. Normally the cords enter the axilla above the first part of the subclavian artery, closely surround its second part, and give off branches around the third part.

Cervical sympathetic ganglia

The superior cervical ganglion lies slightly anterior to the (palpable) transverse process of C2 (axis). The middle cervical ganglion, when present, lies just anterior to the transverse process of C6 (the tubercle of this vertebra is palpable in the anterior neck, often lateral to the cricoid cartilage). The inferior cervical ganglion may be fused with the first thoracic cervical ganglion, forming the stellate or cervicothoracic ganglion. Stellate ganglion block is often used to perform a sympathetic nerve block to the head and neck or to the arm (Ellis et al 2004).

Bonus e-book content

Fig. 33.1 **B**, Sagittal oblique maximum intensity projection (MIP) slab view of the left external carotid artery and some of its branches reconstructed from a CT carotid angiogram. **C**, Coronal oblique MIP view of the right thyrocervical trunk reconstructed from a CT carotid angiogram.

Fig. 33.2 **B**, Sagittal oblique maximum intensity projection view of the right vertebral artery reconstructed from a CT carotid angiogram.

Fig. 33.3 **B**, A volume rendered CT of the head and neck with intravenous contrast medium showing the superficial veins.

Fig. 33.10, The distribution of the cutaneous branches of the trigeminal nerve and of the cervical plexus, and the motor branches of the facial nerve in the face and neck.

Key references

Behnia H, Kheradvar A, Shahrokhi M 2000 An anatomic study of the lingual nerve in the third molar region. J Oral Maxillofac Surg 58:649–51.

The intimate relationship of the lingual nerve to the lower third molar region is a significant factor in the morbidity associated with third molar extractions. This extensive cadaver study reported that in 14% of patients the lingual nerve was located above the lingual crest and that in 22% the nerve was in direct contact with the lingual plate of the alveolar process.

Day JD, Tschabitscher M 1998 Anatomic position of the asterion. Neurosurgery 42:198–9.

The asterion has been used as a landmark in lateral approaches to the posterior fossa. It is not strictly reliable in terms of locating the underlying posterior fossa dura but it does lie directly over the transverse–sigmoid sinus complex. Caution must therefore be taken when placing burr-holes to avoid damage to the venous sinuses with potentially very serious consequences.

Hale SJ, Mirjalili SA, Stringer MD 2010 Inconsistencies in surface anatomy: the need for an evidence-based reappraisal. Clin Anat 23:922–30.

An argument that an evidence-based framework is essential if surface anatomy is to be accurate and clinically relevant.

References

Auerbach JD, Weidner Z, Pill SG et al 2009 The mandibular angle as a landmark for identification of cervical spinal level. Spine 34:1006–11.

Badshah M, Soames R, Ibrahim M et al 2017, Surface anatomy of major anatomical landmarks of the neck in an adult population. Clin Anat 30:781–7.

Balcioglu HA, Kilic C, Akyol M et al 2011 Horizontal migration of pre- and postnatal mental foramen: an anatomic study. Int J Pediatr Otorhinolaryngol 75:1436–41.

Batra APS, Mahajan A, Gupta K 2010 Marginal mandibular branch of the facial nerve: an anatomical study. Indian J Plast Surg 43:60–4.

Behnia H, Kheradvar A, Shahrokhi M 2000 An anatomic study of the lingual nerve in the third molar region. J Oral Maxillofac Surg 58:649–51.

The intimate relationship of the lingual nerve to the lower third molar region is a significant factor in the morbidity associated with third molar extractions. This extensive cadaver study reported that in 14% of patients the lingual nerve was located above the lingual crest and that in 22% the nerve was in direct contact with the lingual plate of the alveolar process.

Bosenberg AT, Kimble FW 1995 Infraorbital nerve block in neonates for cleft lip repair: anatomical study and clinical application. Br J Anaesth 74:506–8.

Charalampidou M, Kjellberg H, Georgiakaki I et al 2008 Masseter muscle thickness and mechanical advantage in relation to vertical craniofacial morphology in children. Acta Odontol Scand 66:23–30.

Chowdhry S, Yoder EM, Cooperman RD et al 2010 Locating the cervical motor branch of the facial nerve: anatomy and clinical application. Plast Reconstr Surg 126:875–9.

Chrcanovic BR, Abreu MH, Custódio AL 2011 A morphometric analysis of supraorbital and infraorbital foramina relative to surgical landmarks. Surg Radiol Anat 33:329–35.

Davies JC, Fattah A, Ravichandiran M et al 2012 Clinically relevant landmarks of the frontotemporal branch of the facial nerve: a three-dimensional study. Clin Anat 25:858–65.

Davies JC, Ravichandiran M, Agur A et al 2016 Evaluation of clinically relevant landmarks of the marginal mandibular branch of the facial nerve: a three–dimensional study with application to avoiding facial nerve palsy. Clin Anat 29:151–6.

Day JD, Tschabitscher M 1998 Anatomic position of the asterion. Neurosurgery 42:198–9.

The asterion has been used as a landmark in lateral approaches to the posterior fossa. It is not strictly reliable in terms of locating the underlying posterior fossa dura but it does lie directly over the transverse–sigmoid sinus complex. Caution must therefore be taken when placing burr-holes to avoid damage to the venous sinuses with potentially very serious consequences.

Ellis H, Feldman S, Harrop-Griffiths W 2004 Anatomy for Anaesthetists, 8th ed. Oxford: Blackwell Science.

Fishel D, Buchner A, Hershkowith A et al 1976 Roentgenologic study of the mental foramen. Oral Surg Oral Med Oral Pathol 41:682–6.

Furukawa S, Wingenfeld L, Takaya A et al 2012 Morphological variation of the carotid artery bifurcation level. Open Access Scientific Reports 1:135. doi:10.4172/scientificreports.135.

Greyling LM, Glanvill R, Boon JM et al 2007 Bony landmarks as an aid for intraoperative facial nerve identification. Clin Anat 20:739–44.

Hale SJ, Mirjalili SA, Stringer MD 2010 Inconsistencies in surface anatomy: the need for an evidence-based reappraisal. Clin Anat 23:922–30.

An argument that an evidence-based framework is essential if surface anatomy is to be accurate and clinically relevant.

Jaffar AA, Hamadah HJ 2003 An analysis of the position of the greater palatine foramen. J Basic Med Sci 3:24–32.

Katakami K, Mishima A, Shiozaki K et al 2008 Characteristics of accessory mental foramina observed on limited cone-beam computed tomography images. J Endod 34:1441–5.

Keough N, Mirjalili SA, Suleman FE et al 2016 The thoracic surface anatomy of adult black South Africans: a reappraisal from CT scans. Clin Anat 29:1018–24.

Liu WM, Chen Q, Liang Y et al 2017 Surgical landmark of mandible angle in the identification of cervical spinal level. J Craniofac Surg 28(6):1582–5.

Liu J, Du L, Xiong X et al. 2017 Radiographic evaluation of the reliability of neck anatomic structures as anterior cervical surgical landmarks. World Neurosurg 103:133–7.

Lo A, Oehley M, Bartlett A et al 2006 Anatomical variations of the common carotid artery bifurcation. ANZ J Surg 76:970–2.

Ma S, Baillie LJ, Stringer MD 2012 Reappraising the surface anatomy of the pterion and its relationship to the middle meningeal artery. Clin Anat 25:330–9.

Mbajiorgu EF, Ekanem AU 2000 A study of the position of the mandibular foramen in adult black Zimbabwean mandibles. Cent Afr J Med 46:184–90.

McKinney P, Katrana DJ 1980 Prevention of injury to the great auricular nerve during rhytidectomy. Plast Reconstr Surg 66:675–9.

Menke RA, Gowgiel JM 1979 Short-needle block anesthesia at the mandibular foramen. J Am Dent Assoc 99:27–30.

Mirjalili SA, Hale SJ, Buckenham T et al 2012a A reappraisal of adult thoracic surface anatomy. Clin Anat 25:827–34.

Mirjalili SA, McFadden SL, Buckenham T et al 2012b Vertebral levels of key landmarks in the neck. Clin Anat 25:851–7.

Mirjalili SA, Muirhead JC, Stringer MD 2012c Ultrasound visualization of the spinal accessory nerve in vivo. J Surg Res 175:e11–16.

Mraiwa N, Jacobs R, Van Cleynenbreugel J et al 2004 The nasopalatine canal revisited using 2D and 3D CT imaging. Dentomaxillofac Radiol 33:396–402.

Navsa N, Tossel G, Boon JM 2005 Dimensions of the neonatal cricothyroid membrane – how feasible is a surgical cricothyroidotomy? Paediatr Anaesth 15:402–6.

Nicholson ML 1985 A study of the position of the mandibular foramen in adult human mandible. Anat Rec 212:110–2.

Nowinski WL, Chua BC, Johnson A et al 2013 Three-dimensional interactive and stereotactic atlas of head muscles and glands correlated with cranial nerves and surface and sectional neuroanatomy. J Neurosci Methods 215:12–18.

Nowinski WL, Thaung TS, Chua BC et al 2015 Three-dimensional stereotactic atlas of the adult human skull correlated with the brain, cranial nerves, and intracranial vasculature. Neuroradiol J 28:190–7.

Pak N, Patel SG, Hashemi Taheri AP et al 2017 A reappraisal of adult thoracic and abdominal surface anatomy in Iranians in vivo using computed tomography. Clin Anat 29:191–6.

Rahmah NN, Murata T, Yako T et al 2011 Correlation between squamous suture and Sylvian fissure: OSIRIX DICOM viewer study. PLoS One 6:e18199.

Raikos A, English T, Yousif AK et al 2017 Topographic anatomy of the great auricular point: landmarks for its localization and classification. Surg Radiol Anat 39:535–40.

Raschke R, Hazani R, Yaremchuk MJ 2013 Identifying a safe zone for midface augmentation using anatomic landmarks for the infraorbital foramen. Aesthet Surg J 33:13–18.

Roth B, Marciniak B, Engelhardt T et al 2008 Anatomic relationship between the internal jugular vein and the carotid artery in preschool children – an ultrasonographic study. Paediatr Anaesth 18:752–6.

Salgarelli AC, Landini B, Bellini P et al 2009 A simple method of identifying the spinal accessory nerve in modified radical neck dissection: anatomic study and clinical implications for resident training. Oral Maxillofac Surg 13:69–72.

Shen XH, Su BY, Liu JJ et al 2016 A reappraisal of adult thoracic and abdominal surface anatomy via CT scan in Chinese population Clin Anat 29:165–74.

Shen XH, Xue HD, Chen Y et al 2017 A reassessment of cervical surface anatomy via CT scan in an adult population. Clin Anat 30:330–5.

Sheng B, Lv F, Xiao Z et al 2012 Anatomical relationship between cranial surface landmarks and venous sinus in posterior cranial fossa using CT angiography. Surg Radiol Anat 34:701–8.

Stringer MD, Mirjalili SA, Meredith SJ et al 2012 Redefining the surface anatomy of the parotid duct: an in vivo ultrasound study. Plast Reconstr Surg 130:1032–7.

Sujatha N, Manjunath KY, Balasubramanyam V 2005 Variations of the location of the greater palatine foramina in dry human skulls. Indian J Dent Res 16:99–102.

Symes A, Ellis H 2005 Variations in the surface anatomy of the spinal accessory nerve in the posterior triangle. Surg Radiol Anat 27:404–8.

Tomaszewska A, Kwiatkowska B, Jankauskas R 2012 The localization of the supraorbital notch or foramen is crucial for headache and supraorbital neuralgia avoiding and treatment. Anat Rec 295:1494–1503.

Toure G, Foy J-P, Vacher C 2015 Surface anatomy of the parotid duct and its clinical relevance. Clin Anat 28:455–9.

Udhaya K, Saraladevi KV, Sridhar J 2013 The morphometric analysis of the mental foramen in adult dry human mandibles: a study on the South Indian population. J Clin Diagn Res 7:1547–51.

Ukoha U, Oranusi CK, Okafor JI et al 2013 Anatomic study of the pterion in Nigerian dry human skulls. Niger J Clin Pract Online 16:325–8.

von Arx T, Friedli M, Sendi P et al 2013 Location and dimensions of the mental foramen: a radiographic analysis by using cone-beam computed tomography. J Endod 39:1522–8.

Wang TM, Kuo KJ, Shih C et al 1988 Assessment of the relative locations of the greater palatine foramen in adult Chinese skulls. Acta Anat (Basel) 132:182–6.

CHAPTER 34

The skull

The skull is the bony skeleton of the head. It houses the brain, the organs of special sense, and the upper parts of the respiratory and digestive systems and provides attachments for many of the muscles of the head and neck. Movement is restricted and is found only in relation to the mandible at the temporomandibular joint and at the atlanto-occipital joint for movement of the head in relation to the neck.

The skull consists of the neurocranium, viscerocranium (facial skeleton) and mandible. The neurocranium may be subdivided into the calvaria (sometimes called the cranial vault) and the basicranium (also known as the cranial base). The neurocranium encloses the brain, intracranial portions of the cranial nerves, blood vessels, meninges and cerebrospinal fluid. Its walls are formed by parts of the frontal, ethmoid, parietal, sphenoid, temporal and occipital bones. The viscerocranium hangs down from the front of the neurocranium and houses the organs of sight, smell and taste, as well as the openings to the respiratory and digestive systems via the nose and mouth, respectively.

Internally, the cranial base can be divided into three regions corresponding to the floor of the anterior, middle and posterior cranial fossae. In clinical parlance, the terms skull base and cranial base are frequently used as though they are synonymous. Indeed, inspection of the inferior surface of a skull confirms that the middle and posterior cranial bases are the same as the middle and posterior skull bases. However, the anterior cranial base and the anterior skull base should not be used interchangeably because the anterior skull base includes the inferior surface of the facial skeleton, whereas the internal surface of the anterior cranial base is the floor of the anterior cranial fossa and may be further subdivided into a midline (central) and two lateral parts. During development, the parts of the skull where the bones are derived by endochondral ossification constitute the chondrocranium; the remaining bones are derived by intramembranous ossification.

The skull is the most complex bony structure in the body. The young adult skull is composed of an average of 28 separate bones, many of which are paired; some in the median plane are single, though symmetric. Most of the vault bones are flat and consist of two tables or plates of compact bone enclosing a narrow layer of relatively dense cancellous marrow (diploic bone). The marrow within the skull bones is a site of haemopoiesis, at least in the young individual. These bones form by intramembranous ossification of a highly vascular connective tissue membrane and have often been referred to as 'dermal' in deference to their alleged ancient phylogenetic origin. The inner table is thinner and more brittle while the outer tends to be thicker and more resilient; this is important to remember when examining fractures to the skull caused by either blunt or sharp trauma. This bone type is also of considerable value in cranial bone grafting in the young, where the two tables can be split to produce an autograft for use in maxillofacial reconstruction. The skull bones vary in thickness in different regions, with the bones of the viscerocranium being rather delicate and therefore particularly susceptible to fracture.

The majority of bones in the skull articulate via fibrous joints called sutures, which facilitate growth rather than movement in the developing skull. The three main sutural morphologies reflect the magnitude of strain placed on them. Thus, the margins of adjacent bones of a suture may be smooth and meet end to end, giving a simple (butt-end) suture (e.g. median palatine suture); may be bevelled, so that the border of one bone overlaps the other (e.g. parietotemporal suture); or may present numerous projections that interlock, giving a serrated jigsaw appearance (e.g. lambdoid suture). The complexity of serrated sutures increases from the inner to the outer surface. Fusion across sutures (synostosis) can start early in the third decade, although its variability precludes using this information to assess age with any degree of accuracy. The process of fusion starts on the internal surface of the cranium first and proceeds externally; the coronal and sagittal sutures are often the first to display synostosis. By middle age, many of the larger sutures will show evidence of synostosis, although there are some that rarely show fusion, e.g. the zygomaticofacial. Premature fusion of sutures during the early growth phase of the skull (craniosynostosis) results in various abnormalities.

The bones forming the base of the skull also play an important role in the overall growth of the face and the neurocranium. They develop mainly via endochondral ossification and the joints between most of them are primary cartilaginous joints. One of the most important is the spheno-occipital synchondrosis, between the body of the sphenoid anteriorly and the basilar part of the occipital bone posteriorly; fusion between them is generally completed between 13 and 18 years of age. Other joints include the occipital synchondroses and the jugular growth plate (or petro-exoccipital articulation).

The two sites of synovial articulation associated with the exterior of the skull are the temporomandibular joint (between the glenoid fossa of the temporal bone and the condylar process of the mandible) and the atlanto-occipital joint (between the condyles of the occipital bone and the superior articular facets of the atlas). Movement at these joints does not facilitate rotation but participates in flexion and extension in the anteroposterior plane and bilateral flexion in the transverse plane.

Many important neurological and vascular structures enter and exit the skull via foramina. The skull is often fractured following direct trauma. In addition to the main foramina, irregular emissary foramina allow veins situated externally on the face and scalp to communicate with those lying intracranially; spread of infection along these routes may have serious clinical consequences (e.g. cavernous sinus thrombosis).

In the account of the skull that follows, only generalized standard views will be considered. A more detailed account of each individual bone will be found associated with the relevant regional text (Berkovitz and Moxham 1994).

FRONTAL (ANTERIOR) VIEW

Viewed from the front, the skull is generally ovoid in shape and is wider above than below (Fig. 34.1). The upper part is formed by the frontal bone, which underlies the forehead region above the orbits. Superomedial to each orbit is a rounded superciliary arch (more pronounced in males), between which there may be a median elevation, the glabella. The glabella may show the remains of the interfrontal (metopic) suture, which usually closes in the first postnatal year (Weinzweig et al 2003) but persists in a small percentage of adult skulls in various ethnic groups. A retained interfrontal suture is usually present in the inferior portion of the suture, a feature known as metopism. The frontal bone articulates with the two nasal bones at the frontonasal sutures, which is marked by a depression at the root of the nose; the point at which the frontonasal and internasal sutures meet is the anthropometric landmark known as the nasion.

The upper part of the face is occupied by the orbits and the bridge of the nose. Each orbital opening is roughly quadrangular in shape, although this can differ depending on ancestral origin (Ch. 44). The upper, supraorbital, margin is formed entirely by the frontal bone, interrupted at the junction of its sharp lateral two-thirds and rounded medial third by the supraorbital notch or foramen, which transmits the supraorbital vessels and nerve. The lateral margin of the orbit is formed largely by the frontal process of the zygomatic bone and is completed above by the zygomatic process of the frontal bone; the frontozygomatic suture between them lies in a palpable depression. The infraorbital margin is formed by the zygomatic bone laterally and the maxilla medially. Both lateral and infraorbital margins are sharp and palpable. The medial margin of the orbit is formed above by the frontal bone and below by the lacrimal crest of the frontal process of the maxilla.

The central part of the face is occupied mainly by the paired maxillae, separated by the anterior nasal aperture. Each maxilla contributes to the upper jaw, the floor and medial wall of the orbital cavity, the lateral wall of the nose, the floor of the nasal aperture and the bone of the cheek. The anterior nasal spine marks the upper limit of the intermaxillary suture at the lower margin of the anterior nasal aperture and is palpable in the nasal septum. The infraorbital foramen transmits the infraorbital vessels and nerve and lies about 1 cm below the middle of the infraorbital margin. The maxillary alveolar process bears the upper teeth. The short, thick zygomatic process of the maxilla has an oblique upper surface that

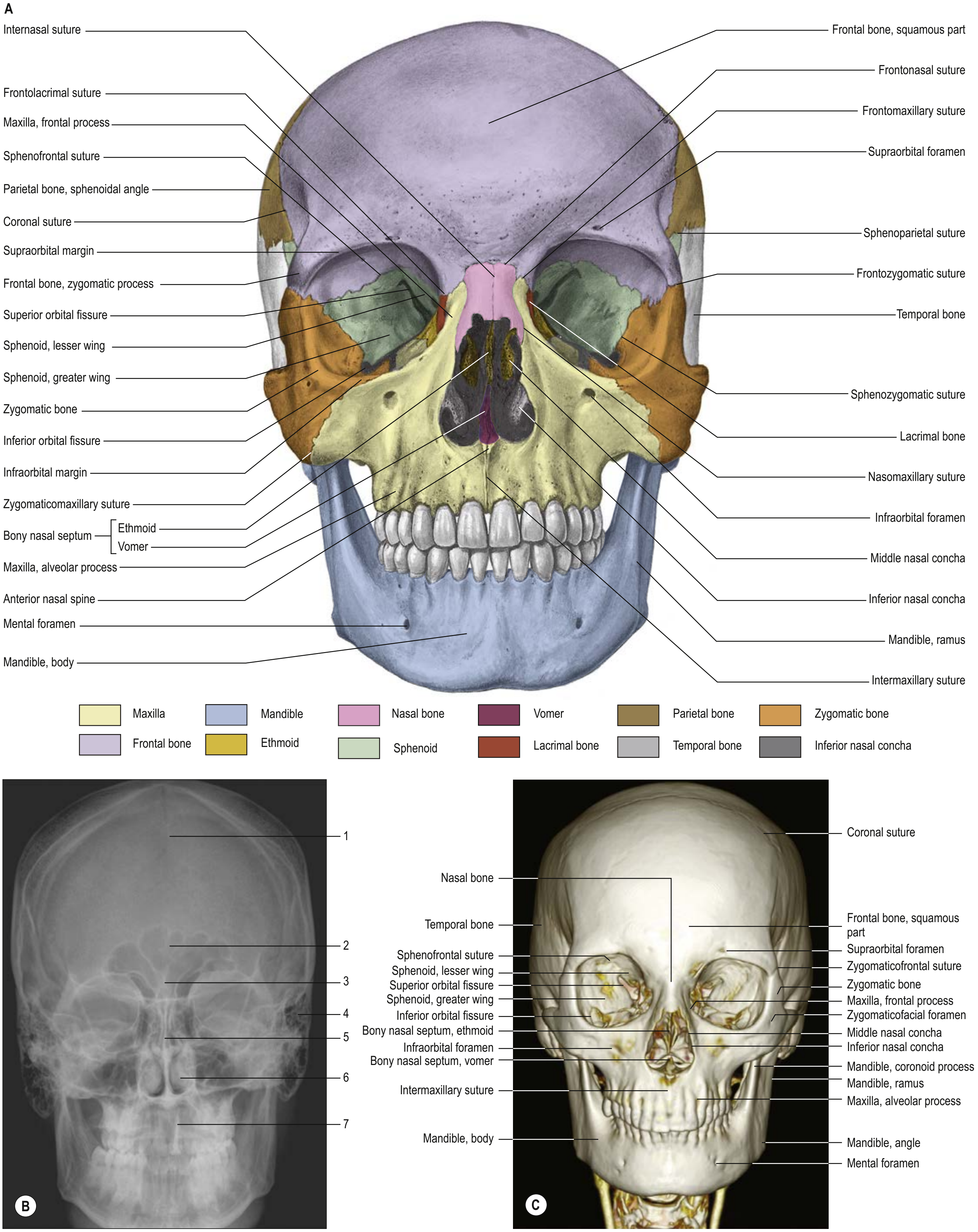
A
Internasal suture
Frontolacrimal suture
Maxilla, frontal process
Sphenofrontal suture
Parietal bone, sphenoidal angle
Coronal suture
Supraorbital margin
Frontal bone, zygomatic process
Superior orbital fissure
Sphenoid, lesser wing
Sphenoid, greater wing
Zygomatic bone
Inferior orbital fissure
Infraorbital margin
Zygomaticomaxillary suture
Bony nasal septum
Ethmoid
Vomer
Maxilla, alveolar process
Anterior nasal spine
Mental foramen
Mandible, body
Frontal bone, squamous part
Frontonasal suture
Frontomaxillary suture
Supraorbital foramen
Sphenoparietal suture
Frontozygomatic suture
Temporal bone
Sphenozygomatic suture
Lacrimal bone
Nasomaxillary suture
Infraorbital foramen
Middle nasal concha
Inferior nasal concha
Mandible, ramus
Intermaxillary suture
Maxilla
Mandible
Nasal bone
Vomer
Parietal bone
Zygomatic bone
Frontal bone
Ethmoid
Sphenoid
Lacrimal bone
Temporal bone
Inferior nasal concha
B
1
2
3
4
5
6
7
C
Nasal bone
Temporal bone
Sphenofrontal suture
Sphenoid, lesser wing
Superior orbital fissure
Sphenoid, greater wing
Inferior orbital fissure
Bony nasal septum, ethmoid
Infraorbital foramen
Bony nasal septum, vomer
Intermaxillary suture
Mandible, body
Coronal suture
Frontal bone, squamous part
Supraorbital foramen
Zygomaticofrontal suture
Zygomatic bone
Maxilla, frontal process
Zygomaticofacial foramen
Middle nasal concha
Inferior nasal concha
Mandible, coronoid process
Mandible, ramus
Maxilla, alveolar process
Mandible, angle
Mental foramen

Fig. 34.1 **A**, The bones of the adult skull, frontal aspect. **B**, An anteroposterior radiograph of the skull and upper cervical spine, young adult. Key: 1, sagittal suture; 2, frontal sinus; 3, crista galli; 4, mastoid air cells; 5, nasal septum; 6, inferior concha; 7, dens of axis. **C**, Volume rendered CT of the head with an anteroposterior view of the skull. (A, Sobotta Atlas of Human Anatomy © Elsevier GmbH, Urban & Fischer, Munich.)

articulates with the zygomatic bone at the zygomaticomaxillary suture. The frontal process of the maxilla ascends posterolateral to the nasal bone to articulate with it medially, the frontal bone superiorly and the lacrimal bone laterally.

The anterior nasal aperture is piriform in shape, wider below than above and bounded by the paired nasal bones and maxillae. The upper boundary of the aperture is formed by the nasal bones while the remainder is formed by the maxillae. In life, several cartilages (septal, lateral nasal, major and minor alar) help to delineate two nasal cavities. The shape of these bones can be used quite successfully to predict the shape of the cartilaginous nose in forensic facial reconstructions (Wilkinson and Rynn 2012).

The lower part of the face, below the external nose, is formed from the alveolar arch of the maxillae and the upper dentition, and the body and alveolar process of the mandible and the lower dentition. In the midline, the mental protuberance produces the characteristic prominence of the chin. The mental foramen, which transmits the mental nerve and accompanying vessels, lies in the same vertical plane as the supraorbital and infraorbital foramina.

Anteroposterior radiographs of the skull clearly show the central location of the paranasal air sinuses in the frontal bone, maxilla and ethmoid. The sinuses exhibit wide anatomical variations which can be useful indicators of identity when postmortem images are compared with antemortem clinical films.

POSTERIOR VIEW

The parietal, temporal and occipital bones form the entirety of the posterior view (Fig. 34.2). The superolateral region is occupied by the parietal bones, the mastoid region of the temporal bones makes up the inferolateral regions, and the central portion is occupied by the squamous portion of the occipital bone, which is the reason why this aspect is also referred to as the occipital view. The parietal bones articulate with the occipital bone at the lambdoid suture, which extends inferiorly into the occipitomastoid and the parietomastoid sutures behind and above the mastoid processes, respectively. The lambda is the anthropometric point where the occipital bone meets the two parietal bones. Accessory sutural bones (or wormian bones) are islands of bone that may be found within a suture. They may arise from separate centres of ossification and they appear to have no clinical significance, being of genetic rather than pathological aetiology; their initial formation is thought to be caused by a degree of dural strain and increased sutural width (Bellary et al 2013). They are most frequent in the lambdoid suture, which is the most tortuous of the sutures. However, they are also often observed within the sagittal and coronal sutures. A large, central interparietal bone is not uncommon and is sometimes referred to as an Inca bone (see Fig. 34.2). Wormian bones are considered to be markers for various congenital diseases, including osteogenesis imperfecta and cleidocranial dysostosis.

The external occipital protuberance is a midline elevation on the occipital bone that can become particularly well developed and palpable in males and is a marker for sex estimation. The location of the protuberance coincides with the anthropometric inion. Superior nuchal lines extend laterally from the protuberance and represent the boundary between the scalp and the neck. Inferior nuchal lines run parallel to, and below, the superior nuchal lines; a set of highest nuchal lines may sometimes develop above the superior lines. The external occipital protuberance, nuchal lines and roughened external surface of the occipital bone between the nuchal lines afford attachment to the muscles of the neck.

SUPERIOR VIEW

Seen from above, the contour of the calvaria varies greatly but is usually ellipsoid, or more strictly, a modified ovoid with its greatest width lying nearer to the occipital pole (Fig. 34.3). Four bones constitute this view and articulate via three well-defined sutures. The squamous part of the frontal bone is anterior, the squamous part of the occipital bone is posterior, and the two parietal bones meet in the midline separating the frontal from the occipital bone. The maximal parietal convexity on each site is palpable at the parietal tuber or eminence; it is most conspicuous in the female (retention of a paedomorphic appearance). The superior and inferior temporal lines run close to the parietal eminence but are best seen in a lateral view.

The coronal suture marks the articulation between the posterior margin of the frontal bone and the anterior margins of the two parietal bones. It descends across the calvaria and projects inferiorly until it meets the junction between the greater wing of the sphenoid and the squamous temporal bone at the pterion. The sagittal suture runs in the midline between the two parietal bones and extends from the bregma anteriorly to the lambda posteriorly. The lambdoid suture delineates the articulation between the posterior borders of the right and left parietal bones and the superior border of the occipital bone.

The bregma represents the position of the anterior fontanelle in the young child. This diamond-shaped, membrane-filled space located between the two frontal and two parietal bones of the developing fetal skull persists until approximately 18 months after birth. A depression can sometimes be found posterior to the bregma (post-bregmatic depression) and is often used as an indicator of sub-Saharan African ancestral origin. The lambda, at the junction of the sagittal and lambdoid sutures, represents the site of the posterior fontanelle, which persists for the first 2–3 months after birth.

A parietal foramen may pierce either or both parietal bones near the sagittal suture about 3.5 cm anterior to the lambda. It transmits a small emissary vein from the superior sagittal sinus. The vertex is the highest point on the skull and it usually occupies a position in the middle third of the sagittal suture.

LATERAL VIEW

The skull, viewed from the side, can be subdivided into three zones: face (anterior), temporal region (middle) and occipital region (posterior)

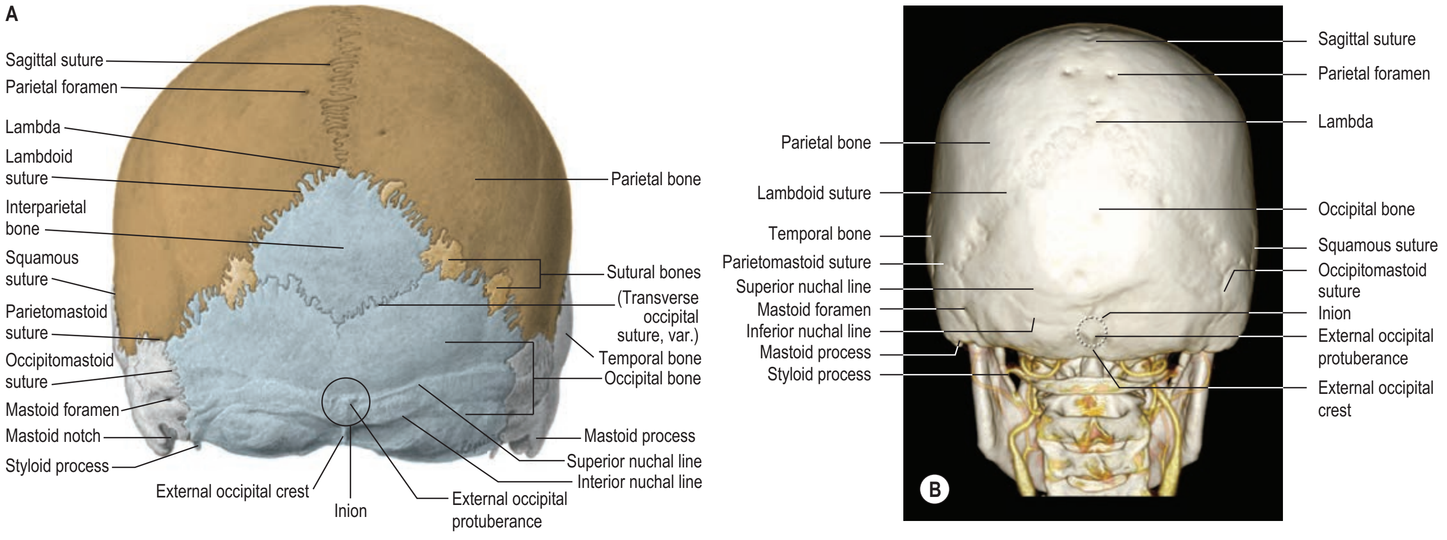
A
Sagittal suture
Parietal foramen
Lambda
Lambdoid suture
Interparietal bone
Squamous suture
Parietomastoid suture
Occipitomastoid suture
Mastoid foramen
Mastoid notch
Styloid process
External occipital crest
Inion
External occipital protuberance
Interior nuchal line
Superior nuchal line
Mastoid process
Occipital bone
Temporal bone
(Transverse occipital suture, var.)
Sutural bones
Parietal bone
Parietal bone
Lambdoid suture
Temporal bone
Parietomastoid suture
Superior nuchal line
Mastoid foramen
Inferior nuchal line
Mastoid process
Styloid process
B
Sagittal suture
Parietal foramen
Lambda
Occipital bone
Squamous suture
Occipitomastoid suture
Inion
External occipital protuberance
External occipital crest

Fig. 34.2 **A**, The bones of the adult skull, posterior aspect. **B**, Volume rendered CT of the head with a posteroanterior view of the skull. (A, Sobotta Atlas of Human Anatomy © Elsevier GmbH, Urban & Fischer, Munich.)

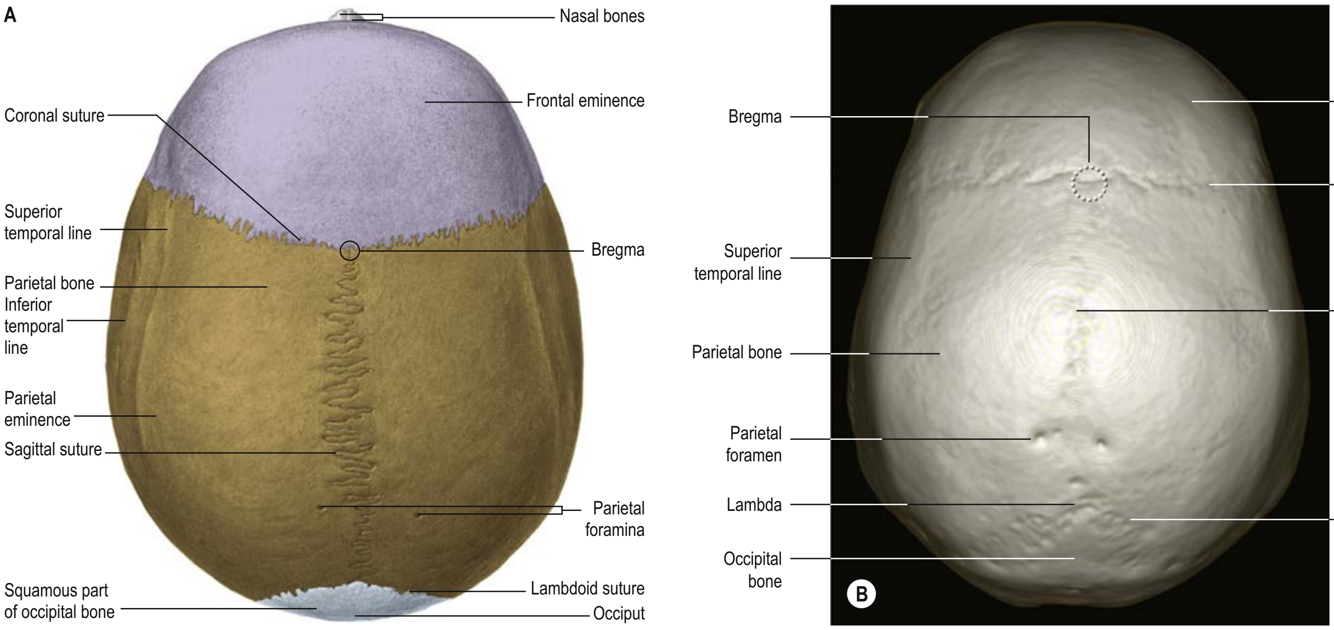

Fig. 34.3 **A**, The bones of the adult skull, superior aspect. **B**, Volume rendered CT of the head with a superior view of the skull. (A, Sobotta Atlas of Human Anatomy © Elsevier GmbH, Urban & Fischer, Munich.)

(Fig. 34.4). The face has been considered in the section on the anterior view of the skull.

The temporal region can be divided into an upper temporal fossa and a lower infratemporal fossa, separated by the position of the zygomatic arch. The upper temporal fossa is bounded inferiorly by the zygomatic arch, superiorly and posteriorly by the temporal lines, and anteriorly by the frontal process of the zygomatic bone. It is continuous inferiorly with the infratemporal fossa deep to the zygomatic arch. The temporal lines often present anteriorly as distinct ridges but become much less prominent as they arch posteriorly across the parietal bone. The inferior temporal line becomes more prominent as it curves down the posterior part of the squamous temporal bone, forming a supramastoid crest at the base of the mastoid process. The superior temporal line gives attachment to the temporal fascia while the inferior temporal line provides attachment for temporalis.

The floor of the temporal fossa is formed by the frontal and parietal bones superiorly and the greater wing of the sphenoid and squamous part of the temporal bone inferiorly. All four bones of one side meet at a roughly H-shaped sutural junction called the pterion. This is an important anthropometric landmark because it commonly overlies both the anterior branch of the middle meningeal artery and the lateral fissure of the cerebral hemisphere (Ma et al 2012). The pterion corresponds to the site of the anterolateral (sphenoidal) fontanelle of the neonatal skull, which closes in the third month after birth.

The vertical suture between the sphenoid and temporal bones, the sphenosquamosal suture, is formed by articulation between the posterior border of the greater wing of the sphenoid and the anterior border of the squamous part of the temporal bone.

The lateral surface of the ramus of the mandible will be described briefly here because it lies within the middle region of this view of the skull. The ramus is a plate of bone projecting upwards from the body of the mandible; its lateral surface gives attachment to masseter. The ramus bears two prominent processes superiorly, the coronoid process anteriorly and the condylar process posteriorly, separated by the mandibular notch. The coronoid process is the site of insertion of temporalis; the condylar process articulates with the mandibular (glenoid) fossa of the temporal bone at the temporomandibular joint. The inferior and posterior borders of the mandible meet at the angle; it is more commonly splayed in the male, reflecting the larger site of attachment for medial pterygoid on the internal surface.

The zygomatic arch stands proud of the rest of the skull, and the temporal and infratemporal fossae communicate via the gap thus created. In life, this space is largely filled by temporalis. The zygomatic bone is the principal bone of the cheek together with the zygomatic processes of the maxilla and temporal bones. The term 'zygomatic arch' is generally restricted to the temporal process of the zygomatic bone and the zygomatic process of the temporal bone, which articulate at the zygomaticotemporal suture. The suture between the zygomatic process of the frontal bone and the frontal process of the zygomatic bone is the frontozygomatic suture; the suture between the maxillary margin of the zygomatic bone and the zygomatic process of the maxilla is the zygomaticomaxillary suture; and the suture between the sphenoid and zygomatic bones is the sphenozygomatic suture. As the zygomatic process of the temporal bone passes posteriorly, it widens to form the articular eminence (tubercle) of the mandibular fossa anteriorly.

The temporal bone is a prominent structure on the lateral aspect of the skull. Its squamous part lies in the floor of the upper temporal fossa and its zygomatic process contributes to the structure of the cheek. Additional components visible in the lateral view of the skull are the mandibular fossa and its articular eminence, the tympanic plate, the external acoustic meatus (external auditory meatus), and the mastoid and styloid processes. The mandibular fossa is bounded in front by the articular eminence and behind by the tympanic plate. The articular eminence provides a surface over which the mandibular condyle glides during mandibular movements and acts to prevent dislocation of the temporomandibular joint. The tympanic plate of the temporal bone contributes most of the margin of the external acoustic meatus; the squamous part forms the posterosuperior region. The external margin is roughened to provide an attachment for the cartilaginous part of the meatus. A small depression, the suprameatal triangle, lies above and behind the meatus and is related to the lateral wall of the mastoid antrum. The mastoid process is an inferior projection of the temporal bone. It lies posteroinferior to the external acoustic meatus and is the site of attachment of sternocleidomastoid. It is in contact behind with the posteroinferior angle of the parietal bone at the parietomastoid suture and with the squamous part of the occipital bone at the occipitomastoid suture. These two sutures meet the lateral end of the lambdoid suture at the asterion. This coincides with the site of the posterolateral fontanelle in the neonatal skull, which closes during the second year. A mastoid foramen may be found near, or in, the occipitomastoid suture; it transmits an emissary vein from the sigmoid sinus. Sutural bones may appear in the parietomastoid suture.

The styloid process lies anterior and medial to the mastoid process and gives attachment to several muscles and ligaments. Its base is partly ensheathed by the tympanic plate and it descends anteromedially, its tip usually reaching a point medial to the posterior margin of the mandibular ramus. The styloid process is very variably developed. Its length ranges from a few millimetres to a few centimetres and increases with age (Krmpotić Nemanić et al 2009).

The infratemporal fossa is an irregular, postmaxillary space deep to the ramus of the mandible. It communicates with the upper temporal fossa deep to the zygomatic arch. It is best visualized when the mandible is removed but, for completeness, is considered here. Its roof is the infratemporal surface of the greater wing of the sphenoid, the lateral pterygoid plate lies medially, and the ramus of the mandible and styloid process lie laterally and posteriorly, respectively. The infratemporal fossa

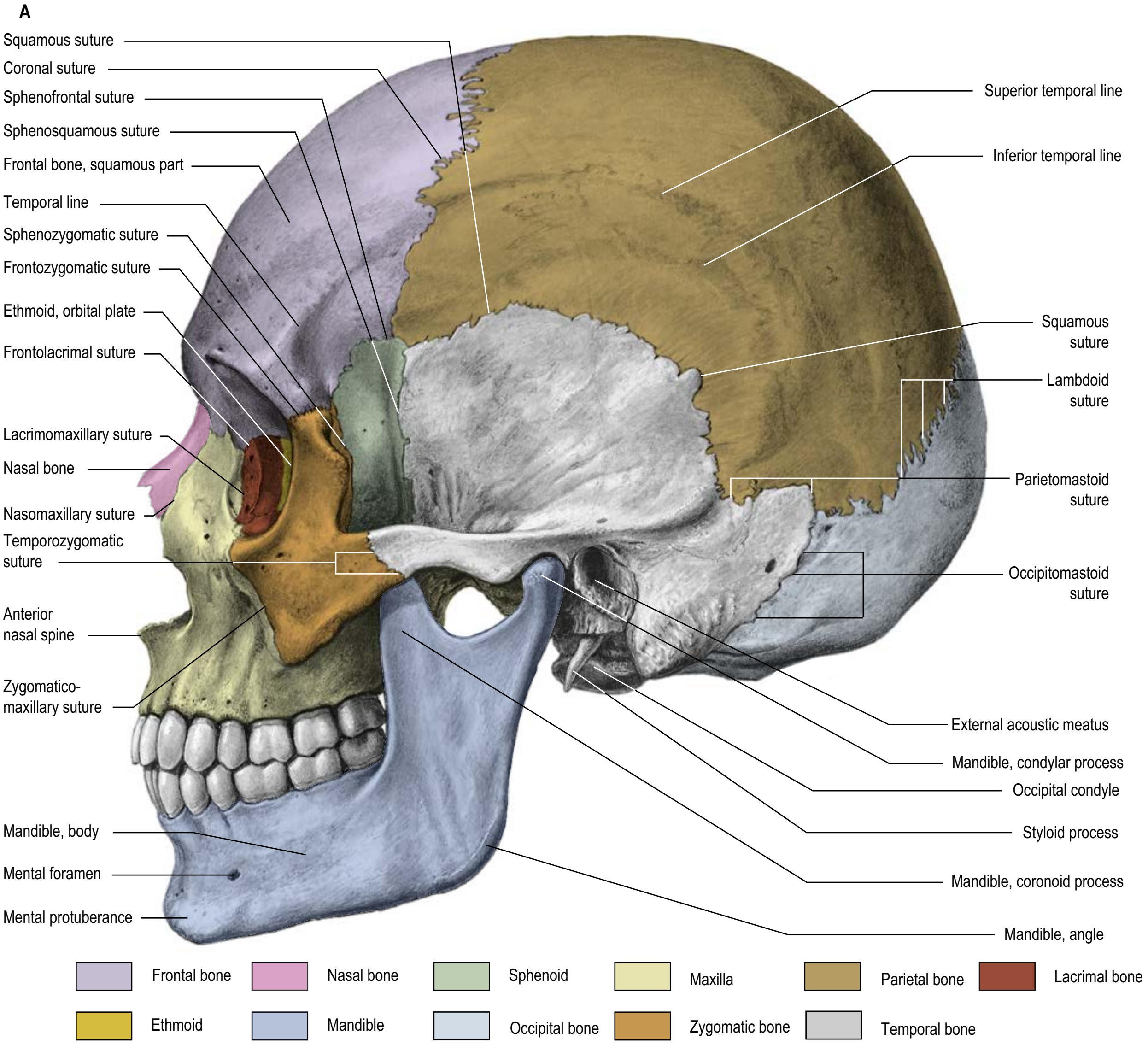
A
Squamous suture
Coronal suture
Sphenofrontal suture
Sphenosquamous suture
Frontal bone, squamous part
Temporal line
Sphenozygomatic suture
Frontozygomatic suture
Ethmoid, orbital plate
Frontolacrimal suture
Lacrimomaxillary suture
Nasal bone
Nasomaxillary suture
Temporozygomatic suture
Anterior nasal spine
Zygomatico-maxillary suture
Mandible, body
Mental foramen
Mental protuberance
Superior temporal line
Inferior temporal line
Squamous suture
Lambdoid suture
Parietomastoid suture
Occipitomastoid suture
External acoustic meatus
Mandible, condylar process
Occipital condyle
Styloid process
Mandible, coronoid process
Mandible, angle
Frontal bone
Nasal bone
Sphenoid
Maxilla
Parietal bone
Lacrimal bone
Ethmoid
Mandible
Occipital bone
Zygomatic bone
Temporal bone

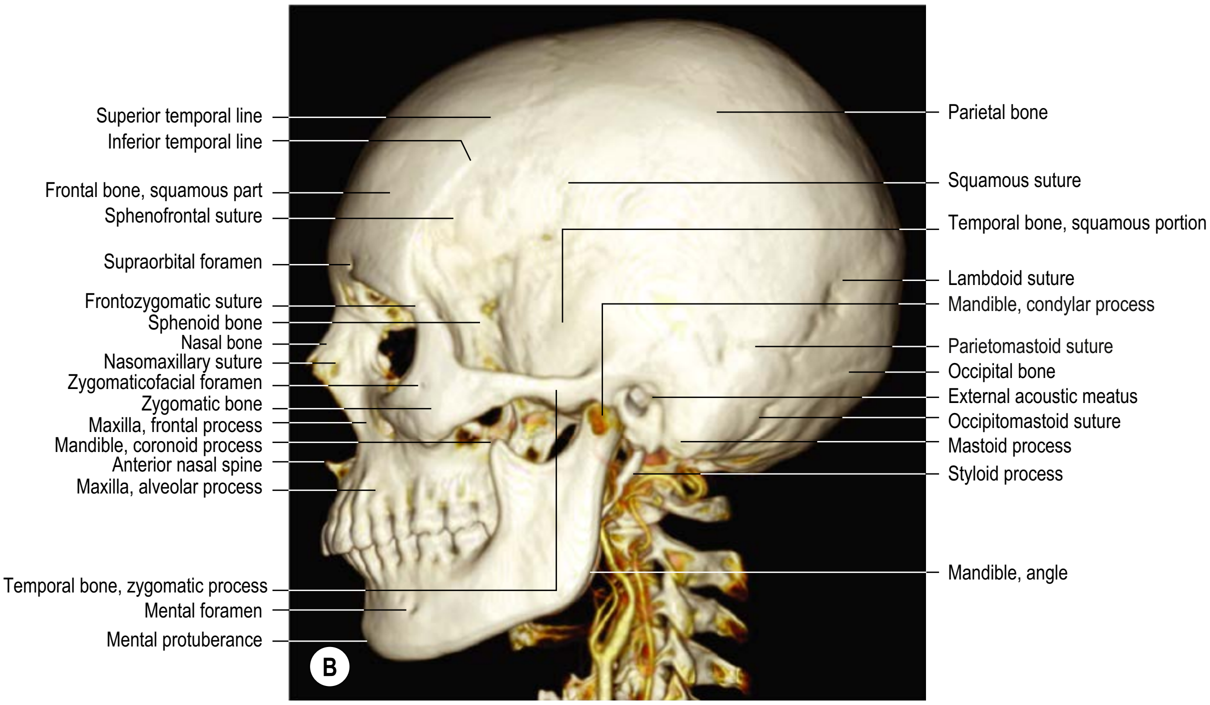
Superior temporal line
Inferior temporal line
Frontal bone, squamous part
Sphenofrontal suture
Supraorbital foramen
Frontozygomatic suture
Sphenoid bone
Nasal bone
Nasomaxillary suture
Zygomaticofacial foramen
Zygomatic bone
Maxilla, frontal process
Mandible, coronoid process
Anterior nasal spine
Maxilla, alveolar process
Temporal bone, zygomatic process
Mental foramen
Mental protuberance
B
Parietal bone
Squamous suture
Temporal bone, squamous portion
Lambdoid suture
Mandible, condylar process
Parietomastoid suture
Occipital bone
External acoustic meatus
Occipitomastoid suture
Mastoid process
Styloid process
Mandible, angle

Fig. 34.4 **A**, The bones of the adult skull, lateral aspect. **B**, Volume rendered CT of the head with a left lateral view of the skull. (C, *continued online*) (A, Sobotta Atlas of Human Anatomy © Elsevier GmbH, Urban & Fischer, Munich.)

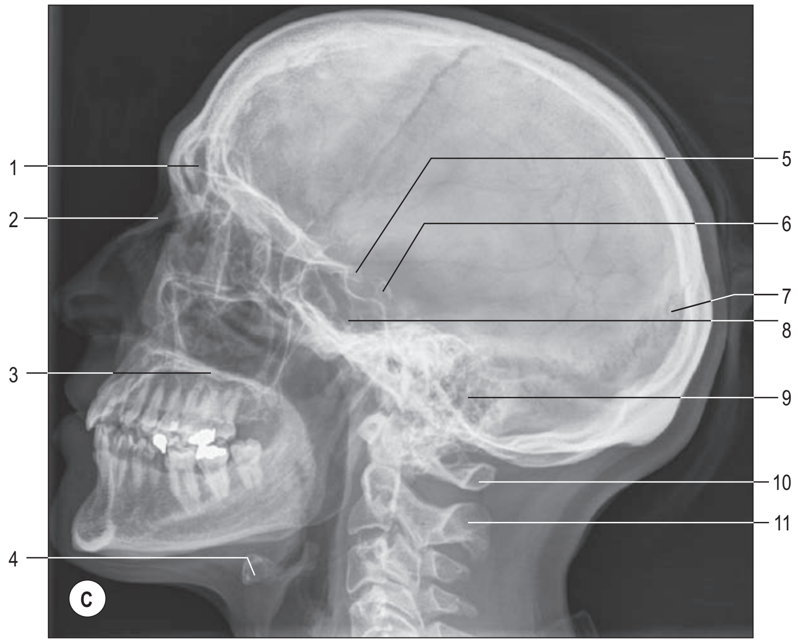

Fig. 34.4, cont'd C A true cephalometric lateral radiograph of the skull and cervical spine, young adult. Key: 1, frontal sinus; 2, nasal bone; 3, hard palate; 4, hyoid bone; 5, anterior clinoid process; 6, posterior clinoid process; 7, lambdoid suture; 8, sphenoidal sinus; 9, mastoid air cells; 10, posterior tubercle of atlas; 11, spinous process of axis.

has no anatomical floor. Its anterior and medial walls are separated above by the pterygomaxillary fissure lying between the lateral pterygoid plate and the posterior wall of the maxilla. The infratemporal fossa communicates with the pterygopalatine fossa through the pterygomaxillary fissure.

INFERIOR VIEW

With the mandible removed, the inferior surface of the skull extends from the upper incisor teeth anteriorly to the superior nuchal lines of the occipital bone posteriorly (Fig. 34.5). The region contains many of the foramina through which structures enter and exit the cranial cavity. The inferior surface may be conveniently subdivided into anterior, middle, posterior and lateral parts. The anterior part contains the hard palate and the dentition of the maxillary arch and lies at a lower level than the rest of the cranial base. The middle and posterior parts may be arbitrarily divided by a transverse plane passing through the anterior margin of the foramen magnum. The middle part is occupied mainly by the sphenoid bone, the apices of the petrous processes of the temporal bones, and the basilar part of the occipital bone. The lateral part contains the zygomatic arches, mandibular fossae, tympanic plates, the styloid and mastoid processes. The posterior part lies in the midline and is formed almost exclusively from the occipital bone. Whereas the middle and posterior parts are directly related to the cranial cavity (the middle and posterior cranial fossae), the anterior part is some distance from the anterior cranial fossa, being separated from it by the nasal cavities.

Anterior part of inferior surface

The bony palate within the superior alveolar arch is formed by the palatine processes of the maxillae anteriorly and the horizontal plates of the palatine bones posteriorly, all meeting at a cruciform system of sutures (see Fig. 34.5). The median palatine suture runs anteroposteriorly and divides the palate into right and left halves. This suture is continuous with the intermaxillary suture between the maxillary central incisor teeth. The transverse palatine (palatomaxillary) sutures run transversely across the palate between the maxillae and the palatine bones. The palate is arched sagittally and transversely; its depth and breadth are variable but are always greatest in the molar region. The incisive fossa lies behind the central incisor teeth, and the lateral incisive foramina, through which incisive canals pass to the nasal cavity, lie in its lateral walls. Median incisive foramina are present in some skulls and open on to the anterior and posterior walls of the fossa. The incisive fossa transmits the nasopalatine nerve and the termination of the greater palatine vessels. When

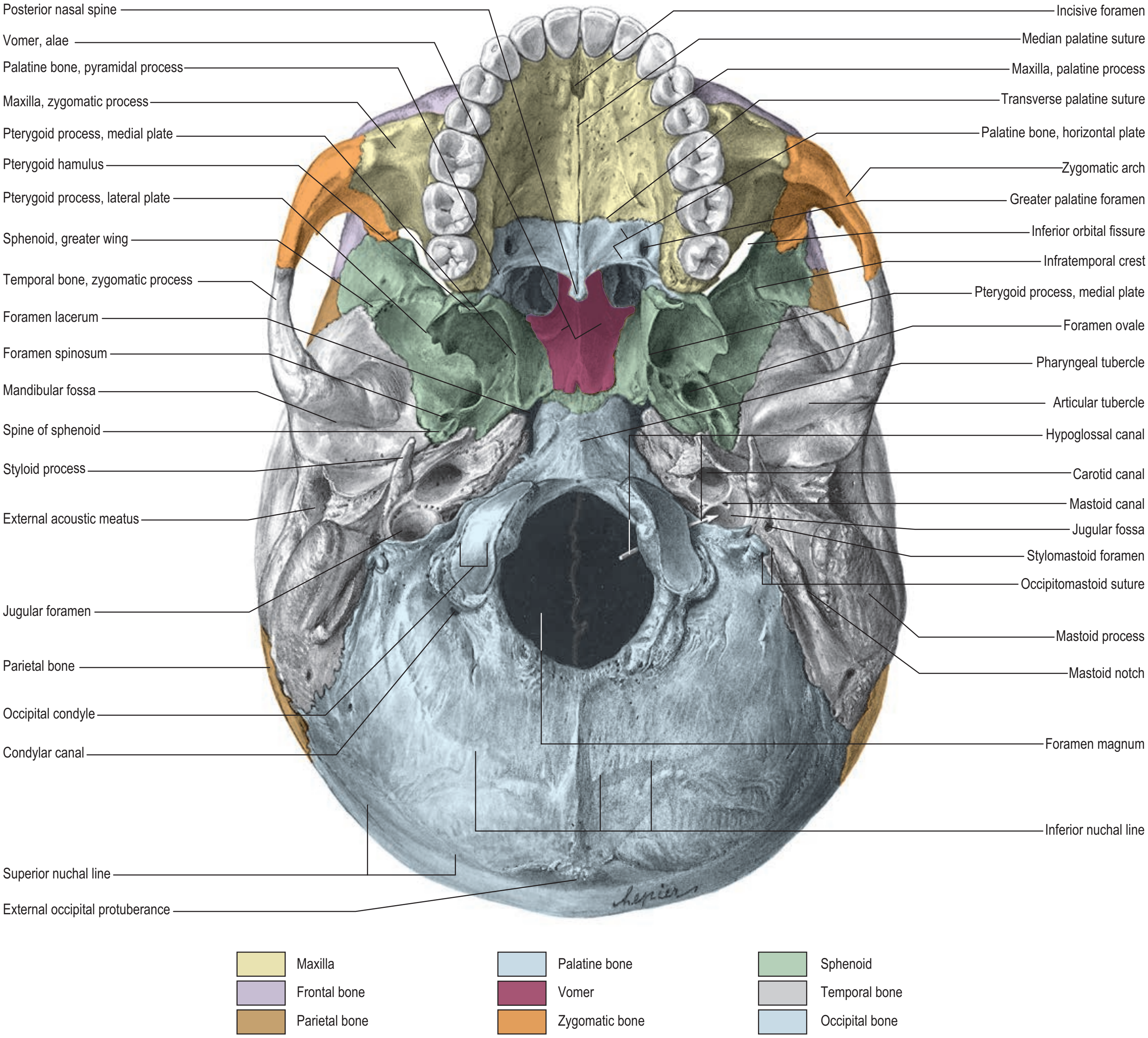
Posterior nasal spine
Vomer, alae
Palatine bone, pyramidal process
Maxilla, zygomatic process
Pterygoid process, medial plate
Pterygoid hamulus
Pterygoid process, lateral plate
Sphenoid, greater wing
Temporal bone, zygomatic process
Foramen lacerum
Foramen spinosum
Mandibular fossa
Spine of sphenoid
Styloid process
External acoustic meatus
Jugular foramen
Parietal bone
Occipital condyle
Condylar canal
Superior nuchal line
External occipital protuberance
Incisive foramen
Median palatine suture
Maxilla, palatine process
Transverse palatine suture
Palatine bone, horizontal plate
Zygomatic arch
Greater palatine foramen
Inferior orbital fissure
Infratemporal crest
Pterygoid process, medial plate
Foramen ovale
Pharyngeal tubercle
Articular tubercle
Hypoglossal canal
Carotid canal
Mastoid canal
Jugular fossa
Stylomastoid foramen
Occipitomastoid suture
Mastoid process
Mastoid notch
Foramen magnum
Inferior nuchal line
Maxilla
Frontal bone
Parietal bone
Palatine bone
Vomer
Zygomatic bone
Sphenoid
Temporal bone
Occipital bone

Fig. 34.5 The external surface of the base of the adult skull. (Sobotta Atlas of Human Anatomy © Elsevier GmbH, Urban & Fischer, Munich.)

median incisive foramina are present, the left nasopalatine nerve usually traverses the anterior foramen and the right nerve traverses the posterior foramen. The greater palatine foramen lies near the lateral palatal border of the transverse palatine suture; a vascular groove, deeper behind and shallower in front, leads forwards from the foramen. The lesser palatine foramina, usually two, lie behind the greater palatine foramen and pierce the pyramidal process of the palatine bone, which is wedged between the lower ends of the medial and lateral pterygoid plates. The palate is pierced by many other small foramina and is marked by pits for palatine glands. Variably prominent palatine crests extend medially from behind the greater palatine foramina. The posterior border projects back as the posterior nasal spine. In the adult, the alveolar arch normally bears a maximum of 16 sockets or alveoli for the teeth; the sockets vary in size and depth. Some are single and some are subdivided by septa, according to the morphology of the dental roots.

The nasal fossae lie above the hard palate and are separated by the nasal septum in the midline. The bony nasal septum is formed from the perpendicular plate of the ethmoid superiorly and the vomer inferiorly. The upper border of the vomer approximates to the inferior aspect of the body of the sphenoid, where it expands into an ala on each side. The two posterior nasal apertures (choanae) are located at the end of the nasal fossae; they are separated by the free posterior border of the vomer and bounded below by the posterior border of the horizontal plates of the palatine bones, above by the sphenoid and laterally by the medial pterygoid plates.

Middle part of inferior surface

The middle part of the inferior surface is made up from the sphenoid, petrous parts of the temporal bones and the basiocciput (see Fig. 34.5). It extends from the posterior nares anteriorly to an artificial line drawn transversely through the anterior margin of the foramen magnum posteriorly. In the adult, the body of the sphenoid fuses with the basiocciput, at the spheno-occipital synchondrosis, to form a midline bar of bone that extends posteriorly to the foramen magnum (internally, this is known as the clivus). The basiocciput bears a small midline pharyngeal tubercle, which gives attachment to the pharyngeal raphe, the highest attachment of the superior pharyngeal constrictor.

The petrous processes of the two temporal bones pass from the lateral sides of the base of the skull and fill the triangular space between the greater wing of the sphenoid anteriorly and the lateral margins of the basiocciput posteriorly. Each petrous process meets the basilar part of the occipital bone at a petro-occipital junction, which is deficient posteriorly at the jugular foramen. The petrosphenoidal junction and the groove for the pharyngotympanic tube lie between the petrous process and the infratemporal surface of the greater wing of the sphenoid. The apex of the petrous process does not meet the spheno-occipital synchondrosis; the deficit so produced is the foramen lacerum.

Pterygoid processes descend from the junction between the greater wing and body of the sphenoid, separated by a pterygoid fossa. Anteriorly, the plates are fused, except inferiorly, where they are separated by the pyramidal process of the palatine bone. Sutures are usually discernible at this site in young skulls. Laterally, the pterygoid plates are separated from the posterior maxillary surface by the pterygomaxillary fissure, which leads into the pterygopalatine fossa. The posterior border of the medial pterygoid plate is sharp, and bears a small projection near the midpoint, above which it is curved and attached to the pharyngeal end of the pharyngotympanic tube. Above, the medial pterygoid plate divides to enclose the scaphoid fossa. Below, it projects as a slender pterygoid hamulus, which curves laterally and is grooved anteriorly by the tendon of tensor veli palatini. The pterygoid hamulus gives origin to the pterygomandibular raphe. The lateral pterygoid plate projects posterolaterally and its lateral surface forms the medial wall of the infratemporal fossa. Superiorly and laterally, the pterygoid process is continuous with the infratemporal surface of the greater wing of the sphenoid bone, which forms part of the roof of the infratemporal fossa. This surface forms the posterolateral border of the inferior orbital fissure and bears an infratemporal crest associated with the origin of the upper part of lateral pterygoid. The infraorbital and zygomatic branches of the maxillary nerve and accompanying vessels pass through the inferior orbital fissure. Laterally, the greater wing of the sphenoid articulates with the squamous part of the temporal bone.

The medial aspect of the greater wing of the sphenoid presents a crescent of foramina of which only the most posterior two, foramen ovale and foramen spinosum, can be viewed on the basal aspect. The foramen ovale lies medial to the foramen spinosum and lateral to the foramen lacerum on the infratemporal surface of the greater wing of the sphenoid bone. It transmits the mandibular division of the trigeminal nerve, the lesser petrosal nerve, the accessory meningeal branch of the maxillary artery and an emissary vein that connects the cavernous venous sinus to the pterygoid venous plexus in the infratemporal fossa. Posterolaterally, the smaller and rounder foramen spinosum transmits the middle meningeal artery and a recurrent meningeal branch of the mandibular nerve. The irregular spine of the sphenoid projects posterolateral to the foramen spinosum. The medial surface of the spine is flat and, with the adjoining posterior border of the greater wing of the sphenoid, forms the anterolateral wall of a groove that is completed posteromedially by the petrous part of the temporal bone. This groove, the auditory sulcus, contains the cartilaginous pharyngotympanic tube, which leads posterolaterally into the bony portion of the tube that lies within the petrous part of the temporal bone. Occasionally, the foramen ovale and foramen spinosum are confluent or the posterior edge of the foramen spinosum may be defective. A small foramen, the sphenoidal emissary foramen (of Vesalius), is sometimes found between the foramen ovale and scaphoid fossa. When present, it contains an emissary vein linking the pterygoid venous plexus in the infratemporal fossa with the cavernous sinus in the middle cranial fossa.

The foramen lacerum is bounded in front by the body and adjoining roots of the pterygoid process and greater wing of the sphenoid bone; posterolaterally, by the apex of the petrous part of the temporal bone; and medially, by the basilar part of the occipital bone. Although nearly 1 cm long, it is not traversed by any major structure. The almost circular carotid canal lies behind and posterolateral to the foramen lacerum in the petrous part of the temporal bone. The internal carotid artery enters the skull through this foramen, ascends in the carotid canal, and turns anteromedially to reach the posterior wall of the foramen lacerum. It ascends through the upper end of the foramen lacerum, accompanied by venous and sympathetic nerve plexuses. Meningeal branches of the ascending pharyngeal artery and emissary veins from the cavernous sinus also traverse the foramen lacerum. In life, the lower part of the foramen lacerum is partially occluded by cartilaginous remnants of the embryological chondrocranium. The pterygoid canal can be seen on the base of the skull at the anterior margin of the foramen lacerum, above and between the pterygoid plates of the sphenoid bone. It leads into the pterygopalatine fossa and transmits the nerve of the pterygoid canal and accompanying blood vessels.

Posterior part of inferior surface

The posterior part of the inferior surface of the skull is predominantly formed by the occipital bone (see Fig. 34.5). Prominent features are the foramen magnum and associated occipital condyles, jugular foramen, mastoid notch and the squamous part of the occipital bone up to the external occipital protuberance and the superior nuchal lines, hypoglossal canals (anterior condylar canals) and condylar canals (posterior condylar canals).

The foramen magnum lies in an anteromedian position and leads into the posterior cranial fossa. It is oval and wider behind, with its greatest diameter being anteroposterior. It contains the lower end of the medulla oblongata, meninges, cerebrospinal fluid, vertebral arteries and veins, and the accessory nerves; the apical ligament of the dens and the tectorial membrane pass through it to attach to the internal basiocciput. Anteriorly, the margin of the foramen magnum is slightly overlapped by the occipital condyles, which project down to articulate with the superior articular facets on the lateral masses of the atlas. Each occipital condyle is oval in outline and orientated obliquely so that its anterior end lies nearer the midline than its posterior end. It is markedly convex anteroposteriorly, less so transversely, and its medial aspect is roughened by ligamentous attachments. The hypoglossal canal is directed laterally and slightly forwards, traverses deep to each condyle and transmits the hypoglossal nerve, a meningeal branch of the ascending pharyngeal artery and an emissary vein from the basilar plexus. A depression, the condylar fossa, lies immediately posterior to the condyle and may contain a (posterior) condylar canal for an emissary vein from the sigmoid sinus. This fossa accommodates the posterior margin of the atlas when the head is fully extended. A jugular process articulates with the petrous part of the temporal bone lateral to each condyle and its anterior free border forms the posterior boundary of the jugular foramen.

Laterally, the occipital bone approximates with the petrous part of the temporal bone anteriorly at the petro-occipital junction, and the mastoid process of the temporal bone more posteriorly at the occipitomastoid suture. The jugular foramen, a large, asymmetric and irregular hiatus, lies at the posterior end of the petro-occipital junction between the jugular process of the occipital bone and the jugular fossa of the petrous part of the temporal bone (see Fig. 42.1C) (Vogl and Bisdas 2009). A number of important structures pass through this foramen: inferior petrosal sinus (anterior); glossopharyngeal, vagus and accessory cranial nerves (middle); and internal jugular vein (posterior). A mastoid canaliculus runs through the lateral wall of the jugular fossa and transmits the auricular branch of the vagus nerve. The canaliculus for the tympanic branch of the glossopharyngeal nerve lies on the ridge between the jugular fossa and the opening of the carotid canal. A small notch, related to the inferior glossopharyngeal ganglion, may be found medially on the upper boundary of the jugular foramen (it is more easily identified internally). The orifice of the cochlear canaliculus may be found at the apex of the notch.

The squamous part of the occipital bone exhibits the external occipital protuberance, supreme, superior and inferior nuchal lines, and the external occipital crest, all of which lie in the midline, posterior to the foramen magnum. The region is roughened for the attachment of muscles whose primary function is extension of the skull at the neck.

Lateral part of inferior surface

The lateral part of the inferior surface consists of the zygomatic arch and infratemporal fossa anteriorly and the mandibular fossa, tympanic plate and styloid and mastoid processes posteriorly (see Fig. 34.5). The anterior structures have been considered earlier in this chapter.

The mandibular fossa is a thin-walled, smooth, concave depression in the temporal bone and is most easily inspected when the mandible is removed. The zygomatic arch extends laterally in front of the fossa and a distinct ridge, the articular eminence, lies anterior to the fossa. Three fissures can be distinguished behind the mandibular fossa. The squamotympanic fissure extends from the spine of the sphenoid, between the mandibular fossa and the tympanic plate of the temporal bone, and curves up the anterior margin of the external acoustic meatus. A thin wedge of bone forming the inferior margin of the tegmen tympani lies within the fissure and divides the squamotympanic fissure into petrotympanic and petrosquamous fissures. The petrotympanic fissure transmits the chorda tympani branch of the facial nerve from the intracranial cavity into the infratemporal fossa. The tympanic plate forms the floor of the external acoustic meatus.

The stylomastoid foramen lies between the mastoid and styloid processes on the lateral aspect of the temporal bone. It transmits the facial nerve and the stylomastoid artery. The distance from the styloid process to the stylomastoid foramen decreases with age (Krmpotić Nemanić et al 2009). A groove, the mastoid notch, lies medial to the mastoid process and gives origin to the posterior belly of digastric. A groove related to the occipital artery often lies medial to the mastoid notch. A mastoid foramen may be present near, or in, the occipitomastoid suture; when present, it transmits an emissary vein from the sigmoid sinus. The external acoustic meatus lies in front of the mastoid process. It is surrounded inferiorly by the tympanic plate, which partly ensheathes the base of the styloid process as the vaginal process.

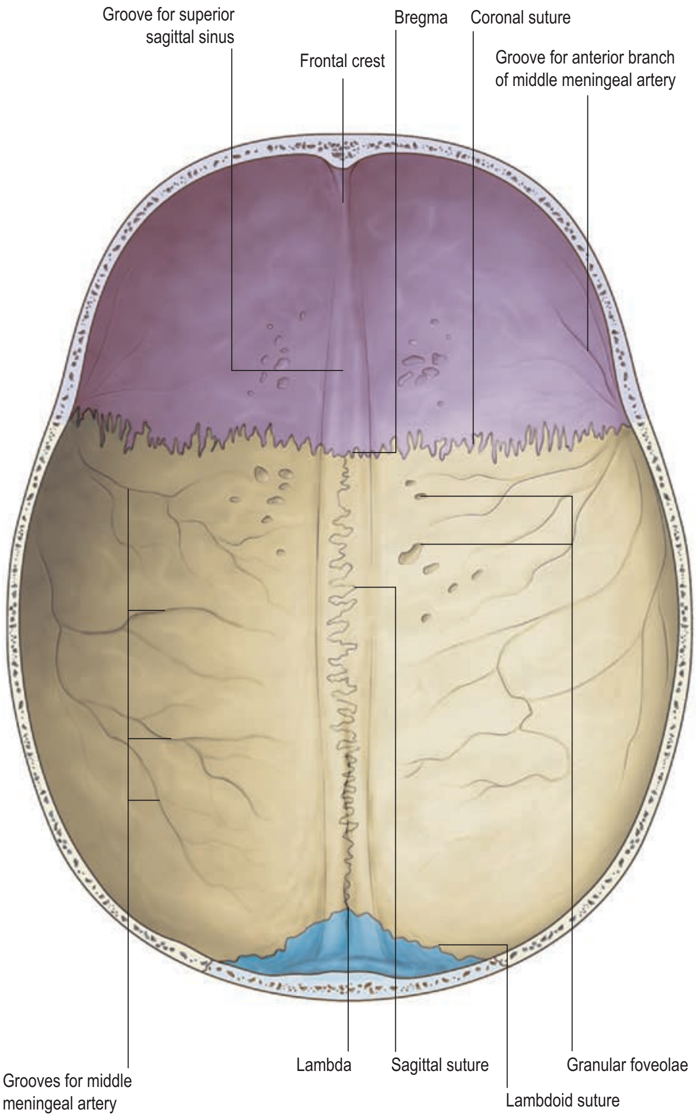
Groove for superior sagittal sinus
Frontal crest
Bregma
Coronal suture
Groove for anterior branch of middle meningeal artery
Grooves for middle meningeal artery
Lambda
Sagittal suture
Granular foveolae
Lambdoid suture

Fig. 34.6 The internal surface of the cranial vault. (With permission from Drake RL, Vogl AW, Mitchell A (eds) Gray's Anatomy for Students, 2nd ed. Elsevier, Churchill Livingstone. Copyright 2010.)

INTERNAL SURFACE OF CALVARIA

The internal surface of the calvaria is deeply concave and includes most of the frontal and parietal bones and the squamous part of the occipital bone, variously united at the coronal, sagittal and lambdoid sutures (Fig. 34.6). Inconstant foramina are seen in the parietal bones near the sagittal sulcus and anterior to the lambdoid suture; they admit emissary veins associated with the superior sagittal sinus. The internal surfaces of the frontal and parietal bones are grooved by furrows that house the frontal and parietal branches of the middle meningeal vessels; the grooves contain the openings of minute channels that admit perforating vessels to the haemopoietic marrow within the diploic bone. Impressions for cerebral gyri are less distinct on the bones of the calvaria than they are on the cranial base.

The falx cerebri, a dural partition that separates the two cerebral hemispheres of the brain, is attached anteriorly to a backward-projecting anteromedian frontal crest. The crest exhibits a groove that widens as it passes back below the sagittal suture and becomes continuous with the sagittal sulcus, which houses the superior sagittal sinus. Irregular depressions, granular foveolae, which become larger and more numerous with age, lie on either side of the sulcus and usually house arachnoid granulations.

CRANIAL FOSSAE (ANTERIOR, MIDDLE, POSTERIOR)

The base of the cranial cavity is divided into three distinct fossae: the anterior, middle and posterior cranial fossae (Fig. 34.7). The floor of the anterior cranial fossa is at the highest level and the floor of the posterior fossa is at the lowest.

Detailed descriptions of the microsurgical anatomy of each region of the cranial base are beyond the scope of this book, and the interested reader is directed in the first instance to Rhoton (2007).

Anterior cranial fossa

The anterior cranial fossa is formed by the frontal, ethmoid and sphenoid bones, and supports the frontal lobes of the cerebral hemispheres. Its floor is composed of the orbital plate of the frontal bone, the cribriform plate and crista galli of the ethmoid bone, and the lesser wings, jugum sphenoidale and prechiasmatic sulcus of the sphenoid.

A perforated plate of bone, the cribriform plate of the ethmoid bone, spreads across the midline between the orbital plates of the frontal bone and is depressed below them, forming part of the roof of the nasal cavity. Olfactory nerves pass from the nasal mucosa to the olfactory bulb of the brain through numerous small foramina in the cribriform plate. Anteriorly, a spur of bone, the crista galli, projects upwards between the cerebral hemispheres and serves as an attachment for the falx cerebri. A depression between the crista galli and the crest of the frontal bone is crossed by the frontoethmoidal suture. It bears the foramen caecum, which is usually a small blind-ended depression formed by the developmental involution of a dural diverticulum that extends through the foramen caecum to the columella; in adults, it occasionally accommodates a vein draining from the nasal mucosa to the superior sagittal sinus. Failure of the foramen caecum to close may cause nasal dermoid cysts and nasoethmoidal encephaloceles in children.

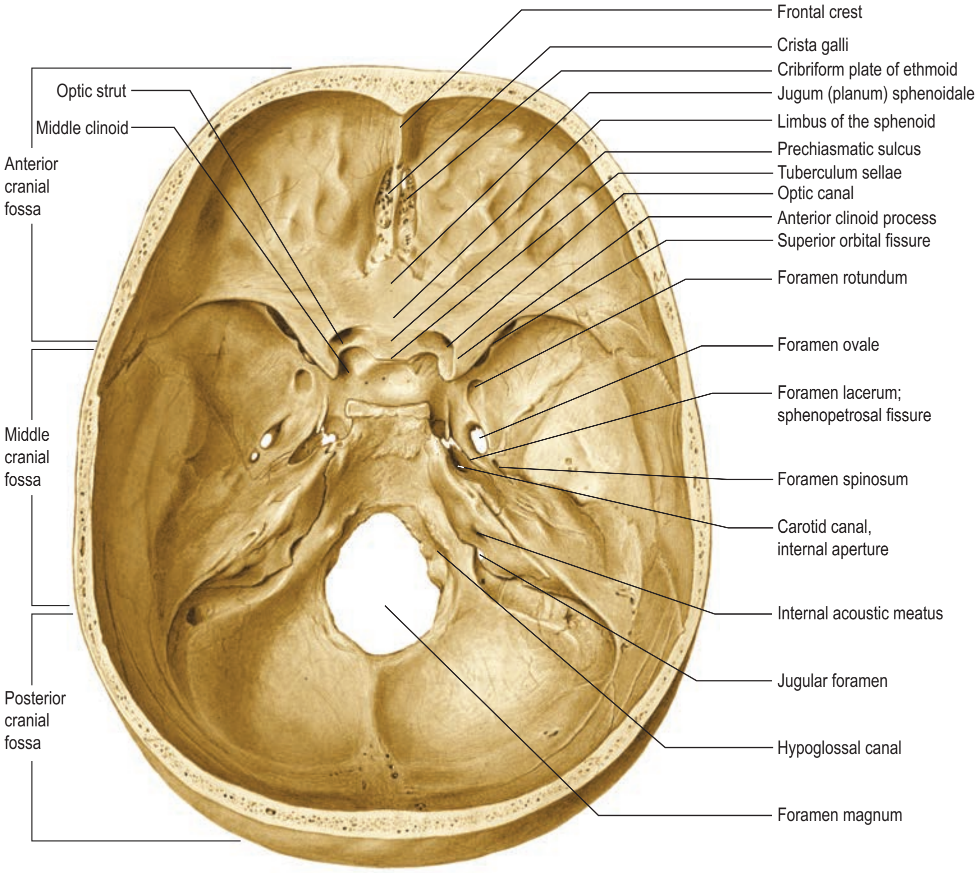

Fig. 34.7 The floor of the cranial cavity showing the cranial fossae. (Sobotta Atlas of Human Anatomy © Elsevier GmbH, Urban & Fischer, Munich.)

The anterior ethmoidal nerve and vessels enter the cranial cavity where the cribriform plate meets the orbital part of the frontal bone. They then pass into the roof of the nasal cavity via a small foramen by the side of the crista galli. The posterior ethmoidal canal, which transmits the posterior ethmoidal nerve and vessels, opens at the junction of the posterolateral corner of the cribriform plate and jugum sphenoidale. The convex orbital plate of the frontal bone separates the brain from the orbit and bears impressions of cerebral gyri and small grooves for meningeal vessels. Posteriorly, it articulates with the anterior border of the lesser wing of the sphenoid laterally and the jugum sphenoidale medially. The jugum sphenoidale is a flat surface on the upper aspect of the sphenoid bone that connects the two lesser wings, also known as the planum sphenoidale. The limbus of the sphenoid bone is a prominent ridge on the body of the sphenoid that forms the posterior border of the jugum sphenoidale and the anterior border of the prechiasmatic sulcus. The latter is an osseous groove that runs transversely between the optic canals. The optic chiasma usually lies above the prechiasmatic sulcus, while the medial orbital surface of the frontal lobes and olfactory tracts lie above the jugum sphenoidale (see Fig. 34.7.)

The posterior boundary of the lesser wing forms the posterior boundary of the anterior cranial fossa; the medial end of the lesser wing constitutes the anterior clinoid process. The lesser wing and the anterior clinoid process join the sphenoid body by two roots that are separated by the optic canal. The anterior root, broad and flat, forms the roof of the optic canal and is continuous with the jugum sphenoidale, while the smaller and thicker posterior root, also known as the optic strut, joins the body of the sphenoid bone at the lateral aspect of the posterior bank of the prechiasmatic sulcus or tuberculum sellae (see Fig. 34.7). The optic strut of the anterior clinoid process separates the optic canal from the superior orbital fissure (Kerr et al 2012). Each optic canal transmits the optic nerve and ophthalmic artery.

Middle cranial fossa

The middle cranial fossa is formed by the sphenoid and temporal bones and supports the temporal lobes of the cerebral hemispheres. It is bounded in front by the posterior aspect of the lesser and greater wings of the sphenoid, behind by the superior border of the petrous part of the temporal bone, laterally by the squamous part of the temporal bone and greater wing of the sphenoid, and medially by the lateral aspect of the sphenoid body, including the carotid sulcus, sella turcica and dorsum sellae.

The middle cranial fossa communicates with the orbits by the superior orbital fissures, each bounded above by a lesser wing, below by a greater wing, and medially by the body of the sphenoid bone and optic strut. The fissures contain the oculomotor, trochlear and abducens nerves, and the lacrimal, frontal and nasociliary branches of the ophthalmic division of the trigeminal nerve, together with filaments from the internal carotid plexus (postganglionic sympathetic), the superior and inferior ophthalmic veins, the orbital branch of the middle meningeal artery, and the recurrent branch of the lacrimal artery.

The central part of the cranial base, located between both middle cranial fossae, is formed by the body of the sphenoid bone, which contains the sphenoidal sinuses. The body of the sphenoid bone is deeply concave and houses the pituitary gland (hypophysis); it is therefore termed the pituitary (hypophysial) fossa, also known as the sella turcica because it resembles the shape of a Turkish saddle (Paluzzi et al 2012). The face and floor of the sella turcica are located within the sphenoidal air sinuses, which is why the most direct surgical route to the pituitary fossa is the trans-sphenoidal approach. The anterior edge of the sella is formed by a bony prominence, the tuberculum sellae, which is continuous anteriorly with the prechiasmatic sulcus; the posterior boundary presents a vertical pillar of bone, the dorsum sellae. The superolateral angles of the dorsum are expanded as the posterior clinoid processes. A fold of dura, the diaphragma sellae, is attached to the anterior and posterior clinoid processes and roofs over the pituitary fossa. The cavernous sinus lies lateral to the pituitary fossa. The lateral wall of the body of the sphenoid contains a shallow carotid sulcus related to the internal carotid artery as it ascends from the carotid canal and runs through the cavernous sinus.

Each anterior clinoid process covers the roof of the cavernous sinus and the paraclinoidal segment of the internal carotid artery as it leaves the cavernous sinus and pierces the dura to enter the intradural space. The anterior clinoid process gives attachment to the anterior petroclinoidal ligament, which forms the free margin of the tentorium cerebelli, and the interclinoidal ligament, which lies between the anterior and posterior clinoids. The middle clinoid process arises from the body of the sphenoid bone at the anterolateral margin of the sella turcica and may be connected to the anterior clinoid process by a thin osseous bar, formed by ossification of the caroticoclinoid ligament. The resulting caroticoclinoid foramen or ring surrounds the paraclinoidal segment of the internal carotid artery (Fernandez-Miranda et al 2012). While anterior and posterior clinoids are always present, middle clinoids are not constant. A recent study revealed that the middle clinoid process was usually identifiable in fine-cut head computed tomogram–angiogram scans, and sometimes had at least one caroticoclinoid ring.

The greater wing of the sphenoid bone contains three consistent foramina and other small variable foramina. The foramen rotundum, situated just below the medial end of the superior orbital fissure, leads forwards into the medial aspect of the inferior orbital fissure and opens into the pterygopalatine fossa; it contains the maxillary nerve (second division of trigeminal nerve).

Behind the foramen rotundum is the foramen ovale, which transmits the mandibular nerve (third division of trigeminal nerve). The foramen spinosum lies just posterolateral to the foramen ovale and transmits the middle meningeal artery and veins; these vessels groove the floor and lateral wall of the middle cranial fossa. The foramen ovale and foramen spinosum open into the underlying infratemporal fossa. When present, the small sphenoidal emissary foramen lies anteromedial to the foramen ovale and lateral to the foramen rotundum; it transmits an emissary vein through which the cavernous sinus and pterygoid plexus communicate.

The foramen lacerum is a misnomer because it is a gap, not a true foramen, formed by the incomplete confluence of the pterygosphenoidal and petroclival fissures. It may therefore also be called the sphenopetroclival synchondrosis. It lies posteromedial to the foramen ovale at the transition between the carotid sulcus of the sphenoid bone and the petrous carotid canal, bounded laterally by the lingula of the sphenoid and the petrolingual ligament extending to the petrous apex. The lower portion of the foramen lacerum is filled with fibrocartilage extending from the pterygosphenoidal fissure, pharyngotympanic tube and basopharyngeal fascia. The upper portion of the foramen contains the laceral segment of the internal carotid artery and should be considered as the rostral extension of the petrous carotid canal (Tauber et al 1999). The only structures that enter or exit the intracranial cavity through the foramen lacerum are the pterygoid (Vidian) nerve and vessels, terminal branches of the ascending pharyngeal artery and small emissary veins connecting the extracranial pterygoid plexus with the intracranial cavernous sinus.

The superior border of the petrous part of the temporal bone separates the middle and the posterior cranial fossae, and is grooved by the superior petrosal sinus. The trigeminal impression, which accommodates the trigeminal ganglion, is situated on the anterior surface of the petrous part of the temporal bone near its apex. A smooth trigeminal notch leads into the impression and lies on the upper border of the petrous part, anteromedial to the groove for the superior petrosal sinus. At the level of the notch, the trigeminal nerve passes from the posterior to the middle cranial fossa, and separates the superior petrosal sinus from the underlying bone. The petrosphenoidal ligament (of Gruber) lies at the anterior end of the trigeminal notch, attached to a minute bony spicule, the petrous tubercle (Iaconetta et al 2003). The ligament runs in a superior, anterior and medial direction to attach to the posterior and lateral aspect of the posterior clinoid. The abducens nerve bends sharply across the upper petrous border and medially over the lateral edge of the dorsum sellae or petrosal process of the sphenoid, and typically passes under the petrosphenoidal ligament to enter the cavernous sinus (Ozveren et al 2002). This interdural space (between dural layers), limited superiorly by the petrosphenoidal ligament, inferiorly by the petrosal process, laterally by the petrous apex, and medially by the dorsum sellae, is known as Dorello's canal (Ambekar et al 2012). It is also defined as the petroclival venous confluence because it is filled with blood from the adjacent venous sinuses, namely: the inferior and superior petrosal, cavernous and basilar plexus (Barges-Coll et al 2010).

Lateral to the trigeminal impression, a narrow groove passes posterolaterally into the hiatus for the greater petrosal nerve (also known as the facial hiatus); the hiatus and groove for the lesser petrosal nerve lies even further laterally (Kakizawa et al 2007). Posterolateral to the facial hiatus, a rounded arcuate eminence is produced by the underlying superior semicircular canal. A line bisecting the angle subtended by the arcuate eminence and the greater petrosal nerve estimates the location of the roof of the internal acoustic meatus (internal auditory canal) in the middle fossa. The petrous segment of the internal carotid artery runs from the carotid foramen to the foramen lacerum within the carotid canal of the petrous part of the temporal bone. The greater petrosal nerve travels above and parallel to the petrous carotid canal, which may be dehiscent. The osseous portion of the pharyngotympanic tube and tensor tympani run parallel and just lateral to the petrous carotid canal within the floor of the middle fossa. The cochlea is situated within the petrous part of the temporal bone, just medial to the posterior aspect of the petrous carotid canal and anterior to the internal acoustic meatus and arcuate eminence. The portion of petrous bone that is limited anteriorly by the mandibular nerve, laterally by the greater petrosal nerve, medially by the superior petrosal sinus, and posteriorly by the internal acoustic meatus and cochlea is named the posteromedial (or Kawase's) triangle of the middle fossa. The surgical procedure known as anterior petrosectomy consists of removal of this bone in order to access the posterior fossa from the middle fossa approach (Kawase et al 1985) (Ch. 43).

The lateral surface of the petrous part of the temporal bone is formed by the tegmen tympani, a thin osseous lamina that separates the tympanic cavity (middle ear) from the middle fossa. Chronically elevated intracranial pressure may cause erosion of the tegmen tympani and spontaneous cerebrospinal fluid otorrhoea. The posterior part of the tegmen tympani forms the roof of the mastoid antrum, lateral to the arcuate eminence, and is also called the tegmen mastoideum. In young skulls, a petrosquamous suture may be visible at the lateral limit of the tegmen tympani but it is obliterated in adults. The tegmen tympani then turns down as the lateral wall of the osseous portion of the pharyngotympanic tube, and its lower border may appear in the squamotympanic fissure. Lateral to the anterior part of the tegmen tympani, the squamous part of the temporal bone is thinned over a small area that coincides with the deepest part of the mandibular fossa.

Posterior cranial fossa

The posterior cranial fossa is formed by the sphenoid, temporal and occipital bones, and contains the cerebellum, pons and medulla oblongata. It is bounded in front by the dorsum sellae, posterior aspects of the body of the sphenoid bone, and the basilar (or clival) part of the occipital bone; behind by the squamous part of the occipital bone; and laterally by the petrous and mastoid parts of the temporal bones and by the lateral (condylar) parts of the occipital bone.

The most prominent feature in the floor of the posterior cranial fossa is the foramen magnum in the occipital bone. The medulla oblongata exits the cranial cavity through the foramen magnum to continue as the spinal cord (see Fig. 35.11). The cerebellum is fully contained within the posterior fossa. When the lower part of the cerebellum, the tonsils, descend abnormally through the foramen magnum, they may cause compression of the medulla at the level of the foramen magnum, a condition called tonsillar herniation or Chiari malformation.

The clivus is a sloping surface that extends from the sella turcica to the foramen magnum, and is formed successively by the dorsum sellae, the posterior part of the body of the sphenoid and the basilar (clival) part of the occipital bone. The spheno-occipital synchondrosis is evident on the clivus of a growing child but not in adults. The clivus is located at the centre of the posterior skull base and separates the nasopharynx from the posterior cranial fossa. Cranial chordomas are malignant tumours that histologically are reminiscent of embryonic notochordal tissue and typically arise within the clival bone (Fernandez-Miranda et al 2014). The clivus reaches its final length at the age of 11 years in both sexes (Krmpotić-Nemanić et al 2005). On each side, the clivus is separated from the petrous part of the temporal bone by a petro-occipital (or petroclival) fissure, filled by a thin plate of cartilage and extending from the foramen lacerum (extracranially) and cavernous sinus (intracranially) to the jugular foramen. The intracranial margins of the fissure are grooved by the inferior petrosal sinus. Chondrosarcomas are malignant tumours composed of transformed cells that produce cartilage; their most common intracranial location is precisely the petroclival fissure.

The jugular foramen is a large opening located between the temporal and occipital bones at the posterior end of the petro-occipital fissure, above and lateral to the foramen magnum. The lower border of the jugular foramen is smooth and is formed by the lateral part of the occipital bone. The upper border is sharp and irregular, and is formed by the petrous part of the temporal bone. It contains a notch, the intrajugular process, which divides the foramen into a large posterolateral compartment, the sigmoid part, which receives the drainage of the sigmoid sinus; and a small anteromedial compartment, the petrosal part, which receives the drainage of the inferior petrosal sinus. The accessory, vagus and glossopharyngeal nerves course in the medial side of the intrajugular process; they lie between the petrosal part (which contains the inferior petrosal sinus accompanied by a meningeal branch of the ascending pharyngeal artery) and the sigmoid part (which contains the sigmoid sinus accompanied by a meningeal branch of the occipital artery). The cochlear canaliculus or aqueduct, which contains the perilymphatic 'duct', is sited in the deepest part of the intrajugular process. The jugular foramina are typically asymmetric: the right foramen is usually larger than the left, reflecting the right dominance of the sigmoid sinus and jugular vein.

The jugular tubercle is a rounded prominence located at the junction of the basilar and lateral parts of the occipital bone, just medial to the jugular foramen. The accessory, vagus and glossopharyngeal nerves cross the posterior portion of the tubercle on their way to the jugular foramen. The hypoglossal (anterior condylar) canal lies just inferior to the jugular tubercle, superior to the occipital condyle, and medial to and below the lower border of the jugular foramen (Morera et al 2010). It transmits the hypoglossal nerve and its recurrent branch, together with the meningeal branch of the ascending pharyngeal artery and an emissary vein that links the (intracranial) basilar plexus with the (extracranial) internal jugular vein. The canal may be divided by bony septa for different rootlets of the hypoglossal nerve. The occipital condyles form the lateral (or condylar) part of the occipital bone, and they lie within the anterior and lateral aspect of the foramen magnum. On each side, their medial surface bears a tubercle that gives attachments to the alar ligaments of the odontoid process, and their inferior surface is convex and articulates with the upper surface of the lateral mass of the atlas. The posterior condylar canal, when present, is located in the extracranial surface behind and above each occipital condyle; its internal orifice is posterolateral to that of the hypoglossal canal and contains the supracondylar vein and a meningeal branch of the occipital artery.

The posterior surface of the petrous part of the temporal bone forms much of the anterolateral wall of the posterior cranial fossa. It contains the internal acoustic meatus, which lies anterosuperior to the jugular foramen, and transmits the facial and vestibulocochlear nerves, the nervus intermedius and labyrinthine vessels. A small subarcuate fossa lined with dura mater lies posteriorly between the internal acoustic meatus and the opening of the vestibular aqueduct. It houses the saccus and ductus endolymphaticus and a small artery and vein. The suprameatal tubercle is a bony prominence located superiorly between the internal acoustic meatus and the petrous ridge (Seoane and Rhoton 1999).

The mastoid part of the temporal bone lies behind the petrous part of the temporal bone in the lateral wall of the posterior cranial fossa. Anteriorly, it is grooved by a wide sigmoid sulcus that runs forwards and downwards, then downwards and medially, and finally forwards to the jugular foramen; it contains the sigmoid sinus. Superiorly, where the groove touches the mastoid angle of the parietal bone, it becomes continuous with a groove that transmits the transverse sinus, and then crosses the parietomastoid suture and descends behind the mastoid antrum. A mastoid foramen, which transmits an emissary vein from the sigmoid sinus and a meningeal branch of the occipital artery, may be sited here. The lowest part of the sigmoid sulcus crosses the occipitomastoid suture and grooves the jugular process of the occipital bone. The right sigmoid sulcus is usually larger than the left.

The squamous part of the occipital bone displays a median internal occipital crest. This runs posteriorly from the foramen magnum to an internal occipital protuberance, gives attachment to the falx cerebelli, and may be grooved by the occipital sinus. The internal occipital protuberance is close to the confluence of the sinuses. It is grooved bilaterally by the transverse sinuses, which curve laterally with an upward convexity to the mastoid angles of the parietal bones. The groove for the transverse sinus is usually deeper on the right, where it is generally a continuation of the superior sagittal sinus, while on the left it is frequently a continuation of the straight sinus. On both sides, the transverse sulcus is continuous with the sigmoid sulcus. Below the transverse sulcus, the internal occipital crest separates two shallow fossae that house the cerebellar hemispheres. The posterior clinoid process and the margins of the grooves for the transverse and superior petrosal sinuses all provide anchorage for the attached margin of the tentorium cerebelli.

DISARTICULATED INDIVIDUAL BONES

Individual bones are described in the appropriate chapters. The bones of the facial skeleton and cranial vault are described in the chapters on the face and scalp (Ch. 36), nose, nasal cavity and paranasal sinuses (Ch. 39), external and middle ear (Ch. 42), and orbit (Ch. 44). The sphenoid and mandible are described in the chapter on the infratemporal fossa (Ch. 38) and the occipital bone is described in the chapter on the back (Ch. 46).

JOINTS

The general characteristics of cranial sutures and the detailed anatomy of the temporomandibular joint and the atlanto-occipital joints are described in Chapters 5, 38 and 46, respectively. Sutural bones are described on page 560.

NEONATAL, PAEDIATRIC AND SENESCENT ANATOMY

The skull at birth

At birth, the calvaria is large in proportion to other skeletal parts, reflecting precocious cerebral maturation. The facial region is relatively small and constitutes only about one-eighth of the neonatal skull, whereas it constitutes about half of the adult skull (Fig. 34.8). Smallness of the face at birth is due mainly to the rudimentary stage of development of the mandible and maxillae; the teeth are unerupted and the maxillae are not yet pneumatized (invaded by air cells). The nose lies almost entirely between the orbits, and the lower border of the nasal aperture is only slightly lower in position than the orbital floors. Bones of the calvaria are unilaminar and lack diploë. Frontal and parietal tuberosities are prominent; in the frontal view, the greatest width occurs between the parietal tuberosities. The glabella, superciliary arches and mastoid processes are not developed and the cranial base is relatively short and narrow.

Ossification is incomplete, and many bones are still in several elements that are united by fibrous tissue or cartilage. The 'os incisivum' is continuous with the maxilla; pre- and postsphenoids may have just united. The two halves of the frontal bone and the mandible; the squamous, lateral and basilar parts of the occipital bone; and the petromastoid and squamotympanic parts of the temporal bone are all separate. The fibrous membrane within which the calvaria forms remains unossified at the six angles of the parietal bones, producing six fontanelles: two single midline (anterior and posterior) and two lateral pairs (sphenoidal/anterolateral and mastoid/posterolateral). The anterior fontanelle is the largest, measuring approximately 4 cm in anteroposterior and 2.5 cm in transverse dimensions. It occupies the junction between the sagittal, coronal and frontal sutures and is rhomboid in shape. The posterior fontanelle lies at the junction between the sagittal and lambdoid sutures and is triangular in shape. The sphenoidal (anterolateral) and mastoid (posterolateral) fontanelles are small and irregular in shape and lie at the sphenoidal and mastoid angles of the parietal bones, respectively.

At birth, the orbits appear relatively large. The developing tooth germs are generally contained within the alveolar crypts, although eruption of the upper central incisor teeth can occur prior to, or shortly after, birth. Temporal bones differ greatly from their adult form. The internal ear, tympanic cavity, auditory ossicles and mastoid antrum are all almost adult in size, the tympanic plate is an incomplete ring that has usually started to fuse with the squamous part, and the mastoid process is absent. The external acoustic meatus is short, straight and wholly cartilaginous. The external aspect of the tympanic membrane faces more inferiorly than laterally, in accord with the basal cranial contour. The stylomastoid foramen is exposed on the lateral surface of the skull, the styloid process has not yet commenced ossification, the mandibular fossa is flat and more lateral, and its articular tubercle is undeveloped. The paranasal sinuses are rudimentary or absent and only the maxillary sinuses are usually identifiable.

The skull is moulded by slow compression during vaginal birth. That part of the scalp that is more central in the birth canal is often temporarily oedematous (caput succedaneum) as a result of interference with venous return. Fontanelles and the openness and width of the sutures allow bones of the cranial vault some overlap during the process of birth; the skull is compressed in one plane with compensatory orthogonal elongation. These deformations disappear within the first week after birth.

Postnatal growth

Although postnatal growth of the calvaria (cranial vault) and facial skeleton usually proceeds in a coordinated fashion, these regions exhibit different rates and temporal periods of expression. In general, early growth of the vault is largely influenced by cerebral maturation while growth of the facial skeleton responds to spatial requirement for the development of the teeth and the muscles of mastication. Growth of the cranial base is largely independent of both vault and facial development, and therefore the three regions will be considered separately. (For further reading, see Belden (1998), Sgouros et al (1999), Sperber et al (2001) and Cunningham et al (2016).

Growth of the calvaria

Growth of the calvaria is rapid during the first year and then continues at a slower rate until the seventh year, when it has reached almost adult dimensions. For most of this period, expansion is largely

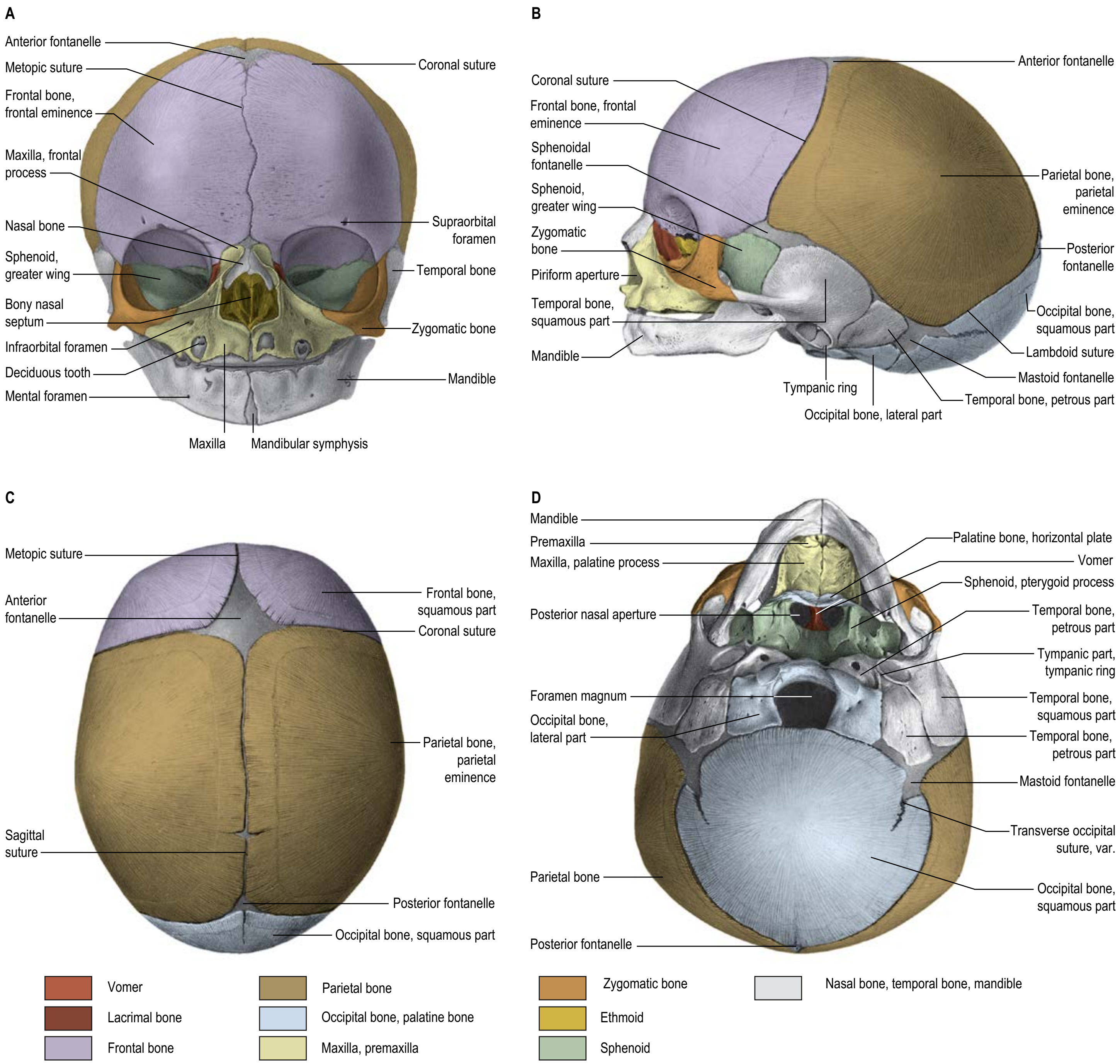
A
Anterior fontanelle
Metopic suture
Frontal bone, frontal eminence
Maxilla, frontal process
Nasal bone
Sphenoid, greater wing
Bony nasal septum
Infraorbital foramen
Deciduous tooth
Mental foramen
Maxilla
Mandibular symphysis
Coronal suture
Supraorbital foramen
Temporal bone
Zygomatic bone
Mandible
B
Coronal suture
Frontal bone, frontal eminence
Sphenoidal fontanelle
Sphenoid, greater wing
Zygomatic bone
Piriform aperture
Temporal bone, squamous part
Mandible
Tympanic ring
Occipital bone, lateral part
Anterior fontanelle
Parietal bone, parietal eminence
Posterior fontanelle
Occipital bone, squamous part
Lambdoid suture
Mastoid fontanelle
Temporal bone, petrous part
C
Metopic suture
Anterior fontanelle
Sagittal suture
Frontal bone, squamous part
Coronal suture
Parietal bone, parietal eminence
Posterior fontanelle
Occipital bone, squamous part
D
Mandible
Premaxilla
Maxilla, palatine process
Posterior nasal aperture
Foramen magnum
Occipital bone, lateral part
Parietal bone
Posterior fontanelle
Palatine bone, horizontal plate
Vomer
Sphenoid, pterygoid process
Temporal bone, petrous part
Tympanic part, tympanic ring
Temporal bone, squamous part
Temporal bone, petrous part
Mastoid fontanelle
Transverse occipital suture, var.
Occipital bone, squamous part
Vomer
Lacrimal bone
Frontal bone
Parietal bone
Occipital bone, palatine bone
Maxilla, premaxilla
Zygomatic bone
Ethmoid
Sphenoid
Nasal bone, temporal bone, mandible

Fig. 34.8 A–D, The neonatal skull: **A**, frontal aspect; **B**, lateral aspect; **C**, superior aspect; D, basal aspect. (Sobotta Atlas of Human Anatomy © Elsevier GmbH, Urban & Fischer, Munich.)

concentric; overall form is determined early in the first year and remains largely unaltered thereafter. However, the shape of the vault is not solely related to cerebral growth, but is also influenced by genetic factors that manifest in an extensive range of shapes and sizes that may be sufficient to allow an evaluation of ethnic origin. During the first and early second years, growth occurs primarily through ossification at apposed margins of bones (which possess an osteogenic layer), accompanied by some accretion and absorption of bone at surfaces in order to adapt to continually altering curvatures. Growth in breadth is said to take place at the sagittal, sphenofrontal, sphenotemporal, occipitomastoid and petro-occipital junctions, while growth in height is said to occur at the frontozygomatic and squamosal sutures, pterion and asterion. During this period, fontanelles are closed by progressive ossification of the bones around them, but separate isolated centres of ossification may develop into sutural bones (Fig. 34.9). The sphenoidal and posterior fontanelles close within 2 or 3 months of birth and the mastoid fontanelles usually close near the end of the first year. Wide variability in both the size and the timing of closure of the anterior fontanelle has been reported, but most will have closed by the middle of the second year and almost all will have closed by 24 months (Pindrik et al 2014).

Early in the first years, the calvarial bones start interlocking at sutural junctions and further expansion is largely achieved by accretion and absorption on external and internal bone surfaces, respectively. At the same time the bones also thicken, although this is not a uniform process. At birth, the vault is unilaminar; the tabular structure with intervening diploë is generally apparent soon thereafter. Thickening of the vault and development of external muscular markings reflect the influences of musculoskeletal maturation. The mastoid processes do not usually develop until the second year and they are pneumatized in the sixth year (Cunningham et al 2016). (For further reading about craniofacial morphology in preterm infants, see Paulsson and Bondemark 2009).

Growth of the cranial base

Growth of the cranial base, which is largely responsible for cranial lengthening, occurs at the cartilaginous joints between the sphenoid and

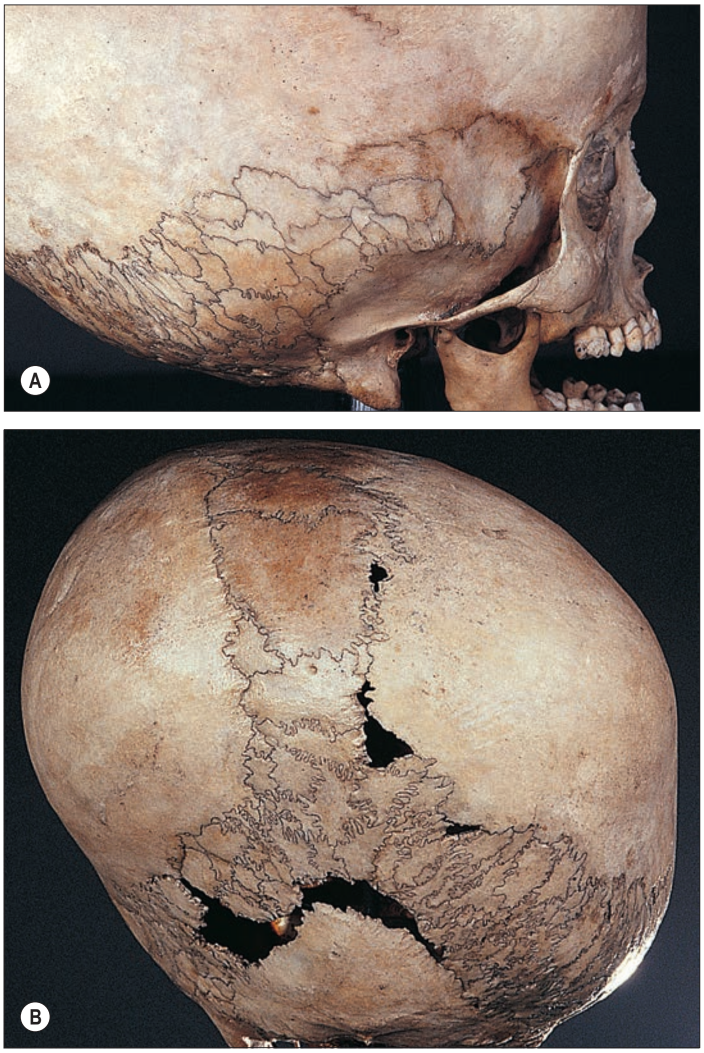

Fig. 34.9 The hydrocephalic skull of a 25-year-old male showing numerous sutural bones. **A**, Lateral view. **B**, Posterior view. (Courtesy of the Museum of the Royal College of Surgeons of England, photograph by Mr J Carr.)

ethmoid anteriorly, and especially between the sphenoid and occipital bones posteriorly (Lieberman et al 2000). Most of the growth occurs during the first five years of life (Sgouros et al 1999), but continues at the spheno-occipital synchondrosis until mid-teenage years. The prolonged period of continued expansion reflects a significant delaying mechanism that allows the continued and relatively late eruption of the permanent dentition. There is some evidence that growth may cease at about 15 years following eruption of the second molars, and this can often lead to insufficient space for growth of the third molars. A pubertal growth spurt has been ascribed to both sexes; it tends to occur some 2 years earlier in females and is likely to continue until the eighteenth year in the male (Ch. 23). The anterior cranial base is significantly shorter in very preterm infants (less than 27 weeks) (Paulsson and Bondemark 2009).

Growth of the facial skeleton

Growth of the facial skeleton occurs over a longer time period than is witnessed for the calvaria. The ethmoid and the orbital and upper nasal cavities have almost completed growth by the seventh year. Orbital and upper nasal growth is achieved by sutural accretion, with deposition of bone preferentially occurring on the facial aspects of the sutural junctions. The maxilla is carried downwards and forwards by expansion of the orbits and nasal septum and by sutural growth, especially at the fontanelles and zygomaticomaxillary and pterygomaxillary sutures. In the first year, growth in width occurs at the symphysis menti and mid-palatal, internasal and frontal sutures; such growth diminishes or even ceases when the symphysis menti and frontal suture close during the first few years, even though the mid-palatal suture persists until mature years. Facial growth continues up to puberty and shows a period of expansion that is linked to the growth spurt and hormonal influences of secondary sexual alteration. After sutural growth, near the end of the second year, expansion of the facial skeleton occurs by surface accretion on the face, alveolar processes and palate, and resorption in the walls of the maxillary sinuses, the upper surface of the hard palate and the labial aspect of the alveolar process. Coordinated growth and divergence of the pterygoid processes reflect deposition and resorption of bone on appropriate surfaces.

Obliteration of the calvarial sutures progresses with age, starting between 20 and 30 years internally and somewhat later on the exterior. Closure times vary greatly. Obliteration usually begins in the coronal or sagittal sutures and then extends into the lambdoid suture. The size of the mandible and maxillae diminish following the loss of teeth and consequent resorption of alveolar bone; this reduces the vertical depth of the face and increases the mandibular angles.

Craniosynostosis

Sutural growth makes an important contribution to growth of the skull, especially during the first few years of life. Premature closure of sutures (craniosynostosis) leads to restriction of growth along the sutures, producing morphological changes that may result in skull deformity (Sharma 2013). Biomechanical forces and genetically determined local expression of growth factors have been implicated in the aetiology of premature fusion but the reasons are not fully understood. Premature fusion may occur in one or more of the cranial sutures; when the sutures around the cranial base are involved, severe limitation of facial bone growth will occur. Metabolic disorders such as rickets and familial hypophosphatasia can also result in synostosis. Raised intracranial pressure with or without hydrocephalus, visual deterioration and mental retardation may result. Scaphocephaly (sagittal craniosynostosis) is the most common and leads to lengthening of the vault in an anteroposterior direction; it can also occur in conjunction with other sutures, e.g. Crouzon's syndrome. Coronal synostosis, either unilateral (plagiocephaly) or bilateral (brachycephaly/oxycephaly), is the next most frequently seen and results in reduced anteroposterior development with marked supraorbital recession. When it is unilateral, the face develops asymmetrically and is rotated away from the side with premature fusion. Metopic craniosynostosis (trigonocephaly) and pansynostosis (turricephaly), where both the coronal and sphenofrontal sutures are involved, are much less common.

Craniofacial dysostosis syndromes, such as Crouzon's, Apert's, Saethre–Chotzen, Pfeiffer's and Carpenter's, show varying degrees of calvarial synostoses that are usually accompanied by a significant lack of growth in the midface. Early release of the calvarial synostoses does not result in normal facial growth, and a midfacial osteotomy at the Le Fort III level is usually required later in life. When significant orbital hypertelorism develops, a transcranial bipartitioning procedure is needed in order to bring the two orbits together.

Altered patterns of skull growth resulting in altered profiles can also be achieved deliberately by affecting sutural growth using binding and other pressure, as has been practised in certain cultures of the world (Fig. 34.10) (Tubbs et al 2006). The earliest known record of the practice is from Iraq and dates back to 45,000 BCE (Gerszten and Gerszten 1995).

Congenital anomalies affecting the skull

A large number of malformations and anomalies affect the bones and associated soft tissue structures of the skull and are the result of a localized error of morphogenesis during embryological development. Many are recognized patterns of malformation that are presumed to share the same aetiology. They do not arise as the result of a single isolated error in morphogenesis and are described as syndromes; specific texts should be consulted for further details.

IDENTIFICATION FROM THE SKULL

There are many ways of identifying an individual; in physical and forensic anthropology, the most important are concerned with determining biological and personal identity (Wilkinson and Rynn 2012). Biological identity pertains to those features that allow an individual to be classified in relation to features present in other individuals, e.g. sex, age, ancestry and stature, whereas personal identity establishes criteria that are characteristic and discriminatory for a particular individual, e.g. DNA, fingerprints, facial appearance and dental information. The skull is a useful source of information for establishing both biological and personal identity and is probably the most studied region of the skeleton.

Sex estimation

The estimation of sex from a juvenile skull is notoriously unreliable. While sexual differences have been detected in measurements of the

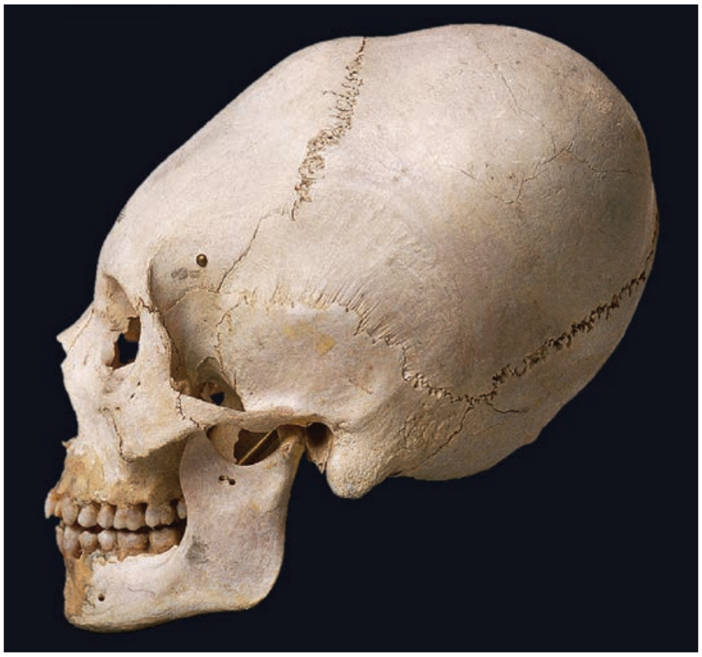

Fig. 34.10 Intentional skull modification: characteristic elongation of the cranial vault produced by head-binding of a newborn. (Courtesy of John Langdon.)

mandible, orbits, tooth size and pattern of dental eruption, they do not reach a level of statistical discrimination that will allow accurate and reliable assessment. It is equally difficult to assign sex to the face of a child because the faces of prepubertal boys and girls are comparable; perceivable sexual dimorphism is not generally manifest until secondary sexual development is under way. Growth in the female face ceases in advance of that of the male and therefore female sex-related characteristics are more paedomorphic. The defining characteristics of sex in an adult skull are therefore male in orientation and reflect the effects of the increased mass of the muscles of mastication, which are attached to the mandible, and of the muscles associated with maintaining the erect head. It is reported that using the skull alone, sex can be predicted with over 80% accuracy in the adult, which is encouraging, given that research has shown that the correct sex can usually be predicted from the adult living face with 96% accuracy.

Generally speaking, a male skull is more robust than the more gracile female skull, although there are obvious genetic, and therefore ancestral, variations that must be considered when attempting to assign sex from a skull. A female forehead is generally higher, more vertical and more rounded than a male forehead (where the frontal eminences are retained). A male mandible is generally more robust and larger than a female mandible; it displays a greater height in the region of the symphysis menti, the chin is squarer, the condyles are larger, the sites of muscle attachments are more pronounced and the gonial angle is generally less than 125°. A male skull generally also has thicker and more rounded orbital margins; pronounced supraorbital ridges; a well-defined glabella in the midline above the root of the nose; more pronounced temporal lines; and a supramastoid crest that extends posterior to the external acoustic meatus.

Other sites of muscle attachment on the skull also reflect the biomechanical requirement to keep the more robust male head erect. They include the mastoid process for sternocleidomastoid, and the nuchal lines, especially the external occipital protuberance, for the attachment of the ligamentum nuchae: both are more robust in a male skull. The male cranial base is generally more robust and the bone is thicker than in a female skull, which means that this area of the skull survives burial particularly well and is therefore of value in sex identification from fragmentary remains.

Age estimation

Age is a continuous variable; establishing chronological age from a skull is predicated on the concept that structures change with age at a relatively constant and predictable rate. The relationship between chronological age and skeletal maturity is closest in the juvenile years, and therefore greater accuracy is achieved in the prediction of age from the juvenile than from the adult skull.

The neonatal skull has been described above. Examples of additional features that allow reliable age determination throughout the subadult years are: development of the nasal spine (by year 3), completion of the hypoglossal canal (by year 4), formation of the foramen of Huschke (by year 5), ossification of the dorsum sellae (by year 5), and fusion of the different parts of the occipital bone (by year 7) (Cunningham et al 2016). The fontanelles are usually all closed by the end of the second year; the posterolateral is the first to close in the first 2 months after birth, and the anterior fontanelle is the last to close around the middle to end of the second year. The mastoid process appears in the second year and the metopic suture between the two frontal bones is usually closed by the end of the first year. The spheno-occipital synchondrosis will fuse between 11 and 16 years in the female and 13 and 18 years in the male, while the vomer and the ethmoid will fuse between 20 and 30 years of age. The last part of the skull to show active age-related growth is the jugular synchondrosis (also known as the jugular growth plate), a small triangular area sited posterolateral to the jugular foramen in the occipitotemporal suture. Fusion here has been reported to commence in the second and third decades, depending on population group, and bilateral fusion may not be completed before the middle of the fourth decade; in a small proportion of individuals, the plate may remain unfused into the sixth decade. Closure of the cranial sutures is age-related but the correlation is not strong and displays strong genetic variation. Thus, while it can be said that suture closure may begin in the early part of the third decade, and it is likely that many of the sutures will be obliterated with advancing age, it is not a reliable means of establishing the age of an individual. See Cunningham et al (2016) for further information on age estimation from the juvenile skeleton.

The most accurate means of estimating age from the skull (of both a living and a deceased individual) is by assessment of dental maturation. Tooth development can be studied throughout the entire juvenile age span (from the early embryo to the adolescent), and importantly, dental age and chronological age have been shown to exhibit a stronger correlation than skeletal and chronological age due to being influenced less by environmental factors compared to the skeleton. Further, the teeth tend to survive inhumation successfully and are remarkably resilient to extrinsic factors, ensuring their value in forensic investigations.

The chronological pattern of dental maturation is well documented and is an extremely important tool for age evaluation. Tooth development can be separated into a number of well-defined stages: deciduous mineralization (crown and root), deciduous emergence and maturation, deciduous root resorption, shedding of deciduous teeth, mineralization (crown and root) of permanent dentition, emergence and maturation of deciduous dentition, and attrition of permanent crowns. These stages do not occur in a linear fashion; while some of the deciduous teeth are emerging, permanent teeth are already being formed. For example, mineralization of the deciduous central incisor commences around the fifteenth week post fertilization, and this is the first tooth to emerge within the first 5 months after birth. All deciduous teeth are in occlusion by around 3 years of age. The first deciduous teeth to be shed are generally the central and lateral incisors around 7 years of age, when the permanent incisors emerge. The last deciduous tooth to be shed is generally the second molar in the tenth year. The first permanent tooth to show mineralization is the first molar, which occurs around the time of birth (sometimes earlier and sometimes later); it is also the first permanent tooth to emerge at around 6 years of age, and it will reach occlusion by the end of the seventh year. The last permanent tooth to emerge is the third molar; the variability of this occurrence makes it of restricted value for age prediction.

The time taken for a crown to form can be calculated from ground sections with considerable accuracy by counting the number of daily cross-striations from the neonatal line. These cross-striations are considered to result from the circadian rhythm inherent in the rate of enamel matrix secretion. For permanent teeth, the time taken for the crown to form can be calculated by counting the number of the enamel striae and multiplying by the individual's periodicity. Patterns of mineralization, emergence and shedding may be supplemented by analyses of tooth length and apical width ratios, cementum apposition, secondary dentine formation, incremental enamel lines, attrition rates, root translucency and dentine transparency (Whittaker and MacDonald 1989). Chemical analysis of the stable isotopes of carbon, oxygen and nitrogen from teeth can provide important information concerning the nature of the diet of an individual and is used in paleodiet analysis and in studies of pathophysiology and nutrition in archaeological and living human populations (Reitsema 2013).

Morphological assignment of ancestry

Physical anthropologists working in both archaeological and forensic arenas are frequently asked to assign a race/ancestry to a given skeleton, in order to facilitate an investigation into an unidentified body (Edgar and Hunley 2009). The traditional view of ancestry is as 'one of the major subdivisions of mankind, regarded as having a common origin and exhibiting a relatively constant set of physical traits' (Bamshad and Olson 2003). However, the usefulness of being able to classify ancestry when attempting to identify an individual from decomposed human remains varies depending on the degree of admixture in the local population compared to the level of admixture in the individual. For example, ancestry does not form part of the biological profile in some South American countries, because the majority of the local population is a mix of several ancestry groups; whereas if a body found in the Highlands of Scotland was assessed as being anything other than of Caucasoid ancestry, it might narrow the field of search considerably.

In forensic/biological anthropology there are at least four broad, overlapping ancestry groups. A relatively high proportion of individuals exhibit a degree of admixture such that variation within a group is often as great as the variation between groups. With the occasional exception (e.g. pelvis (Iscan and Cotton 1985) and femur (Gill 2001)), ancestry is almost exclusively evident in the skull.

Forensic facial approximation, reconstruction and depiction

There are four primary methods of legally identifying a body: DNA, fingerprint, dental and radiological matching. These are all matching processes, meaning that both postmortem and antemortem equivalent data are required for comparison to one another. If the body is past a certain point of decomposition, postmortem data might be unobtainable or corrupted: even DNA is damaged in both fire and water. Alternatively or additionally, the antemortem data might not exist if the individual in life was not on any databases, which is more common than one might suppose: a healthy, law-abiding citizen with perfect teeth might not be on any of these databases. When an investigation into an unidentified body runs into this problem, using forensic facial reconstruction to present an image of the face via the media might be the only way to generate leads for the investigation. Eliciting a recognition reaction from a friend or a family member of a missing person might in turn generate a DNA or fingerprint sample, a set of dental records for comparison, or even a missing person photograph upon which Craniofacial Superimposition can be performed, aligning the 3D skull with the photograph for a direct anatomical comparison, without all the estimations and averages involved in the initial facial reconstruction.

Commonly applied techniques to estimate a face from a skull (Fig. 34.11) combine three areas: the soft tissue depth and pattern across the face; facial feature estimation (eyes, nose, lips and ears all based on separate research); anatomical interpretation of the musculature, including attachment sites and muscle shape. The anatomical methodology is underpinned by scientific standards, anthropometry and morphological patterning in order to predict distinctive facial characteristics. The process can be automated or practitioner-led; although a few practitioners still use traditional clay modelling, most contemporary facial reconstructions are produced using non-invasive clinical/surface imaging, 3D digital technology and photo-editing software. Method summaries are described in a number of anthropology texts (Clement and Ransom 1998, Stephan 2009, Wilkinson 2010, Wilkinson and Rynn 2012).

Bonus e-book content

Fig. 34.4 C, A true cephalometric lateral radiograph of the skull and cervical spine, young adult.

Fig. 34.11 Facial superimposition: a live capture image of the skull has been manipulated into the identical position and size of the face in the photograph.

Key references

Berkovitz BKB, Moxham BJ 1994 Color Atlas of the Skull. London: Mosby–Wolfe.

This atlas gives a clear illustration of the different components of the skull.

Cunningham CA, Scheuer L, Black S 2016 Developmental Juvenile Osteology, 2nd ed. London: Academic Press.

This text was the first to address the subject of the development of the juvenile skeleton in a single volume.

Tubbs RS, Salter EG, Oakes WJ 2006 Artificial deformation of the human skull: a review. Clin Anat 19:372–7.

This article highlights the plasticity of the human skull.

Whittaker DK, MacDonald DG 1989 A Colour Atlas of Forensic Dentistry. London: Wolfe.

An atlas that, although not recent, is an excellent baseline resource for dental anatomy.

Wilkinson C, Rynn C 2012 Craniofacial Identification. Cambridge: Cambridge University Press.

Forensic facial reconstruction is an area that requires an equal amount of scientific and artistic talent. This text addresses this complex subject in an approachable manner.

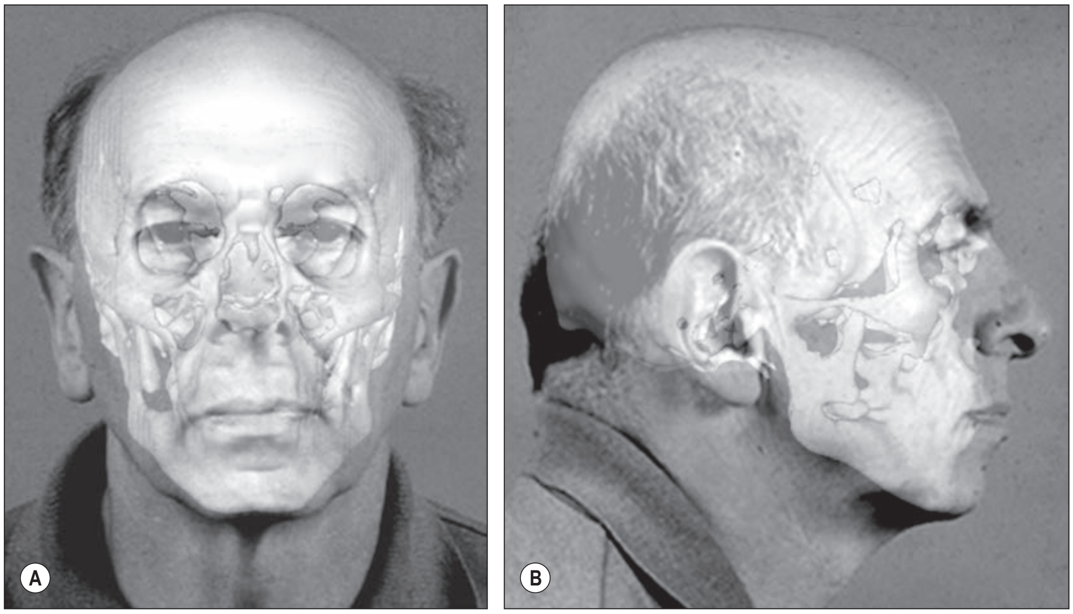

Fig. 34.11 Facial superimposition: a live capture image of the skull has been manipulated into the identical position and size of the face in the photograph. (Courtesy of Professor Caroline Wilkinson and Professor Sue Black, Centre for Anatomy and Human Identification, University of Dundee.)

References

Ambekar S, Sonig A, Nanda A 2012 Dorello's canal and Gruber's ligament: historical perspective. J Neurol Surg B Skull Base 73:430–433.

Bamshad M, Olson S 2003 Does race exist? Sci Am 289:78–85.

This article challenges our perspective on what race is and what that actually means for our modern, diverse world.

Barges-Coll J, Fernandez-Miranda JC, Prevedello DM et al 2010 Avoiding injury to the abducens nerve during expanded endonasal endoscopic surgery: anatomic and clinical case studies. Neurosurgery 67:144–54.

Belden CJ 1998 The skull base and calvaria. Adult and pediatric. Neuroimaging Clin N Am 8:1–20.

Bellary SS, Steinberg A, Mirzayan N et al 2013 Wormian bones: a review. Clin Anat 26:922–7.

Berkovitz BKB, Moxham BJ 1994 Color Atlas of the Skull. London: Mosby–Wolfe.

This atlas gives a clear illustration of the different components of the skull.

Clement J, Ransom DL 1998 Craniofacial Identification in Forensic Medicine. Boca Raton: CRC Press.

Cunningham CA, Scheuer L, Black S 2016 Developmental Juvenile Osteology, 2nd ed. London: Academic Press.

This text was the first to address the subject of the development of the juvenile skeleton in a single volume.

Edgar HJH, Hunley KL 2009 Race reconciled?: How biological anthropologists view human variation. Am J Phys Anthropol 139:1–4.

This reference gives a good overview of how to best describe and interpret human variation in the context of 'race'.

Fernandez-Miranda JC, Tormenti M, Latorre F et al 2012 Endoscopic endonasal middle clinoidectomy: anatomical, radiological, and technical note. Neurosurgery 71:ONS233–9; discussion ONS239.

Fernandez-Miranda JC, Gardner PA, Snyderman C et al 2014 Clival chordomas: a pathological, surgical and radiotherapeutic review. Head Neck 36:892–906.

Gerszten PC, Gerszten E 1995 Intentional cranial deformation: a disappearing form of self-mutilation. Neurosurgery 37:374–381.

Gill GW 2001 Racial variation in the proximal and distal femur: heritability and forensic utility. J Forens Sci 46:791–9.

Iaconetta G, Fusco M, Samii M 2003 The sphenopetroclival venous gulf: a microanatomical study. J Neurosurg 99:366–75.

Iscan MY, Cotton TS 1985 The effect of age on the determination of race from the pelvis. J Hum Evol.14:275–82.

Kakizawa Y, Abe H, Fukushima Y et al 2007 The course of the lesser petrosal nerve on the middle cranial fossa. Neurosurgery 61:15–23.

Kawase T, Toya S, Shiobara R et al 1985 Transpetrosal approach for aneurysms of the lower basilar artery. J Neurosurg 63:857–61.

Kerr RG, Tobler WD, Leach JL et al 2012 Anatomic variation of the optic strut: classification schema, radiologic evaluation, and surgical relevance. J Neurol Surg B Skull Base 73:424–9.

Krmpotić-Nemanić J, Vinter I, Kelovizć Z et al 2005 Postnatal changes of the clivus. Ann Anat 187:277–80.

Krmpotić Nemanić J, Vinter I, Ehrenfreund T et al 2009 Postnatal changes in the styloid process, vagina processus styloidei, and stylomastoid foramen in relation to the function of muscles originating from the styloid process. Surg Radiol Anat 31:43–8.

Lieberman DE, Pearson OM, Mowbray KM 2000 Basicranial influence on overall cranial shape. J Hum Evol 38:291–315.

Ma S, Baillie LJ, Stringer MD 2012 Reappraising the surface anatomy of the pterion and its relationship to the middle meningeal artery. Clin Anat 25:330–9.

Morera VA, Fernandez-Miranda JC, Prevedello DM et al 2010 'Far-medial' expanded endonasal approach to the inferior third of the clivus: the transcondylar and transjugular tubercle approaches. Neurosurgery 66:211–19.

Ozveren MF, Uchida K, Aiso S et al 2002 Meningovenous structures of the petroclival region: clinical importance for surgery and intravascular surgery. Neurosurgery 50:829–36.

Paluzzi A, Fernandez-Miranda JC, Gardner P 2012 Retracing the etymology of terms in neuroanatomy. Clin Anat 25:1005–14.

Paulsson L, Bondemark L 2009 Craniofacial morphology in prematurely born children. Angle Orthodontist 79:276–83.

Pindrik J, Ye X, Ji BG et al 2014 Anterior fontanelle closure and size in full-term children based on head computed tomography. Clin Pediatr (Phila) 53:1149–57.

Reitsema LJ 2013 Beyond diet reconstruction: stable isotope applications to human physiology, health, and nutrition. Am J Hum Biol 225:445–56.

Rhoton AL 2007 Cranial Anatomy and Surgical Approaches. Baltimore: Lippincott Williams & Wilkins.

Seoane E, Rhoton AL Jr 1999 Suprameatal extension of the retrosigmoid approach: microsurgical anatomy. Neurosurgery 44:553–60.

Sgouros S, Natarajan K, Hockley AD et al 1999 Skull base growth in childhood. Pediatr Neurosurg 31:259–68.

Sharma RK 2013 Craniosynostosis. Ind J Plast Surg 46:18–27.

Sperber GH, Guttmann GD, Sperber SM 2001 Craniofacial Development, 4th ed. Ontario, BC: Decker.

Stephan CN 2009 Craniofacial identification: techniques of facial approximation and craniofacial superimposition. Handbook of Forensic Anthropology and Archaeology 25:2304–21.

Tauber M, van Loveren HR, Jallo G et al 1999 The enigmatic foramen lacerum. Neurosurgery 44:386–91.

Tubbs RS, Salter EG, Oakes WJ 2006 Artificial deformation of the human skull: a review. Clin Anat 19:372–7.

This article highlights the incredible plasticity of the human skull.

Vogl TJ, Bisdas S 2009 Differential diagnosis of jugular foramen lesions. Skull Base 19:3–16.

Weinzweig J, Kirschner R, Farley A et al 2003 Metopic synostosis: defining the temporal sequence of normal suture fusion and differentiating it from synostosis on the basis of computed tomography images. Plast Reconstr Surg 112:1211–18.

Whittaker DK, MacDonald DG 1989 A Colour Atlas of Forensic Dentistry. London: Wolfe.

An exceptionally useful atlas that, although not recent, is an excellent baseline resource for dental anatomy.

Wilkinson C 2010 Facial reconstruction -anatomical art or artistic anatomy? J Anat 216: 235–50.

Wilkinson C, Rynn C 2012 Craniofacial Identification. Cambridge: Cambridge University Press.

Forensic facial reconstruction is an area that requires an equal amount of scientific and artistic talent. This text addresses this complex subject in an approachable manner.

CHAPTER

35

Neck

The neck extends from the base of the cranium and the inferior border of the mandible to the thoracic inlet.

SKIN

The skin in the neck is normally under tension. Lines of greatest tension have been termed 'relaxed skin tension lines'; surgical incisions made along these lines are said to heal better with minimal postoperative scarring.

Cutaneous vascular supply and lymphatic drainage

The blood vessels supplying the skin of the neck are derived principally from the facial, occipital, posterior auricular and subclavian arteries. They form a rich network within platysma and in the subdermal plexus, which accounts for the viability of the various skin flaps raised during neck dissection, irrespective of whether or not platysma is included. Great care must be taken in their design to avoid three-point junctions especially if the area has been irradiated previously or is infected, when its viability can be compromised.

The anterior cervical skin is supplied mainly by the superior thyroid artery and the transverse cervical branch of the subclavian artery. The posterior skin is supplied by branches from the occipital artery and the deep cervical and transverse cervical branches of the subclavian artery. The superior skin is supplied by the occipital artery and its upper sternocleidomastoid branch, and the submandibular and submental branches of the facial artery. Inferiorly, the skin is supplied by the transverse cervical and/or suprascapular branches of the subclavian artery.

The pattern of venous drainage of the skin of the neck mirrors the arterial supply: the veins drain into the jugular and facial veins. The profuse blood supply to the facial and neck skin facilitates the design of random flaps, which can often be made larger in this region than elsewhere.

Many lymphatic vessels draining the superficial cervical tissues skirt the borders of sternocleidomastoid to reach the superior or inferior deep cervical nodes. Some pass over sternocleidomastoid and the posterior triangle to drain into the superficial cervical and occipital nodes (see Fig. 35.15). Lymph from the superior region of the anterior triangle drains to the submandibular and submental nodes. Vessels from the anterior cervical skin inferior to the hyoid bone pass to the anterior cervical lymph nodes near the anterior jugular veins, and their efferents go to the deep cervical nodes of both sides, including the infrahyoid, prelaryngeal and pretracheal groups (**Fig. 35.1A**). An anterior cervical node often occupies the suprasternal space (of Burns).

Cutaneous innervation

The cervical skin is innervated by branches of cervical spinal nerves, via both dorsal and ventral rami (see Fig. 47.8). The dorsal rami supply skin over the back of the neck and scalp, and the ventral rami supply skin covering the lateral and anterior portions of the neck, and the angle of the mandible (**Fig. 35.1B**). The dorsal rami of the first, sixth, seventh and eighth cervical nerves have no cutaneous distribution in the neck. The greater occipital nerve mainly supplies the scalp; it comes from the medial branch of the dorsal ramus of the second cervical nerve. The medial branches of the dorsal rami of the third, fourth and fifth cervical nerves pierce trapezius to supply skin over the back of the neck sequentially. The ventral rami of the second, third and fourth cervical nerves supply named cutaneous branches (the lesser occipital, great auricular, transverse cutaneous and supraclavicular nerves), via the cervical plexus (see Fig. 35.1B) (see p. 595 for details of the motor branches of the cervical plexus).

Lesser occipital nerve

The lesser occipital nerve is derived mainly from the second cervical nerve (although fibres from the third cervical nerve may sometimes contribute). It first passes anterior to the plane of the accessory nerve (spinal accessory nerve) before winding around it and becoming anterior to it. It next ascends along the posterior margin of sternocleidomastoid. Near the cranium it perforates the deep fascia and passes up on to the scalp behind the auricle to supply the skin and connect with the great auricular and greater occipital nerves and the auricular branch of the facial nerve. Its auricular branch supplies the skin on the upper third of the medial aspect of the auricle and connects with the posterior branch of the great auricular nerve. The auricular branch is occasionally derived from the greater occipital nerve. It has been suggested that compression or stretching of the lesser occipital nerve contributes to cervicogenic headache (Lucas et al 1994).

Great auricular nerve

The great auricular nerve is the largest ascending branch of the cervical plexus. It arises from the second and third cervical rami, encircles the posterior border of sternocleidomastoid, perforates the deep fascia and ascends on the muscle beneath platysma with the external jugular vein. On reaching the parotid gland, it divides into anterior and posterior branches. The anterior branch is distributed to the facial skin over the parotid gland and connects in the gland with the facial nerve. This cross-innervation between somatic sensory supply (great auricular) and parasympathetic secretomotor fibres to the parotid is considered to be part of the anatomical basis for the phenomenon of gustatory sweating (Frey's syndrome), seen after parotidectomy with its inherent disruption of the secretomotor nerve supply. The posterior branch supplies the skin over the mastoid process and on the back of the auricle (except its upper part); a filament pierces the auricle to reach the lateral surface, where it is distributed to the lobule and concha. Efforts are made to preserve the posterior branch at parotid surgery in order to avoid a sensory deficit of the pinna. The posterior branch communicates with the lesser occipital nerve, the auricular branch of the vagus and the posterior auricular branch of the facial nerve. Division of the greater auricular nerve during neck surgery results in loss of sensation of a variable amount of the lower half of the auricle, which some patients initially find unpleasant.

Transverse cervical cutaneous nerve

The transverse cervical cutaneous nerve arises from the second and third cervical rami. It curves round the posterior border of sternocleidomastoid near its midpoint and runs obliquely forwards, deep to the external jugular vein, to the anterior border of the muscle. It perforates the deep cervical fascia, and divides under platysma into ascending and descending branches that are distributed to the anterolateral areas of the neck. The ascending branches ascend to the submandibular region, forming a plexus with the cervical branch of the facial nerve beneath platysma. Some branches pierce platysma and are distributed to the skin of the upper anterior areas of the neck. The descending branches pierce platysma and are distributed anterolaterally to the skin of the neck, as low as the sternum.

Supraclavicular nerves

The supraclavicular nerves arise from a common trunk formed from rami from the third and fourth cervical nerves and emerge at the posterior border of sternocleidomastoid. Descending under platysma and the deep cervical fascia, the trunk divides into medial, intermediate and lateral (posterior) branches, which diverge to pierce the deep fascia a little above the clavicle. The medial supraclavicular nerves run inferomedially across the external jugular vein and the clavicular and sternal heads of sternocleidomastoid to supply the skin as far as the midline and as low as the second rib. They also supply the sternoclavicular joint. The intermediate supraclavicular nerves cross the clavicle to supply the skin over pectoralis major and deltoid down to the level of the second rib, next to the area of supply of the second thoracic nerve. Overlap between these nerves is minimal. The lateral supraclavicular nerves descend superficially across trapezius and the acromion, supplying the skin of the upper and posterior parts of the shoulder.

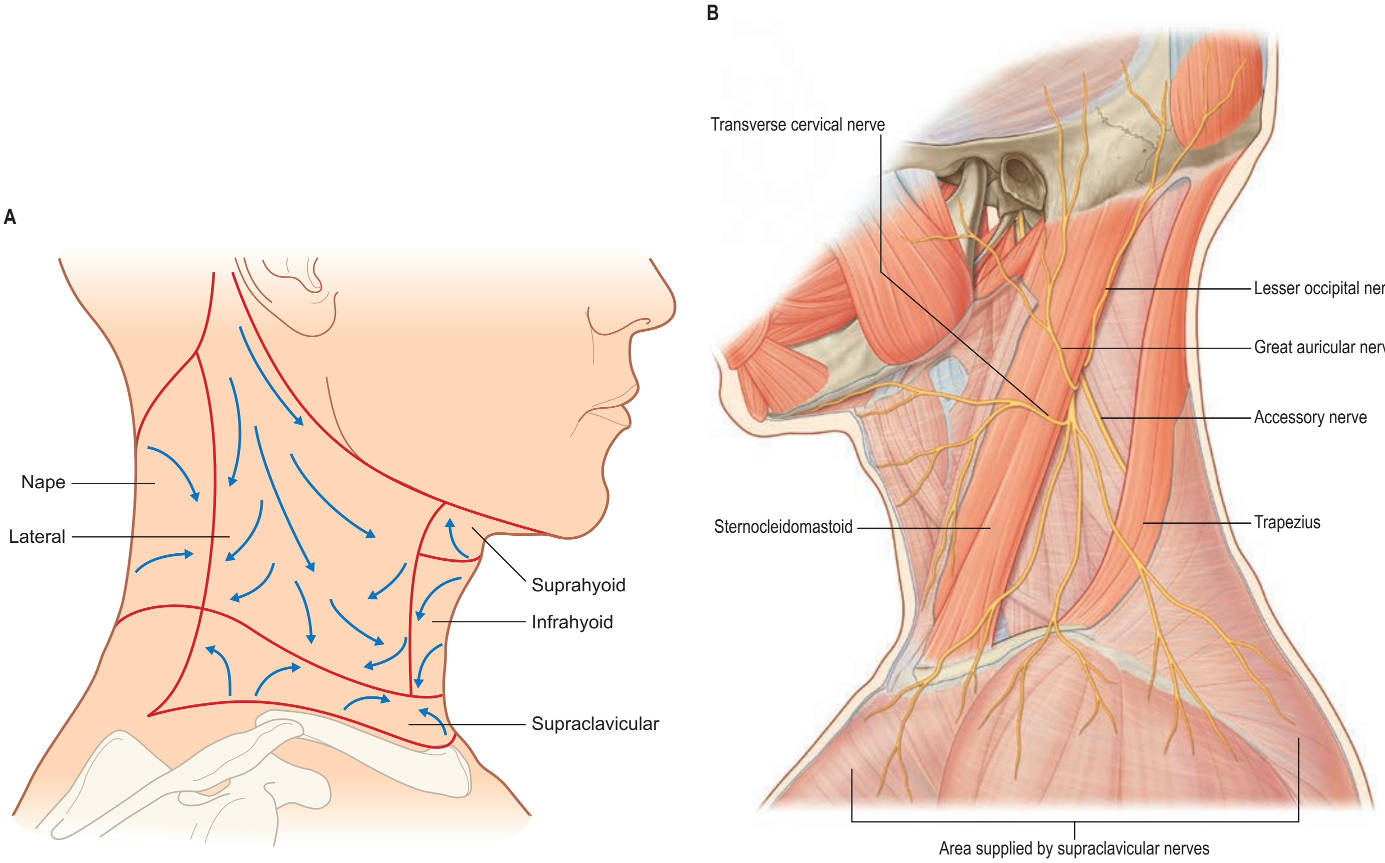
A
Nape
Lateral
Suprahyoid
Infrahyoid
Supraclavicular
B
Transverse cervical nerve
Lesser occipital nerve
Great auricular nerve
Accessory nerve
Sternocleidomastoid
Trapezius
Area supplied by supraclavicular nerves

Fig. 35.1 **A**, Direction of lymphatic drainage of the skin of the neck. The lymphatics of the skin in the suprahyoid region drain to level I, the submental and submandibular lymph nodes. The lymphatics of the skin of the rest of the neck drain to levels II, III and IV, apart from the posterior lateral neck skin lymphatics which drain into the spinal accessory nodes in the posterior triangle (refer to Fig. 35.3B for levels). **B**, The cutaneous branches of the cervical plexus. The accessory nerve is also shown as it crosses the posterior triangle to supply trapezius. Note that the interval between the upper attachments of sternocleidomastoid and trapezius is not normally as extensive as shown here (A, Adapted with permission from Warner L, Jennings C, Watkinson JC 2018 Surgical anatomy of the neck. In: Watkinson JC, Clarke RW (eds) Scott-Brown's Otorhinolaryngology: Head and Neck Surgery, Volume 3, 8th ed. Boca Raton: CRC Press. B, Adapted from Drake RL, Vogl AW, Mitchell A (eds) Gray's Anatomy for Students, 2nd ed. Elsevier, Churchill Livingstone. Copyright 2010.)

BONES, JOINTS AND CARTILAGES

The bones and cartilages of the neck are the cervical vertebrae and the hyoid bone, and the cartilages of the upper respiratory tract, including the larynx. The cervical vertebrae, the occipital bone and the atlanto-occipital and atlanto-axial joints are described in Chapter 46, and the laryngeal cartilages are described in Chapter 41.

Hyoid bone

The U-shaped hyoid bone (**Fig. 35.2**) is suspended from the tips of the styloid processes by the stylohyoid ligaments. It has a body and two greater and two lesser horns or cornua.

Body

The body is irregular, elongated and quadrilateral. Its anterior surface is convex, faces anterosuperiorly, and is crossed by a transverse ridge with a slight downward convexity. A vertical median ridge often bisects the upper part of the body but rarely extends to the lower part. The posterior surface is smooth and concave, faces posteroinferiorly, and is separated from the epiglottis by the thyrohyoid membrane and loose areolar tissue. There is a bursa between the hyoid bone and the membrane. Geniohyoid is attached to most of the anterior surface of the body, above and below the transverse ridge; the medial part of hyoglossus invades the lateral geniohyoid area. The lower anterior surface gives attachment to mylohyoid, the line of attachment lying above sternohyoid medially and omohyoid laterally. The lowest fibres of genioglossus, the hyoepiglottic ligament and (most posteriorly) the thyrohyoid membrane are all attached to the rounded superior border. Sternohyoid is attached to the inferior border medially and omohyoid is attached laterally.

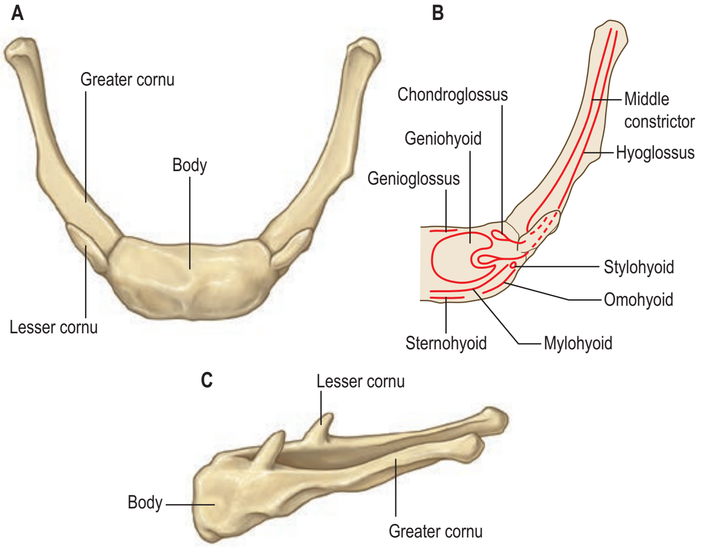
A
Greater cornu
Body
Lesser cornu
B
Chondroglossus
Middle constrictor
Geniohyoid
Hyoglossus
Genioglossus
Stylohyoid
Omohyoid
Sternohyoid
Mylohyoid
C
Lesser cornu
Body
Greater cornu

Fig. 35.2 The hyoid bone. **A**, Anterosuperior aspect. **B**, Anterosuperior aspect, showing the positions of muscular attachments. **C**, Lateral aspect.

Occasionally, the medial fibres of thyrohyoid and, when present, levator glandulae thyroideae, are attached along the inferior border.

The body of the hyoid is removed to excise thyroglossal duct cysts together with its tract (Sistrunk's procedure). During descent from its origin within the tongue base, the duct tract passes either posterior or anterior or through the body of the hyoid, which must be excised in continuity.

Greater cornua

In early life, the greater cornua are connected to the body by cartilage, but after middle age they are usually united by bone. They project backwards (curving posterolaterally) from the lateral ends of the body. They are horizontally flattened and taper posteriorly, and each ends in a tubercle. When the throat is gripped between finger and thumb above the thyroid cartilage, the greater cornua can be identified and the bone can be moved from side to side.

The middle pharyngeal constrictor and, more laterally (i.e. superficially), hyoglossus are attached along the whole length of the upper surface of each greater cornu. Stylohyoid is attached near the junction of the cornu with the body. The fibrous loop for the digastric tendon is attached lateral and a little posterior to hyoglossus. The thyrohyoid membrane is attached to the medial border and thyrohyoid is attached to the lateral border. The oblique inferior surface is separated from the thyrohyoid membrane by fibroareolar tissue.

Lesser cornua

The lesser cornua are two small conical projections at the junctions of the body and greater cornua. At its base, each is connected to the body by fibrous tissue and occasionally to the greater cornu by a synovial joint that occasionally becomes ankylosed.

The middle pharyngeal constrictors are attached to the posterior and lateral aspects of the lesser cornua. The stylohyoid ligaments are attached to their apices and are often partly calcified, and the chondroglossi are attached to the medial aspects of their bases.

Ossification

The hyoid bone develops largely from cartilages of the second (Reichert's cartilage) and third pharyngeal arches: the lesser cornua from the second and the greater cornua from the third. The body appears to develop from a midline mesenchymal condensation of the hypobranchial eminence (Rodríguez-Vázquez et al 2011). Chondrification is seen in embryos at stages 18–20 (42–50 postfertilization days). Ossification of the bone is seen after postmenstrual week 30. The body of the hyoid bone is ossified by postnatal month 4 and the greater cornua by postnatal month 6. Ossification proceeds from six centres, i.e. a pair for the body and one for each cornu. Ossification begins in the greater cornua towards the end of intrauterine life, in the body shortly before or after birth, and in the lesser cornua around puberty. The greater cornual apices remain cartilaginous until the third decade and epiphyses may occur here. They fuse with the body. Synovial joints between the greater and lesser cornua may be obliterated by ossification in later decades.

Joints

The atlanto-occipital and atlanto-axial joints are described in Chapter 46.

TRIANGLES OF THE NECK

Anterolaterally, the neck appears as a somewhat quadrilateral area, limited superiorly by the inferior border of the mandible and a line continued from the angle of the mandible to the mastoid process, inferiorly by the upper border of the clavicle, anteriorly by the anterior median line, and posteriorly by the anterior margin of trapezius. This quadrilateral area can be further divided into anterior and posterior triangles by sternocleidomastoid, which passes obliquely from the sternum and clavicle to the mastoid process and occipital bone (Fig. 35.3). These triangles and subdivisions are somewhat arbitrary because many major structures – arteries, veins, lymphatics, nerves and some viscera – transgress their boundaries without interruption. The triangles provide invaluable assistance in surface anatomical and clinical examination.

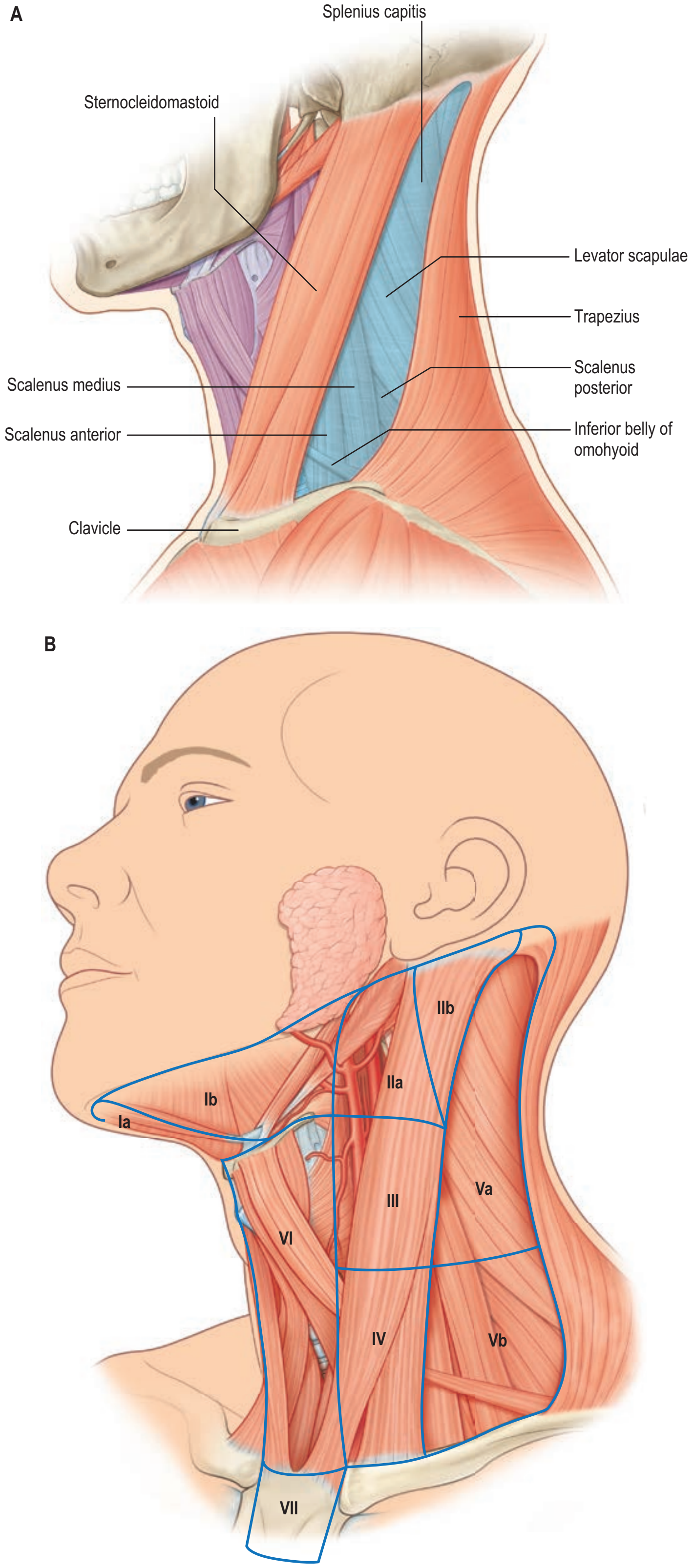

Fig. 35.3 **A**, The anterior and posterior triangles of the neck, left lateral aspect. See the note in the caption to Fig. 35.1B. **B**, Surgical levels of the neck. (A, Adapted with permission from Drake RL, Vogl AW, Mitchell A (eds) Gray's Anatomy for Students, 2nd ed. Elsevier, Churchill Livingstone. Copyright 2010. B, With permission from Brennan P, Standring S, Wiseman S (eds) Gray's Surgical Anatomy. Elsevier. Copyright 2019.)

Anterior triangle of the neck

By tradition, the anterior triangle of the neck is bounded anteriorly by the median line of the neck and posteriorly by the anterior margin of sternocleidomastoid. It should be noted that the bulk of sternocleidomastoid is not included in the delineation of either the anterior or posterior triangles, even though the most important structures in the neck, the major vessels and lymph nodes of levels II, III and IV, lie deep to the muscle (see Fig. 35.3). The base of the triangle is the inferior border of the mandible and its projection to the mastoid process, and the apex is at the manubrium sterni. The anterior triangle can be subdivided into suprahyoid and infrahyoid areas above and below the hyoid bone, and into digastric, submental, muscular and carotid triangles by the passage of digastric and omohyoid across the anterior triangle (see Fig. 35.3). The lymphatic contents of both the anterior and posterior triangles can also be divided into levels I to V, facilitating radiological reporting as well as neck dissection terminology (Fig. 35.3B).

Digastric triangle

The digastric triangle is bordered above by the lower border of the mandible and its projection to the mastoid process, posteroinferiorly by the posterior belly of digastric and by stylohyoid, and anteroinferiorly by the anterior belly of digastric. It is covered by the skin, superficial fascia, platysma and deep fascia, which contain branches of the facial and transverse cutaneous cervical nerves. Its floor is formed by mylohyoid and hyoglossus. The anterior region of the digastric triangle contains the submandibular gland, which has the facial vein superficial to it and the facial artery deep to it. The submental and mylohyoid arteries and nerves lie on mylohyoid. The submandibular lymph nodes are variably related to the submandibular gland. The posterior region of the digastric triangle contains the lower part of the parotid gland. The external carotid artery, passing deep to stylohyoid, curves above the muscle, and overlaps its superficial surface as it ascends deep to the parotid gland before entering it. The internal carotid artery, internal jugular vein and vagus nerve lie deeper and are separated from the external carotid artery by styloglossus, stylopharyngeus and the glossopharyngeal nerve.

Submental triangle

The single submental triangle is demarcated by the anterior bellies of both digastric muscles. Its apex is at the chin, its base is the body of the hyoid bone and its floor is formed by both mylohyoid muscles. It contains lymph nodes and small veins that unite to form the anterior jugular vein. The structures within the digastric and submental triangles are described in more detail with the floor of the mouth.

Muscular triangle

The muscular triangle is bounded anteriorly by the median line of the neck from the hyoid bone to the sternum, inferoposteriorly by the anterior margin of sternocleidomastoid and posterosuperiorly by the superior belly of omohyoid. The triangle contains omohyoid, sternohyoid, sternothyroid and thyrohyoid.

Carotid triangle

The carotid triangle is limited posteriorly by sternocleidomastoid, anteroinferiorly by the superior belly of omohyoid and superiorly by stylohyoid and the posterior belly of digastric. In the living (except the obese), the triangle is usually a small visible triangular depression, sometimes best seen with the head and cervical vertebral column slightly extended and the head contralaterally rotated. The carotid triangle is covered by the skin, superficial fascia, platysma and deep fascia containing branches of the facial and cutaneous cervical nerves. The hyoid bone forms its anterior angle and adjacent floor; it can be located on simple inspection and verified by palpation. Parts of thyrohyoid, hyoglossus and inferior and middle pharyngeal constrictor muscles form its floor. The carotid triangle contains the upper part of the common carotid artery and its division into external and internal carotid arteries. Overlapped by the anterior margin of sternocleidomastoid, the external carotid artery is first anteromedial, then anterior to the internal carotid artery. Branches of the external carotid artery are encountered in the carotid triangle. The superior thyroid artery runs anteroinferiorly, the lingual artery anteriorly with a characteristic upward loop, the facial artery anterosuperiorly, the occipital artery posterosuperiorly and the ascending pharyngeal artery medial to the internal carotid artery. Arterial pulsation greets the examining finger. The superior thyroid, lingual, facial, ascending pharyngeal and sometimes the occipital veins correspond to the branches of the external carotid artery, and all drain into the internal jugular vein. The hypoglossal nerve crosses the external and internal carotid arteries. It curves round the origin of the lower sternocleidomastoid branch of the occipital artery, and at this point the superior root of the ansa cervicalis leaves it to descend anteriorly in the carotid sheath. The internal laryngeal nerve and, below it, the external laryngeal nerve lie medial to the external carotid artery below the hyoid bone. Many structures in this region, such as all or part of the internal jugular vein, associated deep cervical lymph nodes, and the vagus nerve, may be variably obscured by sternocleidomastoid, and, pedantically, are thus 'outside the triangle'.

Posterior triangle of the neck

The posterior triangle is delimited anteriorly by the posterior edge of sternocleidomastoid, posteriorly by the anterior edge of trapezius, and inferiorly by the middle third of the clavicle (see Fig. 35.3). Its apex is between the attachments of sternocleidomastoid and trapezius to the occiput and is often blunted, so that the 'triangle' becomes quadrilateral. The roof of the posterior triangle is formed by the investing layer of the deep cervical fascia. The floor of the triangle is formed by the prevertebral fascia overlying splenius capitis, levator scapulae and the scalene muscles. It is crossed, approximately 2.5 cm above the clavicle, by the inferior belly of omohyoid, which subdivides it into occipital and supraclavicular triangles. The contents of the posterior triangle include fat, lymph nodes (level V), the accessory nerve (which runs in the roof of the triangle, subdivides level Va above and Vb below), cutaneous branches of the cervical plexus, inferior belly of omohyoid, branches of the thyrocervical trunk (transverse cervical and suprascapular arteries), the third part of the subclavian artery, and the external jugular vein. The superficial position of the accessory nerve as it traverses the posterior triangle makes it vulnerable to iatrogenic damage in neck surgery. The anterior and lateral groups of prevertebral muscles form the floor of the posterior triangle.

Occipital triangle

The occipital triangle constitutes the upper and larger part of the posterior triangle, with which it shares the same borders, except that inferiorly it is limited by the inferior belly of omohyoid. Its floor, from above down, is formed by splenius capitis, levator scapulae, and scaleni medius and posterior; semispinalis capitis occasionally appears at the apex. The triangle is covered by skin, superficial and deep fasciae, and inferiorly by platysma. The accessory nerve pierces sternocleidomastoid and crosses levator scapulae obliquely downwards and backwards to reach the deep surface of trapezius. The surface marking of its course is in a line from the junction of the superior third and inferior two-thirds of sternocleidomastoid, to the junction of the inferior third and superior two-thirds of trapezius. Cutaneous and muscular branches of the cervical plexus emerge at the posterior border of sternocleidomastoid. Inferiorly, supraclavicular nerves, transverse cervical vessels and the uppermost part of the brachial plexus cross the triangle. Lymph nodes lie along the posterior border of sternocleidomastoid from the mastoid process to the root of the neck.

Supraclavicular triangle

The supraclavicular triangle is the lower and smaller division of the posterior triangle, with which it shares the same boundaries, except that superiorly it is limited by omohyoid. It corresponds in the living neck with the lower part of a deep, prominent hollow, namely: the greater supraclavicular fossa. Its floor contains the first rib, scalenus medius and the first slip of serratus anterior. Its size varies with the extent of the clavicular attachments of sternocleidomastoid and trapezius, and also the level of the inferior belly of omohyoid. The triangle is covered by skin, superficial and deep fasciae, and platysma, and crossed by the supraclavicular nerves. Just above the clavicle, the third part of the subclavian artery curves inferolaterally from the lateral margin of scalenus anterior across the first rib to the axilla. The subclavian vein is behind the clavicle and is not usually in the triangle, but it may rise as high as the artery and even accompany it behind scalenus anterior. The brachial plexus is partly superior, and partly posterior, to the artery and is always closely related to it. The trunks of the brachial plexus may be palpated easily here if the neck is contralaterally flexed and the examining finger is drawn across the trunks at right-angles to their length. With the musculature relaxed, pulsation of the subclavian artery may be felt and the arterial flow can be controlled by retroclavicular compression against the first rib. The suprascapular vessels pass transversely behind the clavicle, below the transverse cervical artery and vein. The external jugular vein descends behind the posterior border of sternocleidomastoid to end in the subclavian vein. It receives the transverse cervical and suprascapular veins, which form a plexus in front of the third part of the subclavian artery. It is joined occasionally by a small vein that crosses the clavicle anteriorly from the cephalic vein. Other structures within the triangle include the nerve to subclavius, which crosses the triangle, and lymph nodes.

CERVICAL FASCIA

The organization of the layers of the cervical fascia, and of the tissue 'spaces' they enclose, may determine the spread of disease in the head and neck, and facilitates both the differential diagnosis and the surgical management of that disease, particularly in the suprahyoid neck.

Superficial cervical fascia

Like superficial fascia elsewhere in the body, the superficial cervical fascia is not a separate stratum but a zone of loose connective tissue between dermis and deep fascia and is joined to both. It covers platysma but is hardly demonstrable as a separate layer. It may contain considerable amounts of adipose tissue, especially in females, which presumably explains why it is sometimes referred to simply as subcutaneous fat. In the lower cervical region, aponeurotic fibres of platysma gradually fan out in this layer and either become skin ligaments or continue into the fascia covering pectoralis major and deltoid (Nash et al 2005).

Deep cervical fascia

Three layers – superficial investing, middle and deep – are recognized (Fig. 35.4). Details of their precise attachments and contents vary between authors. For further reading, see Som and Curtin (2011).

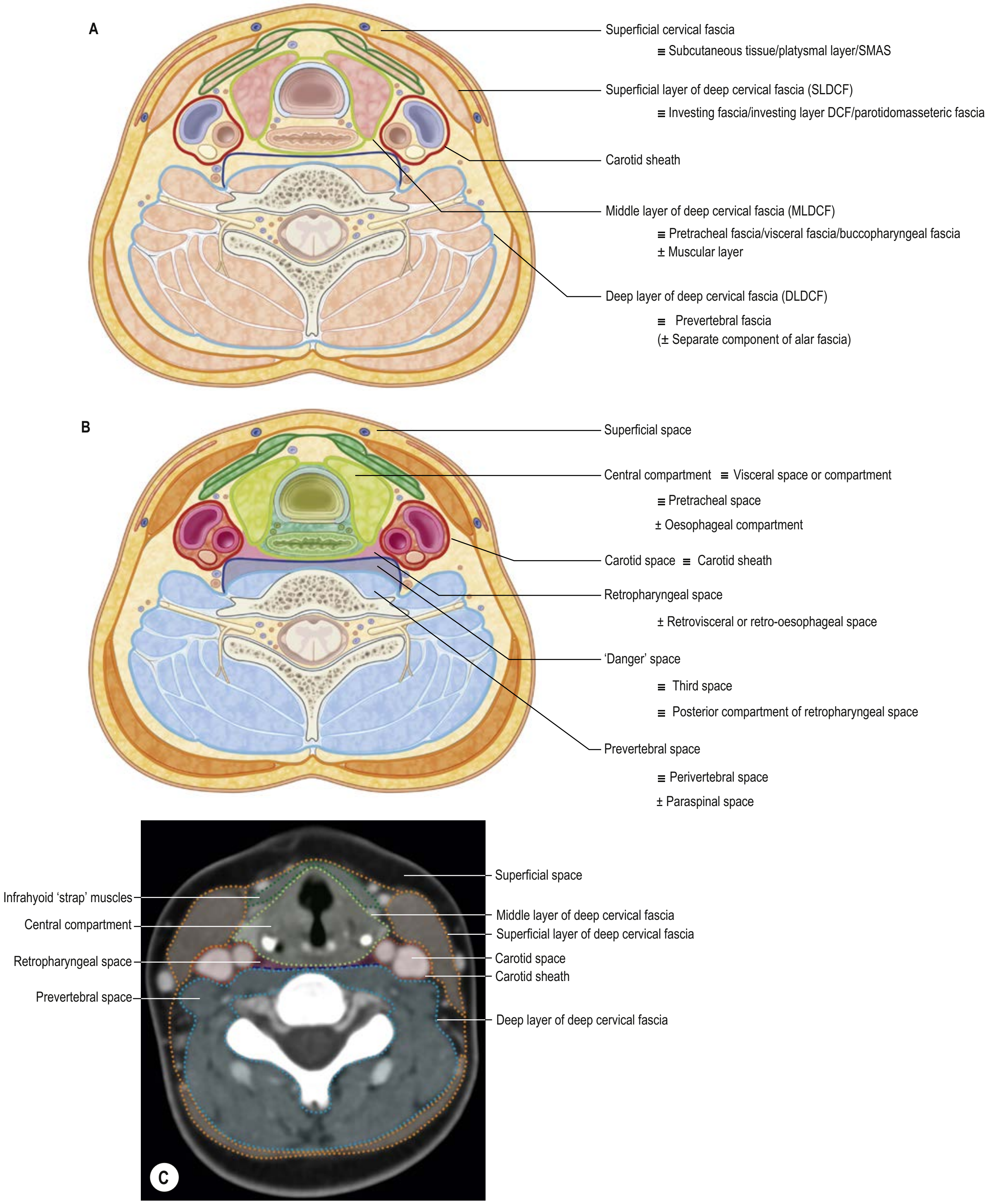
A
Superficial cervical fascia
≡ Subcutaneous tissue/platysmal layer/SMAS
Superficial layer of deep cervical fascia (SLDCF)
≡ Investing fascia/investing layer DCF/parotidomasseteric fascia
Carotid sheath
Middle layer of deep cervical fascia (MLDCF)
≡ Pretracheal fascia/visceral fascia/buccopharyngeal fascia
± Muscular layer
Deep layer of deep cervical fascia (DLDCF)
≡ Prevertebral fascia
(± Separate component of alar fascia)
B
Superficial space
Central compartment ≡ Visceral space or compartment
≡ Pretracheal space
± Oesophageal compartment
Carotid space ≡ Carotid sheath
Retropharyngeal space
± Retrovisceral or retro-oesophageal space
'Danger' space
≡ Third space
≡ Posterior compartment of retropharyngeal space
Prevertebral space
≡ Perivertebral space
± Paraspinal space
Infrahyoid 'strap' muscles
Central compartment
Retropharyngeal space
Prevertebral space
Superficial space
Middle layer of deep cervical fascia
Superficial layer of deep cervical fascia
Carotid space
Carotid sheath
Deep layer of deep cervical fascia
C

Fig. 35.4 **A**, The layers of cervical fascia. Abbreviation: SMAS, superficial musculo-aponeurotic system. **B**, The deep 'spaces' in the neck. **C**, Axial CT of the neck with intravenous contrast medium at the level of C6 showing the deep cervical fascia and deep 'spaces' of the neck; the 'danger' space is at the dashed dark blue line at the posterior aspect of the retropharyngeal space. (A, B, Infrahyoid transverse section of the neck, adapted from McMinn RMH Last's Anatomy. Redrawn with permission from Guidera AK, Dawes PJD, Stringer MD 2012 Cervical fascia: a terminological pain in the neck. ANZ Surg 82:786–91.)

Investing layer of deep cervical fascia

The investing or superficial layer of the deep cervical fascia encircles the neck, ensheathing trapezius and sternocleidomastoid. The portions between trapezius and sternocleidomastoid, and in the anterior triangle of the neck, are formed of areolar tissue, indistinguishable from that in the superficial cervical fascia and deep potential tissue spaces. Superiorly, the deep fascia fuses with periosteum along the superior nuchal line of the occipital bone, over the mastoid process and along the entire base of the mandible. Between the angle of the mandible and the anterior edge of sternocleidomastoid, it is particularly strong. Between the mandible and the mastoid process, it is related to the parotid gland, extending beneath it to become attached to the zygomatic arch. From this region, the strong stylomandibular ligament ascends to the styloid process. Inferiorly, along trapezius and sternocleidomastoid, the investing layer of the deep cervical fascia is attached to the acromion, clavicle and manubrium sterni, fusing with their periostea. A short distance above the manubrium, the investing layer interweaves with aponeurotic fibres of platysma and the fascia investing the strap muscles. It is organized into superficial and deep layers, which are attached to the anterior border of the manubrium, and to the posterior border and the interclavicular ligament, respectively. Between these two layers, a slit-like interval, the suprasternal space, contains a small amount of areolar tissue, the lower parts of the anterior jugular veins and the jugular venous arch, the sternal heads of the sternocleidomastoid muscles and sometimes a lymph node.

Middle layer of deep cervical fascia

Many of the variations in the descriptions of cervical fascia concern the middle layer. (For a detailed discussion, see Som and Curtin (2011).) It is usually subdivided into a muscular layer that surrounds the infrahyoid strap muscles and a visceral layer that includes both the pretracheal and buccopharyngeal fasciae. The visceral layer extends inferiorly from the base of the skull posteriorly and the hyoid bone and thyroid cartilage anteriorly. Laterally, it provides fascial sheaths of varying thickness for the thyroid gland, larynx, trachea, pharynx and oesophagus, and merges with the investing layer of deep cervical fascia and with the carotid sheath (see Fig. 35.4). Inferiorly, it continues into the superior mediastinum along the great vessels and fuses with the fibrous pericardium.

Deep layer of deep cervical fascia

The deep layer of cervical fascia consists of dorsal and ventral layers: the prevertebral and alar fasciae, respectively. In some descriptions, the prevertebral layer is synonymous with the deep layer.

The prevertebral fascia lies closest to the vertebral bodies, covering the anterior surface of longus capitis and longus colli. It extends inferiorly from the skull base, descending in front of longus colli into the superior mediastinum, where it blends with the anterior longitudinal ligament. It passes laterally and posteriorly as the scalene fascia, which covers the scalene muscles, splenius capitis and levator scapulae. All the ventral rami of the cervical nerves are initially behind the prevertebral fascia. The nerves to the rhomboids and serratus anterior and the proximal portions of the phrenic nerve retain this position throughout their course in the neck, but the accessory nerve lies superficial to the prevertebral fascia. As the subclavian artery and the brachial plexus emerge from behind scalenus anterior, they carry the prevertebral fascia downwards and laterally behind the clavicle as the axillary sheath. The prevertebral fascia is attached to the spinous processes of the vertebrae and forms a fascial floor for the posterior triangle of the neck.

The alar fascia is a coronally orientated sheet, attached to the transverse process of the cervical vertebrae. It lies anterior to the prevertebral fascia, from which it is separated by loose connective tissue that fills the so-called danger space (see below), and posterior to the pharynx/oesophagus and the visceral layer of the middle deep cervical fascia, from which it is separated by loose connective tissue that fills the retropharyngeal space (see Fig. 35.4). It passes anterolaterally to fuse with the prevertebral fascia and extends inferiorly from the skull base to about the level of the seventh cervical vertebra (it varies between C6 and T4), where it fuses with the visceral layer of middle cervical fascia, thereby delimiting the lowest extent of the retropharyngeal and danger spaces.

Carotid sheath

The carotid sheath is a condensation of deep cervical fascia around the common and internal carotid arteries, internal jugular vein, vagus nerve and ansa cervicalis. It is thicker around the arteries than the vein, an arrangement that allows the vein to expand. Peripherally, the sheath is connected to adjacent fascial layers by loose areolar tissue. Debate continues as to whether the carotid sheath is formed by all three layers of the deep cervical fascia, or exclusively by the deep or the superficial layer, or whether there is a demonstrable fascial ensheathment (Guidera et al 2012).

Suprapleural membrane (Sibson's fascia)

The suprapleural membrane (Sibson's fascia) serves as a plane of separation between the lower neck and the thorax. It is attached anteriorly to the inner border of the first rib, and posteriorly to the anterior border of the transverse process of the seventh cervical vertebra and is covered and strengthened by a few spreading muscular fibres derived from the scaleni.

Tissue spaces and the spread of infection

The fascial layers of the neck define a number of potential tissue ‘spaces’ above and below the hyoid bone. In health, the tissues within these spaces are closely applied to one another or are filled with relatively loose connective tissue.

Visceral space

The visceral space contains the pharynx, cervical oesophagus, larynx, trachea, thyroid and parathyroid glands, recurrent laryngeal nerves, and the cranial sympathetic trunk. It is bounded anteriorly by the fascia that encloses the infrahyoid strap muscles (muscular layer of middle deep cervical fascia), posteriorly by the alar fascia, and laterally by the carotid sheath on either side. It may be subdivided into an anterior visceral (pretracheal) space and a posterior visceral space. These spaces communicate freely between the levels of the mid-thyroid cartilage and the inferior thyroid artery but are separated inferiorly by the fascia associated with the artery.

Anterior visceral space

This space, also known as the pretracheal space, contains the trachea, thyroid and parathyroid glands, larynx, cervical oesophagus, recurrent laryngeal nerves and the cranial sympathetic trunks. It extends superiorly from the hyoid bone and the attachments of the strap muscles and their fasciae to the hyoid bone and thyroid cartilage down into the anterior portion of the superior mediastinum. It communicates with the posterior visceral space around the sides of the larynx, the caudal portion of the pharynx and the upper cervical oesophagus. It becomes separated from the posterior visceral space at lower levels by dense connective tissue associated with the inferior thyroid artery as the latter approaches the thyroid gland. The portion of the anterior visceral space between the strap fascia and the fascia of the thyroid gland is referred to as the anterior cervical space. Its posterolateral border is either the carotid sheath or the fascia covering sternocleidomastoid. It provides a symmetric landmark on transverse imaging (Smoker and Harnsberger 1991). Infections spreading immediately into the anterior visceral space are usually the result of instrumental or foreign body perforation of the oesophagus.

Posterior visceral space

The posterior visceral space (often referred to as the retropharyngeal space) lies posterior to the pharynx and cervical oesophagus, extending from the skull base down to the superior mediastinum, its caudal limit being the level of fusion between the alar and visceral layers of fascia.

Prevertebral space

The prevertebral tissue space lies between the prevertebral fascia and the vertebral column. It extends from the skull base to the coccyx, enclosing the prevertebral muscles. Infections spread into this space from adjacent vertebrae or their intervertebral discs, the spinal cord, associated nerve roots and spinal nerves. Classically, tuberculosis of the spine breaches the space to a Pott's abscess.

Carotid space

The carotid sheath is a layer of loose connective tissue demarcated by adjacent portions of the investing layer of deep cervical fascia, the pretracheal fascia and the prevertebral fascia. The literature about the carotid space is confusing and best summarized by Som and Curtin (2011).

Danger space

The danger space lies between the alar and prevertebral fasciae, and extends from the skull base down to the posterior mediastinum where the alar, visceral and prevertebral layers of deep cervical fascia fuse. This potential space is closed superiorly, inferiorly and laterally and infections can only enter it by penetrating its walls. Its loose areolar tissue offers a potential route for rapid downward spread of infection, primarily from the retropharyngeal, parapharyngeal or prevertebral spaces, to the posterior mediastinum.

Cellulitis in the neck

Infections arising superiorly, such as molar dental, tonsillar, vertebral or intervertebral disc-related infections can spread through this network of spaces. There are no tissue barriers running horizontally in the neck, which means that delays in treatment can be disastrous as infection with its associated oedema develops and spreads from the infratemporal fossa down to the mediastinum, crosses the midline through the sublingual and submental spaces, and can even track into the axilla. The organisms responsible are often β-haemolytic streptococci or anaerobes: proteolytic enzymes digest the loose connective tissue to open up the spaces.

Apical abscesses of the second and third mandibular molar teeth can perforate the lingual plate of the mandible below and behind the attachment of mylohyoid and its posterior free border. At this point infection spreads directly into the submandibular space and has easy access to the parapharyngeal and pterygoid spaces posteriorly.

Cellulitis of the neck or deep neck space infections are potentially very serious because of the associated swelling. Obstruction of the upper airway and dysphagia can develop in a matter of a few hours: intubation becomes extremely difficult. Urgent drainage of the spaces is necessary, together with establishment of a secure airway usually by tracheostomy. (For further reading see Oliver and Gillespie (2010), Hedge et al (2012), Maroldi et al (2012).)

Understanding the configuration of the cervical fasciae and spaces is also essential for the placement of local cervical plexus anaesthetic blocks to facilitate operations such as thyroidectomy, parathyroidectomy and carotid endarterectomy (Pandit et al 2000).

MUSCLES

The superficial muscles of the neck are platysma, which lies in the subcutaneous tissue of the neck, sternocleidomastoid and trapezius. Sternocleidomastoid is a key landmark because it divides the neck into anterior and posterior triangles; the anterior triangle may be further subdivided into several smaller named triangles (see above). Muscles in the anterior region are organized into supra- and infrahyoid groups. When removing the body of the hyoid in Sistrunk's operation or in revision surgery, these supra- and infrahyoid muscles are detached. They are also detached to mobilize the cervical and intrathoracic trachea by 'dropping the larynx' during upper airway surgery to resect sections of trachea and repair by primary anastomosis. The suprahyoid muscles connect the hyoid bone to the mandible and the base of the skull and include mylohyoid, geniohyoid, stylohyoid and digastric. The infrahyoid (strap) muscles connect the hyoid, sternum, clavicle and scapula and are arranged in a superficial plane (sternohyoid and omohyoid) and a deep plane (sternothyroid and thyrohyoid).

The muscles that form part of the musculoskeletal column in the neck are described in Chapter 46. They can be considered in three groups, anterior, lateral and posterior: very broadly speaking, the muscles in these groups lie anterior, lateral or posterior to the cervical vertebrae. The anterior and lateral groups include longi colli and capitis; recti capitis anterior and lateralis; scaleni anterior, medius, posterior and minimi (the latter are not always present). The posterior muscle group contains the cervical components of the intrinsic muscles of the back, overlaid by some of the extrinsic 'immigrant' muscles of the back that run between the upper limb and the axial skeleton (trapezius, levator scapulae; Ch. 49). The intrinsic muscles are arranged in superficial and deep layers. The superficial layer contains splenius capitis and cervicis. The deeper layers include the transversospinal group (semispinales cervicis and capitis, multifidus and rotatores cervicis), interspinales and intertransversarii, and the suboccipital group (recti capitis posterior major and minor, and obliquus capitis superior and inferior).

The muscles associated with the pharynx and larynx are described in Chapters 40 and 41, respectively.

Platysma

Platysma is a broad sheet of muscle of varying prominence that arises from the fascia covering the upper parts of pectoralis major and deltoid. Its fibres cross the clavicle and ascend medially in the side of the neck. Anterior fibres interlace across the midline with the fibres of the contralateral muscle, below and behind the symphysis menti. Other fibres attach to the lower border of the mandible or to the lower lip or cross the mandible to attach to the skin and subcutaneous tissue of the lower face. Platysma provides an important blood supply to the overlying skin: careful elevation of a myocutaneous flap in the subplatysmal plane, as part of a neck dissection, includes this muscle and its associated blood supply, and minimizes the risk of skin necrosis and wound breakdown.

Vascular supply Platysma is supplied by the submental branch of the facial artery and by the suprascapular artery (from the thyrocervical trunk of the subclavian artery).

Innervation Platysma is innervated by the cervical branch of the facial nerve, which descends on the deep surface of the muscle close to the angle of the mandible.

Actions Contraction diminishes the concavity between the jaw and the side of the neck, and produces tense, oblique ridges in the skin of the neck. Platysma may assist in depressing the mandible, and, via its labial and modiolar attachments, it can draw down the lower lip and corners of the mouth in extreme facial expressions. Surgery that damages the nerve to platysma, the marginal mandibular nerve or the cervical branches of the facial nerve can result in paralysis of the lower lip.

Sternocleidomastoid

Sternocleidomastoid (Fig. 35.5A) descends obliquely across the side of the neck and forms a prominent surface landmark, especially when contracted. It is thick and narrow centrally, and broader and thinner at each end. The muscle is attached inferiorly by two heads. The medial or sternal head is rounded and tendinous, arises from the upper part of the anterior surface of the manubrium sterni, and ascends posterolaterally. The lateral or clavicular head, which is variable in width and contains muscular and fibrous elements, ascends almost vertically from the superior surface of the medial third of the clavicle. The two heads are separated near their attachments by a triangular interval that corresponds to a surface depression, the lesser supraclavicular fossa. As they ascend, the clavicular head spirals behind the sternal head and blends with its deep surface below the middle of the neck, forming a thick, rounded belly. Sternocleidomastoid inserts superiorly by a strong tendon into the lateral surface of the mastoid process from its apex to its superior border, and by a thin aponeurosis into the lateral half of the superior nuchal line. The clavicular fibres are directed mainly to the mastoid process; the sternal fibres are more oblique and superficial, and extend to the occiput. The direction of pull of the two heads is therefore different, and the muscle may be classed as 'cruciate' and slightly 'spiralized'.

Relations The superficial surface of sternocleidomastoid is covered by skin and platysma, between which lie the external jugular vein, the great auricular and transverse cervical nerves, and the superficial lamina of the deep cervical fascia. Near its insertion, the muscle is overlapped by a small part of the parotid gland. The deep surface of the muscle near its origin is related to the sternoclavicular joint and sternohyoid, sternothyroid and omohyoid. The anterior jugular vein crosses deep to it but superficial to the infrahyoid muscles, immediately above the clavicle. The carotid sheath and the subclavian artery are deep to these muscles. Between omohyoid and the posterior belly of digastric, the anterior part of sternocleidomastoid lies superficial to the common, internal and external carotid arteries, the internal jugular, facial and lingual veins, the deep cervical lymph nodes, the vagus nerve and the rami of the ansa cervicalis. The sternocleidomastoid branch of the superior thyroid artery crosses deep to the muscle at the upper border of omohyoid. The posterior part of sternocleidomastoid is related on its internal surface to splenius capitis, levator scapulae and the scalene muscles, the cervical plexus, the upper part of the brachial plexus, the phrenic nerve and the transverse cervical and suprascapular arteries. The occipital artery crosses deep to the muscle at, or under cover of, the lower border of the posterior belly of digastric. At this point, the accessory nerve passes deep to sternocleidomastoid, then pierces and supplies the muscle, before it reappears just above the middle of the posterior border. At its insertion, the muscle lies superficial to the mastoid process, splenius capitis, longissimus capitis and the posterior belly of digastric.

Vascular supply Sternocleidomastoid receives its blood supply from branches of the occipital and posterior auricular arteries (upper part of muscle), the superior thyroid artery (middle part of muscle) and the suprascapular artery (lower part of muscle). A superiorly based flap can be raised on sternocleidomastoid to include a paddle of skin supplied by perforator vessels (Froes et al 1999), and has been used to reconstruct the lips, floor of mouth and inner aspect of the cheeks. It is not

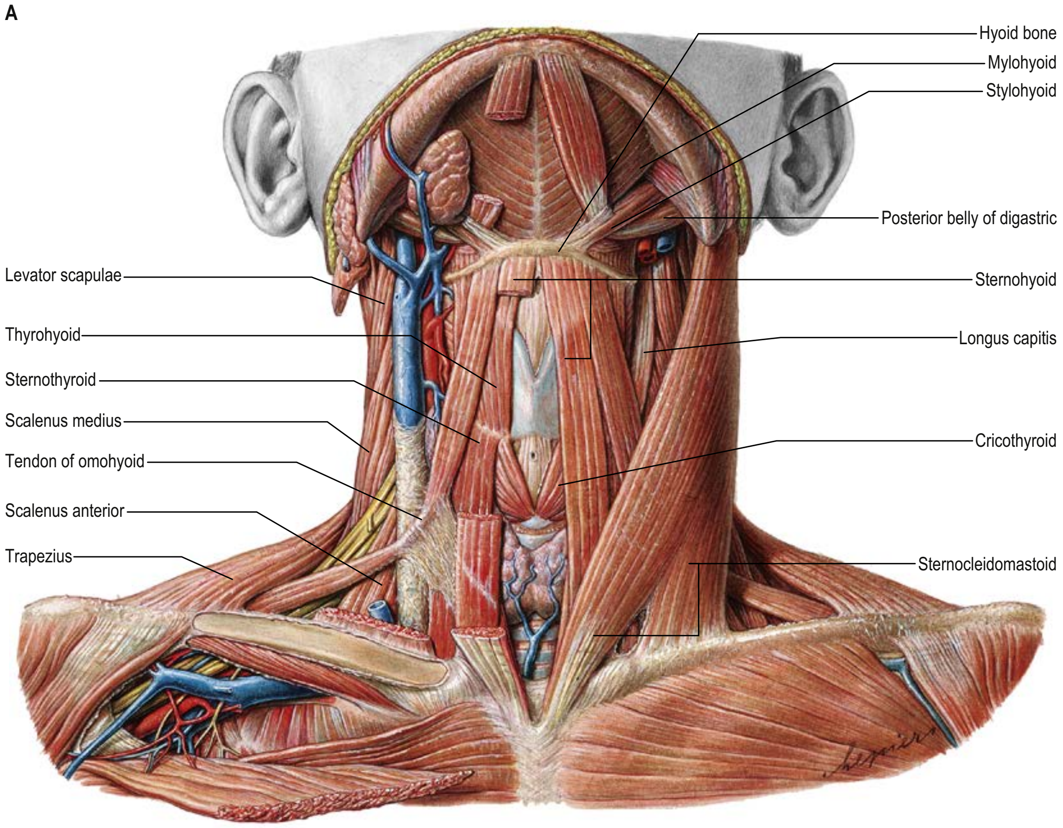
A
Hyoid bone
Mylohyoid
Stylohyoid
Posterior belly of digastric
Levator scapulae
Sternohyoid
Thyrohyoid
Longus capitis
Sternothyroid
Scalenus medius
Cricothyroid
Tendon of omohyoid
Scalenus anterior
Trapezius
Sternocleidomastoid

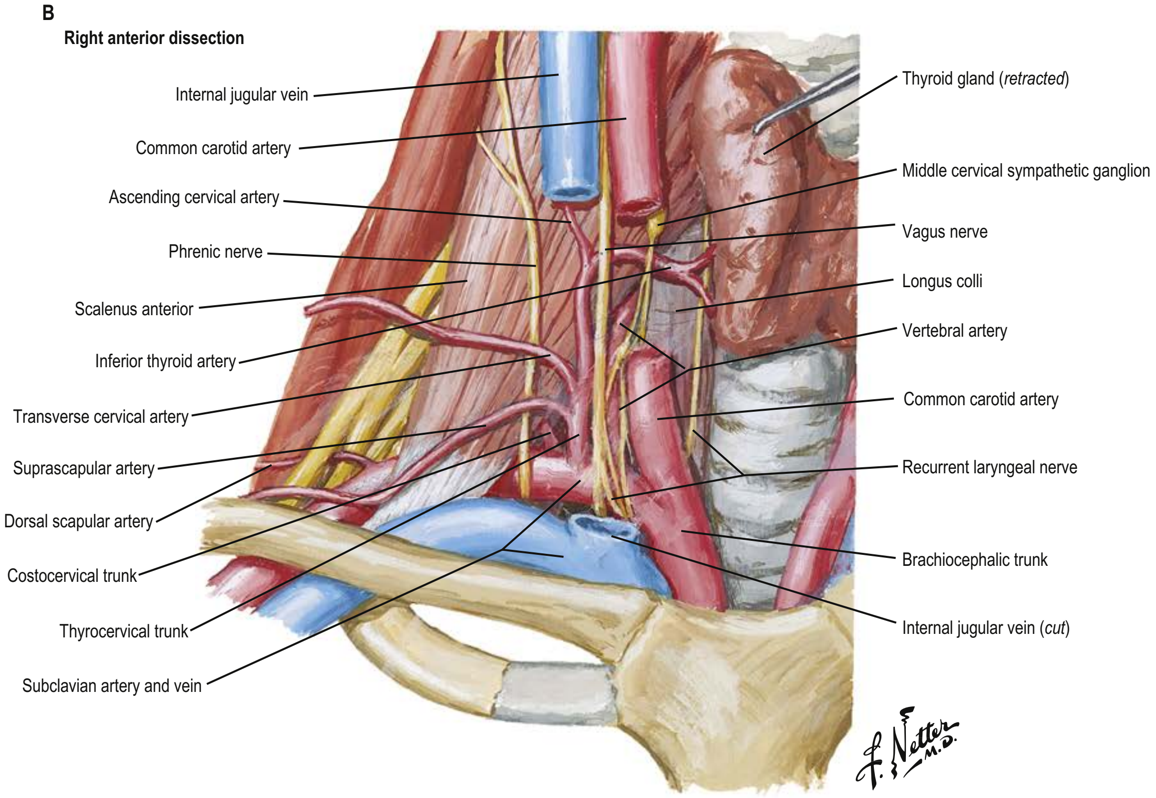
B
Right anterior dissection
Internal jugular vein
Thyroid gland (*retracted*)
Common carotid artery
Middle cervical sympathetic ganglion
Ascending cervical artery
Vagus nerve
Phrenic nerve
Longus colli
Scalenus anterior
Vertebral artery
Inferior thyroid artery
Common carotid artery
Transverse cervical artery
Recurrent laryngeal nerve
Suprascapular artery
Dorsal scapular artery
Brachiocephalic trunk
Costocervical trunk
Internal jugular vein (*cut*)
Thyrocervical trunk
Subclavian artery and vein
F. Netter M.D.

Fig. 35.5 **A**, Muscles of the neck. Note that the head is slightly extended in order to expose the suprahyoid muscles. **B**, Chassaignac's triangle. (A, Sobotta Atlas of Human Anatomy © Elsevier GmbH, Urban & Fischer, Munich; B, with permission from Netter FH Atlas of Human Anatomy, 7th ed. Elsevier. Copyright 2019.)

a very reliable flap and its use has been superseded by microvascular free transfer flaps or by conventional myocutaneous flaps such as the pectoralis major flap.

Innervation Sternocleidomastoid is supplied by the accessory nerve. Branches from the ventral rami of the second, third and sometimes fourth cervical spinal nerves also enter the muscle. Although these cervical rami were believed to be solely proprioceptive, clinical evidence suggests that some of their fibres are motor.

Actions Acting alone, each sternocleidomastoid will tilt the head towards the ipsilateral shoulder, simultaneously rotating the head and turning the face towards the opposite side. This movement happens in an upward, sideways glance. A more common visual movement is a level rotation from side to side, and this probably represents the most frequent use of the sternocleidomastoids. Acting together from below, the muscles draw the head forwards and so help longi colli to flex the cervical part of the vertebral column, which is a common movement in feeding. The two sternocleidomastoids are also used to raise the head when the body is supine; when the head is fixed, they help to elevate the thorax in forced inspiration.

Branchial cysts and fistulae Branchial cysts usually present in the upper neck in early adulthood as fluctuant swellings at the junction of the upper and middle thirds of the anterior border of sternocleidomastoid. The cyst typically passes backwards and upwards through the carotid bifurcation and ends at the pharyngeal constrictor muscles, a course that brings it into intimate association with the hypoglossal, glossopharyngeal and accessory nerves. Great care must be taken to avoid damage to these nerves during surgical removal of a branchial cyst.

Branchial fistulae represent a persistent connection between the second branchial pouch and the cervical sinus. A fistula presents as a small pit adjacent to the anterior border of the lower third of sternocleidomastoid that may weep saliva and become intermittently infected. Excision involves following the tract of the fistula up the neck, often through the carotid bifurcation, and into the distal tonsillar fossa, where it opens into the pharynx.

Branchial cysts, sinuses and fistulae are thought to arise from inclusions of salivary gland tissue in lymph nodes; they may also develop around the parotid gland.

Muscles of the anterior triangle of the neck

Apart from the superficial neck muscles already described, the anterior triangle contains two of the suprahyoid muscles – namely, digastric and stylohyoid – and the four infrahyoid strap muscles (see Fig. 35.5A). The other suprahyoid muscles, namely mylohyoid and geniohyoid, are described with the floor of the mouth in Chapter 37.

Digastric

Digastric has two bellies and lies below the mandible, extending from the mastoid process to the chin (see Fig. 35.5A). The posterior belly, longer than the anterior, is attached in the mastoid notch of the temporal bone and passes downwards and forwards. The anterior belly is attached to the digastric fossa on the base of the mandible near the midline, and slopes downwards and backwards. The two bellies meet in an intermediate tendon that perforates stylohyoid and runs in a fibrous sling attached to the body and greater cornu of the hyoid bone; it is sometimes lined by a synovial sheath. The two bellies of digastric mark out the borders of the submandibular triangle.

Variations Digastric may lack the intermediate tendon and is then attached midway along the body of the mandible. The posterior belly may be augmented by a slip from the styloid process or arise wholly from it. The anterior belly may cross the midline and it is not uncommon for it to fuse with mylohyoid.

Relations Superficial to digastric are platysma, sternocleidomastoid, splenius capitis, longissimus capitis and stylohyoid, the mastoid process, the retromandibular vein, and the parotid and submandibular salivary glands. Mylohyoid is medial to the anterior belly, and hyoglossus, obliquus capitis superior and rectus capitis lateralis, the transverse process of the atlas vertebra, the accessory nerve, internal jugular vein, occipital artery, hypoglossal nerve, internal and external carotid, facial and lingual arteries are all medial to the posterior belly.

Vascular supply The posterior belly is supplied by the posterior auricular and occipital arteries. The anterior belly of digastric receives its blood supply chiefly from the submental branch of the facial artery.

Innervation The anterior belly of digastric is supplied by the mylohyoid branch of the inferior alveolar nerve, and the posterior belly is supplied by the facial nerve. The different innervation of the two parts reflects their separate derivations from the mesenchyme of the first and second branchial arches.

Actions Digastric depresses the mandible and can elevate the hyoid bone. The posterior bellies are especially active during swallowing and chewing.

Stylohyoid

Stylohyoid arises by a small tendon from the posterior surface of the styloid process, near its base. Passing downwards and forwards, it inserts into the body of the hyoid bone at its junction with the greater cornu (and just above the attachment of the superior belly of omohyoid). It is perforated near its insertion by the intermediate tendon of digastric (see Fig. 35.5A). The muscle may be absent or double. It may lie medial to the external carotid artery and may end in the suprahyoid or infrahyoid muscles.

Vascular supply Stylohyoid receives its blood supply from branches of the facial, posterior auricular and occipital arteries.

Innervation Stylohyoid is innervated by the stylohyoid branch of the facial nerve, which frequently arises with the digastric branch, and enters the middle part of the muscle.

Actions Stylohyoid elevates the hyoid bone and draws it backwards, elongating the floor of the mouth.

Stylohyoid ligament

The stylohyoid ligament is a fibrous cord extending from the tip of the styloid process to the lesser cornu of the hyoid bone. It gives attachment to the highest fibres of the middle pharyngeal constrictor and is intimately related to the lateral wall of the oropharynx. Below, it is overlapped by hyoglossus. The ligament is derived from the cartilage of the second branchial arch and may be partially calcified.

Infrahyoid muscles

The infrahyoid muscles are organized so that sternohyoid and omohyoid lie superficially, and sternothyroid and thyrohyoid lie more deeply (see Fig. 35.5A). The muscles are involved in movements of the hyoid bone and thyroid cartilage during vocalization, swallowing and mastication, and are mainly innervated from the ansa cervicalis.

Sternohyoid

Sternohyoid is a thin, narrow strap muscle that arises from the posterior surface of the medial end of the clavicle, the posterior sternoclavicular ligament and the upper posterior aspect of the manubrium (see Fig. 35.5A). It ascends medially and is attached to the inferior border of the body of the hyoid bone. Inferiorly, there is a considerable gap between the muscle and its contralateral fellow, but the two usually come together in the middle of their course and are contiguous above this. Sternohyoid may be absent or double, augmented by a clavicular slip (cleidohyoid), or interrupted by a tendinous intersection.

Vascular supply Sternohyoid is supplied by branches from the superior thyroid artery.

Innervation Sternohyoid is innervated by branches from the ansa cervicalis (C1, 2, 3).

Actions Sternohyoid depresses the hyoid bone after it has been elevated.

Omohyoid

Omohyoid consists of two bellies united at an angle by an intermediate tendon (see Fig. 35.5A). The inferior belly is a flat, narrow band, which inclines forwards and slightly upwards across the lower part of the neck. It arises from the upper border of the scapula, near the scapular notch, and occasionally from the superior transverse scapular ligament. It then passes behind sternocleidomastoid and ends there in the intermediate tendon. The superior belly begins at the intermediate tendon, passes almost vertically upwards near the lateral border of sternohyoid, and is attached to the lower border of the body of the hyoid bone lateral to the insertion of sternohyoid. The length and form of the intermediate tendon vary. It usually lies adjacent to the internal jugular vein at the level of the arch of the cricoid cartilage. The angulated course of the muscle is maintained by a band of deep cervical fascia, attached below to the clavicle and the first rib, that ensheathes the tendon. A variable amount of skeletal muscle may be present in the fascial band; either belly may be absent or double; and the inferior belly may be attached directly to the clavicle and the superior is sometimes fused with sternohyoid.

Vascular supply Omohyoid is supplied by branches from the superior thyroid and lingual arteries.

Innervation The superior belly of omohyoid is innervated by branches from the superior ramus of the ansa cervicalis (C1). The inferior belly is innervated from the ansa cervicalis itself (C1, 2 and 3).

Actions Omohyoid depresses the hyoid bone after it has been elevated. It has been speculated that the muscle tenses the lower part of the deep cervical fascia in prolonged inspiratory efforts, reducing the tendency for soft parts to be sucked inwards.

Sternothyroid

Sternothyroid is shorter and wider than sternohyoid and lies deep and partly medial to it (see Fig. 35.5A). It arises from the posterior surface of the manubrium sterni inferior to the origin of sternohyoid and from the posterior edge of the cartilage of the first rib. It is attached above to the oblique line on the lamina of the thyroid cartilage, where it delineates the upward extent of the thyroid gland. In the lower part of the neck, the muscle is in contact with its contralateral fellow, but the two diverge as they ascend.

Vascular supply Sternothyroid is supplied by branches from the superior thyroid and lingual arteries.

Innervation Sternothyroid is innervated by branches from the ansa cervicalis (C1, 2 and 3).

Actions Sternothyroid draws the larynx downwards after it has been elevated by swallowing or vocal movements. In the singing of low notes, this downward traction would be exerted with the hyoid bone relatively fixed.

Thyrohyoid

Thyrohyoid is a small, quadrilateral muscle that may be regarded as an upward continuation of sternothyroid (see Fig. 35.5A). It arises from the oblique line on the lamina of the thyroid cartilage and passes upwards to attach to the lower border of the greater cornu and adjacent part of the body of the hyoid bone.

Vascular supply Thyrohyoid is supplied by branches from the superior thyroid and lingual arteries.

Innervation Unlike the other infrahyoid muscles, thyrohyoid is not innervated by the ansa cervicalis. In common with geniohyoid, it is supplied by fibres from the first cervical spinal nerve that branch off from the hypoglossal nerve beyond the descendens hypoglossi.

Actions Thyrohyoid depresses the hyoid bone. With the hyoid bone stabilized, it pulls the larynx upwards, e.g. when high notes are sung.

Anterior vertebral muscles

The anterior vertebral group of muscles are longi colli and capitis, and recti capitis anterior and lateralis (**Fig. 35.6**), all of which are flexors of the head and neck to varying degrees. Together with the lateral vertebral muscles, they form the prevertebral muscle group (Sakamoto 2016).

Rectus capitis anterior

Rectus capitis anterior is a short, flat muscle situated behind the upper part of longus capitis. It arises from the anterior surface of the lateral mass of the atlas and the root of its transverse process, and ascends almost vertically to the inferior surface of the basilar part of the occipital bone immediately anterior to the occipital condyle.

Vascular supply Rectus capitis anterior is supplied by branches from the vertebral and ascending pharyngeal arteries.

Innervation Rectus capitis anterior is innervated by branches from the loop between the ventral rami of the first and second cervical spinal nerves.

Actions Rectus capitis anterior flexes the head at the atlanto-occipital joints.

Rectus capitis lateralis

Rectus capitis lateralis is a short, flat muscle that arises from the upper surface of the transverse process of the atlas and inserts into the inferior surface of the jugular process of the occipital bone. In view of its attachments and its relation to the ventral ramus of the first spinal nerve, rectus capitis lateralis is regarded as homologous with the posterior intertransverse muscles.

Vascular supply Rectus capitis lateralis is supplied by branches from the vertebral, occipital and ascending pharyngeal arteries.

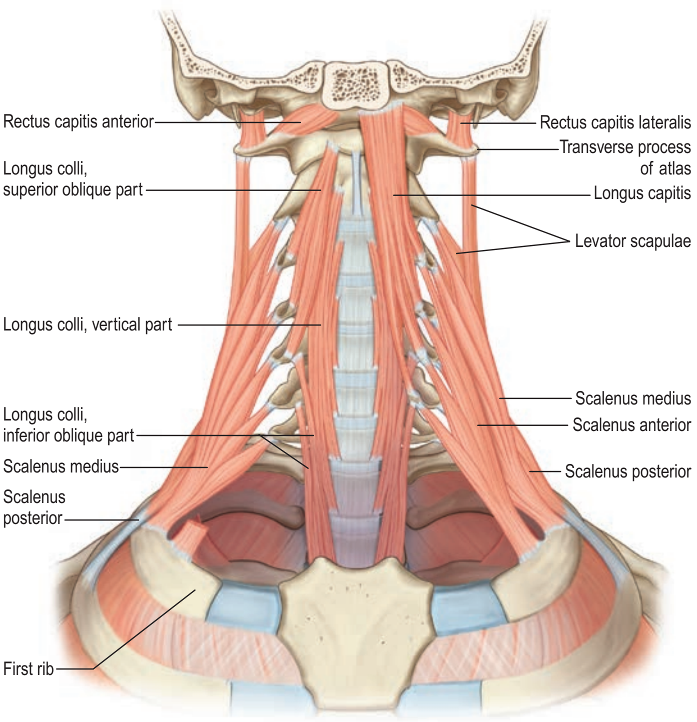

Fig. 35.6 The anterior and lateral vertebral muscles. Scalenus anterior and longus capitis have been removed on the right side.

Innervation Rectus capitis lateralis is innervated by branches from the loop between the ventral rami of the first and second cervical spinal nerves.

Actions Rectus capitis lateralis flexes the head laterally to the same side.

Longus capitis

Longus capitis (see Fig. 35.6) has a narrow origin from tendinous slips from the anterior tubercles of the transverse processes of the third, fourth, fifth and sixth cervical vertebrae, and becomes broad and thick above, where it is inserted into the inferior surface of the basilar part of the occipital bone.

Vascular supply Longus capitis is supplied by the ascending pharyngeal, ascending cervical branch of the inferior thyroid and the vertebral arteries.

Innervation Longus capitis is innervated by branches from the ventral rami of the first, second and third cervical spinal nerves.

Actions Longus capitis flexes the head.

Longus colli

Longus colli (see Fig. 35.6) is applied to the anterior surface of the vertebral column, between the atlas and the third thoracic vertebra. It can be divided into three parts, which all arise by tendinous slips. The inferior oblique part is the smallest, running upwards and laterally from the anterior surfaces of the bodies of the first two or three thoracic vertebrae to the anterior tubercles of the transverse processes of the fifth and sixth cervical vertebrae. The superior oblique part passes upwards and medially from the anterior tubercles of the transverse processes of the third, fourth and fifth cervical vertebrae, to be attached by a narrow tendon to the anterolateral surface of the tubercle on the anterior arch of the atlas. The vertical intermediate part ascends from the anterior surfaces of the bodies of the upper three thoracic and lower three cervical vertebrae to the fronts of the bodies of the second, third and fourth cervical vertebrae.

Vascular supply Longus colli is supplied by branches from the vertebral, inferior thyroid and ascending pharyngeal arteries.

Innervation Longus colli is innervated by branches from the ventral rami of the second, third, fourth, fifth and sixth cervical spinal nerves.

Actions Longus colli flexes the neck forwards. In addition, the oblique parts may flex it laterally, and the inferior oblique part rotates it to the opposite side. Its main antagonist is longissimus cervicis.

Lateral vertebral muscles

Scaleni anterior, medius and posterior extend obliquely between the upper two ribs and the cervical transverse processes. Scalenus minimus (pleuralis) is associated with the suprapleural membrane and cervical pleura, and is described in Chapter 54.

Scalenus anterior

Scalenus anterior lies at the side of the neck deep (posteromedial) to sternocleidomastoid (see Fig. 35.5). Above, it is attached by musculotendinous fascicles to the anterior tubercles of the transverse processes of the third, fourth, fifth and sixth cervical vertebrae. These converge, blend and descend almost vertically, to be attached by a narrow, flat tendon to the scalene tubercle on the inner border of the first rib, and to a ridge on the upper surface of the rib anterior to the groove for the subclavian artery (see Fig. 35.6).

Relations Scalenus anterior forms an important landmark in the root of the neck because the phrenic nerve passes anterior to it and the subclavian artery posterior to it; the brachial plexus lies at its lateral border. The clavicle, subclavius, sternocleidomastoid and omohyoid, lateral part of the carotid sheath, transverse cervical, suprascapular and ascending cervical arteries, subclavian vein, prevertebral fascia and phrenic nerve are all anterior to scalenus anterior. Posteriorly are the suprapleural membrane, pleura, roots of the brachial plexus and the subclavian artery; the latter two separate scalenus anterior from scalenus medius. The proximity of the muscle to the brachial plexus and subclavian artery and vein can give rise to compression syndromes. Below its attachment to the sixth cervical vertebra, the medial border of the muscle is separated from longus colli by an angular interval in which the vertebral artery and vein pass to and from the foramen transversarium of the sixth cervical vertebra. The inferior thyroid artery crosses this interval from the lateral to the medial side near its apex. The sympathetic trunk and its cervicothoracic ganglion are closely related to the posteromedial side of this part of the vertebral artery. On the left side, the thoracic duct crosses the triangular interval at the level of the seventh cervical vertebra and usually comes into contact with the medial edge of scalenus anterior. The musculotendinous attachments of scalenus anterior to anterior tubercles are separated from those of longus capitis by the ascending cervical branch of the inferior thyroid artery.

Chassaignac’s triangle is the space between longus colli and scalenus anterior as it attaches to the tubercle of the sixth cervical vertebra (Chassaignac’s tubercle); the subclavian vein forms the inferior border (**Fig. 35.5B**). This triangle is important surgically because it forms a posterior relation of the internal jugular vein in level IV: nodes in this area (including the scalene nodes) should be specifically explored in selected neck dissection when the vein is preserved. Lymphadenopathy in this location frequently represents metastatic spread from either the thyroid or from a primary site below the clavicles (the ‘rising sun’ sign) which may be of breast, lung, stomach or ovary in origin. The thoracic duct is encountered here, either on the left as a main trunk or as a part of a smaller network of lymphatic channels on either side. Care should be taken to avoid injury to these vessels to prevent a chylous fistula or lymph fluid leaks during neck dissection.

Innervation Scalenus anterior is innervated by branches from the ventral rami of the fourth, fifth and sixth cervical spinal nerves.

Actions Acting from below, scalenus anterior bends the cervical portion of the vertebral column forwards and laterally and rotates it towards the opposite side. Acting from above, the muscle helps to elevate the first rib.

Scalenus medius

Scalenus medius, the largest and longest of the scaleni, is attached above to the transverse process of the axis and the anterior surface of the posterior tubercles of the transverse processes of the lower five cervical vertebrae (see Fig. 35.6). It frequently extends upwards to the transverse process of the atlas. Below it is attached to the upper surface of the first rib between the tubercle of the rib and the groove for the subclavian artery.

Relations The anterolateral surface of the muscle is related to sternocleidomastoid (see Fig. 35.5A). It is crossed anteriorly by the clavicle and omohyoid, and it is separated from scalenus anterior by the subclavian artery and ventral rami of the cervical spinal nerves. Levator scapulae and scalenus posterior lie posterolateral to it. The upper two roots of the nerve to serratus anterior and the dorsal scapular nerve (to the rhomboids) pierce the muscle and appear on its lateral surface.

Innervation Scalenus medius is supplied by branches from the ventral rami of the third to eighth cervical spinal nerves.

Actions Acting from below, scalenus medius bends the cervical part of the vertebral column to the same side. Acting from above, it helps to raise the first rib. The scalene muscles, particularly scalenus medius, are active during inspiration, even during quiet breathing in the erect attitude.

Scalenus posterior

Scalenus posterior is the smallest and most deeply situated of the scalene muscles (see Fig. 35.6). It passes from the posterior tubercles of the transverse processes of the fourth, fifth and sixth cervical vertebrae to the outer surface of the second rib, behind the tubercle for serratus anterior, where it is attached by a thin tendon.

Scalenus posterior is occasionally blended with scalenus medius. The scalene muscles vary a little in the number of vertebrae to which they are attached, in their degree of separation and in their segmental innervation.

Vascular supply All the scalene muscles are supplied by the ascending cervical branch of the inferior thyroid artery. Scalenus posterior receives an additional supply from the superficial cervical artery.

Innervation Scalenus posterior is innervated by branches from the ventral rami of the lower three cervical spinal nerves.

Actions When the second rib is fixed, scalenus posterior bends the lower end of the cervical part of the vertebral column to the same side. When its upper attachment is fixed, it helps to elevate the second rib.

Posterior vertebral muscles

Splenius capitis and splenius cervicis are described in Chapter 46.

VASCULAR SUPPLY AND LYMPHATIC DRAINAGE

Arteries

The common carotid, internal carotid and external carotid arteries provide the major source of blood to the head and neck (**Figs 35.7A, 35.8**). Additional arteries arise from branches of the subclavian artery, particularly the vertebral artery.

The common, internal and external carotid arteries, accompanying veins and nerves all lie in a cleft that is bound posteriorly by the transverse processes of cervical vertebrae and attached muscles, medially by the trachea, oesophagus, thyroid gland, larynx and pharyngeal constrictors, and anterolaterally by sternocleidomastoid and, at different levels, omohyoid, sternohyoid, sternothyroid, digastric and stylohyoid muscles. The common and internal carotid arteries lie within the carotid sheath, accompanied by the internal jugular vein and the vagus nerve.

Common carotid artery

The common carotid arteries differ on the right and left sides with respect to their origins. On the right, the common carotid arises from the brachiocephalic artery as it passes behind the sternoclavicular joint. On the left, the common carotid artery comes directly from the arch of the aorta in the superior mediastinum. The right common carotid, therefore, has only a cervical part whereas the left common carotid has cervical and thoracic parts. Following a similar course on both sides, the common carotid artery ascends, diverging laterally from behind the sternoclavicular joint to the level of the upper border of the thyroid cartilage of the larynx (C3–4 junction), where it divides into external and internal carotid arteries. This bifurcation can sometimes be at a higher or lower level (**Fig. 35.7B**). The angle of bifurcation remains unchanged from infancy to adulthood. However, there is a significant change in the angle of the split between the internal and the external carotid arteries relative to the common carotid artery (Seong et al 2005). The artery may be compressed against the prominent transverse process of the sixth cervical vertebra (Chassaignac's tubercle); above this level it is superficial, and its pulsation can be easily felt.

Relations In the lower part of the neck, the common carotid arteries are separated by a narrow gap that contains the trachea. Above this, the arteries are separated by the thyroid gland, larynx and pharynx. Each artery is contained within the carotid sheath of deep cervical fascia, which also encloses the internal jugular vein and vagus nerve.

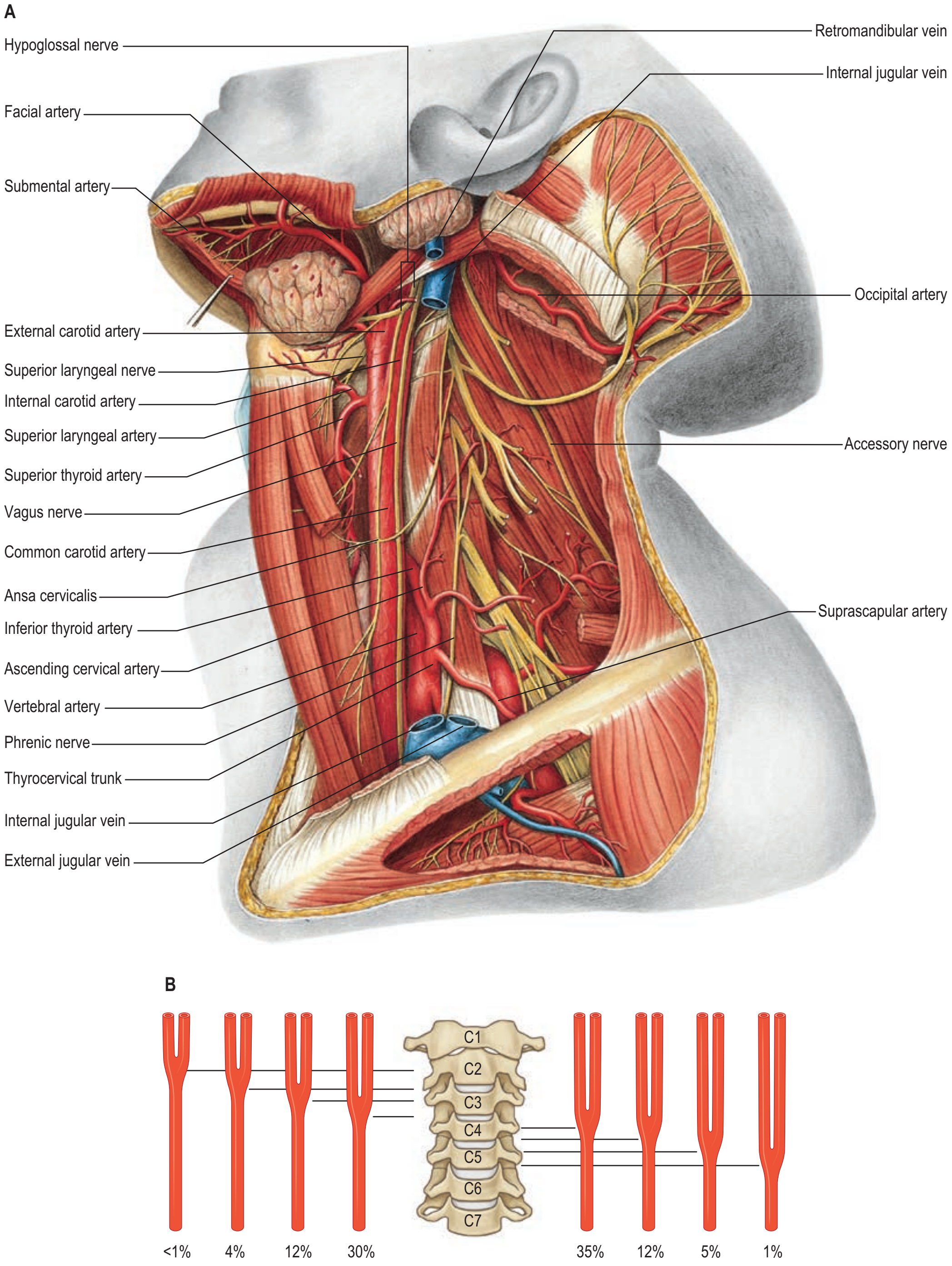
A
Hypoglossal nerve
Facial artery
Submental artery
External carotid artery
Superior laryngeal nerve
Internal carotid artery
Superior laryngeal artery
Superior thyroid artery
Vagus nerve
Common carotid artery
Ansa cervicalis
Inferior thyroid artery
Ascending cervical artery
Vertebral artery
Phrenic nerve
Thyrocervical trunk
Internal jugular vein
External jugular vein
Retromandibular vein
Internal jugular vein
Occipital artery
Accessory nerve
Suprascapular artery
B
C1
C2
C3
C4
C5
C6
C7
<1%
4%
12%
30%
35%
12%
5%
1%

Fig. 35.7 A, Vessels and nerves of the neck, left lateral view. Sternocleidomastoid and the greater part of omohyoid and the internal jugular vein have been removed. Compare with Fig. 35.17, which shows a deeper level of dissection. **B**, The variation in levels of bifurcation of the common carotid artery, related to the cervical vertebrae. (A, B, Sobotta Atlas of Human Anatomy © Elsevier GmbH, Urban & Fischer, Munich.)

The vein lies lateral to the artery, and the nerve lies between them and posterior to both.

The artery is crossed anterolaterally, at the level of the cricoid cartilage, by the intermediate tendon – sometimes the superior belly – of omohyoid. Below omohyoid, it is sited deeply, and covered by skin, superficial fascia, platysma, deep cervical fascia, and sternocleidomastoid, sternohyoid and sternothyroid. Above omohyoid, it is more superficial, and covered merely by skin, superficial fascia, platysma, deep cervical fascia and the medial margin of sternocleidomastoid; it is crossed obliquely from its medial to lateral side by the sternocleidomastoid branch of the superior thyroid artery. The superior root of the ansa cervicalis, joined by its inferior root from the second and third cervical spinal nerves, lies anterior to, or embedded within, the carotid sheath as it crosses it obliquely. The superior thyroid vein usually crosses near the upper border of the thyroid cartilage, and the middle thyroid vein crosses a little below the level of the cricoid cartilage. The anterior jugular vein crosses the common carotid artery above the clavicle, separated from it by sternohyoid and sternothyroid. Posterior to the carotid sheath are the transverse processes of the fourth to sixth cervical vertebrae, to which are attached longus colli, longus capitis and tendinous slips of scalenus anterior. The sympathetic trunk and ascending cervical branch of the inferior thyroid artery lie between the common carotid artery and the muscles. Below the level of the sixth cervical vertebra, the artery is in an angle between scalenus anterior and longus colli, anterior to the vertebral vessels, inferior thyroid and subclavian arteries, sympathetic trunk and, on the left, the thoracic duct. The oesophagus, trachea, inferior thyroid artery, recurrent laryngeal nerve and, at a higher level, the larynx and pharynx are medial to the sheath and its contents. The thyroid gland overlaps it anteromedially. The internal jugular vein lies lateral and, in the lower neck, also anterior to the artery, while the vagus nerve lies posterolaterally in the angle between artery and vein.

On the right side, low in the neck, the recurrent laryngeal nerve crosses obliquely behind the artery. The right internal jugular vein diverges from it below but the left vein approaches and often overlaps its artery.

The right common carotid artery sometimes arises above the level of the sternoclavicular joint, or it may be a separate branch from the aorta. The left common carotid artery varies in origin more than the right and may arise with the brachiocephalic artery. Division of the

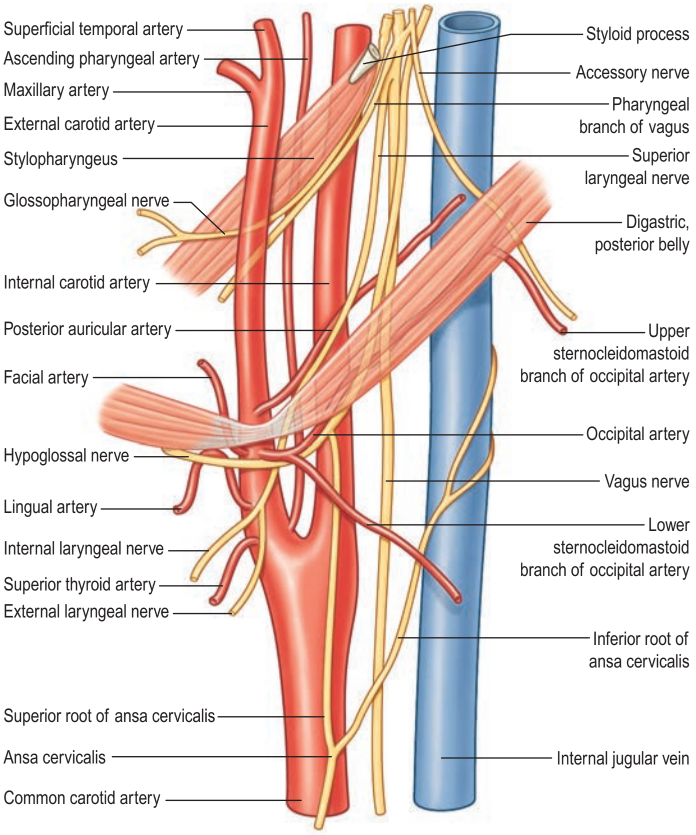

Fig. 35.8 The branches of the external carotid artery. Note the structures that either cross the internal jugular vein and the carotid arteries or intervene between the external and internal carotid arteries.

common carotid may occur higher, near the level of the hyoid bone, or, more rarely, at a lower level alongside the larynx. Very rarely, it ascends without division, so that either the external or internal carotid is absent, or it may be replaced by separate external and internal carotid arteries that arise directly from the aorta, on one side, or bilaterally.

Although the common carotid artery usually has no branches, it may occasionally give rise to the vertebral, superior thyroid, superior laryngeal, ascending pharyngeal, inferior thyroid or occipital arteries.

External carotid artery

The external carotid artery (see Figs 35.7A, 35.8) begins lateral to the upper border of the thyroid cartilage, level with the intervertebral disc between the third and fourth cervical vertebrae. A little curved and with a gentle spiral, it first ascends slightly forwards and then inclines backwards and a little laterally, to pass midway between the tip of the mastoid process and the angle of the mandible. Here, in the substance of the parotid gland behind the neck of the mandible, it divides into its terminal branches, the superficial temporal and maxillary arteries. As it ascends, it gives off several large branches and diminishes rapidly in calibre. In children the external carotid is smaller than the internal carotid, but in adults the two are of almost equal size. At its origin, it is in the carotid triangle and lies anteromedial to the internal carotid artery. It later becomes anterior, then lateral, to the internal carotid as it ascends. At mandibular levels, the styloid process and its attached structures intervene between the vessels; the internal carotid is deep, and the external carotid superficial, to the styloid process. A fingertip placed in the carotid triangle perceives a powerful arterial pulsation, which represents the termination of the common carotid, the origins of external and internal carotids, and the stems of the initial branches of the external carotid.

Relations The skin and superficial fascia, the loop between the cervical branch of the facial nerve and the transverse cutaneous nerve of the neck, the deep cervical fascia and the anterior margin of sternocleidomastoid all lie superficial to the external carotid artery in the carotid triangle. The artery is crossed by the hypoglossal nerve and its vena comitans, and by the lingual, facial and, sometimes, the superior thyroid veins. Leaving the carotid triangle, the external carotid artery is crossed by the posterior belly of digastric and by stylohyoid; it ascends between these muscles and the posteromedial surface of the parotid gland, which it next enters. Within the parotid, the artery lies medial to the facial nerve and the junction of the superficial temporal and maxillary veins. The pharyngeal wall, superior laryngeal nerve and ascending pharyngeal artery are the initial medial relations of the artery. At a higher level, it is separated from the internal carotid artery by the styloid process, styloglossus and stylopharyngeus, glossopharyngeal nerve, pharyngeal branch of vagus nerve and part of the parotid gland. The artery is equally likely to lie medial to the parotid gland, or within it.

The external carotid artery has eight named branches distributed to the head and neck. The superior thyroid, lingual and facial arteries arise from its anterior surface, the occipital and posterior auricular arteries arise from its posterior surface, and the ascending pharyngeal artery arises from its medial surface. The maxillary and superficial temporal arteries are its terminal branches within the parotid gland.

Superior thyroid artery

The superior thyroid artery is the second branch of the external carotid artery. It arises from the anterior surface of the external carotid just below the level of the greater cornu of the hyoid bone (see Figs 35.7A, 35.8). It descends along the lateral border of thyrohyoid to reach the apex of the lobe of the thyroid gland. Lying medially are the inferior constrictor muscle and the external laryngeal nerve; the nerve is often posteromedial, and therefore at risk when the artery is being ligated. Occasionally, it may issue directly from the common carotid.

Branches

The superior thyroid artery supplies the thyroid gland and some adjacent skin. Glandular branches are anterior, which runs along the medial side of the upper pole of the lateral lobe to supply mainly the anterior surface; a branch that crosses above the isthmus to anastomose with its fellow of the opposite side; and posterior, which descends on the posterior border to supply the medial and lateral surfaces and anastomoses with the inferior thyroid artery. A lateral branch sometimes supplies the lateral surface. The superior thyroid artery is often accompanied by the external branch of the superior laryngeal nerve. Care should be taken to preserve this nerve when ligating the superior thyroid artery during surgery because it supplies cricothyroid: iatrogenic damage affects vocal cord function.

The artery has the following named branches: infrahyoid, superior laryngeal, sternocleidomastoid and cricothyroid.

Infrahyoid artery The infrahyoid artery is a small branch that runs along the lower border of the hyoid bone deep to thyrohyoid and anastomoses with its fellow of the opposite side to supply the infrahyoid strap muscles.

Superior laryngeal artery The superior laryngeal artery accompanies the internal laryngeal nerve. Deep to thyrohyoid, it pierces the lower part of the thyrohyoid membrane to supply the tissues of the upper part of the larynx. It anastomoses with its fellow of the opposite side and with the inferior laryngeal branch of the inferior thyroid artery.

Sternocleidomastoid artery The sternocleidomastoid artery descends laterally across the carotid sheath and supplies the middle region of sternocleidomastoid. Like the parent artery itself, it may arise directly from the external carotid artery.

Cricothyroid artery The cricothyroid artery crosses high on the anterior cricothyroid ligament, anastomoses with its fellow of the opposite side and supplies cricothyroid.

Ascending pharyngeal artery

The ascending pharyngeal artery is the first and smallest branch of the external carotid artery. It is a long, slender vessel that arises from the medial (deep) surface of the external carotid artery near the origin of that artery. It is important that it is identified and preserved if the external carotid is being ligated because of its potential to supply to a compromised internal carotid circulation.

The ascending pharyngeal artery ascends between the internal carotid artery and the pharynx to the base of the cranium, crossed by styloglossus and stylopharyngeus; longus capitis is posterior. It gives off numerous small branches to supply longus capitis and longus colli, the sympathetic trunk, the hypoglossal, glossopharyngeal and vagus nerves, and some of the cervical lymph nodes. It anastomoses with the ascending palatine branch of the facial artery and the ascending cervical branch of the inferior thyroid artery. Its named branches are the pharyngeal, inferior tympanic and meningeal arteries.

Pharyngeal artery The pharyngeal artery gives off three or four branches to supply the constrictor muscles of the pharynx and stylopharyngeus. A variable ramus supplies the palate and may replace the ascending palatine branch of the facial artery. The artery descends forwards between the superior border of the superior constrictor and levator veli palatini to the soft palate, and also supplies a branch to the palatine tonsil and the pharyngotympanic tube.

Inferior tympanic artery The inferior tympanic artery is a small branch that traverses the temporal canaliculus with the tympanic branch of the glossopharyngeal nerve and supplies the medial wall of the tympanic cavity.

Meningeal branches The meningeal branches are small vessels that supply the nerves that traverse the foramen lacerum, jugular foramen and hypoglossal canal, and the associated dura mater and adjoining bone. One branch, the posterior meningeal artery, reaches the cerebellar fossa via the jugular foramen, and is usually regarded as the terminal branch of the ascending pharyngeal artery.

Lingual artery

The lingual artery provides the chief blood supply to the tongue and the floor of the mouth (see Figs 35.8, 37.11). It arises anteromedially from the external carotid artery opposite the tip of the greater cornu of the hyoid bone, between the superior thyroid and facial arteries. It often arises with the facial or, less often, with the superior thyroid artery. It may be replaced by a ramus of the maxillary artery. Ascending medially at first, it loops down and forwards, passes medial to the posterior border of hyoglossus and then runs horizontally forwards deep to it. The lingual artery next ascends again almost vertically, and courses sinuously forwards on the inferior surface of the tongue as far as its tip. The further course of the lingual artery is described in Chapter 37.

Relations Its relationship to hyoglossus naturally divides the lingual artery into descriptive 'thirds'. In its first part, the lingual artery is in the carotid triangle. Skin, fascia and platysma are superficial to it, while the middle pharyngeal constrictor muscle is medial. The artery ascends a little medially, then descends to the level of the hyoid bone, and the loop so formed is crossed externally by the hypoglossal nerve. The second part passes along the upper border of the hyoid bone, deep to hyoglossus, the tendons of digastric and stylohyoid, the lower part of the submandibular gland and the posterior part of mylohyoid. Hyoglossus separates it from the hypoglossal nerve and its vena comitans. Here, its medial aspect adjoins the middle constrictor muscle and it crosses the stylohyoid ligament accompanied by lingual veins. The third part is the arteria profunda linguae, which turns upwards near the anterior border of hyoglossus and then passes forwards close to the inferior lingual surface near the frenulum, accompanied by the lingual nerve. Genioglossus is a medial relation, and the inferior longitudinal muscle of the tongue lies lateral to it below the lingual mucous membrane. Near the tip of the tongue, the lingual artery anastomoses with its fellow of the opposite side. Its named branches are the suprahyoid, dorsal lingual and sublingual arteries.

Suprahyoid artery The suprahyoid artery is a small branch that runs along the upper border of the hyoid bone to anastomose with the contralateral artery. It supplies adjacent structures.

Dorsal lingual arteries The dorsal lingual arteries are described in Chapter 37.

Sublingual artery The sublingual artery is described in Chapter 37.

Facial artery

The facial artery (see Figs 35.7, 35.8, 36.25) arises anteriorly from the external carotid in the carotid triangle, above the lingual artery and immediately above the greater cornu of the hyoid bone. In the neck, at its origin, it is covered only by the skin, platysma, fasciae and often by the hypoglossal nerve. It runs up and forwards, deep to digastric and stylohyoid. At first on the middle pharyngeal constrictor, it may reach the lateral surface of styloglossus, separated there from the palatine tonsil only by this muscle and the lingual fibres of the superior constrictor. Medial to the mandibular ramus, it arches upwards and grooves the posterior aspect of the submandibular gland. It then turns down and descends to the lower border of the mandible in a lateral groove on the submandibular gland, between the gland and medial pterygoid. Reaching the surface of the mandible, the facial artery curves round its inferior border, anterior to masseter, to enter the face; its further course is described in Chapter 36. The artery is very sinuous throughout its extent. In the neck, this may be so that the artery is able to adapt to the movements of the pharynx during deglutition, and similarly on the face, so that the artery can adapt to movements of the mandible, lips and cheeks. Facial artery pulsation is most palpable where the artery crosses the mandibular base, and again near the corner of the mouth. There are four branches within the neck and four on the face. The branches in the neck are the ascending palatine, tonsillar, submental and glandular arteries. The branches on the face are described in Chapter 36.

Ascending palatine artery The ascending palatine artery arises close to the origin of the facial artery. It passes up between styloglossus and stylopharyngeus to reach the side of the pharynx, along which it ascends between the superior constrictor of the pharynx and medial pterygoid towards the cranial base. It bifurcates near levator veli palatini. One branch follows this muscle, winding over the upper border of the superior constrictor of the pharynx to supply the soft palate and to anastomose with its fellow of the opposite side and the greater palatine branch of the maxillary artery. The other branch pierces the superior constrictor muscle to supply the tonsil and pharyngotympanic tube, and to anastomose with the tonsillar and ascending pharyngeal arteries (see Fig. 40.7).

Tonsillar artery The tonsillar artery provides the main blood supply to the palatine tonsil. It ascends between medial pterygoid and styloglossus, penetrates the superior constrictor of the pharynx at the upper border of styloglossus, and enters the inferior pole of the tonsil. Its branches ramify in the tonsil and in the musculature of the posterior part of the tongue. The tonsillar artery may sometimes arise from the ascending palatine artery.

Submental artery The submental artery is the largest cervical branch of the facial artery (see Fig. 35.7). It arises as the facial artery separates from the submandibular gland and turns forwards on mylohyoid below the mandible. It supplies the overlying skin and muscles, and anastomoses with a sublingual branch of the lingual and mylohyoid branch of the inferior alveolar artery. At the chin, it ascends over the mandible and divides into superficial and deep branches that anastomose with the inferior labial and mental arteries to supply the chin and lower lip.

Glandular branches Three or four large vessels supply the submandibular salivary gland and associated lymph nodes, adjacent muscles and skin.

Occipital artery

The occipital artery arises posteriorly from the external carotid artery, approximately 2 cm from its origin (see Figs 35.7A, 35.8). At its origin, the artery is crossed superficially by the hypoglossal nerve, which winds round it from behind. The artery next passes backwards, up and deep to the posterior belly of digastric, and crosses the internal carotid artery, internal jugular vein, and hypoglossal, vagus and accessory nerves. Between the transverse process of the atlas and the mastoid process, the occipital artery reaches the lateral border of rectus capitis lateralis. It then runs in the occipital groove of the temporal bone, medial to the mastoid process and attachments of sternocleidomastoid, splenius capitis, longissimus capitis and digastric, and lies successively on rectus capitis lateralis, obliquus capitis superior and semispinalis capitis. Accompanied by the greater occipital nerve, it finally turns upwards to pierce the investing layer of the deep cervical fascia that connects the cranial attachments of trapezius and sternocleidomastoid, and ascends tortuously in the dense superficial fascia of the scalp, where it divides into many branches (see Fig. 46.78).

The occipital artery has two main branches (upper and lower) to the upper part of sternocleidomastoid in the neck. The lower branch arises near the origin of the occipital artery and may sometimes arise directly from the external carotid artery. It descends backwards over the hypoglossal nerve and internal jugular vein, enters sternocleidomastoid and anastomoses with the sternocleidomastoid branch of the superior thyroid artery. The upper branch arises as the occipital artery crosses the accessory nerve and runs down and backwards superficial to the internal jugular vein. It enters the deep surface of sternocleidomastoid with the accessory nerve.

Posterior auricular artery

The posterior auricular artery is a small vessel that branches posteriorly from the external carotid just above digastric and stylohyoid. It ascends between the parotid gland and the styloid process to the groove between the auricular cartilage and mastoid process, and divides into auricular and occipital branches, which are described with the face in

Chapter 36. In the neck, it provides branches that supply digastric, stylohyoid, sternocleidomastoid and the parotid gland. It also gives origin to the stylomastoid artery (described as an indirect branch of the posterior auricular artery in about a third of subjects) that enters the stylomastoid foramen to supply the facial nerve, tympanic cavity, mastoid antrum air cells and semicircular canals. In the young, its posterior tympanic ramus forms a circular anastomosis with the anterior tympanic branch of the maxillary artery.

Internal carotid artery

The internal carotid artery supplies most of the ipsilateral cerebral hemisphere, eye and accessory organs, forehead and, in part, the nose. From its origin at the carotid bifurcation (**Fig. 35.9**; see Fig. 35.8) where there is usually a carotid sinus, it ascends in front of the transverse processes of the upper three cervical vertebrae to the inferior aperture of the carotid canal in the petrous part of the temporal bone. Here, it enters the cranial cavity and turns anteriorly through the cavernous sinus in the carotid groove on the side of the body of the sphenoid bone. It terminates below the anterior perforated substance by division into the anterior and middle cerebral arteries. The internal carotid artery may be divided conveniently into cervical, petrous, cavernous and cerebral parts. Rarely, persistent embryonic branches to the basilar artery from the cervical part of the internal carotid artery may be encountered at the C1–C2 (persistent hypoglossal artery) and C2–C3 (pro-atlantal intersegmental artery) levels.

Relations The internal carotid artery is initially superficial in the carotid triangle, and then passes deeper, medial to the posterior belly of digastric. Except near the skull, the internal jugular vein and vagus nerve are lateral to it within the carotid sheath. The external carotid artery is first anteromedial, but then curves back to lie superficial. Posteriorly, the internal carotid adjoins longus capitis, and the superior cervical sympathetic ganglion lies between them. The superior laryngeal nerve crosses obliquely behind it. The pharyngeal wall lies medial to the artery, which is separated by fat and pharyngeal veins from the ascending pharyngeal artery and superior laryngeal nerve. Anterolaterally, the internal carotid artery is covered by sternocleidomastoid. Below the posterior belly of digastric, the hypoglossal nerve and superior root of the ansa cervicalis and the lingual and facial veins are superficial to the artery. At the level of the digastric, the internal carotid is crossed by stylohyoid and the occipital and posterior auricular arteries. Above digastric, it is separated from the external carotid artery by the styloid process, styloglossus and stylopharyngeus, the glossopharyngeal nerve and the pharyngeal branch of the vagus, and the deeper part of the parotid gland. At the base of the skull, the glossopharyngeal, vagus, accessory and hypoglossal nerves lie between the internal carotid artery and the internal jugular vein, which here has become posterior. The length of the artery varies with the length of the neck and the point of the carotid bifurcation. It may arise from the aortic arch, in which case it lies medial to the external carotid as far as the larynx, where it crosses behind it. The cervical portion is normally straight but may be very tortuous, when it lies closer to the pharynx than usual, very near the tonsil. In children, the tonsillocarotid distance increases with growth to a maximum value of 25 mm (Deutsch et al 1995). The internal carotid artery enters the cranium without giving off any branches. It may occasionally be absent.

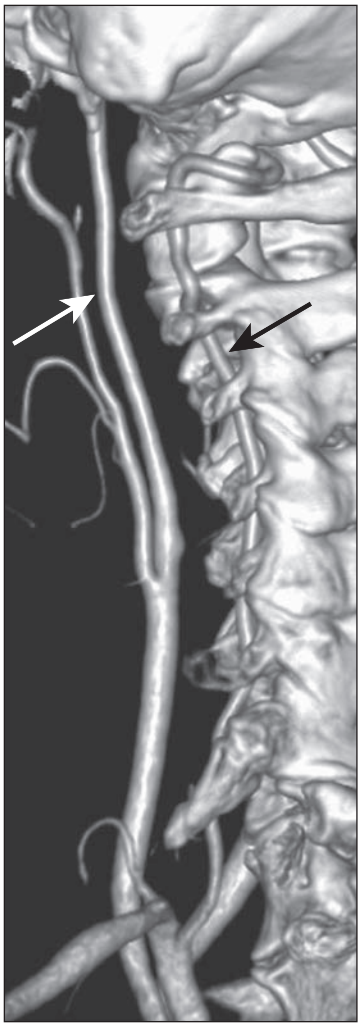

Fig. 35.9 Internal carotid artery anatomy shown on volume rendering of a computed tomographic angiogram. The cervical internal carotid artery (white arrow) is a branchless vessel. Note the course of the vertebral artery (black arrow). (With permission from Kaufman JA, Nesbit GM Carotid and vertebral arteries. In: Kaufman JA, Lee MJ Vascular and Interventional Radiology: The Requisites. Ch. 5. Elsevier, Saunders. Copyright 2014.)

Occlusive atherosclerotic disease within either the internal carotid or common carotid arteries may cause strokes or transient ischaemic attacks (TIAs) characterized by weakness of the contralateral side. Visual disturbances experienced in the ipsilateral eye and classically described as a ‘curtain’ falling down over the visual field (amaurosis fugax), may also occur.

Carotid sinus and carotid body

The common carotid artery has two specialized organs near its bifurcation: the carotid sinus and the carotid body. They relay information concerning the pressure and chemical composition of the arterial blood, respectively, and are innervated principally by the carotid branch(es) of the glossopharyngeal nerve, with small contributions from the cervical sympathetic trunk and the vagus nerve.

The carotid sinus usually appears as a dilation of the lower end of the internal carotid in late adolescence (Seong et al 2005) and functions as a baroreceptor.

The carotid body is a reddish-brown, oval structure, 5–7 mm in height and 2.5–4 mm in width. It lies either posterior to the carotid bifurcation or between its branches, and is attached to, or sometimes partly embedded in, their adventitia. Occasionally, it takes the form of a group of separate nodules. Aberrant miniature carotid bodies, microstructurally similar but with diameters of 600 μm or less, may appear in the adventitia and adipose tissue near the carotid sinus.

The carotid body is surrounded by a fibrous capsule, from which septa divide the enclosed tissue into lobules. Each lobule contains glomus (type I) cells, which are separated from an extensive network of fenestrated sinusoids by sustentacular (type II) cells (**Fig. 35.10**). Glomus cells store a number of peptides, particularly enkephalins, bombesin and neurotensin, and amines including dopamine, serotonin (5-hydroxytryptamine, 5-HT), adrenaline (epinephrine) and noradrenaline (norepinephrine), and are therefore regarded as paraneurones. Unmyelinated axons lie in a collagenous matrix between the sustentacular cells and the sinusoidal endothelium, and many synapse on the glomus cells. They are visceral afferents, which travel in the carotid sinus nerve to join the glossopharyngeal nerve. Preganglionic sympathetic axons and fibres from the carotid sinus synapse on parasympathetic and sympathetic ganglion cells, which lie either in isolation or in small groups near the surface of each carotid body. Postganglionic axons travel to local blood vessels; the parasympathetic efferent fibres are probably vasodilatory and the sympathetic ones are vasoconstrictor.

The carotid body receives a rich blood supply from branches of the adjacent external carotid artery, which is consistent with its role as an arterial chemoreceptor. When stimulated by hypoxia, hypercapnia or increased hydrogen ion concentration (low pH) in the blood flowing through it, it elicits reflex increases in the rate and volume of ventilation via connections with brainstem respiratory centres. The bodies are most prominent in children and normally involute in older age, when they are infiltrated by lymphocytes and fibrous tissue. Individuals with chronic hypoxia, or who live at high altitude or suffer from lung disease, may have enlarged carotid bodies as a result of hyperplasia. Disrupted carotid body maturation may play a role in sudden infant death syndrome (Porzionato et al 2013). Benign and malignant paragangliomas develop in association with succinyl dehydrogenase mutations (SDH).

Other small bodies, resembling carotid bodies and also considered to be chemoreceptors, are present near the arteries of the fourth and sixth pharyngeal arches and hence are found near the aortic arch, ligamentum arteriosum and right subclavian artery; they are supplied by the vagus nerve.

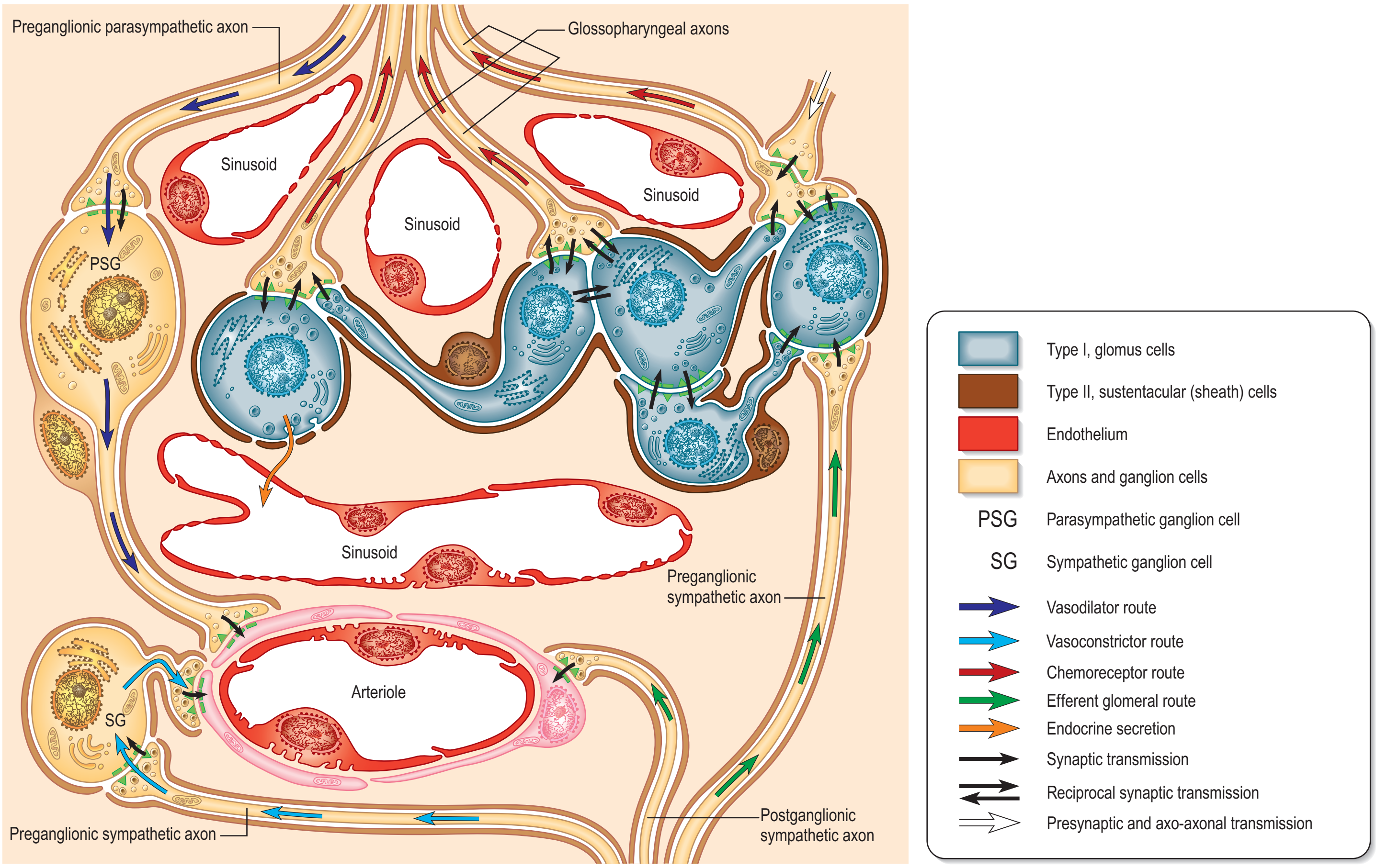
Preganglionic parasympathetic axon
Glossopharyngeal axons
Sinusoid
Sinusoid
Sinusoid
PSG
Sinusoid
Preganglionic sympathetic axon
Arteriole
SG
Preganglionic sympathetic axon
Postganglionic sympathetic axon
Type I, glomus cells
Type II, sustentacular (sheath) cells
Endothelium
Axons and ganglion cells
PSG Parasympathetic ganglion cell
SG Sympathetic ganglion cell
Vasodilator route
Vasoconstrictor route
Chemoreceptor route
Efferent glomeral route
Endocrine secretion
Synaptic transmission
Reciprocal synaptic transmission
Presynaptic and axo-axonal transmission

Fig. 35.10 The cellular, neural and vascular architecture of the carotid body. Functional pathways are indicated.

Subclavian artery

The right subclavian artery arises from the brachiocephalic trunk, the left from the aortic arch (see Fig. 35.18). For description, each is divided into a first part, from its origin to the medial border of scalenus anterior; a second part behind this muscle; and a third part from the lateral margin of scalenus anterior to the outer border of the first rib, where the artery becomes the axillary artery. Each subclavian artery arches over the cervical pleura and pulmonary apex. Their first parts differ, whereas the second and third parts are almost identical.

First part of right subclavian artery

The right subclavian artery branches from the brachiocephalic trunk behind the upper border of the right sternoclavicular joint, and passes superolaterally to the medial margin of scalenus anterior. It usually ascends 2 cm above the clavicle but this varies.

Relations The artery is deep to the skin, superficial fascia, platysma, supraclavicular nerves, deep fascia, clavicular attachment of sternocleidomastoid, sternohyoid and sternothyroid. It is at first behind the origin of the right common carotid artery; more laterally, it is crossed by the vagus nerve, the cardiac branches of the vagus and the sympathetic trunk, and by internal jugular and vertebral veins; the subclavian sympathetic loop encircles it. The anterior jugular vein diverges laterally in front of it, separated by sternohyoid and sternothyroid. Below and behind the artery are the pleura and pulmonary apex; they are separated from the artery by the suprapleural membrane, the ansa subclavia, a small accessory vertebral vein and the right recurrent laryngeal nerve, which winds round the lower and posterior part of the vessel (see Fig. 41.11).

First part of left subclavian artery

The first part of the left subclavian artery springs from the aortic arch, behind the left common carotid, level with the disc between the third and fourth thoracic vertebrae. It ascends into the neck, and then arches laterally to the medial border of scalenus anterior.

Relations In the neck, near the medial border of scalenus anterior, the artery is crossed anteriorly by the left phrenic nerve and the termination of the thoracic duct. Otherwise, anterior relations are the same as those of the first part of the right subclavian artery. Posteriorly and inferiorly, the relations of both vessels are identical but the left recurrent laryngeal nerve, medial to the left subclavian artery in the thorax, is not directly related to its cervical part.

Second part of subclavian artery

The second part of the subclavian artery lies behind scalenus anterior; it is short and constitutes the highest part of the vessel (see Fig. 35.18).

Relations The skin, superficial fascia, platysma, deep cervical fascia, sternocleidomastoid and scalenus anterior are anterior. The right phrenic nerve is often described as being separated from the second part of the subclavian artery by scalenus anterior, whereas it crosses the first part of the left subclavian artery. However, both nerves may sometimes lie anterior to the muscle. The suprapleural membrane, pleura and lung, and the lower trunk of the brachial plexus are posteroinferior; the upper and middle trunks of the plexus are superior; and the subclavian vein is anteroinferior, separated by scalenus anterior.

Third part of subclavian artery

The third part of the subclavian artery descends laterally from the lateral margin of scalenus anterior to the outer border of the first rib, where it becomes the axillary artery. It is the most superficial part of the artery and lies partly in the supraclavicular triangle, where its pulsations may be felt and it may be compressed. The third part of the subclavian artery is the most accessible segment of the artery. Since the line of the posterior border of sternocleidomastoid approximates to the (deeper) lateral border of scalenus anterior, the artery can be felt in the anteroinferior angle of the posterior triangle. It can only be effectively compressed against the first rib: with the shoulder depressed, pressure is exerted down, back and medially in the angle between sternocleidomastoid and the clavicle. The palpable trunks of the brachial plexus may be injected with local anaesthetic allowing major surgical procedures to the arm.

Relations The skin, superficial fascia, platysma, supraclavicular nerves and deep cervical fascia are anterior. The external jugular vein crosses its medial end and here receives the suprascapular, transverse cervical and anterior jugular veins, which collectively often form a venous plexus. The nerve to subclavius descends between the veins and the artery; the latter is terminally behind the clavicle and subclavius, where it is crossed by the suprascapular vessels. The subclavian vein is

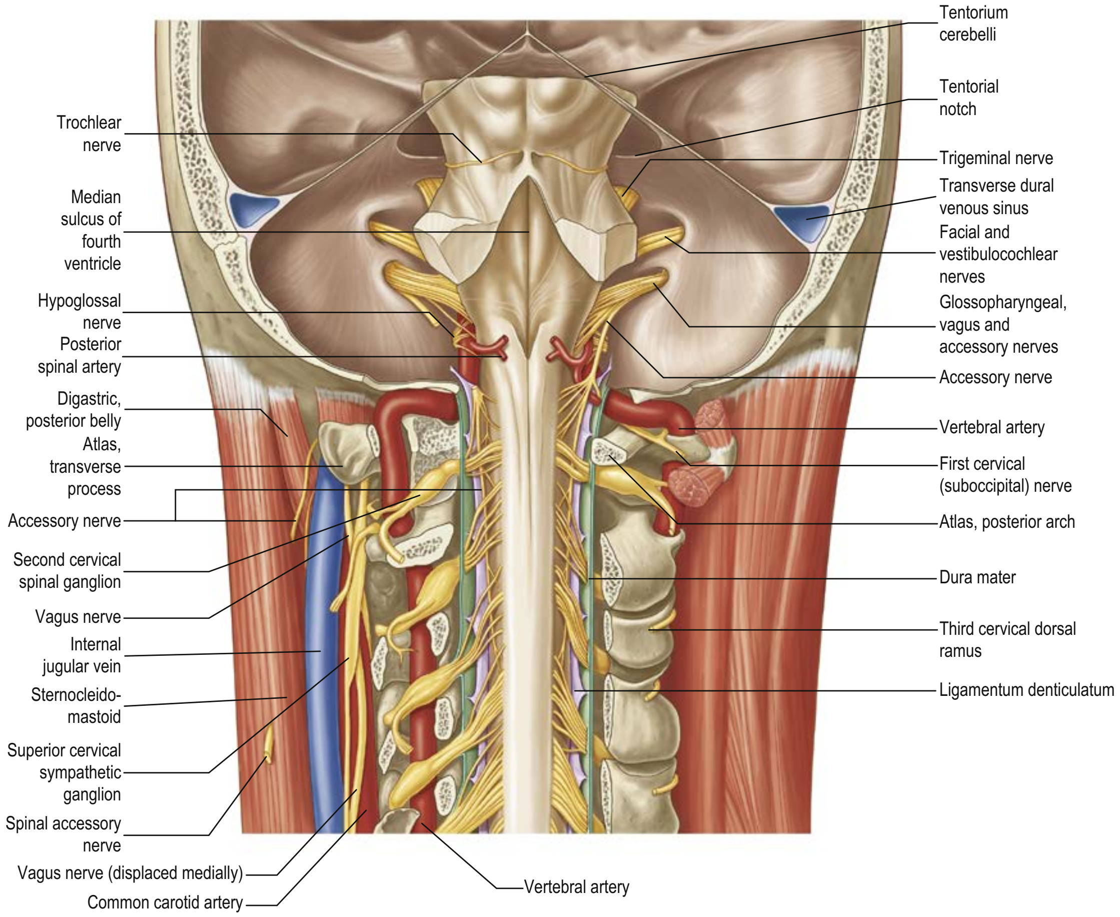
Tentorium cerebelli
Tentorial notch
Trigeminal nerve
Transverse dural venous sinus
Facial and vestibulocochlear nerves
Glossopharyngeal, vagus and accessory nerves
Accessory nerve
Vertebral artery
First cervical (suboccipital) nerve
Atlas, posterior arch
Dura mater
Third cervical dorsal ramus
Ligamentum denticulatum
Trochlear nerve
Median sulcus of fourth ventricle
Hypoglossal nerve
Posterior spinal artery
Digastric, posterior belly
Atlas, transverse process
Accessory nerve
Second cervical spinal ganglion
Vagus nerve
Internal jugular vein
Sternocleido-mastoid
Superior cervical sympathetic ganglion
Spinal accessory nerve
Vagus nerve (displaced medially)
Common carotid artery
Vertebral artery

Fig. 35.11 A dissection of the brainstem and the upper part of the spinal cord after removal of large portions of the occipital and parietal bones, the cerebellum and the roof of the fourth ventricle. On the left side, the foramina transversaria of the atlas and the third, fourth and fifth cervical vertebrae have been opened to expose the vertebral artery. On the right side, the posterior arch of the atlas and the laminae of the succeeding cervical vertebrae have been divided and have been removed, together with the vertebral spines and the contralateral laminae. The tentorium cerebelli and the transverse sinuses have been divided and their posterior portions removed.

anteroinferior and the lower trunk of the brachial plexus is posteroinferior, between the subclavian artery and the scalenus medius (and on the first rib). The upper and middle trunks of the brachial plexus (which are palpable here) and the inferior belly of omohyoid are superolateral. The first rib is inferior.

The right subclavian artery may arise above or below sternoclavicular level; it may be a separate aortic branch and be the first or last branch of the arch. When it is the first branch, it is in the position of a brachiocephalic trunk. When it is the last branch, it arises from the left end of the arch, and ascends obliquely to the right behind the trachea, oesophagus and right common carotid to the first rib. When this happens, the right recurrent laryngeal nerve hooks round the common carotid artery. Sometimes, when the right subclavian artery is the last aortic branch, it passes between the trachea and oesophagus and can cause dysphagia, a condition known as dysphagia lusoria. It may perforate scalenus anterior, and very rarely may pass anterior to it. Sometimes, the subclavian vein accompanies the artery behind scalenus anterior. The artery may ascend as high as 4 cm above the clavicle or it may reach only its upper border. The left subclavian artery is occasionally combined at its origin with the left common carotid artery.

Vertebral artery

The vertebral artery arises from the superoposterior aspect of the first part of the subclavian artery. It passes through the foramina in the transverse processes of all of the cervical vertebrae except the seventh, curves medially behind the lateral mass of the atlas and enters the cranium via the foramen magnum (Fig. 35.11). The artery joins its fellow to form the basilar artery at the lower pontine border. Occasionally, it may enter the cervical vertebral column via the fourth, fifth or seventh cervical vertebra (Fig. 35.12).

Relations The first part, V1, passes back and upwards between longus colli and scalenus anterior, behind the common carotid artery and the vertebral vein. It is crossed by the inferior thyroid artery, and by the thoracic duct on the left side and the right lymphatic duct on the right side. The seventh cervical transverse process, the inferior cervical ganglion and ventral rami of the seventh and eighth cervical spinal nerves lie posterior to the artery. The second part, V2, ascends through the transverse foramina of the remaining cervical vertebrae, accompanied by a large branch from the inferior cervical ganglion and a plexus of veins that form the vertebral vein low in the neck. It lies anterior to the ventral rami of the cervical spinal nerves (C2–C6) and ascends almost vertically

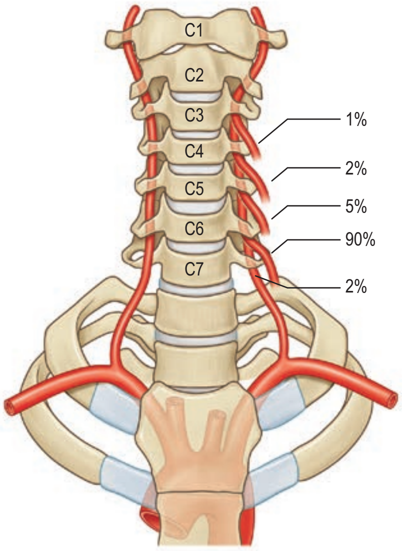
C1
C2
C3
C4
C5
C6
C7
1%
2%
5%
90%
2%

Fig. 35.12 The level of entry of the vertebral artery into the foramina transversaria of the cervical vertebrae. Note that 90% enter at the level of the sixth cervical vertebra. (Sobotta Atlas of Human Anatomy © Elsevier GmbH, Urban & Fischer, Munich.)

to pass through the transverse process of the axis, where it turns laterally to gain access to the transverse foramen of the atlas (see Fig. 35.11). The third part, V3, issues medial to rectus capitis lateralis, and curves backwards and medially behind the lateral mass of the atlas, with the first cervical ventral spinal ramus lying on its medial side. In this position, it lies in a groove on the upper surface of the posterior arch of the atlas, and it enters the vertebral canal below the inferior border of the posterior atlanto-occipital membrane. This part of the artery, covered by semispinalis capitis, lies in the suboccipital triangle. The first cervical dorsal spinal ramus separates the artery from the posterior arch. The fourth part, V4, pierces the dura and arachnoid mater, and ascends anterior to the hypoglossal roots. It inclines anterior to the medulla oblongata and unites with its contralateral fellow to form the midline basilar artery at the lower border of the pons.

Cervical branches of vertebral artery

Spinal branches The spinal branches enter the vertebral canal via the intervertebral foramina and supply the spinal cord and its membranes. They fork into ascending and descending rami, which unite with those above and below, to form two lateral anastomotic chains on the posterior surfaces of the vertebral bodies near the attachment of their pedicles. Branches from these chains supply the periosteum and vertebral bodies, and others communicate with similar branches across the midline; from these connections small rami join similar ones above and below, to form a median anastomotic chain on the posterior surfaces of the vertebral bodies.

Muscular branches Muscular branches arise from the vertebral artery as it curves round the lateral mass of the atlas. They supply the deep muscles of the suboccipital region and anastomose with the occipital, ascending and deep cervical arteries.

Internal thoracic artery

The internal thoracic artery arises inferiorly from the first part of the subclavian artery, 2 cm above the sternal end of the clavicle, opposite the root of the thyrocervical trunk (see Fig. 33.1). It is described further in Chapter 53.

Thyrocervical trunk

The thyrocervical trunk is a short, wide artery that arises from the front of the first part of the subclavian artery near the medial border of scalenus anterior, and divides almost at once into the inferior thyroid, suprascapular and superficial cervical arteries.

Inferior thyroid artery

The inferior thyroid artery loops upwards anterior to the medial border of scalenus anterior, turns medially just below the sixth cervical transverse process, and then descends on longus colli to the lower border of the thyroid gland (see Figs 35.7A, 35.17). It passes anterior to the vertebral vessels and posterior to the carotid sheath and its contents (and usually the sympathetic trunk, whose middle cervical ganglion frequently adjoins the vessel). On the left, near its origin, the artery is crossed anteriorly by the thoracic duct as the latter curves inferolaterally to its termination. Relations between the terminal branches of the artery and recurrent laryngeal nerve are very variable and of considerable surgical importance. The artery usually passes behind the nerve as it nears the gland. However, very close to the gland, the right nerve is equally likely to be anterior, posterior or amongst the branches of the artery, and the left nerve is usually posterior. Together with the inferior thyroid and common carotid arteries, the recurrent laryngeal nerve forms one of the sides of Beahr's triangle (see later). Since the nerve winds around the artery of the sixth branchial arch (aortic arch) on the left side, it is 45° to the midline in its ascent from the chest to the neck. However, on the right side it is slightly more superficial and lateral because it goes around the fourth branchial arch artery (subclavian) in the neck: these variations are important in thyroid surgery and are reversed in dextrocardia. The artery is not accompanied by the inferior thyroid vein.

Muscular branches These supply the infrahyoid muscles, longus colli, scalenus anterior and the inferior pharyngeal constrictor.

Ascending cervical artery The ascending cervical artery is a small branch that arises as the inferior thyroid artery turns medially behind the carotid sheath and ascends on the anterior tubercles of the cervical transverse processes between scalenus anterior and longus capitis. It supplies the adjacent muscles and gives off one or two spinal branches that enter the vertebral canal through the intervertebral foramina to supply the spinal cord and membranes and vertebral bodies, and thereby supplement the spinal branches of the vertebral artery. The ascending cervical artery anastomoses with the vertebral, ascending pharyngeal, occipital and deep cervical arteries.

Inferior laryngeal artery The inferior laryngeal artery ascends on the trachea with the recurrent laryngeal nerve, enters the larynx at the lower border of the inferior constrictor and supplies the laryngeal muscles and mucosa. It anastomoses with its contralateral fellow, and with the superior laryngeal branch of the superior thyroid artery.

Pharyngeal branches These supply the lower part of the pharynx. Tracheal branches supply the trachea and anastomose with the bronchial arteries; oesophageal branches supply the oesophagus and anastomose with the oesophageal branches of the thoracic aorta; inferior and ascending glandular branches supply the posterior and inferior regions of the thyroid gland and anastomose with the contralateral inferior and ipsilateral superior thyroid arteries. The ascending branch also supplies the parathyroid glands.

Suprascapular artery

The suprascapular artery descends laterally across scalenus anterior and the phrenic nerve, posterior to the internal jugular vein and sternocleidomastoid (see Fig. 35.7A). It then crosses anterior to the subclavian artery and brachial plexus, posterior to, and parallel with, the clavicle, subclavius and the inferior belly of omohyoid, to reach the superior scapular border.

Superficial cervical artery

The superficial cervical artery is given off at a higher level than the suprascapular artery. It crosses anterior to the phrenic nerve, scalenus anterior and the brachial plexus, and is covered by the internal jugular vein, sternocleidomastoid and platysma. It crosses the floor of the posterior triangle to reach the anterior margin of levator scapulae and ascends deep to the anterior part of the trapezius, which it supplies, together with the adjoining muscles and the cervical lymph nodes. It anastomoses with the superficial ramus of the descending branch of the occipital artery. About a third of the superficial cervical and dorsal scapular arteries arise in common from the thyrocervical trunk, with a superficial (superficial cervical artery) and a deep (dorsal scapular artery) branch (see Figs 33.1A, 33.2A). The latter passes laterally anterior to the brachial plexus and then posterior to levator scapulae.

Costocervical trunk

On the right, this short vessel arises posteriorly from the second part of the subclavian artery, and, on the left, from its first part. It arches back above the cervical pleura to the neck of the first rib, where it divides into supreme intercostal and deep cervical branches.

Deep cervical artery

The deep cervical artery usually arises from the costocervical trunk (see Fig. 33.1). It is analogous in its first segment to a posterior branch of a posterior intercostal artery, and occasionally is a separate branch of the subclavian artery. It passes back above the eighth cervical spinal nerve between the transverse process of the seventh cervical vertebra and the neck of the first rib (sometimes between the transverse processes of the sixth and seventh cervical vertebrae). It then ascends between semispinales capitis and cervicis to the level of the second cervical vertebra. It supplies adjacent muscles and anastomoses with the deep branch of the descending branch of the occipital artery and branches of the vertebral artery. A spinal branch enters the vertebral canal between the seventh cervical and first thoracic vertebrae.

Dorsal scapular artery

The dorsal scapular artery arises from the third, or less often the second, part of the subclavian artery. It gives off a small branch (which sometimes arises directly from the subclavian artery) to scalenus anterior. It passes laterally through the brachial plexus in front of scalenus medius and then deep to levator scapulae to the superior scapular angle.

Veins

Veins in the neck show considerable variation. They are superficial or deep to the deep fascia but are not entirely separate systems. Superficial veins are tributaries – some with specific names, given below – of the anterior, external and posterior jugular veins (**Figs 35.13–35.14**). They drain a much smaller volume of tissue than the deep veins. The latter drain all but the subcutaneous structures, mostly into the internal jugular vein and also into the subclavian vein.

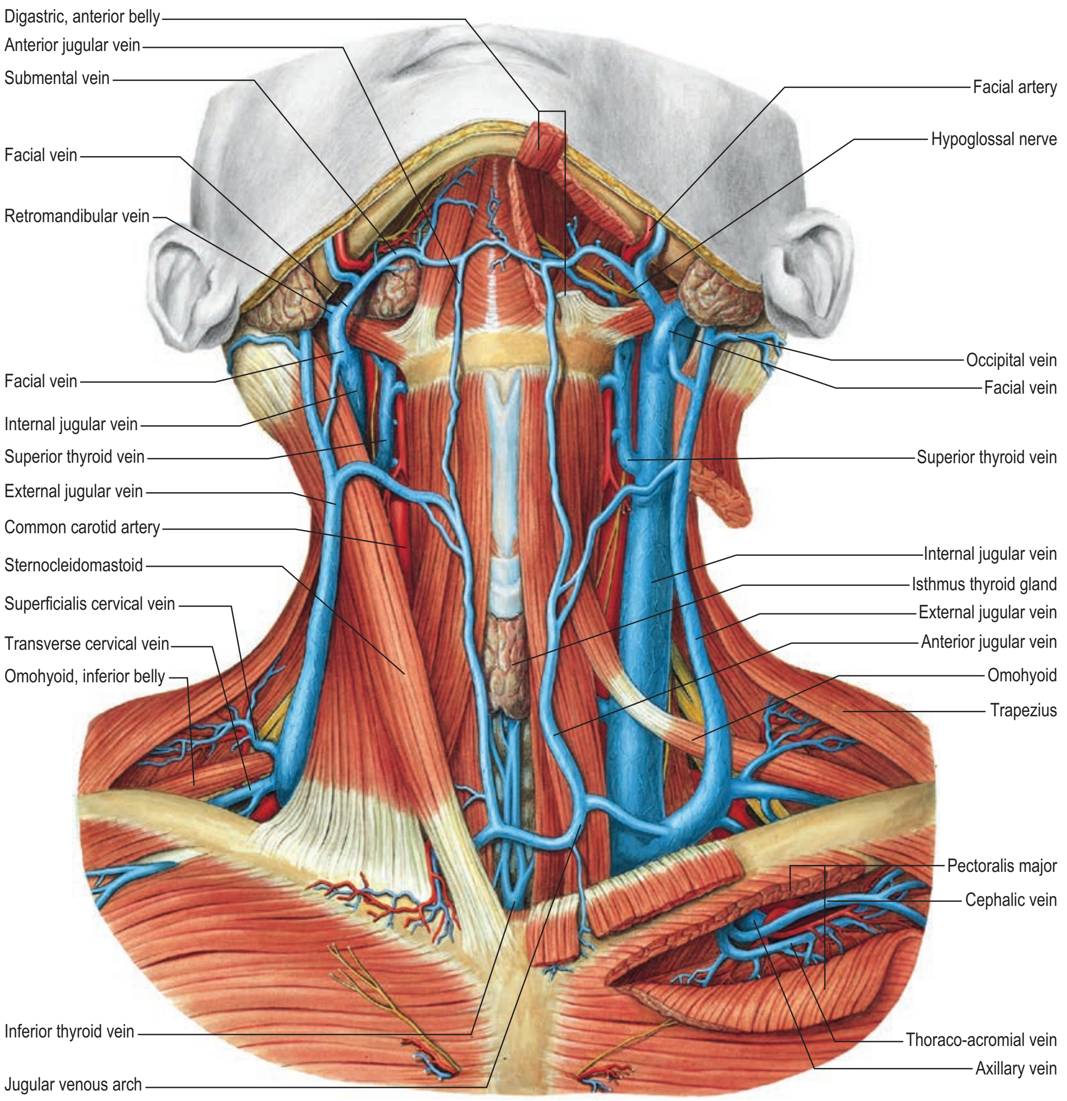
Digastric, anterior belly
Anterior jugular vein
Submental vein
Facial vein
Retromandibular vein
Facial vein
Internal jugular vein
Superior thyroid vein
External jugular vein
Common carotid artery
Sternocleidomastoid
Superficialis cervical vein
Transverse cervical vein
Omohyoid, inferior belly
Inferior thyroid vein
Jugular venous arch
Facial artery
Hypoglossal nerve
Occipital vein
Facial vein
Superior thyroid vein
Internal jugular vein
Isthmus thyroid gland
External jugular vein
Anterior jugular vein
Omohyoid
Trapezius
Pectoralis major
Cephalic vein
Thoraco-acromial vein
Axillary vein

Fig. 35.13 The veins of the neck, seen from the front. The greater part of sternocleidomastoid has been removed on the left side and the cut lower edges have been reflected over the clavicle. (Sobotta Atlas of Human Anatomy © Elsevier GmbH, Urban & Fischer, Munich.)

External jugular vein

The external jugular vein mainly drains the scalp and face, although it also drains some deeper parts. The vein is formed by the union of the posterior division of the retromandibular vein with the posterior auricular vein and begins near the mandibular angle just below or in the parotid gland (see Fig. 33.3A). It descends from the angle to the mid-clavicle, running obliquely, superficial to sternocleidomastoid, to the root of the neck. Here, it crosses the deep fascia and ends in the subclavian vein, lateral or anterior to scalenus anterior. There are valves at its entrance into the subclavian but they do not prevent regurgitation. Its wall is adherent to the rim of the fascial opening. It is covered by platysma, superficial fascia and skin, and is separated from sternocleidomastoid by deep cervical fascia. The vein crosses the transverse cutaneous nerve and lies parallel with the great auricular nerve, posterior to its upper half. In size, the external jugular vein is inversely proportional to the other veins in the neck and may be double. Between the entrance into the subclavian vein and a point approximately 4 cm above the clavicle, the vein is often dilated, producing a so-called sinus.

Tributaries In addition to formative tributaries, the external jugular receives the posterior external jugular and, near its end, transverse cervical, suprascapular and anterior jugular veins. In the parotid gland, it is often joined by a branch from the internal jugular. The occipital vein occasionally joins it.

Posterior external jugular vein

The posterior external jugular vein begins in the occipital scalp and drains the skin and the superficial muscles that lie posterosuperior in the neck. It usually joins the middle part of the external jugular vein.

Anterior jugular vein

The anterior jugular vein arises near the hyoid bone from the confluence of the superficial submandibular veins. It descends between the midline and the anterior border of sternocleidomastoid. Turning laterally, low in the neck, deep to sternocleidomastoid but superficial to the infrahyoid strap muscles, it either joins the end of the external jugular vein or may enter the subclavian vein directly (see Fig. 33.3A). In size, it is usually inverse to the external jugular vein. It communicates with the internal jugular vein and receives the laryngeal veins and sometimes a small thyroid vein. There are usually two anterior jugular veins, united just above the manubrium by a large transverse jugular arch, receiving the inferior thyroid tributaries. They have no valves and may be replaced by a midline trunk.

Internal jugular vein

The internal jugular vein collects blood from the skull, brain, superficial parts of the face and much of the neck. It begins at the cranial base in the posterior compartment of the jugular foramen, where it is continuous with the sigmoid sinus. At its origin, it is dilated as the superior bulb, which lies below the posterior part of the tympanic floor. The internal jugular vein descends in the carotid sheath, and unites with the subclavian vein, posterior to the sternal end of the clavicle, to form the brachiocephalic vein (see Fig. 35.14). Near its termination, the vein dilates into the inferior bulb, above which is a pair of valves. The jugular bulb is a dynamic structure; it forms after 2 years of age and its size stabilizes in adulthood (Friedmann et al 2011).

Relations From above, rectus capitis lateralis, the transverse process of the atlas, levator scapulae, scalenus medius, scalenus anterior, the cervical

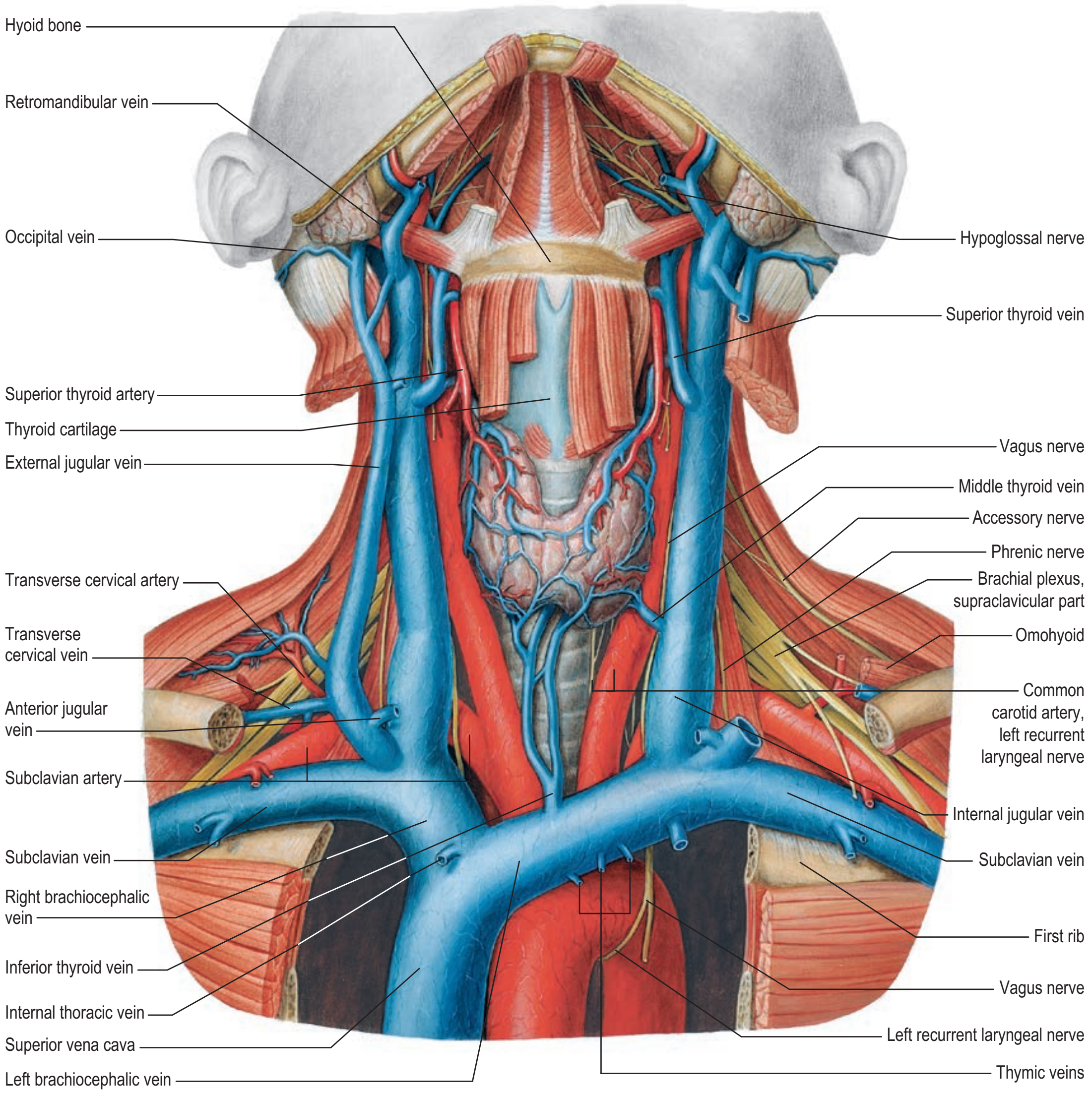
Hyoid bone
Retromandibular vein
Occipital vein
Superior thyroid artery
Thyroid cartilage
External jugular vein
Transverse cervical artery
Transverse cervical vein
Anterior jugular vein
Subclavian artery
Subclavian vein
Right brachiocephalic vein
Inferior thyroid vein
Internal thoracic vein
Superior vena cava
Left brachiocephalic vein
Hypoglossal nerve
Superior thyroid vein
Vagus nerve
Middle thyroid vein
Accessory nerve
Phrenic nerve
Brachial plexus, supraclavicular part
Omohyoid
Common carotid artery, left recurrent laryngeal nerve
Internal jugular vein
Subclavian vein
First rib
Vagus nerve
Left recurrent laryngeal nerve
Thymic veins

Fig. 35.14 The veins of the neck, seen from the front and at a deeper level than shown in Fig. 35.13. Both sternocleidomastoids have been removed, and additional dissection has exposed the thyroid gland and some of the structures that pass through the upper thoracic aperture. (Sobotta Atlas of Human Anatomy © Elsevier GmbH, Urban & Fischer, Munich.)

plexus, the phrenic nerve, thyrocervical trunk, vertebral vein and the first part of the subclavian artery all lie posterior to the vein. On the left, the internal jugular crosses anterior to the thoracic duct. The internal and common carotid arteries and the vagus nerve are medial to the vein, the vagus lying between and posterior to the vessels. The accessory nerve is sometimes found posterior to the vein. Superficially, the internal jugular vein is overlapped above, then covered below, by sternocleidomastoid, and is crossed by the posterior belly of digastric and the superior belly of omohyoid. The parotid gland, styloid process, accessory nerve (almost always), and the posterior auricular and occipital arteries cross the vein superior to the posterior belly of digastric. Between digastric and omohyoid, the sternocleidomastoid arteries and the inferior root of the ansa cervicalis cross the internal jugular vein, the nerve often passing between the vein and the common carotid artery. Below omohyoid, the vein is covered by the infrahyoid muscles and sternocleidomastoid and is crossed by the anterior jugular vein. Deep cervical lymph nodes lie along the internal jugular, mainly on its superficial aspect. At the root of the neck, the right internal jugular vein is separated from the common carotid artery, but the left usually overlaps its artery. At the base of the skull, the internal carotid artery is anterior to the vein, separated from it by the ninth to twelfth cranial nerves.

Tributaries The inferior petrosal sinus, facial, lingual, pharyngeal, superior and middle thyroid veins, and occasionally the occipital vein, are all tributaries of the internal jugular vein. The internal jugular vein may communicate with the external jugular vein. The thoracic duct opens near the union of the left subclavian and internal jugular veins, and the right lymphatic duct opens at the same site on the right.

Inferior petrosal sinus

The inferior petrosal sinus leaves the skull through the anterior part of the jugular foramen, crosses lateral or medial to the ninth to eleventh cranial nerves, and joins the superior jugular bulb.

Facial vein

The initial part of the facial vein as it lies on the face is described in Chapter 36 (see Fig. 33.3A). From the face, it passes over the surface of masseter, crosses the body of the mandible and enters the neck, where it runs obliquely back under platysma. Here it lies superficial to the submandibular gland, digastric and stylohyoid (see Fig. 35.13). Just anteroinferior to the mandibular angle, it is joined by the anterior division of the retromandibular vein, and then descends superficial to the loop of the lingual artery, the hypoglossal nerve and external and internal carotid arteries, to enter the internal jugular near the greater cornu of the hyoid bone, i.e. in the upper angle of the carotid triangle. Near its end, a large branch often descends along the anterior border of sternocleidomastoid to the anterior jugular vein. Its uppermost segment, above its junction with the superior labial vein, is often termed the angular vein.

Tributaries Submental, tonsillar, external palatine (paratonsillar) and submandibular veins, vena comitans of the hypoglossal nerve (sometimes), and pharyngeal and superior thyroid veins are all tributaries of the portion of the facial vein that lies below the mandible.

Lingual vein

The lingual veins follow two routes. The dorsal lingual veins drain the dorsum and sides of the tongue, join the lingual veins accompanying the lingual artery between hyoglossus and genioglossus, and enter the internal jugular near the greater cornu of the hyoid bone. The deep lingual vein begins near the tip of the tongue and runs back, lying near the mucous membrane on the inferior surface of the tongue. Near the anterior border of hyoglossus, it joins a sublingual vein from the sublingual salivary gland to form the vena comitans nervi hypoglossi, which runs back between mylohyoid and hyoglossus with the hypoglossal nerve to join the facial, internal jugular or lingual vein (see Fig. 33.3A).

Pharyngeal veins

The pharyngeal veins begin in a pharyngeal plexus external to the pharynx. They receive meningeal veins and a vein from the pterygoid canal, and usually end in the internal jugular vein, but may sometimes end in the facial, lingual or superior thyroid vein.

Superior thyroid vein

The superior thyroid vein is formed by deep and superficial tributaries corresponding to the arterial branches in the upper part of the thyroid gland (see Figs 35.13–35.14). It accompanies the superior thyroid artery, receives the superior laryngeal and cricothyroid veins, and ends in the internal jugular or facial vein.

Middle thyroid vein

The middle thyroid vein drains the lower part of the thyroid gland and receives veins from the larynx and trachea. It crosses anterior to the common carotid artery to join the internal jugular vein behind the superior belly of omohyoid. The middle thyroid vein is encountered early in thyroid, parathyroid and pharyngeal pouch surgery and usually ligated. It is one of only two structures that lie within the paracarotid tunnel, the other being a non-recurrent laryngeal nerve.

Tympanic body

The tympanic body (glomus jugulare) is ovoid, 0.5 mm long and 0.25 mm broad, and lies in the adventitia of the upper part of the superior bulb of the internal jugular vein. It is similar in structure to the carotid body and is presumed to have a similar function. The predominant cell type has morphological similarities to adrenal chromaffin cells, being derived from the neural crest. Cells obtained from glomus jugulare paragangliomas show spontaneous neurite outgrowth in culture and have vasoactive intestinal peptide (VIP)-like activity. The tympanic body may be present as two or more parts near the tympanic branch of the glossopharyngeal nerve or the auricular branch of the vagus as they lie within their canals in the petrous part of the temporal bone. Tumours of tympanic bodies often involve the adjacent cranial nerves and present with pulsatile tinnitus and a husky voice. These tumours grow into the hypotympanum of the middle ear; intraluminal growth, both proximally and distally, is well recognized.

Subclavian vein

The subclavian vein is a continuation of the axillary vein and extends from the outer border of the first rib to the medial border of scalenus anterior, where it joins the internal jugular vein to form the brachiocephalic vein (see Fig. 35.14). The clavicle and subclavius lie anterior to it; the subclavian artery is posterosuperior, separated by scalenus anterior and the phrenic nerve; and the first rib and pleura are inferior. The vein usually has a pair of valves 2 cm from its end. Its tributaries are the external jugular, dorsal scapular and sometimes the anterior jugular vein. At its junction with the internal jugular, the left subclavian vein receives the thoracic duct, and the right subclavian vein receives the right lymphatic duct.

Vertebral vein

Numerous small tributaries from internal vertebral plexuses leave the vertebral canal above the posterior arch of the atlas and join small veins from local deep muscles in the suboccipital triangle. Their union produces a vessel that enters the foramen in the transverse process of the atlas, forms a plexus around the vertebral artery, and descends through successive transverse foramina to end as the vertebral vein. The vein emerges from the sixth cervical transverse foramen, and descends, at first anterior, then anterolateral, to the vertebral artery. It may join the deep cervical vein before it opens superoposteriorly into the brachiocephalic vein; the opening has a paired valve. As it descends, it passes behind the internal jugular vein and anterior to the first part of the subclavian artery. A small accessory vertebral vein usually descends from the vertebral plexus, traverses the seventh cervical transverse foramen and turns forwards between the subclavian artery and the cervical pleura to join the brachiocephalic vein. The vertebral artery or vein can be encountered deep in Chassaignac's triangle and care should be taken when dissecting this area.

Tributaries The vertebral vein connects with the sigmoid sinus by a vessel in the posterior condylar canal, when the latter exists. It also receives branches from the occipital vein, veins draining the prevertebral muscles, and the internal and external vertebral plexuses. It is joined by the anterior vertebral and deep cervical veins (see below), and sometimes, near its end, by the first intercostal vein.

Anterior vertebral vein

The anterior vertebral vein starts in a plexus around the upper cervical transverse processes, descends near the ascending cervical artery between the attachments of scalenus anterior and longus capitis, and opens into the end of the vertebral vein.

Deep cervical vein

The deep cervical vein accompanies its artery between semispinales capitis and cervicis. It is formed in the suboccipital region by the union of communicating branches of the occipital vein, veins draining the suboccipital muscles, and veins from plexuses around the cervical spines. It passes forwards between the seventh cervical transverse process and the neck of the first rib to end in the lower part of the vertebral vein.

Central venous access

Central venous cannulation permits monitoring of the central venous pressure and the administration of drugs directly into the central circulation.

Internal jugular vein cannulation

Available with the *Gray's Anatomy* e-book

Subclavian vein cannulation

Available with the *Gray's Anatomy* e-book

Lymphatic drainage

Lymph nodes in the head and neck are distributed in terminal and outlying groups (**Fig. 35.15**; see Fig. 33.5). The terminal group is related to the carotid sheath and the nodes it contains are the deep cervical lymph nodes. All lymph vessels of the head and neck drain into this group, either directly from tissues or indirectly through nodes in the outlying groups. Efferents of the deep cervical nodes form the jugular trunk. The right jugular trunk collects lymph from the right arm, right half of the thorax and the right head and neck and terminates in the jugulosubclavian junction or the right lymphatic duct. The left jugular trunk usually enters the thoracic duct, but it may join the internal jugular or subclavian vein. For further reading, see Shah and Patel (2012).

Many vessels draining the superficial cervical tissues skirt the borders of sternocleidomastoid to reach the superior or inferior deep cervical nodes. Others pass to the superficial cervical and occipital nodes. Lymph from the superior region of the anterior triangle drains to the submandibular and submental nodes. Vessels from the anterior cervical skin inferior to the hyoid bone pass to the anterior cervical lymph nodes near the anterior jugular veins. Their efferents go to the deep cervical nodes of both sides, including the infrahyoid, prelaryngeal and pretracheal groups. An anterior cervical node often occupies the suprasternal space. Lymph from tissues of the head and neck internal to the deep fascia drains to the deep cervical nodes directly or through outlying groups that include the retropharyngeal, paratracheal, lingual, infrahyoid, prelaryngeal and pretracheal groups. The lymphatic drainage associated with the nasal region, larynx and oral cavity is described in the appropriate regions. The deep cervical lymphatic nodes lie alongside the carotid sheath, and form superior and inferior groups.

Superior deep cervical nodes The superior deep cervical nodes (level II and III nodes) adjoin the upper part of the internal jugular vein. Most are deep to sternocleidomastoid but a few extend beyond it. One subgroup, consisting of one large and several small nodes, is in a triangular region bounded by the posterior belly of digastric and the facial and internal jugular veins, and is known as the jugulodigastric group. It is concerned especially with drainage of the tongue. Efferents from the upper deep cervical nodes drain to either the lower group or direct to the jugular trunk.

Inferior deep cervical nodes The inferior deep cervical nodes (level IV nodes) are partly deep to sternocleidomastoid and are particularly

The patient is placed in the supine position with the head turned slightly towards the contralateral side. The key anatomical landmarks are the two inferior heads of sternocleidomastoid, which form two sides of a triangle with the clavicle as its base. The internal jugular vein lies between the two heads of the muscle, slightly lateral and anterior to the common carotid artery. In infants and children, cannulation of the vein carries a high incidence of carotid artery puncture; the vein overlaps the artery in the neutral position and head rotation alters the anatomical relation of the two vessels (Hong et al 2010). After the skin has been prepared, local anaesthetic is injected around the apex of the triangle. With one hand palpating the carotid artery, the physician inserts a needle at the apex of the triangle and the tip is directed lateral to the midpoint of the triangle, with a downward angulation of 30°. From a high internal jugular approach, the needle is inserted at the midpoint of the medial border of sternocleidomastoid and directed towards the ipsilateral nipple with a downward angulation of 30–45°. When the left internal jugular vein is cannulated, additional care must be taken to avoid the thoracic duct and the cupula of the pleura, which is higher than on the right side, an arrangement that increases the risk of accidental pneumothorax. The left internal jugular vein is often smaller in diameter than the right (Matthers et al 1992).

Subclavian vein cannulation is performed with the patient supine, the head turned slightly to the contralateral side, and the arms placed by the side. The bed is tilted down by 10° and a small bedroll may be placed between the shoulder blades in order to ensure that the infraclavicular area is more prominent. The skin is cleaned and local anaesthetic injected into the skin 3 cm lateral to the midpoint of the clavicle. The central venous needle is then inserted from the inferior edge of the clavicle towards the suprasternal notch. The needle is directed so that it passes just below the posterior border of the clavicle; care must be taken to avoid downward direction of the needle, which can cause a pneumothorax. Gentle aspiration of the syringe is performed while the needle is being advanced until the subclavian vein is punctured. In children under the age of 3 years, the supraclavicular approach to the subclavian vein is associated with a shorter puncture time and a reduced incidence of guidewire misplacement compared with the infraclavicular approach (Byon et al 2013).

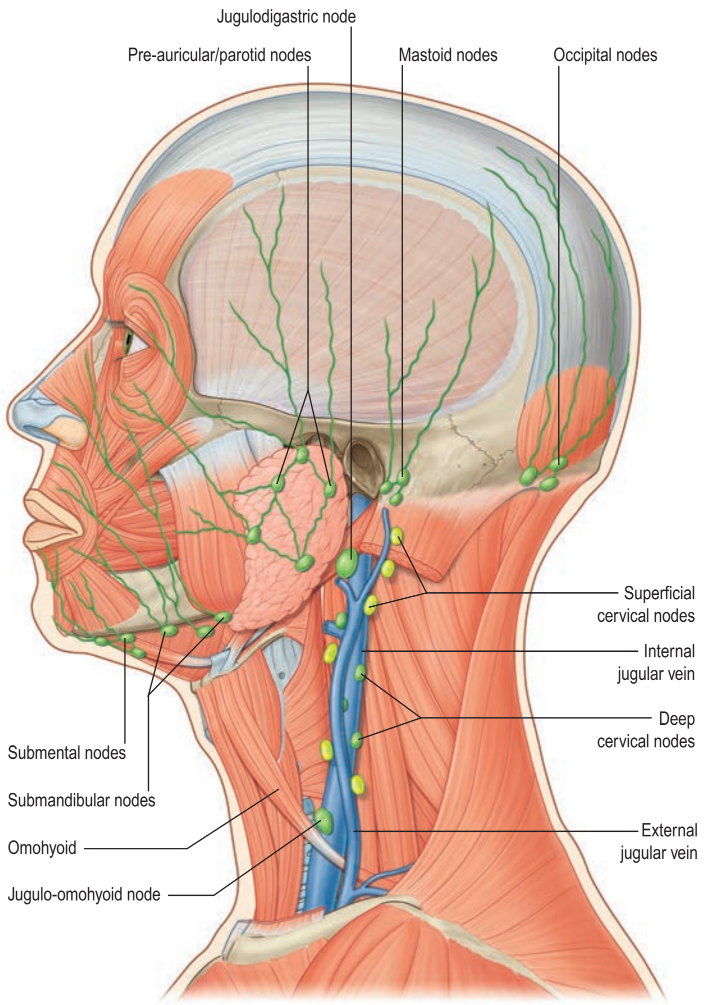

Fig. 35.15 The superficial lymphatic system in the head and neck. The nodes are organized into a superficial group around the head, superficial cervical nodes along the external jugular vein, and deep cervical nodes along the internal jugular vein. (From Drake RL, Vogl AW, Mitchell A (eds) Gray's Anatomy for Students, 2nd ed. Elsevier, Churchill Livingstone. Copyright 2010.)

related to the lower part of the internal jugular vein. Some are closely related to the brachial plexus and subclavian vessels. The jugulo-omohyoid node lies on, or just above, the intermediate tendon of omohyoid, and is concerned especially with lymphatic drainage from the tongue. Efferents from this lower group join the jugular lymph trunk.

Retropharyngeal nodes Retropharyngeal nodes lie between the pharyngeal and prevertebral fasciae and form a median and two lateral groups, the latter anterior to the lateral masses of the atlas along the lateral borders of longus capitis. The nodes receive afferents from the nasopharynx, pharyngotympanic tube and atlanto-occipital and atlanto-axial joints, and drain to the upper deep cervical nodes.

Paratracheal nodes The paratracheal nodes flank both trachea and oesophagus along the recurrent laryngeal nerves. Efferents pass to the corresponding deep cervical nodes.

Infrahyoid prelaryngeal and pretracheal nodes The infrahyoid, prelaryngeal and pretracheal nodes lie beneath the deep cervical fascia. They drain afferents from the anterior cervical nodes, and their efferents join the deep cervical nodes. Infrahyoid nodes are anterior to the thyrohyoid membrane, prelaryngeal nodes lie on the cricovocal membrane, and pretracheal nodes lie anterior to the trachea near the inferior thyroid veins. The paratracheal, infrahyoid, prelaryngeal and pretracheal nodes are important when considering the lymphatic spread of thyroid cancer.

Lingual nodes Lingual nodes are small and inconstant. When present, they are situated on the external surface of hyoglossus and also between the genioglossi. They drain to the upper deep cervical nodes.

Spread of malignant disease in the neck

Cancers arising in the head and neck from regions such as the thyroid gland, larynx, oral cavity and oropharynx, nasopharynx and paranasal sinuses have predictable patterns of spread through the chains of lymph nodes in the neck. It is vitally important to understand these patterns of spread so that the appropriate operation is undertaken for each patient. Clinical experience has shown that the lymph nodes in the neck fall into five distinct groups (see Fig. 33.5, Fig. 35.15). Level I nodes lie in the submandibular triangle bounded by the anterior and posterior bellies of digastric and the lower border of the mandible above. Level I is further divided into level IA (submental triangle) and level IB (submandibular triangle). Level II (upper jugular) nodes lie around the upper portion of the internal jugular vein and the upper part of the accessory nerve. They extend from the skull base to the bifurcation of the common carotid artery or the hyoid bone. Level III (middle jugular) nodes lie around the middle third of the internal jugular vein from the inferior border of level II to the superior belly of omohyoid or the cricothyroid membrane. Level IV (lower jugular) nodes lie around the lower third of the internal jugular vein from the inferior border of level III to the clavicle. The anterior and posterior borders for levels II, III and IV are the lateral border of sternohyoid and the posterior border of sternocleidomastoid, respectively. In other words, deep to sternocleidomastoid in between the anterior and posterior triangles of the neck. Level V (posterior triangle) nodes lie mostly around the lower part of the accessory nerve and the transverse cervical vessels. The accessory nerve divides level V into V_a above and V_b below.

Knowing which levels of nodes are likely to be involved in metastatic spread of a cancer arising in the head and neck helps select the appropriate nodal clearance at surgery. The classic radical neck dissection first described by Crile in 1906 involved a thorough clearance of levels I–V, including the sacrifice of sternocleidomastoid, the internal jugular vein and the accessory nerve. Modified radical neck dissections (functional neck dissections) remove level I–V nodes but spare either or all of sternocleidomastoid, the internal jugular vein and the accessory nerve. Selective neck dissections remove selected groups of nodes, e.g. the supra-omohyoid neck dissection removes level I–III nodes, the lateral neck dissection removes level II–IV nodes, and the posterolateral neck dissection removes level II–V nodes.

Cervical lymphovenous portals

Lymph is returned to the systemic venous circulation via right and left lymphovenous portals that are sited at, or near, the junctions of the internal jugular and subclavian veins (Fig. 35.16). The arrangement of these terminations is variable. Usually, three small lymph trunks converge towards their venous junctions on either side of the body: they are joined on the left side by the larger thoracic duct.

On the right side, the three lymph trunks are the right jugular, right subclavian and right bronchomediastinal trunk. The right jugular trunk extends from the terminal lower deep cervical nodes along the ventrolateral aspect of the internal jugular vein and conveys all the lymph from the right half of the head and neck. The right subclavian trunk drains from the terminal apical axillary group. It extends along the axillary and subclavian veins and conveys lymph from the right upper limb and superficial tissues of the right half of the thoraco-abdominal wall, down to the umbilicus anteriorly and iliac crest posteriorly (and includes much of the breast). The right bronchomediastinal trunk ascends over the trachea towards the lymphovenous portal and conveys lymph from the thoracic walls, the right cupula of the diaphragm and subjacent liver, the right lung, bronchi and trachea, the greater part of the 'right heart' (of clinical parlance, not the geometric right half) and a proportionately small drainage from the thoracic oesophagus.

The three right lymphatic trunks usually open independently (Fig. 35.16B). Their orifices are clustered either on the ventral aspect of the jugulo/subclavian junction, or in the nearby wall of either of the great veins. Sometimes, one or more of the trunks may bifurcate (or even trifurcate) preterminally and then terminate via multiple orifices. Rarely, the three trunks fuse to form a short, single, right lymphatic duct (about 1 cm long) that inclines across the medial border of scalenus anterior at the root of the neck to reach the ventral aspect of the venous junction, where its orifice is guarded by a bicuspid semilunar valve. An incomplete right lymphatic duct may be present if the subclavian and jugular trunks, or any combination of their terminals, are fused. When this occurs, the bronchomediastinal trunk almost invariably opens separately.

On the left, the four trunks that converge on the left lymphovenous portal are the left jugular and left subclavian trunks, which have a disposition corresponding to that of their counterparts on the right; the left bronchomediastinal trunk, which has a drainage similar to that of the right trunk but which drains more of the heart (the 'left' and part of the

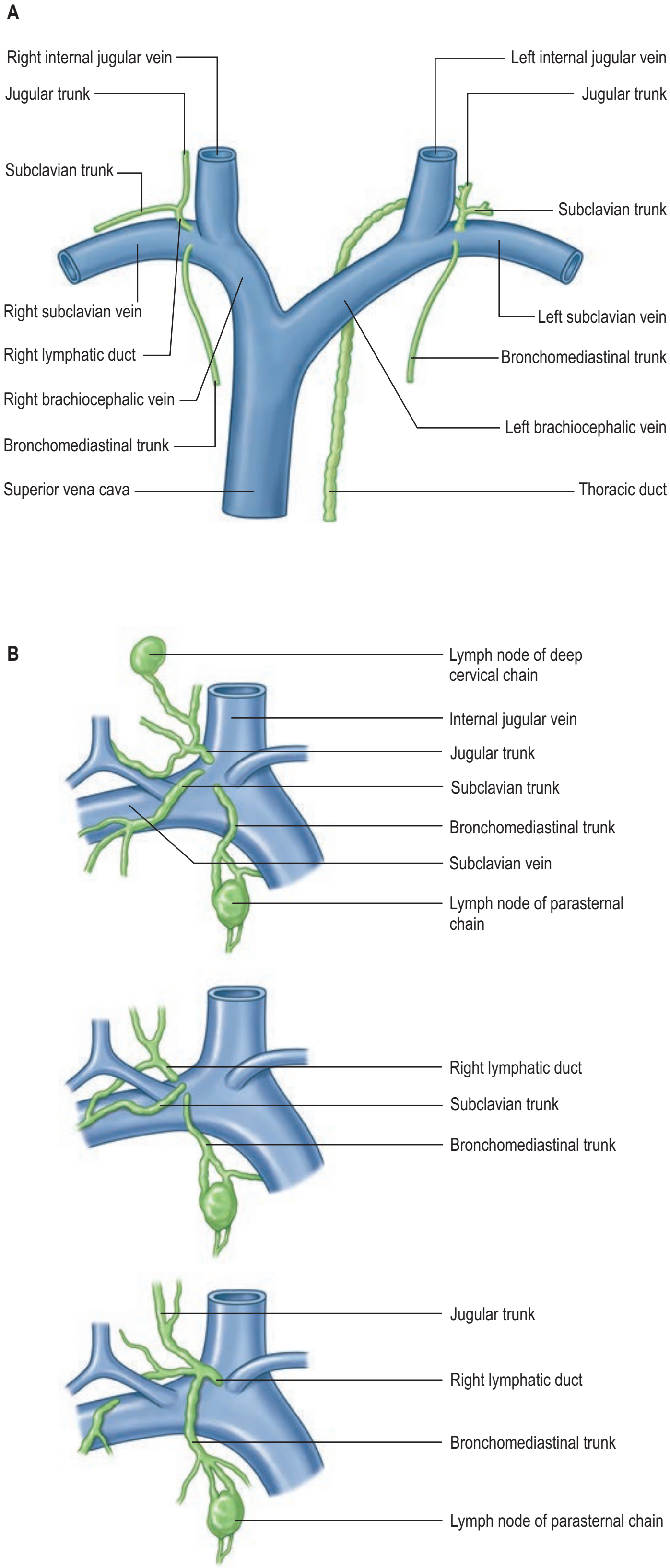
A
Right internal jugular vein
Jugular trunk
Subclavian trunk
Right subclavian vein
Right lymphatic duct
Right brachiocephalic vein
Bronchomediastinal trunk
Superior vena cava
Left internal jugular vein
Jugular trunk
Subclavian trunk
Left subclavian vein
Bronchomediastinal trunk
Left brachiocephalic vein
Thoracic duct
B
Lymph node of deep cervical chain
Internal jugular vein
Jugular trunk
Subclavian trunk
Bronchomediastinal trunk
Subclavian vein
Lymph node of parasternal chain
Right lymphatic duct
Subclavian trunk
Bronchomediastinal trunk
Jugular trunk
Right lymphatic duct
Bronchomediastinal trunk
Lymph node of parasternal chain

Fig. 35.16 **A**, The termination of the right lymphatic trunk and the thoracic duct. **B**, Variations in the terminal lymphatic trunk nodes of the right side. (A, With permission from Drake RL, Vogl AW, Mitchell A (eds) Gray's Anatomy for Students, 2nd ed. Elsevier, Churchill Livingstone. Copyright 2010.)

'right' hearts of clinical parlance) and more of the oesophagus; and the thoracic duct, which drains all of the rest of the body (Fig. 35.16A).

INNERVATION

The skin, joints, viscera and muscles of the neck are innervated by branches of the glossopharyngeal, vagus and accessory nerves, the cervical spinal nerves and the cervical sympathetic trunk.

The first and second cervical dorsal root ganglia lie on the vertebral arches of the atlas and axis respectively. The first cervical ganglion may be absent. Smaller aberrant ganglia sometimes occur on the upper cervical dorsal roots between the ganglia and cord. The upper four cervical roots are small, and the lower four are large. In general, cervical dorsal roots have a thickness ratio to the ventral roots of 3 : 1, which is greater than is seen in other regions. The first dorsal root is an exception, being smaller than the ventral; occasionally, it is absent. The first and second cervical roots are short and run almost horizontally to their exit from the vertebral canal. From the third to the eighth cervical, they slope obliquely down. Obliquity and length increase successively; however, the distance between spinal attachment and vertebral exit never exceeds the height of one vertebra. For details of the neural anastomoses between the upper cervical nerves and branches of the facial, vagus, hypoglossal and accessory nerves, see Shoja et al (2014).

Cervical ventral rami

Cervical ventral rami, except the first, appear between the anterior and posterior intertransverse muscles. The upper four form the cervical plexus, and the lower four, together with most of the first thoracic ventral ramus, form the brachial plexus. Each receives at least one grey ramus communicans, the upper four from the superior cervical sympathetic ganglion, the fifth and sixth from the middle ganglion, and the seventh and eighth from the cervicothoracic ganglion.

The first cervical ventral ramus, the suboccipital nerve, emerges above the posterior arch of the atlas, and passes forwards lateral to its lateral mass and medial to the vertebral artery. It supplies rectus capitis lateralis, emerges medial to it, descends anterior to the transverse process of the atlas and posterior to the internal jugular vein, and joins the ascending branch of the second cervical ventral ramus.

The second cervical ventral ramus issues between the vertebral arches of the atlas and axis. It ascends between their transverse processes, passes anterior to the first posterior intertransverse muscle and emerges lateral to the vertebral artery, generally between longus capitis and levator scapulae. The ramus divides into an ascending branch, which joins the first cervical nerve, and a descending branch, which joins the ascending branch of the third cervical ventral ramus.

The third cervical ventral ramus appears between longus capitis and scalenus medius. The remaining ventral rami emerge between scalenus anterior and the scalenus medius.

Cervical plexus

The cervical plexus is formed by the ventral rami of the upper four cervical nerves, and supplies some neck muscles and the diaphragm, and areas of skin on the head, neck and chest (see Figs 26.6, 35.1). It is situated in the neck opposite a line drawn down the side of the neck from the root of the auricle to the level of the upper border of the thyroid cartilage. It lies deep to the internal jugular vein, the deep fascia and sternocleidomastoid, and anterior to scalenus medius and levator scapulae. Each ramus, except the first, divides into ascending and descending parts, which unite in communicating loops. From the first loop (C2 and 3), superficial branches supply the head and neck; cutaneous nerves of the shoulder and chest arise from the second loop (C3 and 4). Muscular and communicating branches arise from the same nerves. The branches are superficial or deep. The superficial branches perforate the cervical fascia to supply the skin, while the deep branches in general supply muscles. The superficial branches either ascend (the lesser occipital, great auricular and the transverse cutaneous nerves) or descend (supraclavicular nerves). These nerves are described in detail in this chapter on p. 573. The deep branches form medial and lateral series.

Deep branches – medial series

Communicating branches Communicating branches pass from the loop between the first and second cervical rami to the vagus and hypoglossal nerves and to the sympathetic trunk. The hypoglossal branch later leaves the hypoglossal nerve as a series of branches, namely: the meningeal, superior root of ansa cervicalis, nerves to thyrohyoid and to geniohyoid. A branch also connects the fourth and fifth cervical rami. The first four cervical ventral rami each receive a grey ramus communicans from the superior cervical sympathetic ganglion.

The superior root of the ansa cervicalis (descendens hypoglossi) (see Figs 35.7A, 35.8) leaves the hypoglossal nerve where it curves round the occipital artery and then descends anterior to or in the carotid sheath. It contains only fibres from the first cervical spinal nerve. After giving a branch to the superior belly of omohyoid, it is joined by the inferior root of the ansa from the second and third cervical spinal nerves. The two roots form the ansa cervicalis (ansa hypoglossi), from which branches supply sternohyoid, sternothyroid and the inferior belly of omohyoid. Another branch is said to descend anterior to the vessels into the thorax to join the cardiac and phrenic nerves.

Muscular branches Muscular branches supply rectus capitis lateralis (C1), rectus capitis anterior (C1, 2), longus capitis (C1–3) and longus colli (C2–4). The inferior root of the ansa cervicalis and the phrenic nerve are additional muscular branches.

The inferior root of the ansa cervicalis (nervus descendens cervicalis) (see Figs 35.7A, 35.8) is formed by the union of a branch from the second with another from the third cervical ramus. It descends on the lateral side of the internal jugular vein, crosses it a little below the middle of the neck, and continues forwards to join the superior root anterior to the common carotid artery, forming the ansa cervicalis (ansa hypoglossi), from which all infrahyoid muscles except thyrohyoid are supplied. The inferior root almost always comes from the second and third cervical ventral rami, but sometimes from the second to fourth, and occasionally from the third alone. Occasionally, too, it may be derived either from the second alone or from the first to third.

Phrenic nerve The phrenic nerve arises chiefly from the fourth cervical ventral ramus but also has contributions from the third and fifth. It is formed at the upper part of the lateral border of scalenus anterior and descends almost vertically across its anterior surface behind the prevertebral fascia (see Fig 35.7A; **Figs 35.17–35.18**). It descends posterior to sternocleidomastoid, the inferior belly of omohyoid (near its intermediate tendon), the internal jugular vein, transverse cervical and suprascapular arteries and, on the left, the thoracic duct. At the root of the neck, it runs anterior to the second part of the subclavian artery, from which it is separated by scalenus anterior (some accounts state that on the left side the nerve passes anterior to the first part of the subclavian artery), and posterior to the subclavian vein. The phrenic nerve crosses serratus anterior from lateral to medial (lying under the prevertebral fascia) and enters the thorax by crossing medially anterior to the internal thoracic artery.

In the neck, each nerve receives variable filaments from the cervical sympathetic ganglia or their branches and may also connect with internal thoracic sympathetic plexuses.

Accessory phrenic nerve The accessory phrenic nerve is composed of fibres from the fifth cervical ventral ramus that run in a branch of the nerve to subclavius. This lies lateral to the phrenic nerve and descends posterior (occasionally anterior) to the subclavian vein. The accessory phrenic nerve usually joins the phrenic nerve near the first rib but may not do so until near the pulmonary hilum or beyond. The accessory phrenic nerve may be derived from the fourth or sixth cervical ventral rami or from the ansa cervicalis.

Deep branches – lateral series

Communicating branches Lateral deep branches of the cervical plexus (C2, 3, 4) may connect with the accessory nerve within sternocleidomastoid, the posterior triangle or beneath trapezius.

Muscular branches Muscular branches are distributed to sternocleidomastoid (C2, 3, 4), trapezius (C2 and possibly C3), levator scapulae (C3, 4) and scalenus medius (C3, 4). Branches to trapezius cross the posterior triangle obliquely below the accessory nerve.

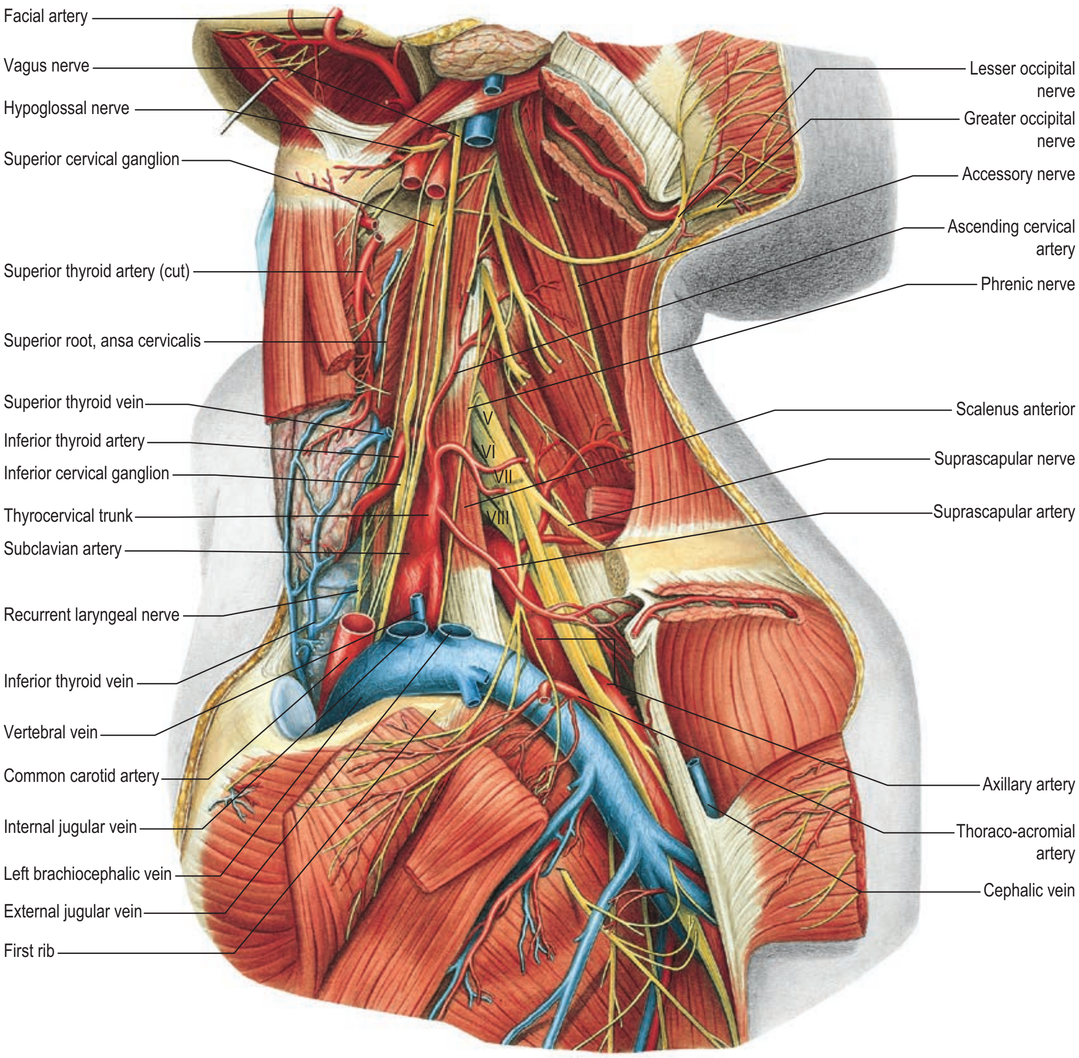
Facial artery
Vagus nerve
Hypoglossal nerve
Superior cervical ganglion
Superior thyroid artery (cut)
Superior root, ansa cervicalis
Superior thyroid vein
Inferior thyroid artery
Inferior cervical ganglion
Thyrocervical trunk
Subclavian artery
Recurrent laryngeal nerve
Inferior thyroid vein
Vertebral vein
Common carotid artery
Internal jugular vein
Left brachiocephalic vein
External jugular vein
First rib
Lesser occipital nerve
Greater occipital nerve
Accessory nerve
Ascending cervical artery
Phrenic nerve
Scalenus anterior
Suprascapular nerve
Suprascapular artery
Axillary artery
Thoraco-acromial artery
Cephalic vein
V
VI
VII
VIII

Fig. 35.17 Vessels and nerves of the neck, left lateral view. The left sternocleidomastoid, the greater part of the infrahyoid group of muscles and numerous vessels have been removed in order to expose deeper structures. Compare with Fig. 35.7A, which shows a more superficial level of dissection. The letters V, VI, VII, VIII refer to the anterior primary rami of C5, C6, C7 and C8, respectively. (Sobotta Atlas of Human Anatomy © Elsevier GmbH, Urban & Fischer, Munich.)

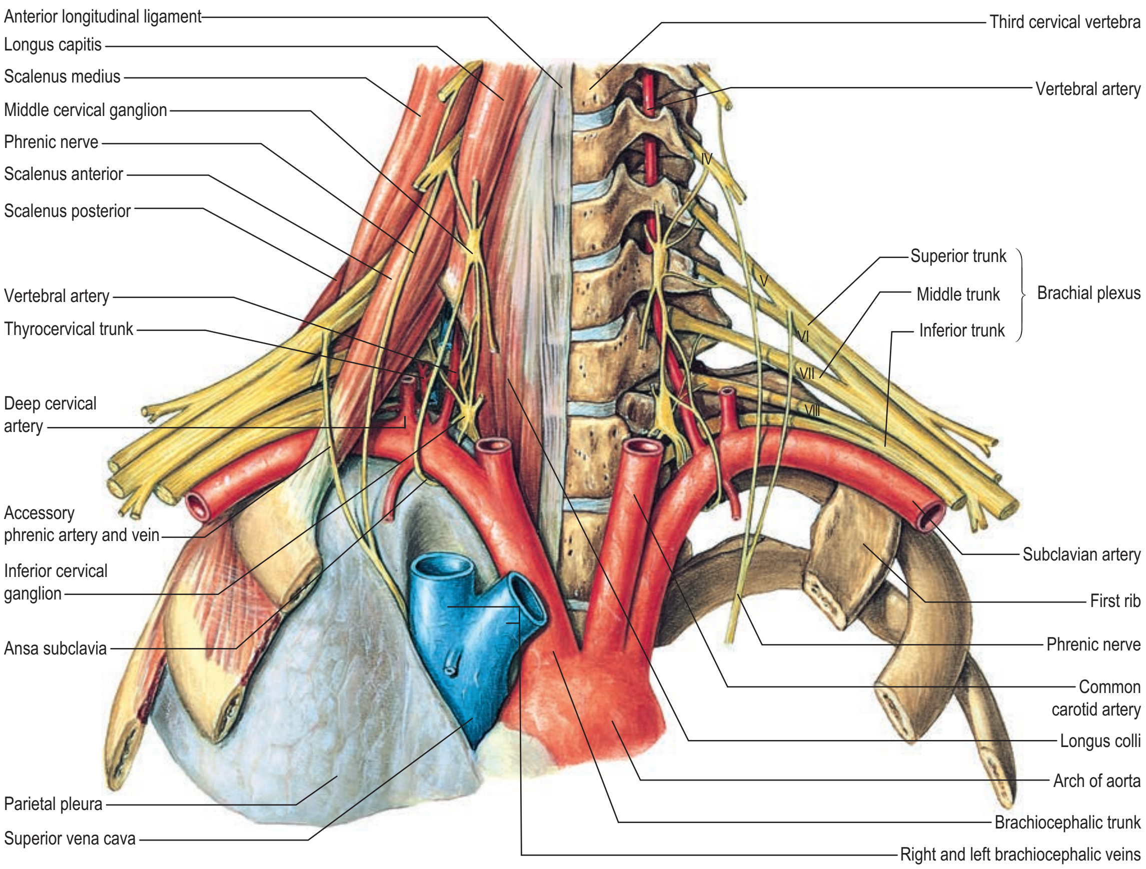
Anterior longitudinal ligament
Longus capitis
Scalenus medius
Middle cervical ganglion
Phrenic nerve
Scalenus anterior
Scalenus posterior
Vertebral artery
Thyrocervical trunk
Deep cervical artery
Accessory phrenic artery and vein
Inferior cervical ganglion
Ansa subclavia
Parietal pleura
Superior vena cava
Third cervical vertebra
Vertebral artery
IV
V
VI
VII
VIII
Superior trunk
Middle trunk
Inferior trunk
Brachial plexus
Subclavian artery
First rib
Phrenic nerve
Common carotid artery
Longus colli
Arch of aorta
Brachiocephalic trunk
Right and left brachiocephalic veins

Fig. 35.18 The root of the neck. Note the sympathetic trunk, the middle and inferior cervical sympathetic ganglia, the trunks of the brachial plexus, the phrenic nerve and the vertebral artery. (Sobotta Atlas of Human Anatomy © Elsevier GmbH, Urban & Fischer, Munich.)

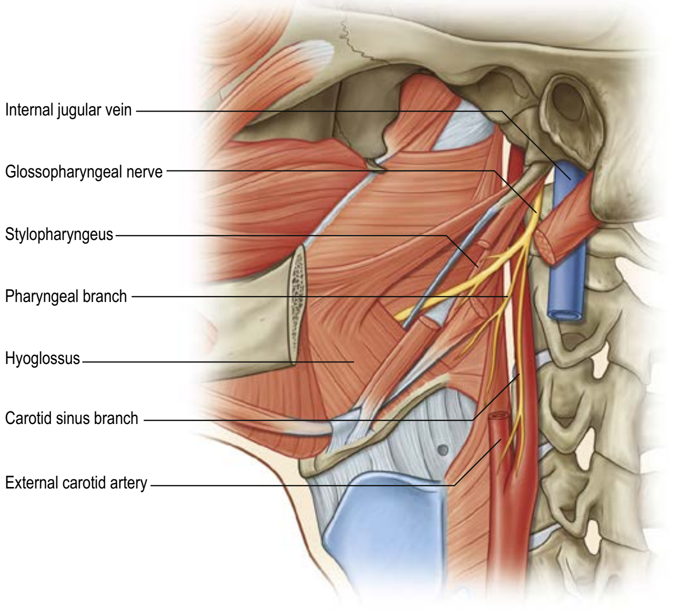
Internal jugular vein
Glossopharyngeal nerve
Stylopharyngeus
Pharyngeal branch
Hyoglossus
Carotid sinus branch
External carotid artery

Fig. 35.19 The glossopharyngeal nerve in the anterior triangle of the neck. (From Drake RL, Vogl AW, Mitchell A (eds) Gray's Anatomy for Students, 2nd ed. Elsevier, Churchill Livingstone. Copyright 2010.)

Brachial plexus

The brachial plexus is formed by the union of the ventral rami of the lower four cervical nerves and the greater part of the ventral ramus of the first thoracic spinal nerve. It may also receive contributions from the fourth cervical and second thoracic spinal nerves. As its name suggests, its branches supply the muscles, joints and skin of the upper limb. The relations and distribution of the nerves derived from the brachial plexus are described in detail in the appropriate chapters in Section 6. However, it is also mentioned here because, at its origin, the brachial plexus lies in the posterior triangle of the neck, in the angle between the clavicle and the lower posterior border of sternocleidomastoid. It emerges between the scaleni anterior and medius, superior to the third part of the subclavian artery, and is covered by platysma, deep fascia and skin, through which it is palpable (see Fig. 35.17). It is crossed by the supraclavicular nerves, the nerve to subclavius, the inferior belly of omohyoid, the external jugular vein and the superficial ramus of the transverse cervical artery. The plexus passes posterior to the medial two-thirds of the clavicle, subclavius and the suprascapular vessels, and lies on the first digitation of serratus anterior and on subscapularis.

Cervical dorsal rami

Each cervical spinal dorsal ramus except the first divides into medial and lateral branches, and all innervate muscles. In general, only medial branches of the second to fourth, and usually the fifth, supply skin. Except for the first (sometimes called the suboccipital nerve) and second, each dorsal ramus passes back medial to a posterior intertransverse muscle, curving round the articular process into the interval between semispinalis capitis and semispinalis cervicis. The cervical dorsal rami are described in detail in Chapter 47.

Cranial nerves

Glossopharyngeal nerve

The glossopharyngeal nerve (see Figs 35.8, 35.11; **Fig. 35.19**) supplies motor fibres to stylopharyngeus, parasympathetic secretomotor fibres to the parotid gland (derived from the inferior salivatory nucleus), sensory fibres to the tympanic cavity, pharyngotympanic tube, fauces, tonsils, nasopharynx, uvula and posterior (postsulcal) third of the tongue, and gustatory fibres from the circumvallate papillae.

The nerve leaves the skull through the anteromedial part of the jugular foramen, anterior to the vagus and accessory nerves, and in a separate dural sheath. In the foramen, it is lodged in a deep groove leading from the cochlear aqueductal depression and is separated by the inferior

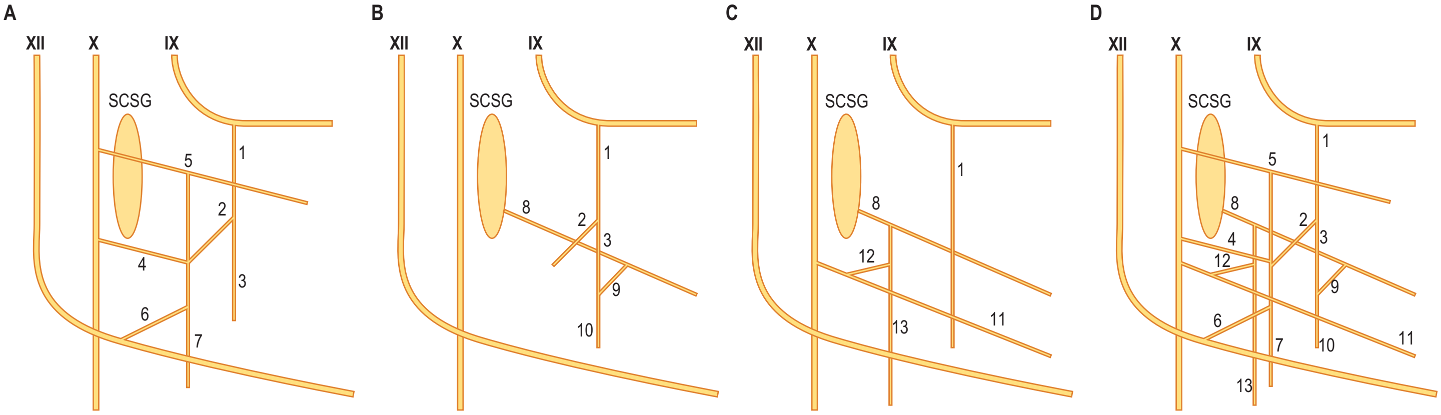

Fig. 35.20 The intercarotid plexus and its main trunks. **A**, Formation of the superficial trunk. **B**, Formation of the intermediate trunk. **C**, Formation of the deep trunk. **D**, Superimposition of **A**, **B** and **C**. Key: 1, carotid sinus nerve; 2, superficial branch of the carotid sinus nerve; 3, deep branch of the carotid sinus nerve; 4, carotid branch of the vagus nerve; 5, pharyngeal branch of the vagus nerve with its carotid branch; 6, carotid branch of the hypoglossal nerve; 7, superficial trunk of the intercarotid plexus; 8, inferior branch of the superior cervical sympathetic ganglion (SCSG); 9, communicating sympathetic branch to the deep branch of the carotid sinus nerve; 10, intermediate trunk of the intercarotid plexus; 11, superior laryngeal nerve; 12, communicating branch of the superior laryngeal nerve to the sympathetic; 13, deep trunk of the intercarotid plexus. (Adapted with permission from Shoja M, Oyesiku NM, Shokouhi G et al 2014 Anastomoses between lower cranial and upper cervical nerves: a comprehensive review with potential significance during skull base and neck operations, part II: glossopharyngeal, vagus, accessory, and hypoglossal nerves and cervical spinal nerves 1–4. Clin Anat 27:118–30.)

petrosal sinus from the vagus and accessory nerves. The groove is bridged by fibrous tissue, which is sometimes calcified. After leaving the foramen, the nerve passes forwards between the internal jugular vein and internal carotid artery, and then descends anterior to the latter, deep to the styloid process and its attached muscles, to reach the posterior border of stylopharyngeus. It curves forwards on stylopharyngeus and either pierces the lower fibres of the superior pharyngeal constrictor or passes between it and the middle constrictor to be distributed to the tonsil, the mucosae of the pharynx and postsulcal part of the tongue, the vallate papillae and oral mucous glands.

Two ganglia, superior and inferior, are situated on the glossopharyngeal nerve as it traverses the jugular foramen. The superior ganglion is in the upper part of the groove occupied by the nerve in the jugular foramen. It is small, has no branches and is usually regarded as a detached part of the inferior ganglion. The inferior ganglion is larger and lies in a notch in the lower border of the petrous part of the temporal bone. Its cells are typical unipolar neurones, whose peripheral branches convey gustatory and tactile signals from the mucosa of the tongue (posterior third, including the sulcus terminalis and vallate papillae) and general sensation from the oropharynx, where it is responsible for initiating the gag reflex.

Communicating branches

The glossopharyngeal nerve communicates with the sympathetic trunk and vagus and facial nerves. Its inferior ganglion is connected with the superior cervical sympathetic ganglion. Two filaments from the inferior ganglion pass to the vagus, one to its auricular branch and the other to its superior ganglion. A branch to the facial nerve arises from the glossopharyngeal nerve below the inferior ganglion and perforates the posterior belly of digastric to join the facial nerve near the stylomastoid foramen.

Branches of distribution

The glossopharyngeal nerve has tympanic, carotid, pharyngeal, muscular, tonsillar and lingual branches.

Tympanic nerve The tympanic nerve leaves the inferior ganglion, ascends to the tympanic cavity through the tympanic canaliculus and divides into branches that contribute to the tympanic plexus on the promontory. The lesser petrosal nerve is derived from the tympanic plexus.

Carotid branch The carotid branch is often double. It arises just below the jugular foramen and descends on the internal carotid artery to the wall of the carotid sinus and to the carotid body. The nerve contains primary afferent fibres from chemoreceptors in the carotid body and from the baroreceptors lying in the carotid sinus wall. It may communicate with the inferior ganglion of the vagus, or with one of its branches, and with a sympathetic branch from the superior cervical ganglion (**Fig. 35.20**).

Pharyngeal branches The pharyngeal branches are three or four filaments that unite with the pharyngeal branch of the vagus and the laryngopharyngeal branches of the sympathetic trunk to form the pharyngeal plexus near the middle pharyngeal constrictor. They constitute the route by which the glossopharyngeal nerve supplies sensory fibres to the mucosa of the pharynx.

Muscular branch The muscular branch supplies stylopharyngeus.

Tonsillar, lingual and lesser petrosal branches The tonsillar, lingual and lesser petrosal branches are described on pages 708–709, 644 and 749, respectively. There are anastomoses between the glossopharyngeal, vagus, greater auricular and other branches of the cervical plexus that may be significant when treating patients with skull base pathology (Shoja et al 2014.)

Lesions of the glossopharyngeal nerve

Damage to the glossopharyngeal nerve is rarely seen without associated involvement of other lower cranial nerves. Transient or sustained hypertension may follow surgical section of the nerve and indicates involvement of the carotid branch. Isolated lesions of the glossopharyngeal nerve lead to loss of sensation over the ipsilateral soft palate, fauces, pharynx and posterior third of the tongue, although this is difficult to assess clinically, and confirmation requires galvanic stimulation. The palatal and pharyngeal (gag) reflexes are reduced or absent and salivary secretion from the parotid gland may also be reduced. Weakness of stylopharyngeus cannot be tested individually. Glossopharyngeal neuralgia consists of episodic brief but severe pain, often precipitated by swallowing and experienced in the throat, behind the angle of the jaw and within the ear. Superior jugular bulb thromboses (e.g. in otitis media) and jugular foramen syndrome (associated with nasopharyngeal carcinoma or a jugular paraganglioma) may cause lesions of the adjacent glossopharyngeal, vagus and accessory nerves, with associated weakness in the muscles supplied in the pharynx and larynx.

Vagus nerve

The vagus is a large mixed nerve. It has a more extensive course and distribution than any other cranial nerve and runs through the neck, thorax and abdomen. Its central connections are described in Chapter 28.

The vagus exits the skull through the jugular foramen, accompanied by the accessory nerve, with which it shares an arachnoid and a dural sheath. Both nerves lie anterior to a fibrous septum that separates them from the glossopharyngeal nerve. The vagus descends vertically in the neck in the carotid sheath, between the internal jugular vein and the internal carotid artery, to the upper border of the thyroid cartilage, and then passes between the vein and the common carotid artery to the root of the neck. Its relationships in this part of its course are therefore similar to those described for these structures (see Figs 35.7A, 35.8, 35.17). Its further course differs on the two sides. The right vagus descends posterior to the internal jugular vein to cross the first part of the subclavian artery and enter the thorax. The left vagus enters the thorax between the left common carotid and subclavian arteries, and behind the left brachiocephalic vein.

After emerging from the jugular foramen, the vagus bears two marked enlargements: a small, round, superior (jugular) ganglion and a larger inferior (nodose) ganglion.

Superior (jugular) ganglion

The superior ganglion is greyish, spherical and approximately 4 mm in diameter. It is connected to the inferior glossopharyngeal ganglion and the sympathetic trunk, the latter by a filament from the superior cervical ganglion.

Inferior (nodose) ganglion

The inferior or nodose ganglion is larger than the superior ganglion, and is elongated and cylindrical in shape with a length of 25 mm and a maximum breadth of 5 mm. It is connected with the hypoglossal nerve, the loop between the first and second cervical spinal nerves, and with the superior cervical sympathetic ganglion. Most visceral afferent fibres have their cell bodies in the nodose ganglion.

Both vagal ganglia are exclusively sensory and contain somatic, special visceral and general visceral afferent neurones. The superior ganglion is chiefly somatic and most of its neurones enter the auricular nerve, whilst neurones in the inferior ganglion are concerned with visceral sensation from the heart, larynx, lungs and the alimentary tract from the pharynx to the transverse colon. Some fibres transmit impulses from taste endings in the vallecula and epiglottis. Large afferent fibres are derived from muscle spindles in the laryngeal muscles. Vagal sensory neurones in the nodose ganglion may show some somatotopic organization. Both ganglia are traversed by parasympathetic and perhaps some sympathetic fibres, but there is no evidence that vagal parasympathetic components relay in the inferior ganglion. Preganglionic motor fibres from the dorsal vagal nucleus and the special visceral efferents from the nucleus ambiguus, which descend to the inferior vagal ganglion, commonly form a visible band, skirting the ganglion in some mammals. These larger fibres probably provide motor innervation to the larynx in the recurrent laryngeal nerve, together with some contribution to the superior laryngeal nerve supplying cricothyroid.

Branches in the neck

The branches of the vagus in the neck are the meningeal, auricular, pharyngeal, carotid body, superior and recurrent laryngeal nerves and cardiac branches.

Meningeal branches Meningeal branches appear to start from the superior vagal ganglion and pass through the jugular foramen to be distributed to the dura mater in the posterior cranial fossa (see Fig. 25.2B).

Auricular branch The auricular branch (Arnold's nerve) arises from the superior vagal ganglion and is joined by a branch from the inferior ganglion of the glossopharyngeal nerve. It passes behind the internal jugular vein and enters the mastoid canaliculus on the lateral wall of the jugular fossa. Traversing the temporal bone, it crosses the facial canal approximately 4 mm above the stylomastoid foramen and here supplies an ascending branch to the facial nerve. Fibres of the nervus intermedius may pass to the auricular branch at this point, which may explain the cutaneous vesiculation in the auricle that sometimes accompanies geniculate herpes. The auricular branch then traverses the tympanomastoid fissure and divides into two rami. One ramus joins the posterior auricular nerve and the other is distributed to the skin of part of the ear and to the external acoustic meatus.

Pharyngeal branch

The pharyngeal branch of the vagus is the main motor nerve of the pharynx (Ch. 40, Pharyngeal plexus). It emerges from the upper part of the inferior vagal ganglion, passes between the external and internal carotid arteries to the upper border of the middle pharyngeal constrictor, and divides into numerous filaments that join rami of the sympathetic trunk and glossopharyngeal nerve to form a pharyngeal plexus. A minute filament, the ramus lingualis vagi, joins the hypoglossal nerve as it curves round the occipital artery.

Branches to the carotid body Branches to the carotid body are variable in number. They may arise from the inferior ganglion or travel in the pharyngeal branch, and sometimes in the superior laryngeal nerve. They form a plexus with the glossopharyngeal rami and branches of the cervical sympathetic trunk.

Superior laryngeal nerve The superior laryngeal nerve is larger than the pharyngeal branch and issues from the middle of the inferior vagal ganglion. It receives a branch from the superior cervical sympathetic ganglion and descends alongside the pharynx, at first posterior, then medial, to the internal carotid artery, and divides into the internal and external laryngeal nerves (see Figs 35.8, 41.12).

The internal laryngeal nerve is sensory to the laryngeal mucosa down to the level of the vocal folds. It also carries afferent fibres from the laryngeal neuromuscular spindles and other stretch receptors. It descends to the thyrohyoid membrane, pierces it above the superior laryngeal artery and divides into an upper and lower branch. The upper branch is horizontal and supplies the mucosa of the pharynx, the epiglottis, vallecula and laryngeal vestibule. The lower branch descends in the medial wall of the piriform recess, supplies the aryepiglottic fold, the mucosa on the back of the arytenoid cartilage and one or two branches to transverse arytenoid (the latter unite with twigs from the recurrent laryngeal to supply the same muscle). The internal laryngeal nerve ends by piercing the inferior pharyngeal constrictor to unite with an ascending branch from the recurrent laryngeal nerve. As it ascends in the neck, it supplies branches, more numerous on the left, to the mucosa and tunica muscularis of the oesophagus and trachea, and to the inferior constrictor.

The external laryngeal nerve, smaller than the internal, descends behind sternohyoid with the superior thyroid artery, but on a deeper plane. It lies first on the inferior pharyngeal constrictor, and then pierces it to curve round the inferior thyroid tubercle and reach cricothyroid, which it supplies: this branch can be damaged when ligating the superior thyroid artery in thyroid surgery. The nerve also gives branches to the pharyngeal plexus and the inferior constrictor. Behind the common carotid artery, the external laryngeal nerve communicates with the superior cardiac nerve and superior cervical sympathetic ganglion.

Recurrent laryngeal nerve The recurrent laryngeal nerve differs, in origin and course, on the two sides. On the right, it arises from the vagus anterior to the first part of the subclavian artery, and curves backwards below and then behind it to ascend obliquely to the side of the trachea behind the common carotid artery. Near the lower pole of the lateral lobe of the thyroid gland, it is closely related to the inferior thyroid artery and crosses either in front of, behind or between its branches. On the left, the nerve arises from the vagus on the left of the aortic arch, curves below it immediately behind the attachment of the ligamentum arteriosum to the concavity of the aortic arch and ascends to the side of the trachea (see Fig. 35.14). As the recurrent laryngeal nerve curves round the subclavian artery, or the aortic arch, it gives cardiac filaments to the deep cardiac plexus. On both sides, the recurrent laryngeal nerve ascends in or near a groove between the trachea and oesophagus. It is closely related to the medial surface of the thyroid gland before it passes under the lower border of the inferior constrictor, and it enters the larynx behind the articulation of the inferior thyroid cornu with the cricoid cartilage. The recurrent laryngeal nerve supplies all laryngeal muscles, except the cricothyroid, and it communicates with the internal laryngeal nerve, supplying sensory filaments to the laryngeal mucosa below the vocal folds. It also carries afferent fibres from laryngeal stretch receptors. The recurrent laryngeal nerve is described further in Chapter 41 (see Figs 41.11, 41.12). Knowledge of the above anatomy is crucial to understanding of both Beahr's triangle (see later) and the principles of thyroid surgery.

Accessory nerve

The accessory nerve (see Figs 35.7A, 35.11, 35.17) arises from an elongated nucleus of motor neurones in the lateral aspect of the ventral horn. Some rootlets emerge directly, while others turn cranially before exiting; their line of exit is irregular rather than linear. They join to form a trunk, the accessory nerve, which ascends intradurally within the vertebral canal between the ligamentum denticulatum and the dorsal roots of the spinal nerves. The nerve enters the skull via the foramen magnum, behind the vertebral artery. It then turns upwards and passes laterally to reach the jugular foramen, which it traverses in a common dural sheath with the vagus, but separated from that nerve by a fold of arachnoid mater.

As the accessory nerve exits the jugular foramen, it runs posterolaterally and passes either medial or lateral to the internal jugular vein; occasionally, it may pass through the vein. The extradural part of the nerve then crosses the transverse process of the atlas and is crossed by the occipital artery before descending obliquely, medial to the styloid process, stylohyoid and the posterior belly of digastric. Running with the superior sternocleidomastoid branch of the occipital artery, it reaches the upper part of sternocleidomastoid and enters its deep surface, to form an anastomosis with fibres from C2 alone, C3 alone, or C2 and C3 (the ansa of Maubrac). It may also communicate with the anterior root of the first cervical nerve (McKenzie branch).

The accessory nerve occasionally terminates in sternocleidomastoid. More commonly, it emerges a little above the midpoint of the posterior border of sternocleidomastoid, generally above the emergence of the great auricular nerve (usually within 2 cm of it) and between 4 and 6 cm from the tip of the mastoid process. However, the point of emergence is very variable. The nerve then crosses the posterior triangle on levator scapulae (see Fig. 35.7A), separated from it by the prevertebral layer of deep cervical fascia and adipose tissue. Here the nerve is relatively superficial within the roof of the posterior triangle and is related to superficial cervical lymph nodes in levels Va and Vb. Some 3–5 cm above the clavicle, it passes behind the anterior border of trapezius, often dividing to form a plexus on its deep surface, which receives contributions from C2–4 (see below), and then enters the deep surface of the muscle.

The cervical course of the accessory nerve follows a line from the lower anterior part of the tragus to the tip of the transverse process of the atlas, and then across sternocleidomastoid and the posterior triangle to a point on the anterior border of trapezius 3–5 cm above the clavicle.

The accessory nerve is thought to provide the sole motor supply to sternocleidomastoid; the second and third cervical nerves are believed to carry proprioceptive fibres from it. The supranuclear pathway of fibres destined for sternocleidomastoid is not simple; current evidence favours bilateral hemispheric innervation, although opinion varies as to the extent of the ipsilateral input. The motor supply to the descending (upper) and transverse (middle) portions of trapezius is primarily from the accessory nerve under predominantly contralateral supranuclear control. Usually, trapezius receives an innervation from the cervical plexus, in most cases from C3 and C4 (Tubbs et al 2011). A study using intraoperative electroneurography and histochemical analyses found that, when present, the cervical fibres did not consistently innervate all three parts of the muscle (descending, transverse and ascending), and that fibres from C2 usually travelled via the accessory nerve, while fibres from C3 and C4 innervated trapezius independently (Pu et al 2008). In addition to their motor contribution, C3 and C4 also carry proprioceptive fibres from trapezius.

On the basis of the incomplete denervation of the muscle that sometimes happens following sacrifice of both the accessory nerve and the cervical plexus, it has been suggested that trapezius receives a partial motor supply from other sources, possibly via thoracic roots. (For a detailed review of the applied surgical anatomy of the accessory nerve plexus, see Brown (2002).)

Sensory ganglia have been described along the course of the intradural portion of the nerve.

Lesions of the accessory nerve

Lesions of the accessory nerve may be sustained centrally, at its exit from the skull or in the neck. The supranuclear fibres that influence motor neurones innervating sternocleidomastoid decussate twice; a lesion of the corticospinal system above the pons therefore produces weakness of the ipsilateral sternocleidomastoid and contralateral trapezius. Episodic contraction of sternocleidomastoid and trapezius, often accompanied by contraction of other muscle groups, e.g. splenius capitis, occurs in spasmodic torticollis, a focal dystonia. In jugular foramen syndrome, caused by pathologies including nasopharyngeal carcinoma or a jugular paraganglioma, lesions of the glossopharyngeal, vagus and accessory nerves coexist. The accessory nerve can be injured more distally in the neck by trauma or by surgical exploration in the posterior triangle. If the accessory nerve is sacrificed as part of a radical or modified neck dissection and if the innervation of trapezius is lost, the patient can develop intractable shoulder pain and dysfunction.

Hypoglossal nerve

The hypoglossal nerve is motor to all the muscles of the tongue except palatoglossus. The hypoglossal rootlets run laterally behind the vertebral artery, collected into two bundles that perforate the dura mater separately opposite the hypoglossal canal in the occipital bone, and unite after traversing it. The canal is sometimes divided by a spicule of bone. The nerve emerges from the canal in a plane medial to the internal jugular vein, internal carotid artery and ninth, tenth and eleventh cranial nerves, and passes inferolaterally behind the internal carotid artery and glossopharyngeal and vagus nerves to the interval between the artery and the internal jugular vein (see Fig. 35.8). Here, it makes a half-spiral turn round the inferior vagal ganglion and is united with it by connective tissue. It then descends almost vertically between the vessels and anterior to the vagus to a point level with the angle of the mandible, becoming superficial below the posterior belly of digastric and emerging between the internal jugular vein and internal carotid artery. Often associated with a plexus of veins around the junction of the common facial and internal jugular veins (vena comitans nervi hypoglossi), excessive bleeding here during neck dissection can lead to nerve damage. The nerve loops round the inferior sternocleidomastoid branch of the occipital artery, crosses lateral to both internal and external carotid arteries and the loop of the lingual artery a little above the tip of the greater cornu of the hyoid, and is itself crossed by the facial vein (see Figs 35.7A, 35.8, 35.17). Its course is described further in Chapter 37.

Communicating branches

The hypoglossal nerve communicates with the sympathetic trunk, the lingual, glossopharyngeal and vagus nerves and the pharyngeal plexus. Near the atlas, it is joined by branches from the superior cervical sympathetic ganglion and a filament from the loop between the first cervical ventral ramus and the ascending branch of the second cervical ventral ramus that leaves the hypoglossal nerve as the upper root of the ansa cervicalis. The vagal connections are close to the skull, and numerous filaments pass between the hypoglossal nerve and the inferior vagal ganglion in the connective tissue that unites them. As the hypoglossal nerve curves round the occipital artery, it receives the ramus lingualis vagi from the pharyngeal plexus. Near the anterior border of hyoglossus, it is connected with the lingual nerve by many filaments that ascend on the muscle.

Branches of distribution

The branches of distribution of the hypoglossal nerve are meningeal, descending, thyrohyoid and muscular nerves.

Meningeal branches Meningeal branches leave the nerve in the hypoglossal canal and return through it to supply the diploë of the occipital bone, the dural walls of the occipital and inferior petrosal sinuses, and much of the floor of the anterior wall of the posterior cranial fossa, probably through pathways other than that of the hypoglossal nerve, e.g. upper cervical spinal nerves (see Fig. 25.3).

Descending branch The descending branch (descendens hypoglossi) contains fibres from the first cervical spinal nerve. It leaves the hypoglossal nerve when it curves around the occipital artery, and runs down on the carotid sheath. It provides a branch to the superior belly of omohyoid before joining the descendens cervicalis to form the ansa cervicalis (see Figs 35.7A, 35.8).

Nerves to thyrohyoid and geniohyoid The nerves to thyrohyoid and geniohyoid arise near the posterior border of hyoglossus and are derived from the first cervical ventral ramus.

Lesions of the hypoglossal nerve

The hypoglossal nerve may be damaged during neck dissection. Complete hypoglossal division causes unilateral lingual paralysis and eventual hemiatrophy; the protruded tongue deviates to the paralysed side, and, on retraction, the wasted and paralysed side rises higher than the unaffected side. The larynx may deviate towards the active side in swallowing, as a consequence of the unilateral paralysis of the hyoid depressors associated with loss of the first cervical ventral ramus, which runs with the hypoglossal nerve. If paralysis is bilateral, the tongue is motionless. Taste and tactile sensibility are unaffected but articulation is slow and swallowing very difficult.

The hypoglossal nerve is often used to reanimate the face in patients, particularly the elderly, when their facial nerves have been transected. Direct end-to-end, end-to-side or split-nerve grafts are reliable and offer a robust, effective and quick alternative to more complex reanimation procedures.

Cervical sympathetic trunk

The cervical sympathetic trunk lies on the prevertebral fascia behind the carotid sheath and contains three interconnected ganglia: the superior, middle and inferior (stellate or cervicothoracic) (see Figs 35.17, 35.18). There may occasionally, however, be two or four ganglia. The cervical sympathetic ganglia send grey rami communicantes to all the cervical spinal nerves but receive no white rami communicantes from them. Their spinal preganglionic fibres emerge in the white rami communicantes of the upper five thoracic spinal nerves (mainly the upper three), and ascend in the sympathetic trunk to synapse in the cervical ganglia. In their course, the grey rami communicantes may pierce longus capitis or scalenus anterior.

Superior cervical ganglion

The superior cervical ganglion is the largest of the three ganglia (see Fig. 35.17). It lies on the transverse processes of the second and third cervical vertebrae and is probably formed from four fused ganglia, judging by its grey rami to C1–4. The internal carotid artery within the carotid sheath is anterior, and longus capitis is posterior. The lower end of the ganglion is united by a connecting trunk to the middle cervical ganglion. Postganglionic branches are distributed in the internal carotid nerve, which ascends with the internal carotid artery into the carotid canal to enter the cranial cavity, and in lateral, medial and anterior branches. They supply vasoconstrictor and sudomotor nerves to the face and neck, dilator pupillae and smooth muscle in the eyelids and orbitalis.

Lateral branches The lateral branches are grey rami communicantes to the upper four cervical spinal nerves and to some of the cranial nerves. Branches pass to the inferior vagal ganglion, the hypoglossal nerve, the superior jugular bulb and associated jugular glomus or glomera, and to the meninges in the posterior cranial fossa. Another branch, the jugular nerve, ascends to the cranial base and divides into two; one part joins the inferior glossopharyngeal ganglion and the other joins the superior vagal ganglion.

Medial branches The medial branches of the superior cervical ganglion are the laryngopharyngeal and cardiac. The laryngopharyngeal branches supply the carotid body and pass to the side of the pharynx, joining glossopharyngeal and vagal rami to form the pharyngeal plexus. A cardiac branch arises by two or more filaments from the lower part of the superior cervical ganglion and occasionally receives a twig from the trunk between the superior and middle cervical ganglia. It is thought to contain only efferent fibres, the preganglionic outflow being from the upper thoracic segments of the spinal cord, and to be devoid of pain fibres from the heart. It descends behind the common carotid artery, in front of longus colli, and crosses anterior to the inferior thyroid artery and recurrent laryngeal nerve. The courses on the two sides then differ. The right cardiac branch usually passes behind, but sometimes in front of, the subclavian artery and runs posterolateral to the brachiocephalic trunk to join the deep (dorsal) part of the cardiac plexus behind the aortic arch. It has other sympathetic connections. About mid-neck, it receives filaments from the external laryngeal nerve. Inferiorly, one or two vagal cardiac branches join it. As it enters the thorax, it is joined by a filament from the recurrent laryngeal nerve. Filaments from the nerve also communicate with the thyroid branches of the middle cervical ganglion. The left cardiac branch, in the thorax, is anterior to the left common carotid artery and crosses in front of the left side of the aortic arch to reach the superficial (ventral) part of the cardiac plexus. Sometimes, it descends on the right of the aorta to end in the deep (dorsal) part of the cardiac plexus. It communicates with the cardiac branches of the middle and inferior cervical sympathetic ganglia and sometimes with the inferior cervical cardiac branches of the left vagus, and branches from these mixed nerves form a plexus on the ascending aorta.

Anterior branches The anterior branches of the superior cervical ganglion ramify on the common and external carotid arteries and the branches of the external carotid, and form a delicate plexus around each, in which small ganglia are occasionally found. The plexus around the facial artery supplies a filament to the submandibular ganglion; the plexus on the middle meningeal artery sends one ramus to the otic ganglion and another, the external petrosal nerve, to the facial ganglion. Many of the fibres coursing along the external carotid and its branches ultimately leave them to travel to facial sweat glands via branches of the trigeminal nerve.

Middle cervical ganglion

The middle cervical ganglion is the smallest of the three and is occasionally absent, in which case it may be replaced by minute ganglia in the sympathetic trunk or may be fused with the superior ganglion. It is usually found at the level of the sixth cervical vertebra, anterior or just superior to the inferior thyroid artery, or it may adjoin the inferior cervical ganglion. It probably represents a coalescence of the ganglia of the fifth and sixth cervical segments, judging by its postganglionic rami, which join the fifth and sixth cervical spinal nerves (but sometimes also the fourth and seventh). It is connected to the inferior cervical ganglion by two or more very variable cords. The posterior cord usually splits to enclose the vertebral artery, while the anterior cord loops down anterior to, and then below, the first part of the subclavian artery, medial to the origin of its internal thoracic branch, and supplies rami to it. This loop is the ansa subclavia and is frequently multiple, lies in close contact with the cervical pleura, and typically connects with the phrenic nerve, and sometimes with the vagus nerve (see Fig. 35.18).

The middle cervical ganglion gives off thyroid and cardiac branches. The thyroid branches accompany the inferior thyroid artery to the thyroid gland. They communicate with the superior cardiac, external laryngeal and recurrent laryngeal nerves, and send branches to the parathyroid glands. Fibres to both glands are largely vasomotor but some reach the secretory cells. The cardiac branch, the largest sympathetic cardiac nerve, arises either from the ganglion itself or more often from the sympathetic trunk cranial or caudal to it. On the right side, it descends behind the common carotid artery and anterior or posterior to the subclavian artery, to the trachea, where it receives a few filaments from the recurrent laryngeal nerve before joining the right half of the deep (dorsal) part of the cardiac plexus. In the neck, it connects with the superior cardiac and recurrent laryngeal nerves. On the left side, the cardiac nerve enters the thorax between the left common carotid and subclavian arteries to join the left half of the deep (dorsal) part of the cardiac plexus. Fine branches from the middle cervical ganglion also pass to the trachea and oesophagus.

Inferior (or cervicothoracic/stellate) ganglion

The inferior cervical ganglion (cervicothoracic/stellate) is irregular in shape and much larger than the middle cervical ganglion (see Fig. 35.18). It is probably formed by a fusion of the lower two cervical and first thoracic segmental ganglia, sometimes including the second and even third and fourth thoracic ganglia. The first thoracic ganglion may be separate, leaving an inferior cervical ganglion above it. The sympathetic trunk turns backwards at the junction of the neck and thorax, and so the long axis of the cervicothoracic ganglion becomes almost anteroposterior. The ganglion lies on or just lateral to the lateral border of longus colli between the base of the transverse process of the seventh cervical vertebra and the neck of the first rib (which are both posterior to it). The vertebral vessels are anterior, and the ganglion is separated from the posterior aspect of the cervical pleura inferiorly by the suprapleural membrane. The costocervical trunk of the subclavian artery branches near the lower pole of the ganglion, and the supreme intercostal artery is lateral.

A small vertebral ganglion may be present on the sympathetic trunk anterior or anteromedial to the origin of the vertebral artery and directly superior to the subclavian artery. When present, it may provide the ansa subclavia. It is also joined to the inferior cervical ganglion by fibres enclosing the vertebral artery and is usually regarded as a detached part of the middle cervical or inferior cervical ganglion. Like the middle cervical ganglion, it may supply grey rami communicantes to the fourth and fifth cervical spinal nerves. The inferior cervical ganglion sends grey rami communicantes to the seventh and eighth cervical and first thoracic spinal nerves, and gives off a cardiac branch, branches to nearby vessels and sometimes a branch to the vagus nerve.

The grey rami communicantes to the seventh cervical spinal nerve vary from one to five (two being the usual number). A third often ascends medial to the vertebral artery in front of the transverse process of the seventh cervical vertebra. It connects with the seventh cervical nerve, and sends a filament upwards through the transverse foramen of the sixth cervical vertebra in company with the vertebral vessels to join the sixth cervical spinal nerve as it emerges from the intervertebral foramen. An inconstant ramus may traverse the transverse foramen of the seventh cervical vertebra. Grey rami to the eighth cervical spinal nerve vary from three to six in number.

The cardiac branch descends behind the subclavian artery and along the anterior aspect of the trachea to the deep cardiac plexus. Behind the artery, it connects with the recurrent laryngeal nerve and the cardiac branch of the middle cervical ganglion (the latter is often replaced by fine branches of the inferior cervical ganglion and ansa subclavia).

The branches to blood vessels form plexuses on the subclavian artery and its branches. The subclavian supply is derived from the inferior cervical ganglion and ansa subclavia, and typically extends to the first part of the axillary artery, although a few fibres may extend further. An extension of the subclavian plexus to the internal thoracic artery may be joined by a branch of the phrenic nerve.

Within the foramina transversaria and intertransverse spaces, the cervical grey rami communicantes form intersegmental arcades as they communicate with one another and the ventral rami of the upper five or six cervical spinal nerves. These arcades accompany the second part of the vertebral artery and create the appearance of a long nerve known as the vertebral nerve. Fine filaments from this nerve and the grey rami communicantes form the vertebral plexus on the surface of the vertebral artery. This plexus contains not only sympathetic efferent fibres but also somatic sensory fibres from the adventitia of the artery with cell bodies in the cervical dorsal root ganglia. The vertebral nerve sends filaments to the posterolateral corners of the cervical intervertebral discs (Bogduk et al 1988), and gives rise to the meningeal branches (sinuvertebral nerves) at each cervical segment. The vertebral plexus, which contains some neuronal cell bodies, continues into the skull along the vertebral and basilar arteries and their branches as far as the posterior cerebral artery, where it meets a plexus from the internal carotid artery. The plexus on the inferior thyroid artery reaches the thyroid gland and connects with the recurrent and external laryngeal nerves, the cardiac branch of the superior cervical ganglion, and the common carotid plexus.

Horner's syndrome

Any condition or injury that destroys the sympathetic trunk ascending from the thorax through the neck into the face results in Horner's syndrome (Bernard–Horner syndrome, oculosympathetic palsy), characterized by a drooping eyelid (ptosis), sunken globe (enophthalmos), narrow palpebral fissure, contracted pupil (meiosis), and vasodilation and lack of thermal sweating (anhydrosis) of the face on the affected side. Classically, this is seen in patients with bronchial carcinomas that have invaded the sympathetic trunk and it is a recognized complication of cervical sympathectomy or a radical neck dissection. Avulsion of the first thoracic nerve from the spinal cord may be diagnosed by development of the syndrome after closed traction lesion of the supraclavicular brachial plexus. Congenital Horner's syndrome has been reported in association with ipsilateral internal carotid artery agenesis (Fons et al 2009). Special features of congenital Horner's syndrome are unilateral straight hair and abnormalities of iris pigmentation in one or both eyes (heterochromia iridis or heterochromia iridum), usually inherited as an autosomal dominant trait and attributed to disruption of the postganglionic sympathetic pathway producing a neurotropic dysgenesis of iris melanocytes (Rennie 2011). Connections between the recurrent laryngeal nerve, the vagus and cervical sympathetic have been linked with Horner’s syndrome complicating thyroidectomy.

VISCERA

The main cervical viscera are the submandibular salivary glands, the thyroid and parathyroid glands, and the cervical portions of the trachea and oesophagus.

Submandibular salivary gland

Each submandibular salivary gland is situated behind and below the ramus of the mandible, in the region of the submandibular triangle, between the anterior and posterior bellies of digastric (see Fig. 37.40A). The gland is described in detail in Chapter 37.

Thyroid gland

The thyroid gland, brownish-red and highly vascular, is placed anteriorly in the lower neck, level with the fifth cervical to the first thoracic vertebrae. It is ensheathed by the pretracheal layer of deep cervical fascia and consists of right and left lobes connected by a narrow, median isthmus. It usually weighs 25 g but this varies. The gland is slightly heavier in females and enlarges during menstruation and pregnancy. Estimation of the size of the thyroid gland is clinically important in the evaluation and management of thyroid disorders and can be achieved non-invasively by means of diagnostic ultrasound. Mean thyroid volume increases with age (Chanoine et al 1991). No significant difference in thyroid gland volume has been observed between males and females from 8 months to 15 years. An enlargement of the thyroid for whatever reason is called a goiter: most swellings are benign, some caused by overactivity (thyrotoxicosis, Graves' disease) and rarely malignant.

The lobes of the thyroid gland are approximately conical. Their ascending apices diverge laterally to the level of the oblique lines on the laminae of the thyroid cartilage, and their bases are level with the fourth or fifth tracheal cartilages. Each lobe is usually 5 cm long, its greatest transverse and anteroposterior extents being 3 cm and 2 cm, respectively. The posteromedial aspects of the lobes are attached to the side of the cricoid cartilage by a lateral thyroid ligament (Berry's ligament). The isthmus connects the lower parts of the two lobes, although occasionally it may be absent. It measures 1.25 cm transversely and vertically, and is usually anterior to the second and third tracheal cartilages, although it can be higher or even sometimes lower because its site and size vary greatly. A conical pyramidal lobe often ascends towards the hyoid bone from the isthmus or the adjacent part of either lobe (more often the left). It is occasionally detached or in two or more parts. A fibrous or fibromuscular band, the levator of the thyroid gland (musculus levator glandulae thyroideae), sometimes descends from the body of the hyoid to the isthmus or pyramidal lobe. (For further reading, see Mohebati and Shaha (2012)).

Ectopic thyroid tissue is rare but may be found around the course of the thyroglossal duct or laterally in the neck, as well as in distant places such as the tongue (lingual thyroid), mediastinum and the subdiaphragmatic organs (Noussios et al 2011). The most frequent location of ectopic thyroid tissue is at the base of the tongue, in particular at the region of the foramen caecum, where it can represent the only thyroid tissue. Small, detached masses of thyroid tissue may be found above the lobes or isthmus as accessory thyroid glands. Vestiges of the thyroglossal duct may persist between the isthmus and the foramen caecum of the tongue, sometimes as accessory nodules or cysts of thyroid tissue near the midline or even in the tongue, where they are called thyroglossal duct cysts.

Surfaces and relations

The convex lateral (superficial) surface of the thyroid gland is covered by sternothyroid: the attachment of this muscle to the oblique thyroid line prevents the upper pole of the gland from extending on to thyrohyoid. Sternohyoid and the superior belly of omohyoid lie more anteriorly, overlapped inferiorly by the anterior border of sternocleidomastoid. The medial surface of the gland is adapted to the larynx and trachea; its superior pole contacts the inferior pharyngeal constrictor and the posterior part of cricothyroid, which separate it from the posterior part of the thyroid lamina and the side of the cricoid cartilage. The external branch of the superior laryngeal nerve is medial to this part of the gland as it passes to supply cricothyroid. Inferiorly, the trachea and, more posteriorly, the recurrent laryngeal nerve and oesophagus (which is closer on the left) are medial relations. The posterolateral surface of the thyroid gland is close to the carotid sheath and overlaps the common carotid artery.

The anterior border of the gland is thin and slants down medially near the anterior branch of the superior thyroid artery. The posterior border is rounded and related inferiorly to the inferior thyroid artery and its anastomosis with the posterior branch of the superior thyroid artery. On the left side, the lower end of the posterior border lies near the thoracic duct. The parathyroid glands are usually related to the posterior border.

The isthmus is covered by sternothyroid, from which it is separated by pretracheal fascia. More superficially it is covered by sternohyoid, the anterior jugular veins, fascia and skin (see Fig. 33.11). The superior thyroid arteries anastomose along its upper border and the inferior thyroid veins leave the gland at its lower border.

Vascular supply and lymphatic drainage

Arteries

The thyroid gland is supplied by the superior and inferior thyroid arteries and sometimes by an arteria thyroidea ima from the brachiocephalic trunk or aortic arch (see Figs 35.14, 35.17). The arteries are large and their branches anastomose frequently both on and in the gland, ipsilaterally and contralaterally. The superior thyroid artery, which is closely related to the external branch of the superior laryngeal nerve, pierces the thyroid fascia and then divides into anterior and posterior branches. The anterior branch supplies the anterior surface of the gland, and the posterior branch supplies the lateral and medial surfaces. The inferior thyroid artery approaches the base of the thyroid gland and divides into superior (ascending) and inferior thyroid branches to supply the inferior and posterior surfaces of the gland. The superior branch also supplies the parathyroid glands. The relationship between the inferior thyroid artery and the recurrent laryngeal nerve is highly variable and of considerable clinical importance; iatrogenic injury to the nerves that supply the larynx represents a major complication of thyroid surgery (Yalçin 2006). The recurrent laryngeal nerve is usually related to the posterior branch of the inferior thyroid artery, which may be replaced by a vascular network (Moreau et al 1998). The most reliable place to identify the recurrent laryngeal nerve is in Beahr's triangle, where the nerve is the third side of this triangle, the other two sides being the inferior thyroid and common carotid arteries. Identification of the recurrent laryngeal nerve can be confirmed by electrical stimulation using a nerve monitor.

Veins

The venous drainage of the thyroid gland is usually via superior, middle and inferior thyroid veins (see Figs 35.13, 35.14, 35.17). The superior thyroid vein emerges from the upper part of the gland, runs with the superior thyroid artery towards the carotid sheath and drains into the internal jugular vein. The middle thyroid vein collects blood from the lower part of the gland; it emerges from the lateral surface of the gland and drains into the internal jugular vein. The inferior thyroid veins arise in a glandular venous plexus that connects with the middle and superior thyroid veins. These veins form a pretracheal plexus, from which the left inferior vein descends to join the left brachiocephalic vein, and the right descends obliquely across the brachiocephalic artery to join the right brachiocephalic vein at its junction with the superior vena cava. The inferior thyroid veins often open via a common trunk into the superior vena cava or left brachiocephalic vein. They drain the oesophageal, tracheal and inferior laryngeal veins and have valves at their terminations.

Lymphatics

Thyroid lymphatic vessels communicate within the gland and the tracheal plexus, passing onwards to prelaryngeal nodes just above the thyroid isthmus and then to pretracheal and paratracheal nodes (level VI). Some may also drain into the brachiocephalic nodes related to the thymus in the superior mediastinum (level VII). Laterally, the gland is drained to the deep cervical nodes (level IV) by vessels lying along the superior thyroid veins. Thyroid lymphatics may drain directly, with no intervening node, to the thoracic duct. In summary, the major lymphatic drainage of the thyroid is to the middle and lower jugular lymph nodes in levels III and IV and to the posterior triangle nodes in level V_b, supplemented by minor drainage to the pretracheal and paratracheal nodes in level VI and to the superior mediastinal nodes in level VII.

Innervation

The thyroid gland receives its innervation from the superior, middle and inferior cervical sympathetic ganglia. Postganglionic fibres from the inferior cervical ganglion form a plexus on the inferior thyroid artery that accompanies the artery to the thyroid gland, and communicates with the recurrent laryngeal nerve and the external branch of the superior laryngeal nerves, the superior cardiac nerve, and the plexus on the common carotid artery.

Imaging

The follicular nature of the thyroid gland is not resolved by current imaging techniques and thus presents a homogeneous texture on cross-sectional imaging (ultrasound, computed tomography, magnetic resonance imaging). Its superficial location makes the thyroid an ideal organ for sonographic examination, facilitating fine needle sampling (FNAC) of any abnormalities (**Fig. 35.21**). The thyroid gland is highly vascular and demonstrates intense contrast enhancement and increased signal on T2-weighted MRI (**Fig. 35.22**). Radionuclide imaging of the thyroid may be performed with technetium (^{99m}Tc) pertechnetate. This readily available radionuclide is trapped by the thyroid in the same way as iodine but is not organified. It yields morphological information and will reveal the presence of ectopic thyroid tissue. Functional data can be obtained with the use of ^{123}iodine or ^{131}iodine, which is trapped and organified. For further reading, see Intenzo et al (2012).

Microstructure

The thyroid gland has a thin capsule of connective tissue that extends into the glandular parenchyma and divides each lobe into irregularly shaped and sized lobules. The functional units of the thyroid are spherical and cyst-like follicles, between 0.02 and 0.9 mm in diameter. Follicles

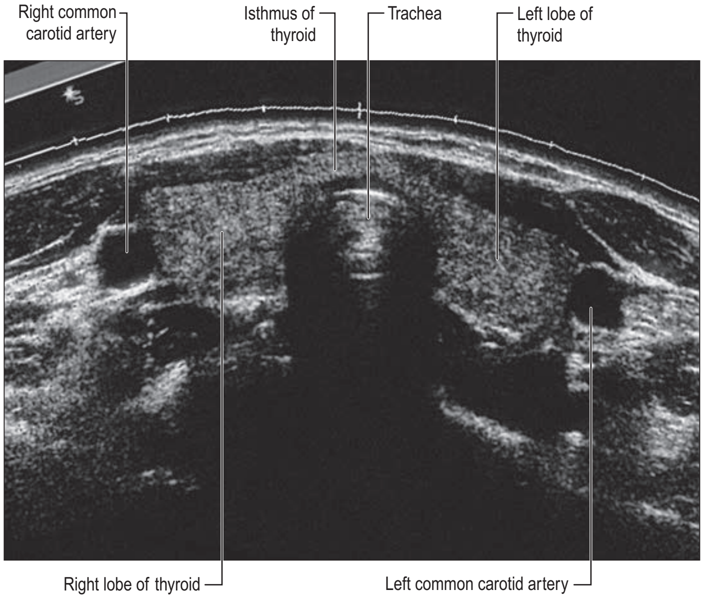

Fig. 35.21 A thyroid sonogram.

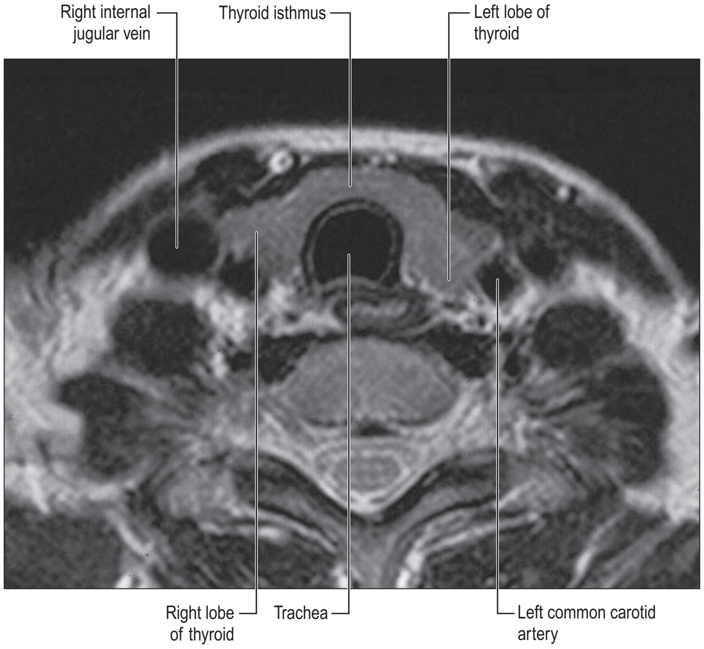

Fig. 35.22 A T2-weighted magnetic resonance image at the level of the thyroid isthmus. Vessels show flow void; compare with Fig. 35.21.

consist of a central colloid core surrounded by a single-layered epithelium resting on a basal lamina (Fig. 35.23). Colloid consists almost entirely of an iodinated glycoprotein, iodothyroglobulin, which is the inactive, stored form of the active thyroid hormones, tri-iodothyronine (T_3) and tetra-iodothyronine or thyroxine (T_4), produced by the follicular epithelial cells. Sufficient iodothyroglobulin is stored extracellularly within follicles to regulate the metabolic activity of the body for up to 3 months. Follicles are surrounded by a delicate connective tissue stroma that contains dense plexuses of fenestrated capillaries, extensive lymphatic networks and sympathetic nerve fibres that supply the arterioles and capillaries. Some nerve fibres end close to the follicular epithelial cells.

Follicular cells Follicular cells vary from squamous or low cuboidal to columnar, depending on their level of activity, which is controlled mainly by circulating hypophysial thyroid-stimulating hormone (TSH, thyrotropin). Resting follicles are large and lined by squamous or low cuboidal epithelium with abundant luminal colloid. Apical microvilli are short in resting cells, but elongate and often branch on stimulation by TSH. Follicles showing differing levels of activity may coexist.

Active follicular cells are highly polarized functionally. The secretion of TSH leads to endocytosis of colloidal droplets at the luminal epithelium (see Fig. 35.23). The hormone stimulates the cells to extend cytoplasmic processes into the luminal colloid and sequester droplets of colloid. The iodinated thyroglobulin in the intracellular colloid droplets is then degraded by follicular cell lysosomes, liberating T_3 and T_4, which pass to the base of the cell, where they are released: they are exported from the thyroid mainly via the blood capillaries and lymphatics. Prolonged high levels of circulating TSH induce follicular cell hypertrophy, progressive resorption of colloid and increased stromal vascularity, and this can result in thyroid enlargement.

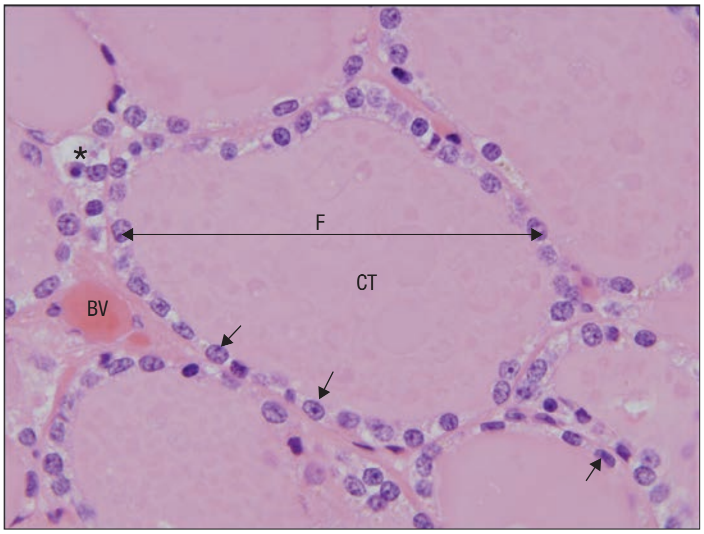

Fig. 35.23 A section through parts of several human thyroid follicles, one of which is labelled (F), showing the follicular epithelium (arrows) enclosing a lumen filled with colloidal thyroglobulin (CT). Calcitonin-secreting C cells are not readily identifiable in routine preparations of human tissue, where they appear as poorly staining (clear) cells within follicles; an example is indicated by the asterisk. A network of blood vessels (BV) within connective tissue septa surrounds the follicles. (Courtesy of Mr Peter Helliwell and the late Dr Joseph Mathew, Department of Histopathology, Royal Cornwall Hospitals Trust, UK.)

Thyroid cancer is usually differentiated and arises from the follicular cells. Following excision any remaining tissue/tumour can be treated with radioactive iodine because the cells retain the ability to both trap and incorporate iodine into tyrosine residues of thyroglobulin. Most differentiated thyroid cancers arise *de novo*. Irradiation of the thyroid in childhood, as might be necessary for the treatment of Hodgkin's lymphoma or as happened in 1986 following the power plant accident in Chernobyl (Ron 2007), is a recognized cause. Routine follow-up is facilitated by serum thyroglobulin measurements: in the athyroid state none should be detectable.

C cells Thyroid parenchyma also contains C (clear) cells, so called because they have pale-staining cytoplasm that is more pronounced in some species than in the human thyroid. C cells are members of the amine precursor uptake and decarboxylation (APUD) system of dispersed neuroendocrine cells. They produce the peptide hormone calcitonin (thyrocalcitonin), which lowers blood calcium by inhibiting bone resorption and calcium recovery from renal tubule ultrafiltrate. C cells populate the middle third of each lateral lobe of the thyroid and are typically found scattered within thyroid follicles, lying inside the basal lamina but not reaching the lumen of the follicle. Occasionally, they occur in clusters in the interfollicular stroma, hence their alternative name of parafollicular cells. C cells give rise to medullary thyroid cancer (MTC) a rare type of malignancy that can be familial and associated with multiple endocrine neoplasia syndromes, i.e. MEN2A when associated with a phaeochromocytoma (benign adrenal tumour) and primary hyperparathyroidism. After excision, patients are followed up both clinically and with serial serum monitoring of plasma calcitonin levels.

Thyroidectomy

Available with the *Gray's Anatomy* e-book

Parathyroid glands

The parathyroid glands are small, yellowish-brown, ovoid or lentiform structures, usually lying between the posterior lobar borders of the thyroid

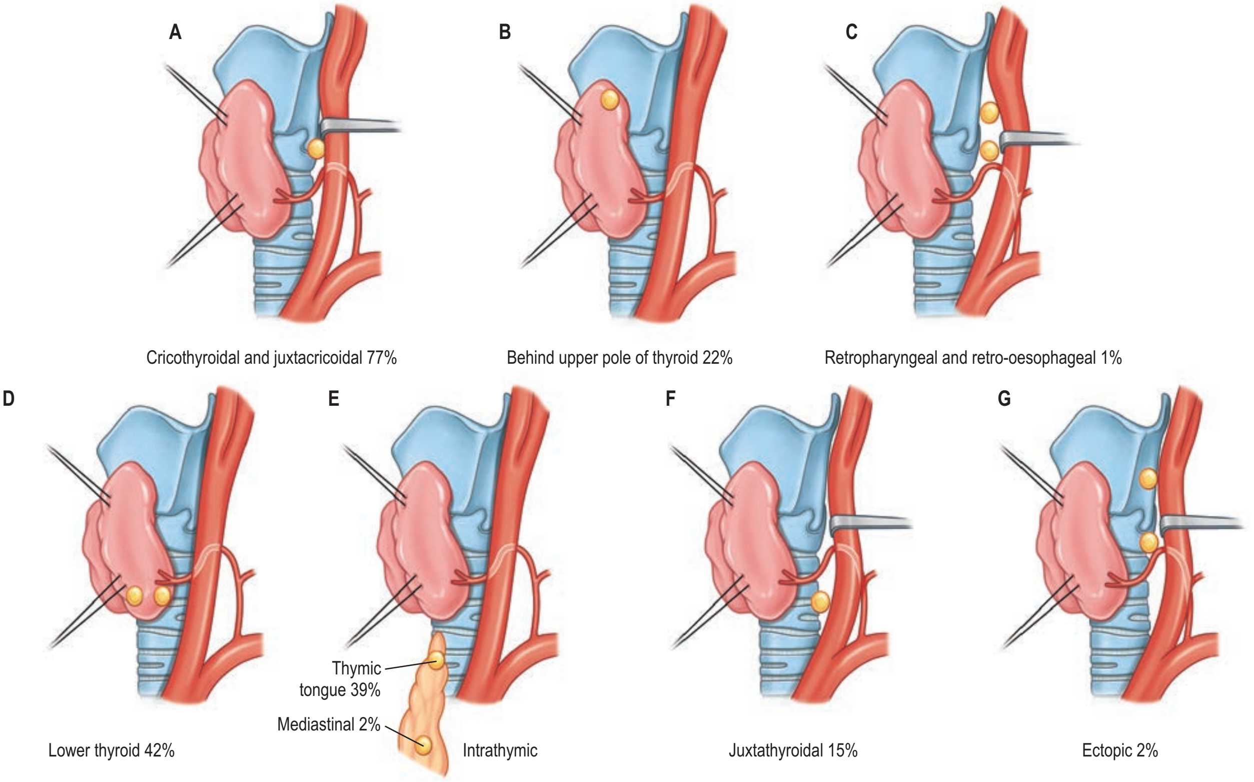
A
B
C
Cricothyroidal and juxtacricoidal 77%
Behind upper pole of thyroid 22%
Retropharyngeal and retro-oesophageal 1%
D
E
F
G
Thymic tongue 39%
Mediastinal 2%
Lower thyroid 42%
Intrathymic
Juxtathyroidal 15%
Ectopic 2%

Fig. 35.24 The distribution of superior (**A**–**C**) and inferior (**D**–**G**) parathyroid glands. **A**, Cricothyroidal and juxtathyroidal. **B**, Behind the upper pole of the thyroid. **C**, Retropharyngeal and retro-oesophageal. **D**, Lower thyroid. **E**, Intrathymic. **F**, Juxtathyroidal. **G**, Ectopic. (H–L, *continued online*)

gland and its capsule (Fig. 35.24). They are commonly 6 mm long, 3–4 mm across and 1–2 mm from posterior to anterior, each weighing about 50 mg. There are usually two on each side, superior and inferior, but there may be more, or only three, or many minute ectopic parathyroid islands scattered in connective tissue in the retro-oesophageal/para-oesophageal space, thyroid, carotid sheath, thyrothymic ligament or the thymus (Taterra et al 2019). Very occasionally, an occult gland may follow a blood vessel into a groove on the surface of the thyroid. Normally, the inferior parathyroids migrate to the inferior thyroid poles, but they may descend with the thymus into the thorax or they may be sessile and remain above their normal level near the carotid bifurcation. The anastomotic connection between the superior and inferior thyroid arteries that occurs along the posterior border of the thyroid gland usually passes very close to the parathyroids, and is a useful aid to their identification.

The superior parathyroid glands are more constant in location than the inferior and are usually to be found midway along the posterior borders of the thyroid gland, although they may be higher. The inferior pair are more variably situated (related to their embryological development) and may be either within the fascial thyroid sheath, below the inferior thyroid arteries and near the inferior lobar poles; or outside the sheath, immediately above an inferior thyroid artery; or in the thyroid gland near its inferior pole. These variations are surgically important (Fig. 35.25). A tumour of the inferior parathyroid situated within the fascial thyroid sheath may descend along the inferior thyroid veins anterior to the trachea into the superior mediastinum, whereas if it is outside the sheath, it may extend postero-inferiorly behind the oesophagus into the posterior mediastinum. The superior parathyroids are usually dorsal, and the inferior parathyroids ventral, to the recurrent laryngeal nerves.

The parathyroid glands are very flattened in cross-section and are not normally visible by current imaging methods, including scintigraphy, unless they are enlarged (see Fig. 35.24).

Vascular supply and lymphatic drainage

Both superior and inferior parathyroid glands are usually supplied by the inferior thyroid arteries; the superior parathyroid may be supplied by the superior thyroid artery or from anastomoses between the superior and inferior thyroid arteries. The glands drain into the plexus of veins on the anterior surface of the thyroid. Lymph vessels are numerous and associated with those of the thyroid and thymus glands.

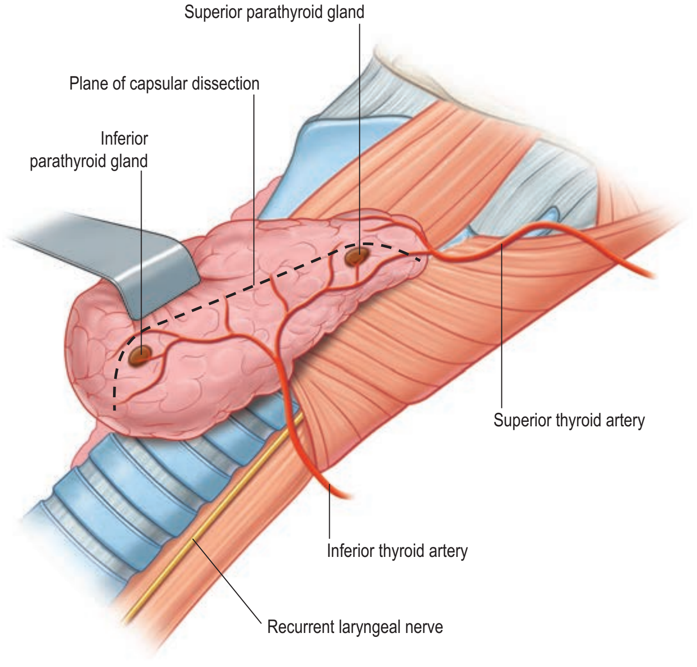
Superior parathyroid gland
Plane of capsular dissection
Inferior parathyroid gland
Superior thyroid artery
Inferior thyroid artery
Recurrent laryngeal nerve

Fig. 35.25 Extracapsular dissection of the thyroid gland preserving the parathyroid glands with their blood supply. The plane of capsular dissection, indicated by the dotted line, allows for mobilization of the parathyroid glands from the thyroid capsule with preservation of their blood supply, and facilitates identification of the recurrent laryngeal nerve. (With permission from Brennan P, Standring S, Wiseman S (eds) Gray's Surgical Anatomy. Elsevier. Copyright 2020.)

Innervation

The nerve supply is sympathetic, either direct from the superior or middle cervical ganglia, or via a plexus in the fascia on the posterior aspect of the thyroid lobe. Parathyroid activity is controlled by variations in blood

Apart from variable enlargement during menstruation and pregnancy, any thyroid swelling is a goitre that may press on related structures. Symptoms most commonly reflect the consequence of pressure on the trachea or on the recurrent laryngeal nerves, and there may also be venous engorgement. During thyroidectomy, care must be taken when ligating the superior and inferior thyroid arteries to avoid iatrogenic injury to adjacent nerves. The external laryngeal nerve runs close to the superior thyroid artery in Joll's triangle, and the recurrent laryngeal nerve runs close to the inferior thyroid artery in Beahr's triangle. Total thyroidectomy may be necessary in the treatment of hyperthyroidism, benign thyroid enlargement in the euthyroid state, and for cancer (which is often combined with a selective neck dissection of the primary major lymph node echelon levels, i.e. III, IV and VI). The parathyroid glands and the recurrent laryngeal nerves are preserved.

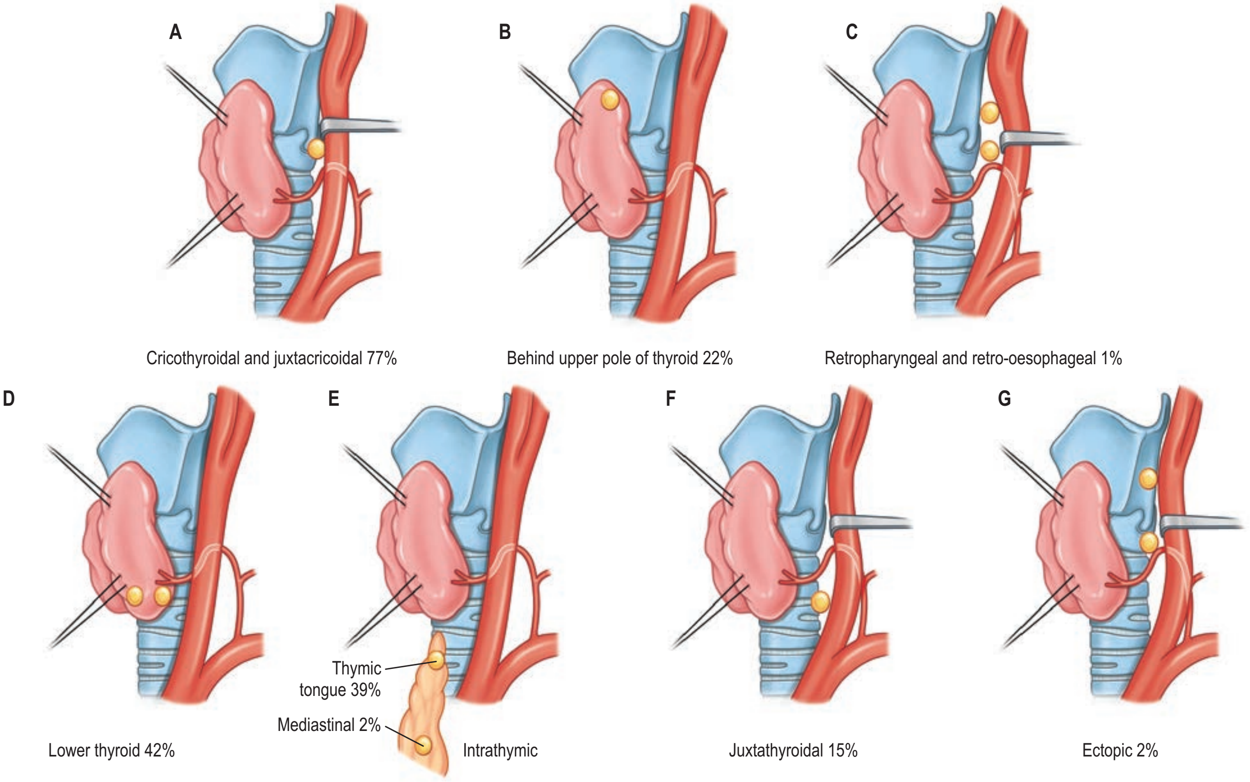
A
B
C
Cricothyroidal and juxtacricoidal 77%
Behind upper pole of thyroid 22%
Retropharyngeal and retro-oesophageal 1%
D
E
F
G
Thymic tongue 39%
Mediastinal 2%
Lower thyroid 42%
Intrathymic
Juxtathyroidal 15%
Ectopic 2%

Fig. 35.24 The distribution of superior (**A**–**C**) and inferior (**D**–**G**) parathyroid glands. **A**, Cricothyroidal and juxtathyroidal. **B**, Behind the upper pole of the thyroid. **C**, Retropharyngeal and retro-oesophageal. **D**, Lower thyroid. **E**, Intrathymic. **F**, Juxtathyroidal. **G**, Ectopic.

Continued

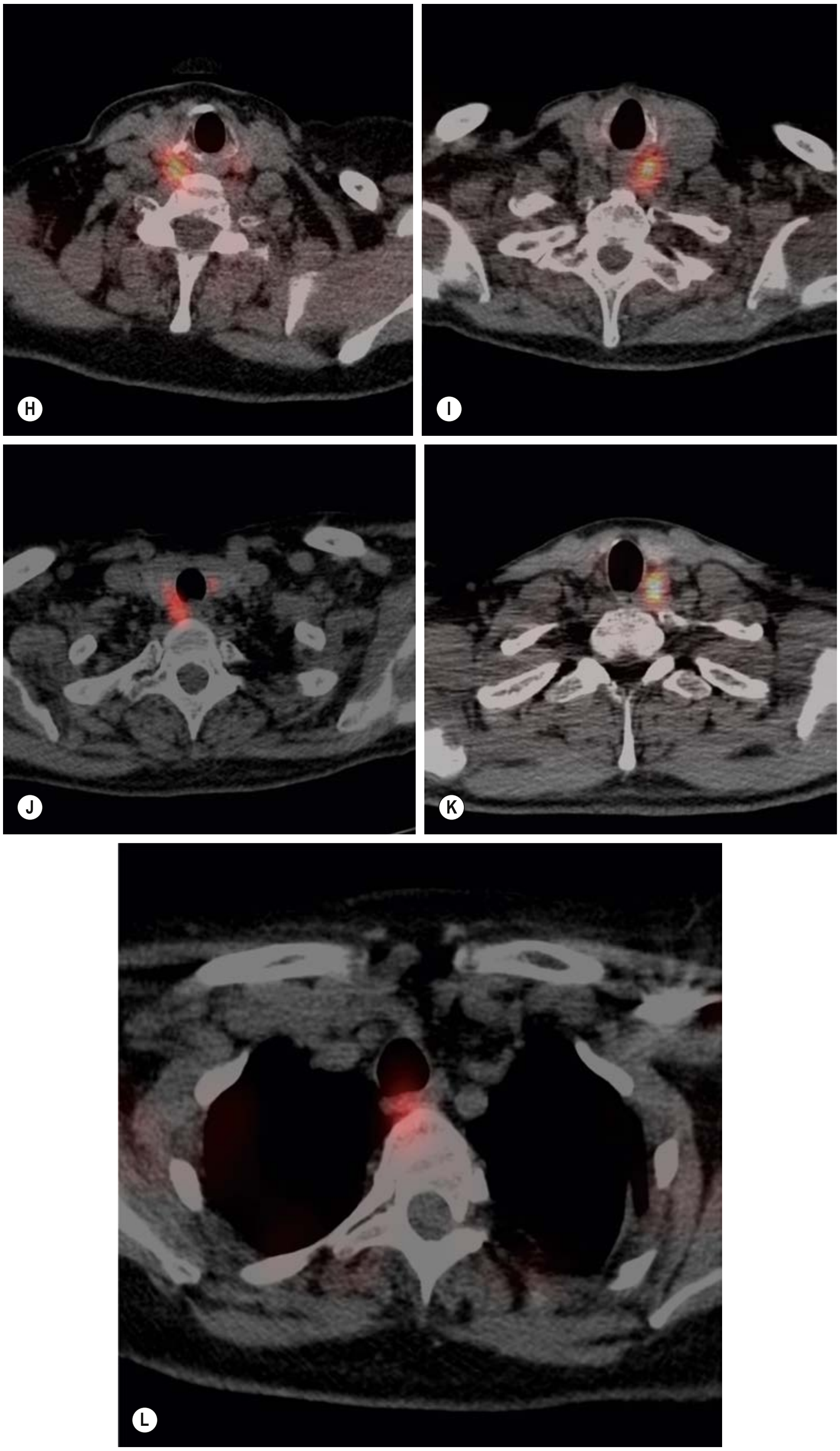

Fig. 35.24, cont'd H–K, Sestamibi SPECT-CT scans showing different positions of the parathyroid glands as adenomas with abnormally increased uptake: **H**, right superior, cricothyroidal and juxtacricoidal; **I**, left superior, cricothyroidal and juxtacricoidal; **J**, right inferior juxtathyroidal; **K**, left inferior paratracheal juxtathyroidal. **L**, Sestamibi SPECT-CT scan showing an ectopic parathyroid gland in a patient with persistent primary hyperparathyroidism after a total thyroidectomy. The increased abnormal uptake is seen in the ectopic gland in a retrotracheal, para-oesophageal position.

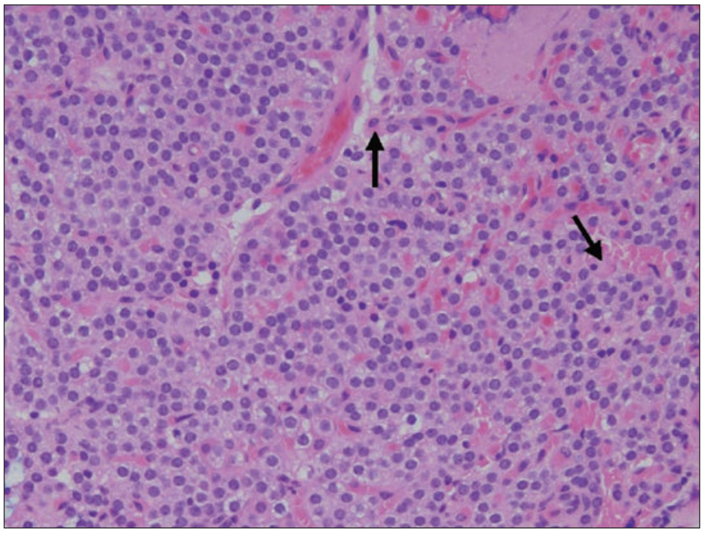

Fig. 35.26 A section of the parathyroid gland, showing clusters and cords of small, tightly packed chief cells surrounded by vascular sinusoids. Scattered oxyphil cells (arrows) are generally larger and more eosinophilic. (Courtesy of Mr Peter Helliwell and the late Dr Joseph Mathew, Department of Histopathology, Royal Cornwall Hospitals Trust, UK.)

calcium level, and is inhibited by a rise and stimulated by a fall. The nerves are believed to be vasomotor but not secretomotor.

Microstructure

Each parathyroid gland has a thin connective tissue capsule with intraglandular septa but lacks distinct lobules. The glands synthesize and secrete parathyroid hormone (PTH, parathormone), a single-chain polypeptide of 84 amino-acid residues concerned with the control of the level and distribution of calcium and phosphorus. In childhood, the gland consists of wide, irregular, interconnecting columns of chief or principal cells separated by a dense plexus of fenestrated sinusoidal capillaries. After puberty, adipose tissue accumulates in the stroma and typically accounts for about one-third of the adult tissue mass, increasing further with age.

Chief cells differ ultrastructurally according to their level of activity. Active chief cells have large Golgi complexes with numerous vesicles and small membrane-bound granules, whereas glycogen granules are most abundant in inactive cells, which have few of the cytoplasmic features of synthetic or secretory activity, and appear histologically as 'clear' cells. In normal human parathyroid glands, inactive chief cells outnumber active cells in a ratio of 3–5 : 1 (**Fig. 35.26**). In contrast to the thyroid, where the activities of adjacent follicular cells are coordinated, individual chief cells of the parathyroid glands go through cycles of secretory activity and rest independently, according to serum calcium levels.

A second cell type, the oxyphil (eosinophil) cell, appears just before puberty and increases in number with age. Oxyphil cells are larger than chief cells and contain more cytoplasm which stains deeply with eosin. Their nuclei are smaller and more darkly staining than those of chief cells, and their cytoplasm is unusually rich in mitochondria. The functional significance of oxyphil cells and their relationship to chief cells are uncertain.

Most parathyroid surgery is undertaken for primary hyperparathyroidism, which is the second commonest cause of hypercalcaemia and usually caused by a solitary parathyroid adenoma. The serum parathormone (PTH) is raised. Such tumours can be localized preoperatively using a combination of radionucleide, ultrasound and CT scanning.

ROOT OF THE NECK

The root of the neck is a zone of transition between four discrete anatomical spaces: the neck, the thorax and both upper limbs (see Fig. 35.18) It contains the subclavian vessels; common carotid artery; trunks of the brachial plexus; sympathetic trunk; phrenic, vagus and recurrent laryngeal nerves (all bilaterally); the terminal portion of the thoracic duct (on the left side only); the terminal portion of the right lymphatic duct (on the right side only); and the oesophagus and trachea (in the midline). The brachiocephalic veins are formed by the union of the internal jugular and subclavian veins at the junction of the neck and thorax, behind the head of the clavicle.

The essential anatomical landmark in orientating and understanding the root of the neck is scalenus anterior, covered by the prevertebral layer of deep cervical fascia. It is important to understand its immediate relations. Anteriorly lie sternocleidomastoid and subclavius, the intermediate tendon of omohyoid, the subclavian vein, branches from the thyrocervical trunk of the first part of the subclavian artery (transverse cervical, suprascapular and ascending cervical arteries), and the phrenic nerve. The nerve lies on the surface of scalenus anterior in the root of the neck, before passing between it and the subclavian vein to enter the superior mediastinum and it is the anatomical key to identifying the muscle intraoperatively. Posteriorly, the roots of the brachial plexus and the second part of the subclavian artery separate scalenus anterior from scalenus medius. Pathologies that cause impingement on either the brachial plexus or the subclavian artery may present clinically as an upper limb compression syndrome. The suprapleural membrane and pleura are intimate posterior relations of scalenus anterior. On each side, the apical (cervical) pleura and the apex of the lung bulge up into the root of the neck. The height to which the apical pleura rises, with reference to the first pair of ribs and costal cartilages, varies in different individuals according to the obliquity of their thoracic inlet. Posteriorly, the apical pleura typically reaches the level of the neck of the first rib, forming a domed roof over each side of the thoracic cavity that is strengthened by the suprapleural membrane. Scalenus anterior covers the anterolateral part of the dome of the pleura, separating it from the subclavian vein. The subclavian artery crosses the dome below its summit, immediately above the vein. The costocervical trunk arches backwards from the subclavian artery and crosses the summit of the dome; its supreme intercostal branch descends behind the dome, between the first intercostal nerve laterally and the first thoracic sympathetic ganglion medially.

Medial relations of scalenus anterior are longus colli and the inferior thyroid artery. The two muscles are separated by an angular interval through which the vertebral artery and vein pass to gain access to the foramen transversarium of the sixth cervical vertebra, and more anteriorly the inferior thyroid artery arches from lateral to medial on its way to the thyroid gland. The area also contains some level IV and scalene nodes within Chassaignac's triangle (see Fig. 35.5B). The cervical sympathetic trunk and the inferior cervical ganglion lie close to the posteromedial aspect of the vertebral artery here. The internal thoracic artery descends from the first part of the subclavian artery, passes behind the brachiocephalic vein and, on the right side, is crossed by the phrenic nerve. The vagus nerve descends anterior to the first part of the subclavian artery, and on the right side only, gives off its recurrent laryngeal branch which usually turns around the lower border of the artery. The terminal portions of the thoracic duct and the right lymphatic duct, on the left and right sides, respectively, cross the triangular interval at the level of the seventh cervical vertebra and come into contact with the medial edge of scalenus anterior.

The axillary sheath, an extension of the prevertebral fascia that accompanies the axillary artery and trunks of the brachial plexus, lies lateral to scalenus anterior.

Cervical rib

A small additional rib (cervical rib) may develop in the root of the neck in association with the seventh cervical vertebra. It is often fibrous in nature, although in some cases it may have undergone ossification. A cervical rib may cause compression of the subclavian artery and the lower roots of the brachial plexus, in which case affected individuals will complain of pain, paraesthesia and even pallor of the affected upper limb, a condition known as thoracic outlet syndrome. The occasional co-occurrence of rudimentary or absent twelfth ribs with cervical ribs indicates that a homeotic shift had occurred over a larger part of the vertebral column in affected fetuses (Bots et al 2011). For further reading on homeotic transformations of vertebrae, see Ten Broek et al (2012).

Oesophagus – cervical portion

The oesophagus is a muscular tube approximately 25 cm long, connecting the pharynx to the stomach. It begins in the neck, level with the lower border of the cricoid cartilage and the sixth cervical vertebra. It descends, largely anterior to the vertebral column, into the superior mediastinum. Generally vertical and median, it inclines to the left as far as the root of the neck, and also bends in an anteroposterior plane to follow the cervical curvature of the vertebral column.

Relations The trachea lies anterior to the oesophagus, attached to it by loose connective tissue. The vertebral column, longus colli and prevertebral layer of deep cervical fascia are posterior, and the common carotid artery and posterior part of the thyroid gland are lateral on each side. In the lower neck, where the oesophagus deviates to the left, it becomes closer to the left carotid sheath and thyroid gland. The thoracic duct ascends for a short distance along its left side. The recurrent laryngeal nerves ascend on each side in or near the tracheo-oesophageal groove.

Vascular supply and lymphatic drainage The cervical part of the oesophagus is mainly supplied by branches from the inferior thyroid arteries. The oesophageal veins drain into the brachiocephalic veins, and lymphatic vessels pass to retropharyngeal, paratracheal or deep cervical lymph nodes in levels III and IV.

Innervation The cervical part of the oesophagus is innervated by the recurrent laryngeal nerves and by the sympathetic plexus around the inferior thyroid artery.

Trachea – cervical portion

The trachea is a tube 10–11 cm long, formed of cartilage and fibromuscular tissue. It descends from the larynx, and extends from the level of the sixth cervical vertebra to the upper border of the fifth thoracic vertebra (see Figs 35.14, 35.22). It lies approximately in the sagittal plane but its point of bifurcation is usually a little to the right. The trachea is flexible and can rapidly alter in length. It is flattened posteriorly, so that in transverse section it is shaped, with some individual variation, like a letter D. Its external transverse diameter is 2 cm in adult males, and 1.5 cm in adult females. The lumen in live adults is 1.2 cm in transverse diameter. In children, the trachea is smaller, more deeply placed and more mobile. Tracheal diameter does not exceed 3 mm in the first postnatal year; during later childhood its diameter in millimetres is about equal to age in years.

Relations The relationships of the trachea to other cervical structures is of clinical significance: tracheostomy is not an uncommon clinical procedure. Anteriorly, the cervical part of the trachea is crossed by skin and by the superficial and deep fasciae. It is also crossed by the jugular arch and overlapped by sternohyoid and sternothyroid. The second to fourth tracheal cartilages are crossed by the isthmus of the thyroid gland, above which an anastomotic artery connects the bilateral superior thyroid arteries. Below and in front are the pretracheal fascia, inferior thyroid veins, thymic remnants and the arteria thyroidea ima (when it exists). In children, the brachiocephalic artery crosses obliquely in front of the trachea at or a little above the upper border of the manubrium. The left brachiocephalic vein may also rise a little above this level. The oesophagus lies posterior to the trachea and separates it from the vertebral column. The paired lobes of the thyroid gland, which descend to the fifth or sixth tracheal cartilage, and the common carotid and inferior thyroid arteries all lie lateral to the trachea. The recurrent laryngeal nerves ascend on each side, in or near the grooves between the sides of the trachea and oesophagus.

Vascular supply and lymphatic drainage The cervical part of the trachea is mainly supplied by branches from the inferior thyroid arteries. The tracheal veins drain into the brachiocephalic veins via the inferior thyroid plexus, and lymphatic vessels drain into the pretracheal and paratracheal nodes.

Innervation The trachea is innervated by branches from the vagi, recurrent laryngeal nerves and sympathetic trunks.

Surgical airway The trachea may be accessed directly in the neck via cricothyroidotomy or tracheostomy. There are numerous indications for performing an elective tracheostomy, including the need to provide prolonged intubation and pulmonary toilet, and management of acute airway obstruction from causes that include laryngeal pathology, trauma (e.g. midface, mandibular or laryngeal fractures), as well as bilateral recurrent laryngeal palsies consequent on thyroid surgery. For detailed descriptions of the operative procedures, appropriate surgical texts should be consulted as well as texts that detail developmental anomalies and anatomical variations (Jarvis 1966, Ger and Evans 1993, Racic et al 2005).

Cricothyroidotomy endangers the cricothyroid artery (a branch of the superior thyroid artery), which is usually found close to the midline, and which reaches the median cricothyroid ligament close to the thyroid cartilage.

Bonus e-book content

Fig. 35.20 The intercarotid plexus and its main trunks.

Fig. 35.24 H–K, Sestamibi SPECT-CT scans showing different positions of the parathyroid glands as adenomas with abnormally increased uptake.

Key references

Bogduk N, Windsor M, Inglis A 1988 The innervation of the cervical intervertebral discs. Spine 13:2–8.

A description of the cervical sinuvertebral nerves, which have an upward course in the vertebral canal, supplying the lateral aspects of the disc at their level of entry and the disc above.

Brown H 2002 Anatomy of the spinal accessory nerve plexus: relevance to head and neck cancer and atherosclerosis. Exp Biol Med 227:570–8.

Data that explain why some patients acquire a severe functional impairment after surgery despite preservation of the accessory nerve. This provides the rationale for conservative neck dissection.

Crile G 1906 Excision of cancer of the head and neck with special reference to the plan of dissection based on one hundred and thirty two operations. J Am Med Assoc 47:1780–6.

A seminal paper that considers the surgical anatomy of radical neck dissection.

Guidera, AK, Dawes PJD, Stringer MD 2012 Cervical fascia: a terminological pain in the neck. ANZ Surg 82:786–91.

A review that provides a critical appraisal of the terms used to describe the cervical fascia in order to achieve consensus and uniformity.

Mohebati A, Shaha AR 2012 Anatomy of thyroid and parathyroid glands and neurovascular relations. Clin Anat 25:19–31.

A review of the pertinent anatomy and embryology of the thyroid and parathyroid glands and the critical structures that lie in their proximity.

Moreau S, de Rugy MG, Babin E et al 1998 The recurrent laryngeal nerve: related vascular anatomy. Laryngoscope 108:1351–5.

An exploration of the considerable variability in the perineural vasculature of the recurrent laryngeal nerve, which lies in close proximity to and is usually supplied by the posterior branch of the inferior thyroid artery.

Smoker WRK, Harnsberger HR 1991 Differential diagnosis of head and neck lesions based on their space of origin. 2. The infrahyoid portion of the neck. Am J Roentgenol 157:155–9.

A pictorial essay that describes the fascia and fascial spaces of the infrahyoid portion of the neck. The contents of each space, the common abnormalities affecting the space, and the characteristic displacements produced by disease in each space are reviewed.

References

Bogduk N, Windsor M, Inglis A 1988 The innervation of the cervical intervertebral discs. Spine 13:2–8.

A description of the cervical sinuvertebral nerves, which have an upward course in the vertebral canal, supplying the lateral aspects of the disc at their level of entry and the disc above.

Bots J, Wijnaendts LC, Delen S et al 2011 Analysis of cervical ribs in a series of human fetuses. J Anat 219:403–9.

Brown H 2002 Anatomy of the spinal accessory nerve plexus: relevance to head and neck cancer and atherosclerosis. Exp Biol Med 227:570–8.

Data that explain why some patients acquire a severe functional impairment after surgery despite preservation of the accessory nerve. This provides the rationale for conservative neck dissection.

Byon HJ, Lee GW, Lee JH et al 2013 Comparison between ultrasound-guided supraclavicular and infraclavicular approaches for subclavian venous catheterization in children–a randomized trial. Br J Anaesth 111:788–92.

Chanoine JP, Toppet V, Lagasse R et al 1991 Determination of thyroid volume by ultrasound from the neonatal period to late adolescence. Eur J Pediatr 150:395–9.

Crile G 1906 Excision of cancer of the head and neck with special reference to the plan of dissection based on one hundred and thirty two operations. J Am Med Assoc 47:1780–6.

A seminal paper that considers the surgical anatomy of radical neck dissection.

Deutsch MD, Kriss VM, Willging JP 1995 Distance between the tonsillar fossa and internal carotid artery in children. Arch Otolaryngol Head Neck Surg 121:1410–2.

Fons C, Vasconcelos M, Vidal M 2009 Agenesis of internal carotid artery in a child with ipsilateral Horner's syndrome. J Child Neurol 24:101–4.

Friedmann DR, Eubig J, McGill M et al 2011 Development of the jugular bulb: a radiologic study. Otol Neurotol 32:1389–95.

Froes LB, De Tolosa EMC, Camargo RDC et al 1999 Blood supply to the human sternocleidomastoid muscle by the sternocleidomastoid branch of the occipital artery. Clin Anat 12:412–6.

Ger R, Evans JT 1993 Tracheostomy: an anatomico-clinical review. Clin Anat 6:337–41.

Guidera, AK, Dawes PJD, Stringer MD 2012 Cervical fascia: a terminological pain in the neck. ANZ Surg 82:786–91.

A review that provides a critical appraisal of the terms used to describe the cervical fascia in order to achieve consensus and uniformity.

Hedge A, Mohan S, Lim WE 2012 Infections of the deep neck spaces. Singapore Med J 53:305–11.

Hong JY, Koo BN, Kim WO et al 2010 Effect of head rotation on overlap and relative position of internal jugular vein to carotid artery in infants and children: a study of the anatomy using ultrasonography. J Crit Care 25:360.e9–360.e13.

Intenzo CM, Dam HQ, Manzone TA et al 2012 Imaging of the thyroid in benign and malignant disease. Semin Nucl Med 42:49–61.

Jarvis JF 1966 Displaced brachiocephalic artery: a potential hazard in tracheostomy. S Afr Med J 40:396–7.

Lucas GDA, Laudanna A, Chopard RP et al 1994 Anatomy of the lesser occipital nerve in relation to cervicogenic headache. Clin Anat 7:90–6.

Maroldi R, Farina D, Ravanelli M et al 2012 Emergency imaging assessment of deep neck space infections. Semin Ultrasound CT MR 33:432–42.

Matthers LH Jr, Smith DW, Frankel L 1992 Anatomical considerations in placement of central venous catheters. Clin Anat 5:89–106.

Mohebati A, Shaha AR 2012 Anatomy of thyroid and parathyroid glands and neurovascular relations. Clin Anat 25:19–31.

A review of the pertinent anatomy and embryology of the thyroid and parathyroid glands and the critical structures that lie in their proximity.

Moreau S, de Rugy MG, Babin E et al 1998 The recurrent laryngeal nerve: related vascular anatomy. Laryngoscope 108:1351–5.

An exploration of the considerable variability in the perineural vasculature of the recurrent laryngeal nerve, which lies in close proximity to and is usually supplied by the posterior branch of the inferior thyroid artery.

Nash L, Nicholson HD, Zhang M 2005 Does the investing layer of the deep cervical fascia exist? Anesthesiology 103:962–8.

Noussios G, Anagnostis P, Goulis DG et al 2011 Ectopic thyroid tissue: anatomical, clinical, and surgical implications of a rare entity. Eur J Endocrinol 165:375–82.

Oliver E, Gillespie M 2005 Deep space neck infections. In: Flint PE (ed) Cummings Otolaryngology Head and Neck Surgery, 5th ed. St Louis: Elsevier, Mosby; Ch. 14, pp. 201–8.

Pandit JJ, Bree S, Dillon P et al 2000 A comparison of superficial versus combined (superficial and deep) cervical plexus block for carotid endarterectomy: a prospective, randomized study. Anesth Analg 91:781–6.

Porzionato A, Macchi V, Stecco C et al 2013 The carotid body in sudden infant death syndrome. Respir Physiol Neurobiol 185:194–201.

Pu YM, Tang EY, Yang XD 2008 Trapezius muscle innervation from the spinal accessory nerve and branches of the cervical plexus. Int J Oral Maxillofac Surg 37:567–72.

Racic G, Matulic J, Roje Z et al 2005 Abnormally high bifurcation of the brachiocephalic trunk as a potential operative hazard: case report. Otolaryngol Head Neck Surg 133:811–13.

Rennie IG 2011 Don't it make my blue eyes brown: heterochromia and other abnormalities of the iris. Eye (Lond) 26:29–50.

Rodríguez-Vázquez JF, Kim JH, Verdugo-López S et al. 2011 Human fetal hyoid body origin revisited. J Anat. 219:143–9.

Ron E 2007 Thyroid cancer incidence among people living in areas contaminated by radiation from the Chernobyl accident. Health Phys 93(5):502–11.

Sakamoto Y 2016 Prevertebral and craniocervical junction muscles. In: Tubbs RS, Shoja MM, Loukas M (eds) Bergman's Comprehensive Encyclopedia of Human Anatomic Variation. New Jersey: Wiley. Ch. 28, pp. 245–53.

Seong J, Lieber BB, Wakhloo AK 2005 Morphological age-dependent development of the human carotid bifurcation. J Biomech 38:453–65.

Shah JP, Patel SJ 2012 Cervical lymph nodes. In: Head and Neck Surgery and Oncology, 4th ed. St Louis: Elsevier, Mosby; pp. 353–94.

Shoja M, Oyesiku NM, Shokouhi G et al 2014 Anastomoses between lower cranial and upper cervical nerves: a comprehensive review with potential significance during skull base and neck operations. Part II: glossopharyngeal, vagus, accessory, and hypoglossal nerves and cervical spinal nerves 1–4. Clin Anat 27:131–44.

Smoker WRK, Harnsberger HR 1991 Differential diagnosis of head and neck lesions based on their space of origin. 2. The infrahyoid portion of the neck. Am J Roentgenol 157:155–9.

A pictorial essay that describes the fascia and fascial spaces of the infrahyoid portion of the neck. The contents of each space, the common abnormalities affecting the space, and the characteristic displacements produced by disease in each space are reviewed.

Som PM, Curtin HD 2011 Head and Neck Imaging, 5th ed. St Louis: Elsevier, Mosby.

Taterra D, Wong LM, Vikse J, et al. 2019 The prevalence and anatomy of parathyroid glands: a meta-analysis with implications for parathyroid surgery. Langenbecks Arch Surg. 404:63–70.

Ten Broek CM, Bakker AJ, Varela-Lasheras I 2012 Evo-devo of the human vertebral column: on homeotic transformations, pathologies and prenatal selection. Evol Biol 39:456–71.

Tubbs RS, Shoja MM, Loukas M et al 2011 Study of the cervical plexus innervation of the trapezius muscle. J Neurosurg Spine 14:626–9.

Yalçin B 2006 Anatomic configurations of the recurrent laryngeal nerve and inferior thyroid artery. Surgery 139:181–7.

Recommended reading

Berkovitz BKB, Kirsch C, Moxham BJ et al 2002 Interactive Head and Neck. London: Primal Pictures.

Cady B, Rossi RL (eds) 1991 Surgery of the Thyroid and Parathyroid Glands. Philadelphia: Elsevier, Saunders.

Kapandji IA 1975 The Physiology of Joints. Edinburgh: Elsevier, Churchill Livingstone.

Lingeman RE 1998 Surgical anatomy. In: Cummings CW et al (eds) Otolaryngology, Head and Neck Surgery, vol. 2, 3rd ed. St Louis: Elsevier, Mosby; pp. 1673–85.

Robbins KT 1998 Neck dissection. In: Cummings CW et al (eds) Otolaryngology, Head and Neck Surgery, vol. 2, 3rd ed. St Louis: Elsevier, Mosby; pp. 1787–819.

Wilson-Pauwels L, Akesson EJ, Stewart PA 1998 Cranial Nerves: Anatomy and Clinical Comments. Toronto: Decker.

CHAPTER 36

Face and scalp

SKIN

The scalp and buccolabial tissues are described here. The structure of the eyelids is discussed in Chapter 44.

Scalp

The scalp extends from the top of the forehead anteriorly to the superior nuchal line posteriorly. Laterally, it projects down to the zygomatic arch and external acoustic meatus. It consists of five layers: skin, subcutaneous tissue, occipitofrontalis (epicranius) and its aponeurosis, subaponeurotic loose areolar tissue and the periosteum of the skull (pericranium).

The skin of the scalp is hairy and rich in sebaceous glands, and is the most common site for sebaceous cysts. The dense subcutaneous connective tissue has the richest cutaneous blood supply in the body. The anterior and posterior muscular bellies of occipitofrontalis are connected by a tough, fibrous, epicranial aponeurosis, and this layer is therefore often called the aponeurotic layer (galea aponeurotica). These three upper layers of the scalp can easily slide on the underlying layer of loose connective tissue. A scalp flap can be raised within the plane between the galea and the pericranium without compromising either the blood or the nerve supply of the scalp because all of these structures lie in the subcutaneous layer (superficial fascia). Anteriorly based subgaleal scalp flaps (bicoronal) provide excellent access to the craniofacial skeleton for the correction of congenital deformity such as craniosynostoses; treatment of craniofacial fractures involving the frontal bone, nasoethmoidal complex, orbit or zygomatic arch; skull-base surgery; or craniotomies. Pericranial flaps can be used to separate the frontal sinus floor from the nasal cavity in the management of fractures of the posterior wall of the frontal sinus (frontal sinus cranialization). Traumatic scalp avulsion may happen if hair becomes trapped in moving machinery or a shearing force is applied in the subgaleal plane during a road traffic accident or fall injury.

The arterial blood supply to the scalp is particularly rich; there are free anastomoses between branches of the occipital and superficial temporal vessels. Scalp lacerations continue to bleed profusely because the elastic fibres of the underlying galea aponeurotica prevent initial vessel retraction. Their repair requires a two-layer closure technique to approximate the galea aponeurotica and skin layers, whereas the pericranial layer, if involved, cannot usually be closed because it retracts.

Eyebrows

The eyebrows are two arched eminences of skin that surmount the orbits. Numerous short, thick hairs are set obliquely in them. Fibres of orbicularis oculi, corrugator and the frontal part of occipitofrontalis are inserted into the dermis of the eyebrows.

Buccolabial tissue

Cheeks

The cheeks are continuous anteriorly with the lips. The external junction is indicated by the nasolabial groove (sulcus) and further laterally by the nasolabial fold, which descends from the side of the nose to the angle of the mouth. The cheek is covered on the outer surface by skin and on the inner surface by mucosa. Each cheek contains the buccinator muscle, and a variable, but usually considerable, amount of adipose tissue, often encapsulated to form a biconcave mass, the buccal fat pad (of Bichat), that is particularly evident in infants. The walls of the cheek contain fibrous connective tissue, vessels, nerves and numerous small buccal mucous (salivary) glands. The buccal fat pad can be used for surgical reconstruction of small intraoral defects of the palate and buccal and retromolar regions.

Lips

The lips are two fleshy folds surrounding the oral orifice. The centre of each lip contains a thick fibrous strand of parallel bundles of skeletal muscle fibres (orbicularis oris, together with incisivus superior and inferior and the direct labial tractors), and their attachments to skin, mucosa or other muscle fibres. The free external surface of each lip is covered by a thin keratinized epidermis and is continuous with the mucosa at the vermilion (red) zone of the lip. The dermis is well vascularized and contains numerous hair follicles, sebaceous glands (Fordyce spots) and sweat glands. Subcutaneous adipose tissue is scanty. The internal mucous surfaces are lined with a thick, non-keratinizing, stratified squamous epithelium. The submucosa is well vascularized and contains numerous minor salivary glands, which may be harvested for histological confirmation of Sjögren's connective tissue disease.

Between the skin and mucosa, the vermilion zone is covered with a specialized keratinized stratified squamous epithelium that is thin near the skin, increases in thickness slightly as the mucosa is approached, and thickens abruptly when true mucosa is reached. The epithelium is covered with transparent, dead squames and its deep surface is highly convoluted, interdigitating with abundant long dermal papillae. The latter carry a rich capillary plexus that imparts a dusky red colour. These surfaces are hairless, their dermis lacks sebaceous, sweat or mucous glands, and they are moistened with saliva by the tip of the tongue. The dense innervation of the lips is reflected in their acute sensitivity to light touch, attributable mainly to the increased density of Meissner's corpuscles (see Fig. 3.29) in the dermal papillae.

The size and curvature of the exposed red-lip surfaces is subject to considerable variation. The attainment of adult dimensions is faster in the upper than in the lower lip; the cutaneous upper lip height normally reaches its adult size at the age of 3 years in females and 6 years in males (Farkas et al 1992). In children, all lip dimensions (distances, areas, volumes) are larger in boys than in girls (Ferrario et al 2000). Upper lip length is significantly shorter in females than in males and follows the growth pattern of the upper airway. Growth plateaus between the ages of 6 and 9 years, increases again from 9 to 16 years, and plateaus between 16 and 18 years (Gonçalves et al 2011).

The line of contact between the lips, the oral fissure, lies just above the incisal edges of the anterior maxillary teeth. On each side, a labial commissure forms the angle (corner) of the mouth, usually near the first premolar tooth. The labial epithelia and internal tissues radiate over the boundaries of the commissure to become continuous with those of the cheek. With age, buccolabial (labiomarginal) grooves appear at the angles of the mouth. On each side, the upper lip is separated from the cheek laterally by the nasolabial groove and is continuous above the nasal ala with the circumalar groove (sulcus). The lower lip is separated from the chin by the mentolabial groove (sulcus).

Externally, the central region of the upper lip presents a shallow vertical groove, the philtrum, limited above by its attachment to the columella of the nose and ending below in a slight tubercle limited by lateral ridges. The lower lip shows a small depression in the midline that corresponds to the tubercle. The junction between the external, hair-bearing skin and the red, hairless surface of the upper lip almost invariably takes the form of a double-curved Cupid's bow. From the centre, it rises rapidly on each side to an apex that corresponds to the lower end of each ridge of the philtrum, and then slopes gently downwards towards the angle of the mouth. The line of contact between the red-lip surfaces is typically almost horizontal. The Cupid's bow is interrupted in cleft lip anomalies.

In the upper lip, a narrow band of smooth tissue related to the subnasal maxillae marks the point at which labial mucosa becomes continuous with gingival mucosa. The corresponding point in the lower lip coincides approximately with the mentolabial sulcus, where the labial mucosa is continuous with mental tissues. The upper and lower lips differ in cross-sectional profile in that neither is a simple fold of uniform thickness. The upper lip has a bulbous asymmetric profile where the skin and red-lip have a slight external convexity, and the adjoining red-lip and mucosa a pronounced internal convexity, creating a mucosal ridge or shelf that can be wrapped around the incisal edges of the parted

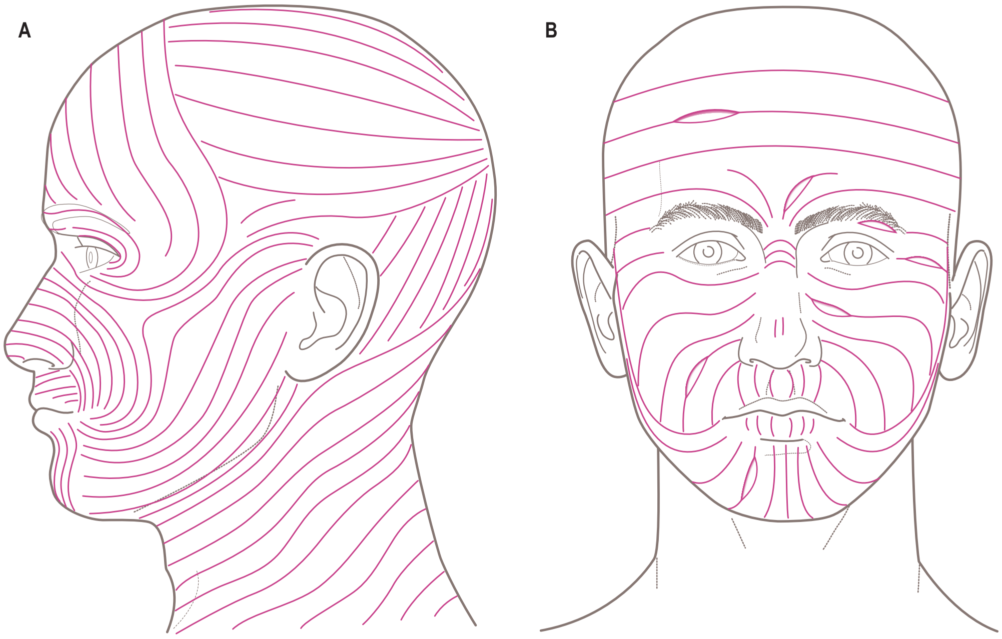

Fig. 36.1 The distribution of relaxed skin tension lines (Kraissl's lines). **A**, Lateral view. **B**, Anterior view.

teeth. The lower lip is on a more posterior plane than the upper lip. In the position of neutral lip contact, the external surface of the lower lip is concave and there is little or no elevation of the internal mucosal surface. The profile of the lips can be modified by muscular activity.

Relaxed skin tension lines and skin flaps on the face

The direction in which facial skin tension is greatest varies regionally. Skin tension lines follow the furrows formed when the skin is relaxed, and are known as 'relaxed skin tension lines' (Borges and Alexander 1962). In the living face, these lines frequently (but not always) coincide with wrinkle lines (**Fig. 36.1**) and can therefore act as a guide in planning elective incisions.

When lesions on the face, such as scars, pigmented lesions and skin cancers, are excised, the dimensions of these lesions often require excision as an ellipse, so that the resulting defect can be closed as a straight line. If the resulting scar is to be aesthetically acceptable, it is important to make the long axis of the ellipse parallel to the natural relaxed skin tension lines, so that the scar will look like a natural skin crease. If the excision line runs contrary to the skin tension lines, the scar may be more conspicuous and will tend to stretch transversely as a result of natural expressive facial movements. When larger lesions are excised, it may be necessary to advance or rotate adjacent soft tissue to fill the defect. The ability to raise these skin flaps is entirely dependent on the regional blood supply; both random pattern and axial pattern skin flaps are used surgically. The richness of the subdermal plexus in the face means that random pattern flaps can be raised with a greater length:breadth ratio than in any other part of the body.

SOFT TISSUE

Fascial layers

Fascia of scalp

The superficial fascia of the scalp is firm, dense and fibroadipose, and adheres closely to both skin and the underlying epicranius and its aponeurosis. Posteriorly, it is continuous with the superficial fascia of the posterior neck, and laterally it is prolonged into the temporal region, where it is looser in texture.

Fascial layers and tissue planes in the face

On the basis of gross dissection and complementary histological studies, four distinct tissue planes are recognized on the face superficial to the plane of the facial nerve and its branches. From superficial to deep, these layers are the skin, a subcutaneous layer of fibroadipose tissue, the superficial musculo-aponeurotic system (SMAS), and the parotid–masseteric fascia.

Subcutaneous fibroadipose tissue

The subcutaneous fibroadipose tissue is a homogeneous layer that is present throughout the face, although the degree of adiposity varies in different parts of the face and with age. Anteriorly, it crosses the nasolabial fold onto the lip. Superiorly, it crosses the zygomatic arch. In both locations, the layer is more fascial than fatty. The fat content of the subcutaneous tissue in the cheek accounts for the cheek mass, and is composed partly by the malar fat pad, a more or less discrete aggregation of fatty tissue inferolateral to the orbital margin.

Superficial musculo-aponeurotic system (SMAS)

The superficial musculo-aponeurotic system (SMAS) is described as a single tissue plane in the face. In some areas it is composed of muscle fibres and elsewhere it is composed of fibrous or fibroaponeurotic tissue; it is not directly attached to bone. When traced below the level of the inferior border of the mandible, it becomes continuous with platysma in the neck. Microdissection has revealed that the SMAS becomes indistinct on the lateral aspect of the face approximately 1 cm below the level of the zygomatic arch. Anteromedially, the SMAS layer blends with the epimysium over some of the mimetic muscles, including zygomaticus major, frontalis and the periorbital fibres of orbicularis oculi (Yousif and Mendelson 1995). In most areas of the face, a distinct sub-SMAS plane can be defined deep to the SMAS that is continuous with the plane between platysma and the underlying investing layer of deep cervical fascia in the neck. However, where the SMAS overlies the parotid gland, it is firmly blended with the superficial layer of the parotid fascia, making it difficult, if not impossible, to define a clear sub-SMAS plane in the region of the parotid.

Parotid–masseteric fascia

The parotid-masseteric fascia is thin, translucent and tough. It covers the parotid duct, the buccal branch of the facial nerve and interconnecting branches from the mandibular nerve where these structures lie on the surface of masseter. Further anteriorly, the parotid–masseteric fascia overlies the buccal fat pad that lies superficial to buccinator and blends with the epimysium on the surface of buccinator. It becomes continuous with the investing layer of deep cervical fascia below the inferior border of the mandible.

Parotid fascia (capsule)

The parotid fascia (parotid capsule) surrounds the parotid gland. Traditionally it was described as an upward continuation of the investing layer of deep cervical fascia in the neck that split to enclose the gland within superficial and deep layers. The superficial layer was thought to be attached superiorly to the zygomatic process of the temporal bone, the cartilaginous part of the external acoustic meatus and the mastoid process, and the deep layer was attached to the mandible, the tympanic plate, and the styloid and mastoid processes of the temporal bone. The current view is that the deep layer of the parotid capsule is derived from the deep cervical fascia but that the superficial layer of the parotid capsule is continuous with the fascia associated with platysma and is a

The following are examples of axial pattern flaps that can be used to reconstruct defects on the face and scalp. The supratrochlear/supraorbital arteries support forehead flaps that are used for nasal reconstruction; there is usually enough skin laxity to allow the majority of the donor site to be closed directly. The frontal branches of the superficial temporal arteries anastomose in the midline, which means that the entire forehead skin can be raised on a narrow pedicle based on just one of the superficial temporal arteries. These flaps can be used to repair many facial defects and also intraoral defects, but the donor site defect cannot be closed directly and must be covered by a skin graft. The parietal branch of the superficial temporal artery and the occipital artery can support hair-bearing flaps from the scalp and are useful for reconstructing defects involving the scalp. The nasolabial flap utilizes the lax skin just lateral to the nasolabial groove. It is not supplied by a named axial artery but rather its blood supply is provided by many small branches from the underlying facial artery that run perpendicular to the skin surface. Nasolabial flaps can be either superiorly or inferiorly based.

component of the SMAS (Mitz and Peyronie 1976, Wassef 1987, Gosain et al 1993). It varies in thickness from a thick fibrous layer anteriorly to a thin translucent membrane posteriorly. It may be traced forwards as a separate layer that passes over the masseteric fascia (also derived from the deep cervical fascia), separated from it by a cellular layer that contains branches of the facial nerve and the parotid duct. Histologically, the parotid fascia is atypical in that it contains muscle fibres in parallel with the fibres of platysma, especially in the lower part of the parotid capsule. Although thin fibrous septa may be seen in the subcutaneous layer histologically, macroscopically there is little evidence of a distinct layer of superficial fascia.

The deep fascia covering the muscles that form the parotid bed (digastric and the styloid group of muscles) contains the stylomandibular and mandibulostylohyoid ligaments. The stylomandibular ligament passes from the styloid process to the angle of the mandible. The more extensive mandibulostylohyoid ligament (angular tract) passes between the angle of the mandible and the stylohyoid ligament for varying distances, generally reaching the hyoid bone. It is thick posteriorly but thins anteriorly in the region of the angle of the mandible. There is some dispute as to whether the mandibulostylohyoid ligament is part of the deep cervical fascia (Ziarah and Atkinson 1981) or lies deep to it (Shimada and Gasser 1988). The stylomandibular and mandibulostylohyoid ligaments separate the parotid gland from the superficial part of the submandibular gland, and so are landmarks of surgical interest.

Temporoparietal and temporal fasciae

Above the level of the zygomatic arch, on the lateral side of the head, the temporoparietal fascia (superficial temporal fascia) constitutes a fascial layer that lies in the same plane as, but is not continuous with, the SMAS. It is quite separate from, and superficial to, the temporal fascia (deep temporal fascia). More superiorly, it blends with the galea aponeurotica. The plane between the temporoparietal fascia and the underlying deep temporal fascia contains loose areolar tissue and a small amount of fat. This tissue plane, the temporoparietal fat pad, is continuous superiorly with the subgaleal plane of loose areolar tissue in the scalp. Running superiorly in the temporoparietal fascia, or just deep to it, are the superficial temporal vessels, the auriculotemporal nerve and its branches, and the temporal branches of the facial nerve. When raising a bicoronal flap, identification of the temporoparietal fat pad helps to separate these two fascial layers, and subsequent dissection in a plane deep to the temporoparietal fascia protects the temporal branch of the facial nerve. The temporal fascia is a dense aponeurotic layer that lies deep to the temporoparietal fat pad and covers temporalis; the superficial fibres of temporalis are attached to the deep surface of the fascia. Superiorly, it is a single layer attached along the length of the superior temporal line, blending with the periosteum. Inferiorly, at approximately the level of the superior orbital rim, the temporal fascia splits into superficial and deep laminae that run downwards and are attached to the lateral and medial margins of the upper surface of the zygomatic arch, respectively. These fascial attachments have a clinical application in the reduction of fractures of the zygomatic complex via a Gillies approach: an instrument is inserted deep to the deep lamina of temporal fascia through a scalp incision and used to elevate depressed zygomatic complex fractures. The fat enclosed between these two layers, the superficial temporal fat pad, contains the zygomatico-orbital branch of the superficial temporal artery and a cutaneous nerve, the zygomaticotemporal branch of the maxillary nerve. The temporal fascia is overlapped by auriculares anterior and superior, the epicranial aponeurosis and part of orbicularis oculi; the superficial temporal vessels and the auriculotemporal nerve ascend over it.

Buccopharyngeal fascia

The buccopharyngeal fascia is a thin layer of fascia that covers buccinator and the superior constrictor of the pharynx (Ch. 40).

Retaining ligaments of the face

The retaining ligaments of the face are fascial bands at specific sites, e.g. the zygomatic ligament (McGregor's patch) and the mandibular ligament. They serve to anchor the skin to the underlying bone. The general cutaneous laxity associated with the ageing process renders facial skin subject to gravitational pull that is resisted by the retaining ligaments. When performing facelift procedures, these ligaments must be surgically divided in order to facilitate redraping of facial skin.

Fascial spaces

The buccal tissue space, lying between the skin and the surface of buccinator, and the infraorbital tissue space, lying between the bony attachments of levator labii superioris and levator anguli oris, can be involved in the spread of odontogenic infection.

BONES OF THE FACIAL SKELETON AND CRANIAL VAULT

The facial skeleton is the anterior part of the skull and includes the mandible. The bones of the nasoethmoidal and zygomaticomaxillary complexes are described here. The mandible is described in Chapter 38.

Parietal bone

The two parietal bones form most of the cranial roof and sides of the skull. Each is irregularly quadrilateral and has two surfaces, four borders and four angles (**Fig. 36.2**).

The external surface is convex and smooth, with a central parietal tuber (tuberosity). Curved superior and inferior temporal lines cross it and form posterosuperior arches. The temporal fascia is attached to the superior line or arch, and temporalis is attached to the inferior line or arch. The epicranial aponeurosis lies above these lines, and part of the temporal fossa lies below. Posteriorly, close to the sagittal (superior) border, an inconstant parietal foramen transmits a vein from the superior sagittal sinus and sometimes a branch of the occipital artery.

The internal surface is concave and marked by impressions of cerebral gyri and by grooves for the middle meningeal vessels. The latter ascend, inclining backwards, from the sphenoidal (anteroinferior) angle and posterior half (or more) of its inferior border. A groove for the superior sagittal sinus lies along the sagittal border and is completed by the groove on the contralateral parietal bone. The falx cerebri is attached to the edges of the groove. Granular foveolae for arachnoid granulations flank the sagittal sulcus and are most pronounced in old age.

The dentated sagittal border, longest and thickest, articulates with the contralateral parietal bone at the sagittal suture. The anterior part of the squamosal (inferior) border is short, thin and truncated, bevelled externally and overlapped by the greater wing of the sphenoid. The middle part of the inferior border is arched, bevelled externally and overlapped by the squamous part of the temporal bone. The posterior part of the inferior border is short, thick and serrated and articulates with the mastoid part of the temporal bone. The frontal border is deeply serrated, bevelled externally above and internally below, and articulates with the frontal bone to form one half of the coronal suture. The occipital border, deeply dentated, articulates with the occipital bone, forming one half of the lambdoid suture.

The frontal (anterosuperior) angle, approximately 90°, is at the bregma, where the sagittal and coronal sutures meet, marking the site of the anterior fontanelle in the neonatal skull. The sphenoidal (anteroinferior) angle lies between the frontal bone and the greater wing of the sphenoid. Its internal surface is marked by a deep groove or canal for the frontal branches of the middle meningeal vessels. The frontal, parietal, sphenoid and temporal bones usually articulate at the pterion, which marks the site of the sphenoidal fontanelle in the embryonic skull. The frontal bone sometimes articulates with the squamous part of the temporal bone, in which case the parietal bone fails to reach the greater wing of the sphenoid bone. The rounded occipital (posterosuperior) angle is at the lambda, the meeting of the sagittal and lambdoid sutures, which marks the site of the posterior fontanelle in the neonatal skull. The blunt mastoid (posteroinferior) angle articulates with the occipital bone and the mastoid portion of the temporal bones at the asterion. Internally, it bears a broad, shallow groove for the junction of the transverse and sigmoid sinuses.

Ossification

Each parietal bone is ossified from two centres that appear in dense mesenchyme near the tuberosity, one above the other at about post-fertilization week 8. These two centres unite early and ossification subsequently radiates from them towards the margins. The angles are therefore the last parts to be ossified, and fontanelles are present at these sites. At birth, the temporal lines are low down; they only reach their final position after the eruption of the molar teeth. Occasionally, the parietal bone is divided by an anteroposterior suture.

Frontal bone

The frontal bone is like half of a shallow, irregular cap and forms the forehead or frons (**Fig. 36.3**). It has three parts and contains two cavities, the frontal sinuses.

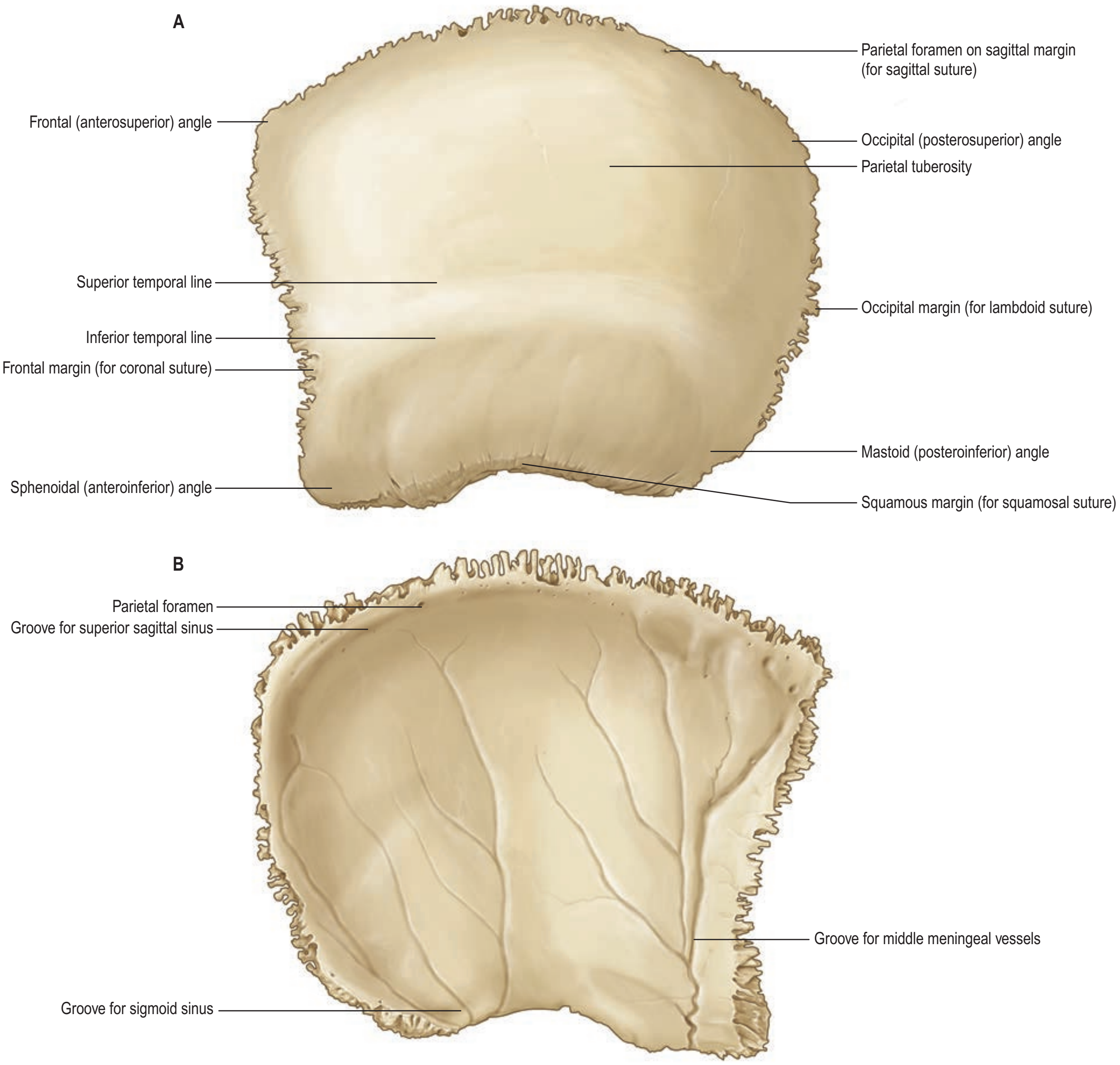
A
Parietal foramen on sagittal margin (for sagittal suture)
Frontal (anterosuperior) angle
Occipital (posterosuperior) angle
Parietal tuberosity
Superior temporal line
Occipital margin (for lambdoid suture)
Inferior temporal line
Frontal margin (for coronal suture)
Mastoid (posteroinferior) angle
Sphenoidal (anteroinferior) angle
Squamous margin (for squamosal suture)
B
Parietal foramen
Groove for superior sagittal sinus
Groove for middle meningeal vessels
Groove for sigmoid sinus

Fig. 36.2 The left parietal bone. **A**, External view. **B**, Internal view.

Squamous part

The squamous part forms the major portion of the frontal bone. Its external surface has a rounded frontal tuber (tuberosity) approximately 3 cm above the midpoint of each supraorbital margin. These tubera vary but are especially prominent in young skulls and more so in adult females than males. Below them, and separated by a shallow groove, are two curved superciliary arches, medially prominent and joined by a smooth median elevated glabella. The arches are more prominent in males: prominence depends partly on the size of the frontal sinuses but is occasionally associated with small sinuses. The curved supraorbital margins of the orbital openings lie inferior to the superciliary arches. The lateral two-thirds of each margin are sharp, the medial one-third is rounded. A supraorbital notch or foramen that transmits the supraorbital vessels and nerve lies at the junction between them and a small frontal notch or foramen may lie medial to the supraorbital notch. The supraorbital margin ends laterally in a strong, prominent zygomatic process that articulates with the zygomatic bone. A line curves posterosuperiorly from the process and divides into superior and inferior temporal lines that continue on the squamous part of the temporal bone. The area of the frontal bone posteroinferior to the temporal lines is the temporal surface and forms the anterior part of the temporal fossa. The parietal (posterior) margin is thick, deeply serrated, and bevelled internally above and externally below. Inferiorly, it becomes a rough, triangular surface that articulates with the greater wing of the sphenoid.

The internal surface of the frontal bone is concave. Its upper, median, part displays a vertical sulcus with edges that unite inferiorly as the frontal crest. The sulcus contains the anterior part of the superior sagittal sinus. The crest ends in a small notch that is completed by the ethmoid bone to form a foramen caecum. The anterior portion of the falx cerebri is attached to the margins of the sulcus and to the frontal crest. The internal surface shows impressions of cerebral gyri, small furrows for meningeal vessels, and granular foveolae near the sagittal sulcus that house arachnoid granulations.

Nasal part

The nasal part of the frontal bone lies between the supraorbital margins. A serrated nasal notch articulates with the nasal bones inferiorly and with the frontal processes of the maxillae and the lacrimal bones laterally. From the centre of the notch posteriorly, the bone projects anteroinferiorly behind the nasal bones and the frontal processes of the maxillae and supports the nasal bridge. The region ends in a sharp nasal spine, on each side of which a small grooved surface partly roofs the ipsilateral nasal cavity. The nasal spine articulates anteriorly with the crest of the nasal bones and posteriorly with the perpendicular plate of the ethmoid bone: it makes a very small contribution to the nasal septum.

Orbital parts

Most of the frontal bone is thick and consists of trabecular tissue lying between two compact laminae. The orbital plates consist entirely of compact bone and are thin and often translucent posteriorly (they can be partly absorbed in old age).

The two orbital plates are curved, triangular laminae separated by a wide ethmoidal notch. They form the largest part of the orbital roofs.

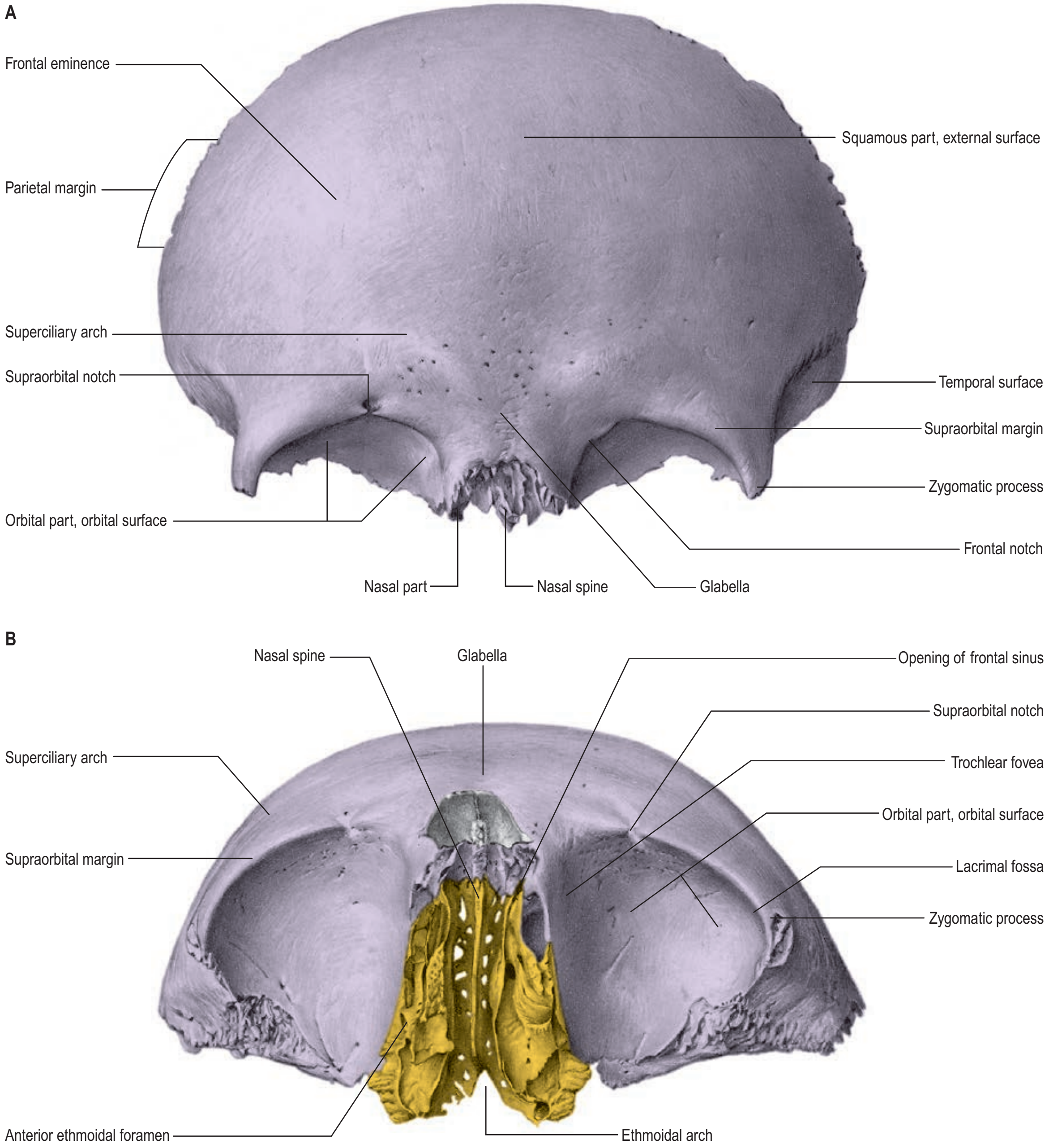
A
Frontal eminence
Squamous part, external surface
Parietal margin
Superciliary arch
Supraorbital notch
Temporal surface
Supraorbital margin
Zygomatic process
Orbital part, orbital surface
Frontal notch
Nasal part
Nasal spine
Glabella
B
Nasal spine
Glabella
Opening of frontal sinus
Supraorbital notch
Superciliary arch
Trochlear fovea
Orbital part, orbital surface
Supraorbital margin
Lacrimal fossa
Zygomatic process
Anterior ethmoidal foramen
Ethmoidal arch

Fig. 36.3 The frontal bone. **A**, Anterior view. **B**, Inferior view, including the articulations between the frontal, ethmoid and nasal bones. (Sobotta Atlas of Human Anatomy © Elsevier GmbH, Urban & Fischer, Munich.)

Their orbital surfaces are smooth and concave and each bears a shallow anterolateral fossa for the lacrimal gland. Their convex cerebral surfaces are marked by frontal gyri and faint grooves for meningeal vessels. On each side, the trochlear fovea (or spine) for attachment of a fibrocartilaginous trochlea through which the tendon of superior oblique plays, lies below and behind the medial end of the supraorbital margin, midway between the supraorbital notch and frontolacrimal suture.

The quadrilateral ethmoidal notch is occupied by the cribriform plate of the ethmoid bone. Inferior to its lateral margins, the bone articulates with the labyrinths of the ethmoid bone, and impressions of the ethmoidal air cells can be seen on this surface. Two transverse grooves across each margin are converted into anterior and posterior ethmoidal canals by articulation with the ethmoid bone; these canals open on the medial orbital wall and transmit the anterior and posterior ethmoidal nerves and vessels. The posterior borders of the orbital plates are thin and serrated, and articulate with the lesser wings of the sphenoid; their lateral parts usually appear in the middle cranial fossa between the greater and lesser wings of the sphenoid.

The frontal sinuses are two irregular cavities that ascend posterolaterally for a variable distance between the frontal laminae. They are separated by a thin septum and usually deflected from the median plane, so that they are rarely symmetric. The sinuses are variable in size and usually larger in males. Their openings lie anterior to the ethmoidal notch and lateral to the nasal spine, and each communicates with the middle meatus in the ipsilateral nasal cavity by a frontonasal canal.

The frontal sinuses are rudimentary at birth and can barely be distinguished. They show a primary expansion with eruption of the first deciduous molars at about 18 months, and again when the permanent molars begin to appear in the sixth year. Growth is slow in the early years but it can be detected radiographically by 6 years. They reach full size after puberty, although, with advancing age, osseous absorption may lead to further enlargement. Their degree of development appears to be linked to the prominence of the superciliary arches, which is thought to be a response to masticatory stresses. The frontal sinuses are described in Chapter 39.

Ossification

The frontal bone is ossified in fibrous mesenchyme from two primary centres that appear in about postfertilization week 8, one near each frontal tuber. Ossification extends superiorly, to form half of the main part of the bone; posteriorly, to form the orbital part; and inferiorly, to form nasal parts. Two secondary centres for the nasal spine appear about the tenth year. At birth, the bone consists of two halves. The median suture usually closes in the first postnatal year but may persist as the metopic suture in a small percentage of individuals (see Fig. 34.8A).

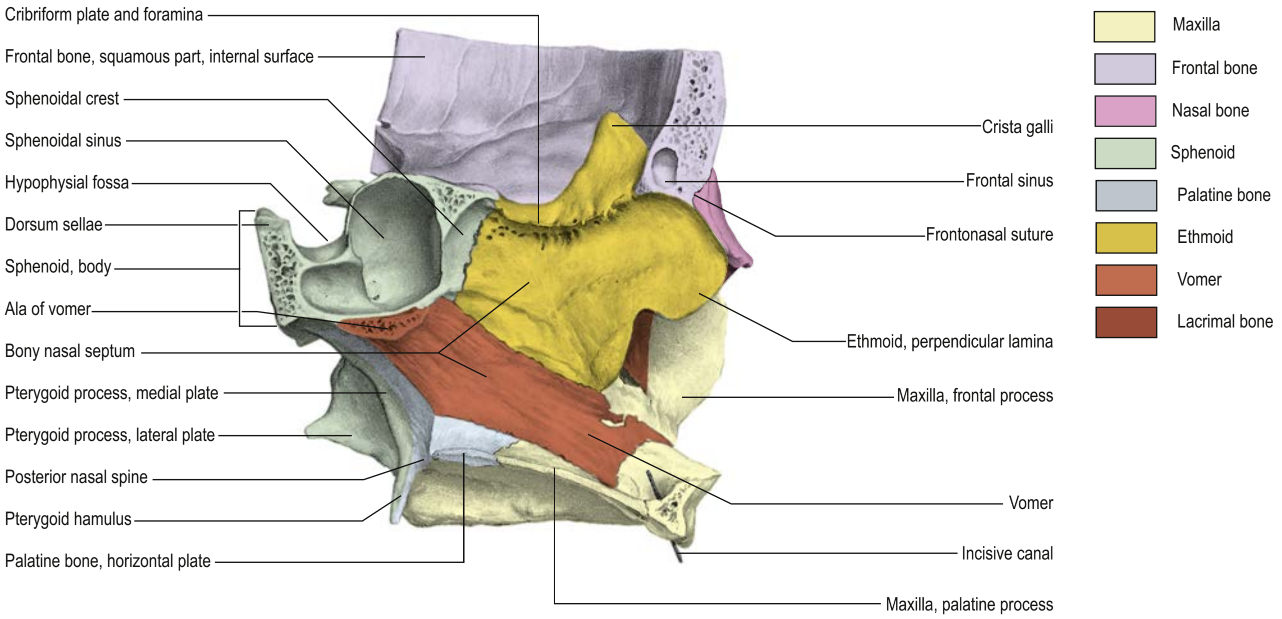

Fig. 36.4 Sagittal view of the facial skeleton, viewed from the right side of the nasal septum, looking towards the left. (Sobotta Atlas of Human Anatomy © Elsevier GmbH, Urban & Fischer, Munich.)

Ethmoid bone

The ethmoid bone is cuboidal and fragile (Figs 36.3B, 36.4–36.6). It lies anteriorly in the cranial base and contributes to the medial walls of the orbit, the nasal septum, and the roof and lateral walls of the nasal cavity. It has a horizontal perforated cribriform plate, a median perpendicular plate, and two lateral labyrinths that contain the ethmoidal air cells.

Cribriform plate and crista galli

The cribriform plate fills the ethmoidal notch of the frontal bone and forms a large part of the nasal roof. It derives its name from the fact that it is penetrated by numerous foramina that transmit branches of the olfactory nerves and their associated meninges. A thick, smooth, triangular, median process, the crista galli, projects upwards from the centre of the cribriform plate. The falx cerebri is attached to its thin and curved posterior border, while its shorter, thick, anterior border articulates with the frontal bone by two small alae, so completing the foramen caecum. Its sides are generally smooth but may show slight bulges that are related to underlying ethmoidal air cells. On both sides of the crista galli, the cribriform plate is narrow and depressed, and is related to the gyrus rectus and the olfactory bulb that lie above it. On each side of the crista anteriorly, there is a small slit occupied by dura mater. Just anterolateral to the slit, a foramen transmits the anterior ethmoidal nerve and vessels to the nasal cavity. A groove runs forwards to the foramen caecum from the anterior ethmoidal canal.

Perpendicular plate

The perpendicular plate is thin, flat, quadrilateral and median. It descends from the cribriform plate to form the upper part of the nasal septum, usually deviating slightly from the midline. Its anterior border articulates with the nasal spine of the frontal bone and the crests of the nasal bones, and its posterior border articulates with the crest of the body of the sphenoid bone above and the vomer below. The thick inferior border is attached to the nasal septal cartilage. Its surfaces are smooth, except for above, where numerous grooves and canals that transmit filaments of the olfactory nerves lead to medial foramina in the cribriform plate.

Ethmoidal labyrinths

The ethmoidal labyrinths consist of thin-walled ethmoidal air cells between two vertical plates. The lateral surface (orbital plate) of the labyrinth is part of the medial orbital wall. The air cells are arranged in anterior and posterior groups separated by the basal lamella (the lateral attachment of the middle concha (turbinate) to the lamina papyracea). Historically the ethmoidal air cells sinuses were subdivided into anterior, middle and posterior ethmoidal air cells, but the nomenclature was inconsistent and confusing, and for clinical purposes, the middle group was incorporated into the anterior group (Stammberger and Kennedy 1995) (Ch. 39). On average, there are 11 anterior ethmoidal air cells, and 7 posterior. In the disarticulated bone, many air cells are open, but in life, and in the articulated skull, they are closed by proximity to adjoining bones, except where they open into the nasal cavity. The superior surface is crossed by two grooves that are converted into the anterior and posterior ethmoidal canals by the frontal bone and shows open air cells that are covered by the edges of the ethmoidal notch of the frontal bone. On the posterior surface, open air cells are covered by the sphenoidal conchae and the orbital process of the palatine bone. The posterior ethmoidal air cells are covered by a thin, smooth, oblong orbital plate that articulates superiorly with the orbital plate of the frontal bone, inferiorly with the maxilla and orbital process of the palatine bone, anteriorly with the lacrimal bone, and posteriorly with the sphenoid bone. The walls of the air cells lying anterior to the orbital plate are completed by the lacrimal bone and frontal process of the maxilla.

A thin, curved uncinate process, variable in size, projects posteroinferiorly from the labyrinth. The upper edge of this process is a medial boundary of the hiatus semilunaris in the middle meatus. The uncinate process appears in the medial wall of the maxillary sinus as it crosses the ostium of the maxillary sinus to articulate with the ethmoidal process of the inferior nasal concha.

The medial surface of the labyrinth forms part of the lateral nasal wall. It appears as a thin lamella that descends from the inferior surface of the cribriform plate and ends as the convoluted middle nasal concha. Superiorly, the surface contains numerous vertical grooves that transmit bundles of olfactory nerves. Posteriorly, it is divided by the narrow, oblique superior meatus, bounded above by the thin, curved superior nasal concha. Posterior ethmoidal air cells open into the superior meatus. The convex surface of the middle nasal concha extends along the entire medial surface of the labyrinth, anteroinferior to the superior meatus. Its lower edge is thick, and its lateral surface is concave and forms part of the middle meatus. The ethmoidal bulla (bulla ethmoidalis) consists of a group of the largest and least variable anterior ethmoidal cells on the lateral wall of the middle meatus, and opens into the meatus, either on the bulla or above it. A curved infundibulum extends up and forwards from the middle meatus and communicates with the anterior ethmoidal sinuses. It typically ascends as the frontonasal duct to include the drainage point for the frontal sinus. (The ethmoidal air cells are described further in Chapter 39.)

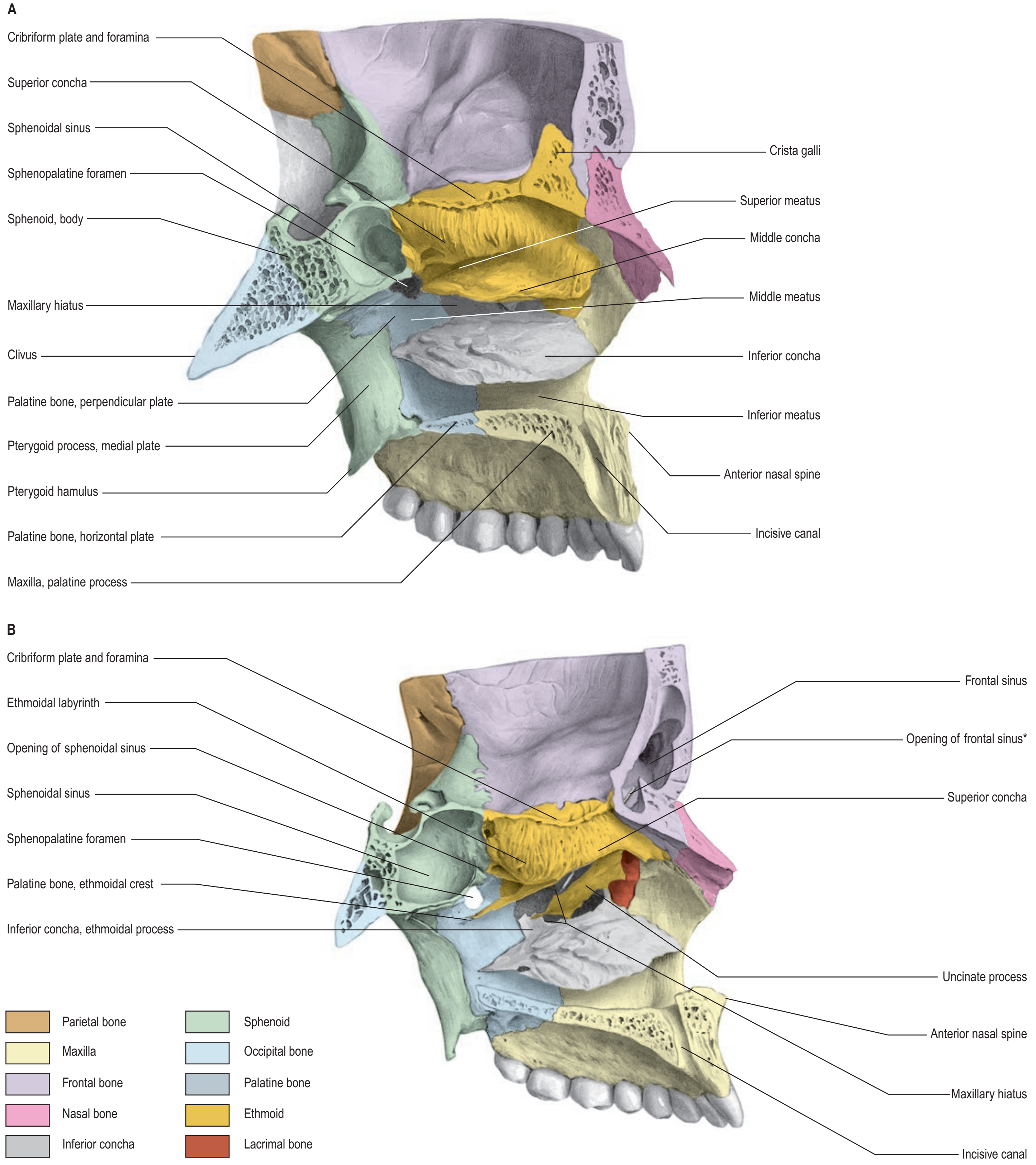
A
Cribriform plate and foramina
Superior concha
Sphenoidal sinus
Sphenopalatine foramen
Sphenoid, body
Maxillary hiatus
Clivus
Palatine bone, perpendicular plate
Pterygoid process, medial plate
Pterygoid hamulus
Palatine bone, horizontal plate
Maxilla, palatine process
Crista galli
Superior meatus
Middle concha
Middle meatus
Inferior concha
Inferior meatus
Anterior nasal spine
Incisive canal
B
Cribriform plate and foramina
Ethmoidal labyrinth
Opening of sphenoidal sinus
Sphenoidal sinus
Sphenopalatine foramen
Palatine bone, ethmoidal crest
Inferior concha, ethmoidal process
Frontal sinus
Opening of frontal sinus*
Superior concha
Uncinate process
Anterior nasal spine
Maxillary hiatus
Incisive canal
Parietal bone
Maxilla
Frontal bone
Nasal bone
Inferior concha
Sphenoid
Occipital bone
Palatine bone
Ethmoid
Lacrimal bone

* Probe located in the passage from the frontal sinus to the middle meatus

Fig. 36.5 A–B, Sagittal views of the facial skeleton, showing the floor of the anterior cranial fossa, the lateral wall of the nasal cavity, the hard palate and the sphenoidal air sinus. In **B**, the middle concha in the lateral wall of the nasal cavity has been removed to reveal the uncinate process. (Sobotta Atlas of Human Anatomy © Elsevier GmbH, Urban & Fischer, Munich.)

Ossification

The ethmoid bone ossifies in the cartilaginous nasal capsule from three centres: one in the perpendicular plate, and one in each labyrinth. The latter two appear in the orbital plates between postmenstrual weeks 13 and 20 and extend into the ethmoidal conchae. At birth, the labyrinths, although ill-developed, are partially ossified, and the remainder are cartilaginous. The perpendicular plate begins to ossify from the median centre during the first year, and fuses with the labyrinths early in the second year. The cribriform plate is ossified partly from the perpendicular plate and partly from the labyrinths. The crista galli ossifies during the second year. The parts of the ethmoid bone unite to form a single bone at around 3 years of age. Ethmoidal air cells begin to develop at about postmenstrual weeks 9–12, and are therefore present at birth; however,

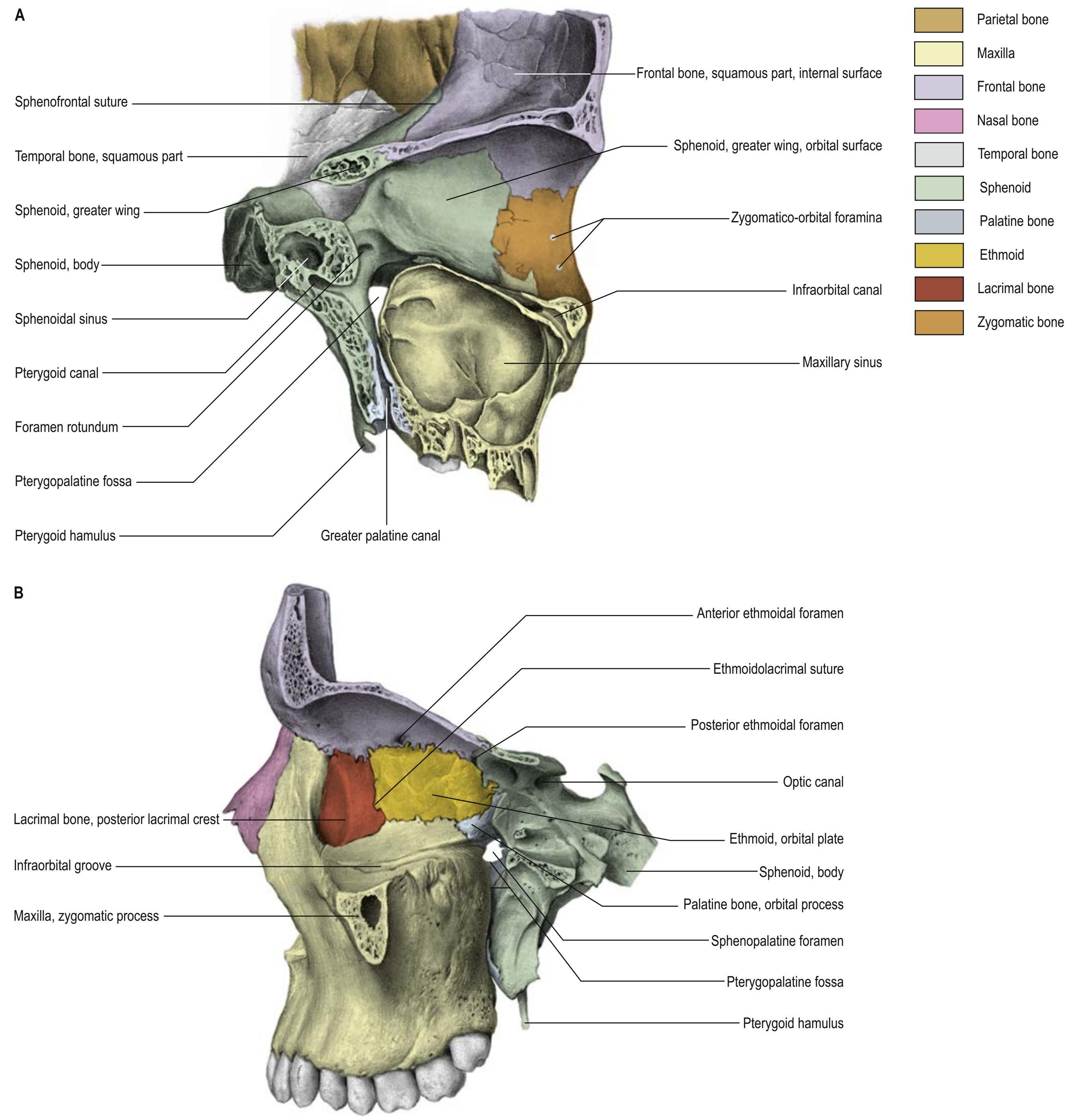
A
Sphenofrontal suture
Temporal bone, squamous part
Sphenoid, greater wing
Sphenoid, body
Sphenoidal sinus
Pterygoid canal
Foramen rotundum
Pterygopalatine fossa
Pterygoid hamulus
Greater palatine canal
Frontal bone, squamous part, internal surface
Sphenoid, greater wing, orbital surface
Zygomatico-orbital foramina
Infraorbital canal
Maxillary sinus
Parietal bone
Maxilla
Frontal bone
Nasal bone
Temporal bone
Sphenoid
Palatine bone
Ethmoid
Lacrimal bone
Zygomatic bone
B
Anterior ethmoidal foramen
Ethmoidolacrimal suture
Posterior ethmoidal foramen
Optic canal
Lacrimal bone, posterior lacrimal crest
Ethmoid, orbital plate
Infraorbital groove
Sphenoid, body
Maxilla, zygomatic process
Palatine bone, orbital process
Sphenopalatine foramen
Pterygopalatine fossa
Pterygoid hamulus

Fig. 36.6 **A**, Sagittal view of the facial skeleton, showing the bones forming the lateral wall of the left orbit and the maxillary air sinus. **B**, The bones forming the medial wall and the floor of the left orbit. (Sobotta Atlas of Human Anatomy © Elsevier GmbH, Urban & Fischer, Munich.)

they are difficult to visualize radiographically until the end of the first year. They grow slowly and have almost reached adult size by the age of 12 years.

Inferior nasal concha

The inferior nasal conchae are curved horizontal laminae in the lateral nasal walls (see Fig. 36.5). Each has two surfaces (medial and lateral), two borders (superior and inferior) and two ends (anterior and posterior). The medial surface is convex, much perforated, and longitudinally grooved by vessels. The lateral surface is concave and part of the inferior meatus. The superior border, thin and irregular, may be divided into three regions: an anterior region articulating with the conchal crest of the maxilla; a posterior region articulating with the conchal crest of the palatine bone; and a middle region with three processes, which are variable in size and form. The lacrimal process is small and pointed and lies towards the front. It articulates apically with a descending process from the lacrimal bone, and at its margins with the edges of the nasolacrimal groove on the medial surface of the maxilla, thereby helping to complete the nasolacrimal canal. Most posteriorly, a thin ethmoidal process ascends to articulate with the uncinate process of the ethmoid bone. An intermediate thin maxillary process curves inferolaterally to articulate with the medial surface of the maxilla at the opening of the maxillary sinus. The inferior border is thick and spongiose, especially in its mid part. The anterior and posterior ends of the inferior nasal concha are more or less tapered, the posterior more so than the anterior.

Ossification

The inferior nasal concha ossifies from one centre that appears at about postmenstrual weeks 17–20 in the incurved lower border of the cartilaginous lateral wall of the nasal capsule. The inferior concha loses continuity with the nasal capsule during ossification.

Lacrimal bone

The lacrimal bones are the smallest and most fragile of the cranial bones and lie anteriorly in the medial walls of the orbits (**Figs 36.5B**, **36.6B**). Each has two surfaces (medial and lateral) and four borders (anterior, posterior, superior and inferior). The lateral (orbital) surface is divided by a vertical posterior lacrimal crest. Anterior to the crest, the anterior edge of a vertical groove articulates with the posterior border of the frontal process of the maxilla to complete the fossa that houses the lacrimal sac. The medial wall of the groove is prolonged by a descending process that contributes to the formation of the nasolacrimal canal by articulating with the lips of the nasolacrimal groove of the maxilla and the lacrimal process of the inferior nasal concha. A smooth part of the medial orbital wall lies behind the posterior lacrimal crest; the lacrimal part of orbicularis oculi is attached to this surface and crest. The surface ends inferiorly in the lacrimal hamulus, which together with the maxilla completes the upper opening of the nasolacrimal canal. The hamulus can appear as a separate lesser lacrimal bone. The anteroinferior region of the medial (nasal) surface is part of the middle meatus. Its posterosuperior part articulates with the ethmoid to complete some of the anterior ethmoidal air cells. The anterior border of the lacrimal bone articulates with the frontal process of the maxilla, the posterior border with the orbital plate of the ethmoid bone, the superior border with the frontal bone, and the inferior border with the orbital surface of the maxilla.

Ossification

The lacrimal bone ossifies from a centre that appears at about postmenstrual week 12 in mesenchyme around the nasal capsule. In later life, the lacrimal bone is subject to patchy erosion.

Nasal bone

The nasal bones are small, oblong, variable in size and form, and placed side by side between the frontal processes of the maxillae, jointly forming the nasal bridge (see Figs 36.4, 36.5, 36.6B). Each nasal bone has two surfaces (external and internal) and four borders (superior, inferior, lateral and mesial). The external surface has a descending concavo-convex profile and is transversely convex. It is covered by procerus and nasalis and perforated centrally by a small foramen that transmits a vein. The internal surface, transversely concave, bears a longitudinal groove that houses the anterior ethmoidal nerve. The superior border, thick and serrated, articulates with the nasal part of the frontal bone. The inferior border, thin and notched, is attached to the lateral nasal cartilage. The lateral border articulates with the frontal process of the maxilla. The medial border, thicker above, articulates with its fellow and projects behind as a vertical crest, so forming a small part of the nasal septum. It articulates from above with the nasal spine of the frontal bone, the perpendicular plate of the ethmoid bone, and the nasal septal cartilage.

Ossification

The nasal bone ossifies from a centre that appears about postmenstrual week 12 in the mesenchyme overlying the cartilaginous anterior part of the nasal capsule.

Vomer

The vomer is thin, flat and almost trapezoid (see Fig. 36.4). It forms the posteroinferior part of the nasal septum and presents two surfaces and four borders. Both surfaces are marked by grooves for nerves and vessels. A prominent groove for the nasopalatine nerve and vessels lies obliquely in an anteroinferior plane. The superior border is thickest, and possesses a deep furrow between projecting alae, which fits and articulates with the rostrum of the body of the sphenoid bone. The alae articulate with the sphenoidal conchae, the vaginal processes of the medial pterygoid plates of the sphenoid bone, and the sphenoidal processes of the palatine bones. Where each ala lies between the body of the sphenoid and the vaginal process, its inferior surface helps to form the vomerovaginal canal. The inferior border articulates with the median nasal crests of the maxilla and palatine bones. The anterior border is the longest and articulates in its upper half with the perpendicular plate of the ethmoid bone. Its lower half is cleft to receive the inferior margin of the nasal septal cartilage. The concave posterior border is thick and bifid superiorly and thin inferiorly and separates the posterior nasal apertures. The anterior extremity of the vomer articulates with the posterior margin of the maxillary incisor crest and descends between the incisive canals.

Inability to identify the vomer during antenatal ultrasound scanning in the first and early second trimesters of pregnancy has been suggested as a marker for trisomy 13 or 21, with a diagnostic accuracy of 0.985 (Mihailovic et al 2012).

Ossification

The nasal septum is initially a plate of cartilage, part of which is ossified superiorly to form the perpendicular plate of the ethmoid. Its anteroinferior region persists as septal cartilage. The vomer is ossified in a layer of connective tissue that covers the cartilage posteroinferiorly on each aspect. At about postfertilization week 8, two centres appear flanking the midline. In postmenstrual week 12 these unite below the cartilage to form a deep groove for the nasal septal cartilage. Union of the bony lamellae progresses anterosuperiorly while the intervening cartilage is absorbed. By puberty, the lamellae are almost united, but evidence of their bilaminar origin remains in the everted alae and anterior marginal groove.

Zygomatic bone

Each zygomatic bone forms the prominence of a cheek, contributes to the floor and lateral wall of the orbit, and the walls of the temporal and infratemporal fossae and completes the zygomatic arch. Each is roughly quadrangular and is described as having three surfaces, five borders and two processes (**Fig. 36.7**).

The lateral (facial) surface is convex and is pierced near its orbital border by the zygomaticofacial foramen that is often double and occasionally absent: when present, it transmits the zygomaticofacial nerve and

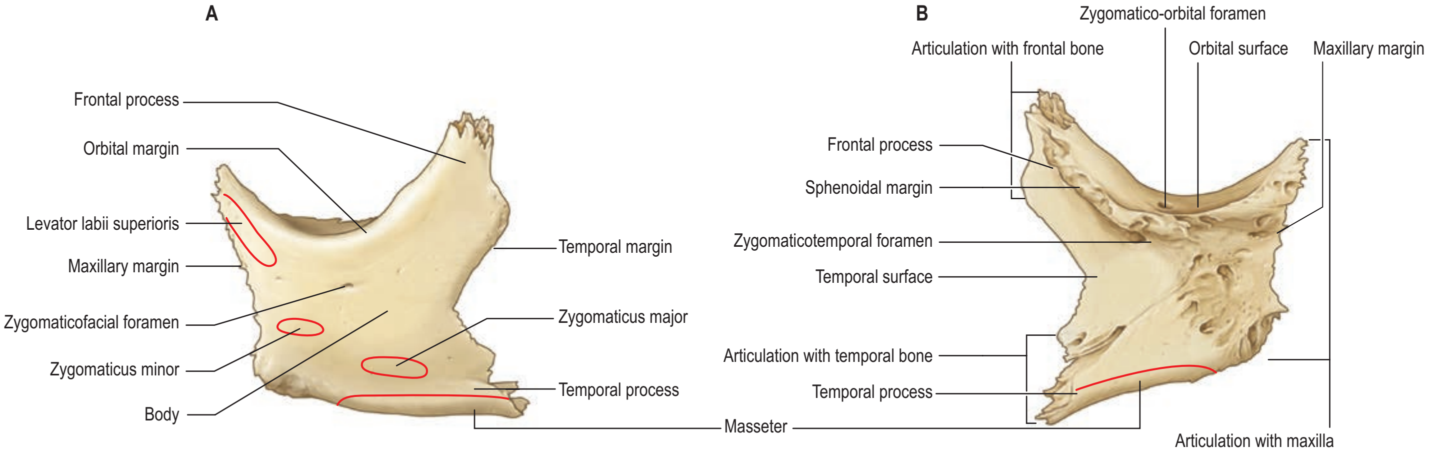

Fig. 36.7 The zygomatic bone. **A**, Anterolateral aspect, showing muscle attachments. **B**, Posterolateral aspect.

vessels. This surface gives attachment to zygomaticus major posteriorly and zygomaticus minor anteriorly. The posteromedial (temporal) surface has a rough anterior area for articulation with the zygomatic process of the maxilla and a smooth, concave posterior area that extends up posteriorly on its frontal process as the anterior aspect of the temporal fossa. It also extends back on the medial aspect of the temporal process as an incomplete lateral wall for the infratemporal fossa. The zygomaticotemporal foramen pierces this surface near the base of the frontal process. The smooth and concave orbital surface forms the anterolateral part of the floor and adjoining lateral wall of the orbit and extends up on the medial aspect of its frontal process. It usually bears zygomatico-orbital foramina that represent the openings of canals leading to the zygomaticofacial and zygomaticotemporal foramina.

The smoothly concave anterosuperior (orbital) border forms the inferolateral circumference of the orbital opening and separates the orbital and lateral surfaces of the bone. The anteroinferior (maxillary) border articulates with the maxilla. Its medial end tapers to a point above the infraorbital foramen. A part of levator labii superioris is attached at this surface. The posterosuperior (temporal) border is sinuous, convex above and concave below, and is continuous with the posterior border of the frontal process and upper border of the zygomatic arch. The temporal fascia is attached to this border. There is often a small, easily palpable, marginal tubercle below the frontozygomatic suture. The posteroinferior border is roughened for the attachment of masseter. The serrated posteromedial border articulates with the greater wing of the sphenoid bone superiorly, and the orbital surface of the maxilla inferiorly. Between these serrated regions a short, concave, nonarticular part usually forms the lateral edge of the inferior orbital fissure: this part is occasionally absent, in which case the fissure is completed by the articulation of the maxilla and sphenoid (or with a small sutural bone between them).

The frontal process, thick and serrated, articulates superiorly with the zygomatic process of the frontal bone and posteriorly with the greater wing of the sphenoid. A tubercle of varying size and form, Whitnall's tubercle, is usually present on its orbital aspect, within the orbital opening and about 1 cm below the frontozygomatic suture. This tubercle provides attachment for the lateral palpebral ligament, the suspensory ligament of the eye, and part of the aponeurosis of levator palpebrae superioris (Ch. 44). The temporal process, directed backwards, has an oblique, serrated end that articulates with the zygomatic process of the temporal bone to complete the zygomatic arch.

Ossification

The zygomatic bone ossifies from one centre that appears in fibrous tissue about postfertilization week 8. The bone is sometimes divided by a horizontal suture into a larger upper and smaller lower part.

Maxilla

The maxillae jointly form the whole of the upper jaw. Each bone forms the greater part of the floor and lateral wall of the nasal cavity, and of the floor of the orbit; contributes to the infratemporal and pterygopalatine fossae; and bounds the inferior orbital and pterygomaxillary fissures. Each maxilla has a body and four processes, namely: the zygomatic, frontal, alveolar and palatine processes (see Fig. 36.6; **Fig. 36.8**).

Body

The body of the maxilla is roughly pyramidal, and has anterior, infratemporal (posterior), orbital and nasal surfaces that enclose the maxillary sinus.

Anterior surface

The anterior surface faces anterolaterally and displays inferior elevations overlying the roots of teeth. There is a shallow incisive fossa above the incisors to which depressor septi is attached. A slip of orbicularis oris is attached to the alveolar border below this fossa, and nasalis is attached superolateral to it. Lateral to the incisive fossa is a larger, deeper canine fossa; levator anguli oris is attached to the bone of this fossa. The incisive and canine fossae are separated by the canine eminence overlying the socket of the canine tooth. The infraorbital foramen lies above the fossa and transmits the infraorbital vessels and nerve. Above the foramen, a sharp border separates the anterior and orbital surfaces of the bone and contributes to the infraorbital margin. Levator labii superioris is attached here above the infraorbital foramen and levator anguli oris is attached below it. Medially, the anterior surface ends at a deeply concave nasal notch, terminating in a pointed process that, with its contralateral fellow, forms the anterior nasal spine. Nasalis and depressor septi are attached to the anterior surface near the notch.

Infratemporal surface

The infratemporal surface is concave and faces posterolaterally, forming the anterior wall of the infratemporal fossa. It is separated from the anterior surface by the zygomatic process and a ridge (jugal crest) that ascends to it from the first molar socket. Near its centre are the openings of two or three alveolar canals that transmit posterior superior alveolar vessels and nerves. Posteroinferior is the maxillary tuberosity, roughened superomedially where it articulates with the pyramidal process of the palatine bone. A few fibres of medial pterygoid are attached here. Above the tuberosity, the smooth anterior boundary of the pterygopalatine fossa is grooved by the maxillary nerve as it passes laterally and slightly upwards into the infraorbital groove on the orbital surface.

Orbital surface

The orbital surface is smooth and triangular and forms most of the floor of the orbit. Anteriorly, its medial border bears a lacrimal notch, behind which it articulates with the lacrimal bone, the orbital plate of the ethmoid and, posteriorly, with the orbital process of the palatine bone. Its posterior border is smoothly rounded and forms most of the anterior edge of the inferior orbital fissure. The infraorbital groove lies centrally. The anterior border is part of the orbital margin and it articulates medially with the lacrimal crest of the frontal process of the maxilla. The infraorbital groove transmits the infraorbital vessels and nerve, and begins midway on the posterior border, where it is continuous with a groove on the posterior surface. It passes forwards into the infraorbital canal, which opens on the anterior surface below the infraorbital margin. Near its midpoint, the infraorbital canal gives off a small lateral branch, the canalis sinuosus, that transmits the anterior superior alveolar nerve and vessels. The canalis sinuosus descends in the orbital floor lateral to the infraorbital canal, curves medially in the anterior wall of the maxillary sinus, and then passes below the infraorbital foramen to the margin of the anterior nasal aperture in front of the anterior end of the inferior concha. It follows the lower margin of the aperture and opens near the nasal septum in front of the incisive canal. The site of the attachment of inferior oblique may be indicated by a small depression in the bone at the anteromedial corner of the orbital surface, lateral to the lacrimal groove.

Nasal surface

The nasal surface displays posterosuperiorly a large, irregular maxillary hiatus that leads into the maxillary sinus. Parts of air sinuses that are completed by articulation with the ethmoid and lacrimal bones lie at the upper border of the hiatus. The smooth concave surface below the hiatus is part of the inferior meatus. Posteriorly, the surface is roughened where it articulates with the perpendicular plate of the palatine bone. This surface is traversed by a groove that descends forwards from the mid-posterior border and is converted into a greater palatine canal by the perpendicular plate. Anterior to the hiatus, a deep nasolacrimal groove, continuous above with the lacrimal groove, makes up about two-thirds of the circumference of the nasolacrimal canal. The rest is contributed by the descending part of the lacrimal bone and the lacrimal process of the inferior nasal concha. The nasolacrimal canal conveys the nasolacrimal duct to the inferior meatus. More anteriorly, an oblique conchal crest articulates with the inferior nasal concha. The concavity below it is part of the inferior meatus, while the surface above it is part of the atrium of the middle meatus.

Zygomatic process

Anterior, infratemporal and orbital surfaces of the maxilla converge at a pyramidal projection, the zygomatic process. Anteriorly, this process merges into the facial surface of the body of the maxilla; posteriorly, it is concave and continuous with the infratemporal surface; superiorly, it is roughly serrated for articulation with the zygomatic bone; and inferiorly, a bony arched ridge, the zygomatico-alveolar ridge or jugal crest, separates the facial (anterior) and infratemporal surfaces.

Frontal process

The frontal process projects posterosuperiorly between the nasal and lacrimal bones. Its lateral surface is divided by a vertical anterior lacrimal crest that gives attachment to the medial palpebral ligament and is continuous below with the infraorbital margin. A small, palpable tubercle at the junction of the crest and orbital surface is a guide to the lacrimal sac. The smooth area anterior to the lacrimal crest merges below with the anterior surface of the body of the maxilla. Parts of orbicularis oculi and levator labii superioris alaeque nasi are attached here. Behind the

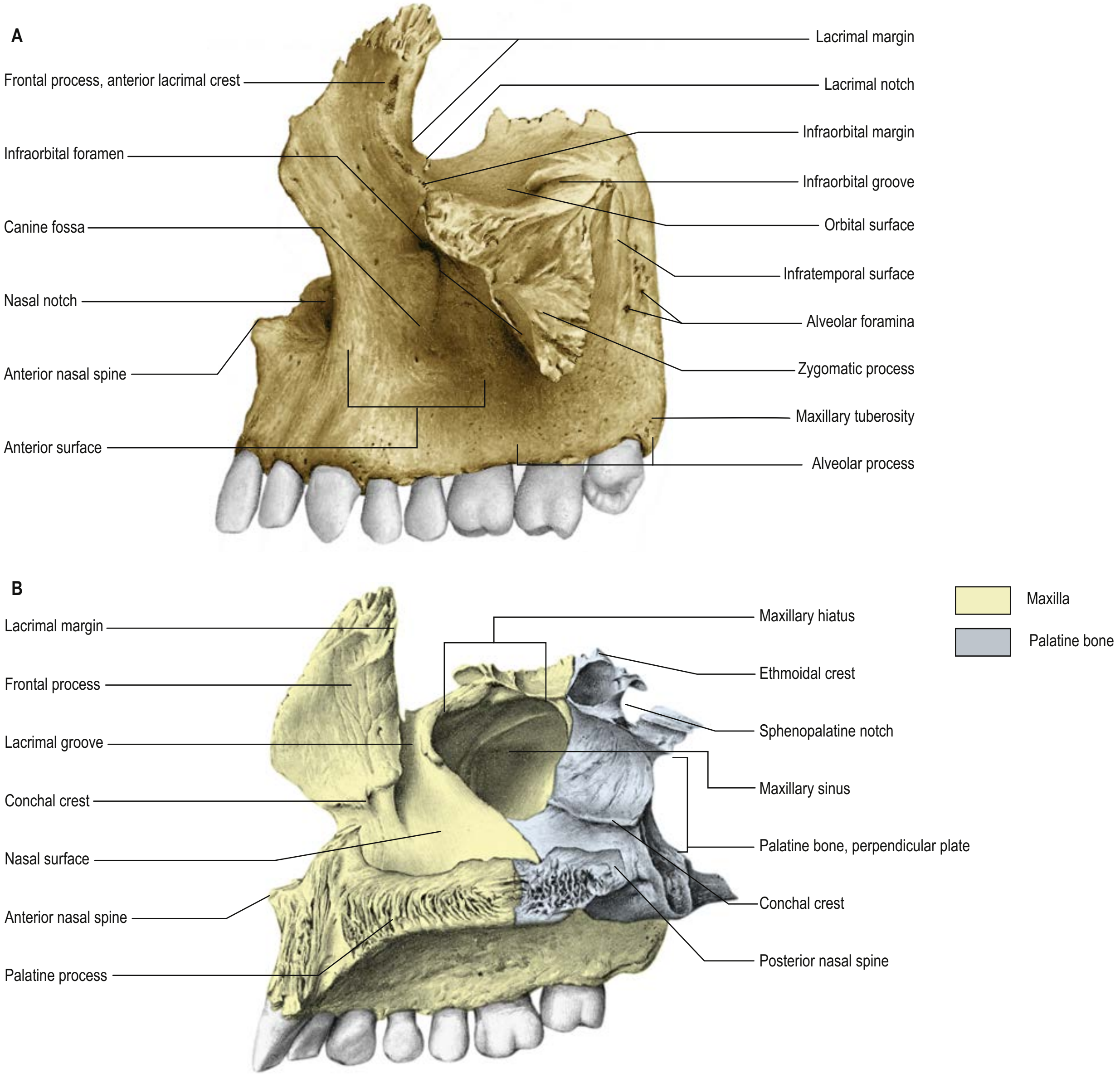
A
Frontal process, anterior lacrimal crest
Infraorbital foramen
Canine fossa
Nasal notch
Anterior nasal spine
Anterior surface
Lacrimal margin
Lacrimal notch
Infraorbital margin
Infraorbital groove
Orbital surface
Infratemporal surface
Alveolar foramina
Zygomatic process
Maxillary tuberosity
Alveolar process
B
Lacrimal margin
Frontal process
Lacrimal groove
Conchal crest
Nasal surface
Anterior nasal spine
Palatine process
Maxillary hiatus
Ethmoidal crest
Sphenopalatine notch
Maxillary sinus
Palatine bone, perpendicular plate
Conchal crest
Posterior nasal spine
Maxilla
Palatine bone

Fig. 36.8 **A**, The maxilla, lateral view. **B**, The maxilla and palatine bone, medial view. (Sobotta Atlas of Human Anatomy © Elsevier GmbH, Urban & Fischer, Munich.)

crest, a vertical groove combines with a groove on the lacrimal bone to complete the lacrimal fossa. The medial surface is part of the lateral nasal wall. A rough subapical area articulates with the ethmoid and closes the anterior ethmoidal air cells. Below this, an oblique ethmoidal crest articulates posteriorly with the middle nasal concha, and anteriorly underlies the agger nasi, a ridge anterior to the concha on the lateral nasal wall. The ethmoidal crest forms the upper limit of the atrium of the middle meatus. The frontal process articulates above with the nasal part of the frontal bone, its anterior border articulates with the nasal bone and its posterior border articulates with the lacrimal bone.

Alveolar process

The alveolar process is thick and arched, wide posteriorly, and socketed for the roots of the upper teeth. The eight sockets on each side vary according to the tooth type. The socket for the canine is deepest, the sockets for the molars are widest and subdivided into three by septa, those for the incisors and second premolar are single, and the socket for the first premolar is usually double. Buccinator is attached to the external alveolar aspect as far forwards as the first molar. In articulated maxillae, the processes form the alveolar arch. Occasionally, a variably prominent maxillary torus is present in the midline of the palate.

Palatine process

The palatine process is thick and horizontal and projects medially from the lowest part of the medial aspect of the maxilla. It forms a large part of the nasal floor and hard palate and is much thicker anteriorly. Its inferior surface is concave and uneven, and with its contralateral fellow it forms the anterior three-quarters of the osseous (hard) palate. The palatine process displays numerous vascular foramina and depressions for palatine glands; posterolaterally, two grooves transmit the greater palatine vessels and nerves. The infundibular incisive fossa is placed between the two maxillae, behind the incisor teeth. The median intermaxillary palatal suture runs posterior to the fossa, and although a little uneven, is usually relatively flat on its oral aspect. Its bony margins are sometimes raised into a prominent longitudinal palatine torus. Two lateral incisive canals, each ascending into its half of the nasal cavity, open in the incisive fossa and transmit the terminations of the greater palatine artery and nasopalatine nerve. Two additional median openings, anterior and posterior incisive foramina, are occasionally present; they transmit the nasopalatine nerves, the left nerve usually passes through the anterior foramen, and the right nerve usually passes through the posterior foramen. On the inferior palatine surface, a fine groove (the incisive suture), extending anterolaterally from the incisive fossa to the interval between the lateral incisor and canine teeth, is prominent in young skulls and can be observed in adult skulls. The superior surface of the palatine process is smooth and concave transversely, and forms most of the nasal floor. The incisive canal lies anteriorly, near its median margin. The lateral border is continuous with the body of the maxilla. The medial border, thicker anteriorly, is raised into a nasal crest that, with its contralateral fellow, forms a groove for the vomer. Anteriorly, this ridge rises higher as an incisor crest, prolonged forwards into a sharp process that, with its fellow, forms an anterior nasal spine. The posterior border is serrated for articulation with the horizontal plate of the palatine bone.

Maxillary sinus

The maxillary sinus is the largest of the paranasal sinuses and is situated in the body of the maxilla. It is described in detail in Chapter 39.

Ossification

The maxilla and premaxilla have primary ossification centres from postfertilization week 7 and three further centres in postfertilization week 8. The pattern of spread of ossification can initially leave an unmineralized zone roughly corresponding to a site where a premaxillary suture can occur. However, this deficiency is soon ossified, and there is no evidence of a separate centre of ossification for the incisor-bearing portion of the maxilla (premaxilla).

The maxillary sinus appears as a shallow groove on the nasal aspect at about postmenstrual weeks 13–16. Though small at birth, the sinus is identifiable radiologically. After birth, it enlarges with the growing maxilla, though it is only fully developed following the eruption of the permanent dentition. The infraorbital vessels and nerve are, for a time, in an open groove in the orbital floor; the anterior part of the groove is subsequently converted into a canal by a lamina that grows in from the lateral side.

At birth, the transverse and sagittal maxillary dimensions are greater than the vertical. The frontal process is prominent, but the body is little more than an alveolar process because the alveoli reach almost to the orbital floor. In adults, the vertical dimension is the greatest, reflecting the development of the alveolar process and enlargement of the sinus. When teeth are lost, the bone reverts towards its infantile shape; its height diminishes, the alveolar process is absorbed, and the lower parts of the bone contract and become reduced in thickness at the expense of the labial wall.

Palatine bone

The palatine bones are posteriorly placed in the nasal cavity, between the maxillae and the pterygoid processes of the sphenoid bones. They contribute to the floor and lateral walls of the nose, to the floor of the orbit and the hard palate, to the pterygopalatine and pterygoid fossae, and to the inferior orbital fissures. Each has two plates (horizontal and perpendicular), arranged as an L-shape, and three processes (pyramidal, orbital and sphenoidal) (**Fig. 36.9**).

Horizontal plate

The horizontal plate is quadrilateral, with two surfaces (nasal and palatine) and four borders (anterior, posterior, lateral and medial). The nasal surface, transversely concave, forms the posterior nasal floor. The palatine surface articulates with its contralateral fellow to form the posterior quarter of the bony palate. There is often a curved palatine crest near its posterior margin. The posterior border is thin and concave; the expanded tendon of tensor veli palatini is attached to it and to its adjacent surface posterior to the palatine crest. Medially, articulating with its contralateral fellow, the posterior border forms a median posterior nasal spine to which musculus uvulae is attached. The anterior border is serrated and articulates with the palatine process of the maxilla. The lateral border is continuous with the perpendicular plate of the palatine bone and is marked by a greater palatine groove. The medial border is thick and serrated, and articulates with its contralateral fellow in the midline, forming the posterior part of the nasal crest that articulates with the posterior part of the lower edge of the vomer.

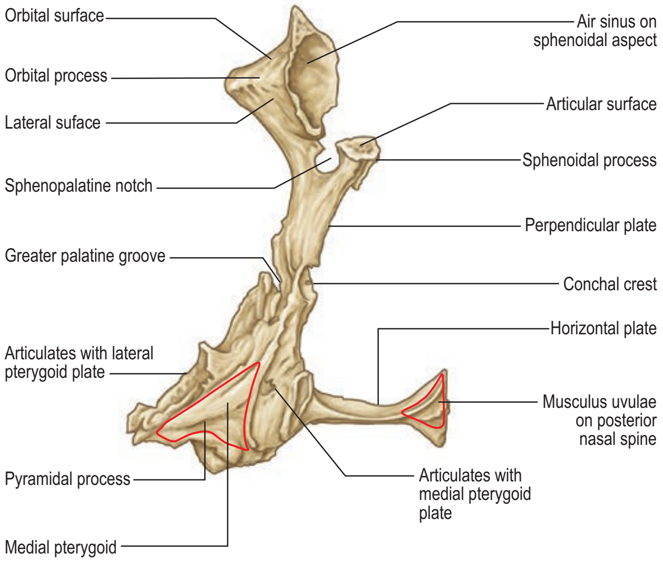

Fig. 36.9 The palatine bone, posterior view.

Perpendicular plate

The perpendicular plate is thin and oblong and has two surfaces (nasal and maxillary) and four borders (anterior, posterior, superior and inferior) (see Figs 36.8B, 36.9). The nasal surface bears two crests (conchal and ethmoidal) and shows areas that contribute to the inferior, middle and superior meatuses. Inferiorly, the nasal surface is concave where it contributes to part of the inferior meatus. Superiorly, a horizontal conchal crest articulates with the inferior concha. Above the conchal crest, the surface presents a shallow depression that forms part of the middle meatus; it is limited superiorly by an ethmoidal crest for the middle nasal concha, above which a narrow, horizontal groove forms part of the superior meatus.

The maxillary surface is largely rough and irregular and articulates with the nasal surface of the maxilla. Posterosuperiorly, it forms a smooth medial wall to the pterygopalatine fossa. Its anterior area, also smooth, overlaps the maxillary hiatus from behind to form a posterior part of the medial wall of the maxillary sinus. A deep, obliquely descending greater palatine groove (converted into a canal by the maxilla) lies posteriorly on this maxillary surface and transmits the greater palatine vessels and nerve.

The anterior border is thin and irregular. Level with the conchal crest, a pointed lamina projects below and behind the maxillary process of the inferior concha; it articulates with it and so appears in the medial wall of the maxillary sinus. The posterior border articulates via a serrated suture with the medial pterygoid plate. It is continuous above with the sphenoidal process of the palatine bone and expands below into its pyramidal process. Orbital and sphenoidal processes project from the superior border and are separated by the sphenopalatine notch, which is converted into a foramen by articulation with the body of the sphenoid. This foramen connects the pterygopalatine fossa to the posterior part of the superior meatus and transmits sphenopalatine vessels and the posterior superior nasal nerves. The inferior border is continuous with the lateral border of the horizontal plate and bears the lower end of the greater palatine groove anterior to the pyramidal process.

Pyramidal process

The pyramidal process slopes down posterolaterally from the junction of the horizontal and perpendicular palatine plates into the angle between the pterygoid plates of the sphenoid bone. On its posterior surface, a smooth, grooved triangular area, limited on each side by rough articular furrows that articulate with the pterygoid plates, completes the lower part of the pterygoid fossa. Anteriorly, the lateral surface articulates with the maxillary tuberosity. This area gives attachment to fibres of the superficial head of medial pterygoid. Posteriorly, a smooth triangular area appears low in the infratemporal fossa between the tuberosity and the lateral pterygoid plate. The inferior surface, near its union with the horizontal plate, bears the lesser palatine foramina that transmit the lesser palatine nerves and vessels.

Orbital process

The orbital process is directed superolaterally from in front of the perpendicular plate and has a constricted ‘neck’. It encloses an air sinus and presents three articular and two non-articular surfaces. Of the articular surfaces, the oblong anterior (maxillary) surface faces down and anterolaterally and articulates with the maxilla. The posterior (sphenoidal) surface is directed up and posteromedially and bears the opening of an air sinus. It usually communicates with the sphenoidal sinus and is completed by a sphenoidal concha. The medial (ethmoidal) surface faces anteromedially and articulates with the labyrinth of the ethmoid bone. The sinus of the orbital process sometimes opens on the surface and communicates with the posterior ethmoidal air cells. More rarely, it opens on both the ethmoidal and sphenoidal surfaces, and communicates with the posterior ethmoidal air cells and the sphenoidal sinus.

Of the non-articular surfaces, the triangular superior (orbital) surface is directed superolaterally to the posterior part of the orbital floor. The lateral surface is oblong, faces the pterygopalatine fossa, and is separated from the orbital surface by a rounded border that forms a medial part of the lower margin of the inferior orbital fissure. This surface may present a groove, directed superolaterally, for the maxillary nerve, and is continuous with the groove on the upper posterior surface of the maxilla. The border between the lateral and posterior surfaces descends anterior to the sphenopalatine notch.

Sphenoidal process

The sphenoidal process is a thin plate that is smaller and lower than the orbital process, and is directed superomedially. Its superior surface articulates with the sphenoidal concha and, above it, with the root of the medial pterygoid plate. It carries a groove that contributes to the formation of the palatovaginal canal. The concave inferomedial surface forms part of the roof and lateral wall of the nasal cavity. Posteriorly, the lateral surface articulates with the medial pterygoid plate, while its smooth anterior region forms part of the medial wall of the pterygopalatine fossa. The posterior border articulates with the vaginal process of the medial pterygoid plate. The anterior border is the posterior edge of the sphenopalatine notch. The medial border articulates with the ala of the vomer.

Ossification

The palatine bone ossifies in mesenchyme from one centre in the perpendicular plate that appears during postfertilization week 8. From this centre, ossification spreads into all parts. At birth, the height of the perpendicular plate equals the width of the horizontal plate, but in adults it is almost twice as great, a change in proportions that accords with those that occur in the maxilla.

Fractures of the facial skeleton

Trauma to the face is common; outcomes are related to the mechanism of the injury in terms of its severity and to delays in treatment. Both soft and hard tissues are affected. Moderate to severe injuries produce facial skeletal disruption that compromises masticatory and orbital function. Inadequate skeletal support of soft tissues contributes to facial asymmetry and the additional loss of soft tissues and subsequent scarring merely compound this. Some fractures pass through foramina, damage branches of the trigeminal nerve and result in sensory deficits. Fracture configurations vary according to the amount of energy absorbed and local anatomical factors that constitute sites of weakness. The direction and magnitude of the applied forces determine the displacement of these fractures, which are modified according to muscle attachments and the state of the dentition, e.g. an unerupted mandibular third molar may produce a weak point at the mandibular angle.

Lateral pterygoid frequently displaces a fractured mandibular condyle medially. Masseter, temporalis and medial pterygoid can stabilize fractures of the mandible when vertically or horizontally favourable, but displace those that are vertically and horizontally unfavourable. Severe injuries to the middle third of the face may result in craniofacial dysjunction, the middle third sliding inferiorly down the angulated and strong anterior skull base, causing an apparent lengthening of the face and a dish-faced appearance. Airway obstruction may result from this downward and backward displacement. Fractures of the anterior mandible may cause loss of support of the muscles controlling the anterior tongue position and may also contribute to loss of the airway.

Although the fractures caused by severe injuries are often complex, it is convenient to describe them as arising in the upper, middle and lower thirds of the face, even though fractures may involve one or more of these areas. Upper third fractures involve the frontal bones. Middle third fractures involve the nasoethmoidal complex, orbit, zygomatic complex and maxilla. Lower third fractures correspond to fractures of the mandible.

Upper third of face

Available with the *Gray's Anatomy* e-book

Middle third of face

Available with the *Gray's Anatomy* e-book

Lower third of face (mandible)

Available with the *Gray's Anatomy* e-book

Campbell's lines

Available with the *Gray's Anatomy* e-book.

Cranial base

Available with the *Gray's Anatomy* e-book.

Skeletal access surgery

Available with the *Gray's Anatomy* e-book.

MUSCLES OF THE FACE

Craniofacial muscles are associated with the orbital margins and eyelids, external nose and nostrils, lips, cheeks and mouth, pinna, scalp and cervical skin, and collectively are often called, not very accurately, 'muscles of facial expression' (Fig. 36.17). Their organization differs from that of muscles in most other regions of the body because there is no deep membranous fascia beneath the skin of the face, and many small slips of muscle that are attached to the facial skeleton insert directly into the skin.

Although these muscles produce movements of the facial skin that reflect emotions, it is usually argued that their primary function is to act as sphincters and dilators of the facial orifices and that the function of facial expression has developed secondarily. Embryologically, they are derived from the mesenchyme of the second branchial arch and so are innervated by the facial nerve. Topographically and functionally, the muscles of facial expression may be subdivided into epicranial, circumorbital and palpebral, nasal, and buccolabial groups (Fig. 36.18).

Epicranial muscle group

Epicranius

Epicranius consists of occipitofrontalis and temporoparietalis.

Occipitofrontalis

Occipitofrontalis covers the dome of the skull from the highest nuchal lines to the eyebrows. It is a broad, musculofibrous layer and consists of four thin, muscular quadrilateral parts, two occipital and two frontal, connected by the epicranial aponeurosis. Each occipital part (occipitalis) arises by tendinous fibres from the lateral two-thirds of the highest nuchal line of the occipital bone and the adjacent region of the mastoid part of the temporal bone to extend forward and join the aponeurosis. The gap between the two occipital parts is occupied by an extension of the epicranial aponeurosis. Each frontal part (frontalis) is adherent to the superficial fascia, particularly of the eyebrows. Although frontalis has no bony attachments of its own, its fibres blend with those of adjacent muscles, procerus, corrugator supercilii and orbicularis oculi, and ascend to join the epicranial aponeurosis anterior to the coronal suture.

Vascular supply Occipitofrontalis is supplied by branches of the superficial temporal, ophthalmic, posterior auricular and occipital arteries.

Innervation The occipital part of occipitofrontalis is supplied by the posterior auricular branch of the facial nerve. The frontal part is supplied by the temporal branches of the facial nerve.

Actions Acting from above, the frontal parts raise the eyebrows and the skin over the root of the nose (e.g. as in expressions of surprise or horror). Acting from below, the frontal parts draw the scalp forwards, throwing the forehead into transverse wrinkles. The occipital parts draw the scalp backwards. Acting alternately, the occipital and frontal parts can move the entire scalp backwards and forwards.

Variations A thin muscular slip, transversus nuchae, is sometimes present. It arises from the external occipital protuberance or from the superior nuchal line, either superficial or deep to trapezius and is frequently inserted with auricularis posterior but may blend with the posterior edge of sternocleidomastoid.

Epicranial aponeurosis

The epicranial aponeurosis covers the upper part of the cranium and, with the epicranial muscle, forms a continuous fibromuscular sheet that extends from the occiput to the eyebrows. Posteriorly, between the occipital

Fractures in the upper third of the face are almost invariably comminuted and are often associated with fractures of the middle third of the face. Fractures of the frontal bone may involve the frontal sinuses and/or orbital roof. If the frontonasal duct is traumatized, its drainage may be impaired predisposing to ascending intracranial infection and mucocele development within the frontal sinuses (Eljamel and Foy 1990; **Fig. 36.10**). This risk may be minimized with frontonasal stents or frontonasal duct and frontal sinus obliteration with autogenous bone graft. Fractures that involve both the anterior and the posterior walls of the frontal sinus also carry a risk of early and delayed intracranial infection, and it is often necessary to obliterate the frontal sinuses or cranialize the frontal sinuses in order to prevent this complication. Cranialization of the frontal sinuses involves the removal of the posterior wall and all frontal sinus mucosa, typically through a frontal craniotomy approach. Fractures of the posterior wall of the frontal sinus may be associated with dural tears (and cerebrospinal rhinorrhoea) that must be repaired at the same time. Fractures involving the orbital roof may be associated with displacement of the globe of the eye, diplopia and supraorbital nerve injury.

The middle third of the face is defined as that area bounded above by a transverse line connecting the two zygomaticofrontal sutures, passing through the frontomaxillary and frontonasal sutures, and limited below by the occlusal plane of the maxillary teeth. Posteriorly, the region is limited by the sphenoethmoidal junction, but it includes the free margins of the pterygoid plates inferiorly. Fractures of the middle third of the facial skeleton (Le Fort 1901) may involve the maxillae, palatine bones, zygomatic bones, zygomatic processes of the temporal bones, nasal bones, vomer, ethmoid bone together with its nasal conchae, and the body and greater and lesser wings of the sphenoid bone. A classification system that subdivides the fractures into central block fractures and those that involve the lateral middle third is now largely of historical value but finds use as an initial description that is later elaborated by defining extensions of the fracture pattern into the upper third and the cranium.

Central middle third of face

The majority of the skeleton of the central middle third is composed of wafer-thin sheets of cortical bone with stronger reinforcements, i.e. the palate and alveolar process; the lateral rim of the piriform aperture extending upwards (via the canine fossa) to the medial orbital rim, and finally to the glabella; the zygomatic buttress and its connections to the inferior and lateral orbital margins and the zygomatic arch; and the orbital rims and the pterygoid plates. Whatever the fracture configuration, pterygoid plate disruption is seen in all examples of maxillary fracture. The strength lies in the facial surface of the skeleton, which, although thin in most areas, is cross-braced. The design is ideally suited to transmit occlusal forces vertically to the cranial base.

Central middle third fractures may involve the nasoethmoidal complex in isolation or as part of a more complex Le Fort pattern of injury. Le Fort I, II or III fractures inevitably involve the infratemporal fossa. The bones of the midface transmit the forces of impact directly to the cranium. The most important strut related to the infratemporal and pterygopalatine fossae is the pterygomaxillary strut. Fractures involving this strut may extend elsewhere to involve the cranial base and orbit. The associated soft tissue damage that accompanies these fractures may damage nerves, blood vessels and muscles. Injuries to the maxillary or mandibular divisions of the trigeminal nerve or the chorda tympani nerve result in altered sensation to the oral cavity, face and jaws, including impaired taste. Fractures extending into the orbit may result in decreased visual acuity, ophthalmoplegia and neural damage to motor nerves. Direct damage to muscles may result in problems with chewing, swallowing, speech, middle ear function and eye movements. Injuries involving the pterygopalatine or otic ganglia interfere with lacrimation, nasal secretions and salivation. Facial deformity with lack of nasal projection, asymmetry and occlusal disturbance and vertical and anteroposterior malposition of the globe, are frequent outcomes of middle third fractures.

Nasoethmoidal complex Fractures can involve the osteocartilaginous framework of the nose in isolation or as part of complex injuries that also involve the paranasal sinuses and/or the orbits (**Fig. 36.11**).

Simple fractures involve the nasal bones and/or frontal process of the maxilla. Only if there is displacement of the bones is a closed reduction of the fracture required. The terminal branch of the anterior ethmoidal nerve and its accompanying vessels are at risk when injuries involve the dorsum of the nose.

Complex nasal injuries may include nasofrontal suture disjunction, nasolacrimal and frontonasal duct injury, and fracture of the ethmoidal complex (Markowitz et al 1991). The skeletal foundation of the nasoethmoidal complex consists of a strong triangular-shaped frame. However, all these structures are fragile and any force sufficient to fracture the frame results in severe comminution and displacement. The ethmoidal air cells act as a crumple zone protecting the cranial base from mechanical forces. A severe impact delivered to the midface, particularly over the bridge of the nose, may result in these structures being driven backwards between the orbits and may result in traumatic hypertelorism, producing an increase in distance between the pupils. Associated displacement of the medial canthal ligaments results in traumatic telecanthus. Increased intercanthal distance may be corrected using microplates, stainless steel

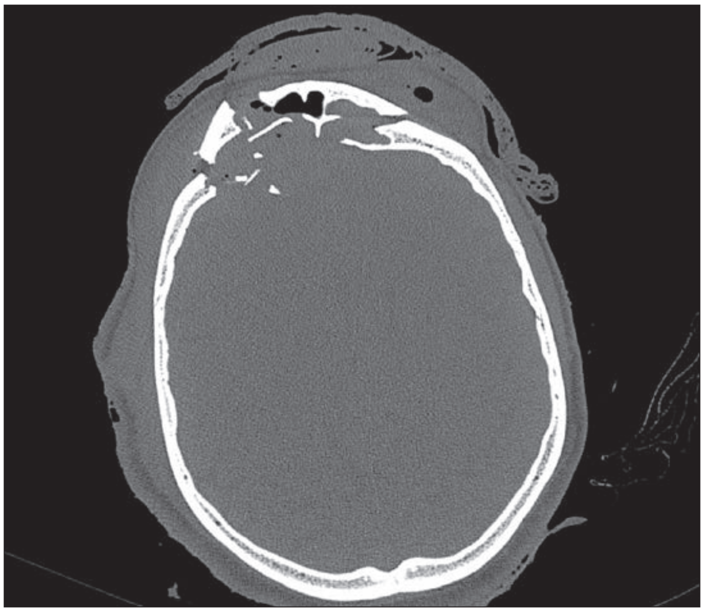

Fig. 36.10 An axial CT of a compound craniofacial fracture with disruption of the anterior and posterior walls of the frontal sinus, torn dura and intracranial bone. Treatment is directed at establishing a safe sinus, i.e. sealing off the frontonasal duct and removing all traces of sinus epithelium. It is also important to establish an intact fronto-orbital bar, to enable an accurate scaffold on which to attach the root of the nose and midface, if implicated in the fracture pattern, and to assure good cosmesis.

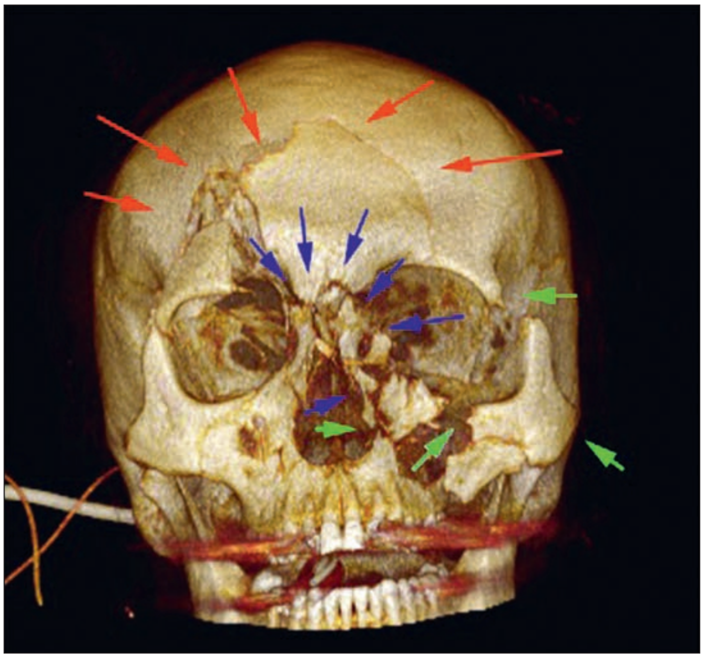

Fig. 36.11 An extended naso-orbito-ethmoid (NOE) fracture. The frontal sinus and frontal bone fracture (red arrows) need to be reconstructed to provide a stable platform for the NOE. The NOE fracture (blue arrows) extends into the anterior maxilla and blends with the extended comminuted zygomatic fracture (green arrows).

wire and acrylic canthal splints. Damage to the lacrimal system requires approximation of the severed canalicular ends or dacryocystorhinostomy. Comminution of the cribriform plates of the ethmoid bone may result in dural tears and cerebrospinal rhinorrhoea. Nasoethmoidal fractures are often combined with more extensive fractures of the frontal bone. The complexity of the injury has implications for subsequent facial reconstruction (Fig. 36.12).

Le Fort I fractures (Guerin's fracture) Le Fort I fractures consist of a horizontal fracture line above the level of the floor of the nose involving the lower third of the nasal septum. The mobile segment consists of the palate, the alveolar process and the lower thirds of the pterygoid plates.

Le Fort II fractures (pyramidal fracture) Le Fort II fractures are pyramidal fractures involving the maxillary bones. From the nasal bridge, the fracture enters the medial wall of the orbit to involve the lacrimal bone and then crosses the inferior orbital rim, usually at the junction of the medial one-third and lateral two-thirds, and often involves the infraorbital foramen. The fracture line then runs beneath the zygomaticomaxillary suture, traversing the lateral wall of the maxillary sinus to extend posteriorly and horizontally across the pterygoid plates. The zygomatic bones and arches remain attached to the skull.

Le Fort III fractures Le Fort III fractures separate the entire midfacial skeleton from the cranial base. The fracture extends through the nasal base, continues posteriorly across the ethmoid bone and then crosses the lesser wing of the sphenoid and, on occasion, involves the optic foramen. Usually, it slopes down medially, passing below the optic foramen to reach the pterygomaxillary fissure and pterygopalatine fossa. From the base of the inferior orbital fissure the fracture runs laterally and upwards, separating the greater wing of the sphenoid from the zygomatic bone to reach the frontozygomatic suture. It also extends downwards and backwards across the pterygopalatine fossa to involve the root of the pterygoid plates. The zygomatic arch is usually fractured at the zygomaticotemporal suture (Le Fort 1901). Open reduction and internal fixation are conducted through aesthetically favourable incisions in the hairline, upper eyelid, oral cavity and lower eyelid (subciliary and transconjunctival) (Fig. 36.13).

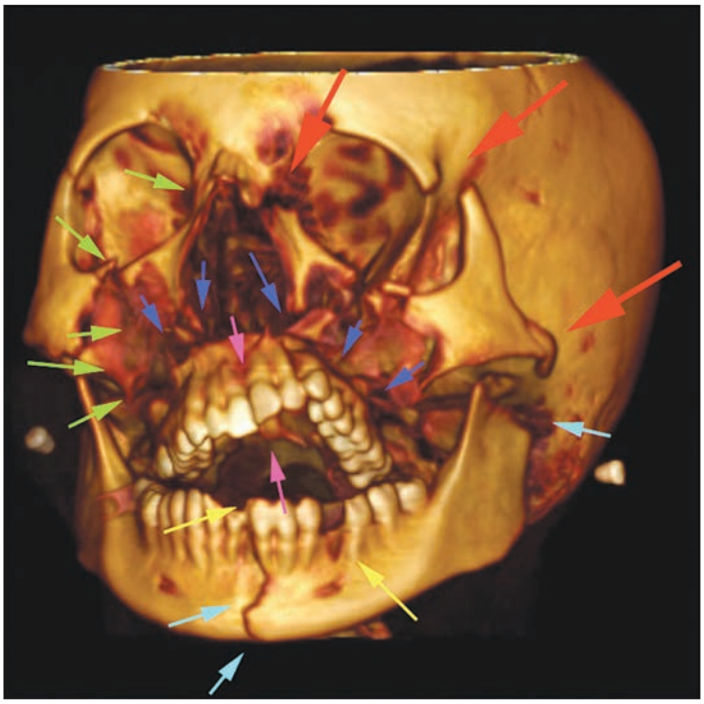

Fig. 36.12 A typical high-energy pan-facial injury. This injury demonstrates several complicated levels of Le Fort type maxillary fracture. The red arrows demonstrate the Le Fort III pattern (although the major fragment is further comminuted). The green arrows demonstrate the Le Fort II pattern, and the dark blue arrows demonstrate the Le Fort I pattern, although the maxilla is itself fractured sagittally (purple arrows). There are also bilateral condylar neck fractures and a mandibular symphysial fracture (light blue arrows). Note the avulsed lower left premolar and dental fracture of the right incisor (yellow arrows). Exclusion of inhaled dental teeth and fragments is important.

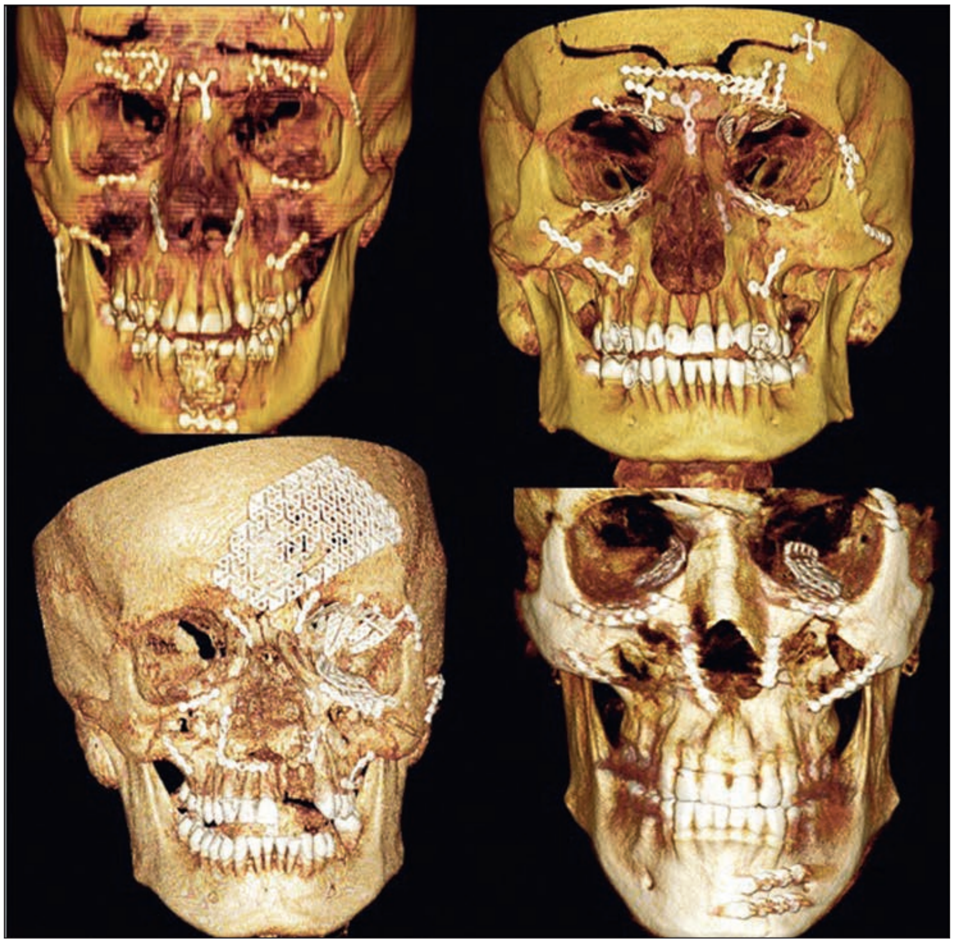

Fig. 36.13 Various examples of plating configurations and titanium alloplastic reconstructions. The aim of surgery is to reconstruct anatomy in order to provide a scaffold on which to overlay the soft tissues.

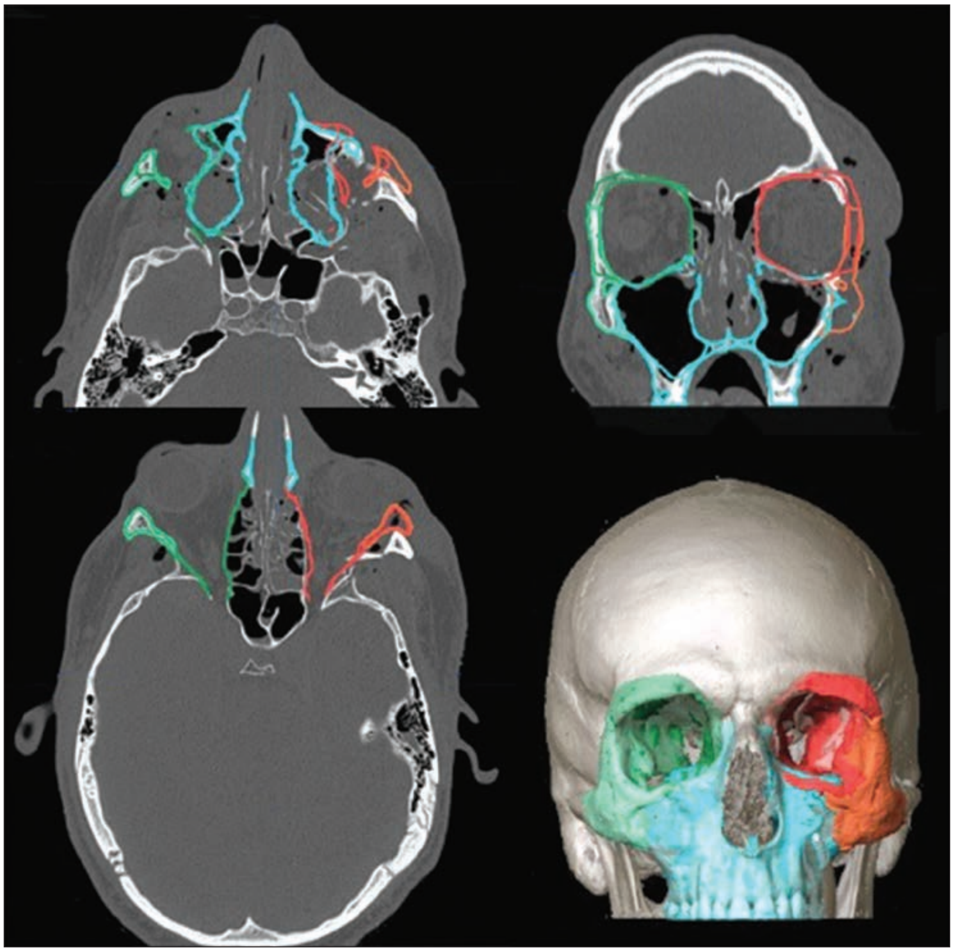

Fig. 36.14 A typical left zygomatic fracture. In this case, navigation planning takes the normal green right side and mirrors to the left. The red and orange outlines indicate where the bone should be. Axial and coronal CTs plus volume rendered reconstruction.

Lateral middle third of face

Fractures of the lateral middle third involve the zygomaticomaxillary complex (Fig. 36.14). The zygomatic bone forms the prominence of the cheek. Since the most common cause of a zygomatic fracture is a blow from a fist, depressed fractures of the zygomaticomaxillary complex are a common injury. These injuries may be sustained in isolation or in association with orbital blowout fractures. Isolated zygomatic arch fractures from a well-directed lateral blow are also common. Classic zygomatic complex fractures involve the zygomaticomaxillary, zygomaticotemporal, zygomaticofrontal and sphenozygomatic sutures. The fracture line extends from the lateral wall of the orbit laterally into the infratemporal fossa at the zygomaticofrontal suture. From this point, it extends inferiorly to join the most lateral aspect of the inferior orbital fissure and continues inferiorly along the posterior surface of the zygomatic buttress, where it communicates with the lateral bulge of the maxillary sinus (antrum). It then runs around the zygomatic buttress, high in the buccal sulcus in the upper molar region to extend upwards towards the infraorbital foramen. It finally runs laterally along the floor of the orbit to reach the lateral extension of the inferior orbital fissure. Clinical signs may include facial asymmetry, infraorbital nerve paraesthesia/anaesthesia, limitation of mouth opening (if there is impingement of the coronoid process by a depressed arch fracture) and signs of orbital blowout fracture (see below).

As zygomatic fractures involve the maxillary sinus (the lateral wall of which is frequently comminuted) and the infratemporal fossa, there is potential for spread of infection between these structures and then via foramina in the cranial base to the middle cranial fossa. Patients with zygomatic complex fractures must be advised to refrain from sneezing or nose-blowing, which may force air from the sinus into the surrounding tissues (surgical emphysema) or into the orbit, resulting in proptosis of the eye. While the zygoma may be reduced transorally (the Keen approach), or via the brow (Dingman approach), or a cheek-hook technique (Poswillo approach), it is perhaps the Gillies temporal approach that is worthy of mention here because it exploits the anatomy of the region (Gillies et al 1927). The incision is hidden in the hairline and the approach depends on the fact that the superior temporal fascia is attached to the superior temporal line of the skull superiorly and the zygomatic arch inferiorly, and that temporalis runs under the arch. An incision through the temporalis fascia, but not through the muscle, allows a metal elevator to be passed from the hairline to the zygomatic arch and body. Outward traction, coupled with rotation, allows precise localization of the bone.

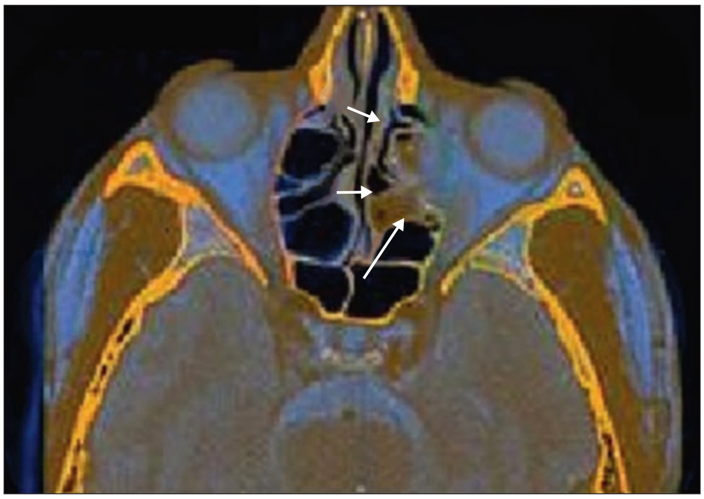

Fig. 36.15 Image fusion of computed tomography and magnetic resonance imaging, showing an extensive left medial orbital wall fracture (arrows). There is obvious herniation of orbital contents and disruption of the soft tissue contents of the orbit.

Orbital fractures The orbit is invariably involved in fractures of the zygomatic bone and in Le Fort II and III fractures and can also be involved in fractures of the frontal bone and extensive nasal complex injuries. Direct blunt trauma to the globe may result in displacement of the globe and fracture of the thin orbital floor (or medial wall) without associated rim involvement and is known as a 'blowout' fracture (Ahmas et al 2006). This protective mechanism of injury helps to maintain the integrity of the globe in preference to the orbital walls. There may be associated herniation of periorbital fat (Fig. 36.15) and/or inferior rectus, resulting in restriction of eye movement, diplopia, ipsilateral lowering of pupillary height, and enophthalmos (due to increased orbital volume) (Manson et al 1986). Fortunately, the optic foramen, situated

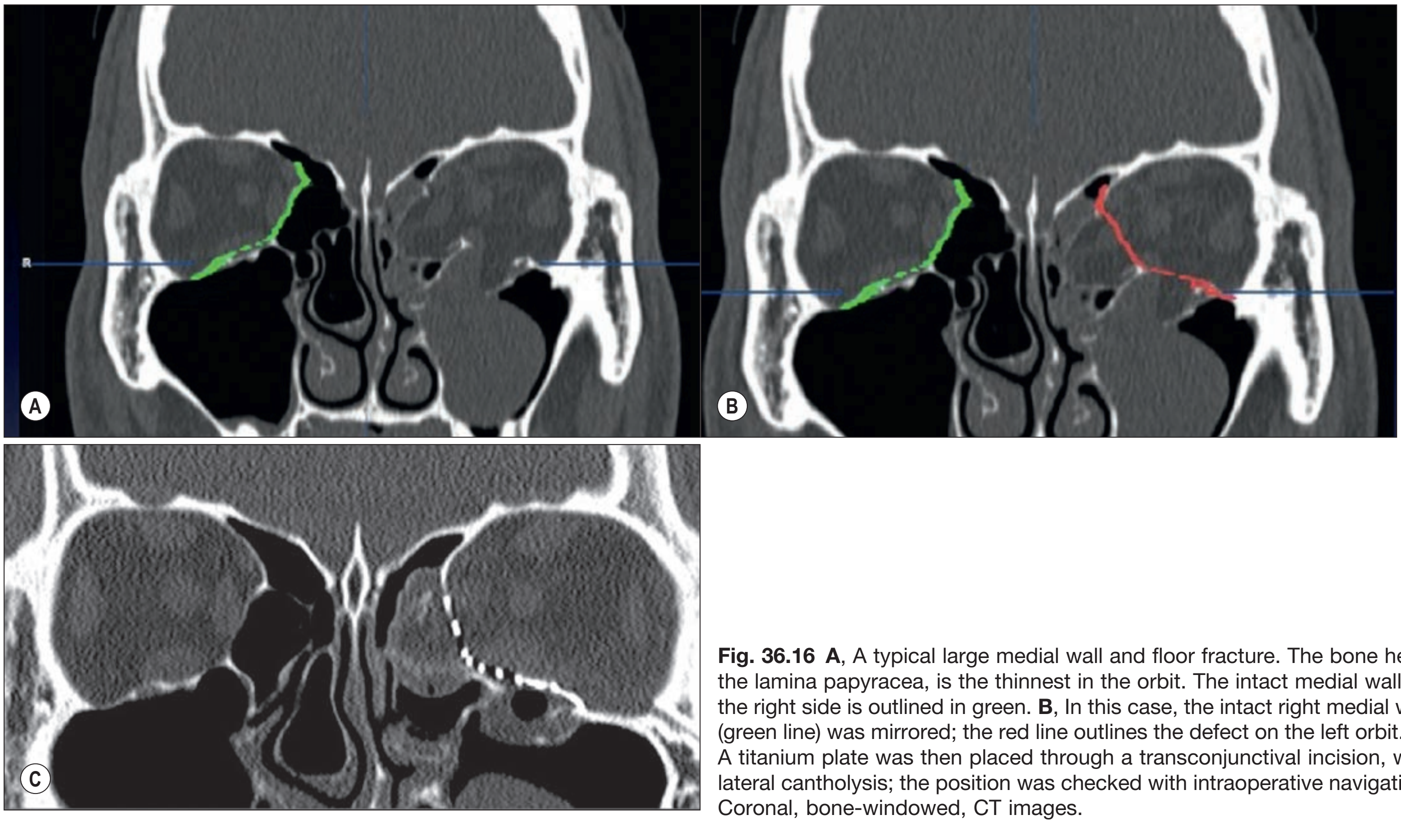

Fig. 36.16 **A**, A typical large medial wall and floor fracture. The bone here, the lamina papyracea, is the thinnest in the orbit. The intact medial wall on the right side is outlined in green. **B**, In this case, the intact right medial wall (green line) was mirrored; the red line outlines the defect on the left orbit. **C**, A titanium plate was then placed through a transconjunctival incision, with lateral cantholysis; the position was checked with intraoperative navigation. Coronal, bone-windowed, CT images.

within the lesser wing of the sphenoid bone, is surrounded by dense bone and is only rarely involved in fractures, which means that direct injury to the optic nerve is unusual. The orbital floor is normally repaired by the insertion of an alloplastic or autogenous graft (Fig. 36.16) (Ellis and Tan 2003).

The mandible is essentially a tubular bone bent into a blunt V shape (Ch. 37). This basic configuration is modified by sites of muscle attachment, principally masseter and medial pterygoid at the angle, and temporalis at the coronoid process. The presence of teeth, particularly those with long roots such as the canines, or of unerupted teeth, produces lines of weakness in the mandible. When the teeth are lost or fail to develop, the subsequent progressive resorption of the alveolar bone means that the mandible reverts to its underlying tubular structure. Like all tubular bones, the strength of the mandible resides in a dense cortical plate, thickened anteriorly and at its lower border, which means that the mandible is strongest anteriorly in the midline and is progressively weaker posteriorly towards the condylar processes. Again, like all tubular bones, the mandible has great resistance to compressive forces, but it fractures at sites of tensile strain. The mandible is liable to particular patterns of distribution of tensile strain when forces are applied to it. Anterior forces applied to the mental symphysis, or over the body of the mandible, lead to strain at the condylar necks and also along the lingual cortical plates on the contralateral side in the molar region. The mandible therefore often fractures at two sites and isolated fractures are relatively unusual. In order of frequency, fractures most commonly involve the neck of the condyle, the angle, the parasymphysial region and the body of the mandible.

Condylar process

The condyle is protected from direct injury by the zygomatic arches. Fractures are usually caused by transmission of force following a blow to the front of the mandible or to the contralateral mandibular body. Fractures are seen at all levels of the condyle (Loukota et al 2005). Except in children, most condylar fractures are not intracapsular but are sustained at the neck and usually run obliquely downwards and backwards from the mandibular notch. The condyle is usually displaced anteromedially (because of the attachment of lateral pterygoid to the temporomandibular joint disc, capsule and anterior border of the neck of the condyle). Most condylar fractures are managed by open reduction and early mobilization.

Angle of mandible

The majority of fractures of the mandible run posteriorly and inferiorly from the alveolar bone to the angle. The presence of a third molar tooth produces a line of weakness and a fracture line will pass through its socket. The unopposed pull of the powerful elevator muscles (masseter, medial pterygoid and temporalis) will typically displace the posterior fragment superiorly, anteriorly and medially.

Ramus and coronoid process

Fractures at the ramus exhibit very little displacement as a consequence of the splinting activity of medial pterygoid medially and masseter laterally (pterygomasseteric sling); their wide attachments to the ramus extend across the fracture lines. Similarly, the coronoid process is rarely displaced significantly because it is splinted by the tendinous insertion of temporalis.

Body of mandible

Most fractures of the body of the mandible are sustained as the result of direct trauma and tend to be concentrated in the first molar or canine region. The more anterior the site of the fracture, the more the upward displacement of the elevators is counteracted by the downward pull of geniohyoid and the anterior belly of digastric. When teeth are present, displacement is limited by the dental occlusion (i.e. further displacement is resisted by the lower and upper teeth), whereas displacement may be considerable in an edentulous patient.

Campbell's lines are five lines that are systematically traced when assessing maxillofacial radiographs. Line 1 joins the two zygomaticofrontal sutures, runs along the superior orbital margins and crosses the midline in the region of the glabella. Line 2 runs along the zygomatic bone and the inferior orbital margin, crosses the frontal process of the maxilla and lateral wall of the nose, and then passes through the nasal septum to follow a similar course to the contralateral zygomatic bone. Line 3 begins at the condyle of the mandible, passes across the mandibular notch and coronoid process of the mandible, then crosses the maxillary sinus from its lateral to medial walls and continues through the lateral wall of the nose at the level of the nasal floor; it follows a similar course on the contralateral side. Line 4 follows the occlusal plane of the upper and lower teeth, and line 5 follows the lower border of the mandible.

The cranial base, regarded clinically as the frontal, ethmoid, sphenoid and occipital bones, is a relatively solid platform inclined at an angle of 45° to the maxillary occlusal plane. Fractures of the cranial base are not readily visible on normal radiographs and are best detected on CT scans. They result in bleeding in the floor of the middle cranial fossa, which often presents as bruising over the mastoid process (Battle's sign). These fractures may be associated with dural tears and escape of cerebrospinal fluid from the nose (rhinorrhoea) or ruptured tympanic membrane (otorrhoea). If the tympanic membrane remains intact, it may appear as blue and bulging (haemotympanum).

The craniofacial skeleton has an excellent blood supply and so can be dismantled as a series of osteoplastic flaps. The surgical disarticulation of the craniofacial skeleton has been used to gain access to otherwise inaccessible sites in order to allow the surgeon to attend to pathology in the skull base, cervical spine and anterior and posterior cranial fossae. The aim is to provide increased and more direct exposure of both the pathology and the adjacent vital structures without the need to resect uninvolved structures. The craniofacial skeleton can be divided into a series of modular osteotomies that permit both independent and conjoined mobilization.

The zygomatic and nasal bones and the maxilla may be exposed, mobilized and pedicled on the overlying soft tissues either unilaterally or bilaterally. These approaches improve access to the nasal cavity, maxillary, ethmoidal and sphenoidal sinuses, the soft palate and nasopharynx, and the infratemporal fossa and pharyngeal space. The exposures may be extended to gain access to the anterior and middle cranial fossae, cavernous sinus, clivus, craniocervical junction and upper cervical vertebrae.

A variety of different access osteotomies have been described and found to be useful in specific clinical situations. Most of the osteotomies described follow the conventional patterns of facial fractures described above. The entire hemimaxilla and zygoma can be mobilized, and pedicled on the soft tissues of the face by making bone cuts that follow the lines of a Le Fort II fracture on one side. The osteotomy is completed by dividing the upper alveolus and palate just to the side of the nasal septum and perpendicular plate of the vomer. The maxilla can be mobilized at the Le Fort I level and down-fractured, pedicled on the palatoglossal muscles and soft tissue attachments, giving good access to the nasopharynx, clivus and upper cervical spine, particularly if the palate is divided in the midline.

Lateral zygomatic osteotomies may be performed to gain access to the orbital apex and infratemporal fossa. The surgical approach is from behind using a hemi- or bicoronal flap. The zygomatic complex is mobilized inferiorly, pedicled on masseter. When combined with a mandibular ramus osteotomy, access is gained to the retromaxillary area and pterygoid space as well as to the infratemporal fossa. In combination with a frontotemporal craniotomy, the zygomatic osteotomy has been used for access to the middle cranial fossa, cavernous sinus, apex of the petrous temporal bone and the interpeduncular cistern.

Dividing the lower lip in the midline and dividing the mandible either in the midline or just in front of the mental foramen, allows the hemi-mandible to be swung laterally. The technique is used to give improved access to the floor of the mouth, the base of the tongue, tonsillar fossa, soft palate, oropharynx, posterior pharyngeal wall, supraglottic larynx and pterygomandibular region. By extending the dissection laterally, access is gained to the pterygoid space, infratemporal fossa and parapharyngeal space. By dissecting more medially, access is gained to the nasopharynx, lower part of the clivus and all seven of the cervical vertebrae. A modification of the mandibular swing procedure increases access up to the skull base, by combining the classic mandibular swing with a horizontal osteotomy of the mandibular ramus above the level of the lingula.

parts of occipitofrontalis, it is attached to the external protuberance and highest nuchal line of the occipital bone. Anteriorly, it splits to enclose the frontal parts and sends a short, narrow prolongation between them. Laterally, the anterior and superior auricular muscles are attached to it; the aponeurosis is thinner and continues over the temporal fascia to the zygomatic arch. It is united to the skin lying over the cranial vault by fibrous superficial fascia, but it is connected more loosely to the underlying pericranium by areolar tissue, an arrangement that allows it to move freely, carrying with it the skin of the scalp.

Temporoparietalis

Temporoparietalis is a variably developed sheet of muscle that lies between the frontal parts of occipitofrontalis and the anterior and superior auricular muscles.

Circumorbital and palpebral muscle group

The circumorbital and palpebral group of muscles are orbicularis oculi, corrugator supercilii and levator palpebrae superioris. The first two are described here; levator palpebrae superioris is described on page 773.

Orbicularis oculi

Orbicularis oculi is a broad, flat, elliptical muscle that surrounds the circumference of the orbit and spreads into the adjacent regions of the eyelids, anterior temporal region, infraorbital cheek and superciliary region (see Fig. 36.18). It has orbital, palpebral and lacrimal parts, and a small ciliary bundle.

The orbital part arises from the nasal component of the frontal bone, the frontal process of the maxilla and from the medial palpebral ligament. The fibres form complete ellipses, without interruption on the lateral side, where there is no bony attachment. The upper orbital fibres blend with the frontal part of occipitofrontalis and corrugator supercilii. Many of them are inserted into the skin and subcutaneous tissue of the eyebrow and constitute depressor supercilii. Inferiorly and medially, the ellipses overlap or blend to some extent with adjacent muscles (levator labii superioris alaeque nasi, levator labii superioris and zygomaticus minor). At the extreme periphery, sectors of complete, and sometimes incomplete, ellipses have a loose areolar connection with the temporal extension of the epicranial aponeurosis.

The palpebral part arises from the medial palpebral ligament, mainly from its superficial surface, and from the bone immediately above and below the ligament. The fibres sweep across the eyelids anterior to the orbital septum, interlacing at the lateral commissure to form the lateral palpebral raphe. A small group of fine fibres, close to the margin of each eyelid behind the eyelashes, constitutes the ciliary bundle.

The lacrimal part arises from the upper part of the lacrimal crest and the adjacent lateral surface of the lacrimal bone. It passes laterally behind the nasolacrimal sac (where some fibres are inserted into the associated fascia) and divides into upper and lower slips. Some fibres are inserted into the tarsi of the eyelids close to the lacrimal canaliculi, but most continue across in front of the tarsi and interlace in the lateral palpebral raphe.

Vascular supply Orbicularis oculi is supplied by branches of the facial, superficial temporal, maxillary and ophthalmic arteries.

Innervation Orbicularis oculi is supplied by temporal and zygomatic branches of the facial nerve.

Actions Orbicularis oculi is the sphincter muscle of the eyelids and plays an important role in facial expression and various ocular reflexes.

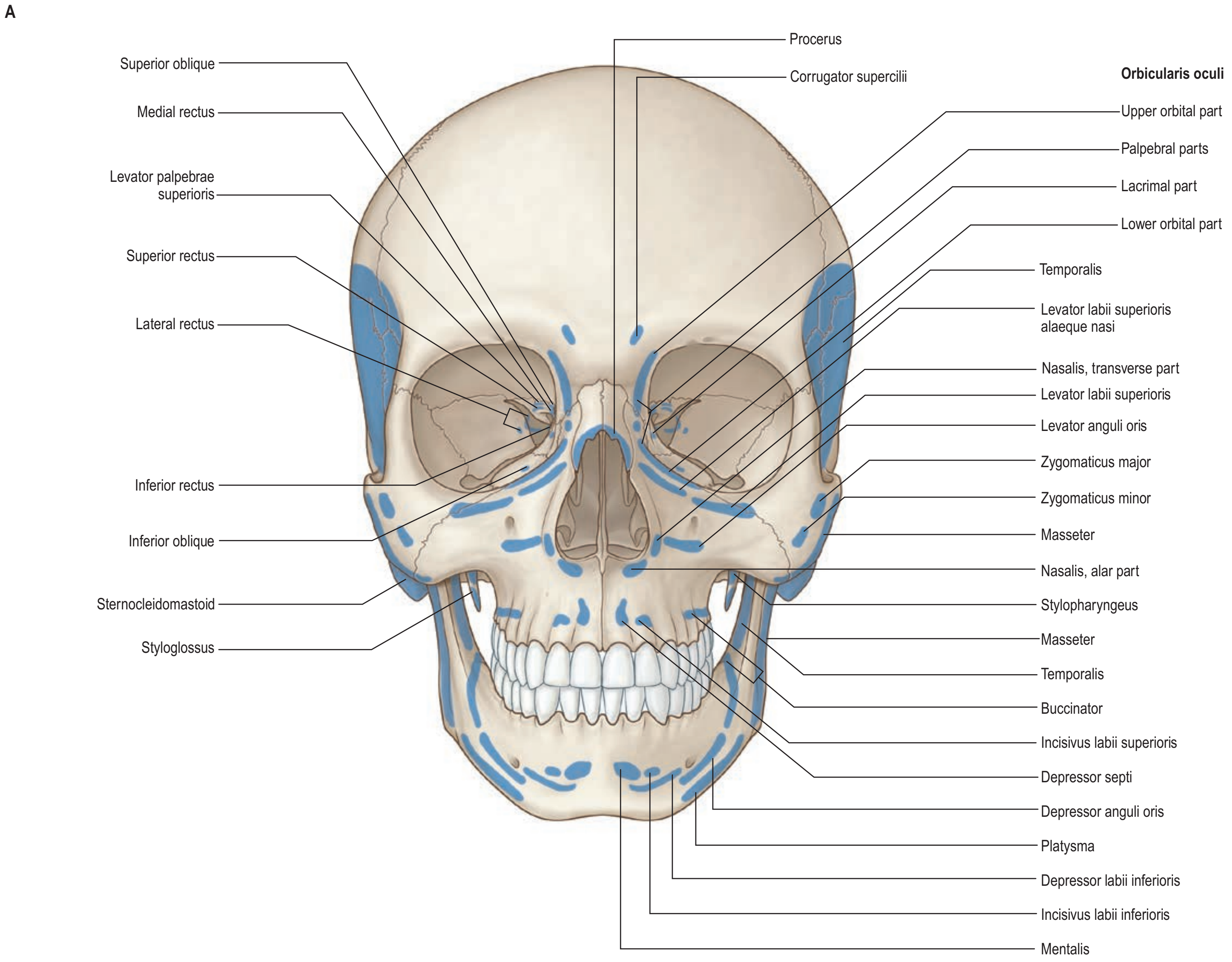
A
Superior oblique
Medial rectus
Levator palpebrae superioris
Superior rectus
Lateral rectus
Inferior rectus
Inferior oblique
Sternocleidomastoid
Styloglossus
Procerus
Corrugator supercilii
Orbicularis oculi
Upper orbital part
Palpebral parts
Lacrimal part
Lower orbital part
Temporalis
Levator labii superioris alaeque nasi
Nasalis, transverse part
Levator labii superioris
Levator anguli oris
Zygomaticus major
Zygomaticus minor
Masseter
Nasalis, alar part
Stylopharyngeus
Masseter
Temporalis
Buccinator
Incisivus labii superioris
Depressor septi
Depressor anguli oris
Platysma
Depressor labii inferioris
Incisivus labii inferioris
Mentalis

Fig. 36.17 A, Anterior view of the skull, showing the muscle attachments.

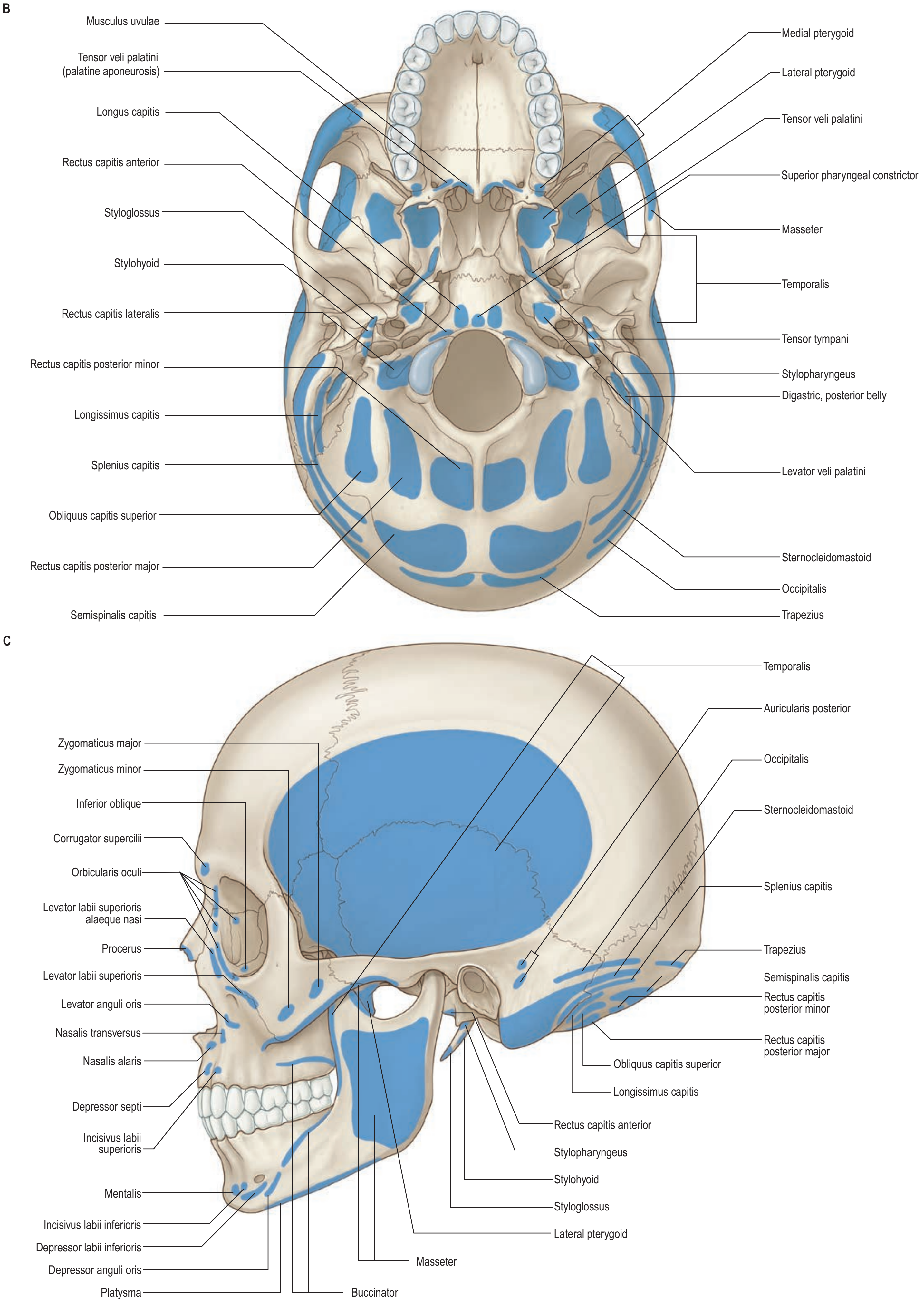
B
Musculus uvulae
Tensor veli palatini (palatine aponeurosis)
Longus capitis
Rectus capitis anterior
Styloglossus
Stylohyoid
Rectus capitis lateralis
Rectus capitis posterior minor
Longissimus capitis
Splenius capitis
Obliquus capitis superior
Rectus capitis posterior major
Semispinalis capitis
Medial pterygoid
Lateral pterygoid
Tensor veli palatini
Superior pharyngeal constrictor
Masseter
Temporalis
Tensor tympani
Stylopharyngeus
Digastric, posterior belly
Levator veli palatini
Sternocleidomastoid
Occipitalis
Trapezius
C
Temporalis
Auricularis posterior
Occipitalis
Sternocleidomastoid
Splenius capitis
Trapezius
Semispinalis capitis
Rectus capitis posterior minor
Rectus capitis posterior major
Obliquus capitis superior
Longissimus capitis
Zygomaticus major
Zygomaticus minor
Inferior oblique
Corrugator supercilii
Orbicularis oculi
Levator labii superioris alaeque nasi
Procerus
Levator labii superioris
Levator anguli oris
Nasalis transversus
Nasalis alaris
Depressor septi
Incisivus labii superioris
Mentalis
Incisivus labii inferioris
Depressor labii inferioris
Depressor anguli oris
Platysma
Buccinator
Masseter
Lateral pterygoid
Styloglossus
Stylohyoid
Stylopharyngeus
Rectus capitis anterior

Fig. 36.17, cont'd B, Basal view of the skull, showing the muscle attachments. **C**, Lateral view of the skull, showing muscle attachments.

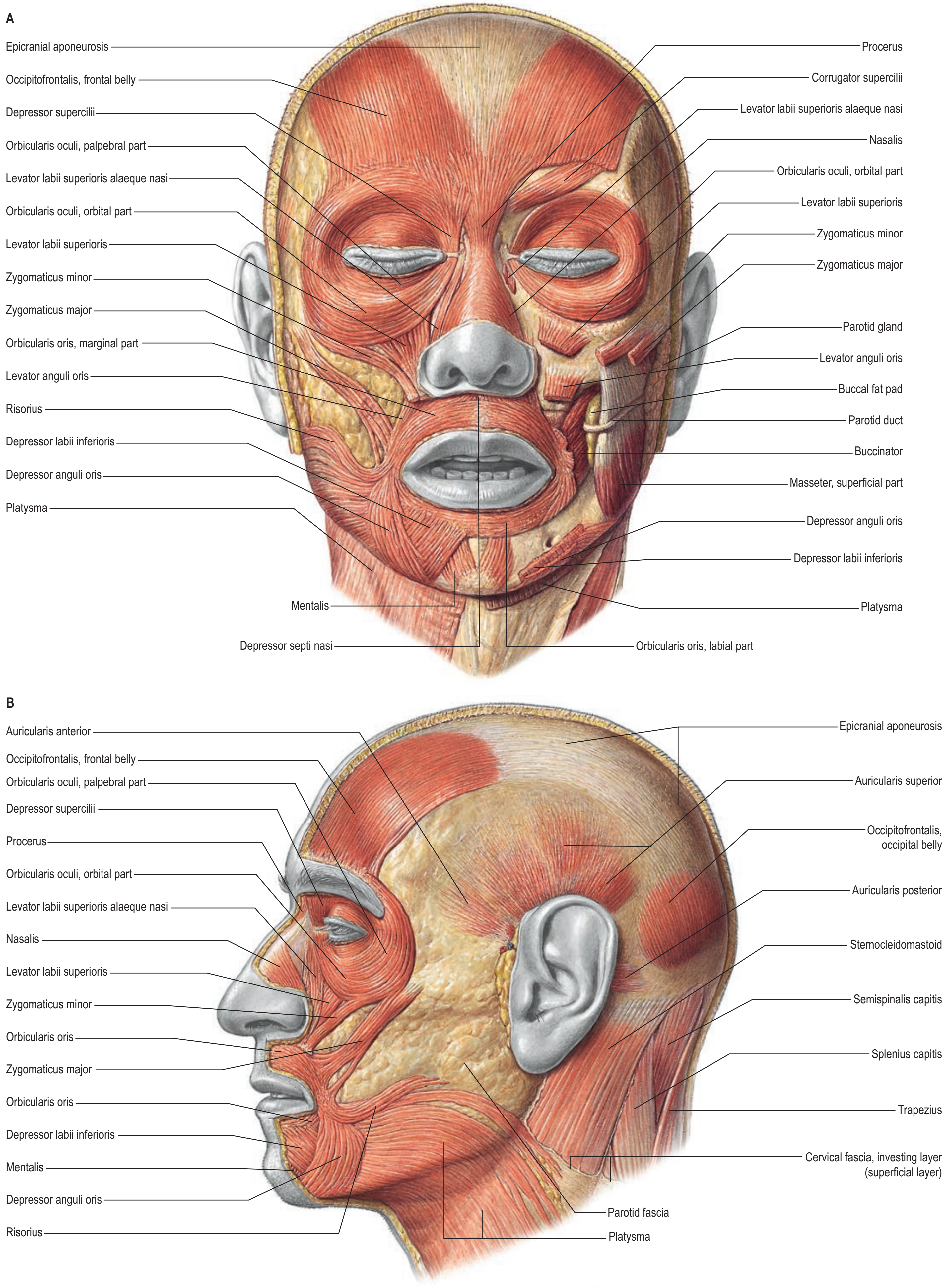
A
Epicranial aponeurosis
Occipitofrontalis, frontal belly
Depressor supercilii
Orbicularis oculi, palpebral part
Levator labii superioris alaeque nasi
Orbicularis oculi, orbital part
Levator labii superioris
Zygomaticus minor
Zygomaticus major
Orbicularis oris, marginal part
Levator anguli oris
Risorius
Depressor labii inferioris
Depressor anguli oris
Platysma
Mentalis
Depressor septi nasi
Procerus
Corrugator supercilii
Levator labii superioris alaeque nasi
Nasalis
Orbicularis oculi, orbital part
Levator labii superioris
Zygomaticus minor
Zygomaticus major
Parotid gland
Levator anguli oris
Buccal fat pad
Parotid duct
Buccinator
Masseter, superficial part
Depressor anguli oris
Depressor labii inferioris
Platysma
Orbicularis oris, labial part
B
Auricularis anterior
Occipitofrontalis, frontal belly
Orbicularis oculi, palpebral part
Depressor supercilii
Procerus
Orbicularis oculi, orbital part
Levator labii superioris alaeque nasi
Nasalis
Levator labii superioris
Zygomaticus minor
Orbicularis oris
Zygomaticus major
Orbicularis oris
Depressor labii inferioris
Mentalis
Depressor anguli oris
Risorius
Epicranial aponeurosis
Auricularis superior
Occipitofrontalis, occipital belly
Auricularis posterior
Sternocleidomastoid
Semispinalis capitis
Splenius capitis
Trapezius
Cervical fascia, investing layer (superficial layer)
Parotid fascia
Platysma

Fig. 36.18 The superficial muscles of the head and neck. **A**, Frontal view. **B–D**, The muscles of the left lateral side of the head and upper part of the neck, shown at progressively deeper levels. (Sobotta Atlas of Human Anatomy © Elsevier GmbH, Urban & Fischer, Munich.)

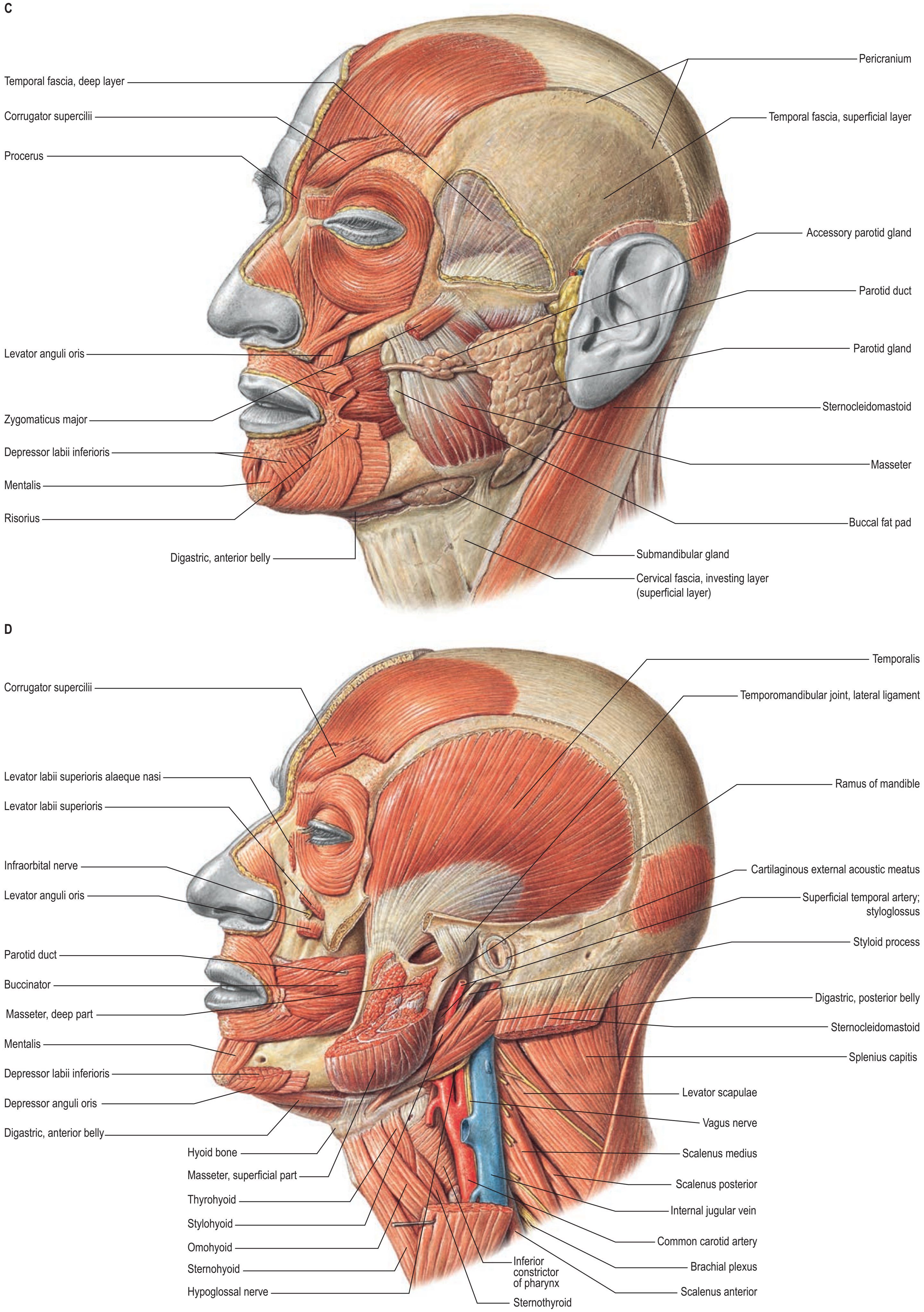
C
Temporal fascia, deep layer
Corrugator supercilii
Procerus
Levator anguli oris
Zygomaticus major
Depressor labii inferioris
Mentalis
Risorius
Digastric, anterior belly
Pericranium
Temporal fascia, superficial layer
Accessory parotid gland
Parotid duct
Parotid gland
Sternocleidomastoid
Masseter
Buccal fat pad
Submandibular gland
Cervical fascia, investing layer (superficial layer)
D
Corrugator supercilii
Levator labii superioris alaeque nasi
Levator labii superioris
Infraorbital nerve
Levator anguli oris
Parotid duct
Buccinator
Masseter, deep part
Mentalis
Depressor labii inferioris
Depressor anguli oris
Digastric, anterior belly
Hyoid bone
Masseter, superficial part
Thyrohyoid
Stylohyoid
Omohyoid
Sternohyoid
Hypoglossal nerve
Inferior constrictor of pharynx
Sternothyroid
Temporalis
Temporomandibular joint, lateral ligament
Ramus of mandible
Cartilaginous external acoustic meatus
Superficial temporal artery; styloglossus
Styloid process
Digastric, posterior belly
Sternocleidomastoid
Splenius capitis
Levator scapulae
Vagus nerve
Scalenus medius
Scalenus posterior
Internal jugular vein
Common carotid artery
Brachial plexus
Scalenus anterior

Fig. 36.18, cont'd

The orbital portion is usually activated under voluntary control. Contraction of the upper orbital fibres produces vertical furrowing above the bridge of the nose, narrowing of the palpebral fissure, and bunching and protrusion of the eyebrows, which reduces the amount of light entering the eyes. Eye closure is largely affected by lowering of the upper eyelid but there is also considerable elevation of the lower eyelid. The palpebral portion can be contracted voluntarily, to close the lids gently as in sleep, or reflexively, to close the lids protectively in blinking. The palpebral part has upper depressor and lower elevator fascicles. The lacrimal part of the muscle draws the eyelids and the lacrimal papillae medially, thereby exerting traction on the lacrimal fascia, and may aid drainage of tears by dilating the lacrimal sac. It may also influence pressure gradients within the lacrimal gland and ducts. This activity may assist in the sinuous flow of tears across the cornea, direct the lacrimal punctum into the lacus lacrimalis, and express secretions of the ciliary and tarsal glands. When the entire orbicularis oculi muscle contracts, the skin is thrown into folds that radiate from the lateral angle of the eyelids. Such folds, when permanent, cause wrinkles (often called 'crow's feet').

Corrugator supercilii

Corrugator supercilii is a small pyramidal muscle located at the medial end of each eyebrow, lying deep to the frontal part of occipitofrontalis and orbicularis oculi, with which it is partially blended (**Fig. 36.18A**). It arises from bone at the medial end of the superciliary arch and its fibres pass laterally and slightly upwards to exert traction on the skin above the middle of the supraorbital margin.

Vascular supply Corrugator supercilii is supplied by branches from adjacent arteries, mainly from the superficial temporal and ophthalmic arteries.

Innervation Corrugator supercilii is innervated by temporal branches of the facial nerve.

Actions Corrugator supercilii cooperates with orbicularis oculi to draw the eyebrows medially and downwards to shield the eyes in bright sunlight. It is also involved in frowning. The combined action of the two muscles produces mainly vertical wrinkles on the supranasal strip of the forehead.

Nasal muscle group

The nasal muscle group consists of procerus, nasalis and depressor septi and is described in Chapter 39.

Buccolabial muscle group

The shape of the mouth and the posture of the lips are controlled by a complex three-dimensional assembly of muscular slips (Yousif and Mendelson 1995). These include elevators, retractors and evertors of the upper lip (levator labii superioris alaeque nasi, levator labii superioris, zygomaticus major and minor, levator anguli oris and risorius); depressors, retractors and evertors of the lower lip (depressor labii inferioris, depressor anguli oris, and mentalis); a compound sphincter (orbicularis oris, incisivus superior and inferior); and buccinator (see Fig. 36.18).

Levator labii superioris alaeque nasi

Levator labii superioris alaeque nasi is described in Chapter 39.

Levator labii superioris

Levator labii superioris arises from the maxilla and zygomatic bone above the infraorbital foramen. Its fibres converge into the muscular substance of the upper lip between the lateral slip of levator labii superioris alaeque nasi and zygomaticus minor.

Vascular supply Levator labii superioris is supplied by the facial artery and the infraorbital branch of the maxillary artery.

Innervation Levator labii superioris is innervated by the zygomatic and buccal branches of the facial nerve.

Actions Levator labii superioris elevates and everts the upper lip. Acting with other muscles, it modifies the nasolabial furrow: in some faces, this furrow is a highly characteristic feature and is often deepened in expressions of sadness or seriousness.

Zygomaticus major

Zygomaticus major arises from the zygomatic bone, just anterior to the zygomaticotemporal suture, and passes to the angle of the mouth where it blends with the fibres of levator anguli oris, orbicularis oris and more deeply placed muscular bands.

Vascular supply Zygomaticus major is supplied by the superior labial branch of the facial artery.

Innervation Zygomaticus major is innervated by the zygomatic and buccal branches of the facial nerve.

Actions

Zygomaticus major draws the angle of the mouth upwards and laterally, as in laughing.

Zygomaticus minor

Zygomaticus minor arises from the lateral surface of the zygomatic bone immediately posterior to the zygomaticomaxillary suture, and passes downwards and medially into the muscular substance of the upper lip. Superiorly, it is separated from levator labii superioris by a narrow triangular interval and, inferiorly, it blends with this muscle.

Vascular supply Zygomaticus minor is supplied by the superior labial branch of the facial artery.

Innervation Zygomaticus minor is innervated by the zygomatic and buccal branches of the facial nerve.

Actions Zygomaticus minor elevates the upper lip, exposing the maxillary teeth. It also assists in deepening and elevating the nasolabial furrow. Acting together, the main elevators of the lip, levator labii superioris alaeque nasi, levator labii superioris and zygomaticus minor, curl the upper lip in smiling and in expressing smugness, contempt or disdain.

Levator anguli oris

Levator anguli oris arises from the canine fossa of the maxilla, just inferior to the infraorbital foramen, and inserts into and below the angle of the mouth. Its fibres mingle there with other muscle fibres (zygomaticus major, depressor anguli oris, orbicularis oris). Some superficial fibres curve anteriorly and attach to the dermal floor of the lower part of the nasolabial furrow. The infraorbital nerve and accompanying vessels enter the face via the infraorbital foramen between the origins of levator anguli oris and levator labii superioris.

Vascular supply Levator anguli oris is supplied by the superior labial branch of the facial artery and the infraorbital branch of the maxillary artery.

Innervation Levator anguli oris is innervated by the zygomatic and buccal branches of the facial nerve.

Actions Levator anguli oris raises the angle of the mouth in smiling and contributes to the depth and contour of the nasolabial furrow.

Malaris

Malaris is a thin sheet of muscle that is sometimes found covering and blending with zygomaticus major and minor and levator labii superioris. It is subject to considerable variation (Zufferey 2013). When present, it is continuous with the inferior limit of orbicularis oculi, from which it is possibly derived. Its fibres incline medially and downwards. Some of its superficial fascicles have a dermal attachment to the nasolabial ridge and sulcus, and others pass directly to the angle of the mouth and to the outer third of the upper lip to intersect with bundles of orbicularis oris.

Mentalis

Mentalis is a conical bundle of fibres lying at the side of the frenulum of the lower lip. The fibres arise from the incisive fossa of the mandible and descend to attach to the skin of the chin.

Vascular supply Mentalis is supplied by the inferior labial branch of the facial artery and the mental branch of the maxillary artery.

Innervation Mentalis is innervated by the mandibular branch of the facial nerve.

Actions Mentalis raises the base of the lower lip and wrinkles the skin of the chin. It helps in protruding and everting the lower lip in drinking and in expressing doubt or disdain.

Depressor labii inferioris

Depressor labii inferioris is a quadrilateral muscle that arises from the oblique line of the mandible, between the symphysis menti and the mental foramen. It passes upwards and medially into the skin and mucosa of the lower lip, blending with its contralateral fellow and with orbicularis oris. Below and laterally, it is continuous with platysma.

Vascular supply Depressor labii inferioris is supplied by the inferior labial branch of the facial artery and the mental branch of the maxillary artery.

Innervation Depressor labii inferioris is innervated by the mandibular branch of the facial nerve.

Actions Depressor labii inferioris draws the lower lip downwards and a little laterally in masticatory activity and may assist in eversion of the lower lip. It contributes to the expressions of irony, sorrow, melancholy and doubt.

Depressor anguli oris

Depressor anguli oris has a long, linear origin from the mental tubercle of the mandible and its continuation, the oblique line, below and lateral to depressor labii inferioris. It converges into a narrow fasciculus that blends at the angle of the mouth with orbicularis oris and risorius, and some fibres continue into levator anguli oris. Depressor anguli oris is continuous below with platysma and cervical fasciae. Some of its fibres may pass below the mental tubercle and cross the midline to interlace with their contralateral fellows, thereby forming transversus menti (the 'mental sling').

Vascular supply Depressor anguli oris is supplied by the inferior labial branch of the facial artery and the mental branch of the maxillary artery.

Innervation Depressor anguli oris is innervated by the buccal and mandibular branches of the facial nerve.

Actions Depressor anguli oris draws the angle of the mouth downwards and laterally in opening the mouth and in expressing sadness. During opening of the mouth, the mentolabial sulcus becomes more horizontal and its central part deepens.

Buccinator

Buccinator is a thin quadrilateral muscle that occupies the interval between the maxilla and the mandible and is the muscle of the cheek (**Fig. 36.18D**). It is attached to the outer surfaces of the alveolar processes opposite the maxillary and mandibular molar teeth, and to the anterior margin of the pterygomandibular raphe. A few fibres also arise from a fine tendinous band that bridges the interval between the maxilla and the pterygoid hamulus, between the tuberosity of the maxilla and the upper end of the pterygomandibular raphe. On its way to the soft palate, the tendon of tensor veli palatini pierces the pharyngeal wall in the small gap that lies behind this tendinous band. The posterior part of buccinator is deeply placed, internal to the mandibular ramus and in the plane of the medial pterygoid plate. Its anterior component curves out behind the third molar tooth to lie in the submucosa of the cheek and lips. The fibres of buccinator converge towards the modiolus near the angle of the mouth. Here the central (pterygomandibular) fibres intersect, those from below cross to the upper part of orbicularis oris, and those from above cross to the lower part. The highest (maxillary) and lowest (mandibular) fibres of buccinator continue forwards to enter their corresponding lips without decussation. As buccinator courses through the cheek and modiolus, substantial numbers of its fibres are diverted internally to attach to submucosa.

Relations Posteriorly, buccinator lies in the same plane as the superior pharyngeal constrictor, which arises from the posterior margin of the pterygomandibular raphe and is covered there by the buccopharyngeal fascia. Superficially, the buccal pad of fat separates the posterior part of buccinator from the ramus of the mandible, masseter and part of temporalis. Anteriorly, the superficial surface of buccinator is related to zygomaticus major, risorius, levator and depressor anguli oris, and the parotid duct. It is crossed by the facial artery, facial vein and branches of the facial and buccal nerves. The deep surface of buccinator is related to the buccal glands and mucous membrane of the mouth. The parotid duct pierces buccinator opposite the third upper molar tooth and lies on the deep surface of the muscle before opening into the mouth opposite the maxillary second molar tooth.

Vascular supply Buccinator is supplied by branches from the facial artery and the buccal branch of the maxillary artery.

Innervation Buccinator is supplied by the buccal branch of the facial nerve.

Actions Buccinator compresses the cheek against the teeth and gums during mastication and assists the tongue in directing food between the teeth. As the mouth closes, the teeth glide over the buccolabial mucosa, which must be retracted progressively from their occlusal surfaces by buccinator and other submucosally attached muscles. When the cheeks have been distended with air, the buccinators expel it between the lips, an activity important when playing wind instruments, and that accounts for the name of the muscle (Latin *buccinator* = trumpeter).

Pterygomandibular raphe

The pterygomandibular raphe is a thin band of tendinous fibres that stretches from the hamulus of the medial pterygoid plate down to the posterior end of the mylohyoid line of the mandible. It is easily palpated medially, where it is covered by the mucous membrane of the mouth. Laterally, it is separated from the ramus of the mandible by a quantity of adipose tissue. It gives attachment to the superior constrictor of the pharynx posteriorly, and the central part of buccinator anteriorly. The pterygomandibular raphe (see Figs 37.1, 37.3) is a useful anatomical landmark for the administration of inferior alveolar nerve blocks because the nerve lies lateral to it.

Orbicularis oris

Orbicularis oris is so named because it was once assumed that the oral fissure was surrounded by a series of complete ellipses of striated muscle that acted together in the manner of a sphincter. In fact, orbicularis oris consists of four substantially independent quadrants (upper, lower, left and right), each containing a larger pars peripheralis and a smaller pars marginalis that are apposed along lines that correspond externally to the lines of junction between the vermilion zone of the lip and the skin. Orbicularis oris is therefore composed of eight segments that are named systematically according to their location. Each segment resembles a fan that has its stem at the modiolus and is open in peripheral segments and almost closed in marginal segments.

Pars peripheralis

In each quadrant, the pars peripheralis has a lateral stem attached to the labial side of the modiolus over its full thickness, from apex to base, including the corresponding upper or lower cornu. Most of these stem fibres are thought to originate within the modiolus (although it is possible that some are direct continuations from the other modiolar muscles). They are reinforced directly by fibres from buccinator (upper fibres and decussating lower central fibres), levator anguli oris and the superficial part of zygomaticus major in the upper lip, and from buccinator (lower fibres and decussating upper central fibres) and depressor anguli oris in the lower lip.

The fibres of orbicularis oris enter their respective superior and inferior labial areas and diverge to form triangular muscular sheets. These are thickest at the junctions between skin and the vermilion zone and become progressively thinner as they reach the limits of the labial region. The greater part of each sheet enters the free lip, where its fibres aggregate into cylindrical bundles orientated parallel to the vermilion zone. Fibres of the direct labial tractors pass to their submucosal attachments between these cylindrical bundles and between the pars peripheralis and pars marginalis. In the upper lip, the highest fibres run near the nasolabial sulcus, a few fibres attach to the sulcus, and a few to the nasal ala and septum. In the lower lip, the lowest fibres reach and are attached to the mentolabial sulcus. A small proportion of the main body of fibres is thought to end in the labial connective tissue, dermis or submucosa as it traverses its quadrant of free lip. Most fibres continue towards the median plane and cross some 5 mm into the opposite half-lip. At this point, the fibres from the two sides interlace on their way to their dermal insertions, creating the ridges of the philtrum of the upper lip and the less marked corresponding depression in the lower lip.

Pars marginalis

The pars marginalis of orbicularis oris is developed to a unique extent in human lips where it is closely associated with speech and the production of some kinds of musical tone. In each quadrant, the pars marginalis consists of a single (occasionally double) band of thin muscle fibres lodged within the tissues of each vermilion zone. At their medial end, the marginal fibres meet and interlace with their contralateral fellows and are then attached to the dermis of the vermilion zone a few millimetres beyond the median plane in a manner similar to pars peripheralis. At their lateral ends, the fibres converge and are attached to the deepest part of the modiolar base along a horizontal strip level with the angle of the mouth.

The relations between the pars marginalis and pars peripheralis are complex. In a full-thickness section of an upper lip at right-angles to the vermilion zone, the cylindrical bundles of the fibres of the pars peripheralis form an S shape, with an external convexity above and an internal convexity below: the classic analogy being to the shank and initial curved part of a hook. Beyond the pars peripheralis, the hook shape is completed by the blunted triangular profile of the pars marginalis that occupies the core of the vermilion zone with its base adjacent to the pars peripheralis and its apex reaching upwards and anteriorly towards the junction between the vermilion zone and the skin. In a similar section through the lower lip, the bundles of the pars peripheralis form a continuous curve that is concave towards the external surface. This is surmounted by the flattened triangular profile of the pars marginalis that curves anteriorly, its apex again nearing the vermilion/cutaneous junction. Thus, throughout the vermilion zones of both lips, the pars marginalis lies substantially anterior to the adjacent bundles of the pars peripheralis. However, as the muscles are traced laterally beyond the vermilion zone and across the angle of the mouth, this relationship alters. The pars marginalis becomes inverted as it wraps progressively around the adjacent edge of the pars peripheralis to reach its deep (submucosal) surface and maintains this position up to its attachment at the modiolar base.

Vascular supply Orbicularis oris is supplied mainly by the superior and inferior labial branches of the facial artery, the mental and infraorbital branches of the maxillary artery, and the transverse facial branch of the superficial temporal artery.

Nerve supply Orbicularis oris is supplied by the buccal and mandibular branches of the facial nerve.

Actions The actions of orbicularis oris are considered in detail in the next section.

Incisivus labii superioris

Incisivus labii superioris has a bony origin from the floor of the incisive fossa of the maxilla above the eminence of the lateral incisor tooth. Initially, it lies deep to the superior part of the pars peripheralis of orbicularis oris. Arching laterally, its fibre bundles become intercalated between, and parallel to, the orbicular bundles. Approaching the modiolus, it is segregated into superficial and deep parts: the former blends partially with levator anguli oris and is attached to the body and apex of the modiolus, and the latter is attached to the superior cornu and base of the modiolus.

Incisivus labii inferioris

Incisivus labii inferioris, an accessory muscle of the orbicularis oris muscle complex, shares many features with incisivus labii superioris. Its osseous attachment is to the floor of the incisive fossa of the mandible, lateral to mentalis and below the eminence of the lateral incisor tooth. Curving laterally and upwards, it blends to some extent with the inferior part of the pars peripheralis of orbicularis oris before reaching the modiolus, where superficial bundles are attached to the apex and body, and deep bundles are attached to the base and inferior cornu.

Platysma

Platysma is described as a muscle of the neck, but it is considered here as a contributor to the orbicularis oris muscle complex. It has mandibular, labial and modiolar parts. Pars mandibularis attaches to the lower border of the body of the mandible. Posterior to this attachment, a substantial flattened bundle separates and passes superomedially to the lateral border of depressor anguli oris where a few fibres join this muscle. The remainder continue deep to depressor anguli oris and reappear at its medial border. Here, they continue within the tissue of the lateral half of the lower lip, as a direct labial tractor, platysma pars labialis. Pars labialis occupies the interval between depressor anguli oris and depressor labii inferioris and is in the same plane as these muscles. The adjacent margins of all three muscles blend and they have similar labial attachments. Platysma pars modiolaris constitutes all the remaining bundles posterior to pars labialis, other than a few fine fascicles that end directly in buccal dermis or submucosa. Pars modiolaris is posterolateral to depressor anguli oris and passes superomedially, deep to risorius, to apical and subapical modiolar attachments.

Risorius

Risorius is a highly variable muscle that ranges in form from one or more slender bundles to a wide, thin, superficial fan. Its peripheral attachments may include some or all of the following: the zygomatic arch, parotid fascia, fascia over the masseter anterior to the parotid, fascia enclosing platysma pars modiolaris, and fascia over the mastoid process. Its fibres converge to apical and subapical attachments at the modiolus.

Vascular supply Risorius is supplied mainly by the superior labial branch of the facial artery.

Nerve supply Risorius is supplied by buccal branches of the facial nerve.

Actions Risorius pulls the angle of the mouth laterally in numerous facial activities, including grinning and laughing.

Movements of the face and lips

Direct labial tractors

Direct labial tractors, as their name suggests, pass directly into the tissues of the lips and not via the modioli. In broad terms, the force exerted by tractors is directed vertically at an approximate right-angle to the oral fissure. Their action will therefore elevate and/or evert the whole, or part, of the upper lip and depress and/or evert the whole, or part, of the lower lip. The tractors are, from medial to lateral, the labial part of levator labii superioris alaeque nasi; levator labii superioris and zygomaticus minor in the upper lip; and depressor labii inferioris and platysma pars labialis in the lower lip.

In both upper and lower lips, the tractors blend into a continuous sheet that divides into a series of superimposed coronal sheets anterior to the muscle bundles of orbicularis oris pars peripheralis as they enter the free lip. The sheets may be divided into three groups at increasing depths from the skin surface, each with a distinct zone of attachment (Fig. 36.19). The superficial group consists of a succession of bundles of fine fibres that curve anteriorly a short distance before being attached in a series of horizontal rows to the dermis between the hair follicles, sebaceous glands and sweat glands. The intermediate group is attached to the dermis of the vermilion zone that they reach by two routes. The more superficial bundles continue past the skin/vermilion junction, then curve posteriorly over orbicularis oris pars marginalis to punctate attachments on the ventral half of the dermis of the vermilion zone. The deeper bundles first pass posteriorly between pars peripheralis and pars marginalis of orbicularis oris, then curve anteriorly to punctate attachments on the dorsal half of the dermis of the vermilion zone. The deep group is closely applied to the anterior surface of orbicularis oris pars peripheralis and sends fine tractor fibres between its parallel bundles to be attached posteriorly into the submucosa and periglandular connective tissue.

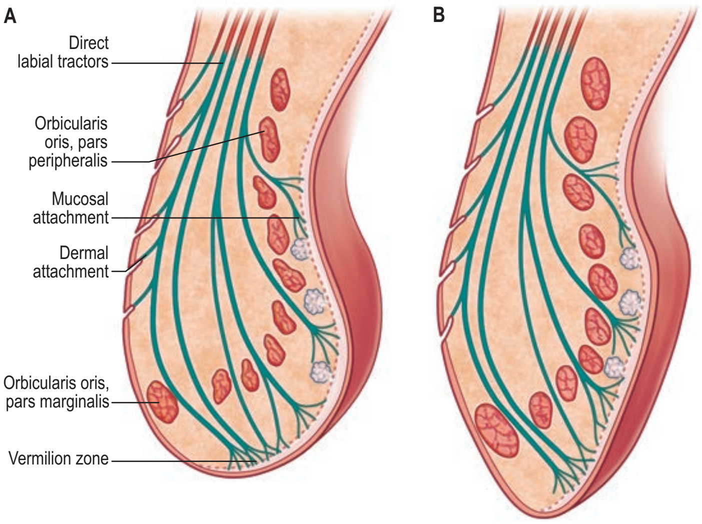

Fig. 36.19 **A**, Sagittal section of the upper lip in repose. On the left is thin skin with oblique hair follicles; on the right is thick mucosa with mucous glands and mucosal shelf; between them is the vermilion zone. **B**, As **A** but slightly contracted, forming a narrowed profile (labial cord).

Movements of the lips

The various groups of direct labial tractors may act together or individually, and their effects may involve a complete labial quadrant or be restricted to a short segment. For example, partial contraction of the superior labial tractors can result in localized elevation of a segment of the upper lip, in a postural expression reminiscent of the 'canine snarl'. Normally, the activity of the tractors is modified by the superimposed activity of orbicularis oris and the modiolar muscles: the resulting actions range from delicate adjustments of the tension and profile of the lip margins to large increases of the oral fissure with eversion of the lips.

Lip protrusion is passive in its initial stages. It may be suppressed by powerful contraction of the whole of orbicularis oris or enhanced by selective activation of parts of the direct labial tractors. However, lip movements must accommodate separation of the teeth brought about by mandibular depression at the temporomandibular joints. Beyond a certain range of mouth opening, labial movements are almost completely dominated by mandibular movements. Thus, over the last 2.5–3 cm inter-incisal distance of wide jaw separation, strong contraction of orbicularis oris cannot effect lip contact. Instead it causes full-thickness inflection of the upper and lower lips, including the vermilion zone, towards the oral cavity, wrapping them around the incisal edges, canine cusps and premolar occlusal surfaces. The involvement of the lips in speech is described in Chapter 41, but some aspects relevant to the actions of orbicularis oris pars marginalis will be described here. Contraction of marginalis is considered to alter the cross-sectional profile of the free margin of the vermilion zone such that both the gentle bulbous profile of the upper lip and the smooth posterosuperior convexity of the lower lip change to a narrow, symmetric, triangular profile. The transformed rims, whose length and tension can be delicately controlled, have been named labial cords and are known to be involved in the production of some consonantal (labial) sounds. A labial cord may also function as a 'vibrating reed' in whistling or playing a wind instrument such as the trumpet.

The modiolus and its role in facial movements

On each side of the face, a number of muscles converge towards a focus just lateral to the angle of the mouth where they interlace to form a dense, compact, mobile, fibromuscular mass called the modiolus. This can be palpated most effectively by using the opposed thumb and index finger to compress the mucosa and skin simultaneously. At least nine muscles, depending on the classification employed, are attached to each modiolus. The muscles lie in different planes, their modiolar stems are often spiralized, and most divide into two bundles, some into three or four, each of them interlacing and attaching in a distinctive way.

The shape and dimensions of the modiolus are subject to individual, age, sexual and ethnic variation. There are no precise histological boundaries because the modiolus is an irregular zone where dense, compact, interlacing tissue grades into the stems of individually recognizable muscles. It has the rough form of a blunt cone that is approximately 10 mm thick from mucosa to dermis, divided approximately equally into basal, central and apical parts. The base is roughly elliptical in outline, extending vertically 20 mm above and 20 mm below a horizontal line through the angle of the mouth and laterally a similar distance from the angle. The blunt apex of the cone is 4 mm across, centred approximately 12 mm lateral to the angle of the mouth. The central body has an oblique fibrous cleft or channel that transmits the facial artery, an arrangement that may limit the extent to which it is compressed by contraction of the buccolabial musculature. The cone shape is modified by two round-edged flanges (cornua) that extend into the lateral free lip tissues above and below the angle of the mouth.

Controlled three-dimensional mobility of the modioli enables them to integrate the activities of the cheeks, lips and oral fissure, the oral vestibule and the jaws. Such activities include biting, chewing, drinking, sucking, swallowing, changes in vestibular contents and pressure, the innumerable subtle variations involved in speech, the modulation (and occasional generation) of musical tones, production of harsher sounds in shouting and screaming, crying, and all the permutations of facial expression, ranging from mere hints to gross distortion, symmetric or asymmetric. Major modiolar movements appear to involve many, if not all, of its associated muscles, and there is little value in considering the actions of the individual muscles in isolation. While the most obvious determinant of modiolar position and mobility is the balance between the forces exerted by muscles that are directly attached to it, another influential factor is the degree of separation or 'gape' between the upper and lower teeth. Starting from the occlusal position, and with the lips maintained in contact, the teeth can be separated by approximately 1.25 cm near the midline, and the mentolabial sulcus descends by a similar distance. With further separation, the lips part, and as gape increases to its maximum, interlabial and interdental distances approach 4 cm, at which point the mentolabial sulcus has descended a further 2 cm. In this posture, the modiolus has descended about 1 cm to lie over the interdental space, into which its basal and surrounding buccal mucosa projects a few millimetres, and its cornua diverge into their respective lips at an obtuse angle to each other, the dispositions of the modiolar muscles being correspondingly modified. The general hexagonal shape of the labial area changes as the mouth and jaws open progressively. In maximal opening, the distance between the superior and inferior boundaries has increased by 3–3.5 cm at the centre; the transverse distance between its lateral angles has decreased by 1 cm and the angles are obtuse; the nasolabial sulci are longer, straighter and more vertical; and the inferior buccolabial sulci are less deep and curved. These soft tissue changes radiate from the bilateral modioli.

With the lips in contact and the teeth in tight occlusion, the modiolus can move a few millimetres in all directions. However, mobility is maximal when there is 2–3 mm clearance between the teeth: the apex of the modiolus may then move vertically upwards 10 mm, downwards 5 mm, posterolaterally 10 mm, and anteromedially 10 mm, these movements being accomplished in the curved planes of the cheek and lips. Specific movements of the modiolus may take place at any point, and along any path, within the boundaries of the envelope of movement thus defined. When the mouth is opened wide, the modiolus becomes immobile. From the neutral position, the modiolus may be displaced superficially along its apicobasal axis for up to 5–10 mm by liquids or solids in the vestibule, or by an increase in air pressure that 'balloons' the cheeks and lips.

Many activities take place in three phases. Initially, a particular modiolar muscle group becomes dominant over its antagonists and the modiolus is rapidly relocated. Next, the modiolus is transiently fixed in this new site by simultaneous contraction of modiolar muscles, principally zygomaticus major, levator anguli oris, depressor anguli oris and platysma pars modiolaris, and this provides a fixed base from which the main physiological effectors, buccinator and orbicularis oris, carry out their specific actions. These actions are usually integrated with partial separation or closure of the jaws, and with varying degrees of activity in the direct labial tractors. All these factors combine to determine the positions of the lips and oral fissure from moment to moment. Modiolar movements may be bilaterally symmetric, unilateral or asymmetric.

Muscles of mastication

Masseter and temporalis, two of the muscles of mastication, are seen on the face. Masseter covers the ramus of the mandible, and temporalis lies over the temporal fossa. These muscles are described in detail with the other main muscles of mastication in Chapter 38.

VASCULAR SUPPLY AND LYMPHATIC DRAINAGE

Arteries

The main arterial supply to the face is derived from the facial and superficial temporal arteries, with additional supply from branches of the maxillary and ophthalmic arteries. The back of the scalp is supplied by the posterior auricular and occipital arteries. There are numerous anastomoses between the branches.

Facial artery

The facial artery arises in the neck from the external carotid artery (see Figs 33.1A, 35.8). It initially lies beneath platysma, passing onto the face at the anteroinferior border of masseter, where its pulse can be felt as it crosses the mandible. The artery is deep to skin, the fat of the cheek and, near the angle of the mouth, zygomaticus major and risorius, and superficial to buccinator and levator anguli oris. It may pass over or through levator labii superioris and pursues a tortuous course along the side of the nose towards the medial corner of the eye. At its termination, it is embedded in levator labii superioris alaeque nasi.

Occasionally, the facial artery barely extends beyond the angle of the mouth, in which case its normal territory beyond this region is taken over by an enlarged transverse facial branch from the superficial temporal artery and by branches from the contralateral facial artery. The facial vein is posterior to the artery and runs a more direct course across the face. At the anterior border of masseter, the two vessels are in contact, whereas in the neck the vein is superficial to the artery. The facial artery

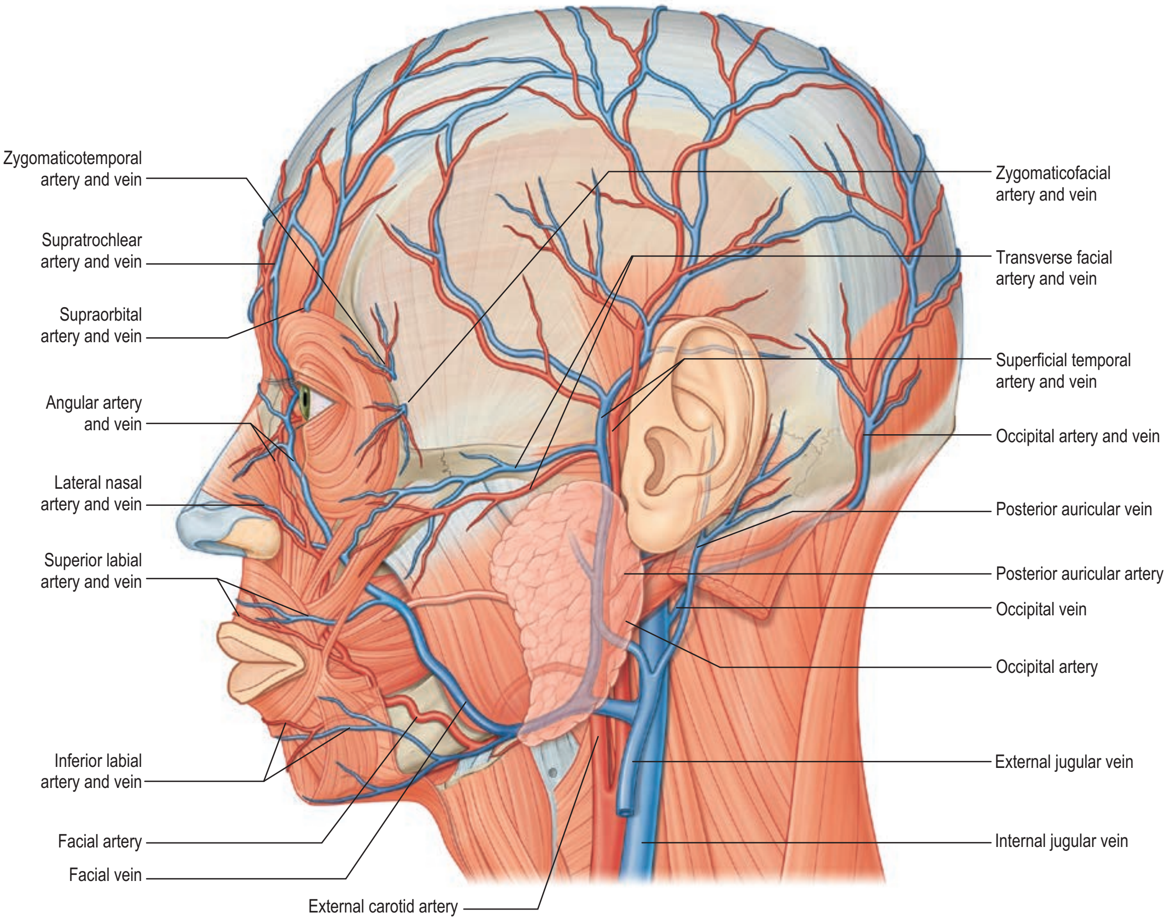
Zygomaticotemporal artery and vein
Supratrochlear artery and vein
Supraorbital artery and vein
Angular artery and vein
Lateral nasal artery and vein
Superior labial artery and vein
Inferior labial artery and vein
Facial artery
Facial vein
External carotid artery
Zygomaticofacial artery and vein
Transverse facial artery and vein
Superficial temporal artery and vein
Occipital artery and vein
Posterior auricular vein
Posterior auricular artery
Occipital vein
Occipital artery
External jugular vein
Internal jugular vein

Fig. 36.20 Arteries and veins of the left side of the face, head and neck and their main branches. The infraorbital artery is shown in Fig. 33.1A.

supplies branches to the muscles and skin of the face (Fig. 36.20). Its named branches on the face are the premasseteric artery, the superior and inferior labial arteries and the lateral nasal artery. The part of the artery distal to its terminal branch is called the angular artery.

Premasseteric artery The premasseteric artery is small and inconstant. When present, it passes upwards along the anterior border of masseter and supplies the surrounding tissues.

Inferior labial artery The inferior labial artery arises near the angle of the mouth, passes upwards and forwards under depressor anguli oris, and then penetrates orbicularis oris to run sinuously near the margin of the lower lip, between the muscle and the mucous membrane. It supplies the inferior labial glands, mucous membrane and muscles, and anastomoses with its contralateral fellow and with the mental branch of the inferior alveolar artery.

Superior labial artery The superior labial artery is larger and more tortuous than the inferior labial artery. It pursues a similar course along the superior labial margin, between the mucous membrane and orbicularis oris, anastomoses with its contralateral fellow, and supplies the upper lip. It gives off an alar branch and a septal branch that ramifies anteroinferiorly in the nasal septum.

Lateral nasal artery The lateral nasal artery is given off by the side of the nose, supplies the dorsum and ala of the nose, and anastomoses with its contralateral fellow. The lateral nasal artery can be replaced by a branch from the superior labial artery.

Superficial temporal artery

The superficial temporal artery is the smaller terminal branch of the external carotid artery (see Figs 33.1A, 36.20). It arises in the parotid gland behind the neck of the mandible, where it is crossed by temporal and zygomatic branches of the facial nerve. Initially deep, it becomes superficial as it passes over the posterior root of the zygomatic process of the temporal bone, where its pulse can be felt. It then ascends in the scalp for approximately 4 cm and divides into frontal (anterior) and parietal (posterior) branches. The artery is accompanied by corresponding veins, and by the auriculotemporal nerve that usually lies just posterior to it.

The superficial temporal artery supplies the skin and muscles at the side of the face and in the scalp, the parotid gland and the temporomandibular joint. It is occasionally biopsied when a histological diagnosis of giant cell arteritis is required. The named branches of the superficial temporal artery are the transverse facial, auricular, zygomatico-orbital, middle temporal, frontal and parietal arteries. The relative sizes of the frontal, parietal and transverse facial branches vary: the frontal and parietal branches may be absent, whereas the transverse facial branch may replace a shortened transverse facial artery arising from the facial artery.

Transverse facial artery The transverse facial artery arises before the superficial temporal artery emerges from the parotid gland. It traverses the gland, crosses masseter between the parotid duct and the zygomatic arch (accompanied by one or two facial nerve branches), and divides into numerous branches that supply the parotid gland and duct, masseter and adjacent skin. The branches anastomose with the facial, masseteric, buccal, lacrimal and infraorbital arteries, and can have a direct origin from the external carotid artery.

Auricular artery The branches of the auricular artery are distributed to the lobule and lateral surface of the auricle and to the external acoustic meatus.

Zygomatico-orbital artery The zygomatico-orbital artery may arise independently from the superficial temporal artery or from its middle temporal or parietal branches. It runs close to the upper border of the zygomatic arch, between the two layers of temporal fascia, to the lateral orbital angle. It supplies orbicularis oculi and anastomoses with the lacrimal and palpebral branches of the ophthalmic artery. A well-developed zygomatico-orbital artery can be associated with a delayed division of the superficial temporal artery into frontal and parietal branches.

Middle temporal artery The middle temporal artery arises just above the zygomatic arch and perforates the temporal fascia to supply temporalis. It anastomoses with the deep temporal branches of the maxillary artery.

Frontal (anterior) branch The frontal branch passes upwards towards the frontal tuberosity and supplies the muscles, skin and pericranium in this region. It anastomoses with its contralateral fellow and with the supraorbital and supratrochlear branches of the ophthalmic artery.

Parietal (posterior) branch The parietal branch is larger than the frontal branch of the superficial temporal artery. It curves upwards and backwards, remains superficial to the temporal fascia, and anastomoses with its contralateral fellow and with the posterior auricular and occipital arteries.

Facial branches of the maxillary artery

The maxillary artery is the larger of the two terminal branches of the external carotid artery. It has three branches that supply the face, namely the mental, buccal and infraorbital arteries (see Figs 33.1A, 33.2A).

Mental artery The mental artery arises from the first part of the maxillary artery as a terminal branch of the inferior alveolar artery. It emerges on to the face from the mandibular canal at the mental foramen, supplies muscles and skin in the chin region, and anastomoses with the inferior labial and submental arteries.

Buccal artery The buccal artery is a branch of the second part of the maxillary artery. It emerges onto the face from the infratemporal fossa, crosses buccinator to supply the cheek, and anastomoses with the infraorbital artery and with branches of the facial artery.

Infraorbital artery The infraorbital artery arises from the third part of the maxillary artery. It runs through the infraorbital foramen and onto the face, supplying the lower eyelid, the lateral aspect of the nose and the upper lip. The infraorbital artery has extensive anastomoses with the transverse facial and buccal arteries and with branches of the ophthalmic and facial arteries.

Facial branches of the ophthalmic artery

The ophthalmic artery is a branch of the internal carotid artery (see Fig. 44.13). Its supratrochlear, supraorbital, lacrimal, medial palpebral and external (dorsal) nasal branches supply the face (see Fig. 36.20).

Supratrochlear artery The supratrochlear artery emerges from the orbit onto the face at the frontal notch. It supplies the medial parts of the upper eyelid, forehead and scalp, and anastomoses with the supraorbital artery and with its contralateral fellow.

Supraorbital artery The supraorbital artery leaves the orbit through the supraorbital notch or foramen. It divides into superficial and deep branches that supply the skin and muscle of the upper eyelid, forehead and scalp. It anastomoses with the supratrochlear artery, the frontal branch of the superficial temporal and its contralateral fellow. At the supraorbital margin, it often sends a branch to the diploë of the frontal bone and can also supply the mucoperiosteum in the frontal sinus.

Lacrimal artery The lacrimal artery appears on the face at the upper lateral corner of the orbit and supplies the lateral part of the eyelids. Within the orbit, it gives off a zygomatic artery that divides into zygomaticofacial and zygomaticotemporal arteries. The zygomaticofacial artery passes through the lateral wall of the orbit to emerge onto the face at the zygomaticofacial foramen and supplies the region overlying the prominence of the cheek. The zygomaticotemporal artery also passes through the lateral wall of the orbit, via the zygomaticotemporal foramen, and supplies the skin over the non-beard part of the temple. The lacrimal artery anastomoses with the deep temporal branch of the maxillary artery and the transverse facial branch of the superficial temporal artery.

Medial palpebral arteries Superior and inferior medial palpebral arteries arise from the ophthalmic artery below the trochlea. They descend behind the nasolacrimal sac to enter the eyelids, where each divides into two branches that course laterally along the edges of the tarsal plates, forming the superior and inferior arches and supplying the eyelids. They anastomose with branches of the supraorbital, zygomatico-orbital and lacrimal arteries. The inferior arch also anastomoses with the facial artery.

External (dorsal) nasal artery The external nasal artery is a terminal branch of the anterior ethmoidal artery that arises from the ophthalmic artery. It emerges at the junction of the nasal bone and the lateral nasal cartilage and supplies the skin covering the external nose.

Occipital artery

The occipital artery arises in the neck from the external carotid artery (see Fig. 35.8). It runs in a groove on the temporal bone, medial to the mastoid process. Accompanied by the greater occipital nerve, the occipital artery enters the posterior scalp by piercing the investing layer of deep cervical fascia that connects the cranial attachments of trapezius and sternocleidomastoid. Tortuous branches run between the skin and the occipital belly of occipitofrontalis, anastomosing with the contralateral occipital, posterior auricular and superficial temporal arteries, as well as with the transverse cervical branch of the subclavian artery. These branches supply the occipital belly of occipitofrontalis and the skin and pericranium associated with the scalp as far forwards as the vertex. The artery may give off a meningeal branch that traverses the parietal foramen.

Posterior auricular artery

The posterior auricular artery arises in the neck from the external carotid artery and ascends between the auricle and mastoid process. It supplies the cranial surface of the auricle via its auricular branch, and the occipital belly of occipitofrontalis and the scalp behind and above the auricle via its occipital branch. The posterior auricular artery anastomoses with the occipital artery.

Veins

The veins of the face are subject to considerable variations; the following description concerns those that are relatively constant (see Fig. 36.20).

Supratrochlear vein

The supratrochlear vein starts on the forehead from a venous network connected to the frontal tributaries of the superficial temporal vein. Veins from this network form a single trunk that descends to the bridge of the nose, near the midline and parallel with its contralateral fellow. The veins are joined by a nasal arch across the nose and then diverge, each joining a supraorbital vein to form the facial vein near the medial canthus of the eye.

Supraorbital vein

The supraorbital vein begins near the zygomatic process of the frontal bone, connecting with branches of the superficial and middle temporal veins. It passes medially above the orbital opening, pierces orbicularis oculi and unites with the supratrochlear vein near the medial canthus of the eye to form the facial vein. A branch passes through the supraorbital notch, where it receives veins from the frontal sinus and frontal diploë, and subsequently connects with the superior ophthalmic vein.

Facial vein

The facial vein is the main vein draining the face. After receiving the supratrochlear and supraorbital veins, it travels obliquely downwards by the side of the nose, passes under zygomaticus major, risorius and platysma, descends to the anterior border of masseter and then passes over the surface of the muscle. It crosses the body of the mandible and runs down in the neck to drain into the internal jugular vein. The facial vein initially lies behind the more tortuous facial artery but it crosses the artery at the lower border of the mandible. The uppermost segment of the facial vein, above its junction with the superior labial vein, is also called the angular vein; any infection of the mouth or face can potentially spread via the angular veins to the cavernous sinuses, resulting in thrombosis.

Tributaries Near its origin, the facial vein connects with the superior ophthalmic vein, both directly and via the supraorbital vein, and so is linked to the cavernous sinus. The facial vein receives tributaries from the side of the nose and, below this, an important deep facial vein from the pterygoid venous plexus. It also receives the inferior palpebral, superior and inferior labial, buccinator, parotid and masseteric veins, and other tributaries that join it below the mandible.

Superficial temporal vein

A widespread venous network across the scalp receives branches from the supratrochlear, supraorbital, posterior auricular and occipital veins. Anterior and posterior tributaries from this network unite above the zygomatic arch to form the superficial temporal vein on each side. The vein accompanies its artery, usually lying behind it, crosses the posterior root of the zygoma and enters the parotid gland, where it joins the maxillary vein to form the retromandibular vein.

Tributaries The tributaries are the parotid veins, rami draining the temporomandibular joint, anterior auricular, transverse facial and middle temporal veins. The middle temporal vein receives the orbital vein (formed by the lateral palpebral veins), pierces the temporal fascia and then passes back between the layers of the fascia to join the superficial temporal vein just above the level of the zygomatic arch.

Buccal, mental and infraorbital veins

The buccal, mental and infraorbital veins drain the cheek and chin regions and pass into the pterygoid venous plexus.

Posterior auricular and occipital veins

The posterior auricular vein arises in a parieto-occipital network that also drains into tributaries of the occipital and superficial temporal veins. It descends behind the auricle to join the posterior division of the retromandibular vein in, or just below, the parotid gland, to form the external jugular vein. It receives a stylomastoid vein and tributaries from the cranial surface of the auricle, drains the region of the scalp behind the ear and drains into the external jugular vein. The occipital vein begins in a posterior network in the scalp, pierces the cranial attachment of trapezius, turns into the suboccipital triangle and joins the deep cervical and vertebral veins. It may be joined by a vein draining the diploë in the occipital bone and then passes to either the internal jugular, posterior auricular, deep cervical or vertebral veins. Emissary veins connect the occipital vein to the intracranial venous sinuses via the mastoid and parietal foramina and through the posterior condylar canal and occipital protuberances.

Lymphatic drainage

Lymph vessels from the frontal region above the root of the nose drain to the submandibular nodes (Fig. 36.21; see Fig. 35.15). Vessels from the rest of the forehead, temporal region, upper half of the lateral auricular aspect and anterior wall of the external acoustic meatus drain to the superficial parotid nodes that lie just anterior to the tragus, either on or deep to the parotid fascia. These nodes also drain lateral vessels from the eyelids and skin of the zygomatic region, and their efferent vessels pass to the upper deep cervical nodes. A strip of scalp above the auricle, the upper half of the cranial aspect and margin of the auricle, and the posterior wall of the external acoustic meatus all drain to the upper deep cervical and posterior auricular nodes. The posterior auricular nodes are superficial to the mastoid attachment of sternocleidomastoid and deep to auricularis posterior and drain to the upper deep cervical nodes. The auricular lobule, floor of the external acoustic meatus and skin over the mandibular angle and lower parotid region all drain to the superficial cervical or upper deep cervical nodes. Superficial cervical nodes lie along the external jugular vein superficial to sternocleidomastoid. Some efferents pass round the anterior border of sternocleidomastoid to the upper deep cervical nodes, while others follow the external jugular vein to the lower deep cervical nodes in the subclavian triangle.

The occipital region of the scalp drains partly to the occipital nodes, and partly to a vessel that runs along the posterior border of sternocleidomastoid to the lower deep cervical nodes. Occipital nodes are commonly superficial to the upper attachment of trapezius but occasionally lie in the superior angle of the posterior triangle.

There are usually three submandibular nodes, internal to the deep cervical fascia in the submandibular triangle. One lies at the anterior pole of the submandibular gland, and two flank the facial artery as it reaches the mandible. Other nodes are often embedded in the gland or deep to it. Submandibular nodes drain a wide area, including vessels from the submental, buccal and lingual groups of nodes, and their efferents pass to the upper and lower deep cervical nodes. The external nose, cheek, upper lip and lateral parts of the lower lip drain directly to the submandibular nodes; the afferent vessels may have a few buccal nodes along their course and near the facial vein. The mucous membrane of the lips and cheek drains to the submandibular nodes, and the lateral part of the cheek drains to the parotid nodes. The central part of the lower lip, buccal floor and tip of the tongue all drain to the submental nodes lying on mylohyoid between the anterior bellies of the digastric muscles. These nodes receive afferents bilaterally, some decussating across the chin and their efferents pass to the submandibular and jugulo-omohyoid nodes.

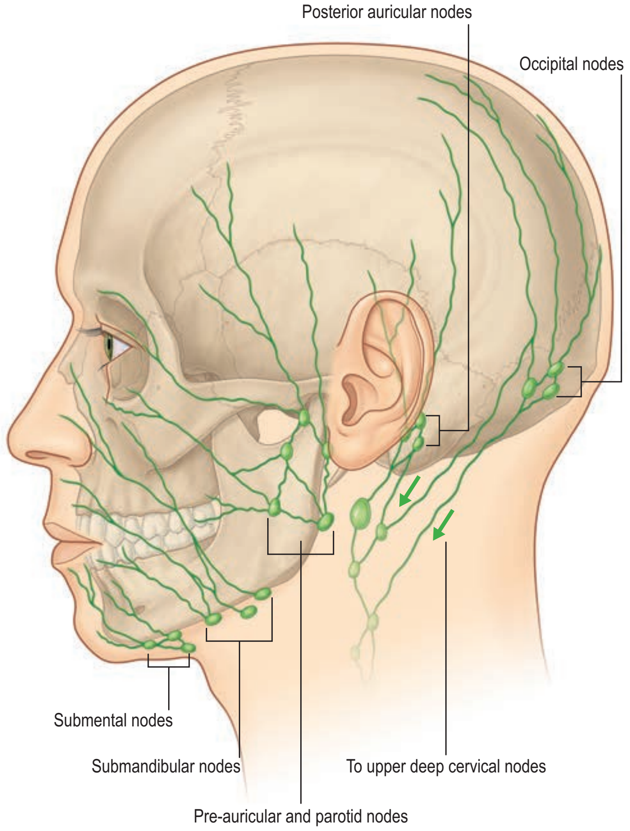
Posterior auricular nodes
Occipital nodes
Submental nodes
Submandibular nodes
To upper deep cervical nodes
Pre-auricular and parotid nodes

Fig. 36.21 Lymphatic drainage of the face and scalp. Arrows indicate the direction of flow. (With permission from Drake RL, Vogl AW, Mitchell A (eds) Gray's Anatomy for Students, 2nd ed. Elsevier, Churchill Livingstone. Copyright 2010.)

INNERVATION

The numerous muscles of facial expression are supplied by the facial nerve, and the two muscles of mastication that relate to the face are innervated by the mandibular division of the trigeminal nerve. The sensory innervation is primarily from the three divisions of the trigeminal nerve, with smaller contributions from the cervical spinal nerves. The detailed innervation of the auricle is considered in Chapter 42.

Trigeminal nerve

Three large areas of the face can be mapped out to indicate the peripheral nerve fields associated with the three divisions of the trigeminal nerve. The fields are not horizontal but curve upwards, reflecting the upwards movement of the facial skin as the skull and brain develop (Fig. 36.22). Embryologically, each division of the trigeminal nerve is associated with a developing facial process that gives rise to a specific area of the adult face: the ophthalmic nerve is associated with the frontonasal process, the maxillary nerve with the maxillary process, and the mandibular nerve with the mandibular process.

Ophthalmic nerve

The cutaneous branches of the ophthalmic nerve supply the conjunctiva, skin over the forehead, upper eyelid and much of the external surface of the nose.

Supratrochlear nerve

The supratrochlear nerve is the smaller terminal branch of the frontal nerve. It runs anteromedially in the roof of the orbit, passes above the trochlea and sends a descending filament to the infratrochlear branch of the nasociliary nerve. The nerve emerges between the trochlea and the supraorbital foramen at the frontal notch, curves up on the forehead close to the bone with the supratrochlear artery, and supplies the conjunctiva and the skin of the upper eyelid. It then ascends beneath the corrugator and the frontal belly of occipitofrontalis before dividing into

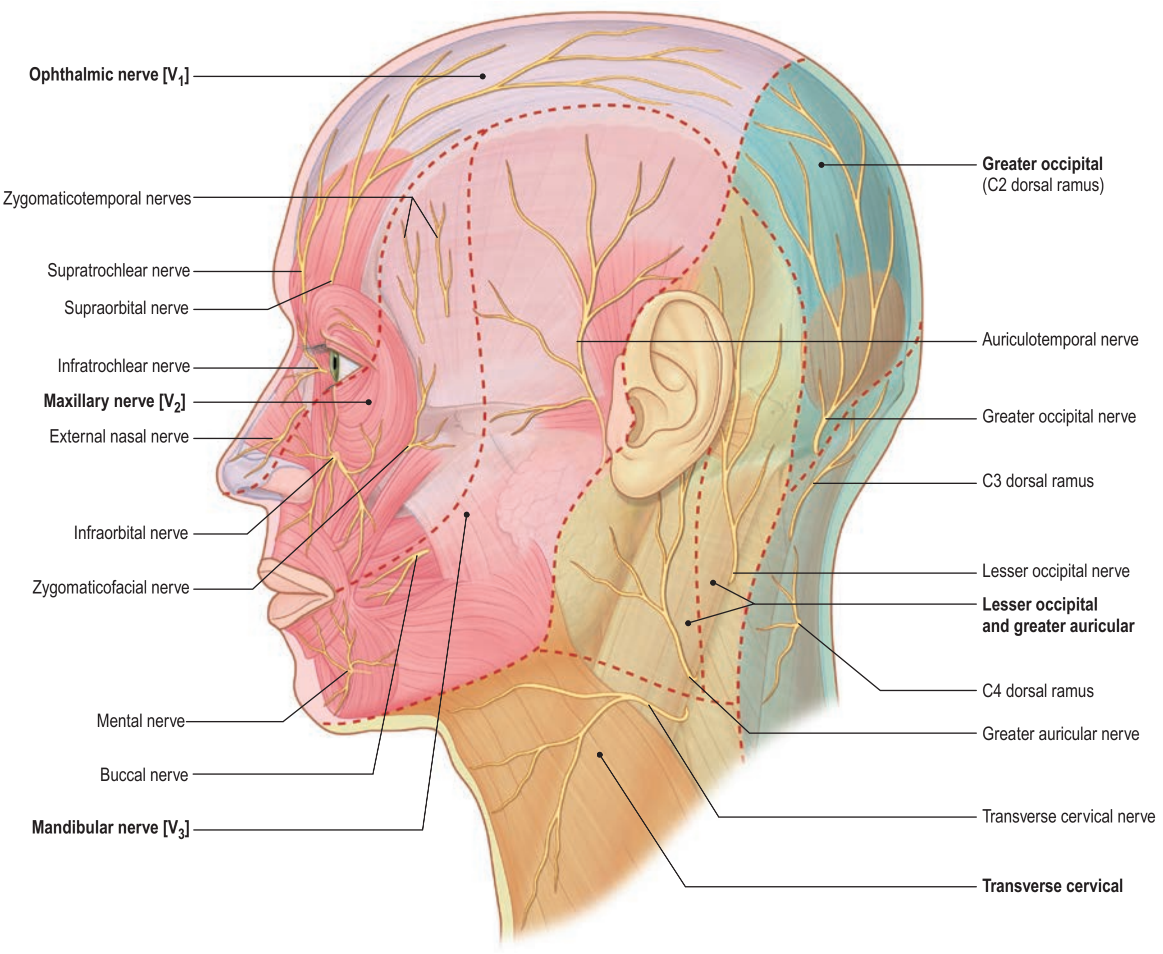
Ophthalmic nerve [V_1]
Zygomaticotemporal nerves
Supratrochlear nerve
Supraorbital nerve
Infratrochlear nerve
Maxillary nerve [V_2]
External nasal nerve
Infraorbital nerve
Zygomaticofacial nerve
Mental nerve
Buccal nerve
Mandibular nerve [V_3]
Greater occipital
(C2 dorsal ramus)
Auriculotemporal nerve
Greater occipital nerve
C3 dorsal ramus
Lesser occipital nerve
Lesser occipital and greater auricular
C4 dorsal ramus
Greater auricular nerve
Transverse cervical nerve
Transverse cervical

Fig. 36.22 Cutaneous innervation of the face and neck, showing dermatomes (in bold, territories outlined with dotted lines). (Adapted with permission from Drake RL, Vogl AW, Mitchell A (eds) Gray's Anatomy for Students, 2nd ed. Elsevier, Churchill Livingstone. Copyright 2010.)

branches that pierce these muscles to supply the skin of the lower forehead near the midline.

Supraorbital nerve

The supraorbital nerve is the larger terminal branch of the frontal nerve. It traverses the supraorbital notch or foramen and supplies palpebral filaments to the upper eyelid and conjunctiva. It ascends on the forehead with the supraorbital artery and divides into medial and lateral branches that supply the skin of the scalp nearly as far back as the lambdoid suture. These branches are at first deep to the frontal belly of occipitofrontalis: the medial branch perforates the muscle to reach the skin, while the lateral branch pierces the epicranial aponeurosis.

Lacrimal nerve

The lacrimal nerve is the smallest of the main ophthalmic branches and pierces the orbital septum to end in the lateral region of the upper eyelid, which it supplies. It anastomoses with filaments of the facial nerve. Occasionally, the lacrimal nerve is absent, in which case it is replaced by the zygomaticotemporal nerve; their relationship is reciprocal, and when the zygomaticotemporal nerve is absent it is replaced by a branch of the lacrimal nerve.

Infratrochlear nerve

The infratrochlear nerve branches from the nasociliary nerve. It leaves the orbit below the trochlea and supplies the skin of the eyelids, the conjunctiva, lacrimal sac, lacrimal caruncle and the side of the nose above the medial canthus.

External nasal nerve

The external nasal nerve is the terminal branch of the anterior ethmoidal nerve. It descends through the lateral wall of the nose and supplies the skin of the nose below the nasal bones, excluding the alar portion around the external nares.

Maxillary nerve

The maxillary nerve passes through the orbit to supply the skin of the lower eyelid, the prominence of the cheek, the alar part of the nose, part of the temple and the upper lip. It has three cutaneous branches: the zygomaticotemporal, zygomaticofacial and infraorbital nerves.

Zygomaticotemporal nerve

The zygomaticotemporal nerve traverses a canal in the zygomatic bone and emerges into the anterior part of the temporal fossa, where it ascends between the bone and temporalis before piercing the temporal fascia about 2 cm above the zygomatic arch to supply the skin of the temple. It communicates with the facial and auriculotemporal nerves. As it pierces the deep layer of the temporal fascia, it sends a slender twig between the two layers of the fascia towards the lateral angle of the eye. It was thought that this branch carried parasympathetic postganglionic fibres from the pterygopalatine ganglion to the lacrimal gland, but it is now known that these fibres usually innervate the lacrimal gland directly.

Zygomaticofacial nerve

The zygomaticofacial nerve traverses the inferolateral angle of the orbit and emerges on the face through a foramen in the zygomatic bone. It perforates orbicularis oculi to supply the skin on the prominence of the cheek and forms a plexus with zygomatic branches of the facial nerve and palpebral branches of the maxillary nerve. Occasionally, the zygomaticofacial nerve is absent.

Infraorbital nerve

The infraorbital nerve emerges onto the face at the infraorbital foramen, where it lies between levator labii superioris and levator anguli oris. It gives off palpebral, nasal and superior labial branches. The palpebral branches ascend deep to orbicularis oculi, pierce the muscle to supply the skin in the lower eyelid and join with the facial and zygomaticofacial nerves near the lateral canthus. Nasal branches supply the skin of the side of the nose and the movable part of the nasal septum and join the external nasal branch of the anterior ethmoidal nerve. Superior labial branches, are large and numerous and descend behind levator labii superioris to supply the skin of the anterior part of the cheek and upper lip. They are joined by branches from the facial nerve to form the infraorbital plexus.

Mandibular nerve

The mandibular nerve supplies the skin over the mandible, the lower lip, the fleshy part of the cheek, part of the auricle of the ear and part of the temple via the buccal, mental and auriculotemporal nerves.

Buccal nerve

The buccal nerve emerges onto the face from behind the ramus of the mandible and passes laterally in front of masseter to unite with the buccal branches of the facial nerve. It supplies the skin over the anterior part of buccinator.

Mental nerve

The mental nerve is the terminal branch of the inferior alveolar nerve. It enters the face through the mental foramen, where it is directed backwards to supply the skin of the lower lip and labial gingivae.

Auriculotemporal nerve

The auriculotemporal nerve emerges onto the face behind the temporomandibular joint and within the superior surface of the parotid gland. It ascends posterior to the superficial temporal vessels, passes over the posterior root of the zygoma, and divides into superficial temporal branches (see Figs 38.20, 38.25). The cutaneous branches of the auriculotemporal nerve supply the tragus and part of the adjoining auricle of the ear and the posterior part of the temple. The nerve may be damaged during parotid gland surgery, resulting in impaired sensation of the tragus and temple. It communicates with the temporofacial division of the facial nerve, usually by two rami that pass anterolaterally behind the neck of the mandible. These communications anchor the facial nerve close to the lateral surface of the condylar process of the mandible and limit its mobility during surgery. Communications with the temporal and zygomatic branches of the facial nerve loop around the transverse facial and superficial temporal vessels.

Facial nerve

The facial nerve emerges from the base of the skull at the stylomastoid foramen and almost immediately gives off the nerves to the posterior belly of digastric and stylohyoid together with the posterior auricular nerve that supplies the occipital belly of occipitofrontalis and some of the auricular muscles (**Fig. 36.23**).

The nerve next enters the parotid gland high up on its posteromedial surface and passes forwards and downwards behind the mandibular ramus. Within the substance of the gland, it branches into superior (temporofacial) and inferior (cervicofacial) trunks, usually just behind and superficial to the retromandibular vein. The trunks branch further to form a parotid plexus (pes anserinus). Five main terminal branches arise from the plexus, diverge within the gland and leave by its anteromedial surface, medial to its anterior margin, to supply the muscles of facial expression (see Fig. 36.23). Six distinctive anastomotic patterns were originally classified by Davis et al (1956) and these are illustrated in **Fig. 36.24**. Numerous microdissection studies have demonstrated considerable individual variation in branching patterns and anastomoses between branches, both within the parotid and on the face (e.g. Lineaweaver et al 1997, Kwak et al 2004): the account that follows is therefore an overview. In surgical terms, these anastomoses are important and presumably explain why accidental or deliberate division of a small branch often fails to result in the expected facial nerve weakness. The surface anatomy of the facial nerve is described in Chapter 33.

The temporal branch usually divides into anterior and posterior rami soon after piercing the parotidomasseteric fascia below the zygomatic arch; there is often a middle (frontal) ramus. These rami cross the arch in subcutaneous tissue lying in the subgaleal space. Their course is extremely variable.

Twigs supply intrinsic muscles on the lateral surface of the auricle and the anterior and superior auricular muscles. They communicate with the zygomaticotemporal branch of the maxillary nerve and the auriculotemporal branch of the mandibular nerve. The more anterior branches supply the frontal belly of occipitofrontalis, orbicularis oculi and corrugator and join the supraorbital and lacrimal branches of the ophthalmic nerve.

Zygomatic branches are generally multiple. They cross the zygomatic bone to the lateral canthus of the eye and supply orbicularis oculi and may also supply muscles innervated by the buccal branch. Twigs communicate with filaments of the lacrimal nerve and the zygomaticofacial branch of the maxillary nerve.

The buccal branch is usually single. It has a close relationship to the parotid duct for about 2.5 cm after emerging from the parotid gland and typically lies below the duct. Superficial branches run beneath the subcutaneous fat and the superficial musculo-aponeurotic system (SMAS). Some branches pass deep to procerus and join the infratrochlear and external nasal nerves. Upper deep branches supply zygomaticus major and levator labii superioris and form an infraorbital plexus with the superior labial branches of the infraorbital nerve. They also supply levator anguli oris, zygomaticus minor, levator labii superioris alaeque nasi and the small nasal muscles (these branches are sometimes described as lower zygomatic branches). Lower deep branches supply buccinator and orbicularis oris and communicate with filaments of the buccal branch of the mandibular nerve.

There are usually two marginal mandibular branches. They run forwards towards the angle of the mandible under platysma, and then

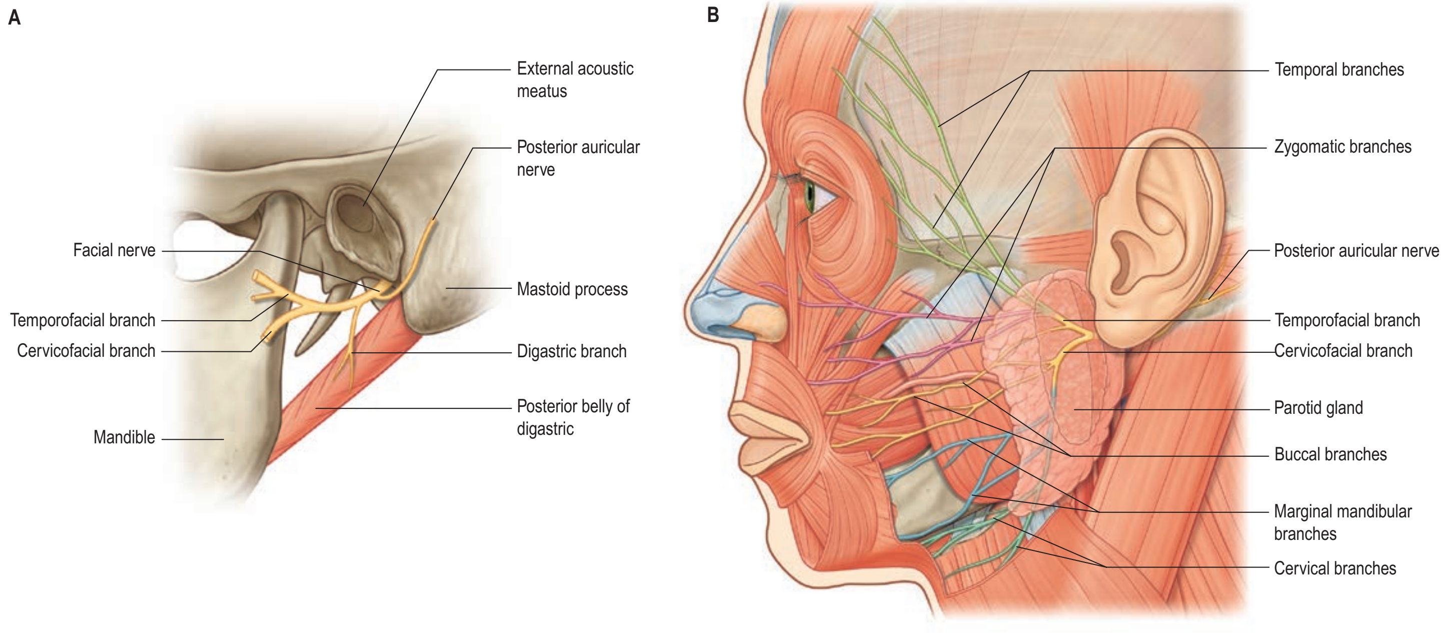

Fig. 36.23 The distribution of the facial nerve. **A**, Branches given off immediately after the nerve exits the stylomastoid foramen. **B**, Branches of the nerve on the face. (With permission from Drake RL, Vogl AW, Mitchell A (eds) Gray's Anatomy for Students, 2nd ed. Elsevier, Churchill Livingstone. Copyright 2010.)

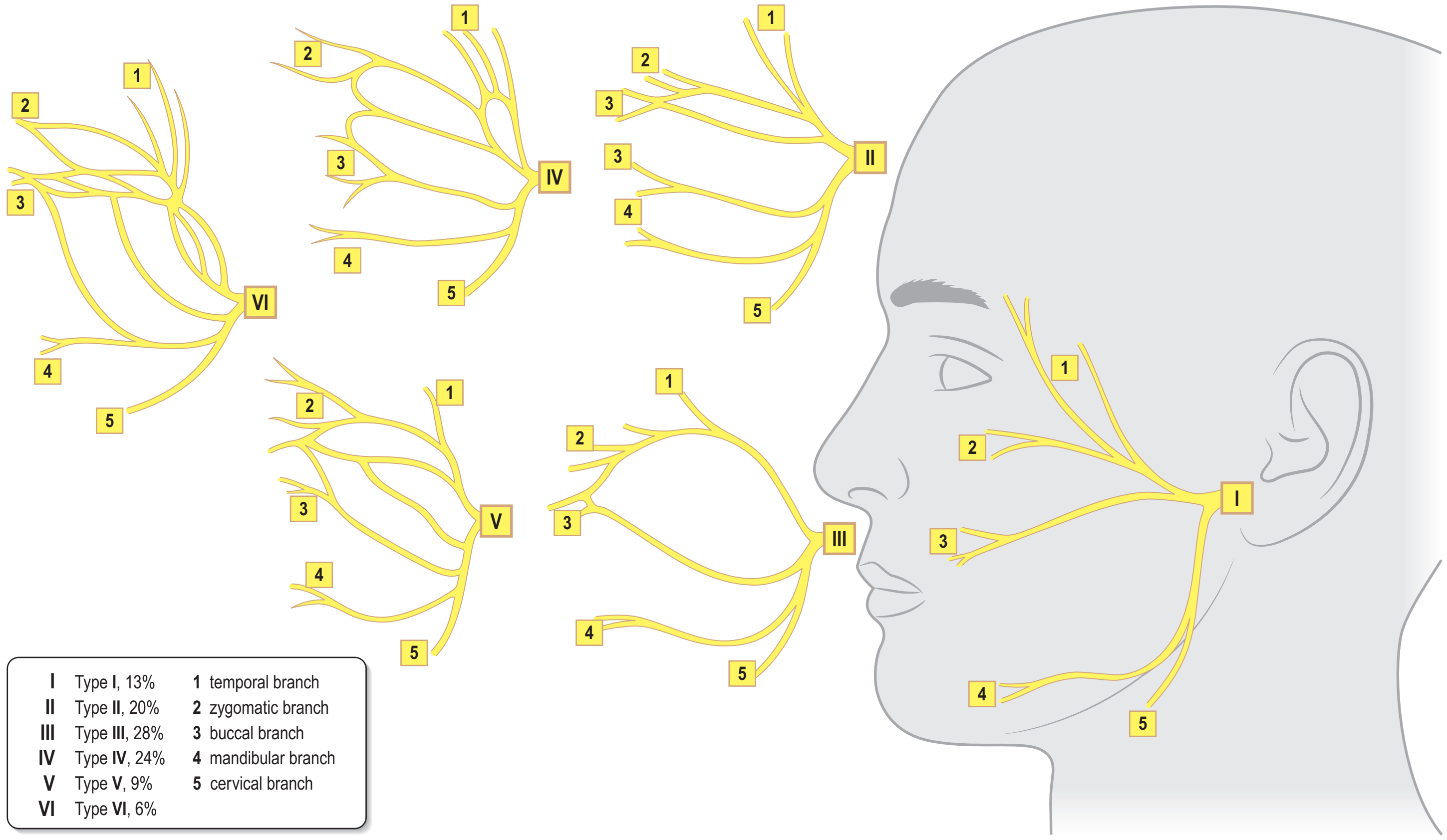

Fig. 36.24 The pattern of branching of the facial nerve. (Adapted with permission from Berkovitz BKB, Moxham BJ 2002 Head and Neck Anatomy. London: Martin Dunitz, and from Davis RA, Anson BJ, Budinger JM et al 1956 Surgical anatomy of the facial nerve and parotid gland based upon a study of 350 cervicofacial halves. Surg Gynecol Obstet 102:385–412, with permission from the American College of Surgeons.)

turn upwards across the body of the mandible to pass under depressor anguli oris. The branches supply risorius and the muscles of the lower lip and chin. Filaments communicate with the mental nerve. The marginal mandibular branch has an important surgical relationship with the inferior border of the mandible.

The cervical branch emerges from the lower part of the parotid gland and runs anteroinferiorly under platysma to the anterior neck. Typically single, it supplies platysma and communicates with the transverse cutaneous cervical nerve.

Cutaneous branches of the facial nerve accompany the auricular branch of the vagus and probably supply small areas on both aspects of the auricle, in the depression of the concha and over its eminence.

Lesions of the facial nerve

Facial paralysis may be due to an upper motor neurone lesion (when frontalis is partially spared because of the bilateral cortical representation of the muscles of the upper part of the face) or a lower motor neurone lesion (when all branches may be involved). Lower motor neurone facial paralysis is most commonly idiopathic (Bell's palsy). There are a large number of other recognized causes that include geniculate herpes zoster (Ramsay Hunt syndrome), malignant tumours of the parotid gland and temporal bone. Iatrogenic damage also accounts for a significant number of palsies, most often acquired in vestibular schwannoma, parotid and middle ear or mastoid surgery (Robinson and Baiungo 2018).

Cervical spinal nerves

Cervical spinal nerves have cutaneous branches that supply areas of skin in the face and scalp (see Fig. 36.22). The named branches are the great auricular and lesser occipital nerves that are part of the cervical plexus and described on page 573 (see Fig. 35.1B), and the greater occipital nerve that is described on page 862 (see Figs 46.78, 47.8).

PAROTID SALIVARY GLAND

The paired parotid glands are the largest of the salivary glands. Each has an average weight of 25 g and is an irregular, lobulated, yellowish mass, lying largely below the external acoustic meatus between the mandible and sternocleidomastoid. The gland also projects forwards onto the surface of masseter (**Fig. 36.23B**). Sometimes, a small and often detached part called the accessory parotid gland (pars accessoria or socia parotidis) lies between the zygomatic arch above and the parotid duct below (Fromer 1977). The overall shape of the parotid gland is variable. Viewed laterally, it is often roughly triangular in outline, whereas other glands are more or less of even width throughout with rounded upper and lower poles.

In its usual inverted pyramidal form, the parotid gland presents superior, superficial, anteromedial and posteromedial surfaces and tapers inferiorly to a blunt apex. The small concave superior surface is related to the cartilaginous part of the external acoustic meatus and posterior aspect of the temporomandibular joint. Here, the auriculotemporal nerve curves round the neck of the mandible, embedded in the parotid capsule. The apex overlaps the posterior belly of digastric and the carotid triangle to a variable extent. The superficial surface is covered by skin and superficial fascia that contains the facial branches of the great auricular nerve, superficial parotid lymph nodes and the posterior border of platysma. It extends upwards to the zygomatic arch, backwards to overlap sternocleidomastoid, downwards to its apex posteroinferior to the mandibular angle, and forwards to lie on masseter below the parotid duct. The anteromedial surface is grooved by the posterior border of the mandibular ramus. It covers the posteroinferior part of masseter, the lateral aspect of the temporomandibular joint and the adjoining part of the mandibular ramus. It passes forwards, medial to the ramus of the mandible, to reach medial pterygoid. The gland may therefore be subdivided into a larger superficial part and a smaller part, the deep 'lobe', deep to the ramus, the two being joined by an isthmus. Branches of the facial nerve emerge on the face from the anterior margin of this surface.

The posteromedial surface is moulded to the mastoid process, sternocleidomastoid, posterior belly of the digastric, and the styloid process and its associated muscles. The external carotid artery grooves this surface before entering the gland, and the internal carotid artery and internal jugular vein are separated from the gland by the styloid process and its associated muscles (**Fig. 36.25**). The anteromedial and posteromedial surfaces meet at a medial margin that may project so deeply that it contacts the lateral wall of the pharynx.

Deep lobe tumours The deep 'lobe' of the gland extends behind the mandibular ramus, where its deep surface lies immediately lateral to

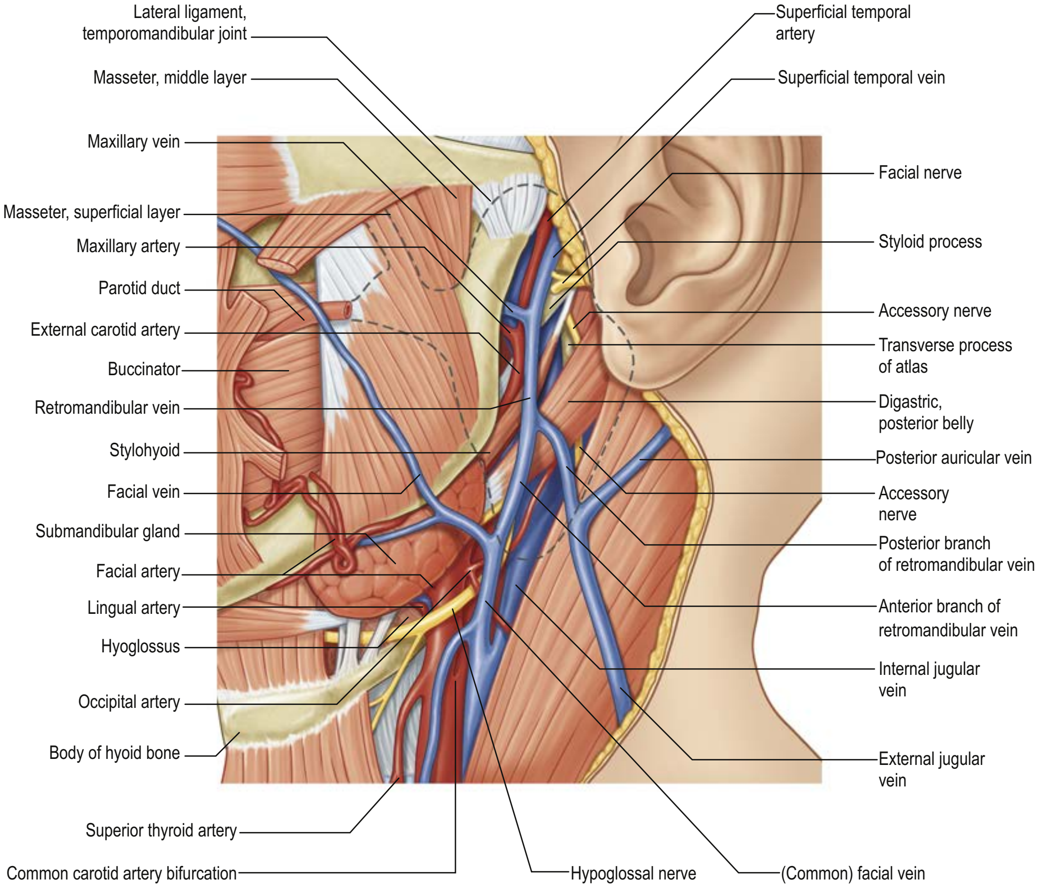
Lateral ligament, temporomandibular joint
Masseter, middle layer
Maxillary vein
Masseter, superficial layer
Maxillary artery
Parotid duct
External carotid artery
Buccinator
Retromandibular vein
Stylohyoid
Facial vein
Submandibular gland
Facial artery
Lingual artery
Hyoglossus
Occipital artery
Body of hyoid bone
Superior thyroid artery
Common carotid artery bifurcation
Hypoglossal nerve
(Common) facial vein
Superficial temporal artery
Superficial temporal vein
Facial nerve
Styloid process
Accessory nerve
Transverse process of atlas
Digastric, posterior belly
Posterior auricular vein
Accessory nerve
Posterior branch of retromandibular vein
Anterior branch of retromandibular vein
Internal jugular vein
External jugular vein

Fig. 36.25 The principal immediate deep relations of the parotid gland. The outline of the parotid gland is indicated by the interrupted black line.

the superior constrictor of the pharynx. When a parotid tumour, either benign or malignant, develops in the deep 'lobe', the mass presents as a swelling in the lateral wall of the oropharynx and not as a facial swelling.

Structures within the parotid gland

The external carotid artery, retromandibular vein and facial nerve, either in part or in whole, traverse the gland and branch within it (Langdon 1998). The external carotid artery enters the posteromedial surface and divides into the maxillary artery, which emerges from the anteromedial surface, and the superficial temporal artery, which gives off its transverse facial branch in the gland and ascends to leave its upper limit (see Fig. 36.23). The posterior auricular artery may also branch from the external carotid artery within the gland, leaving by its posteromedial surface.

The retromandibular vein, formed by the union of the maxillary and superficial temporal veins (which enter near the points of exit of the corresponding arteries), is superficial to the external carotid artery. It descends in the parotid gland and emerges behind the apex of the gland, where it usually divides into an anterior branch that passes forwards to join the facial vein, and a posterior branch that joins the posterior auricular vein to form the external jugular vein. Occasionally, it is not connected to the external jugular vein, which is then small, and the anterior jugular vein is enlarged.

Parotid capsule

The parotid gland is enclosed within an unyielding parotid capsule derived from the investing layer of deep cervical fascia. Acute inflammation of the parotid gland (acute sialadenitis) may cause exquisite pain in the pre-auricular region as a result of capsular stretch and stimulation of the great auricular nerve. The pain is usually exacerbated at mealtimes when the gustatory stimulus to the gland results in further turgor within the capsule. Causes of acute sialadenitis include parotid duct obstruction (calculus, mucus plug and duct stricture) and mumps.

Parotid duct

The average dimensions of the parotid duct are 5 cm long and 3 mm wide (narrower at its oral orifice). The duct begins by the confluence of two main tributaries within the anterior part of the parotid gland. It appears at the anterior border of the upper part of the gland and passes horizontally across masseter, approximately midway between the angle of the mouth and the zygomatic arch (**Fig. 36.18C**; see Figs 36.25, 37.40A). If the duct arises lower down, it may run obliquely upwards. It crosses masseter, turning medially at its anterior border at almost a right angle, and traverses the buccal fat pad and buccinator opposite the crown of the maxillary third molar tooth. The duct then runs obliquely forwards for a short distance between buccinator and the oral mucosa before it opens on a small papilla opposite the crown of the maxillary second molar tooth. The submucosal passage of the duct serves as a valvular mechanism, preventing inflation of the gland with raised intraoral pressures. While crossing masseter, the duct lies between the upper and lower buccal branches of the facial nerve and may receive the accessory parotid duct.

The accessory part of the gland (Fromer 1977) and the transverse facial artery lie above the parotid duct; the buccal branch of the mandibular nerve, emerging from beneath temporalis and masseter, lies just below, at the anterior border of masseter. The parotid duct may be crossed by anastomosing branches between the zygomatic and buccal branches of the facial nerve.

The ramifications of the ductal systems, their patterns and calibres, can be demonstrated radiographically by injecting a radio-opaque substance into the parotid duct via a cannula. In a lateral parotid sialogram, the main duct can be seen to be formed near the centre of the posterior border of the mandibular ramus by the union of two or three ducts that ascend or descend, respectively at right-angles to the main duct. As it crosses the face, the main duct also receives from above five or six ductules from the accessory parotid gland (**Fig. 36.26**). As it curves round the anterior border of masseter, it is often compressed and its shadow is attenuated. Deep lacerations of the cheek, where the integrity of the parotid duct is in doubt, should be explored and repaired using microsurgical techniques to prevent saliva leaking into the soft tissues of the cheek and subsequent sialocele formation.

Vascular supply and lymphatic drainage

The parotid gland receives its arterial supply from the external carotid artery and its branches within and near the gland. The veins drain to the external jugular vein via local tributaries.

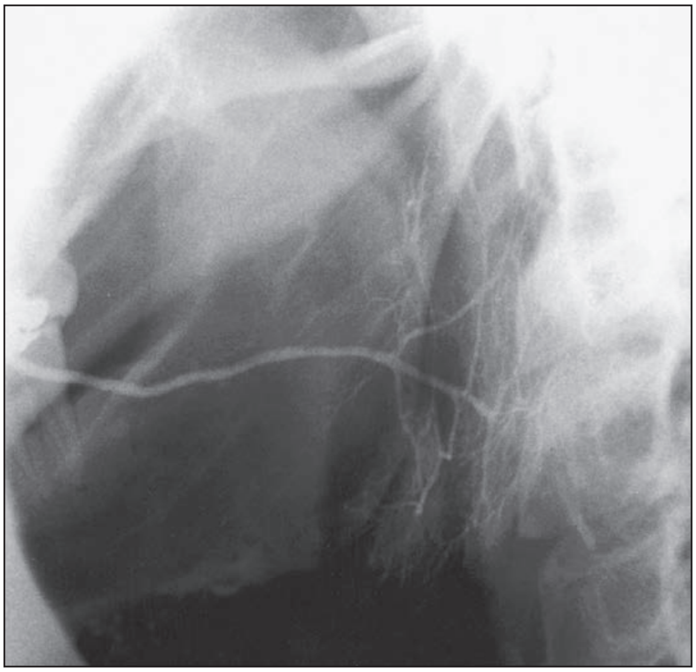

Fig. 36.26 An oblique lateral radiograph showing a normal parotid duct outlined after injection of radio-opaque contrast medium (sialogram). Note that here the main duct is formed by the union of three smaller ducts at the posterior border of the ramus of the mandible. (Courtesy of Dr N Drage.)

Lymph drains to nodes in the skin overlying the parotid gland (pre-auricular nodes) and in the substance of the gland itself. There are usually 10 lymph nodes present in the gland, the majority lying in the superficial part of the gland above the plane related to the facial nerve. Lymph from these parotid nodes drains to the upper deep cervical lymph nodes.

Innervation

Preganglionic nerves travel in the lesser petrosal branch of the glossopharyngeal nerve and synapse in the otic ganglion (see Fig. 33.7). Postganglionic secretomotor fibres reach the gland via the auriculotemporal nerve.

Gustatory sweating

Gustatory sweating (syndrome or auriculotemporal sweating) may occasionally develop after parotid surgery or trauma to the capsule of the gland. It is thought to reflect aberrant innervation of sweat glands on the face by regenerating parasympathetic secretomotor axons that would previously have innervated the parotid gland. Frey's syndrome is characterized by sweating, warmth and redness of the face as a result of salivary stimulation in response to the smell or taste of food. The management of Frey's syndrome is difficult. Denervation by tympanic neurectomy or auriculotemporal nerve avulsion has been advocated but is rarely curative and has been superseded by the subcutaneous infiltration of purified botulinum toxin into the affected area or the use of antiperspirants.

Microstructure of the salivary glands is described in Chapter 37.

Bonus e-book content

Fig. 36.10 A compound craniofacial fracture with disruption of the anterior and posterior walls of the frontal sinus, torn dura mater, and intracranial bone.

Fig. 36.11 An extended naso-orbito-ethmoid (NOE) fracture.

Fig. 36.12 A typical high-energy pan-facial injury.

Fig. 36.13 Various examples of plating configurations and titanium alloplastic reconstructions.

Fig. 36.14 A typical left zygomatic fra6cture.

Fig. 36.15 Image fusion of computed tomography and magnetic resonance imaging, showing an extensive left medial orbital wall fracture.

Fig. 36.16 **A**, A typical large medial wall and floor fracture. **B**, In this case, the intact right medial orbital wall (green line) was mirrored; the red line outlines the defect on the left orbit. **C**, A titanium plate was then placed through a transconjunctival incision, with lateral cantholysis; the position was checked with intraoperative navigation.

Key references

Ahmas F, Kirkpatrick NA, Lyne J et al 2006 Buckling and hydraulic mechanisms in orbital blowout fractures: fact or fiction. J Craniofac Surg 17:438–41.

A paper that does for orbital injuries what Le Fort did for maxillary injuries. The contribution of anatomy to the pathogenesis of floor and medial orbital fractures is elegantly shown.

Borges AF, Alexander JE 1962 Relaxed skin tension lines, Z-plasties on scars, and fusiform excision of lesions. Br J Plast Surg 15:242–54.

A paper that provides the anatomical basis for every incision made on the face.

Eljamel M, Foy P 1990 Post-traumatic CSF fistulae: the case for surgical repair. Br J Neurosurg 4:479–83.

A paper that provides the clinical evidence for management of fractures of the anterior skull base.

Gillies HD, Kilner TP, Stone D 1927 Fractures of the malar–zygomatic compound: with a description of a new X-ray position. Br J Surg 14:651–56.

An old paper but the technique described is a very practical application of exploiting the anatomy of the temporal fossa. The use of temporalis to glide the elevator down to below the arch is insightful.

Langdon JD 1998 Parotid surgery. In: Langdon JD, Patel MF (eds) Operative Maxillofacial Surgery. London: Chapman & Hall; pp. 381–90.

A detailed account of the procedures for the safe dissection of the intraparotid part of the facial nerve.

Le Fort R 1901 Etude expérimental sur les fractures de la mâchoire supérieure. Rec Chir Paris 23:208–27.

A paper that represents the standard way of describing maxillary fractures. Le Fort's classification has endured and still resonates in clinical practice.

Loukota RA, Eckelt U, De Bont L et al 2005 Subclassification of fractures of the condylar process of the mandible. Br J Oral Maxillofac Surg 43:72–3.

A very brief paper that is superb in its simplicity, presenting a logical and pragmatic approach to classifying these injuries, and signposting both surgical difficulty and approach.

Mitz V, Peyronie M 1976 The superficial musculo-aponeurotic system (SMAS) in the parotid and cheek area. Plast Reconstruct Surg 58:80–8.

A paper that provides the anatomical basis for all invasive aesthetic and reconstructive facelift surgery.

Ziarah HA, Atkinson ME 1981 The surgical anatomy of the mandibular distribution of the facial nerve. Br J Oral Surg 19:159–70.

An outline of how the mandibular branch of the facial nerve is at risk in all incisions at the lower border of the mandible, in submandibular gland excision, incision of space-occupying dental infections, and neck dissection. A detailed knowledge of this structure is essential.

References

Ahmas F, Kirkpatrick NA, Lyne J et al 2006 Buckling and hydraulic mechanisms in orbital blowout fractures: fact or fiction. J Craniofac Surg 17:438–41.

A paper that does for orbital injuries what Le Fort did for maxillary injuries. The contribution of anatomy to the pathogenesis of floor and medial orbital fractures is elegantly shown.

Borges AF, Alexander JE 1962 Relaxed skin tension lines, Z-plasties on scars, and fusiform excision of lesions. Br J Plast Surg 15:242–54.

A paper that provides the anatomical basis for every incision made on the face.

Davis RA, Anson BJ, Budinger JM et al 1956 Surgical anatomy of the facial nerve and parotid gland based upon a study of 350 cervicofacial halves. Surg Gynecol Obstet 102:385–412.

Eljamel M, Foy P 1990 Post-traumatic CSF fistulae: the case for surgical repair. Br J Neurosurg 4:479–83.

A paper that provides the clinical evidence for management of fractures of the anterior skull base.

Ellis E 3rd, Tan Y 2003 Assessment of internal orbital reconstructions for pure blowout fractures: cranial bone versus titanium mesh. J Oral Maxillofac Surg 61:442–53.

Farkas LG, Posnick JC, Hreczko TM et al 1992 Growth patterns of the nasolabial region: a morphometric study. Cleft Palate Craniofac J 29:318–24.

Ferrario VF, Sforza C, Schmitz JH et al 2000 Normal growth and development of the lips: a 3-dimensional study from 6 years to adulthood using a geometric model. J Anat 196:415–23.

Fromer J 1977 The human accessory parotid gland: its incidence, nature and significance. Oral Surg Oral Med Oral Pathol 43:671–6.

Gillies HD, Kilner TP, Stone D 1927 Fractures of the malar–zygomatic compound: with a description of a new X-ray position. Br J Surg 14:651–6.

An old paper but the technique described is a very practical application of exploiting the anatomy of the temporal fossa. The use of temporalis to glide the elevator down to below the arch is insightful.

Gonçalves RC, Ravell DB, Ados A 2011 Effects of age and gender on upper airway, lower airway and upper lip growth. Braz Oral Res 25:241–7.

Gosain AK, Yousif NJ, Madiedo G et al 1993 Surgical anatomy of the SMAS: a reinvestigation. Plast Reconstruct Surg 92:1254–63.

Kwak HH, Park HD, Youn KH et al 2004 Branching patterns of the facial nerve and its communication with the auriculotemporal nerve. Surg Radiol Anat 26:494–500.

Langdon JD 1998 Parotid surgery. In: Langdon JD, Patel MF (eds) Operative Maxillofacial Surgery. London: Chapman & Hall; pp. 381–90.

A detailed account of the procedures for the safe dissection of the intraparotid part of the facial nerve.

Le Fort R 1901 Etude expérimental sur les fractures de la mâchoire supérieure. Rec Chir Paris 23:208–27.

A paper that represents the standard way of describing maxillary fractures. Le Fort's classification has endured and still resonates in clinical practice.

Lineaweaver W, Rhoton A, Habal MB 1997 Microsurgical anatomy of the facial nerve. Craniofac Surg 8:6–10.

Loukota RA, Eckelt U, De Bont L et al 2005 Subclassification of fractures of the condylar process of the mandible. Br J Oral Maxillofac Surg 43:72–3.

A very brief paper that is superb in its simplicity, presenting a logical and pragmatic approach to classifying these injuries, and signposting both surgical difficulty and approach.

Manson PN, Grivas A, Rosenbaum A et al 1986 Studies on enophthalmos: II. The measurement of orbital injuries and their treatment by quantitative computed tomography. Plast Reconstr Surg 77:203–14.

Markowitz B, Manson PN, Sargent L et al 1991 Management of the medial canthal tendon in nasoethmoid fractures: the importance of the central fragment in classification and treatment. Plast Reconstr Surg 87:843–5.

Mihailovic T, Stimec BV, Terzic M et al 2012 The absence of the vomer in the first and early second trimester of pregnancy – a new marker of trisomy 21 and trisomy 13. Ultraschall Med 33:E68–74.

Mitz V, Peyronie M 1976 The superficial musculo-aponeurotic system (SMAS) in the parotid and cheek area. Plast Reconstruct Surg 58:80–8.

A paper that provides the anatomical basis for all invasive aesthetic and reconstructive facelift surgery.

Robinson MW, Baiungo J 2018 Facial rehabilitation: evaluation and treatment strategies for the patient with facial palsy. Otolaryngol Clin North Am 51:1151–67.

This paper provides an overview of the strategies for facial nerve reconstruction.

Shimada K, Gasser RF 1988 Morphology of the mandibulo-stylohyoid ligament in human adults. Anat Rec 222:207–10.

Stammberger HR, Kennedy DW, Anatomic Terminology Group 1995 Paranasal sinuses: anatomic terminology and nomenclature. Ann Otol Rhinol Laryngol Suppl 167:7–16.

Wassef M 1987 Superficial fascial and muscular layers in the face and neck: a histological study. Aesth Plast Surg 11:171–6.

Yousif NJ, Mendelson BC 1995 Anatomy of the midface. Clin Plast Surg 22:227–40.

Ziarah HA, Atkinson ME 1981 The surgical anatomy of the mandibular distribution of the facial nerve. Br J Oral Surg 19:159–70.

An outline of how the mandibular branch of the facial nerve is at risk in all incisions at the lower border of the mandible, in submandibular gland excision, incision of space-occupying dental infections, and neck dissection. A detailed knowledge of this structure is essential.

Zufferey JA 2013 Is the malaris muscle the anti-aging missing link of the midface? Eur J Plast Surg 36:345–52.

Further reading

Norman JE de, McGurk M (eds) 1995 Color Atlas and Text of the Salivary Glands. London: Mosby–Wolfe.

CHAPTER 37

Mouth

The mouth extends from the lips and cheeks externally to the anterior pillars of the fauces internally, where it continues into the oropharynx. The mouth can be subdivided into the vestibule external to the teeth and the oral cavity proper internal to the teeth (**Fig. 37.1**). The palate forms the roof of the mouth and separates the oral and nasal cavities. The floor of the mouth is formed by the mylohyoid muscles and is occupied mainly by the tongue. The lateral walls of the mouth are defined by the cheeks and retromolar regions. Three pairs of major salivary glands (parotid, submandibular and sublingual) and numerous minor salivary glands (labial, buccal, palatal, lingual) open into the mouth. The muscles in the mouth and oral cavity are associated with the lips, cheeks, floor of the mouth and tongue. The muscles of the lips and cheeks are described with the face in Chapter 36. The muscles of the soft palate are described with the pharynx in Chapter 40 (Berkovitz and Moxham 2002).

The mouth is concerned primarily with the ingestion and mastication of food, which is mainly the function of the teeth. The mouth is also associated with phonation and ventilation.

CHEEKS

The external features of the cheeks are described in Chapter 36. Internally, the mucosa of the cheek is tightly adherent to buccinator and is thus stretched when the mouth is opened and wrinkled when closed. Ectopic sebaceous glands may be evident as yellow patches (Fordyce spots). Their numbers increase in puberty and in later life.

Few structural landmarks are visible. The parotid duct drains into the cheek opposite the maxillary second molar tooth at a small parotid papilla. A hyperkeratinized line (the linea alba) may be seen at a position related to the occlusal plane of the teeth. In the retromolar region, a fold of mucosa containing the pterygomandibular raphe extends from the upper to the lower alveolus. The entrance to the pterygomandibular space (which contains the lingual and inferior alveolar nerves) lies lateral to this fold and medial to the ridge produced by the anterior border of the ramus of the mandible; this is the site for injection for an inferior alveolar nerve block, commonly used to anaesthetize the ipsilateral lower teeth and gums.

Vascular supply and innervation

The cheek receives its arterial blood supply principally from the buccal branch of the maxillary artery, and is innervated by cutaneous branches of the maxillary division of the trigeminal nerve, via the zygomaticofacial and infraorbital nerves, and by the buccal branch of the mandibular division of the trigeminal nerve.

LIPS

The external features of the lips are described in Chapter 36. The central part of the lips contains orbicularis oris. Internally, the labial mucosa is smooth and shiny, and shows small elevations caused by underlying mucous glands.

The position and activity of the lips are important in controlling the degree of protrusion of the incisors. With normal (competent) lips, the tips of the maxillary incisors lie below the upper border of the lower lip, and this arrangement helps to maintain the 'normal' inclination of

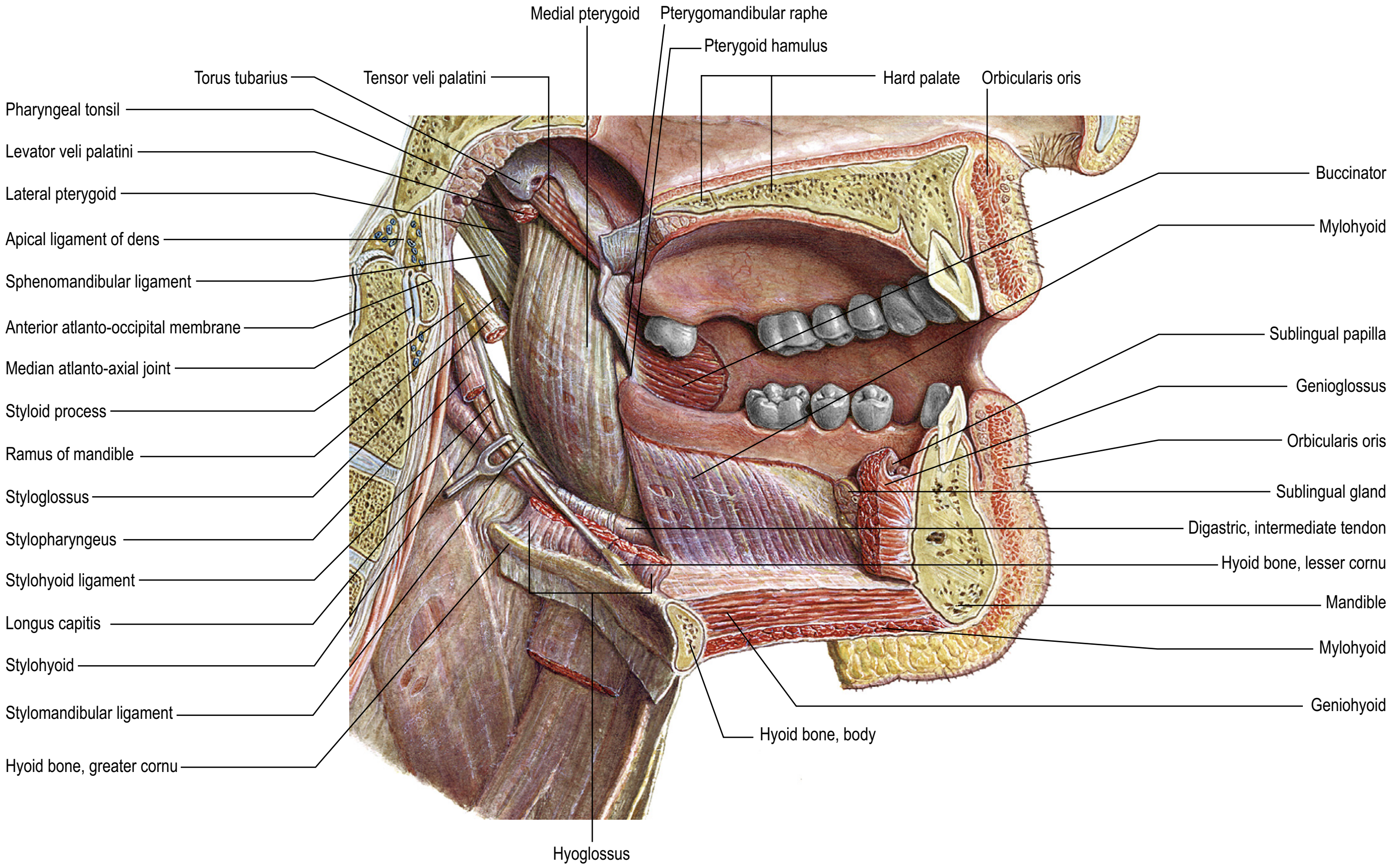
Medial pterygoid
Pterygomandibular raphe
Pterygoid hamulus
Torus tubarius
Tensor veli palatini
Hard palate
Orbicularis oris
Pharyngeal tonsil
Levator veli palatini
Lateral pterygoid
Apical ligament of dens
Sphenomandibular ligament
Anterior atlanto-occipital membrane
Median atlanto-axial joint
Styloid process
Ramus of mandible
Styloglossus
Stylopharyngeus
Stylohyoid ligament
Longus capitis
Stylohyoid
Stylomandibular ligament
Hyoid bone, greater cornu
Buccinator
Mylohyoid
Sublingual papilla
Genioglossus
Orbicularis oris
Sublingual gland
Digastric, intermediate tendon
Hyoid bone, lesser cornu
Mandible
Mylohyoid
Geniohyoid
Hyoid bone, body
Hyoglossus

Fig. 37.1 The oral cavity. The tongue and soft palate have been removed. (Sobotta Atlas of Human Anatomy © Elsevier GmbH, Urban & Fischer, Munich.)

the incisors. When the lips are incompetent, the maxillary incisors may not be so controlled and the lower lip may even lie behind them, thus producing an exaggerated proclination of these teeth. A tight, or overactive, lip musculature may be associated with retroclined maxillary incisors. The lips are kept moist both by tongue deposition of saliva and by numerous minor salivary glands within them. These glands are liable to trauma by the teeth, particularly in the lower lip; this can produce a mucocele as a result of either extravasation of saliva into the submucosal tissues or retention of saliva within the gland or its duct.

Vascular supply and innervation

The lips are mainly supplied by the superior and inferior labial branches of the facial artery. The upper lip is innervated by superior labial branches of the infraorbital nerve, and the lower lip is innervated by the mental branch of the mandibular division of the trigeminal.

ORAL VESTIBULE

The oral vestibule is a slit-like space between the lips or cheeks on one side and the teeth on the other. When the teeth occlude, the vestibule is a closed space that only communicates with the oral cavity proper in the retromolar regions behind the last molar tooth on each side. Where the mucosa that covers the alveolus of the jaw is reflected on to the lips and cheeks, a trough or sulcus is formed, which is called the fornix vestibuli. A variable number of sickle-shaped folds containing loose connective tissue run across the fornix vestibuli. In the midline, these are the upper and lower labial frenula. Other folds may traverse the fornix near the canines or premolars. The folds in the lower fornix are said to be more pronounced than those in the upper fornix (**Fig. 37.2**).

The upper labial frenulum is normally attached well below the alveolar crest. A large frenulum with an attachment near or on the crest may be associated with a midline gap (diastema) between the maxillary first incisors. This can be corrected by simple surgical removal of the frenulum (frenulectomy) because it contains no structures of clinical importance. Prominent frenula may compromise the stability of dentures.

ORAL MUCOSA

The oral mucosa is continuous with the skin at the labial margins (vermilion border) and with the pharyngeal mucosa at the oropharyngeal isthmus. It varies in structure, function and appearance in different regions of the oral cavity and is traditionally divided into lining, masticatory and specialized mucosae (Presland and Dale 2000).

Lining mucosa

The lining mucosa is red in colour, and covers the soft palate, ventral surface of the tongue, floor of the mouth, alveolar processes excluding the gingivae, and the internal surfaces of the lips and cheeks. It has a non-keratinized stratified squamous epithelium, which overlies a loosely fibrous lamina propria, and the submucosa contains some fat deposits and collections of minor mucous salivary glands. The oral mucosa covering the alveolar bone – which supports the roots of the teeth – and the necks (cervical region) of the teeth is divided into two main components. That portion lining the lower part of the alveolus is loosely attached to the periosteum via a diffuse submucosa and is termed the alveolar mucosa. It is delineated from the masticatory gingival mucosa, which covers the upper part of the alveolar bone and the necks of the teeth, by a well-defined junction, the mucogingival junction. The alveolar mucosa appears dark red; the gingival appears pale pink (see Fig. 37.2). These colour differences relate to differences in the type of keratinization and the proximity to the surface of underlying small blood vessels, which may sometimes be seen coursing beneath the alveolar mucosa.

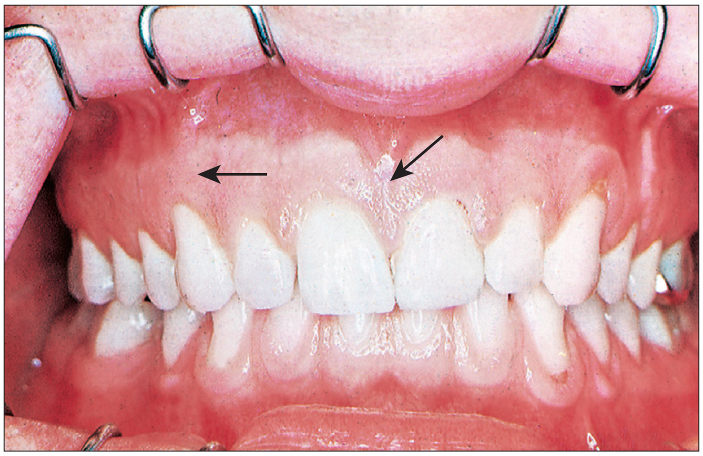

Fig. 37.2 An anterior view of the dentition in centric occlusion, with the lips retracted. Note the pale pink, stippled gingivae and the red, shiny, smooth alveolar mucosa. The degree of overbite is rather pronounced, and the gingiva and its epithelial attachment have receded on to the root of the upper left canine. Note the frena (arrows).

Masticatory mucosa and the gingivae

Masticatory mucosa (mucosa that is subjected to masticatory stress) is bound firmly to underlying bone or to the necks of the teeth, and forms a mucoperiosteum in the gingivae and palatine raphe. Gingival, palatal and dorsal lingual mucosae are keratinized or parakeratinized (Schroeder and Listgarten 1997).

The gingivae may be further subdivided into the attached gingivae and the free gingivae. Attached gingivae are firmly bound to the periosteum of the alveolus and to the teeth, whereas free gingivae, which constitute approximately a 1 mm margin of the gingivae, lie unattached around the cervical region of each tooth. The free gingival groove between the free and attached gingivae corresponds roughly to the floor of the gingival sulcus that separates the inner surface of the attached gingivae from the enamel. The interdental papilla is that part of the gingivae that fills the space between adjacent teeth. The surface of the attached gingivae is characteristically stippled, although there is considerable inter-individual variation in the degree of stippling, and variation according to age, sex and the health of the gingivae. The free gingivae are not stippled. A mucogingival line delineates the attached gingivae on the buccal surface of the upper and lower jaws (see Fig. 37.2) and the lingual surface of the lower jaw from the alveolar mucosa. There is no corresponding obvious division between the attached gingivae and the remainder of the palatal mucosa because this whole surface is orthokeratinized masticatory mucosa, which is pink.

A submucosa is absent from the gingivae and the midline palatine raphe, but is present over the rest of the hard palate. Posterolaterally, it is thick where it contains mucous salivary glands and the greater palatine nerves and vessels, and it is anchored to the periosteum of the maxillae and palatine bones by collagenous septa.

Vascular supply and lymphatic drainage

The gingival tissues derive their blood supply from the maxillary and lingual arteries. The buccal gingivae around the maxillary cheek teeth are supplied by gingival and perforating branches from the posterior superior alveolar artery and by the buccal branch of the maxillary artery. The labial gingivae of anterior teeth are supplied by labial branches of the infraorbital artery and by perforating branches of the anterior superior alveolar artery. The palatal gingivae are supplied primarily by branches of the greater palatine artery.

The buccal gingivae associated with the mandibular cheek teeth are supplied by the buccal branch of the maxillary artery and by perforating branches from the inferior alveolar artery. The labial gingivae around the anterior teeth are supplied by the mental artery and by perforating branches of the incisive artery. The lingual gingivae are supplied by perforating branches from the inferior alveolar artery and by its lingual branch, and by the main lingual artery, a branch of the external carotid artery.

No accurate description is available concerning the venous drainage of the gingivae, although it may be assumed that buccal, lingual, greater palatine and nasopalatine veins are involved. These veins run into the pterygoid plexuses (apart from the lingual veins, which may pass directly into the internal jugular veins).

The lymph vessels of the labial and buccal gingivae of the maxillary and mandibular teeth unite to drain into the submandibular nodes, though in the labial region of the mandibular incisors they may drain into the submental lymph nodes. The lingual and palatal gingivae drain into the jugulodigastric group of nodes, either directly or indirectly through the submandibular nodes.

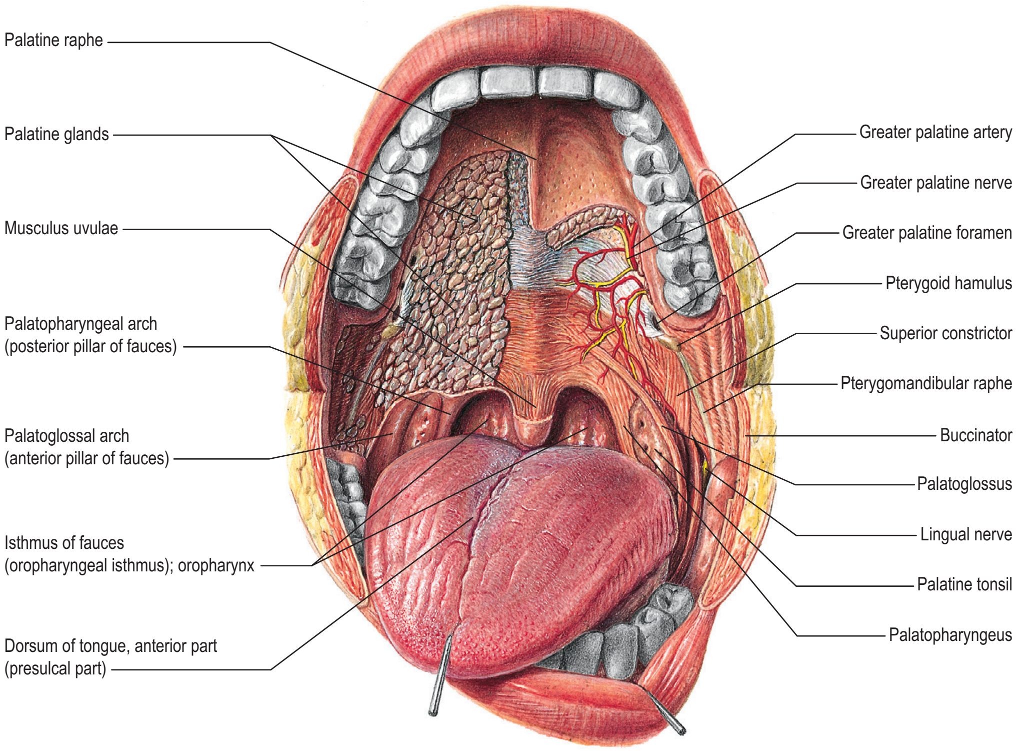

Fig. 37.3 The oral cavity, oropharyngeal isthmus and muscles of the palate. (Sobotta Atlas of Human Anatomy © Elsevier GmbH, Urban & Fischer, Munich.)

Innervation

The nerves supplying the gingivae in the upper jaw come from the maxillary nerve via its greater palatine, nasopalatine, anterior, middle and posterior superior alveolar branches (see Table 37.2). Surgical division of the nasopalatine nerve, e.g. during the removal of an ectopic canine tooth, causes no obvious sensory deficit in the anterior part of the palate, which suggests that the territory of the greater palatine nerve reaches as far forwards as the gingivae lingual to the incisor teeth or that the nerve has large regenerative potential. The mandibular nerve innervates the gingivae in the lower jaw by its inferior alveolar, lingual and buccal branches.

OROPHARYNGEAL ISTHMUS

The oropharyngeal isthmus lies between the soft palate and the dorsum of the tongue, and is bounded on both sides by the palatoglossal arches. Each palatoglossal arch runs downwards, laterally and forwards, from the soft palate to the side of the tongue, and consists of palatoglossus and its covering mucous membrane (**Fig. 37.3**). The approximation of the arches shuts off the mouth from the oropharynx, and is essential for deglutition.

FLOOR OF THE MOUTH

The floor of the mouth is a small, horseshoe-shaped region situated beneath the movable part of the tongue and above the muscular diaphragm formed by the mylohyoid muscles. The fascia of the floor of the mouth lies immediately beneath the oral mucosa and is attached around the inner arc of the mandible, fusing centrally with the connective tissue on the ventral surface of the tongue (Mills et al 2019). The sublingual glands and submandibular ducts are enveloped by the fascial layer, fibres of the anterior part of genioglossus are suspended beneath it, and branches of the lingual nerve, located superficially on the ventral surface of the tongue, lie immediately deep to the fascia. Normal movements of the anterior part of the tongue create tension in the central region of the fascia and elevate it into a midline fold, the lingual frenulum (**Figs 37.4C,D**). Restricted movements of the tongue are commonly attributed to the lingual frenulum tethering the tongue, a condition called ankyloglossia (known colloquially as a 'tongue tie'). Historically, the tongue-tied frenulum has been divided to aid speech but the evidence for this procedure is scanty: there is some evidence that frenotomy may aid breast feeding (NICE 2005, Webb et al 2013).

The lingual frenulum is frequently and erroneously referred to as a 'cord' or 'submucosal band' of connective tissue, whereas the fascial fibres that form the frenulum exhibit a basket-weave orientation across the midline and there are no deep extensions into either genioglossus or the median septum of the tongue (Mills et al 2019). There is therefore no anatomical indication to make deep incisions into muscle when performing a frenotomy, with the attendant risk of iatrogenic injury to the lingual nerve.

The submandibular salivary ducts open into the mouth at the sublingual papilla (caruncle), which is a large, centrally positioned protuberance at the base of the tongue. The sublingual folds lie on either side of the sublingual papilla and cover the underlying submandibular ducts and sublingual salivary glands. The blood supply of the floor of the mouth is described with the blood supply of the tongue. The main muscle forming the floor of the mouth is mylohyoid, with geniohyoid lying immediately above it.

Mylohyoid

Mylohyoid lies superior to the anterior belly of digastric and, with its contralateral fellow, forms a muscular floor for the oral cavity. It is a flat, triangular sheet attached to the whole length of the mylohyoid line of the mandible (**Fig. 37.4A**; see Figs 37.1, 37.10, 37.14). The mylohyoid line is of variable length, sometimes ending before the lower third molar (wisdom) tooth. The posterior fibres of mylohyoid pass medially and slightly downwards to the front of the body of the hyoid bone near its lower border. The middle and anterior fibres from each side decussate in a median fibrous raphe that stretches from the symphysis menti to the hyoid bone. The median raphe is sometimes absent, in which case the two muscles form a continuous sheet, or it may be fused with the anterior belly of digastric. In about one-third of subjects, there is a hiatus in the muscle through which a process of the sublingual gland protrudes. The mylohyoid hiatus is the pathway for a plunging ranula.

Relations The inferior (external) surface is related to platysma, the anterior belly of digastric the superficial part of the submandibular gland, the facial and submental vessels, and the mylohyoid vessels and nerve. The superior (internal) surface is related to geniohyoid, part of hyoglossus and styloglossus, the hypoglossal and lingual nerves, the submandibular ganglion, the sublingual gland, the deep part of the submandibular gland and its duct, the lingual and sublingual vessels, and, posteriorly, the mucous membrane of the mouth (see Fig. 37.14).

Vascular supply Mylohyoid receives its arterial supply from the sublingual branch of the lingual artery, the maxillary artery, via the mylohyoid branch of the inferior alveolar artery, and the submental branch of the facial artery.

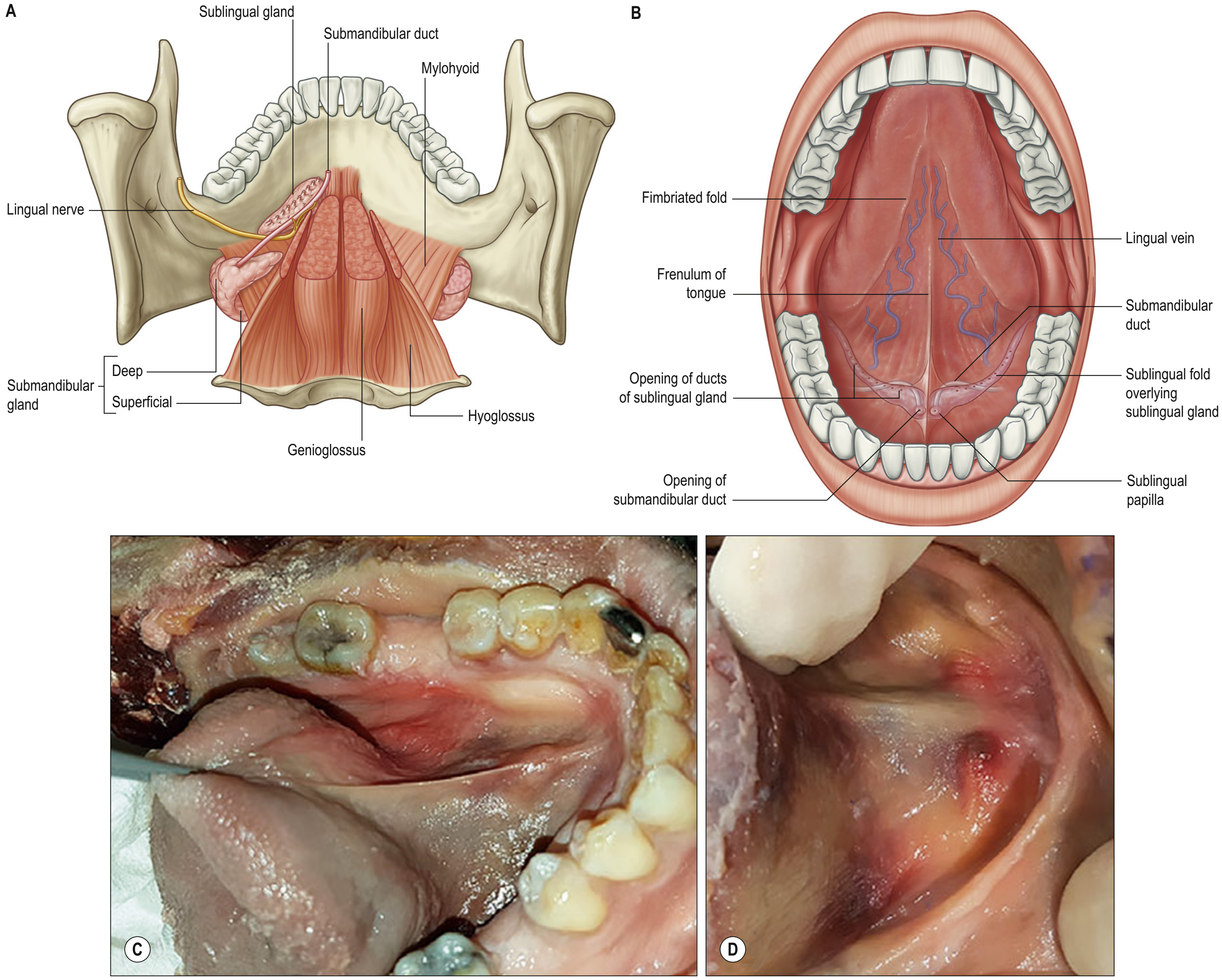
A
Sublingual gland
Submandibular duct
Mylohyoid
Lingual nerve
Submandibular gland
Deep
Superficial
Genioglossus
Hyoglossus
B
Fimbriated fold
Lingual vein
Frenulum of tongue
Submandibular duct
Opening of ducts of sublingual gland
Sublingual fold overlying sublingual gland
Opening of submandibular duct
Sublingual papilla
C
D

Fig. 37.4 The floor of the mouth. **A**, View from above when the bulk of the tongue musculature has been removed. Note the relationships between the lingual nerve and the submandibular duct, and between the submandibular and sublingual salivary glands. **B**, The ventral surface of the tongue, visible when the tip of the tongue is turned upwards. **C**–**D**, Examples of the variable morphology of the lingual frenulum under tension, cadaveric tissue. **C**, Opaque frenulum: mucosa and fascia drawn up to top of fold, genioglossus drawn up into base of frenulum. **D**, Thick/bulky frenulum: genioglossus drawn up into frenulum together with mucosa and fascia. (A, B, With permission from Drake RL, Vogl AW, Mitchell A (eds) Gray's Anatomy for Students, 2nd ed. Elsevier, Churchill Livingstone. Copyright 2010. C, D, With permission from Mills N, Pransky SM, Geddes DT et al 2019 What is a tongue tie? Defining the anatomy of the in-situ lingual frenulum. Clin Anat 32:749–61.)

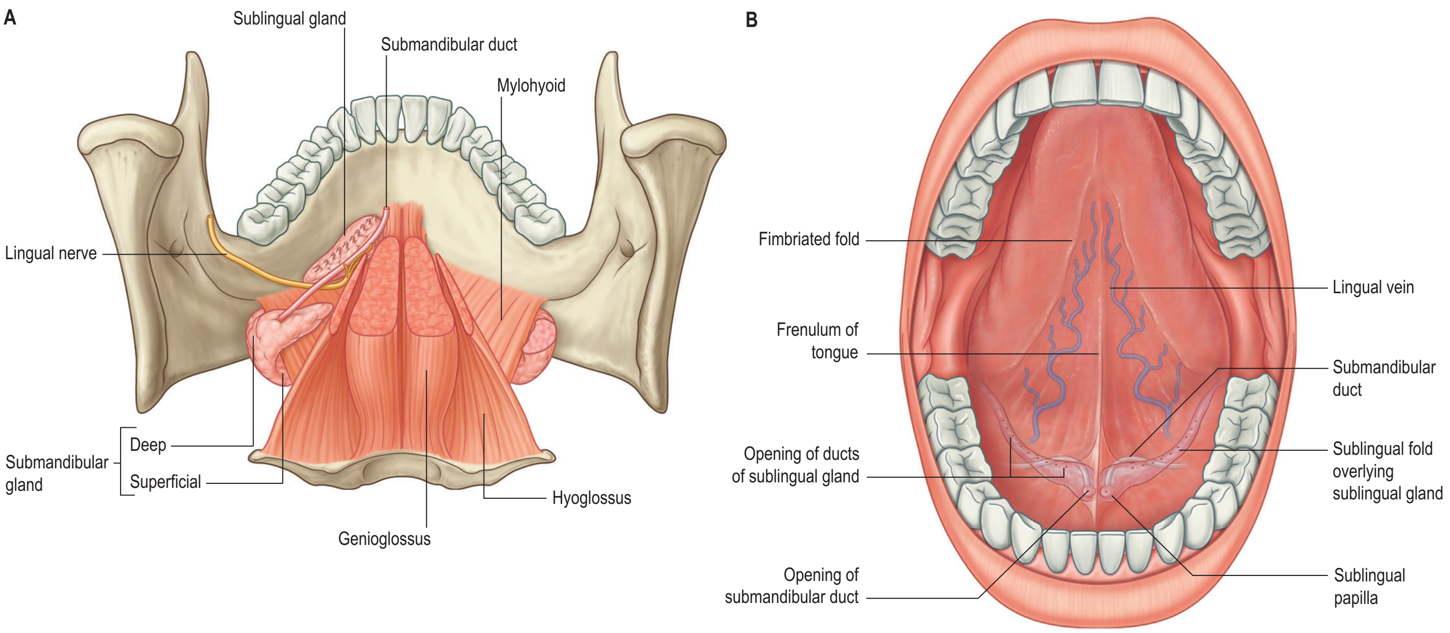

Fig. 37.4 The floor of the mouth. **A**, View from above when the bulk of the tongue musculature has been removed. Note the relationships between the lingual nerve and the submandibular duct, and between the submandibular and sublingual salivary glands. **B**, The ventral surface of the tongue, visible when the tip of the tongue is turned upwards. A, B, With permission from Drake RL, Vogl AW, Mitchell A (eds) Gray's Anatomy for Students, 2nd ed. Elsevier, Churchill Livingstone. Copyright 2010. (C–D, *continued online*)

Innervation. Mylohyoid is supplied by the mylohyoid branch of the inferior alveolar nerve, which can sometimes also supply accessory innervation to the posterior mandibular teeth.

Actions. Mylohyoid elevates the floor of the mouth in the first stage of deglutition. It may also elevate the hyoid bone or depress the mandible.

Geniohyoid

Geniohyoid is a narrow muscle that lies above the medial part of mylohyoid (see Figs 37.9–37.11). It arises from the inferior mental spine (genial tubercle) on the back of the symphysis menti, and runs backwards and slightly downwards to attach to the anterior surface of the body of the hyoid bone. The paired muscles are contiguous and may occasionally fuse with each other or with genioglossus.

Vascular supply. The blood supply to geniohyoid is derived from the lingual artery (sublingual branch).

Innervation. Geniohyoid is supplied by the first cervical spinal nerve, through the hypoglossal nerve.

Actions. Geniohyoid elevates the hyoid bone and draws it forwards, and therefore acts partly as an antagonist to stylohyoid. When the hyoid bone is fixed, geniohyoid depresses the mandible.

PALATE

The palate forms the roof of the mouth and is divisible into two regions, namely: the hard palate in front and soft palate behind.

Soft palate

The soft palate is described with the pharynx in Chapter 40.

Hard palate

The hard palate is formed by the palatine processes of the maxillae and the horizontal plates of the palatine bones (see Figs 36.8B, 36.9, 37.16A). The hard palate is bounded in front and at the sides by the tooth-bearing alveolus of the upper jaw and is continuous posteriorly with the soft palate. It is covered by a thick mucosa bound tightly to the underlying periosteum. In its more lateral regions, it also possesses a submucosa containing the main neurovascular bundle. The mucosa is covered by keratinized stratified squamous epithelium, which shows regional variations and may be ortho- or parakeratinized.

The periphery of the hard palate consists of gingivae. A narrow ridge, the palatine raphe, devoid of submucosa, runs anteroposteriorly in the midline. An oval prominence, the incisive papilla, lies at the anterior extremity of the raphe. It covers the incisive fossa at the oral opening of the incisive canal and also marks the position of the fetal nasopalatine canal. Irregular transverse ridges or rugae, each containing a core of dense connective tissue, radiate outwards from the palatine raphe in the anterior half of the hard palate; their pattern is unique to the individual.

The submucosa in the posterior half of the hard palate contains minor mucous-type salivary glands. They secrete via numerous small ducts, which often drain into a larger duct that opens bilaterally at the paired palatine foveae. These depressions, sometimes a few millimetres deep, flank the midline raphe at the posterior border of the hard palate. They provide a useful landmark for the extent of an upper denture; they cause an overextended denture to become unstable when the soft palate moves during deglutition and mastication. The upper surface of the hard palate is the floor of the nasal cavity and is covered by ciliated respiratory epithelium.

Vascular supply and lymphatic drainage

The palate derives its blood supply principally from the greater palatine artery, a branch of the third part of the maxillary artery. The greater palatine artery descends with its accompanying nerve in the palatine canal, where it gives off two or three lesser palatine arteries, which are transmitted through the lesser palatine canals and foramina to supply the soft palate and tonsil, and anastomose with the ascending palatine branch of the facial artery. The greater palatine artery emerges on to the oral surface of the palate at the greater palatine foramen adjacent to the second maxillary molar and runs in a curved groove near the alveolar border of the hard palate to the incisive canal. It ascends this canal and anastomoses with septal branches of the nasopalatine artery to supply the gingivae, palatine glands and mucous membrane.

The veins of the hard palate accompany the arteries and drain largely to the pterygoid plexus.

Innervation

The sensory nerves of the hard palate are the greater palatine and nasopalatine branches of the maxillary nerve, which all pass through the pterygopalatine ganglion. The greater palatine nerve descends through the greater palatine canal, emerges on the hard palate from the greater palatine foramen, runs forwards in a groove on the inferior surface of the bony palate almost to the incisor teeth and supplies the gums and the mucosa and glands of the hard palate (see Fig. 37.3). It also communicates with the terminal filaments of the nasopalatine nerve. As it leaves the greater palatine canal, it supplies palatine branches to both surfaces of the soft palate. The lesser (middle and posterior) palatine nerves, which are much smaller, descend through the greater palatine canal and emerge through the lesser palatine foramina in the tubercle of the palatine bone to supply the uvula, tonsil and soft palate. The nasopalatine nerves enter the palate at the incisive foramen and are branches of the maxillary nerve that pass through the pterygopalatine ganglion to supply the anterior part of the hard palate behind the incisor teeth.

Fibres conveying taste impulses from the palate probably pass via the palatine nerves to the pterygopalatine ganglion, and travel through it without synapsing to join the nerve of the pterygoid canal and the greater petrosal nerve to the facial ganglion, where their cell bodies are situated. The central processes of these neurones traverse the sensory root of the facial nerve (nervus intermedius) to pass to the gustatory nucleus in the nucleus of the tractus solitarius. Parasympathetic postganglionic secretomotor fibres from the pterygopalatine ganglion run with the nerves to supply the palatine mucous glands.

Tori

Available with the *Gray's Anatomy* e-book

Cysts

Available with the *Gray's Anatomy* e-book

TONGUE

The tongue is a highly muscular organ of deglutition, taste and speech. It is partly oral and partly pharyngeal in position, and is attached by its muscles to the hyoid bone, mandible, styloid processes, soft palate and the pharyngeal wall. It has a root, an apex, a curved dorsum and an inferior surface. Its mucosa is normally pink and moist, and is attached closely to the underlying muscles. The dorsal mucosa is covered by numerous papillae, some of which bear taste buds. Intrinsic muscle fibres are arranged in a complex interlacing pattern of longitudinal, transverse, vertical and horizontal fasciculi, and this allows great mobility. Fasciculi are separated by a variable amount of adipose tissue, which increases posteriorly. The root of the tongue is attached to the hyoid bone and mandible, and between them it is in contact inferiorly with geniohyoid and mylohyoid. The dorsum (posterosuperior surface) is generally convex in all directions at rest. It is divided by a V-shaped sulcus terminalis into an anterior, oral (presulcal) part that faces upwards, and a posterior, pharyngeal (postsulcal) part that faces posteriorly. The anterior part forms about two-thirds of the length of the tongue. The two limbs of the sulcus terminalis run anterolaterally to the palatoglossal arches from a median depression, the foramen caecum, which marks the site of the upper end of the embryonic thyroid diverticulum (thyroglossal duct).

The oral (presulcal) and pharyngeal parts of the tongue differ in their mucosa, innervation and developmental origins.

Oral (presulcal) part

The oral (presulcal) part of the tongue is located in the floor of the oral cavity. It has an apex touching the incisor teeth, a margin in contact with the gums and teeth, and a superior surface (dorsum) related to the hard and soft palates. On each side, in front of the palatoglossal arch, there are four or five vertical folds, the foliate papillae, which represent vestiges of larger papillae found in many other mammals. The mucosa on the inferior (ventral) surface is smooth, purplish and reflected on to the oral floor and gums; it is connected to the oral floor anteriorly by the lingual frenulum. The deep lingual vein, which is visible, lies lateral to the frenulum on either side. The plica fimbriata (fimbriated fold), a fringed mucosal ridge directed anteromedially towards the apex of the tongue, lies lateral to the vein (see Fig. 37.4B). This part of the tongue develops from the lingual swellings of the mandibular arch and from the tuberculum impar, and this embryological derivation explains its sensory innervation.

The dorsal mucosa has a longitudinal median sulcus and is covered by filiform, fungiform and circumvallate papillae (**Fig. 37.5**). It is somewhat thicker than the ventral and lateral mucosae, is directly adherent to underlying muscular tissue with no discernible submucosa, and is covered by numerous papillae. The dorsal epithelium consists of a superficial stratified squamous epithelium, which varies from non-keratinized stratified squamous epithelium posteriorly, to fully keratinized epithelium overlying the filiform papillae more anteriorly. These features probably reflect the fact that the apex of the tongue is subject to greater dehydration than the posterior and ventral parts and is subject to more abrasion during mastication. The underlying lamina propria is a dense fibrous connective tissue, with numerous elastic fibres, and is continuous with similar tissue extending between the fasciculi of the lingual muscles. It contains numerous vessels and nerves from which the papillae are supplied, and also large lymph plexuses and lingual glands.

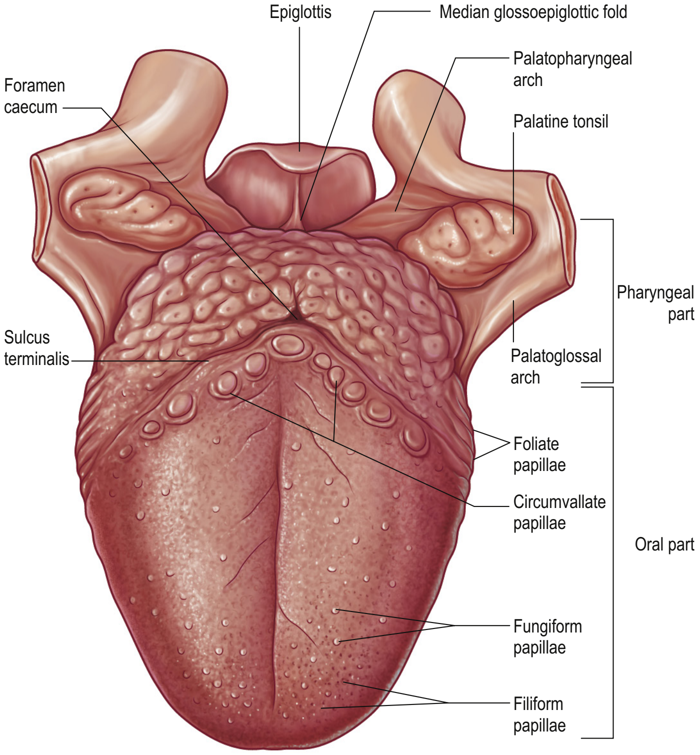

Fig. 37.5 The dorsum of the tongue, adjoining palatoglossal and palatopharyngeal arches, and epiglottis. The palatine tonsils lie in the tonsillar recesses between the palatoglossal and palatopharyngeal arches.

Lingual papillae

Lingual papillae are projections of the mucosa covering the dorsal surface of the tongue (see Fig. 37.5). They are limited to the presulcal part of the tongue, produce its characteristic roughness and increase the area of contact between the tongue and the contents of the mouth. There are four principal types, filiform, fungiform, foliate and circumvallate papillae, and all except the filiform papillae bear taste buds. Papillae are more visible in the living when the tongue is dry.

Filiform papillae

Filiform papillae are minute, conical or cylindrical projections that cover most of the presulcal dorsal area, and are arranged in diagonal rows that extend anterolaterally, parallel with the sulcus terminalis, except at the lingual apex, where they are transverse. They have irregular cores of connective tissue and their epithelium, which is keratinized, may split into whitish fine secondary processes (**Fig. 37.6**). Their functions appear to be to increase the friction between the tongue and food, and to facilitate the movement of particles by the tongue within the oral cavity.

Fungiform papillae

Fungiform papillae occur mainly on the lingual margin but also irregularly on the dorsal surface, where they may occasionally be numerous (see Fig. 37.6). They differ from filiform papillae because they are larger, rounded and deep red in colour, this last reflecting their thin, non-keratinized epithelium and highly vascular connective tissue core. Each usually bears one or more taste buds on its apical surface.

Foliate papillae

Foliate papillae lie bilaterally in two zones at the sides of the tongue near the sulcus terminalis, each formed by a series of red, leaf-like mucosal ridges, covered by a non-keratinized epithelium. They bear numerous taste buds (see Fig. 37.5).

Tori are benign, localized overgrowths of bone found in both the upper (torus palatinus) and lower (torus mandibularis) jaws. Torus palatinus is more common in females, while torus mandibularis is slightly more common in males. Incidence varies from about 0.5% to over 65%: tori are less frequent in Caucasians and more frequent in Eskimos, Mongoloids and other Asian groups. Aetiology is unclear, but torus palatinus may have a hereditary basis (autosomal dominant) (García-García et al 2010).

In the upper jaw, the enlargement is typically seen in the midline. In the lower jaw, it is usually on the lingual aspect in the canine/premolar region and may be unilateral or bilateral. A torus mandibularis may also affect the buccal surface of the mandible. Tori vary considerably in size, and tend to increase in size with age. They may be related to functional adaptations: there is some evidence that their incidence is decreased when fewer teeth are present in the jaws. No treatment is necessary unless they interfere with the construction of satisfactory removable dentures.

Remnants of the nasopalatine ducts or of epithelium persisting during the fusion of palatine processes may proliferate and give rise to non-neoplastic cysts that most often develop in the anterior midline of the hard palate.

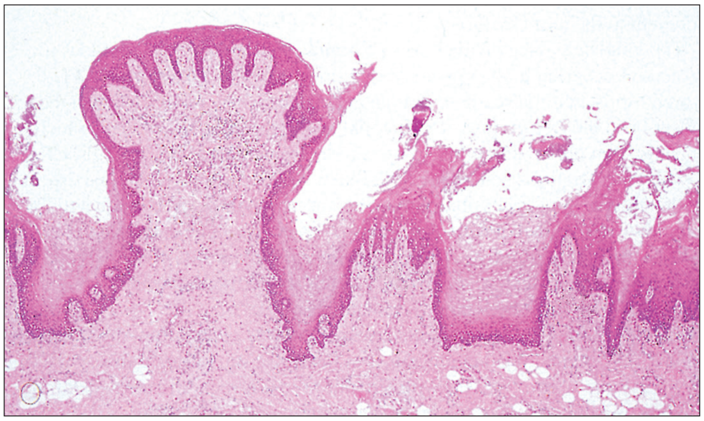

Fig. 37.6 The dorsal surface of the anterior tongue showing non-keratinized fungiform papilla (left) and two keratinized filiform papillae (centre and right) with non-keratinized regions between. (With permission from Young B, Heath JW 2000 Wheater's Functional Histology. Edinburgh: Churchill Livingstone.)

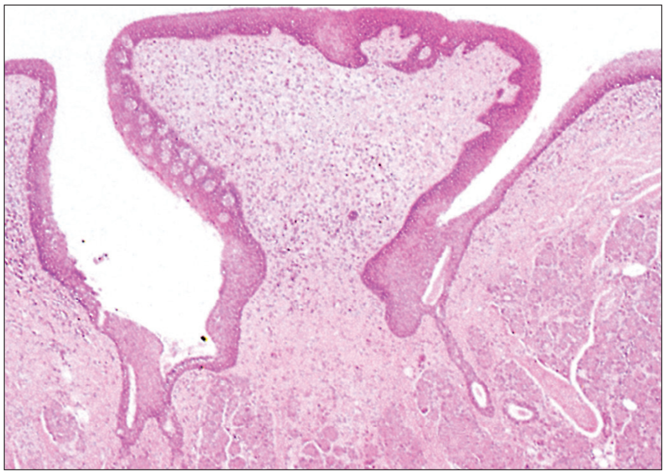

Fig. 37.7 A section through a circumvallate papilla. Serous glands (of von Ebner) empty via ducts into the base of the trench. Numerous taste buds (pale structures on the inner wall of the cleft, left side) are contained within the stratified epithelium of the papillary wall. (With permission from Young B, Heath JW 2000 Wheater's Functional Histology. Edinburgh: Churchill Livingstone.)

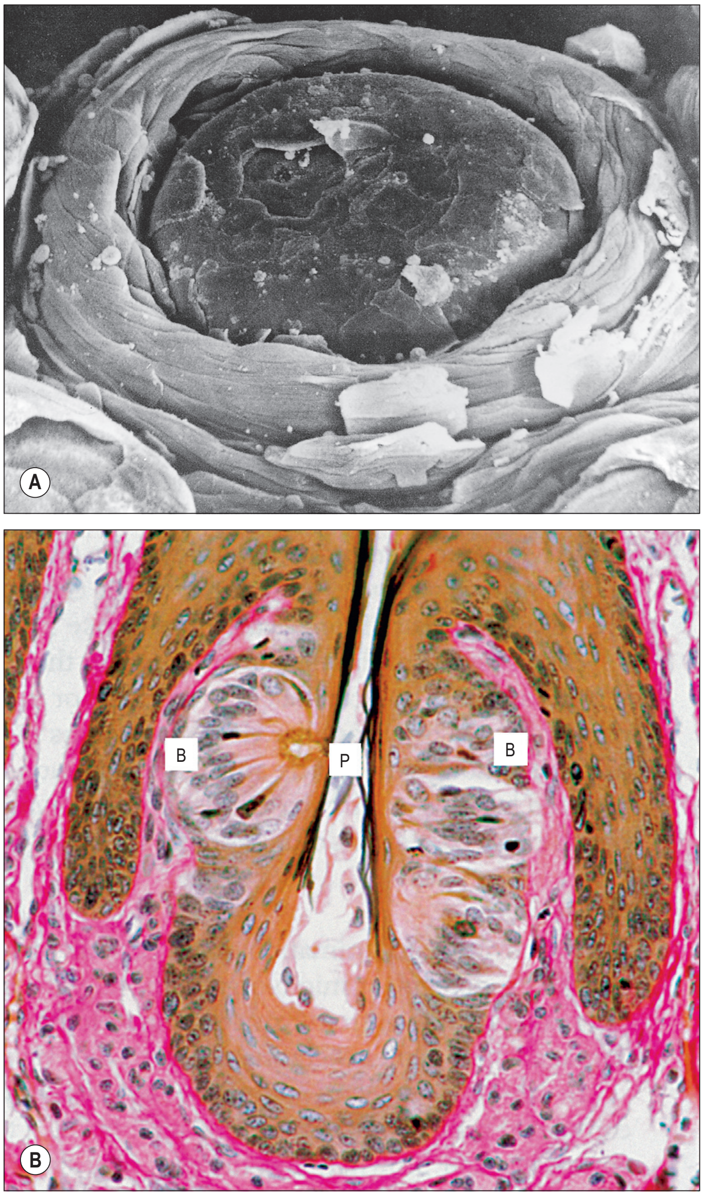

Fig. 37.8 A circumvallate papilla. **A**, A scanning electron micrograph showing a circumvallate papilla surrounded by a trench. **B**, A histological section of a circumvallate papilla showing pale barrel-shaped taste buds (B) in its walls. Key, P, apical pore. (A, Courtesy of S Franey and with permission from Berkovitz BKB, Holland GR, Moxham BJ 2009 Oral Anatomy, Embryology and Histology, 4th ed. Edinburgh: Mosby. B, With permission from Dr JB Kerr, Monash University, from Kerr JB 1999 Atlas of Functional Histology. London: Mosby.)

Circumvallate papillae

Circumvallate papillae are large cylindrical structures, varying in number from 8 to 12, which form a V-shaped row immediately in front of the sulcus terminalis on the dorsal surface of the tongue (see Fig. 37.5). Each papilla, 1–2 mm in diameter, is surrounded by a slight circular mucosal elevation (vallum or wall), which is separated from the papilla by a circular sulcus (**Figs 37.7–37.8**). The papilla is narrower at its base than its apex and the entire structure is generally covered with non-keratinized stratified squamous epithelium. Numerous taste buds are scattered in both walls of the sulcus, and small serous glands (of von Ebner) open into the sulcal base.

Muscles

The tongue is divided by a median fibrous septum that is attached to the body of the hyoid bone. There are extrinsic and intrinsic muscles in each half, the former extending outside the tongue and moving it bodily, the latter wholly within it and altering its shape. The extrinsic musculature consists of four pairs of muscles, namely: genioglossus, hyoglossus, styloglossus (and chondroglossus) and palatoglossus.

Genioglossus

Genioglossus is triangular in sagittal section, lying near and parallel to the midline. It arises from a short tendon attached to the superior genial tubercle behind the mandibular symphysis, above the origin of geniohyoid. From this point, it fans out backwards and upwards (**Fig. 37.9**). The inferior fibres of genioglossus are attached by a thin aponeurosis to the upper anterior surface of the hyoid body near the midline (a few fasciculi passing between hyoglossus and chondroglossus to blend with the middle constrictor of the pharynx). Intermediate fibres pass backwards into the posterior part of the tongue, and superior fibres ascend forwards to enter the whole length of the ventral surface of the tongue from root to apex, intermingling with the intrinsic muscles. The muscles of opposite sides are separated posteriorly by the lingual septum. Anteriorly, they are variably blended by decussation of fasciculi across the midline.

Genioglossus is regarded as the main upper airway dilator muscle. EMG studies have revealed respiratory-related activities in the muscle that appear to be modulated by changes in airway pressure during quiet breathing and by changes in head and jaw posture: this behaviour may be part of a reflex mechanism to maintain airway patency (Cheng et al 2008, Cai et al 2016).

The attachment of the genioglossi to the genial tubercles prevents the tongue from sinking back and obstructing respiration; anaesthetists pull the mandible forwards to obtain the full benefit of this connection. In infants and children, 'chin lift' and 'jaw thrust' are standard resuscitative manoeuvres that rely on this anatomical arrangement to relieve obstruction of the pharynx by the tongue falling back.

Vascular supply. Genioglossus is supplied by the sublingual branch of the lingual artery and the submental branch of the facial artery.

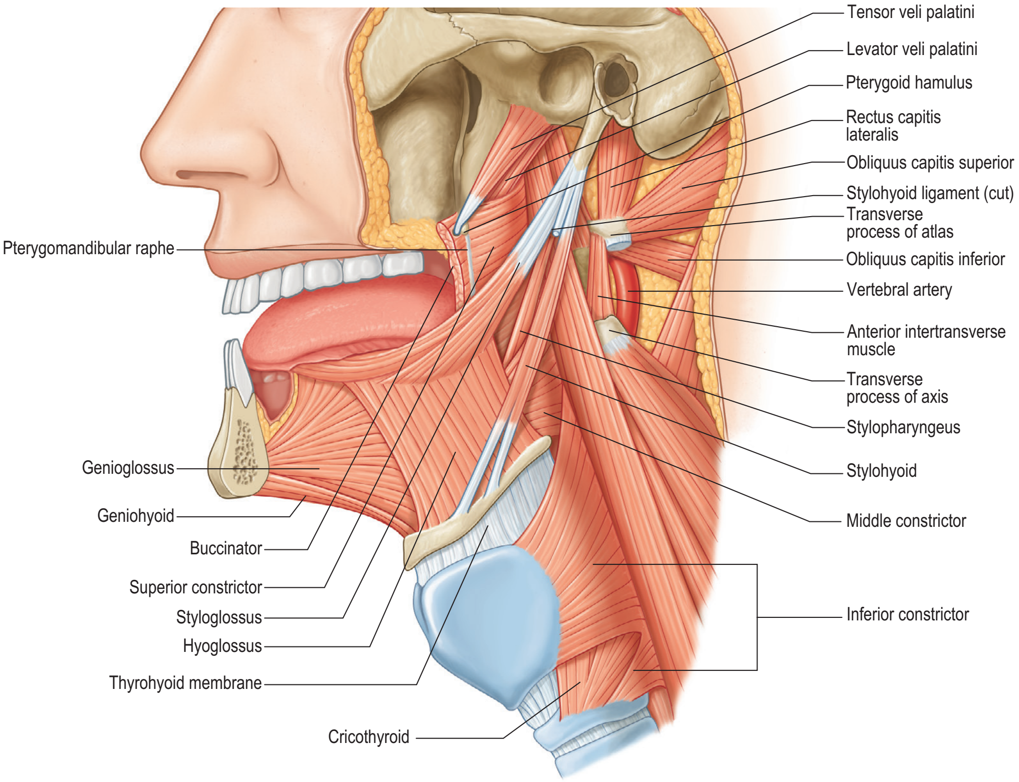
Tensor veli palatini
Levator veli palatini
Pterygoid hamulus
Rectus capitis lateralis
Obliquus capitis superior
Stylohyoid ligament (cut)
Transverse process of atlas
Obliquus capitis inferior
Vertebral artery
Anterior intertransverse muscle
Transverse process of axis
Stylopharyngeus
Stylohyoid
Middle constrictor
Inferior constrictor
Pterygomandibular raphe
Genioglossus
Geniohyoid
Buccinator
Superior constrictor
Styloglossus
Hyoglossus
Thyrohyoid membrane
Cricothyroid

Fig. 37.9 Muscles of the tongue and pharynx. Palatoglossus is not shown here but is depicted in (Fig. 40.3A).

Innervation. Genioglossus is innervated by the hypoglossal nerve.

Actions. Genioglossus brings about the forward traction of the tongue to protrude its apex from the mouth. Acting bilaterally, the two muscles depress the central part of the tongue, making it concave from side to side. Acting unilaterally, genioglossus pushes the tongue to the contralateral side.

Hyoglossus

Hyoglossus is thin and quadrilateral, and arises from the whole length of the greater cornu and the front of the body of the hyoid bone (see Fig. 37.9). It passes vertically up to enter the side of the tongue between styloglossus laterally and the inferior longitudinal muscle medially. Fibres arising from the body of the hyoid overlap those from the greater cornu.

Relations. Hyoglossus is related at its superficial surface to the digastric tendon, stylohyoid, styloglossus and mylohyoid, the lingual nerve and submandibular ganglion, the sublingual gland, the deep part of the submandibular gland and duct, the hypoglossal nerve and the deep lingual vein. By its deep surface it is related to the stylohyoid ligament, genioglossus, the middle constrictor and the inferior longitudinal muscle of the tongue, and the glossopharyngeal nerve. Posteroinferiorly, it is separated from the middle constrictor by the lingual artery. This part of the muscle is in the lateral wall of the pharynx, below the palatine tonsil. Passing deep to the posterior border of hyoglossus are, in descending order: the glossopharyngeal nerve, stylohyoid ligament and lingual artery.

Vascular supply. Hyoglossus is supplied by the sublingual branch of the lingual artery and the submental branch of the facial artery.

Innervation. Hyoglossus is innervated by the hypoglossal nerve.

Actions. Hyoglossus depresses the tongue.

Chondroglossus

Sometimes described as a part of hyoglossus, this muscle is separated from it by some fibres of genioglossus, which pass to the side of the pharynx. It is about 2 cm long, and arises from the medial side and base of the lesser cornu and the adjoining part of the body of the hyoid. It ascends to merge into the intrinsic musculature between hyoglossus and genioglossus. A small slip occasionally springs from the cartilago triticea and enters the tongue with the posterior fibres of hyoglossus.

Vascular supply, innervation and actions. These are similar to those described for hyoglossus.

Styloglossus

Styloglossus is the shortest and smallest of the three muscles attached to the styloid process (see Fig. 37.9). It arises from the anterolateral aspect of the styloid process near its apex, and from the styloid end of the stylomandibular ligament (Mérida-Velasco et al 2006). Passing downwards and forwards, it divides at the side of the tongue into a longitudinal part, which enters the tongue dorsolaterally to blend with the inferior longitudinal muscle in front of hyoglossus, and an oblique part, overlapping hyoglossus and decussating with it.

Vascular supply. Styloglossus is supplied by the sublingual branch of the lingual artery.

Innervation. Styloglossus is innervated by the hypoglossal nerve.

Actions. Styloglossus draws the tongue up and backwards.

Stylohyoid ligament

The stylohyoid ligament is a fibrous cord that extends from the tip of the styloid process to the lesser cornu of the hyoid bone (see Fig. 37.9). It gives attachment to some fibres of styloglossus and the middle constrictor of the pharynx, and is closely related to the lateral wall of the oropharynx. Below it is overlapped by hyoglossus. The ligament is derived embryologically from the second branchial arch. It may be partially calcified.

Palatoglossus

Palatoglossus is closely associated with the soft palate in function and innervation, and is described with the other palatal muscles (Ch. 40).

Intrinsic muscles

The intrinsic muscles of the tongue are the bilateral superior and inferior longitudinal, the transverse and the vertical (**Fig. 37.10**).

Superior longitudinal

The superior longitudinal muscle constitutes a thin stratum of oblique and longitudinal fibres lying beneath the mucosa of the dorsum of the tongue. It extends forwards from the submucous fibrous tissue near the epiglottis and from the median lingual septum to the lingual margins. Some fibres are inserted into the mucous membrane (see Fig. 37.11B).

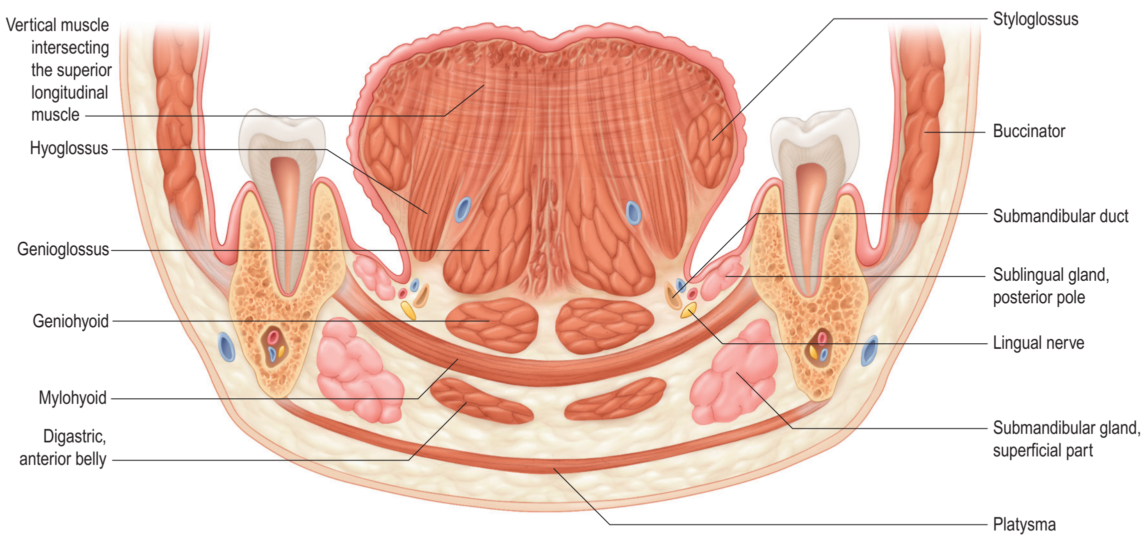
Vertical muscle intersecting the superior longitudinal muscle
Hyoglossus
Genioglossus
Geniohyoid
Mylohyoid
Digastric, anterior belly
Styloglossus
Buccinator
Submandibular duct
Sublingual gland, posterior pole
Lingual nerve
Submandibular gland, superficial part
Platysma

Fig. 37.10 A coronal section through the tongue, the mouth and the body of the mandible opposite the lower first molar tooth.

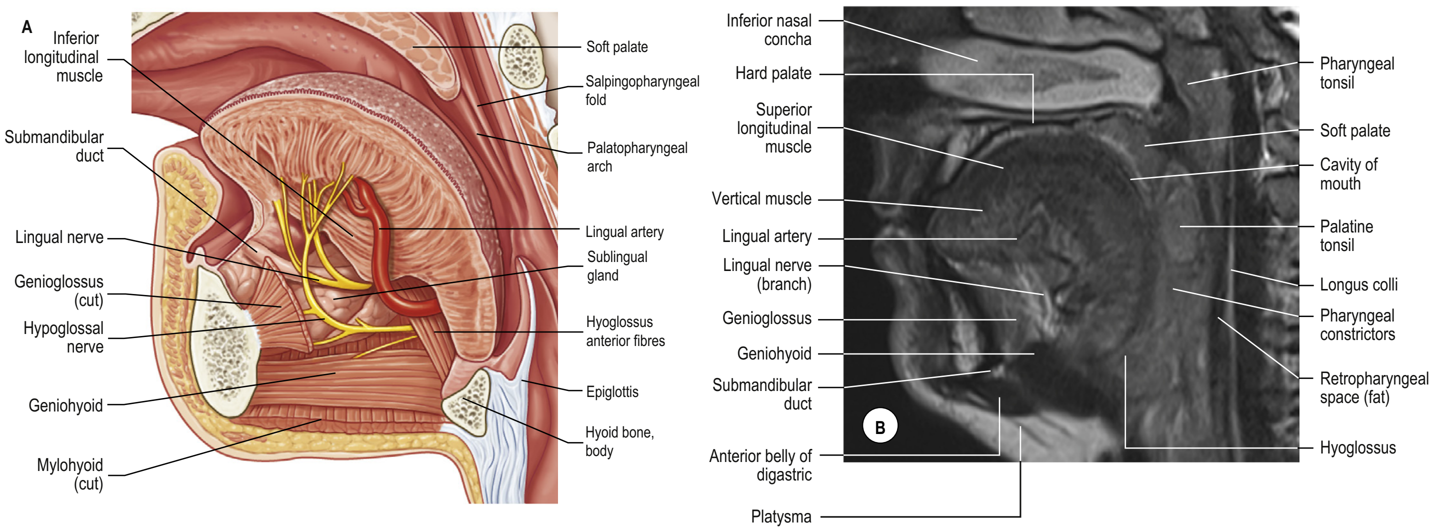
A
Inferior longitudinal muscle
Submandibular duct
Lingual nerve
Genioglossus (cut)
Hypoglossal nerve
Geniohyoid
Mylohyoid (cut)
Soft palate
Salpingopharyngeal fold
Palatopharyngeal arch
Lingual artery
Sublingual gland
Hyoglossus anterior fibres
Epiglottis
Hyoid bone, body
Inferior nasal concha
Hard palate
Superior longitudinal muscle
Vertical muscle
Lingual artery
Lingual nerve (branch)
Genioglossus
Geniohyoid
Submandibular duct
Anterior belly of digastric
Platysma
B
Pharyngeal tonsil
Soft palate
Cavity of mouth
Palatine tonsil
Longus colli
Pharyngeal constrictors
Retropharyngeal space (fat)
Hyoglossus

Fig. 37.11 **A**, The left half of the tongue, viewed from the medial side, showing the lingual artery and ramifications of the hypoglossal and lingual nerves. **B**, Sagittal T2-weighted MRI showing the lingual artery and muscles of the tongue.

Inferior longitudinal

The inferior longitudinal muscle is a narrow band of muscle close to the inferior lingual surface between genioglossus and hyoglossus. It extends from the root of the tongue to the apex. Some of its posterior fibres are connected to the body of the hyoid bone. Anteriorly, it blends with styloglossus (see Fig. 37.11A).

Transverse

The transverse muscles pass laterally from the median fibrous septum to the submucous fibrous tissue at the lingual margin, blending with palatopharyngeus.

Vertical

The vertical muscles extend from the dorsal to the ventral aspects of the tongue in the anterior borders (see Fig. 37.11B).

Vascular supply of intrinsic muscles. The intrinsic muscles are supplied by the lingual artery.

Innervation of intrinsic muscles. All intrinsic lingual muscles are innervated by the hypoglossal nerve.

Actions. The intrinsic muscles are presumed to largely function as muscular hydrostats, altering the shape of the tongue (Sanders et al 2013). Thus, contraction of the superior and inferior longitudinal muscles tend to shorten the tongue, but the former also turns the apex and sides upwards to make the dorsum concave, while the latter pulls the apex down to make the dorsum convex. The transverse muscle narrows and elongates the tongue, while the vertical muscle makes it flatter and wider. Acting alone or in pairs and in endless combination, the intrinsic muscles give the tongue precise and highly varied mobility, important not only in alimentary function but also in speech.

Vascular supply and lymphatic drainage

Lingual artery

The tongue and the floor of the mouth are supplied chiefly by the lingual artery, which arises from the anterior surface of the external carotid artery. It passes between hyoglossus and the middle constrictor of the pharynx to reach the floor of the mouth, accompanied by the lingual veins and the glossopharyngeal nerve. At the anterior border of hyoglossus, the lingual artery bends sharply upwards (Fig. 37.11). It is covered by the mucosa of the tongue and lies between genioglossus medially and the inferior longitudinal muscle laterally. Near the tip of the tongue, it anastomoses with its contralateral fellow; this contribution is important in maintaining the blood supply to the tongue in any surgical resection of the tongue. The branches of the lingual artery form a rich anastomotic network, which supplies the musculature of the tongue, and a very dense submucosal plexus. Named branches of the lingual artery in the floor of the mouth are the dorsal lingual, sublingual and deep lingual arteries.

Dorsal lingual arteries

The dorsal lingual arteries are usually two or three small vessels. They arise medial to hyoglossus and ascend to the posterior part of the dorsum of the tongue. The vessels supply its mucous membrane and the palatoglossal arch, tonsil, soft palate and epiglottis. They anastomose with their contralateral fellows.

Sublingual artery

The sublingual artery arises at the anterior margin of hyoglossus. It passes forwards between genioglossus and mylohyoid to the sublingual gland, and supplies the gland, mylohyoid and the buccal and gingival mucous membranes. One branch pierces mylohyoid and joins the submental branches of the facial artery. Another branch courses through the mandibular gingivae to anastomose with its contralateral fellow. A single artery arises from this anastomosis and enters a small foramen (lingual foramen) on the mandible, situated in the midline on the posterior aspect of the symphysis immediately above the genial tubercles.

Deep lingual artery

The deep lingual artery is the terminal part of the lingual artery and is found on the inferior surface of the tongue near the lingual frenulum.

In addition to the lingual artery, the tonsillar and ascending palatine branches of the facial and ascending pharyngeal arteries also supply tissue in the root of the tongue. In the region of the valleculae, epiglottic branches of the superior laryngeal artery anastomose with the inferior dorsal branches of the lingual artery.

Lingual veins

The lingual veins are formed from the union of the dorsal lingual and deep lingual veins and the vena comitans of the hypoglossal nerve. The veins draining the tongue follow two routes. Dorsal lingual veins drain the dorsum and sides of the tongue, join the lingual veins accompanying the lingual artery between hyoglossus and genioglossus, and empty into the internal jugular vein near the greater cornu of the hyoid bone. The deep lingual vein begins near the tip of the tongue and runs back just beneath the mucous membrane on the inferior surface of the tongue. It joins a sublingual vein from the sublingual salivary gland near the anterior border of hyoglossus and forms the vena comitans nervi hypoglossi, which runs back with the hypoglossal nerve between mylohyoid and hyoglossus to join the facial, internal jugular or lingual vein. The lingual veins usually join the facial and retromandibular veins (anterior division) to form the common facial vein, which drains into the internal jugular vein.

Lymphatic drainage

The mucosa of the pharyngeal part of the dorsal surface of the tongue contains many lymphoid follicles aggregated into dome-shaped groups: the lingual tonsils. Each group is arranged around a central deep crypt, or invagination, which opens on to the surface epithelium. The ducts of mucous glands open into the bases of the crypts. Small isolated follicles also occur beneath the lingual mucosa. The lymphatic drainage of the tongue can be divided into three main regions: marginal, central and dorsal. The anterior region of the tongue drains into marginal and central vessels, and the posterior part of the tongue behind the circumvallate papillae drains into the dorsal lymph vessels. The more central regions may drain bilaterally, and this must be borne in mind when planning to remove malignant tumours of the tongue that are approaching the midline. If the tumour has a propensity for lymphatic spread, both cervical chains may be involved.

Marginal vessels

Marginal vessels from the apex of the tongue and the lingual frenulum area descend under the mucosa to widely distributed nodes. Some vessels pierce mylohyoid as it contacts the mandibular periosteum to enter either the submental or anterior or middle submandibular nodes, or else to pass anterior to the hyoid bone to the jugulo-omohyoid node. Vessels arising in the plexus on one side may cross under the frenulum to end in contralateral nodes. Efferent vessels of median submental nodes pass bilaterally. Some vessels pass inferior to the sublingual gland and accompany the companion vein of the hypoglossal nerve to end in jugulodigastric nodes. One vessel often descends further to reach the jugulo-omohyoid node, and passes either superficial or deep to the intermediate tendon of digastric.

Vessels from the lateral margin of the tongue cross the sublingual gland, pierce mylohyoid and end in the submandibular nodes. Others end in the jugulodigastric or jugulo-omohyoid nodes. Vessels from the posterior part of the lingual margin traverse the pharyngeal wall to the jugulodigastric lymph nodes (Fig. 37.12).

Central vessels

The regions of the lingual surface draining into the marginal or central vessels are not distinct. Central lymphatic vessels ascend between the fibres of the two genioglossi; most pass between the muscles and diverge to the right or left to follow the lingual veins to the deep cervical nodes, especially the jugulodigastric and jugulo-omohyoid nodes. Some pierce mylohyoid to enter the submandibular nodes.

Dorsal vessels

Vessels draining the postsulcal region and the circumvallate papillae run posteroinferiorly. Those near the median plane may pass bilaterally. They turn laterally, joining the marginal vessels, and all pierce the pharyngeal wall, passing around the external carotid arteries to reach the jugulodigastric and jugulo-omohyoid lymph nodes. One vessel may descend posterior to the hyoid bone, perforating the thyrohyoid membrane to end in the jugulo-omohyoid node.

Innervation

All of the muscles of the tongue, with the exception of palatoglossus, are supplied by the hypoglossal nerve. Palatoglossus is supplied via the pharyngeal plexus (Ch. 40).

The sensory innervation of the tongue reflects its embryological development: the anterior two-thirds (presulcal part) is derived from first arch mesenchyme and the posterior one-third (postsulcal part) is derived from third arch mesenchyme. The nerve of general sensation to the anterior two-thirds is the lingual nerve. Taste sensation travels in the chorda tympani branch of the facial nerve. The nerve supplying both general and taste sensation to the posterior third is the glossopharyngeal nerve. An additional area in the region of the valleculae is supplied by the internal laryngeal branch of the vagus nerve.

Proprioceptive nerve endings have been observed in the tongue, although the precise nerve pathways await full clarification. Anaesthetizing the lingual nerve does not appear to affect tongue movement, suggesting that proprioception does not pass along this nerve either directly or via the chordae tympani. Loss of proprioceptive nerve endings following section of the hypoglossal nerve suggests that the proprioceptive pathway involves the hypoglossal nerve directly or indirectly via its connections with the upper three cervical spinal nerves.

Hypoglossal nerve

The course of the hypoglossal nerve in the neck is described in Chapter 35. After crossing the loop of the lingual artery a little above the tip of the greater cornu of the hyoid, it inclines upwards and forwards on hyoglossus, passing deep to stylohyoid, the tendon of digastric and the posterior border of mylohyoid. Between mylohyoid and hyoglossus, the hypoglossal nerve lies below the deep part of the submandibular gland, the submandibular duct and the lingual nerve, with which it communicates. It then passes on to the lateral aspect of genioglossus, continuing forwards in its substance as far as the tip of the tongue (Fig. 37.11A). It distributes fibres to styloglossus, hyoglossus and genioglossus and to the intrinsic muscles of the tongue. Cadaveric tongues stained using Sihler's stain (a whole mount nerve staining technique that renders a large specimen transparent while counterstaining all nerves) or acetylcholinesterase or silver stains show the basic mammalian intralingual pattern of hypoglossal nerve distribution but with notable differences, even from non-human primates. Thus, many muscle fibres, particularly in the transverse group of intrinsic muscles, contain multiple *en grappe* motor end-plates (suggesting that they are some variant of slow tonic muscle fibres). Presumably, these specializations facilitate the fine motor control of tongue shape that is required in speech and swallowing (Mu and Sanders 2010) (Fig. 37.13). If the nerve suffers either iatrogenic or pathological damage, the tongue, on protrusion, will deviate towards the affected side and there may also be wasting of the muscles on the affected side.

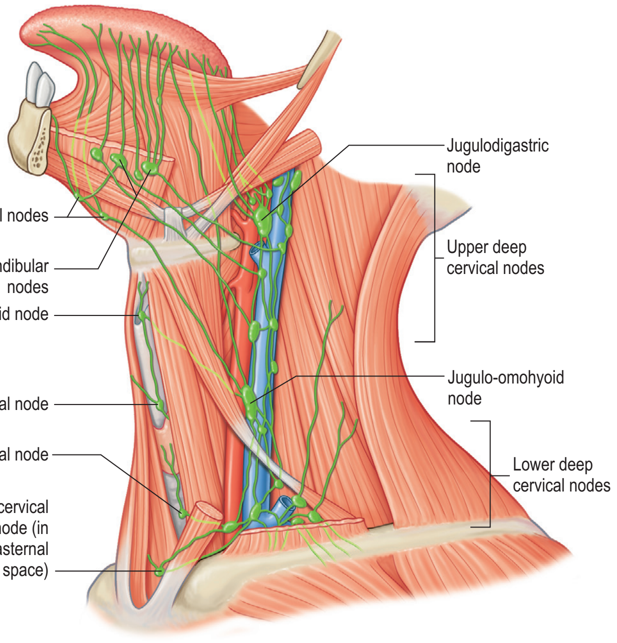

Fig. 37.12 Lymphatic drainage of the tongue: sternocleidomastoid has been removed to expose the chain of deep cervical lymph nodes.

Lingual nerve

The lingual nerve is sensory to the mucosa of the floor of the mouth, mandibular lingual gingivae and mucosa of the presulcal part of the tongue (excluding the circumvallate papillae). It also carries postganglionic parasympathetic fibres from the submandibular ganglion to the sublingual and anterior lingual glands.

The lingual nerve arises from the posterior trunk of the mandibular nerve in the infratemporal fossa (see Fig. 38.23), where it is joined by the chorda tympani branch of the facial nerve and often by a branch of the inferior alveolar nerve. It then passes below the mandibular attachment of the superior pharyngeal constrictor and pterygomandibular raphe, closely applied to the periosteum of the medial surface of the mandible. Here it lies opposite the distal (posterior) root of the third molar tooth, where it is covered only by the gingival mucoperiosteum. In about 1 in 7 cases, the lingual nerve may be located above the lingual bony plate and is susceptible to damage during surgery in the region. It next passes medial to the mandibular attachment of mylohyoid, which carries it progressively away from the mandible, and separates it from the alveolar bone covering the mesial root of the third molar tooth. The lingual nerve then passes downwards and forwards on the deep surface of mylohyoid (i.e. the surface nearer the mucosa covering the floor of the mouth), crossing the lingual sulcus beneath the mucosa. In this position, it lies on the deep portion of the submandibular gland, which bulges over the top of the posterior border of mylohyoid. It passes below the submandibular duct, which crosses it from medial to lateral, and curves upwards, forwards and medially to enter the tongue by medial and lateral branches (see Fig. 37.11; **Fig. 37.14**). Within the tongue, the medial branch sends small branches to the medial part of the ventrolateral tongue, and the lateral branch runs along the lateral border of the tongue and sends larger branches to innervate the mucosa of the anterior tip of the tongue. The lingual nerve is connected to the submandibular ganglion (see Fig. 38.23) by two or three branches. It forms connecting loops with twigs of the hypoglossal nerve at the anterior margin of hyoglossus (Fitzgerald and Law 1958) and within the tongue (Zur et al 2004).

The lingual nerve is at risk during surgical removal of (impacted) lower third molars: patients occasionally develop lingual sensory disturbance postoperatively but this is rarely persistent (Renton 2011). The nerve is also at risk during operations to remove the submandibular salivary gland because the duct must be dissected from the lingual nerve, and because its connection to the submandibular ganglion pulls it into the operating field.

Glossopharyngeal nerve

The glossopharyngeal nerve is distributed to the posterior third of the tongue and the circumvallate papillae. It communicates with the lingual nerve. The course of the glossopharyngeal nerve in the neck is described in Chapter 35.

Taste

The sense of taste is dependent on scattered groups of sensory cells, the taste buds, which occur in the oral cavity and pharynx, and are particularly plentiful on the lingual papillae of the dorsal lingual mucosa.

Taste buds

Taste buds are microscopic barrel-shaped epithelial structures found on all types of lingual papillae (except filiform papillae). They contain chemosensory taste receptor cells in synaptic contact with the terminals of gustatory nerves (the facial, glossopharyngeal or vagus nerves). Taste buds are most abundant on the posterior parts of the tongue, especially around the walls of the circumvallate papillae and their surrounding sulci, where there is an average of 250 taste buds for each of the 8–12 papillae (see Fig. 37.7). Over 1000 taste buds are distributed over the sides of the tongue, particularly over the more posterior folds of the foliate papillae, whereas they are rare, and sometimes even absent, on fungiform papillae. Taste buds have been described on the fetal epiglottis and lingual aspect of the soft palate but most disappear from these sites during postnatal development.

Microstructure of taste buds

Each taste bud is a barrel-shaped cluster of 50–150 fusiform cells, which lies within an oval cavity in the epithelium and converges apically on a gustatory pore, a 2 μm wide opening on the mucosal surface. The whole structure is about 70 μm in height by 40 μm across and is separated by a basal lamina from the underlying lamina propria (see Fig. 37.8B). A small fasciculus of afferent nerve fibres penetrates the basal lamina and spirals around the sensory cells. Chemical substances dissolved in the oral saliva diffuse through the gustatory pores of the taste buds to reach the taste receptor cell membranes, where they cause membrane depolarization. At the ultrastructural level, four distinct cell types have been described within the taste bud: the relatively undifferentiated type IV cells are distinguished by their basal position and the presence of intermediate filaments; type I cells have a dark appearance, while types II and III cells are lighter. Types I and III cells may form synapses with intragemmal nerves. The exposed parts of the receptor cells bear numerous apical microvilli which provide a large surface area for contact with the chemicals dissolved in the saliva.

Innervation of taste buds

Individual gustatory nerves may diverge to innervate widely separated taste buds, or they may innervate more than one sensory cell in each bud. The terminals of several different nerve fibres may converge on individual taste buds. Nerve fibres either branch in the periphery of a taste bud to form a perigemmal plexus, or form an intragemmal plexus within the bud itself. Perigemmal fibres contain various neuropeptides including calcitonin gene-related peptide (CGRP) and substance P, and appear to represent free sensory endings. Intragemmal fibres branch within the taste bud and each forms a series of synapses with the bases of the taste receptor cells.

The gustatory nerve for the anterior part of the tongue, excluding the circumvallate papillae, is the chorda tympani, which travels via the lingual nerve. Taste buds in the inferior surface of the soft palate are innervated mainly by the facial nerve but may also be supplied by the glossopharyngeal nerve. Taste buds in the circumvallate papillae, pharyngeal (postsulcal) part of the tongue and in the palatoglossal arches and the oropharynx are innervated by the glossopharyngeal nerve, and those in the extreme pharyngeal part of the tongue and epiglottis are innervated by the internal laryngeal branch of the vagus.

Central connections

On entering the brainstem, gustatory afferents constitute the tractus solitarius and terminate in the rostral third of the nucleus solitarius of the medulla oblongata.

Taste discrimination

It is difficult to separate the perceptions of taste and smell because the oral and nasal cavities are continuous. Indeed, much of what is perceived as 'taste' is more properly described as 'flavour' and is the result of airborne odorants from the oral cavity that pass through the nasopharynx to the olfactory area above it (Linden 1998).

Perceived sensations of taste are the results of the central processing of a complex pattern of responses from taste receptor cells located in the taste buds on the surface of the tongue. Five canonical tastes, bitter (typically quinine), sweet (typically sugars), umami (typically monosodium glutamate), sour (typically acids) and salty are detected on the tongue (Smith and Margolskee 2006, Kapsimali and Barlow 2012, Liman et al 2014). There are three major classes of taste cells: Type I cells degrade or absorb neurotransmitters and some may transduce salty taste. Type II cells are receptors that bind sweet, bitter, or umami compounds: they do

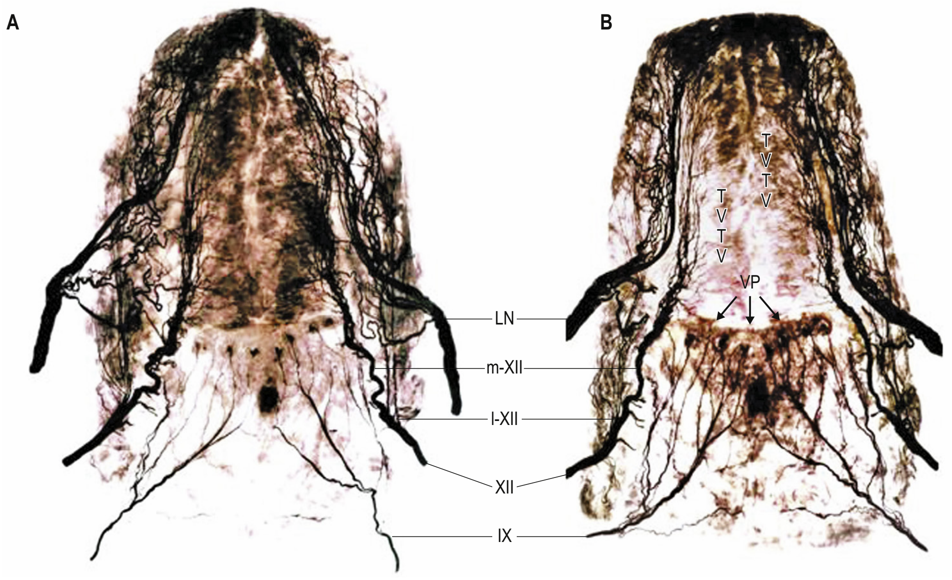

Fig. 37.13 A–**B**, Entire nerve maps of an adult human tongue, Sihler's stain. Several muscles, including genioglossus and the posterior transverse (T) and vertical (V) intrinsic muscles, were removed in order to track individual nerves. The hypoglossal nerve (XII) and its lateral (l-XII) and medial (m-XII) branches lie between the lingual (LN) and glossopharyngeal (IX) nerves in the posterior part of the tongue. The lateral branch is derived from the main trunk of the hypoglossal nerve as either a short single branch (left side in **A**) or multiple branches (right side in **A** and both sides in **B**). Other abbreviations: VP, vallate papillae. (With permission from Mu L, Sanders I 2010 Human tongue neuroanatomy: nerve supply and motor endplates. Clin Anat 23:777–91.)

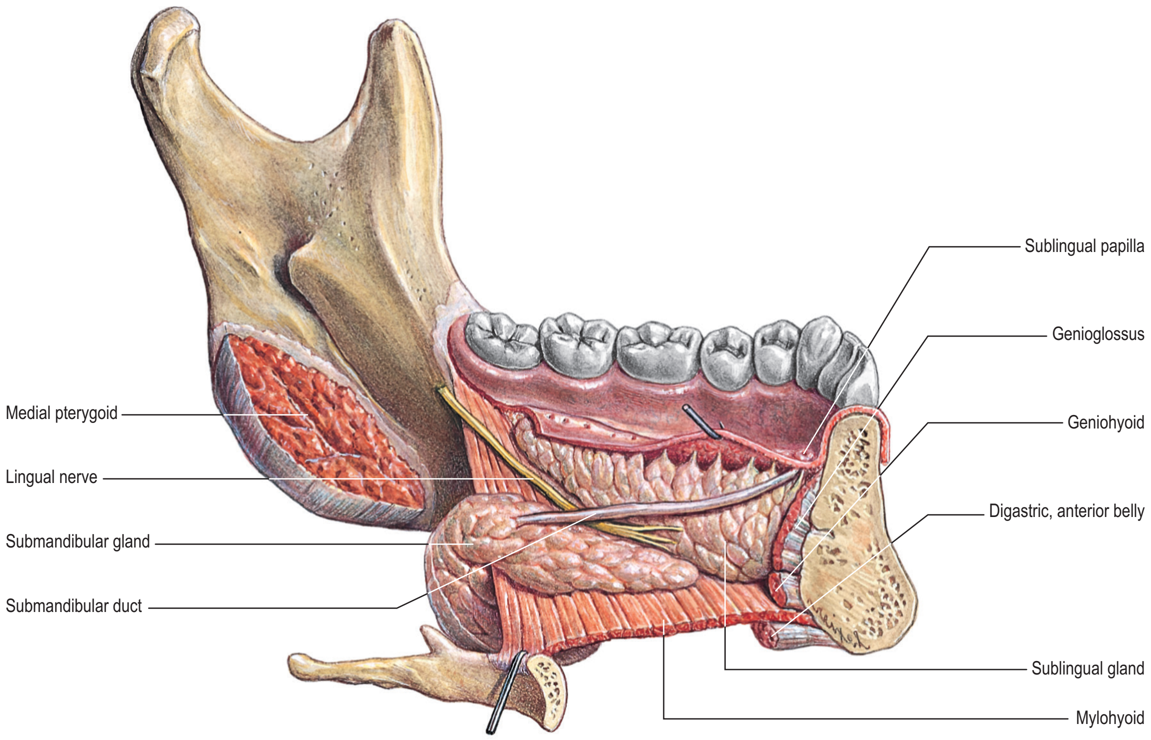

Fig. 37.14 The lingual nerve, submandibular duct, and submandibular and sublingual salivary glands in the floor of the mouth; lingual aspect, left side. (Sobotta Atlas of Human Anatomy © Elsevier GmbH, Urban & Fischer, Munich.)

not form ultrastructurally identifiable synapses but gustatory afferents are closely apposed to them. Each type II cell expresses taste GPCRs specific for only one taste quality. Type III (presynaptic) cells express proteins associated with synapses and form synaptic junctions with nerve terminals (Chaudhari and Roper 2010). Bitter chemicals are detected by a small family of receptors structurally related to rhodopsin: they may detect either one or a few specific bitter chemicals or many bitter chemicals. The tastes of sweet and umami are evoked by a relatively small number of molecules that signal either calorie-rich (sweet) or protein-rich foods (umami) and are sensed by a single type of GPCR, a heterodimer of a common subunit and a unique subunit. The structurally divergent receptors for sugars, bitter chemicals and amino acids all employ a common canonical phosphoinositide-based signalling pathway. In humans, salty taste is generated mainly by sodium ions and is amiloride-insensitive: it appears to be mediated by a nonselective cation pathway that as yet is less well documented than in experimental animals. In newborn infants, oral sucrose has been shown to reduce procedural pain from single events; the mechanism of this nociceptive effect is not yet fully understood (Stevens et al 2013).

The taste bud complex is an extremely dynamic system in which there is a rapid turnover of receptor cells: the lifespan of receptor cells produced by the division of epithelial stem cells (basal cells) is approximately 10 days. The gustatory nerves are therefore continually sprouting new processes, forming new synapses with young cells, and retracting synaptic connections with dying cells. It has been calculated that at any one time less than one-third of the cells in a single taste bud are fully innervated. An intact nerve supply is necessary for the normal survival and function of taste buds. If the nerve supply is interrupted, the taste buds degenerate and slough off, although they will reappear and can return to normal function following nerve regeneration.

Autonomic innervation of the tongue

The parasympathetic secretomotor innervation of the various lingual mucous glands is via the chorda tympani branch of the facial nerve, which synapses in the submandibular ganglion; postganglionic branches are distributed to the lingual mucosa either via the lingual nerve or via plexuses around the lingual arteries.

The postganglionic sympathetic supply to lingual glands and vessels arises from the carotid plexus (fibres derived from neurones in the superior cervical ganglion) and enters the tongue through plexuses around the lingual arteries. Isolated neurones, perhaps postganglionic parasympathetic neurones, have been reported in the postsulcal region and presumably innervate glandular tissue and vascular smooth muscle.

TEETH

Introduction and terminology

Humans have two generations of teeth: the deciduous (primary) dentition (Fig. 37.15) and the permanent (secondary) dentition. The first deciduous teeth erupt into the mouth at about 6 months after birth and all of the deciduous teeth have erupted by 3 years of age. The first permanent molar erupts around 6 years, and thence the deciduous teeth are exfoliated one by one, to be replaced by their permanent successors. A complete permanent dentition is present when the third molars erupt at around the age of 18–21 years. In the complete deciduous dentition, there are 20 teeth, 5 in each jaw quadrant. In the complete permanent dentition, there are 32 teeth, 8 in each jaw quadrant (Berkovitz et al 2009).

There are three basic tooth forms in both dentitions: incisiform, caniniform and molariform. Incisiform teeth (incisors) are cutting teeth and have thin, blade-like crowns. Caniniform teeth (canines) are piercing or tearing teeth and have a single, stout, pointed, cone-shaped crown. Molariform teeth (molars and premolars) are grinding teeth and possess a number of cusps on an otherwise flattened biting surface. Premolars are bicuspid teeth that are restricted to the permanent dentition and replace the deciduous molars.

The tooth-bearing region of the jaws can be divided into four quadrants: the right and left maxillary and mandibular quadrants. A tooth may thus be identified according to the quadrant in which it is located (e.g. a right maxillary tooth or a left mandibular tooth). In both the deciduous and permanent dentitions, the incisors may be distinguished according to their relationship to the midline. Thus, the incisor nearest the midline is the central (first) incisor and the incisor that is more laterally positioned is termed the lateral (second) incisor. The permanent premolars and the permanent and deciduous molars can also be distinguished according to their mesiodistal relationships. The molar most mesially positioned is designated the first molar, and the one behind it is the second molar. In the permanent dentition, the tooth most distally positioned is the third molar. The mesial premolar is the first premolar, and the premolar behind it is the second premolar.

The terminology used to indicate tooth surfaces is shown in Fig. 37.16B. The aspect of teeth adjacent to the lips or cheeks is termed labial or buccal, that adjacent to the tongue being lingual (or palatal in the maxilla). Labial and lingual surfaces of an incisor meet medially at a mesial surface and distally at a distal surface, terms that are also used to describe the equivalent surfaces of premolar and molar (postcanine) teeth. On account of the curvature of the dental arch, mesial surfaces of postcanine teeth are directed anteriorly and distal surfaces are directed posteriorly. Thus, the point of contact between the central incisors is the datum point for mesial and

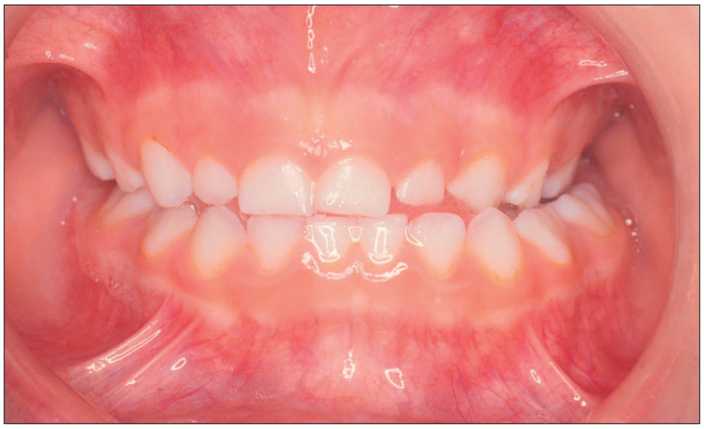

Fig. 37.15 The primary dentition. An anterior view of the complete deciduous (primary) dentition at age 3 years. (Courtesy of Miss Victoria Clark.)

Natal and/or neonatal teeth (teeth present at birth and teeth erupted within the first month of life, respectively) are rare, with an incidence of 1 in 3000 births. More than 90% of natal and neonatal teeth are prematurely erupted deciduous mandibular incisors, while less than 10% are supernumerary. Several syndromes have been associated with natal teeth, namely: Ellis–van Creveld, Hallermann–Streiff, Jadassohn–Lewandowski and Pierre Robin syndromes. Histological features are failure of root formation, a large vascular pulp, irregular dentine formation and a failure of cementum formation (Mhaske et al 2013).

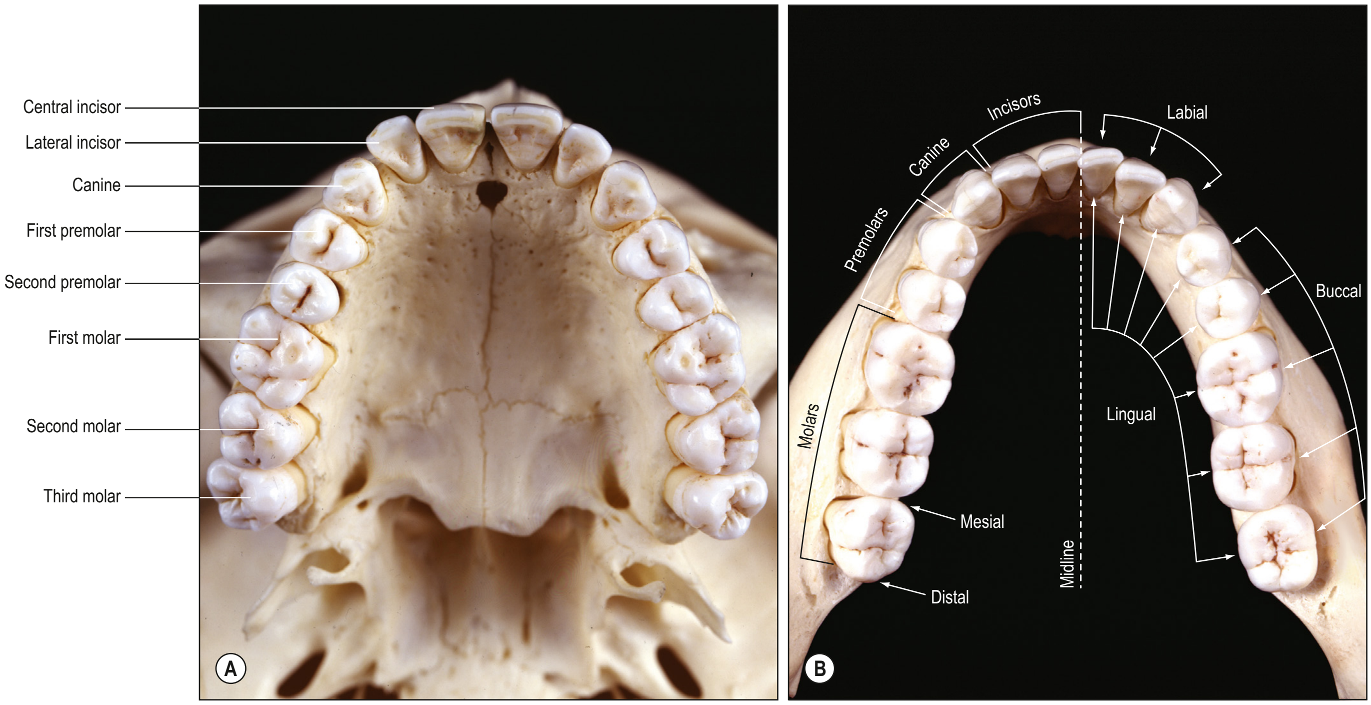

Fig. 37.16 The permanent teeth: occlusal aspect. **A**, The upper dental arch. **B**, The lower dental arch. The terminology employed for the identification of teeth according to their location is shown in the lower jaw; the same terminology is used to describe the teeth in the upper jaw.

distal. The biting or occlusal surfaces of postcanine teeth are tuberculated by cusps that are separated by fissures forming a pattern characteristic of each tooth. The biting surface of an incisor is the incisal edge.

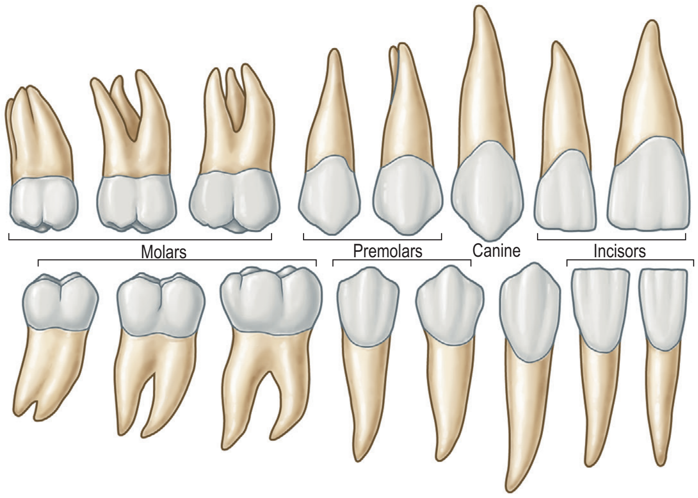

Fig. 37.17 The permanent upper and lower teeth of the right side: labial and buccal surfaces.

Tooth morphology

There are two incisors, a central and a lateral, in each half jaw or quadrant (Figs 37.16–37.17). In labial view, the crowns are trapezoid, and the maxillary incisors (particularly the central) are larger than the mandibular. On eruption, the biting or incisal edges initially have three tubercles or mamelons, which are rapidly removed by wear. In mesial or distal view, their labial profiles are convex while their lingual surfaces are concavo-convex (the convexity near the cervical margin is caused by a low ridge or cingulum, which is prominent only on upper incisors). The roots of incisors are single and rounded in maxillary teeth, but flattened mesiodistally in mandibular teeth. The upper lateral incisor may be congenitally absent or may have a reduced form (peg-shaped lateral incisor).

Behind each lateral incisor is a canine tooth with a single cusp (hence the American term cuspid) instead of an incisal edge. The maxillary canine is stouter and more pointed than the mandibular canine, whose cusp tip is inclined lingually. The canine root, which is the longest of any tooth, produces a bulge (canine eminence) on the alveolar bone externally, particularly in the upper jaw. Although canines usually have single roots, those of the lower jaw may sometimes be bifid.

Distal to the canines are two premolars, each with a buccal and lingual cusp (hence the term bicuspid). The occlusal surfaces of the maxillary premolars are oval (the long axis is buccopalatal) and a mesiodistal fissure separates the two cusps. In buccal view, premolars resemble the canines but are smaller. The maxillary first premolar has two roots (one buccal, one palatal) but may have one root, or very rarely three roots (two buccal and one palatal); this makes the tooth more likely to fracture on removal. The maxillary second premolar usually has one root. The occlusal surfaces of the mandibular premolars are more circular or squarer than those of the upper premolars. The buccal cusp of the mandibular first premolar towers above a diminutive lingual cusp to which it is connected by a ridge separating the mesial and distal occlusal pits. In the mandibular second premolar, a mesiodistal fissure usually separates a buccal from two smaller lingual cusps. Each lower premolar has one root, but very rarely the root of the first is bifid. Rarely, lower second premolars fail to develop.

Posterior to the premolars are three molars whose size decreases distally. Each has a large rhomboid (upper jaw) or rectangular (lower jaw) occlusal surface with four or five cusps. The maxillary first molar has a cusp at each corner of its occlusal surface, and the mesiopalatal cusp is connected to the distobuccal by an oblique ridge. A smaller cusplet or tubercle (cusplet of Carabelli) usually appears on the mesiopalatal cusp (most commonly in Caucasian groups). The tooth has three widely separated roots: two buccal, of which the mesiobuccal is larger and broader and the distobuccal is rounder and smaller, and one large palatal. Their proximity to the maxillary air sinus is thought to be the reason first molar roots are wide apart and second and third molar roots are converged. The smaller maxillary second molar has a reduced or occasionally absent distopalatal cusp. Its three roots show varying degrees of fusion. The maxillary third molar, the smallest, is very variable in form. It usually has three cusps (the distopalatal being absent) and commonly the three roots are fused.

The mandibular first molar has three buccal and two lingual cusps on its rectangular occlusal surface, the smallest cusp being distal. The cusps of this tooth are all separated by fissures. It has two widely separated roots: one mesial and one distal. The smaller mandibular second molar is like the first, but has only four cusps (it lacks the distal cusp of the first molar) and its two roots are closer together. The mandibular third molar is smaller still and, like the upper third molar, is variable in form. Its crown may resemble that of the lower first or second molar and its roots are frequently fused. One or more third molars (upper or lower) often fail to develop.

The cementum-covered roots of teeth lie in sockets or alveoli, to which they are anchored by the periodontal ligament. The five permanent teeth in each quadrant in front of the molars generally have a single root except for the upper first premolar that has two roots, one buccal and one palatal. The roots are rounded in cross-section and taper towards the apex. The roots of the lower incisors are flattened mesiodistally. The upper permanent molars have three roots (two buccal and one palatal) while the lower molars have two roots, one mesial and one distal. The roots of the molar teeth tend to shorten and fuse as one passes from the first to the third molars. When a tooth first erupts, only about two-thirds of the root has formed and it takes a further three years for the root to complete its formation.

The unmineralized central core of the root contains the vital dental pulp, where it is known as the root canal. Generally, there is one canal present in each root. Exceptions to this are the mesiobuccal root of upper molars, which normally has two canals and the mesial root of lower molars which also usually has two canals.

If the pulp becomes infected following dental caries, one form of treatment may require the pulp to be removed and replaced by an inert material (root canal therapy). Clearly, it is important to know the number of root canals present in the tooth so that each is filled during the procedure. Three-dimensional radiographs are now available to aid assessment. Should an abscess develop at the apex of a tooth, the important structures related to each tooth must be considered if extraction becomes necessary to avoid iatrogenic complications. Among the most important of these are the maxillary sinus for the upper premolars and molars, the mental nerve for lower premolars and the lingual and inferior alveolar nerves for the lower third molars. The same structures must be avoided when placing dental implants.

Deciduous teeth

The incisors, canine and premolars of the permanent dentition replace two deciduous incisors, a deciduous canine and two deciduous molars in each jaw quadrant (Figs 37.18–37.19). The deciduous incisors and canine are shaped like their successors but are smaller and whiter and become extremely worn in older children. The deciduous second molars resemble the first permanent molars rather than their successors, the premolars. The upper first deciduous molar has a triangular occlusal surface (its rounded 'apex' is palatal), and a fissure separates a double buccal cusp from the palatal cusp. The lower first deciduous molar is long and narrow; its two buccal cusps are separated from its two lingual cusps by a zigzagging mesiodistal fissure. Both deciduous molars have large buccal protuberances on their mesial aspect. Upper deciduous molars have three roots (fusion of the palatal and distobuccal root is commonplace), and lower deciduous molars have two roots. These roots diverge more than those of permanent teeth because each developing premolar tooth crown is accommodated directly under the crown of its deciduous predecessor. The roots of deciduous teeth are progressively resorbed by osteoclast-like cells (odontoclasts) prior to being shed.

Eruption of teeth

Information on the sequence of development and eruption of teeth into the oral cavity (Fig. 37.20) is important in clinical practice and also in forensic medicine and archaeology. Dental development is one of the best indicators of chronological age when no record of birth exists (Garn et al 1965). The tabulated data provided in Table 37.1 are largely based on European-derived populations and there is evidence of ethnic variation. When a permanent tooth erupts, about two-thirds of the root is formed and it takes about another 3 years for the root to be completed. For deciduous teeth, root completion is more rapid. The developmental stages of initial calcification and crown completion are less affected by environmental influences than is eruption, the timing of which may be modified by several factors such as early tooth loss and severe malnutrition.

Fig. 37.21 shows the panoramic appearance of the dentition seen with orthopantomograms at the time of birth and at 2½, 6½, 10 and 16 years of age.

Dental alignment and occlusion

It is possible to bring the jaws together so that the teeth meet or occlude in many positions. When opposing occlusal surfaces meet with maximal 'intercuspation' (i.e. maximum contact), the teeth are said to be in centric occlusion. In this position, the lower teeth are normally opposed symmetrically and lingually with respect to the upper. Some important features of centric occlusion in a normal (idealized) dentition may be noted. Each lower postcanine tooth is slightly in front of its upper equivalent and the lower canine occludes in front of the upper. Buccal cusps of the lower postcanine teeth lie between the buccal and palatal cusps of the upper teeth. Thus, the lower postcanine teeth are slightly lingual and mesial to their upper equivalents. Lower incisors bite against the palatal surfaces of upper incisors, the latter normally obscuring about one-third of the crowns of the lower. This vertical overlap of incisors in centric occlusion is the overbite.

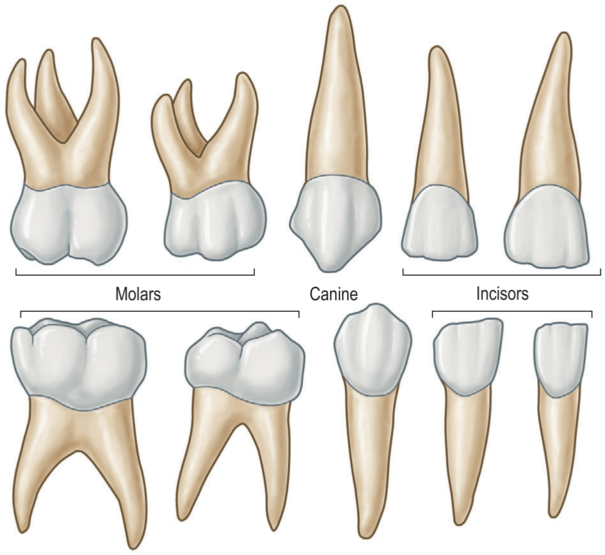

Fig. 37.18 The deciduous upper and lower teeth of the right side; labial and buccal surfaces.

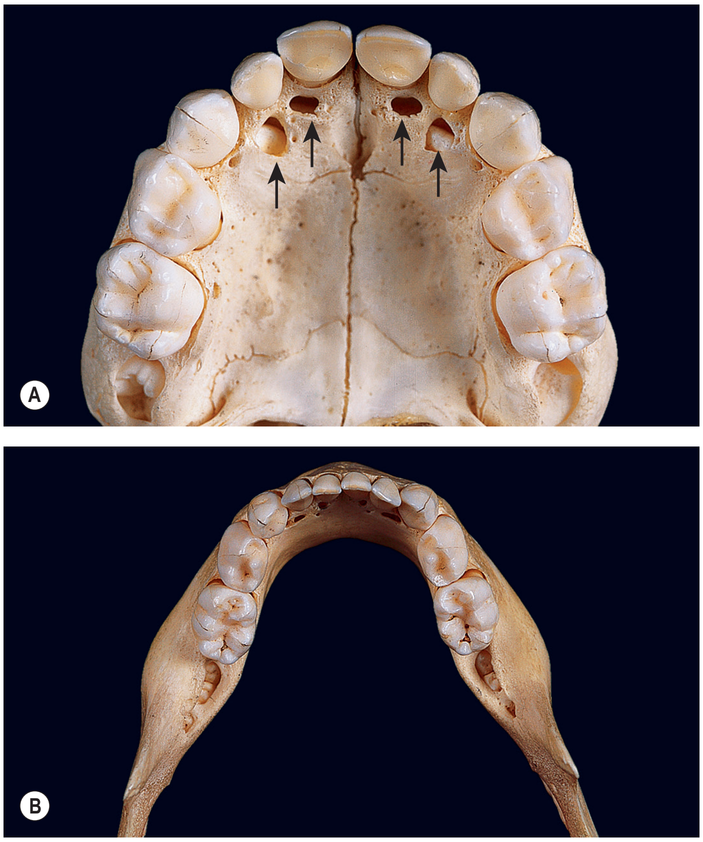

Fig. 37.19 **A**, Upper deciduous dentition: note the channels (arrows) leading to the developing permanent teeth. **B**, Lower deciduous dentition. (With permission from Berkovitz BKB, Moxham BJ 1994 Color Atlas of the Skull. London: Mosby.)

The extent to which upper incisors are anterior to lowers is termed the overjet. In the most habitual jaw position, the resting posture, the teeth are slightly apart, the gap between them being the freeway space or interocclusal clearance. During mastication, especially with lateral jaw movements, the food is comminuted, which facilitates the early stages of digestion.

The ideal occlusion is a rather subjective concept. If there is an ideal occlusion, it can only presently be defined in broad functional terms. Therefore, the occlusion can be considered 'ideal' when the teeth are aligned such that the masticatory loads are within physiological range and act through the long axes of as many teeth in the arch as possible; mastication involves alternating bilateral jaw movements (and not habitual, unilateral biting preferences as a result of adaptation to occlusal interference); lateral jaw movements occur without undue mechanical interference; in the rest position of the

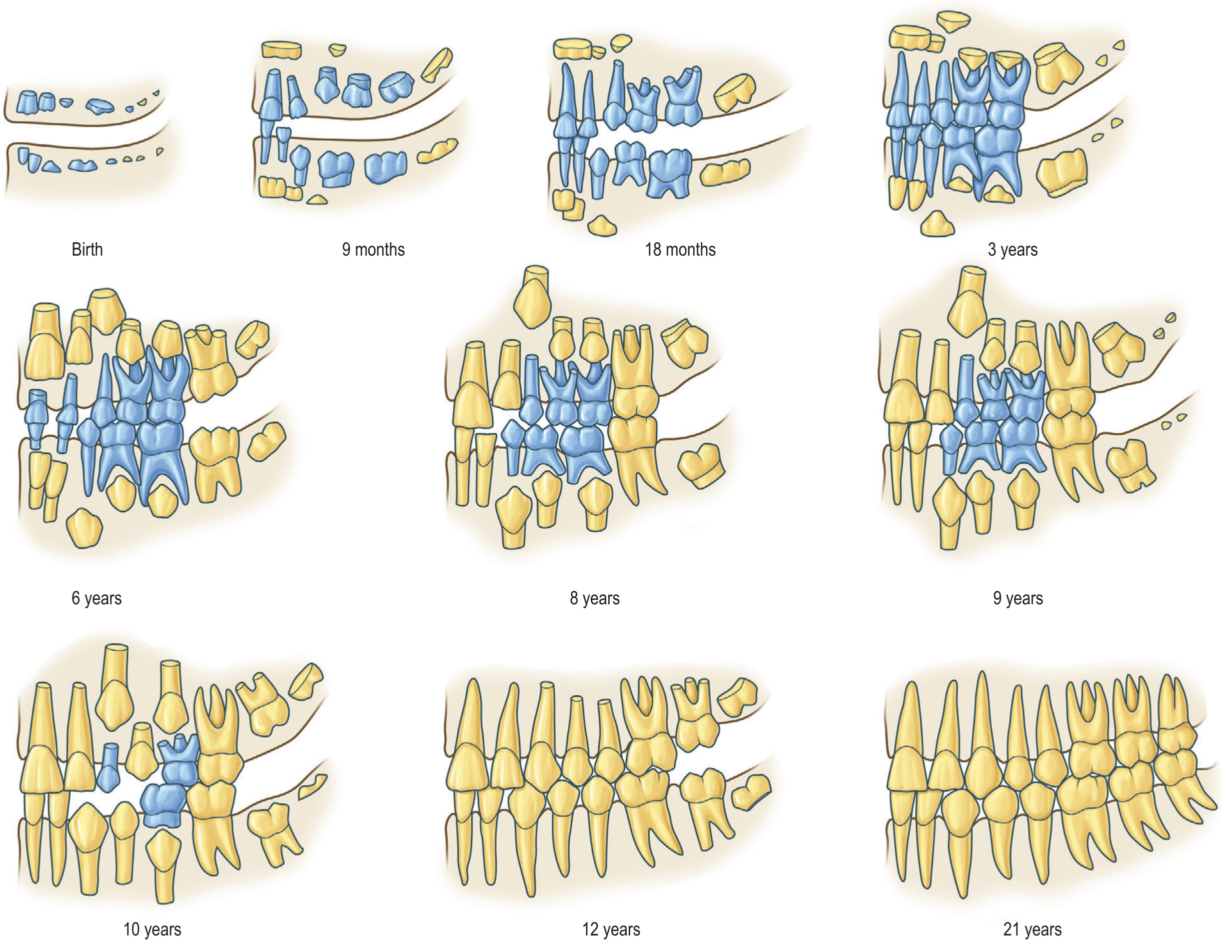

Fig. 37.20 The development of the deciduous (blue) and permanent (yellow) teeth. (Modified with permission from Schour I, Massler M 1941 The development of the human dentition. J Am Dent Assoc 28:1153–60.)

jaw, the gap between teeth (the freeway space) is correct for the individual concerned; and the tooth alignment is aesthetically pleasing to its possessor.

Variations from the ideal occlusion may be termed malocclusions (although these could be regarded as normal, since they are more commonly found in the population: the majority of the population in the USA has some degree of occlusal 'disharmony'). However, the majority of malocclusions should be regarded as anatomical variations rather than abnormalities, as they are rarely involved in masticatory dysfunction or pain, although they may be aesthetically displeasing.

Variations in tooth number, size and form

Available with the Gray's Anatomy e-book.

General arrangement of dental tissues

A tooth consists of a crown covered by very hard translucent enamel and a root covered by yellowish bone-like cementum (Fig. 37.26A). These meet at the neck or cervical margin. A longitudinal ground section (Fig. 37.26B) reveals that the body of a tooth is mostly dentine with an enamel covering over 2 mm thick, while the cementum is much thinner. The dentine surrounds a central pulp cavity, expanded at its coronal end into a pulp chamber and narrowed in the root as a pulp canal, opening at or near its tip by an apical foramen, occasionally multiple. The pulp is a soft connective tissue, continuous with the periodontal ligament via the apical foramen. It contains vessels for the support of the dentine and sensory nerves.

The root is surrounded by alveolar bone, its cementum separated from the osseous socket (alveolus) by the connective tissue of the periodontal ligament, approximately 0.2 mm thick (Fig. 37.27). Coarse bundles of collagen fibres, embedded at one end in cementum, cross the periodontal ligament to enter the osseous alveolar wall, these inserting bundles of collagen being termed Sharpey's fibres. Near the cervical margin, the tooth, periodontal ligament and adjacent bone are covered by the gingiva. On its internal surface, the gingiva is attached to the tooth surface by the junctional epithelium, a zone of profound clinical importance because just above it is a slight recess, the gingival sulcus. As the sulcus is not necessarily self-cleansing, dental plaque may accumulate in it and this predisposes to periodontal disease.

Enamel

Enamel is an extremely hard and rigid material that covers the crowns of teeth. It is a heavily mineralized epithelial cell secretion, containing 95–96% by weight crystalline apatites (88% by volume) and less than 1% organic matrix. The organic matrix comprises mainly unique enamel proteins, amelogenins and non-amelogenins such as enamelins and tuftelins. Although comprising a very small percentage of the weight and volume of enamel, the organic matrix permeates the whole of enamel. As its formative cells are lost from the surface during tooth eruption, enamel is incapable of further growth. Repair is limited to the remineralization of minute carious lesions.

Enamel reaches a maximum thickness of 2.5 mm over cusps and thins at the cervical margins. It is composed of closely packed enamel prisms or rods. In longitudinal section, enamel prisms extend from close to the enamel–dentine junction to within 20 μm of the surface, where they are generally replaced by prismless (non-prismatic, aprismatic) enamel (Fig. 37.28A). In cross-section, the prisms are mainly horseshoe-shaped and are arranged in rows that are staggered, such that the tails of the prisms in one row lie between the heads of the prism in the row above (prism pattern 3) (Fig. 37.28B) and the tails are directed rootwards. The appearance of prism boundaries results from sudden changes in crystallite orientation. Prisms have a diameter of approximately 5 μm, and are packed with flattened hexagonal hydroxyapatite crystals, far larger than those found in collagen-based mineralized tissues.

Two types of incremental lines are visible in enamel: short-term and long-term. At intervals that average 4 μm – with a range of 2–3 μm at the enamel–dentine junction and 4–6 μm in outer enamel – along its length, each prism is crossed by a line, probably reflecting diurnal swelling and shrinking in diameter during its growth. This short-term daily growth line is known as a cross-striation (Fig. 37.28C). The longer-term incremental lines pass from the enamel–dentine junction obliquely to the surface, where they end in shallow furrows, perikymata, visible on newly erupted teeth (Fig. 37.28D). Each line, known as an enamel stria (of Retzius) (Fig. 37.28E), usually represents a period of between 7 and 9 days of enamel growth with a modal value of 9 days. This is known as

The incidence of variation in number and form, which is often related to ethnicity, is rare in deciduous teeth but not uncommon in the permanent dentition. One or more teeth may fail to develop, a condition known as hypodontia. Conversely, additional or supernumerary teeth may form, producing hyperdontia (Fig. 37.22). The third permanent molar is the most frequently missing tooth. In declining order of incidence, other missing teeth are the maxillary lateral incisors, maxillary or mandibular second premolars, mandibular central incisors and maxillary first premolars.

Malformations of teeth can be related to variations in number, size and shape.

Variations in number

Anodontia refers to a complete absence of teeth and this condition is very rare but may be found in some cases of ectodermal dysplasia. More commonly in ectodermal dysplasia a few teeth are present, often malformed. Areas where the teeth are absent lack alveolar process so there is little bone naturally available to receive an implant.

Hypodontia. refers to the condition where just one or two teeth are absent. The most frequently affected teeth are the permanent third molars, then the permanent maxillary second incisors, followed by the second premolars. Having seen the important part played by certain transcription factors during organogenesis, it is not surprising to find in both mice and humans that an absence of teeth has been associated with mutations in *Pax1* and *Msx1* genes.

Hyperdontia. describes an increase in tooth number and affects the maxillary arch much more commonly than the mandibular dentition. The extra teeth are usually situated on the palatal aspect of the permanent incisors or distal to the molars. More rarely, additional premolars develop. Supernumerary teeth in the incisor region can often impede the eruption of the permanent teeth (Figs 37.23–37.24) and indeed this is often the first indication of their presence. A supernumerary tooth situated between the central incisors is known as a mesiodens. Teeth may be unusually large (macrodontia) or small (microdontia), e.g. the crowns of maxillary central incisors may be abnormally wide mesiodistally. A common variant of the maxillary lateral incisor has a small, peg-shaped crown. Epidemiological studies reveal that hyperdontia tends to be associated with macrodontia, and hypodontia with microdontia (Fig. 37.25), the most severely affected individuals representing the extremes of a continuum of variation. Together with family studies, this indicates that the causation is multifactorial, combining polygenic and environmental influences.

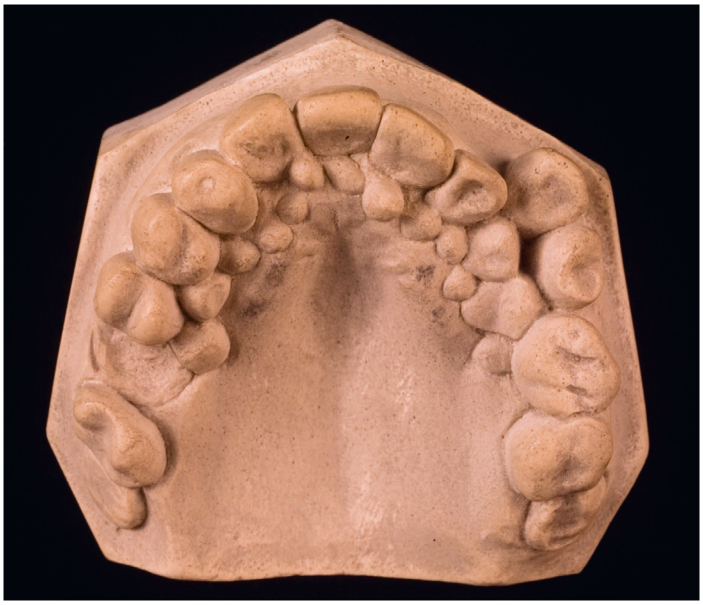

Fig. 37.22 A plaster cast of the maxilla of a 25-year-old male showing 1 supplemental premolar and 12 peg-shaped supernumerary teeth on the palatal side of the permanent teeth. (With permission from Berkovitz BKB, Holland GR, Moxham BJ 2009 Oral Anatomy, Histology and Embryology, 4th ed. Edinburgh: Mosby. Courtesy of Royal College of Surgeons of England.)

Some differences in the form of teeth display geographical variation and are of anthropological and forensic interest. Mongoloid dentitions tend to have shovel-shaped maxillary incisors with enlarged palatal marginal ridges. The additional cusp of Carabelli is commonly found on the mesiopalatal aspect of maxillary first permanent or second deciduous molars in Caucasian but rarely in Mongoloid dentitions. In African races, the mandibular second permanent molar often has five rather than four cusps.

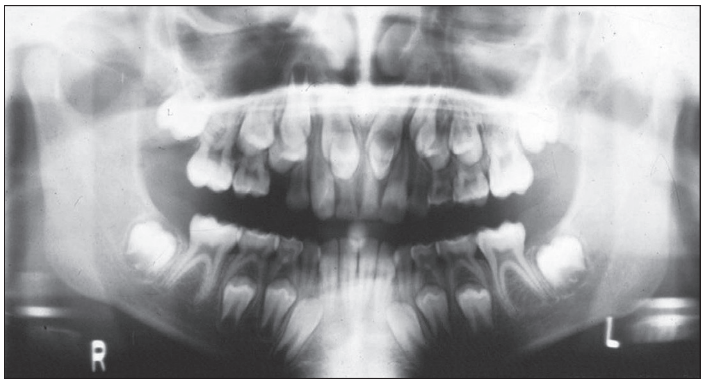

Fig. 37.23 An orthopantomogram showing supernumerary teeth in the upper incisor region preventing the exfoliation of the upper primary central incisors and impeding the eruption of the upper permanent central incisors. (Courtesy of Miss Victoria Clark.)

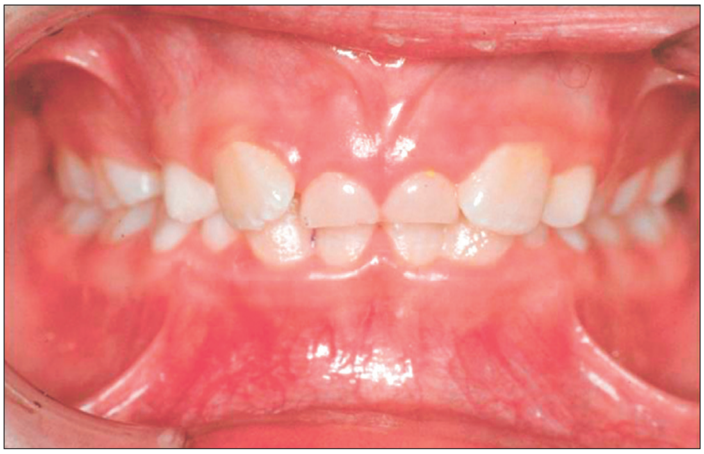

Fig. 37.24 A child with retained maxillary central deciduous incisors caused by the presence of supernumerary teeth. (Courtesy of Miss Victoria Clark.)

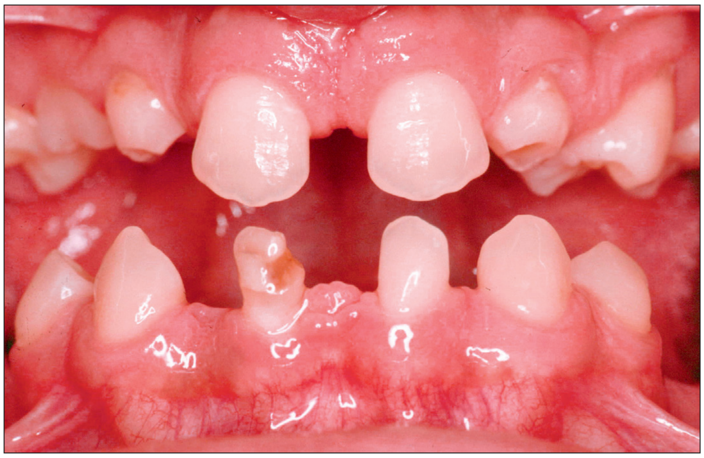

Fig. 37.25 A child with mixed dentition showing hypodontia and microdontia (small conical-shaped teeth). (Courtesy of Miss Victoria Clark.)

Variation in size

Microdontia is the term given to describe a tooth very much reduced in size. Microdontia generally affects individual teeth, usually the maxillary second incisor and the third molar. Occasionally, however, many teeth in the same dentition may be affected, in which case the teeth may be spaced apart. Microdontia may accompany clefts of the lip or palate, Ehlers–Danlos syndrome, hypopituitary disorders and ectodermal disorders. A frequent variation in shape is the peg-shaped maxillary lateral incisor.

Where a tooth is unusually large, the condition is referred to as macrodontia (megadontia) and usually affects individual teeth.

Variation in shape

Abnormal tooth shapes may be seen as a result of congenital syphilis. The incisors may be notched (Hutchinson's incisors) and the molars may have numerous small protrusions on the enamel surface (mulberry molars).

Gemination, fusion and concrescence of teeth

Gemination refers to a situation during development where a tooth germ splits to give the appearance of a large, double tooth. The tooth count in such situations is normal.

Rarely during development, there is **fusion** and union of two adjacent tooth germs. Although in both gemination and fusion, the appearance can suggest a 'double' tooth, in fusion the total number of teeth is one fewer than normal.

Concrescence. is caused by hypercementosis of adjacent roots as the fusion happens after the teeth are formed. It is rarely noticed until one of the teeth is due for extraction when it is found that the other tooth is displaced as well and surgical separation is necessary. It particularly affects second and third molar teeth.

Odontomes

During development a tooth germ may form a tumour-like mass of hard tissue called an odontome which may be asymptomatic or associated with a localized swelling. An odontome may be found in the anterior region of the maxilla, where its presence may prevent eruption of an anterior tooth, or it may be encountered in the posterior region of the jaws, where it may prevent a posterior tooth from erupting. When the odontome consists of many small, discrete, simple, tooth-like structures (denticles), each containing the normal arrangement of dental tissues, it is referred to as a compound odontome. Where the calcified mass bears no resemblance to rudimentary teeth and the dental tissues are arranged haphazardly, it is termed a complex odontome.

An invaginated odontome has been termed 'dens in dente' ('tooth within a tooth): it results either from downward proliferation of a portion of the internal enamel epithelium of the enamel organ into the dental papilla or from retarded growth of part of the tooth germ. It presents on the fully erupted tooth as an extremely deep pit and most commonly affects the permanent maxillary second incisor. The full range of dental tissues (including cementum and bone from incorporation of the dental follicle) may be associated with the 'infolded' organ.

Ameloblastomas

During tooth development, components of the enamel organ may undergo abnormal proliferation to form a tumour. In its simplest form this odontogenic tumour may appear as a benign cyst, often multilocular, that is most commonly seen in the mandible between the ages of 30 and 50 years. Histologically, its main component is strands of epithelial tissue that may resemble pre-ameloblasts, with the nuclei showing a reversal of polarity.

TABLE 37.1 **Chronology of the human dentition**

Dentition	Tooth	First evidence of calcification (weeks *in utero* for deciduous teeth)	Crown completed (postnatal years)	Eruption (postnatal years)	Root completed (years)
Deciduous upper	i1	14	1½ months	10 (8–12) months	1½
	i2	16	2½ months	11 (9–13) months	2
	C	17	9 months	19 (16–22) months	3¼
	m1	15½	6 months	16 (13–19) months	2½
	m2	19	11 months	29 (25–33) months	3
Deciduous lower	i1	14	2½ months	8 (6–10) months	1½
	i2	16	3 months	13 (10–16) months	1½
	C	17	9 months	20 (17–23) months	3¼
	m1	15½	5½ months	16 (14–18) months	2¼
	m2	18	10 months	27 (23–31) months	3
Permanent upper	I1	3–4 months	4–5	7–8	10
	I2	10–12 months	4–5	8–9	11
	C	4–5 months	6–7	11–12	13–15
	P1	1½–1¾ years	5–6	10–11	12–13
	P2	2–2¼ years	6–7	10–12	12–14
	M1	At birth	2½–3	6–7	9–10
	M2	2½–3 years	7–8	12–13	14–16
	M3	7–9 years	12–16	17–21	18–25
Permanent lower	I1	3–4 months	4–5	6–7	9
	I2	3–4 months	4–5	7–8	10
	C	4–5 months	6–7	9–10	12–14
	P1	1¾–2 years	5–6	10–12	12–13
	P2	2¼–2½ years	6–7	1–12	13–14
	M1	At birth	2½–3	6–7	9–10
	M2	2½–3 years	7–8	11–13	14–15
	M3	8–10 years	12–16	17–21	18–25

Adapted with permission from Ash MM 1993 Dental Anatomy, Physiology and Occlusion. Philadelphia: WB Saunders.

an individual's periodicity and it is constant in all teeth from the same individual. Periodicities of 6, 10, 11 and perhaps even 12 days have been reported, but collectively they account for less than 10% of the observed periodicities in large samples of teeth (Reid and Dean 2006).

A prominent striation, the neonatal line, is formed in teeth whose mineralization spans birth. Neonatal lines are present in the enamel and dentine of teeth mineralizing at the time of birth (all the deciduous teeth and the first permanent molars) and are therefore of forensic importance, indicating that an infant has survived for a few days after birth. They reflect a disturbance in mineralization during the first few days after birth. Other accentuated lines can be observed throughout enamel growth; these are generally reflections in disturbances in ameloblast secretion caused by illness or nutritional deficiencies. In serious cases, these disturbances will manifest as hypoplasia (enamel thinning on the tooth surface).

Dentine

Dentine is a yellowish avascular tissue that forms the bulk of a tooth. It is a tough and compliant composite material, with a mineral content of 70% dry weight (largely crystalline hydroxyapatite with some calcium carbonate) and 20% organic matrix (type I collagen, glycosaminoglycans and phosphoproteins). Its conspicuous feature is the regular pattern of microscopic dentinal tubules, 3 µm in diameter, which extend from the pulpal surface to the enamel–dentine junction. The tubules show lateral and terminal branching near the enamel–dentine junction (Fig. 37.29A) and may project a short distance into the enamel (enamel spindles). Each tubule encloses a single cytoplasmic process of an odontoblast whose cell body lies in a pseudostratified layer that lines the pulpal surface. Processes are believed to extend the full thickness of dentine in newly erupted teeth, but in older teeth they may be partly withdrawn and occupy only the pulpal third, while the outer regions contain probably only extracellular fluid. The diameter of the dentine tubule is narrowed by deposition of peritubular dentine. This is different from normal dentine (intertubular dentine) because it is more highly mineralized and lacks a collagenous matrix. Peritubular dentine can therefore be identified by microradiography (Fig. 37.29B). In time, it may completely fill the tubule, a process that gives rise to translucent dentine and that commences in the apical region of the root.

The outermost zone (10–20 µm) of dentine differs in the crown and the root. In the crown, it is referred to as mantle dentine and differs in the orientation of its collagen fibres. In the root, the peripheral zone presents a granular layer – with less overall mineral – beyond which is a hyaline layer that lacks a tubular structure and may function to produce a good bond between the cementum and dentine.

Dentine is formed slowly throughout life, and so there is always an unmineralized zone of predentine at the surface of the mineralized dentine, adjacent to the odontoblast layer at the periphery of the pulp. Biochemical changes within the mineralizing matrix mean that predentine stains differently to the matrix of the mineralized dentine. The predentine–dentine border is generally scalloped, because dentine mineralizes both linearly and as microscopic spherical aggregates of crystals (calcospherites). Dentine, like enamel, is deposited incrementally, and exhibits both short- and long-term incremental lines (Dean 2000). Long-term lines are known as Andresen lines and in the mid-axial region are approximately 20 µm apart; they represent increments of about 6–12 days (Fig. 37.29C). Daily incremental lines (von Ebner lines) in the mid-axial plane are typically 4 µm apart; they are considerably closer together (1–2 µm apart) at the enamel–dentine junction and in root dentine. Where mineralization spans birth (i.e. all deciduous teeth and usually the first permanent molars), a neonatal line is formed in dentine similar to that which is seen in enamel, and it signals the abrupt change in both environment and nutrition that occurs at birth. As with enamel, disturbances in growth of dentine will exhibit as accentuated lines, commonly called contour lines of Owen.

Primary dentine formation proceeds at a steady but declining rate as first the crown and then the root is completed. A slow and intermittent deposition of dentine (regular secondary dentine) continues throughout life and further reduces the size of the pulp chamber; it is distinguished from primary dentine by the reduction and less regular arrangement of dentinal tubules within it. The presence of the odontoblast process means that dentine is a vital tissue. It responds to adverse external stimuli – such as rapidly advancing caries, excessive wear or tooth breakage – by forming poorly mineralized dead tracts, in which the odontoblasts of the affected region die and the tubules remain empty (tertiary dentine). A dead tract may be sealed from the pulp by a thin zone of sclerosed dentine and the deposition of irregular (tertiary) dentine by newly differentiated pulp cells (Fig. 37.30).

Dental pulp

Dental pulp provides the nutritive support for the synthetic activity of the odontoblast layer. It is a well-vascularized, soft, loose connective tissue, enclosed by dentine and continuous with the periodontal ligament via apical and accessory foramina. Several thin-walled arterioles enter by the apical foramen and run longitudinally within the pulp to an extensive subodontoblastic plexus. Blood flow rate per unit volume of tissue is greater in the pulp than in other oral tissues, and tissue fluid pressures within the pulp appear to be unusually high.

As well as typical connective tissue cells, pulp uniquely contains the cell bodies of odontoblasts whose long processes occupy the dentinal tubules. Pulp also has dendritic antigen-presenting cells. Approximately 60% of pulpal collagen is type I, and the bulk of the remainder is type III. As dentine deposition increases with age, the pulp recedes until the whole of the crown may be removed without accessing the pulp.

Dental pulp is extensively innervated by postganglionic vasoconstrictor sympathetic nerve fibres from the superior cervical ganglion, which enter with the arterioles, and by myelinated (Aδ) and unmyelinated (C) sensory nerve fibres from the trigeminal ganglion, which traverse the pulp longitudinally and ramify as a plexus (Raschkow's plexus) beneath the odontoblast layer (Figs 37.31–37.32). Here, any myelinated nerve fibres lose their myelin sheaths and continue into the odontoblast layer, and some enter the dentinal tubules, especially the region beneath the cusps. Stimulation of dentine, whether by thermal, mechanical or osmotic means, evokes a pain response. Pulp nerves release numerous neuropeptides such as CGRP, substance P and neuropeptide Y that maintain homeostasis within the pulp.

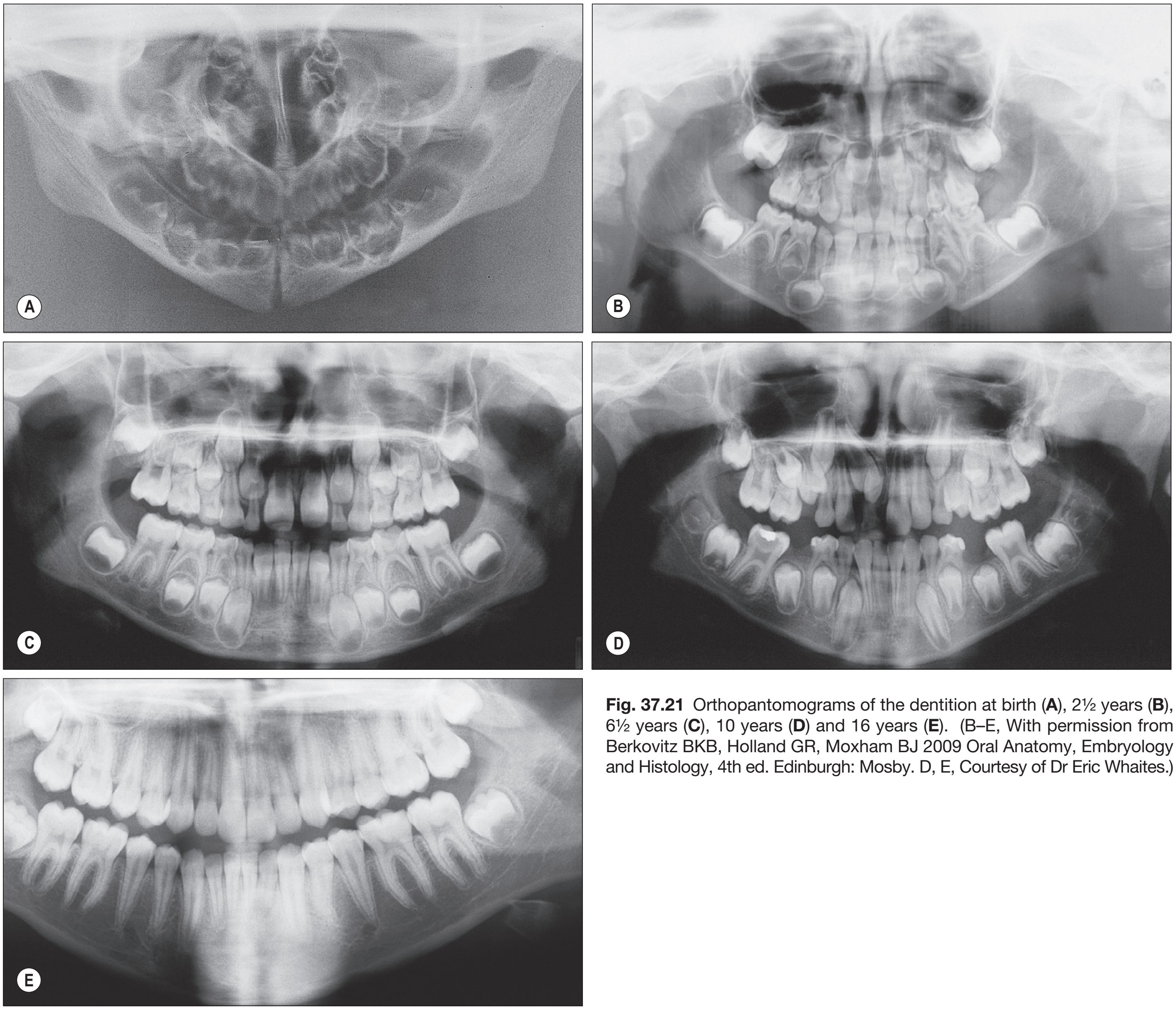

Fig. 37.21 Orthopantomograms of the dentition at birth (**A**), 2½ years (**B**), 6½ years (**C**), 10 years (**D**) and 16 years (**E**). (B–E, With permission from Berkovitz BKB, Holland GR, Moxham BJ 2009 Oral Anatomy, Embryology and Histology, 4th ed. Edinburgh: Mosby. D, E, Courtesy of Dr Eric Whaites.)

Cementum

Cementum is a bone-like tissue that covers the dental roots, and is 50% by weight mineralized (mainly hydroxyapatite crystals). However, unlike bone, cementum is avascular and lacks nerves. The cementum generally overlaps the enamel slightly, although it may meet it end on. Occasionally, the two tissues may fail to meet, in which case dentine is exposed in the mouth. If the exposed dentinal tubules remain patent, then the teeth may be sensitive to stimuli such as cold water. In older teeth, the root may become exposed in the mouth as a consequence of occlusal drift and gingival recession, and cementum is often abraded away by incorrect tooth brushing and dentine is exposed.

Like bone, cementum is perforated by Sharpey's fibres, which represent the attachment bundles of collagen fibres in the periodontal ligament (extrinsic fibres). New layers of cementum, which are deposited incrementally throughout life to compensate for tooth movements, incorporate new Sharpey's fibres. Incremental lines are irregularly spaced. The first (primary) cementum to be formed is thin (up to 200 μm) and acellular, and contains only extrinsic fibres. Cementum formed later (secondary cementum) towards the root apex is produced more rapidly and contains cells, the cementocytes, lying in lacunae joined by canaliculi. The latter are mainly directed towards their source of nutrients from the periodontal ligament. This cementum contains mainly intrinsic collagen fibres of cementoblastic origin, which lie parallel to the surface. Varying arrangements of layering between cellular and acellular cement occur. With increasing age, cellular cement may reach a thickness of a millimetre or more around the apices and at the branching of the roots, where it compensates for the loss of enamel by attrition. Cementum is not remodelled but small areas of resorption with evidence of repair may be seen.

Periodontal ligament

The principal functions of the periodontal ligament are to support the teeth, generate the force of tooth eruption and provide sensory information about tooth position and forces to facilitate reflex jaw activity during chewing movements. The periodontal ligament is a soft, dense, fibrous connective tissue 0.2 mm wide, which contains cells associated with the development and maintenance of alveolar bone (osteoblasts and osteoclasts) and of cementum (cementoblasts and odontoclasts). It also contains a network of epithelial cells (epithelial cell rests of Malassez, ERM cells), which are embryological remnants of an epithelial root sheath. Although their function remains speculative, ERM cells have been implicated in root development and protection against root resorption, and in reparative/regenerative functions of the pulp and periodontal tissues such as apexogenesis and periodontal healing (Keinan and Cohen 2013). Proliferation of ERM cells may play a role in the evolution of odontogenic cysts and tumours.

The majority of collagen fibres of the periodontal ligament are arranged as variously orientated dense fibre bundles that connect alveolar bone and cementum, and which may help to resist movement in specific directions (Fig. 37.33). About 80% of the collagen in the periodontal ligament is type I, most of the remainder being type III. The rate of turnover of collagen is probably the highest of any site in the

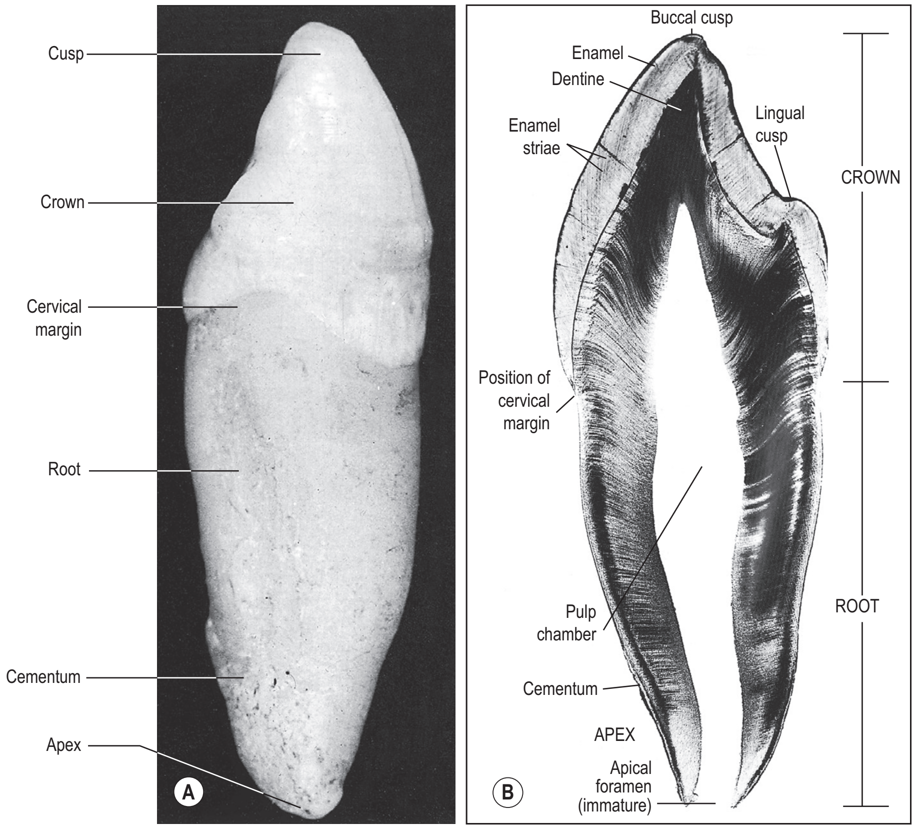

Fig. 37.26 The principal parts of a tooth. **A**, An extracted upper right canine tooth viewed from its mesial aspect. The root is covered by cementum (partially removed), and the curved cervical margin is convex towards the cusp of the tooth. **B**, Ground section of a young (permanent) lower first premolar tooth sectioned in the buccolingual longitudinal plane, photographed with transmitted light. The enamel striae are incremental lines of enamel growth (compare with Fig. 37.31). Within the dentine, the lines of the dentinal tubules are visible, forming S-shaped curves in the apical region but straighter in the root.

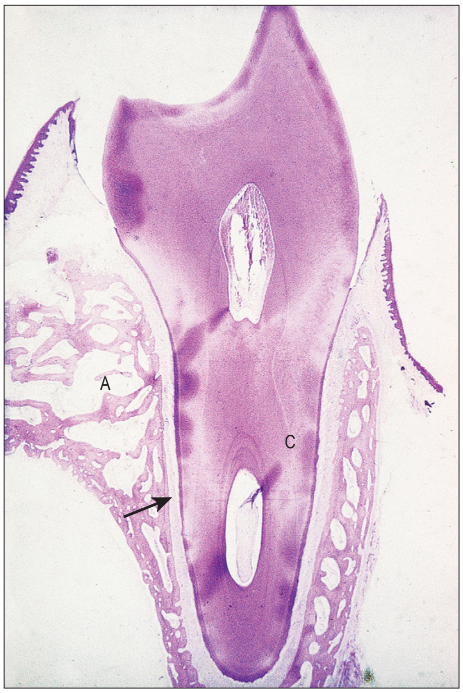

Fig. 37.27 Demineralized section of a tooth with its root attached to the surrounding bone by the periodontal ligament. Key: A, alveolar bone; C, root of tooth lined by cementum. Arrow indicates the periodontal space. (Courtesy of Dr D Lunt.)

body, for reasons that are as yet unclear. A very small volume of fibres are oxytalan (pre-elastin) fibres. Fibroblast density in human periodontal ligament tissue decreases with age (Krieger et al 2013).

The periodontal ligament is innervated by autonomic and sensory nerve fibres, the former carrying vasomotor information and the latter carrying nociceptive and proprioceptive information. Three types of nerve endings have been identified: free nerve endings (originating from myelinated and unmyelinated nerve fibres); Ruffini-like endings (mostly found at the apical part of the periodontal ligament); and lamellated corpuscles (for further reading, see Huang et al (2011)). The periodontal ligament has a rich blood supply; the vessels tend to lie towards the bone side of the periodontal ligament and the capillaries are fenestrated (see below for further details).

Alveolar bone

That part of the maxilla or mandible that supports and protects the teeth is known as alveolar bone. An arbitrary boundary at the level of the root apices of the teeth separates the alveolar processes from the body of the mandible or the maxilla (Fig. 37.34). Like bone in other sites, alveolar bone functions as a mineralized supporting tissue, gives attachment to muscles, provides a framework for bone marrow and acts as a reservoir for ions, especially calcium. It is dependent on the presence of teeth for its development and maintenance, and requires functional stimuli to maintain bone mass. Where teeth are congenitally absent – as in anodontia, for example – it is poorly developed, and it atrophies after tooth extraction, which can cause difficulties in the prosthodontic rehabilitation of patients.

The alveolar tooth-bearing portion of the jaws consists of outer and inner alveolar plates. The individual sockets are separated by plates of bone termed the interdental septa, while the roots of multirooted teeth are divided by inter-radicular septa. The compact layer of bone that lines the tooth socket has been called either the cribriform plate, on account of its content of vascular (Volkmann's) canals, which pass from the alveolar bone into the periodontal ligament; or bundle bone, because numerous bundles of Sharpey's fibres pass into it from the periodontal ligament (Fig. 37.35).

In clinical radiographs, the bone lining the alveolus commonly appears as a continuous dense white line about 0.5–1 mm thick: the lamina dura (Fig. 37.36). However, this appearance gives a misleading impression of the density of alveolar bone; the X-ray beam passes tangentially through the socket wall, and so the radiopacity of the lamina dura is an indication of the quantity of bone the beam has passed through, rather than the degree of mineralization of the bone. Superimposition also obscures the Volkmann's canals. Chronic infections of the dental pulp spread into the periodontal ligament, which leads to resorption of the lamina dura around the root apex (see Fig. 37.36). The presence of a continuous lamina dura around the apex of a tooth therefore usually indicates a healthy apical region (except in acute infections where resorption of bone has not yet begun).

On the labial and buccal aspects of upper teeth, the two cortical plates usually fuse, and there is very little cancellous bone between them, except where the buccal bone thickens over the molar teeth near the root of the zygomatic arch. It is easier and more convenient to extract upper and lower teeth by widening the tooth socket in a buccal direction due to its thinness. Anteriorly in the lower jaw, labial and lingual plates are thin, but in the molar region the buccal plate is thickened as the external oblique line. Near the lower third molar, the lingual bone is much

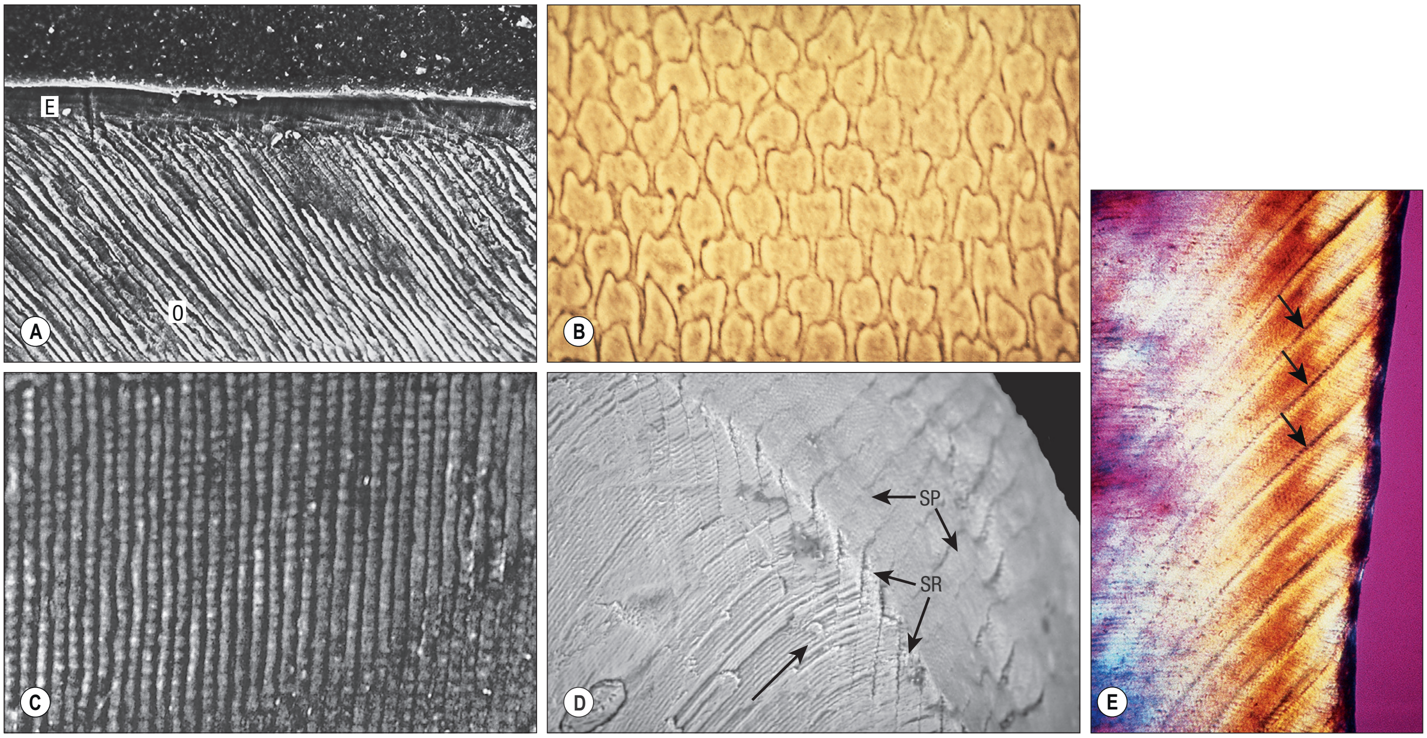

Fig. 37.28 Enamel. **A**, Scanning electron micrograph of acid-etched outer enamel (O) showing enamel prisms, approximately 5 μm wide. A layer of prismless enamel (E) is evident on the surface. **B**, Ground cross-section showing the cross-sectional keyhole (fish scale) appearance of enamel prisms (pattern 3). **C**, Ground longitudinal section showing prisms (vertical lines) and cross-striations (horizontal lines); viewed with phase contrast. **D**, Low-power scanning electron micrograph illustrating the relationship of enamel prism direction (long arrow), striae of Retzius (SR) and surface perikymata (SP). **E**, Ground longitudinal section showing enamel striae (arrows); viewed between crossed polarizing filters. (A, Courtesy of Professor D Whittaker. B, C, With permission from Berkovitz BKB, Holland GR, Moxham BJ 2009 Oral Anatomy, Embryology and Histology, 4th ed. Edinburgh: Mosby. D, With permission from Kelley J, Smith TM 2003 Age at first molar emergence in early Miocene *Afropithecus turkanensis* and life-history evolution in the Hominoidea. J Hum Evol 44:307–29. E, Courtesy of Dr AD Beynon.)

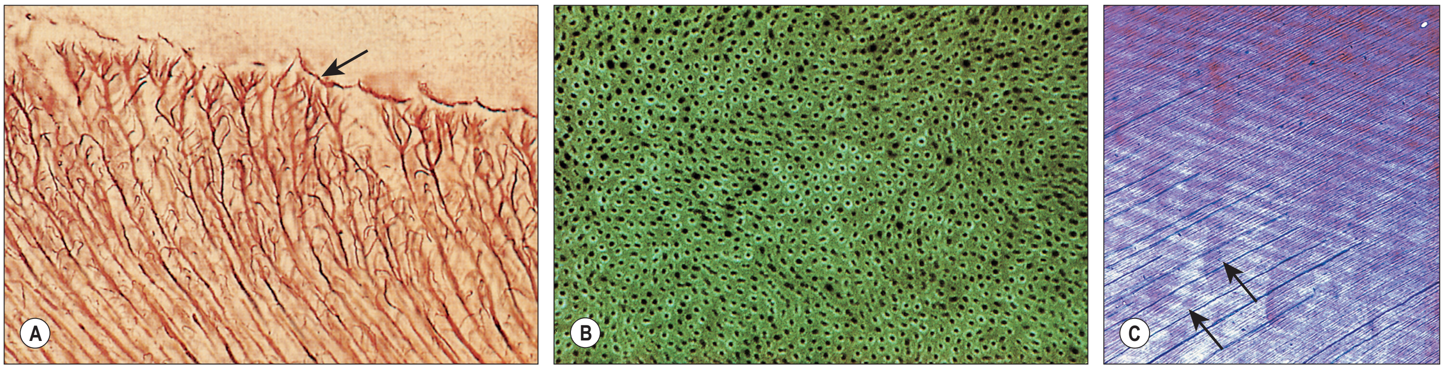

Fig. 37.29 Dentine. **A**, Ground longitudinal section showing branching of dentine tubules near the enamel–dentine junction (arrow). **B**, Microradiograph of transversely sectioned dentinal tubules surrounded by a more radiopaque and therefore more mineralized zone of peritubular dentine. **C**, Ground longitudinal section showing alternate light and dark bands representing long-period incremental lines (Andresen lines; viewed in polarized light). The bands are orientated approximately at right-angles to the direction of the dentinal tubules (arrows). (With permission from Berkovitz BKB, Holland GR, Moxham BJ 2009 Oral Anatomy, Embryology and Histology, 4th ed. Edinburgh: Mosby; B, Courtesy of Dr G Mckay.)

thinner than the buccal and it is important to realize that the lingual nerve is easily damaged by poor technique during tooth extraction.

Vascular supply and lymphatic drainage of the teeth and supporting structures

The main arteries to the teeth and their supporting structures are derived from the maxillary artery, one of the two terminal branches of the external carotid artery. The upper teeth are supplied by branches from the superior alveolar arteries, and the lower teeth by branches from the inferior alveolar arteries.

Superior alveolar arteries

The upper jaw is supplied by posterior, middle and anterior superior alveolar (dental) arteries. The posterior superior alveolar artery usually arises from the third part of the maxillary artery in the pterygopalatine fossa. It descends on the infratemporal surface of the maxilla, and divides to give branches that enter the alveolar canals to supply molar and premolar teeth, adjacent bone and the maxillary sinus, and other branches that continue over the alveolar process to supply the gingivae. The middle and anterior superior alveolar arteries are branches from the infraorbital artery.

The infraorbital artery often arises with the posterior superior alveolar artery. It enters the orbit posteriorly through the inferior orbital fissure and runs in the infraorbital groove and canal with the infraorbital nerve. When the small middle superior alveolar artery is present, it runs down the lateral wall of the maxillary sinus and forms anastomotic arcades with the anterior and posterior vessels, terminating near the canine tooth. The anterior superior alveolar artery curves through the canalis sinuosus to supply the upper incisor and canine teeth and the mucous membrane in the maxillary sinus. The canalis sinuosus swerves laterally from the infraorbital canal and inferomedially below it in the wall of the maxillary sinus, following the rim of the anterior nasal aperture, between the alveoli of canine and incisor teeth and the nasal cavity. It ends near the nasal septum where its terminal branch emerges. The canal may be up to 55 mm long.

Inferior alveolar artery

The inferior alveolar (dental) artery, a branch of the first part of the maxillary artery, descends in the infratemporal fossa posterior to the inferior alveolar nerve. Here, it lies between bone laterally and the sphenomandibular ligament medially. Before entering the mandibular foramen it gives off a mylohyoid branch, which pierces the sphenomandibular ligament to descend with the mylohyoid nerve in its groove on the inner surface of the ramus of the mandible. The mylohyoid artery ramifies superficially on the muscle and anastomoses with the submental branch of the facial artery. The inferior alveolar artery then traverses the mandibular canal with the inferior alveolar nerve to supply the mandibular molars and premolars, and divides into the incisive and mental branches near the first premolar.

The incisive branch continues below the incisor teeth (which it supplies) to the midline, where it anastomoses with its fellow, although few anastomotic vessels cross the midline. In the canal, the arteries supply the mandible, tooth sockets and teeth via branches that enter the minute hole at the apex of each root to supply the pulp. The mental artery leaves the mental foramen and supplies the chin; it anastomoses with the submental and inferior labial arteries. Near its origin, the inferior alveolar artery has a lingual branch, which descends with the lingual nerve to supply the lingual mucous membrane. The pattern of branching of the inferior alveolar artery reflects that of the nerves of the same name.

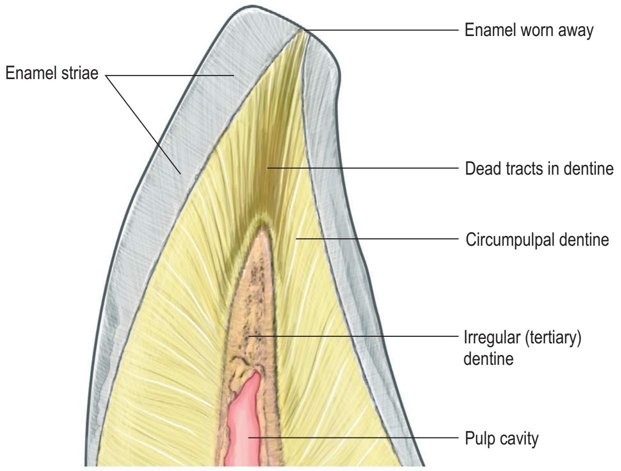
Enamel worn away
Enamel striae
Dead tracts in dentine
Circumpulpal dentine
Irregular (tertiary) dentine
Pulp cavity

Fig. 37.30 Longitudinal ground section of an incisor tooth.

Arterial supply of periodontal ligaments

The periodontal ligaments supporting the teeth are supplied by dental branches of the alveolar arteries. One branch enters the alveolus apically and sends two or three small rami into the dental pulp through the apical foramen, and other rami into the periodontal ligament. Interdental arteries ascend in the interdental septa, sending branches at right-angles into the periodontal ligament, and terminate by communicating with gingival vessels that also supply the cervical part of the ligament. The periodontal ligament therefore receives its blood from three sources: from the apical region; ascending interdental arteries; and descending vessels from the gingivae. These vessels anastomose with each other, which means that when the pulp of a tooth is removed during endodontic treatment, the attachment tissues of the tooth remain vital.

Venous drainage of the teeth

Veins accompanying the superior alveolar arteries drain the upper jaw and teeth anteriorly into the facial vein, or posteriorly into the pterygoid venous plexus. Veins from the lower jaw and teeth collect either into larger vessels in the interdental septa or into plexuses around the root apices and thence into several inferior alveolar veins. Some of these veins drain through the mental foramen to the facial vein; others drain via the mandibular foramen to the pterygoid venous plexus.

Lymphatic drainage of the teeth

The lymph vessels from the teeth usually run directly into the ipsilateral submandibular lymph nodes. Lymph from the mandibular incisors, however, drains into the submental lymph nodes. Occasionally, lymph from the molars may pass directly into the jugulodigastric group of nodes.

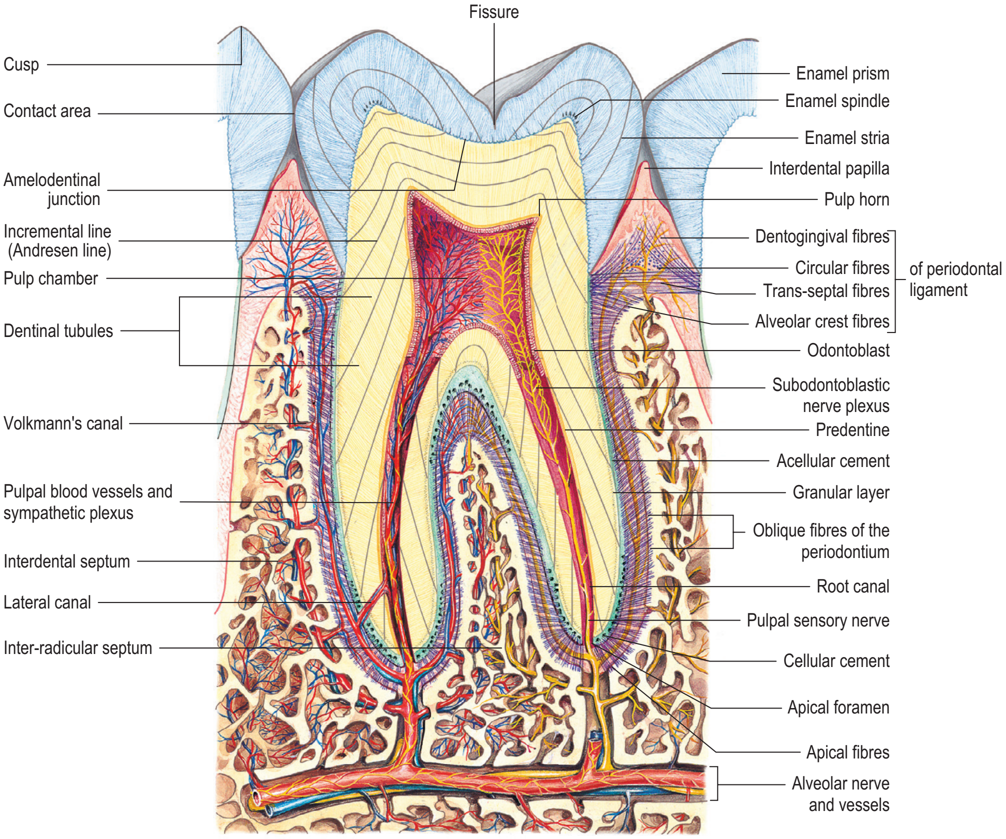
Fissure
Cusp
Contact area
Amelodentinal junction
Incremental line (Andresen line)
Pulp chamber
Dentinal tubules
Volkmann's canal
Pulpal blood vessels and sympathetic plexus
Interdental septum
Lateral canal
Inter-radicular septum
Enamel prism
Enamel spindle
Enamel stria
Interdental papilla
Pulp horn
Dentogingival fibres
Circular fibres
Trans-septal fibres
Alveolar crest fibres
of periodontal ligament
Odontoblast
Subodontoblastic nerve plexus
Predentine
Acellular cement
Granular layer
Oblique fibres of the periodontium
Root canal
Pulpal sensory nerve
Cellular cement
Apical foramen
Apical fibres
Alveolar nerve and vessels

Fig. 37.31 Longitudinal section of a tooth and its surrounding tissues.

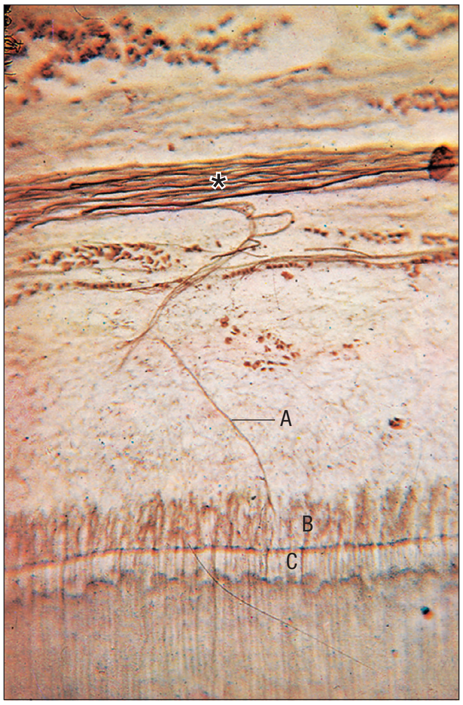

Fig. 37.32 Longitudinal demineralized section of a tooth stained with a silver impregnation technique. Note the small bundle of nerves within the pulp (*); one of the fine axons from the bundle (A) passes between the odontoblasts (B) lining the surface of the predentine (C).

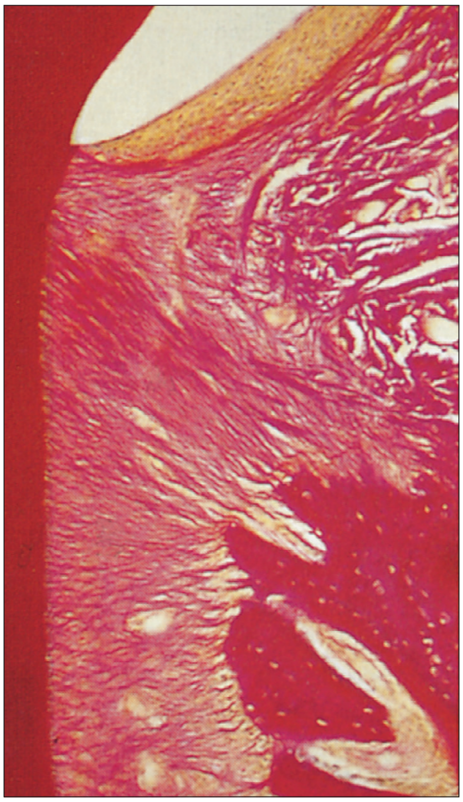

Fig. 37.33 Decalcified longitudinal section of a tooth showing groups of periodontal ligament fibres (the alveolar crest fibres and the horizontal fibres) in the region of the alveolar crest. Van Gieson stain. (With permission from Berkovitz BKB, Holland GR, Moxham BJ 2009 Oral Anatomy, Embryology and Histology, 4th ed. Edinburgh: Mosby.)

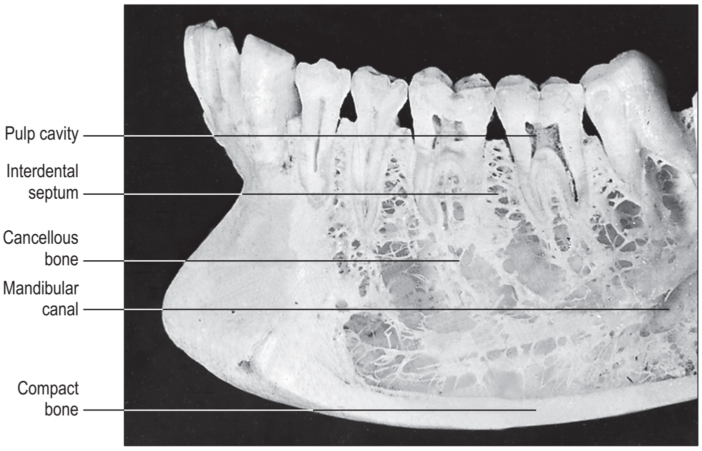

Fig. 37.34 The anterior part of the left side of the mandible; superficial bone has been removed on the buccal side to show the roots of a number of teeth, some of which have also been sectioned vertically. Note the cortical plate of compact bone lining the sockets of the teeth (the lamina dura of radiographs; see Fig. 37.37), and the flat table of bone surmounting the interdental bone septa. In this specimen, the mandibular canal is widely separated from the roots of the teeth, a variable condition.

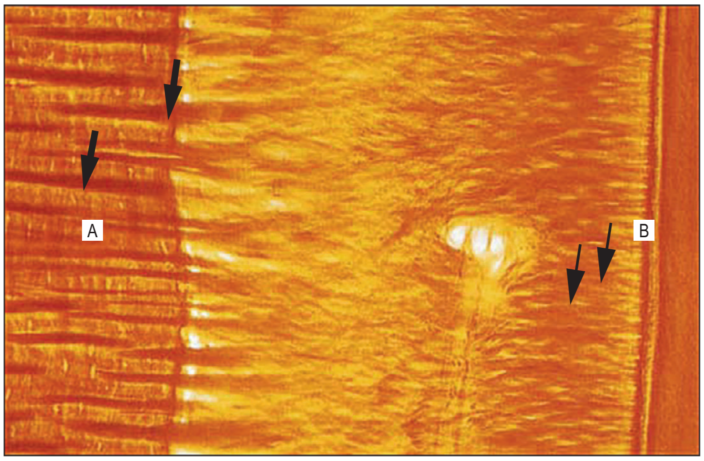

Fig. 37.35 Decalcified section of a root of a tooth showing Sharpey's fibres from the periodontal ligament entering alveolar bone (A). The Sharpey's fibres in bone (thick arrows) are seen to be thicker, but less numerous, than those entering the cementum (B) on the tooth surface (thin arrows). Van Gieson stain. (With permission from Berkovitz BKB, Holland GR, Moxham BJ 2009 Oral Anatomy, Embryology and Histology, 4th ed. Edinburgh: Mosby.)

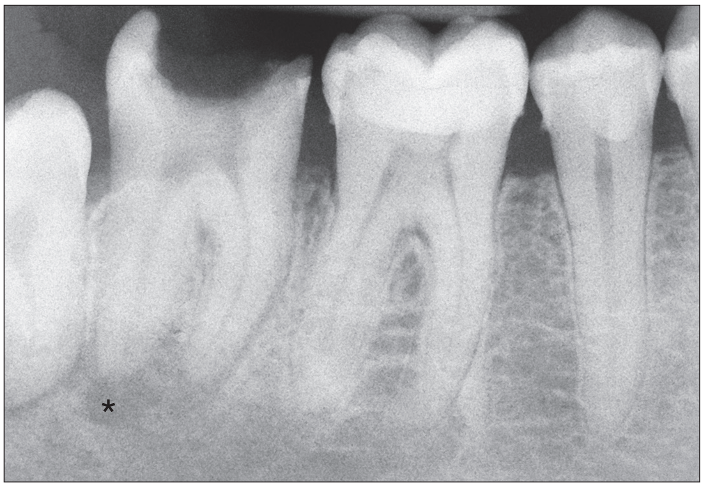

Fig. 37.36 A bite-wing radiograph of teeth and surrounding bone. Note the different radiopacities of enamel and dentine. In a healthy tooth, such as the first molar illustrated here, the lamina dura is complete and appears as a radiopaque line. In the case of the adjacent second molar tooth, in which the bulk of the crown has been lost due to dental caries, an abscess (*) has formed at the base of the tooth and, as a result, the lamina dura has lost its continuity. (Courtesy of Ms Nadine White.)

Innervation of the teeth

The regional innervation of the teeth and gingivae is shown in Table 37.2. The teeth in the upper jaw are supplied by the superior alveolar nerves, while those in the lower jaw are supplied by the inferior alveolar nerve (Rodella et al 2012).

Superior alveolar nerves

The teeth in the upper jaw are supplied by the three superior alveolar (dental) nerves that arise from the maxillary nerve in the pterygopalatine fossa or in the infraorbital groove and canal. The posterior superior alveolar (dental) nerve leaves the maxillary nerve in the pterygopalatine fossa and runs anteroinferiorly to pierce the infratemporal surface of the maxilla, at which point it is possible to perform a local anaesthetic block that will anaesthetize the pulps of the premolar and molar ipsilateral teeth; it then descends under the mucosa of the maxillary sinus. After supplying the lining of the sinus, the nerve divides into small branches that link up as the molar part of the superior alveolar plexus, supplying twigs to the molar teeth. It also supplies a branch to the upper gingivae and the adjoining part of the cheek.

The middle superior alveolar (dental) nerve arises from the infraorbital nerve as it runs in the infraorbital groove, and runs downwards and forwards in the lateral wall of the maxillary sinus. It ends in small branches that link up with the superior dental plexus, supplying small rami to the upper premolar teeth. This nerve is variable, and it may be duplicated or triplicated, or absent.

The anterior superior alveolar (dental) nerve leaves the lateral side of the infraorbital nerve near the midpoint of its canal and traverses the canalis sinuosus in the anterior wall of the maxillary sinus. It curves first under the infraorbital foramen, then passes medially towards the nose, and finally turns downwards and divides into branches to supply the incisor and canine teeth. It assists in the formation of the superior dental plexus and it gives off a nasal branch, which passes through a minute canal in the lateral wall of the inferior meatus to supply the mucous membrane of the anterior area of the lateral wall as high as the opening of the maxillary sinus, and the floor of the nasal cavity. It communicates with the nasal branches of the pterygopalatine ganglion and finally emerges near the root of the anterior nasal spine to supply the adjoining part of the nasal septum.

Inferior alveolar (dental) nerve

The course of the inferior alveolar nerve in the infratemporal fossa is described in Chapter 38. Just before entering the mandibular canal, the inferior alveolar nerve gives off a small mylohyoid branch that pierces the sphenomandibular ligament and enters a shallow groove on the medial surface of the mandible, following a course roughly parallel to its parent nerve. It passes below the origin of mylohyoid to lie on the superficial surface of the muscle, between it and the anterior belly of digastric, both of which it supplies. It gives a few filaments to supply the skin over the point of the chin.

In the mandibular canal, the inferior alveolar nerve runs downwards and forwards, generally below the apices of the teeth until below the first and second premolars, where it divides into terminal incisive and mental branches. The incisive branch continues forwards in a bony canal or in a plexiform arrangement, giving off branches to the first premolar, canine and incisor teeth, and the associated labial gingivae. The lower central incisor teeth receive a bilateral innervation, fibres probably crossing the midline within the periosteum to re-enter the bone via numerous canals in the labial cortical plate.

TABLE 37.2 Innervation of the teeth and gingivae

Maxilla	Nasopalatine nerve			Greater palatine nerve					Palatal gingivae
	Anterior superior alveolar nerve			Middle superior alveolar nerve		Posterior superior alveolar nerve			Teeth
	Infraorbital nerve			Posterior superior alveolar nerve and buccal nerve					Buccal gingivae
	1	2	3	4	5	6	7	8	Tooth position
Mandible	Mental nerve				Buccal nerve and perforating branches of inferior alveolar nerve				Buccal gingivae
	Incisive nerve				Inferior alveolar nerve				Teeth
	Lingual nerve and perforating branches of inferior alveolar nerve								Lingual gingivae

With permission from Berkovitz BKB, Holland GR, Moxham BJ 2009 Oral Anatomy, Embryology and Histology, 4th ed. Edinburgh: Mosby.

The mental nerve passes upwards, backwards and outwards to emerge from the mandible via the mental foramen between and just below the apices of the premolar teeth. It immediately divides into three branches, two of which pass upwards and forwards to form an incisor plexus labial to the teeth, supplying the gingiva (and probably the periosteum). From this plexus and the dental branches, fibres turn downwards and then lingually to emerge on the lingual surface of the mandible on the posterior aspect of the symphysis or opposite the premolar teeth, probably communicating with the lingual or mylohyoid nerve. The third branch of the mental nerve passes through the intermingled fibres of depressor anguli oris and platysma to supply the skin of the lower lip and chin. Branches of the mental nerve also communicate with terminal filaments of the mandibular branch of the facial nerve.

Variations in the fascicular organization of the inferior alveolar nerve are clinically important when extracting impacted third molars. The nerve may appear as a single bundle lying a few millimetres below the roots of the teeth, or it may lie much lower and almost reach the lower border of the bone, so that it gives off a variable number of large rami that pass anterosuperiorly towards the roots before dividing to supply the teeth and interdental septa. Only rarely is it plexiform. The nerve may lie on the lingual or buccal side of the mandible (slightly more commonly on the buccal side). Even when the third molar tooth is in a normal position, the nerve may be so intimately related to it that it grooves its root. Exceptionally, the nerve may be similarly related to the second molar.

Pain sensation in teeth

The teeth are supplied by nociceptors that generate pain sensation of a very high order. The mechanism underlying this sensitivity is of considerable clinical significance and is controversial. Currently, the most widely accepted view is that fluid movements through the dentine tubules stimulate nerve endings at the periphery of the dental pulp (hydrodynamic hypothesis).

Local analgesia

Available with the *Gray's Anatomy* e-book

SALIVARY GLANDS

Salivary glands are compound, tubuloacinar exocrine glands whose ducts open into the oral cavity. They secrete saliva, a fluid that lubricates food to assist deglutition, moistens the buccal mucosa, which is important for speech, and provides an aqueous solvent necessary for taste and a fluid seal for sucking and suckling. Salivary glands also secrete digestive enzymes, e.g. salivary amylase, and antimicrobial agents, e.g. immunoglobulin A (IgA), lysozyme and lactoferrin, into saliva. Most salivary IgA is derived from the blood by passive leakage mainly via gingival crevicular epithelium (Brandtzaeg 2013). Conditions in which there is a significant decrease in the production of saliva (xerostomia) may result in periodontal inflammation and dental caries. An illustration of the position of the major salivary glands and their ducts is given in Fig. 37.40.

The major salivary glands are the paired parotid, submandibular and sublingual glands. In addition, there are numerous minor salivary glands scattered throughout the mouth.

Approximately 0.5 l of saliva is secreted per day. Salivary flow rates are typically 0.3 ml/min when unstimulated, and rise to 1.5–2 ml/min when stimulated. Flow rate is negligible during sleep. In the unstimulated state, the parotid gland contributes 20%, the submandibular gland 65%, and the sublingual and minor salivary glands 15% of the daily output of saliva: when stimulated, the parotid contribution rises to 50%. Parasympathetic impulses usually evoke most of the fluid secretion into saliva, mainly acting through M3 muscarinic cholinergic receptors. Sympathetic impulses elicit exocytosis of protein storage granules in acinar cells in some experimental animals, but the sparse sympathetic (adrenergic) innervation of human sublingual and minor salivary glands is mainly associated with the vasculature and not the parenchyma (Proctor and Carpenter 2007, Proctor 2016). Several aquaporins (transmembrane protein channels) are expressed in salivary glands, including the acinar and ductal cells involved in the formation of saliva: AQP5 appears to play a major role in saliva secretion (Delporte et al 2016).

The failure of complete anaesthesia to the mandibular teeth following an inferior alveolar nerve block, which is meant to anaesthetize the nerve before its entrance into the mandibular canal, indicates that there are alternative pathways for sensory nerves to the teeth. Knowledge of these alternative pathways is important in helping clinicians to obtain complete dental anaesthesia. These alternative pathways involve anatomical variation in the distribution of the inferior alveolar nerve, the buccal branch of the mandibular nerve, the mylohyoid nerve, the lingual nerve, the deep temporal nerves and the cervical plexus. The inferior alveolar nerve may give multiple branches before entering the mandibular canal, one or more of which may escape anaesthesia following inferior alveolar nerve block. They may then re-enter the mandible via small accessory foramina in the retromolar region to supply sensation to the molar teeth (**Fig. 37.37**). The buccal branch of the mandibular nerve, which supplies the buccal gingivae of the molar teeth, may also possess a branch that passes through a small retromolar foramen to supply the molar teeth. The mylohyoid nerve is primarily a motor nerve supplying mylohyoid and the anterior belly of the digastric, but it carries sensory fibres that may enter the mandible via one or more small retromental foramina in the vicinity of the genial tubercles to supply some sensation to the anterior teeth. Communications exist between the inferior alveolar and lingual nerves. If the lingual nerve is not anaesthetized during an inferior alveolar nerve block, this pathway could account for any remaining sensation in the teeth. Although the deep temporal nerves are primarily motor, it has been suggested that terminal branches may pass from the substance of temporalis to enter the mandible through foramina in the retromolar region to supply some sensation to molar teeth. In the cervical plexus, the great auricular nerve, formed by the anterior primary rami of the second and third cervical spinal nerves, supplies skin over the angle of the mandible. It is possible that this nerve may provide a branch that penetrates the mandible to supply one or more of the cheek teeth.

If a successful inferior alveolar nerve block does not completely anaesthetize teeth in a jaw quadrant, additional local injections of anaesthetic solution around the tooth in question may be necessary to block the alternative pathways described above. In addition, there is the possibility of overlap across the midline involving the incisive and mylohyoid nerves. In children, there is evidence to suggest that the lingula is variable in position and its position from the occlusion plane increases with age. It is therefore not considered an appropriate landmark for inferior alveolar nerve block (Ezoddini Ardakani et al 2010).

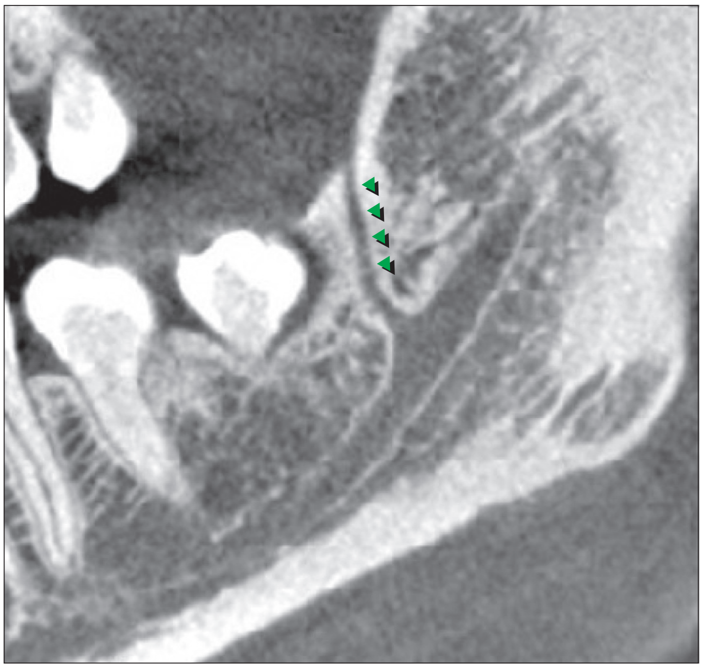

Fig. 37.37 A bifid inferior alveolar canal in which a branch of the inferior alveolar nerve enters the mandible through an accessory foramen in the retromolar region (arrowed) to supply sensation to the molar teeth. (Courtesy of Dr Clare Gleeson.)

Impacted mandibular third molars In many subjects, there is a disproportion between the size of the teeth and the size of the jaws, such that there is insufficient space for all the teeth to erupt. As the third mandibular molar teeth (the wisdom teeth) are the last to erupt, they are often impeded in their eruption and either become impacted or remain unerupted deeply within the jaw bone. If the tooth is completely covered by bone and mucosa, it is very unlikely to cause any symptoms, and the subject remains unaware of its presence unless the tooth is seen on a routine dental radiograph. Very rarely, the surrounding dental follicle may undergo cystic degeneration, which can 'hollow out' the jaw, usually the mandible, to a considerable degree. The developing cyst may displace the tooth as it expands and the tooth may end up as far away as the condylar neck or coronoid process.

More commonly, the erupting wisdom tooth erupts partially before impacting against the distal aspect of the second molar. When this occurs, symptoms are common due to recurrent soft tissue inflammation and infection around the partially erupted tooth caused by food impaction. This condition is known as pericoronitis and, if the infecting organism is virulent, the infection may rapidly spread into the adjacent tissue spaces as described elsewhere (see below and Ch. 38). The tooth only merits surgical removal if the patient suffers a severe bout or multiple bouts of pericoronitis. Surgery is not immediately indicated because it is associated with a degree of morbidity: the lingual and inferior alveolar nerves, which are often in close proximity to the tooth, may be damaged during its removal. The lingual nerve passes across the surface of the periosteum lingually to the lower wisdom tooth, separated from the tooth only by a cortical plate of bone no thicker than an eggshell. Damage to this nerve results in altered sensation (paraesthesia) to the ipsilateral side of the tongue and floor of mouth.

A major problem when extracting mandibular third molar teeth, especially if they are impacted, is possible damage to the inferior alveolar nerve. Indeed, surgical treatment may only necessitate the removal of the crown, leaving behind the roots (after suitable root filling). Maxillary third molars are only rarely impacted because they erupt posteroinferiorly. A clear radiograph is required before any tooth extraction is undertaken in order to alert the dental surgeon to any problems that may be encountered. For example, although the inferior alveolar nerve and its accompanying vessels generally lie beneath the roots of the third permanent molar in the mandibular canal, the neurovascular bundle may occupy a higher position, close to the roots, and may even run between the roots. This may be evident in routine periapical or orthopantomograph radiographs as a constriction or deviation of the mandibular canal or as a radiolucent canal overlying the roots of the third molar (**Fig. 37.38**). In this situation, the inferior alveolar nerve is at risk during extraction of third molars; damage to the nerve may result in paraesthesia in the distribution of the mental nerve, with consequent altered sensation or numbness in the lower lip. The root of a mandibular premolar may occasionally be unusually long and may be in close relationship to the mental nerve, which may then be at risk during extraction of this tooth.

Routine radiographs are no longer considered satisfactory for revealing the close relationship of the inferior alveolar nerve to the third molars; cone beam computed tomography (CBCT) is the method of choice to show this relationship in three dimensions. CBCT is also routinely used prior to insertion of a dental implant to determine not only the exact position of the inferior alveolar nerve and its mental branch but also the topography of the surrounding bone, to establish whether it is suitable for receiving a dental implant.

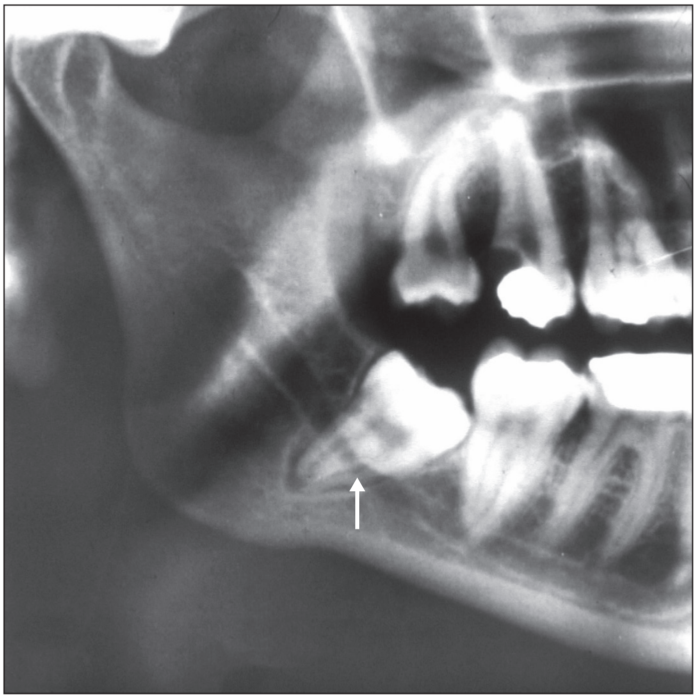

Fig. 37.38 A radiograph showing that the mandibular canal containing the inferior alveolar canal and its contents (arrow) are closely related to the roots of the impacted permanent mandibular third molar. (With permission from Berkovitz BKB, Holland GR, Moxham BJ 2009 Oral Anatomy, Histology and Embryology, 4th ed. Edinburgh, Mosby.)

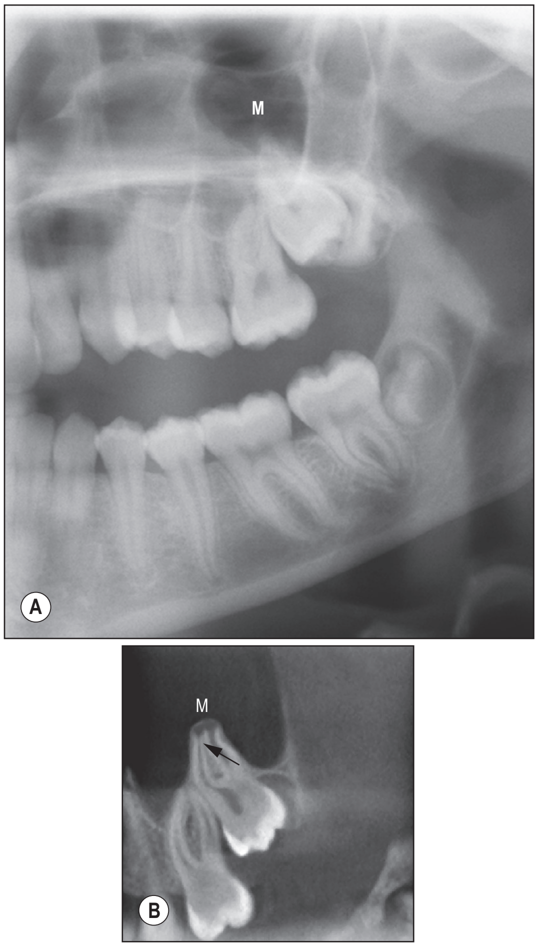

Fig. 37.39 A, A routine orthopantomogram showing the roots of the permanent maxillary molar teeth and the maxillary sinus (M): the precise relationship of the root apices to the floor of the maxillary sinus is unclear. **B**, Cone beam computed tomography of the same patient shown in **A**; the image in the sagittal plane clearly shows the two buccal root apices (arrow) of the permanent maxillary second molar tooth invaginating into the maxillary sinus (M). (Courtesy of Dr J Davies.)

It is technically possible to achieve profound regional anaesthesia by depositing local anaesthetic solution adjacent to the trigeminal nerve trunks or their branches within the infratemporal fossa. These injections can either be performed transorally (posterior superior alveolar nerve block, maxillary nerve block, inferior alveolar nerve block, lingual nerve block and mandibular nerve block) or, rarely, by an external route through the skin of the face (maxillary nerve block, inferior alveolar nerve block and mandibular nerve block).

In the case of the mandible, the anterior teeth can be anaesthetized by simple diffusion techniques, as the bone is relatively thin. However, this is not adequate for the cheek teeth due to the increased thickness of the bone. In this case, the inferior alveolar nerve has to be anaesthetized before it enters the inferior alveolar canal. The needle has to be placed within the pterygomandibular space to achieve a successful inferior alveolar nerve block. The lingual nerve is also usually blocked, as it lies close to the inferior alveolar nerve. Because of the other structures within the infratemporal fossa, it is important for the operator to have a detailed knowledge of the anatomy in this region in order to understand, and therefore try to avoid, the complications that may arise. Any damage to blood vessels in the infratemporal fossa, including the pterygoid venous plexus, can lead to haematoma formation. In extreme cases, bleeding can track through the inferior orbital fissure, resulting in a retrobulbar haematoma, which can lead to loss of visual acuity or blindness. Intravascular injection of local anaesthetic solution (which usually contains adrenaline (epinephrine)) can have profound systemic effects, and for this reason an aspirating syringe is always used to check that the needle has not entered a vessel prior to injection (vessels in this area that theoretically may be entered include the maxillary and internal carotid arteries). If the needle is placed too medially, it may enter medial pterygoid; if directed too laterally, it may penetrate temporalis. In either case, there will be a lack of anaesthesia, followed later by trismus. If the needle is placed too deeply, anaesthetic solution may cause a temporary facial nerve palsy resulting from conduction block in the facial nerve in the region of the parotid gland. Local anaesthetic solution may enter the orbit via the inferior orbital fissure and give orbital symptoms, the most likely being a temporary paralysis of the abducens nerve with loss of activity of lateral rectus.

The root apices of the maxillary cheek teeth are close to, and may even invaginate, the maxillary sinus. The permanent tooth most commonly involved is the upper second molar, followed by the first molar; less frequently, premolars and the third molar may be involved. The likelihood of cavitation of the maxillary sinus increases significantly after tooth extraction. During removal of fractured root apices in this region, care must therefore be taken to ensure that the root fragment is not pushed into the sinus. Similarly, during root canal treatment, care must be taken to ensure that any filling material is not pushed into the sinus. When routine radiographs fail to provide sufficient definition of the close relationship between the floor of the maxillary sinus and root apices, CBCT may be necessary to provide additional detail (Fig. 37.39).

Parotid gland

The parotid gland is the largest salivary gland and is almost entirely serous. The parotid duct runs through the cheek and drains into the mouth opposite the maxillary second permanent molar tooth. The parotid gland is described in detail in Chapter 36. A sialogram of the parotid duct is illustrated in Fig. 37.40A,B.

Submandibular salivary gland

The submandibular gland is irregular in shape and about the size of a walnut. It is a mixed serous and mucous tubuloacinar gland (predominantly serous). It has a larger superficial and a smaller deep part that are continuous with each other around the posterior border of mylohyoid.

Superficial part of the submandibular gland

The superficial part of the gland is situated in the digastric triangle, where it reaches forwards to the anterior belly of digastric and back to the stylomandibular ligament, by which it is separated from the parotid gland. Above, it extends medial to the body of the mandible. Below, it usually overlaps the intermediate tendon of digastric and the insertion of stylohyoid. This part of the submandibular gland presents inferior, lateral and medial surfaces, and is partially enclosed between two layers of deep cervical fascia that extend from the greater cornu of the hyoid bone. The superficial layer is attached to the lower border of the mandible and covers the inferior surface of the gland. The deep layer is attached to the mylohyoid line on the medial surface of the mandible and covers the medial surface of the gland.

The inferior surface, covered by skin, platysma and deep fascia, is crossed by the facial vein and the cervical branch of the facial nerve. Near the mandible, the submandibular lymph nodes are in contact with the gland and some may be embedded within it.

The lateral surface is related to the submandibular fossa on the medial surface of the body of the mandible and the mandibular attachment of medial pterygoid. The facial artery grooves its posterosuperior part, lies at first deep to the gland and then emerges between its lateral surface and the mandibular attachment of the medial pterygoid to reach the lower border of the mandible.

The medial surface is related anteriorly to mylohyoid, from which it is separated by the mylohyoid nerve and vessels and branches of the submental vessels. More posteriorly, it is related to styloglossus, the stylohyoid ligament and the glossopharyngeal nerve, which separate it from the pharynx. In its intermediate part, the medial surface is related to hyoglossus, from which it is separated by styloglossus, the lingual nerve, submandibular ganglion, hypoglossal nerve and deep lingual vein (sequentially from above down). Below, the medial surface is related to the stylohyoid muscle and the posterior belly of digastric.

Deep part of the submandibular gland

The deep part of the gland extends forwards to the posterior end of the sublingual gland. It lies between mylohyoid inferolaterally, hyoglossus and styloglossus medially, the lingual nerve superiorly, and the hypoglossal nerve and deep lingual vein inferiorly (see Figs 37.14, 37.40A).

Vascular supply and lymphatic drainage

The arteries supplying the gland are branches of the facial and lingual arteries. The lymph vessels drain into the deep cervical group of lymph nodes (particularly the jugulo-omohyoid node), interrupted by the submandibular nodes.

Innervation

The secretomotor supply to the submandibular gland is derived from the submandibular ganglion (parasympathetic). The vasomotor supply is derived from the superior cervical ganglion (sympathetic).

Submandibular ganglion

The submandibular ganglion is a small, fusiform body that lies on the upper part of hyoglossus, superior to the deep part of the submandibular gland and inferior to the lingual nerve, to which it is connected by several filaments. The posterior filament is the motor, parasympathetic root that conveys preganglionic fibres from the superior salivatory nucleus in the brainstem via the facial, chorda tympani and lingual nerves to the ganglion, where they synapse. Five or six postganglionic secretomotor branches from the ganglion supply the submandibular gland and its duct, and the sublingual and anterior lingual glands, by travelling either through the anterior filaments that connect the

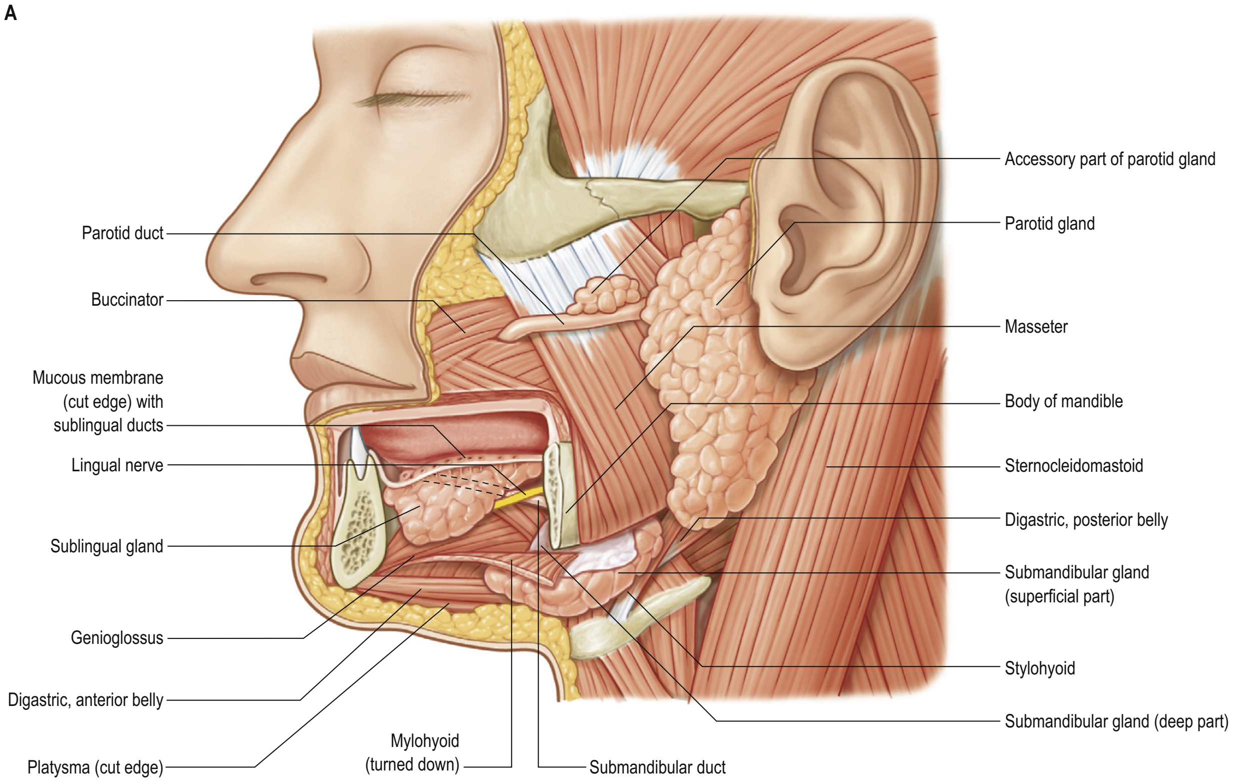
A
Accessory part of parotid gland
Parotid gland
Parotid duct
Buccinator
Masseter
Mucous membrane (cut edge) with sublingual ducts
Body of mandible
Lingual nerve
Sternocleidomastoid
Digastric, posterior belly
Sublingual gland
Submandibular gland (superficial part)
Genioglossus
Stylohyoid
Digastric, anterior belly
Submandibular gland (deep part)
Platysma (cut edge)
Mylohyoid (turned down)
Submandibular duct

Fig. 37.40 **A**, The salivary glands of the left side. The cranial region of the superficial part of the submandibular gland has been excised and mylohyoid has been cut and turned down to expose a portion of the deep part of the gland. (B–C, *continued online*)

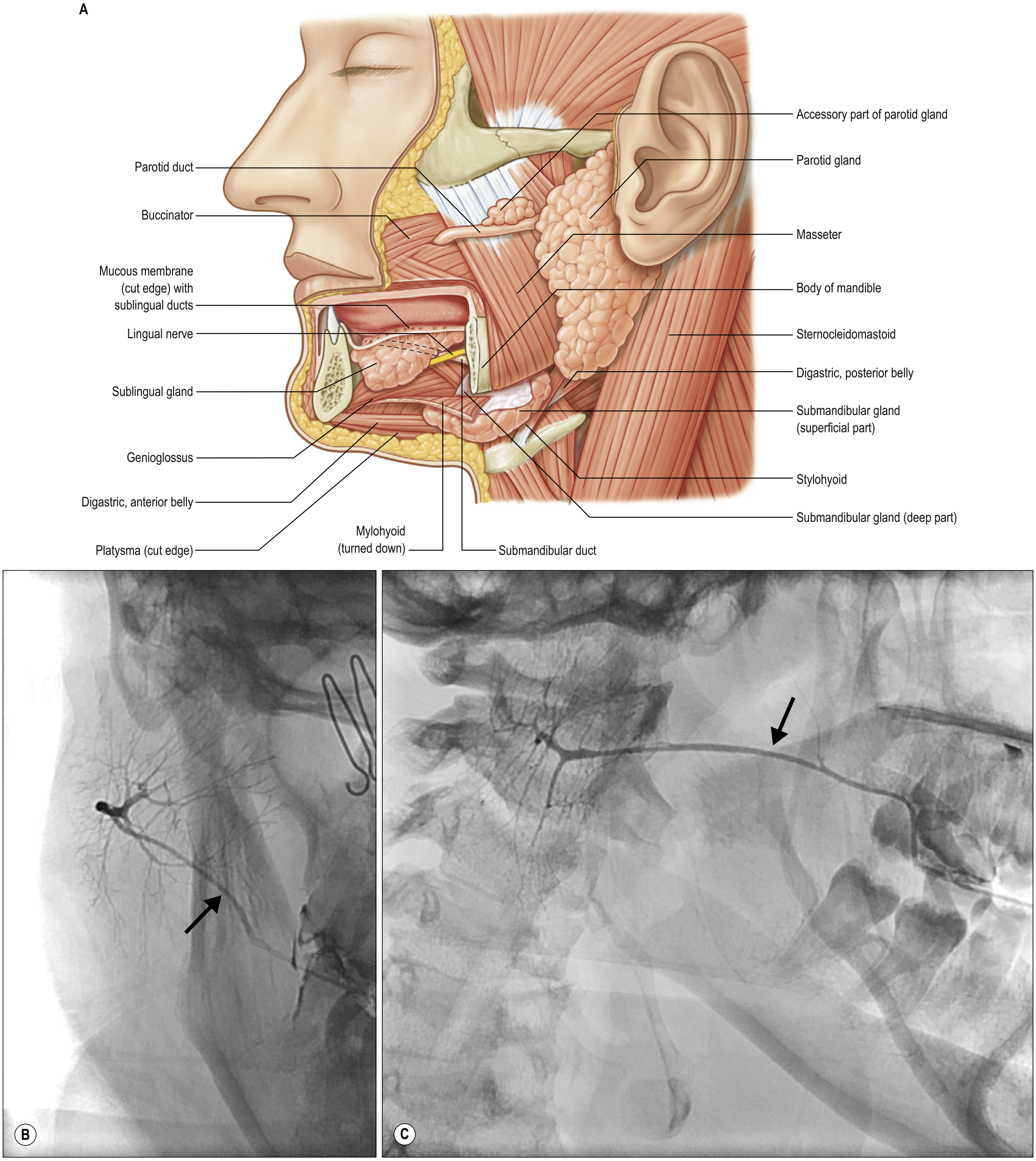
A
Accessory part of parotid gland
Parotid gland
Parotid duct
Buccinator
Masseter
Mucous membrane (cut edge) with sublingual ducts
Body of mandible
Lingual nerve
Sternocleidomastoid
Digastric, posterior belly
Sublingual gland
Submandibular gland (superficial part)
Genioglossus
Stylohyoid
Digastric, anterior belly
Submandibular gland (deep part)
Platysma (cut edge)
Mylohyoid (turned down)
Submandibular duct
B
C

Fig. 37.40 **A**, The salivary glands of the left side. The cranial region of the superficial part of the submandibular gland has been excised and mylohyoid has been cut and turned down to expose a portion of the deep part of the gland. **B–C**, A normal parotid sialogram: **B**, frontal view; **C**, oblique view. The main duct (arrow) has been cannulated in order to fill the gland with contrast medium.

submandibular gland to the lingual nerve or along adjacent blood vessels to their targets. Neuronal cell bodies and small ganglia have been described in the interlobular connective tissue stroma of human submandibular ganglia, close to salivary parenchymal cells and blood vessels (Tosios et al 2010). The sympathetic root is derived from the plexus on the facial artery and consists of postganglionic fibres from the superior cervical ganglion that traverse the submandibular ganglion without synapsing. These fibres are vasomotor to the blood vessels of the submandibular and sublingual glands. Sensory fibres derived from the lingual nerve may also pass through the ganglion.

Submandibular duct

The submandibular duct is about 5 cm long and has a thinner wall than the parotid duct. It begins from numerous tributaries in the superficial part of the gland and emerges from the medial surface of this part of the gland behind the posterior border of mylohyoid. It traverses the deep part of the gland, and then passes at first up and slightly back for approximately 5 mm, this sharp bend over the free edge of mylohyoid being known as the genu of the duct. It then runs forwards between mylohyoid and hyoglossus, passing between the sublingual gland and genioglossus to open in the floor of the mouth on the summit of the sublingual papilla at the side of the frenulum of the tongue (see Figs 37.4, 37.14). It lies between the lingual and hypoglossal nerves on hyoglossus but, at the anterior border of the muscle, it is crossed laterally by the lingual nerve, terminal branches of which ascend on its medial side. As the duct traverses the deep part of the gland, it receives small tributaries draining this part of the gland. It has been suggested previously that the genu of the duct predisposes to the stasis of saliva and thereby encourages salivary stone (sialolith) formation, but this is somewhat controversial and largely unproven.

Like the parotid gland, the duct system of the submandibular gland can be visualized by sialography (Fig. 37.41).

Sublingual salivary gland

The sublingual gland is the smallest of the main salivary glands. It is a mixed serous and mucous tubuloacinar gland in which mucous cells predominate. Each sublingual gland is narrow, flat, shaped like an almond, and weighs approximately 4 g. It lies on mylohyoid and is covered by the mucosa of the floor of the mouth, which is raised as a sublingual fold (see Figs 37.4, 37.14). The deep part of the submandibular gland lies behind; the sublingual fossa of the mandible is lateral; genioglossus is medial and separated from the sublingual gland by the lingual nerve and submandibular duct.

The sublingual gland is made up two parts. A posterior part, which is not always present, is referred to as the greater sublingual gland, from which a main duct (Bartholin's duct) arises to drain either directly onto the sublingual papilla or to join the submandibular duct. This duct may be visualized occasionally in a submandibular sialogram (see Fig. 37.41). An anterior, lesser sublingual gland is always present and consists of a mass of small glands, numbering from 7 to 15, from which a short main duct drains onto the sublingual fold.

Vascular supply, lymphatic drainage and innervation

The arterial supply to the sublingual gland is from the sublingual branch of the lingual artery and the submental branch of the facial artery. Lymphatic drainage is to the submental nodes.

Secretomotor parasympathetic innervation is from the chorda tympani nerve via the submandibular ganglion.

Ranula

Available with the *Gray's Anatomy* e-book

Minor salivary glands

The minor salivary glands of the mouth include the labial, buccal, palatoglossal, palatal and lingual glands. The labial and buccal glands contain both mucous and serous elements. The palatoglossal glands are mucous glands and are located around the pharyngeal isthmus. The palatal glands are mucous glands and occur in both the soft and hard palates. The anterior and posterior lingual glands are mainly mucous. The anterior glands are embedded within muscle near the ventral surface of the tongue and open by means of four or five ducts near the lingual frenulum, and the posterior glands are located in the root of the tongue. The deep posterior lingual glands are predominantly serous. Serous glands (of von Ebner) occur around the circumvallate papillae; their secretion is watery, and they probably assist in gustation by spreading taste stimuli over the taste buds and then washing them away.

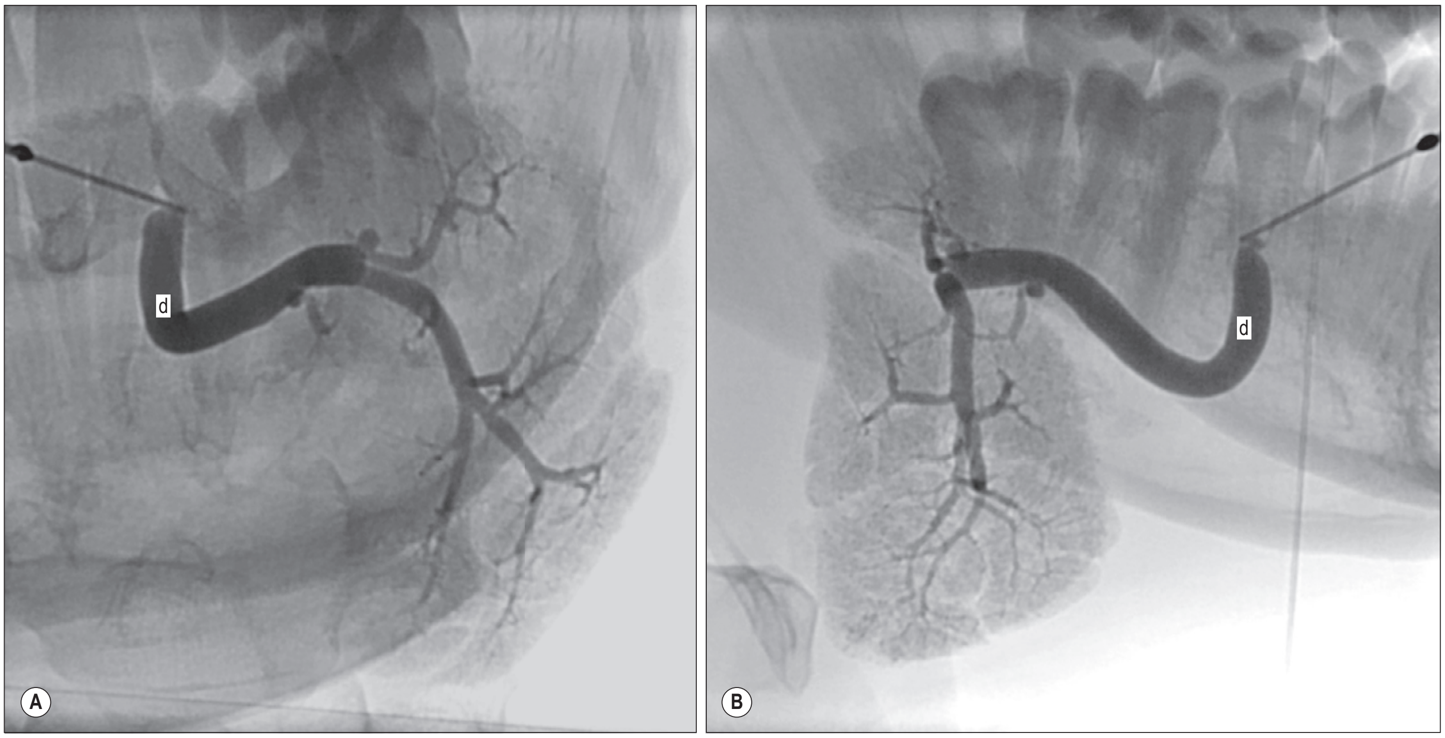

Fig. 37.41 A normal left submandibular sialogram. **A**, Frontal view; **B**, oblique view from the opposite side of the jaw. The main duct (d) has been cannulated in the floor of the mouth in order to fill the gland with contrast medium.

Microstructure

Salivary glands have numerous lobes composed of smaller lobules separated by dense connective tissue that is continuous with the capsule of the gland, and contains excretory (collecting) ducts, blood vessels, lymph vessels, nerve fibres and small ganglia. Each lobule has a single duct, whose branches terminate at dilated secretory 'end-pieces', which are tubular or acinar in shape (Fig. 37.43). Their primary secretion is modified as it flows through intercalated, striated and excretory ducts into one or more main ducts that discharge saliva into the oral cavity. They contain a variable amount of intralobular adipose tissue; adipocytes are particularly numerous in the parotid gland.

The secretory end-pieces of the human parotid gland are almost exclusively serous acini (Fig. 37.44A); mucous tubules or acini are rare. In the submandibular gland, secretory units are predominantly serous acini, with some mucous tubules and acini (Fig. 37.44B). Mucous tubules are often associated with groups of serous cells at their blind ends, appearing as crescent-shaped serous demilunes in routine histological preparations. However, this appearance is a fixation artefact, as tissue prepared by rapid freezing methods lacks serous demilunes and the serous secretory cells align with mucous cells around a common lumen (Yamashina et al 1999). In the sublingual gland, mucous tubules and acini predominate (Fig. 37.44C) but serous cells also occur, as acini or as serous demilunes.

Serous cells are approximately pyramidal in shape. Their nuclei vary in shape and position, but are more rounded and situated less basally than in mucous cells. Apically, the cytoplasm is filled by proteinaceous secretory (zymogen) granules with high amylase activity. Additionally, serous cells secrete kallikrein, lactoferrin and lysozyme, an antibacterial enzyme whose synthesis has been localized in particular to the serous demilunes of the submandibular and sublingual glands, and which is important in the defence against oral pathogens. In the human parotid and submandibular glands, zymogen granules also show a positive periodic acid–Schiff staining reaction, which indicates the presence of polysaccharides, and some texts refer to these cells as seromucous. Mucous cells are cylindrical and have flattened, basal nuclei. Their apical cytoplasm is typically packed with large, pale-staining and electron-translucent secretory droplets. The histological appearance of serous and mucous cells will vary according to the stage in the secretory cycle.

Ducts

Intercalated, striated (both intralobular) and extralobular collecting ducts lead consecutively from the secretory end-pieces. The lining cells of intercalated ducts are flat nearest the secretory end-piece but become cuboidal. Intercalated ducts function primarily as a conduit for saliva but, together with the striated ducts, may also modify its content of electrolytes and secrete IgA. Striated ducts are lined by a low columnar epithelium and are so called because their lining cells have characteristic basal striations. The latter are regions of highly infolded basal plasma membrane, between which lie columns of vertically aligned mitochondria. The nuclei are consequently displaced by the basal striations from a typical ductal basal position to a central or even apical location (see Fig. 37.44). Infolding of the basal plasma membrane and local abundance of mitochondria are typical features of epithelial cells that actively transport electrolytes. Here, the cells transport potassium and bicarbonate into saliva; they produce a hypotonic saliva by reabsorbing sodium and chloride ions in excess of water. Striated ducts modify electrolyte composition and secrete IgA (Ch. 4), lysozyme and kallikrein. The intralobular ductal system of the sublingual gland is less well developed than that of the parotid and submandibular glands.

Collecting ducts are metabolically relatively inert conduits that run within interlobular connective tissue septa in the glands. They transport saliva to the main duct, which opens on to the mucosal surface of the buccal cavity. The lining epithelium of collecting ducts varies. It may be pseudostratified columnar, stratified cuboidal or columnar in the larger ducts, and has a distinct basal layer. It becomes a stratified squamous epithelium near the buccal orifice.

Myoepithelial cells

Myoepithelial cells are contractile cells that lie between the basal laminae and the epithelial cells proper and extend numerous cytoplasmic processes around the serous acini and intercalated ducts (Ogawa 2003). They express both an epithelial and a smooth muscle

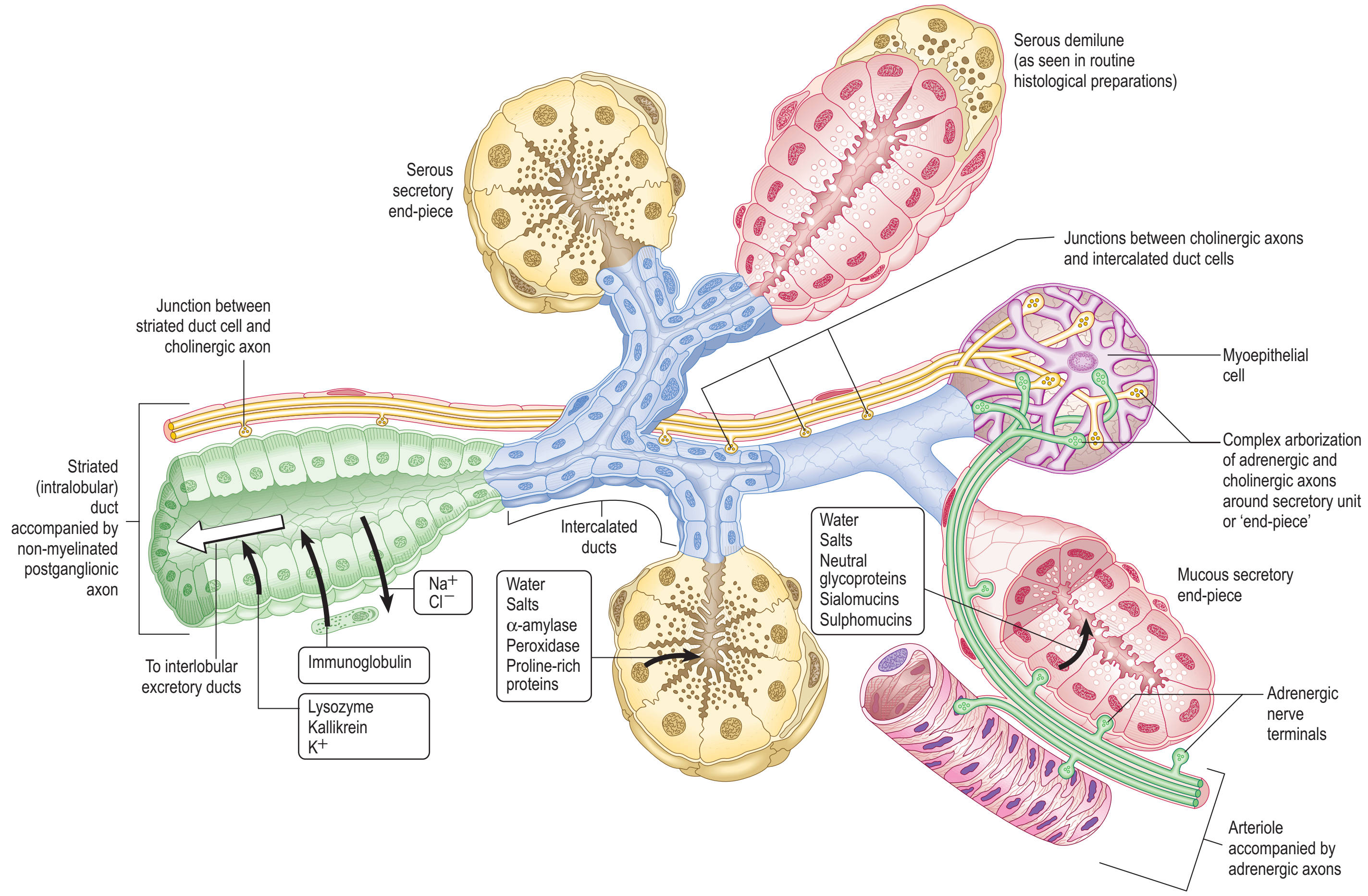
Serous demilune (as seen in routine histological preparations)
Serous secretory end-piece
Junctions between cholinergic axons and intercalated duct cells
Junction between striated duct cell and cholinergic axon
Myoepithelial cell
Complex arborization of adrenergic and cholinergic axons around secretory unit or 'end-piece'
Striated (intralobular) duct accompanied by non-myelinated postganglionic axon
Intercalated ducts
Na+ Cl−
Water Salts Neutral glycoproteins Sialomucins Sulphomucins
Mucous secretory end-piece
Water Salts α-amylase Peroxidase Proline-rich proteins
Immunoglobulin
To interlobular excretory ducts
Lysozyme Kallikrein K+
Adrenergic nerve terminals
Arteriole accompanied by adrenergic axons

Fig. 37.43 The architecture of a generalized salivary gland. Solid black arrows indicate the direction of transport of salivary components, and the open white arrow the direction of salivary flow. The innervation of the ducts, secretory units and arterioles is shown.

If the ducts draining any salivary gland become obstructed, the gland itself is at risk of developing a retention cyst where the retained secretions dilate the gland itself rather like a balloon. This phenomenon is seen mostly in the minor salivary glands that line the lips and oral cavity, where it is known as a mucocele. Trauma, such as persistent lip biting, results in scarring of the overlying oral mucosa and obstruction of the small drainage duct. When trauma occurs in the floor of the mouth and obstructs the drainage duct/s of the sublingual gland, the resulting retention cyst is known as a ranula. (Ranula is the Latin name for a frog and is used here because the tense cystic swelling is said to resemble the throat of a croaking frog.)

A ranula usually presents as a large, tense, bluish swelling anteriorly in the floor of the mouth just to one side of the midline, which often displaces the tongue (Fig. 37.42). Occasionally, the developing retention cyst herniates through a midline dehiscence where the two mylohyoid muscles fail to meet in the midline anteriorly, and then the ranula may present as a submental swelling or as a combined submental and floor-of-mouth swelling, a 'plunging' ranula (Harrison et al 2013). The treatment for a ranula is excision of the sublingual gland responsible.

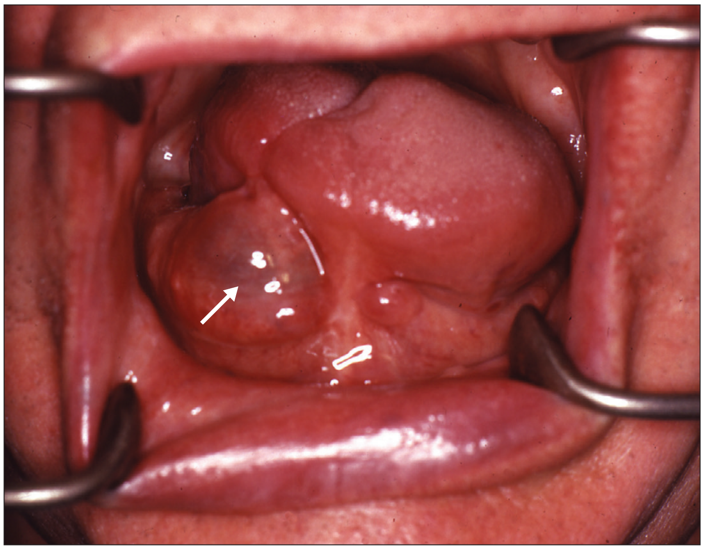

Fig. 37.42 A ranula (arrow) in the floor of the mouth, caused by trauma that damaged the floor of the mouth and the sublingual gland. (With permission from Berkovitz BKB, Holland GR, Moxham BJ 2009 Oral Anatomy, Histology and Embryology. 4th ed. Edinburgh: Mosby. Courtesy of Dr JD Harrison.)

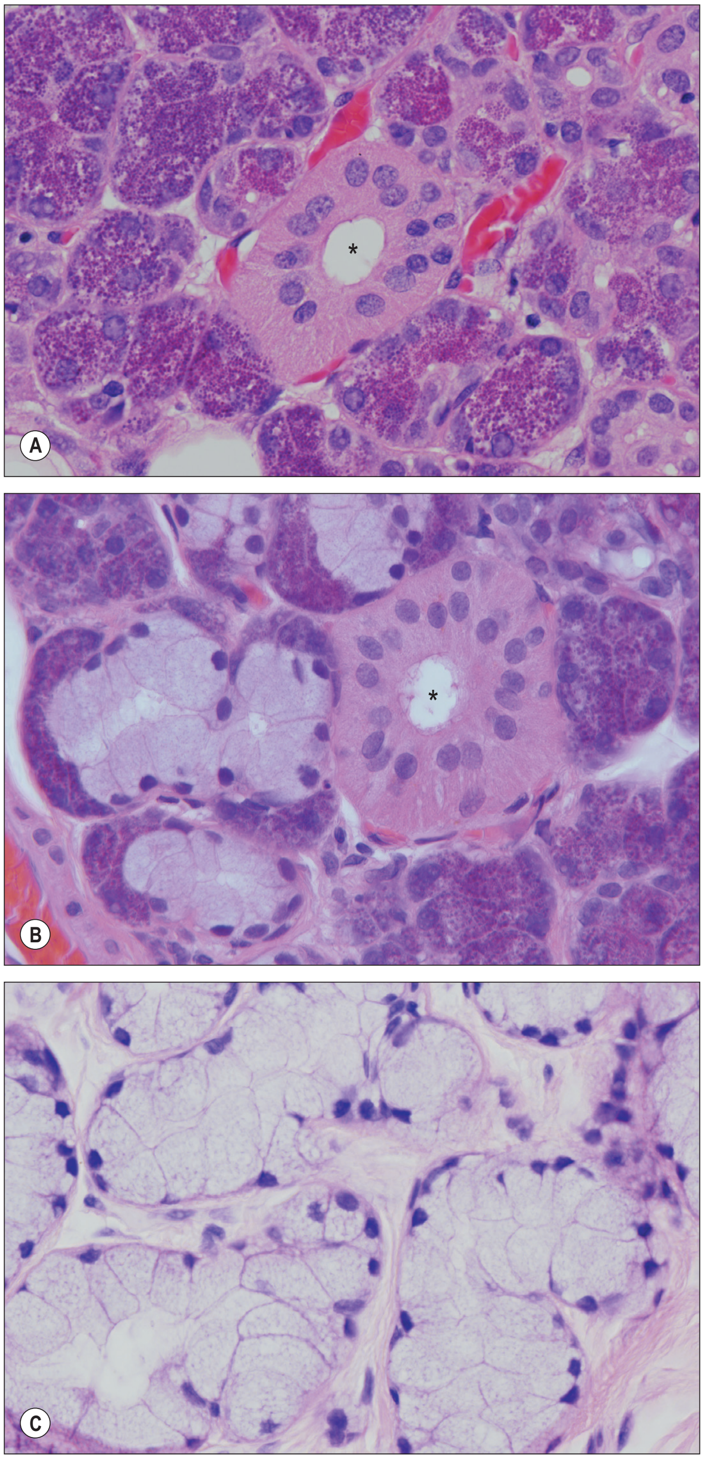

Fig. 37.44 The microstructure of the salivary glands. **A**, The parotid gland. **B**, Mixed secretory units of the submandibular gland. **C**, Mucous acini in the sublingual gland. Asterisks indicate the lumen of a striated duct. (Courtesy of Mr Peter Helliwell and the late Dr Joseph Mathew, Department of Histopathology, Royal Cornwall Hospitals Trust, UK.)

phenotype, being immunoreactive for high molecular weight cytokeratins (CK5/6, 34_E12 and CK14) and smooth muscle markers (actin, myosin, and calponin) (Shah et al 2016). Myoepithelial cells associated with ducts are more fusiform in shape and are aligned along the length of the duct.

Although stimulated by the autonomic nervous system, the precise functional role of myoepithelial cells in salivary secretion awaits clarification (Garrett 1998, Proctor 2016). Functional studies clearly indicate that myoepithelial activity can accelerate the initial outflow of saliva, reduce luminal volume, contribute to the secretory pressure, support the underlying parenchyma, reduce back-permeation of fluid and help salivary flow to overcome increases in peripheral resistance (although, if this is excessive, it may lead to sialectatic damage of striated ducts, thereby increasing overall permeability).

Basal cells

A population of basal cells is present in the striated and collecting ducts (Riva et al 1992). They are sparsely distributed in the striated ducts and more densely distributed in the collecting ducts, in which they form a continuous layer as the ducts pass further towards the hilum. A small population of basal cells is found on the abluminal surface of ductal cells associated with both striated and collecting ducts. These cells can be distinguished from other parenchymal cells by a combination of their morphology, their co-expression of cytokeratin 14 and the anti-apoptotic factor cl-2, and a proliferative index of about 3%, which is the highest of any cell in the region. Basal cells have been implicated as potential stem cells during turnover and/or cell regeneration in salivary glands and during metaplasia, when oncocytes and sebaceous cells may appear. However, some cell division is seen in all parenchymal cell types, including myoepithelial cells, and all these cells may be involved in salivary gland regeneration. (For further reading on salivary gland regeneration see Holmberg and Hoffman 2014.)

Lymph nodes

Lymph nodes are situated both on the surface and within the parotid gland, but are not found within the other salivary glands.

Control of salivary gland activity

The observed wide and rapid variation in the composition, quantity and rate of salivary secretion in response to various stimuli suggests an elaborate control mechanism. Secretion may be continuous but at a low resting level, and may also occur spontaneously. It is mainly a response to the drying of the oral and pharyngeal mucosae. A rapid increase can be superimposed on the resting level, e.g. during mastication or when stimulated by the autonomic innervation. The controlled variation in the activity of the many types of salivary effector cells (serous, seromucous and mucous secretory cells, myoepithelial cells, epithelial cells of all the ductal elements and the smooth muscle of local blood vessels) affects the quantity and quality of saliva. There is no clear evidence that circulating hormones evoke secretion directly at physiological levels but they may alter the response of glandular cells to neural stimuli.

The control of salivation depends on reflex nerve impulses. The afferent inputs to the reflex arc pass to brainstem salivatory centres, especially from taste and mechanoreceptors in the mouth. A variety of other sensory modalities in and around the mouth are also involved, e.g. smell, for certain aspects of submandibular secretion in humans. The afferent input is integrated centrally by the salivatory centres, which are themselves influenced by higher centres. The latter may provide facilitatory or inhibitory influences, which presumably explains why the mouth becomes dry under stress. The efferent drive to the glands passes via parasympathetic and sympathetic outputs from the centres. Relatively little is known about the connections of the preganglionic parasympathetic neurones in the salivatory centres, and virtually nothing is known about either the central location of the sympathetic preganglionic neurones, or the output pathways. No peripheral inhibitory mechanisms exist in the glands (Garrett et al 1999).

The typical pattern of innervation is shown in Fig. 37.43, but details vary in different glands and with age. Only the more constant features are illustrated and described here. Cholinergic nerves often accompany ducts and arborize freely around secretory end-pieces, but adrenergic nerves usually enter glands along arteries and ramify with them. The main secretomotor nerves are predominantly unmyelinated axons; the few myelinated axons that have been seen are presumably either preganglionic efferent or visceral afferent. Within the glands, the nerve fibres intermingle, such that cholinergic and adrenergic axons often lie in adjacent invaginations of one Schwann cell. Secretion and vasoconstriction are mediated via separate sympathetic axons. A single parasympathetic axon may, through serial *en passant* terminals, induce vasodilation, secretion and myoepithelial contraction.

Secretory end-pieces are usually the most densely innervated structures in the gland; individual cells often have both cholinergic and adrenergic innervation. Secretion of water and electrolytes, which creates the foundation for the volume of saliva secreted, is the outcome of a complex set of processes that is largely induced by parasympathetic impulses. Secretion of protein is an ongoing constitutive process wherever it occurs. The regulated exocytosis of pre-packaged proteins, which is the principal source of protein secretion into saliva, depends on the relative levels of activity in sympathetic and parasympathetic fibres.

The ductal elements of salivary glands can markedly modify the composition of saliva. They are less densely innervated than secretory end-pieces but their activity is also under neural control. Adrenal aldosterone promotes resorption of sodium and release of potassium into saliva by striated ductal cells, as it does in kidney tubules. Myoepithelial contraction is stimulated mainly by adrenergic innervation but there may be an additional role for cholinergic axons.

Age changes in salivary glands

A wide range of age changes has been documented in salivary glands. In neonates, acini and ducts are immature and widely separated by abundant vascular connective tissue. After the age of 6 months, glandular structure is more compact and there are numerous lymphocytic foci (Scott 1979). Over the age of 50 years, the amount of glandular tissue decreases and the amount of fibrous tissue, adipocytes, inflammatory cells and oncocytes increases. An increase in duct volume has also been described, although it may in part reflect shrinkage of acini, giving the appearance of duct-like forms (Scott 1986).

With such a significant loss of parenchyma (in both major and minor glands), it might be assumed that there would be a reduction in the amount of saliva produced in the aged population, giving rise to the clinical condition of xerostomia (dry mouth). However, in healthy, unmedicated individuals, this is not the case. This could be interpreted as the result of salivary glands being able to produce more saliva than is needed but is more likely to be a secondary effect related to the increased use of medication (many drugs depress salivary production and many, such as antidepressants and antihistamines, are anticholinergic). Saliva is important in the maintenance of oral health; decreased secretion from the salivary glands results in an increased incidence in oral conditions such as periodontal disease, dental caries and candidal infections ('thrush').

TISSUE SPACES AROUND THE JAWS

The dissemination of infection in soft tissues is influenced by the natural barriers presented by bone, muscle and fascia. However, the tissue spaces around the jaws are primarily defined by muscles, principally mylohyoid, buccinator, masseter, medial pterygoid, superior constrictor and orbicularis oris (**Fig. 37.45**). None of these 'spaces' are actually empty and they should merely be regarded as potential spaces that are normally occupied by loose connective tissue. It is only when inflammatory products such as hyaluronase destroy the loose connective tissue that a definable space is produced.

The spaces are paired except for the submental, sublingual and palatal spaces.

Potential tissue spaces around the lower jaw

The important potential tissue spaces of the lower jaw are the submental, submandibular, sublingual, buccal, submasseteric, parotid, pterygomandibular, peritonsillar, parapharyngeal and retropharyngeal spaces (see Fig. 37.45) (Langdon et al 2002).

The submental and submandibular spaces are located below the inferior border of the mandible beneath mylohyoid, in the suprahyoid region of the neck. The submental space lies beneath the chin in the midline, between the mylohyoid muscles and the investing layer of deep cervical fascia. It is bounded laterally by the two anterior bellies of the digastric muscles. The submental space communicates posteriorly with the two submandibular spaces. The submandibular space is situated between the anterior and posterior bellies of the digastric muscle and communicates with the sublingual space around the posterior free border of mylohyoid. The sublingual space lies in the floor of the mouth, above the mylohyoid muscles, and is continuous across the midline; it communicates with the submandibular spaces over the posterior free borders of the mylohyoid muscles, helped by the submandibular gland's slight extension over this edge.

The remaining tissue spaces are illustrated in **Fig. 37.45B**. The buccal space is located in the cheek, on the lateral side of buccinator. The submasseteric spaces are a series of spaces between the lateral surface of the ramus of the mandible and masseter; they are formed because the fibres of masseter have multiple insertions on to most of the lateral surface of the ramus. The pterygomandibular space lies between the medial surface of the ramus of the mandible and medial pterygoid, and the parotid space lies behind the ramus of the mandible, in and around the parotid gland. The parapharyngeal space is bounded by the superior constrictor of the pharynx and the medial surface of medial pterygoid. It is restricted to the infratemporal region of the head and the suprahyoid region of the neck, and communicates with the retropharyngeal space, which itself extends into the retrovisceral space in the lower part of the neck (the tissue spaces of the neck are described in Chapter 35 and those of the pharynx in Chapter 40). The peritonsillar space lies around the palatine tonsil between the pillars of the fauces, and is part of the intrapharyngeal space. It is bounded by the medial surface of the superior constrictor of the pharynx and its mucosa.

Potential tissue spaces around the upper jaw

The tissue spaces of the upper jaw, the canine (infraorbital), palatal and infratemporal spaces, are usually associated with spread of infection from the teeth. The canine space associated with the canine fossa lies between levator labii superioris and the zygomaticus muscles. The palatal space is not truly a tissue space in the hard palate, since the mucosa there is firmly bound to the periosteum. However, inflammation can strip away some of this periosteum to produce a well-circumscribed abscess. The infratemporal space is the upper extremity of the pterygomandibular space and is closely related to the maxillary tuberosity and therefore the upper molars.

Dental abscess

Abscesses developing in relation to the apices of roots ultimately penetrate the surrounding bone where it is thinnest. The position of the resultant swelling in the soft tissues is largely determined by the relationship between muscle attachments and the sinus (the path taken by the infected material) in the bone. Thus, in the lower incisor region, because the labial bone is thin, abscesses generally appear as a swelling in the labial sulcus, above the attachment of mentalis. The abscess may open below mentalis, when it will point beneath the chin. If an abscess from a lower postcanine tooth opens below the attachment of buccinator, the swelling is in the face; if it opens above, the swelling is in the buccal sulcus of the mouth. If an abscess opens lingually above mylohyoid, the swelling is in the lingual sulcus; if it is below, the swelling is in the neck. Third molar abscesses tend to track into the neck rather than the mouth because mylohyoid ascends posteriorly and the termination of its attachment is variable, sometimes terminating before the position of the third molar and thereby allowing relatively unhindered access into the tissue spaces of the neck.

Apart from canine teeth, which have long roots, abscesses on upper teeth usually open buccally below, rather than above, the attachment of buccinator. Because its root apex is occasionally curved towards the palate, abscesses of the upper lateral incisors may track into the palatal submucosa. Abscesses of upper canines often open facially just below the orbit. Here, the swelling may obstruct drainage in the angular part of the facial vein, which has no valves, and it is therefore possible for infected material to travel via the angular and ophthalmic veins into the cavernous sinus, potentially causing a cavernous sinus thrombosis. Abscesses on the palatal roots of upper molars usually open on the palate. Upper second premolars and first and second molars are related to the maxillary sinus. When this is large, the root apices of these teeth may be separated from its cavity solely by the lining mucosa. Sinus infections may stimulate the nerves entering the teeth, simulating toothache in the ipsilateral premolars and molars; this phenomenon is known as referred pain. Upper first premolars and third molars may be closely related to the maxillary sinus.

With loss of teeth, alveolar bone is extensively resorbed. Thus, in the edentulous mandible, the mental nerve, originally inferior to premolar roots, may lie near the crest of the bone. In the edentulous maxilla, the sinus may enlarge to approach the oral surface of the bone. Both of these facts are of importance when planning surgery in this area.

Severe systemic infections during the time the teeth are developing may lead to faults in enamel, which are visible as horizontal lines (cf. Harris's growth lines).

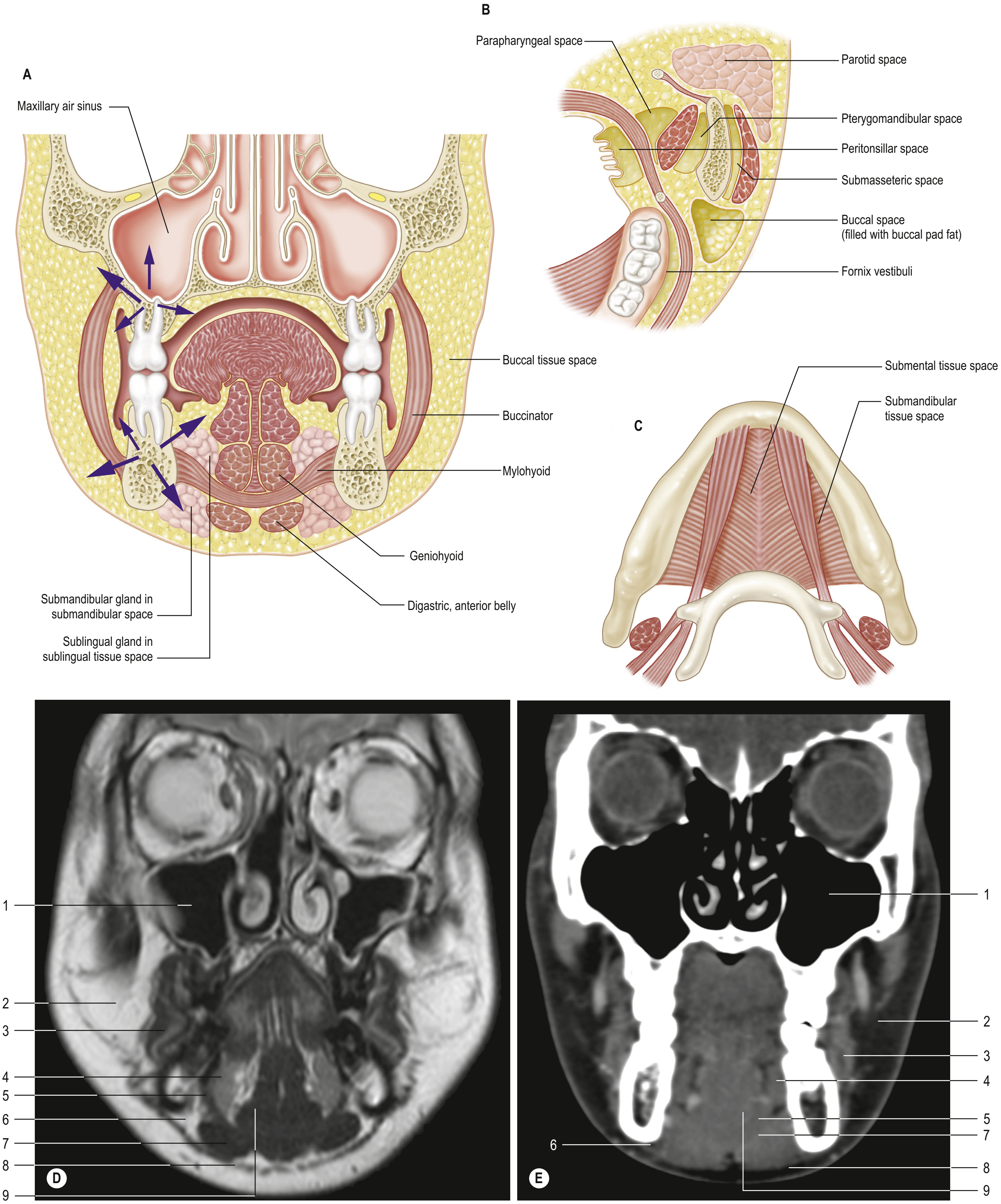
A
Maxillary air sinus
Buccal tissue space
Buccinator
Mylohyoid
Geniohyoid
Digastric, anterior belly
Submandibular gland in submandibular space
Sublingual gland in sublingual tissue space
B
Parapharyngeal space
Parotid space
Pterygomandibular space
Peritonsillar space
Submasseteric space
Buccal space (filled with buccal pad fat)
Fornix vestibuli
C
Submental tissue space
Submandibular tissue space
D
1
2
3
4
5
6
7
8
9
E
1
2
3
4
5
7
6
8
9

Fig. 37.45 Potential tissue spaces around the jaws. **A**, Coronal section showing the sublingual and submandibular spaces in the floor of the mouth and the possible routes for the spread of infections from periapical dental abscesses (left). **B**, Horizontal section through the mandibular molar region showing the associated tissue spaces. **C**, Inferior view of the floor of the mouth (suprahyoid region of the neck) showing the position of the submandibular and sublingual tissue spaces. **D**, Coronal T2-weighted MRI and **E**, coronal CT with intravenous contrast medium, (different individual, soft tissue window setting) through the face showing the spaces around the jaw. Key: 1, maxillary air sinus; 2, buccal tissue space; 3, buccinator; 4, sublingual gland in the sublingual space; 5, mylohyoid; 6, submandibular space; 7, digastric, anterior belly; 8, platysma; 9, geniohyoid. There are small mucosal polyps in the left maxillary air sinus in **D**, a common finding. (B, C, With permission from Berkovitz BKB, Moxham BJ 2002 Head and Neck Anatomy. London: Martin Dunitz.)

Bonus e-book content

Fig. 37.4 C–D, Examples of the variable morphology of the lingual frenulum under tension, cadaveric tissue. **C,** Opaque frenulum: mucosa and fascia drawn up to top of fold, genioglossus drawn up into base of frenulum. **D**, Thick/bulky frenulum: genioglossus drawn up into frenulum together with mucosa and fascia.

Fig. 37.13 A–B, Entire nerve maps of an adult human tongue, Sihler's stain.

Fig. 37.15 The primary dentition.

Fig. 37.22 A plaster cast of the maxilla of a 25-year-old male showing 1 supplemental premolar and 12 peg-shaped supernumerary teeth on the palatal side of the permanent teeth.

Fig. 37.23 An orthopantomogram showing supernumerary teeth in the upper incisor region preventing the exfoliation of the upper primary central incisors and impeding the eruption of the upper permanent central incisors.

Fig. 37.24 A child with retained maxillary central deciduous incisors caused by the presence of supernumerary teeth.

Fig. 37.25 A child with mixed dentition showing hypodontia and microdontia (small conical-shaped teeth).

Fig. 37.37 A bifid inferior dental canal in which a branch of the inferior alveolar nerve enters the mandible through an accessory foramen in the retromolar region to supply sensation to the molar teeth.

Fig. 37.38 A radiograph showing that the mandibular canal containing the inferior alveolar canal and its contents are closely related to the roots of the impacted permanent mandibular third molar.

Fig. 37.39 A, A routine orthopantomogram showing the roots of the permanent maxillary molars, molar teeth and the maxillary sinus. **B**, Cone beam computed tomography of the same patient.

Fig. 37.40 B–C, A normal parotid sialogram: **B**, frontal view; **C**, oblique view.

Fig. 37.42 A ranula in the floor of the mouth, caused by trauma that damaged the floor of the mouth and the sublingual gland.

Key references

Berkovitz BKB, Holland GR, Moxham BJ 2018 Oral Anatomy, Histology and Embryology, 5th ed. Edinburgh: Mosby.

A textbook that describes in detail the gross morphology, histology and development of human teeth.

Garrett JR 1998 Myoepithelial activity in salivary glands. In: Garrett JR, Ekström J, Anderson LC (eds) Glandular Mechanisms of Salivary Secretion. Frontiers in Oral Biology, vol. 10. Basel: Karger, pp. 132–52.

A paper that discusses the activity of myoepithelial cells in the secretory process.

Garrett JR, Ekström J, Anderson LC (eds) 1999 Neural Mechanisms of Salivary Secretion. Frontiers of Oral Biology, vol. 11. Basel: Karger.

A book that contains much basic information concerning the role of nerves in the secretory process of salivary glands.

Langdon J, Berkovitz BKB, Moxham BJ 2002 Infection and the infratemporal fossa and associated tissue spaces. In: Langdon J, Berkovitz BKB, Moxham BJ (eds) Surgical Anatomy of the Infratemporal Fossa. London: M. Dunitz, pp. 77–99.

A chapter that describes the tissue spaces in the floor of the mouth and how they become involved in the spread of infection.

Reid DJ, Dean CM 2006 Variation in modern human enamel formation times. J Hum Evol 50:329–46.

A paper that describes variations in the formation times of modern teeth from two populations (South Africa and Northern Europe) using incremental lines in enamel.

Renton T 2011 Minimising and managing iatrogenous trigeminal nerve injuries in relation to dental procedures. In: Birch R Surgical Disorders of the Peripheral Nerves. Berlin: Springer. Ch. 11, pp. 501–25.

A chapter that describes surgical techniques for avoiding damage to branches of the mandibular nerve during tooth extraction.

Scott J 1986 Structure and function in aging human salivary glands. Gerontology 5:149–58.

A paper that gives quantitative information on changes that occur in the parenchyma of the major salivary glands with age, and discusses the results in terms of xerostomia.

Yamashina S, Tamaki H, Katsumata O 1999 The serous demilune of the rat sublingual gland is an artificial structure produced by conventional fixation. Arch Histol Cytol 62:347–54.

A paper that describes the steps needed to avoid fixation artefacts when studying the histological appearance of salivary glands.

References

Berkovitz BKB, Holland GR, Moxham BJ 2018 Oral Anatomy, Histology and Embryology, 5th ed. Edinburgh: Mosby.

A textbook that describes in detail the gross morphology, histology and development of human teeth.

Berkovitz BKB, Moxham BJ 2002 Head and Neck Anatomy: A Clinical Reference. London: M. Dunitz.

Brandtzaeg P 2013 Secretory immunity with special reference to the oral cavity. J Oral Microbiol 5:10.3402/jom.v5i0.20401.

Cai M, Brown EC, Hatt A et al 2016 Effect of head and jaw position on respiratory-related motion of the genioglossus. J Appl Physiol (1985) 120:758—765.

Chaudhari N, Roper SD 2010 The cell biology of taste. J Cell Biol 190: 285–96.

Cheng S, Butler JE, Gandevia SC et al 2008 Movement of the tongue during normal breathing in awake healthy humans. J Physiol 586: 4283–94.

Dean MC 2000 Incremental markings in enamel and dentine: what they can tell us about the way teeth grow. In: Teaford M, Smith MM, Ferguson M (eds) Development, Function and Evolution of Teeth. Cambridge: Cambridge University Press.

Delporte C, Bryla A, Perret J 2016 Aquaporins in salivary glands: from basic research to clinical applications. Int J Mol Sci 17:166.

Ezoddini Ardakani F, Bahrololoumi Z, Zangouie Booshehri M et al 2010 The position of lingula as an index for inferior alveolar nerve block injection in 7–11-year-old children. J Dent Res Dent Clin Dent Prospects 4:47–51.

Fitzgerald MJ, Law ME 1958 The peripheral connexions between the lingual and hypoglossal nerves. J Anat 92:178–188.

García-García AS, Martínez-González JM, Gómez-Font R et al 2010 Current status of the torus palatinus and torus mandibularis. Med Oral Patol Oral Cir Bucal 15:e353–60.

Garn SM, Lewis AB, Kerewsky RS 1965 Genetic, nutritional and maturational correlates of dental development. J Dent Res 44:228–42.

Garrett JR 1998 Myoepithelial activity in salivary glands. In: Garrett JR, Ekström J, Anderson LC (eds) Glandular Mechanisms of Salivary Secretion. Frontiers in Oral Biology, vol. 10. Basel: Karger, pp. 132–52.

A paper that discusses the activity of myoepithelial cells in the secretory process.

Garrett JR, Ekström J, Anderson LC (eds) 1999 Neural Mechanisms of Salivary Secretion. Frontiers of Oral Biology, vol. 11. Basel: Karger.

A book that contains much basic information concerning the role of nerves in the secretory process of salivary glands.

Harrison JD, Kim A, Al-Ali S et al 2013 Post-mortem investigation of mylohyoid hiatus and hernia: aetiological factors of plunging ranula. Clin Anat 26:693–9.

Holmberg KV, Hoffman MP. 2014 Anatomy, biogenesis and regeneration of salivary glands. Monogr Oral Sci 24:1–13.

Huang Y, Corpas LS, Martens W et al 2011 Histomorphological study of myelinated nerve fibres in the periodontal ligament of human canine. Acta Odontol Scand 69:279–86.

Kapsimali M, Barlow LA. 2012 Developing a sense of taste. Semin Cell Dev Biol 24:200–9.

Keinan D, Cohen RE 2013 The significance of epithelial rests of Malassez in the periodontal ligament. J Endod 39:582–7.

Krieger E, Hornikel S, Wehrbein H 2013 Age-related changes of fibroblast density in the human periodontal ligament. Head Face Med 9:22.

Langdon J, Berkovitz BKB, Moxham BJ 2002 Infection and the infratemporal fossa and associated tissue spaces. In: Langdon J, Berkovitz BKB, Moxham BJ (eds) Surgical Anatomy of the Infratemporal Fossa. London: M. Dunitz, pp. 77–99.

A chapter that describes the tissue spaces in the floor of the mouth and how they become involved in the spread of infection.

Liman ER, Zhang YV, Montell C. 2014 Peripheral coding of taste. Neuron 81(5):984–1000.

Linden RWA (ed) 1998 The Scientific Basis of Eating: Taste and Smell, Salivation, Mastication and Swallowing and their Dysfunctions. Frontiers of Oral Biology, vol. 9. Basel: Karger.

Mérida-Velasco JR, Rodríguez-Vazquez JF, de la Cuadra Blanco C et al 2006 Origin of the styloglossus muscle in the human fetus. J Anat 208:649–53.

Mhaske S, Yuwanati MB, Mhaske A et al 2013 Natal and neonatal teeth: an overview of the literature. ISRN Pediatr 2013:956269.

Mills N, Pransky SM, Geddes DT et al 2019 What is a tongue tie? Defining the anatomy of the in–situ lingual frenulum. Clin Anat 32:749–61.

Mu L, Sanders I 2010 Human tongue neuroanatomy: nerve supply and motor endplates. Clin Anat 23:777–91.

NICE (National Institute for Health and Clinical Excellence) 2005 Division of ankyloglossia (tongue-tie) for breastfeeding. London: NICE.

Ogawa Y 2003 Immunocytochemistry of myoepithelial cells in the salivary glands. Prog Histochem Cytochem 38:343–426.

Presland RB, Dale BA 2000 Epithelial structural proteins of the skin and oral cavity: function in health and disease. Crit Rev Oral Biol Med 11:383–408.

Proctor GB 2016 The physiology of salivary secretion. Periodontol 2000 70:11–25.

Proctor GB, Carpenter GH 2007 Regulation of salivary gland function by autonomic nerves. Auton Neurosci Basic Clin 133: 3–18.

Reid DJ, Dean CM 2006 Variation in modern human enamel formation times. J Hum Evol 50:329–46.

A paper that describes variations in the formation times of modern teeth from two populations (South Africa and Northern Europe) using incremental lines in enamel.

Renton T 2011 Minimising and managing iatrogenous trigeminal nerve injuries in relation to dental procedures. In: Birch R (ed) Surgical Disorders of the Peripheral Nerves. Berlin: Springer. Ch. 11, pp. 501–25.

A chapter that describes surgical techniques for avoiding damage to branches of the mandibular nerve during tooth extraction.

Riva A, Serra GP, Proto E et al 1992 The myoepithelial and basal cells of ducts of human major salivary glands: a SEM study. Arch Histol Cytol 55:Suppl:115–24.

Rodella LF, Buffoli B, Labanca M et al 2012 A review of the mandibular and maxillary nerve supplies and their clinical relevance. Arch Oral Biol 57:323–34.

Sanders I, Mu L, Amirali A, Su H, Sobotka S 2013 The human tongue slows down to speak: muscle fibers of the human tongue. Anat Rec (Hoboken) 296:1615–27.

Schroeder HE, Listgarten MA 1997 The gingival tissues: the architecture of periodontal protection. Periodontol 2000 13:91–120.

Scott J 1979 Qualitative and quantitative changes in the histology of the human submandibular salivary gland during postnatal growth. J Biol Buccale 7:341–52.

Scott J 1986 Structure and function in aging human salivary glands. Gerontology 5:149–58.

A paper that gives quantitative information on changes that occur in the parenchyma of the major salivary glands with age, and discusses the results in terms of xerostomia.

Shah AA, Mulla AF, Mayank M 2016 Pathophysiology of myoepithelial cells in salivary glands. J Oral Maxillofac Pathol 20:480–90.

Smith DV, Margolskee RF 2006 Making sense of taste. Scientific American 16:84–92.

Stevens B, Yamada J, Lee GY et al 2013 Sucrose for analgesia in newborn infants undergoing painful procedures. Cochrane Database of Systematic Reviews 1:CD001069.

Tosios KI, Nikolakis M, Prigkos AC et al 2010 Nerve cell bodies and small ganglia in the connective tissue stroma of human submandibular glands. Neurosci Lett 475:53–5.

Webb AN, Hao W, Hong P 2013 The effect of tongue-tie division on breastfeeding and speech articulation: a systematic review. Int J Pediatr Otorhinolaryngol 77:635–46.

Yamashina S, Tamaki H, Katsumata O 1999 The serous demilune of the rat sublingual gland is an artificial structure produced by conventional fixation. Arch Histol Cytol 62:347–54.

A paper that describes the steps needed to avoid fixation artefacts when studying the histological appearance of salivary glands.

Zur KB, Mu L, Sanders I 2004 Distribution pattern of the human lingual nerve. Clin Anat 17:88–92.

CHAPTER

38

Infratemporal and pterygopalatine fossae and temporomandibular joint

INFRATEMPORAL FOSSA

The infratemporal fossa lies deep to the ramus of the mandible. It communicates with the temporal fossa superiorly deep to the zygomatic arch; the orbit anteriorly through the inferior orbital fissure; the pterygopalatine fossa medially through the pterygomaxillary fissure; the middle fossa through the foramina ovale and spinosum. It contains lateral and medial pterygoid, the mandibular division of the trigeminal nerve, the chorda tympani (facial nerve), the otic ganglion, the maxillary artery and the pterygoid venous plexus.

The infratemporal fossa has a roof and anterior, lateral and medial walls, and is open to the neck posteroinferiorly, which means that it has no anatomical floor. Approximately 80% of the roof is formed by the infratemporal surface of the greater wing of the sphenoid. The remainder is formed by the infratemporal surface of the temporal bone, ending at the articular eminence of the temporomandibular joint and the spine of the sphenoid on the deep medial aspect. The roof contains the foramina ovale and spinosum. The anterior wall is formed by the posterior surface of the maxilla, ending inferiorly at the maxillary tuberosity. The inferior orbital fissure forms the upper limit of the anterior wall, meeting the pterygomaxillary fissure at right-angles. The medial wall is formed anteriorly by the lateral pterygoid plate of the pterygoid process of the sphenoid, and more posteromedially by the pharynx and tensor and levator veli palatini. It contains the pterygomaxillary fissure, across which structures pass between the infratemporal and pterygopalatine fossae (**Fig. 38.1**). The lateral wall is formed by the medial surface of the ramus of the mandible.

Lateral pterygoid provides a key to understanding the relationships of structures within the infratemporal fossa. This muscle lies in the roof of the fossa and runs anteroposteriorly in a more or less horizontal plane from the region of the pterygoid plates to the mandibular condyle. Branches of the mandibular nerve and the main origin of medial pterygoid are deep relations and the maxillary artery is superficial. The buccal branch of the mandibular nerve passes between the two heads of lateral pterygoid. Medial pterygoid and the lingual and inferior alveolar nerves emerge below its inferior border, and the deep temporal nerves and vessels emerge from its upper border. The pterygoid venous plexus lies around and within lateral pterygoid and is important in the spread of infection.

Bones

The sphenoid bone, the paired maxillae and temporal bones, the palatine bones and the mandible collectively provide the skeletal framework to the infratemporal and pterygopalatine regions. The mandible and the two temporal bones articulate at the right and left temporomandibular joints. The disarticulated maxilla and palatine bone are described in Chapter 36, the temporal bone is described in Chapter 42, and the sphenoid and mandible are described here.

Sphenoid

The sphenoid lies in the base of the skull between the frontal, temporal and occipital bones. It has a central body, paired greater and lesser wings that spread laterally from the body, and two pterygoid processes that descend from the junction of the body and greater wings (**Fig. 38.3**).

Body

The body of the sphenoid is cuboidal. It contains two air sinuses separated by a septum. Its cerebral (superior) surface articulates anteriorly with the cribriform plate of the ethmoid bone via the smooth jugum sphenoidale, which is related to the overlying gyri recti and olfactory tracts. The jugum is bounded behind by the anterior border of the sulcus chiasmaticus leading laterally to the optic canals. The tuberculum sellae is posterior; behind it is the deeply concave sella turcica that houses the hypophysis cerebri within the hypophysial fossa. The anterior edge of the sella turcica is completed laterally by two middle clinoid processes. Posteriorly, the sella turcica is bounded by a square dorsum sellae with superior angles that bear variable posterior clinoid processes. The diaphragma sella and the tentorium cerebelli are attached to the clinoid processes. On each side, below

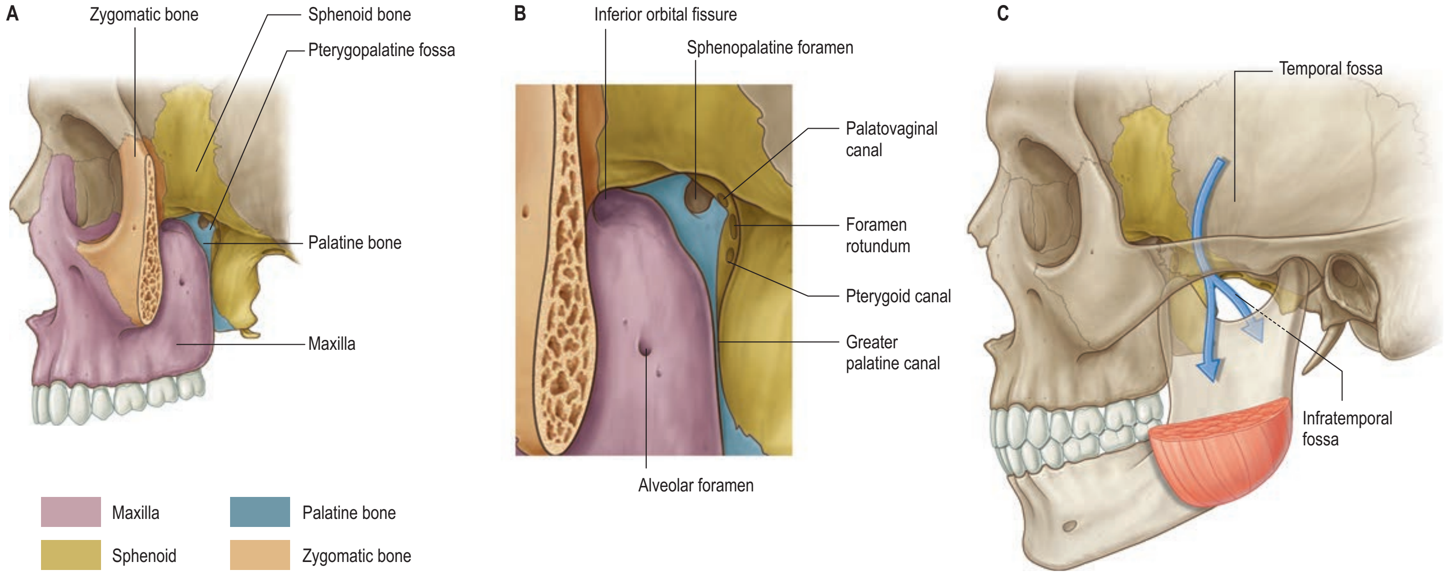

Fig. 38.1 **A**, The pterygopalatine fossa after detachment of the mandible and removal of the zygomatic arch. **B**, Anteromedial view. **C**, Lateral view; the arrows show that the floor of the temporal fossa is open medially to the infratemporal fossa and laterally to the region containing the masseter. (With permission from Drake RL, Vogl AW, Mitchell A (eds), Gray's Anatomy for Students, 2nd ed. Elsevier, Churchill Livingstone. Copyright 2010.)

There is a lack of consensus in the surgical literature with regard to both the boundaries and contents of the infratemporal fossa. Thus, the fossa is sometimes defined as the anatomical space beneath the floor of the middle fossa, incorporating the remainder of the subcranial temporal bone as part of the roof, with the exception of the glenoid fossa of the temporomandibular joint. In this description, the fossa is limited posteriorly by the prevertebral fascia and includes the internal carotid artery, the internal jugular vein, the lower cranial nerves, the cervical sympathetic trunk, and the styloid process with its attached muscles and ligaments. Alternatively, the 'extended' infratemporal fossa is said to consist of the parapharyngeal and masticator spaces (**Fig. 38.2**) (Bejjani et al 1998, Falcon et al 2010, Hosseini et al 2012, Joo et al 2013).

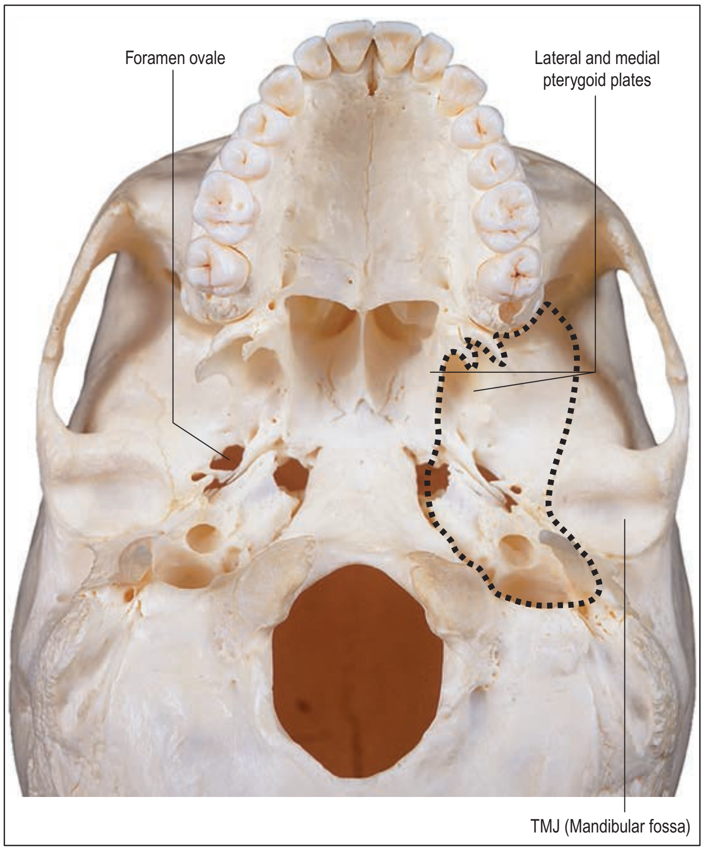

Fig. 38.2 The 'extended' infratemporal fossa. The boundaries of the infratemporal fossa are delineated by the dotted line. Note that the lateral pterygoid plate and pharyngotympanic tube constitute the medial wall of the fossa, and that the temporomandibular joint (TMJ) forms part of its lateral wall. The carotid and jugular foramina lie in the posterior part of this extended infratemporal fossa. (Adapted with permission from Berkovitz BKB, Moxham BJ, Telling D 1994 Color Atlas of the Skull, London, Mosby, and Hosseini SMS, Razfar A, Carrau RL et al 2012 Endonasal transpterygoid approach to the infratemporal fossa: correlation of endoscopic and multiplanar CT anatomy. Head and Neck 34:313–20.)

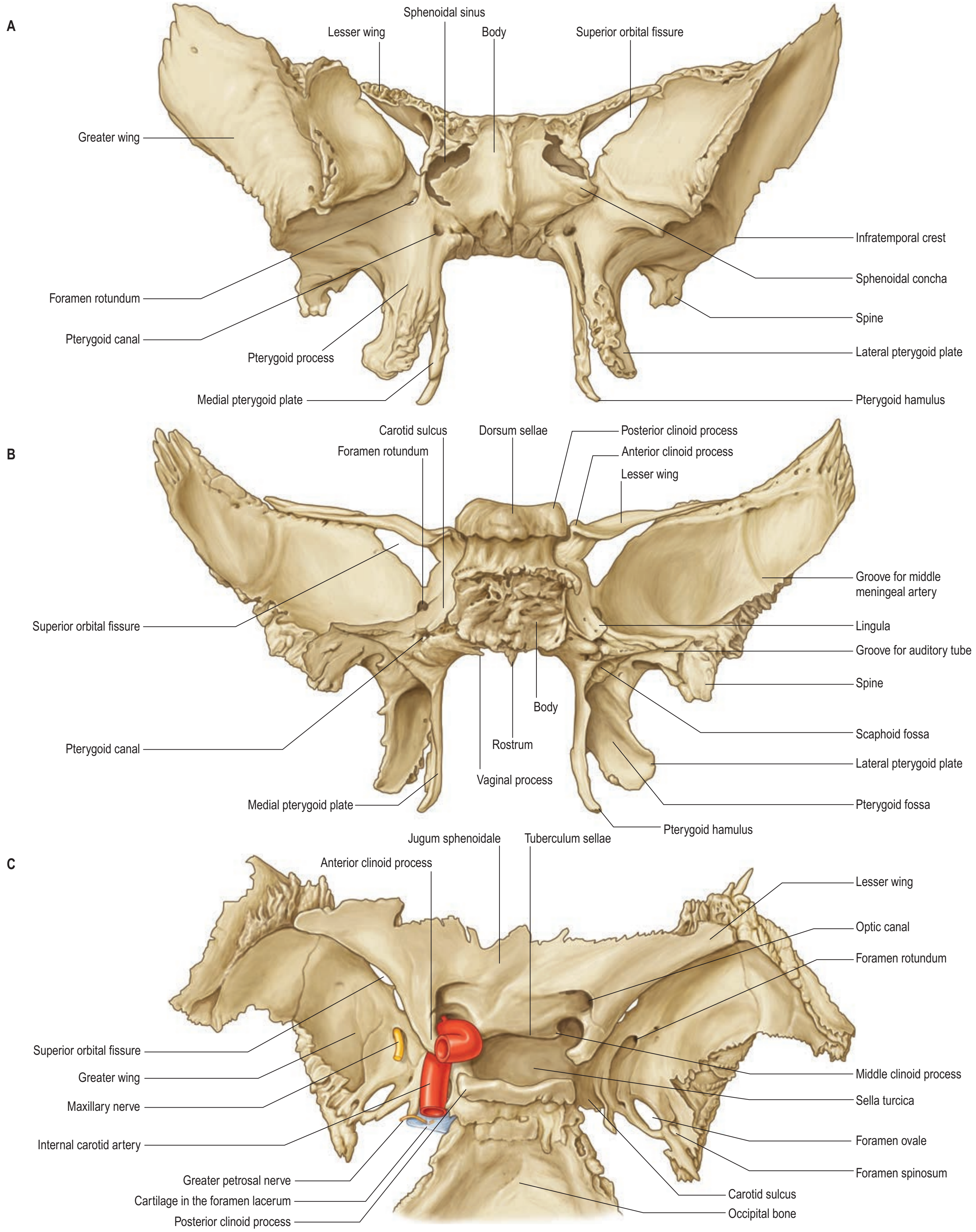
A
Sphenoidal sinus
Lesser wing
Body
Superior orbital fissure
Greater wing
Infratemporal crest
Sphenoidal concha
Foramen rotundum
Spine
Pterygoid canal
Lateral pterygoid plate
Pterygoid process
Medial pterygoid plate
Pterygoid hamulus
B
Carotid sulcus
Dorsum sellae
Posterior clinoid process
Foramen rotundum
Anterior clinoid process
Lesser wing
Groove for middle meningeal artery
Superior orbital fissure
Lingula
Groove for auditory tube
Spine
Body
Scaphoid fossa
Pterygoid canal
Rostrum
Lateral pterygoid plate
Vaginal process
Medial pterygoid plate
Pterygoid fossa
Pterygoid hamulus
C
Jugum sphenoidale
Tuberculum sellae
Anterior clinoid process
Lesser wing
Optic canal
Foramen rotundum
Superior orbital fissure
Middle clinoid process
Greater wing
Sella turcica
Maxillary nerve
Foramen ovale
Internal carotid artery
Foramen spinosum
Greater petrosal nerve
Carotid sulcus
Cartilage in the foramen lacerum
Occipital bone
Posterior clinoid process

Fig. 38.3 The sphenoid bone. **A**, Anterior view. **B**, Posterior view. **C**, Superior view. (Sobotta Atlas of Human Anatomy © Elsevier GmbH, Urban & Fischer, Munich.)

the dorsum sellae, a small petrosal process articulates with the apex of the petrous part of the temporal bone. The body of the sphenoid slopes directly into the basilar part of the occipital bone posterior to the dorsum sellae and together these bones form the clivus. In the growing child, this is the site of the spheno-occipital synchondrosis: premature closure of this joint gives rise to the skull appearances seen in achondroplasia.

The lateral surfaces of the body are united with the greater wings and the medial pterygoid plates. A broad carotid sulcus accommodates both the internal carotid artery and the cranial nerves associated with the cavernous sinus above the root of each wing. The sulcus is deepest posteriorly and is overhung medially by the petrosal part of the temporal bone. Its sharp lateral margin, the lingula, continues back over the posterior opening of the pterygoid canal.

A median triangular bilaminar sphenoidal crest on the anterior surface of the body of the sphenoid makes a small contribution to the nasal septum. The anterior border of the crest articulates with the perpendicular plate of the ethmoid bone, and a sphenoidal sinus opens on either side of it. In the articulated state, the sphenoidal sinuses are closed anteroinferiorly by the sphenoidal conchae that are almost inevitably destroyed when disarticulating a dried skull. Each half of the anterior surface of the body of the sphenoid possesses a superolateral depressed area joined to the ethmoidal labyrinth that completes the posterior ethmoidal sinuses; a lateral margin that articulates with the orbital plate of the ethmoid above and the orbital process of the palatine bone below; and an inferomedial, smooth, triangular area that forms the posterior nasal roof. The orifice of a sphenoidal sinus lies near the superior angle of this triangular area.

The inferior surface of the body of the sphenoid bears a median triangular sphenoidal rostrum, embraced above by the diverging lower margins of the sphenoidal crest. The narrow anterior end of the rostrum fits into a fissure between the anterior parts of the alae of the vomer, and the posterior ends of the sphenoidal conchae flank the rostrum, articulating with its alae. A thin vaginal process projects medially from the base of the medial pterygoid plate on each side of the posterior part of the rostrum, behind the apex of the sphenoidal concha.

Greater wings

The greater wings of the sphenoid curve broadly superolaterally from the body. Posteriorly, each is triangular, fitting the angle between the petrous and squamous parts of the temporal bone at a sphenosquamosal suture. The cerebral surface contributes to the anterior part of the middle cranial fossa. Deeply concave, its undulating surface is adapted to the anterior gyri of the temporal lobe of the cerebral hemisphere. The foramen rotundum lies anteromedially and transmits the maxillary nerve. The foramen ovale, posterolateral to the foramen rotundum, transmits the mandibular nerve, accessory meningeal artery and sometimes the lesser petrosal nerve, although the latter nerve may have its own canaliculus innominatus medial to the foramen spinosum. When present, a small emissary sphenoidal foramen (foramen of Vesalius) transmits a small vein from the cavernous sinus, and can lie medial to the foramen ovale (on one or both sides). The foramen spinosum lies behind the foramen ovale and transmits the middle meningeal artery and meningeal branch of the mandibular nerve.

The lateral surface is vertically convex and divided by a transverse infratemporal crest into temporal (upper) and infratemporal (lower) surfaces. Temporalis is attached to the temporal surface. The infratemporal surface is directed downwards and, with the infratemporal crest, is the site of attachment of the upper fibres of lateral pterygoid. It contains the foramen ovale and foramen spinosum. The small downward-projecting spine of the sphenoid lies posterior to the foramen spinosum; the sphenomandibular ligament is attached to its tip. The medial side of the spine bears a faint anteroinferior groove for the chorda tympani nerve and appears in the lateral wall of the sulcus for the pharyngotympanic tube. A ridge passes downwards to the front of the lateral pterygoid plate, medial to the anterior end of the infratemporal crest, and forms a posterior boundary of the pterygomaxillary fissure.

The quadrilateral orbital surface of the greater wing faces anteromedially and forms the posterior part of the lateral wall of the orbit. It has a serrated upper edge that articulates with the orbital plate of the frontal bone, and a serrated lateral margin that articulates with the zygomatic bone. Its smooth inferior border is the posterolateral edge of the inferior orbital fissure, and its sharp medial margin forms the inferolateral edge of the superior orbital fissure, on which a small tubercle gives partial attachment to the common anular ocular tendon. Below the medial end of the superior orbital fissure, a grooved area forms the posterior wall of the pterygopalatine fossa that is pierced by the foramen rotundum.

The irregular margin of the greater wing, from the body of the sphenoid to the spine, is an anterior limit of the medial half of the foramen lacerum. It contains the posterior aperture of the pterygoid canal and its lateral half articulates with the petrous part of the temporal bone at a sphenopetrosal synchondrosis. The sulcus tubae inferior to the synchondrosis contains the cartilaginous pharyngotympanic (auditory) tube. Anterior to the spine of the sphenoid the concave squamosal margin is serrated, bevelled internally below and externally above, for articulation with the squamous part of the temporal bone. The tip of the greater wing, bevelled internally, articulates with the sphenoidal angle of the parietal bone at the pterion. Medial to this, a triangular rough area articulates with the frontal bone; its medial angle is continuous with the inferior boundary of the superior orbital fissure, and its anterior angle joins the zygomatic bone by a serrated articulation. Fractures of the zygomatic bone preferentially pass through this articulation with the greater wing because it is a line of weakness in the lateral orbit.

Lesser wings

The lesser wings of the sphenoid are triangular pointed plates that protrude laterally from the anterosuperior regions of the body. The superior surface of each wing is smooth and related to the frontal lobe of the cerebral hemisphere. The inferior surface is a posterior part of the orbital roof and upper boundary of the superior orbital fissure and overhangs the middle cranial fossa. The posterior border projects into the lateral fissure of the cerebral hemisphere. The medial end of the lesser wing forms the anterior clinoid process: the anterior and middle clinoid processes are sometimes united to form a caroticoclinoid foramen. The lesser wing is connected to the body by a thin, flat anterior root and a thick, triangular posterior root (the optic strut), between which lies the optic canal. The optic strut extends from the base of the anterior clinoid process to the body and separates the optic canal from the superior orbital fissure. The optic canal is bounded by the body of the sphenoid medially, the lesser wing superiorly, and the optic strut inferiorly and laterally.

Superior orbital fissure

The superior orbital fissure connects the cranial cavity with the orbit. It is bounded medially by the body of the sphenoid; above by the lesser wing of the sphenoid; below by the medial margin of the orbital surface of the greater wing; and laterally, between the greater and lesser wings, by the frontal bone. The contents of the superior orbital fissure are described in Chapter 44 (see Fig. 44.4).

Pterygoid processes

The pterygoid processes descend perpendicularly from the junctions of the greater wings and body. Each consists of a medial and lateral plate with upper parts that are fused anteriorly. The plates are separated below by the angular pterygoid fissure: the margins of the fissure articulate with the pyramidal process of the palatine bone and diverge behind. Medial pterygoid lies in the cuneiform pterygoid fossa between the plates. Above is the small, oval, shallow scaphoid fossa, formed by division of the upper posterior border of the medial plate. Part of tensor veli palatini is attached to the fossa. The anterior surface of the root of the pterygoid process is broad and triangular: it forms the posterior wall of the pterygopalatine fossa and is pierced by the anterior opening of the pterygoid canal.

Lateral pterygoid plate

The lateral pterygoid plate is broad, thin and everted. The lateral surface forms part of the medial wall of the infratemporal fossa and the lower part of lateral pterygoid is attached to it. The medial surface is the lateral wall of the pterygoid fossa and most of the deep head of medial pterygoid is attached to it. The upper part of its anterior border is a posterior boundary of the pterygomaxillary fissure, and the lower part articulates with the palatine bone. The posterior border is free.

Medial pterygoid plate

The medial pterygoid plate is narrower and longer than the lateral. Its lower end is continued into an unciform projection, the pterygoid hamulus, which curves laterally. The pterygomandibular raphe is attached to the hamulus, and the tendon of tensor veli palatini winds around the hamulus. The lateral surface forms the medial wall of the pterygoid fossa and the medial surface provides a lateral boundary for the posterior nasal aperture. The medial plate is prolonged above on the inferior aspect of the body of the sphenoid as a thin vaginal process that articulates anteriorly with the sphenoidal process of the palatine bone and medially with the ala of the vomer. The plate articulates with the posterior border of the perpendicular plate of the palatine bone in the lower part of its anterior margin. Inferiorly, it bears a furrow that is converted anteriorly into the palatovaginal canal by the sphenoidal process of the palatine bone. The palatovaginal canal transmits pharyngeal branches of the maxillary artery and pterygopalatine ganglion. The pharyngobasilar fascia is attached to the whole of the posterior margin of the medial plate, and the superior pharyngeal constrictor is attached to its lower end. The small pterygoid tubercle is found at the upper end of the plate, just below the posterior opening of the pterygoid canal. The processus tubarius, which supports the cartilaginous pharyngeal end of the pharyngotympanic tube, projects back near the midpoint of the margin of the medial pterygoid plate.

Though adjacent, the medial and lateral pterygoid plates have distinct roles. The lateral plate is the province of the infratemporal fossa and masticator space, forming part of the medial boundary of the infratemporal fossa and providing attachment for the lateral and medial pterygoids. The medial plate is functionally related to the pharynx, providing attachment for the pharyngobasilar fascia, superior constrictor and pterygomandibular raphe.

Midface fractures Midface fractures at Le Fort I, II and III levels invariably involve the pterygoid plates at different levels; displacement of the outlines of these bones radiographically confirms the diagnosis. Midface fractures and current classification of these injuries are described and discussed in Chapter 36.

Sphenoidal conchae

The sphenoidal conchae are two thin, curved small plates, attached anteroinferiorly to the body of the sphenoid bone. The superior concave surface of each forms the anterior wall and part of the floor of a sphenoidal sinus. *In situ*, each has vertical quadrilateral anterior and horizontal triangular posterior parts. The anterior part consists of a superolateral depressed area that completes the posterior ethmoidal sinuses and joins below with the orbital process of a palatine bone, and a smooth and triangular inferomedial area that forms part of the nasal roof and is perforated above by a round opening connecting the sphenoidal sinus and spheno-ethmoidal recess.

Anterior parts of the two bones meet in the midline and protrude as the sphenoidal crest. The horizontal part appears in the nasal roof and completes the sphenopalatine foramen. Its medial edge articulates with the rostrum of the sphenoid and the ala of the vomer. Its apex, directed posteriorly, is superomedial to the vaginal process of the medial pterygoid plate and joins the posterior part of the ala. A small conchal part sometimes appears in the medial wall of the orbit, lying between the orbital plate of the ethmoid anteriorly, the orbital process of the palatine bone inferiorly and the frontal bone superiorly.

Ossification

Until postmenstrual weeks 25–32, the sphenoid body has a presphenoidal part, anterior to the tuberculum sellae and continuous with the lesser wings, and a postsphenoidal part, consisting of the sella turcica and dorsum sellae, that is integral with the greater wings and pterygoid processes. Much of the bone is preformed in cartilage. There are six ossification centres for the presphenoidal parts and eight centres for the postsphenoidal parts.

Presphenoidal part

At about postfertilization weeks 8–9 (postmenstrual week 10–11), a centre appears in each wing, lateral to the optic canal; two bilateral centres appear in the presphenoidal body a little later. Each sphenoidal concha has a centre that appears superoposteriorly in the nasal capsule during postmenstrual weeks 17–20. As it enlarges, it partly surrounds a posterosuperior expansion of the nasal cavity that becomes the sphenoidal sinus. The posterior conchal wall is absorbed and the sinus invades the presphenoidal component. The concha fuses with the ethmoidal labyrinth in the fourth year and with the sphenoid and palatine bones before puberty; its anterior deficiency persists as an opening for the sphenoidal sinus.

Postsphenoidal part

The first centres appear in the greater wings at about postmenstrual week 11, one in the basal cartilage of each wing below the foramen rotundum. These centres only contribute to the root of the greater wing (near the foramen rotundum and pterygoid canal). The remainder of the greater wing and the lateral pterygoid plate are ossified in mesenchyme. Two centres flanking the sella turcica appear between postmenstrual weeks 13 and 16 and soon fuse. The medial pterygoid plates are also ossified in 'membrane', a centre in each probably appearing in about postmenstrual weeks 9 or 10. The hamulus is chondrified during postmenstrual weeks 9–12 and begins to ossify at once. The medial and lateral pterygoid plates join at about postmenstrual weeks 21–24. A centre for each lingula appears during postmenstrual weeks 13–16 and soon joins the body. The neonatal optic canal is relatively large and has a keyhole or 'figure of eight' shape rather than the circular profile seen in the adult (Lang 2001).

Postnatal details

Presphenoidal and postsphenoidal parts fuse at about postmenstrual weeks 29–32; an unciform cartilage persists after birth in the lower parts of this junction. At birth, the bone is tripartite and consists of a central part (body and lesser wings) and two lateral parts that each consist of a greater wing and pterygoid process. During the first year, the greater wings and body unite around the pterygoid canals, and the lesser wings extend medially above the anterior part of the body, meeting to form the smooth, elevated jugum sphenoidale. By the twenty-fifth year, the sphenoid and occipital bones are completely fused. An occasional vascular foramen, often erroneously termed the craniopharyngeal canal, is occasionally seen in the anterior part of the hypophysial fossa.

Although the sphenoidal sinus can be identified between postmenstrual weeks 13 and 16 as an evagination of the posterior part of the nasal capsule, by full-term birth (notionally postmenstrual week 40) it represents an outgrowth of the spheno-ethmoidal recess. Pneumatization of the body of the sphenoid has been identified from 4 postnatal months and a distinct cell is visible by 2 years. Pneumatization spreads first into the presphenoid and later invades the postsphenoid part. The sinus reaches full size in adolescence, but often enlarges further by absorption of its walls as age advances.

Certain parts of the sphenoid are connected by ligaments that may occasionally ossify, e.g. the pterygospinous ligament between the sphenoidal spine and the upper part of the lateral pterygoid plate; the interclinoid ligament between the anterior and posterior clinoid processes; and the caroticoclinoid ligament between the anterior and middle clinoid processes.

Premature synostosis of the junction between pre- and postsphenoidal parts, or of the spheno-occipital suture, produces a characteristic appearance, obvious in profile, of an abnormal depression of the nasal bridge.

Stylohamular plane

Available with the *Gray's Anatomy* e-book

Mandible

The mandible is the largest, strongest and lowest bone in the face. It has a horizontally curved body that is convex forwards, and two broad rami that ascend posteriorly (**Fig. 38.5**). The body of the mandible supports the mandibular teeth within the alveolar process. The rami bear the coronoid and condylar processes. Each condyle articulates with the adjacent temporal bone at the temporomandibular joint.

Body

The body has external and internal surfaces separated by upper and lower borders. Anteriorly, the upper external surface shows an inconstant faint median ridge indicating the site of the fused symphysis menti. Inferiorly, this ridge divides to enclose a triangular mental protuberance; its base is centrally depressed but raised on each side as a mental tubercle. The mental protuberance and mental tubercles constitute the chin. The mental foramen, from which the mental neurovascular bundle emerges, lies midway between the upper and lower borders of the body, below either the interval between the premolar teeth, or the second premolar tooth. The posterior border of the foramen is smooth and accommodates the nerve as it emerges posterolaterally. A faint external oblique line ascends backwards from each mental tubercle and sweeps below the mental foramen, becoming more marked as it continues into the anterior border of the ramus.

The lower border of the body, the base, extends posterolaterally from the mandibular symphysis into the lower border of the ramus behind the third molar tooth. The anterior belly of digastric is attached to a rough digastric fossa near the midline on each side. Behind the fossa, the base of the body is thick and rounded, with a slight anteroposterior convexity that changes to a gentle concavity as the ramus is approached, giving the base an overall sinuous profile.

The upper border, the alveolar part, contains 16 alveoli for the roots of the lower teeth. It consists of buccal and lingual plates of bone joined by interdental and inter-radicular septa. Near the second and third molar teeth, the external oblique line is superimposed on the buccal plate. As is the case in the maxilla, the form and depth of the mandibular tooth sockets is related to the morphology of the roots of the mandibular teeth. The sockets of the incisor, canine and premolar teeth usually contain a single root, while those for the three molar teeth each contain two or three roots. The third molar is variable in its position and root presentation: it may be impacted vertically, horizontally, mesially or distally, and its roots may be bulbous, hooked, divergent or convergent, and occasionally embrace the mandibular (inferior dental) canal. The internal surface of the mandible is divided by an oblique mylohyoid line that gives attachment to mylohyoid and, above its posterior end, to the superior pharyngeal constrictor, some retromolar fascicles of buccinator, and the pterygomandibular raphe behind the third molar. The mylohyoid line extends from a point approximately 1 cm from the upper border behind the third molar as far forwards as the mental symphysis; it is sharp and distinct near the molars but faint further forwards. The mylohyoid groove extends downwards and forwards from the ramus below the posterior part of the mylohyoid line and contains the mylohyoid neurovascular bundle. The area below the line is a slightly concave submandibular fossa and is related to the submandibular gland.

A plane exists between the pharyngeal side wall and the infratemporal fossa/masticator space. It is readily identified by palpating the tip of the styloid process and with gentle blunt finger dissection passing anteriorly and medially to the pterygoid hamulus at the lower border of the medial pterygoid plate. Termed the 'stylohamular plane' (Friedman et al 1981), it defines the medial and superior boundaries of the infratemporal fossa and is the medial boundary for tumours confined to the infratemporal fossa. With resections using the stylohamular plane as a guide, the internal carotid artery, internal jugular vein and the vagus nerve should not be at risk because they are deep to the styloid apparatus (Fig. 38.4).

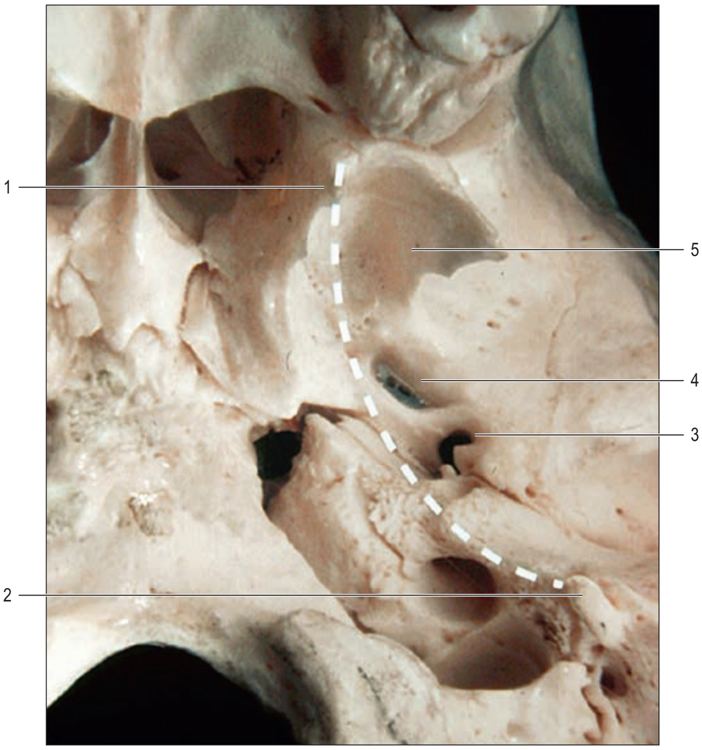

Fig. 38.4 The stylohamular plane (dotted line). Key: 1, pterygoid hamulus; 2, styloid process; 3, foramen spinosum; 4, foramen ovale; 5, lateral pterygoid plate.

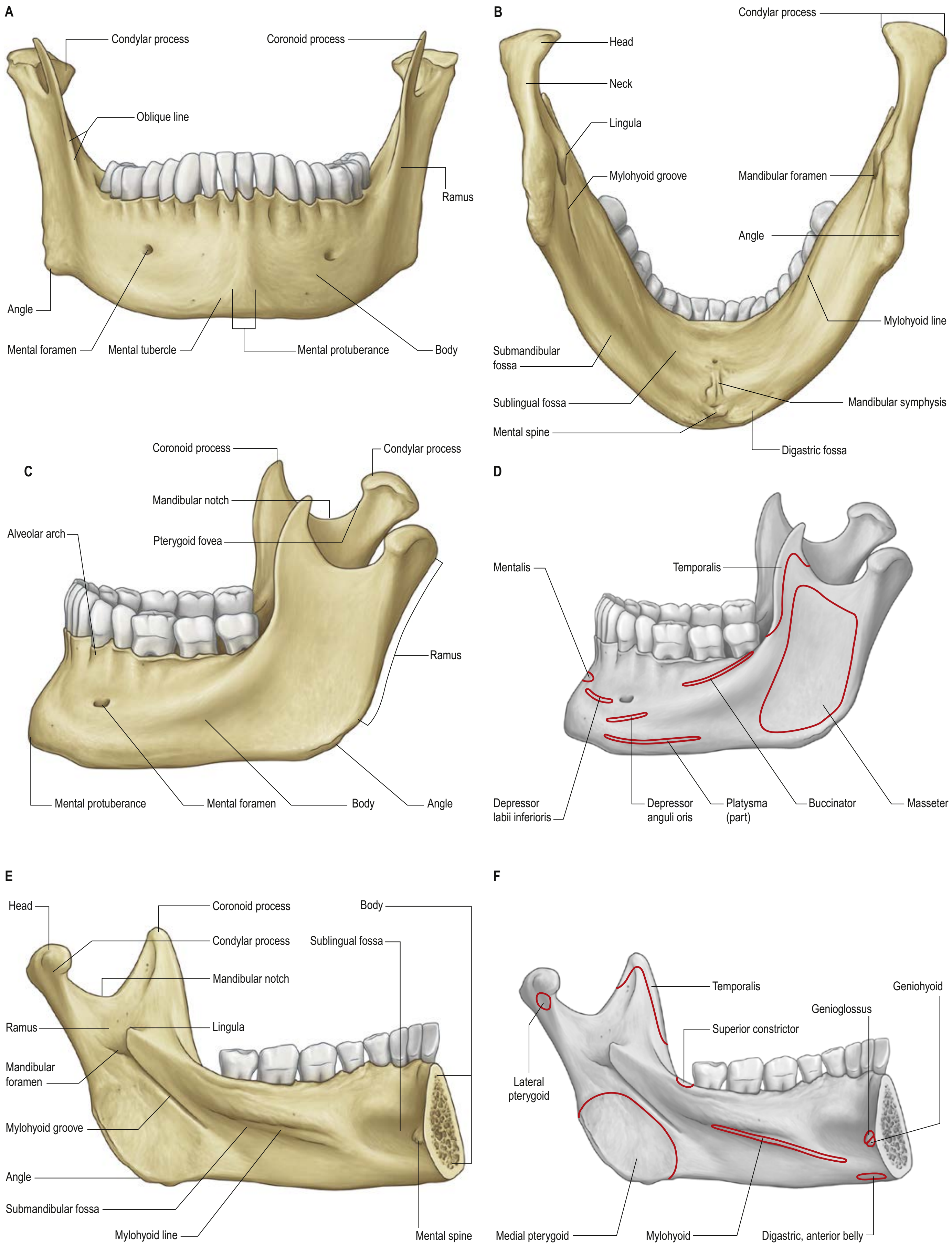
A
Condylar process
Coronoid process
Oblique line
Ramus
Angle
Mental foramen
Mental tubercle
Mental protuberance
Body
B
Condylar process
Head
Neck
Lingula
Mylohyoid groove
Mandibular foramen
Angle
Mylohyoid line
Submandibular fossa
Sublingual fossa
Mandibular symphysis
Mental spine
Digastric fossa
C
Coronoid process
Condylar process
Mandibular notch
Alveolar arch
Pterygoid fovea
Ramus
Mental protuberance
Mental foramen
Body
Angle
D
Mentalis
Temporalis
Depressor labii inferioris
Depressor anguli oris
Platysma (part)
Buccinator
Masseter
E
Head
Coronoid process
Body
Condylar process
Sublingual fossa
Mandibular notch
Ramus
Lingula
Mandibular foramen
Mylohyoid groove
Angle
Submandibular fossa
Mylohyoid line
Mental spine
F
Temporalis
Geniohyoid
Genioglossus
Superior constrictor
Lateral pterygoid
Medial pterygoid
Mylohyoid
Digastric, anterior belly

Fig. 38.5 The adult mandible. **A**, Anterior view. **B**, Inferior view. **C**, Lateral view (with muscle attachments in **D**). **E**, Internal view (with muscle attachments in **F**). (Sobotta Atlas of Human Anatomy © Elsevier GmbH, Urban & Fischer, Munich.)

The area above the line widens anteriorly into a triangular sublingual fossa and is related to the sublingual gland; the bone is covered by mucosa above the sublingual fossa as far back as the third molar. In an edentulous subject, it may be necessary to reduce any ridge-like prominence of the mylohyoid line so that dentures can fit without traumatizing the overlying oral mucosa.

Above the anterior ends of the mylohyoid lines, the posterior symphysial aspect bears a small elevation that is often divided into upper and lower parts, the mental spines (genial tubercles). The spines are sometimes fused to form a single eminence, or they may be absent, in which case their position is indicated merely by an irregularity of the surface. Genioglossus is attached to the upper part, and geniohyoid is attached to the lower part. Midline lingual (genial) foramina, above and/or below the genial tubercles, and lateral lingual foramina in the premolar region are present in most mandibles and are of importance in the vascular supply to the symphysis. A rounded elevation of compact bone, the torus mandibularis, sometimes develops above the mylohyoid line; it is most prominent in the premolar region, is usually bilateral and only of clinical significance if repeatedly traumatized.

Ramus

The mandibular ramus is quadrilateral. It has two surfaces (lateral and medial), four borders (superior, inferior, anterior and posterior) and two processes (coronoid and condylar). The lateral surface is relatively featureless and bears the (external) oblique ridge in its lower part. On the medial surface, the mandibular foramen lies midway between the anterior and posterior borders of the ramus, about level with the occlusal surfaces of the teeth. The inferior alveolar neurovascular bundle passes through the foramen to gain access to the mandibular canal. The foramen is overlapped anteromedially by a thin, sharp, triangular spine, the lingula, to which the sphenomandibular ligament is attached, and which is the landmark for an inferior alveolar local anaesthetic block injection. There is often a small prominence on the lateral surface of the ramus level with the lingula that forms a guide during surgical exposure of the lateral surface for osteotomies of the vertical ramus. Below and behind the foramen, the mylohyoid groove runs obliquely downwards and forwards.

The inferior border is continuous with the mandibular base and meets the posterior border at the angle, which is typically everted in males but frequently inverted in females. The thin superior border bounds the mandibular incisure (sigmoid or mandibular notch, incisura semilunaris), which is surmounted in front by the somewhat triangular, flat coronoid process and behind by the condylar process. The thick, rounded posterior border extends from the condyle to the angle, and is gently convex backwards above and concave below. The anterior border is thin above, where it is continuous with the edge of the coronoid process, and thicker below, where it is continuous with the external oblique line. The temporal crest is a ridge that descends on the medial side of the coronoid process from its tip to the bone just behind the third molar tooth. The triangular depression between the temporal crest and the anterior border of the ramus is the retromolar fossa (retromolar trigone).

The ramus and its processes provide attachment for the four primary muscles of mastication: masseter to the lateral surface; medial pterygoid to the medial surface; temporalis to the coronoid process and anterior ramus; the inferior head of lateral pterygoid to the condyle. The thickness of the ramus decreases markedly behind the external oblique line laterally, the temporal crest medially, and above the lingual, and there may be fusion of the lateral and medial cortical plates. This is of importance in mandibular ramus osteotomies and also influences the frequency of fractures of the mandibular angle.

Antilingula

Available with the *Gray's Anatomy* e-book

Mandibular canal

The mandibular foramen leads into the mandibular canal, which runs downwards and forwards within the ramus, gently curving inferiorly within the body under the roots of the molar teeth, with which it communicates by small openings, and ascending in the premolar region to the mental foramen. The canal is not always easy to define on plain X-rays, especially anterior to the mental foramen. Its walls may be formed either by a thin layer of cortical bone or, more frequently, by trabecular bone. Although the buccal–lingual and superior–inferior positions of the canal vary considerably between mandibles, in general, the mandibular canal is situated nearer the lingual cortical plate in the posterior two-thirds of the bone, and closer to the labial cortical plate in the anterior third. Bilateral symmetry (location of the canal in each half of the mandible) is reported to be common. Near the mental foramen, the inferior alveolar nerve branches into the mental nerve, which ultimately leaves the mandible via the mental foramen, and the incisive nerve, which remains within the bone and supplies the anterior teeth. The mental nerve may extend anteriorly for 2–3 mm within the mandible before curving back to the mental foramen (the 'anterior loop' of the mental nerve). Appreciation of the three-dimensional course of the mandibular canal during its passage through the mandible from the mandibular to the mental foramina is essential if damage to the inferior alveolar nerve is to be avoided in third molar surgery, mandibular osteotomies, dental implant surgery and harvesting of mandibular bone grafts.

Coronoid process

The coronoid process projects upwards and slightly forwards as a triangular plate of bone. Its posterior border bounds the mandibular incisure and its anterior border continues into that of the ramus.

Coronoid hyperplasia

Available with the *Gray's Anatomy* e-book

Condylar process

The mandibular condyle varies considerably in both size and shape. It consists of a core of cancellous bone covered by a thin outer layer of compact bone; the intra-articular aspect is covered by layers of fibrocartilage. When viewed from above, the condyle is roughly ovoid in outline, its anteroposterior dimension (approximately 1 cm) being roughly half its mediolateral dimension. The long axis of the condyle is at right-angles to that of the mandibular ramus but, as a result of the flare of the ramus, the lateral pole of the condyle is slightly anterior to the medial: if the long axes of the two condyles are extended, they meet at an obtuse angle, varying from 145° to 160°, at the anterior border of the foramen magnum. The slender neck of the condyle expands transversely upwards and joins the ramus to the articular head. The pterygoid fovea, a small depression on the anterior surface of the neck below the articular surface, receives part of the attachment of the inferior head of lateral pterygoid. The condyle is one of the most common sites for mandibular fractures.

Condylar hyper- and hypoplasia

Available with the *Gray's Anatomy* e-book

Accessory foramina

Accessory mandibular foramina are usually unnamed and infrequently described, and yet they are numerous. They may transmit auxiliary nerves to the teeth (from facial, mylohyoid, buccal, transverse cervical cutaneous, lingual and other nerves), and their occurrence is significant in dental anaesthetic blocking techniques. The innervation of the teeth is discussed in Chapter 37. The accessory lingual foramina in the mandibular symphysis are particularly relevant in dental implant surgery and osteotomies, e.g. genioplasty, at this site.

Ossification

The mandible forms in dense fibromembranous tissue lateral to the inferior alveolar nerve and its incisive branch, and also in the lower parts of Meckel's cartilage (first branchial arch). Each half is ossified from a centre that appears near the mental foramen between postfertilization days 42 and 50. From this site, ossification spreads medially and posterocranially to form the body and ramus, first below, and then around, the inferior alveolar nerve and its incisive branch. Ossification then spreads upwards, initially forming a trough, and later crypts, for the developing teeth. From postmenstrual week 10, Meckel's cartilage below the incisor rudiments is surrounded and invaded by bone. The mandibular condyle and coronoid process do not develop from the primary (Meckel's) cartilage but from secondary cartilages that appear later (**Fig. 38.6**). A conical mass, the condylar cartilage, extends from the mandibular head downwards and forwards in the ramus, and contributes to its growth in height. Although it is largely replaced by bone by midfetal life, its proximal end persists as proliferating cartilage under the fibrous articular lining until about the third decade. Another secondary cartilage, which soon ossifies, appears along the anterior coronoid border, and disappears before birth. One or two cartilaginous nodules also occur at the symphysis menti. These may ossify as variable mental ossicles in symphysial fibrous tissue between postmenstrual weeks 25 and 28; they unite with adjacent bone before the end of the first postnatal year.

Age changes in the mandible

At birth, the two halves of the mandible are united by a fibrous symphysis menti (**Fig. 38.7B**). The anterior ends of both rudiments are covered

The term 'antilingula' has been used to describe an inconstant bony prominence on the lateral aspect of the ramus. This localized bulge, initially thought to be the result of the entrance of the inferior alveolar neurovascular bundle into the medial ramus, has been used as a guide to the position of the mandibular foramen in mandibular osteotomies. However, there is little correlation between the position of the antilingula and the mandibular foramen. It has been suggested that the prominence (when present) on the lateral ramus could reflect the insertion of fibres of masseter (Lang 1995, Hogan and Ellis 2006, Park et al 2014).

The availability of computed tomography (CT), cone beam CT (CBCT) imaging and computer-assisted intraoperative navigation permits the assessment of the course of the mandibular canal throughout its length both prior to and during any surgical procedure that could place the inferior alveolar nerve and/or the mental nerve at risk (Aizenbud et al 2012, Wittwer et al 2012).

Elongation of the coronoid process may be found bilaterally or unilaterally, resulting in progressive, painless restriction of mandibular opening, as a result of the impingement of the coronoid process on the medial aspect of the zygomatic arch(es) or on the posterior maxilla. This rare condition is more common in patients with ankylosis (fusion) of the temporomandibular joint as a reactive response to attempted muscle function against resistance and more common in males. It usually presents in the middle of the third decade, although it has been reported in neonates. The aetiology is unknown. Treatment involves the resection of the coronoid process(es) (McLoughlin et al 1995, Satoh et al 2006, Mulder et al 2012).

Hyperplasia of the mandibular condyle is a rare unilateral condition that results in facial asymmetry and an altered occlusion (bite). The condition may present at any age; if it develops prior to puberty, growth may not cease at the end of the growth period. Reports vary as to male : female ratio. Although condylar hyperplasia is said to be self-limiting, removal of the growth site in the condyle may be necessary to arrest the condition. Correction of the asymmetry of the jaw is usually performed; however, self-correction of the asymmetry has been reported. A variety of classification systems have been suggested (Obwegeser and Make 1986, Nitzan et al 2008, Nitzan 2009, Wolford et al 2014).

Condylar hypoplasia is also uncommon. It is often associated with more extensive craniofacial anomalies, particularly hemifacial microsomia, where many of the first arch structures fail to develop fully and with failure of the development of the whole temporomandibular articulation. The condition has been subclassified by Pruzansky (1969) and a modified version by Kaban et al (1981): currently the OMENS classification is widely used to assess both bone and soft tissue defects (Vento et al 1991).

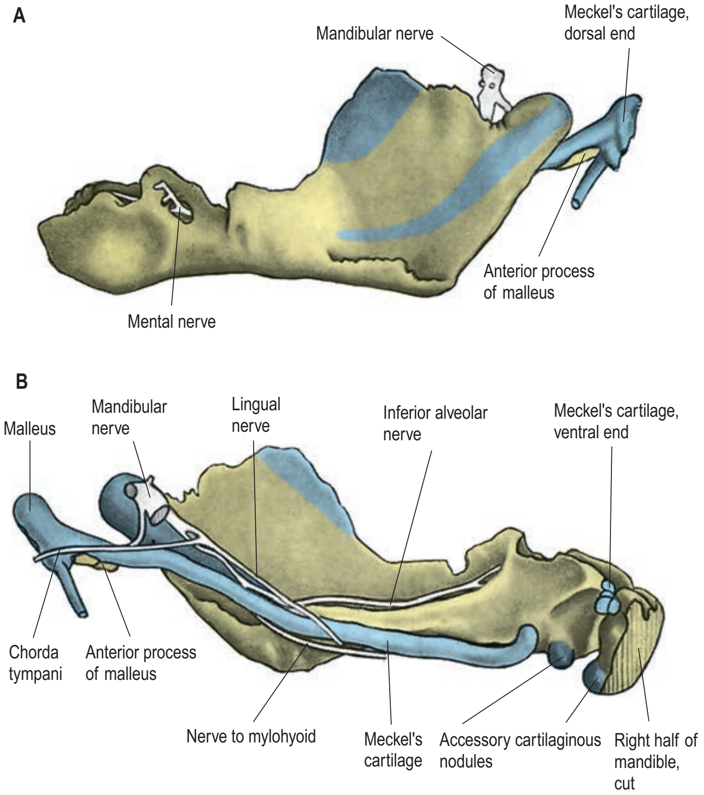
A
Mandibular nerve
Meckel's cartilage, dorsal end
Anterior process of malleus
Mental nerve
B
Malleus
Mandibular nerve
Lingual nerve
Inferior alveolar nerve
Meckel's cartilage, ventral end
Chorda tympani
Anterior process of malleus
Nerve to mylohyoid
Meckel's cartilage
Accessory cartilaginous nodules
Right half of mandible, cut

Fig. 38.6 The left half of a mandible of a human embryo, 95 mm long. **A**, Lateral aspect. **B**, Medial aspect. Blue: cartilage; yellow: bone. (Courtesy of A Low.)

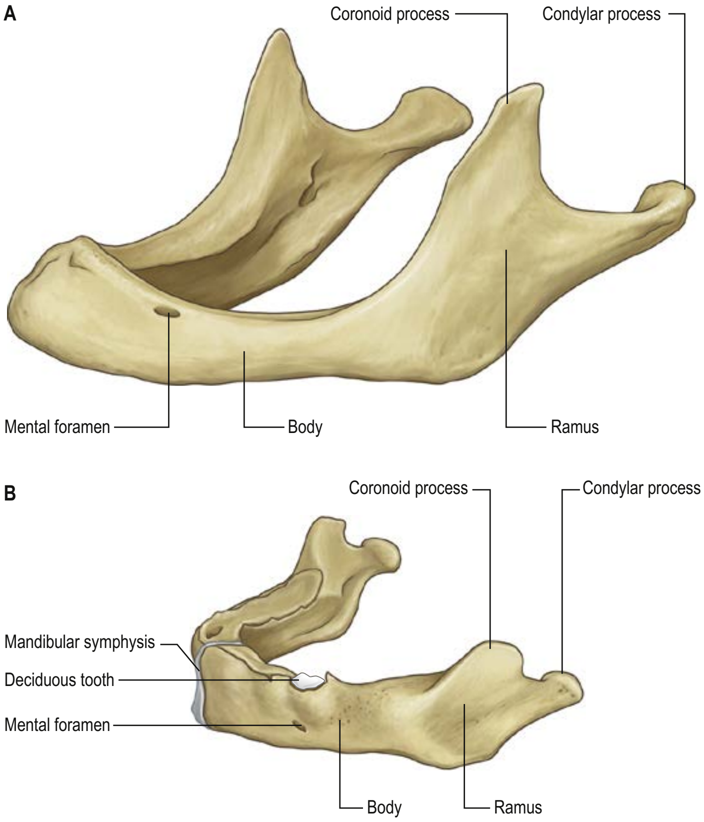

Fig. 38.7 **A**, An edentulous mandible; note the position of the mental foramen. **B**, A neonatal mandible. (Sobotta Atlas of Human Anatomy © Elsevier GmbH, Urban & Fischer, Munich.)

by cartilage, separated only by a symphysis. Until fusion occurs, new cells are added to each cartilage from symphysial fibrous tissue, and ossification on its mandibular side proceeds towards the midline. When the latter process overtakes the former and ossification extends into median fibrous tissue, the symphysis fuses. At this stage, the body is a mere shell, which encloses the imperfectly separated sockets of deciduous teeth. The mandibular canal is near the lower border, and the mental foramen opens below the first deciduous molar and is directed forwards. The condyle is almost in line with the occlusal plane of the mandible and the coronoid projects above the condyle. During the first three postnatal years, the two halves join at their symphysis from below upwards, although separation near the alveolar margin may persist into the second year. The body elongates, especially behind the mental foramen, providing space for three additional teeth. During the first and second years, as a chin develops, the mental foramen alters direction; it no longer faces forwards but now faces backwards, as in the adult mandible, and accommodates the changing direction of the emerging mental nerve.

In general terms, increase in height of the body of the mandible is achieved primarily by formation of alveolar bone associated with the developing and erupting teeth, although some bone is also deposited on the lower border. Increase in length of the mandible is accomplished by deposition of bone on the posterior surface of the ramus and concomitant compensatory resorption on the anterior surface (accompanied by deposition of bone on the posterior surface of the coronoid process and resorption on the anterior surface of the condylar process); a part of the ramus is therefore modelled into an addition to the mandibular body. Increase in width of the mandible is produced by deposition of bone on the outer surface of the mandible and resorption on the inner surface. An increase in the comparative size of the ramus compared with the body of the mandible occurs during postnatal growth and tooth eruption.

The role of the condylar cartilages in mandibular growth remains controversial. One view suggests that continued proliferation of this cartilage is primarily responsible for the increase in both the mandibular length and the height of the ramus. Alternatively, there is persuasive experimental evidence that proliferation of the condylar cartilage is an adaptive response to function, rather than being genetically determined. Condylar growth and remodelling have been shown to be influenced significantly by local factors – notably, movement and loading of the temporomandibular joint – and to be relatively immune to systemic influences such as vitamin C and D deficiency. Considering the changes that occur in the dentition throughout life, continuous adaptation of the temporomandibular articulation is required in order to maintain functional occlusal alignment between the upper and lower arches of teeth; this adaptation is thought to be largely the result of ongoing condylar remodelling.

In adults, alveolar and subalveolar regions are about equal in depth, and the mental foramen appears midway between the upper and lower borders. If teeth are lost, alveolar bone is resorbed, and both the mental foramen and the mandibular canal come to lie closer to the superior border (Fig. 38.7A). The mental foramen is placed higher than the mandibular canal posterior to it, and so resorption of the alveolus in edentulous patients exposes the nerve at the foramen, i.e. prior to the nerve in the mandibular canal (Cawood and Howell 1988, Lang 1995, Eufinger et al 1997).

Bone resorption in the mandible

Available with the *Gray's Anatomy* e-book

Blood supply of the mandible

The blood supply to the body of the mandible is derived from its principal nutrient artery, the inferior alveolar artery, and from the vessels supplying genioglossus, geniohyoid and the anterior belly of digastric (all muscles attached to the lingual aspect of the body of the mandible between the mental foramina). The blood supply to these muscles is from the sublingual branch of the lingual artery and the submental branch of the facial artery. Branches of these vessels may perforate the lingual cortical plate through lateral lingual foramina in the premolar region and genial foramina in the midline (when these foramina are present) (Fig. 38.10). Anastomoses are common. A branch of the submental artery may anastomose with the mental artery, permitting retrograde vascular supply to the body and symphysis (relevant in mandibular fractures). The vascular supply to the mandibular symphysis is of importance in dental implant surgery. The ramus, including the mandibular angle, is supplied by the inferior alveolar artery and from the vessels supplying masseter and medial pterygoid. Vessels supplying temporalis supply the coronoid process. The vascular supply to the

The pattern of bone resorption (atrophy) of the mandible following the loss of teeth is said to be in a centrifugal ('down and out') direction, compared to a centripetal direction in the maxilla. These differences produce a progressive increase in the incongruity of the alveolar processes of the jaws. Bone loss is not limited to the alveolar part; it can involve the base (basal bone) to varying degrees. Progressive remodelling of the mandible and maxilla accompany the bone loss; it is not limited to the body of the mandible but also involves the coronoid process and the mandibular condyle, and reduction in both the height and width of the ramus. This bone loss has implications in denture construction, dental implant surgery and mandibular fractures (**Figs 38.8–38.9**) (Cawood and Howell 1988, Eufinger et al 1997, Sutton et al 2004, Ellis and Price 2008, Aziz and Najjar 2009).

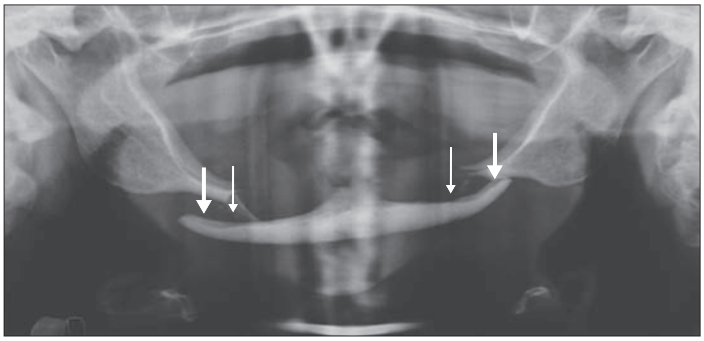

Fig. 38.9 Orthopantomogram showing a bilateral fracture of an edentulous atrophic mandible. There is complete loss of the alveolar process, extending into the underlying basal bone. The mental foramen (narrow arrows) and the mandibular canal (broad arrows) are at the superior border.

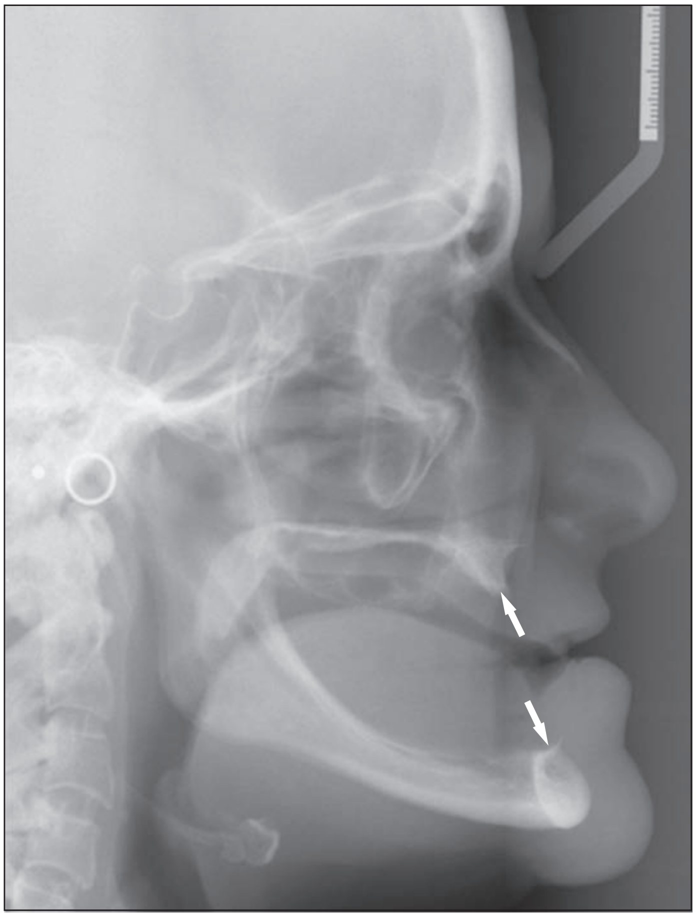

Fig. 38.8 Lateral skull radiograph showing the opposing direction (arrows) of resorption ('atrophy') of the mandible and maxilla, resulting in increasing incongruity between the jaws. The resorption involves the alveolus and the basal bone. (Courtesy of Dr Alf Nastri, Royal Melbourne Hospital.)

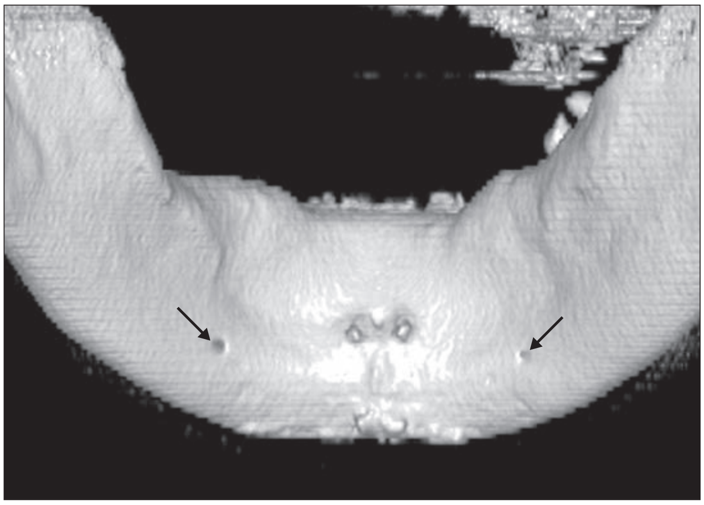

Fig. 38.10 A CT image showing the lateral lingual foramina (arrows). (Courtesy of Dr Koh Nakajima, with permission from Nakajima K, Tagaya A, Otonari-Yamamoto M et al 2014 Composition of the blood supply in the sublingual and submandibular spaces and its relationship to the lateral lingual foramen of the mandible. Oral Surg Oral Med Oral Pathol Oral Radiol 117:e32–8.)

mandibular condyle, temporomandibular joint and the individual masticatory muscles is described below (McDonnel et al 1994, Janfanza et al 2001, Jacobs et al 2007, Romanos et al 2012, Nakajima et al 2014).

Endosseous blood supply to the mandible via lingual foramina

Available with the *Gray's Anatomy* e-book

Tissue spaces

The contents of the infratemporal fossa are contained within a well-defined space that is bounded by and incorporates the masticatory muscles and is termed the masticator space (Fernandes et al 2013). It contains temporalis, masseter, medial and lateral pterygoid, the ramus and coronoid process of the mandible, the mandibular nerve and otic ganglion, the maxillary artery and the pterygoid venous plexus, and part of the buccal fat pad anterolaterally. The masticator space is closed posteriorly by the attachment of the deep cervical fascia, medial pterygoid and masseter (pterygomasseteric sling), and anteriorly, lateral to the ramus, by the firm attachment of masseter (the submasseteric space is a 'potential' space). Above the level of the zygomatic arch, the temporal fascia provides both the superior and lateral limits, by its attachments to the superior temporal line and the zygomatic arch, respectively. Below the zygomatic arch, the investing layer of deep cervical fascia (superficial layer of deep cervical fascia) splits into two laminae to enclose masseter, the lower part of temporalis and medial pterygoid, further defining the boundaries of the masticator space. The superficial (lateral) lamina covers masseter and is attached to the zygomatic arch, and the deep (medial) lamina runs on the deep surface of medial pterygoid, attaching to the skull base medial to the foramen ovale (Guidera et al 2014). This fascial covering of the masticatory muscles is considered to be distinct from the parotid fascia (capsule). The superficial temporal space lies between the temporal fascia laterally and temporalis medially. The deep temporal space, like the submasseteric space, is a 'potential' space between temporalis laterally and the temporal fossa of the skull medially. Both spaces are in communication with the remainder of the masticator space inferiorly. There is a view that the upper limit of the masticator space should be at the level of the zygomatic arch, on the grounds that since both temporal spaces communicate with the remainder of the masticator space, a single masticator space incorporates the temporal fascia, muscles and temporal spaces. Medial to the ramus of the mandible, the pterygomandibular space (part of the masticator space) communicates freely with the pterygopalatine fossa, offering little resistance to the spread of infection or tumours. Posteriorly penetrating maxillary tumours directly involve the masticator space/infratemporal fossa and the pterygopalatine fossa. Resection of the masticator space has been termed a 'compartment' resection of the mandible (Blanchaert and Ord 1998, McMahon et al 2013) (**Fig. 38.12**).

TEMPOROMANDIBULAR JOINT

The temporomandibular joint (TMJ) is a synovial joint between the glenoid fossa (mandibular fossa) of the temporal bone and the mandibular condyle. It is unusual in that its articular surfaces are lined by fibrocartilage, rather than by hyaline cartilage: fibrocartilage is less susceptible to degeneration and has a greater repair capacity. The joint cavity is divided into upper and lower compartments ('spaces') by a fibrocartilaginous articular disc.

The anterior limit of the glenoid fossa is the articular eminence. This transverse ridge of dense bone, tilted down at an angle of approximately 25° to the occlusal plane, forms most of the articular surface of the mandibular fossa. It is strongly convex in the sagittal plane with a slight concavity in the coronal plane and extends out laterally to the zygomatic arch as the articular tubercle. The articular eminence may contain air cells from the mastoid in around 5% of cases on CT scan (Ladeira et al 2013), which may be clinically relevant when the eminence is surgically reduced or screws are placed for fixation. The roof of the glenoid fossa is thin and often translucent when held to the light, confirmation that this is not a major load-bearing area of the joint (Hylander 2006). The posterior wall is formed by the tympanic plate, which also forms the anterior wall of the external acoustic meatus.

The anterior articular area of the fossa (articular fossa) is formed entirely from the squamous portion of the temporal bone and lined by articular tissue that extends anteriorly beyond the articular summit on to the preglenoid plane. The squamotympanic fissure marks the junction with the posterior non-articular (tympanic) area. The tegmen tympani, a bony plate of the petrous temporal, intervenes in the medial aspect of the fissure, where the squamotympanic fissure becomes the petrotympanic fissure. The postglenoid tubercle at the root of the zygomatic arch, just anterior to the squamotympanic fissure, separates the squamotympanic fissure laterally from the tympanic plate.

The condylar head, tilted forwards on the neck at an angle of approximately 30° (physiological anteversion), articulates with the fossa on its anterior and superior surfaces. Like the eminence, both its slope and shape are variable and influenced by age, function and dentition. In the coronal plane, its shape varies from that of a gable (particularly marked in those whose diet is hard) to roughly horizontal (in the edentulous).

It is probably impossible to measure the pressure developed on the articular surfaces of the human jaw joint when biting: direct measurement of loads across the joint in animals has demonstrated significant intermittent loading during mastication. However, there is irrefutable theoretical evidence based on Newtonian mechanics that the jaw joint is a weight-bearing joint. With a vertical bite force of 500 N on the left first molar, the right condyle must support a load of well over 300 N (Osborn 1995). The non-working condyle is more loaded than the condyle on the working side, which may help explain why patients with a fractured condyle choose to bite on the side of the fracture.

Fibrous capsule

The lower part of the joint is surrounded by tight fibres that attach the condyle of the mandible to the disc (collateral ligament). The upper part of the joint is surrounded by loose fibres that attach the disc to the temporal bone (**Fig. 38.13**). Thus, the articular disc is attached separately to the temporal bone and to the mandibular condyle, forming what could be considered two joint capsules. These attachments stabilize the disc but allow rotation over the condyle. Longer fibres joining the condyle directly to the temporal bone may be regarded as reinforcing. The capsule is attached superiorly to the anterior edge of the preglenoid plane, posteriorly to the lips of the squamotympanic fissure, between these to the edges of the articular fossa, and inferiorly to the periphery of the neck of the mandible.

Ligaments

The ligaments of the temporomandibular joint are the temporomandibular (lateral), sphenomandibular and stylomandibular ligaments.

Temporomandibular (lateral) ligament

The broad temporomandibular ligament reinforces the joint capsule laterally and is attached superiorly to the articular tubercle on the root of the zygomatic process of the temporal bone (see Fig. 38.13). It extends downwards and backwards at an angle of approximately 45° to the horizontal, and is attached to the lateral surface and posterior border of the neck of the condyle, deep to the parotid gland. A short, almost horizontal band of collagen connects the articular tubercle anteriorly to the lateral pole of the condyle posteriorly and may function to prevent posterior displacement of the resting condyle and initiate translation of the condyle on mouth opening.

Sphenomandibular ligament

The sphenomandibular ligament is medial to, and normally separate from, the capsule (see Fig. 38.13). It is a flat, thin band that descends from the spine of the sphenoid. It widens as it reaches the lingula of the mandibular foramen, having an average width at its insertion into the mandible of about 12 mm. Some fibres traverse the medial end of the petrotympanic fissure and attach to the anterior malleolar process: they represent a vestige of the dorsal end of Meckel's cartilage.

With the jaw closed, there is approximately 5 mm slack within the ligament. It becomes taut when the jaw is about half open. Superiorly, lateral pterygoid, the auriculotemporal nerve and the maxillary artery and vein are lateral to the ligament, the nerve and vessels running between the ligament and the condylar neck. The chorda tympani nerve lies medially and occasionally grooves the spine of the sphenoid. Anteroinferiorly, the inferior alveolar nerve and vessels and a parotid lobule separate the ligament from the ramus of the mandible. The vessels and nerves to mylohyoid pierce the ligament adjacent to the lingula. Medial pterygoid is inferolateral. The sphenomandibular ligament is separated from the pharynx by fat and a pharyngeal vein.

The endosseous supply of the mandibular symphysis via the lingual foramina, and the rich vascular supply to the anterior floor of the mouth are of particular importance in dental implant surgery and osteotomies, e.g. genioplasty, at this site.

Foramina at the level of, or above, the genial tubercle (superior genial foramen) and below the genial tubercle (inferior genial foramen) are almost always found (McDonnel et al 1994, Jacobs et al 2007). Lateral lingual foramina are usually identified, with an average distance above the lower border of the mandible of 5 mm (Romanos et al 2012). The superior genial foramen may contain a branch of the lingual artery and nerve. The inferior foramen may contain a branch of the sublingual or submental arteries and a branch of the mylohyoid nerve. The lateral foramen may contain a branch of the submental artery (Jacobs et al 2007, Nakajima et al 2014). Although the relative contributions from the individual vessels vary, anastomoses between these perforating vessels and the inferior alveolar artery, within the mandible, are common. The soft tissues in the anterior floor of the mouth adjacent to the mandible are supplied by contributions from the sublingual, submental and mylohyoid arteries; there are considerable anastomoses between them (Flanagan 2003, Loukas et al 2008, Romanos et al 2012, Nakajima et al 2014). Brisk, potentially life-threatening haemorrhage has been reported with dental implant placement in the mandibular symphysis, usually associated with perforation of the lingual cortical plate of the mandible (Woo et al 2006, Loukas et al 2008, Dubois et al 2010, Romanos et al 2012) (**Fig. 38.11**) and death has resulted from genioplasty, secondary to haemorrhage in the anterior floor of the mouth (personal communication). The precise source of the haemorrhage can be difficult to detect and may arise from both within the mandible and the soft tissues in the floor of the mouth, from any of the above-named vessels. The anastomoses between the vessels may result in haemorrhage on both sides of mylohyoid and thus into the sublingual and the submental/submandibular spaces bilaterally. As the lateral and midline lingual foramina are closer to the lower border of the mandible, caution with longer implants has been recommended in this region.

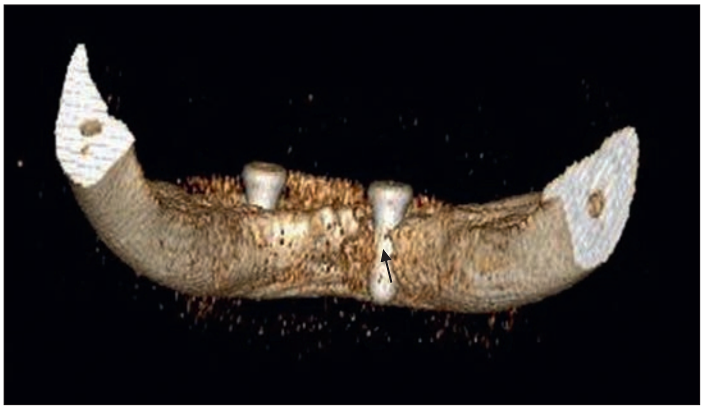

Fig. 38.11 A three-dimensional reformatted CT image showing an implant perforating the lingual cortical plate (arrow), leading to haemorrhage in the anterior floor of the mouth. A tracheostomy was required to secure the airway. (With permission from Dubois L, de Lange J, Baas E et al 2010 Excessive bleeding in the floor of the mouth after endosseous implant placement: a report of two cases. Int J Oral Maxillofac Surg 39:412–15.)

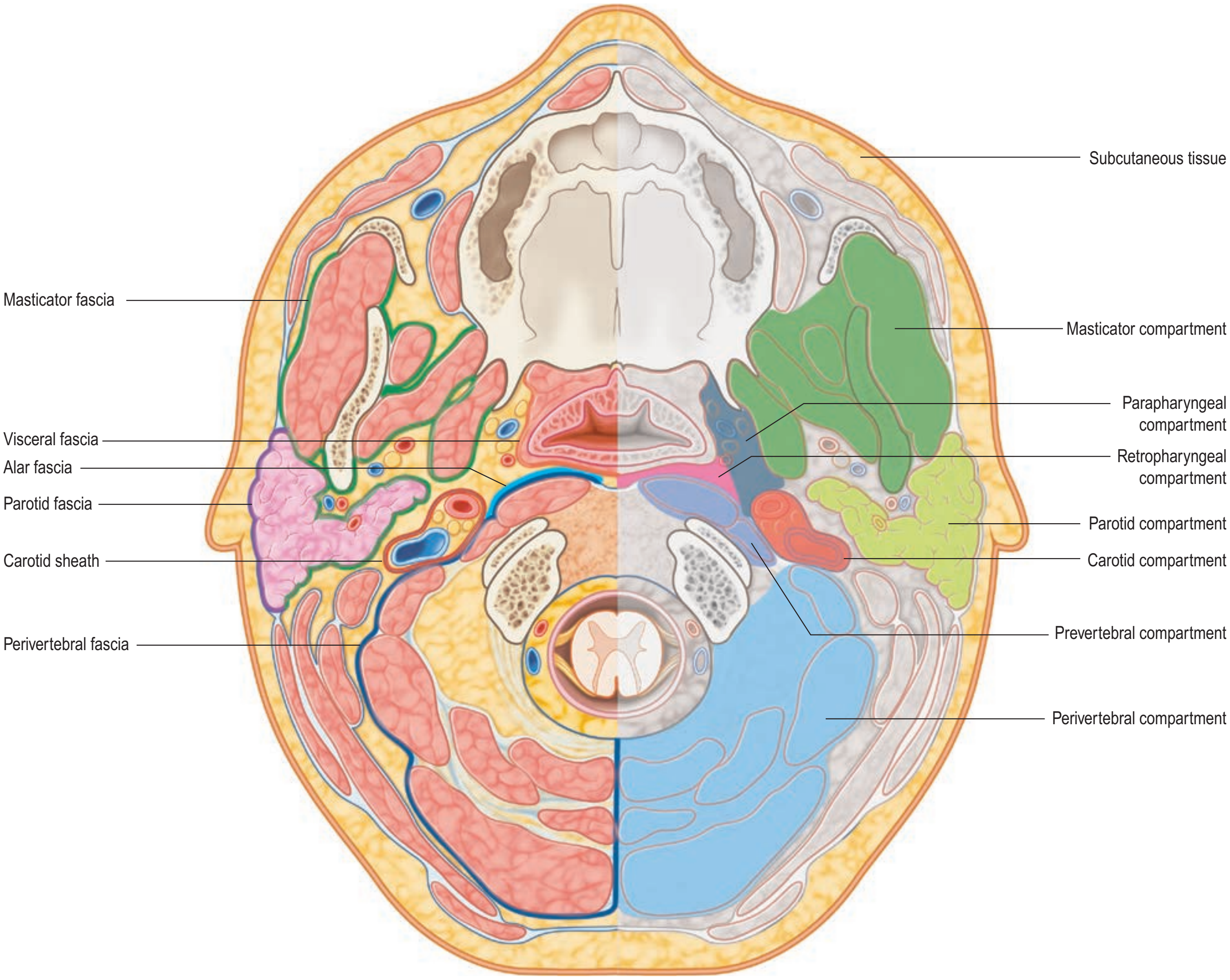

Fig. 38.12 A transverse section at the level of the hard palate demonstrating the cranial fascia (left) and associated compartments (right). (With permission from Guidera AK, Dawes PJD, Fong A et al 2014 Head and neck fascia and compartments: no space for spaces. Head Neck 36:1058–68.)

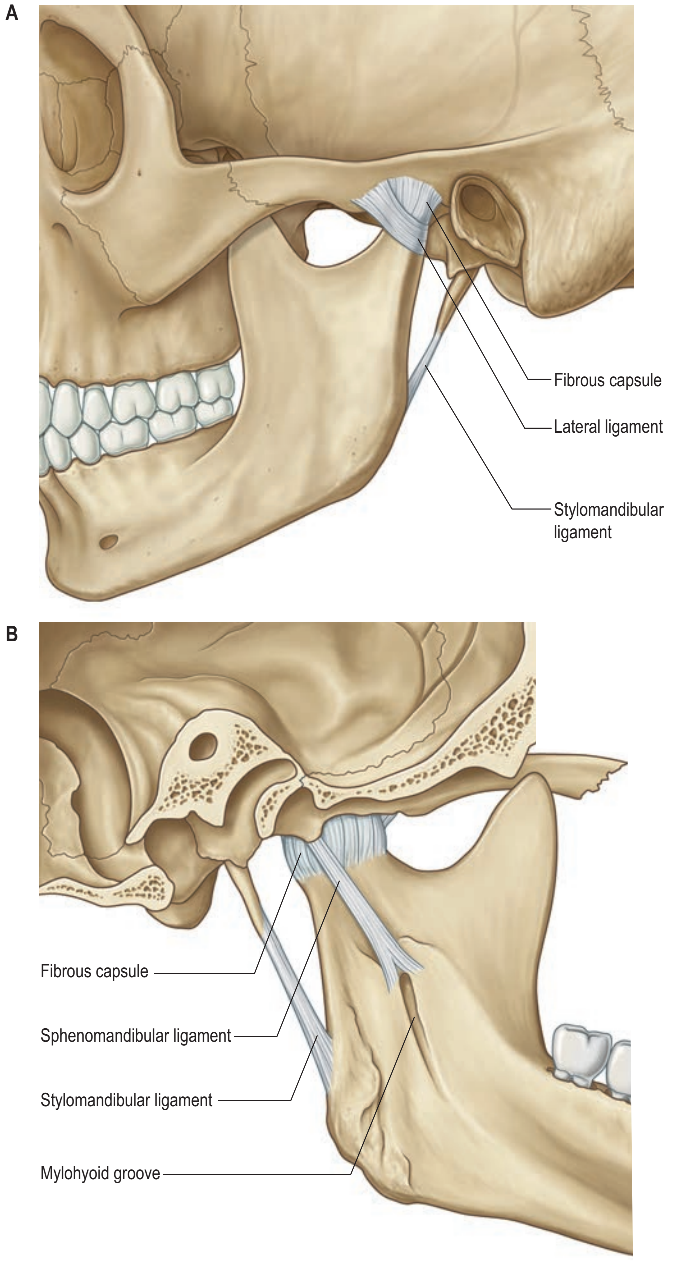

Fig. 38.13 The left temporomandibular joint. **A**, Lateral aspect. **B**, Medial aspect.

Stylomandibular ligament

The stylomandibular ligament is a thickened band of deep cervical fascia that stretches from the apex and adjacent anterior aspect of the styloid process to the angle and posterior border of the mandible (see Fig. 38.13). Its position and orientation indicate that it cannot mechanically constrain any normal movements of the mandible and does not seem to warrant the status of a ligament of the joint.

Synovial membrane

The synovial membrane lines the inside of the capsule of the joint but does not cover the disc or the articular surfaces (condyle, fossa or articular eminence). The synovium is most abundant in the bilaminar zone of the articular disc, forming loose folds posteriorly when the condyle is positioned in the glenoid fossa. These folds disappear when the condyle is protruded and the synovium is stretched.

Synovial fluid and joint lubrication

The coefficient of friction between the articulating surfaces of the temporomandibular joint is almost zero (Nickel et al 2006), reflecting the net result of a combination of adequate joint lubrication, the surface structure of the articulating surfaces and the articular disc. Joint lubrication depends on the synovial fluid, which also provides protection and nutrition to the articular surfaces and is the sole supplier of nutrients to the avascular disc. Surface active phospholipids (SAPLs) and hyaluronic acid are the key lubricants of the joint and act to protect the articular surfaces. Abnormalities of the joint lubrication system, e.g. changes resulting from uncontrolled oxidative stress, may play a role in the onset of some temporomandibular joint disorders such as anchored disc phenomenon (Nitzan 2001).

Articular surfaces

The anterior and superior surfaces of the mandibular condyle and the articular eminence and preglenoid plane of the squamous temporal bone are the principal articulating surfaces of the joint, as reflected in the thickness of the articular tissue covering these surfaces. The fibrocartilaginous covering of the condyle is composed of four distinct layers (De Bont et al 1984). The most superficial layer consists of densely packed fibres of type I collagen arranged mostly parallel to the articular surface and aligned in an anteroposterior direction (this can be seen as striation on arthroscopy – **Video 38.1**). This covers a thin cellular layer, the proliferative zone that is continuous with the cambial layer of the periosteum beyond the margins of the joint. The third layer, of hypertrophic cartilage, is rich in intercellular matrix and contains chondrocytes scattered throughout its depth and randomly orientated fibres of collagen type II. The fourth layer, immediately above the subchondral bone, is the zone of calcification. Although the number of chondrocytes within the hypertrophic zone decreases with age, undifferentiated mesenchymal cells have been identified in postmortem specimens of all ages (Hansson et al 1977), indicating a persistent capacity for proliferation and repair in condylar cartilage and may explain why condylar remodelling occurs throughout life (Toller 1974, Robinson 1993).

Articular disc

The articular disc divides the joint into a superior (discotemporal) space and an inferior (discomandibular) space, both filled with synovial fluid. The transversely oval disc is composed of avascular dense fibrous connective tissue with some chondrification in areas of maximum loading (**Fig. 38.14**). It has a thick margin forming a peripheral anulus and a central depression in its lower surface that accommodates the articular surface of the mandibular condyle. The depression probably develops as a mechanical response to pressure from the condyle as it rotates inside the anulus. The disc is stabilized on the condyle in three ways. Its edges are fused with the part of the capsular ligament that surrounds the lower joint compartment tightly and is attached around the neck of the condyle; well-defined bands in the capsular ligament attach the disc to the medial and lateral poles of the condyle (collateral ligaments); the thick anulus prevents the disc sliding off the condyle (self-centring capability), provided that the condyle and disc are firmly lodged against the articular fossa (as is normally the case).

In sagittal section, the disc has three distinct parts, namely an anterior band, a thinner intermediate zone and a posterior band. The posterior band is the thickest. Its upper surface is concavo-convex where it fits against the convex articular eminence and the concavity of the articular fossa. Posteriorly, the disc is attached to a richly vascularized and innervated region, the bilaminar zone (posterior attachment), that splits into two laminae: unlike the rest of the disc, its normal function is to provide attachment rather than intra-articular support. The upper lamina is composed of fibroelastic tissue and is attached to the squamotympanic fissure. A condensation of elastic fibres in the medial portion of the upper lamina is visible as the posterior oblique protuberance on arthroscopy (see Video 38.1). The lower lamina is composed of fibrous non-elastic tissue and is attached to the posterior aspect of the condyle. The intervening connective tissue between the upper and lower laminae contains a vascular plexus and is well innervated, but the central part of the disc itself is avascular and not innervated. With anterior movement of the disc–condyle complex, the volume of the posterior attachment increases as a result of the negative pressures generated, resulting in an influx of blood into the venous plexus: this pumping mechanism is important in the nutrition of the joint (Stegenga and de Bont 2006).

Upper and lower joint compartments

The upper joint space contains approximately 1.2 ml of synovial fluid and the lower approximately 0.9 ml. Both spaces may be considerably distended with fluid for diagnostic purposes in temporomandibular joint arthrography, for therapeutic purposes in arthrocentesis, and to improve access and visibility in arthroscopy. Both joint spaces

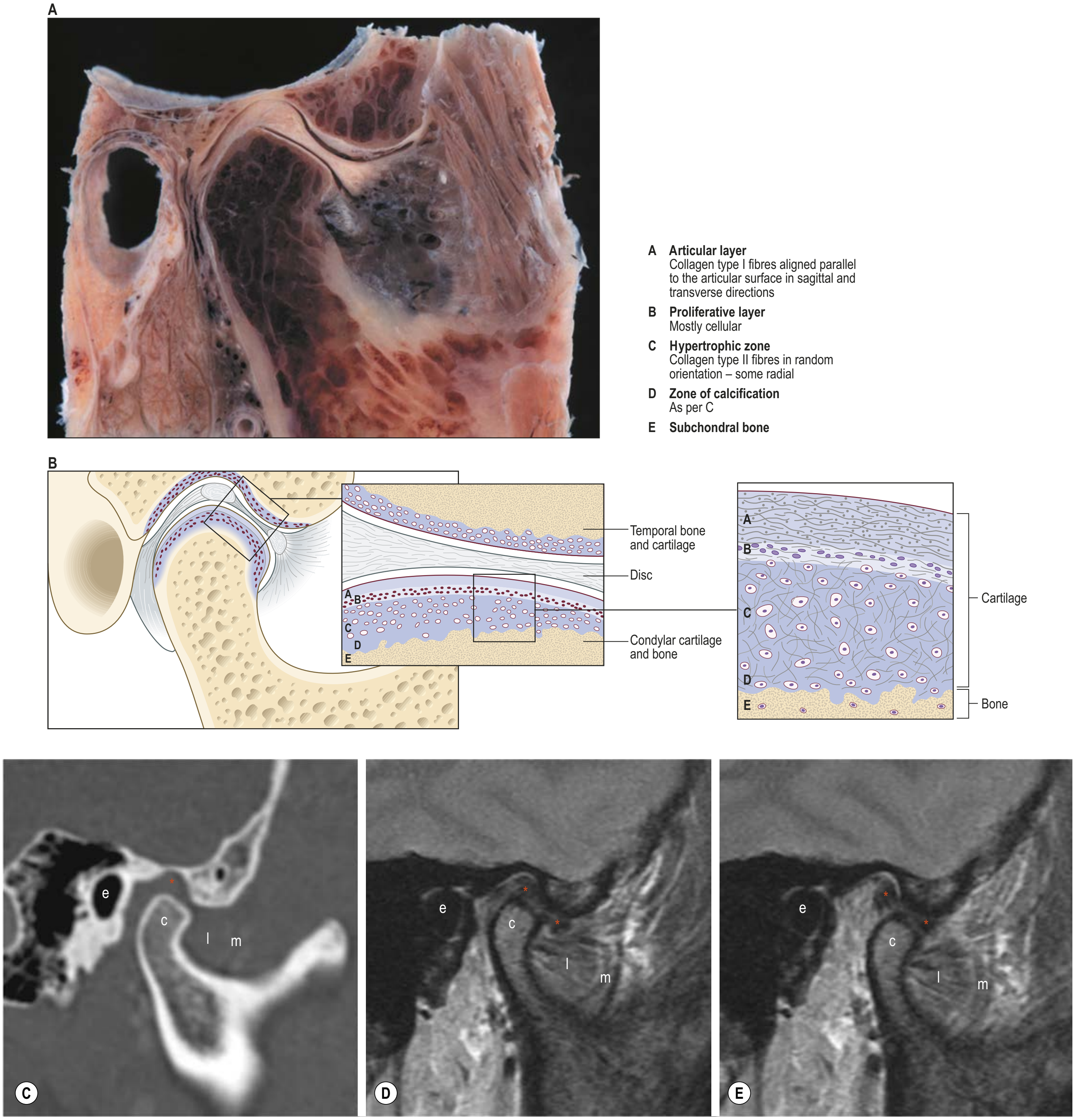
A
A Articular layer
Collagen type I fibres aligned parallel to the articular surface in sagittal and transverse directions
B Proliferative layer
Mostly cellular
C Hypertrophic zone
Collagen type II fibres in random orientation – some radial
D Zone of calcification
As per C
E Subchondral bone
B
Temporal bone and cartilage
Disc
Condylar cartilage and bone
A
B
C
D
E
Cartilage
Bone
e
c
l
m
*
C
D
E

Fig. 38.14 Sagittal sections through the right temporomandibular joint. **A**, Note the relationship of the external acoustic meatus and articular disc to the mandibular condyle. **B**, The microstructure of condylar cartilage. **C**, Contrast enhanced CT (bone window setting) in the sagittal plane through the closed temporomandibular joint. **D**, Proton density sagittal MRI through the closed joint. **E**, Same MRI acquisition parameters as for **D**, but with the mouth open. Note the relationship of the external acoustic meatus (e) to the condylar process of the mandible (c) and the articular disc (*), which deforms on opening. Lateral pterygoid muscle fibres (l) are seen in close relationship to the maxillary vessels (m). (A, Courtesy of Professor Cristina Manzanares Céspedes, Anatomy and Human Embryology Unit, Bellvitge Campus, University of Barcelona.)

have an anterior and posterior recess or pouch, and are lined by synovium, which has a grey hue when viewed through an arthroscope (see Video 38.1).

Functions of the articular disc

The articulating surfaces of the mandibular condyle and the articular fossa are highly incongruent. Wear of the articular surfaces may be reduced by the presence of a deformable articular disc, which not only distributes compressive joint loading over a larger contact area but also significantly reduces the frictional force on the condyle and the articular fossa by separating slide and rotation into different joint compartments.

The disc may aid joint lubrication by storing fluid squeezed out from loaded areas to create a weeping lubricant. Its flexibility, due to its high water content and viscoelastic properties, allows it to function almost like a fluid, further reducing friction within the joint and so aiding joint lubrication. The friction between the articulating surfaces in the absence of the disc is 2–3 times greater than with the disc *in situ*.

The role of the disc in relation to joint stability is controversial. One view is that a deformable and viscoelastic disc stabilizes the condyle within the joint by filling the changing and irregular joint space created during movement. The disc moves in an almost congruent manner relative to the condyle controlled by neuromuscular forces: the upper head of

The anterior portion of the disc is attached to part of the upper head of lateral pterygoid and this muscle may aid in anterior translation of the disc during joint function. Hyperactivity of lateral pterygoid is thought to contribute to anterior disc displacement and possibly dislocation of the condyle, and for this reason injection of botulinum toxin is found to be helpful in the management of both of these conditions.

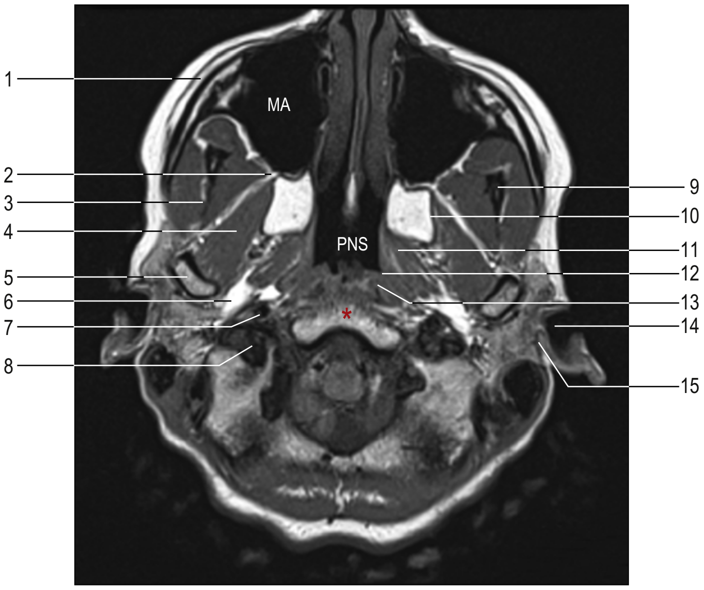

Fig. 38.15 An axial T1-weighted MRI at the level of the external acoustic meatus. Key: 1, body of zygoma; 2, pterygopalatine fossa; 3, temporalis; 4, lateral pterygoid; 5, condyle; 6, parapharyngeal fat stripe; 7, internal carotid artery; 8, jugular bulb/foramen; 9, coronoid process; 10, lateral pterygoid plate; 11, torus tubarius; 12, fossa of Rosenmüller; 13, longus colli; 14, external auditory meatus; 15, superficial lobe of parotid gland. Abbreviations: MA, maxillary antrum; PNS, postnasal space. *, anterior arch of atlas.

lateral pterygoid anteriorly and the elastic tissue in the bilaminar region posteriorly together pull the disc forwards or backwards and the shape of the disc with its thick, 'self-seating' anulus helps to prevent it sliding off the condyle. An alternative view is that a slippery articular disc doubles the number of virtually friction-free sliding surfaces, and so destabilizes the condyle in the same way that stepping on a slippery object destabilizes the foot. These two roles are not mutually exclusive. A deformable disc stabilizes the condyle within the joint whilst, by doubling the friction-free surfaces, the disc–condyle assembly slides freely under compressive loading and so is 'destabilized'.

Relations

Superiorly, the roof of the glenoid fossa has a mean thickness of 0.9 mm (range 0.2–4 mm). It separates the upper joint space from the middle cranial fossa. This bony partition is occasionally fenestrated by inflammatory processes or inadvertently during surgery to the joint, particularly for release of ankylosis, and, rarely, by the condyle being driven superiorly by violent trauma to the mandible. The foramen of Hushke (a tympanic foramen found in some 4% of cadaveric dissections) may communicate directly with the middle cranial fossa or middle ear (Lacout et al 2005). The maxillary artery and its proximal branches, most notably the middle meningeal artery, lie medially, just beyond the joint capsule. The uppermost part of the parotid capsule enclosing the branches of the facial nerve that supply the muscles of the upper face, including orbicularis oculi, are lateral to the joint capsule, and the thread-like nerves are at risk during surgical approach to the joint. The upper part of the infratemporal fossa, which contains the two heads of lateral pterygoid, is anterior to the condyle (Fig. 38.15). This is the space, anterior to the articular eminence, into which the condyle is displaced in cases of dislocation of the temporomandibular joint, or fracture/dislocation of the condylar head due to the vector of pull from lateral pterygoid attached to the anterior condylar neck. Posteriorly, the tympanic plate and tegmen tympani separate the joint from the middle ear cavity. Perforation through this thin, bony wall into the middle ear is a recognized complication of temporomandibular joint arthroscopy.

Vascular supply and innervation

The joint derives its arterial supply from the superficial temporal artery laterally and the maxillary artery medially. Penetrating vessels that supply lateral pterygoid may also supply the condyle. Veins drain the anterior aspect of the joint and associated tissues into the plexus surrounding lateral pterygoid; posteriorly, they drain into the vascular region that separates the two laminae of the bilaminar region of the disc. Positive and negative pressure produced by forward and backward movement of the condyle shunts blood between these regions. Lymphatics drain deeply to the upper cervical lymph nodes surrounding the internal jugular vein.

The articular tissues and the dense part of the articular disc have no nerve supply. The nerve supply to the temporomandibular joint is from branches from the mandibular division of the trigeminal nerve, mostly through the auriculotemporal branch, and branches from the masseteric and deep temporal nerves. Postganglionic sympathetic nerves supply the tissues associated with the capsular ligament and the looser posterior bilaminar extension of the disc. The temporomandibular joint capsule, lateral ligament and retroarticular tissues all contain mechanoreceptors and nociceptors: the input from mechanoreceptors provides a source of proprioceptive sensation that helps control mandibular posture and movement.

Jaw movements

Movements of the condyle in the temporomandibular joint

The major function of the mandible is to exert, via the teeth, the force necessary to break down food into smaller particles and so facilitate digestion. Pure vertical movements of the lower teeth create a crushing force that is ineffective in breaking up tough fibrous food. Humans use a lateral movement of the lower jaw to create a shear force that enhances the effectiveness of the power stroke of mastication. Bodily lateral movement of the whole jaw, the Bennett shift, is insignificant. Extensive lateral movement is only possible when the jaw is rotated horizontally about one condyle while the other condyle slides backwards and forwards. The temporomandibular joint is structurally adapted to accommodate both sliding/translation and rotation/hinging in a sagittal plane. Sliding/translation occurs because the capsular ligament that surrounds the upper joint compartment is loose, whereas the capsular ligament that encloses the lower joint compartment is tight, and only allows the condyle to rotate over the depression inside the anulus of the articular disc. The normal range of maximum mouth opening measured between the upper and lower incisor tips is 35–50 mm, the first 15–25 mm of which is due to hinging of the condyle; the remainder is due to condylar translation. The adult range of movements is reached at around 10 years in females and 15 years in males. Lateral excursions of the chin (including protrusion) can normally achieve 8–12 mm of movement at the lower incisors. At the limit of normal opening, the condyle has translated on to the peak or just beyond the peak of the articular eminence. Translation beyond this results in subluxation (temporary) and dislocation (longer standing) of the joint, when the condyle lies anterior and superior to the peak of the articular eminence.

Symmetric opening

Symmetric jaw opening is associated with preparation for incising. At the start, each mandibular condyle rotates in the lower joint compartment inside the anulus of its disc. After a few degrees of opening, the condyle continues rotating inside its disc and, in addition, both slide forwards down the articular eminence of the upper joint compartment. Without this forward slide or translation, it becomes impossible to continue opening the jaw beyond a gape of approximately 25 mm.

Opinions differ as to why this forward slide should occur. A cadaveric condyle slides forwards when the jaw is rotated open, suggesting that this is not a neuromuscular response but rather the result of mechanical constraints. When the jaw is rotated open, the temporomandibular ligament rapidly becomes taut (Osborn 1995). The taut ligament acts as a constraint that allows the mandible only two rotary movements: it can swing about the upper attachment of the ligament and rotate about the lower attachment. The lower end of the taut ligament acts as a moving fulcrum that converts the downward and backward pull of the opening rotary force (created at the front by digastric and geniohyoid) into one that drives the condyle upwards and forwards into the concavity of the overlying articular disc. This now pushes the disc forward. Swing about the upper attachment creates space above for the disc to slide further forwards, which is possible because the upper part of the capsular ligament is loose. The two movements, rotation and swing, are inextricably linked by the taut ligament and, via the condyle, combine to keep the disc in firm contact with the articular eminence while the jaw is opened. The disc is stabilized by its tight attachment to the condyle (collateral ligament) and by the thickened margins of its anulus that prevent it sliding through the thinner compressed region between the centre of the condyle and the articular eminence.

The articular disc is designed to withstand compressive and shearing loads. It has viscoelastic properties that allow it to deform when loaded and to conform to the surfaces causing this deformation. Removal of the disc increases surface friction within the joint by 2–3 times compared to joints with an intact disc. Long-term follow-up of patients who have had the disc removed ('discectomy') demonstrates that the joint undergoes significant remodelling similar to that seen in osteoarthrosis. There is flattening, slight roughening and sclerosis of the condylar head and articular fossa. These changes, which are believed to be adaptive responses of the condyle and fossa to the absence of an intervening disc, collectively produce a broader contact, decreasing the load per unit area. A layer of fibrous tissue (scar) also forms between the surfaces and synovial tissue may reform over this area providing a 'neo-disc'.

The main purpose of collagen in tissue is to resist tensile forces. The orientation of the collagen fibres in the disc varies in the individual regions, reflecting the direction of the tensile forces imparted to the disc. In the intermediate zone, these fibres are predominantly orientated in an anteroposterior direction. Around the periphery, they form a ring-like structure with a three-dimensional framework of fibrils. In the posterior and anterior bands, their predominant orientation is lateral–medial and superior–inferior. Type 1 collagen, similar to that found in the superficial layers of the head of the condyle and the articular fossa, predominates in the disc.

Chondroitin sulphate and dermatan sulphate are the principal glycosaminoglycans (GAGs) in the intercellular matrix. GAGs are very hydrophilic and play an important role in the resistance and distribution of compressive load applied to the temporomandibular joint. Their concentration varies with the area of the disc and is highest in the superficial layer of the intermediate zone (Nickel and McLachlan 1994, Detamore and Athanasiou 2003, Paegle et al 2003, Obrez and Gallo 2006, Tanaka et al 2006, Miloro and Henrickson 2010).

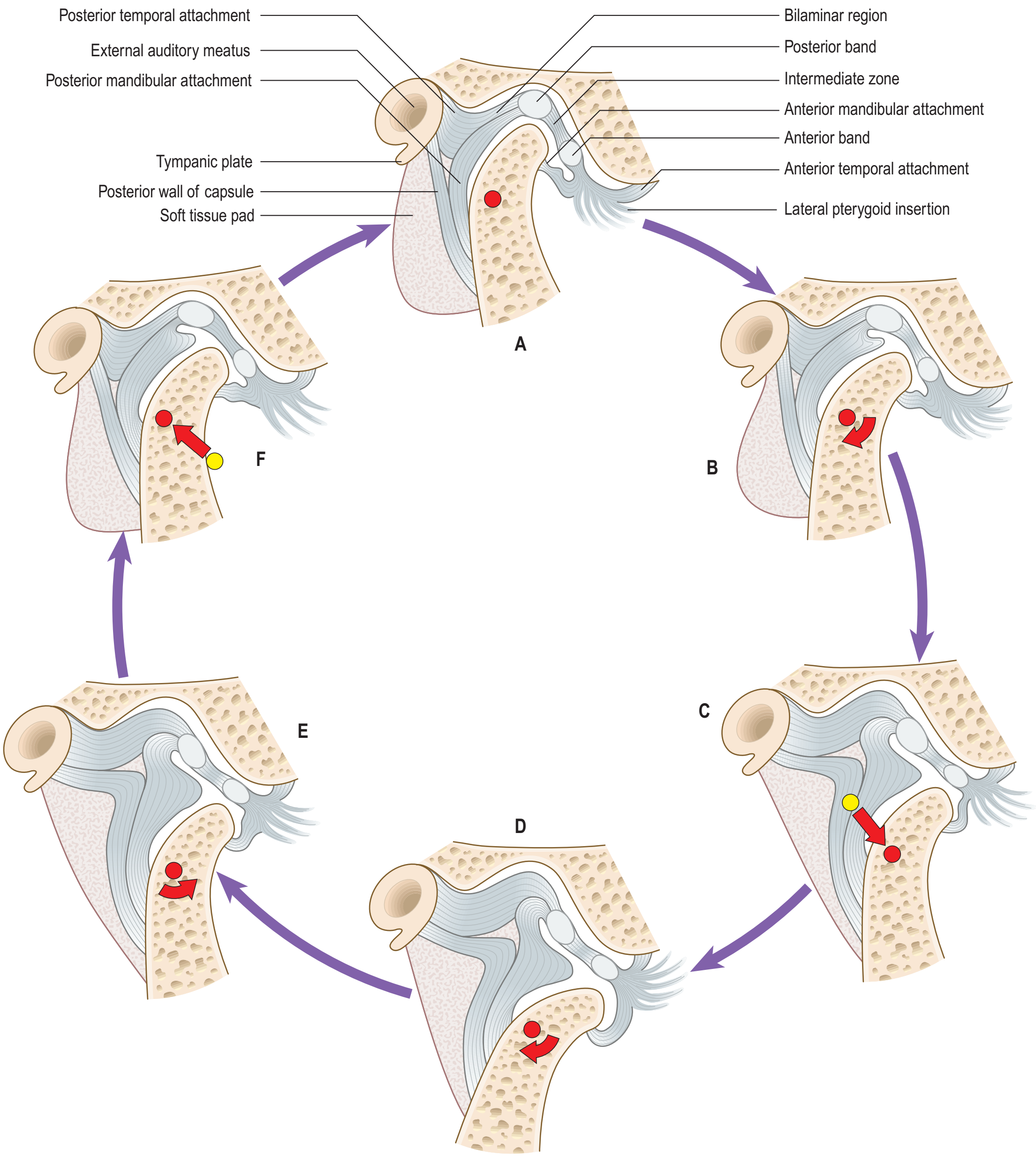
Posterior temporal attachment
External auditory meatus
Posterior mandibular attachment
Tympanic plate
Posterior wall of capsule
Soft tissue pad
Bilaminar region
Posterior band
Intermediate zone
Anterior mandibular attachment
Anterior band
Anterior temporal attachment
Lateral pterygoid insertion
A
B
C
D
E
F

Fig. 38.16 Changing relationships of the condyle of the mandible, the articular disc and the articular surface of the temporal bone during one complete opening (A → D) and closing (D → A) cycle of the mouth.

As forward slide of the condyle continues, the controlling influence exerted by the temporomandibular ligament diminishes. The lingula of the mandible moves away from the spine of the sphenoid, tautening the originally slack sphenomandibular ligament, which now acts in the same way as the temporomandibular ligament, to maintain the condyle against the articular eminence. Symmetric opening thus appears to consist of at least three separate phases: an early phase controlled by the temporomandibular ligament and articular eminence; a short middle phase in which either both temporomandibular and sphenomandibular ligaments, or neither, act to constrain movements; and a late phase controlled by the sphenomandibular ligament and articular eminence.

Changes in disc position during movement

With the teeth in occlusion, the condyle is in the glenoid fossa and the intra-articular disc sits on the condylar head, with its posterior band at the 12 o'clock position from the centre of the condylar head in the sagittal plane (Fig. 38.16A). As mouth opening begins (Fig. 38.16B), the condyle rotates within the lower joint space and the disc remains stationary. At about mid-opening, the condyle and disc begin to move forwards together so that their relative position is maintained (Fig. 38.16C). At maximum gape (Fig. 38.16D), the condylar head slides further anteriorly than the disc and the disc is rotated backwards relative to the condyle by the pull of the elastic superior lamina of the posterior attachment, so that the anterior band of the articular disc is above the summit of the condyle. This differential movement results in the disc moving only about half the distance of the condyle. Mouth closure involves the disc moving back in tandem with the condyle under the influence of the elastic fibres in the upper lamina of the bilaminar area posterior to the disc itself (Fig. 38.16E), which also reverses its angular rotation (Fig. 38.16F) to resume the starting position of the cycle.

Eccentric jaw opening

Jaw movement during mastication can be divided into three parts: opening, closing and power strokes. Eccentric jaw opening is associated with preparing for the power stroke of mastication. The mandibular condyle on the non-working side slides back and forth during lateral movements associated with the power stroke on the working side. Although the jaw muscles now have the major control over mandibular movements, the temporomandibular and sphenomandibular ligaments keep the condyle firmly against its articular eminence during opening.

Eccentric and symmetric jaw closing

During closure of the jaw, the masticatory muscles act in combination to force the joint surfaces together. This compresses the joint tissues and potentially shortens the ligaments so that they no longer constrain jaw movements. Under these conditions, jaw movements and the positions of the condyles are controlled by neuromuscular processes, within the limits of constraints imposed by the articular eminence, the occluding surfaces of the teeth and the presence of food between them. The non-working condyle moves the furthest, and is the most heavily loaded, during the power stroke of mastication. The loads on each joint, balancing and working, drive each condyle more forcefully into its articular eminence.

The envelope of motion

The envelope of motion is the volume of space within which all movements of a point on the mandible have to occur because the limits are set by anatomical features: the shape or size of the upper and lower

Changes in disc position may become out of phase with the condyle, causing obstruction to smooth mandibular movement. The disc is typically pulled anteromedially by lateral pterygoid, preventing forward translation of the condyle. With the disc in this position, the posterior band of the disc is anterior to the condyle, obstructing forward translation of the condyle. As the force from the condyle on the disc increases, the elastic posterior attachments of the disc are stretched until the resistance to movement is overcome and the disc reduces into a normal relationship with the condyle, a movement that is associated with an audible click (audible to the patient and occasionally to others). Once the normal disc–condyle relation is re-established, the mouth is free to achieve maximum opening (see Fig. 38.16C,D). The disc may then snap back anterior to the condyle on mouth closure. This phenomenon is called reciprocal clicking or disc displacement with reduction. If the disc remains completely anterior to the condylar head and does not reduce into a normal relationship with the condyle during opening, the condyle may be prevented from further forward translation and mouth opening is restricted. This common clinical condition is known as disc displacement without reduction.

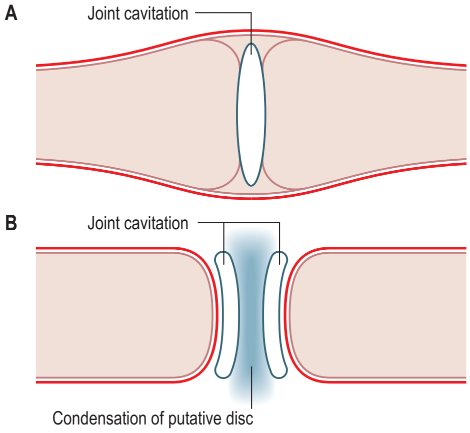

Fig. 38.17 A–B, Development of the temporomandibular joint; the temporal and condylar components of the joint develop from two separate condensations of neural crest mesenchyme.

jaws, tooth contacts, and the attachment of muscle and ligaments. The mandibular movements at these extremes are termed 'border movements'.

In consciously controlled movement of the jaw from the rest position to the fully opened position, the trajectory of the mandibular incisal edge is two-phased. The first phase is a hinge-like movement during which the condyles are retruded within the mandibular fossae. When the teeth are opened by approximately 25 mm, the second phase of opening occurs by anterior movement or protrusion of the condyles down the articular eminences with further rotation. If conscious effort is used, a closure path can then be followed in which the jaw is closed to an extreme protruded tooth contact position, after which it has to be retruded to the starting position. Similar considerations apply to lateral movements: mandibular rotation around a retruding condyle and the protraction of the opposite condyle are anatomically limiting factors that are rarely encountered in normal function.

Although all mandibular movement occurs within or along the border movements, knowledge of the extent of border movements provides little information on the nature of the movements during chewing or on the free ('empty'), habitual movements during both opening and closing, that have a more limited trajectory.

Disc position and internal derangement

Available with the *Gray's Anatomy* e-book

Development of the temporomandibular joint

Unlike the development of most synovial joints, where a single blastema cavitates to form a joint space and the articulating bones are derived from the same condensation of tissue, the temporomandibular joint develops from separate condensations of mesenchyme that coalesce to form the joint. It is first seen at the end of the embryonic period in postfertilization week 8, when condensations of neural crest mesenchyme for the mandibular condyle and the zygomatic process of the squamous part of the temporal bone appear. Chondrogenesis is seen in the mandibular condyle at the end of postfertilization week 9 (postmenstrual week 11), when the articular disc and inferior joint cavity appear. The superior joint cavity is seen from postmenstrual week 13 and endochondral ossification of the mandibular condylar cartilage is seen from postmenstrual week 17. The articular surfaces of the bones that form the joint are covered by a persisting layer of proliferative cells continuous with the periosteum that surrounds each bone (Fig. 38.17).

Muscles

The four principal muscles of mastication are medial and lateral pterygoid, temporalis and masseter: their actions produce movements of the mandible at the temporomandibular joints. The infratemporal fossa contains medial and lateral pterygoid and the tendon of temporalis. Masseter lies on the face, on the lateral surface of the ramus of the mandible, but will be considered here.

Masseter

Masseter (Fig. 38.18) is a quadrilateral multipennate muscle consisting of three layers that blend anteriorly. The superficial layer is the largest.

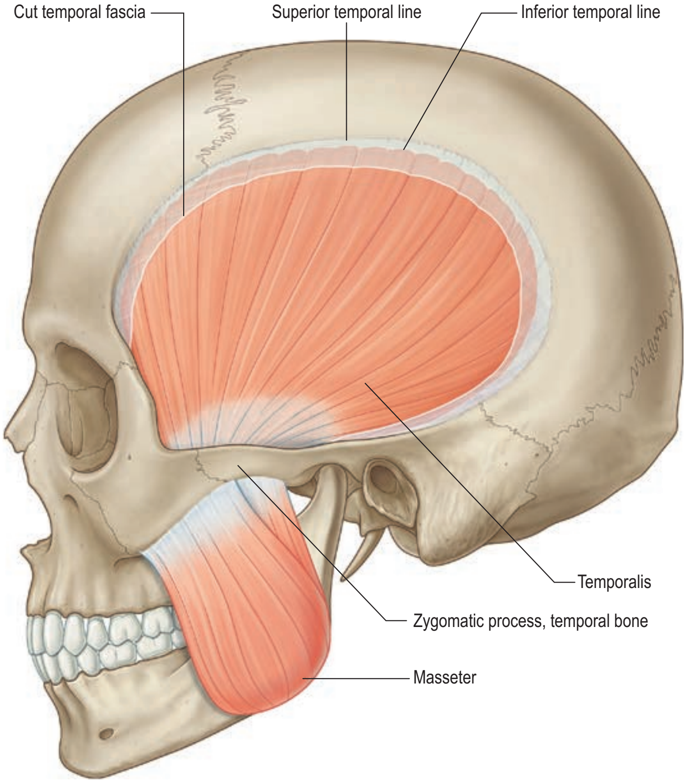

Fig. 38.18 Masseter and temporalis muscles. (Adapted with permission from Drake RL, Vogl AW, Mitchell A (eds) Gray's Anatomy for Students, 2nd ed. Elsevier, Churchill Livingstone. Copyright 2010.)

It arises by a thick aponeurosis from the maxillary process of the zygomatic bone and from the anterior two-thirds of the inferior border of the zygomatic arch. Its fibres pass downwards and backwards and are attached to the angle and lower posterior half of the lateral surface of the mandibular ramus. The superficial fibres are angled approximately 10° from the vertical, as is visible in lean individuals. In the coronal (frontal) plane, the muscle forms a 10° angle with the mandibular ramus. Intramuscular tendinous septa in this layer are responsible for the ridges on the surface of the ramus. The middle layer arises from the medial aspect of the anterior two-thirds of the zygomatic arch and from the lower border of the posterior third of this arch and is attached to the central part of the ramus of the mandible. The deep layer arises from the deep surface of the zygomatic arch and is attached to the upper part of the mandibular ramus and its coronoid process. The deep fibres run vertically and are evident just anterior to the temporomandibular joint, where they are not covered by the more superficial layers. There is still debate as to whether fibres of masseter are attached to the anterolateral part of the articular disc of the temporomandibular joint. Hypertrophy of the masseter may present either unilaterally or bilaterally. The aetiology is uncertain, but may be related to a clenching habit; there may be an associated prominence of the mandibular angle. Treatment can involve surgical reduction of the deep aspect of the muscle and contouring of the mandibular angle or, more commonly, injections of botulinum toxin to prevent function of the motor end plates with associated muscle atrophy.

Relations Skin, platysma, risorius, zygomaticus major, the parotid gland and duct, branches of the facial nerve and the transverse facial branches of the superficial temporal vessels are all superficial relations. Temporalis and the ramus of the mandible lie deep to masseter. The anterior margin of masseter is separated from buccinator and the buccal branch of the mandibular nerve by a buccal pad of fat and crossed by the facial vein. The posterior margin of the muscle is overlapped by the parotid gland. The masseteric nerve and artery reach the deep surface of masseter by passing over the mandibular incisure (mandibular notch).

Vascular supply Masseter is supplied by the masseteric branch of the maxillary artery, the facial artery and the transverse facial branch of the superficial temporal artery.

Innervation Masseter is supplied by the masseteric branch of the anterior trunk of the mandibular nerve.

Abnormalities of disc position (collectively known as internal derangements) can be a cause of joint noises (clicking), limitation of jaw movement and/or pain. The position of the disc is considered to be normal when, with the mandible at rest, the posterior band is positioned in the 12 o'clock position from the centre of the condyle in the sagittal plane. Displacement of the disc anteromedially is most common. MRI and arthrography have demonstrated that, although disc position and clinical symptoms are often linked, a significant proportion of subjects with apparently normal temporomandibular joint function have disc displacement on imaging and, conversely, patients with normally positioned discs may have severe restriction of mouth opening. Similarly, individuals with displaced discs who have undergone disc repositioning surgery often show functional improvement despite persistent displacement of their intra-articular disc and vice versa. Limited mouth opening is not always related to disc displacement or non-reducibility but may be the result of impaired joint lubrication, disc mobility and muscle spasm. In an otherwise asymptomatic jaw with normal movements, an anteriorly 'displaced' disc could be considered a normal variant (Stegenga and de Bont 2006) or, at the least, not an indication for treatment.

It would appear that the adaptive remodelling capacity of the joint (both the mandibular condyle and articular fossa) and adequate joint lubrication are important for maintaining function of the temporomandibular joint.

Actions Masseter elevates the mandible to occlude the teeth in mastication, and has a minor effect in side-to-side movements, protraction and retraction. Its electrical activity in the resting position of the mandible is minimal.

Submasseteric space infections

Available with the *Gray's Anatomy* e-book

Temporalis

Temporalis (see Figs 38.18, 38.20) arises from the whole of the temporal fossa up to the inferior temporal line, other than the part formed by the zygomatic bone, and from the deep surface of the temporal fascia. Its fibres converge and descend into a tendon that passes through the gap between the zygomatic arch and the side of the skull anterior and medial to the articular eminence. A plane exists beneath the temporal fascia attached to the superior surface of the zygomatic arch, and the muscle passing beneath the arch. An elevator introduced into this plane through an incision above the hairline may therefore be placed beneath a fractured zygomatic arch or bone in order to reduce the fracture (Gillies approach). Temporalis is attached to the medial surface, apex, anterior and posterior borders of the coronoid process and to the anterior border of the mandibular ramus almost up to the third molar tooth. Its anterior fibres are orientated vertically, the most posterior fibres almost horizontally, and the intervening fibres with intermediate degrees of obliquity, in the manner of a fan. Fibres of temporalis may occasionally gain attachment to the articular disc. Though less common than enlargement of masseter, hypertrophy of temporalis may develop unilaterally or bilaterally, producing prominence of the temporal fossa, which may be considered unsightly; botulinum toxin injections to prevent function of the motor end plates of the muscle fibres is the preferred treatment for this condition.

Relations Skin, auriculares anterior and superior, temporal fascia, superficial temporal vessels, the auriculotemporal nerve, temporal branches of the facial nerve, the zygomaticotemporal nerve, the epicranial aponeurosis, the zygomatic arch and masseter are all superficial relations. The posterior relations of temporalis are the temporal fossa above and the major components of the infratemporal fossa below. The masseteric vessels and nerve traverse the mandibular notch posterior to the tendon of temporalis. The anterior border of the muscle is separated from the zygomatic bone by an extension of the buccal fat pad.

Vascular supply

Temporalis is supplied by anterior and posterior deep temporal branches from the second part of the maxillary artery that enter its deep aspect, and middle temporal branches from the superficial temporal artery that enter its lateral aspect. There are significant vascular anastomoses within the muscle.

Innervation Temporalis is supplied by the anterior, middle and posterior deep temporal branches of the anterior trunk of the mandibular nerve.

Actions Temporalis elevates the mandible and so closes the mouth and approximates the teeth. This movement requires both the upward pull of the anterior fibres and the backward pull of the posterior fibres because the head of the mandibular condyle rests on the articular eminence when the mouth is open. The muscle also contributes to side-to-side grinding movements. The posterior fibres retract the mandible after it has been protruded. These fibres are almost horizontal and so are the only source of mandibular retrusion.

Lateral pterygoid

Lateral pterygoid is a short, thick muscle with two heads (Fig. 38.20). The upper (superior) head arises from the infratemporal surface and infratemporal crest of the greater wing of the sphenoid bone. The lower (inferior) head arises from the lateral surface of the lateral pterygoid plate. The fibres from the two heads converge and pass backwards and laterally, to be inserted into a depression, the pterygoid fovea, on the anterior aspect of the neck of the mandible. A part of the upper head may be attached to the capsule of the temporomandibular joint and to the anterior and medial borders of the articular disc. Unlike the other muscles of mastication, lateral pterygoid is not pennate, and few Golgi tendon organs are associated with its attachments.

Relations The mandibular ramus and masseter, the maxillary artery (which crosses either deep or superficial to lateral pterygoid), the superficial head of medial pterygoid and the tendon of temporalis are all superficial relations. The deep head of medial pterygoid, the sphenomandibular ligament, the middle meningeal artery and the mandibular nerve are all deep relations. The upper border is related to the temporal and masseteric branches of the mandibular nerve and the lower border is related to the lingual and inferior alveolar nerves. A deeply placed posterior superior alveolar nerve block has been known also to anaesthetize the lingual nerve. The buccal nerve and the maxillary artery pass

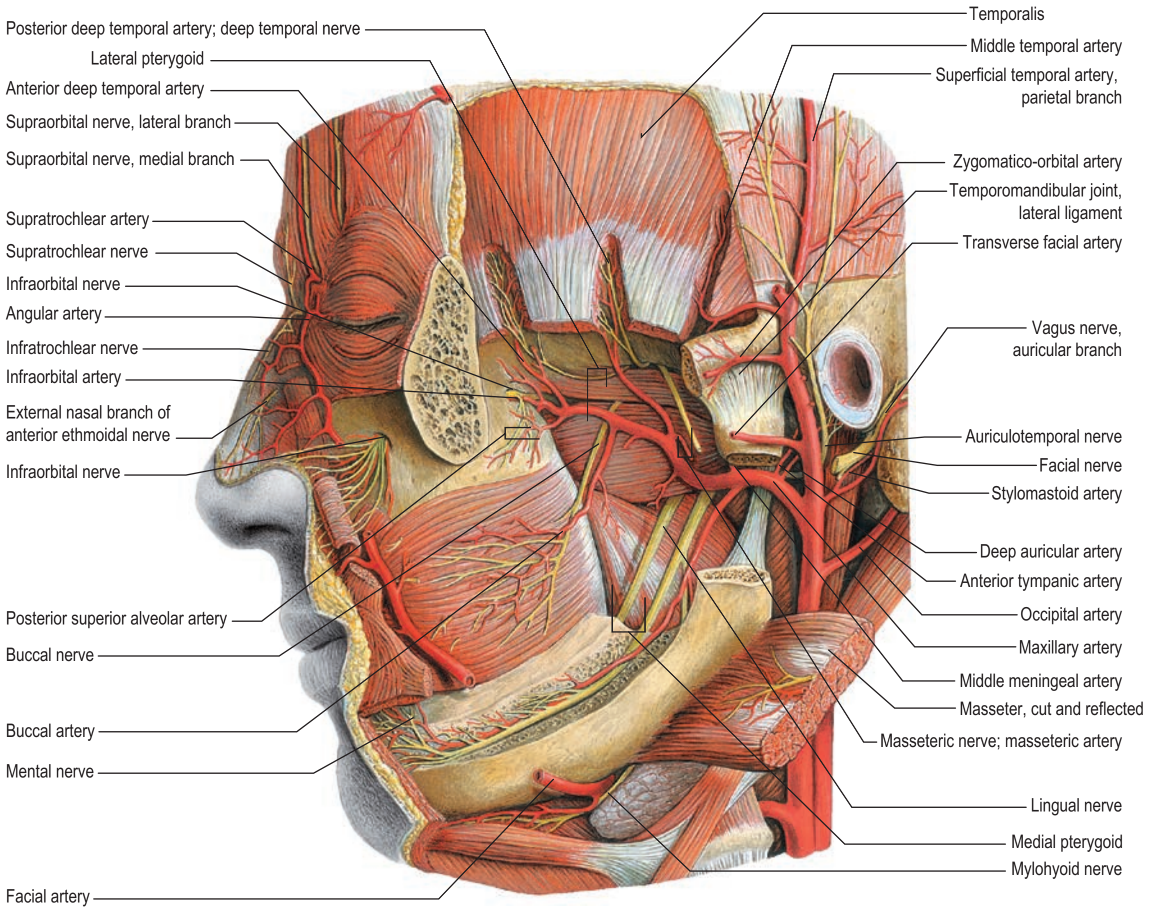
Posterior deep temporal artery; deep temporal nerve
Lateral pterygoid
Anterior deep temporal artery
Supraorbital nerve, lateral branch
Supraorbital nerve, medial branch
Supratrochlear artery
Supratrochlear nerve
Infraorbital nerve
Angular artery
Infratrochlear nerve
Infraorbital artery
External nasal branch of anterior ethmoidal nerve
Infraorbital nerve
Posterior superior alveolar artery
Buccal nerve
Buccal artery
Mental nerve
Facial artery
Temporalis
Middle temporal artery
Superficial temporal artery, parietal branch
Zygomatico-orbital artery
Temporomandibular joint, lateral ligament
Transverse facial artery
Vagus nerve, auricular branch
Auriculotemporal nerve
Facial nerve
Stylomastoid artery
Deep auricular artery
Anterior tympanic artery
Occipital artery
Maxillary artery
Middle meningeal artery
Masseter, cut and reflected
Masseteric nerve; masseteric artery
Lingual nerve
Medial pterygoid
Mylohyoid nerve

Fig. 38.20 Arteries and nerves of the head; deeper lateral regions. Most of the zygomatic arch and the ramus and body of the mandible have been removed; masseter has been cut and reflected laterally. (Sobotta Atlas of Human Anatomy © Elsevier GmbH, Urban & Fischer, Munich.)

Infection around a mandibular third molar tooth sometimes tracks backwards, lateral to the mandibular ramus, and purulence localizes in the submasseteric tissue space deep to the attachment of masseter to the ramus of the mandible. An abscess lying deep to this thick muscle produces little visible swelling but is accompanied by profound muscle spasm and severe limitation of jaw opening (trismus).

The arterial supply is axial, i.e. the vessels run the entire length of the muscle. It is this vascular arrangement that permits the use of temporalis as an inferiorly based pedicled flap, either dynamic or static (increased length being obtained with division of the coronoid process), for the reconstruction of a variety of local facial and oral defects and in the treatment of facial paralysis. The temporalis fascia can be incorporated with the flap. The muscle may be split longitudinally (along its long axis), retaining its axial supply from individual arteries: the vessels are identified at operation with Doppler ultrasound if necessary. A further vascular advantage is that the arterial supply is disposed medially (deep temporal) and laterally (middle temporal), and there are few vessels in the mid-sagittal plane, which means that splitting the muscle flap in the sagittal plane is possible (Fig. 38.19) (Cheung 1996).

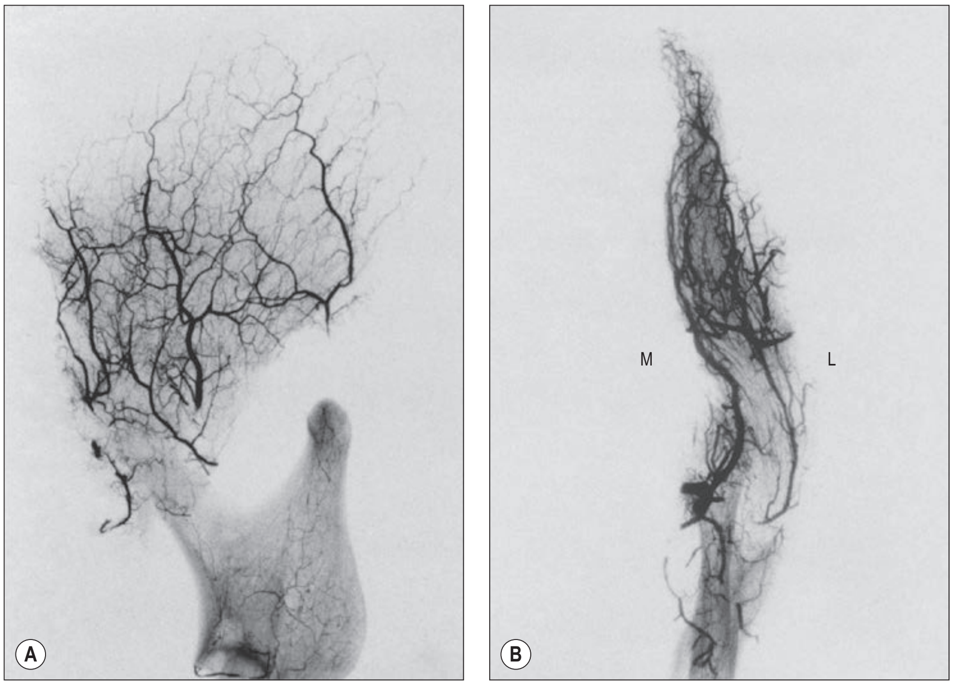

Fig. 38.19 The arterial network of the human temporalis. **A**, Lateral plane. **B**, Coronal plane. In the lateral plane, the muscle is supplied by the three primary arteries: the anterior deep temporal artery in the anterior portion, the posterior deep temporal artery in the mid-portion and the middle deep temporal artery in the posterior portion. In the coronal plane, the arterial distribution is concentrated mainly lateral (L) and medial (M) with less vascular density in the mid-sagittal region of the muscle. (With permission from Cheung LK 1996 The vascular anatomy of the human temporalis muscle: implications for surgical splitting techniques. Int J Oral Maxillofac Surg 25:414–421.)

between the two heads of lateral pterygoid. In temporomandibular joint dysfunction syndrome, spasm of lateral pterygoid can give rise to tenderness when palpating high in the buccal sulcus behind the maxillary tuberosity (the pterygoid sign).

Vascular supply Lateral pterygoid is supplied by the ascending palatine branch of the facial artery and by pterygoid branches of the maxillary artery given off as the artery crosses the muscle.

Innervation The nerves to lateral pterygoid (one for each head) arise from the anterior trunk of the mandibular nerve, deep to the muscle. The upper head and the lateral part of the lower head are innervated by a branch given off from the buccal nerve. The medial part of the lower head is innervated by a branch that arises directly from the anterior trunk of the mandibular nerve.

Actions Lateral pterygoid has assumed a specialized role in mandibular opening that is mediated by its horizontally orientated fibres. When left and right muscles contract together, the condyle is pulled forwards and slightly downwards. This protrusive movement alone has little or no function except to assist in opening the jaw. Digastric and geniohyoid are the main jaw opening muscles: unlike lateral pterygoid, when acting alone, they rotate the jaw open, provided other muscles attached to the hyoid prevent it from being pulled forwards. If only one lateral pterygoid contracts, the jaw rotates about a vertical axis passing roughly through the opposite condyle and is pulled medially towards the opposite side. This contraction, together with that of the adjacent medial pterygoid (both attached to the lateral pterygoid plate), provides most of the strong medially directed component of the force used when grinding food between teeth of the same side. It is arguably the most important function of the lower head of lateral pterygoid.

It is often stated that the upper head is used to pull the articular disc forwards when the jaw is opened. However, electromyographic studies (e.g. McNamara 1973, Juniper 1981) have demonstrated that the upper and lower heads are reciprocally innervated, so that the lower head contracts during mouth opening whilst the upper head relaxes, the situation reversing during closure. An explanation for this surprising activity is as follows (Osborn 1995). Most of the power of a clenching force is due to contractions of masseter and temporalis. The associated backward pull of temporalis is greater than the associated forward pull of (superficial) masseter, and so their combined jaw-closing action potentially pulls the condyle backwards. This is prevented by the simultaneous contraction of the upper head of lateral pterygoid, which stabilizes the condylar head against the articular eminence during closure, particularly during biting and mastication.

Medial pterygoid

Medial pterygoid is a thick, quadrilateral muscle with two heads (see Fig. 38.20). Mirroring masseter (which lies laterally), its fibres descend posteroinferiorly at an angle of about 10° to the vertical. In the coronal plane, the muscle forms a 30° angle with the ramus. The major component is the deep head which arises from the medial surface of the lateral pterygoid plate of the sphenoid bone and is therefore deep to the lower head of lateral pterygoid. The small, superficial head arises from the maxillary tuberosity and the pyramidal process of the palatine bone, and therefore lies on the lower head of lateral pterygoid. The fibres of medial pterygoid descend posterolaterally and are attached by a strong tendinous lamina to the posteroinferior part of the medial surface of the ramus and angle of the mandible, as high as the mandibular foramen and almost as far anteriorly as the mylohyoid groove. This area of attachment is often ridged. Inferior alveolar nerve block injection can occasionally cause haemorrhage into the muscle, which may give rise to painful trismus. Medial pterygoid and masseter act together to support the angle of the mandible as the pterygomasseteric sling: their strong muscle attachments resist lengthening of the mandibular ramus surgically.

Relations The lateral surface of medial pterygoid is related to the mandibular ramus, from which it is separated above its insertion by lateral pterygoid, the sphenomandibular ligament, the maxillary artery, the inferior alveolar vessels and nerve, the lingual nerve and a process of the parotid gland. The medial surface is related to tensor veli palatini and is separated from the superior pharyngeal constrictor by styloglossus and stylopharyngeus and by some areolar tissue.

Vascular supply Medial pterygoid derives its main arterial supply from the pterygoid branches of the maxillary artery.

Innervation Medial pterygoid is innervated by the medial pterygoid branch of the mandibular nerve.

Actions The medial pterygoids assist in elevating the mandible. Acting with the lateral pterygoids, they protrude it. When the medial and lateral pterygoids of one side act together, the corresponding side of the mandible is rotated both forwards and to the opposite side, with the opposite mandibular head as a vertical axis. Alternating activity in the left and right sets of muscles produces side-to-side movements, which are used to triturate food.

Pterygospinous ligament

The pterygospinous ligament, which is occasionally replaced by muscle fibres, stretches between the spine of the sphenoid bone and the posterior border of the lateral pterygoid plate near its upper end. It is sometimes ossified, and then completes a foramen that transmits the branches of the mandibular nerve to temporalis, masseter and lateral pterygoid.

Vascular supply and lymphatic drainage

Maxillary artery

The maxillary artery, the larger terminal branch of the external carotid artery, arises behind the neck of the mandible and is at first embedded in the parotid gland. It then crosses the infratemporal fossa to enter the pterygopalatine fossa through the pterygomaxillary fissure. The artery is widely distributed to the mandible, maxilla, teeth, muscles of mastication, palate, nasal cavity and cranial dura mater (see Fig. 38.20; **Fig. 38.21**). It will be described in three parts: mandibular, pterygoid and pterygopalatine.

The mandibular part runs horizontally by the medial surface of the ramus and passes between the neck of the mandible and the sphenomandibular ligament, parallel with and slightly below the auriculotemporal nerve. It next crosses the inferior alveolar nerve and skirts the lower border of lateral pterygoid. The pterygoid part ascends obliquely forwards medial to temporalis and is usually superficial to the lower head of lateral pterygoid. When it runs deep to lateral pterygoid, it lies between the muscle and branches of the mandibular nerve and may project as a lateral loop between the two parts of lateral pterygoid. Asymmetry in this pattern of distribution may occur between the right and left infratemporal fossae. Where the maxillary artery runs superficial to the lower head of lateral pterygoid, the most common pattern is that the artery passes lateral to the inferior alveolar, lingual and buccal nerves. Less frequently, only the buccal nerve crosses the artery laterally, and rarely the artery can pass deep to all the branches of the mandibular nerve. The pterygopalatine part passes between the two heads of lateral pterygoid to reach the pterygomaxillary fissure before it passes into the pterygopalatine fossa, where it terminates as the third part of the maxillary artery. The mandibular part of the maxillary artery has five branches that all enter bone. The branches are the deep auricular, anterior tympanic, middle meningeal, accessory meningeal and inferior alveolar arteries. The pterygoid part of the maxillary artery has five branches that do not enter bone but supply muscle, and include the deep temporal, pterygoid, masseteric and buccal arteries. The branches of the pterygopalatine part of the artery accompany similarly named branches of the maxillary nerve (including those associated with the pterygopalatine ganglion) and are described on pp. 682–683.

Deep auricular artery

The deep auricular artery pierces the osseous or cartilaginous wall of the external acoustic meatus and supplies the skin of the external acoustic meatus and part of the tympanic membrane. A small branch contributes to the arterial supply of the temporomandibular joint.

Anterior tympanic artery

The anterior tympanic artery passes through the petrotympanic fissure to supply part of the lining of the middle ear and accompanies the chorda tympani nerve.

Middle meningeal artery

The middle meningeal artery is the main source of blood to the calvaria (**Fig. 38.22**). It may arise either directly from the first part of the maxillary artery or from a common trunk with the inferior alveolar artery. When the maxillary artery lies superficial to lateral pterygoid, the middle meningeal artery is usually the first branch of the maxillary artery: this is not usually the case when the maxillary artery takes a deep course in relation to the muscle. The middle meningeal artery ascends between the sphenomandibular ligament and lateral pterygoid, passes between the two roots of the auriculotemporal nerve, and leaves the infratemporal fossa through the foramen spinosum to enter the cranial cavity medial

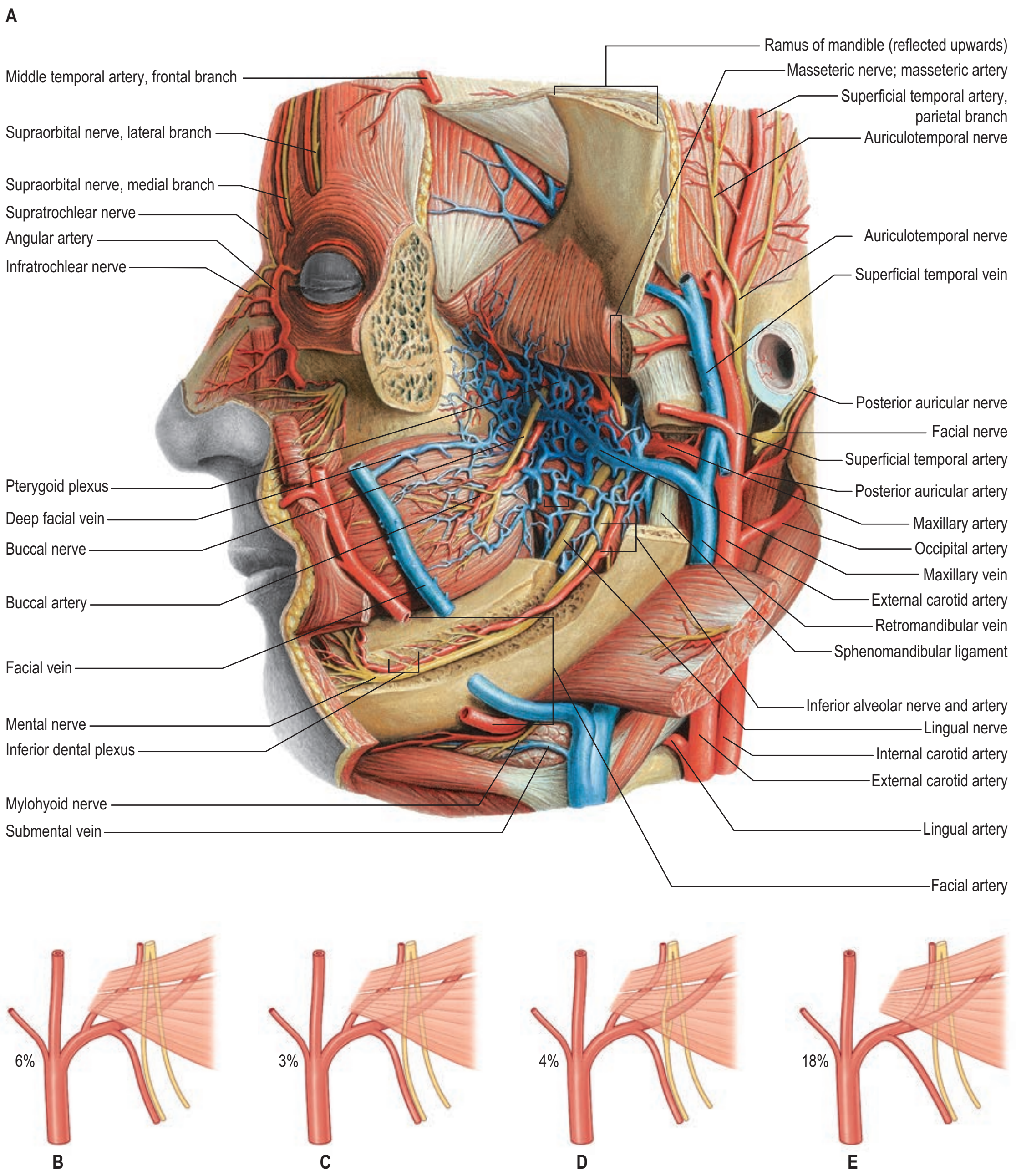
A
Middle temporal artery, frontal branch
Supraorbital nerve, lateral branch
Supraorbital nerve, medial branch
Supratrochlear nerve
Angular artery
Infratrochlear nerve
Pterygoid plexus
Deep facial vein
Buccal nerve
Buccal artery
Facial vein
Mental nerve
Inferior dental plexus
Mylohyoid nerve
Submental vein
Ramus of mandible (reflected upwards)
Masseteric nerve; masseteric artery
Superficial temporal artery, parietal branch
Auriculotemporal nerve
Auriculotemporal nerve
Superficial temporal vein
Posterior auricular nerve
Facial nerve
Superficial temporal artery
Posterior auricular artery
Maxillary artery
Occipital artery
Maxillary vein
External carotid artery
Retromandibular vein
Sphenomandibular ligament
Inferior alveolar nerve and artery
Lingual nerve
Internal carotid artery
External carotid artery
Lingual artery
Facial artery
6%
B
3%
C
4%
D
18%
E

Fig. 38.21 A, Vessels and nerves of the head, exposed at a level deeper than that shown in Fig. 38.20. Note the pterygoid venous plexus. **B–E**, Variations in the course of the maxillary artery. **B**, The maxillary artery passes medial to lateral pterygoid, and to the lingual and inferior alveolar nerves. **C**, The artery passes between the lingual and inferior alveolar nerves. **D**, The artery passes through a loop formed by the inferior alveolar nerve. **E**, The middle meningeal artery branches off distal to the inferior alveolar artery. (Sobotta Atlas of Human Anatomy © Elsevier GmbH, Urban & Fischer, Munich.)

to the midpoint of the zygomatic bone. Its further course is described in Chapter 25.

Accessory meningeal artery

The accessory meningeal artery runs through the foramen ovale into the middle cranial fossa and may arise directly from the maxillary artery or as a branch of the middle meningeal artery itself. In its course in the infratemporal fossa, the accessory meningeal artery is closely related to tensor veli palatini and levator veli palatini and usually runs deep to the mandibular nerve. Although it runs intracranially, its main distribution is extracranial, principally to medial pterygoid, lateral pterygoid (upper head), tensor veli palatini, the greater wing and pterygoid processes of the sphenoid, branches of the mandibular nerve and the otic ganglion. The accessory meningeal artery is sometimes replaced by several separate small arteries.

Inferior alveolar artery

The inferior alveolar artery descends in the infratemporal fossa posterior to the inferior alveolar nerve, between the ramus laterally and the sphenopalatine ligament medially. It gives off two anterior branches before entering the mandibular foramen. The further course of the artery is described in Chapter 37.

Deep temporal arteries

The arterial supply to the temporalis in the coronal plane is concentrated mainly on its medial and lateral aspects. The anterior and posterior branches of the deep temporal arteries pass between temporalis and the pericranium, producing shallow grooves in the bone. They anastomose with the middle temporal branch of the superficial temporal artery situated laterally (Cheung 1996). The anterior deep temporal artery anastomoses with the lacrimal artery by small branches that perforate the zygomatic bone and greater wing of the sphenoid.

Masseteric artery

The masseteric artery is small and accompanies the masseteric nerve as it passes through the mandibular incisure (notch), posterior to the tendon of temporalis, to enter the deep surface of masseter (see Fig. 38.20). Its branches can also supply the temporomandibular joint. The masseteric artery anastomoses with the masseteric branches of the facial artery and with the transverse facial branch of the superficial temporal artery. This vessel is at risk and may cause considerable bleeding if damaged when the sigmoid notch is entered or split surgically.

Pterygoid arteries

The pterygoid arteries are irregular in number and origin, and are distributed to lateral and medial pterygoid.

Buccal artery

The buccal artery runs obliquely forwards between medial pterygoid and the attachment of temporalis, accompanying the lower part of the buccal branch of the mandibular nerve to supply the skin and mucosa over buccinators (see Fig. 38.21A). It anastomoses with branches of the facial and infraorbital arteries. A small lingual branch may be given off to accompany the lingual nerve and supply structures in the floor of the mouth.

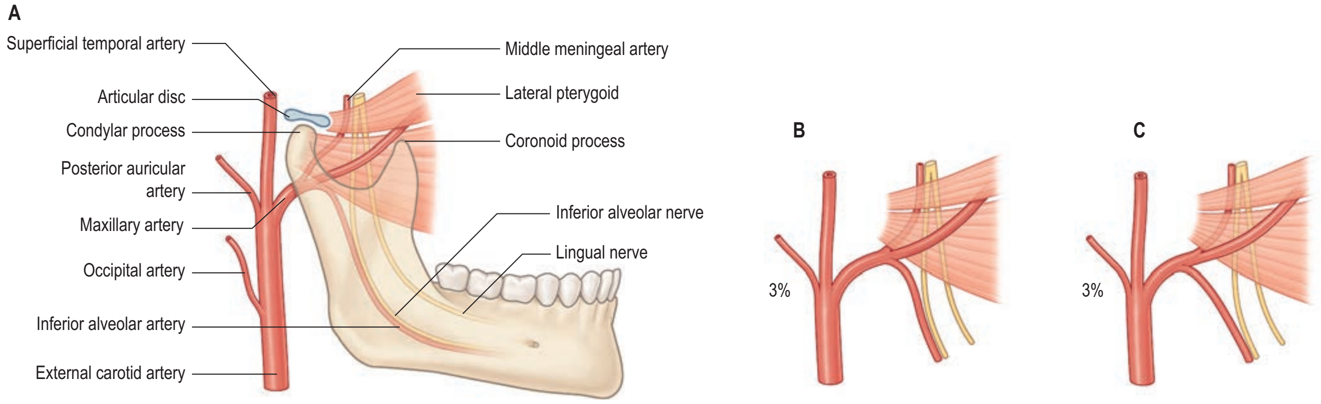

Fig. 38.22 Variations in the origin of the middle meningeal artery. **A**, The middle meningeal artery branches off proximal to the inferior alveolar artery. **B**, The artery branches off opposite the inferior alveolar artery. **C**, The artery branches off distal to the inferior alveolar artery. (Sobotta Atlas of Human Anatomy © Elsevier GmbH, Urban & Fischer, Munich.)

Maxillary veins and the pterygoid venous plexus

Maxillary vein

The maxillary vein is a short trunk that accompanies the first part of the maxillary artery (see Fig. 38.21A). It is formed from the confluence of veins from the pterygoid plexus and passes back between the sphenomandibular ligament and the neck of the mandible to enter the parotid gland. It unites within the substance of the gland with the superficial temporal vein to form the retromandibular vein.

Pterygoid venous plexus

The pterygoid plexus of veins consists of copious large calibre veins that surround the pterygoid segment of the maxillary artery. It is found partly between temporalis and lateral pterygoid, and partly between the two pterygoid muscles. Sphenopalatine, deep temporal, pterygoid, masseteric, buccal, alveolar (dental), greater palatine and middle meningeal veins and a branch or branches from the inferior ophthalmic vein are all tributaries. The plexus is connected with the facial vein via the deep facial vein; with the cavernous sinus through veins that pass through the sphenoidal emissary foramen (of Vesalius), foramen ovale and foramen lacerum; and with the orbit via the inferior ophthalmic vein(s). Its deep temporal tributaries often connect with tributaries of the anterior diploic veins and thus with the middle meningeal veins.

Lymphatic drainage

Lymphatic drainage of the infratemporal fossa (and the temporal fossa) is to the superior deep cervical nodes.

Innervation

The infratemporal fossa contains the major subdivisions of the mandibular branch of the trigeminal nerve, together with the chorda tympani, which enters the fossa and joins the lingual nerve, and the otic ganglion, which is functionally related to the parotid gland. The main sensory branches of the mandibular nerve extend beyond the infratemporal fossa and their distribution to the face is described in Chapter 36.

Mandibular nerve

The mandibular nerve is the largest trigeminal division and is a mixed nerve. Its sensory branches supply the teeth and gingivae of the mandible, the skin in the temporal region, part of the auricle, including the external acoustic meatus and tympanic membrane, and the lower lip, the lower part of the face and the mucosa of the anterior two-thirds (presulcal part) of the tongue and the floor of the oral cavity (see Figs 38.20, 38.21A; **Fig. 38.23**). The motor branches innervate the muscles of mastication. The large sensory root emerges from the lateral part of the trigeminal ganglion and exits the cranial cavity through the foramen ovale. The small motor root passes under the ganglion and through the foramen ovale to unite with the sensory root just outside the skull. As it descends from the foramen ovale, the nerve is usually around 4 cm from the surface and a little anterior to the neck of the mandible. The mandibular nerve immediately passes between tensor veli palatini medially, and lateral pterygoid laterally, and gives off a meningeal branch and the nerve to medial pterygoid from its medial side. The nerve then divides into a small anterior and large posterior trunk. The anterior division gives off branches to the four main muscles of mastication and a buccal branch that is sensory to the cheek. The posterior division gives off three main sensory branches, the auriculotemporal, lingual and inferior alveolar nerves, and motor fibres that supply mylohyoid and the anterior belly of digastric.

As is the case with the extraocular muscles, the masticatory muscles function as a group; only when pathology intervenes do their individual actions, or lack of action, become apparent. Wasting of the masticatory muscles, most evident in the temporal fossa, happens when tumours affect the motor root of the mandibular nerve. The mandible deviates to the side of the pathology as a result of the unopposed action of the contralateral lateral and medial pterygoids.

Meningeal branch (nervus spinosus)

The meningeal branch re-enters the cranium through the foramen spinosum with the middle meningeal artery. It divides into anterior and posterior branches that accompany the main divisions of the middle meningeal artery and supply the dura mater in the middle cranial fossa and, to a lesser extent, in the anterior fossa and calvaria.

Nerve to medial pterygoid

The nerve to medial pterygoid is a slender ramus that enters the deep aspect of the muscle. It supplies one or two filaments that pass through the otic ganglion without interruption to supply tensor tympani and tensor veli palatini.

Anterior trunk of mandibular nerve

The anterior trunk of the mandibular nerve gives rise to the buccal nerve, which is sensory, and the masseteric, deep temporal and lateral pterygoid nerves, which are all motor.

Buccal nerve

The buccal nerve passes between the two heads of lateral pterygoid (see Fig. 38.23). It descends deep to the tendon of temporalis, passes laterally anterior to masseter, and anastomoses with the buccal branches of the facial nerve. It carries motor fibres to lateral pterygoid that are given off as the buccal nerve passes through the muscle. It may also give off the anterior deep temporal nerve. The buccal nerve supplies sensation to the skin over the anterior part of buccinator and the buccal mucous membrane, and the posterior part of the buccal gingivae adjacent to the second and third molar teeth.

Nerve to masseter

The nerve to masseter passes laterally above lateral pterygoid, on to the skull base, anterior to the temporomandibular joint and posterior to the tendon of temporalis. It crosses the posterior part of the mandibular notch with the masseteric artery, ramifying on and then entering the deep surface of masseter. Its articular branches innervate the temporomandibular joint.

Deep temporal nerves

There are usually two deep temporal nerves, anterior and posterior; there may be a middle branch. The nerves pass superior to lateral pterygoid to enter the deep surface of temporalis.

The anterior deep temporal nerve can arise from the buccal nerve, and the posterior deep temporal nerve can arise from the nerve to masseter. Branches from the buccal and masseteric nerves may supply the inferior aspect of the muscle independently from the deep temporal nerves. Discrete neuromuscular subunits based on the anterior, middle and posterior deep temporal nerves have been identified within the muscle, suggesting the possibility of individual dynamic muscle flaps, each with a different vector, in the treatment of facial palsy (Chang et al 2013) (**Fig. 38.24**).

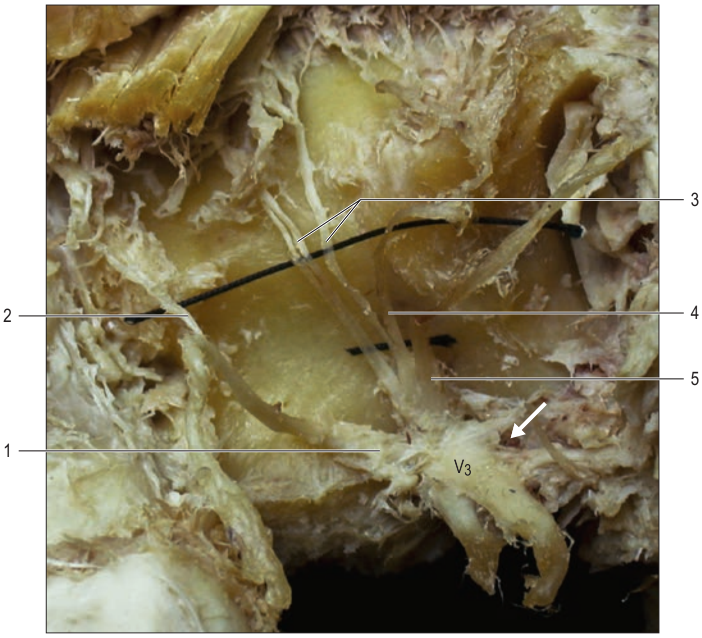

Fig. 38.24 The foramen ovale, inferolateral view. Nerves supplying temporalis originate from the anterior trunk of the mandibular division of the trigeminal nerve V_3 (arrow). Key: 1, (long) buccal nerve; 2, anterior deep temporal nerve; 3, middle deep temporal nerve; 4, posterior deep temporal nerve; 5, nerve to masseter. (Courtesy of David Cantelmi, University of Toronto, Canada. With permission from Chang Y, Cantelmi D, Wisco J et al 2013 Evidence for the functional compartmentalization of the temporalis muscle: a 3-dimensional study of innervation. J Oral Maxillofac Surg 71:1170–7.)

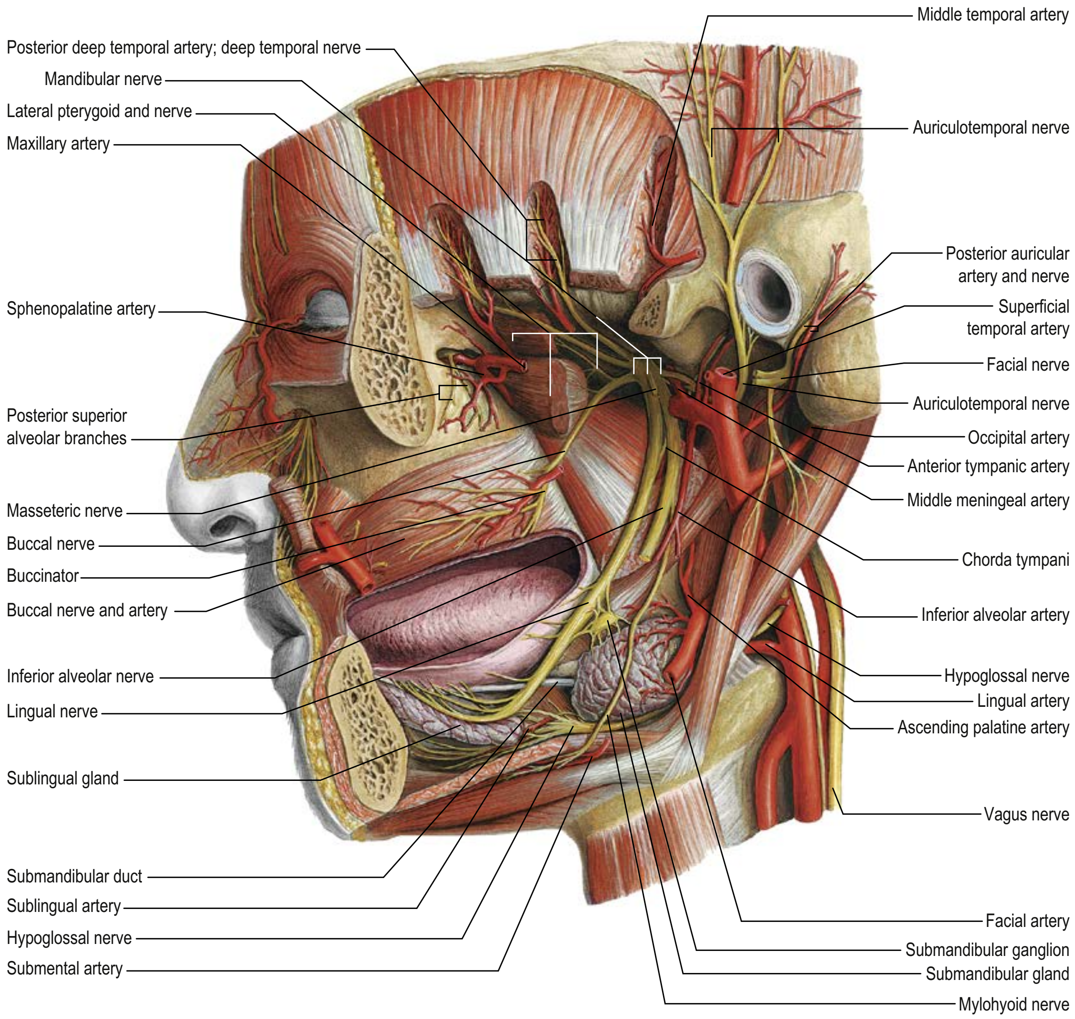
Posterior deep temporal artery; deep temporal nerve
Mandibular nerve
Lateral pterygoid and nerve
Maxillary artery
Sphenopalatine artery
Posterior superior alveolar branches
Masseteric nerve
Buccal nerve
Buccinator
Buccal nerve and artery
Inferior alveolar nerve
Lingual nerve
Sublingual gland
Submandibular duct
Sublingual artery
Hypoglossal nerve
Submental artery
Middle temporal artery
Auriculotemporal nerve
Posterior auricular artery and nerve
Superficial temporal artery
Facial nerve
Auriculotemporal nerve
Occipital artery
Anterior tympanic artery
Middle meningeal artery
Chorda tympani
Inferior alveolar artery
Hypoglossal nerve
Lingual artery
Ascending palatine artery
Vagus nerve
Facial artery
Submandibular ganglion
Submandibular gland
Mylohyoid nerve

Fig. 38.23 Arteries and nerves of the head, deepest lateral regions. Compare with Figs 38.20 and 38.21A. (Sobotta Atlas of Human Anatomy © Elsevier GmbH, Urban & Fischer, Munich.)

Nerve to lateral pterygoid

The nerve to lateral pterygoid enters the deep surface of the muscle and may arise separately from the anterior division of the mandibular nerve or from the buccal nerve.

Posterior trunk of mandibular nerve

The posterior trunk of the mandibular nerve is larger than the anterior and is mainly sensory, although it receives fibres from the motor root for the nerve to mylohyoid. It divides into auriculotemporal, lingual and inferior alveolar (dental) nerves (see Fig. 38.23).

Auriculotemporal nerve

The auriculotemporal nerve usually has two roots that encircle the middle meningeal artery. It runs back under lateral pterygoid on the surface of tensor veli palatini, passes between the sphenomandibular ligament and the neck of the mandible, and then runs laterally posterior to the temporomandibular joint related to the upper part of the parotid gland. Emerging from behind the joint, it ascends over the posterior root of the zygoma, posterior to the superficial temporal vessels, and divides into superficial temporal branches. It communicates with the facial nerve and otic ganglion. The rami to the facial nerve, usually two, pass anterolaterally behind the neck of the mandible to join the facial nerve at the posterior border of masseter. Filaments from the otic ganglion join the roots of the auriculotemporal nerve close to their origin. The sensory distribution of the auriculotemporal nerve on the face is described in Chapter 36.

Lingual nerve

The lingual nerve is sensory to the mucosa of the anterior two-thirds of the tongue, the floor of the mouth and the mandibular lingual gingivae. It arises from the posterior trunk of the mandibular nerve and at first runs beneath lateral pterygoid and superficial to tensor veli palatini, where it is joined by the chorda tympani branch of the facial nerve, and often by a branch of the inferior alveolar nerve. Emerging from under cover of lateral pterygoid, the lingual nerve then runs downwards and forwards on the surface of medial pterygoid (see Fig. 38.23), and is thus carried progressively closer to the medial surface of the mandibular ramus. It becomes intimately related to the bone a few millimetres below and behind the junction of the vertical ramus and horizontal body of the mandible. Here it lies anterior to, and slightly deeper than, the inferior alveolar nerve. It next passes below the mandibular attachment of the superior pharyngeal constrictor and pterygomandibular raphe, closely applied to the periosteum of the medial surface of the mandible, until it lies opposite the posterior root of the third molar tooth, where it is covered only by the gingival mucoperiosteum. At this point, it usually lies approximately 3 mm below the alveolar crest with a mean distance from the bone of 2 mm. In more than 25% of cases, the nerve may be in direct contact with the bone at this site, but sometimes it lies above the alveolar crest. It next passes medial to the mandibular origin of mylohyoid, which carries it progressively away from the mandible and separates it from the alveolar bone that covers the mesial root of the third molar tooth (Pogrel et al 1995). The rest of the nerve is described with the oral cavity in Chapter 37.

Inferior alveolar (dental) nerve

The inferior alveolar nerve descends behind lateral pterygoid. At the lower border of the muscle, the nerve passes between the sphenomandibular ligament and the mandibular ramus and enters the mandibular canal via the mandibular foramen (Barker and Davies 1972). Below lateral pterygoid, it is accompanied by the inferior alveolar artery (see Fig. 38.23), a branch of the first part of the maxillary artery that also enters the canal with associated veins. The subsequent course of the inferior alveolar nerve is described in Chapter 37.

Neural anastomoses with the mandibular nerve

Available with the *Gray's Anatomy* e-book

Otic ganglion

The otic ganglion is a small (major diameter 3–4 mm), oval, flat reddish-grey ganglion situated just below the foramen ovale. It is a peripheral

There are anastomoses between branches of the mandibular division of the trigeminal nerve and branches of the facial nerve. The connection between the lingual nerve and the chorda tympani (facial nerve) is the most familiar interconnection. Connections have also been demonstrated between the auriculotemporal nerve and branches of the facial nerve (**Fig. 38.25**); the buccal branch of the mandibular division of the trigeminal nerve and the buccal and zygomatic branches of the facial via the 'communicating buccal nerve'; and between the mental nerve and the buccal and marginal mandibular branch of the facial nerve. The functional significance of these neural connections is unclear, but may be related to the proprioceptive innervation of the facial musculature (Shoja et al 2014). A branch from the auriculotemporal nerve may join the inferior alveolar nerve within the infratemporal fossa with evident implications for referred pain.

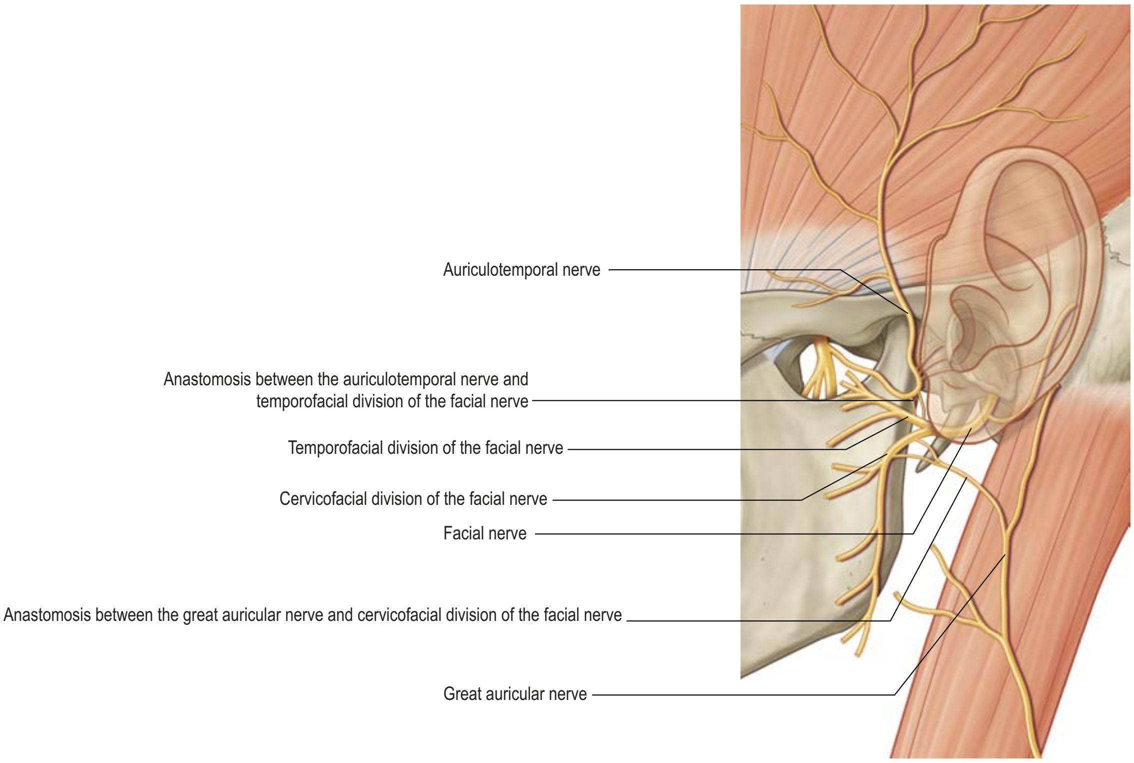
Auriculotemporal nerve
Anastomosis between the auriculotemporal nerve and temporofacial division of the facial nerve
Temporofacial division of the facial nerve
Cervicofacial division of the facial nerve
Facial nerve
Anastomosis between the great auricular nerve and cervicofacial division of the facial nerve
Great auricular nerve

Fig. 38.25 Anastomoses of the auriculotemporal nerve with the temporofacial division of the facial nerve, and of the great auricular nerve with the cervicofacial division of the facial nerve in the parotid and periparotid regions. (With permission from Shoja MM, Oyesiku NM, Grissenauer CJ et al 2014 Anastomoses between lower cranial and upper cervical nerves: a comprehensive review with potential significance during skull base and neck operations, Part 1: Trigeminal, facial and vestibulocochlear nerves. Clin Anat 27:118–30.)

parasympathetic ganglion related topographically to the mandibular nerve but connected functionally with the glossopharyngeal nerve (see Fig. 42.11). Near its junction with the trigeminal motor root, the mandibular nerve lies lateral to the ganglion, tensor veli palatini lies medially, separating the ganglion from the cartilaginous part of the pharyngotympanic tube, and the middle meningeal artery is posterior to the ganglion. The otic ganglion usually surrounds the origin of the nerve to medial pterygoid. It has three roots, parasympathetic motor, sympathetic and sensory: only the parasympathetic fibres relay in the ganglion (see Fig. 33.7). The parasympathetic fibres arise from cell bodies in the inferior salivatory nucleus and travel in the lesser petrosal branch of the glossopharyngeal nerve. The lesser petrosal nerve runs intracranially in the middle cranial fossa on the anterior surface of the petrous temporal bone and passes through either the foramen ovale or the sphenopetrosal fissure or the innominate canal of Arnold (a canal in the greater wing of the sphenoid close to the foramen spinosum), to join the otic ganglion where it synapses. Postganglionic fibres pass by a communicating branch to the auriculotemporal nerve to reach the parotid gland. The sympathetic root arises from a plexus on the middle meningeal artery. It contains postganglionic vasomotor fibres from the superior cervical sympathetic ganglion that pass through the otic ganglion and join the parasympathetic fibres to travel via the auriculotemporal nerve to the parotid gland. Sensory fibres from the parotid gland are derived from the auriculotemporal nerve. Clinical observations suggest that in humans the parotid gland also receives secretomotor parasympathetic fibres through the chorda tympani.

Branches

The otic ganglion is connected by branches to the chorda tympani nerve and the nerve of the pterygoid canal. These branches may form an additional pathway by which gustatory fibres from the anterior two-thirds of the tongue reach the geniculate ganglion without passing through the middle ear: they do not synapse in the otic ganglion. Motor branches to tensor veli palatini and tensor tympani, derived from the nerve to medial pterygoid, pass through the ganglion without synapsing. (For further reading, see Senger et al (2014).)

Chorda tympani

The chorda tympani nerve enters the infratemporal fossa by passing through the medial end of the petrotympanic fissure posterior to the capsule of the temporomandibular joint. The nerve descends medial to the spine of the sphenoid bone, which it sometimes grooves, lying posterolateral to tensor veli palatini. It is crossed medially by the middle meningeal artery, the roots of the auriculotemporal nerve and the inferior alveolar nerve (see Fig. 38.23). It joins the posterior aspect of the lingual nerve at an acute angle. It carries taste fibres from the anterior two-thirds of the tongue and efferent preganglionic parasympathetic secretomotor fibres destined for the submandibular ganglion in the floor of the mouth.

Spread of infection from the infratemporal fossa

Infections from most teeth in the upper jaw or the anterior part of the lower jaw usually drain harmlessly into the oral cavity, either via the vestibule buccally, or via the palate or mouth lingually. In contrast, a pericoronitis that affects a mandibular third molar tooth that communicates with the oral cavity, or, less commonly, either a dental abscess associated with this tooth, or a postoperative infection, can spread along tissue planes. Spread may be buccal, submandibular, submental, parapharyngeal, sublingual, or less commonly, submasseteric and, rarely, infratemporal. The main symptom caused by infection of the pterygomandibular space is trismus (painful reflex muscle spasm) that usually affects medial pterygoid. There are few anatomical barriers to the spread of infection from this space. When the submandibular, sublingual and submental areas are affected either unilaterally or bilaterally (bilateral involvement is known as Ludwig's angina), there is a risk of airway obstruction. Infection may (potentially) spread further, usually to the parapharyngeal, and occasionally to the retropharyngeal spaces, with the possibility of spread into the mediastinum inferiorly. Superior spread can even reach the orbit via the inferior orbital fissure. Life-threatening cavernous sinus thrombosis is a remote possibility once infection has spread to the orbit, with further spread directly through the superior orbital fissure into the cranial cavity. Infection can also spread to the cavernous sinus from the pterygoid plexus and ophthalmic veins (Smyth 2007, Guidera et al 2014) (**Fig. 38.26**).

PTERYGOPALATINE FOSSA

The pterygopalatine fossa is a small pyramidal space below the apex of the orbit on the lateral side of the skull. Placed between the infratemporal fossa laterally and the nasopharynx medially, it functions as a neurovascular conduit. The body of the sphenoid forms the roof, the posterior boundary is the root of the pterygoid process and adjoining anterior surface of the greater wing of the sphenoid, and the anterior boundary is the superomedial part of the infratemporal surface (posterior wall) of the maxilla. The perpendicular plate of the palatine bone, with its orbital and sphenoidal processes, forms the medial boundary, and the pterygomaxillary fissure is the lateral boundary. There are two openings in the posterior wall of the pterygopalatine fossa: the foramen rotundum, which transmits the maxillary nerve, and the pterygoid canal (Vidian canal), which transmits the nerve of the pterygoid canal (Vidian nerve). When the anterior aspect of the pterygoid plate is examined in a disarticulated sphenoid, the foramen rotundum is seen to lie above and lateral to the pterygoid canal (see Figs 38.3A–B).

The fossa communicates with the nasal cavity via the sphenopalatine foramen; with the orbit via the medial end of the inferior orbital fissure; and with the infratemporal fossa via the pterygomaxillary fissure, which lies between the posterior aspect of the maxilla and the pterygoid process of the sphenoid and transmits the maxillary artery. It also communicates with the middle fossa via the foramen rotundum and the pterygoid canal, and with the oral cavity via the greater palatine canal, which opens in the posterolateral aspect of the hard palate. Its proximity to these adjacent areas permits the ready spread of both tumours and infection.

The main contents of the pterygopalatine fossa are the third part of the maxillary artery, the maxillary nerve and many of its branches, and the pterygopalatine ganglion.

Maxillary artery

The maxillary artery passes through the pterygomaxillary fissure from the infratemporal fossa into the pterygopalatine fossa, where it terminates as the third (pterygopalatine) part of the maxillary artery. The artery has a variable and tortuous course in its short passage through the pterygopalatine fossa, where it gives off numerous branches, including the posterior superior alveolar and infraorbital arteries and the artery of the pterygoid canal (Vidian artery), and terminates in the sphenopalatine and greater palatine arteries.

Posterior superior alveolar artery

The posterior superior alveolar artery arises from the maxillary artery within the pterygopalatine fossa and runs through the pterygomaxillary fissure on to the maxillary tuberosity. It gives off branches that penetrate the bone here to supply the maxillary molar and premolar teeth and the maxillary air sinus, and other branches that supply the buccal mucosa. Occasionally, the posterior superior alveolar artery arises from the infraorbital artery.

Infraorbital artery

The infraorbital artery enters the orbit through the inferior orbital fissure. It runs on the floor of the orbit in the infraorbital groove and infraorbital canal, and emerges onto the face at the infraorbital foramen to supply the lower eyelid, part of the cheek, the side of the external nose, and the upper lip. Within the infraorbital canal it gives off the anterior superior alveolar artery that runs downwards to supply the anterior teeth and the anterior part of the maxillary sinus. A middle superior alveolar artery is often described. When present, it branches from the infraorbital artery within the infraorbital canal and runs inferiorly along the lateral wall of the maxillary sinus towards the region of the canine and lateral incisor teeth, anastomosing with the anterior and posterior superior alveolar arteries.

Artery of the pterygoid canal

The artery of the pterygoid canal (Vidian artery) usually arises as a branch of the distal part of the maxillary artery or sometimes as a branch of the petrous segment of the internal carotid artery. It passes through the pterygoid canal and anastomoses with the pharyngeal, ethmoidal and sphenopalatine arteries in the pterygopalatine fossa and with the ascending pharyngeal, accessory meningeal, ascending palatine and descending palatine arteries in the oropharynx and around the pharyngotympanic tube. Through these complex anastomoses, the artery of the pterygoid canal contributes to the supply of part of the pharyngotympanic tube, the tympanic cavity and the upper part of the pharynx. It can also anastomose with the artery of the foramen rotundum and so

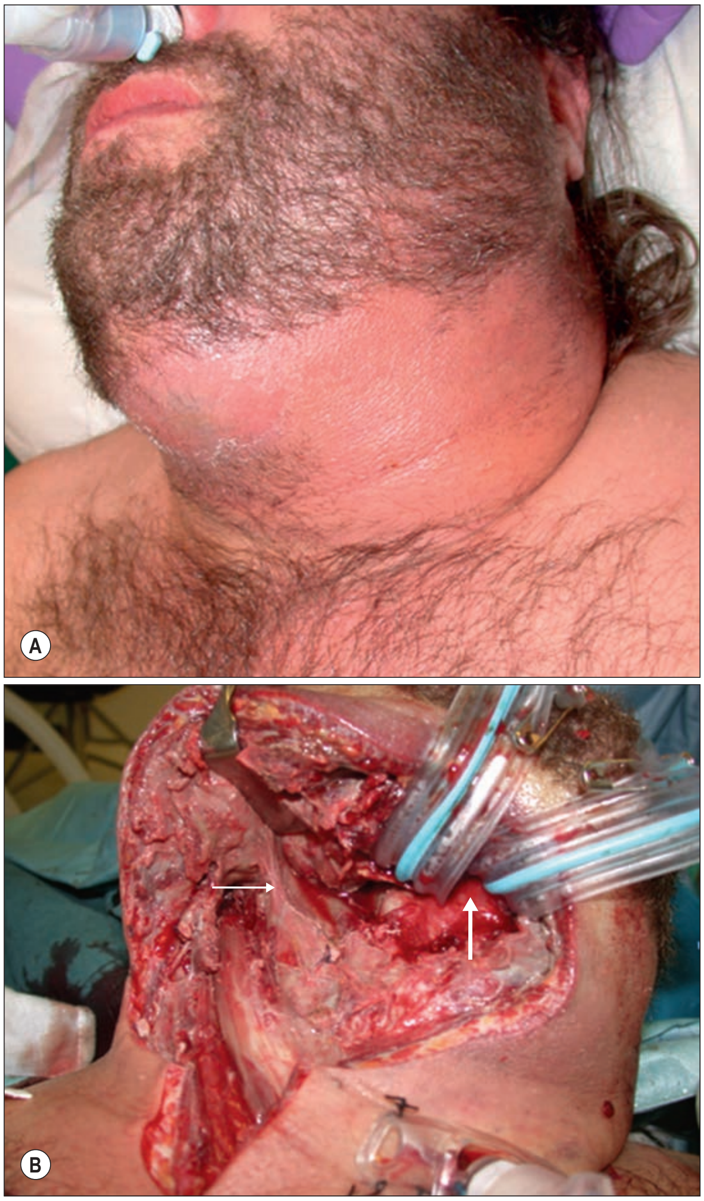

Fig. 38.26 **A**, Ludwig's angina: spread of infection from an infected lower left third molar to the pterygomandibular space and thence into the submandibular, sublingual and submental spaces bilaterally. The infection is life-threatening due to restricted mouth opening and a compromised airway. **B**, In this case, the airway was secured with awake fibreoptic intubation followed by tracheostomy. Aggressive through-and-through drainage was initiated (note the grey discoloration of the tissues). Prior to the availability of antibiotics, Ludwig's angina had a mortality rate of 75%. Aggressive early treatment with surgical drainage and intravenous antibiotics has reduced the mortality to approximately 5%. The narrow white arrow indicates the cut edge of mylohyoid. The broad white arrow indicates through-and-through corrugated drains. (With permission from Smyth AG 2007 Management of orofacial infections. In: Ward-Booth P, Schendel SA, Hausamen JE (eds) Maxillofacial Surgery, 2nd ed. Edinburgh: Churchill Livingstone.)

Some authors describe anterior and posterior 'compartments' of the pterygopalatine fossa, where the anterior compartment contains the third part of the maxillary artery and its branches, and the posterior compartment contains the maxillary division of the trigeminal nerve and the nerve of the pterygoid canal, together with the pterygopalatine ganglion and its branches (**Figs 38.27–38.28**) (Alfieri et al 2003, Cavallo et al 2005, Falcon et al 2010).

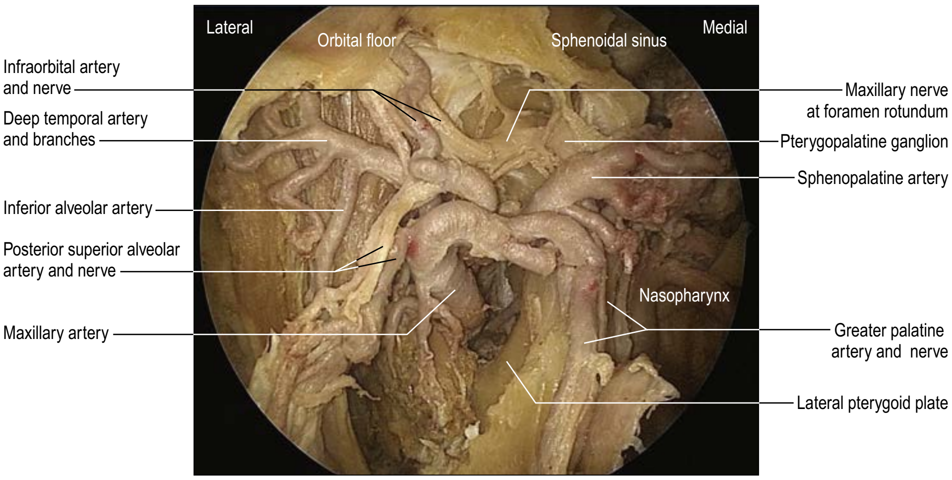
Lateral
Orbital floor
Sphenoidal sinus
Medial
Infraorbital artery and nerve
Deep temporal artery and branches
Inferior alveolar artery
Posterior superior alveolar artery and nerve
Maxillary artery
Maxillary nerve at foramen rotundum
Pterygopalatine ganglion
Sphenopalatine artery
Nasopharynx
Greater palatine artery and nerve
Lateral pterygoid plate

Fig. 38.27 An endoscopic view demonstrating the anterior (vascular) compartment of the right pterygopalatine fossa (00 lens endoscope). The vascular structures are anterior to the neural structures. Fat has been removed. (Image courtesy of Professor C Snyderman, University of Pittsburgh Medical Center.)

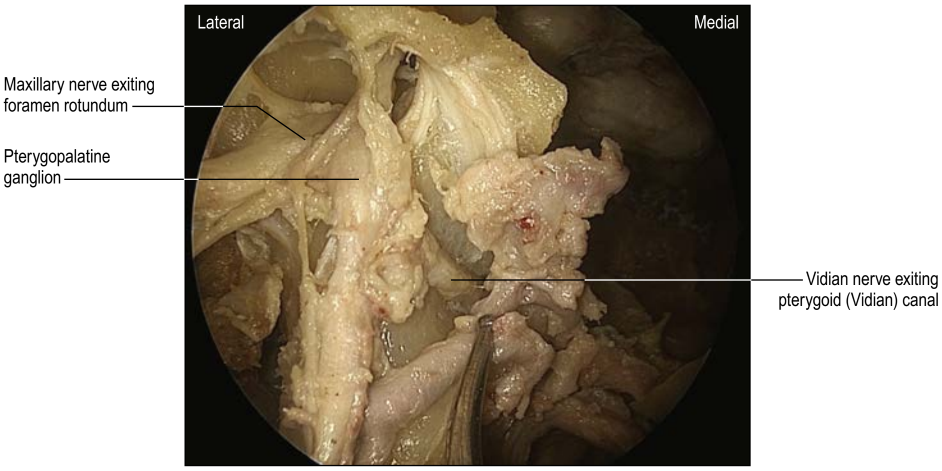
Lateral
Medial
Maxillary nerve exiting foramen rotundum
Pterygopalatine ganglion
Vidian nerve exiting pterygoid (Vidian) canal

Fig. 38.28 An endoscopic view demonstrating the posterior (neural) compartment of the right pterygopalatine fossa (00 lens endoscope). The principal vascular structures and fat have been removed. (Image courtesy of Professor C Snyderman, University of Pittsburgh Medical Center.)

communicate with branches of the cavernous portion of the internal carotid artery.

Pharyngeal artery

The pharyngeal branch of the maxillary artery passes through the palatovaginal canal, accompanying the nerve of the same name, and is distributed to the mucosa of the nasal roof, nasopharynx, sphenoidal air sinus and pharyngotympanic tube.

Greater (descending) palatine artery

The greater palatine artery leaves the pterygopalatine fossa through the greater (anterior) palatine canal, within which it gives off two or three lesser palatine arteries. The greater palatine artery supplies the inferior meatus of the nasal cavity, then passes on to the roof of the hard palate at the greater (anterior) palatine foramen and runs forwards to supply the hard palate and the palatal gingivae of the maxillary teeth. It gives off a branch that runs up into the incisive canal to anastomose with the nasopalatine artery and so contribute to the arterial supply of the nasal septum. The lesser palatine arteries emerge on to the palate through the lesser (posterior) palatine foramen, or foramina, and supply the soft palate.

Sphenopalatine artery

The sphenopalatine artery and the greater palatine artery are the terminal branches of the maxillary artery. The sphenopalatine artery is the principal artery that supplies the mucosa of the nasal cavity. It passes through the sphenopalatine foramen posterior to the superior meatus. From here, its posterior lateral nasal branches ramify over the turbinates and meatuses and anastomose with the ethmoidal arteries and nasal branches of the greater palatine artery to supply the frontal, maxillary, ethmoidal and sphenoidal air sinuses. The sphenopalatine artery next crosses anteriorly on the inferior surface of the sphenoid and ends on the nasal septum in a series of posterior septal branches that anastomose with the ethmoidal arteries (see Fig. 39.9).

Spatial arrangement of the neurovascular contents in the pterygopalatine fossa

Available with the *Gray's Anatomy* e-book

Maxillary nerve

The maxillary division of the trigeminal nerve is wholly sensory (**Fig. 38.30**). It gives off many of its branches in the pterygopalatine fossa. These can be subdivided into those that come directly from the nerve, and those that are associated with the pterygopalatine parasympathetic ganglion. Named branches from the main trunk are meningeal, ganglionic, zygomatic, posterior, middle and anterior superior alveolar and infraorbital nerves. Named branches from the pterygopalatine ganglion are orbital, nasopalatine, posterior superior nasal, greater (anterior) palatine, lesser (posterior) palatine and pharyngeal.

The meningeal branch is given off in the middle fossa. The maxillary nerve leaves the skull via the foramen rotundum to enter the upper part of the pterygopalatine fossa. As it crosses the fossa, the nerve gives off two large ganglionic branches containing fibres destined for the nasal cavity, palate and pharynx, and that pass through the pterygopalatine ganglion without synapsing. It then inclines sharply laterally on the posterior surface of the orbital process of the palatine bone and on the upper part of the posterior surface of the maxilla in the inferior orbital fissure (which is continuous posteriorly with the pterygopalatine fossa): it lies outside the orbital periosteum and gives off its zygomatic and then posterior superior alveolar branches. About halfway between the orbital apex and the orbital rim, the maxillary nerve turns medially to enter the infraorbital canal as the infraorbital nerve. The subsequent course of the maxillary nerve is described in Chapter 36.

Meningeal nerve

The meningeal branch of the maxillary nerve arises within the middle cranial fossa and runs with the middle meningeal vessels. It contributes to the innervation of the dura mater.

Ganglionic branches

There are usually two ganglionic branches that connect the maxillary nerve to the pterygopalatine ganglion.

Zygomatic nerve

The zygomatic branch of the maxillary nerve leaves the pterygopalatine fossa through the inferior orbital fissure together with the maxillary nerve. Its subsequent course is described in Chapter 36 (p. 631).

Posterior superior alveolar nerve

The posterior superior alveolar nerve leaves the maxillary nerve in the pterygopalatine fossa. Its subsequent course and distribution are described in Chapter 37.

Infraorbital nerve

The infraorbital nerve can be regarded as the terminal branch of the maxillary nerve. It leaves the pterygopalatine fossa to enter the orbit at the inferior orbital fissure, and its subsequent course and distribution are described in Chapter 36 (p. 631).

Orbital branches

Fine orbital branches enter the orbit through the inferior orbital fissure and supply orbital periosteum. Some fibres also pass through the posterior ethmoidal foramen to supply the sphenoidal and ethmoidal sinuses. The orbital branches are believed to join branches of the internal carotid nerve to form a 'retro-orbital' plexus, from which orbital structures such as the lacrimal gland and orbitalis receive an autonomic innervation (Ruskell 2004).

Nasopalatine nerve

The nasopalatine nerve leaves the pterygopalatine fossa through the sphenopalatine foramen and enters the nasal cavity. It passes across the cavity to the posterior part of the nasal septum, runs downwards and forwards on the septum in a groove in the vomer, and then turns down through the incisive fossa in the anterior part of the hard palate to enter the roof of the mouth (see Fig. 39.13). When an anterior and a posterior incisive foramen exist in this fossa, the left nasopalatine nerve usually passes through the anterior foramen and the right nerve passes through the posterior foramen. The nasopalatine nerve supplies the lower part of the nasal septum and the anterior part of the hard palate, where it communicates with the greater palatine nerve. The nasopalatine artery, a branch of the maxillary artery, accompanies the nasopalatine nerve and ends in the incisive canal, where it anastomoses with the greater palatine artery and the septal branch of the superior labial artery.

Posterior superior nasal nerves (lateral and medial)

The posterior superior alveolar nerves enter the posterior nasal cavity through the sphenopalatine foramen. Lateral posterior superior nasal nerves (about six) innervate the mucosa lining the posterior parts of the superior and middle nasal turbinates and the posterior ethmoidal sinuses. Two or three medial posterior superior nasal nerves cross the nasal roof below the opening of the sphenoidal sinus to supply the mucosa of the posterior parts of the roof and nasal septum.

Palatine nerves (greater and lesser)

The greater and lesser palatine nerves pass downwards from the pterygopalatine ganglion through the greater palatine canal. The greater palatine nerve descends through the greater palatine canal, emerges on the hard palate from the greater palatine foramen and runs forwards in a groove on the inferior surface of the bony palate almost to the incisor teeth. It supplies the gingivae, mucosa and glands of the hard palate and communicates with the terminal filaments of the nasopalatine nerve. In the greater palatine canal, it gives off posterior inferior nasal branches that emerge through the perpendicular plate of the palatine bone and ramify over the inferior turbinate and walls of the middle and inferior meatuses. As it leaves the greater palatine canal, it gives off branches that are distributed to both surfaces of the adjacent part of the soft palate (see Fig. 37.3).

The lesser (middle and posterior) palatine nerves are much smaller than the greater palatine nerve. They descend through the greater palatine canal, from which they diverge low down to emerge through the lesser palatine foramina in the tubercle or pyramidal process of the palatine bone. They innervate the uvula, tonsil and soft palate.

Fibres conveying taste impulses from the palate probably travel via the palatine nerves to the pterygopalatine ganglion. They pass through the ganglion without synapsing and leave via the greater petrosal nerve. Their cell bodies are located in the geniculate ganglion and their central processes pass via the sensory root of the facial nerve (nervus intermedius) to the gustatory nucleus in the nucleus of the tractus solitarius.

Pharyngeal nerve

The pharyngeal branch of the maxillary nerve leaves the pterygopalatine ganglion posteriorly. It passes through the palatovaginal canal with the pharyngeal branch of the maxillary artery and supplies the mucosa of the nasopharynx posterior to the pharyngotympanic tube.

The communication between the internal and external carotid arteries via the artery of the pterygoid canal is one of a number of collateral vascular pathways that exist between the external carotid artery and branches of the petrous and intracavernous segments of the internal carotid artery. Albeit small and difficult to demonstrate angiographically, these vascular connections may nevertheless provide the arterial supply for arteriovenous malformations, dural-based fistulae and skull base tumours, and may also compensate for occlusion of the internal carotid artery. They also pose a risk of inadvertent embolization of the brain parenchyma during interventional angiography of the external carotid artery system.

There are extensive communications between the artery of the pterygoid canal and the highly vascular nasopharyngeal mucosa. Embolization of branches of the external carotid artery can result in incomplete obliteration of a vascular nasopharyngeal lesion when the artery of the pterygoid canal arises from the internal carotid artery. The collateral circulation provided by the artery of the pterygoid canal can help to maintain cerebral circulation if there is stenosis of the petrous internal carotid artery proximal to the point where the artery of the pterygoid canal joins it, because blood flow in the post-stenotic segment of the internal carotid artery will be supplemented from the external carotid artery via the artery of the pterygoid canal (**Fig. 38.29**) (Allen et al 2005, Takeuchi et al 2005, Tubbs et al 2007).

As the greater palatine artery runs the length of the hard palate, it permits axial mucoperiosteal flaps to be raised, if necessary bilaterally, for the reconstruction of local defects. It is also possible to pedicle the entire mucoperiosteum of the hard palate on a single greater palatine artery. The vascular supply to the denuded palatal bone is sufficient, presumably from its nasal surface, to permit regeneration of the palatal soft tissue. Contracture of the regenerated tissue does not occur because the defect lies over the palatal bone (Gullane and Arena 1977, Gullane and Arena 1985, Salins and Benjamin 2009).

Ligation of the sphenopalatine artery may be necessary in the control of refractory epistaxis. It is usually located endoscopically at the postero-inferior end of the middle turbinate. Multiple branches may be encountered. The sphenopalatine artery provides the axial blood supply to the nasal septal mucosal flap (nasoseptal flap) used in endoscopic skull-base repair, a reflection of its contribution to the vascular supply to the nasal cavity (Hadad et al 2006).

The maxillary artery and its branches are located in a plane anterior to the maxillary nerve, pterygopalatine ganglion and the nerve of the pterygoid canal. This spatial arrangement is particularly relevant in endoscopic approaches to the pterygopalatine fossa (**Video 38.2**). The veins accompanying the third (pterygopalatine) part of the maxillary artery, in common with those accompanying the second (pterygoid) part, are in the form of a venous plexus. Profuse haemorrhage may be encountered from this pterygopalatine venous plexus.

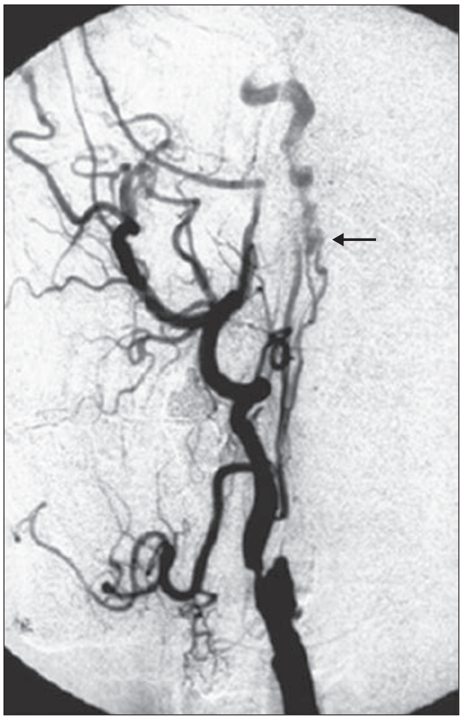

Fig. 38.29 A right common carotid angiogram, left anterior oblique view. The ascending pharyngeal artery provides a collateral blood flow to the petrous internal carotid artery via the artery of the pterygoid canal (arrow). (With permission from Takeuchi M, Kuwayama N, Kubo M et al 2005 Vidian artery as a collateral channel between the external and occluded internal carotid arteries. Neuro Med Chir (Tokyo) 45:470–1.)

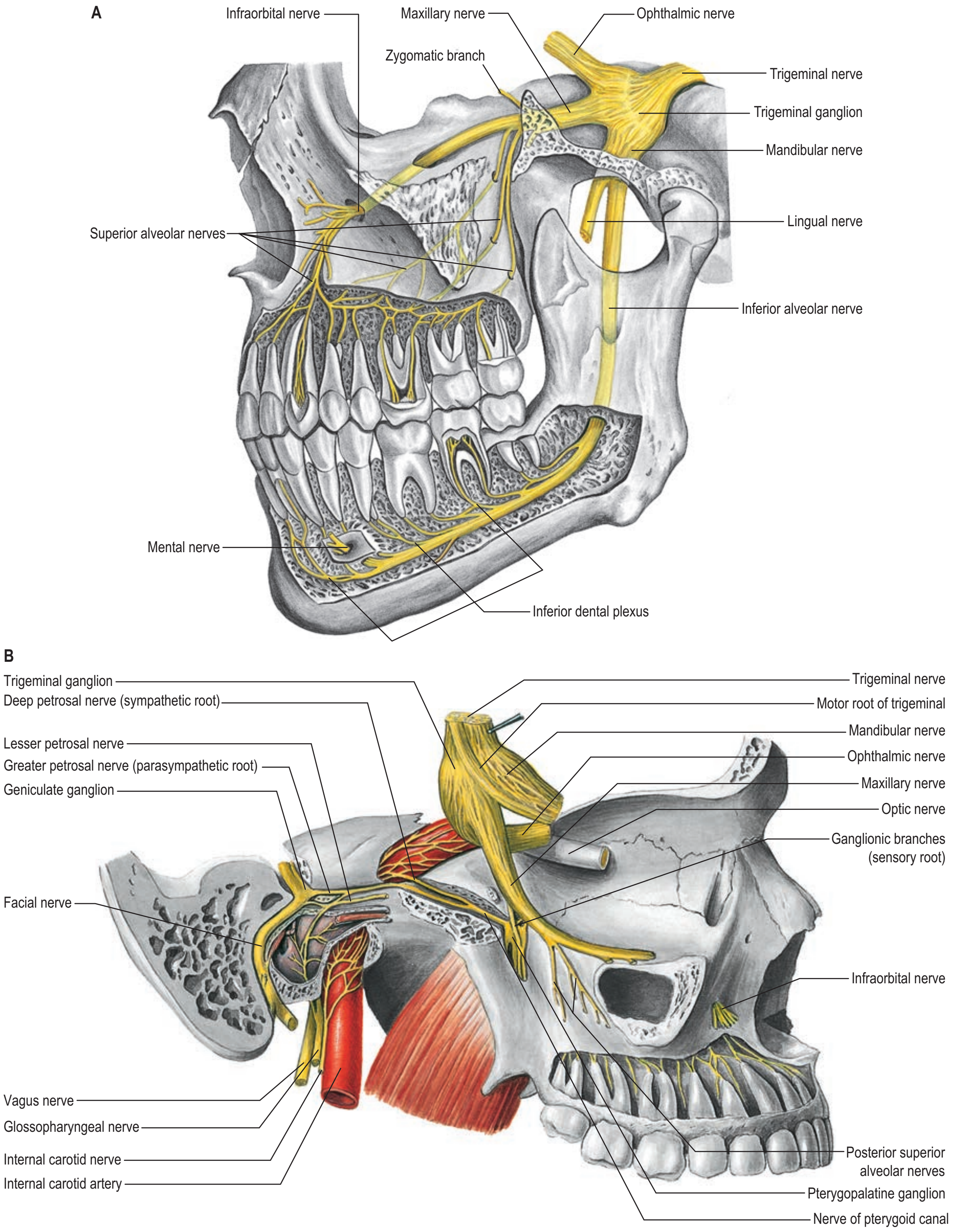
A
Infraorbital nerve
Maxillary nerve
Ophthalmic nerve
Zygomatic branch
Trigeminal nerve
Trigeminal ganglion
Mandibular nerve
Lingual nerve
Superior alveolar nerves
Inferior alveolar nerve
Mental nerve
Inferior dental plexus
B
Trigeminal ganglion
Deep petrosal nerve (sympathetic root)
Lesser petrosal nerve
Greater petrosal nerve (parasympathetic root)
Geniculate ganglion
Facial nerve
Vagus nerve
Glossopharyngeal nerve
Internal carotid nerve
Internal carotid artery
Trigeminal nerve
Motor root of trigeminal
Mandibular nerve
Ophthalmic nerve
Maxillary nerve
Optic nerve
Ganglionic branches (sensory root)
Infraorbital nerve
Posterior superior alveolar nerves
Pterygopalatine ganglion
Nerve of pterygoid canal

Fig. 38.30 **A**, Maxillary and mandibular nerves. **B**, The nerves of the pterygoid canal and the pterygopalatine ganglion. The trigeminal ganglion has been lifted forwards out of the trigeminal impression. Note the sympathetic plexus on the internal carotid artery. (Sobotta Atlas of Human Anatomy © Elsevier GmbH, Urban & Fischer, Munich.)

Neural anastomoses with the maxillary nerve

Available with the *Gray's Anatomy* e-book

Pterygopalatine ganglion

The pterygopalatine ganglion, known colloquially as the 'ganglion of hay fever', is the largest of the peripheral parasympathetic ganglia, and is well protected, deep in the pterygopalatine fossa. Immediately anterior to the pterygoid canal, the ganglion lies below and medial to the foramen rotundum and the maxillary nerve and lateral to the sphenopalatine foramen (see Fig. 38.30B). It is flattened and reddish-grey in colour and lies just below the maxillary nerve as it crosses the pterygopalatine fossa. The majority of the 'branches' of the ganglion are connected with it morphologically but not functionally, because they are primarily sensory branches of the maxillary nerve and so pass through the ganglion without synapsing to enter the ganglionic branches of the maxillary nerve.

Preganglionic parasympathetic fibres destined to synapse in the pterygopalatine ganglion run initially in the greater petrosal branch of the facial nerve, and then in the nerve of the pterygoid canal (Vidian nerve) after the greater petrosal unites with the deep petrosal nerve. The nerve of the pterygoid canal enters the ganglion posteriorly. Postganglionic parasympathetic fibres leave the ganglion: some may join the maxillary nerve via a ganglionic branch and then travel via its zygomatic and zygomaticotemporal branches to the lacrimal gland, but most are thought to travel by orbital branches to the gland. The parasympathetic supply to the pre-ocular part of the central artery of the retina is believed to be derived mainly from the pterygopalatine ganglion and is vasodilatory.

Connections between the zygomaticotemporal branch of the maxillary nerve and the temporal branches of the facial nerve, and the zygomaticofacial branch of the maxillary nerve and the zygomatic branches of the facial nerve have been demonstrated (Shoja et al 2014). It was once thought that the connection between the zygomaticotemporal and lacrimal nerves in the orbit provided parasympathetic secretomotor fibres to the lacrimal gland, but that is now less certain. It is more likely that the postganglionic orbital branches pass through the inferior orbital fissure and innervate the lacrimal gland directly (Ruskell 2004).

Preganglionic secretomotor fibres of uncertain origin also travel in the nerve of the pterygoid canal and synapse in the pterygopalatine ganglion: postganglionic fibres are distributed to palatine, pharyngeal and nasal mucous glands via palatine and nasal branches of the maxillary nerve.

Postganglionic sympathetic fibres pass through the ganglion without synapsing and supply blood vessels and orbitalis. They arise in the superior cervical ganglion and travel via the internal carotid plexus and deep petrosal nerve to enter the pterygopalatine ganglion within the nerve of the pterygoid canal.

General sensory fibres destined for distribution via orbital, nasopalatine, superior alveolar, palatine and pharyngeal branches of the maxillary division of the trigeminal nerve run through the ganglion without synapsing.

Bonus e-book content

Fig. 38.2 The 'extended' infratemporal fossa.

Fig. 38.4 The stylohamular plane.

Fig. 38.8 The opposing direction of resorption ('atrophy') of the mandible and maxilla, resulting in increasing incongruity between the jaws.

Fig. 38.9 A bilateral fracture of an edentulous atrophic mandible.

Fig. 38.10 A CT image showing the lateral lingual foramina.

Fig. 38.11 A three-dimensional reformatted CT image showing an implant perforating the lingual cortical plate, leading to haemorrhage in the anterior floor of the mouth.

Fig. 38.12 A transverse section at the level of the hard palate demonstrating the cranial fascia and associated compartments.

Fig. 38.19 The arterial network of the human temporalis muscle.

Fig. 38.24 The foramen ovale, inferolateral view.

Fig. 38.25 Anastomoses of the auriculotemporal nerve with the temporofacial division of the facial nerve, and of the great auricular nerve with the cervicofacial division of the facial nerve in the parotid and periparotid regions.

Fig. 38.26 Ludwig's angina: spread of infection from an infected lower left third molar to the pterygomandibular space and thence into the submandibular, sublingual and submental spaces bilaterally.

Fig. 38.27 An endoscopic view demonstrating the anterior (vascular) compartment of the right pterygopalatine fossa (00 lens endoscope).

Fig. 38.28 An endoscopic view demonstrating the posterior (neural) compartment of the right pterygopalatine fossa (00 lens endoscope).

Fig. 38.29 A right common carotid angiogram, left anterior oblique view.

Video 38.1 Temporomandibular joint arthroscopy demonstrating intracapsular anatomy.

Video 38.2 Endoscopic anatomy of the infratemporal and pterygopalatine fossae.

Key references

Barker BCW, Davies PL 1972 The applied anatomy of the pterygomandibular space. Br J Surg 10:43–55.

A description of the relationships of the structures within the pterygomandibular space, with particular reference to anaesthesia associated with an inferior alveolar nerve block.

Cavallo LM, Messina A, Gardner P et al 2005 Extended endoscopic endonasal approach to the pterygopalatine fossa: anatomical study and clinical considerations. Neurosurg Focus 19:1–7.

A detailed description of the anatomy of the pterygopalatine fossa and its bony landmarks and contents, when approached endoscopically.

Cawood J, Howell RA 1988 A classification of the edentulous jaws. Int J Oral Maxillofac Surg 17:232–6.

Analysis of the pattern of bone resorption in edentulous maxillae and mandibles in 300 dried skulls, from which a classification system of alveolar resorption is derived.

Cheung LK 1996 The vascular anatomy of the human temporalis muscle: implications for surgical splitting techniques. Int J Oral Maxillofac Surg 25:414–21.

A cadaveric study of 15 cadavers/30 temporalis muscle specimens to assess the territory supplied by each of the three principal nutrient arteries (angiosomes) and the clinical implications of the results.

Guidera AK, Dawes PJD, Fong A et al 2014 Head and neck fascia and compartments: no space for spaces. Head Neck 36:1058–68.

A comprehensive review of the fascia of the head and neck and its associated compartments, aiding the understanding of the variable and, at times, misleading terminology.

Juniper RP 1981 The superior pterygoid muscle. Br J Oral Surg 19:121–8.

An electromyographic study in human subjects demonstrating that the superior and inferior heads of the lateral pterygoid have opposing (antagonistic) action. The superior head is active during closure – particularly the terminal closing phase and on clenching, stabilizing the condyle against the articular eminence.

Lang J 1995 Mandible. In: Clinical Anatomy of the Masticatory Apparatus and Peripharyngeal Spaces. New York: Thieme; pp. 19–41.

Detailed anatomical descriptions – including measurements – of the maxilla and mandible, the infratemporal fossa and its contents, and the temporomandibular joint, relating these to clinical practice.

Nitzan DW 2001 The process of lubrication impairment and its involvement in temporomandibular joint disc displacement. J Oral Maxillofac Surg 59:36–45.

An overview of the lubrication of the temporomandibular joint and its possible role in disc displacement.

Romanos GE, Gupta B, Crespi R 2012 Endosseous arteries in the anterior mandible: literature review. Int J Oral Maxillofac Implants 27:90–4.

A review of the literature on the blood supply of the anterior mandible (symphysis), in particular via nutrient arteries entering the midline and lateral lingual foramina; its relevance to clinicians is discussed.

Stegenga B, de Bont LGM 2006 TMJ disc derangements. In: Laskin DM, Greene CS, Hylander WL (eds) TMDs: An Evidence-Based Approach to Diagnosis and Treatment. Hanover Park: Quintessence; pp. 125–36.

An analysis of the possible aetiology and mechanism of disc derangement/internal derangement of the temporomandibular joint and its clinical course.

References

Aizenbud D, Ciceu C, Hazan-Molina H et al 2012 Relationship between inferior alveolar nerve imaging and neurosensory impairment following bilateral sagittal split osteotomy in skeletal class III cases with mandibular prognathism. Int J Oral Maxillofac Surg 41:461–8.

Alfieri A, Jho H, Schettino R et al 2003 Endoscopic endonasal approach to the pterygopalatine fossa: anatomic study. Neurosurgery 52:374–80.

Allen JW, Alastra JG, Nelson PK 2005 Proximal intracranial internal carotid artery branches: prevalence and importance for balloon occlusion test. J Neurosurg 102:45–52.

Aziz SR, Najjar T 2009 Management of the edentulous/atrophic mandible fracture. Atlas Oral Maxillofacial Surg Clin North Am 17:75–9.

Barker BCW, Davies PL 1972 The applied anatomy of the pterygomandibular space. Br J Surg 10:43–55.

A description of the relationships of the structures within the pterygomandibular space, with particular reference to anaesthesia associated with an inferior alveolar nerve block.

Bejjani GK, Sullivan B, Salas-Lopez E et al 1998 Surgical anatomy of the infratemporal fossa: the styloid diaphragm revisited. Neurosurgery 43:842–52.

Blanchaert RH, Ord RA 1998 Vertical ramus compartment resection of the mandible for deeply invasive tumours. J Oral Maxillofacial Surg 56:15–22.

Cavallo LM, Messina A, Gardner P et al 2005 Extended endoscopic endonasal approach to the pterygopalatine fossa: anatomical study and clinical considerations. Neurosurg Focus 19:1–7.

A detailed description of the anatomy of the pterygopalatine fossa and its bony landmarks and contents, when approached endoscopically.

Cawood J, Howell RA 1988 A classification of the edentulous jaws. Int J Oral Maxillofac Surg 17:232–6.

Analysis of the pattern of bone resorption in edentulous maxillae and mandibles in 300 dried skulls, from which a classification system of alveolar resorption is derived.

Chang Y, Cantanelmi D, Wisco J et al 2013 Evidence for the functional compartmentalization of the temporalis muscle: a 3-dimensional study of innervation. J Oral Maxillofac Surg 71:1170–7.

Cheung LK 1996 The vascular anatomy of the human temporalis muscle: implications for surgical splitting techniques. Int J Oral Maxillofac Surg 25:414–21.

A cadaveric study of 15 cadavers/30 temporalis muscle specimens to assess the territory supplied by each of the three principal nutrient arteries (angiosomes) and the clinical implications of the results.

De Bont LGM, Boering G, Havinga P et al 1984 Spatial arrangement of collagen fibrils in the articular cartilage of the mandibular condyle. J Oral Maxillofac Surg 42:306–13.

Detamore MS, Athanasiou KA 2003 Structure and function of the temporomandibular joint disc: implications for tissue engineering. J Oral Maxillofac Surg 61:494–506.

Dubois L, de Lange J, Baas E et al 2010 Excessive bleeding in the floor of the mouth after endosseous implant placement: a report of two cases. Int J Oral Maxillofac Surg 39:412–5.

Ellis E, Price C 2008 Treatment protocol for fractures of the atrophic mandible. J Oral Maxillofac Surg 66:421–35.

Eufinger H, Gellrich NC, Sandmann D et al 1997 Descriptive and metric classification of jaw atrophy. Int J Oral Maxillofac Surg 26:23–8.

Falcon RT, Rivera-Serrano CM, Miranda JF et al 2010 Endoscopic endonasal dissection of the infratemporal fossa: anatomic relationships and importance of eustachian tube in the endoscopic skull base surgery. Laryngoscope 121:31–41.

Fernandes T, Lobo JC, Castro R et al 2013 Anatomy and pathology of the masticator space. Insights Imaging 4:605–16.

Flanagan D 2003 Important arterial supply of the mandible, control of an arterial haemorrhage, and report of a haemorrhagic incident. J Oral Implantology 29:165–73.

Friedman WH, Katsantonis GP, Copper MH et al 1981 Stylo-hamular dissection: a new method for en-bloc resection of malignancies of the infratemporal fossa. Laryngoscope 91:1869–79.

Guidera AK, Dawes PJD, Fong A et al 2014 Head and neck fascia and compartments: no space for spaces. Head Neck 36:1058–68.

A comprehensive review of the fascia of the head and neck and its associated compartments, aiding the understanding of the variable and, at times, misleading terminology.

Gullane PJ, Arena S 1977 Palatal island flap for reconstruction of oral defects. Arch Otolaryngol 103:598–603.

Gullane PJ, Arena S 1985 Extended palatal island mucoperiosteal flap. Arch Otolaryngol 111:330–5.

Hadad G, Bassagasteguy L, Carrau RL 2006 A novel reconstructive technique after endoscopic expanded endonasal approaches: vascular pedicle nasoseptal flap. Laryngoscope 116:1882–6.

Hansson T, Oberg T, Carlsson GE et al 1977 Thickness of the soft tissue layers and the articular disc in the temporomandibular joint. Acta Odont Scand 35:77–83.

Hogan G, Ellis E 2006 The 'antilingula' – fact or fiction. J Oral Maxillofac Surg 64:1248–54.

Hosseini SMS, Razfar A, Carrau RL et al 2012 Endonasal transpterygoid approach to the infratemporal fossa: correlation of endoscopic and multiplanar CT anatomy. Head Neck 34:313–20.

Hylander WL 2006 Functional anatomy and biomechanics of the masticatory apparatus. In: Laskin DM, Greene CS, Hylander WL (eds) TMDs: An Evidence-Based Approach to Diagnosis and Treatment. Hanover Park: Quintessence; pp. 3–34.

Jacobs R, Lambrichts I, Liang X et al 2007 Neovascularisation of the anterior jaw bones revisited using high-resolution magnetic resonance imaging. Oral Surg Oral Med Oral Pathol Oral Radiol Endod 103:683–93.

Janfanza PJ, Nadol JB, Galla RJ et al 2001 Surgical Anatomy of the Head and Neck. Philadelphia: Lippincott, Williams & Wilkins; pp. 358–9.

Joo W, Funaki T, Yoshioka F et al 2013 Microsurgical anatomy of the infratemporal fossa. Clin Anat 26:455–69.

Juniper RP 1981 The superior pterygoid muscle. Br J Oral Surg 19:121–8.

An electromyographic study in human subjects demonstrating that the superior and inferior heads of the lateral pterygoid have opposing (antagonistic) action. The superior head is active during closure – particularly the terminal closing phase and on clenching, stabilizing the condyle against the articular eminence.

Kaban LB, Mulliken JB, Murray JE. 1981 Three-dimensional approach to analysis and treatment of hemifacial macrosomia. Cleft Palate J. 18:90–9.

Lacout A, Marsot-Dupuch K, Smoker WR et al 2005 Foramen tympanicum, or foramen of Huschke: pathologic cases and anatomic CT study. Am J Neuroradiol 26:1317–23.

Ladeira DBS, Barbosa GLR, Nascimento MCC et al 2013 Prevalence and characteristics of pneumatisation of the temporal bone evaluated by cone beam computed tomography. Int J Oral Maxillofac Surg 42:771–5.

Lang J 1995 Mandible. In: Clinical Anatomy of the Masticatory Apparatus and Peripharyngeal Spaces. New York: Thieme; pp. 19–41.

Detailed anatomical descriptions – including measurements – of the maxilla and mandible, the infratemporal fossa and its contents, and the temporomandibular joint, relating these to clinical practice.

Lang J 2001 Skull Base and Related Structures. Atlas of Clinical Anatomy, 2nd ed. Stuttgart: Schattauer; pp. 1–5.

Loukas M, Kinsella CR, Kapos T et al 2008 Anatomical variation in arterial supply of the mandible with special regard to implant placement. Int J Oral Maxillofac Surg 37:367–71.

McDonnel D, Reza NM, Todd ME 1994 The mandibular lingual foramen: a consistent arterial foramen in the middle of the mandible. J Anat 184:363–9.

McLoughlin PM, Hopper C, Bowley NB 1995 Hyperplasia of the mandibular coronoid process: an analysis of 31 cases and a review of the literature. J Oral Maxillofac Surg 53:250–5.

McMahon JD, Wong LS, Crowther J et al 2013 Patterns of local recurrence after primary resection of cancers that arise in the sinonasal region and the maxillary alveolus. Br J Oral Maxillofac Surg 51:389–93.

McNamara JA Jr 1973 The independent function of the two heads of the lateral pterygoid muscle. Am J Anat 138:197–205.

Miloro M, Henrickson B 2010 Discectomy as the primary surgical option for internal derangement of the temporomandibular joint. J Oral Maxillofac Surg 68:782–9.

Mulder CH, Kalaykova RA, Gortzak T 2012 Coronoid process hyperplasia: a systematic review of the literature from 1995. Int J Oral Maxillofac Surg 41:1483–9.

Nakajima K, Tagaya A, Otonari-Yamamoto M et al 2014 Composition of the blood supply in the sublingual and submandibular spaces and its relationship to the lateral lingual foramen of the mandible. Oral Surg Oral Med Oral Pathol Oral Radiol 117:e32–8.

Nickel JC, Iwasaki LR, Beatty MW et al 2006 Static and dynamic loading effects on temporomandibular joint disc tractional forces. J Dent Res 85:809–13.

Nickel JC, McLachlan KR 1994 In vitro measurement of the frictional properties of the temporomandibular joint disc. Arch Oral Biol 39:323–30.

Nitzan D 2009 Mandibular asymmetry secondary to TMJ active condylar hyperplasia (ACH). Br J Oral Maxillofac Surg 47:502–4.

Nitzan DW 2001 The process of lubrication impairment and its involvement in temporomandibular joint disc displacement. J Oral Maxillofac Surg 59:36–45.

An overview of the lubrication of the temporomandibular joint and its possible role in disc displacement.

Nitzan DW, Katsnelson A, Bermanis I et al 2008 The clinical characteristics of condylar hyperplasia: experience with 61 patients. J Oral Maxillofac Surg 66:312–18.

Obrez A, Gallo LM 2006 Anatomy and function of the TMJ. In: Laskin DM, Greene CS, Hylander WL (eds) TMDs: An Evidence-Based Approach to Diagnosis and Treatment. Hanover Park: Quintessence; pp. 35–52.

Obwegeser HL, Make MS 1986 Hemimandibular hyperplasia – hemimandibular elongation. J Maxillofac Surg 14:183–208.

Osborn JW 1995 Internal derangement and the accessory ligaments around the temporomandibular joint. J Oral Rehab 22:731–740.

Paegle DI, Holmund AB, Hjerpe A 2003 Matrix glycosaminoglycans in the temporomandibular joint in patients with painful clicking and chronic closed lock. Int J Oral Maxillofac Surg 32:397–400.

Park KR, Kim SY, Kim GJ 2014 Anatomic study to determine a safe surgical reference point for mandibular ramus osteotomy. J Craniomaxillofac Surg 42:22–7.

Pogrel MA, Renaut A, Schmidt B et al 1995 The relationship of the lingual nerve to the mandibular third molar region. J Oral Maxillofac Surg 53:1178–81.

Pruzansky S 1969 Not all dwarfed mandibles are alike. Birth Defects 1:120–9.

Robinson PD 1993 Articular cartilage of the temporomandibular joint – can it regenerate? Ann R Coll Surg Engl 75:231–6.

Romanos GE, Gupta B, Crespi R 2012 Endosseous arteries in the anterior mandible: literature review. Int J Oral Maxillofac Implants 27:90–4.

A review of the literature on the blood supply of the anterior mandible (symphysis), in particular via nutrient arteries entering the midline and lateral lingual foramina; its relevance to clinicians is discussed.

Ruskell GL 2004 Distribution of pterygopalatine ganglion efferents to the lacrimal gland in man. Exp Eye Res 78:329–35.

Salins P, Benjamin P 2009 Anatomic basis for reconstruction of retromolar region: significance of palatal flap. J Oral Maxillofac Surg 67:1141–8.

Satoh J, Ohno D, Aizawa T et al 2006 Bilateral coronoid hyperplasia in an adolescent: report of a case and review of the literature. J Oral Maxillofac Surg 64:334–8.

Senger M, Stoffels HJ, Angelov DN 2014 Topography, syntopy and morphology of the human otic ganglion: a cadaver study. Ann Anat 196:327–35.

Shoja MM, Oyesiku NM, Grissenauer CJ et al 2014 Anastomoses between lower cranial and upper cervical nerves: a comprehensive review with potential significance during skull base and neck operations. Part 1: Trigeminal, facial and vestibulocochlear nerves. Clin Anat 27:118–30.

Smyth AG 2007 Management of orofacial infections. In: Ward-Booth P, Schendel SA, Hausamen JE (eds) Maxillofacial Surgery, 2nd ed. Edinburgh: Churchill Livingstone; Ch. 80, pp. 1550–71.

Stegenga B, de Bont LGM 2006 TMJ disc derangements. In: Laskin DM, Greene CS, Hylander WL (eds) TMDs: An Evidence-Based Approach to Diagnosis and Treatment. Hanover Park: Quintessence; pp. 125–36.

An analysis of the possible aetiology and mechanism of disc derangement/internal derangement of the temporomandibular joint and its clinical course.

Sutton DN, Lewis BRK, Patel M et al 2004 Changes in facial form relative to progressive atrophy of the edentulous jaws. Int J Oral Maxillofac Surg 33:676–82.

Takeuchi M, Kuwayama N, Kubo M et al 2005 Vidian artery as a collateral channel between the external and occluded internal carotid arteries. Neuro Med Chir (Tokyo) 45:470–1.

Tanaka E, Dalla-Bona DA, Iwabe T et al 2006 The effect of removal of the disc on the friction in the temporomandibular joint. J Oral Maxillofac Surg 64:1221–4.

Toller PA 1974 Temporomandibular arthropathy. Proc R Soc Med 67:153–9.

Tubbs RS, Hansasuta A, Loukas M et al 2007 Branches of the petrous and cavernous segments of the internal carotid artery. Clin Anat 20:596–601.

Vento AR, LaBrie RA, Mulliken JB 1991 The O.M.E.N.S. classification of hemifacial microsomia. Cleft Palate Craniofac J 28:68–76; discussion 77.

Wittwer G, Adeyemo WL, Beinemann J et al 2012 Evaluation of risk of injury to the inferior alveolar nerve with classical sagittal split osteotomy technique and proposed alternative surgical techniques using computer-assisted surgery. Int J Oral Maxillofac Surg 41:79–86.

Wolford LM, Movahed R, Perez DE 2014 A classification system for conditions causing condylar hyperplasia. J Oral Maxillofac Surg 72:567–95.

Woo BM, Al-Bustani S, Ueeck BA 2006 Floor of mouth haemorrhage and life-threatening airway obstruction during immediate implant placement in the anterior mandible. Int J Oral and Maxillofac Surg 35:961–4.

CHAPTER
39

Nose, nasal cavity and paranasal sinuses

Box 39.1 and **Table 39.1** set out the different anatomical and clinical terms that are applied to some of the structures described in this chapter.

Box 39.1 A note on terminology

‘The advent of endoscopic sinus surgery led to a resurgence of interest in the detailed anatomy of the internal nose and paranasal sinuses. However, the official *Terminologia Anatomica* used by basic anatomists omits many of the structures of surgical importance. This led to numerous clinical anatomy papers and much discussion about the exact names and definitions for the structures of surgical relevance. The European position paper on the anatomical terminology of the internal nose and paranasal sinuses was conceived to re-evaluate the anatomical terms in common usage by endoscopic sinus surgeons and to compare this with the official *Terminologia Anatomica*’ (Lund et al 2014).

Where appropriate, the terms used in this chapter are those commonly used in surgical practice as set out in the ‘European position paper on the anatomical terminology of the internal nose and paranasal sinuses’ (see Table 39.1). Conflicts inevitably arise but hopefully have been minimized. The terms ‘concha’ and ‘turbinate’ are often used interchangeably but anatomists rarely use the latter term, while clinicians rarely use the former; in this chapter, concha is used to describe the bony structure seen in dried skulls, while turbinate is used to describe the bony structures, together with their overlying soft tissue and mucosa, that are encountered during surgery. ‘Ethmoturbinal’ does not appear in *Terminologia Anatomica* but is the collective term for the superior and middle turbinates, occasionally supplemented by a supreme turbinate. With regard to the terms ‘skull base’ and ‘cranial base’, although they are frequently used as though synonymous (the term ‘skull base’ is favoured in the position paper), the anterior skull base includes the inferior surface of the facial skeleton and will therefore be distinguished from the anterior cranial base, which is delimited by the inner and outer surfaces of the anterior cranial fossa (Ch. 34).

NOSE

The nose is the first part of the upper respiratory tract and is responsible for warming, humidifying and, to some extent, filtering inspired air. It also houses the olfactory epithelium, which contains olfactory receptor neurones responsible for detecting airborne odorant molecules.

The nose may be subdivided into an external nose, which opens anteriorly on to the face through the nostrils or nares, and an internal chamber, divided sagittally by a septum into right and left cavities, which open posteriorly into the nasopharynx through the posterior nasal apertures or choanae. The nasal cavities are housed in a supporting framework composed of bone and fibroelastic cartilages. The larger bones in this framework contain air-filled spaces lined with respiratory epithelium, described collectively as the paranasal sinuses. The sinuses and the nasolacrimal ducts drain into the nasal cavity via openings in its lateral walls (**Fig. 39.1**).

EXTERNAL NOSE

The external nose is a pyramidal structure located in the midline of the midface and attached to the facial skeleton. Its upper angle or root is continuous with the forehead, and its free tip forms the apex, which projects anteriorly. The overall shape of the external nose is very variable. The lateral surfaces of the nose unite in the median plane to form the dorsum, which is narrowest at the medial canthus. The lobule is an area containing the tip of the nose. Its base contains two ellipsoidal apertures, the external nares or nostrils, which open on to its inferior surface, separated by the nasal septum and columella. The columella usually projects below the alar margin. The alar sulcus is a groove in the skin bounding the nasal alae above and joining the nasiolabial sulcus. Below, it curves towards the tip of the nose but does not reach it.

Facial and nasal proportions

Available with the *Gray’s Anatomy* e-book

Skin and soft tissue

The skin and soft tissue covering the nose vary in thickness. They are usually thin over the dorsum in the mid third, especially at the osseocartilaginous junction, the rhinion, and loosely connected to the nasal aponeurosis and the muscle fibres that fan out within it. It is thicker over the nasofrontal angle, and at the tip, where it has numerous large sebaceous glands and is more adherent. These variations affect the final nasal contour and profile after rhinoplasty.

The skin of the nose is separated from the underlying osteocartilaginous framework by four layers. These are the superficial fatty panniculus; the fibromuscular layer, a continuation of the facial superficial musculo-aponeurotic system (SMAS) (Ch. 36); the deep fatty layer; and the periosteum or perichondrium.

Soft tissue areas of the nose

Four soft tissue areas of the nose lack cartilaginous support. They have been given numerous eponymous names and descriptions, but were reclassified by Huizing (2003).

Paraseptal soft tissue area

The supratip area contains the paired lateral cartilages, which gradually separate from the septum to a level just above the septal angle. The amount of flare varies, and encloses a small paraseptal soft tissue triangle on each side of the septum.

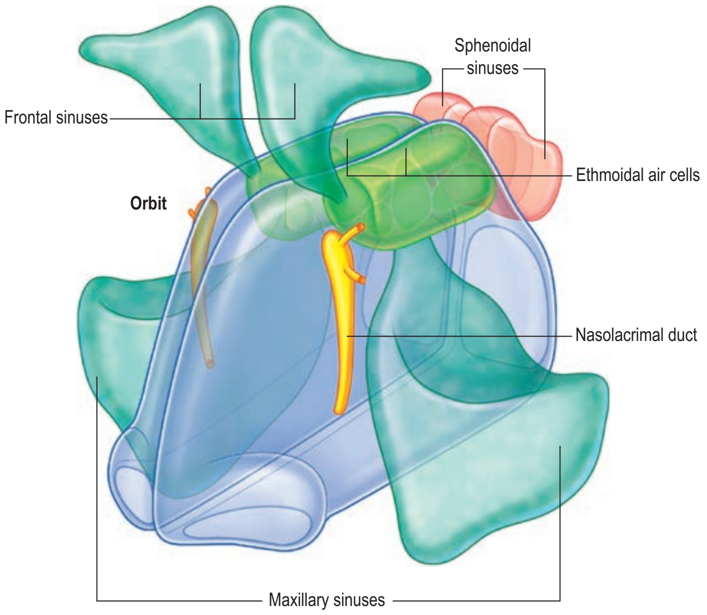

Fig. 39.1 An overview of the spatial relationships between the nasal cavity, paranasal sinuses and nasolacrimal ducts. (With permission from Drake RL, Vogl AW, Mitchell A (eds) Gray’s Anatomy for Students, 2nd ed. Elsevier, Churchill Livingstone. Copyright 2010.)

TABLE 39.1 **Surgical and anatomical terminology**

	Present 'surgical' terminology	Rhinological and anatomical synonyms (textbooks, literature)	*Terminologia Anatomica 1*	Suggested English terminology (position paper)	Frequency of variant in literature*
1	**Nasal cavity**	Inner nose Cavum nasi	Cavitas nasi	***Nasal cavity***	
1.1	Lateral nasal wall	Lateral nasal wall	n.e.	***Lateral nasal wall***	
1.2	Floor of nasal cavity	Nasal floor	n.e.	***Nasal floor***	
1.3	Nasal septum	Septum nasi	Septum nasi	***Nasal septum***	
1.3.1	Cartilaginous portion	Cartilaginous part of the nasal septum Cartilaginous segment Septal cartilage Lamina quadrangularis	Pars cartilaginea (septi nasi) Cartilago septi nasi	***Septal cartilage***	
1.3.2	Bony part	Bony/osseous septum Bony/osseous part of the nasal septum	Pars ossea septi nasi	***Bony septum***	
1.3.2.1	Lamina perpendicularis	Perpendicular plate of ethmoid	Lamina perpendicularis ossis ethmoidalis	***Perpendicular plate of ethmoid***	
1.3.2.2	Vomer	Vomer	Pars ossea septi nasi	***Vomer***	
1.3.3	Membranous portion	Membranous portion	Pars membranacea septi nasi	***Membranous portion (of nasal septum)***	
1.3.4	Jacobson's organ	Vomero-nasal organ	Organum vomeronasale	***Vomero-nasal organ***	
1.3.5	Septal tubercle	Tuberculum septi nasi tubercle of Zuckerkandl Morgagni's tubercle Septal swell body	n.e.	***Septal tubercle***	
1.4	Inferior turbinate	Inferior nasal turbinate Maxilloturbinal Concha inferior Lower turbinate	Concha nasi inferior	***Inferior turbinate***	
1.4.1	Inferior meatus	Inferior nasal meatus Lower nasal meatus	Meatus nasi inferior	***Inferior meatus***	
1.4.1.1	Nasolacrimal duct opening	Hasner's valve (Naso)lacrimal duct ostium Ostium lacrimale	Apertura/ostium ductus nasolacrimalis	***Nasolacrimal duct opening***	
1.5	Middle turbinate	Middle nasal turbinate First (persisting) ethmoturbinal First ethmoidal turbinate Middle concha Concha media	Concha nasi media	***Middle turbinate***	
1.5.1	Basal lamella of middle turbinate	Ground lamella of middle turbinate Third basal lamella	n.e.	***Basal lamella of middle turbinate***	
1.5.2	Paradoxically curved middle turbinate	Concave middle turbinate Inverse middle turbinate	n.e.	***Paradoxical middle turbinate***	3–26%
1.5.3	Concha bullosa (of middle turbinate)	Bullosa middle turbinate/concha	n.e.	***Concha bullosa (of middle turbinate)***	17–36% ~50% in Turkish
1.5.3.1	Interlamellar cell	Interlamellar cell	n.e.	***Interlamellar cell***	
1.6	Middle meatus	Meatus medius Middle nasal meatus	Meatus nasi medius	***Middle meatus***	
1.7	Ostiomeatal complex	Ostiomeatal complex	n.e.	***Ostiomeatal complex***	
1.8	Superior turbinate	Superior nasal turbinate Second (persisting) ethmoturbinal Second ethmoidal turbinate Superior concha Concha superior	Concha nasi superior	***Superior turbinate***	
1.8.1	Concha bullosa (of superior turbinate)	Concha bullosa (of superior turbinate)	n.e.	***Concha bullosa (of superior turbinate)***	1–2%
1.9	Superior meatus	Superior nasal meatus Upper nasal meatus	Meatus nasi superior	***Superior meatus***	
1.10	Supreme turbinate	Supreme nasal turbinate Third (persisting) ethmoturbinal Third ethmoidal turbinate Supreme concha Highest nasal concha Concha (nasalis) suprema (Morgagni)	Concha nasi suprema	***Supreme turbinate***	
1.11	Supreme meatus	Supreme nasal meatus	n.e.	***Supreme meatus***	
2	**Spheno-ethmoidal recess**	Recessus spheno-ethmoidalis	Recessus sphenoethmoidalis	***Spheno-ethmoidal recess***	
3	**Sphenopalatine foramen**	Foramen of sphenopalatine artery	Foramen sphenopalatinum	***Sphenopalatine foramen***	
4	**Olfactory cleft**	Olfactory ridge Olfactory groove Olfactory fissure Olfactory area	Sulcus olfactorius	***Olfactory cleft***	

Continued

TABLE 39.1 **Surgical and anatomical terminology—cont'd**

	Present 'surgical' terminology	Rhinological and anatomical synonyms (textbooks, literature)	*Terminologia Anatomica 1*	Suggested English terminology (position paper)	Frequency of variant in literature*
4.1	Olfactory fibre(s)	Olfactory fibre(s) Fila olfactoria	Fila olfactoria (sing: filum olfactorium)	***Olfactory fibre(s)***	
5	**Choana (plur: choanae)**	Posterior nasal aperture(s) Nares posteriores	Choana (plur: choanae) Apertura nasalis posterior	***Choana***	
6	**Maxillary sinus**	Maxillary antrum	Sinus maxillaris	***Maxillary sinus***	
6.1	Maxillary sinus ostium	Maxillary opening	n.e.	***Maxillary sinus ostium***	
6.1.1	Accessory maxillary ostium (plur: ostia)	Additional maxillary sinus ostium	n.e.	***Accessory ostium***	5% normal 25% CRS patients
6.1.2	Maxillary hiatus	Maxillary hiatus	Hiatus maxillaris	***Maxillary hiatus***	
6.2	Infraorbital nerve canal	Infraorbital canal	Canalis infraorbitalis	***Infraorbital canal***	
6.3	Zygomatic recess	Recessus zygomaticus	n.e.	***Zygomatic recess***	
6.4	Alveolar recess	Recessus alveolaris	n.e.	***Alveolar recess***	
6.5	Prelacrimal recess	Prelacrimal recess	n.e.	***Prelacrimal recess***	
6.6	Lacrimal eminence	Eminentia lacrimalis Bulging of nasolacrimal duct	n.e.	***Lacrimal eminence***	
6.7	Canine fossa	Canine fossa Fossa canina	Fossa canina	***Canine fossa***	
6.8	Anterior (nasal) fontanelle	Fontanella nasal anterior	n.e.	***Anterior fontanelle***	
6.9	Posterior (nasal) fontanelle	Fontanella nasal posterior	n.e.	***Posterior fontanelle***	
6.10	Maxillary artery	(Internal) maxillary artery	Arteria maxillaris	***Maxillary artery***	
7	**Ethmoidal complex**	Ethmoid Ethmoidal sinus(es) Ethmoidal labyrinth Labyrinthus ethmoidalis	Cellulae ethmoidales	***Ethmoidal complex***	
7.1	Anterior ethmoidal cells	Anterior ethmoid Sinus ethmoidalis anterior Cells of anterior ethmoid Anterior ethmoid complex	Cellulae ethmoidales anteriores	***Anterior ethmoidal cells***	
7.2	Middle ethmoidal cells		Cellulae ethmoidales mediae	***t.b.a.***	
7.3	Posterior ethmoidal cells	Posterior ethmoid Sinus ethmoidalis posterior Dorsal ethmoidal cells Cells of posterior ethmoid	Cellulae ethmoidales posteriores	***Posterior ethmoidal cells***	
7.4	Anterior ethmoidal artery	Anterior ethmoidal artery	Arteria ethmoidalis anterior	***Anterior ethmoidal artery***	
7.5	Middle ethmoidal artery	Third ethmoidal artery Accessory ethmoidal artery Intermediate ethmoidal artery Arteria ethmoidalis tertia (40%)	n.e.	***Accessory ethmoidal artery***	(Var) up to 45% if it equates to any situation where >2 arteries
7.6	Posterior ethmoidal artery	Posterior ethmoidal artery	Arteria ethmoidalis posterior	***Posterior ethmoidal artery***	
8	**Anterior ethmoidal complex**	Anterior ethmoidal cells	Cellulae ethmoidales anteriores	***Anterior ethmoidal complex***	
8.1	Agger nasi	Operculum conchae mediae	Agger nasi	***Agger nasi***	
8.1.1	Agger nasi cell	Pneumatized agger nasi Agger cell	n.e. (cellula ethmoidalis anterior)	***Agger nasi cell***	>90%
9	**Uncinate process**	Uncinate process	Processus uncinatus	***Uncinate process***	
9.1	Deflected uncinate process	Doubled middle turbinate Anteriorly curved uncinate process Everted uncinate process	n.e.	***Everted uncinate process***	5–22%
9.2	Aerated uncinate process	Bullous uncinate process Pneumatized uncinate process	n.e.	***Aerated uncinate process***	1–2%
9.3	Basal lamella of uncinate process	Ground lamella of uncinate process Uncinate lamella First basal lamella	n.e.	***Basal lamella of uncinate process***	
9.4	Hiatus semilunaris	Semilunar hiatus Hiatus semilunaris inferior Semilunar gap	Hiatus semilunaris	***Inferior semilunar hiatus***	
9.4	Hiatus semilunaris (superior)	Hiatus semilunaris superior Hiatus semilunaris posterior Superior semilunar hiatus	n.e.	***Superior semilunar hiatus***	(Var)
9.5	Ethmoidal bulla	Bulla ethmoidalis	Bulla ethmoidalis	***Ethmoidal bulla***	
9.5.1	Non-pneumatized ethmoidal bulla	Torus bullaris	n.e.	***t.b.a.***	8%
9.5.2	Bulla lamella	Second ground lamella Basal lamella of ethmoidal bulla Second basal lamella	n.e.	***Basal lamella of ethmoidal bulla***	
9.5.3	Suprabullar recess	Sinus lateralis Suprabullar cell Recessus bullaris	n.e.	***Suprabullar recess***	71%
9.5.4	Retrobullar recess	Hiatus semilunaris superior	n.e.	***Retrobullar recess***	94%

TABLE 39.1 Surgical and anatomical terminology—cont'd

	Present 'surgical' terminology	Rhinological and anatomical synonyms (textbooks, literature)	*Terminologia Anatomica 1*	Suggested English terminology (position paper)	Frequency of variant in literature*
9.5.5	Supraorbital recess	Supraorbital cell Supraorbital ethmoid cell Cellula orbitalis	n.e.	***Supraorbital recess***	(Var) 17%
9.5.6	Infraorbital cell	Haller cell Orbito-ethmoidal cell	n.e.	***Infraorbital cell***	4–15%
9.6	Ethmoidal infundibulum	Ethmoidal infundibulum	Infundibulum ethmoidale	***Ethmoidal infundibulum***	
9.6.1	Terminal recess	Terminal recess of ethmoidal infundibulum Recessus terminalis	n.e.	***Terminal recess***	(Var) 49–85%
9.7	Frontal recess	Recessus frontalis Frontal outflow tract	n.e.	***Frontal recess***	
9.7.1	Infundibular cells	Infundibular cells	n.e.	***Anterior ethmoidal cells***	(Var)
9.7.2	Lacrimal cells	Lacrimal cells	n.e.	***Anterior ethmoidal cells***	(Var) 33%
9.7.3	Nasofrontal duct	Frontal outflow tract Frontal recess	Ductus nasofrontalis	***t.b.a.***	
9.7.4	Maxillary crest	Lacrimal crest Maxillary line	n.e.	***Lacrimal bulge***	
9.7.5	Ethmoidal crest	Crista ethmoidalis Ethmoidal crest of the palatine bone	Crista ethmoidalis	***Ethmoidal crest***	
9.7.6	Frontal sinus drainage pathway	Nasofrontal duct Frontal outflow tract Frontal recess	n.e.	***Frontal sinus drainage pathway***	
10	**Frontal sinus**	Frontal sinus	Sinus frontalis	***Frontal sinus***	
10.1	Interfrontal septum	Frontal sinus septum	Septum sinuum frontalium	***Frontal intersinus septum***	
10.2	Frontal sinus infundibulum	Frontal sinus infundibulum	n.e.	***Frontal sinus infundibulum***	
10.3	Intrafrontal cells	Frontal sinus cells Kuhn type 3/4 cells	Bullae frontales (sing: bulla frontalis)	***Frontoethmoidal cells***	(Var)
10.4	Intersinus septal cell	Intersinus septal cell	n.e.	***Intersinus septal cell***	
10.5	Frontal bulla	Frontal bulla	n.e. (cellula ethmoidalis anterior)	***t.b.a.***	(Var)
10.6	Frontal sinus ostium	Frontal ostium Opening of frontal sinus	Apertura sinus frontalis	***Frontal sinus opening***	
10.7	Frontal beak	Nasal beak Superior nasal spine	Spina frontalis (ossis frontalis) Spina nasalis interna	***Frontal beak***	
11	**Posterior ethmoidal complex**	Posterior ethmoidal cells	Cellulae ethmoidales posteriores	***Posterior ethmoidal complex***	
11.1	Onodi cell	Spheno-ethmoidal cell Gruenwald cell	n.e. (cellula ethmoidalis posterior)	***Sphenoethmoidal cell***	4–65% 8–14% Caucasians, 26–29% Asians
11.2	Basal lamella of superior turbinate	Fourth basal lamella	n.e.	***Basal lamella of superior turbinate***	
11.3	Lamina papyracea	Medial orbital wall Papyraceous lamina	Lamina orbitalis ossis ethmoidalis	***Lamina papyracea***	
11.4	Orbital apex	Orbital apex	n.e.	***Orbital apex***	
11.5	Anulus of Zinn	Common tendinous ring Common anular tendon	Anulus tendineus communis	***Anulus of Zinn***	
11.6	Ophthalmic artery	Ophthalmic artery	Arteria ophthalmica	***Ophthalmic artery***	
12	**Sphenoid sinus**	Sphenoid sinus	Sinus sphenoidalis	***Sphenoid sinus***	
12.1	Intersphenoidal septum	Intersphenoidal septum Sphenoid sinus septum	Septum sinuum sphenoidalium	***Sphenoid intersinus septum***	
12.2	Accessory sphenoidal septum (plur: septa)	Incomplete sphenoidal septations Partial sphenoidal septations Sphenoid sinus subseptations	n.e.	***Sphenoid septations***	(Var) 76%
12.3	Sphenoid sinus ostium	Sphenoid (sinus) ostium Sphenoid (sinus) opening Natural sphenoid ostium	Ostium (apertura) sinus sphenoidalis (plur: ostia sinuum sphenoidalium)	***Sphenoid sinus ostium***	
12.4	Planum sphenoidale	Sphenoid sinus roof Jugum sphenoidale Sphenoidal yoke	Jugum sphenoidale	***Planum sphenoidale***	
12.5	Sellar floor	Floor of sella Sellar bulge	n.e.	***Sellar floor***	
12.6	Vidian canal	Pterygoid canal Canalis nervi pterygoidei	Canalis pterygoideus	***Pterygoid (Vidian) canal***	
12.7	Foramen rotundum	Canalis rotundus Round foramen	Foramen rotundum	***Foramen rotundum***	

Continued

TABLE 39.1 Surgical and anatomical terminology—cont'd

	Present 'surgical' terminology	Rhinological and anatomical synonyms (textbooks, literature)	*Terminologia Anatomica 1*	Suggested English terminology (position paper)	Frequency of variant in literature*
12.8	Lateral recess of sphenoid sinus	Lateral recess of sphenoid sinus	n.e.	***Lateral recess of sphenoid sinus***	(Var)
12.9	Optic tubercle	Optical nerve tubercle Prominentia nervi optici	Tuberculum nervi optici	***Optic nerve tubercle***	
12.9.1	Optic nerve canal	Eminentia nervi optici Optic nerve bulging Optic nerve canal contour	Canalis opticus	***Optic nerve canal***	(Var)
12.9.2	Carotid artery prominence	Prominentia canalis carotici	n.e.	***Carotid artery bulge***	(Var)
12.9.3	Optico-carotid recess	Carotid-optical recess Infraoptical recess	n.e.	***Optico-carotid recess***	(Var)
12.9.4	Sternberg's canal	Canalis craniopharyngicus lateralis	n.e.	***Lateral craniopharyngeal (Sternberg's) canal***	4% adults
13	**Sphenoidal rostrum**	Rostrum	Rostrum sphenoidale	***Sphenoid rostrum***	
14	**Vomerovaginal canal**	Vomerovaginal canal	Canalis vomerovaginalis	***Vomerovaginal canal***	
15	**Palatovaginal canal**	Palatovaginal canal	Canalis palatovaginalis	***Palatovaginal canal***	
16	**Skull base**	Cranial base Basicranium	Basis cranii	***Skull base***	
16.1	Inner skull base	Internal surface of cranial base	Basis cranii interna	***Inner skull base***	
17	**Anterior cranial fossa**	Anterior cranial fossa	Fossa cranii anterior	***Anterior cranial fossa***	
17.1	Olfactory fossa	Ethmoidal notch Fovea ethmoidalis	n.e.	***Olfactory fossa***	
17.2	Cribriform plate	Lamina cribrosa Roof of inner nose	Lamina cribrosa (ossis ethmoidalis)	***Cribriform plate***	
17.2.1	Cribriform foramina	Cribriform openings	Foramina cribrosa	***Cribriform foramina***	
17.2.2	Lateral lamella of cribriform plate	Lateral lamella of cribriform plate	n.e.	***Lateral lamella of cribriform plate***	
17.3	Ethmoidal roof	Foveae ethmoidales (ossis frontalis)	n.e.	***Ethmoidal roof***	
17.4	Crista galli	Crista galli	Crista galli	***Crista galli***	
17.4.1	Pneumatized crista galli	Pneumatized crista galli	n.e.	***Pneumatized crista galli***	13%
17.5	Foramen caecum	Foramen caecum	Foramen caecum	***Foramen caecum***	Open (Var: 1.4%)
18	**Middle cranial fossa**	Middle cranial fossa	Fossa cranii media	***Middle cranial fossa***	
18.1	Sella	Hypophysial fossa Pituitary fossa	Sella turcica	***Sella (turcica)***	
18.2	Sellar tubercle	Suprasellar notch	Tuberculum sellae	***Tuberculum sellae***	
18.3	Dorsum sellae	Dorsum sellae	Dorsum sellae	***Dorsum sellae***	
18.4	Anterior clinoid process	Anterior clinoid process	Processus clinoideus anterior (plur: processus clinoidei anteriores)	***Anterior clinoid process***	Pneumatized (Var: 16.5%)
18.5	Posterior clinoid process	Posterior clinoid process	Processus clinoideus posterior (plur: processus clinoidei posteriores)	***Posterior clinoid process***	
19	**Posterior cranial fossa**	Posterior cranial fossa	Fossa cranii posterior	***Posterior cranial fossa***	
19.1	Clivus	Clivus	Clivus	***Clivus***	

Abbreviations: n.e., non existent; sing., singular; plur., plural; t.b.a., to be abandoned.

*The frequency of specific variations in the anatomy varies considerably in the literature, which relates to the definitions used, the methodology utilized, i.e. anatomical dissection or imaging, whether the study included normal controls and/or patients with chronic rhinosinusitis (CRS), and the ethnicity of the subjects.

With permission from Lund VJ, Stammberger H, Fokkens WJ et al 2014 European position paper on the anatomical terminology of the internal nose and paranasal sinuses. Rhinology 50:Suppl 24:1–34.

The proportions of the nose and face, both from in front and from the side, are of enormous significance to the rhinoplastic surgeon. Aesthetic proportions of the nose vary depending on sex, age, ethnicity and facial characteristics; however, ranges of normality are described to assist in aesthetic assessment (Akguner et al 1998). The female nose is slightly smaller and narrower than the male nose; it is often slightly concave in profile view, with a slightly obtuse nasolabial angle (increased tip rotation). In terms of overall proportion, the face may be divided into horizontal thirds and vertical fifths, with the nose occupying the middle section of each. The width of the nose is roughly 70% of the length; the width of the alar base is usually equal to the intercanthal distance. The height of the nose is defined by tip projection, where the proportion of the length of a line from the tip to the alar groove to the length of a line from nasion to alar groove is in the range of 0.55–0.60. The nasolabial angle, reflecting upward rotation of the nose from the upper lip, normally lies within a range of 105–120° in females and 90–105° in males. On basal view, the nose is roughly shaped as an equilateral triangle. The nares usually measure 1.5–2 cm anteroposteriorly and 0.5–1 cm transversely, and are narrower in front; they occupy approximately two-thirds of the height of the base. The midline columella, containing the caudal end of the nasal septum and the medial crura of the lower lateral cartilages, usually extends 3–5 mm below the nares on lateral views (Fig. 39.2).

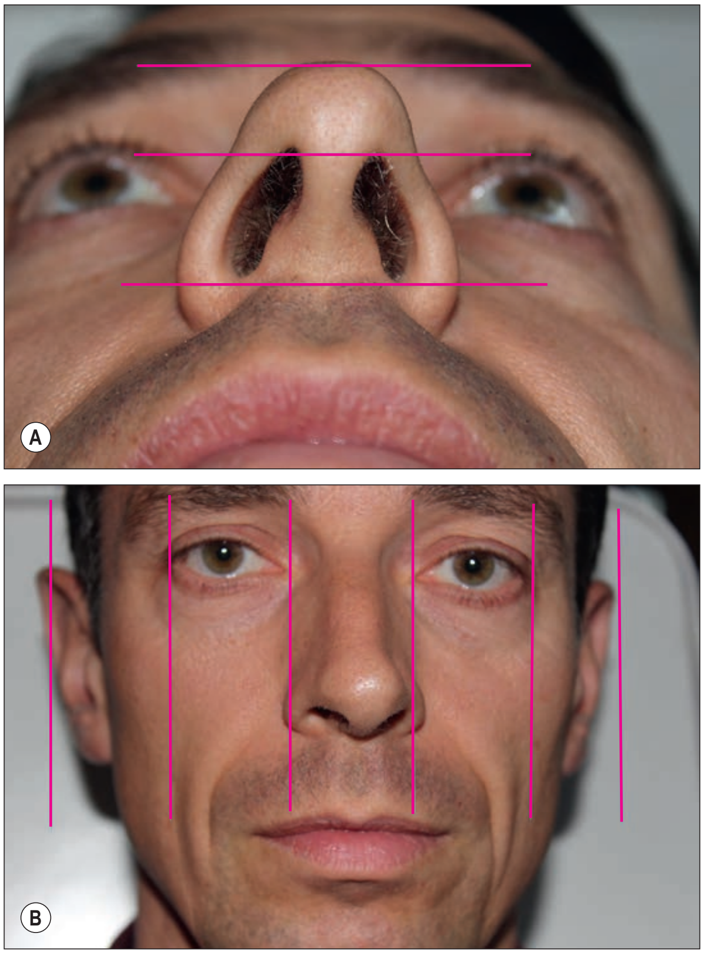

Fig. 39.2 The adult male nose. **A**, Basal view. **B**, Frontal view. The face can be divided into horizontal thirds and vertical fifths, with the nose filling the central segment in terms of both width and height. The basal view may also be divided into horizontal thirds, with the nostrils filling the lower two-thirds.

Lateral soft tissue area

The lateral margin of the lateral cartilage, the piriform aperture and the cranial margin of the lateral crus of the major alar cartilage enclose a triangle containing loose fibroareolar tissue, the transverse portion of nasalis, and one or more small sesamoid cartilages.

Caudal lobular notch

The domal segment of the intermediate crus of the major alar cartilage has a small indentation. The apex of the nostril is a soft tissue triangle with little soft tissue separating the internal and external skin. Incisions in this area may cause unsightly scarring and deformity.

Alar soft tissue area

The lateral crus fails to extend to the lateral limit of the lobule, forming the fourth soft tissue area.

Bones and cartilage

Bony skeleton of the external nose

The piriform aperture has sharp edges. It is bounded below and laterally by the maxilla and above by the nasal bones (Fig. 39.3). The lateral part of the inferior edge of the piriform aperture merges into its lateral wall, which is formed by the frontal process of the maxilla. It is bounded above by the nasal part of the frontal bone and superomedially by the lateral edge of the nasal bone.

The paired nasal bones vary in thickness and width, which is of significance in planning osteotomies. They are thickest and widest at the nasofrontal suture, narrow at the nasofrontal angle before they widen, and become thinner 9–12 mm below the nasofrontal angle. They average 25 mm in length but this can vary widely. The perpendicular plate of the ethmoid bone (part of the bony nasal septum) articulates with the undersurface of the nasal bones and provides support to the dorsum of the nose. A midline bony spine deep to the fused nasal bone projects inwards to articulate with the perpendicular plate of the ethmoid and fuses with the fibrous tissue connecting the lateral nasal cartilages and cartilaginous septum. This is known as the keystone area and provides essential support to the nasal dorsum (Simon et al 2013).

Fractures of the nasal bones The most common injury to the facial skeleton is a fracture of the nasal bones. In simple fractures, the break often occurs between the proximal thicker bone and the thinner bone distally. Displaced fractures require reduction to avoid cosmetic deformity. The terminal branch of the anterior ethmoidal nerve and its accompanying vessels are at risk when injuries involve the dorsum of the nose.

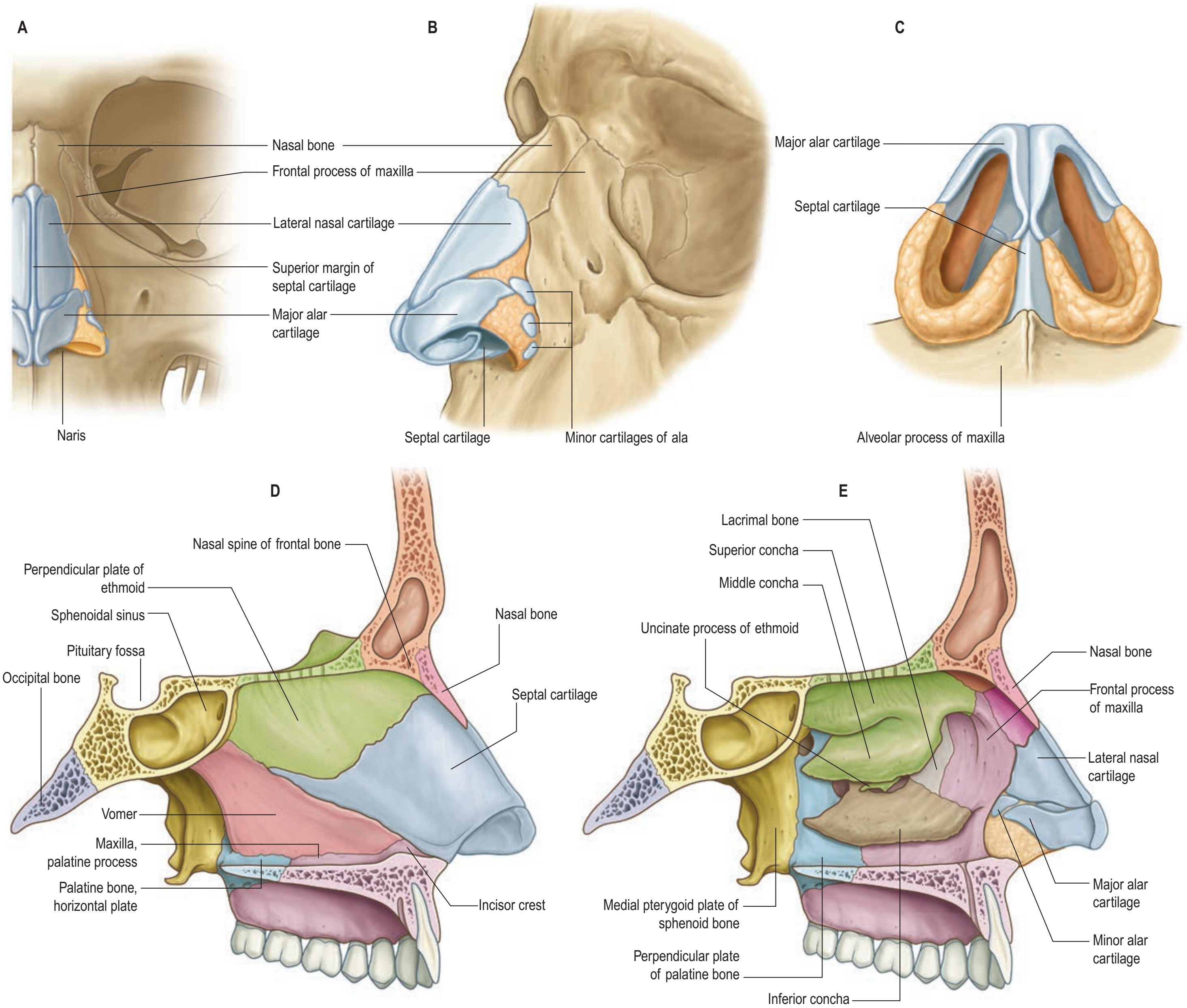
A
B
C
Nasal bone
Frontal process of maxilla
Lateral nasal cartilage
Superior margin of septal cartilage
Major alar cartilage
Major alar cartilage
Septal cartilage
Naris
Septal cartilage
Minor cartilages of ala
Alveolar process of maxilla
D
Nasal spine of frontal bone
Perpendicular plate of ethmoid
Sphenoidal sinus
Pituitary fossa
Occipital bone
Nasal bone
Septal cartilage
Vomer
Maxilla, palatine process
Palatine bone, horizontal plate
Incisor crest
E
Lacrimal bone
Superior concha
Middle concha
Uncinate process of ethmoid
Nasal bone
Frontal process of maxilla
Lateral nasal cartilage
Major alar cartilage
Minor alar cartilage
Medial pterygoid plate of sphenoid bone
Perpendicular plate of palatine bone
Inferior concha

Fig. 39.3 The bony and cartilaginous skeletons of the nose. **A**, The external nose, frontal view. **B**, The external nose, lateral view. **C**, An inferior view of the cartilages. **D**, The nasal cavity, medial wall. **E**, The nasal cavity, lateral wall (left side).

The medial crus has two components, a footplate segment and a columellar segment, which angulate with each other in two planes; they diverge in the basal plane, and rotate upwards in the lateral plane. There is usually asymmetry in the pairs of medial crura.

The medial crus joins the intermediate crus at what is usually the most convex point of the columella, known as the columellar breakpoint.

The intermediate crus is also described in two components. The lobular segment is usually flared and forms the transition between the medial crus and the domal segment of the intermediate crus. The domal segment may be convex, producing an aesthetically pleasing tip; flat, giving a 'boxy' appearance; or convex, producing a 'double-dome'. The domal or tip-defining points are usually formed by the most anterior projection of the domal segment. The amount of divergence of the domes, and the thickness of the overlying soft tissue envelope, determine the relative position of the tip-defining points. The dome projects up to 8–10 mm caudal, and 3–6 mm anterior, to the anterior septal angle, the difference between the two creating the supratip break-point. Disruption of this relationship with rhinoplasty, with loss of projection of the tip, may produce a 'polybeak' deformity.

Classically, transverse connective tissue fibres have been described binding the medial and intermediate crura; interdomal, intercrural and septocrural ligaments have been described. Cadaveric studies by Zhai et al (1995) disputed the presence of transverse fibres, and found that all connective tissue fibres run parallel to the cartilages. These findings notwithstanding, the fibrous connections along the length of the medial and intermediate crura form a single functional unit in the tip.

The large lateral crus determines the shape of the alar lateral wall. Medially, it is a continuation of the intermediate crus, while laterally it connects with accessory cartilages. It runs at the caudal edge of the alar rim in the anterior half, then moves cephalically, leaving a soft tissue area in the rim laterally. Typically, the longitudinal axis of the lateral crus forms an angle of 45° with the septum. More vertical, or cephalic, positioning results in a 'parenthesis' tip deformity.

The lateral crus may take a highly variable position, being either convex or concave, or a combination of both, in medial and lateral portions; asymmetry from side to side has been reported in over half of anatomical specimens.

A chain of lateral accessory cartilages with dense fibrous attachments connect to the lateral crus and the piriform aperture, and to the anterior nasal spine through connection in the floor of the nose.

Tip support

The inherent strength and shape of the cartilaginous framework, and its attachments to surrounding structures, provide support to the tip of the nose. Typically, 'major' and 'minor' tip support mechanisms are described.

Major tip support mechanisms The major mechanisms supporting the tip are: the size, shape and strength of the major alar cartilages; the medial crural footplate attachment to the caudal part of the septum; the attachment of the caudal border of the lateral cartilages to the cephalic border of the major alar cartilages; and the cartilaginous dorsal septum.

Minor tip support mechanisms The minor mechanisms supporting the tip are: the ligamentous sling spanning the domes of the lower lateral cartilages (i.e. the interdomal ligament); the sesamoid complex of major alar cartilages; the attachment of the major alar cartilages to the overlying skin/soft tissue envelope; the nasal spine; and the membranous septum.

Rhinoplasty approaches, either through an intercartilaginous incision between the lateral and the major alar cartilages (closed rhinoplasty), or through an incision caudal to the major alar cartilages and degloving the entire cartilaginous framework (open rhinoplasty), disrupt the tip support mechanisms; the integrity of these mechanisms must be restored during the procedure to prevent loss of tip support and subsequent tip ptosis.

Cartilaginous skeleton of the external nose

The cartilaginous framework consists of the paired lateral and major cartilages and several minor alar nasal cartilages (see Fig. 39.3).

Lateral (superior/upper lateral) nasal cartilage

The lateral nasal cartilage is triangular, and its anterior margin is thicker than the posterior margin. The upper part fuses with the septal cartilage, but anteroinferiorly, it may be separated from it by a narrow fissure. The superior margin of the lateral nasal cartilage is attached to the nasal bone and frontal process of the maxilla, and the inferior margin is connected by fibrous tissue to the lateral crus of the major alar cartilage. Laterally, the cartilage is attached indirectly to the margins of the piriform aperture by loose fibroareolar connective tissue, which may also contain one or more small sesamoid cartilages. The angle formed between the caudal end of the lower lateral and the septum, the internal nasal valve, is usually between 10 and 15° and represents the narrowest cross-sectional area and the area of greatest airflow resistance. Structural abnormalities in this area are likely to produce symptomatic nasal obstruction.

Major alar (lower lateral) cartilage

The major alar cartilage is a highly complex, thin, flexible plate, which is integral to the nasal lobule. It lies below the upper lateral cartilage and curves acutely around the anterior part of its naris. The medial part, the narrow medial crus (septal process), is loosely connected by fibrous tissue to its contralateral counterpart and to the anteroinferior part of the septal cartilage. The intermediate crus forms the margin of the apex of the nostril. The domes give rise to the tip-defining points of the nose. The lateral crus lies lateral to the naris and runs superolaterally away from the margin of the nasal ala. The upper border of the lateral crus of the major alar cartilage is attached by fibrous tissue to the lower border of the lateral nasal cartilage. Its lateral border is connected to the frontal process of the maxilla by a tough fibrous membrane containing three or four minor alar cartilages. The junction between the lateral crura of the major alar and lateral cartilages is variable; the two edges may form a 'scroll', with an outcurving of the lateral cartilage meeting an incurving of the major alar cartilage, in which case the lateral crus is then the more lateral at the junction. The lateral crus is shorter than the lateral margin of the naris; the most lateral part of the margin of the ala nasi is fibroadipose tissue covered by skin. In front, the angulations or 'domes' between the medial and lateral crurae of the major alar cartilages are separated by a notch palpable at the tip of the nose.

Alar cartilage morphology

Available with the *Gray's Anatomy* e-book

Muscles

The nasal muscle group includes procerus, nasalis, dilator naris anterior, depressor septi and levator labii superioris alaeque nasi (**Fig. 39.4**; see Figs 36.17, 36.18). These muscles are involved in respiration and facial expression. Any or all of these muscles may be absent in cleft lip deformities with corresponding functional and aesthetic consequences.

Procerus

Procerus is a small pyramidal muscle that lies close to, and is often partially blended with, the medial side of the frontal part of occipitofrontalis. It arises from a fascial aponeurosis attached to the periosteum covering the lower part of the nasal bone, the perichondrium covering the upper part of the lateral nasal cartilage, and the aponeurosis of the transverse part of nasalis. It is inserted into the glabellar skin over the lower part of the forehead between the eyebrows.

Vascular supply Procerus is supplied mainly by branches from the facial artery.

Innervation Procerus is supplied by temporal and lower zygomatic branches from the facial nerve (a supply from the buccal branch has been described).

Actions Procerus draws down the medial angle of the eyebrow and produces transverse wrinkles over the bridge of the nose. It is active in frowning and 'concentration', and helps to reduce the glare of bright sunlight. Not surprisingly, it is a common target in non-surgical facial rejuvenation techniques, using botulinum toxin.

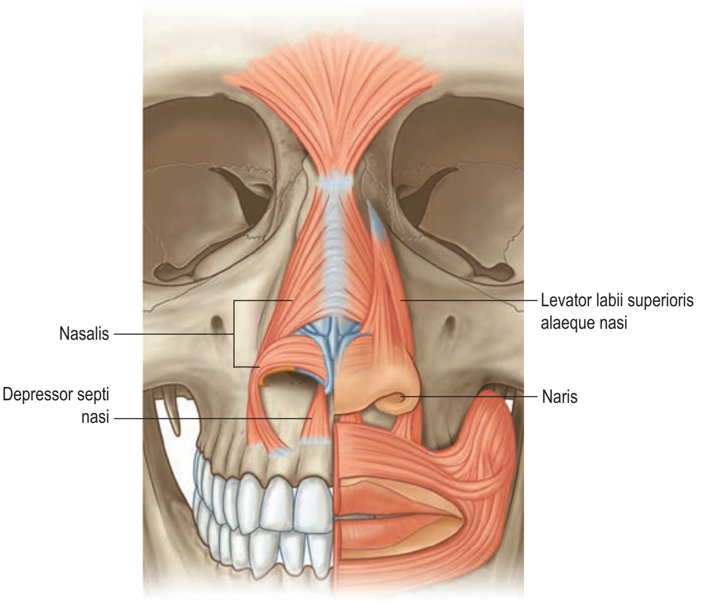

Fig. 39.4 The nasal musculature. (With permission from Drake RL, Vogl AW, Mitchell A (eds) Gray's Anatomy for Students, 2nd ed. Elsevier, Churchill Livingstone. Copyright 2010.)

Nasalis

Nasalis consists of transverse and alar components. The transverse part (compressor naris) is attached to the maxilla above and lateral to the incisive fossa, and lateral to the alar part. Its fibres pass upwards and medially, and expand into a thin aponeurosis that merges with its counterpart across the bridge of the nose, with the aponeuroses of procerus, and with fibres from levator labii superioris alaeque nasi. Fibres from the transverse part may also blend with the skin of the nasolabial and alar folds. The alar part (pars alaris or dilator naris posterior) is attached to the maxilla above the lateral incisor and canine, lateral to the bony attachment of depressor septi, and medial to the transverse part, with which it partly merges. Its fibres pass upwards and anteriorly, and are attached to the skin of the ala above the lateral crus of the lower lateral cartilage, and to the posterior part of the mobile septum. The pars alaris helps to produce the upper ridge of the philtrum.

Dilator naris anterior (also known as apicis nasi or the small dilator muscle of the nose) is a very small muscle attached to the upper lateral cartilage, the alar part of nasalis, the caudal margin of the lateral crus and the lateral alar crus. It encircles the naris and acts as a primary dilator of the nostril.

Vascular supply Nasalis is supplied by branches from the facial artery and from the infraorbital branch of the maxillary artery.

Innervation Nasalis is supplied by the buccal branch of the facial nerve. It may also be supplied by the zygomatic branch of the facial nerve.

Actions The transverse part compresses the nasal aperture at the junction of the vestibule and the nasal cavity. The alar parts draw the alae and posterior part of the columella downwards and laterally, and so assist in widening the nares and in elongating the nose. They are active immediately before inspiration. Dilator naris anterior and the alar part of nasalis (dilator naris posterior) probably function to prevent collapse of the nasal valve during inspiration. Their electromyographic activity is directly proportional to ventilatory resistance and is modified by signals that travel from pulmonary mechano- and pressure receptors via afferent vagal pathways to the brainstem respiratory centre; the efferent limb of the reflex arc runs in the facial nerve.

Depressor septi

Depressor septi lies immediately deep to the mucous membrane of the upper lip. It is usually attached to the periosteum covering the maxilla above the central and lateral incisors and the anterior nasal spine, and to the fibres of orbicularis oris above the central incisor. Its fibres pass to the columella, the mobile part of the nasal septum and the base of the medial crus of the nasal cartilage. A few muscle slips may pass between the medial crura into the nasal tip. Depressor septi may be absent or rudimentary.

Vascular supply Depressor septi is supplied by the superior labial branch of the facial artery.

Innervation Depressor septi is innervated by the buccal branch, and sometimes by the zygomatic branch, of the facial nerve.

Actions Depressor septi pulls the columella, the tip of the nose and the nasal septum downwards. It tenses the nasal septum at the start of nasal inspiration and, with the alar part of nasalis, widens the nasal aperture, as well as causing the nose to 'dip' when some people smile.

Levator labii superioris alaeque nasi

Levator labii superioris alaeque nasi arises from the upper part of the frontal process of the maxilla and, passing obliquely downwards and laterally, divides into medial and lateral slips. The medial slip blends into the perichondrium of the lateral crus of the major alar cartilage of the nose and the skin over it. The lateral slip is prolonged into the lateral part of the upper lip, where it blends with levator labii superioris and orbicularis oris. Superficial fibres of the lateral slip curve laterally across the front of levator labii superioris and attach along the floor of the dermis at the upper part of the nasolabial furrow and ridge.

Vascular supply Levator labii superioris alaeque nasi is supplied by the facial artery and the infraorbital branch of the maxillary artery.

Innervation Levator labii superioris alaeque nasi is innervated by zygomatic and superior buccal branches of the facial nerve.

Actions The lateral slip raises and everts the upper lip and raises, deepens and increases the curvature of the top of the nasolabial furrow. The medial slip pulls the lateral crus superiorly, displaces the circumalar furrow laterally, and modifies its curvature; it is a dilator of the naris. Depressor septi and the medial slip of levator labii superioris alaeque nasi are sometimes described as secondary nasal dilators; there is little evidence that either of these muscles has any direct influence on the nasal valve.

Anomalous nasal muscles

Anomalous, inconstant, nasal muscles have been described. They include anomalous nasi, attached to the frontal process of the maxillae, transverse part of nasalis and the upper lateral cartilage (i.e. in a region normally devoid of muscle), and compressor narium minor, which passes between the anterior part of the lower lateral cartilage and the skin near the margins of the nares. The existence of a small levator septi nasi has been questioned.

Superficial musculo-aponeurotic system (SMAS)

Available with the *Gray's Anatomy* e-book

Cutaneous vascular supply and lymphatic drainage

Nasal skin receives its blood supply from branches of the facial, ophthalmic and infraorbital arteries. The alae and lower part of the nasal septum are supplied by lateral nasal and septal branches of the facial artery, and the lateral aspects and dorsum of the nose are supplied by the dorsal nasal branch of the ophthalmic artery and the infraorbital branch of the maxillary artery. The venous networks draining the external nose do not run parallel to the arteries but correspond to arteriovenous territories of the face. The frontomedian region of the face, including the nose, drains to the facial vein, and the orbitopalpebral area of the face, including the root of the nose, drains to the ophthalmic veins. The connections of the veins of the nose, upper lip and cheek (the 'danger triangle of the face') with the drainage area of the valveless ophthalmic veins, and hence to the cavernous sinus, are clinically significant because they can be a route for spreading infection that initiates thrombosis of the major intracranial sinuses. Lymph drainage is primarily to the submandibular group of nodes, although lymph draining from the root of the nose drains to superficial parotid nodes.

Cutaneous innervation

Nasal skin is innervated by the infratrochlear and external nasal branches of the nasociliary nerve (ophthalmic division, trigeminal nerve), and the nasal branch of the infraorbital nerve (maxillary division, trigeminal nerve).

NASAL CAVITY

The nasal cavity is an irregular space between the roof of the mouth and the cranial base. It is wider below than above, and widest and vertically deepest in its central region, where it is divided by a vertical, midline, osseocartilaginous septum. The bony part of the septum reaches the posterior limit of the cavity.

The nasal cavity communicates with the paranasal sinuses and opens into the nasopharynx through a pair of oval openings, the posterior nasal apertures or choanae. The latter are separated by the posterior border of the vomer, and each is limited above by the vaginal process of the medial pterygoid plates, laterally by the perpendicular plate of the palatine bone and the medial pterygoid plate, and below by the horizontal plate of the palatine bone (Fig. 39.5). The parameters of the intranasal spaces depend on age and gender: growth is usually completed by the age of 16 (Samoliński et al 2007). The adult choana typically measures 2.5 cm in vertical height and 1.3 cm transversely; size is not usually affected by deviations of the nasal septum. The vomerovaginal and palatovaginal canals are found in the roof of this region.

Each half of the nasal cavity has a vestibule, roof, floor, medial (septal) and lateral walls.

Nasal vestibule

The nasal vestibule lies just inside the naris. It is limited above and behind by a curved ridge, the limen nasi, raised where the greater ala of the lateral cartilaginous crus overlaps the lower edge of the lateral nasal cartilage on each side. On the septal side of the nasal cavity, the superior edge of the medial crus of the major alar cartilage (the medial intumescence) marks the boundary between the nasal vestibule and the nasal cavity. The medial wall of the vestibule is formed by a mobile septum consisting of the columella (which does not contain cartilage) and the underlying medial crura of the alar cartilages.

Roof

The roof is horizontal in its central part and slopes downwards in front and behind (Fig. 39.3D–E). The anterior slope is formed by the nasal spine of the frontal bones and by the nasal bones. The central region is formed by the cribriform plate of the ethmoid bone, which separates the nasal cavity from the floor of the anterior cranial fossa. It contains numerous small perforations that transmit the olfactory nerves and their ensheathing meningeal layers, and a separate anterior foramen that transmits the anterior ethmoidal nerve and vessels. The height of the cranial base is greatest anteriorly; hence, when dissecting along the cranial base during sinus surgery, it is safest to do so from back to front, addressing the lower-lying posterior region first to avoid inadvertent intracranial penetration. Posteriorly, the roof of the nasal cavity is formed by the anterior aspect of the body of the sphenoid, interrupted on each side by an opening of a sphenoidal sinus, and the sphenoidal conchae or superior conchae.

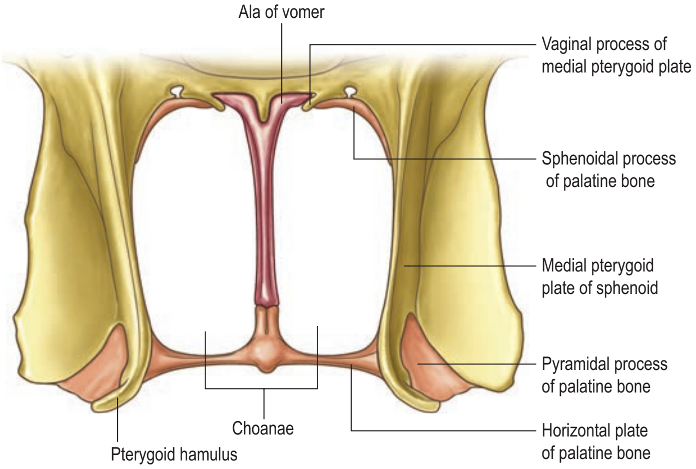
Ala of vomer
Vaginal process of medial pterygoid plate
Sphenoidal process of palatine bone
Medial pterygoid plate of sphenoid
Pyramidal process of palatine bone
Choanae
Horizontal plate of palatine bone
Pterygoid hamulus

Fig. 39.5 A posterior view of the choanae.

Although each muscle is independent in terms of innervation and function, the mimetic muscles of the nose form a continuous layer with connections between all the muscular and ligamentous components (Saban et al 2008). Thus, the superficial musculo-aponeurotic system is continuous from the nasofrontal process to the nasal tip, splitting at the caudal end of the lateral cartilage into superficial and deep layers, each with medial and lateral components (Oneal et al 1999). Dissection in rhinoplasty is usually performed in a sub-superficial musculo-aponeurotic system plane. (For further information on the superficial musculo-aponeurotic system, see Ch. 36).

Floor

The floor of the nasal cavity is smooth and concave transversely, and slopes up from the anterior to the posterior apertures. The greater part is formed by the palatine processes of the maxillae, which articulate posteriorly with the horizontal plates of the palatine bones at the palatomaxillary suture (see Fig. 39.3D–E). Anteriorly, near the septum, a small infundibular opening in the bone of the nasal floor leads into the incisive canals that descend to the incisive fossa; this opening is marked by a slight depression in the overlying mucosa.

The floor of the nose may be deficient as a result of congenital clefting of the hard and/or soft palate.

Medial wall

The medial wall of each nasal cavity is the nasal septum, a thin sheet of bone (posteriorly) and cartilage (anteriorly) that lies between the roof and floor of the cavity (see Figs 36.4, 39.3D).

Bony septum

The septum is usually relatively featureless but sometimes exhibits ridges or bony spurs. The posterosuperior part of the septum and its posterior border are formed by the vomer, which extends from the body of the sphenoid to the nasal crest of the palatine bones and maxilla (see Fig. 36.4). The nasopalatine nerves and vessels groove its surface. (The nasopalatine artery, also known as the septal artery, is a branch of the maxillary artery; it leaves the pterygopalatine fossa through a canal inside the palatine bone, runs parallel to the nasopalatine nerve and ends in the incisive canal, where it anastomoses with the greater palatine artery.) The anterosuperior part of the septum is formed by the perpendicular plate of the ethmoid, which is continuous above with the cribriform plate and the frontal bone. Other bones that make minor contributions to the septum at the upper and lower limits of the medial wall are the nasal bones and the nasal spine of the frontal bones (anterosuperior), the rostrum and crest of the sphenoid (posterosuperior), and the nasal crests of the maxilla and palatine bones (inferior).

Cartilaginous septum

The septal cartilage is almost quadrilateral and may extend back (especially in children) for some distance between the vomer and the perpendicular plate of the ethmoid. Its anterosuperior margin is connected above to the posterior border of the internasal suture, and the distal end of its superior portion is continuous with the upper lateral cartilages. The anteroinferior border is connected by fibrous tissue on each side to the medial crurae of the major alar cartilage. Anteroinferiorly, the cartilaginous septum is attached to the anterior nasal spine, formed by anterior projections of each maxillary crest, and it has a strong, tongue-in-groove attachment with the premaxilla and vomer. The cartilaginous septum anterior to the spine is essential in tip support and should not be excised during septal surgery in order to prevent columellar retraction or loss of tip support. The posterosuperior border joins the perpendicular plate of the ethmoid, while the posteroinferior border is attached to the vomer and, anterior to that, to the nasal crest and anterior nasal spine of the maxilla. The anteroinferior part of the nasal septum between the nares is devoid of cartilage and is therefore called the membranous septum; it is continuous with the columella anteriorly.

Above the incisive canals, at the lower edge of the septal cartilage, a depression pointing downwards and forwards is all that remains of the nasopalatine canal, which connected the nasal and buccal cavities in early fetal life. Near this recess, a minute orifice leads back into a blind tubule, 2–6 mm long, that lies on each side of the septum and houses remnants of the vomeronasal organ (see below).

Lateral wall

The lateral wall of the nasal cavity is formed anteroinferiorly by the maxilla and its anterior and posterior fontanelles (bony deficiencies in the medial wall of the maxilla that are obliterated to varying degrees by fibrous tissue); posteriorly by the perpendicular plate of the palatine bone; and superiorly by the labyrinth of the ethmoid bone (**Fig. 39.6**; see Figs 39.3E, 36.5). It contains three projections of variable size: the inferior, middle and superior nasal conchae or turbinates. (A note on terminology. 'Concha' is the TA-compliant anatomical term; 'turbinate' is the preferred clinical term. In what follows, 'concha' refers to the bony structure seen in dried skulls, while 'turbinate' refers to that bony structure together with the overlying soft tissues and mucosa that are encountered during surgery).

The conchae curve inferomedially in general, each roofing a groove, or meatus, which is open to the nasal cavity. The middle concha may also curve inferolaterally; less commonly, it may often be expanded by an enclosed air cell to form a so-called 'concha bullosa', or occasionally may have a concave medial surface, known as a paradoxical turbinate. The main features of the lateral nasal wall are a rounded elevation, the bulla ethmoidalis, and a curved cleft, the hiatus semilunaris, formed by the posterior edge of the uncinate process and the anterior face of the ethmoidal bulla. This constitutes the medial limit of the ethmoidal infundibulum, a slit-like space that leads towards the maxillary ostium. The maxillary ostium is normally found lateral to the anteroinferior aspect of the uncinate process. The latter may have its predominant attachment to either the lateral nasal wall (>50%), the anterior cranial fossa, or the middle concha, or may have multiple sites of attachment (Netto et al 2015). Where the uncinate process is attached determines whether the frontal sinus drains lateral to the ethmoidal infundibulum or into it. If the uncinate process is attached to the lateral wall, the frontal sinus will drain into the middle meatus and not into the ethmoidal infundibulum, whereas with the other configurations, the sinus will drain into the infundibulum, and thus near or into the maxillary ostium. Agger nasi air cells are anterior ethmoidal air cells that lie anterior to the ethmoidal bulla (see Fig. 39.6). The posterior fontanelle lies posterior to the uncinate process where there is no bone in the medial wall of the maxillary sinus, inferoposterior to the hiatus, and frequently has an accessory opening (**Fig. 39.7**).

Inferior concha and inferior meatus

The inferior concha is a thin, curved, independent bone (for more details see Ch. 36). It articulates with the nasal surface of the maxilla and the perpendicular plate of the palatine bone. Its free lower border is gently curved and the subjacent inferior meatus reaches the nasal floor. The inferior meatus is the largest meatus, extending along almost all the lateral nasal wall. It is deepest at the junction of its anterior and middle thirds, where it admits the inferior opening of the nasolacrimal canal. The canal is formed by the articulations between the lacrimal groove of the maxilla, the descending process of the lacrimal bone and the lacrimal process of the inferior concha. During postnatal development, the ostium of the nasolacrimal duct moves upwards and is increasingly hidden under the over-arching inferior concha. Inconsistent epithelial folds (the valve of Hasner) may remain at its distal opening.

Middle concha and middle meatus

The middle concha is a medial process of the ethmoidal labyrinth and may be pneumatized (concha bullosa). Pneumatization that is restricted to the vertical lamella of the concha above the level of the ostiomeatal complex is termed an interlamellar cell of Grunwald (lamellar bulla, or conchal neck air cell). The middle concha extends back to articulate with the perpendicular plate of the palatine bone. The region beneath it is the middle meatus, which is deeper in front than behind, lies below and lateral to the middle concha, and continues anteriorly into a shallow fossa above the vestibule, termed the atrium of the middle meatus.

Sphenopalatine foramen

The sphenopalatine foramen, in reality a fissure, transmits the sphenopalatine artery and nasopalatine and superior nasal nerves from the pterygopalatine fossa. It is posterior to the middle meatus, and bounded above by the body and concha of the sphenoid, below by the superior border of the perpendicular plate of the palatine bone, and in front and behind by the orbital and sphenoidal processes of the palatine bone, respectively. The crista ethmoidalis, a small bony crest formed by the attachment of the basal lamella of the middle turbinate to the ascending palatine bone, is found anterior to the foramen, and is a reliable surgical landmark.

Ethmoturbinals

The ethmoturbinals are the superior and middle turbinates, occasionally supplemented by a supreme turbinate. They appear during weeks 9 and 10 of gestation as multiple folds on the developing lateral nasal wall and subsequently fuse into three or four ridges, each with an anterior (ascending) and a posterior (descending) ramus, separated by grooves. The first ridge develops into the agger nasi and the uncinate process. The second is thought to become the ethmoidal bulla and the fourth, if present, develops into the superior and supreme turbinates. The third is known as the basal lamella of the middle turbinate.

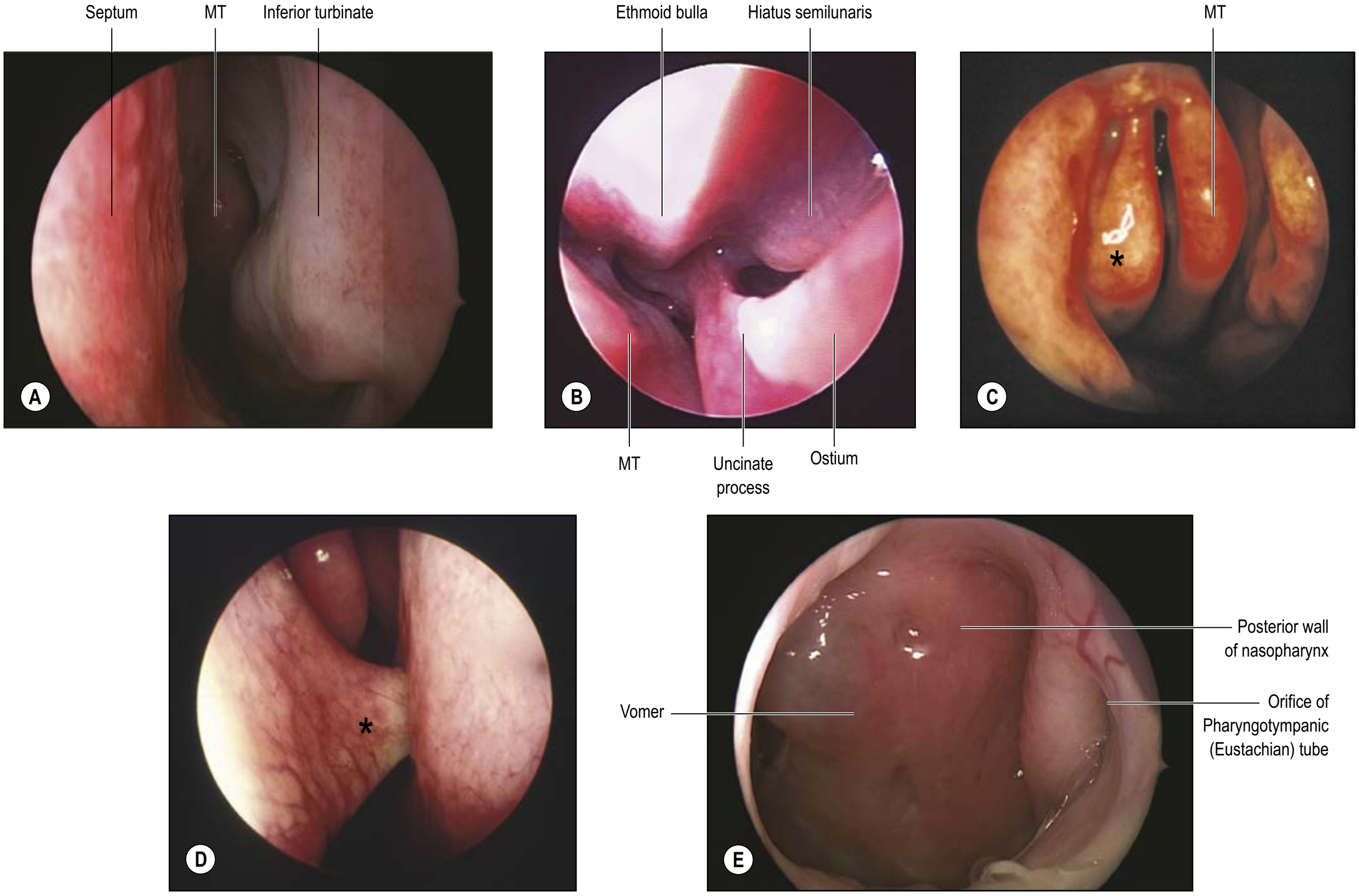
Septum
MT
Inferior turbinate
Ethmoid bulla
Hiatus semilunaris
MT
A
B
MT
Uncinate process
Ostium
C
*
*
D
Posterior wall of nasopharynx
Vomer
Orifice of Pharyngotympanic (Eustachian) tube
E

Fig. 39.7 **A**, An endoscopic view of the nasal cavity showing inferior and middle turbinates (MT). **B**, A view of the middle meatus and left lateral wall of the nose. **C**, An endoscopic view of the nose showing the middle turbinate and the pneumatized uncinate process in the middle meatus (asterisk). **D**, An endoscopic view of the nose demonstrating a deviated nasal septum (asterisk) making contact with the left inferior turbinate. **E**, An endoscopic view of the posterior nasal space.

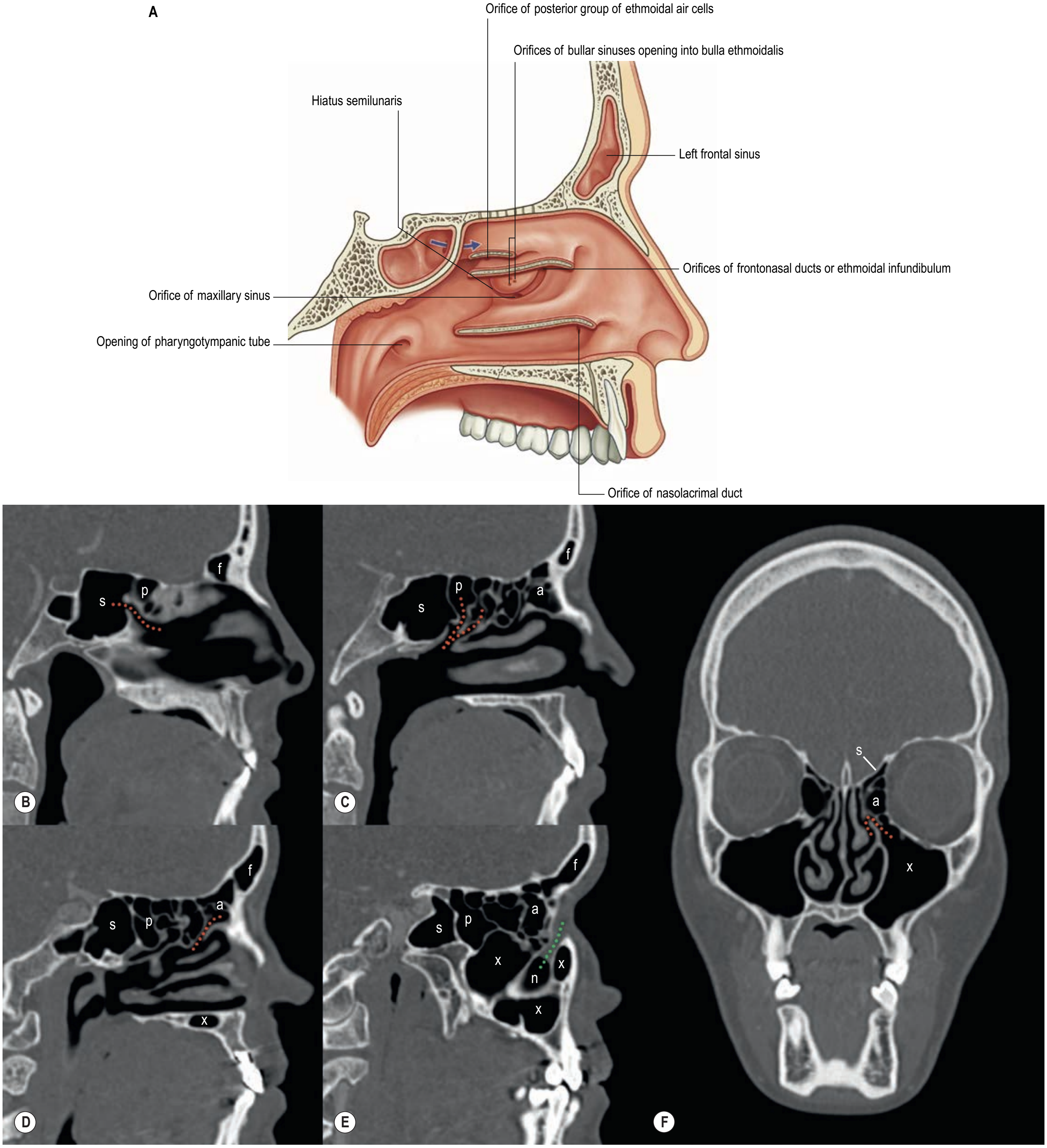
A
Orifice of posterior group of ethmoidal air cells
Orifices of bullar sinuses opening into bulla ethmoidalis
Hiatus semilunaris
Left frontal sinus
Orifices of frontonasal ducts or ethmoidal infundibulum
Orifice of maxillary sinus
Opening of pharyngotympanic tube
Orifice of nasolacrimal duct
B
s
p
f
C
s
p
a
f
D
s
p
a
f
x
E
s
p
a
f
x
n
x
x
F
s
a
x

Fig. 39.6 **A**, The lateral wall of the nasal cavity. The conchae/turbinates have been removed to show the positions of the ostia of the paranasal sinuses and the nasolacrimal duct. The blue arrow passes through the orifice of the sphenoidal sinus into the sphenoethmoidal recess. **B**–**E**, Sagittal CT reconstructions through the left nasal cavity from medial to lateral. **F**, Coronal plane reconstruction through the maxillary air sinuses. The subject was given intravenous contrast medium and the images are viewed with bone window settings. Key: a, anterior ethmoidal air cells; f, frontal air sinus; n, nasal cavity; p, posterior ethmoidal air cells; s, sphenoidal air sinus; x, maxillary air sinus. The path from each air space to the nasal cavity is shown in dashed red and the path of the nasolacrimal duct is dashed green. (A, With permission from Drake RL, Vogl AW, Mitchell A (eds) Gray's Anatomy for Students, 2nd ed. Elsevier, Churchill Livingstone. Copyright 2010.)

Attachments of the basal lamella of the middle turbinate

An understanding of the attachment of the middle turbinate to the roof and lateral wall of the nose is essential when undertaking sinus surgery. Anteriorly, it attaches to the crista ethmoidalis of the maxilla, and posteriorly it attaches to the crista ethmoidalis of the palatine bone, anterior to the sphenopalatine foramen. In between these points, the insertion lies in three different planes. The anterior third inserts vertically into the cranial base. The middle third turns laterally across the cranial base to the lamina papyracea, where it turns inferiorly; it may be indented by either anterior or posterior ethmoidal cells, but separates the two groups of cells. The posterior third runs horizontally, attaching to the lamina and the medial wall of the middle turbinate.

Superior concha and superior meatus

The superior concha is a medial process of the ethmoidal labyrinth and presents as a small curved lamina, posterosuperior to the middle concha. It roofs the superior meatus and is the shortest and shallowest of the three conchae. Above the superior concha, the sphenoidal sinus opens into the triangular sphenoethmoidal recess, which separates the superior concha and anterior aspect of the body of the sphenoid. The superior meatus is a short oblique passage extending about halfway along the upper border of the middle concha. The posterior ethmoidal sinuses open, via a variable number of apertures, into its anterior part.

Highest (supreme) nasal concha

Occasionally, a fourth concha, the highest or supreme nasal concha, appears on the lateral wall of the sphenoethmoidal recess. The passage immediately below it is called the supreme nasal meatus; it may contain an opening for the posterior ethmoidal sinus.

Functions of the nasal turbinates

In vivo, the conchae are covered with a thick, vascular, glandular soft tissue layer with pseudostratified columnar epithelium. They contain erectile tissue, modulated by trigeminal innervation detecting airflow and temperature; congestion and decongestion of the venous sinusoids regulate nasal resistance. The turbinates are essential for filtration, heating and humidification of inspired air. They direct airflow to the olfactory cleft, and some areas receive direct innervation from the olfactory bulb. Hypertrophy of the turbinates in allergy or environmental irritation results in nasal obstruction.

Nasal airflow and the nasal cycle

Available with the *Gray's Anatomy* e-book

Nasal and olfactory mucosae

Nasal mucosa

The lining of the anterior part of the nasal cavity and vestibule is continuous with the skin, and consists of keratinized stratified squamous epithelium overlying a connective tissue lamina propria. Inferiorly, the skin bears coarse hairs (vibrissae), which curve towards the naris and help to arrest the passage of particles in inspired air. In males, after middle age, these hairs increase considerably in size. Further posteriorly, at the limen nasi, this changes into a mucosa, lined initially by non-keratinizing stratified squamous epithelium, and then by pseudostratified ciliated (respiratory) epithelium rich in goblet cells (see Fig. 2.2D). Respiratory epithelium forms most of the surface of the nasal cavity, i.e. it covers the conchae, meatuses, septum, floor and roof, except superiorly in the olfactory cleft, where the olfactory epithelium is present. It is adherent to the periosteum or perichondrium of the neighbouring skeletal structures. In some areas, cells of the respiratory epithelium may be low columnar or cuboidal, and the proportion of ciliated to non-ciliated cells is variable.

There are numerous seromucous glands within the lamina propria of the nasal mucosa. Their secretions make the surface sticky so that it traps particles in the inspired air. The mucous film is continually moved by ciliary action (the mucociliary escalator or rejection current) posteriorly into the nasopharynx at a rate of 6 mm per minute. Palatal movements transfer the mucus and its entrapped particles to the oropharynx for swallowing, but some also enters the nasal vestibule anteriorly. The secretions of the nasal mucosa contain the bacteriocides lysozyme, β-defensin and lactoferrin, and also secretory immunoglobulins (IgA). The mucosa is continuous with the nasopharyngeal mucosa through the posterior nasal apertures, the conjunctiva through the nasolacrimal duct and lacrimal canaliculi, and the mucosa of the sphenoidal, ethmoidal, frontal and maxillary sinuses through their openings into the meatuses.

The mucosa is thickest and most vascular over the conchae, especially at their extremities, and also on the anterior and posterior parts of the nasal septum and between the conchae. The mucosa is very thin in the meatuses, on the nasal floor and in the paranasal sinuses. Its thickness reduces the volume of the nasal cavity and its apertures significantly. The lamina propria contains cavernous vascular tissue with large venous sinusoids.

Olfactory mucosa

Olfactory mucosa (Fig. 39.8) covers approximately 5 cm^2 of the posterior upper parts of the lateral nasal wall, including the upper part of the vertical portion of the middle concha (where it is interspersed with respiratory epithelium in a chequerboard fashion) and the opposite part of the nasal septum, the superior concha, the sphenoethmoidal recess, the upper part of the perpendicular plate of the ethmoid and the portion of the roof of the nose that arches between the septum and lateral wall, including the underside of the cribriform plate (constituting the olfactory cleft or groove). It consists of a yellowish-brown pigmented pseudostratified epithelium, containing olfactory receptor neurones, sustentacular cells and two classes of basal cell, lying on a subepithelial lamina propria containing subepithelial olfactory glands (of Bowman) and bundles of axons derived from the olfactory receptor neurones that course through the mucosa on their way to the cribriform plate. The glands secrete a predominantly serous fluid through ducts that open on to the epithelial surface. These secretions form a thin fluid layer in which sensory cilia and the microvilli of the sustentacular cells are embedded.

Olfactory receptor neurones Olfactory receptor neurones are bipolar. Their cell bodies and nuclei are located in the middle zone of the olfactory epithelium. Each neurone has a single unbranched apical dendrite, 2 µm in diameter, which extends to the epithelial surface; and a basally directed unmyelinated axon, 0.2µm in diameter, which passes in the opposite direction, penetrates the basal lamina and enters the lamina propria. The tips of the dendrites project into the overlying secretory fluid and are expanded into characteristic endings (knobs) (**Fig. 39.8B**). Groups of up to 20 cilia radiate from the circumference of each ending and extend for long distances parallel to the epithelial surface. Internally, the short proximal part of each cilium has the '9 + 2' pattern of microtubules typical of motile cilia, while the longer distal trailing end contains only the central pair of microtubules. The olfactory cilia lack dynein arms and are thought to be non-motile; their primary purpose is to increase the surface area of sensory receptor membrane available for the efficient detection of odorant molecules transferred across the mucous layer by odorant-binding proteins. Mature olfactory neurones express olfactory marker protein (OMP), an abundant cytoplasmic protein involved in olfactory signal transduction (see Fig. 39.8D). Each olfactory receptor neurone expresses receptors for a single odorant molecule (or very few). In humans, over 1000 genes code for functional odorant receptors; the number of functional genes is much higher in macrosmotic animals (Buck and Axel 1991). Although neurones with the same receptor specificity are randomly distributed within anatomical zones of the epithelium, their axons all converge on the same glomerulus in the olfactory bulb. Specific odours activate a unique spectrum of receptor neurones, which in turn activate restricted groups of glomeruli and their second-order neurones.

The axons form small intraepithelial fascicles among the processes of sustentacular and basal cells. The fascicles penetrate the basal lamina and are immediately surrounded by olfactory ensheathing cells. Groups of up to 50 such fascicles join to form larger olfactory nerve rootlets that pass through the cribriform plate of the ethmoid bone, wrapped in meningeal sheaths. They immediately enter the overlying olfactory bulbs, where they synapse in glomeruli with mitral cells and, to a lesser extent, with smaller tufted cells (Ch. 32, p. 517).

Microvillar cells Microvillar cells occupy a superficial position in the olfactory epithelium. They are flask-shaped and electron-lucent, and the apical end of each cell gives rise to a tuft of microvilli that project into the mucus layer lining the nasal cavity (see Fig. 39.8B). Cell counts in longitudinal sections reveal that microvillar cells occur with a density that is approximately one-tenth of the density of ciliated olfactory neurones; their function and origin have yet to be determined.

Sustentacular cells Sustentacular, or supporting, cells are columnar cells that separate and partially ensheathe the olfactory receptor

The paired nasal valves are critical regulators of nasal airflow and resistance. Each is divided into external and internal portions, although often only the internal portion is regarded as the 'nasal valve' or flow-limiting segment. The external valve is made up of the ala, the skin of the vestibule, the nasal sill and the contour of the medial crus of the lower lateral cartilage. The external valve has a tendency to collapse at high flow rates, even in normal individuals.

The upper lateral cartilages are in continuity with the superior border of the nasal septum. A valve-like mechanism exists at its distal end that regulates nasal airflow. The nasal valve area and internal nasal valve are two entities that should not be confused. The nasal valve area is the narrowest portion of the nasal passage. It is bounded medially by the septum and the tuberculum of Zuckerkandl, and superiorly and laterally by the caudal margin of the upper lateral cartilage, its fibroadipose attachment to the piriform aperture and the anterior end of the inferior turbinate; inferiorly, it consists of the floor of the piriform aperture. The nasal valve, on the other hand, is the specific slit-like segment between the caudal margin of the upper lateral cartilage and the septum. It is measured in degrees and normally ranges between 10 and 15°. Dilator naris anterior and the alar part of nasalis support the nasal valves.

Airflow dynamics are recognized as playing a key role in conditioning (i.e. warming, humidifying and filtering) inspired air; however, these dynamics are still poorly understood (Churchill et al 2004, Boyce and Eccles 2006). It is generally agreed that airflow within the nose is both laminar and turbulent. Inspired air is forced to pass through the nasal valve and then expands as it passes further into the nasal cavity, which offers little airflow resistance. This sudden change in speed and pressure produces turbulence and eddies. These currents allow adequate contact of inspired air with respiratory epithelium and facilitate odorant transport to the olfactory area. Chewing also affects nasal airflow; pulses of aroma-laden air are pumped out of the mouth into the retronasal region with each chew.

The cross-sectional area of the nasal airway depends on the dimensions of the septal partition and inferior turbinates (which are modulated by changes in the dimensions of the erectile tissue that covers them), and on the stability of the lateral nasal walls during breathing. The nasal cycle is an alternating fluctuation of nasal engorgement and airflow through the nasal passages, with period lengths ranging from 1 to 5 hours. The mechanism involves changes in sympathetic tone to the venous erectile tissue of the nasal mucosa; increased sympathetic vasoconstriction causes resistance to fall. These alterations in the thickness and contours of the mucosal surfaces are visible as a swelling or shrinkage of the nasal lining, and may serve to protect the mucosae from desiccation. The pacemaker for the cycle is believed to lie within the suprachiasmatic nucleus. The rhythmicity of the cycle decreases with age.

Nasal obstruction

Disturbances of the normal airflow pattern, whether produced by mucocutaneous or skeletal changes within the nose, affect normal nasal breathing and are usually perceived as some form of nasal obstruction.

The septum may be displaced by injury or by disproportionate growth of the cartilage that may cause it to bend; sometimes, the deviation may cause unilateral nasal obstruction. Variations in the anatomy of the lateral nasal wall, usually associated with variations in the size and position of the anterior ethmoidal cells, may obstruct frontal or maxillary sinus drainage, e.g. frontal cells, supraorbital ethmoidal cells, and infraorbital or Haller's cells, which represent an extension of anterior ethmoidal pneumatization along the infraorbital margin, sometimes within the roof of the maxillary sinus (see below).

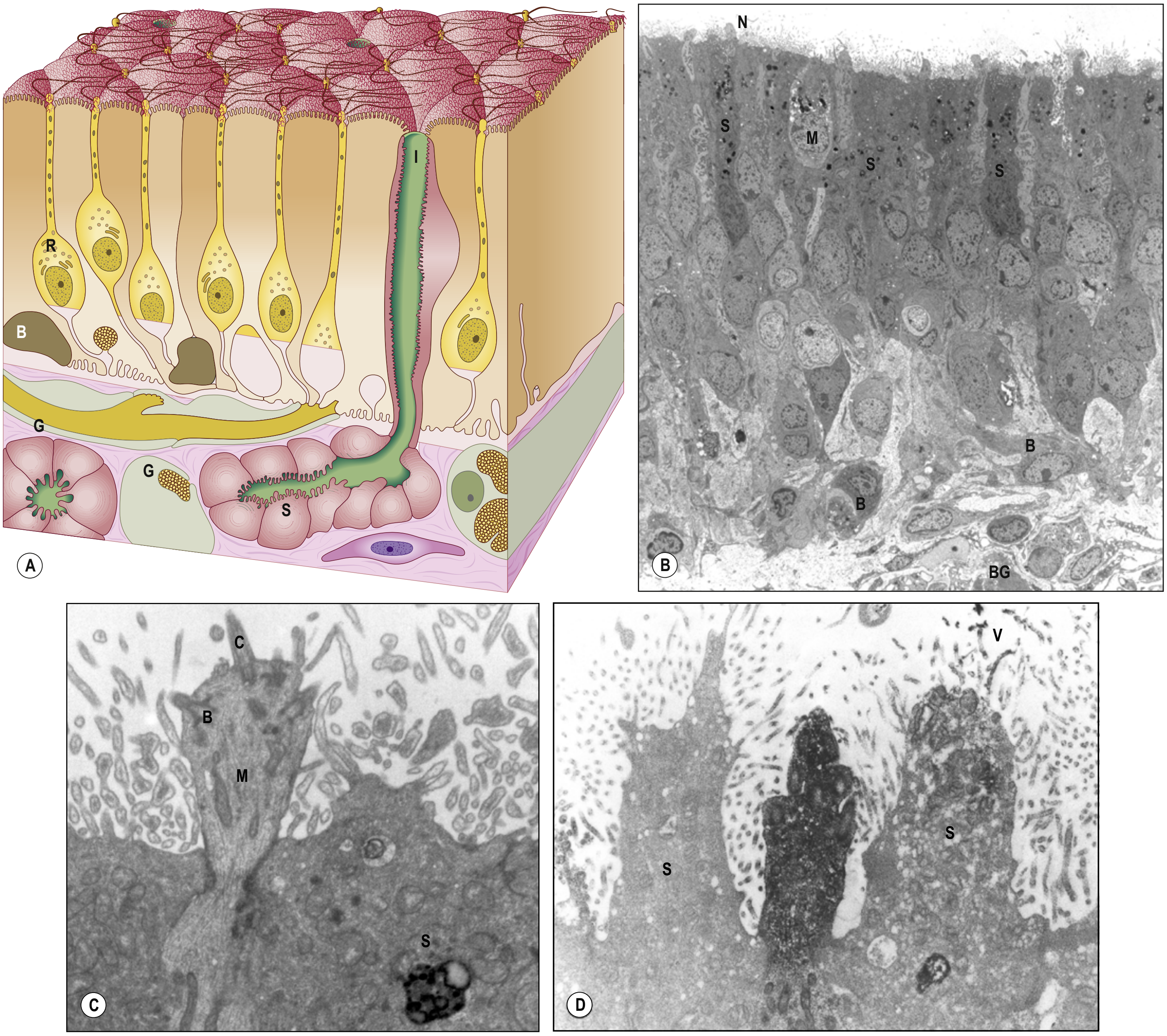

Fig. 39.8 **A**, The chief cytological features of the olfactory epithelium. Receptor cells (neurones) (R) are situated among columnar sustentacular cells. The axons of the receptor cells emerge from the epithelium in bundles enclosed by ensheathing glial cells (G). Rounded globose basal cells (B) and flattened horizontal basal cells (not shown) lie on the basal lamina, and the subepithelial glands (of Bowman) (S) open on to the surface via their intraepithelial ducts (I). At the surface are cilia of the receptor cells and microvilli of the supporting cells. **B**–**D**, Longitudinal sections through human olfactory epithelium. **B**, Ciliated olfactory receptor neurones with characteristic expanded ends (N) project into the nasal lumen. The edge of a Bowman's gland (BG) lies deeper in the lamina propria. Other abbreviations: B, basal cells resting on the basal lamina; M, microvillar cell; S, supporting or sustentacular cells containing electron-dense material. **C**, A higher-power view of the expanded end of an olfactory receptor neurone. The electron-dense, osmiophilic material within the adjacent supporting cell (S) is thought to contribute to the pigmentation of the olfactory epithelium. Other abbreviations: B, basal body with projecting 'feet'; C, olfactory cilium; M, microtubules. **D**, A section of human olfactory epithelium immunostained with anti-OMP (olfactory marker protein). An immunopositive olfactory receptor neurone lies between two unstained supporting cells (S). Other abbreviations: V, microvilli. (B–D, Courtesy of Professor Bruce Jafek, Department of Otolaryngology, University of Colorado, Denver, USA; see Jafek 1983.)

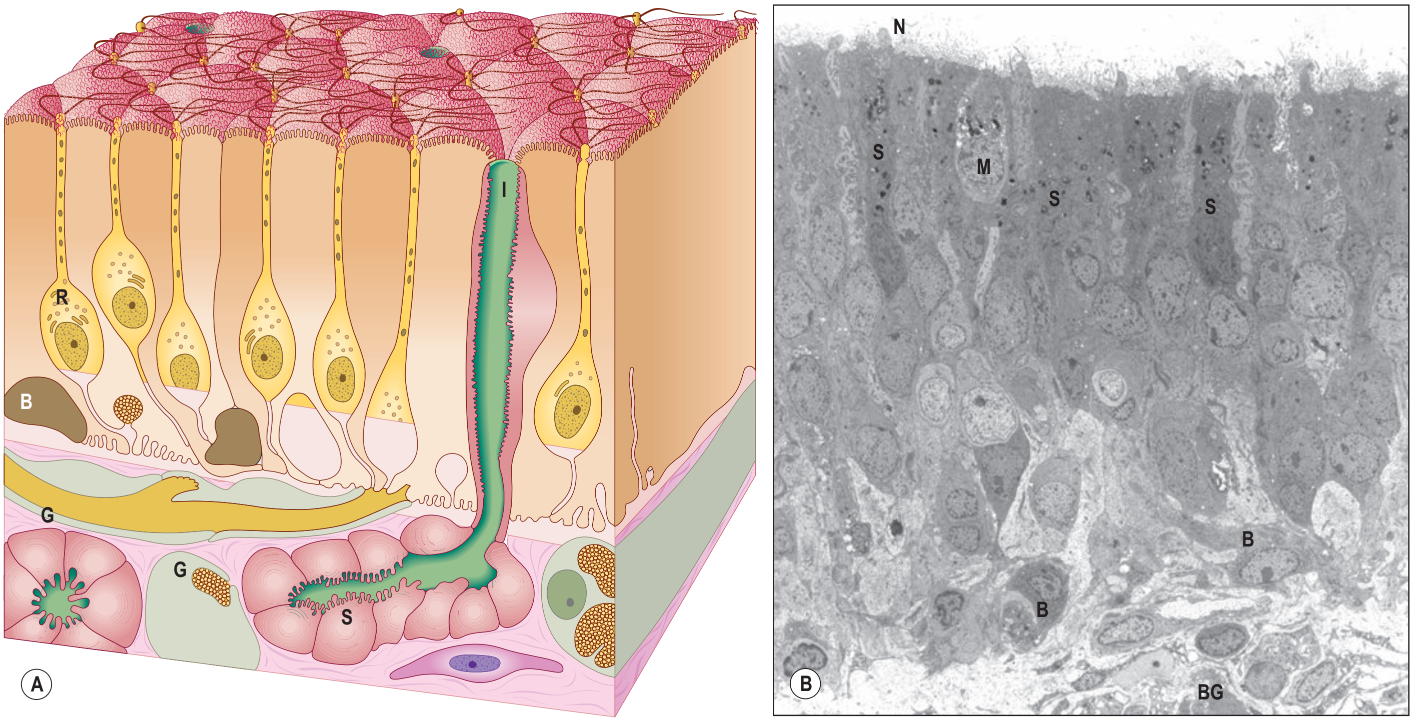

Fig. 39.8 **A**, The chief cytological features of the olfactory epithelium. Receptor cells (neurones) (R) are situated among columnar sustentacular cells. The axons of the receptor cells emerge from the epithelium in bundles enclosed by ensheathing glial cells (G). Rounded globose basal cells (B) and flattened horizontal basal cells (not shown) lie on the basal lamina, and the subepithelial glands (of Bowman) (S) open on to the surface via their intraepithelial ducts (I). At the surface are cilia of the receptor cells and microvilli of the supporting cells. **B–D**, Longitudinal sections through human olfactory epithelium. **B**, Ciliated olfactory receptor neurones with characteristic expanded ends (N) project into the nasal lumen. The edge of a Bowman's gland (BG) lies deeper in the lamina propria. Other abbreviations: B, basal cells resting on the basal lamina; M, microvillar cell; S, supporting or sustentacular cells containing electron-dense material. (B, Courtesy of Professor Bruce Jafek, Department of Otolaryngology, University of Colorado, Denver, USA; see Jafek 1983.) **C–D**, *continued online*

neurones. Their large nuclei form a layer superficial to the neuronal nuclei within the epithelium. The cells are capped by numerous long, irregular, microvilli, which lie in the secretory fluid layer that covers the surface of the epithelium, intermingled with the trailing ends of the cilia on the olfactory receptor endings. Their expanded bases contain numerous lamellated dense bodies, which are the remnants of secondary lysosomes, and which contribute significantly to the pigmentation of the olfactory area (see Fig. 39.8B,C). The granules gradually accumulate with age, and because these cells are long-lived, the intensity of pigmentation also increases with age. Neighbouring sustentacular cells are linked by desmosomes close to the epithelial surface, an arrangement that helps to stabilize the epithelium mechanically. Sustentacular cells and olfactory receptor neurones are linked by tight junctions at the level of the epithelial surface.

Basal cells There are horizontal and globose basal cells. Horizontal basal cells are flattened against the basal lamina. Their nuclei are condensed and their darkly staining cytoplasm contains numerous intermediate filaments of the cytokeratin family, inserted into desmosomes between the basal cells and surrounding sustentacular cells. Globose cells are rounded or elliptical in shape, and have pale, euchromatic nuclei and pale cytoplasm. They form a distinct zone that is slightly internal to the basal surface of the epithelium and characterized by mitotic figures; globose basal cells are the immediate source of new olfactory receptor neurones.

Olfactory ensheathing cells Olfactory ensheathing cells share properties with astrocytes and non-myelinating Schwann cells, but also possess distinctive features that indicate they are a separate class of glia. Developmentally, they are derived from the olfactory placode rather than the neural crest. They ensheathe olfactory axons in a unique manner throughout their entire course and accompany them into the olfactory bulb, where they contribute to the glia limitans. In recent years, olfactory ensheathing cells have been the focus of intense experimental scrutiny in the search for a source of transplantable glia capable of supporting neuronal regeneration within the central nervous system, possibly in the treatment of paraplegia.

Olfactory glands Olfactory (Bowman's) glands are branched tubulo-alveolar structures that lie beneath the olfactory epithelium and secrete their products on to the epithelial surface through narrow, vertical ducts. Their secretions, which include defensive substances, lysozyme, lactoferrin, IgA and sulphated proteoglycans, together with odorant-binding proteins that increase the efficiency of odour detection, bathe the dendritic endings and cilia of the olfactory receptors. The fluid acts as a solvent for odorant molecules, allowing their diffusion to the sensory receptors.

Turnover of olfactory receptor neurones

Available with the *Gray's Anatomy* e-book

Vascular supply and lymphatic drainage

Many of the vessels and nerves supplying the nasal cavities arise within the pterygopalatine fossa and these origins are described in Chapter 38.

Arteries

Branches of the ophthalmic, maxillary and facial arteries supply different territories within the walls, floor and roof of the nasal cavity (Fig. 39.9). They ramify to form anastomotic plexuses within and deep to the nasal mucosa. Anastomoses also occur between some larger arterial branches. The anterior and posterior ethmoidal branches of the ophthalmic artery supply the ethmoidal and frontal sinuses and the roof of the nose (including the septum). The anterior ethmoidal artery usually runs within the bone of the anterior skull base, unless this is well pneumatized with a supraorbital cell, in which case the artery is more likely to be positioned away from the skull base and to be more prone to surgical damage (Fig. 39.10). The anterior ethmoidal artery is usually exposed and ligated within the orbit through a medial canthal incision. That will arrest most bleeds high up in the nasal cavity. It can also be encountered unexpectedly in an anterior ethmoidal cell and cause brisk bleeding if ruptured or accidentally transected. Worse still, the transected proximal end of the artery may retract into the orbit continuing to bleed and causing an orbital haematoma that requires rapid exploration.

Olfactory receptor neurones are lost and replaced throughout life. Individual receptor cells have a variable lifespan, thought to average 1–3 months. Stem cells situated near the base of the epithelium undergo periodic mitotic division throughout life, giving rise to new olfactory receptor neurones, which then grow a dendrite to the olfactory surface and an axon to the olfactory bulb. The cell bodies of these new receptor neurones gradually move apically until they reach the region just below the supporting cell nuclei. When they degenerate, dead neurones either are shed from the epithelium or are phagocytosed by sustentacular cells. The rate of receptor cell loss and replacement increases after exposure to damaging stimuli but declines slowly with age, a phenomenon that presumably contributes to diminishing olfactory sensory function in old age. Biopsy specimens from normosmic adults have revealed that patchy replacement of olfactory with respiratory epithelium occurs even in young healthy adults (Paik et al 1992, Holbrook et al 2005).

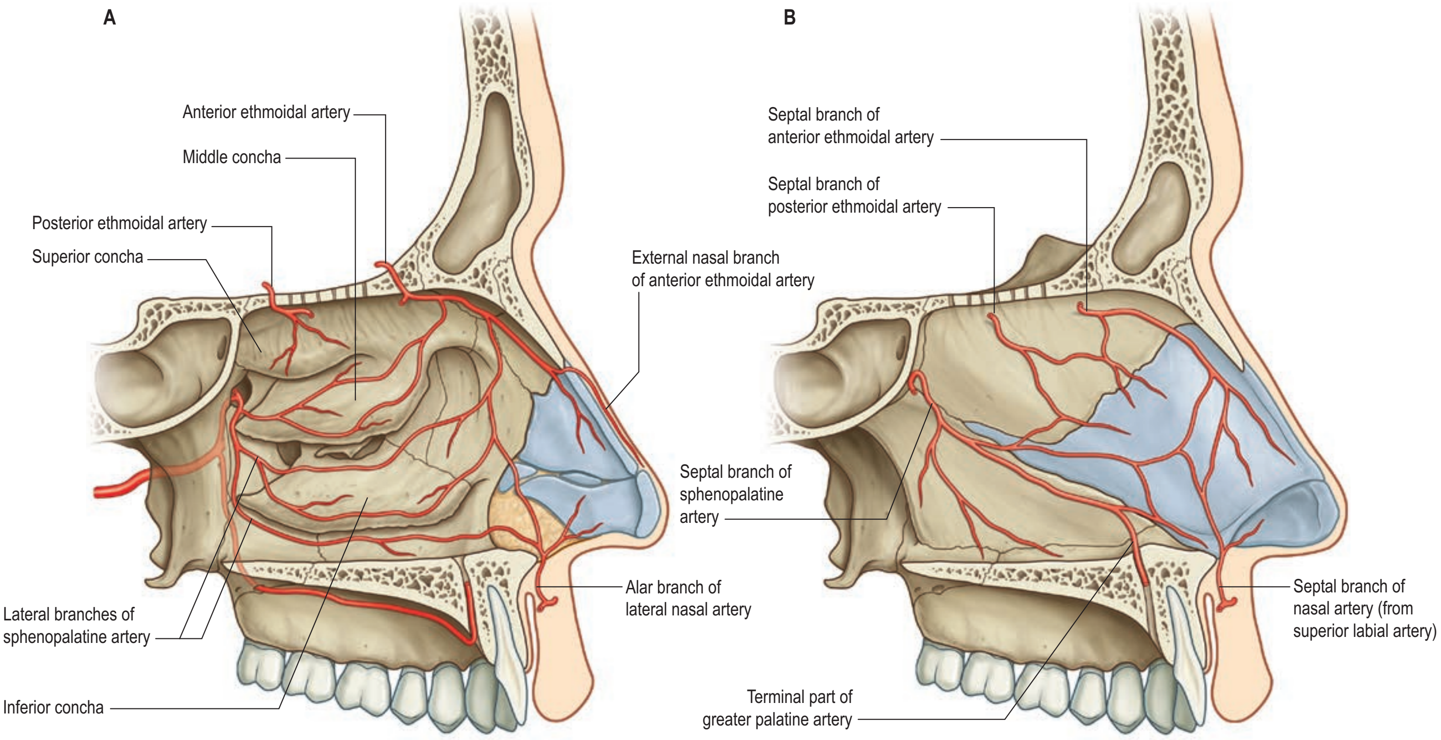
A
B
Anterior ethmoidal artery
Middle concha
Posterior ethmoidal artery
Superior concha
Lateral branches of sphenopalatine artery
Inferior concha
External nasal branch of anterior ethmoidal artery
Septal branch of sphenopalatine artery
Alar branch of lateral nasal artery
Septal branch of anterior ethmoidal artery
Septal branch of posterior ethmoidal artery
Septal branch of nasal artery (from superior labial artery)
Terminal part of greater palatine artery

Fig. 39.9 The arterial supply of the nasal cavity. **A**, The lateral wall of the left nasal cavity. **B**, The medial wall of the left nasal cavity. (With permission from Drake RL, Vogl AW, Mitchell A (eds) Gray's Anatomy for Students, 2nd ed. Elsevier, Churchill Livingstone. Copyright 2010.)

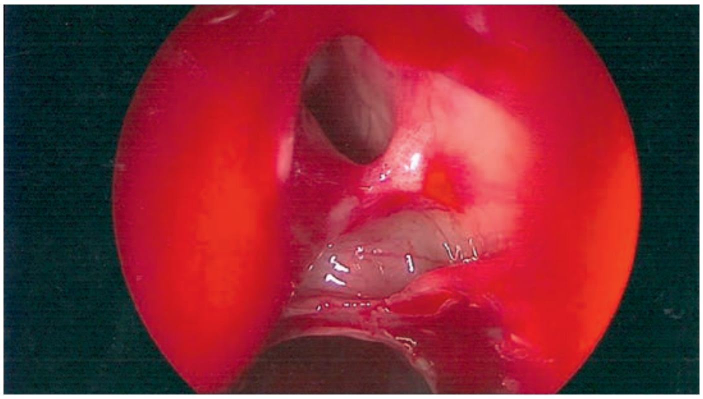

Fig. 39.10 *In vivo* demonstration of the anterior ethmoidal artery exposed in the anterior ethmoidal cells, after removing the anterior face of the ethmoid bulla. Inadvertent damage during sinus dissection may allow retraction of the stump into the orbit, with ongoing bleeding leading to development of an orbital haematoma

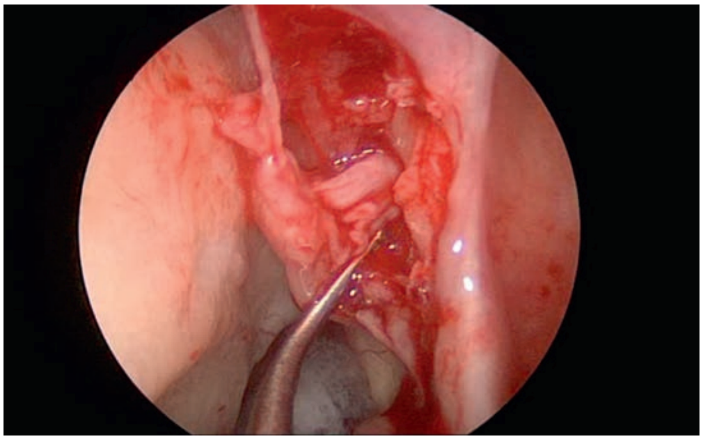

Fig. 39.11 *In vivo* demonstration of the sphenopalatine artery (main trunk, with smaller branch inferiorly demonstrated with the pointer) emerging from the sphenopalatine foramen, behind the crista ethmoidalis. The posterior wall of the maxillary sinus is visible through a large antrostomy, and a mucosal flap has been elevated to demonstrate the vessels.

A middle ethmoid artery may be identified in 20–30% of sinus cavities (Wang et al 2014). The sphenopalatine branch of the maxillary artery supplies the mucosa of the turbinates, meatuses and posteroinferior part of the nasal septum, i.e. it is the principal vessel supplying the nasal mucosa. The artery comes out of a fissure (erroneously termed a foramen), and normally divides before it enters the nasal cavity behind the crista ethmoidalis into posterior lateral nasal and posterior septal branches (Fig. 39.11). Sometimes, the artery may divide before it leaves the foramen. The number and distribution of its branches show great variation, with a median of three branches (Eordogh et al 2018). The greater palatine branch of the maxillary artery supplies the region of the inferior meatus. A branch crosses the sphenoidal rostrum, below its natural ostium, to supply the nasal septum. This is utilized to provide pedicled, vascularized nasoseptal flaps in skull-base reconstruction. Its terminal part ascends through the incisive canal to anastomose on the septum with branches of the sphenopalatine and anterior ethmoidal arteries, and with the septal branch of the superior labial artery. This septal region (Little's area or Kiesselbach's plexus) is a common site of bleeding from the nose. The infraorbital artery and the superior, anterior and posterior alveolar branches of the maxillary artery supply the mucosa of the maxillary sinus. The pharyngeal branch of the maxillary artery supplies the sphenoidal sinus.

Nose bleeds

Available with the *Gray's Anatomy* e-book

Veins

A rich submucosal cavernous plexus is especially dense in the posterior part of the septum and in the middle and inferior turbinates (Fig. 39.12). Numerous arteriovenous anastomoses are present in the deep layer of the mucosa and around the mucosal glands. The cavernous turbinate plexuses resemble those in erectile tissue; the nasal cavity is susceptible to blockage, should they become engorged. Veins from the posterior part of the nose generally pass to the sphenopalatine vein that runs back through the sphenopalatine foramen to drain into the pterygoid venous plexus. The anterior part of the nose is drained mainly through veins accompanying the anterior ethmoidal arteries, and these veins subsequently pass into the ophthalmic or facial veins. Injection of vasoconstrictive agents or corticosteroids during surgery, particularly to the inferior turbinates, may permit access to the intracranial and ophthalmic circulations. Blindness has been reported in rare cases following such injections. A few veins pass through the cribriform plate to connect with those on the orbital surface of the frontal lobes of the brain. When the foramen caecum is patent, it transmits a vein from the nasal cavity to the superior sagittal sinus.

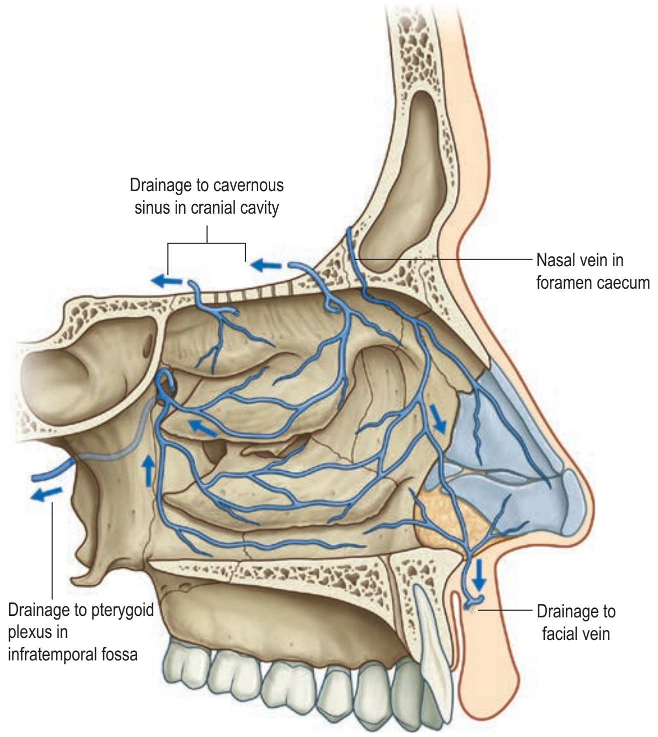
Drainage to cavernous sinus in cranial cavity
Nasal vein in foramen caecum
Drainage to pterygoid plexus in infratemporal fossa
Drainage to facial vein

Fig. 39.12 The venous drainage of the nasal cavity: the lateral wall of the left nasal cavity. (With permission from Drake RL, Vogl AW, Mitchell A (eds) Gray's Anatomy for Students, 2nd ed. Elsevier, Churchill Livingstone. Copyright 2010.)

Lymphatic drainage

Lymph vessels from the anterior region of the nasal cavity pass superficially to join those draining the external nasal skin and end in the submandibular nodes. The rest of the nasal cavity, paranasal sinuses, nasopharynx and pharyngeal end of the pharyngotympanic tube all drain to the upper deep cervical nodes, either directly or through the retropharyngeal nodes. The posterior nasal floor probably drains to the parotid nodes.

Innervation

Olfaction is mediated via the olfactory nerves. General sensation (touch, pain and temperature) from the nasal mucosa is carried by branches of the ophthalmic and maxillary divisions of the trigeminal nerves (Fig. 39.13). Trigeminal fibres close to, and within, the epithelial layer are sensitive to noxious chemicals, e.g. ammonia and sulphur dioxide. Autonomic fibres innervate mucous glands and control cyclical and reactive vasomotor activity.

Sensory (trigeminal) innervation

The anterior ethmoidal branch of the nasociliary nerve leaves the cranial cavity through a small slit near the crista galli and enters the roof of the nasal cavity, where it runs in a groove on the inner surface of the nasal bone, supplying the roof of the nasal cavity. It gives off a lateral internal branch to supply the anterior part of the lateral wall, and a medial internal branch to the anterior and upper parts of the septum, before emerging at the inferior margin of the nasal bone as the external nasal nerve to supply the skin of the external nose to the nasal tip; damage following nasal trauma may result in paraesthesia of the tip. The infraorbital nerve supplies the nasal vestibule. The anterior superior alveolar nerve supplies part of the septum, the floor near the anterior nasal spine and the anterior part of the lateral wall as high as the opening of the maxillary sinus; the lateral posterior superior nasal and the posterior inferior nasal branches of the greater palatine nerve together supply the posterior three-quarters of the lateral wall, roof and floor; the medial posterior superior nasal nerves and the nasopalatine nerve supply the inferior part of the nasal septum; and branches from the nerve of the pterygoid canal supply the upper and posterior part of the roof and septum.

Autonomic innervation

The deep petrosal nerve (postganglionic sympathetic fibres) and the greater petrosal nerve (preganglionic parasympathetic fibres) converge

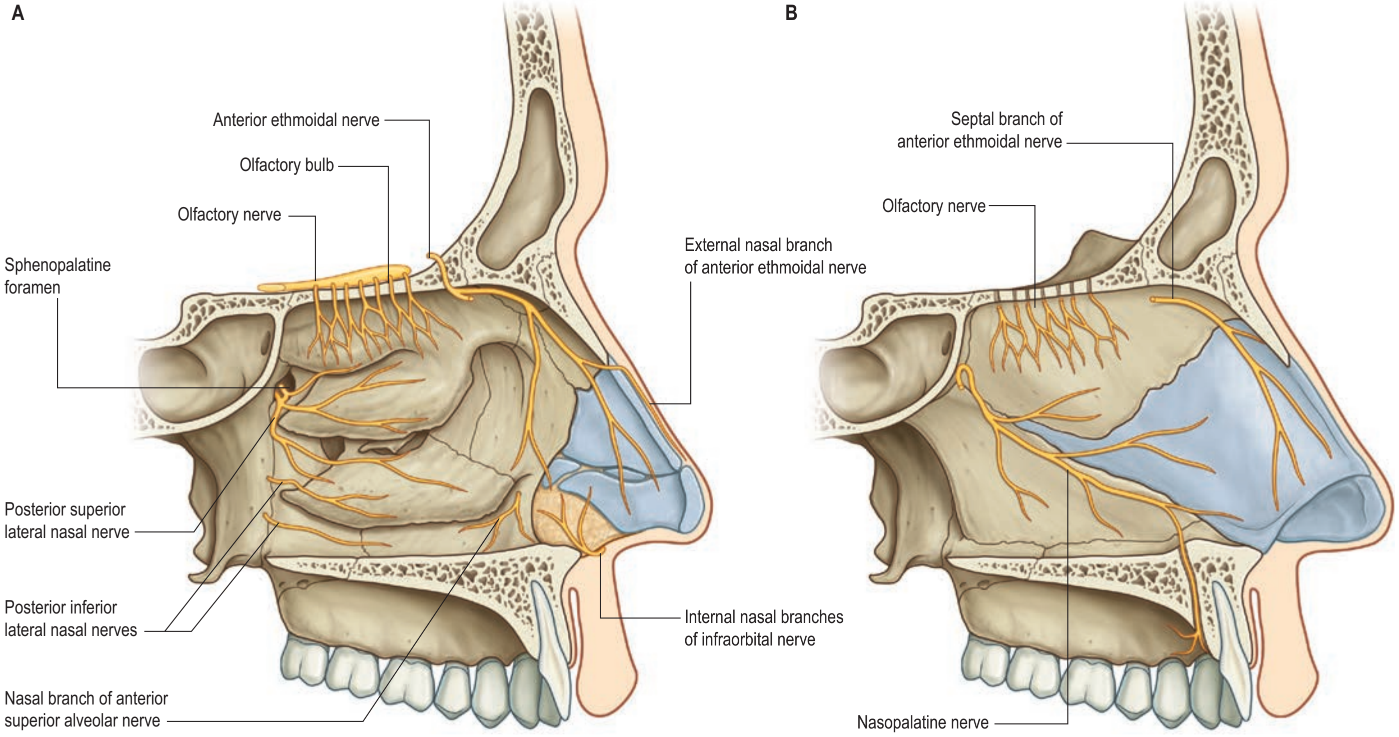
A
B
Anterior ethmoidal nerve
Olfactory bulb
Olfactory nerve
Sphenopalatine foramen
External nasal branch of anterior ethmoidal nerve
Posterior superior lateral nasal nerve
Posterior inferior lateral nasal nerves
Nasal branch of anterior superior alveolar nerve
Internal nasal branches of infraorbital nerve
Septal branch of anterior ethmoidal nerve
Olfactory nerve
Nasopalatine nerve

Fig. 39.13 The innervation of the nasal cavity. **A**, The lateral wall of the left nasal cavity. **B**, The medial wall of the left nasal cavity. (With permission from Drake RL, Vogl AW, Mitchell A (eds) Gray's Anatomy for Students, 2nd ed. Elsevier, Churchill Livingstone. Copyright 2010.)

The vast majority of nose bleeds, particularly in children, occur as a result of digital trauma to the anastomosis of arterioles and veins in Little's area, on the nasal septum just inside the nasal vestibule. This area is amenable to cautery when required. In older patients, brisker bleeding may occur as a result of the spontaneous rupture of arteries further back in the nose. These may be controlled by applying pressure with a nasal pack, but where this fails, knowledge of the pattern of arterial blood supply to the nasal cavity permits interruption of the appropriate blood supply by ligation or embolization of the feeding vessel. The sphenopalatine artery may be ligated under endoscopic visualization as it enters the nose through the sphenopalatine foramen. The ethmoidal arteries may be exposed within the orbit and ligated to arrest bleeding high up in the nasal cavity. The maxillary artery may be exposed surgically behind the posterior wall of the maxillary sinus and ligated, or alternatively it may be identified radiologically, using a radiopaque dye, so that it may be blocked by embolization (Simmen and Jones 2010).

to form the nerve of the pterygoid canal (Vidian nerve in the Vidian canal). The canal enters the pterygopalatine fossa, and the nerve joins the pterygopalatine ganglion, where the parasympathetic fibres synapse, but the sympathetic fibres pass through without synapsing (Ch. 38). The nerve of the pterygoid canal is an important landmark to the petrous portion of the internal carotid artery, and may also rarely be transected to treat intractable rhinorrhoea. Sympathetic postganglionic vasomotor fibres are distributed to the nasal blood vessels. Postganglionic parasympathetic fibres derived from the pterygopalatine ganglion provide the secretomotor supply to the nasal mucous glands, and are distributed via branches of the maxillary nerves.

Olfactory nerves

Olfactory nerves are bundles of very small axons derived from olfactory receptor neurones in the olfactory mucosa. The axons are unmyelinated, and in varying stages of maturity, reflecting the constant turnover of olfactory neurones that takes place in the olfactory epithelium. Bundles of axons surrounded by olfactory ensheathing cells form a plexiform network in the subepithelial lamina propria of the mucosa. The bundles unite into as many as 20 branches that cross the cribriform plate in lateral and medial groups, and enter the overlying olfactory bulb, where they end in glomeruli. Each branch is ensheathed by dura mater and pia arachnoid as it passes through the cribriform plate (**Fig. 39.14**). The dura subsequently becomes continuous with the nasal periosteum, and the pia arachnoid merges with the connective tissue sheaths surrounding the nerve bundles, an arrangement that may favour the spread of infection into the cranial cavity from the nasal cavity.

In severe injuries involving the anterior cranial fossa, the olfactory bulb may be separated from the olfactory nerves or the nerves may be torn, producing anosmia, i.e. loss of olfaction. Fractures may involve the meninges, so that cerebrospinal fluid may leak into the nose, resulting in cerebrospinal rhinorrhoea. Such injuries open up avenues for intracranial infection from the nasal cavity.

Vomeronasal organ

Available with the *Gray's Anatomy* e-book

PARANASAL SINUSES

The paranasal sinuses are the frontal, ethmoidal, sphenoidal and maxillary sinuses, housed within the bones of the same name (**Fig. 39.15** , see Figs 39.1, 39.14–39.25). They all open into the lateral wall of the nasal cavity by small apertures that permit both the equilibration of air between the various air spaces and the clearance of mucus from the sinuses into the nose via a mucociliary escalator. The detailed position of these apertures, and the precise form and size of each of the sinuses, vary enormously between individuals (Lang 1989, Navarro 1997, Beale et al 2009). Respiratory epithelium extends through the apertures of the paranasal sinuses to line their cavities, a feature that unfortunately favours the spread of infections. Sinus mucosa is thinner and less vascular, and has fewer goblet cells, than nasal mucosa. Cilia are always present in the mucosa near the apertures but less evenly distributed elsewhere within the sinuses.

The functions of the paranasal sinuses remain speculative. They clearly add some resonance to the voice, and also allow the enlargement of local areas of the skull while minimizing a corresponding increase in bony mass. It is likely that such growth-related changes serve to strengthen particular regions, e.g. the alveolar processes of the maxillae when the secondary dentition erupts, but they may also function in contouring the head to provide visual signals indicating the individual's status in a social context (e.g. gender, sexual maturity and group identity).

Most sinuses are rudimentary or absent at birth, but enlarge appreciably during the eruption of the permanent teeth and after puberty, events that significantly alter the size and shape of the face.

Development of the paranasal sinuses and anatomical variations in childhood

At birth, both small ethmoidal and maxillary sinuses are present, but the frontal sinus is nothing more than an out-pouching from the nasal cavity, and there is no pneumatization of the sphenoid bone. Understanding the development of the sinuses at each stage of childhood is essential for interpreting pathology and planning surgery. Cadaveric and radiological studies have provided normative data for sinus development.

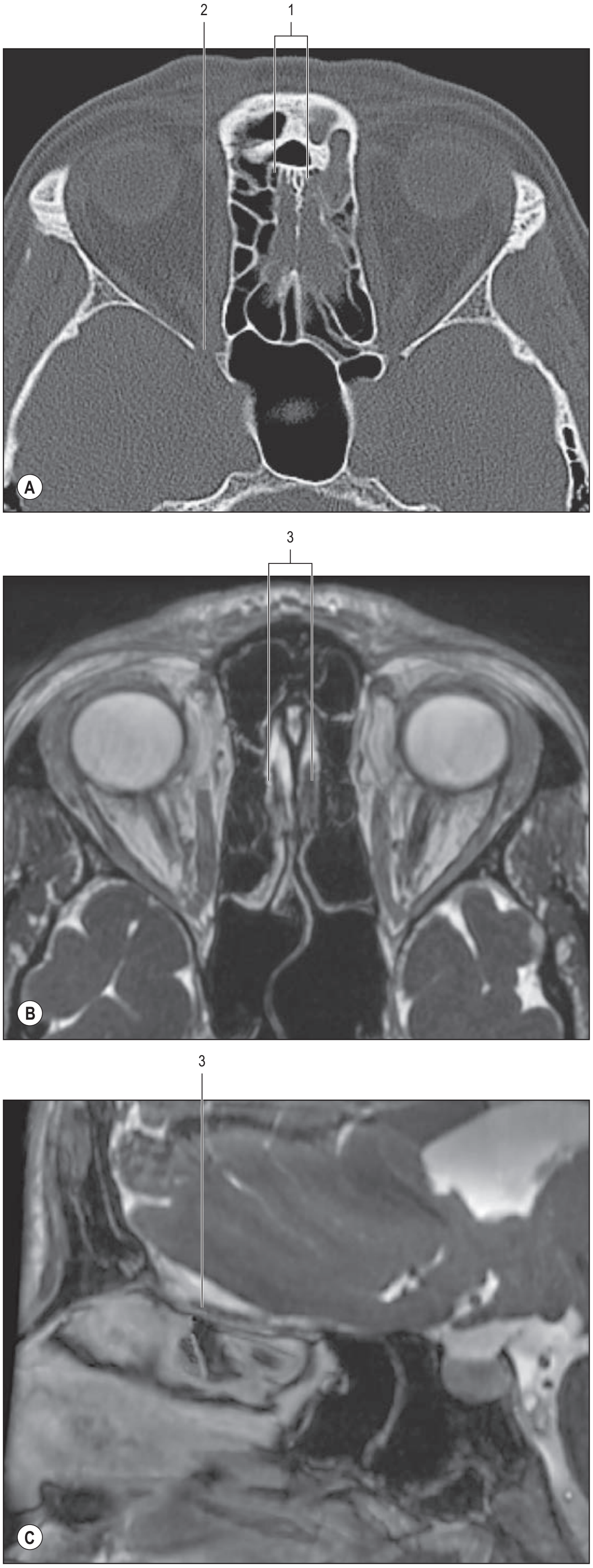

Fig. 39.14 Axial (**A–B**) and sagittal (**C**) scans through the olfactory groove. **A**, Computed tomogram (CT). **B–C**, Magnetic resonance fast imaging employing steady-state acquisition (FIESTA) sequence. Key: 1, ethmoid plate; 2, inferior orbital fissure; 3, olfactory bulb. (With permission from Linn J Cranial nerves. In: Naidich TP, Castillo M, Cha S et al (eds) Imaging of the Brain. Elsevier, Saunders. Copyright 2013.)

In most amphibians, reptiles and mammals, the vomeronasal organ is the peripheral sensory organ of the accessory olfactory system. In these animals, paired vomeronasal organs are located either at the base of the nasal septum or in the roof of the mouth, and are involved in chemical communication that is often, but not exclusively, mediated via pheromones. In many macrosomatic animals, the vomeronasal organ consists of a vomeronasal duct that contains chemosensory cells, and a vomeronasal nerve that terminates centrally in the accessory olfactory bulb. The vomeronasal organ exists in the developing human fetus but its existence in the adult has long been controversial. A bilateral structure in the anteroinferior wall of the nasal septum just dorsal to the paraseptal cartilages, which is presumed to be analogous to the vomeronasal organ of other vertebrates, has been demonstrated in adult human tissue; while there is no evidence that this structure has any neuroreceptive function, it has been suggested that it might have an as yet unknown endocrine function (Wessels et al 2014).

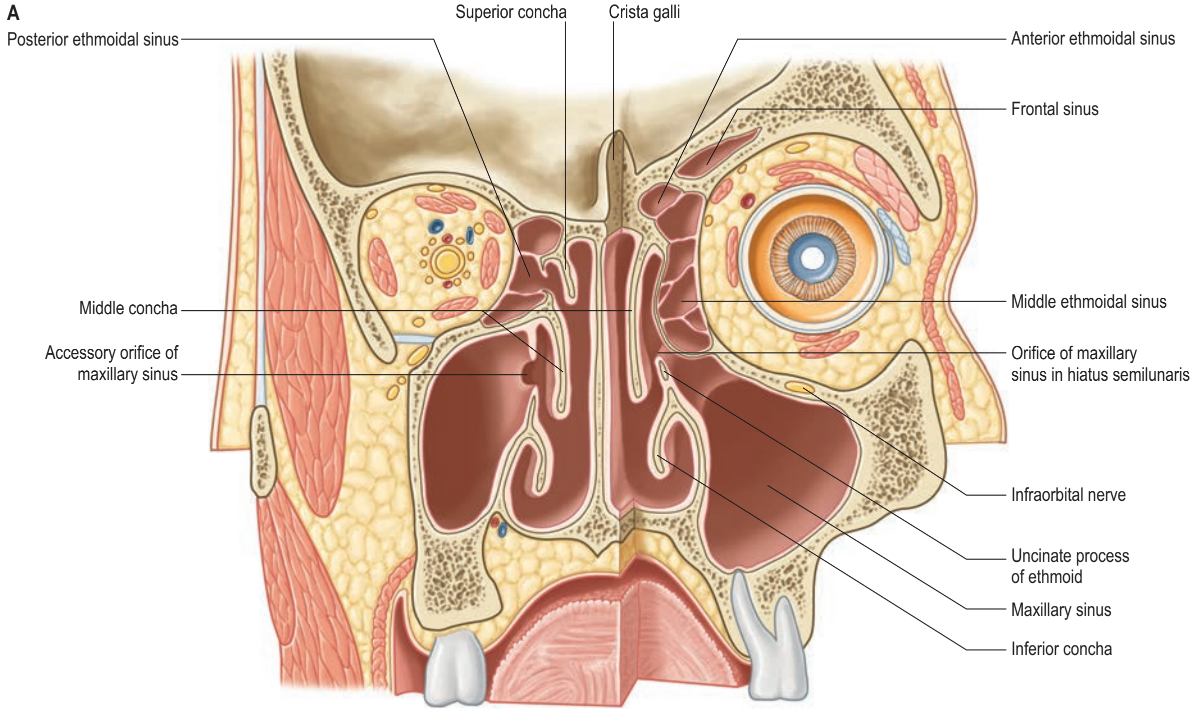

Fig. 39.15 **A**, A coronal section through the nasal cavity, viewed from the posterior aspect. The plane of the section on the right side is more anterior. The normal orifice of the maxillary sinus is shown on the right side and an accessory orifice on the left side. **B–D**, *continued online*

Birth

Available with the *Gray's Anatomy* e-book

1–4 years

Available with the *Gray's Anatomy* e-book

4–8 years

Available with the *Gray's Anatomy* e-book

8–12 years

Available with the *Gray's Anatomy* e-book

Variations in sinus development

Available with the *Gray's Anatomy* e-book

Frontal sinus

The paired frontal sinuses are posterior to the superciliary arches, between the outer and inner tables of the frontal bone (**Figs 39.16–39.17**). Each usually underlies a triangular area on the surface of the face, its angles formed by the nasion, a point 3 cm above the nasion and the junction of the medial third and lateral two-thirds of the supraorbital margin. The two sinuses are rarely symmetric, since the septum between them usually deviates from the median plane. Each sinus may be further divided into a number of communicating recesses by incomplete bony septa.

The average dimensions of an adult frontal sinus are: height 3.2 cm; breadth 2.6 cm; and depth 1.8 cm. Each usually has a frontal portion that extends upwards above the medial part of the eyebrow, and an orbital portion that extends back into the medial part of the roof of the orbit. One or both sinuses may rarely be hypoplastic or even absent; racial differences have been reported. The prominence of the superciliary arches is no indication of the presence or size of the frontal sinuses. They are more prominent in males, and lend the forehead an obliquity that contrasts with the vertical or convex profile typical of children and females.

The aperture of each frontal sinus opens either into the anterior part of the corresponding middle meatus by the ethmoidal infundibulum as a frontonasal recess (rather than a duct), or medial to the hiatus semilunaris if the uncinate process is attached to the lateral nasal wall or an agger nasi cell (Kuhn 2002). The frontal recess is actually the most anterior part of the anterior ethmoidal complex but is described here because of its importance in the drainage of the frontal sinus. Its lateral wall is the lamina papyracea; the medial wall is formed by the middle turbinate; and posteriorly, the wall is made up of either the cranial base, in a suprabullar recess, or the insertion of the bulla, if this reaches the cranial base. Anteriorly, the wall extends from the frontal sinus proper to the anterior attachment of the middle turbinate. In its simplest form, it takes the shape of an inverted funnel, forming an hourglass shape with the floor of the frontal sinus. However, the frontal recess is often narrowed both from in front and from behind by anterior ethmoidal cells, such that it may be highly convoluted (see Fig. 39.17).

These frontoethmoidal cells may be classified with regard to their attachments to the inner walls of the frontal sinus and relationship to the frontal recess as anterior or posterior, medial or lateral (Lund et al 2014), or with regard to their relationship with the agger nasi cell or the ethmoid bulla (Wormald et al 2016) (**Table 39.2**).

Vascular supply, lymphatic drainage and innervation

The frontal sinuses receive their arterial supply from the supraorbital and anterior ethmoidal arteries. The veins drain into an anastomotic vein in the supraorbital notch that connects the supraorbital and superior ophthalmic veins. Lymphatic drainage is to the submandibular nodes. The sinuses are innervated by branches of the supraorbital nerves (general sensation) and the orbital branches of the pterygopalatine ganglia (parasympathetic secretomotor fibres).

Sphenoidal sinus

The sphenoidal sinuses are two large, irregular cavities within the body of the sphenoid and therefore lie posterior to the upper part of the nasal cavity (**Figs 39.18–39.19**). Each opens into the corresponding sphenoethmoidal recess via an aperture high on the anterior wall of the sinus. The sphenoid ostium is usually medial to the superior turbinate, although the height of the ostium is highly variable. The average dimensions of the adult sphenoid are: vertical height 2 cm; transverse breadth 1.8 cm; and anteroposterior depth 2.1 cm. The sinuses are usually separated by a septum that usually deviates from the midline, so that they are unequal in size and form. Their lumina may be further partially divided by bony laminae and accessory septa, especially in the region of former synchondroses, and these septa commonly insert on to the internal carotid artery. Occasionally, one sinus overlaps the other above and, rarely, they intercommunicate. Bony ridges, produced by the internal carotid artery, pterygoid canal, maxillary branch of trigeminal and sometimes the optic nerve, may project into the sinuses from their lateral walls. The sphenoidal sinuses are related above to the optic chiasma and hypophysis cerebri, and on each side to the internal carotid artery and cavernous sinus. One or both sinuses may partially encircle the

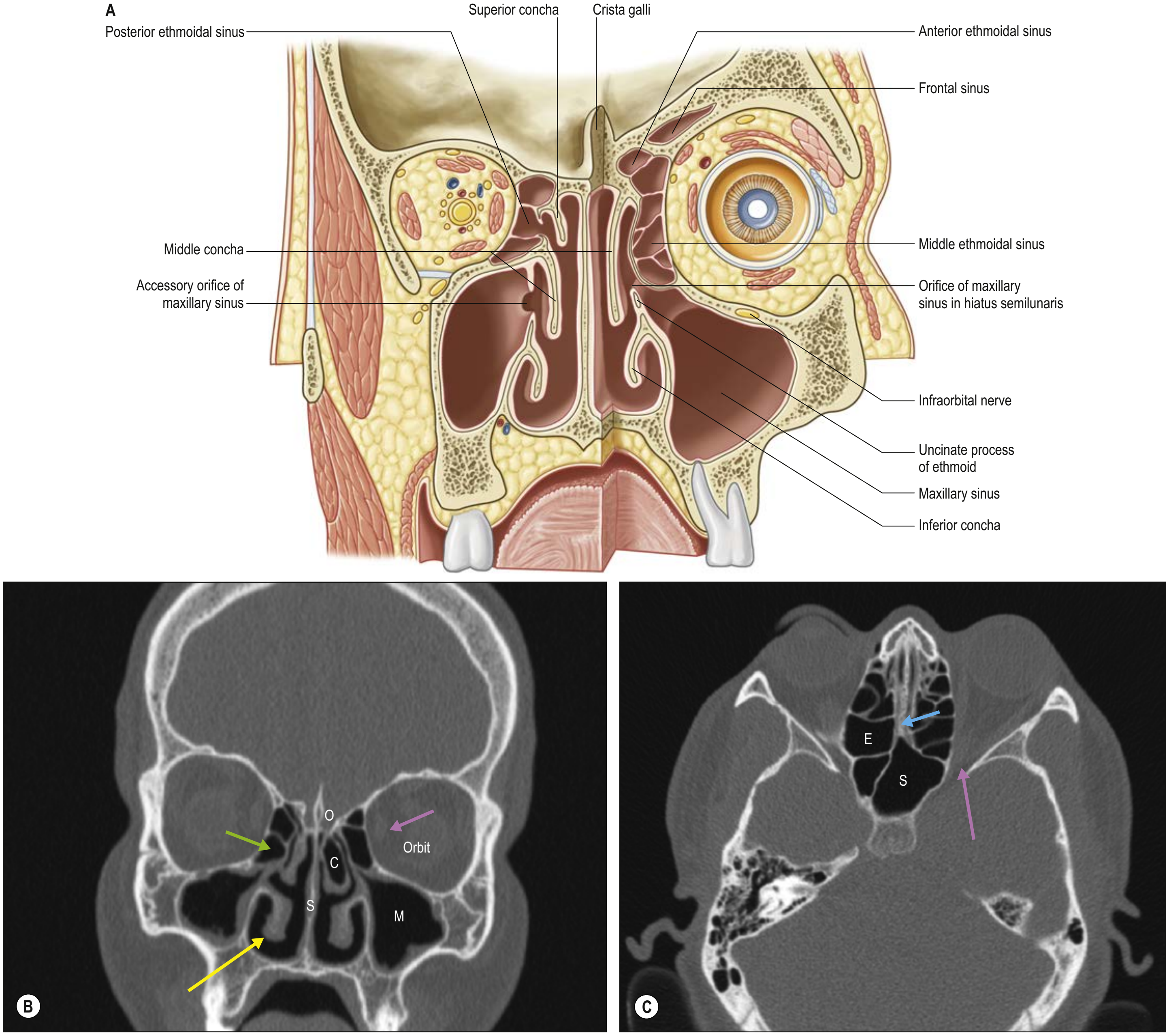
A
Posterior ethmoidal sinus
Superior concha
Crista galli
Anterior ethmoidal sinus
Frontal sinus
Middle concha
Middle ethmoidal sinus
Accessory orifice of maxillary sinus
Orifice of maxillary sinus in hiatus semilunaris
Infraorbital nerve
Uncinate process of ethmoid
Maxillary sinus
Inferior concha
O
Orbit
C
S
M
B
E
S
C

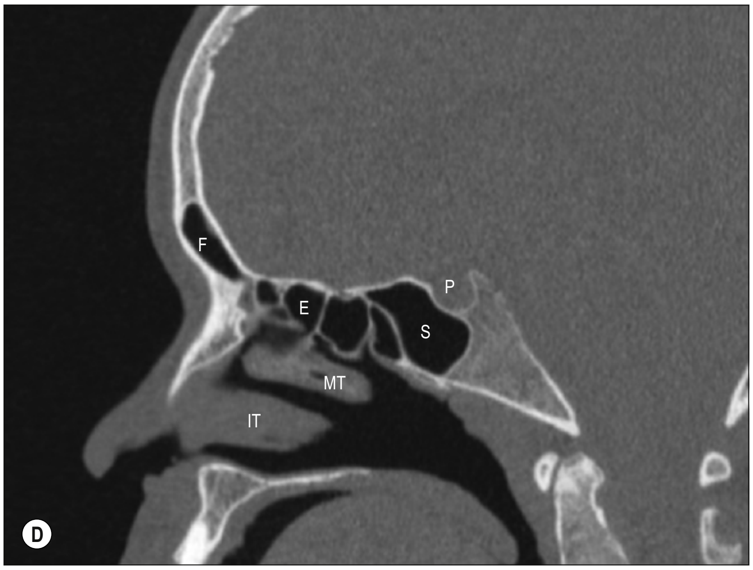

Fig. 39.15 **A**, A coronal section through the nasal cavity, viewed from the posterior aspect. The plane of the section on the right side is more anterior. The normal orifice of the maxillary sinus is shown on the right side and an accessory orifice on the left side. **B–D**, Spiral CT images. **B**, Coronal section. Medial rectus (purple arrow); inferior turbinate (yellow arrow); anterior ethmoidal air cells (green arrow). Abbreviations: C, concha bullosa (pneumatized middle turbinate); M, maxillary sinus; O, olfactory cleft; S, nasal septum. **C**, Axial section. Medial rectus (blue arrow); orbital apex (purple arrow). Abbreviations: E, ethmoidal sinus; S, sphenoidal sinus. **D**, Sagittal section. Abbreviations: E, ethmoidal sinus; F, frontal sinus; IT, inferior turbinate; MT, middle turbinate; P, pituitary fossa; S, sphenoidal sinus.

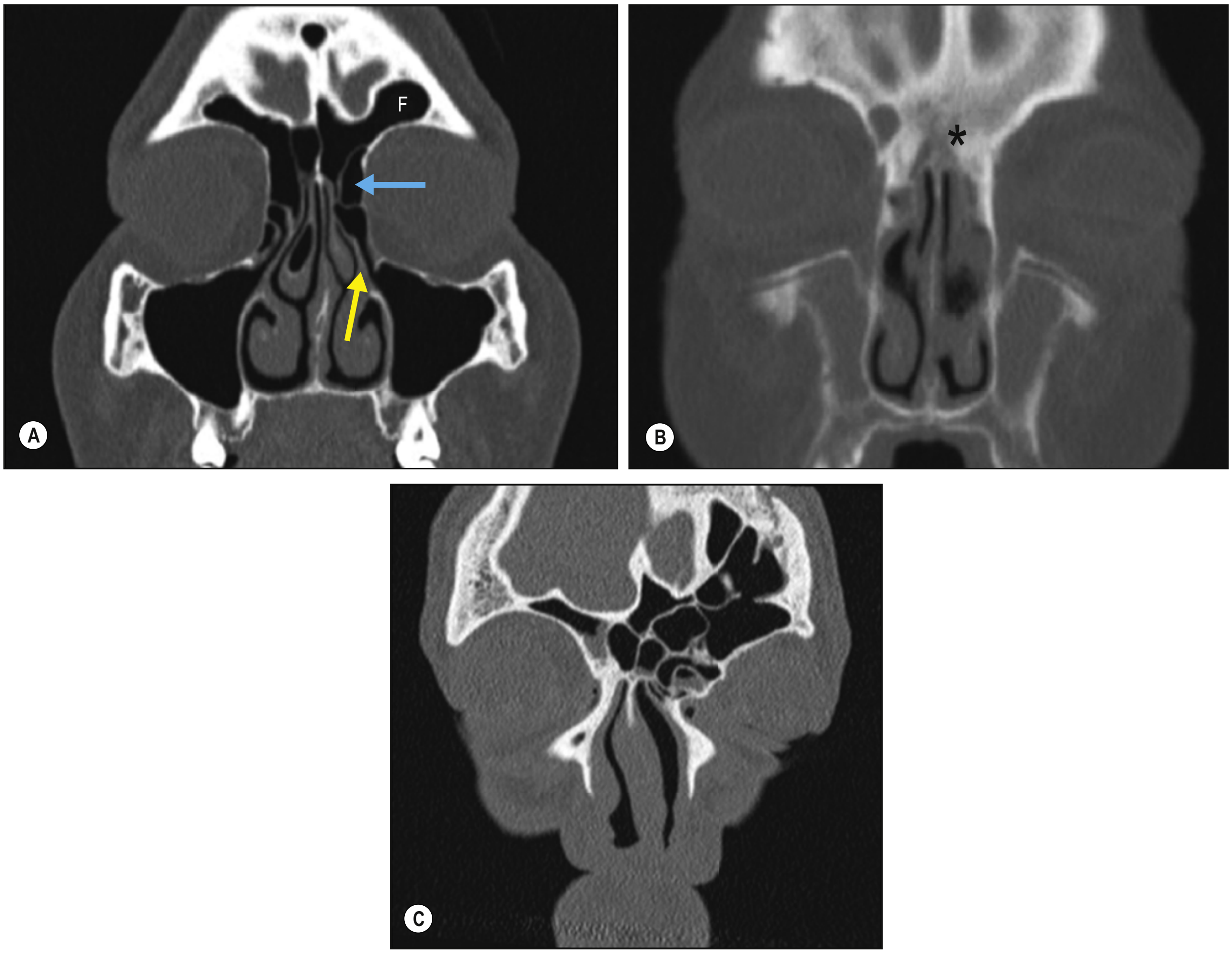

Fig. 39.17 **A**, A coronal CT demonstrating the frontal sinus (F), agger nasi cell (blue arrow) and uncinate process inserting into the middle turbinate (yellow arrow). **B**, An absent frontal sinus (asterisk). **C**, A coronal CT demonstrating variations in the frontal sinus with multiple cells within the frontal recess.

The turbinates at birth are usually bulky and the inferior and middle meatuses are underdeveloped. The uncinate, hiatus semilunaris and ethmoidal bulla are already well-defined, fixed landmarks, and both the anterior and posterior ethmoidal cells are already almost completely developed in terms of number but not size. The cells are separated by connective tissue, which becomes compressed with subsequent expansion of the cells. The ethmoid complex ranges from 8 to 12 mm in length, 1 to 3 mm in width and 1 to 5 mm in height; the complexes expand rapidly in size in the first few years of life. The maxillary sinus is roughly spherical, with a volume of 6–8 cm^3, and measures 10 mm in length, 4 mm in height and 3 mm in width. It lies initially medial to the orbit, but projects laterally under the orbit by the end of the first year of life. The sphenoid is devoid of air, although a blind mucosal sac may sometimes be identified. At birth, the sphenoid has two major ossification centres; failure of fusion between the two may give rise to anatomical variations such as a persistent 'craniopharyngeal canal'. The Eustachian tube is found within the nasal cavity, behind the posterior end of the inferior turbinate. The frontal sinus is no more than a small out-pouching that drains into the infundibulum.

The supreme turbinate has usually disappeared, while the remaining three turbinates reduce relatively in size. The inferior meatus develops and contributes to the nasal airway. The maxillary sinus enlarges rapidly up to the age of 4 years, reaching laterally as far as the infraorbital canal, and inferiorly to the attachment of the inferior turbinate; it ranges between 22 and 30 mm in length, 12 and 18 mm in height and 11 and 19 mm in width. The ethmoidal cells enlarge in all directions, starting anteriorly and then progressing posteriorly. By the age of 4, they are well developed; variants such as the agger nasi cell, infraorbital cell and concha bullosa are identifiable. Sphenoidal pneumatization commences around 7 months of age; a distinct cell is visible by the age of 2 years. By 4 years of age, it is roughly pea-sized, with a diameter of 4–8 mm. The frontal sinus is the last to develop and is imperceptible in infants less than 1 year old. It begins to pneumatize after the age of 2, gradually enlarging as an out-pouching from the anterior ethmoids. Early growth is slow; by 4 years, the vertical height reaches only half the height of the orbit (between 6 and 9 mm in height) (Wolf et al 1993).

TABLE 39.2 Comparison of classification of frontal sinus cells

Kuhn classification (Kuhn 2002)	European position paper (Lund et al 2014)	International Frontal Sinus Anatomy Classification (Wormald at al 2016)
Agger nasi – most anterior ethmoid, anterior to attachment of middle turbinate	Agger nasi cell	Agger nasi cell
Type 1 – single frontal cell above the agger	Anterior and lateral fronto-ethmoidal cell	Supra-agger cell (not extending into frontal sinus)
	Posterior fronto-ethmoidal cell	Supra-bulla cell (not extending into frontal sinus)
Type 2 – tier of cells above agger	Anterior fronto-ethmoidal cells	Supra-agger frontal cell (extending into frontal sinus)
	Posterior fronto-ethmoidal cells	Supra-bulla frontal cell (extending into frontal sinus)
Type 3 – single massive cell above agger extending into frontal sinus	Anterior fronto-ethmoidal cells	Supra-agger frontal cell (extending into frontal sinus)
Type 4 – single isolated cell within frontal sinus (artefact of coronal plane imaging)	Posterior fronto-ethmoidal cells	Supra-bulla frontal cell (extending into frontal sinus)
	Medial (and usually anterior) fronto-ethmoidal cell	Frontal septal cell
	Supraorbital recess – extension over orbit	Supraorbital ethmoid cell

The Kuhn nomenclature was developed based on coronal imaging alone, and has been rendered obsolete by new multi-planar imaging techniques. Both the European and International classifications, while using different terminology, highlight the relationship of frontoethmoidal cells to the drainage pathway of the frontal sinus, thereby facilitating anatomical understanding and surgical approaches.

By 8 years, the sinuses have expanded in all directions. The maxillary sinus has reached the maxillary bone laterally and the plane of the hard palate, becoming tetrahedral in shape. It ranges from 34 to 38 mm in length, 22 to 26 mm in height and 18 to 24 mm in width. The dental buds of unerupted teeth are closely related to the floor of the sinus. The ethmoidal cells continue to enlarge, but more slowly than before; the posterior cells become larger than the anterior cells.

Pneumatization into the vertical plate of the frontal bone does not usually begin until the fifth year, at which time the frontal sinus may be identified radiologically. The frontal sinus pneumatizes rapidly and begins to pneumatize into the vertical plate of the frontal bone; its height reaches the orbital roof at 8 years (Ruf and Pancherz 1996).

By 12 years, the sinuses have almost reached adult proportions. The maxillary sinus pneumatizes into the maxillary alveolus after eruption of the permanent dentition, so that the floor of the sinus now sits 4–5 mm below the level of the floor of the nasal cavity. The ethmoidal sinuses reach adult size, and the frontal sinuses extend into the frontal bone, continuing to enlarge until puberty. The sphenoidal sinus reaches its full size by the age of 14 years.

Asymmetry in the size and shape of the sinuses, hypoplasia and anatomical variants are common (Navarro 1997). Unilateral or bilateral maxillary hypoplasia occurs infrequently; the condition is rarely bilateral. Variation in the pneumatization of almost all the bony lamellae found in the nasal cavity and paranasal sinuses have been described. Pneumatization of an ethmoidal cell into the middle concha creates a concha bullosa, and inferolaterally creates an infraorbital cell. The degree of pneumatization of the sphenoid is highly variable but aplasia is very rare. In contrast, unilateral aplasia of the frontal sinus is present in 15% of adults, and present bilaterally in 5%.

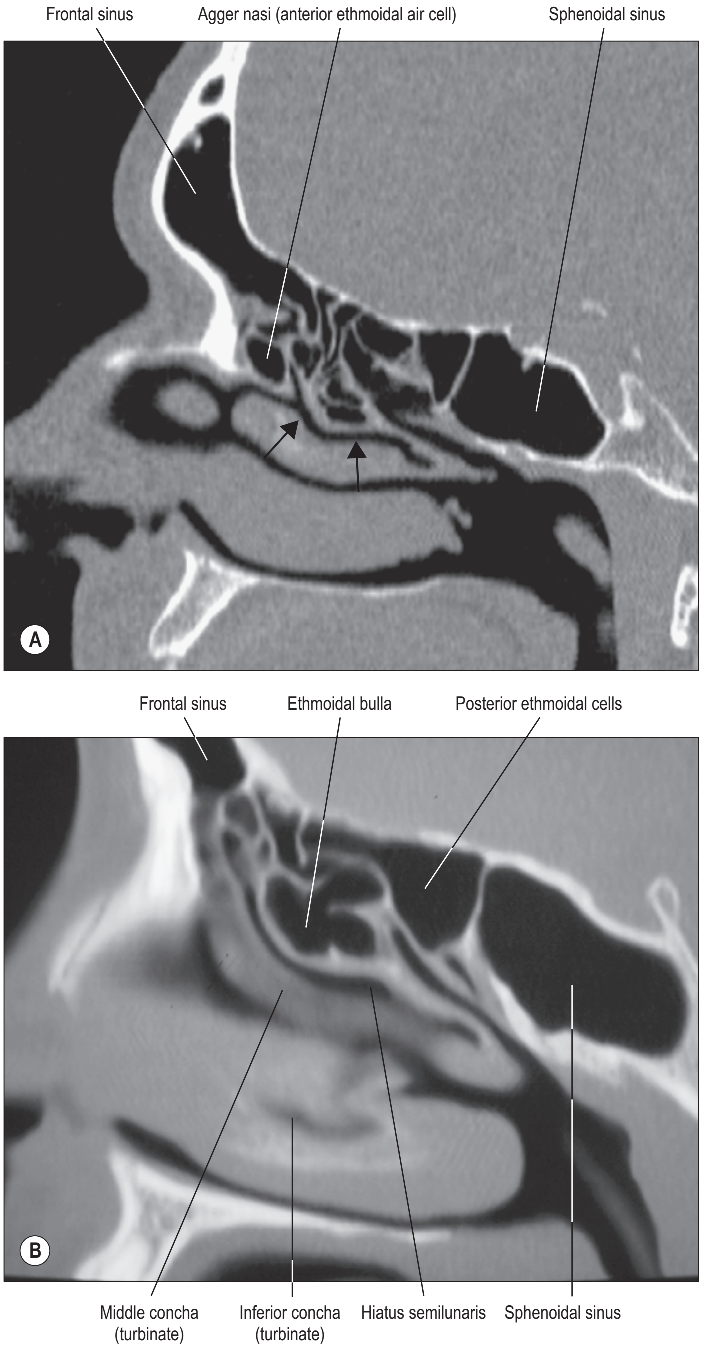
Frontal sinus
Agger nasi (anterior ethmoidal air cell)
Sphenoidal sinus
A
Frontal sinus
Ethmoidal bulla
Posterior ethmoidal cells
B
Middle concha (turbinate)
Inferior concha (turbinate)
Hiatus semilunaris
Sphenoidal sinus

Fig. 39.16 A–B, Sagittal CT scans showing the frontal, ethmoidal and sphenoidal sinuses. Arrows indicate the hiatus semilunaris in **A**. (A, Courtesy of Professor D. Bell.)

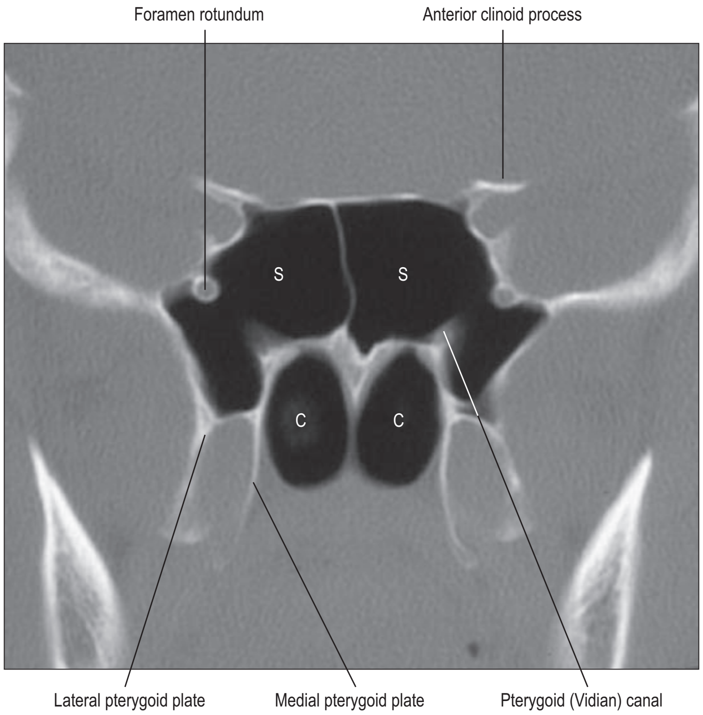
Foramen rotundum
Anterior clinoid process
S
S
C
C
Lateral pterygoid plate
Medial pterygoid plate
Pterygoid (Vidian) canal

Fig. 39.18 A coronal CT scan showing the sphenoidal air sinus. Abbreviations: C, posterior choanae; S, sphenoidal sinus.

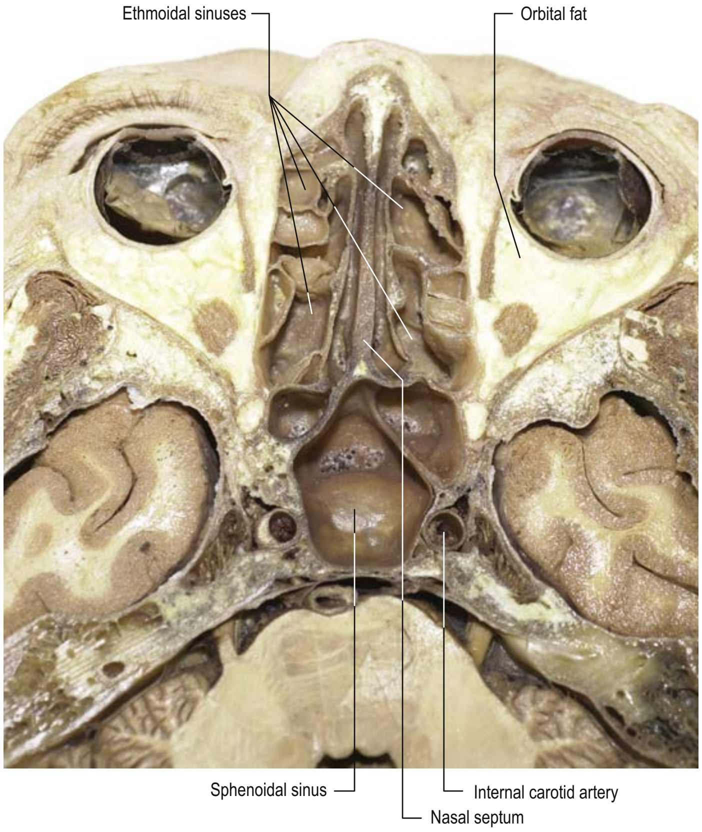
Ethmoidal sinuses
Orbital fat
Sphenoidal sinus
Internal carotid artery
Nasal septum

Fig. 39.19 A horizontal section of the head showing the ethmoidal and sphenoidal sinuses. (With permission from Berkovitz BKB, Moxham BJ 2002 Head and Neck Anatomy. London: Martin Dunitz.)

optic canal. Dehiscences in the osseous walls may occasionally leave their mucosa in contact with the overlying dura mater, optic nerve or carotid artery.

The extent of pneumatization of surrounding bone is highly variable. Sometimes, a lateral recess may extend into the greater and lesser wings of the sphenoid or the pterygoid processes, separating the pterygoid (Vidian) canal and foramen rotundum, and may even invade the basilar part of the occipital bone almost to the foramen magnum. A posterior ethmoidal sinus may extend posterosuperior to the relatively smaller sphenoidal sinuses. In such cases, the sphenoid is medial and inferior to this sphenoethmoidal cell (Onodi cell), which itself will be closely related to the optic nerve and carotid artery. An attempt to approach the sphenoid through a sphenoethmoidal cell places these structures at risk of injury. Sphenoethmoidal cells are readily identified on computed tomographic (CT) imaging, where a horizontal bar can be seen in the coronal plane. The anterior clinoid process may be pneumatized in up to 15% of sphenoidal cells.

The shape and position of the sphenoidal sinus are of clinical importance in an endoscopic trans-sphenoidal surgical approach to the hypophysis cerebri. The sinuses may be classified into three main types: sellar, the most common type, in which the sinus extends for a variable distance beyond the tuberculum sellae; presellar, in which the sinus occasionally extends posteriorly towards, but not beyond, the tuberculum sellae; and conchal, the rarest type, in which a small sinus is separated from the sella turcica by approximately 10 mm of trabecular bone. The anterior midline septum often becomes deviated to one side posteriorly; identification of this septation is important prior to surgery (Fig. 39.20).

Vascular supply, lymphatic drainage and innervation

The sphenoidal sinuses receive their arterial supply from the posterior ethmoidal branches of the ophthalmic arteries and nasal branches of the sphenopalatine arteries. Venous drainage is through the posterior ethmoidal veins draining into the superior ophthalmic veins. Lymph drainage is to the retropharyngeal nodes. The sinuses are innervated by the posterior ethmoidal branches of the ophthalmic nerves (general sensation) and the orbital branches of the pterygopalatine ganglia (parasympathetic secretomotor fibres).

Ethmoidal sinuses

The ethmoidal sinuses differ from the other paranasal sinuses in that they are formed of multiple thin-walled cavities in the ethmoidal labyrinth (see Figs 39.16, 39.17, 39.19). The number and size of the cavities vary, from 3 large to 18 small sinuses on each side. They lie between the upper part of the nasal cavity and the orbit, and are separated from the latter by the paper-thin lamina papyracea or orbital plate of the ethmoid (this presents a poor barrier to infection, which may therefore spread into the orbit). Pneumatization may extend into the middle concha, or into the body and wings of the sphenoid bone lateral to the sphenoidal sinus. (There is a view that the ethmoidal sinuses are aerated after birth, rather than pneumatized, as happens with the other paranasal sinuses (Jankowski 2013).)

The ethmoidal sinuses are divided clinically into anterior and posterior groups on each side, distinguished by their embryological development, sites of communication with the nasal cavity, their mucociliary drainage, and their relation to the basal lamella of the middle turbinate. (Cells wrongly designated previously as belonging to a middle group are now included with the anterior group (Stammberger and Kennedy 1995).) The anterior and posterior groups are separated from each other by the basal lamella; this may be indented by cells from either group and therefore it forms a rather tortuous barrier between them. Within each group, the sinuses are only partially separated by incomplete bony septa.

Anterior ethmoidal sinuses

Up to 11 anterior ethmoidal air cells drain into the ethmoidal infundibulum, a three-dimensional, funnel-shaped cleft between the uncinate and lateral wall of the nose, by one or more orifices. The most anterior group, developmental remnants of the first ethmoturbinals, are the agger nasi cells. These cells are almost always present. They are medial relations of the lacrimal sac and duct, and invaginate beneath the frontal sinus on the lateral wall of the nasal cavity anteriorly. Removal of the superior walls of the agger nasi, 'uncapping the egg', is a key part of surgery of the frontal recess. The ethmoidal bulla, arising from the second ethmoturbinal of the nose, consists of a group of the largest and least variable anterior ethmoidal cells. The cleft between the posterior edge of the uncinate bone and the face of the ethmoidal bulla is known as the hiatus semilunaris. When the bullar lamella reaches the cranial base, this forms the posterior wall of the frontal recess. In other cases, a suprabullar recess may be found. Infraorbital (Haller) cells may develop medially beneath the orbital floor (**Fig. 39.21**).

Posterior ethmoidal sinuses

Up to seven posterior ethmoidal air cells usually drain by a single orifice into the superior meatus; one may drain into the supreme meatus when present, and one or more into the sphenoidal sinus (**Fig. 39.22**). The posterior group lies very close to the optic canal and optic nerve; optic nerve injury is a devastating potential complication of endoscopic sinus surgery, particularly if a sphenoethmoidal cell (Onodi cell) is present. The reported incidence varies widely (3.5–51%). The sphenoethmoidal cell is usually regarded as the most posterior ethmoidal cell that pneumatizes lateral and superior to the sphenoidal sinus, and is intimately associated with the optic nerve; it may contain a tuberculum nervi optici, where the optic canal bulges into the wall of the cell. Pneumatization of the posterior ethmoid cells inferolaterally may create a retromaxillary cell (Herzallah et al 2016).

Roof of the ethmoid bone

The ethmoid bone is open superiorly; the roof is closed by the orbital plate of the frontal bone. Ethmoidal air cells indent this plate; each one is a 'fovea ethmoidalis'. The thin, lateral cribriform lamella (one of the thinnest parts of the cranial base) forms the medial wall of the roof, extending from the middle turbinate to the cribriform plate, and the lateral wall of the olfactory fossa or niche. The olfactory fossa varies in depth and is frequently asymmetrical; it is at risk during sinus surgery.

Uncinate process

The uncinate process is a thin, hook-shaped bone that articulates with the perpendicular plate of the palatine bone and the ethmoidal process of the inferior concha. Its posterosuperior margin is free, forming the hiatus semilunaris with the ethmoidal bulla. It may sometimes reflect medially into the middle meatus and usually overlies the ostium of the maxillary sinus. It is frequently removed during sinus surgery (Becker 1994).

Vascular supply and innervation

The ethmoidal sinuses receive their arterial supply from nasal branches of the sphenopalatine artery and the anterior and posterior ethmoidal branches of the ophthalmic artery. Venous drainage is by the corresponding veins. The lymphatics of the anterior group drain to the submandibular nodes, and those of the posterior group to the retropharyngeal nodes. The sinuses are innervated by the anterior and posterior ethmoidal branches of the ophthalmic nerves (general sensation) and the orbital branches of the pterygopalatine ganglia (parasympathetic secretomotor fibres).

Maxillary sinus

The maxillary sinus is the largest of the paranasal sinuses. It usually fills the body of the maxilla and is pyramidal in shape (see Figs 36.8B, 39.15; **Fig. 39.23**). The base is medial and forms much of the lateral wall of the nasal cavity. The floor, which often lies below the nasal floor, is formed by the alveolar process and part of the palatine process of the maxilla. It is related to the roots of the teeth, especially the second premolar and first molar, but may extend posteriorly to the third molar tooth and/or anteriorly to incorporate the first premolar, and sometimes the canine. Defects in the bone overlying the roots are not uncommon. The roof of the sinus forms the major part of the floor of the orbit. It contains the infraorbital canal, which may exhibit dehiscences. The lateral truncated apex of the pyramid extends into the zygomatic process of the maxilla, and may reach the zygomatic bone, in which case it forms the zygomatic recess, which throws a V-shaped shadow over the antrum on a lateral radiograph.

The facial surface of the maxilla forms its anterior wall, and is grooved internally by a delicate canal (canalis sinuosus) that houses the anterior superior alveolar nerve and vessels as they pass forwards from the infraorbital canal. The prelacrimal recess, the most anteromedial part of the maxillary sinus, may be accessed anterior to the nasolacrimal duct to provide surgical access to the anterior wall of the maxillary sinus (Zhou et al 2013). The posterior wall is formed by the infratemporal surface of the maxilla: it contains alveolar canals that may produce ridges in the sinus and that also conduct the posterior superior alveolar vessels and nerves to the molar teeth. The medial wall is deficient posterosuperiorly at the maxillary hiatus, a large opening that is partially closed in an articulated skull by portions of the perpendicular plate of the palatine bone, the uncinate process of the ethmoid bone, the inferior nasal concha, the lacrimal bone and the overlying nasal mucosa, to form an ostium and anterior and posterior fontanelles. The ostium usually opens into the inferior part of the ethmoidal infundibulum, and thence into the middle meatus, via the hiatus semilunaris (the hiatus forms the area above the superior edge of the uncinate process). The ostium is not normally visible on examination of the nose, without prior resection of the uncinate process. The fontanelles are covered only by periosteum and mucosa, and may contain accessory ostia that may be visible on nasendoscopy and CT. All of the openings are nearer the roof than the floor of the sinus, which means that the natural drainage of the maxillary sinus is reliant on an intact mucociliary escalator; the cilia of the sinus mucoperiosteum normally beat towards the ostium.

The maxillary sinus may be incompletely divided by septa; complete septa are very rare. The thinness of its walls is clinically significant in determining the spread of tumours from the maxillary sinus. A tumour may push up the orbital floor and displace the eyeball; project into the nasal cavity, causing nasal obstruction and bleeding; protrude on to the cheek, causing swelling and numbness if the infraorbital nerve is damaged; spread back into the infratemporal fossa, causing restriction of mouth opening due to pterygoid muscle damage and pain; or spread down into the mouth, loosening teeth and causing malocclusion. Extraction of molar teeth may damage the floor, and impact may fracture its walls. Rarely, hypoplasia of one maxillary antrum is present.

Ostiomeatal complex

The term ostiomeatal complex, or ostiomeatal unit, refers to the area that includes the maxillary sinus ostium, ethmoidal infundibulum and the hiatus semilunaris (**Fig. 39.24**); it is a functional complex rather than a clearly defined anatomical structure. The complex is the common pathway for drainage of secretions from the maxillary and anterior group of ethmoidal sinuses; where the uncinate process attaches to the lateral nasal wall, the complex also drains the frontal sinus.

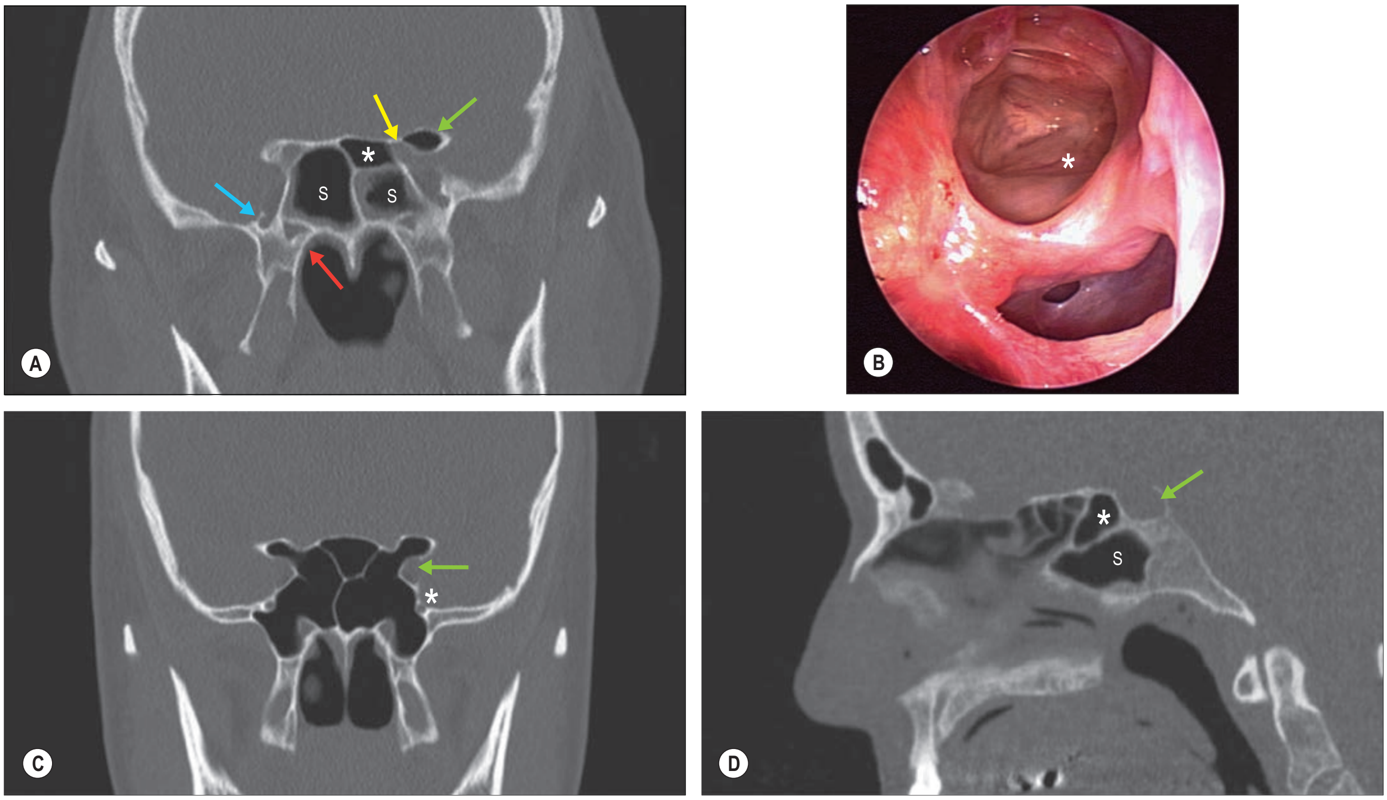

Fig. 39.20 **A**, A coronal CT demonstrating a normal right-sided sphenoidal sinus and a small left-sided sphenoidal sinus (S). The left sphenoethmoidal cell is also shown (asterisk). Pneumatization of the left anterior clinoid process (green arrow) means that the optic nerve (yellow arrow) lies exposed within the sphenoethmoidal cell. The foramen rotundum (blue arrow) and pterygoid (Vidian) canal (red arrow) can also be seen. **B**, An endoscopic view of a right Onodi cell; the optic nerve is visible in the posterolateral wall of the cell (asterisk). **C**, A coronal CT demonstrating well-pneumatized sphenoidal sinuses. The foramen rotundum (asterisk) and internal carotid artery (arrow) are also shown. **D**, A sagittal CT demonstrating the sphenoidal sinus (S), pituitary fossa (arrow) and posterior sphenoethmoidal cell (asterisk).

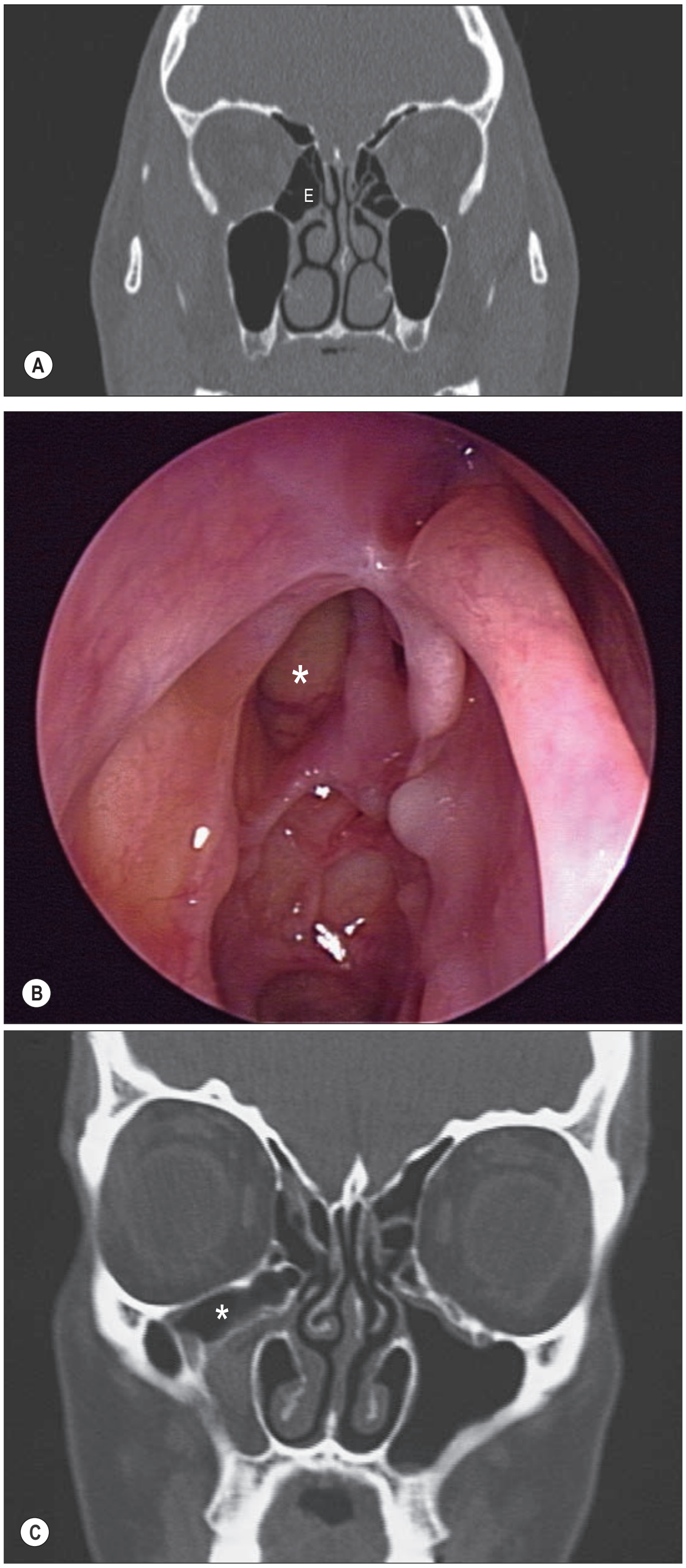

Fig. 39.21 **A**, The anterior ethmoidal air cells (E). **B**, An endoscopic view showing a partially opened agger nasi cell (asterisk). **C**, An infraorbital ethmoidal cell (Haller cell, asterisk), seen as a variation of anterior ethmoidal anatomy.

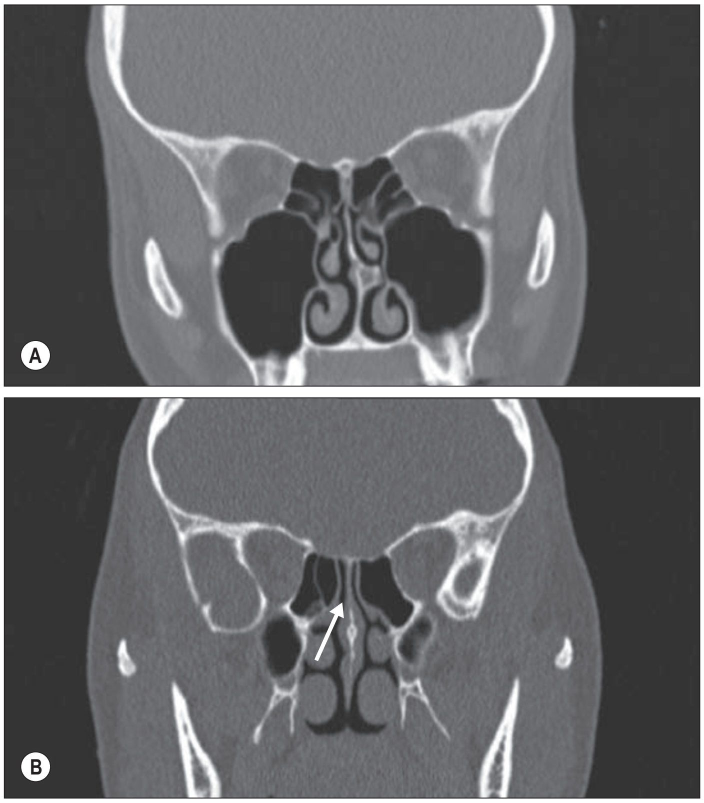

Fig. 39.22 **A**, A coronal CT demonstrating the posterior ethmoidal cells. A bony spur can be seen in the nasal septum. **B**, The posterior ethmoidal air cells and the sphenoethmoidal recess (arrow).

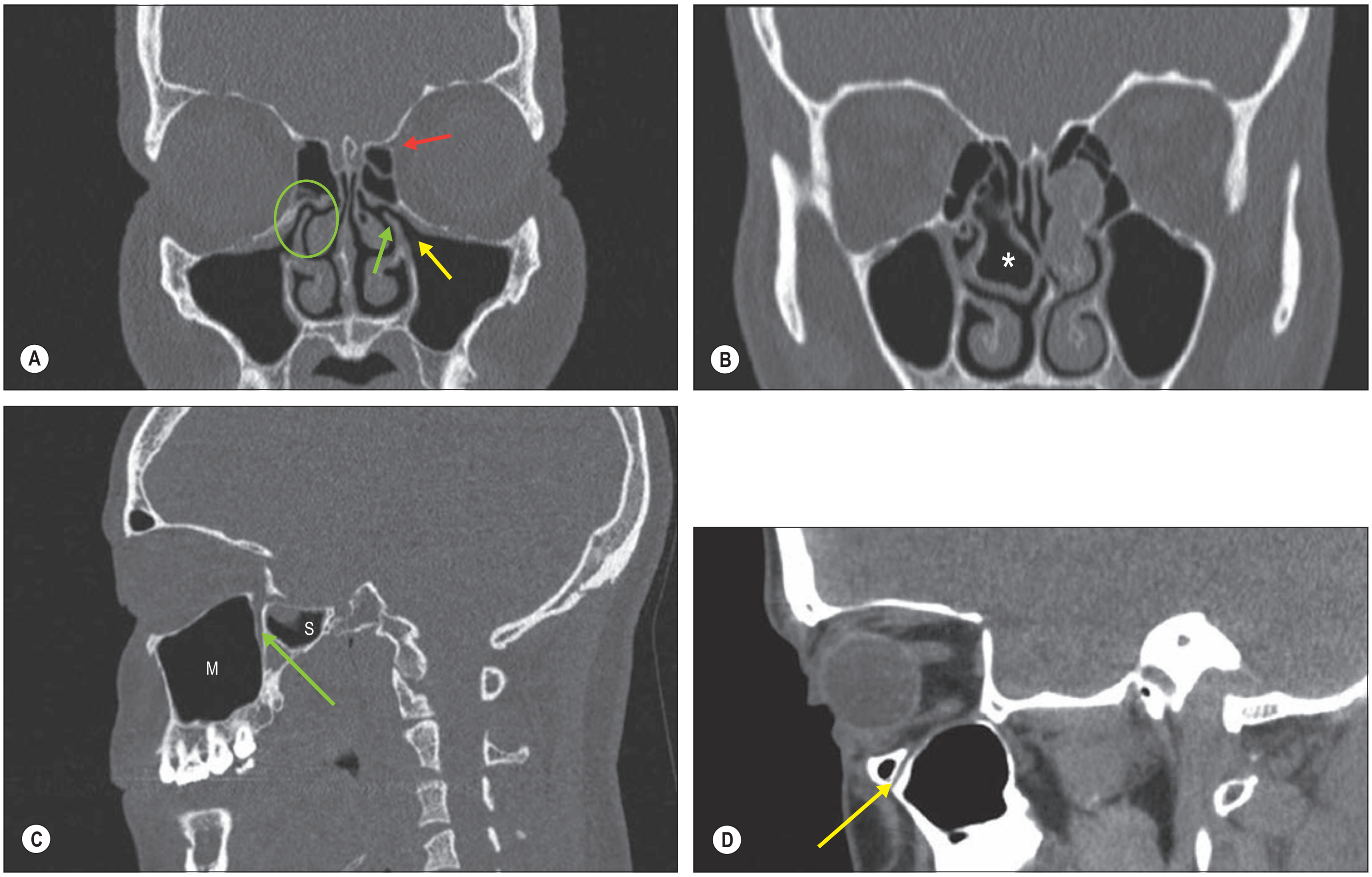

Fig. 39.23 **A**, A coronal section demonstrating the maxillary and anterior ethmoidal sinuses. The ostiomeatal complex (ringed) and infundibulum (yellow arrow) are shown. The anterior ethmoidal artery can be seen leaving the orbit (red arrow). The uncinate process is also visible (green arrow). **B**, A coronal CT demonstrating the maxillary sinuses and a right-sided, pneumatized middle concha (concha bullosa; asterisk). **C**, A sagittal CT demonstrating the relationship between the posterior wall of the maxillary sinus (M), the pterygopalatine fossa (arrow) and a lateral extension of the sphenoidal sinus (S). **D**, A sagittal CT showing the course of the infraorbital nerve through the maxillary sinus (arrow).

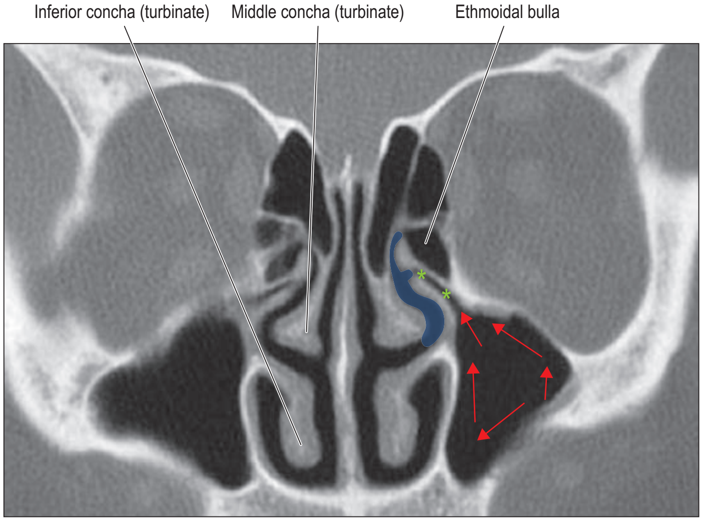

Fig. 39.24 A coronal CT scan through the ostiomeatal complex. Red arrows indicate the direction of mucociliary flow; The blue is quite hard to discern - suggest that it is brighter. This might mean that the green stars also have to be brighter in order to distinguish them from the blue. the middle meatus; and the green stars, the infundibulum.

Vascular supply, lymphatic drainage and innervation

The arterial supply of the maxilla is derived mainly from the maxillary arteries via the anterior, middle and posterior superior alveolar branches and from the infraorbital and greater palatine arteries. Branches of the posterior superior alveolar artery and the infraorbital artery form an anastomosis in the bony wall of the sinus, which also supplies the mucous membrane that lines the nasal chambers. An extraosseous anastomosis frequently exists between the posterior superior alveolar artery and the infraorbital artery. The intra- and extraosseous anastomoses form a double arterial arcade that supplies the lateral antral wall and, partly, the alveolar process. Veins corresponding to the arteries drain into the facial vein or pterygoid venous plexus on either side. Lymph drainage is to the submandibular nodes. The sinuses are innervated by the infraorbital and anterior, middle and posterior superior alveolar branches of the maxillary nerves (general sensation), and nasal branches of the pterygopalatine ganglia (parasympathetic secretomotor fibres).

Imaging of the paranasal sinuses

Standard radiological images are no longer recommended in the diagnosis of rhinosinusitis because of their poor specificity and sensitivity, although they may be used to confirm the presence of acute frontal or maxillary sinusitis that has failed to respond to medical treatment and requires urgent drainage. CT defines anatomical variations but should not be used in isolation for diagnosis because 1 in 3 asymptomatic individuals show incidental mucosal changes (Fig. 39.25). Spiral CT provides good-quality axial, coronal and sagittal images that facilitate an appreciation of the size and relationship of the paranasal sinuses (see Fig. 39.15B–D). Multiplanar and 3D reconstruction techniques have allowed enhanced understanding of the sinus anatomy and suggest that the concept of discrete sinus cells may be an artefact of planar imaging and dissection; in reality, the sinus air cells are likely to be more interconnected than currently described (Vaid and Vaid 2015).

Spread of infection from the sinuses

Uncontrolled paranasal sinus infection can cause very significant morbidity. In the pre-antibiotic era, it was often associated with mortality from meningitis and brain abscess. Paranasal sinus infection has the potential to spread to the orbit, cavernous sinuses, meninges and brain. The ability to overcome infection at this site depends on the virulence of the infecting organism, the speed with which appropriate treatment is delivered, innate immunity and individual anatomical aspects of the sinuses that may predispose to spread of infection. Normal mucociliary clearance of the nasal and paranasal mucosa becomes impaired very quickly with the onset of infection and the patency of drainage pathways become paramount. The middle meatus forms the common drainage pathway for the anterior ethmoidal, frontal and maxillary sinuses. The posterior ethmoidal and sphenoidal sinuses drain into the superior meatus and sphenoethmoidal recess. Endoscopic examination will usually show infected mucus draining from these areas in this situation (Simmen and Jones 2005).

The bony walls of the sinuses are paper-thin in places and dehiscences of them, particularly of the lamina papyracea and cribriform plate of the ethmoids, the lateral wall of the sphenoid, and the orbital and posterior walls of the frontal sinus, bring infected sinus mucosa into direct contact with orbital periosteum, the dura of the anterior cranial fossa and the cavernous sinus. Septic thrombophlebitis then develops and infection spreads rapidly by this route. Sequelae can include blindness, intra- and extradural collections, cavernous sinus thrombosis, meningitis, frontal lobe abscess and osteomyelitis of the cranial vault if diploic veins are involved.

Bonus e-book content

Fig. 39.2 The adult male nose. **A**, Basal view. **B**, Frontal view.

Fig. 39.7 **A**, An endoscopic view of the nasal cavity showing inferior and middle turbinates. **B**, A view of the middle meatus and left lateral wall of the nose. **C**, An endoscopic view of the nose showing the middle turbinate and the pneumatized uncinate process in the middle meatus. **D**, An endoscopic view of the nose demonstrating a deviated nasal septum making contact with the left inferior turbinate. **E**, An endoscopic view of the posterior nasal space.

Fig. 39.8 **C**, A higher-power view of the expanded end of an olfactory receptor neurone. **D**, A section of human olfactory epithelium immunostained with anti-OMP (olfactory marker protein).

Fig. 39.15 **B**, A coronal section of the skull. **C**, An axial section of the skull. **D**, A sagittal section of the skull.

Fig. 39.17 **A**, A coronal CT demonstrating the frontal sinus, agger nasi cell and uncinate process inserting into the middle turbinate. **B**, An absent frontal sinus. **C**, A coronal CT demonstrating variations in the frontal sinus with multiple cells within the frontal recess.

Fig. 39.20 **A**, A coronal CT demonstrating a normal right-sided sphenoidal sinus and a small left-sided sphenoidal sinus. **B**, An endoscopic view of a right Onodi cell; the optic nerve is visible in the posterolateral wall of the cell. **C**, A coronal CT demonstrating well-pneumatized sphenoidal sinuses. **D**, A sagittal CT demonstrating the sphenoidal sinus, pituitary fossa and posterior sphenoethmoidal cell.

Fig. 39.21 **A**, The anterior ethmoidal air cells. **B**, An endoscopic view showing a partially opened agger nasi cell. **C**, An infraorbital ethmoidal cell (Haller cell), seen as a variation of anterior ethmoidal anatomy.

Fig. 39.22 **A**, A coronal CT demonstrating the posterior ethmoidal cells. **B**, The posterior ethmoidal air cells and the sphenoethmoidal recess.

Fig. 39.23 **A**, A coronal section demonstrating the maxillary and anterior ethmoidal sinuses. **B**, A coronal CT demonstrating the maxillary sinuses and a right-sided, pneumatized middle concha (concha bullosa). **C**, A sagittal CT demonstrating the relationship between the posterior wall of the maxillary sinus, the pterygopalatine fossa and a lateral extension of the sphenoidal sinus. **D**, A sagittal CT showing the course of the infraorbital nerve through the maxillary sinus.

Fig. 39.25 Imaging of the paranasal sinuses (CT1–4). Anatomical variants within the sinuses are so common that 'normal' scans are in fact an exception. A series of images from three patients demonstrate examples of several of the variants in pneumatization, size and symmetry of the sinuses that are frequently found. While obstruction of sinus drainage has been attributed to anatomical variants in series B and C, the variants described may also be found in the absence of obstruction. **Series A** is a single patient series demonstrating anatomical variants in the pneumatization of the uncinate and middle turbinates and asymmetry between sides. **Series B** is a single patient series demonstrating a well pneumatized sphenoid sinus and anatomical obstruction to drainage of the right frontal sinus. **Series C** is a single patient series demonstrating anatomical obstruction to the drainage of the left frontal sinus and bilateral conchae bullosae.

Table 39.1 Surgical and anatomical terminology.

Table 39.2 Comparison of classification of frontal sinus cells.

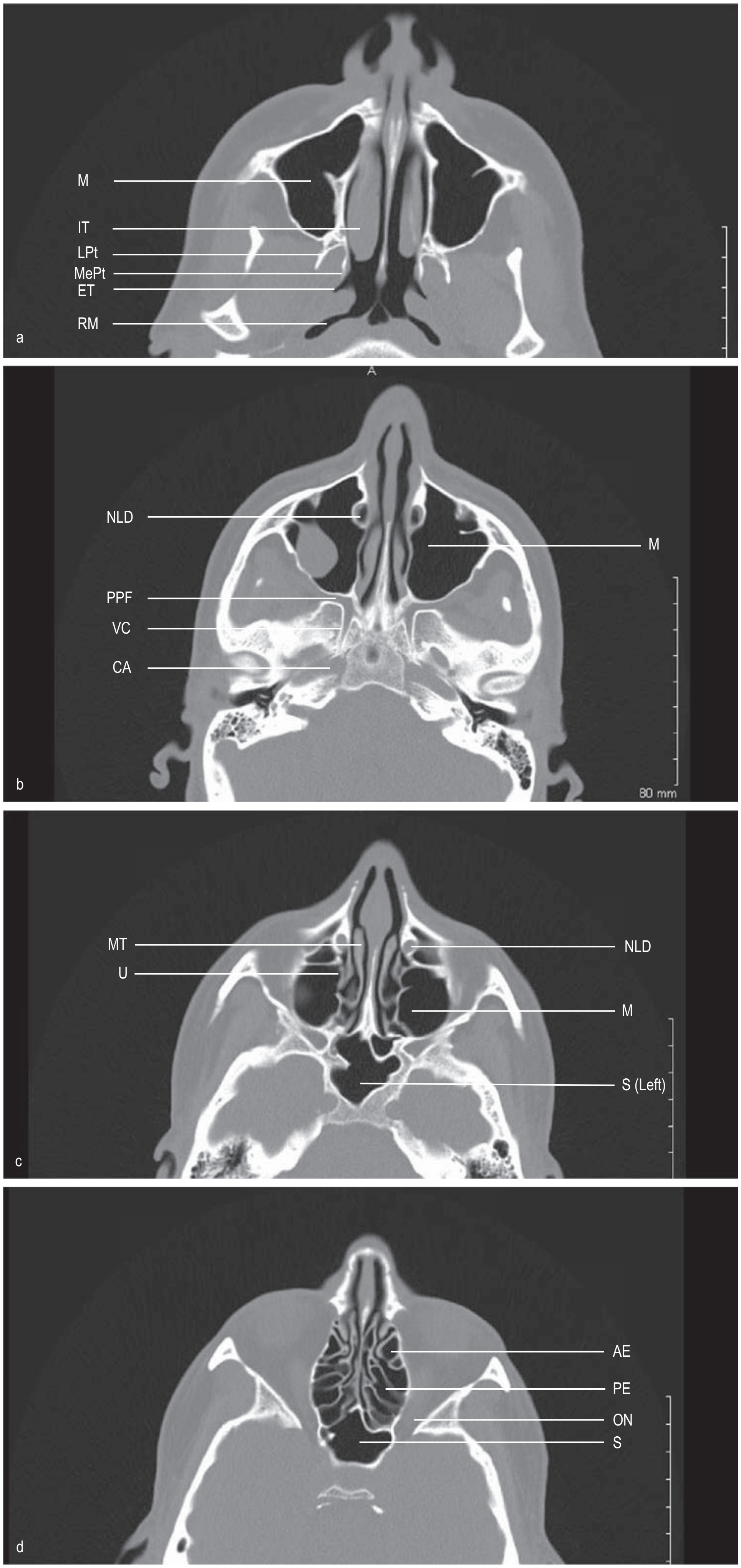

Fig. 39.25 CT imaging of the paranasal sinuses. Anatomical variants within the sinuses are so common that ‘normal’ scans are in fact an exception. The following series of images from three patients demonstrate examples of several of the variants in pneumatization, size and symmetry of the sinuses that are frequently found. While obstruction of sinus drainage has been attributed to anatomical variants in series B and C, the variants described may also be found in the absence of obstruction. **Series A** (a-m) is a single patient series demonstrating anatomical variants in the pneumatization of the uncinate and middle turbinates and asymmetry between sides. (a-d, axial; e-k, coronal; l-m, sagittal). **Series B** (n-v) is a single patient series demonstrating a well pneumatized sphenoid sinus and anatomical obstruction to drainage of the right frontal sinus. (n-r, coronal; s, axial; t-v, sagittal) **Series C** (w-z) is a single patient series demonstrating anatomical obstruction to the drainage of the left frontal sinus and bilateral conchae bullosae. (w,y,z, coronal; x, sagittal) Abbreviations: AC, anterior clinoid process; AE, anterior ethmoidal cell; AEA, anterior ethmoidal artery; AFE, anterior fronto-ethmoidal cell; AN, agger nasi cell; ANS, anterior nasal spine; BNS, bony nasal septum; CA, carotid canal; CG, crista galli; CN, cribriform niche; CS, cartilagenous septum; EB, ethmoid bulla (bulla ethmoidalis); ET Eustachian tube orifice; F, frontal sinus; FR, foramen rotundum; IC, incisive canal; ICA, internal carotid artery; IO, infraorbital cell; ION, infraorbital nerve; IT, inferior turbinate; LP, lamina papyracea; LPt, lateral pterygoid plate; M, maxillary antrum; MePt, medial pterygoid plate; MR, medial rectus; MT, middle turbinate; NLD, nasolacrimal duct; O, olfactory cleft; OC, optic canal; OCR, optico-carotid recess; OMC, ostiomeatal complex; ON, optic nerve; PA, piriform aperture; PE, posterior ethmoid cell; PEA, posterior ethmoid artery; PF, pituitary fossa; PPE, perpendicular plate ethmoid; PPF, pterygopalatine fossa; RM, fossa of Rosenmuller; S, sphenoid sinus; SO, superior oblique; ST, superior turbinate; SuT, supreme turbinate; U, uncinate; VC, Vidian canal; V, vomer. Asterisk denotes structure with anatomical variant.

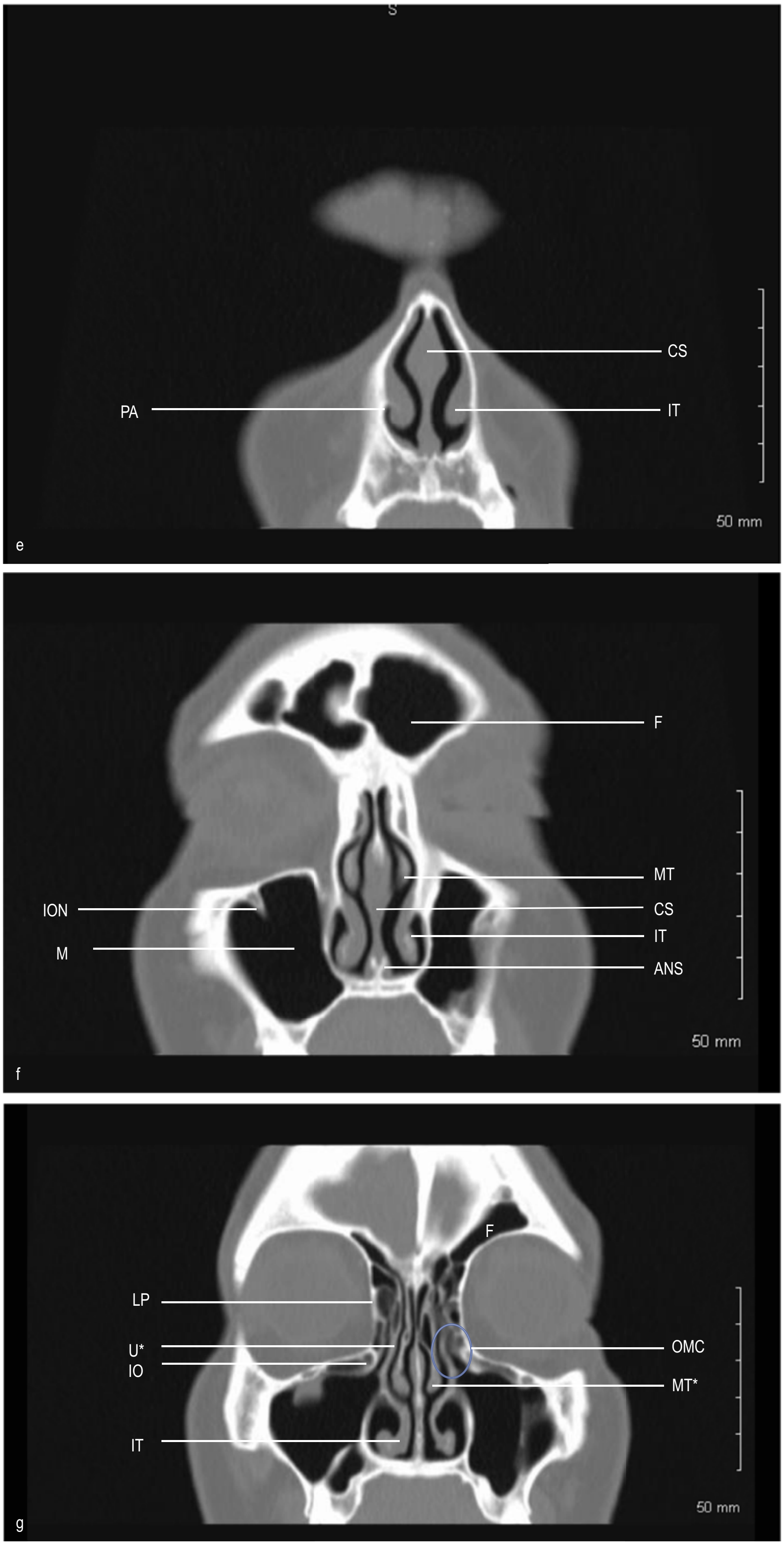
S
CS
PA
IT
50 mm
e
F
MT
ION
CS
M
IT
ANS
50 mm
f
F
LP
U*
IO
OMC
MT*
IT
50 mm
g

Fig. 39.25, cont'd

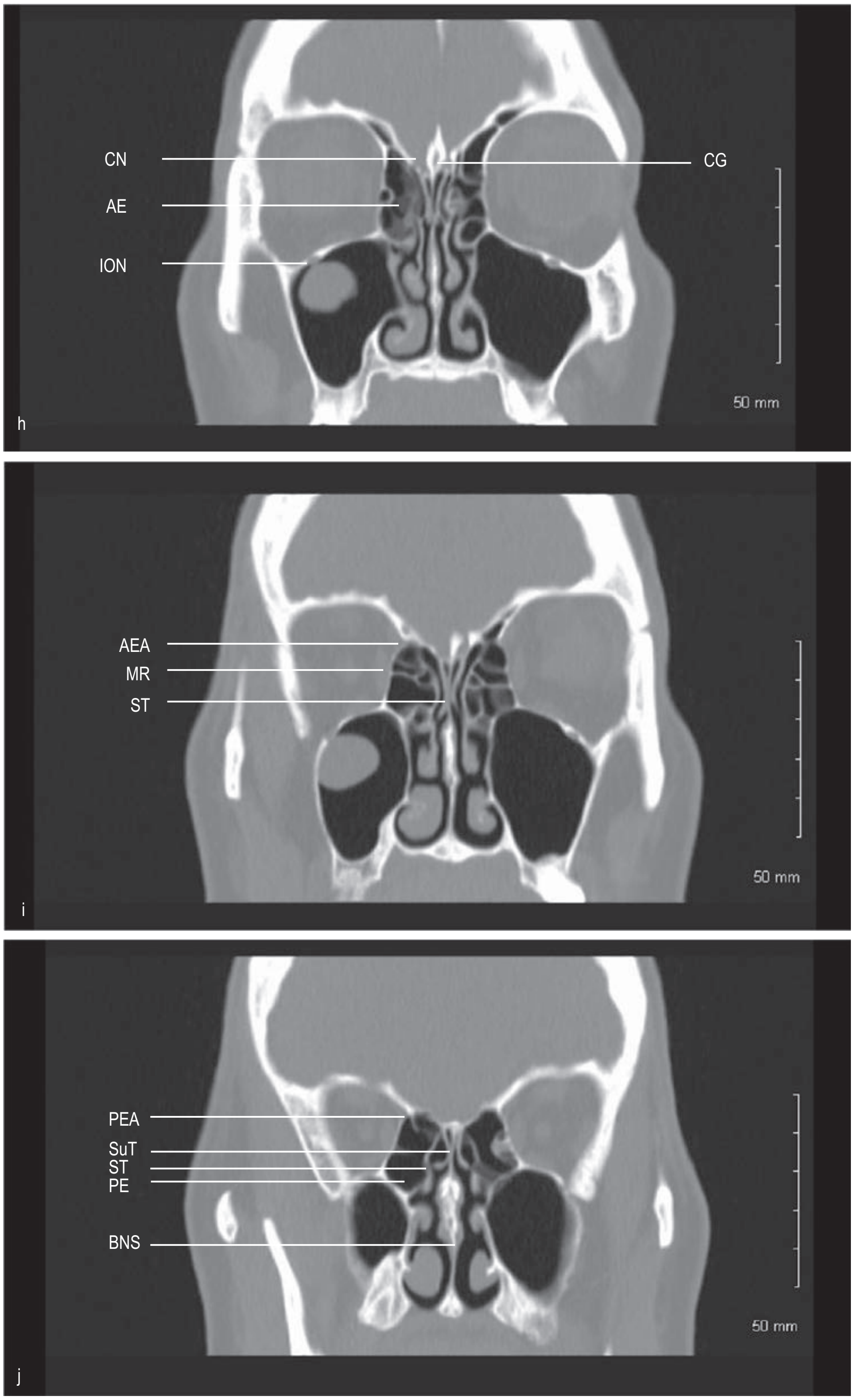
CN
AE
ION
CG
50 mm
h
AEA
MR
ST
50 mm
i
PEA
SuT
ST
PE
BNS
50 mm
j

Fig. 39.25, cont'd *Continued*

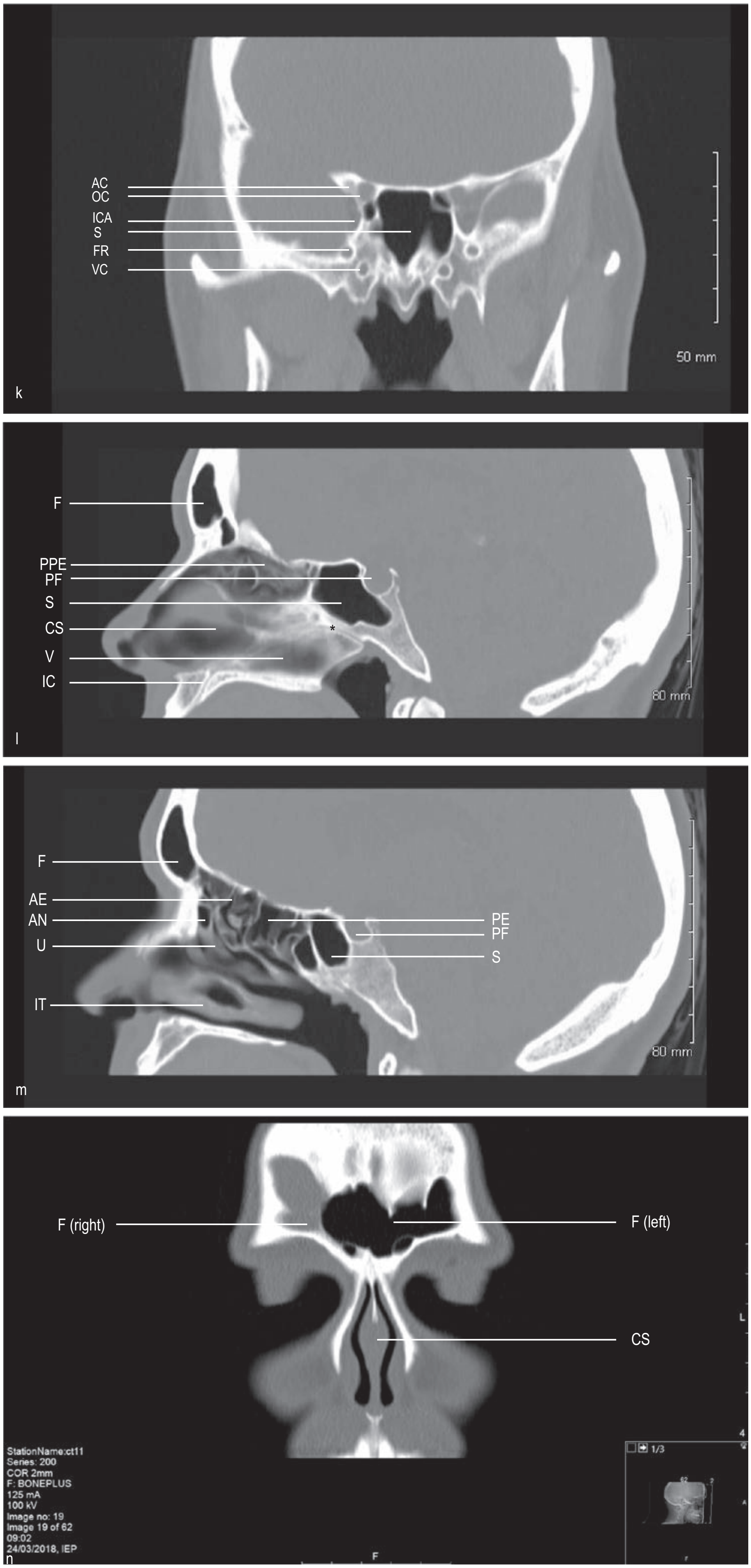
AC
OC
ICA
S
FR
VC
50 mm
k
F
PPE
PF
S
CS
*
V
IC
80 mm
l
F
AE
AN
U
IT
PE
PF
S
80 mm
m
F (right)
F (left)
CS
StationName:ct11
Series: 200
COR 2mm
F: BONEPLUS
125 mA
100 kV
Image no: 19
Image 19 of 62
09:02
24/03/2018, IEP
n
F

Fig. 39.25, cont'd

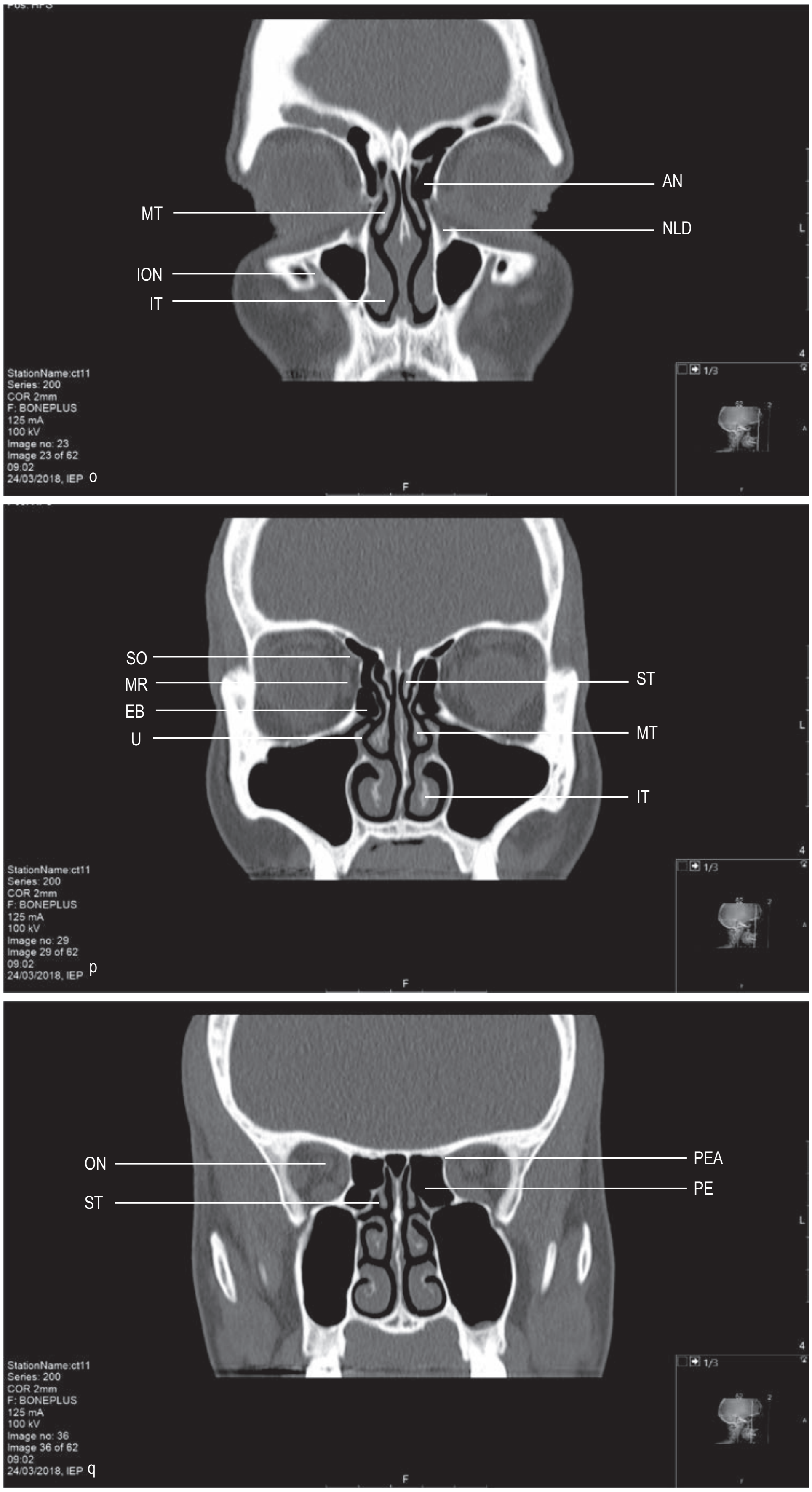
AN
MT
NLD
ION
IT
StationName:ct11
Series: 200
COR 2mm
F: BONEPLUS
125 mA
100 kV
Image no: 23
Image 23 of 62
09:02
24/03/2018, IEP
o
SO
MR
EB
U
ST
MT
IT
StationName:ct11
Series: 200
COR 2mm
F: BONEPLUS
125 mA
100 kV
Image no: 29
Image 29 of 62
09:02
24/03/2018, IEP
p
ON
ST
PEA
PE
StationName:ct11
Series: 200
COR 2mm
F: BONEPLUS
125 mA
100 kV
Image no: 36
Image 36 of 62
09:02
24/03/2018, IEP
q

Fig. 39.25, cont'd

Continued

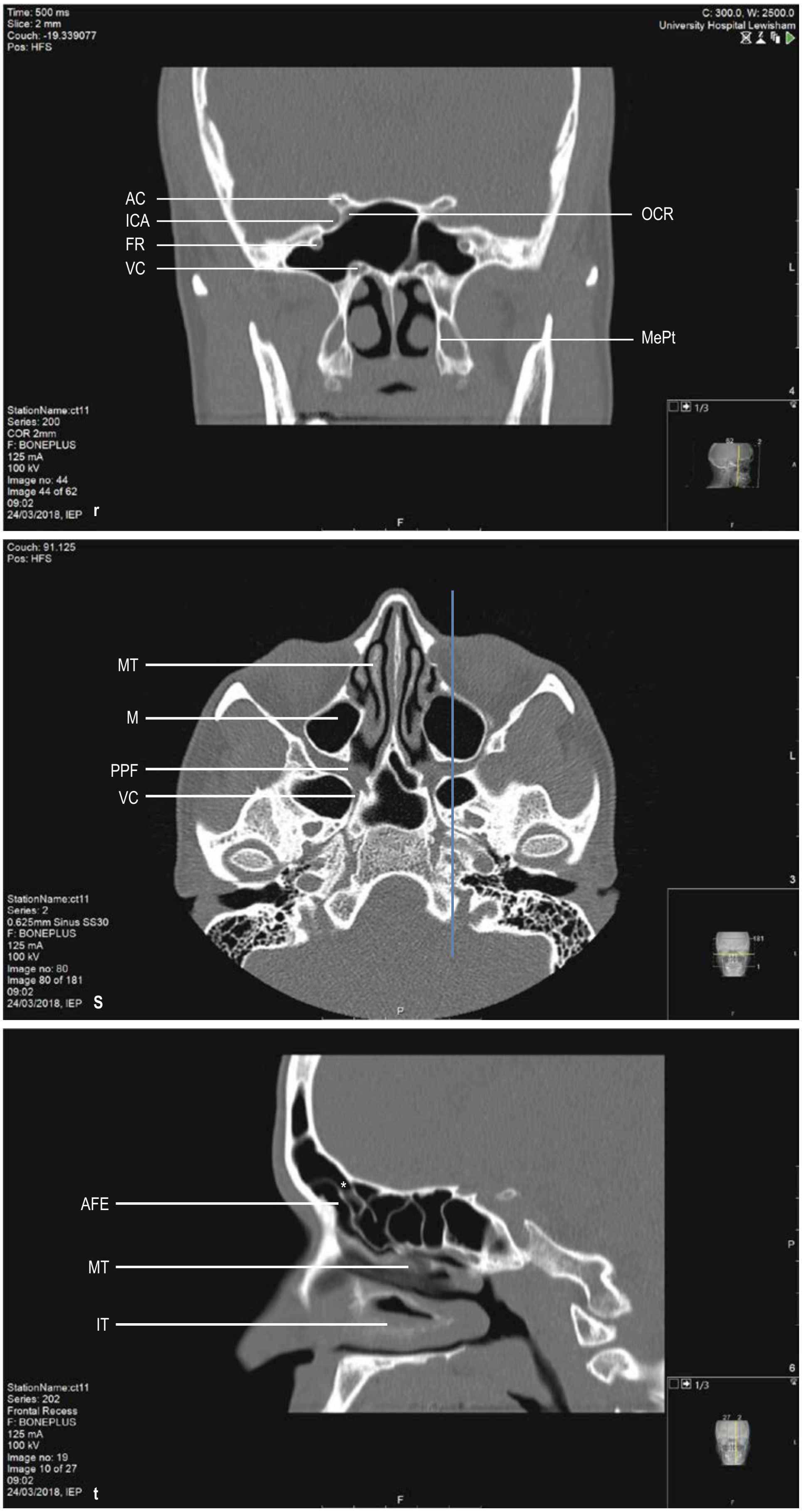
Time: 500 ms
Slice: 2 mm
Couch: -19.339077
Pos: HFS
C: 300.0, W: 2500.0
University Hospital Lewisham
AC
ICA
FR
VC
OCR
MePt
StationName:ct11
Series: 200
COR 2mm
F: BONEPLUS
125 mA
100 kV
Image no: 44
Image 44 of 62
09:02
24/03/2018, IEP
r
1/3
L
F
Couch: 91.125
Pos: HFS
MT
M
PPF
VC
StationName:ct11
Series: 2
0.625mm Sinus SS30
F: BONEPLUS
125 mA
100 kV
Image no: 80
Image 80 of 181
09:02
24/03/2018, IEP
s
L
P
AFE
*
MT
IT
StationName:ct11
Series: 202
Frontal Recess
F: BONEPLUS
125 mA
100 kV
Image no: 19
Image 10 of 27
09:02
24/03/2018, IEP
t
1/3
P
F

Fig. 39.25, cont'd

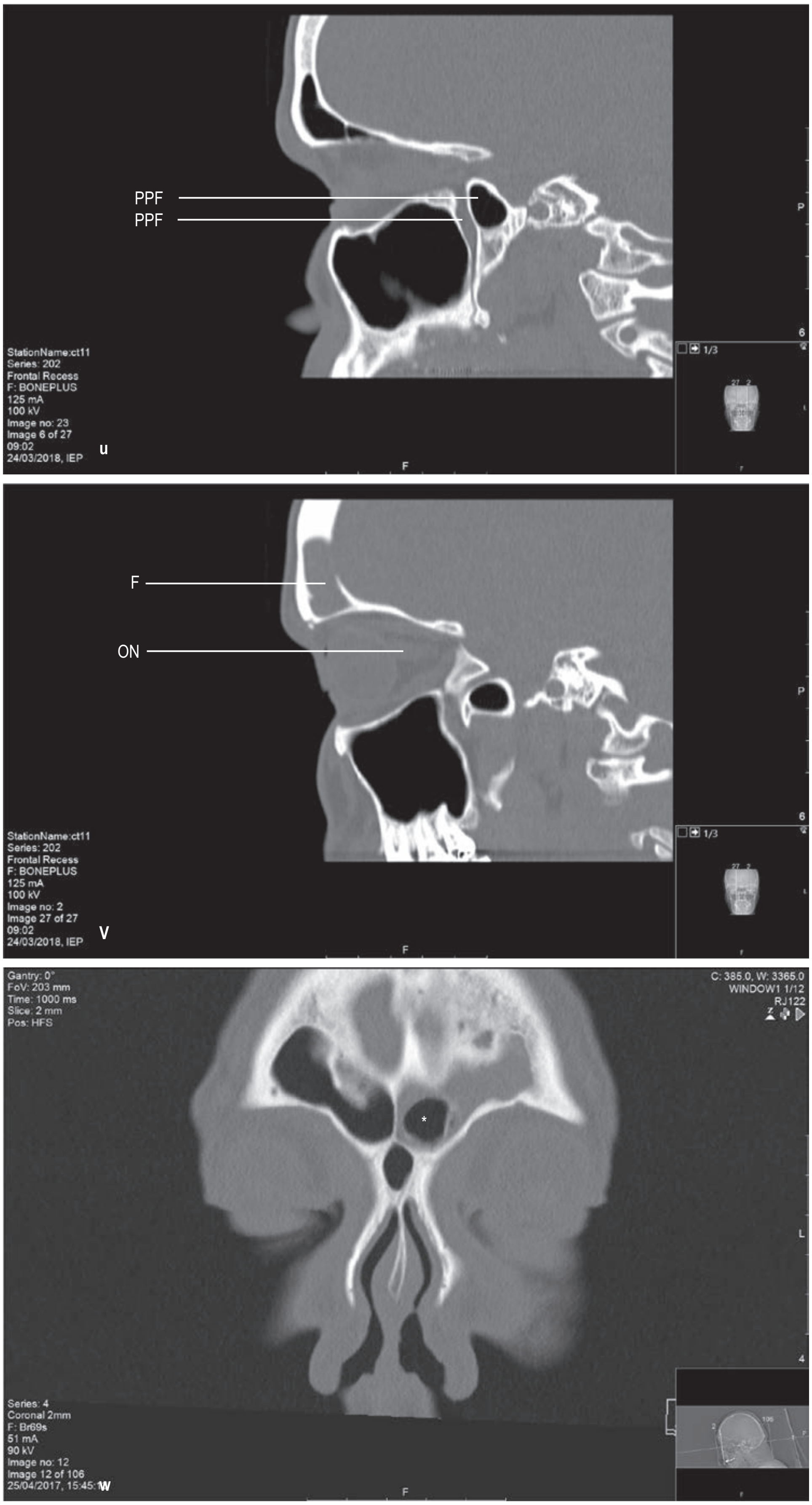
PPF
PPF
StationName:ct11
Series: 202
Frontal Recess
F: BONEPLUS
125 mA
100 kV
Image no: 23
Image 6 of 27
09:02
24/03/2018, IEP
u
F
ON
StationName:ct11
Series: 202
Frontal Recess
F: BONEPLUS
125 mA
100 kV
Image no: 2
Image 27 of 27
09:02
24/03/2018, IEP
v
Gantry: 0°
FoV: 203 mm
Time: 1000 ms
Slice: 2 mm
Pos: HFS
C: 385.0, W: 3365.0
WINDOW1 1/12
RJ122
*
Series: 4
Coronal 2mm
F: Br69s
51 mA
90 kV
Image no: 12
Image 12 of 106
25/04/2017, 15:45:1
w

Fig. 39.25, cont'd

Continued

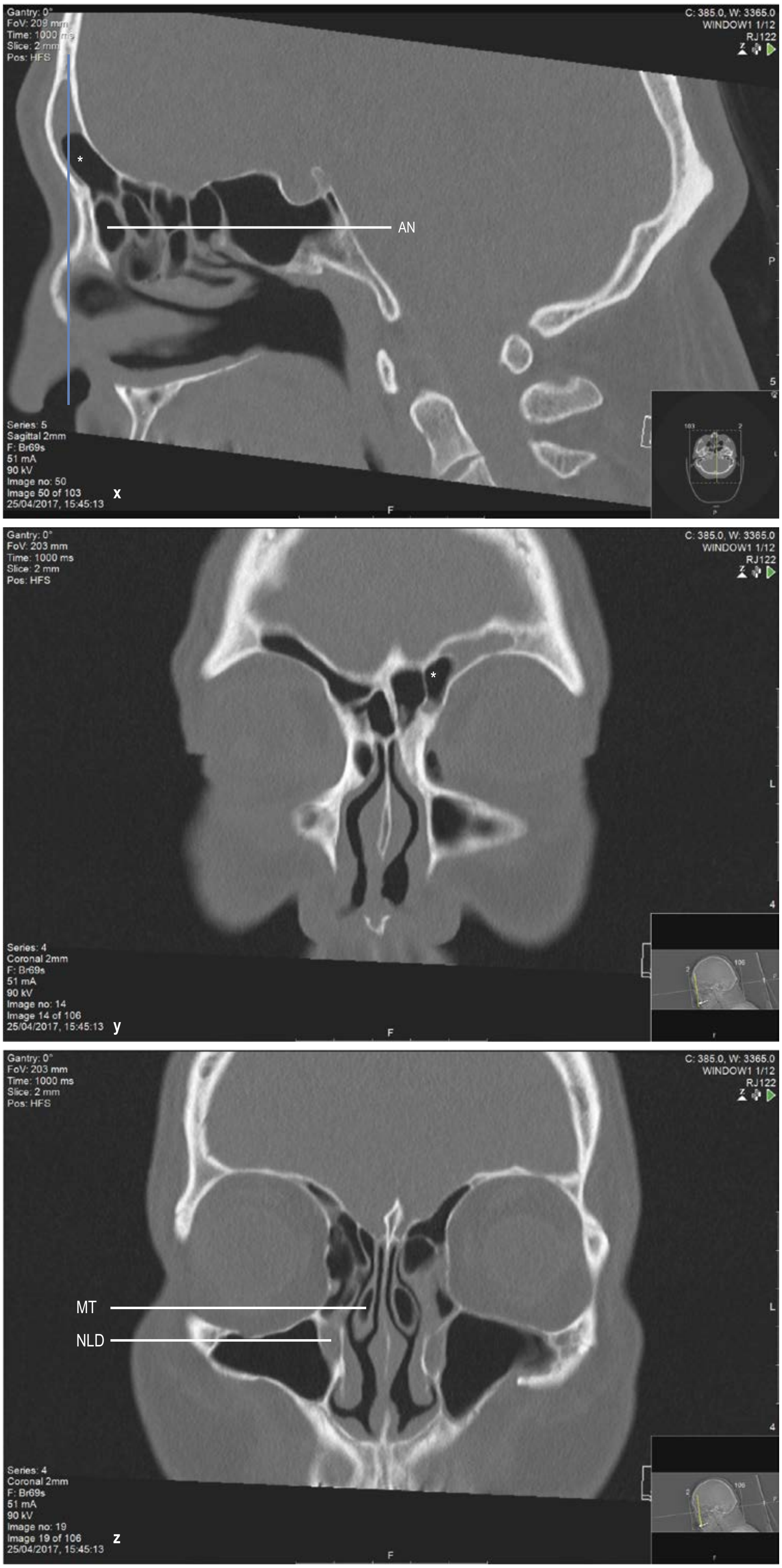
Gantry: 0°
FoV: 203 mm
Time: 1000 ms
Slice: 2 mm
Pos: HFS
C: 385.0, W: 3365.0
WINDOW1 1/12
RJ122
*
AN
P
5
Series: 5
Sagittal 2mm
F: Br69s
51 mA
90 kV
Image no: 50
Image 50 of 103
25/04/2017, 15:45:13
x
F
Gantry: 0°
FoV: 203 mm
Time: 1000 ms
Slice: 2 mm
Pos: HFS
C: 385.0, W: 3365.0
WINDOW1 1/12
RJ122
*
L
4
Series: 4
Coronal 2mm
F: Br69s
51 mA
90 kV
Image no: 14
Image 14 of 106
25/04/2017, 15:45:13
y
F
Gantry: 0°
FoV: 203 mm
Time: 1000 ms
Slice: 2 mm
Pos: HFS
C: 385.0, W: 3365.0
WINDOW1 1/12
RJ122
MT
NLD
L
4
Series: 4
Coronal 2mm
F: Br69s
51 mA
90 kV
Image no: 19
Image 19 of 106
25/04/2017, 15:45:13
z
F

Fig. 39.25, cont'd

Key references

Becker S 1994 Applied anatomy of the paranasal sinuses with emphasis on endoscopic sinus surgery. Ann ORL 103:3–32.

A review of serial cadaveric sections in three planes, analysed with specific attention to the anatomy of the paranasal sinuses as it pertains to endoscopic sinus surgery.

Buck L, Axel R 1991 A novel multigene family may encode odorant receptors: a molecular basis for odor recognition. Cell 65:175–87.

The 2004 Nobel Prize in Physiology or Medicine was awarded to Axel and Buck for their discoveries of the genetic determinants of the olfactory receptors and the organization of the olfactory system in humans.

Huizing E 2003 Incorrect terminology in nasal anatomy and surgery, suggestions for improvement. Rhinology 41:129–33.

A discussion of the limitations of the current nomenclature for the anatomy of the external nose, with suggestions for an improved terminology.

Jafek BW 1983 Ultrastructure of human nasal mucosa. Laryngoscope 93:1576–99.

A study that characterizes the normal ultrastructure of human nasal mucosa, emphasizing the differences between olfactory and respiratory epithelia.

Kuhn F 2002 Lateral Nasal Wall and Sinus Surgical Anatomy: Contemporary Understanding. Maintenance Manual for Lifelong Learning, 2nd ed. American Academy of Otolaryngology/Head and Neck Surgery Foundation. Dubuque: Kendall/Hunt Publishing Company; pp. 203–14.

Excellent descriptions and diagrams of sinus anatomy and common variations.

Lang J 1989 Clinical Anatomy of the Nose, Nasal Cavity and Paranasal Sinuses. Stuttgart: Thieme.

A study with the emphasis on exact measurements between surgical landmarks, with application to surgical procedures.

Lund VJ, Stammberger H, Fokkens WJ et al 2014 European position paper on the anatomical terminology of the internal nose and paranasal sinuses. Rhinology 50:Suppl 24:1–34.

A re-evaluation of the anatomical terms in common usage by endoscopic sinus surgeons and comparison with Terminologia Anatomica.

Navarro JAC 1997 The Nasal Cavity and Paranasal Sinuses: Surgical Anatomy. Berlin: Springer.

A study that emphasizes anatomical variations and their surgical importance, with CT imaging accompanying three-plane dissections.

Oneal R, Beil R, Schlesinger J 1999 Surgical anatomy of the nose. Otolaryngol Clin North Am 32:145–79.

A classification of the subcutaneous tissue of the external nose is included in this discussion of surgical anatomy.

Simmen D, Jones N 2005 Manual of Endoscopic Sinus Surgery and Its Extended Applications. Stuttgart: Thieme.

An extensive range of clinical images illustrate operative sinus procedures.

Simmen DB, Jones NS 2010 Epistaxis. In: Flint PW, Haughey BH, Lund VJ et al (eds) Cummings Otolaryngology: Head and Neck Surgery, 5th ed. Elsevier, Mosby; Ch. 45, pp. 682–93.

A description of the vascular anatomy of the nasal cavity and the surgical approaches to control epistaxis.

Stammberger H, Kennedy DW (eds) 1995 Paranasal sinuses: anatomic terminology and nomenclature. Ann Otol Rhinol Laryngol (Suppl 167) 104 Part 2:7–16.

A consensus on the preferred modern usage of potentially confusing or ambiguous terms in sinus anatomy.

References

Akguner M, Barutcu A, Karaca C 1998 Adolescent growth patterns of the bony and cartilaginous framework of the nose: a cephalometric study. Ann Plast Surg 41:66–9.

Beale TJ, Madani G, Morley SJ 2009 Imaging of the paranasal sinuses and nasal cavity: normal anatomy and clinically relevant anatomical variants. Semin Ultrasound CT MR 30:2–16.

Becker S 1994 Applied anatomy of the paranasal sinuses with emphasis on endoscopic sinus surgery. Ann Oto Rhinol aryngol 103:3–32.

A review of serial cadaveric sections in three planes, analysed with specific attention to the anatomy of the paranasal sinuses as it pertains to endoscopic sinus surgery.

Boyce J, Eccles R 2006 Do changes in nasal airflow have any physiological or pathological effect on the nose and paranasal sinuses? A systematic review. Clin Otolaryngol 31:15–19.

Buck L, Axel R 1991 A novel multigene family may encode odorant receptors: a molecular basis for odor recognition. Cell 65:175–87.

The 2004 Nobel Prize in Physiology or Medicine was awarded to Axel and Buck for their discoveries of the genetic determinants of the olfactory receptors and the organization of the olfactory system in humans.

Churchill SE, Shackleford LL, Georgi JN et al 2004 Morphological variation and airflow dynamics in the human nose. Am J Human Biol 16:625–38.

Eordogh M, Grimm A et al 2018 Anatomy of the sphenopalatine artery and its implications for transnasal surgery. Rhinology 56: 82–8.

Herzallah IR, Saati FA, Marglani OA et al 2016 Retromaxillary pneumatization of posterior ethmoid cells. Otolaryngol Head Neck Surg 155:340–6.

Holbrook EH, Leopold DA, Schwob JE 2005 Abnormalities of axon growth in human olfactory mucosa. Laryngoscope 115:2144–54.

Huizing E 2003 Incorrect terminology in nasal anatomy and surgery, suggestions for improvement. Rhinology 41:129–33.

A discussion of the limitations of the current nomenclature for the anatomy of the external nose, with suggestions for an improved terminology.

Jafek BW 1983 Ultrastructure of human nasal mucosa. Laryngoscope 93:1576–99.

A study that characterizes the normal ultrastructure of human nasal mucosa, emphasizing the differences between olfactory and respiratory epithelia.

Jankowski R 2013 The Evo-Devo Origin of the Nose, Anterior Skull Base and Midface. Berlin: Springer.

Kuhn F 2002 Lateral Nasal Wall and Sinus Surgical Anatomy: Contemporary Understanding. Maintenance Manual for Lifelong Learning, 2nd ed. American Academy of Otolaryngology/Head and Neck Surgery Foundation. Dubuque: Kendall/Hunt Publishing Company; pp. 203–14.

Excellent descriptions and diagrams of sinus anatomy and common variations.

Lang J 1989 Clinical Anatomy of the Nose, Nasal Cavity and Paranasal Sinuses. Stuttgart: Thieme.

A study with the emphasis on exact measurements between surgical landmarks, with application to surgical procedures.

Lund VJ, Stammberger H, Fokkens WJ et al 2014 European position paper on the anatomical terminology of the internal nose and paranasal sinuses. Rhinology 50:Suppl 24:1–34.

A re-evaluation of the anatomical terms in common usage by endoscopic sinus surgeons and comparison with Terminologia Anatomica.

Navarro JAC 1997 The Nasal Cavity and Paranasal Sinuses: Surgical Anatomy. BerlIn: Springer.

A study that emphasizes anatomical variations and their surgical importance, with CT imaging accompanying three-plane dissections.

Netto B, Piltcher OB, Meotti CD et al 2015 Computer tomography imaging study of the superior attachment of the uncinate process. Rhinology 53:187–91.

Oneal R, Beil R, Schlesinger J 1999 Surgical anatomy of the nose. Otolaryngol Clin North Am 32:145–79.

A classification of the subcutaneous tissue of the external nose is included in this discussion of surgical anatomy.

Paik SI, Lehman MN, Seiden AM et al 1992 Human olfactory biopsy: the influence of age and receptor distribution. Arch Otolaryngol Head Neck Surg 118:731–8.

Ruf S, Pancherz H 1996 Development of the frontal sinus in relation to somatic and skeletal maturity: a cephalometric roentgenographic study at puberty. Eur J Orthodont 18:491–7.

Saban Y, Amodeo CA, Hammou JC et al 2008 An anatomical study of the nasal superficial musculoaponeurotic system: surgical applications in rhinoplasty. Arch Facial Plast Surg 10:109–15.

Samoliński BK, Grzanka A, Gotlib T 2007 Changes in nasal cavity dimensions in children and adults by gender and age. Laryngoscope 117:1429–33.

Simmen D, Jones N 2005 Manual of Endoscopic Sinus Surgery and Its Extended Applications. Stuttgart: Thieme.

An extensive range of clinical images illustrate operative sinus procedures.

Simmen DB, Jones NS 2010 Epistaxis. In: Flint PW, Haughey BH, Lund VJ et al (eds) Cummings Otolaryngology: Head and Neck Surgery, 5th ed. Philadelphia: Elsevier, Mosby; Ch. 45, pp. 682–93.

A description of the vascular anatomy of the nasal cavity and the surgical approaches to control epistaxis.

Simon PE, Lam K, Sidle D et al 2013 The nasal keystone region: an anatomical study. JAMA Facial Plast Surg 15:235–7.

Stammberger H, Kennedy DW (eds) 1995 Paranasal sinuses: anatomic terminology and nomenclature. Ann Otol Rhinol Laryngol (Suppl 167) 104 Part 2:7–16.

A consensus on the preferred modern usage of potentially confusing or ambiguous terms in sinus anatomy.

Vaid S, Vaid N 2015 Normal anatomy and anatomic variants of the paranasal sinuses on computed tomography. Neuroimaging Clin North Am. 25:527–48.

Wang L, Youssef A et al 2014 Endoscopic anatomy of the middle ethmoid artery. Int Forum of Allergy Rhinology 4: 164–8.

Wessels Q, Hoogland PV, Vorster W 2014 Anatomical evidence for an endocrine activity of the vomeronasal organ in humans. Clin Anat 27:856–60.

Wolf G, Anderhuber W, Kuhn F 1993 Development of the paranasal sinuses in children: implications for paranasal sinus surgery. Ann Otol Rhinol Laryngol 102:705–11.

Wormald PJ, Hosemann W et al 2016 The International Frontal Sinus Anatomy Classification (IFAC) and classification of the extent of endoscopic frontal sinus surgery. Int Forum Allergy Rhinol 6:677–96.

Zhai LJ, Bruintjes TD, Boschma T et al 1995 The interdomal ligament does not exist. Rhinology 33:135–7.

Zhou B, Han DM, Cui SJ et al 2013 Intranasal endoscopic prelacrimal recess approach to maxillary sinus. Chin Med J 126:1276–80.

CHAPTER

40

Pharynx

The pharynx is a 12–14 cm long musculomembranous tube shaped like an inverted cone. It extends from the cranial base to the lower border of the cricoid cartilage (the level of the sixth or seventh cervical vertebrae), where it becomes continuous with the oesophagus. The width of the pharynx varies constantly because it is dependent on muscle tone, especially of the constrictors. At rest, the pharyngo-oesophageal junction is closed as a result of tonic closure of the upper oesophageal sphincter; during sleep, muscle tone is low and the dimensions of the pharynx are markedly decreased (which may give rise to snoring and sleep apnoea). The pharynx is limited above by the posterior part of the body of the sphenoid and the basilar part of the occipital bone, and it is continuous with the oesophagus below. Behind, it is separated from the cervical part of the vertebral column and the prevertebral fascia covering longus colli and longus capitis, by loose connective tissue in the retropharyngeal space above and the retrovisceral space below.

The muscles of the pharynx are three circular constrictors and three longitudinal elevators. The constrictors resemble three overlapping cones that arise from structures at the sides of the head and neck and pass posteriorly to insert into a midline fibrous band, the pharyngeal raphe. The arterial supply to the pharynx is derived from branches of the external carotid artery, particularly the ascending pharyngeal artery, but also from the ascending palatine and tonsillar branches of the facial artery, the maxillary artery (greater palatine and pharyngeal arteries and the artery of the pterygoid canal), and dorsal lingual branches of the lingual artery. The pharyngeal veins begin in a plexus external to the pharynx, receive meningeal veins and a vein from the pterygoid canal, and usually end in the internal jugular vein. Lymphatic vessels from the pharynx and cervical oesophagus pass to the deep cervical nodes, either directly or via the retropharyngeal or paratracheal nodes. The motor and sensory innervation is principally via branches of the pharyngeal plexus.

The pharynx lies behind, and communicates with, the nasal, oral and laryngeal cavities via the nasopharynx, oropharynx and laryngopharynx, respectively (**Figs 40.1–40.2**). Its lining mucosa is continuous with that lining the pharyngotympanic tubes, nasal cavity, mouth and larynx. The retropharyngeal and parapharyngeal spaces surround the pharynx. The retropharyngeal space lies anterior to the prevertebral and alar fascia and thus to the alar space (so-called danger space) that lies between them (Scali et al 2015). For further reading, including reviews of some of the more important historical literature, see Wood-Jones (1940), Hollinshead (1982), Graney et al (1998), Flint et al (2010).

NASOPHARYNX

Boundaries

The nasopharynx lies above the soft palate and behind the posterior nares, which allow free respiratory passage between the nasal cavities and the nasopharynx (see Figs 40.1–40.2). The nasal septum separates the two posterior nares, each of which measures approximately 25 mm vertically and 12 mm transversely. Just within these openings lie the posterior ends of the inferior and middle nasal turbinates (Ch. 39). The nasopharynx has a roof, a posterior wall, two lateral walls and a floor. All are rigid boundaries except the floor, which can be raised or lowered by the soft palate: the cavity of the nasopharynx is therefore never obliterated by muscle action, unlike the cavities of the oro- and laryngopharynx. The nasal and oral parts of the pharynx communicate through the pharyngeal isthmus, which lies between the posterior border of the soft palate and the posterior pharyngeal wall. Elevation of the soft palate and constriction of the palatopharyngeal sphincter close the isthmus during swallowing.

The roof and posterior wall form a continuous concave slope that leads down from the nasal septum to the oropharynx. It is bounded above by mucosa overlying the posterior part of the body of the sphenoid, and further back by the basilar part of the occipital bone as far as the pharyngeal tubercle. Further down, the mucosa overlies the pharyngobasilar fascia and the upper fibres of the superior constrictor, and behind these, the anterior arch of the atlas. A lymphoid mass, the pharyngeal tonsil (adenoid, nasopharyngeal tonsil), lies in the mucosa of the upper part of the roof and posterior wall in the midline.

The lateral walls of the nasopharynx display a number of important surface features. On either side, each receives the opening of the pharyngotympanic tube (auditory or Eustachian tube), situated 10–12 mm behind and a little below the level of the posterior end of the inferior nasal concha (see Figs 40.1, 40.2). The tubal aperture is approximately triangular in shape and is bounded above and behind by the tubal elevation that consists of mucosa overlying the protruding pharyngeal end of the cartilage of the pharyngotympanic tube. A vertical mucosal fold, the salpingopharyngeal fold, descends from the tubal elevation behind the aperture (see Fig. 40.2) and covers salpingopharyngeus in the wall of the pharynx (**Fig. 40.3**); a smaller salpingopalatine fold extends from the anterosuperior angle of the tubal elevation to the soft palate in front of the aperture. As levator veli palatini enters the soft palate, it produces an elevation of the mucosa immediately around the tubal opening (see Fig. 40.3). A small variable mass of lymphoid tissue, the tubal tonsil, lies in the mucosa immediately behind the opening of the pharyngotympanic tube. Further behind the tubal elevation there is a variable depression in the lateral wall, the lateral pharyngeal recess (fossa of Rosenmüller), located between the posterior wall of the nasopharynx and the salpingopharyngeal fold. The floor of the nasopharynx is formed by the nasal, upper surface of the soft palate.

The relations of the nasopharynx are important in understanding the spread of nasopharyngeal carcinoma (Chong and Ong 2008, Hyare et al 2010). The mucosa of the nasopharynx is separated from the parapharyngeal space by the buccopharyngeal and pharyngobasilar fasciae. The carotid space, enclosed by the carotid sheath, lies posterior and lateral to the parapharyngeal space. The glossopharyngeal, vagus, accessory and hypoglossal nerves lie within the upper part of the carotid space and come to lie within the superior part of the parapharyngeal space together with the sympathetic chain. The carotid sheath is partially deficient at this level, becoming confluent with the retrostyloid compartment of the parapharyngeal space (Warshafsky et al 2012).The foramen lacerum lies superolateral to the fossa of Rosenmüller. The foramen ovale lies still further laterally and transmits the mandibular division of the trigeminal nerve, which passes through the parapharyngeal space and then the masticator space to innervate the muscles of mastication. The retropharyngeal space is posterior to the nasopharynx. The cartilagenous pharyngotympanic tube and levator veli palatine pass through a deficiency in the pharyngobasilar fascia around the sinus of Morgagni. Nasopharyngeal carcinoma typically spreads along the pharyngotympanic tube, causing secretory otitis media. It breaches the pharyngobasilar fascia anteriorly to infiltrate the pterygoid muscles and invades intracranial space through the foramen ovale by perineural spread along the mandibular nerve (Hyare et al 2010).

Microstructure of non-tonsillar nasopharynx The nasopharyngeal epithelium anteriorly is ciliated, pseudostratified respiratory in type with goblet cells (see Fig. 2.2D). The ducts of mucosal and submucosal seromucous glands open onto its surface. Posteriorly, the respiratory epithelium changes to non-keratinized stratified squamous epithelium which continues into the oropharynx and laryngopharynx. The transitional zone between the two types of epithelium consists of columnar epithelium with short microvilli instead of cilia. Superiorly, this zone meets the nasal septum; laterally, it crosses the orifice of the pharyngotympanic tube; and it passes posteriorly at the union of the soft palate and the lateral wall. Numerous mucous glands surround the tubal orifices.

Innervation Much of the mucosa of the nasopharynx behind the pharyngotympanic tube is supplied by the pharyngeal branch of the pterygopalatine ganglion, which traverses the palatovaginal canal with a pharyngeal branch of the maxillary artery.

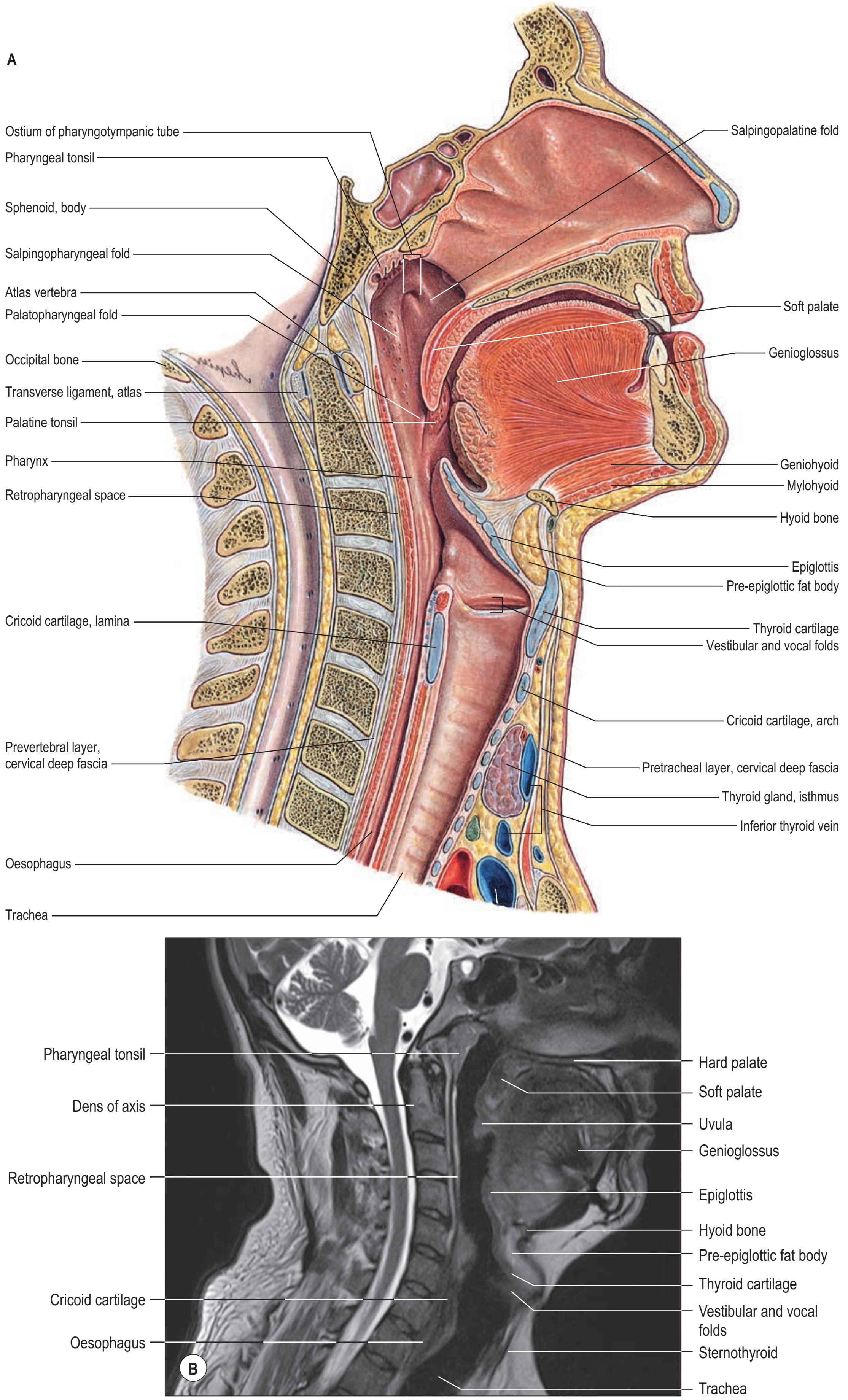
A
Ostium of pharyngotympanic tube
Pharyngeal tonsil
Sphenoid, body
Salpingopharyngeal fold
Atlas vertebra
Palatopharyngeal fold
Occipital bone
Transverse ligament, atlas
Palatine tonsil
Pharynx
Retropharyngeal space
Cricoid cartilage, lamina
Prevertebral layer,
cervical deep fascia
Oesophagus
Trachea
Salpingopalatine fold
Soft palate
Genioglossus
Geniohyoid
Mylohyoid
Hyoid bone
Epiglottis
Pre-epiglottic fat body
Thyroid cartilage
Vestibular and vocal folds
Cricoid cartilage, arch
Pretracheal layer, cervical deep fascia
Thyroid gland, isthmus
Inferior thyroid vein
B
Pharyngeal tonsil
Dens of axis
Retropharyngeal space
Cricoid cartilage
Oesophagus
Hard palate
Soft palate
Uvula
Genioglossus
Epiglottis
Hyoid bone
Pre-epiglottic fat body
Thyroid cartilage
Vestibular and vocal folds
Sternothyroid
Trachea

Fig. 40.2 A, Sagittal section through the head and neck, including the nasal and oral cavities but excluding the intracranial region. **B**, Corresponding sagittal T2-weighted magnetic resonance image (MRI) through the neck that includes the posterior cranial fossa, cerebellum and cervical spinal cord. (A, Sobotta Atlas of Human Anatomy © Elsevier GmbH, Urban & Fischer, Munich.)

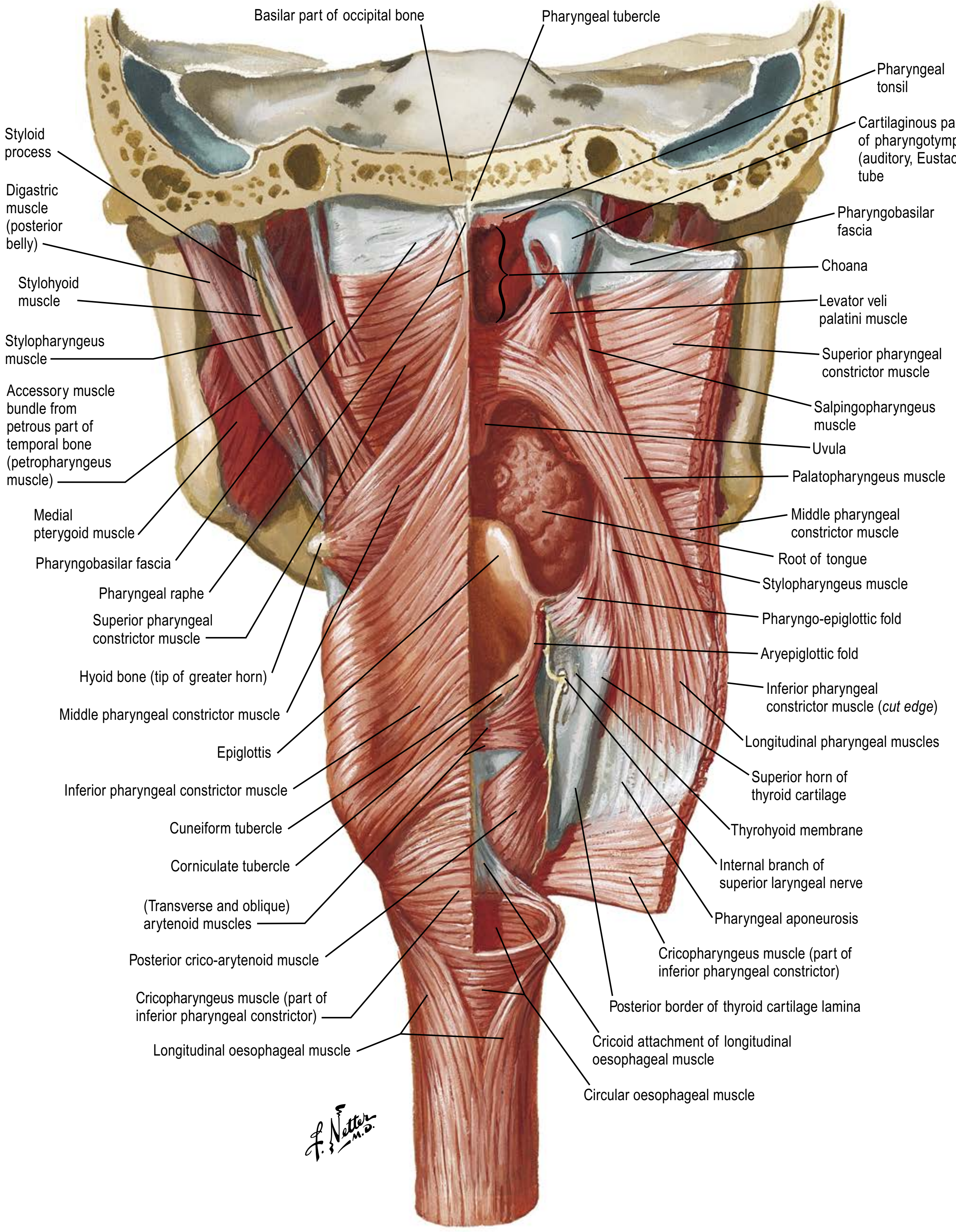
Basilar part of occipital bone
Pharyngeal tubercle
Styloid process
Digastric muscle (posterior belly)
Stylohyoid muscle
Stylopharyngeus muscle
Accessory muscle bundle from petrous part of temporal bone (petropharyngeus muscle)
Medial pterygoid muscle
Pharyngobasilar fascia
Pharyngeal raphe
Superior pharyngeal constrictor muscle
Hyoid bone (tip of greater horn)
Middle pharyngeal constrictor muscle
Epiglottis
Inferior pharyngeal constrictor muscle
Cuneiform tubercle
Corniculate tubercle
(Transverse and oblique) arytenoid muscles
Posterior crico-arytenoid muscle
Cricopharyngeus muscle (part of inferior pharyngeal constrictor)
Longitudinal oesophageal muscle
Pharyngeal tonsil
Cartilaginous part of pharyngotympanic (auditory, Eustachian) tube
Pharyngobasilar fascia
Choana
Levator veli palatini muscle
Superior pharyngeal constrictor muscle
Salpingopharyngeus muscle
Uvula
Palatopharyngeus muscle
Middle pharyngeal constrictor muscle
Root of tongue
Stylopharyngeus muscle
Pharyngo-epiglottic fold
Aryepiglottic fold
Inferior pharyngeal constrictor muscle (*cut edge*)
Longitudinal pharyngeal muscles
Superior horn of thyroid cartilage
Thyrohyoid membrane
Internal branch of superior laryngeal nerve
Pharyngeal aponeurosis
Cricopharyngeus muscle (part of inferior pharyngeal constrictor)
Posterior border of thyroid cartilage lamina
Cricoid attachment of longitudinal oesophageal muscle
Circular oesophageal muscle
F. Netter M.D.

Fig. 40.1 The nasopharynx, oropharynx and laryngopharynx, exposed by cutting the median pharyngeal raphe and reflecting the constrictor muscles laterally on either side, posterior view. (With permission from Netter FH, Atlas of Human Anatomy, 7th ed. Elsevier. Copyright 2019.)

Pharyngeal tonsil

The pharyngeal tonsil (adenoid, nasopharyngeal tonsil) is a median mass of mucosa-associated lymphoid tissue (MALT; see Ch. 4, 'Lymphoid tissues') situated in the roof and posterior wall of the nasopharynx (Fig. 40.4). At its maximal size (during the early years of life), it is shaped like a truncated pyramid, often with a vertically orientated median cleft, so that its apex points towards the nasal septum and its base to the junction of the roof and posterior wall of the nasopharynx (Papaioannou et al 2013).

The free surface of the pharyngeal tonsil is marked by folds that radiate forwards and laterally from a median blind recess, the pharyngeal bursa (bursa of Luschka) that extends backwards and up. The recess marks the rostral end of the embryological notochord: it is present in

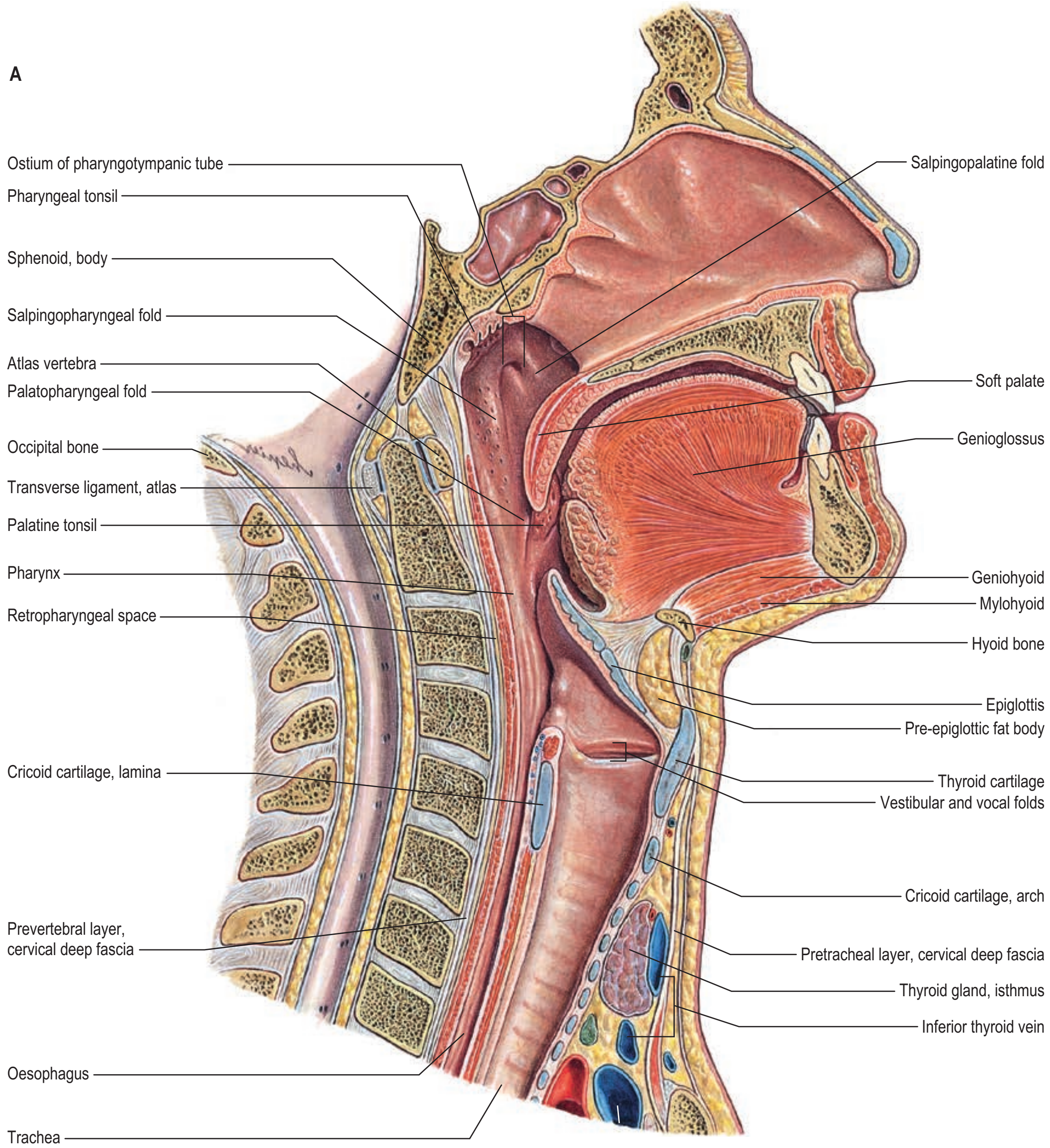
A
Ostium of pharyngotympanic tube
Pharyngeal tonsil
Sphenoid, body
Salpingopharyngeal fold
Atlas vertebra
Palatopharyngeal fold
Occipital bone
Transverse ligament, atlas
Palatine tonsil
Pharynx
Retropharyngeal space
Cricoid cartilage, lamina
Prevertebral layer, cervical deep fascia
Oesophagus
Trachea
Salpingopalatine fold
Soft palate
Genioglossus
Geniohyoid
Mylohyoid
Hyoid bone
Epiglottis
Pre-epiglottic fat body
Thyroid cartilage
Vestibular and vocal folds
Cricoid cartilage, arch
Pretracheal layer, cervical deep fascia
Thyroid gland, isthmus
Inferior thyroid vein

Fig. 40.2 **A**, Sagittal section through the head and neck, including the nasal and oral cavities but excluding the intracranial region. (Sobotta Atlas of Human Anatomy © Elsevier GmbH, Urban & Fischer, Munich.) (B, *continued online*)

the fetus and the young but only occasionally present in the adult. The number and position of the folds and of the deep fissures that separate them vary. A median fold may pass forwards from the pharyngeal bursa towards the nasal septum, or a fissure may extend forwards from the bursa, dividing the nasopharyngeal tonsil into two distinct halves that reflect its paired developmental origins (see Fig. 40.4).

The prenatal origins of the pharyngeal tonsil are described in Chapter 17. After birth, it initially grows rapidly, but usually undergoes a degree of involution and atrophy from the age of 8–10 years: hypoplasia may still be present in adults up to the seventh decade (and still cause problems because of its volume). Relative to the volume of the nasopharynx, the tonsil is largest at 5 years, which may account for the frequency of nasal obstruction in preschool children, and could be an indication for adenoidectomy in this age group.

Vascular supply and lymphatic drainage The arterial supply of the pharyngeal tonsil is derived from the ascending pharyngeal and ascending palatine arteries, the tonsillar branches of the facial artery, the pharyngeal branch of the maxillary artery and the artery of the pterygoid canal (see Fig. 40.7). In addition, a nutrient or emissary vessel to the neighbouring bone, the basisphenoidal artery, which is a branch of the inferior hypophysial arteries, supplies the bed of the pharyngeal tonsil and is a possible cause of persistent post-adenoidectomy haemorrhage in some patients.

Numerous communicating veins drain the pharyngeal tonsil into the internal submucous and external pharyngeal venous plexuses. They emerge from the deep lateral surface of the tonsil and join the external palatine (paratonsillar) veins to pierce the superior constrictor, either to join the pharyngeal venous plexus or unite to form a single vessel that enters the facial or internal jugular vein. They may also connect with the pterygoid venous plexus.

Microstructure The pharyngeal tonsil is covered laterally and inferiorly mainly by ciliated respiratory epithelium that contains scattered small patches of non-keratinized stratified squamous epithelium. Its superior surface is separated from the periosteum of the sphenoid and occipital bones by a connective tissue hemicapsule. The fibrous framework of the tonsil, consisting of a mesh of collagen type III (reticular) fibres supporting a lymphoid parenchyma similar to that in the palatine tonsil, is anchored to the hemicapsule. The nasopharyngeal epithelium lines a series of mucosal folds around which the lymphoid parenchyma is organized into follicles and extrafollicular areas. Internally, the tonsil is subdivided into 4–6 lobes by connective tissue septa, which arise from the hemicapsule and penetrate the lymphoid parenchyma. Seromucous glands lie within the connective tissue, and their ducts extend through the parenchyma to reach the nasopharyngeal surface.

Functions The pharyngeal tonsil forms part of the circumpharyngeal lymphoid ring (Waldeyer's ring) and therefore presumably contributes to the defence of the upper respiratory tract. The territories served by its lymphocytes are uncertain but may include the nasal cavities, nasopharynx, pharyngotympanic tubes and the middle and inner ears.

Thornwaldt's cyst is an embryonic remnant of the persisting cranial end of the notochord that sometimes develops if the pharyngeal bursa is occluded (Fig. 40.5). Usually benign and asymptomatic, these cysts can become infected; symptoms include halitosis, occipital headache and postnasal drip (Yuca and Varsak 2012).

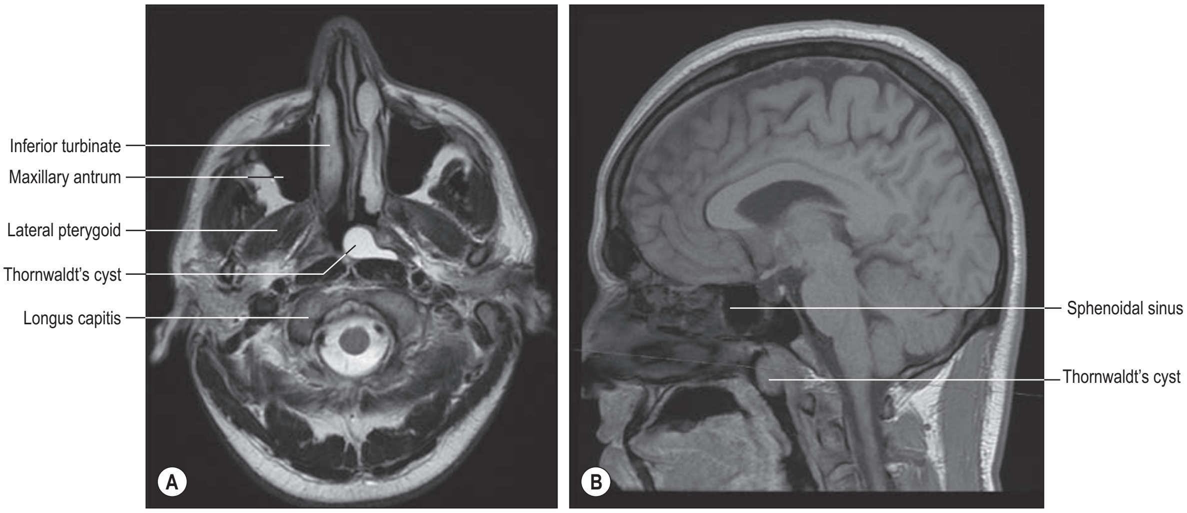
Inferior turbinate
Maxillary antrum
Lateral pterygoid
Thornwaldt's cyst
Longus capitis
A
Sphenoidal sinus
Thornwaldt's cyst
B

Fig. 40.5 Thornwaldt's cyst. Magnetic resonance images: **A**, axial view; **B**, sagittal view.

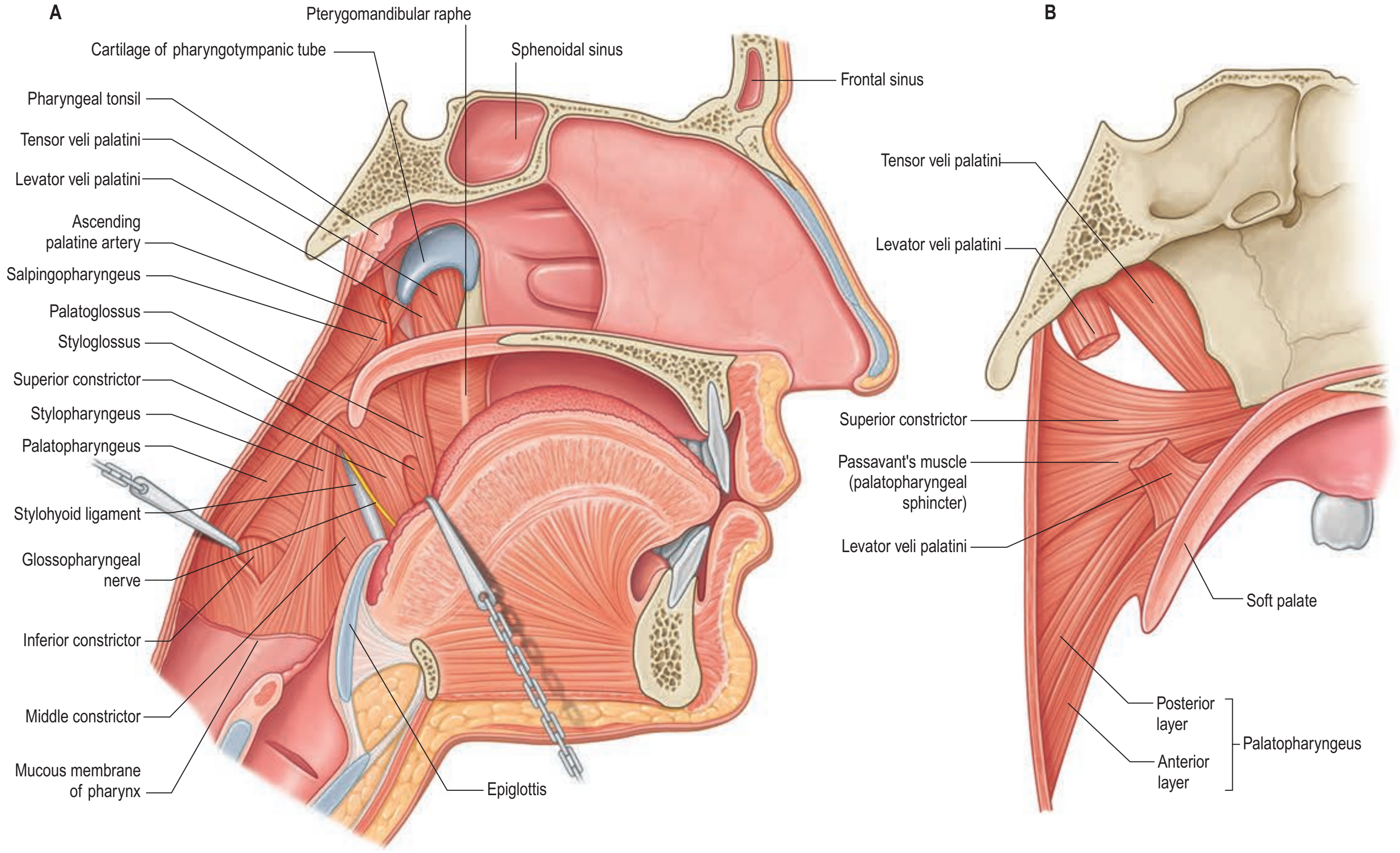
A
Pterygomandibular raphe
Cartilage of pharyngotympanic tube
Sphenoidal sinus
Pharyngeal tonsil
Tensor veli palatini
Levator veli palatini
Ascending palatine artery
Salpingopharyngeus
Palatoglossus
Styloglossus
Superior constrictor
Stylopharyngeus
Palatopharyngeus
Stylohyoid ligament
Glossopharyngeal nerve
Inferior constrictor
Middle constrictor
Mucous membrane of pharynx
Epiglottis
B
Frontal sinus
Tensor veli palatini
Levator veli palatini
Superior constrictor
Passavant's muscle (palatopharyngeal sphincter)
Levator veli palatini
Soft palate
Posterior layer
Anterior layer
Palatopharyngeus

Fig. 40.3 **A**, The interior of the pharynx, exposed by removal of the mucous membrane, sagittal section. The bodies of the cervical vertebrae have been removed, the cut posterior wall of the pharynx retracted dorsolaterally and palatopharyngeus reflected dorsally to show the cranial fibres of the inferior constrictor. The dorsum of the tongue has been pulled ventrally to display a part of styloglossus in the angular interval between the mandibular and the lingual fibres of origin of the superior constrictor. **B**, Muscles of the left half of the soft palate and adjoining part of the pharyngeal wall, sagittal section.

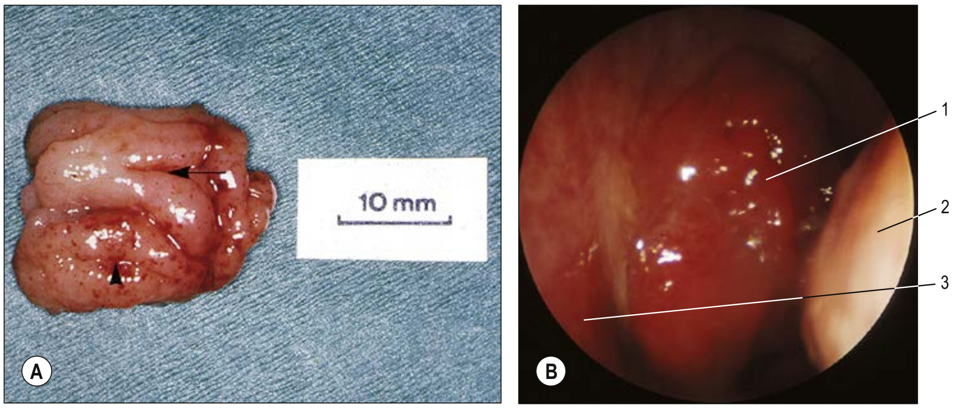

Fig. 40.4 **A**, A pharyngeal tonsil following adenoidectomy by curettage. The rostral surface is to the left; surface folds radiate forwards from a median recess (arrow). In this example, the impression left by contact with the left Eustachian cushion is evident laterally (arrowhead). **B**, A transnasal endoscopic view of a pharyngeal tonsil. Key: 1, pharyngeal tonsil (in posterior naris); 2, inferior concha (posterior view); 3, posterior end of nasal septum. (A, Specimen provided by Professor MJ Gleeson, School of Medicine, King's College London. B, Courtesy of Mr Simon A Hickey.)

Adenoidectomy

Available with the *Gray's Anatomy* e-book

Pharyngotympanic tube

The pharyngotympanic tube (see Figs 40.9A–B, 42.6) connects the tympanic cavity to the nasopharynx. It has several functions related to maintaining the health of the middle ear, including pressure equalization on both aspects of the tympanic membrane, mucociliary clearance and 'drainage', and protection from the influences of the nasopharyngeal environment and loud sounds. Approximately 36 mm long, it descends anteromedially from the tympanic cavity to the nasopharynx at an angle of approximately 45° with the sagittal plane and 30° with the horizontal (these angles increase with age and elongation of the cranial base). It is formed partly by cartilage and fibrous tissue, and partly by bone.

The cartilaginous part, which is approximately 24 mm long, is formed by a triangular plate of cartilage, the greater part of which is in the posteromedial wall of the tube. Its apex is attached by fibrous tissue to the circumference of the jagged rim of the bony part of the tube, and its base is directly under the mucosa of the lateral nasopharyngeal wall, forming a tubal elevation (torus tubarius; Eustachian cushion) behind the pharyngeal orifice of the tube (see Fig. 37.1). The upper part of the cartilage is bent laterally and downwards, producing a broad medial lamina and narrow lateral lamina. In transverse section, it is hook-like and incomplete below and laterally, where the canal is composed of fibrous tissue. The cartilage is fixed to the cranial base in the groove between the petrous part of the temporal bone and the greater wing of

Surgical removal of the pharyngeal tonsil (adenoid) is commonly performed to clear nasopharyngeal obstruction and as part of the treatment of chronic secretory otitis media. A variety of methods are employed, including suction micro-debridement and diathermy with per-nasal endoscopic control. Blind curettage is becoming less common. The newer endoscopic techniques avoid many of the complications previously seen with blind curettage and caused by hyperextension of the cervical spine, such as damage to the prevertebral fascia, anterior spinal ligaments and tubal orifice. Direct vision and diathermy also facilitate haemostasis. Removal of the pharyngeal tonsil in children with submucosal clefts can result in velopharyngeal insufficiency and cause excessive nasality of speech and nasal regurgitation: submucosal clefts are usually visible by careful clinical examination including palpation before surgery. Previous repair of a cleft palate is also a contraindication for adenoidectomy (Gray and Pinborough-Zimmerman 1998, Raol and Hartnick 2015).

the sphenoid and ends near the root of the medial pterygoid plate. In adults, the cartilaginous and bony parts of the tube are not in the same plane, the former descending a little more steeply than the latter. The diameter of the tube is greatest at the pharyngeal orifice and least at the junction of the two parts (the isthmus), increasing again towards the tympanic cavity. At birth, the pharyngotympanic tube is about half its adult length, more horizontal and its bony part is relatively shorter and much wider.

The bony part, approximately 12 mm long, is oblong in transverse section, with its greater dimension in the horizontal plane. It starts from the anterior tympanic wall and gradually narrows to end at the junction of the squamous and petrous parts of the temporal bone, where it has a jagged margin for the attachment of the cartilaginous part. The carotid canal lies medially.

The mucosa of the pharyngotympanic tube is continuous with the nasopharyngeal and tympanic mucosae. The bony canal is lined by a prolongation of the low cuboidal, ciliated mucosa that lines the middle ear. The histology changes to pseudostratified, ciliated, columnar epithelium typical of the upper respiratory tract after the bony/cartilaginous junction. Within the cartilaginous tube, the floor contains numerous mucus-producing goblet cells and is heavily rugated, whereas the walls in the upper half of the tube contain fewer goblet cells and are generally smooth. Mucosal folding is a feature of the childhood tube; the increased surface area and concomitant increased numbers of ciliated cells are presumed to facilitate improved clearance of the mucociliary blanket. Folds decrease with age up to the age of 20 years, when adult characteristics are reached. Mucous glands predominate in neonates; mucous, serous and mixed glands are present in equal amounts in young children; and serous glands predominate in later life (Orita et al 2002). (For further reading see Sade (1989), Bluestone (1998), O'Reilly and Sando (2010).)

Relations Salpingopharyngeus is attached to the inferior part of the cartilaginous tube near its pharyngeal opening. The petrous part of the temporal bone and levator veli palatini, which arises partly from the medial lamina of the tube, are posteromedial. Anterolaterally, tensor veli palatini separates the tube from the otic ganglion, the mandibular nerve and its branches, the chorda tympani nerve and the middle meningeal artery.

Vascular supply The osseous part of the pharyngotympanic tube is supplied by the tubal artery (a branch of the accessory meningeal artery) and the caroticotympanic branches of the internal carotid artery. The cartilaginous part of the tube is supplied by the deep auricular and pharyngeal branches of the maxillary artery, the ascending palatine artery (usually a branch of the facial artery but sometimes branching directly from the external carotid artery) and the ascending pharyngeal branch of the external carotid artery. The veins of the pharyngotympanic tube usually drain to the pterygoid venous plexus.

Innervation The pharyngotympanic tube is innervated by filaments from the tympanic plexus and from the pharyngeal branch of the pterygopalatine ganglion. The tympanic plexus ramifies on the promontory in the middle ear cavity and is formed by the tympanic branch of the glossopharyngeal nerve and caroticotympanic nerves of sympathetic origin (see Fig. 42.11).

Equalization of pressure At rest, the cartilaginous part of the pharyngotympanic tube is closed at the nasopharyngeal orifice. In normal individuals, the tube opens in order to equalize middle ear pressure to ambient pressure. Analysis of slow-motion video-endoscopy reveals four stages in tubal opening. Initially, the soft palate is elevated, the lateral pharyngeal wall moves medially and the medial lamina of the pharyngotympanic tube rotates medially (levator veli palatini is thought to open the distal part of the tube). The lateral wall of the pharyngotympanic tube moves laterally, so that the orifice is dilated both laterally and vertically. Tubal dilation propagates from distal to proximal by the action of dilator tubae. Finally, the proximal cartilaginous tube adjacent to the junctional region opens. Opening usually lasts for 0.3–0.5 sec but is prolonged during yawning. Closure depends on adhesion of the intraluminal mucous blanket, elastic forces of the supporting tissues, and the hydrostatic pressure of venous blood.

Pharyngotympanic tube dysfunction is a very common pathology. Young children, having an immature tube and a prominent adenoid, often present with persistent serous fluid in the middle ear or recurrent middle ear infections. Older children and adults also present with pharyngotympanic tube dysfunction, often caused by a respiratory tract infection, associated oedema and hypersecretion of the mucosal glands. The presenting symptoms are hearing loss, aural fullness, autophony and tinnitus. Nasal decongestants usually help but sometimes the insertion of ventilation tubes (grommets) is required temporarily.

OROPHARYNX

Boundaries

The oropharynx extends from below the soft palate to the upper border of the epiglottis (see Figs 40.1–40.2). It opens into the mouth through the oropharyngeal isthmus, demarcated by the palatoglossal arch, and faces the pharyngeal aspect of the tongue. Its lateral wall consists of the palatopharyngeal arch and palatine tonsil (see Fig. 37.3). Posteriorly, it is level with the bodies of the second, and upper part of the third, cervical vertebrae (see Fig. 40.2).

Soft palate

The soft palate is a mobile flap suspended from the posterior border of the hard palate, sloping down and back between the oral and nasal parts of the pharynx (see Figs 40.2–40.3). The boundary between the hard and soft palate is readily palpable and may be distinguished by a change in colour, the soft palate being a darker red with a yellowish tint. The soft palate is a thick fold of mucosa enclosing an aponeurosis, muscular tissue, vessels, nerves, lymphoid tissue and mucous glands; almost half its thickness is represented by numerous mucous glands that lie between the muscles and the oral surface of the soft palate. The latter is covered by a stratified squamous epithelium, while the nasal surface is covered with a ciliated columnar epithelium. Taste buds are found on the oral aspect of the soft palate.

In most individuals, two small pits, the fovea palatini, may be seen, one on each side of the midline; they represent the orifices of ducts from some of the minor mucous glands of the palate. In its usual relaxed and pendant position, the anterior (oral) surface of the soft palate is concave and has a median raphe. The posterior aspect is convex and continuous with the nasal floor, the anterosuperior border is attached to the posterior margin of the hard palate, and the sides blend with the pharyngeal wall. The inferior border is free and hangs between the mouth and pharynx. A median conical process, the uvula, projects downwards from its posterior border (see Fig. 37.3). It may be congenitally bifid and associated with submucous cleft palate, hypoplastic orifice of the pharyngotympanic tube and absence of the salpingopharyngeal folds.

The anterior third of the soft palate contains little muscle and consists mainly of the palatine aponeurosis. This region is less mobile and more horizontal than the rest of the soft palate and is the chief area acted on by tensor veli palatini.

A small bony prominence, produced by the pterygoid hamulus, can be felt just behind and medial to each upper alveolar process, in the lateral part of the anterior region of the soft palate. The pterygomandibular raphe (a tendinous band between buccinator and the superior constrictor) passes downwards and outwards from the hamulus to the posterior end of the mylohyoid line (see Fig. 40.8). When the mouth is opened wide, this raphe raises a fold of mucosa that indicates the internal, posterior boundary of the cheek; it is an important landmark for an inferior alveolar nerve block (Ch. 37). (For further reading, see Wood-Jones (1940).)

Palatine aponeurosis. A thin, fibrous, palatine aponeurosis, composed of the expanded tendons of the tensor veli palatini muscles, strengthens the soft palate. It is attached to the posterior border and inferior surface of the hard palate behind any palatine crests and extends medially from behind the greater palatine foramina. It is thick in the anterior two-thirds of the soft palate but very thin further back. Near the midline, it encloses the musculus uvulae. All the other palatine muscles are attached to the aponeurosis.

Palatoglossal and palatopharyngeal arches. The lateral wall of the oropharynx presents two prominent folds, the palatoglossal and palatopharyngeal folds (anterior and posterior pillars of the fauces, respectively) (see Figs 37.3, 40.6A). The palatoglossal arch, the anterior fold, runs from the soft palate to the side of the tongue and contains palatoglossus. The palatopharyngeal arch, the posterior fold, projects more medially and passes from the soft palate to merge with the lateral wall of the pharynx; it contains palatopharyngeus. A triangular tonsillar fossa (tonsillar sinus) lies on each side of the oropharynx between the diverging palatopharyngeal and palatoglossal arches and contains the palatine tonsil.

Vascular supply The arterial supply of the soft palate is usually derived from the ascending palatine branch of the facial artery. Sometimes, this is replaced or supplemented by a branch of the ascending pharyngeal artery, which descends forwards between the superior border of the superior constrictor and levator veli palatini and accompanies the latter to the soft palate. The veins of the soft palate usually drain to the pterygoid venous plexus.

Innervation General sensation from most of the soft palate is carried by branches of the lesser palatine nerve (a branch of the maxillary nerve) and from the posterior part of the palate by pharyngeal branches from the glossopharyngeal nerve and from the plexus around the tonsil (formed by tonsillar branches of the glossopharyngeal and lesser palatine nerves). The special sensation of taste from taste buds in the oral surface of the soft palate is carried in the lesser palatine nerve; the taste fibres initially travel in the greater petrosal nerve (a branch of the facial nerve) and pass through the pterygopalatine ganglion without synapsing. The lesser palatine nerve also carries the secretomotor supply to most of the mucosa of the soft palate, via postganglionic branches from the pterygopalatine ganglion. Postganglionic secretomotor parasympathetic fibres may pass to the posterior parts of the soft palate from the otic ganglion (which receives preganglionic fibres via the lesser petrosal branch of the glossopharyngeal nerve). Postganglionic sympathetic fibres run from the carotid plexus along arterial branches supplying the palate.

Obstructive sleep apnoea and snoring

Available with the *Gray's Anatomy* e-book

Palatine tonsil

The palatine tonsils form part of the circumpharyngeal lymphoid ring. Each tonsil is an ovoid mass of lymphoid tissue situated in the lateral wall of the oropharynx (Fig. 40.6; see Figs 37.3, 37.5). Size varies according to age, individual anatomy and pathological status (tonsils may be hypertrophied and/or inflamed), and it is therefore difficult to define the 'normal' appearance of the palatine tonsil. For the first 5 or 6 years of life, the tonsils increase rapidly in size, usually reaching a maximum at puberty, when they average 20–25 mm in vertical, and 10–15 mm in transverse, diameters, and project conspicuously into the oropharynx. Between the ages of 1 and 11 years, the palatine tonsils and the adenoid grow proportionally to the lower facial skeleton (Arens et al 2002). Tonsillar involution begins at puberty, when the reactive lymphoid tissue begins to atrophy and by old age only a little tonsillar lymphoid tissue remains.

The long axis of the tonsil is directed from above, downwards and backwards. Its medial, free, surface usually presents a pitted appearance. The pits, 10–20 in number, lead into a system of blind-ending, often highly branching, crypts that extend through the whole thickness of the tonsil and almost reach the connective tissue hemicapsule. In a healthy tonsil, the openings of the crypts are fissure-like and the walls of the crypt lumina are collapsed so that they are in contact with each other. The human tonsil is polycryptic: the branching crypt system reaches its maximum size and complexity during childhood. The mouth of a deep tonsillar cleft (intratonsillar cleft, recessus palatinus) opens in the upper part of the medial surface of the tonsil. Often erroneously called the supratonsillar fossa, it is not yet situated above the tonsil but within its substance. The mouth of the cleft is semilunar, curving parallel to the convex dorsum of the tongue in the sagittal plane. The upper wall of the recess contains lymphoid tissue that extends into the soft palate as the pars palatina of the palatine tonsil. After the age of 5 years, this embedded part of the tonsil diminishes in size. There is a tendency for the whole tonsil to involute from the age of 14 years and for the tonsillar bed to flatten out. During young adult life, a mucosal fold, the plica triangularis, stretches back from the palatoglossal arch down to the tongue. It is infiltrated by lymphoid tissue and frequently represents the most prominent (anteroinferior) portion of the tonsil. It rarely persists into middle age.

The lateral or deep surface of the tonsil spreads downwards, upwards and forwards. Inferiorly, it invades the dorsum of the tongue; superiorly, it invades the soft palate; and, anteriorly, it may extend for some distance under the palatoglossal arch. This deep, lateral aspect is covered by a layer of fibrous tissue, the tonsillar hemicapsule. This is separable with ease for most of its extent from the underlying muscular wall of the pharynx, formed here by the superior constrictor and sometimes by the anterior fibres of palatopharyngeus, with styloglossus on its lateral side. Anteroinferiorly, the hemicapsule adheres to the side of the tongue and to palatoglossus and palatopharyngeus. In this region, the tonsillar artery, a branch of the facial artery, pierces the superior constrictor to enter the tonsil, accompanied by venae comitantes. An important and sometimes large vein, the external palatine or paratonsillar vein, descends from the soft palate lateral to the tonsillar hemicapsule before piercing the pharyngeal wall. Haemorrhage from this vessel from the upper angle of the tonsillar fossa may complicate tonsillectomy. The muscular wall of the tonsillar fossa separates the tonsil from the ascending palatine artery, and occasionally from the tortuous facial artery, which may lie near the pharyngeal wall at the lower tonsillar level. The glossopharyngeal

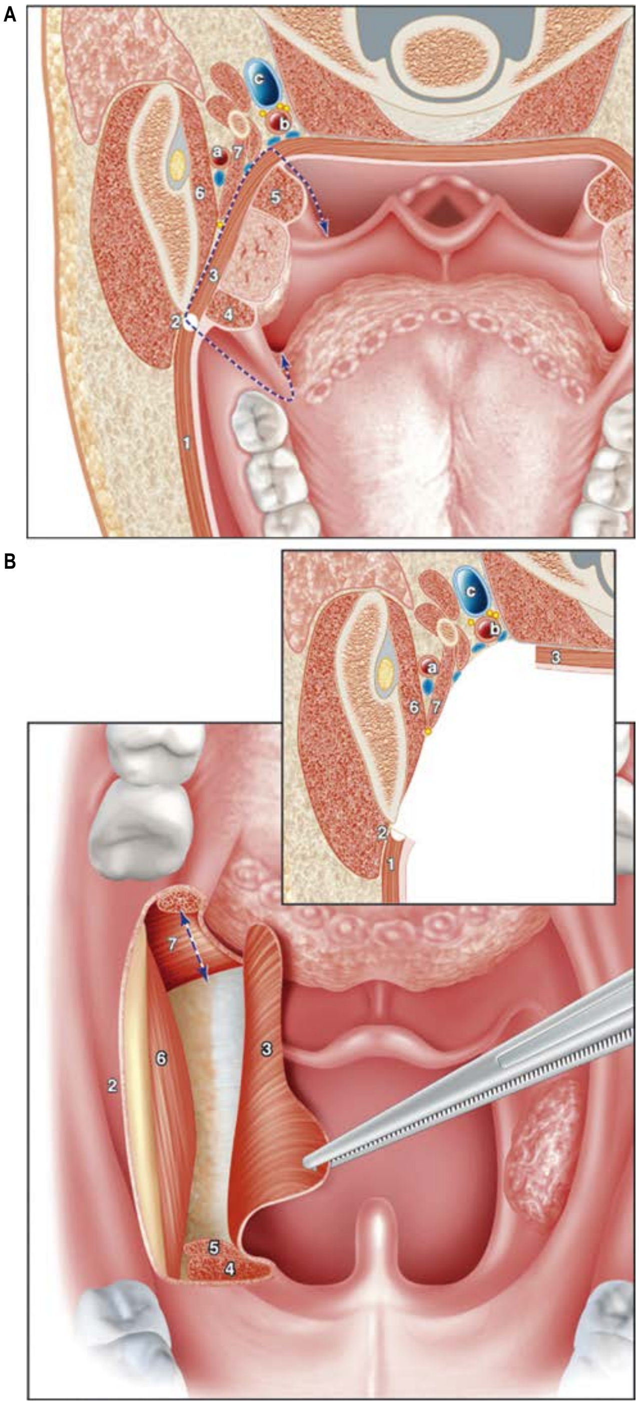

Fig. 40.6 **A**, Anatomical cross-section of the surgical approach in transoral lateral oropharyngectomy. **B**, Velar section and visualization of styloglossus. Key: 1, buccinator; 2, pterygomandibular raphe; 3, pharyngeal constrictor; 4, palatoglossus; 5, palatopharyngeus; 6, medial pterygoid; 7, styloglossus; a, external carotid artery; b, internal carotid artery; c, internal jugular vein. Blue dotted line indicates further transection of styloglossus. Yellow dots indicate cranial nerves IX, X, XI and XII. (Adapted from Rubin F, Laccourreye O, Weinstein GS et al 2017 Transoral lateral oropharyngectomy. Eur Ann Otorhinolaryngol Head Neck Dis 134:419–22.)

The pharyngeal airway is kept patent in awake individuals by the combined dilating action of genioglossus, tensor veli palatini, geniohyoid and stylohyoid, which act to counter the negative pressure generated in the lumen of the pharynx during inspiration. The tone in the muscles is reduced during sleep, and is also affected by alcohol and other sedatives, hypothyroidism and a variety of neurological disorders. If the dilator muscle tone is insufficient, the walls of the pharynx may become apposed. Intermittent pharyngeal obstruction may cause snoring, and complete obstruction results in apnoea, hypoxia and hypercarbia leading to arousal and sleep disturbance. Obstructive sleep apnoea (OSA) is a serious syndrome affecting up to 4% of middle-aged people. It has potentially life-threatening consequences. The pathophysiological causes of OSA include an anatomically small upper airway, in which augmented pharyngeal dilator muscle activation can maintain airway patency when the individual is awake but not when asleep, coupled with instability in the respiratory control system. Individuals with OSA may demonstrate some or all of the following anatomical features: an increase in soft palate length and thickness; a retrusive or short mandible; lowered hyoid bone position; increased amount of fat in the soft palate and parapharyngeal tissues. While these studies differ in their assessment of the relative incidence and significance of these factors, they all confirm thatthe anatomical changes in OSA have the combined effect of both narrowing and shortening the airway. At the same time, physiological mechanisms that exist to ensure that the airways remain dilated and patent seem to suffer a sleep-induced fall in activity in OSA sufferers. The muscles primarily responsible for maintaining a dilated airway under normal conditions are the muscles that control the position of the hyoid bone, the infrahyoid and suprahyoid muscles, the muscles of the tongue, especially genioglossus, and the muscles that move the soft palate. (For further reading, see Ison et al (1997), Malhotra and White (2002), Fogel et al (2004), Johal et al (2007).)

The gold standard for very severe, life-threatening obstructive sleep apnoea is tracheostomy. Moderately severe OSA may respond to continuous positive airway pressure (CPAP) via a closely fitting facemask that inflates the pharynx and counters its tendency to collapse. Mild sleep apnoea is best managed at least initially by weight loss and a mandibular repositioning device that opens the mouth slightly and brings the mandible forwards, thus preventing the tongue base from falling backwards. An alternative surgical approach involves reduction in the length of the soft palate, removal of the tonsils and plication of the tonsillar pillars by uvulopalatopharyngoplasty (UPPP).

nerve lies immediately lateral to the muscular wall of the tonsillar fossa (see Figs 40.3A, 40.6A); it is at risk if the wall is pierced and is commonly temporarily affected by oedema following tonsillectomy, resulting in a disturbance of taste (Ohtsuka et al 2002). The internal carotid artery lies approximately 25 mm behind and lateral to the tonsil. In some individuals, the styloid process may be elongated and deviate towards the tonsillar bed where it can be felt.

Microstructure Each tonsil is a mass of lymphoid tissue associated with the oropharyngeal mucosa and fixed in its position, unlike most other examples of mucosa-associated lymphoid tissue. It is covered on its oropharyngeal aspect by non-keratinized stratified squamous epithelium. The whole of the tonsil is supported internally by a delicate meshwork of fine collagen type III (reticulin) fibres which are condensed in places to form more robust connective tissue septa that also contain elastin. These septa partition the tonsillar parenchyma, and merge at their ends with the dense irregular fibrous hemicapsule on the deep aspect of the tonsil and with the lamina propria on the pharyngeal surface. Blood vessels, lymphatics and nerves branch or join within the connective tissue condensations. The hemicapsule forms its lateral boundary with the oropharyngeal wall, and with the mucosa that covers its highly invaginated free surface.

The 10–20 crypts formed by invagination of the free surface mucosa are narrow tubular epithelial diverticula that often branch within the tonsil and frequently are packed with plugs of desquamated epithelial cells, lymphocytes and bacteria, that may calcify. The epithelium lining the crypts is mostly similar to that of the oropharyngeal surface, i.e. stratified squamous, but there are also patches of reticulated epithelium, which is much thinner and has a complex structure that is of great importance in the immunological function of the tonsil.

Reticulated epithelium Reticulated epithelium lacks the orderly laminar structure of stratified squamous epithelium. Its base is deeply invaginated in a complex manner so that the epithelial cells, with their slender branched cytoplasmic processes, provide a coarse mesh to accommodate the infiltrating lymphocytes and macrophages. The basal lamina of this epithelium is discontinuous. Although the oropharyngeal surface is unbroken, the epithelium may become exceedingly thin in places, so that only a tenuous cytoplasmic layer separates the pharyngeal lumen from the underlying lymphocytes. Epithelial cells are held together by small desmosomes, anchored into bundles of keratin filaments. Interdigitating dendritic cells (antigen-presenting cells, APCs) are also present. The intimate association of epithelial cells and lymphocytes facilitates the direct transport of antigen from the external environment to the tonsillar lymphoid cells, i.e. reticulated epithelial cells are functionally like the microfold (M) cells of the gut. The total surface area of the reticulated epithelium has been estimated at 295 cm^2 for an average palatine tonsil, reflecting the complex branched nature of the tonsillar crypts.

Tonsillar lymphoid tissue There are four lymphoid compartments in the palatine tonsils. Lymphoid follicles, many with germinal centres, are arranged in rows roughly parallel to neighbouring connective tissue septa. Their size and cellular content varies in proportion to the immunological activity of the tonsil. The mantle zones of the follicles, each with closely packed small lymphocytes, form a dense cap, always situated on the side of the follicle nearest to the mucosal surface. These cells are the products of B-lymphocyte proliferation within the germinal centres. Extrafollicular, or T-lymphocyte, areas contain a specialized microvasculature including high endothelial venules (HEVs), through which circulating lymphocytes enter the tonsillar parenchyma. The lymphoid tissue of the reticulated crypt epithelium contains predominantly IgG- and IgA-producing B lymphocytes (including some mature plasma cells), T lymphocytes and antigen-presenting cells. There are numerous capillary loops in this subsurface region.

Vascular supply and lymphatic drainage The arterial blood supply to the palatine tonsil is derived from branches of the external carotid artery (see Fig. 40.6; **Fig. 40.7**). Three arteries enter the tonsil at its lower pole. The largest is the tonsillar artery, a branch of the facial artery, or sometimes of the ascending palatine artery. It ascends between medial pterygoid and styloglossus, perforates the superior constrictor at the upper border of styloglossus, and ramifies in the tonsil and posterior lingual musculature. The other arteries found at the lower pole are the dorsal lingual branches of the lingual artery which enter anteriorly, and a branch from the ascending palatine artery which enters posteriorly to supply the lower part of the palatine tonsil. The upper pole of the tonsil also receives branches from the ascending pharyngeal artery which enter the tonsil posteriorly, and from the descending palatine artery and its branches, the greater and lesser palatine arteries. All of these arteries enter the deep surface of the tonsil, branch within the connective tissue septa, narrow to become arterioles and then give off capillary loops into the follicles, interfollicular areas and the cavities within the base of the reticulated epithelium. The capillaries rejoin to form venules, many with high endothelia, and the veins return within the septal tissues to the hemicapsule as tributaries of the pharyngeal drainage. The tonsillar artery and its venae comitantes often lie within the palatoglossal fold and may haemorrhage if this fold is damaged during surgery.

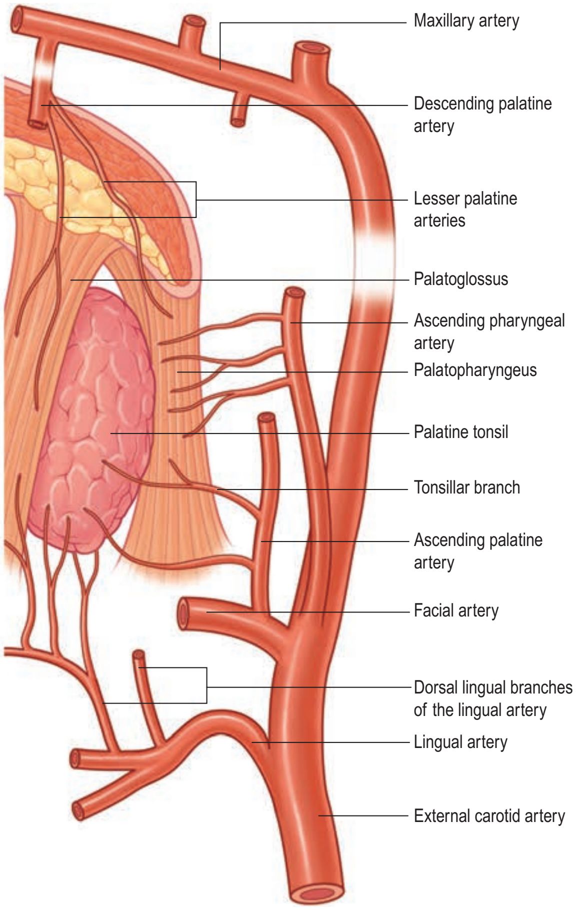

Fig. 40.7 The arterial supply to the palatine tonsil.

Unlike lymph nodes, the palatine tonsils do not possess afferent lymphatics or lymph sinuses. Instead, dense plexuses of fine lymphatic vessels surround each follicle and form efferent lymphatics that pass towards the hemicapsule, pierce the superior constrictor, and drain to the upper deep cervical lymph nodes directly (especially the jugulodigastric nodes) or indirectly through the retropharyngeal lymph nodes. The jugulodigastric nodes are typically enlarged in tonsillitis, when they project beyond the anterior border of sternocleidomastoid and are palpable superficially 1–2 cm below the angle of the mandible; when enlarged, they represent the most common swelling in the neck.

Innervation The tonsillar region is innervated by tonsillar branches of the maxillary and glossopharyngeal nerves. The fibres from the maxillary nerve pass through, but do not synapse in, the pterygopalatine ganglion; they are distributed through the lesser palatine nerves and form a plexus (the circulus tonsillaris) around the tonsil together with the tonsillar branches of the glossopharyngeal nerve. Nerve fibres from this plexus are also distributed to the soft palate and the region of the oropharyngeal isthmus. The tympanic branch of the glossopharyngeal nerve supplies the mucous membrane lining the tympanic cavity. Infection, malignancy and postoperative inflammation of the tonsil and tonsillar fossa may therefore be accompanied by pain referred to the ear.

Tonsillectomy

Available with the *Gray's Anatomy* e-book

Waldeyer's ring

Waldeyer's ring is a circumpharyngeal ring of mucosa-associated lymphoid tissue that surrounds the openings into the digestive and respiratory tracts. It is made up anteroinferiorly by the lingual tonsil, laterally by

Surgical removal of the palatine tonsils is most commonly undertaken for children who suffer from excessive episodes of acute tonsillitis. Other indications include airway obstruction caused by extremely large or infected palatine tonsils and a recurrent peritonsillar abscess. Tonsils are also removed in an older age group when malignancy is suspected. Tonsillectomy using a guillotine is no longer practised because it was associated with an unacceptable incidence of postoperative haemorrhage. Most tonsils are now removed by dissection in the plane of the fibrous hemicapsule, followed by ligation or electrocautery to the vessels that are divided during the procedure. The nerve supply to the tonsil is so diffuse that tonsillectomy under local anaesthesia can be performed successfully by local infiltration rather than by blocking the main nerves. Surgical access to the glossopharyngeal nerve and/or the styloid process may be achieved by separating the fibres of superior constrictor.

the palatine and tubal tonsils, and posterosuperiorly by the pharyngeal tonsil (adenoid) and smaller collections of lymphoid tissue in the intertonsillar intervals.

LARYNGOPHARYNX

Boundaries

The laryngopharynx is situated behind the entire length of the larynx (known clinically as the hypopharynx) and extends from the superior border of the epiglottis, where it is delineated from the oropharynx by the lateral glossoepiglottic folds, to the inferior border of the cricoid cartilage, where it becomes continuous with the oesophagus (see Figs 40.1–40.2). The laryngeal inlet lies in the upper part of its incomplete anterior wall, and the posterior surfaces of the arytenoid and cricoid cartilages lie below this opening.

Piriform fossa A small piriform fossa lies on each side of the laryngeal inlet, bounded medially by the aryepiglottic fold and laterally by the thyroid cartilage and thyrohyoid membrane. Branches of the internal laryngeal nerve lie beneath its mucous membrane. At rest, the laryngopharynx extends posteriorly from the lower part of the body of the third cervical vertebra to the upper part of the body of the sixth cervical vertebra. During deglutition, the laryngopharynx may be elevated considerably by the hyoid elevators.

Inlet of larynx The obliquely sloping inlet of the larynx lies in the anterior part of the laryngopharynx and is bounded above by the epiglottis, below by the arytenoid cartilages of the larynx, and laterally by the aryepiglottic folds (see Fig. 40.1). Below the inlet, the anterior wall of the laryngopharynx is formed by the posterior surface of the cricoid cartilage.

PHARYNGEAL FASCIA

The two named layers of fascia in the pharynx are the pharyngobasilar and buccopharyngeal fasciae. The fibrous layer that supports the pharyngeal mucosa is thickened above the superior constrictor to form the pharyngobasilar fascia (see Fig. 40.10). It is attached to the basilar part of the occipital bone and the petrous part of the temporal bone medial to the pharyngotympanic tube, and to the posterior border of the medial pterygoid plate and the pterygomandibular raphe. Inferiorly, it diminishes in thickness but is strengthened posteriorly by a fibrous band, the median pharyngeal raphe of the constrictors. The buccopharyngeal fascia covers the superior constrictor and passes forwards over the pterygomandibular raphe to cover buccinator.

PHARYNGEAL TISSUE SPACES

Pharyngeal tissue spaces can be subdivided into peripharyngeal and intrapharyngeal spaces: the terms ‘deep neck’ space, subdivided into supra- and infra-hyoid spaces, are commonly used clinically. The peripharyngeal suprahyoid neck spaces include the submandibular and submental spaces anteriorly, the retropharyngeal space posteriorly and the parapharyngeal spaces laterally. The retropharyngeal space is an area of loose connective tissue that lies behind the pharynx and anterior to the prevertebral fascia, extending upwards to the base of the skull and downwards to the retrovisceral space in the infrahyoid part of the neck. Each parapharyngeal space passes laterally around the pharynx and is continuous with the retropharyngeal space. However, unlike the retropharyngeal space, it is a space that is restricted to the suprahyoid region. It is bounded medially by the pharynx, laterally by the pterygoid muscles (where it is part of the infratemporal fossa) and by the sheath of the parotid gland, superiorly by the base of the skull, and inferiorly by suprahyoid structures, particularly the sheath of the submandibular gland. It may be helpful to think of the retropharyngeal space as shaped like an inverted pyramid extending from the base of the skull to the greater cornu of the hyoid bone. The parapharyngeal space can be subdivided into an anterior, prestyloid, compartment and a posterior, retrostyloid, compartment (Maran et al 1984). The prestyloid compartment contains the retromandibular portion of the parotid gland and minor or ectopic salivary glandular tissue, branches of the mandibular division of the mandibular nerve, maxillary artery, ascending pharyngeal artery and a pharyngeal venous plexus, fat and lymph nodes (Shin et al 2001). The retrostyloid compartment contains the internal carotid artery, the internal jugular vein, the glossopharyngeal, vagus, accessory and hypoglossal nerves, the sympathetic chain, fat and lymph nodes. The fascia surrounding the carotid is incomplete at the level above the mandibular angle (hence the term carotid space). Any of these structures may be damaged by penetrating injuries directed posterolaterally in the region; more lateral injuries may result in penetration of the parotid gland.

An intrapharyngeal space potentially exists between the inner surface of the constrictor muscles and the pharyngeal mucosa. Infections in this space are either restricted locally or spread through the pharynx into the retropharyngeal or parapharyngeal spaces. The peritonsillar space is an area of loose connective tissue between the palatine tonsil and superior constrictor that lies around the palatine tonsil between the pillars of the fauces. Infections in the intratonsillar space usually spread up or down the intrapharyngeal space, or through the pharynx into the parapharyngeal space. The pharyngeal mucosal space contains the mucosa of the nasopharynx, oropharynx and hypopharynx as well as the lymphoid tissue of Waldeyer’s ring, adenoid, palatine tonsils, minor salivary glands, the torus tubarius, pharyngobasilar fascia and the cartilage of the pharyngotympanic tubes.

Tissue spaces between the layers of cervical fascia are described in Chapter 35 on pages 578 and 579; tissue spaces around the larynx are described in Chapter 41 on page 726.

Spread of infection

Available with the *Gray’s Anatomy* e-book

Tumours

Available with the *Gray’s Anatomy* e-book

MUSCLES OF THE SOFT PALATE AND PHARYNX

The muscles of the soft palate and pharynx are levator veli palatini, tensor veli palatini, palatoglossus, palatopharyngeus, musculus uvulae, salpingopharyngeus, stylopharyngeus, and the superior, middle and inferior constrictors.

Levator veli palatini

Levator veli palatini arises by a small tendon from a quadrilateral roughened area on the medial end of the inferior surface of the petrous part of the temporal bone, in front of the lower opening of the carotid canal (see Fig. 40.3; **Figs 40.8–40.10**). Additional fibres arise from the inferior aspect of the cartilaginous part of the pharyngotympanic tube and from the vaginal process of the sphenoid bone. At its origin, the muscle is inferior rather than medial to the pharyngotympanic tube and only crosses medial to it at the level of the medial pterygoid plate. It passes medial to the upper margin of the superior constrictor and anterior to salpingopharyngeus. Its fibres spread in the medial third of the soft palate between the two strands of palatopharyngeus to attach to the upper surface of the palatine aponeurosis as far as the midline, where they interlace with those of the contralateral muscle. Thus, the two levator muscles form a sling above and just behind the palatine aponeurosis.

Vascular supply The blood supply of levator veli palatini is derived from the ascending palatine branch of the facial artery and the greater palatine branch of the maxillary artery (Freelander 1992).

Innervation Levator veli palatini is innervated via the pharyngeal plexus.

Actions The primary role of the two levator veli palatini muscles is to elevate the almost vertical posterior part of the soft palate and pull it slightly backwards; during swallowing, the soft palate is elevated so that it touches the posterior wall of the pharynx, separating the nasopharynx from the oropharynx. By additionally pulling on the lateral walls of the nasopharynx posteriorly and medially, the levator veli palatini muscles also narrow that space. They have little or no effect on the pharyngotympanic tube.

Tensor veli palatini

Tensor veli palatini arises from the scaphoid fossa of the pterygoid process and posteriorly from the medial aspect of the spine of the sphenoid bone (see Figs 38.3, 40.3, 40.8–40.10). Between these two sites, it is attached to the anterolateral membranous wall of the pharyngotympanic tube (including its narrow isthmus where the cartilaginous medial two-thirds meets the bony lateral third). Some fibres may be continuous with those of tensor tympani. Inferiorly, the fibres converge on a delicate tendon that turns medially around the pterygoid hamulus to pass through the attachment of buccinator to the palatine aponeurosis and

Infection that spreads into the parapharyngeal space causes pain and trismus. There may be swelling in the oropharynx that extends up to the uvula, displacing it to the contralateral side, and dysphagia. Posterior spread from the parapharyngeal space into the retropharyngeal space will produce bulging of the posterior pharyngeal wall, dyspnoea and nuchal rigidity. Involvement of the carotid sheath may cause thrombosis of the internal jugular vein and nerve palsies of the glossopharyngeal, vagus, accessory and hypoglossal nerves. If the infection continues to spread unchecked, mediastinitis can ensue. A virulent infection in the retropharyngeal space may spread through the alar fascia into the underlying danger space. Infection in this tissue space may also descend into the thorax and even below the respiratory diaphragm, giving rise to chest and shoulder pain, severe dyspnoea and retrosternal discomfort.

Pharyngeal infection from mucosa-associated lymph tissues such as the palatine tonsil, or as a result of a penetrating injury (e.g. from an ingested foreign body), can result in the spread of infection into the tissue spaces of the neck adjacent to the pharynx. This is an extremely serious and life-threatening situation, not only because of the rapidity with which it can involve the superior mediastinum but also because of associated critical airways obstruction.

Primary tumours of the parapharyngeal space are rare. More commonly tumours from adjacent spaces displace the easily identifiable parapharyngeal space on imaging, helping the radiologist to determine the origin of the tumour (Warshafsky et al 2012). Tumours that develop within the prestyloid compartment of the parapharyngeal space most often develop from either ectopic minor salivary tissue, the deep lobe of the parotid gland or in lymph nodes. Those in the post-styloid compartment of the parapharyngeal space are derived from lower cranial nerves in the carotid sheath or vascular tumours arising from the carotid body or the inferior vagal ganglion (Gupta et al 2012). All these tumours, with the exception of those arising in lymph nodes, present late because they grow slowly, produce few symptoms and tend to expand internally rather than externally. Internal expansion and compression of the pharynx often gives rise to a 'plummy' quality of the voice and snoring. Those that cause nerve palsies tend to develop slowly, which means that there is time for local accommodation to take place, but also that symptoms can be very subtle initially and overlooked by the patient. Voice change, dysphagia and aspiration becomes more obvious in later stages of the disease.

Several surgical approaches have been described for the management of parapharyngeal space tumours, including transcervical, transparotid, combined transcervical–transparotid and transoral approaches. Submandibulectomy and mandibulotomy are occasionally necessary (Mydlarz and Agrawal 2014, Sheahan 2014, Paderno et al 2015). Transoral robotic surgery (TORS) can be used for parapharyngeal tumour resection but is mainly, and much more frequently, employed in oropharyngeal tumour resection (see Fig. 40.6) (Baskin et al 2018). As has happened in other areas of surgery where minimally invasive approaches have either become or are becoming the norm, an appreciation of 'inside-out' anatomy, in this case the complex transoral (medial to lateral) anatomy of the oropharynx and parapharyngeal spaces, is increasingly important for the surgeon (Dallan et al 2011, Moore et al 2012, Lim et al 2013, Prades et al 2014,Wang et al 2014, Gun and Ozer 2015, Yarlagadda and Grillone 2015, Gun et al 2016). Very large tumours with significant superior extension may require a lateral skull base approach for safe resection.

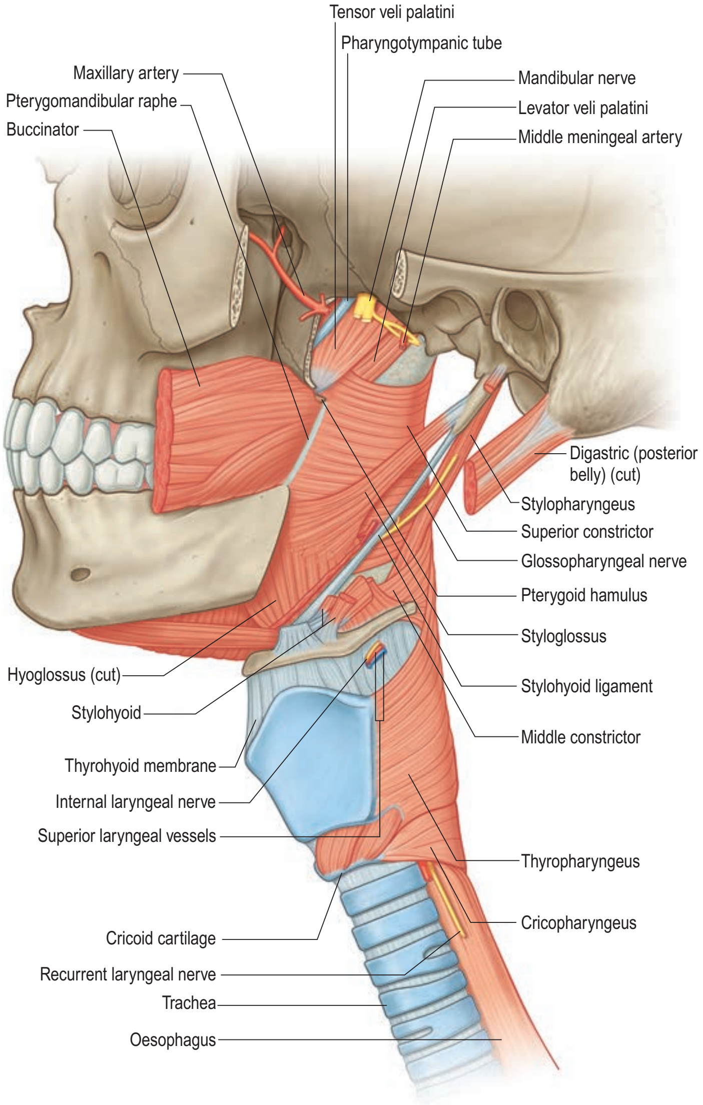

Fig. 40.8 Muscles of the pharynx, lateral view.

the osseous surface behind the palatine crest on the horizontal plate of the palatine bone. There is a small bursa between the tendon and the pterygoid hamulus.

The muscle is thin and triangular, and lies lateral to the medial pterygoid plate, pharyngotympanic tube and levator veli palatini. Its lateral surface contacts the upper and anterior part of medial pterygoid, the mandibular, auriculotemporal and chorda tympani nerves, the otic ganglion and the middle meningeal artery. Tensor veli palatini is connected with the styloid process through the tensor vascular styloid fascia, dividing the parapharyngeal space into pre- and retro-styloid portions (Gupta et al 2012).

Dilator tubae Some fibres of tensor veli palatini that arise from the hamulus of the medial pterygoid plate are attached to the short lateral lamina of the cartilage of the pharyngotympanic, to a condensation of connective tissue lateral to the tubal wall and to a portion of Ostmann's fat pad; these fibres are sometimes referred to as dilator tubae.

Vascular supply The blood supply of tensor veli palatini is derived from the ascending palatine branch of the facial artery and the greater palatine branch of the maxillary artery (Freelander 1992).

Innervation The motor innervation of tensor veli palatini is derived from the mandibular nerve via the nerve to medial pterygoid and reflects the development of the muscle from the first branchial arch.

Actions Tensor veli palatini is said to have three anchoring points on which it isometrically contracts: the pterygoid hamulus, Ostmann's fat pad and medial pterygoid (O'Reilly and Sando 2010). Acting together, the two tensor veli palatini muscles tauten the soft palate, principally its anterior part, and depress it by flattening its arch. Acting unilaterally, the muscle pulls the soft palate to one side. Although contraction of both muscles will slightly depress the anterior part of the soft palate, it is often assumed that the increased rigidity aids palatopharyngeal closure. A primary role of the tensor is to open the pharyngotympanic tube, e.g. during deglutition and yawning, via its dilator tubae component, and so aid equalization of air pressure between the middle ear and nasopharynx.

Palatoglossus

Palatoglossus is narrower at its middle than at its ends (see Figs 40.3, 40.6). Together with its overlying mucosa, it forms the palatoglossal arch or fold (see Fig. 37.3). It arises from the oral surface of the palatine aponeurosis, where it is continuous with its contralateral fellow. It extends forwards, downwards and laterally in front of the palatine tonsil to the side of the tongue. Some of its fibres spread over the dorsum of the tongue, while others pass deeply into its substance to intermingle with fibres of the intrinsic transverse muscle.

Vascular supply Palatoglossus receives its blood supply from the ascending palatine branch of the facial artery and from the ascending pharyngeal artery.

Innervation Palatoglossus is innervated via the pharyngeal plexus and is therefore unlike all the other muscles of the tongue, which are supplied by the hypoglossal nerve.

Actions Palatoglossus elevates the root of the tongue and approximates the palatoglossal arch to its contralateral fellow, thus shutting off the oral cavity from the oropharynx.

Palatopharyngeus

Palatopharyngeus and its overlying mucosa form the palatopharyngeal arch (see Fig. 37.3). Within the soft palate, palatopharyngeus is composed of two fasciculi that are attached to the upper surface of the palatine aponeurosis; they lie in the same plane but are separated from each other by levator veli palatini (see Figs 40.3, 40.9). The thicker, anterior fasciculus arises from the posterior border of the hard palate as well as the palatine aponeurosis, where some fibres interdigitate across the midline. The posterior fasciculus is in contact with the mucosa of the pharyngeal aspect of the palate and joins the posterior band of the contralateral muscle in the midline. The two layers unite at the posterolateral border of the soft palate and are joined by fibres of salpingopharyngeus. Passing laterally and downwards behind the tonsil, palatopharyngeus descends posteromedial to and in close contact with stylopharyngeus, to be attached with it to the posterior border of the thyroid cartilage. Some fibres end on the side of the pharynx, attached to pharyngeal fibrous tissue, and others cross the midline posteriorly, decussating with those of the contralateral muscle. Palatopharyngeus thus forms an incomplete internal longitudinal muscular layer in the wall of the pharynx.

Passavant's muscle (palatopharyngeal sphincter) The existence of a Passavant's muscle remains controversial (Cho et al 2013). It has been described as a part of the superior constrictor and palatopharyngeus muscles (see Fig. 40.3B). An alternative view holds that it is a distinct palatine muscle that arises from the anterior and lateral parts of the upper surface of the palatine aponeurosis, lies lateral to levator veli palatini, blends internally with the upper border of the superior constrictor, and encircles the pharynx as a sphincter-like muscle. Whatever its origin, when it contracts, it forms a ridge (Passavant's ridge) when the soft palate is elevated. Ciliated, 'respiratory' epithelium covers the superior surface in continuity with the superior aspect of the soft palate and changes to stratified, squamous epithelium inferiorly along the line of attachment of the palatopharyngeal sphincter to the palate. The muscle is hypertrophied in cases of complete cleft palate.

Vascular supply Palatopharyngeus receives its arterial supply from the ascending palatine branch of the facial artery, the greater palatine branch of the maxillary artery and the pharyngeal branch of the ascending pharyngeal artery.

Innervation Palatopharyngeus is innervated via the pharyngeal plexus.

Actions Acting together, the palatopharyngei pull the pharynx up, forwards and medially, and thus shorten it during swallowing. They also approximate the palatopharyngeal arches and draw them forwards.

Musculus uvulae

Musculus uvulae arises from the posterior nasal spine of the palatine bone and the superior surface of the palatine aponeurosis and lies between

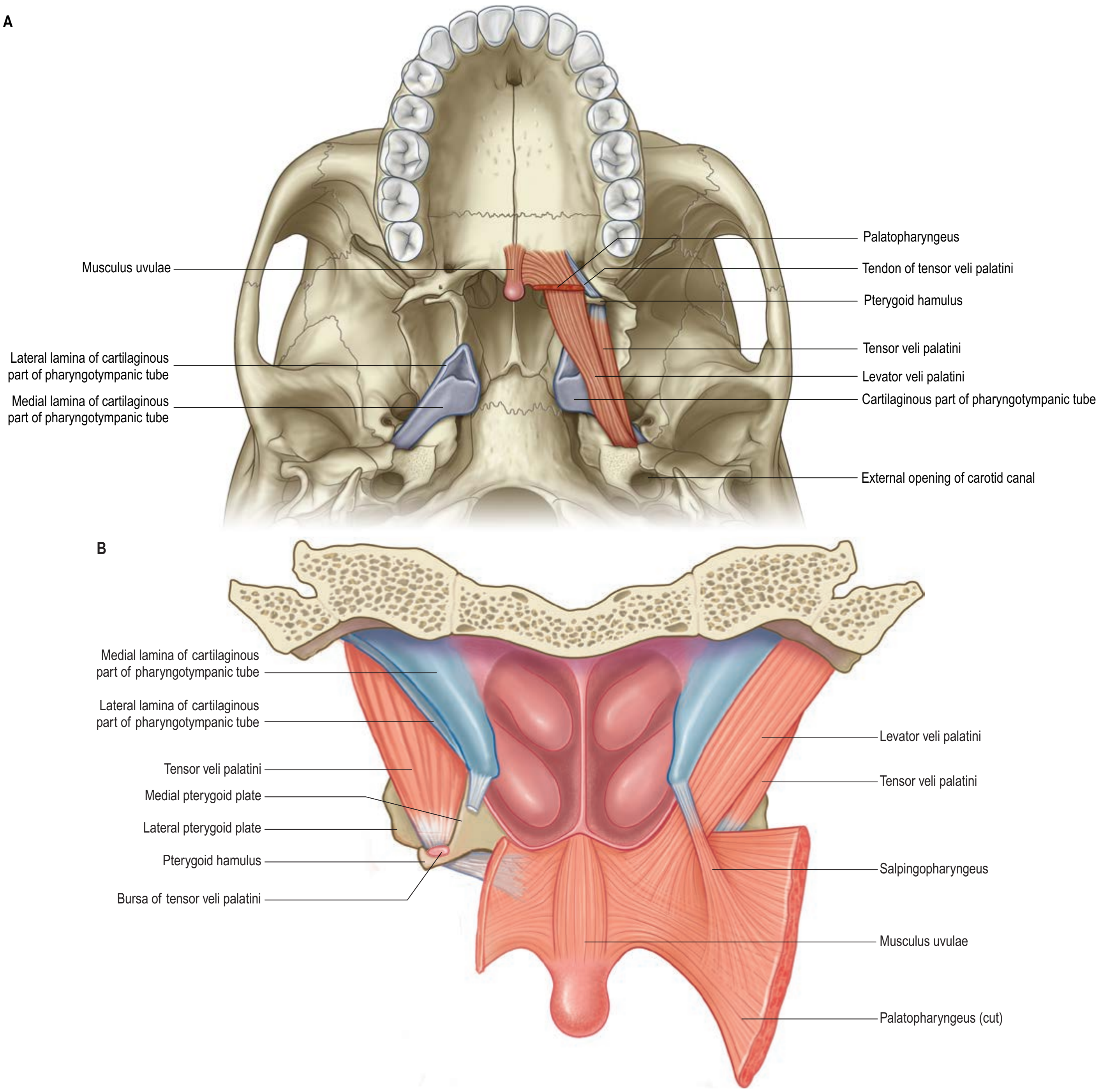
A
Musculus uvulae
Lateral lamina of cartilaginous part of pharyngotympanic tube
Medial lamina of cartilaginous part of pharyngotympanic tube
Palatopharyngeus
Tendon of tensor veli palatini
Pterygoid hamulus
Tensor veli palatini
Levator veli palatini
Cartilaginous part of pharyngotympanic tube
External opening of carotid canal
B
Medial lamina of cartilaginous part of pharyngotympanic tube
Lateral lamina of cartilaginous part of pharyngotympanic tube
Tensor veli palatini
Medial pterygoid plate
Lateral pterygoid plate
Pterygoid hamulus
Bursa of tensor veli palatini
Levator veli palatini
Tensor veli palatini
Salpingopharyngeus
Musculus uvulae
Palatopharyngeus (cut)

Fig. 40.9 Muscles of the soft palate. **A**, Inferior view. **B**, Superior view.

the two laminae of the aponeurosis (see Figs 40.1, 40.9). It runs posteriorly above the sling formed by levator veli palatini and inserts beneath the mucosa of the uvula. The two sides of the muscle are united along most of its length.

Vascular supply The blood supply of musculus uvulae is derived from the ascending palatine branch of the facial artery and the descending palatine branch of the maxillary artery.

Innervation The nerve supply to musculus uvulae is innervated via the pharyngeal plexus.

Actions By retracting the uvular mass and thickening the middle third of the soft palate, musculus uvulae aids levator veli palatini in palatopharyngeal closure. The two muscles run at right-angles to each other and their contraction raises a 'levator eminence' that helps seal off the nasopharynx.

Salpingopharyngeus

Salpingopharyngeus arises from the inferior part of the cartilage of the pharyngotympanic tube near its pharyngeal opening and passes downwards within the salpingopharyngeal fold to blend with palatopharyngeus (see Figs 40.1, 40.3A, 40.9).

Vascular supply Salpingopharyngeus receives its arterial supply from the ascending palatine branch of the facial artery, the greater palatine branch of the maxillary artery and the pharyngeal branch of the ascending pharyngeal artery.

Innervation Salpingopharyngeus is innervated via the pharyngeal plexus.

Actions Salpingopharyngeus elevates the pharynx and may also assist tensor veli palatini to open the cartilaginous end of the pharyngotympanic tube during swallowing.

Stylopharyngeus

Stylopharyngeus is a long slender muscle, cylindrical above and flat below. It arises from the medial side of the base of the styloid process, descends along the side of the pharynx, and passes between the superior and middle constrictors to spread out beneath the mucous membrane (see Figs 37.9, 40.3, 40.8, 40.10). Some fibres merge into the constrictors and the lateral glossoepiglottic fold, while others join fibres of

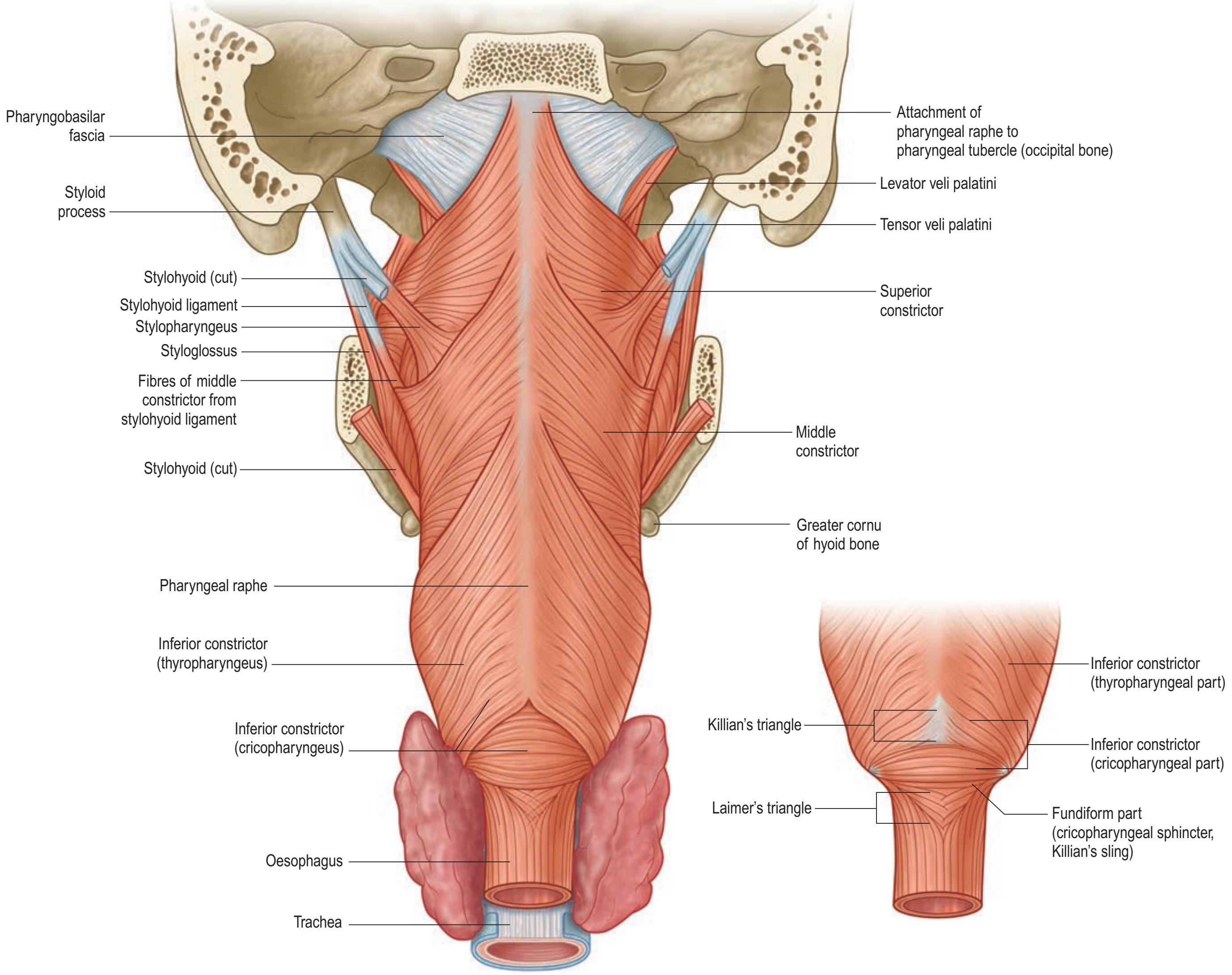
Pharyngobasilar fascia
Styloid process
Stylohyoid (cut)
Stylohyoid ligament
Stylopharyngeus
Styloglossus
Fibres of middle constrictor from stylohyoid ligament
Stylohyoid (cut)
Pharyngeal raphe
Inferior constrictor (thyropharyngeus)
Inferior constrictor (cricopharyngeus)
Oesophagus
Trachea
Attachment of pharyngeal raphe to pharyngeal tubercle (occipital bone)
Levator veli palatini
Tensor veli palatini
Superior constrictor
Middle constrictor
Greater cornu of hyoid bone
Killian's triangle
Laimer's triangle
Inferior constrictor (thyropharyngeal part)
Inferior constrictor (cricopharyngeal part)
Fundiform part (cricopharyngeal sphincter, Killian's sling)

Fig. 40.10 Muscles of the pharynx and the pharyngobasilar fascia, posterior view.

palatopharyngeus and are attached to the posterior border of the thyroid cartilage. The glossopharyngeal nerve curves round the posterior border and the lateral side of stylopharyngeus and passes between the superior and middle constrictors to reach the tongue in most patients.

Vascular supply Stylopharyngeus receives its arterial supply from the pharyngeal branch of the ascending pharyngeal artery.

Innervation Stylopharyngeus is innervated by the glossopharyngeal nerve.

Actions Stylopharyngeus elevates the pharynx and larynx.

Superior constrictor

The superior constrictor is a quadrilateral sheet of muscle and is thinner than the other two constrictors. It is attached anteriorly to the pterygoid hamulus (and sometimes to the adjoining posterior margin of the medial pterygoid plate), the posterior border of the pterygomandibular raphe, the posterior end of the mylohyoid line of the mandible and, by a few fibres, to the side of the tongue (see Figs 40.1, 40.3, 40.8). The fibres curve back into a median pharyngeal raphe that is attached superiorly to the pharyngeal tubercle on the basilar part of the occipital bone.

Relations The upper border of the superior constrictor is separated from the cranial base by a crescentic interval that contains levator veli palatini, the pharyngotympanic tube and an upward projection of pharyngobasilar fascia. The lower border is separated from the middle constrictor by stylopharyngeus and the glossopharyngeal nerve (see Fig. 40.8). Anteriorly, the pterygomandibular raphe separates the superior constrictor from buccinator, and, posteriorly, the superior constrictor lies on the prevertebral muscles and fascia, from which it is separated by the retropharyngeal space. The buccopharyngeal fascia, ascending pharyngeal artery, pharyngeal venous plexus, glossopharyngeal and lingual nerves, middle constrictor, medial pterygoid, stylopharyngeus, styloglossus and the stylohyoid ligament all lie laterally. Palatopharyngeus and the tonsillar capsule lie medially.

Vascular supply The arterial supply of the superior constrictor is derived mainly from the pharyngeal branch of the ascending pharyngeal artery and the tonsillar branch of the facial artery.

Innervation The superior constrictor is innervated via the pharyngeal plexus.

Actions The superior constrictor constricts the upper part of the pharynx.

Middle constrictor

The middle constrictor is a fan-shaped sheet attached anteriorly to the lesser cornu of the hyoid and the lower part of the stylohyoid ligament (the chondropharyngeal part of the muscle), and to the whole of the upper border of the greater cornu of the hyoid (the ceratopharyngeal part) (see Figs 40.8, 40.10). The lower fibres descend deep to the inferior constrictor to reach the lower end of the pharynx; the middle fibres pass transversely, and the superior fibres ascend and overlap the superior constrictor. All fibres insert posteriorly into the median pharyngeal raphe (Sakamoto 2014).

Relations The glossopharyngeal nerve and stylopharyngeus pass through a small gap between the middle and superior constrictors, and the internal laryngeal nerve and the laryngeal branch of the superior thyroid artery pass between the middle and inferior constrictors. The prevertebral fascia and longus colli and longus capitis are posterior; the superior constrictor, stylopharyngeus and palatopharyngeus are internal; and the carotid vessels, pharyngeal plexus of nerves and some lymph nodes are lateral. Near its hyoid attachment, the middle constrictor lies deep to hyoglossus, from which it is separated by the lingual artery.

Vascular supply The arterial supply of the middle constrictor is derived mainly from the pharyngeal branch of the ascending pharyngeal artery and the tonsillar branch of the facial artery.

Innervation The middle constrictor is innervated via the pharyngeal plexus.

Actions The middle constrictor constricts the middle part of the pharynx during swallowing.

Inferior constrictor

The inferior constrictor is the thickest of the three constrictor muscles and is usually described in two parts: thyropharyngeus and cricopharyngeus (see Figs 40.8, 40.10). Thyropharyngeus arises from the oblique line of the thyroid lamina, a strip of the lamina behind this, and by a small slip from the inferior cornu. Some additional fibres arise from a tendinous cord that loops over cricothyroid. Cricopharyngeus arises from the side of the cricoid cartilage between the attachment of cricothyroid and the articular facet for the inferior thyroid cornu. Some authors have described cricopharyngeus as consisting of a superficial upper oblique portion – the pars oblique – and a lower, deeper, transverse portion – the pars fundiformis. The upper part attaches to the median raphe while the lower part forms a circular band that lacks a median raphe. The area demarcated by the pars oblique and pars fundiformis of cricopharyngeus is termed Killian's dehiscence (or Killian's triangle). A second triangular area, Laimer's triangle, can be identified beneath cricopharyngeus between the longitudinal fibres of the oesophagus as they pass laterally on either side to attach to the cricoid cartilage; only the circular muscle of the oesophagus forms the wall here. Both triangles are postulated to be sites of weakness in the wall of the pharynx and oesophagus and are therefore areas where diverticula could potentially form. Both cricopharyngeus and thyropharyngeus spread posteromedially to join the contralateral muscle. Thyropharyngeus is inserted into the median pharyngeal raphe, and its upper fibres ascend obliquely to overlap the middle constrictor; however, cricopharyngeus blends with the circular oesophageal fibres around the narrowest part of the pharynx.

Relations The buccopharyngeal fascia is external; the prevertebral fascia and muscles are posterior; the thyroid gland, common carotid artery and sternothyroid are lateral; and the middle constrictor, stylopharyngeus, palatopharyngeus and the fibrous lamina are internal. The internal laryngeal nerve and laryngeal branch of the superior thyroid artery reach the thyrohyoid membrane by passing between the inferior and middle constrictors. The external laryngeal nerve descends on the superficial surface of the muscle, just behind its thyroid attachment, and pierces its lower part. The recurrent laryngeal nerve and the laryngeal branch of the inferior thyroid artery ascend deep to its lower border to enter the larynx.

Vascular supply The arterial supply of the inferior constrictor is derived mainly from the pharyngeal branch of the ascending pharyngeal artery and the muscular branches of the inferior thyroid artery.

Innervation Both parts of the inferior constrictor are usually innervated via the pharyngeal plexus. Although controversial, available evidence in humans suggests that cricopharyngeus is also supplied by the recurrent laryngeal nerve and the external branch of the superior laryngeal nerve (Sakamoto 2013).

Actions Thyropharyngeus constricts the lower part of the pharynx. Cricopharyngeus is the main component of the upper oesophageal sphincter, or pharyngo-oesophageal high-pressure zone, the other parts being thyropharyngeus and the proximal cervical oesophagus. (The extent to which the lower fibres of thyropharyngeus and the upper fibres of the oesophageal musculature are involved in closing the upper end of the oesophagus appears to depend on the physiological state, whereas cricopharyngeus always participates in closure.) The upper oesophageal sphincter is defined manometrically as a region of elevated intraluminal pressure, 2–4 cm long, located at the junction of the hypopharynx and cervical oesophagus.

Cricopharyngeus contains about 40% of endomysial connective tissue, much of which is elastic, but it lacks muscle spindles (Bonnington et al 1988, Brownlow et al 1989). It contains both slow-twitch type I and fast-twitch type II fibres, a structural arrangement that underpins the various functions of the upper oesophageal sphincter, i.e. maintaining constant basal tone, yet being able to relax and contract rapidly during swallowing, belching and vomiting. The tonic activity of cricopharyngeus between swallows prevents influx of air during inspiration and tracheobronchial aspiration and pharyngeal reflux of oesophageal contents during oesophageal peristalsis. For further reading, see Lang and Shaker (2000).

Hypopharyngeal diverticula

Available with the *Gray's Anatomy* e-book

PHARYNGEAL PLEXUS

Almost all of the nerve supply to the pharynx, whether motor or sensory, is derived from the pharyngeal plexus, which is formed by the pharyngeal branches of the glossopharyngeal and vagus nerves with contributions from the superior cervical sympathetic ganglion. The plexus lies on the external surface of the pharynx, especially on the middle constrictor. Filaments from the plexus ascend or descend external to the superior and inferior constrictors before branching within the muscular layer and mucosa of the pharynx.

The pharyngeal branch of the vagus supplies all the muscles of the soft palate (excluding tensor veli palatini, which is supplied by the mandibular division of the trigeminal via the nerve to medial pterygoid) and all the muscles of the pharynx (excluding stylopharyngeus, which is supplied by the glossopharyngeal nerve). It emerges from the upper part of the inferior vagal ganglion and consists of axons arising from neuronal cell bodies in the nucleus ambiguus. The nerve passes between the external and internal carotid arteries to reach the upper border of the middle pharyngeal constrictor and subsequently divides into numerous filaments that contribute to the pharyngeal plexus. It also gives off a minute filament, the ramus lingualis vagi, which joins the hypoglossal nerve as it curves round the occipital artery.

Whether a 'cranial root' of the accessory nerve serves as the conduit for the major motor drive to the pharyngeal plexus, albeit via the vagus nerve, is a matter of debate. The plexiform connections that may be demonstrated between the accessory nerve and the vagus nerve within the posterior cranial fossa are too variable and insubstantial to support this function.

ANATOMY OF SWALLOWING (DEGLUTITION)

Swallowing involves a series of activities that take place within a matter of seconds. Traditionally described as a reflex, the process is more properly regarded as programmed motor behaviour. Swallowing is initiated when food or liquid stimulates sensory nerves in the oropharynx. In a 24-hour period, an average person swallows between 600 and 1000 times but, of these, only some 150 will relate to feeding; the remainder clear saliva and are less frequent at night (Sato and Nakashima 2006, 2007).

Eating and drinking are basic human pleasures and problems associated with swallowing can impact dramatically on the quality of life. Swallowing disorders are usually symptoms of other complex diseases; an inability to swallow may adversely affect nutritional status and therefore indirectly exacerbate the underlying disease. Aside from the risk of asphyxiation through choking, swallowing disorders can also be a direct cause of morbidity and mortality as a result of aspiration of food, liquid or possibly refluxed gastric acid contents, causing bacterial infection or tissue damage.

Swallowing in the adult human has usually been studied in relation to swallowing solid or liquid food carried out on command. For descriptive purposes, the process has been traditionally divided into four phases: oral preparatory, oral transit/transfer, pharyngeal and oesophageal (in this traditional view some have only recognized three phases, combining the two oral phases of preparation and transit into a single oral phase). While this sequence of events may still be appropriate for describing the swallowing of liquids, it is not sufficiently detailed to represent the way in which solid food is prepared for swallowing, where suitably processed food is passed in stages to the oropharynx and valleculae until a swallow is initiated. Oral and pharyngeal stages overlap when swallowing solid food, but perhaps less so when swallowing saliva or other liquids. It is more appropriate to speak of an oral preparatory and an oral transit phase when describing the swallowing of liquids, but inappropriate when considering the swallowing of solid food. (For further reading, see Hiiemae and Palmer 1999, 2003, Matsuo and Palmer 2008, Mioche et al 2002, Palmer et al 2007.)

Hypopharyngeal diverticula arise in the lower portion of the pharynx through areas of weakness in the pharyngeal wall. The pharyngeal mucosa that lies between cricopharyngeus and thyropharyngeus is relatively unsupported by pharyngeal muscles (the dehiscence of Killian). A delay in the relaxation of cricopharyngeus, which can happen when the swallowing mechanism becomes discoordinated, generates a zone of elevated pressure adjacent to the mucosa in the dehiscence. The result is the development of a pulsion diverticulum (a pouch of prolapsing mucosa), also known as Zenker's diverticulum, which breaches the thin muscle wall adjacent to the sixth cervical vertebra and expands, usually a little to the left side, into the parapharyngeal potential space. This may trap portions (or all) of the passing food bolus, resulting in regurgitation of old food, aspiration pneumonia, halitosis and weight loss. Treatment may involve open excision or inversion of the pouch to prevent it filling, coupled with division of the circular fibres of cricopharyngeus, to prevent the build-up of pressure in the region and recurrence of the pouch. Endoscopic stapling, or laser-assisted diverticulotomy has become popular, first-line, treatment and avoids open surgery for most patients.

The majority of hypopharyngeal diverticula arise either between the two parts of cricopharyngeus (where the upper oblique and lower transverse fibres diverge) or below cricopharyngeus (where the longitudinal fibres of the oesophagus diverge in Laimer's triangle). Some arise between cricopharyngeus and thyropharyngeus. Diverticula are usually midline but may arise laterally below cricopharyngeus.

Oral preparatory phase

In the oral preparatory phase, liquids are taken into the mouth and held there either on the floor of the mouth or against the hard palate by the upward movement of the tongue. During swallowing, the muscles that dilate the pharyngotympanic tube are activated during a pause in the expiratory phase of respiration. Throughout this first phase, the soft palate is fully lowered by contraction of palatoglossus and palatopharyngeus, and the posterior part of the tongue is simultaneously elevated; the apposed soft palate and tongue form a tight seal that helps to prevent premature leakage of the bolus into the oropharynx before the airways are fully protected. Slight leakage of fluid does sometimes happen; the tendency for there to be leakage because of imperfect sealing increases with age.

Oral transit/transfer phase

In the oral transit/transfer phase, the liquid in the oral cavity is transported through the palatoglossal and palatopharyngeal arches into the oropharynx. Genioglossus raises both the tongue tip and the part of the tongue immediately behind the tip so that they come into contact with the alveolar ridge. Orbicularis oris and buccinator remain contracted, keeping the lips and cheeks taut and the liquid central in the oral cavity. The liquid is accommodated in a shallow midline gutter that forms along the dorsum of the tongue, probably as a result of the co-contraction of the styloglossi and the genioglossi, aided by the superior longitudinal and transverse fibres of the intrinsic muscles. The mandible is elevated and the mouth is closed. The floor of the mouth and the anterior and middle portions of the tongue are elevated by co-contraction of the suprahyoid group of muscles (mylohyoid, digastric, geniohyoid and stylohyoid); the effectiveness of the suprahyoid muscles is increased as they contract against a fixed mandible (the mouth does not have to be closed to swallow, but it is much harder to swallow if it is open). Contraction of stylohyoid elevates the more posterior parts of the tongue and empties the longitudinal gutter. At the same time, the tongue flattens, probably as a result of the contraction of hyoglossus and some of the intrinsic lingual muscles, especially the vertical fibres. The elevated, flattened tongue pushes the liquid against the hard palate, and the sides of the tongue seal against the maxillary alveolar processes, helping to move the liquid further posteriorly. Contraction of styloglossus and mylohyoid completes the elevation of the posterior part of the tongue. At the same time, the posterior oral seal relaxes and the posterior tongue moves forwards; the overall effect is of a cam-like action of the tongue, sweeping or squeezing the liquid towards the pillars of the fauces, finally delivering it to the oropharynx and initiating the pharyngeal stage of swallowing, where the pharyngeal aperture is initially increased and then closed.

Oral phases when swallowing solids

When solid food is swallowed, the process is slightly different from that just described for swallowing liquids. Food is mixed with saliva and reduced to smaller pieces by the processes of chewing. When it has been converted to a suitable consistency to be swallowed, it is transferred to the oropharynx and valleculae, where it can be retained for a few seconds prior to swallowing. During this time, chewing may continue; the bolus is progressively augmented in one or more stages until a swallow is initiated and the pharyngeal phase begins. In this part of the 'oral phase for solid food', the essential action is chewing; the mandible is moved by the action of the jaw elevators and depressors, and the food is reduced by the grinding action of the teeth and simultaneously mixed with saliva. The lips are maintained as a tight labial seal by the contraction of orbicularis oris; buccinator performs a similar function for the cheeks. In this way, the sulci are closed, the vestibule normally remains empty, and any food that enters the vestibule is returned to the oral cavity proper. Buccinator keeps the cheeks taut, ensuring that they are kept clear of the occlusal surfaces and that the food remains in place under the occlusal surfaces of the molar teeth. Loss of the nerve supply to buccinator as a result of damage to the facial nerve results in painful and repeated lacerations of the cheeks. It was thought that the soft palate was depressed throughout this phase. It is now recognized that the posterior seal is not tight, and that the oral cavity and oropharynx remain in communication, permitting addition of material to the bolus while chewing continues. Spillage may happen because the soft palate is not in continuous contact with the posterior part of the tongue, as was once thought (Hiiemae and Palmer 1999). Bolus formation appears to involve several cycles of transporting food from the anterior to the posterior part of the tongue through the palatoglossal and palatopharyngeal arches until a bolus accumulates on the oropharyngeal surface of the tongue (retrolingual loading), the valleculae and within the oropharynx. Throughout this phase, the lateral and rotatory tongue movements that deliver the food to the teeth for grinding and reduction are crucial for normal bolus formation because they ensure that the food is positioned under the occlusal surfaces of the teeth. If effective tongue movements are not achieved, chewing will be compromised. Movements of the tongue are also cyclical in phase with the movements of the jaw and hyoid bone. As the jaw is depressed, the tongue is also depressed and moves anteriorly. As the jaw is elevated, the tongue is retracted so that it no longer lies under the anterior teeth as they as are brought together by jaw elevation. These coordinated actions help to ensure that the tongue is not bitten during chewing.

Chewing continues until all the food has been moved posteriorly, a process that can last from less than 1 second to as much as 10 seconds. The oral preparatory, oral transport and pharyngeal phases of swallowing therefore overlap when solid food is being swallowed. As pieces of food are prepared in the mouth, they are moved to the posterior part of the tongue or on into the oropharynx in a similar manner to that used to transport liquids. The end of this phase of swallowing is marked by the tongue propelling the prepared bolus of food to the posterior part of the oral cavity and then on into the oropharynx to initiate the swallow. Contact with either the posterior wall of the oropharynx or the mucosa overlying the palatoglossal and palatopharyngeal arches was once thought to be necessary to initiate a swallow; it is now known that there is a great degree of variability in the position of the bolus at the time at which a swallow is initiated.

Pharyngeal phase

The delivery of the bolus to the oropharynx triggers the pharyngeal phase of the swallow. This phase, which is involuntary and is the most critical stage of swallowing, involves the pharynx changing from being an air channel (between the posterior nares and laryngeal inlet) to a food channel (from the fauces to the upper end of the oesophagus). The airway is protected from aspiration during swallowing by hyolaryngeal elevation, and by resetting respiratory rhythm so that airflow ceases briefly as the bolus passes through the hypopharynx; the total time that elapses from the bolus triggering the pharyngeal phase to the re-establishment of the airway is barely 1 second. Thus, there are two aspects of the process to be examined: the transport of the food down the pharynx and through the upper oesophageal sphincter, and the absolute need to protect the airways throughout this time.

The nasopharynx is sealed off from the oropharynx by activation of the superior pharyngeal constrictor and contraction of a subset of palatopharyngeal fibres to form a variable, ridge-like structure (Passavant's ridge; Cho et al 2013), against which the soft palate is elevated. From an evolutionary perspective, this ridge represents the remnant of a sphincter that encircled a more highly placed larynx; a high laryngeal position is the norm in other mammals and in the human infant (see below), but not in the human adult. Interestingly, the pharyngeal ridge becomes hypertrophic in an infant with a cleft palate, presumably in an attempt to produce a seal to the nasal airway. Ineffective velopharyngeal closure may result in nasal regurgitation of food.

The airway is sealed at the laryngeal inlet by closure of the glottis. The epiglottis is retroflexed over the laryngeal aditus as a result of passive pressure from the base of the tongue and active contraction of the aryepiglottic muscles. The conventional view that laryngeal closure during swallowing takes place from inferior to superior, i.e. the vocal folds adduct first and the epiglottis covers the arytenoids and glottis last, has been challenged by studies using simultaneous electromyography and fibreoptic endoscopic evaluation of swallowing (FEES). These studies have reported that the aryepiglottic folds close before vocal fold adduction during a swallow. The sequence of events that close the glottis may alter according to the type of swallow and consistency of the bolus (Steele and Miller 2010). To prevent aspiration of material, irrespective of its consistency, the hyoid bone and larynx are raised and pulled anteriorly with precise timing by the suprahyoid muscles and the longitudinal muscles of the pharynx (Kendall et al 2001). In this way, the laryngeal inlet is brought forwards under the bulge of the posterior tongue, i.e. out of the path of the bolus. This action helps expand the hypopharyngeal space and relax the upper oesophageal sphincter, which is also raised by several centimetres. The bolus passes over the reflected anterior surface of the epiglottis and is swept through the laryngopharynx to the upper oesophageal sphincter.

Breathing is suspended briefly during swallowing; the larynx is closed and the soft palate is elevated while there is active neural inhibition of ventilation. Swallowing is normally initiated during an expiration, which is then inhibited during the swallow (typically for a period of 0.5–1.5

seconds). Resumption of expiration provides a degree of protection against any residues of solid food that might remain uncleared within the pharynx following the swallow being inhaled into the airway. The bolus is moved by sequential contraction of the pharyngeal constrictor muscles superiorly behind the bolus. At the same time, the pharynx is shortened and elevated as palatoglossus and palatopharyngeus contract against the raised and fixed soft palate. The sequential contraction of the constrictor muscles is often assumed to be the driving force that propels the bolus towards the oesophagus. Evidence that the head of the bolus moves faster than the wave of pharyngeal contraction suggests that, at least in some situations, the kinetic energy imparted to the bolus as it is expelled from the mouth into the oropharynx may be sufficient to carry it through the pharynx. This energy is generated by pressure gradients created within the pharynx by the tongue's driving force, the hypopharyngeal suction pump, and the 'stripping action' of the pharyngeal constrictors (Nishino et al 1985).

The tongue driving force (tongue thrust pressure force) is a positive pressure that squeezes the bolus towards the laryngopharynx. It is generated by the upward movement of the tongue pressing the bolus against the contracting pharyngeal wall and requires a tight nasopharyngeal seal (created by elevation of the soft palate). There is a view that the tongue driving force is the most important factor responsible for moving the bolus down the pharynx. The hypopharyngeal suction pump is caused by the elevation and anterior movement of the hyoid and larynx. This creates a negative pressure in the laryngopharynx, drawing the bolus towards the oesophagus, aided by a more negative pressure inside the oesophagus. The pharyngeal constrictors generate a positive pressure wave behind the bolus. Their sequential contraction may facilitate clearance ('stripping') of the pharyngeal walls and piriform sinuses. Residues that remain in the valleculae reflect inadequate tongue force generation at the end of the oral phase of swallowing.

At the end of this phase, the bolus is propelled towards the upper oesophageal sphincter. At rest, this sphincter is closed by active contraction. Cricopharyngeus relaxes prior to the bolus arriving and the sphincter is then opened actively by the combined action of the suprahyoid muscles in moving the larynx anteriorly and superiorly, and passively by pressure from the arriving bolus. The upper oesophageal sphincter thus differs in its action from that of other sphincters where opening is generally passive and a consequence of pressures generated by the movements towards them of fluids or solids.

Gag reflex

Traditionally, the stimulus for triggering a swallow has been regarded as contact with the posterior wall of the pharynx, since this is usually where the gag reflex is triggered (see page 450.e1). However, many regions of the oropharynx, when appropriately stimulated by the presence of food or liquid, are capable of triggering a swallow, although some regions are more sensitive than others, e.g. the area over the palatoglossal arches. Moreover, there appears to be little relationship between a functioning gag reflex and the ability to swallow normally because individuals with a reduced or absent gag reflex can swallow safely. Conversely, the presence of a brisk and clear gag reflex is not always associated with the ability to swallow safely.

Oesophageal phase

The third, or oesophageal, stage begins after the relaxation of the upper oesophageal sphincter has allowed the bolus to enter the oesophagus. This is a true peristaltic movement, in that a muscular relaxation in front of the bolus and subsequent constriction behind the bolus move it towards the stomach. Sequential waves of contractions of the oesophageal musculature now propel the bolus down to the lower oesophageal sphincter, which opens momentarily to admit the bolus to the stomach. The oesophageal phase of swallowing is much more variable than the other phases and lasts between 8 and 20 seconds.

Swallowing pattern generator

The patterning and timing of striated muscle contraction during swallowing are generated at a brainstem level in a network of neural circuits that collectively form a central swallowing pattern generator. Experimental neurophysiological and tracer studies in animals have shown that the swallowing pattern generator includes several brainstem motor nuclei and two groups of interneurones in the dorsal and ventral medulla: a dorsal swallowing group and a ventral swallowing group. The dorsal swallowing group is located in the nucleus of the solitary tract and possibly in the adjacent reticular formation, and contains neurones that generate the swallowing pattern, probably triggered by convergent information from both cortical and peripheral inputs. The afferent feedback from the branches of the superior laryngeal nerve that innervate the valleculae, epiglottis and supraglottic part of the larynx, and which relay through the nucleus of the solitary tract, facilitates laryngeal closure during swallowing (Jafari et al 2003). The ventral swallowing group is in the ventrolateral medulla above the nucleus ambiguus and contains neurones that act as 'switches', distributing the swallowing drive to motoneurone pools in the trigeminal, facial and hypoglossal nuclei and in the nucleus ambiguus.

The patterns of activation in the smooth muscle of the lower part of the oesophagus are generated locally in intramural plexuses driven by vagal autonomics.

Supramedullary influence on swallowing

Techniques including transcranial magnetic stimulation, cortical evoked potentials, positron emission tomography and functional magnetic resonance imaging (fMRI) have all been exploited in the study of volitional swallowing in humans (Thexton 1998, Thexton and Crompton 1998, Harris et al 2005). Thus far, these studies have shown that numerous cortical and subcortical regions (primary motor and sensory cortices, operculum, supplementary motor area and cingulate cortex, insula, parietal cortical areas, basal regions and cerebellum) are recruited in swallowing, although, as yet, the functional contributions made by each region have not been established, and it is not known how they influence the swallowing pattern generator. The most consistent cortical activation occurs in the primary motor and somatosensory cortices. Perhaps not surprisingly, the greatest area of fMRI activation in the primary motor cortex occurs over the portion of the precentral gyrus where the face, tongue and pharynx are represented; there is evidence for functional asymmetry between the right and left oral sensorimotor cortices (Martin et al 2004). The activity of the swallowing pattern generator is coordinated with other medullary reflexes, e.g. it is difficult to elicit a swallow when the cortical masticatory centres are stimulated. (For further reading on the motor control of oropharyngeal swallowing, see Humbert and German (2013), and on the role of sensory feedback from the oropharynx in swallowing, see Michou and Hamdy (2009).)

Swallowing in the neonate

In the adult, the tip of the epiglottis is significantly lower than the inferior edge of the soft palate. In the neonate, the larynx is high in the neck and the epiglottis may extend above the soft palate so that the laryngeal airway is in direct continuity with the posterior nares (**Figs 40.11–40.12**); a potential space is therefore formed between the soft palate above, the epiglottis behind and the tongue anteroinferiorly. In other mammals with an oropharyngeal anatomy similar to that of the human infant, up to 14 cycles of tongue movement or oral phases cause the accumulation of food in this space. Subsequent emptying of the space is a single event followed by movement of the bolus down the oesophagus. The ratio of accumulation cycles to swallow events in the human neonate is approximately 1.5 : 1, which is lower than in other mammals but still implies some temporary accumulation. In the case of a liquid bolus, accumulated material may be passed laterally to the epiglottis through the piriform fossae rather than over the flexed epiglottis, although it is not known whether this happens in the human infant. (For further reading, see Delaney and Arvedson (2008).)

Swallow safety is critical at all ages. In the neonate, where coordination of suckling, swallowing and breathing is not fully developed, the potential risk of airway obstruction and/or aspiration of ingested milk or other material during swallowing is reduced because the intranarial larynx prevents the bolus from entering the larynx before and after a swallow. (Neonates born at term demonstrate an increase in suck and swallow rates over the course of the first 4weeks; efficiency of feeding, measured as volume of nutrient per suck and per swallow, doubles over the course of the neonatal period (Qureshi et al 2002).)

The change towards adult anatomy and coordination of the phases of swallowing starts a few months after birth (Kelly et al 2007). Differential growth in length of the human pharynx causes the larynx to take up its low adult position and the epiglottis to lose contact with the soft palate; the larynx reaches its final position around the time of puberty. The adult anatomy does not allow any significant accumulation of food immediately anterior to the epiglottis, which means that the transport of food through the fauces has to bear a 1 : 1 relationship to pharyngeal and oesophageal transit. Moreover, the lowered larynx compromises the previously protected airway; the hyoid and larynx are therefore raised and pulled forwards during a swallow in order to minimize the risk of deglutitive aspiration.

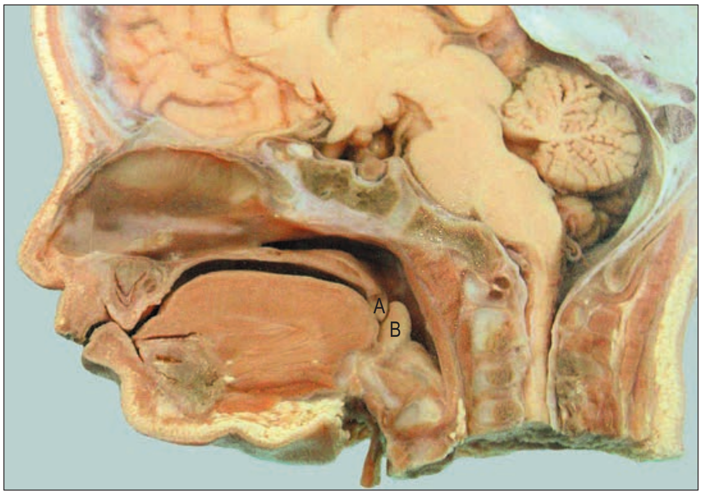

Fig. 40.11 A sagittal section of the head of a neonate. Note the relatively high position of the larynx, the opening being at the level of the soft palate (A). Other abbreviations: B, epiglottis. (With permission from Berkovitz BKB, Holland GR, Moxham BJ 2002 Oral Anatomy, Embryology and Histology, 3rd edn. Edinburgh: Mosby.)

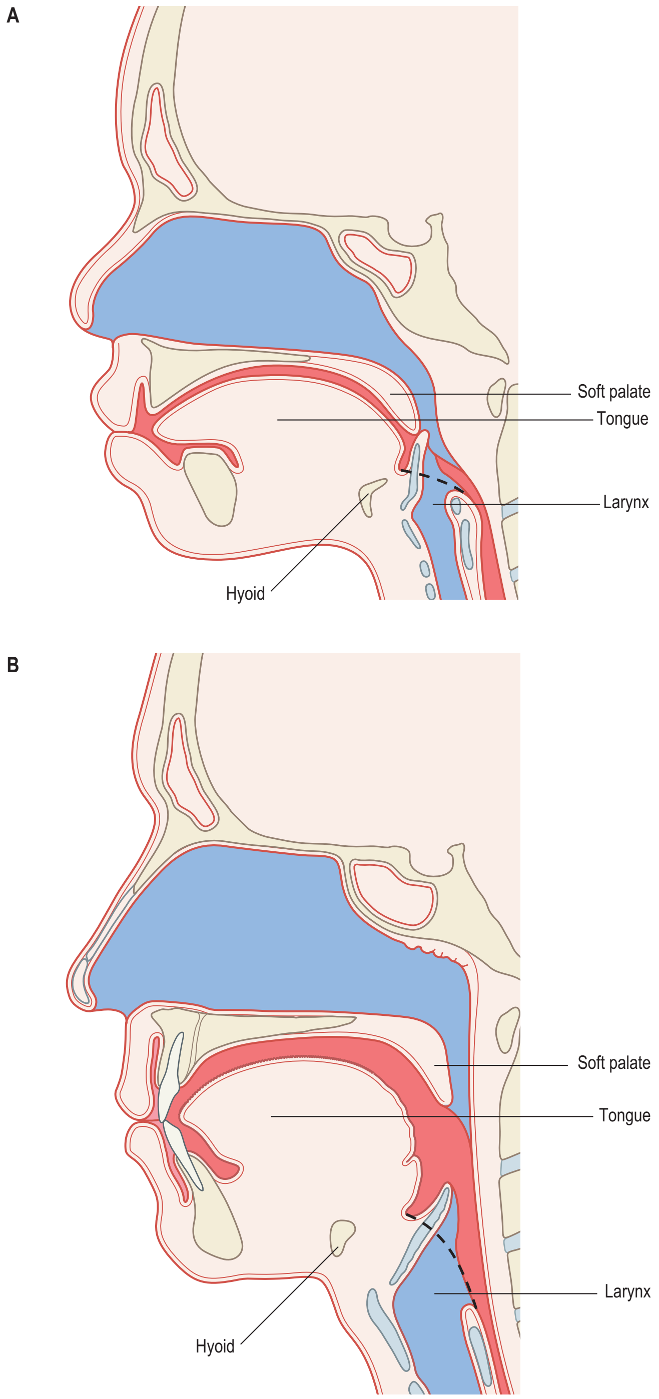

Fig. 40.12 A sagittal section of the head and neck in an infant (**A**) and adult (**B**) human. The food way and the airway are shaded in red and blue, respectively. **A**, In the infant human, the oral cavity is small and the tongue and palate are flatter. **B**, In the adult human, the larynx is lower in the neck, and the food way and airway cross in the pharynx. (Adapted with permission from Matsuo K, Palmer JB 2008 Anatomy and physiology of feeding and swallowing – normal and abnormal. Phys Med Rehabil Clin North Am 19:691–707.)

Dysphagia

Dysphagia is a symptom of many diseases and can arise from anatomical or functional deficits anywhere along the path from the oral cavity to the stomach or from a failure of neural control resulting from congenital malformations, trauma, stroke or neurodegenerative diseases within the central nervous system. Loss of muscle strength affecting tongue propulsion or pharyngeal contraction will impair the initiation of the swallow and/or bolus transport. This will result in retention of residues within the pharynx following a swallow. Residues may also accumulate in the valleculae and piriform sinuses. Failure to protect the airways adequately may result in the penetration of swallowed material food or liquid into the vestibule of the larynx. Aspiration will result if the material then passes through the vocal folds, which may result in airway obstruction or aspiration pneumonia. Penetration may sometimes occur in normal individuals.

Pharyngostomy

Loss of control of the pharyngeal phase of swallowing, e.g. due to neurological disease or ablative head and neck surgery, may result in aspiration of food, especially fluids, leading to pneumonia. This problem may be addressed surgically by pharyngostomy: more recently, percutaneous gastrostomy is favoured and more comfortable for the patient.

In cervical pharyngostomy, a tube may be passed through the cervical skin, fascia and platysma directly into the piriform fossa (Patil et al 2006). This is achieved by passing a curved forcep into the piriform fossa and pushing it laterally, displacing the contents of the carotid sheath and tenting up the platysma and cervical skin from the inside. By cutting down onto the forcep, it is possible to grasp the feeding tube and pull it into the piriform fossa prior to feeding it on into the oesophagus. The tract formed by such a puncture epithelializes and may be used for long-term alimentation.

Bonus e-book content

Fig. 40.2 B, Sagittal T2-weighted magnetic resonance image (MRI) through the neck that includes the posterior cranial fossa, cerebellum and cervical spinal cord.

Fig. 40.5 Thornwaldt's cyst.

Fig. 40.11 A sagittal section of the head of a neonate.

Key references

Flint PW, Haughey BH, Lund VJ et al 2010 Cummings Otolaryngology: Head and Neck Surgery, vols 2 and 3, 5th ed. Philadelphia: Elsevier, Mosby.
Two volumes that contain comprehensive descriptions of the anatomy, physiology and pathology of the pharynx and palate.

Graney DO, Retruzzelli GJ, Myers EW 1998 Anatomy. In: Cummings CW, Fredrickson JM, Harker LA et al (eds) Otolaryngology: Head and Neck Surgery, vol 2, 3rd ed. St Louis: Elsevier, Mosby; pp. 1327–48.
A concise account of the anatomy of the pharynx, highlighting features of clinical relevance.

Hollinshead WH 1982 Anatomy for Surgeons, vol I: The Head and Neck, 3rd ed. Philadelphia: Harper & Row.
An older textbook that provides a valuable account of the anatomy of the pharynx and of tissue spaces in the neck. It is also a thorough guide to the earlier literature.

Matsuo K, Palmer JB 2008 Anatomy and physiology of feeding and swallowing – normal and abnormal. Phys Med Rehabil Clin North Am 19:691–707.
A review of swallowing focusing on the process model of feeding.

O'Reilly RC, Sando I 2010 Anatomy and physiology of the Eustachian tube. In: Flint PW, Haughey BH, Lund VJ et al (eds) Cummings Otolaryngology: Head and Neck Surgery, 5th ed. St Louis: Elsevier, Mosby; Ch. 131, pp. 1866–75.
A review of the clinical anatomy and physiology of the pharyngotympanic tube.

References

Arens R, McDonough JM, Corbin AM et al 2002 Linear dimensions of the upper airway structure during development: assessment by magnetic resonance imaging. Am J Respir Crit Care Med 165:117–22.

Baskin RM, Boyce BJ, Amdur R et al 2018 Transoral robotic surgery for oropharyngeal cancer: patient selection and special considerations. Cancer Manag Res 10:839–46.

Bluestone CD 1998 Anatomy and physiology of the Eustachian tube. In: Cummings CW, Fredrickson JM, Harker LA et al (eds) Otolaryngology: Head and Neck Surgery, vol 4, 3rd ed. St Louis: Elsevier, Mosby; pp. 3003–25.

Bonnington A, Mahon M, Whitmore I 1988 A histological study of the cricopharyngeus muscle in man. J Anat 156:27–37.

Brownlow H, Whitmore I, Willan PLT 1989 A quantitative study of the histochemical and morphometric characteristics of the human cricopharyngeus muscle. J Anat 166:67–75.

Cho JH, Kim JK, Lee H-Y et al 2013 Surgical anatomy of the soft palate. Laryngoscope 123:2900–4.

Chong VFH, Ong CK 2008 Nasopharyngeal carcinoma. Eur J Radiol 66:437–47.

Dallan I, Seccia V, Muscatello L et al 2011 Transoral endoscopic anatomy of the parapharyngeal space: a step-by-step logical approach with surgical considerations. Head Neck 33:557–61.

Delaney AL, Arvedson JC 2008 Development of swallowing and feeding: prenatal through first year of life. Dev Disabil Res Rev 14:105–17.

Flint PW, Haughey BH, Lund VJ et al 2010 Cummings Otolaryngology: Head and Neck Surgery, vols 2 and 3, 5th ed. Philadelphia: Elsevier, Mosby.

Two volumes that contain comprehensive descriptions of the anatomy, physiology and pathology of the pharynx and palate.

Fogel RB, Malhotra A, White DP 2004 Sleep 2: Pathophysiology of obstructive sleep apnoea/hypnoea syndrome. Thorax 59:159–63.

Freelander E 1992 Blood supply of the human levator and tensor veli palatini muscles. Clin Anat 5:34–44.

Graney DO, Retruzzelli GJ, Myers EW 1998 Anatomy. In: Cummings CW, Fredrickson JM, Harker LA et al (eds) Otolaryngology: Head and Neck Surgery, vol 2, 3rd ed. St Louis: Elsevier, Mosby; pp. 1327–48.

A concise account of the anatomy of the pharynx, highlighting features of clinical relevance.

Gray SD, Pinborough-Zimmerman J 1998 Velopharyngeal incompetence. In: Cummings CW et al (eds) Otolaryngology: Head and Neck Surgery, vol 5: Pediatric Otolaryngology, 3rd ed. St Louis: Elsevier, Mosby; pp. 174–87.

Gun R, Durmus K, Kucur C et al 2016 Transoral surgical anatomy and clinical considerations of lateral oropharyngeal wall, parapharyngeal space, and tongue base. Otolaryngol Head Neck Surg 154:480–5.

Gun R, Ozer E 2015 Surgical anatomy of oropharynx and supraglottic larynx for transoral robotic surgery: Transoral Surgical Anatomy for TORS. J Surg Oncol 112:690–6.

Gupta A, Chazen JL, Phillips CD 2012 Imaging evaluation of the parapharyngeal space. Otolaryngol Clin North Am 45:1223–32.

Harris ML, Julyan P, Kulkarni B et al 2005 Mapping metabolic brain activation during human volitional swallowing: a positron emission tomography study using [18F]fluorodeoxyglucose. J Cereb Blood Flow Metab 25:520–6.

Hiiemae KM, Palmer JB 1999 Food transport and bolus formation during complete feeding sequences on foods of different initial consistency. Dysphagia 14:31–42.

Hiiemae KM, Palmer JB 2003 Tongue movements in feeding and speech. Crit Rev Oral Biol Med 14:413–29.

Hollinshead WH 1982 Anatomy for Surgeons, vol I: The Head and Neck, 3rd ed. Philadelphia: Harper & Row.

An older textbook that provides a valuable account of the anatomy of the pharynx and of tissue spaces in the neck. It is also a thorough guide to the earlier literature.

Humbert IA, German RZ 2013 New directions for understanding neural control in swallowing: the potential and promise of motor learning. Dysphagia 28:1–10.

Hyare H, Wisco JJ, Alusi G et al 2010 The anatomy of nasopharyngeal carcinoma spread through the pharyngobasilar fascia to the trigeminal mandibular nerve on 1.5 T MRI. Surg Radiol Anat 32:937–44.

Ison S, Remmers JE, Tanaka A et al 1997 Anatomy of pharynx in patients with obstructive sleep apnea and in normal subjects. J Appl Physiol 84:1319–26.

Jafari S, Prince RA, Kim DY et al 2003 Sensory regulation of swallowing and airway protection: a role for the internal superior laryngeal nerve in humans. J Physiol 550:287–304.

Johal AMA, Patel SI, Battagel JM 2007 The relationship between craniofacial anatomy and obstructive sleep apnoea: a case-controlled study. J Sleep Res 16:319–26.

Kelly BN, Huckabee ML, Jones RD et al 2007 The first year of human life: coordinating respiration and nutritive swallowing. Dysphagia 22:37–43.

Kendall KA, Leonard RJ, McKenzie SW 2001 Accommodation to changes in bolus viscosity in normal deglutition: a videofluoroscopic study. Ann Otol Rhinol Laryngol 110:1059–65.

Lang IM, Shaker R 2000 An overview of the upper esophageal sphincter. Curr Gastroenterol Rep 2:185–90.

Lim CM, Mehta V, Chai R et al 2013 Transoral anatomy of the tonsillar fossa and lateral pharyngeal wall: Anatomic dissection with radiographic and clinical correlation: Tonsillar Fossa Anatomy. Laryngoscope 123:3021–25.

Malhotra A, White DP 2002 Obstructive sleep apnoea. Lancet 360:237–45.

Maran AGD, Mackenzie IJ, Murray JAM 1984 The parapharyngeal space. J Laryngol Otol 98:371–89.

Martin RE, MacIntosh BJ, Smith RC et al 2004 Cerebral areas processing swallowing and tongue movement are overlapping but distinct: a functional magnetic resonance imaging study. J Neurophysiol 92:2428–43.

Matsuo K, Palmer JB 2008 Anatomy and physiology of feeding and swallowing – normal and abnormal. Phys Med Rehabil Clin North Am 19:691–707.

A review of swallowing focusing on the process model of feeding.

Michou E, Hamdy S 2009 Cortical input in control of swallowing. Curr Opin Otolaryngol Head Neck Surg 17:166–71.

Mioche L, Hiiemae KM, Palmer JB 2002 A postero-anterior videofluorographic study of the intra-oral management of food in man. Arch Oral Biol 47:267–80.

Moore EJ, Janus J, Kasperbauer J 2012 Transoral robotic surgery of the oropharynx: clinical and anatomic considerations. Clin Anat 25:135–41.

Mydlarz WK, Agrawal N 2014 Transparotid and transcervical approaches for removal of deep lobe parotid gland and parapharyngeal space tumors. Oper Techn Otolaryngol Head Neck Surg, 25:234–9.

Nishino T, Yonezawa T, Honda Y 1985 Coordination of swallowing and respiration in unconscious subjects. J Appl Physiol 70:988–93.

Ohtsuka K, Tomita H, Murakami G 2002 Anatomy of the tonsillar bed: topographical relationship between the palatine tonsil and the lingual branch of the glossopharyngeal nerve. Acta Oto-Laryngologica 122:99–109.

O'Reilly RC, Sando I 2010 Anatomy and physiology of the Eustachian tube. In: Flint PW, Haughey BH, Lund VJ et al (eds) Cummings Otolaryngology: Head and Neck Surgery, 5th ed. St Louis: Elsevier, Mosby; Ch. 131, pp. 1866–75.

A review of the clinical anatomy and physiology of the pharyngotympanic tube.

Orita Y, Sando I, Hirsch BE et al 2002 Postnatal development of the eustachian tube glands. Laryngoscope 112:1647–52.

Paderno A, Piazza C, Nicolai P 2015 Recent advances in surgical management of parapharyngeal space tumors: Curr Opin Otolaryngol Head Neck Surg 23:83–90.

Palmer JB, Hiiemae KM, Matsuo K et al 2007 Volitional control of food transport and bolus formation during feeding. Physiol Behav 91:66–70.

Papaioannou G, Kambas I, Tsaoussoglou M et al 2013 Age-dependent changes in the size of adenotonsillar tissue in childhood: implications for sleep-disordered breathing. J Pediatr 162:269–74.

Patil PM, Warad NM, Patil RN et al 2006 Cervical pharyngostomy: an alternative approach to enteral feeding. Oral Surg Oral Med Oral Pathol Oral Radiol Endod 102:736–40.

Prades JM, Gavid M, Asanau A et al 2014 Surgical anatomy of the styloid muscles and the extracranial glossopharyngeal nerve. Surg Radiol Anat 36:141–6.

Qureshi MA, Vice FL, Taciak VL et al 2002 Changes in rhythmic suckle feeding patterns in term infants in the first month of life. Dev Med Child Neurol 44:34–9.

Raol N, Hartnick CJ 2015 Anatomy and physiology of velopharyngeal closure and insufficiency. In: Surgery for Pediatric Velopharyngeal Insufficiency, vol. 76. Basel: Karger: pp. 1–6.

Sade J (ed) 1989 Basic Aspects of the Eustachian Tube and Middle Ear Disease. Geneva: Kugler & Ghedini.

Sakamoto Y 2013 Interrelationships between the innervations from the laryngeal nerves and the pharyngeal plexus to the inferior pharyngeal constrictor. Surg Radiol Anat 35:721–8.

Sakamoto Y 2014 Gross anatomical observations of attachments of the middle pharyngeal constrictor. Clin Anat 27:603–9.

Sato K, Nakashima T 2006 Human adult deglutition during sleep. Ann Otol Rhinol Laryngol 115:334–9.

Sato K, Nakashima T 2007 Sleep-related deglutition in children. Ann Otol Rhinol Laryngol 116:747–53.

Scali F, Nash LG, Pontell ME 2015 Defining the morphology and distribution of the alar fascia: a sheet plastination investigation. Ann Otol Rhinol Laryngol 124(10): 814–19.

Sheahan P 2014 Transcervical approach for removal of benign parapharyngeal space tumors. Oper Techn Otolaryngol Head Neck Surg 25(3):227–33.

Shin JH, Lee HK, Kim SY et al 2001 Imaging of parapharyngeal space lesions: focus on the prestyloid compartment. Am J Roentgenol 177(6):1465–70.

Steele CM, Miller AJ 2010 Sensory input pathways and mechanisms in swallowing: a review. Dysphagia 25:323–33.

Thexton A 1998 Some aspects of swallowing. In: Harris M, Edgar M, Meghji S (eds) Clinical Oral Science. Oxford: Wright; pp. 150–66.

Thexton AJ, Crompton AW 1998 The control of swallowing. In: Linden RWA (ed) The Scientific Basis of Eating. Taste and Smell, Salivation, Mastication and Swallowing and their Dysfunctions. Frontiers of Oral Biology Series, vol 9. Basel: Karger; pp. 168–222.

Wang C, Kundaria S, Fernandez-Miranda J et al 2014 A description of arterial variants in the transoral approach to the parapharyngeal space. Clin Anat 27:1016–22.

Warshafsky D, Goldenberg D, Kanekar SG 2012 Imaging anatomy of deep neck spaces. Otolaryngol Clin North Am 45(6):1203–21.

Wood-Jones I 1940 The nature of the soft palate. J Anat 77:147–70.

Yarlagadda BB, Grillone GA 2015 Anatomic considerations in transoral robotic surgery. In: Grillone GA, Jalisi S (eds), Robotic Surgery of the Head and Neck. New York: Springer; pp. 13–27.

Yuca K, Varsak YK 2012 Thornwaldt's cyst. Eur J Gen Med 9:(Suppl 1)26–9.

CHAPTER 41

Larynx

The larynx is an air passage, a sphincter and an organ of phonation, and extends from the tongue to the trachea. It projects ventrally between the great vessels of the neck and is covered anteriorly by skin, fasciae and the infrahyoid strap muscles that lower the hyoid bone and the larynx. Above, it opens into the laryngopharynx and forms its anterior wall; below, it continues into the trachea (see Fig. 40.2). It is mobile on deglutition. At rest, the larynx lies opposite the third to sixth cervical vertebrae in adult males; it is somewhat higher in children and adult females. In infants between 6 and 12 months, the tip of the epiglottis (the highest part of the larynx) lies a little above the junction of the dens and body of the axis vertebra (Mijallili et al 2012). Until puberty, male and female larynges are similar in size. After puberty, the male larynx enlarges considerably in comparison with that of the female; all the cartilages increase in both size and weight, the thyroid cartilage projects in the anterior midline of the neck, and its sagittal diameter nearly doubles. The male thyroid cartilage continues to increase in size until 40 years of age, after which no further growth occurs.

For further reading, including an introduction to the more important historical literature, see Berkovitz et al (2000), Blitzer et al (2009), Dickson and Maue-Dickson (1982), Kaplan (1971), Hollinshead (1982), Tucker (1993).

SKELETON OF THE LARYNX

The skeletal framework of the larynx is formed by a series of cartilages interconnected by ligaments and fibrous membranes and moved by a number of muscles (**Figs 41.1–41.3**). The hyoid bone is attached to the larynx; it is usually regarded as a separate structure with distinctive functional roles and is described in the chapter on the neck (Ch. 35). The laryngeal cartilages are the midline, single thyroid, cricoid and epiglottic cartilages, and the paired arytenoid, cuneiform, corniculate and tritiate cartilages.

The thyroid, cricoid and the greater part of the arytenoid cartilages consist of hyaline cartilage and may undergo mottled calcification as age advances, starting about the twenty-fifth year in the thyroid cartilage and somewhat later in the cricoid and arytenoids. By the sixty-fifth year, these cartilages commonly appear patchily dense in radiographs. The corniculate, cuneiform, tritiate and epiglottic cartilages and the apices of the arytenoid are composed of elastic fibrocartilage, with little tendency to calcify (Munir Turk 1993).

The surface anatomy of the laryngeal cartilages is described on pages 554 and 555.

Epiglottis

The epiglottis is a thin, leaf-like plate of elastic cartilage that projects obliquely upwards behind the tongue and hyoid body, and in front of the laryngeal inlet (see Figs 41.2–41.3, 41.5). Its free end, which is broad and round, and occasionally notched in the midline, is directed upwards. Its attached part, or stalk (petiole, petiolus), is long and narrow and is connected by the elastic thyroepiglottic ligament to the back of the laryngeal prominence of the thyroid cartilage just below the thyroid notch. Its sides are attached to the arytenoid cartilages by aryepiglottic folds (which contain the aryepiglottic muscle) (see Fig. 41.6). Its free upper anterior, or lingual, surface is covered by mucosa (the epithelium is non-keratinized stratified squamous), which is reflected on to the pharyngeal aspect of the tongue and the lateral pharyngeal walls as a median glossoepiglottic, and two lateral glossoepiglottic, folds. This arrangement produces a depression, the vallecula, on each side between the median and lateral folds (see Fig. 41.5B). The lower part of its anterior surface, behind the hyoid bone and thyrohyoid membrane, is connected to the upper border of the hyoid by an elastic hyoepiglottic ligament, and separated from the thyrohyoid membrane by adipose tissue, which constitutes the clinically important pre-epiglottic space (see Fig. 41.5). The smooth posterior, or laryngeal, surface is transversely concave and vertically concavo-convex, and is covered by ciliated respiratory mucosa; its lower projecting part is called the tubercle. This surface forms the oblique anterior wall of the laryngeal vestibule. The cartilage is posteriorly pitted by small mucous glands (**Fig. 41.3D**) and is perforated

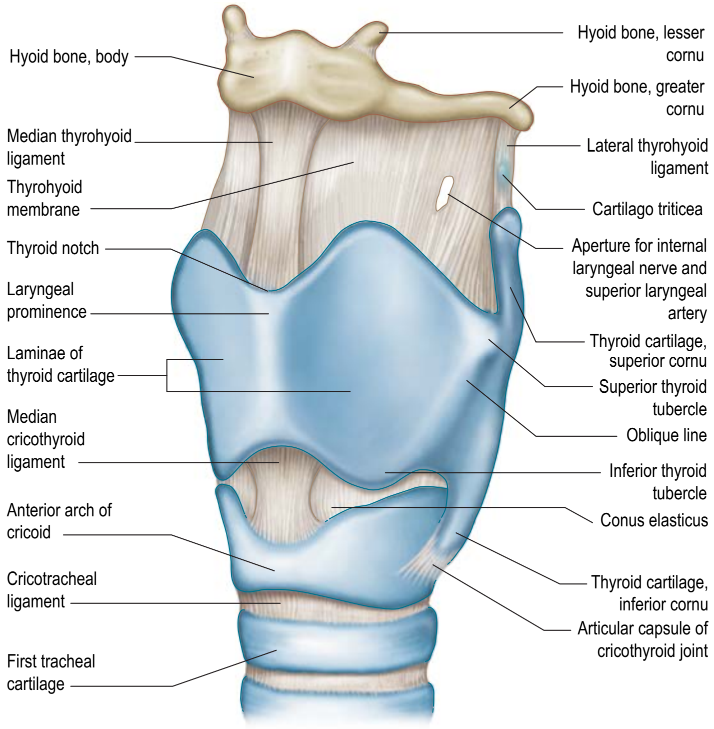
Hyoid bone, body
Median thyrohyoid ligament
Thyrohyoid membrane
Thyroid notch
Laryngeal prominence
Laminae of thyroid cartilage
Median cricothyroid ligament
Anterior arch of cricoid
Cricotracheal ligament
First tracheal cartilage
Hyoid bone, lesser cornu
Hyoid bone, greater cornu
Lateral thyrohyoid ligament
Cartilago triticea
Aperture for internal laryngeal nerve and superior laryngeal artery
Thyroid cartilage, superior cornu
Superior thyroid tubercle
Oblique line
Inferior thyroid tubercle
Conus elasticus
Thyroid cartilage, inferior cornu
Articular capsule of cricothyroid joint

Fig. 41.1 Anterolateral view of the laryngeal cartilages and ligaments.

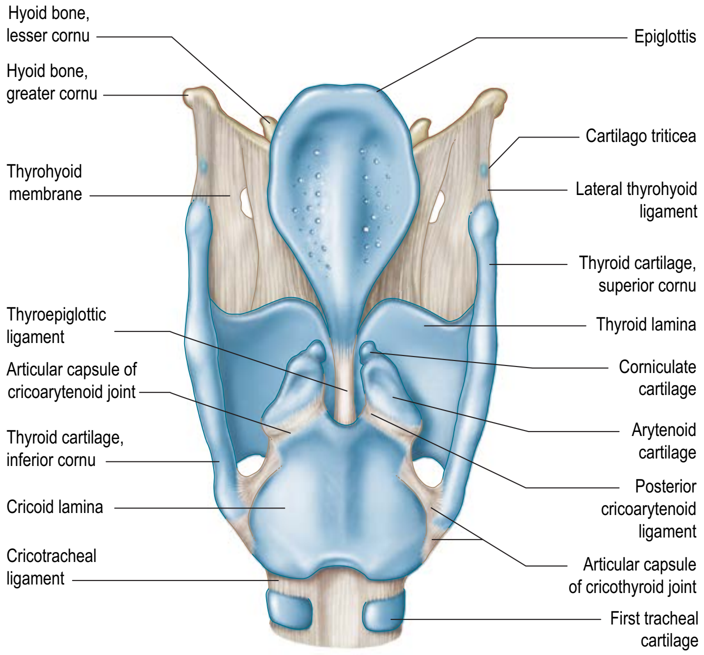
Hyoid bone, lesser cornu
Hyoid bone, greater cornu
Thyrohyoid membrane
Thyroepiglottic ligament
Articular capsule of cricoarytenoid joint
Thyroid cartilage, inferior cornu
Cricoid lamina
Cricotracheal ligament
Epiglottis
Cartilago triticea
Lateral thyrohyoid ligament
Thyroid cartilage, superior cornu
Thyroid lamina
Corniculate cartilage
Arytenoid cartilage
Posterior cricoarytenoid ligament
Articular capsule of cricothyroid joint
First tracheal cartilage

Fig. 41.2 Posterior view of the laryngeal cartilages and ligaments.v

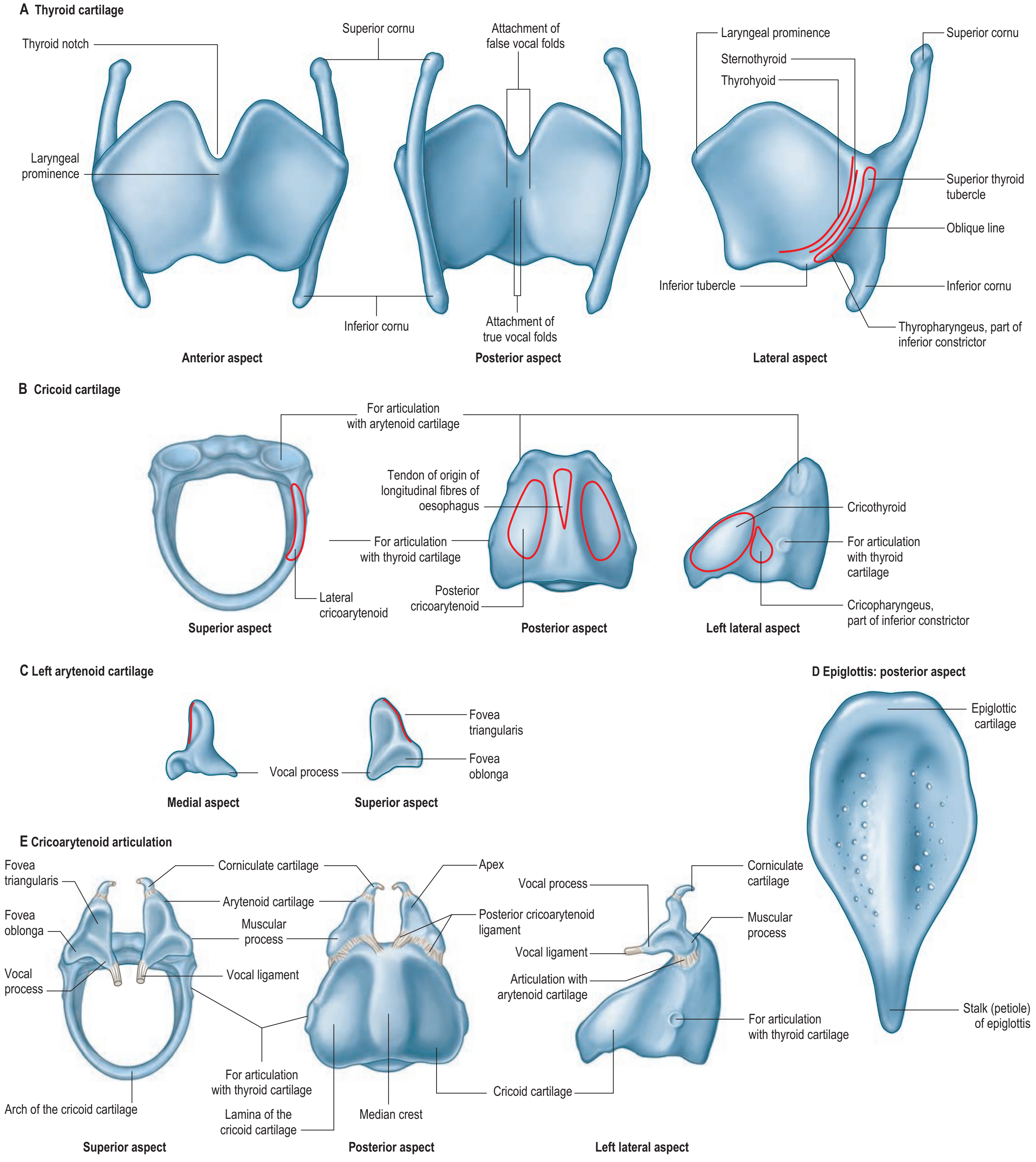
A Thyroid cartilage
Thyroid notch
Superior cornu
Attachment of false vocal folds
Laryngeal prominence
Superior cornu
Sternothyroid
Thyrohyoid
Laryngeal prominence
Superior thyroid tubercle
Oblique line
Inferior tubercle
Inferior cornu
Inferior cornu
Attachment of true vocal folds
Thyropharyngeus, part of inferior constrictor
Anterior aspect
Posterior aspect
Lateral aspect
B Cricoid cartilage
For articulation with arytenoid cartilage
Tendon of origin of longitudinal fibres of oesophagus
Cricothyroid
For articulation with thyroid cartilage
For articulation with thyroid cartilage
Lateral cricoarytenoid
Posterior cricoarytenoid
Cricopharyngeus, part of inferior constrictor
Superior aspect
Posterior aspect
Left lateral aspect
C Left arytenoid cartilage
D Epiglottis: posterior aspect
Fovea triangularis
Vocal process
Fovea oblonga
Medial aspect
Superior aspect
Epiglottic cartilage
E Cricoarytenoid articulation
Fovea triangularis
Corniculate cartilage
Apex
Corniculate cartilage
Vocal process
Fovea oblonga
Arytenoid cartilage
Muscular process
Posterior cricoarytenoid ligament
Muscular process
Vocal ligament
Vocal process
Vocal ligament
Articulation with arytenoid cartilage
For articulation with thyroid cartilage
For articulation with thyroid cartilage
Stalk (petiole) of epiglottis
Cricoid cartilage
Arch of the cricoid cartilage
Lamina of the cricoid cartilage
Median crest
Superior aspect
Posterior aspect
Left lateral aspect

Fig. 41.3 Cartilages of the larynx: thyroid (**A**), cricoid (**B**), arytenoid (**C**), epiglottis (**D**), cricoarytenoid joint (**E**). The attachments of the false vocal folds (vestibular ligaments; above) and the true vocal folds (vocal ligaments; below) are shown in **A**, posterior aspect. Note the pitted surface of the epiglottis (**D**).

by branches of the internal laryngeal nerve and fibrous tissue, which means that the posterior surface of the epiglottis is in continuity through these perforations with the pre-epiglottic space.

Functions of the epiglottis

During swallowing, the hyoid bone moves upwards and forwards, and the epiglottis is bent posteriorly as a result of passive pressure from the base of the tongue and active contraction of the aryepiglottic muscles. Normally, the epiglottis diverts food and liquids away from the laryngeal inlet and into the lateral food channels. It is not essential for respiration or phonation.

Whether downward movement of the epiglottis is a passive process, produced by a combination of the weight of food or liquid on its lingual surface and forces originating elsewhere in the hyoid and larynx, or whether it is an active process brought about by active muscular control, remains the subject of debate. Neither scheme seems to explain epiglottic movement satisfactorily. It is likely that a combination of processes is taking place, in which passive forces originating in the tongue, hyoid and larynx are transmitted to the epiglottis by the hyoepiglottic ligaments while the base of the epiglottis is actively moved by thyroarytenoid and muscles of the laryngeal inlet (Logemann et al 1992, Vandaele et al 1994). Safe swallowing is still possible without an epiglottis, as after a supraglottic laryngectomy, but great care and training is necessary.

Thyroid cartilage

The thyroid cartilage is the largest of the laryngeal cartilages (see Figs 41.1–41.3). It consists of two quadrilateral laminae with anterior borders that fuse along their inferior two-thirds at a median angle to form the subcutaneous laryngeal prominence ('Adam's apple'). This projection is most distinct at its upper end and is well marked in men but less visible in women. Above, the laminae are separated by a V-shaped superior thyroid notch or incisure. Posteriorly, the laminae diverge, and their posterior borders are prolonged as slender horns: the superior and inferior cornua. A shallow ridge, the oblique line, curves downwards and forwards on the external surface of each lamina; it runs from the superior thyroid tubercle, lying a little anterior to the root of the superior cornu, to the inferior thyroid tubercle on the inferior border of the lamina. Often, the oblique line is barely visible or is just a faint line and only the tubercles are prominent. Sternothyroid, thyrohyoid and thyropharyngeus (part of the inferior pharyngeal constrictor) are attached to the oblique line, usually as little more than a tendon (**Fig. 41.3A**).

The internal surface of the lamina is smooth. Above and behind, it is slightly concave and covered by mucosa. The thyroepiglottic ligament, the paired vestibular and vocal ligaments, the thyroarytenoid, thyroepiglottic and vocalis muscles, and the stalk of the epiglottis are all attached to the inner surface of the cartilage, in the angle between the laminae. The true vocal folds lie 6–9 mm below the median thyroid notch. The superior border of each lamina is concave posteriorly and convex anteriorly, dropping sharply to form the thyroid notch; the thyrohyoid membrane is attached along the superior border (see Figs 41.1–41.2). The inferior border of each lamina is concave posteriorly and nearly straight anteriorly; the two parts are separated by the inferior thyroid tubercle. Anteriorly, the thyroid cartilage is connected to the cricoid cartilage by the median (anterior) cricothyroid ligament, which is the thickened medial portion of the conus elasticus.

The anterior border of each thyroid lamina fuses with its partner at an angle of approximately 90° in men and approximately 120° in women. The shallower angle in men is associated with the larger laryngeal prominence, the greater length of the vocal folds, and the resultant deeper pitch of the voice. The posterior border is thick and rounded and receives fibres of stylopharyngeus and palatopharyngeus. The superior cornu, which is long and narrow, curves upwards, backwards and medially, and ends in a conical apex to which the lateral thyrohyoid ligament is attached. The inferior cornu is short and thick, and curves down and slightly anteromedially. On the anteromedial surface of its lower end there is a small oval facet for articulation with the side of the cricoid cartilage; this facet is variable and is only sometimes well defined.

Cricoid cartilage

The cricoid cartilage is attached below to the trachea and articulates with the thyroid cartilage and the two arytenoid cartilages by synovial joints. It forms a complete ring around the airway, the only laryngeal cartilage to do so (**Fig. 41.3B**). It is smaller, but thicker and stronger, than the thyroid cartilage, and has a narrow curved anterior arch and a broad, flatter posterior lamina.

Cricoid arch

The cricoid arch is vertically narrow in front (5–7 mm in height) and widens posteriorly towards the lamina. Cricothyroid is attached to the external aspect of its front and sides, and cricopharyngeus (part of the inferior pharyngeal constrictor) is attached behind cricothyroid. The arch is palpable below the laryngeal prominence, from which it is separated by a depression containing the conus elasticus. The inferior border of the cartilage is nearly horizontal and is circular in outline, whereas the upper border is more elliptical.

Cricoid lamina

The cricoid lamina is approximately quadrilateral in outline, and 2–3 cm in vertical dimension. It bears a posterior median vertical ridge that creates posterior concavities on either side. The two bundles of the longitudinal layer of oesophageal muscle fibres (muscularis externa) are attached by a tendon to the upper part of the ridge. Posterior cricoarytenoid attaches to a shallow depression on either side of the ridge.

A discernible circular synovial facet, facing posterolaterally, sometimes marks the junction of the lamina and arch; it indicates the site where the cricoid articulates with the inferior thyroid cornu. The inferior border of the cricoid is horizontal and joined to the first tracheal cartilage by the cricotracheal ligament (see Fig. 41.1). The superior border runs obliquely up and back and gives attachment anteriorly to the thick median cricothyroid ligament, and laterally to the conus elasticus (see Fig. 41.1) and lateral cricoarytenoid. The posterosuperior aspect of the lamina presents a shallow median notch, on each side of which is a smooth, oval, convex facet, directed upwards and laterally, for articulation with the base of an arytenoid cartilage.

The internal surface of the cricoid cartilage is smooth and lined by mucosa.

Subglottic stenosis

Available with the *Gray's Anatomy* e-book

Arytenoid cartilage

The paired arytenoid cartilages articulate with the lateral parts of the superior border of the cricoid lamina (see Fig. 41.2; **Figs 41.3C,E**). Each is pyramidal and has three surfaces, two processes, a base and an apex. The posterior surface, which is triangular, smooth and concave, is covered by the transverse arytenoid muscle. The anterolateral surface is convex and rough. Near the apex of the cartilage there is an elevation from which a crest curves back, down and then forwards to the vocal process. The lower part of this arcuate crest separates two depressions (foveae). The upper is triangular (fovea triangularis), and the vestibular ligament is attached to it. The lower is oblong (fovea oblonga). Vocalis and thyroarytenoid are attached to it. The medial surface is narrow, smooth and flat, and is covered by mucosa; its lower edge forms the lateral boundary of the intercartilaginous part of the rima glottidis. The base is concave, with a smooth surface for articulation with the lateral part of the upper border of the cricoid lamina. Its round, prominent lateral angle, or muscular process, projects backwards and laterally; it gives attachment to posterior cricoarytenoid behind and lateral cricoarytenoid in front. The vocal ligament is attached to its pointed anterior angle (vocal process), which projects horizontally forwards. The apex curves backwards and medially to articulate with the corniculate cartilage.

Corniculate cartilages

The corniculate cartilages are two conical nodules of elastic cartilage that articulate with the apices of the arytenoid cartilages, elongating them posteromedially (see Figs 41.2, 41.3E). They lie in the posterior parts of the aryepiglottic mucosal folds and are sometimes fused with the arytenoid cartilages.

Cuneiform cartilages

The cuneiform cartilages are two small, elongated, club-like nodules of elastic cartilage, one in each aryepiglottic fold anterosuperior to the corniculate cartilages, and are visible as whitish elevations through the mucosa.

Tritiate cartilages (cartilago triticea)

The tritiate cartilages are two small nodules of elastic cartilage, situated one on either side above the larynx within the posterior free edge of the thyrohyoid membrane, about halfway between the superior cornu of the thyroid cartilage and the tip of the greater cornu of the hyoid bone (see Figs 41.1–41.2). Their functions are unknown, although they may serve to strengthen this connection.

Other inconstant or supernumerary cartilages can be present in the larynx. They are the small, paired sesamoid cartilages, found at the lateral edges of the arytenoid cartilages, and a single inter-arytenoid cartilage, enclosed by the cricopharyngeal ligament.

Calcification of laryngeal cartilages

The thyroid, cricoid and most of the arytenoid cartilages consist of hyaline cartilage and may therefore become calcified. This process normally starts at about 18 years of age. Initially, it involves the lower and posterior part of the thyroid cartilage, and subsequently spreads to involve the remaining cartilages, calcification of the arytenoid cartilage starting at its base. The degree and frequency of calcification of the thyroid and cricoid cartilages appear to be less in females.

Subglottic stenosis is usually acquired by damage to the cricoid ring by prolonged intubation in premature babies (Walner et al 2009). In contrast, congenital subglottic stenosis is uncommon. It is usually seen in children sporadically. Familial cases are rare but have been reported and born to consanguineous parents, suggesting a strong genetic link (Manickavasagam et al 2014). When congenital, it is caused by a small and narrow cricoid ring and may present with stridor and sometimes with just prolonged episodes of croup. Tracheostomy is necessary for nearly 50% of children and a 2% mortality has been reported in a very large series (Holinger et al 1976). Some children may be managed by regular dilatation and a few grow out of the disorder.

The tip and upper portion of the vocal process of the arytenoid cartilage consists of non-calcifying, elastic cartilage. This may have considerable functional significance: the vocal process may bend at the elastic cartilage during adduction and abduction, and the two arytenoid cartilages will contact mainly at their 'elastic' superior portions during adduction.

JOINTS

Cricothyroid joint

The joints between the inferior cornua of the thyroid cartilage and the sides of the cricoid cartilage are synovial. Each is enveloped by a capsular ligament strengthened posteriorly by fibrous bands (see Figs 41.1–41.2; **Fig. 41.4**). Both capsule and ligaments are rich in elastin fibres. The primary movement at the joint is rotation around a transverse axis that passes transversely through both cricothyroid joints. There is some controversy as to whether the cricoid or thyroid cartilage rotates more. The effect of this rotation is to move the cricoid and thyroid cartilages relative to one another in such a way as to bring together or approximate the lamina of the thyroid cartilage and the arch of the cricoid cartilage ('closing the visor'). When the joint is in a neutral position, the ligaments are slack and the cricoid can glide, to a limited extent, in horizontal and vertical directions on the thyroid cornua. The effect of these movements is to lengthen the vocal folds, provided the arytenoid cartilages are stabilized at the cricoarytenoid joint. This may also increase vocal fold tension. For further reading, see Vilkman et al (1987), Hammer et al (2010).

There is a significant amount of variation in the shape of the cricothyroid facet, which can vary from a well-defined facet to a nearly flat surface with just a slight protuberance or to no obvious definable facet. The shape of the facet determines the degree of horizontal and vertical gliding possible at the joint. The degree of elongation of the vocal folds has been shown to vary between 3% and 12%. It has been suggested that this variation might be one factor in determining the success of cricothyroid approximation surgery to raise the pitch of the voice in male to female transsexuals (Hammer et al 2010, Windisch et al 2010, Storck et al 2011, Chen et al 2012).

Cricoarytenoid joint

The cricoarytenoid joints are a pair of synovial joints between the facets on the lateral parts of the upper border of the lamina of the cricoid cartilage and the bases of the arytenoids (see Figs 41.2, 41.3E, 41.4). Each joint is enclosed by a capsular ligament and strengthened by a ligament that, although traditionally called the posterior cricoarytenoid ligament, is largely medial in position.

The cricoid facets are elliptical, convex and obliquely directed laterally, anteriorly and downwards. The long axes of the two facets intersect posteriorly at an angle of about 50°. Two movements take place at this joint. The first is rotation of the arytenoid cartilages at right-angles to the long axis of the cricoid facet (dorso-medio-cranial to ventro-latero-caudal). This causes each vocal process to swing laterally or medially to increase or decrease the width of the rima glottidis. This movement is sometimes referred to as a rocking movement of the arytenoid cartilages. There is also a gliding movement, by which the arytenoids approach or recede from one another, the direction and slope of their articular surfaces imposing a forward and downward movement on lateral gliding. The movements of gliding and rotation are associated. Hence medial gliding happens with medial rotation and lateral gliding with lateral rotation. This results in adduction or abduction of the vocal folds respectively. When viewed from above, foreshortening can give the illusion that the arytenoid cartilages are rotating about their vertical axes, but the shape of the facets prevents such movement happening (Selbie et al 1998). Some authors maintain that rotatory movement about a vertical axis can take place (Liu et al 2013). The posterior cricoarytenoid ligaments limit forward movements of the arytenoid cartilages on the cricoid cartilage. It has been suggested that the 'rest' position of the cricoarytenoid ligament is a major determinant of the position of a denervated vocal fold (England et al 1996).

Arytenocorniculate joints

Synovial or cartilaginous joints link the arytenoid and corniculate cartilages.

Innervation of the cricothyroid, cricoarytenoid and arytenocorniculate joints

The cricothyroid, cricoarytenoid and arytenocorniculate joints are innervated by branches of the recurrent laryngeal nerves that arise either independently or from branches of the nerve to the laryngeal muscles. The capsules of the laryngeal joints contain numerous lamellated (Pacinian) corpuscles, Ruffini corpuscles and free nerve endings (Bradley 2000).

SOFT TISSUES

The skeletal framework of the larynx is joined to surrounding structures by extrinsic membranes. It is also interconnected by intrinsic ligaments and fibroelastic membranes, of which the thyrohyoid and quadrangular membranes, together with the conus elasticus, are the most significant. The thyrohyoid membrane is external to the larynx, whereas the paired quadrangular membranes and conus elasticus are internal. The named ligaments are the median (anterior) cricothyroid ligament, the hyoepiglottic, thyroepiglottic and the cricotracheal ligaments.

Extrinsic ligaments and membranes

Thyrohyoid membrane

The thyrohyoid membrane is a broad, fibroelastic layer attached below to the superior border of the thyroid cartilage lamina and the front of

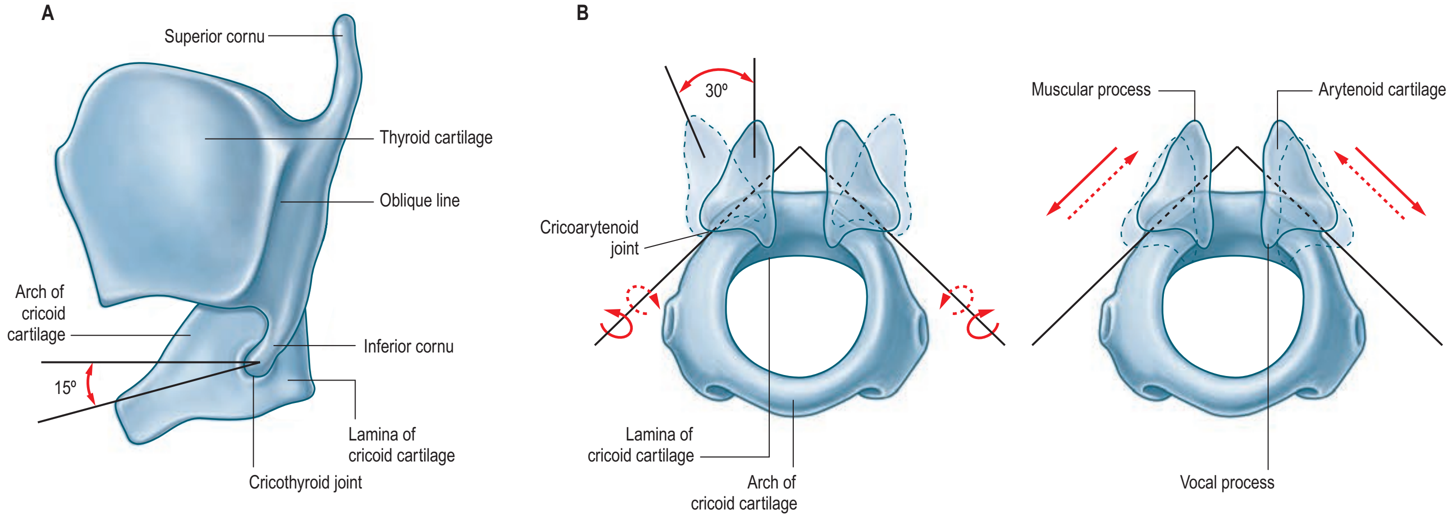

Fig. 41.4 **A**, Lateral view of the cricothyroid joint. **B**, An anterosuperior view of the cricoarytenoid joint.

its superior cornua and above to the superior margin of the body and greater cornua of the hyoid (see Figs 41.1–41.2; **Fig. 41.5C**). It thus ascends behind the concave posterior surface of the hyoid, separated from its body by a bursa that facilitates the ascent of the larynx during swallowing. Its medial portion is thickened, forming the median thyrohyoid ligament. The more lateral, thinner, parts are pierced by the superior laryngeal vessels and internal laryngeal nerves (see Fig. 41.1). Externally, it is in contact with thyrohyoid and omohyoid, and with the body of the hyoid bone. Its inner surface is related to the lingual surface of the epiglottis and the piriform fossae of the pharynx. The round, fold-like, elastic lateral thyrohyoid ligaments form the posterior borders of the thyrohyoid membrane and connect the tips of the superior thyroid cornua to the posterior ends of the greater hyoid cornua. For further reading, see Bosma and Bartner (1993).

Hyo- and thyroepiglottic ligaments

The epiglottis is attached to the hyoid bone and thyroid cartilage by the extrinsic hyoepiglottic and intrinsic thyroepiglottic ligaments, respectively (**Fig. 41.5A**).

Cricotracheal ligament

The cricotracheal ligament unites the lower border of the cricoid to the first tracheal cartilage and is continuous with the perichondrium of the trachea (see Fig. 41.1).

Intrinsic ligaments and membranes

The fibroelastic structures of the larynx lie within the cartilaginous skeleton of the larynx, beneath the laryngeal mucosa (**Fig. 41.5**). They form a discontinuous sheet, separated on both sides of the larynx by a horizontal cleft between the vestibular and vocal ligaments. Its upper part, the quadrangular membrane, lies within the walls of the upper part of the laryngeal cavity, the laryngeal vestibule, and extends between the arytenoid cartilages and the sides of the epiglottis. Its lower part, the conus elasticus, lies within the walls of the lower part of the laryngeal cavity, the infra-glottic cavity and connects the thyroid, cricoid and arytenoid cartilages.

Quadrangular membrane

Each quadrangular membrane passes from the lateral margin of the epiglottis to the apex and fovea triangularis of the ipsilateral arytenoid cartilage. It is often poorly defined, especially in its upper portion. The upper and lower borders of the membrane are free. The upper border slopes posteriorly to form the aryepiglottic ligament, which constitutes the central component of the aryepiglottic fold. Posteriorly, it passes through the fascial plane of the oesophageal suspensory ligament, and helps to form the median corniculopharyngeal ligament, which extends into the submucosa adjacent to the cricoid cartilage. This ligament may exert vertical traction on the tissues of the laryngopharynx. The cuneiform cartilages lie within the aryepiglottic folds. The lower border of the quadrangular membrane forms the vestibular ligament within the vestibular fold.

Cricothyroid membrane and conus elasticus

The conus elasticus is that part of the fibroelastic membrane found in the lower part of the cavity of the larynx. The terminology used to describe this structure is confusing, as different terms may be used to describe apparently similar structures. Two synonyms for the conus elasticus that are commonly found in the literature are the cricovocal membrane and the cricothyroid membrane. The conus elasticus consists of three distinct parts: right and left lateral parts and a thickened median portion. The term conus elasticus is frequently applied to the lateral parts, while the median part is often called either the median or the anterior cricothyroid ligament.

Median (anterior) cricothyroid ligament The median or anterior cricothyroid ligament is the thickened central portion of the conus elasticus. Inferiorly, it is attached to the upper border of the midline region of the cricoid arch and it extends upwards to attach to the inferior border of the thyroid cartilage, passing on to the inner surface of the thyroid angle as far superiorly as the attachment of thyroarytenoid.

Conus elasticus The lateral parts of the conus elasticus are thinner than the median cricothyroid ligament. Inferiorly, the conus elasticus

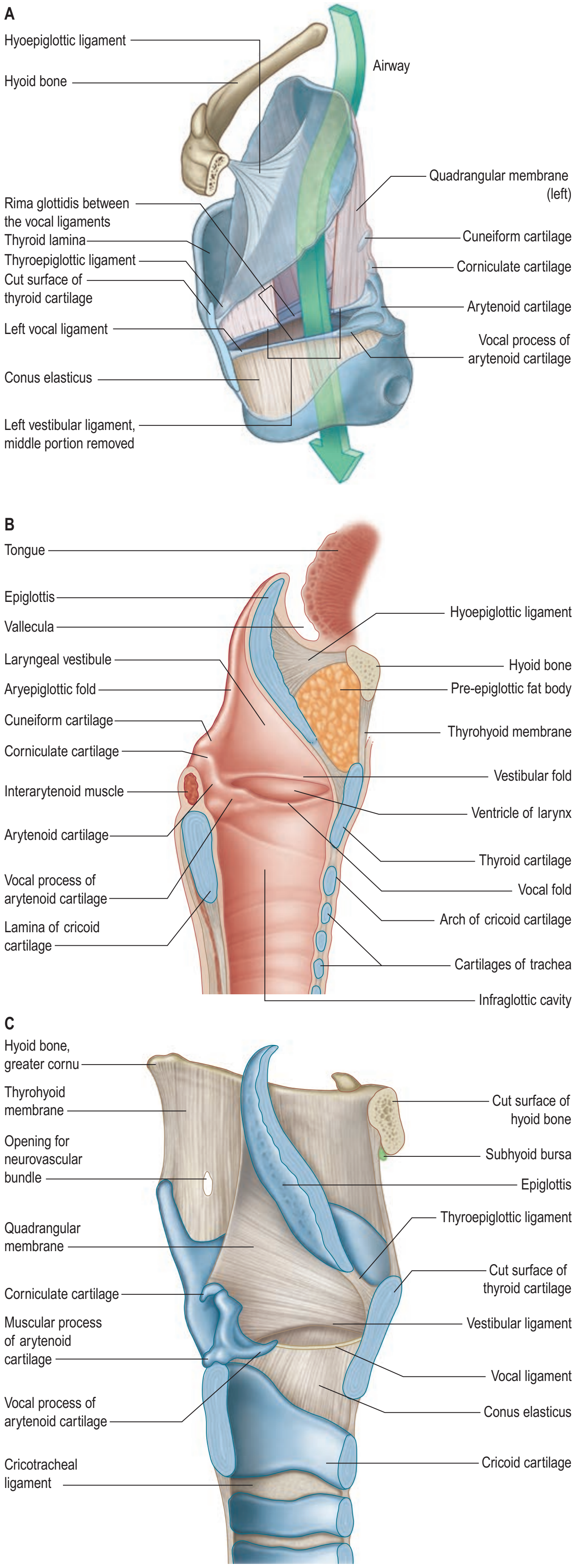
A
Hyoepiglottic ligament
Hyoid bone
Airway
Quadrangular membrane (left)
Rima glottidis between the vocal ligaments
Thyroid lamina
Thyroepiglottic ligament
Cut surface of thyroid cartilage
Cuneiform cartilage
Corniculate cartilage
Arytenoid cartilage
Left vocal ligament
Vocal process of arytenoid cartilage
Conus elasticus
Left vestibular ligament, middle portion removed
B
Tongue
Epiglottis
Vallecula
Hyoepiglottic ligament
Laryngeal vestibule
Hyoid bone
Aryepiglottic fold
Pre-epiglottic fat body
Cuneiform cartilage
Thyrohyoid membrane
Corniculate cartilage
Vestibular fold
Interarytenoid muscle
Ventricle of larynx
Arytenoid cartilage
Thyroid cartilage
Vocal process of arytenoid cartilage
Vocal fold
Lamina of cricoid cartilage
Arch of cricoid cartilage
Cartilages of trachea
Infraglottic cavity
C
Hyoid bone, greater cornu
Thyrohyoid membrane
Cut surface of hyoid bone
Opening for neurovascular bundle
Subhyoid bursa
Epiglottis
Thyroepiglottic ligament
Quadrangular membrane
Cut surface of thyroid cartilage
Corniculate cartilage
Vestibular ligament
Muscular process of arytenoid cartilage
Vocal ligament
Vocal process of arytenoid cartilage
Conus elasticus
Cricotracheal ligament
Cricoid cartilage

Fig. 41.5 A–B, Sagittal sections of the left side of the larynx, showing the laryngeal membranes (**A**) and the interior aspect (**B**) of the left half of the larynx. **C**, The quadrangular membrane viewed from the left side. (A, With permission from Drake RL, Vogl AW, Mitchell A (eds) Gray's Anatomy for Students, 2nd ed. Elsevier, Churchill Livingstone. Copyright 2010.)

attaches to the superior cricoid arch and the cricoid lamina. Superiorly, it extends upwards within the thyroid lamina to attach anteriorly to the inner surface of the thyroid cartilage (just below its midpoint) and posteriorly to the tip and upper surface of the vocal process and fovea oblonga of the arytenoid cartilage. Between these anterior and posterior attachments, the upper edges of the conus elasticus are free, thickened and aligned horizontally, forming the vocal ligaments. Each vocal ligament lies within a mucosa-covered vocal fold, covered on its internal surface by the mucosal lining of the larynx, and externally by the lateral cricoarytenoid and thyroarytenoid muscles (Reidenbach 1995).

The conus elasticus derives its name from the cone or funnel shape produced by the superior and medial curving of its walls between its inferior and superior attachments that is thought to maximize the efficient flow of air towards the rima glottidis during phonation (Lenneberg 1967).

LARYNGEAL CAVITY

The laryngeal cavity extends from the laryngeal inlet opening into the pharynx down to the lower border of the cricoid cartilage, where it continues into the trachea (see Fig. 41.5; **Fig. 41.6**). The walls of the cavity are formed of the fibroelastic membranes described above and lined with mucous membrane that folds over the free edges of these membranes within the larynx. On either side, the continuity of the fibroelastic membrane is interrupted between the upper vestibular and lower true vocal folds.

The folds project into the lumen of the cavity and divide it into upper and lower parts, separated by a middle portion between the two sets of folds that lead into the laryngeal ventricle. The upper folds are the vestibular (ventricular or false vocal) folds; the median aperture between them is the rima vestibuli. The lower pair are the (true) vocal folds (or vocal folds), and the aperture between them is the rima glottidis. The true vocal folds are the primary source of phonation, whereas the vestibular folds normally do not contribute directly to sound production. The supraglottis is a clinical term sometimes used in tumour staging; it refers to all those parts of the larynx that lie above the glottis and comprises the laryngeal inlet (formed of the laryngeal surface of the epiglottis and arytenoid cartilages, and the laryngeal aspects of the aryepiglottic folds), the laryngeal vestibule and the vestibular folds. Other terms that are used clinically in tumour staging are the glottis, defined as the anterior and inferior surfaces of the true vocal folds and the anterior and posterior commissures. The subglottis is defined as the region below the glottis that extends to the inferior border of the cricoid cartilage.

Microstructure of the larynx

The laryngeal mucosa is continuous with that of the pharynx above and the trachea below. It lines the entire inner surface of the larynx, including the ventricle and saccule. The mucosa is thickened over the vestibular folds, where it is the chief component, and is thinner over the vocal folds, where it overlies the vocal ligaments. It is loosely adherent to the anterior surface of the epiglottis but firmly attached to the floor of the valleculae. On the aryepiglottic folds, it is reinforced by a considerable amount of fibrous connective tissue and it adheres closely to the laryngeal surfaces of the cuneiform and arytenoid cartilages.

The laryngeal epithelium is mainly a ciliated, pseudostratified respiratory epithelium (see Fig. 2.2D) where it covers the inner aspects of the larynx, including the lower part of the posterior, laryngeal surface of the epiglottis. It provides a mucociliary clearance mechanism shared with most of the respiratory tract. The vocal folds are covered by non-keratinized, stratified squamous epithelium where they contact each other. This important variation protects the tissue from the effects of the considerable mechanical stresses that act on the surfaces of the vocal folds. Certain parts of the larynx are subject to the abrasive effects of swallowed food and are also covered by non-keratinized, stratified squamous epithelium. These are the 'exterior' surfaces of the larynx, which merge with the laryngopharynx and oropharynx (including the anterior, lingual and upper, posterior surfaces of the epiglottis and the upper parts of the aryepiglottic folds) (Sato 2018).

The laryngeal mucosa has numerous mucous glands, especially over the epiglottis, where the cartilage is pitted, and along the margins of the aryepiglottic folds anterior to the arytenoid cartilages, where they are known as the arytenoid glands. Many large glands in the saccules of the larynx secrete periodically over the vocal folds during phonation. Seromucinous tubule-alveolar glands in the saccule, posterior surface of the epiglottis and the aryepiglottic folds, and goblet cells all secrete mucus in the respiratory epithelium. The free edges of the vocal folds are devoid of glands, and their stratified epithelium is vulnerable to drying and requires the secretions of neighbouring glands. The epithelial surfaces of the vocal folds are lined by microvilli that may retain the lubricating secretions and help to ensure an even distribution of mucus. Poorly lubricated folds would appear to increase resistance to airflow, which means that higher subglottal pressures are needed to initiate and sustain phonation. Taste buds, like those in the tongue, are present on the posterior epiglottic surface and aryepiglottic folds, and less often in other laryngeal regions. Laryngeal stretch-, touch- and pressure-sensitive mechanoreceptors provide perceptual and proprioceptive afferent information for a variety of essential functions, including airway protection, breathing, deglutition, speech and voice (Hammer and Krueger 2014).

Upper part

The upper part of the laryngeal cavity consists of the laryngeal inlet (aditus), the aryepiglottic fold and the laryngeal vestibule.

Laryngeal inlet (aditus)

The upper part of the laryngeal cavity is entered by the laryngeal inlet (aditus laryngis), an approximately triangular aperture between the larynx and pharynx. This faces backwards and somewhat upwards because the anterior wall of the larynx is much longer than the posterior. It slopes downwards and forwards in its upper part because of the oblique inclination of the epiglottis. The inlet is bounded anteriorly by the upper edge of the epiglottis, posteriorly by the transverse mucosal fold between the two arytenoids (posterior commissure), and on each side by the edge of a mucosal ridge, the aryepiglottic fold, that runs between the side of the epiglottis and the apex of the arytenoid cartilage. The midline groove between the two corniculate tubercles is termed the interarytenoid notch.

Aryepiglottic fold

The aryepiglottic fold contains ligamentous and muscular fibres. The ligamentous fibres represent the free upper border of the quadrangular membrane (see Fig. 41.5). The muscle fibres are continuations of the oblique arytenoids (see Fig. 41.10D). The posterior part of the aryepiglottic fold contains two oval swellings, one above and in front, the other behind and below, that mark the positions of the underlying cuneiform and corniculate cartilages, respectively. They are separated by a shallow vertical furrow that is continuous below with the opening of the laryngeal ventricle.

Laryngeal vestibule

The laryngeal vestibule is the region between the laryngeal inlet and vestibular folds. It is wide above, narrow below, and higher anteriorly than posteriorly. The anterior wall is formed by the posterior surface of the epiglottis, the lower part of which (epiglottic tubercle) bulges backwards a little. The lateral walls, higher in front and shallow behind, are formed by the medial surfaces of the aryepiglottic folds. The posterior wall consists of the interarytenoid mucosa above the vestibular folds.

Middle part

The middle part of the laryngeal cavity is the smallest and extends from the rima vestibuli above to the rima glottidis below. On each side it contains the vestibular folds, the ventricle and the saccule of the larynx.

Vestibular folds and ligaments

The narrow vestibular ligament represents the thickened lower border of the quadrangular membrane (see Fig. 41.5C). It is fixed in front to the thyroid angle below the epiglottic cartilage and behind to the anterolateral surface of the arytenoid cartilage above its vocal process. With its covering of mucosa, it is termed the vestibular (ventricular or false vocal) fold (see Figs 41.5B, 41.6). The presence of a loose vascular

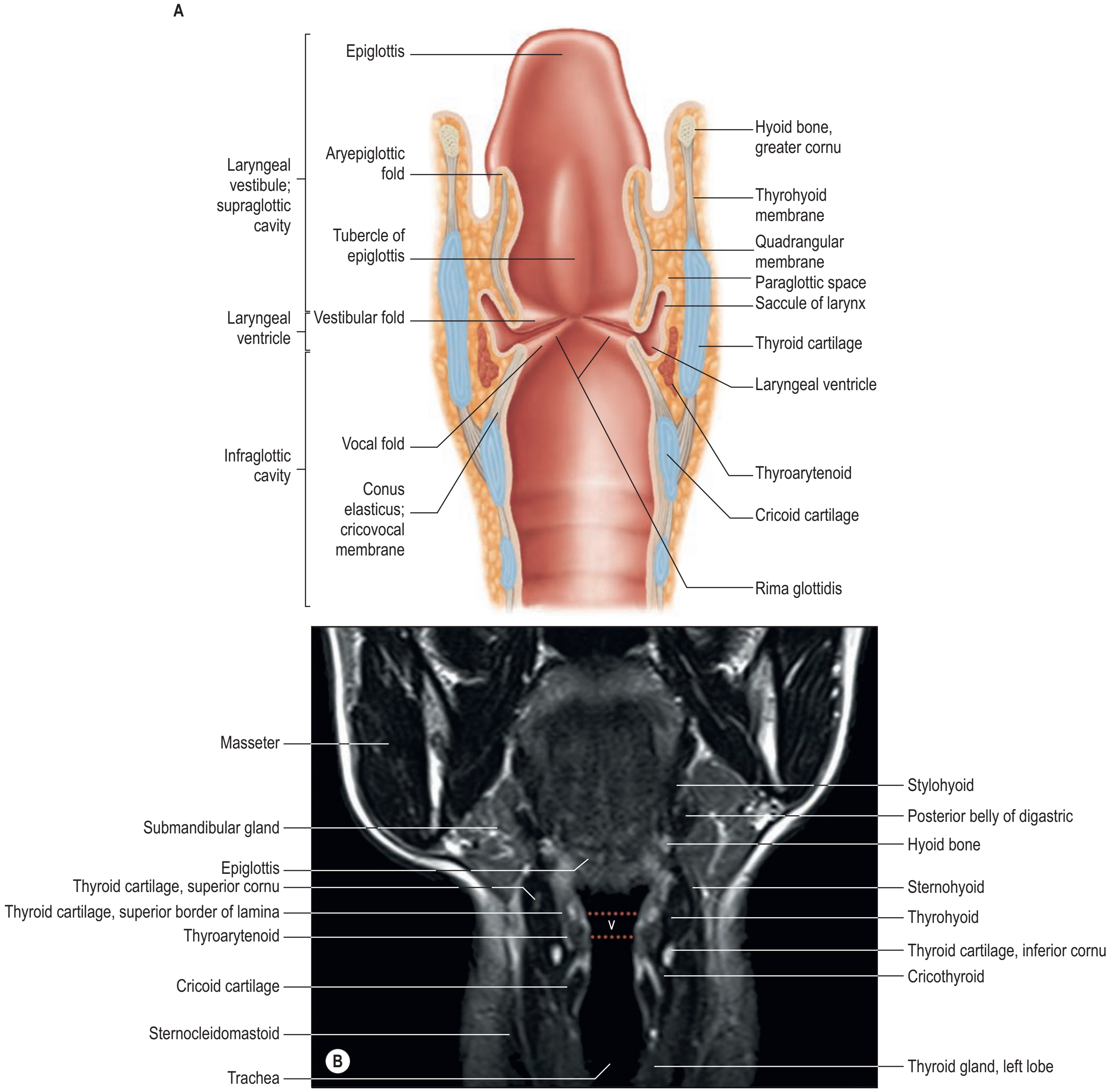
A
Epiglottis
Laryngeal vestibule; supraglottic cavity
Aryepiglottic fold
Tubercle of epiglottis
Laryngeal ventricle
Vestibular fold
Infraglottic cavity
Vocal fold
Conus elasticus; cricovocal membrane
Hyoid bone, greater cornu
Thyrohyoid membrane
Quadrangular membrane
Paraglottic space
Saccule of larynx
Thyroid cartilage
Laryngeal ventricle
Thyroarytenoid
Cricoid cartilage
Rima glottidis
Masseter
Submandibular gland
Epiglottis
Thyroid cartilage, superior cornu
Thyroid cartilage, superior border of lamina
Thyroarytenoid
Cricoid cartilage
Sternocleidomastoid
Trachea
B
V
Stylohyoid
Posterior belly of digastric
Hyoid bone
Sternohyoid
Thyrohyoid
Thyroid cartilage, inferior cornu
Cricothyroid
Thyroid gland, left lobe

Fig. 41.6 A–C, Coronal sections through the larynx and proximal trachea. **A**, Posterior aspect. **B**, T2-weighted MRI. The limits of the laryngeal vestibule (V) are set by the dotted red lines; the supraglottic cavity is above and the infraglottic cavity is below. (*C, continued online*)

mucosa lends the vestibular folds a pink appearance *in vivo*, as they lie above and lateral to the vocal folds. Muscle fibres of thyroarytenoid can be observed within the vestibular folds, though they are variable in extent between individuals. Their function is disputed, with some authors suggesting that they cause adduction and downward movement on the vestibular folds (Reidenbach 1991, Moon and Alipour 2013). The vestibular (ventricular) folds are not the primary sound source in phonation, but they can be used to produce a rough quality of voice known as 'false fold phonation' or 'dysphonia plicae ventricularis'.

Ventricle of the larynx

The laryngeal ventricle (also known as the laryngeal sinus) is a slit between the vestibular folds above and the true vocal folds below (see Figs 41.5–41.6). On each side, it extends from a narrow opening in the wall of the middle part of the laryngeal cavity into a fusiform recess that extends upwards into the laryngeal wall, lateral to the vestibular fold, and opens anteriorly into the saccule.

Saccule of the larynx

The saccule is a conical pouch of variable size. It curves slightly backwards and ascends forwards from the anterior end of the ventricle, between the vestibular fold and thyroid cartilage (see Fig. 41.6), occasionally reaching the upper border of the cartilage or even beyond, when it protrudes through the thyrohyoid membrane. The orifice of the saccule is guarded by a delicate fold of mucosa, the ventriculosaccular fold.

The saccule has a fibrous capsule that is continuous below with the vestibular ligament. It is covered medially by a few muscular fasciculi from the apex of the arytenoid cartilage that pass forwards between the saccule and vestibular mucosa into the aryepiglottic fold. Laterally, it is separated from the thyroid cartilage by the thyroepiglottic muscle, which compresses the saccule, so that its secretions are expressed onto the vocal folds (which lack glands), to lubricate and protect them against desiccation and infection. The saccule has a greater density of mucous glands in the submucosa than elsewhere in the larynx. The glands open onto its luminal surface.

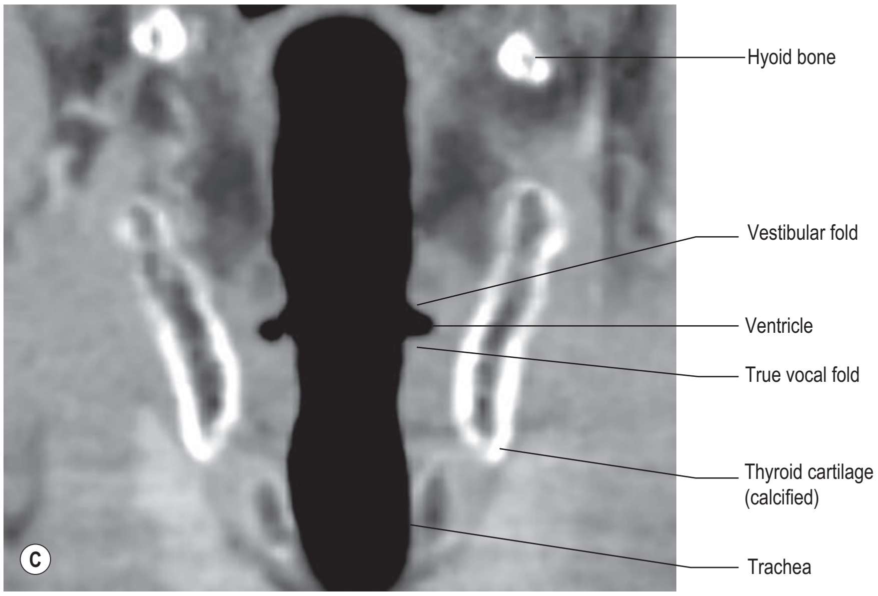
Hyoid bone
Vestibular fold
Ventricle
True vocal fold
Thyroid cartilage (calcified)
Trachea
C

Fig. 41.6 **C**, CT. Note the calcified thyroid cartilage.

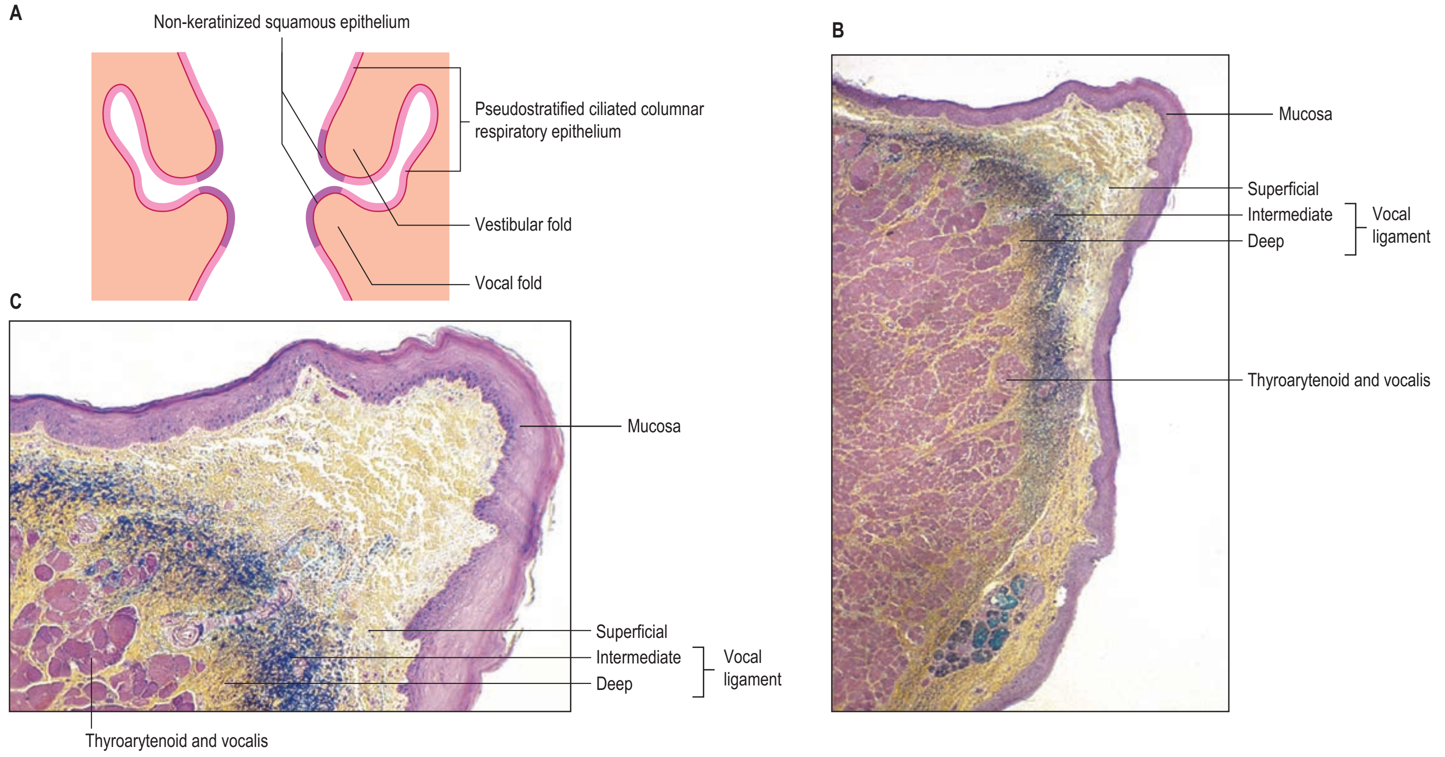
A
Non-keratinized squamous epithelium
Pseudostratified ciliated columnar respiratory epithelium
Vestibular fold
Vocal fold
B
Mucosa
Superficial
Intermediate
Deep
Vocal ligament
Thyroarytenoid and vocalis
C
Mucosa
Superficial
Intermediate
Deep
Vocal ligament
Thyroarytenoid and vocalis

Fig. 41.7 **A**, Coronal view of the laryngeal cavity, showing the distribution of the mucous membrane in the laryngeal cavity. **B**, Structure of the true vocal folds at low power, ×40, stained with Movat's pentachrome stain. **C**, True vocal folds at high power, ×100; Movat's pentachrome stain. The non-keratinized squamous epithelium is shown forming a mucosal layer over the superficial part of the lamina propria, along with the three layers of the lamina propria, with thyroarytenoid and vocalis lying deep to the deep layer of the lamina propria. At higher magnification, the deeper yellow staining of the collagen in the deep layer of the lamina propria compared to the superficial layer indicates a greater degree of cross-linking. (B,C, Adapted with permission from Courey MS 1998 The professional voice, In: Cummings CW et al (eds) Otolaryngology: Head and Neck Surgery, vol 4, 3rd ed. St Louis: Mosby; pp. 3003–25.)

Laryngoceles and saccular cysts

Available with the *Gray's Anatomy* e-book

Vocal folds and ligaments

The vocal folds serve several functions. They protect the airway by closing during swallowing; they are responsible for generation of a cough by closing firmly and then moving rapidly apart during exhalation; they facilitate the Valsalva manoeuvre by closing the glottis and raising intrathoracic pressure, hence also increasing intra-abdominal pressure, such as during defaecation, parturition, or lifting heavy weights; and they are concerned with sound production. The free thickened upper edge of the conus elasticus forms the vocal ligament (see Fig. 41.5C). It stretches back on either side from the midlevel of the thyroid angle to the vocal processes and fovea oblonga of the arytenoids. When covered by mucosa, it is termed the vocal fold or vocal cord (vocal fold is the preferred clinical term) (see Figs 41.5B, 41.6). The vocal folds lie on either side of an aperture, the rima glottidis, and form the anterolateral three-fifths of its edges. The posterior two-fifths of the edges of the rima glottidis are formed by the medial surfaces of the arytenoid cartilages including the vocal processes of the arytenoid cartilages.

Each vocal fold consists of five layers: mucosal epithelium, lamina propria (which has three layers) and a muscular layer (fibres of thyroarytenoid and vocalis) (**Fig. 41.7**). The mucosa overlying the vocal ligament is thin and the epithelial cell layer is attached to the underlying superficial lamina propria by a basement membrane. It lies on the ligament, and so the vocal fold appears pearly white *in vivo*. At birth, the lamina propria consists of a single layer of cells. It becomes a bilaminar structure by 2 months of age and trilaminar (as defined by distinct regions of differential cell populations and cell density) by 7 years of age (Hartnick et al 2005). The most superficial layer (also known as Reinke's space) is hypocellular and consists mainly of loose fine collagen (reticular fibres) and elastic fibres. It is only loosely attached to the underlying vocal ligament that extends along the length of the free margin of the vocal ligament and a little way onto the superior surface of the fold; oedema readily collects here in disease. The middle layer consists predominantly of elastic fibres and the deep layer consists predominantly of collagen fibres; these two layers collectively form the vocal ligament (Sato 2018). The orientation of the collagen and elastin fibres in the middle and deep layers is parallel to that of the fibres of vocalis (Hartnick et al 2005). Thyroarytenoid and vocalis form the fifth layer of the vocal folds. These muscles shorten, relax and aid adduction of the vocal folds.

There are alternative descriptions of the soft tissues of the vocal folds. Some authors describe only two layers: the body (the deep layer of the lamina propria and muscle) and the cover (the mucosa and superficial and intermediate layers of the lamina propria). Others divide the soft tissues of the vocal folds into three layers: the mucosal layer (the mucosa and the superficial layer of the lamina propria), the vocal ligament (the intermediate and deep layers of the lamina propria) and the muscle layer (Titze 1994).

The site where the vocal folds meet anteriorly, the anterior commissure, is the region where fibres of the vocal ligament pass through the thyroid cartilage to blend with the overlying perichondrium. The point at which the vocal ligaments are attached to the thyroid cartilage is known as Broyles' ligament: it can be an anatomical escape pathway for primary tumours arising on the vocal fold.

The maculae flavae are located at the anterior and posterior end of each vocal ligament and can form mucosal bulges that are sometimes visible on endoscopic examination of the larynx through the mucosa as whitish-yellow masses. The vocal folds are connected to the thyroid cartilage anteriorly via the anterior maculae flavae and the anterior commissure tendon, and posteriorly via the posterior maculae flavae. The maculae flavae themselves are described as being formed of dense masses of stellate cells with a morphology markedly different from that of fibroblasts, surrounded by a dense extracellular matrix. The function of the maculae flavae remains unclear but it has been suggested that they play a critical role in the metabolism of the extracellular matrix of the vocal folds (Awd Allah et al 2009, Fayoux et al 2004, Sato et al 2010a, 2010b, Sato 2018).

Laryngeal carcinoma

Available with the *Gray's Anatomy* e-book

Laryngoceles and saccular cysts are air- or fluid-filled enlargements, respectively, of the saccule. A laryngocele is a herniation of the saccular mucosa. The aetiology is uncertain: repeated, sustained high transglottal pressures (such as in trumpet playing) may be a possible cause of acquired symptoms, and some cases may be the result of congenital enlargement of the saccule. Growth of a laryngocele is constrained by the surrounding tissues, and so it expands upwards into the paraglottic space anterior to the piriform fossa, and superiorly to expand the ary-epiglottic fold and reach the vallecula (internal laryngocele). It can extend to the thyrohyoid membrane, which it may pierce to form an external laryngocele, and where it may be palpable in the neck. Symptoms include hoarseness, stridor and dysphagia. The laryngeal saccule may also become pathologically enlarged as a result of obstruction of the ventricular aditus by inflammation, scarring, or compression by a tumour. An expanding, mucus-filled cyst forms as the glandular secretions accumulate: saccular cysts can expand in a similar direction to a laryngocele and may also pierce the thyrohyoid membrane. In addition to hoarseness and stridor, acute respiratory obstruction may result if the contents of the cyst become infected, especially in the young.

Reinke's oedema

Available with the *Gray's Anatomy* e-book

Vocal fold nodules

Available with the *Gray's Anatomy* e-book

Rima glottidis

The rima glottidis is the aperture between the vocal folds anteriorly and the arytenoid cartilages posteriorly (Fig. 41.8). It is bounded behind by the mucosa that passes between the arytenoid cartilages at the level of the vocal folds. The rima glottidis is customarily divided into two regions: an anterior intermembranous part, which makes up about three-fifths of its anteroposterior length and is formed by the underlying vocal ligament; and a posterior intercartilaginous part, formed by the vocal processes of the arytenoid cartilages. The rima glottidis is the narrowest part of the larynx, with an average anteroposterior diameter in adult males of 21.1 mm, and in adult females of 15.1 mm (Friedrich and Lichtenegger 1997); other studies have reported measurements that vary by up to 2 mm. Its width and shape vary with the movements of the vocal folds and arytenoid cartilages during respiration and phonation.

Lower part

The lower part of the laryngeal cavity, the infraglottic cavity (also known as the subglottic cavity), extends from the vocal folds to the lower border of the cricoid. In transverse section, it is elliptical above and wider and circular below, and is continuous with the trachea. Its walls are lined by respiratory mucosa and are supported by the cricothyroid ligament above and the cricoid cartilage below (Reidenbach 1998). The walls of this part of the laryngeal cavity are said to be exponentially curved, a feature that may serve to accelerate the airflow towards the glottis with the minimum loss of energy (Lenneberg 1967).

Laryngoscopic examination

The laryngeal inlet, the structures around it, and the cavity of the larynx can all be inspected using flexible endoscopy, usually via the nasal cavity and nasopharynx. The epiglottis appears relatively short because it is viewed along its long axis, but its tubercle is visible. From the epiglottic margins, the aryepiglottic folds can be traced posteromedially and the cuneiform and corniculate elevations recognized. The pink vestibular folds and pearly white vocal folds are easily seen. When the rima glottidis is wide open, the anterior arch of the cricoid cartilage, the tracheal mucosa and cartilages may also be seen (see Fig. 41.8) and the piriform fossae inspected.

Laryngeal obstruction and trauma

The mucosa of the upper larynx is highly sensitive and contact with foreign bodies excites immediate coughing. Large foreign bodies may obstruct the laryngeal inlet or rima glottidis and suffocation may ensue. Smaller particles may enter the trachea or bronchi, or lodge in the laryngeal ventricle and cause reflex closure of the glottis, termed laryngospasm. Inflammation of the upper larynx, e.g. secondary to infection or the effects of smoke inhalation, may swell the mucosa by effusion of fluid into the loose submucous tissue (oedema of the supraglottis). The effusion neither involves nor extends below the vocal folds because the mucosa here is bound directly to the vocal ligaments and there is no submucous tissue. Laryngotomy below the vocal folds through the cricothyroid ligament, or tracheotomy below the cricoid cartilage, may be necessary to bypass the obstruction above and restore ventilation.

The consequences of trauma to the larynx resulting from either blunt or penetrating injuries may lead to any or all of the following: oedema, haematoma, fracture, dislocations or paralysis. Trauma at the level of the rima glottidis may result in thyroid cartilage fracture and displacement of the fragments into the vocal folds posteriorly with consequent oedema. Suicidal wounds are usually made through the thyrohyoid membrane, damaging the epiglottis, superior thyroid vessels, external and internal carotid arteries, and internal jugular veins. Less frequently, these wounds are inflicted above the hyoid, so that the lingual muscles, lingual and facial vessels are damaged. Caustic substances swallowed accidentally or during a suicide attempt, the ingestion of hot liquids and the inspiration of hot gases may all result in serious laryngeal damage. Radiotherapy as part of the treatment for neck cancer can cause radiation burns within the larynx (Myer 2004).

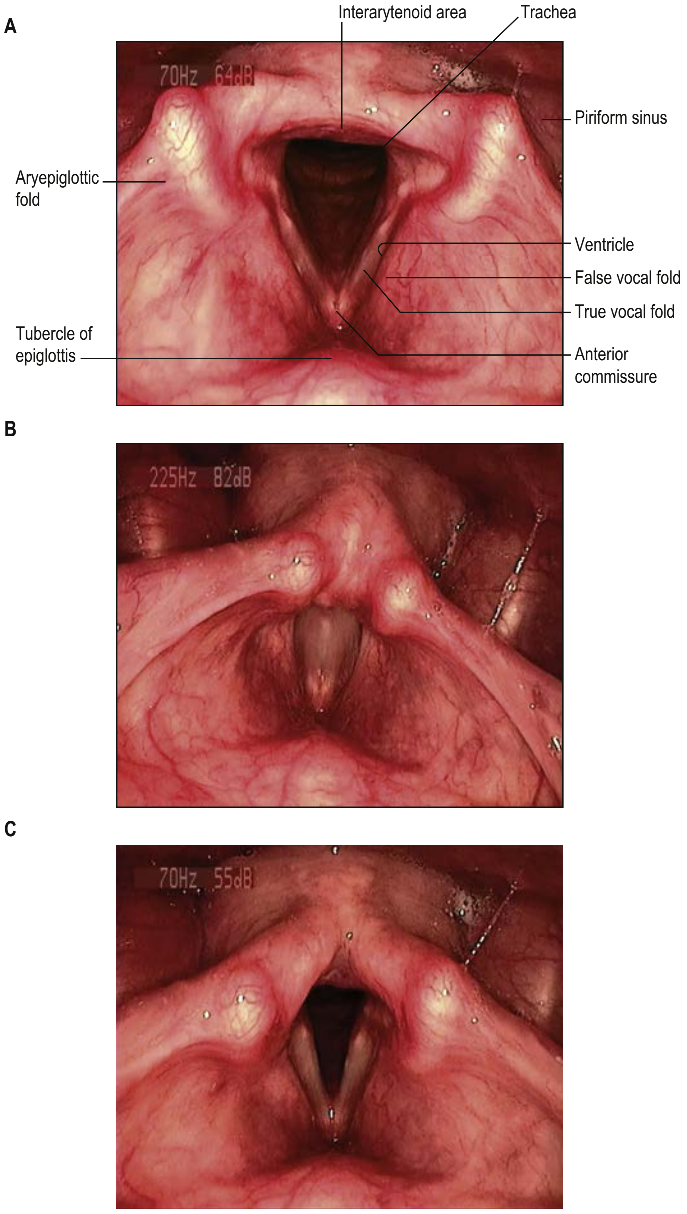

Fig. 41.8 Endoscopic view of the larynx with flexible chip-tip endoscope **A**, Forced inspiration: vocal folds are maximally abducted. **B**, Phonation: vocal folds are adducted. **C**, Quiet respiration: vocal folds are moderately abducted.

THE PAEDIATRIC LARYNX

The paediatric larynx differs markedly from its adult counterpart in size, position, consistency and shape. Although it is about one-third adult size, it is proportionately larger: the lumen is short and funnel-shaped, and disproportionately narrower. The infant larynx lies higher in the neck than the adult larynx (see Fig. 40.11). At rest, the upper border of the infant epiglottis is at the level of the second or third cervical vertebra, and when the larynx is elevated, it reaches the level of the first cervical vertebra. This high position enables an infant to use its nasal airway to breathe while suckling. It also means that the larynx is protected somewhat by the jaw. The epiglottis is X-shaped, with a furled petiole, and the laryngeal cartilages are softer and more pliable than in the adult larynx (which may predispose to airway collapse in inspiration, leading to the clinical picture of laryngomalacia). The thyroid cartilage is shorter and broader, lies closer to the hyoid bone in the neonate and has a relatively short thyrohyoid ligament. Neither the superior notch nor the laryngeal prominence is as marked as it is in the adult. The cricoid cartilage is the same shape as in the adult. Calcification of the cricoid cartilage has been noted as early as 7 years of age (Strauss 2000). The arytenoid cartilages are larger in proportion to the larynx as a whole

Squamous cell carcinoma is by far the most common laryngeal malignancy. The pattern of spread is determined by anatomical features at the site of origin and this influences its management and potential outcomes (Kirchner and Carter 1987, Welsh et al 1989).

Supraglottic tumours arising from the laryngeal surface of the epiglottis can spread through the perforations in the epiglottic cartilage and into the pre-epiglottic space. Because the supraglottis is not directly involved in voice production, tumours in this area most commonly present with a feeling of a persistent lump in the throat and possibly pain on swallowing often radiating to the ipsilateral ear. It is only in the later stages that they present with airway obstruction. If the tumour has spread towards the vocal fold, hoarseness will also be present. Inferior spread into the paraglottic space is more common and may extend as far as the subglottis or even beyond the larynx. Spread in this space medializes the vocal fold, as can be seen on careful laryngoscopy when assessing the tumour stage, and subsequently confirmed by scans. Lateral spread into the piriform sinus is a feature of tumours that arise lower down in the supraglottis on the vestibular folds. Deeper invasion infiltrates the thyroarytenoid muscle, fixing the fold, and eventually the thyroid and arytenoid cartilages.

Ventricular tumours often obstruct mucus outflow from the saccule to cause a saccular cyst or mucocele. Further infiltration of the paraglottic space and transglottic spread ultimately fixes the vocal fold through muscle invasion and, more rarely, direct involvement of the cricoarytenoid joint or infiltration of the recurrent laryngeal nerve. Fixation of the vocal fold is a good indicator of a tumour within the paraglottic space and this is reflected in the TNM staging system as an adverse sign.

Tumours of the true vocal folds almost always present in the first instance with voice change (dysphonia). Glottic tumours tend to spread by local growth in the first instance, when they may be contained in Reinke's space for some time. The paucity of lymphatics in the vocal fold slows tumour progression, allowing time for the patient to present to a clinician with a relatively small tumour load that will only have caused a chronic husky voice. This anatomical feature also accounts for the relative lack of nodal metastases associated with small glottic tumours. The proximity of anterior fold tumours to the thyroid cartilages, separated only by a thin layer of connective tissue, predisposes to cartilage invasion. Spread of tumour via Broyles' ligament to the outside of the larynx changes the tumour stage from a T1 lesion to a T4 lesion, with both therapeutic and survival implications. More posterior fold tumours tend to invade the vocalis muscle and fix it.

Subglottic tumours tend to spread circumferentially and, by so doing, impair the airway dramatically. The management of laryngeal carcinomas is largely dictated by the stage at presentation. Very small tumours of the glottis can be resected or treated by radiotherapy. Organ sparing protocols using radiotherapy and sometimes chemotherapy are often employed for larger tumours in the first instance. Surgical resection, laryngectomy, is indicated for those with advanced disease that have nodal metastases and also for salvage when other therapies have failed.

Any oedema in the superficial lamina propria (Reinke's space) is termed Reinke's oedema. It results in an increase in density of the vocal fold, and hence a drop in the pitch of the voice. The oedema can persist because there is very poor lymphatic drainage from the edges of the vocal folds (Liu et al 2006). Vocal abuse may initiate such changes, but the condition is nearly always confined to smokers.

Vocal fold nodules are chronic lesions of the vocal folds and develop most commonly as the result of persistent overuse (or misuse) of the voice, which results in an increase in the collision forces of the vocal folds. Nodules normally develop at the point of maximum contact of the vocal folds, i.e. at the junction of the anterior third and the posterior two-thirds of the vocal ligament. Excessive trauma at this point, e.g. when singing with poor technique or forcing the voice, initially produces subepithelial haemorrhage or bruising. Over time this results in pathological changes such as subepithelial scarring (singer's or screamer's nodes). Nodules increase vocal fold mass and affect vocal fold closure; the persistent posterior glottal opening causes hoarseness, a breathy voice, reduced vocal intensity and an inability to produce higher frequencies of vibration. These changes can cause a cycle in which increasing vocal effort is required by way of compensation, and this exacerbates the problem (Aronson and Bless 2009).

and so are more prominent; the aryepiglottic folds are disproportionately large. The vocal folds are 4–4.5 mm long, which is relatively shorter than either in childhood or in the adult, and consequently the proportion of the rima glottidis that is intramembranous is smaller in the neonate. The ventricle of the larynx is small, whereas the saccule of the larynx is often considerably larger than it is in adult life.

The mucosa of the vestibule is more loosely attached than it is in the adult larynx and it exhibits multiple submucosal glands. Inflammation of the vestibule can result in rapid and severe oedema. The mucosa is also lax in the infraglottic cavity and swelling here rapidly causes severe respiratory obstruction because of the disproportionately narrower lumen (3.5 mm in diameter in neonates). The neonatal infraglottic cavity extends posteriorly as well as inferiorly, which is an important consideration when passing an endotracheal tube (Litman et al 2003). The infraglottic airway rapidly increases in size during the first two years of life (Eckel et al 1999). By about the third year, sexual differences become apparent: the larynx is larger in boys, although the angle between the thyroid laminae is more pronounced in girls. At puberty, these changes increase and there is greater enlargement of the male larynx.

Congenital anomalies of the larynx include aplasia and hypoplasia of the epiglottis, high-rising epiglottis, bifid epiglottis, saccular cysts, vocal fold palsy, laryngeal atresia, laryngocele, laryngo-tracheo-oesophageal cleft and laryngeal web. Laryngo-tracheo-oesophageal cleft is due to failure of fusion of the posterior cricoid lamina and abnormal development of the tracheo-oesophageal septum, resulting in a posterior sagittal communication between the larynx and pharynx. For further reading, see Adewale (2009), Hudgins et al (1997), Pracy (1983), Sapienza et al (2004) and Wheeler et al (2009).

PARALUMENAL SPACES

A number of potential spaces lie between the laryngeal cartilages and the ligaments and membranes that support them. The three main spaces are the pre-epiglottic, the paraglottic and the subglottic spaces. Their precise definition, and the extent to which they communicate with one another, remain controversial. They are not closed compartments and so their existence does not preclude the spread of tumours. An awareness of the anatomy of these spaces, and the potential pathways of tumour spread from them, has significantly influenced the surgical approach to disease in this region (Welsh et al 1983).

Pre-epiglottic space

Its name implies that the pre-epiglottic space (**Fig. 41.9**) lies anterior to the epiglottis. The upper part of this space also extends beyond the lateral margins of the epiglottis, an arrangement that gives the space the form of a horseshoe and has led to the suggestion that periepiglottic space would be a more appropriate term for this region (Reidenbach 1996a). The space is primarily filled with adipose tissue and does not appear to contain any lymph nodes.

The upper boundary is formed by the weak hyoepiglottic membrane, strengthened medially as the median hyoepiglottic ligament; the anterior boundary is the thyrohyoid membrane, strengthened medially as the median thyrohyoid ligament; and the lower boundary is the thyroepiglottic ligament, continuous laterally with the quadrangular membrane behind. The greater cornu of the hyoid bone forms its upper lateral border. Inferolaterally, the pre-epiglottic space is in continuity with the paraglottic space, from where it is can be invaded by tumour. It is also in continuity with the mucosa of the laryngeal surface of the epiglottis via multiple perforations in the cartilage of the epiglottis (Reidenbach 1996a).

Paraglottic space

The paraglottic space (see Fig. 41.6) is a region of adipose tissue that contains the internal laryngeal nerve, the laryngeal ventricle, and all or part of the laryngeal saccule. It is bounded laterally by the thyroid cartilage and thyrohyoid membrane, superomedially by the quadrangular membrane, inferomedially by the conus elasticus, and posteriorly by the piriform fossa. The lower border of the thyroid cartilage is inferior, and the paraglottic space is continuous inferiorly with the space between the cricoid and thyroid cartilages. Posteroinferiorly, adipose tissue extends towards the cricothyroid joint. Superiorly, the paraglottic space is usually continuous with the pre-epiglottic space, although the two spaces may be separated by a fibrous septum. Consensus is lacking as to the precise boundaries between these two spaces. For example some authorities exclude thyroarytenoid from the paraglottic space and include it as the posterolateral inferior border of the pre-epiglottic space (Reidenbach 1996b).

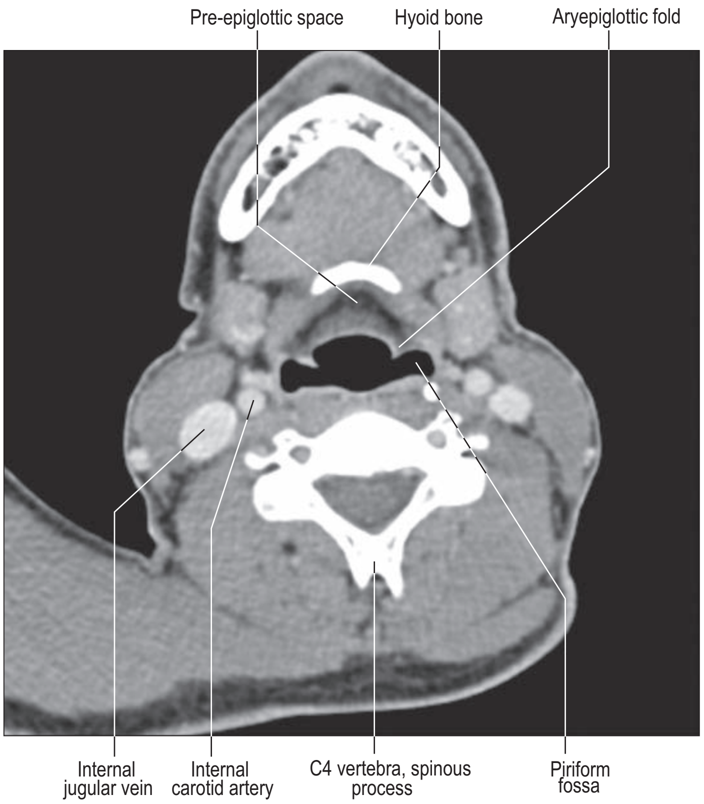

Fig. 41.9 Contrast-enhanced axial computed tomogram of the neck of a 42-year-old male showing the pre-epiglottic space and piriform fossa. (Courtesy of Dr Ivan Zammit.)

Subglottic space

The subglottic space is bounded laterally by the conus elasticus, medially by the mucosa of the infraglottic cavity, and above by the undersurface of Broyles' ligament in the midline. It is continuous below with the inner surface of the cricoid cartilage and its mucosa (Reidenbach 1998).

MUSCLES

The muscles of the larynx may be divided into extrinsic and intrinsic groups.

Extrinsic muscles

The extrinsic muscles connect the larynx to neighbouring structures and are responsible for moving it vertically during phonation and swallowing. They include the infrahyoid strap muscles, thyrohyoid, sternothyroid and sternohyoid (see Ch. 35), and the inferior constrictor muscle of the pharynx (see Ch. 40). Two of the three elevator muscles of the pharynx, stylopharyngeus and palatopharyngeus (see Ch. 40), are also connected directly to the thyroid cartilage, mainly to the posterior aspect of the thyroid laminae and cornua.

The role of the extrinsic muscles during respiration appears to be variable; the larynx has been seen to rise, descend or barely move during inspiration. The extrinsic muscles can affect the pitch and the quality of the voice by raising or lowering the larynx, and geniohyoid elevates and anteriorly displaces the larynx, particularly during deglutition.

Elevation of the larynx decreases the length and calibre of the laryngopharynx and thus shortens the vocal tract overall. This tends to raise both the formant frequencies as well as the fundamental frequency and may be one way by which an increase in pitch is achieved, though a change in pitch is not an inevitable consequence of this movement. The raising of the larynx may also be accompanied by forward or backward movement of the tongue because of the attachment of the tongue to the hyoid bone. These movements may facilitate alveolar or velar articulations, respectively.

The larynx is lowered by contraction of the infrahyoid muscles. This increases the length of the laryngopharynx, tending to lower both the formant frequencies and the fundamental frequency, though, again, a pitch change is not inevitable. Another effect of lowering the larynx will be to decrease supraglottal pressure and this will facilitate the articulation of voiced stops and fricatives (to a lesser extent). Voice quality can also be varied by the height of the larynx and this is an important factor contributing to the variations in quality of voice between different speakers.

Intrinsic muscles

The intrinsic muscles are the cricothyroid, posterior and lateral cricoarytenoid, transverse interarytenoid and oblique arytenoid, aryepiglotticus, thyroarytenoid and its subsidiary part, vocalis, and thyroepiglotticus; all are confined to the larynx in their attachments, and all but the transverse interarytenoid are paired (**Fig. 41.10**). Whereas most of the intrinsic muscles lie internally, under cover of the thyroid cartilage or the mucosa, the cricothyroids appear on the outer aspect of the larynx's cartilaginous framework.

The intrinsic laryngeal muscles may be placed in three groups according to their main actions. The posterior and lateral cricoarytenoids and oblique and transverse interarytenoids vary the degree of abduction and adduction of the vocal folds and thus the dimensions and the degree of opening of the rima glottidis. The cricothyroids, posterior cricoarytenoids, thyroarytenoids and vocalis regulate the length and tension of the vocal folds. In reality, the obliquity of the cricoarytenoid facets means that some overlap in function between these two muscle groups is inevitable. Thus, alterations in the dimensions of the rima glottidis will produce small changes in vocal fold length and shortening the vocal folds will also result in a degree of adduction. The third group of muscles is the oblique arytenoids, aryepiglottic and thyroepiglottic muscles, which modify the laryngeal inlet. Bilateral pairs of muscles usually act in concert with each other.

Neuromuscular spindles have been found in all human laryngeal muscles, the maximum number being found in the transverse interarytenoid (Blitzer et al 2009). The control of phonation requires very considerable neuromuscular coordination, and effective proprioception would appear to be essential to this capacity. The mass of muscle related to adduction far outweighs that related to abduction.

Anatomical variations Numerous variations in the anatomy of the intrinsic muscles have been described in the literature. The more frequently found ones are described in the main text. A particularly comprehensive source documenting these variations was published as long ago as 1875 by Fürbringer. Later authors have studied many of these variations but estimates of their frequency often vary significantly between the various studies; the functional significance of many of these variations is not clear.

Oblique arytenoid and aryepiglotticus

The oblique arytenoids and transverse interarytenoid are often considered to be two parts of the same muscle (known as the interarytenoid), in which case it is said to have two parts: transverse and oblique.

The oblique arytenoids lie superficial to the transverse arytenoid and are sometimes considered to be part of it. They cross each other obliquely at the back of the larynx, each extending from the back of the muscular process of one arytenoid cartilage to the apex of the opposite one (**Fig. 41.10C, D**). Some fibres continue laterally round the arytenoid apex into the aryepiglottic fold, forming the aryepiglottic muscle (aryepiglotticus).

Vascular supply Oblique arytenoid receives its blood supply from the laryngeal branches of the superior and inferior thyroid arteries.

Innervation Oblique arytenoid is innervated by the recurrent laryngeal nerve.

Actions The oblique arytenoids and aryepiglottic muscles act as a sphincter of the laryngeal inlet by adducting the aryepiglottic folds and approximating the arytenoid cartilages to the tubercle of the epiglottis. Their poor development limits their capacity to act as a sphincter of the inlet. The oblique arytenoids are weak adductors of the vocal folds and may be more effective in this action than the transverse interarytenoid because of the superior mechanical advantage.

Transverse interarytenoid

Transverse interarytenoid is a single, unpaired muscle deep to the oblique arytenoids (**Fig. 41.10C**). It bridges the gap at the back of the larynx between the two arytenoid cartilages and fills their concave posterior surfaces. It is attached to the back of the muscular process and adjacent lateral border of both arytenoids.

Vascular supply Transverse interarytenoid receives its blood supply from the laryngeal branches of the superior and inferior thyroid arteries.

Innervation Transverse interarytenoid is innervated by the recurrent laryngeal nerves. It also receives branches from the internal laryngeal nerve, although there is debate as to whether these branches contain any distinct motor input. The nerves form a dense, but highly variable, plexus.

Actions Transverse interarytenoid pulls the arytenoid cartilages towards each other, closing the posterior, intercartilaginous, part of the rima glottidis (see Fig. 41.10C).

Posterior cricoarytenoid

Posterior cricoarytenoid arises from the posterior surface of the cricoid lamina (**Fig. 41.10A**). Its fibres ascend laterally and converge to insert on the upper and posterior surfaces of the muscular process of the ipsilateral arytenoid cartilage. The highest fibres run almost horizontally, the middle run obliquely, and the lowest are almost vertical; some reach the anterolateral surface of the arytenoid cartilage. An additional strip of muscle, ceratocricoid, is occasionally seen in relation to the lower border of posterior cricoarytenoid, arising from the cricoid cartilage and inserting on to the posterior aspect of the inferior cornu of the thyroid cartilage.

Vascular supply Posterior cricoarytenoid receives its blood supply from the laryngeal branches of the superior and inferior thyroid arteries.

Innervation Posterior cricoarytenoid is innervated by the recurrent laryngeal branch of the vagus.

Actions The posterior cricoarytenoids are the only laryngeal muscles that open the rima glottidis. They rotate the arytenoid cartilages laterally around an axis that passes through the long axis of the facets of the cricoarytenoid joints, producing separation of the vocal processes and the attached vocal folds (see Fig. 41.10A). They also pull the arytenoids backwards, assisting the cricothyroids to lengthen the vocal folds. The most lateral fibres draw the arytenoid cartilages laterally, and so the rima glottidis becomes triangular when the posterior cricoarytenoid muscles contract. The posterior cricoarytenoids are active in the production of unvoiced sounds.

Lateral cricoarytenoid

Lateral cricoarytenoid is attached anteriorly to the upper border of the cricoid arch. It ascends obliquely backwards to be attached to the front of the muscular process of the ipsilateral arytenoid cartilage (**Fig. 41.10B**).

Vascular supply Lateral cricoarytenoid receives its blood supply from the laryngeal branches of the superior and inferior thyroid arteries.

Innervation Lateral cricoarytenoid is innervated by a variable number of branches of the anterior terminal division of the recurrent laryngeal nerve. In the majority of cases, these branches arise over the muscle itself.

Actions Lateral cricoarytenoid rotates the arytenoid cartilage in a direction opposite to that of posterior cricoarytenoid, and so closes the rima glottidis (see Fig. 41.10B). As it does so, it brings the tips of the vocal processes together, closing the ligamentous part of the rima glottidis, an action known as medial compression. The action of lateral cricoarytenoid in adducting the vocal folds is therefore distinct and complementary to that of the oblique arytenoid and transverse interarytenoid muscles. Contraction of lateral cricoarytenoid also results in shortening and relaxing of the vocal folds.

Cricothyroid

Cricothyroid is attached anteriorly to the external aspect of the arch of the cricoid cartilage (**Fig. 41.10F**). Its fibres pass backwards and diverge into two groups: a lower 'oblique' part, which slants backwards and laterally to the anterior border of the inferior cornu of the thyroid; and a superior 'straight' part, which ascends more steeply backwards to the posterior part of the lower border of the thyroid lamina. The medial borders of the paired cricothyroids are separated anteriorly by a triangular gap occupied by the median cricothyroid ligament.

Vascular supply Cricothyroid is supplied by the cricothyroid artery, a branch of the superior thyroid artery, which crosses high on the cricothyroid ligament to communicate with its contralateral fellow.

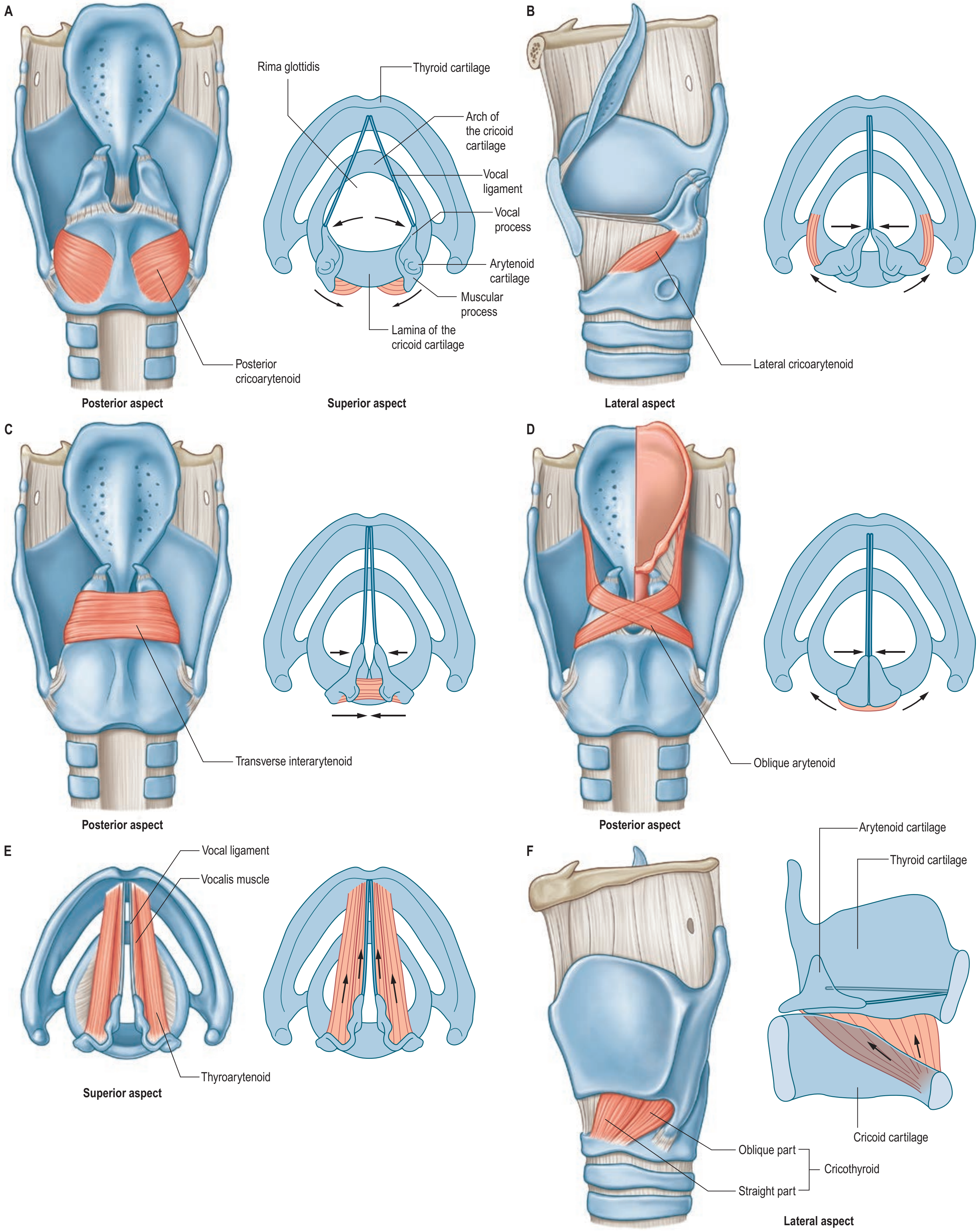
A
Rima glottidis
Thyroid cartilage
Arch of the cricoid cartilage
Vocal ligament
Vocal process
Arytenoid cartilage
Muscular process
Lamina of the cricoid cartilage
Posterior cricoarytenoid
Posterior aspect
Superior aspect
B
Lateral cricoarytenoid
Lateral aspect
C
Transverse interarytenoid
Posterior aspect
D
Oblique arytenoid
Posterior aspect
E
Vocal ligament
Vocalis muscle
Thyroarytenoid
Superior aspect
F
Arytenoid cartilage
Thyroid cartilage
Cricoid cartilage
Oblique part
Cricothyroid
Straight part
Lateral aspect

Fig. 41.10 The intrinsic muscles of the larynx in posterior or lateral views, with their actions shown alongside in a superior view. The arrows indicate the direction of movement of the cartilage in each case. For details, see text.

Innervation Unlike the other intrinsic muscles of the larynx, cricothyroid is innervated by the external branch of the superior laryngeal nerve, and not by the recurrent laryngeal nerve.

Actions Cricothyroid lengthens and hence stretches the vocal folds, increasing their tension. It does this by shortening the space between the inferior border of the thyroid cartilage and the cricoid cartilage, an action that increases the distance between the tip of the vocal process of the arytenoid cartilage and the posterior surface of the lamina of the thyroid cartilage. Rotation happens at the cricothyroid joint (see above). At the same time, the posterior part of cricothyroid pulls the thyroid cartilage forwards, a gliding action that also lengthens the vocal folds. In increasing the tension of the vocal folds, the pitch (frequency) of the voice rises. Some authors consider that cricothyroid has a slight adductive action in moving the vocal folds to a more paramedian position as they are lengthened and thinned (Mu and Sanders 2009, Wadie et al 2013). Others have attributed the relative sparing of abduction in lesions of the recurrent laryngeal nerve to a weak abductive action of cricothyroid. These contradictory views are currently unresolved.

Thyroarytenoid and vocalis

Thyroarytenoid is a broad, thin muscle, lying lateral to the vocal fold, conus elasticus, laryngeal ventricle and saccule (Fig. 41.10E). It is attached anteriorly to the lower half of the angle of the thyroid cartilage, and to the cricothyroid ligament. Its fibres pass backwards, laterally and upwards to the anterolateral surface of the arytenoid cartilage. The lower and more medial fibres form a band that, in coronal section, appears as a triangular bundle attached to the lateral surface of the vocal process and to the fovea oblonga on the anterolateral surface of the arytenoid cartilage. This bundle, the vocalis muscle, is viewed by some authors as simply a medial part of the thyroarytenoid and by others as a distinct and separate muscle. The vocalis is parallel with, and just lateral to, the vocal ligament. It is said to be thicker behind than in front, because many deeper fibres start from the vocal ligament and do not extend to the thyroid cartilage. (An alternative view is that all its fibres loop and intertwine as they pass from the thyroid to the arytenoid cartilage.) A few fibres extend along the wall of the ventricle from the lateral margin of the arytenoid cartilage to the side of the epiglottis. Superior thyroarytenoid, an inconstant small muscle, lies on the lateral surface of the main mass of thyroarytenoid; when present, it extends obliquely from the thyroid angle to the muscular process of the arytenoid cartilage.

Vascular supply Thyroarytenoid receives its arterial blood supply from the laryngeal branches of the superior and inferior thyroid arteries.

Innervation All parts of thyroarytenoid are supplied by the recurrent laryngeal nerve. It also receives a communicating branch from the external laryngeal nerve, although it is not clear whether such branches carry motor or sensory fibres.

Actions The thyroarytenoids draw the arytenoid cartilages towards the thyroid cartilage, thereby shortening and relaxing the vocal ligaments. At the same time, they rotate the arytenoids medially in opposition to the action of posterior cricoarytenoid to approximate the vocal folds and so aid closure of the rima glottidis. Pitch control is achieved by a complex interaction of the intrinsic laryngeal muscles which affect the tension and stiffness of the vocal folds: shortening and slackening of the vocal folds (when cricothyroid relaxes) results in a drop in pitch. Conversely, increasing tension of the vocal folds (when cricothyroid contracts) causes the pitch to rise.

Thyroepiglotticus

Many of the fibres of thyroarytenoid are prolonged into the aryepiglottic fold, where some terminate, and others continue to the epiglottic margin as thyroepiglotticus. The thyroepiglotticus muscles can widen the inlet of the larynx by their action on the aryepiglottic folds.

VASCULAR SUPPLY AND LYMPHATIC DRAINAGE

The blood supply of the larynx is derived mainly from the superior and inferior laryngeal arteries (Fig. 41.11). Rich anastomoses exist between the corresponding contralateral laryngeal arteries and between the ipsilateral laryngeal arteries. The superior laryngeal arteries supply the greater part of the tissues of the larynx, from the epiglottis down to the level of the vocal folds, including the majority of the laryngeal musculature. The inferior laryngeal artery supplies the region around cricothyroid, while its posterior laryngeal branch supplies the tissue around posterior cricoarytenoid (Trotoux et al 1986).

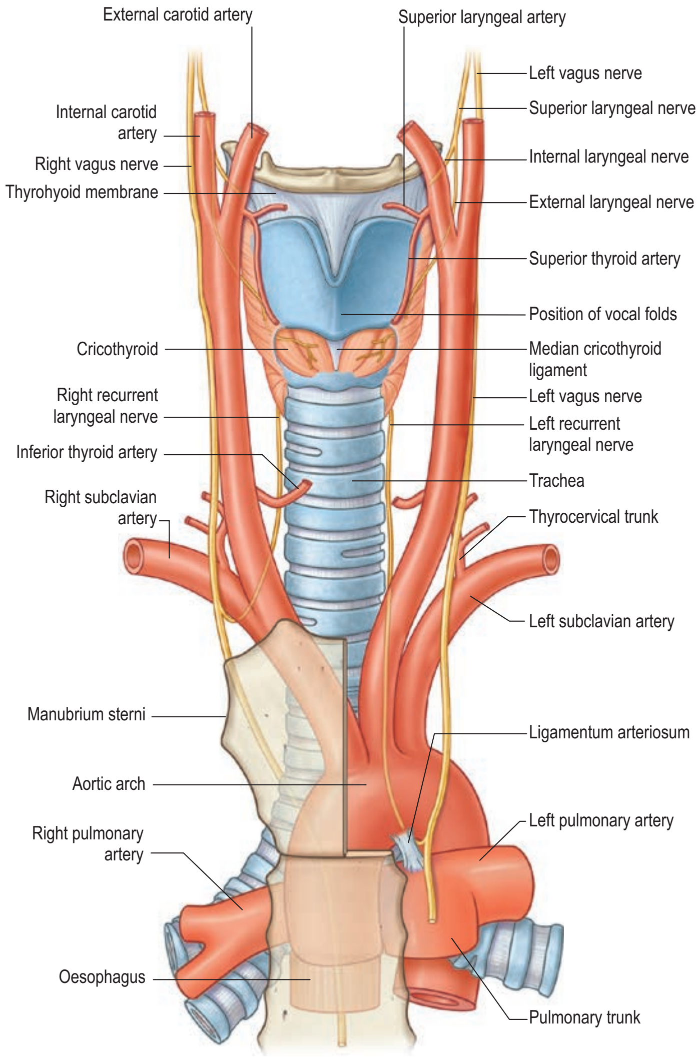

Fig. 41.11 An anterior view of the blood supply and innervation of the larynx. (With permission from Drake RL, Vogl AW, Mitchell A (eds) Gray's Anatomy for Students, 2nd ed. Elsevier, Churchill Livingstone. Copyright 2010.)

Arteries and veins

Superior laryngeal artery

The superior laryngeal artery is normally derived from the superior thyroid artery, a branch of the external carotid artery, as this artery passes down towards the upper pole of the thyroid gland (see Figs 35.7A, 41.11). Sometimes, however, it arises directly from the external carotid artery between the origins of the superior thyroid and lingual arteries or, less commonly, from the common carotid artery or carotid bifurcation (Vazquez et al 2009). The superior laryngeal artery runs down towards the larynx, with the internal branch of the superior laryngeal nerve lying above it. It enters the larynx by penetrating the thyrohyoid membrane and divides into a number of branches that supply the larynx from the tip of the epiglottis down to the inferior margin of thyroarytenoid. It anastomoses with its contralateral fellow and with the inferior laryngeal branch of the inferior thyroid artery.

Cricothyroid artery

The cricothyroid artery arises from the superior thyroid artery and may contribute to the supply of the larynx. It follows a variable course, either superficial or deep to sternothyroid. If superficial, it may be accompanied by branches of the ansa cervicalis, and if deep, it may be related to the external laryngeal nerve. It can anastomose with the artery of the opposite side and with the laryngeal arteries.

Inferior laryngeal artery

The inferior laryngeal artery is smaller than the superior laryngeal artery. It is a branch of the inferior thyroid artery, which arises from

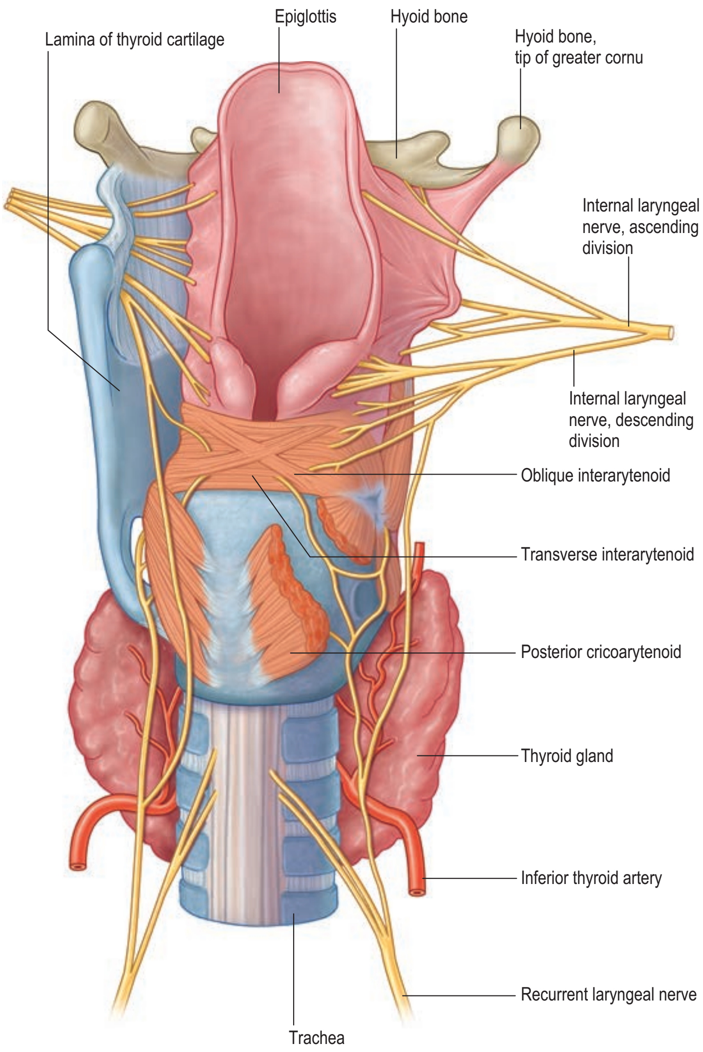
Lamina of thyroid cartilage
Epiglottis
Hyoid bone
Hyoid bone, tip of greater cornu
Internal laryngeal nerve, ascending division
Internal laryngeal nerve, descending division
Oblique interarytenoid
Transverse interarytenoid
Posterior cricoarytenoid
Thyroid gland
Inferior thyroid artery
Recurrent laryngeal nerve
Trachea

Fig. 41.12 Posterior view of the laryngeal innervation.

the thyrocervical trunk of the subclavian artery (see Fig. 35.17). It ascends on the trachea with the recurrent laryngeal nerve, enters the larynx at the lower border of the inferior constrictor, just behind the cricothyroid articulation, and supplies the laryngeal muscles and mucosa. The inferior laryngeal artery anastomoses with its contralateral fellow and with the superior laryngeal branch of the superior thyroid artery.

A posterior laryngeal artery of variable size has been described as a regular feature that arises as an internal branch of the inferior thyroid artery.

Superior and inferior laryngeal veins

Venous return from the larynx is via superior and inferior laryngeal veins, which run parallel to the laryngeal arteries and are tributaries of the superior and inferior thyroid veins, respectively. The superior thyroid vein drains into the internal jugular vein, and the inferior thyroid vein usually drains into the left brachiocephalic vein.

Lymphatic drainage

The vocal folds, with their paucity of lymphatics at their edges, provide a clear demarcation between the upper and lower areas of the larynx. Above the vocal folds, the rich network of lymph vessels draining the supraglottic part of the larynx accompany the superior laryngeal artery, pierce the thyrohyoid membrane, and end in the upper deep cervical lymph nodes, often bilaterally. The supraglottic lymphatics also communicate with those at the base of the tongue. Below the vocal folds, some of the lymph vessels of the infraglottic cavity pass through the conus elasticus to reach the prelaryngeal (Delphian) and/or pretracheal and paratracheal lymph nodes, while others accompany the inferior laryngeal artery and join the lower deep cervical nodes (Welsh et al 1983, Werner et al 2003).

Nodal spread of laryngeal tumours

The upper deep cervical lymph nodes act as pathways for the spread of malignant tumours of the supraglottic larynx. Up to 40% of these tumours will have undergone such spread at the time of clinical presentation. As stated previously, the glottis is very poorly endowed with lymphatic vessels; some 95% of malignant tumours confined to the glottis will present only with a change in voice or airway obstruction, but will not show signs of spread to adjacent lymph nodes at presentation. Tumours of the subglottic larynx will often spread to the paratracheal lymph node chain prior to clinical presentation. The presenting symptoms are usually voice change and airway obstruction rather than a mass in the neck. The paratracheal lymph nodes occupy a deep-seated position in the root of the neck and so their enlargement may remain occult. They must be looked for carefully at surgery and included in any radiation field.

INNERVATION

The larynx is innervated by the internal and external branches of the superior laryngeal nerve, the recurrent laryngeal nerve and sympathetic nerves (see Fig. 41.11; **Fig. 41.12**). Conventionally, the internal laryngeal nerve is described as sensory, the external laryngeal nerve as motor, and the recurrent laryngeal nerve as mixed. The internal laryngeal nerve is sensory down to the vocal folds, the recurrent laryngeal nerve is sensory below the vocal folds, and there is overlap between the territories innervated by the two nerves at the vocal folds themselves. All the intrinsic muscles of the larynx are supplied by the recurrent laryngeal nerve except for cricothyroid, which is supplied by the external laryngeal nerve. A number of anastomoses between the internal, external and recurrent laryngeal nerves have been described, with varying estimates of their incidence. Chronologically, the oldest recorded is that between the recurrent laryngeal nerve and the internal laryngeal branch of the superior laryngeal nerve (Galen's anastomosis). The majority of these anastomoses are found on the posterior surface of the larynx, forming what has been described as a laryngeal plexus to parallel the pharyngeal plexus. Their precise nature and function are unclear, but since some are thought to convey motor fibres, it is reasonable to assume that functions commonly ascribed to the three laryngeal nerves may be more complex than the conventional descriptions imply, which may have potential clinical implications (Sanders et al 1993, Sato and Shimada 1995, Furlan et al 2002, Naidu et al 2014).

The detailed course of the vagus in the neck is described in Chapter 35.

Superior laryngeal nerve

The superior laryngeal nerve arises from the middle of the inferior vagal ganglion. It receives one or more communications from the superior cervical sympathetic ganglion; most frequently, the connection is with the external laryngeal nerve. The sympathetic communication contributes to the innervation of the carotid body (Monfared et al 2002) and the thyroid gland (Sun and Chang 1991). Though the superior laryngeal nerve usually lies on the medial side of the internal carotid artery, it may be found on the lateral side of the artery. The superior laryngeal nerve divides into two branches: a smaller, external and a larger, internal branch, approximately 1.5 cm below the ganglion. Rarely, both branches may arise from the ganglion.

Internal laryngeal nerve

The internal laryngeal nerve passes forwards approximately 7 mm before piercing the thyrohyoid membrane, usually at a higher level than the superior thyroid artery (Durham and Harrison 1962). It splits into superior, middle and inferior branches on entering the larynx. The superior branch supplies the mucosa of the piriform fossa. The large middle branch is distributed to the mucosa of the ventricle, specifically the quadrangular membrane, and therefore probably conveys the afferent component of the cough reflex. The inferior ramus is mainly distributed to the mucosa of the ventricle and subglottic cavity. On the medial wall of the piriform fossa, descending branches give twigs to the interarytenoid muscle and share a number of communicating branches with the recurrent laryngeal nerve (Sanders and Mu 1998).

External laryngeal nerve

The external laryngeal nerve continues downwards and forwards on the lateral surface of the inferior constrictor, to which it contributes some small branches. Indeed, the nerve is sometimes located within the fibres of the constrictor muscle. It passes beneath the attachment of sternothyroid to the oblique line of the thyroid cartilage and supplies cricothyroid. A communicating nerve continues from the posterior surface of cricothyroid, crosses the piriform fossa and enters thyroarytenoid, where it anastomoses with branches from the recurrent laryngeal nerve. It has been suggested that these communicating branches may provide both additional motor components to thyroarytenoid and sensory fibres to the mucosa in the region of the subglottis. An anastomosis between the external and internal laryngeal nerves has also been described in some cases (Kochilas et al 2008).

The close relationship of the external laryngeal nerve to the superior thyroid artery puts the nerve at potential risk when the artery is clamped during thyroid lobectomy, particularly when it is close to the artery (in approximately 20% of cases), or where, instead of crossing the superior thyroid vessels approximately 1 cm or more above the superior pole of the gland, it actually passes below this point (in some 20% of cases) (Cernea et al 1992, Kierner et al 1998). The external laryngeal nerve is also at risk in parathyroidectomy, carotid endarterectomy and anterior cervical spine procedures.

Recurrent laryngeal nerve

The recurrent laryngeal nerve enters the larynx by passing either deep to (usually) or between (sometimes) the fibres of cricopharyngeus at its attachment to the lateral aspect of the cricoid cartilage. It supplies cricopharyngeus as it passes. At this point, the nerve is in intimate proximity to the posteromedial aspect of the thyroid gland. The main trunk divides into two or more branches, usually below the lower border of the inferior constrictor, although branching may take place higher up. The anterior branch is mainly motor and is sometimes called the inferior laryngeal nerve (although this term is best avoided to prevent any confusion with a former synonym for the recurrent laryngeal nerve), while the posterior branch is mainly sensory. The anterior branch of the recurrent laryngeal nerve ascends posterior to the cricothyroid joint and its ligament (Shindo et al 2005). It is usually covered by fibres of posterior cricoarytenoid at this point. It bends over the joint, continuing forwards over the lateral cricoarytenoid muscle before terminating within thyroarytenoid. The anterior branch of the recurrent laryngeal nerve first innervates posterior cricoarytenoid by one or more branches, then innervates interarytenoid and lateral cricoarytenoid, and terminates in thyroarytenoid, which it also supplies (see also Maranillo et al 2005).

The recurrent laryngeal nerve forms several anastomoses with the superior laryngeal nerves (see Fig. 41.12). The posterior branch of the recurrent laryngeal nerve ascends deep to posterior cricoarytenoid to join the descending branch of the internal laryngeal nerve. The ansa Galeni, lying on the interarytenoid muscles, forms a direct connection between the recurrent and internal laryngeal nerves (see Fig. 41.12). There is also a complex anastomosis within and over the posterior surface of the interarytenoid muscles, and, less frequently, anastomoses on the cricoid lamina and thyroarytenoid that form connections with the internal laryngeal nerve (Sanudo et al 1999, Furlan et al 2002).

The recurrent laryngeal nerve does not always lie in a protected position in the tracheo-oesophageal groove but may be slightly anterior to it (more often on the right), and it may be markedly lateral to the trachea at the level of the lower part of the thyroid gland. The upper part of the nerve has a close but variable relationship to the inferior thyroid artery. On the right, it is as often anterior to, or posterior to, or intermingled with, the terminal branches of the artery. On the left, the nerve is usually posterior to the artery, though occasionally it lies anterior to it. The stated incidences of these relationships vary between different authors. The recurrent laryngeal nerve has a highly variable branching pattern (**Fig. 41.13**) (Henry et al 2016).

External to its capsule, the thyroid gland is covered by the visceral layer of deep cervical fascia which splits into two layers at the posterior border of the gland. The anterior layer covers the entire medial surface of each lobe. At, or just above, the isthmus, this layer is conspicuously thickened to form the lateral ligament of the thyroid gland, which attaches the gland to the trachea and the lower part of the cricoid cartilage. The posterior layer passes behind the oesophagus and pharynx to become attached to the prevertebral fascia. A compartment is thus formed on each side of the midline, lateral to the trachea and oesophagus; it contains fat, the recurrent laryngeal nerve and terminal parts of the inferior thyroid artery. The nerve may be lateral or medial to the lateral ligament of the thyroid gland and sometimes may be embedded in it.

A very rare anomaly that is of relevance to laryngeal pathology and surgery is the so-called ‘non-recurrent’ laryngeal nerve, where the right recurrent laryngeal nerve arises directly from the vagus nerve trunk high up in the neck and enters the larynx close to the inferior pole of the thyroid gland. Only the right side is affected, and it is always associated with an abnormal origin of the right subclavian artery from the aortic arch on the left side. If unrecognized, a non-recurrent laryngeal nerve may be susceptible to injury during surgery. It may also potentially be compressed by small tumours of the thyroid gland (Friedman et al 1986).

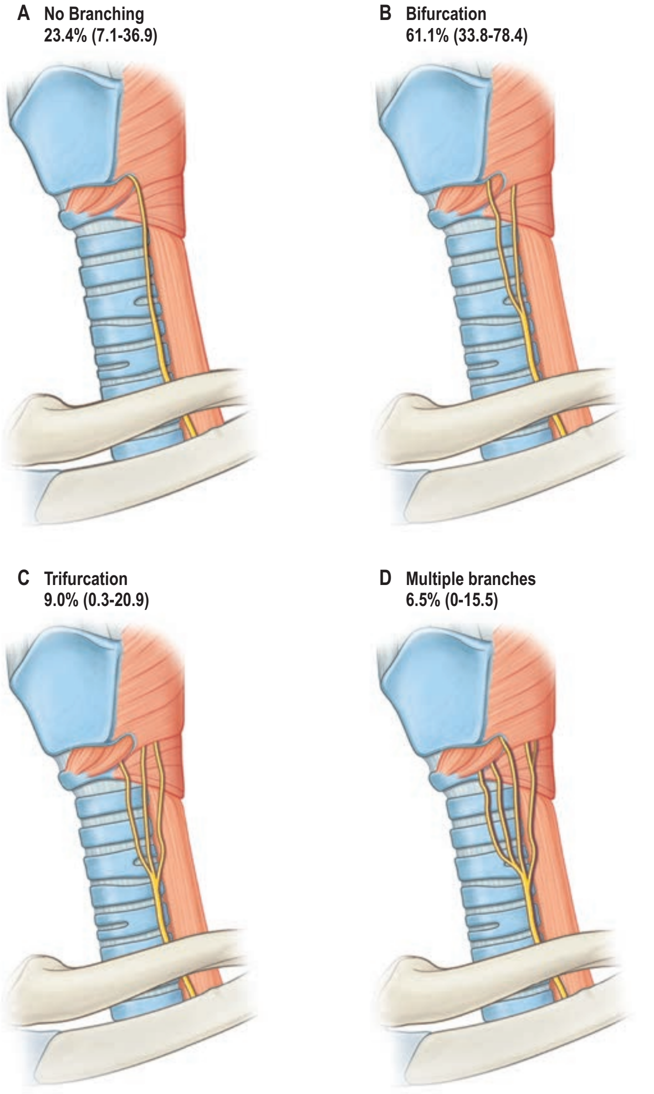

A No Branching
23.4% (7.1-36.9)

B Bifurcation
61.1% (33.8-78.4)

C Trifurcation
9.0% (0.3-20.9)

D Multiple branches
6.5% (0-15.5)

Fig. 41.13 Types of extralaryngeal branching patterns of the recurrent laryngeal nerve, with their pooled cadaver prevalence rates, presented as pooled prevalence rate (95% confidence interval). (Adapted with permission from Henry BM, Vikse J, Graves MJ et al 2016 Extralaryngeal branching of the recurrent laryngeal nerve: a meta-analysis of 28,387 nerves. Langenbecks Arch Surg 401:913–23.)

Interconnections and laryngeal nerve anastomoses

Anastomotic communications between the internal, external and recurrent laryngeal nerves probably explain why normal or near normal voice function can be present following neck surgery when one or more branches of these nerves have been divided (Naidu et al 2014, Henry et al 2017). Numerous communications have been described. Galen's anastomosis is the direct communication between the posterior branches of the internal and recurrent laryngeal nerves: it may be a single or double trunk or a plexus. The cricoid communication connects branches that originate bilaterally from the recurrent laryngeal nerve with the superior branch of the deep portion of the arytenoid plexus. The thyroarytenoid communication links the ascending branch of the recurrent laryngeal nerve and the descending branch from the anterior branch of the internal laryngeal nerve. The arytenoid plexus links the anterior branch of the recurrent laryngeal nerve with the arytenoid branch of the inferior laryngeal nerve. There are also communications between the external laryngeal and recurrent laryngeal nerves and the internal and external laryngeal nerves. The anastomosis between the recurrent laryngeal nerve and the sympathetic trunk probably explains why ptosis is a rare complication following thyroidectomy.

Lesions of the vagus nerve and recurrent laryngeal nerve paralysis

The consequences of vagal nerve lesions are complex, reflecting the long course of the nerve and the possible involvement of three of its branches, namely the pharyngeal, superior laryngeal and recurrent laryngeal nerves. Collectively, these nerves innervate the muscles of the larynx, soft palate and pharynx, and injury may therefore have deleterious effects on phonation and/or soft palate movements and/or swallowing. A lesion of the vagus nerve above the level at which the pharyngeal branch is given off will affect both the superior and recurrent laryngeal nerves. This causes immobility of the vocal fold on the affected side and imparts a breathy voice with lack of pitch and limited loudness. The affected fold is paralysed and lies in the so-called 'cadaveric' position halfway between abduction and adduction. If the lesion is unilateral, the voice is weak and hoarse, but if it is bilateral, phonation is almost absent, the vocal pitch cannot be altered, and the cough is weak and ineffective. There will also be a degree of hypernasality because of the effects on movements of the soft palate caused by paralysis of levator veli palatini. Unilateral palsies impact very significantly on the quality of life of the patient because of impaired vocalization and a tendency to aspirate. Bilateral palsies are extremely serious and a tracheostomy may be required to protect the airway.

A lesion affecting the superior laryngeal nerve may be unilateral or bilateral. Complete section is most likely during the ligation of the vessels forming the vascular pedicle of the superior pole of the thyroid gland during thyroid lobectomy. Unilateral lesions may result in the vocal folds appearing relatively normal and the effect on voice is barely noticeable and is often overlooked. A more detailed examination may detect some shortening of the vocal folds on the affected side with asymmetric tilt of the epiglottis and the anterior larynx canted towards the unaffected side. The result is a mildly hoarse voice with loss of pitch control. Bilateral superior laryngeal nerve lesions result in shortening of both vocal folds, the overhanging of the epiglottis over the folds and reduced tilt between the thyroid and cricoid cartilage. Effects on the voice are correspondingly greater, with reduced loudness and pitch but variable breathiness.

Damage to the internal laryngeal nerve causes loss of mechanoreceptive and proprioceptive sensation from the larynx. Unilateral loss produces a feeling that something is stuck in the throat, whereas bilateral loss will result in aspiration and can cause dysphagia, with a risk of choking.

Unilateral complete palsy of the recurrent laryngeal nerve is more common on the left side, presumably because the nerve is longer on this side. There is isolated paralysis of all the laryngeal muscles on the affected side except cricothyroid, which is innervated by the external laryngeal nerve. The patient may be asymptomatic or have a hoarse, breathy voice and there will be diminished ability to manipulate pitch. The hoarseness may be permanent or may become less severe with time as the contralateral fold develops the ability to hyperadduct and oppose the paralysed fold, thereby closing the glottis during phonation and coughing, although this is seldom enough to restore full voice quality. There may be aspiration of food and drink. Bilateral lesions of the recurrent laryngeal nerve result in both vocal folds being paralysed and taking up a paramedian position. Phonation can be nearly normal because the vocal folds lie so close to the midline, but there will be audible stridor and a compromised airway.

Clinically, the position of the vocal fold in the acute phase after section of the recurrent laryngeal nerve is very variable. Though stridor is more common after bilateral lesions and sometimes only audible to the educated ear, the folds may be sufficiently abducted so that there is little problem with airway obstruction at rest, although the voice is always weaker in this situation. The folds are slightly more widely separated in chronic lesions, which renders the voice weaker but with a less precarious airway. Atrophy and fibrosis of paraglottic muscles probably affect the position of paralysed vocal folds in chronic lesions to a greater degree than variations in the strength of the apposing adductor and abductor muscle groups.

For many years, conventional wisdom held that movements of abduction were affected to a greater degree than those of adduction when the recurrent laryngeal nerve was partially damaged (Semon's law). This effect was thought to reflect the internal segregation within the recurrent laryngeal nerve of axons supplying the laryngeal abductor muscles. The hypothesis was later undermined by the demonstration that axons destined for particular laryngeal muscles are randomly distributed within the nerve. The weak abductive action of cricothyroid that is said to produce lengthening of the vocal folds has been suggested as the explanation for the relative sparing of abduction in these lesions, but is difficult to reconcile with the alternative view that cricothyroid may be a slight adductor of the vocal folds (Mu and Sanders 2009, Wadie et al 2013). It is likely that predicting the effect of partial lesions of the recurrent laryngeal nerve is complicated by the variable patterns of anastomoses between the laryngeal nerves. For further reading, see Aronson and Bless (2009) and Blitzer et al (2009).

Autonomic innervation

Parasympathetic secretomotor fibres run with both the superior and the recurrent laryngeal nerves to mucous glands throughout the larynx. Postganglionic sympathetic fibres run to the larynx with its blood supply and originate in the superior and middle cervical ganglia. A variable number of paraganglia are located on the internal and recurrent laryngeal nerves. Histochemical evidence suggests that one population of neurones in these ganglia have a parasympathetic function while a second population may secrete dopamine (Maranillo et al 2008, Ibanez et al 2010).

ANATOMY OF SPEECH

The principal biological function of the larynx is to act as a sphincter controlling the entry of foreign bodies into the airways and to regulate airflow during ventilation. Thus, the glottis is opened widely during ventilation and is closed tightly during swallowing. The larynx can also close tightly during exertion (effort closure) to regulate thoracic and abdominal pressure during activities such as defecation or parturition, or to fix the thorax to increase mechanical advantage when using the arms to lift objects. The importance of the latter activity should not be underestimated. One of the many problems reported by patients who have undergone a laryngectomy is a loss of power in their arms when trying to lift heavy objects.

The larynx is much more than a simple valve that opens and closes. In addition to its sphincteric functions, its location means that it is perfectly placed to act as a sound source, or voice, that forms the basis of many sounds in human speech. The musculoskeletal structure of the larynx is under exquisite neuromuscular control, allowing it to modify the expiratory stream to produce highly complex patterns of sound of varying loudness, frequency and duration. The ability to execute these complex movements depends largely on specific areas of the cerebral hemispheres that are involved in the motor aspects of language, such as speech and writing, and sensory manifestations of language, including reading and understanding the spoken word. Central control of voice production involves two parallel pathways: a limbic pathway responsible for the control of innate non-verbal and emotional vocalizations, and a larynx-specific motor cortical pathway responsible for regulating the motor control necessary for voluntary voice production. For further reading, see Atkinson and McHanwell (2002), Clark et al (2007), Kaplan (1971), Laver (1980), Sataloff (2017), Titze (1994) and Zemlin (1998).

Overview of speech production

All speech requires an input of energy. For all sounds in Western European languages, and most sounds in other languages, this energy takes the form of a pulmonary expiration. This continuous airflow is converted into a vibration within the larynx by a mechanism called phonation, in which the vocal folds vibrate periodically, interrupting the column of air as it leaves the lungs and converting it into a series of discrete puffs of air. Speech sounds that are produced by vocal fold vibration in this way are said to be voiced. Speech sounds that are produced without vocal fold vibration are termed unvoiced sounds.

The larynx is an inadequate sound source to produce the complex sounds required for comprehensible speech; the laryngeal 'buzz' that is produced by phonation is very quiet and cannot be varied sufficiently to produce the complex range of sounds that is human speech. Amplification and modification of the sound takes place in the supralaryngeal vocal tract, which may be considered as a 17 cm long tube, narrow at the larynx and broadening out proximally as it passes through the pharynx, oral and nasal cavities. This tube acts as a passive amplifier of the sound. (The analogy here is of a megaphone: cupping the hands round the lips lengthens the vocal tract and increases the volume of speech.) The supralaryngeal vocal tract modifies the basic vibration of the larynx by altering its geometry, length and calibre: it provides a series of resonators that can dampen or amplify certain sound frequencies and can transiently interrupt the exhaled air flow and modify it to produce speech. This process is known as articulation. The range of sounds that the human vocal tract is capable of producing is very wide, although any one human language will employ a subset of these sounds to convey meaning. The study of the integration of laryngeal sound production and articulation to produce complex speech is known as phonetics.

Muscular control of the airstream

Normal vegetative ventilation involves rhythmic movements of the thoracic cage that are produced by intercostal muscles, the diaphragm and a number of accessory muscles in the neck, arm and abdomen that have one attachment to some part of the thoracic cage. The thorax is capable of responding mechanically to widely varying demands for oxygen. From a tidal volume at rest of 500 ml and a respiratory rate of 12 per minute, ventilation can increase in fit individuals during vigorous exercise to tidal volumes of 4.5 litres and respiratory rates of 20–25 per minute.

Normal ventilatory patterns are considerably modified during speech, reflecting the special demands that speech places on ventilation. The main source of energy for the production of speech sounds is a pulmonary expiration, although other mechanisms are possible. In order for speech to be produced, sufficient pressure has to be generated beneath the vocal folds. This subglottal pressure (the difference between the air pressures above and below the vocal folds) has to be sustained above a minimum level throughout an utterance. It sets the vocal folds into vibration if the sound is to be voiced or generates airflow for an unvoiced sound. The minimum subglottal pressure needed for speech production is 7 cm H_2O and this increases when loud sounds are produced or when sounds are stressed.

The need to generate sufficient sustained pressure means that speech ventilation is markedly non-rhythmical. At the onset of an utterance, inspiration is typically 1.5 litres, which is deeper than for normal quiet ventilation, ensuring that sufficient air is taken in to maintain adequate subglottal pressure for the duration of the utterance. Inspiration is also quicker, 0.5 seconds rather than 2–3 seconds. Expiration is much longer than normal, perhaps lasting up to 30 seconds, reflecting the fact that the vocal tract is more constricted at the larynx to ensure that pauses for further inspirations are made at suitable points in an utterance. At the end of the first inspiration during running speech, lung volumes do not fully return to resting levels. Conversational speech normally takes place at a higher range of lung capacities than operate in normal quiet ventilation.

The non-rhythmical pattern during speech requires greater inspiratory effort, and for most people it involves a greater use of the diaphragm, usually in combination with the abdominal muscles that are attached to the lower ribs and stabilize the costal attachments of the diaphragm to increase the effectiveness of its action. The main differences are seen in expiration. Speech takes place at higher lung volumes, which means that greater recoil forces are stored in the elastic tissues of the lungs and the ribcage. The generation of subglottal pressure is the product of these elastic recoil forces and the muscular forces generated by the expiratory muscles. At the onset of an utterance, unrestrained recoil forces would generate excessive subglottal pressures that would be wasteful of air, and hence energy, and would affect the loudness of speech. Conversely, towards the end of an utterance, as recoil forces decline, subglottal pressure would fall without additional muscular exertion. Therefore, early in an utterance, inspiratory muscles, particularly the external intercostals and parasternal parts of the internal intercostals, continue to contract, relaxing slowly to counteract the effects of excessive passive elastic recoil. As the recoil forces decline below the point where they can maintain the minimum subglottal pressure needed for phonation, expiratory muscles contract to maintain subglottal pressure as lung air volume nears its resting expiratory level. The main muscles involved are the costal parts of the internal intercostals and the subcostal and transversus thoracis muscles. Their actions are aided by contraction of the anterior abdominal muscles to compress the abdomen. Accessory muscles such as latissimus dorsi may also come into play, but normally these accessory muscles are only active at the end of a very long or loud utterance, or in patients whose ventilatory function is compromised.

Though subglottal pressure tends to remain fairly constant during an utterance, it rises when sounds are stressed, and falls during the production of unvoiced sounds when the larynx is less constricted. At these times, compensatory mechanisms are required to ensure that pressure is maintained; the precise mechanisms have yet to be elucidated but the internal intercostal muscles have been implicated. The anterior abdominal muscles are also active in singing and shouting, and in attempts to speak without the pause necessary for inspiration. Contrary to popular belief, the diaphragm plays little part in the regulation of expiratory force. Unlike the intercostal muscles, the diaphragmatic musculature is sparsely supplied with muscle spindles, and therefore control of the diaphragm is poorly regulated; minute changes can be effected more successfully using the intercostal and anterior abdominal muscles.

Though the expiratory airflow from the lungs is the source of energy for most speech sounds, other sources of airflow are also used. The larynx can be used to generate airflow. The sound /p/ is produced by closing the larynx and then raising it with the lips closed, using the larynx like a piston. Opening the lips then releases a puff of air. This is called an ejective and is an example of egressive glottalic airflow. Ingressive glottalic airflow is also possible, though less effective; examples are not found in English but do in some African and native American languages. A third kind of airflow is velaric, in which the back of the tongue is raised against a lowered soft palate and the vocal tract is closed anterior to that point, either at the lips or with the tongue against the hard palate. This produces a click and is rare. A non-linguistic example in English is the sound made in encouraging a horse. Ingressive pulmonary airflow, such as is found in a groan or a gasp, is theoretically possible, but none of the world's languages employ this as a source of airflow.

After removal of the larynx, e.g. following laryngeal cancer, patients can be taught to swallow air, store it in a segment of the oesophagus and then use it as the energy source to produce egressive oesophageal airflow (oesophageal speech). Speech in these circumstances tends to have a belching quality. Laryngectomy patients always produce phrases that are shorter than normal, and so prostheses incorporating valves and surgical shunts are often inserted to provide a larger egressive airstream by diverting air from the respiratory tract into the oesophagus.

Phonation

The default position of the rima glottidis is open, to maintain patency of the airway during respiration. In quiet respiration, the anterior intermembranous part of the rima glottidis is triangular when viewed from above. Its apex is anterior and its base posterior, and it is represented by an imaginary line approximately 8 mm long connecting the anterior ends of the arytenoid vocal processes. The intercartilaginous part between the medial surfaces of the arytenoids is rectangular, as the two vocal processes lie parallel to each other. During forced respiration, the rima glottidis is widened and the vocal folds are fully abducted to increase the airway (see Fig. 41.8). The arytenoid cartilages rotate laterally, and this moves their vocal processes apart, and converts the rima glottidis into a diamond shape in which both intermembranous and intercartilaginous parts are triangular. The greatest width of the rima glottidis is at the point of the attachments of the vocal folds to the vocal processes.

During speech, the true vocal folds vibrate to act as a source of sound for subsequent speech. There have been a number of theories to explain the mechanism that produces this vibration but these are now only of historic interest. The aerodynamic–myoelastic theory is generally accepted as the mechanism underlying vocal fold vibration, although it does not account for all aspects of phonation.

At the onset of an utterance, during an expiration, the true vocal folds are adducted: the lateral cricoarytenoids and transverse interarytenoids bring together both the intermembranous and intercartilaginous parts of the rima glottidis, actions that either close the glottis completely or reduce the space between the vocal folds to a linear chink. The mucous membrane covering the interarytenoid muscles, the interarytenoid fold, intrudes into the larynx when these muscles adduct the arytenoids, and so aids closure of the intercartilaginous part of the rima glottidis. The vocal folds are also tensed, an essential prerequisite for vibration. These actions cause a build-up of subglottal pressure that continues until a point is reached when the muscular force of adduction is no longer sufficient to resist the rising pressure, and the membranous portions of the vocal folds are forced open a little, releasing air into the supralaryngeal vocal tract. The subglottal pressure falls when the subglottic and supraglottic cavities become continuous and the vocal folds begin to close. Two mechanisms bring about closure. If adductive tension is sustained, then the vocal folds will close. In addition, rapid closure is aided by a physical process, the Bernoulli effect. The forcing of air from a region of high to low pressure through a narrow space causes an increase in the kinetic energy of the molecules at the edge of the space. The effect of this is to lower pressure in the space between the folds at the level of the folds themselves, and this negative pressure simply sucks the folds together because they are mobile. This causes a rise once more in the subglottal pressure and the cycle is repeated. The effect is to cause the release of a series of puffs of air into the supralaryngeal vocal tract at a frequency of many times per second, which is perceived as a sound of a particular frequency (**Figs 41.14–41.15**, **Video 41.1**).

The source of energy for the vibration does not come from the larynx itself. The vocal folds do not behave like the prongs of a tuning fork; their predominant motion is in the horizontal plane at right-angles to the movement of the air column, and there is little vertical movement.

The energy is derived from the motion of the air generated by the muscular and recoil forces in the thorax, and the larynx is simply chopping that column into a series of segments.

The aerodynamic–myoelastic theory does not explain how vocal fold vibration is sustained; nor does it account for the very obvious muco-undulatory component of vocal fold vibration that is visible when the larynx is viewed stroboscopically. Without further input of energy, the vibration of the vocal folds as described above would not be sustained but would be damped and gradually diminish. For vibration to continue there has to be additional energy input. The analogy here is with a child on a swing. For the motion to continue, either the parent has to push the child at an appropriate point in the cycle, or the child has to sustain the motion for themselves by swinging their legs at the crucial point in the swing cycle. In the case of phonation, the source of this additional energy is unclear. It may come from the inertia of the air column itself, i.e. once the vocal folds close, the air column will continue moving upwards because inertia creates a negative pressure above the folds. Alternatively, the energy could come from the manner in which the folds open and close. As the subglottal pressure rises, the lower portion of the fold opens first and the upper edge of the fold is last to open, and when the subglottal pressure falls, the folds close from the bottom edge. It has been suggested that this non-uniform closure creates different shapes within the glottis that may result in differing negative pressures at different phases of the cycle. It also produces a vertical wave-like motion in the folds, termed the muco-undulatory component (or 'mucosal wave'). The analogy here is with a flag blowing in the wind, and it reflects the differing stiffness of the various layers of the vocal folds described above. This vertical component will impart a negligible amount of energy to the air column, but it is likely to impart harmonics to the basic laryngeal vibration.

The sound that results from the process of phonation has three characteristics: a frequency that is perceived as pitch, an intensity that is perceived as loudness, and a timbre perceived as voice quality.

The fundamental frequency of the human voice is determined by the resting length of the vocal folds and varies with age and sex. The frequency range of human speech is from 60 to 500 Hz, with an average of approximately 120 Hz in males, 200 Hz in females and 270 Hz in children. The mechanism of frequency alteration is not entirely clear. An increase in subglottal pressure will cause the frequency of phonation to rise. During an utterance, however, subglottal pressure appears to remain fairly constant, which suggests that the mechanism of frequency alteration resides in intrinsic changes within the vocal folds. Variations in frequency (pitch changes) during an utterance are determined by the complex interrelationships between length, tension and thickness of the vocal folds; one of these variables cannot be altered without affecting the other two parameters to some extent. Gross changes to the vocal folds demonstrate the effects of these variables. Inflamed and swollen vocal folds are much thicker than normal and result in a hoarse voice. At puberty, growth of the thyroid cartilage in males lengthens the vocal folds and lowers the fundamental frequency, and the voice 'breaks' as a result. During panic, the vocal folds may be tensed, which means that the cry for help is a high-pitched squeak.

Pitch is increased by lengthening the vocal folds, as may be confirmed during direct endoscopic examination of the larynx. At first sight this may seem counterintuitive but, as the vocal folds are lengthened, there will be a consequent thinning and stretching. Although an analogy is often drawn between the vocal folds and vibrating strings, a better analogy is that of a rubber band: if a rubber band is lengthened, the tension will increase but the thickness will decrease. The vocal folds may be lengthened by up to 50% of their resting length. It is likely that the initial pitch setting is achieved by action of the cricothyroids, and that fine adjustments can then be made using the vocalis muscles. Paralysis of both cricothyroids, which is usually associated with loss of the neurones that are distributed via the superior laryngeal nerve (as a result of damage to the vagal nuclei in brainstem stroke), results in permanent hoarseness and inability to vary the pitch of the voice. It is important to remember that, once the vocal folds are set in motion, they will deviate from their original setting as they vibrate. Auditory feedback of the sounds produced is used to make minute compensatory adjustments to length, tension and thickness in order to maintain a constant pitch.

Any lengthening of the vocal folds tends to thin them. The thickness can be increased by the vocalis part of thyroarytenoid: as vocalis shortens, it will relax the vocal folds and at the same time increase their thickness. Changes in the tension of the vocal folds are produced by the same muscles that change their length, namely: cricothyroid, posterior cricoarytenoid and vocalis, probably acting isometrically.

Articulation

Available with the *Gray's Anatomy* e-book

Production of vowels

Available with the *Gray's Anatomy* e-book

Production of consonants

Available with the *Gray's Anatomy* e-book

Bonus e-book content

Fig. 41.6 C, CT. Note the calcified thyroid cartilage.

Fig. 41.14 A video montage of the normal phonatory cycle, obtained using a rigid 70° Hopkins rod endoscope with stroboscopic illumination.

Fig. 41.15 The position of the vocal folds during a cycle of vocal fold vibration (phonatory cycle).

Fig. 41.16 Sagittal view of the left side of the head, showing the supralaryngeal vocal tract, the articulators and places of articulation.

Video 41.1 Stroboscopic examination of the vocal folds.

Key references

Blitzer A, Brin MF, Ramig LO 2009 Neurologic Disorders of the Larynx, 2nd ed. New York: Thieme.
A book dealing with the evaluation, diagnosis and management of sensory and motor disorders of the larynx. It also includes topics on the normal anatomy and physiology of the larynx.

Dickson DR, Maue-Dickson W 1982 Anatomical and Physiological Bases of Speech. Boston: Little, Brown.
Some highly detailed descriptions of the structure of the larynx.

Friedrich G, Lichtenegger R 1977 Surgical anatomy of the larynx. J Voice 11:345–55.
A cadaveric study providing detailed anatomical measurements.

Hollinshead WH 1982 Anatomy for Surgeons. Vol I: The Head and Neck, 3rd ed. Philadelphia: Harper & Row.
An older textbook that contains useful information not otherwise readily available. A guide to the earlier literature.

Kaplan HM 1971 Anatomy and Physiology of Speech. New York: McGraw–Hill.
A thorough and comprehensive description of laryngeal anatomy and physiology.

Sataloff RT 2017 Clinical anatomy and physiology of the voice. In: Professional Voice: The Science and Art of Clinical Care, 4th ed. San Diego: Plural Publishing.
A very comprehensive discussion within a textbook on clinical care of professionals' voices.

Sato, K 2018 Functional Histoanatomy of the Human Larynx. Singapore: Springer Nature.
A beautifully illustrated and highly detailed microstructural textbook.

Welsh LW, Welsh JJ, Rizzo TA 1983 Laryngeal spaces and lymphatics: current anatomic concepts. Ann Otol Rhinol Laryngol Suppl 105:19–31.
A description of the 'tissue spaces' and lymphatic drainage of the larynx and their importance in determining the route of spread of tumours.

Werner JA, Dünne AA, Myers JN 2003 Functional anatomy of the lymphatic drainage system of the upper aerodigestive tract and its role in metastasis of squamous cell carcinoma. Head Neck 25:322–32.
A discussion of the routes of lymphatic drainage from the larynx and related structures.

The mechanism by which loudness is increased is the subject of less debate. Loud sounds are produced by increasing subglottal pressure. This is achieved, in turn, by changing the opening quotient of the glottis (the ratio of the time spent in the open phase of the cycle to the total cycle time). In normal speech, this ratio is usually around 0.5, but in very loud speech it can fall to 0.3.

Timbre or voice quality refers to the harsh or mellow quality of the voice. The quality of the voice that can be consciously altered is, to a certain extent, a function of the harmonic frequencies produced by the vocal folds. Alteration of the shape of the supraglottic vocal tract accentuates different harmonics, altering the quality of the voice. Changes in harmonic frequencies facilitate production of different vowels and allows for a 'bright' or 'dark' sound in the voice.

Nearly all languages make the fundamental distinction between voiced and unvoiced sounds. Voicing has been described above. In unvoiced sounds, the vocal folds are not vibrating and will usually be opened under the action of posterior cricoarytenoid. The energy from the airstream is then used by other parts of the vocal tract to generate sound, normally by constricting or stopping the airflow. Phonation is not an all-or-nothing process, but is subject to considerable modification and adjustment. In modal voice, i.e. speaking using habitual pitch, forces acting on the vocal folds are moderate, pressures are sustained, and air is conserved. However, phonation can take place when the vocal folds are more open than usual, resulting in breathy phonation with more air escaping per phonatory cycle than usual. Some languages in South Asia exploit the difference between breathy and non-breathy sounds, whereas in spoken English, a breathy voice is simply recognized as a feature of some speakers. At the other end of the spectrum is vocal creak, where the vocal folds are more closed than normal. Different speakers will habitually employ different laryngeal settings that contribute to their particular voiced quality. In whispering, the intramembranous part of the rima glottidis is closed but the intercartilaginous part remains open, producing a characteristic Y-shaped rima glottidis and a greater loss of air at each phonatory cycle.

With regards to speech, the main function of the larynx is to act as a sound source, but it can also function in speech as an airstream generator and as an articulator.

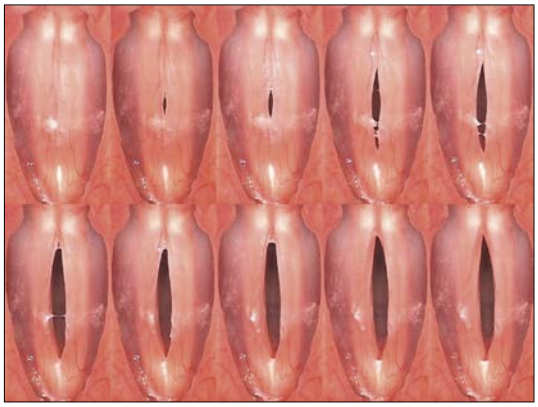

Fig. 41.14 A video montage of the normal phonatory cycle, obtained using a rigid 70° Hopkins rod endoscope with stroboscopic illumination. (Courtesy of Professor Paul Carding.)

The sound produced by phonation is not a pure tone because several harmonics at multiples of the fundamental frequency are also generated. Harmonics give a note of a particular frequency its defining characteristics. An 'A' played on an oboe or violin is immediately recognizable as coming from one or other instrument because of the different harmonics generated by the design of the instrument. The harmonic spectra of individual voices differ and will also vary depending upon the mode of phonation adopted. In the human vocal tract, the fundamental frequency and its harmonics are transmitted to the column of air that extends from the vocal folds to the exterior, mainly through the mouth. Part of the airstream can also be diverted through the nasal cavities when the soft palate is depressed to allow air into the nasopharynx. The supralaryngeal vocal tract acts as a selective resonator in which length, shape and volume can be varied by the actions of the muscles of the pharynx, soft palate, fauces, tongue, cheeks and lips; the relative positions of the upper and lower teeth, which are determined by the degree of opening and protrusion or retraction of the mandible; and alterations in the tension of the walls of the column, especially in the pharynx. Thus, the fundamental frequency (pitch) and

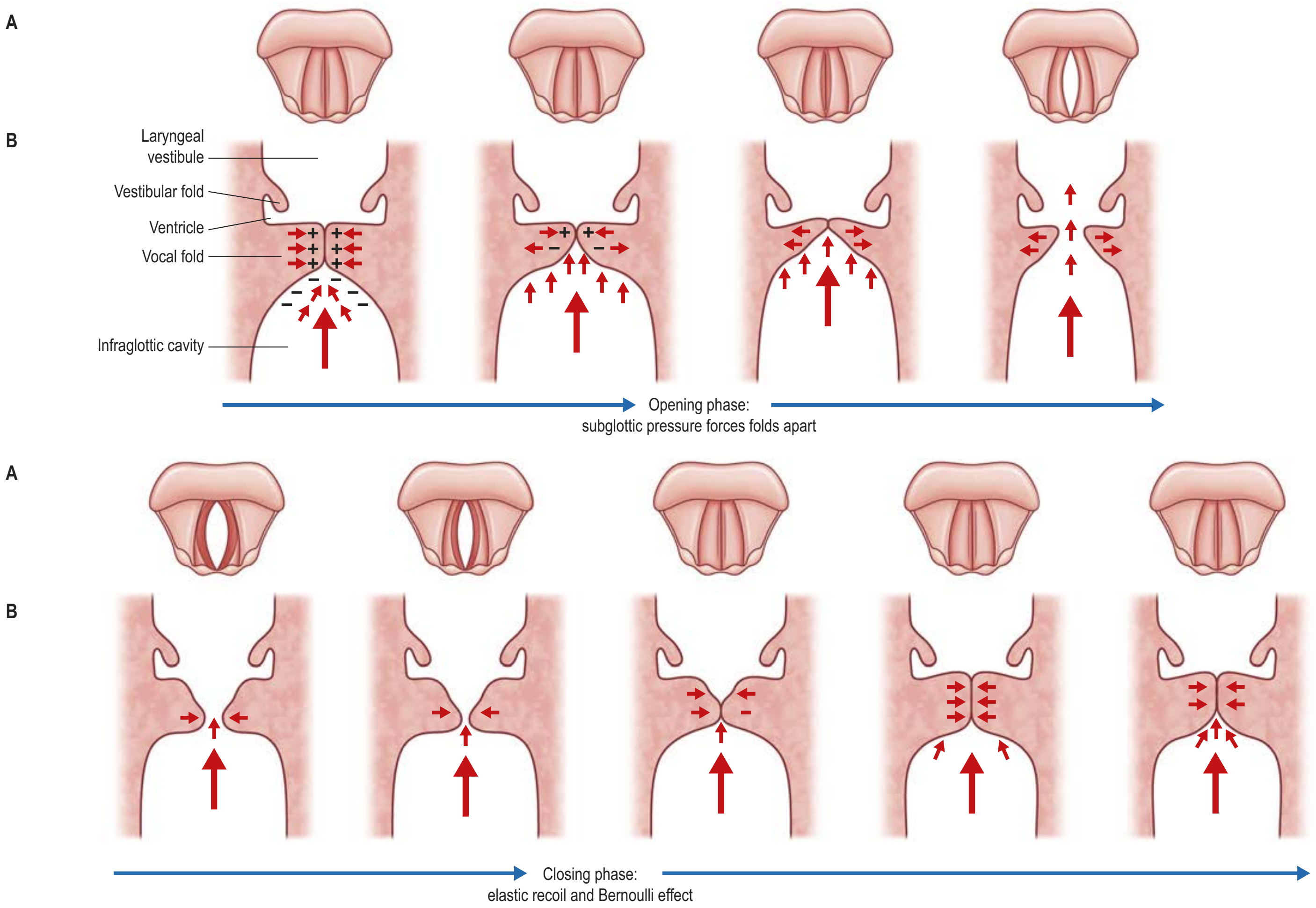

Fig. 41.15 The position of the vocal folds during a cycle of vocal fold vibration (phonatory cycle). **A**, Superior view. **B**, Coronal view.

harmonics produced by the passage of air through the glottis are modified by changes in the supralaryngeal vocal tract.

Harmonics may be amplified or dampened. The fundamental frequency and its associated harmonics may also be raised or lowered by appropriate elevation or depression of the hyoid bone and the larynx as a unit. This is achieved by the selective actions of the extrinsic laryngeal muscles that can shorten or lengthen the resonating column, and to some extent, also alter the geometry of the walls of the air passages. Analysis of the human voice shows that it has a very similar pattern of harmonics for all fundamental frequencies, determined by the vocal tract acting as a selective filter and resonator. This maintains a constant quality of voice without which intelligibility would be lost (recorded speech played back without its harmonics is completely unintelligible). Each human voice is unique and it has been suggested that the unique frequency spectrum of each individual voice could be used for personal identification.

During articulation, the egressive airstream is given a rapidly changing specific quality by the articulatory organs, the lips, oral cavity, tongue, teeth, palate, pharynx and nasal cavity. The discipline of phonetics primarily deals with the way in which speech sounds are produced, and consequently with the analysis of the mode of production of speech sounds by the vocal apparatus. In order to analyse the way in which the articulators are used in different speech sounds, words are broken down into units called phonemes, which are defined as the minimal sequential contrastive units used in any language.

The human vocal tract can produce many more phonemes than are employed in any one language. Not all languages have the same phonemes, and within the same language, the phonemes can vary in different parts of the same country and in other countries where that language is also spoken. Reproducing phonemes that are not used in native speech is difficult because such phonemes require unfamiliar positioning of the speech organs. A native speaker of any language can quickly recognize the origins of anyone attempting to use their language as a second language. The second-language speaker will usually speak it with an accent characteristic of their own first language because they are using the familiar configurations of their vocal tract for each phoneme instead of the correct positioning.

All vowel sounds require phonation by vibration of the vocal folds. Each vowel sound has its own characteristic higher harmonics (frequency spectrum) that exhibit peaks of energy at certain frequencies. These energy peaks are always higher multiples of the fundamental frequencies and are called formants. Formants are the result of the combined effects of phonation, selective resonance of the vocal tract, and the properties of the head as a radiator of sound. The sounds of the different vowels are determined by the shape and size of the mouth, and the positions of the tongue and lips are the most important variables. The tongue may be placed high or low (close and open vowels), or further forwards or back (front and back vowels), and the lips may be rounded or spread.

The production of consonants always involves some degree of constriction of the vocal tract. There are many more consonants than vowels, and, in general, consonants cannot be combined to produce syllables. The classification of consonants is complex and beyond the remit of this book; what follows is a summary (for fuller details, a textbook of phonetics should be consulted).

Consonants may be classified on the basis of where the constriction happens, termed the place of articulation; the degree or extent of constriction, termed the manner of articulation; the shape of the constriction, termed the stricture; and whether or not there is vibration of the vocal folds, when consonants are described as voiced or unvoiced, respectively.

Consonants may also be classified as labial, dental, alveolar, velar, uvular, pharyngeal or glottic, depending on whether the point of maximum constriction occurs at the level of the lips, teeth, bony ridge behind the teeth, palate, uvula, pharynx or glottis, respectively (Fig. 41.16). Different parts of the tongue can be used in combination with the above places of articulation. Phoneticians divide the tongue into the tip, anterior edge, the front part of the dorsum, the centre and back parts of the remaining dorsum, and a most posterior part (the root). These divisions bear no obvious relationship to the anatomical landmarks on the tongue, but they are useful in describing the part of the dorsum of the tongue that contacts other areas of the mouth. Similarly, the manner of articulation can vary from a complete closure to a slight narrowing. An actual closure of the vocal tract is called a stop. A narrowing that is sufficient to produce turbulence of the air in the vocal tract, and which is perceived as a rustling sound, is termed a fricative. Approximants involve a degree of closure insufficient to produce turbulence but with closure greater than that for a vowel. Nasals involve a stoppage in the oral cavity with the soft palate lowered to allow airflow through the nose, and, unlike stops, they can be sustained. Stricture describes the shape of the constriction, e.g. a lateral consonant involves depression of the sides of the tongue, while a grooved consonant is produced by grooving the dorsum of the tongue. Consonants can be produced with the vocal folds vibrating, when they are termed voiced, or without vocal fold vibration, in which case they are termed unvoiced.

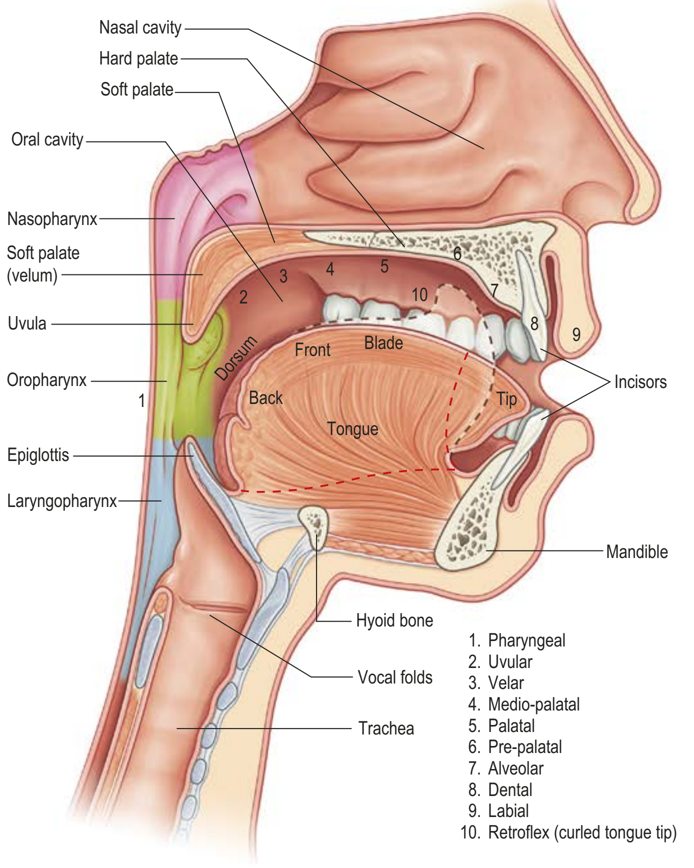

Fig. 41.16 Sagittal view of the left side of the head, showing the supralaryngeal vocal tract, the articulators and places of articulation. The red broken line indicates the tongue position during retroflexion (10).

The best way to illustrate these classificatory systems in operation is by contrasting the production of different consonant pairs in which only one or two parameters have been changed. The /p/ of peat, the /b/ of beat and the /m/ of meat are all bilabial stops, meaning that they are produced by bringing together the lips. The /b/ and the /m/ are voiced but the /p/ is not. The contrast between the /b/ and the /p/ is in the differing way in which the airstreams are produced. The /b/ is produced with a closure of the vocal folds producing sounds (hence it is a 'voiced' consonant) during pulmonary airflow, while the /p/ is produced with the glottis open – hence is unvoiced – and the glottis is then raised using the larynx as a piston to compress the air in the supralaryngeal vocal tract prior to the stop being released. The /m/ differs from the other two stops in being a nasal in which the soft palate is lowered to allow air to escape through the nasal cavity; unlike the other two stops, it can be sustained as in a sound of approval. Bilabial stops can be contrasted with the labiodental fricatives /f/ of feet and the /v/ of veal, both of which are produced by retracting the lower lip beneath the upper teeth. Neither involves a complete closure but both produce a significant constriction of the vocal tract with audible turbulence: the /f/ is unvoiced, while the /v/ is voiced. The sh sound (/ʃ/) in ship is also a fricative involving a grooving of the tongue and is associated with significant audible turbulence; it may be contrasted with the lateral approximant /l/ in law, in which the sides of the tongue are lowered. In this case, it is the nature of the stricture that is different and the degree of closure, e.g. in the case of the approximant /l/, closure is insufficient to produce turbulence. The sh sound in ship can be compared to the /k/ in keen, where the position of the tongue is different: in /k/ the tongue blade contacts the soft palate, while in sh the tongue tip or the blade contact the postalveolar region. The most dramatic example of the difference between voiced and unvoiced sounds may be appreciated if the /s/ sound in sip is compared with the /z/ in zip. If the larynx is loosely palpated while making a sustained unvoiced 'ssssss' sound, no vibration is felt, but if the 'ssssss' is commuted into a prolonged voiced 'zzzzzz', then vibration in the larynx should be readily detectable. The position of the tongue and other articulators is exactly the same for both /s/ and /z/; the difference between them is the presence or absence of phonation.

References

Adewale L 2009 Anatomy and assessment of the pediatric airway. Paediatr Anaesth 19 (Suppl 1):1–8.

Aronson AE, Bless DM 2009 Clinical Voice Disorders, 4th ed. New York: Thieme.

A comprehensive summary of the organic disorders of voice due to laryngeal structural changes and neurological disease, as well as psychogenic voice disorders.

Atkinson M, McHanwell S 2002 Basic Medical Science for Speech and Language Therapy Students. London: Whurr.

Awd Allah RS, Dkhil MA, Farhoud E 2009 Fibroblasts in the human vocal fold mucosa: an ultrastructural study of different age groups. Singapore Med J 50:201–7.

Berkovitz BKB, Moxham BJ, Hickey S 2000 The anatomy of the larynx. In: Ferlito A (ed.) Diseases of the Larynx. London: Chapman & Hall; pp. 25–44.

A description of all aspects of laryngeal anatomy, together with a very useful bibliography.

Blitzer A, Brin MF, Ramig LO 2009 Neurologic Disorders of the Larynx, 2nd ed. New York: Thieme.

A book dealing with the evaluation, diagnosis and management of sensory and motor disorders of the larynx. It also includes topics on the normal anatomy and physiology of the larynx.

Bosma JF, Bartner MA 1993 Ligaments of the larynx and the adjacent pharynx and esophagus. Dysphagia 8:23–8.

Bradley RM 2000 Sensory receptors of the larynx. Am J Med 108:47S–57S.

Cernea CR, Ferraz AR, Nishio S et al 1992 Surgical anatomy of the external laryngeal branch of the external laryngeal nerve. Head Neck 14:380–3.

Chen S, Wang H, Fong AH et al 2012 Micro-CT visualization of the cricothyroid joint cavity in cadavers. Laryngoscope 122:614–21.

Clark J, Yallop C, Fletcher J 2007 An Introduction to Phonetics and Phonology, 3rd ed. Oxford: Blackwell.

Dickson DR, Maue-Dickson W 1982 Anatomical and Physiological Bases of Speech. Boston: Little, Brown.

Some highly detailed descriptions of the structure of the larynx.

Durham FC, Harrison TS 1962 The surgical anatomy of the superior laryngeal nerve. Surg Gynecol Obstet 118:33–44.

Eckel HE, Koebke J, Sittel C et al 1999 Morphology of the human larynx during the first five years of life studied on whole organ serial sections. Ann Otol Rhinol Laryngol 108:232–8.

England RKJ, Wilde AD, McIlwain JC 1996 The posterior cricoarytenoid ligaments and their relationship to the cadaveric position of the vocal cord. Clin Otolaryngol 21:425–8.

Fayoux P, Devisme L, Merrot O et al 2004 Histologic structure and development of the laryngeal macula flava. Ann Otol Rhinol Laryngol 113:498–504.

Friedman M, Toriumi DM, Grybauskas V et al 1986 Nonrecurrent laryngeal nerves and their clinical significance. Laryngoscope 96:87–90.

Friedrich G, Lichtenegger R 1977 Surgical anatomy of the larynx. J Voice 11:345–55.

A cadaveric study providing detailed anatomical measurements.

Fürbringer M 1875 Beitrag zur Kenntnis der Kehlkopfmuskulatur. Jena: Hermann Dufft.

Furlan JC, Brandão LG, Ferraz AR 2002 Prevalence of Galen's anastomosis: an anatomical and comparative study. J Laryngol Otol 116:823–5.

Hammer GP, Windisch G, Prodinger PM et al 2010 The cricothyroid joint – functional aspects with regard to different types of its structure. J Voice 24:140–5.

Hammer MJ, Krueger MA 2014 Voice-related modulation of mechanosensory detection thresholds in the human larynx. Exp Brain Res 232:13–20.

Hartnick CJ, Rehbar R, Prasad V 2005 Development and maturation of the pediatric human vocal fold lamina propria. Laryngoscope 115:4–15.

Henry BM, Vikse J, Graves MJ et al 2016 Extralaryngeal branching of the recurrent laryngeal nerve: a meta-analysis of 28,387 nerves. Langenbecks Arch Surg 401:913–23.

An important discussion of the variable anatomy of the recurrent laryngeal nerve.

Henry BM, Pękala PA, Sanna B et al 2017 The anastomoses of the recurrent laryngeal nerve in the larynx: a meta-analysis and systematic review. J Voice. 31:495–503.

Holinger PH, Kutnick, SL, Schild, JA et al 1976 Subglottic stenosis in infants and children. Ann Otol Rhinol Laryngol 85:591–9.

Hollinshead WH 1982 Anatomy for Surgeons. Vol I: The Head and Neck, 3rd ed. Philadelphia: Harper & Row.

An older textbook that contains useful information not otherwise readily available. A guide to the earlier literature.

Hudgins PA, Siegel J, Jacobs I et al 1997 The normal paediatric larynx on CT and MR. Am J Neuroradiol 18:239–45.

Ibanez M, Valderrama-Canales FJ, Maranillo E et al 2010 Human laryngeal ganglia contain both sympathetic and parasympathetic cell types. Clin Anat 23:673–82.

Kaplan HM 1971 Anatomy and Physiology of Speech. New York: McGraw-Hill.

A thorough and comprehensive description of laryngeal anatomy and physiology.

Kierner AC, Aigner M, Burian M 1998 The external branch of the superior laryngeal nerve: its topographical anatomy as related to surgery of the neck. Arch Otolaryngol Head Neck Surg 124:301–3.

Kirchner JA, Carter D 1987 Intralaryngeal barriers to the spread of cancer. Acta Otolaryngol (Stockh) 103:503–13.

Kochilas X, Bibas A, Xenellis J et al 2008 Surgical anatomy of the external branch of the superior laryngeal nerve and its clinical significance in head and neck surgery. Clin Anat 21:99–105.

Laver J 1980 The Phonetic Description of Voice Quality. Cambridge: Cambridge University Press.

Lenneberg EH 1967 Biological Foundations of Language. New York: Wiley.

Litman RS, Weissend EE, Shibata D et al 2003 Developmental changes of laryngeal dimensions in unparalyzed, sedated children. Anesthesiology 98:41–45.

Liu M, Chen S, Liang L et al 2013 Microcomputed tomography visualisation of the cricoarytenoid joint cavity in cadavers. J Voice 27:778–85.

Liu YH, Xu SC, Tu LL et al 2006 A rich lymphatic network exists in the inferior surface of the vocal cord. Surg Radiol Anat 28:125–8.

Logemann JA, Kahrilas JC, Pauloski BR et al 1992 Closure mechanisms of laryngeal vestibule during swallow. Am J Physiol 262:G338–44.

Manickavasagam J, Yapa S, Bateman ND et al 2014 Congenital familial subglottic stenosis: a case series and review of literature. Intl J Pediatr Otorhinolaryngol 78:359–62.

Maranillo E, Leon X, Orus C et al 2005 Variability in nerve patterns of the adductor muscle group supplied by the recurrent laryngeal nerve. Laryngoscope 115:358–62.

Maranillo E, Vazquez T, Ibanez M et al 2008 Anatomic study of human laryngeal ganglia: number and distribution. Clin Anat 21:641–6.

Mijallili, SA, McFadden SL, Buckenham T et al 2012 Anatomical planes: are we teaching accurate surface anatomy? Clin Anat 25:819–26.

Monfared A, Gorti G, Kim D 2002 Microsurgical anatomy of the laryngeal nerves as related to thyroid surgery. Laryngoscope 112:386–92.

Moon J, Alipour F 2013 Muscular anatomy of the human ventricular folds. Ann Otol Rhinol Laryngol 122:561–7.

Mu L, Sanders I 2009 The human cricothyroid muscle: three muscle bellies and their innervation patterns. J Voice 23:21–8.

Munir Turk L, Hogg DA 1993 Age changes in the human laryngeal cartilages. Clin Anat 6:154–62.

Myer CM 2004 Trauma of the larynx and craniofacial structure: airway implications. Ped Anaesth 14:103–6.

Naidu L, Lazarus L, Partab P et al 2014 Laryngeal nerve 'anastomoses'. Folia Morphol (Warsz) 73:30–6.

Pracy R 1983 The infant larynx. J Laryngol Otol 97:933–47.

Reidenbach MM 1991 The muscular tissue of the vestibular folds of the larynx. Eur Arch Otorhinolaryngol 255:365–7.

Reidenbach MM 1995 Normal topography of the conus elasticus. Anatomical bases for the spread of laryngeal cancer. Surg Radiol Anat 17:107–11.

Reidenbach MM 1996a The periepiglottic space: topographic relations and histological organisation. J Anat 188:173–82.

Reidenbach MM 1996b The paraglottic space and transglottic cancer: anatomic considerations. Clin Anat 9:244–51.

Reidenbach MM 1998 Subglottic region: normal topography and possible clinical implications. Clin Anat 11:9–21.

Sanders I, Mu L 1998 Anatomy of the human internal superior laryngeal nerve. Anat Rec 252:646–56.

Sanders I, Wu BL, Mu L et al 1993 The innervation of the human larynx. Arch Otolaryngol Head and Neck Surg 119:934–9.

Sanudo J-R, Maranillo E, León X et al 1999 An anatomical study of anastomoses between the laryngeal nerves. Laryngoscope 109:983–7.

Sapienza CM, Ruddy BH, Baker S 2004 Laryngeal structure and function in the pediatric larynx: clinical applications. Lang Speech Hearing Serv Sch 35:299–307.

Sataloff RT 2017 Clinical anatomy and physiology of the voice. In: Professional Voice: The Science and Art of Clinical Care, 4th ed. San Diego: Plural Publishing.

A very comprehensive discussion within a textbook on clinical care of professionals' voices.

Sato K 2018 Functional Histoanatomy of the Human Larynx. Singapore: Springer Nature.

A beautifully illustrated and highly detailed microstructural textbook.

Sato I, Shimada K 1995 Arborization of the inferior laryngeal nerve and internal nerve on the posterior surface of the larynx. Clin Anat 8:379–87.

Sato K, Umeno H, Nakashima T 2010a Functional histology of the macula flava in the human vocal fold – part 1: its role in the adult vocal fold. Folia Phoniatr Logop 62:178–84.

Sato K, Umeno H, Nakashima T 2010b Functional histology of the macula flava in the human vocal fold – part 2: its role in the growth and development of the vocal fold. Folia Phoniatr Logop 62:263–70.

Selbie WS, Zhang L, Levine WS et al 1998 Using joint geometry to determine the motion of the cricoarytenoid joint. J Acoust Soc Am 103:1115–27.

Shindo ML, Wu JC, Park EE 2005 Surgical anatomy of the recurrent laryngeal nerve revisited. Otolaryngol Head Neck Surg 133:514–9.

Storck C, Gehrer R, Fischer C et al 2011 The role of the cricothyroid joint anatomy in cricothyroid approximation surgery. J Voice 25:632–7.

Strauss S 2000 Sonographic appearance of cricoid cartilage calcification in healthy children. Am J Roentgenol 174:223–8.

Sun SQ, Chang RW 1991 The superior laryngeal nerve loop and its surgical implications. Surg Radiol Anat 13:175–80.

Titze IR 1994 Principle of Voice Production. Englewood Cliffs, NJ: Prentice–Hall.

Trotoux J, German MA, Bruneau X 1986 La vascularisation du larynx. Ann Oto-laryngol (Paris) 103:389–97.

Tucker HM 1993 The Larynx, 2nd ed. New York: Thieme.

Vandaele DJ, Perlman AL, Cassell MD 1994 Intrinsic fibre architecture and attachments of the human epiglottis and their contributions to the mechanism of deglutition. J Anat 186:1–15.

Vazquez T, Cobiella R, Maranillo E et al 2009 Anatomical variations of the superior thyroid and superior laryngeal arteries. Head Neck 31:1078–85.

Vilkman EA, Pitkanen R, Suominen H 1987 Observations on the structure and the biomechanics of the cricothyroid articulation. Acta Otolaryngol (Stockh) 103:117–26.

Wadie M, Adam SI, Sasaki CT 2013 Development, anatomy and physiology of the larynx. In: Shaker R, Belafsky PC, Postma GN et al (eds) Principles of Deglutition: A Multidisciplinary Text for Swallowing and Its Disorders. New York: Springer Science+Business Media.

Walner DL, Loewen MS, Kimura RE 2009 Neonatal subglottic stenosis – incidence and trends. Laryngoscope 111:48–51.

Welsh LW, Welsh JJ, Rizzo TA 1983 Laryngeal spaces and lymphatics: current anatomic concepts. Ann Otol Rhinol Laryngol Suppl 105:19–31.

A description of the 'tissue spaces' and lymphatic drainage of the larynx and their importance in determining the route of spread of tumours.

Welsh LW, Welsh JJ, Rizzo TA 1989 Internal anatomy of the larynx and the spread of cancer. Ann Otol Rhinol Laryngol 98:228–34.

Werner JA, Dünne AA, Myers JN 2003 Functional anatomy of the lymphatic drainage system of the upper aerodigestive tract and its role in metastasis of squamous cell carcinoma. Head Neck 25:322–32.

A discussion of the routes of lymphatic drainage from the larynx and related structures.

Wheeler M, Coté CJ, Todres ID 2009 The pediatric airway. In: Coté CJ, Lerman J, Todres ID (eds) A Practice of Anesthesia for Infants and Children, 4th ed. Philadelphia: Elsevier, Saunders; pp. 238–243.

Windisch G, Hammer GP, Prodinger PM et al 2010 The functional anatomy of the cricothyroid joint. Surg Radiol Anat 32:135–9.

Zemlin WR 1998 Speech and Hearing Science: Anatomy and Physiology, 4th ed. Boston: Allyn & Bacon.

CHAPTER 42

External and middle ear

By convention, the ear is subdivided into three parts: the external, middle and inner ear. It is largely, but not entirely, contained within the temporal bone. The ears not only receive, modulate, conduct, amplify and discriminately analyse the complex pressure waves that are sound, but also contain the end organs of balance.

TEMPORAL BONE

Each temporal bone consists of four components: the squamous, petromastoid and tympanic parts and the styloid process (Fig. 42.1). The squamous part has a shallow mandibular fossa associated with the temporomandibular joint (Ch. 38). The petromastoid part is relatively large; its petrous portion houses the auditory apparatus and is formed of compact bone. In contrast, the mastoid process is trabecular and variably pneumatized. The tympanic part has the form of a thin and incomplete ring whose ends are fused with the squamous part. The styloid process gives attachment to the styloid group of muscles. The temporal bone contains four canals: the external acoustic meatus (external auditory canal), visible on the lateral surface, through which sound waves travel to the tympanic membrane; the internal acoustic meatus (internal auditory canal), evident on the medial surface, through which the facial and vestibulocochlear nerves pass; the facial (Fallopian) canal, through which the facial nerve passes from the internal acoustic meatus to the stylomastoid foramen and neck; and the carotid canal, through which the internal carotid artery passes from the neck to the foramen lacerum and cavernous sinus.

Squamous part

The squamous part lies anterosuperiorly and is thin and partly translucent. Its external temporal surface is smooth, slightly convex, and forms part of the temporal fossa, to which temporalis muscle is attached. Above the external acoustic meatus, it is grooved vertically by the middle temporal artery, a branch of the superficial temporal artery (Daraei and Mattox 2018). The supramastoid crest curves backwards and upwards across its posterior part and gives attachment to the temporal fascia. The junction between the squamous and mastoid parts is approximately 1.5 cm below this crest, and traces of the squamomastoid suture may persist. The suprameatal triangle, a depression marking the position of the mastoid antrum (which is medial to the triangle at a depth of approximately 1.25 cm), lies between the anterior end of the supramastoid crest and the posterosuperior quadrant of the external acoustic meatus. The triangle usually contains a small suprameatal spine anteriorly.

The internal cerebral surface of the squamous part is concave and contains depressions that correspond to convolutions of the temporal lobe of the cerebral hemisphere. This surface is grooved by the middle meningeal vessels. Its lower border is fused to the anterior region of the petrous part but traces of a petrosquamosal suture often appear in adult bones. The superior border is thin and bevelled internally; it overlaps the inferior border of the parietal bone at the squamosal suture. Posteriorly, it forms an angle with the mastoid element. The anteroinferior border, thin above and thick below, meets the greater wing of the sphenoid bone; it is bevelled internally above, and bevelled externally below.

The squamous part has a zygomatic process and a mandibular fossa.

Zygomatic process

The zygomatic process juts forwards from the lower region of the squamous part. Its triangular posterior aspect has a broad base that is directed laterally, presenting superior and inferior surfaces. The zygomatic process then twists anteromedially, so that its surfaces become medial and lateral.

The superior surface of the posterior part is concave. The inferior surface is bounded by anterior and posterior roots, converging into the anterior part of the process. The tubercle of the zygomatic root gives attachment to the lateral temporomandibular ligament at the junction of the roots. The posterior root is prolonged forwards above the external acoustic meatus, its upper border continuing into the supramastoid crest. Very rarely, the squamous part is perforated above the posterior root by a squamosal foramen, which transmits the petrosquamous sinus. The anterior root juts almost horizontally from the squamous part. Its inferior surface, with an anteroposterior convexity, forms a short semi-cylindrical articular tubercle and comes into contact with the articular disc of the temporomandibular joint. The tubercle forms the anterior limit of the mandibular fossa.

The anterior part of the zygomatic process is thin and flat, and the temporal fascia is attached to its superior border. The inferior border is short and arched and gives origin to some fibres of masseter. The lateral surface is convex. The medial surface is concave and provides further attachment for part of masseter. The anterior end is deeply serrated and slopes obliquely posteroinferiorly to articulate with the temporal process of the zygomatic bone, forming the zygomatic arch. Anterior to the articular tubercle, a small triangular area forms part of the roof of the infratemporal fossa; it is continuous behind with the anterior root and in front with the infratemporal crest of the greater wing of the sphenoid.

Mandibular fossa

The mandibular fossa is limited in front by the articular eminence of the zygomatic process. It presents an anterior articular area, formed by the squamous part, and a posterior non-articular area, formed by the tympanic element. The articular surface is smooth, oval and concave, and contacts the articular disc of the temporomandibular joint. Unlike most other synovial joints, it is lined by fibrous tissue rather than hyaline cartilage, reflecting its intramembranous development. The non-articular area sometimes contains part of the parotid gland. A small, conical postglenoid tubercle separates the articular surface laterally from the tympanic plate.

Posteriorly, the mandibular fossa is separated from the tympanic part by the squamotympanic fissure. Rarely, a postglenoid foramen exists anterior to the external acoustic meatus in the line of fusion of the squamous and tympanic parts. When present, it replaces the squamosal foramen noted above and transmits the petrosquamous sinus. Medially, a projection from the petrous part of the temporal bone (tegmen tympani) comes to lie within the squamotympanic fissure, further dividing it into petrotympanic and petrosquamous fissures. The petrotympanic fissure leads into the tympanic cavity and contains an anterior malleolar ligament and the anterior tympanic branch of the maxillary artery. The anterior opening of the anterior canaliculus for the chorda tympani nerve lies at the medial end of the fissure.

Petromastoid part

The petromastoid part of the temporal bone, although morphologically one element, is more conveniently described as two parts, namely: mastoid and petrous parts.

Mastoid part

The mastoid part is the posterior region of the temporal bone and has an outer surface roughened by the attachments of the occipital belly of occipitofrontalis and auricularis posterior. A mastoid foramen, of variable size, number and position, traversed by a vein from the sigmoid sinus and a small dural branch of the occipital artery, frequently lies near its posterior border. The foramen may be in the occipital or occipitotemporal suture; it may sometimes be parasutural or may be absent. The mean length of the mastoid emissary vein from its point of origin to its point of termination is 7.2 cm (range 3.8–11.8 cm). It can be a significant source of bleeding in retrosigmoid and far lateral approaches to the skull base, usually controlled by the repetitive applications of surgical wax. It is of considerable clinical importance to craniofacial surgeons when operating on complex craniosynostotic patients, where the emissary vein may be the sole dominant drainage pathway of the brain (Louis et al 2009, Kim et al 2014).

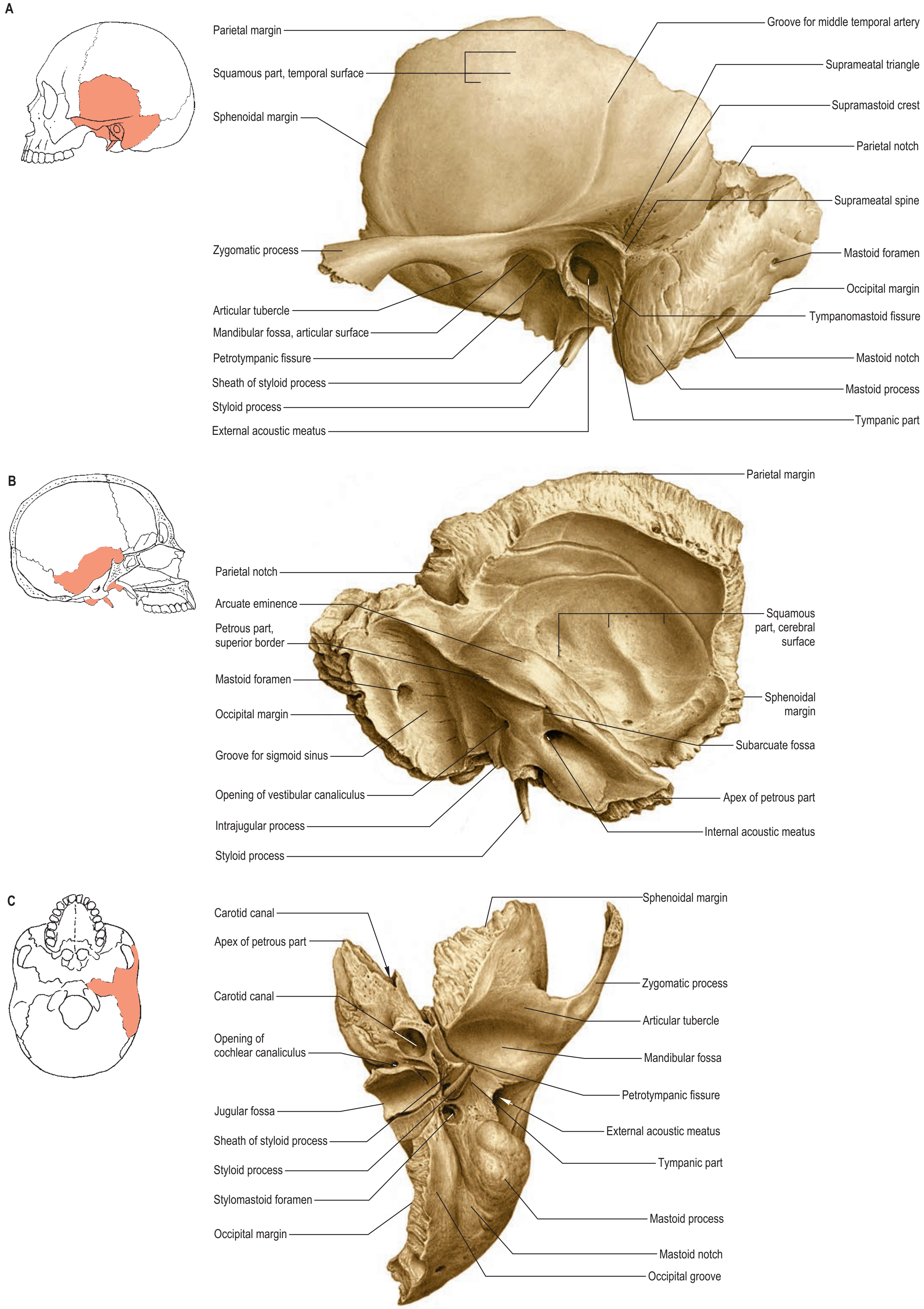
A
Parietal margin
Squamous part, temporal surface
Sphenoidal margin
Zygomatic process
Articular tubercle
Mandibular fossa, articular surface
Petrotympanic fissure
Sheath of styloid process
Styloid process
External acoustic meatus
Groove for middle temporal artery
Suprameatal triangle
Supramastoid crest
Parietal notch
Suprameatal spine
Mastoid foramen
Occipital margin
Tympanomastoid fissure
Mastoid notch
Mastoid process
Tympanic part
B
Parietal margin
Parietal notch
Arcuate eminence
Petrous part, superior border
Mastoid foramen
Occipital margin
Groove for sigmoid sinus
Opening of vestibular canaliculus
Intrajugular process
Styloid process
Squamous part, cerebral surface
Sphenoidal margin
Subarcuate fossa
Apex of petrous part
Internal acoustic meatus
C
Carotid canal
Apex of petrous part
Carotid canal
Opening of cochlear canaliculus
Jugular fossa
Sheath of styloid process
Styloid process
Stylomastoid foramen
Occipital margin
Sphenoidal margin
Zygomatic process
Articular tubercle
Mandibular fossa
Petrotympanic fissure
External acoustic meatus
Tympanic part
Mastoid process
Mastoid notch
Occipital groove

Fig. 42.1 The left temporal bone. **A**, Lateral aspect. **B**, Medial aspect. **C**, Inferior aspect. (Sobotta Atlas of Human Anatomy © Elsevier GmbH, Urban & Fischer, Munich.)

The mastoid part projects down as the conical mastoid process and is larger in adult males. Sternocleidomastoid, splenius capitis and longissimus capitis are all attached to its lateral surface, and the posterior belly of digastric is attached to a deep mastoid notch on its medial aspect. The occipital artery runs in a shallow occipital groove that lies medial to the mastoid notch. The internal surface of the mastoid process bears a deep, curved sigmoid sulcus for the sigmoid venous sinus; the sulcus is separated from the underlying innermost mastoid air cells by a thin lamina of bone.

The superior border of the mastoid part is thick and serrated for articulation with the mastoid angle of the parietal bone. The posterior border is also serrated and articulates with the inferior border of the occipital bone between its lateral angle and jugular process. The mastoid element is fused with the descending process of the squamous part; below, it appears in the posterior wall of the tympanic cavity.

Petrous part

The petrous part is a mass of bone that is wedged between the sphenoid and occipital bones in the cranial base; it contains the labyrinth. It is inclined superiorly and anteromedially, and has a base, apex, three surfaces (anterior, posterior and inferior) and three borders (superior, posterior and anterior).

The base would correspond to the part that lies on the base of the skull and is separated from the squamous part by a suture. However, this suture disappears soon after birth. The subsequent development of the mastoid processes means that the precise boundaries of the base are no longer identifiable.

The apex, blunt and irregular, is angled between the posterior border of the greater wing of the sphenoid and the basilar part of the occipital bone. It contains the anterior opening of the carotid canal and limits the foramen lacerum posterolaterally.

The anterior surface contributes to the floor of the middle cranial fossa (Ch. 34) and is continuous with the cerebral surface of the squamous part (although the petrosquamosal suture often persists late in life). The whole surface is adapted to the inferior temporal gyrus. Behind the apex is a trigeminal impression for the trigeminal ganglion. Bone anterolateral to this impression roofs the anterior part of the carotid canal but is often deficient. A ridge separates the trigeminal impression from another hollow behind, which partly roofs the internal acoustic meatus and cochlea. This, in turn, is limited behind by the arcuate eminence, which is raised by the superior (anterior) semicircular canal but is not necessarily directly over it. Laterally, the anterior surface roofs the vestibule and, partly, the facial canal. Between the squamous part laterally and the arcuate eminence and the hollows just described medially, the anterior surface is formed by the tegmen tympani, a thin plate of bone that forms the roof of the mastoid antrum and extends forwards above the tympanic cavity and the canal for tensor tympani. The lateral margin of the tegmen tympani meets the squamous part at the petrosquamosal suture, turning down in front as the lateral wall of the canal for tensor tympani and the osseous part of the pharyngotympanic tube; its lower edge is in the squamotympanic fissure. Anteriorly, the tegmen bears a narrow groove related to the greater petrosal nerve (which passes posterolaterally to enter the bone by a hiatus anterior to the arcuate eminence). The groove passes forwards to the foramen lacerum. A smaller and similar hiatus and groove may be found more laterally; they are related to the lesser petrosal nerve (which runs to the foramen ovale). The posterior slope of the arcuate eminence overlies the posterior and lateral semicircular canals. Lateral to the eminence, the posterior part of the tegmen tympani roofs the mastoid antrum.

The posterior surface contributes to the anterior part of the posterior cranial fossa and is continuous with the internal surface of the mastoid part. The opening of the internal acoustic meatus lies near its centre. A small slit leading to the vestibular aqueduct lies behind the opening of the meatus, almost hidden by a thin plate of bone. This contains the saccus and ductus endolymphaticus together with a small artery and vein. The terminal half of the saccus endolymphaticus protrudes through the slit between the periosteum and dura mater. The subarcuate fossa lies above these openings.

The irregular inferior surface is part of the exterior of the cranial base. Near the apex of the petrous part, a quadrilateral area is partly associated with the attachment of levator veli palatini and the cartilaginous pharyngotympanic tube, and partly connected to the basilar part of the occipital bone by dense fibrocartilage. Behind this region is the large, circular opening of the carotid canal, and behind the opening of the canal is the jugular fossa, which is of variable depth and size, and contains the superior jugular bulb. The inferior ganglion of the glossopharyngeal nerve lies in a triangular depression anteromedial to the jugular fossa (below the internal acoustic meatus). At its apex is a small opening into the cochlear canaliculus, occupied by the perilymphatic duct (a tube of dura mater) and a vein draining from the cochlea to the internal jugular vein. A canaliculus for the tympanic nerve from the glossopharyngeal nerve lies on the ridge between the carotid canal and the jugular fossa. The mastoid canaliculus for the auricular branch of the vagus nerve is laterally positioned in the jugular fossa. Behind the jugular fossa, the rough quadrilateral jugular surface is covered by cartilage that joins it to the jugular process of the occipital bone.

The superior border, the longest, is grooved by the superior petrosal sinus. The attached margin of the tentorium cerebelli is fixed to the edges of the groove except at its medial end, where it is crossed by the roots of the trigeminal nerve. The posterior border, intermediate in length, bears a sulcus medially, which forms, together with the occipital bone, a gutter for the inferior petrosal sinus. Behind this, the jugular fossa contributes (together with the occipital bone) to the jugular foramen and is notched by the glossopharyngeal nerve. Bone on either or both sides of the jugular notch may meet the occipital bone and divide the jugular foramen into two or three parts. The anterior border is joined laterally to the squamous part of the temporal bone at the petrosquamosal suture; medially, it articulates with the greater wing of the sphenoid bone.

Two canals exist at the junction of the petrous and squamous parts, one above the other, separated by a thin osseous plate and both leading to the tympanic cavity; the upper canal contains tensor tympani, while the lower canal is the pharyngotympanic tube.

Tympanic part

The tympanic part of the temporal bone is a curved plate below the squamous part and anterior to the mastoid process. Internally, it fuses with the petrous part and appears between this and the squamous part, where it is inferolateral to the auditory orifice. Behind, it fuses with the squamous part and mastoid process, and is the anterior limit of the tympanomastoid fissure. Its concave posterior surface forms the anterior wall, floor and part of the posterior wall of the external acoustic meatus. The tympanic membrane is attached to a narrow tympanic sulcus on its medial surface. The quadrilateral concave anterior surface is the posterior wall of the mandibular fossa and may contact the parotid gland. Its rough lateral border forms most of the margin of the osseous part of the external acoustic meatus and is continuous with its cartilaginous part. Laterally, the upper border is fused with the back of the postglenoid tubercle; medially, it forms the posterior edge of the petrotympanic fissure. The inferior border is sharp and splits laterally to form, at its root, the sheath of the styloid process (vaginal process). Centrally, the tympanic part is thin and is often perforated. The stylomastoid foramen lies between the styloid and mastoid processes; it represents the external end of the facial canal, contains part of the aponeurosis of the posterior belly of digastric, and transmits the facial nerve and stylomastoid artery.

Styloid process

The styloid process is slender and pointed, and projects anteroinferiorly from the inferior aspect of the temporal bone. Its length may vary considerably, normally ranging from 2.83 to 4.16 cm. In some patients it may be much longer and be the cause of severe, neuralgic pain in the ipsilateral pharynx when swallowing (Eagle's syndrome) as the glossopharyngeal nerve rubs against the process. Mechanical impingement of the cervical carotid artery with an excessively long styloid process has been implicated as a cause of arterial dissection with the consequences that flow from that (Muthusami 2013, Jelodar et al 2018, Ledesma-Montes et al 2018). Most often the styloid process is almost straight but can show a curvature, an anteromedial concavity being most common. Its proximal part (tympanohyal) is ensheathed by the tympanic plate, especially anterolaterally, while muscles and ligaments are attached to its distal part (stylohyal). *In vivo*, its relationships are important. The styloid process is covered laterally by the parotid gland; the facial nerve crosses its base; the external carotid artery crosses its tip, embedded in the parotid; and medially, the process is separated from the beginning of the internal jugular vein by the attachment of stylopharyngeus.

External acoustic meatus

The temporal bone contains the bony (osseous) part of the external acoustic meatus.

Ossification

The four temporal components ossify independently (Fig. 42.2). The squamous part is ossified in a sheet of condensed mesenchyme from a single centre near the zygomatic roots, which appears in embryonic

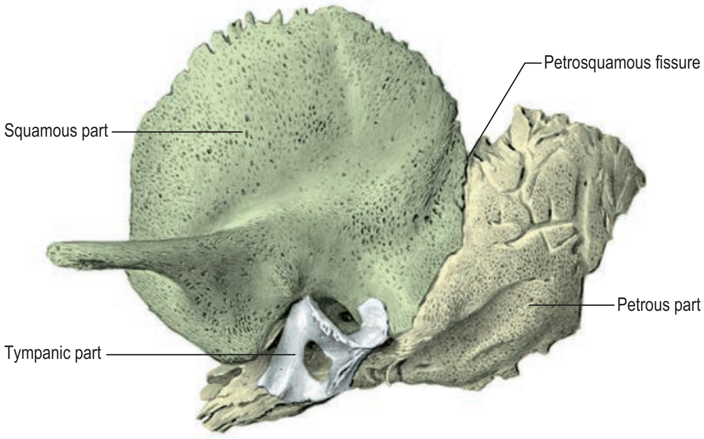

Fig. 42.2 The left temporal bone at birth. (Sobotta Atlas of Human Anatomy © Elsevier GmbH, Urban & Fischer, Munich.)

stages 21–23 (postfertilization week 8). The petromastoid part has several centres that appear in the cartilaginous otic capsule during postmenstrual weeks 17–20; as many as 14 have been described. These centres vary in order of appearance. Several are small and inconstant and soon fuse with others. The otic capsule is almost fully ossified by postmenstrual week 24. The tympanic part is also ossified in mesenchyme from four centres that appear at about postmenstrual week 14. At birth, it is an incomplete tympanic ring that is deficient above; its concavity is grooved by a tympanic sulcus for the tympanic membrane. The malleolar sulcus housing the anterior malleolar process, chorda tympani and anterior tympanic artery, inclines obliquely downwards and forwards across the medial aspect of the anterior part of the ring. The styloid process develops from two centres at the cranial end of the cartilage in the second visceral or hyoid arch: a proximal centre for the tympanohyal appears before birth, and the centre for the distal stylohyal appears after birth. The tympanic ring unites with the squamous part shortly before birth; the petromastoid fuses with it and the tympanohyal during the first postnatal year. The stylohyal does not unite with the rest of the process until after puberty and may never do so.

Once ossified, the tympanic cavity, mastoid antrum and the posterior end of the pharyngotympanic tube become surrounded by bone. The petrous part forms the roof, floor and medial wall of the cavity, while the squamous and tympanic parts, together with the tympanic membrane, form its lateral wall. At birth, the middle and inner ears are adult size, and the tympanic cavity, mastoid antrum, tympanic membrane and auditory ossicles are all almost adult size. The anterior process does not join the malleus until 6 months later. The internal acoustic meatus is approximately 6 mm in horizontal diameter, 4 mm in vertical diameter and 7 mm in length at birth, and the adult diameters are 7.7 mm and 11 mm, respectively.

After birth and apart from general growth, the tympanic ring extends posterolaterally to become cylindrical, growing into a fibrocartilaginous tympanic plate, which forms the adjacent part of the external acoustic meatus at this stage. This growth is not equal but is rapid in the anterior and posterior regions, which meet and blend. Thus, for a time, an opening (foramen of Huschke) exists in the floor; it usually closes at about the fifth year but is sometimes permanent. The external acoustic meatus is relatively as long in children as it is in adults, but the canal is fibrocartilaginous, whereas its medial two-thirds are osseous in adults. Surgical access to the tympanic cavity is via the mastoid antrum, and in children it is necessary to remove only a thin scale of bone in the suprameatal triangle to reach the antrum. The tympanic plate ensheathes the styloid process by posterior extension and extends medially over the petrous bone to the carotid canal.

Initially, the mandibular fossa is shallow, facing more laterally, but it then deepens and ultimately faces downwards. Posteroinferiorly, the squamous part grows down behind the tympanic ring to form the lateral wall of the mastoid antrum. The mastoid part is at first flat, so that the stylomastoid foramen and rudimentary styloid process are immediately behind the tympanic ring. The mastoid part becomes invaded by air cells, especially at puberty. The lateral mastoid region grows downwards and forwards to form the mastoid process, which means that the styloid process and stylomastoid foramen become inferior. Descent of the foramen lengthens the facial canal. The mastoid process is not perceptible until late in the second year; consequently, the facial nerve is relatively superficial and susceptible to damage during surgical exploration during this period. The subarcuate fossa gradually fills and is almost obliterated.

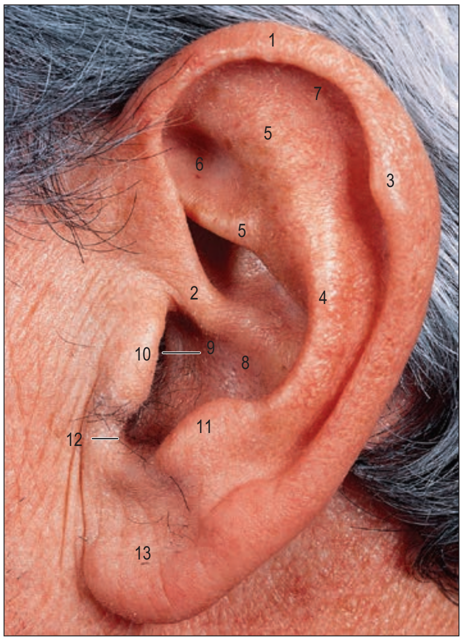

Fig. 42.3 The lateral surface of the left auricle. Key: 1, helix; 2, crus of helix; 3, auricular tubercle; 4, antihelix; 5, crura of antihelix; 6, triangular fossa; 7, scaphoid fossa; 8, concha of auricle; 9, external acoustic meatus; 10, tragus; 11, antitragus; 12, intertragic notch; 13, lobule of auricle. (With permission from Berkovitz BKB, Moxham BJ 2002 Head and Neck Anatomy. London: Martin Dunitz.)

In the neonate, the petrous and squamous parts of the temporal bone are usually partially separated by the petrosquamous fissure, which opens directly into the mastoid antrum of the middle ear. Rarely, the fissure closes in infants during the first year, but it sometimes remains unclosed up to the age of 19 years and can be a route for the spread of infection from the middle ear to the meninges. There is a bimodal growth pattern in the lateral surface dimensions of the temporal bone in children; marked increases in dimension take place from birth to the age of 4 years but little growth is seen between the ages of 4 and 20 years (Simms and Neely 1989). The neonatal pharyngotympanic tube (Eustachian tube) is about half the length of its adult counterpart. Its opening from the middle ear cavity is as large as it is in the adult but the pharyngeal opening in the nasal part of the pharynx is relatively smaller. The course of the pharyngotympanic tube is horizontal in the newborn, whereas in the adult it passes from the middle ear downwards, forwards and medially.

EXTERNAL EAR

The external ear consists of the auricle (pinna) and the external acoustic meatus. The auricle projects to a variable and individual degree from the side of the head. It collects sound waves and conducts them along the external acoustic meatus inwards towards the ear drum, the tympanic membrane. The auricle thus acts as the first element of a series of stimulus modifiers in the auditory apparatus.

Auricle (pinna)

The lateral surface of the auricle is irregularly concave, faces slightly forwards, and displays numerous eminences and depressions (Fig. 42.3). It has a prominent curved rim, the helix. This usually bears a small tubercle posterosuperiorly, Darwin's tubercle, which is quite pronounced during postmenstrual weeks 21–24. The antihelix is a curved prominence, parallel and anterior to the posterior part of the helix; it divides above into two crura that flank a depressed triangular fossa. The curved depression between the helix and antihelix is the scaphoid fossa. The antihelix encircles the deep, capacious concha of the auricle, which is incompletely divided by the crus or anterior end of the helix. The conchal area above this, the cymba conchae, overlies the suprameatal triangle of the temporal bone, which can be felt through it, and which overlies the mastoid antrum. The tragus is a small curved flap below the crus of the helix and in front of the concha; it projects posteriorly, partly overlapping the meatal orifice. The antitragus is a small tubercle opposite the tragus and is separated from it by the intertragic incisure or notch. Below it is the lobule, composed of fibrous and adipose tissues. It is soft, unlike the majority of the auricle, which is firm and is supported by elastic cartilage. The cranial surface of the auricle presents elevations that correspond to the depressions on its lateral surface and after which they are named (e.g. eminentia conchae, eminentia fossae triangularis).

At birth, most of the linear dimensions of the auricle are approximately three-quarters of their adult size; the length and height of the tragus are less than half of their adult size. Width dimensions mature between the ages of 5 and 11 years; length dimensions mature between 12 and 16 years (Purkait 2013).

Common congenital anomalies

Developmental anomalies of the branchial arches may produce a grossly misshapen or microtic auricle, sometimes with associated anomalies of the middle ear and significant hearing loss. Deformity of the auricle may be the result of hereditary factors, exposure to teratogens or unusual intrauterine positioning. A number of common anomalies have been recognized; they carry descriptive names or eponyms (Porter and Tan 2005) (**Table 42.1**).

Skin

The skin of the auricle continues into the external acoustic meatus to cover the outer surface of the tympanic membrane. It is thin, has no dermal papillae, and is closely adherent to the cartilaginous and osseous parts of the canal; inflammation of the canal skin is very painful because of this firm attachment to the underlying structures. The thick subcutaneous tissue of the cartilaginous part of the meatus contains numerous ceruminous glands that secrete wax, or cerumen. Their coiled tubular structure resembles that of sweat glands. The secretory cells are columnar when active but cuboidal when quiescent; they are covered externally by myoepithelial cells. Ducts open either on to the epithelial surface or into the nearby sebaceous gland of a hair follicle. Cerumen prevents the maceration of meatal skin by trapped water. Antibacterial properties have been attributed to cerumen but the evidence for this is lacking (Campos et al 2000, Pata et al 2003).

Two types of wax, wet and dry, are recognized. They are genetically determined (Yoshiura et al 2006). Overproduction, accumulation or impaction of wax may completely occlude the meatus. This may hinder sound from reaching the tympanic membrane and so restrict its natural vibration. Although ceruminous glands and hair follicles are largely limited to the cartilaginous meatus, a few small glands and fine hairs are also present in the roof of the lateral part of the bony meatus. The warm, humid environment of the relatively enclosed meatal air aids the mechanical responses of the tympanic membrane.

Cartilaginous framework

The auricle is a single thin plate of elastic fibrocartilage covered by skin, its surface moulded by eminences and depressions (Fig. 42.4). It is connected to the surrounding parts by ligaments and muscles, and is continuous with the cartilage of the external acoustic meatus. There is no cartilage in the lobule or between the tragus and the crus of the helix, where the gap is filled by dense fibrous tissue. Anteriorly, where the helix curves upwards, there is a small cartilaginous projection: the spine of the helix. Its other extremity is prolonged inferiorly as the tail of the helix and it is separated from the antihelix by the fissura antitragohelicina (antitragohelicine fissure). The cranial aspect of the cartilage bears the eminentia conchae and eminentia scaphae, which correspond to the depressions on the lateral surface. The two eminences are separated by a transverse furrow, the sulcus antihelicis transversus, which corresponds to the inferior crus of the antihelix on the lateral surface. The eminentia conchae is crossed by an oblique ridge, the ponticulus, for the attachment of auricularis posterior. There are two fissures in the auricular cartilage, one behind the crus of the helix and another in the tragus.

Ligaments

Anterior and posterior extrinsic ligaments connect the auricle with the temporal bone. The anterior ligament extends from the tragus and the spine of the helix to the root of the zygomatic process of the temporal bone. The posterior ligament passes from the posterior surface of the concha to the lateral surface of the mastoid process. Two main intrinsic ligaments connect individual auricular cartilages: a strong fibrous band passes from the tragus to the helix, thereby completing the meatus anteriorly and forming part of the boundary of the concha; and another band passes between the antihelix and the tail of the helix. Less prominent bands exist on the cranial aspect of the auricle.

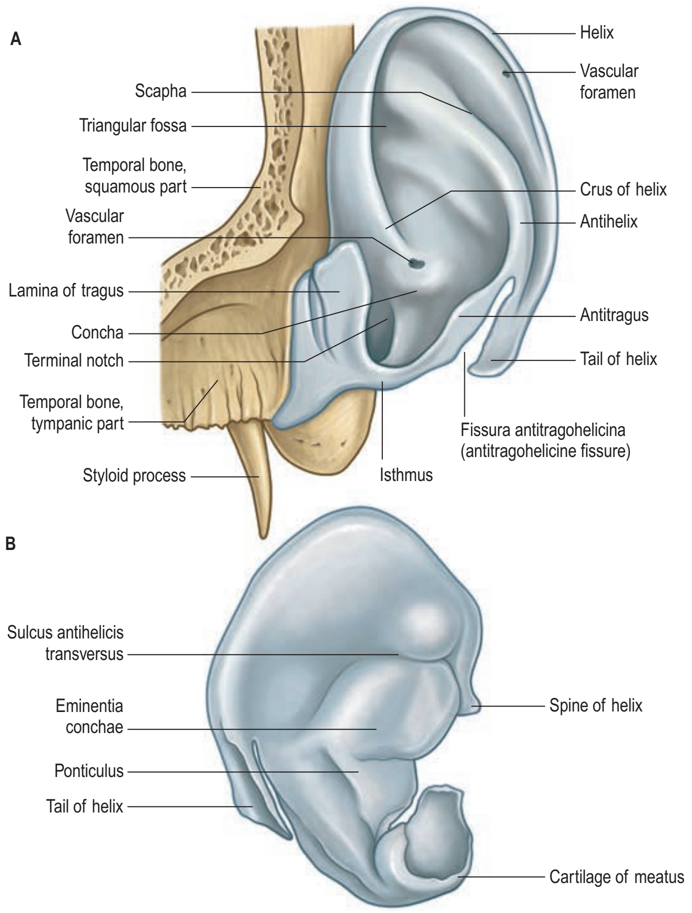

Fig. 42.4 The auricular cartilages of the left ear. **A**, Lateral surface. **B**, Medial surface.

Auricular muscles

Extrinsic auricular muscles connect the auricle to the skull and scalp, and move the auricle as a whole. Intrinsic auricular muscles connect the different parts of the auricle.

Extrinsic muscles

The extrinsic auricular muscles are the auriculares anterior, superior and posterior (Fig. 42.5B). The smallest of the three is auricularis anterior, a thin fan of pale fibres that arise from the lateral edge of the epicranial aponeurosis and converge to attach to the spine of the helix. The largest of the three, auricularis superior, is also thin and fan-shaped, and converges from the epicranial aponeurosis via a thin, flat tendon to attach to the upper part of the cranial surface of the auricle. The auricularis posterior consists of two or three fleshy fasciculi that arise by short aponeurotic fibres from the mastoid part of the temporal bone and insert into the ponticulus on the eminentia conchae.

Vascular supply The arterial supply of the extrinsic auricular muscles is derived mainly from the posterior auricular artery.

Innervation Auriculares anterior and superior are supplied by temporal branches of the facial nerve, and auricularis posterior is supplied by the posterior auricular branch of the facial nerve.

Actions In humans, these muscles have very little obvious effect. Despite the paucity of auricular movement, auditory stimuli may evoke patterned responses from these small muscles and electromyography can detect the 'crossed acoustic response' that was once used to determine objective measurements of auditory threshold levels. It has been superseded in clinical neuro-otology by computer-averaged brainstem evoked response audiometry.

Intrinsic muscles

The intrinsic auricular muscles are helicis major and minor, tragicus, antitragicus, transversus auriculae and obliquus auriculae (Fig.

TABLE 42.1 **Common anomalies of the auricle (see Chapter 16)**

Anomaly	Structural defect	Figure
Anotia	Complete absence of the auricle. Anotia and microtia may arise consequent to developmental disturbances between postfertilization weeks 6 and 8 (embryonic stages 15–23).	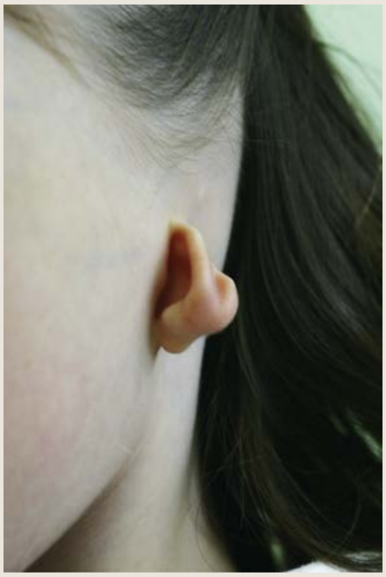
Cryptotia (Hidden ear, pocket ear)	The upper pole of the auricle is buried beneath the temporal skin	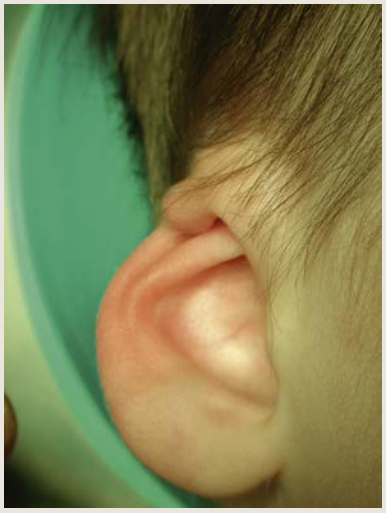
Microtia	Diminutive ear; this is usually an isolated congenital anomaly but is sometimes associated with recognized syndromes, e.g. fetal alcohol syndrome, maternal diabetic syndrome, thalidomide or isotretinoin exposure	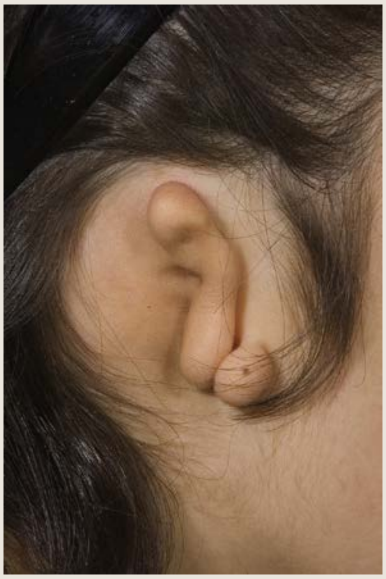

Continued

TABLE 42.1 Common anomalies of the auricle (see Chapter 16)—cont'd

Anomaly	Structural defect	Figure
Polyotia (Mirror ear)	Caused by the persistence of pre-auricular tissue that would normally be included in the auricle; the persistent tissue lies in front of the tragus in the posterior aspect of the cheek	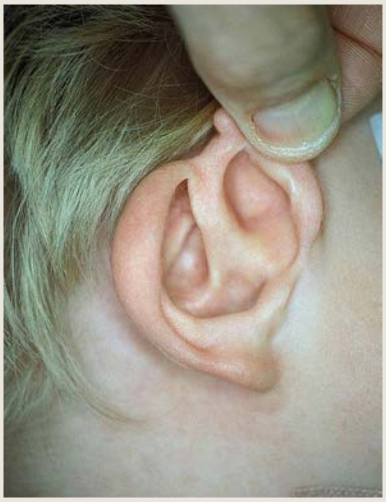
Stahl's bar ('Satiro's ear', 'lop ear')	Common congenital deformity of the auricle in which the helix is flattened and the upper crus of the antihelix is duplicated. This produces a ridge of cartilage running from the antihelix to the rim of the helix, causing a pointing of the ear and a reversal of the normal concavity of the scaphoid fossa. The upper part of the auricle may flop over	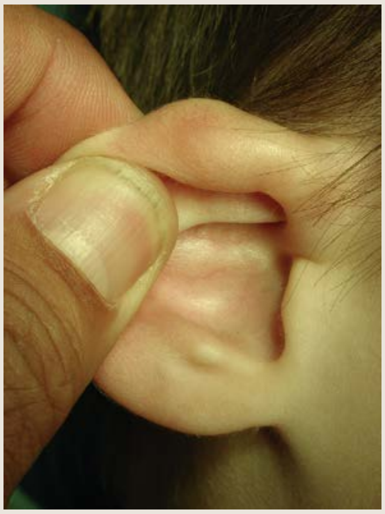
Prominent ears (Bat ear)	The antihelical fold is either absent or inadequate	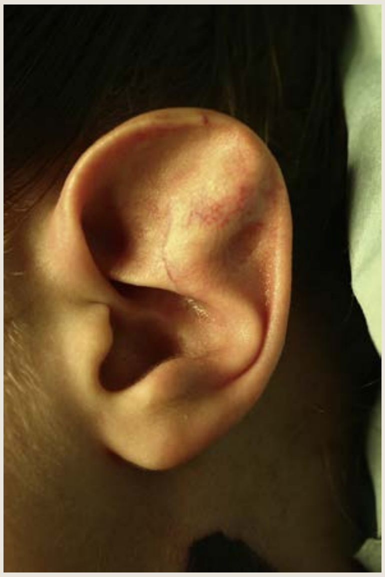

TABLE 42.1 Common anomalies of the auricle (see Chapter 16)—cont'd

Anomaly	Structural defect	Figure
Pre-auricular sinus	The result of failure of fusion of the first and second branchial arches. Clinically, pre-auricular sinuses may become chronically infected and require surgical excision. This may be technically demanding, given the close proximity to the facial nerve and auricular tubercles around the dorsal end of the first branchial cleft. The sinuses may be simple pits or complex branching sinuses that occasionally extend deeply towards the external acoustic meatus so that they lie close to the facial nerve. There is debate as to whether the anomalies are epithelial inclusions between the hillocks or remnants of the first branchial cleft	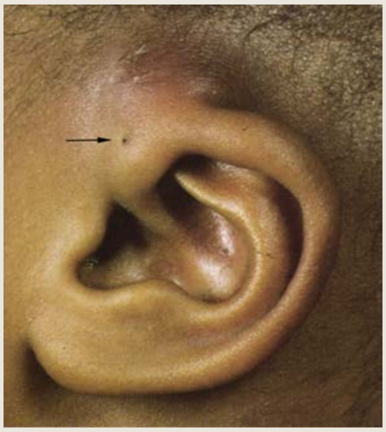

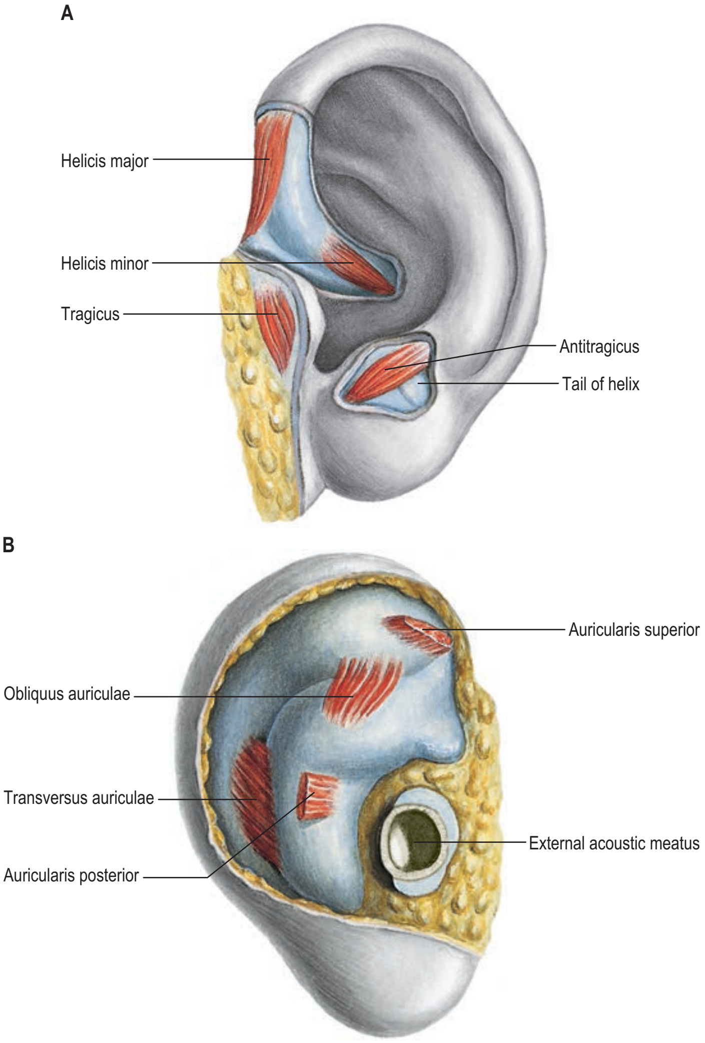

Fig. 42.5 The extrinsic and intrinsic auricular muscles of the left ear. Auricularis anterior is not illustrated. (Sobotta Atlas of Human Anatomy © Elsevier GmbH, Urban & Fischer, Munich.)

42.5A). Helicis major is a narrow vertical band on the anterior margin of the helix, passing from its spine to its anterior border, where the helix is about to curve back. Helicis minor is an oblique fasciculus covering the crus of the helix. Tragicus is a short, flattened, vertical band on the lateral aspect of the tragus. Antitragicus passes from the outer part of the antitragus to the tail of the helix and the antihelix. Transversus auriculae, located on the cranial aspect of the auricle, consists of scattered fibres – partly tendinous, partly muscular, which extend between the eminentia conchae and the eminentia scaphae. Obliquus auriculae, also located on the cranial aspect of the auricle, consists of a few fibres that extend from the upper and posterior parts of the eminentia conchae to the eminentia scaphae.

Vascular supply The intrinsic auricular muscles are supplied by branches of the posterior auricular and superficial temporal arteries.

Innervation The intrinsic auricular muscles on the lateral aspect of the auricle are innervated by the temporal branches of the facial nerve, and those on the cranial aspect of the auricle are innervated by the posterior auricular branch of the facial nerve.

Actions The intrinsic muscles modify auricular shape minimally, if at all, in most human ears: helicis major can draw the auricle forwards and upwards. Rare individuals can modify the shape and position of their external ears.

Vascular supply and lymphatic drainage

Arteries The superficial temporal and posterior auricular arteries provide the blood supply to the auricle. Each has three to five branches contribute to a helical rim arcade that ensures a good arterial blood supply to potential watershed areas. The posterior auricular artery gives off three to seven branches that run radially along the posterior side of the auricular cartilage to the helical rim, where they connect with the helical rim arcade. It also gives off two to four perforating branches that pierce the auricular cartilage to reach the anterior surface of the auricle at the base of the helical root and at the cavum conchae near the antitragus. They supply the anterior surface of the auricle, part of the external acoustic meatus and contribute to the helical rim arcade (Zilinsky et al 2017). This rich anastomotic network of vessels at the helical rim provides a solid basis for reconstructive surgical strategies.

Veins Auricular veins correspond to the arteries of the auricle. Arteriovenous anastomoses are numerous in the skin of the auricle and are thought to be important in the regulation of core temperature.

Lymphatic drainage The posterior aspect of the auricle drains to nodes at the mastoid tip. The tragus and upper part of the auricle drain into pre-auricular nodes, while the remainder of the auricle drains to upper deep cervical lymph nodes.

Innervation

The sensory innervation of the auricle is complex and not fully determined. This is perhaps because the external ear represents an area where skin originally derived from a branchial region meets skin originally derived from a postbranchial region. The sensory nerves involved are the great auricular nerve, which supplies most of the cranial surface and the posterior part of the lateral surface (helix, antihelix, lobule); the lesser occipital nerve, which supplies the upper part of the cranial surface; the auricular branch of the vagus, which supplies the concavity of the concha and posterior part of the eminentia; the auriculotemporal nerve, which supplies the tragus, crus of the helix and the adjacent part of the helix; and the facial nerve, which, together with the auricular branch of the vagus, probably supplies small areas on both aspects of the auricle, in the depression of the concha and over its eminence. The details of the cutaneous innervation derived from the facial nerve require further clarification. It is possible that, as the auricular branch of the vagus traverses the temporal bone and crosses the facial canal, approximately 4 mm above the stylomastoid foramen, it contributes an ascending branch to the facial nerve and that, in this way, fibres of the vagus are carried via the facial nerve to the auricle.

External acoustic meatus

The external acoustic meatus extends from the concha to the tympanic membrane; it is approximately 2.5 cm from the floor of the concha and approximately 4 cm from the tragus. It has two structurally different parts: its lateral third is cartilaginous, and its medial two-thirds is osseous (Fig. 42.6). It forms an S-shaped curve, directed at first medially, anteriorly and slightly up (pars externa), then posteromedially and up (pars media), and lastly anteromedially and slightly down (pars interna). It is oval in section; its greatest diameter is obliquely inclined posteroinferiorly at the external orifice but is nearly horizontal at its medial end. There are two constrictions: one near the medial end of the cartilaginous part, and the other, the isthmus, in the osseous part about 2 cm from the bottom of the concha. The tympanic membrane, which closes its medial end, is obliquely set, which means that the floor and the anterior wall of the meatus are longer than its roof and posterior wall.

The lateral, cartilaginous part is approximately 8 mm long. It is continuous with the auricular cartilage and attached by fibrous tissue to the circumference of the osseous part. The meatal cartilage is deficient posterosuperiorly, and the gap is occupied by a sheet of collagen. Two or three deep fissures (of Santorini) exist in its anterior part. Tumours of the external acoustic meatus escape the confines of the canal through these fissures and spread into the adjacent soft tissues; the extent of these fissures, which are subject to individual variation, influence outcomes by accelerating the spread of the tumour into the soft tissue of skull base.

The osseous part is approximately 16 mm long and is narrower than the cartilaginous part. In sagittal section, it is oval or elliptical, and it is directed anteromedially and slightly downwards, with a slight posterosuperior convexity. Its medial end is smaller than the lateral end and it terminates obliquely. The anterior wall projects medially approximately 4 mm beyond the posterior and is marked, except above, by a narrow tympanic sulcus or anulus, to which the perimeter of the tympanic membrane is attached. Its lateral end is dilated and mostly rough for the attachment of the meatal cartilage. The anterior, inferior and most of the posterior parts of the osseous meatus are formed by the tympanic

740

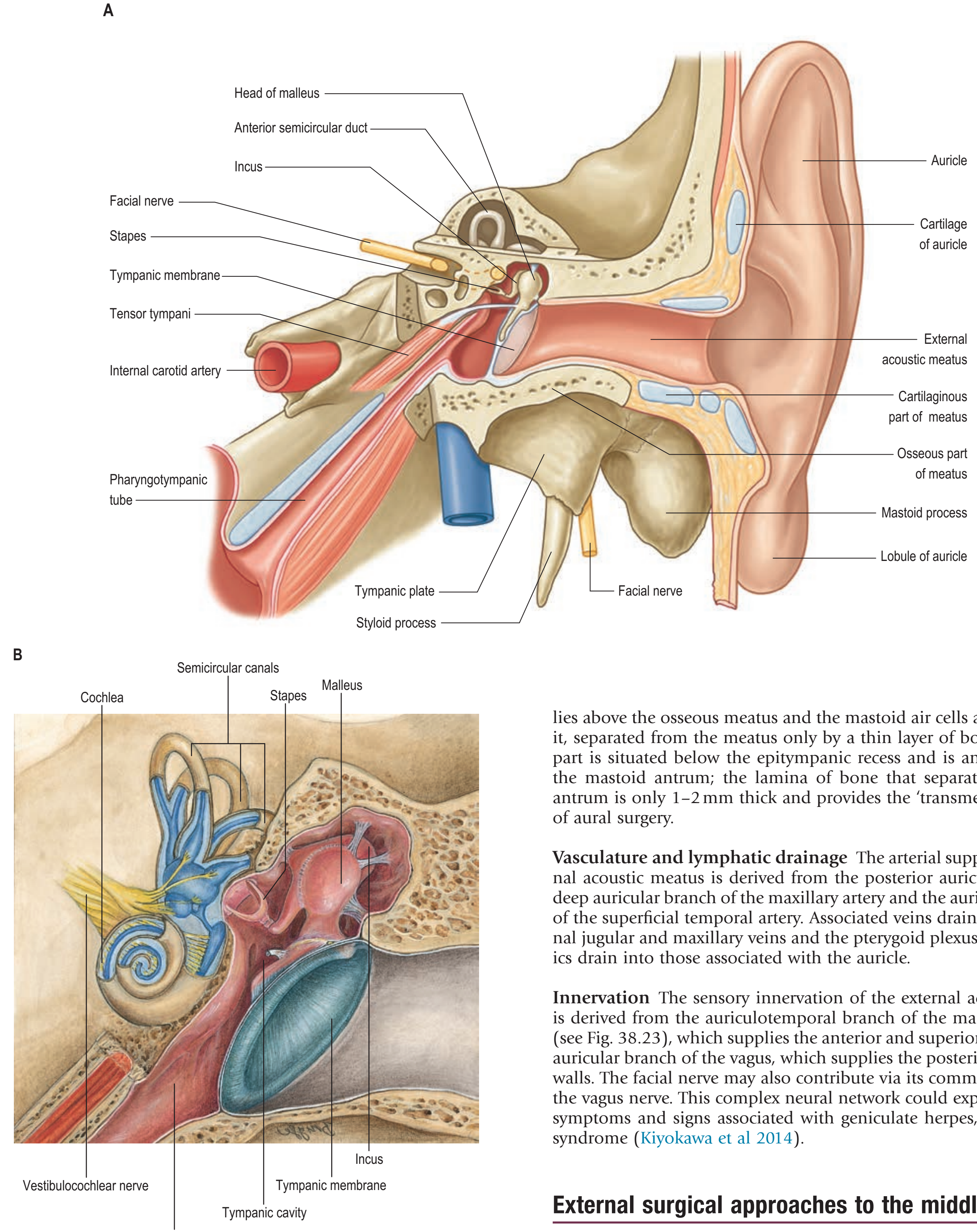
A
Head of malleus
Anterior semicircular duct
Incus
Facial nerve
Stapes
Tympanic membrane
Tensor tympani
Internal carotid artery
Pharyngotympanic tube
Tympanic plate
Styloid process
Facial nerve
Auricle
Cartilage of auricle
External acoustic meatus
Cartilaginous part of meatus
Osseous part of meatus
Mastoid process
Lobule of auricle
B
Semicircular canals
Cochlea
Stapes
Malleus
Incus
Vestibulocochlear nerve
Tympanic membrane
Tympanic cavity
Pharyngotympanic tube

Fig. 42.6 The external, middle and inner regions of the left ear. **A**, Anterior aspect. **B**, A more detailed view of the relationships of structures in the middle and inner ear. (B, Sobotta Atlas of Human Anatomy © Elsevier GmbH, Urban & Fischer, Munich.)

plate of the temporal bone, which in the fetus is only a tympanic ring. The posterosuperior region is formed by the squamous part of the temporal bone. The outer wall of the meatus is bounded above by the posterior zygomatic root, below which there may be a suprameatal spine.

Relations of the meatus The condylar process of the mandible lies anterior to the meatus and is partially separated from the cartilaginous part by a small portion of the parotid gland. A blow on the chin may cause the condyle to break into the meatus. The middle cranial fossa lies above the osseous meatus and the mastoid air cells are posterior to it, separated from the meatus only by a thin layer of bone. Its deepest part is situated below the epitympanic recess and is anteroinferior to the mastoid antrum; the lamina of bone that separates it from the antrum is only 1–2 mm thick and provides the 'transmeatal approach' of aural surgery.

Vasculature and lymphatic drainage The arterial supply of the external acoustic meatus is derived from the posterior auricular artery, the deep auricular branch of the maxillary artery and the auricular branches of the superficial temporal artery. Associated veins drain into the external jugular and maxillary veins and the pterygoid plexus. The lymphatics drain into those associated with the auricle.

Innervation The sensory innervation of the external acoustic meatus is derived from the auriculotemporal branch of the mandibular nerve (see Fig. 38.23), which supplies the anterior and superior walls, and the auricular branch of the vagus, which supplies the posterior and inferior walls. The facial nerve may also contribute via its communication with the vagus nerve. This complex neural network could explain the varied symptoms and signs associated with geniculate herpes, Ramsay Hunt syndrome (Kiyokawa et al 2014).

External surgical approaches to the middle ear

Surgical access to the middle ear can be achieved by a number of methods. Provided the external acoustic meatus is wide enough, the tympanic membrane can be elevated by incising the skin of the bony meatus circumferentially, leaving a vascular pedicle superiorly. The canal skin is then elevated from the underlying bone until the fibrous anulus of the tympanic membrane is visualized. This can then be elevated from the tympanic groove and the middle ear mucosa incised to allow the tympanic membrane to be reflected forwards and upwards. This per-meatal approach is called a tympanotomy and is used for stapedectomy, ossiculoplasty, myringoplasty and the removal of small middle-ear tumours: today, many of these procedures are undertaken endoscopically.

If the external acoustic meatus is too narrow to allow adequate visualization of the middle ear, or if access is required to the mastoid aditus and antrum, it is necessary to displace the superficial soft tissues. There are two main external approaches to the middle ear: the endaural approach and the postauricular approach.

The endaural approach involves making an incision in the notch between the tragus and the helix. This is carried down to expose the lower margin of temporalis muscle and the bone of the external acoustic meatus. The cartilaginous meatus is separated from the bony meatus and reflected laterally as a conchomeatal flap. The bony meatus can then be widened by drilling away bone (canalplasty). This gives more space to manipulate the delicate structures of the middle ear, as well as improving subsequent visualization of the tympanic membrane when the incision has healed.

The postauricular approach involves making an incision approximately 1 cm behind the postauricular skin crease and deepening the incision to the periosteum of the mastoid process, dividing the posterior auricular muscles on the way. Grafts can be harvested from the temporalis fascia. The periosteum is incised and elevated to expose the bony external acoustic meatus from behind. The skin over the junction of the bony and cartilaginous meatus is incised to allow the cartilage of the auricle and meatus to be swung forwards on its blood supply and so expose the bony meatus and mastoid process. Access can then be gained by drilling and elevating a tympanomeatal skin flap, as described for the endaural approach.

Temporalis fascia is the most popular tissue used as a free graft for repair of the tympanic membrane because it is easily obtained. In recent years, tragal perichondrium has become a popular alternative; it has the additional advantage that the cartilage can also be harvested and used to reinforce the repair.

More extensive resections of the temporal bone are undertaken using extended pre- or postauricular incisions into the temporal region and neck. The blood supply of the auricle is sufficient to maintain viability despite significant elevation and undermining.

MIDDLE EAR

The middle ear is an irregular, laterally compressed space in the petrous part of the temporal bone. It is lined with mucous membrane and filled with air, which reaches it from the nasopharynx via the pharyngotympanic tube (see Fig. 42.6; Fig. 42.7). The middle ear contains three small bones – the malleus, incus and stapes, collectively called the auditory ossicles – which form an articulated chain connecting the lateral and medial walls of the cavity, and which transmit the vibrations of the tympanic membrane across the cavity to the cochlea.

The essential function of the middle ear is to transfer energy efficiently from relatively weak vibrations in the elastic, compressible air in the external acoustic meatus to the incompressible fluid around the delicate receptors in the cochlea. Mechanical coupling between the two systems must match their resistance to deformation or 'flow', i.e. their impedance, as closely as possible. Aerial waves of low amplitude and low force per unit area arrive at the tympanic membrane, which has 15–20 times the area of the stapedial footplate that contacts the perilymph in the inner ear; the force per unit area generated by the footplate is increased by a similar amount, while the amplitude of vibration is almost unchanged.

Protective mechanisms incorporated into the design of the middle ear include the presence of the pharyngotympanic tube (to equalize pressure on both sides of the delicate tympanic membrane); the shape of the articulations between the ossicles; and the reflex contractions of stapedius and tensor tympani in response to sounds of fairly high intensity (preventing damage caused by sudden or excessive excursions of the ossicles).

The space within the middle ear can be subdivided into three parts. These are the mesotympanum or tympanic cavity proper, which is opposite the tympanic membrane; the epitympanum or attic, which is above the level of the membrane, and contains the head of the malleus and the body and short process of the incus; and the hypotympanum, which is in the floor of the cavity between the jugular bulb and the lower margin of the tympanic membrane. The vertical and anteroposterior diameters of the mesotympanum and hypotympanum are each approximately 15 mm; the transverse diameter is 6 mm superiorly and 4 mm inferiorly, narrowing to 2 mm opposite the umbo. The cavity is bounded laterally by the tympanic membrane and medially by the lateral wall of the internal ear, the promontory. It communicates posteriorly with the mastoid antrum and the mastoid air cells, and anteriorly with the nasopharynx via the pharyngotympanic tube (see Fig. 42.6).

The tympanic cavity and mastoid antrum, auditory ossicles and structures of the internal ear are all almost fully developed at birth and subsequently alter little; almost all of the volume changes are due to expansion of the epitympanic space (Osborn et al 2011). In the fetus, the cavity contains a gelatinous tissue that has practically disappeared by birth, when it is filled by a fluid that is absorbed when air enters via the pharyngotympanic tube. The tympanic cavity is a common site of infection in childhood.

Boundaries of the tympanic cavity

The tympanic cavity has a roof, a floor and lateral, medial, posterior and anterior walls. The sections that follow describe the bony anatomy of the middle ear. The mucosal lining has been well documented from an anatomical and functional standpoint (Gleeson et al 1991). With the advent of middle ear endoscopy in the live patient at surgery, finer detail of the mucosal folds within the middle ear cavity have been documented in a way never possible before. In future, the role of these folds will become apparent in both health and disease (Marchioni et al 2013, Nogueira et al 2013, Tarabichi et al 2013, Li et al 2018).

Roof

A thin plate of compact bone, the tegmen tympani, separates the cranial and tympanic cavities, and forms much of the anterior surface of the petrous temporal bone. It is prolonged posteriorly as the roof of the mastoid antrum and anteriorly it covers the canal for tensor tympani. In youth, the unossified petrosquamosal suture may allow the spread of infection from the tympanic cavity to the meninges. In adults, veins from the tympanic cavity traverse this suture to reach the superior petrosal or petrosquamous sinus and thus may also transmit infection to these structures through a process of thrombophlebitis.

Longitudinal fractures of the middle cranial fossa almost always involve the tympanic roof, accompanied by dislocation of the ossicular chain, rupture of the tympanic membrane, or a fractured roof of the osseous external acoustic meatus, which can be seen as a notch on otoscopy. Such injuries usually cause bleeding from the ear, with escape of cerebrospinal fluid if the dura mater has been torn (CSF otorrhoea).

Floor

The floor of the tympanic cavity is a narrow, thin, convex plate of bone that separates the cavity from the superior bulb of the internal jugular vein. The bone may be patchily deficient, in which case the tympanic cavity and the vein are separated only by mucous membrane and fibrous tissue. Alternatively, the floor is sometimes thick and may contain some accessory mastoid air cells. A small aperture for the tympanic branch of the glossopharyngeal nerve lies near the medial wall.

Lateral wall

The lateral wall consists mainly of the tympanic membrane but also contains the ring of bone to which the membrane is attached. The lateral epitympanic bony wall is wedge-shaped in section and its sharp inferior portion is known as the outer attic wall or scutum. This part is easily eroded or blunted by cholesteatoma, a feature easily detected on computed tomography (CT) scans. There is a deficiency or notch in the upper part of this ring, close to which are the small openings of the anterior and posterior canaliculi for the chorda tympani and the petrotympanic fissure. The posterior canaliculus for the chorda tympani is situated in the angle between the posterior and lateral walls of the tympanic cavity just behind the tympanic membrane, at a variable position approximately level with the upper end of the handle of the malleus. This variable position or entrance into the tympanic cavity should be kept in mind when mobilizing the chorda tympani in stapes surgery. It may not reflect inferiorly to the extent desired and can be easily damaged in the process. Within the mastoid, the chorda tympani passes into a minute canal that descends in front of the facial canal and ends in it about 6 mm above the stylomastoid foramen. This canal and the chorda tympani should not be mistaken for the main trunk of the facial nerve when skeletonizing the facial (Fallopian) canal during surgery. The canaliculus transmits the chorda tympani and a branch of the stylomastoid artery to the tympanic cavity. The chorda tympani leaves the tympanic cavity through the anterior canaliculus, which opens at the medial end of the petrotympanic fissure.

The petrotympanic fissure is a mere slit approximately 2 mm in length, which opens just above and in front of the ring of bone to which the tympanic membrane is attached. It contains the anterior process and anterior ligament of the malleus and transmits the anterior tympanic branch of the maxillary artery to the tympanic cavity.

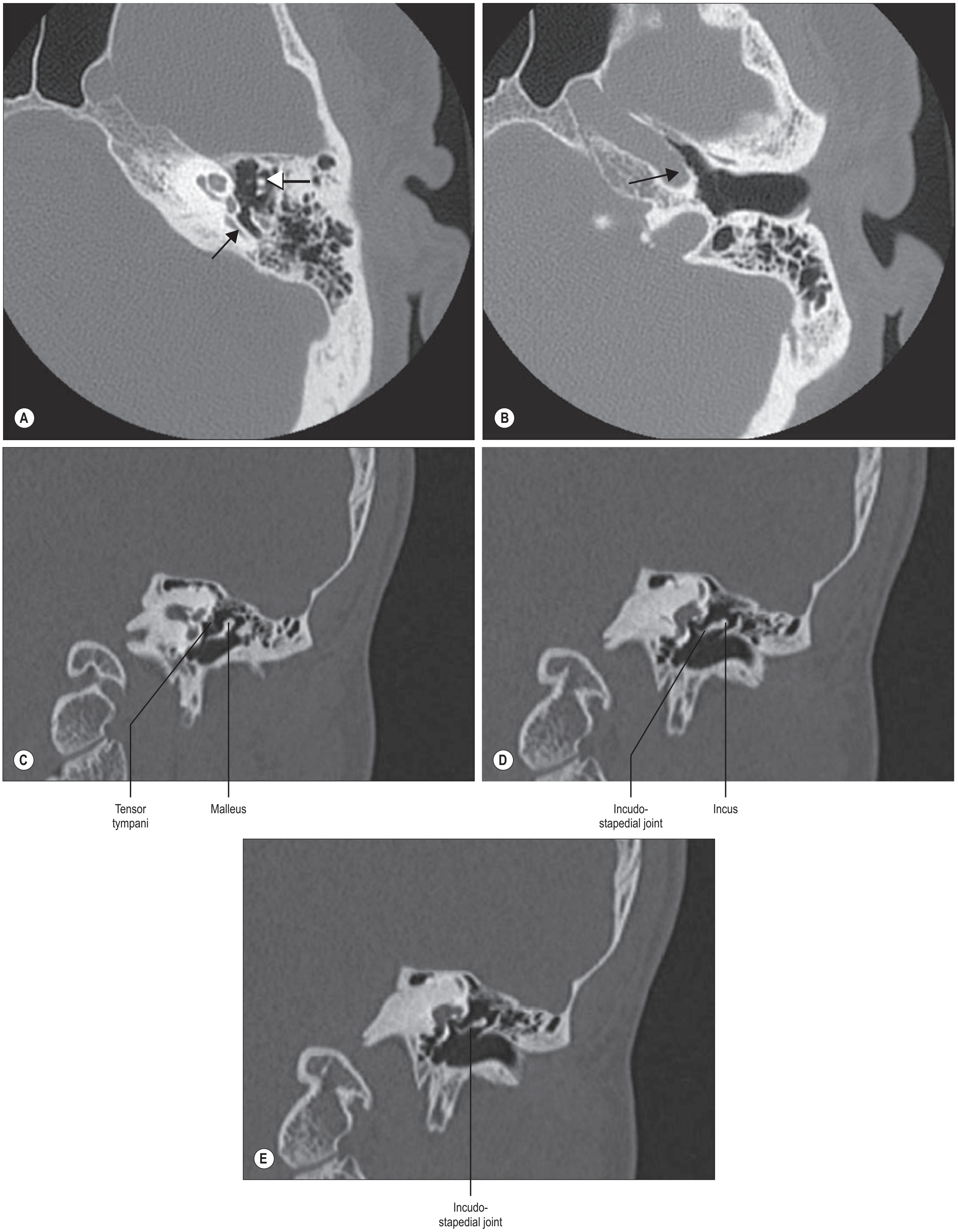
A
B
C
D
Tensor tympani
Malleus
Incudo-stapedial joint
Incus
E
Incudo-stapedial joint

Fig. 42.7 **A**, An axial CT scan at the level of the ossicular mass (white arrow) in the epitympanum, showing the mastoid antrum and its relationship to the lateral (horizontal) semicircular canal (black arrow). **B**, An axial CT scan at the level of the entrance of the pharyngotympanic tube, showing its relationship to the internal carotid artery (black arrow). Coronal CT scans showing details of the ossicular mass. **C**, Malleus and tensor tympani. **D** and **E**, Incus and incudostapedial joint. (A, B, Courtesy of Dr Steven Connor.)

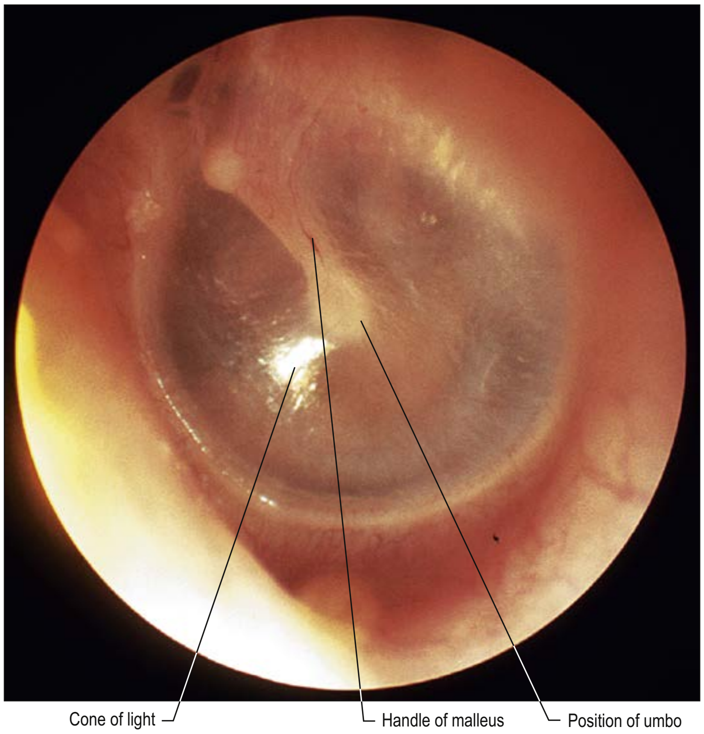

Fig. 42.8 An auroscopic view of the left tympanic membrane. Note that a bright cone of light is seen in the anteroinferior quadrant of the membrane when it is illuminated. (Courtesy of Mr Simon A Hickey.)

Tympanic membrane

The tympanic membrane separates the tympanic cavity from the external acoustic meatus (Fig. 42.8; see Fig. 42.6). It is thin, semi-transparent and almost oval, though somewhat broader above than below. It lies obliquely, at an angle of approximately 55° with the meatal floor in adults. Its longest, anteroinferior diameter is 9–10 mm, and its shortest is 8–9 mm. Most of its circumference is a thickened fibrocartilaginous ring or anulus, which is attached to the tympanic sulcus at the medial end of the meatus. The anulus contains radially orientated smooth muscle cells in several locations that possibly play a role in controlling blood flow or maintaining tension (Henson et al 2005). The sulcus is deficient superiorly, i.e. it is notched. Two bands, the anterior and posterior malleolar folds, pass from the ends of this notch to the lateral process of the malleus. The small triangular part of the membrane, the pars flaccida, lies above these folds and is lax and thin. The major part of the tympanic membrane, the pars tensa, is taut. The handle of the malleus is firmly attached to the internal surface of the tympanic membrane as far as its centre, which projects towards the tympanic cavity. The inner surface of the membrane is thus convex and the point of greatest convexity is termed the umbo. Although the membrane as a whole is convex on its inner surface, its radiating fibres are curved with their concavities directed inwards.

Microstructure

Histologically, the tympanic membrane is composed of an outer cuticular layer, an intermediate fibrous layer and an inner mucous layer.

The cuticular stratum is continuous with the thin skin of the meatus. It is keratinized, stratified squamous in type, devoid of dermal papillae and hairless. Its subepithelial tissue is vascularized and may develop a few peripheral papillae. Ultrastructurally, it is typically 10 cells thick and has two zones: a superficial layer of non-nucleated squames, and a deep zone that resembles the epidermal prickle cell layer (stratum spinosum). There are numerous desmosomes between cells, the deepest of which lie on a continuous basal lamina but lack epithelial pegs and hemidesmosomes. The cells of this stratum have a propensity for lateral migration and differentiation not shared with any other stratified squamous epithelia in the body.

The fibrous stratum consists of an external layer of radiating fibres that diverge from the handle of the malleus, and a deep layer of circular fibres, which are plentiful peripherally but sparse and scattered centrally. Ultrastructurally, the filaments are 10 nm in diameter and are linked at 25 nm intervals. They have a distinctive amino acid composition and may consist of a protein peculiar to the tympanic membrane. Small groups of collagen fibrils appear at 11 postmenstrual weeks, interspersed with small bundles of elastin microfibrils. Older specimens contain more typically cross-banded collagen fibrils and an amorphous elastin component. The fibrous stratum is replaced by loose connective tissue in the pars flaccida.

The mucous stratum is a part of the mucosa of the tympanic cavity and is thickest near the upper part of the membrane. It consists of a single layer of very flat cells, with overlapping interdigitating boundaries and desmosomes and tight junctions between adjacent cells. The cytoplasm contains only a few organelles; the luminal surfaces of these apparently metabolically inert cells have a few irregular microvilli and are covered by an amorphous electron-dense material. There are no ciliated columnar cells.

Innervation

The tympanic membrane is mainly innervated by the auriculotemporal nerve and appears to perceive only pain. There is a minor, inconstant and overlapping sensory supply from the facial, glossopharyngeal and vagus nerves.

The auricular branch of the vagus arises from the superior vagal ganglion and is joined soon after by a ramus from the inferior ganglion of the glossopharyngeal nerve. It passes behind the internal jugular vein and enters the mastoid canaliculus on the lateral wall of the jugular fossa. It traverses the temporal bone and crosses the facial canal about 4 mm above the stylomastoid foramen. At this point, it supplies an ascending branch to the facial nerve. Fibres of the nervus intermedius may pass to the auricular branch of the vagus here, which may explain the cutaneous vesiculation that sometimes accompanies geniculate herpes. The auricular branch then traverses the tympanomastoid fissure and divides into two rami. One ramus joins the posterior auricular nerve and the other is distributed to the skin of part of the cranial surface of the auricle, the posterior wall and floor of the external acoustic meatus, and to the adjoining part of the outer surface of the tympanic membrane. The auricular branch therefore contains somatic afferent nerve fibres, which probably terminate in the spinal trigeminal nucleus. Stimulation of the vagus nerve, e.g. in syringing the ear, can cause a reflex bradycardic reaction on heart rate. From a practical point of view, the tympanic membrane can be anaesthetized for minor procedures like myringotomy by the application of topical anaesthetic agents. For more complicated surgical procedures, e.g. tympanoplasty, it is possible to provide sufficient anaesthesia by local infiltration at the level of the bony and cartilaginous external acoustic meatus.

Otitis media

It is assumed that acute otitis media usually arises as a result of ascending infection from the nasopharynx via the pharyngotympanic tube to the middle ear cleft. From there, it may extend to the mastoid aditus and antrum. Swelling secondary to the infection may result in the closure of both exits from the middle ear, i.e. the pharyngotympanic tube and the aditus, with subsequent accumulation of pus under pressure, which causes lateral bulging and inflammation of the tympanic membrane. The latter may burst, releasing mucopurulent discharge into the external acoustic meatus, which results in a release of the pressure in the middle ear and a diminution in the levels of pain. After a brief period, the discharge dries up and, for the most part, the resultant perforation of the tympanic membrane heals. Normal ventilation and drainage of mucus from the middle ear are restored once the swelling and function of the pharyngotympanic tube resolve. On occasion, the process will fail to produce a perforation of the tympanic membrane and the inflammatory exudates will not drain. The immune defence system sterilizes the exudates of organisms, resulting in a sterile mucoid effusion, otitis media with effusion or glue ear (see below). The effusion may cause protracted deafness because its relatively incompressible nature prevents free vibration of the tympanic membrane (Bluestone and Klein 2002).

Myringoplasty

Persistent perforation of the tympanic membrane caused by infection or trauma leads to hearing impairment and predisposes to continuing infection as a result of contamination with organisms from the external acoustic meatus. This condition is known as chronic suppurative otitis media of the tubotympanic type. Myringoplasty is a surgical procedure that uses a connective tissue scaffold or graft to support healing of the perforation. The most common technique involves the elevation of the tympanic anulus and the placement of a piece of fibrous connective tissue, e.g. part of the fibrous deep fascia that invests the lateral surface of temporalis or the perichondrium of the tragal cartilage, on to the undersurface of the tympanic membrane to close the perforation. The healed

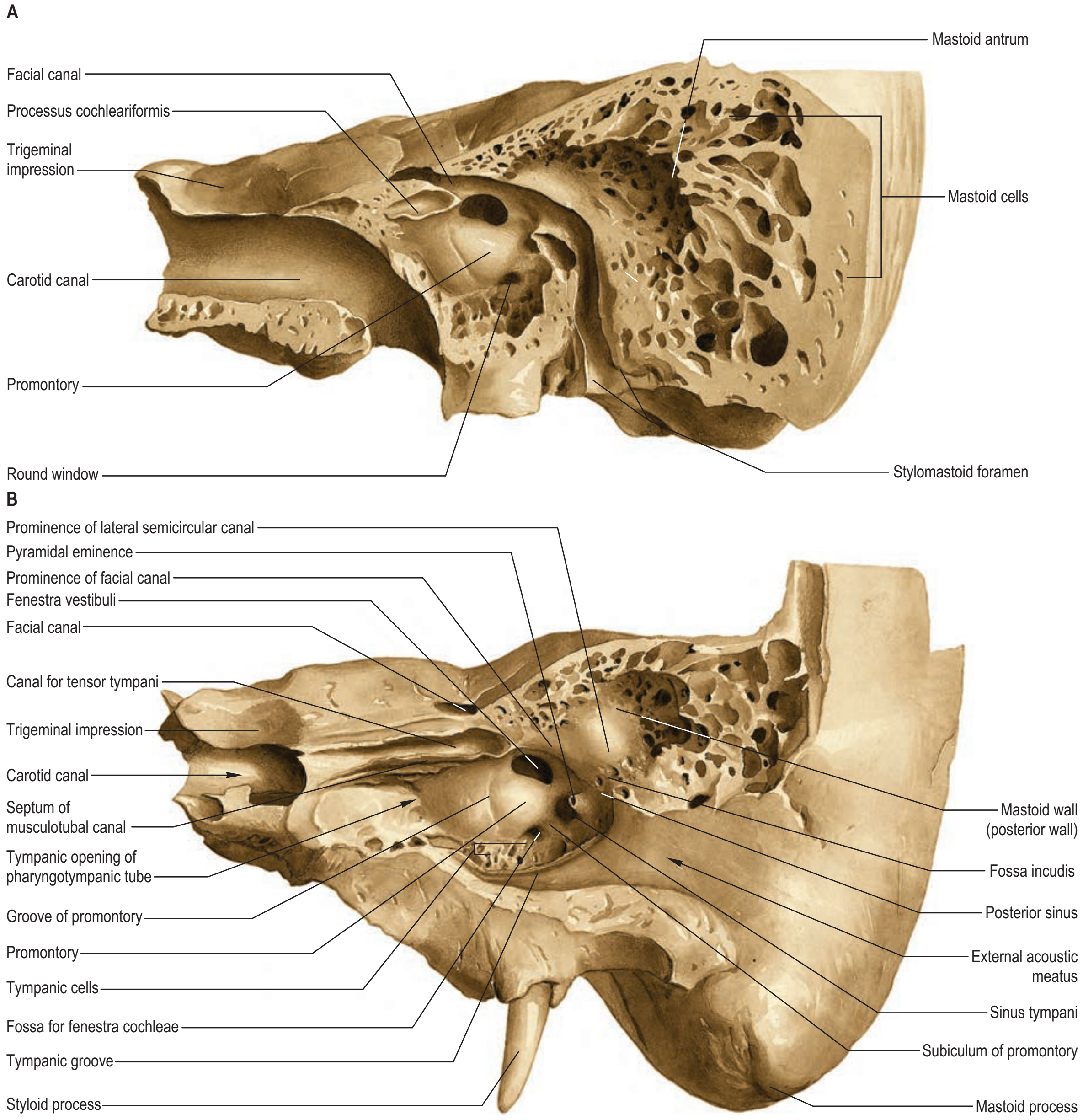
A
Facial canal
Processus cochleariformis
Trigeminal impression
Carotid canal
Promontory
Round window
Mastoid antrum
Mastoid cells
Stylomastoid foramen
B
Prominence of lateral semicircular canal
Pyramidal eminence
Prominence of facial canal
Fenestra vestibuli
Facial canal
Canal for tensor tympani
Trigeminal impression
Carotid canal
Septum of musculotubal canal
Tympanic opening of pharyngotympanic tube
Groove of promontory
Promontory
Tympanic cells
Fossa for fenestra cochleae
Tympanic groove
Styloid process
Mastoid wall (posterior wall)
Fossa incudis
Posterior sinus
External acoustic meatus
Sinus tympani
Subiculum of promontory
Mastoid process

Fig. 42.9 The medial wall of the left tympanic cavity, anterolateral aspect. **A**, The lateral wall and adjacent parts of the anterior and superior walls have been removed; the facial canal and carotid canal have been opened. **B**, A section along the axis of the petrous part of the temporal bone. (Sobotta Atlas of Human Anatomy © Elsevier GmbH, Urban & Fischer, Munich.)

edges of the perforation are stripped of epithelium to encourage healing and scar formation. The fibrous tissue supports the healing tympanic membrane and may, in part, be incorporated into the repair. Once the perforation is healed, the vibratory function of the tympanic membrane is usually restored to normal.

Medial wall

The medial wall of the tympanic cavity is also the lateral boundary of the internal ear. Its features are the promontory, fenestra vestibuli (fenestra ovalis, oval window), fenestra cochleae (fenestra rotunda, round window) and the facial prominence (Fig. 42.9).

The promontory is a rounded prominence furrowed by small grooves that lodge the nerves of the tympanic plexus. It lies over the lateral projection of the basal turn of the cochlea. A minute spicule of bone frequently connects the promontory to the pyramidal eminence of the posterior wall. The apex of the cochlea lies near the medial wall of the tympanic cavity, anterior to the promontory. A depression behind the promontory is known as the sinus tympani.

The fenestra vestibuli is a kidney-shaped opening situated above and behind the promontory and leading from the tympanic cavity to the vestibule of the inner ear. Its long diameter is horizontal and its convex border is directed upwards. It is occupied by the base of the stapes, the footplate; the circumference of the footplate is attached to the margin of the fenestra by an anular ligament.

The fenestra cochleae is situated below and a little behind the fenestra vestibuli, from which it is separated by a posterior extension of the promontory, called the subiculum. Occasionally, another ridge of bone, the ponticulus, leaves the promontory above the subiculum and runs to the pyramid on the posterior wall of the cavity. The fenestra cochleae lies completely under the overhanging edge of the promontory in a deep hollow or niche, and is placed very obliquely. In dried specimens, it opens anterosuperiorly from the tympanic cavity into the scala tympani of the cochlea, but in life it is closed by the secondary tympanic membrane. This is somewhat concave towards the tympanic cavity and convex towards the cochlea. It is bent so that its posterosuperior third forms an angle with its anteroinferior two-thirds. The membrane is composed of an external layer derived from the tympanic mucosa; an internal layer, derived from the cochlear lining membrane; and an intermediate, fibrous layer.

The prominence of the facial nerve canal indicates the position of the upper part of the bony facial (Fallopian) canal, which contains the facial nerve. The canal crosses the medial tympanic wall from the cochleariform process anteriorly, runs just above the fenestra vestibuli, and then curves down into the posterior wall of the cavity. Its lateral wall may be partly deficient.

Posterior wall

The posterior wall of the tympanic cavity is wider above than below. Its main features are the aditus to the mastoid antrum, the pyramid and the fossa incudis (see Fig. 42.9).

The aditus to the mastoid antrum is a large irregular aperture that leads back from the epitympanic recess into the upper part of the mastoid antrum. A rounded eminence on the medial wall of the aditus, above and behind the prominence of the facial nerve canal, corresponds to the position of the lateral semicircular canal.

The pyramidal eminence is situated just behind the fenestra vestibuli and in front of the vertical part of the facial nerve canal. It is hollow and contains the stapedius muscle. Its summit projects towards the fenestra vestibuli and is pierced by a small aperture that transits the tendon of stapedius. The cavity in the pyramidal eminence is prolonged down and back in front of the facial nerve canal; it communicates with the canal by an aperture through which a small branch of the facial nerve passes to stapedius.

The fossa incudis is a small depression in the lower and posterior part of the epitympanic recess. It contains the short process of the incus, which is fixed to the fossa by ligamentous fibres.

Mastoid antrum

The mastoid antrum is an air sinus in the petrous part of the temporal bone. Its topographical relations are of considerable surgical importance. The aditus to the mastoid antrum, which leads back from the epitympanic recess, opens in the upper part of its anterior wall. The lateral semicircular canal lies medial to the aditus. The descending part of the facial nerve canal is anteroinferior. The medial wall is related to the posterior semicircular canal. The sigmoid sinus lies some distance posteriorly; the distance can be extremely variable and is dependent on the degree of pneumatization of the mastoid. The roof is formed by the tegmen tympani, and so the antrum lies below the middle cranial fossa and the temporal lobe of the brain. The floor has several openings that communicate with the mastoid air cells. The lateral wall, which offers the usual surgical approach to the cavity, is formed by the postmeatal process of the squamous part of the temporal bone. This is only 2 mm thick at birth but increases at an average rate of 1 mm a year, attaining a final thickness of 12–15 mm. In adults, the lateral wall of the antrum corresponds to the suprameatal triangle (Macewen's triangle) on the outer surface of the skull. This is palpable through the cymba conchae. The superior side of the triangle, the supramastoid crest, is level with the floor of the middle cranial fossa; the anteroinferior side, which forms the posterosuperior margin of the external acoustic meatus, indicates approximately the position of the descending part of the facial nerve canal; and the posterior side, formed by a posterior vertical tangent to the posterior margin of the external acoustic meatus, is anterior to the sigmoid sinus.

The adult capacity of the mastoid antrum is variable, but on average is 1 ml, with a general diameter of 10 mm. Unlike the other air sinuses in the skull, it is present at birth, and indeed is then almost adult in size, although it is at a higher level relative to the external acoustic meatus than it is in adults. In the very young, the thinness of the lateral antral wall and the absence or underdevelopment of the mastoid process mean that the stylomastoid foramen and emerging facial nerve are very superficially situated.

Mastoid air cells

Though the mastoid antrum is well developed at birth, the mastoid air cells are merely minute antral diverticula at this stage. As the mastoid develops in the second year, the air cells gradually extend into it and by the fourth year they are well formed, although their greatest growth occurs at puberty. They vary considerably in number, form and size. Usually, they interconnect and are lined by a mucosa with squamous non-ciliated epithelium, continuous with that in the mastoid antrum and tympanic cavity. They may fill the mastoid process, even to its tip, and some may be separated from the sigmoid sinus and posterior cranial fossa only by extremely thin bone, which is occasionally deficient (see Fig. 42.9). Some may lie superficial to, or even behind, the sigmoid sinus, and others may be present in the posterior wall of the descending part of the facial nerve canal. Those in the squamous part of the temporal bone may be separated from deeper cells in the petrous part by a plate of bone in the line of the squamomastoid suture (Körner's septum). Sometimes, they extend only minimally into the mastoid process, in which case the process consists largely of dense bone or trabecular bone containing bone marrow. Varieties of the mastoid process are recognized. The three types most commonly described are pneumatized (with many air cells); sclerotic or diploic (with few or no air cells); and mixed (contain both air cells and bone marrow).

The mastoid process may sometimes have no air cells at all. Alternatively, air cells may extend beyond the mastoid process into the squamous part of the temporal bone above the supramastoid crest; into the posterior root of the zygomatic process of the temporal bone; into the osseous roof of the external acoustic meatus just below the middle cranial fossa; or into the floor of the tympanic cavity very close to the superior jugular bulb. Rarely, a few may excavate the jugular process of the occipital bone. An important group may extend medially into the petrous part of the temporal bone, even to its apex, and are related to the pharyngotympanic tube, carotid canal, labyrinth and abducens nerve. Some investigators maintain that these are not continuous with the mastoid cells but grow independently from the tympanic cavity. All of these extensions of the mastoid air cells are pathologically important since infection may spread to the structures around them. (For further reading on the mastoid air cells and other pneumatized regions of the temporal bone, see Allam (1969)).

Innervation. The mastoid air cells are innervated by a meningeal branch of the mandibular division of the trigeminal nerve.

Mastoiditis

Mastoiditis is a potentially dangerous, life-threatening condition that develops as a result of the spread of bacterial infection from the tympanic cavity via the aditus to the mastoid antrum and associated mastoid air cells. Occasionally, the infection may spread through the tegmen tympani to the dura mater of the middle cranial fossae, to cause meningitis or a temporal lobe abscess. Similar spread may be seen into the posterior cranial fossa and cerebellum.

Infection may spread laterally through the cortical bone of the lateral aspect of the mastoid process to form a subperiosteal postauricular abscess (Bezold's abscess), or through the cortical bone of the tip of the mastoid process to the attachment of the posterior belly of digastric and sternocleidomastoid, which stimulates painful muscular contraction and torticollis.

Anterior wall

The inferior, larger area of the anterior wall of the tympanic cavity is narrowed by the approximation of the medial and lateral walls of the cavity (see Fig. 42.6). It is a thin lamina and forms the posterior wall of the carotid canal. It is perforated by the superior and inferior caroticotympanic nerves and the tympanic branch or branches of the internal carotid. The canals for tensor tympani and the osseous part of the pharyngotympanic tube open above it, the canal for tensor tympani being superior to that for the pharyngotympanic tube. Both canals incline downwards and anteromedially, to open in the angle between the squamous and petrous parts of the temporal bone, and are separated by a thin, osseous septum. The canal for tensor tympani and the bony septum runs posterolaterally on the medial tympanic wall and ends immediately above the fenestra vestibuli. Here, the posterior end of the septum is curved laterally to form a pulley, the processus cochleariformis (cochleariform process), which is a surgical landmark for the identification of the geniculate ganglion of the facial nerve. The tendon of tensor tympani turns laterally over the pulley before attaching to the upper part of the handle of the malleus.

Pharyngotympanic tube blockage in children

The pharyngotympanic tube serves to ventilate the middle ear, exchanging nasopharyngeal air with the air in the middle ear, which has been altered in its composition via transmucosal gas exchange with the haemoglobin in the blood vessels of the mucosa. The tube also carries mucus from the middle ear cleft to the nasopharynx as a result of ciliary transport.

In children, the pharyngotympanic tube is relatively narrow. It is prone to obstruction when the mucosa swells in response to infection or allergic challenge; obstruction results in a relative vacuum being created in the middle ear secondary to transmucosal gas exchange, and this in turn promotes mucosal secretion and the formation of a middle ear effusion. Because of the collapsibility of the pharyngotympanic tube, the vacuum thus created can overcome the distending effect of the muscles of the tube and 'lock' the tube shut. The resultant persistent middle ear effusion, otitis media with effusion (glue ear), can cause hearing loss by splinting the tympanic membrane and impeding its vibration. It can also provide an ideal environment for the proliferation of bacteria, with the result that an acute otitis media may develop (see above). It is possible to relieve the vacuum and unlock the tube, and then remove the effusion by myringotomy, i.e. by surgically creating a hole in the tympanic membrane. This hole will generally heal rapidly, and it is common practice to insert a flanged ventilation tube (a grommet or tympanostomy tube) to keep the hole open. Migration of the outer squamous layer of the tympanic membrane eventually displaces the tube and the myringotomy heals.

Auditory ossicles

A chain of three mobile ossicles – the malleus, incus and stapes – transfers sound waves across the tympanic cavity from the tympanic membrane to the fenestra vestibuli. The malleus is attached to the tympanic membrane, and the base (footplate) of the stapes is attached to the rim of the fenestra vestibuli. The incus is suspended between them and articulates with both bones.

Malleus

The malleus is the largest of the ossicles and is shaped somewhat like a mallet (Fig. 42.10). It is 8–9 mm long and has a head, neck, handle (manubrium) and anterior and lateral processes. The head is the large upper end of the bone and is situated in the epitympanic recess. It is ovoid in shape, articulates posteriorly with the incus, and is covered elsewhere by mucosa. The cartilaginous articular facet for the incus is narrowed near its middle and consists of a larger upper part and a smaller lower part, orientated almost at right-angles to each other. Opposite the constriction, the lower margin of the facet projects in the form of a process, the spur of the malleus. The neck is the narrowed part below the head, and inferior to this is an enlargement from which the anterior and lateral processes project. The lateral process has a cartilaginous cap that articulates with the tympanic membrane (Michaelides et al 2018).

The handle of the malleus is connected by its lateral margin to the tympanic membrane by a narrow core of dense connective tissue, surrounded by loose connective tissue. It varies in width along the manubrium (De Greef et al 2016) (see Figs 42.6, 42.8). It is directed downwards, medially and backwards. It decreases in size towards its free end, which is curved slightly forwards and is flattened transversely. Near the upper end of its medial surface there is a slight projection to which the tendon of tensor tympani is attached. The anterior process is a delicate bony spicule, directed forwards from the enlargement below the neck, and connected to the petrotympanic fissure by ligamentous fibres. In fetal life, it is the longest process of the malleus and is continuous in front with Meckel's cartilage. The lateral process is a conical projection from the root of the handle of the malleus. It is directed laterally and is attached to the upper part of the tympanic membrane and, via the anterior and posterior malleolar folds, to the sides of the notch in the upper part of the tympanic sulcus.

Ossification

The cartilaginous precursor of the malleus originates as part of the dorsal end of Meckel's cartilage. With the exception of its anterior process, the malleus ossifies from a single endochondral centre that appears near the future neck of the bone during postmenstrual weeks 13–16. The anterior process ossifies separately in dense connective tissue and joins the rest of the bone during postmenstrual weeks 21–24.

Incus

The incus is shaped less like an anvil, from which it is named, than a premolar tooth with its two diverging roots. It has a body and two processes (see Fig. 42.10). The body is somewhat cubical but laterally compressed. On its anterior surface, it has a saddle-shaped facet for articulation with the head of the malleus. The long process, rather more than half the length of the handle of the malleus, descends almost vertically, behind and parallel to the handle. Its lower end bends medially and ends in a rounded lenticular process, the medial surface of which is covered with cartilage and articulates with the head of the stapes. The short process, somewhat conical, projects backwards and is attached by ligamentous fibres to the fossa incudis in the lower and posterior part of the epitympanic recess. The presence of a single nutrient vessel within the long process of the incus and the absence of any collateral circulation render this segment of the bone susceptible to aseptic necrosis following middle ear infections.

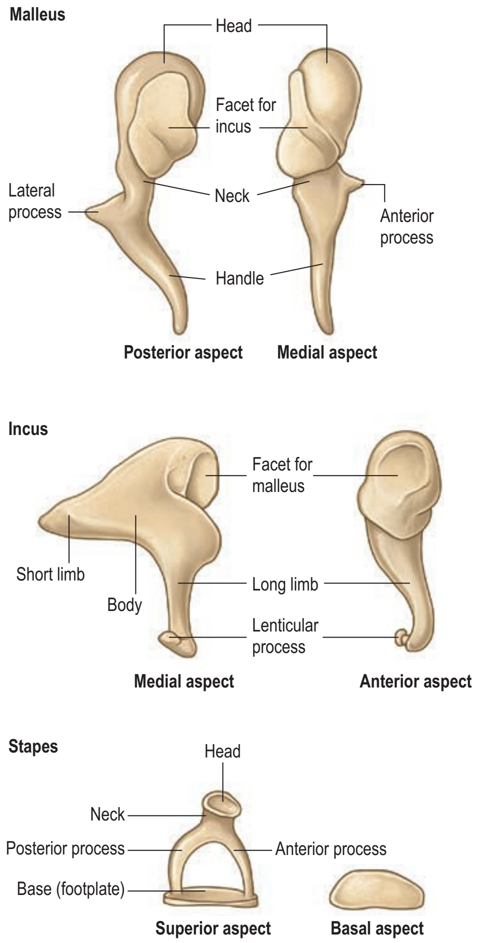

Fig. 42.10 The left auditory ossicles.

Ossification

The incus has a cartilaginous precursor continuous with the dorsal extremity of Meckel's cartilage. Ossification often spreads from a single centre in the upper part of its long process during postmenstrual weeks 13–16; the lenticular process may have a separate centre.

Stapes

The stapes has a head, neck, two limbs (processes or crura) and a base (footplate) (see Fig. 42.10). The head (caput) is directed laterally and has a small cartilaginous facet for articulation with the lenticular process of the incus. The neck is the constricted part supporting the head, and the tendon of stapedius is attached to its posterior surface. The processes diverge from the neck and are connected at their ends by a flattened oval plate, the base, which forms the footplate of the stapes. The footplate is attached to the margin of the fenestra vestibuli by a ring of fibres (the anular ligament). The anterior process is shorter, thinner and less curved than the posterior.

Ossification

The stapes is preformed in the perforated dorsal moiety of the hyoid arch cartilage of the fetus. Ossification starts from a single endochondral centre that appears in the base during postmenstrual weeks 13–16 and then gradually spreads through the limbs of the stapes to reach the head.

At birth, the auditory ossicles have achieved their full adult size and configuration. They increase in density during the first years of life as marrow cavities are replaced with endosteal bone and fine trabeculae (Isaacson 2014).

Ossicular ligaments

The ossicles are connected to the tympanic walls by ligaments (see Fig. 42.6B): three for the malleus and one each for the incus and stapes. Some are mere mucosal folds that carry blood vessels and nerves to and from the ossicles and their articulations, and others contain a central, strong band of collagen fibres.

The anterior ligament of the malleus stretches from the neck of the malleus, just above the anterior process, to the anterior wall of the tympanic cavity near the petrotympanic fissure. Some of its collagen fibres traverse this fissure to reach the spine of the sphenoid, and others continue into the sphenomandibular ligament. The latter, like the anterior malleolar ligament, is derived from the perichondrial sheath of Meckel's cartilage. The anterior malleolar ligament may contain muscle fibres, called laxator tympani or musculus externus mallei. The lateral ligament of the malleus is a triangular band that stretches from the posterior part of the border of the tympanic incisure to the head of the malleus. The superior ligament of the malleus connects the head of the malleus to the roof of the epitympanic recess.

The posterior ligament of the incus connects the end of its short process to the fossa incudis. The superior ligament of the incus is little more than a mucosal fold passing from the body of the incus to the roof of the epitympanic recess.

The vestibular surface and rim of the stapedial base are covered with hyaline cartilage. The cartilage encircling the base is attached to the margin of the fenestra vestibuli by a ring of elastic fibres, the anular ligament of the base of the stapes. The posterior part of this ligament is much narrower than the anterior part; it acts as a kind of hinge on which the stapedial base moves when stapedius contracts and during acoustic oscillation.

Ossicular articulations

The ossicular articulations are typical synovial joints. The incudomalleolar joint is saddle-shaped and the incudostapedial joint is a ball and socket articulation. The articular surfaces are covered with articular cartilage, and each joint is enveloped by a capsule that is rich in elastic tissue and lined by synovial membrane. Versican, fibronectin, elastin and hyaluronan have been co-localized in the attachments of tensor tympani and stapedius to the malleus and stapes, respectively, and in the anular ligament of the incudostapedial joint in histological sections of adult middle ears (Kawase et al 2012). Co-localization between elastic fibres and hyaluronan in the middle ear appears to be a postnatal maturational event, possibly an adaptation to acoustic oscillation producing multidirectional mechanical stress (Takanashi et al 2013).

Movements of the auditory ossicles

The handle of the malleus follows all movements of the tympanic membrane. The malleus and incus rotate together around an axis that runs from the short process and posterior ligament of the incus to the anterior ligament of the malleus. When the tympanic membrane and handle of the malleus move inwards (medially), the long process of the incus moves in the same direction and pushes the stapedial footplate towards the labyrinth and the perilymph contained within the labyrinth. The movement of the perilymph causes a compensatory outward bulging of the secondary tympanic membrane. These events are reversed when the tympanic membrane moves outwards. If the movement of the tympanic membrane is considerable, the incus does not follow the full outward excursion of the malleus and merely glides on it at the incudomalleolar joint, so preventing a dislocation of the footplate of the stapes from the fenestra vestibuli. When the handle of the malleus is carried medially, the spur at the lower margin of the head of the malleus locks the incudomalleolar joint, and this necessitates an inward movement of the long process of the incus. The joint is unlocked again when the handle of the malleus is carried outwards. The three bones together act as a bent lever so that the stapedial footplate does not move in the fenestra vestibuli like a piston, but rocks on a fulcrum at its anteroinferior border where the anular ligament is thick. The rocking movement around a vertical axis, which is like a swinging door, is said to happen only at moderate intensities of sound. With loud, low-pitched sounds, the axis becomes horizontal, and the upper and lower margins of the stapedial footplate oscillate in opposite directions around this central axis, thus preventing excessive displacement of the perilymph.

Otosclerosis and other causes of stapes fixation, stapedectomy and stapedotomy

Otosclerosis is a localized disease of the bone derived from the embryonic otic capsule in which lamellar bone is replaced by woven bone of greater thickness and vascularity. It may develop spontaneously but is often seen in pedigrees and accelerated by pregnancy; the inherited form is associated with mutations of the *RELN* gene. The position of the focus of new bone formation determines its effect on the function of the ear. When new bone develops around the footplate of the stapes, it may fix the footplate to the margin of the fenestra vestibuli and prevent it from moving. This impedes the passage of vibrations of the tympanic membrane passing through the ossicular chain to the inner ear, producing a conductive hearing loss. Otosclerosis affecting other parts of the otic capsule is thought to cause a sensorineural element to the overall hearing loss.

The footplate may be fixed by conditions other than otosclerosis. Rarely it may be fixed from birth, congenital fixation, but more commonly is the result of chronic otitis media causing dense scarring throughout the middle ear cleft known as tympanosclerosis, or associated with other temporal bone anomalies, e.g. Wardenberg syndrome (Melzer et al 2016). Whatever the cause, the result is a conductive hearing loss.

Stapedectomy is a surgical procedure designed to bypass the fixation of the stapes footplate caused by otosclerosis. The tympanic membrane is temporarily elevated for access to the middle ear and, under microscopic control, the incudostapedial joint is disarticulated. The limbs of the stapes and stapedius are then both divided and the superstructure of the stapes removed. Formerly the entire footplate was removed (stapedectomy) but nowadays a small hole (stapedotomy) is then made in the fixed footplate of the stapes using a microdrill, laser or hand reamer to expose the membranous inner ear bathed in perilymph. A small graft of connective tissue is used to cover the hole with a flexible membrane. A piston usually measuring 4.5 mm in length and 0.4 mm in width and made of Teflon or titanium that incorporates an open hook at one end is crimped onto the long process of the incus and placed so that the free end of the piston engages the membrane covering the footplate perforation (Luers and Hüttenbrink 2015). The tympanic membrane is then returned. The connection between the tympanic membrane and the inner ear is thus reconstituted and hearing restored.

Stapedectomy or stapedotomy for congenital fixation carries the risk of a 'gusher' as perilymph flows vigorously and seemingly endlessly from the vestibule of the labyrinth once the footplate is perforated. Staunching the flow is best achieved by placing a free muscle graft between the long process of the incus and the oval window. Direct suction over the oval window must be avoided at all costs because it might cause rupture of the inner ear membranes and result in a very significant or complete hearing loss in the ear.

Muscles

There are two intratympanic muscles: tensor tympani and stapedius (Anderson 1976).

Tensor tympani

Tensor tympani is a long, slender muscle that occupies the bony canal above the osseous part of the pharyngotympanic tube, from which it is separated by a thin bony septum (see Fig. 42.6). It arises from the cartilaginous part of the pharyngotympanic tube and the adjoining region of the greater wing of the sphenoid, as well as from its own canal. It passes back within its canal, and ends in a slim tendon which bends laterally round the pulley-like processus cochleariformis and attaches to the handle of the malleus, near its root (see Fig. 42.12).

Vascular supply Tensor tympani receives its arterial blood supply from the superior tympanic branch of the middle meningeal artery.

Innervation Tensor tympani is innervated by a branch of the nerve to medial pterygoid (a ramus of the mandibular division of the trigeminal nerve), which traverses the otic ganglion without interruption to reach the muscle.

Actions Tensor tympani draws the handle of the malleus medially, and so tenses the tympanic membrane and helps to damp sound vibrations; its action also pushes the base of the stapes more tightly into the fenestra vestibuli.

Stapedius

Stapedius arises from the wall of a conical cavity in the pyramidal eminence on the posterior wall of the tympanic cavity, and from its continuation anterior to the descending part of the facial nerve canal. Its minute tendon emerges from the orifice at the apex of the pyramid and passes forwards to attach to the posterior surface of the neck of the stapes. The muscle is of an asymmetric bipennate form. It contains numerous small motor units, each of only 6–9 muscle fibres; a few neuromuscular spindles exist near the myotendinous junction.

Vascular supply Stapedius receives its arterial blood supply from branches of the posterior auricular, anterior tympanic and middle meningeal arteries.

Innervation Stapedius is supplied by a branch of the facial nerve that is given off in the facial canal.

Actions Stapedius helps to damp down excessive sound vibrations. It opposes the action of tensor tympani (which pushes the stapes more tightly into the fenestra vestibuli). Paralysis of stapedius results in hyperacusis.

Stapedial and tensor tympani reflexes. When noises are loud, and immediately before speaking, a reflex contraction of stapedius and tensor tympani takes place that helps damp down the movement of the ossicular chain before vibrations reach the internal ear. The afferent pathways involve the auditory component of cranial nerve VIII, and higher centres prior to speech. The efferent pathway involves the facial nerve (stapedius) and the mandibular nerve (tensor tympani).

Vascular supply and lymphatic drainage

A number of arteries supply the walls and contents of the tympanic cavity. The deep auricular, anterior tympanic and stylomastoid arteries are larger than the others.

The deep auricular branch of the first part of the maxillary artery often arises with the anterior tympanic artery. It ascends in the parotid gland behind the temporomandibular joint, pierces the cartilaginous or bony wall of the external acoustic meatus and supplies its cuticular lining, the exterior of the tympanic membrane and the temporomandibular joint.

The anterior tympanic branch of the first part of the maxillary artery ascends behind the temporomandibular joint and enters the tympanic cavity through the petrotympanic fissure. It ramifies on the interior of the tympanic membrane and forms a vascular circle around it with the posterior tympanic branch of the stylomastoid artery. It also anastomoses with twigs of the artery of the pterygoid canal and caroticotympanic branches of the internal carotid artery in the mucosa of the tympanic cavity.

The stylomastoid branch of the occipital or posterior auricular arteries supplies the posterior part of the tympanic cavity and mastoid air cells. It also enters the stylomastoid foramen to supply the facial nerve and semicircular canals. In the young, its posterior tympanic branch forms a circular anastomosis with the anterior tympanic artery.

The smaller arteries supplying the tympanic cavity include the petrosal branch of the middle meningeal artery, which enters through the hiatus for the greater petrosal nerve; the superior tympanic branch of the middle meningeal artery, which traverses the canal for tensor tympani; an inferior tympanic branch from the ascending pharyngeal artery, which traverses the tympanic canaliculus together with the tympanic branch of the glossopharyngeal nerve, to supply the medial wall of the tympanic cavity; a branch from the artery of the pterygoid canal, which accompanies the pharyngotympanic tube; and a tympanic branch or branches from the internal carotid artery, which is given off in the carotid canal and perforates the thin anterior wall of the tympanic cavity.

The mastoid air cells and dura mater are also supplied by a mastoid branch from the occipital artery. It is small in size and sometimes absent. When present, it enters the cranial cavity via the mastoid foramen near the occipitomastoid suture. In early fetal life, a stapedial artery traverses the stapes.

The veins from the tympanic cavity terminate in the pterygoid venous plexus and the superior petrosal sinus. A small group of veins runs medially from the mucosa of the mastoid antrum through the arch formed by the superior (anterior) semicircular canal and emerges on to the posterior surface of the petrous temporal bone at the subarcuate fossa. These veins drain into the superior petrosal sinus and are the remains of the large subarcuate veins of childhood. They represent a potential route for the spread of infection from the mastoid antrum to the meninges.

Lymphatic vessels of the tympanic and antral mucosae drain to the parotid or upper deep cervical lymph nodes. Vessels draining the tympanic end of the pharyngotympanic tube probably end in the deep cervical nodes.

Innervation

The tympanic cavity contains the tympanic plexus and the facial nerve. Branches from the plexus and the facial nerve supply structures within the tympanic cavity but also leave the cavity to supply structures on the face.

Tympanic plexus

The nerves that constitute the tympanic plexus ramify on the surface of the promontory on the medial wall of the tympanic cavity. They are derived from the tympanic branch of the glossopharyngeal nerve and the caroticotympanic nerves (Fig. 42.11). The former arises from the inferior ganglion of the glossopharyngeal nerve and reaches the tympanic cavity via the tympanic canaliculus for the tympanic nerve. The superior and inferior caroticotympanic nerves are postganglionic sympathetic fibres that are derived from the carotid sympathetic plexus and traverse the wall of the carotid canal to join the plexus.

The tympanic plexus supplies branches to the mucosa of the tympanic cavity, pharyngotympanic tube and mastoid air cells. It sends a branch to the greater petrosal nerve via an opening anterior to the fenestra vestibuli. The lesser petrosal nerve, which may be regarded as the continuation of the tympanic branch of the glossopharyngeal nerve, traverses the tympanic plexus. It occupies a small canal below that for the tensor tympani. It runs past, and receives a connecting branch from, the geniculate ganglion of the facial nerve. The lesser petrosal nerve emerges from the anterior surface of the temporal bone via a small opening lateral to the hiatus for the greater petrosal nerve and then traverses either the foramen ovale or the sphenopetrosal fissure or the innominate canal (of Arnold) to join the otic ganglion. Postganglionic secretomotor fibres leave this ganglion in the auriculotemporal nerve to supply the parotid gland. In former times, the operation of tympanic neurectomy was undertaken to reduce salivation in patients who drooled and to diminish facial sweating in those with Frey's syndrome following parotidectomy; less invasive and more effective procedures are employed nowadays.

Facial nerve

The facial nerve consists of intracranial (cisternal), intratemporal and extratemporal portions. The intratemporal portion is further

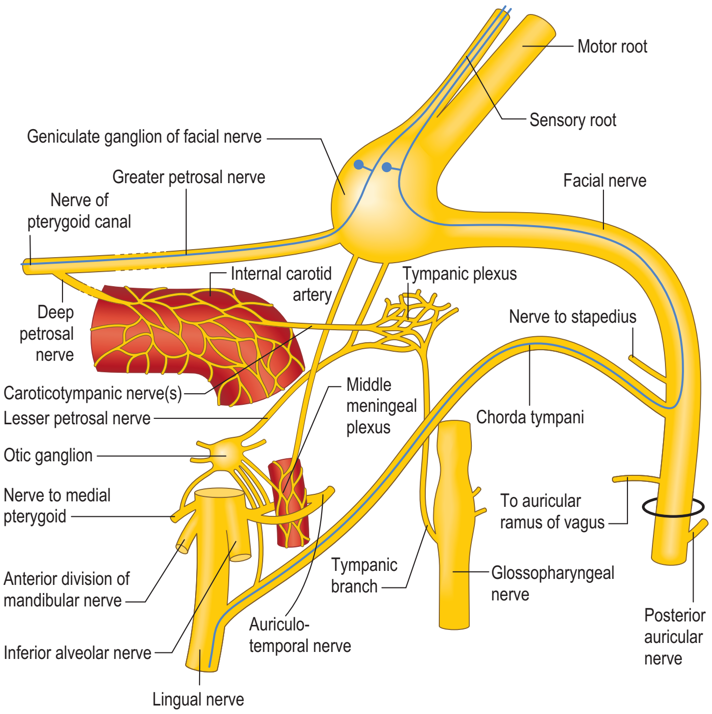

Fig. 42.11 The intracranial branches of the facial and glossopharyngeal nerves and the connections of the tympanic plexus and the otic ganglion. The course of the taste fibres from the mucous membrane of the palate and from the anterior presulcal part of the tongue is represented by the blue lines.

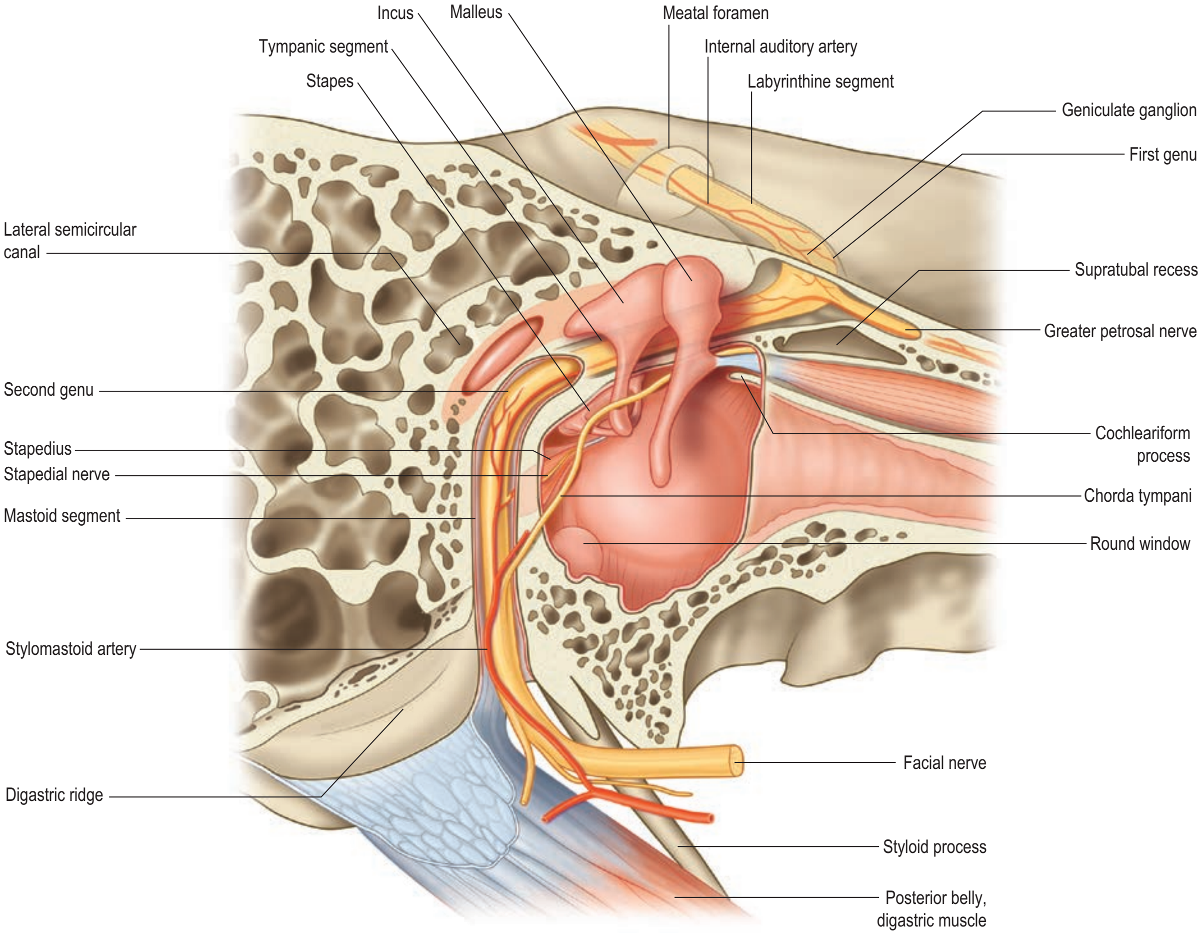

Fig. 42.12 A schematic diagram to illustrate the relationships of the facial nerve within the temporal bone. For simplicity, the course of the labyrinthine segment of the facial nerve has been portrayed more superiorly than it is in life. At the first genu, it turns sharply on itself and passes deeply to the internal auditory meatus. In an anatomically correct diagram, its course viewed from the lateral perspective (as shown here) would be obscured by the ossicular mass. The facial nerve is vulnerable to injury at several sites within the temporal bone and the neck. The labyrinthine and perigeniculate segments are susceptible to compression, ischaemia and transection in both longitudinal and transverse fractures of the temporal bone. The narrowing of the facial (Fallopian) canal at the meatal foramen has been implicated in the pathogenesis of idiopathic facial palsy (Bell's palsy). At the first genu, the facial nerve is tethered by the greater petrosal nerve, increasing its susceptibility to iatrogenic shearing injuries when it is mobilized in re-routing procedures to enable access to tumours. The facial (Fallopian) canal containing the tympanic segment of the facial nerve may be dehiscent above and distal to the oval window; as a result, the nerve is easily and inadvertently damaged in middle ear surgery for cholesteatoma or stapedectomy. The mastoid segment of the facial nerve is lateral to the tympanic anulus where it is at risk of surgical trauma in meatoplasty surgery around the external acoustic meatus. (Redrawn from Francis HW 2010 Anatomy of the temporal bone, external ear, and middle ear. In: Flint PW, Haughey BH, Lund VJ et al (eds) Cummings Otolaryngology: Head and Neck Surgery, 5th ed. Mosby; Ch 127, pp. 1821–30.)

divided into meatal, labyrinthine, tympanic (horizontal) and mastoid (vertical) segments (Fig. 42.12). The cisternal segment emerges from the ventrolateral aspect of the caudal border of the pons. The meatal segment enters the porus acusticus of the internal acoustic meatus accompanied by the nervus intermedius, the vestibulocochlear nerve and the labyrinthine vessels. In this part of its course, the nerve lacks a fibrous sheath or endoneurium and is surrounded by a thin layer of arachnoid. The motor root, which supplies the muscles of the face, and the nervus intermedius, which contains sensory fibres concerned with the perception of taste and parasympathetic (secretomotor) fibres to various glands, are still separate components; they usually merge within the meatus. The labyrinthine segment runs from the fundus of the internal acoustic meatus to the geniculate ganglion, where the nerve makes the first bend or genu (see Fig. 42.11). The labyrinthine segment is the shortest and narrowest part of the facial nerve; it lacks anastomosing arterial cascades, which renders it susceptible to vascular compression. The tympanic segment initially curves around the oval window niche, then lies just anterior and inferior to the lateral semicircular canal and bends again at the second genu to become the mastoid segment, which is the longest of the petrous segments and runs from the pyramidal process to the stylomastoid foramen. The tympanic and mastoid segments of the facial nerve are supplied by the facial arch, formed by the petrosal branch of the middle meningeal artery and the stylomastoid branch of the posterior auricular artery. The extratemporal course of the facial nerve is described in Chapter 36 (pages 632 and 633).

The branches that arise from the facial nerve within the temporal bone can be divided into those that come from the geniculate ganglion and those that arise within the facial canal.

The main branch from the geniculate ganglion is the greater (superficial) petrosal nerve, a branch of the nervus intermedius. The greater petrosal nerve passes anteriorly, receives a branch from the tympanic plexus and traverses a hiatus on the anterior surface of the petrous part of the temporal bone. It enters the middle cranial fossa, runs forwards in a groove on the bone above the lesser petrosal nerve, and then passes beneath the trigeminal ganglion to reach the foramen lacerum. Here it is joined by the deep petrosal nerve from the internal carotid sympathetic plexus, to become the nerve of the pterygoid canal (Vidian nerve). The greater petrosal nerve contains parasympathetic fibres destined for the pterygopalatine ganglion, and taste fibres from the palate. The geniculate ganglion also communicates with the lesser petrosal nerve.

The nerve to stapedius arises from the facial nerve in the facial nerve canal behind the pyramidal eminence of the posterior wall of the tympanic cavity and passes forwards through a small canal to reach the muscle.

The chorda tympani (see Figs 42.11, 42.12) leaves the facial nerve some 6 mm above the stylomastoid foramen and runs anterosuperiorly in a canal to enter the tympanic cavity via the posterior canaliculus. It then curves anteriorly in the substance of the tympanic membrane between its mucous and fibrous layers, and crosses medial to the upper part of the handle of the malleus to the anterior wall of the tympanic cavity, where it enters the anterior canaliculus. It exits the skull at the petrotympanic fissure, and its further course is described on page 682. The chorda tympani contains parasympathetic fibres that supply the submandibular and sublingual salivary glands via the submandibular ganglion and taste fibres from the anterior two-thirds of the tongue.

Dehiscences of the facial nerve canal

The facial nerve may be somewhat variable in its anatomical course through the temporal bone (Proctor and Nasger 1982, Proctor 1991). It may split into two or three strands, starting at the geniculate ganglion, and then make its way across the promontory to the stylomastoid foramen, or pass a few millimetres posteriorly to its second genu, before it turns inferiorly posterior to the fossa incudis, a position where it is particularly vulnerable during surgical exploration of the mastoid antrum. The more proximal the division into strands, the more bizarre is the subsequent course. More distal bifurcations pass either side of the fenestra vestibuli. It may be dehiscent, particularly in its second part, when it occasionally overhangs the stapes, or run inferior to the stapedial superstructure, a position that renders it vulnerable during surgery to the stapes (Barnes et al 2001). The motor fibres to the face may be carried through the chorda tympani, which is then enlarged. When this is the case, the distal facial nerve dwindles to a fibrous strand in a narrowed stylomastoid foramen. In chronic bone disease in the tympanic cavity, the facial nerve may be exposed in its canal. Inflammation may lead to facial paralysis of the infranuclear or lower motor neurone type.

Bell's palsy

Bell's palsy is the eponym given to an idiopathic lower motor neurone facial palsy. It may be complete or partial, and is characterized by a flaccid paralysis of the ipsilateral muscles of facial expression; decreased lacrimation in the ipsilateral eye (which is controlled by neurones in the greater petrosal nerve); and hyperacusis or decreased tolerance of loud noises in the ipsilateral ear as a result of paralysis of stapedius. Its cause remains the subject of speculation but is most probably a herpes virus infection (Zandian et al 2014). Magnetic resonance imaging studies suggest that there are inflammatory changes in labyrinthine and perigeniculate segments of the facial nerve. In the vast majority of cases, spontaneous full recovery takes place after a few weeks.

Tympanic mucosa

The mucosa of the tympanic cavity is pale, thin and slightly vascular. It is continuous with that of the pharynx, via the pharyngotympanic tube, and covers the ossicles, muscles and nerves in the cavity to form the inner layer of the tympanic membrane and the outer layer of the secondary tympanic membrane. It also spreads into the mastoid antrum and air cells. The middle ear mucosa is a mucus-secreting respiratory mucosa bearing cilia on its surface. The precise distribution of the mucociliary epithelium varies in normal middle ears, being more widespread in the young. Three distinct mucociliary pathways have been identified – epitympanic, promontorial and hypotympanic – the latter being the largest. Each of these pathways coalesces at the tympanic orifice of the pharyngotympanic tube (Gleeson et al 1991).

The mucosa forms several vascular folds that extend from the tympanic walls to the ossicles: one descends from the roof of the cavity to the head of the malleus and the upper margin of the body of the incus, and a second surrounds the stapedius. Other folds invest the chorda tympani nerve and tensor tympani. The folds separate off saccular recesses that give the interior of the tympanic cavity a somewhat honeycombed appearance; these mucosal folds have been described in greater detail by Proctor (1964). Of note, the superior recess of the tympanic membrane, Prussak's space, lies between the neck of the malleus and the pars flaccida, bounded by the lateral malleolar fold (Marchioni et al 2013). This space can play an important role in the retention of keratin and subsequent development of cholesteatoma.

Cholesteatoma

Cholesteatoma is the name given to keratinizing squamous epithelium within the middle ear. There is debate as to how such epithelium comes to be in the middle ear. Theories include development from embryological cell rests, metaplasia from inflamed mucoperiosteum, and aberrant migration of squamous epithelium either through a perforation in the tympanic membrane (usually in the pars flaccida or posterosuperior pars tensa) or within an area of tympanic membrane atelectasis where the tympanic membrane becomes adherent to the medial wall of the tympanic cavity. It is likely that all of these processes may be implicated at some time. A feature of cholesteatoma that remains poorly understood is its ability to erode bone, by activating osteoclasts, thus allowing the epithelium to proliferate and invade, destroying the temporal bone and carrying infection to the soft tissues. Cholesteatoma can therefore cause deafness through damage to the ossicles and inner ear; problems with balance through damage to the vestibule and semicircular canals; facial palsy through ischaemia and necrosis of the facial nerve; and intracranial sepsis. Treatment involves microsurgical dissection of the invading sac of epithelium with, wherever possible, preservation of the delicate structures just listed.

Bonus e-book content

Table 42.1 Common anomalies of the auricle.

Key references

Proctor B 1991 The anatomy of the facial nerve. Otolaryngol Clin North Am 24:479–504.

The course of the facial nerve from its origin in the human brainstem to its termination in the muscles of facial expression is reviewed in detail. Its relationship to important adjacent structures is emphasized.

Proctor B, Nager GT 1982 The facial canal: normal anatomy, variations and anomalies. Ann Otol Rhinol Laryngol 91:33–61.

A detailed anatomical description, emphasizing the relations of the facial canal to adjacent structures and variations in the course of the canal.

References

Allam AF 1969 Pneumatization of the temporal bone. Ann Otol Rhinol Laryngol 78:49–64.

Anderson SD 1976 The intratympanic muscles. In: Hinchcliffe R (ed) Scientific Foundations of Otolaryngology. London: Heinemann; pp. 257–80.

Barnes G, Liang J, Hall S et al 2001 Development of the Fallopian canal in humans – a morphologic and radiologic study. Otol Neurotol 22:931–7.

Bluestone C, Klein J 2002 Otitis media, atelectasis and Eustachian tube dysfunction. In: Bluestone CD, Stool SE (eds) Pediatric Otolaryngology, vol. 1, 4th ed. Philadelphia: Elsevier, Saunders; pp. 474–86.

Campos A, Betancor L, Arias A et al 2000 Influence of human wet cerumen on the growth of common and pathogenic bacteria of the ear. J Laryngol Otol 114:925–9.

Daraei P, Mattox DE 2018 Landmarks for the preservation of the middle temporal artery during mastoic surgery: cadaveric dissection study. Am J Otolaryngol 39:6–9.

De Greef D, Goyens J, Pintelon I et al 2016 On the connection between the tympanic membrane and the malleus. Hear Res 340:50–9.

Gleeson M, Felix H, Neivergelt J 1991 Quantitative and qualitative analysis of the human middle ear mucosa. In: Sade J (ed) The Eustachian Tube, Basic Aspects. Amsterdam: Kugler & Ghedini; pp. 125–31.

Henson MM, Madden VJ, Rask-Andersen H et al 2005 Smooth muscle in the annulus fibrosus of the tympanic membrane in bats, rodents, insectivores and humans. Hear Res 200:29–37.

Isaacson G 2014 Endoscopic anatomy of the pediatric middle ear. Otolaryngol Head Neck Surg 150:6–15.

Jelodar S, Ghadirian H, Ketababchi M et al 2018 Bilateral ischemic stroke due to carotid artery compression by abnormally elongated styloid process at both sides: a case report. J Stroke Cerebrovasc Dis 27: e89-e91.

Kawase T, Shibata S, Katori Y et al 2012 Elastic fiber-mediated enthesis in the human middle ear. J Anat 221:331–40.

Kim LK, Ahn CS, Fernandes AE 2014 Mastoid emissary vein: anatomy and clinical relevance in plastic and reconstructive surgery. J Plast Reconstr Aesthet Surg 67:775–80.

Kiyokawa J, Yamaguchi K, Okada R et al 2014 Origin, course and distribution of nerves to the posterosuperior wall of the external acoustic meatus. Anat Sci Int 89:238-45.

Ledesma-Montes C, Hernadez-Guerrero JC, Jininee-Farfan MD 2018 Length of the ossified stylohyoid complex in Eagle syndrome. Eur Arch Otorhinolaryngol 275:2095–100.

Li B, Doan P, Gruhl RR et al 2018 Endoscopic anatomy of the tensor fold and anterior attic. Otolaryngol Head Neck Surg 158:358–63.

Louis RG, Loukas M, Wartmann CT et al 2009 Clinical anatomy of the mastoid and occipital emissary veins in a large series. Sur Radiol Anat 31:139–44.

Luers JC, Hüttenbrink KB 2015 Surgical anatomy and pathology of the middle ear. J Anat 228:338–53.

Marchioni D, Piccinini A, Alicandri-Ciufelli M et al 2013 Endoscopic anatomy and ventilation of the epitympanum. Otolaryngol Clin North Am 46:165–78.

Melzer JM, Eliason M, Conley GS 2016 Congenital stapes malformation: rare conductive hearing loss in a patient with Waardenburg syndrome. Laryngoscope 126:992–5.

Michaelides E, Kanasl A, Rutter S et al 2018 The malleus cap: anatomical description of cartilage of the lateral process of the malleus. Am J Otolaryngol 39:208–11.

Muthusami PO, Kesavadas C, Sylaja PN et al 2013 Implicating the long styloid process in cervical carotid artery dissection. Neuroradiology 55:861–7.

Nogueira JE, Mattioli F, Presutti L et al Endoscopic anatomy of the retrotympanum. Otolaryngol Clin North Am 46:179–88.

Osborn AJ, Oghalai JS, Vrabec JT 2011 Middle ear volume as an adjunct measure in congenital aural atresia. Int J Pediatr Otorhinolaryngol 75:910–14.

Pata YS, Ozturk C, Akbas Y et al 2003 Has cerumen a protective role in recurrent external otitis? Am J Otolaryngol 24:209–212.

Porter CJW, Tan ST 2005 Congenital auricular anomalies: topographic anatomy, embryology, classification and treatment strategies. Plast Reconstr Surg 115:1701–12.

Proctor B 1964 The development of the middle ear spaces and their surgical significance. J Otolaryngol 78:631–49.

Proctor B 1991 The anatomy of the facial nerve. Otolaryngol Clin North Am 24:479–504.

The course of the facial nerve from its origin in the human brainstem to its termination in the muscles of facial expression is reviewed in detail. Its relationship to important adjacent structures is emphasized.

Proctor B, Nager GT 1982 The facial canal: normal anatomy, variations and anomalies. Ann Otol Rhinol Laryngol 91:33–61.

A detailed anatomical description, emphasizing the relations of the facial canal to adjacent structures and variations in the course of the canal.

Purkait R 2013 Progression of growth in the external ear from birth to maturity: a 2-year follow-up study in India. Aesthetic Plast Surg 37:605–16.

Simms DL, Neely JG 1989 Growth of the lateral surface of the temporal bone in children. Laryngoscope 99:795–9.

Takanashi Y, Shibata S, Katori Y et al 2013 Fetal development of the elastic-fiber-mediated enthesis in the human middle ear. Ann Anat 195:441–8.

Tarabichi M, Marchioni D, Presutti L et al 2013 Endoscopic transcanal ear anatomy and dissection. Otolaryngol Clin North Am 46:131–54.

Yoshiura K, Kinoshita A, Ishida T et al 2006 A SNP in the *ABCC11* gene is the determinant of human earwax type. Nat Genet 38:324–30.

Zilinsky I, Erdmann D, Weissman O et al 2017 Reevaluation of the arterial blood supply of the auricle. J Anat 230:315–24.

Zandian A, Osiro S, Hudson R et al 2014 The neurologist's dilemma: a comprehensive clinical review of Bell's palsy, with emphasis on current management trends. Med Sci Monit 20:83–90.

Recommended reading

Anson BJ, Donaldson JA 1976 The Surgical Anatomy of the Temporal Bone and Ear. Philadelphia: Saunders.

Phelps PD, Lloyd GAS 1990 Diagnostic Imaging of the Ear, 2nd ed. Berlin: Springer.

Wright A 1997 Anatomy and ultrastructure of the human ear. In: Kerr GA (ed) Scott Brown's Otolaryngology, vol. 1, 6th ed. London: Butterworth–Heinemann; pp. 1–50.

CHAPTER

43

Inner ear

The inner ear contains the organ of hearing and the organs of balance. All are located within the labyrinth, a series of interlinked cavities in the petrous temporal bone containing interconnected membranous sacs and ducts. All spaces within the labyrinth are filled with fluid. The different sacs contain sensory epithelia consisting of supporting cells and mechanosensory cells, the hair cells that underlie acoustico-lateralis sensory systems in all vertebrates. In humans, there are six such mechanosensory epithelia: the organ of Corti within the cochlea (the hearing organ); the utricle and saccule (static balance organs); and the cristae of the semicircular canals (dynamic balance organs). Whilst sharing the same basic structure, hair cells and the accessory systems that surround them show specific adaptations to each of the different sensory modalities.

The disarticulated temporal bone is described in detail in Chapter 42. The internal acoustic meatus (internal auditory canal) and bony and membranous labyrinths are described here.

OSSEOUS (BONY) LABYRINTH

The bony labyrinth consists of the vestibule (sacculus and utriculus/ saccule and utricle), semicircular canals and cochlea, which are all cavities lined by periosteum and which contain the membranous labyrinth (**Fig. 43.1**). The bone is denser and harder than the other parts of the petrous bone, and it is therefore possible, particularly in young skulls, to dissect the bony labyrinth out from the petrous temporal bone.

The osseous and membranous labyrinths are filled with fluid (**Fig. 43.2**). The gap between the internal wall of the osseous labyrinth and the external surface of the membranous labyrinth is filled with perilymph, a clear fluid with an ionic composition similar to that of other extracellular fluids, i.e. low in potassium ions and high in sodium and calcium. The membranous labyrinth contains endolymph, a fluid with an ionic composition more like that of cytosol, i.e. high in potassium ions and low in sodium and calcium. Moreover, the endolymphatic compartment has an electrical potential that, at least within the cochlea, is approximately 80 mV more positive than the perilymphatic compartment (the endolymphatic potential). These differences in ionic composition and potential, maintained by homeostatic tissues in the walls of the labyrinth, are essential to maximize the sensitivity of the mechanosensory hair cells that convert the vibrations set up in the inner ear fluids by head or sound movements into electrical signals that are transmitted via the vestibulocochlear nerve to the vestibular and cochlear nuclei, respectively, in the brainstem.

Vestibule

The vestibule is the central part of the bony labyrinth and lies medial to the tympanic cavity, posterior to the cochlea and anterior to the semicircular canals (see Fig. 43.1). It is somewhat ovoid in shape but flattened transversely, and (on average) measures 5 mm from front to back and vertically, and 3 mm across. In its lateral wall is the opening of the oval window (fenestra vestibuli), into which the base of the stapes inserts, and to which the base of the stapes is attached by an annular ligament. Anteriorly, on the medial wall, is a small spherical recess that contains the saccule; it is perforated by several minute holes, the macula cribrosa media, which transmit fine branches of the vestibular nerve to the saccule. Behind the recess is an oblique vestibular crest, the anterior end of which forms the vestibular pyramid. This crest divides below to enclose a small depression, the cochlear recess, which is perforated by vestibulocochlear fascicles as they pass to the vestibular end of the cochlear duct. Posterosuperior to the vestibular crest, in the roof and medial wall of the vestibule, is the elliptical recess (**Fig. 43.1B**), which contains the utricle. The pyramid and adjoining part of the elliptical recess are perforated by a number of holes, the macula cribrosa superior; those in the former transmit nerves to the utricle and those in the latter transmit

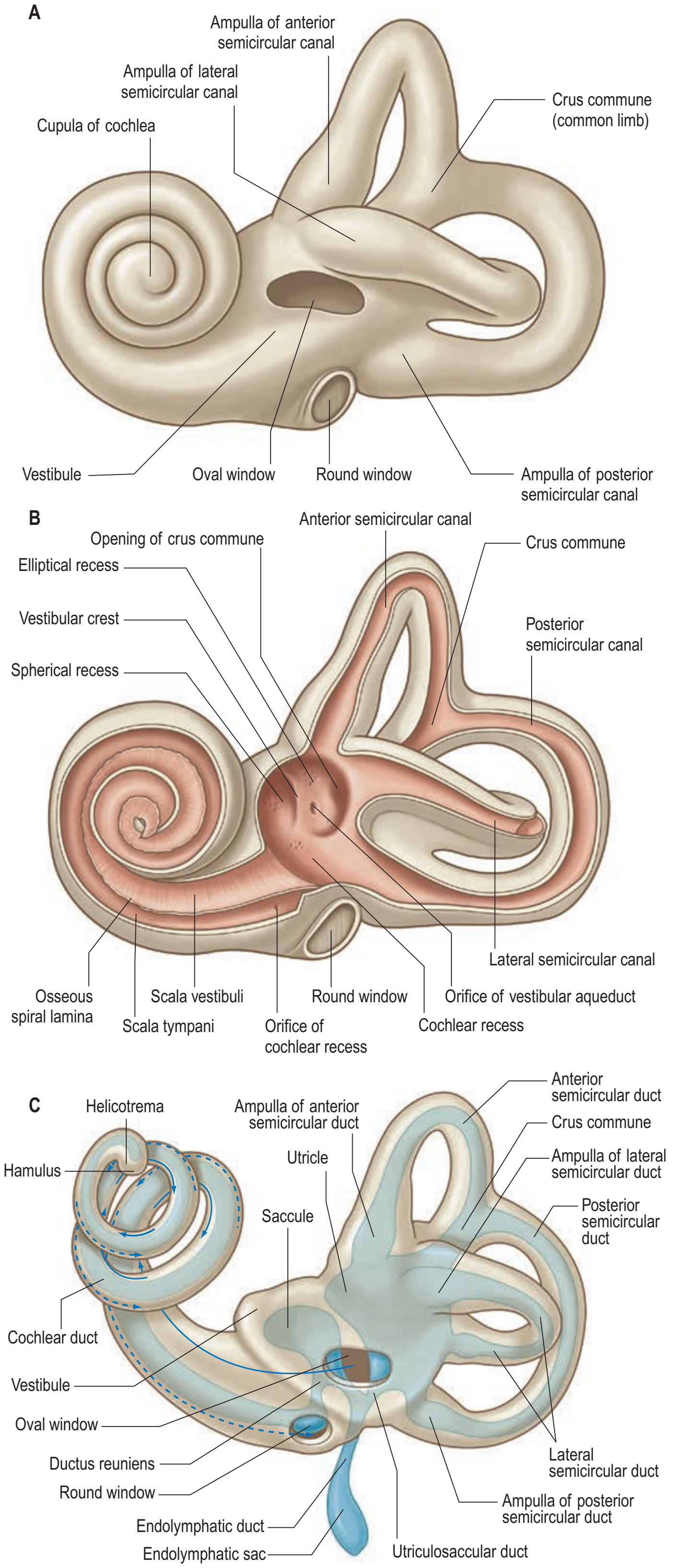
A
Ampulla of anterior semicircular canal
Ampulla of lateral semicircular canal
Cupula of cochlea
Crus commune (common limb)
Vestibule
Oval window
Round window
Ampulla of posterior semicircular canal
B
Opening of crus commune
Anterior semicircular canal
Elliptical recess
Crus commune
Vestibular crest
Posterior semicircular canal
Spherical recess
Lateral semicircular canal
Osseous spiral lamina
Scala vestibuli
Scala tympani
Round window
Orifice of cochlear recess
Orifice of vestibular aqueduct
Cochlear recess
C
Helicotrema
Ampulla of anterior semicircular duct
Anterior semicircular duct
Crus commune
Hamulus
Utricle
Ampulla of lateral semicircular duct
Saccule
Posterior semicircular duct
Cochlear duct
Vestibule
Oval window
Ductus reuniens
Round window
Lateral semicircular duct
Ampulla of posterior semicircular duct
Endolymphatic duct
Endolymphatic sac
Utriculosaccular duct

Fig. 43.1 The bony labyrinth. **A**, Lateral aspect. **B**, Interior. **C**, The membranous labyrinth (blue) projected on to the bony labyrinth.

Continued

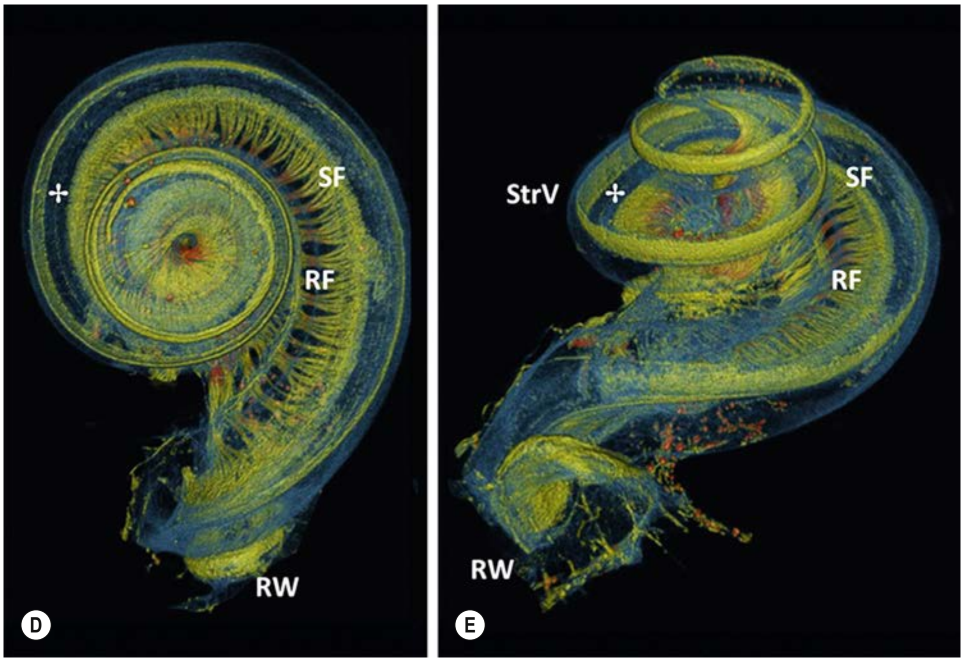

Fig. 43.1, cont'd **D–E**, 3D renderings of the cochlea and round window. Fresh cadaveric temporal bones were postfixed with osmium tetroxide, decalcified with EDTA and scanned using micro-CT at 5.5 μm voxel resolution: colour rendering is based on intensities in order to differentiate between neural tissue (yellow), bone and membranous structures (blue). The viewpoint is on the apex (**D**) and basal turn (**E**) of the cochlea. Radially oriented nerve fibre bundles (RF) connect to hair cells on the organ of Corti (+). Abbreviations: RW, round window; SF, spirally oriented nerve fibre bundles; StrV, stria vascularis. (D, E, With permission from Van den Boogert T, van Hoof, Handschuh S et al 2018 Optimization of 3D-visualization of micro-anatomical structures of the human inner ear in osmium tetroxide contrast enhanced micro-CT scans. Front Neuroanat 12:1–11.) (**F–I,** *continued online*)

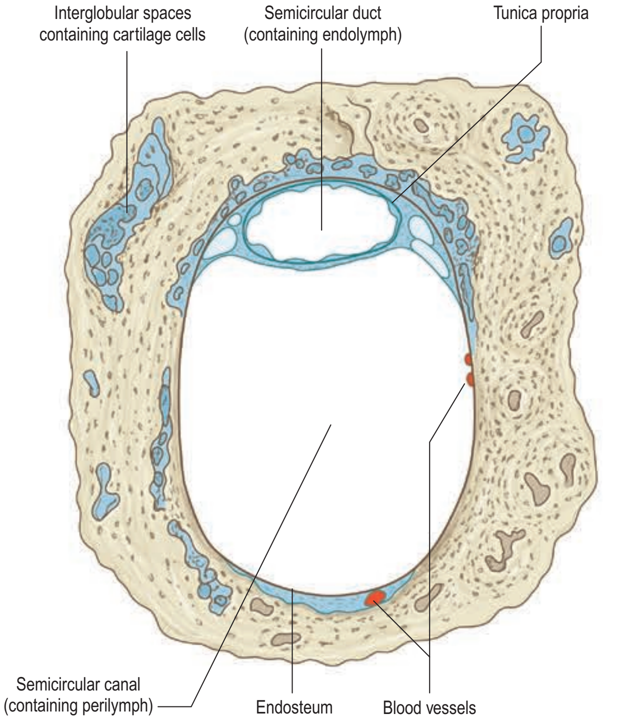
Interglobular spaces containing cartilage cells
Semicircular duct (containing endolymph)
Tunica propria
Semicircular canal (containing perilymph)
Endosteum
Blood vessels

Fig. 43.2 A transverse section through the left posterior semicircular canal and duct.

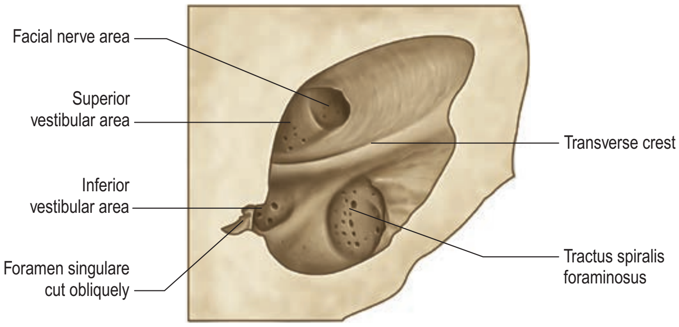

Fig. 43.3 The fundus of the left internal acoustic meatus, exposed by a section through the petrous part of the left temporal bone nearly parallel to the line of its superior border.

nerves to the ampullae of the anterior and lateral semicircular canals (see Fig. 43.1B). The region of the pyramid and elliptical recess corresponds to the superior vestibular area in the internal acoustic meatus (see Fig. 43.3). The vestibular aqueduct opens below the elliptical recess. It reaches the posterior surface of the petrous bone and contains one or more small veins and part of the membranous labyrinth, the endolymphatic duct (**Fig. 43.1C**). In the posterior part of the vestibule are the five openings of the semicircular canals; in its anterior wall is an elliptical opening that leads into the scala vestibuli of the cochlea.

Semicircular canals

The three semicircular canals – anterior (superior), posterior and lateral (horizontal) – are located posterosuperior to the vestibule (see Fig. 43.1). They are compressed from side to side and each forms approximately two-thirds of a circle. They are unequal in length but similar in diameter along their lengths, except where they bear a terminal swelling, an ampulla, which is almost twice the diameter of the canal.

The anterior semicircular canal is 15–20 mm long. It is vertical in orientation and lies transverse to the long axis of the petrous temporal bone under the anterior surface of its arcuate eminence. The eminence may not accurately coincide with this semicircular canal but may instead be adapted to the occipitotemporal sulcus on the inferior surface of the temporal lobe of the brain. The ampulla at the anterior end of the canal opens into the upper and lateral part of the vestibule. Its other end unites with the upper end of the posterior canal to form the crus commune (common limb), which is 4 mm long, and opens into the medial part of the vestibule.

The posterior semicircular canal is also vertical but curves backwards almost parallel with the posterior surface of the petrous bone. It is 18–22 mm long and its ampulla opens low in the vestibule, below the cochlear recess where the macula cribrosa inferior transmits nerves to it. Its upper end joins the crus commune.

The lateral canal is 12–15 mm long and its arch runs horizontally backwards and laterally. Its anterior ampulla opens into the upper and lateral angle of the vestibule, above the oval window and just below the ampulla of the anterior canal; its posterior end opens below the opening of the crus commune.

The two lateral semicircular canals of the two ears are often described as being in the same plane and the anterior canal of one side as being almost parallel with the opposite posterior canal. However, measurements of the angular relations of the planes of the semicircular osseous canals in 10 human skulls led Blanks et al (1975) to suggest that the planes of the three ipsilateral canals are not completely perpendicular to each other. The angles were measured as: lateral/anterior 111.76 ± 7.55°,

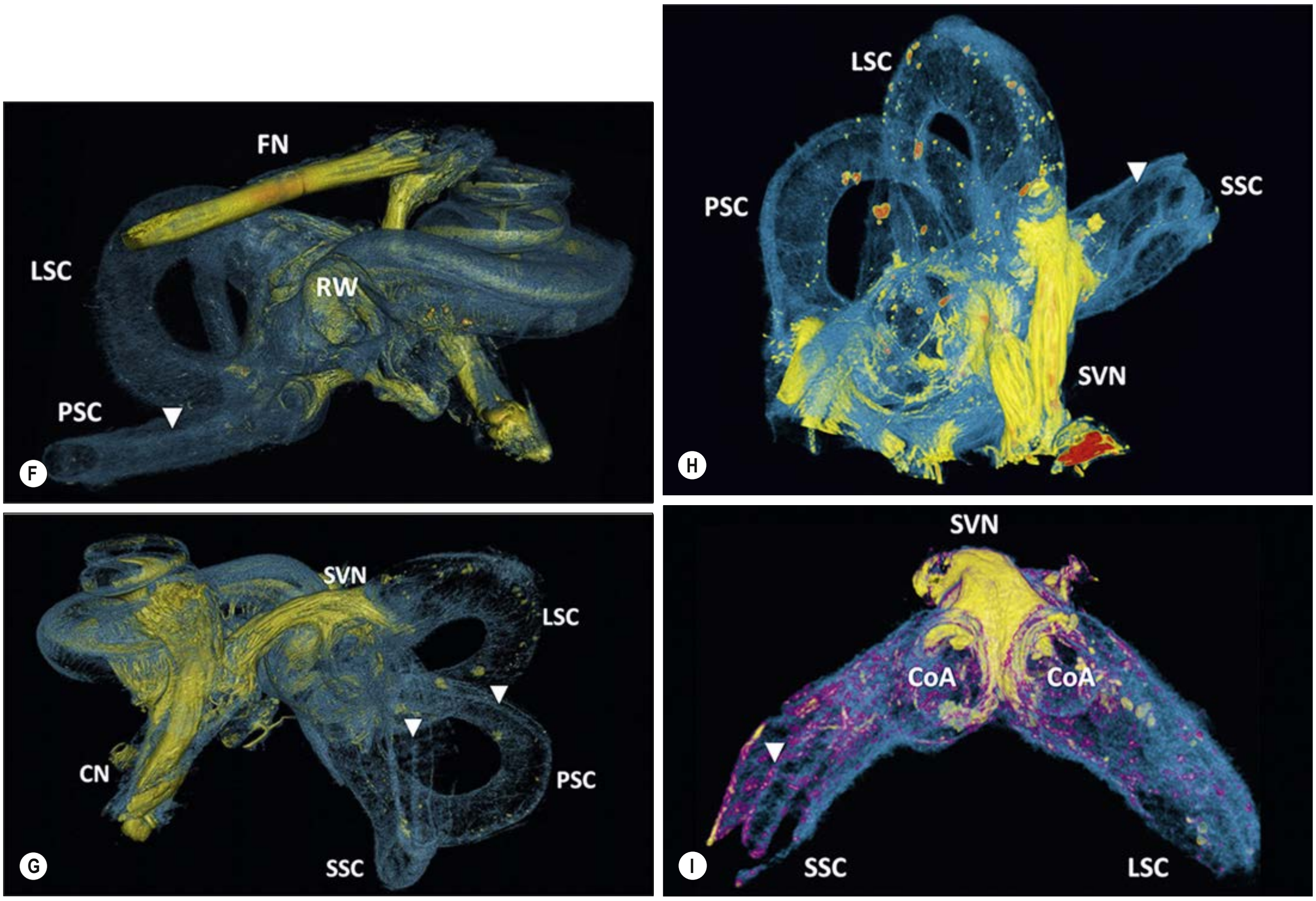

Fig. 43.1 F–I, Cadaveric tissue has been processed as in Fig. 43.1 D–E. **F, G**. 3D renderings of the entire labyrinth of two processed samples viewed from different perspectives. **F**, The cochlear nerve was removed during dissection. **G,** The relationship of the superior branch of the vestibular nerve (SVN) and the cupulae of the lateral and superior semicircular canals (LSC and SSC). The membranous labyrinth may be discerned from its bony encasement (arrowheads). **H,** The posterior, lateral and superior semicircular canals (PSC, LSC, SSC) and the SVN. **I**, The relationship of the SVN and the cristae of the ampullae (CoA) of the SSC and LSC. The membranous labyrinth may be discerned from its bony encasement (arrowheads). Other abbreviations: CN, cochlear nerve; FN, facial nerve; RW, round window. (With permission from Van den Boogert T, van Hoof, Handschuh S et al 2018 Optimization of 3D-visualization of micro-anatomical structures of the human inner ear in osmium tetroxide contrast enhanced micro-CT scans. Front Neuroanat 12:1–11.)

anterior/posterior 86.16 ± 4.72°, posterior/lateral 95.75 ± 4.66°. The planes of similarly orientated canals of the two sides also showed some departure from being parallel: left anterior/right posterior 24.50 ± 7.19°, left posterior/right anterior 23.73 ± 6.71°, left lateral/right lateral 19.82 ± 14.93°. The same observers (Curthoys et al 1977) also measured the dimensions of the canals. The mean radii of the osseous canals were found to be as follows: lateral 3.25 mm, anterior 3.74 mm, posterior 3.79 mm. The diameters of the osseous canals are 1 mm (minor axis) and 1.4 mm (major axis). The membranous ducts within them are much smaller, but are also elliptical in transverse section, and have major and minor axes of 0.23 and 0.46 mm (see Fig. 43.2). Representative means for ampullary dimensions are as follows: length 1.94 mm, height 1.55 mm. Phylogenetic studies suggest that the arc sizes of the semicircular canals in humans and other primates may be functionally linked to sensory control of body movements. The angulation and dimensions of the canals may be related to locomotor behaviour and possibly to agility, or more specifically to the frequency spectra of natural head movements (see review by Spoor and Zonneveld (1998)).

Cochlea

The cochlea (from the Greek *cochlos* for snail) is the most anterior part of the labyrinth, lying in front of the vestibule (see Figs 43.1, 43.9A). It is 5 mm from base to apex, and 9 mm across its base. Its apex, or cupula, points towards the anterosuperior area of the medial wall of the tympanic cavity (see Fig. 43.9A). Its base faces the bottom of the internal acoustic meatus and is perforated by numerous apertures for the cochlear nerve. The cochlea has a conical central bony core, the modiolus, and a spiral canal runs around it. A delicate osseous spiral lamina (or ledge) projects from the modiolus, partially dividing the canal (see Fig. 43.9B). Within this bony spiral lies the membranous cochlear duct, attached to the modiolus at one edge and to the outer cochlear wall by its other edge. There are therefore three longitudinal channels within the cochlea. The middle canal (the cochlear duct or scala media) is blind and ends at the apex of the cochlea; its flanking channels communicate with each other at the modiolar apex at a narrow slit, the helicotrema (see Fig. 43.1C). Two distensible membranes form the upper and lower bounds of the scala media. One is Reissner's membrane, the thin vestibular membrane that separates the scala media from the scala vestibuli. The other is the basilar membrane, which forms the partition between the scala media and the scala tympani. The organ of Corti, the sensory epithelium of hearing, sits on the inner surface of the basilar membrane. At the base of the scala vestibuli is the oval window (fenestra vestibuli), which leads on to the vestibular cavity but is sealed by the footplate of the stapes. The scala tympani is separated from the tympanic cavity by the secondary tympanic membrane at the round window (fenestra cochleae). The central cochlear core, the modiolus, has a broad base near the lateral end of the internal acoustic meatus, where it corresponds to the spiral tract (tractus spiralis foraminosus). There are several openings in this area for the fascicles of the cochlear nerve: those for the first 1½ turns run through the small holes of the spiral tract, and those for the apical turn run through the hole that forms the centre of the tract. Canals from the spiral tract go through the modiolus and open in a spiral sequence into the base of the osseous spiral lamina. Here the small canals enlarge and fuse to form Rosenthal's canal, a spiral canal in the modiolus that follows the course of the osseous spiral lamina and contains the spiral ganglion (see Fig. 43.9B). The main tract continues through the centre of the modiolus to the cochlear apex.

The osseous cochlear canal spirals for about 2¾ turns around the modiolus and is 35 mm long. At its first turn, the canal bulges towards the tympanic cavity, where it underlies the promontory. At the base of the cochlea, the canal is 3 mm in diameter but it becomes progressively reduced in diameter as it spirals apically to end at the cupula. In addition to the round and oval windows, which are the two main openings at its base, the canal has a third, smaller opening for the cochlear aqueduct or canaliculus. The latter is a minute funnel-shaped canal that runs to the inferior surface of the petrous temporal bone; it transmits a small vein to the inferior petrosal sinus and connects the subarachnoid space to the scala tympani.

The osseous or primary spiral lamina is a ledge that projects from the modiolus into the osseous canal like the thread of a screw (see Fig. 43.9B). It is attached to the inner edge of the basilar membrane and ends in a hook-shaped hamulus at the cochlear apex, partly bounding the helicotrema (see Fig. 43.1C). From Rosenthal's canal, many tiny canals, the habenula perforata, radiate through the osseous lamina to its rim, where they each carry a fascicle of the cochlear nerve through the foramen nervosum to the organ of Corti. A secondary spiral lamina projects inwards from the outer cochlear wall towards the osseous spiral lamina and is attached to the outer edge of the basilar membrane. It is most prominent in the lower part of the first turn; the gap between the two laminae increases progressively towards the cochlear apex, which means that the basilar membrane is wider at the apex of the cochlea than at the base.

Microstructure of the bony labyrinth

The wall of the bony labyrinth is lined by fibroblast-like perilymphatic cells and extracellular matrix fibres (see Fig. 43.2). The morphology of the cells varies in different parts of the labyrinth. Where the perilymphatic space is narrow, as in the cochlear aqueduct, the cells are reticular or stellate in form; they give off sheet-like cytoplasmic extensions that cross the extracellular space. Where the space is wider, as in the scalae vestibuli and tympani of the cochlea and much of the vestibule, the perilymphatic cells on the periosteum and the external surface of the membranous labyrinth are extremely flat and resemble a squamous epithelium. Elsewhere, on parts of the perilymphatic surface of the basilar membrane, the cells are cuboidal.

Recent evidence suggests that micropores or canaliculi (canaliculi perforantes) (0.2–23.0 μm diameter) are more widely distributed within the bony surfaces lining the perilymphatic space than was previously suspected; they are numerous in the peripheral and modiolar portions of the osseous spiral lamina and the floor of the scala tympani, but sparse in the osseous wall of the scala vestibuli. The proposal that these canaliculi normally provide an extensive fluid communication channel between the scala tympani and the spiral canal of the cochlea could have implications not only for novel drug-based cochlear therapies delivered via the scala tympani and the delivery of stem cells or appropriate cell lines into the deafened cochlea, but also for the design of implanted perimodiolar electrode arrays (Shepherd and Colreavy 2004). (For further reading about the changes in the inner ear that are induced by implanted cochlear electrodes, both acute and long-term, see Keifer et al (2006).)

Composition of inner ear fluids

Perilymph resembles cerebrospinal fluid in ionic composition, particularly in the scala tympani. Its composition differs a little between the two cochlear scalae: concentrations of potassium, glucose, amino acids and proteins are greater in the scala vestibuli. This has led to the suggestion that perilymph in the scala vestibuli is derived from plasma via the endothelial boundary of the cochlear blood vessels, whereas the perilymph in the scala tympani contains some cerebrospinal fluid derived from the subarachnoid spaces via the cochlear canaliculus. However, the lack of significant bulk flow suggests that perilymph homeostasis is predominantly locally regulated. Perilymph contains approximately 5 mM K^+, 150 mM Na^+, 120 mM Cl^- and 1.5 mM $Ca2^+$.

The membranous labyrinth is filled with endolymph, a fluid produced by the marginal cells of the stria vascularis and the dark cells of the vestibule (see review by Wangemann and Schacht (1996)) (see Figs 43.9B, C). Whatever their relative contributions, endolymph probably circulates in the labyrinth; it enters the endolymphatic sac, where it is transferred into the adjacent vascular plexus via the specialized epithelium of the sac. Pinocytotic removal of fluid may also take place in other labyrinthine regions.

Endolymph contains greater K^+ (150 mM) and Cl^- (130 mM) concentrations and lower Na^+(2 mM) and $Ca2^+$ (20 μM) concentrations than perilymph. The high K^+ concentration is important for the function of the mechanosensory hair cells and is maintained by the actions of the lateral wall, which contains two tissues, namely: the spiral ligament and the stria vascularis. Together, these tissues promote the recirculation of K^+ from perilymph back to endolymph by uptake via potassium channels and gap junctional communication. Gap junctions are formed from connexins; their importance to this process is emphasized by the fact that mutations in connexins, the most common being GJB2 (connexin 26), are significant causes of genetic hearing loss (Duman and Tekin 2013). The vestibular regions may not have an endolymphatic potential, as their lateral wall structure is simplified compared to that of the cochlea, although the difference in K^+ concentration between endolymph and perilymph remains important.

Internal acoustic meatus

The internal acoustic meatus (internal acoustic/auditory canal) is separated from the internal ear at its lateral fundus by a vertical plate divided unequally by a transverse (falciform) crest (**Fig. 43.3**). Five nerves – facial, nervus intermedius, cochlear, superior and inferior vestibular – pass through openings in the vertical plate, above and below the transverse crest. The facial and superior vestibular nerves enter canals that are superior to the crest. The facial nerve is anterior to the superior vestibular nerve, from which it is separated at the lateral end of the meatus by a vertical ridge of bone (Bill's bar). The nervus intermedius lies between the facial motor root and the superior vestibular nerve, to which it may be adherent. The superior vestibular area contains openings for nerves to the utricle and anterior and lateral semicircular ducts. Below the crest, an anterior cochlear area contains a spiral of small holes, the tractus spiralis foraminosus, which encircles the central cochlear canal. Behind this, the inferior vestibular area contains openings for saccular nerves, and most posteroinferiorly, a single hole (foramen singulare) admits the nerve to the posterior semicircular duct. High-resolution synchrotron radiation phase contrast imaging with 3D renderings of undecalcified human temporal bones has delineated a blind-ending extension of the cerebellopontine cistern into the fundus of the internal acoustic meatus (the acoustic-facial cistern) and a system of arachnoid pillars that pass between the walls of this cistern and the cranial nerves that lie within the meatus and possibly provide structural support for the nerves (Mei et al 2019). It has been suggested that vascular loops in the internal acoustic meatus from the anterior inferior cerebellar artery might be a source of pulsatile tinnitus, but loops are found just as commonly in patients without pulsatile tinnitus.

MEMBRANOUS LABYRINTH

The membranous labyrinth is separated from the periosteum by a space that contains perilymph and a web-like network of fine blood vessels (see Figs 43.1C, 43.2). It can be divided into two major regions: the vestibular apparatus and the cochlear duct.

Vestibular apparatus

The vestibular apparatus consists of three semicircular ducts that communicate with the utricle, a membranous sac leading into a smaller chamber, the saccule, via the utriculosaccular duct. This Y-shaped duct has a side branch to the endolymphatic duct, which passes to the endolymphatic sac, a small but functionally important expansion situated under the dura of the petrous temporal bone. From the saccule, a narrow canal, the ductus reuniens, leads to the base of the cochlear duct. These various ducts and sacs form a closed system of intercommunicating channels (see Fig. 43.1C). Endolymph is resorbed into the cerebrospinal fluid from the endolymphatic sac, which therefore provides the site for the drainage of endolymph for the entire membranous labyrinth.

The terminal fibres of the vestibular nerve are connected to the five specialized sensory epithelia (two maculae and three cristae) in the walls of the membranous labyrinth. Maculae are flat plaques of sensory hair cells and supporting cells, and are found in the utricle and saccule. The cristae (crests) are ridges bearing sensory hair cells and supporting cells. They are found in the walls of the ampullae near the utricular openings of the three semicircular canals, one for each canal.

Utricle

The utricle is the larger of the two major vestibular sacs. It is an irregular, oblong, dilated sac that occupies the posterosuperior region of the vestibule (see Fig. 43.1C) and contacts the elliptical recess (where it is a blind-ended pouch) and the area inferior to it.

The macula of the utricle (or utriculus) is a specialized neurosensory epithelium lining the membranous wall and is the largest of the vestibular sensory areas (**Fig. 43.4**). It is triangular or heart-shaped in surface view and lies horizontally with its long axis orientated anteroposteriorly and its sharp angle pointing posteriorly (**Fig. 43.5**). It is flat except at the anterior edge, where it is gently folded in on itself, and it measures 2.8 mm long by 2.2 mm wide. The mature form of the macula is reached early in development, but in the adult a bulge is often present on the anterolateral border; there is sometimes an indentation at the anteromedial border. The epithelial surface is covered by the otolithic membrane (statoconial membrane), a gelatinous structure in which many small crystals, the otoconia (otoliths, statoliths), are embedded. A curved ridge, the 'snowdrift line', runs along the length of the otolithic membrane. It corresponds to a narrow crescent of underlying sensory epithelium termed the striola, 0.13 mm wide. The density of sensory hair cells in this strip of epithelium is 20% less than in the rest of the macula. The striola is convex laterally and runs from the medial aspect of the anterior margin in a posterior direction towards, but not reaching, the posterior pole. The part of the macula medial to the striola is called the pars interna and is slightly larger than the pars externa, which is lateral to it. The significance of this area is that the sensory cells are functionally and anatomically polarized with respect to the midline of the striola (see Fig. 43.5). The macula in each utricle is approximately horizontal when the head is in its normal position. Linear acceleration of the head in the horizontal plane will result in the otolithic membrane lagging behind the movement of the membranous labyrinth as a result of the inertia produced by its mass. The membrane thus maximally stimulates one group of hair cells by deflecting their bundles towards the striola whilst inhibiting others by deflecting their bundles away from it. Hence each horizontal movement of the head will produce a specific pattern of firing in utricular afferent nerve fibres.

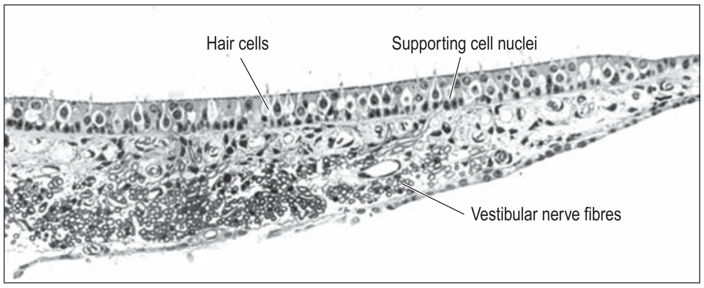

Fig. 43.4 A section of the utricular macula from a guinea pig, showing the relative positions of the hair cells and supporting cell nuclei. Semi-thin resin section, toluidine blue stain. (The inner ear is extremely vulnerable to hypoxia and situated in one of the hardest bones in the body, which means that well-fixed human tissue is rarely obtained for histology. Guinea pigs are one of the most frequently used animal models of human hearing and their inner ear ultrastructure is very similar.) (Courtesy of RM Walsh, DN Furness and CM Hackney, The Institute of Science and Technology in Medicine, School of Life Sciences, Keele University.)

Saccule

The saccule (or sacculus) is a slightly elongated, globular sac lying in the spherical recess near the opening of the scala vestibuli of the cochlea (see Fig. 43.1C). The saccular macula is an almost elliptical structure, 2.6 mm long and 1.2 mm at its widest point. Its long axis is orientated anteroposteriorly but, in contrast to the utricular macula, the saccular macula lies in a vertical plane on the wall of the saccule. Its elliptical shape is very slightly distorted by a small anterosuperior bulge. Like the utricular macula, it is covered by an otolithic (statoconial) membrane and possesses a striola similar to that of the utricle, 0.13 mm wide, which extends along its long axis as an S-shaped strip about which the sensory cells are functionally and anatomically polarized (see Fig. 43.5). The part of the macula above the striola is termed the pars interna, and that below it, the pars externa. The operation of the saccule is similar to that of the utricle. However, because of its vertical orientation, the saccule is particularly sensitive to linear acceleration of the head in the vertical plane and is, therefore, a major gravitational sensor when the head is in an upright position. It is also particularly sensitive to movement along the anteroposterior axis.

Semicircular ducts

The lateral, anterior and posterior semicircular ducts follow the course of their osseous canals. Throughout most of their length they are securely attached, by much of their circumference, to the osseous walls. They are approximately one-quarter of the diameter of their osseous canals (see Fig. 43.2). The medial ends of the anterior and posterior ducts fuse to form a single common duct, the crus commune, before entering the utricle. The lateral end of each canal is dilated to form an ampulla, within the ampulla of the osseous canal. The short segment of duct between the ampullae and utricle is the crus ampullaris.

The membranous wall of each ampulla contains a transverse elevation (septum transversum), on the central region of which is a saddle-shaped sensory ridge, the ampullary crest, containing hair cells and supporting cells. It is broadly concave on its free edge along most of its length and has a concave gutter (planum semilunatum) at either end between the ridge and the duct wall. Sectioned across the ridge, the crests of the lateral and anterior semicircular ducts have smoothly rounded corners; the posterior crest is more angular. A vertical plate of gelatinous extracellular material, the cupula, is attached along the free edge of the crest (**Fig. 43.6**). It projects far into the lumen of the ampulla so that it is

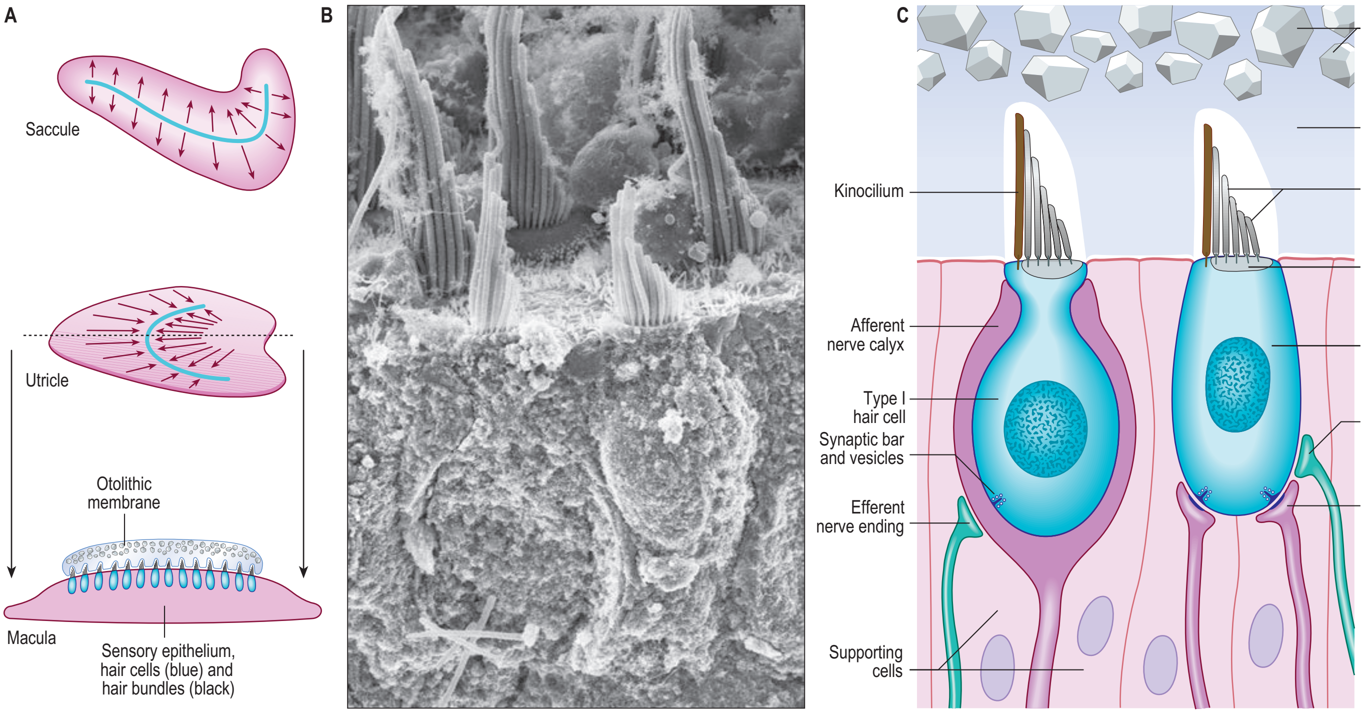

Fig. 43.5 **A**, The morphological organization of the saccular and utricular maculae and the relationship of their hair cells to the otolithic membrane. The utricular macula has been tilted in the plane of the page to emphasize that it lies horizontally, whereas the saccular macula lies vertically when the head is in an upright position. Note the different shapes of the maculae, the position of the striola as indicated by a curved line in each case, and the different orientations of their stereociliary bundles. The arrows indicate the excitatory direction of deflection. **B**, A scanning electron micrograph of a fracture of a utricular macula (guinea pig) showing a type I hair cell (left) and a type II hair cell (right). **C**, The differing innervation patterns of the two types of hair cell. (B, Courtesy of DN Furness, The Institute of Science and Technology in Medicine, School of Life Sciences, Keele University.)

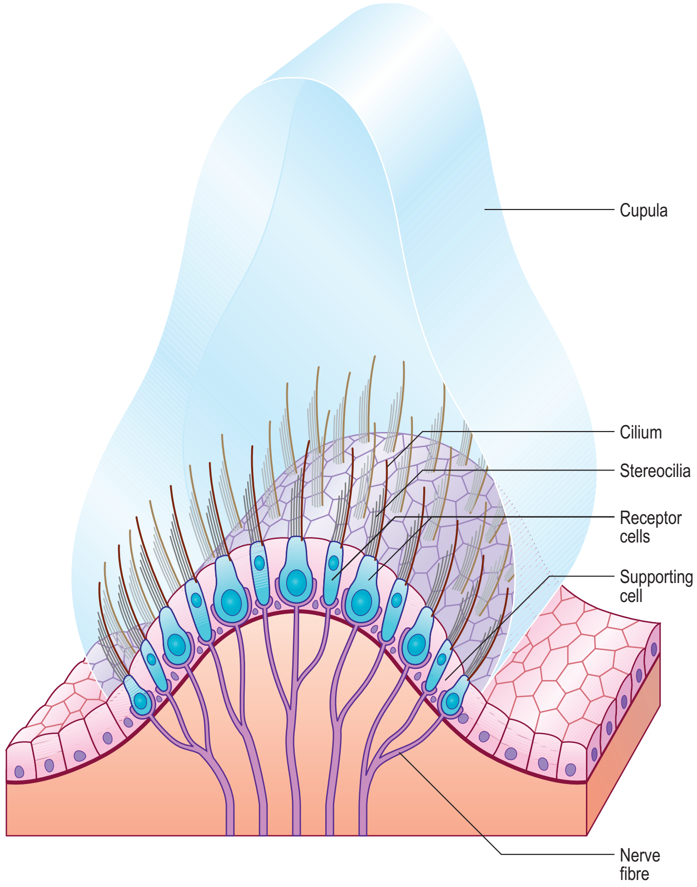

Fig. 43.6 A section of an ampullary crest.

readily deflected by movements of endolymph derived from head rotations within the duct, by means of which stimuli are delivered to the sensory hair cells. The three semicircular ducts in their canals thus detect angular accelerations during tilting or turning movements of the head in all three different planes of three-dimensional space.

Microstructure of the vestibular system

The maculae and crests detect the orientation of the head with respect to gravity and changes in head movement by means of the mechanosensitive hair cells. These hair cells are in synaptic contact with afferent and efferent endings of the vestibular nerve on their basolateral aspect. The entire epithelium lies on a bed of thick, fibrous connective tissue containing myelinated vestibular nerve fibres and blood vessels. The axons lose their myelin sheaths as they perforate the basal lamina of the sensory epithelium. There are two types of sensory hair cell in the vestibular system, type I and type II (see Figs 43.5, 43.8).

Type I vestibular sensory cells measure 25 μm in length, with a free surface of 6–7 μm in diameter. The basal part of the cell does not reach the basal lamina of the epithelium. Each cell is typically bottle-shaped, with a narrow neck and a rather broad, rounded basal portion containing the nucleus (see Fig. 43.5). The apical surface is characterized by 30–50 stereocilia (large, regularly arranged, modified microvilli about 0.25 μm across) and a single kinocilium (with the typical '9+2' arrangement of microtubules characteristic of true cilia). The kinocilium is considerably longer than the stereocilia, and may attain 40 μm, whereas the stereocilia are of graded lengths. They are characteristically arranged in regular rows behind the kinocilium in descending order of height, the longest being next to the kinocilium (**Fig. 43.7**). The kinocilium emerges basally from a typical basal body, with a centriole immediately beneath it.

Close to the inner surface of their basal two-thirds, every cell contains numerous synaptic ribbons with associated synaptic vesicles. The postsynaptic surface of an afferent nerve ending encloses the greater part of the sensory cell body in the form of a cup (chalice or calyx). Efferent nerve fibres make synapses with the external surface of the calyx, rather than directly with the sensory cell.

The kinocilium confers structural polarity on the bundle, which relates to functional polarity. The stereocilia and kinocilium are all interconnected by fine extracellular filaments of various types, called cross links. One in particular, the tip link, connects the shorter stereocilia in each row with adjacent stereocilia in the taller row next to it (see Fig. 43.7). The tip link is common to all types of hair cell and is thought to play a central role in transduction; mutations in the proteins that comprise the tip link are significant in Usher syndrome, which is characterized by decreased vestibular function, hearing loss and visual abnormalities. Deflection of the bundle towards the kinocilium results in depolarization of the hair cell and increases the rate of neurotransmitter release from its base. Deflection away from the kinocilium hyperpolarizes the hair

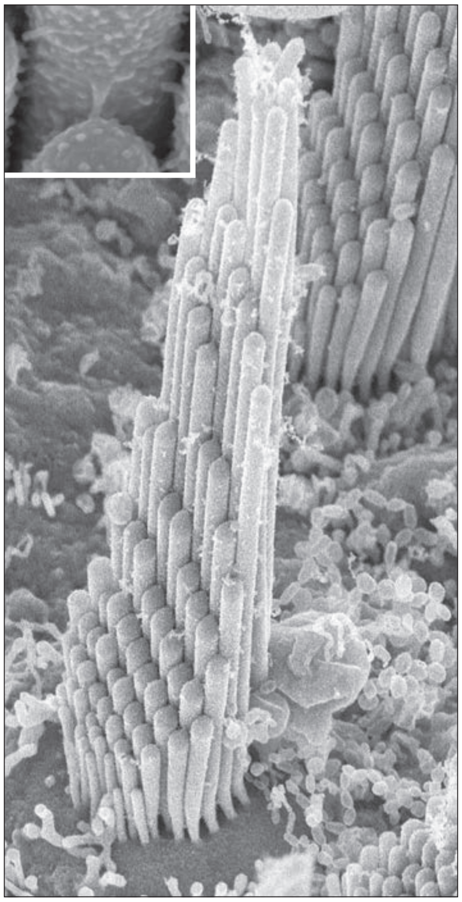

Fig. 43.7 A scanning electron micrograph of a stereociliary bundle from the utricle (guinea pig). The stereocilia are arranged in rows of increasing height towards the tallest element, the kinocilium. Deflection in the direction of the kinocilium results in depolarization of the hair cell. The inset shows a tip link connecting a short stereocilium tip to the tall stereocilium side behind. (Courtesy of DN Furness, School of Life Sciences, Keele University.)

cell and reduces the release of neurotransmitter. How deflections produce these responses will be considered in more detail later.

There is much greater variation in the sizes of type II sensory cells (see Fig. 43.5B,C; **Fig. 43.8**). Some are up to 45 μm long and almost span the entire thickness of the sensory epithelium, whereas others are shorter than type I cells. They are mostly cylindrical, but otherwise resemble type I cells in their contents and the presence of an apical kinocilium and stereocilia. However, their kinocilia and stereocilia tend to be shorter and less variable in length. The most striking difference between type I and II cells is their efferent nerve terminals: type II cells receive several efferent nerve boutons containing a mixture of small clear and dense-core vesicles around their bases, and afferent endings are small expansions rather than chalices.

Polarization allows the hair cells to have specific orientations that optimize their function within each sensory organ. In the maculae, they are arranged symmetrically on either side of the striola. In the utricle, the kinocilia are positioned on the side of the sensory cell nearest to the striola so that the excitatory direction is towards the midline. In the saccule, the structural and functional polarity is the opposite, i.e. away from it. In the ampullary crests, the cells are orientated with their rows of stereocilia at right-angles to the long axis of the semicircular duct. In the lateral crest, the kinocilia are on the side towards the utricle, whereas in the anterior and posterior crests they are away from it. These different arrangements are important functionally because any given acceleration of the head maximally depolarizes one group of hair cells and maximally inhibits a complementary set, thus providing a unique representation of the magnitude and orientation of any movement (for further details, see Furness (2002)).

The type I and II sensory cells are set within a matrix of supporting cells that reach from the base of the epithelium to its surface and form rosettes round the sensory cells, as seen in surface view. Although their form is irregular, they can easily be recognized by the position of their nuclei, which tend to lie below the level of sensory cell nuclei and just above the basal lamina (see Fig. 43.4). The apices of the supporting cells are attached by tight junctions to neighbouring supporting cells and to the hair cells to produce the reticular lamina, a composite layer that forms a plate that is relatively impermeable to cations other than via the mechanosensitive transduction channels of the hair cells.

The otolithic membrane is a layer of extracellular material divided into two strata. The external layer is composed of otoliths or otoconia, which are barrel-shaped crystals of calcium carbonate with angular ends, up to 30 μm long, and heterogeneous in distribution. They are attached to a more basal gelatinous layer into which the stereocilia and kinocilia of the sensory cells are inserted (see Fig. 43.5). The gelatinous material consists largely of glycosaminoglycans associated with fibrous protein.

Epley manoeuvre

Available with the *Gray's Anatomy* e-book

Endolymphatic duct and sac

The endolymphatic duct runs in the osseous vestibular aqueduct and becomes dilated distally to form the endolymphatic sac. This is a structure of variable size, which may extend through an aperture on the posterior surface of the petrous bone to end between the two layers of the dura on the posterior surface of the petrous temporal bone near the sigmoid sinus (see Fig. 43.1C). The surface cells throughout the entire endolymphatic duct resemble those lining the non-specialized parts of the membranous labyrinth and consist of squamous or low cuboidal epithelium. The epithelial lining and subepithelial connective tissue become more complex where the duct dilates to form the endolymphatic sac. An intermediate or rugose segment and a distal sac can be distinguished. In the intermediate segment, the epithelium consists of light and dark cylindrical cells. Light cells are regular in form and have numerous long surface microvilli with endocytic invaginations between them and large clear vesicles in their apical region. In contrast, dark cells are wedge-shaped and have a narrow base, few apical microvilli and dense, fibrillar cytoplasm.

The endolymphatic sac has important roles in the maintenance of vestibular function. Endolymph produced elsewhere in the labyrinth is absorbed in this region, probably mainly by the light cells. Damage to the sac, or blockage of its connection to the rest of the labyrinth, causes endolymph to accumulate; this produces hydrops, which affects both vestibular and cochlear function. The epithelium is also permeable to leukocytes, including macrophages, which can remove cellular debris from the endolymph, and to various cells of the immune system that contribute antibodies to this fluid.

Cochlear duct

The cochlear duct is a spiral tube that runs within the bony cochlea (see Figs 43.1C, **Fig. 43.9**). The osseous spiral lamina projects for part of the distance between the modiolus and the outer wall of the cochlea and is attached to the inner edge of the basilar membrane. Above it is a thickened ridge of endosteum called the spiral limbus. The endosteum of the outer wall is thickened to form a spiral cochlear ligament that projects inwards as a triangular basilar crest attached to the outer rim of the basilar membrane. Immediately above this is a concavity, the external spiral sulcus (sulcus spiralis externus), above which the thick, highly vascular periosteum projects as a spiral prominence. Above the prominence is a specialized, thick epithelial layer, the stria vascularis. A second, thinner vestibular membrane, Reissner's membrane, extends from the spiral limbus to the outer wall of the cochlea, where it is attached above the stria. Reissner's membrane consists of two layers of squamous epithelial cells separated by a basal lamina. The side facing the scala vestibuli bears flattened perilymphatic cells, with tight junctions between them, creating a diffusion barrier. The endolymphatic side is lined by squamous epithelial cells with many microvilli; these are also joined by tight junctions and are involved in ion transport. The canal thus enclosed between the scala tympani and the scala vestibuli is the cochlear duct (see Fig. 43.9B). It is triangular in cross-section throughout the length of the cochlea. The closed upper end, the lagena, is attached to the cupula. The lower end of the duct turns medially, narrowing into the ductus reuniens, and connects with the saccule (see Fig. 43.1C).

The organ of Corti, the sensory epithelium of the cochlea, sits on the basilar membrane. The apices of the sensory hair cells and the supporting cells it contains are joined by tight junctions to form the reticular lamina. The diffusion barriers that line the cochlear duct ensure that the apices of the sensory hair cells are bathed in endolymph, whereas their lateral and basal regions are bathed in perilymph.

The stria vascularis lies on the outer wall of the cochlear duct, above the spiral eminence (see Fig. 43.9B–C). It has a special stratified epithelium containing a dense intraepithelial capillary plexus and three cell types: superficial marginal, dark or chromophil cells; intermediate light, or chromophobe cells; and basal cells. The endolymphatic surface consists only of the apices of marginal cells. The intermediate and basal cells lie deeper within the stria and send cytoplasmic processes towards the surface, between the deeper parts of the marginal cells. The long descending cytoplasmic processes of the marginal dark cells and the ascending processes of the intermediate and basal cells envelop the intraepithelial capillaries. The stria vascularis is involved in ion transport and helps to produce the unusual ionic composition of endolymph. It is the source of the large positive endocochlear electrical potential, maintenance of which is directly dependent on adequate oxygenation of the epithelial cells, provided by the intraepithelial capillary plexus.

The osseous spiral lamina consists of two plates of bone between which are canals for the cochlear nerve fibres. On the upper plate, the periosteum is thickened to form the spiral limbus (limbus laminae spiralis) (see Fig. 43.9B). It ends externally in the internal spiral sulcus, which in section is shaped like a C. Its upper part, the overhanging limbic edge, is the vestibular labium, and the lower tapering part is the tympanic labium, which is perforated by small holes (the habenula perforata) for branches of the cochlear nerve. The upper surface of the vestibular labium is crossed at right-angles by furrows, separated by numerous elevations, the auditory teeth (dentes acustici). The limbus is covered by a layer that appears superficially to be squamous epithelium; however, only the cells over the 'teeth' are flat, and those in the furrows are flask-shaped interdental cells. The epithelium is continuous with the epithelium in the internal spiral sulcus and on the inferior surface of Reissner's membrane. During development, the interdental cells secrete some of the material that forms the tectorial membrane. The limbus contains fibrocytic cells interspersed with extracellular matrix.

Basilar membrane

The basilar membrane stretches from the tympanic lip of the osseous spiral lamina to the basilar crest of the spiral ligament (see Fig. 43.9B–C). It consists of two zones. The thin zona arcuata stretches from the spiral limbus to the bases of the outer pillar cells and supports the organ of Corti. It is composed of compact bundles of small (8–10 nm diameter) collagenous filaments, mainly radial in orientation. The outer, thicker zona pectinata starts beneath the bases of the outer pillar cells and is attached to the crista basilaris. The basilar membrane is trilaminar in the zona pectinata, but the upper and lower layers fuse at its attachment to the crista basilaris. The length of the basilar membrane is 35 mm; its width increases from 0.21 mm basally to 0.36 mm at its

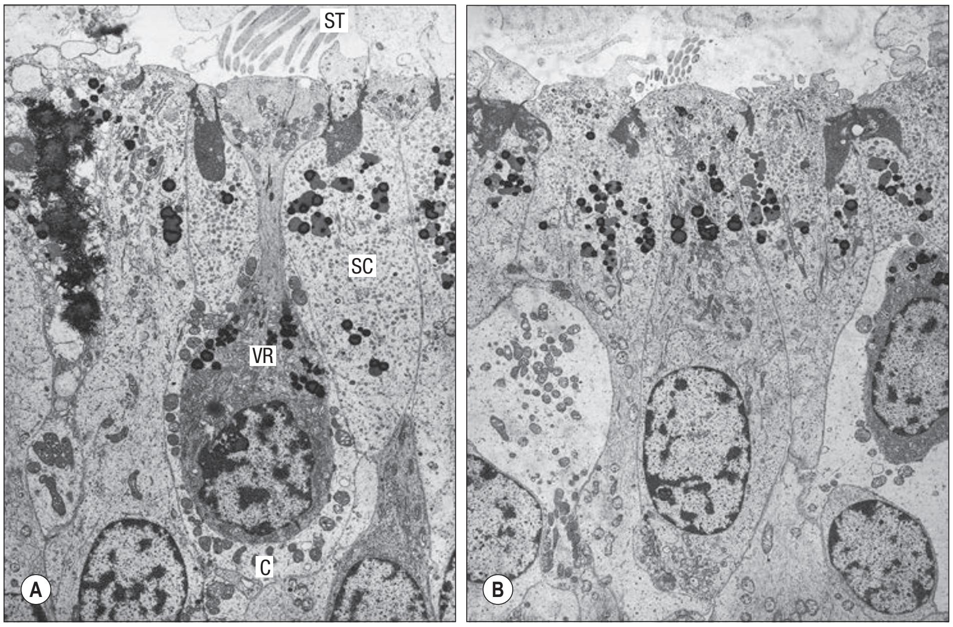

Fig. 43.8 Human vestibular hair cells (transmission electron micrographs). **A**, Type I cell (VR) bearing an apical group of stereocilia (ST) seen in a vertical section through the macula. Note that the hair cell is bottle-shaped, and that much of it is enclosed in the calyceal ending (C) of an afferent nerve terminal. Other abbreviations: SC, supporting cells. **B**, Human type II vestibular hair cell. A bouton-type afferent nerve terminal is in contact with the basal part. (Courtesy of H Felix, M Gleeson and L-G Johnsson, ENT Department, University of Zurich and GKT School of Medicine, London.)

Benign paroxysmal positional vertigo is a condition in which a sensation of rotation with associated nystagmus is induced by adopting a particular position (with the abnormal ear dependent). It is believed that calcium carbonate crystals from the otoliths become freed from the otolithic membrane and, in certain positions, drop into the ampulla of the posterior semicircular duct, possibly becoming adherent to the cupula and rendering it gravity-sensitive. In certain positions, the alignment of the axis of the posterior semicircular canal with gravity results in the displacement of the cupula and the activation of the vestibulo-ocular reflex, leading to compensatory nystagmoid eye movements in response to apparent head movements.

Epley's canalith repositioning procedure relies on the adoption of a series of body postures designed to allow the aberrant crystals (or canaliths) to float out of the posterior semicircular duct and to stick to the wall of the vestibule. Cure rates in excess of 80% have been recorded and the procedures have largely superseded surgical procedures designed to denervate the ampulla of the posterior semicircular duct in its canal (singular neurectomy) or obliterate the canal completely (Furman and Cass 1999).

The spiral ligament is lateral to the stria vascularis. It is composed of thick collagenous fibres interspersed with fibrocytic cells of several different types, and root cells that send large processes into the ligament from the region of the basilar crest. There is an extensive capillary network that parallels that of the stria vascularis. The fibrocytes and the root cells express connexins and have gap junctional systems (Jagger et al 2010) that allow transcellular transport of ions, although the two types of cell are not directly coupled. It is thought that potassium recycling from perilymph to endolymph is mediated partly through these gap junctional networks emanating from the Deiters' cells underlying the sensory hair cells. Late-onset hearing loss (DFN3) is thought to be the result of fibrocyte degeneration (Minowa et al 1999).

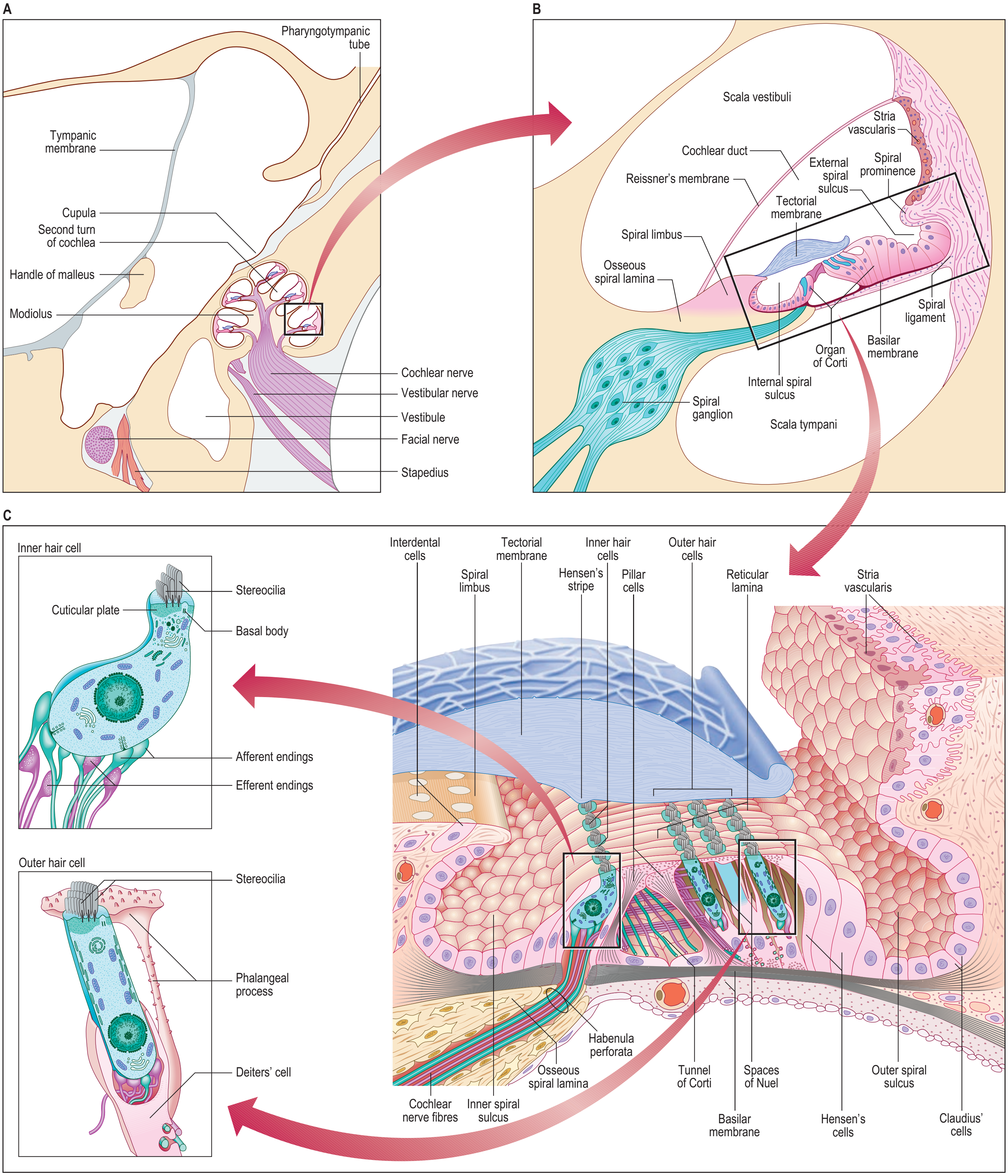
A
Pharyngotympanic tube
Tympanic membrane
Cupula
Second turn of cochlea
Handle of malleus
Modiolus
Cochlear nerve
Vestibular nerve
Vestibule
Facial nerve
Stapedius
B
Scala vestibuli
Stria vascularis
Cochlear duct
External spiral sulcus
Spiral prominence
Reissner's membrane
Tectorial membrane
Spiral limbus
Osseous spiral lamina
Spiral ligament
Basilar membrane
Organ of Corti
Internal spiral sulcus
Spiral ganglion
Scala tympani
C
Inner hair cell
Stereocilia
Cuticular plate
Basal body
Afferent endings
Efferent endings
Outer hair cell
Stereocilia
Phalangeal process
Deiters' cell
Interdental cells
Spiral limbus
Tectorial membrane
Hensen's stripe
Inner hair cells
Pillar cells
Outer hair cells
Reticular lamina
Stria vascularis
Habenula perforata
Osseous spiral lamina
Cochlear nerve fibres
Inner spiral sulcus
Tunnel of Corti
Spaces of Nuel
Basilar membrane
Hensen's cells
Outer spiral sulcus
Claudius' cells

Fig. 43.9 The cochlea. **A**, A horizontal section through the left temporal bone showing the position of the cochlea with respect to the tympanic cavity. **B**, A section through the second turn of the cochlea seen in **A**. The modiolus is to the left. **C**, The structure of the cochlear organ of Corti and stria vascularis, showing the arrangement of the various types of cell and their overall innervation. The organization of the inner and outer hair cells and their synaptic connections are also depicted. **A** and **B** are drawn from histological sections.

apex, accompanied by corresponding narrowing of the osseous spiral lamina and a decrease in the thickness of the basilar crest. The lower or tympanic surface of the basilar membrane is covered by a layer of vascular connective tissue and elongated perilymphatic cells. One vessel, the spiral vessel (vas spirale), is larger; it lies immediately below the tunnel of Corti.

Organ of Corti

The organ of Corti consists of a series of epithelial structures that lie on the zona arcuata of the basilar membrane (see Fig. 43.9B–C). The more central of these structures are two rows of cells: the internal (inner) and external (outer) pillar cells. The bases of the pillar cells are expanded, and rest contiguously on the basilar membrane, but their rod-like cell bodies are widely separated. The two rows incline towards each other and come into contact again at the heads of the pillars, enclosing between them and the basilar membrane the tunnel of Corti, which has a triangular cross-section (see Fig. 43.9C). Internal to the inner pillar cells is a single row of inner hair cells. External to the outer pillar cells are three or four rows of outer hair cells. The bases of the outer hair cells are cupped by supporting cells called outer phalangeal (Deiters') cells, except for a gap where cochlear axons synapse with them. The apical ends of the hair cells and apical processes of the supporting cells form a regular mosaic called the reticular lamina, which is covered by the tectorial membrane, a gel-like structure projecting from the spiral limbus. The reticular lamina is impervious to ions and thus maintains the electrochemical gradient between the fluids surrounding the apices and the basolateral membranes of the sensory hair cells. A narrow gap separates the tectorial membrane from the reticular lamina except where the apical stereocilia of the outer hair cells project to make contact with it.

In addition to the tunnel of Corti, other intercommunicating spaces, the spaces of Nuel, surround the outer hair cells. This entire intercommunicating complex of spaces of Nuel and tunnel of Corti is filled with perilymph, which diffuses through the matrix of the basilar membrane. The fluid in these spaces is also sometimes called the cortilymph; it is possible that there are minor alterations in perilymphatic composition within it because it is exposed to the activities of synaptic endings and specialized excitable cells.

Each pillar cell has a base or crus, an elongated scapus (rod) and an upper end or caput (head) (see Fig. 43.9C); each crus and caput are in contact, but the scapi are separated by the tunnel of Corti. Electron microscopy shows many microtubules, 30 nm in diameter, arranged in linked parallel bundles of 2000 or more in the scapus, originating in the crus and diverging above the scapus to terminate in the head region. The nucleus is situated in the foot-like expansion resting on the basal lamina.

There are almost 6000 inner pillar cells. Their bases rest on the basilar membrane near the tympanic lip of the internal spiral sulcus, and their bodies form an angle of approximately 60° with the basilar membrane. Their heads resemble the proximal end of the ulna, with deep concavities for the heads of the outer pillar cells, which they overhang to form the top of the tunnel of Corti. There are almost 4000 outer pillar cells. They are longer and more oblique than the inner pillar cells and form an angle of approximately 40° with the basilar membrane. Their heads fit into the concavities on the heads of the inner pillar cells and project externally between the first row of outer hair cells as thin processes that contact the processes of the Deiters' cells. The distances between the bases of the inner and outer pillar cells increase from the cochlear base to its apex, whereas the angles they make with the basilar membrane diminish.

Cochlear hair cells are the sensory transducers of the cochlea; collectively, they detect the amplitude and frequency of the sound waves that enter the cochlea. All cochlear hair cells have a common pattern of organization. They are elongated cells with a group of modified apical microvilli or stereocilia (which contain parallel arrays of actin filaments), similar to those of vestibular hair cells, and a group of synaptic contacts with cochlear nerve fibres at their rounded bases (**Fig. 43.10**). The inner hair cells form a single row along the inner edge of inner pillar cells (and the spiral tunnel), whereas the outer hair cells are arranged in three or, in some regions of the human cochlea, in four or even five rows, interspersed with supporting cells (**Fig. 43.10A**). These two groups have distinctive roles in sound reception; the differences in their detailed structure reflect this functional divergence. There are 3500 inner hair cells and 12,000 outer hair cells. The two sets of hair cells lean towards each other apically at about the same angles as the neighbouring inner and outer pillar cells. The geometric arrangement of these cells is very precise, and this pattern is closely related to the sensory performance of the cochlea.

The inner hair cells are pear-shaped and slightly curved; the narrower end is directed towards the surface of the organ of Corti and the wider basal end is positioned some distance above the inner end of the basilar membrane (see Fig. 43.9C). The inner hair cells are surrounded by inner border cells and by inner phalangeal cells, which are attached externally to the heads of the inner pillar cells. The flat apical surface of each inner hair cell is elliptical when viewed from above, its long axis directed in the direction of the row of hair cells (see Fig. 43.10A). The breadth of the apex exceeds that of the inner pillar cells so that each inner hair cell is related to more than one inner pillar cell. The apex bears 50–60 stereocilia, arranged in several ranks of progressively ascending height, the tallest on the strial side. The tips of the shorter rows are connected diagonally to the sides of the adjacent taller stereocilia by thin filaments called tip links; each stereocilium is also connected to all its neighbours by a variety of lateral links. The height of a stereociliary row varies along the length of the cochlea, being tallest at the apex and shortest at its base. The stereociliary bases insert into a transverse lamina of dense fibrillar material, the cuticular plate, which lies immediately beneath the apical surface of each inner hair cell. The cuticular plate includes a small aperture containing a basal body. During development, a kinocilium containing microtubules is anchored here, a condition that persists in vestibular hair cells.

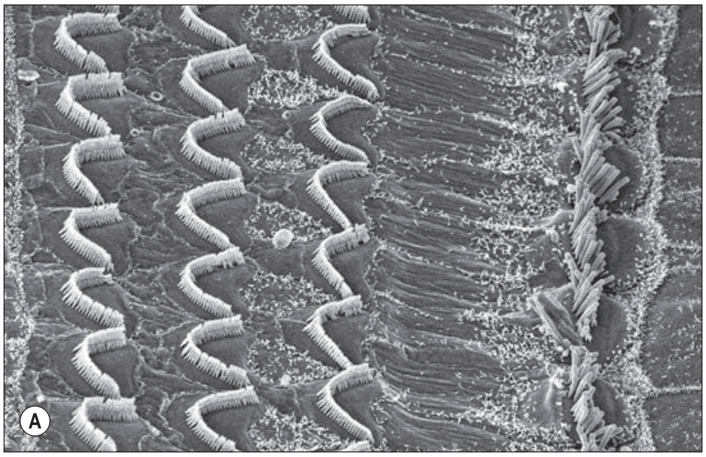

Fig. 43.10 Scanning electron micrographs of the surface of the organ of Corti (guinea pig). **A**, The reticular lamina. Three rows of V-shaped stereociliary bundles can be seen protruding from the apices of the outer hair cells. They are separated from the single row of inner hair cells (which have relatively linear stereociliary bundles) by the apices of the inner pillar cells. (Courtesy of DN Furness, School of Life Sciences, Keele University.) (B, *continued online*)

At its base, each inner hair cell forms 10 or more synaptic contacts with afferent endings, each being marked by a presynaptic structure similar to the ribbon synapses of the retina. Occasionally, an efferent synapse makes direct contact with a hair cell base but these are usually presynaptic to the terminal expansions of afferent endings, rather than to the hair cell itself.

Outer hair cells are long cylindrical cells that are nearly twice as tall as the inner hair cells (see Figs 43.9C, 43.10A). There is a gradation of length: the outermost row is longest in any one cochlear region, and those of the cochlear apex are taller than those of the base. They are surrounded by the apical or phalangeal processes of the Deiters' cells or, on the internal side of the inner row, by the heads of the outer pillar cells. The stereocilia, which may number up to 100 per cell, are arranged in three rows of graded heights; the tallest is on the outer side. The rows are arranged in the form of a V or W, depending on cochlear region, the points of the angles directed externally. The stereocilia are also graded in height according to cochlear region; those of the cochlear base are shortest. Like those of inner hair cells, the stereocilia possess tip links (see Fig. 43.10B) and other filamentous connections with their neighbours and are inserted at their narrow bases into a cuticular plate. The tallest stereocilia are embedded in shallow impressions on the underside of the tectorial membrane.

The rounded nucleus is positioned near the base of the cell. Below the nucleus are a few ribbon-like synapses associated with afferent endings of the cochlear nerve. The latter are fewer in number and smaller than the cluster of efferent boutons that contact the base of the cell. The neurotransmitter at the afferent synapse in both inner and outer hair cells is glutamate whereas that of the efferent endings is acetylcholine, although other neurotransmitters or neuromodulators have been demonstrated.

Cochlear hair cells respond with phenomenal speed and sensitivity to sound vibrations that cause submicron deflections of their stereociliary hair bundles. Outer hair cells not only detect these vibrations but also generate force to increase auditory sensitivity and frequency discrimination. (See Fettiplace and Hackney (2006) for further details about the sensory and motor functions of auditory hair cells.)

Deiters' or phalangeal cells lie between the rows of outer hair cells. Their expanded bases lie on the basilar membrane and their apical ends partially envelope the bases of the outer hair cells (see Fig. 43.9C; **Fig. 43.11**). Each has a finger-like (phalangeal) process that extends diagonally upwards between the hair cells to the reticular membrane, where it forms a plate-like expansion that fills the gaps between hair cell apices.

Five or six rows of columnar supporting cells or external limiting cells, such as Hensen's cells and Claudius' cells, lie external to the Deiters' cells (see Fig. 43.9C).

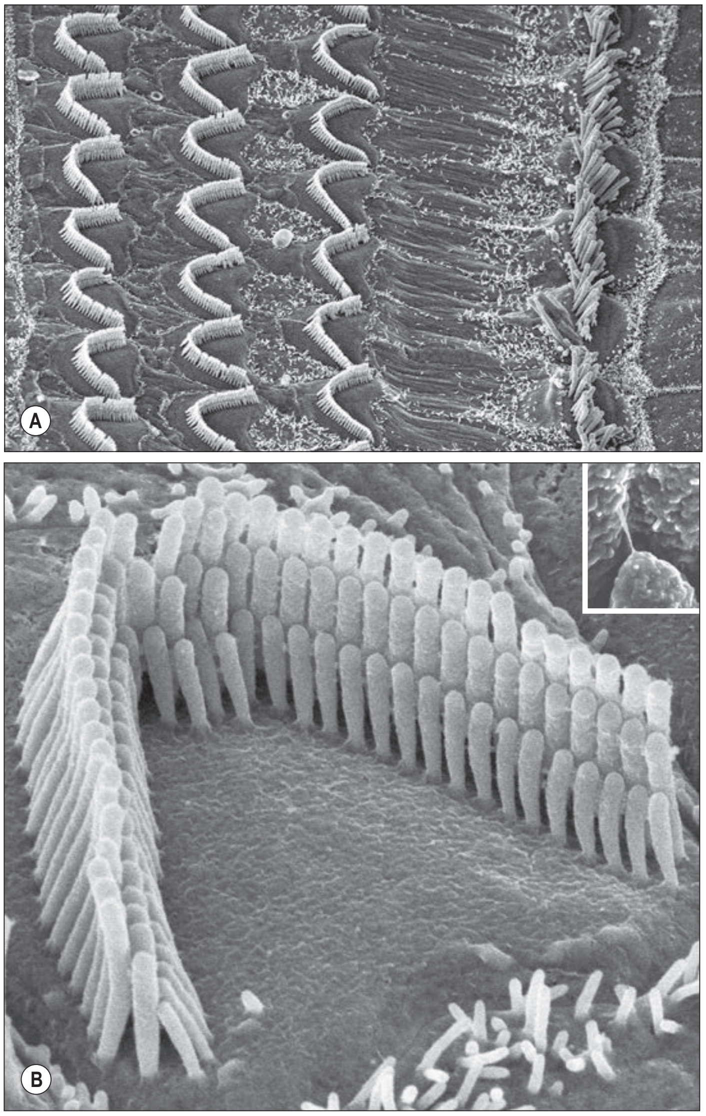

Fig. 43.10 Scanning electron micrographs of the surface of the organ of Corti (guinea pig). **A**, The reticular lamina. Three rows of V-shaped stereociliary bundles can be seen protruding from the apices of the outer hair cells. They are separated from the single row of inner hair cells (which have relatively linear stereociliary bundles) by the apices of the inner pillar cells. **B**, The stereociliary bundle of one outer hair cell, showing three rows of stereocilia increasing in height; deflection of the stereocilia in the direction of the tallest row results in depolarization of the hair cell. Microvilli can be seen on the surface of Deiters' cells (front right). The inset shows a tip link connecting a short stereocilium tip to the side of the tall stereocilium behind. (Courtesy of DN Furness, School of Life Sciences, Keele University.)

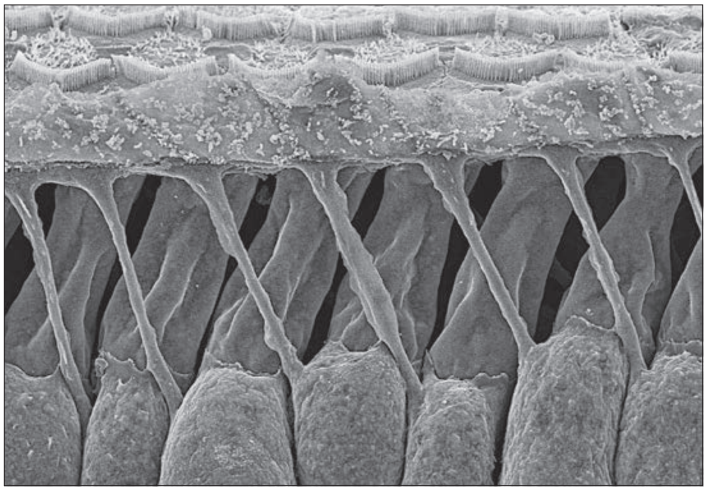

Fig. 43.11 A scanning electron micrograph of a portion of the organ of Corti (guinea pig), dissected to expose the outer row of outer hair cells and their attendant Deiters' cells with narrow phalangeal processes. The stereociliary bundles of two rows of outer hair cells are visible above the reticular lamina. (Courtesy of DN Furness, School of Life Sciences, Keele University.)

The apices of the hair cells and supporting cells that form the reticular lamina are linked by tight junctions, adherens junctions and desmosomes. This arrangement is significant for two reasons. The reticular lamina creates a highly impermeable barrier to the passage of ions other than via the mechanotransducer channels in the stereociliary membranes. It also forms a rigid support between the apices of the hair cells, coupling them mechanically to the movements of the underlying basilar membrane, which causes lateral shearing movements between the stereocilia and the overlying tectorial membrane. If there is hair cell loss as a result of trauma such as excessive noise, or ototoxic drugs, the supporting cells expand rapidly to fill the gap, disturbing the regular pattern of the reticular lamina (phalangeal scars) but restoring its function.

Hair cell mechanotransduction

Mechanotransduction is central to both hearing and balance and is a phenomenon that is shared by all the sensory hair cells of vestibular and auditory epithelia. The basic mechanism is the same in all of the different types of hair cell and is dependent on common features of the hair bundle: specifically, the 'staircase' array of stereocilia and the tip links connecting the tips of shorter and adjacent taller stereocilia. Deflections of the bundle in an excitatory (depolarizing) direction cause tension in the tip link, which acts to open non-specific cationic mechanoelectrical transduction channels. The identity of these channels is now thought to be a protein, transmembrane channel-like protein 1 (TMC1), which, together with several known accessory proteins, is located in the membrane at the lower end of the tip link. Mutations in TMC1 are one of the commonest forms of genetic hearing loss. Influx of potassium and calcium ions through these channels, depolarizes the cell and leads to calcium influx through basolateral voltage-gated calcium channels, which causes release of neurotransmitter. The hair cells also have basolateral potassium channels that allow efflux of potassium into perilymph. The tip link that is central to this process consists of two molecules of cadherin 23 and two molecules of protocadherin 15, forming a strong twisted strand (Hackney and Furness 2013). The importance of this structure is emphasized by the fact that mutations in these cadherins underlie deaf-blindness conditions (Usher syndrome).

The sensitivity of mechanotransduction is greatly increased by the combination of the hair-cell membrane potential (−70 mV) and the endolymphatic potential (+80 mV), producing an overall driving potential of up to 150 mV. It is therefore vital to maintain a high potassium concentration, despite its depletion from endolymph during detection of acoustic or balance stimuli.

Tectorial membrane

The tectorial membrane overlies the sulcus spiralis internus and organ of Corti, and is a stiff, gelatinous plate (see Fig. 43.9B–C). It contains collagen types II, V and IX, interspersed with glycoproteins (tectorins), which contribute approximately half of the total protein.

In transverse section, the tectorial membrane has a characteristic shape. The underside is nearly flat and the upper surface is convex, and it is thin on the modiolar side where it is attached to the vestibular labium of the spiral limbus. Its outer part forms a thickened ridge, overhanging the edge of the reticular lamina. The lower surface is relatively smooth, except where the stereocilia of the outer hair cells are embedded in the membrane, leaving a pattern of W- or V-shaped indentations and an S-shaped ridge called Hensen's stripe, which projects towards the stereocilia of the inner hair cells. The interdental cells of the spiral limbus are believed to secrete the membrane.

VASCULAR SUPPLY

Arteries

The inner ear is principally supplied by the labyrinthine artery. The stylomastoid branch of either the occipital artery or the posterior auricular artery (see Fig. 35.8) also supplies the semicircular canals.

Labyrinthine artery

The labyrinthine artery arises from the basilar artery, sometimes from the anterior inferior cerebellar artery. It divides at the bottom of the internal acoustic meatus into cochlear and vestibular branches. The cochlear branch divides into 12–14 twigs, which traverse the canals in the modiolus and are distributed as a capillary plexus to the spiral lamina, basilar membrane, stria vascularis and other cochlear structures. Vestibular arterial branches supply the utricle, saccule and semicircular ducts.

Veins

Descriptions of the venous drainage of the inner ear are often conflicting, presumably reflecting both normal variation and the existence of connections between the veins that provide the potential for collateral circulation. Veins draining the vestibule and semicircular canals accompany the arteries. They pass towards the utricle to form the vein of the vestibular aqueduct, which empties into either the sigmoid or inferior petrosal sinus. The vein of the cochlear aqueduct (inferior cochlear vein) usually drains into either the inferior petrosal sinus or the superior bulb of the internal jugular vein. It is formed by the union of the common modiolar and vestibulocochlear veins and provides almost all of the venous outflow of the cochlea (Wright and Roland 2013). The common modiolar vein is formed by the union of the anterior and posterior spiral veins near the basal cochlear turn; the vestibulocochlear vein is formed by the confluence of the anterior and posterior vestibular veins and the vein of the round window. When present, a labyrinthine vein drains the apical and middle cochlear coils into either the posterior part of the superior petrosal sinus or the transverse sinus or the inferior petrosal sinus.

For details of the microvasculature of the cochlea of humans and other mammals, see Axelsson (1988).

INNERVATION

Vestibulocochlear nerve

The vestibulocochlear nerve emerges from the cerebellopontine angle. It courses through the posterior cranial fossa in close association with the facial nerve, nervus intermedius and labyrinthine vessels. Together with these structures, it enters the petrous temporal bone via the porus acusticus of the internal acoustic meatus, and divides into an anterior trunk, the cochlear nerve, and a posterior trunk, the vestibular nerve (Fig. 43.12A). Both contain the centrally directed axons of bipolar neurones, together with a smaller number of efferent fibres that arise from brainstem neurones and terminate on cochlear and vestibular sensory cells. In humans, the intratemporal portion of the vestibulocochlear nerve consists of two histologically distinct portions: a central glial zone adjacent to the brainstem, and a peripheral or non-glial zone (Bridger and Farkashidy 1980). In the glial zone, the axons are supported by central neuroglia, whereas in the non-glial zone they are ensheathed by Schwann cells. The non-glial zone sometimes extends into the cerebellopontine angle medial to the internal acoustic meatus in human vestibulocochlear nerves. During development, a gap of several weeks has been reported between the onset of Schwann cell myelination distally and glial myelination proximally; it has been suggested that the gap may coincide with the time of the final maturation of the organ of Corti.

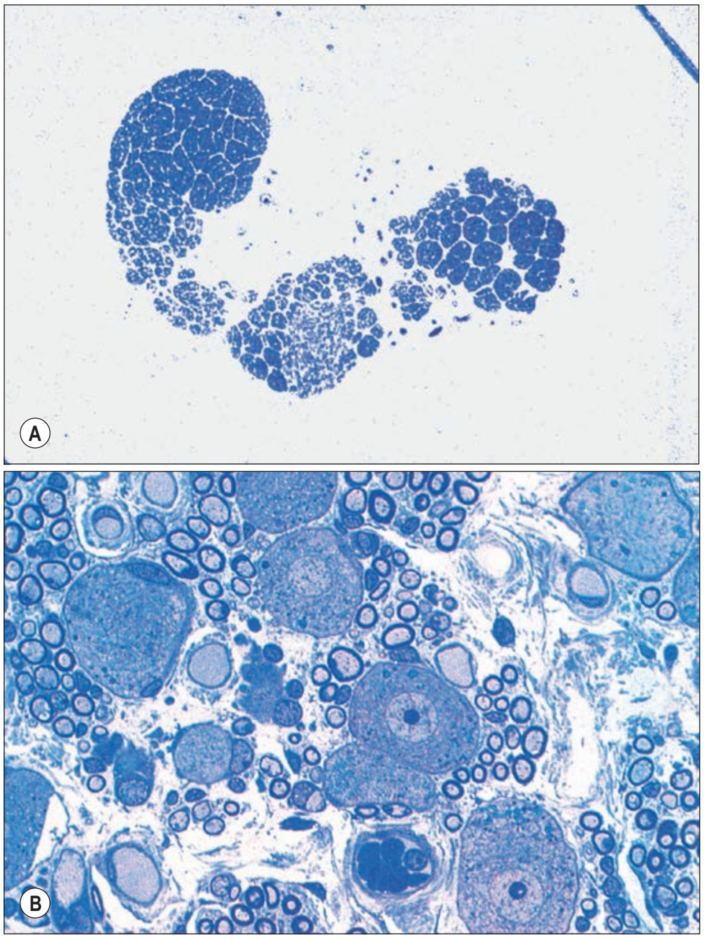

Fig. 43.12 The vestibulocochlear nerve (human). **A**, A transverse section. The cochlear nerve (the comma-shaped profile on the left) abuts the inferior division of the vestibular nerve (right). The singular nerve is a separate fascicle between the superior and inferior divisions of the vestibular nerve. **B**, A portion of a vestibular ganglion, showing neuronal perikarya, myelinated axons and small blood vessels. (Toluidine blue stained resin sections courtesy of H Felix, M Gleeson and L-G Johnsson, ENT Department, University of Zurich and School of Medicine, King's College London.)

(For further details about the development of the human cochlear nerve, see Ray et al (2005).)

In audiological practice, it is important to distinguish between intratemporal and intracranial lesions. However, this surgical distinction does not correlate with the precise anatomical description of peripheral and central portions of the auditory and vestibular systems. Clinically, the term 'peripheral auditory lesion' is used to describe lesions peripheral to the spiral ganglion, and the term 'peripheral vestibular disturbance' includes lesions of the vestibular ganglion and the entire vestibular nerve.

Vestibular nerve

The cell bodies of the bipolar neurones that contribute to the vestibular nerve lie in the vestibular ganglion, which is situated in the trunk of the nerve within the lateral end of the internal acoustic meatus (**Fig. 43.12B**). Their peripheral processes innervate the maculae of the utricle and saccule and the ampullary crests of the semicircular ducts (see below). Their axons travel to the central nervous system in the vestibular nerve, which enters the brainstem at the cerebellopontine angle and terminates in the vestibular nuclear complex. Neurones in this complex project to motor nuclei in the brainstem and upper spinal cord, and to the cerebellum and thalamus. Thalamic efferent projections pass to a cortical vestibular area that is probably located near the intraparietal sulcus in area 2 of the primary somatosensory cortex.

Vestibular (Scarpa's) ganglion

The cell bodies of the neurones in the vestibular ganglion vary considerably in size: their circumferences range from 45 to 160 μm (Felix et al 1987). No topographically ordered distribution relating to size has been found. The cell bodies are notable for their abundant granular endoplasmic reticulum, which in places forms Nissl bodies, and prominent Golgi complexes. They are covered by a thin layer of satellite cells and are often arranged in pairs, closely abutting each other so that only a thin layer of endoneurium separates the adjacent coverings of satellite cells. This arrangement has led to speculation that ganglion cells may affect each other directly by electrotonic spread (ephaptic transmission: see Felix et al (1987)).

Two distinct sympathetic components have been identified in the vestibular ganglion: a perivascular adrenergic system derived from the stellate ganglion, and a blood vessel-independent system derived from the superior cervical ganglion.

Intratemporal vestibular nerve

The peripheral processes of the vestibular ganglion cells are aggregated into definable nerves, each with a specific distribution. The main nerve divides at and within the ganglion into superior and inferior divisions, which are connected by an isthmus. The superior division, the larger of the two, passes through the small holes in the superior vestibular area at the fundus of the internal acoustic meatus (see Fig. 43.3) and supplies the ampullary crests of the lateral and anterior semicircular ducts via the lateral and anterior ampullary nerves, respectively. A secondary branch of the lateral ampullary nerve supplies the macula of the utricle; however, the greater part of the utricular macula is innervated by the utricular nerve, which is a separate branch of the superior division. Another branch of the superior division supplies part of the saccule.

The inferior division of the vestibular nerve passes through small holes in the inferior vestibular area (see Fig. 43.3) to supply the remainder of the saccule and the posterior ampullary crest via saccular and singular branches, respectively; the latter passes through the foramen singulare. Occasionally, a very small supplementary or accessory branch innervates the posterior crest; it is probably a vestigial remnant of the crista neglecta, an additional area of sensory epithelium found in some other mammals but seldom in humans.

Afferent and efferent cochlear fibres are also present in the inferior division of the vestibular nerve but leave at the anastomosis of Oort to join the main cochlear nerve (see review by Warr (1992)). Another anastomosis, the vestibulofacial anastomosis, is situated more centrally between the facial and vestibular nerves and is the point at which fibres originating in the intermediate nerve pass from the vestibular nerve to the main trunk of the facial nerve.

There are approximately 20,000 fibres in the vestibular nerve, of which 12,000 travel in the superior division and 8000 travel in the inferior division. The distribution of fibre diameters is bimodal, with peaks at 4 μm and 6.5 μm. The smaller fibres go mainly to the type II hair cells and the larger fibres tend to supply the type I hair cells. In addition to the afferents, efferent and autonomic fibres have been identified. Efferent fibres synapse exclusively with the afferent calyceal terminals around type I cells and usually with the afferent boutons on type II cells, although a few are in direct contact with the cell bodies of type II cells. The autonomic fibres do not contact vestibular sensory cells but terminate beneath the sensory epithelia.

Anatomy of balance and posture

The vestibular labyrinths on each side of the head are arranged symmetrically with respect to each other. Vestibular sensory pathways are concerned with perception of the position of the head in space and movement of the head; they also establish important connections for reflex movements that govern the equilibrium of the body and the fixity of gaze.

The vestibular system consists of two otolithic organs – the utricle and the saccule – and three semicircular ducts in their osseous canals. The otolithic organs detect linear acceleration due to gravitational pull (gravito-inertial acceleration) and the direction of other linear accelerations such as the up-and-down movements of the head that occur in running. They also respond when the head is tilted relative to gravity: so-called pitch (forward and backward tilting) and roll (side-to-side tilting) movements. The semicircular canals detect angular accelerations resulting from rotations of the head or body.

The stereocilia in the apical hair bundles of the mechanosensitive hair cells in each of these organs are embedded in an overlying accessory gel-like structure, the otolithic membrane (in the utricle and the saccule) and the cupula (in the semicircular ducts). Their apical surfaces are bathed in endolymph; tight junctional complexes between the apices of the hair cells and their adjacent supporting cells separate the endolymph from the perilymph that bathes their basolateral surfaces. As noted earlier, deflection of the stereocilia (caused by displacements of their overlying accessory membranes by fluid movements in the membranous labyrinth) produces either an increased or a decreased rate of opening of the mechanotransduction channels at their tips, depending on whether they are deflected towards or away from the tallest row, respectively. The change in the membrane potential of the receptor cell is signalled to the brain as a change in the firing frequency of the vestibular nerve afferents (either an increase or a decrease of the basal resting discharge, depending on the direction of stimulation). The signals are compared centrally with visual and somatosensory signals, which also signal the position of the head in space (for a more detailed account, see Furness (2002)).

Semicircular canals

Angular acceleration and deceleration of the head cause a counterflow of endolymph in the semicircular ducts in the semicircular canals, which deflects the cupula of each crista and displaces the stereociliary/kinociliary bundles. When a steady velocity of head movement is reached, the endolymph rapidly adopts the same velocity as the surrounding structures because of friction with the canal walls, so that the cupula and receptor cells return to their resting state. The three semicircular canals are orientated approximately at right-angles to each other, which means that all possible directions of acceleration can be detected. Directional sensitivity to head movement is coded by opposing receptor signals: the left and right semicircular canals of each functional pair (e.g. the left and right anterior canals) respond oppositely to any movement of the head that affects them (**Fig. 43.13**). Some vestibular neurones receive a bilateral input from vestibular receptors, enabling them to compare the discharge rates of right and left canal afferents, a mechanism that increases the sensitivity of the system.

Maculae

In the maculae, the weight of the otoconial crystals creates a gravitational pull on the otoconial membrane and thus on the stereociliary bundles of the sensory cells that are inserted into its base. Because of this, they are able to detect the static orientation of the head with respect to gravity. They also detect shifts in position according to the extent to which the stereocilia are deflected. The two maculae are set at right-angles to each other, and the cells of both are orientated functionally in opposite directions across their striolar boundaries. Movement causes depolarization of the hair cells on one side of the striola and hyperpolarization of cells on the other side; because the striola is curved, small groups of hair cells on the macular epithelium each respond to a specific direction of head tilt or linear acceleration (**Fig. 43.14**). Moreover, because the otoconia have a collective inertia/momentum, linear acceleration and deceleration along the anteroposterior axis can be detected by the lag or overshoot of the otoconial membrane with respect to the epithelial surface, and so the saccular macula is able to signal these changes of velocity.

The macular receptors can also be stimulated by low-frequency sound, which sets up vibratory movements in the otoconial membrane, although this appears to require relatively high sound levels. Efferent synapses on the afferent endings of the type I sensory cells and on the bases of type II cells receive inputs from the brainstem that appear to be inhibitory. They serve to reduce the activity of the afferent fibres either indirectly, in the case of the type I cells, or directly, for the type II cells.

Visual reflexes

The vestibular system plays a major role in the control of visual reflexes, which allow the fixation of gaze on an object in spite of movements of the head, and require the coordinated movements of the eye, neck and upper trunk. Constant adjustments of the visual axes are achieved chiefly through the medial longitudinal fasciculus, which connects the vestibular nuclear complex with neurones in the oculomotor, trochlear and abducens nuclei and with upper spinal motor neurones (**Fig. 43.15**; see Fig. 44.12), and also by the vestibulospinal tracts. See Chapter 29 for further information about the vestibulo-ocular reflex.

Abnormal activity of the vestibular input or central connections has various effects on these reflexes, e.g. the production of nystagmus. This can be elicited by the caloric test, a clinical test of vestibular function, by syringing the external acoustic meatus with water above or below body temperature, a procedure that appears to stimulate the cristae of the lateral semicircular duct directly. Spontaneous high activity in the afferent fibres of the vestibular nerve is seen in Ménière's disease, in which those affected experience a range of disturbances, including the sensation of dizziness and nausea, the latter reflecting the vestibular input to the vagal reflex pathway.

Cochlear nerve

Intratemporal cochlear nerve

The cochlear nerve connects the organ of Corti to the cochlear nuclei and related nuclei of the brainstem. The cochlear nerve lies inferior to the facial nerve throughout the internal acoustic meatus (see above). It becomes intimately associated with the superior and inferior divisions of the vestibular nerve, which are situated in the posterior compartment of the canal and leaves the internal acoustic meatus in a common fascicle (see Fig. 43.12A).

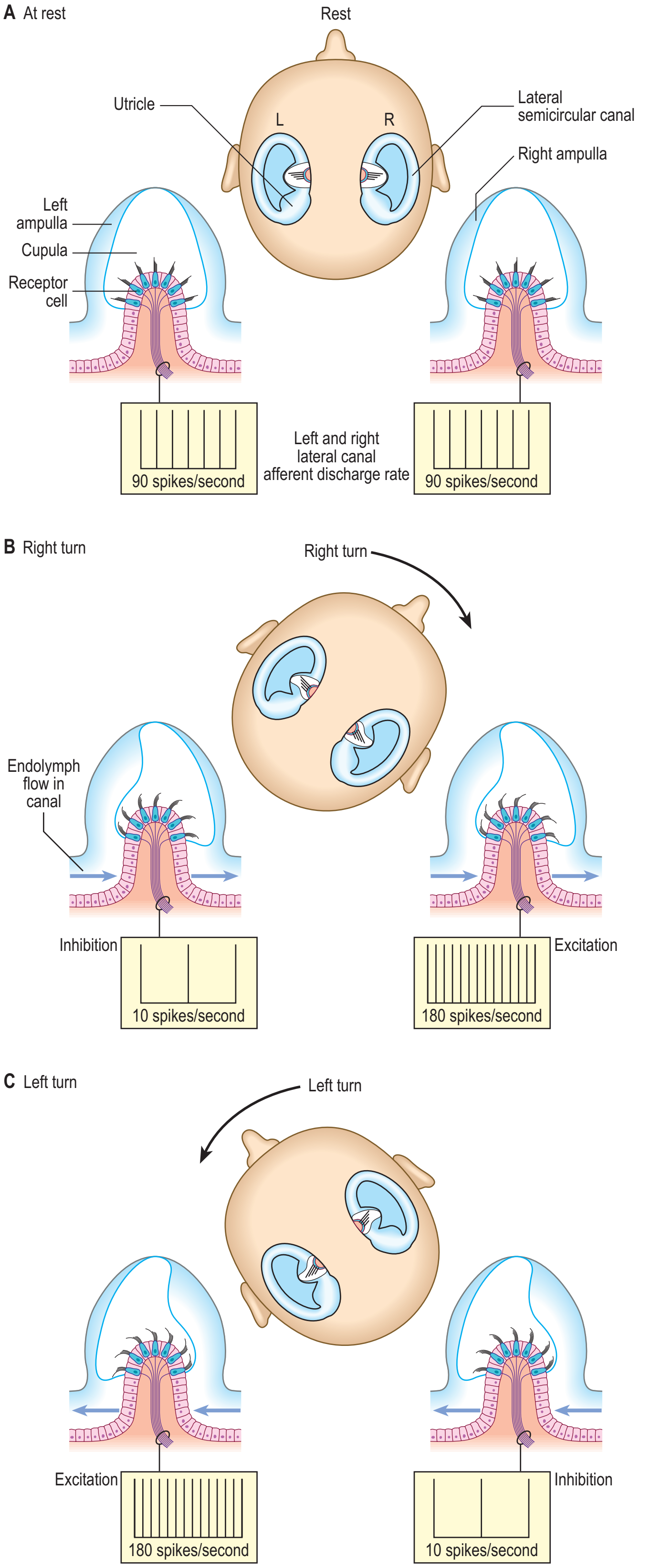

Fig. 43.13 The response of the lateral semicircular canals to head rotation in the horizontal plane. The firing rates of afferents from the left and right lateral canals are equivalent at rest (**A**). However, when the head is turned to the right (**B**) or to the left (**C**), receptor depolarization and afferent fibre excitation occurs on the side to which the head turns; there is inhibition on the contralateral side.

There are 30,000–40,000 nerve fibres in the human cochlear nerve (for review, see Nadol (1988)). Their fibre diameter distribution is

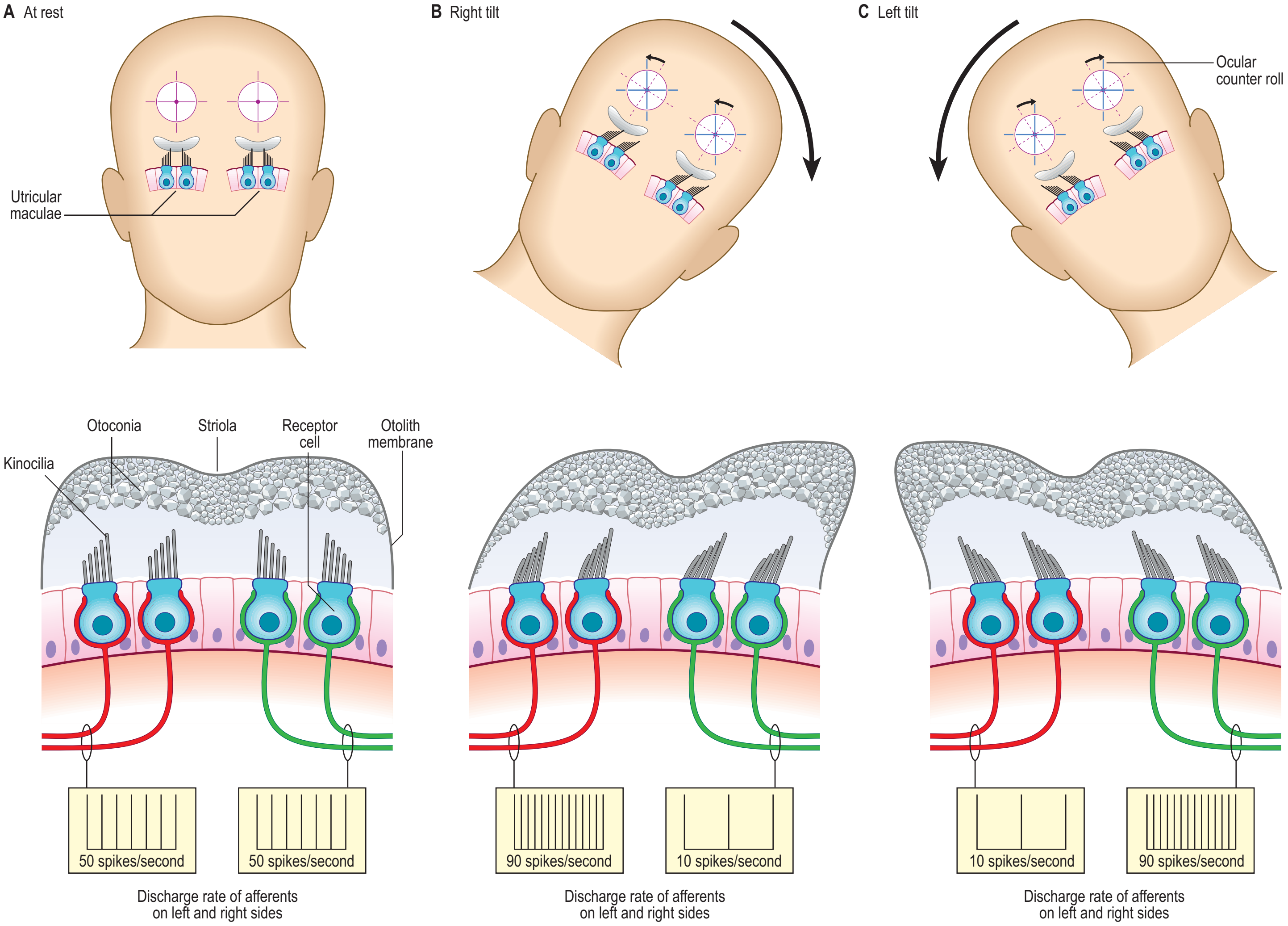

Fig. 43.14 Head tilt is encoded by a macular map of directional space. These diagrams depict the responses of the utricular maculae to head tilt. Firing rates in the vestibular afferents that innervate receptors on either side of the striola (red and green lines) are equivalent when the head is upright (**A**). When the head is tilted to the right (**B**) or to the left (**C**) the stereocilia are deflected by displaced otoconia; hair cells on the upward slope side of the striola increase their firing rate, while those on the downward slope decrease their firing rate.

unimodal, and ranges from 1 to 11 µm, with a peak at 4–5 µm. Functionally, the nerve contains both afferent and efferent somatic fibres, together with adrenergic postganglionic sympathetic fibres from the cervical sympathetic system.

Afferent cochlear innervation

The afferent fibres are the axons of bipolar neurones that lie in the spiral ganglion in the modiolus (see Fig. 43.9B; **Fig. 43.16**). There are two types of ganglion cell: most (90–95%) are large type I cells, while the remainder are smaller type II cells (see review by Nadol (1988)). Type I cells contain a prominent spherical nucleus, abundant ribosomes and many mitochondria; in many mammals (although possibly not in humans), they are surrounded by myelin sheaths. In contrast, type II cells are smaller and always unmyelinated, and have a lobulated nucleus. The cytoplasm of type II cells is enriched with neurofilaments but has fewer mitochondria and ribosomes than type I cells.

Basilar fibres Basilar fibres are the peripheral processes of type II ganglion cells and are afferent to the outer hair cells. They take an independent spiral course, turning towards the cochlear apex near the bases of the inner hair cells. They run for a distance of about five pillar cells before turning radially again and crossing the floor of the tunnel of Corti, often diagonally, to form part of the outer spiral bundle.

Outer spiral bundles The afferent fibres of the bundles of the outer spiral group course towards the basal part of the cochlea, continually branching off *en route* to supply several outer hair cells. The outer spiral bundles also contain efferent fibres (see below).

Efferent cochlear fibres

The efferent nerve fibres in the cochlear nerve are derived from the olivocochlear system (see reviews by Warr (1992), Guinan (1996)). Within the modiolus, the efferent fibres form the intraganglionic spiral bundle, which may be one or more discrete groups of fibres situated at the periphery of the spiral ganglion (**Fig. 43.17**). There are two main groups of olivocochlear efferents: lateral and medial. The lateral efferents come from small neurones in and near the lateral superior olivary nucleus and arise mainly, but not exclusively, ipsilaterally. They are organized into inner spiral fibres that run in the inner spiral bundle before terminating on the afferent axons that supply the inner hair cells. The medial efferents originate from larger neurones in the vicinity of the medial superior olivary nucleus, and the majority arise contralaterally. They are myelinated and cross the tunnel of Corti to synapse with the outer hair cells mainly by direct contact with their bases, although a few synapse with the afferent terminals. The efferent innervation of the outer hair cells decreases along the organ of Corti from cochlear base to apex, and from the first (inner) row to the third. The efferents use acetylcholine, γ-aminobutyric acid (GABA) or both as their neurotransmitter. They may also contain other neurotransmitters and neuromodulators.

Activity of the medial efferents inhibits cochlear responses to sound; the strength of the activity grows slowly with increasing sound level. They are believed to modulate the micromechanics of the cochlea by altering the mechanical responses of the outer hair cells, thus changing their contribution to frequency selectivity and sensitivity. The lateral efferents related to the inner hair cells also respond to sound. They make contacts most commonly with the inner radial afferent fibres rather than the inner hair cell base (see Fig. 43.9C) and appear to modify transmission through the afferents. The cholinergic fibres may excite the radial fibres, while those containing GABA may inhibit them, although

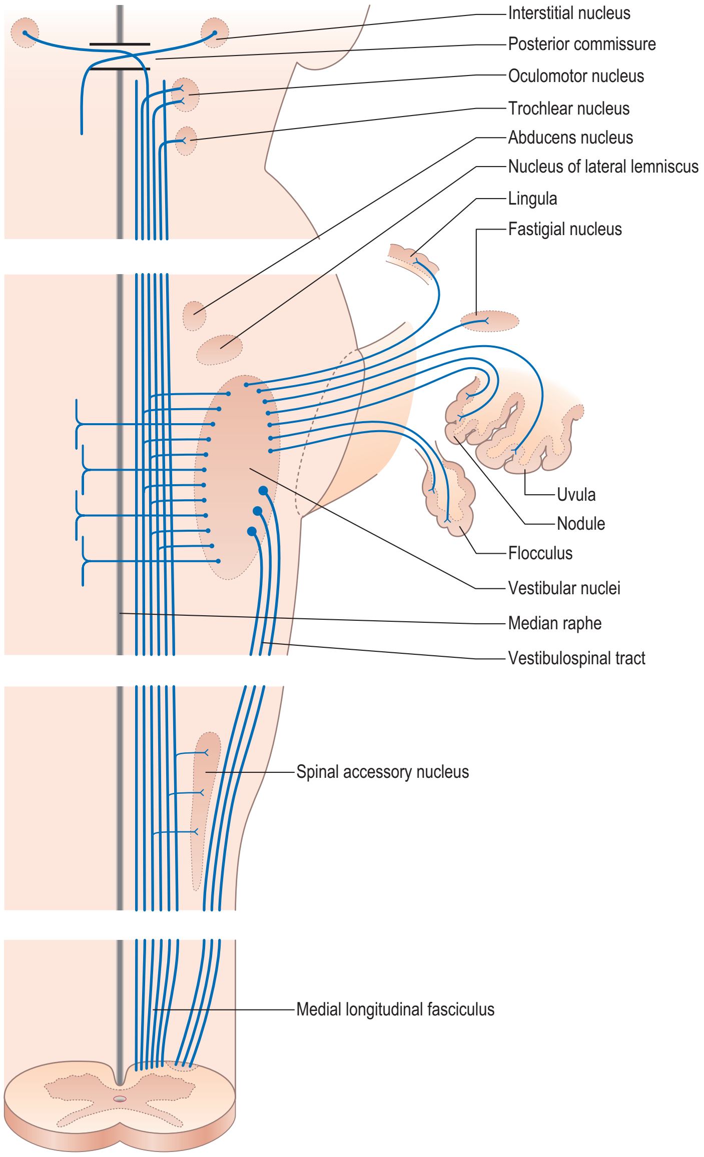
Interstitial nucleus
Posterior commissure
Oculomotor nucleus
Trochlear nucleus
Abducens nucleus
Nucleus of lateral lemniscus
Lingula
Fastigial nucleus
Uvula
Nodule
Flocculus
Vestibular nuclei
Median raphe
Vestibulospinal tract
Spinal accessory nucleus
Medial longitudinal fasciculus

Fig. 43.15 Some of the fibre components of the medial longitudinal fasciculus.

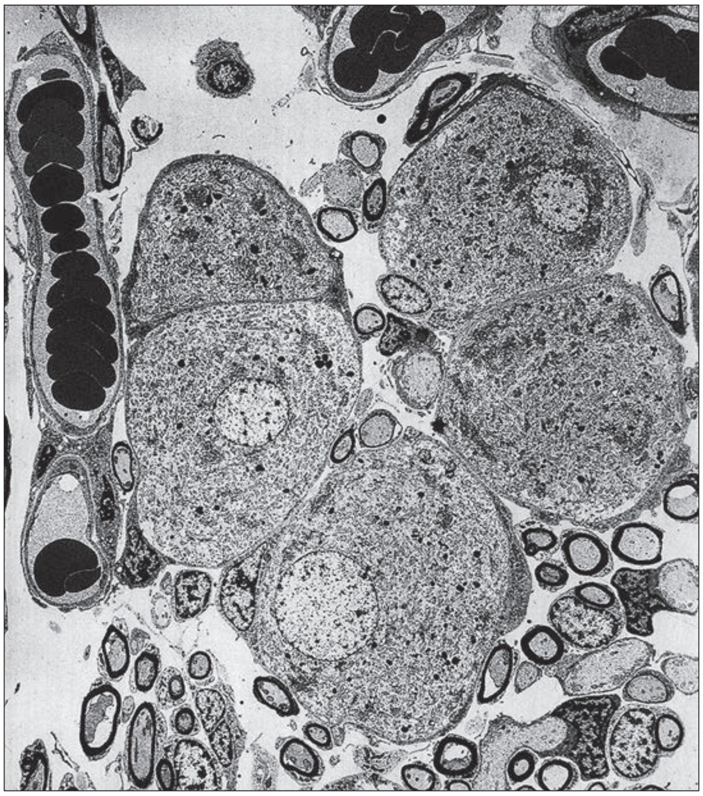

Fig. 43.16 A transmission electron micrograph showing several type II ganglion cells and axons in a human spiral ganglion. Note the absence of myelin from the surrounding sheaths of the ganglion cells. (Courtesy of H Felix, M Gleeson and L-G Johnsson, ENT Department, University of Zurich and GKT School of Medicine, London.)

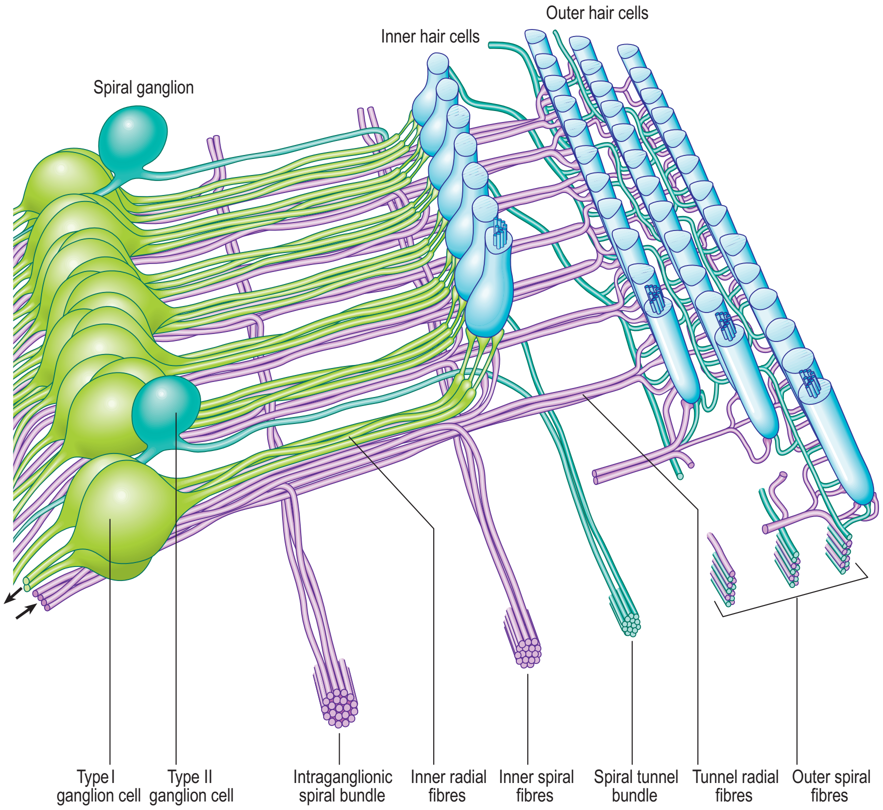
Outer hair cells
Inner hair cells
Spiral ganglion
Type I ganglion cell
Type II ganglion cell
Intraganglionic spiral bundle
Inner radial fibres
Inner spiral fibres
Spiral tunnel bundle
Tunnel radial fibres
Outer spiral fibres

Fig. 43.17 A simplified view of the innervation of the organ of Corti. Note the contrast between the convergent afferent innervation of the inner hair cells (approximately 10 fibres to each cell) and the divergent supply of the outer hair cells (1 afferent fibre to 10 cells).

their role is less well understood than that of the medial efferents (see review by Guinan (1996)).

Autonomic cochlear innervation

Autonomic nerve endings appear to be entirely sympathetic. Two adrenergic systems have been described within the cochlea: a perivascular plexus derived from the stellate ganglion and a blood vessel-independent system derived from the superior cervical ganglion. Both systems travel with the afferent and efferent cochlear fibres and seem to be restricted to regions away from the organ of Corti. The sympathetic nervous system may cause primary and secondary effects in the cochlea by remotely altering the metabolism of various cell types and by influencing the blood vessels and nerve fibres with which it makes contact.

ANATOMY OF HEARING

Sound waves entering the external ear are converted into electrical signals in the cochlear nerve by the peripheral auditory system (**Fig. 43.18**). The axons in the cochlear nerve constitute the auditory component of the vestibulocochlear nerve and terminate in the dorsal and ventral cochlear nuclei (Ch. 28); onward connections make up the ascending (central) auditory pathway.

Peripheral auditory system

Vibrations in the air column in the external acoustic meatus cause a comparable set of vibrations in the tympanic membrane and auditory ossicles. The chain of ossicles acts as a lever that increases the force per unit area at the round window by 1.2 times while the reduction in size of the round window compared with the tympanic membrane increases the force per unit area of the oscillating surface a further 17 times. This overcomes the inertia of the cochlear fluids and produces in them pressure waves that are conducted almost instantaneously to all parts of the basilar membrane. The latter varies continuously in width, mass and stiffness from the basal to the apical end of the cochlea. Each part of the basilar membrane vibrates, but only the region tuned to a specific frequency will respond maximally to a pure tone entering the ear. A wave of mechanical motion, the travelling wave, is propagated along the basilar membrane to the position where it responds maximally and then dies away again. With increasing frequency, the locus of maximum amplitude moves progressively from the apical to the basal end of the cochlea. The pattern of vibrations in the basilar membrane thus varies with the intensity and frequency of the acoustic waves reaching the perilymph. Because of the arrangement of the hair cells on the basilar membrane, these oscillations generate a largely transverse shearing force between the outer hair cells and the overlying tectorial membrane (in which the apices of the hair cell stereocilia are embedded). This movement depends on the mechanical properties of the entire organ of Corti, including its cytoskeleton, which stiffens this structure. The inner hair cell stereocilia, which probably do not touch the tectorial membrane, although they come very close to it, are likely to be stimulated by local movements of the endolymph. Displacement of the stereociliary bundle of a hair cell activates mechanoelectrical transduction channels near the tips of its stereocilia, and this allows potassium and calcium ions from the endolymph to enter the hair cell (see earlier and overview by Fettiplace and Hackney (2006)). This induces a depolarizing receptor potential

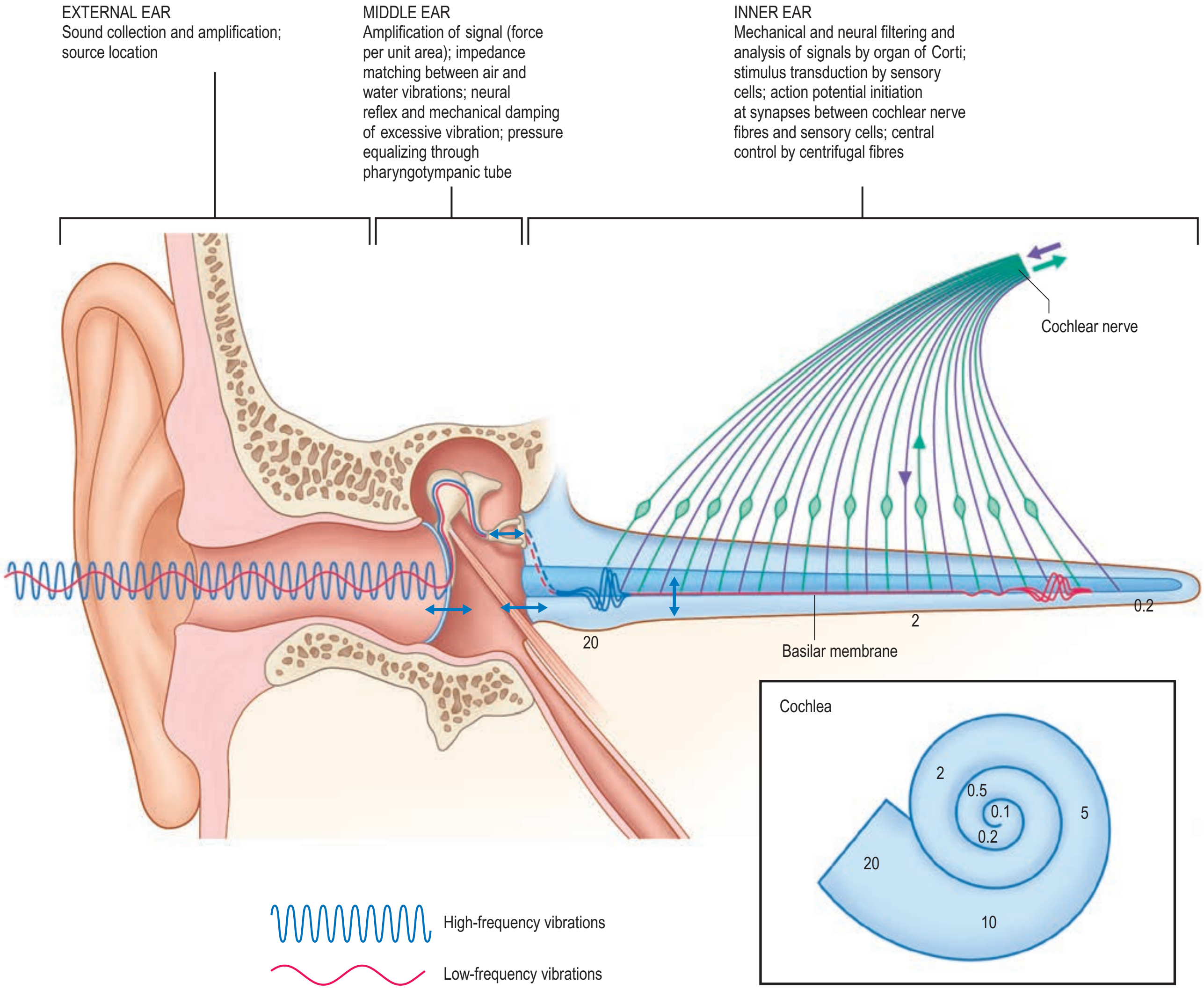
EXTERNAL EAR
Sound collection and amplification; source location
MIDDLE EAR
Amplification of signal (force per unit area); impedance matching between air and water vibrations; neural reflex and mechanical damping of excessive vibration; pressure equalizing through pharyngotympanic tube
INNER EAR
Mechanical and neural filtering and analysis of signals by organ of Corti; stimulus transduction by sensory cells; action potential initiation at synapses between cochlear nerve fibres and sensory cells; central control by centrifugal fibres
Cochlear nerve
20
2
0.2
Basilar membrane
Cochlea
2
0.5
0.1
0.2
5
20
10
High-frequency vibrations
Low-frequency vibrations

Fig. 43.18 The principal activities of the peripheral auditory apparatus. For clarity, the cochlea is depicted as though it had been uncoiled, but it is normally coiled as in the inset. Different sound frequencies differentially excite different regions of the cochlea, the specific locations being given in kHz from 0.1 to 20 kHz in humans. Note that the frequency map is logarithmic, so that each decade occupies an equivalent distance on the basilar membrane. The components are drawn roughly to scale for the human ear, in which the cochlea is 35 mm in length. The points of maximal stimulation of the basilar membrane by high-frequency and low-frequency vibrations, together with their transmission pathways through the external and middle ear, are also indicated.

and the release of neurotransmitter on to the cochlear afferents at the base of the cell. In this way, a specific group of auditory axons is activated at the position of maximal basilar membrane vibration.

The mechanical behaviour of the basilar membrane is responsible for a broad discrimination between different frequencies (passive tuning; see overview by Ashmore (2002)), but fine frequency discrimination in the cochlea appears to be related to physiological differences between the hair cells. Individual tuning of hair cells may result from differences in shape, stereociliary length, or possibly variations in the molecular composition of sensory membranes and may have a role in cochlear amplification (active tuning).

The activity of the outer hair cells appears to play an important part in regulating inner hair-cell sensitivity at specific frequencies. Outer hair cells can change length when stimulated electrically at frequencies of many thousands of cycles per second. The rapidity of these changes in length indicates a novel type of motile mechanism, which is believed to depend on conformational changes in prestin, a protein that displays piezoelectricity and is located in the plasma membrane of the cells (Fettiplace and Hackney 2006, Hudspeth 2014) (**Fig. 43.19**). When the membrane potential of the outer hair cells changes, they generate forces along their axes. When the mechanoelectrical transduction channels open, they are thought to oppose the viscous forces that tend to damp down the vibration of the cochlear partition and adjust the mechanics of the organ of Corti on a cycle-by-cycle basis. Alternatively, they may alter the mechanics of the partition more slowly under the influence of the efferent pathway. At a particular frequency, an increase in the intensity of stimulus is signalled by an increase in the rate of discharge in individual cochlear axons. At greater intensities, it is signalled by the number of activated cochlear axons (recruitment).

The respective roles of the two groups of hair cells have been much debated, particularly since differences in their innervation and physiological behaviour have become apparent. Because of their rich afferent supply, inner hair cells are believed to be the major source of auditory signals in the cochlear nerve. Some evidence for this view is based on the finding that animals treated with antibiotics that are specifically toxic to outer hair cells are still able to hear, but their sensitivity and frequency discrimination is impaired.

Some electrical responses of the cochlea can be recorded with extracellular electrodes. The most significant is the endolymphatic potential, a steady potential recordable between the cochlear duct and the scala tympani, which is caused by the different ionic compositions of their fluids. As the resting potential of hair cells is approximately 70 mV (negative inside) and the endolymphatic potential is positive in the cochlear duct, the total transmembrane potential across the apices of hair cells is 150 mV. This is a greater resting potential than is found anywhere else in the body and provides the driving force for mechanotransduction and for the cochlear amplifier.

Under stimulation by sound, a rapid oscillatory cochlear microphonic potential can be recorded. It matches the frequency of the stimulus and movements of the basilar membrane precisely and appears to depend on fluctuations in the conductance of hair cell membranes, probably of the outer hair cells. At the same time, an extracellular summating potential develops, a steady direct current shift related to the (intracellular) receptor potentials of the hair cells. Cochlear nerve fibres then begin to respond with action potentials that are also recordable from the cochlea. Intracellular recording of auditory responses from inner hair cells has confirmed that these cells resemble other receptors; their steady receptor potentials are related in size to the amplitude of the acoustic stimulus. At the same time, afferent axons are stimulated by synaptic action at the bases of the inner hair cells. They fire more rapidly as the vibration of the basilar membrane increases in amplitude, up to a threshold that depends on the sensitivity of the specific nerve fibre involved. Each inner hair cell is contacted by axons with response thresholds that range from 0 decibels sound pressure level (dBSPL), the approximate threshold of human hearing, to those that respond to intensities in excess of 100 dBSPL; the loudest sound tolerable is around 120 dBSPL. Each axon responds most sensitively to the frequency represented by its particular cochlear location, its characteristic frequency (see Fig. 43.18).

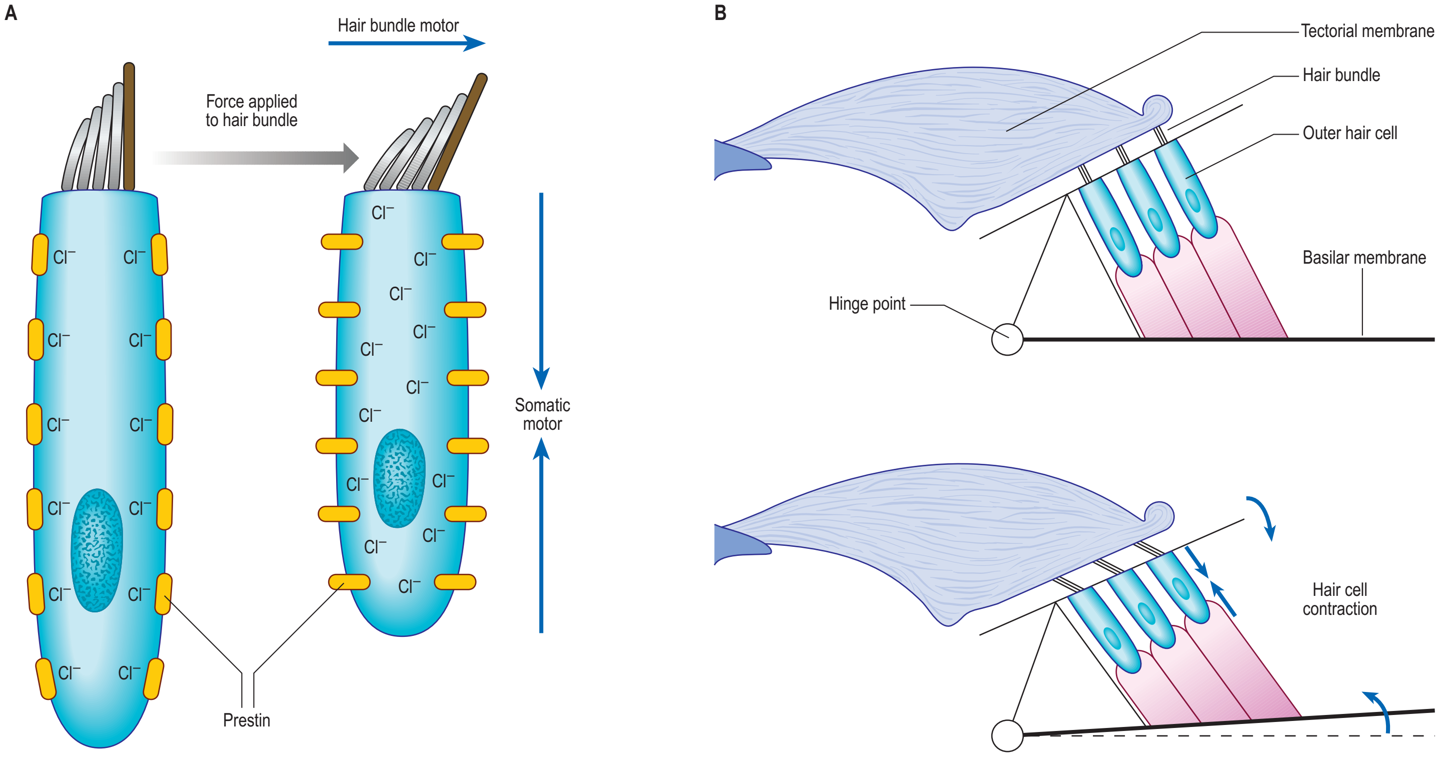

Fig. 43.19 The putative motors of outer hair cells. Outer hair cells can generate force, mechanically boosting sound-induced vibrations of the hair bundle and augmenting frequency tuning. Two mechanisms have been advanced to explain this cochlear amplifier: the somatic motor and the hair bundle motor. **A**, In the resting state, Cl^- ions are bound to prestin molecules in the lateral membrane of the hair cell. When force is applied to the hair bundle, the cell is depolarized, the Cl^- ions dissociate and the prestin changes conformation, reducing its area in the plane of the membrane and shortening the hair cell body (the somatic motor). Adaptation of mechanoelectrical transduction (MET) channels, which are activated by bending of the stereocilia at their tapered base, also causes the hair bundle to produce extra force in the direction of the stimulus (the hair bundle motor). The amplitudes of the hair bundle movements have been exaggerated to illustrate the concept. **B**, The effects of the somatic motor (blue arrows) on the organ of Corti mechanics, which leads to downward motion of the reticular lamina (the upper surface of the organ of Corti) and a negative deflection of the hair bundle. This is a negative feedback pathway, as a positive deflection of the hair bundle causes outer hair cell depolarization, cell contraction and opposing motion of the bundle (see Fettiplace and Hackney (2006)).

Central auditory pathway

The primary afferents of the auditory pathway arise from cell bodies in the spiral ganglion of the cochlea. The axons travel in the vestibulocochlear nerve, which enters the brainstem at the cerebellopontine angle. Afferent fibres bifurcate, and terminate in the dorsal and ventral cochlear nuclei (**Fig. 43.20**; Ch. 28). The dorsal cochlear nucleus projects via the dorsal acoustic stria to the contralateral inferior colliculus. The ventral cochlear nucleus projects via the trapezoid body or the intermediate acoustic stria to relay centres in either the superior olivary complex, the nuclei of the lateral lemniscus, or the inferior colliculus. The superior olivary complex is dominated by the medial superior olivary nucleus, which receives direct input from the ventral cochlear nucleus on both sides and is involved in localization of sound by measuring the time difference between afferent impulses arriving from the two ears.

The inferior colliculus consists of a central nucleus and two cortical areas. The dorsal cortex lies dorsomedially, and the external cortex lies ventromedially. Secondary and tertiary fibres ascend in the lateral lemniscus. They converge in the central nucleus, which projects to the ventral division of the medial geniculate body of the thalamus. The external cortex receives both auditory and somatosensory input. It projects to the medial division of the medial geniculate body and, together with the central nucleus, also projects to olivocochlear cells in the superior olivary complex and to cells in the cochlear nuclei. The dorsal cortex receives input from the auditory cortex and projects to the dorsal division of the medial geniculate body. Connections also run from the nucleus of the lateral lemniscus to the deep part of the superior colliculus, to coordinate auditory and visual responses.

The ascending auditory pathway crosses the midline at several points both below and at the level of the inferior colliculus. However, the input to the central nucleus of the inferior colliculus and higher centres has a clear contralateral dominance; during the initial stages of cortical auditory processing, each hemisphere responds most strongly to the contralateral ear. The medial geniculate body is connected reciprocally to the primary auditory cortex, which lies in the posterior half of the superior temporal gyrus and also dives into the lateral sulcus as the transverse temporal gyri (Heschl's gyri). Secondary areas of the auditory cortex are located in an adjacent belt region, and other regions of auditory association cortex have been described in a parabelt region beyond the secondary cortex.

The corpus callosum, particularly the posterior third of the body, contains auditory interhemispheric fibres that originate from the primary and second auditory cortices. Asymmetries of minicolumn number in primary and auditory association cortex have been correlated with axonal fibre numbers in the subregions of the corpus callosum through which they project (Chance et al 2006).

The presence of tonotopic gradients in the primary auditory cortex is well established in animals and in humans. Hemispheric differences for frequency selectivity (i.e. the ability of the cochlea to separate the acoustic frequencies along its length like an acoustic prism) and tonotopic organization have been reported, e.g. the right hemisphere appears to be most responsive to acoustic sound features such as pitch, whereas the left hemisphere seems to be more involved in processing temporal dynamics such as the phonological aspects of speech. Morphological asymmetries favouring the left hemisphere in the planum temporale and Heschl's gyri have been correlated with left hemispheric dominance for language functions but a direct link between structure and function has not been clearly established; studies often show relative rather than absolute differences in hemispheric specialization for particular attributes.

The transformation of the physical characteristics of sound into 'auditory objects' is thought to occur in the transition from primary to secondary auditory cortex. (For a critical perspective on auditory objects, see Griffiths and Warren (2004).)

Hearing loss

Sensorineural hearing loss is the most prevalent form of hearing impairment. It refers commonly to loss or damage of the sensory hair cells or their innervation but can also result from lateral wall degeneration and loss of the endolymphatic potential. The hair cells are particularly

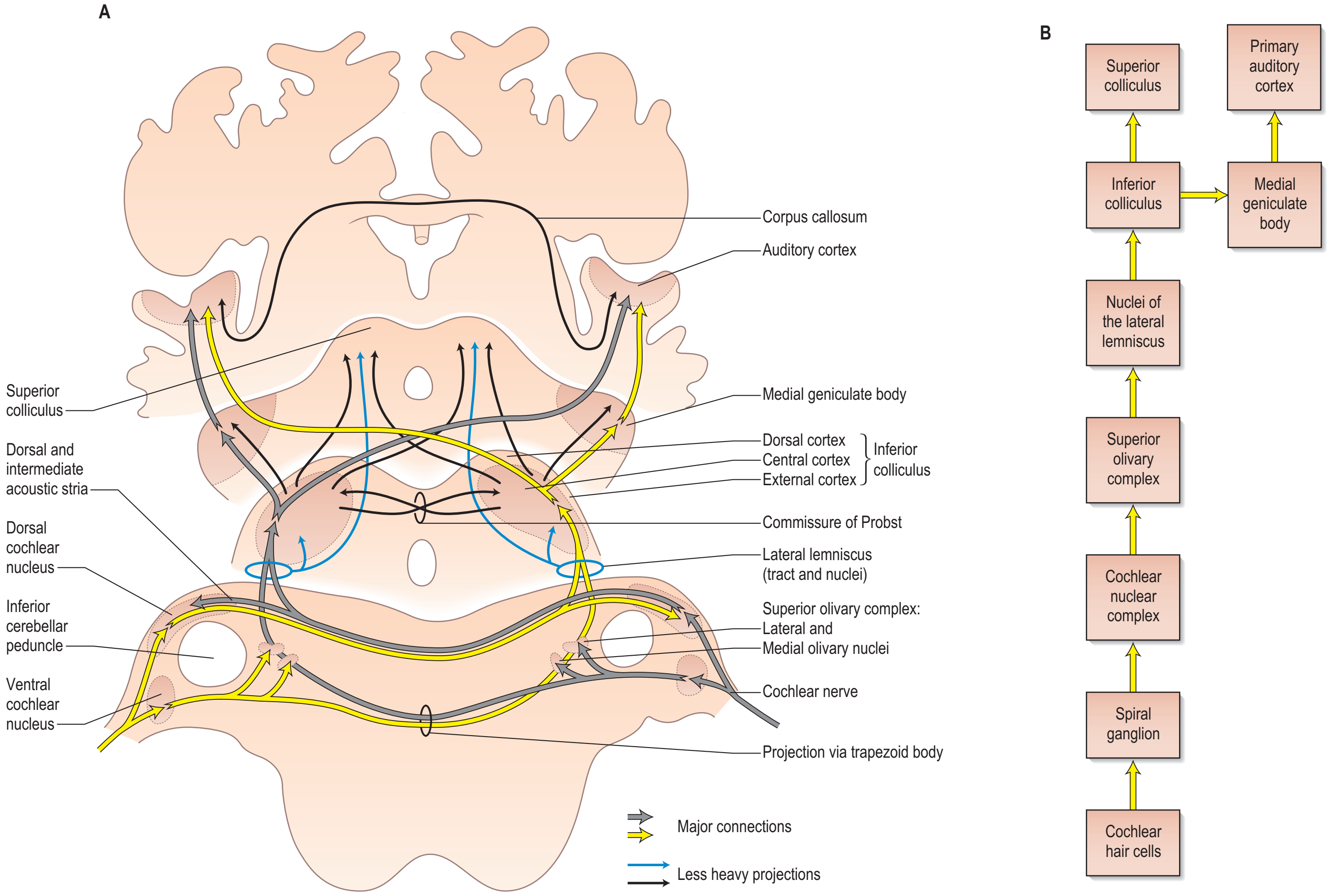
A
Corpus callosum
Auditory cortex
Superior colliculus
Medial geniculate body
Dorsal cortex
Central cortex
External cortex
Inferior colliculus
Dorsal and intermediate acoustic stria
Commissure of Probst
Dorsal cochlear nucleus
Lateral lemniscus (tract and nuclei)
Inferior cerebellar peduncle
Superior olivary complex:
Lateral and
Medial olivary nuclei
Ventral cochlear nucleus
Cochlear nerve
Projection via trapezoid body
Major connections
Less heavy projections
B
Superior colliculus
Primary auditory cortex
Inferior colliculus
Medial geniculate body
Nuclei of the lateral lemniscus
Superior olivary complex
Cochlear nuclear complex
Spiral ganglion
Cochlear hair cells

Fig. 43.20 The main features of the human ascending auditory pathway. **A**, A series of sections showing that ipsilateral and commissural connections occur at most levels in this system. The major connections are shown by the thicker arrows; thinner arrows denote less heavy projections. **B**, The main stations of the auditory pathway.

vulnerable to mechanical trauma produced by high-intensity noise and to changes in their physiological environment caused by infection or hypoxia. These can lead to rapid degenerative processes that result in hair cell loss, often by apoptosis, and produce either hearing loss or vestibular dysfunction. These changes can be induced by drugs such as the aminoglycoside antibiotics, some diuretics and certain anticancer drugs. A decrease in cochlear sensitivity, presbyacusis, almost invariably occurs with age; hair cells at the high frequency end of the cochlea tend to be lost first. At least 60% of hearing loss may have a genetic basis, a significant proportion may be non-syndromic, and most of these genes are inherited in an autosomal recessive mode (Ch. 16).

Ménière's disease is a distressing disorder of the inner ear characterized by episodes of hearing loss, tinnitus and vertigo. Histological examination of an affected ear reveals endolymphatic hydrops (swelling of the endolymphatic spaces), suggesting poor drainage of the endolymph via the endolymphatic sac.

Whilst some forms of conductive deafness are amenable to treatment, at present sensorineural hearing loss is irreversible. The main treatment options are an external hearing aid or a cochlear implant (CI). The external hearing aid is inserted into the auditory canal and provides amplified input to the inner ear, utilizing the residual hearing of the patient.

Surgical approaches to the inner ear

Available with the *Gray's Anatomy* e-book

Bonus e-book content

Fig. 43.1 F–I, 3D renderings of the entire labyrinth and of the superior branch of the vestibular nerve.

Fig. 43.7 A scanning electron micrograph of a stereociliary bundle from the utricle (guinea pig).

Fig. 43.8 Human vestibular hair cells (transmission electron micrographs).

Fig. 43.10 B, The stereociliary bundle of one outer hair cell, showing three rows of stereocilia increasing in height; deflection of the stereocilia in the direction of the tallest row results in depolarization of the hair cell. Microvilli can be seen on the surface of Deiters' cells. The inset shows a tip link connecting a short stereocilium tip to the side of the tall stereocilium behind.

Fig. 43.21 A radiographic image of a cochlear implant in situ.

Key references

Duman D, Tekin M 2013 Autosomal recessive nonsyndromic deafness genes: a review. Front Biosci 17:2213–36.

A review that summarizes genes and mutations reported in families with ARNSHL. Mutations in GJB2, *encoding connexin 26, make this gene the most common cause of hearing loss in many populations. Other relatively common deafness genes include* SLC26A4, MYO15A, OTOF, TMC1, CDH23 *and* TMPRSS3.

Fettiplace R, Hackney CM 2006 The sensory and motor roles of auditory hair cells. Nat Rev Neurosci 7:19–29.

A description of proteins involved in the sensory and motor functions of auditory hair cells, with evidence for each force generator.

Guinan J Jr 1996 Physiology of olivocochlear efferents. In: Dallos P, Popper AN, Fay RR (eds) The Cochlea. New York: Springer; pp. 435–502.

A comprehensive description of the efferent innervation of the cochlea and its function.

Wangemann P, Schacht J 1996 Homeostatic mechanisms in the cochlea. In: Dallos P, Popper AN, Fay RR (eds) The Cochlea. New York: Springer; pp. 130–5.

A review of inner ear fluids (perilymph and endolymph), how they are produced and their possible functional significance.

Hearing impairment is the most common disabling sensory defect in humans. Two causes of deafness are usually distinguished: conductive hearing loss and sensorineural hearing loss.

Conductive hearing loss may result from trauma to the external or middle ears, blockage of the external acoustic meatus, or disruption of the tympanic membrane (e.g. by intense sounds or extreme pressure changes). It may also result from acute or chronic infection associated with a perforation of the tympanic membrane, as in acute otitis media. The ossicular chain may be disrupted by trauma, avascular necrosis of the long process of the incus following a middle ear infection or cholesteatoma. The most common cause of a conductive hearing loss is a middle ear effusion (glue ear), in which fluid that has replaced the normally air-filled middle ear impedes the movements of the tympanic membrane. Other less common causes include tympanosclerosis, in which calcium plaques are formed in the tympanic membrane and middle ear mucosa that stiffen the tympanic membrane and limit the mobility of the ossicular chain. Similarly, new bone laid down around the oval window and footplate of the stapes, otosclerosis, impedes stapes mobility and imparts a conductive hearing loss.

Cochlear implants consist of an external microphone and sound processor on the side of the head behind the external ear, adjacent to a subcutaneous receiver attached to a multichannel electrode. The electrode is inserted into the inner ear (see below for surgical approaches) and is advanced as far as feasible along the cochlear spiral (**Fig. 43.21**). The sound processor transmits a digitized representation of environmental sound to the implant which converts it to electrical pulses along the electrode. The signal is spatially segregated through the different channels of the electrode and stimulates functional cochlear nerve fibres that remain within the deaf ear. Thus the different frequency components of the sound stimulus are presented along the tonotopic axis to stimulate as closely as possible the spiral ganglion neurones that in the intact ear would represent them. This generates a pattern of auditory nerve firing representing different frequency components along the auditory pathway, restoring some measure of sensitivity and frequency selectivity.

The design of cochlear and, more recently, vestibular implants, particularly their electrodes and processing algorithms, is a rapidly advancing science, but is hampered by suboptimal information about the three-dimensional (3-D) neural architecture of the labyrinth and cochlea. Improved imaging techniques that preserve some of the smaller neural structures that might otherwise be destroyed by dissection techniques are being developed to answer this deficiency. For example, osmium tetroxide (OsO_4) contrast enhanced micro-CT scanning of the inner ear in combination with post acquisition image processing using noise reduction and edge preserving filters before segmentation (see Fig. 43.1D–I) (van den Boogert et al 2018).

The inner ear may be approached surgically in a number of ways. Many drugs, e.g. gentamicin and steroids, are now injected through the intact tympanic membrane, where they diffuse through the round window membrane to access the inner ear. The promontory that overlies the basal turn of the cochlea and the oval window may be opened through a tympanotomy (per-meatal elevation of the tympanic membrane). The semicircular canals are generally accessed by a transmastoid approach. In days gone by, such an approach would be used to fenestrate the lateral canal in the management of otosclerosis. The advent of stapes prostheses and stapedectomy rendered this operation obsolete. However, the transmastoid approach is the workhorse for much middle and inner ear surgery because it gives a wide exposure of all the vital structures. For patients with profound hearing loss, enlarging the mastoid aditus inferiorly (posterior tympanotomy) to produce a triangle bounded above by the fossa incudis, superficially by the chorda tympani and deeply by the descending portion of the facial nerve, gives access to the round window so that it can be instrumented and a multichannel cochlear electrode inserted into the scala tympani of the cochlea so that it lies against the spiral lamina and can stimulate the adjacent fibres of the cochlear nerve. This is then connected to the cochlear implant device, which is housed in an extension of the mastoid cavity. Posterior canal obliteration for cupulolithiasis not responsive to Epley's manoeuvre is also undertaken through the mastoid. The endolymphatic sac may be approached by elevating the cortical bone of the anterolateral wall of the posterior cranial fossa, anterior to the sigmoid venous sinus and posterior to the posterior semicircular canal (below a line extended from the axis of the lateral semicircular canal). Decompression of the sac or a shunt procedure is favoured by some for the management of Ménière's disease. Superior canal dehiscences, as seen in Minor's syndrome, are repaired either through the mastoid or by using a middle fossa approach. In patients with intractable Ménière's disease, the whole of the labyrinth can be removed through the mastoid. Vestibular nerve section and the removal of vestibular schwannomas are generally undertaken through retrosigmoid, retrolabyrinthine, translabyrinthine or middle fossa approaches. The choice of approach is dictated or influenced by the size of the tumour, desire or need to preserve hearing, and the surgeon's choice. In recent years, the development of auditory brainstem implants has brought hope to those with profound hearing loss associated with neurofibromatosis type 2 or cochlear nerve aplasia. These devices are similar to a cochlear implant but the electrodes are placed directly into the cochlear nucleus within the brainstem through a retrosigmoid approach.

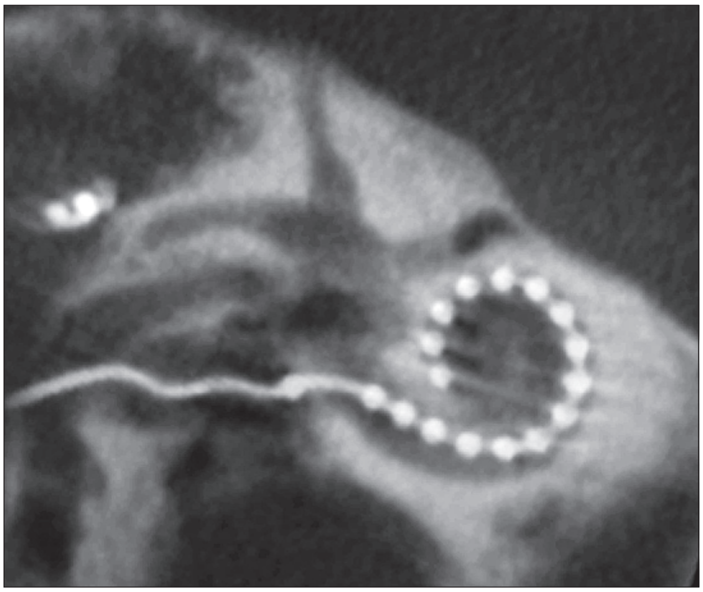

Fig. 43.21 Radiographic image of a cochlear implant (CI) *in situ*. The CI has an external microphone that detects the acoustic signal and converts it to a digital signal with both temporal and spatial components. The signal is transmitted via an external coil using radiofrequencies to an internal telemetry coil connected to a sound processor: the two coils are held in place by magnets. The processed signal is sent to an intracochlear multichannel electrode array and the electrodes in the CI stimulate the the surviving spiral ganglion neurones. The internal device includes a ground electrode that is placed beneath the temporalis muscle for current return.

References

Ashmore J 2002 The mechanics of hearing. In: Roberts D (ed) Signals and Perception: The Fundamentals of Human Sensation. Basingstoke and New York: Palgrave Macmillan; pp. 3–16.

Axelsson A 1988 Comparative anatomy of cochlear blood vessels. Am J Otolaryngol 9:278–90.

Blanks RH, Curthoys IS, Markham CH 1975 Planar relationships of the semicircular canals in man. Acta Otolaryngol 80:185–96.

Bridger MW, Farkashidy J 1980 The distribution of neuroglia and Schwann cells in the 8th nerve of man. J Laryngol Otol 94:1353–62.

Chance SA, Casanova MF, Switala AE et al 2006 Minicolumnar structure in Heschl's gyrus and planum temporale: asymmetries in relation to sex and callosal fiber number. Neuroscience 143:1041–50.

Curthoys IS, Blanks RH, Markham CH 1977 Semicircular canal radii of curvature (R) in cat, guinea pig and man. J Morphol 115:1–15.

Duman D, Tekin M 2013 Autosomal recessive nonsyndromic deafness genes: a review. Front Biosci 17:2213–36.

A review that summarizes genes and mutations reported in families with ARNSHL. Mutations in GJB2, *encoding connexin 26, make this gene the most common cause of hearing loss in many populations. Other relatively common deafness genes include* SLC26A4, MYO15A, OTOF, TMC1, CDH23 *and* TMPRSS3.

Felix H, Hoffman V, Wright A, Gleeson MJ 1987 Ultrastructural findings on human Scarpa's ganglion. Acta Otolaryngol Suppl 436:85–92.

Fettiplace R, Hackney CM 2006 The sensory and motor roles of auditory hair cells. Nat Rev Neurosci 7:19–29.

A description of proteins involved in the sensory and motor functions of auditory hair cells, with evidence for each force generator.

Furness DN 2002 The vestibular system. In: Roberts D (ed) Signals and Perception: The Fundamentals of Human Sensation. Basingstoke and New York: Palgrave Macmillan; pp. 77–90.

Furman JM, Cass SP 1999 Benign paroxysmal positional vertigo. N Engl J Med 341:1590–6.

Griffiths TD, Warren JD 2004 What is an auditory object? Nat Rev Neurosci 5:887–92.

Guinan J Jr 1996 Physiology of olivocochlear efferents. In: Dallos P, Popper AN, Fay RR (eds) The Cochlea. New York: Springer; pp. 435–502.

A comprehensive description of the efferent innervation of the cochlea and its function.

Hackney CM, Furness DN 2013 The composition and role of cross links in mechanoelectrical transduction in vertebrate sensory hair cells. J Cell Sci 126:1721–31.

Hudspeth AJ 2014 Integrating the active process of hair cells with cochlear function. Nat Rev Neurosci 15:600–14.

Jagger DJ, Nevill G, Forge A 2010 The membrane properties of cochlear root cells are consistent with roles in potassium recirculation and spatial buffering. J Assoc Res Otolaryngol 11:435–48.

Keifer J, Böhnke F, Adunka O et al 2006 Representation of acoustic signals in the human cochlea in presence of a cochlear implant electrode. Hearing Res 221:36–43.

Mei X, Schart-Morén N, Li H et al 2019 Three-dimensional imaging of the human internal acoustic canal and arachnoid cistern: a synchrotron study with clinical implications. J Anat 234:316–26.

Minowa O, Ikeda K, Sugitani Y et al 1999 Altered cochlear fibrocytes in a mouse model of DFN3 nonsyndromic deafness. Science 285:1408–11.

Nadol JB 1988 Comparative anatomy of the cochlea and auditory nerve in mammals. Hear Res 34:253–66.

Ray B, Roy TS, Wadhwa S et al 2005 Development of the human fetal cochlear nerve. Hearing Res 202:74–86.

Shepherd RK, Colreavy MP 2004 Surface microstructure of the perilymphatic space: implications for cochlear implants and cell- or drug-based therapies. Arch Otolaryngol Head Neck Surg 130:518–23.

Spoor F, Zonneveld F 1998 Comparative review of the human bony labyrinth. Am J Phys Anthropol Suppl 27:211–51.

Van den Boogert T, van Hoof, Handschuh S et al 2018 Optimization of 3D-visualization of micro-anatomical structures of the human inner ear in osmium tetroxide contrast enhanced micro-CT scans. Front Neuroanat 12:1–11.

Wangemann P, Schacht J 1996 Homeostatic mechanisms in the cochlea. In: Dallos P, Popper AN, Fay RR (eds) The Cochlea. New York: Springer; pp. 130–5.

A review of inner ear fluids (perilymph and endolymph), how they are produced and their possible functional significance.

Warr WB 1992 Organization of olivocochlear efferent systems in mammals. In: Webster DB, Popper AN, Fay RR (eds) Mammalian Auditory Pathway: Neuroanatomy. New York: Springer; pp. 410–48.

Wright CG, Roland PS 2013 Vascular trauma during cochlear implantation: a contributor to residual hearing loss? Otol Neurotol 34:402–7.

CHAPTER

44

Orbit and accessory visual apparatus

BONY ORBIT

The bony orbits are skeletal cavities located on either side of the root of the nose that serve as sockets for the eyes and associated tissues. The walls of each orbit protect the eye from injury, provide points of attachment for six extraocular muscles that allow the accurate positioning of the visual axis, and determine the spatial relationship between the two eyes, which is essential for both binocular vision and conjugate eye movements.

By convention, each cavity is considered to approximate to a quadrilateral pyramid with its base at the orbital opening, narrowing to its apex along a posteromedially directed axis. Each orbit has a roof, floor and medial and lateral walls. The medial walls lie approximately 25 mm apart in adults and are nearly parallel. The angle between the medial and lateral walls is about 45°. The compromise between protection and ensuring a good field of view dictates that each eyeball is located anteriorly within the orbit. The eyeball thus occupies only one-fifth of the volume of the orbit (**Fig. 44.1**); the remainder of the cavity is filled with extraocular muscles, vessels and nerves that are contained within and supported by orbital fat and connective tissue. In brief, the orbit transmits the optic, oculomotor, trochlear and abducens nerves, branches of the ophthalmic and maxillary divisions of the trigeminal nerve and the ophthalmic vessels. The ciliary parasympathetic ganglion is located towards the rear of the orbit, lateral to the optic nerve and medial to lateral rectus. The orbit also contains components of the lacrimal system, which is responsible for the production and drainage of tears.

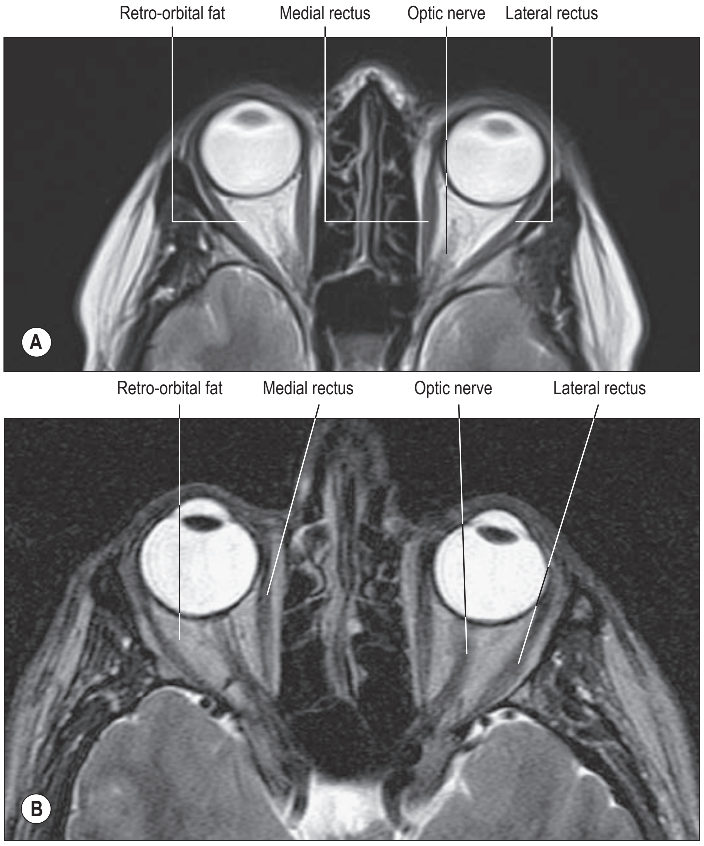

Fig. 44.1 **A**, A T2-weighted axial magnetic resonance imaging (MRI) scan through the mid-orbit. **B**, Note the optic nerve in its entirety. (Courtesy of Dr Timothy Beale FRCR, Royal National Throat Nose and Ear Hospital, London.)

There is a strong correlation between the pattern of orbital growth and eyeball growth. Orbital growth is most rapid during the first 12–24 months of life and most parameters reach 86–96% of adult values by the age of 8 years (Escaravage and Dutton 2013). Orbital volumes are larger in boys than in girls throughout childhood (Bentley et al 2002).

Roof

The roof of the orbit is formed principally by the thin orbital plate of the frontal bone (**Fig. 44.2**). It is gently concave on its orbital aspect, which separates the contents of the orbit and the brain in the anterior cranial fossa. Anteromedially, it contains the frontal sinus and displays a small trochlear fovea, sometimes surmounted by a small spine, where the cartilaginous trochlea (pulley) for superior oblique is attached. Anterolaterally, there is a shallow fossa that houses the orbital part of the lacrimal gland. The roof slopes down significantly towards the apex, joining the lesser wing of the sphenoid, which completes the roof. The optic canal lies between the roots of the lesser wing and is bounded medially by the body of the sphenoid.

Medial wall

The medial wall of the orbit is formed principally by the orbital plate (lamina papyracea) of the ethmoid bone (see Fig. 44.2). This paper-thin, rectangular plate covers the middle and posterior ethmoidal air cells, providing a route by which infection can spread into the orbit. The ethmoid articulates with the medial edge of the orbital plate of the frontal bone at a suture that is interrupted by anterior and posterior ethmoidal foramina. Posteriorly, it articulates with the body of the sphenoid, which forms the medial wall of the orbit to its apex. The lacrimal bone lies anterior to the ethmoid; it contains a fossa for the nasolacrimal sac that is limited in front by the anterior lacrimal crest on the frontal process of the maxilla and behind by the posterior lacrimal crest of the lacrimal bone (to which the lacrimal part of orbicularis oculi and lacrimal fascia are attached). A descending process of the lacrimal bone at the lower end of the posterior lacrimal crest contributes to the formation of the upper part of the nasolacrimal canal, which is completed by the maxilla (**Fig. 44.3**). During development, the medial wall of the orbit doubles in length, with disproportionate enlargement of its anterior half. Growth is rapid during the first 6 years of life and gradual between 7 years and adulthood (Isaacson and Monge 2003).

Floor

The floor of the orbit is mostly formed by the orbital plate of the maxilla, which articulates with the zygomatic bone anterolaterally and the small triangular orbital process of the palatine bone posteromedially (see Fig. 44.3). The floor is thin and forms most of the roof of the maxillary sinus. Not quite horizontal, it ascends a little laterally. Anteriorly, it curves into the lateral wall, and posteriorly, it is separated from the lateral wall by the inferior orbital fissure, which connects the orbit posteriorly to the pterygopalatine fossa, and more anteriorly to the infratemporal fossa. The medial lip is notched by the infraorbital groove. The latter passes forwards and sinks into the floor to become the infraorbital canal, which opens on the face at the infraorbital foramen; the infraorbital groove, canal and foramen contain the infraorbital nerve and vessels. Proportionally more pure orbital fractures involve the floor, particularly in the region of the infraorbital groove (Burm et al 1999). The classic ‘blowout fracture’ leaves the orbital rim intact and typically entraps soft tissue structures, leading to diplopia, impaired ocular motility and enophthalmos; infraorbital nerve involvement leads to ipsilateral sensory disturbance of the skin of the midface.

Lateral wall

The lateral wall of the orbit is formed by the orbital surface of the greater wing of the sphenoid posteriorly and the frontal process of the zygomatic bone anteriorly; the bones meet at the sphenozygomatic suture. The

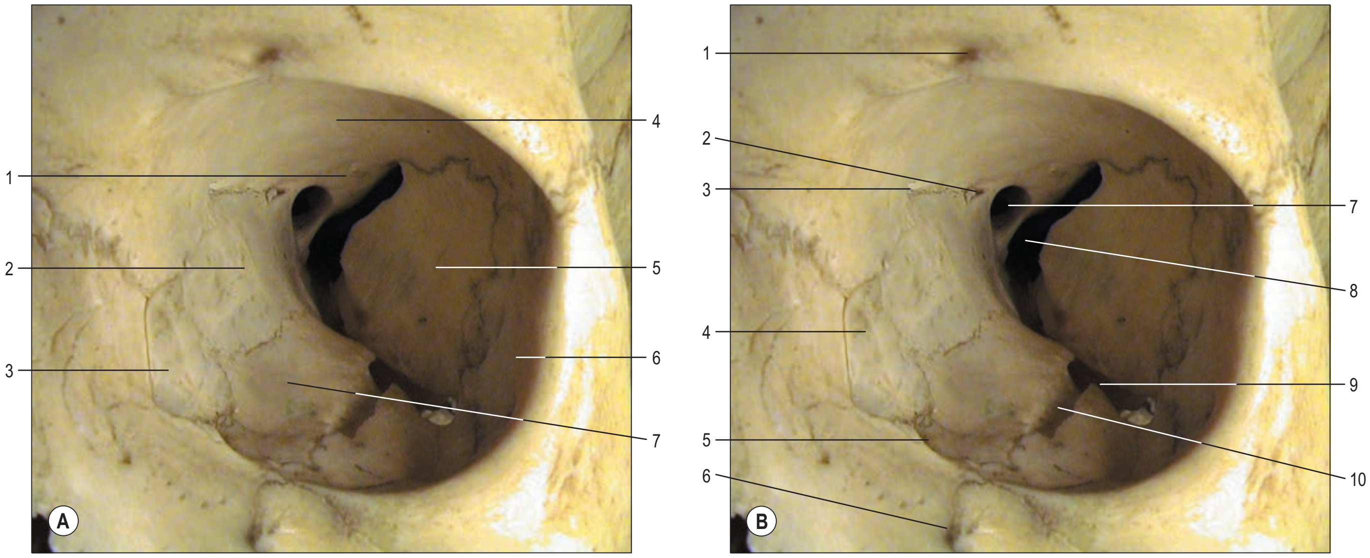
1
2
3
4
5
6
7
A
1
2
3
4
5
6
7
8
9
10
B

Fig. 44.2 An anterior view of the left orbit indicating the bones forming the walls (**A**) and the principal apertures (**B**). **A**, Key: 1, lesser wing of sphenoid; 2, orbital plate of ethmoid; 3, lacrimal bone; 4, orbital plate of frontal bone; 5, greater wing of sphenoid; 6, zygomatic; 7, orbital plate of maxilla. **B**, Key: 1, supraorbital foramen; 2, posterior ethmoidal foramen; 3, anterior ethmoidal foramen; 4, lacrimal fossa; 5, (canal for) nasolacrimal duct; 6, infraorbital foramen; 7, optic canal; 8, superior orbital fissure; 9, inferior orbital fissure; 10, infraorbital groove.

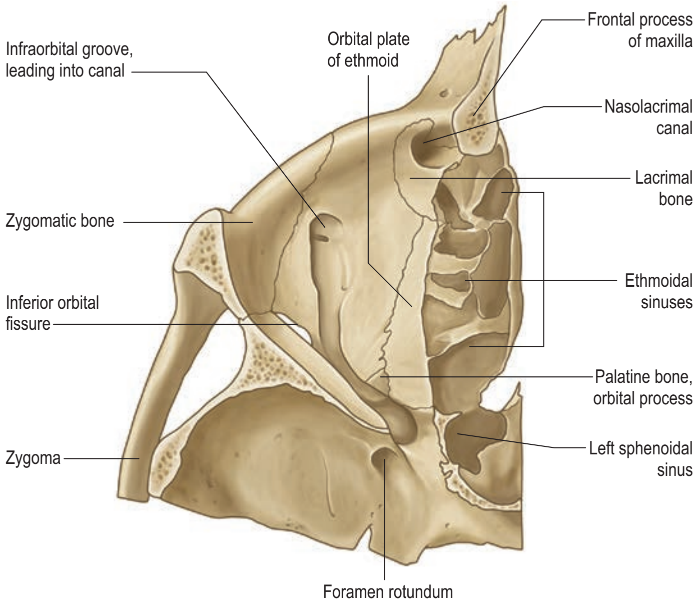
Infraorbital groove, leading into canal
Orbital plate of ethmoid
Frontal process of maxilla
Nasolacrimal canal
Lacrimal bone
Zygomatic bone
Ethmoidal sinuses
Inferior orbital fissure
Palatine bone, orbital process
Left sphenoidal sinus
Zygoma
Foramen rotundum

Fig. 44.3 A horizontal section through the floor of the left orbit and the adjacent ethmoidal and sphenoidal sinuses, viewed from above.

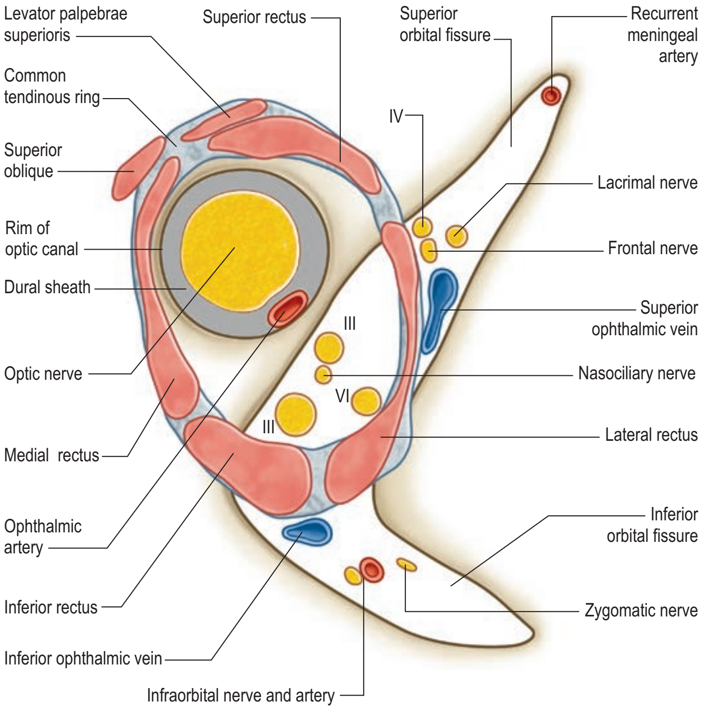
Levator palpebrae superioris
Superior rectus
Superior orbital fissure
Recurrent meningeal artery
Common tendinous ring
IV
Superior oblique
Lacrimal nerve
Rim of optic canal
Frontal nerve
Dural sheath
Superior ophthalmic vein
III
Optic nerve
Nasociliary nerve
VI
III
Lateral rectus
Medial rectus
Ophthalmic artery
Inferior orbital fissure
Inferior rectus
Zygomatic nerve
Inferior ophthalmic vein
Infraorbital nerve and artery

Fig. 44.4 The common tendinous ring: muscle origins have been superimposed. The relative positions of the nerves and vessels that enter the orbital cavity by passing through the superior orbital fissure or optic canal are shown. Note that the attachments of levator palpebrae superioris and superior oblique lie external to the common tendinous ring but are attached to it. The ophthalmic veins frequently pass through the ring. The recurrent meningeal artery (a branch of the ophthalmic artery) is often conducted from the orbit to the cranial cavity through its own foramen. Abbreviations: III, oculomotor nerve; IV, trochlear nerve; VI, abducens nerve.

zygomatic surface contains the openings of minute canals for the zygomaticofacial and zygomaticotemporal nerves, the former near the junction of the floor and lateral wall, and the latter at a slightly higher level, sometimes near the suture. The orbital tubercle, to which the lateral palpebral ligament, the check ligament of lateral rectus and the aponeurosis of levator palpebrae are all attached, lies just inside the midpoint of the lateral orbital margin. The lateral wall is the thickest wall of the orbit, especially posteriorly, where it separates the orbit from the middle cranial fossa. Anteriorly, the lateral wall separates the orbit and the infratemporal fossa. The lateral wall and roof are continuous anteriorly but are separated posteriorly by the superior orbital fissure, which lies between the greater wing (below) and lesser wing (above) of the sphenoid, and communicates with the middle cranial fossa. The fissure tapers laterally but widens at its medial end, its long axis descending posteromedially. Where the fissure begins to widen, its inferolateral edge shows a projection, often a spine, for the lateral attachment of the common tendinous ring (see Fig. 44.4). An inferior orbital fissure, which runs from the superolateral end of the superior orbital fissure towards the orbital floor, is sometimes associated with an anastomosis between the middle meningeal and infraorbital arteries.

Orbital fissures and foramina

Optic canal

The lesser wing of the sphenoid is connected to the body of the sphenoid by a thin, flat anterior root and a thick, triangular posterior root. The optic canal lies between these (see Fig. 44.2) and connects the orbit to the middle cranial fossa, transmitting the optic nerve and its meningeal sheaths, and the ophthalmic artery. The common tendinous ring, which gives origin to the four recti, is attached to the bone near the superior, medial and lower margins of the orbital opening of the canal (see Fig. 44.4). The growth of the optic canal continues from the fetal period into adulthood with an increase in both the length and width of the canal (Prado et al 2007).

Superior orbital fissure

The superior orbital fissure is the gap between the greater and lesser wings of the sphenoid, bounded medially by the body of the sphenoid, and closed at its anterior extremity by the frontal bone (see Fig. 44.2). It connects the cranial cavity with the orbit and transmits the oculomotor, trochlear and abducens nerves, branches of the ophthalmic nerve and the ophthalmic veins (see Fig. 44.4).

Inferior orbital fissure

The inferior orbital fissure is bounded above by the greater wing of the sphenoid, below by the maxilla and the orbital process of the palatine bone, and laterally by the zygomatic bone (see Fig. 44.2). The maxilla and sphenoid often meet at the anterior end of the fissure, excluding the zygomatic bone. The inferior orbital fissure connects the orbit with the pterygopalatine and infratemporal fossae and transmits the infraorbital and zygomatic branches of the maxillary nerve and accompanying vessels (see Fig. 44.4), orbital rami from the pterygopalatine ganglion and a connection between the inferior ophthalmic vein and pterygoid venous plexus. A small maxillary depression may mark the attachment of inferior oblique anteromedially, lateral to the lacrimal hamulus.

Ethmoidal foramina

The anterior and posterior ethmoidal foramina usually lie in the fronto-ethmoidal suture (see Fig. 44.2). The posterior foramen may be absent, and occasionally there is a middle ethmoidal foramen. The foramina open into canals that transmit their vessels and nerves into the ethmoidal sinuses, anterior cranial fossa and nasal cavity.

Orbitomeningeal (cranio-orbital) foramina

Available with the *Gray's Anatomy* e-book

Common tendinous ring

The common tendinous ring is a fibrous anulus that surrounds the optic canal and part of the superior orbital fissure at the apex of the orbit and gives origin to the four recti (**Fig. 44.4**). The optic nerve and ophthalmic artery enter the orbit via the optic canal, and so lie within the common tendinous ring. The superior and inferior divisions of the oculomotor nerve, the nasociliary branch of the ophthalmic nerve, and the abducens nerve also enter the orbit within the common tendinous ring, but they do so via the superior orbital fissure (see Fig. 44.15). The trochlear nerve and the frontal and lacrimal branches of the ophthalmic nerve all enter the orbit through the superior orbital fissure but lie outside the common tendinous ring. Structures that enter the orbit through the inferior orbital fissure lie outside the common tendinous ring. The close anatomical relationship of the optic nerve and other cranial nerves at the orbital apex means that lesions in this region may lead to a combination of visual loss from optic neuropathy and ophthalmoplegia from multiple cranial nerve involvement (Yeh and Foroozan 2004).

ORBITAL CONNECTIVE TISSUE AND FAT

The orbit contains a complex arrangement of connective tissue that forms a supporting framework for the eyeball and also influences ocular rotations and compartmentalizes orbital fat (**Fig. 44.5**). Certain regions have anatomical and clinical significance, including the orbital septum, fascial sheath of the eye, 'check' ligaments, suspensory ligament and periosteum. The notion that orbital connective tissues function as extraocular muscle pulleys and influence ocular motility has gained widespread acceptance (Demer 2002, Miller 2007, Guo et al 2016).

Orbital septum

The orbital septum is a weak membranous sheet, attached to the orbital rim where it becomes continuous with the periosteum (see Fig. 44.5). It extends into each eyelid and blends with the tarsal plates and, in the upper eyelid, with the superficial lamella of levator palpebrae superioris. The orbital septum is thickest laterally, where it lies in front of the lateral palpebral ligament. It passes behind the medial palpebral ligament and nasolacrimal sac, but in front of the pulley of superior oblique. The septum is pierced above by levator palpebrae superioris and below by a fibrous extension from the sheaths of inferior rectus and inferior oblique. The lacrimal, supratrochlear, infratrochlear and supraorbital nerves and vessels pass through the septum from the orbit *en route* to the face and scalp. Clinically, the septum is an important anatomical reference that differentiates pre- and post-septal (orbital) cellulitis.

Fascial sheath of the eyeball

A thin fascial sheath, the fascia bulbi (Tenon's capsule), envelops the eyeball from the optic nerve to the corneoscleral junction, separating it from the orbital fat and forming a socket for the eyeball (see Fig. 44.5;**Fig. 44.6**). The ocular aspect of the sheath is loosely attached to the sclera by delicate bands of episcleral connective tissue. Posteriorly, it is traversed by ciliary vessels and nerves. It fuses with the sclera and with the sheath of the optic nerve where the latter enters the eyeball; attachment to the sclera is strongest in this position and again anteriorly, just behind the corneoscleral junction at the limbus. Injection of local anaesthetics via a cannula into the space between the fascia bulbi and the sclera (sub-Tenon's anaesthesia) has become a popular technique for many ophthalmic surgical procedures (Davison et al 2007).

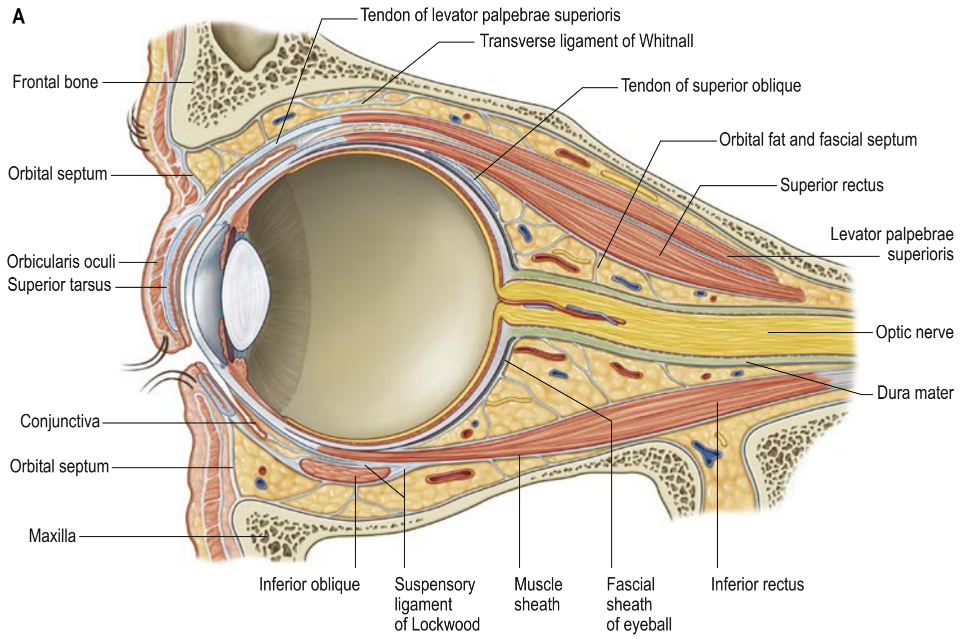
A
Tendon of levator palpebrae superioris
Transverse ligament of Whitnall
Frontal bone
Tendon of superior oblique
Orbital fat and fascial septum
Superior rectus
Orbital septum
Levator palpebrae superioris
Orbicularis oculi
Superior tarsus
Optic nerve
Dura mater
Conjunctiva
Orbital septum
Maxilla
Inferior oblique
Suspensory ligament of Lockwood
Muscle sheath
Fascial sheath of eyeball
Inferior rectus

Fig. 44.5 A, The contents of the orbit, sagittal section. (B, *continued online*)

The orbit may also be connected with the cranial cavity via inconstant canals, including an A-type orbitomeningeal foramen with the anterior cranial fossa, or a metopic canal, Warwick's foramen, accessory opening of the foramen rotundum or an M-type orbitomeningeal foramen with the middle cranial fossa (Regoli and Bertelli 2017).

One or more orbitomeningeal (cranio-orbital) foramina are present in at least one orbital cavity in approximately 60% of individuals (Macchi et al 2016). These foramina usually lie close to the superior orbital fissure, either in the frontal bone, or the greater wing of the sphenoid, or along the frontosphenoidal suture. They typically transmit the meningolacrimal artery (an orbital branch of the middle meningeal artery that supplies the lacrimal gland), but may also also transmit the anastomosis between the recurrent branch of the lacrimal artery and the middle meningeal artery. Although usually small in calibre, approximately 5% of orbits have an orbitomeningeal foramen large enough to transmit important vessels that could be a source of severe bleeding during deep orbital surgery.

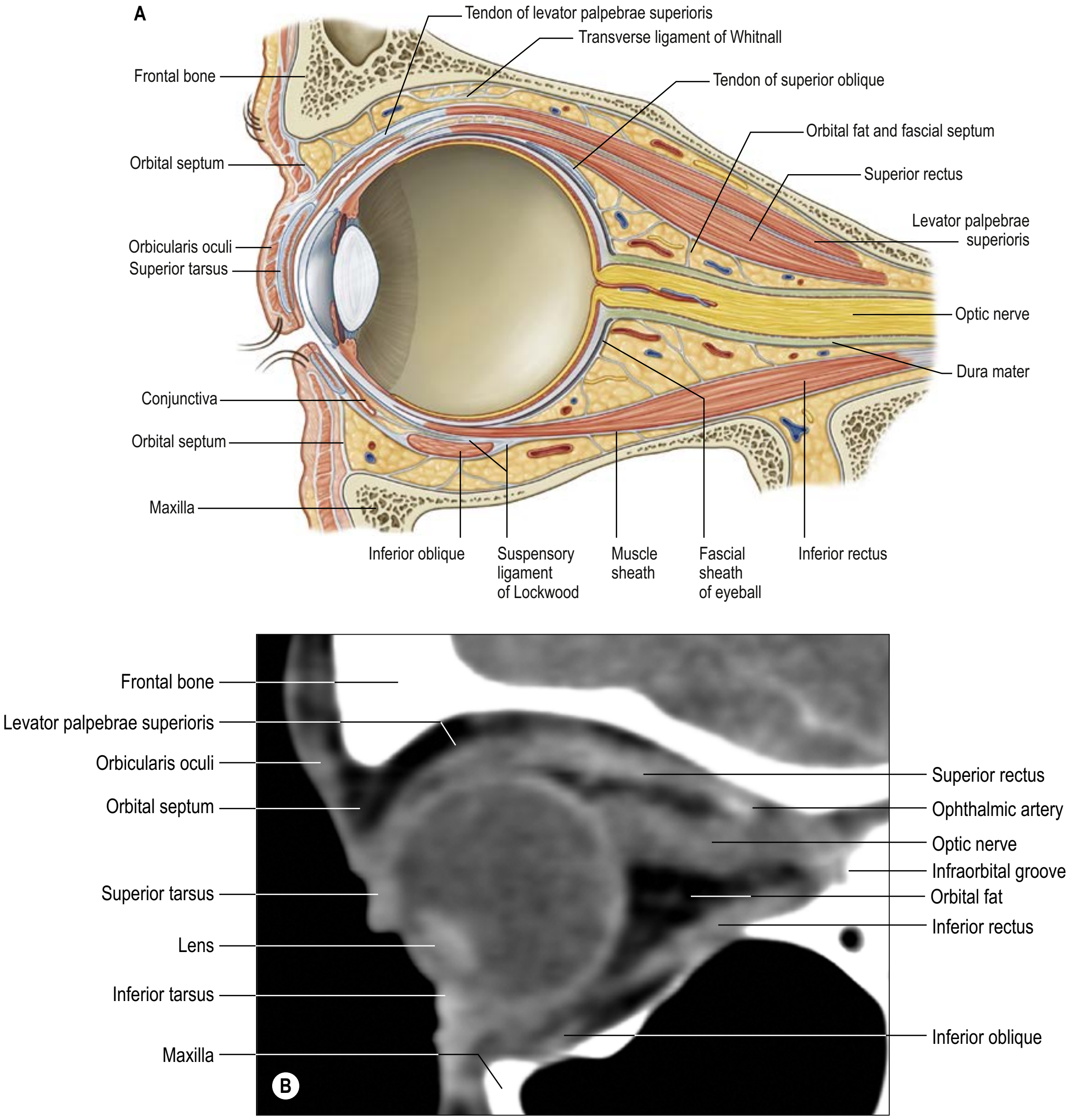
A
Tendon of levator palpebrae superioris
Transverse ligament of Whitnall
Frontal bone
Tendon of superior oblique
Orbital fat and fascial septum
Orbital septum
Superior rectus
Levator palpebrae superioris
Orbicularis oculi
Superior tarsus
Optic nerve
Dura mater
Conjunctiva
Orbital septum
Maxilla
Inferior oblique
Suspensory ligament of Lockwood
Muscle sheath
Fascial sheath of eyeball
Inferior rectus
Frontal bone
Levator palpebrae superioris
Orbicularis oculi
Orbital septum
Superior tarsus
Lens
Inferior tarsus
Maxilla
B
Superior rectus
Ophthalmic artery
Optic nerve
Infraorbital groove
Orbital fat
Inferior rectus
Inferior oblique

Fig. 44.5 **A**, The contents of the orbit, sagittal section. **B**, A sagittal oblique CT scan with contrast medium through the orbit; the subject was looking towards their feet.

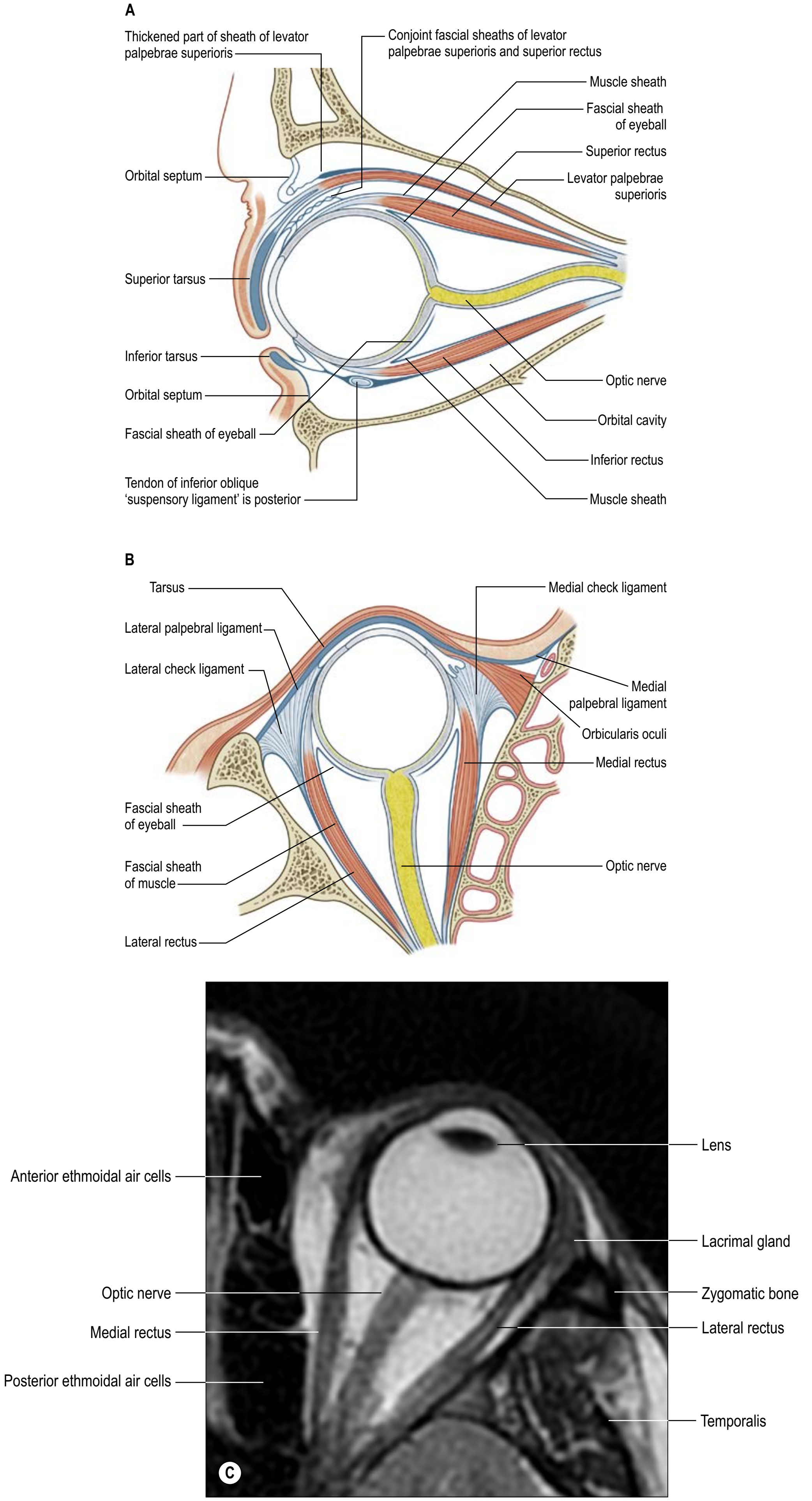
A
Thickened part of sheath of levator palpebrae superioris
Conjoint fascial sheaths of levator palpebrae superioris and superior rectus
Muscle sheath
Fascial sheath of eyeball
Superior rectus
Levator palpebrae superioris
Orbital septum
Superior tarsus
Inferior tarsus
Orbital septum
Fascial sheath of eyeball
Tendon of inferior oblique 'suspensory ligament' is posterior
Optic nerve
Orbital cavity
Inferior rectus
Muscle sheath
B
Tarsus
Lateral palpebral ligament
Lateral check ligament
Medial check ligament
Medial palpebral ligament
Orbicularis oculi
Medial rectus
Fascial sheath of eyeball
Fascial sheath of muscle
Lateral rectus
Optic nerve
Anterior ethmoidal air cells
Optic nerve
Medial rectus
Posterior ethmoidal air cells
Lens
Lacrimal gland
Zygomatic bone
Lateral rectus
Temporalis
C

Fig. 44.6 **A**, The orbital fascia, sagittal section. **B**, The orbital fascia, horizontal section. **C**, An axial T2-weighted MRI scan through the left orbit.

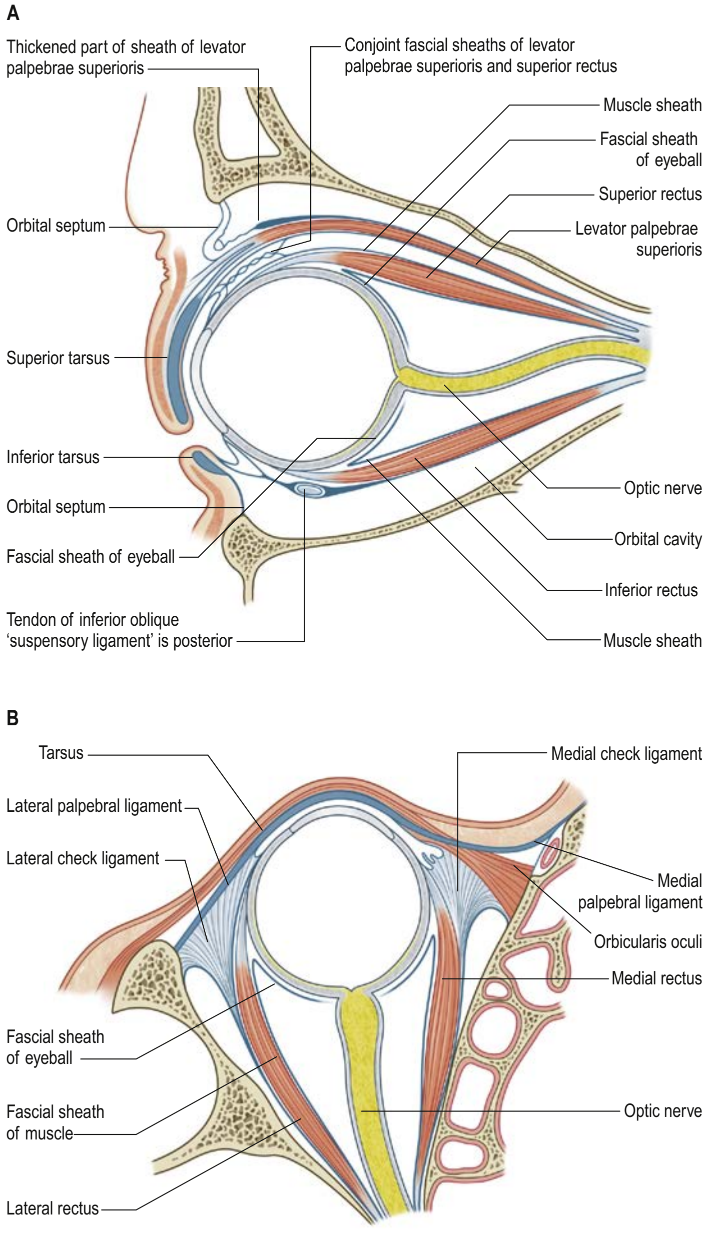
A
Thickened part of sheath of levator palpebrae superioris
Conjoint fascial sheaths of levator palpebrae superioris and superior rectus
Muscle sheath
Fascial sheath of eyeball
Superior rectus
Levator palpebrae superioris
Orbital septum
Superior tarsus
Inferior tarsus
Orbital septum
Fascial sheath of eyeball
Tendon of inferior oblique 'suspensory ligament' is posterior
Optic nerve
Orbital cavity
Inferior rectus
Muscle sheath
B
Tarsus
Lateral palpebral ligament
Lateral check ligament
Fascial sheath of eyeball
Fascial sheath of muscle
Lateral rectus
Medial check ligament
Medial palpebral ligament
Orbicularis oculi
Medial rectus
Optic nerve

Fig. 44.6 **A**, The orbital fascia, sagittal section. **B**, The orbital fascia, horizontal section. (C, *continued online*)

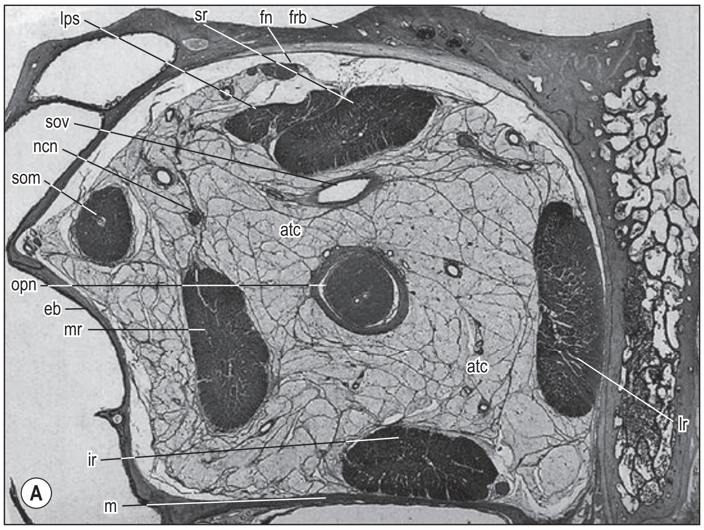
lps
sr
fn
frb
sov
ncn
som
atc
opn
eb
mr
atc
lr
ir
m
A

Fig. 44.7 **A**, A coronal section through the left orbit (viewed from in front), cut through a plane passing 5 mm behind the posterior pole of the globe. Abbreviations: atc, adipose tissue compartments; eb, ethmoid bone; fn, frontal nerve; frb, frontal bone; ir, inferior rectus; lps, levator palpebrae superioris; lr, lateral rectus; m, maxilla (bone); mr, medial rectus; ncn, nasociliary nerve; opn, optic nerve; som, superior oblique; sov, superior ophthalmic vein; sr, superior rectus. (With permission from Koornneef L 1977 The architecture of the musculo-fibrous apparatus in the human orbit. Acta Morphol Neerl Scand 15:35–64.) (B, *continued online*)

The fascia bulbi is perforated by the tendons of the extraocular muscles and is reflected on to each as a tubular sheath, the muscular fascia. The sheath of superior oblique reaches the fibrous pulley (trochlea) associated with the muscle. The sheaths of the four recti are very thick anteriorly but are reduced posteriorly to a delicate perimysium. Just before they blend with the fascia bulbi, the thick sheaths of adjacent recti become confluent and form a fascial ring.

Expansions from the muscular fascia are important for the attachments they make. Those from the medial and lateral recti are triangular and strong, and are attached to the lacrimal and zygomatic bones, respectively; since they may limit the actions of the two recti, they are termed the medial and lateral check ligaments (see Fig. 44.6). Other extraocular muscles have less substantial check ligaments, and the capacity of any of them actually to limit movement has been questioned.

The sheath of inferior rectus is thickened on its underside and blends with the sheath of inferior oblique. These two, in turn, are continuous with the fascial ring noted earlier and therefore with the sheaths of the medial and lateral recti. Since the latter are attached to the orbital walls by check ligaments, a continuous fascial band, the suspensory ligament of the eye, is slung like a hammock below the eye, providing sufficient support such that, even when the maxilla (forming the floor of the orbit) is removed, the eye will retain its position.

The thickened fused sheath of inferior rectus and inferior oblique also has an anterior expansion into the lower eyelid, where, augmented by some fibres of orbicularis oculi, it attaches to the inferior tarsus as the inferior tarsal muscle; contraction of inferior rectus in downward gaze therefore also draws the lid downward. The sheath of levator palpebrae superioris is also thickened anteriorly, and just behind the aponeurosis it fuses inferiorly with the sheath of superior rectus. It extends forwards between the two muscles and attaches to the upper fornix of the conjunctiva.

Other extensions of the fascia bulbi pass medially and laterally, and attach to the orbital walls, forming the transverse ligament of the eye. This structure is of uncertain significance, but presumably plays a part in drawing the fornix upwards in gaze elevation and may act as a fulcrum for levator movements. Other numerous finer fasciae form radial septa that extend from the fascia bulbi and the muscle sheaths to the periosteum of the orbit, and so provide compartments for orbital fat (Koornneef 1977). They also prevent the gross displacement of orbital fat, which could interfere with the accurate positioning of the two eyes that is essential for binocular vision.

The periosteum of the orbit is only loosely attached to bone. Behind, it is united with the dura mater surrounding the optic nerve and, in front, it is continuous with the periosteum of the orbital margin, where it gives off a stratum that contributes to the orbital septum. It also attaches to the trochlea and, as the lacrimal fascia, forms the roof and lateral wall of the fossa for the nasolacrimal sac.

Orbital connective tissue pulleys

There is mounting evidence that challenges the traditional view that the recti are attached only at their origin and scleral insertion. The concept that orbital connective tissue sheaths elastically coupled to the orbital walls function as pulleys was initially proposed as an explanation for the observed orbital stability of rectus muscle paths (Miller 1989). Each pulley consists of an encircling sleeve of collagen located within the fascia bulbi, near the equator of the globe. Elastic fibres and bundles of smooth muscle confer the required internal rigidity to the structure (Demer 2002). Although the original model described a passive pulley system, the current view is that fibres from the orbital surface of the muscle insert into the pulley sleeve to allow small longitudinal movements. This 'active pulley hypothesis' provides a better explanation for normal ocular kinematics (Miller 2007, Guo et al 2016).

Orbital fat

The spaces between the main structures of the orbit are occupied by fat, particularly in the region between the optic nerve and the surrounding cone of muscles (see Fig. 44.5; **Fig. 44.7**). Fat also lies between the muscles and periosteum, and is limited anteriorly by the orbital septum. Collectively, the fat helps to stabilize the position of the eyeball and also forms a socket within which the eye can rotate. Conditions resulting in an increased overall volume of orbital fat with associated swelling of

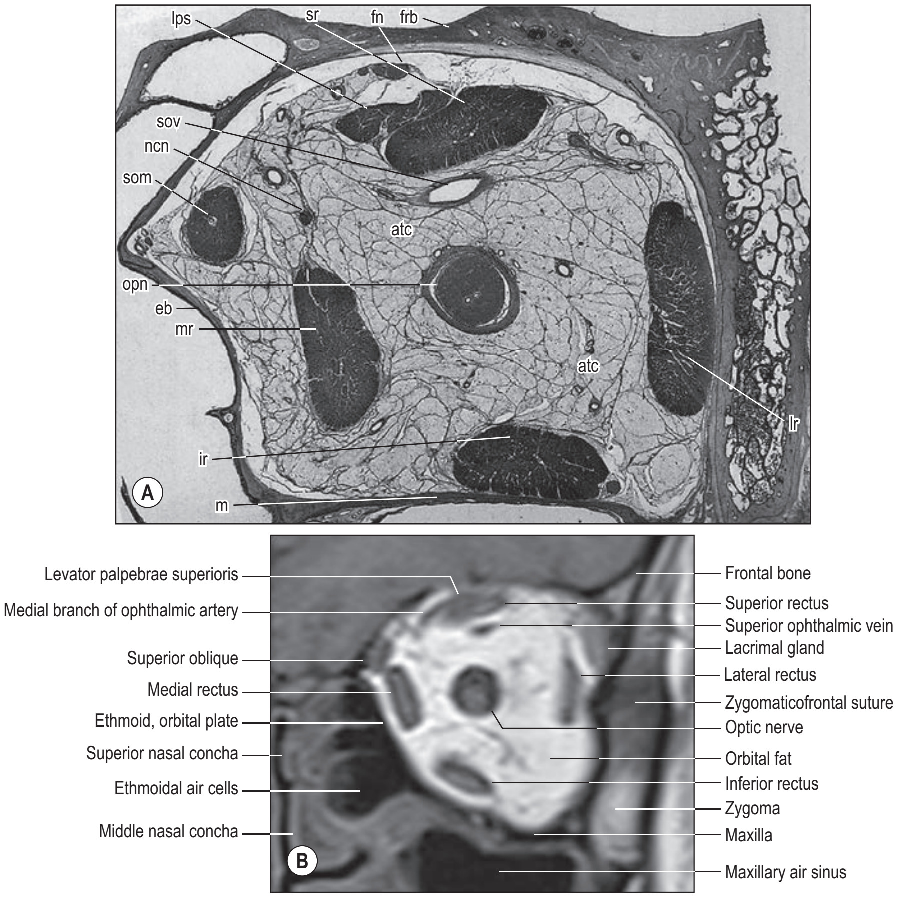
lps
sr
fn
frb
sov
ncn
som
atc
opn
eb
mr
atc
lr
ir
A
m
Levator palpebrae superioris
Medial branch of ophthalmic artery
Superior oblique
Medial rectus
Ethmoid, orbital plate
Superior nasal concha
Ethmoidal air cells
Middle nasal concha
B
Frontal bone
Superior rectus
Superior ophthalmic vein
Lacrimal gland
Lateral rectus
Zygomaticofrontal suture
Optic nerve
Orbital fat
Inferior rectus
Zygoma
Maxilla
Maxillary air sinus

Fig. 44.7 **A**, A coronal section through the left orbit (viewed from in front), cut through a plane passing 5 mm behind the posterior pole of the globe. Abbreviations: atc, adipose tissue compartments; eb, ethmoid bone; fn, frontal nerve; frb, frontal bone; ir, inferior rectus; lps, levator palpebrae superioris; lr, lateral rectus; m, maxilla (bone); mr, medial rectuB260.787 s; ncn, nasociliary nerve; opn, optic nerve; som, superior oblique; sov, superior ophthalmic vein; sr, superior rectus. **B**, Coronal T1-weighted MRI scan through the left orbit, cut through a plane 5 mm behind the posterior pole of the globe. (A, With permission from Koornneef L 1977 The architecture of the musculo-fibrous apparatus in the human orbit. Acta Morphol Neerl Scand 15:35–64.)

the extraocular muscles, e.g. hyperthyroidism (Graves' disease), may lead to forward protrusion of the eyeball (exophthalmos).

EXTRAOCULAR MUSCLES

Extraocular muscles are specialized skeletal muscles with several unique morphological, cellular and molecular properties (Spencer and Porter 2006). There are seven extraocular (extrinsic) muscles associated with the eye. Levator palpebrae superioris is an elevator of the upper eyelid, and the other six, i.e. four recti (superior, inferior, medial and lateral) and two obliques (superior and inferior), are capable of moving the eye in almost any direction. Complete congenital absence of the extraocular muscles, thought to represent a severe form of congenital fibrosis syndrome, has been described (Brady et al 1992). Rarely, humans have deep orbital bands consistent with supernumerary extraocular muscles (Khitri and Demer 2010).

Levator palpebrae superioris

Levator palpebrae superioris is a thin, triangular muscle that arises from the inferior aspect of the lesser wing of the sphenoid, above and in front of the optic canal, and separated from it by the attachment of superior rectus (see Fig. 44.4). It has a short narrow tendon at its posterior attachment and broadens gradually, then more sharply as it passes anteriorly above the eyeball. The muscle ends in front in a wide aponeurosis. Some of its tendinous fibres pass straight into the upper eyelid to attach to the anterior surface of the tarsus, while the rest radiate and pierce orbicularis oculi to pass to the skin of the upper eyelid. A thin lamina of smooth muscle, the superior tarsal muscle, passes from the underside of levator palpebrae superioris to the upper margin of the superior tarsus (see Fig. 44.20).

The connective tissue sheaths of the adjoining surfaces of levator palpebrae superioris and superior rectus are fused (see Fig. 44.5). Where the two muscles separate to reach their anterior attachments, the fascia between them forms a thick mass to which the superior conjunctival fornix is attached; this is usually described as an additional attachment of levator palpebrae superioris. Traced laterally, the aponeurosis of the levator passes between the orbital and palpebral parts of the lacrimal gland to attach to the orbital tubercle of the zygomatic bone. Medially, it loses its tendinous nature as it passes closely over the reflected tendon of superior oblique, and continues on to the medial palpebral ligament as loose strands of connective tissue.

Vascular supply Levator palpebrae superioris receives its arterial supply both directly from the ophthalmic artery and indirectly from its supraorbital branch.

Innervation Levator palpebrae superioris is innervated by a branch of the superior division of the oculomotor nerve that enters the inferior surface of the muscle. Sympathetic fibres to the smooth muscle component of levator palpebrae superioris (superior tarsal muscle) are derived from the plexus surrounding the internal carotid artery; these nerve fibres may join the oculomotor nerve in the cavernous sinus and pass forwards in its superior branch.

Actions Levator palpebrae superioris elevates the upper eyelid. During this process, the lateral and medial parts of its aponeurosis are stretched and thus limit its action; the elevation is also checked by the orbital septum. Elevation of the eyelid is opposed by the palpebral part of orbicularis oculi. Levator palpebrae superioris is linked to superior rectus by a check ligament, and so the upper eyelid elevates when the gaze of the eye is directed upwards.

The position of the eyelids depends on reciprocal tone in orbicularis oculi and levator palpebrae superioris, and on the degree of ocular protrusion. In the opened position, the upper eyelid covers the upper part of the cornea, while the lower lid lies just below its lower margin. The eyes are closed by movements of both lids, produced by the contraction of the palpebral part of orbicularis oculi and relaxation of levator palpebrae superioris. In looking upwards, the levator contracts and the upper lid follows the ocular movement. At the same time, the eyebrows are usually raised by the frontal parts of occipitofrontalis to diminish their overhang. The lower lid lags behind ocular movement, so that more sclera is exposed below the cornea and the lid is bulged a little by the lower part of the elevated eye. When the eye is depressed, both lids move; the upper retains its normal relation to the eyeball and still covers about a quarter of the cornea, whereas the lower lid is depressed because the extension of the thickened fascia of inferior rectus and inferior oblique pull on its tarsus as the former contracts.

The palpebral apertures are widened in states of fear or excitement by contraction of the superior and inferior tarsal muscles as a result of increased sympathetic activity. Lesions of the sympathetic supply result in drooping of the upper eyelid (ptosis), as seen in Horner's syndrome.

The recti

The four recti are approximately strap-shaped; each has a thickened middle part that thins gradually to a tendon (**Figs 44.8–44.9**). They are attached posteriorly to a common tendinous ring that encircles the superior, medial and inferior margins of the optic canal, continues laterally across the inferior and medial parts of the superior orbital fissure, and is attached to a tubercle or spine on the margin of the greater wing of the sphenoid (see Fig. 44.4). The tendinous ring is closely adherent to the dural sheath of the optic nerve medially and to the surrounding periosteum. Inferior rectus, part of medial rectus and the lower fibres

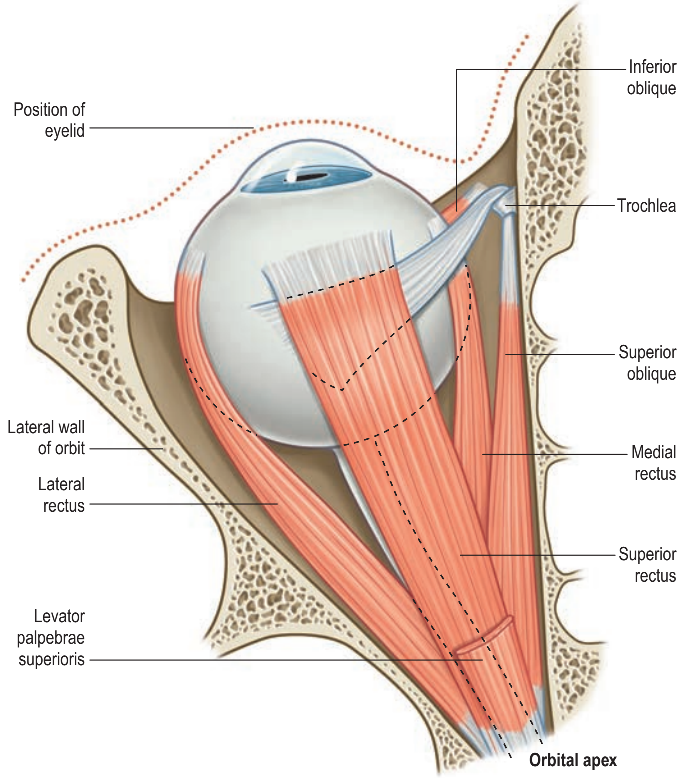

Fig. 44.8 The extraocular muscles viewed from above.

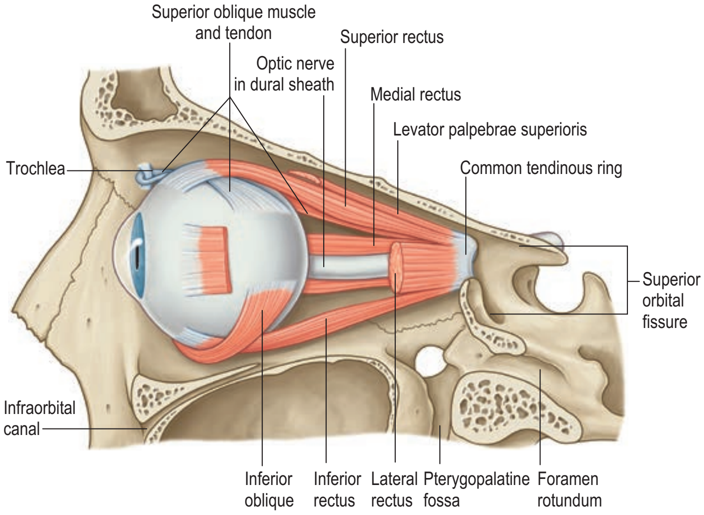

Fig. 44.9 The muscles of the left orbit, lateral view.

of lateral rectus are all attached to the lower part of the ring, whereas superior rectus, part of medial rectus and the upper fibres of lateral rectus are all attached to the upper part. A second small tendinous slip of lateral rectus is attached to the orbital surface of the greater wing of the sphenoid, lateral to the common tendinous ring.

Each rectus muscle passes forwards, in the position implied by its name, to be attached anteriorly by a tendinous expansion into the sclera. However, before their scleral attachment, the recti make functionally important connections with orbital connective tissue that influence muscle action (see p. 772).

Superior rectus

Superior rectus is slightly larger than the other recti. It arises from the upper part of the common tendinous ring, above and lateral to the optic canal. Some fibres also arise from the dural sheath of the optic nerve. The fibres pass forwards and laterally (at an angle of approximately 25° to the median plane of the eye in the primary position) to insert into the upper part of the sclera, approximately 8 mm from the limbus (see Fig. 44.8). The insertion is slightly oblique, the medial margin more anterior than the lateral margin.

Vascular supply Superior rectus receives its arterial supply both directly from the ophthalmic artery and indirectly from its supraorbital branch.

Innervation Superior rectus is innervated by the superior division of the oculomotor nerve that enters the inferior surface of the muscle.

Actions Superior rectus moves the eye so that the cornea is directed upwards (elevation) and medially (adduction). To obtain upward movement alone, the muscle must function with inferior oblique. Superior rectus also causes intorsion of the eye (i.e. medial rotation). Because a check ligament extends from superior rectus to levator palpebrae superioris, elevation of the eye also results in elevation of the upper eyelid. For more detailed discussion of its actions, see page 775.

Inferior rectus

Inferior rectus arises from the common tendinous ring, below the optic canal. It runs along the orbital floor in a similar direction to superior rectus (i.e. forwards and laterally) and inserts obliquely into the sclera below the cornea, approximately 6.5 mm from the limbus (see Fig. 44.9).

Vascular supply Inferior rectus receives its arterial supply from the ophthalmic artery and from the infraorbital branch of the maxillary artery.

Innervation Inferior rectus is innervated by a branch of the inferior division of the oculomotor nerve that enters the superior surface of the muscle.

Actions The principal activity of inferior rectus is to move the eye so that it is directed downwards (depression). It also causes the eye to deviate medially and extorts the eye (i.e. produces lateral rotation). To obtain downward movement alone, inferior rectus must function with superior oblique. A fibrous extension from inferior rectus to the inferior tarsus of the eyelid causes the lower eyelid to be depressed when the muscle contracts. For more detailed discussion of its actions, see page 775.

Medial rectus

Medial rectus is slightly shorter than the other recti but is the strongest of the group. It arises from the medial part of the common tendinous ring, and also from the dural sheath of the optic nerve, passing horizontally forwards along the medial wall of the orbit, below superior oblique (see Figs 44.8–44.9). It inserts into the medial surface of the sclera, approximately 5.5 mm from the limbus and slightly anterior to the other recti.

Vascular supply Medial rectus receives its arterial supply from the ophthalmic artery.

Innervation Medial rectus is innervated by a branch from the inferior division of the oculomotor nerve that enters the lateral surface of the muscle.

Actions Medial rectus moves the eye so that it is directed medially (adducted). The two medial recti acting together are responsible for convergence of the eyes. For more detailed discussion of its actions, see page 775.

Lateral rectus

Lateral rectus arises principally from the lateral part of the common tendinous ring and bridges the superior orbital fissure (see Fig. 44.4); some fibres also arise from a spine on the greater wing of the sphenoid. The muscle passes horizontally forwards along the lateral wall of the orbit to insert into the lateral surface of the sclera, approximately 7 mm from the limbus (see Fig. 44.8).

Vascular supply Lateral rectus receives its arterial supply from the ophthalmic artery directly and/or from its lacrimal branch.

Innervation Lateral rectus is innervated by the abducens nerve by branches that enter the medial surface of the muscle.

Actions Lateral rectus moves the eye so that it is directed laterally (abducted). For more detailed discussion of its actions, see page 775.

The obliques

Superior oblique

Superior oblique is a fusiform muscle that arises from the body of the sphenoid superomedial to the optic canal and the tendinous attachment of the superior rectus (see Fig. 44.4). It runs forwards to end in a round tendon that passes through a fibrocartilaginous loop, the trochlea, attached to the trochlear fossa of the frontal bone (see Fig. 44.8). Tendon and trochlea are separated by a delicate synovial sheath. The tendon subsequently descends posterolaterally and inferior to superior rectus, and is attached to the sclera in the superolateral part of the posterior quadrant behind the equator, between the superior and lateral recti.

Vascular supply Superior oblique receives its arterial supply directly from the ophthalmic artery and indirectly from its supraorbital branch.

Innervation Superior oblique is innervated by the trochlear nerve, which enters the superior surface of the muscle.

Actions Superior oblique is inserted into the posterior part of the eyeball; when it contracts, the back of the eyeball is elevated, and the front of the eyeball is depressed (particularly in the adducted position). Superior oblique also moves the eye laterally (abducted) and intorts the eyeball. For more detailed discussion of its actions, see page 775.

Inferior oblique

Inferior oblique is a thin, narrow muscle that lies near the anterior margin of the floor of the orbit. It arises from the orbital surface of the maxilla lateral to the nasolacrimal fossa and ascends posterolaterally, at first between inferior rectus and the orbital floor, and then between the eyeball and lateral rectus. It is inserted into the lateral part of the sclera behind the equator of the eyeball, in the inferolateral part of the posterior quadrant between the inferior and lateral recti, near, but slightly posterior to, the attachment of superior oblique (see Fig. 44.9). The muscle broadens and thins, and, in contrast to the other extraocular muscles, its tendon is barely discernible at its scleral attachment.

Vascular supply Inferior oblique receives its arterial supply from the ophthalmic artery and from the infraorbital branch of the maxillary artery.

Innervation Inferior oblique is innervated by a branch of the inferior division of the oculomotor nerve that enters the orbital surface of the muscle.

Actions Inferior oblique is inserted into the posterior part of the eyeball; when it contracts, the back of the eyeball is depressed and the front of the eyeball is elevated (particularly in the adducted position). The muscle moves the eye laterally (abduction) and also causes extorsion. For more detailed discussion of its actions, see page 775.

Minor muscles of the eyelids

Several smooth muscles are associated with the orbit, although they are not directly attached to the eyeball. Orbitalis, the orbital muscle of Müller, lies at the back of the orbit and spans the infraorbital fissure. Its functions are uncertain but its contraction may produce a slight forward protrusion of the eyeball. The superior and inferior tarsal muscles are small muscle laminae inserted into the upper and lower eyelids, and are described in more detail with the tarsal plates (p. 775). All three minor muscles receive a sympathetic innervation from the superior cervical ganglion via the internal carotid plexus.

Movements of the eyes

Movements of the eyes involve rotations around a centre of rotation within the globe. For practical purposes, this can be considered to lie 13.5 mm behind the corneal apex. Normal eye movements are binocular. Movements of the eyes in the same direction are termed versions, whilst those in opposite directions are termed vergences. Eye movements are often accompanied by corresponding movements of the eyelids, particularly in upgaze, where the activity of levator palpebrae superioris is closely coupled to that of superior rectus. The following section describes the ocular motor system in terms of the actions of individual extraocular muscles, the diversity of eye movements and their neural control.

Actions of the extraocular muscles

Levator palpebrae superioris elevates the upper lid, and its antagonist is the palpebral part of orbicularis oculi. The degree of elevation, which, apart from blinking, is maintained for long periods during waking hours, is a compromise between ensuring an adequate exposure of the cornea and controlling the amount of incident light. In bright sunshine, the latter can be reduced by lowering the upper lid, so limiting glare. The role of the superior tarsal muscle is less clear. Its tonus is related to sympathetic activity, and since ptosis is a consequence of impairment of its sympathetic nerve supply, it may function as an accessory elevator of the upper eyelid.

Six extraocular muscles rotate the eyeball in directions that depend on the geometrical relation between their bony and global (scleral) attachments (**Fig. 44.10**), which are altered by the ocular movements themselves. For convenience, each muscle will be considered in isolation, but it must be appreciated that any movement of the eyeball alters the tension and/or length in all six muscles. It is useful to consider the four recti and two obliques as separate groups (remembering always that they act in concert) because they form more obvious groupings as antagonists or synergists. The extrinsic ocular muscles collectively position the eyeball in the orbital cavity and prevent its anteroposterior movements, other than a slight retraction during blinks, because the recti exert a posterior traction while the obliques pull the eyeball to some degree anteriorly. They may be assisted by various 'check ligaments' (see above). A simplified description of the actions of the extraocular muscles is summarized in **Fig. 44.11**.

Of the four recti, the medial and lateral exert comparatively straightforward forces on the eyeball. Being approximately horizontal, when the visual axis is in its primary position, i.e. directed to the horizon, they rotate the eye medially (adduction) or laterally (abduction) about an imaginary vertical axis. They are antagonists. The visual axis can be swept through a horizontal arc by reciprocal adjustment of their lengths. When, as is usual, both eyes are involved, the medial and lateral recti of each eye either can adjust both visual axes in a conjugate movement from point to point at infinity (their axes remaining parallel), or they can converge or diverge the axes to or from nearer or more distant objects of attention in the visual field.

The medial and lateral recti do not rotate the eye around its horizontal axis and so cannot elevate or depress the visual axes as gaze is transferred from nearer to more distant objects or the reverse. This movement requires the superior and inferior recti (aided by the two oblique muscles). It is important to remember that the orbital axis does not correspond with the visual axis in its primary position but diverges from it at an angle of approximately 23° (**Fig. 44.10A**) (the value varies between individuals, and depends on the angle between the orbital axes and the median plane). Thus, the simple rotation caused by an isolated superior rectus, analysed with reference to the three hypothetical ocular axes, appears more complex, being primarily elevation (horizontal axis), and secondarily a less powerful medial rotation (vertical axis) and slight intorsion (anteroposterior axis) in which the midpoint of the upper rim of the cornea (often referred to as '12 o'clock') is rotated medially. These actions, compounded as a single, simple rotation, are easily appreciated when it is seen that the direction of traction of superior rectus runs in a posteromedial direction from its attachment in front, which is anterior to the equator and superior to the cornea, to its bony attachment near the orbital apex (see Fig. 44.10). Inferior rectus pulls in a similar direction to superior rectus but rotates the visual axis downwards about the horizontal axis. It rotates the eye medially on a vertical axis but its action around the anteroposterior axis extorts the eye, i.e. rotates it so that the corneal '12 o'clock' point turns laterally. The combined, equal contractions of the superior and inferior recti therefore rotate the eyeball medially, since their effects around the horizontal and anteroposterior axes are opposed. In binocular movements, they assist the medial recti in converging the visual axes, and by reciprocal adjustment can elevate or depress the visual axes. As the eyeball is rotated laterally, the lines of traction of the superior and inferior recti approach the plane of the anteroposterior ocular axis (see Fig. 44.10), and so their rotational effects about this and the vertical ocular axis diminish. In abduction to approximately 23°, they become almost purely an elevator and depressor, respectively, of the visual axis.

Superior oblique acts on the eye from the trochlea and, since the attachment of inferior oblique is, for practical purposes, vertically below this, both muscles approach the eyeball at the same angle, being attached in approximately similar positions in the superior and inferior posterolateral ocular quadrants (see Fig. 44.10). Superior oblique elevates the posterior aspect of the eyeball, and inferior oblique depresses it, which means that the former rotates the visual axis downwards and the latter rotates it upwards, and both movements occur around the horizontal axis. When the eye is in the primary position, the obliquity of both muscles means that they pull in a direction posterior to the vertical axis and both therefore rotate the eye laterally around this axis. With regard to the anteroposterior axis, in isolation, superior oblique intorts the eye and inferior oblique extorts it. Like the superior and inferior recti, therefore, the two obliques have a common turning movement around the vertical axis but are opposed forces in respect of the other two. Acting in concert, they could therefore assist the lateral rectus in abducting the visual axis, as in divergence of the eyes in transferring attention from near to far. Again, like the superior and inferior recti, the directions of traction of the oblique muscles also vary with ocular position, such that they become more nearly a pure elevator and a depressor as the eye is adducted.

Ocular rotations are, for the most part, under voluntary control, whereas torsional movements cannot be initiated at will. When the head is tilted in a frontal plane, reflex torsions occur. Any small lapse in the concerted adjustment of both eyes produces diplopia.

Movements that shift or stabilize gaze

The role of eye movements is to bring the image of objects of visual interest on to the fovea of the retina and to hold the image steady in order to achieve the highest level of visual acuity. Several types of eye movement are required to ensure that these conditions are met. Moreover, the movements of both eyes must be near perfectly matched to achieve the benefits of binocularity. Both voluntary and reflex movements are involved and may be so classified. Alternatively, they may be grouped into those movements that shift gaze as visual interest changes, and those that stabilize gaze by maintaining a steady image on the retina. They have distinct characteristics, and are generated by different neural mechanisms in response to different stimuli, but share a common final motor pathway. Movements that shift or stabilize gaze include saccades, vergence, pursuit and vestibular-generated reflexes (Leigh and Zee 2015).

Saccadic activity is almost omnipresent in human vision. Thus, both visual axes are endlessly and rapidly transferred to new points of interest in any part of the visual field. Binocular gaze is frequently made to travel routes of the most variable complexity in examining objects of interest in the field, and both visual axes must be maintained with sufficient accuracy to avoid diplopia. In so-called 'fixation' of a focus of attention, whether uniocular or binocular, the visual axis is not 'fixed' in a perfectly steady manner but undergoes minute, but measurable, flicking (of a few minutes or even seconds of arc) across the true line of fixation. These microsaccades are rapid and surprisingly complex. When interest changes to another feature of the visual scene, the eyes execute a fast or saccadic movement to take up fixation. If the required rotation is small, the saccade is accurate, whereas small supplementary corrective saccades are needed if the shift is substantial. Saccades may also occur in response to other, i.e. non-visual, exteroceptive stimuli (e.g. auditory, tactile or centrally evoked). They may be volitional or reflex. As an example of the latter, in reading a line of print, the eyes make three or four jerky saccades rather than following the line smoothly; the line is usefully imaged only when the eye is stationary, which means that little of the line is seen by the centre of the fovea. In general, reaction times and movements are measured in microseconds, amplitude varies from seconds of arc to many degrees, with an accuracy of 0.2° or better, and the velocity of a large saccade may reach 500° sec^{-1}. The speed of saccades is assured by an initial, slightly excessive, contraction of the appropriate muscles to overcome orbital viscous resistance. The necessary deceleration when the target is fixated is largely dependent on the elasticity of the extraocular muscles and orbital soft tissues, and not on antagonistic muscular activity.

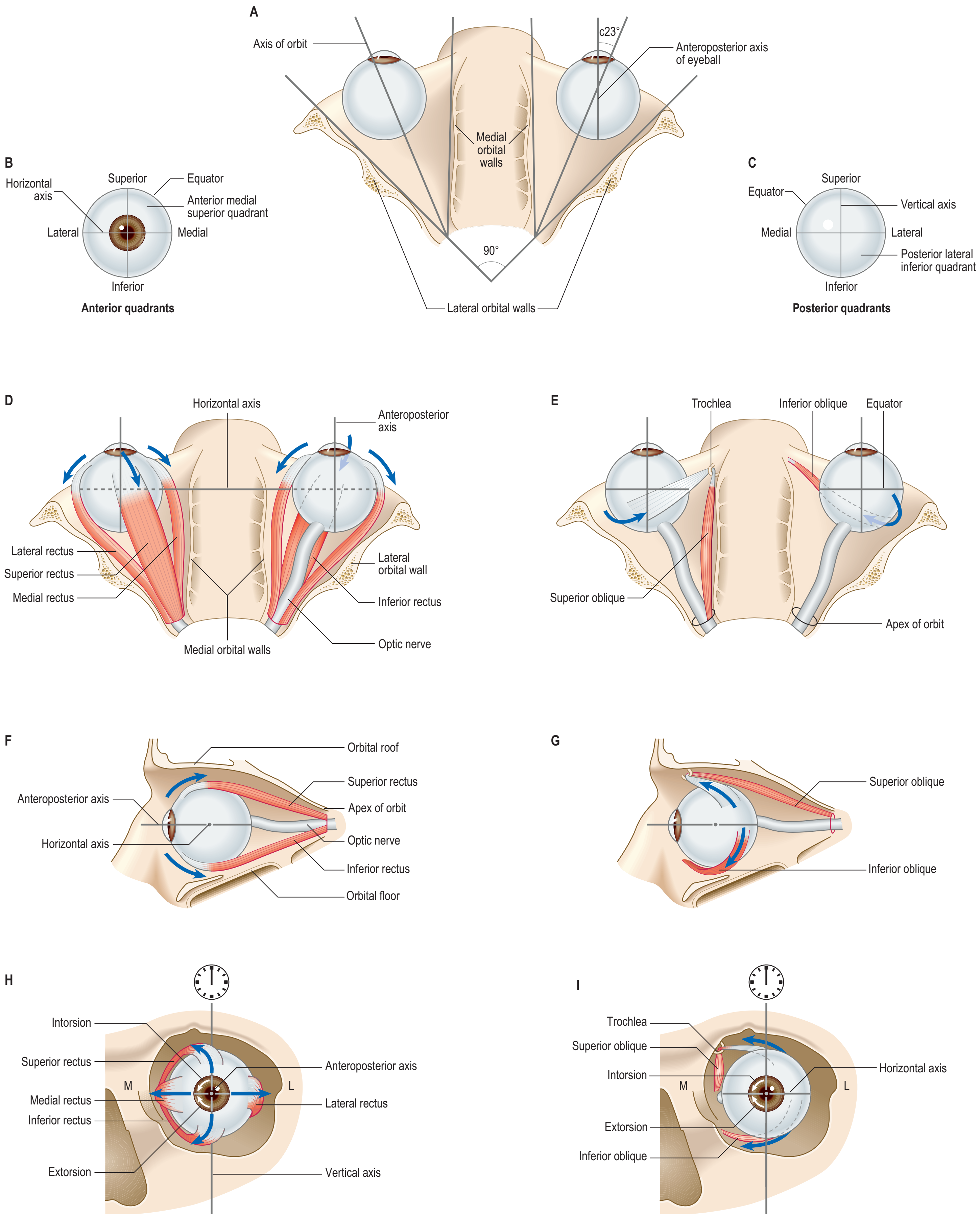
A
Axis of orbit
c23°
Anteroposterior axis of eyeball
Medial orbital walls
90°
Lateral orbital walls
B
Horizontal axis
Superior
Equator
Anterior medial superior quadrant
Lateral
Medial
Inferior
Anterior quadrants
C
Equator
Superior
Vertical axis
Medial
Lateral
Posterior lateral inferior quadrant
Inferior
Posterior quadrants
D
Horizontal axis
Anteroposterior axis
Lateral rectus
Superior rectus
Medial rectus
Lateral orbital wall
Inferior rectus
Medial orbital walls
Optic nerve
E
Trochlea
Inferior oblique
Equator
Superior oblique
Apex of orbit
F
Orbital roof
Anteroposterior axis
Superior rectus
Apex of orbit
Horizontal axis
Optic nerve
Inferior rectus
Orbital floor
G
Superior oblique
Inferior oblique
H
Intorsion
Superior rectus
M
L
Anteroposterior axis
Medial rectus
Lateral rectus
Inferior rectus
Extorsion
Vertical axis
I
Trochlea
Superior oblique
Intorsion
M
L
Horizontal axis
Extorsion
Inferior oblique

Fig. 44.10 The geometrical basis of ocular movements. **A**, The relationship between the orbital and ocular axes, with the eyes in the primary position, where the visual axes are parallel. **B–C**, The ocular globe in anterior and posterior views to show conventional geometry. **D**, The orbits from above, showing the medial and lateral recti and the superior rectus (left) and the inferior rectus (right), indicating turning moments primarily around the vertical axis. **E**, The superior (left) and inferior (right) oblique muscles showing turning moments primarily around the vertical and also anteroposterior axes. **F**, A lateral view to show the actions of the superior and inferior recti around the horizontal axis. **G**, A lateral view to show the action of the superior and inferior oblique muscles around the anteroposterior axis. **H**, An anterior view to show the medial rotational movement of the superior and inferior recti around the vertical axis. Conventionally, the 12 o'clock position indicated is said to be intorted (superior rectus) or extorted (inferior rectus), as indicated by the small arrows on the cornea. **I**, An anterior view to show the torsional effects of the superior oblique (intorsion) and inferior oblique (extorsion) around the anteroposterior axis, as indicated by the small arrows on the cornea.

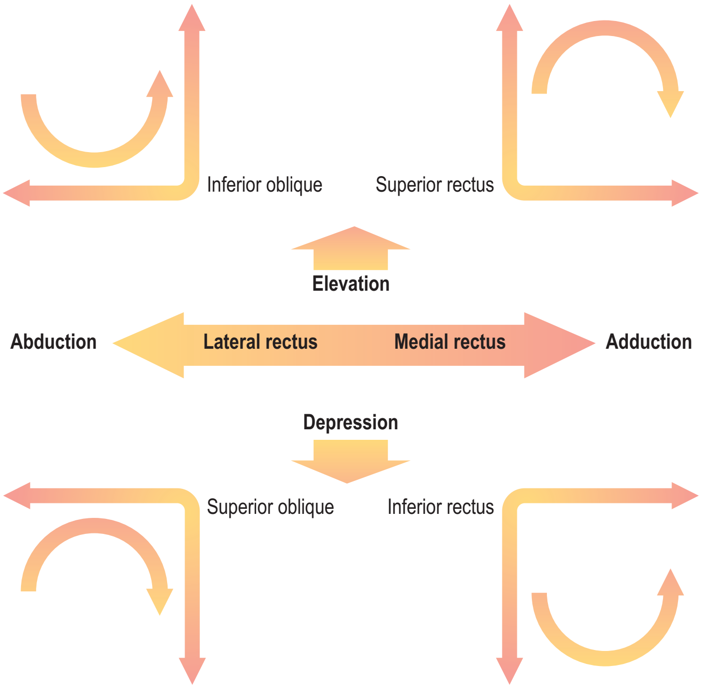

Fig. 44.11 A simplified summary of the actions of the extraocular muscles. Clockwise and anticlockwise curved arrows represent intorsion and extorsion, respectively.

Vergence is a relatively slow movement permitting maintenance of single binocular vision of close objects. The eyes converge towards the midline between the two eyes to achieve imagery of the object on both foveas. The view of the object at the two eyes is not quite the same and the disparity is used to assess depth. In addition, the pupils constrict and the eyes accommodate to achieve sharp, focused images. These three activities constitute the near reflex (Ch. 45).

Pursuit eye movements are used to track a moving object of visual interest, maintaining the image approximately on the fovea. They are usually preceded by a saccade to capture the image but, unlike saccades, pursuit movements are slow and motivated by vision. If the angular shift required to track a moving object is large or the object is moving swiftly, the initial saccade is frequently inaccurate and one or more small corrective saccades are made before tracking begins. Because the stimulus is visual, the pursuit system response is subject to a relatively long latency (approximately 100 msec); the limitation in performance this imposes may be offset by a predictive capacity when object movement follows a regular pattern, and the eye movements adjust in anticipation of the speed and direction of the object. Smooth pursuit performance declines with age and is commonly impaired in cerebellar disease.

The vestibular apparatus induces a variety of reflex eye movements to compensate for the potentially disruptive effects on vision caused by head and body movement (Ch. 43). Receptors in the semicircular canals respond to active or passive rotational (angular) accelerations of the head. When the body makes substantial rotational movements, a vestibulo-ocular reflex generates a cycle of responses involving both the shifting and stabilizing of gaze. Body rotation is matched by counter-rotation of the eyes so that gaze direction is unaltered and clear vision is maintained. Physical constraint limits the rotation to 30° or less and is followed by a rapid saccadic movement of the eyes to another object in the visual scene and the cycle is repeated. Vision is therefore clear throughout most of the cycle while the image is stationary, but at the cost of no useful vision during the brief periods of the saccades. The reflex is efficient and rapid; this speed could not be generated by the visual system, which is slow relative to the short latency of vestibular receptors.

Other reflexes generated by the vestibular system, which induce compensatory eye movements to stabilize gaze, are activated during brief head movements. When the head is sharply rotated in any direction, the eyeball rotates by an equal amount in the opposite direction in response to the stimulation of semicircular canal cristae (angular acceleration), and gaze is undisturbed. Brief rotational movements are commonly combined with translational movements (linear acceleration) that are monitored by otolith organs. For example, a linear displacement occurs in walking as the head bobs vertically with each stride, and a rotational displacement occurs as the head rolls, invoking otolith and canal responses, respectively, to stabilize the retinal image. Vestibular disease incurring the loss of the rapid, fine compensatory eye movements in locomotion destabilizes the retinal image, blurs vision and may render locomotion intolerable.

The otoliths also respond to the pull of gravity, generating static vestibulo-ocular reflexes associated with head tilt. When static otolith orientation is changed, e.g. when the head is tilted upwards or downwards, the eyes counter-rotate to maintain fixation of the horizontal meridian. Lateral tilt towards a shoulder generates a torsional counter-rotation equal and in opposite direction by the two eyes, a movement that cannot be made voluntarily: because the foveal image is unaffected by torsional movements, there is no visual penalty.

The optokinetic response is another visually mediated reflex that stabilizes retinal imagery when a visual scene is rotated about a stationary subject. As the scene changes, the eyes follow and hold the retinal image steady until the eyes shift rapidly in the opposite direction to another area of the visual scene. The stimulus is the full field of vision, rather than small objects within it, and the alternating slow and fast phases of movement that are generated describe optokinetic nystagmus. This reflex functions in collaboration with the rotational vestibulo-ocular reflex. In sustained rotations of the body, the vestibulo-ocular reflex fades because of the mechanical arrangements of the semicircular canals. In darkness, the reflex, which is initially compensatory, loses velocity, and after approximately 45 seconds the eyes become stationary. With a visual input, the reflex is sustained by the optokinetic response, and because the reflex is already initiated, the relative delay of visual input is overcome. The usual method of evoking optokinetic nystagmus in the laboratory or clinic is to present a horizontally moving pattern of vertical black-on-white stripes while the head of the subject is held stationary.

Neural control of gaze

Although the detailed anatomical substrates for the different types of eye movement differ, they share common neural circuitry that lies mainly in the pons and midbrain, for horizontal and vertical gaze movements, respectively (Fig. 44.12). The common element for all types of horizontal gaze movements is the abducens nucleus. It contains motor neurones that innervate the ipsilateral lateral rectus and interneurones that project via the medial longitudinal fasciculus to the contralateral oculomotor nucleus, which controls medial rectus. A lesion of the abducens nucleus leads to a total loss of ipsilateral horizontal conjugate gaze. A lesion of the medial longitudinal fasciculus produces slowed or absent adduction of the ipsilateral eye, usually associated with jerky movements (nystagmus) of the contralateral abducting eye, a syndrome called internuclear ophthalmoplegia (Leigh and Zee 2015). The gaze motor command involves specialized areas of the reticular formation of the brainstem, which receive a variety of supranuclear inputs. The main region for the generation of horizontal saccades is the paramedian pontine reticular formation, located on each side of the midline in the central paramedian part of the tegmentum, and extending from the pontomedullary junction to the pontopeduncular junction. Each paramedian pontine reticular formation contains excitatory neurones (referred to as 'burst' neurones) that discharge at high frequencies just prior to and during ipsilateral saccades. Excitatory burst neurones make monosynaptic connections with the ipsilateral abducens nucleus. Omnipause neurones in the pontine nucleus raphe interpositus, located in the midline between the rootlets of the abducens nerves, discharge tonically during fixation but stop firing immediately prior to a saccade. They appear to exert an inhibitory influence on the burst neurones and act as a switch to change from fixation to saccadic mode (Ramat et al 2007).

The tonic activity of neurones in the nucleus prepositus hypoglossi and medial vestibular nucleus is thought to provide an eye position signal to maintain the eccentric position of the eye against the viscoelastic forces in the orbit. These forces tend to move the eyeball back to looking straight ahead, i.e. the primary position, after a saccade. Vestibular nuclei and the perihypoglossal complex project directly to the abducens nuclei: these projections probably also carry smooth pursuit signals, via the cerebellum.

The final common pathway for vertical gaze movements is formed by the oculomotor and trochlear nuclei. The rostral interstitial nucleus of the medial longitudinal fasciculus contains both excitatory burst neurones that discharge in relation to up-and-down vertical saccadic movements and project to motor neurones involved in vertical gaze, and omnipause neurones that act similarly to those for horizontal gaze. The rostral interstitial nucleus of the medial longitudinal fasciculus projects through the posterior commissure to its equivalent on the other side of the mesencephalon for upgaze, as well as directly to the ipsilateral

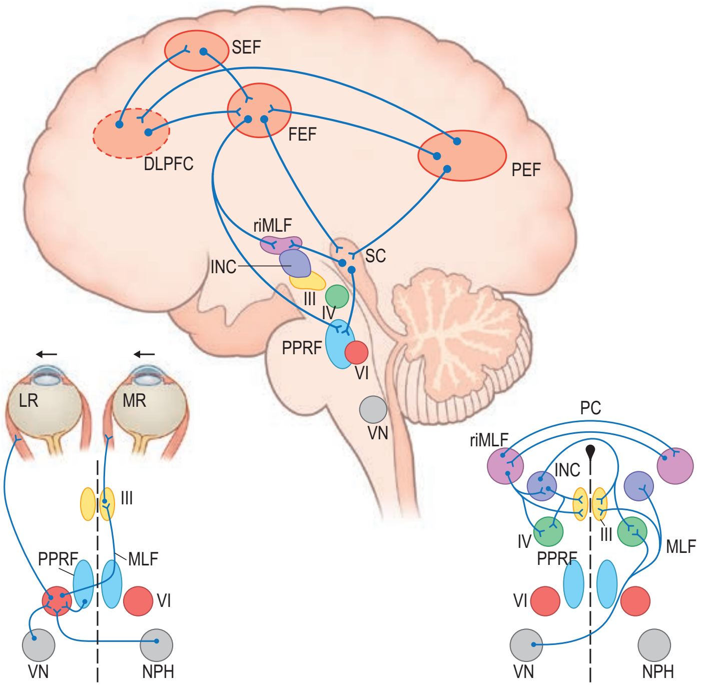

Fig. 44.12 A summary of the control of eye movements. The central drawing shows the supranuclear connections from the frontal eye field (FEF) and the posterior eye field (PEF) to the superior colliculus (SC), rostral interstitial nucleus of the medial longitudinal fasciculus (riMLF), and the paramedian pontine reticular formation (PPRF). The diagram on the left shows the brainstem pathways for horizontal gaze. Axons from the PPRF travel to the ipsilateral abducens nucleus innervating lateral rectus (LR). Abducens internuclear axons cross the midline and travel in the medial longitudinal fasciculus (MLF) to the neuronal pool in the oculomotor nucleus (III) that innervates medial rectus (MR) of the contralateral eye. The diagram on the right shows the brainstem pathways for vertical gaze. Important structures include the riMLF, PPRF, the interstitial nucleus of Cajal (INC) and the posterior commissure (PC). Other abbreviations: DLPFC, dorsolateral prefrontal cortex; IV, trochlear nucleus; NPH, nucleus propositus hypoglossi; SEF, supplementary eye field; VI, abducens nucleus; VN, vestibular nucleus.

oculomotor and trochlear nuclei for downgaze (see Fig. 44.12). Neurones in and around the interstitial nucleus of Cajal, which lies slightly caudal to the rostral interstitial nucleus of the medial longitudinal fasciculus, provide signals for vertical gaze holding. Vertical gaze palsies can affect upgaze, downgaze or both. Lesions within the posterior commissure predominantly give rise to disturbances in upgaze, associated with other signs of dorsal midbrain syndrome, e.g. pupillary abnormalities (light–near dissociation). Discrete lesions placed more ventrally in the region of the rostral interstitial nucleus of the medial longitudinal fasciculus may cause mixed up-and-down, or mainly downgaze disturbances (Leigh and Zee 2015).

The cerebellum and cerebral hemispheres play important roles in the control of eye movements. The vestibulocerebellum (flocculus and nodule) is involved in gaze holding, smooth pursuit and the vestibulo-ocular reflex (Ch. 29). The dorsal vermis and fastigial nucleus are involved in programming accurate saccades and smooth pursuit. The cerebral hemispheres are also involved in the programming and coordination of saccadic and pursuit conjugate eye movements. The frontal eye field, the supplementary eye field, the dorsolateral prefrontal cortex and the parietal eye field are all involved in eye movement control: these areas are interconnected and send projections to the superior colliculus and other brainstem ocular motor centres. Although the anatomical location of cortical gaze control areas has been well characterized in non-human primates, their precise location in the human brain is yet to be definitively established and appears to vary depending on the method used (Amiez and Petrides 2009).

Two parallel pathways are involved in the cortical generation of saccades. An anterior system originates in the frontal eye field and projects, both directly and via the superior colliculus, to the brainstem saccadic generators. This pathway also passes indirectly via the basal ganglia to the superior colliculus. Projections from the frontal cortex influence cells in the pars reticularis of the substantia nigra, via a relay in the caudate nucleus. An inhibitory pathway from the pars reticulata projects directly to the superior colliculus. This may be a gating circuit related to voluntary saccades, especially of the memory-guided type. A posterior pathway originates in the parietal eye field and passes to the brainstem saccadic generators via the superior colliculus. This pathway is important for triggering reflexive saccades.

The smooth pursuit system has developed relatively independently of the saccadic oculomotor system to maintain foveation of a moving target, although there are inevitable interconnections between the two. The first task is to identify and code the velocity and direction of a moving target. This is largely performed by secondary visual areas at the parietal–occipital–temporal lobe junction (human homologue of the middle temporal visual area (V5) and medial superior temporal visual area of monkeys). Descending pathways from these posterior cortical areas project to a group of nuclei that lie in the basal part of the pons, which in turn transfer the pursuit signal bilaterally to the cerebellum and ultimately to ocular motor neurones.

The vestibulo-ocular reflex maintains coordination of vision during movement of the head and results in a compensatory conjugate eye movement that is equal but opposite to the movement of the head. This essentially three-neurone arc consists of primary vestibular neurones that project to the vestibular nuclei; secondary neurones that project from these nuclei directly to the abducens and oculomotor nuclei; and tertiary neurones that innervate the extraocular muscles. Vestibular neurones responding to head rotation also respond to optokinetic stimuli, which means that the neural substrate is likely to include both the visual and vestibular systems.

Several cortical areas contribute to vergence movements. Posterior visual areas are responsible for sensory processing and generating reflexive, stimulus-linked movements, whereas the frontal cortex (frontal and supplementary eye fields) is more concerned with volitional, self-initiated movements (Leigh and Zee 2015). These cortical regions project to the midbrain supraocular motor area, which encodes vergence eye movements and sends excitatory projections to medial rectus and lateral rectus motoneurones that generate convergence and divergence, respectively.

VASCULAR SUPPLY AND LYMPHATIC DRAINAGE

Arteries

Orbital vascular anatomy displays noteworthy inter-individual variation (Hayreh 2006): the usual pattern and more common variations are presented below. The main vessel supplying orbital structures is the ophthalmic artery (**Fig. 44.13**). Its terminal branches anastomose on the face and scalp with those of the facial, maxillary and superficial temporal arteries, and in so doing establishing connections between the external and internal carotid arteries. The infraorbital branch of the maxillary artery, which anastomoses with the middle meningeal artery, may also supply orbital structures.

Ophthalmic artery

The ophthalmic artery leaves the internal carotid artery as it exits the cavernous sinus medial to the anterior clinoid process. It enters the orbit by the optic canal, inferolateral to the optic nerve and continues forwards for a short distance before turning medially by crossing (almost always) over or under the optic nerve (see Fig. 44.13A). The main trunk of the artery continues along the medial wall of the orbit between the superior oblique and lateral rectus, and divides into supratrochlear (frontal) and dorsal nasal branches at the medial end of the upper eyelid. Although the order of branches from the ophthalmic artery is quite variable, there are several consistent branches, including the central retinal artery, muscular branches, ciliary arteries, lacrimal artery, supraorbital artery, anterior and posterior ethmoidal arteries, meningeal branch, medial palpebral arteries, supratrochlear artery and dorsal nasal artery (Hayreh and Dass 1962a). Many of the branches of the ophthalmic artery accompany sensory nerves with the same name and have a similar distribution to these nerves. Variations in the origin and course of the ophthalmic artery have been described (Huynh-Le et al 2005, Hayreh 2006, Bertelli et al 2017).

Central retinal artery

The small central artery of the retina is the first branch of the ophthalmic artery. It begins below the optic nerve and, for a short distance, lies in the dural sheath of the nerve. It enters the inferomedial surface of the nerve 6.4–15.2 mm behind the eye, and runs to the retina (accompanying the central retinal vein) along its axis. The further distribution of the central retinal artery is described in Chapter 45.

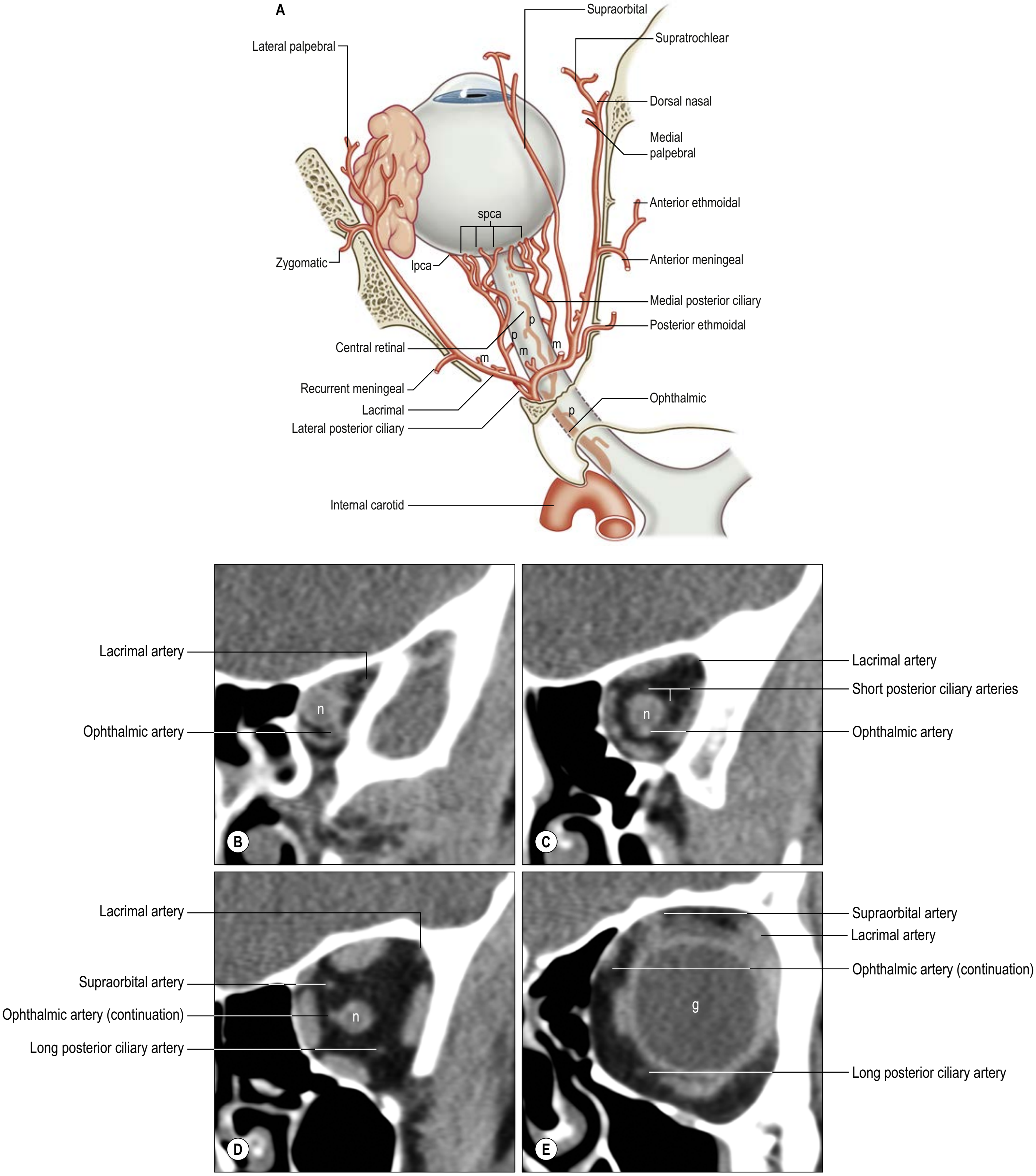
A
Supraorbital
Supratrochlear
Lateral palpebral
Dorsal nasal
Medial palpebral
Anterior ethmoidal
spca
Zygomatic
lpca
Anterior meningeal
Medial posterior ciliary
p
Posterior ethmoidal
p
m
m
m
Central retinal
Recurrent meningeal
Lacrimal
Lateral posterior ciliary
Ophthalmic
p
Internal carotid
Lacrimal artery
Ophthalmic artery
n
B
Lacrimal artery
Short posterior ciliary arteries
n
Ophthalmic artery
C
Lacrimal artery
Supraorbital artery
Ophthalmic artery (continuation)
Long posterior ciliary artery
n
D
Supraorbital artery
Lacrimal artery
Ophthalmic artery (continuation)
g
Long posterior ciliary artery
E

Fig. 44.13 A, Dorsal view of the left eye showing the orbital distribution of the ophthalmic artery. **B–E**, Coronal CT sections through the left orbit from posterior to anterior, showing arterial branches. Contrast medium has been given to the patient. Abbreviations: g, globe; lpca, long posterior ciliary artery; m, muscular arteries; n, optic nerve; p, pial arteries; spca, short posterior ciliary arteries.

Muscular branches

Branches to the extraocular muscles frequently spring from a common trunk to form superior and inferior groups, most of which accompany branches of the oculomotor nerve. The inferior branch contains most of the anterior ciliary arteries. Other muscular vessels branch from the lacrimal and supraorbital arteries or from the trunk of the ophthalmic artery.

Ciliary arteries

The ciliary arteries are distributed in long and short posterior, and in anterior groups (see Fig. 44.13A). Long posterior ciliary arteries, usually two, pierce the sclera near the optic nerve, pass anteriorly along the horizontal meridian and join the major arterial circle of the iris (see Fig. 45.8). About seven short posterior ciliary arteries pass close to the optic nerve to reach the eyeball, where they divide into 15–20 branches. They pierce the sclera around the optic nerve to supply the choroid, and anastomose with twigs of the central retinal artery at the optic disc (see Fig. 45.30). Anterior ciliary arteries arise from muscular branches of the ophthalmic artery. They reach the eyeball on the tendons of the recti, form a circumcorneal subconjunctival vascular zone, and pierce the sclera near the sclerocorneal junction to end in the major arterial circle of the iris.

Lacrimal artery

The lacrimal artery is a large branch that usually leaves the ophthalmic artery near its exit from the optic canal (see Fig. 44.13A), although it occasionally arises before the ophthalmic artery enters the orbit. It accompanies the lacrimal nerve along the upper border of lateral rectus, supplies and traverses the lacrimal gland, and ends in the eyelids and conjunctiva as the lateral palpebral arteries. The latter run medially in the upper and lower lids and anastomose with the medial palpebral arteries. The lacrimal artery gives off one or two zygomatic branches. One reaches the temporal fossa via the zygomaticotemporal foramen and anastomoses with the deep temporal arteries. The other reaches the cheek by the zygomaticofacial foramen and anastomoses with transverse facial and zygomatico-orbital arteries. A recurrent meningeal branch, usually small, passes back via the lateral part of the superior orbital fissure to anastomose with the middle meningeal artery. This branch is sometimes large and replaces the lacrimal artery, in which case it becomes a more significant contributor to the orbital blood supply (Hayreh and Dass 1962b, Uchino et al 2013).

Supraorbital artery

The supraorbital artery leaves the ophthalmic artery where it crosses the optic nerve (see Fig. 44.13A), and ascends medial to superior rectus and levator palpebrae superioris. It accompanies the supraorbital nerve between the periosteum and levator palpebrae superioris, passes through the supraorbital foramen or notch, and divides into superficial and deep branches. These supply the skin, muscles and frontal periosteum, and anastomose with the supratrochlear artery and with the frontal branch of the superficial temporal artery and its contralateral fellow (see Fig. 36.20). The supraorbital artery supplies superior rectus and levator palpebrae superioris, sends a branch across the trochlea to the medial canthus, and often sends a branch to the diploë of the frontal bone at the supraorbital margin; it may also supply the mucoperiosteum in the frontal sinus.

Posterior ethmoidal artery

The posterior ethmoidal artery runs through the posterior ethmoidal canal and supplies the posterior ethmoidal air sinuses. Entering the cranium, it gives off a meningeal branch to the dura mater, and nasal branches that descend into the nasal cavity via the cribriform plate, and anastomoses with branches of the sphenopalatine artery (see Fig. 39.9).

Anterior ethmoidal artery

The anterior ethmoidal artery passes with its accompanying nerve through the anterior ethmoidal canal to supply the ethmoidal and frontal air sinuses. Entering the cranium, it gives off a meningeal branch to the dura mater, and nasal branches that descend into the nasal cavity with the anterior ethmoidal nerve (see Fig. 39.9). It runs in a groove on the deep surface of the nasal bone to supply the lateral nasal wall and septum. A terminal branch appears on the nose between the nasal bone and the upper nasal cartilage (see Fig. 39.9).

Meningeal branch

A meningeal branch, usually small, passes back through the superior orbital fissure or its own foramen to the middle cranial fossa, where it anastomoses with the middle meningeal artery. It is sometimes large, in which case it becomes a major contributor to the orbital blood supply.

Medial palpebral arteries

Above the trochlea, two medial palpebral arteries branch separately from the ophthalmic artery and join the lateral palpebral arteries to complete the arterial arcades supplying the upper and lower eyelids.

Supratrochlear artery

The supratrochlear artery is a terminal branch of the ophthalmic artery. It leaves the orbit superomedially with the supratrochlear nerve, ascends on the forehead to supply the skin, muscles and pericranium, and anastomoses with the supraorbital artery and with its contralateral fellow.

Dorsal nasal artery

The dorsal nasal artery is the other terminal branch of the ophthalmic artery and emerges from the orbit between the trochlea and medial palpebral ligament. It gives a branch to the upper part of the nasolacrimal sac and then divides into two branches. One branch anastomoses with the terminal part of the facial artery, and the other runs along the dorsum of the nose, supplies its outer surface and anastomoses with its contralateral fellow and the lateral nasal branch of the facial artery.

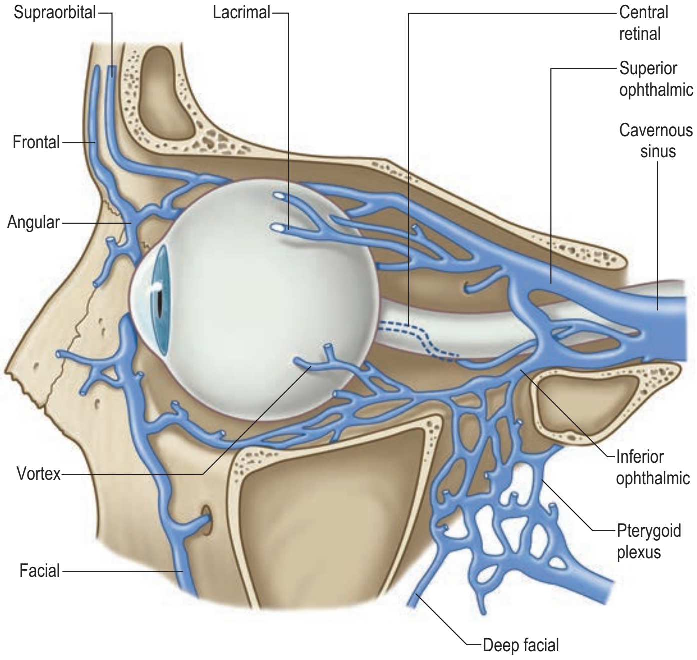

Fig. 44.14 The principal veins of the orbit.

Infraorbital branch of the maxillary artery

The infraorbital branch of the maxillary artery enters the orbit through the inferior orbital fissure (see Fig. 38.20). Accompanying the infraorbital nerve, it passes along the infraorbital groove of the maxilla in the floor of the orbit before entering the infraorbital canal, and comes out on to the face through the infraorbital foramen. While in the infraorbital groove, it gives off branches that supply inferior rectus and inferior oblique, the nasolacrimal sac and, occasionally, the lacrimal gland.

Veins

The orbit is drained by the superior and inferior ophthalmic veins and the infraorbital vein (**Fig. 44.14**). The veins of the eyeball mainly drain into the vortex veins; the retinal veins drain into the central retinal vein.

Superior and inferior ophthalmic veins

The superior and inferior ophthalmic veins link the facial and intracranial veins, and are devoid of valves. The superior ophthalmic vein forms posteromedial to the upper eyelid from two tributaries that connect anteriorly with the facial and supraorbital veins. It runs with the ophthalmic artery, lying between the optic nerve and superior rectus, and receives the corresponding tributaries, the two superior vortex veins of the eyeball, and the central vein of the retina. The central retinal vein sometimes drains directly into the cavernous sinus, although it still gives a communicating branch to the superior ophthalmic vein. The superior ophthalmic vein may also receive the inferior ophthalmic vein. It traverses the superior orbital fissure, usually above the common tendinous ring of the recti, and ends in the cavernous sinus.

The inferior ophthalmic vein begins in a network near the anterior region of the orbital floor and medial wall. It runs backwards on inferior rectus and across the inferior orbital fissure, and then either joins the superior ophthalmic vein or passes through the superior orbital fissure, within or below the common tendinous ring, to drain directly into the cavernous sinus. The inferior ophthalmic vein receives tributaries from inferior rectus and inferior oblique, the nasolacrimal sac, the eyelids and the two inferior vortex veins of the eyeball. It communicates with the pterygoid venous plexus by a branch that passes through the inferior orbital fissure, and may also communicate with the facial vein across the inferior margin of the orbit.

Infraorbital vein

The infraorbital vein runs with the infraorbital nerve and artery in the floor of the orbit, and passes backwards through the inferior orbital fissure into the pterygoid venous plexus. It drains structures in the floor of the orbit and communicates with the inferior ophthalmic vein; it may also communicate with the facial vein on the face.

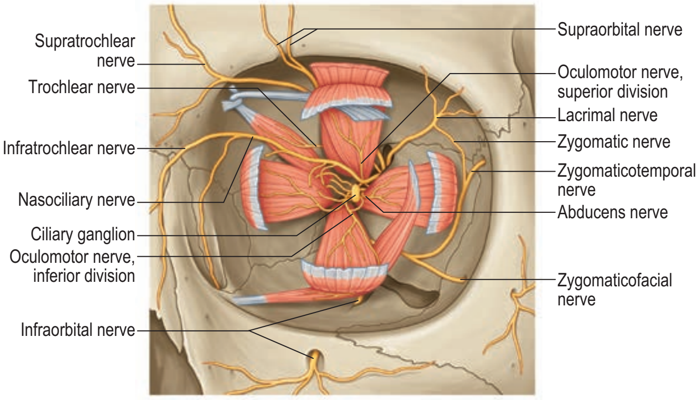
Supratrochlear nerve
Trochlear nerve
Infratrochlear nerve
Nasociliary nerve
Ciliary ganglion
Oculomotor nerve, inferior division
Infraorbital nerve
Supraorbital nerve
Oculomotor nerve, superior division
Lacrimal nerve
Zygomatic nerve
Zygomaticotemporal nerve
Abducens nerve
Zygomaticofacial nerve

Fig. 44.15 The left orbit viewed from in front, showing motor and sensory nerves and the origins of the extraocular muscles. Note that in this figure the trochlear nerve is shown inserting on the inferior aspect of the superior oblique, whereas it more commonly inserts on the superior surface of the muscle. (With permission from Dutton JJ 1994 Atlas of Clinical and Surgical Orbital Anatomy. Philadelphia: Saunders.)

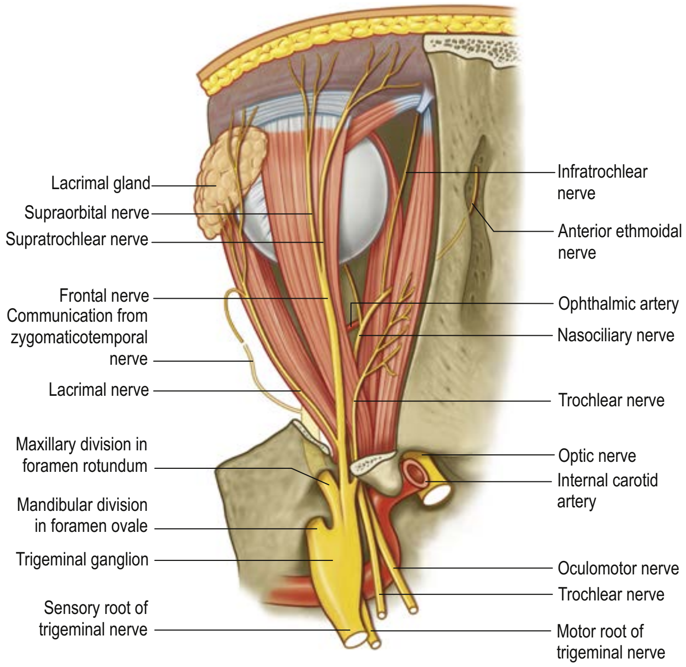
Lacrimal gland
Supraorbital nerve
Supratrochlear nerve
Frontal nerve
Communication from zygomaticotemporal nerve
Lacrimal nerve
Maxillary division in foramen rotundum
Mandibular division in foramen ovale
Trigeminal ganglion
Sensory root of trigeminal nerve
Infratrochlear nerve
Anterior ethmoidal nerve
Ophthalmic artery
Nasociliary nerve
Trochlear nerve
Optic nerve
Internal carotid artery
Oculomotor nerve
Trochlear nerve
Motor root of trigeminal nerve

Fig. 44.16 The nerves of the left orbit, superior aspect.

Lymphatic drainage

Lymphatic vessels other than those draining the conjunctiva have not been identified.

INNERVATION

Somatic and autonomic motor and somatic sensory nerves are found in the orbit (Figs 44.15–44.17). The oculomotor, trochlear and abducens nerves supply the extraocular muscles. Parasympathetic fibres travelling in the oculomotor nerve (from cell bodies in the Edinger–Westphal nucleus) supply sphincter pupillae and the ciliary muscle (ciliaris) via the ciliary ganglion, and those travelling in the facial nerve (from cell bodies in the lacrimal portion of the superior salivatory nucleus) innervate the lacrimal gland and choroid via the pterygopalatine ganglion. Postganglionic sympathetic fibres arising (from cell bodies in the superior cervical ganglion) supply dilator pupillae. Both sympathetic and parasympathetic nerves supply the arteries. The sensory nerves within the orbit are the optic, ophthalmic and maxillary nerves (the maxillary nerve and most of the ophthalmic branches only pass through the orbit *en route* to supply the face and jaws).

Oculomotor nerve

The oculomotor nerve is the third cranial nerve (see Fig. 44.15). It innervates levator palpebrae superioris and four of the extraocular muscles (superior, inferior and medial rectus and inferior oblique), and also conveys parasympathetic fibres that relay in the ciliary ganglion.

For descriptive purposes, the nerve is usually divided into cisternal, cavernous and orbital portions: surgically oriented classifications derived from combined microsurgical and endoscopic cadaveric dissection studies have proposed five or seven parts (Iaconetta et al 2010, Park et al 2017).

The cisternal portion of the oculomotor nerve emerges from the midbrain, either through the medial sulcus of the crus cerebri in the caudal part of the interpeduncular fossa or through the medial or the middle part of the crus cerebri. It usually passes forwards and laterally through the interpeduncular cistern between the posterior communicating artery and the superior cerebellar artery: this portion of the nerve is supplied by the P1 and P2 segments of the posterior cerebral artery. The pupilloconstrictor fibres lie superficially on the dorsomedial surface of the cisternal portion of oculomotor nerve, a location that renders them vulnerable to aneurysmal compression (Kerr and Hollowell 1964, Shechtman et al 2007): in contrast, a pupil-sparing palsy of the oculomotor nerve is pathognomonic of an ischaemic lesion, which tends to involve the central region of the nerve.

The oculomotor nerve next passes inferolateral to the posterior communicating artery and inferomedial to the uncus and enters the roof of the cavernous sinus through the oculomotor trigone. This cavernous portion of the nerve passes along the lateral dural wall of the cavernous sinus, dividing into superior and inferior divisions that run beneath the trochlear and ophthalmic nerves. The two divisions enter the orbit through the superior orbital fissure, within the common tendinous ring of the recti, separated by the nasociliary branch of the ophthalmic nerve.

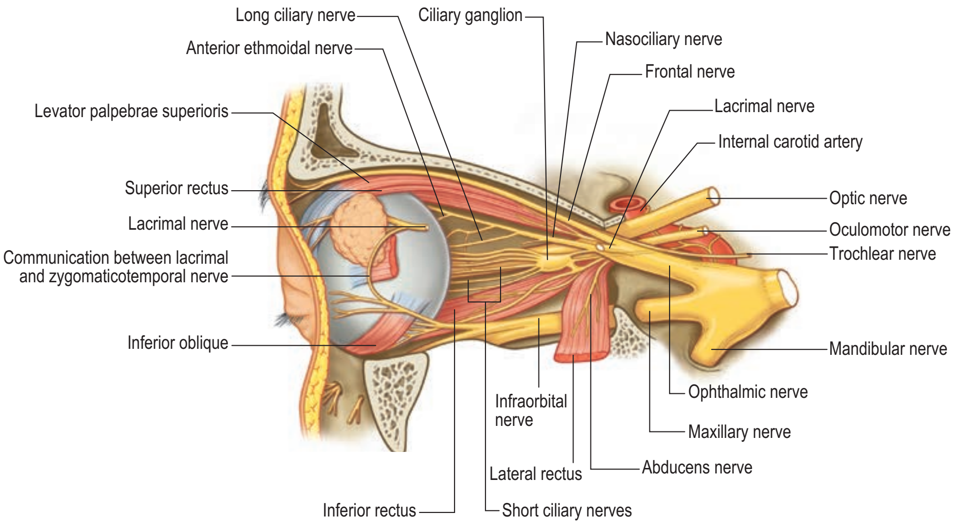
Long ciliary nerve
Ciliary ganglion
Anterior ethmoidal nerve
Nasociliary nerve
Frontal nerve
Lacrimal nerve
Internal carotid artery
Levator palpebrae superioris
Superior rectus
Lacrimal nerve
Communication between lacrimal and zygomaticotemporal nerve
Inferior oblique
Optic nerve
Oculomotor nerve
Trochlear nerve
Mandibular nerve
Ophthalmic nerve
Maxillary nerve
Abducens nerve
Infraorbital nerve
Lateral rectus
Inferior rectus
Short ciliary nerves

Fig. 44.17 The nerves of the left orbit and the ciliary ganglion, lateral aspect.

The superior division of the oculomotor nerve passes above the optic nerve to enter the inferior (ocular) surface of superior rectus. It supplies this muscle and gives off a branch that runs to innervate levator palpebrae superioris. The inferior division of the oculomotor nerve divides into medial, central and lateral branches. The medial branch passes beneath the optic nerve to enter the lateral (ocular) surface of medial rectus; the central branch runs downwards and forwards to enter the superior (ocular) surface of inferior rectus; the lateral branch travels forwards on the lateral side of inferior rectus to enter the orbital surface of inferior oblique and also communicates with the ciliary ganglion to distribute parasympathetic fibres to sphincter pupillae and the ciliary muscle.

Trochlear nerve

The trochlear nerve is the fourth cranial nerve and innervates superior oblique exclusively. It has the longest intracranial course and the smallest diameter of all of the cranial nerves, and is also the only cranial nerve to emerge from the dorsal surface of the brainstem, lateral to the lower edge of the inferior colliculus. The cisternal portion of the nerve courses anterolaterally, winding round the cerebral peduncle toward the tentorium cerebelli through the quadrigeminal and ambient cisterns. It passes anteriorly along the infratentorial groove of the tentorium cerebelli and penetrates the roof of the cavernous sinus at the junction of the anterior and posterior petroclinoid dural folds. The cavernous portion continues along the lateral wall of the cavernous sinus below the oculomotor nerve, crossing this nerve at the level of the optic strut to become the most superior structure in the cavernous sinus. The trochlear nerve enters the orbit through the superior orbital fissure outside the common tendinous ring, above levator palpebrae superioris and medial to the frontal and lacrimal nerves (see Fig. 44.16). The orbital portion runs medially across levator palpebrae superioris and superior rectus to reach superior oblique: its branches typically end on the posterior one-third of the muscle, most often on the medial aspect (Joo and Rhoton 2015).

Abducens nerve

The abducens nerve is the sixth cranial nerve and exclusively innervates lateral rectus. It has a long and tortuous intracranial course and is tightly attached to the skull base at the level of the petrous apex. The nerve usually exits the pontomedullary sulcus as a single trunk medial to the facial nerve, runs upward, anteriorly and laterally between the pons and clivus, pierces the inner layer of dura mater and runs through the inferior venous compartment of the petroclival venous confluence in a bow-shaped canal, Dorello's canal. It then bends sharply across the upper border of the petrous part of the temporal bone to enter the cavernous sinus, where it lies lateral to the internal carotid artery (unlike the oculomotor, trochlear, ophthalmic and maxillary nerves, which merely invaginate the lateral dural wall of the sinus) but medial to all the other nerves coursing through the cavernous sinus. It enters the orbit through the inferomedial part of the superior orbital fissure, within the common tendinous ring, at first below, and then between, the two divisions of the oculomotor nerve and lateral to the nasociliary nerve (see Fig. 44.15). It passes forwards to enter the medial (ocular) surface of lateral rectus, most often in the posterior one-third of the muscle (Joo et al 2012).

Optic nerve

The optic nerve is the second cranial nerve and contains the axons of retinal ganglion cells (Ch. 45). The two optic nerves join to form the optic chiasma, which is usually positioned over the diaphragma sellae and pituitary gland (normofixed), although it may be prefixed (above the tuberculum sellae) or postfixed (above the dorsum sellae). The axons representing the temporal visual fields decussate within the chiasma. The optic nerve is usually described in four parts, intracranial (~10 mm), intracanalicular (~10 mm), intraorbital (25–30 mm) and intraocular (1 mm). The intracranial part arises from the optic chiasma in the suprasellar cistern. It is surrounded by the optic sheath and its dorsal surface is covered by the falciform ligament. The intracanalicular part passes through the optic canal together with the ophthalmic artery. This is the weakest point of the anterior visual pathway because the nerve is fixed to its bony surroundings by fibrous adhesions. The intraorbital part passes forwards, laterally and downwards, and pierces the sclera at the lamina cribrosa, slightly medial to the posterior pole. It has a somewhat tortuous course within the orbit to allow for movements of the eyeball (Demer 2016). The subarachnoid space surrounding the intracranial part is continuous with the subarachnoid space around the intracanalicular and intraorbital parts; the dural sheath surrounding the optic nerve originates at the level of the optic canal and accompanies the optic nerve to the sclera.

The intraorbital part of optic nerve has important relationships with other orbital structures (see Fig. 44.4). As it leaves the optic canal, it lies superomedial to the ophthalmic artery, and is separated from lateral rectus by the oculomotor, nasociliary and abducens nerves, and sometimes by the ophthalmic veins. It is closely related to the origins of the four recti, whereas more anteriorly, where the muscles diverge, it is separated from them by a substantial amount of orbital fat. Just beyond the optic canal, the ophthalmic artery and the nasociliary nerve cross the optic nerve to reach the medial wall of the orbit. The central artery of the retina enters the substance of the optic nerve about halfway along its length. Near the back of the eyeball, the optic nerve becomes surrounded by the long and short ciliary nerves and vessels.

Ophthalmic nerve

The ophthalmic division of the trigeminal nerve arises from the trigeminal ganglion in the middle cranial fossa. It passes forwards along the lateral dural wall of the cavernous sinus, giving off three main branches – the lacrimal, frontal and nasociliary nerves – just before it reaches the superior orbital fissure (see Figs 44.16–44.17). These branches subsequently travel through the orbit to supply targets that are primarily in the upper part of the face (see Fig. 36.22).

Lacrimal nerve

The lacrimal nerve enters the orbit through the superior orbital fissure, outside the common tendinous ring and lateral to the frontal and trochlear nerves. It passes forwards along the lateral wall of the orbit on the superior border of lateral rectus, and travels through the lacrimal gland and the orbital septum to supply the conjunctiva and skin covering the lateral part of the upper eyelid. The nerve also communicates with the zygomatic branch of the maxillary nerve, which may carry some postganglionic parasympathetic fibres from the pterygopalatine ganglion to the lacrimal gland (see orbital branches from pterygopalatine ganglion, below).

Frontal nerve

The frontal nerve is the largest branch of the ophthalmic nerve. It enters the orbit through the superior orbital fissure outside the common tendinous ring, and lies between the lacrimal nerve laterally and the trochlear nerve medially. It passes forwards towards the rim of the orbit on levator palpebrae superioris; about halfway along this course, it divides into the supraorbital and supratrochlear nerves.

Supraorbital nerve

The supraorbital nerve, the larger of the two terminal branches of the frontal nerve, continues forwards along levator palpebrae superioris until it leaves the orbit through the supraorbital notch or foramen. It emerges on to the forehead and supplies the mucous membrane that lines the frontal sinus, the conjunctiva and skin covering the upper eyelid, and the skin over the forehead and scalp. The postganglionic sympathetic fibres that innervate the sweat glands of the supraorbital area probably travel in the supraorbital nerve, having entered the ophthalmic nerve via its communication with the abducens nerve within the cavernous sinus.

Supratrochlear nerve

The supratrochlear nerve runs medially above the trochlea for the tendon of superior oblique. It gives a descending branch to the infratrochlear nerve and ascends on to the forehead through the supraorbital notch (or foramen) to supply the conjunctiva and skin covering the upper eyelid and the forehead.

Nasociliary nerve

The nasociliary nerve is intermediate in size between the frontal and lacrimal nerves, and is more deeply placed in the orbit, which it enters through the common tendinous ring, lying between the two rami of the oculomotor nerve. It crosses the optic nerve with the ophthalmic artery and runs obliquely below superior rectus and superior oblique to reach the medial orbital wall, where it gives off the anterior and posterior ethmoidal nerves. The nasociliary nerve also has long ciliary and infratrochlear branches and a connection with the ciliary ganglion.

Anterior ethmoidal nerve

The anterior ethmoidal nerve passes through the anterior ethmoidal foramen and canal, and enters the cranial cavity. It runs forwards in a groove on the upper surface of the cribriform plate beneath the dura mater, and descends through a slit lateral to the crista galli into the nasal cavity, where it occupies a groove on the internal surface of the nasal bone and gives off the medial and lateral internal nasal branches. For a description of the subsequent distribution of the anterior ethmoidal nerve, see Chapter 39.

Posterior ethmoidal nerve

The posterior ethmoidal nerve leaves the orbit by the posterior ethmoidal foramen and supplies the ethmoidal and sphenoidal sinuses.

Infratrochlear nerve

The infratrochlear nerve leaves the orbit below the trochlea and supplies the skin of the eyelids, the conjunctiva, lacrimal sac, lacrimal caruncle and the side of the nose above the medial canthus.

Long ciliary nerves

Two or three long ciliary nerves branch from the nasociliary nerve as it crosses the optic nerve. They accompany the short ciliary nerves, pierce the sclera near the attachment of the optic nerve, and run forwards between the sclera and choroid. They supply the ciliary body, iris and cornea, and contain postganglionic sympathetic fibres for the dilator pupillae from neurones in the superior cervical ganglion. An alternative pathway for the supply of the dilator pupillae is via the sympathetic root associated with the ciliary ganglion (**Fig. 44.18**; see p. 799).

Ramus communicans to the ciliary ganglion

The ramus communicans to the ciliary ganglion usually branches from the nasociliary nerve as the latter enters the orbit lateral to the optic nerve. It is sometimes joined by a filament from the internal carotid sympathetic plexus or from the superior ramus of the oculomotor nerve as it enters the posterosuperior angle of the ganglion.

Maxillary nerve

Most of the branches of the maxillary division of the trigeminal nerve arise in the pterygopalatine fossa. They include the zygomatic and infraorbital nerves, which pass into the orbit through the inferior orbital fissure (see Figs 38.30, 44.17).

Zygomatic nerve

The zygomatic nerve lies close to the base of the lateral wall of the orbit. It divides soon after entering the orbit into two branches, the zygomaticotemporal and the zygomaticofacial nerves, which run within the orbit for only a short distance before passing on to the face through the lateral wall of the orbit. Either they may enter separate canals within the zygomatic bone or the zygomatic nerve itself may enter the bone before dividing. For a description of the distribution of the zygomaticotemporal and zygomaticofacial nerves on the face, see Chapter 36.

Infraorbital nerve

The infraorbital nerve initially lies in the infraorbital groove on the floor of the orbit (see Fig. 44.2). As it approaches the rim of the orbit, it runs into the infraorbital canal, through which it passes to emerge onto the face at the infraorbital foramen. It supplies the skin of the lower eyelid and possibly the conjunctiva. For a description of the subsequent distribution of the infraorbital nerve on the face, see Chapter 36.

Ciliary ganglion

The ciliary ganglion is a parasympathetic ganglion concerned with the innervation of the ciliary muscle and sphincter pupillae. It is a small, flat, reddish-grey swelling, 1–2 mm in diameter, connected to the nasociliary nerve, and located near the apex of the orbit in loose fat approximately 1 cm in front of the medial end of the superior orbital fissure (see Fig.44.17). It lies between the optic nerve and lateral rectus, usually lateral to the ophthalmic artery. Its neurones, which are multipolar, are larger than those found in typical autonomic ganglia; a very small number of more typical neurones are also present.

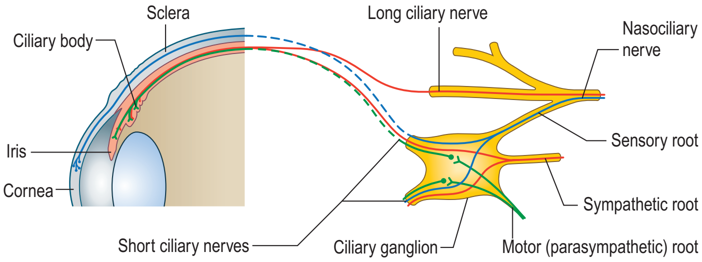

Fig. 44.18 The ciliary ganglion, with its roots and branches of distribution. Key: red, sympathetic fibres; green, parasympathetic fibres; blue, sensory fibres. Alternative pathways are given for the sympathetic fibres.

Its connections or roots (motor, sensory and sympathetic) enter or leave the ganglion posteriorly (see Fig. 44.18). Eight to ten delicate filaments, termed the short ciliary nerves, emerge anteriorly from the ganglion, arranged in two or three bundles, the lower being larger. They run forwards sinuously with the ciliary arteries, above and below the optic nerve, and divide into 15–20 branches that pierce the sclera around the optic nerve and run in small grooves on the internal scleral surface. They convey parasympathetic, sympathetic and sensory fibres between the eyeball and the ciliary ganglion; only the parasympathetic fibres synapse in the ganglion.

The parasympathetic root, derived from the branch of the oculomotor nerve to the inferior oblique, consists of preganglionic fibres from the Edinger–Westphal nucleus, which relay in the ganglion. Postganglionic fibres travel in the short ciliary nerves to the sphincter pupillae and ciliary muscle. More than 95% of these fibres supply the ciliary muscle, which is much the larger muscle in volume.

The sympathetic root contains fibres from the plexus around the internal carotid artery within the cavernous sinus. These postganglionic fibres, derived from the superior cervical ganglion, form a fine branch that enters the orbit through the superior orbital fissure inside the common tendinous ring. The fibres may pass directly to the ganglion, or may join the nasociliary nerve and travel to the ganglion in its sensory root; either way, they traverse the ganglion without synapsing to emerge into the short ciliary nerves and are distributed to the blood vessels of the eyeball. Sympathetic fibres innervating dilator pupillae may sometimes travel via the short ciliary nerves (rather than the more usual route via the ophthalmic, nasociliary and long ciliary nerves).

The sensory fibres that pass through the ciliary ganglion are derived from the nasociliary nerve. They enter the short ciliary nerves and carry sensation from the cornea, the ciliary body and the iris.

Orbital branches of the pterygopalatine ganglion

Several rami orbitales arise dorsally from the pterygopalatine ganglion and enter the orbit through the inferior orbital fissure. Branches leave the orbit through the posterior ethmoidal air sinus. There is strong experimental evidence from animal studies that postganglionic parasympathetic branches pass directly to the lacrimal gland, ophthalmic artery and choroid.

EYELIDS, CONJUNCTIVA AND LACRIMAL SYSTEM

The exposed ocular surface is protected by retractable eyelids and by a tear film produced mainly by the lacrimal gland, with contributions from glands within the eyelid and conjunctiva (a transparent mucous membrane that covers the inner surface of the eyelid and the exposed surface of the sclera) (see Fig. 45.1).

Eyelids

The eyelids (palpebrae) are two folds of modified skin that cover the anterior surface of the eye (**Fig. 44.19**). By their reflex closure, achieved by contraction of orbicularis oculi, they protect the eyes from injury and shield them from excessive light. Periodic blinking maintains a thin film

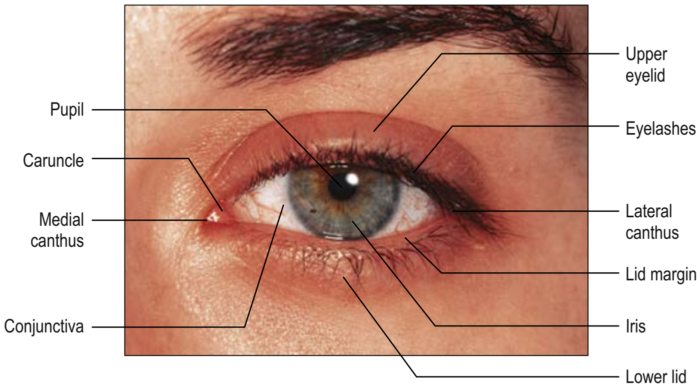

Fig. 44.19 The eyelids and anterior aspect of the eyeball. (With permission from Berkovitz BKB, Moxham BJ 2002 Head and Neck Anatomy. London: Martin Dunitz.)

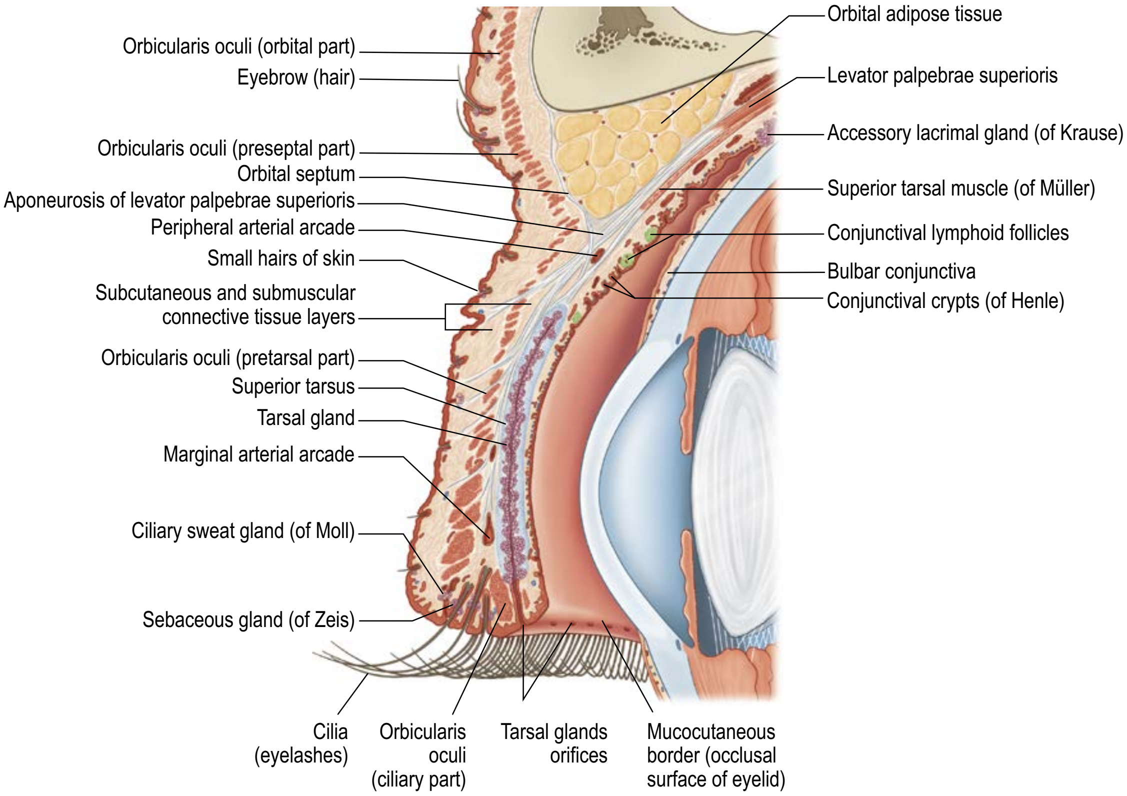
Orbicularis oculi (orbital part)
Eyebrow (hair)
Orbicularis oculi (preseptal part)
Orbital septum
Aponeurosis of levator palpebrae superioris
Peripheral arterial arcade
Small hairs of skin
Subcutaneous and submuscular connective tissue layers
Orbicularis oculi (pretarsal part)
Superior tarsus
Tarsal gland
Marginal arterial arcade
Ciliary sweat gland (of Moll)
Sebaceous gland (of Zeis)
Cilia (eyelashes)
Orbicularis oculi (ciliary part)
Tarsal glands orifices
Mucocutaneous border (occlusal surface of eyelid)
Orbital adipose tissue
Levator palpebrae superioris
Accessory lacrimal gland (of Krause)
Superior tarsal muscle (of Müller)
Conjunctival lymphoid follicles
Bulbar conjunctiva
Conjunctival crypts (of Henle)

Fig. 44.20 The upper eyelid and anterior segment of the eye, sagittal section.

of tears over the cornea that prevents desiccation; movement of the eyelids during blinking helps ensure the even distribution of the tear film and facilitates tear outflow through the nasolacrimal drainage system.

The upper eyelid is larger and more mobile than the lower eyelid and contains an elevator muscle, levator palpebrae superioris (see above). A transverse opening, the palpebral fissure, lies between the free margins of the lids, which join at their extremities (termed the medial and lateral canthus). The lateral canthus is relatively featureless. The medial canthus is approximately 2 mm lower than the lateral canthus; this distance is increased in some Asiatic groups. It is separated from the eyeball by a small triangular space, the lacrimal lake (lacus lacrimalis), in which a small, reddish body called the lacrimal caruncle is situated. The caruncle represents an area of modified skin containing some fine hairs and is mounted on the plica semilunaris, a fold of conjunctiva that is believed by some to be a vestige of the nictitating membrane of other animals.

A small elevation, the lacrimal papilla, is located on each palpebral margin approximately one-sixth of the way along from the medial canthus of the eye. A small aperture in the centre of the papilla, the punctum lacrimale, forms the opening to the lacrimal drainage system. The mean external diameter of the punctum is 0.6 mm (assessed on anterior segment optical coherence tomography *in vivo*): previous values of 0.2–0.3 mm diameter derived from cadaveric studies likely reflect fixation-induced tissue shrinkage (Timlin et al 2016). The margin of the eyelid lateral to the lacrimal papilla bears the eyelashes and is termed the ciliary part of the eyelid. The margin medial to the papilla lacks eyelashes and forms the lacrimal part of the eyelid.

When looking straight ahead, the upper eyelid overlaps the upper part of the cornea by 2–3 mm, whereas the lower lid margin lies just below the corneoscleral junction (limbus). When the eyelids are closed, the upper lid moves down to cover the whole of the cornea. Malposition of the lower eyelid is common, particularly in the elderly. Ectropion describes the rolling out of the lower eyelid so that it is no longer in contact with the cornea, leading to epiphora (watering). Entropion describes the inversion of the eyelid with corresponding inturning of the eyelashes (trichiasis), which contact the cornea and cause irritation.

Each eyelid margin is 2–3 mm from front to back. The anterior two-thirds is skin and the posterior third is conjunctival mucosa. A narrow 'grey line' lies anterior to the mucocutaneous junction and corresponds to the location of the ciliary (marginal) part of orbicularis oculi. It is an important surgical landmark, since an incision at this point affords a relatively bloodless plane along which the eyelid can be split into anterior and posterior lamellae. The eyelashes lie in front of the grey line, and the circular openings of the tarsal (Meibomian) glands lie behind it. The tarsal glands are often visible through the palpebral conjunctiva, when the eyelids are everted, as a series of parallel, faint yellow lines arranged perpendicular to the lid margins.

Eyelashes are short, thick, curved hairs, arranged in double or triple rows. The upper lashes, which are longer and more numerous, curve upwards, while those in the lower lid curve down, so that upper and lower lashes do not interlace when the lids are closed.

The eyelids pass to adjacent facial skin without obvious demarcation, although their limits are clearly defined in pathological conditions such as oedema. Various skin folds or furrows are of topographical interest. A prominent superior palpebral furrow or fold lies approximately opposite the upper margin of the tarsal plate and is deeply recessed when the lids are open. A prominent feature of Asian eyes is an absent or very low eyelid skin fold, which together with an inferior extension of the pre-aponeurotic fat pad gives rise to a fuller upper eyelid appearance and a narrower palpebral fissure (Saonanon 2014). Furthermore, Asians typically have a skin flap, the epicanthus, which begins laterally in the superior palpebral fold and progresses medially to cover the medial canthus. Infant Caucasians frequently have a transient epicanthus that sometimes persists in the adult. A less prominent inferior palpebral furrow occupies a similar position in the skin of the lower lid and deepens on downward gaze. A nasojugal furrow extends obliquely from the medial lower margin of the bony orbit to the cheek, and a malar furrow may be seen laterally along the inferior orbital rim in middle age, but only infrequently and faintly in the young.

The palpebral fissure undergoes complex changes during infancy (Fox 1966, Paiva et al 2001). At birth, the fissure is relatively narrow, but then widens considerably giving rise to the rounder appearance of the palpebral fissure in infancy as compared to that of the adult. The peak level of growth in the horizontal dimension of the palpebral fissure is reached between the ages of 17 and 19 years, in the vertical dimension between 10 and 13 years (Park et al 2008).

Structure

From its anterior surface inwards, each eyelid consists of skin, subcutaneous connective tissue, fibres of the palpebral part of orbicularis oculi (see Fig. 36.18A), submuscular connective tissue, the tarsal plate (tarsus), tarsal glands and orbital septum, and the palpebral conjunctiva (Fig. 44.20). The upper lid also contains the aponeurosis of levator palpebrae superioris. The skin is extremely thin and is continuous at the palpebral margins with the conjunctiva. The subcutaneous connective tissue is very delicate, seldom contains any adipose tissue, and lacks elastic fibres.

The palpebral part of orbicularis oculi is subdivided anatomically into marginal, pretarsal and preseptal parts. The palpebral muscle fibre bundles are thin and pale, and lie parallel with the palpebral margins. Deep to them is the submuscular connective tissue, a loose fibrous layer that is continuous in the upper lid with the subaponeurotic layer of the scalp; effusions of blood or pus at this level can therefore pass down from the scalp into the upper eyelid. The main nerves lie in the submuscular layer, which means that local anaesthetics should be injected deep to orbicularis oculi.

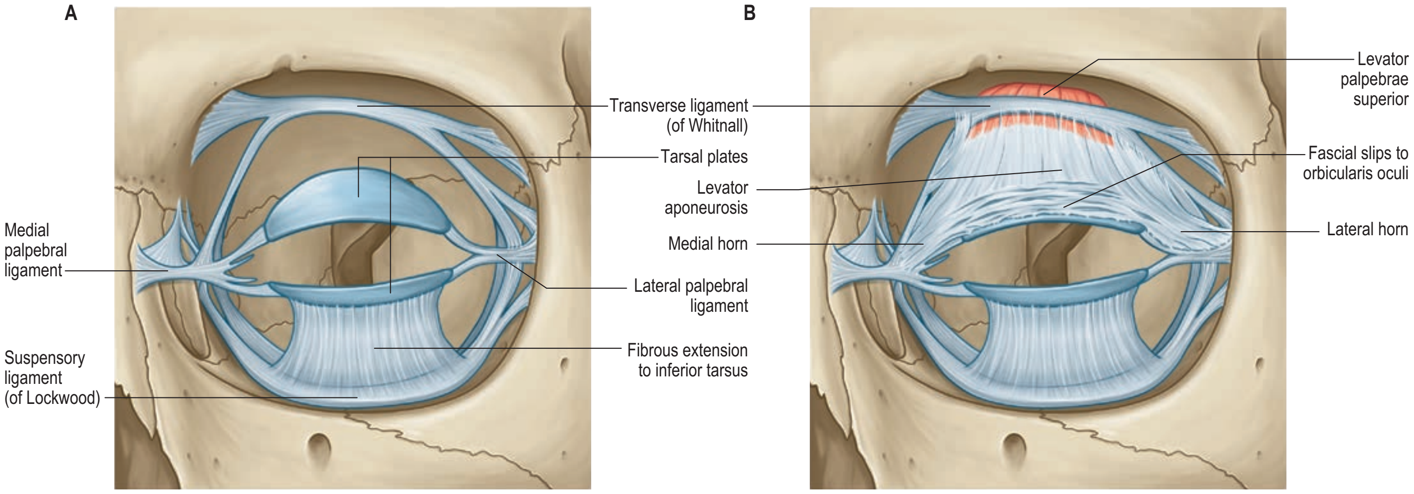
A
B
Transverse ligament (of Whitnall)
Tarsal plates
Levator aponeurosis
Medial horn
Lateral palpebral ligament
Fibrous extension to inferior tarsus
Medial palpebral ligament
Suspensory ligament (of Lockwood)
Levator palpebrae superior
Fascial slips to orbicularis oculi
Lateral horn

Fig. 44.21 **A**, The tarsal plates and their attachments. **B**, The anterior insertion of levator palpebrae superioris.

Tarsal plates

The tarsal plates (**Fig. 44.21A**) are thin, elongated, crescent-shaped plates of firm, dense fibrous tissue approximately 2.5 cm long. There is one in each eyelid to provide support and determine eyelid form. Each is convex and conforms to the configuration of the anterior surface of the eyeball. The free ciliary border is straight and adjacent to the eyelash follicles. The orbital border is convex and attached to the orbital septum. The superior tarsus, the larger of the two, is semi-oval, approximately 10 mm in height centrally; its inferior edge is parallel to, and approximately 2 mm from, the lid margin. The smaller inferior tarsus is narrower and approximately 4 mm in vertical height.

The tarsal plates are connected to the margins of the orbit by the orbital septum and by the medial and lateral palpebral (canthal) ligaments (see Fig. 44.21A). The medial palpebral ligament passes from the medial ends of the two tarsal plates to the anterior lacrimal crest and the frontal process of the maxilla. It splits at its insertion into the tarsal plates to surround the lacrimal canaliculi, and lies in front of the nasolacrimal sac and the orbital septum. The lateral palpebral ligament is relatively poorly developed. It passes from the lateral ends of the tarsal plates to a small tubercle on the zygomatic bone within the orbital margin and is more deeply situated than the medial palpebral ligament. It lies beneath the orbital septum and the lateral palpebral raphe of orbicularis oculi.

The deepest fibres of the aponeurosis of levator palpebrae superioris are attached to the anterior surface of the superior tarsus (see Fig. 44.21B). The superior and inferior tarsal plates are also associated with a thin lamina of smooth muscle forming the superior and inferior tarsal muscles, respectively. Opposite the equator of the eye, the superior tarsal muscle passes from the inferior face of levator palpebrae superioris to a fibrous extension that projects to the upper margin of the superior tarsus (see Fig. 44.20). The muscle is innervated by the sympathetic nervous system and, on contraction, elevates the eyelid. Although it may be regarded as supplementing the action of the levator muscle, its full role is not clear. The mild ptosis that is a characteristic feature of Horner's syndrome is the result of an interruption to the sympathetic supply to the superior tarsal muscle. A corresponding but less prominent inferior tarsal muscle in the lower eyelid unites the inferior border, and possibly also the anterior surface, of the inferior tarsus to the capsulopalpebral fascia, which is the anterior expansion of the fused fascial sheath of inferior rectus and inferior oblique. Contraction of inferior rectus during downward gaze therefore also pulls the lower lid downwards. The lower lid is capable of depressing by 4–5 mm, although it is not equipped with a striated muscle counterpart to the levator of the upper lid.

Palpebral glands

Tarsal (Meibomian) glands are modified sebaceous glands embedded in the tarsi (**Fig. 44.22**): they secrete meibum, a lipid rich secretion that mixes with aqueous tears during the blink to form the tear film (Butovich 2017). There are between 20 and 40 individual tarsal glands in the upper eyelid and 20 to 30 in the lower, arranged in approximately parallel rows perpendicular to the eyelid margin: their number declines with age (Arita et al 2017). Tarsal glands occupy the full tarsal height and are therefore longer centrally where the tarsi are higher. Each gland consists of a long central canal surrounded by numerous rounded secretory acini (Obata 2002). Differentiated acinar cells secrete into the central canal in a holocrine process. Basal cells in the acini do not contain lipid droplets: differentiating cells undergo a centripetal movement accompanied by enlargement of the cells and lipogenesis. Each canal is lined at its orifice by stratified epithelium and opens on the free palpebral margin just anterior to the mucocutaneous junction.

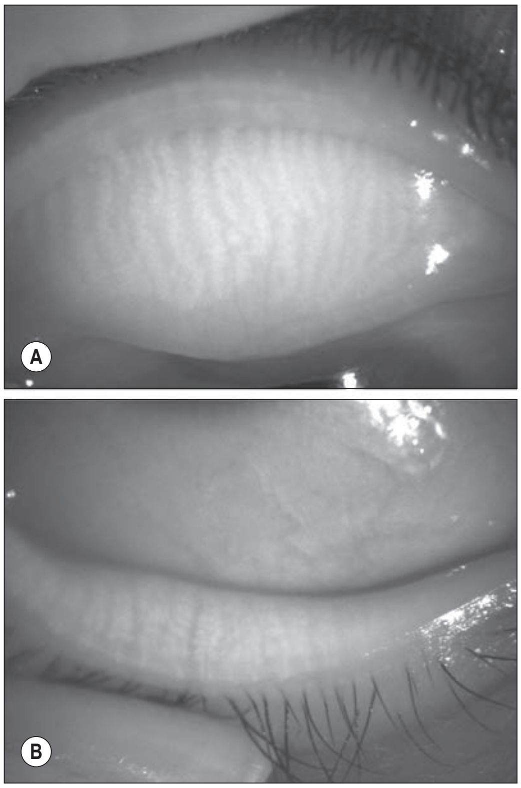

Fig. 44.22 Tarsal (Meibomian) glands in the upper (**A**) and lower (**B**) eyelids imaged by noninvasive infrared meibography. Meibomian glands can be seen as areas of high reflectivity. Glands in the upper lid are longer and more slender. (From Arita R, Fukuoka S, Morishige N 2017 New insights into the morphology and function of Meibomian glands. Exp Eye Res. 163:64–71.)

The secretion of the tarsal glands spreads over the margins of the eyelids, and so an oily layer is drawn over the tear film as the palpebral fissure opens after a blink, reducing evaporation and contributing to tear film stability. The presence of the oily, hydrophobic secretions of tarsal glands along the margins of the eyelids also inhibits the spillage of tears on to the face. Obstruction of the tarsal gland ducts by lipid and cellular debris may result in lipogranulomatous inflammation and the clinical manifestations of an internal hordeolum or chalazion: glandular dysfunction is a major cause of evaporative dry eye.

Small sebaceous glands (of Zeis) and sweat glands (of Moll) are associated with the eyelashes (see Fig. 44.20) and are prone to infection, producing an external hordeolum (stye).

Vascular supply and lymphatic drainage

The arterial supply to the eyelids is derived principally from the medial and lateral palpebral branches of the ophthalmic artery. Their branches course laterally along the tarsal edges to form superior and inferior arcades (two in the upper eyelid and one in the lower). The eyelids are also supplied by branches of the infraorbital, facial, transverse facial and superficial temporal arteries.

The veins that drain the eyelids are larger and more numerous than the arteries; they pass either superficially to veins on the face and forehead, or deeply to the ophthalmic veins within the orbit.

The lymph vessels that drain the eyelids and conjunctiva start in a superficial plexus beneath the skin, and in a deep plexus in front of and behind the tarsi. These plexuses communicate with one another, and medial and lateral sets of vessels arise from them. The lateral lymph vessels drain the whole thickness of the lateral part of the upper and lower lids and pass laterally from the lateral canthus to end in the superficial and deep parotid lymph nodes. The medial lymph vessels drain the skin over the medial part of the upper eyelid, the whole thickness of the medial half of the lower lid and the caruncle and follow the course of the facial vein to end in the submandibular group of lymph nodes.

Innervation

The ophthalmic and maxillary divisions of the trigeminal nerve innervate the eyelids. The upper eyelid is supplied mainly by the supraorbital branch of the frontal nerve. Additional contributions come from the lacrimal nerve, the supratrochlear branch of the frontal nerve, and the infratrochlear branch of the nasociliary nerve. The nerve supply to the lower eyelid is derived principally from the infraorbital branch of the maxillary nerve, with small contributions from the lacrimal and infratrochlear nerves.

Conjunctiva

The conjunctiva is a thin, transparent mucous membrane that extends from the eyelid margins anteriorly, providing a lining to the lids, before turning sharply on itself to form the fornices; from here, it is reflected on to the globe to cover the sclera up to its junction with the cornea. The conjunctiva thus forms a sac that opens anteriorly through the palpebral fissure (**Fig. 44.23**). At the free palpebral margins, the conjunctiva is continuous with the skin of the eyelids, the lining epithelium of the ducts of the tarsal glands, and with the lacrimal canaliculi and lacrimal sac (see below). The continuity between the conjunctiva and the nasolacrimal duct and nasal mucosa is important in the spread of infection.

Conjunctival goblet cells contribute the mucin component of the preocular tear film and play a central role in the defence of the ocular surface against microbial infection. The conjunctiva is conventionally divided into five regions: marginal, tarsal, orbital, bulbar and limbal): the marginal, tarsal and orbital regions are collectively referred to as the palpebral conjunctiva (see Fig. 44.23).

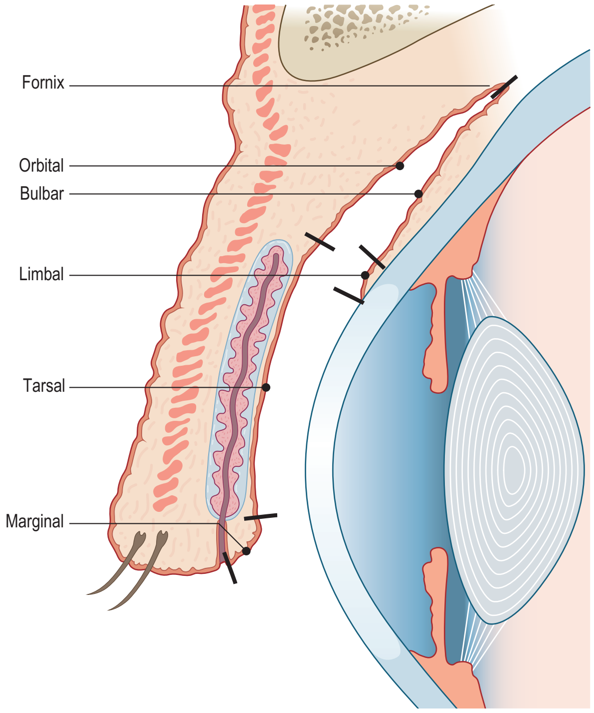

Fig. 44.23 The regions of the conjunctiva, sagittal section.

The marginal zone extends from a line immediately posterior to the openings of the tarsal glands and passes around the eyelid margin to continue on the inner surface of the lid as far as the subtarsal groove (a shallow sulcus that marks the marginal border of the tarsus). The tarsal conjunctiva is highly vascular and is firmly attached to the underlying tarsal plate. The orbital zone extends as far as the fornices, which mark the line of reflection of the conjunctiva from the lids on to the eyeball. The conjunctiva is more loosely attached to underlying tissues over the orbital zone and so folds readily. Elevations of the conjunctival surface in the form of papillae and lymphoid follicles (part of the mucosa-associated lymphoid tissue, MALT) are commonly observed in this region (Knop and Knop 2002).

Ducts of the lacrimal gland open into the lateral part of the superior fornix. The bulbar conjunctiva is loosely connected to the eyeball over the exposed sclera; it is thin and transparent, and readily permits the visualization of conjunctival and episcleral blood vessels. The loose attachment of the conjunctiva to the fascial sheath of the globe (Tenon's capsule) in this region means that the conjunctiva is freely movable here, but as the bulbar conjunctiva approaches the cornea, its surface becomes smoother and its attachment to the sclera increases. The limbal conjunctiva extends approximately 1–1.5 mm around the cornea and contains a dense network of capillaries.

Structure

The conjunctiva is composed of an epithelial layer and an underlying fibrous layer or substantia propria. The type of the epithelium and the thickness of the substantia propria vary with location. At the margin of the lids, the epithelium is non-keratinized stratified squamous and 10–12 cells thick. The epithelium of the tarsal conjunctiva thins to two or three layers and consists of columnar and flat surface cells. Near the fornices, the cells are taller, and a trilaminar conjunctival epithelium covers much of the bulbar conjunctiva. It thickens closer to the corneoscleral junction and then changes to stratified squamous epithelium typical of the cornea. A proportion of limbal conjunctival epithelial cells serve as stem cells for the corneal epithelium, which means that this region of the conjunctiva is essential for maintaining corneal integrity.

Mucous-secreting goblet cells are scattered within the conjunctival epithelium. They show a marked regional variation in density, being most frequent in conjunctival regions normally covered by the eyelids, and reduced in number within exposed inter-palpebral locations (Doughty 2012).

The substantia propria, or fibrous layer, is thickest at the fornix and thinnest over the tarsi where conjunctival attachment is firmest. With the exception of the tarsal conjunctiva, the substantia propria adjacent to the epithelium is mainly loose. It merges with the fibrous fascia bulbi and episclera in the limbal and bulbar regions, and is loosely attached to the sheaths of the recti. At the fornix, it is continuous with orbital fascial tissues and has loose attachments to the overlying tendon of levator palpebrae superioris and the superior tarsal muscle fascia superiorly, an arrangement that provides support for the fornix during eyeball rotation.

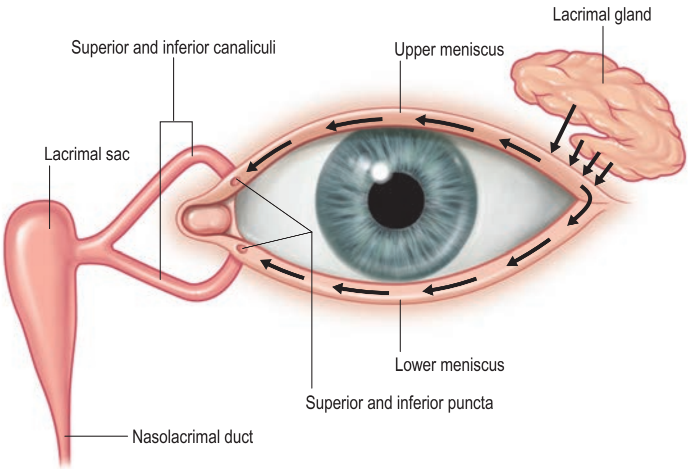

Fig. 44.24 A representation of tear dynamics on the ocular surface. Tears are produced by the lacrimal gland and flow within the upper and lower meniscus. Tears drain sequentially through the puncta, canaliculi, lacrimal sac and nasolacrimal duct.

Vascular supply and lymphatic drainage

The arteries of the palpebral conjunctiva are derived from the vascular arcades of the eyelids. Many of the small vessels of the eyelid drain to the conjunctival veins, which, in turn, pass back to the orbital and facial veins. The substantia propria of the tarsal and orbital conjunctiva is richly vascular. A dense capillary network is arranged in a single subepithelial lamina, a distribution that meets the metabolic requirement of the cornea during sleep, when oxygen is available to the cornea only through this vascular system. The bulbar conjunctiva receives blood from the palpebral arcades and from the anterior ciliary arteries that reach the conjunctiva on the orbital surface of the recti. The veins drain by the same route and join the ophthalmic veins.

Lymphatics drain into pre-auricular and submandibular lymph nodes.

Innervation

The conjunctiva is innervated by sensory nerves from the same ophthalmic and maxillary branches of the trigeminal nerve that serve the eyelids. Autonomic nerve fibres are abundant in the conjunctiva, particularly in bulbar and limbal regions, and are probably vasomotor in function.

Lacrimal system

The lacrimal system consists of structures responsible for the production of tears (principally, the main lacrimal gland with a contribution from accessory lacrimal glands) and the lacrimal drainage pathway that collects the tear fluid and conveys it into the nasal cavity (paired lacrimal canaliculi, lacrimal sac and nasolacrimal duct) (**Fig. 44.24**).

The total tear volume is approximately 7 µl. It is distributed within the precorneal tear film (1–2 µl), and along the upper and lower marginal tear strips (5–6{ ts}µl), wedge-shaped menisci that run along the posterior border of the lid margins and join together at the canthi. Reflex tear secretion, as measured by the Schirmer test in the unanaesthetized eye, decreases with increasing age when investigated in the 20–80-year-old age range. Tear volume and the concentration of the tear proteins lysozyme and lactoferrin also decrease with age (Rocha et al 2008).

Lacrimal gland

The lacrimal gland is the primary producer of the aqueous component of the tear layer. Its secretion is a watery fluid with an electrolyte content similar to that of plasma. It contains several proteins that play key roles in protecting the ocular surface from microbial infection (e.g. lysozyme, lactoferrin, immunoglobulin A (IgA)) and in maintaining ocular surface epithelial integrity.

The lacrimal gland consists of orbital and palpebral parts that are continuous posterolaterally around the concave lateral edge of the aponeurosis of levator palpebrae superioris. The orbital part, about the size and shape of an almond, lodges in a shallow fossa on the medial aspect of the zygomatic process of the frontal bone, just within the orbital margin. It lies above levator palpebrae superioris and, laterally, above lateral rectus. Its lower surface is connected to the sheath of levator palpebrae superioris and its upper surface is connected to the orbital periosteum. Its anterior border is in contact with the orbital septum and its posterior border attached to the orbital fat. The palpebral part, about one-third the size of the orbital part, is subdivided into two or three lobules and extends below the aponeurosis of levator palpebrae superioris into the lateral part of the upper lid, where it is attached to the superior conjunctival fornix and is visible through the conjunctiva when the lid is everted. The lacrimal gland reduces in size with age (Tamboli et al 2011) and may be congenitally absent (Keith and Boldt 1986).

The main ducts of the lacrimal gland, up to 12 in number, discharge into the conjunctival sac at the superior lateral fornix. Those from the orbital part penetrate the aponeurosis of levator palpebrae superioris to join those from the palpebral part, which means that excision of the palpebral part is functionally equivalent to total removal of the gland (Maitchouk et al 2000).

Numerous small accessory lacrimal glands (of Krause and of Wolfring) account for approximately 10% of the total lacrimal secretory mass: their presence may in part explain why the ocular surface does not dry up after extirpation of the main lacrimal gland (Stevenson et al 2016), although their contribution to basal tear secretion is controversial (Conrady et al 2016). The glands of Krause are found in the conjunctival fornices, particularly in the superior fornix. The glands of Wolfring lie along the nonmarginal border of both tarsal plates. The accessory lacrimal glands are structurally and histologically similar to the main lacrimal gland (Obata 2006) but apparently lack parasympathetic innervation.

Microstructure

The lacrimal gland is lobulated and tubulo-acinar in form. Its secretory units are acini similar to those found in the salivary glands (**Fig. 44.25**) (Ruskell 1975). Acini consist of secretory cells that discharge their product into a central lumen continuous with an intercalated duct

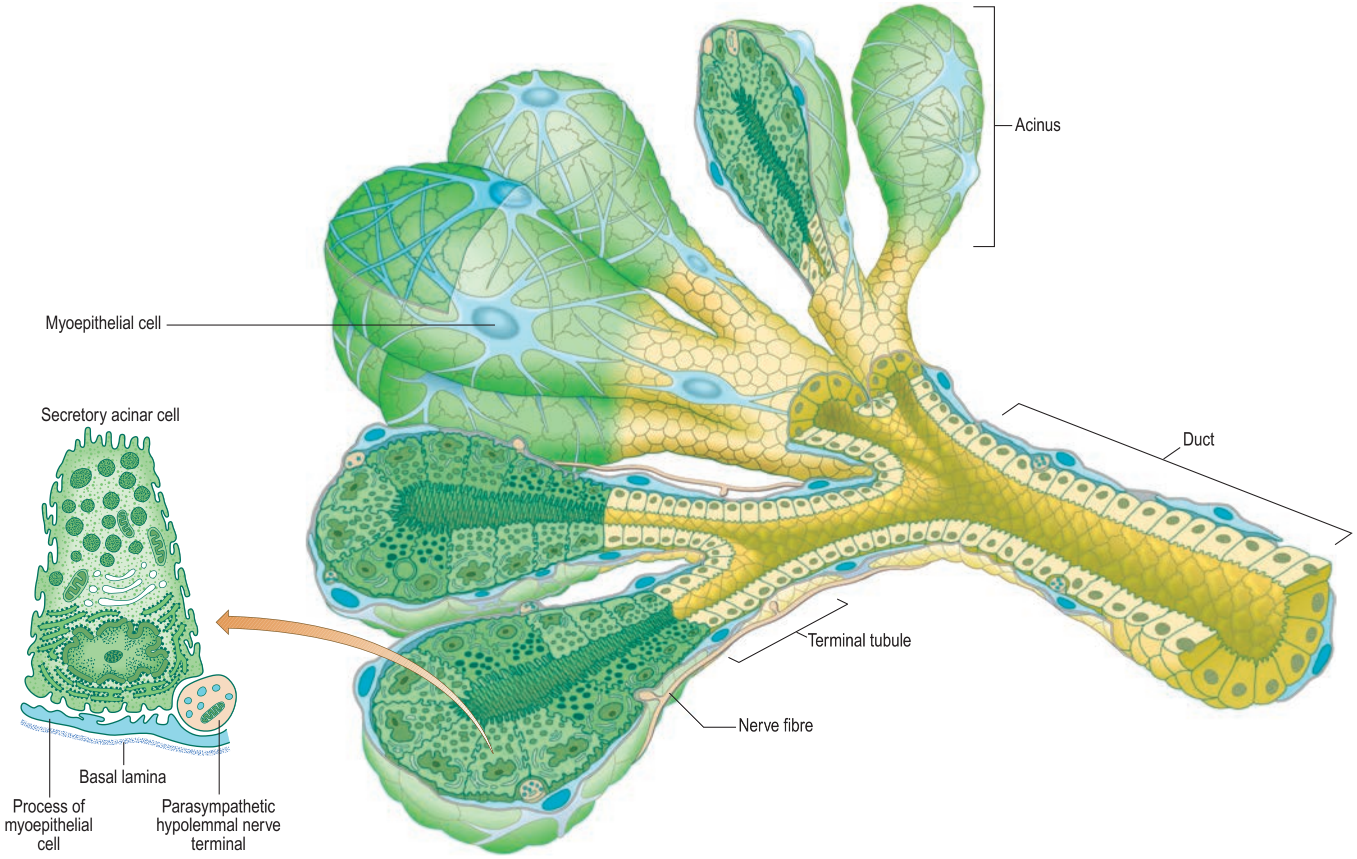

Fig. 44.25 The organization of the secretory units in the lacrimal gland.

formed from a single layer of epithelial cells that lack secretory granules. Myoepithelial cells extend processes around the perimeter of acini and ducts; their contraction imparts a mechanical force on the acini and ducts, which promotes the expulsion of tears from the gland. The interstices of the gland are composed of loose connective tissue that contains numerous immune cells, mainly B-lymphocytes and plasma cells (particularly IgA-secreting cells). The ageing gland exhibits histological changes including diffuse atrophy and periductal fibrosis.

Vascular supply

The lacrimal gland receives its arterial blood supply from the lacrimal branch of the ophthalmic artery. It may also receive blood from the infraorbital artery. Venous drainage is into the superior ophthalmic vein.

Innervation

The lacrimal gland is innervated by secretomotor postganglionic parasympathetic fibres from the pterygopalatine ganglion (Ch. 38). They reach the gland either via zygomatic and lacrimal branches of the maxillary nerve, or by passing directly from the ganglion (Ruskell 2004). Postganglionic sympathetic fibres from the superior cervical ganglion supply the lacrimal gland and may be involved in the regulation of blood flow and the modulation of gland secretion (Dartt 2009).

Lacrimation reflex

The lacrimation reflex produces a significant increase in tear volume and is elicited by thermal, mechanical or chemical stimulation of polymodal nociceptors in the conjunctiva and cornea (Situ and Simpson 2010). The afferent limb of the reflex involves branches of the ophthalmic nerve, with an additional contribution from the infraorbital nerve if the conjunctiva of the lower eyelid is involved. Corneal afferents travelling in these nerves terminate in the nucleus of the spinal tract of the trigeminal nerve: experimental tract tracing studies in animals have implicated the transition between the trigeminal subnuclei caudalis and interpolaris as an important area that projects to preganglionic parasympathetic neurones lying close to or within the superior salivatory nucleus and to the facial motor nucleus, both regions involved in the efferent limb of the blinking reflex (Meng and Kurose 2013). The neural mechanism for controlling and maintaining basal tear production is less clear. Lacrimation may also occur in response to emotional triggers without any irritation of ocular structures, when it may be accompanied by alterations in the mimetic facial muscles, vocalizations and sobbing (Gračanin et al 2014): emotional lacrimation is thought to be mediated by limbic projections to the superior salivatory nucleus.

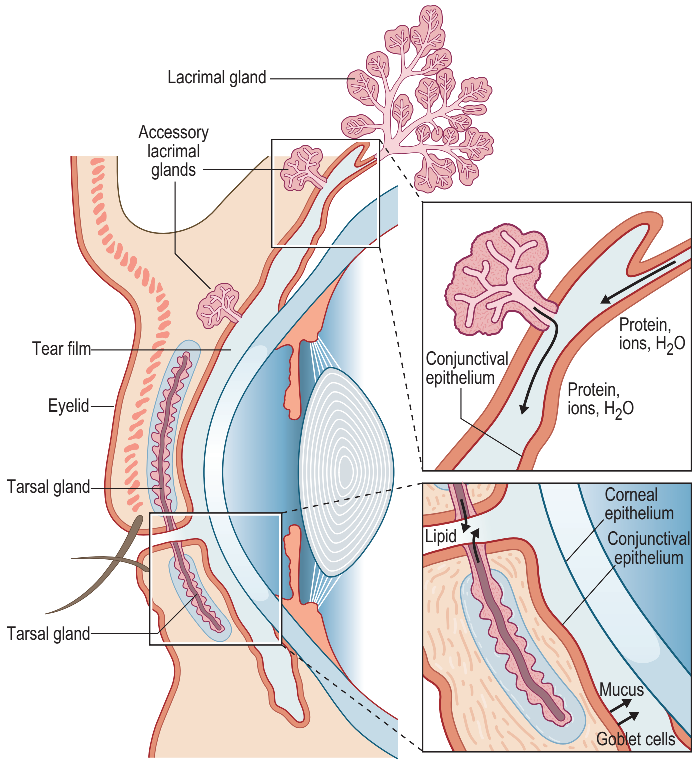

Fig. 44.26 Orbital glands that contribute the various components of the preocular tear film. The aqueous component (consisting primarily of proteins, ions and water) is produced by the main and accessory lacrimal glands. Tarsal glands in the eyelids produce the lipid layer of the tear film, and the mucous component is derived from conjunctival goblet cells.

Preocular tear film

The tear film is a complex fluid 2–5 μm thick that covers the exposed parts of the ocular surface framed by the eyelid margins. Classically, the tear film has been regarded as a trilaminar structure, with a superficial lipid layer (secreted by the tarsal glands) that overlies an aqueous phase (derived from the main and accessory lacrimal glands) and an inner mucinous layer (produced mainly by conjunctival goblet cells) (**Fig. 44.26**). Recent evidence suggests that the preocular tear film behaves as a single dynamic functional unit consisting of a muco-aqueous gel layer, lying beneath, but partially integrated with, an overlying lipid layer (Willcox et al 2017).

The tear film performs a number of important functions. By smoothing out irregularities of the corneal epithelium, it creates an even surface of good optical quality that is reformed with each blink. The air–tear interface forms the principal refractive surface of the optical system of the eye. Since the cornea is avascular, it is dependent on the tear film for its oxygen provision. When the eye is open, the tear film is in a state of equilibrium with the oxygen in the atmosphere, and gaseous exchange takes place across the tear–epithelial interface. The constant turnover of the tear film also provides a mechanism for the removal of metabolic waste products. Tears play a major role in the defence of the eye against microbial colonization; the washing action of the tear fluid reduces the likelihood of microbial adhesion to the ocular surface, and the tears contain a host of protective antimicrobial proteins. There is clinical evidence that tear fluid secretion may increase as a compensatory response to the loss of tear film stability caused by deficiency of the oily layer (Arita et al 2017).

Lacrimal drainage pathway

There is a constant turnover of tears; their production is matched by elimination. Some tears are lost by evaporation or absorption across the conjunctiva, but the majority are eliminated via the nasolacrimal drainage system (see Fig. 44.24). Tears collect at the medial canthal angle, where they drain into the puncta of the upper and lower lids. The puncta drain into lacrimal canaliculi running just below the margins of the eyelids. Each lid contains one canaliculus, approximately 10 mm long, that passes vertically from its punctum for about 2 mm, then widens to form an ampulla, before passing medially (horizontally) towards the lacrimal sac: the superior canaliculus is smaller and shorter than its inferior counterpart. The canaliculi are at first anterior to the crura of the medial canthal ligament, then pass either through or around the crura to lie posterior to the canthal ligament and continue to the lacrimal sac within the fascial tissue of the posterior arm of the canthal ligament (Dutton 2011). The canaliculi almost always unite to form a common canaliculus (1–2 mm long) before entering the posterolateral wall of the lacrimal sac at the common internal punctum (Maliborski and Różycki 2014). An inconstant fold has been described at this point, but it is not clear whether it constitutes a barrier to reflux of tears into the lacrimal sac. Effective drainage involves a number of mechanisms, including capillary attraction, contraction of the lacrimal part of orbicularis oculi associated with the vertical part of each canaliculus and the closing and opening phases of blinking (Beigi et al 2015). Overproduction of tears or their inadequate or blocked drainage leads to epiphora (welling of tears in the eye and lid margin overspill onto the cheek). Congenital absence of lacrimal puncta, supernumerary lacrimal puncta and canaliculi, have all been described (Satchi and McNab 2010).

The mucosa lining the canaliculi is a non-keratinized stratified squamous epithelium lying on a basement membrane and surrounded by a lamina propria rich in elastic fibres: the canaliculi are therefore easily dilated when probed. Striated muscle fibres of orbicularis oculi interweave on each side of a canaliculus in a manner suggesting a sphincter-like spiralling, and supporting the claim that lumen size is regulated on blinking, possibly facilitating tear drainage.

The lacrimal sac is the closed upper end of the nasolacrimal duct. It is approximately 12 mm long and lies in a fossa in the lacrimal bone (with a variable contribution from the frontal process of the maxilla) in the anterior part of the medial wall of the orbit (see Fig. 44.2). The sac is bounded anteriorly by the anterior lacrimal crest of the maxilla and posteriorly by the posterior lacrimal crest of the lacrimal bone. Its closed upper end is laterally flattened, its lower part is rounded and merges into the nasolacrimal duct, and the lacrimal canaliculi open into its lateral wall near its upper end.

A layer of lacrimal fascia, continuous with the orbital periosteum, passes between the lacrimal crest of the maxilla and the lacrimal bone. It forms a roof and lateral wall to the lacrimal fossa and separates the lacrimal sac from the medial palpebral ligament anteriorly and the lacrimal part of orbicularis oculi posteriorly. A plexus of minute veins lies between the fascia and the sac. The upper half of the lacrimal fossa is related medially to the anterior ethmoidal sinuses, and the lower half to the anterior part of the middle meatus. The lacrimal sac has a fibroelastic wall and is lined internally by mucosa that is continuous with the conjunctiva through the lacrimal canaliculi, and with the nasal mucosa through the nasolacrimal duct (Paulsen 2003).

The nasolacrimal duct is approximately 18 mm long, and descends from the lacrimal sac to open anteriorly in the inferior meatus of the nose at an expanded orifice. A fold of mucosa (plica lacrimalis) forms an imperfect valve just above its opening (ostium lacrimalis). The duct runs down an osseous canal formed laterally and anteriorly by the lacrimal sulcus of the frontal process and the body of maxilla, and medially and posteriorly by the lacrimal sulcus of the lacrimal bone and the lacrimal process of the inferior nasal concha. It is narrowest in the middle and is directed downwards, backwards and a little laterally. The mucosa of the lacrimal sac and the nasolacrimal duct has a bilaminar columnar epithelium, ciliated in places. A rich plexus of veins forms erectile tissue around the duct; engorgement of these veins may obstruct the duct. Congenital nasolacrimal duct obstruction has been reported to trouble 5–20% of newborns: the obstruction is due to the failure of nasolacrimal duct to fully canalise at birth and typically resolves spontaneously during the early months of life (Sathiamoorthi et al 2018).

Bonus e-book content

Fig. 44.5 B, A sagittal oblique CT scan with contrast medium through the orbit; the subject was looking towards their feet.

Fig. 44.6 C, An axial T2-weighted magnetic resonance imaging (MRI) scan through the left orbit.

Fig. 44.7 B, A coronal T1-weighted MRI scan through the left orbit, cut through a plane 5 mm behind the posterior pole of the globe.

Key references

Bertelli E, Regoli M, Bracco S 2017 An update on the variations of the orbital blood supply and hemodynamic. Surg Radiol Anat 39(5):485–496.

A review of the blood supply to the orbit focusing on: (a) variations of the ophthalmic artery origin; (b) contribution of the external carotid artery to the orbital blood supply; (c) orbital haemodynamics.

Dartt DA 2009 Neural regulation of lacrimal gland secretory processes: relevance in dry eye diseases. Prog Retin Eye Res 28:155–177.

A review that focuses on the neural regulation of lacrimal gland secretion under normal and dry eye conditions.

Demer JL 2002 The orbital pulley system: a revolution in concepts of orbital anatomy. Ann N Y Acad Sci 956:17–32.

A study that provides a comprehensive structural investigation of the orbital pulley system and discusses its putative role in influencing ocular rotation.

Knop E, Knop N 2002 A functional unit for ocular surface immune defence formed by the lacrimal gland, conjunctiva and lacrimal drainage system. Adv Exp Med Biol 506B:635–644.

A review of the structural organization of eye-associated lymphoid tissues and their role in the immune defence of the eye.

Koornneef L 1977 The architecture of the musculo-fibrous apparatus in the human orbit. Acta Morphol Neerl Scand 15:35–64.

A study using serial histological sections and thicker tissue slices of whole orbits to reconstruct the spatial organization of the orbital connective tissue system.

Leigh RJ, Zee DS 2015 The Neurology of Eye Movement, 5th ed. Oxford: Oxford University Press.

The definitive textbook describing the neurological basis of normal eye movements and ocular motility disorders.

Miller JM 2007 Understanding and misunderstanding extraocular muscle pulleys. J Vis 7:10.1–15.

A discussion of the issues and controversies regarding the role of extraocular muscle pulleys in health and disease.

Ruskell GL 1975 Nerve terminals and epithelial cell variety in the human lacrimal gland. Cell Tiss Res 138:121–136.

The first comprehensive description of the ultrastructure of the human lacrimal gland.

Willcox MDP, Argüeso P, Georgiev GA et al 2017 TFOS DEWS II Tear Film Report. Ocul Surf 15:366-403.

Part of the 2017 Tear Film and Ocular surface Dry Eye Workshop Report (TFOS DEWS II) dealing with the structure and function of the preocular tear film and its role in dry eye disease.

References

Amiez C, Petrides M 2009 Anatomical organization of the eye fields in the human and non-human primate frontal cortex. Prog Neurobiol 89:220–30.

Arita R, Fukuoka S, Morishige N. 2017 New insights into the morphology and function of meibomian glands. Exp Eye Res 163:64–71.

Bentley RP, Sgouros S, Natarajan K et al 2002 Normal changes in orbital volume during childhood. J Neurosurg 96:742–6.

Bertelli E, Regoli M, Bracco S. 2017 An update on the variations of the orbital blood supply and hemodynamic. Surg Radiol Anat 39:485–96.

A review of the blood supply to the orbit focusing on: (a) variations of the ophthalmic artery origin; (b) contribution of the external carotid artery to the orbital blood supply; (c) orbital haemodynamics.

Beigi B, Gupta D, Luo YH et al 2015 Punctal function in lacrimal drainage: the 'pipette sign' and functional ectropion. Clin Exp Optom 98:366–9.

Brady AP, Stack JP, O'Keeffe M 1992 Congenital absence of extraocular muscles: MR demonstration. J Comput Assist Tomogr 16:490–1.

Burm JS, Chung CH, Oh SJ 1999 Pure orbital blowout fracture: new concepts and importance of medial orbital blowout fracture. Plast Reconstr Surg 103:1839–49.

Butovich IA 2017 Meibomian glands, meibum, and meibogenesis. Exp Eye Res 163:2–16.

Conrady CD, Joos ZP, Patel PCK 2016 Review: the lacrimal gland and its role in dry eye. J Ophthalmol 2016:7542929.

Dartt DA 2009 Neural regulation of lacrimal gland secretory processes: relevance in dry eye diseases. Prog Retin Eye Res 28:155–77.

A review that focuses on the neural regulation of lacrimal gland secretion under normal and dry eye conditions.

Davison M, Padroni S, Bunce C et al 2007 Sub-Tenon's anaesthesia versus topical anaesthesia for cataract surgery. Cochrane Database Syst Rev 3:CD006291.

Demer JL 2002 The orbital pulley system: a revolution in concepts of orbital anatomy. Ann N Y Acad Sci 956:17–32.

A study that provides a comprehensive structural investigation of the orbital pulley system and discusses its putative role in influencing ocular rotation.

Demer JL 2016 Optic nerve sheath as a novel mechanical load on the globe in ocular duction. Invest Ophthalmol Vis Sci 57:1826–38.

Doughty MJ 2012 Goblet cells of the normal human bulbar conjunctiva and their assessment by impression cytology sampling. Ocul Surf 10:149–69.

Dutton JD 2011 Atlas of Clinical and Surgical Orbital Anatomy, 2nd ed. Philadelphia: Elsevier.

Escaravage GK Jr, Dutton JJ 2013 Age-related changes in the pediatric human orbit on CT. Ophthal Plast Reconstr Surg 29:150–6.

Fox SA 1966 The palpebral fissure. Am J Ophthalmol 62:73–8.

Gračanin A, Bylsma LM, Vingerhoets AJ 2014 Is crying a self-soothing behavior? Front Psychol 28:502.

Guo H, Gao Z, Chen W 2016 The biomechanical significance of pulley on binocular vision. Biomed Eng Online 15(Suppl 2):137.

Hayreh SS, Dass R 1962a The ophthalmic artery. II. Intra-orbital course. Br J Ophthal 46:165–85.

Hayreh SS, Dass R 1962b The ophthalmic artery: I. Origin and intra-cranial and intra-canalicular course. Br J Ophthalmol 46:65–98.

Hayreh SS 2006 Orbital vascular anatomy. Eye (Lond) 20:1130–44.

Huynh-Le P, Natori Y, Sasaki T 2005 Surgical anatomy of the ophthalmic artery: its origin and proximal course. Neurosurgery 57(4 Suppl):236–41.

Iaconetta G, de Notaris M, Cavallo LM et al 2010 The oculomotor nerve: microanatomical and endoscopic study. Neurosurgery 66:593–601.

Isaacson G, Monge JM 2003 Arterial ligation for pediatric epistaxis: developmental anatomy. Am J Rhinol 17:75–81.

Joo W, Yoshioka F, Funaki T et al 2012 Microsurgical anatomy of the abducens nerve. Clin Anat 25:1030–42.

Joo W, Rhoton AL Jr 2015 Microsurgical anatomy of the trochlear nerve. Clint Anat 28:857–64.

Keith CG, Boldt DW 1986 Congenital absence of the lacrimal gland. Am J Ophthalmol 102:800–1.

Kerr FW, Hollowell OW 1964 Location of pupillomotor and accommodation fibres in the oculomotor nerve: experimental observations on paralytic mydriasis. J Neurol Neurosurg Psychiat 27473–81.

Khitri MR, Demer JL 2010 Magnetic resonance imaging of tissues compatible with supernumerary extraocular muscles. Am J Ophthalmol 150:925–31.

Knop E, Knop N 2002 A functional unit for ocular surface immune defence formed by the lacrimal gland, conjunctiva and lacrimal drainage system. Adv Exp Med Biol 506B:635–44.

A review of the structural organization of eye-associated lymphoid tissues and their role in the immune defence of the eye.

Koornneef L 1977 The architecture of the musculo-fibrous apparatus in the human orbit. Acta Morphol Neerl Scand 15:35–64.

A study using serial histological sections and thicker tissue slices of whole orbits to reconstruct the spatial organization of the orbital connective tissue system.

Leigh RJ, Zee DS 2015 The Neurology of Eye Movement, 5th ed. Oxford: Oxford University Press.

The definitive textbook describing the neurological basis of normal eye movements and ocular motility disorders.

Macchi V, Regoli M, Bracco S et al 2016 Clinical anatomy of the orbitomeningeal foramina: variational anatomy of the canals connecting the orbit with the cranial cavity. Surg Radiol Anat 38:165–77.

Maitchouk DY, Beuerman RW, Ohta T et al 2000 Tear production after unilateral removal of the main lacrimal gland in squirrel monkeys. Arch Ophthalmol 118:246–52.

Maliborski A, Różycki R 2014 Diagnostic imaging of the nasolacrimal drainage system. Part I. Radiological anatomy of lacrimal pathways. Physiology of tear secretion and tear outflow. Med Sci Monit 20:628–38.

Meng ID, Kurose M 2013 The role of corneal afferent neurons in regulating tears under normal and dry eye conditions. Exp Eye Res 117:79–87.

Miller JM 1989 Functional anatomy of normal human rectus muscles. Vision Res 29:223–40.

Miller JM 2007 Understanding and misunderstanding extraocular muscle pulleys. J Vis 7:10.1–15.

A discussion of the issues and controversies regarding the role of extraocular muscle pulleys.

Obata H 2002 Anatomy and histopathology of human Meibomian gland. Cornea 21(Supp1 2):S70–74.

Obata H 2006 Anatomy and histopathology of the human lacrimal gland. Cornea 25(10 Suppl 1):S82–89.

Paiva RS, Minare-Filho AM, Cruz AA 2001 Palpebral fissures changes in early childhood. J Pediatr Ophthalmol Strabismus 38:219–23.

Park DH, Choi WS, Yoon SH et al 2008 Anthropometry of Asian eyelids by age. Plast Reconstr Surg 121:1405–13.

Park HK, Rha HK, Lee KJ et al 2017 Microsurgical anatomy of the oculomotor nerve. Clin Anat 30:21–31.

Paulsen F 2003 The human nasolacrimal ducts. Adv Anat Embryol Cell Biol 170:1–106.

Prado PA, Ribeiro EC, De Angelis MA, Smith RL 2007 Biometric study of the optic canal during cranial development. Orbit 26:107–11.

Ramat S, Leigh RJ, Zee DS et al 2007 What clinical disorders tell us about the neural control of saccadic eye movements. Brain 130:10–35.

Regoli M, Bertelli E 2017 The revised anatomy of the canals connecting the orbit with the cranial cavity. Orbit 36:110–17.

Rocha EM, Alves M, Rios JD et al 2008 The aging lacrimal gland: changes in structure and function. Ocul Surf 6:162–74.

Ruskell GL 1975 Nerve terminals and epithelial cell variety in the human lacrimal gland. Cell Tiss Res 138:121–136.

The first comprehensive description of the ultrastructure of the human lacrimal gland.

Ruskell GL 2004 Distribution of pterygopalatine ganglion efferents to the lacrimal gland in man. Exp Eye Res 78:329–35.

Saonanon P 2014 Update on Asian eyelid anatomy and clinical relevance. Curr Opin Ophthalmol 25:436–42.

Satchi K, McNab AA 2010 Double lacrimal puncta: clinical presentation and potential mechanisms of epiphora. Ophthalmology 117:180–3.

Sathiamoorthi S, Frank RD, Mohney BG 2018 Spontaneous resolution and timing of intervention in congenital nasolacrimal duct obstruction. JAMA Ophthalmol 136:1281–6.

Shechtman DL, Woods AD, Tyler JA 2007 Pupil sparing incomplete third nerve palsy secondary to a cavernous sinus meningioma: challenges in management. Clin Exp Optom 90:132–8.

Situ P, Simpson TL 2010 Interaction of corneal nociceptive stimulation and lacrimal secretion. Invest Ophthalmol Vis Sci 51:5640–5.

Spencer RF, Porter JD 2006 Biological organization of the extraocular muscles. Prog Brain Res 151:43–80.

Stevenson W, Pugazhendhi S, Wang M 2016 Is the main lacrimal gland indispensable? Contributions of the corneal and conjunctival epithelia. Surv Ophthalmol 61:616–27.

Tamboli DA, Harris MA, Hogg JP et al 2011 Computed tomography dimensions of the lacrimal gland in normal Caucasian orbits. Ophthalmic Plast Reconstr Surg 27:453–6.

Timlin HM, Keane PA, Day AC et al 2016 Characterizing the lacrimal punctal region using anterior segment optical coherence tomography. Acta Ophthalmol 94:154–9.

Uchino A, Saito N, Takahashi M et al 2013 Persistent dorsal ophthalmic artery and ophthalmic artery arising from the middle meningeal artery diagnosed by MR angiography at 3 T. Surg Radiol Anat 35:775–82.

Willcox MDP, Argüeso P, Georgiev GA et al 2017 TFOS DEWS II Tear Film Report. Ocul Surf 15: 366–403.

Part of the 2017 Tear Film and Ocular surface Dry Eye Workshop Report (TFOS DEWS II) dealing with the structure and function of the preocular tear film and its role in dry eye disease.

Yeh S, Foroozan R 2004 Orbital apex syndrome. Curr Opin Ophthalmol 15:490–8.

CHAPTER

45

Eye

The outer surface of the eye is composed of parts of two spheres with different radii. The anterior segment, part of the smaller sphere, is formed by the transparent cornea and accounts for approximately 7% of the ocular surface. The posterior segment of the eyeball is part of the larger sphere formed externally by the opaque sclera (Fig. 45.1).

Internal to the sclera is a vascular, pigmented layer consisting of three continuous parts that collectively make up the uveal tract: a thin choroid lying posteriorly, a thicker ciliary body and an anterior iris that is displaced from the outer coat and terminates at the pupillary aperture. The internal surface of the choroid is covered by the photosensory retina, which terminates anteriorly at the ora serrata; the latter also marks the junction between the ciliary body and choroid. The vasculature of the choroid supplies nutrients to the avascular outer retina.

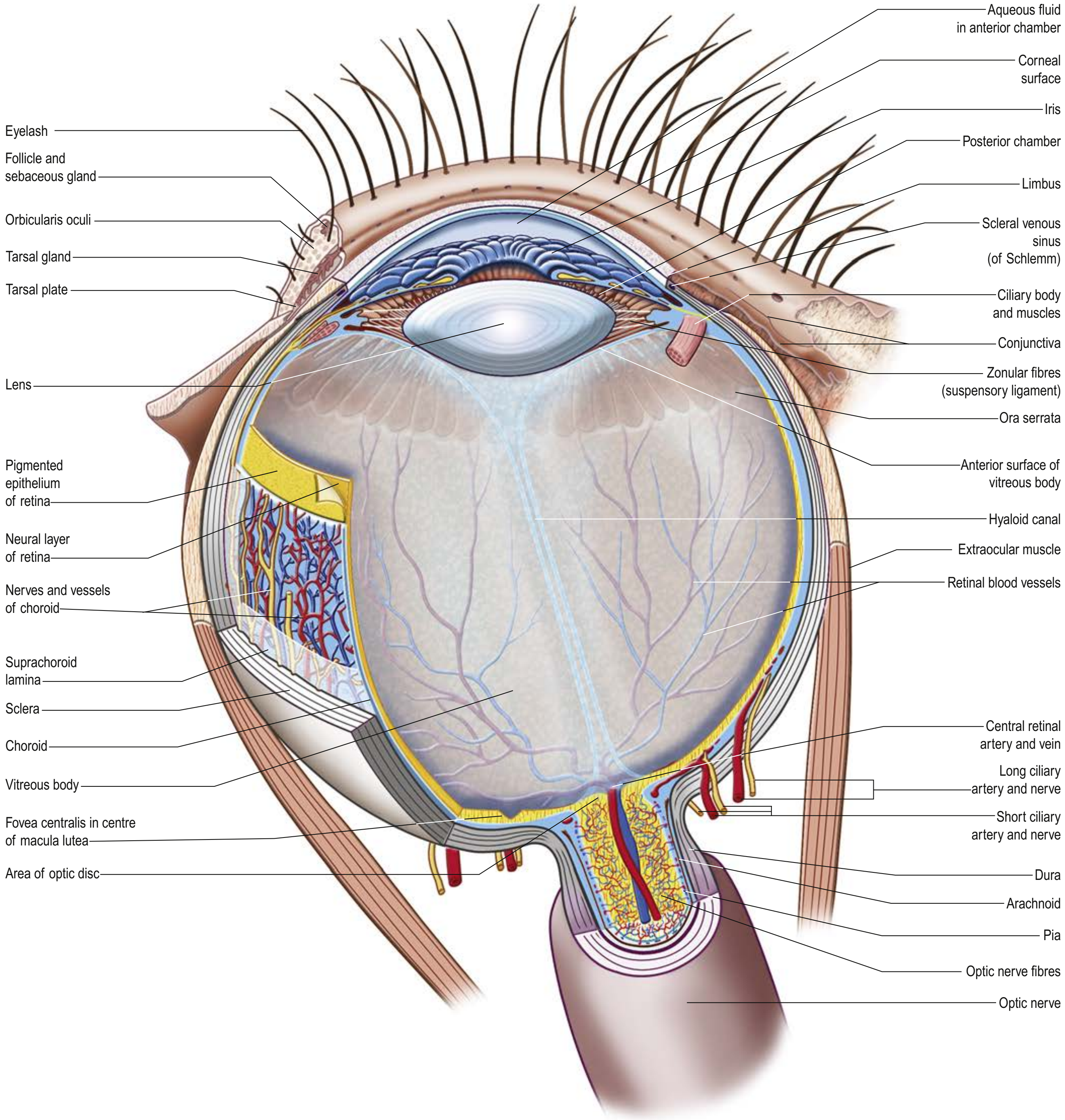
Eyelash
Follicle and sebaceous gland
Orbicularis oculi
Tarsal gland
Tarsal plate
Lens
Pigmented epithelium of retina
Neural layer of retina
Nerves and vessels of choroid
Suprachoroid lamina
Sclera
Choroid
Vitreous body
Fovea centralis in centre of macula lutea
Area of optic disc
Aqueous fluid in anterior chamber
Corneal surface
Iris
Posterior chamber
Limbus
Scleral venous sinus (of Schlemm)
Ciliary body and muscles
Conjunctiva
Zonular fibres (suspensory ligament)
Ora serrata
Anterior surface of vitreous body
Hyaloid canal
Extraocular muscle
Retinal blood vessels
Central retinal artery and vein
Long ciliary artery and nerve
Short ciliary artery and nerve
Dura
Arachnoid
Pia
Optic nerve fibres
Optic nerve

Fig. 45.1 The left eye and part of the lower eyelid in horizontal section, viewed from above. Parts have been cut away to show internal structures.

The ocular lens is located immediately behind the iris and is suspended from the ciliary body via zonular fibres (suspensory ligament) (see Fig. 45.1). Smooth muscles within the ciliary body regulate the tension exerted on the elastic lens and hence determine its shape, thereby adjusting the focus of the eye in the process of accommodation. The iris, which does not allow the transmission of light due to a heavily pigmented posterior surface, also contains smooth muscle, allowing it to regulate the size of the pupillary aperture.

The iris and lens separate the eye into three chambers. The largest, the vitreous chamber, is filled with the gel-like vitreous humour, and lies posterior to the lens, comprising about two-thirds of the volume of the eye (see Fig. 45.1). The spaces between the lens and iris, and the iris and cornea, are, respectively, the posterior and anterior chambers of the eye. Both are filled with aqueous humour, which is produced by the epithelium of the ciliary body, travels through the pupil, circulates in the anterior chamber and is drained principally through the canal of Schlemm at the iridocorneal filtration angle. Aqueous humour provides metabolic support to the avascular lens and cornea.

The sole purpose of the eyes and their associated structures within the bony orbit is to form a good image on a healthy retina. The photoreceptors of the retina transduce the optical radiation into neurobiological activity and other cells within the retina then begin to process the output of the photoreceptors. The retinal signal is transferred via the optic nerve, along the visual pathway (see Fig. 45.32) to various regions within the brain, where further processing results in visual perception.

OUTER COAT

The fibrous outer coat of the eye consists of the opaque posterior sclera and the transparent anterior cornea. Together they form a semi-elastic protective covering enclosing the eye, which, when made turgid by intraocular pressure, determines the optical geometry of the eye and ensures its shape is not distorted when it moves. The sclera also provides attachments for the extraocular muscles, and its smooth external surface rotates easily on the adjacent tissues of the orbit when these muscles contract (Ch. 44). The opacity of the sclera helps ensure that only light that enters the eye through the pupil reaches the retina. The cornea, on the other hand, not only admits light but also its covering tear film is the major refractive surface of the eye.

Sclera

The sclera accounts for approximately 93% of the outer coat of the eye. Anteriorly, it is continuous with the cornea at the corneoscleral junction, known as the limbus (see Fig. 45.1). It is punctured by a number of foramina containing nerves and blood vessels, most notably the optic foramen, which lies 3 mm medial to the midline and 1 mm below the horizontal and houses the optic nerve. Smaller openings contain anterior ciliary arteries that penetrate anteriorly, vortex veins that cross the sclera equatorially, and the long and short ciliary nerves and arteries that enter posteriorly. There is considerable individual variation in scleral dimensions; for example, it is often thicker in males. The sclera is thickest at the posterior pole (just less than 1 mm) and decreases anteriorly, reaching a minimum equatorially at about half this thickness, before increasing somewhat on approaching the limbus. It also thins approaching the optic nerve. The sclera is thinner when the eye is elongated in myopia.

The external surface of the sclera is covered by a delicate episcleral lamina of loose fibrovascular tissue, which contains blood vessels and is in contact with the inner surface of the fascial sheath of the eyeball. Anteriorly, the external scleral surface is covered by conjunctiva, which is reflected onto it from the posterior surfaces of the eyelids. The scleral internal surface adjacent to the choroid is attached to it by a delicate fibrous layer, the suprachoroid lamina, which contains numerous fibroblasts and melanocytes. Anteriorly, the inner sclera is attached to the ciliary body by the lamina supraciliaris. Posteriorly, at the optic nerve, the outer half of the sclera turns back to become continuous with the dura mater, while the inner half is modified to form a perforated plate, the lamina cribrosa sclerae. The optic nerve fascicles pass through these minute orifices, while the central retinal artery and vein pass through a larger, central aperture. The lamina cribrosa sclerae is the weakest part of the sclera and bulges outwards (a cupped disc) when intraocular pressure is raised chronically, as in glaucoma.

Like the cornea, the scleral stroma is composed mainly of densely packed collagen embedded in a matrix of proteoglycans, which are mixed with occasional elastic fibres and fibroblasts. However, in contrast to the cornea, scleral collagen fibrils show a large variation in diameter and spacing, and the lamellae branch and interlace extensively. This arrangement of fibres results in increased light scatter, which is responsible for the opaque, dull-white appearance of the sclera, and imparts a high tensile strength to the sclera to resist the pull of the extraocular muscles and contain the intraocular pressure. Collagen fibre bundles are arranged circumferentially around the optic disc and the orifices of the lamina cribrosa. The fibres of the tendons of the recti intersect scleral fibres at right-angles at their attachments, and then interlace deeper in the sclera. Although the sclera acts as a conduit for blood vessels, scleral vessels are few and mainly disposed in the episcleral lamina, especially close to the limbus. Its sensory nerve supply is surprisingly rich, accounting for the intense pain associated with scleral inflammation (Watson and Young 2004).

A forward pointing ridge of scleral tissue, the scleral spur, lies between the anterior ciliary body and the posterior edges of the canal of Schlemm and trabecular meshwork (**Figs 45.2, 45.3A**). Collagen fibres within this spur are orientated in a circular fashion, and it contains an increased number of elastic fibres.

Scleral development is under active regulation to ensure an eye of the correct axial length to produce a focused image (Wallman and Winawer 2004).

Filtration angle and aqueous drainage

Aqueous humour drains from the eye mainly through the trabecular meshwork into the canal of Schlemm at the iridocorneal (filtration) angle, formed between the posterior aspect of the limbus and the base of the iris (see Fig 45.2; **Fig. 45.3**). The trabecular meshwork is continuous anteriorly with Descemet's membrane and the endothelium of the cornea. Aqueous humour filters from the anterior chamber through interconnected spaces among loose trabecular fibres, most of which are attached to the anterior, external aspect of the scleral spur. Of the remainder, most are continuous with longitudinal fibres of the ciliary muscle, some of which attach to the posterior internal aspect of the scleral spur. The trabecular meshwork provides sufficient resistance to aqueous humour outflow to

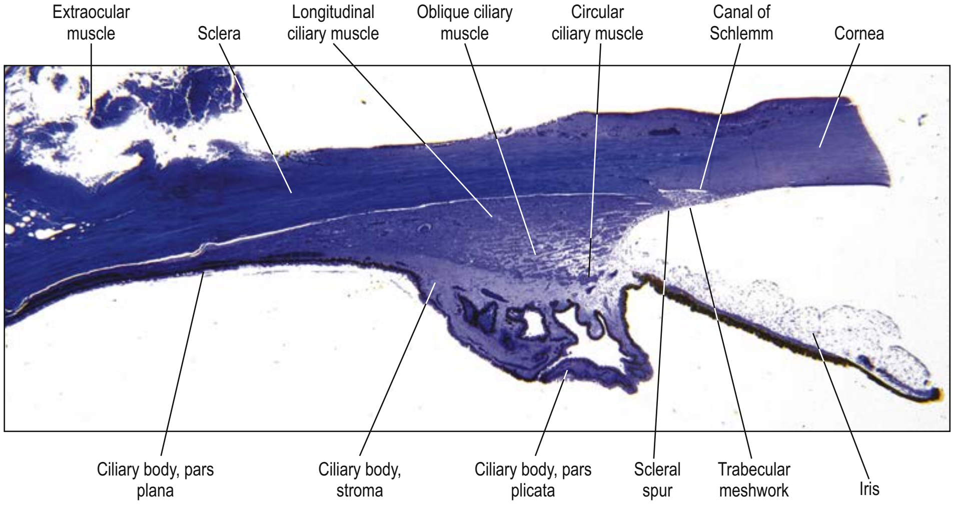

Fig. 45.2 A meridional section through the anterior eye, highlighting the ciliary body and drainage apparatus.

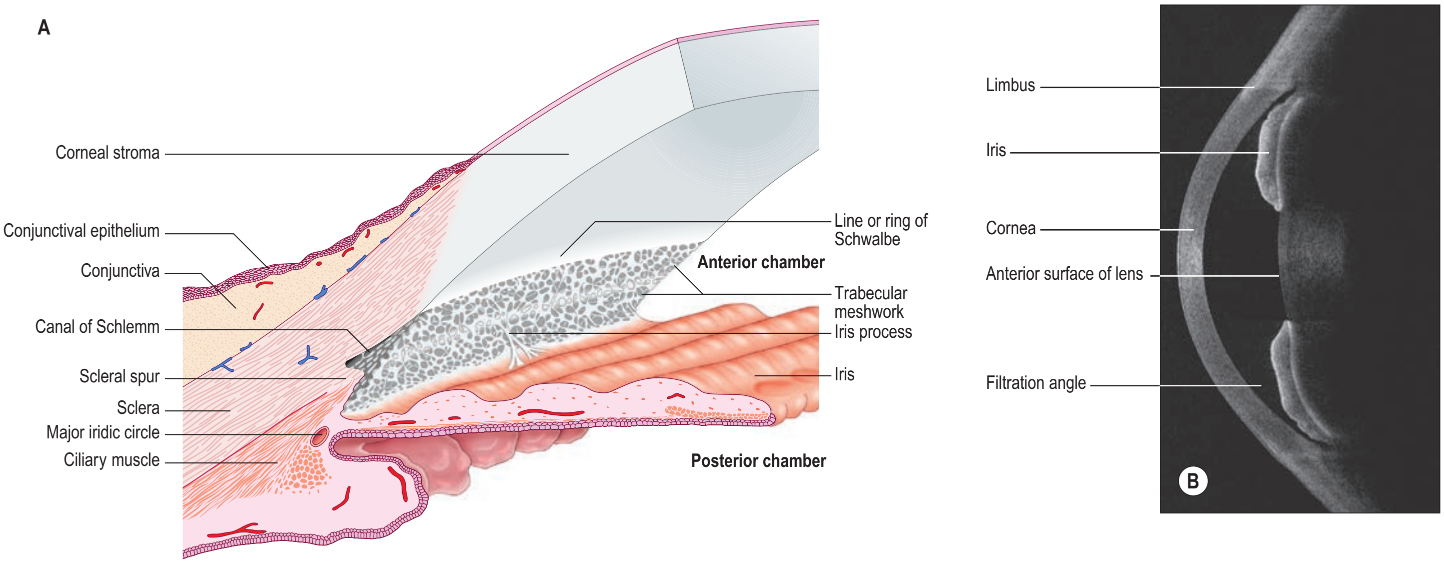
A
Corneal stroma
Conjunctival epithelium
Conjunctiva
Canal of Schlemm
Scleral spur
Sclera
Major iridic circle
Ciliary muscle
Line or ring of Schwalbe
Anterior chamber
Trabecular meshwork
Iris process
Iris
Posterior chamber
Limbus
Iris
Cornea
Anterior surface of lens
Filtration angle
B

Fig. 45.3 **A**, A schematic representation of the tissues bordering the anterior chamber angle. The trabecular meshwork is an anulus of tissue spanning the angle; its meshes are shown in transverse section opposite the canal of Schlemm and partly attached to the scleral spur. A single iris process bridges the angle, connecting the trabecular meshwork to the anterior tissues of the iris. **B**, An optical coherence tomography (OCT) *in vivo* image of the anterior segment of a 60-year-old Caucasian female taken in dim room light. (B, Courtesy of Mr Gus Gazzard, Consultant Ophthalmic Surgeon, Moorfields Eye Hospital, London.)

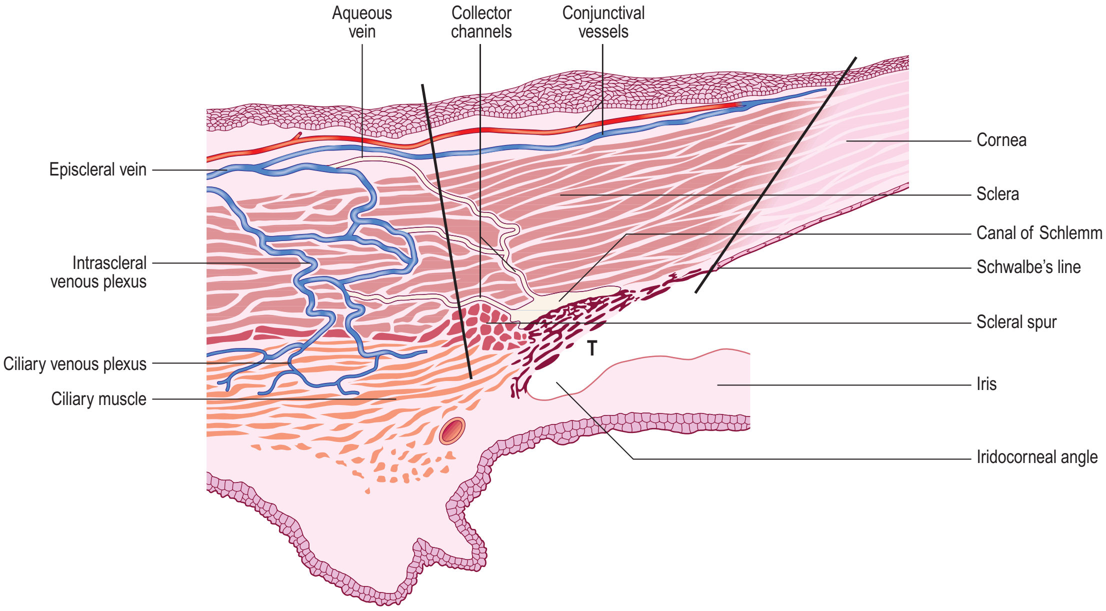
Aqueous vein
Collector channels
Conjunctival vessels
Episcleral vein
Intrascleral venous plexus
Ciliary venous plexus
Ciliary muscle
Cornea
Sclera
Canal of Schlemm
Schwalbe's line
Scleral spur
T
Iris
Iridocorneal angle

Fig. 45.4 Tissues of the filtration angle in section. The approximate borders of the limbal region are indicated by the solid lines. Aqueous humour drains from the anterior chamber at T through the trabecular meshwork into the canal of Schlemm, from where it flows through collector channels, either to the intrascleral venous plexus, where it mixes with blood from the ciliary venous plexus, or directly to the surface tissues of the eye as an aqueous vein. The aqueous vein is shown joining an episcleral vein at the surface to form a laminated vessel. Aqueous and blood drain posteriorly in episcleral veins, which, in turn, join anterior ciliary veins.

generate an intraocular pressure of approximately 15 mmHg. It also acts as a filter and has the capacity to phagocytose particulate matter.

The canal of Schlemm (sinus venosus sclerae) is an anular endothelial canal located near the internal surface of the sclera close to the limbus. In cross-section, the canal appears as an oval cleft, with an outer wall that grooves the sclera. Posteriorly, it extends as far as the anterior edge of the scleral spur. The canal of Schlemm may be double or multiple in parts of its course, and its walls are constructed of a continuous single thin endothelial layer. Passage of aqueous humour to the canal probably occurs via giant pinocytotic vacuoles and associated transcellular pores, which form on the inner face of the endothelium and discharge into the canal at the outer face. Aqueous humour passes through a plexus of fine intrascleral vessels that connect the canal of Schlemm with episcleral veins (Fig. 45.4). Normally, the canal does not contain blood; pressure gradients prevent the reflux of blood, even though the channels between the canal and veins have no valves. However, in venous congestion, blood may enter the canal; the continuous endothelial outer wall of the canal prevents further reflux.

An alternative route for aqueous outflow, the uveoscleral pathway, has been described (Fautsch and Johnson 2006, Goel et al 2010). Estimates of aqueous drained by this route in humans vary from under 5% to as much as 54% (Alm and Nilsson 2009). Since there is no epithelial barrier between the anterior chamber and the ciliary body, aqueous humour is able to enter the loose connective tissue in front of the ciliary muscle and pass between the muscle fibres into the supraciliary and suprachoroidal spaces, where it can be absorbed by vessels that drain the uvea. Clinically, aqueous outflow via this route can be increased by topical prostaglandin analogues, which are first-line therapy for the treatment of open angle glaucoma.

Any interference with the drainage of aqueous increases intraocular pressure and may lead to glaucoma, which can be either 'primary', or secondary to a specific ocular anomaly or disease. Primary glaucoma can be either 'closed angle', where the filtration angle is narrowed by the proximity of the iris root to the cornea, or, more commonly 'open angle', where aqueous access to angle tissues is unimpeded. In the most common form of primary open angle glaucoma, age-related pathological changes within the trabecular meshwork reduce the facility of aqueous drainage, thus raising intraocular pressure (Gabelt and Kaufman 2005). Sustained raised pressure leads to progressive defects in the visual field, because of either direct mechanical damage to retinal ganglion cell axons (particularly at the optic nerve head), or impairment of the optic nerve head blood supply, or both.

Differences in drainage angle morphology most probably underlie variations in the prevalence of primary angle closure glaucoma (Wang et al 2012); drainage through both the canal of Schlemm and the uveoscleral pathway is decreased in old age. As the lens grows throughout life, while

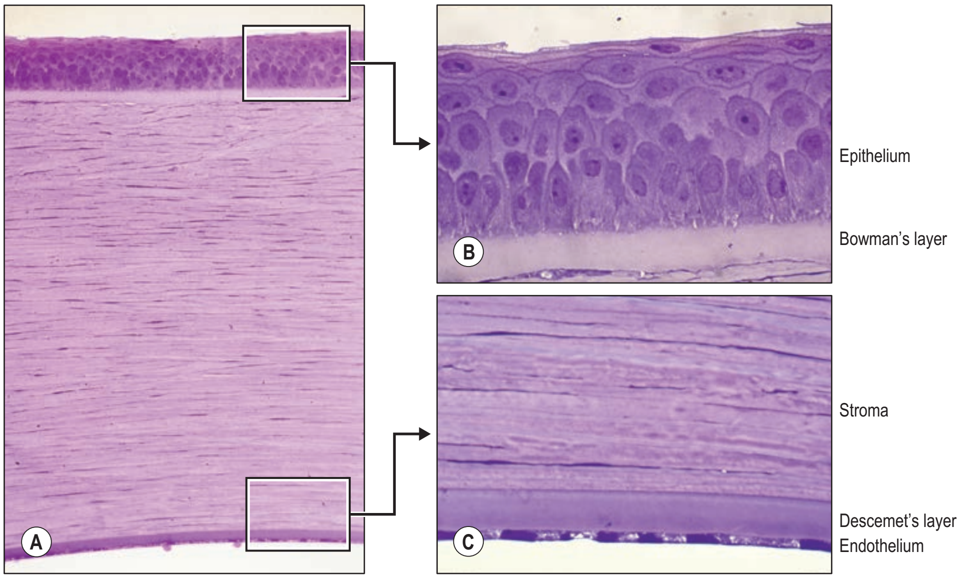

Fig. 45.5 **A**, A low-power light micrograph of the five layers of the cornea. **B**, A high-power light micrograph of the corneal epithelium and Bowman's layer. **C**, A high-power light micrograph of the corneal endothelium, Descemet's layer and part of the stroma. The darkly staining cells in the stroma are keratocytes.

the eye ceases to enlarge after the age of about 15, the depth of the anterior chamber will decrease with age, impairing aqueous drainage.

Cornea

The avascular cornea is the anterior transparent part of the outer coat. Convex anteriorly, it projects from the sclera as a dome-shaped elevation with an area of 1.1 cm^2 in adults, forming approximately 7% of the external tunic area. Since it is more curved (average radius, r = 7.8 mm) than the sclera (r = 11.5 mm), a slight sulcus sclerae marks the corneoscleral junction. The high corneal curvature of the neonate cornea decreases to reach adult levels within a relatively short space of time (Friling et al 2004).

The cornea is approximately 670 µm thick close to the corneoscleral junction, and on average 537 µm at its centre (Wolfs et al 1997). At the nasal and temporal limbus, the transition from cornea to sclera is in a line that is approximately perpendicular to the cornea; this transition is more oblique superiorly and inferiorly, with the sclera overlapping the cornea to a greater extent anteriorly. Consequently, when viewed from the front, the corneal perimeter is slightly elliptical, because its horizontal diameter (11.7 mm) is a little greater than its vertical (10.6 mm). Its posterior perimeter is circular (diameter 11.7 mm).

Since the cornea carries most of the optical power of the eye, changes to its shape can have a significant impact on the refractive state of the eye (p. 802). This has been used to advantage in numerous techniques for correcting refractive error, such as laser refractive surgery.

Microscopically, the cornea traditionally consists of five layers. Arranged anterioposteriorly, these are the corneal epithelium, anterior limiting lamina (Bowman's layer), substantia propria (stroma), posterior limiting lamina (Descemet's membrane) and endothelium (Fig. 45.5).

Corneal epithelium

The corneal epithelium accounts for approximately 10% of the corneal thickness (50 µm). It usually consists of 5–6 layers of cells (Fig. 45.5B) that protect the ocular surface from mechanical abrasion, form a permeability barrier (to small molecules, water and ions) and prevent the entry of pathogens. The deepest cells are columnar with flat bases, rounded apices and large round or oval nuclei. Outside these are 2–3 layers of polyhedral (often wing-shaped) cells. In the more superficial layers, the cells become progressively flatter and present a smooth, optically perfect surface when covered by the tear film. Scanning electron microscopy of surface cells reveals extensive finger-like and ridge-like projections (microvilli and microplicae). A complex network of tight junctions links the superficial cells, consistent with their barrier function.

Anterior limiting lamina (Bowman's layer)

The anterior limiting lamina, which lies internal to the corneal epithelium, contains a dense mass of collagen fibrils set in a matrix similar to that of the substantia propria. It is 12 µm thick, is readily distinguishable from the substantia propria because it does not contain fibroblasts, and appears amorphous by light microscopy (see Fig. 45.5B).

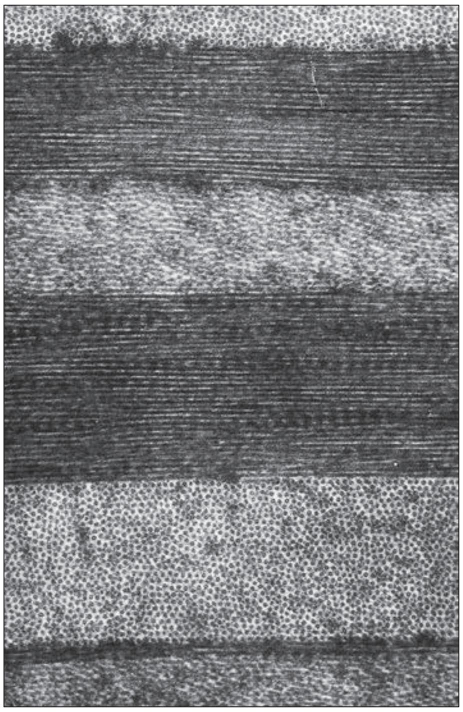

Fig. 45.6 An electron micrograph of the stroma of the human cornea, showing the geometric precision of the alternation in direction of adjacent layers of fibres. (Courtesy of John Marshall, St Thomas' Hospital, London.)

Substantia propria (stroma)

The substantia propria is approximately 500µm thick and forms the bulk of the cornea. It is a compact and transparent layer, composed of 200–250 sequential lamellae, each made up of fine parallel collagen fibrils mainly of type I collagen. Flat dendritic interconnecting fibroblasts (keratocytes) form a coarse mesh between the lamellae. Alternate lamellae are typically orientated at large angles to each other (Fig. 45.6). X-ray diffraction indicates that they run along two preferred directions, superior–inferior and nasal–temporal, to account for the additional tensile stress exerted by the recti along these meridians (Boote et al 2005). Each lamella is approximately 2 µm thick and of variable width (10–250 µm or, rarely, more). In the central cornea, fibrils within the lamellae have a similar diameter of approximately 31 nm. This increases slightly with age and approaching the limbus. The small size of the fibrils (much smaller than the wavelength of light), the regularity of their spacing (maintained by collagen–proteoglycan interactions) and the careful control of corneal hydration, are the principal factors that determine stromal transparency. Light scattered by the collagen fibrils is eliminated by destructive interference in all directions other than forwards.

Surgically, the anterior cornea can be separated from the posterior Descemet's membrane and the endothelium by the injection of air into the corneal stroma. However, the cleavage plane is somewhat anterior to Descemet's layer and it has been suggested that the remaining posterior corneal stroma represents a distinct, sixth, layer within the cornea. This pre-Descemet's layer, which is approximately 10 µm wide in aged eyes, is characterized by lamellae of collagen and a lack of keratocytes (Dua et al 2013): unlike the traditional five layers of the cornea, it is not readily discernible in light micrographs (**Fig. 45.5C**) and is probably best regarded as a posterior variation of the corneal stroma rather than a distinct corneal layer.

A common finding in the elderly is arcus senilis, a complete or partial ring, usually white or grey in colour, seen externally at the corneal margin caused by cholesterol, phospholipid and triglyceride deposits within the stroma.

Posterior limiting lamina (Descemet's layer)

The posterior limiting lamina covers the substantia propria posteriorly. It is thin and apparently homogeneous, and is regarded as the basement membrane of the endothelium (see Fig. 45.5C). Some 4 µm thick at birth, it may increase to 12 µm by the eighth decade.

Endothelium

The endothelium covers the posterior surface of the cornea and consists of a single layer of squamous cells (see Fig. 45.5C) with prominent interdigitations between adjacent cells, which are also connected by tight and gap junctions. When viewed *en face*, the endothelium appears as a mosaic of polygonal (typically hexagonal) cells. As these cells have a limited capacity for mitosis, in response to pathology, trauma, age and prolonged contact lens wear, the endothelial mosaic becomes less regular, and shows a greater variation in cell size (pleomorphism) and shape (polymegathism), as cells spread to fill gaps caused by cell loss. The numerous mitochondria and prominent rough endoplasmic reticulum within these cells reflects their high metabolic activity. Thus, for example, active pumping mechanisms largely control the degree of corneal hydration.

Corneal innervation

The cornea is innervated by numerous branches of the ophthalmic nerve, which either form an anular plexus around the periphery of the cornea or pass directly from the sclera and enter the corneal stroma radially as 70–80 small groups of fibres. On entering the cornea, the few myelinated nerves lose their myelin sheaths and ramify throughout the anterior corneal stroma in a delicate reticulum, their terminal filaments forming an intricate subepithelial plexus. Axon bundles from this plexus cross the anterior limiting membrane and form a sub-basal plexus from which individual beaded axons pass to more superficial epithelial layers, eventually terminating as free nerve endings. Corneal nerves provide the afferent arm of the blink and lacrimation reflexes (Ch. 44) and may also have a neurotrophic function (Müller et al 2003). Corneal sensitivity to mechanical and chemical stimuli declines with age, and may be related to a decrease in the density or sensitivity of corneal nociceptors.

Corneoscleral junction (limbus)

The limbus marks the transitional zone between the cornea and sclera (see Fig. 45.3B). Here, the corneal epithelium merges with the epithelium of the conjunctiva, which thickens (up to 12 cells). Bowman's layer terminates, and the corneal stromal collagen loses its regularity. The capillaries of the conjunctiva and episclera end in loops near the limbus, ensuring the avascularity of the cornea. Internally, Descemet's membrane disperses into the fibres of the trabecular meshwork and the corneal endothelium is continuous with that covering the trabeculae. The limbus forms a convenient surface landmark for ocular surgery and intravitreal injection. A position 4 mm posterior to the limbus, for example, indicates the pars plana of the ciliary body (orbiculus ciliaris) in adults, through which safe surgical access to the posterior segment of the eye can be achieved.

The corneal epithelium does not possess stem cells and its replacement depends on the centripetal migration of cells from the edges of the cornea. These cells are the progeny of mitotic limbal stem cells located within radially orientated epithelial ingrowths (palisades of Vogt).

UVEA

The vascular tunic of the eye consists of the choroid, ciliary body and iris, which collectively form a continuous structure, the uvea (see Fig. 45.1). The choroid covers the internal scleral surface and extends forwards to the ora serrata. The ciliary body continues forwards from the choroid to the circumference of the iris, which is a circular diaphragm behind the cornea and in front of the lens, forming an almost central aperture, the pupil.

Choroid

The choroid is a thin, highly vascular, pigmented layer that lines almost five-sixths of the eye posteriorly. Its mean thickness, measured by optical coherence tomography, is approximately 230 µm (Arora et al 2012), and is greatest behind the macula. These dimensions are influenced by several factors because the choroid thins with age (Park and Oh 2013), and its thickness is correlated with axial length, central corneal thickness, time of day and various pathological conditions such as angle closure.

The choroid is pierced by the optic nerve where it is firmly adherent to the sclera. Elsewhere, its external surface is only loosely connected to the sclera by the suprachoroid layer (lamina fusca). Internally, it is attached to the retinal pigment epithelium, and at the optic disc is continuous with the pia-arachnoid tissues around the optic nerve.

Four layers can be identified in transverse section. Starting externally, these are the suprachoroid, vascular stroma, choriocapillaris and lamina vitrea (Bruch's membrane) (**Fig. 45.7**; see also Fig. 45.22).

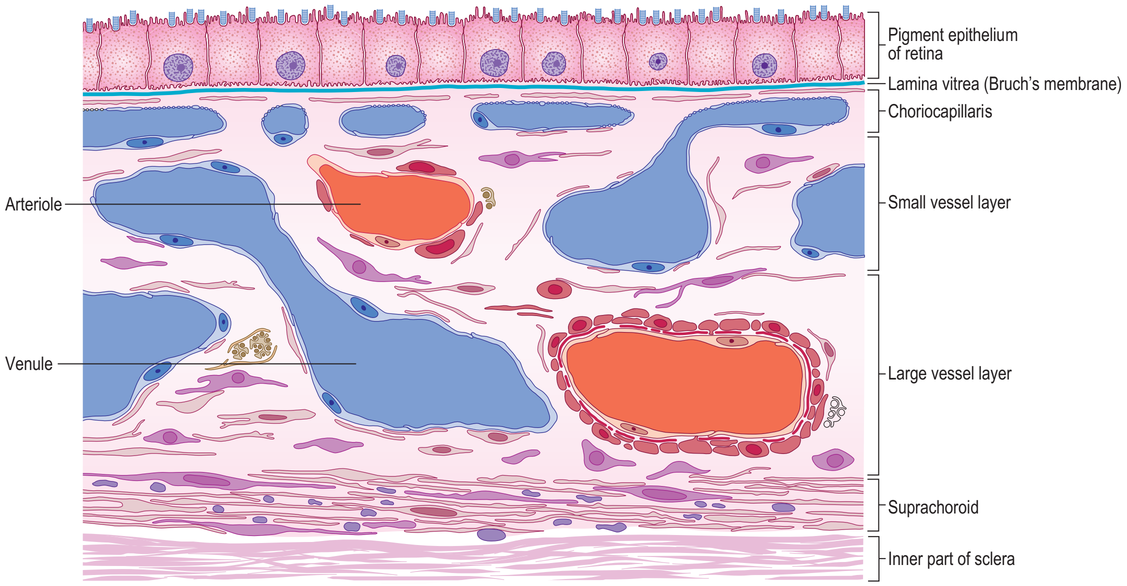

Fig. 45.7 A drawing of a histological section through the choroid close to the posterior pole.

Suprachoroid

The suprachoroid covers the external surface of the choroid; it is approximately 30 µm thick and composed of delicate non-vascular lamellae, each one a network of fine collagen and elastic fibres, fibroblasts and melanocytes. Ciliary nerves and long posterior ciliary arteries pass forwards to the anterior uvea in this layer.

Vessel layer (stroma)

Internal to the suprachoroid is a layer composed mainly of arteries and veins, but with some loose connective tissue containing scattered pigment cells. Like the retinal pigment epithelium, these melanocytes absorb light that traverses the retina but is not absorbed by the photoreceptors, so preventing internal reflection. They also help limit the passage of light through the sclera to the retina.

The blood supply of the choroid, as well as the rest of the uvea, is summarized in **Fig. 45.8**. Short posterior ciliary arteries enter the eye through the sclera near the optic nerve and supply the posterior choroid. These vessels branch and gradually decrease in size as they approach the retinal border. The choroidal stroma can be divided into an outer layer of larger vessels (Haller's layer) and an inner layer of smaller vessels (Sattler's layer), which eventually give rise to the choriocapillaris (see Fig. 45.7). Long posterior ciliary arteries and recurrent branches of anterior ciliary arteries supply the anterior part of the choriocapillaris.

Veins within the choroid converge spirally onto four, or very occasionally more, principal vortex veins that pierce the sclera behind the equator to reach tributaries of the ophthalmic veins.

The vessels of the choroid have a rich autonomic vasomotor supply.

The blood flow through the choroid is high, a feature probably associated with an intraocular pressure of 15–20 mmHg: a venous pressure above 20 mmHg is therefore required to maintain circulation. The choroidal perfusion rate exceeds that required to supply nutrients and may serve to cool the retina during exposure to bright light.

Choriocapillaris

The choriocapillaris provides nutrients to the avascular outer five layers of the retina and is composed of large (up to 20 µm thick), densely packed, freely anastomosing, fenestrated capillaries. Pericytes are found mainly on the scleral surface, while most fenestrations face the retina. The permeability of choriocapillaris is exceptionally high, compared to other structures that are invested with fenestrated capillaries.

Lamina vitrea (Bruch's membrane)

The lamina vitrea lies between the choriocapillaris and the retinal pigment epithelium, and is derived from both. Under the light microscope, it appears as a thin (2–4 µm) homogeneous layer: its thickness increases with age. It consists of five layers: a central elastic fibre mesh with flanking internal and external layers of collagen and the basal laminae of the choriocapillaris and retinal pigment epithelium.

The lamina vitrea regulates the passage of fluid and solutes from the choroidal capillaries to the retina. With increasing age, lipid-containing extracellular deposits (drusen) may accumulate between the basal lamina of the retinal pigment epithelium and the inner collagenous layer of this membrane. The deposits impair the exchange of gases, nutrients and metabolites between the choroidal blood and the outer layers of the retina, contributing to chorioretinal diseases such as age-related macular degeneration (Curcio and Johnson 2013). The age-related impairment of the transport of retinoids across the lamina vitrea

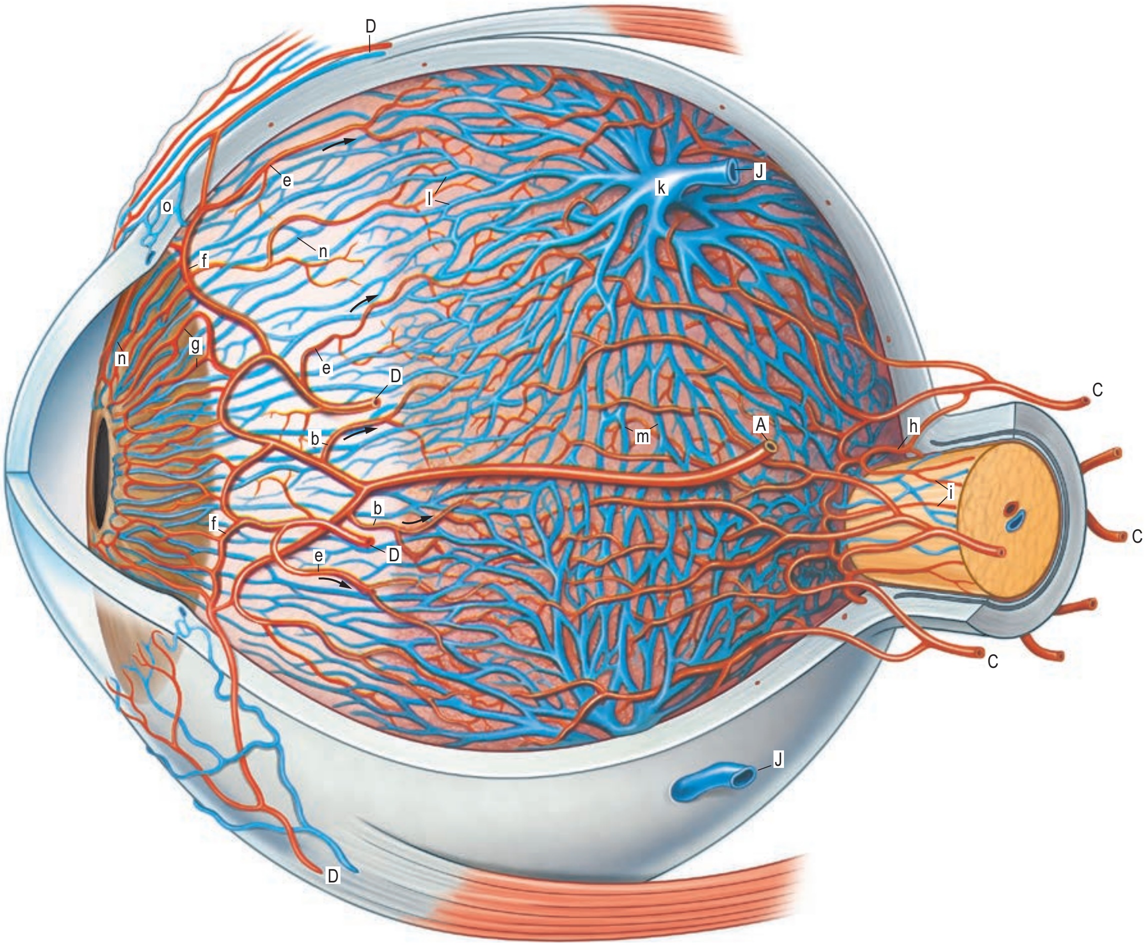

Fig. 45.8 The vasculature of the uveal tract. The long posterior ciliary arteries, one of which is visible (A), branch at the ora serrata (b) and feed the capillaries of the anterior part of the choroid. Short posterior ciliary arteries (C) divide rapidly to form the posterior part of the choriocapillaris. Anterior ciliary arteries (D) send recurrent branches to the choriocapillaris (e) and anterior rami to the major arterial circle (f). Branches from the circle extend into the iris (g) and to the limbus. Branches of the short posterior ciliary arteries (C) form an anastomotic circle (of Zinn) (h) round the optic disc, and twigs from this (i) join an arterial network on the optic nerve. The vortex veins (J) are formed by the junctions (k) of suprachoroidal tributaries (l). Smaller tributaries are also shown (m, n). The veins draining the scleral venous sinus (o) join anterior ciliary veins and vorticose tributaries. (With permission from Hogan MJ, Alvarado JA, Weddell JE 1971 Histology of the Human Eye. Philadelphia: WB Saunders.)

contributes to the slower rate of dark adaptation in older individuals. During sight-threatening choroidal neovascularization, as develops with wet age-related macular degeneration, vessels enter the retina from the choroid through breaks in the lamina vitrea.

Ciliary body

The ciliary body serves to anchor the lens via zonular fibres (suspensory ligaments) and by the contraction of its smooth muscle, it changes the refractive power of the lens (accommodation). Its anterior internal surface is also the source of aqueous humour, while posteriorly its inner surface is contiguous with the vitreous humour and secretes several of its components. The anterior ciliary arteries and the long posterior ciliary arteries meet in the anterior ciliary body at the major iridic circle; the major nerves to all anterior tissues of the eyeball pass through the ciliary body.

Externally, the ciliary body may be represented by a line that extends from approximately 1.5 mm posterior to the limbus (corresponding also to the scleral spur) to a line 7.5–8 mm posterior to this on the temporal side, and 6.5–7 mm on the nasal side. The ciliary body is thus slightly eccentric. It projects posteriorly from the scleral spur, which is its attachment, with a meridional width varying from 5.5 to 6.5 mm. Internally, it exhibits a posteriorly crenated or scalloped periphery, the ora serrata, where it is continuous with the choroid and retina (**Figs 45.9–45.10**). Anteriorly, it is confluent with the periphery of the iris, and externally, it bounds the iridocorneal angle of the anterior chamber.

In cross-section, the ciliary body is composed of four layers. From internal to external, these are a double layer of epithelial cells, the stroma, ciliary muscle and a supraciliary layer (see Fig. 45.2).

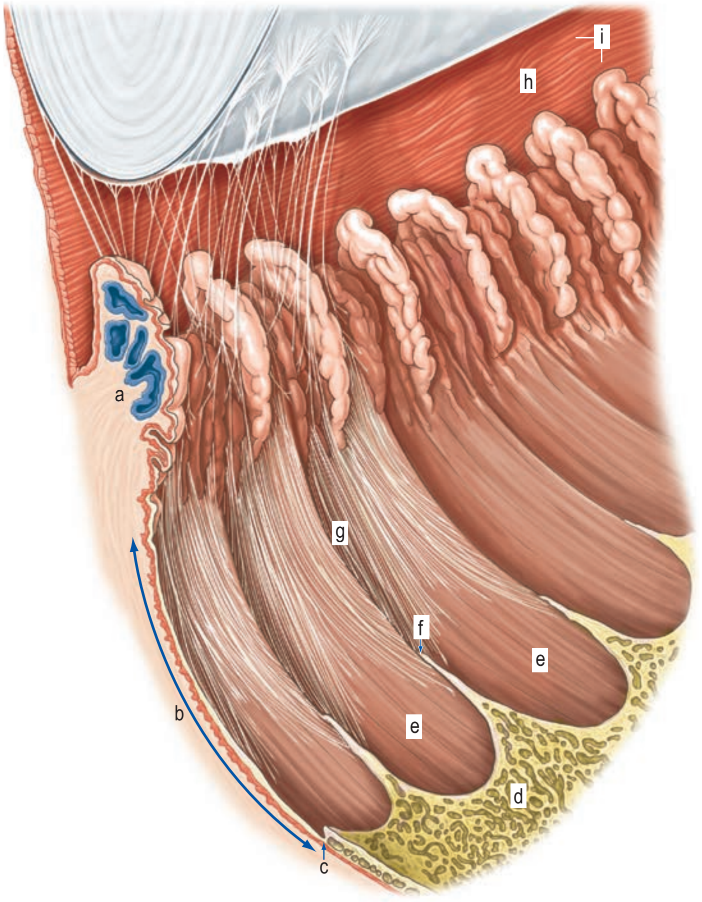

Fig. 45.9 The ciliary region seen from the ocular interior. Above is the periphery of the lens, attached by the zonular fibres (suspensory ligament) to the processes of the pars plicata (corona ciliaris) of the ciliary body (a). The pars plana ciliaris (orbiculus ciliaris) (b) has a scalloped boundary, the ora serrata (c), which separates it from the retina (d). Flanking the 'dentate bays' (e) of the ora serrata are the dentate processes (f), with which linear ridges or striae (g) are continuous; the striae extend forwards between the main ciliary processes, providing an attachment for the longer zonular fibres. The posterior aspect of the iris shows radial (h) and circumferential (i) sulci. (With permission from Hogan MJ, Alvarado JA, Weddell JE 1971 Histology of the Human Eye. Philadelphia: WB Saunders.)

Meridionally, the ciliary body can be divided into two parts (see Figs 45.2, 45.9–45.10). Anteriorly, the ridged pars plicata (corona ciliaris) surrounds the base of the iris and accounts for about one-third of the ciliary body. Posteriorly, the relatively smooth and thin pars plana (orbiculus ciliaris) lies adjacent to the ora serrata and forms a convenient access point for instruments during vitreoretinal surgery and for intraocular injection. The whole ciliary body is covered internally by a double epithelium, in which the inner layer is unpigmented, while the outer layer contains melanin. At the ora serrata, the retinal pigment epithelium is continuous with the outer pigmented epithelium of the pars plana, while the neural retina is replaced by inner unpigmented ciliary epithelium (see Fig. 45.24). Anteriorly, this double epithelium continues over the pars plicata until it merges with the double epithelium on the posterior surface of the iris (where the inner layer of cells also accumulates melanin). The anterior pars plicata is ridged meridionally by 70–80 ciliary processes radiating from the base of the iris (see Figs 45.9–45.10). In the young eye, these process are approximately parallel-sided structures, but in the adult, their flanks become less regular and appear thicker. A minor ridge, or ciliary plica, lies in the valley between most of the processes. The crests of the processes are less pigmented, giving them the appearance of light striae, from which the name ciliary is derived. The zonular fibres attached to the lens extend into the valleys between the ciliary processes and pass beyond them to fuse with the basal lamina of the superficial epithelial layer of pars plana. Their sites of attachment are marked by striae that pass back from the valleys of the pars plicata, across the pars plana, almost as far as the apices of the dentate processes of the ora serrata (see Fig. 45.9).

Ciliary epithelium

The ciliary epithelium consists of two layers of cells that are derived embryonically from the two layers of the optic cup. The inner, superficial, layer consists of columnar cells over the pars plana, and cuboidal cells over the ciliary processes of the pars plicata; it becomes irregular and more flattened between the processes. These cells contain little or no pigment. The outer layer of the ciliary epithelium, in contrast, contains cuboidal cells that are loaded with melanin. Normally, the two layers are firmly united, but fluid may separate them pathologically. The pigment layer is attached to the stroma of the ciliary body by its basal lamina, which continues back into the basal lamina of the choroid. Because of the invagination of the optic cup during development, a basal lamina covers the free surface of the bilayer, which is continuous with the internal limiting membrane of the retina.

The ciliary epithelium is responsible for the secretion of aqueous humour, while the outer pigmented epithelium additionally contributes to the eye's 'black box effect', like the retinal pigment epithelium, choroidal pigment and posterior iris epithelium, absorbing stray light to enhance image quality. Several changes in epithelial cell morphology may contribute to an age-related decrease in aqueous humour secretion (Gabelt and Kaufman 2005).

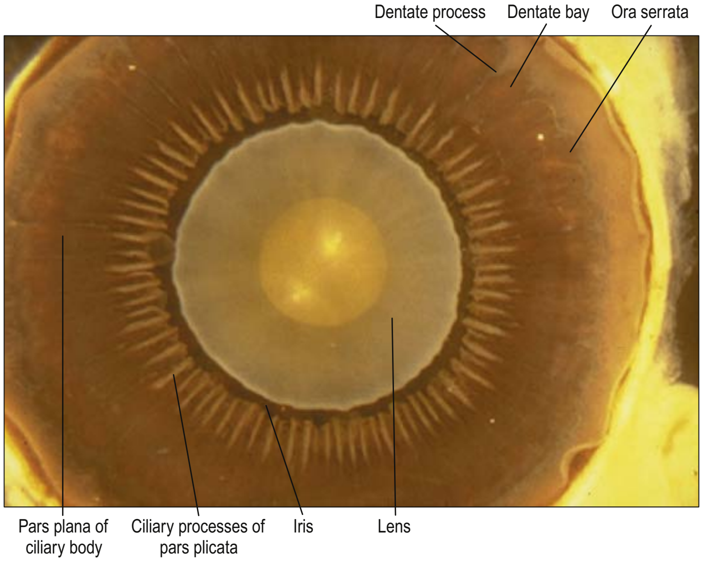

Fig. 45.10 The posterior aspect of the anterior half of the eye, showing the termination of the neural retina at the ora serrata and the ciliary body. The lens has retained sufficient transparency to reveal the iris border; the crenated perimeter of the lens is due to tension imposed by the attached zonular fibres (unseen).

Ciliary stroma

The ciliary stroma is composed largely of loose bundles of collagen between the ciliary muscle and overlying processes and extending into both of them. It also contains numerous larger branches of the ciliary vessels. A dense reticulum of large (up to 35 μm in diameter) fenestrated capillaries is concentrated in the ciliary processes, facilitating the passage of substances from the blood plasma during aqueous production. Anteriorly, near the root of the iris, the major iridic (arterial) circle (see Fig. 45.8) is formed by anastomosis between the anterior ciliary arteries and long posterior ciliary arteries, branches of the ophthalmic artery (see Fig. 44.13). Ciliary veins, also draining the iris, pass posteriorly to join the vortex veins of the choroid.

Ciliary muscle

Ciliary muscle is composed of smooth muscle cells, most of which are attached to the scleral spur and arranged in three different orientations. The outermost fibres are meridional or longitudinal and pass posteriorly into the stroma of the choroid. The innermost fibres swerve acutely from the spur to run circumferentially as a sphincter near the periphery of the lens. Obliquely interconnecting radial fibres run between these two muscular strata, frequently forming an interweaving lattice (see Fig. 45.2; **Fig. 45.11**). Contraction of ciliary muscle results in changes in lens curvature during the process of accommodation. Its contraction also increases aqueous drainage through the trabecular meshwork.

Accommodation reflex

At rest, distant objects are focused on the retina in an emmetropic eye. In order to focus closer things, the dioptric power of the eye has to be increased, which is achieved by increasing the curvature of the lens. At rest, the lens is under tension from the zonular fibres (suspensory ligaments) and hence flattened. On accommodation, the ciliary muscle contracts, moving the ciliary body forwards and inwards towards the optic axis. All parts of the muscle act in concert and tension on the zonular fibres is relaxed. As the lens is covered by an elastic capsule, once tension on it is released, it assumes a more convex shape suitable for focusing closer objects. The radius of curvature of the anterior lens surface changes most during accommodation. This classic view of accommodation, first proposed in principal by Helmholtz over 100 years ago, remains generally accepted, although details of the roles of various ocular structures continue to be debated (Charman 2008).

Information from the retina passing to the visual cortex does not constitute the afferent limb of a simple reflex in the usual sense of the term but permits the visual areas to assess the clarity of objects in the visual field. Cortical efferent information passes to the pretectal area and thence to the Edinger–Westphal nucleus, which contains preganglionic parasympathetic neurones whose axons travel in the oculomotor nerve and synapse in the ciliary ganglion within the orbit (**Fig. 45.12**). Postganglionic fibres (short ciliary nerves) innervate the ciliary muscle, causing it to contract. There is also a sparse sympathetic innervation of ciliary muscle, which has a very limited capacity to relax the muscle.

Accommodation is usually accompanied by constriction of the pupil following contraction of the sphincter pupillae, and convergent eye movements caused by contraction of the medial, superior and inferior recti (all innervated by the oculomotor nerve). This near triad, which serves to improve image quality, may become disrupted in various diseases.

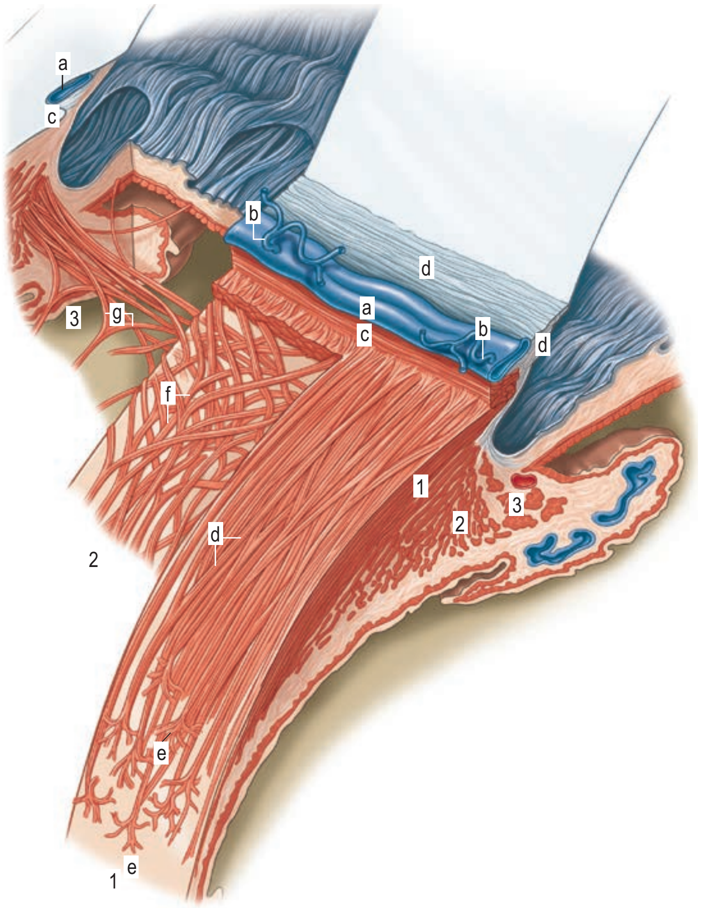

Fig. 45.11 The ciliary muscle and its components. The meridional or longitudinal (1), radial or oblique (2), and circular or sphincteric (3) layers of muscle fibres are displayed by successive removal towards the ocular interior. The cornea and sclera have been removed, leaving the canal of Schlemm (a), collecting venules (b), scleral spur (c) and trabecular meshwork (d). The meridional fibres (1) often display acutely angled junctions (d) and terminate in epichoroidal stars (e). The radial fibres meet at obtuse angles (f) and similar junctions, at even wider angles (g), occur in the circular ciliary muscle. (With permission from Hogan MJ, Alvarado JA, Weddell JE 1971 Histology of the Human Eye. Philadelphia: WB Saunders.)

Supraciliary layer

The thin supraciliary layer separates the sclera from the ciliary muscle and is largely composed of collagen fibres derived from the two layers it divides. It also forms the alternative uveoscleral route (other than the canal of Schlemm) for the drainage of aqueous humour (pp. 791-792).

Iris

The iris is an adjustable diaphragm around a central aperture (slightly medial to true centre), the pupil. It lies between the cornea and lens and is immersed in aqueous fluid (see Fig. 45.1), partially dividing the anterior segment into an anterior chamber, enclosed by the cornea and iris, and a posterior chamber, situated between the iris and the lens anterior to the vitreous. The efficacy of the iris as a light stop is mainly due to a densely pigmented posterior double epithelium. The pupillary aperture is adjusted by the action of two muscles, the dilator and sphincter pupillae.

Seen from the front, the iris is divided into a large ciliary zone adjacent to the ciliary body and a smaller, inner, pupillary zone (**Fig. 45.13**). The two regions join at the collarette. The anterior surface of the iris often contains large depressions (crypts of Fuchs), and at the pupillary margin, the posterior pigmented epithelium is visible as the pupillary ruff.

In transverse section, several subdivisions of the iris are evident (**Fig. 45.14**). From anterior to posterior, they are an anterior border layer, the stroma (which contains the sphincter pupillae), and two pigmented epithelial layers, the most anterior of which contains the dilator pupillae. It is thinnest at its root (approximately 200 μm), where the ciliary body is attached, and thickest at the collarette.

Anterior border layer

The anterior surface of the iris is not a distinct epithelium but a modified layer of the iris stroma, formed mainly by an increased number of fibroblasts that constitute a network on the anterior surface with a layer of underlying melanocytes. At the outer periphery of the iris, the anterior border layer blends with the trabecular connective tissue of the iridocorneal angle; at the pupillary margin, it meets the epithelium of the posterior surface of the iris.

The colour of the iris is a product of the combined effect of reflection/absorption by the iridial connective tissue and the concentration of pigment in the anterior border layer and, to a lesser extent, in the iris stroma. The distribution of pigment is often irregular, which produces a flecked appearance. When pigment is largely absent, other than in the posterior epithelial layers (the condition at birth), the iris is light blue. Those with dark irises are not only less likely to be dazzled by bright light, they also have a lower corneal sensitivity to chemical irritants, and mydriatic drugs are less effective. Iris colour also correlates with the incidence of ocular diseases such as cataract and uveal melanoma (Sun et al 2014). The insubstantial and variable nature of the anterior iris

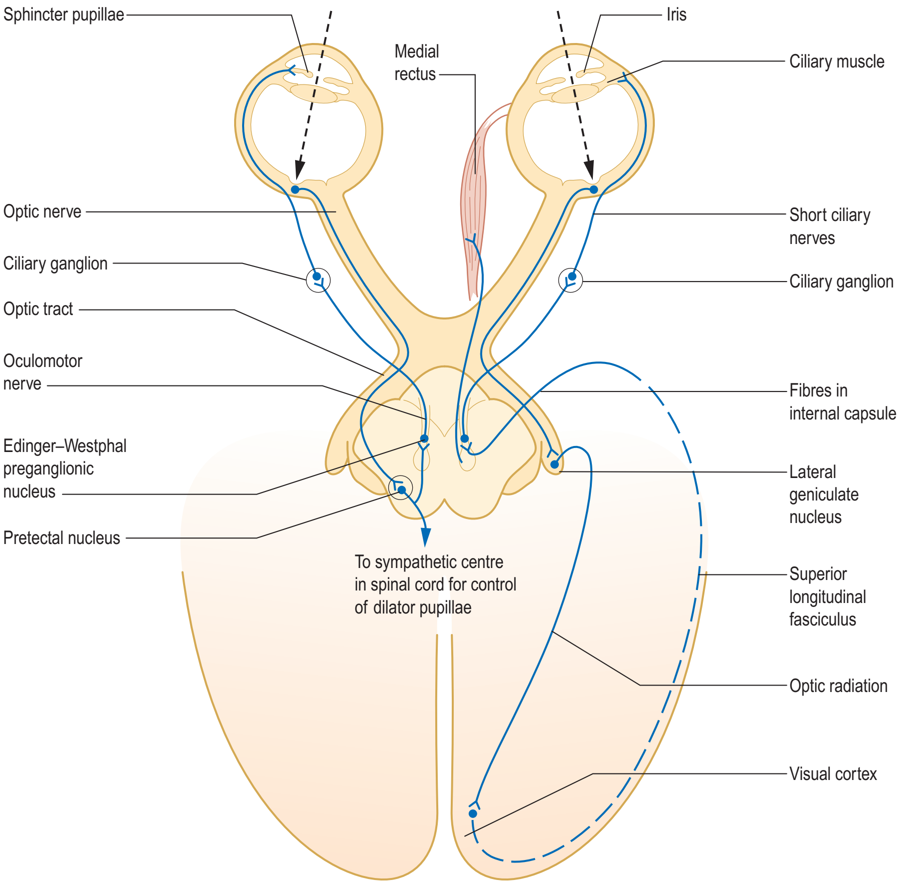
Sphincter pupillae
Iris
Medial rectus
Ciliary muscle
Optic nerve
Short ciliary nerves
Ciliary ganglion
Ciliary ganglion
Optic tract
Oculomotor nerve
Fibres in internal capsule
Edinger–Westphal preganglionic nucleus
Lateral geniculate nucleus
Pretectal nucleus
To sympathetic centre in spinal cord for control of dilator pupillae
Superior longitudinal fasciculus
Optic radiation
Visual cortex

Fig. 45.12 The neural pathways of the pupillary light reflex (left) and the accommodation reflex (right). (From Oxford Textbook of Functional Anatomy, Vol 3 Head and Neck, MacKinnon P, Morris J (eds) 1990. With permission of Oxford University Press.)

gives every iris a unique external appearance, which can be used for individual identification.

Stroma

The stroma of the iris is formed of fibroblasts, melanocytes and a loose collagenous matrix but no elastic tissue. The intercellular spaces appear to communicate freely with the anterior chamber. A few large, heavily pigmented 'clump cells' may be present; these are phagocytes and contain lysosomes and ingested melanosomes. The stroma also contains vessels and nerves. An aggregation of smooth muscle cells near the pupillary margin forms the anular contractile sphincter pupillae (see below).

Epithelial layers

The epithelial surface covering the iris posteriorly is a continuation of the bilaminar epithelium of the ciliary body and is formed from the two layers of the optic cup. The pupil, through which this epithelium curves for a short distance on to the anterior surface as the pigment ruff, corresponds to the opening of the optic cup.

The layer of epithelial cells nearest the stroma is, perhaps confusingly, termed the anterior epithelium, although it lies posterior to the stroma. Its cells are pigmented, as are those of the corresponding layer in the ciliary epithelium. They give rise to the dilator pupillae. Vitreal to this stratum is a layer of heavily pigmented cells, the posterior epithelium, which is continuous with the inner non-pigmented layer of the ciliary epithelium. As is readily apparent from *in vivo* scans, the pupillary region of the iris rests on the front surface of the lens (see Fig. 45.3B). Its posterior surface therefore bears numerous radial ridges that facilitate the movement of aqueous humour from the posterior to the anterior chamber. Adjacent epithelial cells are extensively joined by various junctions that ensure the layer can withstand the excursions of the iris during changes in pupillary size (**Fig. 45.15**).

Muscles of the iris

Sphincter pupillae

The sphincter pupillae is a flat anulus of smooth muscle approximately 750 µm wide and 150 µm thick that lies anterior to, and largely separated from, the epithelium covering the posterior iris. Its densely packed, fusiform muscle cells are often arranged in small bundles, as in the ciliary muscle, and pass circumferentially around the pupil (see Fig. 45.13). Collagenous connective tissue lies in front of and behind the muscle fibres. It is very dense posteriorly, where it binds the sphincter to the pupillary end of the dilator muscle and is attached to the epithelial layer at the pupil margin. Small axons, mostly non-myelinated, ramify in the connective tissue between bundles.

Dilator pupillae

The dilator (dilatator) pupillae forms a thin layer that lies immediately anterior to the epithelium of the posterior surface of the iris. Its 'fibres' are the muscular processes of the anterior layer of this epithelium, whose cells are therefore myoepithelial. Myofilaments are present throughout these cells but are more abundant in their fusiform basal muscular processes, which are approximately 4 µm thick, 7 µm wide and 60 µm in length. They form a layer 3–5 elements thick through most of the iris, from its periphery to the outer perimeter of the sphincter, which it slightly overlaps. Here the dilator thins out and sends spurs to blend with the sphincter. Unlike the apical parts of the myoepithelial cells, these have a basal lamina and are joined by gap junctions like those between the sphincteric muscle cells. Small, unmyelinated axons pass between, and terminate on, their muscular processes (see Fig. 45.15).

Innervation of muscles of the iris

The iris is innervated mainly by the long and short ciliary nerves. Short ciliary nerves, which contain parasympathetic, postganglionic, myelinated axons derived from the ciliary ganglion (see Figs 44.17, 44.18, 45.12), innervate the sphincter pupillae, losing their myelin well before entering the muscle. The dilator is supplied with sympathetic, non-myelinated, postganglionic fibres from the superior cervical ganglion whose routes are less well established. An additional small fraction of nerve endings in the dilator and sphincter muscles have been identified as parasympathetic and sympathetic, respectively, in experimental animal studies, including those on primates. The nerve fibres form plexuses within the iris, from which fibres extend to innervate the two muscles, the vessels and the anterior border layer; some fibres may be afferent (trigeminal) and others are vasomotor.

Pupillary light reflex

In young adults pupillary diameter normally varies from around 2 mm when fully constricted (miosis) in bright light to at least 8 mm when dilated in darkness (mydriasis), and has an even wider range under the influence of drugs. Resting pupil size over a range of light levels declines with age (senile miosis), contributing to reduced visual sensitivity in

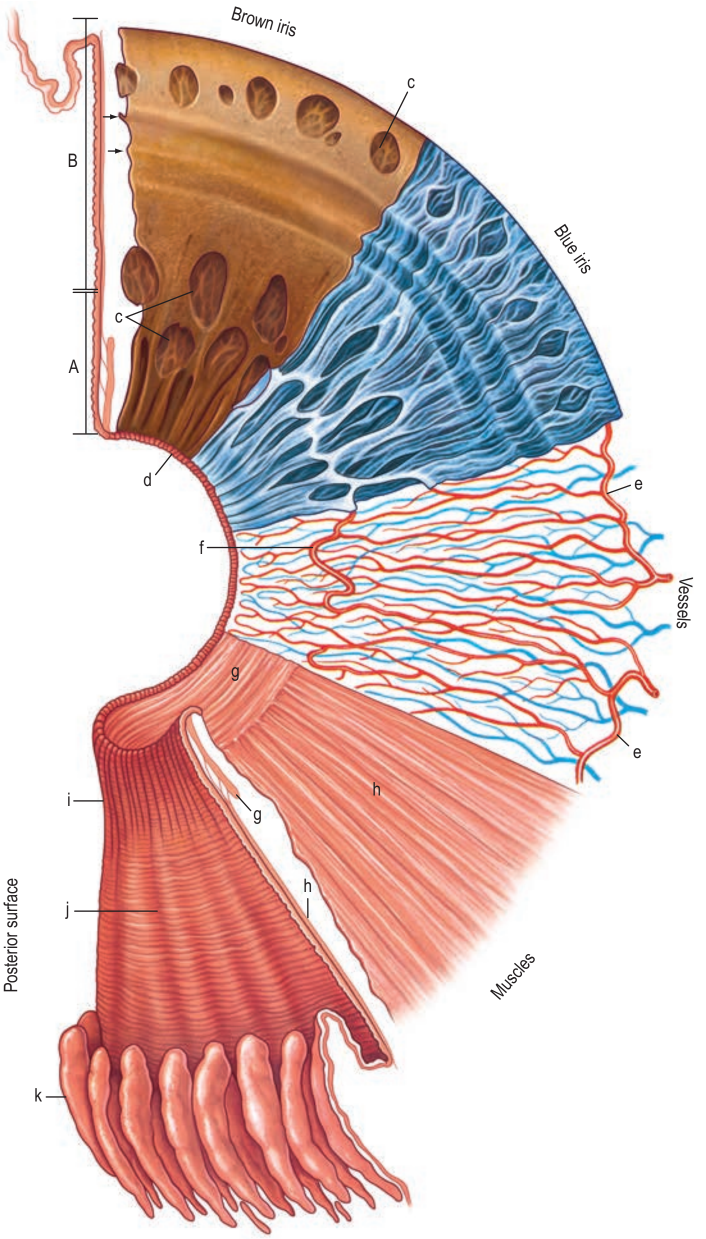

Fig. 45.13 The surfaces and internal strata of the iris, composite view. In a clockwise direction from above, the pupillary (A) and ciliary (B) zones are shown in successive segments. The first (brown iris) shows the anterior border layer and the openings of crypts (c). In the second segment (blue iris), the layer is much less prominent and the trabeculae of the stroma are more visible. The third segment shows the iridial vessels, including the major arterial circle (e) and the incomplete minor arterial circle (f). The fourth segment shows the muscle stratum, including the sphincter (g) and dilator (h) of the pupil. The everted 'pupillary ruff' of the epithelium on the posterior aspect of the iris (d) appears in all segments. The final segment, folded over for pictorial purposes, depicts this aspect of the iris, showing radial folds (i and j) and the adjoining ciliary processes (k). Circular contraction furrows are shown (arrows) in the ciliary portion of the iris. (With permission from Hogan MJ, Alvarado JA, Weddell JE 1971 Histology of the Human Eye. Philadelphia: WB Saunders.)

the elderly. Variations in pupil area in different light levels (maximally a factor of 16) will obviously affect the amount of light impinging on the retina. However, compared to the total range of illumination within which humans can maintain some degree of vision (approximately 10 log units), this effect, though important, is small. Most mechanisms for dark/light adaptation are retinal, and neural or biochemical in nature. Enhancing visual acuity by restricting light to the centre of the lens, and thereby decreasing the amount of spherical aberration, is at least as important a function of pupillary constriction.

If only one eye is illuminated, the pupil of that eye constricts (direct response), as does the pupil of the contralateral, unilluminated, eye (consensual response). While change in pupillary diameter is usually considered a reflex response to changes in light level, the pupil also constricts on viewing near objects and in response to painful stimuli; it can also be influenced by more complex cortical factors.

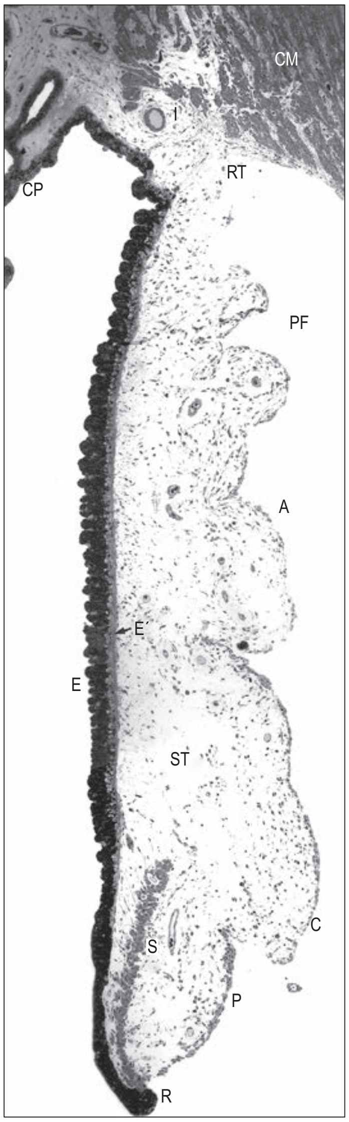

Fig. 45.14 A meridional section of the iris. The posterior surface is lined with a double epithelium (E, E′); the arrow points to the processes of the anterior layer of the epithelium forming the dilator pupillae muscle. The iris is in a contracted state, as shown by the thickened epithelium opposite the dilator muscle and thinning opposite the sphincter, and by the shortness of the pupillary zone. Abbreviations: A, anterior border layer; C, collarette; CM, ciliary muscle; CP, ciliary processes; I, major iridic circle; P, pupillary region of the iris; PF, folds in anterior surface towards the root; R, pupillary ruff; RT, root; S, sphincter pupillae muscle; ST, stroma.

In pupillary constriction, light acting on both traditional retinal photoreceptors (rods and cones) and on intrinsically photosensitive retinal ganglion cells (p. 807) gives rise to activity in retinal ganglion cells that is conducted along the optic nerve, through the optic chiasma and along the optic tract. Although the majority of tract fibres end in the lateral geniculate nucleus of the thalamus (see Fig. 45.32), a small number leave the optic tract before it reaches the thalamus, at the superior brachium, and synapse in the olivary pretectal nucleus. The information is relayed from the pretectal nucleus by short neurones that synapse bilaterally on preganglionic parasympathetic neurones in the Edinger–Westphal nucleus (in the oculomotor nerve complex in the rostral midbrain). Efferent impulses pass along parasympathetic fibres carried by the oculomotor nerve to the orbit, where they synapse in the ciliary ganglion. Postganglionic fibres travel in the short ciliary nerves to the sphincter pupillae, which reduces the size of the pupil when it contracts (see Fig. 45.12).

Pupillary dilation is brought about by lessening the parasympathetic drive to the sphincter (see above) and by sympathetic activation of the dilator. Sympathetic preganglionic fibres arise from neurones in the intermediolateral cell column in segments C8–T2 of the spinal cord, a region termed the ciliospinal center of Budge (and Waller), and pass via the sympathetic trunk to the superior cervical ganglion. Postganglionic neurones travel up the neck next to the internal carotid artery as the internal carotid nerve; at the level of the cavernous sinus, the nerve breaks up to form an interweaving network of fibres, the carotid plexus, around the carotid artery. Some of the axons from the plexus form the sympathetic root of the ciliary ganglion, passing through the ciliary ganglion without synapsing (see Fig. 44.18), and innervating the iris dilator via short ciliary nerves travelling within the choroid. Other postganglionic sympathetic fibres bypass the ciliary ganglion and reach the dilator in long ciliary nerves, which are branches of the nasociliary nerve. Neurones supplying the long and short ciliary nerves enter the orbit by the superior orbital fissure (Ch. 44). Some sympathetic fibres additionally reach the eye via the optic canal (Ruskell 2003).

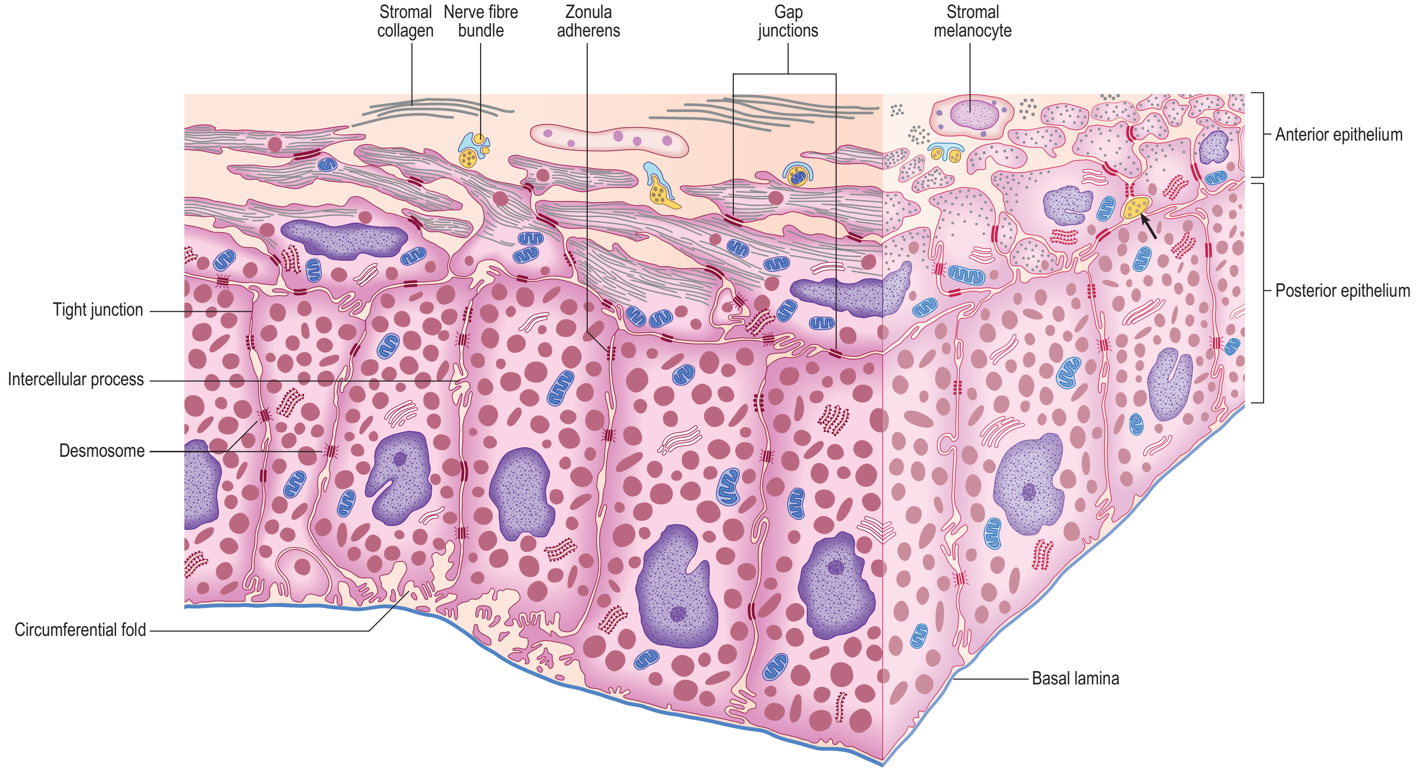

Fig. 45.15 The posterior structures of the iris. The dilator pupillae is shown in transverse section on the right and in longitudinal section on the left (the arrow shows a rarer deeper nerve terminal).

Vascular supply of the iris

The iris receives its blood supply from the long posterior and anterior ciliary arteries (see Fig. 45.8). On reaching the attached root of the iris, both long ciliary arteries divide into an upper and a lower branch. The branches anastomose with the corresponding contralateral arteries, and with the anterior ciliary arteries, to form the major iridic circle (circulus arteriosus major) at the base of the iris (see Figs 45.13–45.14). Vessels converge from this circle towards the free margin of the iris, where they form loops and become veins. At the level of the collarette, arteries and veins anastomose to form an incomplete minor iridic circle (circulus arteriosus minor). The smaller arteries and veins are very similar in their structure and are often slightly helical when the pupil is dilated, allowing them to adapt to changes in iridial shape as the pupil varies in size. All of the vessels, including the capillaries, have a non-fenestrated endothelium and a prominent, often thick, basal lamina. There is no elastic lamina in the arteries or veins, and there are few smooth muscle cells, especially in the veins. Connective tissue in the tunica media is loose, whereas the adventitia is remarkably dense and collagenous, so that it appears to form almost a separate tube.

LENS AND HUMOURS

The cornea, aqueous humour, lens and vitreous humour, often collectively termed the ocular media, serve to form an image on the retina by transmitting and refracting light. Additionally, the aqueous provides nutrients to the avascular cornea and lens, and removes their metabolic waste, as well as generating the intraocular pressure that maintains the shape of the eye.

Aqueous humour

Aqueous humour is derived from the plasma within the fenestrated capillaries of the ciliary processes and is actively secreted into the posterior chamber by the overlying epithelium. Thereafter, it passes around the equator of the lens and flows through the pupil into the anterior chamber, where it circulates before being drained at the iridocorneal angle either through the trabecular meshwork into the canal of Schlemm or via the ciliary muscle using an alternative uveoscleral pathway (pp. 791–792).

The major component of aqueous, like plasma, is water and the composition of the two fluids is broadly similar, although they do differ in the concentration of some electrolytes and organic solutes. In the interests of optical clarity, the blood–aqueous barrier also ensures a very low concentration of protein in the aqueous (generally less than 1% of the level in plasma). Inflammation of the anterior uvea can lead to a breakdown of this barrier and the presence of protein in the aqueous, resulting in light scatter that is manifest clinically as ‘flare’.

Lens

The lens is an encapsulated, biconvex body bathed in aqueous humour, which serves to selectively transmit light and adjust the focus of the eye. Posteriorly, it contacts the hyaloid fossa of the vitreous humour. Anteriorly, it forms a ring of contact with the posterior border of the pupillary region of the iris but, further away from the axis of the lens, the gap between the lens and iris increases to form the posterior chamber of the eye (see Fig. 45.1; **Fig. 45.16**). The lens is encircled by the ciliary processes and is attached to the ciliary body by the zonular fibres (suspensory ligaments), which issue mainly from the pars plana. Collectively, the zonular fibres form the zonule that holds the lens in place and transmits the forces that stretch the lens.

The anterior convexity of the lens is less steep than that of the posterior surface. The central points of these surfaces are the anterior and posterior poles of the lens and a line connecting them is its axis. The marginal circumference of the lens is its equator.

The dimensions of the lens are optically and clinically important, and change with age as a consequence of continuous growth. Its equatorial diameter at birth is 6.5 mm, increasing rapidly at first, then more slowly to 9.0 mm at 15 years of age, and even more gradually to reach 9.5 mm in the ninth decade. Its axial dimension increases from 3.5–4.0 mm at birth to 4.75–5.0 mm at age 95. The lens flattens during the first decade of life (Mutti et al 1998). Average adult radii of the anterior and posterior surfaces of the lens are 10 mm and 6 mm, respectively. These reduce in later life, the anterior surface increasing most in curvature as the lens thickens, so that, in old age, the lens pushes the iris forwards slightly, predisposing the elderly eye to angle closure glaucoma.

The lens consists of three layers (**Fig. 45.17**). Its bulk is composed of elongated cells (lens fibres), which anteriorly, as far as the equator, are covered by a single layer of epithelial cells, and the whole is enclosed by the outer lens capsule. The lens is avascular and devoid of nerve fibres or other structures that might affect its transparency. Its surface forms a very effective barrier against invasion by cells or elements of the immune system, and so creates an immunologically sequestered environment. It is unique as it retains all the cells formed throughout its life.

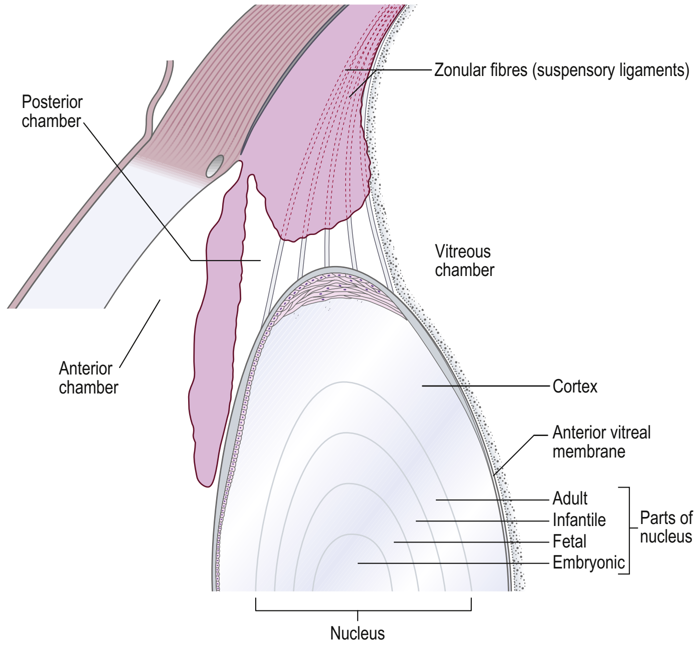

Fig. 45.16 A sagittal section through part of the lens and related structures. The cortex is distinguished from the nucleus, which is composed of embryonic, fetal, infantile and adult parts. The capsule is drawn in blue, exaggerated in thickness 100 times, and is based on observations from a 35-year-old.

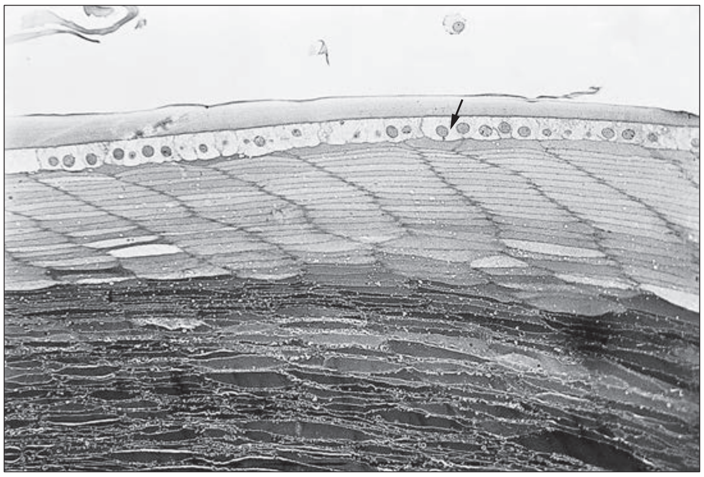

Fig. 45.17 A section through the anterior layers of the lens. The thin capsule covers the single row of epithelial cells (arrow), and the lens substance is composed of regularly stacked younger fibres and more densely stained and complex older deeper fibres.

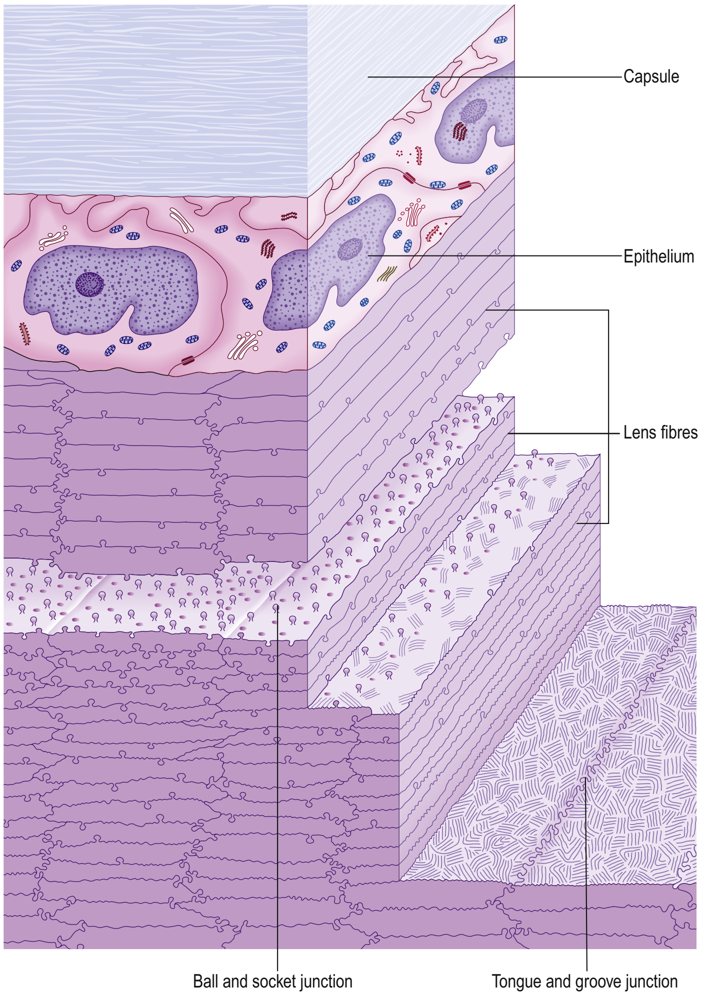

Fig. 45.18 The mechanical junctions between lens fibres. There are no junctions immediately below the epithelium. Ball and socket junctions develop in deeper layers; these are subsequently eliminated towards the nucleus, where tongue and groove junctions gradually form. Angle joints are present at most levels.

Lens capsule

The lens capsule is a basement membrane that covers the surface of the lens. Although it is thick compared to most membranes, its molecular composition is similar to that of other, thinner, membranes, consisting of various classes of collagen as well as a range of glycosaminoglycans and glycoproteins (Danysh and Duncan 2009). Its thickness, and the fact it remains intact for decades after removal of the lens fibres, permits cataract removal and the implantation of intraocular lenses.

The capsule is derived from the anterior lens epithelial cells and their fetal precursors, and is firmly attached to the epithelium anteriorly and to lens fibres posteriorly. It is elastic, a property it owes mainly to the arrangement of its collagen, and which is central to the process of accommodation. Capsule thickness varies with position on the lens surface and age. One view is that, in adults, it is thicker at the anterior pole (11–15 μm) and equator (7.2 μm) than at the posterior pole (3.5 μm), with a band of increased thickness in the midperiphery between the anterior pole and equator (13.5–16 μm) and a lesser maximum between the posterior pole and the equator (4–9 μm) (see Fig. 45.16). While capsular thickness at the anterior pole and in the anterior midperiphery increases with age, thickness at the posterior pole and equator remains unchanged, while in the posterior midperiphery it decreases in older individuals (Barraquer et al 2006). Zonular fibres, composed of thin (4–7 nm) fibrils with hollow centres resembling fibrils associated with elastic connective tissue, insert into the capsule near the equator.

Lens epithelium

The anterior surface of the lens between the outer capsule and the underlying lens fibres is covered by a layer of simple, roughly cuboidal (10 μm high and 13 μm wide), epithelial cells that, in surface view, are polygonal (see Fig. 45.17). These cells differentiate into lens fibres; they undergo mitosis at a germinative zone just anterior to the equator and are displaced towards the equator, where they synthesize characteristic lens fibre proteins and undergo extreme elongation. As other cells follow suit, the earlier cells come to occupy a deeper position within the lens stroma.

Lens fibres

The inwardly displaced epithelial cells elongate further in both an anterior and a posterior direction, becoming up to 12 mm long, depending on age and position in the lens. Fibres near the surface at the equator are nucleated; the nuclei form a short, S-shaped bow, which extends inwards from the surface. The deeper fibres lose their nuclei and most other organelles.

Variations in lens fibre structure and composition make it possible to distinguish a softer cortical zone, made up of younger fibres, and a firmer central part, representing the older nucleus. The nucleus can be further subdivided into layers representing the age at which the fibres within them were formed.

In cross-section, individual fibres are flattened hexagons measuring approximately 10 μm by 2 μm (see Fig. 45.16). They are tightly packed, and fibres are firmly attached to their neighbours by a variety of interlocking junctions (**Fig. 45.18**). Lens fibres are also in contact through desmosomes and numerous gap junctions.

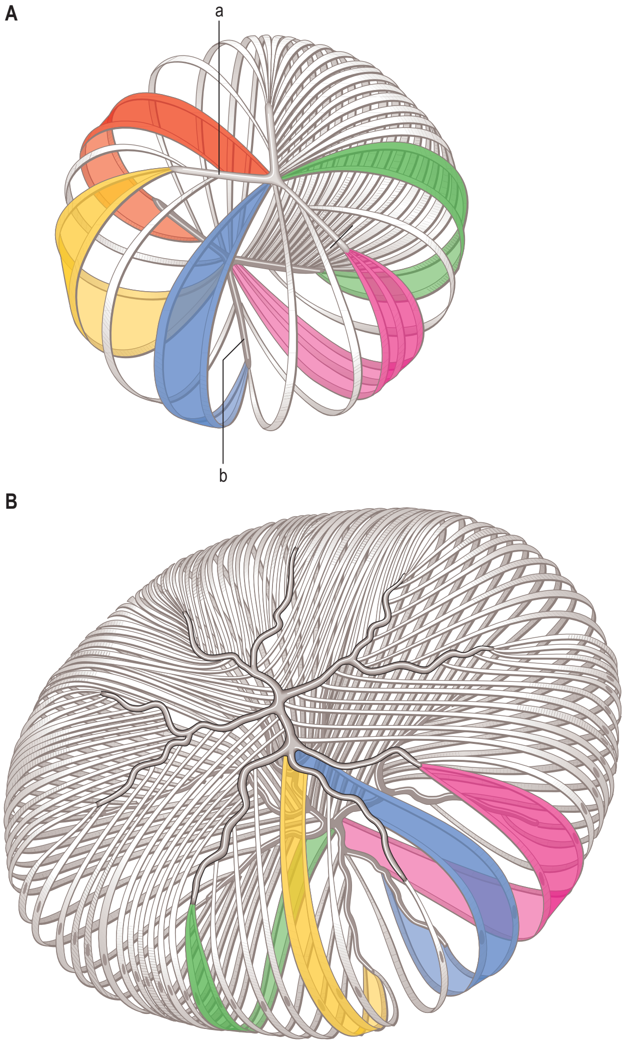

Fig. 45.19 The structure of the fetal (**A**) and adult (**B**) human lens, showing the major details of arrangement of the lens fibres. The anterior (a) and posterior (b) triradiate sutures are shown in the fetal lens. Fibres pass from the apex of an arm of one suture to the angle between two arms at the opposite pole, as shown in the coloured segments. Intermediate fibres show the same reciprocal behaviour. The suture pattern becomes much more complex as successive strata are added to the exterior of the growing lens, and the original arms of each triradiate suture show secondary and tertiary dichotomous branchings. (With permission from Hogan MJ, Alvarado JA, Weddell JE 1971 Histology of the Human Eye. Philadelphia: WB Saunders.)

All lens fibres cross a plane passing through the equator and terminate on both the anterior and posterior lens surfaces at 'sutures'. These radiate out from the poles towards the equator and represent lines of linearly registered, interlocking junctions between terminating lens fibres. In fetuses, the sutures on the anterior surface of the lens form a triradiate pattern centred on the anterior pole resembling the limbs of an upright letter Y (Fig. 45.19A). Posteriorly, the sutural configuration is similar but inverted. The sutures increase in number and complexity as a consequence of lens growth and other changes in the arrangement of lens fibres (Fig. 45.19B). Fibres that start near the central axis of the lens anteriorly terminate posteriorly on a suture near the periphery, and *vice versa*.

Lens fibres contain crystallins, proteins that are responsible for the transparency and refractile properties, and for much of the elasticity, of the lens. At least three varieties coexist – α, β and γ, their relative proportions changing throughout life. They have very high concentrations and form up to 60% of the lens fibre mass, giving these cells a higher protein content than any other bodily tissue. Variations in their concentration in different parts of the lens give rise to regional differences in refractive index, correcting for the spherical and chromatic aberrations which might otherwise be the case in a homogeneous lens.

Lens transparency is largely the result of the regular packing of crystallins within its fibres, as well as the avascularity of the lens and the absence of fibre organelles. Apart from transmitting the visible spectrum, the lens also serves to prevent potentially damaging UVA radiation from reaching the retina using a variety of chromophores such as various kynurenine derivatives. Shorter wavelengths (UVB) are removed by the cornea. At birth, the lens is colourless and transmits all wavelengths from the infra-red to the near-ultraviolet well. However, throughout life, due largely to post-translational modification of its proteins, the amount of short wavelength radiation transmitted diminishes until, in old age, the lens takes on an amber tinge as it absorbs visible radiation too, decreasing blue sensitivity in older people. In cataract, these changes are more pronounced. Lens fluorescence also increases with age, reducing contrast of the retinal image (Zelentsova et al 2017).

Ocular refraction

Refraction takes place when light is obliquely incident on the interface between media of different refractive indices. Approximately two-thirds (40 dioptres) of the total refractive power of the unaccommodated eye is effected by the tear film covering the curved cornea, as its refractive index is similar to that of water (1.333), while that of air is close to unity. The remaining approximately 20 dioptres of the eye's power is the result of refraction by the lens, whose refractive index varies from 1.386 at its periphery to 1.406 at its core, which is higher than that of the surrounding media. The main value of the lens is its ability to vary its dioptric power during the process of accommodation, allowing an increase in refraction of 12 dioptres when viewing close objects in the young. This decreases with age, being halved at 40 years and reduced to one dioptre or less at 60 years (presbyopia).

Disorders of refraction

An unaccommodated eye is said to be emmetropic when the refracting structures are so related to its length that the retina receives a focused image of a distant object. Although the majority of eyes are emmetropic, a large, and increasing, minority have errors of refraction (ametropia) that can take three different forms. In myopia, the eye is too long for its refractive power and distant objects are focused in front of the retina when relaxed; closer objects will be in focus and, consequently, the eye is said to be 'short-sighted'. Conversely, in hyperopia (long sight), the eye is too short for its refractive power and, when it is relaxed, distant objects are focused behind the retina. In astigmatism, the refractive power of the eye is not the same in different meridians, which are approximately 90° apart in regular astigmatism.

Normally, emmetropia is assured during development both by the active control of the sclera's biomechanical and biochemical properties and changes in the optical features of the eye's refractive elements, a process known as emmetropization (Wallman and Winawer 2004). A resting focal plane behind the retina results in scleral growth causing axial elongation of the globe until the focused image and the position of the retina are coincident. On the other hand, light focused in front of the retina retards scleral growth, reducing axial length. In ametropia, this process fails.

The causes of refractive errors such as myopia are both genetic and environmental. Not only have several candidate genes been identified, but also factors such as increased near work and lack of outdoor activity have all been linked to myopia (Wallman and Winawer 2004, Flitcroft 2013). This has led to a recent increase in the incidence of myopia to epidemic proportions, with a prevalence of over 80% in the adult population of some East Asian cities (Rose et al 2008). Fortunately, errors of refraction are amenable to correction using spectacle or contact lenses and by various forms of refractive surgery.

As noted above, the ability to change the power of the lens through accommodation diminishes during the fifth decade to an extent that neither the corrected ametrope nor the emmetrope is able to focus near objects clearly, and reading spectacles become necessary. Many factors could potentially result in such loss of accommodation, but it seems likely that the main cause is the continued growth of the lens, rather than a reduced ability of the ciliary muscle to contract (Strenk et al 2005). This is offset to a very limited extent by the reduction of the pupil aperture with age, which increases the depth of focus but at the cost of creating the further problem of requiring greater illumination.

Other errors of refraction are the concomitants of eye disease, especially those that affect the cornea. Corneal curvature, for example, may be sufficiently altered as a residual defect of past disease to cause irregular astigmatism. In keratoconus, the cornea is thinned and steepened centrally, distorting the refracting surface. A dislocated lens, caused, for example, by Marfan syndrome, also disrupts the refractive status of the eye.

Vitreous humour

The vitreous humour occupies about four-fifths of the eyeball. Posteriorly, it is in contact with the retina, while further forwards it abuts the ciliary body, zonular fibres and lens. Its anterior surface is hollowed into a deep concavity, the hyaloid fossa, fitting the shape of the lens (see Fig. 45.1). It is colourless, consisting of approximately 99% water, but is not entirely structureless. At its perimeter (cortex), it has a gel-like consistency (100–300 μm thick); nearer the centre, it contains a more liquid zone. Hyaluronan, in the form of long glycosaminoglycan chains, fills the whole vitreous. In addition, the vitreous contains a random loose network of type II collagen fibrils, which are densest in the cortex and occasionally grouped into fibres. The cortex also contains scattered cells, hyalocytes, which possess the characteristics of mononuclear phagocytes and may contribute to the production of hyaluronan. Normally in a resting state, they can be actively phagocytic in inflammatory conditions. Hyalocytes are not present in the cortex bordering the lens.

The liquid vitreous is absent at birth, appears first at 4 or 5 years, and increases to occupy half the vitreous space by the seventh decade. Vitreous liquefaction results in an increased incidence of posterior vitreous detachment and associated floaters in the elderly. The cortex is most dense at the pars plana of the ciliary body adjacent to the ora serrata, where attachment is strongest, and this is often referred to as the vitreous base. Elsewhere, the vitreous also has a firm (peripapillary) attachment at the edge of the optic disc. The adherence of the vitreous to the retina can result in traction on the retina if the vitreous shrinks, such as happens in old age, producing macular holes or peripheral breaks, possibly leading to retinal detachment.

A narrow hyaloid canal runs from the optic nerve head to the central posterior surface of the lens (see Fig. 45.1). In the fetus, this contains the hyaloid artery, which normally disappears about 6 weeks before birth. The canal persists in adult life as a very delicate fibrous structure and is of no functional importance.

RETINA

The retina is a sheet of cells, ranging in thickness from less than 100 μm at its edge to a maximum of around 300 μm at the foveal rim. It lines the inner posterior surface of the eyeball, sandwiched between the choroid externally and the vitreous humour internally, and terminates anteriorly at the ora serrata: it covers around 70% of the inner surface area of the globe (see Fig. 45.1).

When viewed with an ophthalmoscope to show the fundus oculi, the most prominent feature is the blood vessels emanating from and entering the optic disc (**Fig. 45.20A**).The 'central retina' or macula (diameter 5–6 mm) is centred temporal and inferior to the disc. The middle of the macula, the fovea and foveola, is easily identified with an ophthalmoscope as an avascular area with a yellow tinge (see Fig. 45.20A). The lack of blood vessels at the foveola is even more apparent in a fluorescein angiogram (**Fig. 45.20B**). The peripheral retina lies outside the macula.

Microstructure

The retina is composed of a variety of epithelial, neural and glial cell types. When seen in transverse section, their distribution is conventionally described in 10 layers (**Fig. 45.21**). These layers are evident in histological sections (**Fig. 45.22**), but can also be seen *in vivo* using optical coherence tomography (**Fig. 45.23**). Embryologically, the retina is derived from the two layers of the invaginated optic vesicle (Ch. 15). Nine layers develop from the inner layer of the optic vesicle and form the neural retina. The outermost layer becomes a stratum of cuboidal pigment cells, the retinal pigment epithelium (layer 1), that separates the choroid from the neural retina.

The outermost layer of the neural retina contains the light-sensitive parts of the photoreceptors, which convert the optical image into neural activity. From the photoreceptors, neural activity flows radially to bipolar and ganglion cells, and laterally via horizontal cells in the outer retina and amacrine cells in the inner retina. Photoreceptors synaptically contact each other and bipolar and horizontal cells in the outer plexiform layer (layer 5), while bipolar, amacrine and ganglion cells synapse in the inner plexiform layer (layer 7). The axons of ganglion cells run towards the optic disc in the nerve fibre layer (layer 9), where they leave the retina as the optic nerve, which transmits the retinal output to the visual areas of the brain where visual processing is completed. Although most neural activity flows from the photoreceptors towards the brain, some information flow takes place in the opposite direction via centripetal fibres in the optic nerve and interplexiform cells in the retina that connect the inner and outer plexiform layers.

The classic 10-layered appearance of the retina is absent in the optic nerve head, the fovea and foveola, and the ora serrata. At the optic nerve head, the axons of the retinal ganglion cells leave the retina to form the optic nerve and all the other neural cell types are missing. At the fovea and foveola, the inner five layers of the retina are 'pushed aside'. At the ora serrata, where the retina borders the ciliary body (see Fig. 45.10), the retinal pigment epithelium merges with the outer pigmented epithelium of the ciliary body, while the neural retina borders the inner unpigmented ciliary epithelium; the retina is thinnest at this point. The normal layered arrangement of the neural retina approaching the ora serrata is frequently

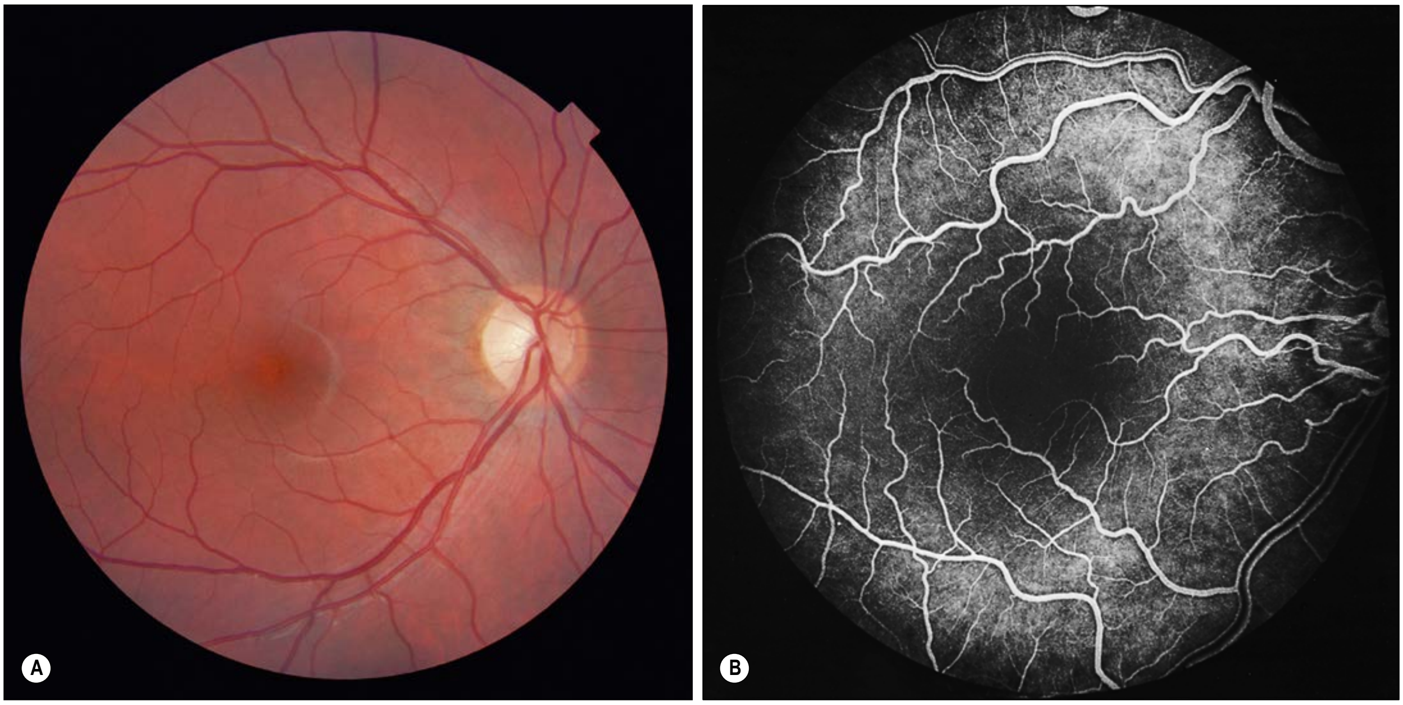

Fig. 45.20 A, A fundus photograph of the right eye of a 19-year-old Caucasian female. The central retinal vessels are seen emanating from the optic disc. Retinal arteries are narrower and lighter in colour, and generally are vitreal to the veins. The avascular centre of the macular region, with its associated macular pigment, can be seen temporal to the disc. **B**, A fluorescein angiogram showing the macular region of a right eye. The main macular vessels are approaching from the right. The elderly subject has considerable macular pigmentation that masks fluorescence from the choroidal circulation.

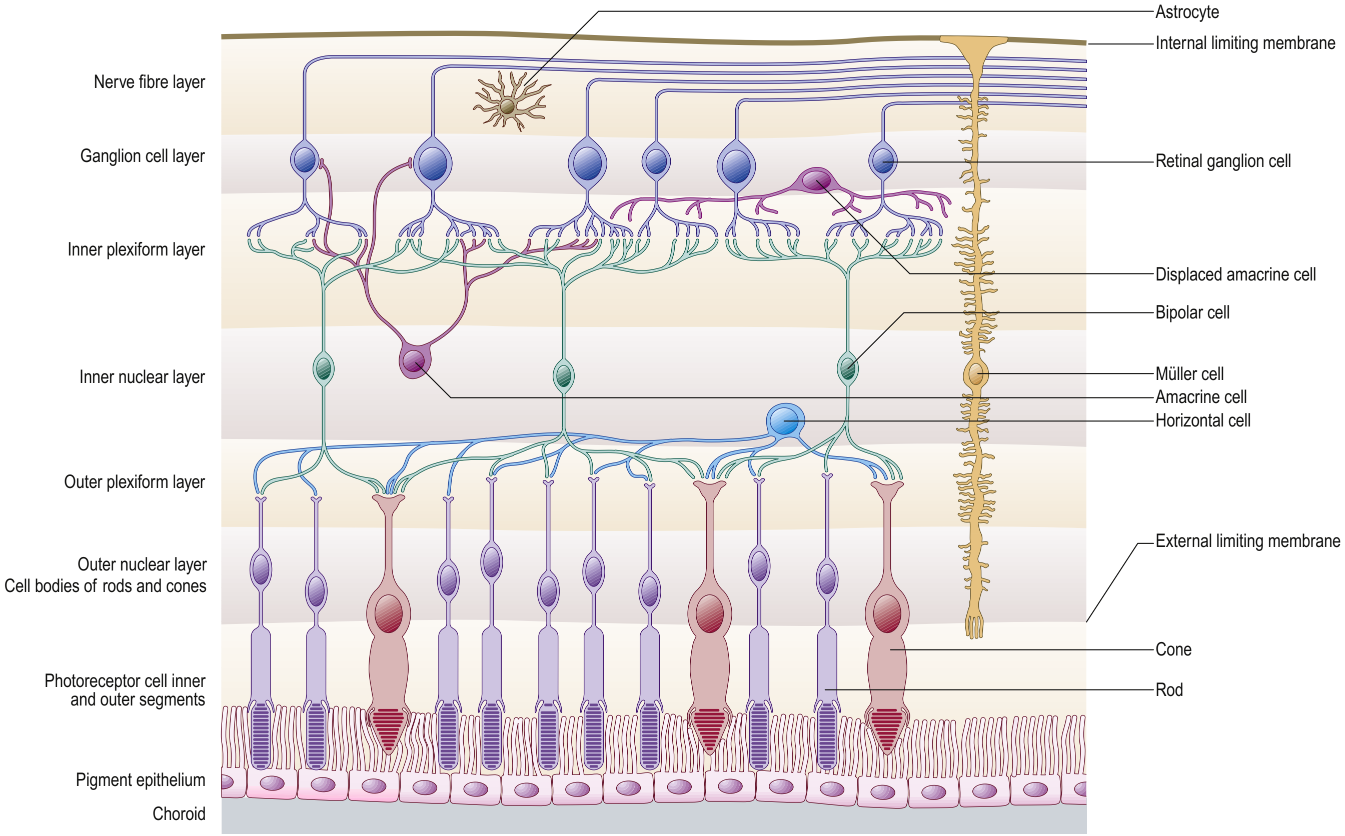
Nerve fibre layer
Ganglion cell layer
Inner plexiform layer
Inner nuclear layer
Outer plexiform layer
Outer nuclear layer
Cell bodies of rods and cones
Photoreceptor cell inner and outer segments
Pigment epithelium
Choroid
Astrocyte
Internal limiting membrane
Retinal ganglion cell
Displaced amacrine cell
Bipolar cell
Müller cell
Amacrine cell
Horizontal cell
External limiting membrane
Cone
Rod

Fig. 45.21 Neural cells whose cell bodies and interconnections account for the layered appearance of the retina in histological section (compare with Fig. 45.22). Also shown are the two principal types of neuroglial cell in the retina (although microglia are also present, they are not shown).

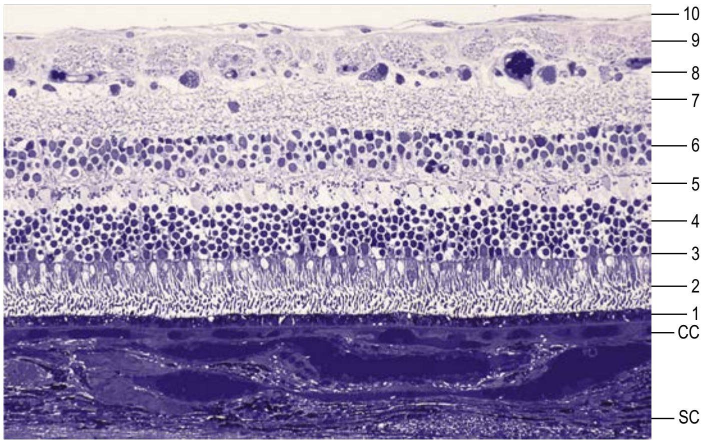
10
9
8
7
6
5
4
3
2
1
CC
SC

Fig. 45.22 A transverse section of the retina and choroid. The 10 layers of the retina are shown. Key: 1, pigment epithelial layer; 2, rod and cone layer; 3, external limiting membrane; 4, outer nuclear layer; 5, outer plexiform layer; 6, inner nuclear layer; 7, inner plexiform layer; 8, ganglion cell layer; 9, nerve fibre layer; 10, internal limiting membrane. Abbreviations: CC, choriocapillaris; SC, suprachoroid.

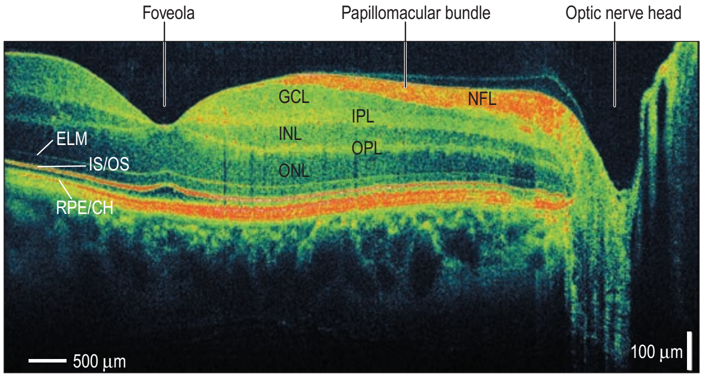
Foveola
Papillomacular bundle
Optic nerve head
GCL
NFL
IPL
INL
OPL
ONL
ELM
IS/OS
RPE/CH
500 μm
100 μm

Fig. 45.23 A high-definition optical coherence tomography (OCT) *in vivo* image of the human retina. The image has approximately 2 μm axial resolution, is 8 mm long and consists of 10,000 axial scans. The image is expanded in the vertical direction to permit better visualization of retinal layers. Abbreviations: ELM, external limiting membrane; GCL, ganglion cell layer; INL, inner nuclear layer; IPL, inner plexiform layer; IS/OS, boundary between the photoreceptor inner and outer segments; NFL, nerve fibre layer; ONL, outer nuclear layer; OPL, outer plexiform layer; RPE/CH, retinal pigment epithelium and choriocapillaris. (Courtesy of Professor James Fujimoto, Department of Electrical Engineering and Computer Science, MIT, Boston, USA.)

disrupted by cysts in older individuals (Fig. 45.24). Insufficiency in the vascular supply from the choriocapillaris leads to localized ovoid areas of outer retinal atrophy, known as paving stone (cobblestone) degeneration in the peripheral retina: the condition occurs in about one-third of adults, especially older individuals or those with increased axial length.

Cells of the retina

Retinal pigment epithelium

In the central retina the retinal pigment epithelium is composed of approximately cuboidal cells (12 μm height × 14 μm diameter) that become flatter and wider (60 μm) in the periphery. They form a single continuous layer that extends from the periphery of the optic disc to the ora serrata. The cells are flat in radial section, hexagonal or pentagonal in surface view, and number 4–6 million. Their cytoplasm, especially the apical portion, contains numerous melanosomes. The basal surface contains many small invaginations that increase the surface area for exchange of substances with the choriocapillaris. Apically, the cells bear longer (5–7 μm), heavily pigmented, microvilli that contact, or project between, the outer segments of the photoreceptors. The tips of rod outer segments are more deeply inserted into these invaginations than those of cones. The different embryological origins of the retinal pigment epithelium and neural retina mean that the attachments between these two layers are unsupported by junctional complexes; the neural retina and retinal pigment epithelium are therefore easily parted (retinal detachment).

Retinal pigment epithelium cells play a major role in the turnover of rod and cone photoreceptive components. Their cytoplasm contains the phagocytosed tips of rods and cones undergoing lysosomal destruction. The final products of this process are lipofuscin granules. Disturbances in this phagocytic activity of the retinal pigment epithelium can lead to retinal disease (Kevany and Palczewski 2010).

Light reaching the outer retina but missing the photoreceptors is absorbed by the retinal pigment epithelium, which, like melanin elsewhere in the eye, prevents such stray light degrading image quality. A zone of tight junctions between adjacent cells also allows the epithelium to function as a blood–retinal barrier between the neural retina and the vascular system of the choroid. The retinal pigment epithelium is required for the regeneration of bleached visual pigment and may have antioxidant properties. It also secretes a variety of growth factors necessary for the integrity of the choriocapillaris endothelium and the photoreceptors and produces a number of immunosuppressive factors. A failure of any of the diverse functions of the retinal pigment epithelium could result in compromised retinal function (Strauss 2005).

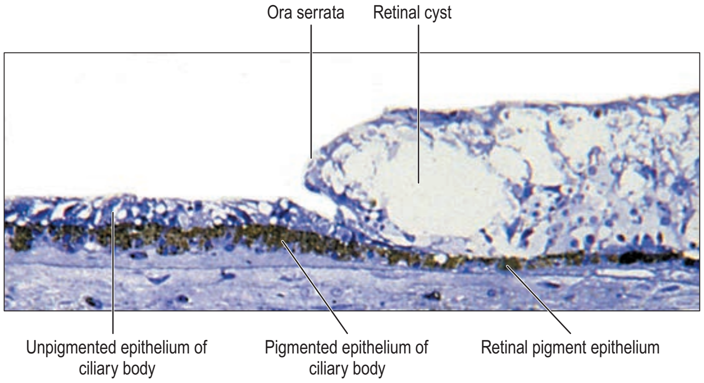
Ora serrata
Retinal cyst
Unpigmented epithelium of ciliary body
Pigmented epithelium of ciliary body
Retinal pigment epithelium

Fig. 45.24 The junction between the retina and ciliary body (ora serrata). The retinal pigment epithelium is continuous with the outer, pigmented epithelium of the ciliary body, while the neural retina abuts the inner, unpigmented epithelium of the ciliary body. The layered appearance that is apparent elsewhere in the neural retina is disrupted adjacent to the ora serrata by cystic degeneration.

The cells of the retinal pigment epithelium undergo several age-related morphological changes, many of which precede the onset of age-related macular degeneration (Boulton and Dayhaw-Baker 2001). In addition to various pleomorphic changes, lipofuscin granules accumulate with age, while the density of melanin granules decreases: the fundus therefore appears darker in the young. Retinal pigment epithelial cells are amitotic: an overall decrease in cell density with age has often been reported, although this is not a universal observation.

Rods and cones

Rods and cones are the 'image-forming' photoreceptors of the outer retina and function at low (scotopic) and higher (photopic) light levels, respectively. Both are long, radially orientated structures with a similar organization, although details differ (Fig. 45.25). From the choroidal end inwards, the cells consist of outer and inner segments connected by a thin connecting cilium (together making up layer 2 of the retina), a cell body containing the nucleus, and a synaptic terminal (either a more complex pedicle for cones or a simpler rod spherule) where they

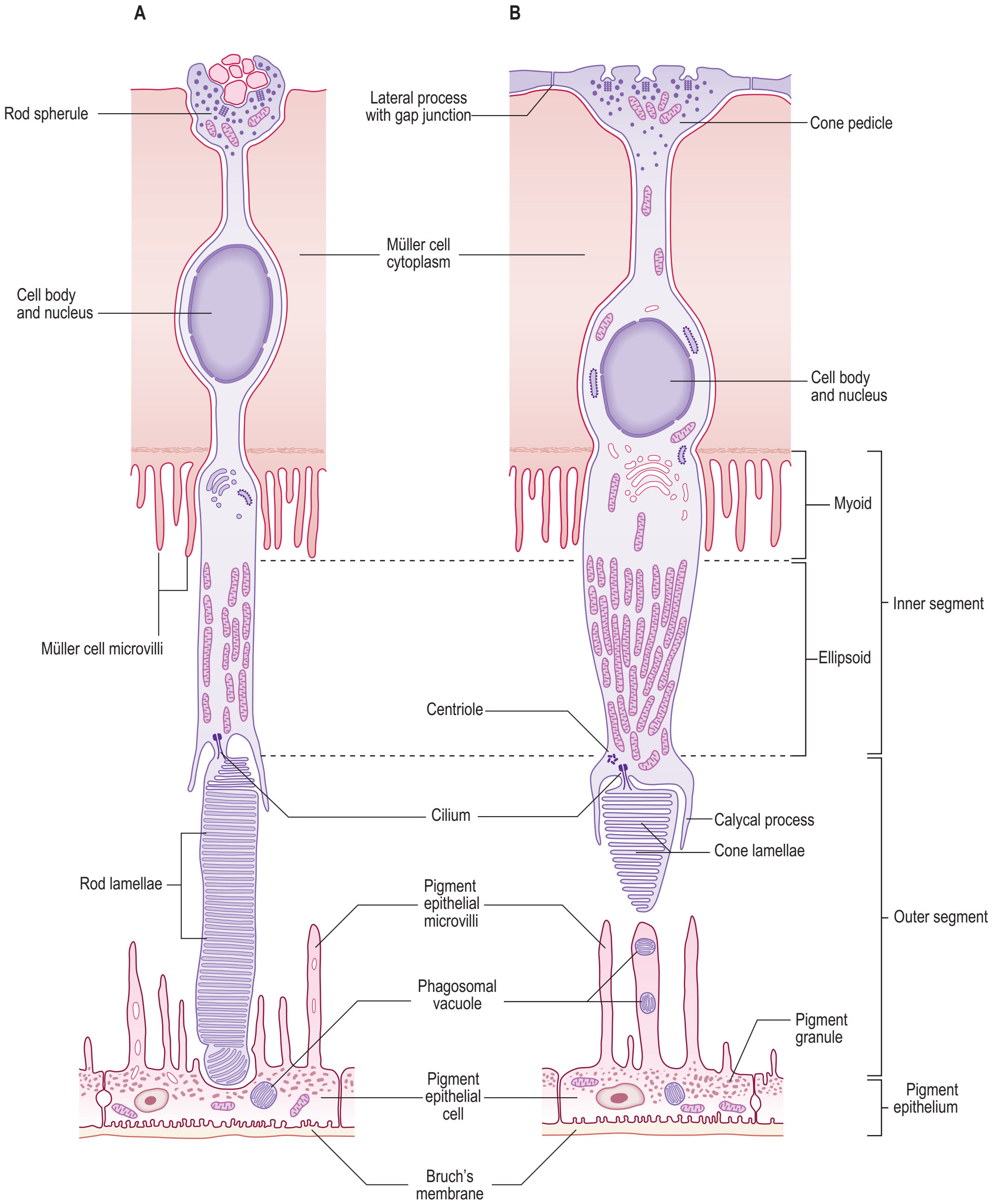
A
B
Rod spherule
Lateral process with gap junction
Cone pedicle
Müller cell cytoplasm
Cell body and nucleus
Cell body and nucleus
Myoid
Inner segment
Müller cell microvilli
Ellipsoid
Centriole
Cilium
Calycal process
Cone lamellae
Rod lamellae
Pigment epithelial microvilli
Outer segment
Phagosomal vacuole
Pigment granule
Pigment epithelial cell
Pigment epithelium
Bruch's membrane

Fig. 45.25 The major features of a retinal rod cell (**A**) and a retinal cone cell (**B**). The relative size of the pigment epithelial cells has been exaggerated for illustrative purposes.

make synaptic connections with adjacent bipolar and horizontal cells and with other cone or rod cells within the outer plexiform layer.

The nuclei of the rods and cones form the outer nuclear layer (layer 4). The cone nuclei are relatively large and oval, and generally form a single layer that often penetrates the external limiting membrane (layer 3). They also contain less heterochromatin than those of rods and thus usually stain more lightly. Rod nuclei are round and smaller, stain more darkly, and form several layers vitreal to the cone nuclei.

The external limiting membrane is not, in fact, a membrane at all, although it appears as such in the light microscope; rather, it is a series of zonulae adherentes between photoreceptors and the glial (Müller) cells that separate them. These junctions most likely serve to anchor the photoreceptors and prevent leakage of the interphotoreceptor matrix that surrounds the photoreceptor outer and inner segments.

Rod outer segments are cylindrical and consist of around 1000 flattened, lobulated, membranous discs. These form as deep infoldings of the plasma membrane at the base of the outer segment; they 'bud off' after formation so that the discs are not attached to the plasma membrane and are free-floating within the outer segment. Cone outer segments are generally shorter and, as their name implies, often conical (especially in the peripheral retina). Cone discs do not bud off after formation and remain as infoldings of the plasma membrane.

The inner segment of both rods and cones is divided into an outer, mitochondria-rich, ellipsoid and an inner myoid that contains endoplasmic reticulum. In most of the retina, these inner segments are much wider in cones (5–6 µm at their widest point) than rods (1.5 µm) (**Fig. 45.26**). In both rods and cones, proteins are manufactured within the myoid and incorporated into the newly formed discs at the base of the outer segment. In rods, as new discs are added, old discs are pushed up the outer segment and eventually phagocytosed by the retinal pigment epithelium. Cone discs are also phagocytosed but the incorporation of new proteins within the discs is more diffuse (Nguyen-Legros and Hicks 2000). While all rods within the retina have a similar structure, the cones at the foveola are highly modified compared to those situated more peripherally and, in many ways, resemble rods with a longer outer segment and a thinner inner segment.

Light is absorbed by rhodopsins, visual pigments consisting of a protein, opsin, that spans the membrane of the outer segment discs, bound to a light-absorbing chromophore, retinal, which is an aldehyde of vitamin A_1. Such rhodopsins have a smooth, bell-shaped absorption profile with a point of maximum absorbance (λ_{max}), indicating the wavelength at which they are most sensitive. Humans possess four different opsins, resulting in four spectrally distinct visual pigments: one located within the rods (λ_{max} 498 nm) and three within different populations of cones absorbing maximally at the short (λ_{max} 420 nm), middle (λ_{max} 534 nm) and longer (λ_{max} 563 nm) wavelength end of the visible spectrum. The three cone classes are sometimes referred to as the blue, green and red cones but are better classed as S, M and L cones. The action of light is to isomerize the retinal, separating it from the opsin, a process which, via a G-protein coupled enzyme cascade and a second messenger system, results in the closure of cation channels in the receptor outer segment membrane, leading to a hyperpolarization of the photoreceptor, and a consequent decrease in the release of glutamate from its synapses.

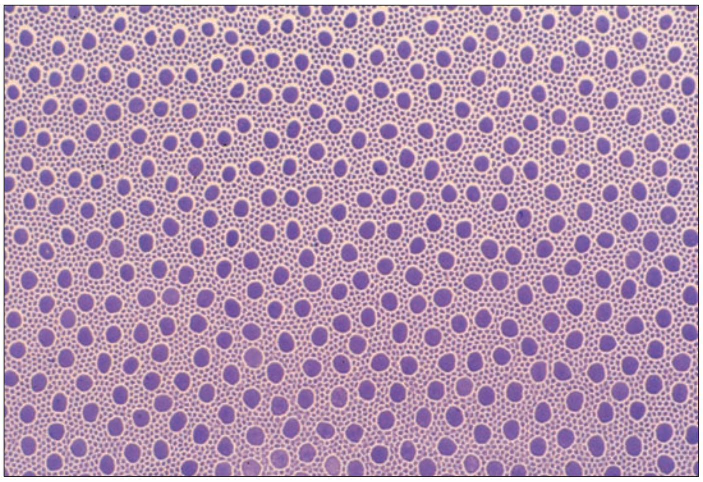

Fig. 45.26 Tangential section of a human retina in the parafovea cut at the level of the inner/outer segments, showing the 'mosaic' of both the larger cones and the more numerous, but smaller, rods. Photoreceptors at the top of the image are sectioned at a level closer to the retinal pigment epithelium than receptors lower in the figure. The reduction in size of the cones at the top of the figure is explained by the conical shape of their outer segment. If the figure were continued upwards, representing sections closer to the retinal pigment epithelium, the size of the cones would continue to decrease and the amount of surrounding white space would increase. Rod outer segment diameter, however, would change little.

The human retina contains, on average, 4.6 million cones and 92 million rods, although there is significant inter-individual variation (Curcio et al 1990). The number of central rods declines by about 30% with age, whereas the number of foveal cones remains stable (Curcio et al 1993). Although cones populate the whole retina, their density is highest in the foveola, where approximately 7000 cones reach an average density equivalent to 199,000 cones/mm^2; this area is entirely rod-free. Going outwards from the foveola, rod numbers rise, reaching a peak density (>150,000 rods/mm^2) in a horizontal elliptical ring at an eccentricity of 2–5 mm, thereafter declining once more towards the periphery. Cone density is 40–45% higher in the nasal retina compared to the temporal retina, and slightly higher inferiorly than superiorly.

The number of S cones in all human retinae is similar, making up less than 10% of all cones (Curcio et al 1991, Hofer et al 2005). The distribution of S cones is relatively even throughout the retina, although they are absent from the central fovea. The relative proportions of L and M cones shows a much greater degree of variation between individuals, the L : M cone ratio varies from close to unity to over 10. The distribution of L and M cones is more irregular than that of S cones and appears random with some indication of clumping (Bowmaker et al 2003, Hofer et al 2005).

The high packing density of cones at the foveola, achieved by decreasing inner segment diameter, ensures maximal resolution, while the presence of more than one spectral cone type allows colour vision. S cones probably contribute little to spatial resolution because they are absent from the foveola. Rod-based vision provides high sensitivity, but with relatively low spatial discrimination and no ability to distinguish wavelengths. Although many of the functional differences between rods and cones rely on the different properties of the photoreceptors themselves, their connectivity to other retinal neurones is equally important.

Horizontal cells

Horizontal cells are inhibitory interneurones. Their dendrites and axons extend laterally within the outer plexiform layer, making synaptic contacts with cone pedicles and rod spherules, and, via gap junctions at the tips of their dendrites, with each other. Their cell bodies lie in the outer part of the inner nuclear layer (layer 6). Three morphological types of horizontal cell can be distinguished in the human retina (Kolb et al 1992). The dendrites of HI and HIII cells contact cones, and their axons terminate on rods. Both the axons and dendrites of HII cells synapse only with cones.

Bipolar cells

Bipolar cells are radially orientated neurones. Their dendrites synapse on photoreceptors, horizontal cells and interplexiform cells in the outer plexiform layer. Their somata are located in the inner nuclear layer, and axonal branches in the inner plexiform layer synapse with dendrites of ganglion cells or amacrine cells. Golgi staining has identified nine distinct types of bipolar cell in the human retina (Kolb et al 1992), eight of which contact cones exclusively, and the remaining type synapses only on rods.

Cone bipolars are of three major morphological types: midget, S (blue) cone and diffuse, according to their connectivity and size. Midget cone bipolar cells either invaginate the cone pedicle or synapse on its base (flat subtype). In the central retina, each midget bipolar cell contacts only a single cone (2–3 in the periphery), forming part of a one-to-one channel from cone to ganglion cell that mediates high spatial resolution. S cones form part of a short-wavelength mediating channel, while the larger diffuse cone bipolars are connected to up to 10 cones and are thought to signal luminosity rather than colour.

Cone bipolar cells can also be of two physiological types, according to their response to the light-induced decrease in glutamate release from the photoreceptors to which they are synaptically connected. If illumination of the photoreceptors with a point of light causes a depolarization of the connected bipolar cell, it is said to be an 'ON' bipolar, contacting the cone by 'sign-inverting' synapses with metabotropic receptors. However, if cones are connected to an 'OFF' bipolar cell via 'sign-conserving' synapses with ionotropic receptors, illumination of the photoreceptor will result in hyperpolarization of the bipolar cell. Illumination of a concentric area of surrounding photoreceptors causes the opposite response in bipolar cells to illumination within their dendritic field. This inhibition is mediated via horizontal cells and gives rise to the

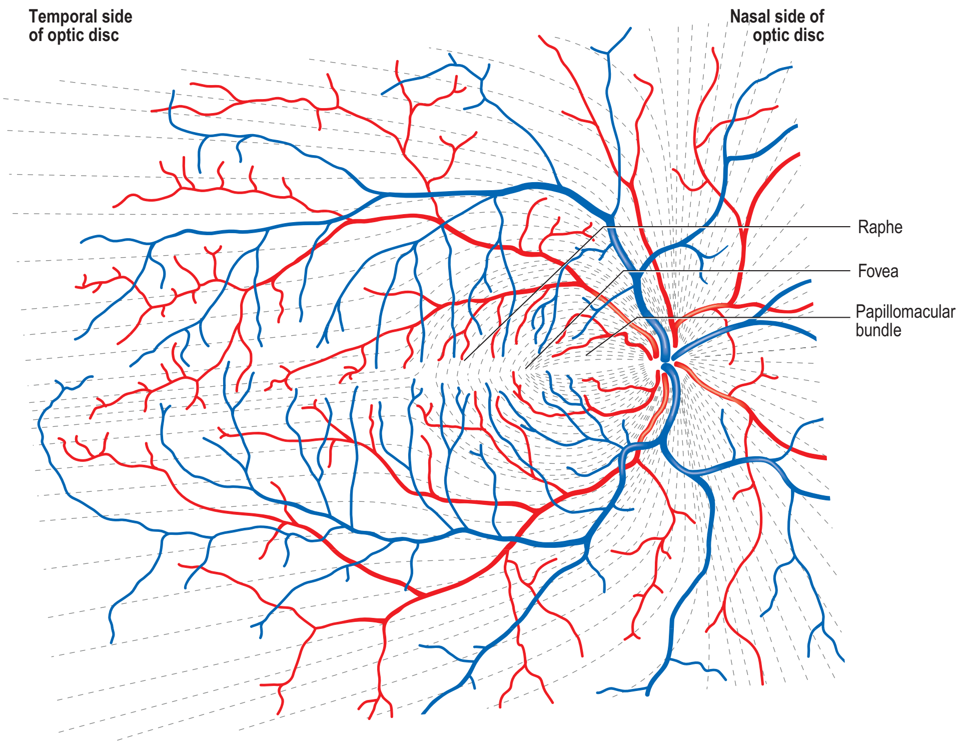

Fig. 45.27 Directions of axons (dashed lines) and blood vessels of the nerve fibre layer of the retina of the right eye. Axons pass radially on the nasal side of the optic disc, whereas fibres on the temporal side avoid crossing the fovea by arching around it. Some of the fibres from the fovea and central region pass straight to the optic disc and others arch above and below the horizontal; together, these form the papillomacular bundle. A raphe is formed by the central fibres temporal to the fovea. Venules are shown crossing in front of arteries; the reverse relationship is probably the more common pattern. All vessels issue from the disc on the right of the figure; the larger temporal branches tend to arch around the central region of the retina and do not approach the fovea. The peripheral retina and most of the nasal retina are not shown.

antagonistic centre-surround type receptive field that is characteristic of all levels of the visual system up to and including the occipital cortex.

The single morphological type of rod bipolar cell contacts 30–35 rods in the central retina, increasing to 40–45 rods in the periphery. Such convergence serves to increase the absolute sensitivity of the rod system. All rod bipolar cells are 'ON-centre' and do not contact ganglion cells directly, but synapse with a class of amacrine cell (AII), which then contacts cone bipolar cells.

The inner plexiform layer can be divided into two main layers: an outer layer containing the synaptic endings of 'OFF' cone bipolar cells, and an inner layer of 'ON' cone and rod bipolar cell synapses.

Amacrine cells

Most amacrine cells lack typical axons and, consequently, their dendrites make both incoming and outgoing synapses. Each neurone has a cell body either in the inner nuclear layer near its boundary with the inner plexiform layer, or on the outer aspect of the ganglion cell layer, when it is known as a displaced amacrine cell. The processes of amacrine cells make a variety of synaptic contacts in the inner plexiform layer with bipolar and ganglion cells, as well as with other amacrine cells.

The various classes of amacrine cell serve a number of important functions. AII cells play an essential role in the rod pathway (see above). Other cells appear to be important modulators of photoreceptive signals and serve to adjust or maintain relative colour and luminosity inputs under changing light conditions. They are probably also responsible for some of the complex forms of image analysis known to take place within the retina, such as directional movement detection. Up to 24 different morphological types of amacrine cell are recognized in humans (Kolb et al 1992); coupled to their neurochemical complexity, this makes them perhaps the most diverse neural cell type in the body.

Interplexiform cells

Interplexiform cells, often regarded as a subclass of amacrine cells, generally have cell bodies in the inner nuclear layer. They are postsynaptic to cells in the inner retina and send signals against the general direction of information flow in the retina, synapsing with bipolar, horizontal and photoreceptor cells in the outer plexiform layer. Although their function is uncertain, it is likely that, through the release of γ-aminobutyric acid (GABA) and dopamine, they adjust some aspect of retinal function such as sensitivity.

Ganglion cells

The human retina contains 0.7–1.5 million ganglion cells, the output neurones of the retina (Curcio and Allen 1990). Their number declines with age, in glaucoma, and possibly other conditions such as Alzheimer's disease.

Ganglion cell dendrites synapse with processes of bipolar and amacrine cells in the inner plexiform layer. Ganglion cell bodies, together with displaced amacrine cells, form the ganglion cell layer of the retina (layer 8). They form a single layer throughout most of the retina, but become progressively more numerous near the macula, where they are ranked in up to 10 rows, reaching a peak density of up to 38,000/mm^2 in a horizontally orientated elliptical ring 0.4–2.0 mm from the foveal centre. Their number diminishes again towards the fovea, from which they are almost totally excluded.

Up to 15 ganglion cell types have been identified in the mammalian retina based on their morphology, physiology and target area in the brain; each type is presumed to be functionally distinct. For example, some project to different regions of the lateral geniculate nucleus and form three parallel visual pathways involved in conscious visual perception: the magnocellular and parvocellular systems and a pathway carrying the S cone signal (Wässle 2004). Midget ganglion cells (P cells) contact only single midget bipolar cells in the central retina, which, in turn, connect to single cones, giving each cone a 'private line' out of the retina and ensuring optimal acuity. The large dendritic field of parasol cells (M cells) is consistent with a role in motion detection. Parasol and midget ganglion cells together make up around 80% of human retinal ganglion cells. The remaining cells (approximately 200,000) project to the superior colliculus of the midbrain, the thalamic pulvinar, the pretectum and the accessory optic system, and contribute to various subconscious visual reflexes such as the pupillary and accommodation responses (see Fig. 45.12). A population of around 3000 large, intrinsically light-sensitive ganglion cells, containing the retinal-based visual pigment melanopsin (λ_{max} 479 nm), form a network of extensive overlapping dendrites (Dacey et al 2005). These 'inner retinal photoreceptors' also receive input from the rods and cones and provide a 'non-image forming' system that monitors overall levels of illumination. They are the major route by which the eye influences circadian rhythms via the suprachiasmatic nucleus and they contribute to light-evoked pupillary constriction via projections to the olivary pretectal nucleus. Axons of some of these photosensitive ganglion cells project to the lateral geniculate nucleus, where they are thought to provide the visual system with information relating to brightness, for example contributing to light adaptation and contrast sensitivity.

Ganglion cell axons form the nerve fibre layer on the inner surface of the retina. They run parallel to the surface of the retina, converging on the optic nerve head where they leave the eye as the optic nerve. Fibres from the medial (nasal) retina approach the disc in a simple radial pattern (**Fig. 45.27**), whereas axons from the lateral (temporal) retina take an arcuate route as they avoid the fovea. Axons from the macula form a papillomacular fasciculus that passes almost straight to the disc. The thickness of the nerve fibre layer increases dramatically near the optic disc as fibres from the peripheral retina traverse more central areas. The other retinal layers thin towards the edge of the disc; all neural elements of the retina other than ganglion cell axons are excluded at the disc.

Axons of retinal ganglion cells are surrounded by the processes of radial glial cells and retinal astrocytes. They are almost always unmyelinated within the retina; an optical advantage because myelin is refractile. Although a few small axons may be myelinated, in general myelination does not start until axons enter the optic disc and become part of the optic nerve.

Retinal glial cells

There are three types of retinal glial cells: radial Müller cells, astrocytes and microglia. Müller cells form the predominant glial element of the retina. Astrocytes are largely confined to the ganglion cell and nerve fibre layers. Small numbers of microglial cells are scattered throughout the neural part of the retina.

Müller cells span almost the entire thickness of the neural retina, ensheathing and separating the various neural cells except at synaptic sites. They constitute much of the total retinal volume, and almost totally fill the space between neural elements. Their nuclei lie within the inner nuclear layer; from this region each cell body extends a single thick fibre that runs radially outwards, giving off complex lateral lamellae that branch among the processes of the outer plexiform layer. Apically, each central process terminates at the external limiting membrane, from which microvilli project for a short distance into the space between the rod and cone inner segments (fibre baskets) (see Fig. 45.25). On the inner surface of the retina, the main Müller cell process expands into a terminal foot plate that contacts those of neighbouring glial cells and forms part of the internal limiting membrane (see below).

Müller cells have numerous functions (Reichenbach and Bringmann 2013). Like astrocytes, they contact blood vessels, especially capillaries of the inner nuclear layer; their basal laminae fuse with those of perivascular cells or vascular endothelia, contributing to the formation of the blood–retinal barrier. They maintain the stability of the retinal extracellular environment, for example by regulation of potassium levels, uptake of neurotransmitter, removal of debris, storage of glycogen, provision of neuroprotective support to the photoreceptors and mechanical support to the whole neural retina. They are also involved in the regeneration of cone visual pigments; some may be a source of stem cells; and they may act as light guides, conveying light from the inner retina to the photoreceptors, overcoming some of the optical disadvantages of an 'inverted' retina.

The cell bodies of retinal astrocytes lie within the nerve fibre layer and their processes branch to form sheaths around ganglion cell axons. The close association between astrocytes and blood vessels in the inner retina suggests that they contribute to the blood–retinal barrier. Retinal microglia are scattered mostly within the inner plexiform layer. Their radiating branched processes spread mainly parallel to the retinal plane, giving them a star-like appearance when viewed microscopically from the surface of the retina. They can act as phagocytes; their number increases in the injured retina.

The inner border of the retina is formed by the internal limiting membrane (layer 10), which consists of collagen fibres and proteoglycans from the vitreous, a basement membrane (which is continuous with the basal lamina of the ciliary epithelium), and the plasma membrane of expanded Müller cell terminal foot plates. It is 0.5–2 µm thick in the posterior retina and thickens with age. The internal limiting membrane is involved in fluid exchange between the vitreous and the retina, and, perhaps through the latter, with the choroid. Its other functions include anchorage of retinal glial cells, and inhibition of cell migration into the vitreous humour.

Modifications of the central retina

The central retina, or area centralis, clinically referred to as the macula, constitutes around 3% of the retinal surface area. It is composed of four concentric areas: starting with the innermost, these are the foveola (0.35 mm diameter, equivalent of an angular subtense at the nodal point of around 1.25°); the fovea (1.5 mm, 5.2°); the parafovea (2.5 mm, 8.6°); and the loosely defined perifovea (5–6 mm, 20°). The foveola, which contains no rods or S cones, is centred about 3 mm temporal and 1 mm inferior to the optic disc (see Fig. 45.20A). In the foveola and surrounding fovea, all the inner retinal layers beyond the outer nuclear layer have been displaced peripherally, so that the retina is approximately half as thick as it is elsewhere (see Fig. 45.23; **Fig. 45.28**). This foveal pit is created by the processes that connect foveal and foveolar photoreceptor cell bodies to their synapses running almost parallel to the retinal surface before connecting to postreceptoral retinal neurones outside the fovea. These oblique 'axons', along with associated Müller cells, form the Henle fibre layer. Aspects of normal macular morphology, such as the central retinal thickness and the steepness of the foveal slope, show significant individual variation. Aged foveas are less symmetric along the midline than their younger counterparts and have steeper slopes.

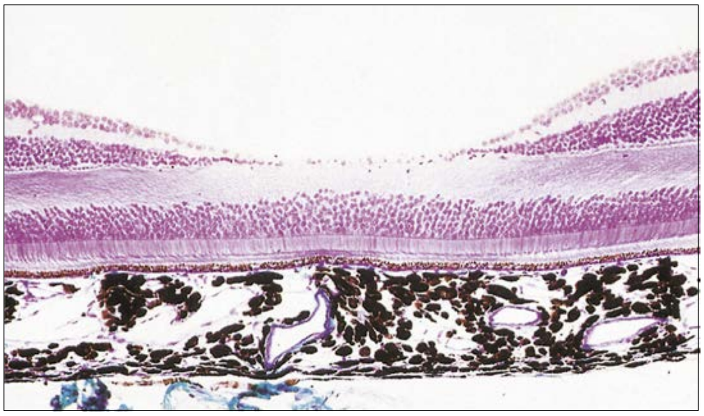

Fig. 45.28 A section through the fovea centralis. (With permission from Young B, Heath JW 2000 Wheater's Functional Histology. Edinburgh: Churchill Livingstone.)

The macula lutea is a horizontally elliptical yellow area centred on the foveola. It is formed by high concentrations of a macular pigment composed of the carotenoids lutein, zeaxanthin and meso-zeaxanthin and which absorb short wavelengths (400–530 nm). This pigment is localized in the fibrous Henle and inner plexiform layers, mainly within Műller cells and therefore largely absent in the central foveola. The density of pigment and its spatial distribution vary by more than an order of magnitude between individuals, and are influenced by factors including age, gender, smoking and diet. One function of macular pigment is to protect the photoreceptors from photo-oxidative damage; it has been hypothesized that low levels may be associated with retinal pathologies such as age-related macular degeneration (Lima et al 2016).

The increased packing density of cones in the foveola and their lack of convergence with ganglion cells, combined with the absence of the inner retinal layers, including blood vessels, from the central macula (reducing light scatter), collectively ensure that visual resolution is highest in this part of the retina. Acuity may be further enhanced by the macular pigment, which, apart from having antioxidant properties and removing potentially harmful short-wave radiation, will absorb those wavelengths most prone to chromatic aberration and Rayleigh scatter.

Vascular supply

The retina has a dual arterial supply and both parts are necessary to maintain retinal function. The outer five layers of the retina are avascular and rely on an indirect supply from the choroidal capillaries (p. 795). The inner retina receives a direct blood supply through capillaries connected to branches of the central retinal artery and vein. Only the inner retinal circulation will be described here.

The central retinal artery enters the optic nerve as a branch of the ophthalmic artery 6.4–15.2 mm behind the eyeball (Kocabiyik et al 2005), and travels within the optic nerve to its head, where it passes through the lamina cribrosa. At this level, it divides into equal superior and inferior branches, each of which, after a few millimetres, give off nasal and temporal branches that supply the 'quadrants' of the retina (see Fig. 45.27). Although similar retinal veins unite to form the central retinal vein, the courses of the arteries and veins do not correspond exactly. These vessels mainly run within the nerve fibre and ganglion cell layers of the retina, a course that accounts for their clarity when seen through an ophthalmoscope (see Fig. 45.20A), and explains why they can serve as an easily accessible indicator of cardiovascular disease. Arteries often cross veins, usually lying superficial to them; in severe hypertension, the arteries may press on the veins and cause visible dilations distal to these crossings. The vitreal location of arteries, their lighter, bright red coloration and smaller diameter in comparison to veins allow the two vessel types to be distinguished ophthalmoscopically. The detailed pattern of the inner retinal vessels is unique and therefore can be used as a source of biometric information for individual recognition.

From the four major arteries within the inner retina, dichotomous branches run from the posterior pole to the periphery, supplying the whole retina (Zhang 1994). Arteries and veins ramify in the nerve fibre layer, near the internal limiting membrane, and arterioles pass deeper into the retina to supply capillary beds. Venules return from these beds to larger superficial veins that converge towards the disc to form the central retinal vein.

Retinal capillary networks are often in three different layers, the number of layers depending on location. Radial peripapillary capillaries are the most superficial of the capillary networks and lie within the inner nerve fibre layer. A layer of inner capillaries runs within the nerve fibre and ganglion cell layers, and an outer capillary layer is located in the inner plexiform and inner nuclear layers (**Fig. 45.29**). Approaching the fovea, capillaries are restricted to two layers, and terminal capillaries eventually join to form a single-layered macular capillary ring, producing a capillary-free zone 450–500 µm in diameter at the fovea. This avascular region is clearly visible in a fluorescein angiogram (Fig. 45.20B). Capillaries become less numerous in the peripheral retina and are absent from a zone approximately 1.5 mm wide adjoining the ora serrata.

The territories of the arteries that supply a particular quadrant do not overlap, nor do the branches within a quadrant anastomose with each other, which means that a blockage in a retinal artery causes loss of vision in the corresponding part of the visual field. The only exception to this end-arterial pattern is in the vicinity of the optic disc. Here, the posterior ciliary arteries enter the eye near the disc and their rami not only supply the adjacent choroid, but also form an anastomotic circle in the sclera around the head of the optic nerve (circle of Zinn/Haller) (**Fig. 45.30**). Branches from this ring join the pial arteries of the nerve (see below). Small cilioretinal arteries derived from any arteries in this region may enter the eye in up to 50% of individuals and contribute to the central retinal vasculature; they may preserve visual function following occlusion of the central retinal artery. Small retinociliary veins may sometimes be present.

The structure of retinal blood vessels resembles that of vessels elsewhere, except that the arteries lack an internal elastic lamina, and their adventitia may contain muscle cells. Capillaries are non-fenestrated; endothelial cells are joined by complex tight junctions, fulfilling the requirements of a blood–retinal barrier. Perivascular cells, including pericytes and glia, play key roles in the development and maintenance of the blood–retinal barrier (Bharadwaj et al 2013). Selective loss of pericytes happens early in the development of diabetic retinopathy and has been linked to the characteristic pathological changes seen in this condition (Park et al 2017). Within the optic nerve, the central artery is innervated by sympathetic and parasympathetic nerves; this innervation does not extend to the retinal vessels. The cholinergic parasympathetic supply is derived mainly from the pterygopalatine ganglion and is vasodilatory (Ch. 38). The adrenergic postganglionic sympathetic supply originates in the superior cervical ganglion and travels via a plexus around the internal carotid and ophthalmic arteries; it is unclear whether it elicits vasoconstriction or dilation (Bergua et al 2013).

Although inner retinal blood vessels lie between the incoming light and the photoreceptors, they are not perceived because their location is constant. In marked contrast, the growth of new retinal vessels (neovascularization) is one of the major sight-threatening complications of diseases such as diabetes and retinopathy of prematurity.

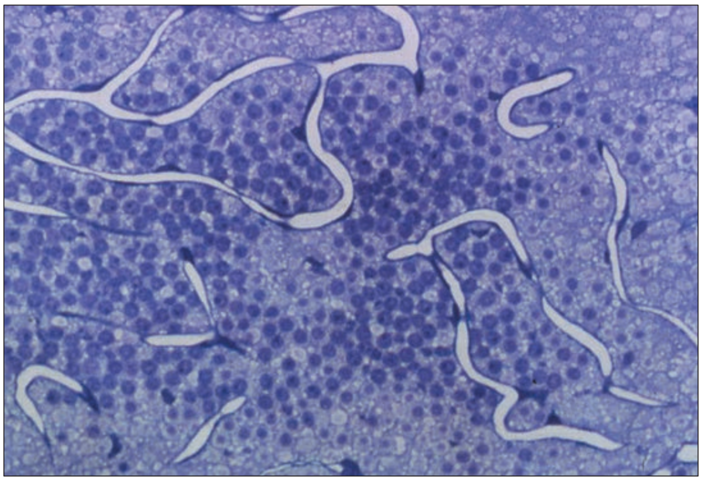

Fig. 45.29 A tangential section of the retina at the level of the inner nuclear layer, highlighting the dense network of capillaries.

Retinopetal innervation

The human retina receives efferent innervation via axons within the optic nerve. Although there are only a small number of these retinopetal neurones, they branch extensively within the retina. They emerge at the optic disc, course through the nerve fibre layer, and give off orthogonal branches that ramify in the inner plexiform layer (Repérant et al 2006). One set of axons arises from perikarya in the posterior hypothalamus and uses histamine as a neurotransmitter, while other serotoninergic fibres arise from cell bodies in the dorsal raphe. These neurones are not specialized for vision; they project to many other targets in the central nervous system besides the retina, forming components of an ascending arousal system (Gastinger et al 2006). Histamine is released during the day in the inner plexiform layer and activates receptors located on cone pedicles, horizontal cell perikarya and ON bipolar cell dendrites via volume transmission. Histamine also decreases the absolute sensitivity of the retina to light and, possibly, modulates retinal blood flow (Vila et al 2012).

Optic nerve head

The axons of more than a million retinal ganglion cells converge at the optic nerve head and leave the eye by penetrating the sclera to form the optic nerve. The optic nerve head represents that part of the optic nerve lying within the bulb of the eye. Since all retinal neural elements, apart from ganglion cell axons, are absent from this region, it is insensitive to light and forms the 'blind spot'.

Histologically, the optic nerve head can be divided into three zones (see Fig. 45.30): prelaminar (the anterior part terminating at the vitreous); laminar (formed by the lamina cribrosa); and postlaminar (continuous with the retrobulbar optic nerve). The surface view of the optic nerve head, usually seen with an ophthalmoscope, is referred to as the optic disc (Fig. 45.20A).

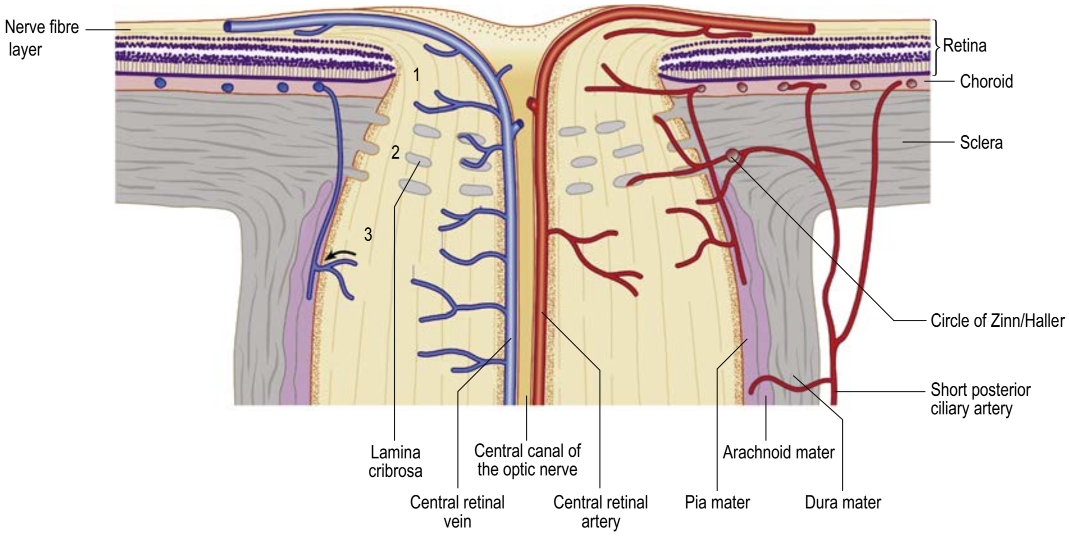

Fig. 45.30 Vessels of the optic nerve head. The dotted areas represent the principal glial membranes. Arteries are represented on the right and veins on the left. The prelaminar, laminar and postlaminar zones are indicated by 1–3, respectively.

Prelaminar zone

The inner surface of the optic nerve head is covered by an astroglial membrane (of Elschnig) that is continuous with the internal limiting membrane of the retina. At the centre of the disc, the layer of astrocytes thickens into a central meniscus (of Kuhnt). Retinal ganglion cells turn into the optic nerve head accompanied by astrocytes that gradually increase in number posteriorly, eventually forming a sieve-like structure, the glial lamina cribrosa, through which the nerve fibres pass as separate fasciculi. A collar of astrocytes several cells thick (the intermediary tissue of Kuhnt) separates the optic nerve from the terminating outer layers of the retina at the perimeter of the optic nerve head. It continues posteriorly and forms a barrier between the optic nerve head and the choroid (the border tissue of Jacoby) (Anderson and Hoyt 1969).

Laminar zone

The lamina cribrosa is composed of discrete trabeculae of collagenous and elastic connective tissue that extend from the sclera to form a meshwork through which the optic nerve fascicles and central retinal vessels pass. Each trabecula has a lining of astrocytes continuous with the astrocytes that form the glial lamina cribrosa.

Postlaminar zone

The optic nerve thickens in the postlaminar zone as its axons become myelinated. The reflected sclera, and the dura mater with which it is continuous, invest the nerve together with the arachnoid and pia mater. Fine fibrous septa penetrate the optic nerve from the pia mater, dividing it into 300–400 fascicles, and giving pial blood vessels access to the nerve.

Optic disc

The optic disc is a region of great clinical importance because it is visible by ophthalmoscopy (see Fig. 45.20A). Oedema of the disc (papilloedema) may be the first sign of raised intracranial pressure that has been transmitted into the subarachnoid space around the optic nerve. The disc is also sensitive to raised intraocular pressure present in glaucoma and shows characteristic structural changes as a result of loss of retinal ganglion cells.

The optic disc is superomedial to the posterior pole of the eye, and so lies away from the visual axis. It is round or oval, and usually approximately 1.6 mm in transverse diameter and 1.8 mm in vertical diameter, although its appearance is very variable. In light-skinned individuals, the general retinal hue is a bright terracotta-red, with which the pale pink of the disc contrasts sharply; the central part of the disc is usually even paler and may be light grey. These differences are due in part to the degree of vascularization of the two regions, which is much less at the optic disc, and to the total absence of choroidal or retinal pigment cells. In individuals with strongly melanized skin, both the retina and disc are darker. The optic disc rarely projects sufficiently to justify the term papilla, although it is usually a little elevated on its lateral side, where the papillomacular nerve fibres turn into the optic nerve (see Fig. 45.27). Typically, there is a slight depression where the retinal vessels traverse its centre.

Vascular supply

The prelaminar region is supplied mainly by branches of the central retinal artery. Branches from the short posterior ciliary arteries form a circle, often incomplete, within the sclera around the optic nerve head (circle of Zinn/Haller) and centripetal branches from this structure supply the laminar region of the optic nerve head (see Fig. 45.30). The short posterior ciliary arteries may also give off centripetal branches directly to supply the lamina, as well as branches that pass anteriorly to augment the prelaminar blood supply. In the postlaminar region, arteries from the prepapillary choroid and circle of Zinn pass retrogradely as pial vessels, providing centripetal branches that supply the optic nerve. More posteriorly, the optic nerve receives pial arterioles directly from the posterior ciliary arteries. The central retinal artery may also contribute some centrifugal branches in this region.

The central retinal vein drains the optic nerve head at all levels; other drainage pathways are minor.

VISUAL PATHWAY

The visual pathway includes the interneurones of the retina, retinal ganglion cells whose axons project via the optic nerve, chiasma and optic tract to the lateral geniculate nucleus and neurones within the lateral geniculate nucleus that project via the optic radiation to the primary visual cortex (Fig. 45.31). It is important to remember that visual space is optically inverted by the crystalline lens when relating the spatial location of neurones within the visual pathway to corresponding visual field locations.

Retinal ganglion cell axons, on entering the optic nerve, initially maintain their relative retinal positions, with axons from the fovea forming a lateral wedge. Such retinotopic mapping is largely maintained within the optic nerve, although nearer the chiasma the foveal axons take a position in the centre of the optic nerve while temporal fibres occupy their previous lateral location.

At the chiasma, a substantial rearrangement of axons takes place. Most axons arising from the nasal half of a line bisecting the fovea within each retina cross in the chiasma to enter the contralateral optic tract. Fibres from the temporal hemi-retinas do not generally cross in the chiasma. Classically, the axons within the optic tract were thought to maintain their topographic order and each tract was assumed to be a single representation of the contralateral hemifield. However, it is now clear that axons are mainly organized in functional groupings, larger superficial axons representing the magnocellular pathway and deeper axons originating from midget ganglion cells and forming the parvocellular pathway. This arrangement is chronotopic, the deeper axons developing earlier during axogenesis than the more superficial ones (Reese 1993).

The lateral geniculate nucleus contains cells arranged in six laminae (see Fig. 30.6). The contralateral nasal retina projects to laminae 1, 4 and 6, whereas the ipsilateral temporal retina projects to layers 2, 3 and 5. Layers 1 and 2 contain magnocellular cells; the remaining layers are parvocellular. Unlike the optic tract, there is a point-to-point retinotopic arrangement between corresponding points in each hemiretina so that the contralateral visual field is mapped within each lateral geniculate nucleus.

Axons from the lateral geniculate nucleus run in the retrolenticular part of the internal capsule and form the optic radiation. This curves dorsomedially to the primary visual cortex, located around and within the depths of the calcarine sulcus in the occipital lobe (also known as the striate cortex, Brodmann area 17, or V1) (see Fig. 32.12). The visual cortex also has a strict retinotopic organization. Fibres representing the lower half of the visual field sweep superiorly to reach the visual cortex above the calcarine sulcus, while those representing the upper half of the visual field curve inferiorly into the temporal lobe (Meyer's loop) before reaching the visual cortex below the calcarine sulcus. The periphery of the retina is represented anteriorly within the visual cortex, and the macula is mapped towards the posterior pole, occupying a disproportionately large area that reflects the high number of foveal retinal ganglion cells that subserve the enhanced acuity of this region.

The primary visual cortex is connected to prestriate and other cortical regions where further processing of visual stimuli takes place.

Almost all (90%) of the retinal ganglion cell axons terminate on neurones in the lateral geniculate nucleus. Extrageniculate axons (10%) leave the optic tract before the lateral geniculate nucleus: they may leave the optic chiasma dorsally and project to the suprachiasmatic nucleus of the hypothalamus, or may branch off the optic tract at the superior brachium and project to the superior colliculus, pretectal areas and inferior pulvinar.

Visual field defects

The basis for clinical assessment of damage to the visual pathway is an understanding of the retinotopic projections within the pathway. Plotting visual field loss frequently reveals the approximate location of the causative lesion and sometimes its nature. Since retinal lesions can be visualized with an ophthalmoscope, field testing might appear to be redundant for such defects, but is still helpful in assessing the extent of the damage and may be the key factor in confirming a diagnosis. For example, field defects in glaucoma that are a consequence of damage to the nerve fibre bundles at the optic nerve head, may be detectable ophthalmoscopically, but confirmation of the diagnosis frequently depends on field assessment. Early defects consist of one or more areas of paracentral focal field loss, progressing to arcuate scotomas. The shape of the defect corresponds to the anatomical arrangement of ganglion cell axons.

As far as the location of lesions central to the retina is concerned, deficits in the vision of one eye are usually attributable to optic nerve lesions. Lesions of the optic chiasma, involving crossing nerve fibres, produce a bilateral field loss, as exemplified by a pituitary adenoma. The tumour expands upwards from the pituitary fossa, usually compressing the inferior midline of the chiasma, and eventually produces bitemporal hemianopia, starting with an early loss in the upper temporal quadrants (bitemporal quadrantanopia).

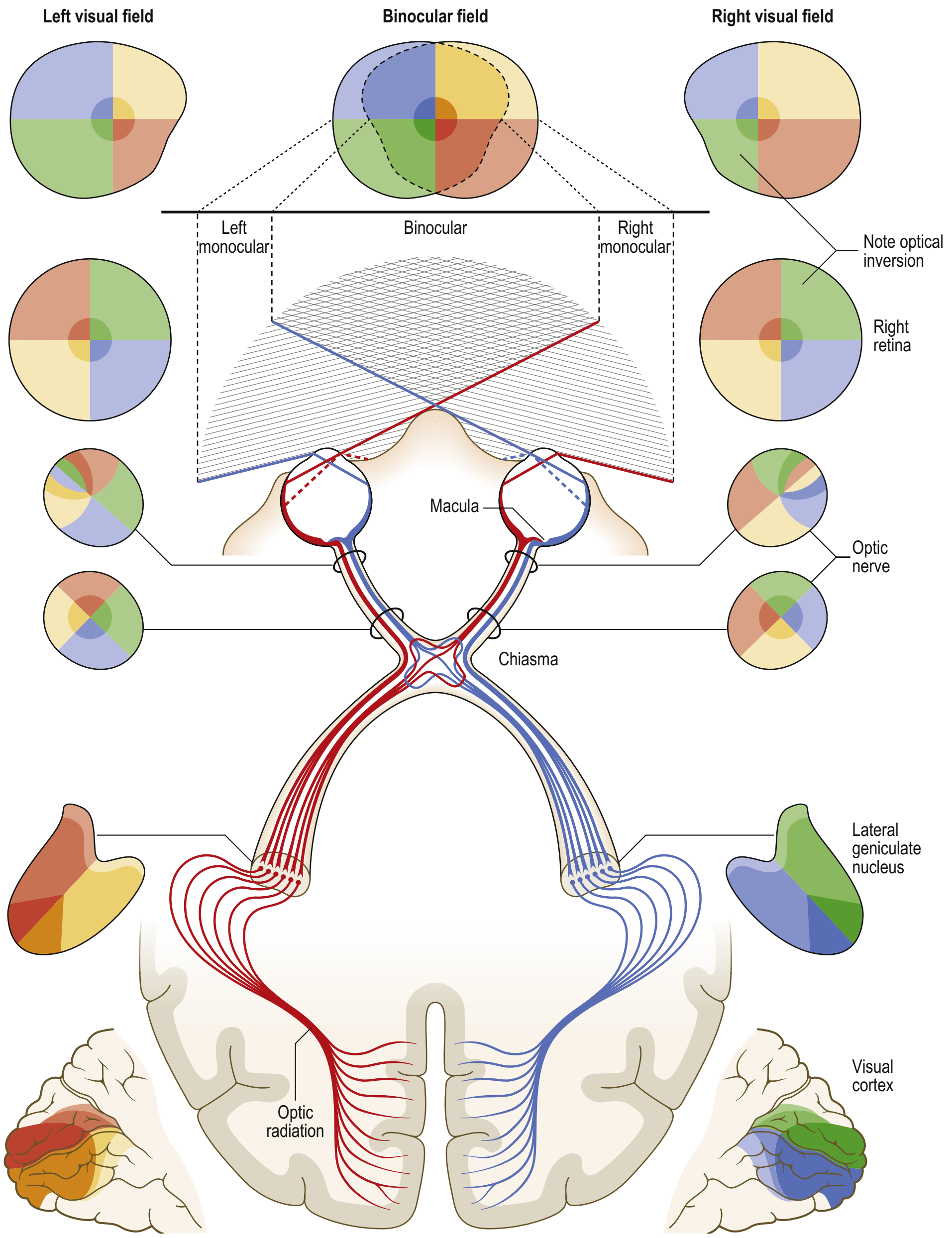

Fig. 45.31 The visual pathway (simplified), showing the spatial arrangement of neurones and their fibres in relation to the quadrants of the retinae and visual fields. The proportions at various levels are not exactly to scale. In particular, the macula is exaggerated in size in the visual fields and retinae. In each quadrant of the visual field, and in the parts of the visual pathway subserving it, two shades of each respective colour are used; the paler shade denotes the peripheral field and the darker shade denotes the macular part of the quadrant. From the lateral geniculate nucleus onwards, these two shades are both made more saturated to denote intermixture of neurones from both retinae, the palest shade being reserved for parts of the visual pathway concerned with monocular vision.

Since the optic tract contains contralateral nasal and ipsilateral temporal retinal projections, damage to the tract will cause a homonymous contralateral visual field loss. Although complete disruption of the tract results in contralateral hemianopia, the incomplete spatial segregation of axons within the tract, described above, makes the field losses following smaller lesions harder to interpret. However, they do show substantial incongruity (dissimilar defects in the fields of the two eyes) and often specific functional deficits, consistent with the partial segregation of functionally distinct axons from the two half-retinas (Reese 1993). Incongruity is most marked in defects of the optic tract, less obvious in optic radiation defects, and usually absent in cortically induced field defects, thus providing an additional clue in assessing location of the cause.

Lesions of the optic radiations are usually unilateral, and commonly vascular in origin. Field defects therefore develop abruptly, in contrast to the slow progression of defects associated with tumours, and the resulting hemifield loss follows the general rule that visual field defects central to the chiasma are on the opposite side to the lesion. Little or no incongruity is seen in visual cortical lesions, but they commonly display the phenomenon of macular sparing, the central 5–10° visual field being retained in an otherwise hemianopic defect.

Key references

Arora KS, Jefferys JL, Maul EA et al 2012 The choroid is thicker in angle closure than in open angle and control eyes. Inv Ophthalmol Vis Sci 53:7813–18.
An investigation of some of the factors affecting choroidal thickness measured in vivo.

Boote C, Dennis S, Huang YF et al 2005 Lamellar orientation in human cornea in relation to mechanical properties. J Struct Biol 149:1–6.
The quantification by X-ray scattering of the arrangement of collagen fibres in the human corneal stroma.

Charman WN 2008 The eye in focus: accommodation and presbyopia. Clin Exp Optom 91:207–25.
A summary of the various mechanisms of accommodation and the reasons for the decline of accommodative amplitude with age.

Curcio CA, Sloan KR, Kalina RE et al 1990 Human photoreceptor topography. J Comp Neurol 292:497–523.
The first description of the distribution of rods and cones in the human retina using modern methods.

Dacey DM, Liao H-S, Peterson BB et al 2005 Melanopsin-expressing ganglion cells in primate retina signal colour and irradiance and project to the LGN. Nature 433:749–54.
Although directly light-sensitive melanopsin-containing retinal ganglion cells were first described in rodents, this is the first description of their occurrence in primates.

Kolb H, Linberg KA, Fisher SK 1992 Neurons of the human retina – a Golgi study. J Comp Neurol 318:147–87.
The most comprehensive description of the morphology of neural cell types in the human retina.

Reichenbach A, Bringmann A 2013 New functions of Müller cells. Glia 61:651–78.

A review of the many functions of Müller cells, some of them only recently proposed.

Strauss O 2005 The retinal pigment epithelium in visual function. Phys Rev 85:845–81.

A review of the many functions of the retinal pigment epithelium and their role in various disease processes.

Wallman J, Winawer J 2004 Homeostasis of eye growth and the question of myopia. Neuron 43:447–68.

A review of the mechanisms of emmetropization and the causes of myopia.

Wang D, Qi M, He M et al 2012 Ethnic differences of anterior chamber area and volume and its association with angle width. Inv Ophthalmol Vis Sci 53:3139–44.

An optical coherence tomography (OCT) investigation showing differences in the morphology of the anterior chamber between Caucasians and people with a Chinese heritage.

References

Alm A, Nilsson SFE 2009 Uveoscleral outflow – a review. Exp Eye Res 88:760–8.

Anderson DR, Hoyt W 1969 Ultrastructure of intraorbital portion of human and monkey optic nerve. Arch Ophthalmol 82:506–30.

Arora KS, Jefferys JL, Maul EA et al 2012 The choroid is thicker in angle closure than in open angle and control eyes. Inv Ophthalmol Vis Sci 53:7813–18.

An investigation of some of the factors affecting choroidal thickness measured in vivo.

Barraquer RI, Michael R, Abreu R et al 2006 Human lens capsule thickness as a function of age and location along the sagittal lens perimeter. Invest Ophthalmol Vis Sci 47:2053–60.

Bergua A, Kapsreiter M, Neuhuber WL et al 2013 Innervation pattern of the preocular human central retinal artery. Exp Eye Res 110:142–7.

Bharadwaj AS, Appukuttan B, Wilmarth PA et al 2013 Role of the retinal vascular endothelial cell in ocular disease. Prog Retinal Eye Res 32:102–80.

Boote C, Dennis S, Huang YF et al 2005 Lamellar orientation in human cornea in relation to mechanical properties. J Struct Biol 149:1–6.

The quantification by X-ray scattering of the arrangement of collagen fibres in the human corneal stroma.

Boulton M, Dayhaw-Barker P 2001 The role of the retinal pigment epithelium: topographical variation and ageing changes. Eye 15:384–9.

Bowmaker JK, Parry JWL, Mollon JD 2003 The arrangement of L and M cones in human and a primate retina. In: Mollon JD, Pokorny J, Knoblauch K (eds) Normal and Defective Colour Vision. Oxford: Oxford University Press.

Charman WN 2008 The eye in focus: accommodation and presbyopia. Clin Exp Optom 91:207–25.

A summary of the various mechanisms of accommodation and the reasons for the decline of accommodative amplitude with age.

Curcio CA, Allen KA 1990 Topography of ganglion cells in human retina. J Comp Neurol 300:5–25.

Curcio CA, Allen KA, Sloan KR et al 1991 Distribution and morphology of human cone photoreceptors stained with anti-blue opsin. J Comp Neurol 312:610–24.

Curcio CA, Johnson M 2013 Structure, function, and pathology of Bruch's membrane. In: Ryan SJ, Schachat AP, Wilkinson CP et al (eds) Retina, 5th ed. Oxford: Elsevier.

Curcio CA, Millican CL, Allen KA et al 1993 Aging of the human photoreceptor mosaic: evidence for selective vulnerability of rods in central retina. Invest Ophthalmol Vis Sci 34:3278–96.

Curcio CA, Sloan KR, Kalina RE et al 1990 Human photoreceptor topography. J Comp Neurol 292:497–523.

The first description of the distribution of rods and cones in the human retina using modern methods.

Dacey DM, Liao H-S, Peterson BB et al 2005 Melanopsin-expressing ganglion cells in primate retina signal colour and irradiance and project to the LGN. Nature 433:749–54.

Although directly light-sensitive melanopsin-containing retinal ganglion cells were first described in rodents, this is the first description of their occurrence in primates.

Danysh BP, Duncan MK 2009 The lens capsule. Exp Eye Res 88:151–64.

Dua HS, Faraj LA, Said DG et al 2013 Human corneal anatomy redefined: a novel pre-Descemet's layer (Dua's layer). Ophthalmology 120:1778–85.

Fautsch MP, Johnson DH 2006 Aqueous humor outflow: what do we know? Where will it lead us? Inv Ophthalmol Vis Sci 47:4181–7.

Flitcroft DI 2013 Is myopia a failure of homeostasis? Exp Eye Res 114:16–24.

Friling R, Weinberger D, Kremer I et al 2004 Keratometry measurements in preterm and full term newborn infants. Br J Ophthalmol 88:8–10.

Gabelt BAT, Kaufman PL 2005 Changes in aqueous humor dynamics with age and glaucoma. Prog Retinal Eye Res 24:612–37.

Gastinger MJ, Tian N, Horvath T et al 2006 Retinopetal axons in mammals: emphasis on histamine and serotonin. Curr Eye Res 31:655–67.

Goel M, Picciani RG, Lee RK et al 2010 Aqueous humor dynamics: a review. Open Ophthalmol J 4:52–9.

Hofer H, Carroll J, Neitz J et al 2005 Organization of the human trichromatic cone mosaic. J Neurosci 25:9669–79.

Kevany BM, Palczewski K 2010 Phagocytosis of retinal rod and cone photoreceptors. Physiology 25:8–15.

Kocabiyik N, Yalcin B, Ozan H 2005 The morphometric analysis of the central retinal artery. Ophthal Physiol Opt 25:375–8.

Kolb H, Linberg KA, Fisher SK 1992 Neurons of the human retina – a Golgi study. J Comp Neurol 318:147–87.

The most comprehensive description of the morphology of neural cell types in the human retina.

Lima VC, Rosen RB, Farah M 2016 Macular pigment in retinal health and disease. Int J Retina Vitreous 2:19.

Müller LJ, Marfurt CF, Kruse F et al 2003 Corneal nerves: structure, contents and function. Exp Eye Res 76:521–42.

Mutti DO, Zadnik K, Fusaro RE et al 1998 Optical and structural development of the crystalline lens in childhood. Invest Ophthalmol Vis Sci 39:120–33.

Nguyen-Legros J, Hicks D 2000 Renewal of photoreceptor outer segments and their phagocytosis by the retinal pigment epithelium. Int Rev Cytol 196:245–313.

Park DY, Lee J, Kim J et al 2017 Plastic roles of pericytes in the blood–retinal barrier. Nat Commun 8:15296.

Park KA, Oh SY 2013 Choroidal thickness in healthy children. Retina 33:1971–6.

Reese BE 1993 Clinical implications of the fibre order in the optic pathway of primates. Neurol Res 15:83–6.

Reichenbach A, Bringmann A 2013 New functions of Müller cells. Glia 61:651–78.

A review of the many functions of Müller cells, some of them only recently proposed.

Repérant J, Ward R, Miceli D et al 2006 The centrifugal visual system of vertebrates: a comparative analysis of its functional anatomical organization. Brain Res Rev 52:1–57.

Rose KA, Morgan IG, Smith W 2008 Myopia, lifestyle, and schooling in students of Chinese ethnicity in Singapore and Sydney. Arch Ophthalmol 126:527–30.

Ruskell G 2003 Access of autonomic nerves through the optic canal, and their orbital distribution in man. Anat Rec A Discov Mol Cell Evol Biol 275:973–78.

Strauss O 2005 The retinal pigment epithelium in visual function. Phys Rev 85:845–81.

A review of the many functions of the retinal pigment epithelium and their role in various disease processes.

Strenk SA, Strenk LM, Koretz JF 2005 The mechanism of presbyopia. Prog Retinal Eye Res 24:379-93.

Sun HP, Lin Y, Pan CW 2014 Iris color and associated pathological ocular complications: a review of epidemiologic studies. Int J Ophthalmol-Chi 7:872.

Vila A, Satoh H, Rangel C et al 2012 Histamine receptors of cones and horizontal cells in Old World monkey retinas. J Comp Neurol 20:528–43.

Wallman J, Winawer J 2004 Homeostasis of eye growth and the question of myopia. Neuron 43:447–68.

A review of the mechanisms of emmetropization and the causes of myopia.

Wang D, Qi M, He M et al 2012 Ethnic differences of anterior chamber area and volume and its association with angle width. Inv Ophthalmol Vis Sci 53:3139–44.

An optical coherence tomography (OCT) investigation showing differences in the morphology of the anterior chamber between Caucasians and people with a Chinese heritage.

Wässle H 2004 Parallel processing in the mammalian retina. Nature Rev Neurosci 5:747–57.

Watson PG, Young RD 2004 Scleral structure: organisation and disease. A review. Exp Eye Res 278:609–23.

Wolfs RC, Klaver CC, Vingerling JR et al 1997 Distribution of central corneal thickness and its association with intraocular pressure: The Rotterdam Study. Am J Ophthalmol 123:767–72.

Zelentsova EA, Yanshole LV, Fursova AZ et al 2017 Optical properties of the human lens constituents. J Photochem Photobiol B 173:318–24.

Zhang HR 1994 Scanning electron-microscopic study of corrosion casts on retinal and choroidal angioarchitecture in man and animals. Prog Retinal Eye Res 13:243–70.

CHAPTER

46

Back

Most clinical disorders of the back present as low back pain with or without associated lower limb pain, weakness or numbness, and so, historically, most attention has been paid to the anatomy of the lower (lumbosacral) back. In this Section, the term 'back' will include the whole of the posterior aspect of the trunk and of the neck. The whole of this region has great clinical importance but its anatomy has often been neglected. Recent understanding of the detailed topography of the bony and soft tissue elements of the lower back owes much to the work of Bogduk (2012).

The soft tissues of the back of the trunk and neck include the skin and subcutaneous fat, the underlying fascial layers and the musculature. The deep, 'true' or epaxial muscles lie within compartments in their own fascial 'skeleton'. The bony framework to which the muscles and fasciae attach includes elements of the axial skeleton, i.e. the vertebral column and occiput, elements of the pectoral and pelvic girdles, and the ribs. The occiput is described below, the scapula in Chapter 49, the ribs in Chapter 53 and the pelvis in Chapter 77.

SKIN

The skin of the back of the trunk is thick and highly protective, but has low discriminatory sensation. The superficial fascia is thick and fatty in most areas of the back. Its attachment to the deeper fascial layers is strong in the midline, especially in the neck, but becomes weaker more laterally. The skin of the back of the neck is thicker than that of the front of the neck, but thinner than that of the back of the trunk. The quantity, texture and distribution of hair vary with sex, race and the individual, though well-defined hair tracts have been delineated (**Fig. 46.1**).

Lines of skin tension run horizontally in the cervical and lumbosacral regions but form segments of two adjacent circles in the thoracic region (**Fig. 46.2**).

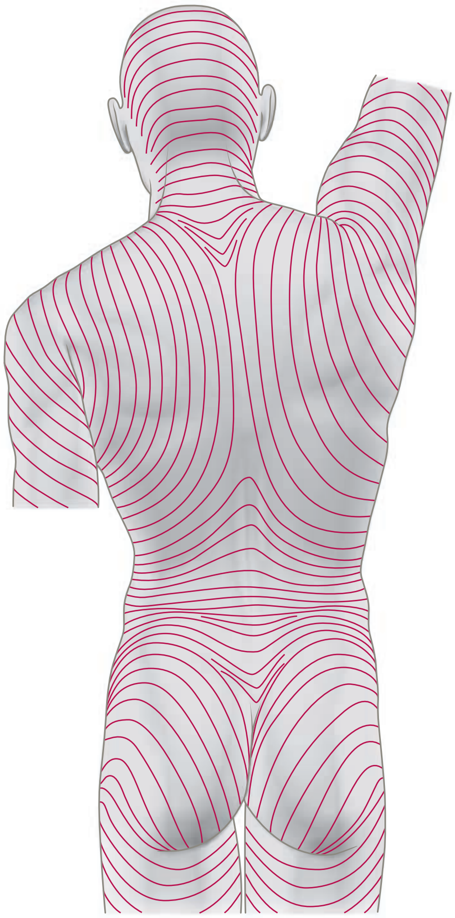

Fig. 46.2 Lines of skin tension on the dorsum of the trunk and head. (With permission from Kraissl CL, Plast Reconstruct Surg 8: 1–28, 1951, Lippincott Williams and Wilkins.)

Cutaneous innervation and dermatomes

The skin of the back of the neck and trunk is innervated by the dorsal (posterior primary) rami of the spinal nerves (see Fig. 47.8). The spinal nerves involved include C2–C5, T2–L3, S2–S4 and Co1. The pattern of their dermatomes is shown in **Fig. 46.3**. There is about half a segment of overlap between these cutaneous 'strips'; the strips supplied by the dorsal rami do not correspond exactly to those served by ventral rami, and differ slightly in both width and position. In the cervical and upper thoracic regions (down to T6) skin is supplied by the medial branches of the dorsal rami, while in the lower thoracic, lumbar and sacral regions it is supplied by the lateral branches.

Cutaneous vascular supply and lymphatic drainage

The skin of the back of the trunk receives its arterial blood supply mainly from musculocutaneous branches of posterior intercostal, lumbar and lateral sacral arteries (**Fig. 46.4**), which all accompany the cutaneous branches of their respective dorsal rami. In addition, there is a supply from the dominant vascular pedicles of the superficial (extrinsic) back muscles. The skin over the scapula is supplied by branches of the suprascapular, dorsal scapular and subscapular arteries. The skin of the back of the neck is supplied mainly from the occipital and deep cervical arteries. The superficial cervical or transverse cervical artery supplies the skin of the lower part of the back of the neck (Cormack and Lamberty 1994).

Veins drain the skin of the back of the neck into tributaries of the occipital and deep cervical veins. The skin of the back of the trunk drains into the azygos system, via tributaries of the posterior intercostal and lumbar veins.

Lymph from the skin of the back of the neck drains into occipital, lateral deep cervical and axillary nodes (**Fig. 46.5**). From the back of the trunk, drainage is to the posterior (subscapular) axillary nodes and to the lateral superficial inguinal nodes.

FASCIAL LAYERS

The main fascial layers in the axial and paraxial regions of the trunk and neck are the thoracolumbar fascia, the deep cervical fascia and the prevertebral, endothoracic, retroperitoneal and posterior parts of the pelvic fasciae (the latter four layers collectively form the continuous prevertebral plane). Other important structures with fascial components are the ligamentum nuchae and the aponeurosis of erector spinae (see below).

Thoracolumbar fascia

The thoracolumbar (lumbodorsal) fascia covers the deep muscles of the back and the trunk. Above, it passes anterior to serratus posterior superior and is continuous with the superficial lamina of the deep cervical fascia on the back of the neck. In the thoracic region, the

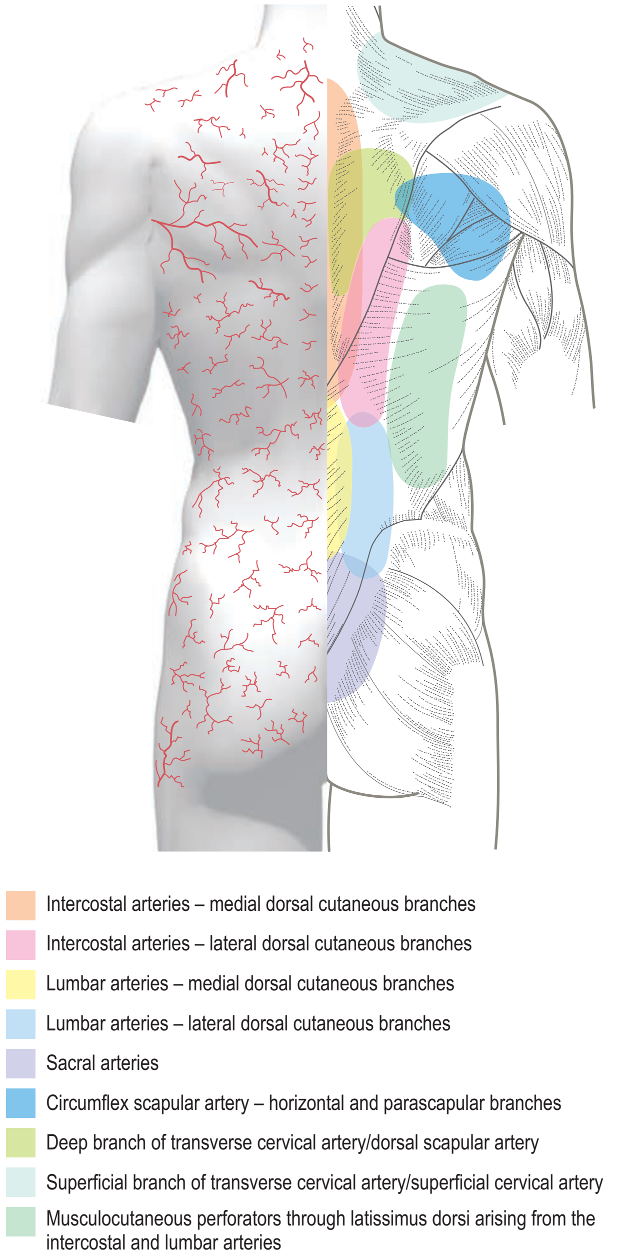
Intercostal arteries – medial dorsal cutaneous branches
Intercostal arteries – lateral dorsal cutaneous branches
Lumbar arteries – medial dorsal cutaneous branches
Lumbar arteries – lateral dorsal cutaneous branches
Sacral arteries
Circumflex scapular artery – horizontal and parascapular branches
Deep branch of transverse cervical artery/dorsal scapular artery
Superficial branch of transverse cervical artery/superficial cervical artery
Musculocutaneous perforators through latissimus dorsi arising from the intercostal and lumbar arteries

Fig. 46.4 Areas of cutaneous arterial supply on the dorsum of the trunk. (Redrawn with permission from Cormack GC, Lamberty BGH 1994 The Arterial Anatomy of Skin Flaps. Edinburgh: Churchill Livingstone.)

thoracolumbar fascia provides a thin fibrous covering for the extensor muscles of the vertebral column and separates them from the muscles connecting the vertebral column to the upper extremity. Medially, it is attached to the spines of the thoracic vertebrae, and laterally to the angles of the ribs. In the lumbar region, the thoracolumbar fascia is in three layers (Fig. 46.6; see Fig. 61.1). The posterior layer is attached to the spines of the lumbar and sacral vertebrae and to the supraspinous ligaments. The middle layer is attached medially to the tips of the lumbar transverse processes and the intertransverse ligaments, below to the iliac crest, and above to the lower border of the twelfth rib and the lumbocostal ligament. The anterior layer covers quadratus lumborum and is attached medially to the anterior surfaces of the lumbar transverse processes behind the lateral part of psoas major; below, it is attached to the iliolumbar ligament and the adjoining part of the iliac crest; above, it forms the lateral arcuate ligament. The posterior and middle layers unite to form a tough raphe at the lateral margin of erector spinae, and at the lateral border of quadratus lumborum they are joined by the anterior layer to form the aponeurotic origin of transversus abdominis. At sacral levels, the posterior layer is attached to the posterior superior iliac spine and posterior iliac crest, and fuses with the underlying erector spinae aponeurosis. Bogduk (2012) describes two laminae in the posterior layer at lumbar levels, with varying orientation of the constituent collagen fibres relating to the biomechanical function of the fascia. The posterior and middle layers of the thoracolumbar fascia and the vertebral column together form an osteofascial compartment that encloses the erector spinae muscle group.

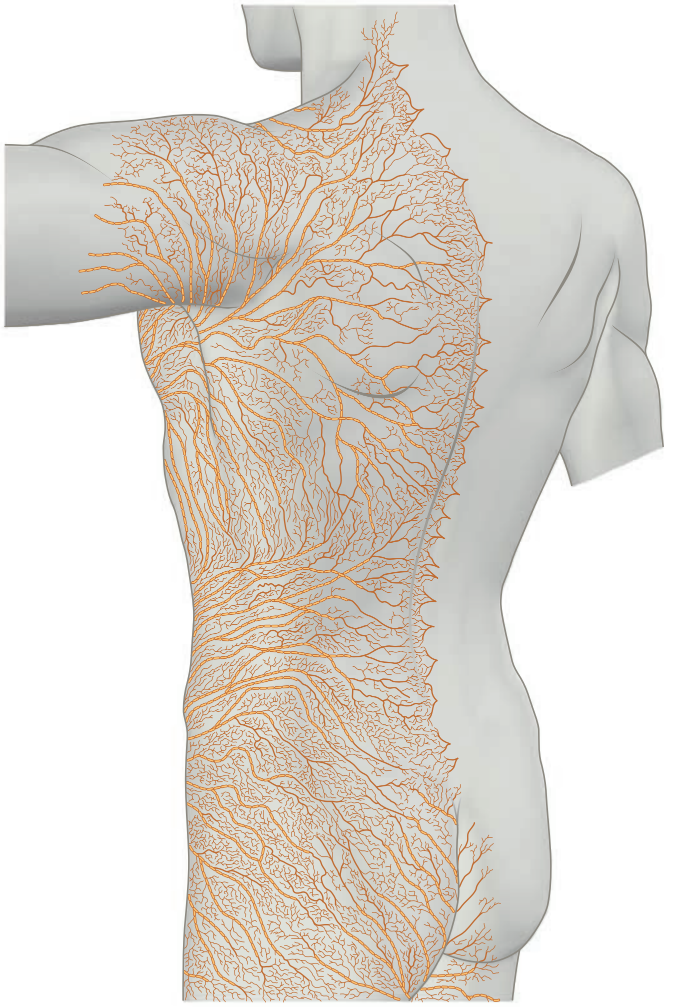

Fig. 46.5 Cutaneous lymphatics on the dorsum of the trunk. (With permission from Romanes GJ (ed) 1964 Cunningham's Textbook of Anatomy, 10th ed. London: Oxford University Press.)

The attachments of the fascia, especially those that assure continuity with the abdominal wall musculature, putatively give it an important role in lifting, though the exact details of this role remain controversial. The fascia may also play an important role in load transfer between the trunk and the limbs: its tension is affected by the actions of latissimus dorsi, gluteus maximus and the hamstrings. Additionally, the thoracolumbar fascia contains nociceptive nerve endings that may be responsible for some forms of back pain. Other mechanisms related to the thoracolumbar fasciae that have been implicated as a possible source of back pain include tissue deformation due to injury or immobility, resulting in impaired proprioceptive signalling and possibly an increase in pain sensitivity, and increased sensitivity of the thoracolumbar fascia in conditions involving other tissues innervated by the same spinal nerve (Willard et al 2012).

Deep cervical fascia

The investing layer of the deep cervical fascia forms the deep fascia of the posterior aspect of the neck (see Fig. 35.4A). It attaches in the midline to the external occipital protuberance, the ligamentum nuchae and the spine of the seventh cervical vertebra, and splits to enclose trapezius on each side. Inferiorly, the posterior part of the investing layer attaches with trapezius to the spine and acromion of the scapula.

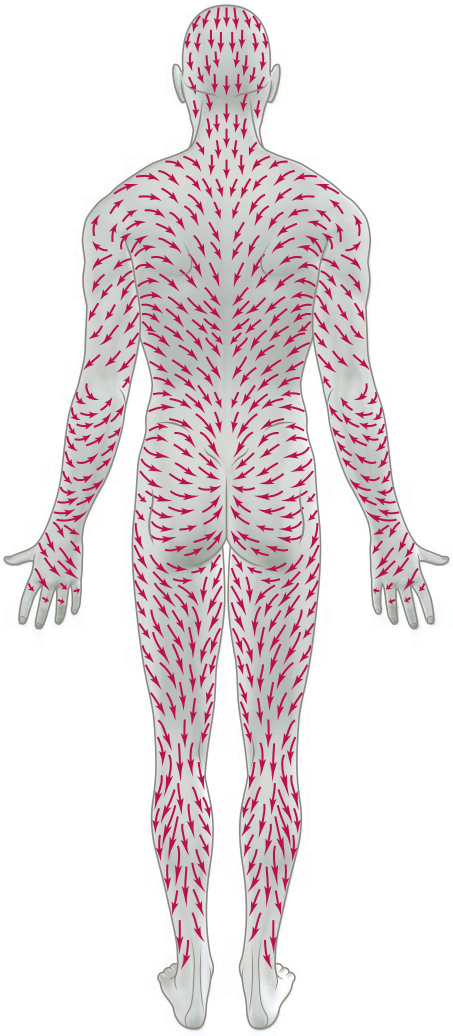

Fig. 46.1 Hair tracts on the dorsal surface of the body. (Adapted with permission from Wood Jones F (ed) 1949 Buchanan's Manual of Anatomy, 8th ed. London: Baillière Tindall and Cox.)

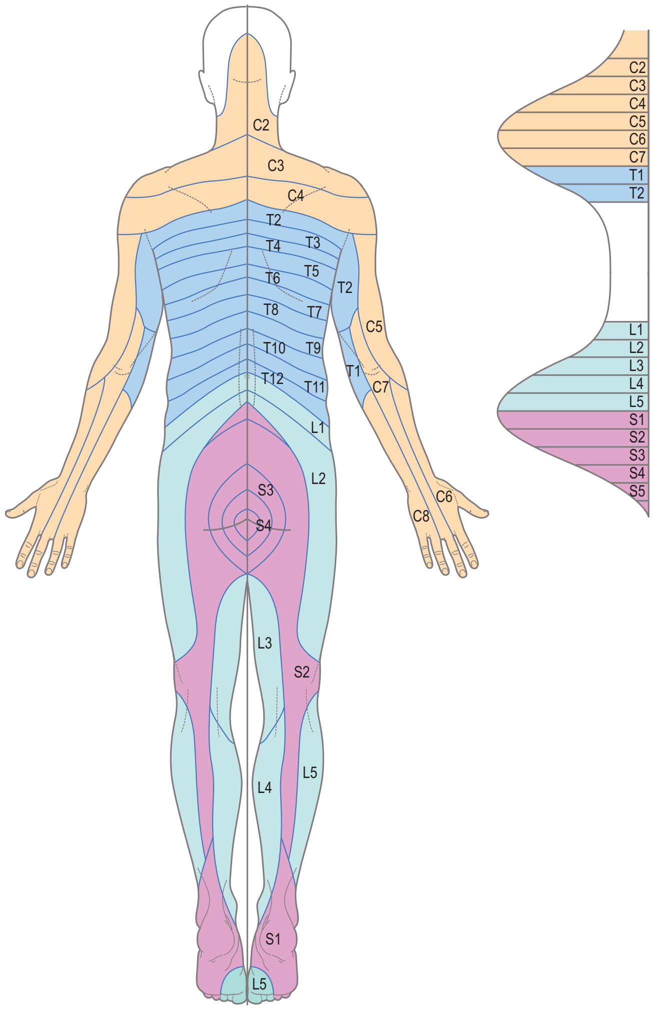
C2
C3
C4
T2
T4
T3
T6
T5
T2
T8
T7
C5
T10
T9
T12
T11
T1
C7
L1
L2
S3
S4
C6
C8
L3
S2
L5
L4
S1
L5
C2
C3
C4
C5
C6
C7
T1
T2
L1
L2
L3
L4
L5
S1
S2
S3
S4
S5

Fig. 46.3 Dermatomes on the dorsal surface of the body. The small diagram shows the regular arrangement of dermatomes in the upper and lower limbs of the embryo. Maps of dermatome distribution are useful in clinical neurology as a guide to identify the location of pathology in patients with peripheral sensory deficits, but it is important to remember that they are approximations (Ch. 24). (Adapted with permission from Moffat DB 1993 Lecture Notes on Anatomy, 2nd ed. Oxford: Blackwell Scientific.)

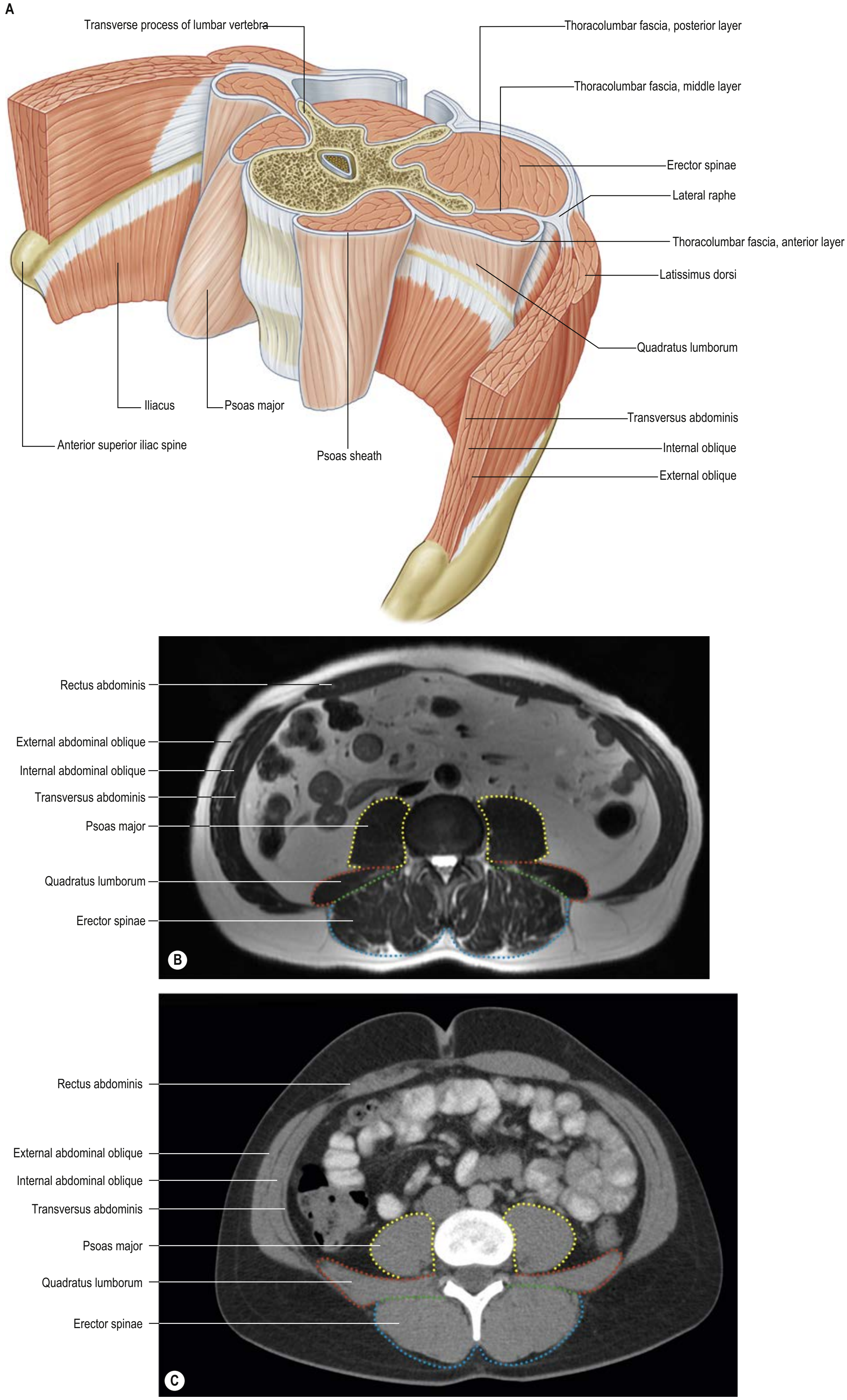
A
Transverse process of lumbar vertebra
Thoracolumbar fascia, posterior layer
Thoracolumbar fascia, middle layer
Erector spinae
Lateral raphe
Thoracolumbar fascia, anterior layer
Latissimus dorsi
Quadratus lumborum
Transversus abdominis
Internal oblique
External oblique
Iliacus
Psoas major
Anterior superior iliac spine
Psoas sheath
Rectus abdominis
External abdominal oblique
Internal abdominal oblique
Transversus abdominis
Psoas major
Quadratus lumborum
Erector spinae
B
Rectus abdominis
External abdominal oblique
Internal abdominal oblique
Transversus abdominis
Psoas major
Quadratus lumborum
Erector spinae
C

Fig. 46.6 A, Muscles and fasciae of the posterior abdominal wall. **B**, An axial T2-weighted MR image through the lower abdomen at the level of L3. **C**, Axial CT with intravenous and oral contrast medium through the lower abdomen at the same level. Psoas sheath (yellow); thoracolumbar fascia, anterior layer (red), middle layer (green), posterior layer (blue).

BONES

Occipital bone

The occipital bone forms much of the back and base of the cranium (**Fig. 46.7**). It is trapezoid and internally concave, and encloses the foramen magnum. It has four parts: basilar (basioccipital), which is the quadrilateral part in front of the foramen magnum; squamous, which is the expanded plate posterosuperior to the foramen; and two lateral (condylar or exoccipital), one on each side of the foramen magnum. The latter is anteromedian and wider behind, with an anteroposterior diameter greater than its transverse diameter.

The occipital bone provides attachment for a number of the muscles of the neck and upper part of the back (longus capitis; recti capitis anterior, lateralis, posterior major and minor; superior oblique; semispinalis capitis; splenius capitis; occipitofrontalis; trapezius; sternocleidomastoid), and articulates with the first cervical vertebra at the atlanto-occipital joints.

Squamous part

The squamous part is an expanded plate posterosuperior to the foramen magnum, convex externally and concave internally. On its external surface, the external occipital protuberance lies midway between its summit and the foramen magnum. On each side, two curved lines extend laterally from this protuberance. The upper one, faintly marked and often almost imperceptible, is the highest nuchal line, and the lower one is the superior nuchal line. The epicranial aponeurosis is attached to the medial part of the highest nuchal line. The median external occipital crest is often faint; it descends from the external occipital protuberance to the foramen magnum. On each side, an inferior nuchal line spreads laterally from the midpoint of the crest.

The internal surface of the squamous part is divided into four deep fossae by an irregular internal occipital protuberance and by ridged sagittal and horizontal extensions from the protuberance. The two superior fossae are triangular and adapted to the occipital poles of the cerebral hemispheres; the inferior fossae are quadrilateral and shaped to accommodate the cerebellar hemispheres. A wide groove with raised banks, the superior sagittal sulcus, ascends from the protuberance to the superior angle of the squamous part. The posterior part of the falx cerebri is attached to the margins of the sulcus. A prominent internal occipital crest descends from the protuberance and bifurcates near the foramen magnum, and provides an attachment for the falx cerebelli. The occipital sinus, sometimes double, lies in this attachment. A small vermian fossa may exist at the lower end of the internal occipital crest; when present, it is occupied by part of the inferior cerebellar vermis. On each side, a wide sulcus for the transverse sinus extends laterally from the internal occipital protuberance; the tentorium cerebelli is attached to the margins of these sulci. The right sulcus is usually larger than the left, and passes into the sulcus for the superior sagittal sinus, whereas the left usually receives the straight sinus. The position of the confluence of the sinuses is indicated by a depression on one side of the protuberance.

The position of the fetal posterior fontanelle coincides with the junction between the superior angle of the squamous part of the occipital bone and the occipital angle of the parietal bone on either side. The lateral angles of the squamous part are marked internally by the ends of the transverse sulci and project between the parietal and temporal bones. The lambdoid borders extend from superior to lateral angles and are serrated for articulation with the occipital borders of the parietal bones at the lambdoid suture. The mastoid borders extend from the lateral angles to the jugular processes, articulating with the mastoid parts of the temporal bones. A variety of sutural bones (ossicles) may occur at or near the lambda, e.g. the 'interparietal' (Inca bone or ossicle of Goethe).

Muscle attachments The occipital part of occipitofrontalis is attached to the lateral part of the highest nuchal line (**Fig. 46.7C**). Trapezius attaches to the medial third of the superior nuchal line and to the external occipital protuberance. Sternocleidomastoid attaches to the lateral half of the superior nuchal line, with splenius capitis just below the lateral third of that line. Semispinalis capitis is attached to the medial part of the area between the superior and inferior nuchal lines; obliquus capitis superior attaches to the lateral part of this area. Rectus capitis posterior major attaches to the lateral part of the inferior nuchal line and to the bone immediately below, and rectus capitis posterior minor attaches to the medial part of the inferior nuchal line and to the bone between that line and the foramen magnum.

Basilar part

The basilar part extends anterosuperiorly from the foramen magnum. In young skulls, it presents a rough and uneven surface where it is joined to the body of the sphenoid by a growth cartilage (spheno-occipital synchondrosis). This plate has fully ossified by the twenty-fifth year, at which time the occipital and sphenoid bones are fused.

The inferior surface bears a small pharyngeal tubercle, about 1 cm in front of the foramen magnum, which gives attachment to the fibrous pharyngeal raphe. A small depression immediately anterior to the occipital condyle may occasionally be replaced by a small precondylar tubercle. The anterior atlanto-occipital membrane is attached to the anterior margin of the foramen magnum.

The superior surface has the form of a broad groove that slopes upwards and forwards from the foramen magnum, directly into the basilar part of the sphenoid; together, these bones form the clivus. The lateral margins articulate below with the petrous part of the temporal bones.

Muscle attachments Longus capitis is attached anterolateral to the pharyngeal tubercle, and rectus capitis anterior is attached to the small depression anterior to the occipital condyle (see Fig. 46.7C).

Lateral (condylar) parts

The lateral (condylar) parts of the occipital bone flank the foramen magnum. On their inferior surfaces are occipital condyles for articulation with the superior articular facets of the atlas vertebra. The condyles are oval or reniform, their long axes converging anteromedially. The articular surfaces, wholly convex, face inferolaterally. They are occasionally constricted and a condyle may be in two parts (as may be the reciprocal surfaces of the atlas vertebra). A tubercle gives attachment to an alar ligament medial to each articular facet. The hypoglossal (anterior condylar) canal, which is situated anteriorly above each condyle, starts internally a little above the anterolateral part of the foramen magnum and continues anterolaterally. It may be partly or wholly divided by a spicule of bone and transmits the hypoglossal nerve and a meningeal branch of the ascending pharyngeal artery. A condylar fossa, behind each condyle, fits the posterior margin of the superior facet of the atlas vertebra in full extension of the skull. Its floor is sometimes perforated by a posterior condylar canal for a sigmoid emissary vein. A quadrilateral plate, the jugular process, projects laterally from the posterior half of each condyle, and contributes the posterior part of the jugular foramen. The jugular process is indented in front by a jugular notch, which may be partly divided by a small intrajugular process projecting anterolaterally. A paramastoid process sometimes projects downwards and may even articulate with the transverse process of the atlas vertebra. Laterally, the jugular process has a rough quadrilateral or triangular area that is joined to the jugular surface of the temporal bone by cartilage; it begins to ossify at around 25 years.

An oval jugular tubercle overlies the hypoglossal canal on the superior surface of the occipital condyle. Its posterior part often bears a shallow furrow for the glossopharyngeal, vagus and accessory nerves. A deep groove containing the end of the sigmoid sinus curves anteromedially around a hook-shaped process to end at the jugular notch. The posterior condylar canal opens into the posterior cranial fossa near the medial end of the groove.

Muscle attachments Rectus capitis lateralis attaches to a roughened area on the inferior surface of the jugular process (see Fig. 46.7C).

Ossification

Above the highest nuchal lines, the squamous part of the occipital bone is developed in a fibrous membrane and is ossified from two centres (one on each side) from about postmenstrual week 10. This part of the occipital bone may remain separate as the interparietal bone. The remainder of the occipital bone is preformed in cartilage. Below the highest nuchal lines, the squamous part ossifies from two centres that appear in about postmenstrual week 10 and soon unite. The two components of the squamous part unite during postmenstrual weeks 9–12; the line of their union is recognizable at birth. The remainder of the cartilage of the occipital bone is ossified from five centres: two each for the lateral parts appear during postmenstrual week 11, and one for the basilar part appears around postmenstrual week 9.

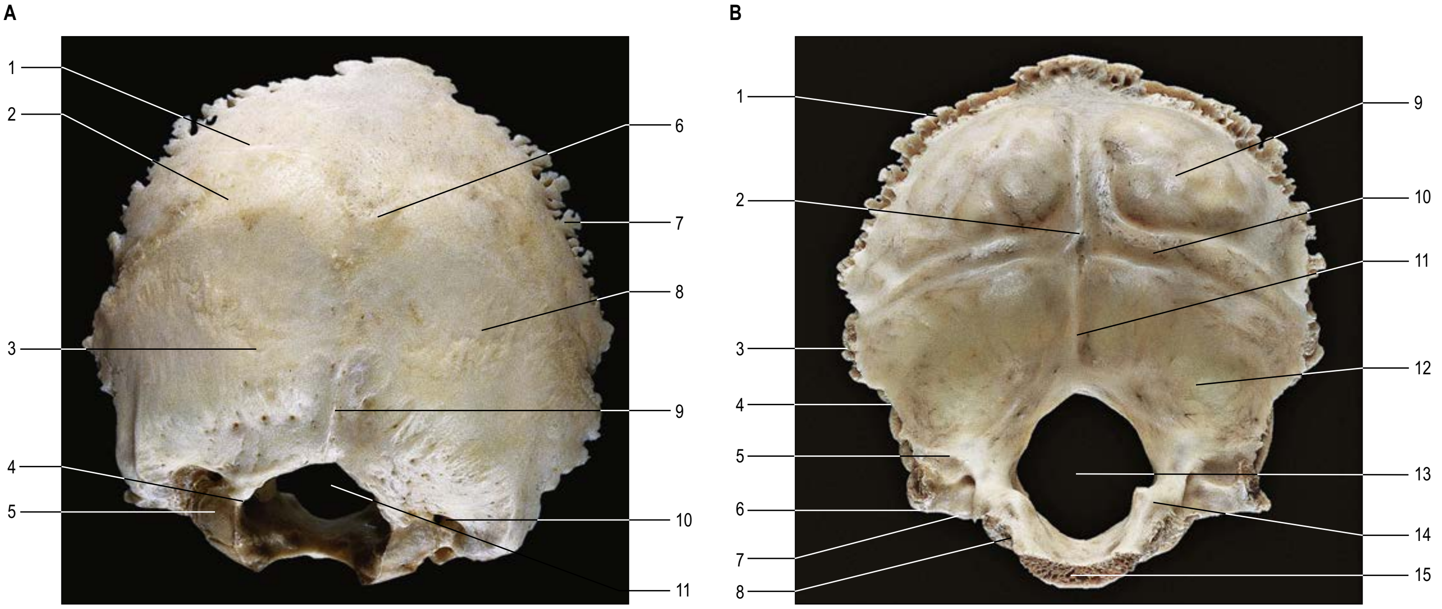
A
1
2
3
4
5
6
7
8
9
10
11
B
1
2
3
4
5
6
7
8
9
10
11
12
13
14
15

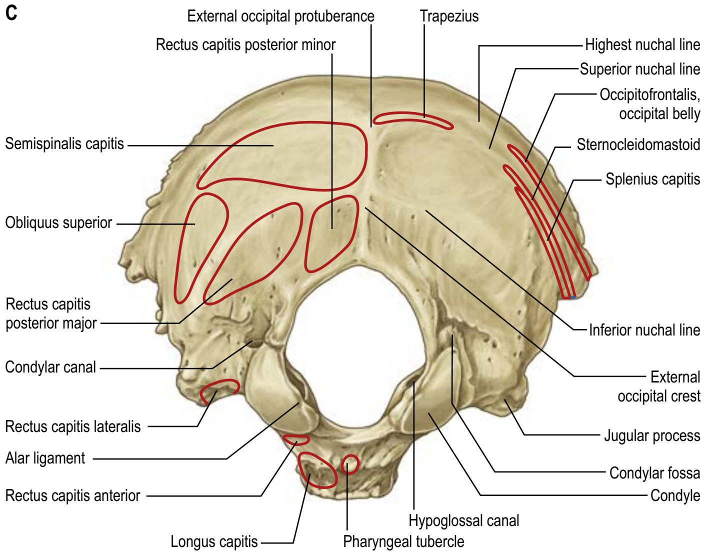
C
External occipital protuberance
Trapezius
Rectus capitis posterior minor
Highest nuchal line
Superior nuchal line
Occipitofrontalis, occipital belly
Semispinalis capitis
Sternocleidomastoid
Splenius capitis
Obliquus superior
Rectus capitis posterior major
Inferior nuchal line
Condylar canal
External occipital crest
Rectus capitis lateralis
Jugular process
Alar ligament
Condylar fossa
Rectus capitis anterior
Condyle
Hypoglossal canal
Longus capitis
Pharyngeal tubercle

Fig. 46.7 The occipital bone. **A**, External surface. Key: 1, highest nuchal line; 2, superior nuchal line; 3, inferior nuchal line; 4, hypoglossal canal; 5, occipital condyle; 6, external occipital protuberance; 7, lambdoid margin; 8, squamous part; 9, external occipital crest; 10, condylar canal; 11, foramen magnum. **B**, Internal surface. Key: 1, lambdoid margin; 2, internal occipital protuberance at 'confluence of sinuses'; 3, lateral angle; 4, mastoid margin; 5, groove for sigmoid sinus; 6, jugular process; 7, jugular notch; 8, groove for inferior petrosal sinus; 9, cerebral fossa; 10, groove for transverse sinus; 11, internal occipital crest; 12, cerebellar fossa; 13, foramen magnum; 14, jugular tubercle; 15, margin of basilar part for articulation with body of sphenoid. **C**, Muscle attachments. (A, B, With permission from Berkovitz BKB, Moxham BJ 1994 Colour Atlas of the Skull. London: Mosby.)

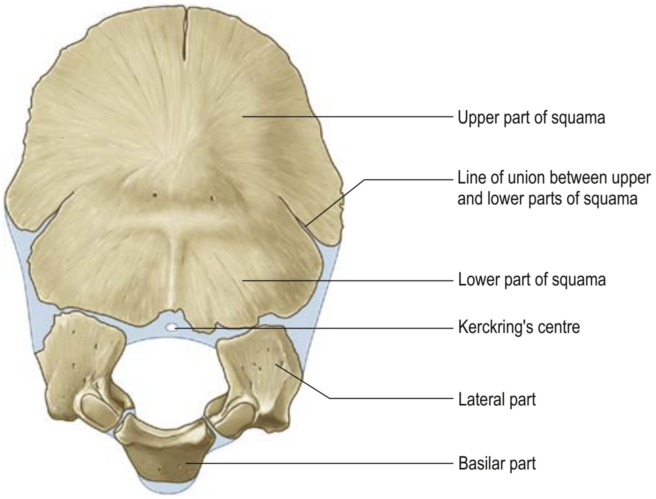
Upper part of squama
Line of union between upper and lower parts of squama
Lower part of squama
Kerckring's centre
Lateral part
Basilar part

Fig. 46.8 The occipital bone of a neonate, external surface. Parts of the chondrocranium that are still unossified are shown in blue.

At birth, the occipital bone consists of four separate parts (Fig. 46.8) – a basilar part, two lateral parts and a squamous part – all joined by cartilage and forming a ring around the foramen magnum. The squamous and lateral parts fuse together from the second year. The lateral parts fuse with the basilar part during years three and four, but fusion may be delayed until the seventh year.

Vertebral column

The vertebral column is a curved linkage of individual bones or vertebrae (Fig. 46.9). A continuous series of vertebral foramina runs through the articulated vertebrae posterior to their bodies, and collectively constitutes the vertebral canal, which transmits and protects the spinal cord and nerve roots, their coverings and vasculature (Fig. 46.10; see Fig. 47.2). A series of paired lateral intervertebral foramina transmits the spinal nerves and their associated vessels between adjacent vertebrae. The linkages between the vertebrae include cartilaginous interbody joints and paired synovial facet (zygapophysial) joints, together with a complex of ligaments and overlying muscles and fasciae. The muscles directly concerned with vertebral movements and attached to the column lie mainly posteriorly. Several large muscles producing major spinal movements lie distant from the column and without direct attachment to it, e.g. the anterolateral abdominal wall musculature. Movements of the column and the muscles concerned are described on page 840. The column as a whole receives its vascular supply and innervation according to general anatomical principles, which are considered below.

Vertebral column morphology is influenced externally by mechanical and environmental factors and internally by genetic, metabolic and hormonal factors. These all affect its ability to react to the dynamic forces of everyday life, such as compression, traction and shear. These dynamic forces can vary in magnitude and are much influenced by occupation, locomotion and posture.

The adult vertebral column usually consists of 33 vertebral segments. Each presacral segment (except the first two cervical) is separated from its neighbour by a fibrocartilaginous intervertebral disc. The functions of the column are to support the trunk, to protect the spinal cord and nerves, and to provide attachments for muscles. It is also an important site of haemopoiesis throughout life. Its total length in males is about 70 cm and in females about 60 cm. The intervertebral discs contribute about one-quarter of this length in young adults, though there is some diurnal variation in this contribution. Approximately 8% of overall body length is accounted for by the cervical spine, 20% by the thoracic, 12% by the lumbar and 8% by the

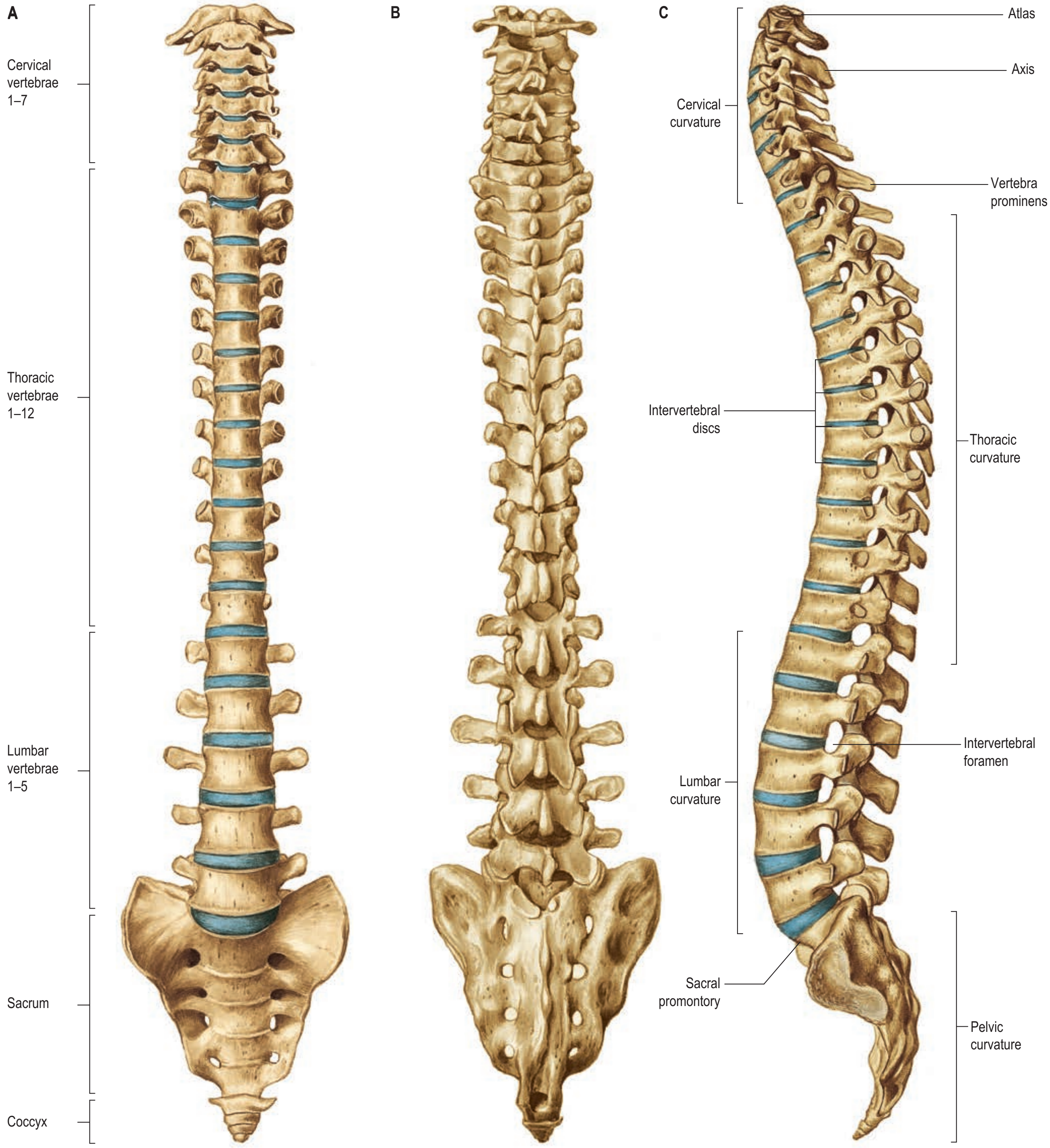
A
Cervical vertebrae 1–7
Thoracic vertebrae 1–12
Lumbar vertebrae 1–5
Sacrum
Coccyx
B
C
Atlas
Axis
Cervical curvature
Vertebra prominens
Intervertebral discs
Thoracic curvature
Intervertebral foramen
Lumbar curvature
Sacral promontory
Pelvic curvature

Fig. 46.9 The vertebral column. **A**, Anterior aspect. **B**, Posterior aspect. **C**, Lateral aspect. (Sobotta Atlas of Human Anatomy © Elsevier GmbH, Urban & Fischer, Munich.)

sacrococcygeal regions. Although the usual number of vertebrae is 7 cervical, 12 thoracic, 5 lumbar, 5 sacral and 4 coccygeal, this total is subject to frequent variability, and there have been reports of variation between 32 and 35 bones. The demarcation of groups by their morphological characteristics may be blurred: thus there may be thoracic costal facets on the seventh cervical vertebra, giving it the appearance of an extra thoracic vertebra; lumbar-like articular processes may be found on the lowest thoracic vertebra; or the fifth lumbar vertebra may be wholly or partially incorporated into the sacrum. As a result of these changes in transition between vertebral types, there may be 23–25 mobile presacral vertebrae.

Anterior aspect

The anterior aspect of the column is formed by the anterior surfaces of the vertebral bodies and of the intervertebral discs (see Fig. 46.9A). It has important anatomical relations at all levels and should be considered in continuity. It forms part of several clinically significant junctional or transitional zones, including the prevertebral/retropharyngeal zone of the neck, the thoracic inlet, the diaphragm and the pelvic inlet. The anterior aspect of the column is covered centrally by the anterior longitudinal ligament, which forms a fascial plane with the prevertebral and endothoracic fascia and with the subperitoneal areolar tissue of the posterior abdominal wall. Infection and other pathological processes may spread along this fascial plane.

Lateral aspect

The lateral aspect of the vertebral column is arbitrarily separated from the posterior by articular processes in the cervical and lumbar regions and by transverse processes in the thoracic region (see Fig. 46.9C). Anteriorly, it is formed by the sides of vertebral bodies and intervertebral discs. The oval intervertebral foramina, behind the bodies and between the pedicles, are smallest at the cervical and upper thoracic levels, and increase progressively in size in the thoracic and upper

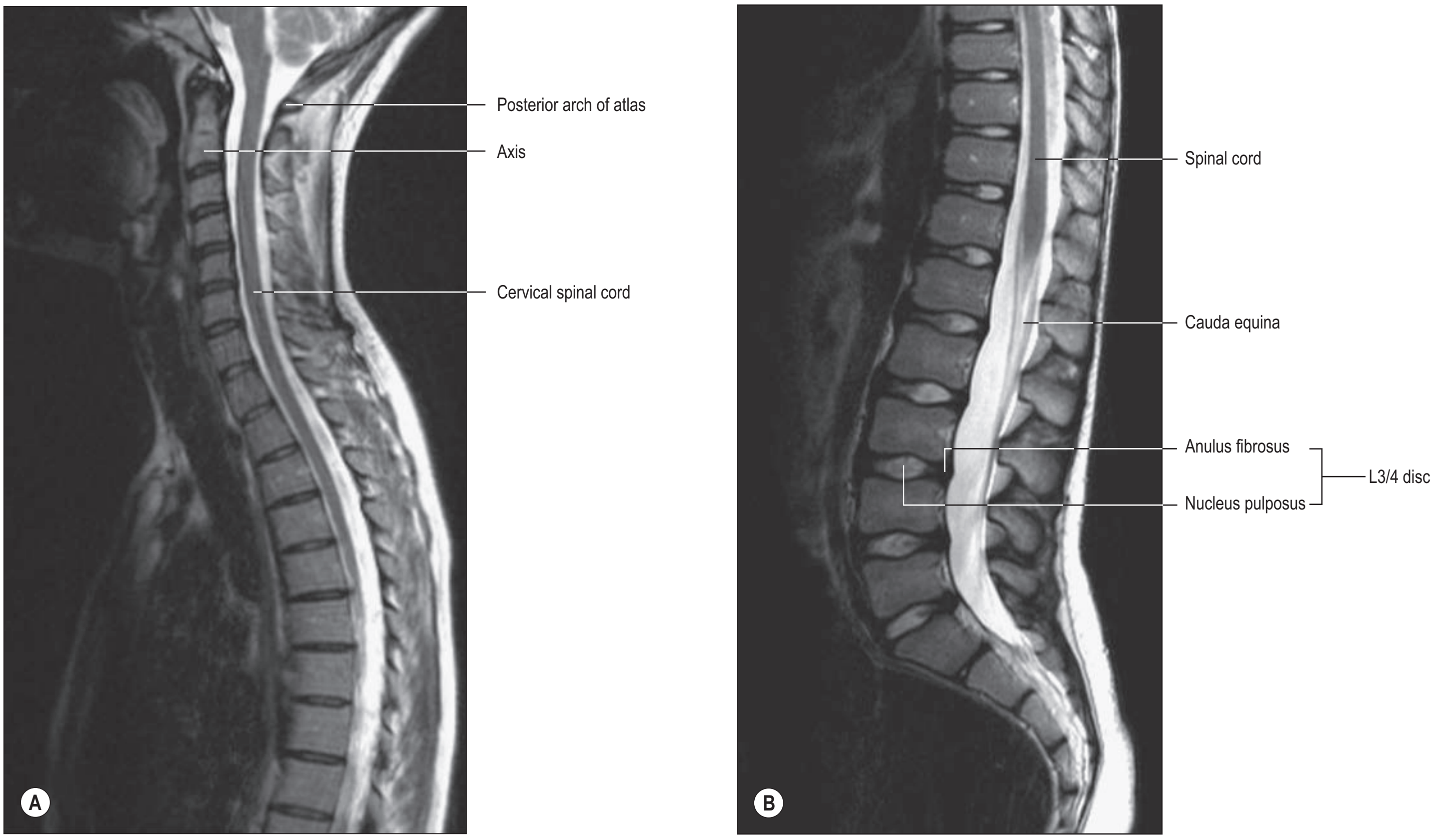

Fig. 46.10 A sagittal magnetic resonance (MR) image of the cervical and upper thoracic (**A**) and lower thoracic and lumbar (**B**) spine.

lumbar regions. The lumbosacral (L5/S1) intervertebral foramen is the smallest of the lumbar foramina (Fig. 46.11). The foramina permit communication between the lumen of the vertebral canal and the paravertebral soft tissues (a 'paravertebral space' is sometimes described), which may be important in the spread of tumours and other pathological processes. The lateral aspects of the column have important anatomical relations, some of which vary considerably between the two sides.

Posterior aspect

The posterior aspect of the column is formed by the posterior surfaces of the laminae and spinous processes, their associated ligaments and the facet joints (Fig. 46.9B). It is covered by the deep muscles of the back.

Structural defects of the posterior bony elements

Deformity and bony deficiency may occur at several sites within the posterior elements. The laminae may be wholly or partially absent, or the spinous process alone may be affected, with no abnormalities in the overlying soft tissues (spina bifida occulta). A defect may occur in the bone that joins the superior and inferior articular processes (pars interarticularis): this condition is spondylolysis, and may be developmental or result from acute or fatigue fracture. If such defects are bilateral, the column becomes unstable at that level, and forward displacement of that part of the column above (cranial to) the defects may occur: this is spondylolisthesis (Fig. 46.12). Abnormality of the laminar bone, or degenerative changes in the facet joints, may also lead to similar displacement in the absence of pars defects. The deformity of the vertebral canal resulting from severe spondylolisthesis may lead to neural compression and subsequent damage (Fig. 46.13). Much more rarely, bony defects may occur elsewhere in the posterior elements, e.g. in the pedicles.

Detailed anatomical relations of all aspects of the vertebral column at the various levels are best appreciated by the study of horizontal (axial) sections and images (see Figs 46.47B and 46.74).

Curvatures

Embryonic and fetal curvatures

The embryonic body appears flexed, with primary thoracic and pelvic curves that are convex dorsally. The fetal body is affected by the available space for movement, for example, increased flexion of the spine is seen in oligohydramnios (Albequerque et al 2002). The general fetal movements that have been observed from 11–14 postmenstrual weeks may lead to the appearance of secondary spinal curvatures in the sagittal plane (Bagnall et al 1977, Lu et al 2016). A cervical lordosis appears towards the end of the first trimester and reflects the development of function in the muscles responsible for head extension: the early development of a gasp reflex, which involves head extension and flexion of the arms, may be a contributory factor. A lumbosacral lordosis has been demonstrated in fetuses of 23–-40 postmenstrual weeks, but does not appear to be correlated with gestational age, suggesting that it is not related to growth but may be genetically determined (Been and Kalichman 2014).

Neonatal curvatures

In the neonate, the vertebral column has no fixed curvatures. It is particularly flexible and, if dissected free from the body, it can easily be bent (flexed or extended) into a perfect half-circle. A slight sacral curvature can be seen, which develops as the sacral vertebrae ossify and fuse. The thoracic part of the column is the first to develop a relatively fixed curvature, which is concave anteriorly. An infant can usually support its head at 3 or 4 months, sit upright at around 9 months, and will commence walking between 12 and 15 months. These functional changes exert a major influence on the development of the secondary curvatures in the vertebral column and changes in the proportional size of the vertebrae, in particular in the lumbar region. The secondary lumbar curvature becomes important in maintaining the centre of gravity of the trunk over the legs when walking starts, and thus changes in body proportions exert a major influence on the subsequent shape of curvatures in the vertebral column.

Adult curvatures

In adults, the cervical curve is a lordosis (convex forwards), and the least marked. It extends from the atlas to the second thoracic vertebra, with its apex between the fourth and fifth cervical vertebrae. Sexual dimorphism has been described in the cervical curvatures. The thoracic curve is a kyphosis (convex dorsally). It extends between the second and the eleventh and twelfth thoracic vertebrae, and its apex lies between the sixth and ninth thoracic vertebrae. This curvature is caused by the increased posterior height of the thoracic vertebral bodies. The lumbar curve is also a lordosis. It has a greater

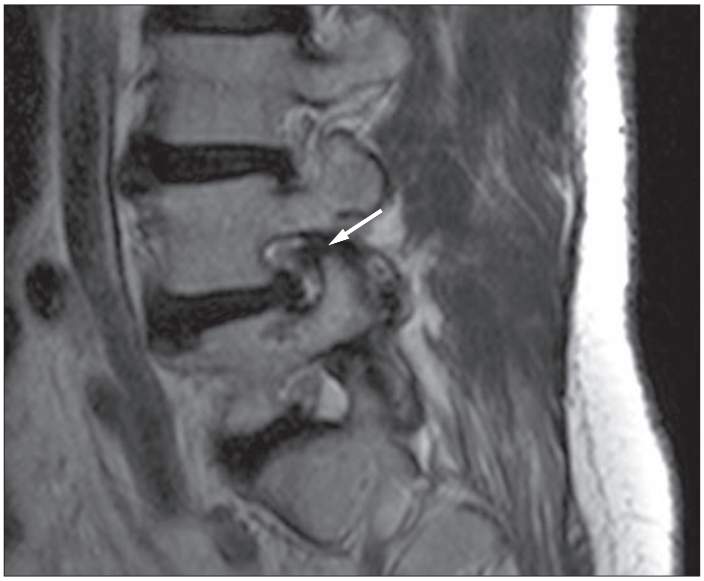

Fig. 46.11 A sagittal MR image of the lumbar spine showing the L5–S1 intervertebral foramen (neuroforamen) and a pathologically narrowed L4–L5 intervertebral foramen (arrow). This narrowing, known as lumbar foraminal stenosis, results in leg pain with an L4 sensory distribution.

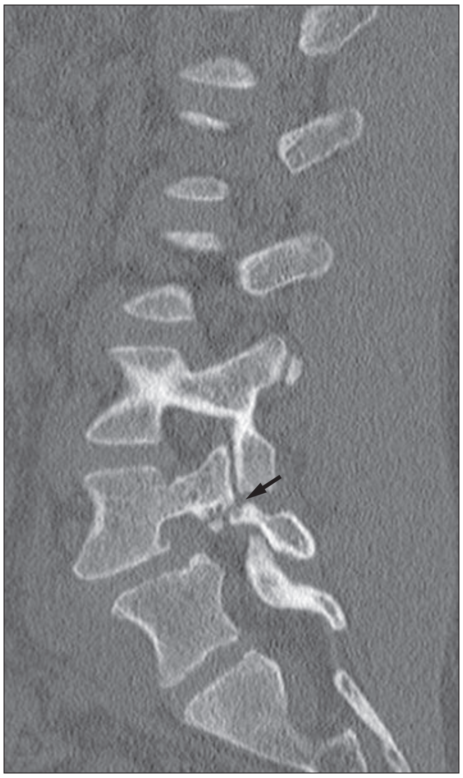

Fig. 46.12 A sagittal CT image of the lumbar spine showing the left side of an isthmic spondylolisthesis resulting from bilateral fractures of the pars interarticularis (arrow).

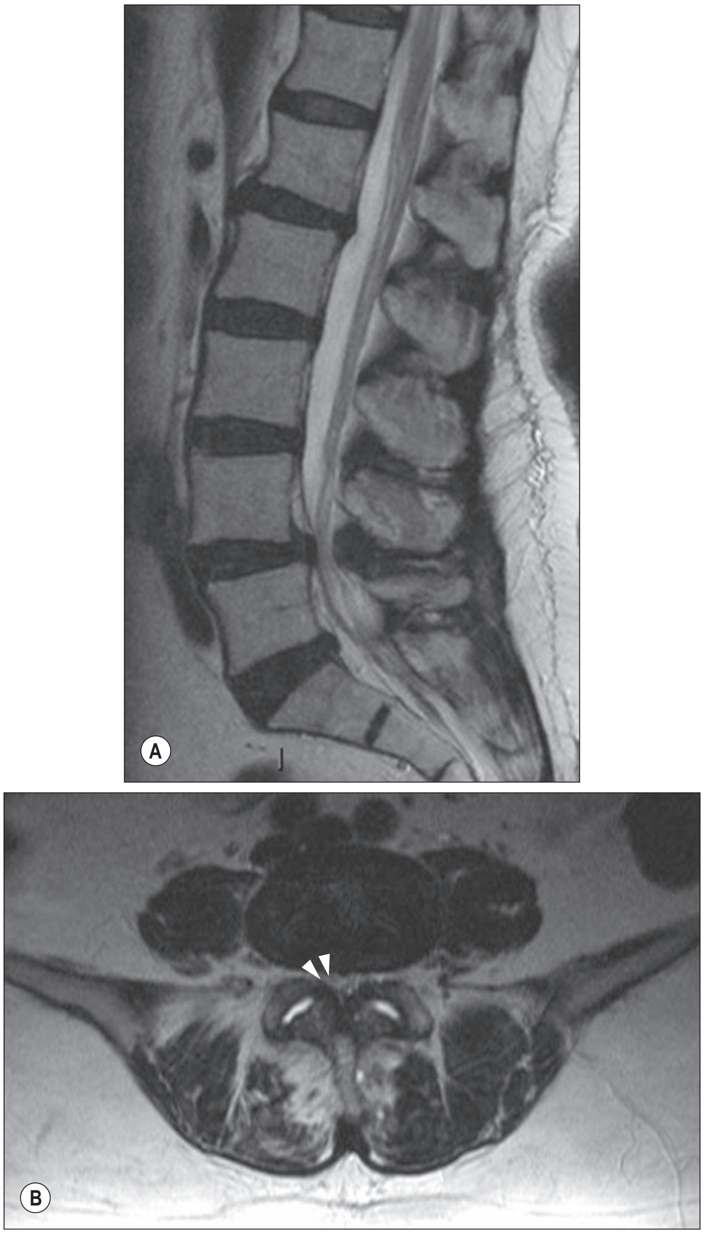

Fig. 46.13 (**A**) Sagittal and (**B**) axial MR images of a degenerative spondylolisthesis at L4–L5. This condition is accompanied by massive superior articular facet hypertrophy and subsequent critical central and lateral recess stenosis (arrowheads).

magnitude in females and extends from the twelfth thoracic vertebra to the lumbosacral angle; there is an increased convexity of the last three segments as a result of the greater anterior height of the intervertebral discs and some posterior wedging of the vertebral bodies. Its apex is at the level of the third lumbar vertebra. The pelvic curve is concave anteroinferiorly and involves the sacrum and coccygeal vertebrae. It extends from the lumbosacral junction to the apex of the coccyx.

The presence of these curvatures means that the cross-sectional profile of the trunk changes with spinal level. The anteroposterior diameter of the thorax is much greater than that of the lower abdomen. In the normal vertebral column, there are well-marked curvatures in the sagittal plane and no lateral curvatures other than in the upper thoracic region, where there is often a slight lateral curvature, convex to the right in right-handed persons, and to the left in the left-handed. Compensatory lateral curvature may also develop to cope with pelvic obliquity, such as that imposed by inequality of leg length. The sagittal curvatures are present in the cervical, thoracic, lumbar and pelvic regions (see Fig. 46.9). These curvatures have developed with rounding of the thorax and pelvis as an adaptation to bipedal gait.

Vertebral column in the elderly

In older people, age-related changes in the structure of bone lead to broadening and loss of height of the vertebral bodies. These changes are more severe in females. The bony changes in the vertebral column are accompanied by changes in the collagen content of the discs and by decline in the activity of the spinal muscles. This leads to progressive decline in vertebral column mobility, particularly in the lumbar spine. The development of a 'dowager's hump' in the mid-thoracic region in females, caused by age-related osteoporosis, increases the thoracic kyphosis and cervical lordosis. Overall, these changes in the vertebral column lead directly to loss of total height in the individual.

As discs desiccate, there is often a straightening of the cervical spine and development of subsequent cervical kyphosis. This, coupled with narrowing of the spinal canal, can lead to increased risk of neurological damage of the cervical spinal cord, in addition to pain.

In mid-lumbar vertebrae, the width of the body increases with age. In males there is a relative decrease of posterior to anterior body height: anterior height decreases relative to width in both males and females. Twomey et al (1983) observed a reduction in bone density of lumbar vertebral bodies with age, principally as a result of a reduction in transverse trabeculae (more marked in females as a result of postmenopausal osteoporosis), which was associated with increased diameter and increasing concavity in their juxtadiscal surfaces (end-plates).

Other changes affect the vertebral bodies. Osteophytes (bony spurs) may form from the compact cortical bone on the anterior and lateral surfaces of the bodies. Although individual variations occur, these changes appear in most individuals from 20 years onwards. They are most common on the anterior aspect of the body and never involve the ring epiphysis. Osteophytic spurs are frequently asymptomatic but may result in diminished movements within the spine.

Vascular supply and lymphatic drainage

Arteries

The vertebral column, its contents and its associated soft tissues all receive their arterial supply from derivatives of dorsal branches of the embryonic intersegmental somatic arteries (see Fig. 13.18). The named artery concerned depends on the level of the column. These intersegmental vessels persist in the thoracic and lumbar regions as the posterior intercostal and lumbar arteries (**Figs 46.14–46.16**). In the cervical and sacral regions, longitudinal anastomoses between the intersegmental vessels persist as longitudinal vessels, which themselves give spinal branches to the vertebral column. In the neck, the postcostal anastomosis becomes most of the vertebral artery, while the post-transverse anastomosis forms most of the deep cervical artery (**Figs 46.17–46.19**). The ascending cervical artery and the lateral sacral artery are persistent parts of the precostal anastomosis.

In the thorax and abdomen, the primitive arterial pattern is retained by the paired branches of the descending aorta, which supply the vertebral column (**Fig. 46.20**; see Fig. 46.14). On each side, the main trunk of the artery (posterior intercostal or lumbar) passes around the vertebral body, giving off primary periosteal and equatorial branches to the body, and then a major dorsal branch. The latter gives off a spinal branch that enters the intervertebral foramen, before itself supplying the facet joints, the posterior surfaces of the laminae and the overlying muscles and skin. There is free anastomosis between these dorsal articular and soft tissue branches, extending over several segments (Crock and Yoshizawa 1976, Boelderl et al 2002). At cervical and sacral levels, the longitudinally running arteries described above have direct spinal branches. The spinal branches are the main arteries of supply to all bony elements of the vertebrae and to the dura and epidural tissues, and also contribute to the supply of the spinal cord and nerve roots via radicular branches. As they enter the vertebral canal, the spinal arteries divide into postcentral, prelaminar and radicular branches. The postcentral branches, which are the main nutrient arteries to the vertebral bodies and to the periphery of the intervertebral discs, anastomose beneath the posterior longitudinal ligament with their fellows above and below, as well as across the midline (**Fig. 46.20B**). This anastomosis also supplies the anterior epidural tissues and dura. The majority of the vertebral arch, the posterior epidural tissues and dura, and the ligamentum flavum are supplied by the prelaminar branches and their anastomotic plexus on the posterior wall of the vertebral canal. (For further reading on the arterial supply and venous drainage of the vertebral column and spinal cord, see Crock (1996), Parke et al (2011).)

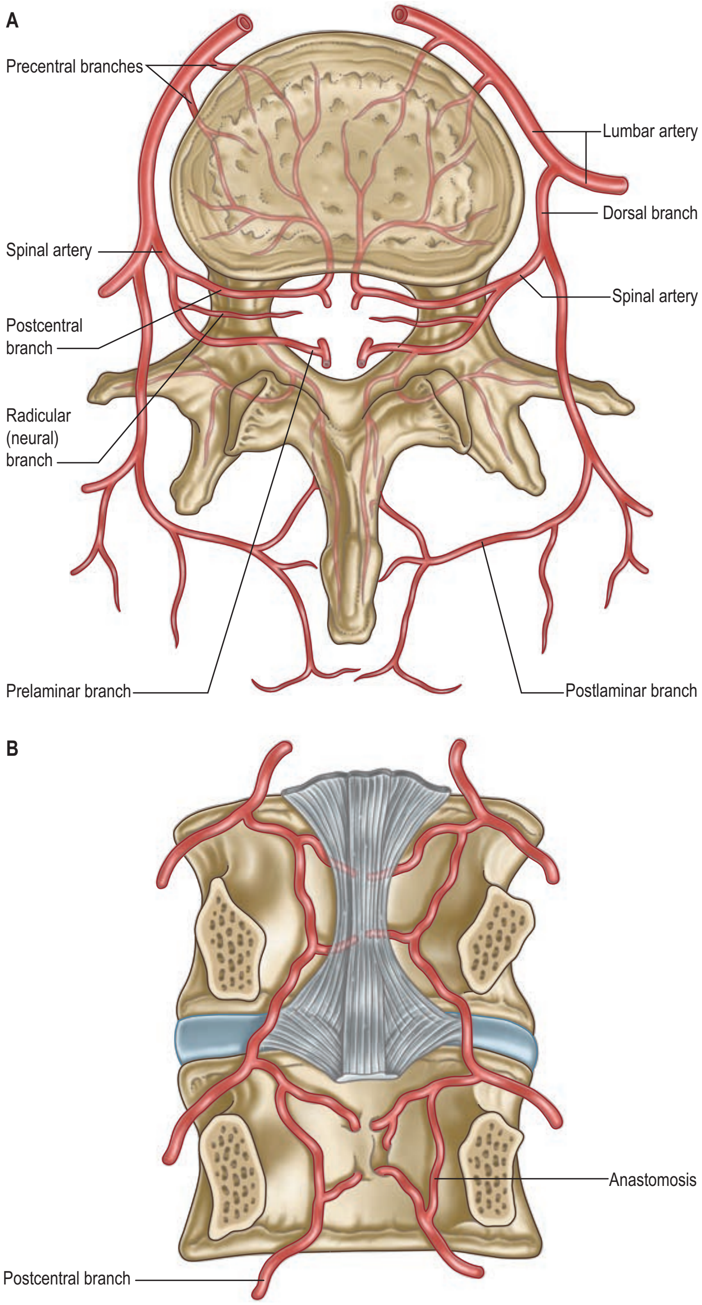

Fig. 46.20 The arterial supply to the vertebrae and the contents of the vertebral canal. **A**, The branching pattern of the lumbar segmental arteries. **B**, Arterial anastomoses between postcentral branches of spinal arteries within the vertebral canal. (C, *continued online*)

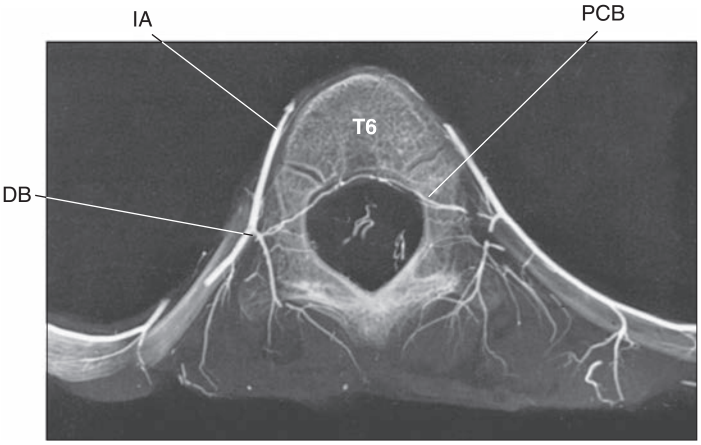

Fig. 46.14 A vertical radiograph of a section through T6 of a specimen from a 6-year-old child injected with barium sulphate. The intercostal arteries (IA) give rise to dorsal branches (DB) that provide spinal branches to the vertebral canal and posterior branches to the arch and dorsal musculature. Posterior central branches (PCB) send vessels into the vertebral body. Note the fine anterior central and anterior laminar and posterior laminar vessels and the neurocentral synchondrosis. (With permission from Parke WW, Bono CM, Garfin SR 2011 Applied anatomy of the spine. In: Herkowitz HN, Garfin SR, Eismont FJ et al (eds) Rothman-Simeone The Spine, 6th ed. Saunders, Elsevier.)

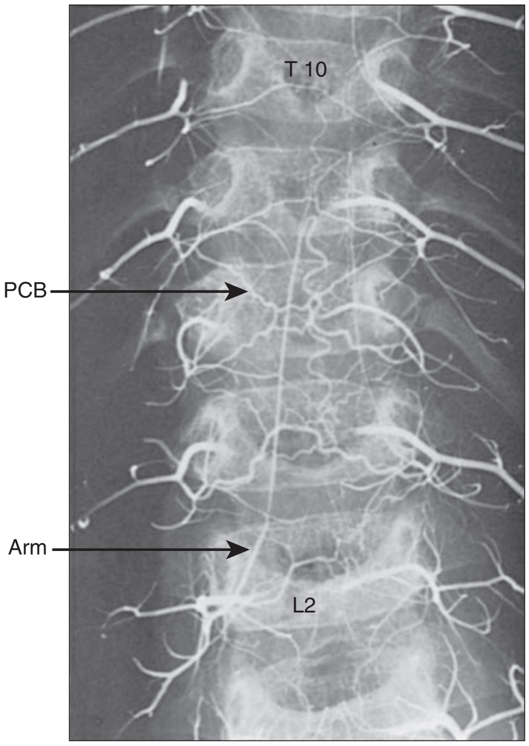

Fig. 46.15 Anteroposterior arteriogram of the lower thoracic and upper lumbar vertebrae in a 6-year-old child injected with barium sulphate. The interlocking anastomotic pattern formed by the posterior central branches (PCB) and the manner in which four branches converge over the centre of the dorsum of the body of each vertebra are well shown. The arteria radicularis magna (Arm) forms a major contribution to the anterior spinal artery of the cord and can be seen arising at L2. (With permission from Parke WW, Bono CM, Garfin SR 2011 Applied anatomy of the spine. In: Herkowitz HN, Garfin SR, Eismont FJ et al (eds) Rothman-Simeone The Spine, 6th ed. Saunders, Elsevier.)

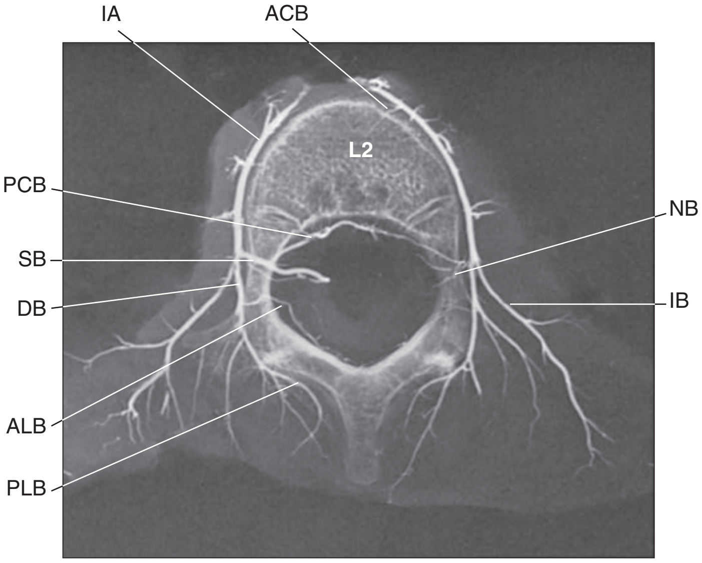

Fig. 46.16 Vertical radiograph of a section through a lumbar vertebra of a 6-year-old child injected with barium sulphate. The vascularity of the lumbar vertebra may be regarded as the archetypal pattern from which other regions evolved variations. The segmental lumbar artery gives rise to numerous anterior central branches (ACB) that penetrate the cortical bone of the body. The spinal branch (SB) sends prominent posterior central branches (PCB) to the dorsum of the body, whereas the dorsal branch (DB) supplies the anterior (ALB) and posterior (PLB) laminar branches. Neural branches (NB) follow the nerve roots to the cord. In this section, the arteria radicularis magna is seen as a neural branch on the right side. Other abbreviations: IA, intercostal arteries; IB, intercostal branches. (With permission from Parke WW, Bono CM, Garfin SR 2011 Applied anatomy of the spine. In: Herkowitz HN, Garfin SR, Eismont FJ et al (eds) Rothman-Simeone The Spine, 6th ed. Saunders, Elsevier.)

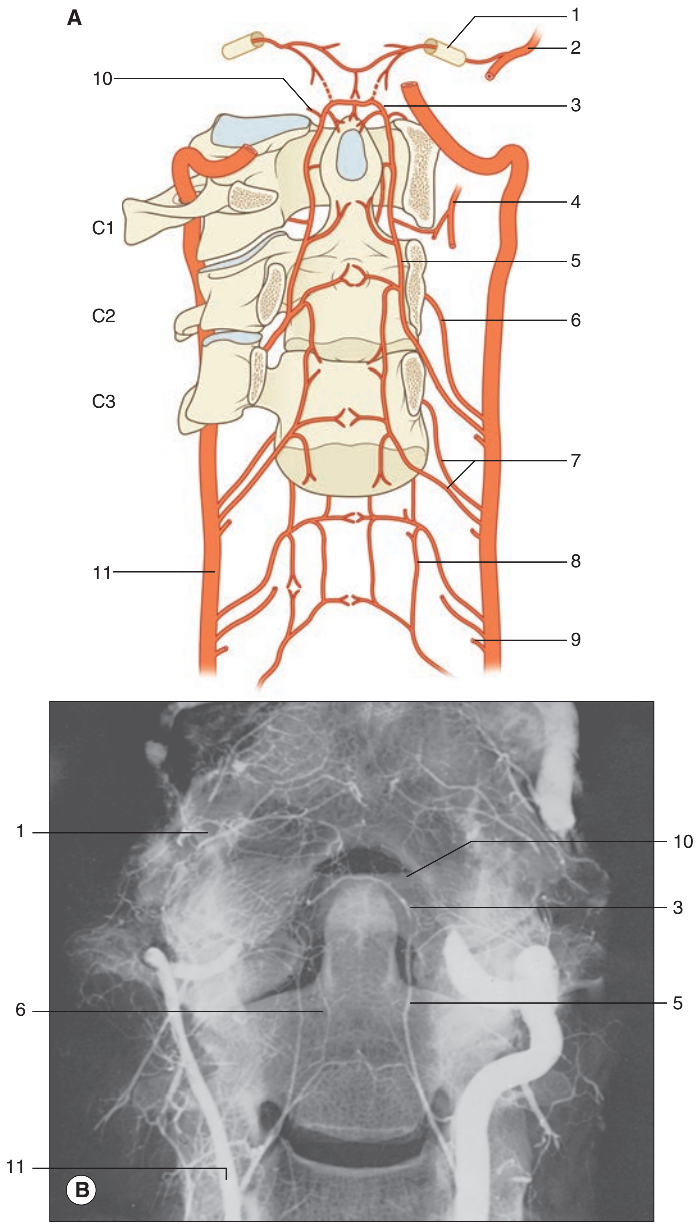

Fig. 46.17 **A**, The arterial supply to the bodies of the upper cervical vertebrae and the odontoid process. Numerical designations apply to the same structures in **B**. Key: 1, meningeal artery in hypoglossal canal; 2, occipital artery; 3, apical arcade of odontoid process; 4, ascending pharyngeal artery giving collateral branch beneath anterior arch of atlas; 5, posterior ascending artery; 6, anterior ascending artery; 7, precentral and postcentral arteries to typical cervical vertebral body; 8, anterior spinal plexus; 9, medullary branch of vertebral artery: radicular, prelaminar, and meningeal branches are also found at each level; 10, collateral to ascending pharyngeal artery passing rostral to anterior arch of atlas; 11, left vertebral artery. (With permission from Parke WW, Bono CM, Garfin SR 2011 Applied anatomy of the spine. In: Herkowitz HN, Garfin SR, Eismont FJ et al (eds) Rothman-Simeone The Spine, 6th ed. Saunders, Elsevier.)

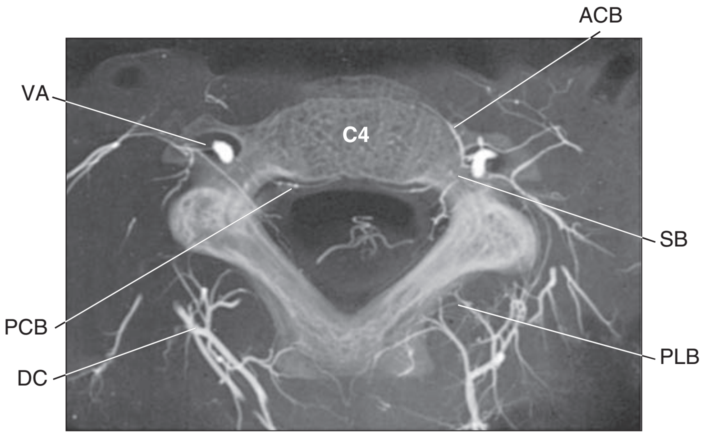

Fig. 46.18 A vertical radiograph of a section through the fourth cervical vertebra of a 6-year-old child injected with barium sulphate. The deep cervical artery (DC) provides the posterior laminar branches (PLB). Vertebral arteries show numerous anastomoses with other cervical arteries and send spinal branches (SB) that form posterior central branches (PCB) of the body and anterior laminar branches of the arch. Anterior central branches (ACB) may arise independently from the vertebral arteries (VA). (With permission from Parke WW, Bono CM, Garfin SR 2011 Applied anatomy of the spine. In: Herkowitz HN, Garfin SR, Eismont FJ et al (eds) Rothman-Simeone The Spine, 6th ed. Saunders, Elsevier.)

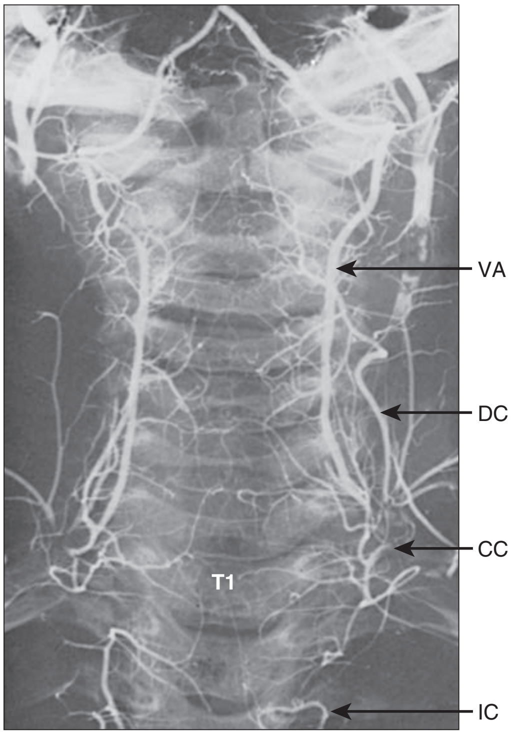

Fig. 46.19 An arteriogram of the cervical and upper thoracic regions of the 6-year-old spine seen in Figs 46.16 and 46.18. The vertebral artery (VA) and deep cervical branch (DC) of the costocervical trunk (CC) supply segmental branches to each vertebra. The costocervical artery also typically supplies T1 and T2, but in this case T2 receives a high intercostal (IC) branch on the left side. (With permission from Parke WW, Bono CM, Garfin SR 2011 Applied anatomy of the spine. In: Herkowitz HN, Garfin SR, Eismont FJ et al (eds) Rothman-Simeone The Spine, 6th ed. Saunders, Elsevier.)

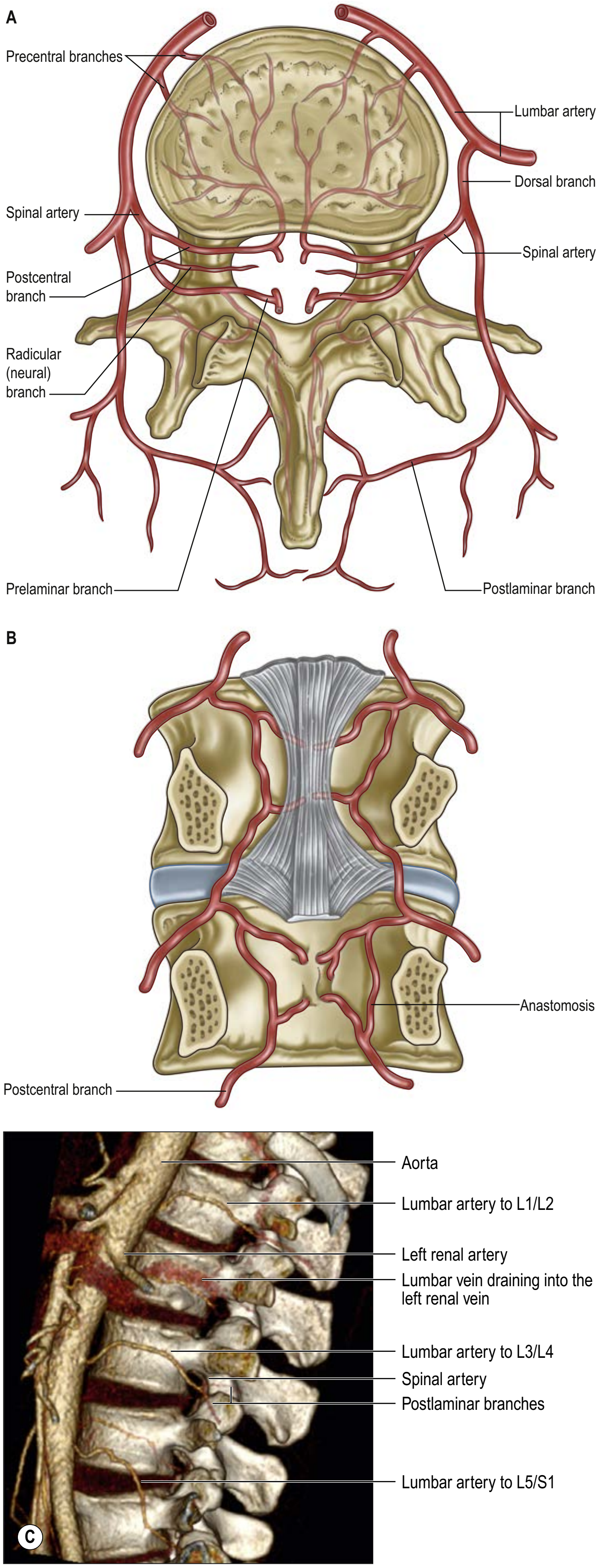
A
Precentral branches
Lumbar artery
Dorsal branch
Spinal artery
Spinal artery
Postcentral branch
Radicular (neural) branch
Prelaminar branch
Postlaminar branch
B
Anastomosis
Postcentral branch
Aorta
Lumbar artery to L1/L2
Left renal artery
Lumbar vein draining into the left renal vein
Lumbar artery to L3/L4
Spinal artery
Postlaminar branches
Lumbar artery to L5/S1
C

Fig. 46.20 The arterial supply to the vertebrae and the contents of the vertebral canal. **A**, The branching pattern of the lumbar segmental arteries. **B**, Arterial anastomoses between postcentral branches of spinal arteries within the vertebral canal. **C**, Virtual rendering of a CT aortogram showing the lumbar spinal arterial supply, viewed from the left.

Veins

Veins of the vertebral column form intricate plexuses along the entire column, external and internal to the vertebral canal (**Fig. 46.21**) (Groen et al 2004). Both groups are devoid of valves, anastomose freely with each other, and join the intervertebral veins. Interconnections are widely established between these plexuses and longitudinal veins early in fetal life. When development is complete, the plexuses drain into the caval and azygos/ascending lumbar systems via named veins that accompany the arteries described above.

The veins also communicate with cranial dural venous sinuses and with the deep veins of the neck and pelvis. The venous complexes associated with the vertebral column can dilate considerably, and can form alternative routes of venous return in patients with major venous obstruction in the neck, chest or abdomen. The absence of valves allows pathways for the wide and sometimes paradoxical spread of malignant disease and sepsis. Pressure changes in the body cavities are transmitted through these venous plexuses and thus to the cerebrospinal fluid, though the cord itself may be protected from such congestion by valves in the small veins that drain from the cord into the internal vertebral plexus.

External vertebral venous plexuses

The external vertebral venous plexuses are anterior and posterior. They anastomose freely, and are most developed in the cervical region. Anterior external plexuses are anterior to the vertebral bodies, communicate with basivertebral and intervertebral veins, and receive tributaries from vertebral bodies. Posterior external plexuses lie posterior to the vertebral laminae and around spines and transverse and articular processes. They anastomose with the internal plexuses and join the vertebral, posterior intercostal and lumbar veins.

Internal vertebral venous plexuses

The internal vertebral venous plexuses are embedded in epidural fat, supported by a network of collagenous fibres (Chaynes et al 1998). These thin-walled channels receive tributaries from the bones, red bone marrow and spinal cord. (For the venous drainage of the spinal cord, see Fig. 47.15). They form a denser network than the external plexuses and are arranged vertically as four interconnecting longitudinal vessels: two anterior and two posterior.

The anterior internal plexuses are large plexiform veins on the posterior surfaces of the vertebral bodies and intervertebral discs. They flank the posterior longitudinal ligament, beneath which they are connected by transverse vessels into which the large basivertebral veins open. The posterior internal plexuses, on each side in front of the vertebral arches and ligamenta flava, anastomose with the posterior external plexuses via veins that pass through and between the ligaments. The internal plexuses interconnect by venous rings near each vertebra. Around the foramen magnum, they form a dense network connecting with vertebral veins, occipital and sigmoid sinuses, the basilar plexus, the venous plexus of the hypoglossal canal and the condylar emissary veins.

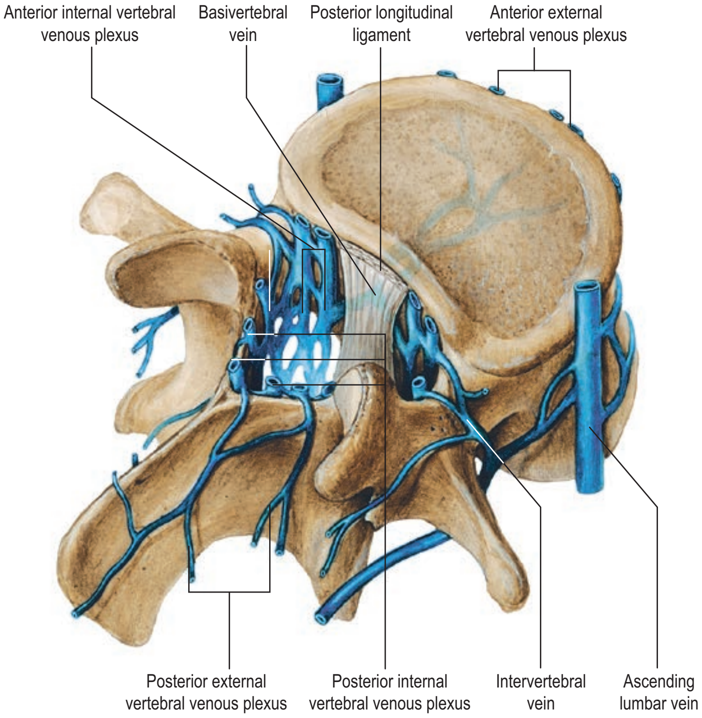
Anterior internal vertebral venous plexus
Basivertebral vein
Posterior longitudinal ligament
Anterior external vertebral venous plexus
Posterior external vertebral venous plexus
Posterior internal vertebral venous plexus
Intervertebral vein
Ascending lumbar vein

Fig. 46.21 Venous drainage of the vertebral column. Note that the basivertebral vein is shown beneath (i.e. anterior to) the posterior longitudinal ligament. (Sobotta Atlas of Human Anatomy © Elsevier GmbH, Urban & Fischer, Munich.)

Basivertebral veins

The basivertebral veins are paired valveless veins that drain the pars spongiosa of the vertebral bodies into the internal and external vertebral venous plexuses. In each segment, they emerge horizontally from foramina in the vertebral bodies. Posteriorly, they drain into the transverse branches of the anterior internal vertebral plexuses. Anteriorly, they drain directly into the anterior external vertebral venous plexus. The basivertebral veins enlarge in advanced age.

Intervertebral veins

Branches of the anterior internal plexuses drain into retrocorporal veins that join the posterior internal venous plexuses to form intervertebral veins. As their name suggests, these veins accompany the spinal nerves through intervertebral foramina; they drain in craniocaudal sequence into the vertebral, posterior intercostal, lumbar and lateral sacral veins. Upper posterior intercostal veins may drain into the caval system via brachiocephalic veins, whereas the lower intercostals drain into the azygos system. Lumbar veins are joined longitudinally in front of the transverse processes by the ascending lumbar veins, in which they may terminate. Alternatively, they may proceed around the vertebral bodies to drain into the inferior vena cava. Whether the basivertebral or intervertebral veins contain effective valves is uncertain, but experimental evidence strongly suggests that their blood flow can be reversed (Batson 1957). This may explain how pelvic neoplasms, e.g. carcinoma of the prostate, may metastasize in vertebral bodies: the cells spread into the internal vertebral plexuses via their connections with the pelvic veins when blood flow is temporarily reversed by raised intra-abdominal pressure or postural alterations (Pearce 2006).

Lymphatic drainage

Little is known in detail about the lymphatic drainage of the vertebral column and its associated soft tissues. In general, deep lymphatic vessels tend to follow the arteries. The cervical vertebral column drains to deep cervical nodes, the thoracic to (posterior) intercostal nodes and the lumbar column to lateral aortic and retro-aortic nodes. The pelvic part of the column drains to lateral sacral and internal iliac nodes.

Innervation

The innervation of the vertebral column and its associated soft tissues has been studied in greatest detail in the lumbar region (see Fig. 46.61). The account given here relies particularly on the work of Bogduk (2012), to whose textbook on the lumbosacral spine the interested reader is referred. See also the work of Groen et al (1990).

Innervation is derived from the spinal nerves where they branch, in and just beyond the intervertebral foramina. There is an input from the sympathetic system either via grey rami communicantes or directly from thoracic sympathetic ganglia. The branches of the spinal nerve concerned are the dorsal ramus and the recurrent meningeal or sinuvertebral nerves (usually more than one at each level) (see Fig. 47.7). The dorsal ramus branches to supply the facet joints, periosteum of the posterior bony elements, overlying muscles and skin. The exact origin and branching pattern of the sinuvertebral nerves is controversial, but they may be best considered as recurrent branches of the ventral rami. They receive the sympathetic input described above, then re-enter the intervertebral foramina to supply the structures that form the walls of the vertebral canal, the dura and epidural soft tissues. Their subsequent course is described on page 867.

Vertebrae: general features

A typical vertebra has a ventral body; a dorsal vertebral (neural) arch, extended by lever-like processes; and a vertebral foramen, which is occupied in life by the spinal cord, meninges and their vessels (**Fig. 46.22**).

Opposed surfaces of adjacent bodies are bound together by intervertebral discs of fibrocartilage. The complete column of bodies and discs forms the strong but flexible central axis of the body and supports the

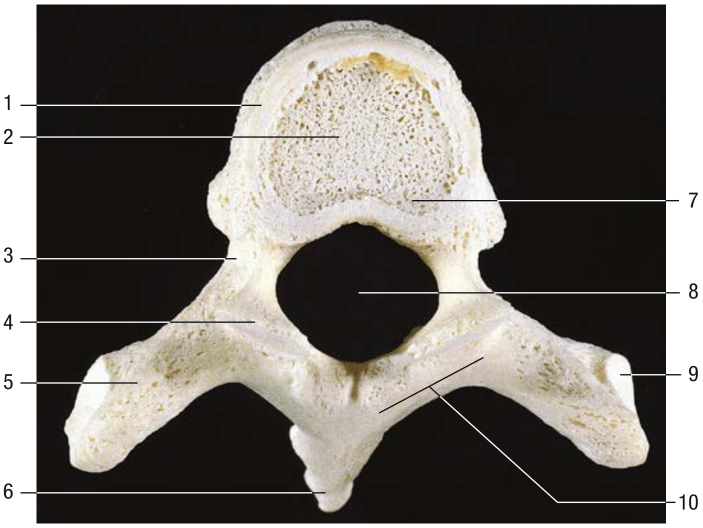

Fig. 46.22 The fourth thoracic vertebra, superior aspect. Key: 1, bone derived from anular epiphysis; 2, vertebral body – bone derived from centrum; 3, pedicle; 4, superior articular facet; 5, transverse process; 6, spinous process; 7, vertebral body, bone derived from neural arch; 8, vertebral foramen; 9, costal facet; 10, lamina.

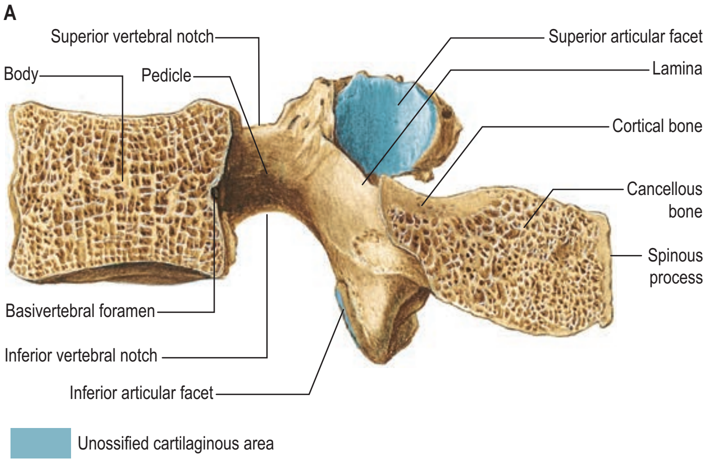

Fig. 46.23 **A**, A median sagittal section through a lumbar vertebra. (Sobotta Atlas of Human Anatomy © Elsevier GmbH, Urban & Fischer, Munich.) (B, *continued online*)

full weight of the head and trunk. It also transmits even greater forces generated by muscles attached to it directly or indirectly. The foramina form a vertebral canal for the spinal cord, and between adjoining vertebral arches, near their junctions with vertebral bodies, intervertebral foramina transmit mixed spinal nerves, smaller recurrent nerves, and blood and lymphatic vessels.

The cylindroid vertebral body varies in size, shape and proportions in different regions of the vertebral column. Its superior and inferior (discal) surfaces vary in shape from approximately flat (but not parallel) to sellar, with a raised peripheral smooth zone, formed from an 'anular' epiphysial disc, within which the surface is rough. These differences in texture reflect variations in the early structure of intervertebral discs. In the horizontal plane, the profiles of most bodies are convex anteriorly, but concave posteriorly where they complete the vertebral foramen. Most sagittal profiles are concave anteriorly but flat posteriorly. Small vascular foramina appear on the front and sides, and posteriorly there are small arterial foramina and a large irregular orifice (sometimes double) for the exit of basivertebral veins (Fig. 46.23). The adult vertebral body is not coextensive with the developmental centrum but includes parts of the neural arch posterolaterally.

Viewed anteriorly, there is a cephalocaudal increase in vertebral body width from the second cervical to the third lumbar vertebra, which is associated with an increased load-bearing function. The increase is linear in the neck but not in the thoracic and lumbar regions. There is some variation in size of the last two lumbar bodies, but thereafter width diminishes rapidly to the coccygeal apex. In the two lowest lumbar vertebrae, there is an inverse relation between the areas of the upper and lower surfaces of the bodies and the size of the pedicles and transverse processes.

On each side, the vertebral arch has a vertically narrower ventral part – the pedicle – and a broader lamina dorsally. Paired transverse, superior and inferior articular processes project from their junctions. There is a median dorsal spinous process.

Pedicles are short, thick, rounded dorsal projections from the superior part of the body at the junction of its lateral and dorsal surfaces; the concavity formed by the curved superior border of the pedicle is shallower than the inferior one (see Fig. 46.23). When vertebrae articulate by the intervertebral disc and facet joints, these adjacent vertebral notches contribute to an intervertebral foramen. The complete perimeter of an intervertebral foramen consists of the notches, the dorsolateral aspects of parts of adjacent vertebral bodies and the intervening disc, and the capsule of the synovial facet joint (see Fig. 46.25). The laminae are directly continuous with the pedicles. They are vertically flattened and curve dorsomedially.

Lateral to the spinous processes, vertebral grooves contain the deep dorsal muscles. At cervical and lumbar levels, these grooves are shallow and mainly formed by laminae. In the thoracic region, they are deeper, broader and formed by the laminae and transverse processes. The laminae are broad for the first thoracic vertebra and narrow for the second to seventh, then broaden again from the eighth to eleventh, but become narrow thereafter down to the third lumbar vertebra.

The spinous process (vertebral spine) projects dorsally and often caudally from the junction of the laminae. Spines vary considerably in size, shape and direction. They lie approximately in the median plane and project posteriorly, although in some individuals a minor deflection of the processes to one side may be seen. The spines act as levers for muscles that control posture and active movements (flexion/extension, lateral flexion and rotation) of the vertebral column.

The paired superior and inferior articular processes (zygapophyses) arise from the vertebral arch at the pediculolaminar junctions. The superior processes project cranially, bearing dorsal facets that may also have a lateral or medial inclination, depending on level. Inferior processes run caudally with articular facets directed ventrally, again with a medial or lateral inclination that depends on vertebral level. Articular processes of adjoining vertebrae thus contribute to the synovial zygapophysial or facet joints, and form part of the posterior boundaries of the intervertebral foramina. These joints permit limited movement between vertebrae; mobility varies considerably with vertebral level.

Transverse processes project laterally from the pediculolaminar junctions as levers for muscles and ligaments, particularly those concerned in rotation and lateral flexion. In the cervical region, the transverse processes are anterior to the articular processes, lateral to the pedicles and between the intervertebral foramina. In the thoracic region, they are posterior to the pedicles, considerably behind those of the cervical and lumbar processes. In the lumbar region, the transverse processes are anterior to the articular processes, but posterior to the intervertebral foramina. There is considerable regional variation in the structure and length of the transverse processes. In the cervical region, the transverse process of the atlas is long and broad, which allows the rotator muscles maximum mechanical advantage. Breadth varies little from the second to the sixth cervical vertebra, but increases in the seventh. In thoracic vertebrae, the first is widest, and breadth decreases to the twelfth, where the transverse elements are usually vestigial. The transverse processes become broader in the upper three lumbar vertebrae, and diminish in the fourth and fifth. The transverse process of the fifth lumbar vertebra is the most robust. It arises directly from the body and pedicle to allow for force transmission to the pelvis through the iliolumbar ligament.

The thoracic transverse processes articulate with ribs, but at other levels the mature transverse process is a composite of a 'true' transverse process and an incorporated costal element. Costal elements develop as basic parts of neural arches in mammalian embryos, but become independent only as thoracic ribs. Elsewhere, they remain less developed and fuse with the 'transverse process' of descriptive anatomy (see Fig. 18.11C).

Vertebrae are internally trabecular and have an external shell of compact bone perforated by vascular foramina (see Fig. 46.23). The shell is thin on the superior and inferior body surfaces but thicker in the arch and its processes. The trabecular interior contains red bone marrow and one or two large ventrodorsal canals that contain the basivertebral veins. Pubertal adolescents have higher trabecular bone density than prepubertal children.

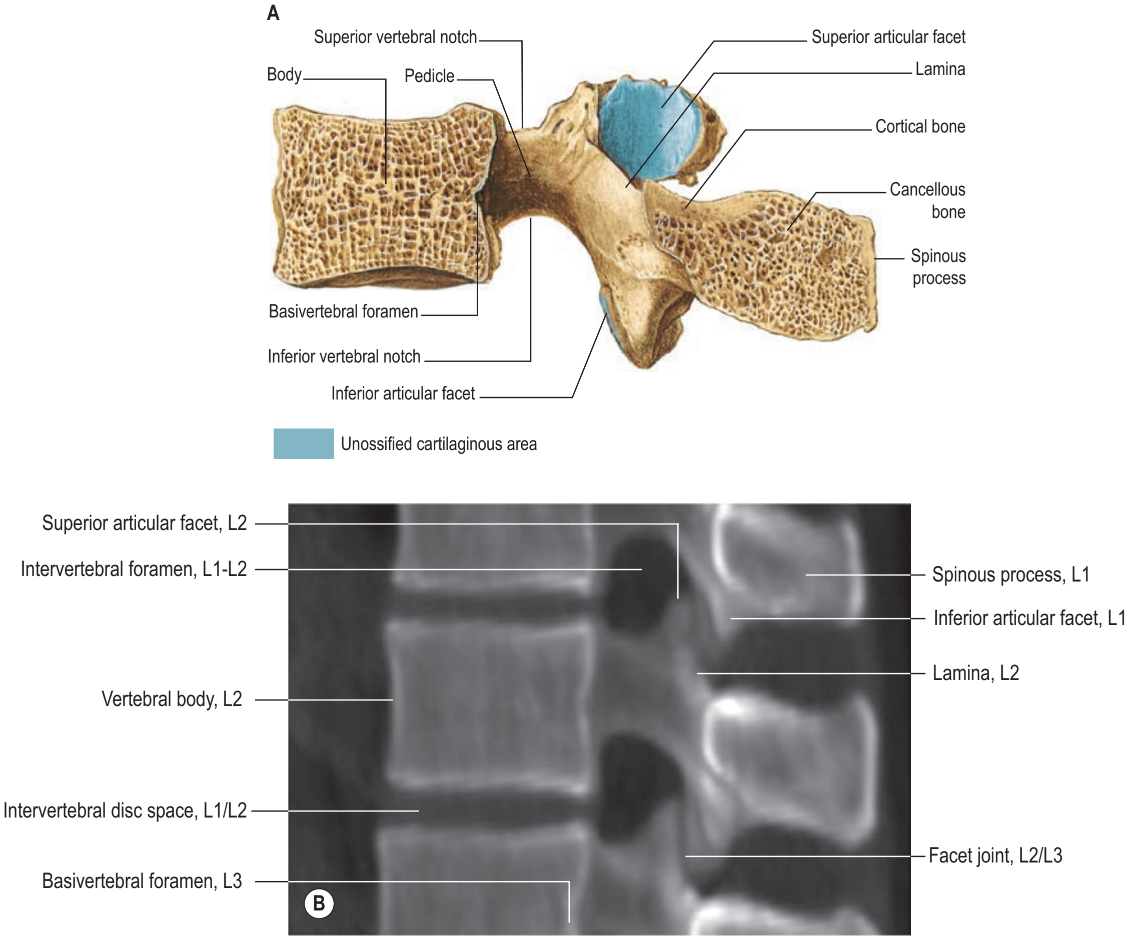
A
Superior vertebral notch
Body
Pedicle
Superior articular facet
Lamina
Cortical bone
Cancellous bone
Spinous process
Basivertebral foramen
Inferior vertebral notch
Inferior articular facet
Unossified cartilaginous area
Superior articular facet, L2
Intervertebral foramen, L1-L2
Vertebral body, L2
Intervertebral disc space, L1/L2
Basivertebral foramen, L3
B
Spinous process, L1
Inferior articular facet, L1
Lamina, L2
Facet joint, L2/L3

Fig. 46.23 **A**, A median sagittal section through a lumbar vertebra. **B**, A volume rendered sagittal CT slab through the right half of the body of the second lumbar vertebra, viewed from the left; compression trabeculae of the cancellous bone can be seen running vertically in the central aspect of the body. (A, Sobotta Atlas of Human Anatomy © Elsevier GmbH, Urban & Fischer, Munich.)

Sexual dimorphism in vertebrae has received little attention, but Taylor and Twomey (1984) have described radiological differences in adolescent humans and have reported that female vertebral bodies have a lower ratio of width to depth. Vertebral body diameter has also been used as a basis for sex prediction in the analysis of skeletal material (MacLaughlin and Oldale 1992).

Vertebral canal

The vertebral canal (**Fig. 46.24**) extends from the foramen magnum to the sacral hiatus, and follows the vertebral curves. In the cervical and lumbar regions, which exhibit free mobility, it is large and triangular, but in the thoracic region, where movement is less, it is small and circular. These differences are matched by variations in the diameter of the spinal cord and its enlargements. In the lumbar region, the vertebral canal decreases gradually in size between L1 and L5, with a greater relative width in the female.

For clinical purposes, it is useful to consider the vertebral canal as having three zones. These are a central zone, between the medial margins of the facet joints, and two lateral zones, beneath the facet joints and entering the intervertebral foramina. Each lateral zone, which passes into and just beyond the intervertebral foramen, can be further subdivided into subarticular (lateral recess), foraminal and extraforaminal regions (MacNab and McCulloch 1990). The lateral zone thus described forms the canal of the spinal nerve (the radicular or 'root' canal). The central zone of the canal is a little narrower than the radiological interpedicular distance if the lateral recess is considered to be part of the radicular canal rather than part of the central zone.

Spinal stenosis

Narrowing (stenosis) of the vertebral canal may occur at single or multiple spinal levels, and mainly affects the lumbar and cervical regions. Stenosis may affect the central canal and the 'root canals', either together or separately. There is a developmental form of the condition that mainly affects the central canal but more commonly the stenosis is degenerative, and results from intervertebral disc narrowing and osteoarthritic changes in the facet joints. This latter combination is more likely to narrow the intervertebral foramen and the 'root canal', even though the sectional profile of the vertebral canal in affected lumbar vertebrae typically changes from the shape of a bell to that of a trefoil. The lumbosacral intervertebral foramen, which is normally the smallest in the region, is particularly liable to such stenosis. Severe spinal stenosis may compress the spinal cord and compromise its arterial supply. More localized 'root canal' stenosis will present with the clinical features of spinal nerve compression, but without the tension signs that characterize the stretching of nerve roots over a prolapsed disc. Ischaemia of the nerves and roots may provoke more damage than the actual physical compression of the neural tissue.

Intervertebral foramina

Intervertebral foramina are the principal routes of entry to and exit from the vertebral canal, and are closely related to the main intervertebral articulations. (Minor routes occur between the median, often partly fused, margins of the ligamenta flava.) The same general arrangement applies throughout the vertebral column, between the axis and sacrum, although there are some quantitative and structural regional variations. Because of their construction, contents and susceptibilities to multiple disorders, the intervertebral foramina are loci of great biomechanical, functional and clinical significance. The specializations cranial to the axis and at sacral levels are described with the individual bones and articulations.

The boundaries of a generalized intervertebral foramen (**Fig. 46.25**) are, anteriorly, from above downwards, the posterolateral aspect of the superior vertebral body, the posterolateral aspect of the intervertebral symphysis (including the disc), and a small (variable) posterolateral part of the body of the inferior vertebra; superiorly, the compact bone of the deep arched inferior vertebral notch of the vertebra above; inferiorly, the compact bone of the shallow superior vertebral notch of the vertebra below; and posteriorly, a part of the ventral aspect of the fibrous capsule of the facet synovial joint. Cervical intervertebral foramina are distinct in having superior and inferior vertebral notches of almost equal depth, which, in accord with the direction of the pedicles, face anterolaterally. External to them, and oriented in the same direction, is a transverse process. The thoracic and lumbar intervertebral foramina face laterally and their transverse processes are posterior. In addition, the anteroinferior boundaries of the first to tenth thoracic foramina are formed by the articulations of the head of a rib and the capsules of double synovial joints (with the demifacets on adjacent vertebrae and the intra-articular ligament between the costocapitular ridge and the intervertebral symphysis). Lumbar foramina lie between the two principal lines of vertebral attachment of psoas major. The walls of each foramen are covered throughout by fibrous tissue, which is in turn periosteal (though the presence of a true periosteum lining the vertebral canal is controversial: Newell (1999)), perichondrial, anular and capsular. The more lateral parts of the foramina may be crossed at a variable level by narrow fibrous bands, the transforaminal ligaments (for detail of these ligaments, see Bogduk (2012)). The true foramen is the foraminal region of the canal of the spinal nerve (the radicular or 'root' canal). A foramen contains a segmental mixed spinal nerve and its sheaths, from two to four recurrent meningeal (sinuvertebral) nerves, variable numbers of spinal arteries, and plexiform venous connections between the internal and external vertebral venous plexuses. These structures, particularly the nerves, may be affected by trauma or one of the many disorders that may affect tissues bordering the foramen. In particular, nerve compression and irritation may be caused by intervertebral disc prolapse, or by bony entrapment as the size of the foramen decreases (**Fig. 46.26**). This decrease may result from facet joint osteoarthritis, osteophyte formation, disc degeneration and degenerative spondylolisthesis, all of which may lead to lateral or foraminal spinal stenosis.

Cervical vertebrae

The cervical vertebrae (**Figs 46.27–46.28**) are the smallest of the moveable vertebrae, and are characterized by a foramen in each transverse process. The first, second and seventh have special features and will be considered separately. The third, fourth and fifth cervical are almost identical, and the sixth, while typical in its general features, has minor distinguishing features.

Typical cervical vertebra

A typical cervical vertebra (**Figs 46.29–46.30**) has a small, relatively broad vertebral body. The pedicles project posterolaterally and the longer laminae posteromedially, enclosing a large, roughly triangular vertebral foramen; the vertebral canal here accommodates the cervical enlargement of the spinal cord. The pedicles attach midway between the discal surfaces of the vertebral body, so the superior and inferior vertebral notches are of similar depth. The laminae are thin and slightly curved, with a thin superior and slightly thicker inferior border. The spinous process ('spine') is short and bifid, with two tubercles that are often unequal in size. The junction between lamina and pedicle bulges laterally between the superior and inferior articular processes to form an articular pillar ('lateral mass') on each side. The transverse process is morphologically composite around the foramen transversarium. Its dorsal and ventral bars terminate laterally as corresponding tubercles. The tubercles are connected, lateral to the foramen, by the costal (or intertubercular) lamella; these three elements represent morphologically the capitellum, tubercle and neck of a cervical costal element (see Fig. 18.11C). The attachment of the dorsal bar to the pediculolaminar junction represents the morphological transverse process, and the attachment of the ventral bar to the ventral body represents the capitellar process. In all but the seventh cervical vertebra, the foramen transversarium normally transmits the vertebral artery and vein and a branch from the cervicothoracic ganglion (vertebral nerve).

The vertebral body has a convex anterior surface. The discal margin gives attachment to the anterior longitudinal ligament. The posterior surface is flat or minimally concave, and its discal margins give attachment to the posterior longitudinal ligament. The central area displays several vascular foramina, of which two are commonly relatively larger. These are the basivertebral foramina, which transmit basivertebral veins to the anterior internal vertebral plexus. The superior discal surface is saddle-shaped, formed by flange-like lips, uncinate processes, which arise from most of the lateral circumference of the upper margin of the vertebral body. Uncinate processes are rudimentary at birth and are usually found on the third to seventh cervical vertebra in the adult. The uncinate processes on the vertebra below articulate with the corresponding bevelled surfaces on the inferior aspect of the vertebra above. Whether uncovertebral joints are synovial joints has proved controversial since their description by von Luschka in 1858; the demonstration of synoviocytes in the lateral joint capsule tissue of elderly uncovertebral joints suggests that they should be regarded as synovial joints (Hartman 2014) (see Fig.

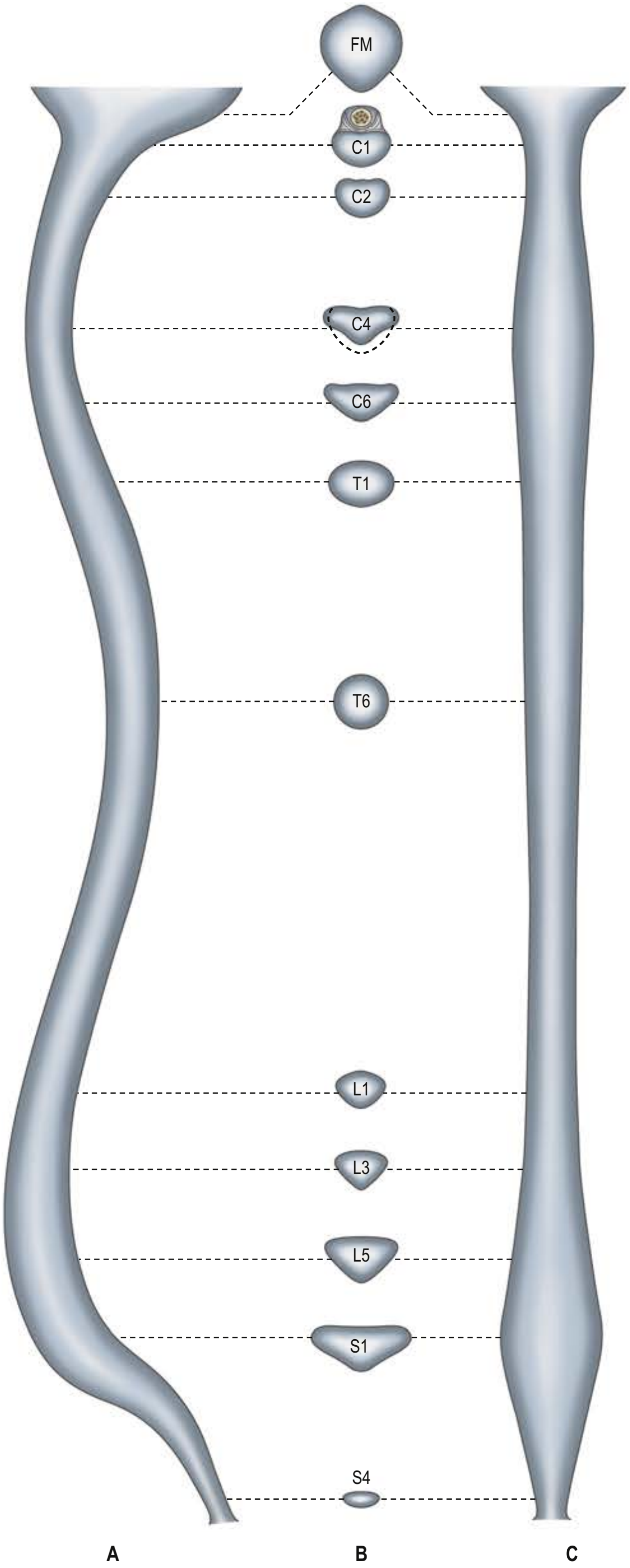

Fig. 46.24 The vertebral canal in section. **A**, Sagittal view. **B**, Transverse (axial) view. **C**, Coronal view. Abbreviation: FM, foramen magnum.

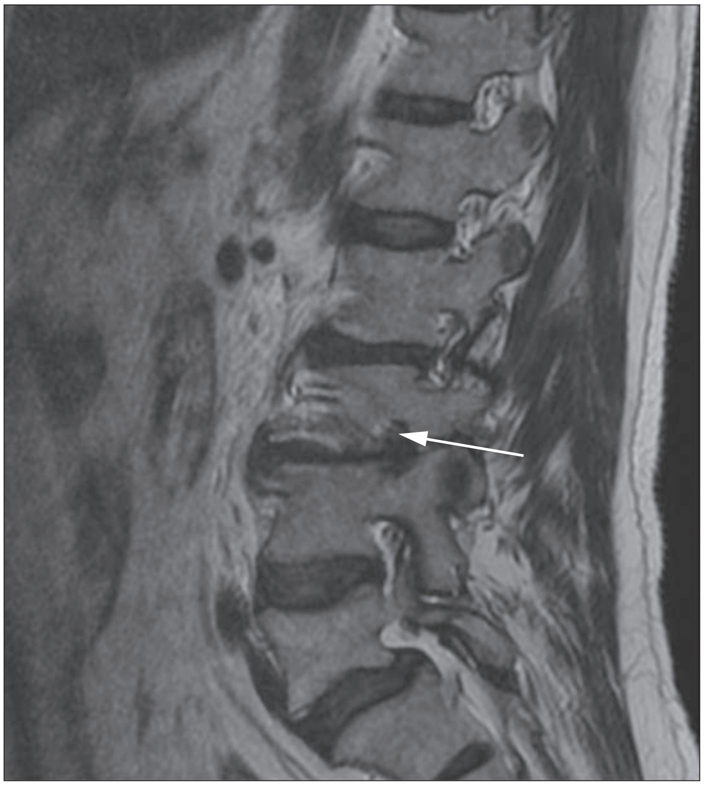

Fig. 46.26 A sagittal T1-weighted MRI showing a markedly reduced L3–L4 foraminal volume secondary to advanced disc degeneration resulting in bony neural entrapment of the L3 spinal nerve (arrow).

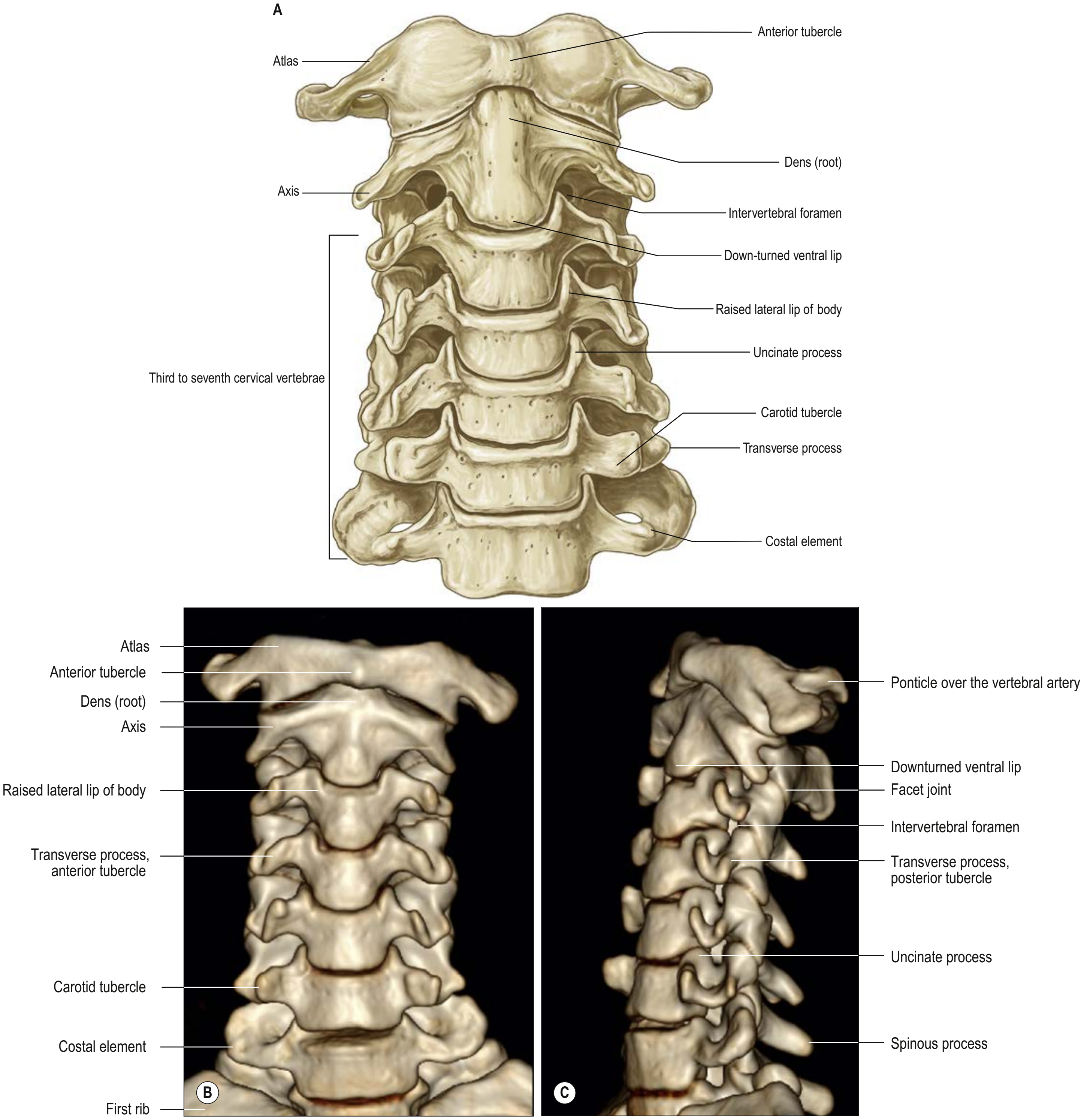
A
Atlas
Anterior tubercle
Dens (root)
Axis
Intervertebral foramen
Down-turned ventral lip
Raised lateral lip of body
Third to seventh cervical vertebrae
Uncinate process
Carotid tubercle
Transverse process
Costal element
Atlas
Anterior tubercle
Dens (root)
Axis
Raised lateral lip of body
Transverse process, anterior tubercle
Carotid tubercle
Costal element
First rib
B
Ponticle over the vertebral artery
Downturned ventral lip
Facet joint
Intervertebral foramen
Transverse process, posterior tubercle
Uncinate process
Spinous process
C

Fig. 46.27 **A**, Cervical vertebrae (anterior aspect). **B**–**C**, Volume rendered CT of the cervical spine: **B**, anterior view; **C**, oblique view.

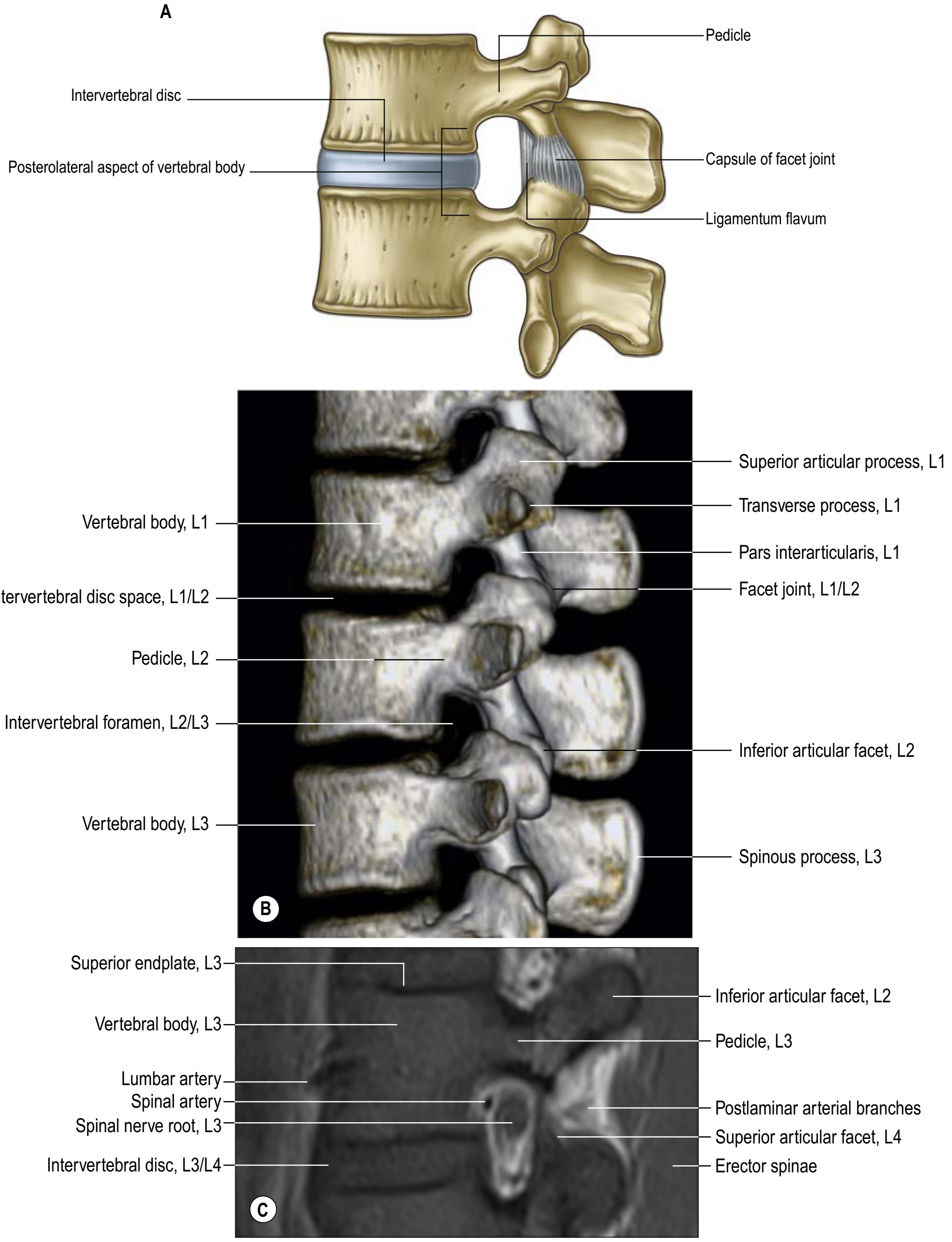
A
Intervertebral disc
Posterolateral aspect of vertebral body
Pedicle
Capsule of facet joint
Ligamentum flavum
Superior articular process, L1
Transverse process, L1
Vertebral body, L1
Pars interarticularis, L1
Intervertebral disc space, L1/L2
Facet joint, L1/L2
Pedicle, L2
Intervertebral foramen, L2/L3
Inferior articular facet, L2
Vertebral body, L3
Spinous process, L3
B
Superior endplate, L3
Inferior articular facet, L2
Vertebral body, L3
Pedicle, L3
Lumbar artery
Spinal artery
Postlaminar arterial branches
Spinal nerve root, L3
Superior articular facet, L4
Intervertebral disc, L3/L4
Erector spinae
C

Fig. 46.25 **A**, The boundaries of an intervertebral foramen. **B**, A volume rendered CT of the upper lumbar spine viewed from the left, showing the intervertebral foraminal boundaries. **C**, A sagittal T1-weighted MRI at L3 showing the L3-L4 intervertebral foramen. In this sequence, adipose tissue is bright and seen surrounding the neurovascular structures passing through the foramen.

46.59). The inferior discal surface is also concave; the concavity is produced mainly by a broad projection from the anterior margin, which partly overlaps the anterior surface of the intervertebral disc. The discal surfaces of cervical vertebrae are so shaped in order to restrict both lateral and anteroposterior gliding movements during articulation. The paired ligamenta flava extend from the superior border of each lamina below to the roughened inferior half of the anterior surfaces of the lamina above. The superior part of the anterior surface of each lamina is smooth, like the immediately adjacent surfaces of the pedicles, which are usually in direct contact with the dura mater and cervical root sheaths to which they may become loosely attached. The spinous process of the sixth cervical vertebra is larger and is often not bifid.

The superior articular facets, flat and ovoid, are directed superoposteriorly, whereas the corresponding inferior facets are directed mainly anteriorly, and lie nearer the coronal plane than the superior facets. In children, facet joint angle decreases until 10 years of age and remains unchanged thereafter (Kasai et al 1996). The dorsal rami of the cervical spinal nerves curve posteriorly, close to the anterolateral aspects of the lateral masses, and may actually lie in shallow grooves, especially on the third and fourth pairs. The dorsal root ganglion of each cervical spinal nerve lies between the superior and inferior vertebral notches of adjacent vertebrae. The large anterior ramus passes posterior to the vertebral artery, which lies on the concave upper surface of the costal lamella; the concavity of the lamellae increases from the fourth to the sixth vertebra. The fourth to sixth anterior tubercles are elongated and rough for muscle attachment. The sixth, the carotid tubercle (Chassaignac's tubercle), is the longest (**Fig. 46.31**). The carotid artery can be forcibly compressed in the groove formed by the vertebral bodies and the larger anterior tubercles, especially the sixth. The posterior tubercles are rounded and more laterally placed than the anterior, and all but the sixth are also more caudal; the sixth is at about the same level as the anterior.

Muscle attachments The ligamentum nuchae and numerous deep extensors, including semispinalis thoracis and cervicis, multifidus, spinales and interspinales, are all attached to the spinous processes. Tendinous slips of scalenus anterior, longus capitis and longus colli are attached to the fourth to sixth anterior tubercles. Splenius, longissimus and iliocostalis cervicis, levator scapulae and scalenus posterior and

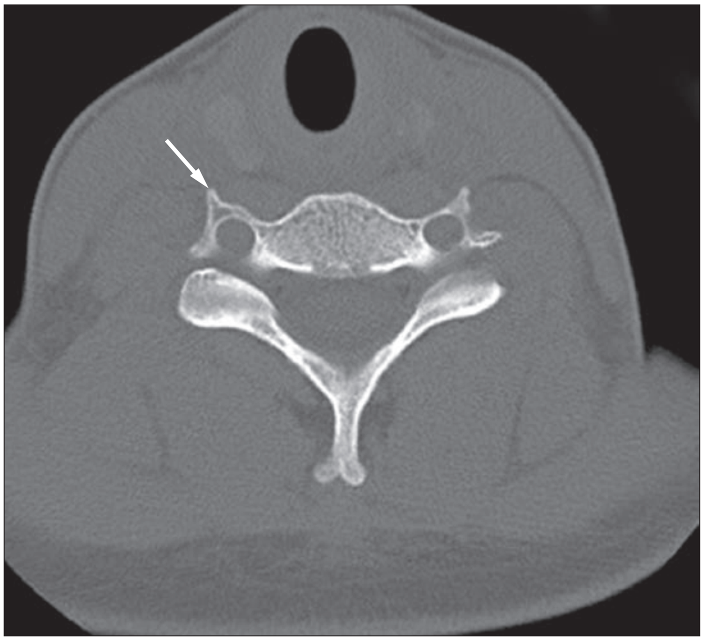

Fig. 46.31 An axial CT scan showing the carotid tubercle (Chassaignac's tubercle) (arrow). This bony landmark is useful for identification of the C6 vertebra by palpation. Note the bifid spinous process of C6.

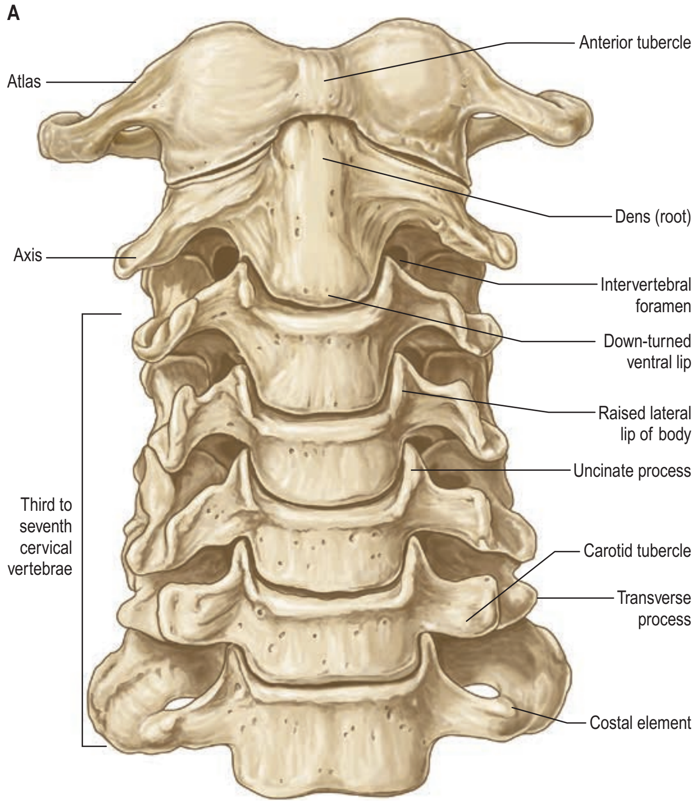
A
Atlas
Anterior tubercle
Dens (root)
Axis
Intervertebral foramen
Down-turned ventral lip
Raised lateral lip of body
Uncinate process
Third to seventh cervical vertebrae
Carotid tubercle
Transverse process
Costal element

Fig. 46.27 **A**, Cervical vertebrae (anterior aspect). (B–C, *continued online*)

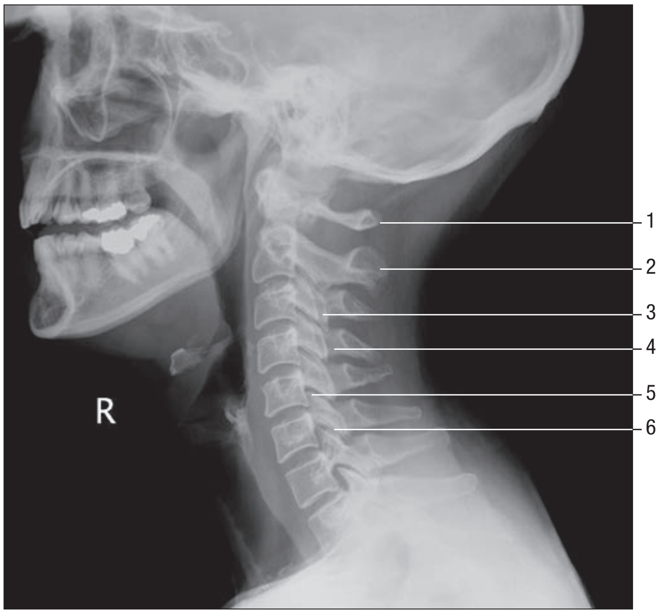

Fig. 46.28 A lateral radiograph of the cervical spine. Key: 1, C1 posterior tubercle; 2, C2 spinous process; 3, C3 inferior articular process; 4, C4 lamina; 5, C6 superior articular facet; 6, C6/7 facet (zygapophysial) joint.

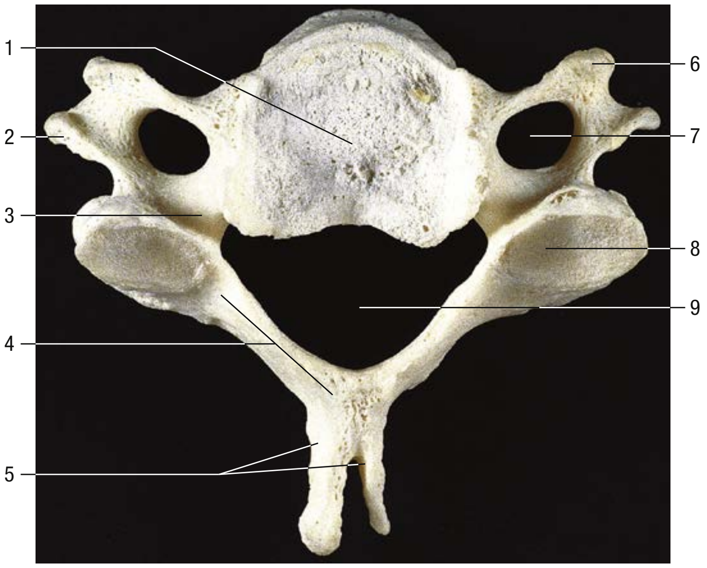

Fig. 46.29 Fourth cervical vertebra, superior aspect. Key: 1, body; 2, posterior tubercle of transverse process; 3, pedicle; 4, lamina; 5, bifid spinous process; 6, anterior tubercle of transverse process; 7, foramen transversarium; 8, superior articular facet; 9, vertebral foramen.

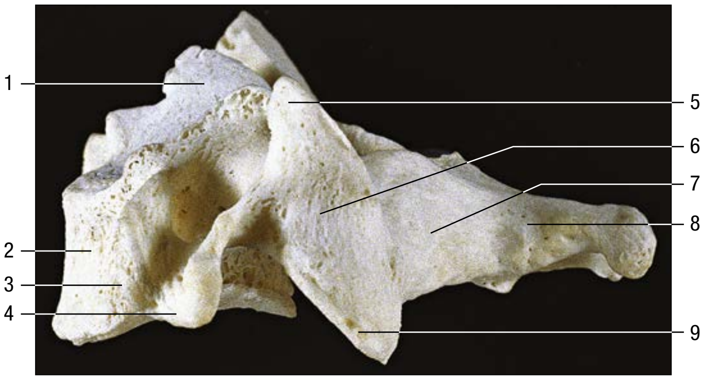

Fig. 46.30 Fourth cervical vertebra, lateral aspect. Key: 1, uncinate process; 2, body; 3, anterior tubercle of transverse process; 4, posterior tubercle of transverse process; 5, superior articular process; 6, lateral mass; 7, lamina; 8, spinous process; 9, inferior articular process.

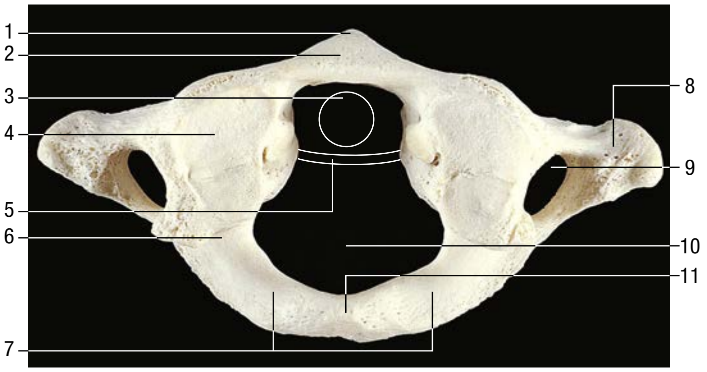
1
2
3
4
5
6
7
8
9
10
11

Fig. 46.32 The first cervical vertebra (atlas), superior aspect. Key: 1, anterior tubercle; 2, anterior arch; 3, outline of dens; 4, superior articular facet, on lateral mass (bipartite facet in this specimen); 5, outline of transverse ligament; 6, groove for vertebral artery and C1 (beneath bony overhang from lateral mass here); 7, posterior arch; 8, transverse process; 9, foramen transversarium; 10, vertebral foramen; 11, posterior tubercle.

medius are all attached to the posterior tubercles. Shallow anterolateral depressions on the anterior surface of the body lodge the vertical parts of longus colli.

Ossification Cervical vertebrae ossify according to the standard vertebral pattern described in Chapter 18. Incomplete segmentation ('block vertebra') is common in the cervical spine and most commonly involves the axis and third cervical vertebra. There is a general caudal to cranial gradient in the growth of ossification centres and closure of synchondroses in the atlas and axis (Karwacki and Schneider 2012).

Atlas, C1

The atlas, the first cervical vertebra (Fig. 46.32), supports the head. It is unique in that it fails to incorporate a centrum, whose expected position is occupied by the dens, a cranial protuberance from the axis. The atlas consists of two lateral masses connected by a short anterior and a longer posterior arch. The transverse ligament retains the dens against the anterior arch.

The transverse ligament divides the vertebral canal into two compartments (Fig. 46.33). The anterior third (approximately) of the canal is occupied by the dens. The posterior compartment is occupied by the

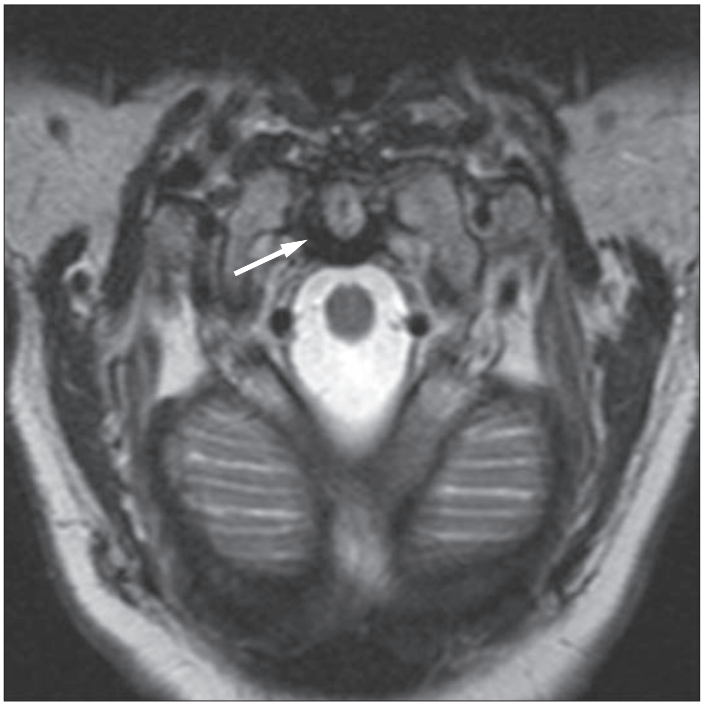

Fig. 46.33 An axial MR image showing an intact transverse ligament (arrow).

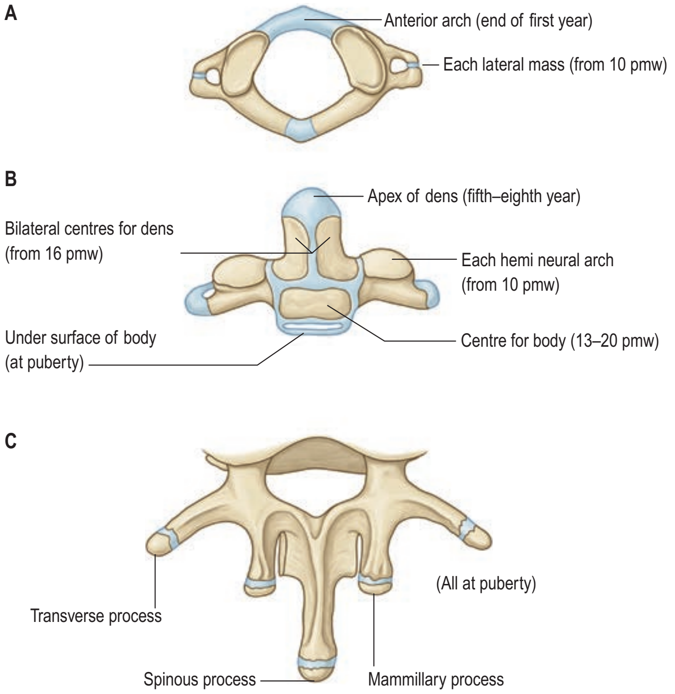
A
Anterior arch (end of first year)
Each lateral mass (from 10 pmw)
B
Apex of dens (fifth–eighth year)
Bilateral centres for dens (from 16 pmw)
Each hemi neural arch (from 10 pmw)
Under surface of body (at puberty)
Centre for body (13–20 pmw)
C
(All at puberty)
Transverse process
Spinous process
Mammillary process

Fig. 46.34 Ossification in the vertebral column. **A**, Atlas. **B**, Axis. **C**, Lumbar vertebra. Abbreviation: pmw, postmenstrual week.

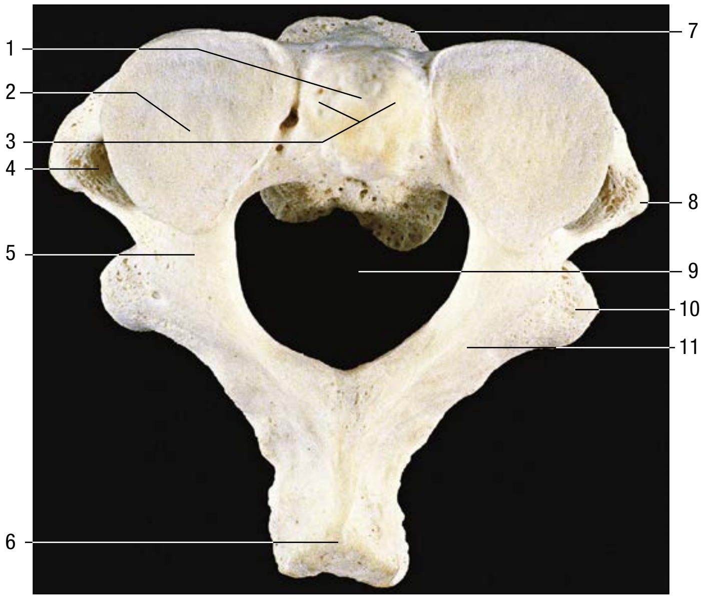

Fig. 46.36 The second cervical vertebra (axis), superior aspect. Key: 1, dens – attachment of apical ligament; 2, superior articular facet on lateral mass; 3, dens – attachments of alar ligaments; 4, foramen transversarium; 5, pedicle; 6, spinous process; 7, body; 8, transverse process; 9, vertebral foramen; 10, inferior articular process; 11, lamina.

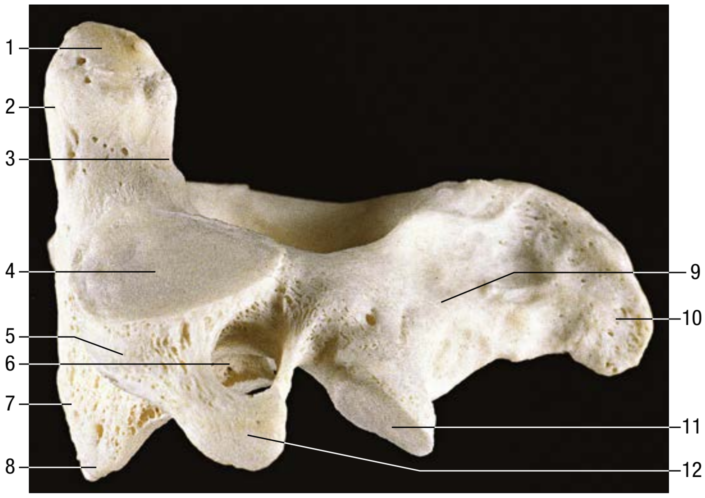

Fig. 46.37 The second cervical vertebra (axis), lateral aspect. Key: 1, dens – attachment of alar ligament; 2, facet for anterior arch of atlas; 3, groove for transverse ligament of atlas; 4, superior articular facet; 5, lateral mass; 6, divergent foramen transversarium; 7, body; 8, ventral lip of body; 9, lamina; 10, spinous process; 11, inferior articular facet; 12, transverse process.

spinal cord and its coverings, and the cord itself takes up about half of this space (i.e. the cord, like the dens, occupies one-third of the canal).

The anterior arch is slightly convex anteriorly, and carries a roughened anterior tubercle to which is attached the anterior longitudinal ligament (which is cylindrical at this level). Its upper and lower borders provide attachment for the anterior atlanto-occipital membrane and diverging lateral parts of the anterior longitudinal ligament. The posterior surface of the anterior arch carries a concave, almost circular, facet for the dens.

The lateral masses are ovoid, their long axes converging anteriorly. Each bears a kidney-shaped superior articular facet for the respective occipital condyle, which is sometimes completely divided into a larger anterior and a smaller posterior part (Lang 1986). The inferior articular facet of the lateral mass is almost circular and is flat or slightly concave. It is orientated more obliquely to the transverse plane than the superior facet, and faces more medially and very slightly backwards. On the medial surface of each lateral mass is a roughened area that bears vascular foramina and a tubercle for attachment of the transverse ligament. In adults, the distance between these tubercles is shorter than the transverse ligament itself, with a mean value of approximately 16 mm.

The posterior arch forms three-fifths of the circumference of the atlantal ring. The superior surface bears a wide groove for the vertebral artery and venous plexus immediately behind, and is variably overhung by the lateral mass; the first cervical nerve intervenes. The flange-like superior border gives attachment to the posterior atlanto-occipital membrane, and the flatter inferior border to the highest pair of ligamenta flava. The posterior tubercle is a rudimentary spinous process, roughened for attachment of the ligamentum nuchae.

The transverse processes are longer than those of all cervical vertebrae except the seventh (see Fig. 46.27). They act as strong levers for the muscles that make fine adjustments to keep the head balanced. Maximum atlantal width varies from 74 to 95 mm in males and 65 to 76 mm in females, and this affords a useful criterion for assessing sex in human remains. The apex of the transverse process, which is usually broad, flat and palpable between the mastoid process and ramus of the mandible, is homologous with the posterior tubercle of typical cervical vertebrae; the remaining part of the transverse process consists of the costal lamella. A small anterior tubercle is sometimes visible on the anterior aspect of the lateral mass. The costal lamella is sometimes deficient, which leaves the foramen transversarium open anteriorly.

Muscle attachments The superior oblique parts of longus colli are attached on each side of the anterior tubercle. The anterior surface of the lateral mass gives attachment to rectus capitis anterior. Rectus capitis posterior minor is attached just lateral to the posterior tubercle. Rectus capitis lateralis is attached to the transverse process superiorly, and obliquus capitis superior is located more posteriorly. Obliquus capitis inferior is attached laterally on the apex, below which are slips of levator scapulae, splenius cervicis and scalenus medius.

Ossification The atlas is commonly ossified from three centres arising from postmenstrual week 10 (Fig. 46.34). One appears in each lateral mass from postmenstrual week 10 onwards, gradually extending into the posterior arch where they unite between the third and fourth years, usually directly but occasionally through a separate centre. At birth, the anterior arch is fibrocartilaginous, and a separate centre appears about the end of the first year. This unites with the lateral masses between the sixth and eighth years, the lines of union extending across anterior parts of the superior articular facets. Occasionally, the anterior arch is formed by the extension and ultimate union of centres in the lateral masses and sometimes from two lateral centres in the arch itself.

The central part of the posterior arch may be absent and replaced by fibrous tissue. Frequently, bony spurs arise from the anterior and posterior margins of the groove for the vertebral artery. These are sometimes referred to as ponticles; they occasionally convert the

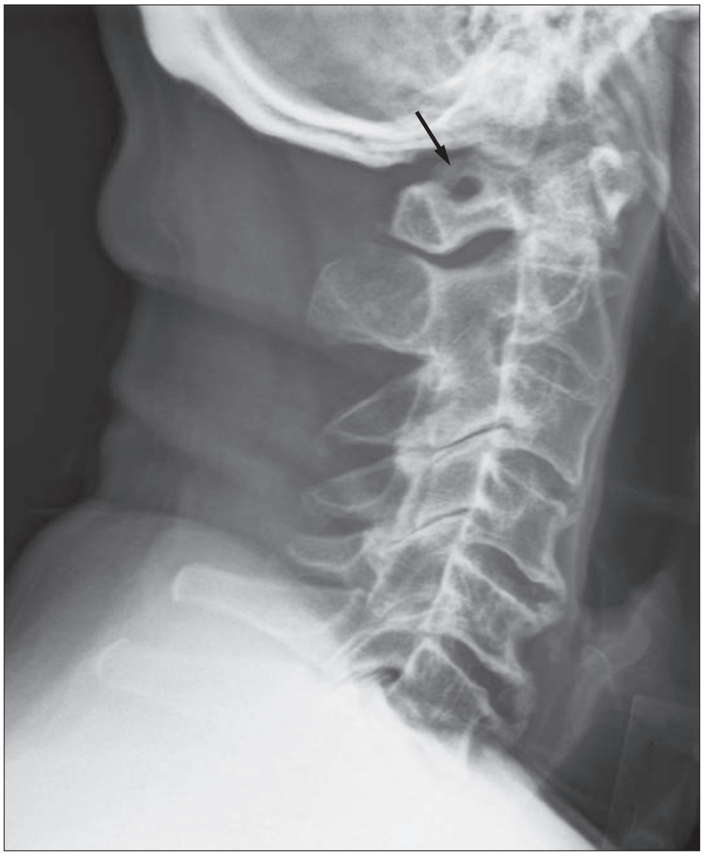

Fig. 46.35 A lateral cervical radiograph demonstrating a posterior ponticle forming the roof of a tunnel over the vertebral artery (arrow).

groove into a foramen, the arcuate foramen or posticus ponticus (Fig. 46.35), which may increase the risk of injury to the vertebral artery in surgical procedures involving the C1 arch (Klimo et al 2007). More often, the foramen is incomplete superiorly. Rarely, the atlas may be wholly or partially assimilated into (fused with) the occiput.

Axis, C2

The axis, the second cervical vertebra (Figs 46.36–46.37), acts as an axle for rotation of the atlas and head around the strong dens (odontoid process), which projects cranially from the superior surface of the body.

The dens is conical in shape with a mean length of 15 mm in adults. It may be tilted a little, up to 14°, posteriorly or, less often, anteriorly on the body of the axis; it may also tilt laterally up to 10°. The posterior surface bears a broad groove for the transverse ligament, which is covered in cartilage. The apex is pointed, and from this point arises the apical ligament. The alar ligaments are attached to the somewhat flattened posterolateral surfaces above the groove for the transverse ligament. The anterior surface bears an ovoid articular facet for the anterior arch of the atlas, and the surface is pitted by many vascular foramina, which are most numerous near the apex.

The body consists of less compact bone than the dens. It is composite, and consists of the partly fused centra of the atlas and axis, and a rudimentary disc (synchondrosis) between them, which usually remains detectable deep within the body of the axis throughout life. Large ovoid articular facets are present on either side of the dens at the junction of the body and vertebral arch; they are flat or slightly convex for articulation with the masses of the atlas. The facets lie in a plane anterior to the plane of the uncovertebral (Luschka) articulations, with which they are, in part, homologous. The somewhat triangular, downward-projecting anterior border gives attachment to the anterior longitudinal ligament. Posteriorly, the lower border receives the posterior longitudinal ligament and the membrana tectoria.

The pedicles are stout, and the superior surface carries part of the superior articular facet, which also projects laterally and downwards on to the transverse process. The anterolateral surface is deeply grooved by the vertebral artery, running beneath the thin lateral part of the inferior surface of the superior articular facet, which can become quite thin. The inferior surface of each pedicle bears a deep, smooth inferior intervertebral notch, in which the large root sheath of the third cervical nerve lies. The interarticular part of the pedicle is short and lies between the relatively small inferior posterior articular process (which is located at the pediculolaminar junction and bears a small anteriorly facing facet) and the superior articular surface.

The transverse process is pointed, projects inferiorly and laterally, and arises from the pediculolaminar junction and the lateral aspect of the interarticular area of the pedicle. The rounded tip is homologous with the posterior tubercle of a typical cervical vertebrae. The foramen transversarium is directed laterally as the vertebral artery turns abruptly laterally under the superior articular facet. Small anterior tubercles may be present near the junction of the costal lamella with the body.

The laminae are thick and give attachment to the ligamenta flava.

The spinous process is large, with a bifid tip and a broad base, which is concave inferiorly. The ligamentum nuchae is attached to the apical notch.

Muscle attachments The anterior surface of the body carries a deep depression on each side for the attachment of the vertical part of longus colli. Levator scapulae, scalenus medius and splenius cervicis are all attached to the tips of the transverse processes, and the intertransverse muscles are attached to their upper and lower surfaces. The lateral surfaces of the spinous process give origin to obliquus capitis inferior, and rectus posterior major is attached a little more posteriorly. The inferior concavity of the process receives semispinalis and spinalis cervicis, multifidus more deeply, and the interspinales near the apex.

Arterial supply Small branches arise mainly from the vertebral artery at the level of the intervertebral foramen for the third cervical nerve and form paired anterior and posterior longitudinal channels, branches of which enter the dens near the base and near the apex. The anterior channel also receives numerous twigs from nearby branches of the external carotid artery via branches to longus colli and the ligaments of the apex; hence avascular necrosis does not occur after fracture of the base of the dens.

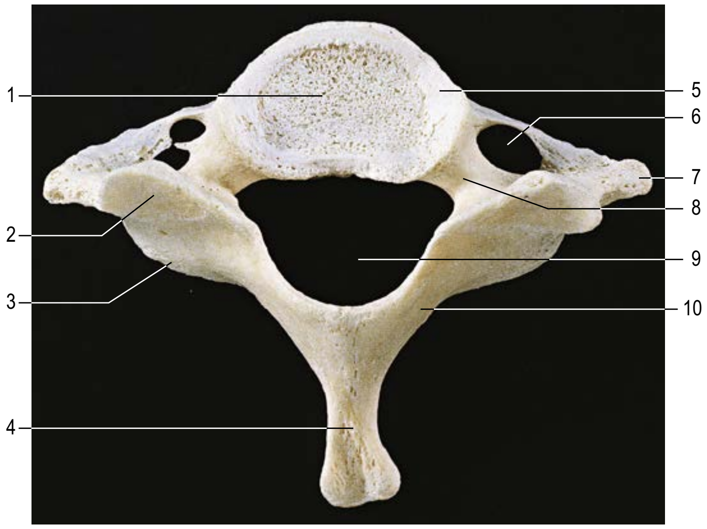

Fig. 46.40 The seventh cervical vertebra, superior aspect. Key: 1, body; 2, superior articular facet; 3, inferior articular process; 4, spinous process; 5, uncinate process; 6, foramen transversarium (foramina are asymmetric in this specimen); 7, transverse process; 8, pedicle; 9, vertebral foramen; 10, lamina.

Ossification The axis is ossified from five primary and two secondary centres (see Fig. 46.34). The vertebral arch has two primary centres and the centrum one, as in a typical vertebra. The former appear from about postmenstrual week 10, and that for the centrum during postmenstrual weeks 13–20. The dens is largely ossified from bilateral centres, identified from postmenstrual week 16 and joining before birth to form a conical mass, deeply cleft above by cartilage. This cuneiform cartilage forms the apex of the odontoid process. A centre appears in it which shows considerable individual variation in both time of appearance and time of fusion to the rest of the dens; it most often appears between 5 and 8 years, but sometimes even later, fusing with the main mass in about the twelfth year. The cartilage was thought to be part of the cranial sclerotomal half of the first cervical segment or pro-atlas. It has also been suggested that the apical centre for the dens is itself derived from the pro-atlas, which may also contribute to lateral atlantal masses. The dens is separated from the body by a cartilaginous disc, the circumference of which ossifies while its centre remains cartilaginous until old age; possible rudiments of adjacent epiphyses of atlas and axis may occur in the disc. A thin epiphysial plate is formed inferior to the body around puberty.

Ossification may sometimes be incomplete. Thus the apical cuneiform centre may fail to fuse with the dens, or the dens itself may fail to fuse with the body, instead forming an os odontoideum (Fig. 46.38). This is likely to result from minor trauma in early childhood causing disruption of the developing dens rather than being a congenital failure (Klimo et al 2007). Interposition of the transverse ligament may prevent union of fractures through the base of the dens (Fig. 46.39). Hypoplasia of the dens is usually accompanied by atlanto-occipital assimilation and basilar invagination. Abnormalities of the dens are common, and can result in atlanto-axial subluxation. In some skeletal dysplasias there is abnormal ossification in which the dens ossifies separately and much later than the atlantal centrum. This is probably a result of abnormal mobility in the cartilaginous anlage, and normal ossification may be restored if motion is prevented by surgical fusion.

Seventh cervical vertebra, vertebra prominens, C7

The seventh cervical vertebra, the vertebra prominens (Fig. 46.40), has a long spinous process that is visible at the lower end of the nuchal furrow. It ends in a prominent tubercle for the attachment of the ligamentum nuchae and the muscles detailed below. The thick and prominent transverse processes lie behind and lateral to the foramina transversaria. The latter transmit vertebral veins but not the vertebral artery, and each is often divided by a bony spicule. The costal lamella is relatively thin and may be partly deficient. It is grooved superiorly for the anterior ramus of the seventh cervical nerve and usually carries a small and inconspicuous anterior tubercle. The posterior tubercle is prominent. The suprapleural membrane is attached to the anterior border of the transverse process.

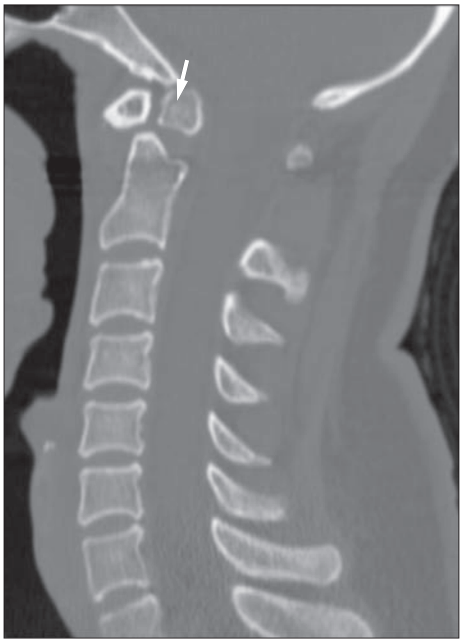

Fig. 46.38 A sagittal CT scan reconstructed image demonstrating an os odontoideum (arrow).

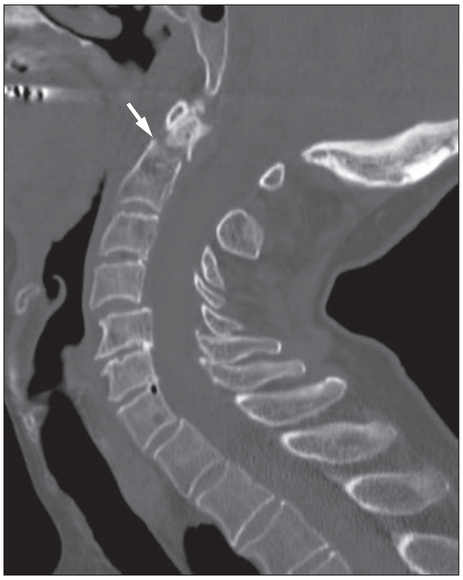

Fig. 46.39 A sagittal CT scan reconstructed image of a type II odontoid fracture (arrow). These fractures involve the base of the dens and have a high non-union rate.

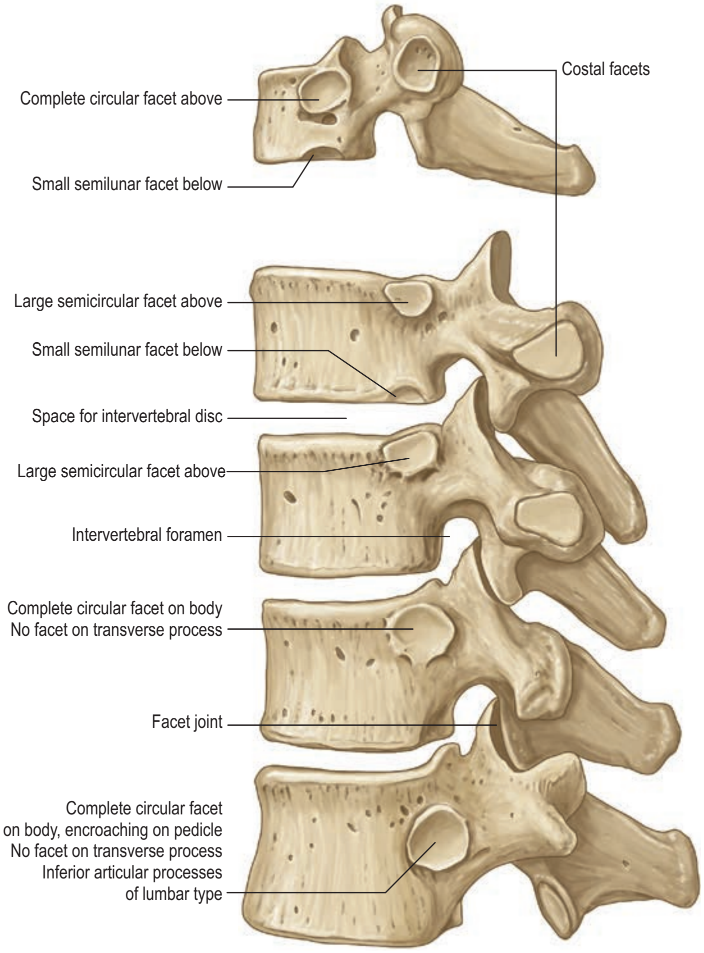
Costal facets
Complete circular facet above
Small semilunar facet below
Large semicircular facet above
Small semilunar facet below
Space for intervertebral disc
Large semicircular facet above
Intervertebral foramen
Complete circular facet on body
No facet on transverse process
Facet joint
Complete circular facet
on body, encroaching on pedicle
No facet on transverse process
Inferior articular processes
of lumbar type

Fig. 46.41 The first, ninth, tenth, eleventh and twelfth thoracic vertebrae, lateral aspect.

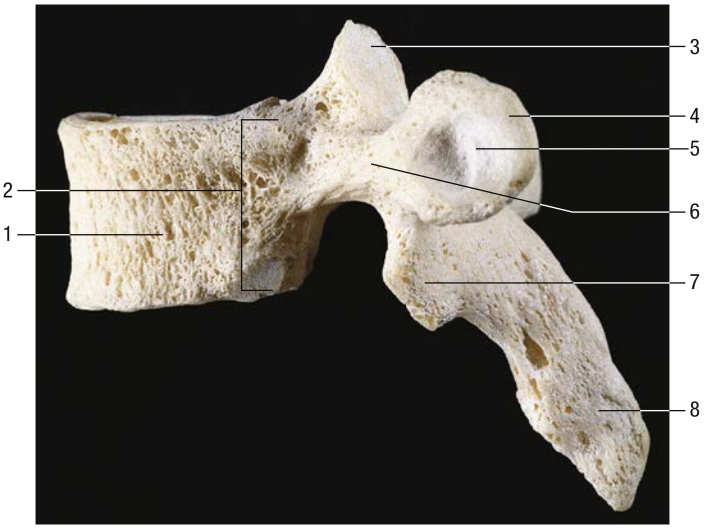

Fig. 46.42 The fourth thoracic vertebra, lateral aspect. Key: 1, body; 2, costocapitular demifacets; 3, superior articular facet; 4, transverse process; 5, costotubercular facet; 6, pedicle; 7, inferior articular process; 8, spinous process.

The costal lamella of the transverse process may be separate as a cervical rib. The foramina transversaria may be asymmetric; sometimes one is absent if the costal lamella is undeveloped.

Muscle attachments Trapezius, spinalis capitis, semispinalis thoracis, multifidus and interspinales all attach to the tubercle of the spinous process. The anterior border of the transverse process receives the attachment of scalenus minimus (pleuralis), when present. The first pair of levatores costarum is attached to the transverse processes.

Ossification Ossific centres for the costal processes appear between postmenstrual weeks 21 and 24 and join the body and transverse processes between the fifth and sixth years; they may remain separate and grow anterolaterally as cervical ribs. Separate ossific centres may, on occasion, also occur in the costal processes of the fourth to sixth cervical vertebrae.

Thoracic vertebrae

Thoracic vertebrae in general

All thoracic vertebral bodies display lateral costal facets and all but the lowest two or three transverse processes also have facets (**Fig. 46.41**). The facets articulate with the head of the rib (costocapitular facet) and its tubercle (costotubercular facet), respectively.

The body is typically a waisted cylinder (**Fig. 46.42**) except where the vertebral foramen encroaches, and transverse and anteroposterior dimensions are almost equal. On each side there are two costal facets (which are really demifacets): the superior and usually larger pair at the upper border are anterior to the pedicles, while the inferior pair at the lower border are anterior to the vertebral notches. The vertebral foramen (see Fig. 46.22) is small and circular, so the pedicles do not diverge as they do in cervical vertebrae; the thoracic spinal cord is smaller and more circular than the cervical cord. The laminae are short, thick and broad, and overlap from above downwards. The spinous process slants downwards. The thin and almost flat superior articular processes project from the pediculolaminar junctions and face posteriorly and a little superolaterally. The inferior processes project down from the laminae and their facets are directed forwards and a little superomedially. The large, club-like transverse processes also project from the pediculolaminar junctions. Each passes posterolaterally and bears, near its tip, anterior oval facets for articulation with the tubercle of the corresponding rib.

The bodies of upper thoracic vertebrae gradually change from cervical to thoracic in type, and the lower change from thoracic to lumbar. The body of the first is typically cervical, its transverse diameter being almost twice the anteroposterior; the second retains a cervical shape but its two diameters differ less. The third body is the smallest, and has a convex anterior aspect unlike the flattened first and second thoracic vertebrae. The remaining bodies increase in size and, because of its increased anteroposterior diameter, the fourth is typically 'heart-shaped'. The fifth to eighth increase their anteroposterior dimension but change little transversely. These four, in transverse section, are asymmetric, their left sides being flattened by pressure of the thoracic aorta. The rest increase more rapidly in all measurements, so that the body of the twelfth resembles that of a typical lumbar vertebra. These modifications may contribute to the greater range of flexion–extension seen at the cervical and lumbar ends of the thoracic vertebral column.

The anterior and posterior longitudinal ligaments are attached to the borders of the bodies. The capsular and radiate ligaments of the costovertebral joints are attached around the margins of the costal facets.

The dimensions and angles of thoracic pedicles change progressively from the upper thoracic spine distally: there is a successive caudal increase in thickness. These changing relationships have a significant bearing on the placement of pedicle screws in spinal surgery (Wood 2013). The superior vertebral notch is recognizable only in the first thoracic vertebra, whereas the inferior notch is deep in all. Ligamenta flava are attached at the upper borders and lower anterior surfaces of the laminae.

Thoracic transverse processes shorten in caudal succession. In the upper five or six vertebrae, the costal facets are concave and face anterolaterally, and at lower levels the facets are flatter and face superolaterally and slightly forwards. The costotransverse ligament is attached to the anterior surface medial to the facet; the lateral costotransverse ligament is attached to its tuberculated apex and the superior costotransverse ligament is attached to its lower border.

Thoracic spines overlap from the fifth to the eighth vertebra, whose spine is the longest and most oblique. Supraspinous and interspinous ligaments are attached to the spines.

The first and ninth to twelfth thoracic vertebrae

The first and ninth to twelfth thoracic vertebrae display additional atypical features. The first thoracic vertebra (see Fig. 46.41) resembles a cervical vertebra in its body, both in shape and in the distinctive posterolateral 'lipping' that forms the anterior border of the superior vertebral notch. There are circular superior costal facets for articulation with the whole facet on the head of the first rib. The smaller, semilunar inferior facets articulate with a demifacet on the head of the second rib. The upper costal facet is often incomplete, in which case the first rib articulates with the seventh cervical vertebra and the intervening disc. A small, deep depression often occurs below the facet. The long, thick spine is horizontal and commonly as prominent as that of the seventh cervical vertebra. The ninth vertebra (see Fig. 46.41) often fails to articulate with the tenth ribs, in which case the inferior demifacets are absent. The tenth thoracic vertebra (see Fig. 46.41) only articulates with the tenth pair of ribs, so that superior facets only appear on the body. These are usually large and semilunar, but are oval when the tenth ribs fail to articulate with the ninth vertebra and intervening disc. The transverse process may or may not bear a facet for the tubercle of the tenth rib. The eleventh thoracic vertebra (see Fig. 46.41) articulates only with the heads of the eleventh ribs. The circular costal facets are close to the upper border of the body and extend on to the pedicles. The small transverse processes lack articular facets. The eleventh and twelfth thoracic spinous processes are triangular, with blunt apices and a horizontal lower and an oblique upper border. The twelfth thoracic vertebra (see Fig. 46.41) articulates with the heads of the twelfth ribs by circular facets somewhat below the upper border, spreading on to the pedicles. The body is large and the vertebra has some lumbar features. The transverse process is replaced by three small tubercles: the superior is largest, projects upwards and corresponds to a lumbar mammillary process, though it does not lie as close to the superior articular process; the lateral tubercle is the homologue of a transverse process; and the inferior is the homologue of a lumbar accessory process. The superior and inferior processes are surprisingly long in some specimens.

A change in orientation of articular processes from thoracic to lumbar type usually occurs at the eleventh thoracic vertebra, but sometimes at the twelfth or tenth. In the transitional vertebra the superior articular processes are thoracic, and face posterolaterally, while the inferior are transversely convex and face anterolaterally. The transitional vertebra marks the site of a sudden change of mobility from predominantly rotational to predominantly flexion–extension.

Muscle attachments Longus colli arises from the upper three thoracic vertebral bodies, lateral to the anterior longitudinal ligament, and psoas major and minor arise from the sides of the twelfth near its lower border. Upper and lower borders of the transverse processes provide attachment for the intertransverse muscles or their fibrous vestiges. The posterior surfaces of the transverse processes provide attachment for the deep dorsal muscles, and levator costae is attached posteriorly on the apex. Trapezius, rhomboid major and minor, latissimus dorsi, serratus posterior superior and inferior, and many deep dorsal muscles are attached to the spines. Rotatores attach to the posterior aspects of the laminae.

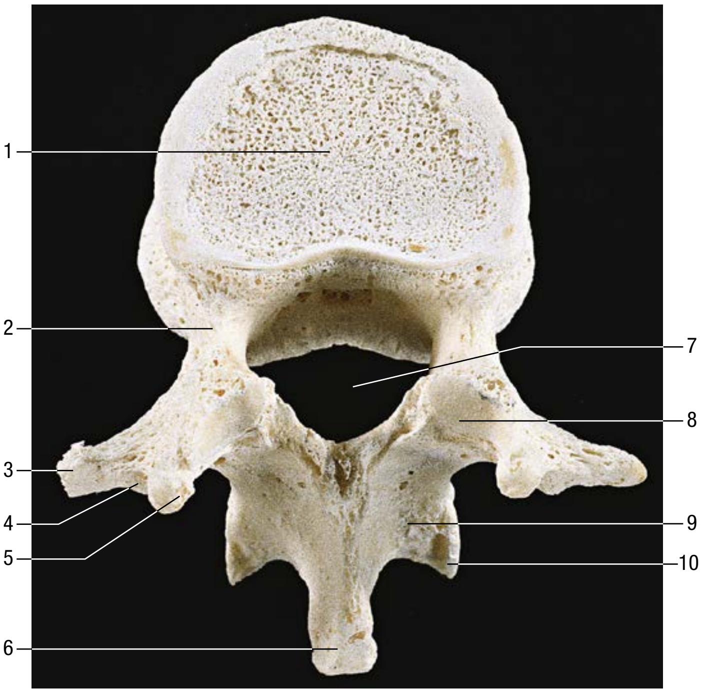

Fig. 46.43 The first lumbar vertebra, superior aspect. Key: 1, body; 2, pedicle; 3, transverse process; 4, accessory process; 5, mammillary process; 6, spinous process; 7, vertebral foramen; 8, superior articular facet; 9, lamina; 10, inferior articular facet.

Ossification Thoracic vertebrae all ossify according to the standard vertebral pattern described in Chapter 18.

Lumbar vertebrae

Lumbar vertebrae in general

The five lumbar vertebrae are distinguished by their large size and the absence of costal facets and transverse foramina. The body is wider transversely (**Fig. 46.43**; see Fig. 46.47B). The vertebral foramen is triangular, larger than at thoracic levels but smaller than at cervical levels. The pedicles are short. The spinous process is almost horizontal, quadrangular and thickened along its posterior and inferior borders. The superior articular processes bear vertical concave articular facets facing posteromedially, with a rough mammillary process on their posterior borders (**Fig. 46.44A**). The inferior articular processes have vertical convex articular facets that face anterolaterally. The transverse processes are thin and long, except on the more substantial fifth pair. A small accessory process marks the posteroinferior aspect of the root of each transverse process. The accessory and mammillary processes are linked by a fine ligament, the mammillo-accessory ligament, which is sometimes ossified, and beneath which runs the medial branch of the dorsal primary ramus of the spinal nerve (Bogduk 2012).

Strong paired pedicles arise posterolaterally from each body near its upper border. Superior vertebral notches are shallow and the inferior ones are deep. The laminae are broad and short, but do not overlap as much as those of the thoracic vertebrae. The fifth spine is the smallest, and its apex is often rounded and down-turned. Upper lumbar superior articular processes are further apart than inferior ones, but the difference is slight in the fourth and negligible in the fifth. The articular facets are reciprocally concave (superior) and convex (inferior), which allows flexion, extension, lateral bending and some degree of rotation. There are sex differences in the angle of inclination and depth of curvature of the articular facets. The facets are sometimes asymmetric.

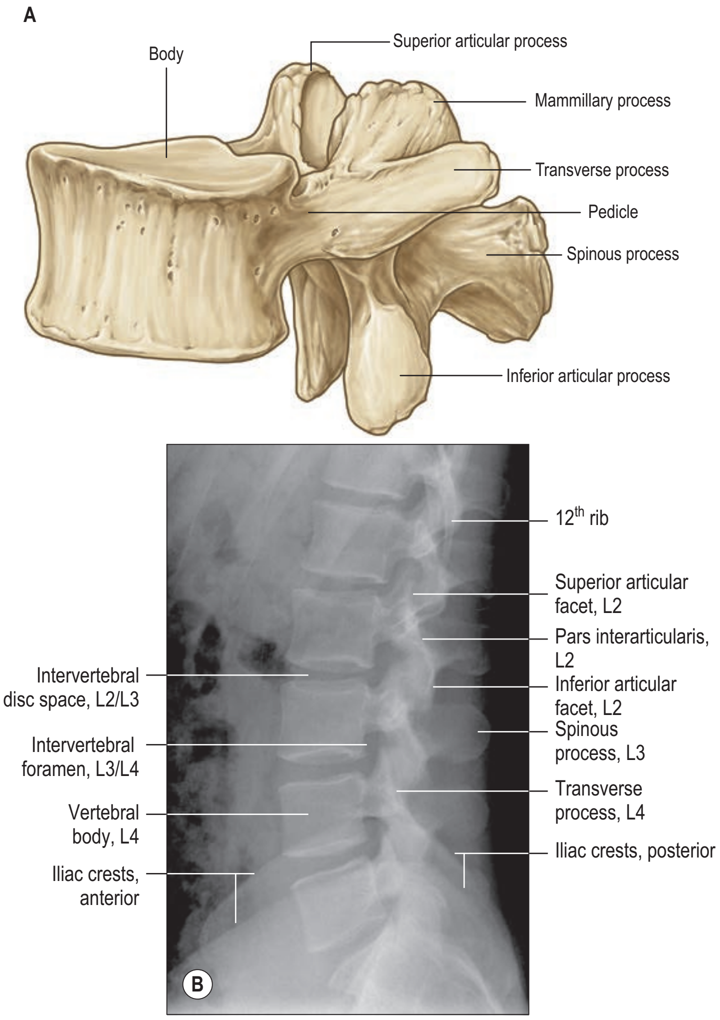
A
Body
Superior articular process
Mammillary process
Transverse process
Pedicle
Spinous process
Inferior articular process
12th rib
Superior articular facet, L2
Pars interarticularis, L2
Inferior articular facet, L2
Spinous process, L3
Transverse process, L4
Iliac crests, posterior
Intervertebral disc space, L2/L3
Intervertebral foramen, L3/L4
Vertebral body, L4
Iliac crests, anterior
B

Fig. 46.44 The lumbar spine. **A**, A typical lumbar vertebra, lateral aspect. **B**, Lateral radiograph of the lumbar spine.

Transverse processes, except the fifth, are anteroposteriorly compressed and project posterolaterally. The lower border of the fifth transverse process is angulated, and passes laterally and then superolaterally to a blunt tip; the whole process presents a greater upward inclination than the fourth. The angle on the inferior border may represent the tip of the costal element and the lateral end the tip of the true transverse process. The lumbar transverse processes increase in length from first to third and then shorten (**Fig. 46.45**). The fifth pair incline both upwards and posterolaterally. The costal element is incorporated in the mature transverse process.

On average, the adult spinal cord ends at the level of the middle third of the body of the first lumbar vertebra, which means that the first lumbar vertebral foramen usually contains the conus medullaris. The cord may terminate above or below this level (Saifuddin et al 1998) (Ch. 47); lower lumbar vertebral foramina contain the cauda equina and spinal meninges (**Fig. 46.46**; see Fig. 46.10B). Variation occurs in the sagittal and coronal dimensions of the lumbar vertebral canal, both within and between normal populations.

The fifth lumbar vertebra (**Fig. 46.47**) has a massive transverse process that is continuous with the whole of the pedicle and encroaches on the body. The body is usually the largest and markedly deeper anteriorly, so contributing to the lumbosacral angle.

Segmentation anomalies (sacralization) are considered below with the sacrum. The costal element of the first lumbar vertebra may form a short lumbar rib, which articulates with the transverse process, but not usually with the body, of the vertebra.

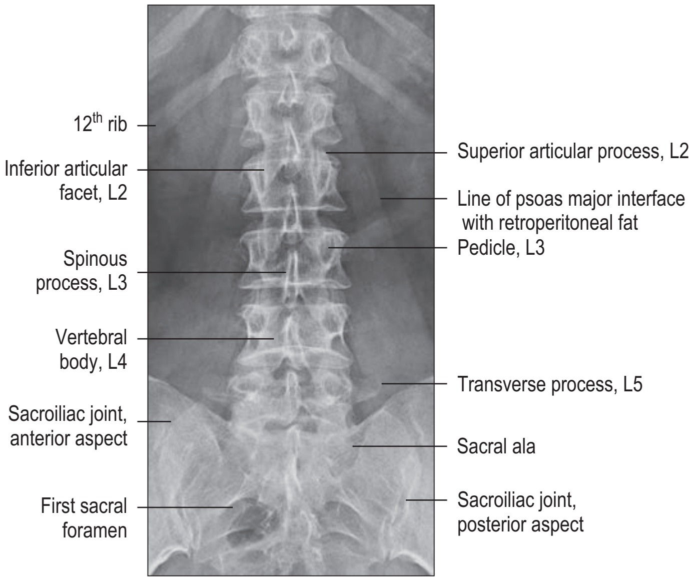
12th rib
Inferior articular facet, L2
Spinous process, L3
Vertebral body, L4
Sacroiliac joint, anterior aspect
First sacral foramen
Superior articular process, L2
Line of psoas major interface with retroperitoneal fat
Pedicle, L3
Transverse process, L5
Sacral ala
Sacroiliac joint, posterior aspect

Fig. 46.45 An anteroposterior radiograph of the lumbar spine.

Muscle and fascial attachments Upper and lower borders of lumbar bodies give attachment to the anterior and posterior longitudinal ligaments. The upper bodies (three on the right, two on the left) give attachments to the crura of the respiratory diaphragm lateral to the anterior longitudinal ligament. Posterolaterally, psoas major is attached to the upper and lower margins of all the lumbar bodies, and between them, tendinous arches carry its attachments across their concave sides (see Fig. 61.7). The posterior lamella of the thoracolumbar fascia, erectores spinae, spinales thoracis, multifidi, interspinal muscles and ligaments, and supraspinous ligaments are all attached to spinous processes. All lumbar transverse processes present a vertical ridge on the anterior surface, nearer the tip, which marks the attachment of the anterior layer of the thoracolumbar fascia, and separates the surface into medial and lateral areas for psoas major and quadratus lumborum, respectively. The middle layer of the fascia is attached to the apices of the transverse processes; the medial and lateral arcuate ligaments attach to the vertical ridge on the anterior aspect of the first pair, and the iliolumbar ligament attaches to the apices of the fifth pair. Posteriorly, the transverse processes are covered by deep dorsal muscles, and fibres of longissimus thoracis are attached to them and to their accessory processes. The ventral lateral intertransverse muscles are attached to their upper and lower borders, while the dorsal attach cranially to the accessory process and caudally to the upper border of the transverse process. The mammillary process, homologous with the superior tubercle of the twelfth thoracic vertebra, gives attachment to multifidus and the medial intertransverse muscle. The latter also attaches to the accessory process, which is sometimes difficult to identify.

Ossification Lumbar vertebrae ossify according to the standard vertebral pattern described in Chapter 18 but also have two additional centres for the mammillary processes. A pair of scale-like epiphyses usually appear on the tips of the costal elements of the fifth lumbar vertebra (see Fig. 46.34C).

Sacrum

The sacrum is a large, triangular fusion of five vertebrae and forms the posterosuperior wall of the pelvic cavity, wedged between the two hip (innominate) bones (see Fig. 77.8). Its blunted, caudal apex articulates with the coccyx and its superior, wide base with the fifth lumbar vertebra at the lumbosacral angle. It is set obliquely and curved longitudinally, the dorsal surface is convex, and the pelvic surface is concave; this ventral curvature increases pelvic capacity (**Figs 46.48–46.51**). Between base and apex are dorsal, pelvic and lateral surfaces and a sacral canal. In childhood, individual sacral vertebrae are connected by cartilage, and the adult bone retains many vertebral features. The sacrum

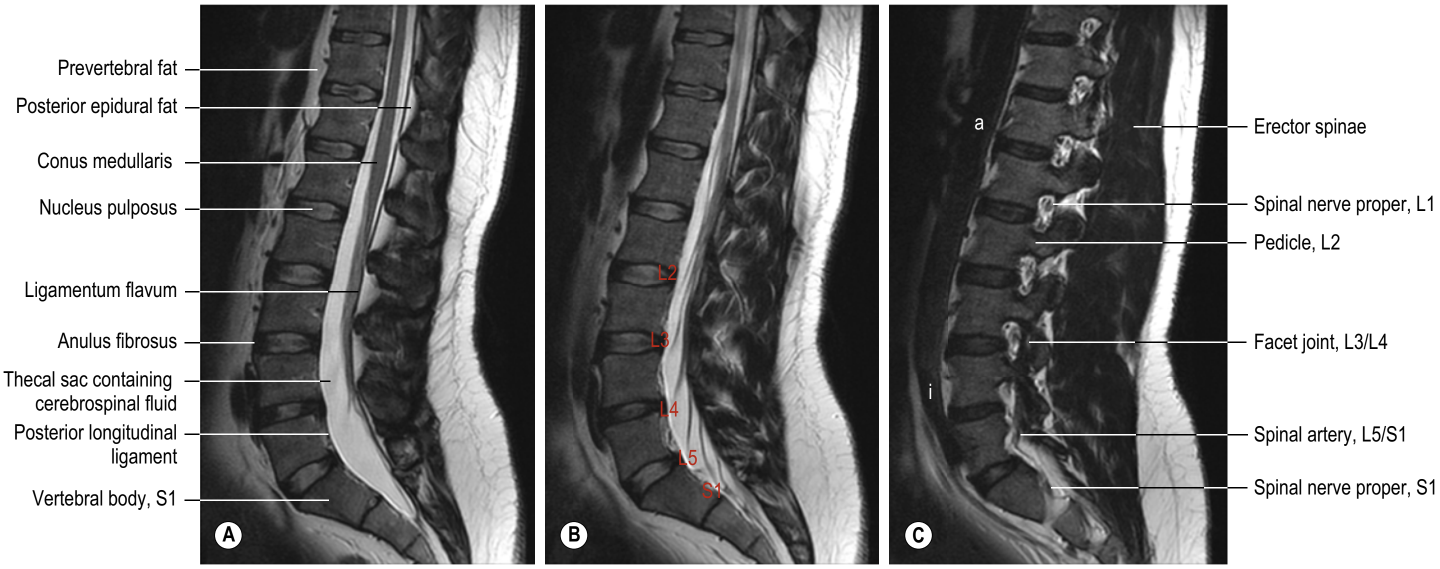
Prevertebral fat
Posterior epidural fat
Conus medullaris
Nucleus pulposus
Ligamentum flavum
Anulus fibrosus
Thecal sac containing cerebrospinal fluid
Posterior longitudinal ligament
Vertebral body, S1
A
L2
L3
L4
L5
S1
B
a
i
C
Erector spinae
Spinal nerve proper, L1
Pedicle, L2
Facet joint, L3/L4
Spinal artery, L5/S1
Spinal nerve proper, S1

Fig. 46.46 **A**-**C**, Sagittal T2-weighted MRIs of the lumbar spine from median sagittal to left (para)sagittal. Note how the spinal nerve roots in the cauda equina descend from the level of the conus to pass out laterally through their respective intervertebral foramina, as labelled in **B**. Key: a, aorta; i, left common iliac artery.

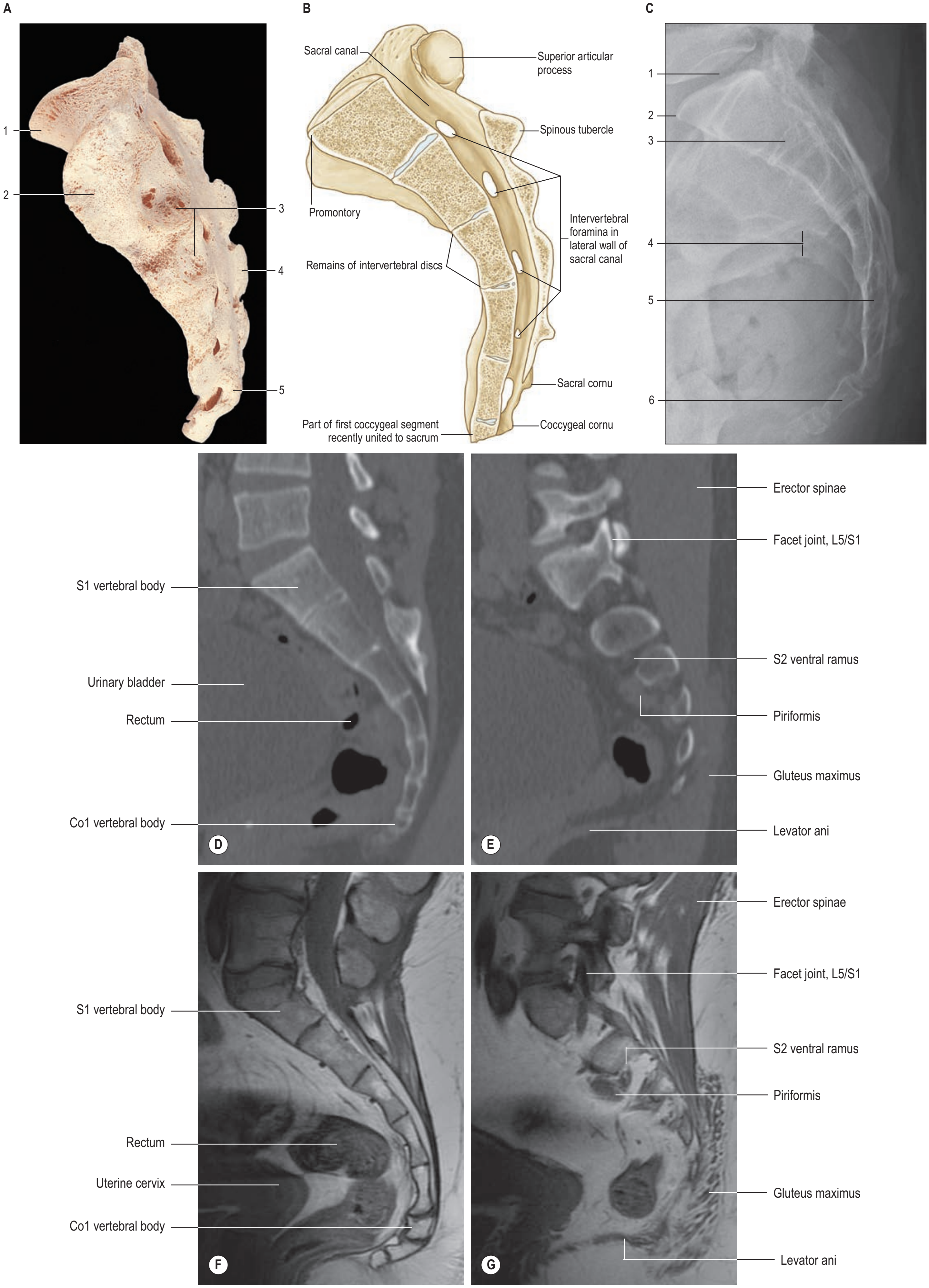
A
B
C
1
2
3
4
5
Sacral canal
Superior articular process
Spinous tubercle
Promontory
Intervertebral foramina in lateral wall of sacral canal
Remains of intervertebral discs
Sacral cornu
Part of first coccygeal segment recently united to sacrum
Coccygeal cornu
1
2
3
4
5
6
S1 vertebral body
Urinary bladder
Rectum
Co1 vertebral body
D
E
Erector spinae
Facet joint, L5/S1
S2 ventral ramus
Piriformis
Gluteus maximus
Levator ani
S1 vertebral body
Rectum
Uterine cervix
Co1 vertebral body
F
G
Erector spinae
Facet joint, L5/S1
S2 ventral ramus
Piriformis
Gluteus maximus
Levator ani

Fig. 46.51 **A**, The sacrum, lateral aspect. Key: 1, promontory; 2, auricular (articular) surface; 3, attachments of interosseous sacroiliac ligaments; 4, spinous process; 5, sacral cornu (left). **B**, A midline sagittal section through the sacrum. **C**, A lateral radiograph of the sacrum. Key: 1, L5–S1 disc; 2, sacral promontory; 3, S1–2 disc; 4, greater sciatic notches; 5, S4; 6, Co1. **D**, **E**, Midline sagittal and left sagittal CTs in a male. **F**, **G**, A T1-weighted MRI through the sacrum in a female.

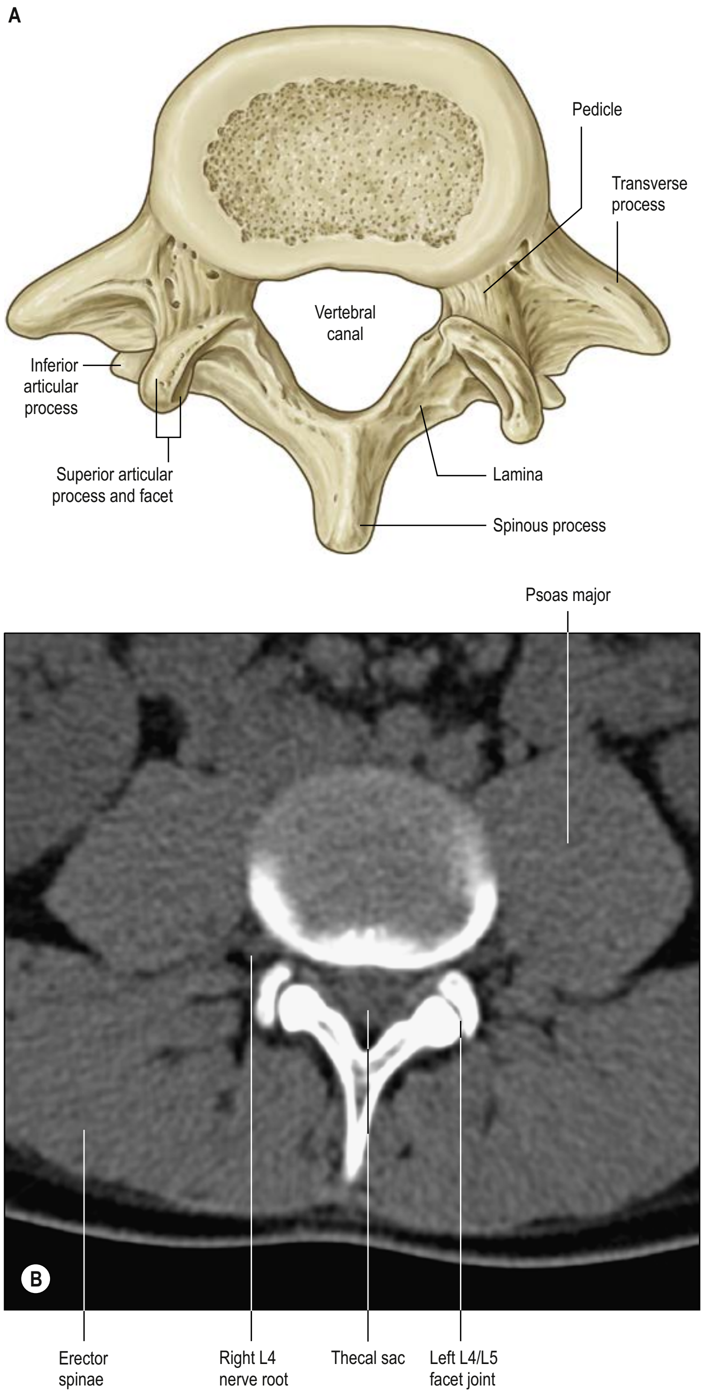
A
Pedicle
Transverse process
Vertebral canal
Inferior articular process
Superior articular process and facet
Lamina
Spinous process
Psoas major
B
Erector spinae
Right L4 nerve root
Thecal sac
Left L4/L5 facet joint

Fig. 46.47 Lumbar vertebrae. **A**, Fifth lumbar vertebra, superior aspect. **B**, Normal axial plane CT image through the lumbar spine at the level of the fourth lumbar vertebra.

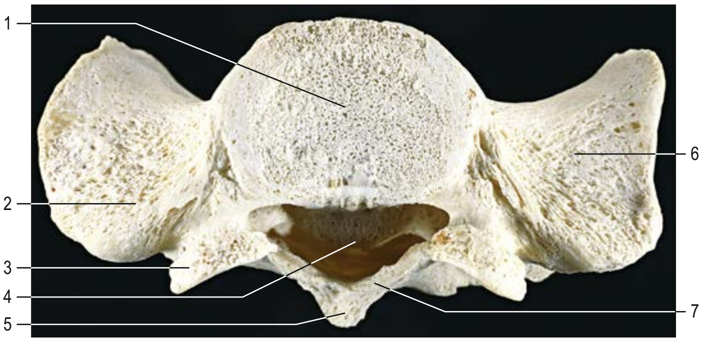

Fig. 46.48 The sacrum, superior aspect (base). Key: 1, body of S1; 2, posterosuperior ala (transverse process element); 3, superior articular process; 4, sacral canal; 5, spinous process of S1; 6, anterosuperior ala (costal element); 7, lamina.

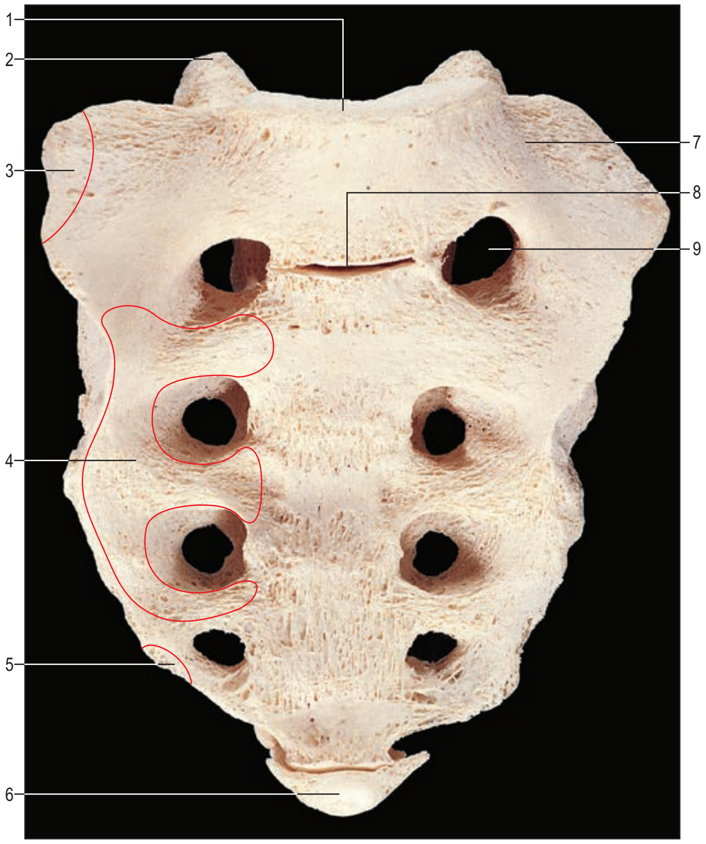

Fig. 46.49 The sacrum, anterior (pelvic) surface. Key: 1, upper border of body of S1 (sacral promontory); 2, superior articular process of S1; 3, attachment of iliacus; 4, attachment of piriformis; 5, attachment of coccygeus; 6, coccyx; 7, ala; 8, incompletely fused S1–S2 intervertebral joint; 9, first pelvic sacral foramen.

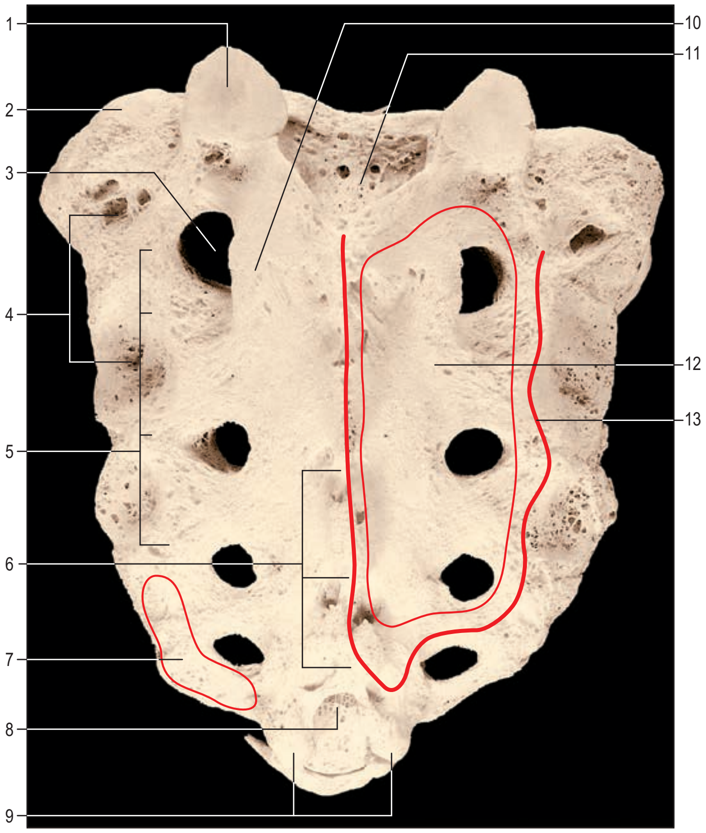
1
2
3
4
5
6
7
8
9
10
11
12
13

Fig. 46.50 The sacrum, posterior (dorsal) surface. Key: 1, superior articular facet of S1; 2, ala; 3, first dorsal sacral foramen; 4, attachments of interosseous sacroiliac ligaments; 5, lateral crest and transverse tubercles; 6, median crest and spinous processes; 7, attachment of gluteus maximus; 8, sacral hiatus; 9, cornua; 10, intermediate crest and articular tubercle (inferior articular process); 11, posterior surface of body of S1 forming anterior wall of sacral canal; 12, area of attachment of multifidus (bounded by thin line); 13, attachment of erector spinae aponeurosis (thick line).

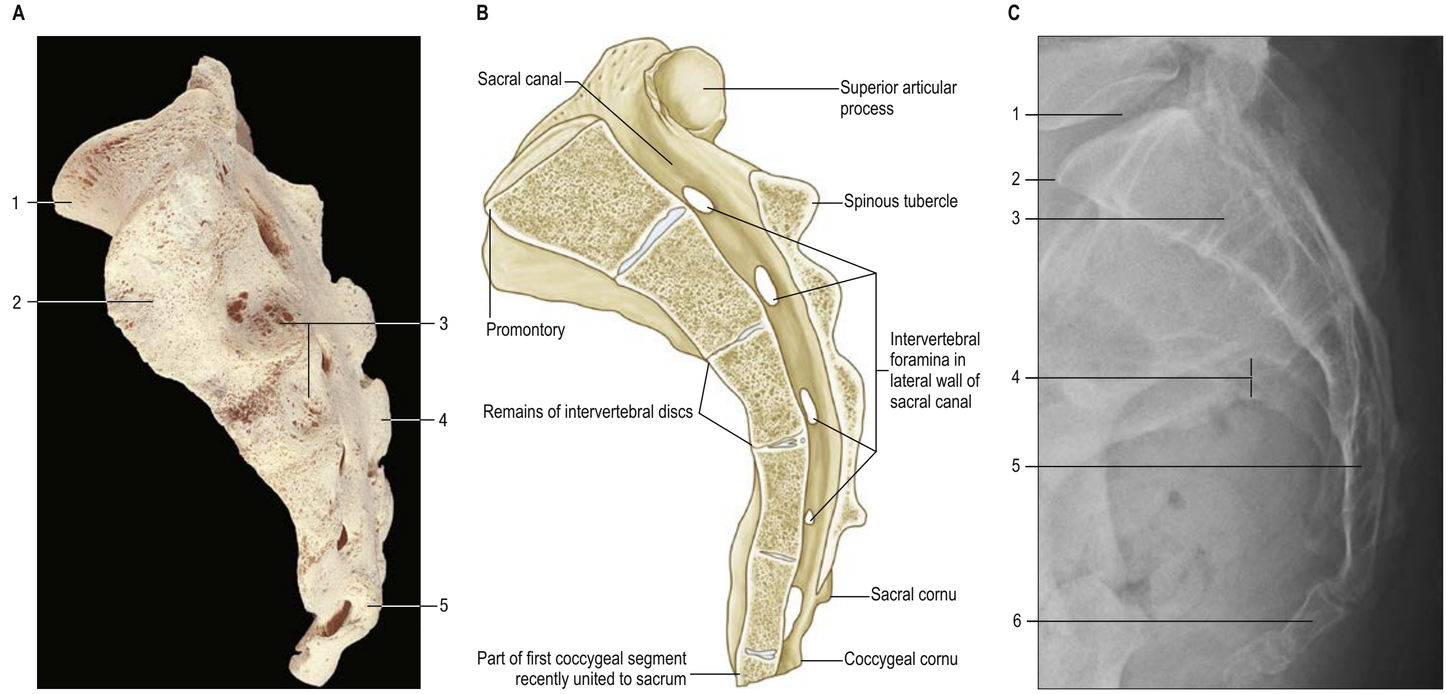
A
1
2
3
4
5
B
Sacral canal
Superior articular process
Spinous tubercle
Promontory
Intervertebral foramina in lateral wall of sacral canal
Remains of intervertebral discs
Sacral cornu
Part of first coccygeal segment recently united to sacrum
Coccygeal cornu
C
1
2
3
4
5
6

Fig. 46.51 **A**, The sacrum, lateral aspect. Key: 1, promontory; 2, auricular (articular) surface; 3, attachments of interosseous sacroiliac ligaments; 4, spinous process; 5, sacral cornu (left). **B**, A midline sagittal section through the sacrum. **C**, A lateral radiograph of the sacrum. Key: 1, L5–S1 disc; 2, sacral promontory; 3, S1–S2 disc; 4, greater sciatic notches; 5, S4; 6, Co1. (D–G, *continued online*)

consists of trabecular bone enveloped by a shell of compact bone of varying thickness.

Base The base (see Fig. 46.48) is the upper surface of the first sacral vertebra, the least modified from the typical vertebral plan. The body is large and wider transversely, and its anterior projecting edge is the sacral promontory. The vertebral foramen is triangular; its pedicles are short and diverge posterolaterally. The laminae are oblique, inclining down posteromedially to meet at a spinous tubercle. The superior articular processes project cranially, with concave articular facets directed posteromedially to articulate with the inferior articular processes of the fifth lumbar vertebra. The posterior part of each process projects backwards and its lateral aspect bears a rough area homologous with a lumbar mammillary process.

The transverse process is much modified as a broad, sloping mass that projects laterally from the body, pedicle and superior articular process. It is formed by the fusion of the transverse process and the costal element to each other and to the rest of the vertebra, and forms the upper surface of the sacral lateral mass or ala.

Terminal fibres of the anterior and posterior longitudinal ligaments are attached to the ventral and dorsal surfaces of the first sacral body. Its upper laminar borders receive the lowest pair of ligamenta flava. The ala is smooth superiorly, concave medially and rough laterally, and covered almost entirely by psoas major. The smooth area is grooved obliquely by the lumbosacral trunk. The rough area is for the lower band of the iliolumbar ligament, which lies lateral to the fifth lumbar spinal nerve and to the anterior sacroiliac ligament.

Pelvic surface The anteroinferior pelvic surface (see Fig. 46.49) is vertically and transversely concave, but the second sacral body may produce a convexity. Four pairs of pelvic sacral foramina communicate with the sacral canal through intervertebral foramina, and transmit ventral rami of the upper four sacral spinal nerves. The large area between the right and left foramina, which is formed by the flat pelvic aspects of the sacral bodies, bears evidence of their fusion at four transverse ridges. The longitudinal bars between the foramina are costal elements, which fuse to the vertebrae. Lateral to the foramina, the costal elements unite. Posteriorly, they unite with the transverse processes to form the lateral part of the sacrum, which expands basally as the ala.

The first three sacral ventral rami emerge from the pelvic sacral foramina and pass anterior to piriformis. The sympathetic trunks descend in contact with bone, medial to the foramina, as do the median sacral vessels in the midline. Lateral to the foramina, lateral sacral vessels are related to bone. Ventral surfaces of the first, second and part of the third sacral bodies are covered by parietal peritoneum and crossed obliquely, left of the midline, by the attachment of the sigmoid mesocolon. The rectum is in contact with the pelvic surfaces of the third to fifth sacral vertebrae and with the bifurcation of the superior rectal artery between the rectum and third sacral vertebra.

Dorsal surface The posterosuperior aspect of the dorsal surface bears a raised, interrupted, median sacral crest with four (sometimes three) spinous tubercles, which represent fused sacral spines (see Fig. 46.50). Below the fourth (or third) tubercle there is an arched sacral hiatus in the posterior wall of the sacral canal. This hiatus is produced by the failure of the laminae of the fifth sacral vertebra to meet in the median plane, and as a result the posterior surface of the body of that vertebra is exposed on the dorsal surface of the sacrum. Flanking the median crest, the posterior surface is formed by fused laminae, and lateral to this are four pairs of dorsal sacral foramina. Like the pelvic foramina, they lead into the sacral canal through intervertebral foramina, and each transmits the dorsal ramus of a sacral spinal nerve. Medial to the foramina, and vertically below each articular process of the first sacral vertebra, is a row of four small tubercles, which collectively constitute the intermediate sacral crest. These are sometimes termed articular tubercles, and represent fused contiguous articular processes. The inferior articular processes of the fifth sacral vertebra are free and project downwards at the sides of the sacral hiatus as sacral cornua, connected to coccygeal cornua by intercornual ligaments. The interrupted roughened crest to the lateral side of the dorsal sacral foramina is the lateral sacral crest, which is formed by fused transverse processes, whose apices appear as a row of transverse tubercles.

The upper three sacral spinal dorsal rami pierce multifidus as they emerge via dorsal foramina.

Lateral surface The lateral surface (**Fig. 46.51A**) is a fusion of transverse processes and costal elements. It is wide above and rapidly narrows in its lower part. The broad upper part bears an auricular surface for articulation with the ilium, and the area posterior to this is rough and deeply pitted by the attachment of ligaments. The auricular surface, borne by costal elements, is like an inverted letter L. The shorter, cranial limb is restricted to the first sacral vertebra; the caudal limb descends to the middle of the third. Beyond this, the lateral surface is non-articular and reduced in breadth. Caudally, it curves medially to the body of the fifth sacral vertebra at the inferior lateral angle, beyond which the surface becomes a thin lateral border. A variable accessory sacral articular facet sometimes occurs, posterior to the auricular surface.

The auricular surface is covered by hyaline cartilage, and formed entirely by costal elements. It shows cranial and caudal elevations and

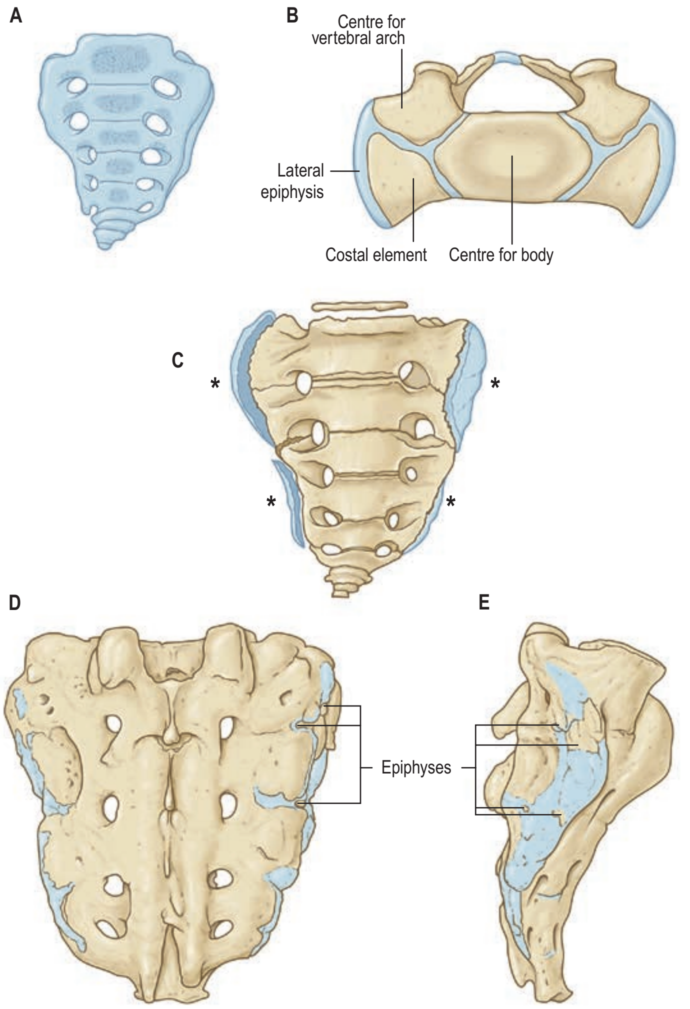

Fig. 46.52 Ossification of the sacrum and coccyx. **A**, At birth. **B**, The base of the sacrum of a child about 4 years old. **C**, At the twenty-fifth year: epiphysial plates for each lateral surface are marked by asterisks. **D–E**, The epiphyses of the costal and transverse process of the sacrum at the eighteenth year.

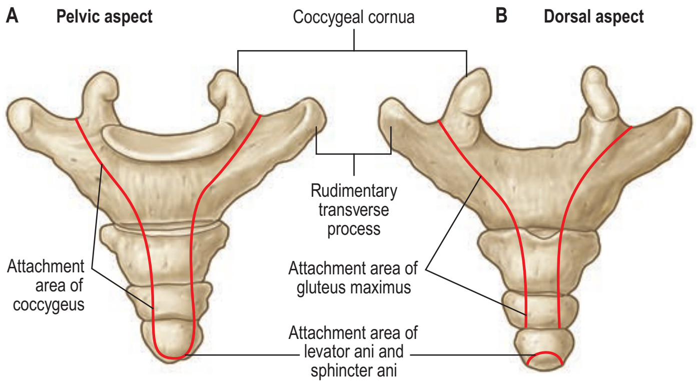
A
Pelvic aspect
Coccygeal cornua
B
Dorsal aspect
Rudimentary transverse process
Attachment area of coccygeus
Attachment area of gluteus maximus
Attachment area of levator ani and sphincter ani

Fig. 46.53 The coccyx. **A**, Anterior (pelvic) aspect. **B**, Posterior (dorsal) aspect.

an intermediate depression, behind which a third elevation is visible in the elderly. The surface becomes more corrugated with age. The rough area behind the auricular surface shows two or three marked depressions for the attachment of strong interosseous sacroiliac ligaments. Below the auricular surface the sacrotuberous and sacrospinous ligaments are attached between gluteus maximus dorsally and coccygeus ventrally.

Apex The apex is the inferior aspect of the fifth sacral vertebral body, and bears an oval facet for articulation with the coccyx.

Sacral canal The sacral canal (**Fig. 46.51B**) is formed by sacral vertebral foramina, and is triangular in section (see Fig. 46.48). Its upper opening, seen on the basal surface, appears to be set obliquely. The inclination of the sacrum means that it is directed cranially in the standing position. Each lateral wall presents four intervertebral foramina, through which the canal is continuous with pelvic and dorsal sacral foramina. Its caudal opening is the sacral hiatus. The canal contains the cauda equina and the filum terminale, and the spinal meninges. Opposite the middle of the sacrum, the subarachnoid and subdural spaces close; the lower sacral spinal roots and filum terminale pierce the arachnoid and dura mater at that level. The filum terminale with its meningeal coverings emerges below the sacral hiatus and passes downwards across the dorsal surface of the fifth sacral vertebra and sacrococcygeal joint to reach the coccyx. The fifth sacral spinal nerves also emerge through the hiatus medial to the sacral cornua, and groove the lateral aspects of the fifth sacral vertebra.

Muscle attachments The pelvic surface gives attachment to piriformis in its second to fourth segments, to iliacus superolaterally, and to coccygeus inferolaterally. The dorsal surface gives attachment to the aponeurosis of erector spinae along a U-shaped area of spinous and transverse tubercles, covering multifidus, which occupies the enclosed area (see Fig. 46.50). On the lateral border below the auricular surface, gluteus maximus is attached dorsal and coccygeus is attached ventral to the sacrotuberous and sacrospinous ligaments.

Ossification The sacrum resembles typical vertebrae in the ossification of its segments (**Fig. 46.52**). Primary centres for the centrum and each half vertebral arch appear from postmenstrual week 19. Primary centres for the costal elements of the upper three or more segments appear superolateral to the pelvic sacral foramina, from postmenstrual weeks 21–24. Each costal element unites with its half vertebral arch between the second and fifth years, and the conjoined element so formed unites anteriorly with the centrum and posteriorly with its opposite fellow at about the eighth year. Thereafter, the upper and lower surfaces of each sacral body are covered by an epiphysial plate of hyaline cartilage, which is separated from its neighbour by the fibrocartilaginous precursor of an intervertebral disc. Laterally, successive conjoined vertebral arches and costal elements are separated by hyaline cartilage; a cartilaginous epiphysis, sometimes divided into upper and lower parts, develops on each auricular and adjacent lateral surface. Soon after puberty, the fused vertebral arches and costal elements of adjacent vertebrae begin to coalesce from below upwards. At the same time, individual epiphysial centres develop for the upper and lower surfaces of bodies, spinous tubercles, transverse tubercles and costal elements.

The costal epiphysial centres appear at the lateral extremities of the hyaline cartilages between adjacent costal elements; two anterior and two posterior centres appear in each of the intervals between the first, second and third sacral vertebrae. Ossification spreads from these into the auricular epiphysial plates. One costal epiphysial centre, placed anteriorly, occurs in each remaining interval and from them ossification spreads to the epiphysial plate covering the lower part of the lateral surface of the sacrum. Sacral bodies unite at their adjacent margins after the twentieth year, but the central and greater part of each intervertebral disc remains unossified up to or beyond middle life.

Variants The sacrum may contain six vertebrae, by development of an additional sacral element or by incorporation of the fifth lumbar or first coccygeal vertebra. Inclusion of the fifth lumbar vertebra (sacralization) is usually incomplete and limited to one side. In the most minor degree of the abnormality, a fifth lumbar transverse process is large and articulates, sometimes by a synovial joint, with the sacrum at the posterolateral angle of its base. Reduction of sacral constituents is less common but lumbarization of the first sacral vertebra does occur; it remains partially or completely separate. The bodies of the first two sacral vertebrae may remain unfused when the lateral masses are fused. The dorsal wall of the sacral canal may be variably deficient, due to imperfect development of laminae and spines. Orientation of the superior sacral articular facets displays wide variation, as does the sagittal curvature of the sacrum. Asymmetry (facet tropism) of the superior facets alters the relation between the planes of the two lumbosacral facet joints.

Coccyx

The coccyx (**Fig. 46.53**) is a small, triangular bone and is often asymmetric in shape. It usually consists of four fused rudimentary vertebrae, although the number varies from three to five, and the first is sometimes separate. The bone is directed downwards and ventrally from the sacral apex; its pelvic surface is tilted upwards and forwards, its dorsum downwards and backwards. Orientation varies with mobility and between individuals.

The base or upper surface of the first coccygeal vertebral body has an oval, articular facet for the sacral apex. Posterolateral to this, two coccygeal cornua project upwards to articulate with sacral cornua; they are homologues of the pedicles and superior articular processes of other vertebrae. A rudimentary transverse process projects superolaterally from each side of the first coccygeal body and may articulate or fuse with the inferolateral sacral angle, completing the fifth sacral foramina.

The second to fourth coccygeal vertebrae diminish in size and are usually mere fused nodules. They represent rudimentary vertebral bodies, though the second may show traces of transverse processes and pedicles.

The gap between the fifth sacral body and the articulating cornua represents, on each side, an intervertebral foramen that transmits the fifth sacral spinal nerve. The dorsal ramus descends behind the rudimentary transverse process, and the ventral ramus passes anterolaterally between the transverse process and sacrum.

Muscle and ligament attachments The lateral parts of the pelvic surface, including the rudimentary transverse processes, give attachment to the levatores ani and coccygei. The anterior sacrococcygeal ligament is attached to the front of the first and sometimes second coccygeal vertebral bodies. The cornua give attachment to the intercornual ligaments. The lateral sacrococcygeal ligament connects the transverse process to the inferolateral sacral angle. Gluteus maximus is attached to the dorsal surface, and both levator ani and sphincter ani externus are attached to the tip of the bone. The median area gives attachment to the deep and superficial posterior sacrococcygeal ligaments, the superficial descending from the margins of the sacral hiatus and sometimes closing the sacral canal. The filum terminale, which is situated between the two ligaments, blends with them on the dorsum of the first coccygeal vertebra.

Ossification Each coccygeal segment is ossified from one primary centre. A centre in the first segment appears about birth and its cornua may soon ossify from separate centres. Remaining segments ossify at wide intervals up to the twentieth year or later. Segments slowly unite: union between the first and second is frequently delayed until 30 years. The coccyx often fuses with the sacrum in later decades, especially in females.

LIGAMENTS OF THE VERTEBRAL COLUMN

Anterior longitudinal ligament

The anterior longitudinal ligament (Fig. 46.54B) is a strong band extending along the anterior surfaces of the vertebral bodies. It is broader caudally, and thicker and narrower in thoracic than in cervical and lumbar regions, and is also relatively thicker and narrower opposite vertebral bodies than at the levels of intervertebral symphyses. It extends from the basilar part of the occipital bone to the anterior tubercle of C1 and the front of the body of C2, and then continues caudally to the front of the upper sacrum. Its longitudinal fibres are strongly adherent to the intervertebral discs, hyaline cartilage end-plates and margins of adjacent vertebral bodies, and are loosely attached at intermediate levels of the bodies, where the ligament fills their anterior concavities, flattening the vertebral profile. At these various levels, ligamentous fibres blend with the subjacent periosteum, perichondrium and periphery of the anulus fibrosus. The anterior longitudinal ligament has several layers. The most superficial fibres are the longest and extend over three or four vertebrae, the intermediate extend between two or three, and the deepest from one body to the next. Laterally, short fibres connect adjacent vertebrae.

Posterior longitudinal ligament

The posterior longitudinal ligament (Fig. 46.55) lies on the posterior surfaces of the vertebral bodies in the vertebral canal, attached between the body of C2 and the sacrum, and continuous with the membrana tectoria above. Its smooth, glistening fibres, attached to intervertebral discs, hyaline cartilage end-plates and adjacent margins of vertebral bodies, are separated between attachments by basivertebral veins and the venous channels that drain them into anterior internal vertebral plexuses. At cervical and upper thoracic levels the ligament is broad and of uniform width, but in lower thoracic and lumbar regions it is denticulated, narrow over vertebral bodies and broad over discs. Its superficial fibres bridge three or four vertebrae, while deeper fibres extend

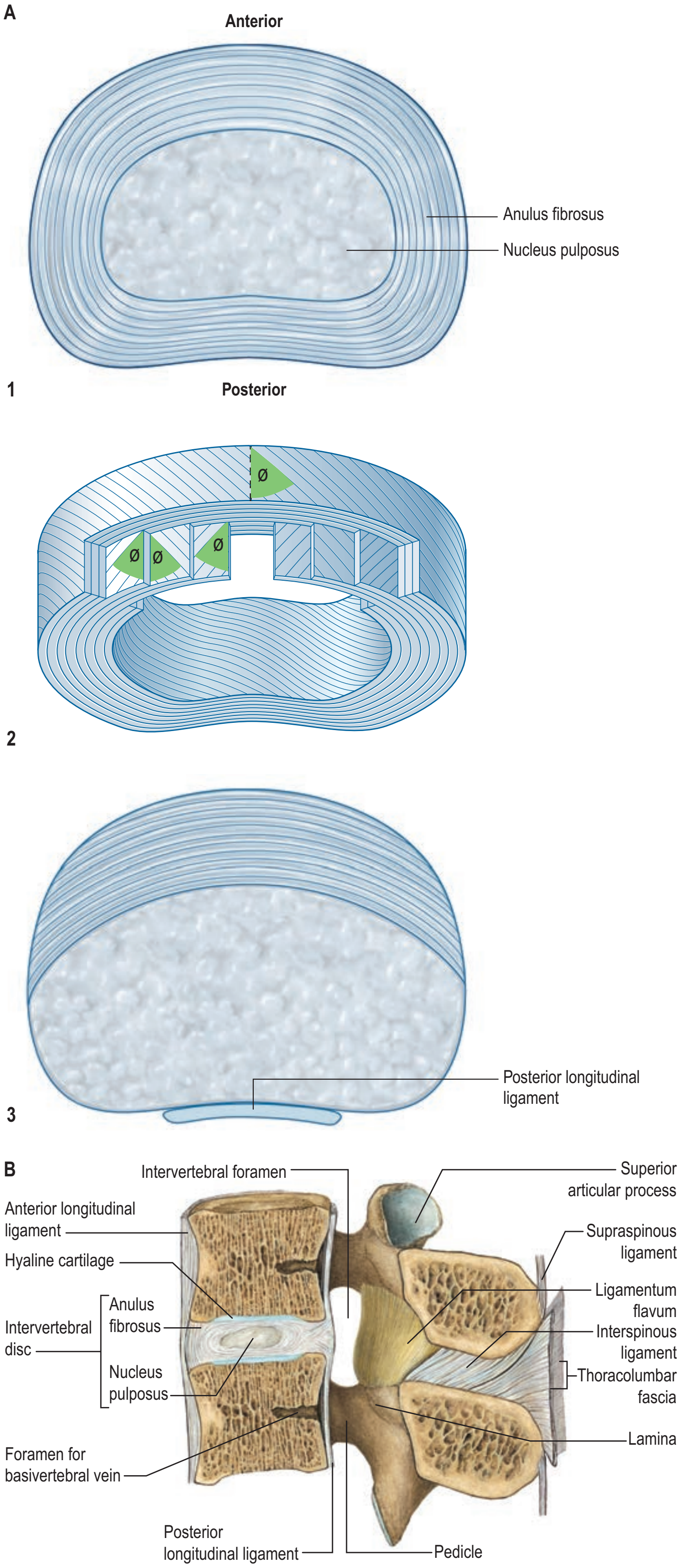

Fig. 46.54 A, The main structural features of an intervertebral disc. For clarity, the number of fibrocartilaginous laminae has been greatly reduced. Note the alternating obliquity of collagen fascicles in adjacent laminae. Key: 1, lumbar disc; 2, detailed structure of anulus fibrosus; ø = approximately 65°; 3, cervical disc. **B**, A median sagittal section through the upper lumbar vertebral column showing discs and ligaments. (A, After Bogduk N 1997 Clinical Anatomy of the Lumbar Spine and Sacrum, 3rd ed. Edinburgh: Churchill Livingstone. B, Sobotta Atlas of Human Anatomy © Elsevier GmbH, Urban & Fischer, Munich.)

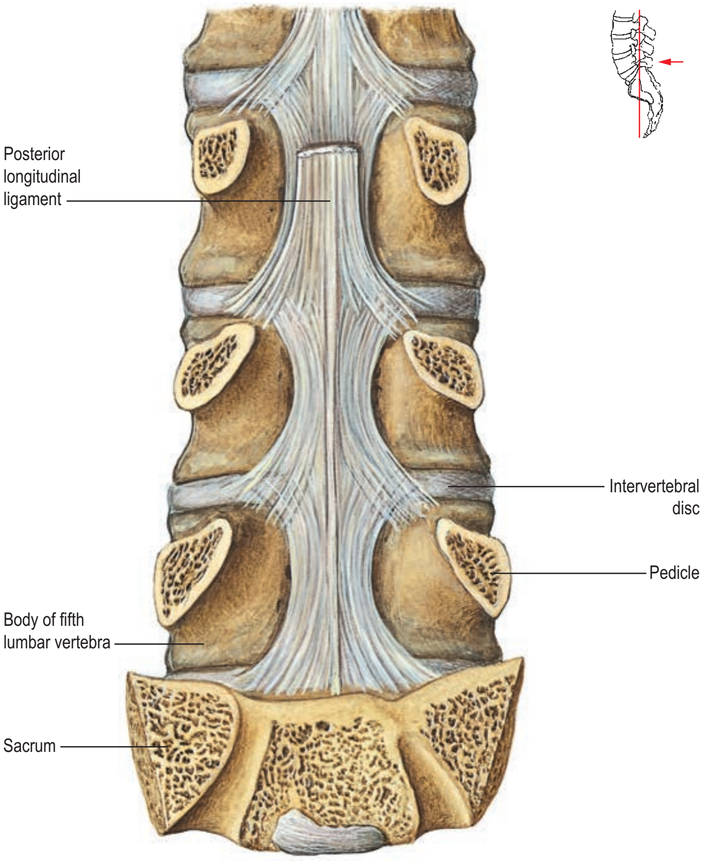
Posterior longitudinal ligament
Intervertebral disc
Pedicle
Body of fifth lumbar vertebra
Sacrum

Fig. 46.55 The posterior longitudinal ligament in the lumbar region. (Sobotta Atlas of Human Anatomy © Elsevier GmbH, Urban & Fischer, Munich.)

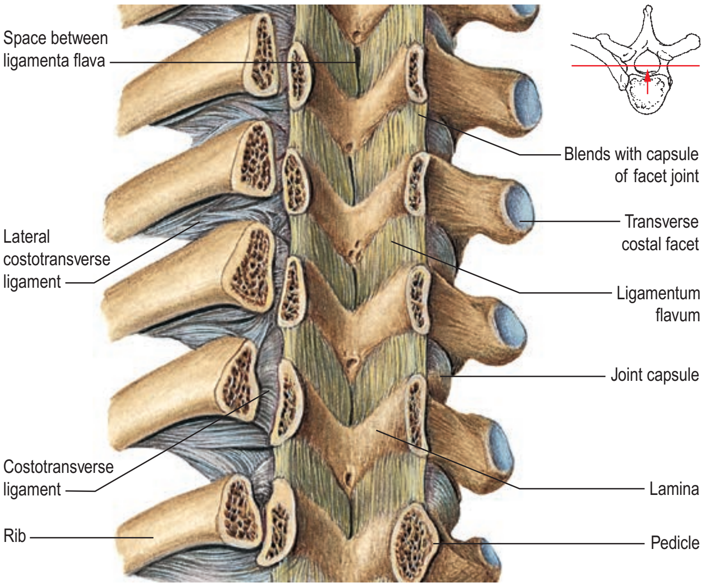
Space between ligamenta flava
Blends with capsule of facet joint
Transverse costal facet
Lateral costotransverse ligament
Ligamentum flavum
Joint capsule
Costotransverse ligament
Lamina
Rib
Pedicle

Fig. 46.56 The ligamenta flava and costotransverse ligaments, ventral aspect. (Sobotta Atlas of Human Anatomy © Elsevier GmbH, Urban & Fischer, Munich.)

between adjacent vertebrae as perivertebral ligaments, which are close to and, in adults, fused with the anulus fibrosus of the intervertebral disc. The layers of the posterior longitudinal ligament and the relationship of the ligament to associated membranes in the epidural space are fully discussed by Loughenbury et al (2006).

Ligamenta flava

The ligamenta flava (see Fig. 46.54B; **Fig. 46.56**) connect laminae of adjacent vertebrae in the vertebral canal. Their attachments extend from facet joint capsules to the point where laminae fuse to form spines. Here their posterior margins meet and are partially united; the intervals between them admit veins that connect the internal and posterior external vertebral venous plexuses. Their predominant tissue is yellow elastic tissue, whose almost perpendicular fibres descend from the lower anterior surface of one lamina to the posterior surface and upper margin of the lamina below. The anterior surface of the ligaments is covered by a fine, continuous, smooth lining membrane (Newell 1999). The ligaments are thin, broad and long in the cervical region, thicker in the thoracic and thickest at lumbar levels. They arrest separation of the laminae in spinal flexion, preventing abrupt limitation, and also assist restoration to an erect posture after flexion, perhaps protecting discs from injury.

The morphology and histology of the ligamentum flavum have been studied in the thoracolumbar region (Viejo-Fuertes et al 1998). On a macroscopic level, it has two layers, superficial and deep, where the fibres run in opposite directions. The superficial layer is innervated by medial branches from the dorsal roots of the spinal nerves. The deep layer is innervated by sinuvertebral nerves. This innervation appears to become increasingly poorer with age-related degeneration.

Interspinous ligaments

Interspinous ligaments (see Fig. 46.54B) connect the facing edges of consecutive spinous processes, and extend ventrally as far as the ligamentum flavum and dorsally to the supraspinous ligament, when this ligament is present (see below). They differ structurally at thoracic, lumbar and cervical levels. The thoracic interspinous ligaments are narrow and elongated, whereas those at lumbar levels are thick and quadrilateral, and occur as closely applied pairs, the left and right ligaments being separated by a narrow or potential cleft. In the lumbar ligaments, collagen fibres run obliquely inferiorly and ventrally, and only the deepest fibres are truly ligamentous. The more dorsal fibres are derived from tendons of longissimus thoracis that dip into the interspinous space to gain attachment to the superior edge of the spinous process rather than to its tip. Distinctive interspinous ligaments are not evident at cervical levels, where they are represented by the median septum of the ligamentum nuchae as it passes between the cervical spinous processes.

Supraspinous ligament

The supraspinous ligament (see Fig. 46.54B) is a strong, fibrous cord that connects the tips of spinous processes from C7 to L3 or L4. It is regularly deficient. The most superficial fibres extend over three or four vertebrae, the deeper span two or three, and the deepest connect adjacent spines and are continuous with the interspinous ligament. Most of the ligament is formed by the tendons of muscles with posterior midline attachments, i.e. semispinalis, longissimus, trapezius and latissimus dorsi. Only the most superficial fibres lack any connection with muscle. Below L4, the ligament is replaced by the decussating fibres of latissimus dorsi.

Intertransverse ligaments

Intertransverse ligaments run between adjacent transverse processes. At cervical levels, they consist of a few, irregular fibres that are largely replaced by intertransverse muscles; in the thoracic region, they are cords intimately blended with adjacent muscles; and in the lumbar region, they are thin and membranous. For the detailed anatomy of the lumbar intertransverse ligaments, see Bogduk (2012).

Ligamentous instability

Damage to the ligaments controlling stability of the column may occur in the absence of evident bony pathology. This is particularly prevalent in inflammatory disease of the upper cervical spine, where rheumatoid arthritis may weaken or destroy the ligaments on which atlanto-axial stability depends (**Fig. 46.57**). The transverse ligament is stronger than the dens, which therefore usually fractures before the ligament ruptures. The alar ligaments are weaker, and combined head flexion and rotation may avulse one or both alar ligaments; rupture of one side results in an increase of about one-third in the range of rotation to the opposite side. Pathological softening of the transverse and adjacent ligaments or of the lateral atlanto-axial joints results in atlanto-axial subluxation,

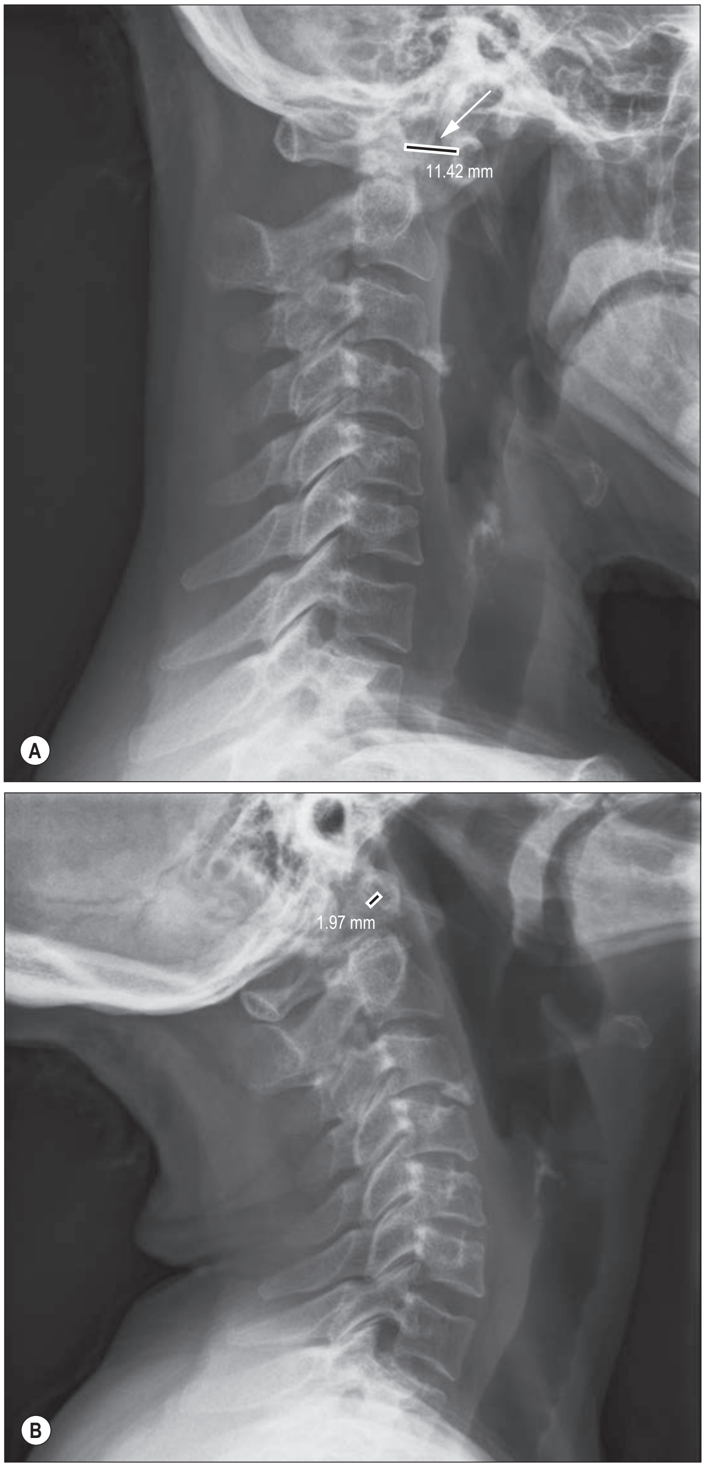

Fig. 46.57 Atlanto-axial instability in the setting of rheumatoid arthritis. Note the marked widening of the atlanto–dens interval seen on extension radiographs (arrow) (**A**), when compared with flexion (**B**).

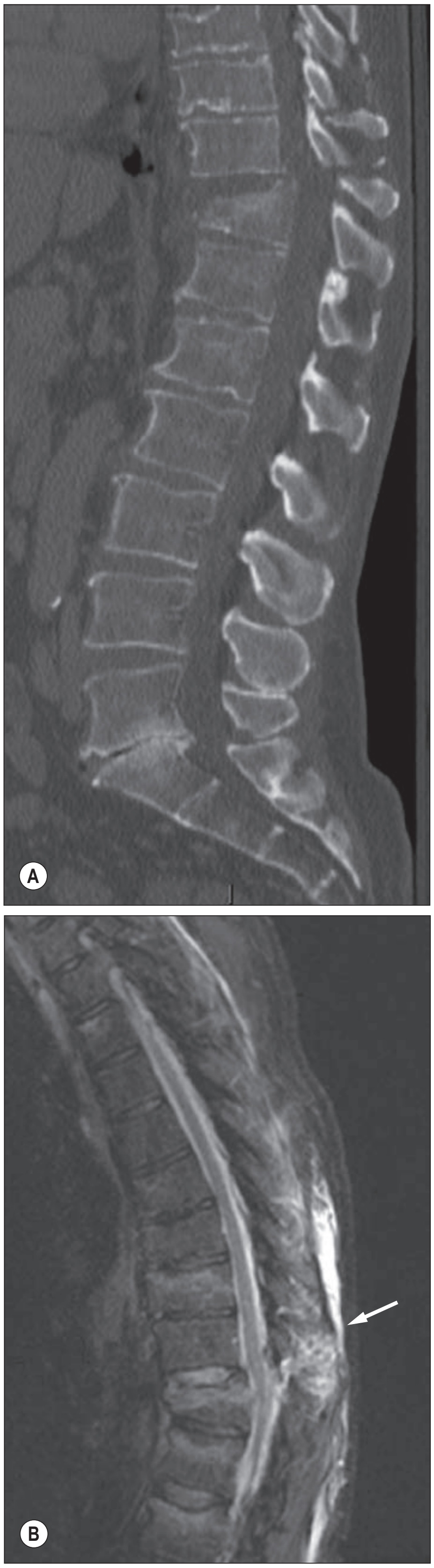

Fig. 46.58 **A**, A sagittal CT reconstruction showing an osseous and ligamentous injury at T10–T11 sustained by a 54-year-old male after a major compression injury. **B**, The MR image shows gross disruption of the supraspinous and interspinous ligaments (arrow).

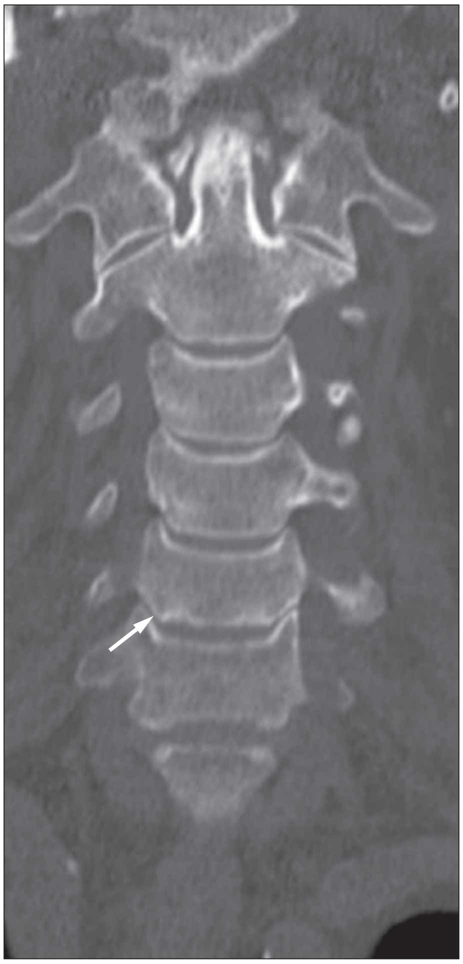

Fig. 46.59 A coronal CT reconstruction: note uncovertebral 'joint' (arrow).

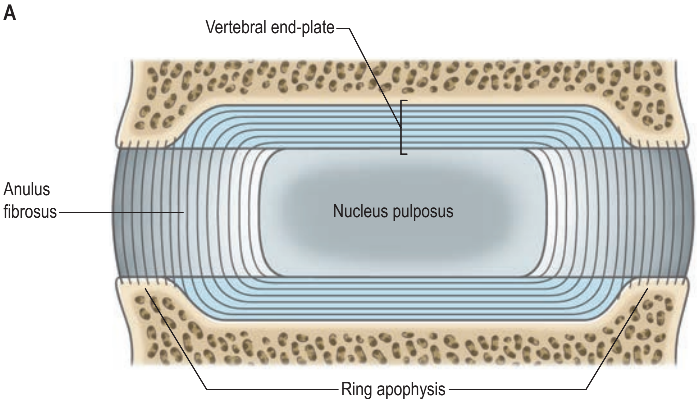

Fig. 46.60 **A**, The structure of the vertebral end-plate: the collagen fibres of the inner two-thirds of the anulus fibrosus sweep around into the vertebral end-plate and form its fibrocartilaginous component. The peripheral fibres of the anulus are anchored into the bone of the ring apophysis. (With permission from Bogduk N 2012 Clinical Anatomy of the Lumbar Spine and Sacrum, 5th ed. Edinburgh: Churchill Livingstone.) (B–D, *continued online*)

which may cause spinal cord injury. Ligamentous damage may also occur in spinal injuries (**Fig. 46.58**), particularly at cervical levels. Damage may also occur as a result of spinal surgery where ligament removal in addition to bone removal (such as partial facet resection) may result in iatrogenic instability.

Developmental laxity of ligaments may also lead to problems with instability, especially if there is an episode of trauma; this combination is probably responsible for atlanto-axial rotational instability. Laxity of cervical spinal ligaments may be a normal variant in children and lead to diagnostic difficulties. In radiographs of the upper cervical spine in children aged less than 8 years, a deceptive appearance of subluxation ('pseudosubluxation') may result from a combination of ligamentous laxity and facet orientation. This usually occurs between C2 and C3 but may occasionally be seen at C3/C4. Clinical and other radiological features should facilitate the correct diagnosis.

JOINTS

All vertebrae from C2 to S1 articulate by secondary cartilaginous joints (symphyses) between their bodies, synovial joints between their articular processes, and fibrous joints between their laminae, transverse and spinous processes. In the cervical region, from C3 to C7, joints have been described between the uncinate or neurocentral processes of the inferior vertebral body and the bevelled lateral border of the superior body at each level. These small uncovertebral or neurocentral 'joints' are absent at birth, do not contain synovium, and are probably clefts in the intervertebral discs (**Fig. 46.59**).

Intervertebral joints

Joints between the vertebral bodies

Joints between vertebral bodies are symphyses. Typical vertebral bodies are united by anterior and posterior longitudinal ligaments and by fibrocartilaginous intervertebral discs between sheets of hyaline cartilage (vertebral end-plates).

Articulating surfaces: intervertebral discs The intervertebral discs are the chief bonds between the adjacent surfaces of vertebral bodies from C2 to the sacrum. Except at the sites of the uncovertebral (neurocentral) joints of Luschka, disc outlines correspond with the adjacent bodies. Their thickness varies in different regions and within individual discs. Each disc consists of an outer lamellated anulus fibrosus and an inner nucleus pulposus (see Fig. 46.54A).

In cervical and lumbar regions the discs are thicker anteriorly, contributing to the anterior convexity of the vertebral column. In the thoracic region they are nearly uniform, and the anterior concavity is largely due to the vertebral bodies. Discs are thinnest in the upper thoracic region and thickest in the lumbar region. They adhere to thin layers of cartilage on the superior and inferior vertebral surfaces, the vertebral end-plates. The latter do not reach the periphery of the vertebral bodies but are encircled by ring apophyses. The end-plates contain both hyaline cartilage and fibrocartilage. The fibrocartilaginous component lies nearer to the disc and is sometimes considered not to be part of the end-plate itself. The fibrocartilaginous components of the end-plates above and below the nucleus pulposus, together with the innermost lamellae of the anulus fibrosus, form a flattened sphere of collagen that surrounds and encloses the nucleus (**Fig. 46.60**). The overall proportion of fibrocartilage in the end-plate increases with age. While all discs are attached to the anterior and posterior longitudinal ligaments, discs in the thoracic region are additionally tied laterally, by intra-articular ligaments, to the heads of ribs articulating with adjacent vertebrae. Intervertebral discs form about one-quarter of the length of the postaxial vertebral column; cervical and lumbar regions make a greater contribution than the thoracic and are thus more pliant.

Anulus fibrosus. The anulus fibrosus has a narrow outer collagenous zone and a wider inner fibrocartilaginous zone. Its lamellae, which are convex peripherally when seen in vertical section, are incomplete collars. The internal vertical concavity of the lamellae conforms to the surface profile of the nucleus pulposus. In all quadrants of the anulus, about half the lamellae are incomplete; the proportion increases in the posterolateral region. The exact nature of the interlamellar substance remains in some doubt. Posteriorly, lamellae join in a complex manner. Fibres in the rest of each lamella are parallel and run obliquely between vertebrae at about 65° to the vertical (see Fig. 46.54A). Fibres in successive lamellae cross each other obliquely in opposite directions, thus limiting rotation. The obliquity of fibres in deeper zones varies in different lamellae. Posterior fibres may sometimes be predominantly vertical, which possibly predisposes them to herniation.

This standard description of the anulus may not apply at all spinal levels; a cadaveric study indicates that the anulus is usually incomplete posteriorly in adult cervical discs (Mercer and Bogduk 1999) (see Fig. 46.54A).

Nucleus pulposus. The nucleus pulposus is better developed in cervical and lumbar regions and lies between the centre of the disc and its posterior surface. At birth it is large, soft and gelatinous, and is composed of mucoid material. It contains a few multinucleated notochordal cells and is invaded by cells and collagen fibres from the inner zone of the adjacent anulus fibrosus. Notochordal cells disappear in the first decade, and the mucoid material is gradually replaced by fibrocartilage,

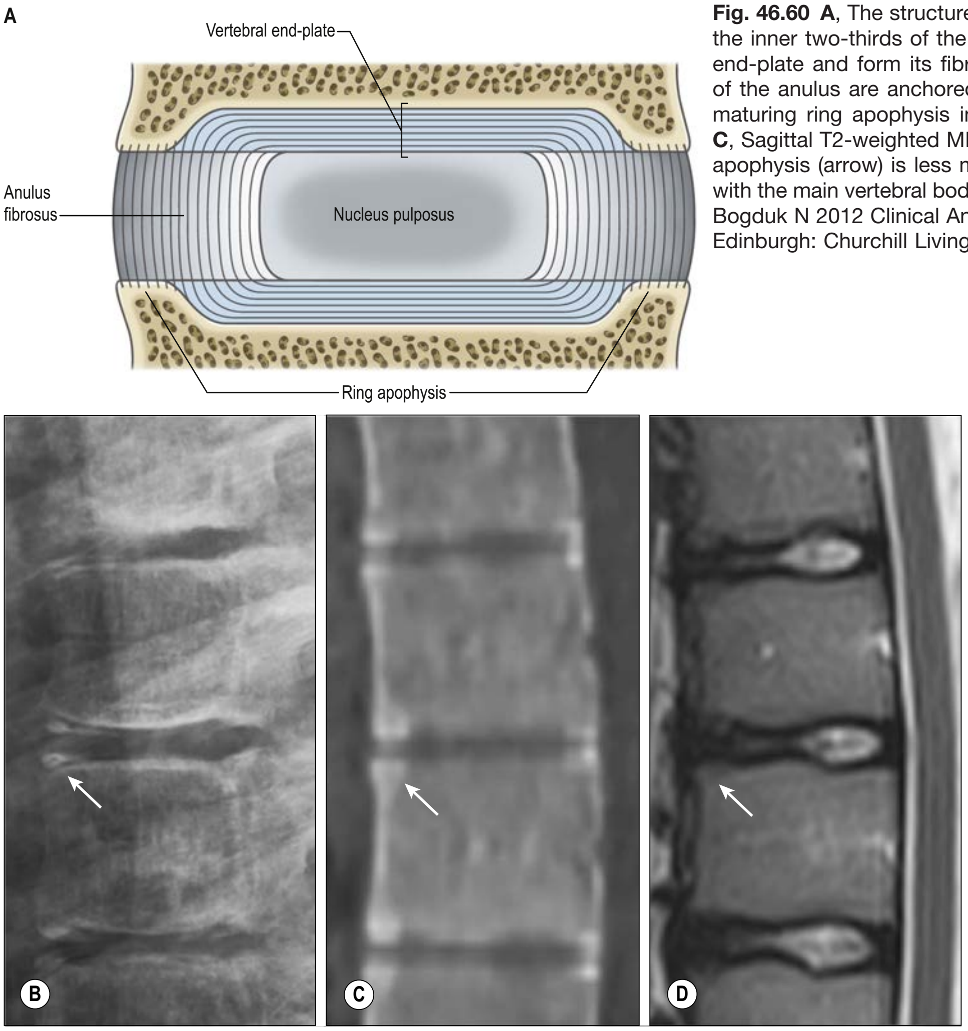

Fig. 46.60 **A**, The structure of the vertebral end-plate: the collagen fibres of the inner two-thirds of the anulus fibrosus sweep around into the vertebral end-plate and form its fibrocartilaginous component. The peripheral fibres of the anulus are anchored into the bone of the ring apophysis. **B**–**D**, The maturing ring apophysis in the mid-thoracic spine. **B**, Lateral radiograph. **C**, Sagittal T2-weighted MRI. **D**, Sagittal CT multiplanar reconstruction. The apophysis (arrow) is less mature in **B** (16 years old), having started to fuse with the main vertebral body in **C** and **D** (late teens). (A, With permission from Bogduk N 2012 Clinical Anatomy of the Lumbar Spine and Sacrum, 5th ed. Edinburgh: Churchill Livingstone.)

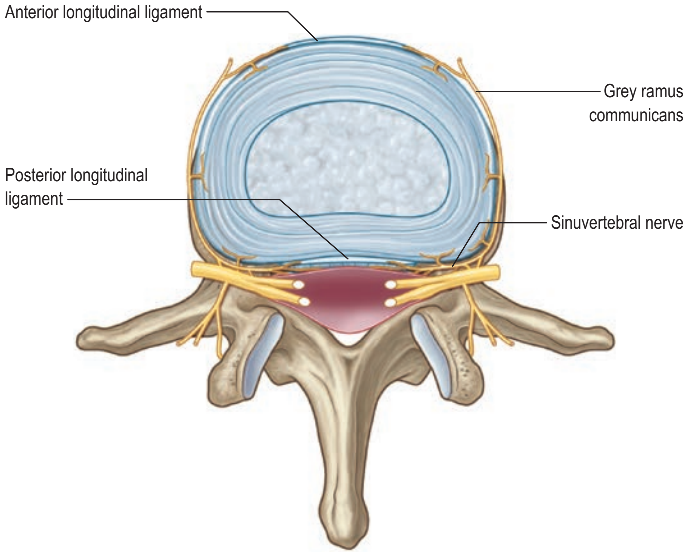
Anterior longitudinal ligament
Grey ramus communicans
Posterior longitudinal ligament
Sinuvertebral nerve

Fig. 46.61 Innervation of a lumbar intervertebral disc. Branches of the grey rami communicantes and the sinuvertebral nerves are shown entering the disc and the anterior and posterior longitudinal ligaments. Branches of the sinuvertebral nerves also supply the ventral aspect of the dural sac and the dural nerve root sleeve.

derived mainly from the anulus fibrosus and the plates of hyaline cartilage adjoining the vertebral bodies. The nucleus pulposus becomes less differentiated from the remainder of the disc as age progresses, and gradually becomes less hydrated and increasingly fibrous. The type II collagen of the nucleus becomes more like the type I of the anulus as its fibril diameter increases. The quantity of aggregated proteoglycans in the nucleus decreases, while the keratan sulphate/chondroitin sulphate ratio increases. As increased cross-linking occurs between collagen and the proteoglycans, the discs lose their water-binding capacity and become stiffer and more liable to injury. Contrary to what was previously thought, it has now been shown that lumbar discs do not decrease in overall height as a part of normal ageing. The anulus gradually loses height as its radial bulge increases, but the nucleus retains height and may increase in convexity as it increasingly indents the endplate. Loss of trunk height with age results from a decrease in vertebral body height (Bogduk 2012). When the disc is not loaded, pressure in the nucleus pulposus is low at all ages.

For a review of the structure and function of the human intervertebral disc, see Adams and Dolan (2005).

Ligaments The ligaments associated with the joints between the vertebral bodies are described on pages 853.

Vascular supply Small offshoots of spinal branches of arteries supplying the vertebral column form an anastomosis on the outer surface of the anulus fibrosus and supply its most peripheral fibres. Normal discs are otherwise avascular and are dependent for their nutrition on diffusion from vertebral bone beneath adjacent end-plates and from the peripheral anulus. Vascular and avascular parts differ in their reaction to injury. Venous drainage is via the external and internal vertebral venous plexuses to the intervertebral veins and thence to the larger named veins that drain the vertebral column. Lymphatic drainage of the vertebral column is briefly considered above. Nothing specific is known about the lymphatic drainage of the disc.

Innervation The nerve supply of intervertebral discs has been studied in detail in the lumbar region (Fig. 46.61). The outer third of the anulus is innervated by the sinuvertebral nerves; each sinuvertebral nerve supplies both the disc at the level of its spinal nerve of origin and the disc one level above. The anterior part of the anulus is supplied by the sympathetic (preganglionic, grey ramus communicans) rather than by the mixed nerve. In damaged and degenerate discs, the nerves may penetrate more centrally into the disc substance. The sinuvertebral nerves are condensations within extensive nerve plexuses that lie on the posterior longitudinal ligament. Similar plexuses have been demonstrated anteriorly, covering the anterior longitudinal ligament, and laterally in the fetus.

Relations and 'at risk' structures Posterior, lateral and anterior relations of the intervertebral disc are important in the planning of interventional investigative and therapeutic procedures ranging from discography to open disc surgery. The posterolateral surface of the disc forms the anterior boundary of the intervertebral foramen on each side, and so is closely related to the spinal nerve and its accompanying vessels. More centrally, the disc is related posteriorly to the dura mater covering the spinal cord and the cauda equina. Anterior relations of the discs vary considerably with vertebral level, but important 'at risk' structures include the pharynx and oesophagus, the descending aorta and

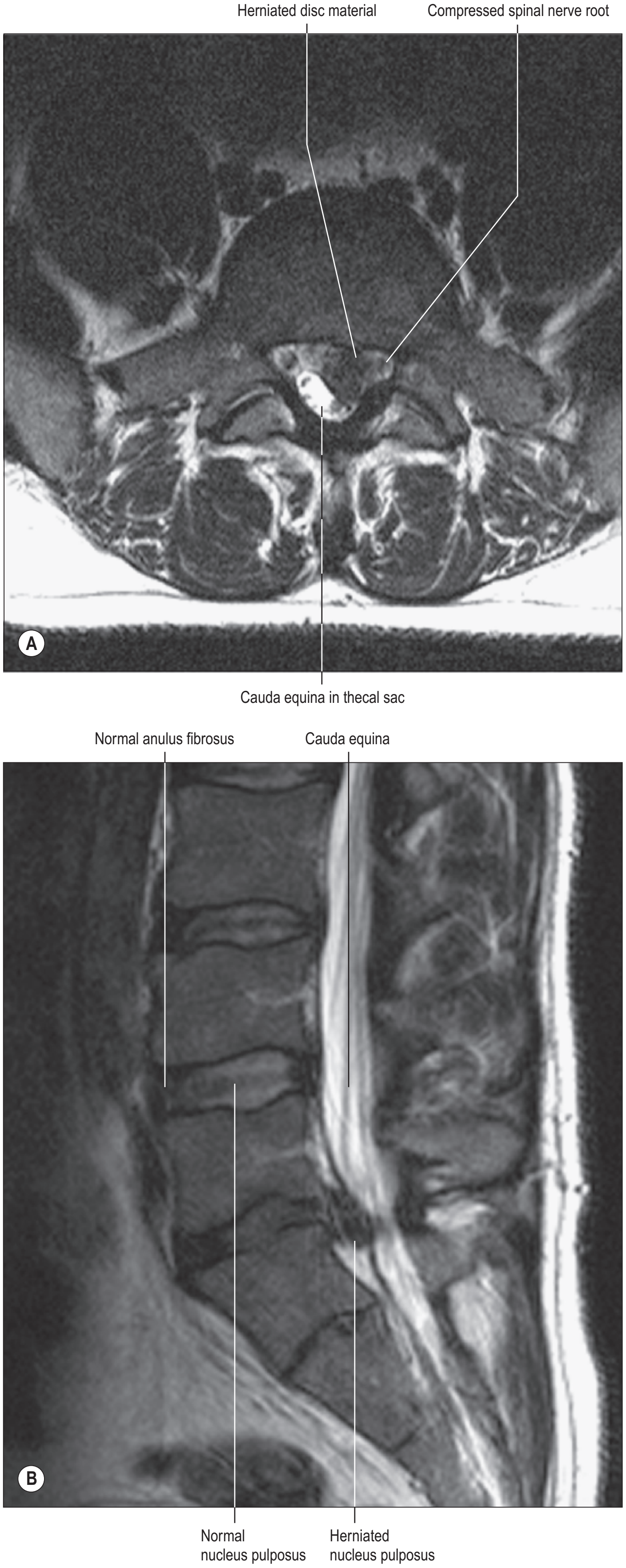

Fig. 46.62 Left posterolateral disc extrusion. **A**, Axial view. **B**, Sagittal view.

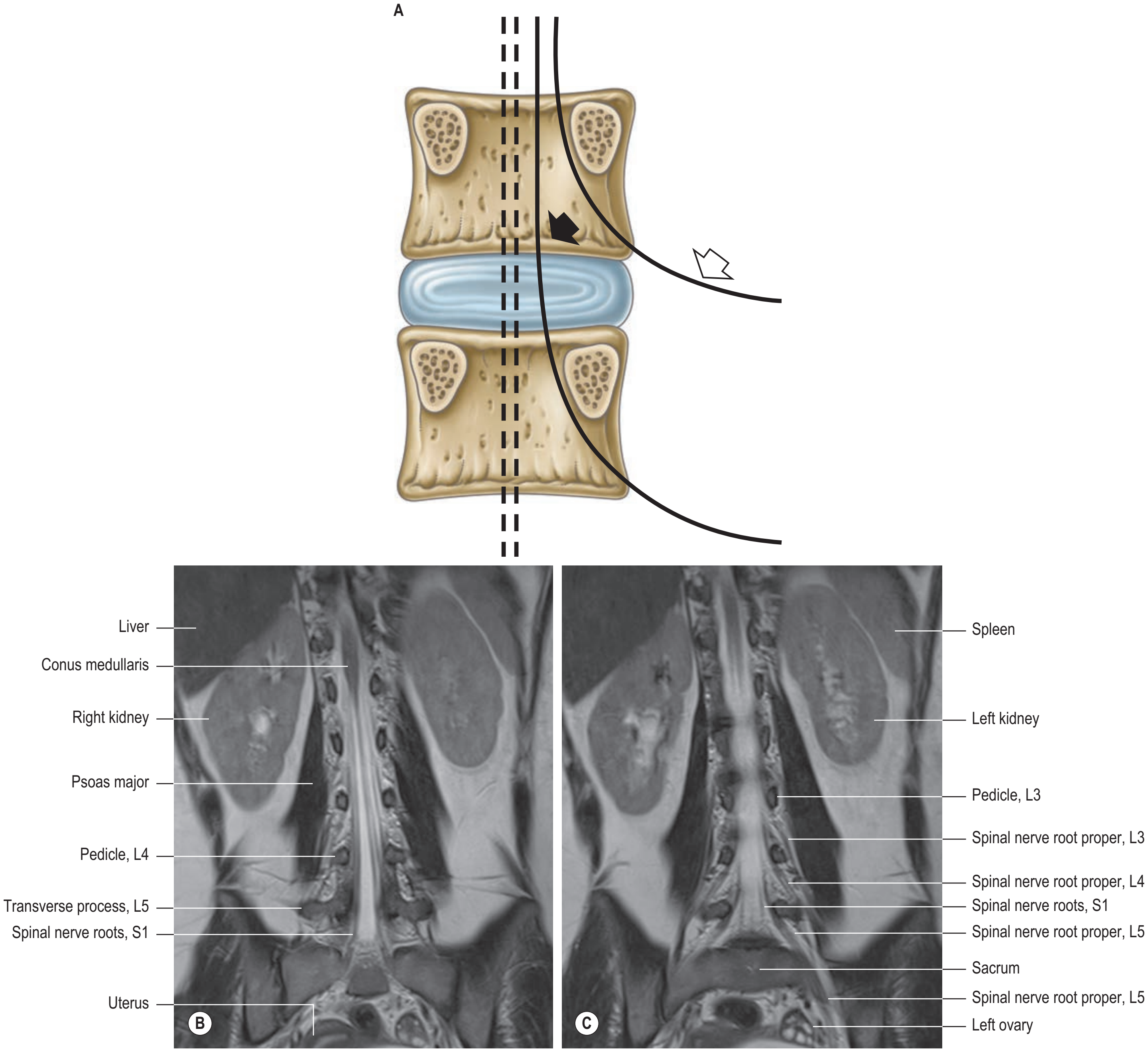
A
Liver
Conus medullaris
Right kidney
Psoas major
Pedicle, L4
Transverse process, L5
Spinal nerve roots, S1
Uterus
B
C
Spleen
Left kidney
Pedicle, L3
Spinal nerve root proper, L3
Spinal nerve root proper, L4
Spinal nerve roots, S1
Spinal nerve root proper, L5
Sacrum
Spinal nerve root proper, L5
Left ovary

Fig. 46.63 **A**, Exiting and traversing nerve roots. The upper root (open arrow) is the exiting root at this level; the lower (closed arrow) is the traversing root here, which becomes the exiting root at the level below. The dotted roots are traversing roots of the lower segment. **B**–**C**, T2-weighted coronal MRIs from posterior to anterior in a teenage female investigated for scoliosis, showing the lumbosacral spinal nerve roots descending from the conus medullaris and exiting through the intervertebral foramina.

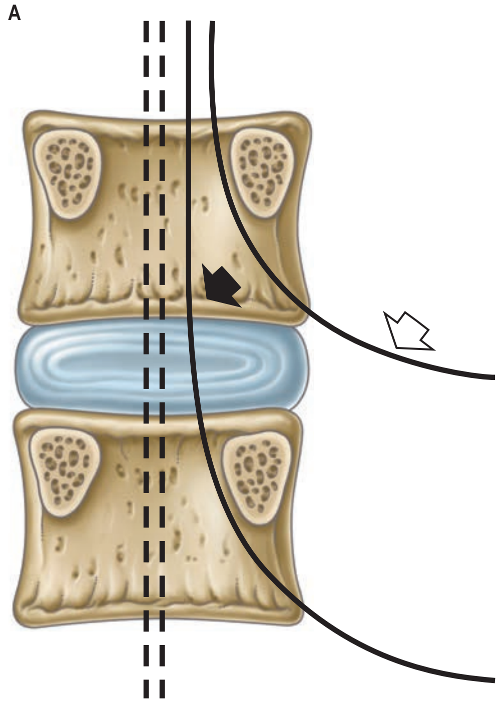

Fig. 46.63 **A**, Exiting and traversing nerve roots. The upper root (open arrow) is the exiting root at this level; the lower (closed arrow) is the traversing root here, which becomes the exiting root at the level below. The dotted roots are traversing roots of the lower segment. (B–C, *continued online*)

the inferior vena cava. Laterally, relations change with level, but the parietal pleura in the thorax, and the sympathetic trunk and psoas muscles in the lumbar region, are important examples.

Prolapsed intervertebral disc A prolapsed intervertebral disc most commonly affects the 20–55-year age group and is most often seen at the L4/L5 and lumbosacral levels. It may also affect the cervical discs, particularly at C5/C6 and C6/C7. The thoracic discs are rarely affected. Acute tearing or chronic degeneration of the posterior lamellae of the anulus fibrosus allows deformation and herniation of the disc contents. The disc most often prolapses just lateral to the posterior longitudinal ligament and can compress one or two spinal nerves unilaterally (Fig. 46.62). Much less commonly, the prolapse is central, in the midline posteriorly. The compression of neural structures may then be bilateral, affecting the cord itself or the whole cauda equina. If the damaged anulus ruptures completely, some of the nuclear tissue may escape into the vertebral and 'root' canals. This sequestrated material may migrate within the canals and cause nerve compression at spinal levels distant from that of the disc rupture. The disc material itself may have an irritative effect on the spinal nerve.

Regarding the anatomy of the vertebral canal and intervertebral foramen in relation to disc prolapse, it is important to understand that one or both of two spinal nerves and their roots may be affected by a single prolapse, depending on the exact site of the prolapse in the horizontal plane. At the level of each disc and foramen, there are two spinal nerves (and their roots) to consider: these are the exiting nerve and the traversing nerve (Fig. 46.63) (MacNab and McCulloch 1990). The nerve usually affected at lumbar levels is the traversing nerve, which crosses the back of the disc on its way to become the exiting nerve at the level below. Thus a lumbosacral (i.e. L5/S1) disc prolapse usually compresses the S1 nerve. However, a prolapse may affect the exiting nerve at its own level. This is especially likely if the prolapse is in the extraforaminal zone of the 'root' canal, the so-called 'far lateral' prolapse. At cervical levels, because the roots and nerve leave the vertebral canal almost horizontally, the prolapse usually affects the exiting nerve. This nerve will still bear the number of the vertebra below the affected disc because cervical nerves exit the canal above the pedicle of their numerically corresponding vertebra. Neurological presentation will include signs and symptoms of spinal nerve damage at the affected level. Thus pain and sensory loss will be dermatomal in distribution. Sensory changes usually precede motor loss.

Internal disruption of a lumbar intervertebral disc is more common than disc prolapse and is now an increasingly recognized cause of back pain. Typically, the nucleus is decompressed and the inner lamellae of the anulus appear to collapse into it.

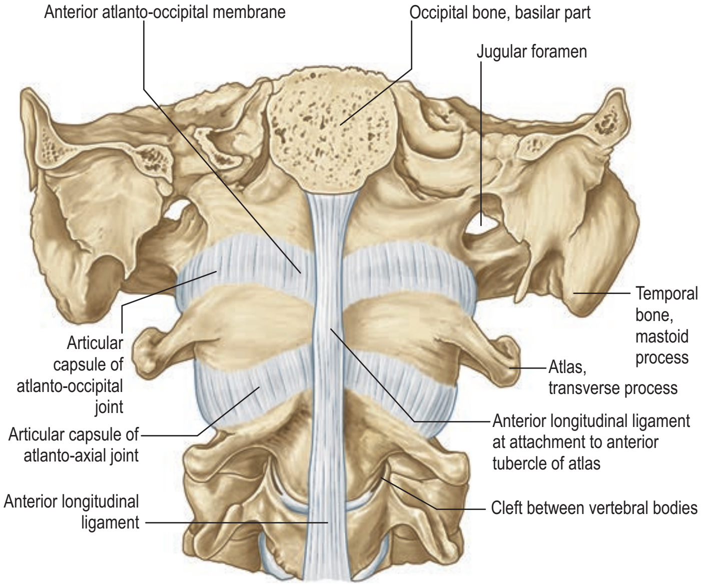
Anterior atlanto-occipital membrane
Occipital bone, basilar part
Jugular foramen
Temporal bone, mastoid process
Articular capsule of atlanto-occipital joint
Atlas, transverse process
Anterior longitudinal ligament at attachment to anterior tubercle of atlas
Articular capsule of atlanto-axial joint
Anterior longitudinal ligament
Cleft between vertebral bodies

Fig. 46.65 The atlanto-occipital and atlanto-axial joints, anterior aspect. On each side a small cleft has been opened between the lateral part of the upper surface of the body of the third cervical vertebra and the bevelled, inferior surface of the body of the axis.

For more detail on disc pathology and its consequences, see Adams and Dolan (2005).

Facet (zygapophysial) joints

Joints between the vertebral articular processes (zygapophyses) are synovial and have long been called zygapophysial joints by anatomists. However, in current clinical practice they are commonly called 'facet joints'. Detailed description of the anatomy of these joints is to be found in Bogduk (2012), where the author explains why the term 'facet joint' is both incorrect and essentially ambiguous, on the grounds that facets are not restricted to zygapophysial articular processes and occur, for example, in both costovertebral and costotransverse joints.

Articulating surfaces Facet joints are of the simple (cervical and thoracic) or complex (lumbar) synovial variety; the articulating surfaces are covered in hyaline cartilage and are carried on mutually adapted articular processes. The size and shape of these processes vary with spinal level and are described with the individual vertebrae.

Fibrous capsule The fibrous capsule is thin and loose and attached peripherally to the articular facets of adjacent articular processes. The capsules are longer and looser in the cervical region. According to Bogduk (2012), the anterior fibrous capsule is replaced entirely by the ligamentum flavum in the lumbar spine.

Intracapsular structures. Bogduk describes two types of intra-articular structure in lumbar facet joints: namely, subcapsular fat and 'meniscoid' structures. The latter structures may be collagenous, fibroadipose or purely adipose, and project into the crevices between non-congruent articular surfaces. They resemble inclusions seen in the small joints of the hand; their function is conjectural.

Ligaments Ligaments that work in conjunction with, and modify the function of, the facet joints throughout the vertebral column are described on pages 853–854.

Synovial membrane The synovium is attached around the periphery of the articular cartilages and lines the fibrous capsule. In the lumbar region, it is reflected over the intracapsular structures described above.

Vascular supply The posterior spinal branches of the arteries that supply the vertebral column form arterial anastomoses around the facet joints. Venous drainage is via the external and internal posterior vertebral venous plexuses to the intervertebral veins and thence to the larger named veins that drain the vertebral column. Lymphatic drainage follows the principles described for the vertebral column.

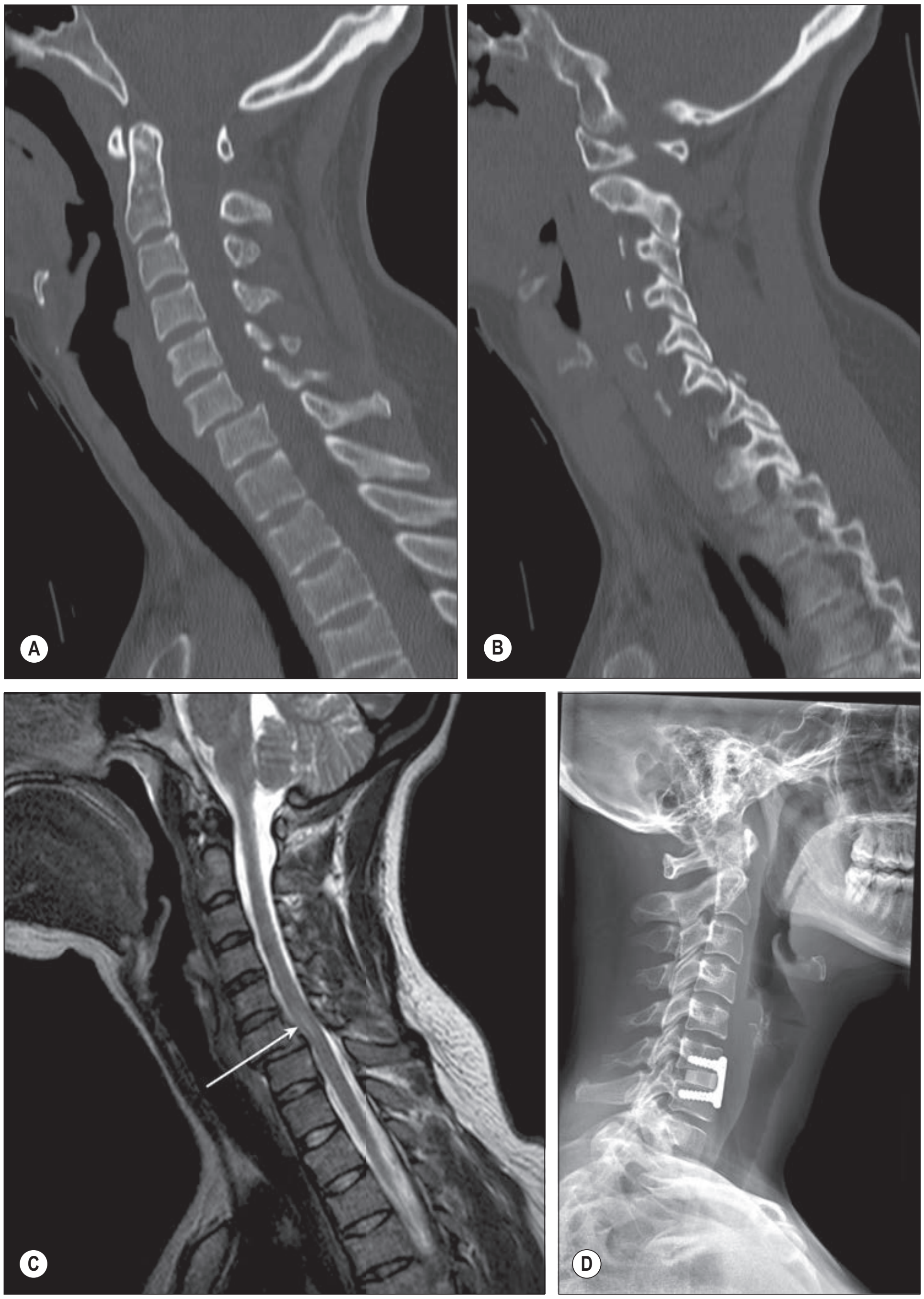

Fig. 46.64 **A**, A sagittal CT reconstruction showing C6–C7 flexion distraction injury with traumatic spondylolisthesis. **B**, A C6–C7 perched facet with a small chip fracture of the superior articular process of C7. **C**, A T2-weighted sagittal MRI with an associated spinal cord contusion (arrow) due to the injury. **D**, Lateral X-ray status post-surgical reduction via anterior cervical discectomy and placement of an allograft and plate and screws.

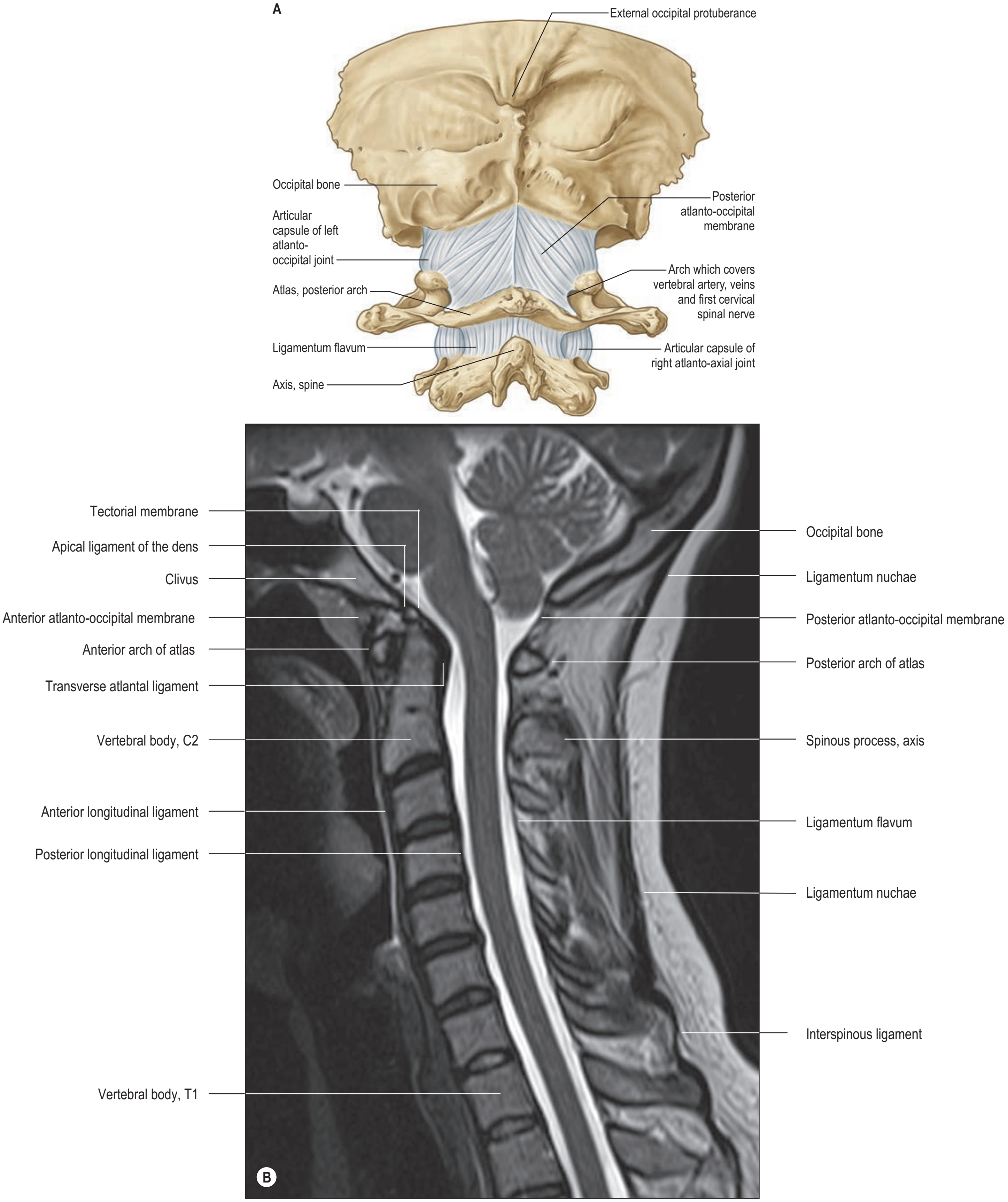
A
External occipital protuberance
Occipital bone
Articular capsule of left atlanto-occipital joint
Posterior atlanto-occipital membrane
Atlas, posterior arch
Arch which covers vertebral artery, veins and first cervical spinal nerve
Ligamentum flavum
Articular capsule of right atlanto-axial joint
Axis, spine
Tectorial membrane
Apical ligament of the dens
Clivus
Anterior atlanto-occipital membrane
Anterior arch of atlas
Transverse atlantal ligament
Vertebral body, C2
Anterior longitudinal ligament
Posterior longitudinal ligament
Vertebral body, T1
Occipital bone
Ligamentum nuchae
Posterior atlanto-occipital membrane
Posterior arch of atlas
Spinous process, axis
Ligamentum flavum
Ligamentum nuchae
Interspinous ligament
B

Fig. 46.66 **A**, The atlanto-occipital and atlanto-axial joints, posterior aspect. **B**, An axial T2-weighted MRI demonstrating the ligamentous structures of the cervical spine.

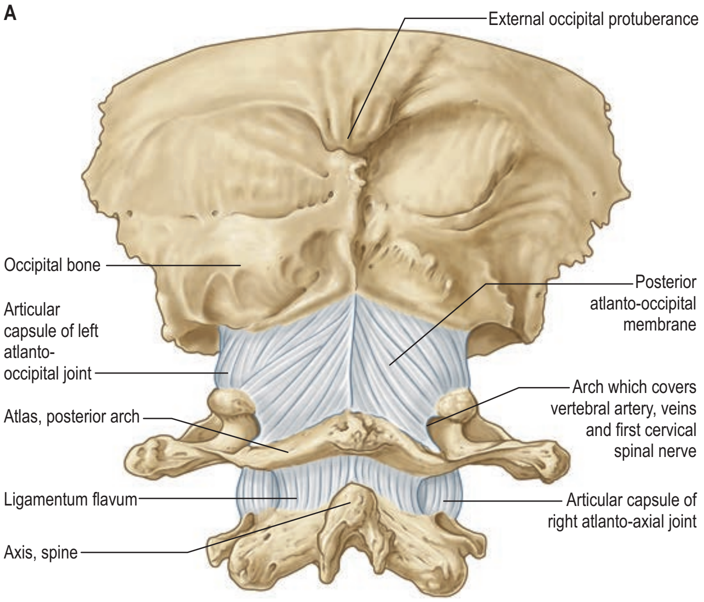
A
External occipital protuberance
Occipital bone
Articular capsule of left atlanto-occipital joint
Posterior atlanto-occipital membrane
Atlas, posterior arch
Arch which covers vertebral artery, veins and first cervical spinal nerve
Ligamentum flavum
Articular capsule of right atlanto-axial joint
Axis, spine

Fig. 46.66 **A**, The atlanto-occipital and atlanto-axial joints, posterior aspect. (B, *continued online*)

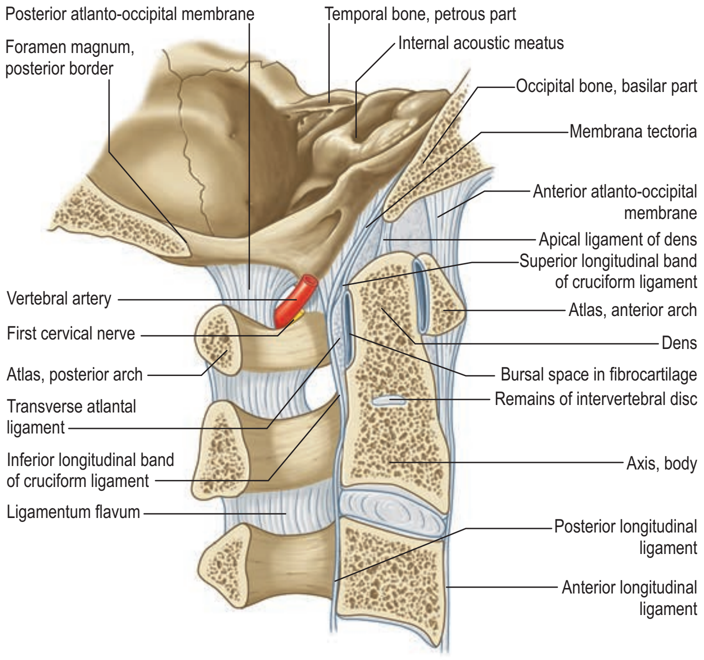
Posterior atlanto-occipital membrane
Temporal bone, petrous part
Foramen magnum, posterior border
Internal acoustic meatus
Occipital bone, basilar part
Membrana tectoria
Anterior atlanto-occipital membrane
Apical ligament of dens
Superior longitudinal band of cruciform ligament
Vertebral artery
Atlas, anterior arch
First cervical nerve
Dens
Atlas, posterior arch
Bursal space in fibrocartilage
Remains of intervertebral disc
Transverse atlantal ligament
Inferior longitudinal band of cruciform ligament
Axis, body
Ligamentum flavum
Posterior longitudinal ligament
Anterior longitudinal ligament

Fig. 46.67 Median sagittal section through the occipital bone and first to third cervical vertebrae.

Innervation The facet joints are profusely innervated by medial branches of the dorsal primary rami of the spinal nerves, which give articular branches to the joints above and below them.

Relations and 'at risk' structures Anteriorly, the capsules of the facet joints form the posterior boundaries of the intervertebral foramina. Posteriorly and laterally, the joints are related to the deep muscles of the back, some of whose fibres attach to the capsules. The joints also lie in close relation to the medial branches of the dorsal rami of the spinal nerves and to their accompanying arteries and veins. Damage to the medial branches of the dorsal rami may denervate the deep back muscles. Access to the facet joints and their related nerves may be required in the diagnosis and treatment of spinal pain.

Additionally, facet joints can be subluxed or fractured with trauma. This may compromise the neuroforamen. It is often also associated with displacement of adjacent vertebrae and disc, and so the spinal canal and its contents may be compromised (**Fig. 46.64**).

Lumbar articular tropism In the lumbar region, asymmetric orientation of the facet joints occurs in about one-fifth of the population. Such facet tropism does not appear to predispose to degenerative disc disease.

Craniovertebral joints

The articulation between the cranium and vertebral column is specialized to provide a wider range of movement than those that occur in the rest of the axial skeleton. It consists of the occipital condyles, the atlas and the axis. It functions like a universal joint that permits horizontal and vertical scanning movements of the head, and is adapted for eye–head coordination.

Atlanto-occipital joints

The atlas articulates with the occipital bone of the skull by a pair of synovial joints. The bones are connected by articular capsules and by the anterior and posterior atlanto-occipital membranes (**Figs 46.65–46.66**).

Articulating surfaces Each joint consists of two reciprocally curved articular surfaces, one on the occipital condyle and the other on the lateral mass of the atlas. The atlantal facets are concave and tilted medially.

Fibrous capsules The fibrous capsules surround the occipital condyles and superior atlantal articular facets. They are thicker posteriorly and laterally, where the capsule is sometimes deficient, and may communicate with the joint cavity between the dens and the transverse atlantal ligament.

Ligaments The ligaments are the anterior and posterior atlanto-occipital membranes.

Anterior atlanto-occipital membrane. The anterior atlanto-occipital membrane (see Fig. 46.65; **Fig. 46.67**) is a broad, dense fibrous structure that connects the anterior margin of the foramen magnum to the upper border of the anterior arch of the atlas. Laterally, it blends with the joint capsule; medially, it is strengthened by a median cord, which is the anterior longitudinal ligament stretching between the basilar occipital bone and anterior atlantal tubercle.

Posterior atlanto-occipital membrane. The posterior atlanto-occipital membrane (see Figs 46.66–46.67) is broad but relatively thin, and connects the posterior margin of the foramen magnum to the upper border of the posterior atlantal arch, blending laterally with the joint capsules. It arches over the grooves for the vertebral arteries, venous plexuses and first cervical nerve, and forms the 'floor' of the suboccipital triangle. The ligamentous border of this arch is sometimes ossified. The membrane is usually attached by a soft tissue 'bridge', which may contain muscle or tendon fibres, to rectus capitis posterior minor, and is firmly attached anteriorly to the spinal dura in the same area (Zumpano et al 2006). The ligaments connecting the axis and the occipital bone are functionally involved with the posterior atlanto-occipital membrane.

Synovial membrane The synovial cavities of one or both joints may communicate with that of the posterior component of the median atlanto-axial joint.

Vascular supply The arterial supply of this region is derived from an anastomosis between branches of the deep cervical, occipital and vertebral arteries.

Innervation The joints are innervated by branches of the ventral primary ramus of the first cervical spinal nerves.

Factors maintaining stability Factors maintaining stability include the fibrous capsules, the atlanto-occipital membranes, the shape of the articular surfaces, the ligaments connecting the axis and the occipital bone, the ligamentum nuchae and the posterior neck muscles. The suboccipital muscles play an important proprioceptive and postural role.

Muscles producing movements The orientation and shape of the atlanto-occipital joints allow mainly for flexion–extension, which has a total range of about 15°. Axial rotation and lateral flexion have not been measured in living subjects, but a few degrees of motion in these directions can be produced by forceful movement in cadavers.

The following muscles produce these movements: for flexion – longus capitis and rectus capitis anterior; for extension – recti capitis posteriores major and minor, obliquus capitis superior, semispinalis capitis, splenius capitis and trapezius (cervical part); for lateral flexion – rectus capitis lateralis, semispinalis capitis, splenius capitis, sternocleidomastoid and trapezius (cervical part); and for rotation – obliquus capitis superior, rectus capitis posterior minor, splenius capitis and sternocleidomastoid.

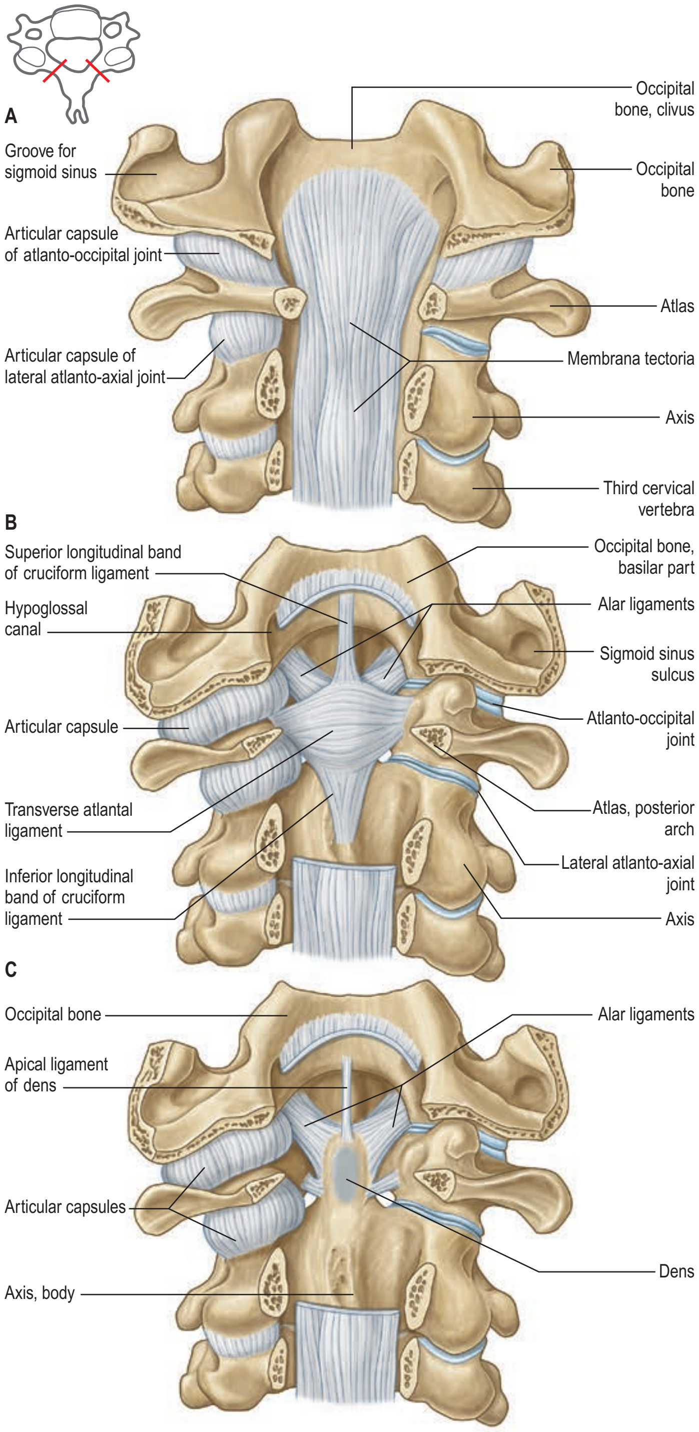

Fig. 46.68 The posterior aspect of the atlanto-occipital and atlanto-axial joints. The posterior part of the occipital bone and the laminae of the cervical vertebrae have been removed and the atlanto-occipital joint cavities opened. (Sobotta Atlas of Human Anatomy © Elsevier GmbH, Urban & Fischer, Munich.)

Relations and 'at risk' structures Posteriorly, the joints are closely related to the vertebral arteries as they pass from the foramina transversaria into the foramen magnum. The dorsal primary ramus of the first cervical nerve and rectus capitis posterior major lie posteromedially and rectus capitis anterior lies anteriorly.

Atlanto-axial joints

The atlas articulates with the axis at three synovial joints. These are a pair between the lateral masses, and a median complex between the dens of the axis and the anterior arch and transverse atlantal ligament.

Articulating surfaces The articular surfaces of the joints between the lateral masses are often classified as planar. The bony articular surfaces are more complex in shape and are usually reciprocally concave in the coronal plane; the medial parts are somewhat convex in the sagittal plane (especially that of the axis). The cartilaginous articular surfaces are usually less concave. The median joint is a pivot between the dens and a ring formed by the anterior arch and transverse atlantal ligament. A vertically ovoid facet on the anterior dens articulates with a facet on the posterior aspect of the anterior atlantal arch.

Fibrous capsules The fibrous capsules for the lateral joints are attached to the articular margins and are thin and loose. Each has a posteromedial accessory ligament attached below to the axial body near the base of its dens, and above to the lateral atlantal mass near the transverse ligament. The fibrous capsule for the median joint is also relatively weak and loose, especially superiorly.

Ligaments Anteriorly, the vertebral bodies are connected by the anterior longitudinal ligament (see Figs 46.65, 46.67): here, a strong, thickened band attaches above to the lower border of the anterior tubercle of the anterior arch of the atlas and below to the front of the axial body. Posteriorly, the vertebral arches are joined by the ligamenta flava (see Figs 46.66–46.67), which are attached to the lower border of the atlantal arch above and to the upper borders of the axial laminae. At this level, these ligaments form a thin membrane, pierced laterally by the second cervical nerves.

Transverse atlantal and cruciform ligaments. The transverse atlantal ligament (**Fig. 46.68**; see Fig. 46.33) is a broad, strong band that arches across the atlantal ring behind the dens; its length varies about a mean of 20 mm. It is attached laterally to a small but prominent tubercle on the medial side of each atlantal lateral mass, and broadens medially where it is covered anteriorly by a thin layer of articular cartilage. It consists almost entirely of collagen fibres, which, in the central part of the ligament, cross one another at an angle to form an interlacing mesh. From its upper margin a strong median longitudinal band arises that inserts into the basilar part of the occipital bone between the apical ligament of the dens and membrana tectoria, and from its inferior surface a weaker and less consistent longitudinal band passes to the posterior surface of the axis. These transverse and longitudinal components together constitute the cruciform ligament. The transverse ligament divides the ring of the atlas into unequal parts (see Figs 46.32–46.33). The posterior two-thirds surrounds the spinal cord and meninges, and the anterior third contains the dens, which the transverse ligament retains in position even when all other ligaments are divided.

Ligaments connecting axis and occipital bone. Ligaments connecting the axis and the occipital bone consist of the membrana tectoria, the paired alar ligaments, the median apical ligament, and the longitudinal components of the cruciform ligament (see Figs 46.67–46.68).

Membrana tectoria Inside the vertebral canal, the membrana tectoria is a broad strong band representing the upward continuation of the posterior longitudinal ligament. Its superficial and deep laminae are both attached to the posterior surface of the axial body. The superficial lamina expands as it ascends to the upper surface of the basilar occipital bone, and attaches above the foramen magnum, where it blends with the cranial dura mater. The deep lamina consists of a strong median band that ascends to the foramen magnum, and two lateral bands that pass to, and blend with, the capsules of the atlanto-occipital joints as they reach the foramen magnum. The membrane is separated from the cruciform ligament of the atlas by a thin layer of loose areolar tissue, and sometimes by a bursa.

Alar ligaments The alar ligaments are thick cords, about 11 mm long, which pass horizontally and laterally from the longitudinally ovoid flattenings on the posterolateral aspect of the apex of the dens to the roughened areas on the medial side of the occipital condyles. In most individuals there is also an anteroinferior band, approximately 3 mm long, which inserts into the lateral mass of the atlas in front of the transverse ligament. Fibres occasionally pass from the dens to the anterior arch of the atlas. In addition, in some 10% of cases a continuous transverse band of fibres, the transverse occipital ligament, passes between the occipital condyles immediately above the transverse ligament. The ligaments consist mainly of collagen fibres arranged in parallel. The main function of the alar ligaments is now considered to be limitation of atlanto-axial rotation, the left becoming taut on rotation to the right and vice versa. The slightly downward movement of the atlas during rotation helps permit a wider range of movement by reducing tension in the alar ligaments, and in the capsules and accessory ligaments of the lateral atlanto-occipital joint.

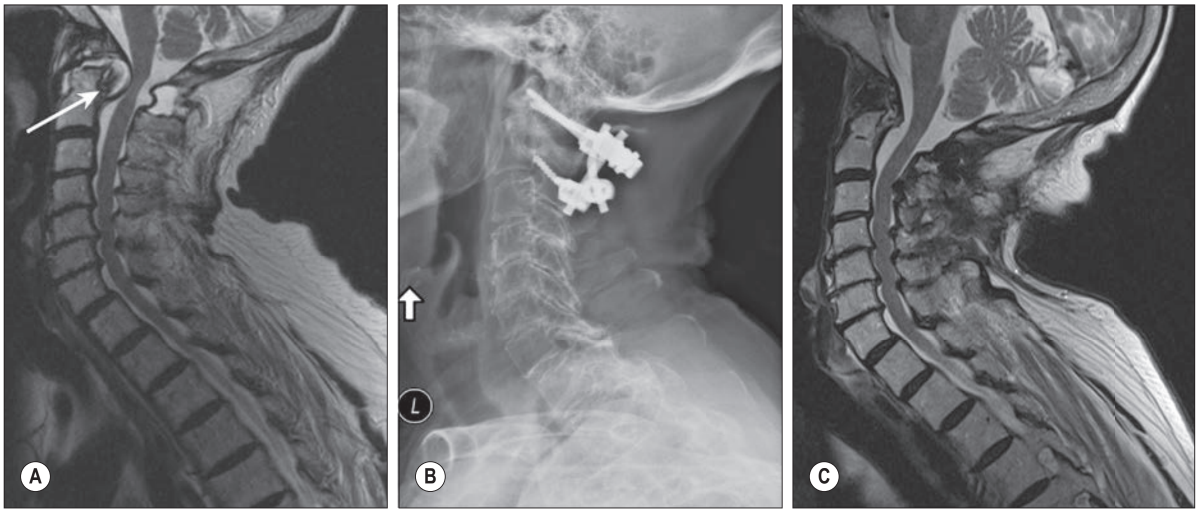

Fig. 46.69 **A**, A T2-weighted MRI showing soft tissue pannus (arrow) compressing the ventral cervicomedullary junction. **B**, A lateral X-ray showing a C1–C2 surgical fusion. **C**, A T2-weighted MRI, 1 year postoperative, showing resorption of the pannus that occurred with stabilization and surgical fusion.

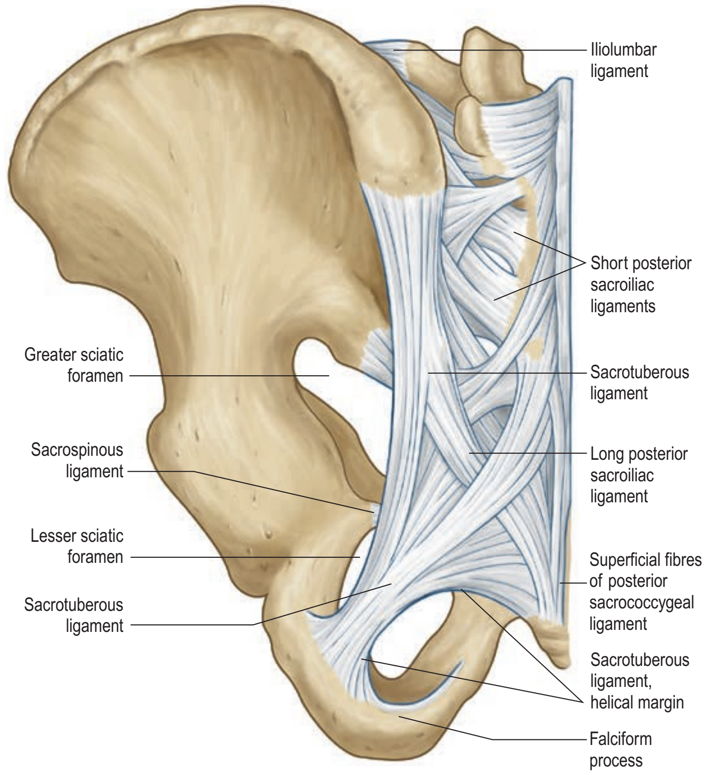
Iliolumbar ligament
Short posterior sacroiliac ligaments
Greater sciatic foramen
Sacrotuberous ligament
Sacrospinous ligament
Long posterior sacroiliac ligament
Lesser sciatic foramen
Superficial fibres of posterior sacrococcygeal ligament
Sacrotuberous ligament
Sacrotuberous ligament, helical margin
Falciform process

Fig. 46.70 Joints and ligaments on the posterior aspect of the left half of the pelvis and the fifth lumbar vertebra.

Apical ligament of the dens The apical ligament of the dens fans out from the apex of the dens into the anterior margin of the foramen magnum between the alar ligaments, and represents the cranial continuation of the notochord and its sheath. It is separated for most of its extent from the anterior atlanto-occipital membrane and cruciform ligament by pads of fatty tissue, though it blends with their attachments at the foramen magnum, and with the alar ligaments at the apex of the dens.

The ligamentum nuchae and the anterior longitudinal ligament also connect cervical vertebrae with the cranium.

Synovial membrane The synovial membranes of the lateral joints have no special features. The median joint has two synovial cavities that sometimes communicate. The synovial cavity of the posterior component of the median joint complex is larger, lying between the horizontally orientated ovoid facet, on the posterior surface of the dens and the cartilaginous anterior surface of the transverse ligament; communication often exists with one or both of the atlanto-occipital joint cavities.

Vascular supply The arterial supply of this region is derived from an anastomosis between branches of the deep cervical, occipital and vertebral arteries.

Innervation The joints are innervated by branches of the ventral primary ramus of the second cervical spinal nerve.

Factors maintaining stability The most important factors maintaining stability are the ligaments, of which the transverse atlantal ligament is the strongest (see Fig. 46.33). The alar ligaments are weaker. Other ligaments connecting the axis and the occipital bone, the fibrous capsules, the ligamentum nuchae and the posterior neck muscles also contribute to stability; the suboccipital muscles play an important proprioceptive and postural role.

Muscles producing movements Movement is simultaneous at all three joints and consists almost exclusively of rotation around the axis. The shape of the articular surfaces is such that, when rotation occurs, the axis ascends slightly into the atlantal ring, limiting stretch on the lateral atlanto-axial joint capsules. Rotation is limited mainly by the alar ligaments, with a minor contribution from the accessory atlanto-axial ligament. The normal range of atlanto-axial rotation is about 40°.

The muscles that produce atlanto-axial rotation act on the cranium, transverse processes of the atlas and spinous process of the axis. They are mainly obliquus capitis inferior, rectus capitis posterior major and splenius capitis of one side, and the contralateral sternocleidomastoid.

Relations and 'at risk' structures The most important 'at risk' relation is the spinal cord, lying posterior to the median atlanto-axial joint. Anteriorly, the atlanto-axial articulations, capsules and ligaments are separated from the buccopharyngeal fascia and superior constrictor by longus capitis and longus colli, the prevertebral fascia and the retropharyngeal (potential) space. Fractures or instability in this region may result in pathological development of soft tissue known as a pannus that may result in spinal cord compromise (**Fig. 46.69**).

Variants of craniovertebral joints

Anomalies of the craniovertebral joints are sometimes seen. Many are minor segmentation anomalies and may be incidental radiological or osteological findings. More severe anomalies may lead to craniocervical instability (Piper and Traynelis 1998).

Lumbosacral junction

Articulations between the fifth lumbar and first sacral vertebrae resemble those between other vertebrae. The bodies are united by a symphysis that includes a large intervertebral disc. The latter is deeper anteriorly at the lumbosacral angle. The synovial facet joints are separated by a wider interval than those above.

Articulating surfaces The reciprocally curved surfaces of the facet joints show considerable individual variation in alignment and shape. Asymmetry (facet tropism) is not unusual.

Ligaments The major ligament associated with the lumbosacral junction is the iliolumbar ligament (see Fig 77.9A; **Fig. 46.70**).

Iliolumbar ligament The iliolumbar ligament is attached to the tip and anteroinferior aspect of the fifth lumbar transverse process, and sometimes has a weak attachment to the fourth transverse process. It radiates laterally and is attached to the pelvis by two main bands. A lower band passes from the inferior aspect of the fifth lumbar transverse process and the body of the fifth lumbar vertebra across the anterior sacroiliac ligament to reach the posterior margin of the iliac fossa. An upper band, part of the attachment of quadratus lumborum, passes to the iliac crest anterior to the sacroiliac joint, and is continuous above with the anterior layer of the thoracolumbar fascia. The lower ligament has a more vertical component that reaches the posterior iliopectineal line; this component is a lateral relation of the L5 ventral ramus. A posterior component of the iliolumbar ligament passes behind quadratus lumborum to attach to the ilium.

In neonates and children, the iliolumbar 'ligament' is muscular; the muscle is gradually replaced by ligament up to the fifth decade of life.

Vascular supply The vascular supply of the lumbosacral junction is derived mainly from the iliolumbar and superior lateral sacral arteries.

Innervation The lumbosacral junction is innervated by branches derived from the fourth and fifth lumbar spinal nerves.

Relations and 'at risk' structures The lumbosacral disc is related anteriorly to the common iliac veins, the median sacral vessels, and the superior hypogastric plexus of nerves. The sympathetic trunks cross it anterolaterally, while the obturator nerves and lumbosacral trunks pass close laterally. The relations of the lumbosacral facet joints are similar to those of the lumbar facet joints (see above).

Sacrococcygeal junction

The sacrococcygeal joint is usually a symphysis between the sacral apex and coccygeal base, united by a thin fibrocartilaginous disc that is somewhat thicker in front and behind than laterally. Its surfaces carry hyaline cartilage that varies from thin veils to small islands. Occasionally, the coccyx is more mobile and the joint is synovial.

Ligaments The anterior sacrococcygeal ligament consists of irregular fibres that descend on the pelvic surfaces of both sacrum and coccyx, and is attached in the same way as the anterior longitudinal ligament.

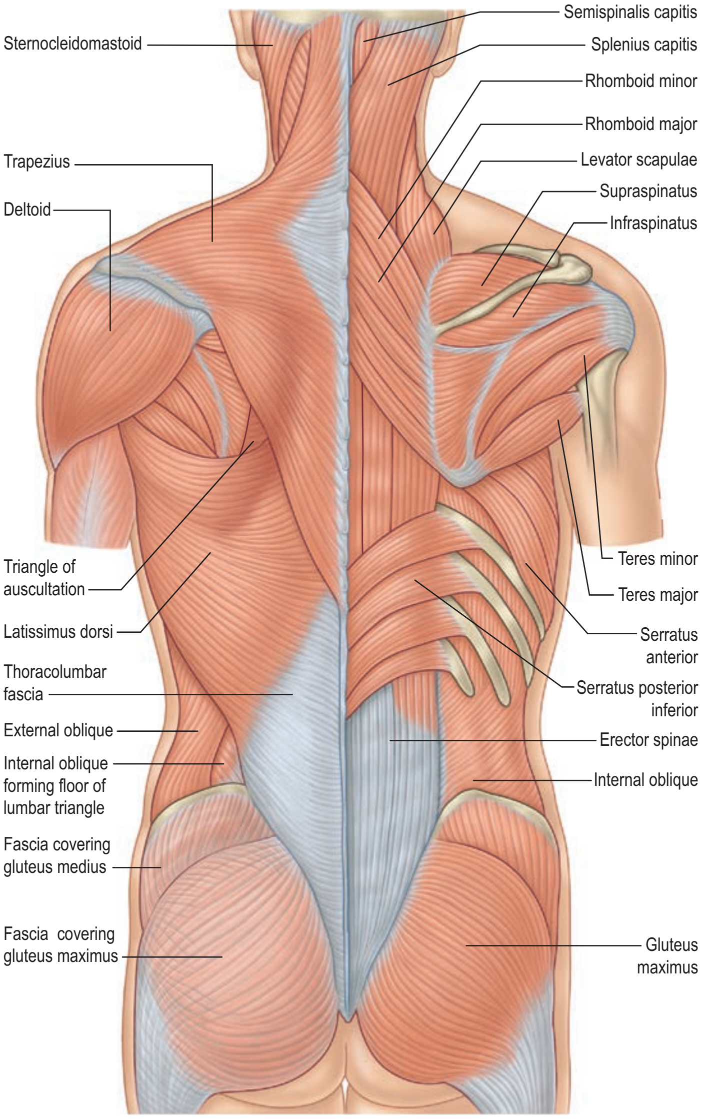
Sternocleidomastoid
Trapezius
Deltoid
Triangle of auscultation
Latissimus dorsi
Thoracolumbar fascia
External oblique
Internal oblique forming floor of lumbar triangle
Fascia covering gluteus medius
Fascia covering gluteus maximus
Semispinalis capitis
Splenius capitis
Rhomboid minor
Rhomboid major
Levator scapulae
Supraspinatus
Infraspinatus
Teres minor
Teres major
Serratus anterior
Serratus posterior inferior
Erector spinae
Internal oblique
Gluteus maximus

Fig. 46.71 Superficial muscles of the back of the neck and trunk. The skin, superficial and deep fasciae (other than gluteofemoral) have been removed on the left; sternocleidomastoid, trapezius, latissimus dorsi, deltoid and external abdominal oblique have been dissected away on the right.

The flat superior posterior sacrococcygeal ligament passes from the margin of the sacral hiatus to the dorsal coccygeal surface, roofing the lower sacral canal (see Fig. 46.70). The deep posterior sacrococcygeal ligament passes from the back of the fifth sacral vertebral body to the dorsum of the coccyx and corresponds to the posterior longitudinal ligament. On each side, the lateral sacrococcygeal ligaments connect the coccygeal transverse processes to the inferolateral sacral angles, completing foramina for the fifth sacral spinal nerves. Similarly, the intercornual ligaments connect the sacral and coccygeal cornua, and a fasciculus connects the sacral cornua to the coccygeal transverse processes.

Vascular supply The arterial supply of the sacrococcygeal junction is derived from the inferior lateral sacral and median sacral arteries.

Innervation The innervation of the sacrococcygeal junction is derived from the lower two sacral and the coccygeal nerves.

Intercoccygeal joints

In the young the intercoccygeal joints are symphyses, with thin discs of fibrocartilage between coccygeal segments. Segments are also connected by extensions of the anterior and posterior sacrococcygeal ligaments. In adult males all segments unite comparatively early, but in females union is later. In advanced age the sacrococcygeal joint becomes obliterated. Occasionally, the joint between the first and second segments is synovial. The apex of the terminal segment is connected to overlying skin by white fibrous tissue.

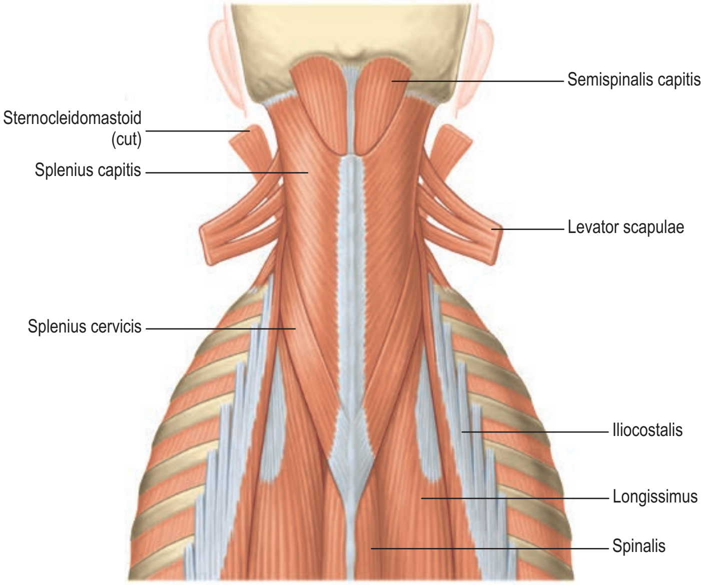
Sternocleidomastoid (cut)
Splenius capitis
Splenius cervicis
Semispinalis capitis
Levator scapulae
Iliocostalis
Longissimus
Spinalis

Fig. 46.72 An axial T2-weighted MRI of the lumbar spine at the level of the L3-L4 intervertebral disc.

MUSCLES

The musculature of the back is arranged in a series of layers, of which only the deeper are true, intrinsic, back muscles (**Fig. 46.71**). The true back muscles are characterized by their position and by their innervation by branches of the posterior (dorsal) rami of the spinal nerves. The true back muscles below the neck lie deep to the posterior layer of the thoracolumbar fascia. In the lumbar region, where the layers of the thoracolumbar fascia are well defined, they occupy the compartment between its posterior and middle layers.

Lying superficial to the true, intrinsic muscles are the extrinsic, 'immigrant' muscles (see Fig. 46.71). The most superficial of these run between the upper limb and the axial skeleton, and consist of trapezius, latissimus dorsi, levator scapulae and the rhomboid muscles. Beneath this layer lie the serratus posterior group, superior and inferior, which are variably developed but usually thin muscles whose function may be respiratory or possibly proprioceptive. All the extrinsic muscles are innervated by ventral rami.

Trapezius, levator scapulae, rhomboid major, rhomboid minor and latissimus dorsi are described in Chapter 49, serratus posterior superior and inferior are described in Chapter 53. The muscles of the posterior abdominal wall are described in Chapter 61.

The intrinsic muscles are also arranged in layers. The more superficial layers contain the splenius muscles in the neck and upper thorax, and the erector spinae group in the trunk as a whole. The deeper layers include the spinotransverse group, which is itself layered into semispinalis, multifidus and the rotatores, and the suboccipital muscles. Deepest of all lie the interspinal and intertransverse muscles. The latter group constitute a mixture of dorsal and ventral spinal muscles. The lumbar intertransversarii mediales, thoracic intertransversarii and medial parts of cervical posterior intertransversarii are innervated by dorsal rami, but the others are supplied by ventral rami.

Muscle attachments and fibre direction Although developmentally the muscles of the back extend caudally as the vertebral column elongates, drawing their nerve supply with them, they have traditionally been described as if their fibres ran caudocranially, so that the 'origins' of the muscles lay distal to their 'insertions'.

It has been shown that in the lumbar spine it is more appropriate morphologically and biomechanically to view the muscles in the reverse direction – from above downwards (Bogduk 2012). It is reasonable to argue that this view may also be applied to the cervical and thoracic muscles, and so for uniformity in this section, all muscles have been described in this way.

Ligamentum nuchae

The ligamentum nuchae is not a ligament of the neck, for it does not connect adjacent bones and lacks the internal structure typical of a ligament. It is a unique arrangement of tendons and fascia between the posterior muscles of the neck. It consists of a dorsal raphe and a median septal portion. The dorsal raphe lies superficially

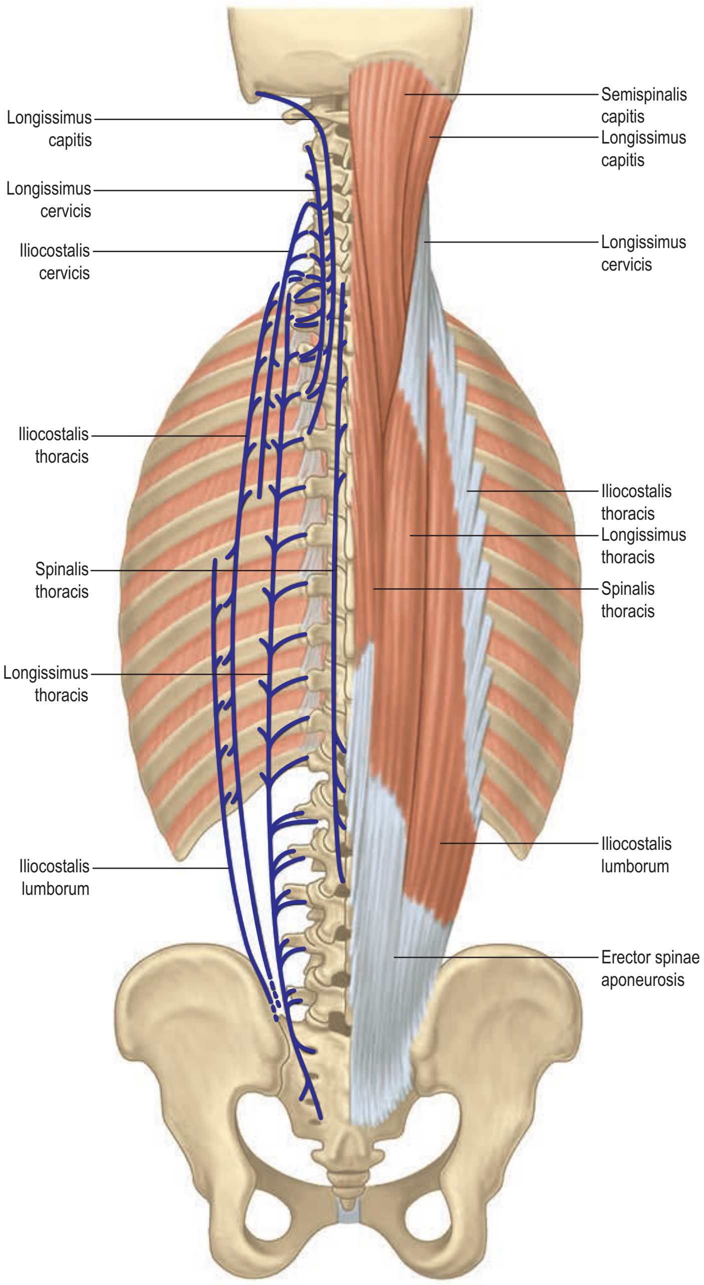

Fig. 46.73 The erector spinae muscle group.

TABLE 46.1 Components of erector spinae and their regional parts

Spinalis	Longissimus	Iliocostalis
Spinalis thoracis	Longissimus capitis	Iliocostalis cervicis
Spinalis cervicis	Longissimus cervicis	Iliocostalis thoracis
Spinalis capitis	Longissimus thoracis	Iliocostalis lumborum

along the posterior midline of the neck. It is attached to the external occipital protruberance superiorly, and the tip of the C7 spinous process inferiorly. In its superior half it consists of the aggregated tendons of the most medial fibres of the cervical portion of trapezius. Because of their longitudinal arrangement, these tendons have been described as forming the funicular portion of the ligamentum nuchae (Mercer and Bogduk 2003). In its inferior half, the funicular portion is joined by the obliquely orientated tendons of splenius capitis and rhomboid minor. Across the midline the tendons of splenius capitis are continuous with those of rhomboid minor on the other side, and they interweave with the tendons of the reciprocal sets of muscles to produce the raphenous structure of the ligamentum nuchae. From the ventral surface of the dorsal raphe, a median fascial septum extends deeply towards the vertebral column and separates semispinalis capitis from its opposite partner. A lateral expansion of the septum extends laterally ventral to semispinalis capitis, separating it from multifidus and semispinalis cervicis. The median continuation of the septum reaches the tips of the cervical spinous processes, and extends into the cervical interspinous spaces as far as the ligamentum flavum. At upper cervical levels, the septum is attached to the external occipital crest and the posterior tubercle of the atlas, and it blends with the posterior atlanto-occipital and posterior atlanto-axial membranes. Passing through these membranes, it is attached to the posterior surface of the dura mater (Dean and Mitchell 2002). Only the dorsal raphe affords attachment to muscles; no muscles arise from the median septum.

Splenius capitis

Attachments Splenius capitis arises from the mastoid process and the rough surface on the occipital bone just below the lateral third of the superior nuchal line. Its fibres pass downwards and medially to reach the midline. The lower fibres insert into the tips of the spinous processes of the seventh cervical and upper three or four thoracic vertebrae and the intervening supraspinous ligaments. The tendons of the upper fibres interlace in the midline with those of the opposite side in the dorsal raphe of the ligamentum nuchae in the lower half of the cervical region (**Fig. 46.72**).

Relations Splenius capitis lies deep to trapezius and covers semispinalis capitis and longissimus capitis. The upper part of the muscle lies beneath sternocleidomastoid. Between sternocleidomastoid and trapezius it forms part of the floor of the posterior triangle of the neck, above and behind levator scapulae.

Vascular supply See below.

Innervation Splenius capitis is innervated by lateral branches of the second and third cervical dorsal rami.

Actions Acting unilaterally, and synergistically with the contralateral sternocleidomastoid, splenius capitis rotates the head to the same side. Acting bilaterally, splenius capitis extends the head.

Splenius cervicis

Attachments Splenius cervicis is confluent with splenius capitis, but covers more caudal regions of the neck and thoracic region (see Fig. 46.72). It arises from the transverse process of the atlas, the tip of the transverse process of the axis and the posterior tubercle of the third cervical vertebra. Its fibres pass downwards and medially, wrapping around the other posterior intrinsic neck muscles, to insert into the third to sixth thoracic spinous processes.

Relations Splenius cervicis lies deep to serratus posterior superior, the rhomboids and trapezius. It covers the upper parts of the erector spinae and the lower semispinalis muscles.

Vascular supply See below.

Innervation Splenius cervicis is innervated by lateral branches of the lower cervical dorsal rami.

Actions Acting unilaterally, splenius cervicis rotates the upper cervical vertebra, in the same way that the splenius capitis rotates the head. Acting bilaterally, splenius cervicis extends the upper cervical spine.

Variations The splenii may be absent or vary in their vertebral attachments. Accessory slips also occur.

Erector spinae

Erector spinae (see Fig. 46.6; **Figs 46.73–46.74**) is a large musculotendinous mass that differs in size and composition at different vertebral levels. It consists of fascicles that assume systematic attachments to homologous parts of the skull, the cervical, thoracic and lumbar vertebrae, the sacrum and the ilium. Individual muscles are defined by the attachments of their fascicles and the regions that they span. There are three muscles, each with three regional parts (**Table 46.1**).

Spinalis Spinalis thoracis is the most medial portion of erector spinae in the thoracic region. It consists of fascicles that arise from the spinous processes of the upper thoracic vertebra and insert into the spinous processes of the eleventh and twelfth thoracic and first two lumbar vertebrae. The number of fascicles and their segmental attachments vary. The fascicles are arranged in an overlapping series of increasingly longer, flat arcs. The shortest fascicles have the lowest origin and highest insertion, and the longest fascicles have the highest origin and lowest

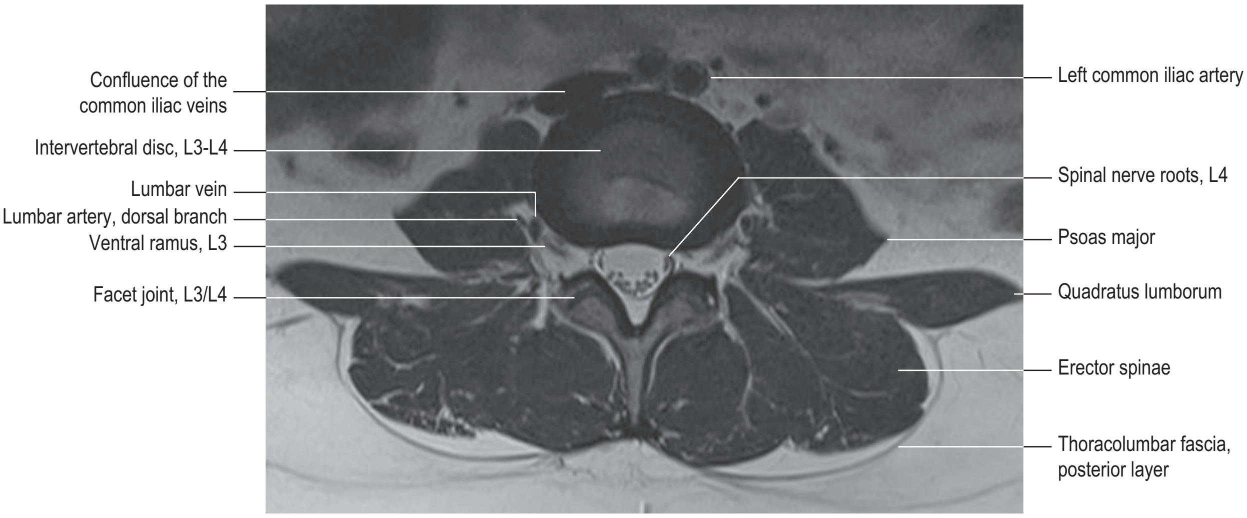
Confluence of the common iliac veins
Intervertebral disc, L3-L4
Lumbar vein
Lumbar artery, dorsal branch
Ventral ramus, L3
Facet joint, L3/L4
Left common iliac artery
Spinal nerve roots, L4
Psoas major
Quadratus lumborum
Erector spinae
Thoracolumbar fascia, posterior layer

Fig. 46.74 An axial MRI of the lumbar spine at the level of the L4-L5 intervertebral disc.

insertion. Laterally, the muscle blends intimately with longissimus thoracis and is considered by some to be a component of that muscle.

Spinalis is irregularly and poorly developed in other regions. When present, spinalis cervicis consists of paramedian fibres that arise variously from the spinous processes of the axis and the third and fourth cervical vertebrae, and insert into the lower part of the ligamentum nuchae and the spine of the seventh cervical vertebra (sometimes also to the first and second thoracic vertebrae). Spinalis capitis is represented by occasional fibres of semispinalis capitis that insert into the spines of the seventh cervical and first thoracic vertebrae instead of reaching the thoracic transverse processes.

Longissimus Longissimus is the central component of erector spinae. It assumes a series of attachments at sites that are homologous to the junction of the transverse and costal elements of the segment. These sites are represented at thoracic levels by the tip of a transverse process and the immediately adjacent posterior surface of the rib; at cervical levels by the transverse process and posterior tubercle; and at lumbar levels by the accessory process (the transverse element) and medial half of the transverse process (the costal element).

Longissimus capitis is a narrow flat band of muscle that arises from the posterior edge of the mastoid process, under cover of splenius capitis and sternocleidomastoid. It descends across the lateral surface of semispinalis capitis and inserts by a series of tendons into the transverse processes of the lower three or four cervical and upper four or so thoracic vertebrae.

Longissimus cervicis is a long thin muscle that arises by tendons from the posterior tubercles of the transverse processes of the second to sixth cervical vertebra. It descends into the thoracic region, between the tendons of longissimus capitis and longissimus thoracis, to insert by tendons into the transverse processes of the upper four or five thoracic vertebrae.

Longissimus thoracis is the largest component of erector spinae. It consists of many small fascicles that are aggregated in a particular manner to produce a very long, and in some places thick, muscle. It has lumbar and thoracic parts.

The lumbar part is formed by fleshy bundles that arise from the accessory process and the medial half or so of the posterior surface of the transverse process of each of the five lumbar vertebrae. The fascicles pass inferiorly and slightly laterally. Those from the first four lumbar vertebrae converge on to a common flat tendon that covers the lateral surface of the muscle and separates it from the lumbar fibres of iliocostalis, for which reason it is called the lumbar intermuscular aponeurosis. The aponeurosis commences in the mid-lumbar region, with a broad irregular base, and inferiorly it tapers to a truncated point that inserts into the medial surface of the ilium just dorsal to the ala of the sacrum. The fascicle from the first lumbar vertebra attaches rostrally and dorsally to the aponeurosis. Successive fascicles attach to it more ventrally and caudally. The fascicle from the fifth lumbar vertebra inserts separately, deep to the intermuscular aponeurosis, into the ventromedial aspect of the ilium and the upper fibres of the dorsal sacroiliac ligament. Medially, the lumbar fibres of longissimus are separated from the multifidus by a wide cleavage plane filled with fat and veins.

The thoracic part consists of fascicles with small, fusiform muscle bellies that have short rostral tendons and long caudal tendons. The muscle bellies are arranged in a tiered fashion across the length of the posterior thoracic wall, with the highest lying medially and the lowest lying laterally. The upper four fascicles arise from the tips of the first four thoracic transverse processes. The succeeding fascicles have bifid tendons that arise from the transverse process and the adjacent rib at each of the lower eight thoracic segments. The long caudal tendons of the thoracic fascicles of longissimus are aggregated in parallel to form a wide aponeurosis, which allows them to assume a variety of caudal insertions. The tendons of the uppermost fascicles insert into the lumbar spinous processes and their supraspinous ligament. Those from the first thoracic segment reach the L1–L2 level, and those from the sixth thoracic segment reach the L5 level. The fascicles from the seventh to ninth thoracic segments reach the median sacral crest, and those from the tenth and eleventh thoracic segments attach transversely across the posterior surface of the third segment of the sacrum. The fascicle from the twelfth thoracic segment reaches the sacrum and dorsal segment of the iliac crest just below where the intermuscular aponeurosis of the lumbar fibres of longissimus inserts into the ilium. The aponeurosis covers the multifidus and the lumbar fibres of longissimus; it extends from the midline as far laterally as the dorsal edge of the lumbar intermuscular aponeurosis, with which it fuses. Within the lumbar intermuscular aponeurosis, the lumbar fibres of longissimus, from L1 to L5, complete the systematic progression of attachments exhibited by the thoracic fibres.

TABLE 46.2 Components of the spinotransverse group

Rotatores	Multifidus	Semispinalis
Rotatores thoracis	Multifidus	Semispinalis cervicis
Rotatores cervicis		Semispinalis thoracis
Rotatores capitis		Semispinalis capitis

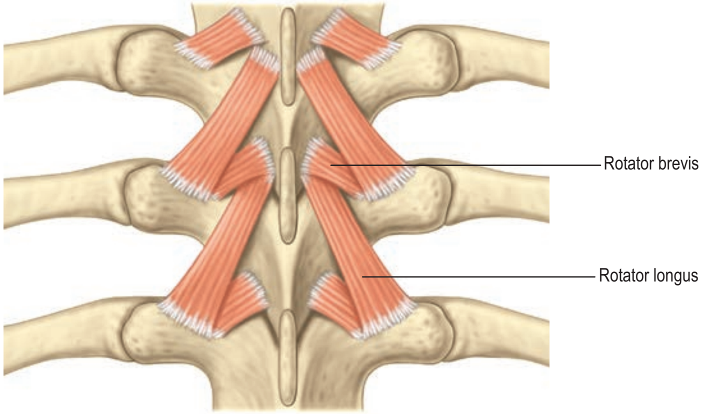

Fig. 46.75 Rotatores (thoracic region). (With permission from Benninghoff, Anatomie, 15th edition © Urban and Schwarzenberg, 1994.)

Iliocostalis Iliocostalis is the most lateral component of the erector spinae. Its fascicles are attached to sites that are homologous with the ribs.

Iliocostalis cervicis consists of slender fascicles that arise by long tendons from the posterior tubercles of the fourth, fifth and sixth cervical vertebrae. They descend over the posterior thorax to insert into the third to sixth ribs at their angles.

Iliocostalis thoracis is a narrow, fusiform muscle. The fibres arise from the back of the transverse process of the seventh cervical vertebra and the superior borders of the angles of the upper six ribs; they lie lateral to iliocostalis cervicis, and insert into the upper borders of the angles of the lower six ribs.

Iliocostalis lumborum consists of lumbar and thoracic parts. The lumbar part is formed by fleshy fascicles that arise from the tips of the first four lumbar transverse processes and the posterior surface of the middle layer of thoracolumbar fascia lateral to these tips. These fascicles descend to the ilium in a laminated fashion, such that those from higher levels cover those from lower levels. They insert into the medial end of the iliac crest and the dorsal segment of the iliac crest, with the fascicle from L4 assuming the most ventral and lateral attachment, and the fascicle from L1 assuming the most dorsal and medial attachment. The attachment to the ilium is largely by fleshy fibres but the more superficial fibres are aponeurotic. The thoracic part consists of eight or nine small fascicles that respectively arise from the lower eight or nine ribs at their angles, lateral to the iliocostalis thoracis. Each fascicle arises from its rib by a ribbon-like tendon. The tendons are longer at high levels but become progressively shorter at lower levels. The muscle bellies of the fascicles are uniform in length, and each gives rise to a caudal tendon. These tendons are aggregated to form a dorsal aponeurosis that covers the lumbar part of iliocostalis lumborum and inserts in a linear fashion into the medial end of the iliac crest and its dorsal segment. Along this line the fascicles are represented serially, such that the fascicle from the twelfth rib attaches most laterally and that from the fourth or fifth rib attaches most medial and inferiorly.

Erector spinae aponeurosis Together, the dorsal aponeuroses of the thoracic fibres of longissimus and the thoracic fibres of iliocostalis lumborum form a wide sheet of parallel tendons known as the erector spinae aponeurosis. It is attached to the lumbar spinous processes and supraspinous ligaments, the median sacral crest, the third sacral segment, the dorsal segment of the iliac crest and the medial end of the iliac crest, and covers multifidus and the lumbar fibres of both longissimus and iliocostalis. Significantly, the erector spinae aponeurosis is formed exclusively by the tendons of the thoracic fibres of longissimus thoracis and iliocostalis lumborum; it does not give rise to the lumbar fibres of these muscles, which are attached independently to the ilium. Some of the more superficial fibres of multifidus may insert into the

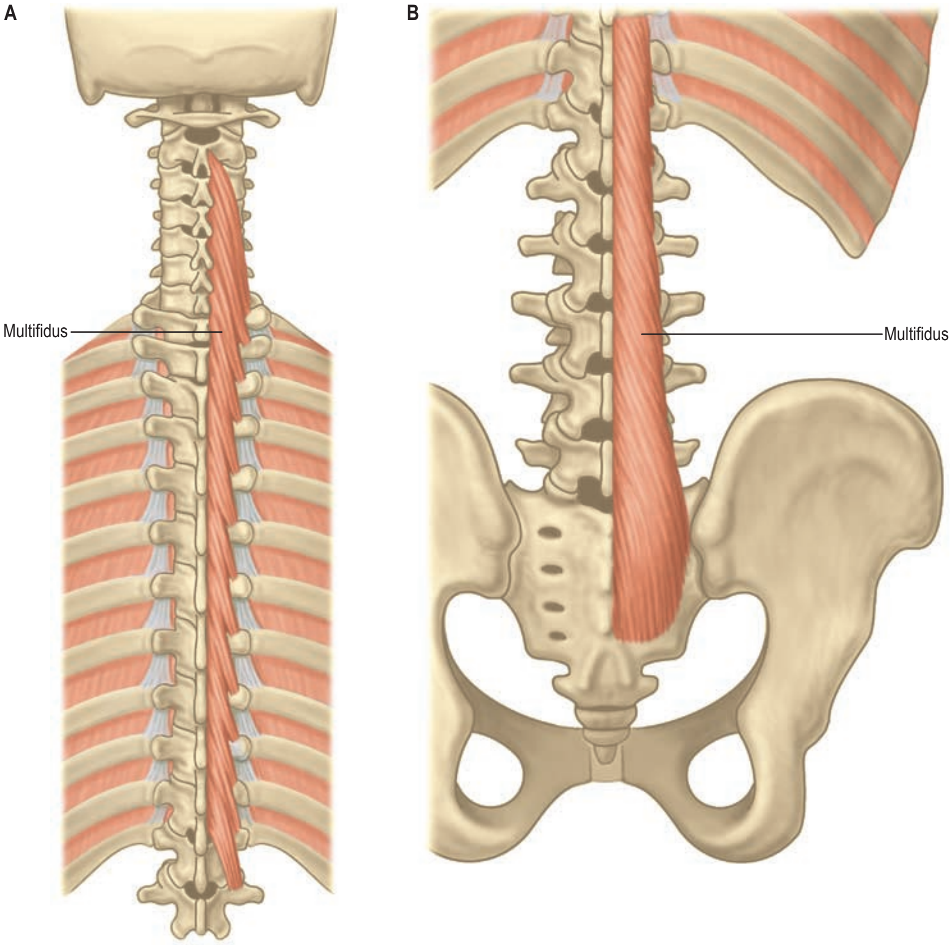

Fig. 46.76 Multifidus. **A**, Cervicothoracic parts. **B**, Lumbosacral parts.

deep surface of the erector aponeurosis over the sacrum, but otherwise the substantive insertion of multifidus is into the sacrum. A portion of the uppermost fibres of gluteus maximus arise from the dorsal surface of the inferolateral corner of the erector spinae aponeurosis. The lumbar intermuscular aponeurosis is a ventral extension of the erector spinae aponeurosis, separating the lumbar fibres of longissimus from those of iliocostalis.

Relations Erector spinae is covered in the lumbar and thoracic regions by the thoracolumbar fascia, and by serratus posterior inferior below and the rhomboids and splenii above. In the lumbar region, it lies in the compartment between the posterior and middle layers of the thoracolumbar fascia.

Vascular supply See below.

Innervation Erector spinae is innervated by the lateral branches of the dorsal rami of the cervical, thoracic and lumbar spinal nerves. At lumbar levels, lateral branches innervate iliocostalis and intermediate branches innervate longissimus.

Actions The thoracic and lumbar components of erector spinae are powerful extensors of the vertebral column. Acting concentrically and bilaterally they can extend the thoracic and lumbar spines whereas acting unilaterally they can laterally flex the trunk. However, more commonly, erectores spinae act eccentrically.

From the upright posture, the trunk can flex forwards under the influence of gravity. This movement is initiated by flexor muscles, such as rectus abdominis, in order to bring the centre of gravity of the trunk forwards. Thereafter, erectores spinae control the descent of the thorax under gravity. When the trunk is fully flexed, many parts of erector spinae cease to contract and become electromyographically silent. In this position, flexion is limited by passive tension in the back muscles, and tension in the thoracolumbar fascia, the posterior spinal ligaments and the intervertebral discs. Similarly, lateral flexion under gravity is controlled by the contralateral erector spinae, with input from the oblique abdominal muscles.

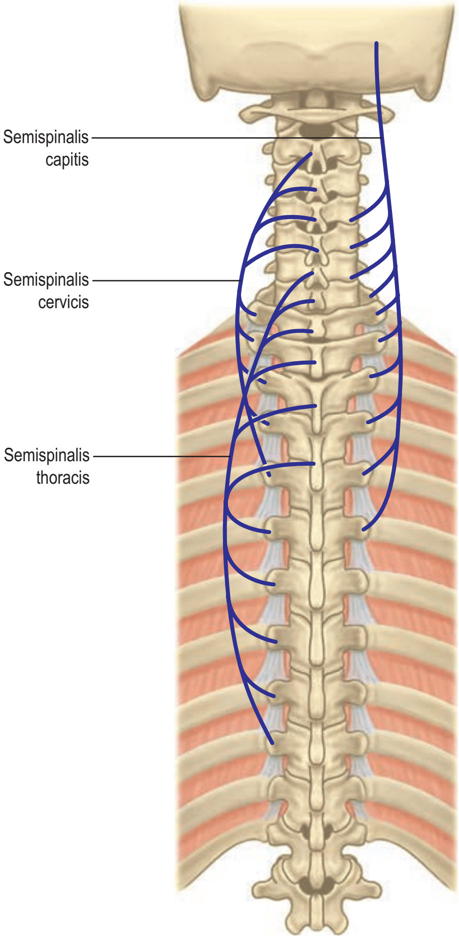

Fig. 46.77 The attachments of semispinalis.

The function of the cervical and capital components of erector spinae has not been determined. These are small muscles with very little force capacity, and are poorly orientated to exercise extension or to control flexion of the head or cervical spine. As putative extensors they are dwarfed by semispinalis and splenius. Axial rotation of the head draws longissimus capitis around the perimeter of the cervical spine, orientating it perhaps so that it is able to restore the head to neutral from the rotated position.

Spinotransverse group

The spinotransverse muscle group consists of muscles where the fascicles span between a spinous process and the transverse elements of vertebrae at various levels below. The muscles are grouped according to the length of their fascicles and the region that they cover (Table 46.2).

Rotatores have the deepest and shortest fascicles, and span one and two segments, whereas the fascicles of multifidus span two, three, four or five segments, and those of semispinalis span about six segments.

Rotatores Rotatores thoracis (Fig. 46.75) consist of 11 pairs of small quadrilateral muscles. The first pair lies between the first and second thoracic vertebrae, and the last between the eleventh and twelfth thoracic vertebrae. One or more may be absent from the upper or lower ends of the series. In each segment, a rotator brevis connects the lower border and lateral surface of the lamina above to the upper, posterior part of the transverse process of the vertebra immediately below; a rotator longus connects the base of the spinous process above to the transverse process two levels below. Rotatores are not obviously present at lumbar and cervical levels, where they may be represented by some of the deeper fascicles of multifidus.

Multifidus At cervical, thoracic and upper lumbar levels, multifidus lies lateral to the spinous processes and covers the laminae of the underlying vertebrae, but at lumbosacral levels it expands to cover the posterior surface of the sacrum (Fig. 46.76). At each segmental level, multifidus is formed by several fascicles that arise from the caudal edge of the lateral surface of the spinous process and from the caudal end of its tip. They radiate caudally to insert into the transverse elements of vertebrae two, three, four and five levels below (Macintosh et al 1986). These sites are represented at cervical levels by the superior articular processes, at thoracic levels by the posterior surface of each transverse process near its base, and at lumbar levels by the mammillary processes. Fascicles that extend beyond the fifth lumbar vertebra insert into the dorsal surface of the sacrum. The longest fascicles from the first and second lumbar vertebrae insert into the dorsal segment of the iliac crest. From each spinous process the shortest fascicles pass inferiorly and laterally to their insertion; the longer fascicles assume a progressively steeper course and are arranged progressively more medially. The fascicles from a given segment are flanked and overlapped dorsolaterally by fascicles from successively higher segments, an arrangement that endows the intact muscle with a laminated structure.

Semispinalis The semispinalis muscles are formed by the longest fascicles of the spinotransverse group. Three divisions are defined essentially by their origins (Fig. 46.77).

Semispinalis cervicis arises from the spinous processes of the second to fifth cervical vertebrae. Its fascicles span about six segments and cover the cervical and thoracic multifidus. They insert by fleshy or tendinous fibres into the posterior surfaces of the upper five or six thoracic transverse processes. The fascicle from the axis is the largest and is composed chiefly of muscle.

Semispinalis thoracis consists of thin, fleshy fascicles that have long tendons at both ends. They arise from the lower two cervical and the upper four thoracic spinous processes, and insert into the transverse processes of the sixth to tenth thoracic vertebrae. They cover the thoracic multifidus.

Semispinalis capitis covers semispinalis cervicis. It arises from the medial part of the area between the superior and inferior nuchal lines of the occipital bone and forms a thick muscle bundle in the suboccipital region. Individual fascicles pass inferiorly, laterally and ventrally from the muscle, ending as flat tendons that insert successively into the superior articular processes of the lower four cervical vertebrae and the tips of the transverse processes of the upper six or seven thoracic vertebrae. The medial part of the muscle in the cervical region is formed by the thoracic fascicles, which are more or less distinct from the rest, and has been called biventer cervicis because it is traversed by an incomplete tendinous intersection.

Semispinalis is not formed in the lumbar region, but vestiges of its caudal tendons are represented as the mammillo-accessory ligaments of the lumbar vertebrae.

Relations At cervical, thoracic and lumbar levels, components of erector spinae lie lateral to the spinotransverse group of muscles. They are covered at cervical levels by splenius, at thoracic levels by spinalis thoracis, and at lumbar levels by the erector spinae aponeurosis. In the neck, semispinalis capitis lies mainly deep to splenius and trapezius, but a small portion may be exposed to form the uppermost part of the floor of the posterior triangle of the neck.

Vascular supply See below.

Innervation Rotatores, multifidus, semispinalis thoracis and semispinalis cervicis are all innervated by the medial branches of the dorsal rami of the appropriate spinal nerves. Semispinalis capitis is innervated by descending branches of the greater occipital nerve (C2) and the third cervical nerve (C3).

Actions All the spinotransverse muscles are extensors. They extend the vertebrae from which they arise, or the head in the case of semispinalis capitis. The predominantly longitudinal orientation of their fascicles precludes any substantive action as rotators. Although rotatores have been presumed to rotate the thoracic vertebrae, this action has not been validated. Axial rotation has been expressly refuted as an action of the lumbar multifidus.

Interspinales

Interspinales are short, paired muscular fasciculi attached above and below to the apices of the spines of contiguous vertebrae, one on either side of the interspinous ligament. They are most distinct in the cervical region, where they consist of six pairs, the first between the axis and third vertebra, and the last between the seventh cervical and first thoracic vertebrae. In the thoracic region they occur between the first and second vertebrae (sometimes between the second and third), and the eleventh and twelfth vertebrae. In the lumbar region there are four pairs between the five lumbar vertebrae. A pair is occasionally found between the last thoracic and first lumbar vertebrae, and another between the fifth lumbar vertebra and the sacrum. Sometimes cervical interspinales span more than two vertebrae.

Intertransversarii

Intertransversarii are small muscles between the transverse processes of the vertebrae. They are best developed in the cervical region, where they consist of posterior and anterior sets of muscles separated by the ventral rami of spinal nerves. Posterior intertransverse muscles are divisible into medial and lateral slips. Each medial slip, the intertransverse muscle 'proper', is often further subdivided into medial and lateral parts by the passage through it of the dorsal ramus of a spinal nerve. There are seven pairs of these muscles, the highest between the atlas and axis, and the lowest between the seventh cervical vertebra and the first thoracic vertebra; the anterior muscles between atlas and axis are often absent. In the thoracic region, intertransversarii consist of single muscles that span between the transverse processes of the last three thoracic and the first lumbar vertebrae. In the lumbar region, they again consist of two sets of muscles. One set, intertransversarii mediales, connects the accessory process of one vertebra with the mammillary process of the next. The other set, intertransversarii laterales, can be divided into ventral and dorsal parts; the ventral parts connect the transverse processes of the lumbar vertebrae, and the dorsal parts connect the accessory processes to the transverse processes of succeeding vertebrae.

Different parts of the intertransversarii in the cervical and lumbar regions are homologous with certain muscles found in the thoracic region. The homologies are determined according to whether the muscle attaches between consecutive transverse elements of the vertebrae, or between transverse and costal elements, or between consecutive costal elements. They are reinforced by the nerve supply of the muscle, and by the relationship between the muscles and certain nerves.

The medial slips of the 'proper' posterior intertransverse muscles of the neck connect consecutive transverse elements, as do the intertransversarii mediales of the lumbar region. These muscles are homologous with the thoracic intertransverse muscles and ligaments. All are supplied by dorsal rami. The lateral slips of the 'proper' posterior intertransverse muscles connect a transverse element to a costal element, as do the intertransversarii laterales dorsales. They are homologous with levatores costarum and are supplied by the ventral rami of spinal nerves. At each level, the medial branch of a dorsal ramus separates the true

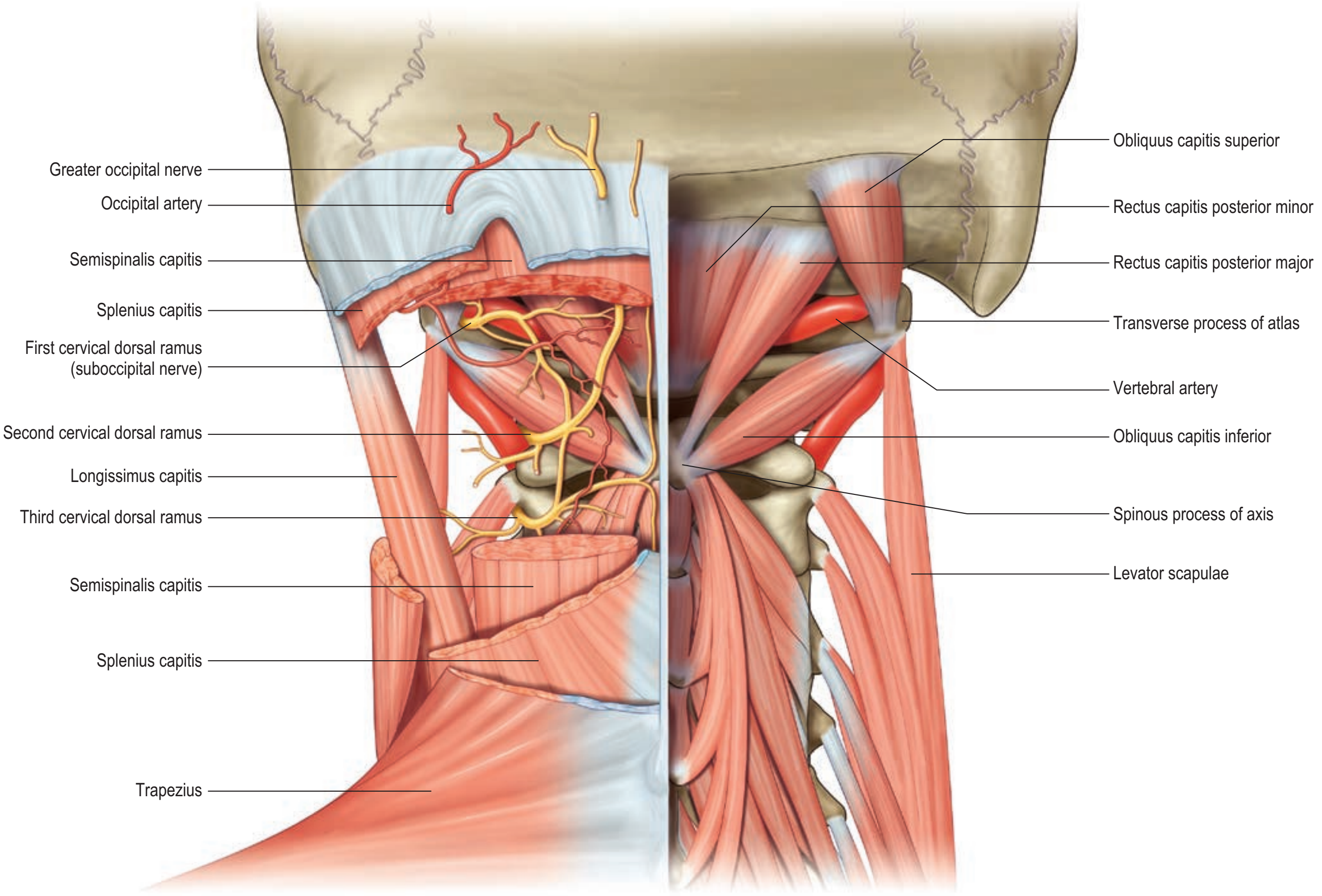
Greater occipital nerve
Occipital artery
Semispinalis capitis
Splenius capitis
First cervical dorsal ramus (suboccipital nerve)
Second cervical dorsal ramus
Longissimus capitis
Third cervical dorsal ramus
Semispinalis capitis
Splenius capitis
Trapezius
Obliquus capitis superior
Rectus capitis posterior minor
Rectus capitis posterior major
Transverse process of atlas
Vertebral artery
Obliquus capitis inferior
Spinous process of axis
Levator scapulae

Fig. 46.78 Suboccipital triangles, posterior view. (From Drake RL, Vogl AW, Mitchell A et al (eds), Gray's Atlas of Anatomy. Elsevier, Churchill Livingstone. Copyright 2008.)

intertransverse muscle from levator costae or its equivalent. The anterior intertransverse muscles of the neck and lateral parts of the posterior intertransversarii connect the costal processes of consecutive vertebrae, as do the intertransversarii laterales ventrales of the lumbar region; they are homologous with the intercostal muscles and are supplied by ventral rami.

Actions of interspinales and intertransversarii The functions of interspinales and intertransversarii have not been established. They are very small muscles and are unlikely to be able to generate enough force to be prime movers of the vertebrae. However, they are richly endowed with muscle spindles; the density approaches that found in the lumbricals of the hand and in the extraocular muscles. It therefore seems reasonable to assume that the short muscles of the back may serve a proprioceptive function in controlling the position of the vertebral column and its movements.

Vascular supply of the true back muscles

The true (intrinsic) muscles of the back receive their blood supply from: the vertebral artery; deep cervical artery; superficial and deep descending branches of the occipital artery; deep branch of the transverse cervical artery (when present); supreme intercostal artery, via dorsal branches of the upper two posterior intercostal arteries; posterior intercostal arteries of the lower nine spaces via dorsal branches; dorsal branches of the subcostal arteries; dorsal branches of the lumbar arteries; dorsal branch of arteria lumbalis ima; and dorsal branches of the lateral sacral arteries.

The detailed pattern of the arterial supply of the deep muscles of the back has been described by Michel Salmon (1994). These muscles are supplied by dorsal branches of the posterior intercostal and lumbar arteries. In the thoracic and upper lumbar regions, where the components of erector spinae run in well-defined longitudinal columns, arterial trunks from these dorsal branches run in the sulci between the columns and between erector spinae and multifidus, giving off branches to supply the muscles. This vascular pattern is less regular in the lumbar region.

Suboccipital muscles

The suboccipital muscles (Fig. 46.78) are four small muscles that connect the occipital bone, atlas and axis posteriorly. They lie inferior to the anterior part of the occipital bone, where three of the muscles form the boundaries of the suboccipital triangle: rectus capitis posterior major lies above and medially; obliquus capitis superior lies above and laterally, and obliquus capitis inferior lies below and laterally. With the head in the anatomical position, the suboccipital triangle lies almost in the horizontal plane.

Rectus capitis posterior major Rectus capitis posterior major is attached by a pointed tendon to the spine of the axis, becomes broader as it ascends, and is attached to the lateral part of the inferior nuchal line and the occipital bone immediately below it. As the muscles of the two sides pass upwards and laterally, they leave between them a triangular space in which parts of recti capitis posteriores minores are visible.

Rectus capitis posterior minor Rectus capitis posterior minor is attached by a narrow pointed tendon to the tubercle on the posterior arch of the atlas. As it ascends, it broadens before attaching to the medial part of the inferior nuchal line and to the occipital bone between the inferior nuchal line and the foramen magnum. Either muscle may be doubled longitudinally. There is usually a soft tissue attachment to the posterior atlanto-occipital membrane, which itself is firmly attached anteriorly to the spinal dura in the same area (Zumpano et al 2006).

Obliquus capitis inferior Obliquus capitis inferior, the larger of the two oblique muscles, passes laterally and slightly upwards from the lateral surface of the spine and the adjacent upper part of the lamina of the axis to the inferoposterior aspect of the transverse process of the atlas.

Obliquus capitis superior Obliquus capitis superior is attached by tendinous fibres to the upper surface of the transverse process of the atlas. It expands in width as it ascends dorsally, and is attached to the occipital bone between the superior and inferior nuchal lines, lateral to semispinalis capitis and overlapping the insertion of rectus capitis posterior major.

Relations of the suboccipital triangle Medially, the suboccipital triangle is covered by a layer of dense adipose tissue, deep to semispinalis capitis. Laterally, it lies under longissimus capitis and sometimes splenius capitis, both of which overlap obliquus capitis superior. The 'floor' of the triangle is formed by the posterior atlanto-occipital membrane and the posterior arch of the atlas. The vertebral artery and the dorsal ramus of the first cervical nerve lie in a groove on the upper surface of the posterior arch of the atlas.

Vascular supply The suboccipital muscles receive their blood supply from the vertebral artery and deep descending branches of the occipital artery.

Innervation All the suboccipital muscles are supplied by the dorsal ramus of the first cervical spinal nerve.

Actions of the suboccipital muscles The suboccipital muscles are involved in extension of the head at the atlanto-occipital joints and rotation of the head and atlas on the axis. Obliquus capitis superior and the two recti are probably more important as postural muscles than as prime movers but this is difficult to confirm by direct observation. Rectus capitis posterior major extends the head and, acting with obliquus capitis inferior, rotates the face towards the ipsilateral side. Rectus capitis posterior minor extends the head. Obliquus capitis superior extends the head and laterally flexes it to the ipsilateral side.

MOVEMENTS OF THE VERTEBRAL COLUMN

Spinal movements between individual vertebrae cannot be measured accurately by skin-surface techniques; only biplanar radiography is sufficient for this purpose. Movements of the entire lumbar spine can be measured using skin-surface techniques, but the results are of limited clinical use because there is high inter- and intra-observer variation (Pearcy et al 1984, Pearcy and Tibrewal 1984).

The intervertebral discs are the principal sites of vertebral column movement. Conversely, at most levels, the extent to which the discs may be deformed is also the limiting factor for motion. Bony deformation in the subchondral bone and articular cartilage may contribute to movement. Regional variations in mobility of the spine depend on the geometry, orientation and properties of the facet joints and related ligamentous complexes. Physiological intervertebral movements usually combine tilting (bending) and gliding (shear), so the instantaneous centre of rotation moves continually during the movement. During flexion and extension of the lumbar vertebrae, the centre of rotation usually lies near the centre of the intervertebral disc when viewed in the transverse plane, close to the superior end-plate of the vertebra below.

The oblique and ovoid articular surfaces of the facet joints ensure that spinal movements in different planes are usually 'coupled' to a certain extent. For example, lateral flexion would cause impingement of the articular surfaces on that side, leading to a posteriorly directed force on the upper vertebra that would act to rotate it about its long axis. Physiologically, coupled movements are variable. Although movements between individual vertebrae are small, their summation gives a large total range to the vertebral column in flexion, extension, lateral flexion and axial rotation. Each pair of vertebrae with its interposed disc and ligaments is termed a motion segment or functional spinal unit.

In flexion, the anterior longitudinal ligament becomes relaxed as the anterior parts of the intervertebral discs are compressed. At its limit, the posterior longitudinal ligament, ligamenta flava, interspinous and supraspinous ligaments, and the posterior fibres of the intervertebral discs are all tensed, the interlaminar intervals widen, the inferior articular processes glide on the superior processes of subjacent vertebrae, and their capsules become taut. Tension of extensor muscles is also important in limiting flexion, e.g. when carrying a load on the shoulders. Flexion is effectively absent in the thoracic region. In forward flexion of the lumbar spine, the muscles normally protect the osteoligamentous spine from injury. However, the margin of safety can be compromised during repetitive or sustained bending by a failure of the spinal reflexes. Once the muscle protection is lost, flexion injury affects first the interspinous ligaments and then the capsules of the facet joints. The ligamentum flavum has such a high content of elastin that it is always under tension, and can be stretched by 80% without damage. This ligament probably functions to provide a constant smooth lining to the vertebral canal, which is never overstretched in flexion and which never goes slack in extension.

In extension, the opposite events occur and there is compression of posterior discal fibres. Extension is limited by tension of the anterior longitudinal ligament, anterior discal fibres and impaction of spines or articular processes. It is marked in cervical and lumbar regions, and much less at thoracic levels, partly because the discs are thinner, but also because of the presence of the ribs and chest musculature. In full extension, the axis of movement passes posterior to the disc, moves forwards as the column straightens and passes into flexion, and reaches the centre of the intervertebral disc in full flexion.

In lateral flexion, which is always combined with 'coupled' axial rotation, intervertebral discs are laterally compressed and contralaterally tensed and lengthened, and motion is limited by tension of antagonist muscles and ligaments. Lateral movements occur in all parts of the column but are greatest in cervical and lumbar regions.

Axial rotation involves twisting of vertebrae relative to each other with accompanying torsional deformation of intervening discs. About 50% of cervical rotation occurs at the atlanto-axial joint. Elsewhere in the column, although movement is slight between individual vertebrae, the range summates to become considerable for the column as a whole. In the postcervical column, the effective range of rotation is greatest at the thoracolumbar junction. There is very little rotation in the remainder of the lumbar region.

In the cervical region, the upward inclination of the superior articular facets allows free flexion and extension. The latter is usually greater, and is checked above by locking of the posterior edges of the superior facets of C1 in the occipital condylar fossae, and below by slipping of the inferior processes of C7 into grooves inferoposterior to the first thoracic superior articular processes. Flexion stops where the cervical convexity is straightened, checked by apposition of the projecting lower lips of vertebral bodies on subjacent bodies. Cervical lateral flexion and rotation are always coupled, and the superomedial inclination of the superior articular facets imparts rotation during lateral flexion.

Cervical motion can be considered to involve the upper (i.e. the atlanto-occipital and atlanto-axial complexes) and the lower cervical spine (C3–C7). Two physiological movements take place at the atlanto-occipital joints: those of flexion–extension and lateral flexion. The atlanto-axial joints allow flexion–extension and rotation. Some studies have suggested that maximum flexion–extension occurs between the occiput and C1; however, Frobin et al (2002) noted between 12.6° and 14.5° at this level, which is less than at some of the other cervical levels. Global cervical flexion ranges from 45° to 58°, depending on the method of assessment, age and sex; older subjects and females exhibit less motion (Trott et al 1996, Ordway et al 1997). At an intersegmental level, motion increases from the second cervical level and peaks at the mid-cervical level (14–17° recorded at C4/C5), before reducing at the junction of the cervical and thoracic spine (9.8–11.5° noted at C6/C7) (Frobin et al 2002). Global ranges of lateral flexion range from 32° to 47°, with a gradual reduction in range with age and sex, while rotational movements range from 63° to 78°. Intersegmental ranges of motion vary from 4.7° to 6° for lateral flexion between C2 and C7, and 2–12° for rotation (White and Panjabi 1990).

In the thoracic region, especially superiorly, all movements are limited, reducing interference with respiration. Lack of upward inclination of the superior articular facets prohibits much flexion, and extension is checked by contact of the inferior articular margins with the laminae and of adjacent spines. Thoracic rotation is freer, though limited by the ribs at upper levels. Its axis is in the vertebral bodies in the mid-thoracic region, and in front of them elsewhere, so that rotation involves some lateral displacement. The direction of articular facets would allow free lateral flexion but this is limited in the upper thoracic region by the resistance of the ribs and sternum. Rotation is usually combined with slight lateral flexion to the same side.

Movement in the thoracic spine is frequently regionalized to upper, mid- and lower thoracic. In the upper thoracic, flexion ranges from 7.8° to 9.5°, increasing to 10–11.4° in the mid-thoracic and 12.5–12.8° in the lower thoracic (Willems et al 1996). Extension is more consistent, ranging from 7.1° to 9.7° throughout the thoracic spine. Lateral flexion is greater in the lower thoracic spine, ranging from 5.6° to 6.2° in the upper thoracic, 7.9° to 8.1° in the mid-thoracic and 11.9° to 13.2° in the lower thoracic. However, rotation is greatest in the mid-thoracic region, being 11.8–15.9° in the upper thoracic, 21.5–25.3° in the mid-thoracic, and 8.3–11.8° in the lower thoracic.

Flexion movements are generally greater than extension or lateral flexion in the lumbar region. Axial rotation occurs about a centre of rotation in the posterior anulus, and is limited by bony contact in the facet joints after only 1–2° of movement. Functional transition between thoracic and lumbar regions is usually between the eleventh and twelfth thoracic vertebrae, where the facet joints usually fit so tightly that slight compression locks them, and prevents all movements but flexion.

During flexion of the lumbar spine there is an unfolding or straightening of the lumbar lordosis. Thus in full flexion the lumbar spine assumes a straight alignment or is curved slightly forwards. Normal ranges of global lumbar flexion are 58° to 72° in those under 40 years old and 40° to 60° in the over-forties; females exhibit a reduced range compared with males (Dvorak et al 1995, McGregor et al 1995). At an intersegmental level, the L3/L4 junction and L4/L5 junction exhibit the greatest mobility – approximately 12° and 13° respectively, while at the lowest level (L5/S1) there is only 9°, and at the upper lumbar levels only 8° and 10°, respectively (Pearcy et al 1984). Movements into extension are the converse of those seen in flexion. Normal ranges of global extension are from 25° to 30° in those under 40 years old and 15° to 20° in those over forty. At an intersegmental level, L5/S1 and L1/L2 exhibit the greatest mobility at approximately 5°, while the remaining levels exhibit less than 5° of extension. Ranges of lateral flexion and rotation in the lumbar spine are reduced compared to other regions of the spine. Global lateral flexion ranges from 20° to 35°, and rotation ranges from 25° to 40°; the ranges of both movements are reduced with age. Assessment of intersegmental rotation and lateral flexion has proven difficult because of the limitations of measurement techniques.

Role of musculature

Although muscles will move the spinal column, the majority of muscular activity is involved in providing stability to maintain posture and to provide a firm platform for limb function. Hence the concept of 'core stability' in modern rehabilitation programmes, especially in sports-related problems.

It is important to recognize the way in which the muscles of the back work in conjunction with those of the abdominal wall, particularly the oblique and transversus muscles, and with those of the lower limbs. The erector spinae group and internal abdominal oblique and transversus abdominis are anatomically and functionally connected by the thoracolumbar fascia (which encloses the former, and into which the latter are inserted). This fascia, together with collagenous tissue within the back muscles, plays an important role in resisting forward bending of the trunk, and during manual handling. The fascia is tensioned primarily by flexing the trunk, although this tension may be enhanced slightly by the lateral pull of the abdominal muscles. It is functionally advantageous to generate tension in the fascia and muscle sheaths because the elastic strain energy stored in these stretched tissues can be used to help bring the trunk to an upright position and so reduce the metabolic cost of the movement (Adams et al 2006). The thoracolumbar fascia may also have an important function in transferring load between the trunk and the lower limbs; tension in the fascia can be increased by the actions of gluteus maximus and the hamstrings as well as by trunk flexion.

Muscles producing vertebral movements

The spinal column is moved both directly by muscles attached to it, and indirectly by muscles attached to other bones. Gravity always plays a part: movements with gravity usually involve the eccentric contraction of antagonists. Flexion is effected by longus capitis and longus colli, scaleni, sternocleidomastoid and rectus abdominis of both sides, aided in the lumbar region by the abdominal obliques; extension by the erector spinae complex and the transversospinalis group, splenius, semispinalis capitis and trapezius of both sides, together with the suboccipital muscles; lateral flexion by ipsilateral longissimus, iliocostalis, abdominal obliques and flexors, and quadratus lumborum; and rotation by sternocleidomastoid, splenius cervicis, abdominal obliques, rotatores and multifidus.

Factors involved in stability

The vertebral column is remarkable in that it combines mobility, stability and load-bearing capacity and also protects its contained neural structures, irrespective of its position. Much of the stability of the vertebral column depends on dynamic muscular control but there are also bony and ligamentous 'static' stabilizers. There is considerable variation between segments of the column in terms of stability and mobility; the most mobile levels are the least stable. The latter are those in which the ratio of intervertebral disc height to vertebral body height is highest. Stability may be compromised by damage to any of these structures.

Trauma may affect any vertebral region. Levels of specialized mobility (e.g. atlanto-axial joint) and the junctions of mobile and relatively fixed regions (e.g. cervicothoracic, thoracolumbar) are particularly vulnerable to severe structural damage, often accompanied by spinal cord and nerve injury. Injuries of the vertebral column may affect purely soft tissue (ligaments, joint capsules and muscles) or may affect bony structures (see Fig. 46.58). Pure ligamentous/capsular injuries leading to instability may be particularly difficult to diagnose in the absence of gross radiological signs. In the cervical spine, subluxation and dislocation of the facet joints commonly occur without or with minimal bony injury because of the orientation of the articular facets (see Fig. 46.65).

Chronic infections of many types (e.g. tuberculosis) may involve the vertebrae and lead to their deformity and collapse, affect their mechanical properties and compromise their neuroprotective function. Acute infections, spreading locally or via the blood stream, may lead to the collection of pus within the vertebral canal, causing spinal cord compression (epidural abscess).

The integrity of the vertebrae may also be affected by malignant disease, most commonly metastatic. Vertebrae have a copious blood supply throughout life, and many of the common cancers (e.g. breast, bronchus) spread via the arterial system. Cancers of the haemopoietic system (e.g. multiple myeloma) also commonly affect the vertebrae. Prostatic carcinoma has a predilection to metastasize to the vertebral column, often using the venous (Batson's plexus) rather than the arterial route (Batson 1957). Metastatic deposits may occur within the epidural space, compressing the contents of the dural sac at multiple levels.

Systemic inflammatory diseases may cause both deformity and instability of the vertebral column. Rheumatoid arthritis inflames facet joints and weakens ligaments, leading to instability, especially in the cervical spine (see Fig. 46.57). Ankylosing spondylitis and other seronegative arthritides affect joints and ligamentous attachments (entheses), leading to ectopic ossification of collagenous structures, fusion (ankylosis) of interbody and facet joints, and loss of the normal spinal curvatures. Widespread new bone formation at and around the joints of the column occurs in DISH (diffuse idiopathic skeletal hyperostosis). Such conditions would seem to increase stability of the column, at the expense of its mobility and function, but an ankylosed spine is very liable to fracture, with an associated risk of neural damage (**Fig. 46.79**).

Full stability and load-bearing capacity both require intact vertebral bodies and intervertebral discs. Earlier views regarding the relative importance of the disc-body complex and the posterior elements have proved somewhat simplistic. Clinical observation led to the 'three-column concept' of spinal stability, in which the column is divided into three longitudinal parts rather than two (Denis 1983). The anterior column is formed by the anterior longitudinal ligament, the anterior half of the vertebral body and the anterior anulus fibrosus. The middle column is made up of the posterior longitudinal ligament, the posterior half of the vertebral body and pedicles, and the posterior anulus fibrosus. The posterior column consists of the vertebral arch and facet joints and the posterior ligamentous complex. The more columns that are affected, the worse is the instability; an injury to two columns is usually unstable.

Although regarded as the most influential system for classifying thoracolumbar spinal injuries, the concept was criticized for oversimplifying the biomechanics of injury. A more recent classification system, aided by improved computed tomographic imaging and magnetic resonance imaging, stresses the importance of the posterior ligamentous complex in determining the stability of the injured spine in addition to the morphology of the injury (compression, translational/rotational or distraction injuries) and the neurological status of the patient (intact, nerve root injury, complete or incomplete spinal cord injury, cauda equina syndrome) (Lee et al 2005).

The elastic deformability of intervertebral discs permits tilting and axial rotation between vertebral bodies, and also helps to reduce vertical accelerations of the head. The main shock-absorbing mechanism of the column stems from the spinal curves, which increase and decrease slightly during locomotion against the restraining tension of the trunk muscles. The elastic strain energy in the stretched tendons of the muscle is responsible for shock absorption.

All ligaments of the column, as well as the facet joint capsules, are important in the maintenance of stability. The anterior longitudinal ligament is very strong, and resists translational displacement (shear) of the vertebrae as well as extension. All the ligaments of the posterior complex resist flexion and rotation, and their integrity determines the range of movements allowed. These ligaments can support the whole column when the muscles are inactive, e.g. in quiet standing. At the limit of lumbar flexion, the column is supported mainly by the thoracolumbar fascia and by collagenous tissue within the electrically silent muscles of the back.

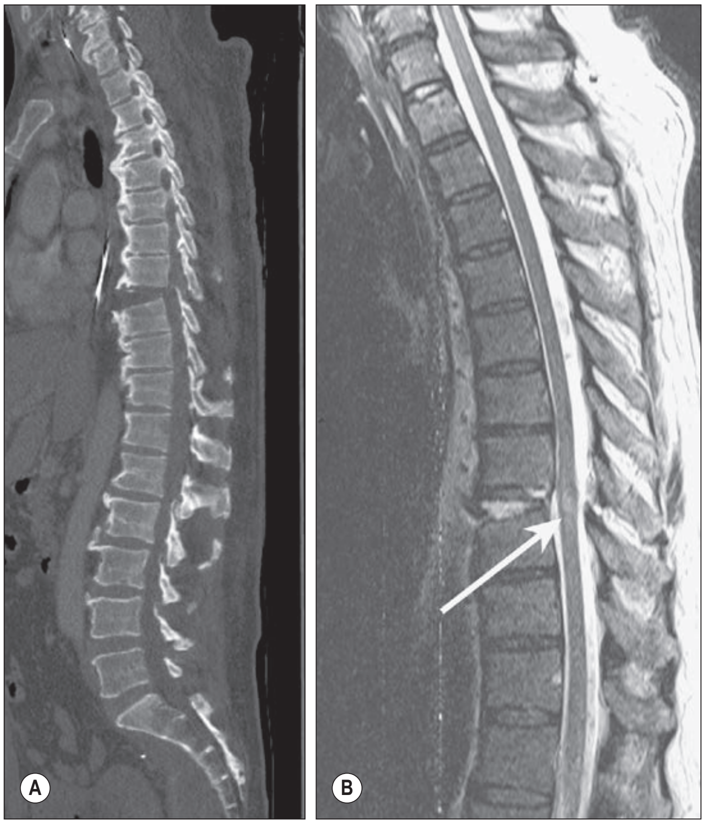

Fig. 46.79 **A**, A sagittal CT reconstruction showing a T8–T9 distraction extension injury in the setting of diffuse idiopathic skeletal hyperostosis. The patient was paraplegic at presentation. **B**, T2-weighted MRI shows abnormal signal throughout the disc space but also spinal cord signal abnormality (arrow) indicating a spinal cord injury.

Both body height and spinal stability are subject to a marked diurnal variation. Body height is affected by changes from recumbency to the upright posture. These diurnal variations appear to be due to changes that occur within the cervical, thoracic and lumbar regions of the spine. Investigations using stereophotogrammetry have demonstrated that 40% of diurnal changes occur in the thoracic spine and affect the degree of kyphosis, and a further 40% in the lumbar spine, but do not affect the lordosis (Wing et al 1992). The greatest change in vertebral column length is found in adolescents and young adults. The height loss occurs within 3 hours of rising in the morning, with an overall loss of about 15 mm.

Although the curvatures within the vertebral column contribute to the changes in height, changes within the intervertebral disc contribute both to observed height loss and to variation in stability. Magnetic resonance imaging investigations reveal a dynamic movement of fluid into and out of an intervertebral disc and adjacent vertebral body over a 24-hour period. Body position affects the movement of fluid. In the early morning, the discs are swollen with water, the intervertebral ligaments and the anulus fibrosus are taut, and the intrinsic bending stiffness and stability of the osteoligamentous spine are relatively high. After several hours of normal activity, the discs lose approximately 20% of their water and height. This change makes the ligaments slack and greatly reduces the bending stiffness of the spine, so that relatively more of the stability of the spine must then be provided by the musculature. The diurnal expulsion of water from intervertebral discs also affects the distribution of compressive loading in the spine. As the day progresses, the hydrostatic pressure in the nucleus pulposus falls, and stress concentrations arise in the anulus fibrosus and facet joints.

Movements are both determined and constrained by the shape and orientation of the facet joints, whose articular surfaces stabilize the column primarily by resisting horizontal gliding (shear) movements and axial rotation. In the most mobile regions, the joint surfaces are flatter and more horizontally placed, as will become apparent if a typical cervical facet joint is compared with a typical lumbar joint.

Certain regions of the vertebral column are further stabilized by additional extraspinal factors. The thoracic spine is stabilized by its position as an integral part of the thoracic cage and by its strong ligamentous linkages with the ribs. The sacrum is effectively a virtually fixed integral element of the bony pelvis.

The contribution to stability conferred by the musculature has been grossly underrated. The whole vertebral column is stabilized by the 'guy-rope' or staying effect of the long muscles that attach it to the girdles, the head and the appendicular skeleton. This effect is particularly marked for erector spinae, which controls global posture and movement. The small and deep muscles of the back are best able to resist shear movements between vertebrae because only they have sufficient angulation to the long axis of the vertebral column to do this effectively. The deep muscles can also fine-tune intervertebral movements.

For most back problems in clinical practice, especially chronic low back pain, enhancing muscle strength, stamina and coordination with the many other muscle groups that contribute to stability, e.g. pelvic girdle muscles, is the most appropriate and effective therapeutic avenue. Only a minority of cases benefit from surgery. Furthermore, iatrogenically damaging the neurovascular supply and neglecting the musculature may explain the relatively high failure rates from surgery. Minimally invasive spine surgery with emphasis on the preservation of soft tissue and muscle envelope may be a useful adjunct in maintaining spinal stability.

Mechanical injury to the vertebral column may be produced by flexion, extension, distraction, rotation, shear or compression; movements that cause damage are commonly combined, e.g. flexion, axial rotation and compression.

POSTURE AND ERGONOMICS

Posture is a descriptive term for the relative position of the body segments during rest or activity. The maintenance of good posture is a compromise between minimizing the load on the spine and minimizing the muscle work required.

The well-balanced erect body has a line of gravity that extends from the level of the external auditory meatus, through the dens of the axis just anterior to the body of the second thoracic vertebra, through the centre of the body of the twelfth thoracic vertebra, and through the rear of the body of the fifth lumbar vertebra to lie anterior to the sacrum. The position of the line of gravity may move anteriorly with locomotion and may vary between individuals.

The normal curvature of the cervical spine is a lordosis. However, as a result of pain, injury or poor ergonomics, this curve can become flattened to give a 'protruding chin' stance, i.e. hypolordosis in the lower cervical spine.

The thoracic spine is held convex posteriorly, and this posture primarily results from the structure of the underlying vertebrae. However, this curve or kyphosis can become exaggerated to give the impression of a rounded back. Poor posture and ergonomics can lead to this exaggerated curvature but other important causes include tuberculosis, a wedge or compression fracture of a vertebral body, Scheuermann's osteochondritis, ankylosing spondylitis, osteoporosis and metastatic carcinoma.

The lumbar spine is held in a lordosis. The degree of this lordosis is determined by the lumbosacral angle and is normally 30–45°. The muscles responsible for this posture include erector spinae, rectus abdominus, the internal and external abdominal obliques, psoas major, iliacus, the gluteal and hamstring muscles. The lordosis can be increased (as a result of weak abdominal muscles and tight hamstring muscles), decreased, flattened (common in people with either acute or chronic low back pain) or reversed.

A common postural deviation seen throughout the spine is scoliosis or lateral curvature of the spine. It can be structural, compensatory or protective. In structural scoliosis, the lateral curvature is associated with vertebral rotation, and both the curve and the rotation become more accentuated on forward flexion. Such a scoliosis is common in adolescent girls and its cause is unknown. Various factors have been proposed as common causes including various genetic and hereditary factors (Latalski et al. 2017). It may also be secondary to an underlying disorder, e.g. muscular dystrophy, spinal muscular atrophy or spina bifida. A compensatory scoliosis occurs when the pelvis is tilted laterally, e.g. as a result of unequal leg length or a fixed abduction or adduction deformity at the hip joint. Usually there is no intrinsic abnormality of the spine itself and the scoliosis disappears when the pelvic tilt is corrected. A sciatic or antalgic scoliosis is a temporary deformity produced by the protective action of muscles in certain painful conditions of the spine.

Spinopelvic balance refers to an ideal spinal alignment that would allow an individual to maintain a standing posture with minimal expenditure of energy (Schwab et al. 2009). Too much of a deviation in the coronal or sagittal planes may lead to increased effort in standing and eventually fatigue, pain and disability.

Ergonomics has been defined as 'the way humans work', and it permits an appreciation of the effects of tasks and the work environment on underlying postural biomechanics. Nachemson (1975) showed that discs were loaded maximally in sitting and in lifting in a forward-leaning position, so sitting posture and lifting have received considerable ergonomic attention.

In sitting, the goal has been to determine the seat type and reclining angle associated with lowest disc pressure and the least paraspinal muscle activity. When sitting with the hips and knees flexed to 90°, the pelvis rotates posteriorly, flattening the lumbar lordosis and consequently increasing the load on the intervertebral discs. Thus it is now advised that, in sitting, the angle between trunk and thigh should be between 105° and 135°, with the sacrum tilted at 16° and the fourth and fifth lumbar vertebrae supported.

In lifting heavy weights, there is considerable initial compression of lumbar intervertebral discs, and large increases in thoracic and intra-abdominal pressure. The compressive force acting on the spine is shared between the vertebral bodies and the vertebral arch. In the lumbar spine, the vertebral arch typically resists 20% of this force once the disc height has been reduced by diurnal fluid expulsion, and when the spine is positioned upright. However, age-related narrowing of the disc can cause more than 50% of the compressive force to be resisted by the vertebral arch, which may explain why osteoarthritis of the facet joints commonly follows disc degeneration.

When lifting, manual handling advisers emphasize the importance of leg lifting as opposed to back lifting. Loads should also be kept close to the body to reduce the lever arm of the load. The use of deep inspiration to raise intra-abdominal pressure while lifting has also been advised, as this is believed to offer further support to the lumbar spine. The spine is at risk when lifting is combined with twisting, lateral bending and asymmetric postures. However, heavy lifting remains one of the key work-related risk factors for the spine together with whole-body vibration, prolonged sitting, twisting and bending.

SURFACE ANATOMY

Skeletal landmarks

Vertebral spines

A furrow runs along the posterior median line from the external occipital protuberance above to the intergluteal cleft (anal cleft, natal cleft) below (**Figs 46.81–46.82**). The furrow is bordered laterally by muscles attaching to, and acting upon, the vertebral column; it is deepest in the mid-lumbar region and shallowest in the distal cervical region. Inferiorly, it widens out into a flattened, triangular area, with an inferior apex that lies at the start of the intergluteal cleft and corresponds approximately to the spinous process of S3. Palpation of the median furrow reveals the sagittal curves of the vertebral column (see Fig. 46.82): the cervical curve is convex anteriorly (lordosis) and extends from the C1 to the T2 vertebra; the thoracic curvature is concave anteriorly (kyphosis) and extends from the T2 to the T12 vertebra; and the lumbar curvature is convex anteriorly and extends from the T12 vertebra to the lumbosacral prominence. The external occipital protuberance is subcutaneous and is palpable on the postero-inferior aspect of the cranium in the midline, especially when it is approached from below. The inion is the most prominent part of this protuberance. The tubercle on the posterior arch of C1 (atlas) is impalpable, whereas the transverse process of C1 is palpable as an indistinct mass through sternocleidomastoid just inferior to the apex of the mastoid process. The spinous process of C2 is the first palpable feature in the median furrow, located several centimetres inferior to the inion (see Fig. 46.81B). The tips of the spinous processes of C3 to C6 are more difficult to palpate because the overlying ligamentum nuchae forms a palpable raised midline ridge, especially when the neck is flexed. The ligamentum nuchae terminates inferiorly at the spinous process of C7 (vertebra prominens), which is the most

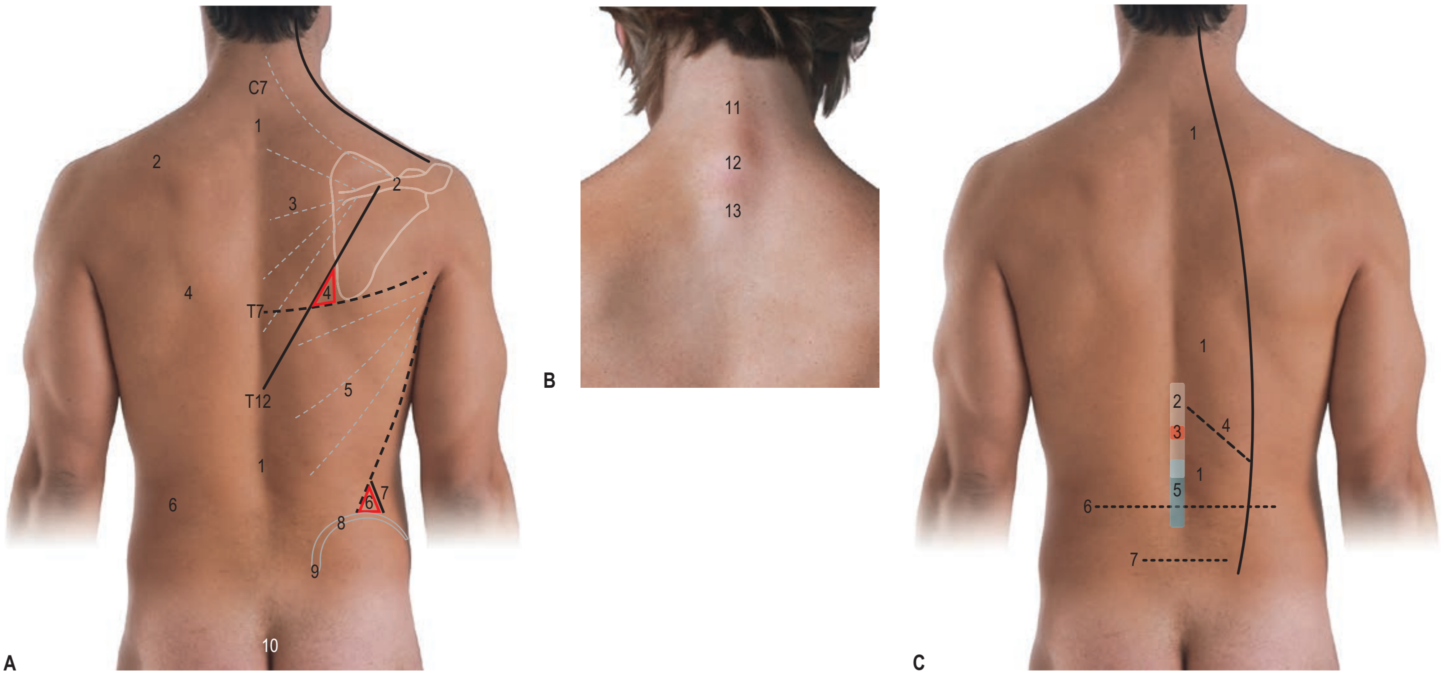

Fig. 46.81 **A**–**C**, Surface anatomy of the back. Key: **A**, 1, posterior median line and the median furrow; 2, spine of the scapula; 3, trapezius (between solid black lines); 4, triangle of auscultation; 5, latissimus dorsi (between dashed black lines); 6, inferior lumbar (Petit's) triangle; 7, external abdominal oblique; 8, iliac crest; 9, posterior superior iliac spine; 10, superior part of intergluteal cleft (approximates the spinous process of S3). **B**, 11, ligamentum nuchae (raised by neck flexion); 12, spinous process of C7 (vertebra prominens); 13, spinous process of T1. **C**, 1, erector spinae (black line represents lateral border); 2, zone of spinal cord termination (white): ranges from the middle third of the vertebral body of T11 to the middle third of the vertebral body of L3; 3, most common level of spinal cord termination (red) at the middle third of the vertebral body of L1; corresponds with the lower part of the T12–L1 interspinous space; 4, rib 12 (dashed black line); 5, zone of supracristal plane intersection with vertebral column (blue): ranges from the L2–L3 interspinous space to the spinous process of L5; 6, highest point of iliac crest marked by the supracristal plane (Tuffier's line): almost always intersects the vertebral column from the vertebral body of L4 to the L4–L5 intervertebral disc; 7, posterior superior iliac spine and interspinous plane, marked by an indentation in the overlying skin. Note the potential overlap between zone 5 (supracristal plane) and the zone 2 (termination of the spinal cord).

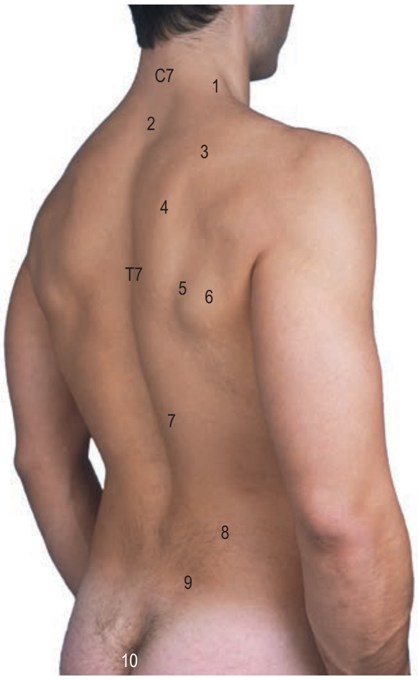

Fig. 46.82 Surface anatomy of the back, oblique view. Key: 1, trapezius (descending part); 2, posterior median line and median furrow; 3, spine of scapula; 4, trapezius (ascending part) overlying erector spinae; 5, triangle of auscultation; 6, inferior angle of scapula; 7, erector spinae; 8, inferior lumbar (Petit's) triangle; 9, posterior superior iliac spine; 10, superior part of intergluteal cleft (approximates the spinous process of S3); C7, T7, spinous processes of C7 and T7, respectively.

superior visible projection in this region. The spinous process of T1 is palpable immediately inferior to that of C7 and is usually more prominent. Identification of the remaining spinous processes of the thoracic vertebrae is not easy, even in a thin subject when the trunk is fully flexed, because they overlap one another in the mid-thoracic region. In the upper and mid-thoracic regions, the tips of the spinous processes lie level with the superior part of the bodies of the vertebrae immediately below, whereas in the lower thoracic region, they lie either opposite the inferior part of their own vertebral body, or the intervertebral disc articulating with the vertebra immediately below (see Table 46.4). The tips of the spinous processes of the lumbar vertebrae can usually be palpated without difficulty, especially if the trunk is flexed. Each lies opposite the inferior part of its own vertebral body and the intervertebral disc articulating with the vertebra below. The interspinous spaces are represented by a palpable depression between adjacent spinous processes.

Spinal levels of viscera

In adults, the spinal cord usually terminates level with the middle third of the vertebral body of L1 (range, middle third of the vertebral body of T11 to middle third of the vertebral body of L3); 25% of spinal cords end below the level of the L1–L2 intervertebral disc (Macdonald et al 1999). In children, the reported level of spinal cord termination varies with age (Van Schoor et al 2015). In children aged 1 year and above, the spinal cord terminates most commonly at the lower third of the vertebral body of L1 (range, lower third of the vertebral body of T12 to L2–L3 intervertebral disc), but may terminate as low as the middle third of the vertebral body of L3 in infants under 1 year of age (Malas et al 2001, Kesler et al 2007, Van Schoor at al 2015). The spinous processes of the vertebrae can be used as landmarks to approximate the levels of thoracic and abdominal viscera. Some of the more important are shown in **Table 46.4** (minor differences between the two sides have been ignored).

Spinal balance and alignment are intimately related to the pelvis. Pelvic parameters have been proposed that allow the relationship of the pelvis to the spine to be mathematically assessed (Schwab et al 2009). Three common measurements include pelvic tilt, pelvic incidence and sacral slope (**Fig. 46.80**). Pelvic tilt is defined as the angle between the vertical and a line through the midpoint of the sacral plate to femoral heads axis. It often reflects a compensatory mechanism: when the spine tilts forward (age- related change, loss of lordosis, increase of kyphosis) an individual will try his/her best to maintain an economic posture and to keep the spine as vertical as possible (i.e. bring the spine over the pelvis). By increasing the pelvic tilt through pelvic retroversion, spinopelvic balance may be maintained, but eventually this may lead to increased fatigue and pain. If decompensation occurs, standing with a forward stooped posture is likely.

Pelvic incidence is defined as the angle between the perpendicular to the sacral plate at its midpoint and the line connecting this point to the axes of the femoral heads. Sacral slope is the angle between the horizontal and the sacral plate. A noted geometric relationship is pelvic incidence = pelvic tilt + sacral slope (Schwab et al 2009) (**Table 46.3**). Lumbar lordosis can be approximated by the equation LL = PI ±9° (based on data from asymptomatic adults with a mean age of 48 years) (Schwab et al 2009). This relationship is useful in surgical planning by spinal surgeons because it allows the surgeon to optimize the extent of lordosis created using various fusion techniques. If too little lordosis is created, there may be continued pain or decompensation because appropriate spinopelvic balance has not been achieved.

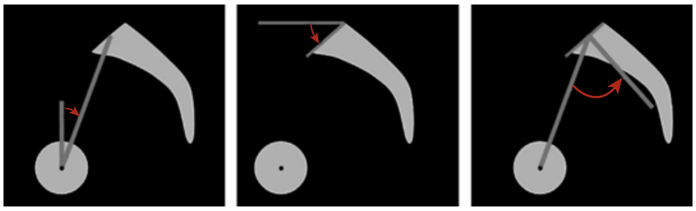
Pelvic tilt Sacral slope Pelvic incidence

Fig. 46.80 Analysis of the pelvis in the sagittal plane is commonly assessed with three angular measurements: pelvic tilt, sacral slope and pelvic incidence. (With permission from Schwab F, Lafage V, Patel A 2009 Sagittal plane considerations and the pelvis in the adult patient. Spine (Phila Pa 1976) 34:1828–33. Figure 2.)

TABLE 46.3 Normative values of pelvic parameters on adult population (mean ± SD)

Age group (years)	Pelvic incidence (°)	Pelvic tilt (°)	Sacral slope (°)
21–40	52 ± 10	13 ± 7	39 ± 9
41–60	53 ± 8	14 ± 6	40 ± 7
>60	51 ± 9	16 ± 9	36 ± 9

With permission from Schwab F, Lafage V, Patel A et al 2009 Sagittal plane considerations and the pelvis in the adult patient. Spine (Phila Pa 1976) 34:1828–33. Table 1.

TABLE 46.4 Vertebral spines and interspinous spaces as landmarks for the viscera

Spine/space	Vertebral body level	Viscera
C5	C6	Cricoid cartilage; start of oesophagus
C7	C7 or C7-T1 disc	Superior limit of the apex of the lung
T3	Superior T4	Common upper level of sternal plane intersection; medial part of scapular spine; superior limit of the oblique fissure of left lung
T4	Superior T5	Common lower level of sternal plane intersection; superior limit of the oblique fissure of right lung
T5 or T5-T6 space	Superior T6	Tracheal bifurcation
T7	Superior T8	Inferior angle of scapula; triangle of auscultation located laterally
T10-T11 space	Superior T11	Inferior vena cava traverses the respiratory diaphragm (classically reported as T8); superior limit of superior pole of the kidney
T11	Inferior T11 or T11-T12 disc	Oesophagus traverses the respiratory diaphragm (classically reported as T10)
T11-T12 space	Superior T12	Aorta traverses the respiratory diaphragm; Origin of the coeliac trunk from the aorta
T12-L1 space	Superior L1	Lowest level of pleural cavity; common level of spinal cord termination (middle of L1) in an adult
L1	Inferior L1 or L1-L2 disc	Transpyloric plane; origin of the superior mesenteric artery from the aorta; renal hilum (classically reported level)
L1-L2 space	Superior/mid L2	Subcostal plane; sometimes marks the transpyloric plane; renal hilum
L2-L3 space	Superior/mid L3	Origin of the inferior mesenteric artery from the aorta; inferior limit of the spinal cord in infants (0-1 year of age)
L3-L4 space	Superior/mid L4	Bifurcation of aorta; possible lumbar puncture insertion site (adult)
L4	Inferior L4 or L4-L5 disc	Supracristal plane (the plane may also align with the L4-L5 interspinous space); used to landmark the needle insertion site for adult lumbar puncture either above (L3-L4 interspinous space) or below (L4-L5 interspinous space)
S2	S2	Termination of subarachnoid space

Scapular landmarks

The shape of the back in the upper thoracic region is determined largely by the scapula and the muscles attached to it. Bony scapular landmarks are most evident when the upper limbs hang by the sides in the anatomical position (see Figs 46.81A, 46.82).

The scapula overlies rib 2 to rib 7. Its superior angle is palpable through trapezius, and its inferior angle through latissimus dorsi; these angles are joined by the medial border of the scapula, which runs vertically. The spine of the scapula runs subcutaneously and is easily palpable from its root medially to the acromial angle and acromion laterally. With the upper limb in the anatomical position, the spinous process of T3 is located level with the spine of the scapula, and the spinous process of T7 is level with the inferior angle.

Posterior pelvic and sacrococcygeal bony landmarks

The entire iliac crest can be palpated in the lower part of the lumbar region of the back. It can be traced posteriorly and superiorly from the anterior superior iliac spine to its tubercle, then around to its highest point, which is located posteriorly, and finally downwards and medially to the posterior superior iliac spine, which is overlaid by an indentation in the skin. For landmarking during lumbar puncture (see Fig. 47.20), a line joining the highest points of the iliac crests (supracristal plane, Tuffier's line) is used. In the majority of individuals, the line intersects the vertebral column at the level of the vertebral body of L4 or L4–L5 intervertebral disc, but it can range from the L2–L3 interspinous space to spinous process of L5 (Render 1996, Walsh et al 2006, Chakraverty et al 2007, Pak et al 2016, Shen et al 2016, Uzun et al 2016) (see Figs 46.81C, 76.19). In most adults the plane intersects the vertebral column inferior to the termination of the spinal cord. Localizing the supracristal plane via palpation may place it at a higher level in females and individuals with a higher body mass index (Kim et al 2007, Hale et al 2010). It is important to remember that the median furrow may not coincide with the median plane when an individual lies in the lateral decubitus position, especially in the lumbar region in subjects with a higher body mass. Careful palpation may be necessary to identify the vertebral spinous processes in this position. The spinous processes of the sacral vertebrae are smaller and less well defined than those of the other vertebrae. When determined by palpation, the plane passing through the posterior superior iliac spines intersects the spinous process of S1 or S2 (range, spinous process of L5 to spinous process of S3) (Chakraverty et al 2007, Kim et al 2007), whereas radiographic assessment shows the plane most commonly intersects the spinous process of S2 (McGaugh et al 2007) (see Fig. 76.19). The latter serves as a useful landmark for the inferior limit of the dural sac in an adult, which is most commonly located level with the inferior part of the vertebral bodies of S1 to S2 (range, L5–S1 intervertebral disc to vertebral body of S4). The tip of the coccyx can be felt deeply near the centre of the intergluteal cleft. Moving the examining finger cranially enables palpation of the raised ridges of the sacral cornua on either side of the midline; they demarcate the sacral hiatus and so form the landmark for performing a caudal anaesthetic block (see Figs 47.21, 47.22, 76.19). The sacral cornua are not developed in very young children, which means that the sacral hiatus cannot be located via palpation (Mirjalili et al 2015).

Musculotendinous landmarks

In the posterior cervical region, a median furrow lies between the cylindrical muscular prominences that are formed mainly by the semispinalis muscles and are accentuated by neck extension against resistance. In the thoracic and lumbar regions, broad elevations produced by the erector spinae muscle group extend for about one hand's breadth on either side of the median furrow between the iliac crest and rib 12 (see Fig. 46.82). The lateral border of this elevation then crosses the ribs in the region of their angles, passing medially as it ascends. The erector spinae muscle group can be demonstrated, or accentuated, by extending the vertebral column against resistance.

Trapezius is a flat, triangular muscle that covers the back of the neck and shoulder (see Figs 46.71 and 46.81A). The two trapezius muscles resemble a trapezium in which two of the angles correspond to the shoulders, the third to the external occipital protuberance and the fourth to the spinous process of T12. On each side, the anterosuperior border of the muscle forms the posterior boundary of the posterior triangle of the neck; it can be seen in muscular subjects, especially during shoulder elevation against resistance or by extension and lateral flexion of the neck against resistance. The ascending (lower) fibres are best seen when an erect individual pushes both hands against a wall with their elbows extended.

Latissimus dorsi occupies the lower half of the back. It passes from the spinous processes of the lower six thoracic vertebrae, the thoracolumbar fascia and the posterior iliac crest, to the posterior axillary fold. In lean individuals, with the arm adducted against resistance, the inferolateral border can easily be traced to the iliac crest. The upper border passes horizontally from the spinous process of T7 to the inferior angle of the scapula and then on to the posterior axillary fold.

The triangle of auscultation (see Figs 46.71, 46.82) lies between the upper border of latissimus dorsi, the lower inferolateral border of trapezius and the inferomedial border of rhomboid major, although for simplicity the medial border of the scapula is often substituted for the latter muscle.

The inferior lumbar (Petit's) triangle (see Figs 46.71, 46.82), one of the sites of a rare primary lumbar hernia, lies inferiorly just lateral to the highest point of the iliac crest, between the inferolateral border of latissimus dorsi, the posterior free border of external abdominal oblique and the iliac crest. The corridor bordered by the triangle is used to enter the retroperitoneal space: the fascia covering the triangle is detached from the iliac crest and the retroperitoneal space can be entered.

CLINICAL EXAMINATION

Clinical examination of the back of the trunk and neck best follows the order of inspection, palpation and movement. The examination will be determined by the circumstances of presentation and by the history, and may include musculoskeletal, neurological and vascular observations. Information relevant to the neurological and vascular examination of the skin and material relating to spinal movements and deeper innervation are found above. Palpation of the region involves careful assessment of the bony and musculotendinous landmarks described above, looking in particular for asymmetry, deformity and tenderness. Note that, apart from the spinous processes, most of the bony elements of the vertebrae and almost all of the intervertebral joints are not palpable from behind. In regions of lordosis (sagittal plane curves of the spine with anterior convexity, i.e. mid-cervical and mid- and lower lumbar), parts of the vertebral column can often be palpated anteriorly with care in well-relaxed, thin subjects. .Examination of the spine requires a careful neurological exam, and may also involve manoeuvres that assess neurology in relation to potential anatomical derangements. For example, the straight leg raise stretches caudal lumbar spinal nerve roots and exacerbates pain in the presence of caudal lumbar pathology such as an L4–L5 or L5–S1 intervertebral disc herniation. Examination of other joints such as the hip or shoulder is also important when examining the spine because pain related to these structures may present similar to radiculopathy and other spinal problems. A careful history and examination of the spine along with neurological and orthopaedic examination should allow the clinician to be fairly certain of the spinal localization of pathological processes.

Bonus e-book content

Fig. 46.1 Hair tracts on the dorsal surface of the body.

Fig. 46.3 Dermatomes on the dorsal surface of the body. The small diagram shows the regular arrangement of dermatomes in the upper and lower limbs of the embryo. Maps of dermatome distribution are useful in clinical neurology as a guide to identify the location of pathology in patients with peripheral sensory deficits, but it is important to remember that they are approximations (Ch. 24).

Fig. 46.11 A sagittal MR image of the lumbar spine showing the L5–S1 intervertebral foramen (neuroforamen) and a pathologically narrowed L4–L5 intervertebral foramen.

Fig. 46.12 A sagittal CT image of the lumbar spine showing the left side of an isthmic spondylolisthesis resulting from bilateral fractures of the pars interarticularis.

Fig. 46.13 (**A**) Sagittal and (**B**) axial MR images of a degenerative spondylolisthesis at L4–L5.

Fig. 46.14 A vertical radiograph of a section through T6 of a specimen from a 6-year-old child injected with barium sulphate.

Fig. 46.15 An anteroposterior arteriogram of the lower thoracic and upper lumbar vertebrae in a 6-year-old child injected with barium sulphate.

Fig. 46.16 A vertical radiograph of a section through a lumbar vertebra of a 6-year-old child injected with barium sulphate.

Fig. 46.17 The arterial supply to the bodies of the upper cervical vertebrae and the odontoid process.

Fig. 46.18 A vertical radiograph of a section through the fourth cervical vertebra of a 6-year-old child, showing vascularity.

Fig. 46.19 An arteriogram of the cervical and upper thoracic regions of the 6-year-old spine seen in Figs 46.16 and 46.18.

Fig. 46.20 **C**, Virtual rendering of a CT aortogram showing the lumbar spinal arterial supply, viewed from the left.

Fig. 46.23 **B**, A volume rendered sagittal CT slab through the right half of the body of the second lumbar vertebra, viewed from the left; compression trabeculae of the cancellous bone can be seen running vertically in the central aspect of the body.

Fig. 46.24 The vertebral canal in section.

Fig. 46.26 A sagittal T1-weighted MRI showing a markedly reduced L3-L4 foraminal volume secondary to advanced disc degeneration resulting in bony neural entrapment of the L3 spinal nerve.

Fig. 46.27 **B–C**, A volume rendered CT of the cervical spine: **B**, anterior view; **C**, oblique view.

Fig. 46.31 An axial CT scan showing the carotid tubercle (Chassaignac's tubercle).

Fig. 46.33 An axial MR image showing an intact transverse ligament.

Fig. 46.35 A lateral cervical radiograph demonstrating a posterior ponticle forming the roof of a tunnel over the vertebral artery.

Fig. 46.38 A sagittal CT scan reconstructed image demonstrating an os odontoideum.

Fig. 46.39 A sagittal CT scan reconstructed image of a type II odontoid fracture.

Fig. 46.51 **D, E**, A midline sagittal and left sagittal CT in a male. **F, G**, A T1-weighted MRI in a female through the sacrum.

Fig. 46.57 Atlanto-axial instability in the setting of rheumatoid arthritis.

Fig. 46.58 **A**, A sagittal CT reconstruction showing an osseous and ligamentous injury at T10–T11 sustained by a 54-year-old male after a major compression injury. **B**, The MR image shows gross disruption of the supraspinous and interspinous ligaments.

Fig. 46.60 **B-D,** The maturing ring apophysis in the mid-thoracic spine.

Fig. 46.63 **B–C**, T2-weighted coronal MRIs from posterior to anterior in a teenage female investigated for scoliosis, showing the lumbosacral spinal nerve roots descending from the conus medullaris and exiting through the intervertebral foramina.

Fig. 46.64 **A**, A sagittal CT reconstruction showing C6–C7 flexion distraction injury with traumatic spondylolisthesis. **B**, A C6–C7 perched facet with a small chip fracture of the superior articular process of C7. **C**, T2 weighted sagittal MRI with an associated spinal cord contusion (arrow) due to the injury. **D**, Lateral X-ray status post-surgical reduction via anterior cervical discectomy and placement of an allograft and plate and screws.

Fig. 46.66 **B**, An axial T2-weighted MRI demonstrating the ligamentous structures of the cervical spine.

Fig. 46.69 **A**, A T2-weighted MRI showing soft tissue pannus (arrow) compressing the ventral cervicomedullary junction. **B**, A lateral X-ray showing a C1–C2 surgical fusion. **C**, T2-weighted MRI, 1 year postoperative, showing resorption of the pannus that occurred with stabilization and surgical fusion.

Fig. 46.74 An axial MRI of the lumbar spine at the level of the L4-L5 intervertebral disc.

Fig. 46.79 **A**, A sagittal CT reconstruction showing a T8–T9 distraction extension injury in the setting of diffuse idiopathic skeletal hyperostosis. The patient was paraplegic at presentation. **B**, T2-weighted MRI shows abnormal signal throughout the disc space but also spinal cord signal abnormality (arrow) indicating a spinal cord injury.

Fig. 46.80 Analysis of the pelvis in the sagittal plane is commonly assessed with three angular measurements: pelvic tilt, sacral slope and pelvic incidence.

Key references

Adams MA, Bogduk N, Burton K et al 2006 The Biomechanics of Back Pain, 2nd ed. Edinburgh: Elsevier, Churchill Livingstone.

A comprehensive and detailed source of information on the functional anatomy, tissue biology and biomechanics of the lumbar spine.

Batson OV 1957 The vertebral vein system. Caldwell Lecture, 1956. Am J Roentgenol Radium Ther Nuclear Med 78:195–212.

A pioneering study of the venous plexuses of the vertebral column, which has become the standard of reference in its field.

Bogduk N 2012 Clinical and Radiological Anatomy of the Lumbar Spine, 5th ed. Edinburgh: Elsevier, Churchill Livingstone.

The most thorough text currently available on the topographical and functional anatomy of the lumbosacral spine. The book incorporates biomechanical and physiological information that is related to the clinical problem of low back pain.

Denis F 1983 The three column spine and its significance in the classification of acute thoracolumbar spinal injuries. Spine 8:817–31.

A seminal paper for the understanding and classification of thoracolumbar instability.

Groen GJ, Baljet B, Drukker J 1990 Nerves and nerve plexuses of the human vertebral column. Am J Anat 188:282–96.

An acetylcholinesterase whole-mount study of human fetal material giving detail of the perivertebral nerve plexuses and of the sinuvertebral nerves.

MacNab I, McCulloch J 1990 Backache, 2nd ed. Baltimore: Williams & Wilkins.

The functional anatomy of the lumbar spine, described as a basis for the clinical management of low back pain.

Mercer S, Bogduk N 1999 The ligaments and anulus fibrosus of human adult cervical intervertebral discs. Spine 24:619–26; discussion 27–8.

A human cadaveric microdissection study showing that the cervical anulus fibrosus is an anterior crescent rather than a uniformly circumferential structure.

Newell RL 1999 The spinal epidural space. Clin Anat (New York, NY) 12:375–9.

A review of the morphological, developmental and topographical aspects of the spinal epidural space.

Viejo-Fuertes D, Liguoro D, Rivel J et al 1998 Morphologic and histologic study of the ligamentum flavum in the thoraco-lumbar region. Surg Radiol Anat: SRA 20:171–6.

A cadaver-based study detailing anatomical and histological findings with regard to the ligamentum flavum.

Willard FH, Vleeming A, Schuenke MD et al 2012 The thoracolumbar fascia: anatomy, function and clinical considerations. J Anat 221:507–36.

A detailed review of the thoracolumbar fascia with regard to functional anatomy and how it plays a role in spinal stability and as a potential pain generator.

References

Adams MA, Bogduk N, Burton K et al 2006 The Biomechanics of Back Pain, 2nd ed. Edinburgh: Elsevier, Churchill Livingstone.

A comprehensive and detailed source of information on the functional anatomy, tissue biology and biomechanics of the lumbar spine.

Adams MA, Dolan P 2005 Spine biomechanics. J Biomech 38: 1972–83.

Albequerque CA, Smoth KR, Saywers TE et al 2002 Relation between oligohydramnios and spinal flexion in the human fetus. Early Hum Dev 68:119–26.

Bagnall KM, Harris PF, Jones PRM 1977 A radiographic study of the human fetal spine. 1. The development of the secondary cervical curvature. J Anat 123:777–82.

Batson OV 1957 The vertebral vein system. Caldwell Lecture, 1956. Am J Roentgenol Radium Ther Nuclear Med 78:195–212.

A pioneering study of the venous plexuses of the vertebral column, which has become the standard of reference in its field.

Been E, Kalichman L 2014 Lumbar lordosis. The Spine Journal 14:87–97.

Boelderl A, Daniaux H, Kathrein A et al 2002 Danger of damaging the medial branches of the posterior rami of spinal nerves during a dorsomedian approach to the spine. Clin Anat (New York, NY) 15:77–81.

Bogduk N 2012 Clinical and Radiological Anatomy of the Lumbar Spine, 5th ed. Edinburgh: Elsevier, Churchill Livingstone.

The most thorough text currently available on the topographical and functional anatomy of the lumbosacral spine. The book incorporates biomechanical and physiological information that is related to the clinical problem of low back pain.

Chakraverty R, Pynsent P, Isaacs K 2007 Which spinal levels are identified by palpation of the iliac crests and the posterior superior iliac spines? J Anat 210:232–6.

Chaynes P, Verdie JC, Moscovici J et al 1998 Microsurgical anatomy of the internal vertebral venous plexuses. Surg Radiol Anat 20:47–51.

Cormack GC, Lamberty BGH 1994 The Arterial Anatomy of Skin Flaps. Edinburgh: Elsevier, Churchill Livingstone.

Crock H 1996 An Atlas of Vascular Anatomy of the Skeleton and Spinal Cord. London: Martin Dunitz.

Crock HV, Yoshizawa H 1976 The blood supply of the lumbar vertebral column. Clin Orthop Relat Res 115:6–21.

Dean NA, Mitchell BS 2002 Anatomic relation between the nuchal ligament (ligamentum nuchae) and the spinal dura mater in the craniocervical region. Clin Anat (New York, NY) 15:182–5.

Denis F 1983 The three column spine and its significance in the classification of acute thoracolumbar spinal injuries. Spine 8:817–31.

A seminal paper for the understanding and classification of thoracolumbar instability.

Dvorak J, Vajda EG, Grob D et al 1995 Normal motion of the lumbar spine as related to age and gender. Eur Spine J 4:18–23.

Frobin W, Leivseth G, Biggemann M et al 2002 Sagittal plane segmental motion of the cervical spine. A new precision measurement protocol and normal motion data of healthy adults. Clin Biomech (Bristol, Avon) 17:21–31.

Groen GJ, Baljet B, Drukker J 1990 Nerves and nerve plexuses of the human vertebral column. Am J Anat 188:282–96.

An acetylcholinesterase whole-mount study of human fetal material giving detail of the perivertebral nerve plexuses and of the sinuvertebral nerves.

Groen RJ, du Toit DF, Phillips FM et al 2004 Anatomical and pathological considerations in percutaneous vertebroplasty and kyphoplasty: a reappraisal of the vertebral venous system. Spine 29:1465–71.

Hartman J 2014 Anatomy and clinical significance of the uncinate process and uncovertebral joint: a comprehensive review. Clin Anat 27:431–40.

Hale SJ, Mirjalili SA, Stringer MD 2010 Inconsistencies in surface anatomy: the need for an evidence-based reappraisal. Clin Anat 23:922–30.

Karwacki GM, Schneider JF 2012 Normal ossification patterns of atlas and axis: a CT study. AJNR Am J Neuroradiol 33:1882–7.

Kasai T, Ikata T, Katoh S et al 1996. Growth of the cervical spine with special reference to its lordosis and mobility. Spine 21:2067–73.

Kesler H, Dias MS, Kalapos P 2007 Termination of the normal conus medullaris in children: a whole-spine magnetic resonance imaging study. Neurosurg Focus 23:E7:1–6.

Kim HW, Ko YJ, Rhee WI et al 2007 Interexaminer reliability and accuracy of posterior superior iliac spine and iliac crest palpation for spinal level estimations. J Manipulative Physiol Ther 30:386–9.

Klimo P Jr, Rao G, Brockmeyer D 2007 Congenital anomalies of the cervical spine. Neurosurg Clin North Am 18:463–78.

Lang J 1986 Craniocervical region, osteology and articulations. Neuro Orthop 1:67–92.

Latalski M, Danielewicz-Bromberek A, Fatyga M, et al 2017 Current insights into the aetiology of adolescent idiopathic scoliosis. Arch Orthop Trauma Surg 137:1327–33.

Lee JY, Vaccaro AR, Lim MR et al 2005 Thoracolumbar injury classification and severity score: a new paradigm for the treatment of thoracolumbar spine trauma. J Orthop Sci 10:671–5.

Loughenbury PR, Wadhwani S, Soames RW 2006 The posterior longitudinal ligament and peridural (epidural) membrane. Clin Anat (New York, NY) 19:487–92.

Lu Y, Yang T, Luo H et al 2016 Visualization and quantitation of fetal movements by real-time three-dimensional ultrasound with live xPlane imaging in the first trimester of pregnancy. Croat Med J 57:474–81.

Macdonald A, Chatrath P, Spector T et al 1999 Level of termination of the spinal cord and the dural sac: a magnetic resonance study. Clin Anat 12:149–52.

Macintosh JE, Valencia F, Bogduk N et al 1986 The morphology of the lumbar multifidus muscles. Clin Biomech (Bristol, Avon) 1:196–204.

MacLaughlin SM, Oldale KN 1992 Vertebral body diameters and sex prediction. Ann Hum Biol 19:285–92.

MacNab I, McCulloch J 1990 Backache, 2nd ed. Baltimore: Williams & Wilkins.

The functional anatomy of the lumbar spine, described as a basis for the clinical management of low back pain.

Malas MA, Salbacak A, Buyukmumcu M et al 2001 An investigation of the conus medullaris termination level during the period of fetal development to adulthood. Kaibogaku Zasshi – Journal of Anatomy 76:453–9.

McGaugh JM, Brisme JM, Dedrick GS et al 2007 Comparing the anatomical consistency of the posterior superior iliac spine to the iliac crest as reference landmarks for the lumbopelvic spine: a retrospective radiological study. Clin Anat 20:819–25.

McGregor AH, McCarthy ID, Hughes SP 1995 Motion characteristics of the lumbar spine in the normal population. Spine 20:2421–28.

Mercer S, Bogduk N 1999 The ligaments and anulus fibrosus of human adult cervical intervertebral discs. Spine 24:619–26; discussion 27–8.

A human cadaveric microdissection study showing that the cervical anulus fibrosus is an anterior crescent rather than a uniformly circumferential structure.

Mercer SR, Bogduk N 2003 Clinical anatomy of ligamentum nuchae. Clin Anat (New York, NY) 16:484–93.

Mirjalili SA, Taghavi K, Frawley G et al 2015. Should we abandon landmark–based technique for caudal anesthesia in neonates and infants? *Pediatric Anesthesia* 25:511–16.

Nachemson A 1975 Towards a better understanding of low-back pain: a review of the mechanics of the lumbar disc. Rheumatol Rehab 14:129–43.

Newell RL 1999 The spinal epidural space. Clin Anat (New York, NY) 12:375–9.

A review of the morphological, developmental and topographical aspects of the spinal epidural space.

Ordway NR, Seymour R, Donelson RG et al 1997 Cervical sagittal range-of-motion analysis using three methods. Cervical range-of-motion device, 3space, and radiography. Spine 22:501–8.

Pak N, Patel SG, Hashemi Taheri AP et al 2016 A reappraisal of adult thoracic and abdominal surface anatomy in Iranians in vivo using computed tomography. Clin Anat 29:191–6.

Parke WW, Bono CM, Garfin SR 2011 Applied anatomy of the spine. In: Herkowitz HN, Garfin SR, Eismont FJ et al (eds) Rothman-Simeone The Spine, 6th ed. Philadelphia: Elsevier, Saunders; Ch. 2, pp. 15–53.

Pearce JMS 2006 The craniospinal venous system. Eur Neurol 56:136–8.

Pearcy M, Portek I, Shepherd J 1984 Three-dimensional X-ray analysis of normal movement in the lumbar spine. Spine 9:294–7.

Pearcy MJ, Tibrewal SB 1984 Axial rotation and lateral bending in the normal lumbar spine measured by three-dimensional radiography. Spine 9:582–7.

Piper JG, Traynelis VC 1998 Congenital malformations of the craniovertebral junction. In: Dickman CA, Spetzler RF, Sonntag VKH (eds) Surgery of the Craniovertebral Junction. New York: Thieme.

Render CA 1996 The reproducibility of the iliac crest as a marker of lumbar spine level. Anaesthesia 51:1070–71.

Saifuddin A, Burnett SJ, White J 1998 The variation of position of the conus medullaris in an adult population. A magnetic resonance imaging study. Spine 23:1452–6.

Salmon M 1994 Arteries of the muscles of the extremities and trunk. In: Taylor GI, Razaboni RM (eds) Anatomic Studies, Book 1. St Louis: Quality Medical Publishing.

Schwab F, Lafage V, Patel A et al 2009 Sagittal plane considerations and the pelvis in the adult patient. Spine (Phila Pa 1976) 34: 1828–33.

Shen XH, Su BY, Liu JJ et al 2016 reappraisal of adult thoracic and abdominal surface anatomy via CT scan in Chinese population. Clin Anat 29:165–74.

Taylor JR, Twomey LT 1984 Sexual dimorphism in human vertebral body shape. J Anat 138:281–6.

Trott PH, Pearcy MJ, Ruston SA et al 1996 Three-dimensional analysis of active cervical motion: the effect of age and gender. Clin Biomech (Bristol, Avon) 11:201–6.

Twomey L, Taylor J, Furniss B 1983 Age changes in the bone density and structure of the lumbar vertebral column. J Anat 136:15–25.

Uzun C, Atman ED, Ustuner E et al 2016 Surface anatomy and anatomical planes in the adult Turkish population. Clin Anat 29:183–90.

Van Schoor AN, Bosman MC, Bosenberg AT 2015 Descriptive study of the differences in the level of the conus medullaris in four different age groups. Clin Anat 28:638–44.

Viejo-Fuertes D, Liguoro D, Rivel J et al 1998 Morphologic and histologic study of the ligamentum flavum in the thoraco-lumbar region. Surg Radiol Anat SRA 20:171–6.

A cadaver-based study detailing anatomical and histological findings with regard to the ligamentum flavum.

Walsh JC, Quinlan JF, Butt K et al 2006 Variation in position of the L4/5 disc inter-space from the anatomical landmark: review of 450 radiographs and clinical applications. Eur J Orthop Surg Traumatol 16:203–6.

White AA, Panjabi MM 1990 Clinical Biomechanics of the Spine, 2nd ed. Philadelphia: JB Lippincott.

Willard FH, Vleeming A, Schuenke MD et al 2012 The thoracolumbar fascia: anatomy, function and clinical considerations. J Anat 221:507–36.

A detailed review of the thoracolumbar fascia with regard to functional anatomy and how it plays a role in spinal stability and as a potential pain generator.

Willems JM, Jull GA, J KF 1996 An in vivo study of the primary and coupled rotations of the thoracic spine. Clin Biomech (Bristol, Avon) 11:311–16.

Wing P, Tsang I, Gagnon F et al 1992 Diurnal changes in the profile shape and range of motion of the back. Spine 17:761–6.

Wood GW II 2103 Spinal anatomy and surgical approaches. In: Canale ST, Beaty JH (eds) Campbell's Operative Orthopaedics, 12th ed. St Louis: Mosby; Ch. 37, pp.1524–58.

Zumpano MP, Hartwell S, Jagos CS 2006 Soft tissue connection between rectus capitis posterior minor and the posterior atlanto-occipital membrane: a cadaveric study. Clin Anat (New York, NY) 19:522–7.

CHAPTER
47

Spinal cord and spinal nerves: gross anatomy

The gross anatomy of the structures that lie within the vertebral canal and their extensions through the intervertebral foramina, the spinal nerve or radicular ('root') canals, is described in this chapter. The internal organization of the spinal cord is described in Chapter 27.

The spinal cord and its blood vessels and nerve roots lie within a meningeal sheath, the theca, which occupies the central zone of the vertebral canal and extends from the foramen magnum, where it is in continuity with the meningeal coverings of the brain, to the level of the second sacral vertebra in the adult. Distal to this level, the dura extends as a fine cord, the filum terminale externum, which fuses with the posterior periosteum of the first coccygeal segment. Tubular prolongations of the dural sheath extend around the spinal roots and nerves into the lateral zones of the vertebral canal and out into the root canals, eventually fusing with the epineurium of the spinal nerves. Between the theca and the walls of the vertebral canal is the epidural (spinal extradural) space, which is loosely filled with fat, connective tissue containing small arteries and lymphatics, and an important venous plexus. Three-dimensional appreciation of the anatomy of the spinal theca and its surroundings is essential for the efficient management of spinal pain and of spinal injuries, tumours and infections. Equally significant clinically is the anatomy of the often-precarious blood supply of the spinal cord and its associated structures. The increasing application and refinement of diagnostic imaging and endoscopic procedures lend a new importance to topographical detail here.

SPINAL CORD

The spinal cord occupies the superior two-thirds of the vertebral canal (**Figs 47.1–47.2**). It is continuous cranially with the medulla oblongata, just below the level of the foramen magnum, at the upper border of the atlas. It terminates caudally as the conus medullaris. During development, the vertebral column elongates more rapidly than the spinal cord, so that there is an increasing discrepancy between the anatomical level of spinal cord segments and their corresponding vertebrae. At stage 23, the vertebral column and spinal cord are the same length and the cord ends at the last coccygeal vertebra. In later fetal life, the conus medullaris lies between the third lumbar and fifth sacral vertebrae. In premature and term neonates, it lies between the first and third lumbar vertebrae, and in children between the ages of 1 and 7 years, it lies between the twelfth thoracic and third lumbar vertebrae (Barson 1970, Vettivel 1991, Malas et al 2001, Kesler et al 2007, Suresh et al 2013). In the adult, the spinal cord terminates on average at the level of the middle third of the body of the first lumbar vertebra (Macdonald et al 1999) (see Fig. 46.81), which corresponds approximately to the transpyloric plane. However, it may end as high as the middle third of the body of the eleventh thoracic vertebra or as low as the middle third of the body of the third lumbar vertebra (Macdonald et al 1999). Its position rises slightly in vertebral flexion, and there is some correlation with the length of the trunk, especially in females. (For dimensional data, consult Barson and Sands (1977).)

The filum terminale, a filament of connective tissue approximately 20 cm long, descends from the apex of the conus medullaris. Its upper 15 cm, the filum terminale internum, is continued within extensions of the dural and arachnoid meninges and reaches the caudal border of the second sacral vertebra. Its final 5 cm, the filum terminale externum, fuses with the investing dura mater, and then descends to the dorsum of the first coccygeal vertebral segment. The filum is continuous above with the spinal pia mater. A few strands of nerve fibres, which probably represent the roots of rudimentary second and third coccygeal spinal nerves, adhere to its upper part. The central canal is continued into the filum for 5–6 mm. A capacious part of the subarachnoid space surrounds the filum terminale internum, and is the site of election for access to the cerebrospinal fluid (CSF) via a lumbar puncture (see below).

The spinal cord varies in transverse width, gradually tapering craniocaudally, except at the levels of the enlargements. It is not cylindrical, being wider transversely at all levels, especially in the cervical segments. The cervical enlargement, the source of the large spinal nerves that supply the upper limbs, extends from the third cervical to the second thoracic segments. Its maximum circumference (approximately 38 mm) is in the sixth cervical segment (a spinal cord segment provides the attachment of the rootlets of a pair of spinal nerves). The lumbar enlargement, the source of the large spinal nerves that supply the lower limbs, extends from the first lumbar to the third sacral segments; the equivalent vertebral levels are the ninth to twelfth thoracic vertebrae. Its greatest circumference (approximately 35 mm) is near the lower part of the body of the twelfth thoracic vertebra, below which it rapidly dwindles into the conus medullaris.

Fissures and sulci extend along most of the external surface. A ventral (anterior) median fissure (sulcus) and a posterior median sulcus and septum almost completely separate the cord into right and left halves; they are joined by a commissural band of nervous tissue that contains a central canal (see Fig. 27.1).

The ventral median fissure extends along the whole ventral surface with an average depth of 3 mm, although it is deeper at caudal levels. It contains a reticulum of pia mater. Dorsal to it is the anterior white commissure. Perforating branches of the spinal vessels pass from the fissure to the commissure to supply the central spinal region. The posterior median sulcus is shallower, and from it a posterior median septum penetrates more than halfway into the cord, almost to the central canal. The septum varies in anteroposterior extent from 4 to 6 mm, and diminishes caudally as the canal becomes more dorsally placed and the cord contracts. The patency of the central canal diminishes with age: a postmortem study found the canal to be patent along the length of the cord in infants under 1 year of age, but occluded in most segments with increasing age after the second decade (Yasui et al 1999).

Dorsal rootlets of spinal nerves enter the cord along a posterolateral sulcus that lies from 1.5 to 2.5 mm lateral to each side of the posterior median sulcus. The white matter between the posteromedian and posterolateral sulci on each side is the dorsal (posterior) funiculus. In cervical and upper thoracic segments, a longitudinal posterointermediate sulcus marks a septum dividing each posterior funiculus into two large tracts on either side, a medial fasciculus gracilis and a lateral fasciculus cuneatus. A ventrolateral (anterolateral) funiculus lies between the posterolateral sulcus and ventral median fissure, and is subdivided into ventral (anterior) and lateral funiculi by ventral spinal rootlets that pass through its substance to issue from the surface of the cord. The ventral funiculus is medial to, and includes, the emerging ventral rootlets, whilst the lateral funiculus lies between the roots and the posterolateral sulcus. In upper cervical segments, nerve rootlets emerge through each lateral funiculus to form the accessory nerve, which ascends in the vertebral canal lateral to the spinal cord and enters the posterior cranial fossa via the foramen magnum (see Fig. 35.11).

Dorsal and ventral roots

The paired dorsal and ventral roots of the spinal nerves are continuous with the spinal cord (**Fig. 47.1F**). They cross the subarachnoid space and traverse the dura mater separately, uniting in or close to their intervertebral foramina to form the (mixed) spinal nerves. Since the spinal cord is shorter than the vertebral column, the more caudal spinal roots descend for varying distances around and beyond the cord to reach their corresponding foramina. In so doing, they form a divergent sheaf of spinal nerve roots, the cauda equina, which is gathered round the filum terminale in the spinal theca, mostly distal to the apex of the cord.

Ventral spinal roots contain efferent somatic and, at some levels, preganglionic sympathetic, axons that extend from neuronal cell bodies in the ventral horns and intermediolateral columns, respectively. There are also afferent nerve fibres in these roots. The rootlets comprising each ventral root emerge from the anterolateral sulcus in groups over an

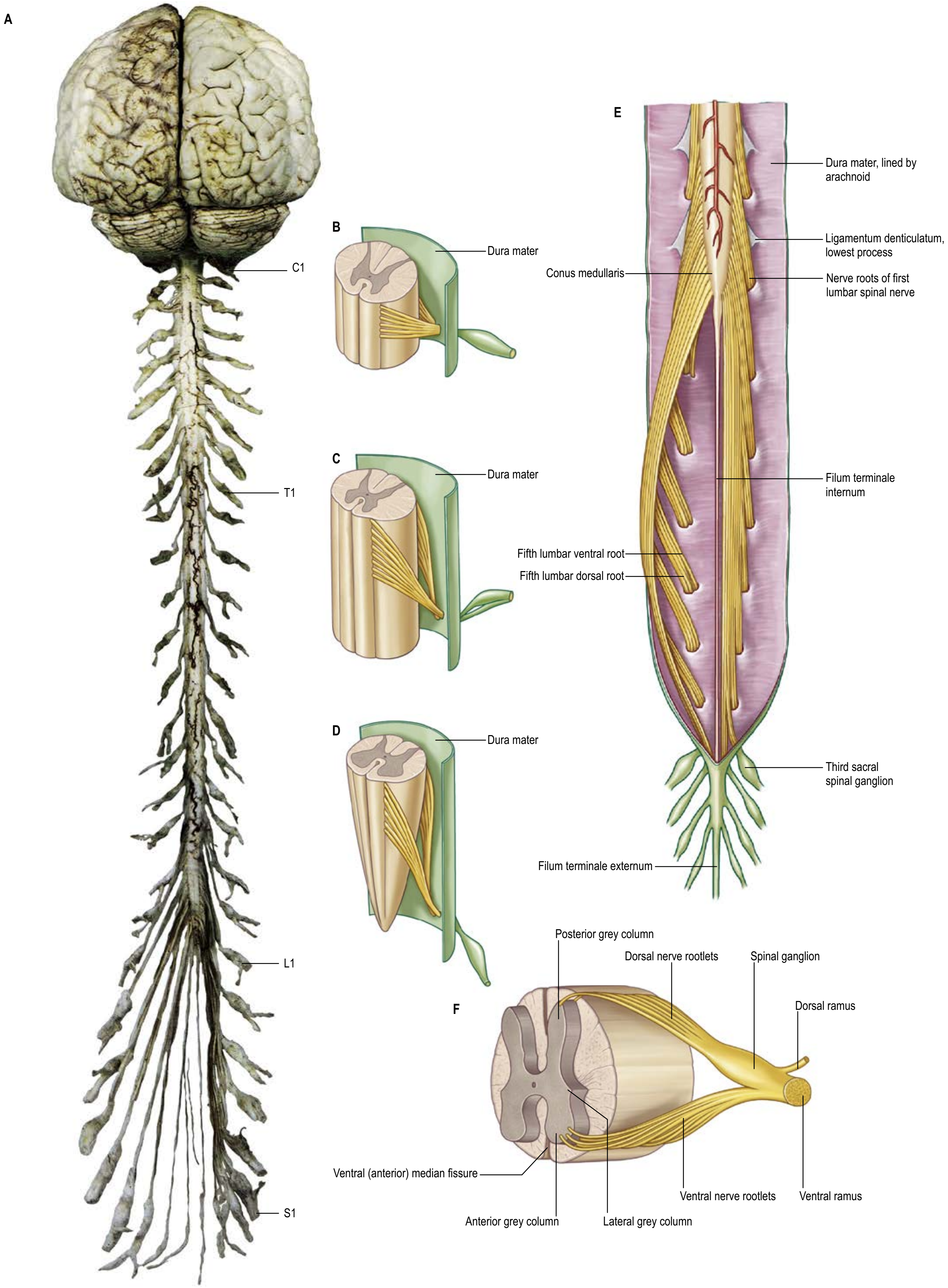
A
C1
T1
L1
S1
B
Dura mater
C
Dura mater
D
Dura mater
E
Dura mater, lined by arachnoid
Ligamentum denticulatum, lowest process
Conus medullaris
Nerve roots of first lumbar spinal nerve
Filum terminale internum
Fifth lumbar ventral root
Fifth lumbar dorsal root
Third sacral spinal ganglion
Filum terminale externum
F
Posterior grey column
Dorsal nerve rootlets
Spinal ganglion
Dorsal ramus
Ventral (anterior) median fissure
Anterior grey column
Lateral grey column
Ventral nerve rootlets
Ventral ramus

Fig. 47.1 **A**, The brain and spinal cord with attached spinal nerve roots and dorsal root ganglia, photographed from the dorsal aspect. Note the fusiform cervical and lumbar enlargements of the cord, and the changing obliquity of the spinal nerve roots as the cord is descended. The cauda equina is undisturbed on the right but has been spread out on the left to show its individual components. **B**–**D**, The formation of a typical spinal nerve, ventral aspect: **B**, cervical level; **C**, thoracic level; **D**, lumbar level. **E**, The lower end of the spinal cord, filum terminale and cauda equina exposed from behind. The dura mater and the arachnoid have been opened and spread out. **F**, A spinal cord segment showing the mode of formation of a typical spinal nerve and the gross relationships of the grey and white matter.

Continued

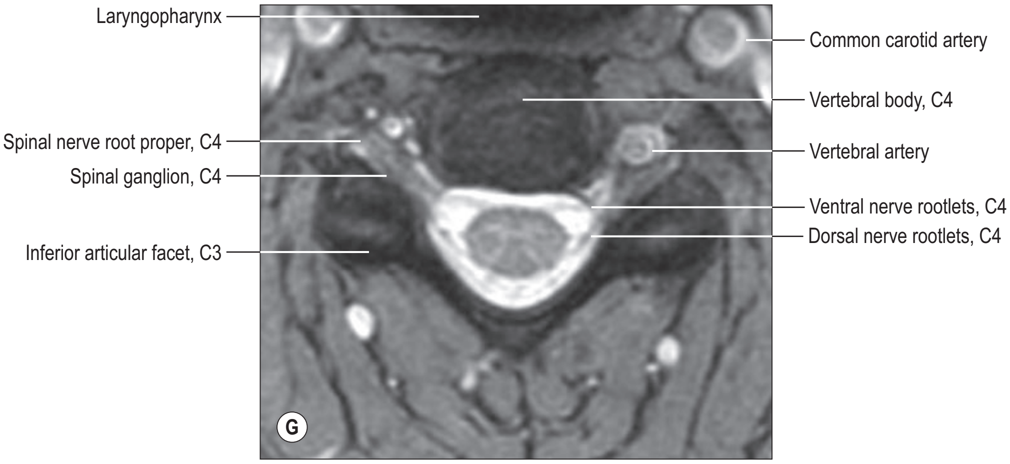
Laryngopharynx
Spinal nerve root proper, C4
Spinal ganglion, C4
Inferior articular facet, C3
Common carotid artery
Vertebral body, C4
Vertebral artery
Ventral nerve rootlets, C4
Dorsal nerve rootlets, C4
G

Fig. 47.1, cont'd G, Axial T2-weighted MRI of the cervical spine at the level of C4 showing the ventral and dorsal nerve rootlets. The grey and white matter of the spinal cord can also be differentiated: white matter is lower signal. (A, Dissection by MCE Hutchinson, photograph by Kevin Fitzpatrick, London. B–D, Sobotta Atlas of Human Anatomy © Elsevier GmbH, Urban & Fischer, Munich.)

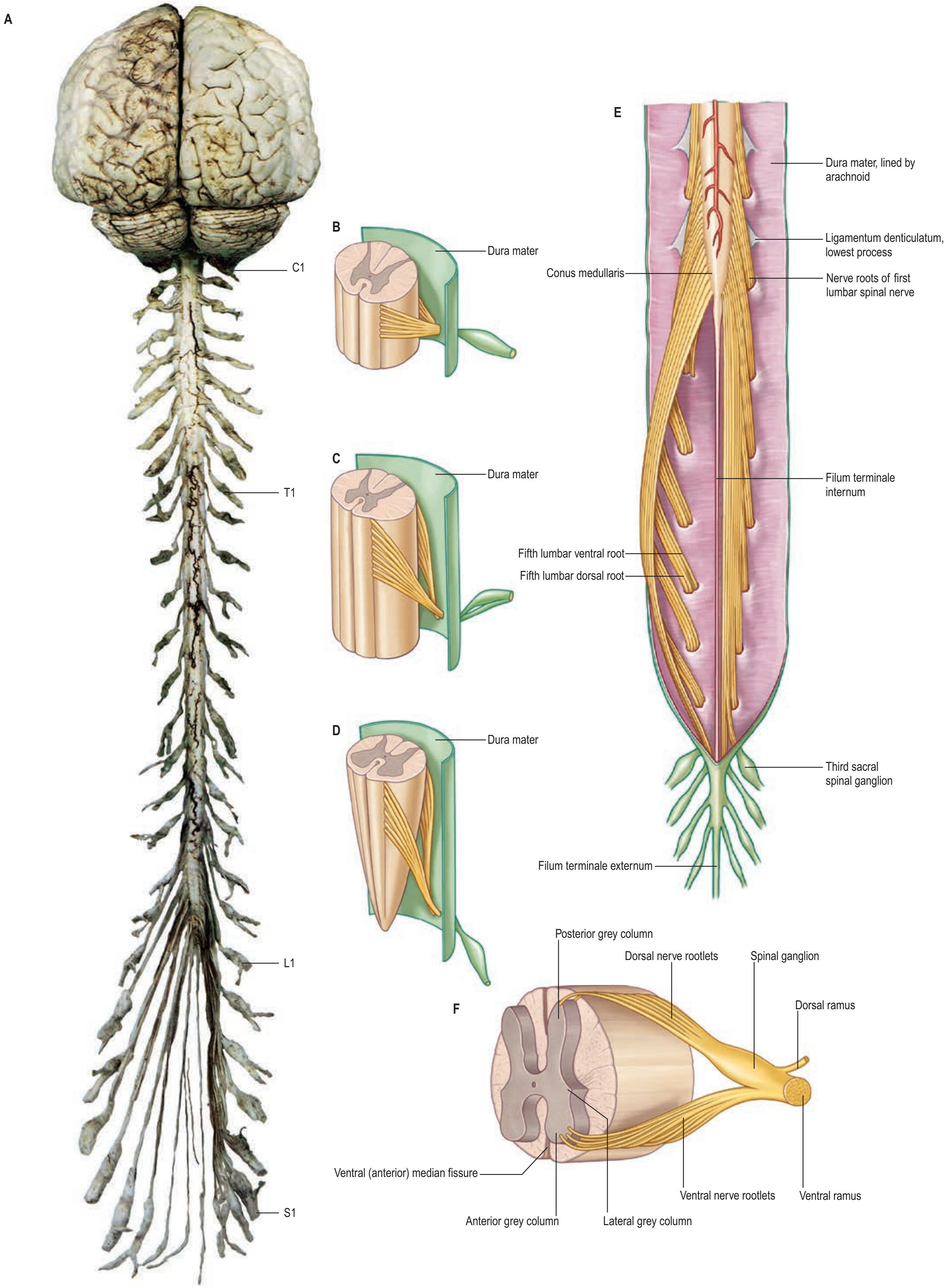
A
C1
T1
L1
S1
B
Dura mater
C
Dura mater
D
Dura mater
E
Dura mater, lined by arachnoid
Ligamentum denticulatum, lowest process
Conus medullaris
Nerve roots of first lumbar spinal nerve
Filum terminale internum
Fifth lumbar ventral root
Fifth lumbar dorsal root
Third sacral spinal ganglion
Filum terminale externum
F
Posterior grey column
Dorsal nerve rootlets
Spinal ganglion
Dorsal ramus
Ventral (anterior) median fissure
Ventral nerve rootlets
Ventral ramus
Anterior grey column
Lateral grey column

Fig. 47.1 **A**, The brain and spinal cord with attached spinal nerve roots and dorsal root ganglia, photographed from the dorsal aspect. Note the fusiform cervical and lumbar enlargements of the cord, and the changing obliquity of the spinal nerve roots as the cord is descended. The cauda equina is undisturbed on the right but has been spread out on the left to show its individual components. **B**–**D**, The formation of a typical spinal nerve, ventral aspect: **B**, cervical level; **C**, thoracic level; **D**, lumbar level. **E**, The lower end of the spinal cord, filum terminale and cauda equina exposed from behind. The dura mater and the arachnoid have been opened and spread out. **F**, A spinal cord segment showing the mode of formation of a typical spinal nerve and the gross relationships of the grey and white matter. (A, Dissection by MCE Hutchinson, photograph by Kevin Fitzpatrick, London. B–D, Sobotta Atlas of Human Anatomy © Elsevier GmbH, Urban & Fischer, Munich.) (G, *continued online*)

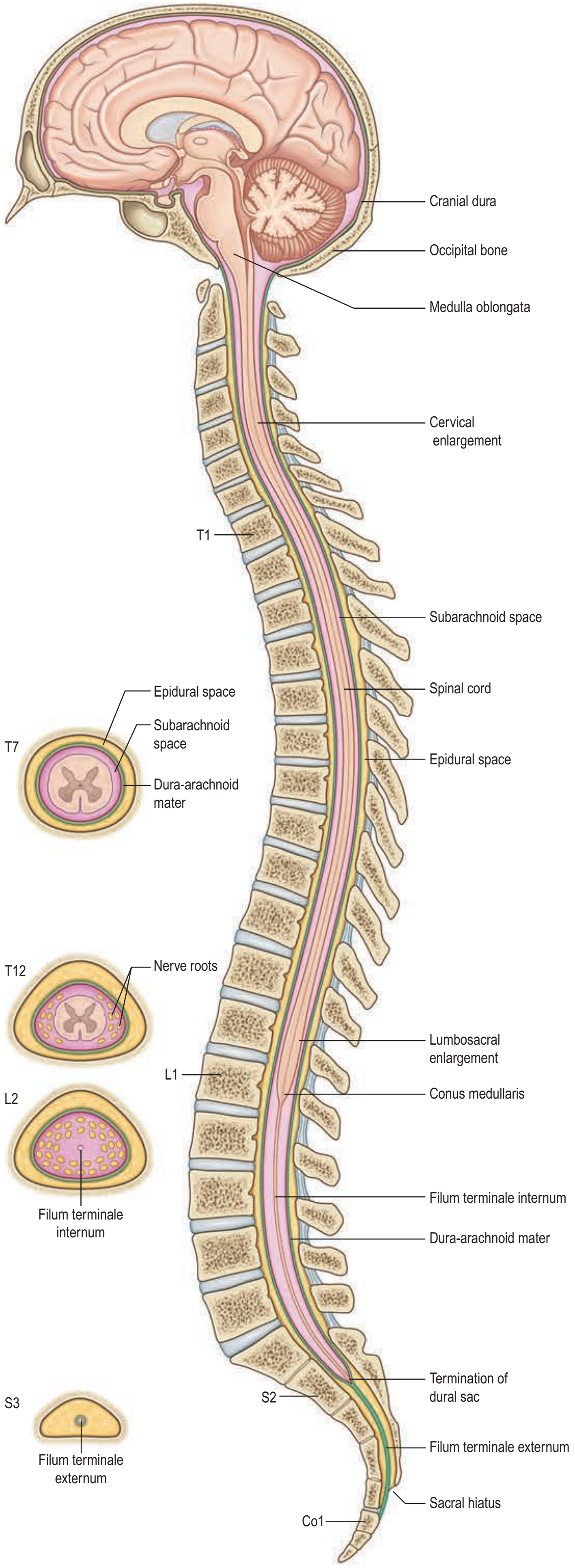

Fig. 47.2 The epidural and subarachnoid spaces.

elongated vertical elliptical area (see Fig. 47.1F). Dorsal spinal roots bear ovoid swellings, the spinal ganglia, one on each root proximal to its junction with a corresponding ventral root in an intervertebral foramen. Each root fans out into 6–8 rootlets before entering the cord in a vertical row in the posterolateral sulcus. Dorsal roots are usually said to contain only afferent axons (both somatic and visceral), which are the central processes of unipolar neurones in the spinal root ganglia, but they may also contain a small number (3%) of efferent fibres and autonomic vasodilator fibres.

Each ganglionic neurone has a single short stem that divides into a medial (central) branch that enters the spinal cord via a dorsal root, and a lateral (peripheral) branch that passes peripherally to a sensory end organ. The central branch is an axon while the peripheral one is an elongated dendrite (but when traversing a peripheral nerve is, in general structural terms, indistinguishable from an axon). The region of spinal cord associated with the emergence of a pair of nerves is a spinal segment but there is no actual surface indication of segmentation. Moreover, the deep neural sources or destinations of radicular fibres may lie far beyond the confines of the 'segment' so defined.

MENINGES

Dura mater

In some areas within the skull, the dura mater can be distinguished from the endosteum, but at the base of the skull around the foramen magnum the two layers are fused and adherent to the bone. Distal to the foramen magnum, within the vertebral column, the dura is distinct from the tissues that line the vertebral canal, and separated from them by the epidural space (see below). The spinal dura mater forms a tube whose upper end is attached to the edge of the foramen magnum and to the posterior surfaces of the second and third cervical vertebral bodies, and also by fibrous bands to the posterior longitudinal ligament, especially towards the caudal end of the vertebral canal. The dural tube narrows at the lower border of the second sacral vertebra. It invests the thin spinal filum terminale, descends to the back of the coccyx, and blends with the periosteum.

Epidural space

The epidural space lies between the spinal dura mater and the tissues that line the vertebral canal (see Fig. 47.2). It is closed above by fusion of the spinal dura with the edge of the foramen magnum, and below by the posterior sacrococcygeal ligament that closes the sacral hiatus. It contains loosely packed connective tissue, fat, a venous plexus, small arterial branches, lymphatics and fine fibrous bands that connect the theca with the lining tissue of the vertebral canal. These bands, the meningovertebral ligaments, are best developed anteriorly and laterally. Similar bands tether the nerve root sheaths or 'sleeves' within their canals. There is also a midline attachment from the posterior spinal dura to the ligamentum nuchae at atlanto-occipital and atlanto-axial levels (Dean and Mitchell 2002). The venous plexus consists of longitudinally arranged chains of vessels, connected by circumdural venous 'rings'. The anteriorly placed vessels receive the basivertebral veins.

The shape of the space within each spinal segment is not uniform, though the segmental pattern is metamerically repeated. It is difficult to define the true shape of the 'space' because it changes with the introduction of fluid or as a result of preservation techniques. In the lumbar region, the dura mater is apposed to the walls of the vertebral canal anteriorly and attached by connective tissue in a manner that permits displacement of the dural sac during movement and venous engorgement. Adipose tissue is present posteriorly in recesses between the ligamentum flavum and the dura. The connective tissue extends for a short distance through the intervertebral foramina along the sheaths of the spinal nerves. Like the main thecal sac, the root sheaths are partially tethered to the walls of the foramina by fine meningovertebral ligaments.

Epidural injections

Contrast media and other fluids injected into the epidural space at the sacral level can spread up to the cranial base. Local anaesthetics injected near the spinal nerves, just outside the intervertebral foramina, may spread up or down the epidural space to affect the adjacent spinal nerves or may pass to the opposite side. The paravertebral spaces of each side communicate via the epidural space, particularly at lumbar levels.

For a review of the morphology of the epidural space and a discussion of the nature of the lining layer of the vertebral canal, see Newell (1999).

A variety of pathological processes can occur within the epidural space, compressing the dura and resulting in pain and potential neurological disturbance. Among the more common pathological entities seen are infection, haematoma and tumours (Figs 47.3–47.4).

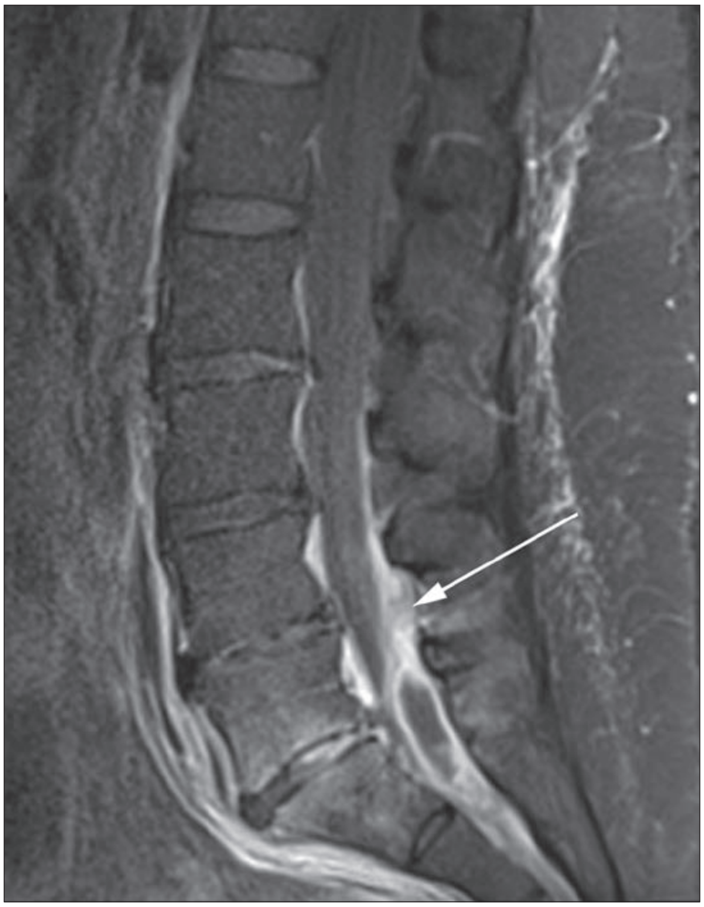

Fig. 47.3 A T1 post-contrast sagittal lumbar spinal magnetic resonance (MR) image showing a spinal epidural abscess (arrow) adherent to the lumbar dura and spinal nerves in a 28-year-old female with a history of intravenous drug abuse.

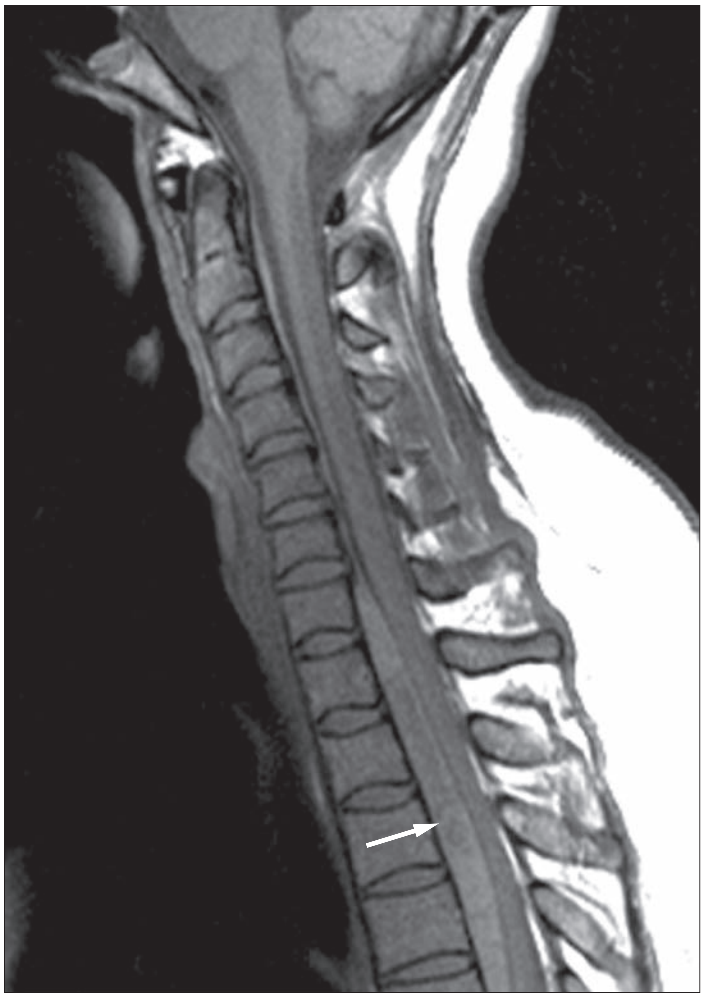

Fig. 47.4 A sagittal thoracic MR image showing a large ventral spinal epidural haematoma (arrow) resulting in severe neck and upper thoracic pain and ataxia.

Subdural space

The subdural space is a potential space in the normal spine because the arachnoid and dura are closely apposed (Haines et al 1993). It does not connect with the subarachnoid space but continues for a short distance along the cranial and spinal nerves. Accidental subdural catheterization may occur during epidural injections. Injection of fluid into the subdural space may damage the cord either by direct toxic effects or by compression of the vasculature.

Arachnoid mater

The spinal arachnoid mater surrounds the spinal cord and is continuous with the cranial arachnoid mater (**Fig. 47.5**). It is closely applied to the deep aspect of the dura mater. At sites where vessels and nerves enter or leave the subarachnoid space, the arachnoid mater is reflected on to the surface of these structures and forms a thin coating of leptomeningeal cells over the surface of both vessels and nerves. Thus a subarachnoid angle is formed as nerves pass through the dura into the intervertebral foramina. At this point, the layers of leptomeninges (arachnoid and pia) fuse and become continuous with the perineurium. The epineurium is in continuity with the dura. Such an arrangement seals the subarachnoid space so that particulate matter does not pass directly from the subarachnoid space into nerves. The existence of a pathway of lymphatic drainage from the CSF is controversial.

Pia mater

The spinal pia mater (see Fig. 47.5) closely invests the surface of the spinal cord and passes into the ventral median fissure. The subpial collagenous layer in the spinal subpial 'space' is thicker than it is in the cerebral region and is continuous with the collagenous core of the ligamentum denticulatum (denticulate ligament).

The ligamentum denticulatum is a flat, fibrous sheet on either side of the spinal cord between the ventral and dorsal spinal roots. Its medial border is continuous with the subpial connective tissue of the cord and its lateral border forms a series of triangular processes, the apices of which are fixed at intervals to the dura mater. The first crosses behind the vertebral artery where it is attached to the dura mater, and is separated by the artery from the first cervical ventral root. Its site of attachment to the dura mater is above the rim of the foramen magnum, just behind the hypoglossal nerve; the accessory nerve ascends on its posterior aspect (see Fig. 35.11). The last of the dentate ligaments lies between the exiting twelfth thoracic and first lumbar spinal nerves and is a narrow, oblique band that descends laterally from the conus medullaris. Changes in the form and position of the dentate ligaments during spinal movements have been demonstrated by cine-radiography. Beyond the conus medullaris, the pia mater continues as a coating of the filum terminale.

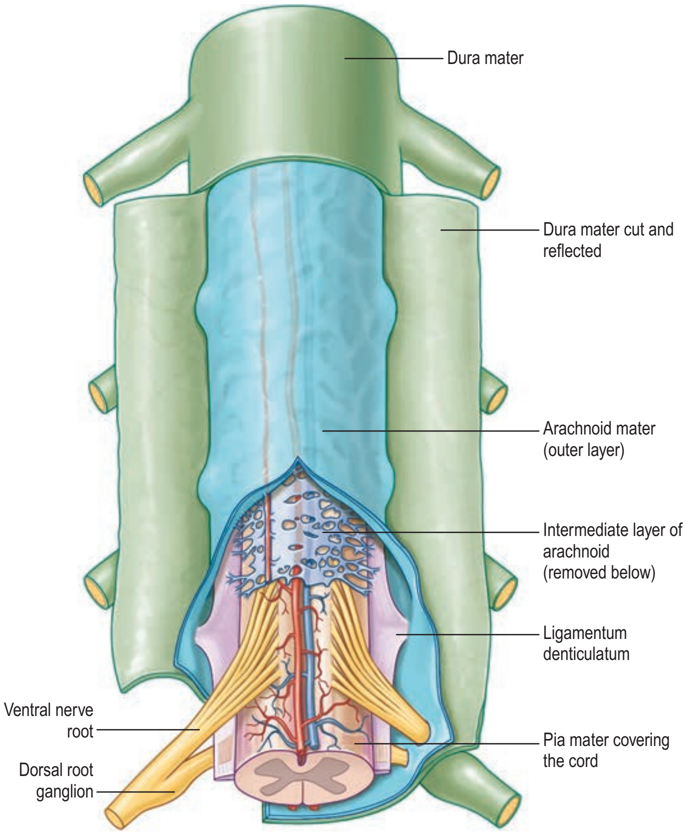
Dura mater
Dura mater cut and reflected
Arachnoid mater (outer layer)
Intermediate layer of arachnoid (removed below)
Ligamentum denticulatum
Ventral nerve root
Pia mater covering the cord
Dorsal root ganglion

Fig. 47.5 Part of the spinal cord exposed from the anterior aspect to show the meningeal coverings.

Intermediate layer

In addition to the well-defined coats of arachnoid and pia mater, the cord is also surrounded by an extensive intermediate layer of leptomeninges. This layer is concentrated in the dorsal and ventral regions, and forms a highly perforated, almost lace-like structure that is focally compacted to form the dorsal, dorsolateral and ventral ligaments of the spinal cord. Dorsally, the intermediate layer is adherent to the deep aspect of the arachnoid mater and forms a discontinuous series of dorsal ligaments that attach the spinal cord to the arachnoid. The dorsolateral ligaments are more delicate and fenestrated, and they extend from the dorsal roots to the parietal arachnoid. As the intermediate layer spreads laterally over the dorsal surface of the dorsal roots, it becomes increasingly perforated and eventually disappears. A similar arrangement is seen over the ventral aspect of the spinal cord but the intermediate layer is less substantial.

The intermediate layer is structurally similar to the trabeculae that cross the cranial subarachnoid space, i.e. it has a collagenous core coated by leptomeningeal cells. The intermediate layers of leptomeninges around the spinal cord may act as a baffle within the subarachnoid space to dampen waves of CSF movement in the vertebral canal. Inflammation within the spinal subarachnoid space may result in extensive fibrosis within the intermediate layer and the complications of chronic arachnoiditis (**Fig. 47.6**).

Coverings and relations of the spinal roots and nerves in the radicular canal

Tubular prolongations of spinal dura mater, closely lined by arachnoid, extend around the spinal roots and nerves as they pass through the lateral zone of the vertebral canal and through the intervertebral foramina (see Fig. 47.5; **Fig. 47.6A**). These prolongations, the spinal nerve sheaths or root sheaths, gradually lengthen as the spinal roots become increasingly oblique. Each individual dorsal and ventral root runs in the subarachnoid space with its own covering of pia mater. Each root pierces the dura separately, taking a sleeve of arachnoid with it, before joining within the dural prolongation just distal to the spinal ganglion. The dural sheaths of the spinal nerves fuse with the epineurium, within or slightly beyond the intervertebral foramina. The arachnoid prolongations within the sheaths do not extend as far distally as their dural coverings, but the subarachnoid space and the CSF it contains extend sufficiently distally to form a radiologically demonstrable root sleeve for each nerve. Shortening or obstruction of this sleeve seen on magnetic resonance imaging (MRI) indicates compression of the spinal nerve. At the cervical level, where the nerves are short and the vertebral movement is greatest, the dural sheaths are tethered to the periosteum of the adjacent transverse processes. In the lumbosacral region, there is less tethering of the dura to the periosteum, though there may be an attachment posteriorly to the facet joint capsule.

CEREBROSPINAL FLUID (CSF)

The cerebrospinal fluid is described in detail in Chapter 25. Although there is free communication between the spinal and cerebral subarachnoid spaces, the mode of circulation of the spinal CSF and the contribution that it makes to the overall circulation of CSF remain uncertain in humans: CSF may be absorbed from the spinal subarachnoid space; spinal arachnoid granulations and villi have been described (Kido et al 1976).

SPINAL NERVES

In those body segments that largely retain a metameric (segmental) structure, e.g. the thoracic region, spinal nerves show a common plan (**Fig. 47.7**). The dorsal, epaxial, ramus passes back lateral to the articular processes of the vertebrae and divides into medial and lateral branches that penetrate the deeper muscles of the back; both branches innervate

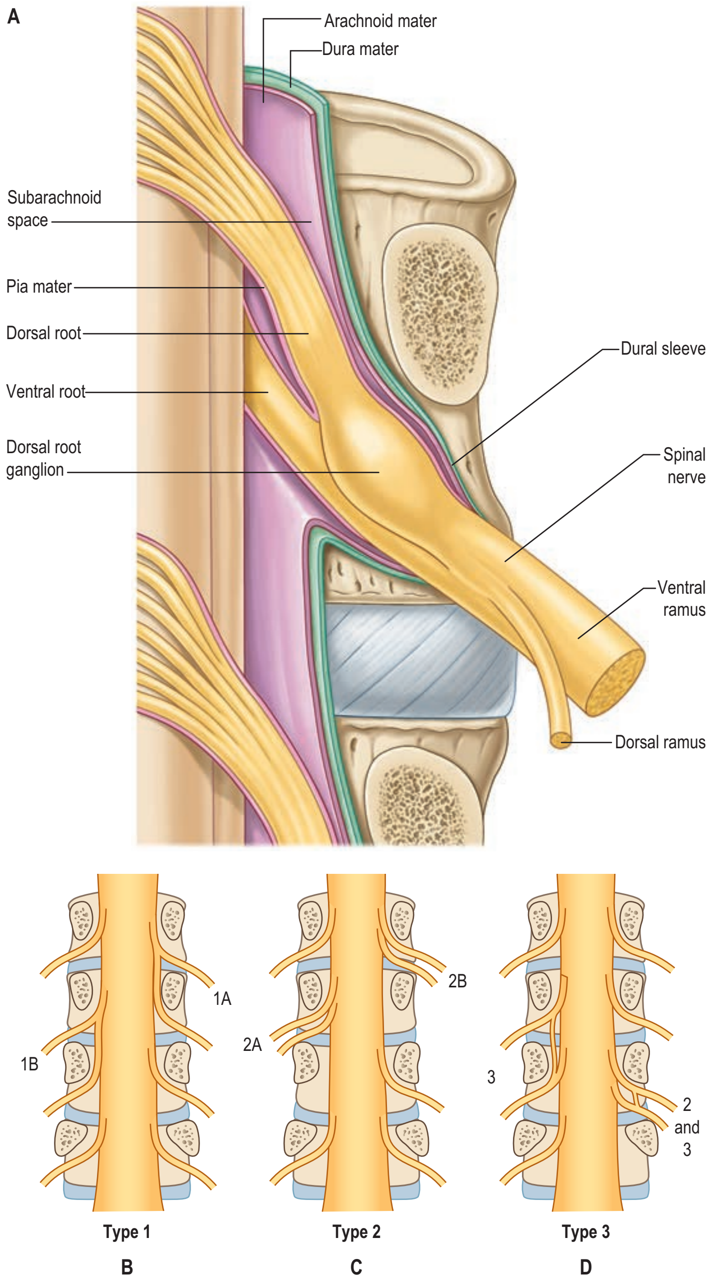
A
Arachnoid mater
Dura mater
Subarachnoid space
Pia mater
Dorsal root
Ventral root
Dorsal root ganglion
Dural sleeve
Spinal nerve
Ventral ramus
Dorsal ramus
1A
1B
2A
2B
3
2 and 3
Type 1
Type 2
Type 3
B
C
D

Fig. 47.6 **A**, A lumbar spinal nerve and its roots and meningeal coverings. **B**–**D**, Extradural anomalies of the lumbar nerve roots.

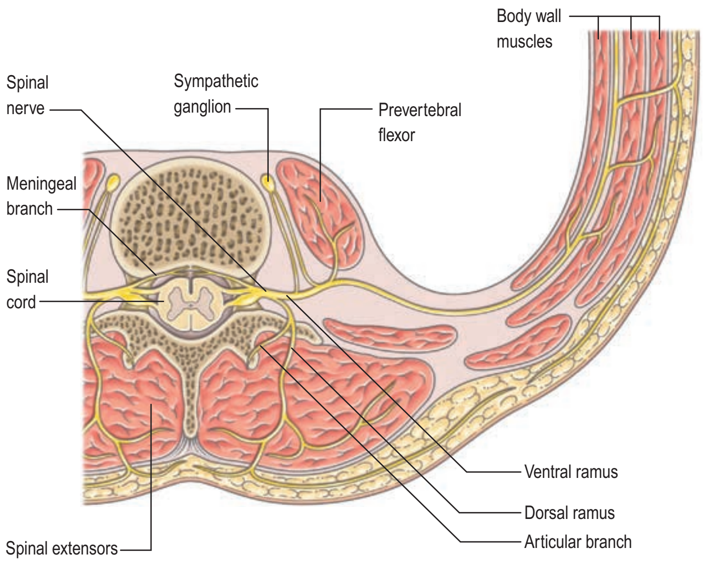
Body wall muscles
Spinal nerve
Sympathetic ganglion
Prevertebral flexor
Meningeal branch
Spinal cord
Ventral ramus
Dorsal ramus
Articular branch
Spinal extensors

Fig. 47.7 The formation and branching pattern of a typical spinal nerve.

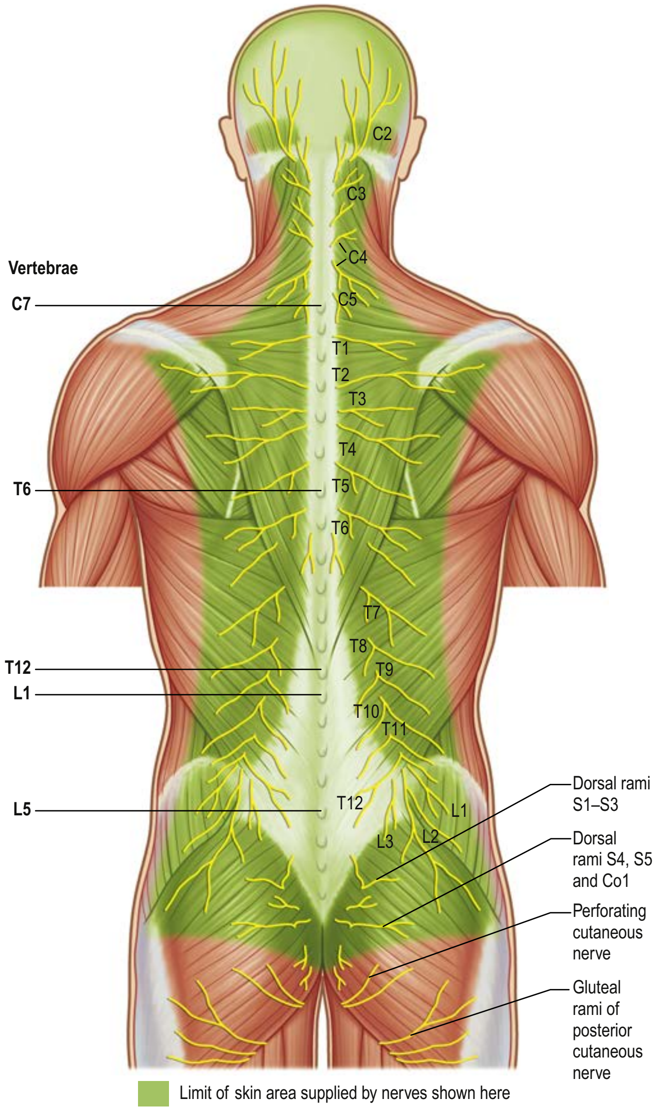
Vertebrae
C7
T6
T12
L1
L5
C2
C3
C4
C5
T1
T2
T3
T4
T5
T6
T7
T8
T9
T10
T11
T12
L1
L2
L3
Dorsal rami S1–S3
Dorsal rami S4, S5 and Co1
Perforating cutaneous nerve
Gluteal rami of posterior cutaneous nerve
🟩 Limit of skin area supplied by nerves shown here

Fig. 47.8 The cutaneous distribution of the dorsal rami of the spinal nerves. The nerves are shown lying on the superficial muscles. The nerves are numbered on the right side; the spines of the seventh cervical, sixth and twelfth thoracic, and first and fifth lumbar vertebrae are labelled on the left side.

the adjacent muscles and supply a band of skin from the posterior median line to the lateral border of the scapula (Fig. 47.8). The ventral, hypaxial, ramus is connected to a corresponding sympathetic ganglion by white and grey rami communicantes. It innervates the prevertebral muscles and curves around in the body wall to supply the lateral muscles of the trunk. Near the mid-axillary line, it gives off a lateral branch that pierces the muscles and divides into anterior and posterior cutaneous branches. The main nerve advances in the body wall, where it supplies the ventral muscles and terminates in branches to the skin.

Spinal nerves are united ventral and dorsal spinal roots, attached in series to the sides of the spinal cord. The term spinal nerve strictly applies only to the short segment after union of the roots and before branching occurs. This segment, the spinal nerve proper, lies in the intervertebral foramen; it is sometimes mistakenly called the ‘nerve root’. There are 31 pairs of spinal nerves: 8 cervical, 12 thoracic, 5 lumbar, 5 sacral and 1 coccygeal. The abbreviations C, T, L, S and Co, with appropriate numerals, are commonly applied to individual nerves as individual ‘root values’. The peripheral nerves emerge through the intervertebral foramina. At thoracic, lumbar, sacral and coccygeal levels, the numbered nerve exits the vertebral canal by passing below the pedicle of the corresponding vertebra, e.g. L4 nerve exits the intervertebral foramen between L4 and L5. However, in the cervical region, nerves C1–C7 pass above their corresponding vertebrae. C1 leaves the vertebral canal between the occipital bone and atlas, and hence is often termed the suboccipital nerve. The last pair of cervical nerves does not have a correspondingly numbered vertebra and C8 passes between the seventh cervical and first thoracic vertebrae. Each nerve is continuous with the spinal cord by ventral and dorsal roots; each dorsal root bears a spinal, sensory ganglion (dorsal root ganglion).

Spinal roots and ganglia

Ventral (anterior) roots

Ventral roots contain axons of neurones in the ventral (anterior) and lateral spinal grey columns. Each emerges as a series of rootlets in two or three irregular rows in an area approximately 3 mm in horizontal width.

Dorsal (posterior) roots

Dorsal roots contain centripetal processes of neurones sited in the spinal ganglia. Each consists of medial and lateral fascicles that both diverge into rootlets that enter the spinal cord along the posterolateral sulcus. The rootlets of adjacent dorsal roots are often connected by oblique filaments, especially in the lower cervical and lumbosacral regions.

Little is known of the detail of the regions of entry and emergence of afferent and efferent rootlets in humans, but these zones of transition between the central and peripheral nervous systems have been extensively described in rodents (Fraher 2000).

Appearance and orientation of roots at each spinal level

The size and direction of spinal nerve roots vary. The upper four cervical roots are small, while the lower four are large. Cervical dorsal roots have a thickness ratio to the ventral roots of 3 : 1, which is greater than in other regions. The first dorsal root is an exception, being smaller than the ventral, and it is occasionally absent. The conventional view is that the first and second cervical spinal roots are short, running almost horizontally to their exits from the vertebral canal, and that from the third to the eighth cervical levels the roots slope obliquely down. Obliquity and length increase successively, although the distance between spinal attachment and vertebral exit never exceeds the height of one vertebra. An alternative view states that upper cervical roots descend, the fifth is horizontal, the sixth to eighth ascend, the first two thoracic roots are horizontal, the next three ascend, the sixth is horizontal and the rest descend (Kubik and Müntener 1969). This view is based on the observation that the cervicothoracic part of the spinal cord grows more in length than other parts.

Thoracic roots, except the first, are small, and the dorsal root only slightly exceeds the ventral in thickness. They increase successively in length. In the lower thoracic region, the roots descend in contact with the spinal cord for at least two vertebrae before emerging from the vertebral canal.

Lower lumbar and upper sacral roots are the largest, and their rootlets are the most numerous. Coccygeal roots are the smallest. Kubik and Müntener (1969) confirm that lumbar, sacral and coccygeal roots descend with increasing obliquity to their exits. The spinal cord ends near the lower border of the first lumbar vertebra, and so the lengths of successive roots rapidly increase; the consequent collection of roots is the cauda equina (**Fig. 47.1A**). The largest roots, and hence the largest spinal nerves, are continuous with the spinal cervical and lumbar enlargements and innervate the upper and lower limbs.

Spinal ganglia (dorsal root ganglia)

Spinal ganglia (dorsal root ganglia, DRG) are large groups of neurones on the dorsal spinal roots. Each is oval and reddish: its size is related to that of its root. A ganglion is bifid medially where the two fascicles of the dorsal root emerge to enter the cord. Ganglia are usually sited in the intervertebral foramina, immediately lateral to the perforation of the dura mater by the roots (see **Fig. 47.1B**). However, the first cervical ganglion lies on the vertebral arch of the atlas, the second lies behind the lateral atlanto-axial joint, the sacral lie inside the vertebral canal, and the coccygeal ganglion usually lies within the dura mater. The first cervical ganglia may be absent. Small aberrant ganglia sometimes occur on the upper cervical dorsal roots between the spinal ganglia and the cord.

Spinal nerves proper

Immediately distal to the spinal ganglia, ventral and dorsal roots unite to form spinal nerves. These very soon divide into dorsal and ventral rami, both of which receive fibres from both roots (see Fig. 47.6A). At all levels above the sacral, this division occurs within the intervertebral foramen. Division of the sacral spinal nerves occurs within the sacral vertebral canal, and the dorsal and ventral rami exit separately through posterior and anterior sacral foramina at each level. Spinal nerves trifurcate at some cervical and thoracic levels, in which case the third branch is called a ramus intermedius. At or distal to its origin, each ventral ramus gives off recurrent meningeal (sinuvertebral) branches and receives a grey ramus communicans from the corresponding sympathetic ganglion. The thoracic and first and second lumbar ventral rami each contribute a white ramus communicans to the corresponding sympathetic ganglia. The second, third and fourth sacral nerves also supply visceral branches, unconnected with sympathetic ganglia, which carry a parasympathetic outflow direct to the pelvic plexuses.

Cervical spinal nerves enlarge from the first to the sixth nerve. The seventh and eighth cervical and the first thoracic nerve are similar in size to the sixth cervical nerve. The remaining thoracic nerves are relatively small. Lumbar nerves are large, increasing in size from the first to the fifth. The first sacral is the largest spinal nerve; thereafter the sacral nerves decrease in size. The coccygeal nerves are the smallest spinal nerves. The size of the spinal nerve and its associated structures within the intervertebral foramen is not in direct relation to the size of the foramen. At lumbar levels, though L5 is the largest nerve, its foramen is smaller than those of L1–L4, which renders this nerve particularly liable to compression.

In the radicular ('root') canal and intervertebral foramen, the spinal nerve is related to the spinal artery of that level and its radicular branch, and to a small plexus of veins. At the outer end of the foramen, the nerve may lie above or below transforaminal ligaments.

Meningeal nerves

Recurrent meningeal (or sinuvertebral) nerves (**Fig. 47.9**) occur at all vertebral levels. They are mixed sensory and sympathetic nerves, represented by numerous fine filaments amongst which one, or two to four, larger trunks may be evident. At cervical levels, the autonomic roots arise from the grey rami that form the vertebral nerve. At thoracic and lumbar levels, each nerve is formed by a somatic root from the ventral ramus and by an autonomic root from the grey ramus communicans of that segment. Each nerve pursues a recurrent course through the intervertebral foramen, passing ventral to the spinal nerve, to enter the vertebral canal, where it divides into ascending, descending and transverse branches. These branches communicate with corresponding branches from the segments above and below, and from the opposite side, forming arcades along the floor of the vertebral canal. Meningeal branches of the arcades form a plexus on the ventral surface of the dural sac and nerve root sleeves that attenuates laterally; the posterior paramedian dura is devoid of nerve endings. Skeletal branches are distributed to the posterior longitudinal ligament, the periosteum of the vertebral bodies, and

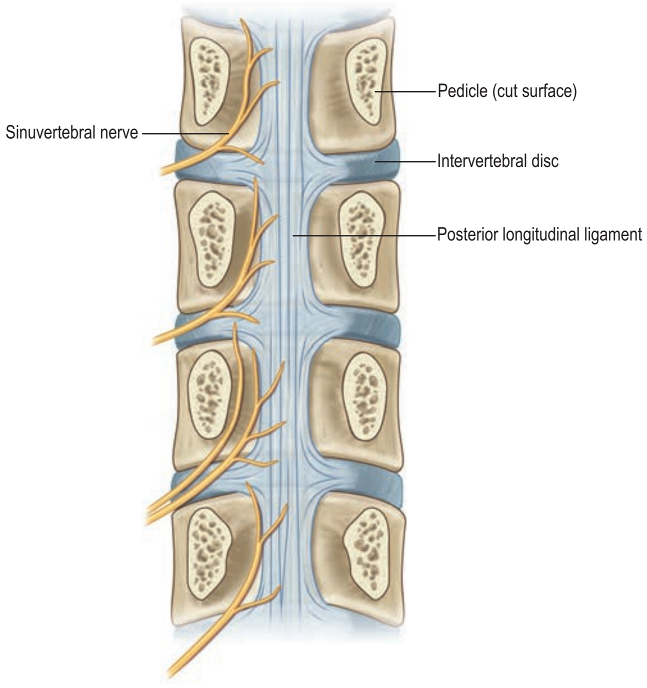

Fig. 47.9 The course and skeletal distribution of the lumbar sinuvertebral nerves. Each nerve supplies the intervertebral disc at its level of entry into the vertebral canal, the disc above, and the intervening posterior longitudinal ligament. In about one-third of cases, the nerve at a particular level may be represented by more than one filament.

to the posterior and posterolateral aspects of the intervertebral discs (Garcia-Cosamalon et al 2010). Vascular branches accompany the veins and arteries of the vertebral canal and those of the vertebral bodies. The upper three cervical meningeal nerves ascend through the foramen magnum into the posterior cranial fossa, where they innervate the dura mater that covers the clivus. *En route*, they innervate the median atlanto-axial joint and its ligaments.

Functional components of spinal nerves

A typical spinal nerve contains somatic efferent fibres and somatic and visceral afferent fibres. Some, but not all, spinal nerves also contain preganglionic autonomic fibres.

Somatic components

Somatic efferent fibres innervate skeletal muscles and are axons of α, β and γ neurones in the spinal ventral grey column. Somatic afferent fibres convey impulses into the central nervous system from receptors in the skin, subcutaneous tissue, muscles, tendons, fasciae and joints; they are peripheral processes of unipolar neurones in the spinal ganglia.

Visceral components

Preganglionic visceral efferent sympathetic fibres are axons of neurones in the spinal intermediolateral grey column throughout the thoracic and upper two or three lumbar segments; they join the sympathetic trunk via corresponding white rami communicantes and synapse with postganglionic neurones that are distributed to smooth muscle, myocardium or exocrine glands. The preganglionic visceral efferent parasympathetic fibres are axons of neurones in the spinal lateral grey column of the second to fourth sacral segments; they leave the ventral rami of corresponding sacral nerves and synapse in pelvic ganglia. The postganglionic axons are distributed mainly to smooth muscle or glands in the walls of the pelvic viscera. Visceral afferent fibres have cell bodies in the spinal ganglia. Their peripheral processes pass through white rami communicantes and, without synapsing, through one or more sympathetic ganglia to end in the walls of the viscera. Some visceral afferent fibres may enter the spinal cord in the ventral roots.

Central processes of ganglionic unipolar neurones enter the spinal cord by dorsal roots and synapse on somatic or sympathetic efferent neurones, usually through interneurones, completing reflex paths. Alternatively, they may synapse with other neurones in the spinal or brainstem grey matter that give origin to a variety of ascending tracts.

Variations of spinal roots and nerves

The courses of spinal roots and nerves in relation to the thecal sac and vertebral and radicular canals may be aberrant. An individual intervertebral foramen may contain a duplicated sheath, nerve and roots, which will then be absent at an adjacent level. Abnormal communications between roots may occur within the vertebral canal. These anomalies have been described and classified for the lumbosacral spine by Neidre and MacNab (1983) (see Fig. 47.6).

Rami of the spinal nerves

Ventral (anterior) primary rami supply the limbs and the anterolateral aspects of the trunk, and in general are larger than the dorsal rami. Thoracic ventral rami run independently and retain a largely segmental distribution. Cervical, lumbar and sacral ventral rami connect near their origins to form plexuses. Dorsal rami do not join these plexuses. The ventral rami are described in the appropriate regional sections.

Dorsal (posterior) primary rami of spinal nerves are usually smaller than the ventral rami and are directed posteriorly. Retaining a segmental distribution, all, except for the first cervical, fourth and fifth sacral and the coccygeal, divide into medial and lateral branches that supply the muscles and skin of the posterior regions of the neck and trunk (see Fig. 47.8).

Cervical dorsal spinal rami

Each cervical spinal dorsal ramus, except the first, divides into medial and lateral branches that all innervate muscles. In general, only medial branches of the second to fourth, and usually the fifth, supply the skin. Except for the first and second, each dorsal ramus passes posteriorly around an articular pillar as far as the root of the transverse process medial to a posterior intertransverse muscle, which it supplies.

First cervical dorsal ramus (suboccipital nerve)

The first cervical dorsal ramus, the suboccipital nerve, is larger than the ventral (see Fig. 46.78). It emerges superior to the posterior arch of the atlas and inferior to the vertebral artery, and enters the suboccipital triangle to supply rectus capitis posterior major and minor, obliquus capitis superior and inferior, and semispinalis capitis. A filament from the branch to inferior oblique joins the second dorsal ramus. The suboccipital nerve occasionally has a cutaneous branch that accompanies the occipital artery to the scalp, and connects with the greater and lesser occipital nerves. It may also communicate with the accessory nerve.

Second cervical dorsal ramus

The second cervical dorsal ramus is slightly larger than the ventral and all the other cervical dorsal rami (see Figs 36.22, 46.78). It runs between the lamina of the axis and inferior oblique, below which it divides into a large medial and smaller lateral branch. The dorsal ramus or its medial branch receives communicating branches from the first cervical dorsal ramus that pass both through and around inferior oblique. A descending communicating branch crosses the C2–C3 facet joint to reach the third cervical dorsal ramus.

Greater occipital nerve

The medial branch, termed the greater occipital nerve, passes transversely across inferior oblique deep to semispinalis capitis, which it innervates. Near the origin of inferior oblique, it turns rostrally along rectus capitis posterior major, where it receives a communicating branch from the third occipital nerve before turning dorsally to pierce semispinalis capitis. It emerges on to the scalp by passing above an aponeurotic sling between trapezius and sternocleidomastoid near their occipital attachments. It ascends with the occipital artery and divides into branches that connect with the third occipital and lesser occipital nerves, and which supply the back of the auricle and the skin of the scalp as far forwards as the coronal suture. The lateral branch of the second cervical dorsal ramus supplies longissimus capitis, semispinalis capitis and splenius capitis, and sends a communicating branch to the lateral branch of the third cervical dorsal ramus.

Greater occipital neuralgia

Greater occipital neuralgia is a syndrome of pain and paraesthesiae felt in the distribution of the greater occipital nerve. This is usually caused by damage or irritation to the greater occipital nerve but more rarely can result from a similar process in the lesser occipital nerve or both greater and lesser occipital nerves. A similar syndrome may be caused by upper facet joint arthritis involving the second cervical root (Vanelderen et al 2010).

Third cervical dorsal ramus

The third cervical dorsal ramus is intermediate in size between the second and fourth. It courses back round the articular pillar of the third cervical vertebra, medial to the posterior intertransverse muscle, and divides into medial and lateral branches. The lateral branch passes dorsally across the surface of semispinalis capitis to supply it and the overlying longissimus capitis and splenius capitis. It receives a communicating branch from the lateral branch of the second cervical dorsal ramus, and sends a similar branch to the lateral branch of the fourth cervical dorsal ramus. The deep medial branch curves dorsally and medially around the waist of the articular pillar before ending in multifidus. It sends an articular branch to the C3–C4 facet joint, and may also send a branch into semispinalis capitis. The superficial medial branch, the third occipital nerve, curves around the lateral and dorsal surfaces of the C2–C3 facet joint, which it supplies. It continues transversely, deep to semispinalis, which it supplies, and sends a communicating branch to the greater occipital nerve. Just above the second cervical spinal process, the third occipital nerve turns dorsally to pierce semispinalis capitis, splenius capitis and trapezius, and becomes cutaneous over a small area immediately below the superior nuchal line. Communicating branches join the cutaneous branches of the greater and lesser occipital nerves.

Dorsal rami of the lower five cervical nerves

The dorsal rami of the lower five cervical nerves curve back round the vertebral articular pillars and divide into lateral and medial branches. The lateral branches supply longissimus cervicis, splenius cervicis and iliocostalis cervicis. The medial branches curve around the lateral and dorsal surfaces of the articular pillar of their segment, deep to semispinalis capitis. They send articular branches to the facet joints above and below their course before entering and supplying multifidus. Terminal branches reach interspinalis at each segment. Cutaneous branches arise consistently from the fourth, and commonly from the fifth, sixth and eighth, but not usually from the seventh medial branches. These branches pass across multifidus or through semispinalis cervicis and turn dorsally around the medial border of semispinalis capitis, to pierce splenius cervicis and trapezius and reach the skin.

Thoracic dorsal spinal rami

At each segmental level, the thoracic dorsal rami pass dorsally through an aperture bounded by the transverse processes superiorly and inferiorly, the facet joint medially, and the superior costotransverse ligament laterally. Thereafter, each dorsal ramus follows a prolonged course laterally, between the anterior lamella of the superior costotransverse ligament anteriorly, and the costolamellar ligament and the posterior lamella of the superior costotransverse ligament posteriorly. In this narrow space, the dorsal ramus divides into lateral and medial branches. The lateral branches continue laterally as far as the costotransverse joint, above which they turn dorsally and inferiorly to supply the levatores costarum, and enter the longissimus thoracis and iliocostalis muscles. Lateral branches from the upper six thoracic dorsal rami remain intramuscular. Those from the lower six levels emerge from iliocostalis lumborum to pierce serratus posterior inferior and latissimus dorsi in line with the costal angles. They descend across as many as four ribs before becoming superficial. The twelfth thoracic lateral branch sends a filament medially along the iliac crest and then passes down to the anterior gluteal skin. Some upper thoracic lateral branches may become cutaneous.

Each medial branch hooks dorsally around the lateral margin of the posterior lamella of the superior costotransverse ligament, lying a variable distance above the tip of the transverse process. At the first to fourth, and at the ninth and tenth thoracic levels, the medial branches cross the superior tip of the transverse process to turn inferiorly and medially across the posterior surface of the transverse process, lying between the attachment sites of multifidus medially and semispinalis laterally. Each nerve continues this oblique course to supply multifidus and semispinalis. At the fifth to eighth thoracic levels, the medial branches assume a course parallel to that of other levels, but do not reach the transverse process, instead passing superior and dorsal to the plane of the transverse processes. At the eleventh and twelfth levels, in keeping with the relatively short transverse processes at these levels, the medial branches run close to the superior articular processes. Each medial branch supplies articular branches to the facet joints above and below its course. Medial branches of the upper six thoracic dorsal rami furnish cutaneous branches that pierce trapezius and the rhomboids to reach the skin near the spinous processes. Cutaneous branches may occasionally arise from the medial branches of the lower six thoracic dorsal rami.

Lumbar dorsal spinal rami

After leaving its spinal nerve, each of the first to fourth lumbar dorsal rami passes through an aperture in the dorsal leaf of the intertransverse ligament just above a transverse process (Fig. 47.10). Each dorsal ramus supplies the overlying medial intertransverse muscle before dividing into lateral and medial branches. The lateral branches supply the longissimus and iliocostalis components of the lumbar erector spinae. The upper three lumbar lateral branches emerge from the lateral border of iliocostalis lumborum and pierce the aponeurosis of latissimus dorsi to become cutaneous. They cross the iliac crest to reach the gluteal skin; some reach as far as the level of the greater trochanter. Medial branches cross the junction of the superior articular process and transverse process, and hook medially between the mammillary and accessory processes, deep to the mammillo-accessory ligament. Medial to the ligament, each medial branch sends articular branches to the facet joints above and below its course, before entering multifidus, which it supplies. Medial branch blocks (see below in the clinical procedure section) are quite useful in the treatment of facet-mediated low back pain. Terminal branches reach interspinalis at each segment.

The fifth dorsal ramus has a longer course than other dorsal rami. It arches over the ala of the sacrum, lying against the root of the first sacral superior articular process. Opposite the base of the lumbosacral joint, it sends a branch into the lowest fibres of longissimus thoracis, and a communicating branch to the first sacral dorsal ramus, before terminating as a branch that hooks around the lumbosacral joint to end in multifidus.

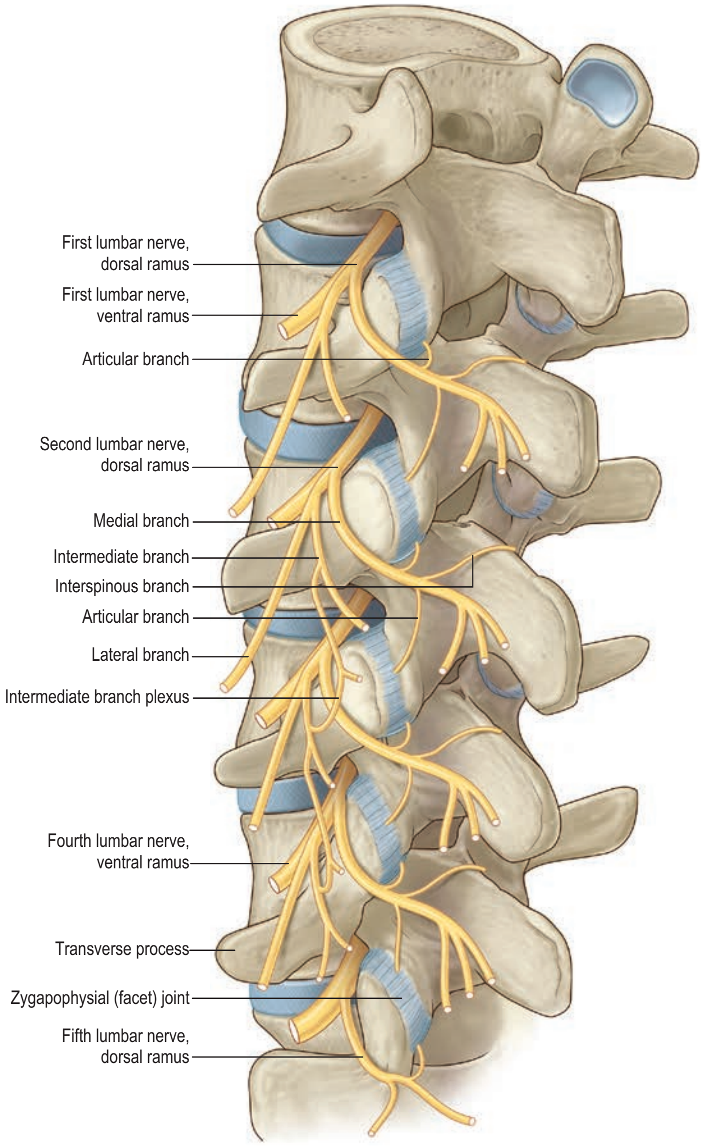
First lumbar nerve, dorsal ramus
First lumbar nerve, ventral ramus
Articular branch
Second lumbar nerve, dorsal ramus
Medial branch
Intermediate branch
Interspinous branch
Articular branch
Lateral branch
Intermediate branch plexus
Fourth lumbar nerve, ventral ramus
Transverse process
Zygapophysial (facet) joint
Fifth lumbar nerve, dorsal ramus

Fig. 47.10 Left posterolateral view of the lumbar spine showing the branches of the lumbar dorsal rami.

Sacral dorsal spinal rami

Sacral dorsal rami are small, diminishing in size inferiorly; other than the fifth, all emerge through the dorsal sacral foramina. The upper three are covered at their exit by multifidus, and divide into medial and lateral branches. Medial branches are small and end in multifidus. Lateral branches join together and with branches of the last lumbar and fourth sacral dorsal rami to form loops dorsal to the sacrum. Branches from these loops run dorsal to the sacrotuberous ligament and form a second series of loops under gluteus maximus. From these, two or three gluteal branches pierce gluteus maximus (along a line from the posterior superior iliac spine to the coccygeal apex) to supply the posterior gluteal skin.

The dorsal rami of the fourth and fifth sacral nerves are small and lie caudal to multifidus. They unite with each other and with the coccygeal dorsal ramus to form loops dorsal to the sacrum; filaments from these supply the skin over the coccyx.

Coccygeal dorsal spinal ramus

The coccygeal dorsal spinal ramus does not divide into medial and lateral branches. It communicates with the fourth and fifth sacral dorsal rami to supply the skin over the coccyx.

VASCULAR SUPPLY OF SPINAL CORD, ROOTS AND NERVES

Arteries

The spinal cord and its roots and nerves are supplied with blood by both longitudinal and segmental vessels (Fig. 47.11). Three major longitudinal vessels, a single anterior and two posterior spinal arteries (each of which is sometimes doubled to pass on either side of the dorsal rootlets) originate intracranially from the vertebral artery and terminate in a plexus around the conus medullaris. The anterior spinal artery forms

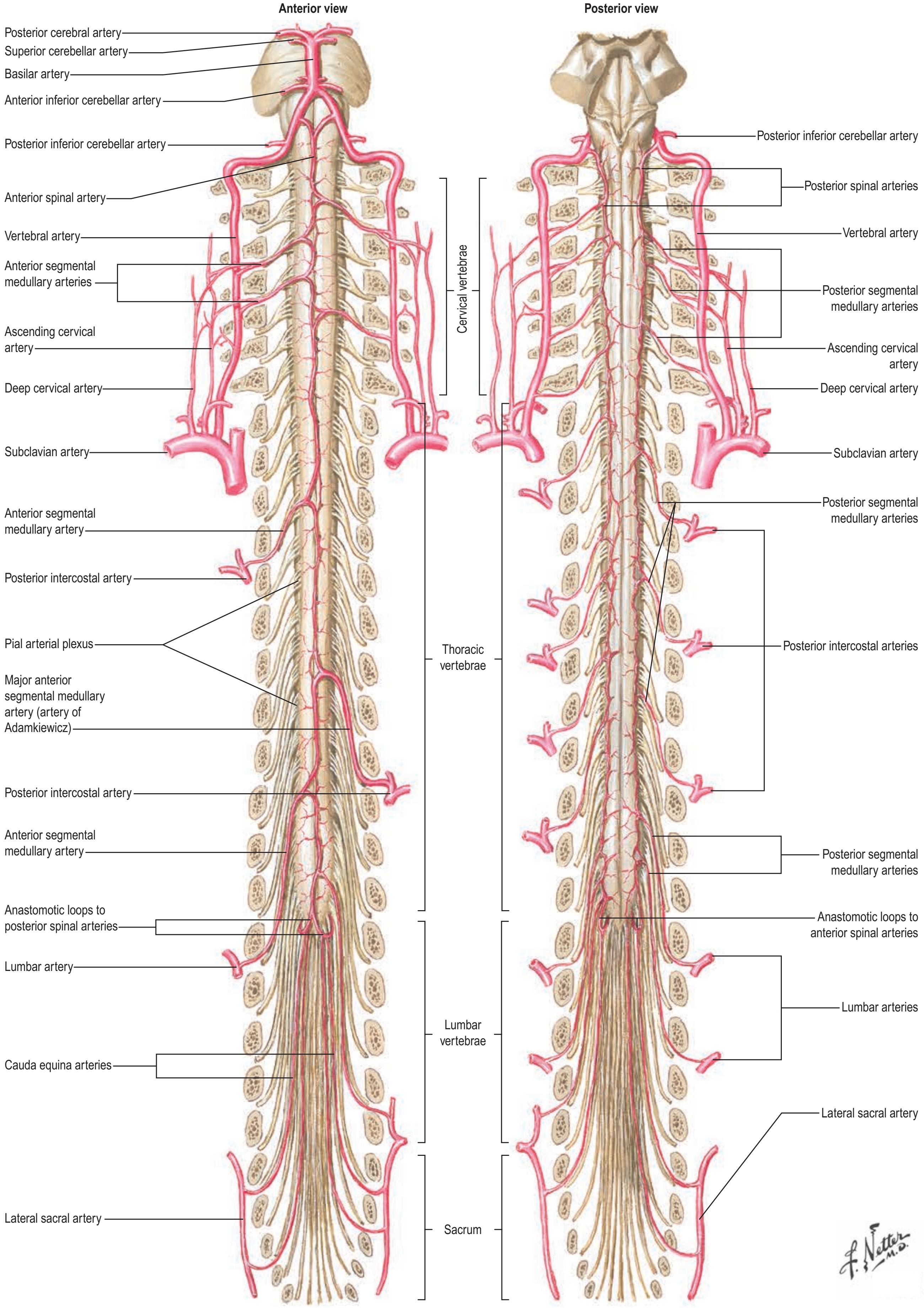
Anterior view
Posterior view
Posterior cerebral artery
Superior cerebellar artery
Basilar artery
Anterior inferior cerebellar artery
Posterior inferior cerebellar artery
Anterior spinal artery
Vertebral artery
Anterior segmental medullary arteries
Ascending cervical artery
Deep cervical artery
Subclavian artery
Anterior segmental medullary artery
Posterior intercostal artery
Pial arterial plexus
Major anterior segmental medullary artery (artery of Adamkiewicz)
Posterior intercostal artery
Anterior segmental medullary artery
Anastomotic loops to posterior spinal arteries
Lumbar artery
Cauda equina arteries
Lateral sacral artery
Cervical vertebrae
Thoracic vertebrae
Lumbar vertebrae
Sacrum
Posterior inferior cerebellar artery
Posterior spinal arteries
Vertebral artery
Posterior segmental medullary arteries
Ascending cervical artery
Deep cervical artery
Subclavian artery
Posterior segmental medullary arteries
Posterior intercostal arteries
Posterior segmental medullary arteries
Anastomotic loops to anterior spinal arteries
Lumbar arteries
Lateral sacral artery
F. Netter M.D.

Fig. 47.11 Arteries of the spinal cord. (Reprinted from Netter Anatomy Illustration Collection, © Elsevier Inc. All Rights Reserved.)

from the fused anterior spinal branches of the vertebral artery, and descends in the ventral median fissure of the cord. Each posterior spinal artery originates either directly from the ipsilateral vertebral artery or from its posterior inferior cerebellar branch, and descends in a posterolateral sulcus of the cord. The segmental arteries are derived in craniocaudal sequence from spinal branches of the vertebral, deep cervical, intercostal and lumbar arteries. These vessels enter the vertebral canal through the intervertebral foramina and anastomose with branches of the longitudinal vessels to form a pial plexus on the surface of the cord. The segmental spinal arteries send anterior and posterior radicular branches to the spinal cord along the ventral and dorsal roots. Most anterior radicular arteries are small and end in the ventral nerve roots or in the pial plexus of the cord. The small posterior radicular arteries also supply the dorsal root ganglia; branches enter at both ganglionic poles to be distributed around ganglion cells and nerve fibres (see also Crock (1996).)

Segmental radiculomedullary feeder arteries

Some radicular arteries, mainly situated in the lower cervical, lower thoracic and upper lumbar regions, are large enough to reach the ventral median fissure, where they divide into slender ascending and large descending branches. These are the anterior radiculomedullary feeder arteries (Dommisse 1975). They anastomose with the anterior spinal arteries to form a single or partly double longitudinal vessel of uneven calibre along the ventral median fissure. The largest anterior medullary feeder, the great anterior radiculomedullary artery of Adamkiewicz, varies in level, arising from a spinal branch of either one of the lower posterior intercostal arteries (T9–T11), or of the subcostal artery (T12), or less frequently of the upper lumbar arteries (L1 and L2). It most often arises on the left side (Carmichael and Gloviczki 1999). Reaching the spinal cord, it sends a branch to the anterior spinal artery below and another to anastomose with the ramus of the posterior spinal artery, which lies anterior to the dorsal roots. It may be the main supply to the lower two-thirds of the cord. Central branches of the anterior spinal artery enter the ventral median fissure, and then turn right or left to supply the ventral grey column, the base of the dorsal grey column, including the dorsal nucleus, and the adjacent white matter (**Fig. 47.12**).

Each posterior spinal artery contributes to a pair of longitudinal anastomotic channels, anterior and posterior to the dorsal spinal roots. These are reinforced by posterior medullary feeders from the posterior radicular arteries. The latter are variable in number and size, but smaller, more numerous and more evenly distributed than the anterior medullary feeders. The anterior channel is joined by a ramus from the descending branch of the great anterior segmental medullary artery of Adamkiewicz. In all longitudinal spinal arteries the width of the lumen is uneven and complete interruptions may occur. At the conus medullaris they communicate by anastomotic loops. Anastomoses other than those between the pial or peripheral spinal arterial branches may be important, e.g. a posterior spinal series of anastomoses between rami of the dorsal divisions of segmental arteries near the spinous processes.

Intramedullary arteries

The central branches of the anterior spinal artery supply about two-thirds of the cross-sectional area of the cord. The rest of the dorsal grey and white columns and peripheral parts of the lateral and ventral white columns are supplied by numerous small radial vessels that branch from posterior spinal arteries and the pial plexus. In a microangiographic study of the human cervical spinal cord, up to six anterior, and eight posterior, radicular spinal arteries were described, and up to eight central branches arose from each centimetre of the anterior spinal artery (Turnbull et al 1966). Abnormalities of blood vessels in the spinal cord can result in clinically significant haemorrhages and neurological events (**Fig. 47.13**)

Spinal cord ischaemia

The spinal cord can rely for neither its transverse nor its longitudinal blood supply entirely on the longitudinal arteries. The anterior longitudinal artery and the intramedullary arteries are functional end-arteries, although overlap of territories of supply has been described (Backes and Nijenhuis 2008). Damage to the anterior longitudinal artery can result in loss of function of the anterior two-thirds of the cord (**Fig. 47.14**). The longitudinal arteries cannot supply the whole length of the cord, and the input of the segmental medullary feeder vessels is essential. This is especially true of the artery of Adamkiewicz, which may effectively carry the major supply for the lower cord; damage to this individual artery compromises perfusion of the distal cord and may be responsible for paraplegia following aortic bypass procedures. For many years, it was assumed that the anterior spinal artery system provided the dominant supply to the cord, but clinical evidence implies that the posterior spinal arteries may be as important as the anterior system in protecting the cord. The mid-thoracic cord, distant from the main anterior medullary feeders, is particularly liable to become ischaemic after periods of hypotension; T4–T9 has been described as the critical vascular zone of the spinal cord, where interference with the circulation is most likely to result in paraplegia.

Veins

Intramedullary veins within the substance of the spinal cord drain into a circumferential plexus of surface veins, the coronal plexus (venous plexus of the pia mater). Six tortuous longitudinal channels are usually identified within this plexus: anterior and posterior spinal veins (anterior and posterior median veins) and four others that run on either side of the ventral and dorsal nerve roots (**Fig. 47.15**). Only the anterior spinal vein, which drains the central grey matter, is consistently complete. It receives sulcal veins and small pial veins from the coronal plexus and is largest in calibre in the lumbosacral region. The posterior spinal vein is frequently variable, appearing plexiform in some segments and as a single channel in others. These vessels connect freely and drain superiorly into the cerebellar veins and cranial sinuses, and segmentally into medullary veins mainly. The segmental veins drain into the intervertebral veins and thence into the external vertebral venous plexuses (see Fig. 46.21), the caval and azygos systems.

Segmental veins

Anterior and posterior radiculomedullary veins run along some of the ventral and dorsal roots. Like the medullary feeder arteries, they are largest in the cervical and lumbar regions of the cord, but do not necessarily occur in the same segments as the medullary feeders. They drain the cord but not the roots themselves. Very small anterior and posterior radicular veins occur in most spinal segments, accompanying and draining the ventral and dorsal roots and some of the cord at the points of entry and exit of the rootlets; they usually drain into the intervertebral veins.

THE EFFECTS OF INJURY

Spinal cord injury and vertebral column injury

Various clinical definitions have been described in the *International Standards Booklet for Neurological and Functional Classification of Spinal Cord Injury*, which was a landmark publication in standardizing the language of the neurological examination as it relates to spinal cord injury (Ditunno et al 1994). 'Tetraplegia' refers to impairment or loss of neural function secondary to a cervical injury. 'Paraplegia' refers to loss of function in the thoracic, lumbar or sacral segments of the cord. 'Dermatome' refers to the area of skin innervated by cutaneous axons in the distribution of a single spinal nerve. 'Myotome' refers to the muscle fibres innervated by the motor axons of a single spinal nerve. 'Neurological level' is the first level where motor and sensory function is normal on both sides of the body. 'Sensory level' refers to the most caudal level with normal sensation on both sides of the body. 'Motor level' refers to the most caudal segment with antigravity strength, providing that the next most rostral level is stronger. 'Complete injury' occurs when there is an absence of motor and sensory function below the motor and sensory levels and absence of function in the lowest sacral segment. 'Incomplete injury' refers to partial preservation of sensory and/or motor function below the neurological levels, as well as evidence of 'sacral sparing' (evidence of preserved function of the lowest sacral segment) (Ditunno et al 2004). 'Spinal shock' refers to the absence of reflexes and motor/sensory function below the level of injury and occurs typically from the time at which spinal cord injury is sustained to 24 hours after injury, followed by a phase of reflex return (Ditunno et al 2004).

In the assessment of a patient with spinal injury and neurological damage, it is important to remember that the level of cord and root injury will not coincide with that of the skeletal damage to the vertebral column. In estimating the vertebral levels of cord segments in the adult, a useful approximation is that, in the cervical region, the tip of a vertebral spinous process corresponds to the succeeding cord segment (i.e. the sixth cervical spine is opposite the seventh spinal segment); at upper thoracic levels, the tip of a vertebral spine corresponds to the cord two segments lower (i.e. the fourth spine is level with the sixth segment),

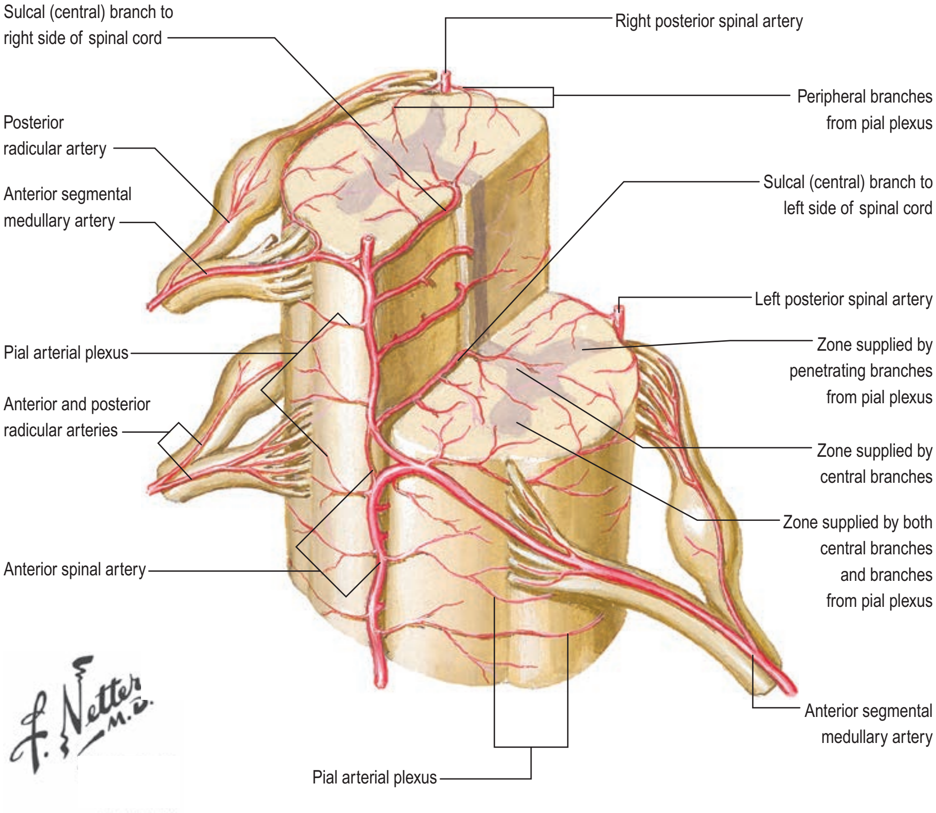
Sulcal (central) branch to right side of spinal cord
Right posterior spinal artery
Peripheral branches from pial plexus
Posterior radicular artery
Anterior segmental medullary artery
Sulcal (central) branch to left side of spinal cord
Left posterior spinal artery
Pial arterial plexus
Zone supplied by penetrating branches from pial plexus
Anterior and posterior radicular arteries
Zone supplied by central branches
Zone supplied by both central branches and branches from pial plexus
Anterior spinal artery
Anterior segmental medullary artery
Pial arterial plexus
F. Netter M.D.

Fig. 47.12 Arterial disposition within the spinal cord. (Reprinted from Netter Anatomy Illustration Collection, © Elsevier Inc. All Rights Reserved.)

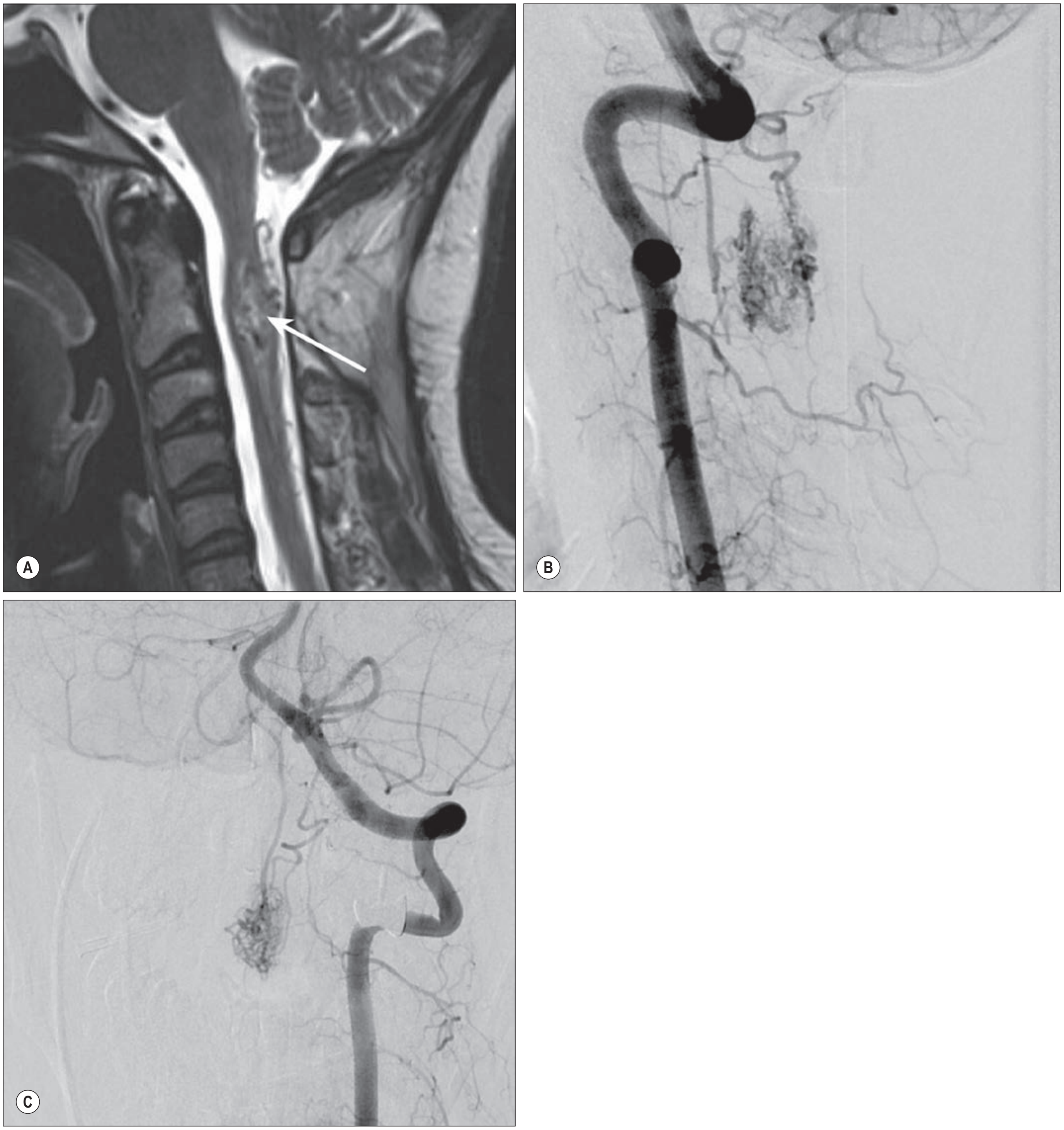

Fig. 47.13 A 35-year-old female presented with sudden onset of weakness secondary to intramedullary cervical spinal cord haemorrhage. A lateral MRI **(A)**, and lateral **(B)** and anteroposterior (AP) **(C)** angiograms show an intramedullary arteriovenous malformation located largely posterior to the body of C2 in the substance of the spinal cord (arrow). (Images courtesy of Dr Michael Alexander.)

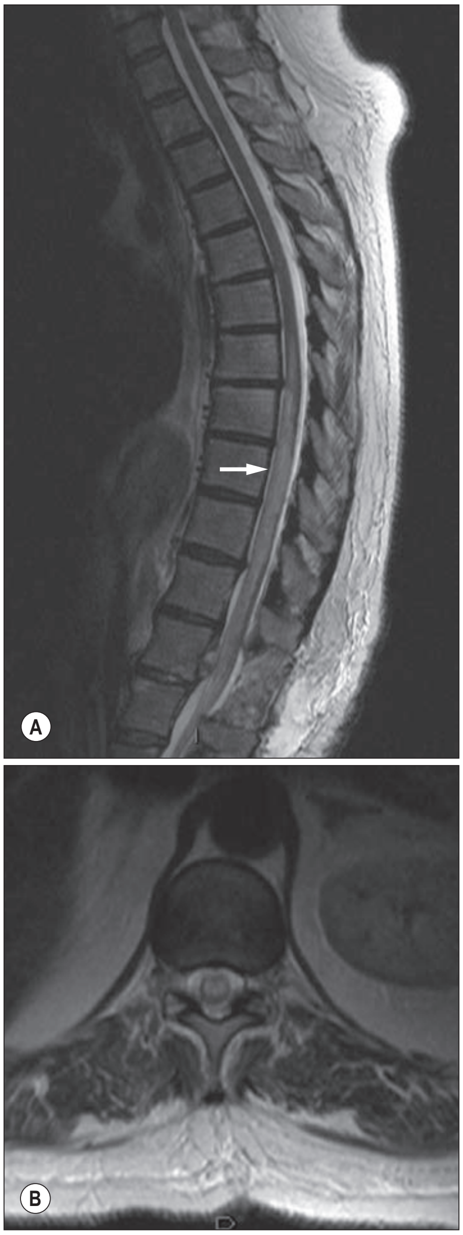

Fig. 47.14 **A**, Sagittal thoracic MR image showing spinal cord ischaemic changes (arrow) secondary to thrombotic occlusion of the artery of Adamkiewicz in a patient with a hypercoagulable disorder. **B**, The changes were noted to be in the distribution of the anterior spinal artery, as seen on this axial image.

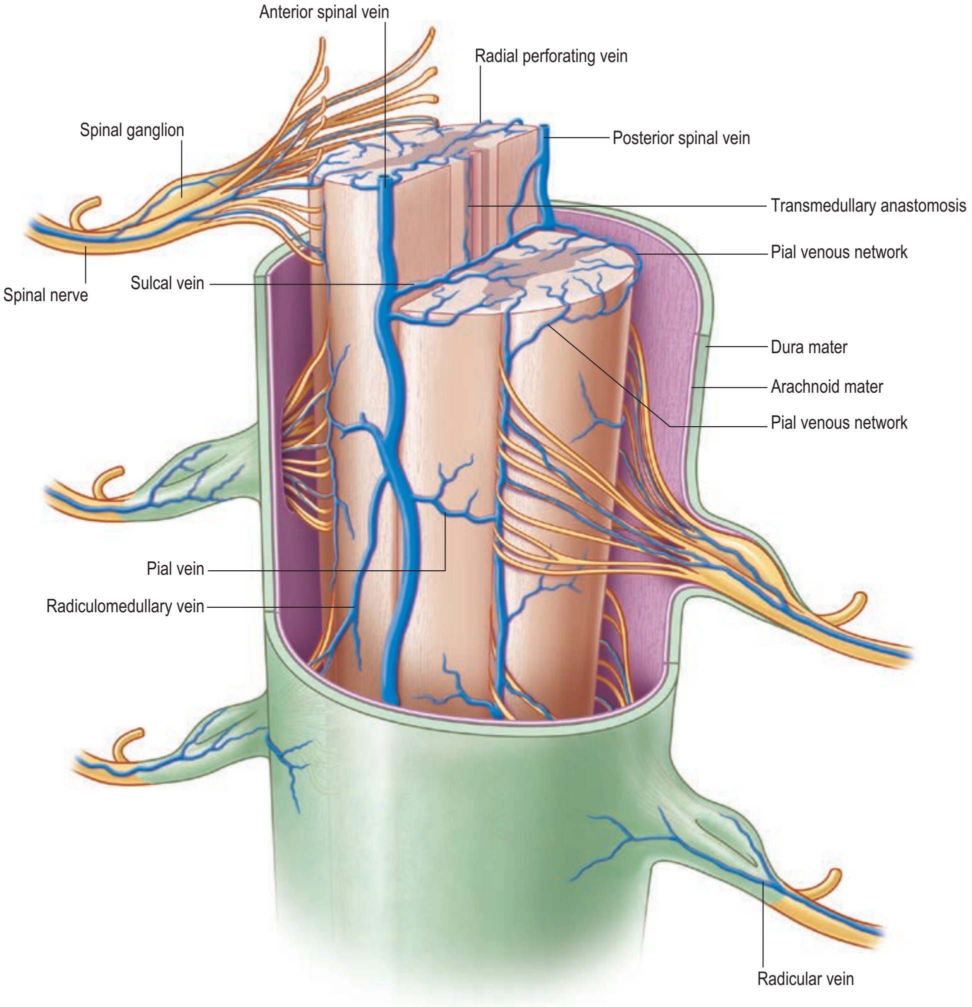

Fig. 47.15 Venous drainage of the spinal cord. (With permission from Miyasaka K, Asano T, Ushikoshi S et al 2000 Vascular anatomy of the spinal cord and classification of spinal arteriovenous malformations. Interv Neuroradiol. 6 Suppl 1:195–8.)

and in the lower thoracic region, there is a difference of three segments (i.e. the tenth thoracic spine is level with the first lumbar segment). The eleventh thoracic spine overlies the third lumbar segment and the twelfth is opposite the first sacral segment. In making this estimate by palpation of the vertebral spines, it is important to remember the relationship of the individual spines to their vertebral bodies. Clinical localization may be off by several levels because other factors may come into play, such as vascular insufficiency or venous obstruction, resulting in the lesion being localized as significantly lower than it actually is (Rousseff and Tzvetanov 2006, Sonstein et al 1996).

Complete division above the fourth cervical segment causes respiratory failure because of the loss of activity in the phrenic and intercostal nerves. Lesions between C5 and T1 paralyse all four limbs (quadriplegia), the effects in the upper limbs varying with the site of injury: at the fifth cervical segment, paralysis is complete; and at the sixth, each arm is positioned in abduction and lateral rotation, with the elbow flexed and the forearm supinated, due to unopposed activity in deltoid, supraspinatus, rhomboid and the brachial flexors (all supplied by the fifth cervical spinal nerves). Upper limb paralysis is less marked in lower cervical lesions. Lesions of the first thoracic segment paralyse small muscles in the hand and damage the sympathetic outflow to the head and neck, resulting in contraction of the pupil, recession of the eyeball, narrowing of the palpebral fissure and loss of sweating in the face and neck (Horner's syndrome). However, sensation is retained in areas innervated by segments above the lesion; thus cutaneous sensation is retained in the neck and chest down to the second intercostal space because this area is innervated by the supraclavicular nerves (C3 and C4). At thoracic levels, division of the cord paralyses the trunk below the segmental level of the lesion, and both lower limbs (paraplegia). The first sacral neural segment is approximately level with the thoracolumbar vertebral junction; injury, which commonly occurs here, paralyses the urinary bladder, the rectum and muscles supplied by the sacral segments, and cutaneous sensibility is lost in the perineum, buttocks, the back of the thighs and the legs, and soles of the feet. The roots of lumbar nerves descending to join the cauda equina may be damaged at this level, causing complete paralysis of both lower limbs. Lesions below the first lumbar vertebra may divide or damage the cauda equina, but severe nerve damage is uncommon and is usually confined to the spinal roots at the level of the trauma. Neurological symptoms may also occur as a result of interference with the spinal blood supply, particularly in the lower thoracic and upper lumbar segments.

Spinal cord injury without radiological abnormality: 'SCIWORA'

The spinal cord may be damaged without radiological evidence of skeletal injury to the vertebral column. This most commonly occurs with motor vehicle accidents but also has been reported with sports injuries and falls. MRI may or may not show evidence of cord injury after SCIWORA occurs; the majority of patients sustaining these injuries have an abnormal MRI scan.

Spinal cord syndromes

Available with the *Gray's Anatomy* e-book

Lesions of the spinal roots, nerves and ganglia

Spinal roots, nerves and ganglia may be damaged in the vertebral and root canals and at the intervertebral foramina. Neurofibromas and schwannomas may occur on the roots and nerves in the root canals (Fig. 47.16). As they enlarge, these tumours become dumbbell-shaped, with both an intraspinal and an extraspinal component in continuity; the clinical picture may thus include paradoxical features as the asymmetric space-occupying lesion grows. Root compression usually presents acutely with pain, which may be severe. The pain, paraesthesias and numbness occur in a dermatomal distribution; dermatomal overlap may make it difficult to demonstrate sensory loss on the trunk. Severe traction injuries of the upper limbs may cause avulsion of spinal roots from the cord in the cervical region.

Typical neural abnormalities include cord oedema, haemorrhage, contusion or transection. Typical extraneural abnormalities include intervertebral disc protrusion or herniation, ligamentum flavum bulging, cervical spondylitis, prevertebral soft tissue oedema, ligamentous abnormalities and/or ossification of the posterior longitudinal ligament. Originally, this was considered a paediatric diagnosis but it has now been shown to be equally common in adults. Spinal stenosis and pre-existing cord compression have been postulated as a risk factor for SCIWORA but clinical series have not supported this (Boese and Lechler 2013, Boese et al 2013).

For cervical spinal injury, several cord syndromes have been described, relating the clinical picture to the anatomy of the neurological lesion within the cord. The most common of these is central cord syndrome, which usually results from hyperextension injury to an osteoarthritic neck, when the major injury is to the central grey matter. This typically gives an incomplete cord injury pattern with greater motor loss in the upper extremities than in the lower limbs. There is also variable sensory loss and neurogenic bladder dysfunction (Pouw et al 2010). In anterior cord syndrome, which may occur in flexion–compression injuries of the neck, the damage occurs in the area of supply of the anterior spinal artery, sparing the posterior columns; the motor loss is usually proportionately greater in the lower than in the upper limbs, while sensory loss is less of a problem. A third syndrome that may be seen with penetrating trauma is Brown–Séquard syndrome. This is an injury directed to one side of the spinal cord, where there is ipsilateral loss of motor function and pinprick sensation and contralateral loss of pain and temperature sensation (Lee et al 1990). The anatomical basis for these symptoms is injury to the ipsilateral posterior columns and corticospinal tract, and injury to the lateral spinothalamic tract, which conveys contralateral pain and temperature sensation (see Ch. 27).

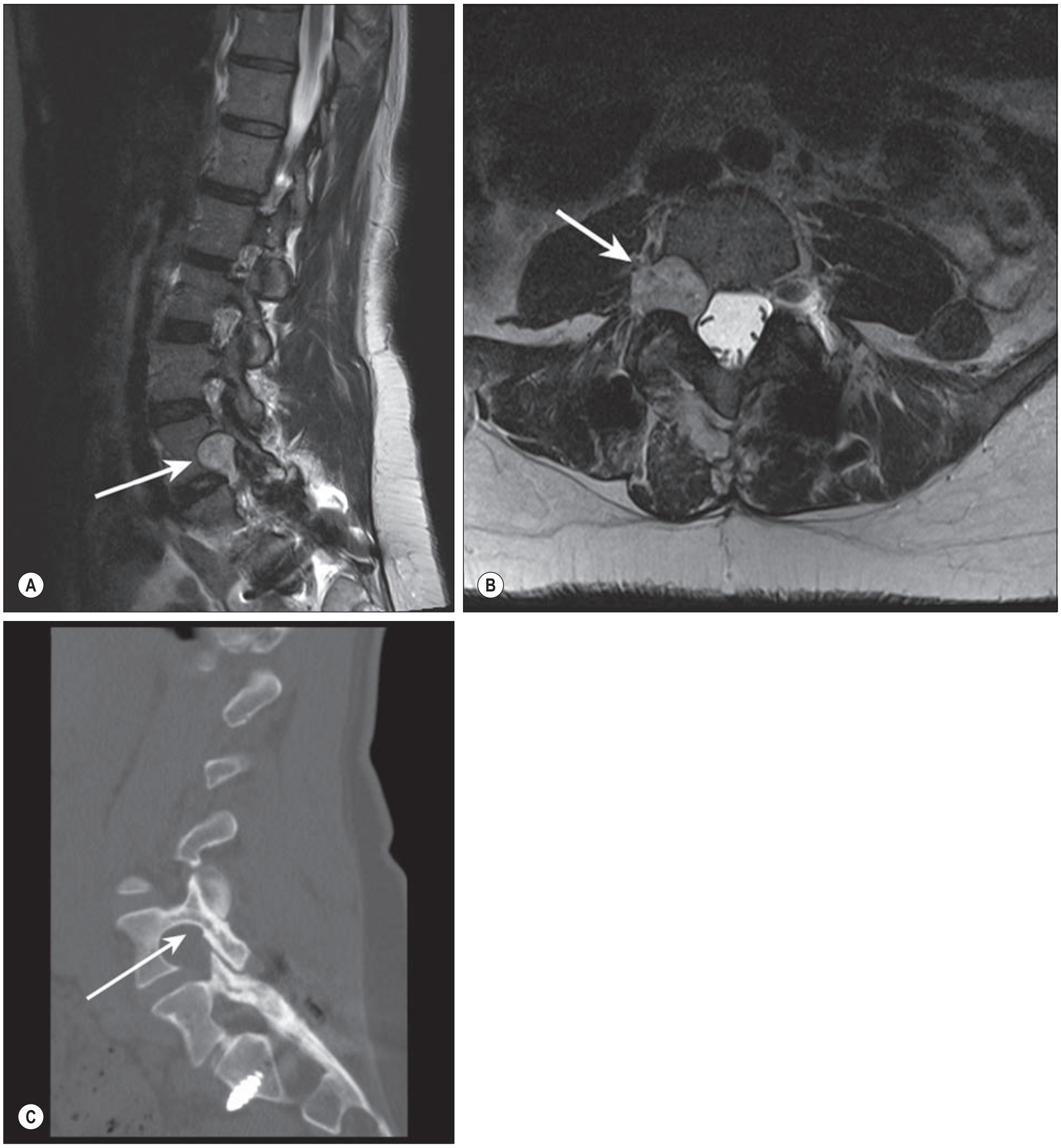

Fig. 47.16 **A**–**B**, MRI sagittal and axial images showing a right L4 nerve root schwannoma (arrows) in a 51-year-old female who presented with right foot numbness and weakness 11 years after L5–S1 spinal fusion procedure. **C**, CT scan shows an enlarged neuroforamen and erosion of the right L4 pedicle (arrow).

The anatomical basis for pain of spinal origin

In the diagnosis and description of pain of spinal origin, it is particularly important to distinguish between radicular pain and somatic referred pain.

Radicular pain is caused by disorders that affect a spinal nerve or its dorsal root ganglion. This type of pain characteristically radiates, along a narrow band, into the area of the limb (or trunk wall) that the spinal nerve supplies, and is typically (although not always) lancinating in quality, not unlike an electric shock.

Referred pain is pain felt in the distribution of a nerve that is not the nerve that innervates the source of pain, although typically these nerves are derived from the same spinal cord segment. Referred pain is felt deeply across a broad area, and is usually aching in quality; although it may radiate into a limb (or around the trunk wall), it is typically constant in location. Patients may find it hard to define the outer boundaries of this pain but they can clearly identify the centre of its distribution. Referred pain can be subdivided into somatic referred pain and visceral referred pain, according to its origin. As its name implies, visceral referred pain is caused by disorders in viscera; in some cases, the referral can be quite remote from the viscus, e.g. cardiac pain that radiates into the neck. Somatic referred pain is caused by disorders of muscular and skeletal structures. Examples include lumbar spinal pain referred to the gluteal region, thigh or leg; cervical spinal pain referred to the upper limb girdle; and cervical or thoracic spinal pain referred to the chest wall, where it may mimic cardiac pain. Often the source of somatic referred pain cannot be determined by clinical examination, and invasive tests are required to pinpoint its location.

Lesions of the conus and cauda equina

Lesions of the conus and cauda equina, e.g. tumours, cause bilateral deficit, often with pain in the back extending into the sacral segments and to the legs. Loss of bladder and erectile function can be early features (**Fig. 47.17**). There are lower motor neurone signs in the legs with fasciculation and muscle atrophy. Sensory loss usually involves the perineal or 'saddle area', as well as other lumbar and sacral dermatomes. There may be congenital abnormalities, e.g. spina bifida, lipomata or diastematomyelia, and the conus may extend below the lower border of L1, often with a tethered filum terminale (**Fig. 47.18**). Extramedullary lesions include prolapsed intervertebral discs. A midline (central) disc protrusion in the lumbar region may present with involvement of the sacral segments only.

Two distinct clinical syndromes, conus medullaris syndrome and cauda equina syndrome, have been described, the latter being much more common. Cauda equina syndrome typically presents in men who have a lumbar disc herniation in the setting of lumbar spinal stenosis, with symptoms of asymmetric saddle anaesthesia and asymmetric lower extremity weakness, and delayed presentation of atonic bladder and flaccid anal sphincter. Conus medullaris syndrome typically presents with symmetric saddle anaesthesia, symmetric motor deficit and earlier atonic bladder and sphincter dysfunction. The usual causes are intradural tumours or vascular lesions (Radcliff et al 2011).

Tethered cord syndrome may be associated with occult or non-occult spinal dysraphism. In its classic form, it refers to an unusually low conus medullaris (although in some 14–18% of cases the position of the conus is anatomically normal). There is some debate as to what constitutes an abnormally low conus, whether below the L1–2 disc space or below the lower border of the body of the L2 vertebra. Most commonly, tethered cord syndrome is associated with a short filum terminale more than 2 mm wide, but it also may be related to an intradural lipoma. Traction on the caudal cord and loss of filum terminale elasticity are thought to predispose to decreased blood flow in the cord, leading to symptoms (Filippidis et al 2010). The clinical presentation varies according to age. In children, the most common presentation includes foot deformities, neurological deficits, spinal deformity and various cutaneous findings such as a lumbar capillary angioma. In adults, the syndrome more commonly presents with perianal pain and leg weakness (see Fig. 47.18) (Pang and Wilberger 1982).

CLINICAL PROCEDURES

Available with the *Gray's Anatomy* e-book

Bonus e-book content

Fig. 47.1 G, Axial T2-weighted MRI of the cervical spine at the level of C4 showing the ventral and dorsal nerve rootlets.

Fig. 47.3 A T1 post-contrast sagittal lumbar spinal magnetic resonance (MR) image showing a spinal epidural abscess adherent to the lumbar dura and spinal nerves in a 28-year-old female with a history of intravenous drug abuse.

Fig. 47.4 A sagittal thoracic MR image showing a large ventral spinal epidural haematoma resulting in severe neck and upper thoracic pain and ataxia.

Fig. 47.12 Arterial disposition within the spinal cord.

Fig. 47.13 A 35-year-old female presented with sudden onset of weakness secondary to intramedullary cervical spinal cord haemorrhage.

Fig. 47.14 A, A sagittal thoracic MR image showing spinal cord ischaemic changes secondary to thrombotic occlusion of the artery of Adamkiewicz in a patient with a hypercoagulable disorder. **B**, The changes were noted to be in the distribution of the anterior spinal artery, as seen on this axial image.

Fig. 47.16 A–B, MRI sagittal and axial images showing a right L4 nerve root schwannoma in a 51-year-old female who presented with right foot numbness and weakness 11 years after L5–S1 spinal fusion procedure. **C**, CT scan shows an enlarged neuroforamen and erosion of the right L4 pedicle.

Fig. 47.17 A sagittal MR image showing a spinal ependymoma, a tumour arising from the filum terminale, which can be seen just below the conus medullaris.

Fig. 47.18 A sagittal MR image showing a tethered filum terminale resulting in low-lying conus.

Fig. 47.19 The lumbar interlaminar window in extension and flexion.

Fig. 47.20 A, A sagittal section illustrating the course of a lumbar puncture needle through skin, subcutaneous tissue, supraspinous ligament, interspinous ligament between the spinous processes, ligamentum flavum, dura mater, into the subarachnoid space and between the nerve roots of the cauda equina. **B**, Horizontal section of a lumbar vertebra illustrating the course of a lumbar puncture needle through (in order) skin, subcutaneous tissue, between the spinous processes and laminae, ligamentum flavum, epidural space, dura mater, into the subarachnoid space and between the nerve roots of the cauda equina.

Fig. 47.21 Palpation of the sacral cornua for caudal epidural injection.

Fig. 47.22 Position of the needle in a caudal epidural injection.

Fig. 47.23 Anteroposterior fluoroscopic image showing a right medial branch block of the L1 and L2 medial branches.

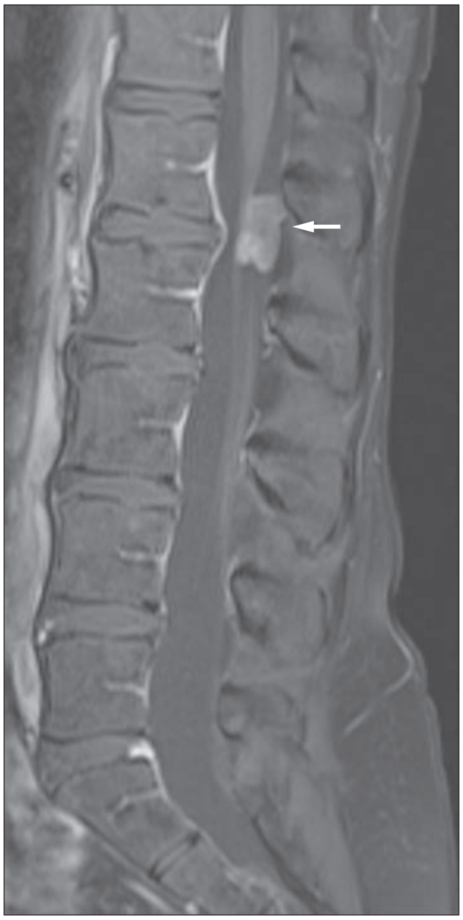

Fig. 47.17 Sagittal MR image showing a spinal ependymoma (arrow), a tumour arising from the filum terminale, which can be seen just below the conus medullaris. The patient presented with pain in the back radiating to the legs. At surgery to resect the ependymoma, it was found to be adherent to the filum terminale.

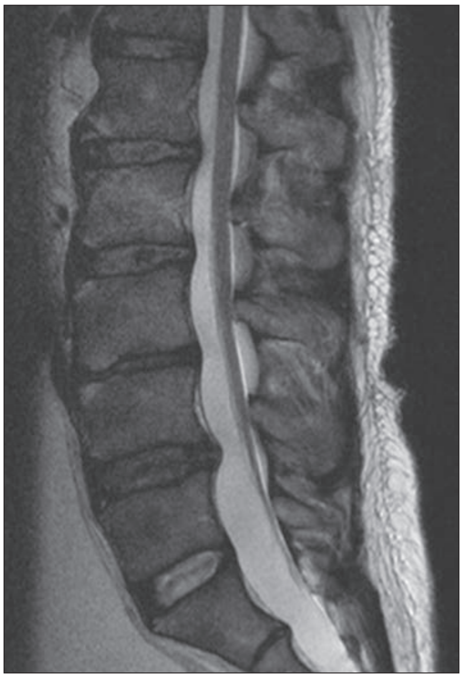

Fig. 47.18 Sagittal MR image showing a tethered filum terminale resulting in low-lying conus. The patient presented with back pain and perineal disturbances consistent with 'tethered cord syndrome'. The end of the conus medullaris was noted to be at the L5 level.

Access to cerebrospinal fluid

The safest approach to the cerebrospinal fluid (CSF) is to enter the lumbar cistern of the subarachnoid space in the midline, well below the level at which the spinal cord normally terminates (see above). The fine needle employed is unlikely to damage the mobile nerve roots of the cauda equina. This procedure is called lumbar puncture. It is also possible to access the CSF by midline puncture of the cerebellomedullary cistern (cisterna magna) (Ch. 25): this is cisternal puncture.

Lumbar puncture: adult

Lumbar puncture in the adult may be performed with the patient either sitting or lying on their side (lateral decubitus) on a firm, flat surface. In each position, the lumbar spine must be flexed as far as possible, in order to separate the vertebral spines maximally and expose the ligamentum flavum in the interlaminar window (**Fig. 47.19**). A line is then taken between the highest points of the iliac crests: this line almost always intersects the vertebral column at the vertebral body of L4 or the L4/L5 intervertebral disc level, but it may range from the L2/L3 interspinous space to the spinous process of L5 (see Fig.76.19). In most adults the plane intersects the vertebral column inferior to the termination of the spinal cord (see Fig. 46.81C). Localizing the supracristal plane via palpation may place it at a higher level in females and individuals with a higher body mass index (Kim et al 2007, Hale et al 2010). With the spines now identified, the skin is anaesthetized and a needle is inserted between the spines of L3 and L4 (or L4 and L5). Exact identification of the level by palpation is difficult (Broadbent et al 2000). The soft tissues that the needle will traverse should also be anaesthetized; care should be taken that the injection of an excessive amount of local anaesthetic does not compromise appreciation of the structures being traversed. These will be, in order: subcutaneous tissue, supraspinous ligament, interspinous ligament, ligamentum flavum, epidural space containing

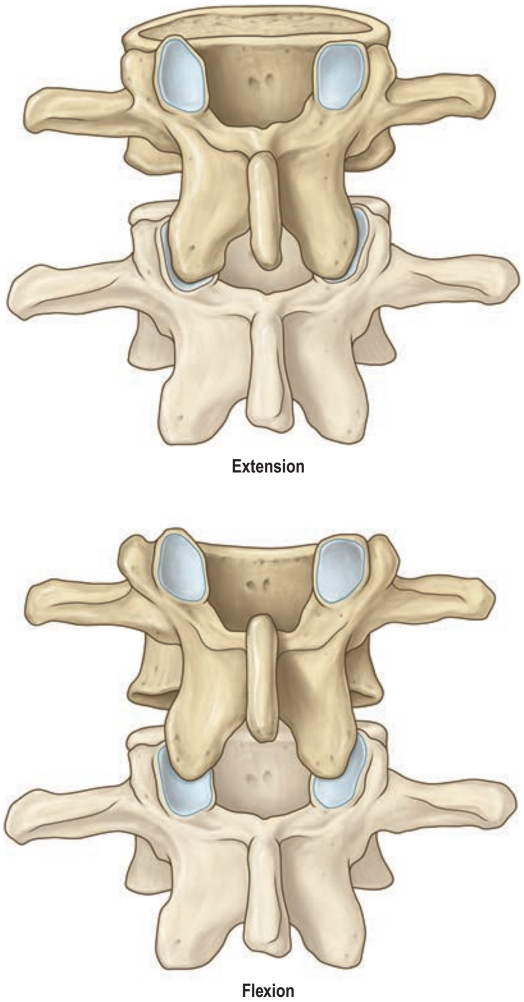

Fig. 47.19 The lumbar interlaminar window in extension and flexion.

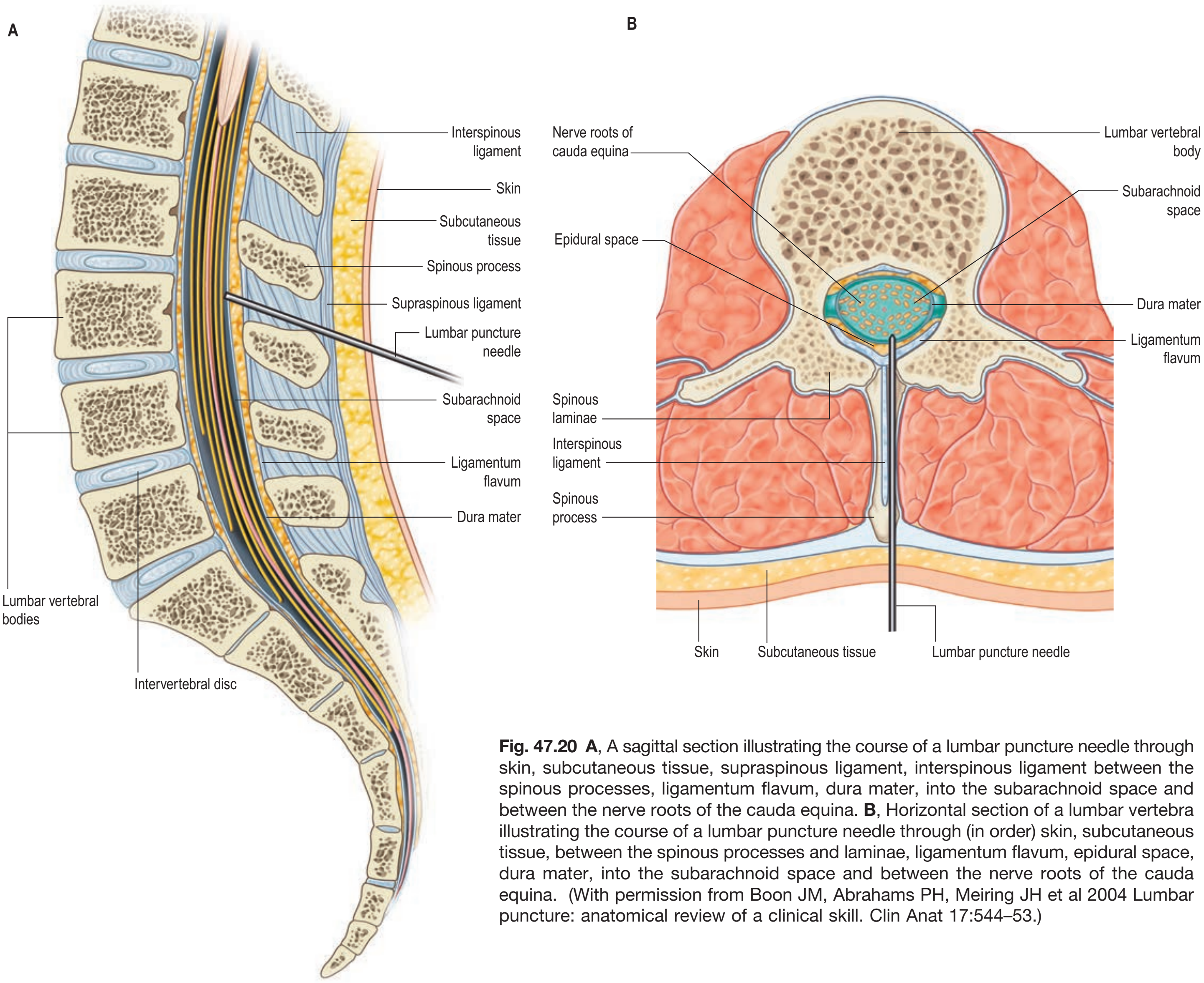
A
Interspinous ligament
Skin
Subcutaneous tissue
Spinous process
Supraspinous ligament
Lumbar puncture needle
Subarachnoid space
Ligamentum flavum
Dura mater
Lumbar vertebral bodies
Intervertebral disc
B
Nerve roots of cauda equina
Epidural space
Spinous laminae
Interspinous ligament
Spinous process
Lumbar vertebral body
Subarachnoid space
Dura mater
Ligamentum flavum
Skin
Subcutaneous tissue
Lumbar puncture needle

Fig. 47.20 **A**, A sagittal section illustrating the course of a lumbar puncture needle through skin, subcutaneous tissue, supraspinous ligament, interspinous ligament between the spinous processes, ligamentum flavum, dura mater, into the subarachnoid space and between the nerve roots of the cauda equina. **B**, Horizontal section of a lumbar vertebra illustrating the course of a lumbar puncture needle through (in order) skin, subcutaneous tissue, between the spinous processes and laminae, ligamentum flavum, epidural space, dura mater, into the subarachnoid space and between the nerve roots of the cauda equina. (With permission from Boon JM, Abrahams PH, Meiring JH et al 2004 Lumbar puncture: anatomical review of a clinical skill. Clin Anat 17:544–53.)

the internal vertebral venous plexus, dura, arachnoid, and finally, the subarachnoid space (Fig. 47.20). The lumbar puncture needle may then be inserted in the midline or just to one side, and angled in the horizontal and sagittal planes sufficiently to pierce the ligamentum flavum in or very near the midline. There is then a slight loss of resistance as the needle enters the epidural space; careful advancement will next pierce the dura and arachnoid to release CSF. For further details about the clinical anatomy of lumbar puncture, see Boon et al (2004).

Lumbar puncture: neonate and infant

The spinal cord usually terminates between the bodies of L1 and L3 lumbar vertebrae from postmenstrual week 28 onwards. In infants (postnatal month 2 to 3 years) and children (3–7 years), the conus medullaris lies most commonly at the lower third of the vertebral body of L1 (range, lower third of the vertebral body of T12 to the L2/L3 intervertebral disc) (Barson 1970, Barson and Sands 1977, Vettivel 1991, Malas et al 2001, Kesler et al 2007, Suresh et al 2013). The supracristal plane most commonly intersects the vertebral column at a slightly higher level in children (L3–L4) than in adults (L4–L4/L5); when located via palpation it may range in position from the L2/L3 to the L5/S1 interspinous space. These differences and the potential overlap between the level of the supracristal plane and the termination of the spinal cord must be borne in mind before undertaking lumbar puncture in the neonate and infant. Ultrasound guidance may be preferable (Baxter et al 2016). A lumbar puncture is performed by placing the infant in a position, either lying or sitting, that gives maximum convex curvature to the lumbar spine. A trocar needle is inserted into the back between the spinous processes of either L3 and L4 or L4 and L5 lumbar vertebrae and into the subarachnoid space below the level of the conus medullaris. The space between L3 and L4 is approximately level with the iliac crests and it is usual to insert the trocar needle into the intervertebral space immediately above or below the iliac crests. The distance from the skin to the subarachnoid space is approximately 1.4 cm in neonates; it increases progressively with age.

Cisternal puncture

In cisternal puncture, the cisterna magna (see Fig. 25.25) is entered by midline puncture through the posterior atlanto-occipital membrane. Further details of this difficult specialist technique are beyond the scope of this book.

Access to the epidural space

The epidural space lies between the spinal dura and the wall of the vertebral canal. It contains epidural fat and a venous plexus. Access to this space, usually in the lumbar region, is required for the administration of anaesthetic and analgesic drugs, and for endoscopy. The caudal route is used mainly for analgesic injections.

Thoracic and cervical epidurals

It is possible to access the epidural space at thoracic and cervical levels, but the specialist techniques required are beyond the scope of this book.

Lumbar epidural

For access to the lumbar epidural space, the approach is as for lumbar puncture. The intention in epidural injection is to avoid dural puncture, so the epidural space should be entered in the midline posteriorly, where the depth of the space is greatest. The skin/epidural distance has been assessed in children at the L3/L4 interspace; 1 mm/kg of body weight is considered to be a useful guideline for infants and children between the ages of 6 months and 10 years (Bösenberg and Gouws 1995). Techniques for entering the epidural space rely on the appreciation of loss of resistance to injection of saline (air is used by some) as the space is entered: saline cannot be injected into the dense ligamentum flavum, but can be injected into the loose tissues of the epidural space. As there is very little distance between the ligamentum flavum and the underlying dura, care must be taken not to continue advancing the needle once loss of resistance has occurred.

Caudal epidural

The route of access to the caudal epidural space is via the sacral hiatus. This means that the space is entered below the level of termination of the dural sac (the subarachnoid space and its contained CSF), which usually extends only to the level of the second sacral segment. Occasionally, the dural sac ends as high as the fifth lumbar vertebra, and very rarely it may extend to the third part of the sacrum, in which case it is occasionally possible to enter the subarachnoid space inadvertently during the course of a sacral nerve block.

With the patient in the lateral position or lying prone over a pelvic pillow, the sacral hiatus is identified by palpation of the sacral cornua (**Fig. 47.21**). These are felt at the upper end of the natal cleft approximately 5 cm above the tip of the coccyx. Alternatively, the sacral hiatus may be approximated by constructing an equilateral triangle based on a line joining the posterior superior iliac spines where the the inferior apex of the triangle overlies the hiatus (see Fig. 76.19). After local anaesthetic infiltration, a needle is introduced at 45° to the skin, in order to penetrate the posterior sacrococcygeal ligament and enter the sacral canal. The puncture of the ligament can usually be felt as the needle is advanced. Once the canal is entered, the hub of the needle is lowered so that the needle may be fed along the canal (**Fig. 47.22**). If the needle is angled too obliquely, it will strike bone, whereas if it is placed too superficially, it will lie outside the canal and any fluid injected can be felt subcutaneously.

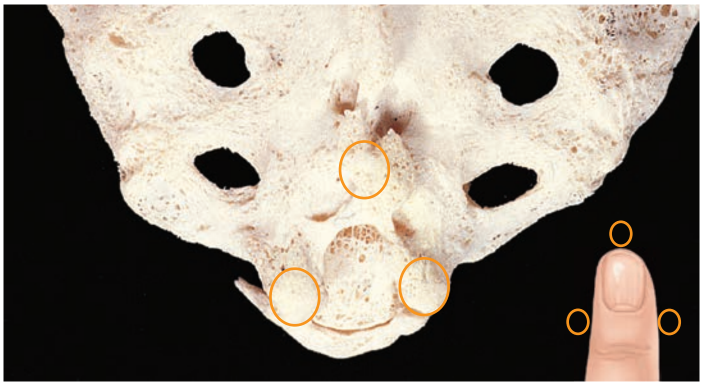
Fig. 47.21 Palpation of the sacral cornua for caudal epidural injection.

Medial branch block

Medial branch block is a clinical procedure that can be used in the diagnosis and treatment of facet-mediated low back pain. The medial branch of the dorsal ramus of each lumbar spinal nerve runs beneath the mammillo-accessory ligament in a groove at the root of the superior articular process of the adjacent facet joint. Each medial branch innervates not only the adjacent facet joint capsule but also the capsule of the facet joint located at the level immediately below it, which means that each facet joint has a dual innervation (Amrhein et al 2016). The L5 spinal nerve is unusual because its dorsal ramus does not have a medial branch; it lies in the groove between the sacral ala and the superior articular facet of S1 (Iannuccilli et al 2013). To achieve complete sensory blockade of a single lumbar facet joint, two separate injections are necessary (to block conduction in the medial branches of the spinal nerves exiting at the level of the joint and at the level immediately above) (**Fig. 47.23**).

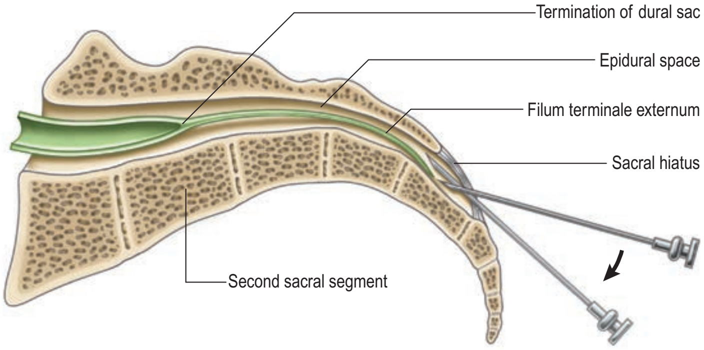

Fig. 47.22 Position of the needle in a caudal epidural injection.

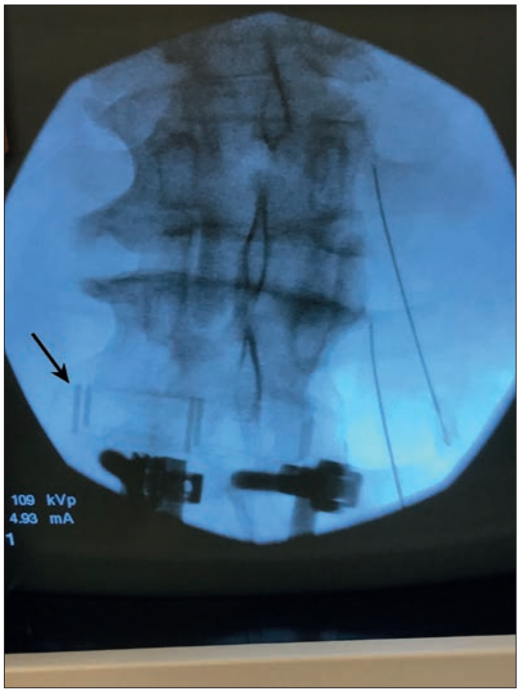

Fig. 47.23 Anteroposterior fluoroscopic image showing a right medial branch block of the L1 and L2 medial branches. The L2–L3 facet joint, which was suspected of being a pain generator after an attempted fusion from a lateral approach was felt to have resulted in nonunion, was rendered anaesthetic. An intervertebral cage is seen in the L3 disc space (arrow). (Image courtesy of Dr Avrom Gart.)

Key references

Crock H 1996 An Atlas of Vascular Anatomy of the Skeleton and Spinal Cord. London: Martin Dunitz.

Ditunno JF Jr, Young W, Donovan WH et al 1994 The International Standards Booklet for Neurological and Functional Classification of Spinal Cord Injury. American Spinal Injury Association. Paraplegia 32:70–80.

A landmark publication standardizing the language of the neurologic exam as it relates to spinal cord injury.

Dommisse G 1975 The Arteries and Veins of the Human Spinal Cord From Birth. Edinburgh: Churchill Livingstone.

Newell RL 1999 The spinal epidural space. Clin Anat (New York, NY) 12:375–379.

Pang D, Wilberger JE Jr 1982 Tethered cord syndrome in adults. J Neurosurg 57:32–47.

A review of a series of adult patients with tethered cord syndrome which compares their clinical presentation to children with similar pathology.

Radcliff KE, Kepler CK, Delasotta LA et al 2011 Current management review of thoracolumbar cord syndromes. Spine J 11:884–892.

An in-depth review on the clinical aspects of cauda equina syndrome and conus medularis syndrome.

References

Amrhein TJ, Joshi AB, Kranz PG 2016 Technique for CT fluoroscopy-guided lumbar medial branch blocks and radiofrequency ablation. AJR Am J Roentgenol 207: 631–4.

Backes WH, Nijenhuis RJ 2008 Advances in spinal cord MR angiography. AJNR Am J Neuroradiol 29:619–31.

Barson AJ 1970 The vertebral level of termination of the spinal cord during normal and abnormal development. J Anat 106:489–97.

Barson AJ, Sands J 1977 Regional and segmental characteristics of the human adult spinal cord. J Anat 123:797–803.

Baxter B, Evans J, Morris R et al 2016 Neonatal lumbar puncture: are clinical landmarks accurate? Arch Dis Child Fetal 2016 101:F448-50.

Boese CK, Lechler P 2013 Spinal cord injury without radiologic abnormalities in adults: a systematic review. J Trauma Acute Care Surg 75:320–30.

Boese CK, Nerlich M, Klein SM et al 2013 Early magnetic resonance imaging in spinal cord injury without radiological abnormality in adults: a retrospective study. J Trauma Acute Care Surg 74:845–8.

Boon JM, Abrahams PH, Meiring JH et al 2004 Lumbar puncture: anatomical review of a clinical skill. Clin Anat 17:544–53.

Bösenberg AT, Gouws E 1995 Skin-epidural distance in children. Anaesthesia 50:895–7.

Broadbent CR, Maxwell WB, Ferrie R e al 2000 Ability of anaesthetists to identify a marked lumbar interspace. Anaesthesia 55:1122–6.

Carmichael S, Gloviczki P 1999 Anatomy of the blood supply to the spinal cord: the artery of Adamkiewicz revisited. Perspect Vasc Surg 12:113–22.

Crock H 1996 An Atlas of Vascular Anatomy of the Skeleton and Spinal Cord. London: Martin Dunitz.

Dean NA, Mitchell BS 2002 Anatomic relation between the nuchal ligament (ligamentum nuchae) and the spinal dura mater in the craniocervical region. Clin Anat (New York, NY) 15:182–5.

Ditunno JF, Little JW, Tessler A 2004 Spinal shock revisited: a four-phase model. Spinal Cord 42:383–95.

Ditunno JF Jr, Young W, Donovan WH et al 1994 The International Standards Booklet for Neurological and Functional Classification of Spinal Cord Injury. American Spinal Injury Association. Paraplegia 32:70–80.

A landmark publication standardizing the language of the neurologic exam as it relates to spinal cord injury.

Dommisse G 1975 The Arteries and Veins of the Human Spinal Cord from Birth. Edinburgh: Churchill Livingstone.

Filippidis AS, Kalani MY, Theodore N et al 2010 Spinal cord traction, vascular compromise, hypoxia, and metabolic derangements in the pathophysiology of tethered cord syndrome. Neurosurg Focus 29:E9 1–4.

Fraher JP 2000 The transitional zone and CNS regeneration. J Anat 196:137–58.

Garcia-Cosamalon J, del Valle ME, Calavia MG et al 2010 Intervertebral disc, sensory nerves and neurotrophins: who is who in discogenic pain? J Anat 217:1–15.

Haines DE, Harkey HL, al-Mefty O 1993 The 'subdural' space: a new look at an outdated concept. Neurosurgery 32:111–20.

Hale SJ, Mirjalili SA, Stringer MD 2010 Inconsistencies in surface anatomy: the need for an evidence-based reappraisal. Clin Anat 23:922–30.

Iannuccilli JD, Prince EA Soares GM 2013 Interventional spine procedures for management of chronic low back pain – a primer. Semin Intervent Radiol 30:307–17.

Kesler H, Dias MS, Kalapos P 2007 Termination of the normal conus medullaris in children: a whole-spine magnetic resonance imaging study. Neurosurg Focus 23:E7.

Kido DK, Gomez DG, Pavese AM Jr et al 1976 Human spinal arachnoid villi and granulations. Neuroradiology 11:221–8.

Kim HW, Ko YJ, Rhee WI et al 2007 Interexaminer reliability and accuracy of posterior superior iliac spine and iliac crest palpation for spinal level estimations. J Manipulative Physiol Ther 30:386–9.

Kubik S, Müntener M 1969 [Topography of the spinal nerve roots. II. The influence of the growth of the dural sac as well as of the curvatures and of the movements of the vertebral column upon the course of spinal nerve roots]. Acta Anatomica 74:149–68. [Article in German.]

Lee HM, Kim NH, Park CI 1990 Spinal cord injury caused by a stab wound – a case report. Yonsei Med J 31:280–4.

Macdonald A, Chatrath P, Spector T et al 1999 Level of termination of the spinal cord and the dural sac: a magnetic resonance study. Clin Anat 12:149–52.

Malas MA, Salbacak A, Büyükmumcu M et al 2001 An investigation of the conus medullaris termination level during the period of fetal development to adulthood. Kaibogaku Zasshi 76:453–9.

Neidre A, MacNab I 1983 Anomalies of the lumbosacral nerve roots. Review of 16 cases and classification. Spine 8:294–9.

Newell RL 1999 The spinal epidural space. Clin Anat (New York, NY) 12:375–9.

Pang D, Wilberger JE Jr 1982 Tethered cord syndrome in adults. J Neurosurg 57:32–47.

A review of a series of adult patients with tethered cord syndrome which compares their clinical presentation to children with similar pathology.

Pouw MH, van Middendorp JJ, van Kampen A et al 2010 Diagnostic criteria of traumatic central cord syndrome. Part 1: A systematic review of clinical descriptors and scores. Spinal Cord 48:652–6.

Radcliff KE, Kepler CK, Delasotta LA et al 2011 Current management review of thoracolumbar cord syndromes. Spine J 11:884–92.

An in-depth review on the clinical aspects of cauda equina syndrome and conus medullaris syndrome.

Rousseff RT, Tzvetanov P 2006 False localising levels in spinal cord compression. NeuroRehabilitation 21:219–22.

Sonstein WJ, LaSala PA, Michelsen WJ et al 1996 False localizing signs in upper cervical spinal cord compression. Neurosurgery 38:445–8; discussion 8–9.

Suresh S, Polaner DM, Coté CJ 2013 Regional anesthesia. In: Coté CJ, Lerman J, Anderson BJ (eds) Practice of Anesthesia for Infants and Children, 5th ed. Philadelphia: Elsevier Saunders; Ch. 41, pp. 835–79.

Turnbull IM, Brieg A, Hassler O 1966 Blood supply of cervical spinal cord in man. A microangiographic cadaver study. J Neurosurg 24:951–65.

Vanelderen P, Lataster A, Levy R et al 2010 8. Occipital neuralgia. Pain Pract 10:137–44.

Vettivel S 1991 Vertebral level of the termination of the spinal cord in human foetuses. J Anat 179:149–61.

Yasui K, Hashizume Y, Yoshida M et al 1999 Age-related morphologic changes of the central canal of the human spinal cord. Acta Neuropathol 97:253–9.

CHAPTER 48

Pectoral girdle and upper limb: overview and surface anatomy

The upper limb is, in mechanical terms, a series of powered, articulated segments which enable the hand to be positioned accurately in space so that it can sense and manipulate its surrounding environment. It is attached to the bony thorax at the sternoclavicular joint, and to the chest wall by a series of powerful flat muscles which stabilize the scapula, allowing it to act as a stable but mobile base on which the limb can function. An extensive range of movement is enabled by a number of factors. The glenohumeral joint is remarkably little constrained and the muscles that both stabilize and move it are powerful. Elbow flexion allows movements close to the trunk, such as eating and attention to personal hygiene, while extension achieves a wide arc of reach for daily activities. Pronation and supination markedly increase the functional capacity of the hand by rotating the forearm through nearly 180°.

In the soft tissues, the deep fascial planes and the synovial sheaths permit the excursion of muscles and tendons against each other and their adjacent structures. Condensations of fascia around the neurovascular bundles segregate them and enhance gliding.

The innervation of the upper limb is complex and rich. There is a particular concentration of specialized sensory organelles in the wrist and hand, not only in the skin but also in the deep afferent system from muscles, tendons and joints. The postganglionic sympathetic vasomotor and sudomotor nerves are especially dense in the palmar skin. The basis of stereognosis, the ability to recognize the qualities of objects and textures, is a combination of stimuli from skin, tendon, muscle and joints. Movement is vital; blindfolded patients cannot identify the nature of an object if it is simply placed on the finger, but recognize it immediately if allowed to create spatial and temporal patterns by feeling the object or material between moving fingers and thumb.

BONES AND JOINTS

The bones of the upper limb include the scapula, clavicle, humerus, radius and ulna (connected by the interosseous membrane along most of their length), the eight bones forming the carpus, five metacarpals and fourteen phalanges (Figs 48.1–48.2). There are two phalanges in the thumb and three in each finger.

The thoracoscapular joint is the platform for function of the upper limb: paralysis of either of the two great muscles, trapezius and serratus anterior, is crippling. The limb is directly attached to the axial skeleton by one bony articulation, the sternoclavicular joint. The glenohumeral joint is shallow and little constrained, whereas the acromioclavicular joint is a plane joint stabilized by strong ligaments. The range of movements provided by these joints and the muscles acting across them is enormous. Arthrodesis of the thoracoscapular joint for facioscapulohumeral dystrophy improves flexion and abduction of the glenohumeral joint, but protraction and retraction are lost. A correctly performed glenohumeral arthrodesis retains powerful adduction, protraction and retraction, but rotation and the limited elevation achieved is dependent on rotation of the scapula. The elbow includes a hinge between the humerus and ulna, and two pivot joints, between the humerus and radius, and between the proximal radius and ulna. This permits a range of about 150° of flexion and extension, and 180° of pronosupination in conjunction with the distal radio-ulnar joint. The wrist complex allows a range of flexion and extension of about 140°, supplemented by some 70° of adduction and abduction. The condylar metacarpophalangeal joint enables 120° of flexion and extension, about 40° of abduction and adduction, and some rotation. Pronation and supination are unique to the primate upper limb. The range of movement of the thumb ray, which rests on the 'saddle' carpometacarpal joint, the qualities of the long muscles and the thenar muscles acting on the ray and the skin of the web space, are unique to humans.

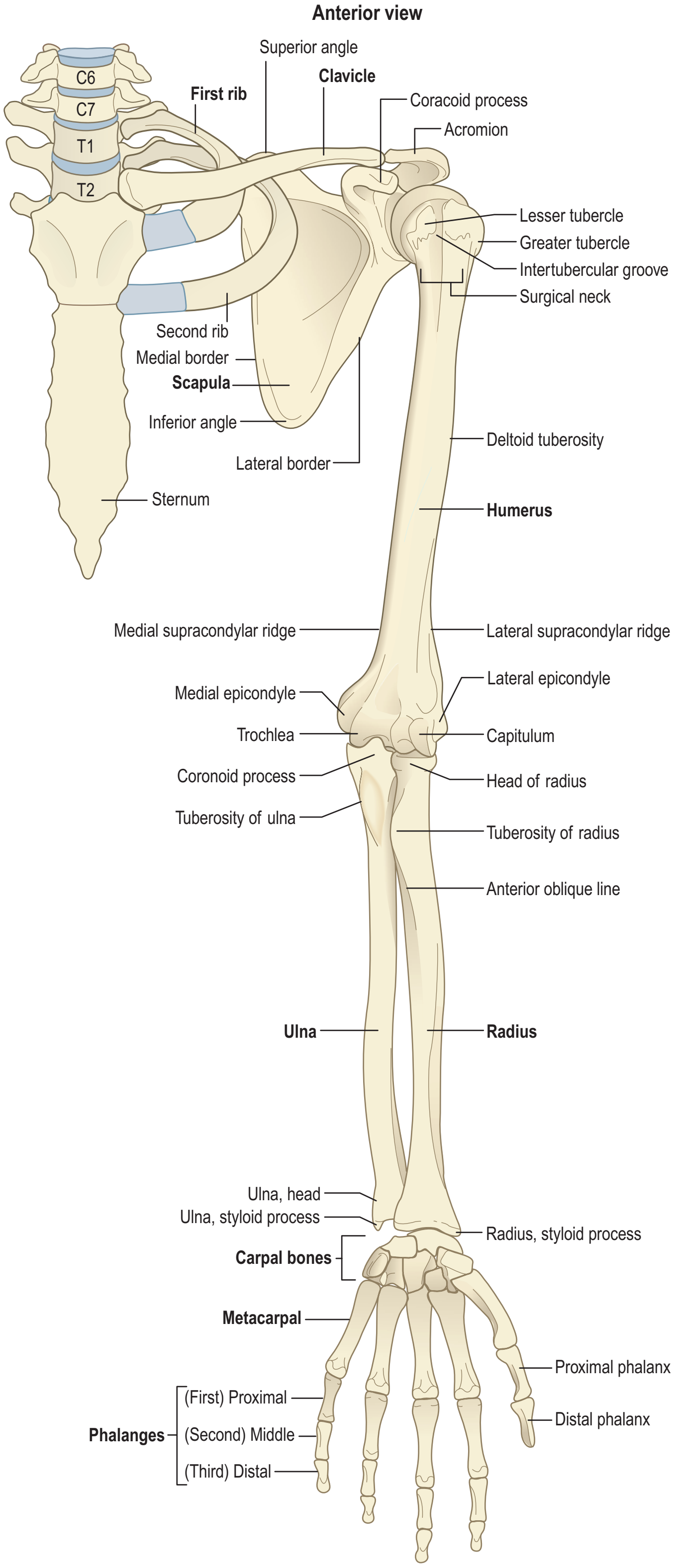
Anterior view
Superior angle
Clavicle
First rib
Coracoid process
Acromion
C6
C7
T1
T2
Lesser tubercle
Greater tubercle
Intertubercular groove
Surgical neck
Second rib
Medial border
Scapula
Inferior angle
Deltoid tuberosity
Lateral border
Sternum
Humerus
Medial supracondylar ridge
Lateral supracondylar ridge
Lateral epicondyle
Medial epicondyle
Trochlea
Capitulum
Coronoid process
Head of radius
Tuberosity of ulna
Tuberosity of radius
Anterior oblique line
Ulna
Radius
Ulna, head
Ulna, styloid process
Radius, styloid process
Carpal bones
Metacarpal
Proximal phalanx
(First) Proximal
Distal phalanx
Phalanges
(Second) Middle
(Third) Distal

Fig. 48.1 The bones of the pectoral girdle and upper limb: anterior view.

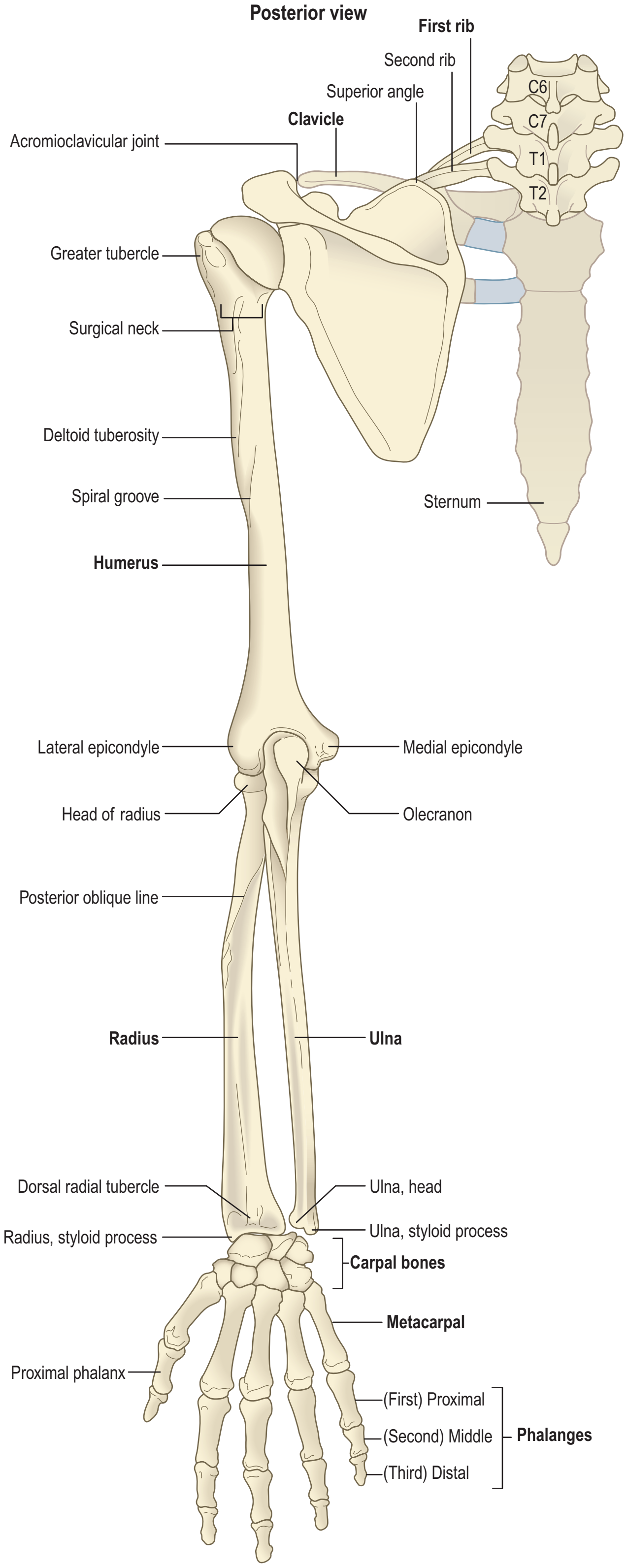

Fig. 48.2 The bones of the pectoral girdle and upper limb: posterior view.

SKIN AND FASCIA

The skin over the front of the neck and posterior triangle is mobile and is sustained by the underlying platysma. Large flaps may be raised safely when platysma is included with the skin. The postaxial skin of the posterior aspect of the neck, shoulder, arm and forearm is thicker and hairy, whereas the glabrous preaxial skin on the anterior surface of the arm and forearm is thinner and more mobile. The situation is reversed in the hand, where the thick palmar skin is firmly secured by a fibrous skeleton to the palmar aponeurosis, whereas the dorsal skin is thinner and more mobile, especially across the joints. The characteristic furrows or creases at the elbow, wrist and interphalangeal joints represent places of anchorage of the deep fascia. The hairy skin of the axilla is especially mobile, permitting the extensive range of movement at the glenohumeral joint; it is rich in sweat glands and their sympathetic nerves. The dense sympathetic innervation in the axilla, the hand and forearm is important in temperature homeostasis. The consequences of scarring from burns or other injury, or badly placed incisions, are severe, and nowhere more so than after a deep burn of the axilla.

The superficial fascia is generally thicker on the dorsal aspect of the neck, shoulder, arm and forearm. Measurement of its thickness in the arm provides a useful measure of obesity. It is an important gliding plane between the skin and the underlying deep fascia. Nerves and vessels are at risk of entrapment or even rupture where they perforate the deep fascia to ramify into the superficial fascia and skin.

The deep fascia, intermuscular septa and the interosseous membrane between the radius and ulna define discrete compartments that enable gliding of segregated structures against one another. The medial and lateral intermuscular septa of the arm and the interosseous membrane also provide wide areas for the attachment of muscles. The various fascial compartments are relevant to the spread of infection and tumour, and are especially important in ischaemia (compartment syndrome).

The prevertebral fascia (see Fig. 35.4A) envelops the phrenic nerve, scalene muscles, cervical ventral rami, cervical sympathetic trunk, and subclavian and vertebral arteries. It projects below the clavicle as the axillary sheath, enveloping the divisions and cords of the brachial plexus with the axillary artery, and continues into the arm as the brachial sheath, surrounding the brachial artery with its venae comitantes, the median nerve and the proximal part of the radial and ulnar nerves. The great muscles of the shoulder and axilla, deltoid, pectoralis major and latissimus dorsi are covered by deep fascia that winds around their deep surfaces to blend with the deep fascia of the arm. This latter is drawn upwards by suspensory condensations of fascia to form the cone-shaped axillary space, an arrangement that is obvious to the reader who traces the anterior surface of pectoralis major with a finger, then follows it round and deep, before thrusting the finger upwards as far at least as the lateral part of the second rib.

The deep fascia of the arm and forearm forms a sleeve that is attached to the medial and lateral intermuscular septa in the arm, to the periosteum of the medial and lateral epicondyles and olecranon at the elbow, and to the periosteum of the ulna and radius. Important condensations, such as the bicipital aponeurosis at the elbow, and the flexor and extensor retinacula at the wrist, are, in turn, subdivided by septa. Discrete compartments within the forearm separate the superficial muscles from the deep. The reader will note the relative mobility of the extensor muscles that traverse the elbow: brachioradialis and the radial extensor muscles of the wrist form the 'mobile wad' of Henry, overlying the deeper compartment containing the posterior interosseous nerve and vessels, supinator, the digital extensors, extensor carpi ulnaris and the long muscles acting on the thumb ray.

Three compartments are found in the anterior aspect of the forearm. The deep flexor compartment contains the anterior interosseous nerve and vessels, flexor pollicis longus, flexor digitorum profundus and pronator quadratus. The superficial compartment contains the radial artery, pronator teres, flexor carpi radialis, palmaris longus and flexor digitorum superficialis. The ulnar nerve and vessels pass in a separate sheath close to the ulna. The anterior deep fascia of the forearm continues into the hand as the palmar aponeurosis, from which a complex arrangement of septa forms the fibrous skeleton of the hand (see Fig. 51.12A). The range of excursion of the main nerves of the upper limb across fixed points such as the first rib, the distal humerus and the distal radius, is some 10–15 mm and is enabled by gliding between the adventitia and the epineurium. More movement occurs within the plane between the epineurium and perineurium, and also within the perineurium itself (Commentary 1.5).

Cutaneous innervation

Bundles of nerves enter the skin deep in the dermis and course towards the skin surface, giving off axons, nearly all unmyelinated, that innervate the associated end organs. The few myelinated axons terminate at hair follicles, Meissner corpuscles and Merkel complexes. The density of innervation of the epidermis is greatest in the proximal segment of the limb and there is little change between the twentieth and eightieth years.

MUSCLES

The sensorimotor cortex controls movements, not individual muscles. Reaching out to catch a flying object, such as a cricket ball, requires the coordination and integrated action of every muscle group in the upper limb, and indeed beyond. This system of complex and refined muscle patterning depends on the integrity of the somatic afferent and efferent pathways in the central nervous system.

The muscles of the upper limb may be grouped according to their origin and the joints on which they act. Muscles arising from the axial skeleton to act on the scapula include trapezius, levator scapulae, the rhomboids and serratus anterior. Muscles arising from the axial skeleton to act on the glenohumeral joint include the sternal head of pectoralis major, pectoralis minor and latissimus dorsi. Muscles passing between the scapula and the proximal humerus control the glenohumeral joint. They include supra- and infraspinatus, subscapularis, teres major and minor, and coracobrachialis. Deltoid and the clavicular head of pectoralis major also belong here, even though they arise in part from the clavicle. The main muscles controlling the elbow include biceps brachii and triceps: the long heads of both muscles traverse the glenohumeral joint to insert on the scapula. The main muscles controlling supination and pronation are biceps brachii and supinator, pronator teres and pronator quadratus. The radiocarpal joint is controlled by extensors carpi radialis longus and brevis, extensor carpi ulnaris, flexors carpi ulnaris and radialis, and palmaris longus. The muscles acting on the thumb ray include the powerful flexor pollicis longus, the much weaker abductor pollicis longus, and extensors pollicis longus and brevis. These last three are essential for thumb function. The unopposed action of flexor pollicis longus leads to the virtually useless thumb in palm posture. The extension and flexion of the metacarpophalangeal and interphalangeal joints of the fingers rest on coordinated activity in extensor digitorum, flexors digitorum superficialis and profundus, and the interosseous and lumbrical muscles. Extensor digitorum alone extends the metacarpophalangeal joints; the long flexors alone flex the interphalangeal joints. The imbalance caused by paralysis of the small muscles leads to 'clawing' deformity (see Fig. 48.27). The small muscles of the hand may be considered as those controlling the thumb ray and web space; adductor pollicis lies deep to the first dorsal interosseous; abductor and flexor pollicis brevis and opponens pollicis are superficial and form the ball of the thumb. The interosseous muscles acting with the lumbricals flex, abduct and adduct the metacarpophalangeal joints and, in conjunction with the long flexor and extensor muscles, enable full extension of the proximal interphalangeal joints. Abductor and opponens digiti minimi and flexor digiti minimi brevis form the hypothenar eminence and act on the little finger.

Many muscles act on more than one joint, for example, the long heads of biceps and triceps flex and extend, respectively the glenohumeral joint as well as the elbow. In addition, biceps brachii is a powerful supinator of the forearm. Extensor carpi radialis longus not only extends the wrist, but also is a powerful abductor of that joint and a flexor of the elbow in pronation. Flexor carpi ulnaris is the most powerful muscle in the forearm; it contributes to elbow flexion, flexes and adducts the wrist, and is active in all sustained movements of the wrist.

Certain muscles are functionally segregated, e.g. the anterior part of deltoid is a powerful flexor of the glenohumeral joint, whereas the posterior part is the most powerful extensor of that joint.

VASCULAR SUPPLY AND LYMPHATIC DRAINAGE

The detailed regional descriptions of these systems in the upper limb are found in Chapters 49–51.

Arteries

The axial vessel is the subclavian artery, which arises from the brachiocephalic trunk on the right and directly from the arch of the aorta on the left (Fig. 48.3). The artery is described in three parts that are successively anteromedial, deep and lateral to scalenus anterior. The second and third parts are in close relation to the seventh and eighth cervical and first thoracic ventral rami, and to the middle and lower trunks of the brachial plexus. The subclavian artery becomes the axillary artery at the outer border of the first rib. The axillary artery is closely related to the divisions of the brachial plexus deep to the clavicle, and to the cords below it. It continues deep to pectoralis minor and becomes the brachial artery at the inferior margin of teres major.

The brachial artery is closely related to the median nerve; both move from the medial side of the arm to the anterior aspect of the elbow, lying medial to the tendon of biceps brachii and deep to the bicipital aponeurosis. The artery divides into the radial and ulnar arteries just distal to the elbow. The ulnar artery is consistently the larger of the two. The common interosseous artery arises close to its origin and subsequently divides into the anterior and posterior interosseous arteries. The anterior interosseous artery, accompanied by the anterior interosseous nerve, lies on the interosseous membrane in the deepest part of the deep flexor compartment. The posterior interosseous artery is separated from the membrane by the deep extensor muscles. The radial and ulnar arteries remain in the flexor compartment of the forearm, the ulnar artery moving towards the ulnar nerve in the proximal quarter of the forearm; it is usually the dominant vessel for the hand. At the wrist, the radial artery passes dorsally and crosses the scaphoid and trapezium.

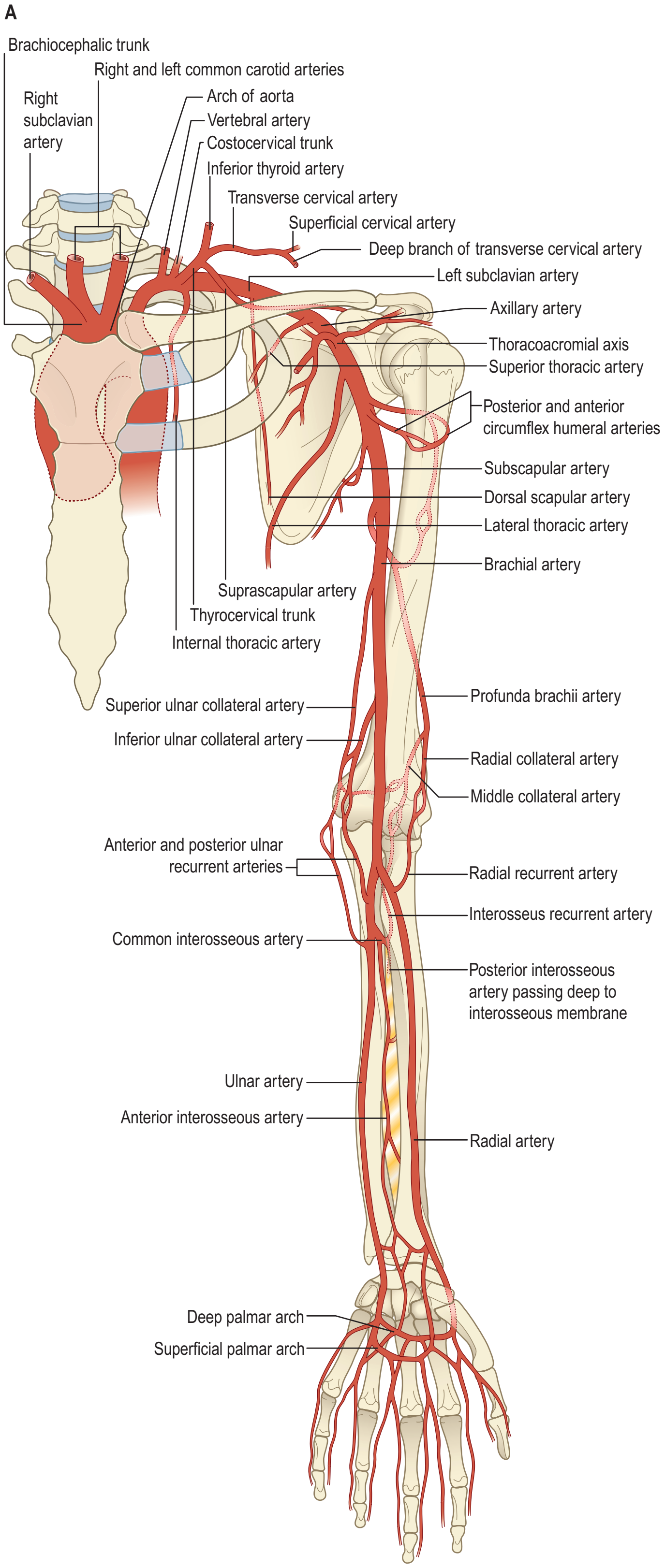
A
Brachiocephalic trunk
Right and left common carotid arteries
Right subclavian artery
Arch of aorta
Vertebral artery
Costocervical trunk
Inferior thyroid artery
Transverse cervical artery
Superficial cervical artery
Deep branch of transverse cervical artery
Left subclavian artery
Axillary artery
Thoracoacromial axis
Superior thoracic artery
Posterior and anterior circumflex humeral arteries
Subscapular artery
Dorsal scapular artery
Lateral thoracic artery
Brachial artery
Suprascapular artery
Thyrocervical trunk
Internal thoracic artery
Superior ulnar collateral artery
Profunda brachii artery
Inferior ulnar collateral artery
Radial collateral artery
Middle collateral artery
Anterior and posterior ulnar recurrent arteries
Radial recurrent artery
Interosseus recurrent artery
Common interosseous artery
Posterior interosseous artery passing deep to interosseous membrane
Ulnar artery
Anterior interosseous artery
Radial artery
Deep palmar arch
Superficial palmar arch

Fig. 48.3 **A**, Arteries of the upper limb. (B–E, *continued online*)

Important branches from the main axial vessels form extensive anastomoses that provide a collateral circulation. For example, the collateral circulation formed by branches of the thyrocervical trunk with the circumflex humeral and subscapular arteries permits survival of the limb after occlusion of either the third part of the subclavian artery, or of the axillary artery deep to the clavicle and pectoralis minor. The

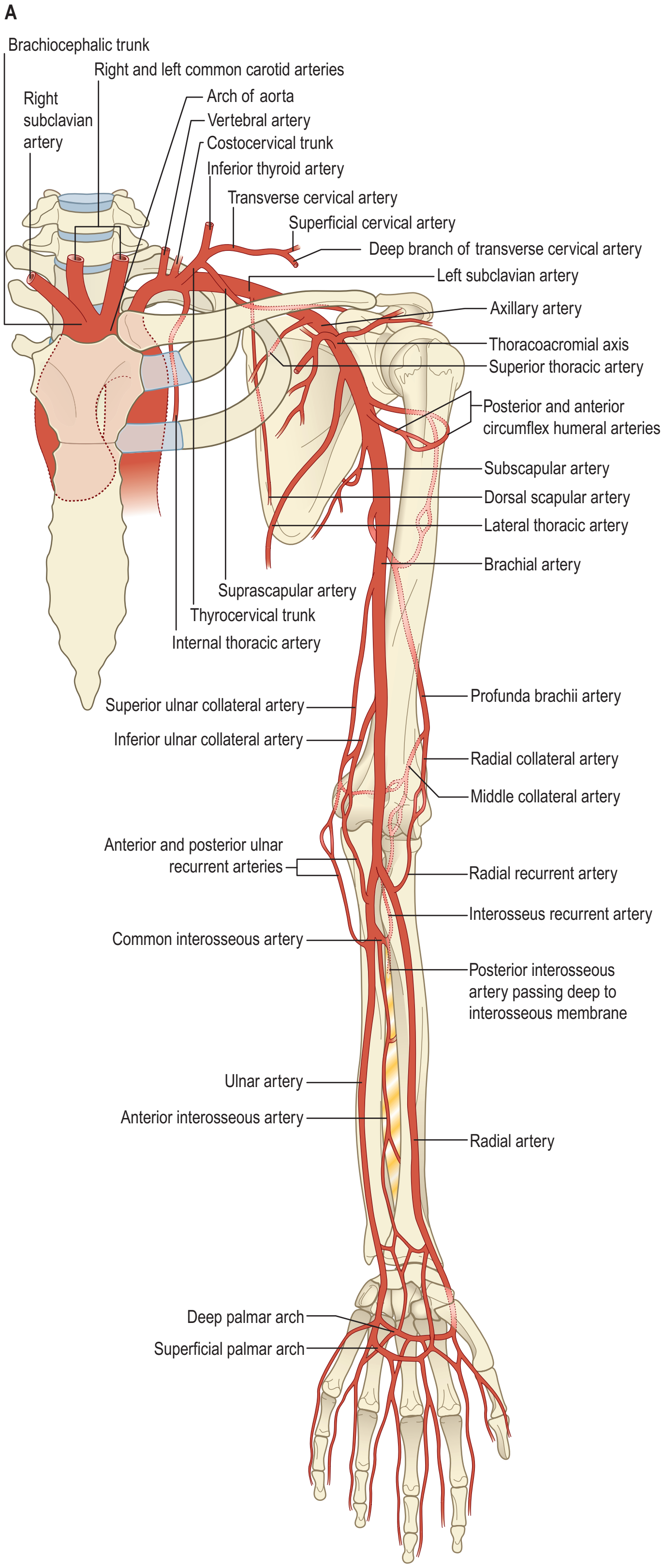
A
Brachiocephalic trunk
Right and left common carotid arteries
Right subclavian artery
Arch of aorta
Vertebral artery
Costocervical trunk
Inferior thyroid artery
Transverse cervical artery
Superficial cervical artery
Deep branch of transverse cervical artery
Left subclavian artery
Axillary artery
Thoracoacromial axis
Superior thoracic artery
Posterior and anterior circumflex humeral arteries
Subscapular artery
Dorsal scapular artery
Lateral thoracic artery
Brachial artery
Suprascapular artery
Thyrocervical trunk
Internal thoracic artery
Superior ulnar collateral artery
Inferior ulnar collateral artery
Profunda brachii artery
Radial collateral artery
Middle collateral artery
Anterior and posterior ulnar recurrent arteries
Radial recurrent artery
Interosseus recurrent artery
Common interosseous artery
Posterior interosseous artery passing deep to interosseous membrane
Ulnar artery
Anterior interosseous artery
Radial artery
Deep palmar arch
Superficial palmar arch

Fig. 48.3 **A**, Arteries of the upper limb.

Continued

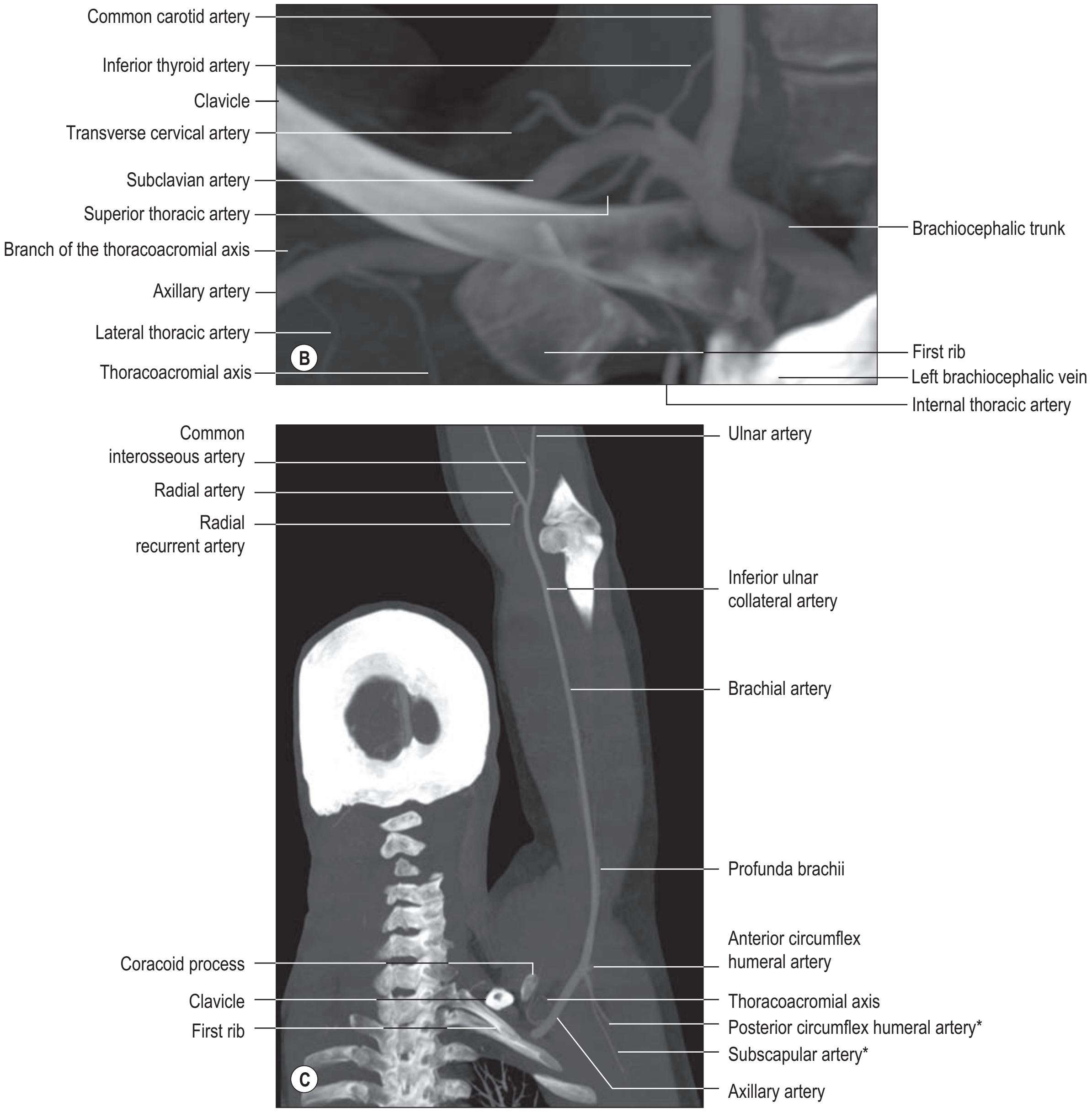
Common carotid artery
Inferior thyroid artery
Clavicle
Transverse cervical artery
Subclavian artery
Superior thoracic artery
Branch of the thoracoacromial axis
Axillary artery
Lateral thoracic artery
Thoracoacromial axis
B
Brachiocephalic trunk
First rib
Left brachiocephalic vein
Internal thoracic artery
Common interosseous artery
Radial artery
Radial recurrent artery
Ulnar artery
Inferior ulnar collateral artery
Brachial artery
Profunda brachii
Coracoid process
Clavicle
First rib
C
Anterior circumflex humeral artery
Thoracoacromial axis
Posterior circumflex humeral artery*
Subscapular artery*
Axillary artery

Fig. 48.3, cont'd B, Coronal oblique maximum intensity projection view of the right subclavian and axillary arteries and their branches from a CT carotid angiogram. Contrast medium was injected via the left arm and can be seen in the brachiocephalic vein. **C**, Coronal oblique maximum intensity projection from a CT angiogram of the left arm from the axillary artery to the arteries in the forearm. The whole arm is abducted above the head to reduce the effect of radiation beam attenuation that would occur if left by the side of the body, hence reducing noise and increasing image quality. *The posterior circumflex humeral and subscapular arteries arise from a common trunk.

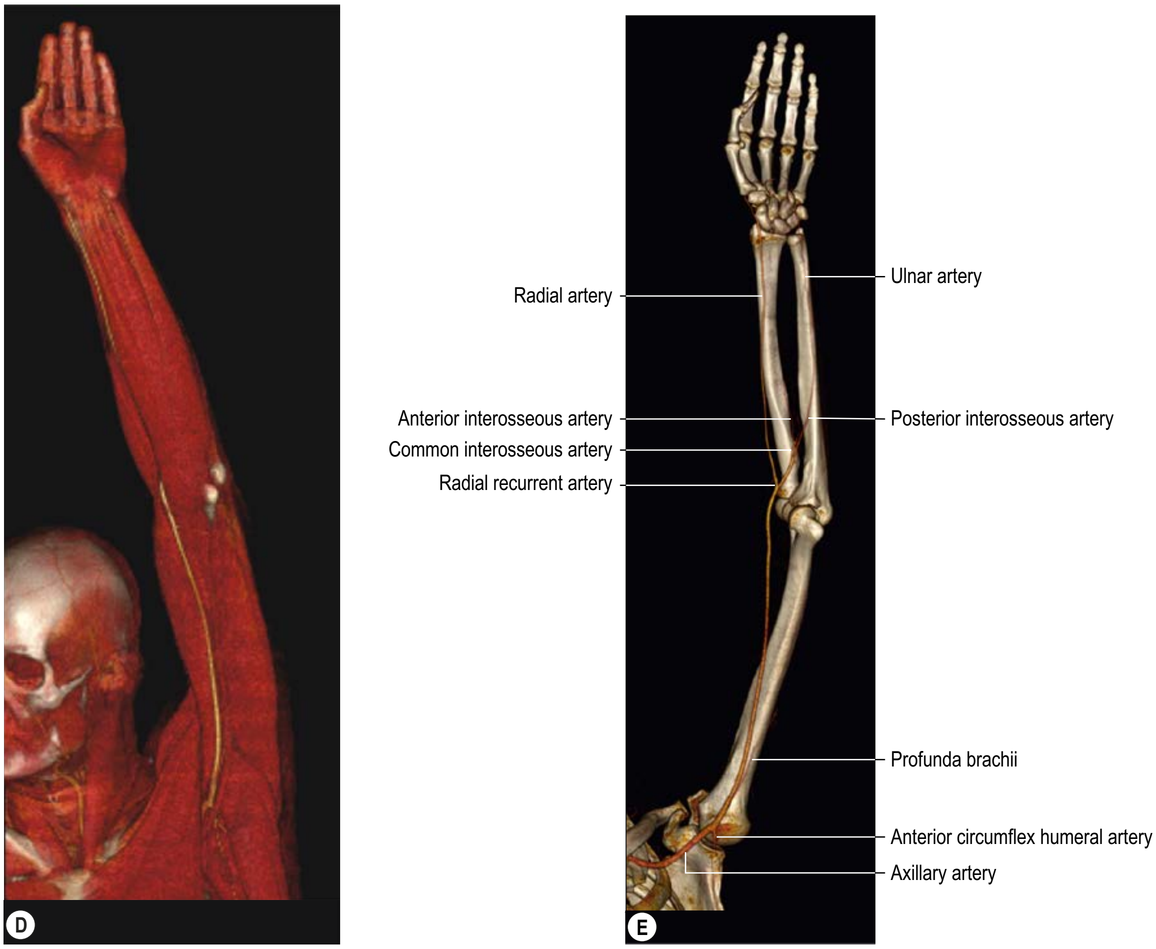
D
E
Radial artery
Ulnar artery
Anterior interosseous artery
Posterior interosseous artery
Common interosseous artery
Radial recurrent artery
Profunda brachii
Anterior circumflex humeral artery
Axillary artery

Fig. 48.3, cont'd D, **E**, A volume rendered CT angiogram of the left arm acquired with the arm abducted and prone.

profunda brachii is an important channel for the posterior muscles of the arm. It accompanies the radial nerve and contributes to the collateral circulation about the elbow with the ulnar collateral and recurrent vessels and the radial collateral and recurrent vessels. The anterior interosseous artery is effectively an end artery. A series of anastomoses between the radial and ulnar arteries, such as the transversely orientated palmar and dorsal arches and the superficial and deep palmar arches, maintain a rich blood supply to the wrist and hand. There are extensive interconnections between these arches and between the dorsal and palmar phalangeal arteries.

Pulses

The pulsation of the subclavian artery is palpable at the lateral margin of sternocleidomastoid and is easily blocked by digital pressure against the first rib. This simple maoeuvre has saved lives and limbs, and should be widely known and rehearsed because it is the best method for emergency control of bleeding from the deeply placed axillary artery. The method was used successfully for high amputation or disarticulation of the shoulder in the Napoleonic wars.

The brachial artery is palpable in the arm in the groove, or valley, between biceps brachii anteriorly and the medial head of triceps brachii posteriorly; it can be traced down to the anterior aspect of the elbow, where it moves towards the midline. The radial and ulnar pulses are palpable at the wrist, where the vessels emerge from under the cover of overlying muscles.

Veins

The upper limb is drained by superficial and deep groups of vessels.

The superficial group starts as an irregular dorsal arch on the back of the hand. The cephalic vein begins at the radial extremity of the arch, and ascends along the lateral aspect of the arm within the superficial fascia to enter the deltopectoral groove. It pierces the deep fascia above the superior margin of pectoralis minor and enters the axillary vein near the tip of the coracoid (Fig. 48.4). The basilic vein drains the ulnar end of the arch, passes along the medial aspect of the forearm, pierces the deep fascia at the elbow, and joins the venae comitantes of the brachial artery to form the axillary vein. The prominent median cubital vein links the cephalic and basilic veins on the flexor aspect of the elbow. It receives a number of tributaries from the flexor aspect of the forearm and gives off the deep median vein, which pierces the fascial roof of the antecubital fossa to join the venae comitantes of the brachial artery.

The deep group of veins drains the tissues beneath the deep fascia of the upper limb and is connected to the superficial system by perforating veins. The deep veins accompany the arteries, usually as venae comitantes, ultimately becoming the axillary, and subsequently the subclavian, vein.

The subclavian vein is the central continuation of the axillary vein. It starts at the outer border of the first rib, which it crosses. Initially deep to the clavicular head of pectoralis major and then to subclavius, which is a buffer between it and the overlying medial portion of the clavicle, the vein then runs deep to the insertion of sternocleidomastoid. Sometimes, only the superior margins of the vein rise above the medial end of the clavicle; sometimes, the entire vein does so. The phrenic nerve and the inferior part of scalenus anterior lie posteriorly. The subclavian vein joins the internal jugular vein to form the brachiocephalic vein at the medial border of scalenus anterior, behind the sternoclavicular joint (see Fig. 35.14). A pair of valves usually lies within 2 cm of this junction. The subclavian vein receives, as tributaries, the external jugular, dorsal scapular and, sometimes, the anterior jugular veins. The trifurcation of subclavian, external and internal jugular veins is demonstrable by a forced expiration (Valsalva) manœuvre, when the distended veins rise up above the sternoclavicular joint, filling the fossa above the jugular notch of the sternum (**Video 48.1**). Main lymphatic vessels join the subclavian veins at, or very close to, this junction with the internal jugular vein. The left subclavian vein receives the thoracic duct; the right receives the right lymphatic duct (see Fig. 35.16). There is a risk of air embolism after wounding of the subclavian, external or internal jugular veins.

Cutaneous blood supply

The blood supply of the skin of the upper limb is generally abundant (Fig. 48.5) and rather more robust than that in the lower limb. Proximally based flaps of skin caused by 'degloving' injury are more likely to survive; even a distally based flap of palmar skin may do so. The skin of the lower leg is notoriously sensitive to the effects of fracture because of rupture of the vessels perforating the deep fascia; this problem is less severe in the upper limb. Three interconnected pathways may be recognized in the

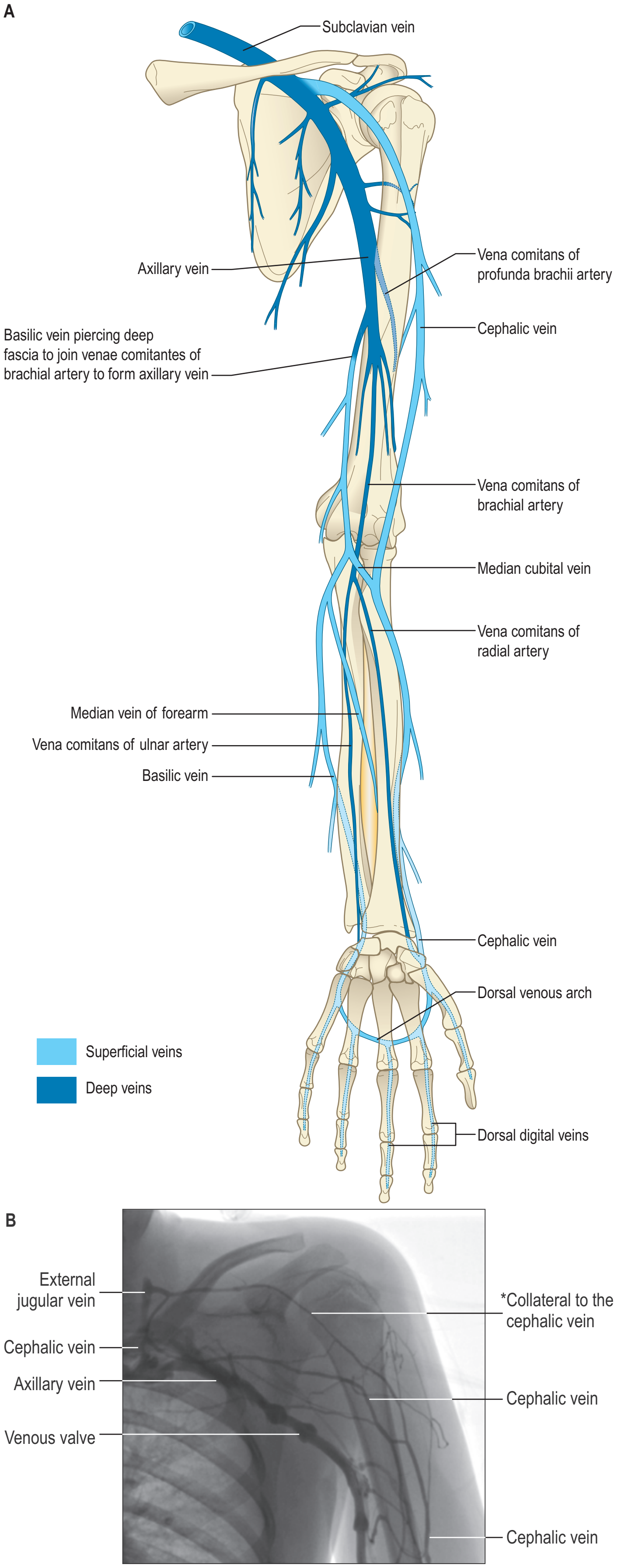
A
Subclavian vein
Axillary vein
Vena comitans of profunda brachii artery
Cephalic vein
Basilic vein piercing deep fascia to join venae comitantes of brachial artery to form axillary vein
Vena comitans of brachial artery
Median cubital vein
Vena comitans of radial artery
Median vein of forearm
Vena comitans of ulnar artery
Basilic vein
Cephalic vein
Dorsal venous arch
Superficial veins
Deep veins
Dorsal digital veins
B
External jugular vein
Cephalic vein
Axillary vein
Venous valve
*Collateral to the cephalic vein
Cephalic vein
Cephalic vein

Fig. 48.4 **A**, The veins of the upper limb. **B**, Venogram of the left arm. There are multiple cephalic vein collaterals, one of which drains into the external jugular vein (*). (C, D, E, *continued online*)

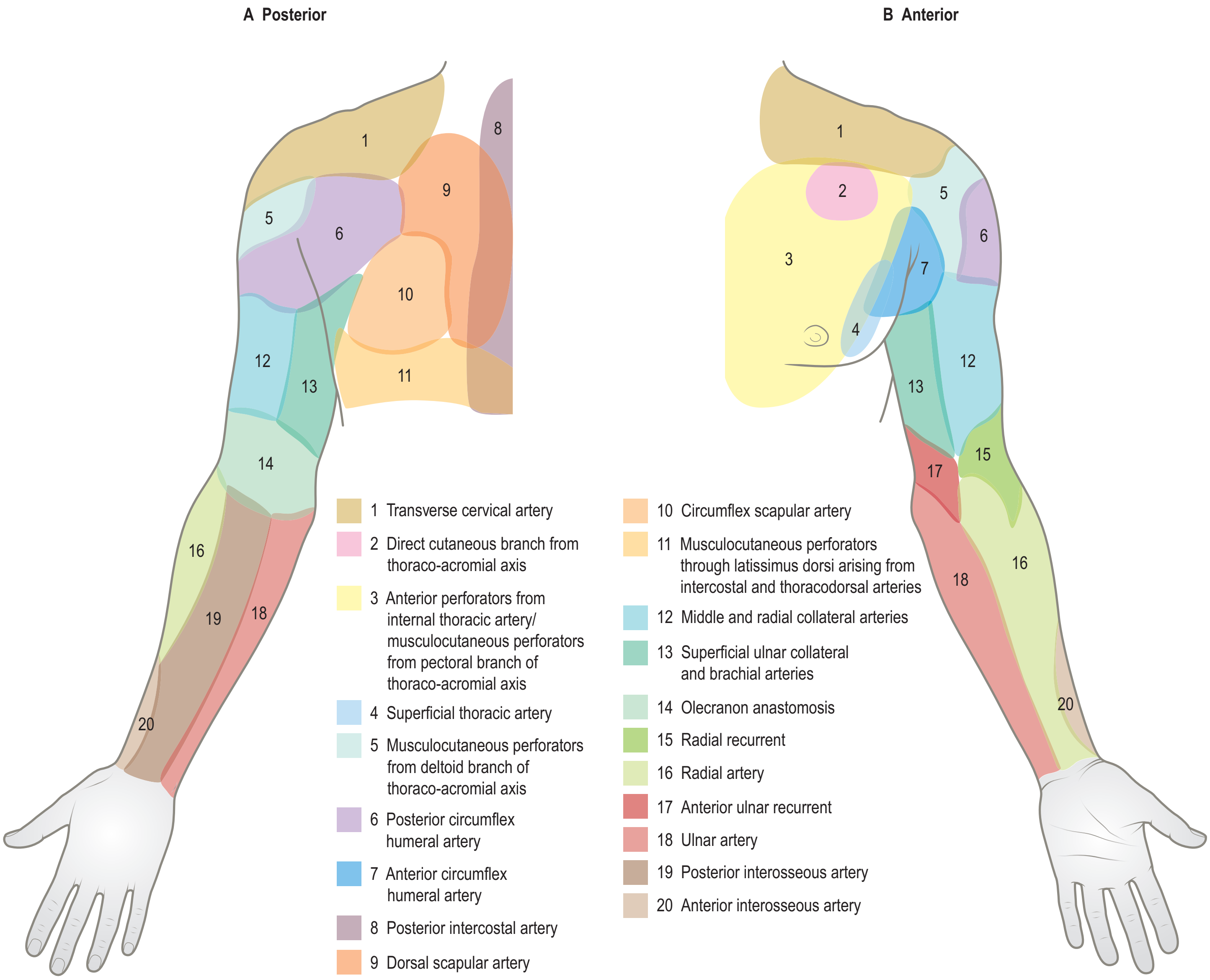
A Posterior
B Anterior
1 Transverse cervical artery
2 Direct cutaneous branch from thoraco-acromial axis
3 Anterior perforators from internal thoracic artery/ musculocutaneous perforators from pectoral branch of thoraco-acromial axis
4 Superficial thoracic artery
5 Musculocutaneous perforators from deltoid branch of thoraco-acromial axis
6 Posterior circumflex humeral artery
7 Anterior circumflex humeral artery
8 Posterior intercostal artery
9 Dorsal scapular artery
10 Circumflex scapular artery
11 Musculocutaneous perforators through latissimus dorsi arising from intercostal and thoracodorsal arteries
12 Middle and radial collateral arteries
13 Superficial ulnar collateral and brachial arteries
14 Olecranon anastomosis
15 Radial recurrent
16 Radial artery
17 Anterior ulnar recurrent
18 Ulnar artery
19 Posterior interosseous artery
20 Anterior interosseous artery

Fig. 48.5 The anatomical territories served by the cutaneous blood supply to the upper limb. (With permission from Cormack GC, Lamberty BGH 1994 The Arterial Anatomy of Skin Flaps, 2nd ed. Edinburgh: Churchill Livingstone.)

upper limb, namely: muscle perforators, deep fasciocutaneous vessels and the direct cutaneous supply.

Muscle perforators

Available with the *Gray's Anatomy* e-book

Fasciocutaneous system

Available with the *Gray's Anatomy* e-book

Direct cutaneous supply

Available with the *Gray's Anatomy* e-book

Lymphatic drainage

Superficial tissues

The subcutaneous tissues of the limbs can be divided into five layers: skin (layer 1); subcutaneous fat (2); superficial fascia (3); loose areolar tissue (4) and deep fascia (5). Layer 2 can be subdivided into a superficial (2a) and deep layer (2c) by a thin transparent horizontal septum (2b) (Tourani et al 2014). The main superficial veins and the superficial nerves are found in layer 4 and the lymphatic collectors in layer 2c and layer 4.

Superficial lymphatic vessels begin in cutaneous plexuses. In the hand, the palmar plexus is denser than the dorsal plexus. Digital plexuses drain along the digital borders to their webs, where they join the distal palmar vessels, which pass back to the dorsal aspect of the hand. The proximal palm drains towards the carpus, medially by vessels that run along its ulnar border, and laterally to join vessels draining the thumb. Several vessels from the central palmar plexus form a trunk that winds round the second metacarpal bone to join the dorsal vessels that drain the index finger and thumb.

In the forearm and arm, superficial vessels run with the superficial veins. Collecting vessels from the hand pass into the forearm on all carpal aspects. Dorsal vessels, after running proximally in parallel, curve successively round the borders of the limb to join the ventral vessels. Anterior carpal vessels run through the forearm parallel with the median vein of the forearm to the cubital region, then follow the medial border of biceps brachii before piercing the deep fascia at the anterior axillary fold to end in the lateral axillary lymph nodes.

Lymph vessels that lie laterally in the forearm receive vessels that curve round the lateral border from the dorsal aspect of the limb. They follow the cephalic vein to the level of the tendon of deltoid, where most incline medially to reach the lateral axillary nodes; a few continue with the vein and drain into the infraclavicular nodes. Vessels lying medially in the forearm are joined by vessels that curve round the medial border of the limb and follow the basilic vein. Proximal to the elbow, some end in supratrochlear lymph nodes whose efferents, together with the medial vessels that have bypassed them, pierce the deep fascia with the basilic vein and end in the lateral axillary nodes or deep lymphatic vessels.

Collecting vessels from the deltoid region pass round the anterior and posterior axillary folds to end in the axillary nodes. The scapular skin drains either to subscapular axillary nodes or by channels that follow the transverse cervical vessels to the inferior deep cervical nodes.

Vessels pass from the deep axial vessels through muscle, perforate the deep fascia and supply the overlying skin. The latissimus dorsi myocutaneous flap based on the thoracodorsal vessels was an important development in plastic and reconstructive surgery, not only for the replacement of lost skin or reconstruction of the breast, but also in the evolution of the free-functioning muscle transfer.

The fasciocutaneous system rests on branches that arise from deep vessels and pass along the intermuscular septa to perforate the deep fascia and ramify over its surface: extensive areas of skin are supplied in this way. The development of fasciocutaneous flaps, either as pedicle flaps or free grafts, has been a revolutionary advance in the treatment of severe wounds. Not only is it possible to replace large areas of lost skin, but also to improve the tissue bed that supports the main nerves thereby enhancing regeneration and relieving neuropathic pain.

The direct cutaneous supply is exemplified in the palmar skin, where branches from the underlying digital vessels pass directly into the overlying skin.

Deeper tissues

Deep lymph vessels follow the main neurovascular bundles (radial, ulnar, interosseous and brachial) to the lateral axillary nodes. They are less numerous than the superficial vessels and communicate with them at intervals. A few lymph nodes occur along the vessels. Scapular muscles drain mainly to the subscapular axillary nodes, and pectoral muscles drain mainly to the pectoral, central and apical nodes.

Efferent vessels from the deep cervical nodes form the jugular trunk. The right jugular trunk drains the right upper limb, the right half of the thorax and the right head and neck, and enters the right thoracic duct or directly enters the right subclavian vein close to its junction with the internal jugular. The left jugular trunk usually enters the thoracic duct, but it may directly enter either the subclavian or internal jugular vein (see Figs 35.16, 49.45).

ACUTE ISCHAEMIA AND COMPARTMENT SYNDROMES IN THE UPPER LIMB

Available with the *Gray's Anatomy* e-book

INNERVATION

The accessory nerve, dorsal scapular nerve, long thoracic nerve (nerve to serratus anterior), suprascapular nerve and nerve to subclavius all innervate muscles that act on the scapulothoracic 'joint' and will therefore be summarized here.

Accessory nerve

The integrity of the accessory nerve is fundamental to thoracoscapular function and essential for scapulohumeral rhythm (Camp and Birch 2011). The intraspinal and intracranial course of the accessory nerve and of the segment of the nerve that lies in the anterior triangle of the neck are described in Chapter 35.

The accessory nerve passes either deep to or through sternocleidomastoid, to enter the posterior triangle in a consistent and important relation to the ascending nerves of the cervical plexus. The great auricular nerve is the key to exposure of the accessory nerve, which emerges, usually as one trunk, 5–10 mm cephalad to the point where the great auricular nerve winds around sternocleidomastoid, and moves from a plane posterior to the muscle to one that is anterior. The general relations of the posterior triangle vary with individual physique, but this relation between the two nerves is reliably consistent. The nerve now runs across the fatty areolar tissue at the apex of the posterior triangle, in close relation to the superior superficial cervical lymph nodes deep to platysma. It is separated from the underlying levator scapulae by this areolar tissue, and then, more deeply, by the prevertebral fascia. One slender branch passes to the upper fibres of trapezius either deep to sternocleidomastoid or just beyond it. The nerve pierces the fascia covering the deep surface of trapezius close to the anterior border of the muscle and then runs caudally about 2 cm from that border. The nerve passes down in a characteristic sinuous fashion, accompanied by slender vessels to the deep, inner face of trapezius. A branch from the cervical plexus (third and fourth cervical ventral rami) joins the nerve just above the clavicle. Intraoperative stimulation of this branch rarely evokes a muscular response; it probably conveys afferent fibres from the middle and lower parts of trapezius. The nerve now turns medially, continuing in parallel to the spine of the scapula about 4 cm above it. At the medial end of the spine, the nerve turns caudally again, passing down parallel to the medial border of the scapula. It divides into terminal muscular branches about 7 cm distal to the scapular spine. Although sternocleidomastoid, and the middle and the lower portions of trapezius, may be partially supplied by branches from the cervical plexus, the upper part of trapezius is innervated solely by the accessory nerve.

Dorsal scapular nerve

The dorsal scapular nerve arises above the clavicle from the proximal segment of the the fifth cervical ventral ramus. It passes posteriorly, piercing scalenus medius, to run down in the plane between levator scapulae and serratus posterior superior and the posterior scalene muscles. It continues along the anterior border of the rhomboid muscles about 1.5 cm medial to the vertebral border of the scapula and is closely related to the dorsal scapular artery. The dorsal scapular nerve innervates the rhomboid muscles and, together with branches from the third and fourth cervical ventral rami, it supplies levator scapulae.

Long thoracic nerve (nerve to serratus anterior)

The long thoracic nerve is formed by branches that arise above the clavicle from the proximal segments of the fifth, sixth and seventh cervical ventral rami. It innervates serratus anterior, a muscle that is essential for the function of the thoracoscapular joint. The muscular branches from the rami join deep to scalenus medius, and the trunk passes down posterolateral to the muscle, on the floor of the posterior triangle deep to the suprascapular nerve. The branches from the fifth and sixth cervical ventral rami are the largest. The nerve follows a sinuous course deep to the investing fascia covering the anterior faces of the digitations of serratus anterior. It is accompanied here by a branch of the thoracodorsal artery, and inclines posterolaterally towards the mid-axillary line.

Suprascapular nerve

The suprascapular nerve, from the fifth and sixth cervical ventral rami, is usually the first branch of the upper trunk, but frequently arises directly from the fifth cervical ventral ramus. It gives motor branches to supraspinatus and infraspinatus and articular branches to the glenohumeral and acromioclavicular joints

Nerve to subclavius

The slender nerve to subclavius, from the fifth and sixth cervical ventral rami, springs from the upper trunk and passes anteriorly. It descends anterior to the plexus and the subclavian artery and passes above the subclavian vein to supply subclavius.

Brachial plexus

The muscles, joints and skin of the upper limb are innervated by the fifth, sixth, seventh and eighth cervical ventral rami and nearly all of the first thoracic ventral ramus, collectively forming the brachial plexus (Figs 48.6–48.7). A branch from the fourth to the fifth cervical ventral ramus which contributes to the innervation of the glenohumeral and elbow flexor muscles is seen occasionally at operation. A muscular contribution from the second thoracic ventral ramus is rare. The rami enter the posterior triangle of the neck between scalenus anterior and medius. Rami from the seventh and eight cervical ventral rami are the largest (C8 contains about 30,000 myelinated axons) and those from the fifth cervical and the first thoracic ventral rami are the smallest (between 15,000 and 20,000 myelinated axons). An adult brachial plexus contains between 120,000 and 150,000 myelinated axons, of which 25% innervate the shoulder girdle and glenohumeral joint. The proportion of motor fibres is greatest in the fifth and eighth cervical

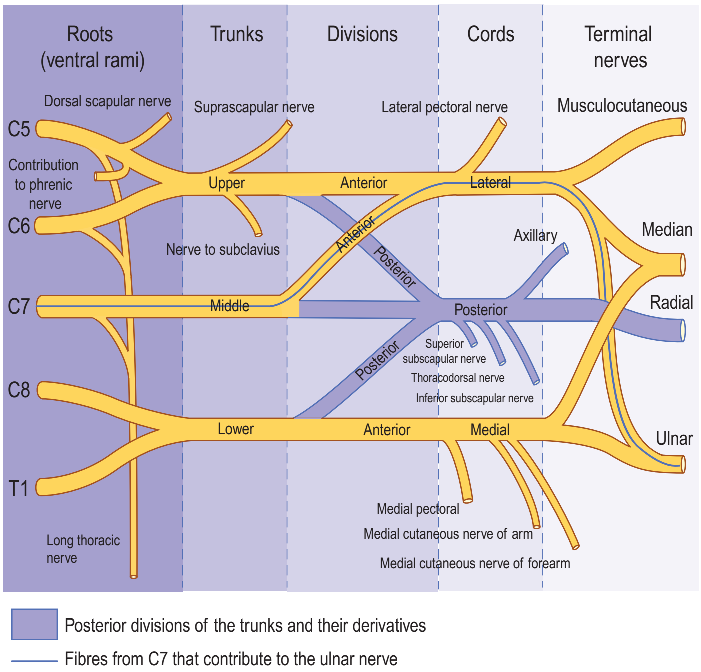

Fig. 48.6 A schematic plan of the brachial plexus. (Adapted with permission from Drake RL, Vogl AW, Mitchell A (eds) Gray's Anatomy for Students, 2nd ed. Elsevier, Churchill Livingstone. Copyright 2010.)

Common examples of the classical compartment syndrome in the upper limb occur in the flexor and extensor compartments of the forearm. Although nerve conduction is lost before muscle contractility, ischaemia is more likely to produce infarction of muscle than necrosis of nerve. Decompression of a nerve embedded within muscle that has become fibrosed by ischaemia usually leads to relief of pain and considerable improvement in sensation and sympathetic function, even when delayed for some months.

Anoxia occurs either because of cessation of flow through a main axial artery or as a result of increasing pressure within an osseofascial compartment caused by bleeding, infusion of fluid or sepsis. It destroys the integrity of the cell membrane and capillary endothelium, which means that the homeostatic balance between the intravascular, extracellular and intracellular spaces is lost. Tissue death is imminent.

The increased permeability of the vascular endothelium leads to an increase in intracompartmental pressure by exudation, which collapses the low-pressure lymphatic and venous systems. The final event is the closure or obstruction of perfusing arterioles to muscles and the extrinsic supply to nerves, when tissue or extravascular pressure exceeds the cortical closing pressure of those vessels. The vicious circle is complete. The fluid entering the compartment cannot get out and continues to leak into the compartment until the pressure is so high that inflow is blocked. Increasing intracompartmental pressure occurs when the collateral circulation is inadequate after occlusion of the main artery or after restoration of flow through that vessel, unless the compartments have been decompressed adequately by fasciotomy. The vascular anastomoses about the joints of the upper limb provide a richer collateral circulation than those found in the lower limb. In a study of nearly 2500 World War II battle casualties, at a time when ligation of damaged arteries was common, ligation of the popliteal artery led to amputation in 346 of 502 limbs. By contrast, the incidence of amputation after ligation was about one-quarter for the subclavian artery, one-third for the axillary artery and more than one-half when the brachial artery was ligated proximal to the profunda brachii artery. These figures are certainly lower in the less contaminated injuries of civilian life, but some degree of post-ischaemic fibrosis is almost inevitable after failure to repair these vessels. The principles of arterial repair include urgent restoration of flow by repair of the artery and restoration of tissue perfusion by decompression. Temporary intraluminal shunts are invaluable, as they buy time and permit adequate stabilization of the skeleton. Application of these principles in current conflicts ensures a remarkably high rate of limb survival and a remarkably low incidence of post-ischaemic fibrosis.

Flow through the brachial artery in adults and in children has been measured by high-resolution ultrasonography. Flow was calculated by the Laplace equation: BF (blood flow) = $[\pi \times (D/2)]^2 \times$ FV (flow velocity). The mean diameter of the brachial artery in children aged between 4 and 5 years is 2.7 mm, which provides a resting flow of about 200 ml per minute. The significance of the diameter of the vessel is emphasized by Poiseuille's law. This is the physical law describing the volume of flow (Φ) of an incompressible uniform viscous liquid, where R is the internal radius of the tube, P the pressure difference between the two ends, η the dynamic fluid viscosity and L the total length of the tube.

$$\Phi = \frac{\pi R^4}{8\eta}\,\frac{[\Delta P]}{L}$$

The diameter of the superior ulnar collateral artery at the elbow in a 5-year-old child is, at most, 1 mm. This calibre provides flow of about 20 ml per minute, assuming that the pressure gradient is the same as that in the brachial artery itself. These facts must be borne in mind by any clinician inclined to the view that cessation of flow through the brachial artery is a matter of little consequence. The collateral channels take hours or days to develop and may be compromised by the original injury or during operation. The radial and ulnar nerves are often entrapped or compressed in fracture dislocations at the elbow, blocking flow through the ulnar and radial collateral systems that accompany these nerves.

The presence of peripheral pulses does not indicate adequate perfusion of the deep intracompartmental tissues, neither does the perfusion of skin or the nail bed when pulses are absent. The cardinal symptom of ischaemic anoxia is severe pain and the cardinal sign is loss of nerve conduction. This can be confirmed during exposure of limb nerves with an inflated tourniquet cuff in position proximally. For about 20 minutes, stimulation of the nerve evokes a brisk muscular response as a consequence of transmission through the neuromuscular junction. This response diminishes and disappears after about 30 minutes, although conduction within the nerve itself can still be detected for up to another 20 minutes. However, direct stimulation of the muscle provokes a twitch that can be elicited for up to several hours. Indeed, it is the loss of this direct response that signifies impending death of the muscle, and with it, death of the limb. The earliest nerve fibres to suffer are the largest, i.e. those conveying vibration and proprioception sense.

Ischaemia and acute compression within neurovascular fascial compartments

Sleeves of fascia surround main nerves and main vessels in some regions, an arrangement that predisposes nerves to injury from ischaemia or compression, or both. The seventh and eighth cervical and first thoracic ventral rami are enclosed in semi-rigid space after they enter the posterior triangle of the neck. This is bounded, posteriorly, by the dorsal part of the first rib, the transverse processes of the cervical vertebrae and by the fascia of levator scapulae. The nerves are embraced by scalenus anterior and scalenus medius, both of which are invested in an unyielding fascia. This is one envelope of the prevertebral fascia that also serves to bind the phrenic nerve down to the anterior face of scalenus anterior. The prevertebral fascia is particularly well developed in front of the vertebral column and also at the base of the posterior triangle, where it envelops the seventh and eighth cervical and first thoracic ventral rami, the phrenic nerve, the cervical sympathetic chain, and the subclavian and vertebral arteries. Infusion of relatively large volumes of fluid, from 10 to 20 ml, deep to the prevertebral fascia for the purpose of inducing regional block may cause tamponade of the radicular vessels that enter the spinal canal and contribute to the anterior spinal artery. Wilbourn (2005) has described the medial brachial fascial compartment, which extends from the axilla to the elbow and is bounded by the tough medial intramuscular septum and the axillary sheath. Bleeding into this compartment is responsible for the majority of infraclavicular plexopathies that follow regional block, and for many of the neurological lesions that result from closed or even open injuries in this region. The anterior interosseous nerve and its accompanying artery may be damaged by compression because of swelling in the deepest part of the flexor compartment of the forearm. The ulnar nerve, accompanied by the ulnar artery, lies in a discrete fascial compartment in the distal two-thirds of the forearm.

Bleeding into the axillary fascia (the medial antebrachial compartment) causes a characteristic, progressive lesion. There is, almost always, pain accompanied by dysaesthesiae; loss of sensation soon follows and then, over the next 2–3 hours, paralysis ensues. Wilbourn's comment bears repeating: Distal pulses are normal as they are with most compartment syndromes because the elevated pressure, although sufficient to collapse the vasa nervorum, is far below mean arterial pressure. Ultrasound, MR and CT may reveal the vascular lesion, but, considering the very brief time available for surgical decompression before irreversible nerve damage occurs, obtaining these is rarely justified.

In one series of 16 patients (Stenning et al 2005), there was, in all cases, an injury to the axillary artery or one of its offsets, caused by dislocation of the shoulder or fracture of the proximal humerus. The diagnosis of continuing bleeding into the axillary sheath was made by the delayed onset of nerve palsy or the deepening of the lesion whilst under observation. A favourable outcome was seen in 87 nerve palsies, where urgent repair of the artery and decompression of the axillary sheath were performed. However, delay in diagnosis and treatment may lead to permanent loss of function.

Case report

After a fracture/dislocation of the shoulder in a 59-year-old man, the patient's complaints of pain and the signs of a deepening nerve lesion were not appreciated for several days. Angiography showed bleeding from the subscapular artery. Two unsuccessful attempts were made to occlude this by embolization. The patient was reviewed at six weeks in right heart failure; haemoglobin was 4.9 g/litre (49 g/dl). He was in great pain and there was a total and deep plexopathy. MRI scan showed an enormous haematoma occupying the axilla and the arm, and suggested continuing bleeding. Treatment was simple: the axillary artery was exposed and controlled above pectoralis minor and the brachial artery exposed and controlled in the arm. More than 4 litres of altered blood were removed from the sac. The defect in the axillary artery was, at most, 2 mm in diameter and it was closed by direct suture. The pain was relieved and there was gradual recovery of the nerves, but the small muscles of the hand never recovered.

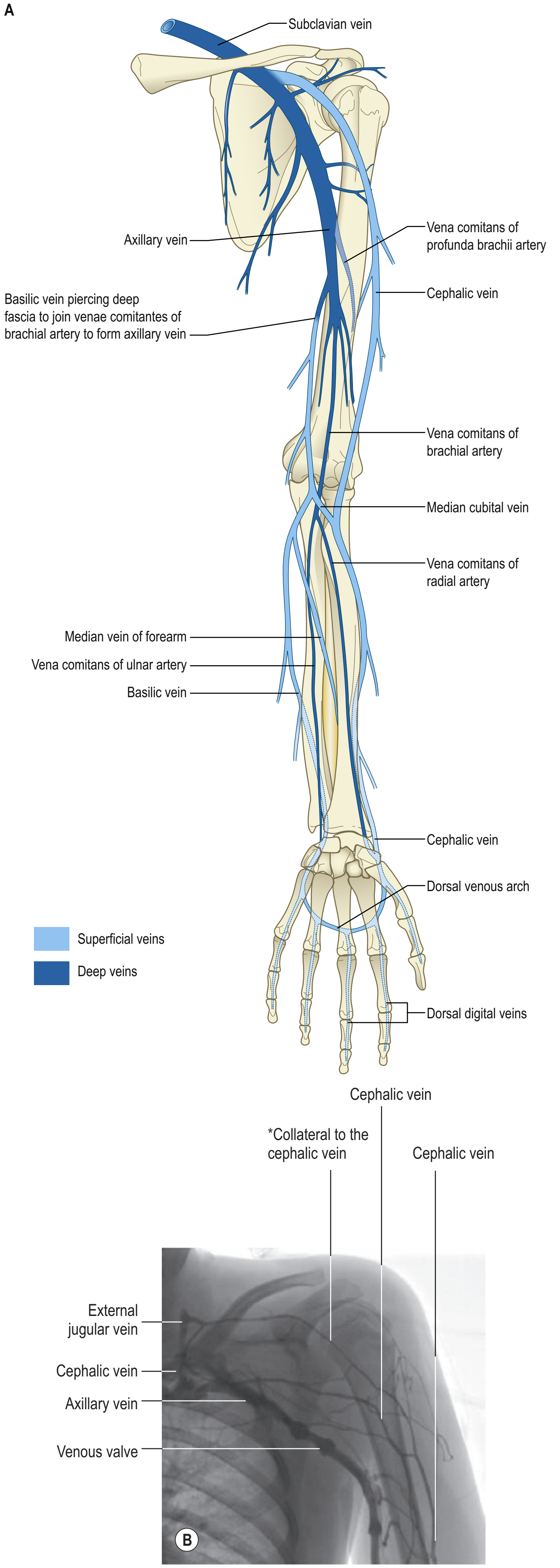
A
Subclavian vein
Axillary vein
Vena comitans of profunda brachii artery
Cephalic vein
Basilic vein piercing deep fascia to join venae comitantes of brachial artery to form axillary vein
Vena comitans of brachial artery
Median cubital vein
Vena comitans of radial artery
Median vein of forearm
Vena comitans of ulnar artery
Basilic vein
Cephalic vein
Dorsal venous arch
Superficial veins
Deep veins
Dorsal digital veins
Cephalic vein
*Collateral to the cephalic vein
Cephalic vein
External jugular vein
Cephalic vein
Axillary vein
Venous valve
B

Fig. 48.4 **A**, The veins of the upper limb. **B**, Venogram of the left arm. There are multiple cephalic vein collaterals, one of which drains into the external jugular vein (*).

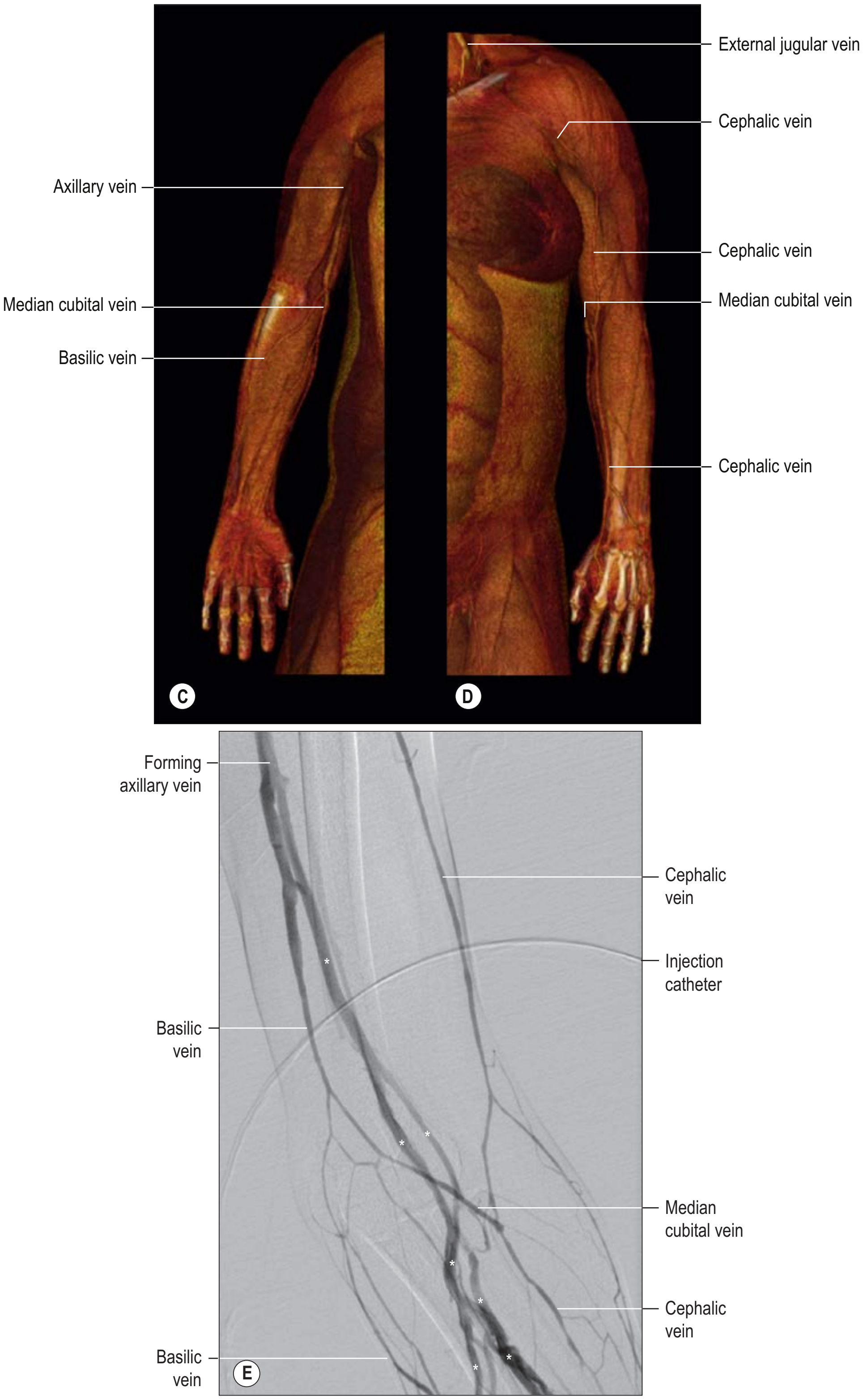
External jugular vein
Cephalic vein
Axillary vein
Cephalic vein
Median cubital vein
Median cubital vein
Basilic vein
Cephalic vein
C
D
Forming axillary vein
Cephalic vein
Injection catheter
Basilic vein
Median cubital vein
Cephalic vein
Basilic vein
E

Fig. 48.4, cont'd C–D, A volume rendered CT venogram of the left arm: **C**, posterior view; **D**, anterior view. **E**, A digital subtraction venogram at the left antecubital fossa, anterior view. Venae comitantes to the arterial tree are marked with asterisks (*) to distinguish them from the superficial veins; these deeper veins are usually less dense because the injection of contrast medium is through a superficial vein.

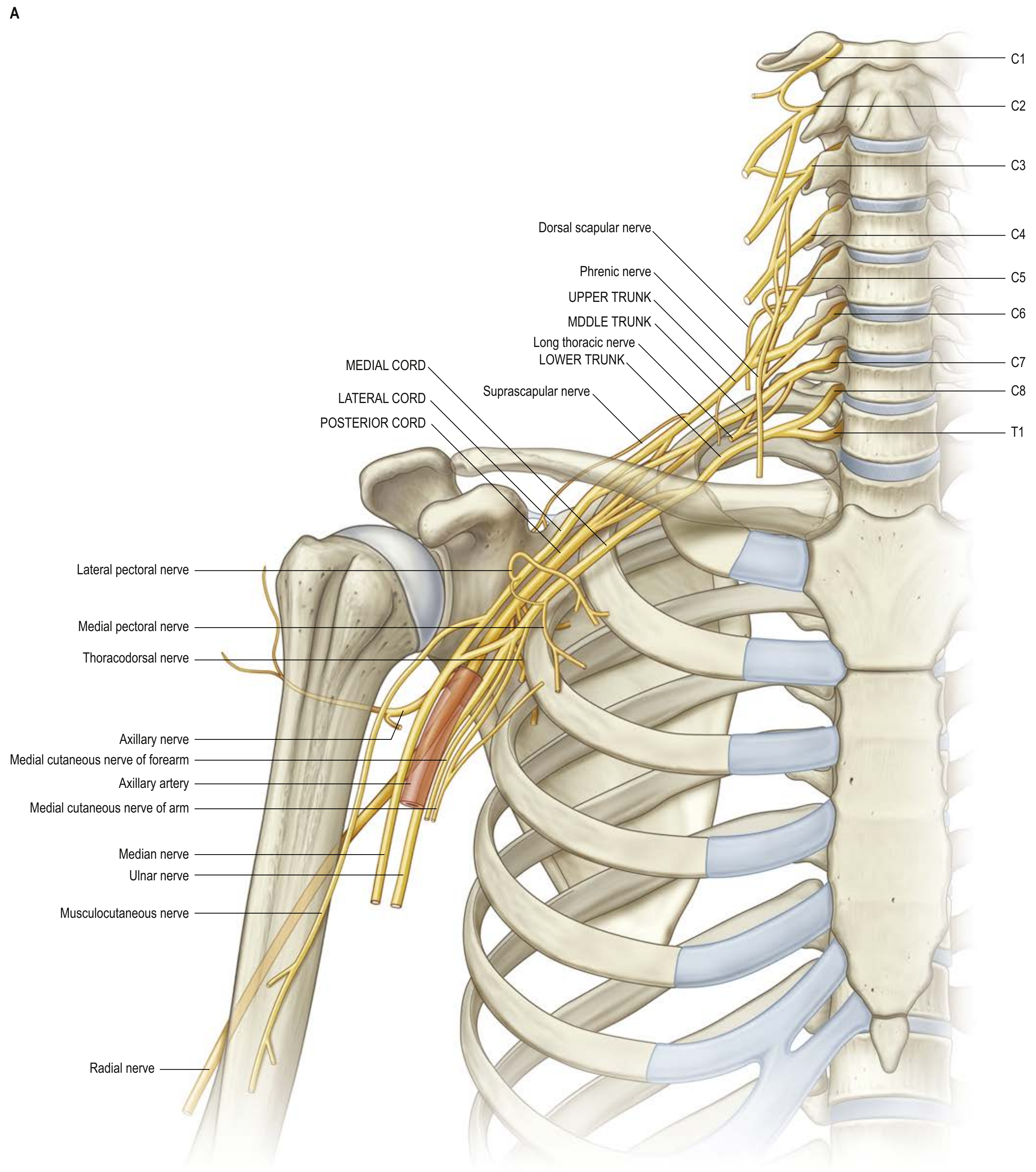
A
C1
C2
C3
Dorsal scapular nerve
C4
Phrenic nerve
C5
UPPER TRUNK
MDDLE TRUNK
C6
Long thoracic nerve
LOWER TRUNK
MEDIAL CORD
C7
LATERAL CORD
Suprascapular nerve
C8
POSTERIOR CORD
T1
Lateral pectoral nerve
Medial pectoral nerve
Thoracodorsal nerve
Axillary nerve
Medial cutaneous nerve of forearm
Axillary artery
Medial cutaneous nerve of arm
Median nerve
Ulnar nerve
Musculocutaneous nerve
Radial nerve

Fig. 48.7 A, The brachial plexus. Note the sequence: ventral (anterior) primary rami; trunks; divisions; cords; nerves. The trunks are upper, middle and lower, and the cords are lateral, medial and posterior, according to their (variable) position in relation to the axillary artery..)

continued

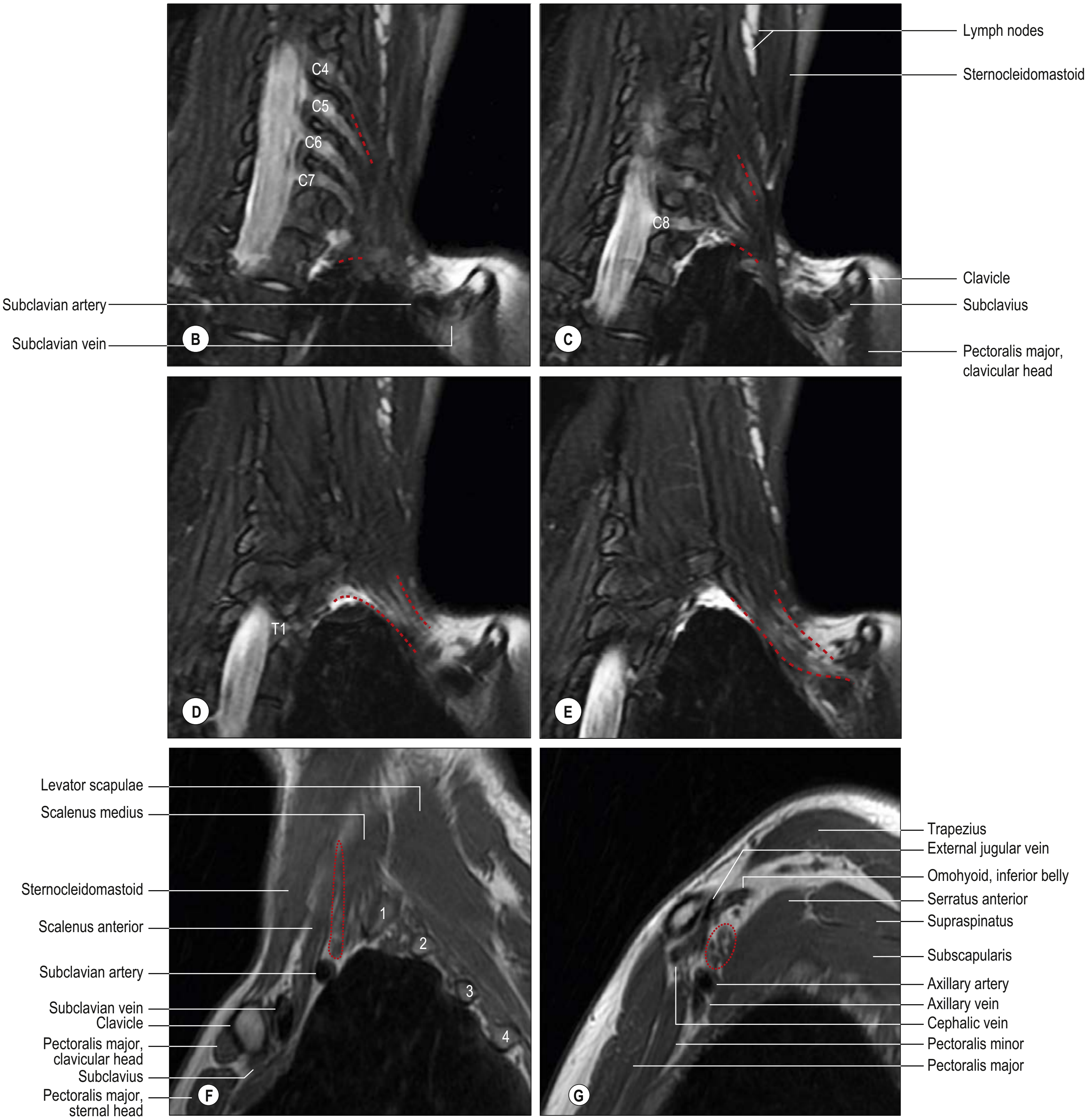
C4
C5
C6
C7
Subclavian artery
Subclavian vein
B
Lymph nodes
Sternocleidomastoid
C8
Clavicle
Subclavius
Pectoralis major, clavicular head
C
T1
D
E
Levator scapulae
Scalenus medius
Sternocleidomastoid
Scalenus anterior
Subclavian artery
Subclavian vein
Clavicle
Pectoralis major, clavicular head
Subclavius
Pectoralis major, sternal head
1
2
3
4
F
Trapezius
External jugular vein
Omohyoid, inferior belly
Serratus anterior
Supraspinatus
Subscapularis
Axillary artery
Axillary vein
Cephalic vein
Pectoralis minor
Pectoralis major
G

Fig. 48.7, cont'd B–E, Sagittal oblique T2-weighted fat saturated MRI of the supraclavicular to retroclavicular left brachial plexus within the dashed red lines, from posterior to anterior; individual spinal nerve roots have been labelled accordingly. **F–G**, Sagittal T1-weighted MRI of the left brachial plexus (viewed from the left), showing its components outlined in dotted red at the interscalene (**F**) and retroclavicular spaces (**G**). The left upper ribs are numbered accordingly. (A, Courtesy of Rolfe Birch, all rights reserved, published in Birch R, Surgical Disorders of the Peripheral Nerve, 2nd ed, 2011. Springer-Verlag, London.)

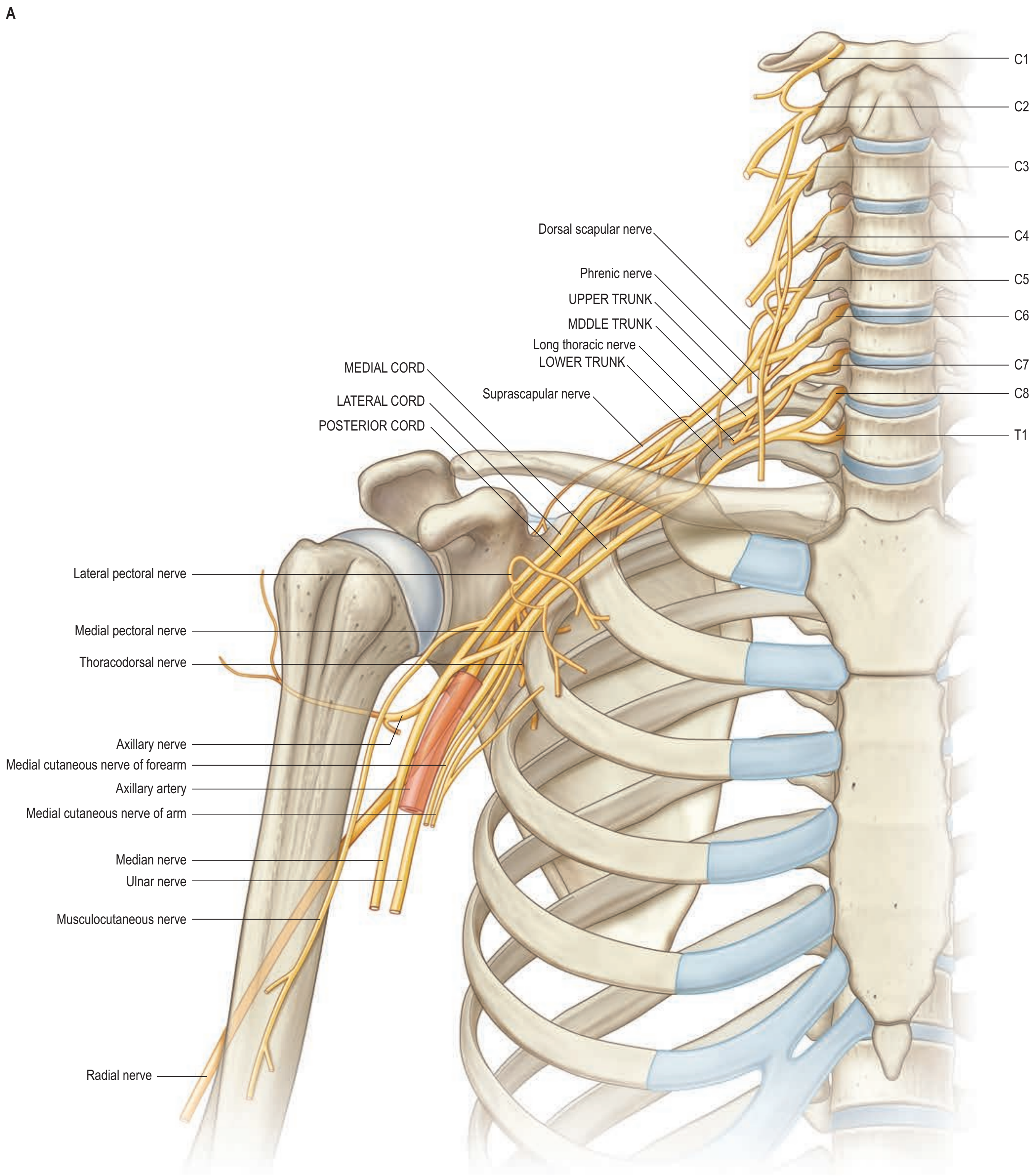
A
C1
C2
C3
C4
C5
C6
C7
C8
T1
Dorsal scapular nerve
Phrenic nerve
UPPER TRUNK
MDDLE TRUNK
Long thoracic nerve
LOWER TRUNK
MEDIAL CORD
LATERAL CORD
POSTERIOR CORD
Suprascapular nerve
Lateral pectoral nerve
Medial pectoral nerve
Thoracodorsal nerve
Axillary nerve
Medial cutaneous nerve of forearm
Axillary artery
Medial cutaneous nerve of arm
Median nerve
Ulnar nerve
Musculocutaneous nerve
Radial nerve

Fig. 48.7 **A**, The brachial plexus. Note the sequence: ventral (anterior) primary rami; trunks; divisions; cords; nerves. The trunks are upper, middle and lower, and the cords are lateral, medial and posterior, according to their (variable) position in relation to the axillary artery. (Courtesy of Rolfe Birch, all rights reserved, published in Birch R, Surgical Disorders of the Peripheral Nerve, 2nd ed, 2011. Springer-Verlag, London.) (B–G, *continued online*)

ventral rami; the sensory contribution is greatest in the seventh cervical ventral ramus. A complex interchange of branches, before the main nerves of the upper limb are formed, produces the trunks, divisions and cords of the brachial plexus.

Blood supply The blood supply to the brachial plexus is derived from vessels which arise from the subclavian and vertebral arteries. Important branches pass from the vertebral artery to the fifth and sixth cervical ventral rami and the more proximal cervical nerves. Branches from the costocervical trunk provide a rich supply to the eighth cervical and first thoracic ventral rami. Extensive contributions come from the suprascapular and superficial cervical arteries that arise from the thyrocervical trunk. In at least one-third of cases, the superficial cervical and dorsal scapular arteries arise from the thyrocervical trunk as the transverse cervical artery. In clinical terms, the arteries arising from the thyrocervical trunk have become the lifeline to the upper limb and must be preserved during operations in cases when the ruptured subclavian artery has not been repaired. The dorsal scapular artery may arise from the third part of the subclavian artery to pass between the upper and middle trunks of the brachial plexus.

Trunks of the brachial plexus

The upper trunk is formed by the fifth and sixth cervical ventral rami, where these nerves emerge from deep to scalenus anterior. The middle trunk is the continuation of the seventh cervical ventral ramus. The lower trunk is formed by the eighth cervical and first thoracic ventral rami, and passes over the anterosuperior surface of the first rib. The first thoracic ventral ramus takes an upward course across the deep face of the neck of the first rib behind the pleura and the vertebral and subclavian arteries towards the lower trunk. The formation of the trunks is fairly consistent; they lie in front of one another rather than side by side, with the subclavian artery passing anteromedially. The phrenic nerve crosses the fifth cervical ventral ramus to pass anteromedially on the surface of scalenus anterior. The upper trunk, its divisions and the suprascapular nerve can all be palpated in the supraclavicular fossa in a subject of normal physique. The examining finger identifies first the subclavian pulse and then the nerves, whilst rolling the fingertip laterally (see Video 48.1).

Divisions of the brachial plexus

The trunks divide into anterior and posterior divisions. The upper trunk divides 2–3 cm above the clavicle, and the divisions of the middle and lower trunk are formed deep to the clavicle. The posterior divisions of the upper and middle trunks are consistently larger than their anterior divisions. The posterior division of the lower trunk is consistently smaller than the anterior division and is absent in about 10% of cases.

Cords of the brachial plexus

The cords are formed by the confluence of divisions: the lateral cord from the anterior divisions of the upper and middle trunks; the posterior cord by all three posterior divisions; and the medial cord by the anterior division of the lower trunk and, sometimes, by a branch from the anterior division of the middle trunks. The divisions of the trunks and the formation of the cords represent an important anatomical and functional differentiation. The posterior divisions and posterior cord innervate postaxial (extensor) musculature; the anterior divisions and the lateral and medial cords innervate preaxial (flexor) musculature.

The formation and relations of the three cords are variable and, indeed, their designations somewhat misleading. Immediately inferior to the clavicle, the posterior cord is lateral, the medial cord is posterior, and the lateral cord is anterior, in relation to the axillary artery; the cords assume their appropriate relations about the axillary artery deep to pectoralis minor. There is considerable variation in this arrangement; most commonly, the axillary artery lies anterior to the three cords and the median nerve.

The branches of the posterior cord, the largest of the three trunks, are consistent. In sequence, they are the upper subscapular, thoracodorsal, lower subscapular, axillary and radial nerves. The branches of the medial cord are usually predictable; the medial pectoral nerve and medial cutaneous nerve of the forearm are succeeded by the division into the medial root of the median nerve and the ulnar nerve. The ulnar nerve may arise as two or three branches. The greatest variation in formation of trunk nerves is found within the lateral cord. Occasionally, the musculocutaneous nerve arises more distally than usual, either directly from the lateral cord as two or three branches or even from the median nerve itself. Sometimes, the highest of these branches enters coracobrachialis no more than 2 or 3 cm below the coracoid process. The lateral root of the median nerve may arise as two or three branches, and in some cases, it appears as a branch of the musculocutaneous nerve.

Terminal branches of the brachial plexus

Axillary (circumflex) nerve

The axillary nerve (fifth and sixth cervical ventral rami) (Fig. 48.8) runs freely in loose fatty tissue in the axilla before turning around subscapularis to pass almost horizontally through the quadrilateral tunnel, where it is accompanied by the posterior circumflex humeral vessels (see Fig. 49.33). It innervates teres minor and deltoid, and the skin overlying deltoid on the lateral aspect of the shoulder.

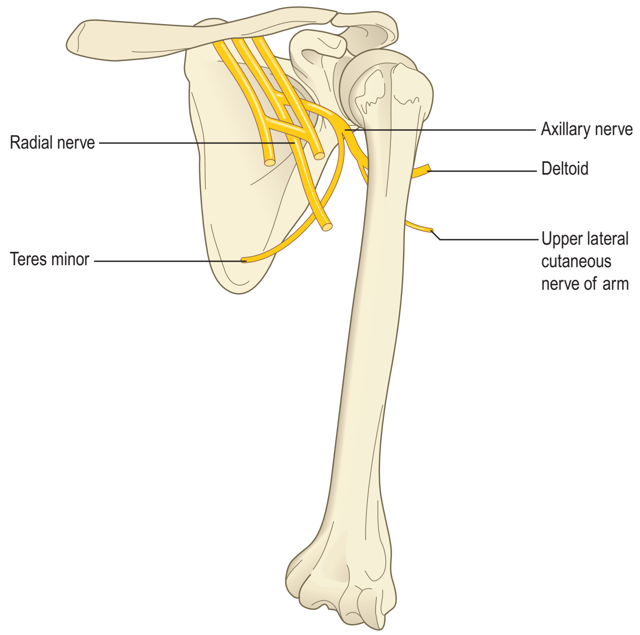

Fig. 48.8 Motor and sensory branches of the axillary nerve. (With permission from O'Brien M, Aids to the Examination of the Peripheral Nervous System, 5th ed. Saunders, Elsevier. Copyright 2010.)

Radial nerve

The radial nerve (fifth, sixth, seventh and eighth cervical and first thoracic ventral rami) is the terminal branch of the posterior cord (Fig. 48.9). It is the largest nerve in the upper limb and the most commonly damaged. Between its origin at the level of the base of the coracoid and its entrance into the spiral groove, where it is accompanied by the profunda brachii artery, the radial nerve is supplied by fewer arteries than elsewhere along its course. The first 8–10 cm of the nerve may not have a nutrient artery and will, therefore, be relatively avascular if the nerve is transected at its origin. The nerve lies closest to the bone where it pierces the lateral intermuscular septum to pass through a short tunnel bounded by bone and unyielding fascia. The nerve is tethered here, a common level of rupture, entrapment or compression.

The nerve to the medial head of triceps arises in the axilla and accompanies the main nerve as it passes through the intermuscular septum. The nerve(s) to the lateral head of triceps arise(s) within the spiral groove; that to the lateral head just before the radial nerve re-enters the anterior compartment. Two cutaneous nerves, the lower lateral cutaneous nerve of the arm and the posterior cutaneous nerve of the forearm, pass away from the main nerve in the final part of the spiral groove and course along the anterior face of the lateral head of triceps to perforate the deep fascia about four fingers'-breadths above the lateral epicondyle. They innervate the skin of the lower lateral arm and the posterior aspect of the forearm. The nerve to brachioradialis is formed about three fingers'-breadths proximal to the lateral epicondyle; the nerve to extensor carpi radialis longus about one finger's-breadth more distal; and that to extensor carpi radialis brevis about one finger's-breadth above the epicondyle. These branches spring from the main nerve as it runs in the valley between brachialis anteriorly and brachioradialis posteriorly, where the nerve may be palpated. At the level of the tip of the lateral epicondyle, the radial nerve divides into the posterior interosseous and superficial radial nerves. Another branch to extensor carpi radialis brevis is usually given off here. The superficial radial nerve innervates the skin over the dorsum of the radial half of the ring, middle and index fingers, and that of the thumb as far as the distal interphalangeal joint. It often provides important sensation on the skin of the thumb web space and the skin on the adjacent sides of the thumb and index.

Median nerve

The median nerve is formed by the union of the lateral root from the lateral cord (sixth and seventh cervical ventral rami), and the medial root from the medial cord (eighth cervical and first thoracic ventral rami), which meet anterior to the third part of the axillary artery (Fig. 48.10). Fibres in the lateral root innervate the palmar skin of the thumb, index and most of the middle finger, pronator teres, flexor carpi radialis and some of flexor digitorum superficialis (Fig. 48.11). The lateral root conveys most of the sympathetic fibres to the median distribution in the hand. The medial root carries fibres to the skin of the medial side of the middle and the lateral side of the ring finger, and also fibres to palmaris longus, flexor digitorum superficialis and the lateral part of flexor digitorum profundus, flexor pollicis longus, pronator quadratus and the median innervated muscles within the hand.

The first branch of the median nerve, to pronator teres, arises 2–3 cm above the medial epicondyle. A second branch, or leash of

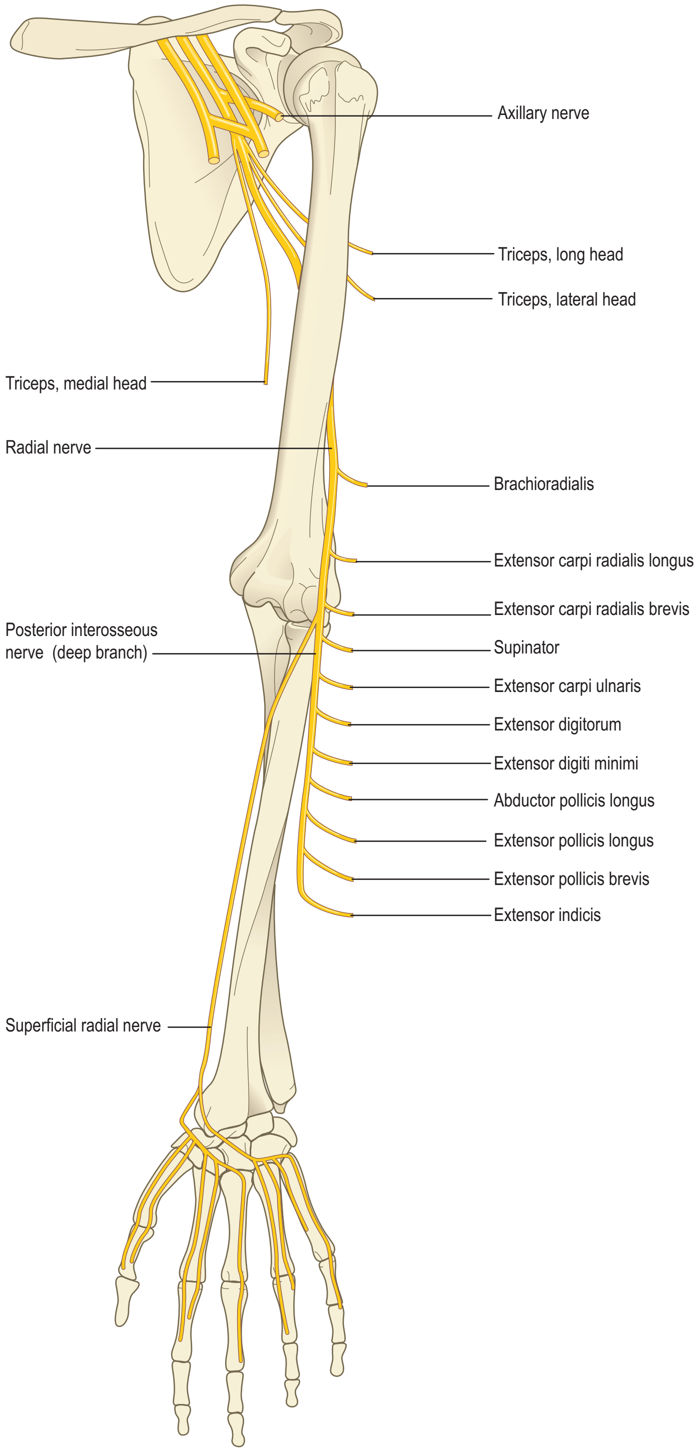
Axillary nerve
Triceps, long head
Triceps, lateral head
Triceps, medial head
Radial nerve
Brachioradialis
Extensor carpi radialis longus
Extensor carpi radialis brevis
Posterior interosseous nerve (deep branch)
Supinator
Extensor carpi ulnaris
Extensor digitorum
Extensor digiti minimi
Abductor pollicis longus
Extensor pollicis longus
Extensor pollicis brevis
Extensor indicis
Superficial radial nerve

Fig. 48.9 Motor and sensory branches of the radial nerve. Variation exists in the cutaneous innervation of the dorsal aspects of the digits. Here, the radial nerve is shown to supply all five digits; the skin of the dorsum of the ring and little fingers is frequently innervated by the dorsal branch of the ulnar nerve. (With permission from O'Brien M, Aids to the Examination of the Peripheral Nervous System, 5th ed. Saunders, Elsevier. Copyright 2010.)

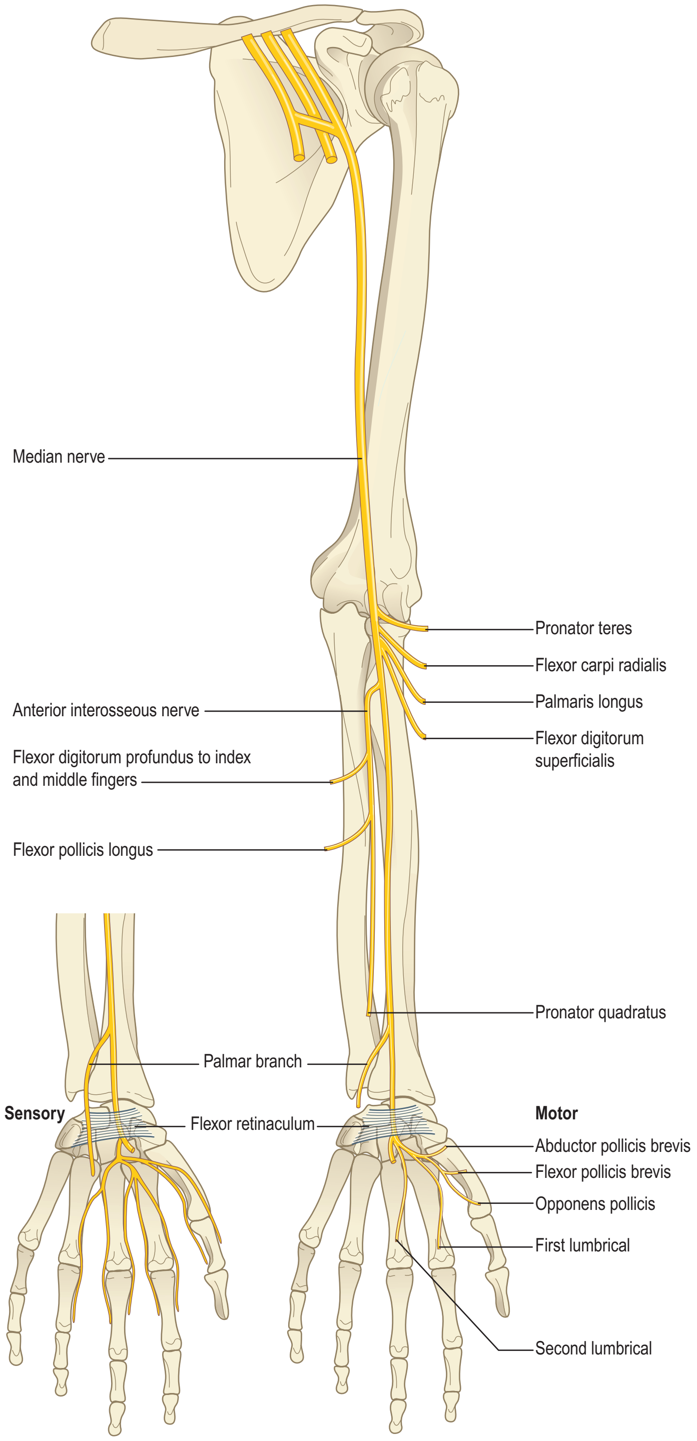
Median nerve
Pronator teres
Flexor carpi radialis
Palmaris longus
Anterior interosseous nerve
Flexor digitorum superficialis
Flexor digitorum profundus to index and middle fingers
Flexor pollicis longus
Pronator quadratus
Palmar branch
Sensory
Flexor retinaculum
Motor
Abductor pollicis brevis
Flexor pollicis brevis
Opponens pollicis
First lumbrical
Second lumbrical

Fig. 48.10 Motor and sensory branches of the median nerve. Flexor pollicis brevis may be supplied by both median and ulnar nerves. (With permission from O'Brien M, Aids to the Examination of the Peripheral Nervous System, 5th ed. Saunders, Elsevier. Copyright 2010.)

branches, arises at the level of the tip of the medial epicondyle and innervates palmaris longus, flexor carpi radialis and flexor digitorum superficialis. Just proximal to the tendinous arcade of flexor digitorum superficialis, the median nerve gives off the anterior interosseous nerve. Accompanied by the anterior interosseous vessels, this large branch dives deeply to pass down along the interosseous membrane and supplies flexor pollicis longus, the radial half of flexor digitorum profundus and pronator quadratus. There is no cutaneous distribution. The main nerve continues in the plane between the superficial and deep digital flexors, supplying two or three branches to the former. The palmar cutaneous nerve arises about 3 cm proximal to the proximal wrist crease (when there are two creases), and passes lateral to the main nerve and superficial to the flexor retinaculum to innervate the skin of the proximal palm. The median nerve passes deep to the flexor retinaculum, into the carpal tunnel, to enter the palm. The nerve to the thenar muscles arises within, or just distal to, the tunnel, usually on the lateral side of the main nerve. The palmar digital nerves are formed within the palm of the hand.

The nerve is palpable along its course in the arm, where it is covered by deep fascia and skin, after emerging from deep to coracobrachialis. It is palpable on the flexor aspect of the elbow, deep to the bicipital aponeurosis, and is accompanied by the brachial artery in this segment of the limb. The median nerve is palpable at the wrist where it emerges from behind the superficial flexor tendons, just lateral to palmaris longus.

Ulnar nerve

The ulnar nerve (seventh and eighth cervical and first thoracic ventral rami) is the continuation of the medial cord (Fig. 48.12). It inclines posteromedially to perforate the medial intermuscular septum about 10 cm proximal to the medial epicondyle and passes through a fibrous

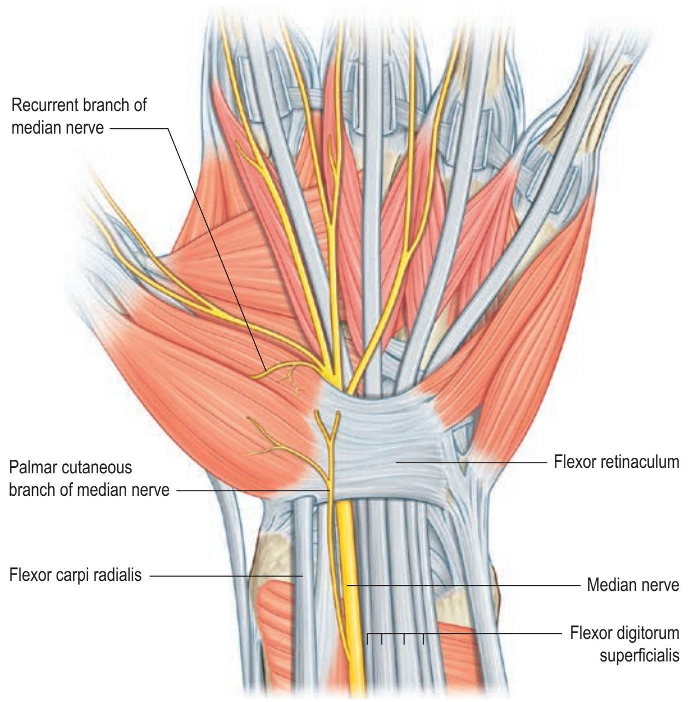
Recurrent branch of median nerve
Palmar cutaneous branch of median nerve
Flexor retinaculum
Flexor carpi radialis
Median nerve
Flexor digitorum superficialis

Fig. 48.11 The normal course of the median nerve and the palmar cutaneous nerve at the wrist. (Courtesy of Rolfe Birch, all rights reserved, published in Birch R, Surgical Disorders of the Peripheral Nerve, 2nd ed, 2011. Springer-Verlag, London.)

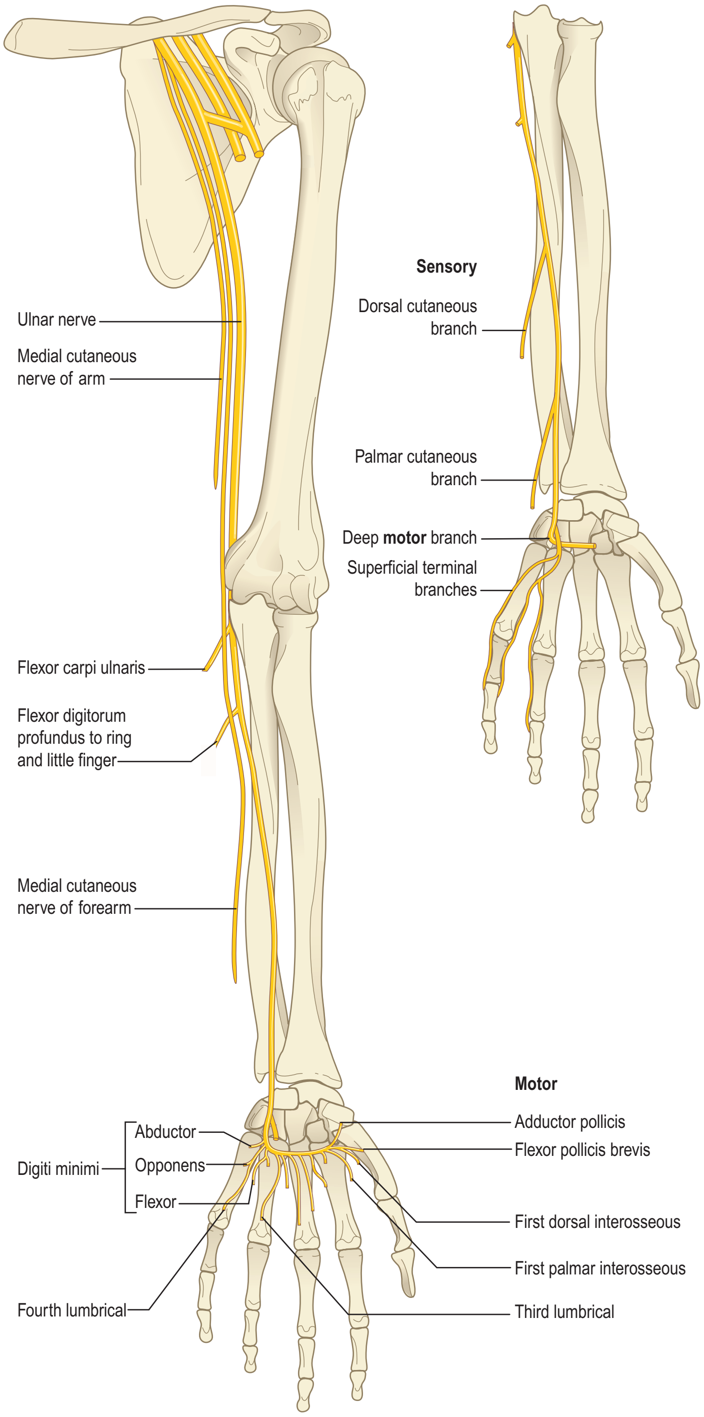
Ulnar nerve
Medial cutaneous nerve of arm
Flexor carpi ulnaris
Flexor digitorum profundus to ring and little finger
Medial cutaneous nerve of forearm
Sensory
Dorsal cutaneous branch
Palmar cutaneous branch
Deep **motor** branch
Superficial terminal branches
Motor
Digiti minimi
Abductor
Opponens
Flexor
Fourth lumbrical
Adductor pollicis
Flexor pollicis brevis
First dorsal interosseous
First palmar interosseous
Third lumbrical

Fig. 48.12 Motor and sensory branches of the ulnar nerve and the medial cutaneous nerves of the arm and the forearm. Flexor pollicis brevis may be supplied by both median and ulnar nerves. (With permission from O'Brien M, Aids to the Examination of the Peripheral Nervous System, 5th ed. Saunders, Elsevier. Copyright 2010.)

canal, the arcade of Struthers, which is between 5 and 6 cm long. The walls of the canal include the medial intermuscular septum and the fascial sheath which invests the medial head of triceps brachii. The nerve next passes behind the medial epicondyle, then between the capsule of the humero-ulnar joint and the overlying arcuate ligament, which joins the two origins of flexor carpi ulnaris, i.e. the nerve passes through the cubital tunnel. It is accompanied by the superior collateral ulnar vessels in the lower third of the arm as far as the entrance to the cubital tunnel, and then by the posteroinferior ulnar collateral vessels. The anastomosis between these vessels permits the use of most of the ulnar nerve as a free vascularized graft, in cases where the parent roots, the seventh and eighth cervical ventral rami and the first thoracic ventral ramus, are irreparable. In the forearm, the nerve runs with the ulnar vessels in a well-defined sheath deep to the anterior margin of flexor carpi ulnaris. It divides into superficial (sensory) and deep (motor) components at the wrist, both passing through the ulnar (Guyon's) canal.

The superficial division innervates the skin of the medial two digits and palmaris brevis. The deep branch passes, with the deep branch of the ulnar artery, between abductor and flexor digiti minimi, pierces opponens digiti minimi and then runs across the deep palmar space with the deep palmar arch. It innervates all the muscles of the hand, except for the first and second (index and middle) lumbricals, abductor pollicis brevis, opponens pollicis and part of flexor pollicis brevis.

A branch to the medial head of triceps is often given off in the distal third of the arm. There are usually two neurovascular pedicles to flexor carpi ulnaris, the first at the exit from the cubital tunnel, the second about one-quarter of the way down the forearm. Several branches pass to flexor digitorum profundus. The dorsal cutaneous nerve arises about 6 cm proximal to the ulnar styloid, winds around the ulna, at first deep to flexor carpi ulnaris, and then subcutaneously. It innervates the skin of the dorsum of the hand and little finger, and the medial side of the ring finger.

The ulnar nerve is palpable in the lower arm and behind the medial epicondyle, where it is subcutaneous. There is an important relation here: a posterior branch of the medial cutaneous nerve of the forearm sweeps across the cubital tunnel and gets in the way of medial surgical exposures. Inadvertent injury may cause severe pain. The ulnar nerve is palpable at the wrist where it emerges from under flexor carpi ulnaris. The dorsal cutaneous branch can be palpated in those of slender physique where it crosses the subcutaneous ulna.

Musculocutaneous nerve

The musculocutaneous nerve (fifth, sixth and seventh cervical ventral rami) is one of the two terminal branches of the lateral cord, the other being the lateral root of the median nerve (Fig. 48.13). This division usually occurs at the level of the third part of the axillary artery, where the lateral cord lies lateral to the vessel, but it may occur more proximally, where the cord is anterior to the second part of the artery. The nerve may also arise as two or three branches from the cord, or even from the median nerve. It supplies coracobrachialis, both heads of biceps brachii and most of brachialis, and continues as the lateral cutaneous nerve of forearm, deep to biceps, before emerging lateral to it about 11 cm above the lateral epicondyle, and then running down the lateral aspect of the forearm. The nerve sometimes innervates the skin over the first metacarpal and the lateral part of the thenar eminence.

Segmental innervation of the upper limb

There is a segmental pattern to the innervation of the upper limb. The most proximal muscles are supplied by branches of the uppermost rami, and the most distal muscles are supplied by branches derived from the

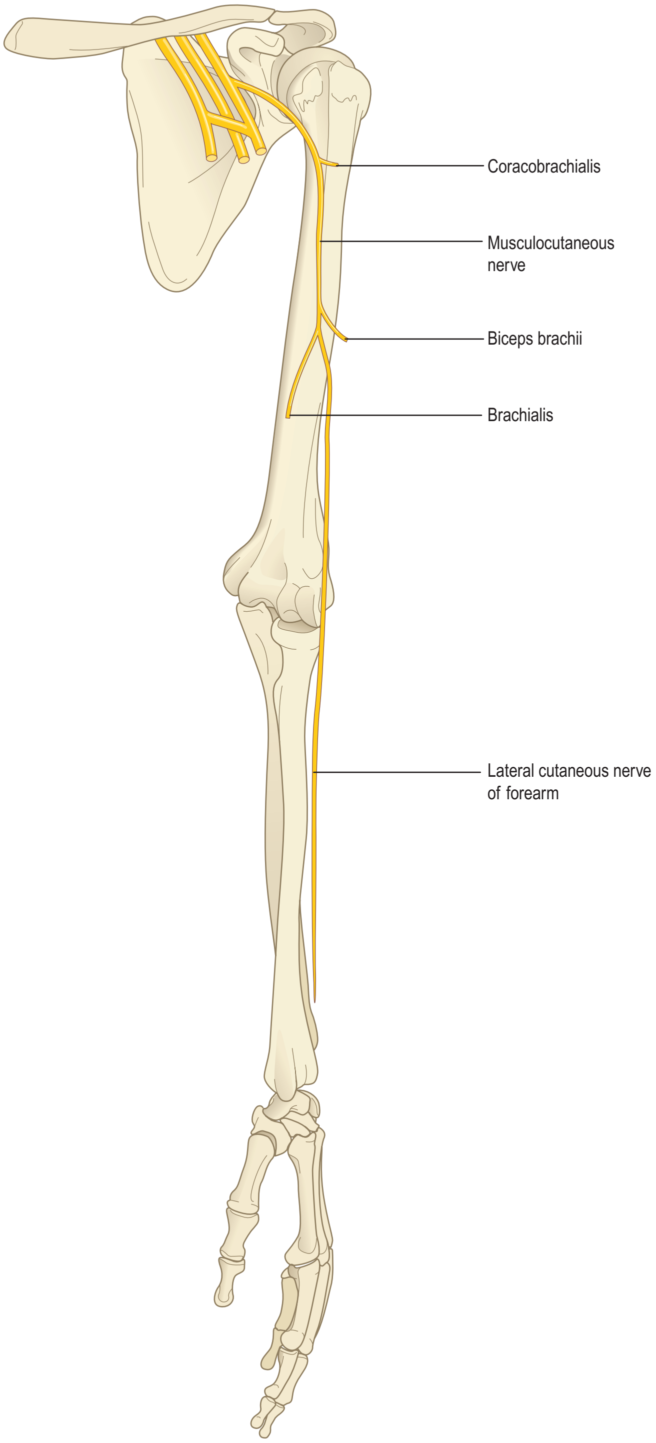

Fig. 48.13 Motor and sensory branches of the musculocutaneous nerve. (With permission from O'Brien M, Aids to the Examination of the Peripheral Nervous System, 5th ed. Saunders, Elsevier. Copyright 2010.)

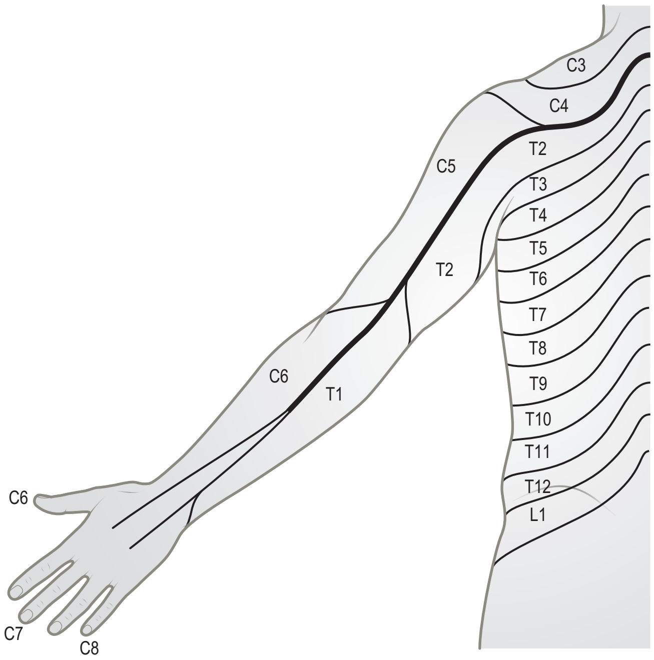

Fig. 48.14 Approximate distribution of the dermatomes on the posterior aspect of the upper limb. (Courtesy of Rolfe Birch, all rights reserved, published in Birch R, Surgical Disorders of the Peripheral Nerve, 2nd ed, 2011. Springer-Verlag, London.)

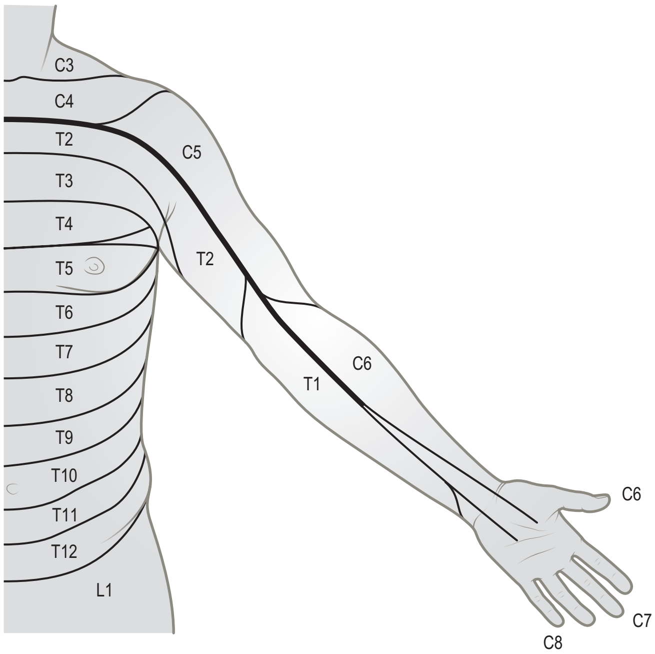

Fig. 48.15 Approximate distribution of the dermatomes on the anterior aspect of the upper limb. (Courtesy of Rolfe Birch, all rights reserved, published in Birch R, Surgical Disorders of the Peripheral Nerve, 2nd ed, 2011. Springer-Verlag, London.)

eighth cervical and first thoracic ventral rami. The segmental pattern of innervation is shown more clearly in the cutaneous supply. The cervical supply has been, as it were, extruded from the supply to the trunk. Thus, in the transition of cutaneous innervation from the skin of the neck to that of the trunk, there is a change from the fourth cervical to the second thoracic segment anteriorly, and a change from the fifth cervical to the second thoracic segment posteriorly (Figs 48.14–48.15; see Figs 24.10, 48.55). (For further reading, see Ladak et al (2014).) The truly autonomous area of cutaneous supply of each main component nerve is small and variable in extent and location.

C5 regularly controls extension, abduction and lateral rotation of the shoulder. C6 usually innervates biceps brachii, brachialis, lateral head of triceps, brachioradialis, extensor carpi radialis longus, and sometimes contributes to the innervation of pronator teres, supinator and flexor carpi radialis. C7 gives widespread innervation throughout the limb; in those unusual instances where it alone is damaged, the patient will note a rather diffuse loss of function throughout the upper limb, often without complete anaesthesia and sometimes without paralysis of any single significant muscle group. C7 consistently supplies latissimus dorsi. C8 innervates the extensors of the digits and of the thumb in at least one-third of cases. T1 innervates these muscles and also the medial head of triceps in at least 10%. Muscles, movements and segmental innervation in the upper limb are set out in Tables 48.1–48.3. Table 48.4 helps to distinguish between upper and lower motor neurone lesions.

Autonomic nerves

The preganglionic sympathetic inflow to the upper limb is derived from neurones in the intermediolateral horn of spinal cord segments T2–T6/7. Myelinated preganglionic axons pass from the spinal nerves to the thoracic

TABLE 48.1 Movements, muscles and segmental innervation in the upper limb

Joint	Movement	Muscle	Innervation	C3	C4	C5	C6	C7	C8	T1
SCAPULA	ELEVATION	Upper trapezius	Accessory n.	▨	■					
		Levator scapulae	Dorsal scapular n.	▨	▨	▨				
	DEPRESSION	Lower trapezius	Accessory n.	▨	■					
	RETRACTION	Middle trapezius	Accessory n.	▨	■					
		Rhomboids	Dorsal scapular n.		▨	▨				
SHOULDER	PROTRACTION	Serratus anterior	Long thoracic n.			■	▨	▨		
	FLEXION	Anterior deltoid	Axillary n.			■	▨			
		Pectoralis major (clavicular head)	Medial and lateral pectoral nn.			■	▨			
		Pectoralis major (sternocostal head)	Medial and lateral pectoral nn.				▨	■	▨	▨
		Coracobrachialis	Musculocutaneous n.			▨	▨	▨		
	EXTENSION	Posterior deltoid	Posterior deltoid			■	▨			
		Infraspinatus	Suprascapular n.			■	▨			
		Teres minor	Axillary n.			■	▨			
		Teres major	Lower subscapular n.			▨	■	▨		
		Latissimus dorsi	Thoracodorsal n.				▨	■	▨	
	VERTICAL ABDUCTION	Middle deltoid	Axillary n.			▩	▩			
		Supraspinatus	Suprascapular n.			■	▨			
	VERTICAL ADDUCTION	Pectoralis major (sternocostal head)	Medial and lateral pectoral nn.				▨	■	▨	
		Latissimus dorsi	Thoracodorsal n.				▨	■	▨	
		Coracobrachialis	Musculocutaneous n.			▨	▨	▨		
	HORIZONTAL ABDUCTION	Posterior deltoid	Axillary n.			■	▨			
	HORIZONTAL ADDUCTION	Pectoralis major (clavicular head)	Medial and lateral pectoral nn.			■	▨			
		Pectoralis minor	Medial and lateral pectoral nn.			▨	▨	■	■	▨
		Anterior deltoid	Axillary n.			■	▨			
	MEDIAL ROTATION	Subscapularis	Upper and lower subscapular nn.			▨	■			
		Teres major	Brachial plexus			▨	▨	▨		
		Latissimus dorsi	Thoracodorsal n.				▨	■	▨	
		Anterior deltoid	Axillary n.			■	▨			
	LATERAL ROTATION	Infraspinatus	Suprascapular n.			■	▨			
		Teres minor	Axillary n.			■	▨			
		Posterior deltoid	Axillary n.			■	▨			
ELBOW	**FLEXION**	Biceps brachii	Musculocutaneous n.			▩	▩			
		Brachialis	Musculocutaneous and radial nn.			▨	■	▨		
		Brachioradialis	Radial n.			▩	▩			
	EXTENSION	Triceps brachii	Radial n.				▩	▩	▩	
	SUPINATION*	Biceps brachii	Musculocutaneous n.			▨	▨			
		Supinator	Posterior interosseous n.				■	▨		
	PRONATION*	Pronator quadratus	Anterior interosseous n.					▨	■	
		Pronator teres	Median n.				▨	■		
WRIST	FLEXION	Flexor carpi radialis	Median n.				▨	▨		
		Palmaris longus	Median n.					▨	▨	
		Flexor carpi ulnaris	Ulnar n.					▨	■	▨
	EXTENSION	Extensor carpi radialis longus	Radial n.			▩	▩			
		Extensor carpi radialis brevis	Posterior interosseous n.					■	▨	
		Extensor carpi ulnaris	Posterior interosseous n.					■	▨	
	ABDUCTION	Extensor carpi radialis longus	Radial n.			▨	■			
		Extensor carpi radialis brevis	Posterior interosseous n.					■	▨	
		Flexor carpi radialis	Median n.				▨	▨		
	ADDUCTION	Extensor carpi ulnaris	Posterior interosseous n.					■	▨	
		Flexor carpi ulnaris	Ulnar n.					▨	■	▨
FINGERS	FLEXION (MP/PIP joints)	Flexor digitorum superficialis	Median n.					▨	■	▨
		Dorsal interossei	Ulnar n.						▨	■
		Palmar interossei	Ulnar n.						▨	
	FLEXION (DIP joints)	Flexor digitorum profundus (lateral)	Anterior interosseous n.					▩	▩	
		Flexor digitorum profundus (medial)	Ulnar n.					▩	▩	
	FLEXION (MP joint)	Flexor digiti minimi brevis	Ulnar n.						▨	■
	EXTENSION (MP/PIP/DIP joints)	Extensor digitorum	Posterior interosseous n.					▩	▩	
		Extensor indicis	Posterior interosseous n.					■	▨	
	EXTENSION (MP/PIP/DIP joints)	Flexor digiti minimi	Posterior interosseous n.					■	▨	
	EXTENSION (PIP/DIP joints)	Lumbricals I and II	usually Median n.						▨	■
		Lumbricals III and IV	ususally Ulnar n.						▨	■
	ABDUCTION	Dorsal interossei	Ulnar n.						▩	▩
	ABDUCTION (thumb fixed)	Abductor pollicis brevis	Median n.						▩	▩
	ABDUCTION	Abductor digiti minimi	Ulnar n.						▨	■
	ADDUCTION	Palmar interossei	Ulnar n.						▨	■
	OPPOSITION	Opponens digit minimi	Ulnar n.						▨	■
THUMB	FLEXION (IP joint)	Flexor pollicis longus	Anterior interosseous n.					▩	▩	
	FLEXION/ROTATION (MP joint)	Flexor pollicis brevis	Median n. and/or ulnar n.						▨	■
	EXTENSION (MP joint)	Extensor pollicis brevis	Posterior interosseous n.					■	▨	
	EXTENSION (IP joint)	Extensor pollicis longus	Posterior interosseous n.					■	▨	
	ABDUCTION	Abductor pollicis longus	Posterior interosseous n.					■	▨	
	ABDUCTION/ROTATION	Abductor pollicis brevis	Median n.						▩	▩
	ADDUCTION/ROTATION	Adductor pollicis	Ulnar n.						▨	■
	ADDUCTION/FLEXION (MP joint)	Palmar interosseous I	Ulnar n.						▨	■
	OPPOSITION	Opponens pollicis	Median n. and ulnar n.						▨	■

Muscles and movements that have diagnostic value are marked in red. Spinal roots have been given the same colour (light peach, dark peach, red) when they innervate a muscle to a similar extent. Red has been used to indicate roots from which there is known to be a dominant contribution.

* These movements occur at the radio-ulnar joints.

Abbreviations: DIP, distal interphalangeal; IP, interphalangeal; MP, metacarpophalangeal; PIP, proximal interphalangeal.

TABLE 48.2 Segmental innervation of the muscles of the upper limb

Nerves	Muscles
C3, C4	Trapezius, levator scapulae
C5	Rhomboids, deltoids, supraspinatus, infraspinatus, teres minor, biceps
C6	Serratus anterior, latissimus dorsi, subscapularis, teres major, pectoralis major (clavicular head), biceps, coracobrachialis, brachialis, brachioradialis, supinator, extensor carpi radialis longus
C7	Serratus anterior, latissimus dorsi, pectoralis major (sternal head), pectoralis minor, triceps, pronator teres, flexor carpi radialis, flexor digitorum superficialis, extensor carpi radialis longus, extensor carpi radialis brevis, extensor digitorum, extensor digiti minimi
C8	Pectoralis major (sternal head), pectoralis minor, triceps, flexor digitorum superficialis, flexor digitorum profundus, flexor pollicis longus, pronator quadratus, flexor carpi ulnaris, extensor carpi ulnaris, abductor pollicis longus, extensor pollicis longus, extensor pollicis brevis, extensor indicis, abductor pollicis brevis, flexor pollicis brevis, opponens pollicis
T1	Flexor digitorum profundus, intrinsic muscles of the hand (except abductor pollicis brevis, flexor pollicis brevis, opponens pollicis)

TABLE 48.3 Segmental innervation of joint movements of the upper limb

Territory	Muscles	Nerves
Shoulder	Abductors and lateral rotators	C5
	Adductors and medial rotators	C6–C8
Elbow	Flexors	C5, C6
	Extensors	C7, C8
Forearm	Supinators	C6
	Pronators	C7, C8
Wrist	Flexors and extensors	C6, C7
Digits	Long flexors and extensors	C7, C8
Hand	Intrinsic muscles	C8, T1

TABLE 48.4 Movements and muscles tested to determine the location of a lesion in the upper limb

Arm movement	Muscle	Upper motor neurone	Root	Reflex	Nerve
Shoulder abduction	Deltoid	++	C5		Axillary
Elbow flexion	Biceps		C5/6	+	Musculocutaneous
	Brachioradialis		C6		Radial
Elbow extension	Triceps	+	C7	+	Radial
Radial wrist extensor	Extensor carpi radialis longus	+	C6		Radial
Finger extensors	Extensor digitorum	+	C7	(+)	Posterior interosseous
Finger flexors	Flexor pollicis longus and flexor digitorum profundus, index		C8	+	Anterior interosseous
	Flexor digitorum profundus, ring and little				Ulnar
Finger abduction	First dorsal interosseous	++	T1		Ulnar
	Abductor pollicis brevis		T1		Median

The muscles listed in the 'Upper motor neurone' column are those that are preferentially affected in upper motor neurone lesions. The root level is the principal supply to a muscle.

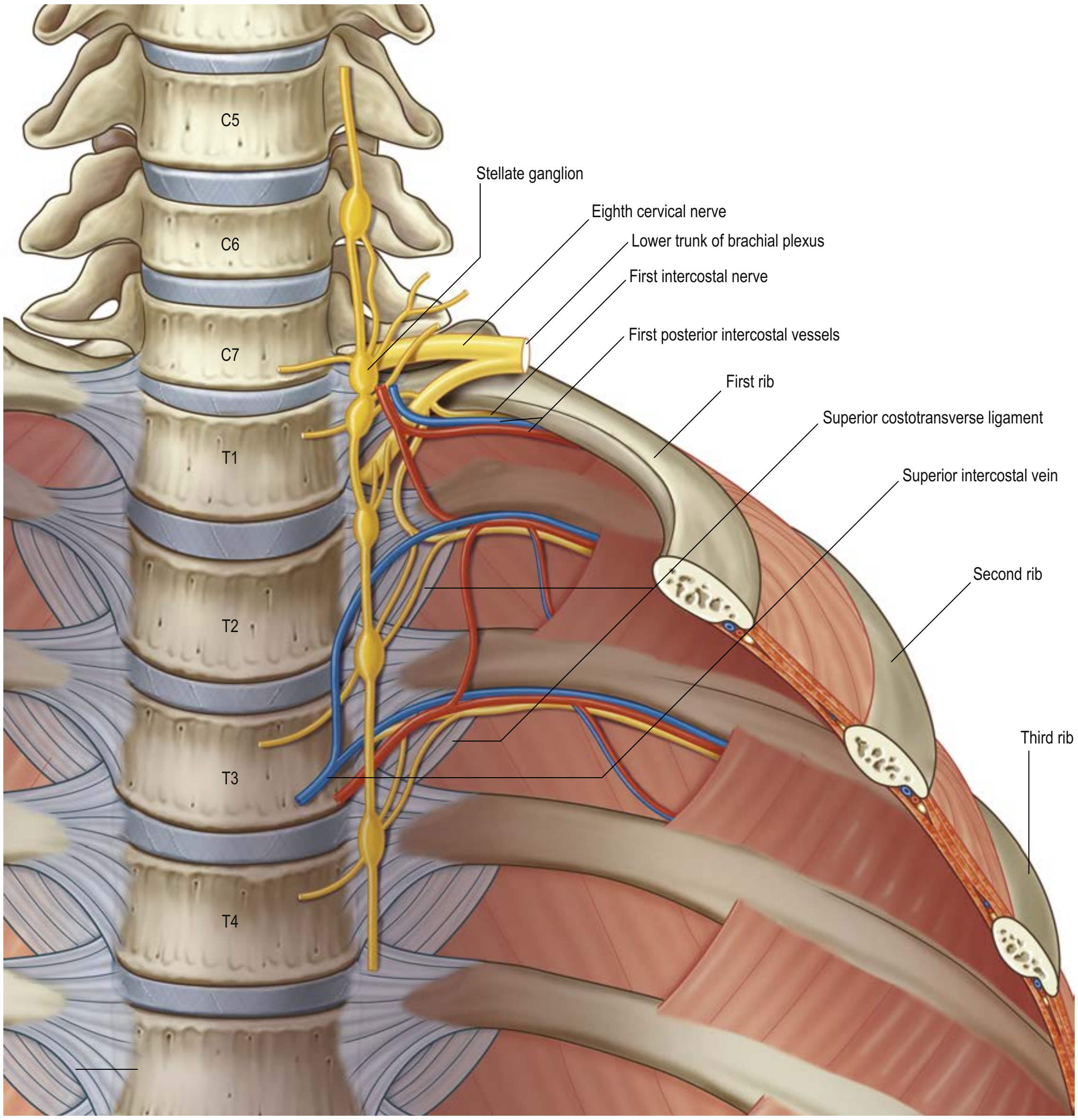
C5
C6
C7
T1
T2
T3
T4
Stellate ganglion
Eighth cervical nerve
Lower trunk of brachial plexus
First intercostal nerve
First posterior intercostal vessels
First rib
Superior costotransverse ligament
Superior intercostal vein
Second rib
Third rib

Fig. 48.16 The relations of the left cervicothoracic (stellate) ganglion. (Courtesy of Rolfe Birch, all rights reserved, published in Birch R, Surgical Disorders of the Peripheral Nerve, 2nd ed, 2011. Springer-Verlag, London.)

sympathetic trunk via white rami communicates. They pass up the trunk to the middle cervical and inferior cervical (stellate or cervicothoracic) ganglia, where they relay.

The unmyelinated postganglionic fibres are distributed by grey rami communicantes to the nerves of origin of the brachial plexus. The fifth and sixth cervical ventral rami receive grey rami from the middle cervical ganglion; the seventh and eighth cervical ventral rami receive grey rami from the inferior cervical ganglion; the first thoracic ventral ramus not only receives a grey ramus from the inferior cervical ganglion but also contributes a white ramus to it (see Fig. 24.13; Fig. 48.16). Interruption of this white ramus is one cause of Horner's (Bernard–Horner) syndrome: drooping eyelid, narrow palpebral fissure, a contracted pupil, and vasomotor with sudomotor paralysis in the ipsilateral face and neck. The sympathetic outflow to the upper limb passes with the peripheral nerves and is particularly rich in the palmar skin of the hand and in the skin of the axilla.

CLINICAL DIAGNOSIS OF FOCAL NERVE LESIONS IN THE UPPER LIMB

Available with the *Gray's Anatomy* e-book

Injuries of the supraclavicular brachial plexus

Available with the *Gray's Anatomy* e-book

NERVES AT RISK FROM MUSCULOSKELETAL INJURY

Available with the *Gray's Anatomy* e-book

THORACIC OUTLET SYNDROMES

Available with the *Gray's Anatomy* e-book

SURFACE ANATOMY

Skeletal landmarks

The clavicle is both visible and palpable from its prominent and relatively rounded medial (sternal) end, which forms the lateral boundary of the jugular (suprasternal) notch, to its flattened lateral end, where it joins the acromion (Fig. 48.53A). The acromioclavicular joint line is palpable as an anteroposteriorly aligned ridge or groove. The anterior, superior and lateral surfaces of the acromion are subcutaneous and palpable (Fig. 48.53C). Posteriorly, the palpable acromial angle marks the junction of the acromion with the spine of the scapula. From this point, the spine of the scapula is subcutaneous and easily visible in subjects of lower body mass, and is palpable to the medial (vertebral) border of the scapula, where it lies opposite the spinous process of T3.

In the acute injury, the object of the clinician must be to recognize the fact of injury as soon as possible after the event, and later, to go on to determine the nerve or nerves affected, the level(s) of injury, and the extent and depth of the lesion(s). The history is important: high injury transfer, open fracture and wounding (be it accidental, criminal, surgical, or all three) indicate a serious lesion and advice from witnesses or emergency paramedical staff is always valuable. Injuries that potentially threaten life or limb complicate closed traction lesions of the supraclavicular brachial plexus in about 20% of cases. It is important to seek occult injuries to the head, spine, thorax, abdomen and pelvis before embarking on treatment of the nerve lesion(s).

The early symptoms of acute nerve injury include: abnormal spontaneous sensations; alteration or loss of sensibility; weakness and paralysis; impairment of function; an awareness of warming and dryness of all or part of an extremity (sometimes); and pain (sometimes). Neuropathic pain is never easy to recognize in an injured patient, who is probably confused, distressed and in pain. It can be distinguished from the pain of fracture or dislocation by loss of sensation; painful, spontaneous sensory symptoms, expressed throughout the territory of the nerve; and by lancinating or shooting pain, radiating into the distribution of the nerve. Constant crushing, bursting or burning pain in an otherwise undamaged hand indicates serious and continuing injury to major trunk nerves more proximally. Progression of sensory loss, with a deep bursting or crushing pain within the muscles of the limb, signifies critical ischaemia.

The main nerves are stretched, ruptured or avulsed from muscle by violent hyperextension–abduction injuries of the arm. The axillary or brachial artery may be damaged by fracture of the proximal humerus or fracture-dislocation of the shoulder but such injuries are relatively uncommon (Menendez and Ring 2015). The axillary nerve and posterior circumflex vessels, which pass almost horizontally posterior to the neck of the humerus, are particularly at risk from anterior dislocation of the head of the humerus. The radial nerve and the profunda brachii artery are relatively fixed where they pass from the anterior to the posterior compartment by perforating the medial intermuscular septum in the axilla, and again when they re-emerge into the anterior compartment by perforating the lateral intermuscular septum. They may be stretched, ruptured or entrapped by displaced fractures of the shaft of the humerus. The median, ulnar and radial nerves may be subjected to traction, or entrapment, by fracture or dislocation about the elbow. The median nerve is severely compressed by fractures or dislocations impinging on the carpal tunnel. All nerves may be transected by wounds from a knife, glass, a bullet or other missile anywhere along their course. The axillary artery and its main branches are commonly involved in nerve injuries. Wounds of the median nerve in the arm commonly extend to the brachial artery, and the ulnar artery is usually involved in wounds to the ulnar nerve in the forearm and at the wrist.

Nerves and their related structures may be displaced by fracture, dislocation or haematoma. The ensuing fibrosis distorts normal anatomical relations; this increases the risk of intraoperative damage when nerves and accompanying vessels are not formally exposed. The incidence of such iatrogenic injuries is increasing and accounts for one-quarter of lesions of the radial nerve: the incidence is even higher for nerves around the elbow.

Injuries to nerves of cutaneous sensation are common after wounds, incisions or vessel puncture. It is remarkable that the elective removal of nerves such as the medial cutaneous nerve of the forearm for the purpose of grafting is followed by pain only very rarely, while lesions of the terminal branches are usually painful. The medial cutaneous nerve of the arm and the intercostobrachial nerve are at risk during operations in the axilla. The posterior cutaneous nerves of the arm and forearm are vulnerable during the lateral approach to the shaft of the humerus. The medial and lateral cutaneous nerves of the forearm are frequently damaged during operations around the elbow. The dorsal branch of the ulnar nerve is at risk during operations on the distal third of the ulna. The superficial radial and lateral cutaneous nerves are frequently injured by interventions on the lateral side of the wrist. Injuries to the palmar cutaneous branch of the median nerve and to the digital nerves are unwelcome complications of operations on the hand. These injuries cause pain, which may become severe. Mechanical allodynia, the perception of light touch as pain, is common; the spread of pain and allodynia beyond the territory of an injured nerve is frequent and indicates central sensitization of other neurones in the dorsal horn of the spinal cord.

Examination

Examination complements the history and the interpretation of symptoms to provide an accurate diagnosis. All findings should be set down in an intelligible record. Unfortunately, the signs of acute nerve injury have to be sought at a time when the patient may be least able to cooperate in an examination: soon after wounding, when there is likely to be distress and when the general condition may be affected by loss of blood and other injuries and/or by drink and drugs. The examination often has to be undertaken in the frequently unfavourable surroundings of an accident department. When the lesion has been inflicted by a surgeon or anaesthetist, the patient's response is likely to be distorted by postoperative pain, by the effects of recent general anaesthesia or by sedative or analgesic drugs. These are inappropriate conditions for a quiet and comprehensive 'neurological examination', and yet this is the time when the fact of nerve injury must at least be recognized if the best result is to be obtained from treatment. The examiner should, at all times, bear in mind the fact that, if there is a wound over the line of a main nerve and if there is any suggestion of loss of sensibility or impairment of motor function in the distribution of that nerve, it must be regarded as having been cut until and unless it is proved otherwise.

Local signs in closed injury

In closed injuries, swelling or ecchymosis and linear abrasions indicate severe soft tissue injury and also the line of application of force (see Fig. 48.29). Peripheral pulses and limb perfusion must be examined and re-examined.

Wound characteristics

It is useful to distinguish between the tidy wound caused by a knife and the untidy, and usually contaminated, wound of open fracture, machinery or gunshot. A further distinction is made between wounds caused by a handgun, rifle and close-range shotgun, the latter being particularly destructive. The injuries of current conflicts are classed as penetrating missile wound; (small) fragment wound; and blast wound, those from mines or improvised explosive devices (IEDs).

Sensation

Sensory loss is determined by response to light touch and pinprick. If circumstances permit, the patient outlines the area of sensory loss, which is then marked by a black skin-marker pen. The surrounding zone of incomplete sensory loss can be similarly marked in red, and the limb then photographed. For clinical examples, see **Figs 48.17–48.27**

Examination of muscles

Selected muscles are examined. The patient lying supine is usually able to demonstrate activity in serratus anterior by lifting the shoulders away from the couch, by means of 'forward shrugging'. It is usually possible to observe the presence of flexion and abduction at the shoulder, flexion and extension of the elbow and wrist, and flexion and extension of the

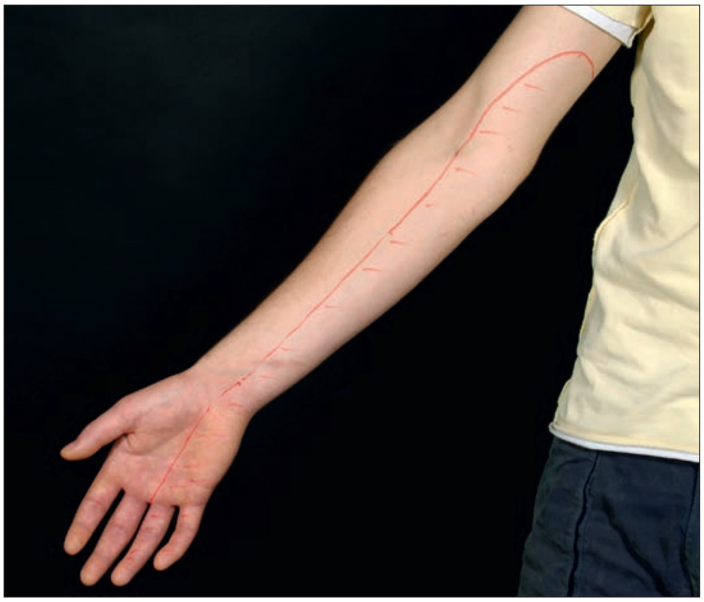

Fig. 48.17 The area of sensory abnormality after transection of C8 and T1. (Courtesy of Rolfe Birch, all rights reserved, published in Birch R, Surgical Disorders of the Peripheral Nerve, 2nd ed, 2011. Springer-Verlag, London.)

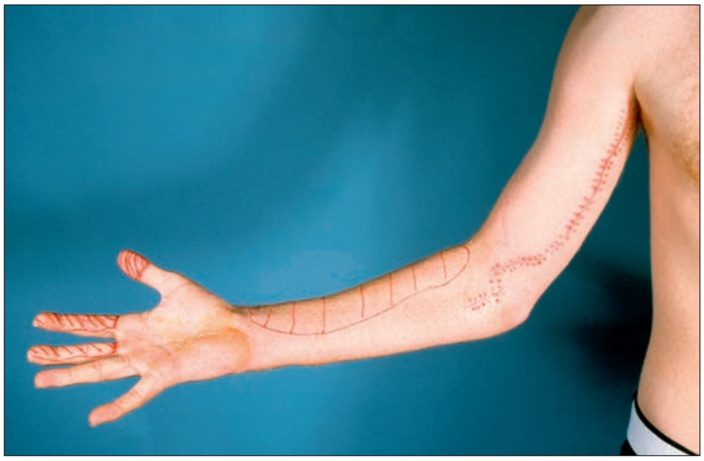

Fig. 48.18 The area of sensory abnormality after section of the lateral cord in the axilla. As in Fig. 48.17, there was no complete loss of sensation. (Courtesy of Rolfe Birch, all rights reserved, published in Birch R, Surgical Disorders of the Peripheral Nerve, 2nd ed, 2011. Springer-Verlag, London.)

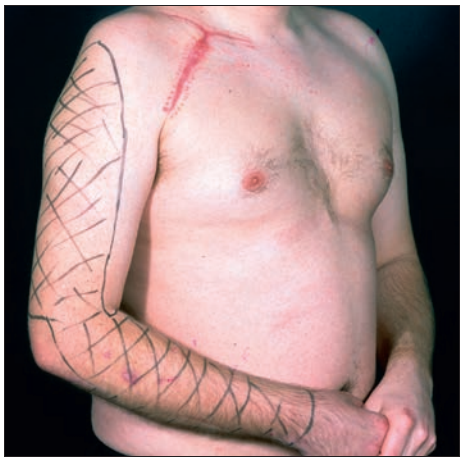

Fig. 48.19 Rupture of the posterior divisions of the trunks of the brachial plexus deep to the clavicle. (Courtesy of Rolfe Birch, all rights reserved, published in Birch R, Surgical Disorders of the Peripheral Nerve, 2nd ed, 2011. Springer-Verlag, London.)

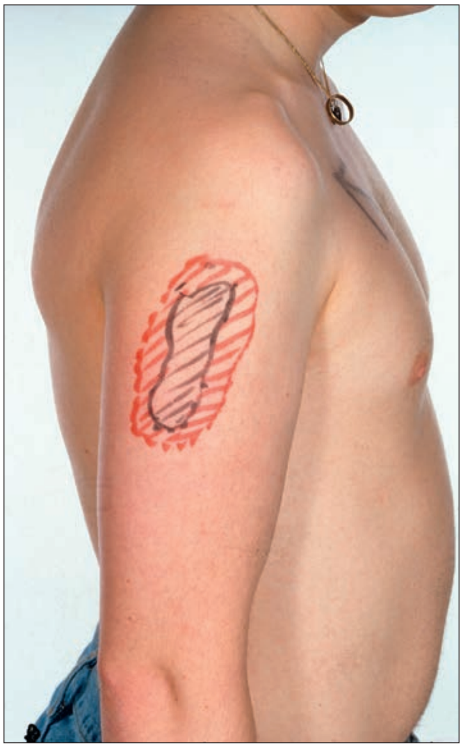

Fig. 48.20 Rupture of the axillary nerve. (Courtesy of Rolfe Birch, all rights reserved, published in Birch R, Surgical Disorders of the Peripheral Nerve, 2nd ed, 2011. Springer-Verlag, London.)

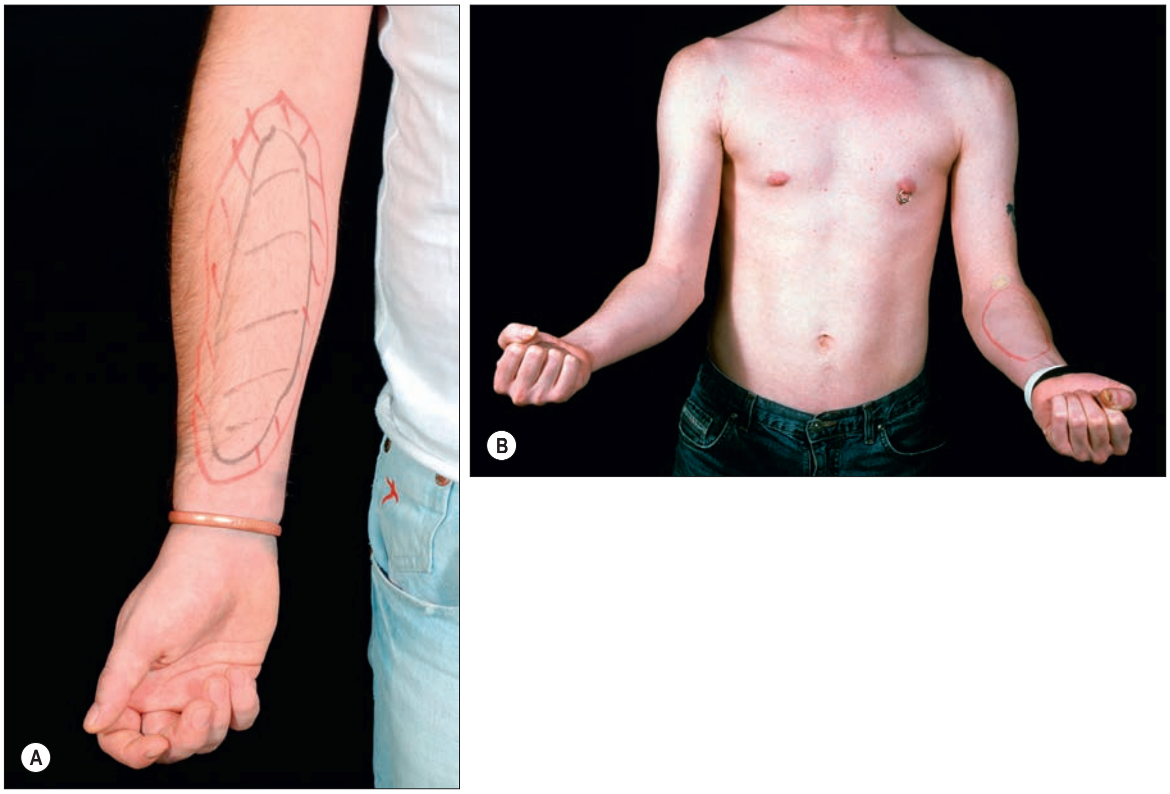

Fig. 48.21 Sensory loss in two cases of rupture of the musculocutaneous nerve. Both patients were able to supinate the forearm fully; the power of elbow flexion was around 30%. (Courtesy of Rolfe Birch, all rights reserved, published in Birch R, Surgical Disorders of the Peripheral Nerve, 2nd ed, 2011. Springer-Verlag, London.)

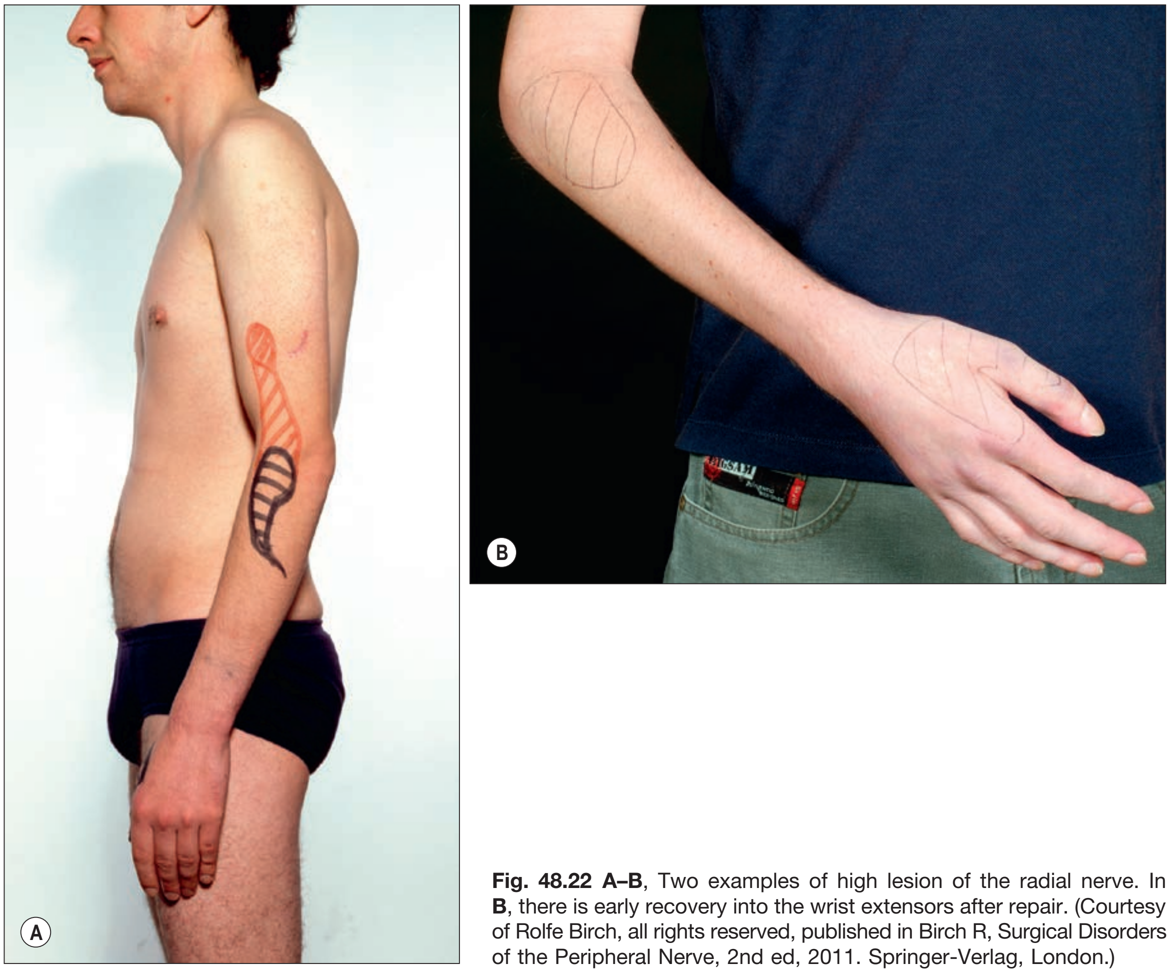

Fig. 48.22 A–B, Two examples of high lesion of the radial nerve. In **B**, there is early recovery into the wrist extensors after repair. (Courtesy of Rolfe Birch, all rights reserved, published in Birch R, Surgical Disorders of the Peripheral Nerve, 2nd ed, 2011. Springer-Verlag, London.)

fingers. The radial, median and ulnar nerves are tested by asking the patient to form an 'O' between the thumb and little finger, to give the 'thumbs up' sign, and to open and close the fingers like a fan. The palmar skin is scrutinized for changes in colour and in sweating (Fig. 48.28). Although this may be more difficult in pigmented skin, such changes are detectable. The standard tendon reflexes are examined.

Secondary examination

A more detailed examination is possible when the patient's condition is stable, and when pain has been controlled. Limb dominance, occupation, marital status, underlying disease and continuing medication are recorded, if this has not already been done. Neuropathic pain is now somewhat easier to recognize because it is less responsive to analgesics than is pain from skeletal injury.

Recognition of the level of a lesion and the depth of injury

A sound grasp of the distribution of the spinal nerves and of the location of the formation and branching of the trunk nerves allows accurate diagnosis of the level of a lesion.

Posterior cord and radial nerve

The extent of the sensory loss is variable. There is no cutaneous sensory loss in lesions confined to the posterior interosseous nerve. The examination of selected muscles is reliable in guiding the clinician to the level of injury. They include, in order: teres major (inferior scapular nerve), latissimus dorsi (thoracodorsal nerve) and deltoid (axillary nerve). Subscapularis (superior scapular nerve) is not an easy muscle to examine.

Paralysis of all three heads of triceps places the injury in the axilla. The nerves to the lateral head of triceps leaves the main nerve rather distally, so that radial palsy, with paralysis of the lateral head but active medial and long heads, points to a lesion in the spiral groove. The nerve to brachioradialis consistently passes away from the main trunk about three fingers'-breadths above the lateral epicondyle, and the nerve to extensor carpi radialis longus leaves the main trunk about 1 cm more distally. One nerve to extensor carpi radialis brevis leaves the main nerve about 1 cm proximal to the lateral epicondyle, and another leaves at the site of division into the superficial radial and posterior interosseous nerves.

Lateral cord, musculocutaneous nerve and lateral root of the median nerve

It seems that most of the median nerve fibres that innervate the skin of the hand pass through the lateral cord. Paralysis involves biceps brachii, brachialis, flexor carpi radialis and pronator teres. That portion of brachialis innervated by the radial nerve may be intact. Division of the musculocutaneous nerve does not lead to loss of elbow flexion because brachioradialis acts as a powerful flexor of the joint (see Fig. 48.21).

Medial cord, medial head of the median and ulnar nerves

The sensory loss does not extend into the arm. If it does, then the medial cutaneous nerve of the arm must be involved. Paralysis is extensive, and includes the long flexor muscles to the digits, the small muscles of the hand, and the smooth muscle associated with the vessels and sweat glands supplying the whole of the ulnar two fingers.

Median nerve

Involvement of the palmar cutaneous nerve is useful in localizing a lesion at the wrist (see Figs 48.25, 48.26), but the extent of paralysis is a more precise guide to the level of a lesion. Injuries in the arm cause paralysis of all muscles innervated by the median nerve, including those arising from the medial epicondyle (flexor carpi radialis, pronator teres, palmaris longus, and part of flexor digitorum superficialis), as well as those innervated by the anterior interosseous nerve (flexor pollicis longus, flexor digitorum profundus to index finger) (see Fig. 48.24). Anterior interosseous palsy is distinguished from high median injury by the absence of any loss of skin sensation. Abductor pollicis brevis is the one small muscle of the hand that is consistently innervated by the median nerve.

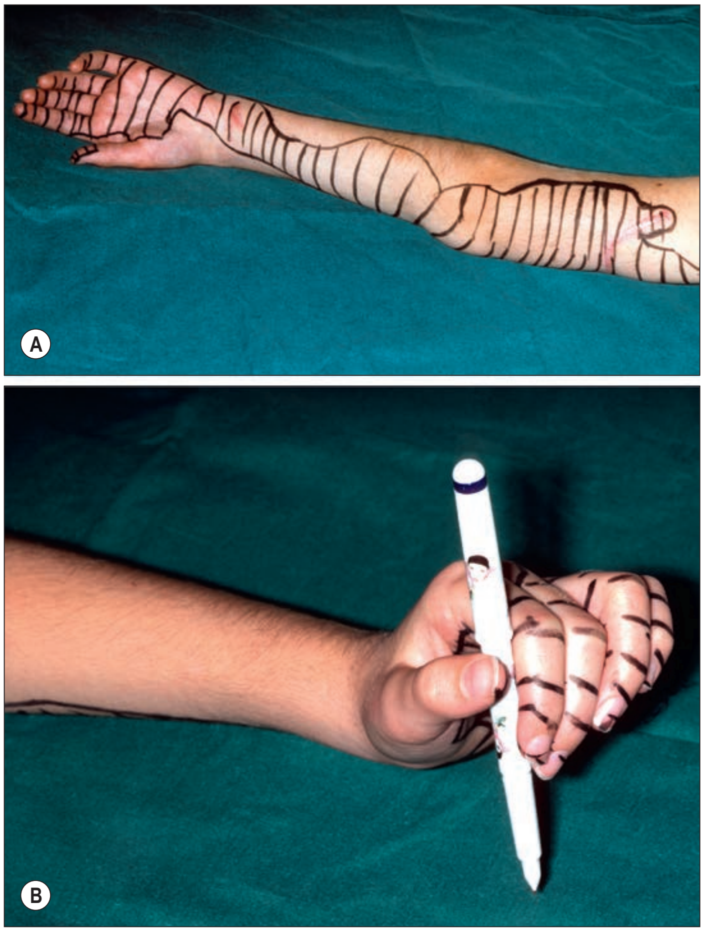

Fig. 48.23 A–B, Transection of the median nerve, ulnar nerve, medial cutaneous nerve of the forearm, and brachial artery, in the arm of a 14-year-old boy. Note the extent of skin innervation provided by the superficial radial and lateral cutaneous nerves of the forearm. The intact radial nerve permits a sort of grasp. (Courtesy of Rolfe Birch, all rights reserved, published in Birch R, Surgical Disorders of the Peripheral Nerve, 2nd ed, 2011. Springer-Verlag, London.)

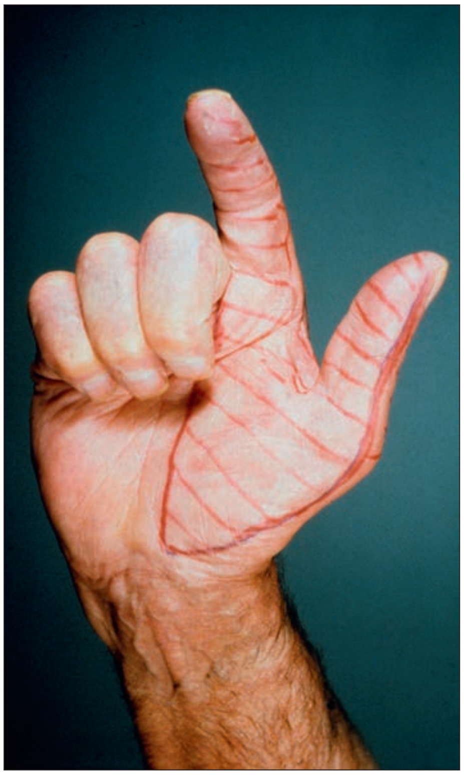

Fig. 48.24 A high median nerve injury; there is no active flexion of the index finger and thumb. (Courtesy of Rolfe Birch, all rights reserved, published in Birch R, Surgical Disorders of the Peripheral Nerve, 2nd ed, 2011. Springer-Verlag, London.)

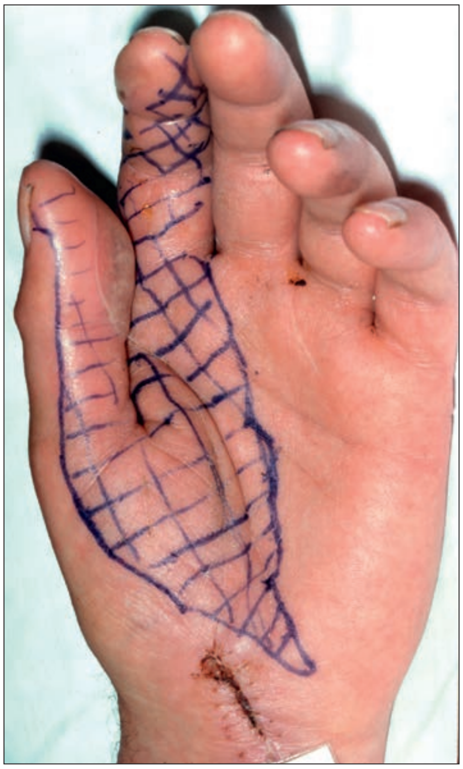

Fig. 48.25 Section of the median nerve and the palmar cutaneous nerve at the wrist. (Courtesy of Rolfe Birch, all rights reserved, published in Birch R, Surgical Disorders of the Peripheral Nerve, 2nd ed, 2011. Springer-Verlag, London.)

Ulnar nerve

The sensory loss is related to the involvement of the dorsal and palmar cutaneous branches (see Fig. 48.27). Ulnar palsy with paralysis of flexor carpi ulnaris places a lesion in the arm. Paralysis confined to the hand places a lesion in the distal half of the forearm. Preservation of the hypothenar muscles with paralysis of the other hand muscles innervated by the ulnar nerve places a lesion in the proximal part of the palm of the hand. There is no cutaneous sensory loss in a palsy of the deep branch of the ulnar nerve. The posture of the digits is characteristic in ulnar nerve lesions.

The examiner should bear in mind the possibility of anatomical variation and also the ability for other muscles to compensate for the actions of those paralysed by what are termed ‘trick movements’. In fact, these muscles are acting appropriately and the movements are real enough (see Fig. 48.23B).

Depth of a lesion

The distinction between conduction block and severance of an axon (axonotmesis or neurotmesis) is sometimes difficult. Serious injuries are likely to cause serious lesions of nerves. Severance of a nerve with a cutaneous sensory component will lead to well-defined loss of sensibility and to complete motor, sudomotor and vasomotor paralysis in the distribution of the nerve. Simple conduction block is likely to produce a patchy loss of sensibility and patchy motor loss. Further, it is likely to bear more heavily on the large axons than on the small ones. Vibration sense and sensibility to light touch are likely to be impaired, whereas pain sensibility may be unaffected. There is a risk of underestimating the severity of a nerve lesion in cases of closed injury and after intraoperative events. Different populations of nerve fibres within a main nerve that has been violently stretched but not ruptured sustain lesions of all grades of severity. Some remain intact, whilst conduction is blocked in others. Some ruptured axons will recover spontaneously, whilst others will not, depending on their cellular microenvironment (see Commentary 1.6).

Testing of sensibility is often difficult soon after wounding, or when nerve injury is associated with fracture of a long bone. The actions of some muscles can be simulated by the actions of others, so that the fact of paralysis can be missed in the early stages after nerve injury. Thus, when the median nerve has been cut, opposition of the thumb can be mimicked by the action of extensor pollicis brevis (posterior interosseous nerve) and abductor pollicis longus (radial nerve). Similarly, abductor

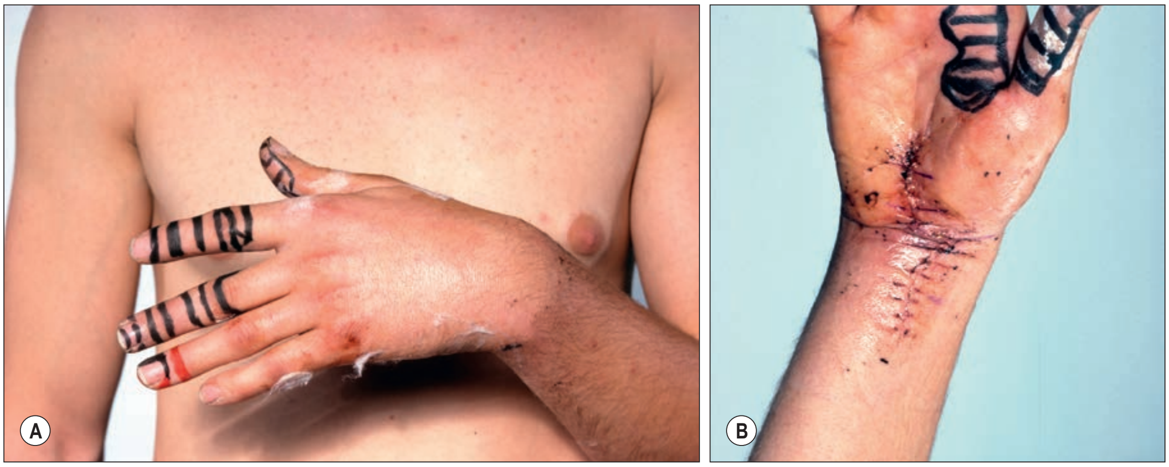

Fig. 48.26 A–B, Typical area of loss of sensibility after division of the median nerve at the wrist, sparing the palmar cutaneous branch. (Courtesy of Rolfe Birch, all rights reserved, published in Birch R, Surgical Disorders of the Peripheral Nerve, 2nd ed, 2011. Springer-Verlag, London.)

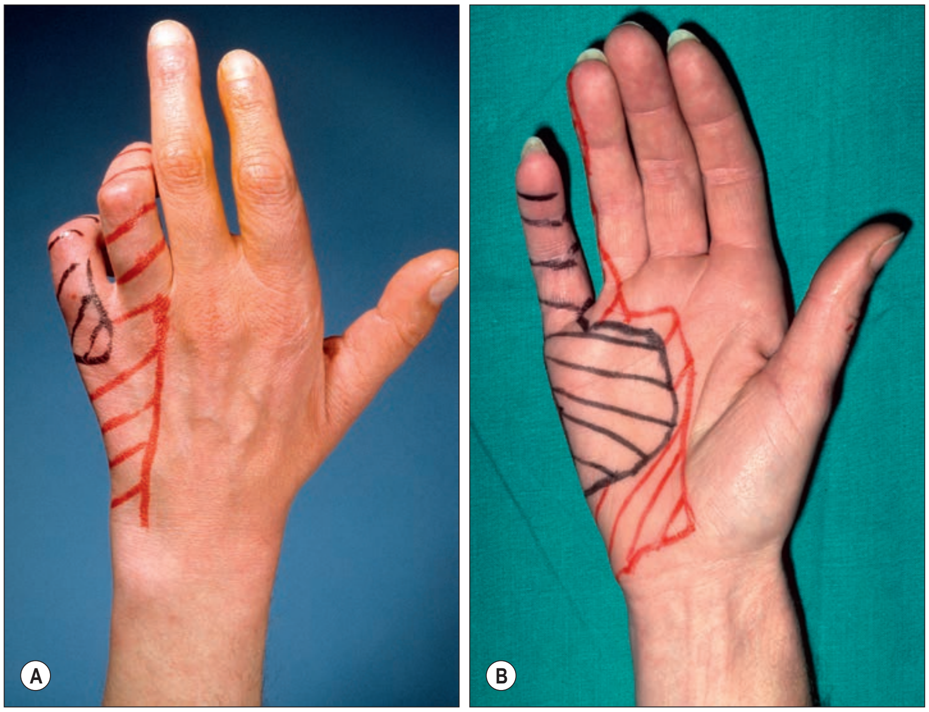

Fig. 48.27 A–B, Area of sensory loss and 'clawing' of little and ring fingers after division of the ulnar nerve in the forearm. (Courtesy of Rolfe Birch, all rights reserved, published in Birch R, Surgical Disorders of the Peripheral Nerve, 2nd ed, 2011. Springer-Verlag, London.)

pollicis longus can imitate the action of the abductor pollicis brevis. It is important to examine both hands, especially in the early days, when there is no wasting to guide the examiner. One almost infallible sign is always present in the first 48 hours after deep injury of a nerve with a cutaneous sensory component: because small, as well as large, fibres are affected, the skin in the distribution of the damaged nerve is warm and dry. In a small child, there may be an abnormal posture of the denervated digits; the 'immersion test' is also helpful. The injured hand or foot is placed, for a few minutes, in warm water; the skin of the denervated digits fails to wrinkle. In ischaemia, the large fibres conveying discriminative sensibility and vibration sense are first affected. It is not easy to test these modalities when ischaemia is developing because of the damage to a main vessel that is associated with a fracture of a long bone, but if action is not taken until superficial sensibility is lost, it will come too late.

Tinel's sign

In closed injuries, percussion of the skin over a nerve in which axons have been ruptured evokes sensations usually described as a wave or surge of pins and needles into the cutaneous distribution of the nerve. This is Tinel's sign and it is a most useful aid to diagnosis. The sign can be elicited on the day of injury in most conscious patients. It indicates not only where the nerve has been injured but also the fact that at least some axons have been ruptured. Tinel's sign can be detected from such 'motor' nerves as the posterior interosseous nerve; sensory symptoms radiate into muscular territory rather than into skin. It is more difficult to elicit the sign over deep-seated nerves such as the axillary, eighth cervical or first thoracic nerves.

Eliciting Tinel's sign in closed lesions

The examiner's finger taps along the course of the nerve from distal to proximal, starting below the presumed level of the lesion. The patient is asked to say when the advancing finger elicits a wave or a surge of pins and needles or abnormal sensations, which may be painful, into the distribution of the nerve, which must be clearly indicated by the examiner. The level of the sign should be measured from a fixed bony point and the distance recorded. At times, the examination is painful and patients need to be warned of this. A Tinel's sign that remains static at the level of a lesion strongly suggests rupture of the nerve or persisting local conditions inimical to spontaneous regeneration.

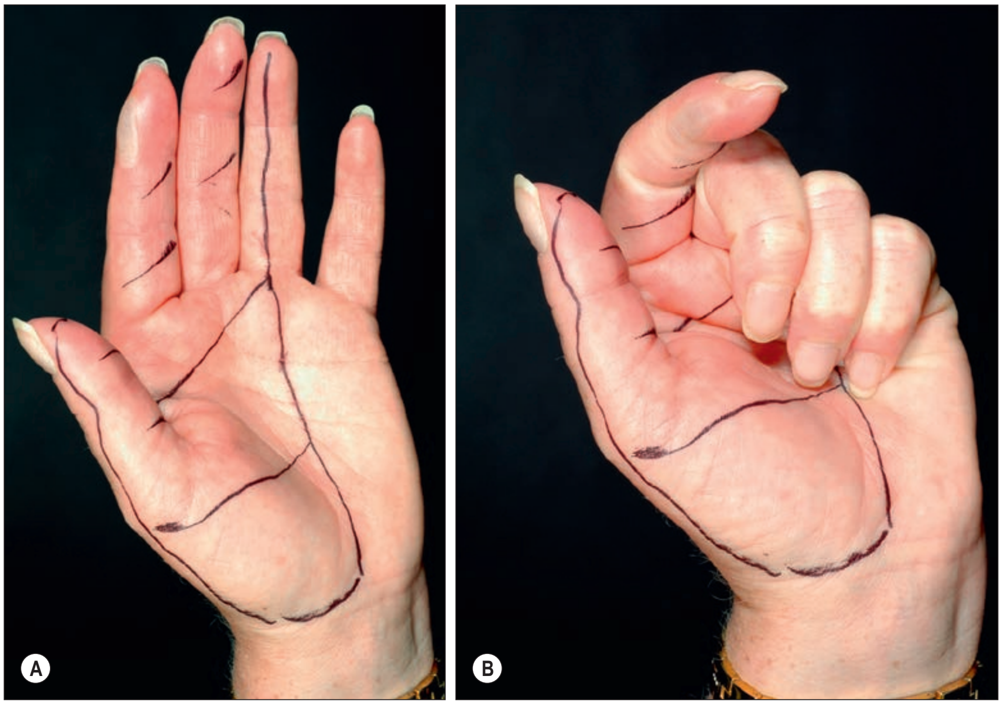

Fig. 48.28 Sympathetic paralysis seen within a few days of transection. **A–B,**Transection of the median nerve at the elbow. (Courtesy of Rolfe Birch, all rights reserved, published in Birch R, Surgical Disorders of the Peripheral Nerve, 2nd ed, 2011. Springer-Verlag, London.)

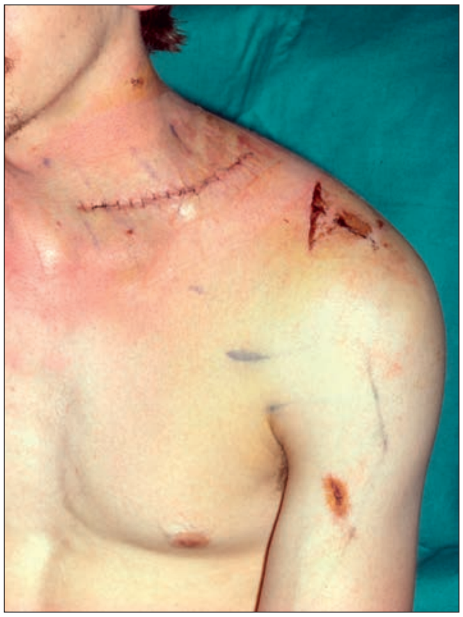

Fig. 48.29 Linear abrasions in the neck indicate separation of the forequarter from the trunk. The abrasion at the tip of the shoulder marks the point of impact against a roadside kerb. Rupture of C5, preganglionic C6–T1. (Courtesy of Rolfe Birch, all rights reserved, published in Birch R, Surgical Disorders of the Peripheral Nerve. 2nd edition, 2011. Springer-Verlag, London.)

The closed traction lesion of the supraclavicular brachial plexus is amongst the worst of all peripheral nerve injuries because of the frequent association with injury to the spinal cord and the usual complication of severe pain. There is one common element: the violent distraction of the forequarter from the head, neck and chest so that the angle between the head and the shoulder is opened. One important physical sign that illustrates this point is the presence of linear abrasions and bruising at the tip of the shoulder (Fig. 48.29). These are often injuries of great violence and motor cyclists in high-speed accidents are particularly at risk. Associated injuries to the head, spine, chest, abdomen, pelvis, long bones and subclavian artery are common.

The most common site of the nerve lesion lies within the spinal canal, affecting the intradural segments of the spinal nerves. These injuries are called preganglionic because the lesion lies between the dorsal root ganglion and the spinal cord. This concept of pre- and postganglionic injury, introduced by Bonney in 1954, is fundamental to diagnosis and treatment. The preganglionic injury is the most common lesion because the union of the ventral and dorsal roots is the weakest link in the long chain between the central nervous system and the periphery. Postganglionic rupture usually involves the ventral ramus, distal to the branching of the dorsal ramus (see Figs 47.1, 47.7). In one series of 200 patients operated on between the years 2000 and 2004, 429 spinal nerves sustained preganglionic rupture, 223 were postganglionic ruptures and the remaining 298 spinal nerves were intact or recovering. The fifth and sixth cervical nerves are somewhat protected by proximal branches to such nerves as the phrenic and long thoracic, and also by the transverse radicular ligaments. The vulnerability of C8 and T1 is enhanced by the increasing obliquity of the roots in the spinal canal and the angulated course of T1.

There are two types of preganglionic, intradural, injury: rupture peripheral to the transitional zone and avulsion central to it (Figs 48.30–48.31; see also Fig. 3.37). The former is more common. The extent of the displacement of the dorsal root ganglion, and the level of rupture of the dura, vary. These patterns are outlined in a classification by Bonney (Birch 2011a) and examples are illustrated in Figs 48.32 and 48.33. Bonney (1954, 1959) showed that the neuronal cell bodies in the dorsal root ganglion in preganglionic injuries remained alive and that conduction within their peripheral axons was maintained, even though the cell body was separated from the spinal cord (Figs 48.34–48.35); the axon reflex is probably maintained by the unmyelinated C fibres. Bonney and Gilliatt (1958) recorded sensory action potentials from peripheral nerves in cases of preganglionic injury; the measurements of persisting peripheral conduction stimulated a profound and lasting interest in conduction in the central pathways. Intraoperative studies of motor and sensory conduction are essential in emergency or urgent exploration of the brachial plexus. The demonstration that myelinated afferent fibres pass through the ventral root in the human (Schenker and Birch 2000) (Fig. 48.36) may be significant in operations to reattach the ruptured ventral root to the spinal cord.

Diagnosis

It is important always to search for occult injuries to the head, chest and spine. Once the diagnosis of injury to the brachial plexus has been made, it should be put to one side while a systematic examination is made of the whole patient. Analysis, history and precise clinical

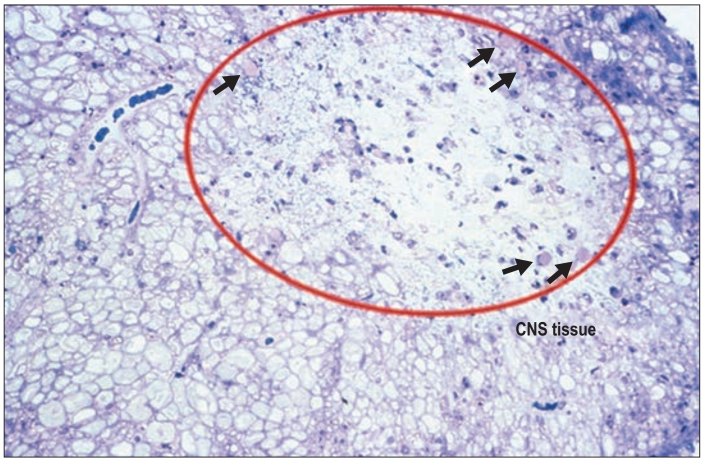

Fig. 48.30 Transverse section of the tip of an avulsed dorsal root at C6 4 days after injury, showing a central avulsion. The tissue in the centre of the section is central nervous system (CNS) tissue, in which glial cells show post-traumatic lytic changes. Corpora amylacea are indicated by arrows. Toluidine blue stained resin section ×100. (Courtesy of the Editor Journal of Bone and Joint Surgery (British), from Schenker M, Birch R 2001 Diagnosis of the level of intradural rupture of the rootlets in traction lesions of the brachial plexus. J Bone Joint Surg Br 83:916–20.)

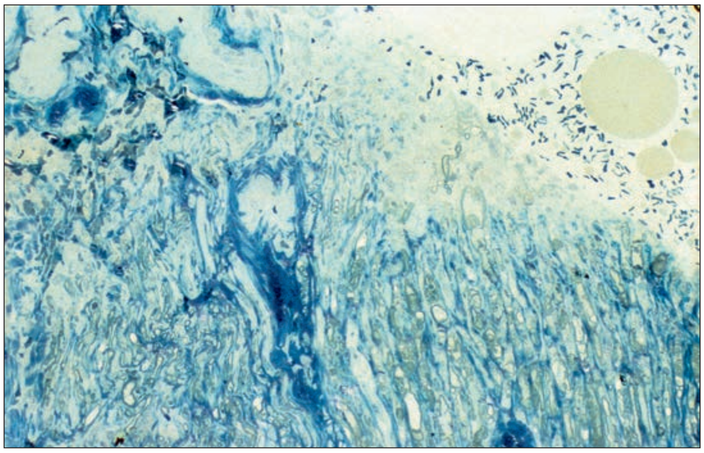

Fig. 48.31 An avulsed ventral root of C6 4 days after injury, showing a peripheral intradural rupture. The nerve tissue at the site of the rupture showed no central nervous system features. The tip is covered by organized blood clot and erythrocytes that interweave with fibrin strands. The myelinated fibres show early signs of Wallerian degeneration. Toluidine blue stained resin section ×200. (Courtesy of Rolfe Birch, all rights reserved, published in Birch R, Surgical Disorders of the Peripheral Nerve. 2nd edition, 2011. Springer-Verlag, London.)

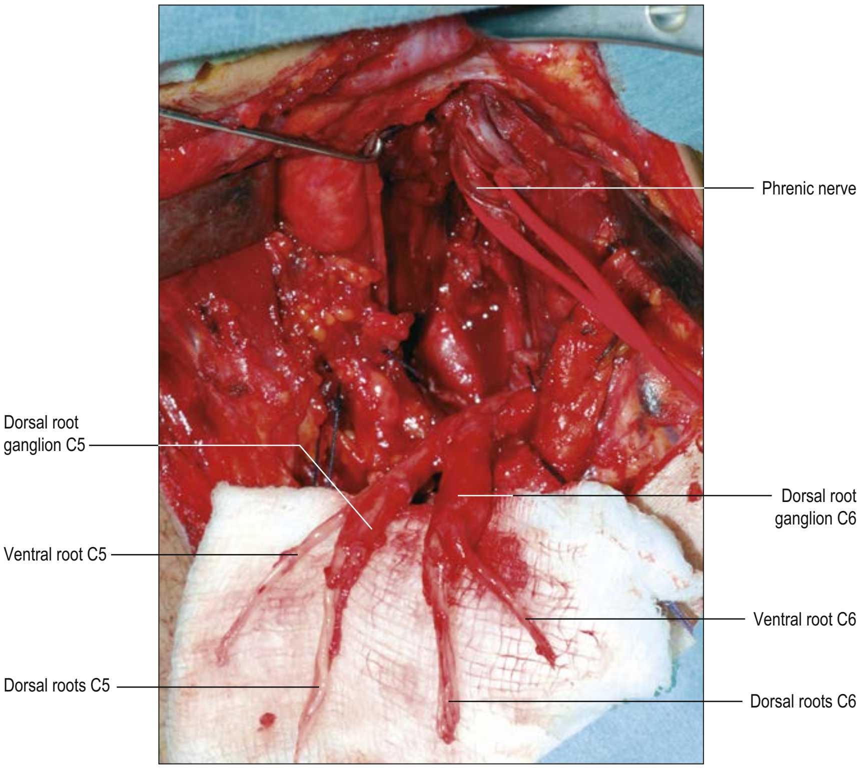

Fig. 48.32 The fifth and sixth cervical nerves avulsed from the spinal cord. The ventral root is easily distinguishable from the dorsal rootlets. Note the dorsal root ganglion, the dural sleeve merging into the epineurium, and the spinal nerve itself. The small pieces of tissue on the proximal ends of the dorsal rootlets (below) are probably portions of the spinal cord. (Courtesy of Rolfe Birch, all rights reserved, published in Birch R, Surgical Disorders of the Peripheral Nerve. 2nd edition, 2011. Springer-Verlag, London.)

examination usually permit an accurate diagnosis of the extent and the level of the neurological injury.

History An understanding of the axis of application of force to the injured limb is very important. A description from witnesses or the patient of the shoulder being violently arrested by an object – stone, tree, kerb or vehicle – while the body is flying through the air confirms that there has been violent stretching of the structures in the posterior triangle of the neck.

Pain Severe pain within a paralysed and anaesthetic limb indicates very serious injury to the spinal nerves. It may be constant, described as crushing, burning or intense pins and needles, and is usually felt in the forearm and hand. Two-thirds of conscious patients who developed such pain did so on the day of injury. The superimposed shooting pain coursing into the dermatome of a spinal nerve signifies preganglionic injury to the nerve (Fig. 48.37). More than one-half of conscious patients experienced this pain on the day of injury (Birch 2011b).

Inspection Inspection of the limb may reveal linear cuts and abrasions passing from the face to the shoulder, indicating distraction of the limb when injury was sustained. Deep bruising is an important sign of tearing of prevertebral muscle or even of the subclavian artery. Increasing swelling in the posterior triangle indicates a collection of spinal fluid, either from nerves avulsed from the spinal cord or from an expanding haematoma, or both. Horner's (Bernard–Horner) syndrome is a strong indicator of preganglionic injury to C8 and T1 and is the result of interruption of the rami between the spinal nerves and the stellate ganglion (see Fig. 48.16).

Sensory loss Sensory loss extending above the clavicle is a sign of preganglionic injury to at least the upper nerves of the brachial plexus (Figs 48.38-48.41).

Muscle weakness Paralysis of serratus anterior and of the ipsilateral hemidiaphragm shows that the lesion is in the most proximal segments of C4–C7 and that these nerves are likely to have sustained preganglionic injury.

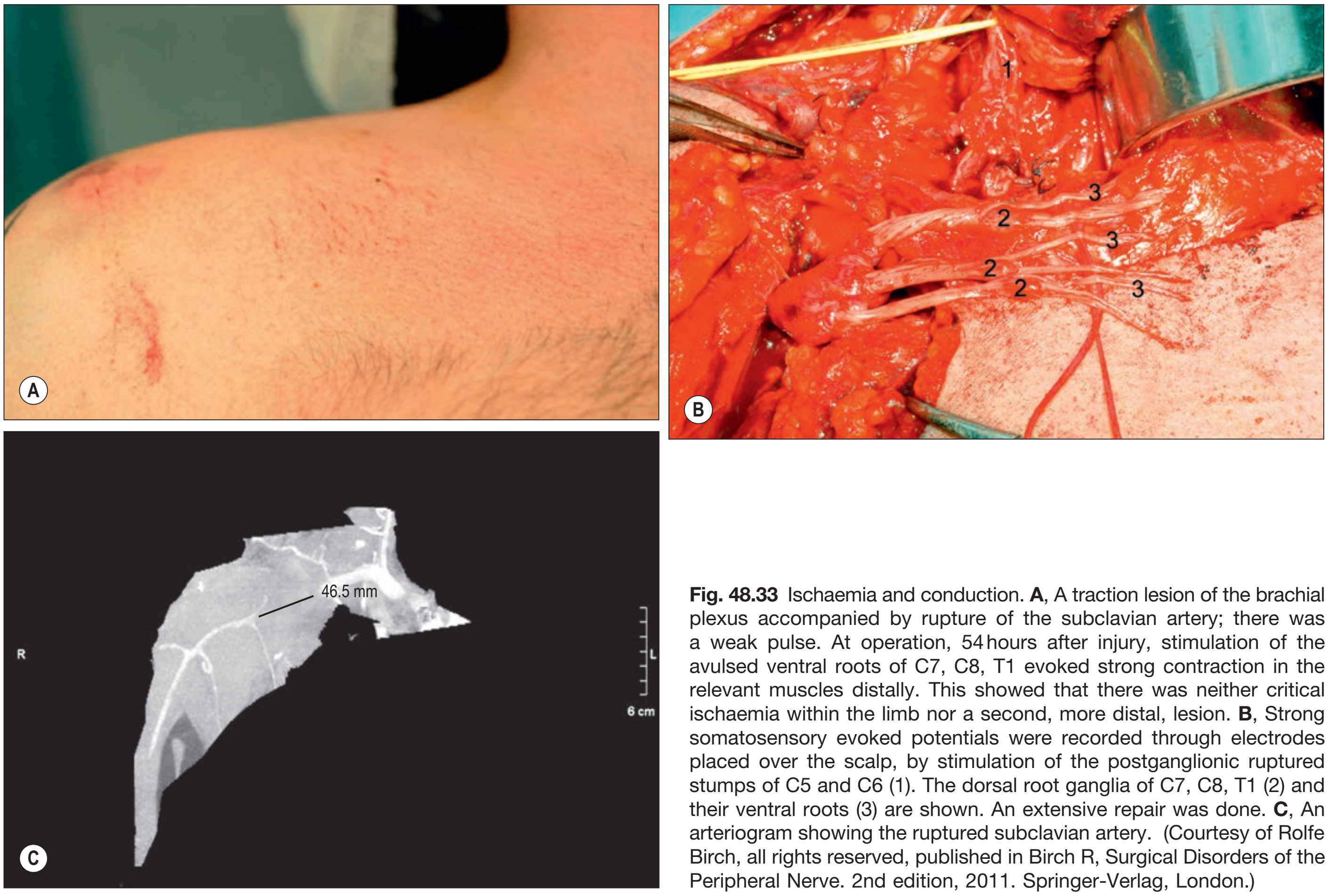
A
B
1
2
2
2
3
3
3
C
46.5 mm
R
L
6 cm

Fig. 48.33 Ischaemia and conduction. **A**, A traction lesion of the brachial plexus accompanied by rupture of the subclavian artery; there was a weak pulse. At operation, 54 hours after injury, stimulation of the avulsed ventral roots of C7, C8, T1 evoked strong contraction in the relevant muscles distally. This showed that there was neither critical ischaemia within the limb nor a second, more distal, lesion. **B**, Strong somatosensory evoked potentials were recorded through electrodes placed over the scalp, by stimulation of the postganglionic ruptured stumps of C5 and C6 (1). The dorsal root ganglia of C7, C8, T1 (2) and their ventral roots (3) are shown. An extensive repair was done. **C**, An arteriogram showing the ruptured subclavian artery. (Courtesy of Rolfe Birch, all rights reserved, published in Birch R, Surgical Disorders of the Peripheral Nerve. 2nd edition, 2011. Springer-Verlag, London.)

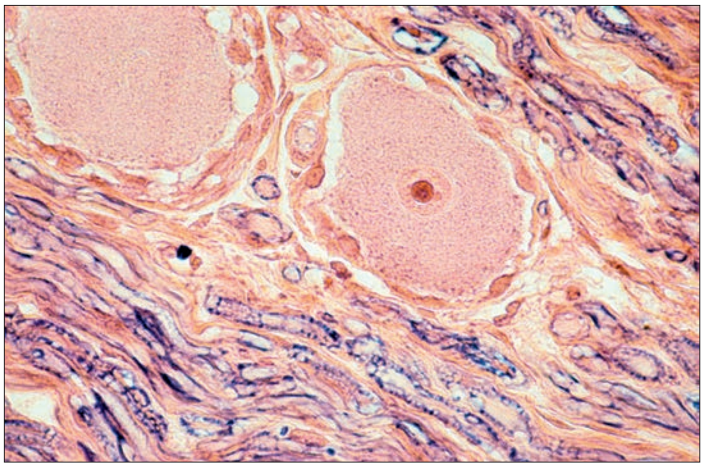

Fig. 48.34 A dorsal root ganglion 6 months after avulsion from the spinal cord. The cell bodies are healthy and there are numerous myelinated fibres. Solochrome cyanin ×960. (Courtesy of Rolfe Birch, all rights reserved, published in Birch R, Surgical Disorders of the Peripheral Nerve. 2nd edition, 2011. Springer-Verlag, London.)

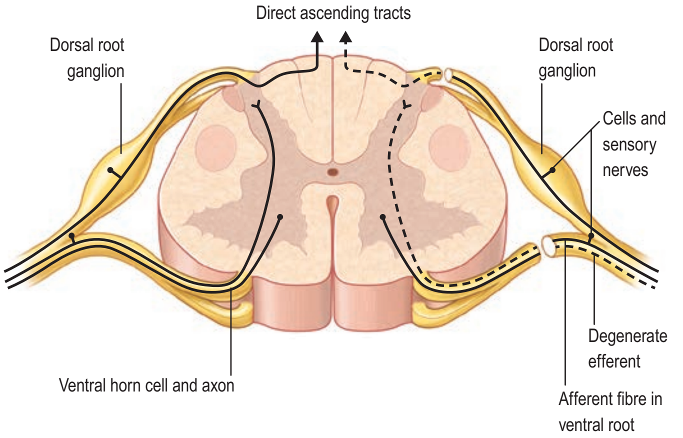
Direct ascending tracts
Dorsal root ganglion
Dorsal root ganglion
Cells and sensory nerves
Degenerate efferent
Ventral horn cell and axon
Afferent fibre in ventral root

Fig. 48.35 The nerve and roots detached from the spinal cord. Note the intact dorsal root ganglion cell, with healthy axons in the detached parts of the roots, and the degeneration of the efferent fibre in the ventral root. (Courtesy of Rolfe Birch, all rights reserved, published in Birch R, Surgical Disorders of the Peripheral Nerve. 2nd edition, 2011. Springer-Verlag, London.)

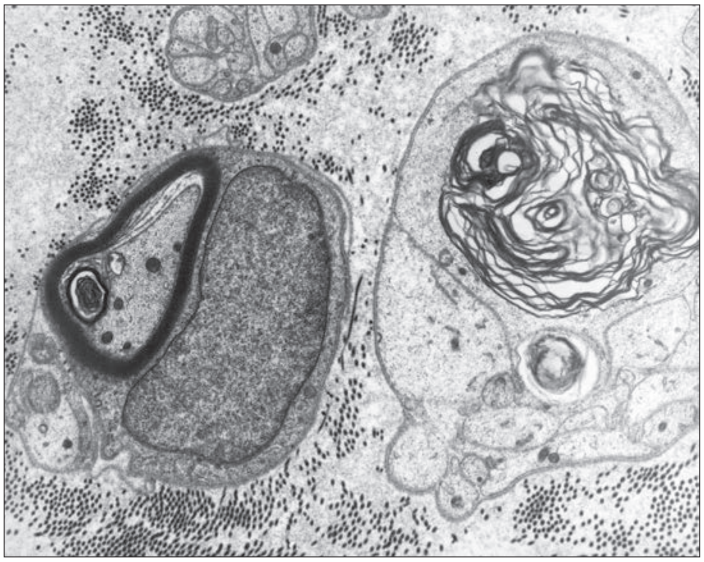

Fig. 48.36 Wallerian degeneration in the ventral root of the eighth cervical nerve 6 weeks after avulsion from the spinal cord. A degenerate efferent myelinated fibre (right) compared to a non-degenerate afferent myelinated fibre (left). EM ×11115. (Courtesy of Rolfe Birch, all rights reserved, published in Birch R, Surgical Disorders of the Peripheral Nerve. 2nd edition, 2011. Springer-Verlag, London.)

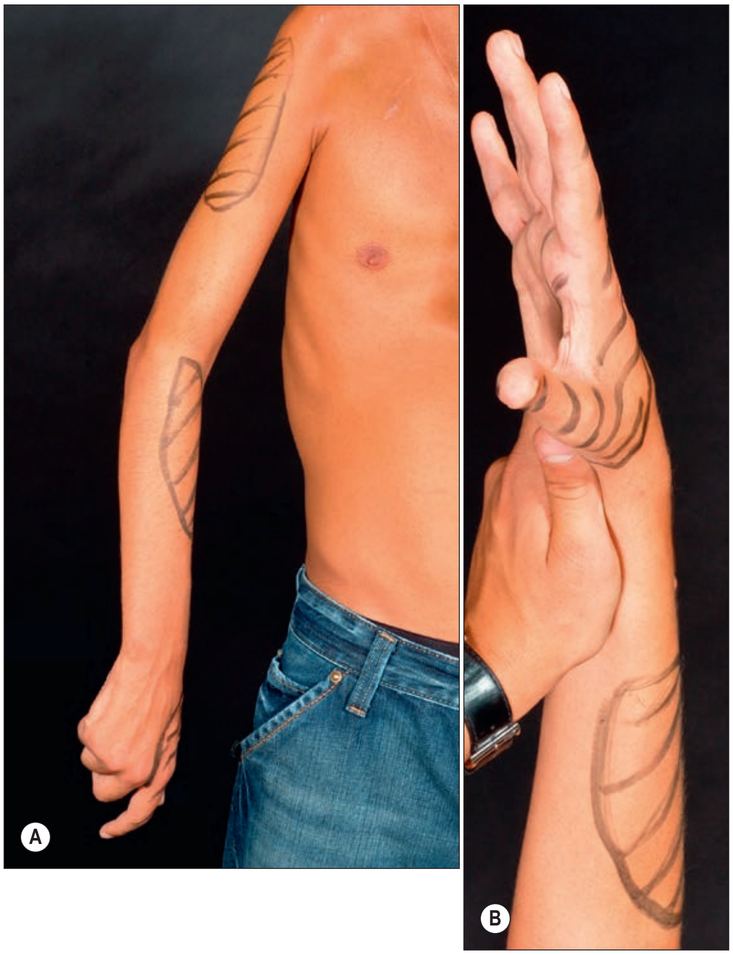

Fig. 48.37 **A–B**, Intense, lightning-like pain was felt in the dermatomes of C5–C7 in this patient on the day of injury; these three nerves were avulsed from the spinal cord. (Courtesy of Rolfe Birch, all rights reserved, published in Birch R, Surgical Disorders of the Peripheral Nerve. 2nd edition, 2011. Springer-Verlag, London.)

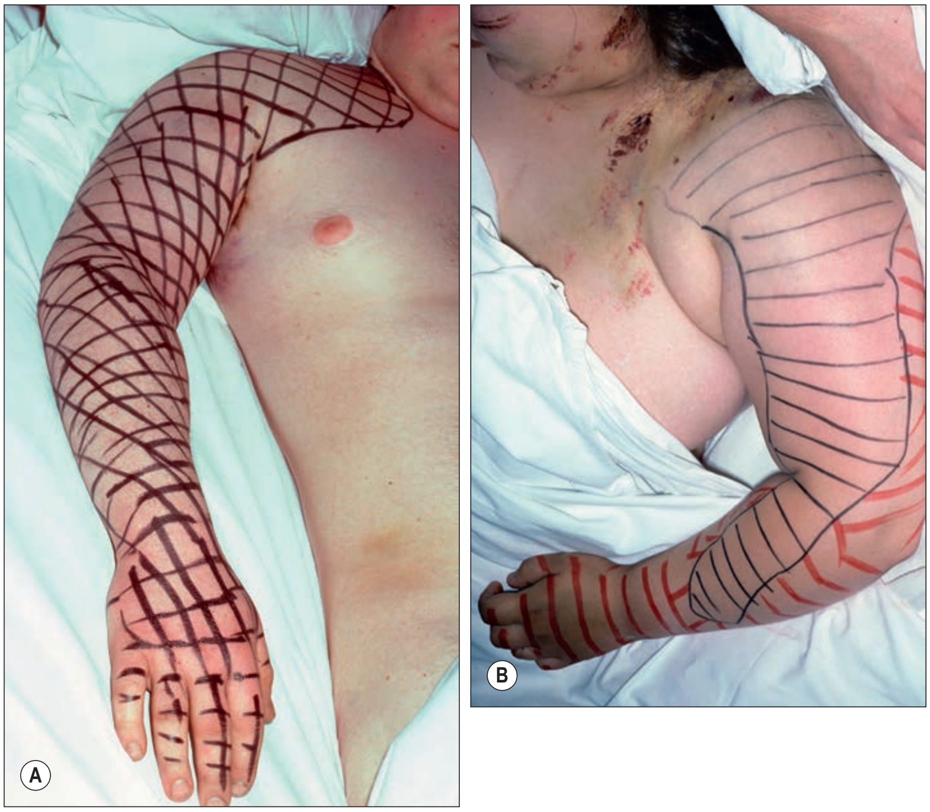

Fig. 48.38 **A–B**, Sensory loss in a complete preganglionic lesion of C4–T1 in two patients. (Courtesy of Rolfe Birch, all rights reserved, published in Birch R, Surgical Disorders of the Peripheral Nerve. 2nd edition, 2011. Springer-Verlag, London.)

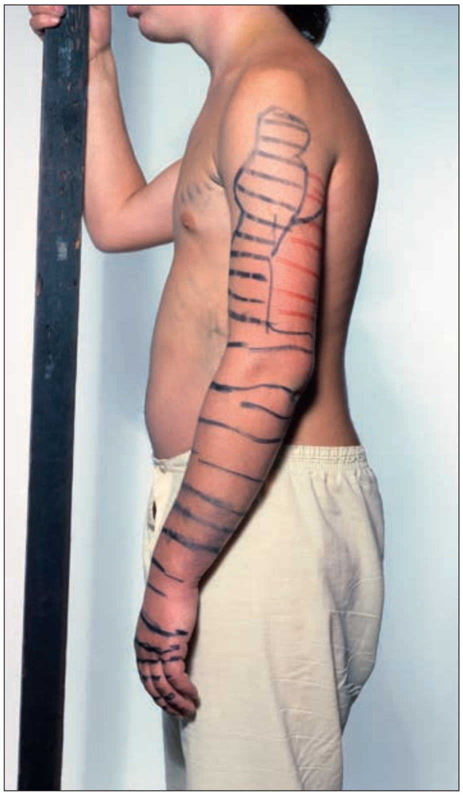

Fig. 48.39 Sensory loss in a preganglionic lesion of C5–T1. C4 innervates the skin of the outer aspect of the shoulder; T2 innervates the skin of the inner aspect of the arm. (Courtesy of Rolfe Birch, all rights reserved, published in Birch R, Surgical Disorders of the Peripheral Nerve. 2nd edition, 2011. Springer-Verlag, London.)

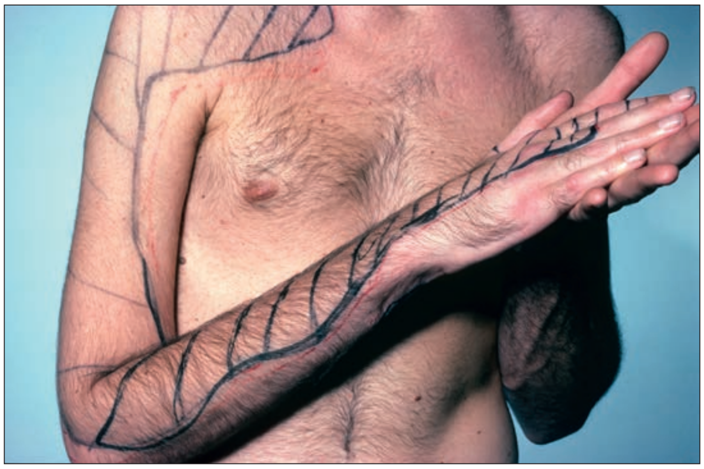

Fig. 48.40 Sensory loss in a preganglionic lesion of C4–C7. (Courtesy of Rolfe Birch, all rights reserved, published in Birch R, Surgical Disorders of the Peripheral Nerve. 2nd edition, 2011. Springer-Verlag, London.)

Recognition of postganglionic rupture Tinel's sign is most valuable in the early detection of ruptures. It is important to advise the patient that percussion in the posterior triangle of the neck may be painful – at times, extremely so. The patient is asked to indicate the region into which they experience radiation of intense 'pins and needles'. When these extend down the outer arm and proximal forearm, then rupture of C5 is likely. When they extend to the lateral aspect of the forearm and thumb, then a similar lesion of C6 may be anticipated. Percussion over a rupture of C7 evokes sensations into the dorsum of the hand; that over a rupture of the lower trunk evokes sensations in the inner aspect of the forearm and little fingers.

It is difficult to overstate the significance of a strong positive Tinel's sign in detecting rupture of a spinal nerve within the posterior triangle: the stronger the sign, the more likely the chances of finding a robust stump. It should be emphasized that Tinel's sign is detectable, in a conscious patient, on the day of injury.

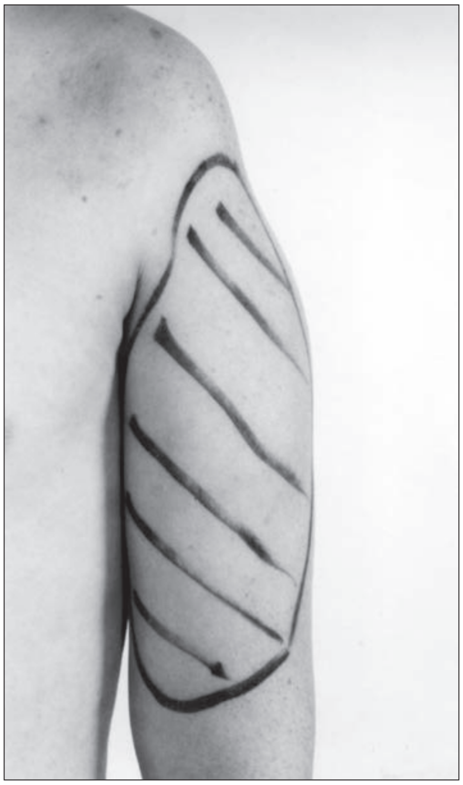

Fig. 48.41 Sensory loss in a preganglionic lesion of C5. The area of sensory loss is usually larger than that seen after rupture of the axillary (circumflex) nerve (see Fig. 49.2). (Courtesy of Rolfe Birch, all rights reserved, published in Birch R, Surgical Disorders of the Peripheral Nerve. 2nd edition, 2011. Springer-Verlag, London.)

Investigations Radiological and imaging studies confirm or modify the clinical diagnosis, but they may also confirm or reveal associated injuries to the spinal column, the spinal cord and the chest. Plain radiographs confirm elevation of the ipsilateral hemidiaphragm and may show tilting of the cervical spine away from the side of injury, which is often associated with fracture or dislocation of the first rib. The condition of roots and evidence of displacement or other abnormalities of the spinal cord are revealed by myelography: more precisely, by computed tomographic (CT) myelography and, increasingly in current practice, by magnetic resonance imaging (MRI).

Patterns of lesions

A survey of the incidence of these lesions in the UK, conducted through the auspices of the British Orthopaedic Association, uncovered 328 patients admitted with complete or partial lesions in 1987 (Goldie and Coates 1992). The lesion was complete in 26.2% of patients; the subclavian artery was ruptured in 5.5%; there were other major injuries in 40%, and a wound in the neck in 5.5%. **Table 48.5** sets out the patterns of injury in 301 patients operated on in 1989–93. Complete lesions accounted for 141 of the cases; 52 patients sustained preganglionic injury to all five spinal nerves. Over the years, there has been a modest decrease in the severity of injury; the proportion of cases with complete preganglionic injury of the fifth to the eighth cervical ventral rami and the first thoracic ventral ramus was 18.7% in the series reported by Rosson (Rosson 1987); 17.3% in those operated on between 1989 and 1993; and less than 8% in patients operated on between 2000 and 2004 (Birch 2011a). However, the incidence of injury to the subclavian artery in the operated cases remains steady over this time at about 10%.

Treatment

The direct object of treatment is rehabilitation. This entails the following steps: provision of accurate diagnosis and prognosis; improvement of prognosis by repair of damaged nerves; relief of pain; palliation of paralysis by custom-made orthoses and by musculotendinous transfers (**Fig. 48.42**); and assistance towards a return to original, appropriately modified or new work or study and to independent living.

Operations should be undertaken as soon as the patient's general condition permits in cases where there is evidently a serious nerve injury (Birch 2011a). There have been important improvements in outcomes over the years. The possibility of reconnection of the avulsed ventral roots to the spinal cord has been realized in a few carefully selected

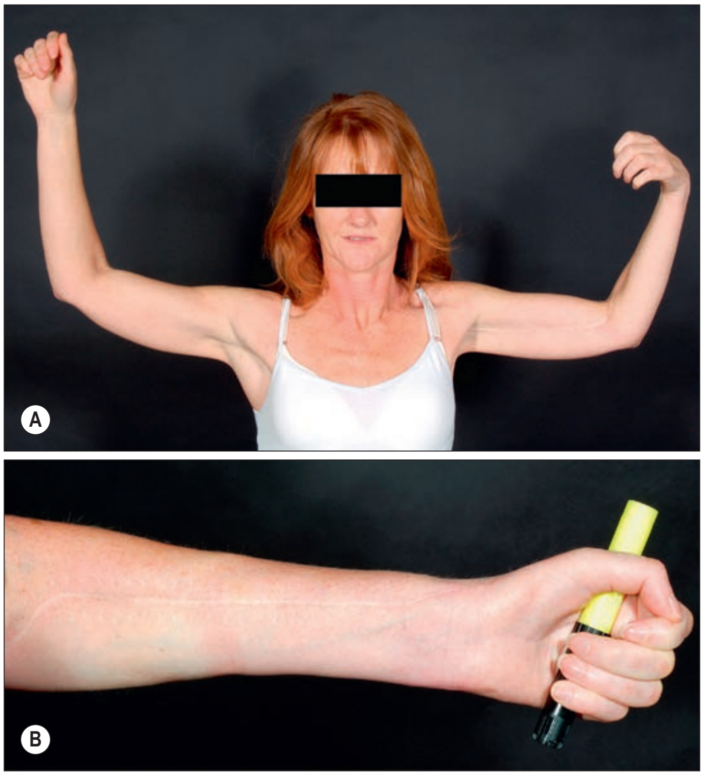

Fig. 48.42 A–B, A woman aged 28 at the time of injury with left-sided rupture of C5, C7, C8 and T1, and a preganglionic lesion of C6. Function is shown at 96 months after repair: wrist extension was regained by transfer of flexor carpi ulnaris to extensor carpi radialis brevis. (Courtesy of Rolfe Birch, all rights reserved, published in Birch R, Surgical Disorders of the Peripheral Nerve. 2nd edition, 2011. Springer-Verlag, London.)

TABLE 48.5 Patterns of injury in 301 consecutively operated supraclavicular lesions (1989–1993)

Pattern of injury	No. of patients
Complete lesions: pre- and postganglionic injuries	141
Ruptures of upper nerves C5 (C6, C7) Intradural ruptures of lower nerves (C6–C8) T1	83
Ruptures of middle nerves (C6) C7 (C8) Intradural above and below	5
Ruptures of lower nerves C8, T1 Intradural ruptures of upper nerves C5–C7	1
Total intradural ruptures of C5–T1	52
Incomplete lesions: some roots intact	153
Damage C5, C6 (C7) Recovering or intact (C7) C8, T1	117
Damage C6–C8 Recovering or intact C5, T1	23
Damage C7, C8, T1 Recovering or intact C5, C6	13

cases (Fig. 48.43). The return of fluid and coordinated muscle action, and of the biceps tendon jerk, suggests some regeneration into the deep afferent pathway, perhaps through myelinated afferent fibres in the ventral root.

Pain relief One of the most pleasing aspects of surgical endeavour has been the finding that reinnervation of muscle is regularly successful in improving pain and this is a strong indication for securing reinnervation of a limb, no matter how limited, in even the most severe injuries (Berman et al 1996, 1998, Kato et al 2006; see Birch 2011a, 2011b, 2011c).

The anatomical arrangements of some of the peripheral nerves make them particularly vulnerable to damage from musculoskeletal injury.

Fractures and dislocations

In the upper limb, the cords of the brachial plexus and the axillary vessels pass in a space bounded by subscapularis (deep) and pectoralis minor (superficial). Anterior displacement of the humeral head or bone fragments forces the nerves and vessels against the deep surface of pectoralis minor, which acts as a guillotine. Rupture of nerves and vessels is frequent in high-energy transfer injuries in younger adults and is common in many lower-energy transfer injuries in the elderly (Fig. 48.44). The proximity to bone of all three main nerves at the elbow renders them vulnerable to skeletal injuries.

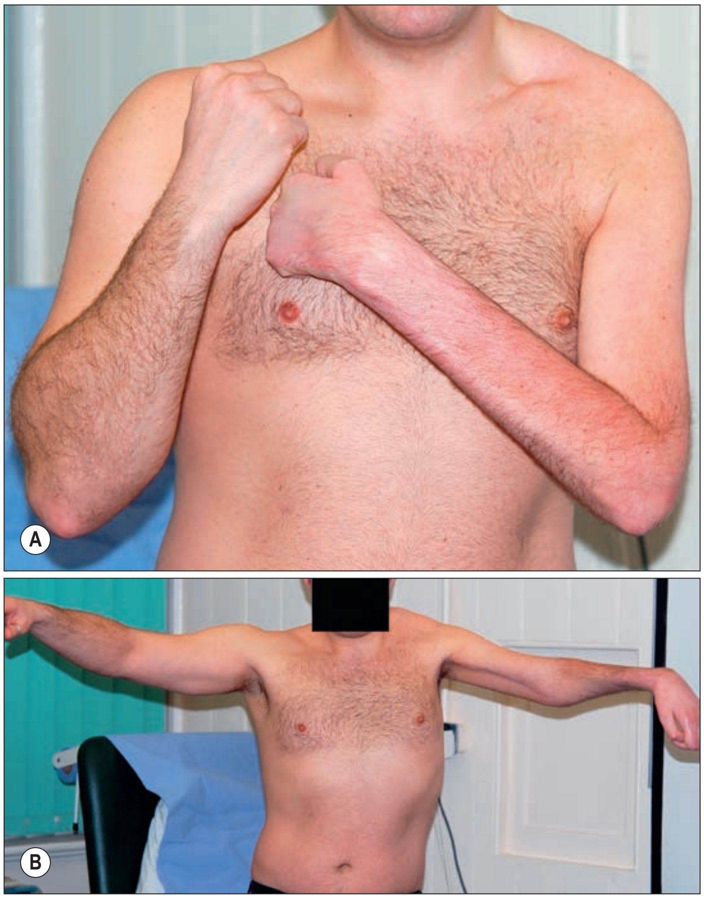

Fig. 48.43 A–B, A 23-year-old man with a left-sided preganglionic lesion of C5–T1. Function is shown at the shoulder and elbow 11 years after reimplantation of the ventral roots of C5, C6, C7. (Courtesy of Rolfe Birch, all rights reserved, published in Birch R, Surgical Disorders of the Peripheral Nerve. 2nd edition, 2011. Springer-Verlag, London.)

In the lower limb, nerve injuries are more common and more serious because of the greater forces involved in serious skeletal injuries. The lumbosacral plexus is at risk in fracture dislocations of the sacroiliac joints, especially when fractures extend into the sacral foramina. The sciatic nerve is damaged by posterior displacement of the femoral head (see Fig. 76.11B).

Tethering of nerves

In the upper limb, the axillary nerve runs in loose fatty tissue in its course anterior to subscapularis. When it turns around that muscle, it enters a quadrilateral tunnel formed by the union of the fasciae of subscapularis cranially, teres major caudally and coracobrachialis laterally, which surrounds the nerve and the posterior circumflex vessels. The neurovascular bundle curves around the inferior border of the tendon of subscapularis, and passes over the superior border of the tendon of teres major, entering a near-horizontal tube. This arrangement puts the nerve at risk during anterior dislocation of the head of the humerus and the frequent complication of bleeding from the posterior circumflex vessels, which strangles the nerve. The radial nerve is at risk from fractures of the shaft of the humerus between the two relatively fixed points of the nerves to the lateral head of triceps and the tunnel through the lateral intermuscular septum.

In the lower limb, the common fibular nerve, which passes above or through piriformis in as many as 30% of cases, is tethered above in relation to piriformis and below at the neck of the fibula. The fascia surrounding biceps femoris and its tendon sweeps around to embrace the nerve; in dislocation of the knee, the muscle frequently avulses the tip of the head of the fibula and is displaced anteriorly, pulling the nerve

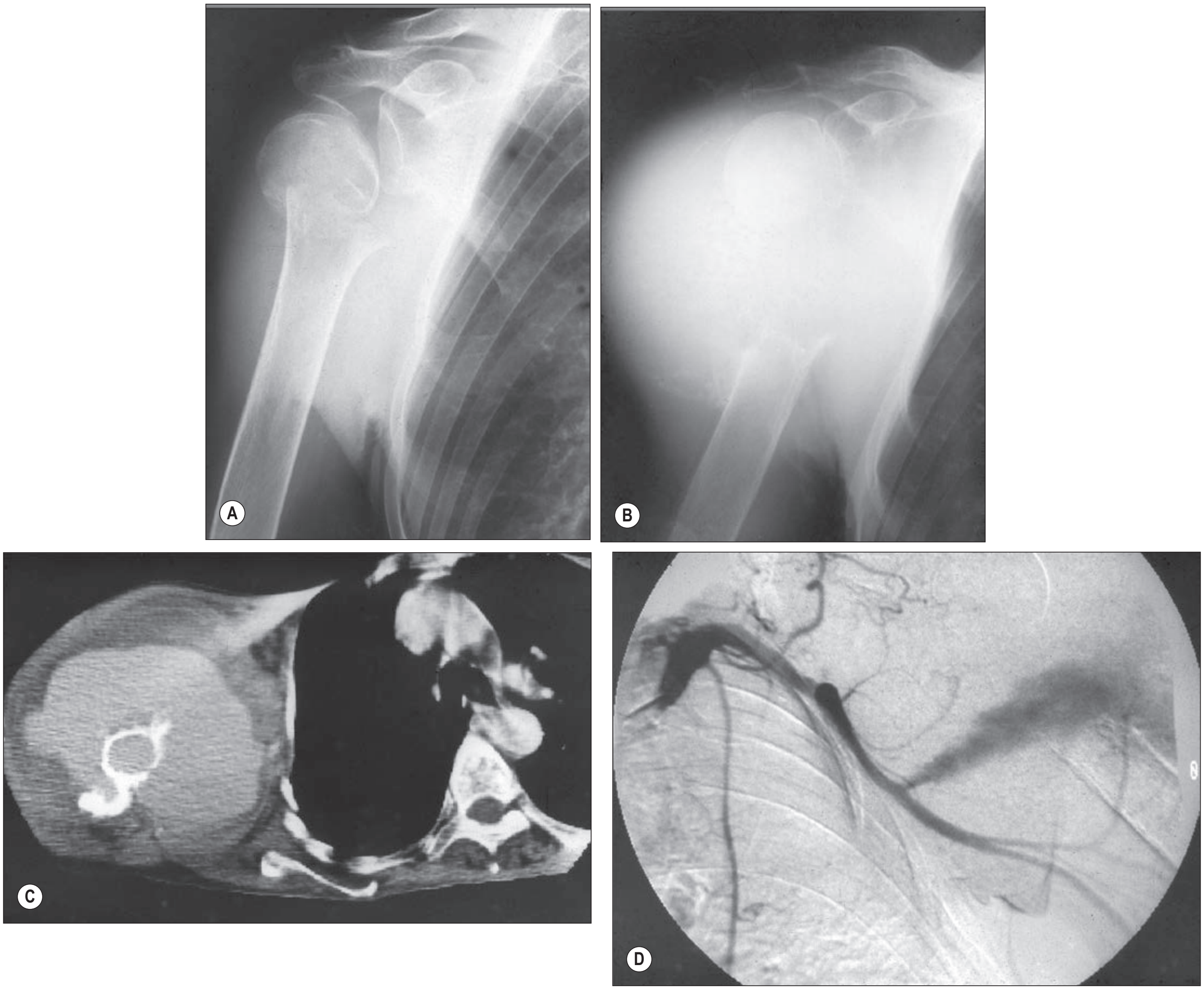

Fig. 48.44 A leaking aneurysm 20 weeks after fracture of the neck of the humerus in an 83-year-old woman. She made a good recovery after repair of the defect. **A**, A radiograph on the day of injury. **B**, A radiograph at 18 weeks. **C**, A magnetic resonance imaging (MRI) scan at 18 weeks. **D**, An angiogram on the day of operation. (Courtesy of Rolfe Birch, all rights reserved, published in Birch R, Surgical Disorders of the Peripheral Nerve. 2nd edition, 2011. Springer-Verlag, London.)

with it. The deep fibular nerve passes rather acutely forwards to enter the anterior compartment of the leg. Refer to Commentary 9.1 for further information on nerve biomechanics.

Fascial arrangements

Sleeves of fascia surround main nerves and main vessels in some regions, an arrangement that predisposes the nerves to injury from ischaemia and compression from bleeding. After the seventh and eighth cervical and first thoracic ventral rami enter the posterior triangle of the neck, they are enclosed in quite a rigid space bounded posteriorly by the dorsal part of the first rib, the transverse processes of the cervical vertebrae and the fascia of levator scapulae. The nerves are embraced by scalenus anterior and scalenus medius, both of which are invested in an unyielding fascia (this is one envelope of the prevertebral fascia that also serves to bind the phrenic nerve down to the anterior face of scalenus anterior). The prevertebral fascia is particularly well developed anterior to the vertebral column and at the base of the posterior triangle, where it envelops the seventh and eight cervical and first thoracic ventral rami, the phrenic nerve, the cervical sympathetic chain, and subclavian and vertebral arteries. Infusion of relatively large volumes of fluid, from 10 to 20 ml, deep to the prevertebral fascia, for the purpose of inducing regional block, may cause tamponade of the radicular vessels that enter the spinal canal and contribute to the anterior spinal artery (Fig. 48.45; see also Figs 47.11–47.12). The medial brachial fascial compartment extends from the axilla to the elbow and is bounded by the tough medial intramuscular septum and the axillary sheath. Bleeding into this compartment is responsible for many infraclavicular plexopathies following regional block or fracture dislocation of the shoulder (Fig. 48.46).

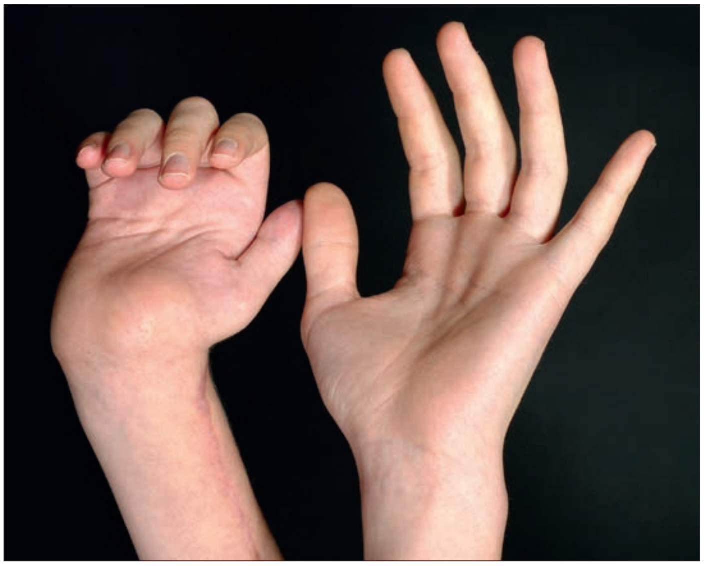

Fig. 48.45 The hands of an 11-year-old boy 7 years after anterior cord infarction caused by interscalene block. (Courtesy of Rolfe Birch, all rights reserved, published in Birch R, Surgical Disorders of the Peripheral Nerve. 2nd edition, 2011. Springer-Verlag, London.)

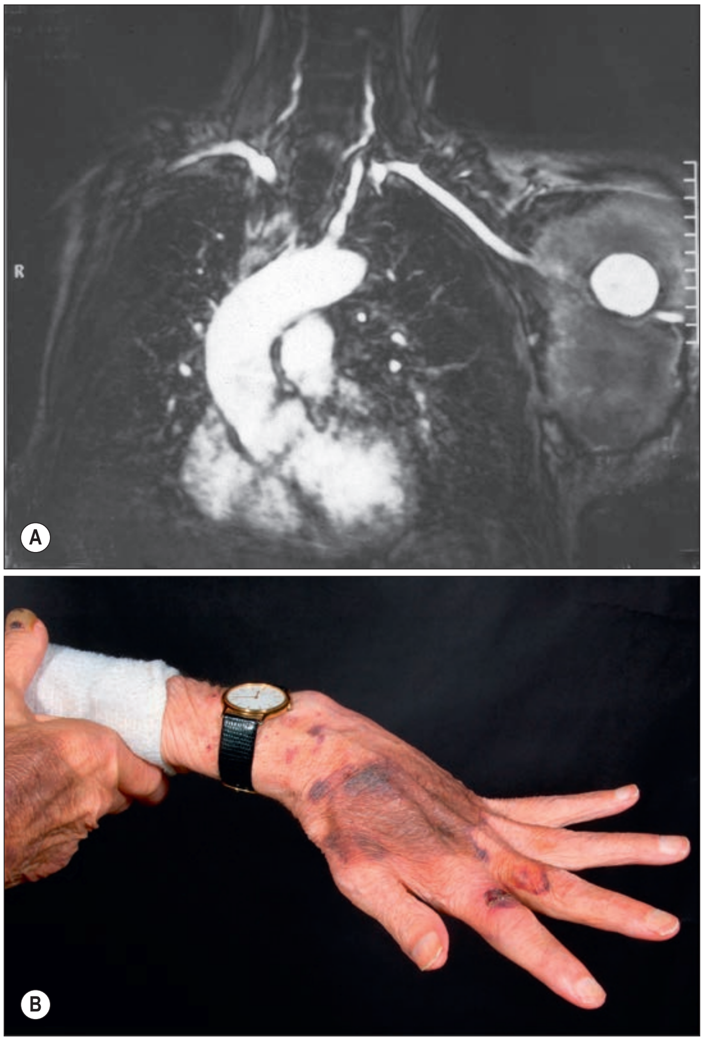

Fig. 48.46 Fracture of the left proximal humerus, complicated by expanding haematoma in a 63-year-old man. Two attempts to occlude the torn posterior circumflex artery by interventional radiology failed. He was seen at 8 weeks, by which time he was in right heart failure and in great pain; he had a complete infraclavicular plexopathy on the left side. Six litres of altered blood were removed from the axilla; his pain was relieved. Recovery was particularly poor in the radial and median nerves. **A**, An MR angiogram before operation. **B**, The left hand 4 years after operation. (Courtesy of Rolfe Birch, all rights reserved, published in Birch R, Surgical Disorders of the Peripheral Nerve. 2nd edition, 2011. Springer-Verlag, London.)

Neurovascular compartments

The anterior interosseous nerve and its accompanying artery may be damaged by compression because of swelling in the deepest part of the flexor compartment of the forearm. The ulnar nerve is accompanied by the ulnar artery in a discrete fascial compartment in the distal two-thirds of the forearm. The deep fibular nerve is accompanied by the anterior tibial artery, an end artery, throughout most of the anterior compartment of the leg; occlusion of this artery causes death of the nerves and muscles of the anterior compartment. The femoral nerve is damaged by haematoma where it passes deep to the thick fascia over iliacus, and it is also at risk from bleeding into the femoral triangle (Fig. 48.47; see Fig. 77.48). The tibial nerve is accompanied by the posterior tibial artery in the distal half of the leg in a sheath of fascia similar to the arrangements for the ulnar vessels and nerve (Fig. 48.48).

Collateral circulation

The collateral circulation at the elbow depends on vessels that run with the three main nerves. This network may maintain an adequate supply to the hand and the extensor muscles of the forearm after acute loss of flow through the brachial artery if there is no associated fracture dislocation. The situation is much worse if the ulnar or radial nerves, with their accompanying vessels, are displaced into a fracture or compressed by haematoma. The collateral circulation at the knee is particularly poor. Acute loss of flow through the popliteal artery, unless urgently restored, invariably leads to extensive death of muscle and nerve, and often to amputation.

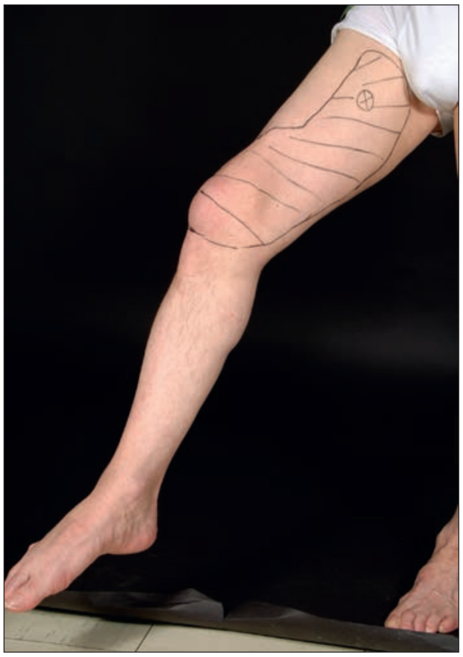

Fig. 48.47 Recovering femoral palsy from a haematoma in the femoral triangle in a 69-year-old farmer who was taking warfarin after aortic valve replacement. Two months previously he had injured his thigh whilst vaulting a gate. He experienced severe pain for 24 hours but this recovered spontaneously. The area of sensory loss is outlined and the site of the Tinel's sign is also marked. Recovery was good but not complete by 6 months. (Courtesy of Rolfe Birch, all rights reserved, published in Birch R, Surgical Disorders of the Peripheral Nerve. 2nd edition, 2011. Springer-Verlag, London.)

Thoracic outlet syndromes (TOS) are amongst the most confusing and controversial of peripheral nerve disorders. Several different entities are grouped under this one heading but they have little in common beyond the presumed site of the lesion. The lower part of the brachial plexus, and the lower trunk in particular, joined at the first rib by the subclavian vessels, run a regular obstacle course on their way to the lower borders of pectoralis minor. Some of the more important obstacles will be described here.

Suprapleural membrane (Sibson's fascia)

In its pure form, the suprapleural membrane is a thin, fan-shaped structure attached anteriorly to the internal border of the first rib, and posteriorly to the anterior border of the transverse process of the seventh cervical vertebra. It covers the apical pleura and intervenes between it and the subclavian artery. The deep part of the membrane may be quite tough and aponeurotic (Fig. 48.49). The extent of its peripheral attachment varies. Scalenus minimus is the muscle that sometimes replaces the deep or posterior part of the membrane; it may be up to 10 mm in diameter in its widest part but is usually much smaller than that. The posterior border of the membrane forms, with the edge of the first rib, the foramen through which the first thoracic nerve escapes.

First rib

The broad first rib (see Fig. 53.9) has a surface that is more horizontal than vertical. It extends over the apical pleura and curves round to the costochondral junction and then to the manubrium (see Fig. 53.8). In the healthy state, the apical pleura is easily separable from the head and neck, and most of the underside of the first rib; anteriorly, it becomes rather adherent to the underside of the rib, in relation to the costochondral junction. Scalenus medius is attached to the upper surface of the rib posteriorly. The upper portion of the nerve to serratus anterior is usually formed in scalenus medius by branches from the fourth, fifth and sixth cervical ventral rami; it emerges from the lateral surface of the muscle to be joined by a contribution from the seventh cervical ventral ramus. Anterior to scalenus medius, the surface of the rib is, in the adult, grooved by the passage of the first thoracic ventral ramus and the lower trunk of the brachial plexus. There is a distinct tubercle at the attachment of scalenus anterior; the subclavian artery lies in a slight depression posterior to the tubercle, and the subclavian vein runs over the upper surface of the rib anterior to the tubercle. The intercostal muscles are attached to

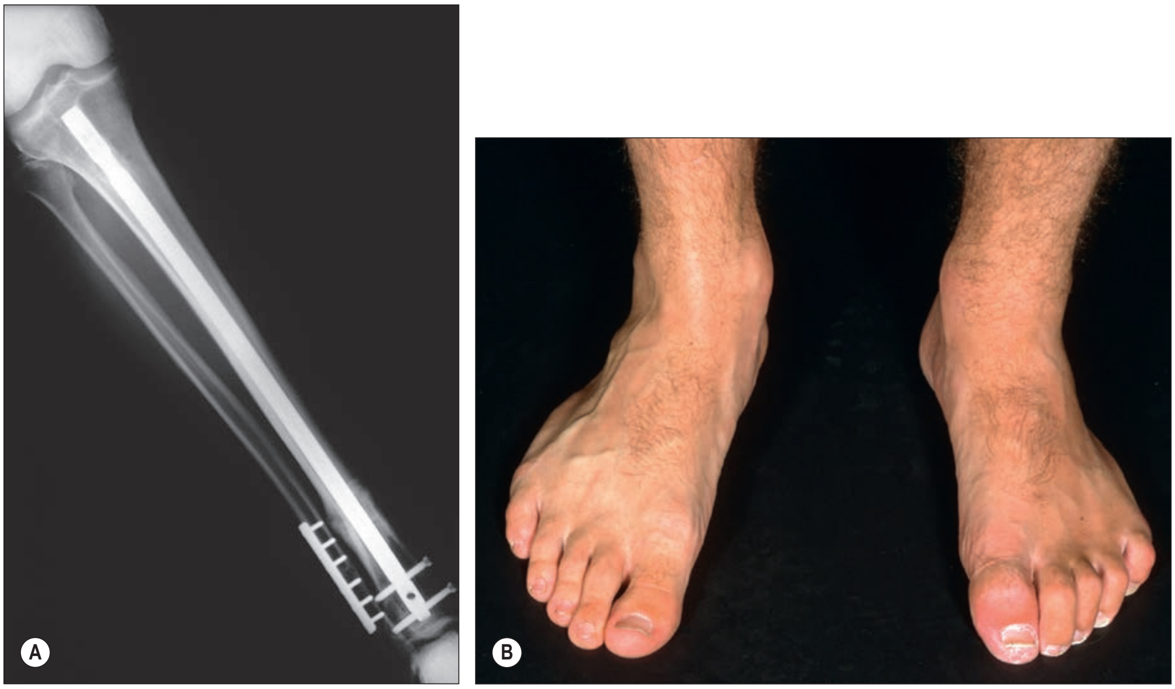

Fig. 48.48 **A**, 'Closed' intramedullary nailing of a fracture of a long bone. The tibial nerve and the posterior tibial artery were involved in the fracture. **B**, The muscles of the deep flexor compartment were fibrosed, causing severe clawing of the toes. (Courtesy of Rolfe Birch, all rights reserved, published in Birch R, Surgical Disorders of the Peripheral Nerve. 2nd edition, 2011. Springer-Verlag, London.)

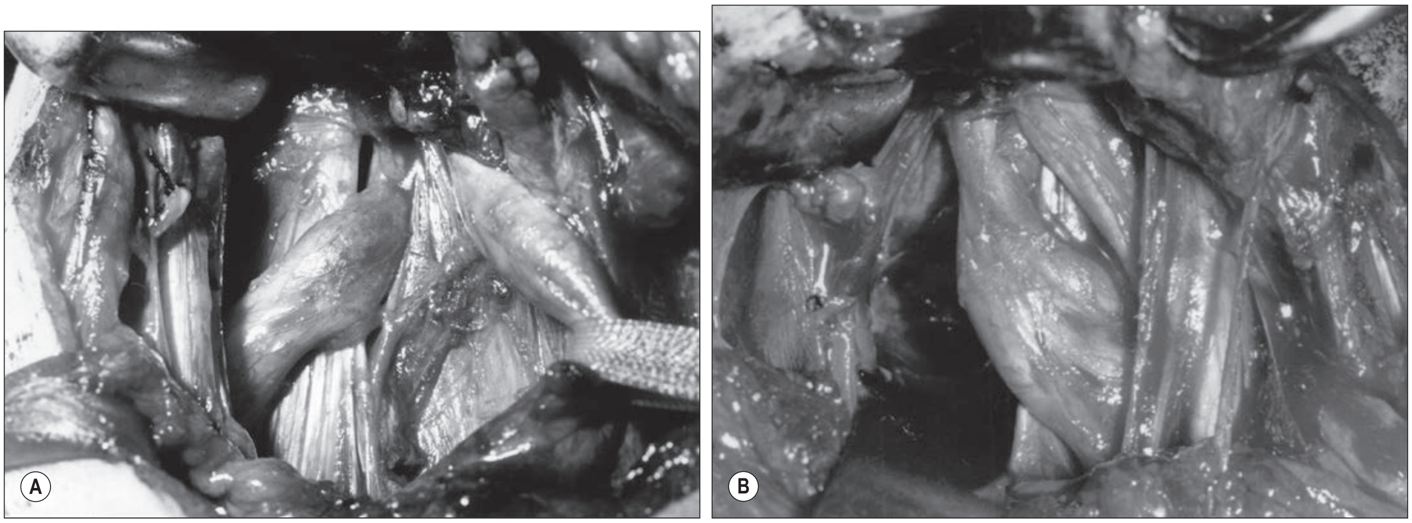

Fig. 48.49 Entrapment of the lower trunk through an anomaly of the suprapleural membrane and scalenus medius. **A**, The right lower trunk is trapped between the aponeurotic edge of scalenus medius posteriorly and the suprapleural membrane anteriorly. **B**, A 'scalenus sickle' and an anomalous scalenus anterior. The left lower trunk passes over the edge of the sickle and behind the part of scalenus anterior that passes posterior to the subclavian artery. (Courtesy of Rolfe Birch, all rights reserved, published in Birch R, Surgical Disorders of the Peripheral Nerve. 2nd edition, 2011. Springer-Verlag, London.)

the edge of the rib. The lower part of the cervicothoracic (stellate) ganglion lies on the head of the first rib, deep to the proximal part of the vertebral artery as it arises from the first part of the subclavian artery (see Fig. 35.18). The major part of the first thoracic ventral ramus is at first below the rib, then medial to its edge. The preganglionic (sympathetic) ramus of the first thoracic ventral ramus connects it to the stellate ganglion; the postganglionic ramus is less noticeable. The size and disposition of scalenus anterior vary: it may bifurcate to include the artery; it may be bulky and its tendon may curve posteriorly round the artery to form a kind of snare. Deep to scalenus anterior, a very thin fascia covers the artery. The phrenic nerve, chiefly derived from the fourth cervical ventral ramus, curves round the muscle to run down anterior to it into the thorax, lying, at first, posterior to the internal jugular vein and crossing behind the subclavian vein. The thoracic duct and the right lymphatic duct enter the brachiocephalic vein at the subclavian–jugular (triradiate) junction on the left and right, respectively. All of the scalene muscles vary in formation and size. Bridges of muscle and fascia may pass between them, altering and diminishing the space available for the neurovascular bundles.

Seventh cervical rib

Estimates of incidence range from 0.004% to 1%. Cervical ribs are asymptomatic in most people. The extent of the rib, which is rarely symmetric bilaterally, ranges from a prolongation and pointing of the seventh cervical transverse process to a complete rib in all respects like a first thoracic rib. The classification proposed by Sargent (1921) is as follows: type 1, prolongation and pointing of the seventh cervical transverse process; type 2, short articulating rib with fibrous prolongation; type 3, jointed rib long enough to carry the eighth cervical nerve; type 4, jointed rib fused at its end with the first rib or articulating with it; and type 5, a complete seventh cervical rib with cartilaginous union to the first costal cartilage or to the manubrium (Fig. 48.50).

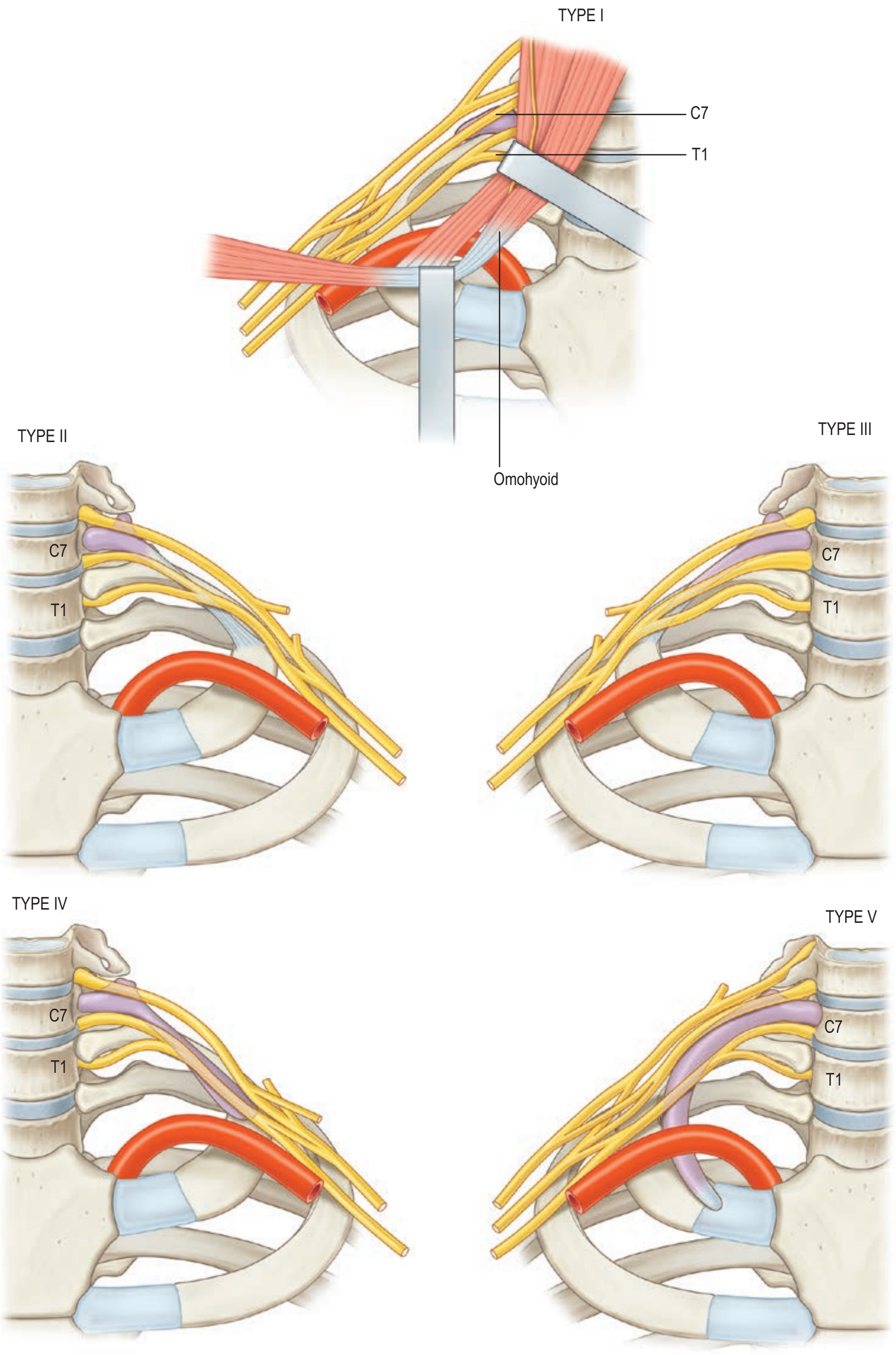

Fig. 48.50 Variations of the seventh cervical rib (purple), ranging from elongation of the seventh cervical transverse process to a virtually complete additional rib (after Sargent 1921). (Courtesy of Rolfe Birch, all rights reserved, published in Birch R, Surgical Disorders of the Peripheral Nerve. 2nd edition, 2011. Springer-Verlag, London.)

Arterial thoracic outlet syndrome

Arterial TOS was the first of the syndromes to be recognized and the first to be treated surgically. Astley Cooper wrote, 'I have seen an exostosis arise from the 6th or 7th cervical vertebrae or perhaps from both' (Cooper and Travers 1817). He went on to describe the case of a woman who came into Guy's Hospital with no pulse at the wrist or elbow and with 'venous redness' of the upper limb, which was cold, 'ennumbed' and painful; she also had a projection of the lower cervical vertebrae towards the clavicle, with consequent pressure on the subclavian artery. Coote (1861) reported the removal of a left seventh cervical rib causing aneurysm of the subclavian artery. Two physicians, Lewis and Pickering (1934), pointed to the mechanism of production of the arterial lesion, namely: intimal breakage with local thrombosis and distal embolization. Arterial affection occurs as the subclavian artery crosses a 'normal' first rib or a seventh cervical rib, commonly one with bony union to, or synchondrosis or synostosis with, a boss on the first rib at about its middle part. The vessel is distorted by the bone and constricted by a leash formed by the tendon of insertion of scalenus anterior. There is commonly dilation of the artery distal to the point of constriction, and the dilation may proceed to the formation of a true aneurysm (Wickham and Martin 1962). Complete obstruction of the main vessel with distal embolization may lead to critical ischaemia. The most dangerous complication is contralateral hemiplegia, doubtless from embolization from a thrombus extending proximally to the carotid vessel (Symonds 1927).

The arterial form of this outlet syndrome is a condition predominantly affecting young women; the occurrence of such symptoms in older individuals must suggest a primary diagnosis of atherosclerosis or other systemic disorder. The symptoms are initially those of Raynaud's disease with episodic blanching and temperature change, episodic pain with muscular activity, and distal ulceration and necrosis. The extremity may be cooler than the unaffected limb and there is likely to be a pulse

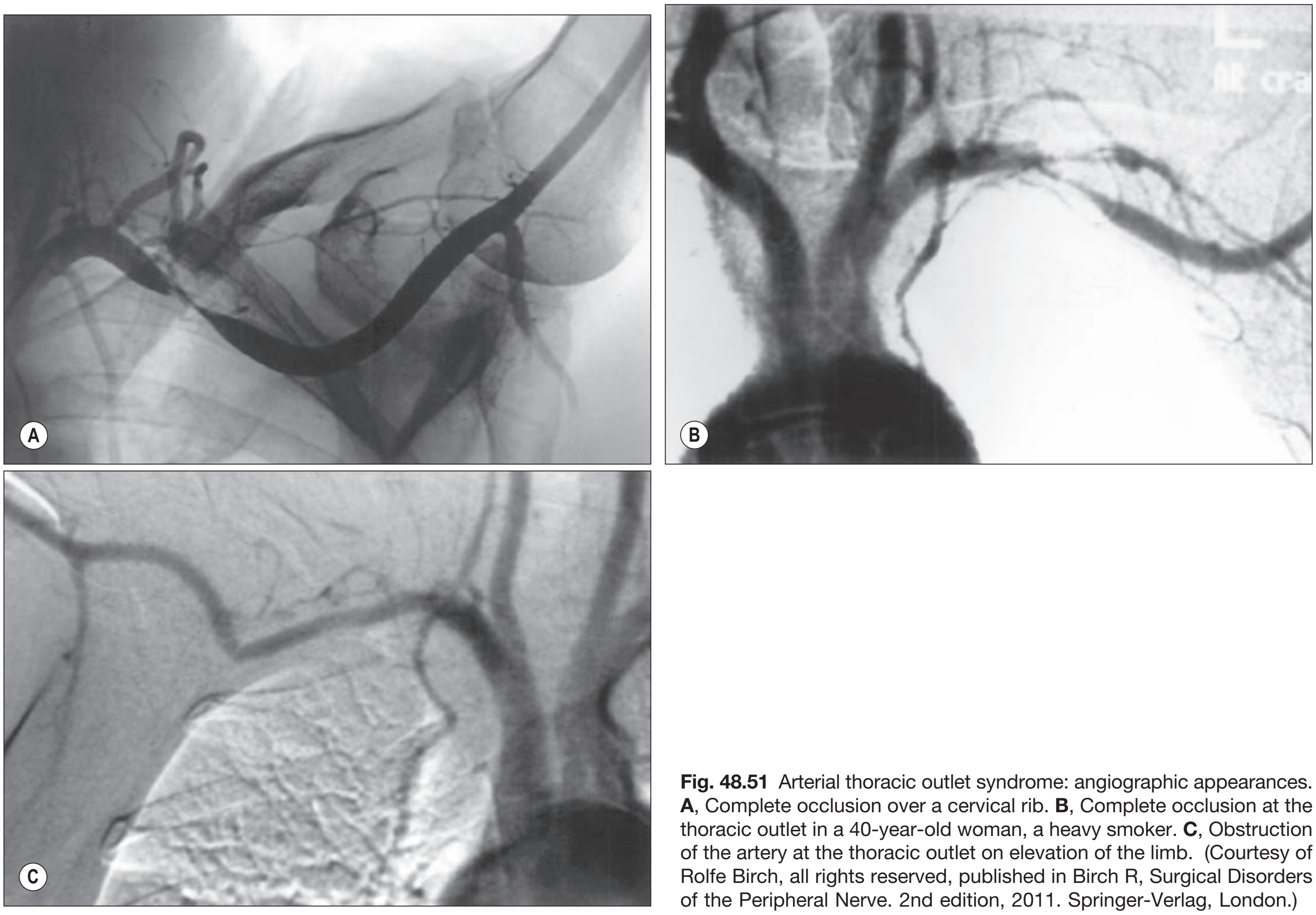

Fig. 48.51 Arterial thoracic outlet syndrome: angiographic appearances. **A**, Complete occlusion over a cervical rib. **B**, Complete occlusion at the thoracic outlet in a 40-year-old woman, a heavy smoker. **C**, Obstruction of the artery at the thoracic outlet on elevation of the limb. (Courtesy of Rolfe Birch, all rights reserved, published in Birch R, Surgical Disorders of the Peripheral Nerve. 2nd edition, 2011. Springer-Verlag, London.)

difference, even the absence of a pulse. Even if the hands are the same colour at rest and slightly dependent, there is likely to be blanching of the affected hand on elevation. The artery is prominent, displaced upwards and anteriorly by the underlying rib; there is a loud bruit and there may be a thrill. Doppler ultrasound examination is likely to show an abnormality: principally, a clamped, monophasic velocity signal anywhere over the arterial tree of the upper limb (Parry and Eastcott 1992). Radiographs will, of course, show a seventh cervical rib if one is present. Magnetic resonance angiography and duplex ultrasonography have generally superseded arteriography in this field, as in others, and will confirm the site and extent of the obstruction, the extent of stenosis and aneurysm formation, and the degree of distal occlusion (**Fig. 48.51**).

Operation is required urgently in cases of critical ischaemia, and soon in cases in which ischaemia is threatened. It may be indicated when a cervical rib is present, causing no symptoms but producing deformity of the subclavian artery sufficient to cause a steady bruit over the vessel, which must surely indicate distortion of the vessel that is likely, in time, to cause intimal breakage and thrombosis. Arterial TOS is uncommon rather than rare and it is potentially dangerous. The bruit from a prominent subclavian artery associated with an underlying seventh cervical rib cannot be ignored and investigations need to be pursued to define the extent of distortion of the artery.

True neurogenic thoracic outlet syndrome

Neurogenic TOS is rare. As Gilliatt (1984) pointed out, a number of cases were seen at the National Hospital for Nervous Diseases, Queen Square, London, UK, in the early years of the last century, with wasting of the thenar muscles that was attributed to a cervical rib. In fact, these patients probably had a carpal tunnel syndrome. The confusion was not resolved for more than 40 years until the application of nerve conduction studies defined the much more common disorder. Gilliatt put the annual incidence of cervical rib syndrome with muscle wasting as low as 1 in 1 million in the general population. The patients are usually young to middle-aged women and the abnormalities are usually confined to one upper limb. The symptoms are insidious and often mild; presentation is delayed for some years, and is usually occasioned by the sudden realization that the hand has become wasted. There is pain in the medial aspect of the forearm and there may also be some blunting of sensibility in that area and in the little finger. The latter is frequently shorter than it is in a normal, age-matched hand, suggesting that the affliction of the fibres in the lower trunk commenced before skeletal maturity. There is wasting of the superficial thenar muscles, which sometimes extends to all of the small muscles of the hands (**Fig. 48.52**) and there may be weakness of the flexor muscles of the forearm, most evident in those innervated by the ulnar nerve. There may be a bruit over the subclavian artery. Radiographs of the neck show rudimentary cervical ribs or elongated transverse processes of the seventh cervical vertebrae. The diagnostic electrophysiological findings were characterized by Gilliatt, Le Quesne and Logue in 1970 and include a small or absent sensory response in the ulnar nerve and the medial cutaneous nerve of the forearm; a normal sensory response in the median nerve; an attenuated compound motor action potential amplitude from abductor pollicis brevis; and a low-amplitude ulnar motor response (Smith and Knight 2011). Operation is indicated in these patients in the expectation of alleviation of pain, improvement in sensation and some improvement in strength; recovery of the wasted small muscles of the hand is rare.

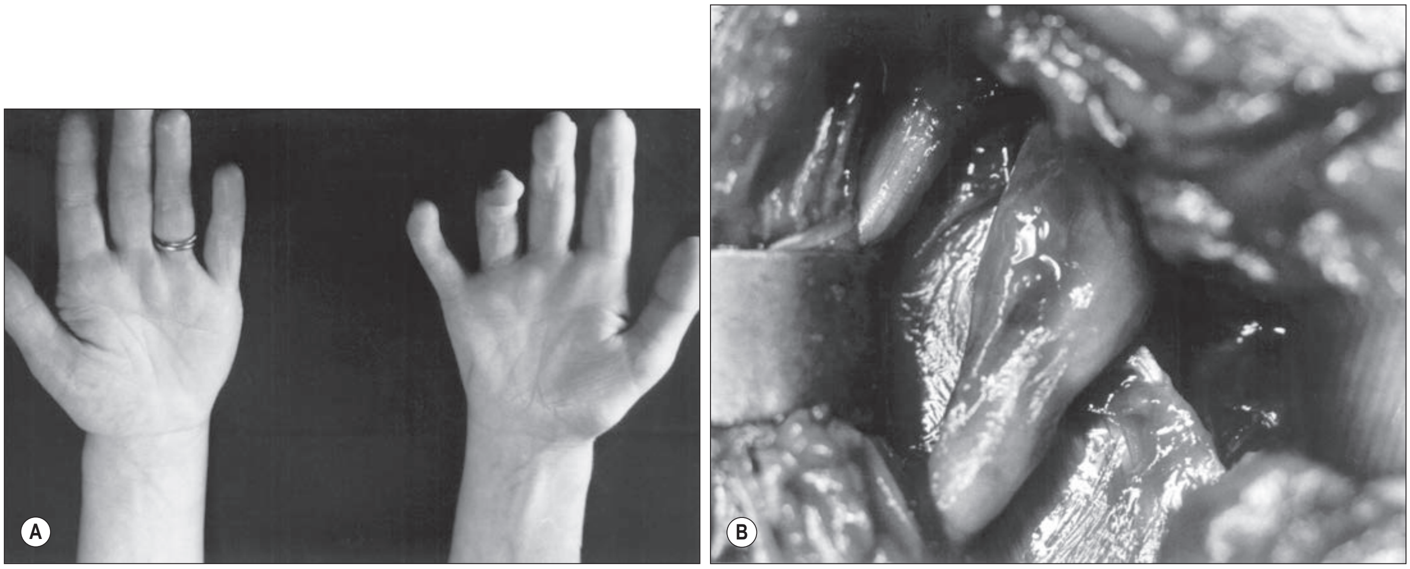

Fig. 48.52 The classical neurogenic outlet syndrome; shortening of the little finger is often evident. **A**, Severe wasting of the intrinsic muscles of the right hand in a 35-year-old woman. **B**, The right lower trunk is seen angulated over a 'scalenus sickle' and there is extreme attenuation of the trunk, which, in the photograph, appears to be rather lateral to the sickle. When the nerve was first exposed at operation, the zone of attenuation was, in fact, at the site of angulation. There was slow improvement after decompression. (Courtesy of Rolfe Birch, all rights reserved, published in Birch R, Surgical Disorders of the Peripheral Nerve. 2nd edition, 2011. Springer-Verlag, London.)

Neural (non-specific/disputed) thoracic outlet syndrome without plain motor signs

Neural TOS without plain motor signs is more common and more difficult. Patients present with symptoms and signs consistent with a diagnosis of TOS but studies of blood flow and nerve conduction are normal. It is important to seek causes of the symptoms beyond the apparent diagnosis and to remember that the presence of a cervical rib does not, of itself, permit a diagnosis of TOS. The urge to advise operation should be tempered with knowledge of the possibility of complications and the high rate of recurrence of symptoms as time passes (Birch 2011d).

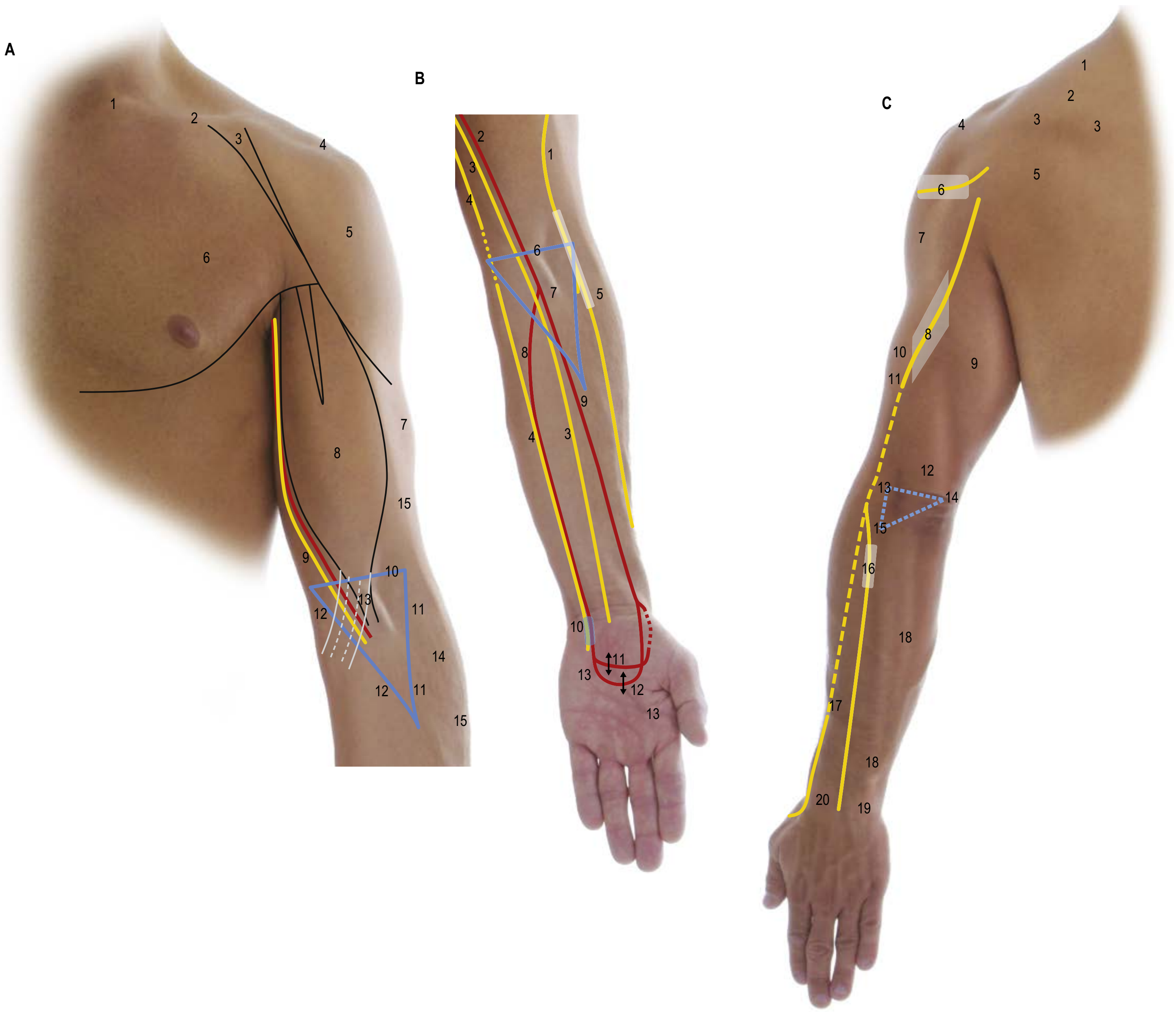

Fig. 48.53 The surface anatomy of the upper limb. **A**, The anterior aspect of the left pectoral girdle, arm and elbow. Key: 1, sternoclavicular joint; 2, clavicle; 3, infraclavicular fossa/deltopectoral triangle, and deltopectoral groove running inferolaterally; 4, acromion; 5, deltoid; 6, pectoralis major; 7, lateral head of triceps; 8, biceps brachii; 9, median nerve and brachial artery running anterior to triceps medial head; 10, epicondylar line and borders of cubital fossa (blue); 11, brachioradialis; 12, pronator teres; 13, biceps tendon (black) and aponeurosis (grey) passing inferomedially; 14, extensor muscle mass of the forearm; 15, cephalic vein. **B**, The anterior aspect of the left elbow, forearm and hand. Key: 1, radial nerve; 2, brachial artery; 3, median nerve; 4, ulnar nerve (dashed part of line shows nerve passing posterior to the medial epicondyle); 5, zone of radial nerve bifurcation (white): 1.0 ± 2.8 cm distal to the lateral epicondyle; 6, cubital fossa borders (blue); 7, biceps tendon with brachial artery bifurcation located medially; 8, ulnar artery; 9, radial artery; 10, pisiform with the ulnar (Guyon's) canal (blue) laterally; 11, deep palmar arch, located 4.0 ± 0.8 cm distal to the distal wrist crease); 12, superficial palmar arch located 5.2 ± 0.8 cm distal to the distal wrist crease); 13, proximal palmar crease. **C**, A posterior view of the left pectoral girdle, arm, elbow and forearm. Key: 1, trapezius; 2, supraspinatus; 3, spine of scapula; 4, acromion; 5, infraspinatus; 6, zone of axillary nerve passing around proximal humerus (white): 6.0 ± 1 cm from proximal humeral margin; 7, deltoid; 8, radial nerve and its zone of passage around spiral (radial) groove (white): enters the spiral groove 47 ± 3% and leaves it 61 ± 3% of the way down a line from greater tubercle to lateral epicondyle of the humerus; 9, triceps, long head; 10, triceps, lateral head; 11, radial nerve piercing lateral intermuscular septum 67 ± 5% of the way down a line from greater tubercle to lateral epicondyle of the humerus; 12, triceps tendon; 13, lateral epicondyle and borders of anconeus triangle (blue dashed line); 14, olecranon and olecranon bursa; 15, radial head; 16, zone of posterior interosseous nerve winding around radial neck (white): 2.5 ± 0.5 cm distal to radial head; 17, superficial radial nerve emerging from between the tendons of brachioradialis and extensor carpi radialis longus approximately 8.5 ± 1.5 cm proximal to radial styloid process; 18, posterior border of ulna; 19, ulnar head; 20, dorsal radial tubercle.

The medial border of the scapula, superior to the level of the scapular spine, is covered by trapezius and, therefore, difficult to palpate. Below the spine, the medial border is palpable down to the inferior angle. Although covered by teres major and latissimus dorsi, the inferior angle is also palpable when approached from below, and can be seen and/or palpated as it moves around the thoracic wall during movements of the pectoral girdle. The inferior angle is located at the level of the spinous process of T7 and overlies the seventh rib; it is a convenient landmark from which the ribs can be counted along the lateral chest wall, e.g. when a thoracotomy is being performed.

The infraclavicular fossa is visible as a small depression in the skin located over the deltopectoral triangle, inferior to the clavicle between the clavicular attachments of pectoralis major and deltoid, at the junction of the convex medial and concave lateral parts of the clavicle (see Fig. 48.53A). The apex of the coracoid process lies approximately 2.5 cm below the clavicle immediately lateral to this fossa, and is covered by the anterior fibres of deltoid. Deep palpation lateral to the coracoid process and through deltoid reveals the lesser tubercle of the humerus below the anterior border of the acromion. The greater tubercle of the humerus is the most lateral bony prominence in the shoulder region and is palpable lateral and inferior to the acromion. The greater and lesser tubercles can be felt moving under an examining finger during lateral and medial glenohumeral joint rotation. The vertical groove of the intertubercular sulcus (bicipital groove) is palpable between the tubercles; regional tenderness occurs in bicipital tendinitis. When the arm is abducted, the head of the humerus can be palpated on deep pressure at the apex of the axilla.

The shaft of the humerus is covered by overlying muscles and is not easily palpable. Distally, the medial epicondyle of the humerus is both visible and palpable, particularly when the elbow is flexed, and can be traced proximally to the medial supracondylar ridge. The ulnar nerve passes posterior to the medial epicondyle and can be rolled from side to side just proximal to the epicondyle (**Fig. 48.53B**). The lateral epicondyle of the humerus is less prominent, but its posterior surface is palpable and its lateral margin can be traced proximally on deep palpation to the lateral supracondylar ridge. Inspection of the posterior surface of an extended elbow reveals a depression lateral to the midline, bounded laterally by the raised mass of the superficial forearm extensor muscles, and medially by the lateral side of the olecranon. The floor of this depression contains the posterior surface of the lateral epicondyle of the humerus superiorly, and the head of the radius covered by the anular ligament inferiorly. Rotations of the radial head are palpable during forearm pronation and supination. The humero-radial part of the elbow joint forms a palpable transverse depression/sulcus between the lateral epicondyle and the radial head.

The posterior surface of the olecranon is subcutaneous; the freely mobile subcutaneous olecranon bursa overlies the olecranon. When the elbow is extended, the apex (tip) of the olecranon lies on a line level with the medial and lateral humeral epicondyles (see Fig. 48.53B). When the elbow is flexed, the apex of the olecranon descends and the three bony points then form a triangle. This relationship is lost following elbow dislocation or avulsion fracture of the olecranon.

The elbow joint is situated 2 cm below a line joining the two humeral epicondyles. It slopes downwards and medially from its lateral extremity. When the elbow is fully extended with the forearm and hand in supination, the valgus angulation at the elbow (carrying angle) is normally 165° in females and 175° in males. The angle is obscured in full forearm pronation and disappears on full elbow flexion, when the shafts of the ulna and humerus are moved into the same plane. The elbow joint can be accessed with a needle from a posterior perspective via the anconeus triangle; the borders of the triangle join the olecranon, radial head and lateral epicondyle of the humerus.

The posterior border of the ulna is subcutaneous and palpable from the olecranon superiorly to the styloid process inferiorly (see Fig. 48.53C). Its position corresponds to the longitudinal furrow that is visible on the posterior forearm when the elbow is fully flexed and marks the border between the anterior and posterior compartments of the forearm. In contrast, the radial shaft is covered by muscles and can only be felt indistinctly. The rounded head of the ulna forms a surface elevation on the medial side of the posterior surface of the wrist (**Fig. 48.54B**), especially when the forearm and hand are pronated. The ulnar styloid process projects distally from the posteromedial aspect of the ulnar head: a palpable depression distal to the ulnar head overlies the ulnar collateral ligament and triangular articular (fibrocartilage) disc covering the distal ulna.

The expanded distal end of the radius forms a slight surface elevation on the lateral side of the wrist and can be traced inferiorly to the radial styloid process, located immediately posterior to the tendon of abductor pollicis longus. The posterior aspect of the lower end of the radius is partly obscured by the extensor tendons but is easily palpated. The prominent dorsal radial (Lister's) tubercle is both visible and palpable, and aligns with the web space between digits 2 (index) and 3 (middle) (see Fig. 48.54B; **Fig. 48.54C**). The tendon of extensor pollicis longus sits medial to the tubercle in extensor compartment III, and the tendons of extensor carpi radialis longus and brevis sit lateral to the tubercle in extensor compartment II.

The dorsal aspects of the trapezium and of each of the metacarpal bones are partially palpable around the margins of the corresponding extensor tendons (see Fig. 48.54B). The heads of the metacarpal bones form the prominences of the knuckles, and are most obvious during flexion of the digits. On the dorsal aspect of the hand, each metacarpophalangeal joint line forms a palpable depression passing lateral and medial to the digital extensor tendon, and alternating digit flexion/extension aids identification. The joint can be aspirated or injected from this perspective. Palpation distal to the metacarpal head reveals the flared base of the corresponding proximal phalanx. The interphalangeal joints are palpable on the dorsolateral and dorsomedial aspects of a flexed digit just distal to the prominences formed by the heads of the proximal and middle phalanges.

The radiocarpal (wrist) joint is identified between the distal ends of the radius and ulna and the proximal carpal bones on flexion and extension of the wrist. There may be three transverse creases, proximal, intermediate and distal, on the flexor aspect of the wrist. Only the distal and intermediate creases are constant; the intermediate may be the de facto proximal crease when there are only two creases. When three creases are present, the most proximal marks the proximal limit of the flexor synovial sheaths, the intermediate overlies the radiocarpal joint and the distal crease sits 0.5 ± 0.3 cm proximal to the proximal border of the flexor retinaculum. The crease overlying the radiocarpal joint gently curves between the radial and ulnar styloid processes (**Fig. 48.54A**). The radial styloid process normally sits 1 cm distal to the ulnar styloid process. Alteration of this arrangement can indicate a fracture.

Four of the carpal bones are palpable. The pisiform is both visible and palpable on the palmar aspect of the medial wrist at the base of the hypothenar eminence. It is often overlain by the distal wrist crease. It can be moved over the articular surface of the triquetrum when the wrist is flexed passively. The hook of the hamate lies approximately 2.5 cm distal to the pisiform, in line with the ulnar border of the ring finger. It can also be located at the intersection of two lines: the index–metacarpal–pisiform line, that joins a point centred on the pisiform to a point overlying the midline of the metacarpal of the index finger at the proximal palmar crease, and the ring–metacarpal line, that joins a point centred on the metacarpal head of the ring finger to a point at the junction of the medial and middle one-thirds of the distal wrist crease (Cobb et al 1993). The hook of the hamate can be felt on deep palpation; the superficial division of the ulnar nerve can often be rolled from side to side over the palmar surface of the hook. The tubercle of the scaphoid is situated at the base of the thenar eminence, in line with the tendon of flexor carpi radialis, and in many individuals forms a small visible elevation. Immediately distal to it, but covered by the muscles of the thenar eminence, the tubercle of the trapezium can be identified on deep palpation.

The distal wrist crease normally sits distal to the lunate, overlies the pisiform and sits within 0.5 ± 0.3 cm (range 0.4–1.1 cm) of the proximal border of the flexor retinaculum (Cobb et al 1993). The proximal and distal edges of the flexor retinaculum, and therefore the surface position of the carpal tunnel, can be mapped according to its palpable bony attachments; medially to the pisiform and the hook of the hamate and laterally to the tubercles of the scaphoid and trapezium (superficial lamina) and to the medial lip of the groove on the trapezium (deep lamina) (see Fig. 48.54A).

Musculotendinous landmarks

Deltoid can be identified when the arm is abducted against resistance. The deltoid tendon is palpable approximately halfway down the lateral aspect of the shaft of the humerus. Its anterior border can be traced superomedially across the anterior aspect of the humerus and the tendon of pectoralis major, to the lateral clavicle; it forms the lateral boundary of the deltopectoral triangle (see Fig. 48.53A, Video 48.1). The posterior border runs superomedially from the posterior aspect of the deltoid tendon and reaches the crest of the scapular spine near its medial end. The normal rounded contour of the shoulder is produced by deltoid covering the lateral aspect of the greater tubercle of the humerus. Shoulder dislocation results in the loss of the normal rounded contour of the shoulder because the greater tubercle is displaced medially, and deltoid consequently descends vertically to its humeral attachment. Supraspinatus and infraspinatus are visible and palpable above and below the scapular spine, respectively (see Fig. 48.53C).

The lower border of pectoralis major forms the anterior axillary fold. It is visible and palpable when an abducted shoulder is adducted against resistance, e.g. by firmly pressing a hand on to the hip. The clavicular head of pectoralis major can be felt and seen to contract when flexing the shoulder from 90° against resistance; the sternocostal head becomes visible when extending a flexed shoulder against resistance.

The posterior axillary fold formed by latissimus dorsi and the underlying teres major reaches a lower level on the humerus than the anterior axillary fold. When the abducted shoulder is adducted against resistance, the posterior axillary fold is accentuated and the lateral border of latissimus dorsi can be traced inferomedially to its attachment to the iliac crest. When the upper limb is raised above the head, the lower five

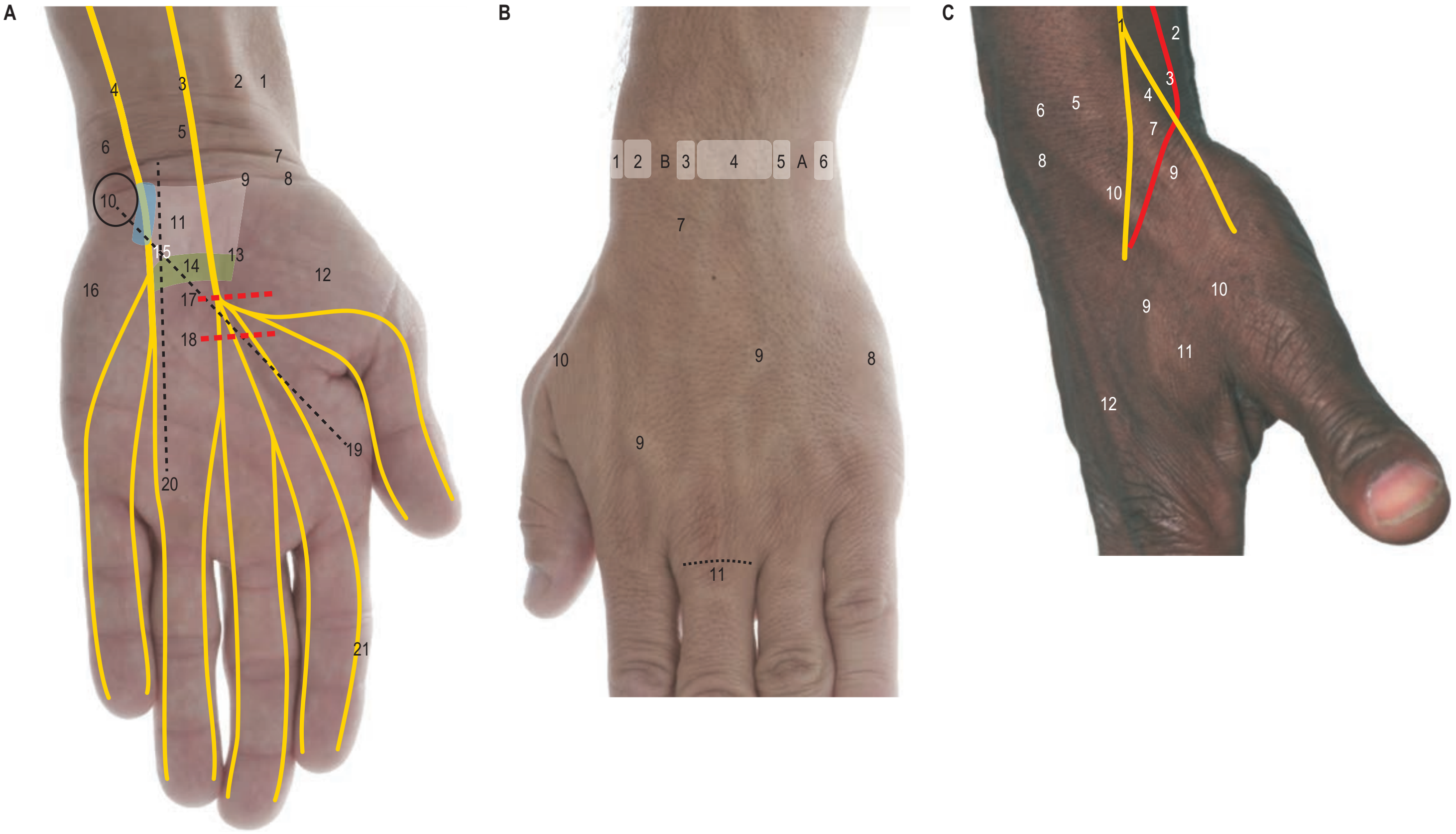

Fig. 48.54 The surface anatomy of the wrist and hand. **A**, The ventral hand and wrist. Key: 1, radial artery; 2, flexor carpi radialis tendon; 3, median nerve; 4, ulnar nerve, passing through the ulnar (Guyon's) canal (blue) in the palm; 5, palmaris longus tendon; 6, flexor carpi ulnaris tendon; 7, proximal transverse wrist crease: marks the line of the radiocarpal (wrist) joint; 8, distal transverse wrist crease: sits 0.5 ± 0.3cm proximal to the proximal boundary of the carpal tunnel; 9, scaphoid tubercle; 10, pisiform (black oval): aligned with distal wrist crease; 11, flexor retinaculum (white shading); 12, thenar eminence; 13, trapezium tubercle; 14, aponeurotic continuation of the flexor retinaculum (green shading); 15, hook of hamate at the intersection of (19) and (20), with the superficial branch of ulnar nerve passing anteriorly; 16, hypothenar eminence; 17, distal extent of deep palmar arterial arch (4.0 ± 0.8 cm from the distal wrist crease); 18, distal extent of superficial palmar arterial arch (5.2 ± 0.8 cm from the distal wrist crease); 19, index–metacarpal–pisiform line; 20, ring–metacarpal line; 21, positions of palmar neurovascular bundles. **B**, The dorsal hand and wrist. Key: 1–6, first to sixth extensor compartments of the wrist; 7, radiocarpal joint needle insertion point; 8, hypothenar eminence; 9, dorsal venous network of the hand; 10, extensor pollicis longus tendon; 11, extensor tendon and metacarpophalangeal joint line; A, head of the ulna; B, dorsal radial (Lister's) tubercle. **C**, The anatomical snuff-box. Key: 1, superficial branch of radial nerve branching 4–5 cm proximal to the radial styloid process; 2, flexor carpi radialis tendon; 3, radial artery; 4, extensor compartment I, containing abductor pollicis longus and extensor pollicis brevis; 5, extensor compartment II, containing the tendons of extensors carpi radialis longus and brevis; 6, dorsal radial (Lister's) tubercle; 7, radial styloid process; 8, radiocarpal (wrist) joint needle insertion point; 9, cephalic vein; 10, extensor pollicis longus tendon; 11, first dorsal interosseous muscle; 12, extensor digitorum tendon.

or six serrations of serratus anterior are visible on the lateral aspect of the thorax, curving downwards and forwards to interdigitate with the serrations of external abdominal oblique.

Biceps brachii produces a visible elevation on the anterior arm; the shallow medial and lateral bicipital grooves marking its medial and lateral borders (see Fig. 48.53A). It tapers superiorly, where it is covered by pectoralis major, and inferiorly where it continues as the biceps tendon just above the elbow joint. Flexion of the elbow against resistance aids identification of the muscle and of the bicipital tendon, which can be held between finger and thumb and traced inferiorly into the cubital fossa. With the elbow held in resisted flexion, the sharp upper margin of the bicipital aponeurosis can be traced passing inferomedially over the elevated mass of the superficial group of forearm flexor muscles. Coracobrachialis passes inferolaterally from the coracoid process, emerges from the lateral axillary wall and forms a rounded ridge near to the upper part of the medial side of biceps.

On the posterior arm, the lateral head of triceps forms a laterally placed elevation, inferior to the posterior border of deltoid (see Fig. 48.53C). Triceps can be made visible by extending the elbow against resistance. On the medial side, the rounded mass produced by the long head of triceps passes superiorly and disappears deep to deltoid.

Brachioradialis is the most superficial muscle on the lateral side of the anterior forearm. When the elbow is flexed against resistance whilst in a mid-pronation–supination position, brachioradialis stands out as a prominent ridge extending upwards beyond the level of the elbow joint to the lower lateral side of the arm. The medial border of brachioradialis marks the boundary between the anterior and posterior compartments of the forearm.

The three borders of the cubital fossa can be mapped out anterior to the elbow by a line joining the medial and lateral humeral epicondyles (superiorly), brachioradialis (laterally) and pronator teres (medially) (see Fig. 48.53A–B). Pronator teres passes inferolaterally from the medial epicondyle to a point approximately halfway down the radial shaft; its rounded belly is palpable and often visible during resisted forearm pronation.

The rounded mass of the superficial forearm flexor muscles is visible in the upper medial forearm, and that of the extensor muscle mass is visible in the upper lateral forearm. The lines of travel of the superficial forearm muscles can be mapped out according to their attachment points. Inflammation of the common flexor or extensor tendons (epicondylitis) can be indicated by tenderness to palpation over their respective tendinous origins on the humeral epicondyles.

Palpating lateral to flexor carpi radialis, 3–4 cm proximal to the wrist crease, reveals the muscle belly of flexor pollicis longus (flexing and extending the thumb will confirm the correct placement of the examining finger). The area on the medial side of flexor carpi radialis tendon is packed with important structures. The median nerve is either covered by, or situated just lateral to, the tendon of palmaris longus. The latter can be identified by gently pinching the tips of the digits together and partially flexing the wrist (see Fig. 48.54A). Near to the wrist, the median nerve lies very close to the skin and can, therefore, be injured by relatively superficial lacerations. When palmaris longus is absent, only a thin covering of subcutaneous fat and deep fascia separate the skin and nerve. The four tendons of flexor digitorum superficialis lie deep to the median nerve; the tendons to the middle and ring fingers lie anterior to those for the index and little fingers as they pass deep to the flexor retinaculum, and can be felt and seen to move during finger flexion and extension. Deeper still are the tendons of flexor digitorum profundus. The broad tendon of flexor carpi ulnaris is easily palpated passing to the pisiform on the medial (ulnar) side of the anterior wrist; the ulnar nerve, artery and venae comitantes lie along its lateral (radial) edge. Any sharp injury that cuts through the tendon usually has enough energy to sever the ulnar neurovascular bundle.

When the thumb is fully extended, the depression of the anatomical snuff-box is visible on the lateral aspect of the wrist immediately distal to the radial styloid process (see Fig. 48.54C). The snuff-box is bounded on its anterolateral side by the tendons of abductor pollicis longus (laterally) and extensor pollicis brevis (immediately medial), and on its posteromedial side by the tendon of extensor pollicis longus. Running a finger along extensor pollicis brevis may enable palpation of the superficial radial nerve, which can be rolled from side to side on the tendon. The cephalic vein passes over the roof of the snuff-box, where it is visible and palpable, and the pulsation of the radial artery can be palpated deeply on its floor.

The tendons located within the six extensor compartments of the wrist are subcutaneous and palpable (see Fig. 48.54B). Compartment I (containing abductor pollicis longus and extensor pollicis brevis) sits over the lateral radius. Regional tenderness to palpation occurs in de Quervain's tenosynovitis. Compartment II (containing extensors carpi radialis longus and brevis) and III (containing extensor pollicis longus) flank the lateral and medial sides of the dorsal radial (Lister's) tubercle, respectively. Compartments V (containing extensor digiti minimi) and VI (containing extensor carpi ulnaris) flank the posterior and medial sides of the ulnar head, respectively. Compartment IV (containing extensors digitorum and indicis) sits between the ulnar head and compartment III. The tendons of extensors carpi radialis longus and brevis can be identified passing over the dorsum of the wrist when the fist is repeatedly clenched and relaxed. The tendons of extensor digitorum are visible and palpable on the dorsal hand with the fingers fully extended. With the wrist in extension and adduction, the tendon of extensor carpi ulnaris is palpable distal to the ulnar styloid as it crosses the wrist. The first dorsal interosseous forms a visible muscular mass on the lateral side of the dorsal hand between the index finger and thumb, especially whilst abducting the index finger against resistance.

The first metacarpal is both visible and palpable on the dorsolateral hand. Its dorsal aspect forms the lateral border of the hand. The raised muscular mass of the thenar eminence, produced by abductor and flexor pollicis brevis overlying opponens pollicis, is located on the lateral side of the palm (see Fig. 48.54A). The less prominent hypothenar eminence is located on the medial side of the palm and is formed by the comparable muscles of the little finger. The medial aspect of the hypothenar eminence forms the medial border of the hand.

Vessels, pulses and nerves

Arteries

The brachial artery travels along the medial arm in the depression posterior to coracobrachialis and subsequently along the groove to the medial side of biceps, to a point just medial to the bicipital tendon at the level of the radial head/neck (see Fig. 48.53A–B). Its pulsations are palpable along this line of travel and proximal to the bicipital aponeurosis, via compression against the humerus. Brachial artery catheterization just proximal to the aponeurosis is used for coronary angiography or cardiac catheterization. The ability to compress the brachial artery against the humerus makes the arm the favoured site for non-invasive blood pressure measurement. The median nerve is intimately related to the brachial artery throughout its course in the arm. Proximally, it sits lateral to the artery; around the midpoint of the arm, it passes anterior to the artery and descends on its medial side to the cubital fossa.

The radial and ulnar arteries originate in the anterior forearm at a point situated medial to the bicipital tendon at the level of the lower head/neck of the radius (see Fig. 48.53B). From here, the ulnar artery passes inferomedially to a point one-third of the way down flexor carpi ulnaris (which passes along a line joining the medial humeral epicondyle to the pisiform). The ulnar artery and nerve then pass inferiorly to a point just lateral to the pisiform along the line of flexor carpi ulnaris, with the ulnar artery lying on the lateral (radial) side of the nerve. The radial artery passes inferolaterally through the forearm, from its point of origin to a point just lateral to the tendon of flexor carpi radialis, anterior to the distal radius. The upper part of its course can be represented by a line that passes deep to the medial part of the elevation produced by brachioradialis on the anterior aspect of the forearm. At the wrist it passes posteriorly, deep to the tendons of abductor pollicis longus and extensor pollicis brevis, and enters the anatomical snuff-box, where its pulsations are palpable.

The radial pulse is palpable on the anterior (volar) aspect of the wrist between the tendon of flexor carpi radialis medially and the radial styloid process laterally. This is the simplest pulse to palpate during routine patient examination. The pulse of the ulnar artery is usually only palpable using deep pressure immediately lateral to the tendon of flexor carpi ulnaris at the wrist; it is difficult to palpate.

The cardinal line of Kaplan is often used to position arteries within the hand and wrist, however, multiple different descriptions of the line are used (Vella et al 2006) thus making it an unreliable reference. The use of bony landmarks and skin creases is preferable. At their most distal extent, the superficial and deep palmar arterial arches are located 5.2 ± 0.8 cm and 4.0 ± 0.8 cm, respectively, distal to the distal wrist crease (McLean et al 2008). Both arterial arches sit proximal to the proximal palmar crease (see Figs 48.53B, 48.54A). The digital neurovascular bundles pass along the medial and lateral sides of the dorsal and palmar (volar) surfaces of the digits, and can be anaesthetized in these positions via the web space.

Sites for arterial cannulation

At the wrist, the radial artery is commonly used for arterial cannulation for arterial blood sampling and blood pressure monitoring. Thrombosis or vasospasm of the radial artery at this site should not normally jeopardize the circulation to the hand since the interconnecting palmar arterial arches provide a collateral circulation to the hand. Allen's test, and ideally Doppler ultrasound, should be performed prior to invasive procedures to determine the presence of collateral circulation from the ulnar artery.

Allen's test

Allen's test examines the patency of the interconnection between the superficial and deep palmar arches, and determines whether either artery is capable of maintaining the arterial supply to the hand in isolation. To perform the test, the radial and ulnar arteries of one hand are compressed by the examiner's thumbs. The forearm is then elevated and the hand exsanguinated by clenching the fist. The hand is then opened while arterial compression is continued. The palm of the hand appears pale, unless there is an anomalous arterial supply, e.g. from a persistent median artery. The rapid return of a normal pink colour to the palmar skin following removal of digital pressure from the ulnar artery suggests it is capable of perfusing the hand adequately in isolation. If the palmar skin remains pale, it must be assumed either that there is a distal obstruction to the artery or that the artery cannot adequately perfuse the hand in isolation. For comparison, the test may be repeated with release of digital pressure on the radial artery.

Veins

The superficial veins of the upper limb are usually visible and palpable, especially when a tourniquet occludes venous return proximally. At the wrist, the cephalic vein consistently passes over the roof of the anatomical snuff-box (see Fig. 48.54C) and the dorsolateral aspect of the distal radius. Here, it sits next to the superficial branch of the radial nerve. The cephalic vein ascends the anterolateral forearm and the lateral arm in the groove lateral to biceps brachii. Superiorly, it ascends the deltopectoral groove to the deltopectoral triangle, where it pierces the clavipectoral fascia to enter the axillary vein.

The median cubital and basilic veins may be identified over the cubital fossa. In the proximal forearm, the cephalic vein runs alongside the lateral cutaneous nerve of the forearm. The veins are frequently covered by fat, especially in the female, which makes them difficult to identify. The median cubital vein usually arises from the cephalic vein approximately 2.5 cm distal to the lateral epicondyle of the humerus, and runs upwards and medially over the bicipital aponeurosis to join the basilic vein approximately 2.5 cm above the transverse skin crease of the elbow. The median vein of the forearm drains the venous plexuses on the palmar surface of the hand. It ascends the anterior forearm and usually joins either the basilic vein or the median cubital vein; sometimes, it divides into two branches, just distal to the elbow, one of which joins the basilic vein and the other the cephalic vein.

Venepuncture

Commonly accessed superficial veins include the cephalic or median cubital vein at the cubital fossa, and the dorsal venous network of the hand. The cephalic vein may also be accessed over the distal radius and anatomical snuff-box. The latter site has many advantages for placing an indwelling cannula when a lengthy period is contemplated, although the vein lies close to the superficial branch of the radial nerve. The superficial veins of the upper limb often sit in close proximity to cutaneous nerves, and may be vulnerable to iatrogenic injury during venepuncture (Wallis et al 2018).

A high bifurcation of the brachial artery is seen occasionally and may produce an anomalous superficial ulnar artery that descends superficial to the common origin of the forearm flexor muscles. When this occurs, the ulnar artery, although deep to the deep fascia, may lie subcutaneously and pass superficial to the bicipital aponeurosis where its pulsation may be observed. Such an artery is therefore at risk of puncture during median cubital vein access.

Lymph nodes

Supratrochlear lymph nodes lie next to the basilic vein in the region of the medial supracondylar ridge of the humerus. If enlarged, they may be palpated along the line of the vein, a few centimetres above the elbow joint.

Nerves

The trunks of the brachial plexus lie in the posterior triangle of the neck posterior to the subclavian artery (its pulsations are palpable), in the angle between the clavicle and the lower posterior border of the clavicular head of sternocleidomastoid. The upper trunk can be palpated by passing the fingers inferiorly along the vertical groove between scalenus anterior and scalenus medius. This interscalene groove can be visualized by asking the subject to sniff (inhale) rapidly through their nose. The divisions of the brachial plexus pass posterior to the middle one-third of the clavicle; the cords of the plexus sit deep to pectoralis minor (landmarked passing inferomedially from the coracoid process) around the second part of the axillary artery. Several of the main branches of the brachial plexus may be damaged along their course in the upper limb by relatively minor procedures (**Table 48.6**).

The axillary nerve and circumflex humeral vessels pass around the posterior and lateral sides of the proximal humerus, close to the surgical neck, approximately 5 cm from the posterior edge, and 6 cm from the anterior edge, of the acromion (Cetik et al 2006). Bono et al (2000) found the axillary nerve to lie 6 ± 1 cm from the proximal humerus, passing within 2 ± 1 cm of the surgical neck of the humerus (see Fig. 48.53C).

The radial nerve passes inferolaterally along, or within 2 cm of, the spiral groove on the posterior humerus (see Fig. 48.53C). The distance from the acromion to a line passing through the humeral epicondyles can be used as a baseline measurement; the radial nerve reaches the spiral groove 47 ± 3%, leaves it 61 ± 3%, and pierces the lateral intermuscular septum 67 ± 5% of the way down this line (Cox et al 2010, Cho et al 2013). The radial nerve then passes inferiorly, approximately 1 cm lateral to the tendon of biceps, and bifurcates into the posterior interosseous and superficial branch of the radial nerve 1 ± 2.8 cm distal to the lateral humeral epicondyle (Cox et al 2010) (see Fig. 48.53B). The posterior interosseous nerve winds around the radial neck 2.5 ± 0.5 cm distal to the radial head (Cox et al 2010); this is an important surgical consideration when making an incision to expose the radial head. The nerve then passes inferiorly through the posterior forearm to a point midway between the ulnar head and the dorsal radial tubercle. The superficial branch of the radial nerve passes inferiorly, deep to brachioradialis, and becomes superficial by passing between brachioradialis and extensor carpi radialis longus approximately 8.5 cm proximal to the radial styloid process (Auerbach et al 1994, Park et al 2010). It then branches 4–5 cm proximal to the radial styloid process and its branches are palpable as they pass over the tendon of extensor pollicis longus where it borders the anatomical snuff-box.

The median nerve is intimately related to the brachial artery throughout its course in the arm. In the forearm, it passes along a line joining a point just medial to the pulsating brachial artery in the cubital fossa to either the tendon of palmaris longus, or to a point just lateral to the tendon at the wrist (see Fig. 48.53B).

The ulnar nerve passes posterior to the medial epicondyle and can be rolled from side to side just proximal to the epicondyle (see Fig. 48.53B). In the forearm and proximal hand, its course corresponds to a line drawn from the base of the posterior aspect of the medial epicondyle of the humerus to the lateral side of the pisiform, where the nerve passes through the ulnar (Guyon's) canal and its superficial branch often passes superficial to the hook of the hamate. Deep pressure at these bony landmarks can produce paraesthesia in the distribution of the nerve. Proximally, the ulnar nerve sits deep to flexor carpi ulnaris; distally, it sits lateral to the tendon of flexor carpi ulnaris and medial to the ulnar artery and its venae comitantes.

Dermatomes

Knowledge of the extent of individual dermatomes is largely based on clinical evidence. The dermatomes of the upper limb arise from the fifth to the eighth cervical and first thoracic ventral rami. The seventh cervical ventral ramus supplies the central part of the hand (**Fig. 48.55**, see Figs 48.14, 48.15). Considerable overlap exists between adjacent dermatomes innervated by nerves derived from consecutive spinal cord segments.

Myotomes

The predominant segmental origin of the nerve supply for each of the muscles of the upper limb and for the movements that take place at the joints of the upper limb are summarized in Tables 48.1–48.4.

Reflexes

Biceps jerk (C5, C6) The elbow is flexed to a right-angle (90°) and the forearm slightly pronated. A finger is placed on the biceps tendon and struck with a percussion hammer; this should elicit elbow flexion and slight supination of the forearm.

Triceps jerk (C6–C8) The upper limb is supported at the wrist and the elbow flexed to a right-angle. Triceps tendon is struck with a percussion hammer just proximal to the olecranon; this should elicit extension of the elbow.

Radial jerk (C7, C8) The radial jerk is a periosteal, and not a tendon, reflex. The elbow is flexed to a right-angle and the forearm placed in the mid-pronation/supination position. The radial styloid is struck with the percussion hammer. This elicits contraction of brachioradialis, which should elicit flexion of the elbow.

Nerve blocks

Brachial plexus There are three common approaches to achieve anaesthetic blockade of the brachial plexus: the interscalene,

TABLE 48.6 Common sites for iatrogenic upper limb nerve injury in primary care

Nerve	Site	Procedure
Axillary	Lateral surface of deltoid	Intramuscular injection
Median	Roof of the cubital fossa	Venepuncture into the basilic or median cubital vein
	Carpal tunnel or midline anterior wrist	Steroid injection into the carpal tunnel
Radial	Lateral border of the cubital fossa or in the groove between brachioradialis and biceps brachialis	Venepuncture into the cephalic vein
Superficial branch of radial	Roof of the anatomical snuff-box	Venepuncture into the cephalic vein
Ulnar	Medial epicondyle	Steroid injection for medial epicondylitis
Lateral and medial cutaneous of forearm	Cubital fossa	Venepuncture

Adapted from Wallis et al., 2018 Adapted from Wallis KA, Hills T, Mirjalili SA 2018 Minimising iatrogenic nerve injury in primary care. Br J Gen Pract 68(673):392–393.

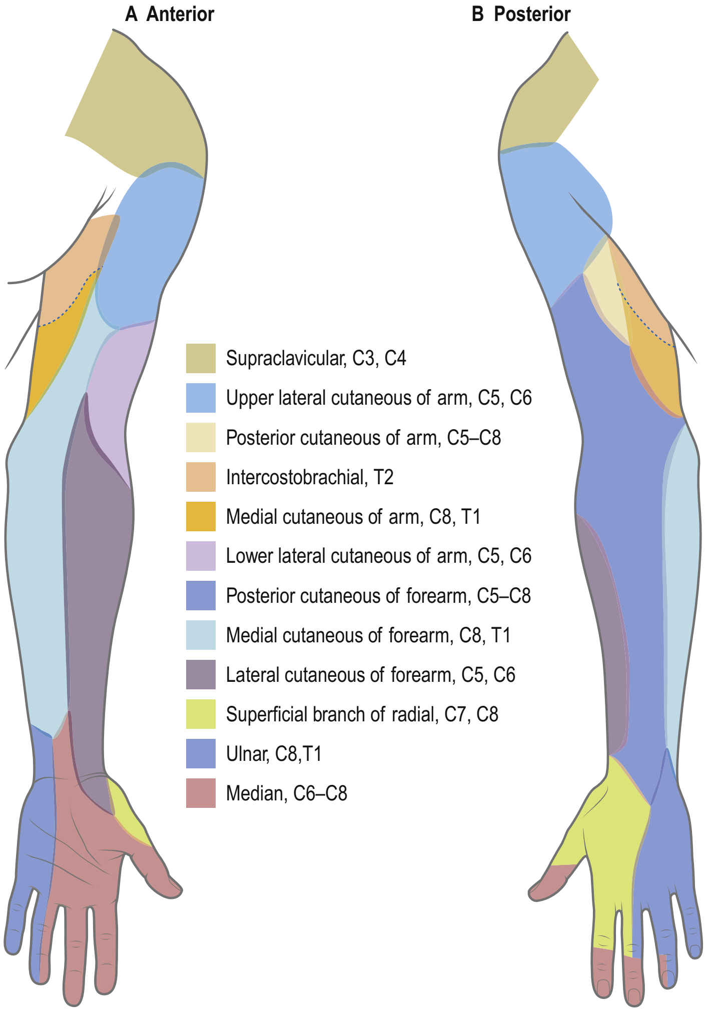
A Anterior
B Posterior
Supraclavicular, C3, C4
Upper lateral cutaneous of arm, C5, C6
Posterior cutaneous of arm, C5–C8
Intercostobrachial, T2
Medial cutaneous of arm, C8, T1
Lower lateral cutaneous of arm, C5, C6
Posterior cutaneous of forearm, C5–C8
Medial cutaneous of forearm, C8, T1
Lateral cutaneous of forearm, C5, C6
Superficial branch of radial, C7, C8
Ulnar, C8,T1
Median, C6–C8

Fig. 48.55 The distribution of skin territories supplied by the cutaneous nerves of the left upper limb. **A**, Viewed from the anterior aspect. **B**, Viewed from the posterior aspect.

supraclavicular and axillary routes. Ultrasound guidance is commonly used.

The interscalene route requires identification of the interscalene groove. The patient is asked to sniff, an action that involves the scalene muscles as accessory muscles of respiration. A needle is inserted perpendicular to the skin and enters the interscalene groove. Paraesthesia may be elicited, and local anaesthetic solution is injected. There is a risk that some local anaesthetic may move in a retrograde direction and reach the cervical epidural space. The proximal nature of the block means that there is almost always some involvement of the phrenic nerve, and sympathetic block (as evidenced by a Horner's syndrome) is universal.

The supraclavicular route places local anaesthetic solution in the plane occupied by the trunks of the brachial plexus as they emerge between scalenus anterior and medius on the first rib, immediately posterior to the third part of the subclavian artery. The site of injection is 2 cm above the midpoint of the clavicle. The needle is directed backwards, inwards and downwards to make contact with the upper surface of the first rib. During this procedure, the patient will usually report paraesthesia within the upper limb, which indicates that the needle is correctly placed; preliminary aspiration ensures that a major vessel has not been punctured. If the first rib is missed, there is the risk of producing a pneumothorax. There is often a transient Horner's syndrome, caused by diffusion of the local anaesthetic towards the stellate ganglion.

The axillary approach blocks the nerves as they group around the axillary artery.

Wrist Anaesthesia of the palm of the hand (except for the lateral surface of the thumb base) can be achieved by blockade of the ulnar and median nerves at the wrist (see Video 51.9). The ulnar nerve may be blocked via a needle inserted lateral to the tendon of flexor carpi ulnaris at the wrist. The median nerve may be blocked via a needle inserted at the level of the proximal wrist crease between the tendons of palmaris longus and flexor carpi radialis.

The radial nerve, which supplies the dorsal skin of the hand, may be blocked by injecting local anaesthetic in the subcutaneous tissues around the dorsolateral wrist, where branches of the nerve can be palpated as they pass over tendon of extensor pollicis longus, especially during resisted extension of the thumb.

Digital nerves

The digital nerves lie on either side of the flexor sheath in a plane immediately anterior to the phalanx. Therefore, the needle should be inserted on either side of the base of the digit, just anterior to the anterolateral margin of the phalanx. A common alternative approach to blocking the digital nerves is via a dorsal skin approach; the needle is inserted through the dorsal skin on either side of the base of the proximal phalanx and advanced towards the palmar location of the digital nerves while the local anaesthetic agent is continually infused. This is thought to be less painful than the palmar approach because the dorsal skin is less sensitive than the palmar skin.

Bonus e-book content

Fig. 48.3 **B**, Coronal oblique MIP from a CT carotid angiogram of the subclavian and axillary arteries. **C**, Coronal oblique MIP from a CT angiogram, from axillary artery to forearm arteries. **D**, **E**, A volume rendered CT angiogram, left arm abducted and prone.

Fig. 48.4 **C–D**, A volume rendered CT venogram of the left arm. **E**, A digital subtraction venogram at the left antecubital fossa.

Fig. 48.7 **B–E,** Sagittal oblique T2-weighted fat saturated MRI of the supraclavicular to retroclavicular left brachial plexus. **F–G,** Sagittal T1-weighted MRI of the left brachial plexus showing its components at the interscalene (**F**) and retroclavicular spaces (**G**).

Fig. 48.17 The area of sensory abnormality after transection of C8 and T1.

Fig. 48.18 The area of sensory abnormality after section of the lateral cord in the axilla.

Fig. 48.19 Rupture of the posterior divisions of the trunks of the brachial plexus.

Fig. 48.20 Rupture of the axillary nerve.

Fig. 48.21 Sensory loss in two cases of rupture of the musculocutaneous nerve.

Fig. 48.22 **A–B**, Two examples of a high lesion of the radial nerve.

Fig. 48.23 **A–B**, Sensory loss after transection of the median nerve, ulnar nerve, medial cutaneous nerve of the forearm, and brachial artery, in the arm of a 14-year-old boy.

Fig. 48.24 A high median nerve injury.

Fig. 48.25 Section of the median and palmar cutaneous nerves at the wrist.

Fig. 48.26 **A–B**, Typical loss of sensibility after division of median nerve at the wrist.

Fig. 48.27 Deficit after division of the ulnar nerve in the forearm.

Fig. 48.28 Sympathetic paralysis following median nerve transection.

Fig. 48.29 Rupture of C5, preganglionic C6–T1.

Bonus e-book content—cont'd

Fig. 48.30 Transverse section of the tip of an avulsed dorsal root at C6 4 days after injury.

Fig. 48.31 Avulsed ventral root of C6 4 days after injury; peripheral intradural rupture.

Fig. 48.32 Avulsion of C5, C6 from the spinal cord.

Fig. 48.33 Ischaemia and conduction.

Fig. 48.34 A dorsal root ganglion 6 months after avulsion from the spinal cord.

Fig. 48.35 The nerve and roots detached from the spinal cord.

Fig. 48.36 Wallerian degeneration, ventral root of C8.

Fig. 48.37 **A–B**, Intense, lightning-like pain was felt in the dermatomes of C5–C7 in this patient on the day of injury; these three nerves were avulsed from the spinal cord.

Fig. 48.38 Sensory loss in a complete preganglionic lesion of C4–T1 in two patients.

Fig. 48.39 Sensory loss in a preganglionic lesion of C5–T1.

Fig. 48.40 Sensory loss in a preganglionic lesion of C4–C7.

Fig. 48.41 Sensory loss in a preganglionic lesion of C5.

Fig. 48.42 **A–B**, Function after 96 months of left-sided rupture of C5–C8, T1.

Fig. 48.43 Function 11 years after reimplantation of the ventral roots of C5–C7.

Fig. 48.44 A leaking aneurysm 20 weeks after fracture of the neck of the humerus.

Fig. 48.45 Consequences of anterior cord infarction caused by interscalene block.

Fig. 48.46 An expanding haematoma complicating fracture of left proximal humerus.

Fig. 48.47 Recovering femoral palsy from haematoma in the femoral triangle.

Fig. 48.48 Consequences of 'closed' intramedullary nailing of a fracture of a long bone.

Fig. 48.49 Anomaly of the suprapleural membrane and scalenus medius: entrapment of the lower trunk.

Fig. 48.50 Variations of the seventh cervical rib.

Fig. 48.51 Arterial thoracic outlet syndrome: angiographic appearances.

Fig. 48.52 The classical neurogenic outlet syndrome.

Table 48.1 Movements, muscles and segmental innervation in the upper limb.

Table 48.2 Segmental innervation of the muscles of the upper limb.

Table 48.3 Segmental innervation of joint movements of the upper limb.

Table 48.4 Tests to determine the location of a lesion in the upper limb.

Table 48.5 Patterns of injury in 301 consecutively operated supraclavicular lesions (1989–93)

Video 48.1 Upper limb surface anatomy.

Key reference

Birch R 2011 Surgical Disorders of the Peripheral Nerves, 2nd ed. London: Springer.

An account of the current state-of-the-art practice of diagnosis and management of surgical lesions of the peripheral nerves, including the brachial plexus.

References

Auerbach DM, Collins ED, Kunkle KL et al 1994 The radial sensory nerve: an anatomic study. Clin Orthop Relat Res 308:241–9.

Berman J, Anand P, Chen L et al 1996 Pain relief from preganglionic injury to the brachial plexus by later intercostal transfer. J Bone Joint Surg Br 78:759–60.

Berman JS, Birch R, Anand P 1998 Pain following human brachial plexus injury with spinal cord root avulsion and the effect of surgery. Pain 75:199–207.

Bono CM, Grossman MG, Hochwald N et al 2000 Radial and axillary nerves: anatomic considerations for humeral fixation. Clin Orthop Relat Res 373:259–64.

Birch R 2011a The closed supraclavicular lesion. In: Surgical Disorders of the Peripheral Nerves, 2nd ed. London: Springer; Ch. 9, pp. 375–429.

Birch R 2011b Pain. In: Surgical Disorders of the Peripheral Nerves, 2nd ed. London: Springer; Ch. 12, pp. 527–62.

Birch R 2011c Rehabilitation. In: Surgical Disorders of the Peripheral Nerves, 2nd ed. London: Springer; Ch. 14, pp. 607–30.

Birch R 2011d Operating on peripheral nerves. In: Surgical Disorders of the Peripheral Nerves, 2nd ed. London: Springer; Ch. 7, pp 231–302.

Bonney G 1954 The value of axon responses in determining the site of lesion in traction lesions of the brachial plexus. Brain 77:588–609.

Bonney G, Gilliatt RW 1958 Sensory nerve conduction after traction lesion of the brachial plexus. Proc R Soc Med 51:365–7.

Bonney G 1959 Prognosis in traction lesions of the brachial plexus. J Bone Joint Surg Br 41:4–35.

Camp SJ, Birch R 2011 Injuries to the spinal accessory nerve: a lesson to surgeons. J Bone Joint Surg Br 93:62–7.

Cetik O, Uslu M, Acar HI et al 2006 Is there a safe area for the axillary nerve in the deltoid muscle? A cadaveric study. J Bone Joint Surg Am 88:2395–9.

Cho H, Lee HY, Gil YC et al 2013 Topographical anatomy of the radial nerve and its muscular branches related to surface landmarks. Clin Anat 26:862–9.

Cobb TK, Cooney WP, An K-N 1993 Relationship of deep structures of the hand and wrist to topographical landmarks. Clin Anat 6:300–7

Cooper A, Travers B 1817 On exostosis. In: Cooper A, Travers B (eds) Surgical Essays, 2nd ed. London: Cox & Son, p. 171.

Coote H 1861 Exostosis of the left transverse process of the seventh cervical vertebra, surrounded by blood vessels and nerves, successful removal. Lancet 1:360–1.

Cox CL, Riherd D, Tubbs RS et al 2010 Predicting radial nerve location using palpable landmarks. Clin Anat 23:420–6.

Gilliatt RW 1984 Thoracic outlet syndrome. In: Dyck PJ, Thomas PK, Lambert EH et al (eds) Peripheral Neuropathy, 2nd ed. Philadelphia: WB Saunders, pp. 1409–24.

Gilliatt RW, Le Quesne PM, Logue V 1970 Wasting of the hand associated with a cervical rib or band. J Neurol Neurosurg Psychiatry 33:615–24.

Goldie BS, Coates CJ 1992 Brachial plexus injuries – a survey of incidence and referral pattern. J Hand Surg [Br] 17:86–8.

Kato N, Htut M, Taggart M et al 2006 The effects of operative delay on the relief of neuropathic pain after injury to the brachial plexus. J Bone Joint Surg Br 88:756–9.

Ladak A, Tubbs RS, Spinner RJ 2014 Mapping sensory nerve communications between peripheral nerve territories. Clin Anat 27:681–90.

Lewis T, Pickering GW 1934 Observations upon maladies in which the blood supply to the digits ceases intermittently or permanently and upon gangrene of the digits: observations relevant to so-called 'Raynaud's disease'. Clin Sci 1:327–66.

McLean KM, Sacks JM, Kuo YR et al 2008 Anatomical landmarks to the superficial and deep palmar arches. Plast Reconstr Surg 121(1):181–5.

Menendez ME, Ring D 2015 A comparison of the Charlson and Elixhauser comorbidity measures to predict inpatient mortality after proximal humerus fracture. J Orthop Trauma 29:488–93.

Park BK, Bun HR, Hwang M et al 2010 Medial and lateral branches of the superficial radial nerve: cadaver and nerve conduction studies. Clin Neurophysiol 121:228–32.

Parry EW, Eastcott HHG 1992 Cervical rib and thoracic outlet syndrome. In: Eastcott HHG (ed) Arterial Surgery, 3rd ed. Edinburgh: Churchill Livingstone, pp. 333–53.

Rosson JW 1987 Disability following closed traction lesions of the brachial plexus sustained in motor cycle accidents. Hand Surg 12B:353–5.

Sargent P 1921 Lesions of the brachial plexus associated with rudimentary ribs. Brain 44:95–124.

Schenker M, Birch R 2000 Intact myelinated fibres in biopsies of ventral spinal roots after preganglionic traction injury to the brachial plexus. A proof that Sherrington's 'wrong way afferents' exist in man? J Anat 197:383–91.

Smith S, Knight R 2011 Clinical neurophysiology in peripheral nerve injuries. In: Birch R (ed) Surgical Disorders of the Peripheral Nerves, 2nd ed. London: Springer; Ch. 6, pp. 191–230.

Stenning M, Drew S, Birch R 2005 Low-energy arterial injury at the shoulder with progressive or delayed nerve palsy. J Bone Joint Surg Br 87:1102–6.

Symonds CP 1927 Cervical rib: thrombosis of subclavian artery, contralateral hemiplegia of sudden onset, probably embolic. Proc R Soc Med 20:1244–5.

Tourani SS, Taylor GI, Ashton MW 2014 Understanding the three-dimensional anatomy of the superficial lymphatics of the limbs. Plast Reconstr Surg 134:1065–74.

Vella JC, Hartigan BJ, Stern PJ 2006 Kaplan's cardinal line. J Hand Surg [Am] 31:912–8.

Wallis KA, Hills T, Mirjalili SA 2018 Minimising iatrogenic nerve injury in primary care. Br J Gen Pract 68:392–3.

Wickham JEA, Martin P 1962 Aneurysm of the subclavian artery in association with cervical abnormality. Br J Surg 50:205–9.

Wilbourn AJ 2005 Brachial plexus injuries. In: Dyck PJ, Thomas PK (eds) Peripheral Neuropathy, 4th ed. Philadelphia: Elsevier, Saunders; Ch. 55, pp. 1339–73.

CHAPTER

49

Shoulder girdle and arm

The upper limb is differentiated to achieve the complex patterns of stereotactic, non-stereotactic and gestural movements (each with a distinct neurological basis) that enable hand function. The combined movements of the shoulder and elbow bring objects in the hand into the visual field, while the great range of the shoulder and pectoral girdle enable a wide reach. Oculospinal afferents appear to be the most important modulators of the shoulder joint stability needed for *reaching*. An object is first reached and then grasped (increasing both superficial and deep peripheral afferent inputs that enhance proximal shoulder girdle stability (Alizadehkhaiyat et al 2011)), before being *retrieved* into the visual field. The requirements of attention to the visual field define the need for stability in the shoulder girdle: the closer the attention to an object in the centre of the field of vision ('macular vision'), the finer the control of the motion and stability of the shoulder girdle.

The joints of the upper limb become more complex proximodistally. The greatest potential for stability is gained through 'close-packing' (the state of a joint where the greatest stability is achieved for the least energy) in the carpus of the hand, while the range of available motion in each joint becomes more restricted. Close-packing occurs through a lesser, more specific, range of movement in the elbow: the flexed elbow with a supinated forearm is the position for carrying the greatest load with the least energy expenditure or the greatest resistance to fatigue. Close-packing occurs in the glenohumeral joint, so providing stability, but it is almost entirely gained through muscular activity. At the extremes of range, through capsular fibre spiralling, it is costly in terms of muscular energy expenditure, especially on a background of age- and gene-dependent musculotendinous degeneration. The scapulothoracic joint is the least intrinsically stable joint in the body and is entirely dependent on muscular activity for its stability and movement around the fulcrum of the acromioclavicular joint.

For the purposes of this chapter, the junction between the 'arm' and the 'elbow joint' will be taken to be the level at which the radial nerve perforates the lateral intermuscular septum to enter the anterior compartment of the arm, and the ulnar nerve perforates the medial intermuscular septum to gain the posterior compartment of the arm at the elbow.

SKIN AND SOFT TISSUES

Skin

Cutaneous vascular supply

The skin over the lateral end of the clavicle is supplied by the supraclavicular artery, which pierces the deep fascia superior to the clavicle and anterior to trapezius. In most cases, this artery arises from the superficial cervical/transverse cervical artery, but it occasionally arises from the suprascapular artery. The area over deltoid is supplied by the anterior and posterior circumflex humeral arteries. The deltoid branch of the thoracoacromial axis contributes to the blood supply of the anterior aspect of the shoulder via musculocutaneous perforators through deltoid.

The blood supply to the skin of the upper arm may be divided into three regions with separate supplies. The deltoid region is supplied by musculocutaneous perforators, and the medial and lateral regions are supplied by fasciocutaneous perforators (Cormack and Lamberty 1994, Salmon, in Taylor and Razaboni 1994).

The deltoid region is supplied by the posterior circumflex humeral artery via musculocutaneous perforators. After exiting from the quadrangular space, it gives off a descending branch that runs down to the insertion of deltoid and the overlying skin, and an ascending branch that passes superiorly towards the acromion and pierces the edge of deltoid and the deep fascia to fan out and supply the overlying skin.

The medial side of the upper arm is supplied by five or six fasciocutaneous perforators that arise from the brachial artery, the superior ulnar collateral artery and, if present, the single artery to biceps brachii. These perforators pass along the medial intermuscular septum to spread out in the deep fascia and anastomose with perforating vessels superiorly and inferiorly, and from the lateral side. There are virtually no musculocutaneous perforators through biceps or triceps.

The lateral side of the upper arm below deltoid is supplied by perforating vessels from the middle collateral and radial collateral arteries (the terminating bifurcation of the profunda brachii). The middle collateral artery sends perforators to the skin via the lateral intermuscular septum between brachioradialis and triceps, while the radial collateral artery gives off cutaneous perforators via the intermuscular septum between brachialis and brachioradialis. These cutaneous vessels anastomose with those from the medial side.

Cutaneous innervation

The skin over the anterior shoulder region is mobile and accommodates the great mobility of the shoulder girdle. The skin over the posterior aspect of the shoulder girdle is thicker and less mobile, being held to the underlying scapula by coarse connective tissue fibres. The cutaneous innervation reflects this difference in skin quality. The supraclavicular nerves (see Fig. 35.1B) are long, mobile nerves passing deep to platysma before piercing the muscle and the investing cervical fascia over or immediately caudal to the clavicle. The medial clavicular skin, including the skin over the sternoclavicular joint, is innervated by the small, often multifilamentous, medial supraclavicular nerve. The skin over the clavicle and over a variable extent of the anterior chest skin, including a variable extent of the anterior axillary fold, is innervated by the large, middle supraclavicular nerve. This nerve is frequently injured by injudicious incisions for the surgical treatment of fractures of the clavicle; a painful neuroma is a common outcome. The skin over the lateral clavicle, acromion and deltoid region is innervated by the lateral supraclavicular nerve or nerves. The floor of the axilla, together with part of the upper medial aspect of the arm, is supplied by the intercostobrachial nerve (lateral branch of the second intercostal nerve). Occasionally, the lateral branch of the third intercostal nerve contributes to the supply of the skin in the floor of the axilla. The lower aspect of the medial side of the upper arm is supplied by the medial cutaneous nerve of the arm. The lateral aspect of the upper arm is supplied by the upper lateral cutaneous nerve (a branch of the axillary nerve) and the lower lateral cutaneous nerve (a branch of the radial nerve). The posterior aspect is supplied by the posterior cutaneous nerve of the arm (a branch of the radial nerve). Fig. 49.1–49.5 illustrate the approximate areas of sensory loss or disturbance after pre- or postganglionic lesions involving C4–T1.

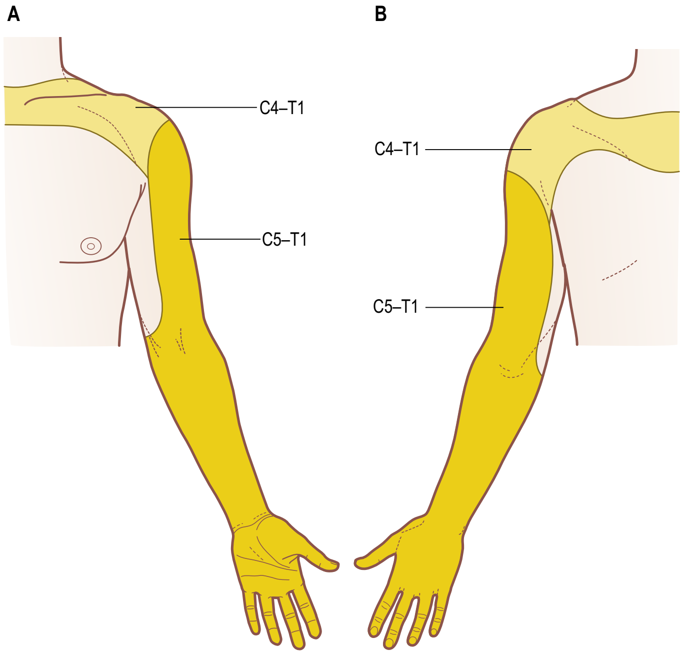

Fig. 49.1 The approximate area of sensory loss or disturbance after proven preganglionic (avulsion) lesion of C4–T1 and C5–T1. **A**, Anterior view. **B**, Posterior view.

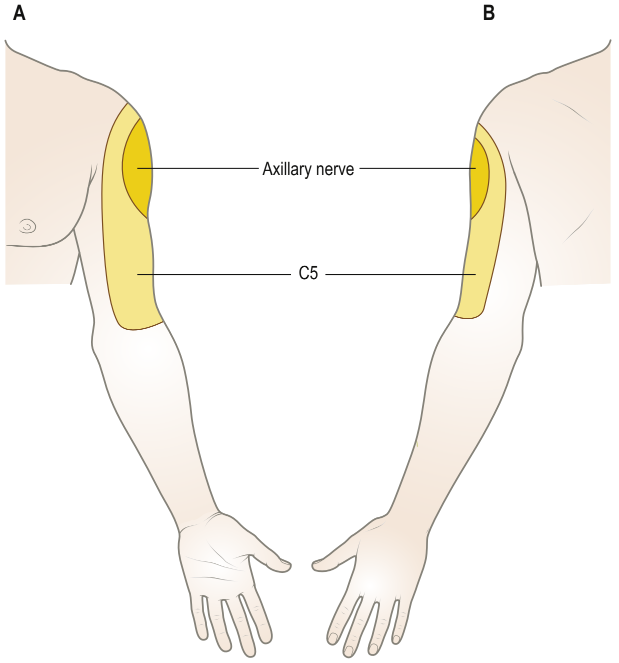

Fig. 49.2 The approximate area of sensory loss or disturbance after complete interruption of C5 and the axillary nerve. **A**, Anterior view. **B**, Posterior view. Sensory loss is greater in C5 lesions than in axillary lesions.

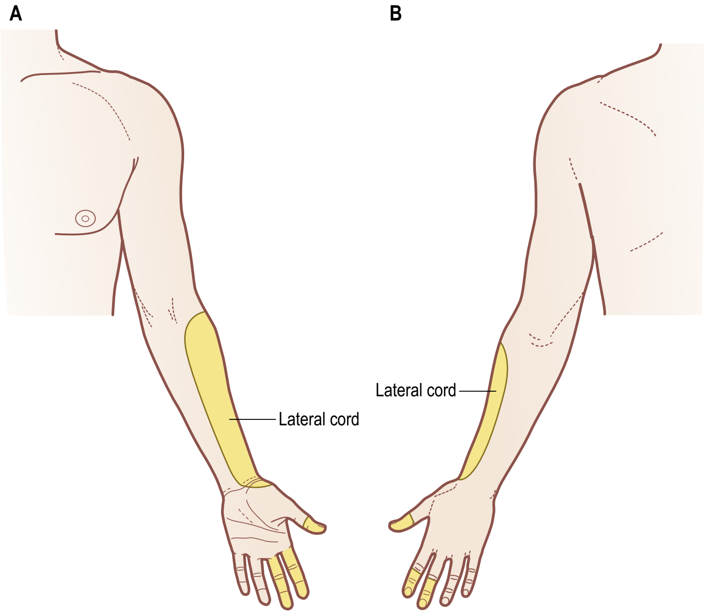

Fig. 49.3 The approximate area of sensory loss or disturbance after complete interruption of the lateral cord. **A**, Anterior view. **B**, Posterior view. Sometimes, loss of sensation is not complete; this is also true of the medial cord.

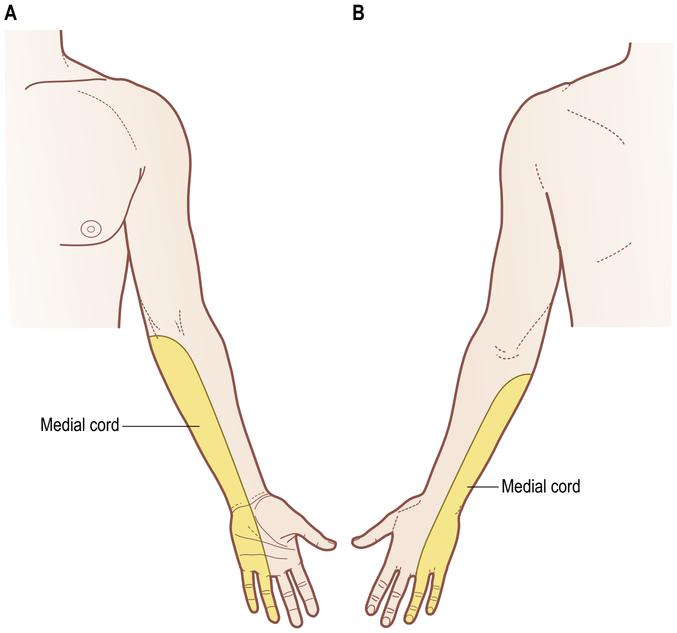

Fig. 49.4 The approximate area of sensory loss or disturbance after complete interruption of the medial cord. **A**, Anterior view. **B**, Posterior view.

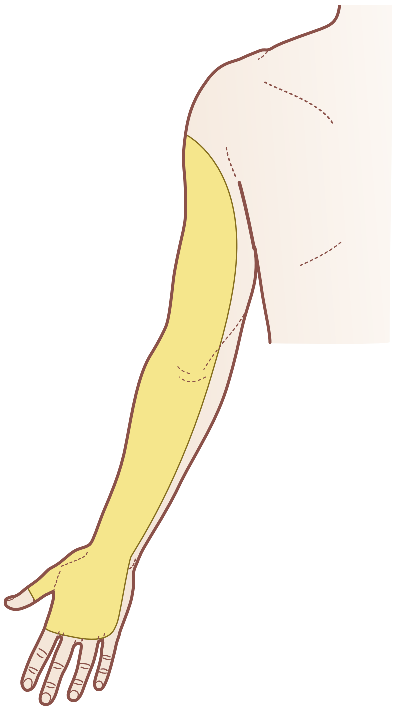

Fig. 49.5 The approximate area of sensory loss or disturbance after complete interruption of the posterior cord. Posterior view.

Soft tissues

Deep fascia

In common with locomotor muscles in the lower limb, the upper limb muscles are attached, in varying degrees, to their surrounding deep fascial envelopes. This arrangement increases the area (footprint) of attachment of a muscle within a fascial compartment, so increasing the effectiveness and efficiency of that muscle. For example, the fasciae overlying the three muscles of the scapular fossae (subscapularis, infraspinatus and supraspinatus) are well attached and thicker medially; the fibro-osseous cuff so formed around the medial parts of the muscles affords a greater area of attachment than would be available if the muscles were attached only to the scapular fossae. The blood supply to the muscles of the upper limb is defined by their fascial compartmentation.

Compartment syndrome of the arm The muscular compartments of the arm (and thigh) are not as well defined as those of the forearm (and leg). Compartment syndrome is less common in trauma of the arm but remains a concern, particularly after extensive reconstruction procedures and high-energy or crushing injuries of the limb.

Fascia over deltoid

The deep fascia over deltoid is thickest anteriorly and posteriorly, and is adherent in a linear fashion to the external aspect of the superficial fibrous septa of the central (lateral) part of that muscle. It blends with the pectoral fascia in front, and with the thick and strong fascia overlying infraspinatus behind. Above, it blends with the periosteum of the lateral part of the clavicle, the thin periosteum of the acromion, the crest of the scapular spine and the cranial part of the medial border of the scapula, caudal to the spine of the scapula, where it blends with the infraspinatus fascia. Below, it is continuous with the deep brachial fascia, blending with the lateral intermuscular septum (Leijnse et al 2008).

Pectoral and axillary fascia

The pectoral fascia is thin over pectoralis major. It is attached medially to the sternum and is continuous with the fascia of the rectus sheath caudally. Cranially, it blends with the periosteum of the clavicle and the anterior aspect of the capsule of the sternoclavicular joint. Laterally, it is continuous with the fascia over deltoid; it forms the roof of the infraclavicular fossa between the muscular attachments of pectoralis major and deltoid to the clavicle. The fascia is loosely adherent to the septum between the sternal and clavicular parts of pectoralis major. Inferolaterally, between pectoralis major and latissimus dorsi, the fascia thickens to form the floor of the axilla as the axillary fascia. At the caudal edge of pectoralis major, a deep lamina of fascia ascends to envelop the caudal border of pectoralis minor; it becomes the clavipectoral fascia at the upper edge of pectoralis minor. The hollow of the armpit is produced mainly by the action of this fascia in tethering the axillary skin to the floor of the axilla; it is sometimes referred to as the suspensory ligament of the axilla. The axillary fascia is pierced by the tail of the breast (see Fig. 53.22A). The pectoral fascia envelops the lateral margin of latissimus dorsi; the deep and superficial layers ensheathe that muscle and are attached behind to the spines of the thoracic and lumbar vertebrae, blending with the thoracolumbar fascia medially and caudally.

Clavipectoral fascia

The clavipectoral fascia is the superior continuation of the deep lamina of the pectoral fascia and the medial continuation of the parietal layer of the subscapular bursal fascia. Laterally, it is continuous with the coraco-acromial ligament above and lateral to the coracoid. It envelops the coracoid blending with the periosteum of the tip of that process, the short head of biceps brachii and coracobrachialis. It covers the interval between those two muscles and pectoralis minor, which it envelops, and then traverses the interval between pectoralis minor and subclavius. It splits around subclavius and is attached to the clavicle anterior and posterior to the groove for subclavius. The posterior layer is contiguous with the deep cervical fascia, a condensation of which forms a tether around the central tendinous part of omohyoid, so indirectly connecting it to the clavicle. The deep aspect of the posterior lamina of the clavipectoral fascia blends with the sheath of the axillary vessels. Medially, it blends with the fascia over the first two intercostal spaces and is attached to the first rib, medial to subclavius. Occasionally, the fascia thickens to form a band between the first rib and coracoid process, the costocoracoid ligament, under which the lateral cord of the brachial plexus is closely applied (Atasoy 2004). The cephalic vein, thoraco-acromial artery and associated veins and lymphatic vessels, and the lateral pectoral nerve all pass through the fascia immediately superior to the upper border of pectoralis minor. This fascia was called the 'clavi-coraco-axillary aponeurosis' by Testut (1904).

Subscapular fascia

The subscapular fascia is thin and attached to the entire circumference of the subscapular fossa. Subscapularis is partly attached to its deep surface medially, which is an example of the extension of the attachment zone of a muscle for more effective action. The fascia extends laterally and blends with the deep layer of the subscapular bursa in front of the tendon of subscapularis and with the external layer of the capsule of the rotator interval of the glenohumeral joint. Inferiorly, it continues as the fascia enveloping teres major.

Infraspinous fascia

The infraspinous fascia covers infraspinatus and is attached to the margins of the infraspinous fossa, except cranially and medially, where there is a loose attachment to the lower aspect of the spine of the scapula. Cranially and laterally, the infraspinatus fascia is continuous with the supraspinatus fascia, creating a single muscular compartment for the two muscles. The deep fibres of deltoid are attached to the infraspinatus fascia over a strip of about 1 cm for the entire length of the spine of the scapula; the examining finger cannot palpate the spine of the scapula from within the space between deltoid and infraspinatus. The fascia is contiguous with the strong lower border of the deltoid fascia along the overlapping posterior border of deltoid.

Supraspinous fascia

The supraspinous fascia completes the osseofibrous compartment containing supraspinatus; it is attached to the scapula around the boundaries of the attachment of supraspinatus. It is thick medially, where supraspinatus attaches to its own fascia, but thinner laterally under the coraco-acromial ligament.

Brachial fascia

The deep fascia of the upper arm, the brachial fascia, is continuous with the fasciae covering deltoid and pectoralis major; it forms a thin, loose covering for the anterior muscles of the arm and a more robust covering for the posterior muscles. Medially, just below the middle of the upper arm, it is perforated by the basilic vein, lymphatic vessels and, at various levels, by branches of the brachial cutaneous nerves.

The fascia is thickest distally, where it contains the brachial muscles in distinct compartments anteriorly and posteriorly, and is defined medially and laterally by tough septa. The lateral intermuscular septum is continuous with the fascia overlying the lateral part of deltoid proximally, and has an upward, thinner extension to the lateral crest of the intertubercular sulcus (groove) contiguous with the fascia over the anterior border of deltoid. It is attached to the supracondylar ridge of the lateral epicondyle of the humerus, and is perforated at the level of the junction of the upper three-fifths and lower two-fifths of the humerus by the radial nerve and the radial collateral branch of the profunda brachii artery passing into the anterior compartment from behind. It provides extension for the zone of attachment of the lateral head of triceps posteriorly, and of brachialis, brachioradialis and extensor carpi radialis longus anteriorly. The medial intermuscular septum extends from the medial lip of the intertubercular sulcus, where it is contiguous with the fascia of teres major, next blends with the aponeurosis of attachment of coracobrachialis to the medial aspect of the humerus, and then passes as a thick septum along the medial aspect of the humerus to the medial supracondylar ridge of the medial epicondyle. It gives attachment to the medial head of triceps posteriorly, and brachialis anteriorly. It is perforated by the ulnar nerve at about the same level as the radial nerve laterally, together with the superior ulnar collateral artery and the posterior branch of the inferior ulnar collateral artery. At the elbow, the brachial fascia is attached to the epicondyles of the humerus, so completing the muscular compartments, and the olecranon of the ulna, and is continuous with the antebrachial fascia.

Axillary neurovascular sheath

The axillary neurovascular sheath is closely contiguous with the posterior aspect of the clavipectoral fascia. The second part of the axillary artery lies behind pectoralis minor; most intimal ruptures of the vessel caused by distraction trauma occur in this part of the vessel.

Spread of infection

Available with the *Gray's Anatomy* e-book

BONES

Clavicle

The clavicle lies almost horizontally at the root of the neck (see Figs 35.13, 48.7A). It is a crank-shaped cantilever that carries the scapula, so enabling the limb to swing clear of the trunk. It transmits part of the weight of the limb to the axial skeleton. The lateral or acromial end of the bone is flattened and articulates with the medial side of the acromion, whereas the medial or sternal end is enlarged and articulates with the clavicular notch of the manubrium sterni and first costal cartilage. The shaft is gently curved and resembles the italic letter *f* in shape, being convex forwards (the antecurve) in its medial two-thirds and concave forwards (the retrocurve) in its lateral third (Fig. 49.6). The inferior aspect of the intermediate two-fifths is grooved in its long axis for the attachment of subclavius. Laterally, the internal architecture of the clavicle is trabecular, with a medullary cavity in the medial two-thirds. The cortical bone is thickest at the transition zone between the antecurve and retrocurve. The female clavicle is typically shorter, thinner, less curved and smoother. Mid-shaft circumference is the most reliable single indicator of sex; a combination of this measurement with weight and length yields more reliable and consistent results. The clavicle is subcutaneous throughout its whole length and accordingly can be palpated for its entire length; the medial (sternal) end forms an expanded, blunt-faced margin of the jugular notch. The anterior border of the lateral (acromial) end is not readily distinguished from the acromion; the attachment of deltoid obscures the anterior aspect of the acromioclavicular joint. By contrast, the posterior border of the lateral end forms the anterior margin of a roughly parabolic hollow under the lateral fibres of trapezius, the posterior border being formed by the anterior border of the spine of the scapula. The hollow will admit at least one palpating finger. If the pulp of the finger is placed on the spine of the scapula as far laterally as the hollow will permit, the nail will inevitably point to the posterior capsule of the acromioclavicular joint; this landmark is always palpable, During forceful flexion/adduction/protraction of the upper limb across the trunk (e.g. when the scapula is wrenched from the lateral end of the clavicle in thoracoscapular dissociation), the axillary sheath containing the axial vessels and cords of the brachial plexus is forced into pectoralis minor, which acts as a fulcrum or guillotine, around which the vessels angle sharply, so rupturing the arterial intima. Acute neural injuries occur as a result of direct injury (traction, compression, or both) to the nerve trunks, causing acute sensorimotor deficits, arterial adventitial haematoma or acute aneurysm expanding within the axillary sheath to cause the syndrome of causalgia (rapidly progressive, severe pain in the distribution of the affected nerve trunks with neural deficits). Arterial thrombosis following intimal rupture is associated with late nerve deficits as a result of inadequate neural perfusion, local scarring with distortion of the axillary sheath and its contents, and poor posture of the affected limb.

The neurovascular bundle enclosed within the sheath is separated from the subscapular fascia by a ‘virtual space’ traversed by the subscapular nerves, an arrangement that permits full excursion of subscapularis without distortion of the neurovascular bundle during normal arm movements. The tip of the coracoid can be likened to the tip of the shaft of a steering oar attached to a vessel (the scapula) tethered within the thick clavipectoral fascia: the effect of pectoralis minor acting as an antagonist of trapezius in scapular position and motion control (see below) is optimized by the wide attachment of the clavipectoral fascia and coraco-acromial ligament to the clavicle and scapula (see Fig. 49.18).

When axillary suppuration occurs, the local fascial arrangement affects the spread of pus. Suppuration may be superficial or deep to the clavipectoral fascia. In the former, an abscess would appear at the edge of the anterior axillary fold or in the groove between deltoid and pectoralis major; in the latter, pus would tend to track upwards in the axillary neurovascular sheath and appear at the root of the neck, taking the direction of least resistance. Lymphangitis in the medial aspect of the arm suggests infection deep to the clavipectoral fascia with lymphatic obstruction. When an axillary abscess is incised, the knife should enter the axillary ‘base’, midway between the anterior and posterior margins and near the thoracic side, to avoid the lateral thoracic, subscapular and axillary vessels on the anterior, posterior and lateral walls, respectively.

even in well-muscled individuals, when other shoulder landmarks can be obscured.

Lateral two-fifths

The lateral two-fifths of the clavicle are flattened and have superior and inferior surfaces, and anterior and posterior borders. The anterior border is concave, thin and roughened, and may be marked by a small deltoid tubercle. The posterior border, also roughened by muscular attachments, is convex backwards. The superior surface is roughened near its margins but is smooth centrally, where it can be felt through the skin. The inferior surface presents two obvious markings. Close to the posterior border, at the junction of the lateral fourth with the rest of the bone, a prominent conoid tubercle gives attachment to the conoid part of the coracoclavicular ligament. A narrow, roughened strip, the trapezoid line, runs forwards and laterally from the lateral side of this tubercle, almost as far as the acromial end (**Fig. 49.6B**). The trapezoid part of the coracoclavicular ligament is attached to it. A small, oval articular facet, for articulation with the medial aspect of the acromion, faces laterally and slightly downwards at the lateral end of the shaft.

Subclavius is attached to the groove on the inferior surface (see Fig. 49.6B). The clavipectoral fascia is attached to the edges of the groove. The posterior edge of the groove runs to the conoid tubercle, where fascia and conoid ligament merge. There is a laterally inclined nutrient foramen lateral to the groove. Deltoid (anteriorly) and trapezius (posteriorly) are attached to the lateral two-fifths of the shaft; both muscles are inserted directly into the clavicle and indirectly into the clavicular periosteum. The coracoclavicular ligaments, attached to the conoid tubercle and trapezoid line (see Fig. 49.6B), transmit the weight of the upper limb to the clavicle, and are counteracted by the cervical part of trapezius, which supports its lateral part (see Fig. 49.18).

Medial three-fifths

The medial three-fifths of the shaft of the clavicle are cylindrical or prismoid in form and have four surfaces, although the inferior surface is often reduced to a mere ridge. The anterior surface is roughened over most of its extent but is smooth and rounded laterally, where it forms the upper boundary of the infraclavicular fossa. The upper surface is roughened medially and smooth laterally. The posterior surface is smooth and featureless medially; its lateral half bears a groove in the long axis of the bone. The inferior surface is marked near its sternal end by a roughened oval impression, which is often depressed below the surface. Its margins give attachment to the costoclavicular ligament, which connects the clavicle to the upper surface of the first rib and its cartilage. Rarely, this area is smooth or raised to constitute an eminence that may form a synovial pseudarthrosis with the upper surface of the first rib; in older subjects, an extra-articular synostosis may form.

The medial three-fifths provide attachment, anteriorly, for the clavicular head of pectoralis major. The clavicular head of sternocleidomastoid is attached to the medial half of the superior surface, but the marking on the bone is not conspicuous. The smooth, posterior surface is devoid of muscular attachments, except at its lower part immediately adjoining the sternal end, where the lateral fibres of sternohyoid are attached. Medially, this surface is related to the lower end of the internal jugular vein (from which it is separated by sternohyoid), the termination of the subclavian vein, and the start of the brachiocephalic vein. More laterally, the clavicle arches in front of the trunks and divisions of the brachial plexus and the third part of the subclavian artery. The thyrocervical trunk and its branches, and the suprascapular and transverse cervical vessels are immediately behind and above the upper aspect of this surface. Subclavius is inserted in the subclavian groove on the inferior surface, and the clavipectoral fascia is attached to the edges of the groove. The posterior lip of the groove is continuous with the conoid tubercle laterally and brings the clavipectoral fascia into continuity with the conoid ligament. A nutrient foramen is found in the lateral end of the groove, running in a lateral direction; the nutrient artery is derived from the suprascapular artery.

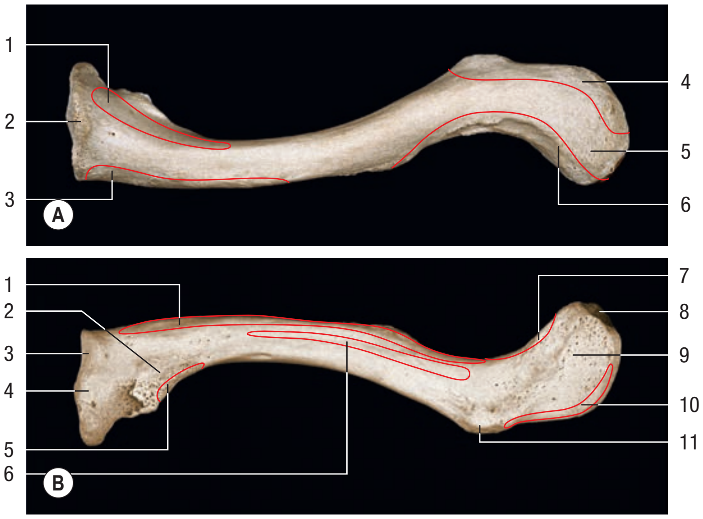

Fig. 49.6 The left clavicle, showing sites of muscular and ligamentous attachment and articular surfaces. **A**, Superior view. Key: 1, sternocleidomastoid (clavicular head); 2, sternal end; 3, pectoralis major; 4, trapezius; 5, acromial end; 6, deltoid. **B**, Inferior view. Key: 1, pectoralis major; 2, for costoclavicular ligament; 3, for first costal cartilage; 4, for sternum; 5, sternohyoid; 6, subclavius; 7, deltoid; 8, for acromion; 9, trapezoid line; 10, trapezius; 11, conoid tubercle.

Sternal end

The sternal end of the clavicle is directed medially, downwards and forwards, and articulates with the clavicular notch of the manubrium sterni. The sternal surface, usually irregular and pitted, is quadrangular (sometimes triangular). Its uppermost part is slightly roughened for attachment of the interclavicular ligament, sternoclavicular capsule and articular disc. Elsewhere, the surface is smooth and articular; it extends on to the inferior surface for a short distance, where it articulates with the first costal cartilage. The sternal end of the clavicle projects upwards beyond the manubrium sterni and can be felt and seen easily, forming the lateral wall of the jugular notch, behind which are the cricoid cartilage, cricothyroid membrane, the lower part of the thyroid cartilage of the larynx and the brachiocephalic vein. The sternal ends of each clavicle thus form a guide to the jugular notch: if the sternal end of the clavicle is displaced backwards (by traumatic dislocation), the landmarks of the notch are lost, the trachea is displaced and there will be difficulty breathing. If the trachea is displaced to one side (for instance, by pneumothorax), the features of the larynx cannot be palpated readily.

Ossification

The clavicle begins to ossify before any other bone in the body. The shaft of the bone undergoes intramembranous ossification in two primary centres, medial and lateral, in stages 18–20 (42–50 postfertilization days). However, the clavicle does not ossify exclusively by intramembranous ossification. Endochondral ossification extends from the shaft to the sternal and acromial ends in stages 20–21. In 14 mm embryos, the clavicle is a band of condensed mesenchyme between the acromion and apex of the first rib, and is continuous with the sternal rudiment. Medial and lateral zones of early cartilage transformation ('precartilage') occur within this band; intramembranous centres of ossification appear and soon fuse in the mesenchyme between them. Sternal and acromial zones become true cartilage into which ossification extends from the shaft. Length increases by interstitial growth of these terminal cartilages, which develop zones of hypertrophy, calcification and advancing endochondral ossification like other growth cartilages. Diameter increases by subperichondral deposition in the extremities and subperiosteal deposition in the shaft. A secondary centre for the sternal end appears in the late teens, or even early twenties, usually 2 years earlier in females (**Fig. 49.7**). Fusion is probably rapid but reliable data are lacking. An acromial secondary centre sometimes develops at around 18–20 years, but this epiphysis is always small and rudimentary, and rapidly joins the shaft. Growth is usually complete by 23 years in both sexes. Epiphyses are endochondral and probably fuse in the same way as they do in long bones.

Scapula

The scapula is a large, triangular bone that lies over the posterolateral chest wall, covering parts of the second to seventh ribs (see Fig. 48.7A),

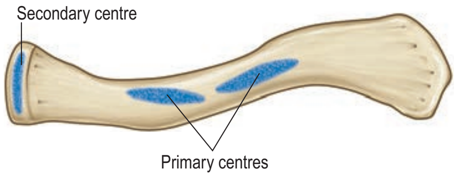

Fig. 49.7 The three constant centres of ossification of the clavicle.

The shaft of the clavicle is usually fractured as a result of a violent impact to the side of the shoulder. The fracture typically occurs at the junction of the lateral two-fifths and medial three-fifths, where the transition from antecurve to retrocurve occurs and the bone changes in cross-sectional shape from its flatter lateral part to a tubular medial part. The weight of the arm causes displacement of the lateral fragment downwards, inwards and into forward (ventral) rotation, a posture maintained even in recumbency partly by the action of subclavius. If the fracture heals in this position, the dimensions and shape of the retroclavicular space are altered, particularly during elevation of the arm above shoulder level, and the brachial plexus (and its perfusion) and the subclavian vessels can be distorted (one of the many causes of the syndrome associated with thoracic outlet obstruction).

Anomalies of clavicular growth and development include defects of ossification, morphology (shape) and length. Defects of ossification in the clavicle and those cranial bones that ossify by intramembranous ossification occasionally coincide, e.g. in cleidocranial dysostosis. Defects of morphology and length occur in the immature clavicle in birth lesions of the brachial plexus; the lateral two-fifths are affected. In a typical case, the acromial end of the clavicle is short and excessively curved ventrally, rotated by up to 90°, while the coracoclavicular ligaments are normal. The coracoid is long and more vertical than usual; the scapula is often small, and the scapular neck region is short with variable glenoid dysplasia. These characteristic defects are predominantly associated with the upper trunk lesion (C5 and C6) that results in a muscular imbalance across the acromioclavicular and glenohumeral joints; the flexor and medial (internal) rotator muscles are relatively short. The short, tight pectoralis minor and coracobrachialis produce a distorting force on the coracoid, which elongates and rotates dorsally. With retropulsion of the humeral head posteriorly, the scapula rotates ventrally, particularly if there is posterior glenoid dysplasia. Deltoid shortening creates a downward distraction on the developing acromion, which lengthens and curves distally. The spine of the scapula is parallel to the body of the scapula rather than dorsally directed, and these deformities cause the acromioclavicular joint to be orientated more horizontally. As a result, the lateral clavicle is excessively curved ventrally. The concept here is that the abnormal shape is driven by asymmetrical muscle paralysis and partial recovery, and that *form* follows the neural lesion. While poor movement (causing a lack of ‘motivation’ for growth in *length*) might explain the clavicular shortening, an equally valid explanation might involve a vascular insufficiency of the lateral ossification centre of the clavicle (with a similar insufficiency of the lateral ossification centres of the scapula for the glenoid): both have a contribution from the suprascapular artery, which is ‘at risk’ during injuries that lead to brachial plexus palsy. Length is a function of perfusion and shortening follows vascular insufficiency (Kambhampati et al 2006).

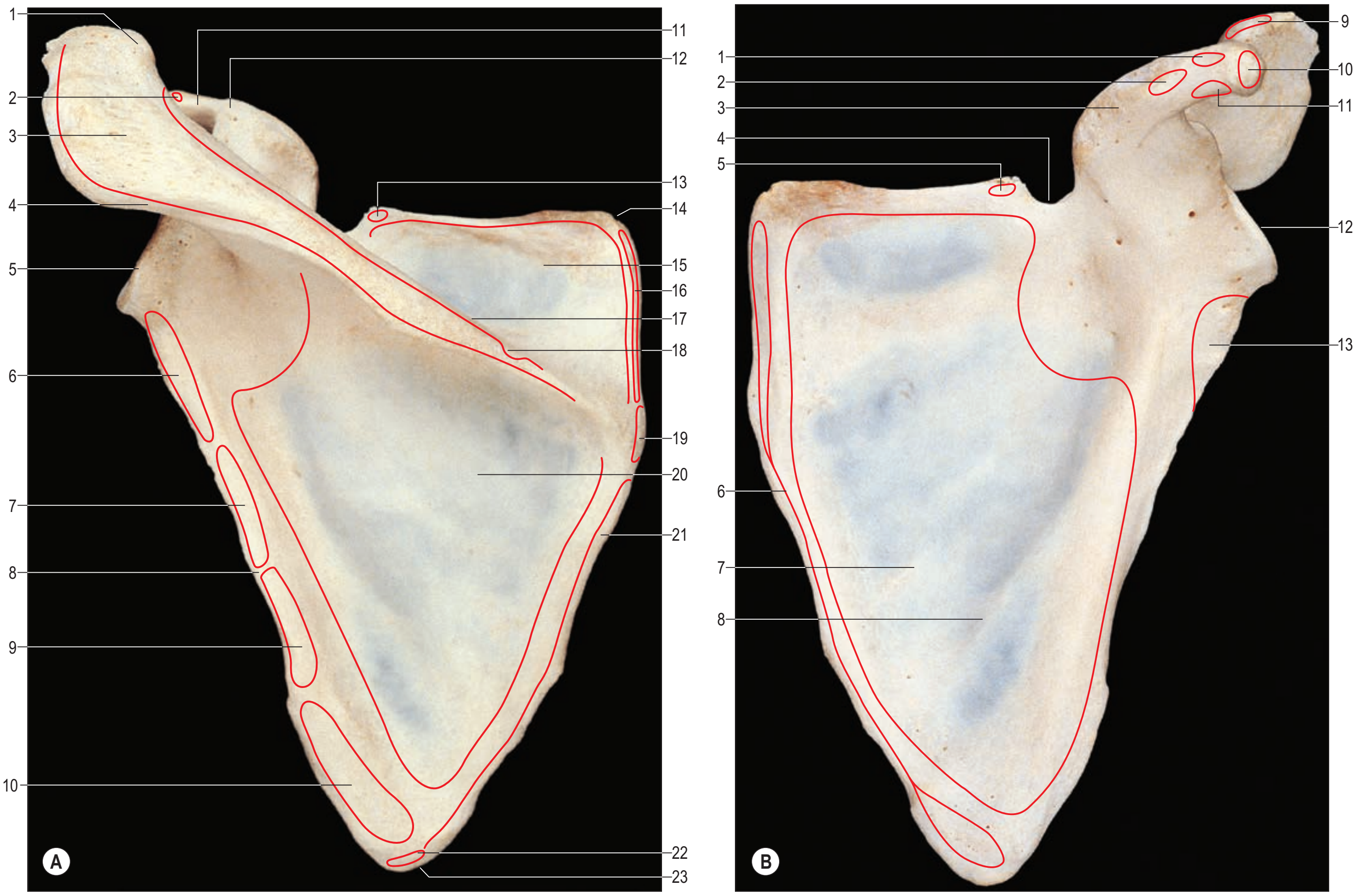

Fig. 49.8 The left scapula, showing sites of muscular and ligamentous attachment and articular surfaces. **A**, Posterior aspect. Key: 1, clavicular facet; 2, biceps brachii (short head); 3, acromion; 4, deltoid; 5, glenoid fossa; 6, triceps brachii (long head); 7 and 9, teres minor; 8, groove for circumflex scapular artery; 10, teres major; 11, conoid tubercle; 12, coracoid process; 13, omohyoid (inferior belly); 14, superior angle; 15, supraspinatus; 16, levator scapulae; 17, spine; 18, trapezius; 19, rhomboid minor; 20, infraspinatus; 21, rhomboid major; 22, latissimus dorsi; 23, inferior angle. **B**, Anterior aspect. Key: 1, attachment of trapezoid ligament; 2, attachment of conoid ligament; 3, acromion process; 4, suprascapular notch; 5, omohyoid (inferior belly); 6, serratus anterior; 7, subscapularis; 8, ridge for intermuscular tendon of subscapularis; 9, deltoid; 10, biceps brachii (short head) and coracobrachialis; 11, pectoralis minor; 12, glenoid fossa; 13, triceps brachii (long head).

with a vertical long (craniocaudal) axis. It has costal and dorsal surfaces; superior, lateral and medial borders; inferior, superior and lateral angles; and three processes: the spine, the acromion and the coracoid process (Figs 49.8–49.9).

The superior and lateral borders and the supraspinous and infraspinous fossae converge laterally at the lateral angle of the scapula. This region comprises the glenoid fossa, the coracoid process and the neck of the scapula. Three robust columns of bone, namely, the lateral border of the spine of the scapula, the coracoid and the lateral border of the scapula, thus converge at the neck region. Load applied through the glenoid fossa or through the coracoid is transmitted into the scapula through these columns, which also provide a robust framework for the scapular body. The main processes, and thicker parts of the scapula, contain trabecular bone for load-bearing; the rest consists of a thin layer of compact bone for muscular attachments.

Costal surface

The costal surface, which is directed medially and forwards when the arm is by the side, is gently concave, especially in its upper part, matching the contour of the chest wall (Fig. 49.8B).

Near the lateral border, there is a longitudinal rounded ridge, prominent near the neck but less so below, which is separated from the lateral border by a narrow, grooved area. Subscapularis arises from the subscapular fossa that comprises nearly the whole of the costal surface, including the grooved area immediately adjoining the lateral border, but excluding the area next to the neck of the bone. Small, fibrous intramuscular septa are attached to four or five roughened ridges that subdivide this surface incompletely into a number of smooth areas. The anterior aspect of the neck is separated from subscapularis by a bursal protrusion of the synovial membrane of the shoulder joint (subscapular 'bursa'). The lower five or six digitations of serratus anterior are attached to an oval area near the inferior angle. The remainder of the muscle is inserted into a narrow strip along the ventral aspect of the medial border, which is wider above, where it receives the large first digitation. The longitudinal thickening of the bone near the lateral border provides a column of the necessary strength to withstand the pull of serratus anterior on the inferior angle during lateral scapular rotation, when the glenoid cavity is turned to face more directly upwards as the arm is raised from the side and carried above the head against gravity.

Dorsal surface

The dorsal surface is divided by the transverse, shelf-like spine of the scapula into two unequal parts: a smaller supraspinous fossa above and an infraspinous fossa below. The fossae are confluent at the spinoglenoid notch between the lateral border of the spine and the dorsal aspect of the neck; their central parts may be very thin (Fig. 49.8A). The supraspinous fossa is bounded superiorly and anteriorly by the superior border, from the suprascapular notch and dorsal aspect of the root of the coracoid laterally, to the superior angle medially; and medially, by the upper part of the medial border. The infraspinous fossa is bounded by the medial and lateral borders and the inferior angle.

Supraspinatus is attached to the medial two-thirds of the supraspinous fossa on the dorsal surface; the fascia that covers the muscle is attached to the margins of the fossa. A fat pad lies between the supraspinatus fascia and the under-surface of trapezius. Teres minor is attached to the upper two-thirds of a flattened strip that adjoins the lateral border. The strip is grooved near its upper end by the circumflex scapular vessels passing between teres minor and the bone as they enter the infraspinous fossa. The lower limit of the attachment of teres minor is indicated by an oblique ridge, which runs from the lateral border to the neighbourhood

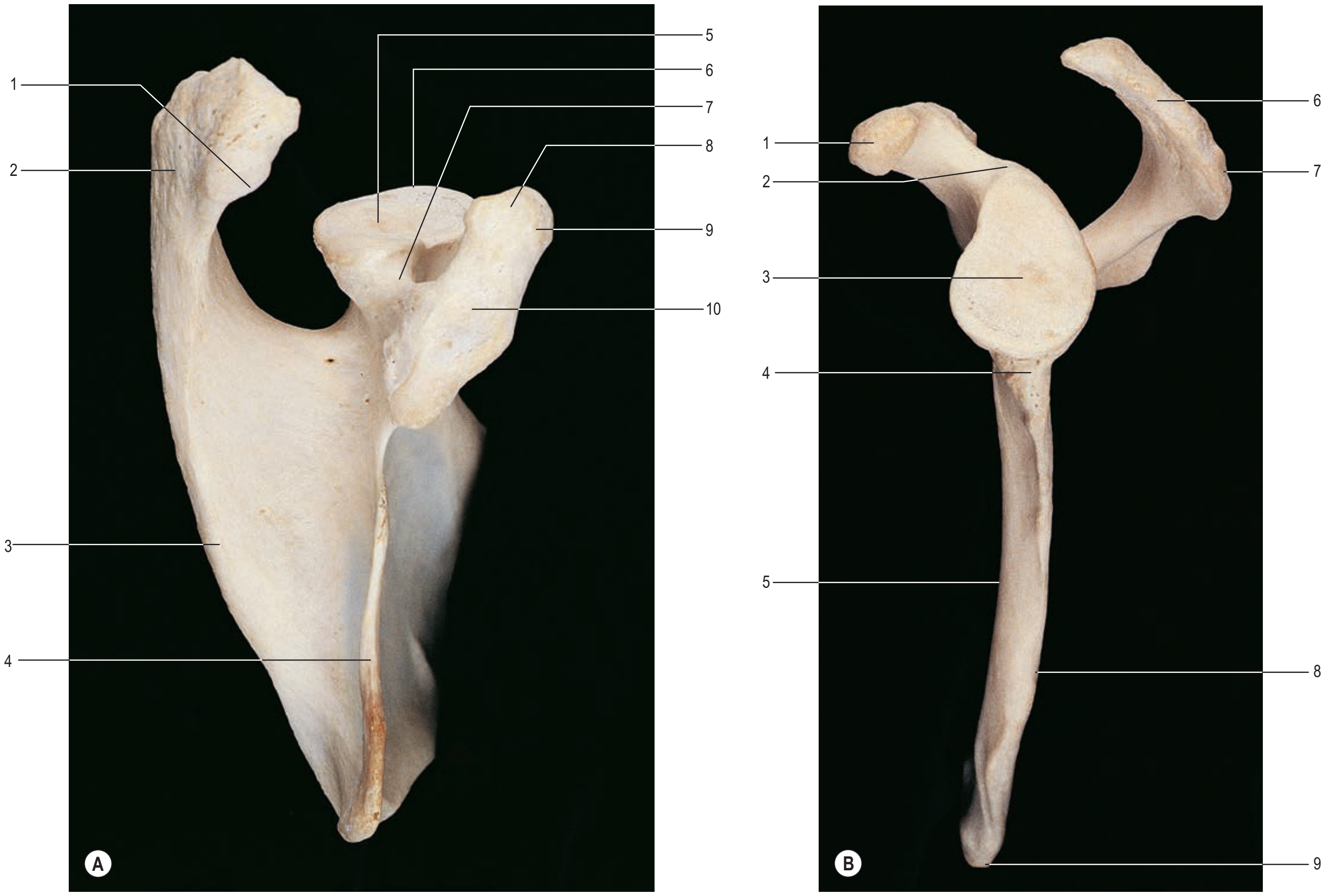

Fig. 49.9 The left scapula, showing sites of muscular and ligamentous attachment and articular surfaces. **A**, Superior aspect. Key: 1, facet for clavicle; 2, acromial process; 3, spine; 4, superior border; 5, head; 6, glenoid fossa; 7, neck; 8, conoid tubercle (for conoid ligament); 9, coracoid process; 10, attachment of trapezoid ligament. **B**, Lateral aspect. Key: 1, coracoid process; 2, supraglenoid tubercle; 3, glenoid fossa; 4, infraglenoid tubercle for long head of triceps brachii; 5, ventral surface; 6, acromion; 7, acromial angle; 8, lateral border; 9, inferior angle.

of the inferior angle and cuts off a somewhat oval area where teres major is attached. The dorsal aspect of the inferior angle may give origin to a small slip that joins the deep surface of latissimus dorsi. The infraspinous fossa is hollowed out laterally but is convex medially. Infraspinatus is attached to the infraspinous fossa, with the exception of an area near the neck of the bone. The strong infraspinatus fascia passes on to teres minor and teres major, and sends fascial partitions between them that reach the bone along the ridges marking the limits of their attachments.

Superior border

The superior border, thin and sharp, is the shortest. At its anterolateral end, it is separated from the root of the coracoid process by the suprascapular notch (see Fig. 49.8B), which can vary in shape and size. Medial to the suprascapular notch, the superior border gives origin to the inferior belly of omohyoid. The notch is bridged by the superior transverse ligament (or suprascapular ligament), which is attached laterally to the root of the coracoid process and medially to the limit of the notch. The ligament is sometimes ossified. The foramen, thus completed, transmits the suprascapular nerve to the supraspinous fossa, whereas the suprascapular vessels pass backwards above the ligament.

Lateral border

The lateral border has a triangular or rhomboidal cross-section. It forms a clearly defined, sharp, roughened ridge that runs sinuously from the inferior angle to the glenoid cavity. At its upper end, it widens into a rough, somewhat triangular, area: the infraglenoid tubercle (Fig. 49.9B). The lateral border separates the attachments of subscapularis and teres minor and major. These muscles project beyond the bone and, with latissimus dorsi below, cover it so completely that it cannot be felt through the skin. The long head of triceps is attached to the infraglenoid tubercle.

The grooved part of the costal surface, the narrow, flat lateral strip of the dorsal surface and the adjacent thickened ridge (see Fig. 49.9B) are often included in the 'lateral column' in surgical practice. By definition, the remainder of the scapular body (costal and dorsal surfaces) and the medial border are called the 'medial column'.

Medial border

The medial border extends from the inferior to the superior angle. It is slightly thickened and flat, and is further thickened at the medial end of the spine. In its lower two-thirds, this border can easily be felt through the skin, but its upper third is more deeply placed and more difficult to palpate. It is thin and often angled opposite the root of the spine. Levator scapulae is attached to a narrow strip, extending from the superior angle to the root of the spine, and rhomboid minor is attached below this, opposite the root of the spine. Rhomboid major is attached to the remainder of the border.

Scapular angles

The inferior angle lies over the seventh rib, or over the seventh intercostal space. It can be felt through the skin and the muscles that cover it, and, when the arm is raised above the head, it can be seen to rotate forwards (protract) around the chest wall; when the arm is lowered, the scapula should restitute (retract) to its original position without a disturbance of rhythm. It is covered on its dorsal aspect by the upper border of latissimus dorsi, a small slip from which is frequently attached to the inferior angle. The superior angle, at the junction of the superior and medial borders, is obscured by the upper part of trapezius. It lies over the dorsal surface of the second rib and can be palpated deeply above and behind the clavicle.

The lateral angle, truncated and broad, comprises the glenoid fossa (cavity) and scapular neck, with the coracoid projecting forwards. When the arm is by the side, the fossa is directed forwards, laterally and slightly upwards. When the arm is raised above the head, it is directed almost straight upwards, i.e. the plane of the fossa is horizontal. The supraglenoid tubercle is a small, rough, sloping area at the cranial margin of the fossa;

it often encroaches on the root of the coracoid process, and is the site of attachment for the tendon of the long head of biceps brachii. The infraglenoid tubercle is a larger, rough area at the caudal margin of the glenoid fossa, at the upper end of the lateral margin, and is the site of attachment for the tendon of the long head of the triceps brachii. The anatomical neck is the region of the scapula extending between the infraglenoid and supraglenoid tubercles anteriorly and posteriorly, lateral to the root of the coracoid process; anteriorly, there is no landmark to distinguish the anatomical neck from the costal surface of the body of the scapula. Posteriorly, the anatomical neck is limited by the spinoglenoid notch at the root of the spine of the scapula. The bone here has an asymmetric, triangular cross-sectional shape; the plane of the anterior surface of the neck makes an acute angle of about 60° with the plane of the glenoid fossa, but the dimension and shape of the posterior surface are more variable.

Spine of the scapula

The spine of the scapula forms a shelf-like projection on the upper part of the dorsal surface of the bone, and is triangular in shape (see Fig. 49.8A). Its lateral border is free, thick and rounded, and bounds the spinoglenoid notch, which lies between it and the dorsal surface of the neck of the bone. Its anterior aspect joins the dorsal surface of the scapula along a line that runs laterally and slightly upwards from the junction of the upper and middle thirds of the medial border. The plate-like body of the bone is bent along this line, which accounts for the concavity of the upper part of the costal surface. The dorsal border is the crest of the spine and is subcutaneous throughout nearly its whole extent. The crest expands into a smooth, triangular area at its medial end. Elsewhere, the upper and lower edges and the surface of the crest are roughened for muscular attachments. The upper surface of the spine widens as it is traced laterally and is slightly hollowed out. Together with the upper area of the dorsal surface of the bone, the upper surface of the spine forms the supraspinous fossa. The lower surface is overhung by the crest at its medial, narrow end, but is gently convex in its wider, lateral portion. Together with the lower area of the dorsal surface of the bone, the lower surface of the spine forms the infraspinous fossa, which communicates with the supraspinous fossa through the spinoglenoid notch.

Supraspinatus is attached to the upper surface of the spine of the scapula; the infraspinatus, by contrast, is not attached to the lower surface of the spine. The flattened triangular area at its root lies opposite the spine of the third thoracic vertebra and is covered by the tendon of trapezius; a bursa intervenes to enable the tendon to play over this part of the bone. The posterior fibres of deltoid are attached to the lower border of the crest and, to a variable extent, to the medial border by attachment to the infraspinatus fascia. The middle fibres of trapezius are attached to the upper border of the crest. The lowest fibres of trapezius terminate in a flat, triangular tendon that glides over the smooth area at the base of the spine and inserts into a rough prominence, erroneously called the deltoid tubercle, on the dorsal or subcutaneous aspect of the spine near its medial end.

Acromion

The acromion projects forwards, almost at right-angles, from the lateral end of the spine, with which it is continuous. The lower border of the crest of the spine becomes continuous with the lateral border of the acromion at the acromial angle, which forms a reliable, subcutaneous, bony landmark. The medial border of the acromion is short and is marked anteriorly by a small, oval facet, directed upwards and medially, for articulation with the lateral end of the clavicle. The lateral border, tip and upper surface of the acromion can all be felt through the skin without difficulty. There may be an accessory articular facet on the inferior surface of the acromion.

The acromion is subcutaneous over its dorsal surface, being covered only by the skin and superficial fascia. The lateral border, which is thick and irregular, and the tip of the process, as far round as the clavicular facet, give origin to the middle fibres of deltoid. The medial aspect of the tip gives attachment, below deltoid, to the lateral end of the coraco-acromial ligament. The articular capsule of the acromioclavicular joint is attached around the margins of the clavicular facet. Behind the facet, the medial border of the acromion gives insertion to the horizontal (middle) fibres of trapezius. The inferior aspect of the acromion is relatively smooth and forms a protective arch over the shoulder joint, together with the coraco-acromial ligament and the coracoid process. The tendon of supraspinatus passes below the overhanging acromion and is separated from it and from deltoid by the subacromial bursa.

Coracoid process

The coracoid process arises from the upper border of the neck of the scapula and its body is bent sharply so as to project forwards and slightly laterally (see Figs 49.8–49.9). When the arm is by the side, the coracoid process points almost straight forwards. Its tip can be felt through the skin and is covered by the anterior fibres of deltoid, about 2.5 cm below the clavicle at the junction of the lateral fifth with the rest of the bone, at the lateral border of the infraclavicular fossa. It forms a short, curved cantilever fixed to the scapula at its base and is displaced by the actions of the muscles attached to its body and tip. Pectoralis minor pulls the coracoid (and, therefore, the scapula) forwards and medially around the chest wall, balanced by trapezius, its antagonist; this action forms the foundation on which coracobrachialis can help support the long lever arm of the humerus during humeral motion, together with its antagonist, the deltoid. During forceful forward elevation of the protracted shoulder girdle, subclavius and pectoralis minor may contribute to deceleration of the limb.

The infraclavicular brachial plexus and the axillary vessels lie below and medial to the coracoid. The acromial branch of the thoraco-acromial artery passes above it, and the sensory branch of the lateral pectoral nerve to the rotator interval capsule, together with accompanying vessels, lies immediately below.

On the dorsal aspect of the coracoid process, at the point where it changes direction, a rough impression forms part of the region of attachment of the conoid portion of the coracoclavicular ligament. The trapezoid portion of the coracoclavicular ligament is attached to the upper aspect of the horizontal part of the process, anterior to the conoid part. Pectoralis minor is attached to the superior and medial aspects of the coracoid process. The wider, medial, end of the coraco-acromial ligament is attached to the lateral border and is continuous inferiorly with the lateral aponeurotic part of the tendon of the short head of biceps brachii. The coracohumeral ligament is attached to the root of the coracoid at its lateral border. The interval between the anterior aspect of the scapular neck immediately medial to the glenoid fossa and the deep surface of the coracoid is often bridged by the glenocoracoid ligament. The inferior aspect of the coracoid process is otherwise smooth and saddle-shaped. When the arm is elevated, the upper border of subscapularis is apposed to, and runs under, this surface, which forms a pulley for the muscle, increasing the power generated during forceful medial (internal) rotation of the shoulder in elevation, such as during a serve in tennis. Coracobrachialis is attached to the deep aspect of the lower part of the medial side and the deep surface of the tip of the process, and the short head of biceps is attached to the lateral side and superficial aspect of the tip.

Scapular movements

Scapular movement is a product of interconnected suspension, motion and articulation mechanisms. The suspension mechanism consists of the scapular articulation with the clavicle and the suspension muscles of the scapula and clavicle, notably trapezius, attached to the lateral clavicle, the acromion and the spine of scapula, and its antagonists pectoralis minor and subclavius. The articulation with the clavicle comprises two linked systems: 'clavicle – acromioclavicular joint – acromion – spine of scapula – lateral scapular angle' and 'clavicle – coracoclavicular ligament – coracoid – lateral scapular angle – spine of scapula'. This mechanism therefore subserves the function of scapular rotation or tilt limited by the ellipsoid range of motion of the lateral clavicle. The motion mechanism consists of the agonist–antagonist force couple of serratus anterior passing to the chest wall anterolaterally, and levator scapulae, rhomboid major, rhomboid minor and serratus posterior (when present), which all pass to the vertebral column medially. This mechanism therefore subserves the function of scapular protraction and retraction around the elliptic paraboloid of the chest wall. The articulation mechanism consists of the scapular neck region and the glenoid fossa, which articulates with the humeral head. The muscles that subserve the function of holding the humeral head on the glenoid through the wide range of motion of the glenohumeral joint are the rotator cuff muscles, which take their attachment from the body of the scapula. This mechanism therefore concerns the relationship between the position and orientation of the glenoid fossa and the scapular body.

Ossification

The cartilaginous scapula is ossified from eight or more centres: one in the body, two each in the coracoid process and the acromion, and one each in the medial border, inferior angle and lower part of the rim of the glenoid cavity (**Fig. 49.10**). The medial part originates from dermomyotomes of somites 17–24 (level of fifth cervical vertebra – level of fifth thoracic vertebra) and the lateral part from somatopleuric mesenchyme. The primary ossification centre for the body appears in stage 23 (53–58 postfertilization days). Ossification begins in the middle of the coracoid process in the first year or, in a small proportion of individuals, before birth; the process joins the rest of the bone about the fifteenth year. At or soon after puberty, centres of ossification occur in the rest of

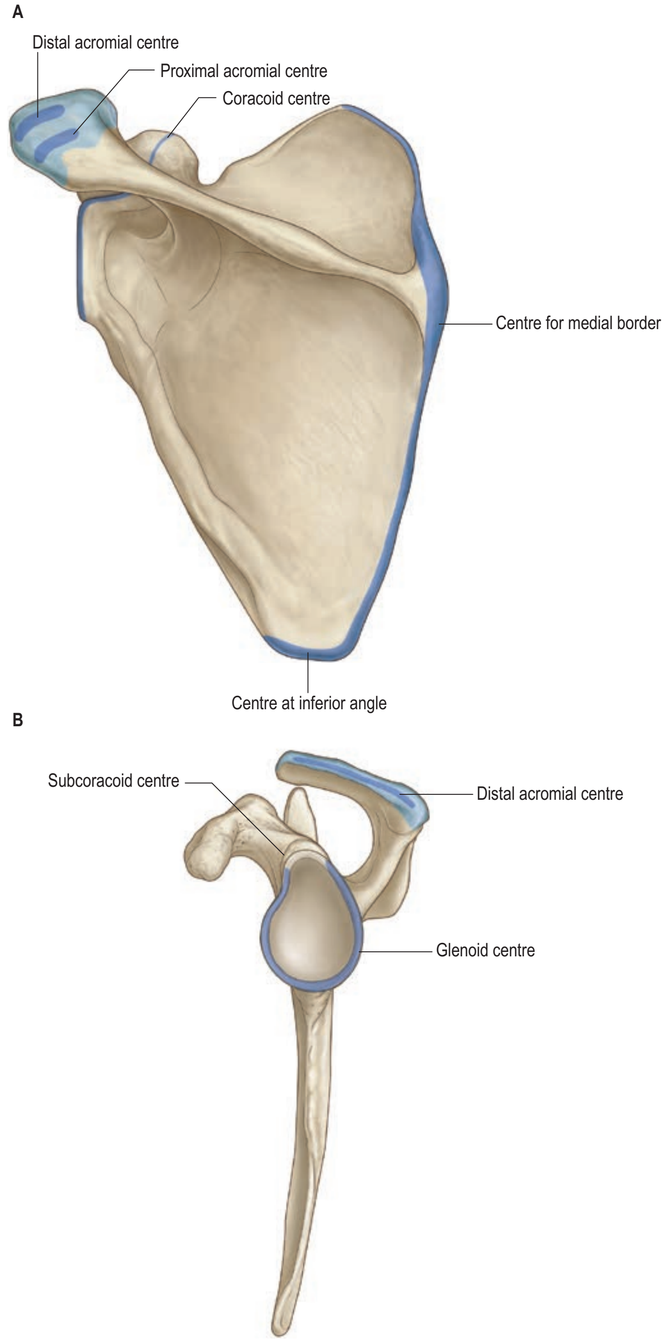

Fig. 49.10 Ossification of the scapula. **A**, Dorsal aspect. **B**, Lateral aspect. (Adapted with permission from Drake RL, Vogl AW, Mitchell A (eds), Gray's Anatomy for Students, 2nd ed. Elsevier, Churchill Livingstone. Copyright 2010.)

the coracoid process (subcoracoid centre), in the rim of the lower part of the glenoid cavity, frequently at the tip of the coracoid process, in the acromion, in the inferior angle and contiguous part of the medial border and in the medial border. A variable area of the upper part of the glenoid cavity, usually the upper third, is ossified from the subcoracoid centre; it unites with the rest of the bone in the fourteenth year in the female and the seventeenth year in the male. A horseshoe-shaped epiphysis appears for the rim of the lower part of the glenoid cavity; thicker at its peripheral than at its central margin, it converts the flat glenoid cavity of the child into the gently concave fossa of the adult. The base of the acromion is formed by an extension from the spine; the rest of the acromion is ossified from two centres that unite and then join the extension from the spine. The various epiphyses of the scapula have all joined the bone by about the twentieth year.

Ligaments

The intrinsic scapular ligaments are strengthening ligaments (coraco-acromial ligament) and bounding ligaments (superior transverse scapular or suprascapular ligament, inferior transverse scapular or spinoglenoid ligament, and the variable glenocoracoid ligament).

Coraco-acromial ligament The coraco-acromial ligament is a strong triangular band between the coracoid process and acromion. It is attached apically to the acromion anterior to the articular surface for the clavicle, and by its base along the whole lateral border of the coracoid. Together with the coracoid process and acromion, it completes an arch above the humeral head. It may be composed of two strong marginal bands with a thinner centre; when pectoralis minor is inserted into the humeral capsule instead of the coracoid process, which happens occasionally, its tendon passes between the bands. The subacromial bursa facilitates movement between the coraco-acromial arch and the subjacent supraspinatus and shoulder joint, functioning as a secondary synovial articulation. When the coraco-acromial ligament is cut, it is impossible to appose the two cut surfaces afterwards: this suggests there is resting tension in the ligament, which forms a 'tension band' between the acromial and coracoid processes of the scapula, so 'pre-tensioning' both processes against the distracting forces of deltoid and trapezius, and pectoralis minor and the conjoined short head of biceps brachii and coracobrachialis, respectively.

Superior transverse scapular (suprascapular) ligament The superior transverse scapular (suprascapular) ligament converts the scapular notch into a foramen; it is sometimes ossified. A flat fasciculus, it narrows towards its attachments to the base of the coracoid process, blending with the lower fibres of the conoid ligament, and to the medial side of the scapular notch. The suprascapular nerve traverses the foramen, and the suprascapular vessels cross above the ligament.

Inferior transverse scapular (spinoglenoid) ligament When present, the inferior transverse scapular ligament is a membranous ligament that may stretch from the lateral border of the spine of the scapula to the glenoid margin (see Fig. 49.33). It forms an arch over the branches of the suprascapular nerve and vessels entering the infraspinous fossa to supply infraspinatus.

Humerus

The humerus, the longest and largest bone in the upper limb, has expanded ends and a shaft (**Figs 49.11–49.12**). The spheroidal humeral head forms an enarthrodial articulation with the glenoid fossa of the scapula. The lesser tubercle projects from the front of the shaft, close to the head, and is limited on its lateral side by the well-marked groove, the intertubercular sulcus, by which it is separated from the greater tubercle. The distal end is adapted to the forearm bones at the elbow joint and carries the medial and lateral epicondyles with the articular surfaces for the radius and ulna between them. The axis between the epicondyles is the inter-epicondylar axis.

The shaft of the human (and primate) humerus is relatively *medially* rotated with respect to the humeral head, compared with quadripedal ancestors; this gives the characteristically greater range of *external* rotation at the glenohumeral joint than that obtaining in other species. This is reflected in the spiroidal architecture of the adult humeral medullary cavity, the arrangement and relationship of the posterior compartment of brachial muscles and the radial nerve, and the disposition to long spiral fractures caused by external twisting forces.

With the arm by the side in the anatomical position, and with the medial and lateral epicondyles in the same (frontal) plane (i.e. the inter-epicondylar axis is in the frontal plane), the humeral *head* is rotated posteriorly at an angle averaging 15–20° in European cadaveric specimens (Boileau and Walch 1997). Since the glenoid fossa of the scapula faces anterolaterally, the humerus is not rotated posteriorly relative to the scapula in the anatomical position. It is important to remember this position of the bone when movements of the arm and forearm are considered; movements are recorded relative to the trunk (starting in the anatomical position) or relative to the scapula, and it is important to define which method is in use.

Proximal end

The proximal end of the humerus consists of the head, anatomical neck, and the greater and lesser tubercles. It joins the shaft at an ill-defined 'surgical neck', which is closely related on its medial side to the axillary nerve and posterior circumflex humeral artery (see Figs 49.22, 49.31, 49.33). The proximal end of the humerus makes up the upper fifth of the length of the bone.

Head

The head of the humerus forms rather less than half a spheroid; in sectional profile, it is spheroidal (strictly, ovoidal) (see Fig. 49.12). Its

The primordial scapula migrates caudally to its usual position at a level between the second and seventh ribs by the end of the embryonic period (53–58 postfertilization days). With further development, the scapula alters shape. Initially, the horizontal diameter exceeds the vertical but the ratio gradually decreases until mature dimensions are reached, an adaptation thought to provide upright hominids with increased range, and therefore freedom of use, of the upper limb. Avian gene-deletion studies have shed light on the development of the scapula. Scapular body development appears to be controlled by the *Emx2* gene, also expressed in the developing mesonephros. The development of the acromion and the spine of the scapula are controlled by the *Pax1* gene, and glenoid and coracoid development is controlled by the *Hoxc6* gene (Huang et al 2000), one of the homeobox genes responsible for somite differentiation and development; development of the glenoid and coracoid appears likely to be more intimately related to the development of the upper limb bud as a whole. The development of the scapular body appears to be independent of that of the processes and glenoid region. Adult scapulae may show a line of fusion across the body and spine of the scapula, suggesting that the primordia of the processes (including the glenoid) and the primordium of the body migrate towards each other; since the trapezius is derived from branchial arch mesoderm it would appear that the development of the spine of the scapula and acromion and trapezius are intimately related, but separate from the body. This hypothesis is supported by the observation that; in the condition of congenital undescended scapular syndrome (Sprengel deformity), the development of the scapular body is altered, and there is intramuscular ossification of variable parts of the medial scapulospinal muscles; the development of the processes (including the glenoid) is unaffected (Dhir and Lambert 2014; Dhir et al 2018). Since the medial border of the scapula develops from the dermomyotomes of somites 17–24 (see above) any vertebral anomalies at this level may result in tethering of scapular structures to the cervical spine, sometimes by an abnormal omovertebral tether (fibrous, chondral, or osseous), that prevents the upper border of the scapula descending to its usual position.

The suprascapular nerve may be entrapped by the ligament if this is thickened or ossified and this may cause the syndrome of neurostenalgia, a typical pain of unremitting burning or aching nature, due to stenosis or distortion of the nerve trunk by extrinsic compression. Weakness of supraspinatus and infraspinatus may subsequently occur. Surgical release of the ligament is often helpful; this may be undertaken by open or arthroscopic surgical exposure and division of the ligament.

A ganglion (an outpouching of the synovial membrane of the glenohumeral joint) may occur immediately behind and above the posterosuperior corner of the glenoid fossa; this can compress the branch of the suprascapular nerve that supplies infraspinatus as it courses around the lateral aspect of the spine of the scapula under the inferior scapular ligament. Since the nerve cannot move aside (it is ‘held’ under the ligament), it can be readily distorted; there is characteristic severe pain, followed by specific atrophy of infraspinatus. Decompression of the ganglion and division of the ligament are curative in the early stage of this syndrome. An intraneural ganglion may arise from the articular branch of the suprascapular nerve; muscular pain and atrophy would be expected to be more rapid than in the case of the synovial ganglion (Spinner et al 2006).

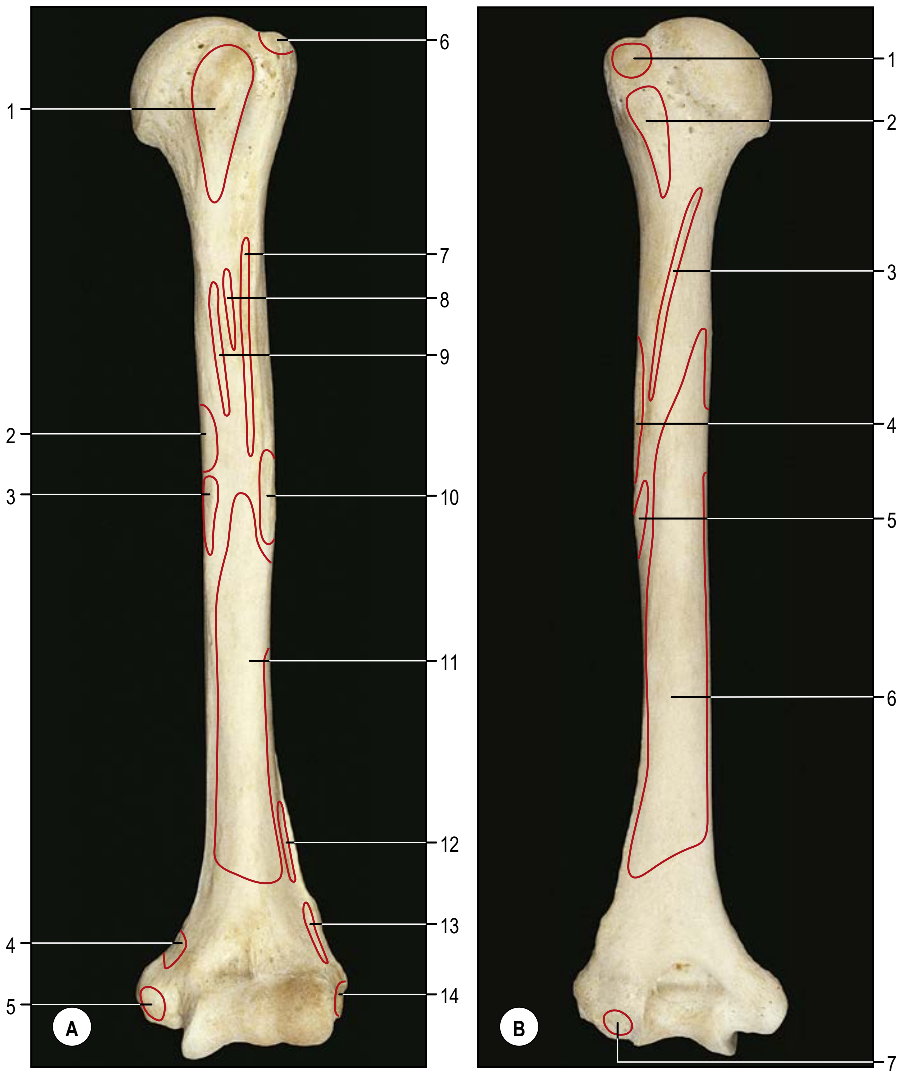

Fig. 49.11 The left humerus showing sites of muscular attachments. **A**, Anterior aspect. Key: 1, subscapularis; 2, triceps brachii (medial head); 3, coracobrachialis; 4, pronator teres (humeral head); 5, common flexor origin; 6, supraspinatus; 7, pectoralis major; 8, latissimus dorsi; 9, teres major; 10, deltoid; 11, brachialis; 12, brachioradialis; 13, extensor carpi radialis longus; 14, common extensor origin. **B**, Posterior aspect. Key: 1, infraspinatus; 2, teres minor; 3, triceps brachii (lateral head); 4, deltoid; 5, brachialis; 6, triceps brachii (medial head); 7, anconeus.

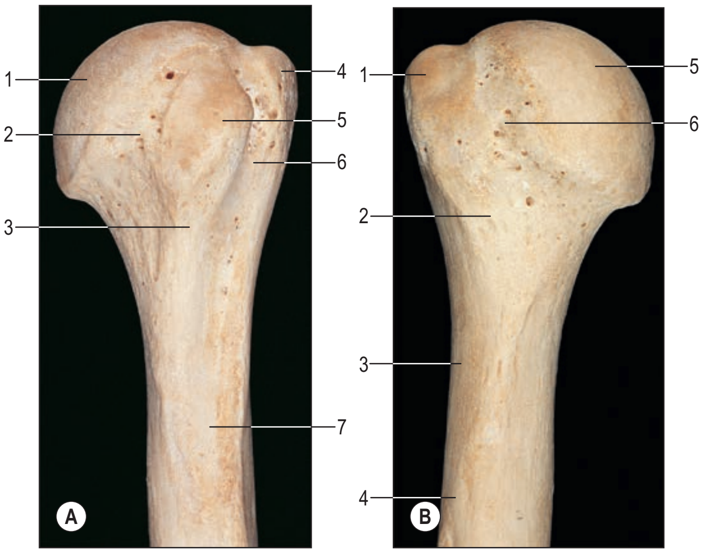

Fig. 49.12 The proximal end of the left humerus. **A**, Anterior aspect. Key: 1, head; 2, anatomical neck; 3, surgical neck; 4, greater tubercle; 5, lesser tubercle; 6, intertubercular sulcus; 7, shaft. **B**, Posterior aspect. Key: 1, greater tubercle; 2, surgical neck; 3, shaft; 4, radial groove; 5, head; 6, anatomical neck.

smooth articular surface is covered with hyaline cartilage that is thicker centrally. When the arm is at rest by the side, it is directed medially, backwards and upwards to articulate with the glenoid cavity of the scapula. The humeral articular surface is much more extensive than the glenoid cavity, which means that only a portion of it is in contact with the cavity in any one position of the arm.

Anatomical neck

The anatomical neck of the humerus immediately adjoins the margin of the head, forming a slight constriction that is least obvious next to the greater tubercle. A slight roughness indicates the line of capsular attachment of the shoulder joint, other than at the intertubercular sulcus, where the long tendon of biceps brachii emerges. Medially, the capsular attachment diverges from the anatomical neck and descends 1 cm or more on to the shaft.

Lesser tubercle

The lesser tubercle is anterior to and just distal to the anatomical neck. It is palpable through the thickness of deltoid about 3 cm below the anterior edge of the acromion. It can be distinguished from the coracoid by rotation of the humerus under the palpating finger; the lesser tubercle slips away from the examining finger, the tip of the coracoid does not. The lateral edge of the lesser tubercle is sharp and forms the medial border of the intertubercular sulcus. Subscapularis is attached to the lesser tubercle (see Fig. 49.11A). The transverse ligament of the shoulder (transverse humeral ligament) is attached to the upper aspect of the lateral margin of the tubercle.

Greater tubercle

The greater tubercle is the most lateral part of the proximal end of the humerus and projects beyond the lateral border of the acromion. Its posterosuperior aspect, near the anatomical neck, bears three smooth, flattened impressions for the attachment of supraspinatus (uppermost), infraspinatus (middle) and teres minor (lowest and placed on the posterior surface of the tubercle) (see Fig. 49.11). The attachments of subscapularis and teres minor are not confined to their respective tubercles, but extend for varying distances on to the adjacent metaphysis. The projecting lateral surface of the tubercle presents numerous vascular foramina and is covered by deltoid, producing the normal rounded contour of the shoulder. A part of the subacromial bursa may cover the upper part of this area and separate it from deltoid. The intertubercular sulcus (bicipital groove) lies between the tubercles. It contains the long tendon of biceps, its synovial sheath, and an ascending branch from the anterior circumflex humeral artery. The rough lateral lip of the groove is marked by the bilaminar tendon of pectoralis major, and its medial lip by the tendon and muscular insertion of teres major. The floor of the groove provides attachment for a frequent upward extension of the tendon of pectoralis major, and for the tendon of latissimus dorsi more caudally (Dancker 2013).

Shaft

The shaft of the humerus is almost cylindrical in its proximal half. Distal to the deltoid tuberosity, it is equilaterally triangular in cross-section, flaring out into a broad isosceles triangular cross-section just above the elbow joint. It can be readily palpated laterally and medially, but the muscles of the anterior and posterior compartments obscure the bone to palpation anteriorly and posteriorly. It has three surfaces and three borders, which are only distinct towards the elbow joint. The shaft comprises the middle three-fifths of the humerus.

Surfaces

The posterior surface, between the medial and lateral borders, is broad, flat and convex distally. The medial head of triceps is attached to the posterior surface over an elongated triangular area, the apex of which is placed on the medial part of the bone above the level of the lower limit of insertion of teres major. The area widens below and covers the whole surface almost down to the lower end of the bone. The lateral head of triceps is attached to a ridge, sometimes rough, that descends obliquely and laterally above the attachment for the medial head. Above triceps, the axillary nerve and the posterior circumflex humeral vessels wind around the bone on the deep surface of deltoid. Below the attachment of the lateral head of triceps, but above the attachment of the medial head, a shallow groove runs from the upper medial aspect of the surface downwards and laterally towards the lateral border; it contains the radial nerve and its branches, and the profunda brachii vessels.

The anterolateral surface is bounded by the anterior and lateral borders, and is smooth and featureless in its upper part, which is covered by deltoid. About, or a little above, the middle of this surface, deltoid is attached to the deltoid tubercle. Further distally, the surface gives origin to the lateral fibres of brachialis, which extend upwards into the floor of the lower end of the groove for the radial nerve (see Fig. 49.11). The nerve perforates the lateral intermuscular septum close to the bone at the level of the junction of the upper three-fifths and lower two-fifths of the humerus, and enters the anterior compartment of the arm close to the anterolateral surface, between brachialis medially and brachioradialis laterally.

The anteromedial surface is bounded by the anterior and medial borders. Below the intertubercular sulcus, the rest of the upper half of the surface is smooth and devoid of muscular attachment; its lower half is occupied by the medial part of brachialis (see Fig. 49.11A). Coracobrachialis is attached to a long rough strip in the middle third of the medial border, posterior to the brachial neurovascular sheath, which lies in close relation to the humerus in the middle third of this surface. The humeral head of pronator teres is attached to a narrow area close to the lowest part of the medial supracondylar ridge; the ridge itself gives attachment to the medial intermuscular septum of the arm.

A little below its midpoint, the nutrient foramen, which is directed downwards, opens close to the medial border. A hook-shaped process of bone, the supracondylar process, ranging from 2 to 20 mm in length, occasionally projects from the anteromedial surface of the shaft, approximately 5 cm proximal to the medial epicondyle. It is curved downwards and forwards, and its pointed apex is connected to the medial border, just above the epicondyle, by a fibrous band, to which part of pronator teres is attached. The foramen completed by this fibrous band usually transmits the median nerve and brachial artery, but sometimes encloses only the nerve, or the nerve plus the ulnar artery (in cases of high division of the brachial artery). A groove that lodges the artery and nerve is usually found posterior to the process.

Anterior border

The anterior border starts on the front of the greater tubercle and runs downwards almost to the lower end of the bone. Its proximal third forms the lateral lip of the intertubercular sulcus and is roughened for muscular attachments. The succeeding portion is also roughened and forms the anterior limit of the deltoid tubercle; the lower half of the border is smooth and rounded.

Lateral border

The lateral border is most conspicuous at the lower end of the bone, where it is thickened to form the lateral supracondylar ridge, and its sharp edge is roughened along its anterior aspect. In its middle and upper thirds, the border is barely discernible, but in a well-marked bone it can be traced upwards to the posterior surface of the greater tubercle. A little above its middle, it is marked by a V-shaped, roughened area: the deltoid tubercle. The limbs of the V are broad; the groove for the radial nerve runs downwards and laterally behind the posterior limb and fades away on the lower part of the anterolateral surface. The lateral intermuscular septum is attached to the lateral border, and is a condensation of the fascia over the lower part of deltoid and the neighbouring brachialis, forming a septum between the anterior and posterior muscular compartments. The septum is most obvious in the lower three-fifths of the arm, and is perforated by the radial nerve and accompanying vessels.

Medial border

The medial border, although rounded, can be identified without difficulty in the lower half of the shaft, where it becomes the medial supracondylar ridge. In its proximal third, the medial border is indistinct until it broadens out to form a triangular area. The lateral border of this area forms the medial lip of the intertubercular sulcus, and the medial border runs upwards as the calcar humerale to the anatomical neck, where it is roughened, with vascular apertures, and forms the area of attachment of the inferior part of the shoulder capsule. In its middle third, the medial border is interrupted by a wide, shallow groove, the radial (spiral) groove that crosses the bone obliquely, passing downwards and forwards from its posterior to its anterior surface.

Fractures of the humeral shaft

Humeral shaft fractures are common; the pattern of the fracture and the displacement of the fragments depend on the force of injury and on the level at which the bone is broken. If there is wide displacement at the time of fracture, closely associated nerves and vessels are at risk of direct injury. Nerves that are ‘fixed’ in relation to the bone and attached septa are at further risk of indirect injury by stretching or, later, by the callus of bone healing. (For a discussion of radial nerve injury and fractures of the humeral shaft, see Lambert (2005).)

Distal end

The distal end of the humerus is described in Chapter 50.

Ossification

The proximal humerus and shaft are ossified from four centres: one each in the shaft, head, greater and lesser tubercles (**Fig. 49.13**). The centre for the shaft appears near its middle in stages 21–22 (50–55 postfertilization days) and gradually extends towards the ends. Most growth occurs at the distal end of the bone. Ossification beginning in the head has been reported between 4 and 6 postnatal months; the greater tubercle starts to ossify during the first year in females and second year in males; the lesser tubercle begins to ossify at about the fifth year.

By the sixth year, the centres for the head and tubercles have joined to form a single large epiphysis, hollowed out on its inferior surface to adapt to the conical upper end of the metaphysis. This macroscopic topography provides for mechanical stability in the physis during growth, although rotational stability is still relatively poor; adolescent proximal humeral physial fracture-separations are commonly unstable in rotation. The proximal humeral epiphysis fuses with the shaft of the humerus at about the thirteenth or fourteenth year in females, beginning on the medial aspect of the physial line, and between the fourteenth to sixteenth year in males.

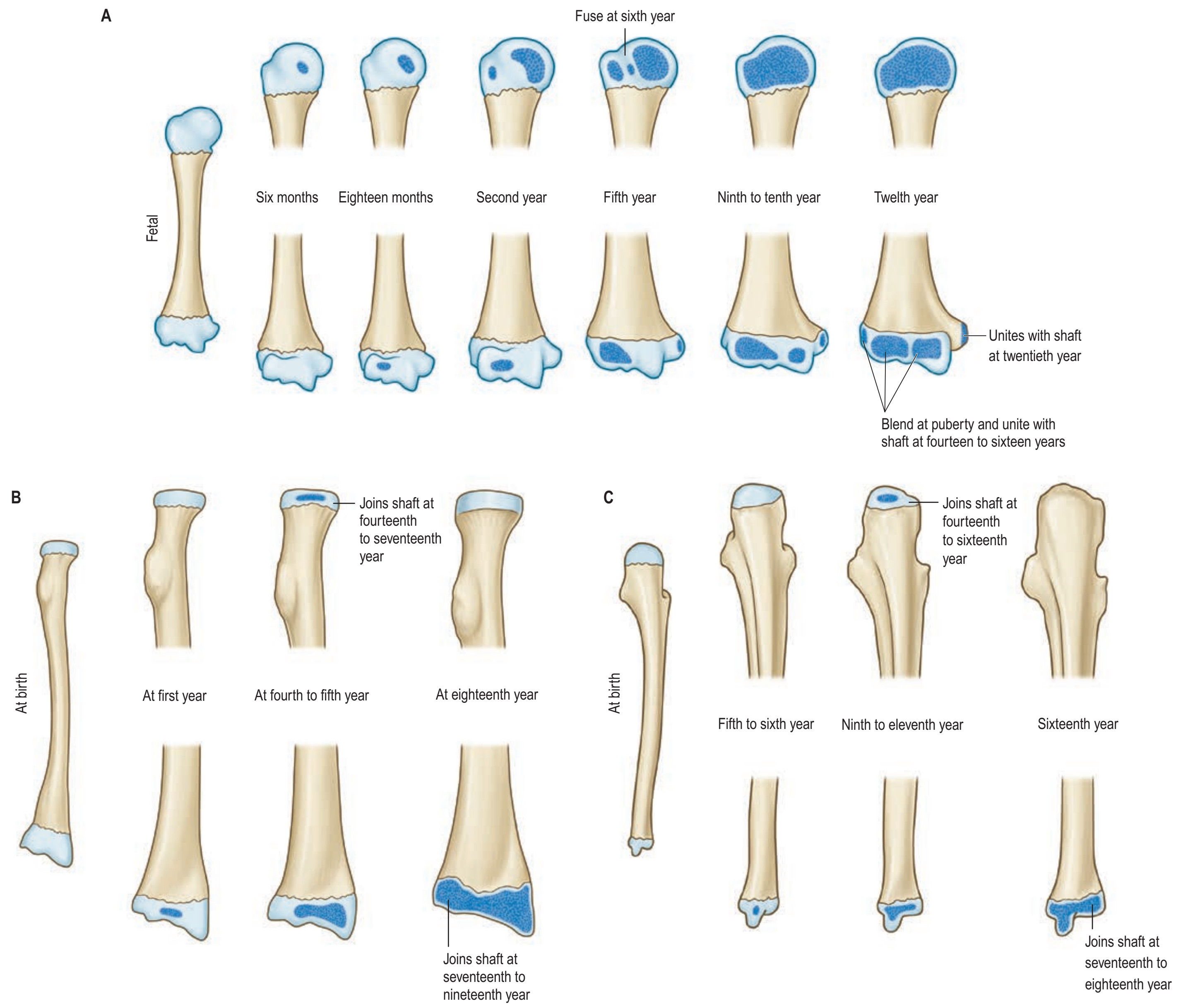
A
Fuse at sixth year
Fetal
Six months
Eighteen months
Second year
Fifth year
Ninth to tenth year
Twelth year
Unites with shaft at twentieth year
Blend at puberty and unite with shaft at fourteen to sixteen years
B
Joins shaft at fourteenth to seventeenth year
At birth
At first year
At fourth to fifth year
At eighteenth year
Joins shaft at seventeenth to nineteenth year
C
Joins shaft at fourteenth to sixteenth year
At birth
Fifth to sixth year
Ninth to eleventh year
Sixteenth year
Joins shaft at seventeenth to eighteenth year

Fig. 49.13 Stages in ossification of (**A**) the humerus, (**B**) the radius and (**C**) the ulna (not to scale).

JOINTS

Sternoclavicular joint

The sternoclavicular joint is a synovial sellar (saddle, or hyperbolic paraboloid) joint with an intra-articular fibrocartilaginous disc. It is the only skeletal articulation between the upper limb and the axial skeleton (Sewell et al 2013).

Articulating surfaces The articulating surfaces are the sternal end of the clavicle and the clavicular notch of the sternum, together with the adjacent superior surface of the first costal cartilage (Fig. 49.14). The larger clavicular articular surface is covered by fibrocartilage, which is thicker than the fibrocartilaginous lamina on the sternum. The joint is convex vertically but slightly concave anteroposteriorly, and is therefore sellar; the clavicular notch of the sternum is reciprocally curved but the two surfaces are not fully congruent. An articular disc completely divides the joint.

Fibrous capsule The capsule is thickened anteriorly and posteriorly, but superiorly and especially inferiorly, it is little more than loose areolar tissue.

Ligaments There are two sets of associated ligaments. The intrinsic ligaments are the anterior and posterior sternoclavicular ligaments; the extrinsic ligaments are the midline interclavicular ligament and the costoclavicular ligaments on each side.

Anterior sternoclavicular ligament The anterior sternoclavicular ligament is broad and attached above to the anterosuperior aspect of the sternal end of the clavicle. It passes inferomedially to the upper anterior aspect of the manubrium, spreading on to the first costal cartilage.

Posterior sternoclavicular ligament The posterior sternoclavicular ligament is a weaker band posterior to the joint. It descends inferomedially from the posterior aspect of the sternal end of the clavicle to the posterior aspect of the upper manubrium.

Interclavicular ligament The interclavicular ligament is continuous above with the deep cervical fascia. It unites the superior aspect of the sternal ends of both clavicles; some fibres are attached to the superior manubrial margin.

Costoclavicular ligament The costoclavicular ligament is like an inverted cone, but short and flattened. It has anterior and posterior laminae that are attached to the upper surface of the first rib and costal cartilage, and ascends to the margins of an impression on the inferior clavicular surface at its medial end. Fibres of the anterior lamina ascend laterally and those of the posterior lamina (which are shorter) ascend medially (see Fig. 49.14). They fuse laterally and are closely related to the attachments of subclavius, particularly the tendon of origin; it can be hard to distinguish the lateral border of the ligament from the tendon. The ligament merges medially with the capsule. It can be ossified in older adults, particularly females. A few deep fibres of pectoralis major attach to the external surface of the ligament, adjacent first rib, first costal cartilage and manubrium sterni.

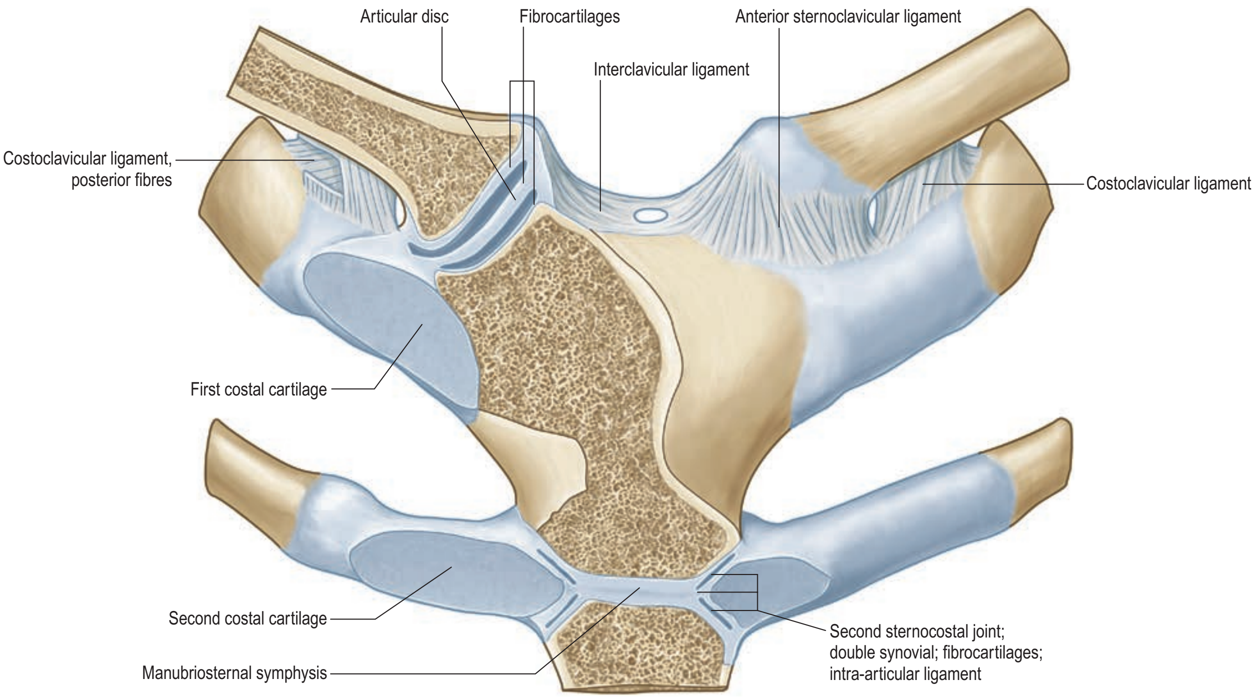
Articular disc
Fibrocartilages
Anterior sternoclavicular ligament
Interclavicular ligament
Costoclavicular ligament, posterior fibres
Costoclavicular ligament
First costal cartilage
Second costal cartilage
Manubriosternal symphysis
Second sternocostal joint; double synovial; fibrocartilages; intra-articular ligament

Fig. 49.14 The sternoclavicular joints, anterior aspect. The joint on the left side is intact and the joint on the right side is shown in coronal section.

Articular disc The fibrocartilaginous articular disc divides the cavity of the joint into two compartments between the sternal and clavicular surfaces. It is attached above to the posterosuperior border of the articular surface of the clavicle, below to the first costal cartilage near its sternal junction, and by the rest of its circumference to the capsule, and therefore adapts to the contour of the clavicular surface. It is thicker peripherally, especially superoposteriorly and inferomedially; the central part of the disc may be perforated in later life.

Vascular supply The sternoclavicular joint is supplied by branches from the internal thoracic and suprascapular arteries.

Innervation The sternoclavicular joint is innervated superficially by branches from the medial supraclavicular nerve and deeply by the nerve to subclavius.

Factors maintaining stability There is almost no bony articular congruence at the sternoclavicular joint. However, the strength of its associated ligaments and the articular disc produce durable stability. These factors make sternoclavicular joint dislocation rare; fracture of the clavicular shaft is far more common for the same force directed along the clavicle. (See Sewell et al (2013) for a review of the mechanisms and treatment of sternoclavicular instability.)

Movements The capsule around the clavicular attachment is more lax. Movements between the clavicle and the disc are more extensive than those between the disc and sternum. The sellar shape of the articular surfaces permits translation or gliding in approximately anteroposterior and vertical planes, with rotation about the long axis of the clavicle. Close-packing coincides with maximum posterior rotation associated with full scapular rotation, i.e. in high elevation of the arm above shoulder height.

In this position, the tension developed in the anterior sternoclavicular ligament and anterior component of the costoclavicular ligament causes the clavicle to undergo an obligatory posterior translation. It also acts as a check-rein on further rotation and displacement, so protecting the relatively weaker posterior sternoclavicular ligament from overload. Although the function of subclavius is unknown, a consideration of the simple biomechanics of forceful elevation of the arm above shoulder height suggests that this muscle has an important role in decelerating the elevating arm, so protecting the medial 'clavicular–costal–sternal' ligamentous structures from recurrent stretching that is likely to accelerate degeneration and injury. The common innervation of the sternoclavicular joint (the deep afferent–mechanoceptor system) and subclavius suggests an intimate functional relationship between these structures. In daily activities, in which the upper limb is used largely in front of the trunk, the sternal end of the clavicle glides on the sternal facet about the fulcrum provided by the costoclavicular ligament. All joints in which polyaxial gliding occurs, producing shear forces (rotation with translation), possess either intra-articular synovial bursae or intra-articular fibrocartilaginous discs; the latter degenerate over time, producing characteristic exophytic degenerative arthritis. In this context, it is interesting that degeneration of the sternoclavicular joint and ossification of the costoclavicular ligaments (claviculocostal synostosis) are almost exclusively found in females above the age of 50 years.

Acromioclavicular joint

The acromioclavicular joint is a synovial plane joint and has an intra-articular fibrocartilaginous disc.

Articulating surfaces The articulating surfaces are between the acromial end of the clavicle and the medial acromial margin (Fig. 49.15). The joint is approximately plane but either surface may be slightly convex, the other usually being reciprocally concave: both surfaces are covered by fibrocartilage. It may appear incongruent at rest. The clavicular surface is a narrow, oval area that faces laterally or inferolaterally and overlaps a corresponding facet on the medial acromial border. The long axis is anteroposterior (Colegate-Stone et al 2010).

Fibrous capsule The capsule completely surrounds the articular margins. It is lined by synovial membrane and is strengthened superiorly by the acromioclavicular ligament and the fibres of the attachment of trapezius, posteriorly by the fibres of attachment of trapezius, and anteriorly by the fibres of attachment of deltoid. The inferior capsule is often incomplete in later life.

Ligaments There are two sets of associated ligaments. The intrinsic ligaments are the acromioclavicular ligaments; the extrinsic ligaments are the coracoclavicular ligaments.

Acromioclavicular ligaments The superior acromioclavicular ligament is quadrilateral. It extends between the upper aspects of the lateral end of the clavicle and the adjoining acromion. Its parallel fibres interlace with the aponeuroses of trapezius and deltoid. The inferior acromioclavicular ligament is thin, and often perforated in later life; it extends between the inferior surface of the lateral end of the clavicle and the adjoining acromion. It provides attachment for the intra-articular disc when this is present and complete.

Coracoclavicular ligament The coracoclavicular ligament connects the clavicle and the coracoid process of the scapula. Though separate from the acromioclavicular joint, it is an efficient and important accessory ligament because it helps to maintain the apposition of the acromion to the clavicle, and so contributes to the suspension mechanism of the scapula (see above). The trapezoid and conoid parts of the ligament,

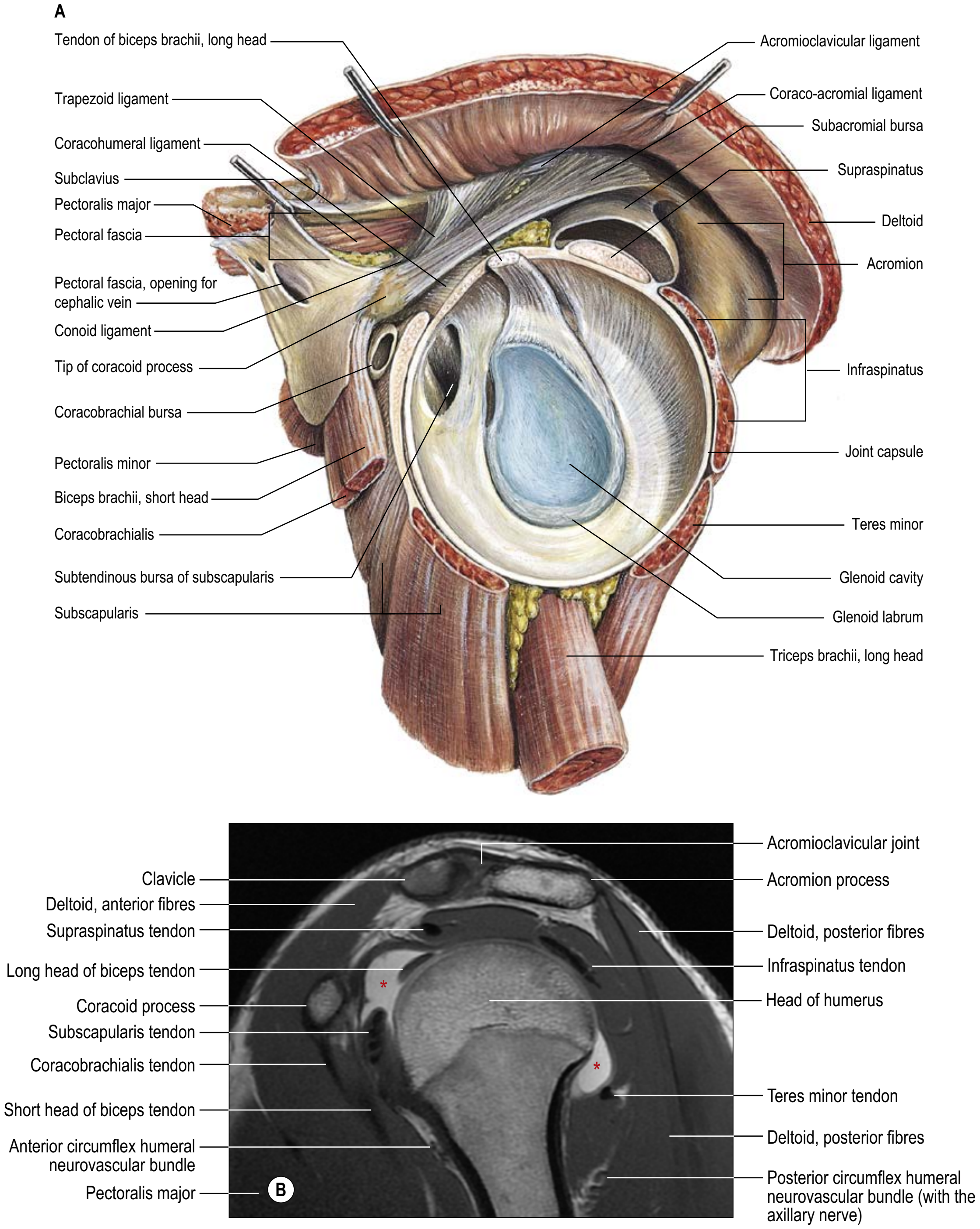
A
Tendon of biceps brachii, long head
Trapezoid ligament
Coracohumeral ligament
Subclavius
Pectoralis major
Pectoral fascia
Pectoral fascia, opening for cephalic vein
Conoid ligament
Tip of coracoid process
Coracobrachial bursa
Pectoralis minor
Biceps brachii, short head
Coracobrachialis
Subtendinous bursa of subscapularis
Subscapularis
Acromioclavicular ligament
Coraco-acromial ligament
Subacromial bursa
Supraspinatus
Deltoid
Acromion
Infraspinatus
Joint capsule
Teres minor
Glenoid cavity
Glenoid labrum
Triceps brachii, long head
Clavicle
Deltoid, anterior fibres
Supraspinatus tendon
Long head of biceps tendon
Coracoid process
Subscapularis tendon
Coracobrachialis tendon
Short head of biceps tendon
Anterior circumflex humeral neurovascular bundle
Pectoralis major
B
Acromioclavicular joint
Acromion process
Deltoid, posterior fibres
Infraspinatus tendon
Head of humerus
Teres minor tendon
Deltoid, posterior fibres
Posterior circumflex humeral neurovascular bundle (with the axillary nerve)
*
*

Fig. 49.15 A, The interior of the left shoulder joint, anterolateral aspect. **B**, Sagittal T1-weighted MR arthrogram of the left shoulder, viewed from the left. Contrast medium is injected into the joint before the acquisition, and then shows up as bright fluid within the distended joint capsule (*). (A, Sobotta Atlas of Human Anatomy © Elsevier GmbH, Urban & Fischer, Munich.)

usually separated by fat or, frequently, by a bursa, connect the posterior (more horizontal) part of the coracoid process and the lateral end of the subclavian groove of the clavicle (Fig. 49.16): these adjacent areas may even be covered by cartilage to form a coracoclavicular joint.

The trapezoid part is anterolateral and is broad, thin and quadrilateral, ascending slightly from the upper coracoid surface to the trapezoid line on the inferior clavicular surface. Its anterior border is free, and its posterior border is joined to the conoid part, forming an angle that projects backwards and upwards. Quadrilateral ligaments twist when the adjoined bones rotate with respect to each other, and as they twist, the apposed surfaces must approach each other; such ligaments, therefore, act to oppose excessive rotation of the adjoining bones.

The conoid part is posteromedial and is a dense, almost vertical, triangular or conical band. Its broader base is attached superiorly to the conoid tubercle of the clavicle; its inferior apex is attached posteromedially to the dorsal surface and root of the coracoid process immediately lateral to the scapular notch, and is contiguous with the superior transverse scapular ligament. Conical ligaments are constructed to oppose distraction; the conoid ligament, therefore, helps to keep the coracoid and the clavicle closely apposed. If the trapezoid ligament is disrupted, the conoid ligament forms a vertical fulcrum around which the coracoid can rotate under the clavicle, particularly if the acromioclavicular ligaments are also disrupted. This is the anatomical basis for the spectrum of acromioclavicular joint dislocation.

Articular disc The articular disc is a complete fibrocartilaginous partition in juvenile and adolescent joints, creating medial and lateral compartments; over time, the centre of the disc perforates, and in adults (more than 20 years old), it is often incomplete inferiorly.

Vascular supply The acromioclavicular joint receives its arterial supply from branches of the suprascapular and thoraco-acromial arteries.

Innervation The acromioclavicular joint is innervated by branches from the suprascapular and lateral pectoral nerves. It has been suggested that the density of nociceptors is greatest in the inferior acromioclavicular ligament and capsule.

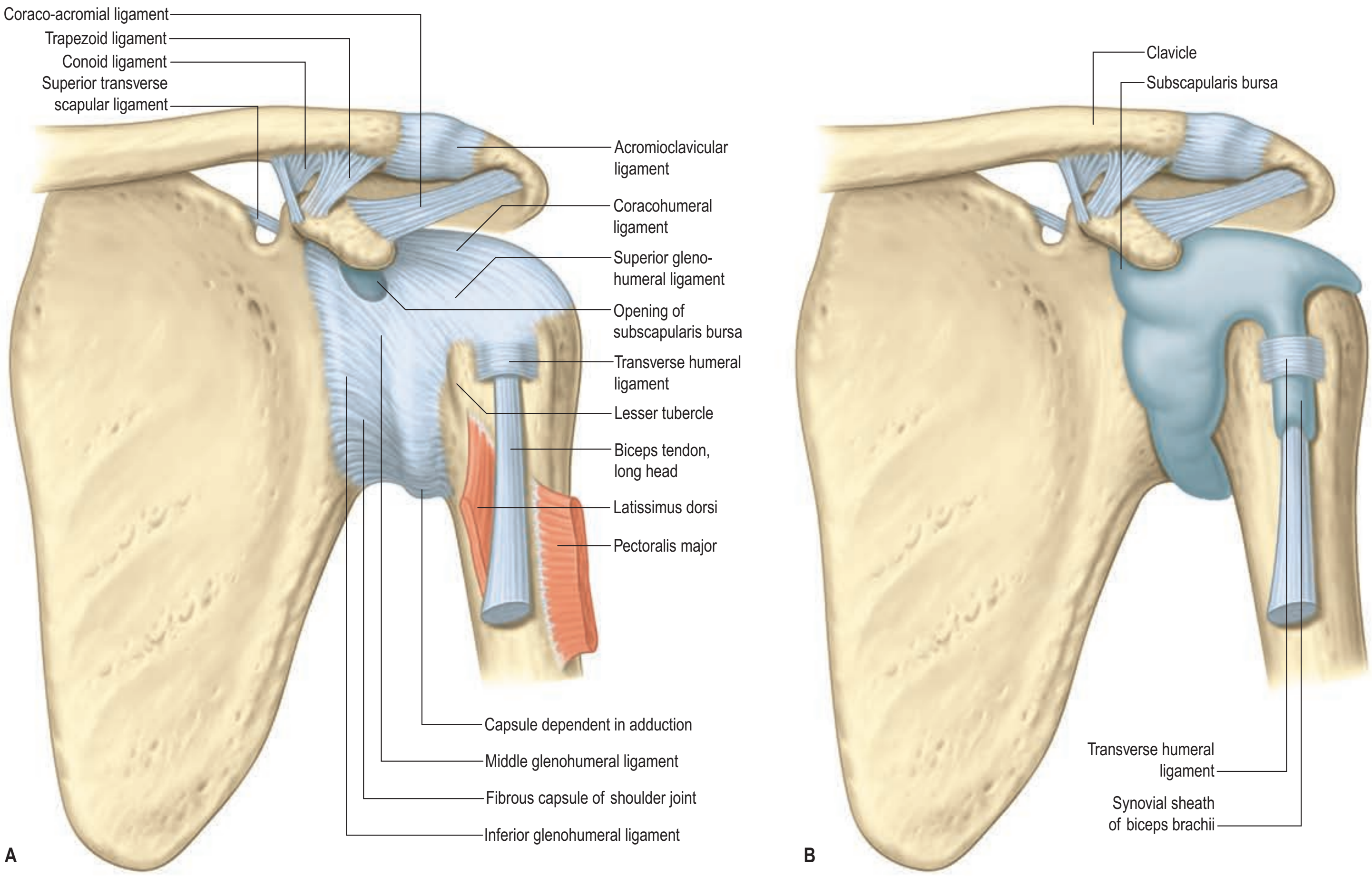
Coraco-acromial ligament
Trapezoid ligament
Conoid ligament
Superior transverse scapular ligament
Acromioclavicular ligament
Coracohumeral ligament
Superior glenohumeral ligament
Opening of subscapularis bursa
Transverse humeral ligament
Lesser tubercle
Biceps tendon, long head
Latissimus dorsi
Pectoralis major
Capsule dependent in adduction
Middle glenohumeral ligament
Fibrous capsule of shoulder joint
Inferior glenohumeral ligament
A
Clavicle
Subscapularis bursa
Transverse humeral ligament
Synovial sheath of biceps brachii
B

Fig. 49.16 **A**, The ligaments associated with the left shoulder, anterior aspect. **B**, A deeper view, showing the subscapularis bursa.

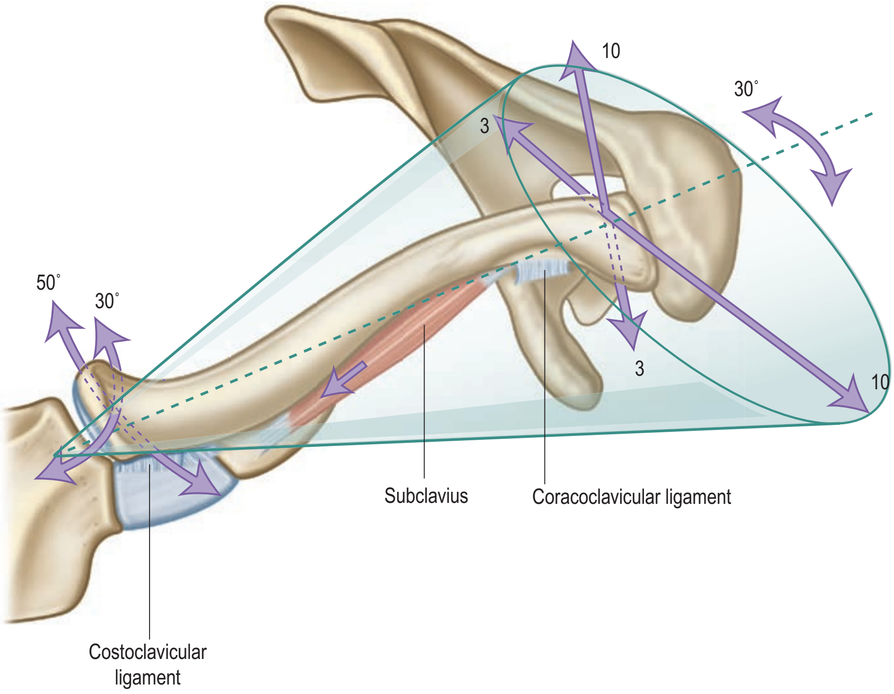
10
30˚
3
50˚
30˚
3
10
Subclavius
Coracoclavicular ligament
Costoclavicular ligament

Fig. 49.17 Clavicular motion about the medial fulcrum of the costoclavicular ligaments immediately lateral to the sternoclavicular joint. The motion of the lateral end of the clavicle is limited by the motion available in the sternoclavicular joint, but based on an extra-articular fulcrum. The movements of the medial end of the clavicle at the sternoclavicular joint are therefore translations or gliding motions: the articular surfaces are configured for this type of motion. The lateral (acromial) end of the clavicle describes an asymmetric conical path during motion of the upper extremity. The maximal range of rotation of the clavicle (subtended by the sternoclavicular joint) is 30°; the maximal range of rotation of the scapula (sternoclavicular and acromioclavicular joints combined) is about 60° with respect to the sternum. The scapula is suspended from the distal clavicle at the acromioclavicular joint, which can be considered as the true joint (the cavity bounded by the acromioclavicular capsule and ligaments); it is also part of an extended articulation that comprises the true joint and the coracoclavicular suspensory ligaments. Arguably, the ligaments might be better defined as the claviculocoracoid ligaments, to acknowledge their role as the spiroid fulcrum around which the body of the scapula, and therefore the glenoid fossa, rotate during protraction and retraction of the scapula. The action of subclavius is to resist upward displacement of the distal clavicle, or to decelerate the clavicle moving into elevation. Linear measurements are given in centimetres.

Factors maintaining stability The acromioclavicular ligaments provide the greatest resistance to anteroposterior displacement of the acromioclavicular joint, while the coracoclavicular ligaments resist rotation and vertical translation of the joint.

Movements Movements at the joint complement those of the sternoclavicular joint (Figs 49.17–49.20). The sternal end of the clavicle is robustly supported by strong ligaments, and a similar, but less robust, arrangement of ligaments suspends the scapula from the lateral end of the bone. The motion of the acromioclavicular joint is limited by its small surface area and the articular capsule.

Movements at the scapulothoracic joint

The sternoclavicular and the acromioclavicular joints, in combination with the fascial space between the scapula and underlying chest wall, are known collectively as the scapulothoracic articulation. Scapular movements on the thoracic wall are facilitated by loose areolar tissue between subscapularis and serratus anterior, and between serratus anterior and the chest wall; the latter gliding plane is the scapulothoracic joint. It is a virtual space. There may be a bursa between the superior angle of the scapula and the dorsal aspect of the second rib.

The three long nerves innervating the scapulothoracic 'joint', i.e. accessory, long thoracic and dorsal scapular, innervate the three major muscle groups of scapulothoracic motion, namely: trapezius, serratus anterior and the medial scapular stabilizing muscles (levator scapulae and the rhomboids).

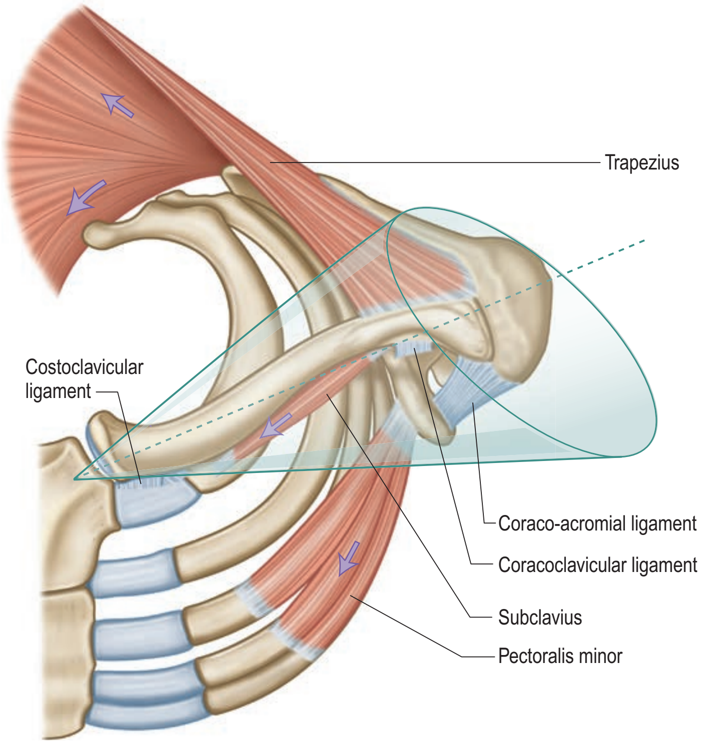

Fig. 49.18 The distal clavicle is moved by trapezius, which has an extensive attachment along the spine of the scapula and the medial aspect of the distal third of the clavicle. The antagonist of trapezial power is pectoralis minor, which, rarely, has an extension or slip of tendon that joins the coraco-acromial ligament. The latter acts as a tension band between the 'outriggers' of the acromion and coracoid. If surgically divided, the cut surfaces of the coraco-acromial ligament cannot be readily reapposed, suggesting a mechanical role in pre-tensioning the acromion and coracoid against the pull of trapezius. Shortening or tightness of pectoralis minor will create fixed protraction of the scapula, which then rotates ventrally around the chest wall. As a consequence, the acromion tilts and the space between it and the cranial surface of the rotator cuff below (the subacromial space) diminishes, creating the conditions in which forceful coaptation of the apposed surface of the rotator cuff and the coraco-acromial ligament may occur. This is the painful condition of 'impingement'.

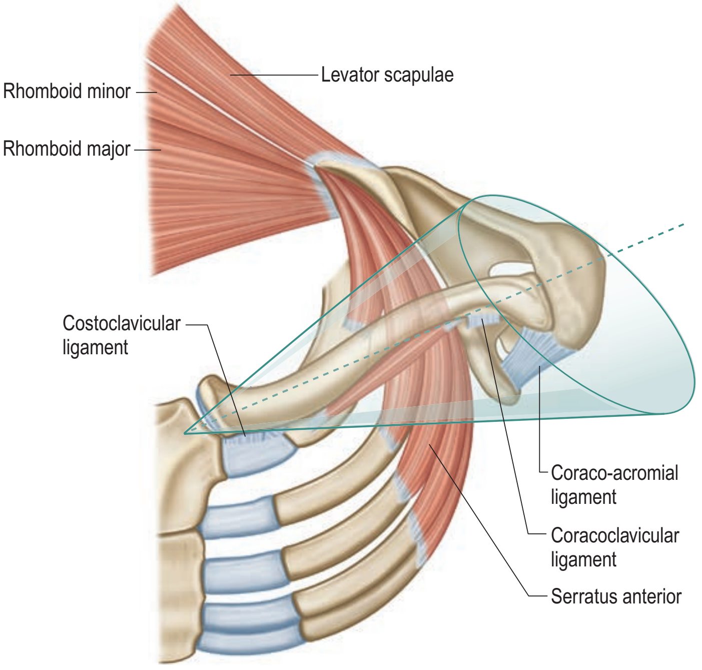

Fig. 49.19 Motion of the medial border of the scapula is governed by the opposing actions of the medial parascapular group (levator scapulae and rhomboids minor and major) and the scapulothoracic group (serratus anterior), causing retraction and protraction, respectively.

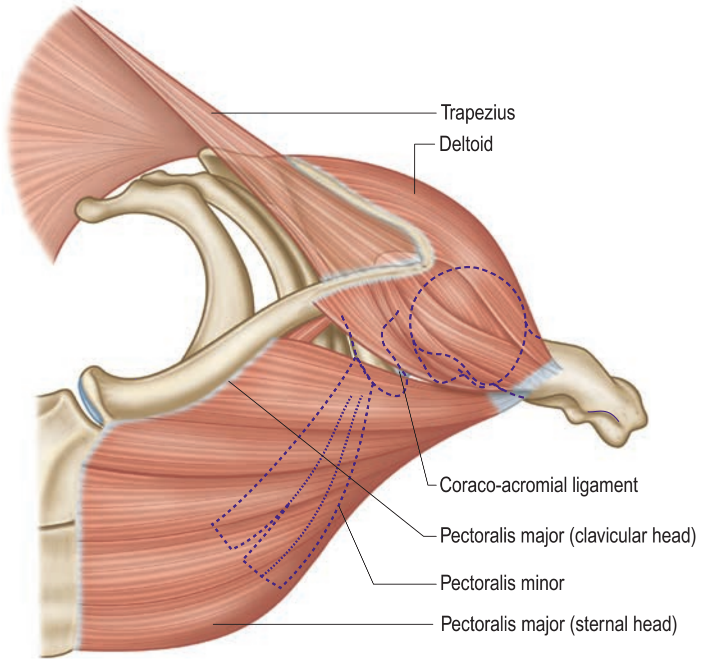
Trapezius
Deltoid
Coraco-acromial ligament
Pectoralis major (clavicular head)
Pectoralis minor
Pectoralis major (sternal head)

Fig. 49.20 The closely related humeral attachments of pectoralis major and deltoid (between one-third and one-half of the way down the shaft of the bone) enable the pectoralis major–deltoid muscular envelope to move the elbow, forearm and hand in space, using the shoulder as a fulcrum for effective delivery of power through a wide range of motion from in front of the trunk to behind. The relative coarseness of these muscles underlies their ability to produce great torque in upper-extremity motion; motion generated by these muscles is 'fine-tuned' by the rotator cuff working concordantly with the outer envelope (each segment or part of the rotator cuff can be said to have an equivalent segment or part in the outer envelope of muscles; this pattern is considered as a force-couple generating stable motion of the humerus on the scapula at the glenoid).

The following account should be read together with the description of movements of the glenohumeral joint. It is important to bear in mind that the purpose of scapular motion is the appropriate positioning of the glenohumeral joint in space, and the purpose of scapular stability is to provide a foundation for glenohumeral motion.

Elevation and depression

Scapular elevation, as in 'shrugging the shoulders', is generated by trapezius acting on the lateral clavicle, acromion and spine of the scapula. If levator scapulae is less active, the scapula rotates laterally (i.e. the inferior angle protracts around the chest wall), with dorsal rotation at the acromioclavicular joint; this is resisted by the rhomboid muscles and controlled by pectoralis minor. If levator scapulae is more active, then the scapula ascends with less rotation. The sternal end of the clavicle, rotating about an anteroposterior axis through the bone above the medial attachment of the costoclavicular ligament, slides down over the articular disc. This is resisted by subclavius and by tension in the costoclavicular ligament and sternoclavicular joint capsule. In scapular depression, ventral rotation occurs at the acromioclavicular joint, and the clavicle slides up on the disc at the sternoclavicular joint. The movements are checked by the cervical fibres of trapezius, the interclavicular and superior sternoclavicular ligaments and the articular disc. Usually, gravity alone is sufficient; when necessary, the lowest part of serratus anterior and pectoralis minor are active depressors.

Protraction and retraction

Protraction (forward movement) round the thoracic wall occurs in pushing, thrusting and reaching movements, usually with some lateral rotation. The acromion advances over the clavicular facet to the limit, and the shoulder is simultaneously advanced by forward movement of the lateral end of the clavicle and posterior translation of its sternal end over the sternal facet, carrying the disc with it. Pectoralis major, together with the anterior sternoclavicular ligament and posterior lamina of the costoclavicular ligament, check backward slide of the sternal end. Serratus anterior and pectoralis minor are prime movers and maintain continuous apposition of the scapula, especially its medial border, in smooth gliding on the thoracic wall, with the rhomboid muscles controlling the rate and

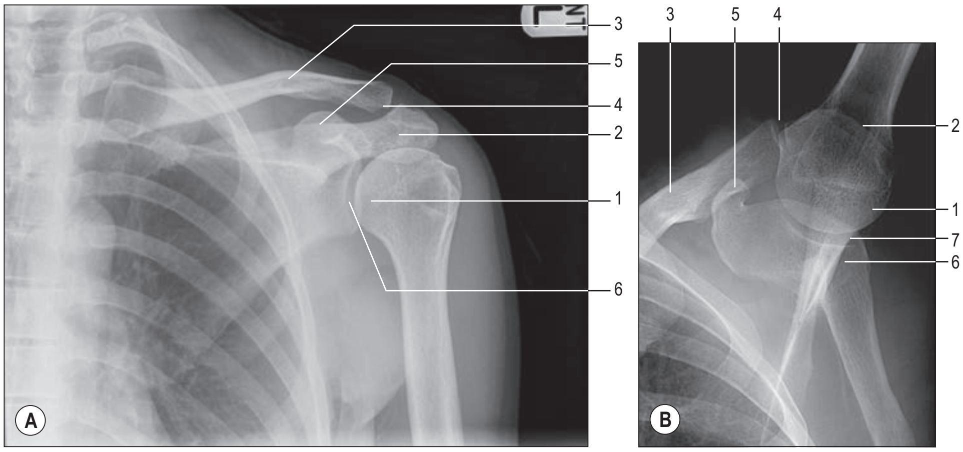

Fig. 49.21 Radiographs of the left shoulder of an 18-year-old female. **A**, Anteroposterior view. **B**, Axillary view with the arm abducted. Key: 1, head of humerus; 2, acromion; 3, clavicle; 4, acromioclavicular joint; 5, coracoid process; 6, glenoid fossa; 7, glenohumeral articulation.

range of motion. The upper part of latissimus dorsi also acts like a strap across the inferior scapular angle in protraction and lateral rotation.

In scapular retraction, i.e. bracing back the shoulders, these movements are reversed and checked at the sternoclavicular joint by the posterior sternoclavicular ligament and anterior lamina of the costoclavicular ligament. Trapezius (horizontal and lower fibres) and the rhomboids are prime movers, while the subclavius and pectoralis minor, enveloped within the clavi-coraco-axillary fascia, appear to decelerate the elevating limb.

Lateral and medial rotation

Lateral (upward) rotation of the scapula increases the range of humeral elevation by turning the glenoid cavity to face almost directly up, e.g. when raising the arm above the head. This movement is always associated with humeral elevation and rotation at the glenohumeral joint, and with protraction of the scapula. Scapular rotation requires movement at both sternoclavicular and acromioclavicular joints; the sternoclavicular joint permits elevation of the lateral end of the clavicle, a movement that is almost complete when the arm is abducted to 90°. The acromioclavicular joint moves in the first 30° of abduction, when the conoid ligament becomes taut, and is subsequently accompanied by clavicular rotation at the sternoclavicular joint around the longitudinal axis of the bone. The medial end is depressed further as the lateral end continues to rise. Some acromioclavicular movement also occurs in the final stages of humeral abduction. Trapezius (cervical fibres) and serratus anterior (the lower part) are prime movers, with the rhomboids providing resistance to motion.

Medial (downward) rotation is usually effected by gravity; gradual active lengthening of trapezius and serratus anterior is sufficient to control it. When more force is needed, levator scapulae, the rhomboids and, in the initial stages, pectoralis minor are prime movers in returning the scapula to a position of rest.

Glenohumeral (shoulder) joint

The glenohumeral joint is a synovial multiaxial spheroidal joint between the roughly hemispherical head of the humerus and the shallow glenoid fossa of the scapula (Fig. 49.21). It is the most mobile joint in the body and the most frequently dislocated. Its anatomy is a compromise between the requirements for motion and stability; both depend on the surrounding muscular and soft tissue envelope more than on the shape and surface area of the articulating surfaces.

The humeral head is held to the concave glenoid fossa by the compressive action of the rotator cuff muscles; the stabilizing mechanism of the glenohumeral joint is one of concavity compression. The rotator cuff muscles are attached to the proximal humerus through a musculotendinous envelope (see below), the deep surface of which fuses with the lateral part of the articular fibrous capsule. The humeral head is then contained in a spherical space bounded medially by the glenoid fossa and elsewhere by the deep surface of the fibrous capsule, a form of osseofibrous acetabulum. The walls of this 'acetabulum' (i.e. the rotator cuff muscles and tendons) are contained within a roughly spherical space bounded by the coracoid anteriorly; the coraco-acromial ligament anterosuperiorly; the acromion and spine of the scapula posteriorly, posterosuperiorly and posterolaterally; and the deep surface of deltoid anterolaterally and laterally. This arrangement creates two gliding planes, one internal (the glenohumeral articular gliding plane) and one external (the subcoracoid–subacromial–subdeltoid plane); the latter is continuous with the plane under the scapula (the scapulothoracic gliding plane). Gliding is facilitated by the synovial lined cavities of the glenohumeral joint and the subcoracoid, subacromial and subdeltoid bursae, which are nearly always contiguous. Infection, inflammation and injury commonly cause adhesions and fibrosis (with subsequent contracture) in these planes; restriction of motion follows, specific to the site and extent of adhesion. The surfaces of both gliding planes are extensive and fibrosis is consequently very restricting.

Articulating surfaces The articular surfaces are reciprocally curved and are correctly termed ovoids. The surface area of the humeral convexity is approximately four times that of the glenoid concavity, which means that only a small portion of the head opposes the glenoid in any position (Figs 49.22–49.23). The radius of curvature of the glenoid fossa in the coronal plane is greater than that of the humeral head, and is deepened by a fibrocartilaginous rim, the glenoid labrum (see Fig. 49.15). Both articular surfaces are covered by hyaline cartilage, thickest centrally and thinner peripherally over the humerus, and *vice versa* over the glenoid cavity. In most positions, their curvatures are not fully congruent and the joint is loose-packed; close-packing (full congruence) is probably only reached with the humerus abducted and laterally rotated.

Glenoid labrum The glenoid labrum is a fibrocartilaginous rim around the glenoid fossa. Anteriorly, it is triangular in section; posteriorly, it is more ovoid; while inferiorly, it may be flattened and almost deficient. It varies in size and thickness. The attachment to the edge of the glenoid fossa is secure superiorly where it blends with the anterior and posterior fasciculi of the long tendon of biceps (Vangsness et al 1994), less secure posteriorly, but relatively more secure anteroinferiorly (Bankart 1923). There may be an aperture between the free deep edge of the labrum and the anterior glenoid rim above the midpoint of the fossa. In slightly less than one-fifth of normal shoulders, there may be no anterior labrum, in which case its place is taken by a cord-like middle glenohumeral ligament. The labrum may be hypoplastic or absent in patients with collagen deficiency but with normal shoulder function (hypermobility syndrome); these shoulders are not necessarily unstable. The labrum deepens the glenoid cavity and so may assist in stabilizing the humeral head on the fossa, although the mechanism of this function remains uncertain. It may protect the bone and probably assists lubrication.

Fibrous capsule A fibrous capsule envelops the joint (see Figs 49.16, 49.22). It is attached medially to the glenoid neck at a variable distance from the glenoid labrum, so forming recesses anterior and posterior to the scapular neck; it includes the supraglenoid tubercle, to which the long head of biceps attaches, and which is therefore intracapsular. Laterally, it is attached to the anatomical neck of the humerus, i.e. near the articular margin, exceptinferomedially, where it descends more than 1 cm on the calcar humerale. The fibres of the capsule are orientated in a spiral fashion, so that, in elevation of the arm, the capsule tightens, so bringing the articular surfaces into closer apposition and contributing to the concavity compression. In some individuals, a deeper band of fibres orientated in a reverse obliquity to the main capsular fibres passes from the region of the lesser tubercle to the lower part of the anterior rim of the glenoid fossa. This is the anterior oblique band; its contribution to stability is uncertain.

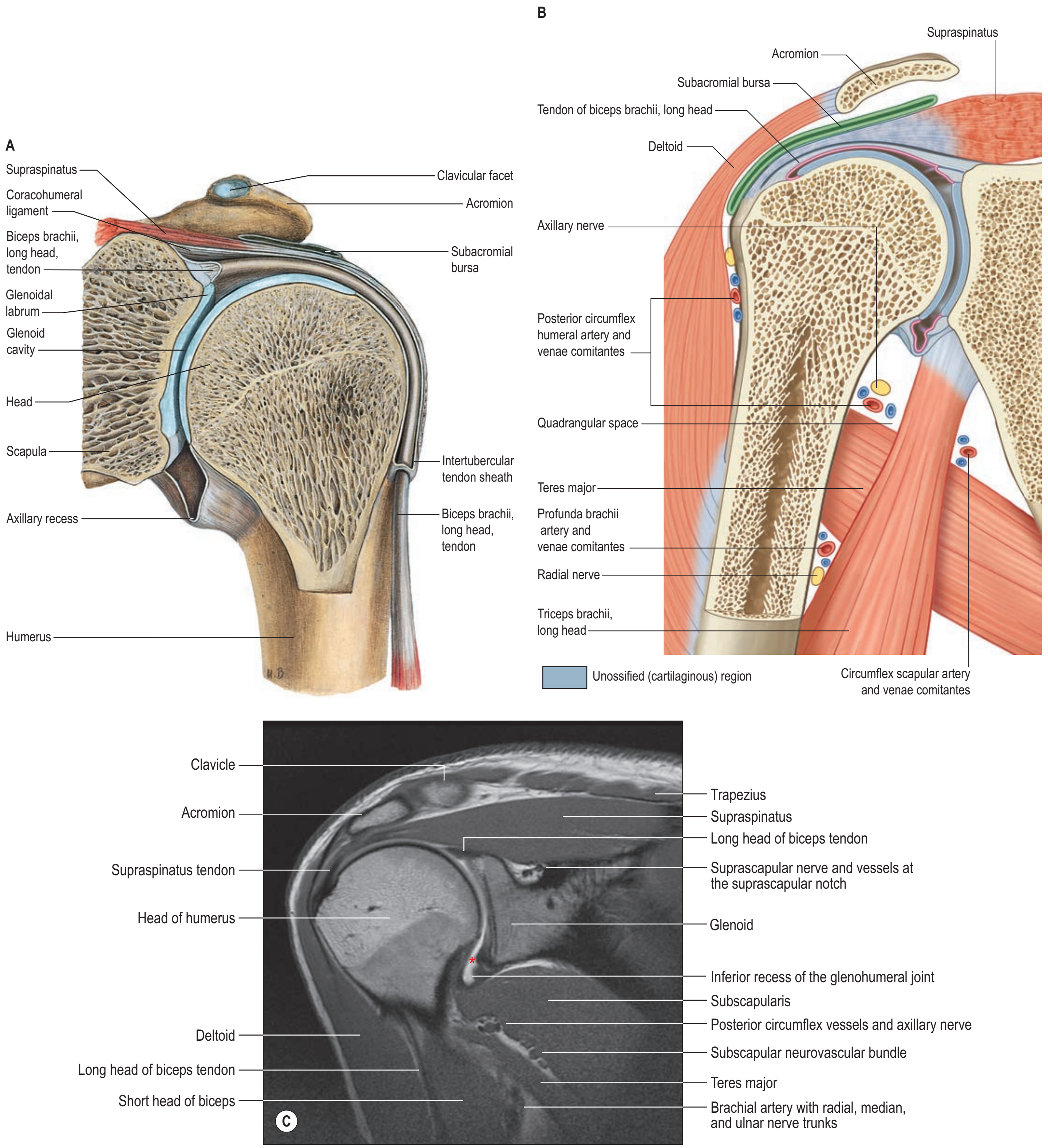
A
Supraspinatus
Coracohumeral ligament
Biceps brachii, long head, tendon
Glenoidal labrum
Glenoid cavity
Head
Scapula
Axillary recess
Humerus
Clavicular facet
Acromion
Subacromial bursa
Intertubercular tendon sheath
Biceps brachii, long head, tendon
B
Supraspinatus
Acromion
Subacromial bursa
Tendon of biceps brachii, long head
Deltoid
Axillary nerve
Posterior circumflex humeral artery and venae comitantes
Quadrangular space
Teres major
Profunda brachii artery and venae comitantes
Radial nerve
Triceps brachii, long head
▨ Unossified (cartilaginous) region
Circumflex scapular artery and venae comitantes
Clavicle
Acromion
Supraspinatus tendon
Head of humerus
Deltoid
Long head of biceps tendon
Short head of biceps
Trapezius
Supraspinatus
Long head of biceps tendon
Suprascapular nerve and vessels at the suprascapular notch
Glenoid
Inferior recess of the glenohumeral joint
Subscapularis
Posterior circumflex vessels and axillary nerve
Subscapular neurovascular bundle
Teres major
Brachial artery with radial, median, and ulnar nerve trunks
*
C

Fig. 49.22 Coronal sections through the left shoulder joint, posterior aspect. **A**, Anterior view. **B**, Posterior view. Note the subacromial bursa and contents of the quadrangular space. **C**, Coronal T1-weighted MR arthrogram of the left shoulder through the anterior aspect of the glenohumeral joint, viewed from posterior to match **B**. Contrast medium is injected into the joint before the acquisition, and then shows up as bright fluid within the joint capsule (*). (A, Sobotta Atlas of Human Anatomy © Elsevier GmbH, Urban & Fischer, Munich.)

The lateral part of the external surface of the fibrous capsule is blended with the tendons of supraspinatus (superiorly), infraspinatus and teres minor (posteriorly), subscapularis (anteriorly) and by the tendon of the long head of triceps at the infraglenoid tubercle (inferiorly). The rotator interval is a medially based, triangular area of uncovered capsule between the superior edge of subscapularis and the anterior edge of supraspinatus, with the base of the coracoid as the medial boundary of the interval. It is reinforced by the coracohumeral ligament, the superior glenohumeral ligament, and fibres from the supraspinatus tendon laterally. The axillary nerve and posterior circumflex humeral vessels are separated from the inferior capsule by the inferior border of subscapularis. The capsule is least supported inferiorly, and subjected to the greatest strain in full abduction, when it is stretched tightly across the humeral head. It is supported in this position by the proximal part of the long head of triceps and the broad bulk of teres major.

There are two openings in the capsule: below the coracoid process, connecting the joint cavity to a bursa that may envelop the upper border of the tendon of subscapularis (anteriorly); and between the humeral tubercles, allowing passage of the long tendon of biceps and its synovial sheath.

Ligaments The ligaments associated with the glenohumeral joint are the glenohumeral (superior, middle and inferior), coracohumeral and

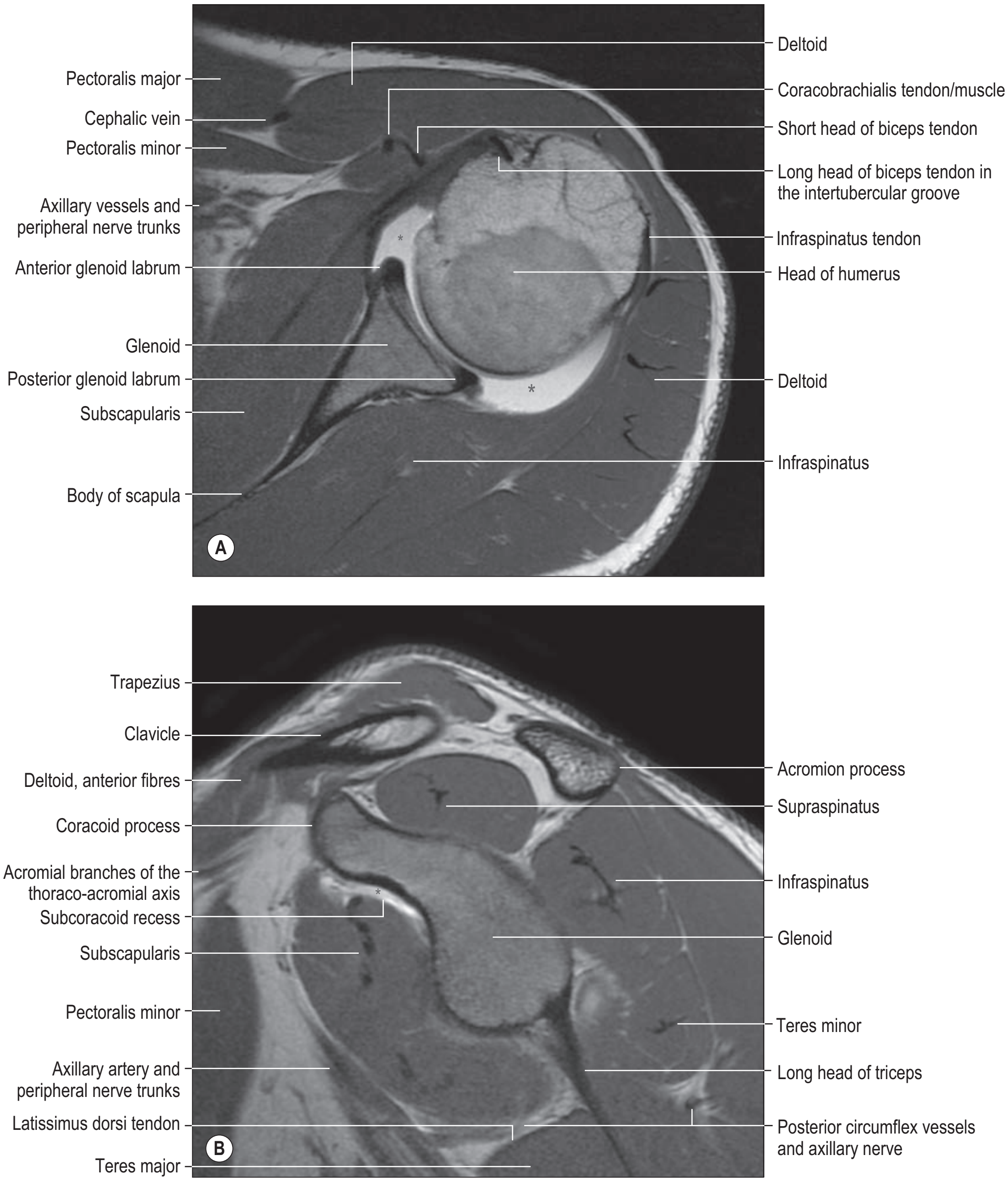
Deltoid
Pectoralis major
Coracobrachialis tendon/muscle
Cephalic vein
Short head of biceps tendon
Pectoralis minor
Long head of biceps tendon in the intertubercular groove
Axillary vessels and peripheral nerve trunks
Infraspinatus tendon
Anterior glenoid labrum
Head of humerus
*
Glenoid
Posterior glenoid labrum
Deltoid
*
Subscapularis
Infraspinatus
Body of scapula
A
Trapezius
Clavicle
Acromion process
Deltoid, anterior fibres
Supraspinatus
Coracoid process
Acromial branches of the thoraco-acromial axis
Infraspinatus
Subcoracoid recess
*
Glenoid
Subscapularis
Pectoralis minor
Teres minor
Axillary artery and peripheral nerve trunks
Long head of triceps
Latissimus dorsi tendon
Posterior circumflex vessels and axillary nerve
B
Teres major

Fig. 49.23 A magnetic resonance arthrogram of the shoulder. **A**, Axial T1-weighted MRI of the left shoulder through the mid-level of the glenohumeral joint. Contrast medium is injected into the joint before the acquisition, and then shows up as bright fluid within the distended joint capsule (*). **B**, Sagittal T1-weighted MRI of the shoulder through the mid-level of the glenohumeral joint. Contrast medium is injected into the joint before the acquisition, and then shows up as bright fluid within the distended joint capsule (*).

transverse humeral. A ligament only restricts a specific motion of a joint when discrete parts of the ligament become tight; this only occurs at the limits of a specific motion of the joint when the ligament acts as a 'check-rein'. For movements that lie within the limit of motion, ligaments have no mechanical role. Mechanoreceptors and nociceptors are clustered at each end of the ligaments, more on the glenoid side than the humeral side (Halata and Baumann 2008). The capsule, ligaments and labrum contain the deep afferent innervation of the glenohumeral joint and therefore contribute to stability of the joint through facilitation of the rotator cuff activity within the normal range of human shoulder motion.

Glenohumeral ligaments Three glenohumeral ligaments, only visible from within the joint, reinforce the capsule anteriorly and inferiorly (**Fig. 49.24**). The superior glenohumeral ligament passes from the supraglenoid tubercle, just anterior to the origin of the long head of biceps, to the humerus at the fovea capitis, near the proximal tip of the lesser tubercle on the medial ridge of the intertubercular sulcus. It forms an anterior cover around the long head of biceps and is part of the rotator interval. Together with the coracohumeral ligament, it is an important stabilizer in the inferior direction, helping to keep the humeral head suspended (the coracohumeral ligament is more robust than the superior glenohumeral ligament).

The middle glenohumeral ligament arises from a wide attachment below the superior glenohumeral ligament, along the anterior glenoid margin as far as the inferior third of the rim, and passes obliquely inferolaterally, enlarging as it does so, to attach to the lesser tubercle deep to the tendon of subscapularis, with which it blends. The width and thickness of this ligament may be as much as 2 cm and 4 mm, respectively. It provides anterior stability between 45° and 60° of abduction in the scapular plane. However, 30% of individuals may not have a middle glenohumeral ligament; these individuals are not more likely to have unstable shoulders. It may be thickened and cord-like in the Buford complex (a congenital glenoidal labrum variant), again with no apparent disadvantage for stability.

The thicker and longer inferior glenohumeral ligament complex is a hammock-like structure with anchor points on the anterior and posterior sides of the glenoid. It arises from the anterior, middle and posterior margins of the glenoid labrum, below the epiphysial line, and passes anteroinferiorly to the inferior and medial aspects of the neck of the humerus. The anterior, superior edge of the inferior ligament is thickened as the anterior band; there is an equivalent, but not so robust, thickening of the posterior capsule: the posterior band. Between the two bands is a region of thin capsule known as the axillary pouch. (For further details, consult Burkart and Debski (2002), Di Giacomo et al (2008).)

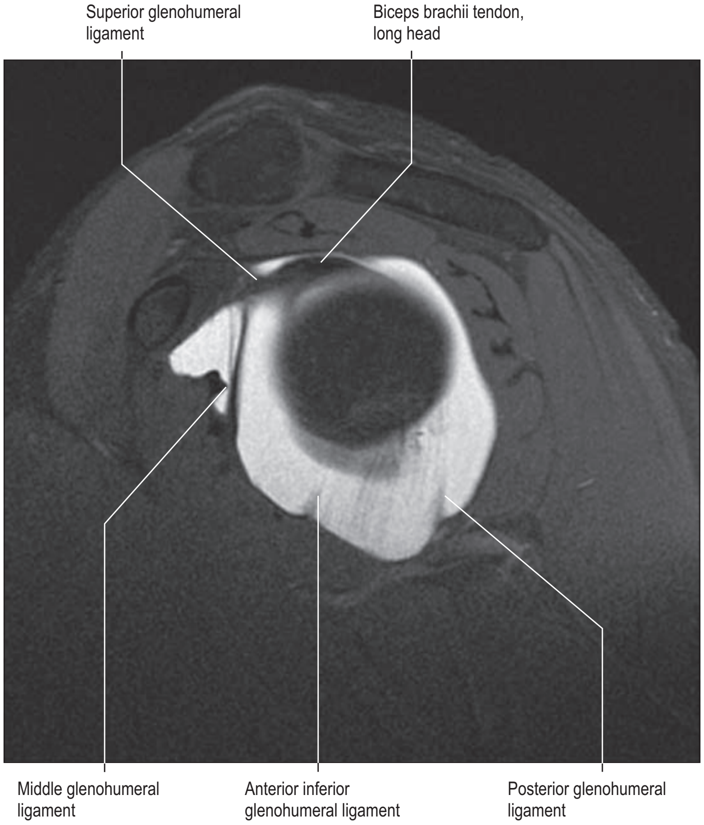
Superior glenohumeral ligament
Biceps brachii tendon, long head
Middle glenohumeral ligament
Anterior inferior glenohumeral ligament
Posterior glenohumeral ligament

Fig. 49.24 A sagittal MR arthrogram of the shoulder of a 28-year-old male. The glenohumeral joint has been distended by intra-articular injection of contrast medium: the glenohumeral ligaments are clearly outlined.

Coracohumeral ligament The coracohumeral ligament is attached to the dorsolateral base of the coracoid process and extends as two bands, which blend with the capsule, to the greater and lesser tubercles (see Fig. 49.16). Portions of the coracohumeral ligament form a tunnel for the biceps tendon on the anterior side of the joint. The rotator interval is reinforced by the coracohumeral ligament. It also blends inferiorly with the superior glenohumeral ligament. The ligament tightens in external rotation of the glenohumeral joint.

Transverse humeral ligament The transverse humeral ligament is a broad band that passes between the humeral tubercles, and is attached superior to the epiphysial line (see Fig. 49.16). It converts the intertubercular sulcus into a canal, and acts as a retinaculum for the long tendon of biceps.

Synovial membrane The synovial membrane lines the capsule and covers parts of the anatomical neck. The long tendon of biceps brachii traverses the joint in a synovial sheath that continues into the intertubercular sulcus as far as the surgical neck of the humerus (see Figs 49.16B, 49.22A). The intra-articular bicipital sheath may be connected to the articular surface of the superior capsule above by a mesotenon, which may be incomplete, presenting as one or several strands. This arrangement can only be the case if the biceps tendon was originally an extra-articular structure and invaginated, with its synovial sheath, into the glenohumeral joint as the upper limb rotated into external rotation relative to the trunk during development.

Bursae Many bursae adjoin the shoulder joint (see Figs 49.15–49.16). They are usually found between the tendon of subscapularis and the capsule, communicating with the joint between the superior and middle glenohumeral ligaments; on the superior acromial aspect; between the coracoid process and capsule; between teres major and the long head of triceps; and anterior and posterior to the tendon of latissimus dorsi. The subacromial bursa, between deltoid and the capsule, does not communicate with the joint cavity but is prolonged under the acromion and coraco-acromial ligament, and between them and supraspinatus: it appears to be attached, together with the subdeltoid fascia, to the acromion. Bursae sometimes occur behind coracobrachialis and between the tendon of infraspinatus and the capsule, occasionally opening into the joint.

Vascular supply The glenohumeral joint is supplied by branches from the anterior and posterior circumflex humeral, suprascapular and circumflex scapular vessels.

Innervation The glenohumeral joint is innervated mainly from the posterior cord of the brachial plexus through the subscapular nerves. The capsule is supplied by the suprascapular nerve (posterior and superior parts), axillary nerve (anteroinferior) and the lateral pectoral nerve (anterosuperior, including the rotator interval capsule).

Factors maintaining stability The articulation between the relatively large humeral head and the shallow glenoid fossa allows a wide range of movement but is a challenge for the stability of the joint.

Movements at the glenohumeral joint

The shoulder is capable of any combination of swing and spin over a range far wider than that of any other joint in the body. Flexion–extension, abduction–adduction, and medial (internal) and lateral (external) rotation all occur at the shoulder. A combination of all of these results in circumduction, which is not a useful movement to record in clinical practice. Although most movement of the shoulder occurs at the glenohumeral joint, the scapulothoracic articulation contributes to overall shoulder movement in all directions, including lateral rotation.

Muscles producing movements The muscles that produce movements at the glenohumeral joint are principally the scapulohumeral and thoracobrachial muscles: deltoid, pectoralis major and latissimus dorsi, assisted by coracobrachialis. The translating effect of these muscles on the shoulder joint is counteracted by the rotator cuff, a group of short muscles (subscapularis, supraspinatus, infraspinatus and teres minor), including teres major, that are attached closer to the joint, and that centre the head of the humerus in the glenoid fossa through the entire range of motion.

Flexion Flexion is carried out by pectoralis major (clavicular part), deltoid (anterior fibres) and coracobrachialis, assisted by biceps. The sternocostal part of pectoralis major is a major force in flexion forwards to the coronal plane from full extension.

Extension Extension is carried out by deltoid (posterior fibres) and teres major, from the dependent position. When the fully flexed arm is extended against resistance, latissimus dorsi and the sternocostal part of pectoralis major act powerfully until the arm reaches the coronal plane.

Abduction Abduction is carried out by supraspinatus and deltoid. The effect of deltoid is mainly upward and, unless opposed, this would displace the humerus upwards. Subscapularis, supraspinatus, infraspinatus and teres minor exert a centralizing force and so apply a balancing force; together with deltoid, they constitute a 'couple' to produce abduction in the scapular plane.

Medial rotation Medial rotation is carried out by pectoralis major, deltoid (anterior fibres), latissimus dorsi, teres major and, with the arm pendant, subscapularis.

Lateral rotation Lateral rotation is carried out by infraspinatus, deltoid (posterior fibres) and teres minor. Lateral rotation is important for clearance of the greater tubercle and its associated tissues as it passes under the coraco-acromial arch during elevation of the arm.

Glenohumeral joint dislocation

The glenohumeral joint is the most frequently dislocated joint in the body. Most dislocations are anterior, and occur when the forearm is forced backwards into greater lateral (external) rotation when it is in abduction, lateral rotation and extension. A dislocated shoulder loses its normal contour because the humeral head is displaced anterior to the glenoid rim and, sometimes, under the coracoid, which means that the acromion process, rather than the greater tubercle, becomes the most lateral bony structure, giving the shoulder a 'squared-off' appearance.

MUSCLES

The shoulder girdle and shoulder joint musculature are arranged in layered, functional groups (Table 49.1). The muscles of the shoulder girdle may suspend or move the scapula; these functions are

In the anatomical analysis of shoulder movements, it is usual to relate humeral movement to the scapula, rather than to conventional anatomical planes. However, in clinical practice, movements *are* related to the conventional anatomical planes. When the arm hangs at rest, the glenoid fossa faces almost equally forwards and laterally, and the humeral capitular and scapular (topographical) axes correspond, although the humerus, relative to the anatomical position, is medially rotated. With the humerus in the anatomical position, i.e. with the inter-epicondylar axis in the frontal plane, the humeral head axis is posteriorly directed, in line with the axis of the scapula.

Using the anatomical description, flexion carries the arm anteromedially on an axis through the humeral head orthogonal to the glenoid fossa at its centre. Abduction and adduction occur in a vertical plane orthogonal to that of flexion–extension and the axis is horizontal, through the humeral head and parallel with the glenoid plane. Pure abduction raises the arm anterolaterally in the plane of the scapula. However, when referred to the trunk, flexion and extension occur in the paramedian plane, and abduction and adduction occur in the coronal plane. In this sense, raising the arm vertically from flexion or raising it from abduction are both accompanied by humeral rotation in opposite directions. Whether 'scapular' or any other plane of abduction is described, these are selections from an infinite series. In scapular abduction, points on the humeral surface pursue vertical cords, but in rotation, they are horizontal. In 'pure' flexion–extension, in a plane orthogonal to the scapula, the axis of movement and the notional 'mechanical axis' are regarded as projected from the centre of the glenoid cavity.

Glenohumeral abduction is about 120° or more (see Fig. 49.21B). Abduction may reach 180° after thoracoscapular arthrodesis for facioscapulohumeral dystrophy (Copeland and Howard 1978). Abduction is restricted to about 45° after glenohumeral arthrodesis. Some 60° of further abduction occurs at the sterno- and acromioclavicular articulations, and contralateral vertebral flexion also aids in bringing the arm to the vertical. During active elevation, movements at the glenohumeral and acromioclavicular joints are simultaneous, except in the initial few degrees, when most, often all, movement is glenohumeral. For every 15° of elevation, glenohumeral movement is said to be 10° and scapular movement 5°, but this ratio is not linear throughout the range of motion. During the initial stages of abduction, the entire rotator cuff counteracts the strong upward component of the pull of deltoid, which would otherwise cause the humeral head to slide up the glenoid surface; the additive turning moments exerted by the combined deltoid and supraspinatus force-couple may then abduct the arm. Deltoid also acts with the other elements of the rotator cuff, according to the position of the arm in space, to maintain rotation, flexion and extension of the arm. It is important to consider the synergistic relation between the rotator cuff and deltoid as a continuum in which the rotator cuff muscles act to provide a stable base on which deltoid can work effectively, whatever the position of the arm.

In flexion, the humerus swings at right-angles to the scapular plane, and scapular rotation cannot increase the elevation (120°) that is obtainable in full flexion. If the fully flexed humerus is also abducted, elevation increases *pro rata* until, when the humerus reaches the scapular plane, i.e. when true abduction is reached, 180° of elevation becomes possible. In medial or lateral rotation, the humerus revolves about one-quarter of a circle around a vertical axis; the range is greatest when the arm is pendant, and least when it is vertical. When the rotational range at the glenohumeral joint is assessed, the forearm should be flexed to a right-angle at the elbow in order to prevent the effects of superadded pronation or supination in the pendant limb. In circumduction, which is a succession of the foregoing movements, the distal end of the humerus describes the base of a cone with its apex at the humeral head. This glenohumeral movement may be greatly increased by scapular movements, e.g. in acts of slinging objects with force.

The peculiar relation of the long head of biceps brachii to the shoulder joint may serve several purposes. By its connection with both the shoulder and elbow, the muscle harmonizes their actions as an elastic connection during all upper limb movements. It helps to prevent the humeral head impinging on the acromion when deltoid contracts and also to steady it in movements of the arm. In paralysis or absence (i.e. in rotator cuff tendon tears) of supraspinatus, the long head of biceps may also help initiate abduction of the arm, particularly when the humerus is laterally rotated.

The axillary nerve and vessels may be injured during dislocation or, more commonly, during inexpert attempts at relocation, particularly in older patients. This can lead to an inability to maintain abduction of the shoulder as a result of paralysis of deltoid. If, after relocation of the joint, the patient cannot *initiate* elevation (abduction) from the pendant position, then there may be an associated rotator cuff rupture and/or suprascapular nerve lesion. If the patient can initiate, but cannot maintain, abduction beyond 15°, then deltoid palsy should be suspected. Patients, particularly the elderly, can have a rotator cuff rupture and an axillary nerve palsy causing deltoid paralysis; it can be difficult to distinguish between the two. There may also be an area of hypoaesthesia or anaesthesia over the distal part of the muscle (sometimes referred to as the 'regimental badge patch' of skin; see Fig. 49.2), reflecting loss of function in the upper lateral cutaneous nerve of the arm (a branch of the axillary nerve), as well as venous occlusive changes (swelling) in the limb. After more violent dislocation, younger patients may have deltoid paralysis and an intact, but stretched, rotator cuff or partial tearing of the tendons, with a suprascapular nerve injury; these patients may have unexpected pain in the supraspinous fossa with weakness of infraspinatus (lateral rotation), as well as the anticipated anterior shoulder pain. Posterior dislocation is rare and typically occurs when violent movements produce marked medial rotation and adduction, e.g. in epileptic seizures or electric shock. The upper limb is held in fixed medial rotation, and external rotation is impossible to perform.

TABLE 49.1 The relationship between functional muscle grouping and actions of the pectoral girdle*

Functional group	Specific muscles	Action
Occipitospinoscapular	Trapezius	Scapular suspension Position and motion of the acromioclavicular joint in relation to the thorax and (neur) axis Deceleration of the lateral clavicle during motion
Thoracoscapular	Pectoralis minor	
Spinoclavicular	Trapezius	
Thoracoclavicular	Subclavius	
Thoracoscapular (medial border)	Levator scapulae Rhomboid minor Rhomboid major Serratus anterior Serratus posterior superior Serratus posterior inferior	Scapular motion Position and motion of the glenohumeral joint in relation to the thorax and (neur)axis
Thoracohumeral	Pectoralis major Latissimus dorsi	Thoracobrachial motion Position of the arm
Scapulohumeral	Deltoid Coracobrachialis Biceps brachii (short head)	
	Teres minor Infraspinatus Supraspinatus Subscapularis Teres major	Concavity compression of the glenohumeral joint
	Triceps brachii (long head) Biceps brachii (long head)	Coordination of shoulder and elbow motion

*As a principle, a muscle will act on a motion segment to alter the position of the distal extent of that segment in space. As an example, deltoid acts on the shoulder joint but its effect is to move the distal extent of the humerus, i.e. the elbow.

interdependent. The muscles of the shoulder joint may stabilize the joint, move the arm on the stable shoulder joint, or coordinate shoulder and elbow movement; these functions are also interdependent. The closer a muscle is to the centre of motion of the joint on which it acts, the greater its effect on the stability of that joint at rest and during motion. The further away from the centre of motion, the greater the effect of the resultant muscular vector on translation of the joint surfaces. As an example, both subscapularis and pectoralis major generate medial rotation of the glenohumeral joint; subscapularis contributes to concavity compression at the glenohumeral joint (i.e. stability), while pectoralis major causes anterior displacement into flexion and adduction in the absence of subscapularis; when these muscles are working synergistically, the arm is both stabilized at the glenohumeral joint, and flexed and adducted.

The clinical examination of the shoulder girdle muscles is demonstrated in Video 48.1.

Muscles of scapular suspension

Trapezius acts on the spine of the scapula, acromion and lateral clavicle to rotate the acromioclavicular joint upwards and dorsally; movement is guided and limited by the length and shape of the clavicle. Pectoralis minor acts to control the position of the coracoid as trapezius acts on the scapula, while subclavius acts to control clavicular elevation and rotation. These muscles act on the processes of the scapula, while the coraco-acromial ligament acts as a tension band between the processes. Disruption of the continuity of this arrangement (fracture of the clavicle or coracoid, or dislocation of the acromioclavicular joint) will have a profound effect on scapular suspension.

Trapezius

Trapezius is derived from head paraxial mesenchyme with neural crest connective tissue, rather than from the dermomyotomes of lower somites, and is therefore unique among shoulder girdle muscles. It is attached to the spine of the scapula and acromion, segments of the scapula for which development is encoded by a single gene (Dhir et al, 2018).

Attachments Trapezius is a flat, triangular muscle that extends over the back of the neck and upper thorax (Fig. 49.25). The paired trapezius muscles form a diamond shape, from which the name is derived. On either side, the muscle is attached to the medial third of the superior nuchal line, external occipital protuberance, ligamentum nuchae, and apices of the spinous processes and their supraspinous ligaments from C7 to T12. The occipital attachment is by a fibrous lamina, which is also adherent to the skin. The spinal attachment is by a broad triangular aponeurosis from the sixth cervical to the third thoracic vertebrae, and by short tendinous fibres below this.

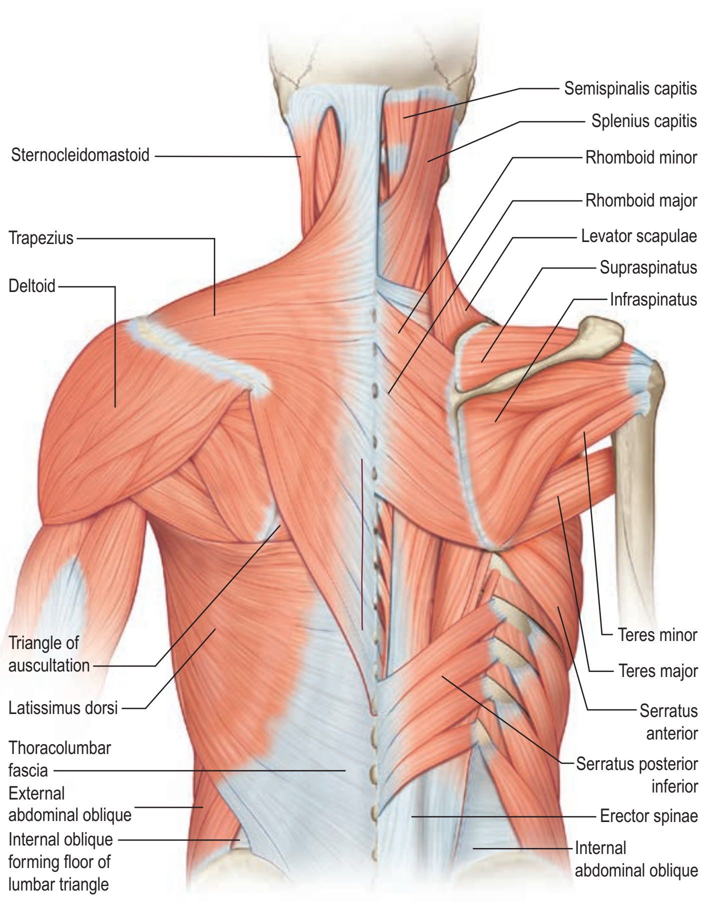

Fig. 49.25 The muscles of the back and shoulder girdles. Superficial muscles are shown on the left. Deeper muscles, revealed after excision of deltoid, latissimus dorsi and trapezius, are shown on the right.

Superior fibres descend, inferior fibres ascend, and the fibres between them are directed horizontally; all converge laterally on the scapula. The superior fibres are attached to the posterior border of the lateral third of the clavicle; the middle fibres to the medial acromial margin and superior lip of the crest of the scapular spine; and the inferior fibres pass into an aponeurosis that glides over a smooth triangular surface at the medial end of the scapular spine and is attached to a tubercle at its lateral apex.

Variants The clavicular attachment of trapezius varies in extent, sometimes reaching mid-clavicle, and occasionally blending with sternocleidomastoid. The vertebral attachment sometimes stops at the eighth thoracic spine. The occipital attachment may be absent. Cervical and dorsal parts are occasionally separate. The inferior part may be hypoplastic or absent.

Vascular supply The upper third of trapezius is supplied by a transverse muscular branch that arises from the occipital artery at the level of the mastoid process. It enters the muscle on its deep surface and gives off several musculocutaneous perforators to the overlying skin. The middle portion of trapezius, together with an area of overlying skin, is supplied by the superficial cervical artery or by a superficial branch of the transverse cervical artery, via musculocutaneous perforators. The lower third of trapezius is supplied by a muscular branch from the dorsal scapular artery, passing medial to the medial border of the scapula. It reaches the deep surface of the muscle either by piercing the rhomboids or by passing between rhomboids major and minor at the level of the base of the spine of the scapula. It anastomoses with the medial and lateral perforating branches of the posterior intercostal arteries.

Innervation Trapezius is innervated by the accessory nerve (see Chs 35 and 48 for more details). Sensory (proprioceptive) branches are derived from the third and fourth cervical ventral rami.

Actions Trapezius cooperates with other muscles in steadying the scapula, controlling it during movements of the arm and maintaining the level and poise of the shoulder. Electromyographic activity is minimal in the unloaded arm, and heavy loads can be suspended with only a small contribution from the upper part; it is the lower part of the muscle that resists lateral rotation of the scapula under load. Acting with levator scapulae, the upper fibres elevate the scapula and, with it, the point of the shoulder; acting with serratus anterior, the lower fibres of trapezius protract and rotate the scapula medially (upwards) so that the arm can be raised above the head; acting with the rhomboids, it retracts the scapula, bracing the shoulder. With the shoulder fixed, trapezius may bend the head and neck backwards and laterally. Trapezius, pectoralis minor, levator scapulae, rhomboids and serratus anterior combine to produce a variety of scapular rotations see below.

If the muscle is denervated, the functions of trapezius cannot be substituted readily by muscle transfer; its unique suite of complex actions suggest that it should rarely, if ever, be used as a muscle for transfer elsewhere.

Testing The upper fibres of trapezius are palpated while the shoulder is shrugged against resistance (see Video 48.1). The lower fibres are palpated during scapular retraction. A better discriminative test is as follows: the hand is brought by medial rotation to the small of the back and the patient is asked to maintain it firmly in this position while the examiner tries to pull the hand off the back. The lower fibres of the trapezius are activated to hold the scapular spine horizontal. Failure to do so implies paresis or paralysis of trapezius, but this must be distinguished from congenital hypoplasia of the lower fibres of the muscle.

Trapezius palsy results in a characteristic posture: the shoulder is tilted laterally and forwards, the acromioclavicular joint is lowered, the superior pole of the scapula is rotated upwards and the inferior pole is displaced medially and, usually, away from the chest wall. This distinguishes trapezius palsy from that of serratus anterior, in which the entire medial border of the scapula tends to elevate away from the chest wall (so-called ‘winging’). The scapula is displaced upwards and towards the spine. The altered posture and disordered motion of the scapula create distortion (narrowing and elongation) of the cervico-axillary sheath and its contents; symptoms of reduced venous return, lymphatic obstruction and disturbed neural perfusion (pain, paraesthesiae, dysaesthesiae) are almost universal.

Pectoralis minor

Attachments Pectoralis minor is a thin, triangular muscle lying posterior (deep) to pectoralis major (see Figs 49.26, 49.47). It arises from the upper margins and outer surfaces of the third to fifth ribs (frequently, second to fourth), near their cartilages, and from the fascia over the adjoining external intercostal muscles. Its fibres ascend laterally under cover of pectoralis major, converging in a flat tendon that is attached to the medial border and upper surface of the coracoid process of the scapula. Part or all of the tendon may appear to cross the coracoid process into the coraco-acromial ligament.

Variants Slips of the muscle are sometimes separated and vary in number and level. In rare cases, one passes from the first rib to the coracoid (pectoralis minimus). The costal attachments can be second to fifth ribs; third to fifth; second to fourth; or third to fourth. The muscle may be present or absent when pectoralis major is absent (in Poland's syndrome).

Relations Pectoralis major, the lateral pectoral nerve and pectoral branches of the thoraco-acromial artery are anterior. The ribs, external intercostals, serratus anterior, the axilla, axillary vessels, lymphatics and brachial plexus are all posterior. The upper border of pectoralis minor is separated from the clavicle by a triangular gap filled by the clavipectoral fascia, behind which are the axillary vessels, lymphatics and nerves. The lateral thoracic artery follows the lower border of the muscle. The medial pectoral nerves pierce and partly supply the muscle.

Vascular supply Pectoralis minor is supplied by pectoral and deltoid branches of the thoraco-acromial and superior and lateral thoracic arteries.

Innervation Pectoralis minor is innervated by branches of the medial and lateral pectoral nerves (fifth, sixth, seventh and eighth cervical and first thoracic ventral rami).

Actions Pectoralis minor assists serratus anterior in drawing the scapula forwards around the chest wall. With levator scapulae and the rhomboids, it rotates the scapula, depressing the point of the shoulder. It resists scapular rotation caused by trapezius. Both pectoral muscles are electromyographically quiescent in normal inspiration, but are active in forced inspiration.

Subclavius

Attachments Subclavius is a long, asymmetric triangular muscle between the clavicle and the first rib (Fig. 49.26). It arises from the junction of the first rib and its costal cartilage by a thick tendon, prolonged at its inferior margin and anterior to the costoclavicular ligament. It passes upwards and laterally to attach by direct muscular fibres into a groove on the undersurface of the middle third of the clavicle; the lower and most lateral fibres are the longest. Subclavius may be attached to the coracoid process or the upper border of the scapula as well as, or instead of, the clavicle.

Relations Posteriorly, subclavius is separated from the first rib by the subclavian vessels and brachial plexus; anteriorly, it is separated from pectoralis major by the anterior lamina of the clavipectoral fascia. The suprascapular artery, which has a variable pattern, descends behind the muscle, passing between it and omohyoid anteriorly and the subclavian vessels posteriorly; the artery, therefore, has a close relationship to the posterior surface of the clavicle, a feature that makes it susceptible to injury during clavicular fracture and surgical fixation.

Vascular supply Subclavius is supplied by the clavicular branch of the thoraco-acromial artery and the suprascapular artery.

Innervation Subclavius is supplied by the nerve to subclavius (fifth and sixth cervical ventral rami). It seems reasonable to assume that a muscle, however apparently insubstantial, that has a unique, solitary nerve supply must have an important function; subclavius is no exception (see above and below).

Actions Subclavius resists accelerated elevation and rotation of the clavicle during elevation of the shoulder girdle, and may help to close-pack the medial end of the clavicle against the articular disc of the sternoclavicular joint for greater stability under load. It is inaccessible to palpation and difficult to investigate by electromyography. Incidentally, it ‘protects’ the subclavian vessels and brachial plexus that lie behind it.

Muscles of scapular motion

Levator scapulae

Attachments Levator scapulae is a slender muscle attached by tendinous slips to the transverse processes of the atlas and axis, and to the posterior tubercles of the transverse processes of the third and fourth cervical vertebrae (see Figs 35.6, 49.25–49.26). It descends diagonally to attach to the medial scapular border between its superior angle and the triangular smooth surface at the medial end of the scapular spine.

Variants Levator scapulae varies considerably in its vertebral attachments and the extent to which it separates into slips. There may be accessory attachments to the mastoid process, occipital bone, first or second rib, the scaleni, trapezius and the serratus muscles.

Vascular supply Levator scapulae receives its arterial supply mainly from the transverse cervical and ascending cervical arteries. The vertebral extremity of the muscle is supplied by branches from the vertebral artery.

Innervation Levator scapulae is innervated directly by branches of the third and fourth cervical spinal nerves, and from the fifth cervical nerve via the dorsal scapular nerve.

Actions Levator scapulae elevates the superior angle of the scapula. If unopposed, this causes a lateral rotation of the scapula. With the cervical vertebral column fixed, levator scapulae acts with trapezius to elevate the scapula or to sustain a weight carried on the shoulder; with the shoulder fixed, the muscle inclines the neck to the same side.

Rhomboid minor

Attachments Rhomboid minor is a small, cylindrical muscle. It runs from the lower ligamentum nuchae and the spines of the seventh cervical and first thoracic vertebrae to the base of a smooth triangular surface at the medial end of the spine of the scapula, where dorsal and ventral layers enclose the inferior border of levator scapulae (see Fig. 49.25). The dorsal layer of rhomboid minor is attached to the rim of the triangular surface, dorsolateral to and below levator scapulae. The ventral layer is strong and wide, extending 2–3 cm medial to and below levator scapulae; here, the fasciae of rhomboid minor and serratus anterior are fused. Rhomboid minor is usually separate from rhomboid major, but the muscles overlap and are occasionally united.

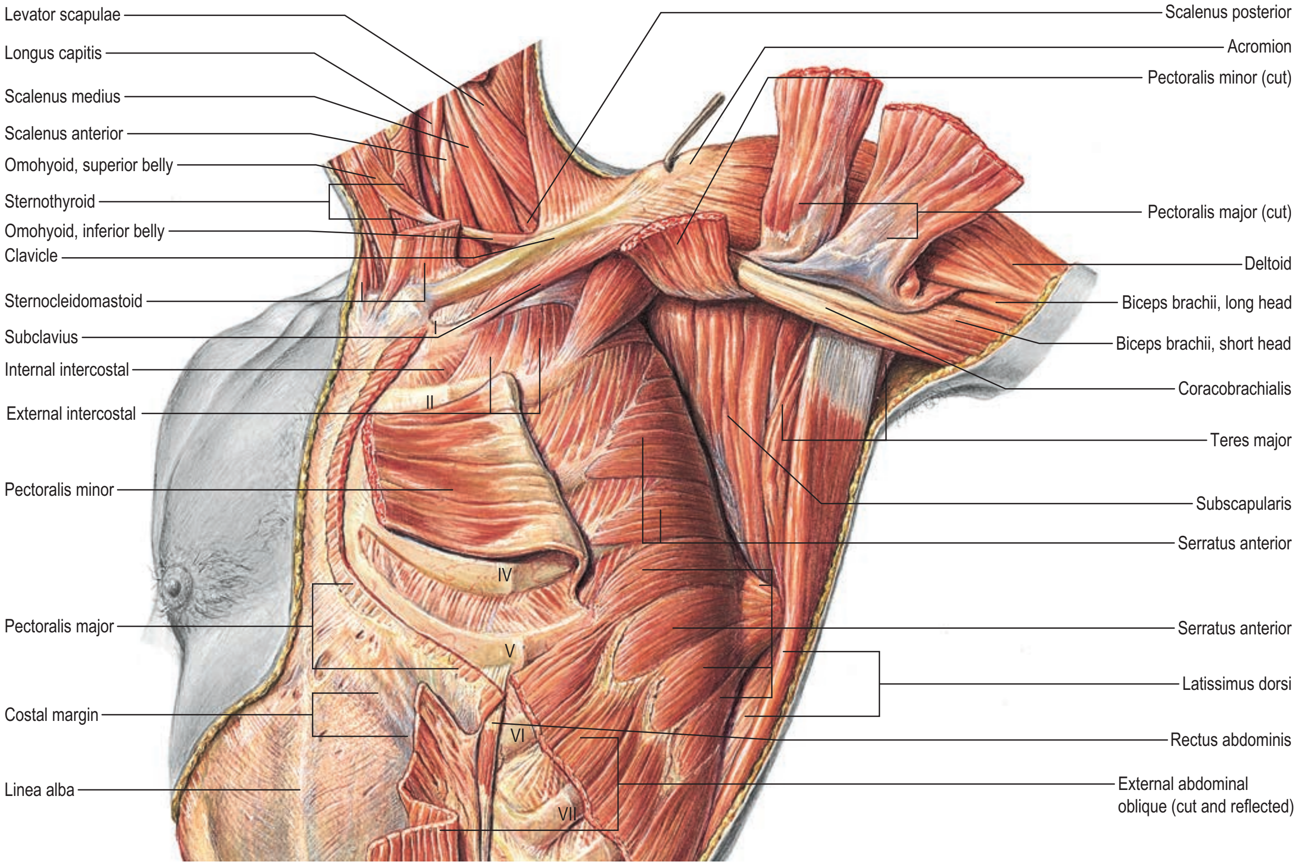
Levator scapulae
Longus capitis
Scalenus medius
Scalenus anterior
Omohyoid, superior belly
Sternothyroid
Omohyoid, inferior belly
Clavicle
Sternocleidomastoid
Subclavius
Internal intercostal
External intercostal
Pectoralis minor
Pectoralis major
Costal margin
Linea alba
Scalenus posterior
Acromion
Pectoralis minor (cut)
Pectoralis major (cut)
Deltoid
Biceps brachii, long head
Biceps brachii, short head
Coracobrachialis
Teres major
Subscapularis
Serratus anterior
Serratus anterior
Latissimus dorsi
Rectus abdominis
External abdominal oblique (cut and reflected)
I
II
IV
V
VI
VII

Fig. 49.26 The deep muscles of the chest and left shoulder girdle, anterior aspect. Roman numerals refer to costal cartilages. (Sobotta Atlas of Human Anatomy © Elsevier GmbH, Urban & Fischer, Munich.)

Variants There is some variability in the vertebral and scapular attachments of rhomboids major and minor. A slip of muscle may extend from the upper border of rhomboid minor to reach the occipital bone (rhomboid occipitalis).

Rhomboid major

Attachments Rhomboid major is a quadrilateral sheet of muscle that arises by tendinous fibres from the spines and supraspinous ligaments of the second to fifth thoracic vertebrae, and descends laterally to the medial border of the scapula between the root of the spine and the inferior angle (see Fig. 49.25). Most of its fibres usually end in a tendinous band between these two points, joined to the medial border by a thin membrane. Occasionally, this is incomplete, in which case some muscular fibres are attached directly into the scapula. The attachments of rhomboid major (and also those of rhomboid minor, levator scapulae and serratus anterior) may be more extensive, with 'folds' or extensions passing to both dorsal and costal aspects of the scapula adjacent to its medial margin.

Vascular supply of the rhomboids Rhomboids major and minor are supplied by the dorsal scapular artery or the deep branch of the transverse cervical artery and by dorsal perforating branches from the upper five or six posterior intercostal arteries.

Innervation of the rhomboids Rhomboids major and minor are innervated by a branch of the dorsal scapular nerve (fourth and fifth cervical ventral rami).

Actions of the rhomboids Both rhomboid major and rhomboid minor retract the medial border of the scapula superiorly and medially, and are used in retraction of the shoulders.

Testing of the rhomboids Rhomboids major and minor can be palpated deep to trapezius on bracing the shoulder back against resistance with the arm in elevation at shoulder level.

Serratus anterior

Attachments Serratus anterior is a large muscular sheet that curves around the thorax. It arises from an extensive costal attachment and inserts on the scapula (see Figs 49.25–49.26). Fleshy digitations arise anteriorly from the outer surfaces and superior borders of the upper eight to ten ribs, and from fasciae that cover the intervening intercostal muscles. The line of origin of the muscle is long and slightly curved, and passes inferolaterally around the thorax. There are three parts: the upper fibres arise from the first and second ribs and intercostal fascia, the middle fibres arise from the third to sixth ribs, and the lower fibres interdigitate with the upper five slips of external oblique. The muscle follows the contour of the chest wall closely, reaching the medial border of the scapula anterior to subscapularis. The first (uppermost) digitation encloses, and is attached to, a triangular area of both the costal and the dorsal surfaces of the superior scapular angle. The next two or three digitations form a triangular sheet that is attached to the costal surface along almost its entire medial border. The lower four or five digitations converge to be attached by musculotendinous fibres to a triangular impression on the costal surface of the inferior angle; they enclose the inferior angle and are also attached to a smaller triangular part of its dorsal surface near its tip.

Variants Digitations may be absent, particularly the first and eighth, and sometimes also the intermediate part. Serratus anterior may be partly fused with levator scapulae, adjacent external intercostals or external oblique.

Vascular supply Serratus anterior is supplied by superior and lateral thoracic arteries, and by branches from the thoracodorsal artery before (occasionally, after) it divides in latissimus dorsi.

Innervation Serratus anterior is innervated by the long thoracic nerve (fifth, sixth and seventh cervical ventral rami), which descends on the external surface of the muscle.

Actions With pectoralis minor, serratus anterior protracts (draws forwards) the scapula, as a prime mover in all reaching and pushing movements. The upper part, with levator scapulae and the upper fibres of trapezius, suspends the scapula; only slight activity is sufficient to support the unloaded arm. The more extensive lower insertion pulls the inferior scapular angle forwards around the thorax, assisting trapezius in upward rotation of the bone, an action that is essential to raising the arm above the head. In the initial stages of abduction, serratus anterior helps other muscles to fix the scapula, so that deltoid acts effectively on the humerus and not the scapula. While deltoid is raising the arm to a right-angle with the scapula, serratus anterior and trapezius are simultaneously rotating the scapula; the combination allows the arm to be raised to the vertical. To effect this upward rotation of the scapula, forward pull on the inferior angle by the lower digitations of serratus anterior is coupled with an upward and medial pull on the lateral end of the clavicle and acromion by the upper fibres of trapezius, and a downward pull on the base of the scapular spine by the lower fibres of trapezius. Conversely, slow downward scapular rotation, assisted by gravity, is achieved by controlled lengthening of these muscles. More powerful downward rotation requires balanced contraction of the upper fibres of serratus anterior, levator scapulae, rhomboids, pectoralis minor and the middle part of trapezius. When weights are carried in front of the body, serratus anterior prevents backward rotation of the scapula. Electromyography shows that serratus anterior is not active in normal human respiration. This may not apply to laboured respiration, e.g. when asthmatics and athletes may be observed to fix the scapula by grasping a rail or other support.

Testing The muscular digitations of serratus anterior can be seen and felt when the outstretched hand pushes against resistance.

When serratus anterior is paralysed, the medial border of the scapula, and especially its lower angle, stand out prominently. The arm cannot be raised fully. Pushing is ineffective; indeed, attempts to do so produce further projection, known as 'winging' of the scapula (Streit et al 2012; see Fig. 49.39).

Serratus posterior superior

Serratus posterior superior is described on page 1008.

Serratus posterior inferior

Serratus posterior inferior is described on page 1008 (see Fig. 49.25).

Muscles of thoracobrachial motion

The large muscles from the trunk to the arm, and from the scapula to the arm, act on the shoulder joint. Pectoralis major and latissimus dorsi are attached to the metaphysis of the humerus below the centre of rotation of the joint, while deltoid and coracobrachialis are attached to the midpoint of the diaphysis or shaft, some way from the centre of rotation of the shoulder joint. These four muscles move the arm in relation to the shoulder joint, so that, although they act through the shoulder joint, their role is to position the elbow joint (and, thus, the hand) in space. The continuous sheet of muscle that is pectoralis major and deltoid positions the elbow through a wide, asymmetrical, conical range of motion from adduction across the trunk with medial rotation, through flexion, abduction and external rotation, into extension at the shoulder. The cervical spinal segmental levels at which this range of movement is represented, C5 and C6, give rise to the anterior division innervation to pectoralis major (thus, pre-axial or predominantly flexor muscles) and the posterior division innervation (thus, post-axial or predominantly extensor muscles) to deltoid. Similarly, coracobrachialis (a flexor and adductor of the abducted arm) is innervated through the anterior division of C5, C6 and (predominantly) C7 segmental levels, while latissimus dorsi is innervated through the posterior division of C6, C7 and C8 (predominantly C7). These are examples of the *movements* of a joint, rather than individual muscles, being subserved in a biologically efficient manner by the minimum number of spinal segmental levels required to achieve the aim of positioning the elbow in space, while maintaining subtlety in effect.

Pectoralis major

Attachments Pectoralis major is a thick, fan-shaped muscle. It arises from the anterior surface of the sternal half of the clavicle (clavicular head); half the breadth of the anterior surface of the sternum down to the level of the sixth or seventh costal cartilage (sternal head); the first to the seventh costal cartilages (first and seventh often omitted); the sternal end of the sixth rib; and the aponeurosis of external oblique (rectus head) (**Fig. 49.27**). The clavicular fibres are usually separated from the sternal fibres by a slight cleft. The muscle converges to a flat tendon, approximately 5 cm wide, that is attached to the lateral lip of the intertubercular sulcus of the humerus. The tendon is bilaminar. The thicker anterior lamina is formed by fibres from the manubrium, joined superficially by clavicular fibres and deeply by fibres from the sternal margin and the second to fifth costal cartilages. Clavicular fibres may be prolonged into the tendon of deltoid. The posterior lamina receives fibres from the sixth (and, often, seventh) costal cartilages, sixth rib, sternum, and aponeurosis of external oblique. Costal fibres join the lamina without twisting. Fibres from the sternum and aponeurosis curve around the lower border, turning successively behind those above them, which means that this part of the muscle is twisted so that the fibres that are lowest at their medial origin are highest at their attachment on the humerus. The posterior lamina reaches higher on the humerus than the anterior, and gives off an expansion that covers the intertubercular sulcus and blends with the capsular ligament of the shoulder joint. An expansion from the deepest part of the lamina lines the intertubercular sulcus at its linear insertion; another expansion descends from its lower border into the deep fascia of the upper arm.

The rounded lower border of pectoralis major forms the anterior axillary fold and becomes conspicuous in abduction against resistance.

Variants The abdominal slip from the aponeurosis of external oblique is sometimes absent. The number of costal attachments and the extent to which the clavicular and costal parts are separated vary. Right and left muscles may decussate across the sternum. A superficial vertical slip, or slips, may ascend from the lower costal cartilages and rectus sheath to blend with sternocleidomastoid or to attach to the upper sternum or costal cartilages. This is sternalis (rectus sternalis).

Relations Skin, superficial fascia, platysma, medial and intermediate supraclavicular nerves, breast tissue and deep fascia are all anterior. The sternum, ribs and costal cartilages, clavipectoral fascia, subclavius, pectoralis minor, serratus anterior, external intercostal muscles and membranes are all posterior. Pectoralis major forms the superficial layer of the anterior axillary wall, and hence lies anterior to the axillary vessels and nerves and the upper parts of biceps brachii and coracobrachialis. Its upper border is separated from deltoid by the infraclavicular fossa, which contains the cephalic vein and deltoid branch of the thoraco-acromial artery. Pectoralis major is separated from latissimus dorsi on the medial axillary wall but the two muscles converge as they approach the lateral axillary wall; the floor of the intertubercular sulcus lies between their attachments.

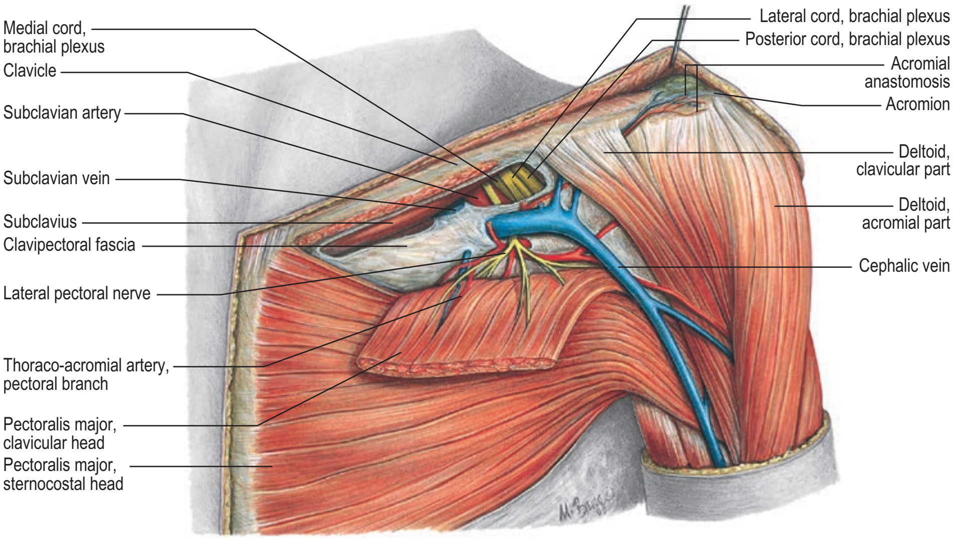
Medial cord, brachial plexus
Clavicle
Subclavian artery
Subclavian vein
Subclavius
Clavipectoral fascia
Lateral pectoral nerve
Thoraco-acromial artery, pectoral branch
Pectoralis major, clavicular head
Pectoralis major, sternocostal head
Lateral cord, brachial plexus
Posterior cord, brachial plexus
Acromial anastomosis
Acromion
Deltoid, clavicular part
Deltoid, acromial part
Cephalic vein

Fig. 49.27 The left deltopectoral groove, dissected to show the clavipectoral fascia and thoraco-acromial axis. (Sobotta Atlas of Human Anatomy © Elsevier GmbH, Urban & Fischer, Munich.)

Vascular supply Pectoralis major is supplied by one dominant vascular pedicle from the pectoral branch of the thoraco-acromial axis, supplemented by several smaller secondary segmental vessels from the deltoid and clavicular branches of the thoraco-acromial axis, and perforating branches of the internal thoracic arteries and superior and lateral thoracic arteries.

Innervation Pectoralis major is supplied through the medial and lateral pectoral nerves. Fibres for the clavicular part are derived from the fifth and sixth cervical ventral rami; those for the sternocostal part are derived from the seventh and eighth cervical ventral rami and first thoracic ventral ramus.

Actions The two parts of pectoralis major can act separately or together. The whole muscle assists adduction and medial rotation of the humerus against resistance. It swings the extended arm forwards and medially, its clavicular part acting with the anterior fibres of deltoid and coracobrachialis; the sternocostal part is relaxed. The opposite movement is usually aided by gravity. When it is resisted, the sternocostal part acts together with latissimus dorsi, teres major and the posterior fibres of deltoid; the clavicular part is relaxed. With the raised arms fixed, e.g. gripping a branch, the same combination of muscles draws the trunk up and forwards. Pectoralis major is active in deep inspiration.

Testing To test the clavicular head, the abducted arm is flexed against resistance. To test the sternocostal head, the arm is adducted against resistance.

Poland's syndrome

Available with the *Gray's Anatomy* e-book

Chondro-epitrochlearis Chondro-epitrochlearis is a rare extra 'head' of pectoralis major, arising deep to the sternal and rectus components of that muscle from the anterior aspect of the fifth, sixth and seventh ribs and their costal cartilages, and in the same plane as pectoralis minor.

Deltoid

Attachments Deltoid is a thick, curved triangle of muscle. It arises from the anterior border and superior surface of the lateral third of the clavicle, the lateral margin and superior surface of the acromion, and the lower edge of the crest of the scapular spine (other than its smooth, medial, triangular surface) (see Figs 49.25, 49.27). The fibres converge inferiorly to a short, substantial tendon that has an extensive attachment which envelops the deltoid tubercle on the lateral aspect of the midshaft of the humerus. Anterior and posterior fibres converge directly to this tendon. The intermediate part is multipennate; four intramuscular septa descend from the acromion to interdigitate with three septa ascending from the deltoid tubercle. The septa are connected by short muscle fibres that provide powerful traction (Leijnse et al 2008). The fasciculi are large, producing a coarse longitudinal striation. The muscle surrounds the glenohumeral articulation on all sides, except inferomedially, giving the shoulder its rounded profile. In contraction, its borders are easily seen and felt. The tendon gives off an expansion into the brachial deep fascia that may reach the forearm.

Variants Deltoid may fuse with pectoralis major or may receive additional slips from trapezius, the infraspinous fascia or the lateral scapular border. Teres minor shares a common innervation and could be considered as a fourth, posteroinferior part of deltoid.

Relations The skin, superficial and deep fasciae, platysma, lateral supraclavicular and upper lateral brachial cutaneous nerves are all superficial. The coracoid process, coraco-acromial ligament, subacromial bursa, tendons of pectoralis minor, coracobrachialis, both heads of biceps brachii, pectoralis major, subscapularis, supraspinatus, infraspinatus, teres minor, long and lateral heads of triceps, circumflex humeral vessels, axillary nerve, and the surgical neck and upper shaft of the humerus, including both tubercles, are all deep. The anterior border of deltoid is separated from pectoralis major proximally by the infraclavicular fossa, which contains the cephalic vein and deltoid branches of the thoraco-acromial artery; distally, these muscles are in contact. The posterior border of deltoid overlies infraspinatus and triceps.

Vascular supply Deltoid is supplied by acromial and deltoid branches of the thoraco-acromial artery; the anterior and posterior circumflex humeral arteries; subscapular artery; and the deltoid branch of profunda brachii.

Innervation Deltoid is innervated by the axillary nerve (fifth and sixth cervical ventral rami).

Actions The deltoid moves the upper limb around the centre of rotation of the glenohumeral joint. Different parts of the muscle can act independently, as well as together. Anterior fibres assist pectoralis major in drawing the arm forwards and rotating it medially. Posterior fibres act as external rotators, and act with latissimus dorsi and teres major in drawing the arm backwards (into extension). The posterior fibres of deltoid provide up to 80% of the external rotation power of the arm when elevated into the plane of the scapula. The multipennate, acromial, part of deltoid is a strong abductor; aided by supraspinatus, it abducts the arm until the inferior joint capsule is tight. Movement takes place in the plane of the body of the scapula, which is the only way that scapular rotation can be fully effective in raising the arm above the head. In true abduction, acromial fibres contract strongly, while clavicular and posterior fibres prevent departure from the plane of motion. In the early stages of abduction, traction on the humerus by deltoid would displace the arm upward, but the humeral head is prevented from translating upward by the synergistic centralizing effect of the rotator cuff muscles (supraspinatus, subscapularis, infraspinatus and teres minor). Electromyography suggests that deltoid contributes little to unresisted medial (internal) or lateral (external) rotation but confirms that it takes part in most other shoulder movements, particularly when resisted, for instance when lifting a weight.

Testing Deltoid can be seen and felt to contract when the arm is abducted against resistance in the scapular plane. Since this motion can also be achieved by supraspinatus, a more specific test for the activity of deltoid is to assess extension against resistance with the arm in 30° abduction in the scapular plane: this reduces the confounding effect of latissimus dorsi and triceps as extensors of the adducted arm. Subtle weakness can be determined using the deltoid lag sign (Hertel et al 1998).

Coracobrachialis

Coracobrachialis is the most medial of the three anterior compartment muscles of the arm. It has a common origin with the short head of biceps brachii. In turn, the short head of biceps shares a common distal attachment with the long head of biceps. The three anterior compartment muscles, therefore, form a single functional group that brings the supinated hand into flexion and medial rotation, towards the face.

Attachments Coracobrachialis arises from a muscular origin on the deep surface of the apex of the coracoid process, deep to the tendon of the short head of biceps brachii, and by muscular fibres from the proximal 5–10 cm of this tendon. It ends on an impression, 3–5 cm in length, midway along the medial border of the humeral shaft between the attachments of the medial head of triceps and brachialis (**Fig. 49.28**), and opposite the insertion of deltoid. Accessory slips may be attached to the lesser tubercle, medial epicondyle or medial intermuscular septum.

Relations Coracobrachialis forms an inconspicuous rounded ridge on the upper medial side of the arm; pulsation of the brachial artery can be felt and often seen in the depression behind it. The muscle is perforated and supplied by the musculocutaneous nerve. Anteriorly, it is related to pectoralis major above and, at its humeral insertion, to the brachial vessels and median nerve, which cross it. The tendons of subscapularis, latissimus dorsi, teres major, the medial head of triceps, the humerus and the circumflex humeral vessels are all posterior. The third part of the axillary artery and proximal parts of the median and musculocutaneous nerves are first medial and become posterior further distally; they may be partially obscured by the muscle if it is bulky. Biceps brachii and brachialis are lateral.

Vascular supply One or more branches from the axillary artery pass deep to the lateral root of the median nerve and the musculocutaneous nerve to reach the deep surface of coracobrachialis. Branches from the anterior circumflex humeral artery supply the deep surface of the muscle. The artery accompanying the musculocutaneous nerve sends a recurrent branch to the coracoid attachment and gives off a series of branches to coracobrachialis during its intramuscular course. Accessory branches from the thoraco-acromial artery supply the superficial part of coracobrachialis.

Innervation Coracobrachialis is innervated by the musculocutaneous nerve (fifth, sixth and seventh cervical ventral rami), the motor nerve to the anterior (flexor) compartment of the upper arm.

Actions Deltoid and coracobrachialis insert into the humerus approximately opposite each other. Coracobrachialis acts as an antagonist to

Poland's syndrome is a rare congenital anomaly, in which there is hypoplasia of the thoracic chest wall muscles and ipsilateral hypoplasia of the arm and hand. It occurs in approximately 1 : 50,000 live births. The major clinical feature is absence of the sternocostal head of pectoralis major and all of pectoralis minor. In addition, there may be hypoplasia of latissimus dorsi, serratus anterior, external oblique, supraspinatus, infraspinatus, deltoid and the intercostal muscles, and hypoplasia of the hemithorax and ribs. Hypoplasia affecting the arm ranges from syndactyly to symbrachydactyly and ectrodactyly. The second, third and fourth fingers are the most affected; the wrist, forearm, upper arm and scapula are variably involved. There may be ipsilateral breast hypoplasia and absent nipple–areolar complex.

The aetiology is unclear. Rib primordia are seen from stage 15 (35–36 postfertilization days) extending laterally and ventrally into hypaxial muscle sheets in the developing chest wall: anomalous vertebral development and other causes of pectoral aplasia would be initiated before this time. It has been suggested that the musculoskeletal anomalies reflect interruption of the early embryonic blood supply in the subclavian and vertebral arteries and/or their branches, during or around the sixth week of development (stages 15–17), the so-called subclavian artery supply disruption sequence (SASDS) (Bavinck and Weaver 1986).

The muscle has an extensive attachment to the lateral crest of the intertubercular sulcus, the medial intermuscular septum and the medial epicondylar ridge. It is innervated by branches of the lateral pectoral nerve that perforate pectoralis minor or pass to the muscle in the plane between pectoralis minor and major. It is noted as a pterygium deep to the anterior axillary wall with a sharply defined inferior border in the axilla, made more noticeable by flexion and medial rotation against resistance with the arm elevated into the scapular plane. With the arm in the elevated position, contraction of the muscle causes a retropulsion of the glenohumeral joint, a rare cause of posterior glenohumeral instability.

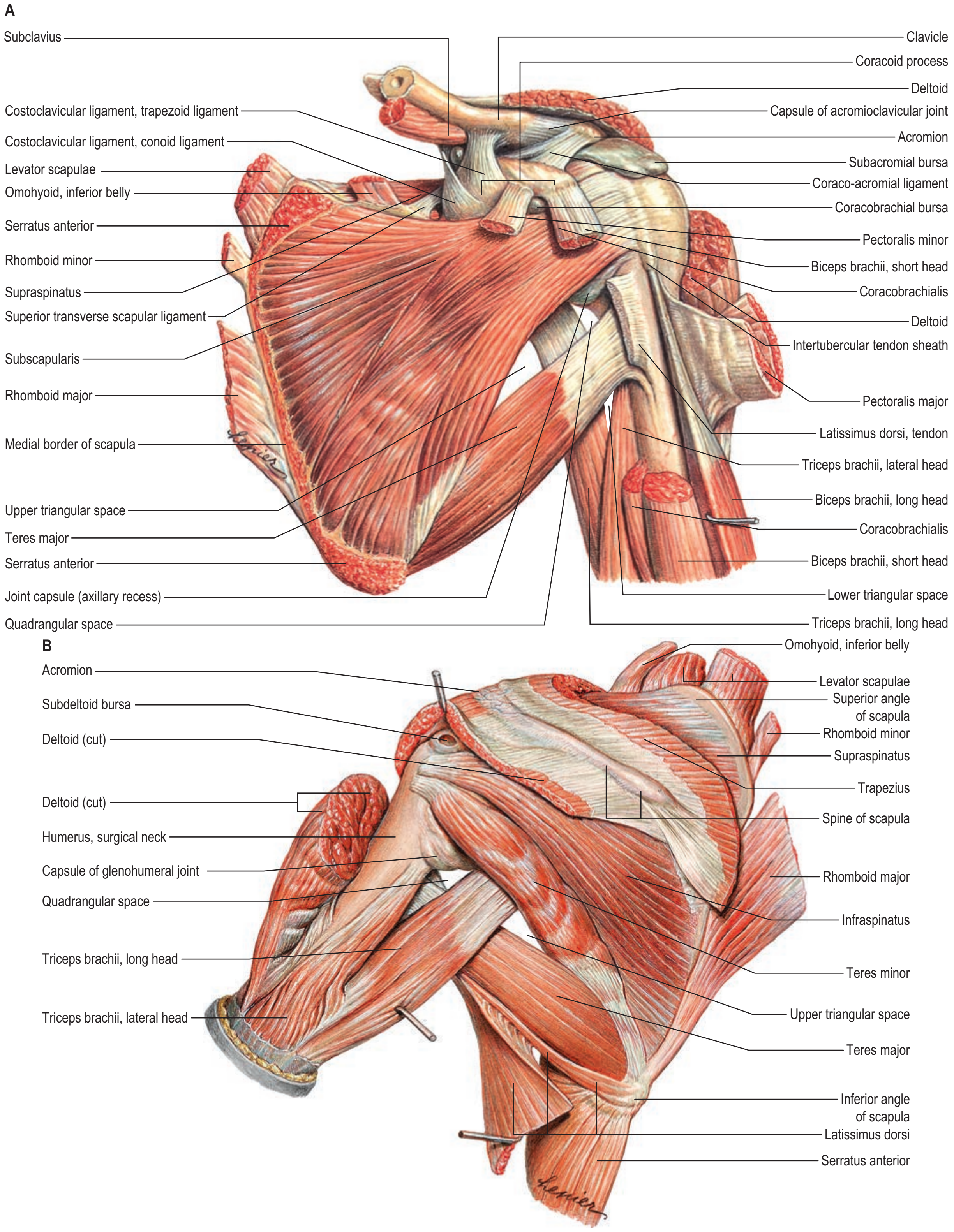
A
Subclavius
Costoclavicular ligament, trapezoid ligament
Costoclavicular ligament, conoid ligament
Levator scapulae
Omohyoid, inferior belly
Serratus anterior
Rhomboid minor
Supraspinatus
Superior transverse scapular ligament
Subscapularis
Rhomboid major
Medial border of scapula
Upper triangular space
Teres major
Serratus anterior
Joint capsule (axillary recess)
Quadrangular space
Clavicle
Coracoid process
Deltoid
Capsule of acromioclavicular joint
Acromion
Subacromial bursa
Coraco-acromial ligament
Coracobrachial bursa
Pectoralis minor
Biceps brachii, short head
Coracobrachialis
Deltoid
Intertubercular tendon sheath
Pectoralis major
Latissimus dorsi, tendon
Triceps brachii, lateral head
Biceps brachii, long head
Coracobrachialis
Biceps brachii, short head
Lower triangular space
Triceps brachii, long head
B
Acromion
Subdeltoid bursa
Deltoid (cut)
Deltoid (cut)
Humerus, surgical neck
Capsule of glenohumeral joint
Quadrangular space
Triceps brachii, long head
Triceps brachii, lateral head
Omohyoid, inferior belly
Levator scapulae
Superior angle of scapula
Rhomboid minor
Supraspinatus
Trapezius
Spine of scapula
Rhomboid major
Infraspinatus
Teres minor
Upper triangular space
Teres major
Inferior angle of scapula
Latissimus dorsi
Serratus anterior

Fig. 49.28 The deep muscles of the left shoulder girdle. **A**, The anterior aspect after removal of the superficial muscles. **B**, Posterior aspect. (Sobotta Atlas of Human Anatomy © Elsevier GmbH, Urban & Fischer, Munich.)

the action of deltoid, particularly when the arm is in abduction and extension; it flexes the arm forwards and medially. In abduction, it acts with the anterior fibres of deltoid to resist departure from the plane of motion.

Testing Coracobrachialis can be tested by palpating its fibres during adduction and medial rotation of the flexed shoulder against resistance. Alternatively, the muscle can be palpated during forceful depression of the elbow against resistance or with the arm by the side.

Latissimus dorsi

Attachments Latissimus dorsi is a large, flat, triangular muscle that sweeps over the lumbar region and lower thorax, and converges to a narrow tendon (see Fig. 49.25). It arises by tendinous fibres from the spines of the lower six thoracic vertebrae anterior to trapezius; from the posterior layer of thoracolumbar fascia, by which it is attached to the spines and supraspinous ligaments of the lumbar and sacral vertebrae; and from the posterior part of the iliac crest. It also springs by muscular fibres from the posterior part (outer lip) of the iliac crest lateral to erector spinae, and by fleshy slips from the three or four lower ribs, interdigitating with external oblique (see Fig. 60.2). From this extensive attachment, fibres pass laterally with different degrees of obliquity (the upper fibres are nearly horizontal, the middle oblique and the lower almost vertical), to form a sheet 12 or 13 mm thick that overlaps the inferior scapular angle, and may attach to it. The muscle curves around the inferolateral border of teres major to gain its anterior surface and ends as a flattened tendon, up to 7 cm long, anterior to the tendon of teres major. It is attached to the floor of the intertubercular sulcus of the humerus with an expansion to the deep fascia (Dancker 2013). The attachment extends higher on the humerus than that of teres major. As the muscle curves round teres major, the fasciculi rotate around each other, so that fibres that originate lowest at the midline insert highest on the humerus, and fibres that originate highest at the midline insert lowest on the humerus. A bursa sometimes occurs between the muscle and the inferior scapular angle. The tendons of latissimus dorsi and teres major are united at their lower borders but separated by a bursa near their humeral attachments.

Latissimus dorsi and teres major together form the posterior axillary fold. When the arm is adducted against resistance, this fold is accentuated, and the whole inferolateral border of latissimus dorsi can be traced to its attachment to the iliac crest. The radial nerve and the branch or branches it supplies to the medial head of triceps are close anterior relations of the tendon of the latissimus dorsi, 3–5 cm medial to the shaft of the humerus, before the radial nerve traverses the lower triangular space and passes into the posterior compartment of the arm (see quadrangular and triangular spaces below).

The lower, lateral margin of latissimus dorsi is usually separated from the posterior border of external oblique by the lumbar triangle. The base of this small triangle is the iliac crest and its floor the internal oblique; it should not be confused with the triangle of auscultation, medial to the scapula, which is bounded above by trapezius, below by latissimus dorsi and laterally by the medial border of the scapula. Part of rhomboid major is exposed in the triangle. If the scapulae are drawn forwards, by folding the arms across the chest, and the trunk is bent forwards, parts of the sixth and seventh ribs and the interspace between them (overlying the apex of the lower pulmonary lobe) become subcutaneous.

Variants Latissimus dorsi commonly receives some additional fibres from the scapula as it crosses the inferior scapular angle. A muscular axillary arch, 7–10 cm in length and 5–15 mm in breadth, may sometimes be present; it crosses from the edge of latissimus dorsi, midway in the posterior fold, and passes anterior to the axillary vessels and nerves to join the tendons of pectoralis major, coracobrachialis or the fascia over biceps brachii. The vertebral and costal attachments of latissimus dorsi may be reduced or, in rare cases, increased. A fibrous slip usually passes from the tendon, near its humeral insertion, to the long head of triceps.

Vascular supply Latissimus dorsi is supplied by a single dominant vascular pedicle, the thoracodorsal artery, itself a continuation of the subscapular artery. The thoracodorsal artery and its accompanying venae comitantes enter the muscle at a single neurovascular hilum on its costal surface, 6–12 cm from the subscapular artery and 1–4 cm medial to the lateral border of the muscle. The artery gives off up to three large branches to serratus anterior before dividing at, or even before, the neurovascular hilum for latissimus dorsi. The basic pattern of branching is a bifurcation into lateral and medial branches. The larger lateral branch follows a course parallel to, and 1–4 cm from, the upper border of the muscle; the smaller branch diverges at an angle of 45° and travels medially. In a small number of cases, the artery trifurcates. This usually yields a small recurrent branch that returns to supply the proximal part of the muscle but, in some cases, it provides a third major branch that supplies the distal part of the muscle. Occasionally, the lateral branch gives off a further collateral to serratus anterior. The major branches give off 5–9 longitudinal branches that travel distally, parallel with the muscle fibres. Musculocutaneous perforators arising from these vessels supply the overlying skin.

In addition to the dominant vascular pedicle, latissimus dorsi is supplied inferiorly by several smaller, secondary, segmental vascular pedicles. These are dorsal perforating arteries derived from the ninth, tenth and eleventh posterior intercostal arteries and the first, second and third lumbar arteries. They all enter the muscle on its deep surface and anastomose within the muscle with branches of the thoracodorsal artery.

Innervation Latissimus dorsi is supplied by the thoracodorsal nerve, from the posterior cord of the brachial plexus (sixth, seventh and eighth cervical ventral rami, predominantly from the seventh cervical ventral ramus). This nerve runs in the neurovascular pedicle and divides approximately 1.5 cm proximal to the point of bifurcation or trifurcation of the thoracodorsal artery. The neural and vascular branches travel together and so the pattern of branching of the nerve follows that of the artery closely.

Actions Latissimus dorsi is active in adduction, extension and, especially, in medial rotation of the humerus. Humeral adduction and extension are most powerful when the initial position of the arm is one of partial abduction or flexion, or a combination of the two. With the sternocostal part of pectoralis major and teres major, it adducts the raised arm against resistance. When the arms are raised above the head, as in climbing, it pulls the trunk upwards and forwards. It takes part in all violent expiratory efforts, such as coughing or sneezing; this is readily confirmed by palpation. Electromyography suggests that latissimus dorsi aids deep inspiration, but it is also active towards the end of forcible expiration, e.g. when blowing a sustained note on a musical instrument. When the arm is elevated, the stretched fibres of latissimus dorsi press on the inferior scapular angle (to which it may also be attached), keeping it in contact with the chest wall. Despite this range of actions, surgical transposition of the muscle does not appear to produce any serious measurable restrictions of normal activity.

Testing Latissimus dorsi is palpated on the lateral chest wall when the abducted arm is adducted against resistance, and can be felt to contract during coughing. The rounded muscular posterior wall of the axilla is formed by teres major, not latissimus dorsi.

Muscles of concavity compression

The function of the rotator cuff muscles is to generate a concavity compressive force in all positions of the arm at the shoulder. The term ‘rotator cuff’ is conventionally taken to mean the tendinous parts of the four rotator cuff muscles: subscapularis, supraspinatus, infraspinatus and teres minor. Since teres minor, parts of infraspinatus and most of subscapularis do not have tendons, this use of the term excludes important parts of the rotator cuff apparatus. In this description, the term ‘rotator cuff’ will be used to define the entire musculotendinous apparatus that centralizes the humeral head on the glenoid. The tendons of the rotator cuff will be referred to specifically.

It is maintained that the inferior capsule of the glenohumeral joint is exposed as a weak part of the capsule, and so predisposed to injury (dislocation). However, in elevation of the arm above 90°, the bulk of teres major forms a muscular buttress to the lower part of the joint and, in this position, clearly draws the humeral head into the glenoid, i.e. it has a centralizing effect. Teres major is a part of the centralizing function of the rotator cuff, and should be considered together with the conventional definition of the rotator cuff.

The mechanism of the rotator cuff has been likened to that of the fibrous ‘endoskeleton’ of the heart, in which the muscular chambers are constructed around the fibrous architecture of the valvular system, and muscle contraction is centralized on this fibrous support. The muscles of the rotator cuff are attached to their tendons in a similar manner: the fibrous architecture of the tendons provides a framework for the action of the rotator cuff so that it always generates a centralizing force on the glenoid (Gagey et al 1993).

The muscles of the rotator cuff combine in three groups (subscapularis and teres major, supraspinatus and infraspinatus, and teres minor) by virtue of their innervation. Subscapularis and teres major are innervated through the subscapular nerves (C5–7, posterior division, posterior cord); supraspinatus and infraspinatus by the suprascapular nerve (C5, C6, upper trunk); and teres minor by the axillary nerve (C5, C6, posterior division, posterior cord). The common origin of their innervation suggests a common final action, namely the generation of the centralizing compression force. In functional terms, supraspinatus and infraspinatus can be considered as one muscle on the grounds that they have the same innervation and the same vascular supply; their attachment to the scapula is a continuum broken only by the spine of scapula for the attachment of trapezius; and their actions are complementary.

Supraspinatus

Attachments Supraspinatus arises from the medial two-thirds of the supraspinous fossa and from the supraspinous fascia (see Fig. 49.28B). The fibres converge, under the acromion, into a thick tendon that passes obliquely through the muscle, crosses above the humeral head, and is attached to the highest facet of the greater tubercle of the humerus. The tendon has a posterior, flatter, component closer to the facet of attachment. The anterior, obliquely directed fibres of supraspinatus are inserted into the anterior aspect of the thick tendon; the more parallel posterior fibres are inserted into both the thick tendon and the flatter component. The thick tendon is contiguous with the transverse humeral and coracohumeral ligaments and forms an anterior pillar to the posterosuperior part of the rotator cuff. The deep surface of the tendon blends into the articular capsule over its distal 1 cm. Fibrocartilage has been described at the tendinous insertion, as in other tendons attached to epiphysial bone.

Vascular supply Supraspinatus is supplied by the suprascapular and dorsal scapular arteries.

Innervation Supraspinatus is innervated by the suprascapular nerve (fifth and sixth cervical ventral rami).

Actions The conventional view is that supraspinatus initiates abduction of the shoulder and assists deltoid in abduction thereafter. However, there is evidence that both supraspinatus and deltoid are involved throughout the range of abduction, including initiation of the movement. In complete axillary nerve lesions (complete, irreversible deltoid palsy), supraspinatus, acting with other cuff muscles, can initiate, regulate, achieve and maintain full abduction of the arm (although endurance is limited). If supraspinatus is detached, torn or paralysed, and deltoid is also paralysed, investigation and surgical exploration and repair of damaged rotator cuff tendon, muscle or nerve supply is considered important. With a functioning rotator cuff but a compromised deltoid (usually due to axillary nerve palsy) the arm is functionally adept and useful while lacking in endurance. In contrast, when the rotator cuff is functionally compromised (whether due to injury or denervation) but deltoid is normal, arm function is potentially poor because stability of the joint is adversely compromised and deltoid cannot readily function to overcome this disability, unless the diameter of the humeral head is sufficiently great to provide a form of 'pulley' for the (enhanced) action of the deltoid. Supraspinatus helps to stabilize the head of the humerus in the glenoid fossa during movements of the glenohumeral joint and when the arm is dependent, even when moderately loaded, supraspinatus assists deltoid in preventing downward displacement of the humerus.

Testing It is extremely difficult to palpate supraspinatus unless trapezius is thin. The tendon of supraspinatus is separated from the coraco-acromial ligament, acromion and deltoid by the large subacromial bursa; when this is inflamed, abduction of the shoulder joint is painful. The tendon is the most frequently torn element of the musculotendinous cuff around the shoulder joint.

Infraspinatus

Attachments Infraspinatus is a thick, triangular muscle that occupies most of the infraspinous fossa (see Fig. 49.28B). It arises by muscular fibres from the medial two-thirds of the fossa, by tendinous fibres from ridges on its surface and from the deep surface of the infraspinous fascia, by which it is separated from teres major and minor. Its fibres converge to a tendon that glides under the lateral border of the spine of the scapula, and then passes across the posterior aspect of the capsule of the shoulder joint to be attached to the middle facet on the greater tubercle of the humerus. The tendon fuses with that of supraspinatus immediately lateral to the thick lateral margin of the spine of the scapula; the fibres of the tendon decussate so that fibres of infraspinatus can be traced to the facet for supraspinatus, and vice versa (Mochizuki et al 2008). The tendon is sometimes separated from the capsule by a bursa that may communicate with the joint cavity. The tendon is flattened, but is thickened in several places, reinforcing its posterior aspect as it attaches to the middle facet. From this region, fibres passing orthogonally within the deeper substance of the tendon of infraspinatus pass forwards into supraspinatus, then pass across the rotator interval to subscapularis. This band of fibres is termed the 'cable' (Burkhart et al 1993), and it provides the mechanical link between the posterosuperior and anterior parts of the rotator cuff, thus ensuring that there is intrinsic coordination of the rotator cuff mechanism. The muscular part of infraspinatus is attached directly to the middle facet on the greater tubercle and is sometimes fused with teres minor laterally; their tendons are usually separable closer to the joint capsule.

Vascular supply Infraspinatus is supplied by the suprascapular and circumflex scapular arteries.

Innervation Infraspinatus is innervated by the suprascapular nerve (fifth and sixth cervical ventral rami).

Actions Infraspinatus is a lateral rotator of the humerus. Together with supraspinatus, subscapularis and teres minor, it helps to stabilize the head of the humerus in the glenoid fossa during shoulder movements.

Teres minor

Attachments Teres minor is a narrow, elongated muscle that arises from the upper two-thirds of a flattened strip on the dorsal surface of the scapula adjoining its lateral border, and from two aponeurotic laminae that separate it from infraspinatus and teres major (see Fig. 49.28B). It runs upwards and laterally. The upper fibres end in a short tendon (which may be absent), attached to the lowest facet on the greater tubercle of the humerus. The lower fibres are attached directly into the humerus distal to this facet and above the origin of the lateral head of triceps. The tendon passes across, and blends with, the lower posterior surface of the capsule of the shoulder joint. Teres minor may be fused with infraspinatus.

Vascular supply Teres minor is supplied by the circumflex scapular artery, which pierces the origin of the muscle as it turns upwards in the infraspinous fossa, and by the posterior circumflex humeral artery.

Innervation Teres minor is innervated by a branch of the axillary nerve that is given off the main trunk as it enters the quadrangular space (fifth and sixth cervical ventral rami).

Actions Teres minor acts as a lateral rotator and weak adductor of the humerus with the arm pendant. Together with supraspinatus, infraspinatus, subscapularis and teres major, it helps to stabilize the head of the humerus in the glenoid fossa during shoulder movements.

Subscapularis

Attachments Subscapularis is a bulky, triangular muscle that fills the subscapular fossa (see Figs 49.26, 49.28A). In its medial two-thirds, the fibres are attached to the periosteum of the costal surface of the scapula. Other fibres arise from tendinous intramuscular septa, attached to ridges on the bone, and from the aponeurosis that covers the muscle and separates it from teres major and the long head of triceps. The fibres converge laterally into a broad tendon above, which has a thickened, rounded upper margin, and is attached to the lesser tubercle of the humerus and the anterior part of the articular capsule, with a wide direct muscular attachment to the lower part of the lesser tubercle. The tendon is separated from the neck of the scapula by the large subscapular bursa, which may communicate with the shoulder joint.

Variation is unusual. A separate inferior slip (subscapularis accessorius) may pass from the lateral border of the scapula to the glenohumeral capsule or to the periosteum medial to the intertubercular sulcus of the humerus, and should be distinguished from the true infraglenoid muscle (Staniek and Brenner 2012).

Relations Subscapularis forms much of the posterior axillary wall. Its anterior surface is apposed inferomedially to serratus anterior, the axillary vessels, brachial plexus and subscapular vessels and nerves, and superolaterally to coracobrachialis and biceps. Its posterior surface is attached to the scapula and glenohumeral capsule. Its lower border contacts teres major and latissimus dorsi. Its upper border is contiguous with the capsule of the rotator interval; at the most lateral extent of the interval, the long tendon of biceps passes lateral to the attachment of subscapularis, covered by the transverse humeral ligament.

Vascular supply Subscapularis is supplied by small branches from the suprascapular, axillary and subscapular arteries.

Innervation Subscapularis is innervated by the upper and lower subscapular nerves (fifth and sixth cervical ventral rami, posterior cord).

Actions Subscapularis is a medial rotator of the humerus. Together with supraspinatus, infraspinatus, teres minor and teres major, it helps to stabilize the head of the humerus in the glenoid fossa during shoulder movements.

The attachment of teres major lies in direct continuity with the attachment of subscapularis on the lesser tubercle. The muscles lie in virtually the same plane as they approach the humerus, they share a similar innervation from the posterior cord of the brachial plexus, and perform the same actions. Like the spinati, subscapularis and teres major might be considered as a functional unit.

Teres major

Attachments Teres major is a large, thick, ovoid muscle that arises from the oval area on the dorsal surface of the inferior scapular angle, and from the fibrous septa interposed between the muscle and teres minor and infraspinatus (see Fig. 49.28A). Its fibres ascend laterally and end in a short, flat tendon, 2–5 cm long, attached to the medial lip of the intertubercular sulcus of the humerus. The tendon lies behind that of latissimus dorsi, from which it is separated by a bursa; the tendons are united along their lower borders for a short distance but are readily separated.

Variants Teres major may be fused with the scapular part of latissimus dorsi, and may send a slip to join the long head of triceps or the brachial fascia.

Vascular supply Teres major is supplied by the thoracodorsal branch of the subscapular artery on its way to latissimus dorsi and by the posterior circumflex humeral artery (Dancker 2013).

Innervation Teres major is innervated by the lower subscapular nerve (fifth, sixth and seventh cervical ventral rami).

Actions Despite its name, teres major has a nerve supply and action that is distinct from teres minor. Teres major draws the humerus backwards and rotates it medially. Electromyographic studies are equivocal about its major role in movement, but its involvement as a contributor to static posture and arm-swinging is not contested. In the elevated arm, teres major both supports the inferior glenohumeral joint capsule and humeral head, and centralizes the humeral head on the cavity of the glenoid, and thus, in functional terms, it is a rotator cuff muscle.

Testing Teres major can be palpated in the posterior axillary fold during adduction of the humerus against resistance.

Rotator cuff disease

The subacromial space is defined inferiorly by the superior surface of the rotator cuff (supraspinatus and the anterior part of infraspinatus); superiorly by the anterior edge and inferior surface of the anterior third of the acromion, the coraco-acromial ligament and the acromioclavicular joint, collectively forming the coraco-acromial arch; posteriorly by the posterior wall of the subacromial bursa. It is occupied by the subacromial bursa, lined by synovial membrane and extending anterolaterally under deltoid as the subdeltoid bursa, which facilitates movement of the rotator cuff under the coraco-acromial arch. The upper surface of the rotator cuff normally impinges, without symptoms, under the coraco-acromial arch when the humerus is abducted, flexed and medially rotated.

If the upper surface of the rotator cuff is damaged, or the bursa is thickened or inflamed, or the undersurface of the coraco-acromial arch is rough, then the impingement can become abrasive, producing the painful ‘impingement syndrome’.

Muscles that coordinate shoulder and elbow motion

The muscles of the upper arm are coracobrachialis, which acts only on the shoulder joint; biceps brachii and triceps, which cross both shoulder and elbow joints; and brachialis, which acts only at the elbow joint. Coracobrachialis is described on page 915.

Anterior compartment of the arm

Biceps brachii

Attachments Biceps brachii derives its name from its two proximally attached ‘heads’ (see Figs 49.15–49.16, 49.26, 49.28A). The short head arises by a thick, flattened tendon from the apex of the coracoid, superficial to the muscular origin of coracobrachialis. The long head starts within the capsule of the shoulder joint as a long narrow, oval tendon running from the supraglenoid tubercle of the scapula at the apex of the glenoidal cavity, where it is variably continuous with the glenoidal labrum. The tendon of the long head is enclosed in a double tubular synovial sheath which may persist as a mesotenon. It arches over the humeral head, in close apposition to it, emerges from the joint under the transverse humeral ligament, and descends in the intertubercular sulcus, where it is retained by the transverse humeral ligament and a fibrous expansion from the tendon of pectoralis major.

The two tendons lead into elongated bellies that, although closely applied, can be separated to within 7 cm or so of the elbow joint. At this joint, they end in a flattened tendon that is attached to the rough posterior area of the radial tuberosity, separated by a bursa from the smooth anterior area of the tuberosity. As the tendon approaches the radius, it spirals so that its anterior surface becomes lateral before being applied to the tuberosity. The tendon has a broad medial expansion, the bicipital aponeurosis, which descends medially across the brachial artery and fuses with the deep fascia over the origins of the flexor muscles of the forearm (Fig. 49.29). The tendon can be split without difficulty as far as the tuberosity: it can thus be confirmed that its anterior and posterior layers receive fibres from the short and long heads, respectively.

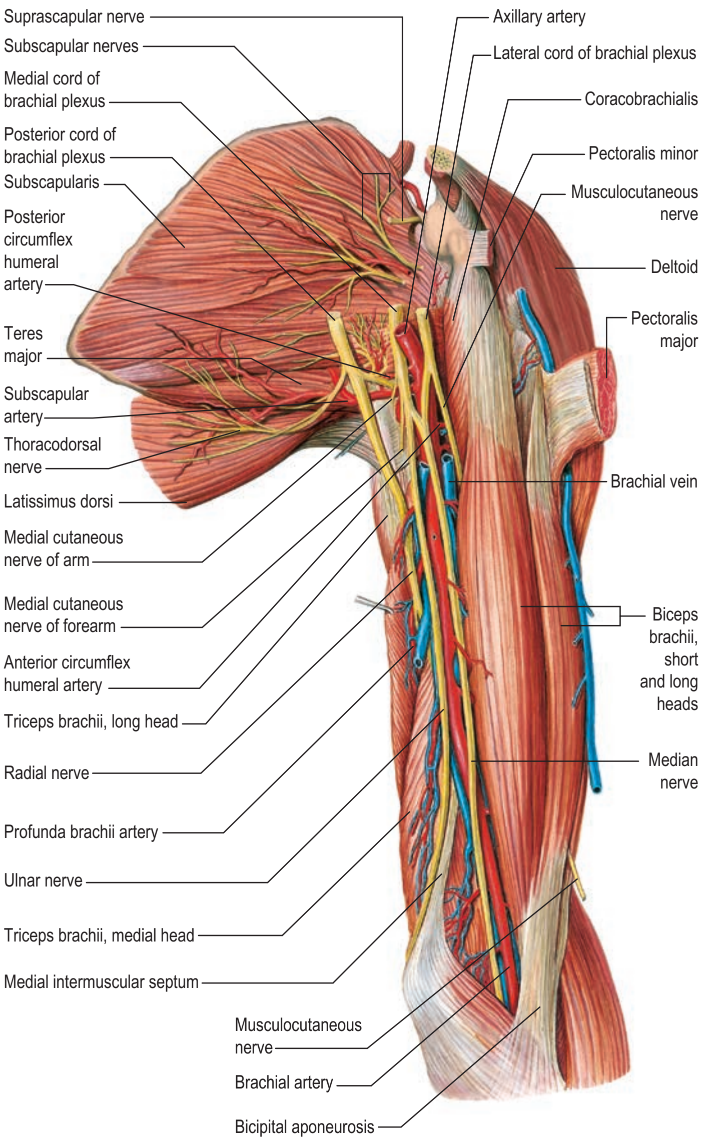
Suprascapular nerve
Subscapular nerves
Medial cord of brachial plexus
Posterior cord of brachial plexus
Subscapularis
Posterior circumflex humeral artery
Teres major
Subscapular artery
Thoracodorsal nerve
Latissimus dorsi
Medial cutaneous nerve of arm
Medial cutaneous nerve of forearm
Anterior circumflex humeral artery
Triceps brachii, long head
Radial nerve
Profunda brachii artery
Ulnar nerve
Triceps brachii, medial head
Medial intermuscular septum
Musculocutaneous nerve
Brachial artery
Bicipital aponeurosis
Axillary artery
Lateral cord of brachial plexus
Coracobrachialis
Pectoralis minor
Musculocutaneous nerve
Deltoid
Pectoralis major
Brachial vein
Biceps brachii, short and long heads
Median nerve

Fig. 49.29 The muscles, vessels and nerves of the left upper arm, anterior aspect. (Sobotta Atlas of Human Anatomy © Elsevier GmbH, Urban & Fischer, Munich.)

Occasionally, a third head arises from the superomedial part of brachialis and is attached to the bicipital aponeurosis and medial side of the tendon of insertion. It usually lies behind the brachial artery but it may consist of two slips that descend in front of and behind the artery. Less often, other slips may spring from the lateral aspect of the humerus or intertubercular sulcus.

Relations Biceps is overlapped proximally by pectoralis major and deltoid. Distally, it is covered only by fasciae and skin, and it forms a conspicuous elevation on the front of the arm. Its long head passes through the shoulder joint; its short head is anterior to the joint. Distally, it lies anterior to brachialis, the musculocutaneous nerve and supinator. Its medial border touches coracobrachialis and overlaps the brachial vessels and median nerve and its lateral border is related to deltoid and brachioradialis.

Vascular supply Biceps brachii is typically supplied by up to eight vessels originating from the brachial artery in the middle third of the arm. These vessels pass laterally, posterior to the median nerve, and divide into ascending and descending branches just before reaching the deep surface of the muscle. Smaller branches arise from the anterior circumflex humeral artery and the deltoid branch of the acromial division of the thoraco-acromial axis.

The arterial supply to biceps brachii is very variable: the main arterial supply may originate from the superior or inferior ulnar collateral arteries, subscapular artery, axillary artery, ulnar or radial arteries (in cases of proximal bifurcation of the brachial artery) or the profunda brachii artery. There is often a single large pedicle that accompanies the nerve to biceps: injury to the muscle and musculocutaneous nerve at this level in the arm commonly results in a fibrotic, atonic muscle with distal sensory dysfunction.

Pain is generated during abduction of the arm in the scapular plane and typically an arc of pain is experienced between 60° and 120° of elevation, the so-called 'impingement arc'. Rotator cuff disease is a painful condition with many causes and severe or chronic impingement of the rotator cuff tendons on the undersurface of the coraco-acromial arch is often a significant factor. The supraspinatus tendon is anatomically affected most by the impingement, which coincides with an area of reduced vascularity in this tendon. When associated with a tendinopathy from age-related degenerative changes within the tendon, impingement may be associated with partial or complete tears of the cuff. Clinically, it causes tenderness over the anterior portion of the acromion in addition to the 'painful arc',

Innervation Biceps brachii is innervated by the musculocutaneous nerve (fifth and sixth cervical ventral rami); separate, often segmental, branches pass to each belly.

Actions Biceps brachii is a powerful supinator, especially in rapid or resisted movements. It flexes the elbow, most effectively, with the forearm supinated, and acts, to a slight extent, as a flexor of the shoulder joint. The long head helps to check upward translation of the humeral head during contraction of deltoid, in synergy with the action of the rotator cuff. Via the bicipital aponeurosis, it is attached to the posterior border of the ulna, the distal end of which is drawn medially in supination. When the elbow is flexed against resistance, the tendon of insertion and bicipital aponeurosis become conspicuous.

Testing With the forearm supinated, biceps brachii can be tested by palpating its fibres during elbow flexion against resistance.

Brachialis

Attachments Brachialis arises from the lower half of the anterior surface of the shaft of the humerus, starting on either side of the insertion of deltoid, and extending distally to within 2.5 cm of the cubital articular surface. It also arises from the intermuscular septa, more from the medial than the lateral, since it is separated distally from the lateral intermuscular septum by brachioradialis and extensor carpi radialis longus. Its fibres converge to a thick, broad tendon that is attached to the ulnar tuberosity and to a rough impression on the anterior aspect of the coronoid.

Brachialis may be divided into two or more parts. It may be fused with brachioradialis, pronator teres or biceps and it may send a tendinous slip to the radius or to the bicipital aponeurosis.

Relations Biceps brachii, the brachial vessels and the musculocutaneous and median nerves are anterior (Fig. 49.30). The humerus and the capsule of the elbow joint are posterior. Pronator teres and the medial intermuscular septum, which separates it from triceps and the ulnar nerve, are medial. The radial nerve, radial recurrent and radial collateral arteries, brachioradialis and extensor carpi radialis longus are all lateral.

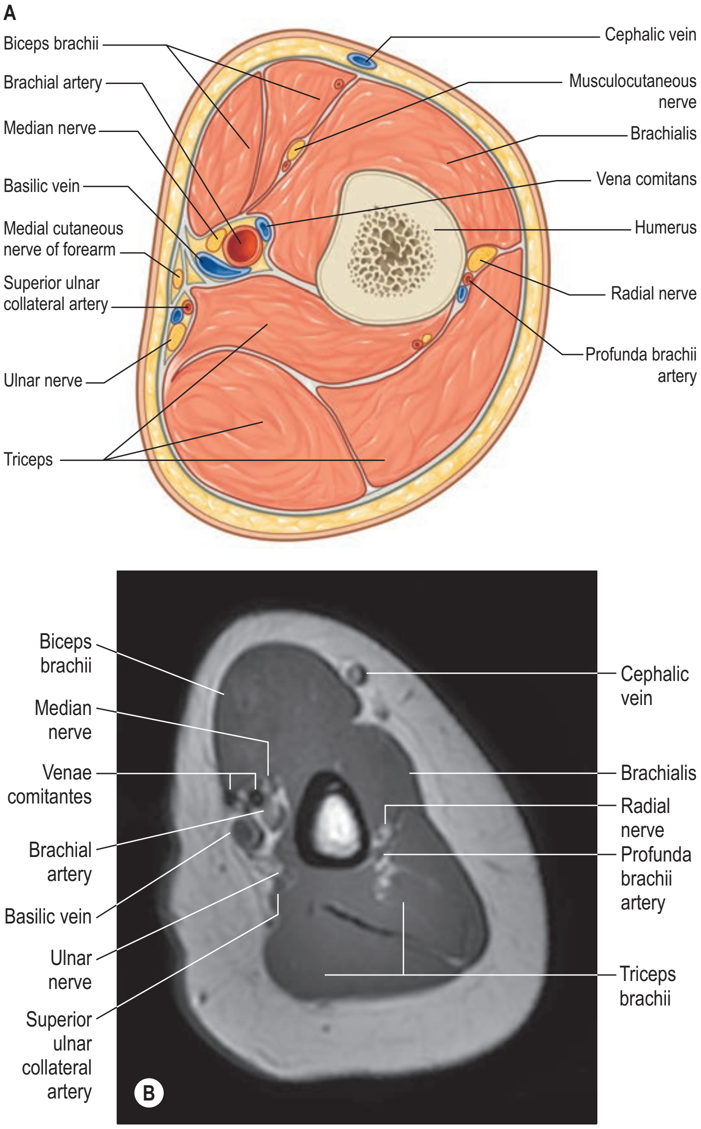

Fig. 49.30 **A**, A transverse section through the left arm, a little below the middle of the shaft of the humerus. **B**, An axial T1-weighted MRI at a similar level.

Vascular supply The blood supply to brachialis typically consists of two main arteries (superior and inferior), supplemented by a system of accessory arteries. The superior main artery originates from the brachial artery distal to the site of origin of the superior ulnar collateral artery and travels laterally to enter the anterior surface of the upper third of the muscle. The inferior main artery originates either from the superior ulnar collateral artery or directly from the brachial artery, and enters the mid-portion of the muscle. The accessory arteries are small and variable in number, origin and course. They can arise from the brachial artery, the superior and inferior ulnar collateral arteries, or the profunda brachii artery. The fact that brachialis has a greater vascular supply than biceps brachii suggests that its metabolic demands are greater: brachialis is the prime flexor of the forearm at the elbow, while biceps has more subtle actions on the shoulder and elbow, coordinating the two joints while positioning the hand in space.

Innervation The musculocutaneous nerve (fifth and sixth cervical ventral rami)) supplies a large medial part of the muscle and the radial nerve (seventh cervical ventral ramus) often, but variably, supplies a small lateral part (Oberlin et al 1994).

Action Brachialis is a flexor of the elbow joint with the forearm either prone or supine, whether or not the movement is resisted.

Testing Brachialis can be tested by palpating its fibres during elbow flexion against resistance.

Posterior compartment of the arm

Triceps

Attachments Triceps fills most of the extensor compartment of the upper arm (see Figs 49.28–49.30). It has three heads (long, lateral and medial), from which it takes its name.

The long head arises by a flattened tendon from the infraglenoid tubercle of the scapula, blending above with the inferior part of the glenohumeral capsule. Its muscular fibres descend medial to the lateral head and superficial to the medial head, and join them to form a common tendon. The lateral head arises by a flattened tendon from a narrow, linear, oblique ridge on the posterior surface of the humeral shaft, and from the lateral intermuscular septum. The origin on the humerus ascends with varying obliquity from its lateral border above the radial groove and behind the deltoid tuberosity to the surgical neck medial to the insertion of teres minor. These fibres also converge to the common tendon. The medial head, which is overlapped posteriorly by the lateral and long heads, has a particularly extensive origin. It is attached to the entire posterior surface of the humeral shaft, below the radial groove from the insertion of teres major to within 2.5 cm of the trochlea; the medial border of the humerus; the medial intermuscular septum; and the lower part of the lateral intermuscular septum. Some muscular fibres reach the olecranon directly; the rest converge to the common tendon (Keener et al 2010). Some fibres from the medial head are attached to the posterior capsule of the elbow joint as articularis cubiti.

The tendon of triceps begins near the middle of the muscle. It is formed of two laminae that are organized in a similar manner to that of the tendon of gastrocnemius and soleus in the posterior compartment of the leg. In the distal half of the superficial part of the muscle, the superficial lamina forms an aponeurotic layer to which the deep fascia of the arm is adherent; the deeper lamina is more vertical. After receiving the muscle fibres, the two laminae unite above the elbow and are attached, for the most part, to the upper surface of the olecranon. On the lateral side, a band of fibres continues down over anconeus to blend with the antebrachial fascia.

Relations The long head of triceps descends between teres minor and major, dividing the wedge-shaped interval between them and the humerus into triangular and quadrangular spaces (see Fig. 49.28). The lateral head of triceps forms an elevation, parallel and medial to the posterior border of deltoid, that stands out prominently when the elbow is actively extended. The mass that lies medial to it, and that disappears under deltoid, is the long head.

Lowering the hand under the influence of gravity by extension at the elbow calls for controlled lengthening of biceps brachii. This is an example of a habitual movement in which muscle tension increases despite increasing length. (This is 'eccentric' loading of a muscle; during such loading, the muscle–tendon junction is at greater risk of rupture. 'Concentric' loading occurs when the muscle shortens as tension increases.) As the hand descends and the elbow extends, the vertical through the centre of gravity of the forearm is carried further from the fulcrum of movement and therefore the turning moment exerted by the load increases and must be matched by an increase in the moment exerted by the muscle.

Vascular supply The blood supply to triceps is derived mainly from the profunda brachii artery and the superior ulnar collateral artery, with an accessory supply from the posterior circumflex humeral artery. The medial head of triceps is supplied on its anterior surface by two or three branches from the superior ulnar collateral artery. The posterior surface is supplied by a large proximal branch from the profunda brachii artery that passes medially anterior to the radial nerve. The long head of triceps is supplied on its anterior surface by two arteries, one arising from the axillary artery anterior to the tendon of latissimus dorsi and the other arising from either the brachial artery or the superior ulnar collateral artery. The posterior surface receives a recurrent branch from the posterior circumflex humeral artery immediately after it has passed through the quadrangular space. The lateral surface receives a number of small branches from the profunda brachii artery in its distal portion. The lateral head of triceps is primarily supplied by branches of the profunda brachii artery, with an additional supply from a branch of the posterior circumflex humeral artery.

Innervation Triceps is innervated by branches from the radial nerve (sixth cervical ventral ramus, lateral head; seventh cervical ventral ramus, long head; eighth cervical ventral ramus, medial head). There are separate branches for each head.

Actions Triceps is the major extensor of the forearm at the elbow joint. The medial head is active in all forms of extension, whereas the lateral and long heads are minimally active, except in extension against resistance, as in thrusting or pushing or supporting body weight on the hands with the elbows semi-flexed. When the flexed arm is extended at the shoulder joint, the long head may assist in drawing back and adducting the humerus to the thorax. The long head supports the lower part of the capsule of the shoulder joint, especially when the arm is raised. Articularis cubiti probably draws up the posterior part of the capsule of the elbow joint during extension of the forearm. In forceful supination of the semi-flexed forearm, involving contraction of both supinator and biceps brachii, triceps contracts synergistically to maintain the semi-flexed position.

Testing Triceps can be tested by palpating its fibres during elbow extension against resistance.

Quadrangular and triangular spaces

The quadrangular space (quadrilateral space; foramen of Velpeau) is more a horizontal cleft or tunnel than a vertical space. It has defined boundaries. Anteriorly, the space is bounded by subscapularis, the capsule of the shoulder joint and teres minor superiorly, teres major inferiorly, the long head of triceps medially and the surgical neck of the humerus laterally. Posteriorly, the quadrangular space is bounded above by teres minor. The axillary nerve and the posterior circumflex humeral artery and vein pass obliquely through the space (see Figs 49.33, 49.47).

There are two triangular spaces (see Figs 49.28, 49.47). The upper triangular space is bounded above by subscapularis anteriorly, teres minor posteriorly, teres major inferiorly and the long head of triceps laterally. The circumflex scapular vessels pass through this space. The lower triangular space (the triangular interval) is bounded above by subscapularis anteriorly, teres major posteriorly, the long head of triceps medially and the humerus laterally. The radial nerve and the profunda brachii vessels pass through this space.

VASCULAR SUPPLY AND LYMPHATIC DRAINAGE

Arteries

Dorsal scapular artery

In the majority of cases, the dorsal scapular artery arises from the third, or less often the second, part of the subclavian artery. It passes laterally through the trunks of the brachial plexus in front of scalenus medius and then deep to levator scapulae to reach the superior scapular angle. Here, it descends with the dorsal scapular nerve under the rhomboids along the medial border of the scapula to the inferior angle. It supplies the rhomboids, latissimus dorsi and the inferior portion of trapezius and the skin over the inferomedial aspect of trapezius via musculocutaneous perforators. It anastomoses with the suprascapular and subscapular arteries and with posterior branches of some posterior intercostal arteries. It sends a small branch to scalenus anterior; sometimes, this arises directly from the subclavian artery.

Variants About one-third of the superficial cervical and dorsal scapular arteries arise as a common vessel, the transverse cervical artery, from the thyrocervical trunk, which then divides into a superficial and a deep branch (superficial cervical and dorsal scapular arteries, respectively) (see Figs 33.1A, 49.31). In this case, the dorsal scapular artery arises near the superior border of the scapula; it passes laterally, anterior to the brachial plexus and then posterior to levator scapulae.

Suprascapular artery

The suprascapular artery usually arises from the thyrocervical trunk of the subclavian artery, although it may arise from the third part of the subclavian artery. It first descends laterally across scalenus anterior and the phrenic nerve, posterior to the internal jugular vein and sternocleidomastoid, then crosses anterior to the subclavian artery and brachial plexus, posterior and parallel with the clavicle, subclavius and the inferior belly of omohyoid, to reach the superior border of the scapula. Here, it passes above (sometimes, under) the superior transverse ligament, separating it from the suprascapular nerve, and enters the supraspinous fossa (**Fig. 49.31**; see Fig. 49.33), where it lies on the bone, and

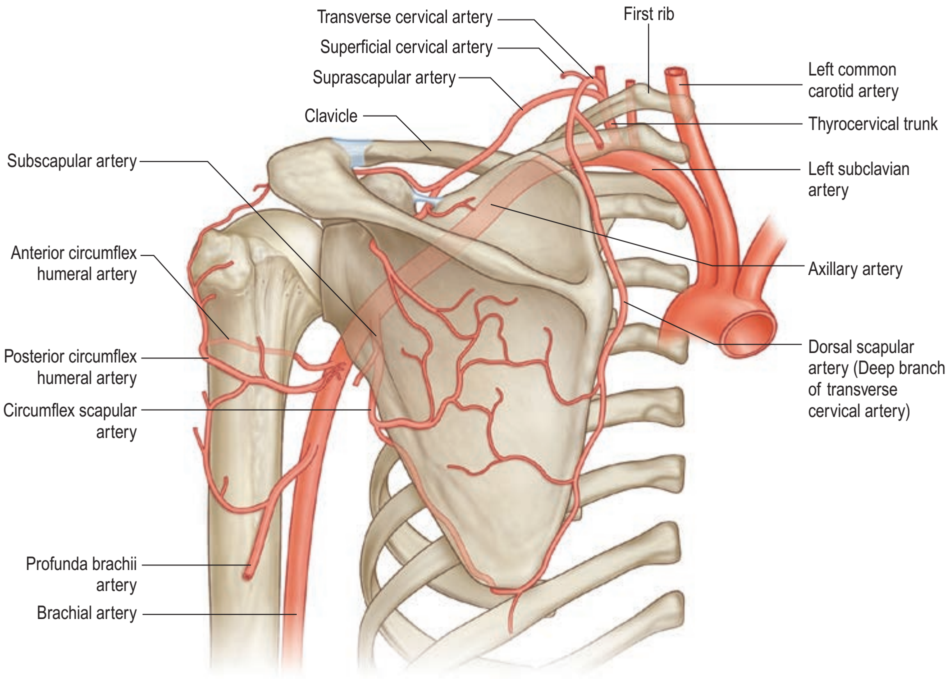
Transverse cervical artery
Superficial cervical artery
Suprascapular artery
Clavicle
First rib
Left common carotid artery
Thyrocervical trunk
Left subclavian artery
Axillary artery
Dorsal scapular artery (Deep branch of transverse cervical artery)
Subscapular artery
Anterior circumflex humeral artery
Posterior circumflex humeral artery
Circumflex scapular artery
Profunda brachii artery
Brachial artery

Fig. 49.31 The scapular anastomosis, left side. (With permission from Drake RL, Vogl AW, Mitchell A (eds), Gray's Anatomy for Students, 2nd ed. Elsevier, Churchill Livingstone. Copyright 2010.)

supplies supraspinatus. It descends behind the scapular neck, and passes through the spinoglenoid notch deep to the inferior transverse ligament to gain the deep surface of infraspinatus, where it anastomoses with the circumflex scapular and deep branch of the transverse cervical artery. Its muscular branches supply sternocleidomastoid, subclavius and infraspinatus. It also gives off a suprasternal branch that crosses the sternal end of the clavicle to supply the skin of the upper thorax, and an acromial branch that pierces trapezius to supply the skin over the shoulder. This last branch anastomoses with the thoraco-acromial and posterior circumflex humeral arteries.

As the suprascapular artery passes over the superior transverse ligament, it gives off a branch that enters the subscapular fossa beneath subscapularis and anastomoses with the subscapular artery and the deep branch of the transverse cervical artery. It also supplies the acromioclavicular and glenohumeral joints, the clavicle and the scapula.

Angiomyosomes

Available with the *Gray's Anatomy* e-book

Supraclavicular artery

This small vessel arises from either the transverse cervical or superficial cervical artery. It pierces the deep fascia just superior to the clavicle and anterior to trapezius, and supplies an area of skin over the lateral end of the clavicle.

Axillary artery

The axillary artery, a continuation of the subclavian artery, begins at the outer border of the first rib and ends nominally at the inferior border of teres major, where it becomes the brachial artery (see Fig. 49.31). Its direction varies with the position of the limb; it is almost straight when the arm is raised at right-angles, concave upwards when the arm is elevated above this level, and convex upwards and laterally when the arm is by the side (**Fig. 49.32**). At first deep, it subsequently becomes superficial, when it is covered only by the skin and fasciae. Pectoralis minor crosses it and so divides it into three parts, which are proximal, posterior and distal to the muscle.

Relations of the first part

The skin, superficial fascia, platysma, supraclavicular nerves, deep fascia, clavicular fibres of pectoralis major and the clavipectoral fascia, lateral pectoral nerve and the loop of communication between the lateral and medial pectoral nerves, and the thoraco-acromial and cephalic veins are all anterior. The first intercostal space and external intercostal, first and second digitations of serratus anterior, long thoracic and medial pectoral nerves, and the medial cord of the brachial plexus are all posterior. The posterior cord of the brachial plexus is lateral and the axillary vein is anteromedial. The first part is enclosed with the axillary vein and brachial plexus in a fibrous axillary sheath, which is continuous with the prevertebral layer of the deep cervical fascia.

Relations of the second part

The skin, superficial and deep fascia, and pectoralis major and minor are all anterior. The posterior cord of the brachial plexus and the areolar tissue between it and subscapularis are posterior. The axillary vein is medial, separated from the artery by the medial cord of the brachial plexus and the medial pectoral nerve. The lateral cord of the brachial plexus is lateral, separating the artery from coracobrachialis. The cords of the brachial plexus thus surround the second part on three sides, with the dispositions implied by their names, and separate it from the vein and adjacent muscles.

Relations of the third part

Pectoralis major and, distal to the muscle, skin and fasciae are anterior. The lower part of subscapularis and the tendons of latissimus dorsi and teres major are posterior. Coracobrachialis is lateral and the axillary vein is medial. Branches of the brachial plexus are arranged as follows: laterally, the lateral root and then trunk of the median nerve and, for a short distance, the musculocutaneous nerve; medially, the medial cutaneous nerve of the forearm between the axillary artery and vein anteriorly, and the ulnar nerve between these vessels posteriorly; anteriorly, the medial root of the median nerve; and posteriorly, the radial and axillary nerves, the latter only to the distal border of subscapularis. The dispositions of the branches of the brachial plexus around the axillary artery have, therefore, altered: there has been a rotation such that the nerves derived from the lateral cord are now more anterior, those from the medial cord more posterior, and those of the posterior cord come to lie more laterally.

Variants

The branches of the axillary artery exhibit considerable variation. An alar thoracic artery, often from the second part, may supply fat and lymph nodes in the axilla. The lateral thoracic artery may be absent, in which case it is replaced by lateral perforating branches of the intercostal arteries; alternatively, it may become, or give off, a direct cutaneous vessel (named the superficial thoracic artery by some sources) that supplies the skin over the lateral border of pectoralis major. In up to one-third of cases, the subscapular artery can arise from a common trunk with the posterior circumflex humeral artery. Occasionally, the subscapular, circumflex humeral and profunda brachii arteries arise in common, and in this case, branches of the brachial plexus surround this common vessel instead of the axillary artery. The posterior circumflex humeral artery may arise from the profunda brachii artery and pass back below teres major, instead of passing through the quadrangular space. Sometimes, the axillary artery divides into radial and ulnar arteries (anomalous 'high division'), and is, occasionally, the source of the anterior interosseous artery.

Angiomyosomes

Available with the *Gray's Anatomy* e-book

Branches

The branches of the axillary artery are one from the first part (superior thoracic), two from the second part (thoraco-acromial, lateral thoracic)

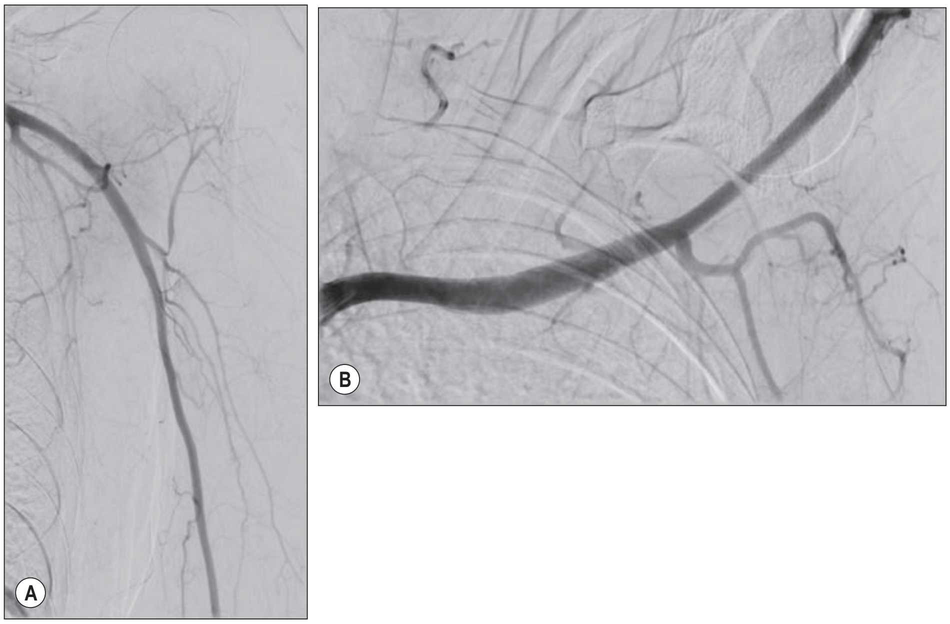

Fig. 49.32 Axillary angiograms. **A**, View with the arm by the side. **B**, View with the arm elevated.

Two branches of the subclavian artery perfuse the dorsal scapular suspension and medial motion muscles (the dorsal scapular artery), the posterosuperior rotator cuff muscles (the suprascapular artery) and the clavicle. These vessels correspond to the equivalent innervation for the same muscles. In this sense, innervation and angiomyotomes correspond. Pain afferents from the muscles, mostly small, unmyelinated axons, travel in the nerves. Ischaemic ('fatigue-related') pain from these three groups of dorsal muscles is felt as a diffuse, burning sensation in the same region as the vascular supply, without radiation or referral, and without respite during rest for a characteristic period, somewhat equivalent to the period over which the symptoms of a chronic ischaemic muscular compartment syndrome may resolve. The suprascapular artery supplies a muscular compartment that is contained in a well-defined and relatively restricting fascia; it is, therefore, not a surprise that the ischaemic ('fatigue-related') pain generated in this compartment may present earlier and be more persistent than elsewhere in muscles less well contained by fascial sheaths.

The axillary artery supplies the muscles of the ventral compartments of the shoulder, including the pectoral–deltoid muscle sheet, the scapulohumeral muscles (other than the posterosuperior rotator cuff) and the shoulder joint, including the scapula (with the serratus muscles) and proximal humerus. Its terminal branch, the brachial artery, supplies the muscles of the anterior compartment of the arm (for the branches of the brachial artery at the elbow and in the forearm, see Ch. 50). The profunda brachii artery, the major proximal branch of the brachial artery, supplies the muscles of the posterior compartment of the arm and the shaft of the humerus.

and three from the third part (subscapular, anterior and posterior circumflex humeral) (see Fig. 49.47).

Superior thoracic artery

The superior thoracic artery is a small vessel that arises from the first part of the axillary artery near the lower border of subclavius; it sometimes arises from the thoraco-acromial artery (see Fig. 49.47). It runs anteromedially above the medial border of pectoralis minor, then passes between it and pectoralis major to gain the thoracic wall. It supplies these muscles and the thoracic wall, and anastomoses with the internal thoracic and upper intercostal arteries.

Thoraco-acromial (acromiothoracic) artery

The thoraco-acromial artery is a short branch that arises from the second part of the axillary artery (see Figs 49.27, 49.47). It is initially overlapped by pectoralis minor, skirting its medial border; it next pierces the clavipectoral fascia and divides into pectoral, acromial, clavicular and deltoid branches, which supply pectoralis major and minor, an area of skin over the clavipectoral fascia, and the anterior portion of deltoid.

Pectoral branch The pectoral branch is the largest branch. It descends between the pectoral muscles, gives a branch to pectoralis minor, and then continues on the deep surface of pectoralis major. It enters the muscle and anastomoses with the intercostal branches of the internal thoracic and lateral thoracic arteries. It gives off perforating branches to the breast, and musculocutaneous perforators to the skin over pectoralis major.

Acromial branch The acromial branch crosses the coracoid process under deltoid, which it supplies, then pierces the muscle and ends on the acromion. It anastomoses with branches of the suprascapular artery, the deltoid branch of the thoraco-acromial artery and the posterior circumflex humeral arteries.

Clavicular branch The clavicular branch ascends medially between the clavicular part of pectoralis major and the clavipectoral fascia. It supplies the sternoclavicular joint and subclavius.

Deltoid branch The deltoid branch often arises with the acromial branch. It crosses pectoralis minor to accompany the cephalic vein between pectoralis major and deltoid, and supplies both muscles.

Lateral thoracic artery

The lateral thoracic artery arises from the second part of the axillary artery. Following the lateral border of pectoralis minor, it passes to the deep surface of pectoralis major as far distally as the fifth intercostal space (see Fig. 49.45). It supplies serratus anterior and the pectoral muscles, the axillary lymph nodes and subscapularis. It anastomoses with the internal thoracic, subscapular and intercostal arteries, and with the pectoral branch of the thoraco-acromial artery. In females, it is large and has lateral mammary branches, which curve round the lateral border of pectoralis major to the breast. In both males and females, it gives off cutaneous branches that pass around the lateral border of pectoralis major to supply the skin in this region.

Subscapular artery

The subscapular artery is the largest branch of the axillary artery (see Figs 49.31, 49.47). It usually arises from the third part of the axillary artery at the distal (inferior) border of subscapularis, which it follows to the inferior scapular angle where it anastomoses with the lateral thoracic and intercostal arteries and the deep branch of the transverse cervical artery. It supplies adjacent muscles and the thoracic wall. It is accompanied distally by the nerve to latissimus dorsi. Approximately 4 cm from its origin, the subscapular artery divides into the circumflex scapular and thoracodorsal arteries.

Circumflex scapular artery

The circumflex scapular artery, the larger of the two terminal branches of the subscapular artery, curves backwards around the lateral border of the scapula, traversing a triangular space between subscapularis above, teres major below and the long head of the triceps laterally (see Fig. 49.33). It enters the infraspinous fossa under teres minor and then divides. One branch (infrascapular) enters the subscapular fossa deep to subscapularis, and anastomoses with the suprascapular and dorsal scapular arteries (or deep branch of the transverse cervical artery). The other branch continues along the lateral border of the scapula between teres major and minor, then, dorsal to the inferior angle, anastomoses with the dorsal scapular artery. Small branches supply the posterior part of deltoid and the long head of triceps, and anastomose with an ascending branch of the profunda brachii artery.

Thoracodorsal artery The other terminal branch of the subscapular artery, the thoracodorsal artery, follows the lateral margin of the scapula, posterior to the lateral thoracic artery, between latissimus dorsi and serratus anterior. Before entering the deep surface of latissimus dorsi, it supplies teres major and the intercostals, and sends one or two branches to serratus anterior. It enters latissimus dorsi muscle with the thoracodorsal nerve; this constitutes the principal neurovascular pedicle to the muscle. It provides numerous musculocutaneous perforators that supply the skin over the superior part of latissimus dorsi. The intramuscular portion of the artery anastomoses with intercostal arteries and lumbar perforating arteries.

Anterior circumflex humeral artery

The anterior circumflex humeral artery arises from the lateral side of the axillary artery at the distal border of subscapularis (see Fig. 49.31). It runs horizontally behind coracobrachialis and the short head of biceps, anterior to the surgical neck of the humerus. Reaching the intertubercular sulcus, it sends an ascending branch to supply the humeral head and shoulder joint (Brooks et al 1993), continues laterally under the long head of biceps and deltoid, and anastomoses with the posterior circumflex humeral artery.

Posterior circumflex humeral artery

The posterior circumflex humeral artery is larger than the anterior (see Fig. 49.31). It branches from the third part of the axillary artery at the distal border of subscapularis and runs backwards with the axillary nerve through a quadrangular space bounded by subscapularis, the capsule of the shoulder joint and teres minor above, teres major below, the long head of triceps medially, and the surgical neck of the humerus laterally (see Fig. 49.22B). It curves round the humeral neck and supplies the shoulder joint, deltoid, teres major and minor, and long and lateral heads of triceps (Gerber et al 1990). It gives off a descending branch that anastomoses with the deltoid branch of the profunda brachii artery and with the anterior circumflex humeral and acromial branches of the suprascapular and thoraco-acromial arteries.

Potential vascular anastomoses around the shoulder girdle: clinical relevance

Available with the *Gray's Anatomy* e-book

Brachial artery

The brachial artery is a continuation of the axillary artery. It begins at the distal (inferior) border of the tendon of teres major and ends about a centimetre distal to the elbow joint (at the level of the neck of the radius) by dividing into the radial and ulnar arteries (see Figs 49.33, 49.44, 50.21–50.22). At first, it is medial to the humerus, but gradually spirals anterior to it until it lies midway between the humeral epicondyles. Its pulsation can be felt throughout the arm.

Relations

The brachial artery is wholly superficial, covered anteriorly only by skin and superficial and deep fasciae. The bicipital aponeurosis crosses it anteriorly at the elbow, separating it from the median cubital vein; the median nerve crosses it lateromedially near the distal attachment of coracobrachialis. Posterior to the artery are the long head of triceps, separated initially by the radial nerve and profunda brachii artery, and then successively by the medial head of triceps, the attachment of coracobrachialis and brachialis. Proximally, the median nerve and coracobrachialis lie laterally and the medial cutaneous nerve of the forearm and ulnar nerve lie medially. Distally, biceps brachii overlaps the artery laterally and the median nerve and basilic vein lie medially. The artery is accompanied by two venae comitantes, connected by transverse and oblique branches. At the elbow, the brachial artery sinks deeply into the triangular intermuscular cubital fossa and its further course is described in Chapter 50 and Chapter 81.

Variants

The brachial artery, with the median nerve, may diverge from the medial border of biceps brachii and descend towards the medial humeral epicondyle, usually behind a supracondylar process from which a fibrous arch crosses the artery, and which then runs behind or through pronator teres to the elbow. Occasionally, the artery divides proximally into two trunks that reunite. Frequently, it divides more proximally than usual into radial, ulnar and common interosseous arteries. Most often, the radial branches arise proximally, Two significant cutaneous branches arise from the circumflex scapular artery as it emerges through the upper triangular space. The superior, or horizontal, branch is a direct cutaneous artery that passes medially at the level of the deep fascia parallel with the spine of the scapula and supplies a band of skin overlying the spine of the scapula. The lower branch (parascapular branch) is also a direct cutaneous vessel that passes in an inferomedial direction, again at the level of the deep fascia, and supplies an area of skin overlying the lateral border of the scapula. Both of these cutaneous vessels provide the anatomical basis of skin flaps that can be surgically raised in this region (scapular flap based on the horizontal branch and parascapular flap based on the lower, parascapular branch) to reconstruct areas of missing tissue elsewhere in the body.

The potential vascular anastomoses around the shoulder girdle are numerous, which means that collateral perfusion of the upper limb is possible in occlusion of the axillary artery or vein. In acute occlusion of the axillary artery, these potential anastomoses are not reliable and clinicians should not rely on anastomotic perfusion of the acutely ischaemic limb. The axillary artery is most ‘at risk’ of occlusion as a result of intimal separation and dissection in its second part, behind pectoralis minor, an injury associated with infraclavicular brachial plexus traction lesions (Birch 2011). Although magnetic resonance imaging with angiography is recommended for the diagnosis of the poorly perfused limb after distraction trauma, the site of intimal rupture is so consistent as to make urgent surgical exploration without imaging a reasonable clinical decision.

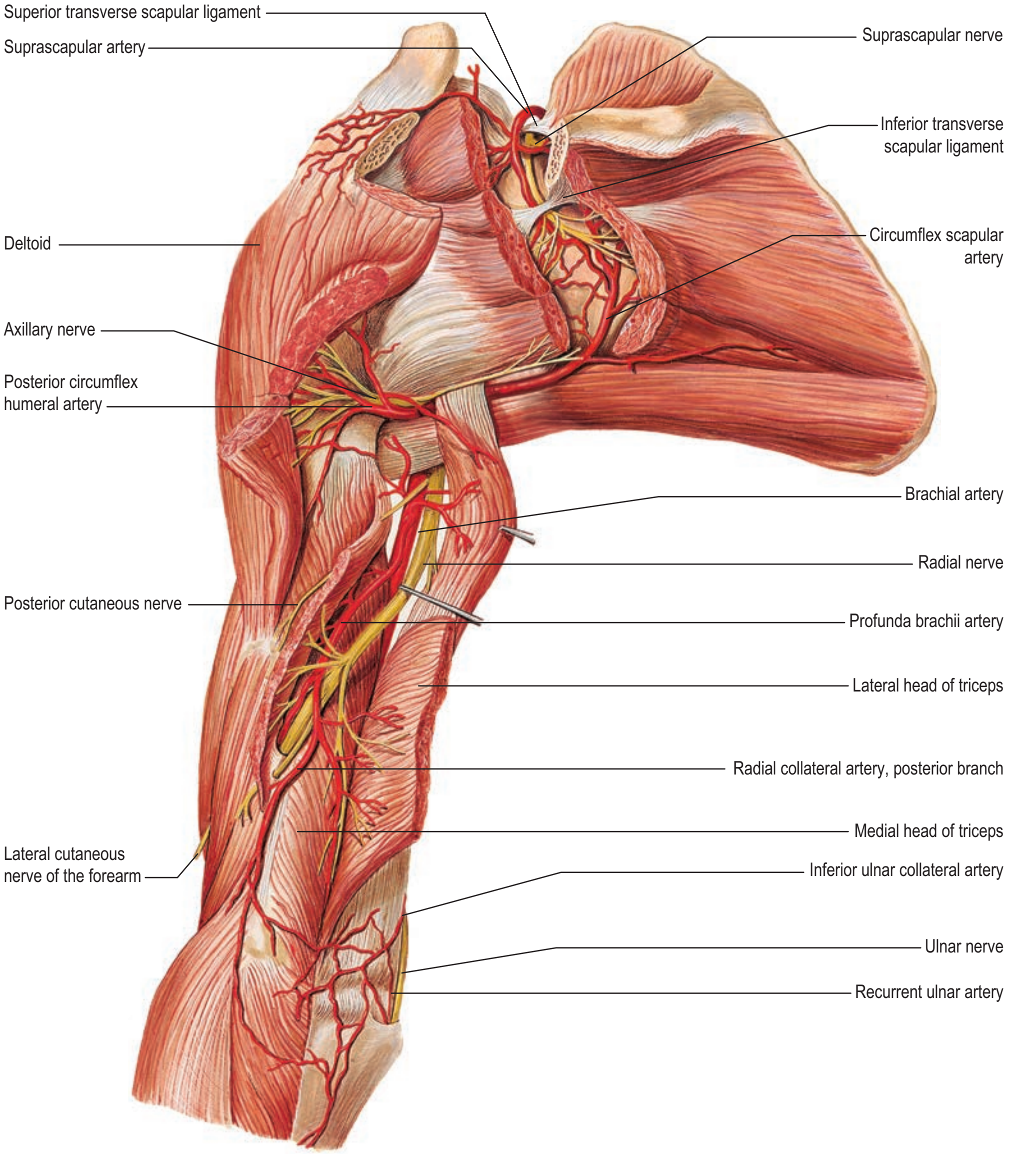
Superior transverse scapular ligament
Suprascapular artery
Deltoid
Axillary nerve
Posterior circumflex humeral artery
Posterior cutaneous nerve
Lateral cutaneous nerve of the forearm
Suprascapular nerve
Inferior transverse scapular ligament
Circumflex scapular artery
Brachial artery
Radial nerve
Profunda brachii artery
Lateral head of triceps
Radial collateral artery, posterior branch
Medial head of triceps
Inferior ulnar collateral artery
Ulnar nerve
Recurrent ulnar artery

Fig. 49.33 Muscles, vessels and nerves of the left upper arm, posterior aspect. (Sobotta Atlas of Human Anatomy © Elsevier GmbH, Urban & Fischer, Munich.)

leaving a common trunk for the ulnar and common interosseous arteries. Sometimes, the ulnar artery arises proximally and the radial and common interosseous arteries form the other division, or the common interosseous may also arise proximally. Slender vasa aberrantia may connect the brachial artery to the axillary artery or to one of the forearm arteries, usually the radial. The brachial artery may be crossed by muscular or tendinous slips from coracobrachialis, biceps brachii, brachialis or pronator teres. Rarely, the median nerve crosses posterior, rather than anterior, to the brachial artery near the insertion of coracobrachialis.

Branches

The branches of the brachial artery are the profunda brachii, nutrient, superior, middle and inferior ulnar collateral, deltoid, muscular, radial and ulnar arteries.

Profunda brachii artery The profunda brachii artery (Fig. 49.33; see Fig. 49.31) is a large branch from the posteromedial aspect of the brachial artery, distal to teres major. It follows the radial nerve closely, at first posteriorly between the long and medial heads of triceps, then in the spiral groove covered by the lateral head of triceps. It supplies muscular branches, and the nutrient artery of the humerus, and finally divides into terminal radial and middle collateral branches. The radial collateral branch pierces the lateral intermuscular septum to reach the anterior aspect of the epicondyle of the humerus in the groove between brachioradialis and brachialis, and takes part in the anastomosis around the elbow. The middle collateral branch runs posterior to the septum and epicondyle.

The profunda brachii may originate from a common origin with the posterior circumflex humeral artery, from the axillary artery proximal to the tendon of latissimus dorsi, or from the distal portion of the axillary artery.

Middle collateral (posterior descending) branch The middle collateral artery is the larger terminal branch of the profunda brachii artery. It arises posterior to the humerus and descends along the posterior surface of the lateral intermuscular septum to the elbow. Proximally, the artery lies between brachialis (anteriorly) and the lateral head of triceps (posteriorly). Distally, it lies between brachioradialis (anteriorly) and the lateral head of triceps (posteriorly). It may pierce the deep fascia and become cutaneous, or remain deep to the fascia, forming an arch with the inferior ulnar collateral artery proximal to the olecranon fossa before anastomosing with the interosseous recurrent artery behind the lateral epicondyle; it gives off about five small fasciocutaneous perforators and often has a small branch that accompanies the nerve to anconeus.

Radial collateral (anterior descending) branch The radial collateral artery accompanies the radial nerve through the lateral intermuscular septum, descending between brachialis and brachioradialis anterior to the lateral epicondyle and anastomosing with the radial recurrent artery. It supplies brachialis, brachioradialis, the radial nerve and a few fasciocutaneous perforators.

Nutrient artery of humerus The nutrient artery of the humerus arises near the mid-level of the upper arm and enters the nutrient canal near the attachment of coracobrachialis, posterior to the deltoid tuberosity; it is directed distally.

Superior ulnar collateral artery The superior ulnar collateral artery arises a little distal to the mid-level of the upper arm, usually from the brachial artery (see Fig. 48.3), but often as a branch from the profunda brachii. It accompanies the ulnar nerve, piercing the medial intermuscular septum to descend in the posterior compartment and supply the medial head of triceps. It passes between the medial epicondyle and olecranon, ending deep to flexor carpi ulnaris by anastomosing with the posterior ulnar recurrent and inferior collateral arteries. A branch sometimes passes anterior to the medial epicondyle and anastomoses with the anterior ulnar recurrent artery.

Middle ulnar collateral artery If present, the middle ulnar collateral artery arises from the brachial artery between the superior and inferior ulnar collateral arteries. It passes anterior to the medial epicondyle, anastomoses with the anterior ulnar recurrent artery, supplies triceps and sends small fasciocutaneous perforators to the skin.

Inferior ulnar collateral (supratrochlear) artery The inferior ulnar collateral artery begins approximately 5 cm proximal to the elbow. It passes medially between the median nerve and brachialis, pierces the medial intermuscular septum and curls round the humerus between triceps and bone (see Figs 48.3, 49.33). It forms an arch proximal to the olecranon fossa with the middle collateral branch of the profunda brachii artery. As it lies on brachialis, it gives off branches that descend anterior to the medial epicondyle to anastomose with the anterior ulnar recurrent artery. Behind the epicondyle, a branch anastomoses with the superior ulnar collateral and posterior ulnar recurrent arteries.

Muscular branches Muscular branches are distributed to coracobrachialis, biceps and brachialis.

Deltoid (ascending) branch The deltoid branch ascends between the lateral and long heads of triceps, and anastomoses with a descending branch of the posterior circumflex humeral artery.

Radial and ulnar arteries The radial and ulnar arteries are described in detail on pages 951 and 951, respectively. For an account of the anastomosis about the elbow, see page 952.

Veins

The deep veins have numerous anastomoses with each other and with the superficial veins.

Axillary vein

The axillary vein is the continuation of the basilic vein (see Fig. 48.4). It begins at the lower border of teres major and ascends to the outer border of the first rib, where it becomes the subclavian vein. It is joined by the brachial vein near subscapularis, and by the cephalic vein near its costal end; other tributaries follow the axillary arterial branches. It lies medial to the axillary artery, which it partly overlaps. The medial pectoral nerve, medial cord of the brachial plexus, ulnar nerve and medial cutaneous nerve of the forearm lie between the artery and the vein. The medial cutaneous nerve of the arm is medial to the vein; the lateral group of axillary lymph nodes is posteromedial. There are a pair of valves near the distal end of the vein, and valves near the ends of the cephalic and subscapular veins.

Subclavian vein

The subclavian vein is a continuation of the axillary vein (see Fig. 48.4). It extends from the outer border of the first rib to the medial border of scalenus anterior, where it joins the internal jugular to form the brachiocephalic vein. The clavicle and subclavius are anterior; the subclavian artery is posterosuperior, separated by scalenus anterior and the phrenic nerve; and the first rib and pleura are inferior. The vein usually has a pair of valves about 2 cm from its end. Its tributaries are the external jugular, dorsal scapular and (sometimes) anterior jugular veins, and, occasionally, a small branch from the cephalic vein that ascends anterior to the clavicle. At its junction with the internal jugular vein, the left subclavian receives the thoracic duct, and the right subclavian vein receives the right lymphatic duct (see Fig. 35.16).

Brachial veins

The brachial veins flank the brachial artery, as venae comitantes with tributaries similar to the arterial branches; they join the axillary vein near the lower margin of subscapularis. The medial branch often joins the basilic vein before it becomes the axillary vein.

Superficial veins

The cephalic vein ascends anterior to the elbow, superficial to a groove between brachioradialis and biceps brachii, crosses superficial to the lateral cutaneous nerve of the forearm, and ascends lateral to biceps and between pectoralis major and deltoid, where it adjoins the deltoid branch of the thoraco-acromial artery (Fig. 49.34). It enters the infraclavicular fossa, passes posterior to the clavicular head of pectoralis major, pierces the clavipectoral fascia, crosses the axillary artery and joins the axillary vein just below clavicular level. It may connect with the external jugular vein by a branch anterior to the clavicle. The median cubital vein is sometimes large, transferring most blood from the cephalic to the basilic vein; when this occurs, the proximal cephalic vein is either absent or much diminished.

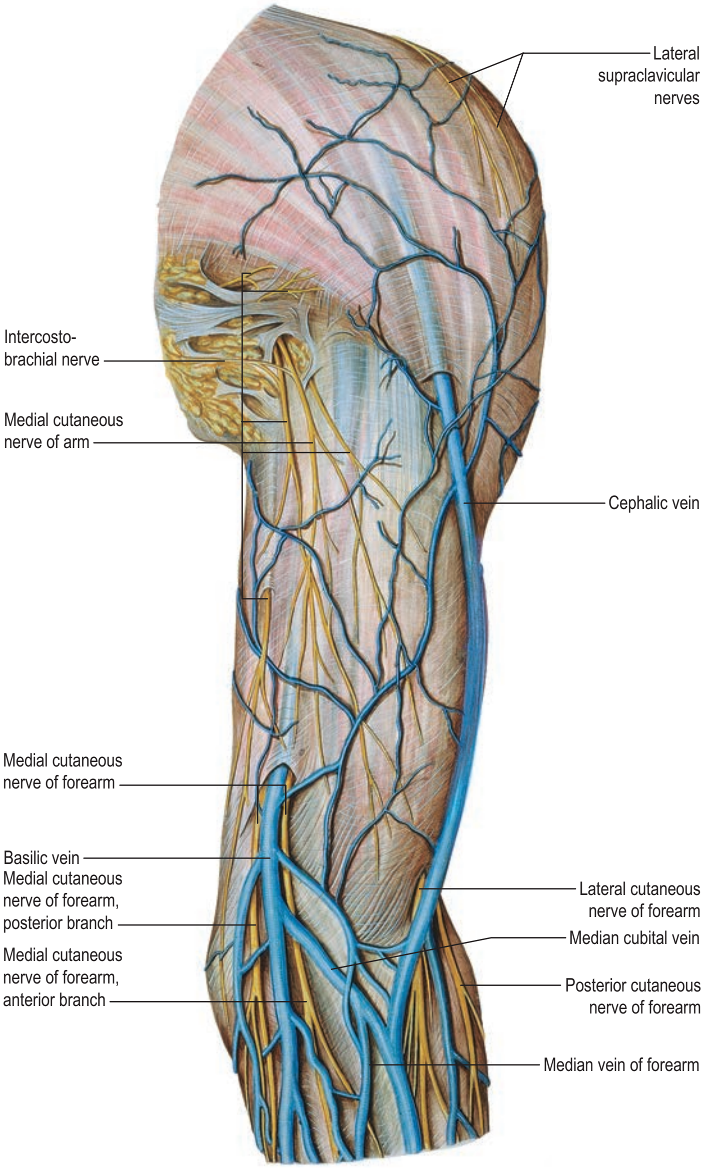
Lateral supraclavicular nerves
Intercosto-brachial nerve
Medial cutaneous nerve of arm
Cephalic vein
Medial cutaneous nerve of forearm
Basilic vein
Medial cutaneous nerve of forearm, posterior branch
Lateral cutaneous nerve of forearm
Median cubital vein
Medial cutaneous nerve of forearm, anterior branch
Posterior cutaneous nerve of forearm
Median vein of forearm

Fig. 49.34 The superficial veins and nerves, left arm, anterior (flexor) aspect. (Sobotta Atlas of Human Anatomy © Elsevier GmbH, Urban & Fischer, Munich.)

Lymphatic drainage

Lymphatics follow the usual pattern, in that superficial lymphatics follow the veins, and deep lymphatics follow the arteries (see Fig. 49.45).

INNERVATION

Brachial plexus

For an overview of the brachial plexus, see Chapter 48 and Figs 48.6–48.7.

In the axilla, the lateral and posterior cords of the brachial plexus are anterior and lateral to the first part of the axillary artery, respectively, and the medial cord is behind the artery. The cords assume their appropriate relations around the second part of the artery, deep to pectoralis major. In the lower axilla, the cords divide into nerves that supply the

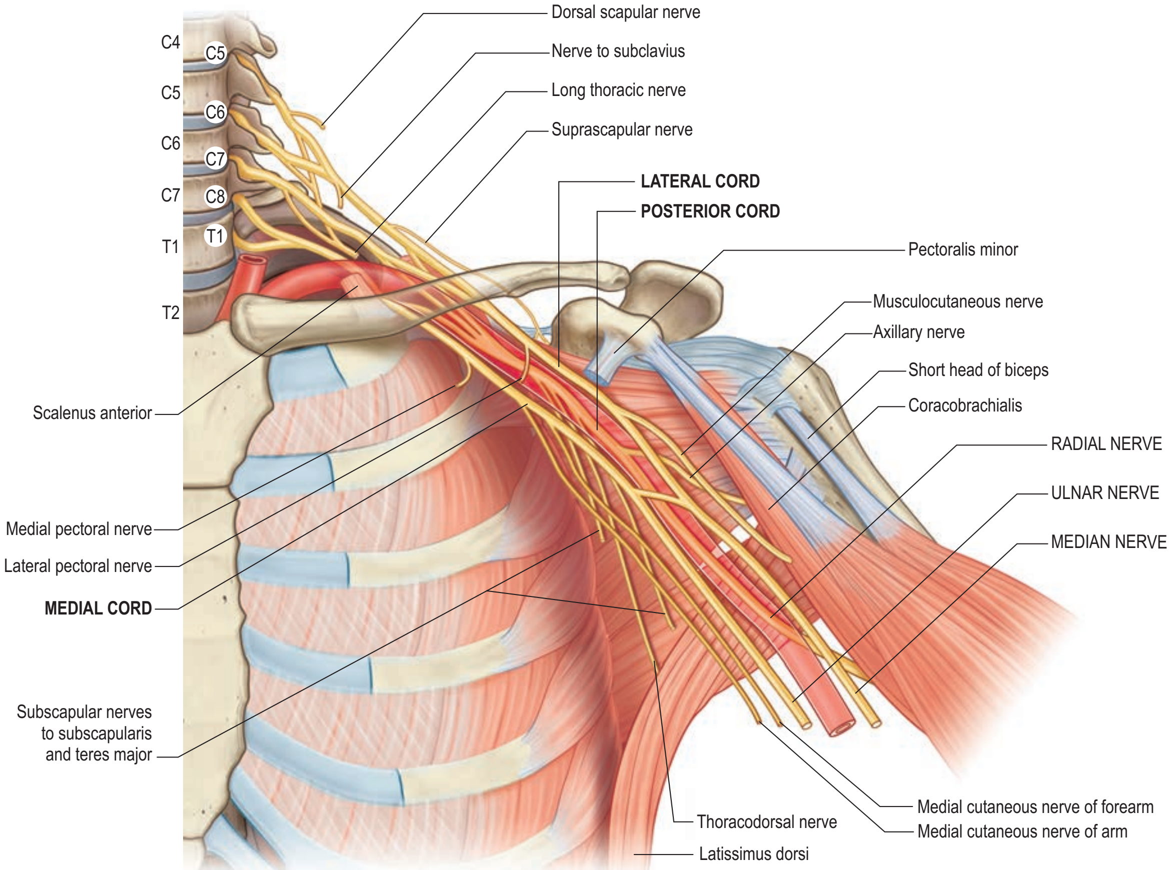
Dorsal scapular nerve
Nerve to subclavius
Long thoracic nerve
Suprascapular nerve
LATERAL CORD
POSTERIOR CORD
Pectoralis minor
Musculocutaneous nerve
Axillary nerve
Short head of biceps
Coracobrachialis
RADIAL NERVE
ULNAR NERVE
MEDIAN NERVE
Medial cutaneous nerve of forearm
Medial cutaneous nerve of arm
Thoracodorsal nerve
Latissimus dorsi
C4
C5
C6
C7
T1
T2
C5
C6
C7
C8
T1
Scalenus anterior
Medial pectoral nerve
Lateral pectoral nerve
MEDIAL CORD
Subscapular nerves
to subscapularis
and teres major

Fig. 49.35 The brachial plexus and its major branches. The axillary artery, shown in red outline, runs anterior to the radial nerve. The vertebral levels are labelled C4–T2; the spinal nerves are labelled C5–T1 (white circles).

upper limb (**Fig. 49.35**). Other than the medial root of the median nerve, these nerves are related to the third part of the artery in the same way as their cords are related to the second part, i.e. branches of the lateral cord are lateral to the artery, branches of the medial cord are medial, and branches of the posterior cord are posterior.

Suprascapular nerve

The suprascapular nerve is a large branch of the upper trunk (fifth and sixth cervical ventral rami) (see Figs 35.17, 49.35). It runs laterally, deep to trapezius and omohyoid, and enters the supraspinous fossa through the suprascapular notch inferior to the superior transverse scapular ligament. It runs deep to supraspinatus and supplies it. It curves round the lateral border of the spine of the scapula with the suprascapular artery to reach the infraspinous fossa, where it gives two branches to infraspinatus and articular rami to the shoulder and acromioclavicular joints. The suprascapular nerve rarely has a cutaneous branch: when present, it pierces deltoid close to the tip of the acromion and supplies the skin of the proximal third of the arm within the territory of the axillary nerve.

Lateral pectoral nerve

The lateral pectoral nerve (fifth and sixth cervical ventral rami) is larger than the medial, and may arise either from the anterior divisions of the upper and middle trunks, or by a single branch from the lateral cord, just above or deep to the clavicle. It crosses anterior to the axillary artery and vein, pierces the clavipectoral fascia and supplies the deep surface of pectoralis major. It sends a branch to the medial pectoral nerve, forming a loop in front of the first part of the axillary artery to supply some fibres to pectoralis minor.

Medial pectoral nerve

The medial pectoral nerve (eighth cervical ventral ramus and first thoracic ventral ramus) branches from the medial cord while the latter lies posterior to the axillary artery and curves forwards between the axillary artery and vein. Anterior to the artery, it joins a ramus of the lateral pectoral nerve and enters the deep surface of pectoralis minor, which it supplies. Two or three branches pierce pectoralis minor and others may pass round its inferior border to end in pectoralis major.

Upper (superior) subscapular nerve

The superior subscapular nerve is smaller than the inferior. It arises from the posterior cord (fifth and sixth cervical ventral rami), enters subscapularis at a high level, and is frequently double.

Lower (inferior) subscapular nerve

The inferior subscapular nerve arises from the posterior cord (fifth and sixth cervical ventral rami). It supplies the lower part of subscapularis and ends in teres major, which is sometimes supplied by a separate branch.

Thoracodorsal nerve

The thoracodorsal nerve arises from the posterior cord (sixth, seventh and eighth cervical ventral rami) between the subscapular nerves. It accompanies the subscapular artery along the posterior axillary wall and supplies latissimus dorsi, reaching its distal border (see Fig. 49.29).

Axillary nerve

The axillary nerve arises from the posterior cord (fifth and sixth cervical ventral rami) (see Figs 49.33, 49.35, 48.8). Initially it is lateral to the radial nerve, posterior to the axillary artery and anterior to subscapularis. At the lower border of subscapularis, it curves back inferior to the humeroscapular articular capsule and, together with the posterior circumflex humeral vessels, traverses a quadrangular space bounded above by subscapularis (anteriorly) and teres minor (posteriorly), below by teres major, medially by the long head of triceps, and laterally by the surgical neck of the humerus. It divides in the space into anterior and posterior branches. The anterior branch curves round the neck of the humerus with the posterior circumflex humeral vessels, deep to deltoid, to reach the anterior part of the muscle. At the level of the anterior border of the acromion, the nerve often consists of two or more thin filaments that supply the anterior deltoid; it gives off a few small cutaneous branches that pierce deltoid and ramify in the skin over its lower part. The posterior branch courses medially and posteriorly along the attachment of the lateral head of triceps, inferior to the glenoid rim. It usually lies medial to the anterior branch in the quadrangular space. It gives off the nerve to teres minor and the upper lateral cutaneous nerve of the arm at the lateral edge of the attachment of the long head of triceps. The nerve to teres minor enters the muscle on its inferior surface. The posterior branch frequently supplies the posterior aspect of deltoid, usually via a separate branch from the main stem, but occasionally from the superior lateral cutaneous nerve of the arm. However, the posterior part of deltoid has a more consistent supply from the anterior branch of the axillary nerve, which should be remembered when performing a posterior deltoid-splitting approach to the shoulder. The upper lateral cutaneous nerve of the arm pierces the deep fascia at the medial border of the posterior aspect of deltoid, and supplies the skin over the lower part of deltoid and the upper part of the long head of triceps. The posterior branch is intimately related to the inferior aspects of the glenoid and shoulder joint capsule. There is often an enlargement or pseudoganglion on the branch to teres minor. The axillary trunk supplies a branch to the shoulder joint below subscapularis.

Injuries to the shoulder girdle involving the accessory, long thoracic, axillary and suprascapular nerves

Available with the *Gray's Anatomy* e-book

Musculocutaneous nerve

The musculocutaneous nerve arises from the lateral cord (fifth, sixth and seventh cervical ventral rami), opposite the lower border of pectoralis minor (**Fig. 49.44**; see Figs 48.13, 49.45). It pierces coracobrachialis a variable distance below the tip of the coracoid process and then descends laterally between biceps brachii and brachialis to the lateral side of the arm. The first branch, to coracobrachialis, may pass into the muscle no more than 2 cm distal to the tip of the coracoid; fibres from the seventh cervical ventral ramus may branch directly from the lateral cord. Branches to biceps brachii and brachialis leave after the musculocutaneous nerve has pierced coracobrachialis. There are usually two branches to brachialis, and the lower branch also supplies the anterior aspect of the elbow joint. The nerve to biceps brachii is consistently accompanied by a vascular pedicle. The nerve now inclines lateral and deep, into the plane between brachialis posteriorly and biceps anteriorly, where it supplies a small branch to the humerus that enters the shaft with the nutrient artery. Below the branches to brachialis, the musculocutaneous nerve continues as the lateral cutaneous nerve of the forearm.

The musculocutaneous nerve has frequent variations. It may run behind coracobrachialis or adhere for some distance to the median nerve and pass behind biceps brachii. Some fibres of the median nerve may run in the musculocutaneous nerve, leaving it to join their proper trunk; less frequently, the reverse occurs, and the median nerve sends a branch to the musculocutaneous nerve. Occasionally, the musculocutaneous nerve also supplies pronator teres and may replace radial branches to the dorsal surface of the thumb.

Medial cutaneous nerve of the arm

The medial cutaneous nerve of the arm (eighth cervical and first thoracic ventral rami) is the smallest and most medial branch of the brachial plexus, arising from the medial cord (see Fig. 49.35). It crosses the axilla, either anterior or posterior to the axillary vein, then passes medial to the axillary vein, communicates with the intercostobrachial nerve, and descends medial to the brachial artery and basilic vein. It pierces the deep fascia at the midpoint of the upper arm to supply the skin over the medial aspect of the distal third of the upper arm (see Fig. 49.34). It connects with the posterior branch of the medial cutaneous nerve of the forearm. Sometimes, the medial cutaneous nerve of the arm and the intercostobrachial nerve are connected in a plexiform manner in the axilla. The intercostobrachial nerve may be large and reinforced by part of the lateral cutaneous branch of the third intercostal nerve. In these cases, it replaces the medial cutaneous nerve of the arm and receives a connection representing the latter from the brachial plexus (occasionally, this connection is absent).

Medial cutaneous nerve of the forearm

The medial cutaneous nerve of the forearm comes from the medial cord (first thoracic ventral ramus) (see Fig. 49.34). It lies initially between the axillary artery and vein, and gives off a ramus that pierces the deep fascia to supply the skin over the biceps, almost to the elbow. The nerve descends medial to the brachial artery, pierces the deep fascia with the basilic vein midway in the arm, and divides into anterior and posterior branches. Its further course is described in Chapter 50 and Chapter 81.

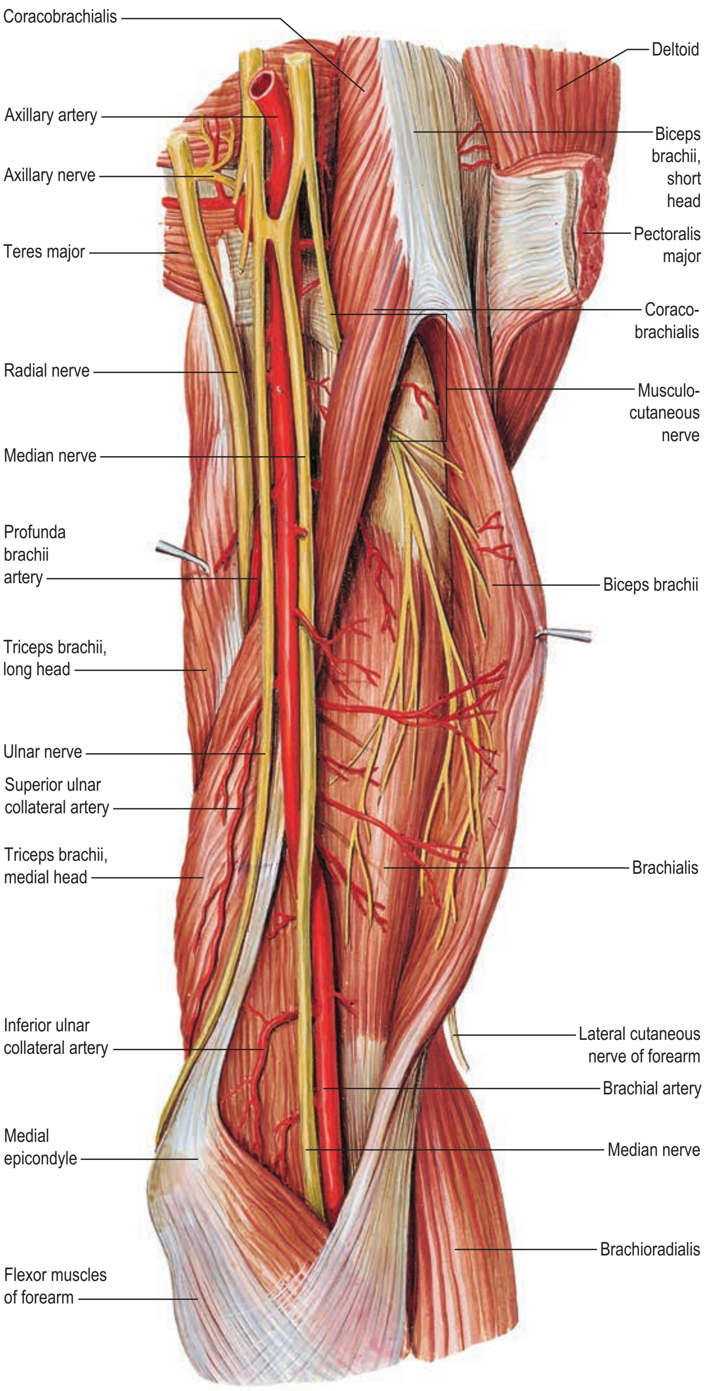

Fig. 49.44 The left upper arm dissected to show the musculocutaneous nerve. Note also the changing relationship of the brachial artery and median nerve. Anterior aspect. (Sobotta Atlas of Human Anatomy © Elsevier GmbH, Urban & Fischer, Munich.)

Median nerve

The median nerve has two roots from the lateral cord (fifth, sixth and seventh cervical ventral rami) and medial cord (eighth cervical and first thoracic ventral rami), which embrace the third part of the axillary artery and unite anterior or lateral to it (see Figs 49.29, 49.35, 49.44, 48.7, 48.10). Some fibres from the seventh cervical ventral ramus often leave the lateral root in the lower part of the axilla. They pass distomedially posterior to the medial root, and usually anterior to the axillary artery, to join the ulnar nerve. Clinically, they are believed to be mainly motor and to supply flexor carpi ulnaris. The median nerve gives off vascular branches to the brachial artery. If the lateral root is small, the musculocutaneous nerve (fifth, sixth and seventh cervical ventral rami) connects with the median nerve in the arm. The further course of the median nerve is described in Chapter 50 and Chapter 81.

Serious mistakes are most common in the diagnosis of severe injuries about the shoulder girdle: diagnosis of injuries to the accessory, long thoracic, axillary and suprascapular nerves is by no means straightforward. Precise but elementary clinical examination is reliable: delay before diagnosis is therefore inexplicable. Matters are not helped by the persistence with which incorrect and discredited ideas about what muscles do continue to be taught. Many nerve injuries in this region are painful and, too often, a patient is passed to a pain clinic without a diagnosis.

Inferior scapulohumeral angle (ISHA)

Assessing the inferior scapulohumeral angle (ISHA) informs the clinician about function at the thoracoscapular and shoulder joints (Fig. 49.36). The ISHA is subtended by the long axis of the humerus and the lateral border of the scapula; the apex of the angle is centred over the glenohumeral joint. Stiffness of the joints is detected by measuring *passive* range, which is normally between 170° and 180°. The excursion between the humerus and the scapula in a healthy adult is between 130° and 140°, i.e. the difference between the ISHA at rest and in full elevation. It is important to remember that full elevation is possible after successful thoracoscapular arthrodesis in scapulohumeral dystrophy (Copeland and Howard 1978). This range of movement occurs at the shoulder joints, mainly the glenohumeral joint, with some involvement of the acromioclavicular and sternoclavicular joints. Successful glenohumeral arthrodesis enables a range of elevation of 30–40°, provided by the thoracoscapular joint.

Accessory nerve

The integrity of the accessory nerve is fundamental to thoracoscapular function and essential for scapulohumeral rhythm. The nerve is usually divided at the apex of the posterior triangle, usually by surgeons, and is a crippling injury. Typically, there is immediate pain, then dropping of the shoulder and a remarkable loss of function. The average ISHA is about 50°. The pain is characteristic: often severe, deep-seated, dull, constant and boring in nature, and felt around the scapula and the posterior aspect of the neck and shoulder. The posture of the scapula is also characteristic: because of the loss of the great suspensory muscle, trapezius, the scapula drops down and away from the spinal column (Fig. 49.37). There is often winging of the scapula, easily distinguished from that caused by paralysis of serratus anterior by the posture of the scapula (Fig. 49.38). The nerve appears to be relatively immune to the harmful effects of delayed repair, even as late as 4 years after injury, with early relief of pain long before there is reinnervation of muscle (Camp and Birch 2011).

Long thoracic nerve

The long thoracic nerve is frequently injured during operations around the first rib, in the posterior triangle and in the axilla, and by misplaced intercostal drains. It is particularly susceptible to involvement in neuralgic amyotrophy. Serratus palsy is usual in preganglionic injury to C5, C6 and C7. Pain and loss of function are usual and are only slightly less than those seen after accessory nerve palsy. The signs are characteristic. The active ISHA is, on average, 130°; this is the only nerve lesion in which the active ISHA actually exceeds the total range of active abduction. The scapula is pulled upwards and towards the spine by the unopposed action of trapezius (Fig. 49.39), an action that is increased by the weight of the limb, which contributes to the winging and is most notable in protraction.

Dislocation of the shoulder: the suprascapular and axillary nerves

Although most nerve lesions in uncomplicated anterior dislocations are benign, it is well to remember the risk to adjacent vessels, more so in high-energy transfer injuries, in older patients and in those with peripheral vascular disease. The consequences of delay in treatment are severe. It is very hard to examine muscles in a patient with a fracture-dislocation of the shoulder. Sensory loss is inconsistent. Consider, for example, a patient after successful reduction of a dislocated shoulder, whose arm is supported in a sling. There are three simple tests: initiation of abduction shows that the suprascapular nerve is intact and that the rotator cuff is not ruptured; abnormal sensibility in the skin over deltoid indicates a lesion of the axillary nerve; and gentle extension of the shoulder on the part of the patient, supported as it is in a sling, means that the examiner can palpate activity in the posterior fibres of deltoid (Figs 49.40–49.41).

The diagnosis of nerve injury is by no means straightforward. All too often, rupture of the axillary nerve is not recognized until deltoid is atrophied, long past the ideal time for repair. The widely held view that deltoid is the abductor of the shoulder is erroneous. Deltoid provides power and stamina, and abduction is initiated and maintained by the suprascapular nerve, acting through supra- and infraspinatus, their tendons and attachments. Disruption of any component of this abductor mechanism interferes with or precludes abduction. Wynn Parry (1981) treated 145 patients in whom paralysis was confined to deltoid. The range of abduction was full or nearly so, and a system of training enabled most patients to return to full military duties. He wrote: 'It must be stressed that these movements providing full abduction and elevation are not trick movements, in the sense usually associated with this word; all the muscles involved normally help to abduct the shoulder. The scapulohumeral rhythm is quite normal and in the later stages of re-education the patient does not even need to rotate the humerus externally to initiate movement.' Seddon (1975) was a little more cautious, finding abduction to about 155° was more usual. The ISHA is diminished by about 20° in uncomplicated ruptures of the axillary nerve when there is no stiffness of the shoulder.

Axillary nerve

The axillary nerve innervates deltoid. Although a good range of elevation is usually maintained by an intact abductor mechanism, strength and stamina are greatly reduced. Early diagnosis of rupture of the axillary

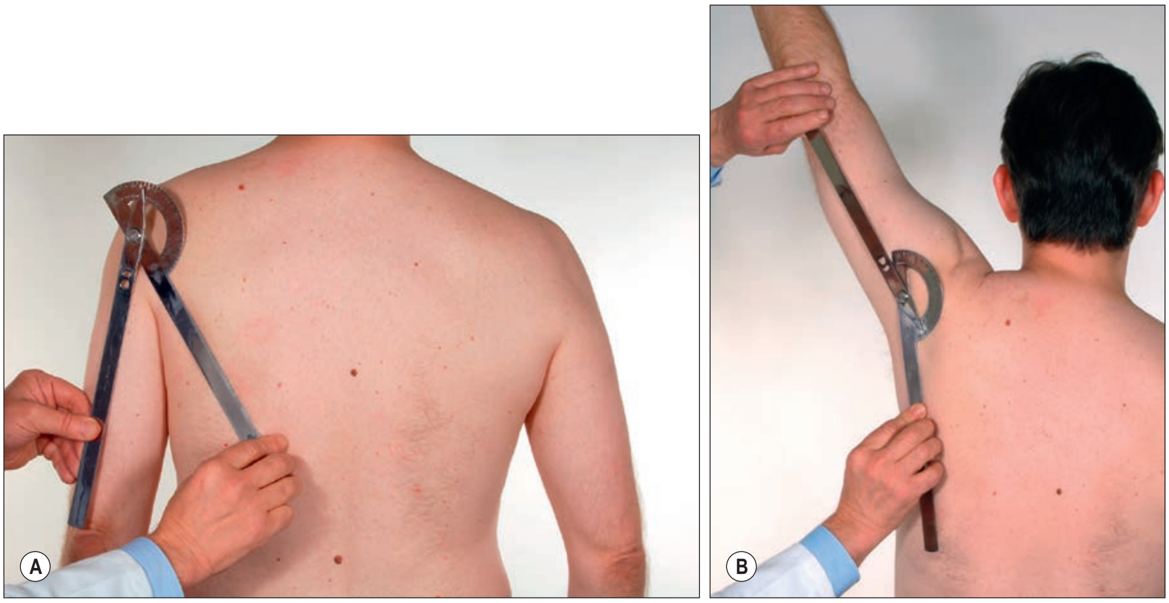

Fig. 49.36 The active inferior scapulohumeral angle (ISHA) in a normal shoulder is about 170°. **A**, At rest. **B**, Arm abducted. (Courtesy of Rolfe Birch, all rights reserved, published in Birch R, Surgical Disorders of the Peripheral Nerve, 2nd ed, 2011. Springer-Verlag, London.)

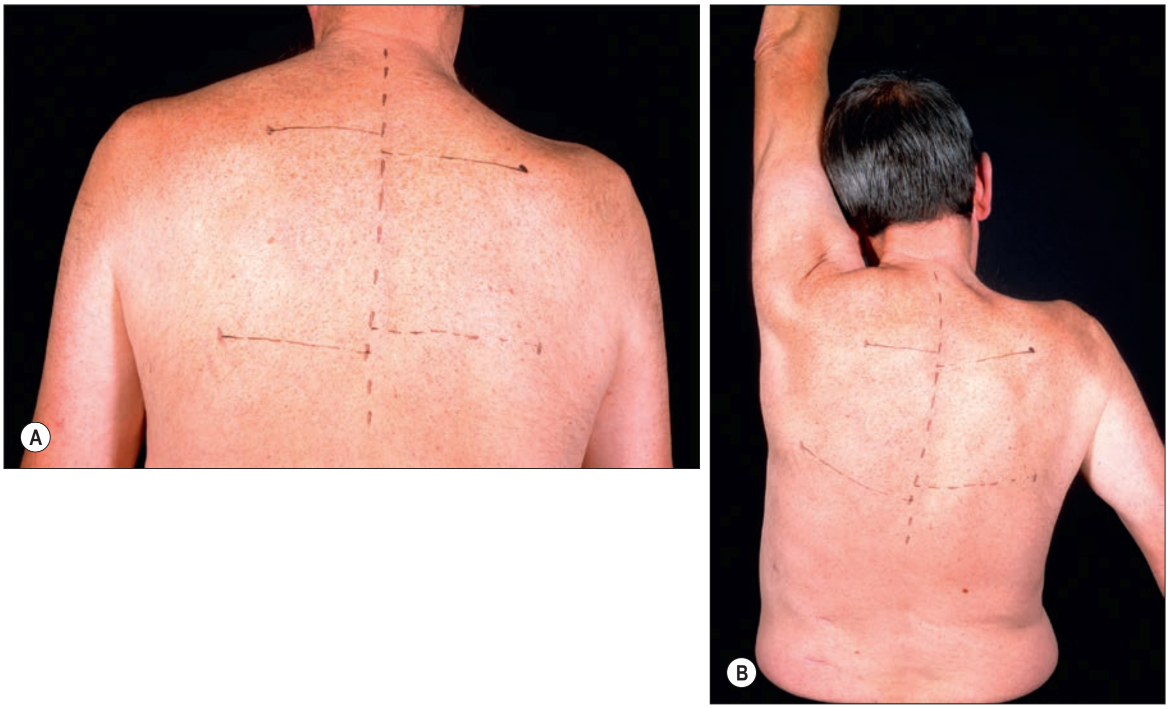

Fig. 49.37 A right accessory nerve palsy. **A**, At rest. **B**, Attempted abduction. The scapula drops down and away from the spine. The active ISHA is 30°. (Courtesy of Rolfe Birch, all rights reserved, published in Birch R, Surgical Disorders of the Peripheral Nerve, 2nd ed, 2011. Springer-Verlag, London.)

nerve can prove difficult; the nerve is deeply seated, which means that Tinel's sign is rarely detectable. Active movement is restricted by pain and by the restraint of any sling. The loss of sensation varies and there may not be complete anaesthesia. Patients with an intact suprascapular nerve and an intact rotator cuff are able to initiate abduction and many can fully elevate the arm, or nearly so. The power of forward flexion and of abduction is reduced to, at most, 30–40% of normal, whereas extension, with the shoulder at 90° of abduction, is 10% or less. One useful test is to palpate the posterior third of deltoid with the fingers and ask the patient to move the elbow gently backwards. It should be possible to detect activity in the muscle when the arm is supported in a sling or by the examiner's arm.

Suprascapular nerve

The suprascapular nerve is essential for abduction and lateral rotation at the glenohumeral joint. When the nerve or the rotator cuff is torn, or both are injured, the ISHA is so reduced that the patient is unable to move the arm away from the body. At rest, the head of the humerus drops inferiorly and migrates proximally in attempted abduction (see Fig. 49.41). In isolated cuff tears, the ISHA opens to about 30° or even more. In isolated axillary palsy, the ISHA is sometimes normal, or, more often, reduced by about 20° (**Figs 49.42–49.43**).

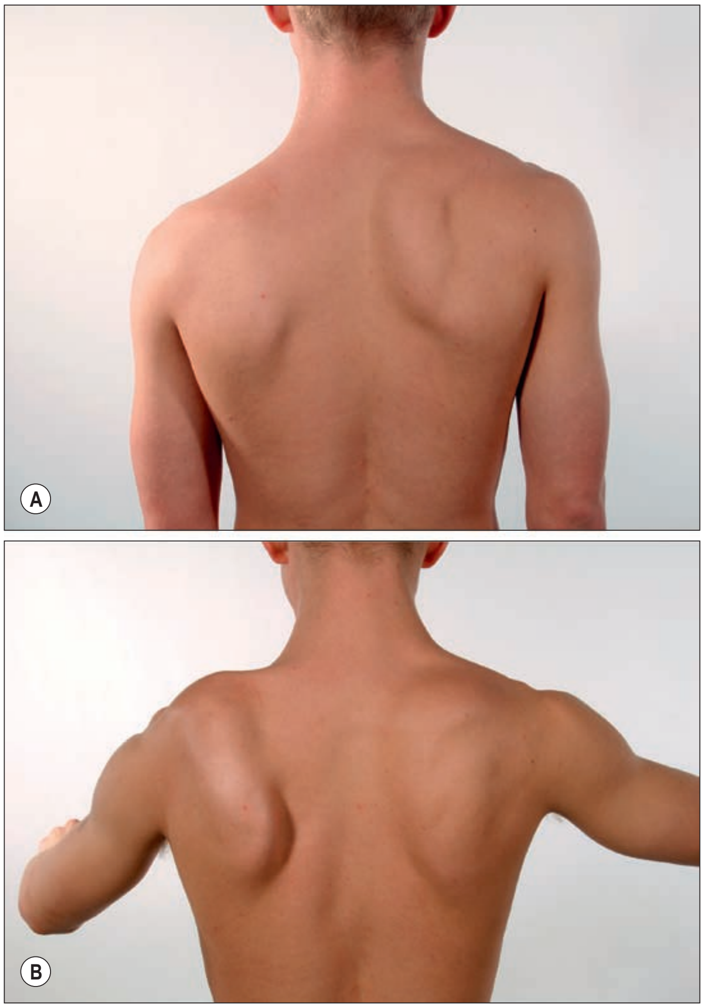

Fig. 49.38 A left accessory nerve palsy. Scapular winging, without prominence of the lower fibres of trapezius, in a case where there is some early recovery into the upper fibres after repair of the accessory nerve. **A**, At rest, the scapula is displaced downwards and away from the spine. **B**, Arm abducted. (Courtesy of Rolfe Birch, all rights reserved, published in Birch R, Surgical Disorders of the Peripheral Nerve, 2nd ed, 2011. Springer-Verlag, London.)

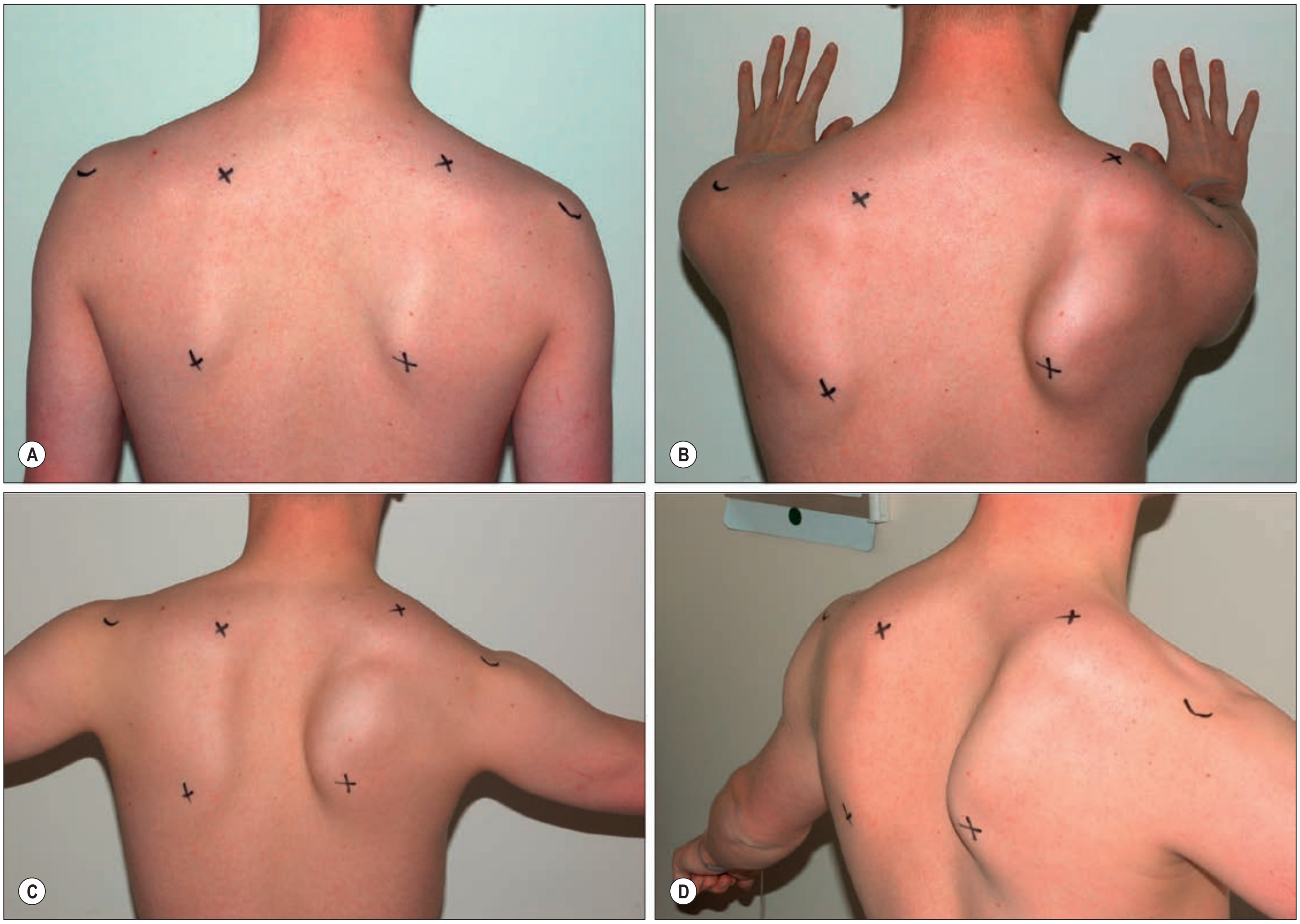

Fig. 49.39 Scapular winging in long thoracic nerve palsy. This is easily distinguishable from the winging provoked by accessory nerve palsy by the position of the scapula, which is drawn upwards and towards the spine by the unopposed action of trapezius, levator scapulae and the rhomboids. **A**, Arms at rest. **B**, Hands pressed against the wall. **C**, Attempted abduction. **D**, Oblique view. (Courtesy of Rolfe Birch, all rights reserved, published in Birch R, Surgical Disorders of the Peripheral Nerve, 2nd ed, 2011. Springer-Verlag, London.)

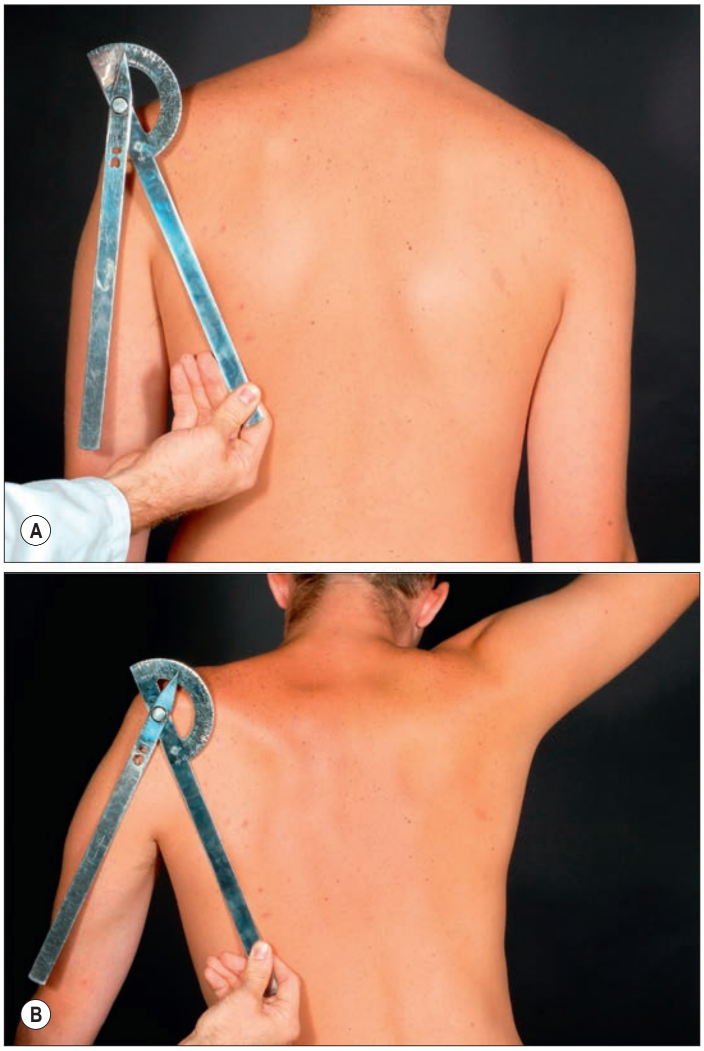

Fig. 49.40 Initiation of abduction, with opening of the active inferior scapulohumeral angle (ISHA), was the first sign of recovery into supraspinatus after repair of the suprascapular nerve. The lesion of the axillary nerve was irreparable. **A**, At rest. **B**, Attempted abduction. (Courtesy of Rolfe Birch, all rights reserved, published in Birch R, Surgical Disorders of the Peripheral Nerve, 2nd ed, 2011. Springer-Verlag, London.)

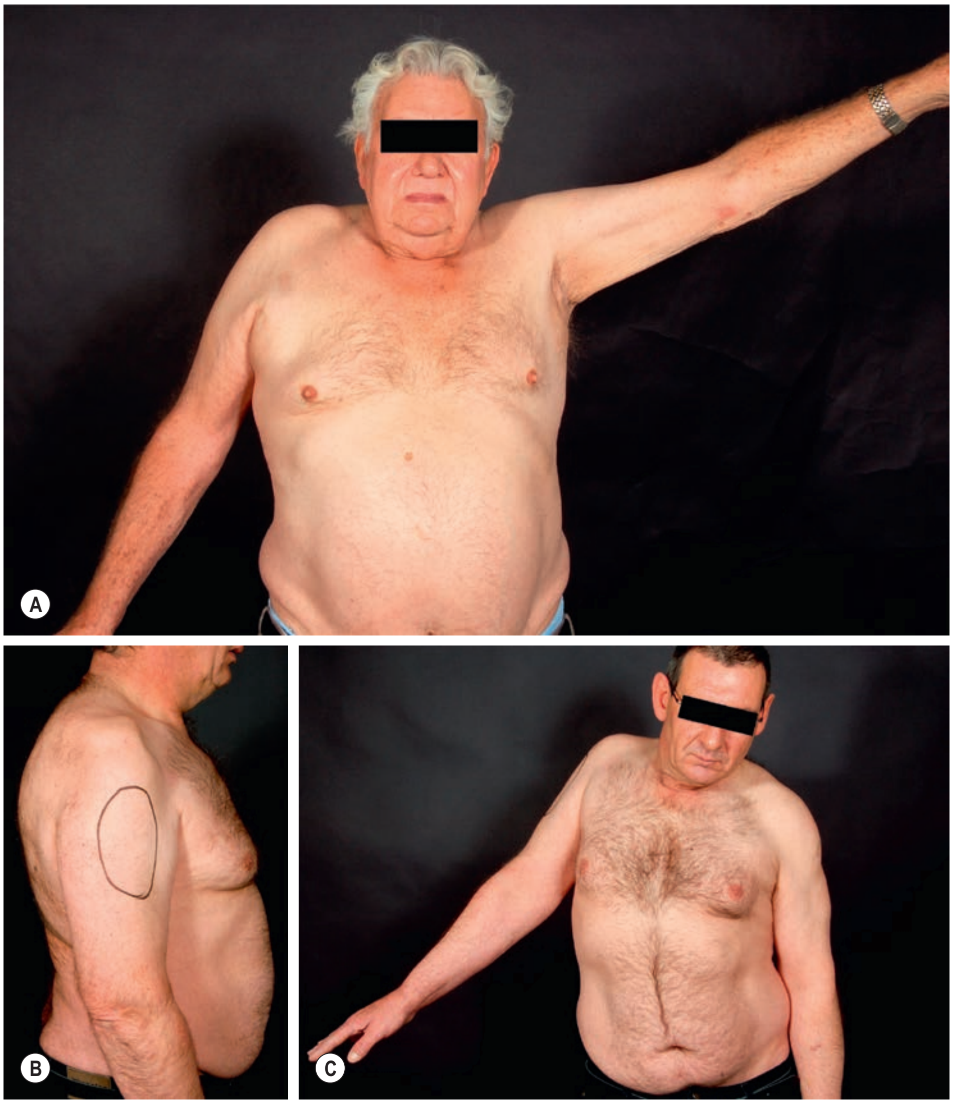

Fig. 49.41 Rupture of the rotator cuff, with lesions of the suprascapular and axillary nerves from fracture-dislocation of the shoulder. **A,** The range of elevation at the right shoulder in a 74-year-old man, in whom there was clear evidence of recovery for both of the nerves. **B**–**C**, This shipwright held on to a cable to rescue a man from the River Thames. The weight of the man and the force of the current were such that he felt the muscles tearing in his right shoulder; then he felt the head of the humerus pulling out from the socket and his arm went dead. Both nerves were recovering. (Courtesy of Rolfe Birch, all rights reserved, published in Birch R, Surgical Disorders of the Peripheral Nerve, 2nd ed, 2011. Springer-Verlag, London.)

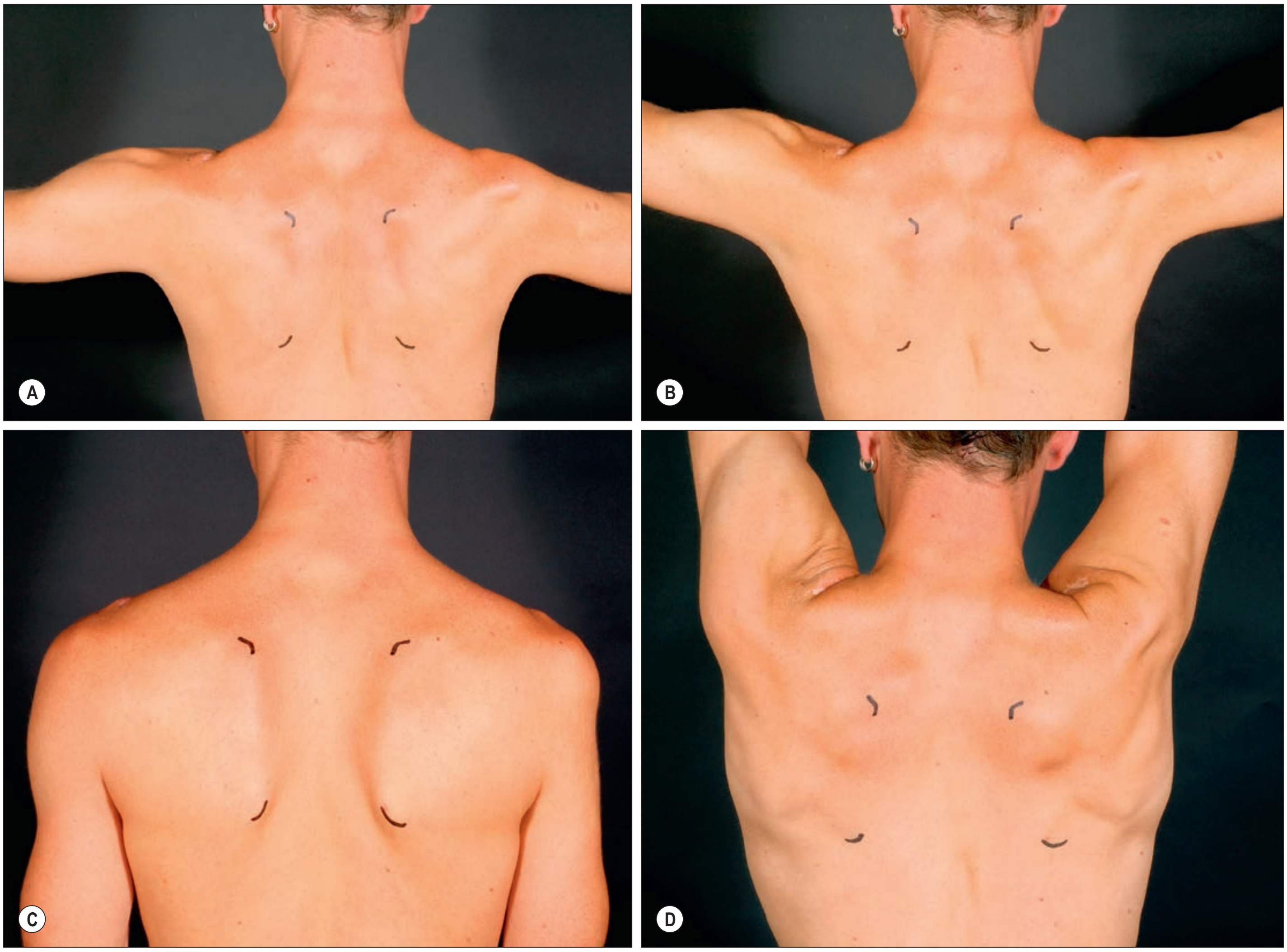

Fig. 49.42 **A-D,** Movement of the scapula in a case of rupture of the right axillary nerve. **D**, The active inferior scapulohumeral angle (ISHA) on the side of the injury is reduced by 20°, showing that 20° of the range of elevation is provided by extra movement at the thoracoscapular joint. (Courtesy of Rolfe Birch, all rights reserved, published in Birch R, Surgical Disorders of the Peripheral Nerve, 2nd ed, 2011. Springer-Verlag, London.)

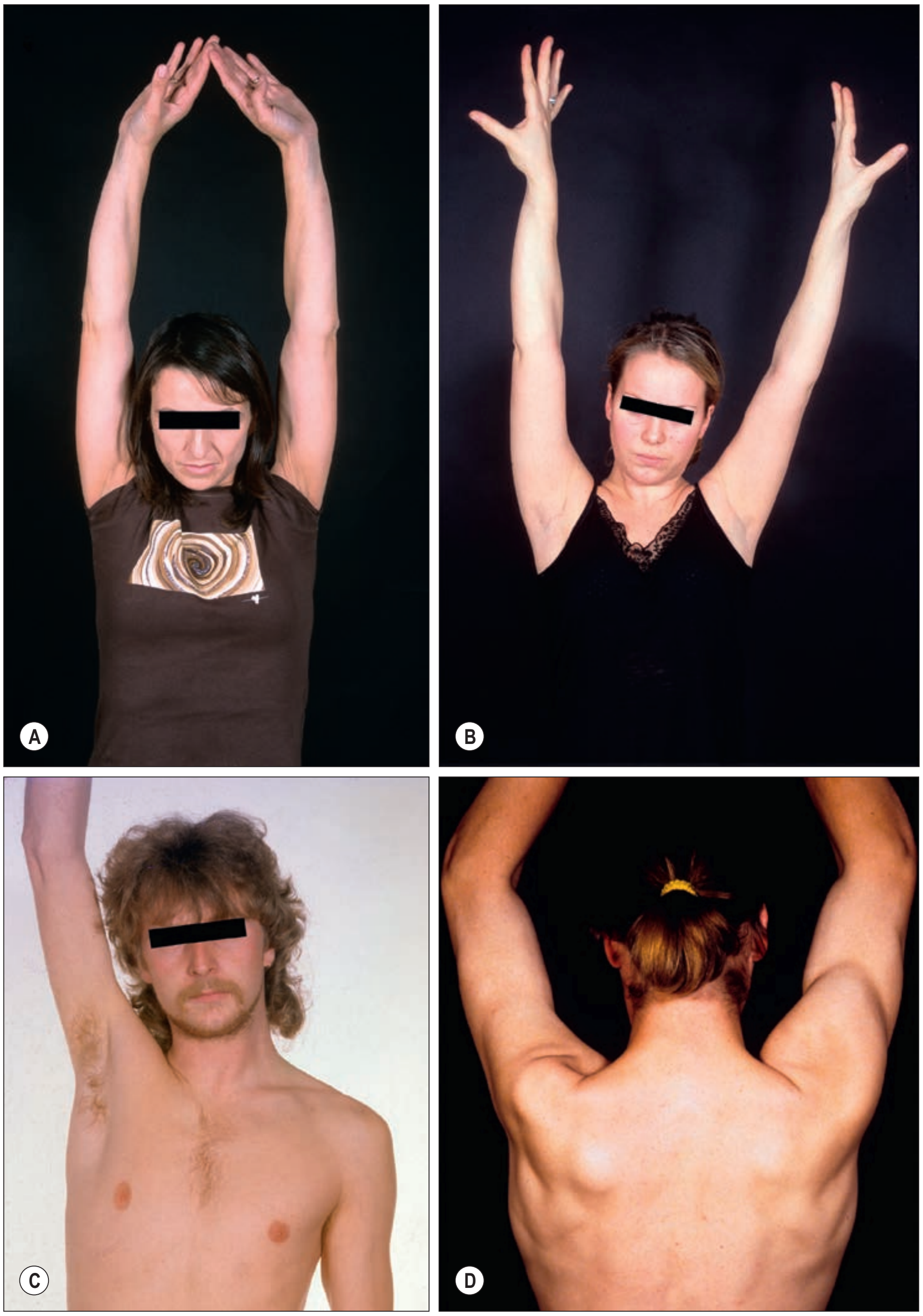

Fig. 49.43 A–D, Elevation of the upper limb in full medial rotation by supraspinatus in the absence of deltoid in four cases of proven rupture of the axillary nerve. Note the activity in the clavicular head of pectoralis major in **C**. (Courtesy of Rolfe Birch, all rights reserved, published in Birch R, Surgical Disorders of the Peripheral Nerve, 2nd ed, 2011. Springer-Verlag, London.)

Ulnar nerve

The ulnar nerve arises from the medial cord (eighth cervical and first thoracic ventral rami) but often receives fibres from the seventh cervical ventral ramus. It usually has no branches in the arm, but occasionally may give a branch to the medial head of triceps (see Figs 49.29, 49.35, 49.44, 48.12). The nerve runs distally through the axilla, medial to the axillary artery and between it and the vein, and continues distally medial to the brachial artery as far as the mid-arm. Here, it pierces the medial intermuscular septum, inclining medially as it descends anterior to the medial head of triceps to the interval between the medial epicondyle and the olecranon. The further course of the ulnar nerve is described in Chapter 50 and Chapter 81.

Radial nerve

The radial nerve is the largest branch of the brachial plexus. It arises from the posterior cord (fifth, sixth, seventh and eighth cervical ventral rami, and occasionally the first thoracic ventral ramus) (see Figs 49.33, 49.35, 49.45, 48.9) and descends behind the third part of the axillary artery and the upper part of the brachial artery, anterior to subscapularis above and the tendons of latissimus dorsi and teres major below, giving branches to the medial head of triceps at this level. With the profunda brachii artery, it inclines dorsally, passing through the lower triangular space below the lower border of teres major, between the long head of triceps and the humerus. Here, it supplies the long head of triceps and gives rise to the posterior cutaneous nerve of the arm, which supplies the skin along the posterior surface of the upper arm. It then spirals obliquely across the back of the humerus, lying posterior to the uppermost fibres of the medial head of triceps, which separate the nerve from the bone in the first part of the spiral groove. It gives off a muscular branch to the lateral head of triceps and a branch that passes through the medial head of triceps to innervate anconeus. On reaching the lateral side of the humerus, the radial nerve pierces the lateral intermuscular septum to enter the anterior compartment of the arm. The further course of the radial nerve is described in Chapter 50 and Chapter 81.

The branches of the radial nerve in the upper arm are: muscular, cutaneous, articular, superficial terminal and posterior interosseous.

Muscular branches

Muscular branches supply triceps, anconeus, brachioradialis, extensor carpi radialis longus and brachialis in medial, posterior and lateral groups. Medial muscular branches arise from the radial nerve on the medial side of the arm and supply the medial and long heads of triceps. The branch to the medial head is a long, slender filament that lies close to the ulnar nerve as far as the distal third of the arm, and is often termed the ulnar collateral nerve. A large posterior muscular branch arises from the nerve as it lies in the humeral groove and divides to supply the medial and lateral heads of triceps and anconeus. The branch to anconeus is a long nerve that descends in the medial head of triceps and partially supplies it; the nerve is accompanied by the middle collateral branch of the profunda brachii artery and passes behind the elbow joint to end in anconeus. Lateral muscular branches arise anterior to the lateral intermuscular septum and supply the lateral part of brachialis, brachioradialis and extensor carpi radialis longus.

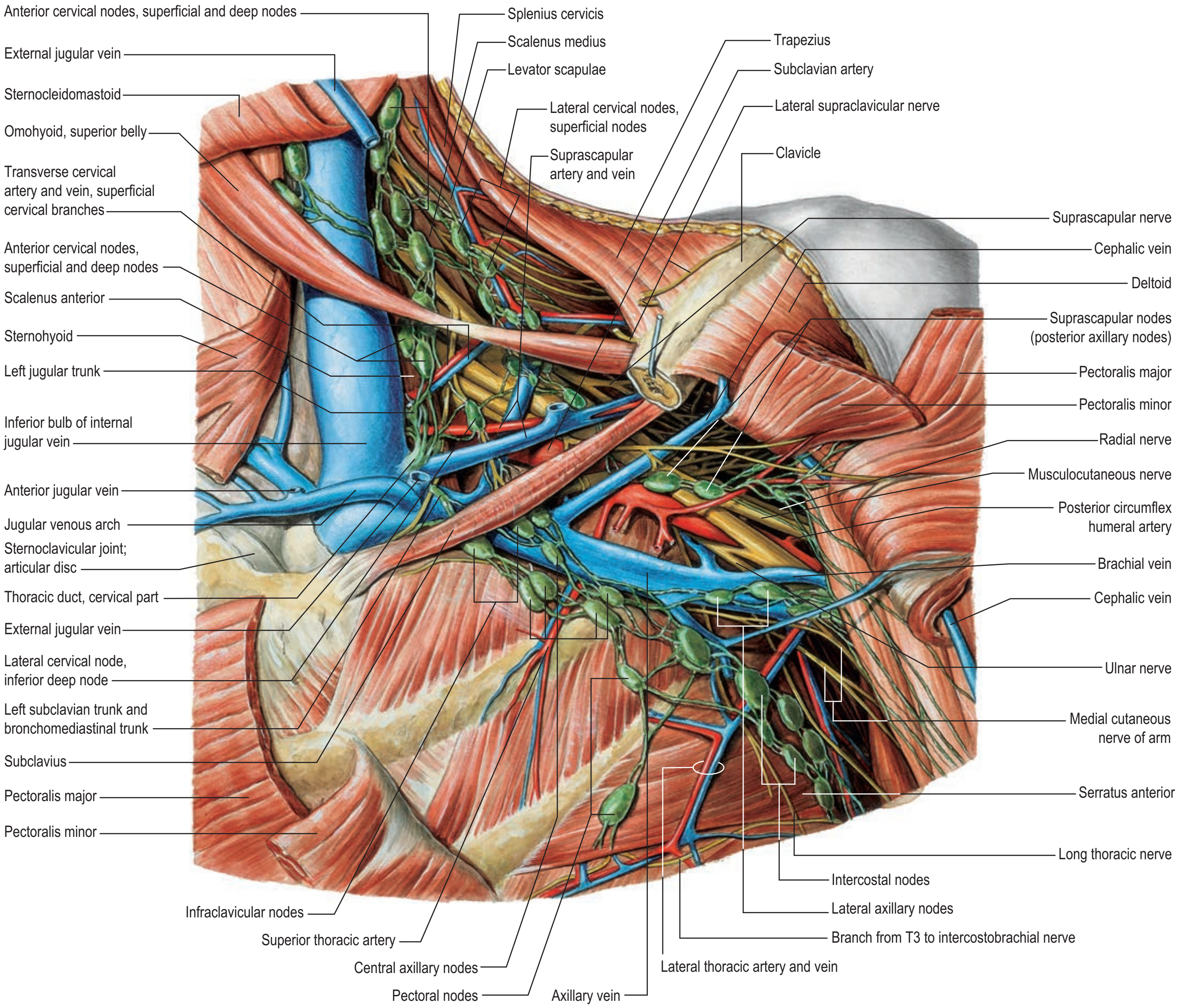
Anterior cervical nodes, superficial and deep nodes
External jugular vein
Sternocleidomastoid
Omohyoid, superior belly
Transverse cervical artery and vein, superficial cervical branches
Anterior cervical nodes, superficial and deep nodes
Scalenus anterior
Sternohyoid
Left jugular trunk
Inferior bulb of internal jugular vein
Anterior jugular vein
Jugular venous arch
Sternoclavicular joint; articular disc
Thoracic duct, cervical part
External jugular vein
Lateral cervical node, inferior deep node
Left subclavian trunk and bronchomediastinal trunk
Subclavius
Pectoralis major
Pectoralis minor
Infraclavicular nodes
Superior thoracic artery
Central axillary nodes
Pectoral nodes
Axillary vein
Splenius cervicis
Scalenus medius
Levator scapulae
Lateral cervical nodes, superficial nodes
Suprascapular artery and vein
Trapezius
Subclavian artery
Lateral supraclavicular nerve
Clavicle
Suprascapular nerve
Cephalic vein
Deltoid
Suprascapular nodes (posterior axillary nodes)
Pectoralis major
Pectoralis minor
Radial nerve
Musculocutaneous nerve
Posterior circumflex humeral artery
Brachial vein
Cephalic vein
Ulnar nerve
Medial cutaneous nerve of arm
Serratus anterior
Long thoracic nerve
Intercostal nodes
Lateral axillary nodes
Branch from T3 to intercostobrachial nerve
Lateral thoracic artery and vein

Fig. 49.45 The left axillary fossa and the deep aspect of the thoracic inlet, anterior aspect. The clavicle has been partially removed and the pectoral muscles have been reflected. (Sobotta Atlas of Human Anatomy © Elsevier GmbH, Urban & Fischer, Munich.)

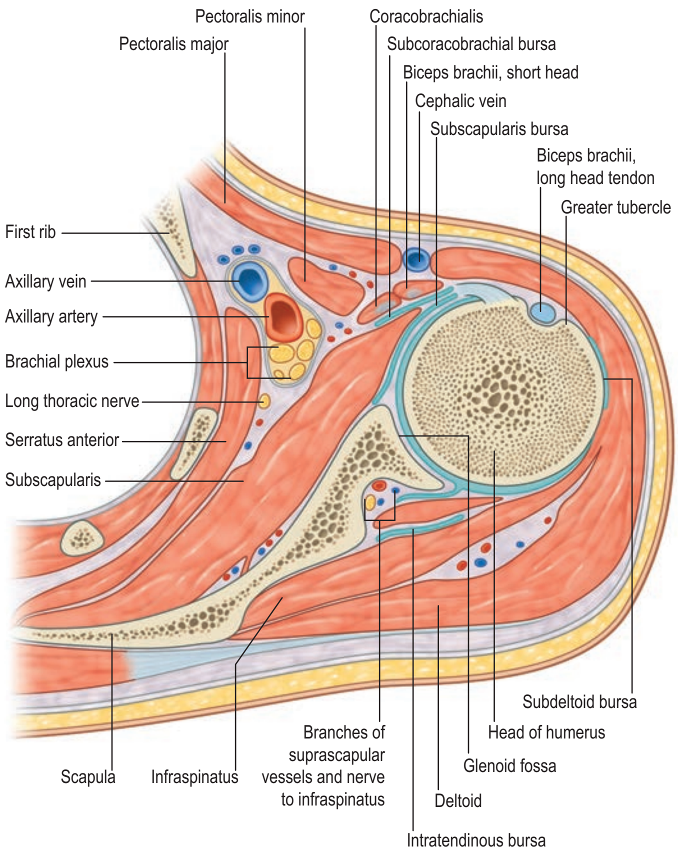
Pectoralis minor
Pectoralis major
Coracobrachialis
Subcoracobrachial bursa
Biceps brachii, short head
Cephalic vein
Subscapularis bursa
Biceps brachii, long head tendon
Greater tubercle
First rib
Axillary vein
Axillary artery
Brachial plexus
Long thoracic nerve
Serratus anterior
Subscapularis
Subdeltoid bursa
Head of humerus
Glenoid fossa
Branches of suprascapular vessels and nerve to infraspinatus
Deltoid
Scapula
Infraspinatus
Intratendinous bursa

Fig. 49.46 A transverse section through the left shoulder joint and axilla, viewed from below.

Cutaneous branches

Cutaneous branches are the posterior and lower lateral cutaneous nerves of the arm and the posterior cutaneous nerve of the forearm.

Posterior cutaneous nerve of the arm. The small posterior cutaneous nerve of the arm arises in the axilla and passes medially to supply the skin on the dorsal surface of the arm nearly as far as the olecranon. It crosses posterior to, and communicates with, the intercostobrachial nerve.

Lower lateral cutaneous nerve of the arm. The lower lateral cutaneous nerve of the arm perforates the lateral head of triceps distal to the deltoid tuberosity, passes to the front of the elbow close to the cephalic vein, and supplies the skin of the lateral part of the lower half of the arm.

Posterior cutaneous nerve of the forearm. The posterior cutaneous nerve of the forearm arises with the lower lateral cutaneous nerve of the arm. Perforating the lateral head of triceps, it descends first lateral in the arm, then along the dorsum of the forearm to the wrist, supplying the skin in its course. Near its termination it joins dorsal branches of the lateral cutaneous nerve of the forearm.

AXILLA

Boundaries

The axilla is a pyramidal region between the upper thoracic wall and the arm (**Figs 49.45–49.46**; see Fig. 49.35). Its blunt apex continues into the root of the neck (cervico-axillary canal) between the external border of the first rib, superior border of the scapula, posterior surface of the clavicle, and the medial aspect of the coracoid process. Its triangular base, which is virtual, can be imagined as facing downwards; it is broad at the chest and narrow at the arm, and corresponds to the skin and a thick layer of axillary fascia between the inferior borders of pectoralis

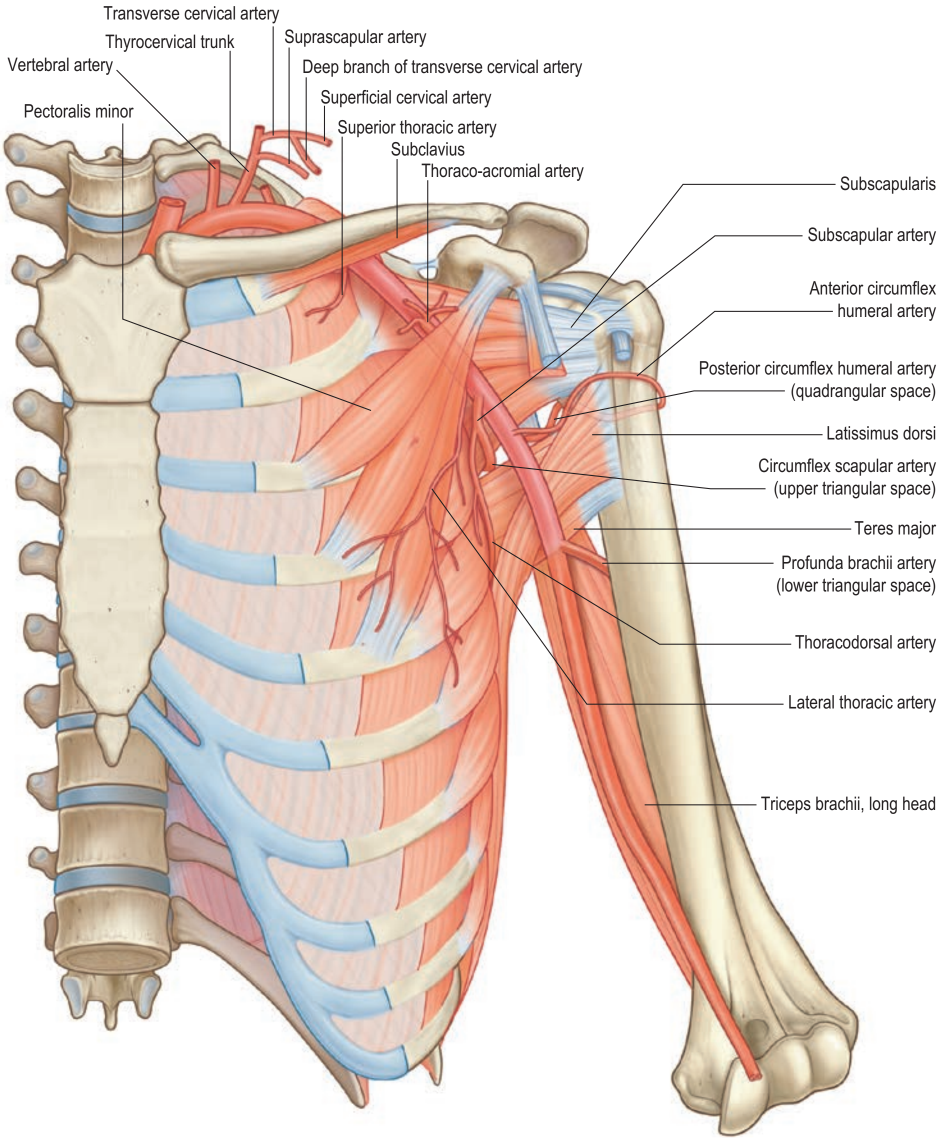
Transverse cervical artery
Thyrocervical trunk
Vertebral artery
Pectoralis minor
Suprascapular artery
Deep branch of transverse cervical artery
Superficial cervical artery
Superior thoracic artery
Subclavius
Thoraco-acromial artery
Subscapularis
Subscapular artery
Anterior circumflex humeral artery
Posterior circumflex humeral artery (quadrangular space)
Latissimus dorsi
Circumflex scapular artery (upper triangular space)
Teres major
Profunda brachii artery (lower triangular space)
Thoracodorsal artery
Lateral thoracic artery
Triceps brachii, long head

Fig. 49.47 The left axillary artery and its branches. (With permission from Drake RL, Vogl AW, Mitchell A (eds), Gray's Anatomy for Students, 2nd ed. Elsevier, Churchill Livingstone. Copyright 2010.)

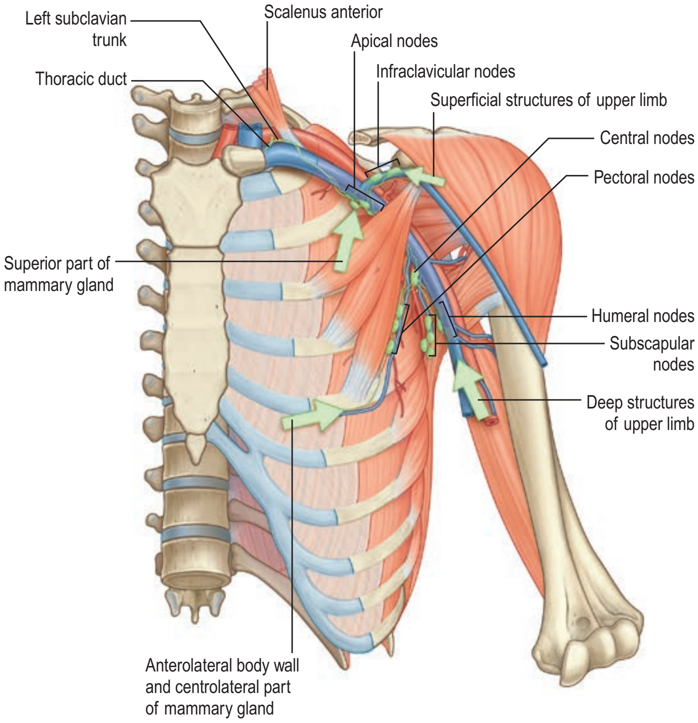
Left subclavian trunk
Thoracic duct
Scalenus anterior
Apical nodes
Infraclavicular nodes
Superficial structures of upper limb
Central nodes
Pectoral nodes
Superior part of mammary gland
Humeral nodes
Subscapular nodes
Deep structures of upper limb
Anterolateral body wall and centrolateral part of mammary gland

Fig. 49.48 Lymph nodes and vessels associated with the left axilla. Arrows indicate the direction of flow. (With permission from Drake RL, Vogl AW, Mitchell A (eds), Gray's Anatomy for Students, 2nd ed. Elsevier, Churchill Livingstone. Copyright 2010.)

major anteriorly and latissimus dorsi posteriorly. It is convex upwards, conforming to the concavity of the armpit.

The anterior wall is formed by pectorales major and minor, the former covering the whole wall, and the latter its intermediate cranial part, with a clear fascial plane between the two muscles. The interval between the upper border of pectoralis minor and the clavicle is occupied by the clavipectoral fascia (see Fig. 49.27). The posterior wall is formed by subscapularis superiorly and teres major and latissimus dorsi inferiorly. The medial 'wall' is convex laterally and is composed of the first four ribs and their associated intercostal muscles, together with the upper part of serratus anterior. The anterior and posterior walls converge laterally; the 'wall' is narrow and consists of the humeral intertubercular sulcus. The lateral angle lodges coracobrachialis and biceps.

Contents

The axilla contains the axillary vessels, the infraclavicular part of the brachial plexus and its branches, lateral branches of some intercostal nerves, many lymph nodes and vessels, loose adipose areolar tissue and, in many instances, the 'axillary tail' of the breast. The axillary vessels and brachial plexus run from the apex to the base along the lateral wall, nearer to the anterior wall; the axillary vein is anteromedial to the artery. The obliquity of the upper ribs means that the neurovascular bundle, after it emerges from behind the clavicle, crosses the first intercostal space, and so its relations are different at upper and lower levels. Thoracic branches of the axillary artery are in contact with the pectoral muscles. The lateral thoracic artery reaches the thoracic wall along the lateral margin of pectoralis minor. Subscapular vessels descend on the posterior wall at the lower margin of subscapularis. The subscapular and thoracodorsal nerves cross the anterior surface of latissimus dorsi at different inclinations. Circumflex scapular vessels wind round the lateral border of the scapula; posterior circumflex humeral vessels and the axillary nerve curve back and laterally around the surgical neck of the humerus (Fig. 49.47; see Fig. 49.31).

No large vessel lies on the medial 'wall', which is crossed proximally only by small branches of the superior thoracic artery. The long thoracic nerve descends on serratus anterior and the intercostobrachial nerve perforates the upper anterior part of this wall, crossing the axilla to its lateral 'wall'.

Axillary lymph nodes

There are between 20 and 30 axillary nodes, divided into five not wholly distinct groups, namely, lateral, anterior (pectoral), posterior (subscapular), central and apical (see Fig. 53.24). Four of the groups are intermediary and only the apical group is terminal. Collectively, they drain the entire upper limb, breast and trunk above the umbilicus.

The lateral group of four to six nodes is posteromedial to the axillary vein; its afferents drain the whole limb, except the vessels that accompany the cephalic vein (**Fig. 49.48**; see Figs 49.45, 53.24). Efferent vessels pass partly to the central and apical axillary groups, and partly to the inferior deep cervical nodes. The anterior group of four or five nodes spreads along the inferior border of pectoralis minor near the lateral thoracic vessels. Their afferents drain the skin and muscles of the supraumbilical anterolateral body wall and breast, and their efferents pass partly to the central and partly to the apical axillary nodes. The posterior group of six or seven nodes lie on the inferior margin of the posterior axillary wall, along the subscapular vessels. Their afferents drain the skin and superficial muscles of the inferior posterior region of the neck and the dorsal aspect of the trunk down to the iliac crest, and their efferents pass to the apical and central axillary nodes. A central group of three or four large nodes embedded in axillary fat receives afferents from all preceding groups, and their efferents drain to the apical nodes. An apical group of six to twelve nodes is partly posterior to the superior part of pectoralis minor and partly above its superior border, extending to the apex of the axilla medial to the axillary vein. The only direct territorial afferents are those that accompany the cephalic vein and/or some that drain the upper peripheral region of the breast; the group drains all the other axillary nodes. Their efferents unite as the subclavian trunk and drain directly to either the jugulosubclavian venous junction, the subclavian vein, the jugular lymphatic trunk or (occasionally) to a right lymphatic duct; the left trunk usually ends in the thoracic duct (see Fig. 35.16). A few efferents from apical nodes usually reach the inferior deep cervical nodes. One or two infraclavicular nodes appear beside the cephalic vein in the groove between pectoralis major and deltoid, just inferior to the clavicle. Their efferents pass through the clavipectoral fascia to the apical axillary nodes. Occasionally, some pass anterior to the clavicle to the inferior deep cervical (supraclavicular) nodes.

Bonus e-book content

Fig. 49.36 The active inferior scapulohumeral angle (ISHA) in a normal shoulder is about 170°.

Fig. 49.37 A right accessory nerve palsy.

Fig. 49.38 A left accessory nerve palsy.

Fig. 49.39 Scapular winging in long thoracic nerve palsy.

Fig. 49.40 Initiation of abduction, with opening of the active inferior scapulohumeral angle (ISHA), was the first sign of recovery into supraspinatus after repair of the suprascapular nerve.

Fig. 49.41 Rupture of the rotator cuff, with lesions of the suprascapular and axillary nerves from fracture-dislocation of the shoulder.

Fig. 49.42 Movement of the scapula following rupture of the right axillary nerve.

Fig. 49.43 Elevation of the upper limb in full medial rotation by supraspinatus in the absence of deltoid in four cases of proven rupture of the axillary nerve.

Key references

Alizadehkhaiyat O, Fisher AC, Kemp GJ et al 2011 Shoulder muscle activation and fatigue during a controlled forceful hand-grip task. J Electromyogr Kinesiol 21:478–82.

A discussion of the principle that purposeful distal muscle activity causes upregulation and facilitation of segments more proximal in the upper limb kinetic chain.

Bankart AS 1923 Recurrent or habitual dislocation of the shoulder-joint. Br Med J 2:1132–3.

The original description of the lesion that consumes so much clinical time.

Birch R 2011 Surgical Disorders of the Peripheral Nerves, 2nd ed. London: Springer-Verlag.

An account of the current state-of-the-art practice of diagnosis and management of surgical lesions of the peripheral nerves, including the brachial plexus.

Boileau P, Walch G 1997 The three-dimensional geometry of the proximal humerus. Implications for surgical technique and prosthetic design. J Bone Joint Surg Br 79:857–65.

The seminal European publication that introduced the science of measurement to the understanding of the morphology of the proximal humerus, and from which all subsequent work takes its lead.

Burkhart SS, Esch JC, Jolson RS 1993 The rotator crescent and rotator cable: an anatomic description of the shoulder's 'suspension bridge'. Arthroscopy 9:611–6.

A description and explanation of the clinical relevance of the anteroposterior capsular ''endoskeleton' or fibrous frame (Gagey et al 1993) of the shoulder that confers stability on the moving humeral head.

Dancker M 2013 The clinical-functional anatomy of the teres major muscle [diploma thesis]. Innsbruck Medical University.

Teres major was little studied until this cadaveric study. The muscle might provide a motor for an absent or insufficient subscapularis; the information given will assist the surgeon in planning transfer of the muscle.

Gagey O, Arcache J, Welby F et al 1993 [Fibrous frame of the rotator cuff. The concept of fibrous lock]. [In French] Rev Chir Orthop Reparatrice Appar Mot 79:452–5.

The seminal anatomical publication that describes the architecture of the collagenous frame of the shoulder, and which also provides a cohesive explanation for the clinical syndromes of rotator cuff failure.

Hertel R, Lambert SM, Ballmer FT 1998 The deltoid extension lag sign for diagnosis and grading of axillary nerve palsy. J Shoulder Elbow Surg 7:97–9.

A description of an example of the value of testing muscle capacity by eccentric activity, a more sensitive clinical method of determining weakness (that is, decrement from normal without testing against the power of the observer) than using resistance against a load (concentric activity).

Leijnse JNAL, Han S-H, Kwon YH 2008 Morphology of deltoid origin and end tendons – a generic model. J Anat 213:733–42.

A description of the internal architecture of deltoid in relation to the discrete functions of the parts of that muscle.

Streit JJ, Lenarz CJ, Shishani Y et al 2012 Pectoralis major tendon transfer for the treatment of scapular winging due to long thoracic nerve palsy. J Shoulder Elbow Surg 21:685–90.

The largest series of the direct or indirect transfer of the sternal head of pectoralis major for insufficiency of serratus anterior in symptomatic scapular dyskinesia.

Taylor GI, Razaboni RM (eds) 1994 Michel Salmon: Anatomic Studies. Book 1, Arteries of the Muscles of the Extremities and the Trunk. Book 2, Arterial Anastomotic Pathways of the Extremities. St Louis: Quality Medical Publishing.

A book that contains the translated work of Dr Michel Salmon: it describes the blood supply to muscle, as well as the anastomotic pathways in the limbs.

Vangsness CT Jr, Jorgenson SS, Watson T et al 1994 The origin of the long head of the biceps from the scapula and glenoid labrum. An anatomical study of 100 shoulders. J Bone Joint Surg Br 76:951–4.

A detailed description of the variation in the cadaveric anatomy of the origin of biceps brachii, permitting more accurate interpretation of the clinical variance of this structure.

References

Alizadehkhaiyat O, Fisher AC, Kemp GJ et al 2011 Shoulder muscle activation and fatigue during a controlled forceful hand-grip task. J Electromyogr Kinesiol 21:478–82.

A discussion of the principle that purposeful distal muscle activity causes upregulation and facilitation of segments more proximal in the upper limb kinetic chain.

Atasoy E 2004 Thoracic outlet syndrome: anatomy. Hand Clin 20:7–14.

Bankart AS 1923 Recurrent or habitual dislocation of the shoulder-joint. Br Med J 2:1132–3.

The original description of the lesion that consumes so much clinical time.

Bavinck JN, Weaver DD 1986 Subclavian artery supply disruption sequence: hypothesis of a vascular etiology for Poland, Klippel-Feil, and Möbius anomalies. Am J Med Genet. 23: 903–18.

Birch R 2011 Surgical Disorders of the Peripheral Nerves, ed 2. London: Springer-Verlag.

An account of the current state-of-the-art practice of diagnosis and management of surgical lesions of the peripheral nerves, including the brachial plexus.

Boileau P, Walch G 1997 The three-dimensional geometry of the proximal humerus. Implications for surgical technique and prosthetic design. J Bone Joint Surg Br 79:857–65.

The seminal European publication that introduced the science of measurement to the understanding of the morphology of the proximal humerus, and from which all subsequent work takes its lead.

Brooks CH, Revell WJ, Heatley FW 1993 Vascularity of the humeral head after proximal humeral fractures. An anatomical cadaver study. J Bone Joint Surg Br 75B:132–6.

Burkart AC, Debski RE 2002 Anatomy and function of the glenohumeral ligaments in anterior shoulder instability. Clin Orthop Relat Res 400:32–9.

Burkhart SS, Esch JC, Jolson RS 1993 The rotator crescent and rotator cable: an anatomic description of the shoulder's ‘suspension bridge’. Arthroscopy 9:611–6.

A description and explanation of the clinical relevance of the anteroposterior capsular thickening linking subscapularis with the posterior rotator cuff, forming part of the fibrous ‘endoskeleton’ or fibrous frame (Gagey et al 1993) of the shoulder that confers stability on the moving humeral head.

Camp SJ, Birch R 2011 Injuries to the spinal accessory nerve: a lesson to surgeons. J Bone Joint Surg Br 93:62–7.

Colegate-Stone T, Allom R, Singh R et al 2010 Classification of the morphology of the acromioclavicular joint using cadaveric and radiological analysis. J Bone Joint Surg Br 92:743–6.

Copeland SA, Howard RC 1978 Thoracoscapular fusion for facioscapulohumeral dystrophy. J Bone Joint Surg Br 60:547–51.

Cormack G, Lamberty B 1994 The arterial anatomy of skin flaps. Edinburgh: Churchill Livingstone.

Dancker M 2013 The clinical-functional anatomy of the teres major muscle [diploma thesis]. Innsbruck Medical University.

Teres major was little studied until this cadaveric study. The muscle might provide a motor for an absent or insufficient subscapularis; the information given will assist the surgeon in planning transfer of the muscle.

Dhir R, Lambert S 2014 The undescended scapular syndrome: Sprengel and the cleithrum. A case series and hypothesis. BJJ 96B(Suppl 11):176.

Dhir R, Chin K, Lambert S 2018 The congenital undescended scapula syndrome: Sprengel and the cleithrum: a case series and hypothesis. J Shoulder Elbow Surg 27:252–9.

Di Giacomo G, Pouliart N, Costantini A et al 2008 Atlas of Functional Shoulder Anatomy. New York: Springer.

Gagey O, Arcache J, Welby F et al 1993 [Fibrous frame of the rotator cuff. The concept of fibrous lock]. [In French] Rev Chir Orthop Reparatrice Appar Mot 79:452–5.

The seminal anatomical publication that describes the architecture of the collagenous frame of the shoulder, and which also provides a cohesive explanation for the clinical syndromes of rotator cuff failure.

Gerber C, Schneeberger AG, Vinh TS 1990 The arterial vascularization of the humeral head. An anatomical study. J Bone Joint Surg Am 72:1486–94.

Halata Z, Baumann K 2008 Mechanoreceptors of the shoulder joint: structure and function. In: Di Giacomo G, Pouliart N, Costantini A et al (eds) Atlas of Functional Shoulder Anatomy. New York: Springer; Ch. 5.1.

Hertel R, Lambert SM, Ballmer FT 1998 The deltoid extension lag sign for diagnosis and grading of axillary nerve palsy. J Shoulder Elbow Surg 7:97–9.

A description of an example of the value of testing muscle capacity by eccentric activity, a more sensitive clinical method of determining weakness (that is, decrement from normal without testing against the power of the observer) than using resistance against a load (concentric activity).

Huang R, Zhi Q, Patel K et al 2000 Dual origin and segmental organisation of the avian scapula. Development 127: 3789–94.

Kambhampati S, Birch R, Cobiella C et al 2006 Posterior subluxation and dislocation of the shoulder in obstetric brachial plexus palsy. J Bone Joint Surg Br 88:213–9.

Keener JD, Chafik D, Kim HM et al 2010 Insertional anatomy of the triceps brachii tendon. J Shoulder Elbow Surg 19:399–405.

Lambert S 2005 Further opinion. Radial nerve palsy associated with fractures of the shaft of the humerus: a systematic review. J Bone Joint Surg Br 87:1647–52.

Leijnse JNAL, Han S-H, Kwon YH 2008 Morphology of deltoid origin and end tendons – a generic model. J Anat 213:733–42.

A description of the internal architecture of deltoid in relation to the discrete functions of the parts of that muscle.

Mochizuki T, Sugaya H, Uomizu M et al 2008 Humeral insertion of the supraspinatus and infraspinatus. New anatomical findings regarding the footprint of the rotator cuff. J Bone Joint Surg Am 90:962–9.

Oberlin C, Béal D, Leechavengvongs S et al 1994 Nerve transfer to biceps muscle using a part of ulnar nerve for C5–C6 avulsion of the brachial plexus: anatomical study and report of four cases. J Hand Surg [Am] 19:232–7.

Sewell MD, Al-Hadithy N, LeLeu A et al 2013 Instability of the sternoclavicular joint: current concepts in classification in treatment and outcomes. Bone Joint J 95:721–31.

Spinner RJ, Amrani KK, Kliot M et al 2006 Suprascapular intraneural ganglia and glenohumeral joint connections. J Neurosurg 104:551–7.

Staniek M, Brenner E 2012 Variations in the anatomy of the anterior-inferior rotator cuff: the ‘infraglenoid muscle’. Ann Anat 194:373–80.

Streit JJ, Lenarz CJ, Shishani Y et al 2012 Pectoralis major tendon transfer for the treatment of scapular winging due to long thoracic nerve palsy. J Shoulder Elbow Surg 21:685–90.

The largest series of the direct or indirect transfer of the sternal head of pectoralis major for insufficiency of serratus anterior in symptomatic scapular dyskinesia.

Taylor GI, Razaboni RM (eds) 1994 Michel Salmon: Anatomic Studies. Book 1, Arteries of the Muscles of the Extremities and the Trunk. Book 2, Arterial Anastomotic Pathways of the Extremities. St Louis: Quality Medical Publishing.

A book that contains the translated work of Dr Michel Salmon: it describes the blood supply to muscle, as well as the anastomotic pathways in the limbs.

Testut L 1904 Traite d'Anatomie Humaine. Cinquieme edition, 1, 804. Paris: O.Doin.

Vangsness CT Jr, Jorgenson SS, Watson T et al 1994 The origin of the long head of the biceps from the scapula and glenoid labrum. An anatomical study of 100 shoulders. J Bone Joint Surg Br 76:951–4.

A detailed description of the variation in the cadaveric anatomy of the origin of biceps brachii, permitting more accurate interpretation of the clinical variance of this structure.

Wynn Parry CB 1981 Rehabilitation of the Hand, 4th ed. London: Butterworth.

CHAPTER

50

Elbow and forearm

SKIN AND SOFT TISSUES

Skin

Cutaneous vascular supply

The skin of the elbow and forearm receives its blood supply from muscle perforators, fasciocutaneous networks and direct cutaneous vessels. The skin of the anterolateral cubital fossa is supplied by muscle perforators arising from the radial collateral and radial recurrent arteries. The skin of the medial cubital fossa receives branches from an anastomosis between the inferior ulnar collateral and the ulnar recurrent arteries. Small direct cutaneous vessels spring from the brachial artery. The skin of the posterolateral aspect of the elbow is supplied by branches of the posterior interosseous recurrent artery and a rich plexus of collateral and anastomosing arteries. The skin of the posteromedial aspect is supplied by branches of the superior and inferior ulnar collateral arteries and the posterior ulnar recurrent artery feeding into the plexus.

The skin of the anterior forearm is supplied by fasciocutaneous perforators; the largest is the inferior cubital artery, which arises from the radial artery at the distal apex of the cubital fossa and extends to midway down the forearm. Fasciocutaneous perforators from the radial artery supply the lateral two-thirds of the anterior surface of the forearm (see Fig. 48.5). The vessels pass in the intermuscular septa between brachioradialis and flexor carpi radialis, and between flexor carpi radialis and flexor digitorum superficialis. Fasciocutaneous perforators from the ulnar artery supply skin over the ulnar side of the anterior forearm and the medial quarter of the posterior forearm from the cubital fossa to the wrist. A small contribution comes from musculocutaneous perforators that pass through brachioradialis and flexor carpi ulnaris.

The skin of the distal third of the lateral forearm is supplied by the terminal perforating branches of the anterior interosseous artery. The central half of the posterior surface of the forearm, from the lateral edge of extensor digitorum, just below the lateral epicondyle of the humerus, to the wrist, is supplied by fasciocutaneous perforators from the posterior interosseous artery that pass along the intermuscular fascia between extensor carpi ulnaris and extensor digiti minimi.

Cutaneous innervation

A small area of skin anterolateral to the elbow is supplied by the lateral cutaneous nerve of the arm. The skin overlying the posterior aspect of the elbow is innervated by the posterior cutaneous nerve of the arm and proximal branches of the posterior cutaneous nerve of the forearm. The lateral cutaneous nerve of the forearm innervates the skin of the anterior half and radial posterior quarter of the forearm. The medial cutaneous nerve of the forearm supplies the skin overlying most of the elbow, the ulnar half of the anterior forearm and the ulnar quarter of the posterior forearm (**Fig. 50.1** and p. 956).

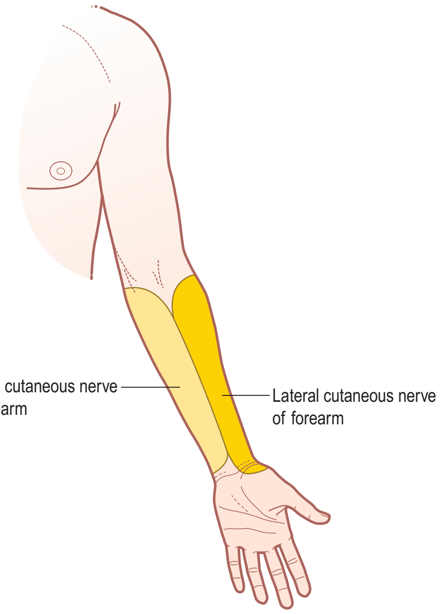
Medial cutaneous nerve of forearm
Lateral cutaneous nerve of forearm

Fig. 50.1 Sensory loss or disturbance after complete section of the medial and lateral cutaneous nerves of the forearm.

Soft tissues

Cubital fossa

The cubital fossa is a triangular depression in the anterior aspect of the upper forearm (see Fig. 48.53) (Macchi et al 2014). It is bounded proximally by the epicondylar line, medially by the lateral margin of pronator teres, and laterally by the medial face of brachioradialis; it is bisected by the tendon of biceps brachii. The deep fascia of the forearm forms its roof. It is continuous with the deep fascia of the anterior arm, attached to the medial and lateral humeral epicondyles and augmented by the bicipital aponeurosis, which sweeps across the medial and inferior part of the fossa to the fascia over the superficial flexor muscles. Supinator and brachialis lie in the floor of the fossa. From medial to lateral, the basilic, median cubital and cephalic veins lie in the superficial fascia. Branches of the medial cutaneous nerve of the forearm are closely related to the basilic vein. The lateral cutaneous nerve of the forearm runs down alongside the lateral edge of the tendon of biceps brachii. Deep to the deep fascia, and from medial to lateral, are the median nerve and the brachial artery, the latter inclining from the medial side of the arm to pass down the fossa close to the midline. The radial and ulnar arteries, with their accompanying veins, originate in the lower part of the fossa. The radial nerve enters the fossa laterally in the groove between brachioradialis and brachialis, and divides into the superficial radial and posterior interosseous nerves above the humero-radial joint. The superficial radial nerve continues down the forearm under cover of brachioradialis.

Compartments of the forearm

The deep fascia, the interosseous membrane and the fibrous intermuscular septa, some of which pass between the deep fascia and bone, divide the forearm into compartments. These include the superficial and deep flexor (anterior) compartments, the extensor (posterior) compartment, and a proximolateral compartment that includes brachioradialis and extensors carpi radialis longus and brevis (the mobile wad) (**Fig. 50.2**). The dense sheath of the antebrachial fascia (the deep fascia of the forearm) is continuous above with the brachial fascia. It is attached to the olecranon, the posterior border of the ulna, and the lateral and medial epicondyles. The fascia is thicker posteriorly and in the lower forearm. It is strengthened above by tendinous fibres from biceps and triceps. Near the wrist, two localized thickenings, the flexor and extensor retinacula, retain the digital tendons in position (Ch. 51). From its deep surface, septa pass between muscles, providing areas of additional attachment. Muscles arise from its inner aspect in the upper forearm. Vessels and nerves pass through apertures in the fascia; a large aperture anterior to the elbow transmits a venous communication between superficial and deep veins.

BONES

Humerus

Distal end of humerus

The distal end of the humerus is a modified condyle; it is wider transversely and has articular and non-articular parts (Figs 50.3–50.4). The articular part is curved forwards, so that its anterior and posterior surfaces lie in front of the corresponding surfaces of the shaft. It articulates with the radius and the ulna at the elbow joint, and is divided by a faint groove into a lateral capitulum and a medial trochlea.

The capitulum is a rounded, convex projection, considerably less than half a sphere, which covers the anterior and inferior surfaces of the lateral part of the condyle of the humerus but does not extend on to its posterior surface. It articulates with the discoid head of the radius, which lies in contact with its inferior surface in full extension of the elbow but slides on to its anterior surface during flexion. The groove of the trochlea winds backwards and laterally from the anterior to the posterior surface of the bone, and is wider, deeper and more symmetrical posteriorly. Anteriorly, the medial flange of the pulley is longer than the lateral, and the surface adjoining its projecting medial margin is convex to accommodate itself to the medial part of the upper surface of the coronoid process of the ulna. These asymmetries entail varying angulation between the humeral and ulnar axes, together with some conjunct rotation. The non-articular part of the condyle includes the medial and lateral epicondyles, and the olecranon, coronoid and radial fossae.

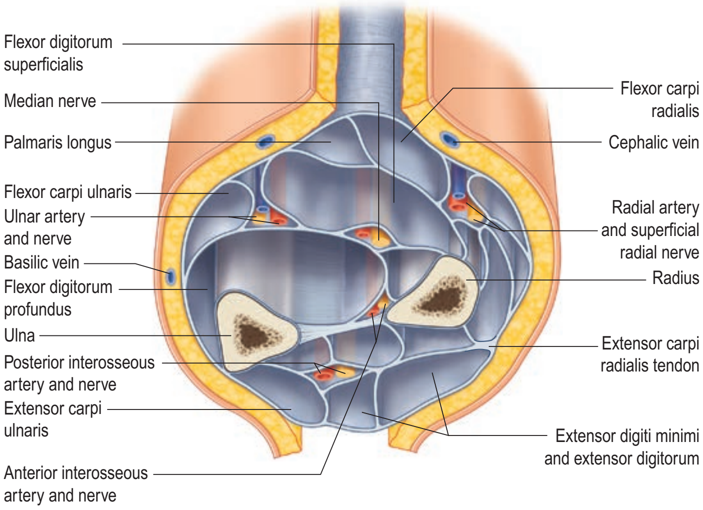
Flexor digitorum superficialis
Median nerve
Palmaris longus
Flexor carpi ulnaris
Ulnar artery and nerve
Basilic vein
Flexor digitorum profundus
Ulna
Posterior interosseous artery and nerve
Extensor carpi ulnaris
Anterior interosseous artery and nerve
Flexor carpi radialis
Cephalic vein
Radial artery and superficial radial nerve
Radius
Extensor carpi radialis tendon
Extensor digiti minimi and extensor digitorum

Fig. 50.2 The compartments of the forearm. A cross-section through the upper third of the left forearm.

Trochlea

The trochlea is a pulley-shaped surface that covers the anterior, inferior and posterior surfaces of the condyle of the humerus medially and articulates with the trochlear notch (greater sigmoid notch) of the ulna. On its lateral side, it is separated from the capitulum by a faint groove; its medial margin projects distally beyond the rest of the bone. When the elbow is extended, the inferior and posterior aspects of the trochlea are in contact with the ulna but, as the joint is flexed, the trochlear notch slides on to the anterior aspect so that its posterior aspect is then left uncovered (Giannicola et al 2015). The downward projection of the medial edge of the trochlea is the principal factor in determining the degree of angulation between the long axis of the humerus and the long axis of the supinated forearm when the elbow is extended.

Medial epicondyle

The medial border of the humerus ends by turning slightly backwards as the medial epicondyle, which forms a conspicuous, blunt projection on the medial side of the condyle. It is subcutaneous and usually visible, especially in passive flexion of the elbow. Its posterior surface is smooth and is crossed by the ulnar nerve, which lies in a shallow sulcus as it enters the forearm. The nerve can be felt and rolled against the bone here; if jarred against the epicondyle, a characteristic tingling sensation results. The lower part of the anterior surface of the medial epicondyle is marked by the attachment of the superficial group of forearm flexors: they arise from the epiphysis for the epicondyle but are entirely extracapsular. A capsular condensation, the ulnar collateral ligament of the elbow, is attached to the medial epicondyle medial to the attachments of these tendons.

Lateral epicondyle

The lateral border of the humerus ends at the lateral epicondyle; its lower portion constitutes the lateral supracondylar ridge. The lateral

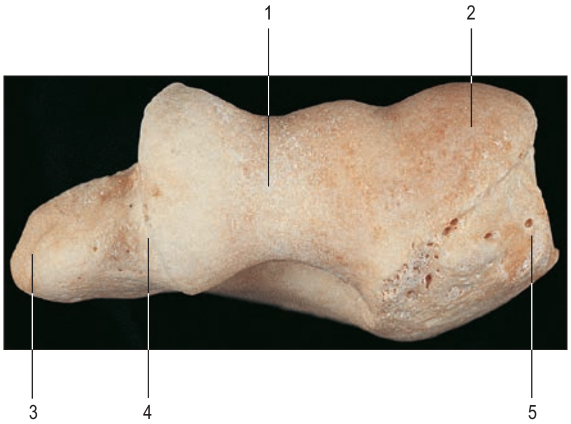

Fig. 50.4 Inferior aspect of the distal end of the left humerus. Key: 1, trochlea; 2, capitulum; 3, medial epicondyle; 4, sulcus for ulnar nerve; 5, lateral epicondyle.

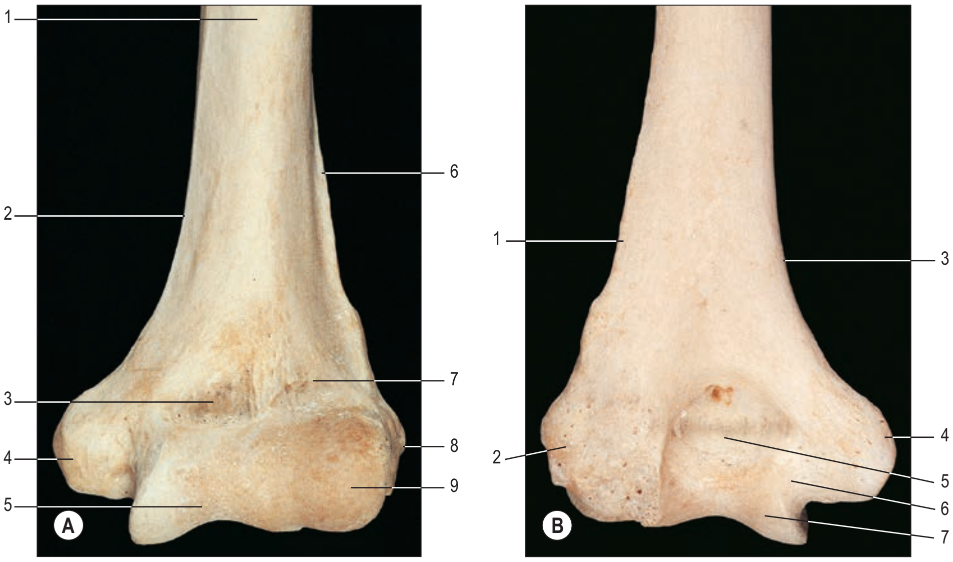
1
2
3
4
5
6
7
8
9
A
1
2
3
4
5
6
7
B

Fig. 50.3 **A**, Anterior aspect of the distal end of the left humerus. Key: 1, shaft; 2, medial supracondylar ridge; 3, coronoid fossa; 4, medial epicondyle; 5, trochlea; 6, lateral supracondylar ridge; 7, radial fossa; 8, lateral epicondyle; 9, capitulum. **B**, Posterior aspect of the distal end of the left humerus. Key: 1, lateral supracondylar ridge; 2, lateral epicondyle; 3, medial supracondylar ridge; 4, medial epicondyle; 5, olecranon fossa; 6, sulcus for ulnar nerve; 7, trochlea.

epicondyle occupies the lateral part of the non-articular portion of the condyle but does not project beyond the lateral supracondylar ridge. It turns slightly forwards, unlike the medial epicondyle, which turns slightly backwards. Its lateral and anterior surfaces show a well-marked impression for the tendons of the superficial group of the extensor muscles of the forearm (see Fig. 49.11A), which arise from the lateral side of the lower humeral epiphysis; like the flexor tendons, they are extracapsular. The posterior surface, which is very slightly convex, is easily felt in a depression visible behind the extended elbow. A small area on the posterior surface gives origin to anconeus. A small tubercle is readily palpable on the lateral epicondyle. The lateral ligamentous complex, a capsular condensation attached to the lateral epicondyle, is immediately anterior and inferior to this tubercle, deep to the origins of the common tendon (see later).

Olecranon, coronoid and radial fossae

The olecranon fossa is a deep hollow on the posterior surface of the condyle, immediately above the trochlea, that lodges the tip of the olecranon of the ulna when the elbow is extended. The floor of the fossa is always thin and may be partially deficient. A similar but smaller hollow, the coronoid fossa, lies immediately above the trochlea on the anterior surface of the condyle and accommodates the anterior margin of the coronoid process of the ulna during flexion of the elbow. A very slight depression, the radial fossa, lies above the capitulum on the lateral side of the coronoid fossa and is related to the margin of the head of the radius in full flexion of the elbow.

Ossification

The distal humerus ossifies as follows. During the first year, ossification begins in the capitulum and extends medially to form the main part of the articular surface. The centre for the medial part of the trochlea appears in the ninth year in females and tenth year in males. Ossification begins in the medial epicondyle in the fourth year in females and the sixth in males, and in the lateral epicondyle in about the twelfth year. The centre for the medial epicondyle forms a separate epiphysis, which is entirely extracapsular, on the posteromedial aspect of the epicondyle. It is separated from the rest of the lower epiphysis by a downgrowth from the shaft, with which it becomes continuous at about the twentieth year. The centres for the lateral epicondyle, capitulum and trochlea coalesce around puberty, and the composite epiphysis consolidates with the shaft in the fourteenth year in females and sixteenth in males.

Radius

The radius is the lateral bone of the forearm (Figs 50.5–50.7). It has expanded proximal and distal ends, the distal being much the broader. The shaft widens rapidly towards its distal end, and is convex laterally and concave anteriorly in its distal part. The radius articulates with the humeral capitulum, the lateral surface of the lateral ridge of the trochlea, the ulna and the carpus.

Proximal radius

The proximal radius includes a head, neck and tuberosity. The head is discoid, its proximal surface a shallow cup for articulation with the humeral capitulum. Its smooth articular periphery is vertically deepest medially, where it contacts the ulnar radial notch. The posterior surface of the radial head is palpable on the posterolateral aspect of the extended elbow. The head overhangs the neck, which is the circumferential constriction immediately below it, particularly laterally. The tuberosity is distal to the medial part of the neck; posteriorly, it is rough, whereas anteriorly, it is usually smooth.

Radial shaft

The radial shaft has a lateral convexity and is triangular in cross-section. The interosseous border is sharp, except proximally, near the tuberosity, and distally, where the interosseous border is the posterior margin of a small, elongated, triangular area, proximal to the ulnar notch. These two areas form the medial surface of the radial shaft. The interosseous membrane is attached to the distal three-quarters of the radial shaft, and connects the radius to the ulna. The anterior surface, between anterior and interosseous borders, is concave transversely and shows a distal anterior curvature. There is a proximally directed nutrient foramen and canal near the midpoint of the shaft. The posterior surface of the shaft, between the interosseous and posterior borders, is largely flat but may be slightly hollow proximally. The lateral surface is gently convex. A finely irregular oval area occurs near the midshaft; further distally, the surface is smooth.

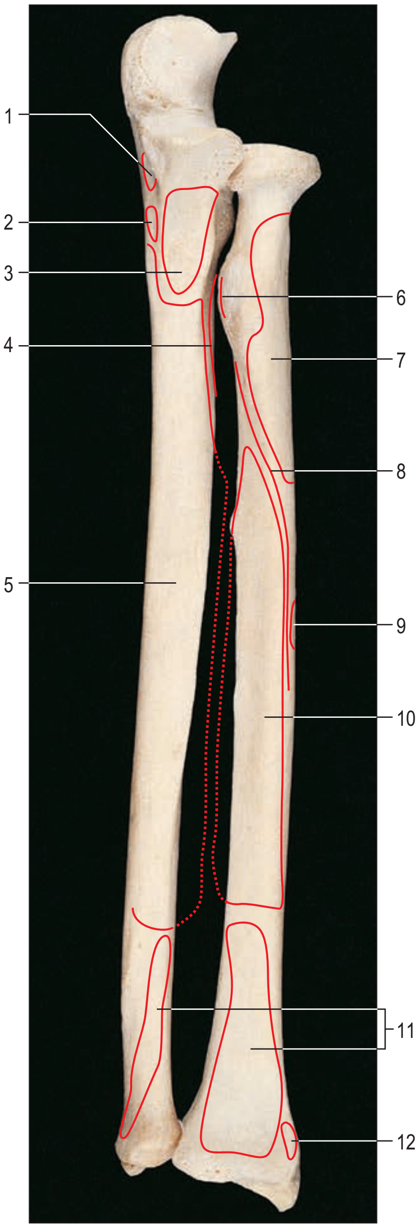

Fig. 50.5 Articulated radius and ulna: anterior view, showing muscle attachments. Note that the hatched lines denote extension of muscular attachments on to the interosseous membrane. Key: 1, flexor digitorum superficialis; 2, pronator teres (ulnar head); 3, brachialis; 4, supinator; 5, flexor digitorum profundus; 6, biceps; 7, supinator; 8, flexor digitorum superficialis (oblique line); 9, pronator teres; 10, flexor pollicis longus; 11, pronator quadratus; 12, brachioradialis.

Distal radius

The distal end of the radius (Fig. 50.8) is the widest part and is four-sided in section. The lateral surface is slightly rough, projecting distally as the radial styloid process. The smooth carpal articular surface is divided by a ridge into medial and lateral areas. The medial distal radial articular surface (lunate fossa) is quadrangular, whereas the lateral part of the articular surface (scaphoid fossa) is triangular and curves on to the styloid process. The anterior surface of the distal radius is a thick, palpable, prominent ridge 2 cm proximal to the thenar eminence. The medial surface is the ulnar notch, which is smooth and anteroposteriorly concave for articulation with the head of the ulna. The posterior surface has a palpable dorsal tubercle (Lister's tubercle), limited medially by an oblique groove and in line with the cleft between the index and middle fingers. Lateral to the tubercle is a wide, shallow groove, divided by a vertical ridge.

Muscular, ligamentous and articular attachments

The proximal articular surface of the radial head and its circumference are covered by hyaline cartilage. The upper rim fits the groove between the capitulum and trochlea and enters the radial fossa in flexion. The articular circumference articulates with the ulnar radial notch and anular ligament, within which it rotates in pronation and supination. The radial

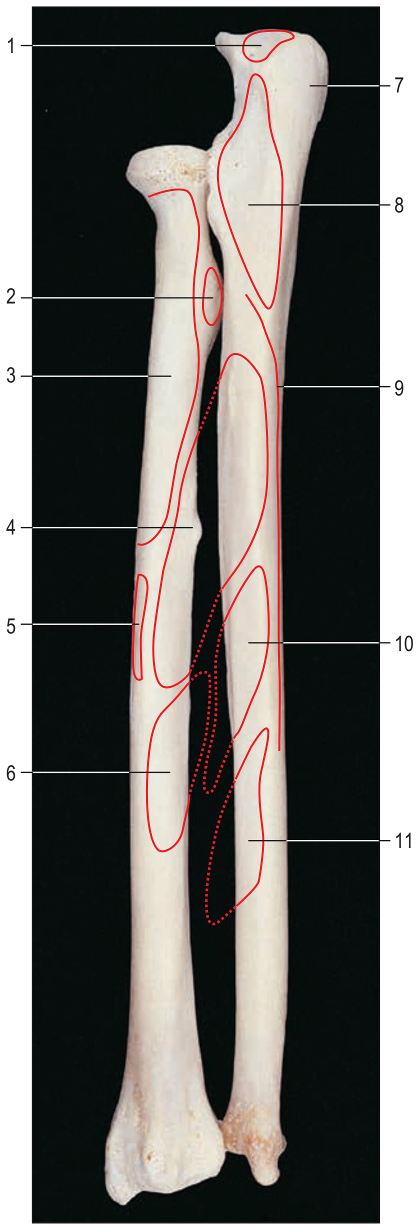

Fig. 50.6 Articulated radius and ulna: posterior view, showing muscle attachments. Key: 1, triceps; 2, biceps; 3, supinator; 4, abductor pollicis longus; 5, pronator teres; 6, extensor pollicis brevis; 7, subcutaneous area; 8, anconeus; 9, posterior border: attachment for common aponeurosis of extensor carpi ulnaris, flexor carpi ulnaris, flexor digitorum profundus; 10, extensor pollicis longus; 11, extensor indicis.

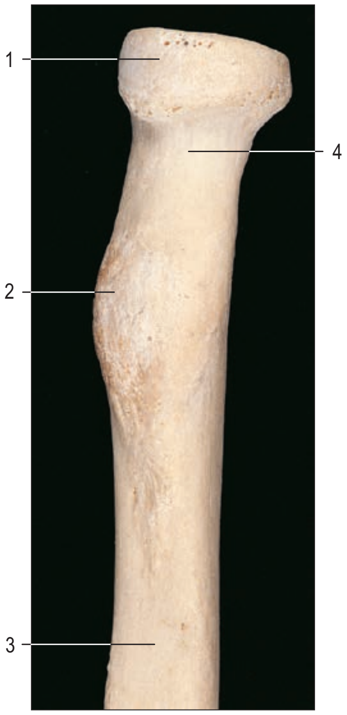

Fig. 50.7 The proximal end of the left radius: anterior view. Key: 1, head; 2, radial tuberosity; 3, shaft; 4, neck.

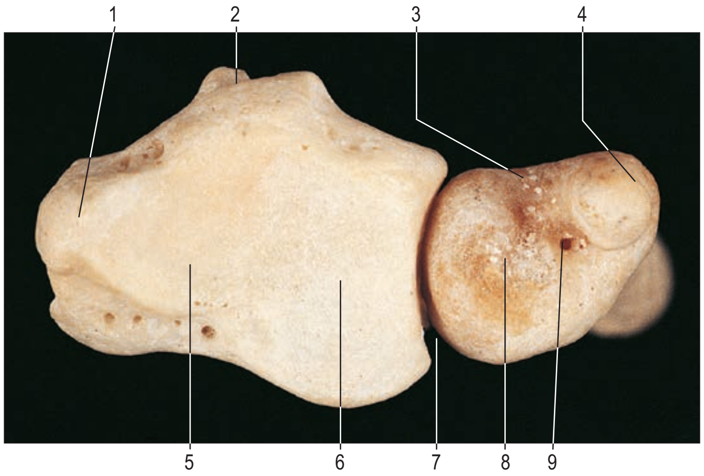

Fig. 50.8 The distal ends of the left radius and ulna. Key: 1, styloid process of radius; 2, dorsal tubercle; 3, groove for tendon of extensor carpi ulnaris; 4, styloid process of ulna; 5, facet for scaphoid; 6, facet for lunate; 7, inferior radio-ulnar articulation; 8, area of contact with articular disc; 9, area for attachment of articular disc. Compare with Fig 51.20A.

neck is enclosed by the narrower distal part of the ligament, from which it is separated by a synovial protrusion from the superior radio-ulnar joint. The posterior area of the tuberosity is marked by the tendon of biceps brachii, which is separated from a smooth anterior area by a bursa. The oblique cord of the interosseous membrane is attached just distal to the bursa.

Flexor digitorum superficialis is attached to the proximal anterior surface of the radius by a thin, wide head. Flexor pollicis longus has an extensive attachment to the proximal two-thirds of the anterior surface of the radial shaft, overlying the nutrient foramen. Pronator quadratus is attached to the distal quarter of the anterior radial shaft; a small, triangular area proximal to the ulnar notch gives attachment to the deepest part of the muscle. Pronator teres is attached to a rough area near the midpoint of the lateral surface of the radial shaft, at its maximal curvature. Proximally, supinator is attached to a long, V-shaped area on the lateral surface of the shaft. Distal to pronator teres, the lateral surface is covered by tendons of brachioradialis, extensor carpi radialis longus and brevis. On the posterior surface, abductor pollicis longus is attached proximally, and extensor pollicis brevis more distally. The remaining surface is devoid of attachments and covered by the long and short extensors of the thumb. The lateral surface, proximal to the styloid process, receives the attachment of brachioradialis and is crossed obliquely, downwards and forwards, by the tendons of abductor pollicis longus and extensor pollicis brevis. The radial styloid process projects beyond that of the ulna, its apex covered by the tendons of abductor pollicis longus and extensor pollicis brevis. The lateral radiocarpal ligament is attached to its tip, and the palmar radiocarpal ligament is attached to the terminal ridge on the anterior surface of the lower end. The base of the triangular articular disc of the inferior radio-ulnar joint is attached to a smooth ridge distal to the ulnar notch. A narrow protrusion of synovial membrane extends proximally from the ulnar notch, anterior to the lower end of the interosseous membrane. The lateral part of the carpal articular surface articulates with the scaphoid, and the medial part with the lateral part of the lunate. In full adduction, the proximal surface of the lunate is wholly in contact with the radius.

The radial dorsal tubercle receives a slip from the extensor retinaculum and is grooved medially by the tendon of extensor pollicis longus. The wide groove lateral to the tubercle contains the tendons of extensor carpi radialis longus laterally and extensor carpi radialis brevis medially, together with their synovial sheaths. Medially, the dorsal surface is grooved by the tendons of extensor digitorum, separated from the bone by the tendons of extensor indicis and the posterior interosseous nerve. The dorsal radiocarpal ligament is attached to the distal margin of this surface.

Vascular supply

The radius is supplied by branches of the radial, ulnar and anterior and posterior interosseous arteries through multiple metaphysial nutrient foramina. Usually, there is one nutrient diaphysial foramen located on the anterior surface of the bone, which is directed proximally towards the elbow. A network of small fascioperiosteal and musculoperiosteal vessels arise from the compartmental vessels and reach the bone via its septal and muscular attachments.

The dorsal metaphysis of the distal radius is richly supplied (Fig. 50.9A). Branches connect the anterior interosseous artery proximally to the dorsal carpal arch distally. These pass through the fourth and fifth extensor compartments of the wrist and provide metaphysial nutrient arteries. Intercompartmental vessels send nutrient arteries to the radius through the retinaculum between the first and second dorsal compartments, and the second and third dorsal compartments. These vessels originate from the radial artery and anterior interosseous arteries, respectively, and anastomose with the dorsal carpal arch.

Ossification

The radius ossifies from three centres. One appears centrally in the shaft in embryonic stage 23, and the others appear in each end (see Figs 49.13, 50.12). Ossification begins in the distal epiphysis towards the end of the first postnatal year and in the proximal epiphysis during the fourth year in females and the fifth year in males. The proximal epiphysis unites with the shaft in the fourteenth year in females and seventeenth year in males, and the distal epiphysis unites with the shaft in the seventeenth and nineteenth years, respectively. A fourth centre sometimes appears in the tuberosity at about the fourteenth or fifteenth year.

Ulna

The ulna is medial to the radius in the supinated forearm. Its proximal end is a massive hook, concave forwards, that articulates with the distal humerus (Figs 50.10–50.11). The lateral border of the shaft is a sharp interosseous crest to which the interosseous membrane is attached. The bone diminishes progressively from its proximal mass throughout almost its whole length, but, at its distal end, expands into a small, rounded head and styloid process. The shaft is triangular in cross-section proximally, and almost cylindrical distally. Along its whole length, the ulna is slightly convex posteriorly. Mediolaterally, its profile is sinuous; the proximal half has a slight curvature that is concave laterally and the distal half a curvature that is concave medially.

Proximal ulna

The proximal end of the ulna has large olecranon and coronoid processes, and trochlear and radial notches that articulate with the humerus and radius, respectively. The olecranon process is more proximal and is bent forwards at its summit like a beak that enters the olecranon fossa of the humerus in extension. Its posterior surface is smooth, triangular and subcutaneous, and its proximal border underlies the 'point' of the elbow. In extension, it can be felt near a line joining the humeral epicondyles, but in flexion, it descends, so that the three osseous points form an isosceles triangle. The relationship between the plane of the dorsal surface of the olecranon and the ulnar shaft, known as the proximal ulna dorsal angulation (PUDA, average 5.7º) is variable. In some individuals, the olecranon plane is flexed, in some it is extended and in some the dorsal surface of the olecranon and the shaft of the ulna are in the same plane:

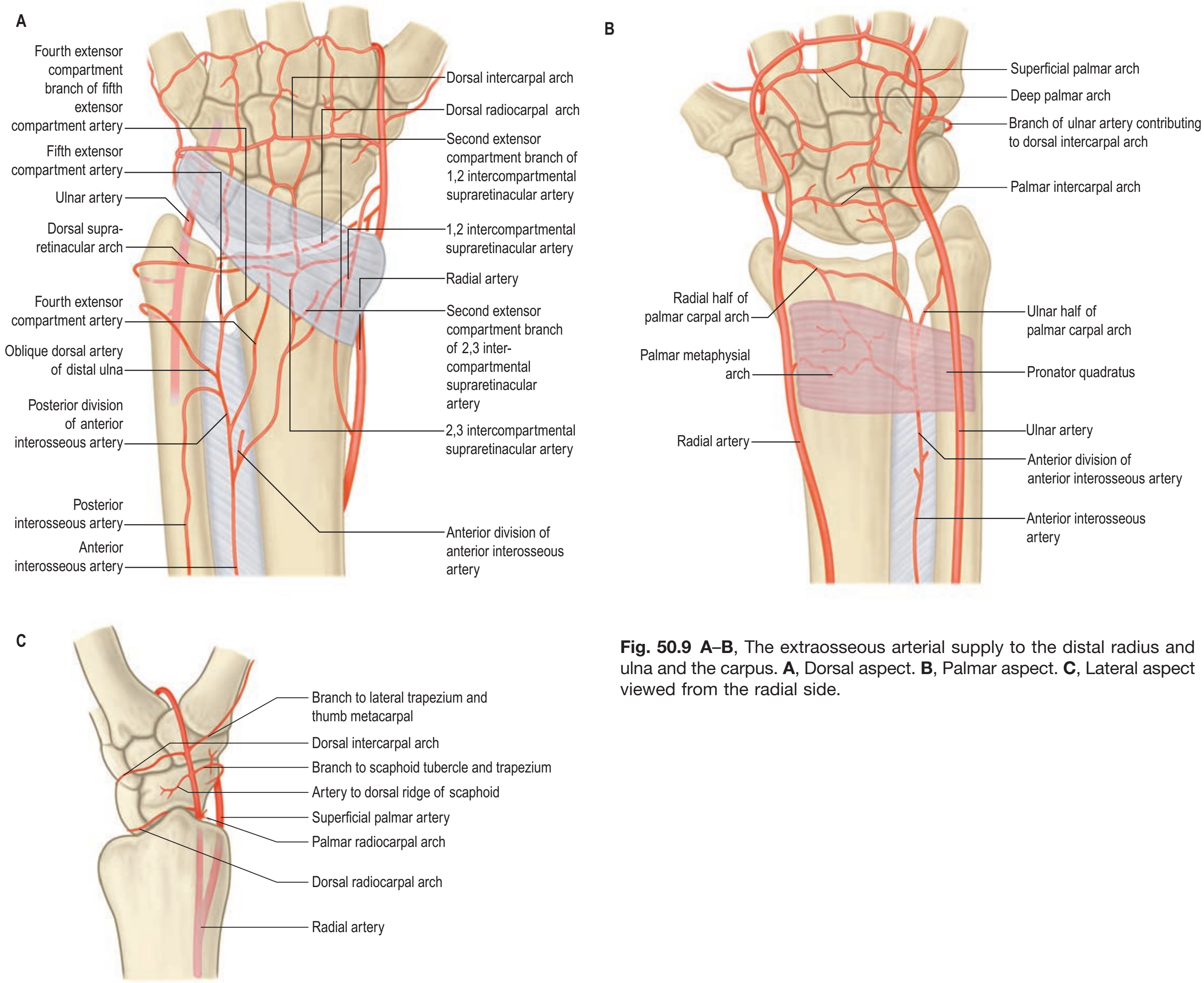
A
Fourth extensor compartment branch of fifth extensor compartment artery
Fifth extensor compartment artery
Ulnar artery
Dorsal supraretinacular arch
Fourth extensor compartment artery
Oblique dorsal artery of distal ulna
Posterior division of anterior interosseous artery
Posterior interosseous artery
Anterior interosseous artery
Dorsal intercarpal arch
Dorsal radiocarpal arch
Second extensor compartment branch of 1,2 intercompartmental supraretinacular artery
1,2 intercompartmental supraretinacular artery
Radial artery
Second extensor compartment branch of 2,3 intercompartmental supraretinacular artery
2,3 intercompartmental supraretinacular artery
Anterior division of anterior interosseous artery
B
Superficial palmar arch
Deep palmar arch
Branch of ulnar artery contributing to dorsal intercarpal arch
Palmar intercarpal arch
Radial half of palmar carpal arch
Palmar metaphysial arch
Radial artery
Ulnar half of palmar carpal arch
Pronator quadratus
Ulnar artery
Anterior division of anterior interosseous artery
Anterior interosseous artery
C
Branch to lateral trapezium and thumb metacarpal
Dorsal intercarpal arch
Branch to scaphoid tubercle and trapezium
Artery to dorsal ridge of scaphoid
Superficial palmar artery
Palmar radiocarpal arch
Dorsal radiocarpal arch
Radial artery

Fig. 50.9 A–B, The extraosseous arterial supply to the distal radius and ulna and the carpus. **A**, Dorsal aspect. **B**, Palmar aspect. **C**, Lateral aspect viewed from the radial side.

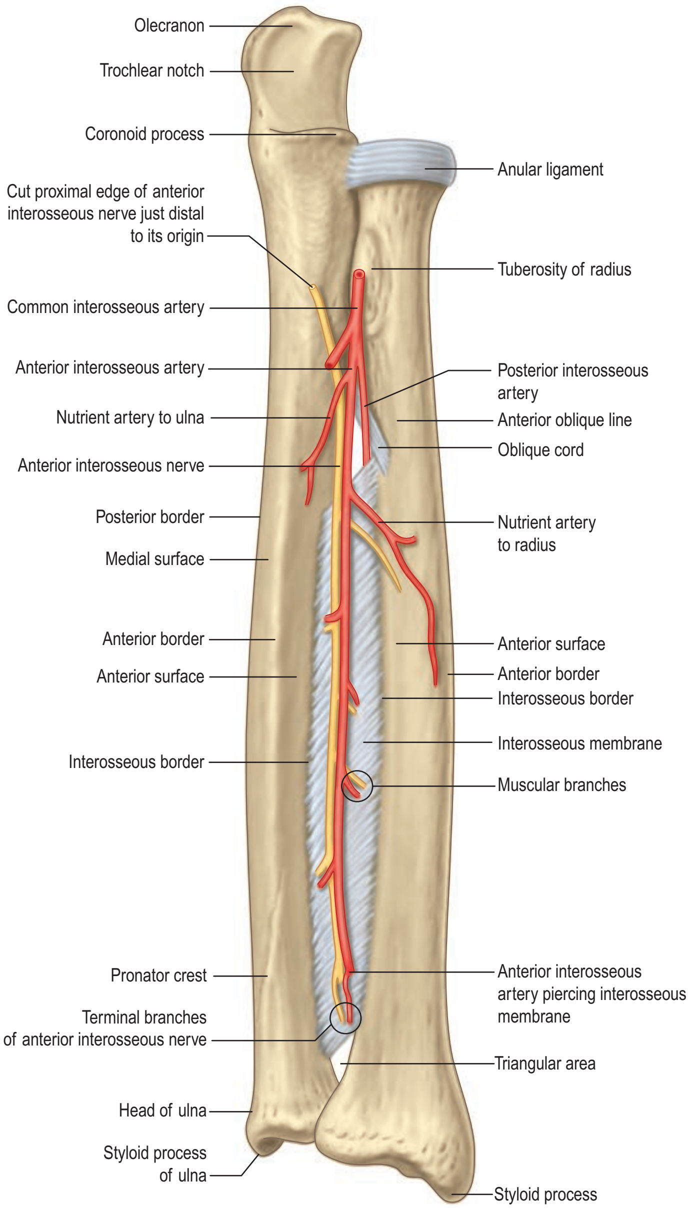
Olecranon
Trochlear notch
Coronoid process
Cut proximal edge of anterior interosseous nerve just distal to its origin
Common interosseous artery
Anterior interosseous artery
Nutrient artery to ulna
Anterior interosseous nerve
Posterior border
Medial surface
Anterior border
Anterior surface
Interosseous border
Pronator crest
Terminal branches of anterior interosseous nerve
Head of ulna
Styloid process of ulna
Anular ligament
Tuberosity of radius
Posterior interosseous artery
Anterior oblique line
Oblique cord
Nutrient artery to radius
Anterior surface
Anterior border
Interosseous border
Interosseous membrane
Muscular branches
Anterior interosseous artery piercing interosseous membrane
Triangular area
Styloid process

Fig. 50.10 Anterior aspect of the interosseous membrane and oblique cord of the forearm: the membrane and cord are syndesmoses.

these differences may explain some of the variability in the range of extension of the normal elbow (Rouleau et al 2010).

The anterior, articular surface of the olecranon forms the proximal area of the trochlear notch. Its base is slightly constricted where it joins the shaft and is the narrowest part of the proximal ulna. The coronoid process projects anteriorly distal to the olecranon. Its proximal aspect forms the distal wall of the trochlear notch and possesses two facets, the anterolateral facet which articulates with the lateral ridge of the trochlea and the anteromedial facet which articulates with the medial ridge. On the lateral surface, distal to the trochlear notch, a shallow, smooth, oval radial notch articulates with the radial head. Distal to the radial notch, the surface is hollow to accommodate the radial tuberosity during pronation and supination. The anterior surface of the coronoid is triangular. Its distal part is the tuberosity of the ulna and its medial border is sharp and bears the small sublime tubercle proximally for insertion of the anterior band of the medial ligament.

The trochlear notch articulates with the trochlea of the humerus. It is constricted at the junction of the olecranon and coronoid processes, where their articular surfaces may be separated by a narrow, rough, non-articular strip. A smooth ridge, adapted to the groove on the humeral trochlea, divides the notch into medial and lateral parts. The medial fits into the trochlear flange. The radial notch, an oval or oblong proximal depression on the lateral aspect of the coronoid process, articulates with the periphery of the radial head and is separated from the trochlear notch by a smooth ridge.

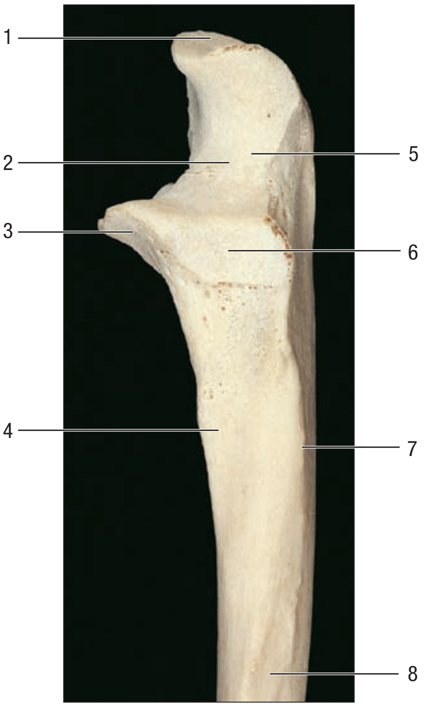

Fig. 50.11 The proximal end of the left ulna: lateral view. Key: 1, olecranon; 2, non-articular strip in trochlear notch; 3, coronoid process; 4, tuberosity; 5, trochlear notch; 6, radial notch; 7, supinator crest; 8, shaft.

Ulnar shaft

The ulnar shaft is triangular in cross-section in its proximal three-quarters, but distally is almost cylindrical (see Figs 50.31–50.32). It has anterior, posterior and medial surfaces and interosseous, posterior and anterior borders. The interosseous border is a conspicuous lateral crest in its middle half. Proximally, it becomes the supinator crest, which is continuous with the posterior border of a depression distal to the radial notch. Distally, it disappears. The rounded anterior border starts medial to the ulnar tuberosity, descends backwards, and is usually traceable to the base of the styloid process. The posterior border, also rounded, descends from the apex of the posterior aspect of the olecranon, and curves laterally to reach the styloid process. It is palpable throughout its length in a longitudinal furrow, most obvious when the elbow is fully flexed.

The anterior surface, between the interosseous and anterior borders, is longitudinally grooved, sometimes deeply (see Fig. 50.10). Proximal to its midpoint, a proximally directed nutrient foramen admits a branch of the anterior interosseous artery. Distally, it is crossed obliquely by a rough, variable prominence, descending from the interosseous to the anterior border. The medial surface, between the anterior and posterior borders, is transversely convex and smooth. The posterior surface, between the posterior and interosseous borders, is divided into three areas. The most proximal is limited by a sometimes faint, oblique line that ascends laterally from the junction of the middle and upper thirds of the posterior border to the posterior end of the radial notch. The region distal to this line is divided into a larger medial and narrower lateral strip by a vertical ridge, which is usually distinct only in its proximal three-quarters.

Distal ulna

The distal end of the ulna is slightly expanded and has a head and styloid process. The head is palpable and visible in pronation on the posteromedial aspect of the wrist. Its lateral convex articular surface fits the radial ulnar notch. Its smooth distal surface is separated from the carpus by an articular disc, the apex of which is attached to a rough area between the articular surface and styloid process. The ulnar styloid process is a short, round, posterolateral projection of the distal end of the ulna, palpable in supination about 1 cm proximal to the plane of the radial styloid. A posterior vertical groove is present between the head and styloid process.

Muscular, ligamentous and articular attachments

The capsule of the elbow joint is attached to the proximal, anterior surface of the olecranon, and the tendon of triceps is attached to its rough posterior two-thirds; the capsule and tendon may be separated by a bursa. The medial surface of the olecranon is marked proximally by the attachment of the posterior and oblique bands of the ulnar collateral ligament and by the ulnar part of flexor carpi ulnaris. The smooth area distal to this is the most proximal attachment of flexor digitorum profundus. Anconeus is attached to the lateral surface of the olecranon and the adjoining posterior surface of the ulnar shaft as far as its oblique line. The posterior surface of the ulna is separated from the skin by a subcutaneous bursa.

Brachialis is attached to the anterior surface of the coronoid process, including the ulnar tuberosity. The oblique and anterior bands of the ulnar collateral ligament and the distal part of the humero-ulnar slip of flexor digitorum superficialis are attached to a small tubercle at the proximal end of the medial border. Further distally, the margin of the coronoid process provides attachment for the ulnar head of pronator teres. An ulnar head of flexor pollicis longus may be attached to the lateral or, more rarely, the medial, border of the coronoid process. Fibres of flexor digitorum profundus are attached to its medial surface. The anular ligament is attached to the anterior rim of the radial notch and, posteriorly, to a ridge at, or just behind, the posterior margin of the notch. The depressed area distal to the notch is limited behind by the supinator crest, and both provide attachment for supinator.

The olecranon area of the trochlear notch is usually divided into three areas. The most medial faces anteromedially, and is grooved to fit the medial flange of the humeral trochlea, with which it makes increasing contact during flexion. A flat intermediate area fits the lateral flange. The most lateral area is a narrow strip that abuts the trochlea in extension. The articular surface is narrower than the base of the olecranon; non-articular areas are related to the synovial processes. The coronoid area of the trochlear notch is also divided; its medial and lateral areas correspond to the medial and intermediate areas of the olecranon. The medial is the deeper, and conforms to the convex medial trochlear flange and is essential for elbow stability. The medial and anterior parts of the capsular ligament are attached to its medial and anterior borders.

The deep fascia of the forearm is attached to the subcutaneous posterior border, which also provides an attachment for the aponeurosis of flexor digitorum profundus in its proximal three-quarters, for flexor carpi ulnaris in its proximal half, and for extensor carpi ulnaris in its middle third. These three muscles are attached to the posterior border through a common blended aponeurosis. The interosseous membrane is attached along the interosseous border, except for a short length proximally.

Flexor digitorum profundus is attached to the proximal three-quarters of the anterior border and medial surface, arising medial to the coronoid process and olecranon. The rough strip across the distal fourth of the anterior surface provides part of the bony attachment for pronator quadratus. Anconeus is attached to the posterior surface proximal to the oblique line and lateral to the olecranon. The narrow strip between the interosseous border and vertical ridge gives rise to the attachment of three deep muscles: abductor pollicis longus arises from the proximal quarter, extensor pollicis longus from the succeeding quarter (sometimes a ridge is interposed between them), and extensor indicis from the third quarter. Extensor carpi ulnaris covers the broad strip medial to the vertical ridge and its tendon grooves the posterior aspect of the distal end of the ulna.

Vascular supply

The ulna receives its vascular supply from branches of the radial, ulnar, anterior and posterior interosseous arteries via multiple metaphysial nutrient foramina. Usually one, but occasionally two, major nutrient diaphysial foramina are located on the anterior surface of the bone, directed proximally towards the elbow. A network of small fascioperiosteal and musculoperiosteal branches given off from the compartmental vessels reaches the bone via septal and muscular attachments.

Ossification

The ulna ossifies from four main centres: one each in the shaft and distal end, and two in the olecranon (see Fig. 49.13; **Fig. 50.12**). Ossification begins in the midshaft in embryonic stages 22 and 23 and extends rapidly. A centre appears in the distal end in the fifth year in females and sixth year in males, and extends into the styloid process. The distal olecranon is ossified as an extension from the shaft, the remainder from two centres, one for the proximal trochlear surface and the other for a thin, scale-like proximal epiphysis on its summit. The proximal epiphysis appears in the ninth year in females and eleventh year in males, and the whole proximal epiphysis has usually joined the shaft by the fourteenth year in females and sixteenth year in males. The distal epiphysis usually unites with the shaft in the seventeenth year in females and eighteenth year in males. Together with the distal humerus, the proximal ulna ossifies in a sequential manner; skeletal maturity may be assessed by observations of elbow radiographs.

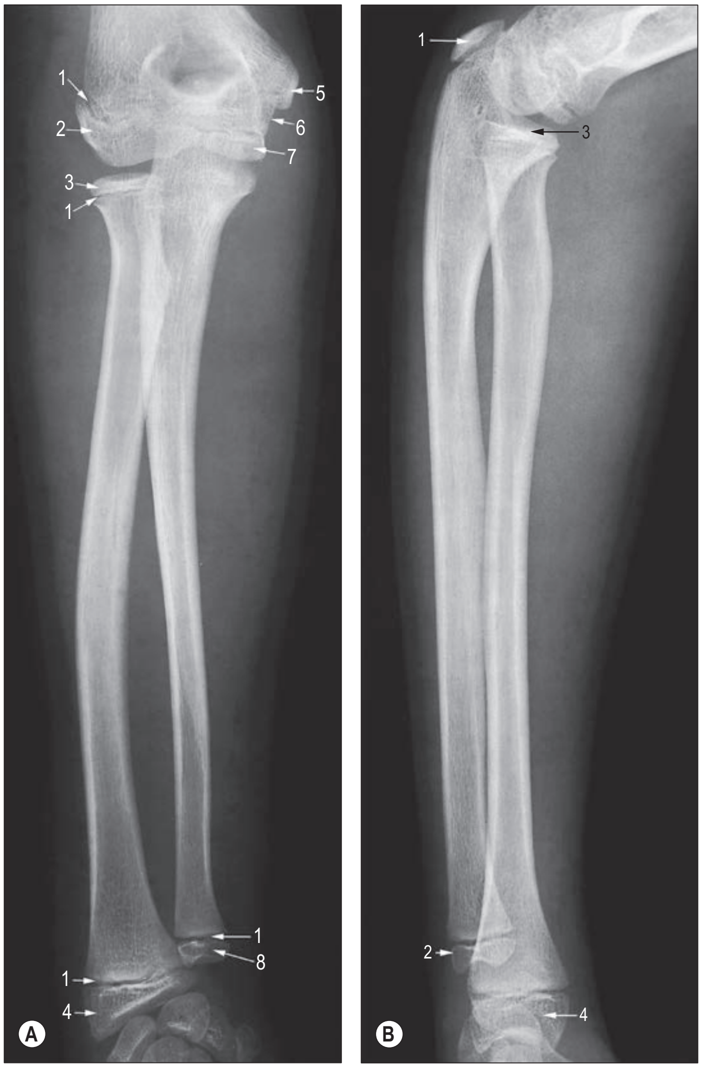

Fig.50.12 Radiographs of the forearm of a girl aged 11 years. **A**, Anteroposterior view. Key: 1, cartilaginous growth plates; 2, conjoined epiphyses of capitulum and lateral epicondyle; 3, proximal radial epiphysis; 4, distal radial epiphysis; 5, epiphysis of medial epicondyle; 6, diaphysial bone; 7, trochlear epiphysis; 8, distal ulnar epiphysis. **B**, Lateral view, semi-flexed at the elbow. Note the epiphyses and adjacent radiotranslucent growth cartilages. Key: 1, olecranon; 2, distal ulnar epiphysis; 3, proximal radial epiphysis; 4, distal radial epiphysis.

JOINTS

The elbow joint acts as a platform for the forearm and hand. The humero-ulnar and humero-radial (radiocapitellar) joints form a complex hinge.

The humero-ulnar joint is continuous with pivot joints between the distal humerus and proximal radius, and between the proximal radius and ulna (Figs 50.13–50.16). There is a high degree of congruity between the deep trochlea of the humerus and the large trochlear notch of the ulna. This stable arrangement is enhanced by strong ulnar (medial) and radial (lateral) collateral ligaments and, in full extension, by the anterior capsule. An arc of 150° of flexion and extension is possible. The configuration of the humero-ulnar joint, between the trochlea and the trochlear notch of the ulna and the distal prolongation of the medial edge of the trochlear pulley, tilts the ulna, forming a 'carrying angle' (approximately 14° in females and 11° in males) between the longitudinal axes of the humerus and ulna when the elbow is fully extended and supinated. These axes become aligned in full flexion as a result of the spiral morphology of the trochlea. The humero-radial joint, in conjunction with synchronous movements at the proximal and distal radio-ulnar joints that are aided by minor contributions from the radiocarpal and carpal joints, allows 180° of pronation and supination of the forearm.

Humero-ulnar and humero-radial joints

The humero-ulnar joint is a complex hinge joint and is continuous with two pivot joints between the distal humerus and proximal radius, and

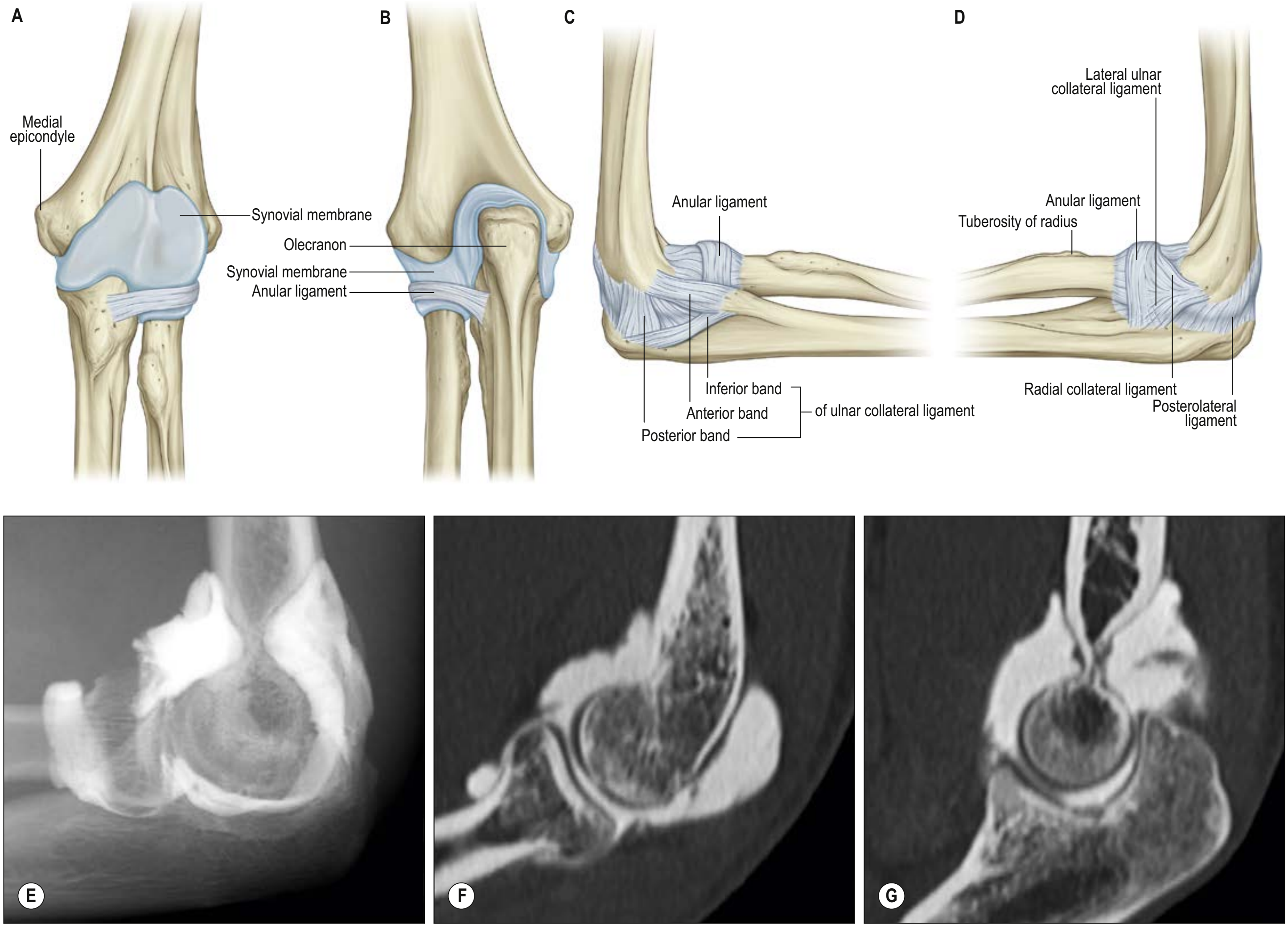
A
Medial epicondyle
Synovial membrane
B
Olecranon
Synovial membrane
Anular ligament
C
Anular ligament
Inferior band
Anterior band
Posterior band
of ulnar collateral ligament
D
Lateral ulnar collateral ligament
Anular ligament
Tuberosity of radius
Radial collateral ligament
Posterolateral ligament
E
F
G

Fig. 50.13 **A–D**, The left elbow joint. **A**, The synovial cavity partially distended: anterior aspect. The fibrous capsule of the elbow joint has been removed but the thick part of the anular ligament has been left *in situ*. Note that the synovial membrane (blue) descends below the lower border of the anular ligament. **B,** The synovial cavity partially distended: posterior aspect of the specimen represented in **A. C**, Medial aspect. **D**, Lateral aspect. **E**, Fluoroscopic arthrogram of the elbow joint. **F, G,** Sagittal CT arthrogram images of the patient in **E**, through the humero-radial joint (**F**) and through the humero-ulnar joint (**G**).

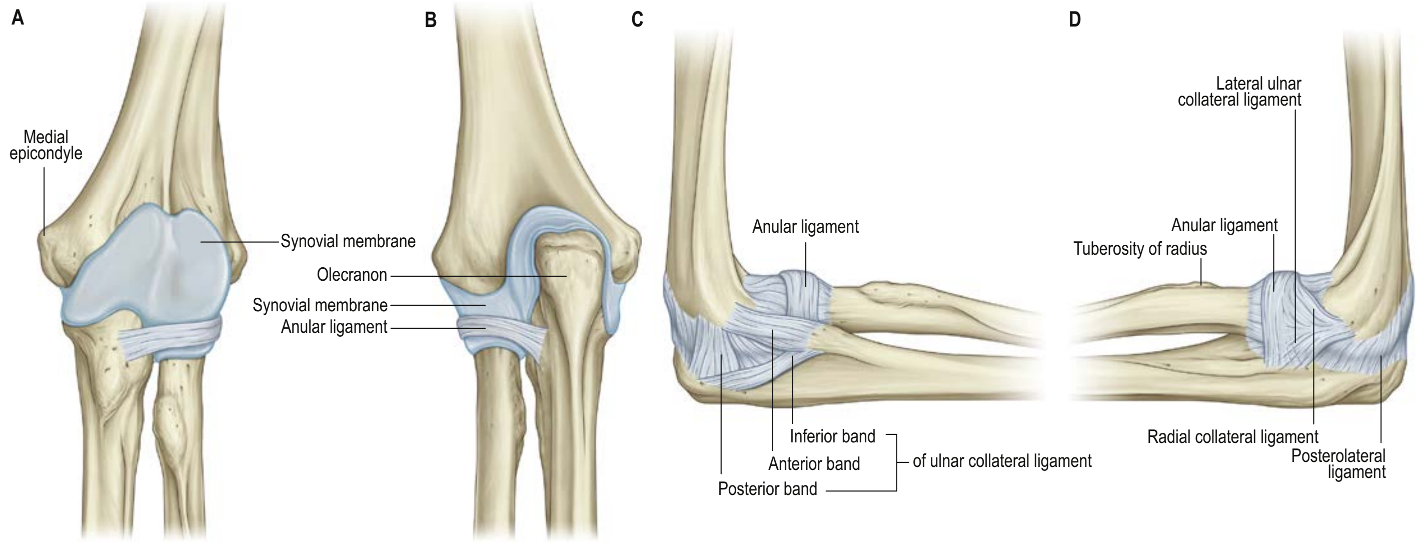

Fig. 50.13 A–D, The left elbow joint. **A**, The synovial cavity partially distended: anterior aspect. The fibrous capsule of the elbow joint has been removed but the thick part of the anular ligament has been left *in situ*. Note that the synovial membrane (blue) descends below the lower border of the anular ligament. **B**, The synovial cavity partially distended: posterior aspect of the specimen represented in **A. C**, Medial aspect. **D**, Lateral aspect. (E–G, *continued online*)

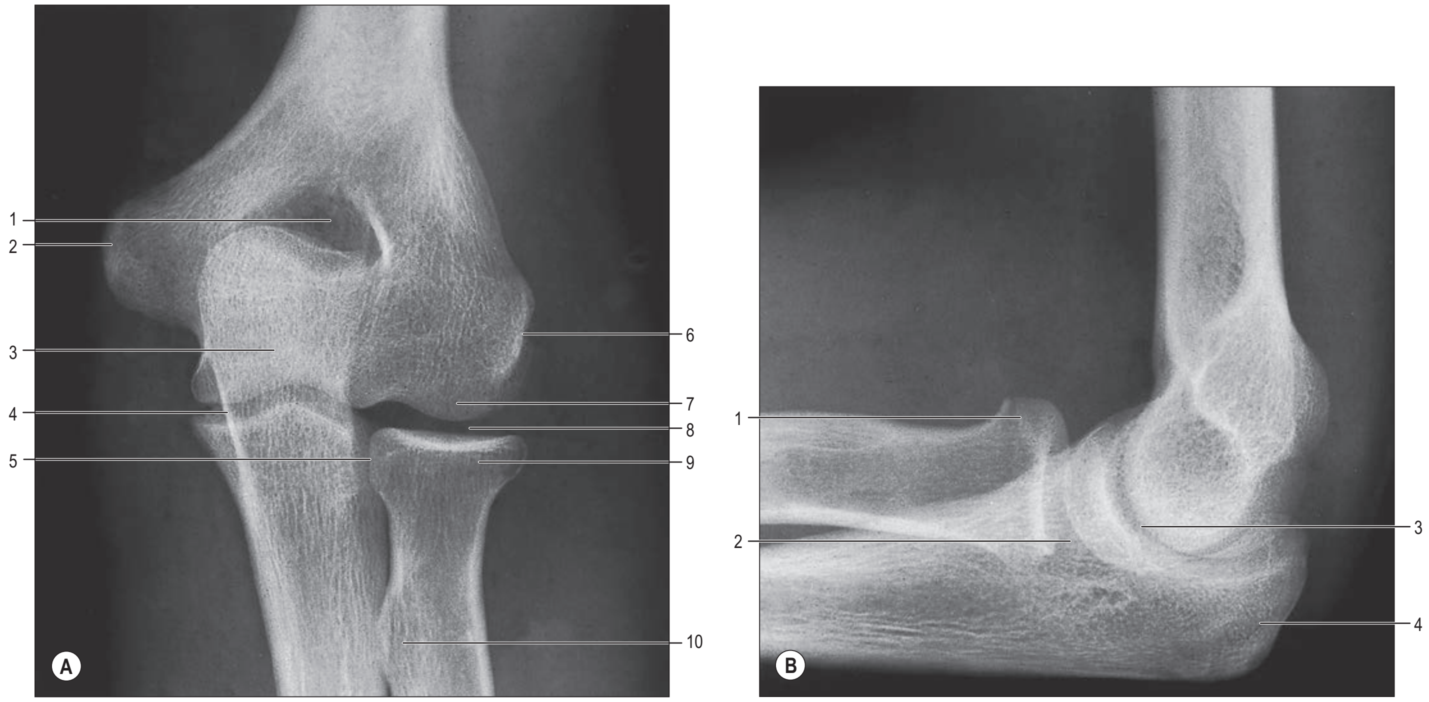

Fig. 50.14 Radiographs of the left elbow joint of an adult. **A**, Anteroposterior view. Key: 1, olecranon fossa; 2, medial humeral epicondyle; 3, shadow of olecranon superimposed on trochlea; 4, humero-ulnar joint; 5, radial head articulating with radial notch of ulna; 6, lateral humeral epicondyle; 7, capitulum; 8, humero-radial joint; 9, head of radius; 10, radial tuberosity. **B**, Lateral view. Key: 1, head of radius; 2, profile of capitulum; 3, profile of trochlea; 4, olecranon.

between the proximal radius and ulna (see Figs 50.13–50.16). There is a high degree of congruity between the deep trochlea of the humerus and the large trochlear notch of the ulna. This stable arrangement is enhanced by strong ulnar (medial) and radial (lateral) collateral ligaments and, in full extension, by the anterior capsule. An arc of 150° of flexion and extension is possible. A range of 180° of pronation and supination is achieved by synchronous movements at the proximal and distal radio-ulnar joints, aided by minor contributions from the radiocarpal and carpal joints.

Articulating surfaces The distal humerus has two distinct articulating surfaces: the trochlea and the capitulum (see Fig. 50.3). The shape of the trochlea is asymmetrical, with a longer medial flange. It is widest posteriorly in the adult. The joint line lies 2 cm distal to the interepicondylar line and is tilted inferomedially. The flexion–extension arc of elbow movement is not that of a simple hinge. Different parts of the distal humerus are in contact with the corresponding articular surface of the proximal ulna throughout the range of movement; in full extension of the elbow, a medial segment of the distal humerus is not in contact with the ulna, whereas in full flexion, a lateral segment is not in contact.

The surface of the trochlear notch has an asymmetrical sellar surface that allows some rotation during swing in the flexion–extension plane. It is predominantly concave in the transverse plane, but convex in the anteroposterior plane. There is a 'bare area' devoid of hyaline cartilage between the olecranon and coronoid areas of the trochlear notch that is covered by fibrofatty tissue and synovium. The humeral capitulum is reciprocally convex with the concavity of the articulating surface of the radial head. The more prominent medial rim of the radial head sits in the groove between the capitulum and trochlea. Contact between the capitulum and radial head is maximal with the elbow in mid-flexion and the forearm in mid-pronation.

Fibrous capsule The fibrous capsule is broad and thin anteriorly. It is attached proximally to the anterior surfaces of the medial epicondyle and humerus above the coronoid and radial fossa, and distally to the edge of the ulnar coronoid process and anular ligament. It may be

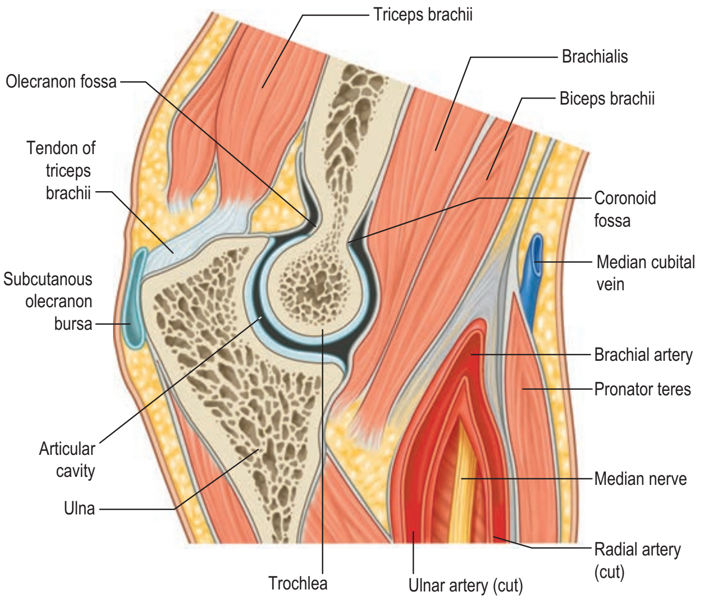

Fig. 50.15 A sagittal section through the left elbow joint: medial aspect. The synovial membrane is shown in blue. (Sobotta Atlas of Human Anatomy © Elsevier GmbH, Urban & Fischer, Munich.)

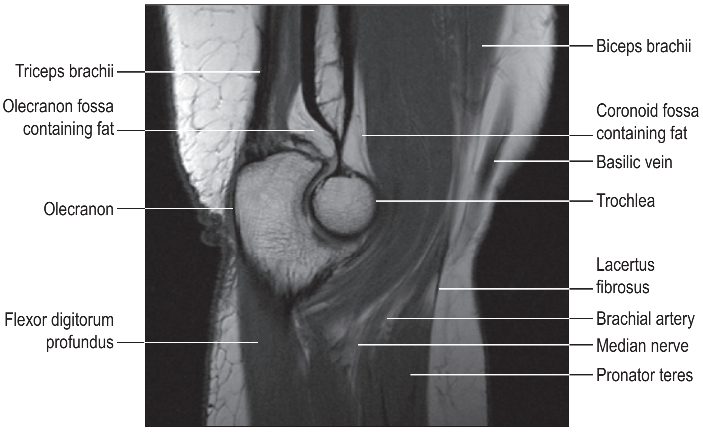

Fig. 50.16 Sagittal proton density weighted MRI through the left elbow joint.

augmented by fibres from brachialis and blends into the ulnar collateral ligament medially and the radial collateral ligament laterally. Posteriorly, the capsule is even thinner and is related to the tendon of triceps and anconeus. It is attached proximally to the superoposterior aspect of the humeral capitulum, the posterior aspect of the medial epicondyle and the olecranon fossa. Only the lowest part of the olecranon fossa is devoid of a capsular attachment. Inferomedially, it reaches the superior and lateral margins of the olecranon and is laterally continuous with the superior radio-ulnar capsule deep to the anular ligament. The olecranon bursa lies between the capsule of the elbow and the insertion of triceps. Inflammation caused by pressure, friction or infection of the bursa can result in marked swelling and limitation in elbow function.

Ligaments The humero-radio-ulnar articulations have ulnar (medial) and radial (lateral) collateral ligamentous complexes (see Fig. 50.13).

Ulnar collateral ligamentous complex The ulnar (medial) collateral ligament complex is triangular and consists of thick anterior, posterior and inferior bands connected by thinner tissue. The strongest and stiffest anterior band is attached by its apex to the anterior aspect of the medial epicondyle midway between the medial trochlea and the apex of the medial epicondyle and by its broader base to a proximal sublime tubercle on the medial margin of the coronoid. The anterior band is taut throughout most of the range of flexion and contributes to the stability of the joint. The posterior band of the ulnar collateral ligament is also triangular in shape; its apex is attached to the back of the medial epicondyle and its distal attachment is the medial margin of the olecranon. The posterior band becomes taut between 90° and full flexion of the elbow. Connecting these two thick bands is a less sturdy inferior oblique band that runs between the olecranon and coronoid processes, converting a depression on the medial margin of the trochlear notch into a foramen, through which the intracapsular fat pad is continuous with the extracapsular fat medial to the joint. The ulnar collateral ligament of the elbow lies beneath triceps, flexor carpi ulnaris, the ulnar nerve and the attachment of flexor digitorum superficialis as it extends from the medial epicondyle to the medial coronoid border.

Radial collateral ligamentous complex The capsule on the lateral aspect of the elbow has interconnecting thickenings that form a broad sling between the humerus and ulna around the radial head. The radial (lateral) collateral ligamentous complex is divided into four elements, the radial collateral ligament, anular ligament, lateral ulnar collateral ligament and posterolateral ligament (Camp et al 2018). The radial collateral ligament is attached low on the lateral epicondyle anterior and inferior to a small tubercle on the lateral epicondyle and inserts distally into the anular ligament which wraps around the radial head from the anterior rim of the radial notch of the ulna to the supinator crest. Proximally, the radial collateral ligament is continuous with the lateral ulnar collateral ligament that arises from the inferior aspect of the tubercle on the lateral epicondyle and inserts into the supinator crest and often gives rise to accessory fibres that cross the anular ligament distally. The posterolateral ligament is more proximal still and extends onto the posterior aspect of the capitulum, creating a hammock behind the radial head that limits dorsal translation (Edwards et al 2018). The posterolateral ligament blends with the bony attachments of supinator and extensor carpi radialis brevis. It is taut throughout most of the range of flexion of the elbow and contributes to the stability of the joint.

Synovial membrane The synovial membrane extends from the articular margins of the humerus and lines the coronoid, radial and olecranon fossae, the flat medial surface of the trochlea, the deep surface of the elbow capsule and the distal part of the anular ligament. A crescentic synovial fold projecting between the proximal radius and ulna contains extrasynovial fat and forms the division between the humero-ulnar and humero-radial joints.

There are three other fat pads between the capsule and synovium; the largest is in the olecranon fossa, where it is pushed into the fossa by triceps during flexion of the elbow. The two other fat pads are in the coronoid and radial fossae, and are pushed into these fossae by brachialis on extension of the elbow. Smaller fat pads covered by synovium project into the joint at the trochlear notch and also cover non-articular areas of bone.

Vascular supply The articular arteries of the elbow are derived from numerous small periarticular anastomoses around the joint (see Fig. 50.29). Of particular note is the blood supply to the radial head, an intracapsular structure supplied by vessels arising from the radial recurrent artery that travels retrogradely up the surface of the bare area of the bone and fans out to supply the whole radial head (Yamaguchi et al 1997).

Innervation The elbow joint is innervated by filaments arising from all of the main nerves supplying the upper limb, except the axillary nerve. The ulnar posterior part is supplied by the ulnar nerve and the medial cutaneous nerve of the forearm; the ulnar anterior part is supplied by the median and musculocutaneous nerves. The radial nerve is the sole supplier of the radial posterior part, and the radial anterior part is innervated by both radial and musculocutaneous nerves (de Kesel et al 2012).

Proximal radio-ulnar joint

The proximal radio-ulnar joint is a uniaxial pivot joint (**Fig. 50.17**).

Articulating surfaces Articulating surfaces include the articulation between the circumference of the radial head and the fibro-osseous ring of the ulnar radial notch and anular ligament.

Fibrous capsule The fibrous capsule of the proximal radio-ulnar joint is continuous with that of the elbow and is attached to the anular ligament.

Ligaments The proximal radio-ulnar joint has anular and quadrate ligaments.

Anular ligament The anular ligament is the principal stabilizer of the joint. It is a strong composite band that winds around four-fifths of the

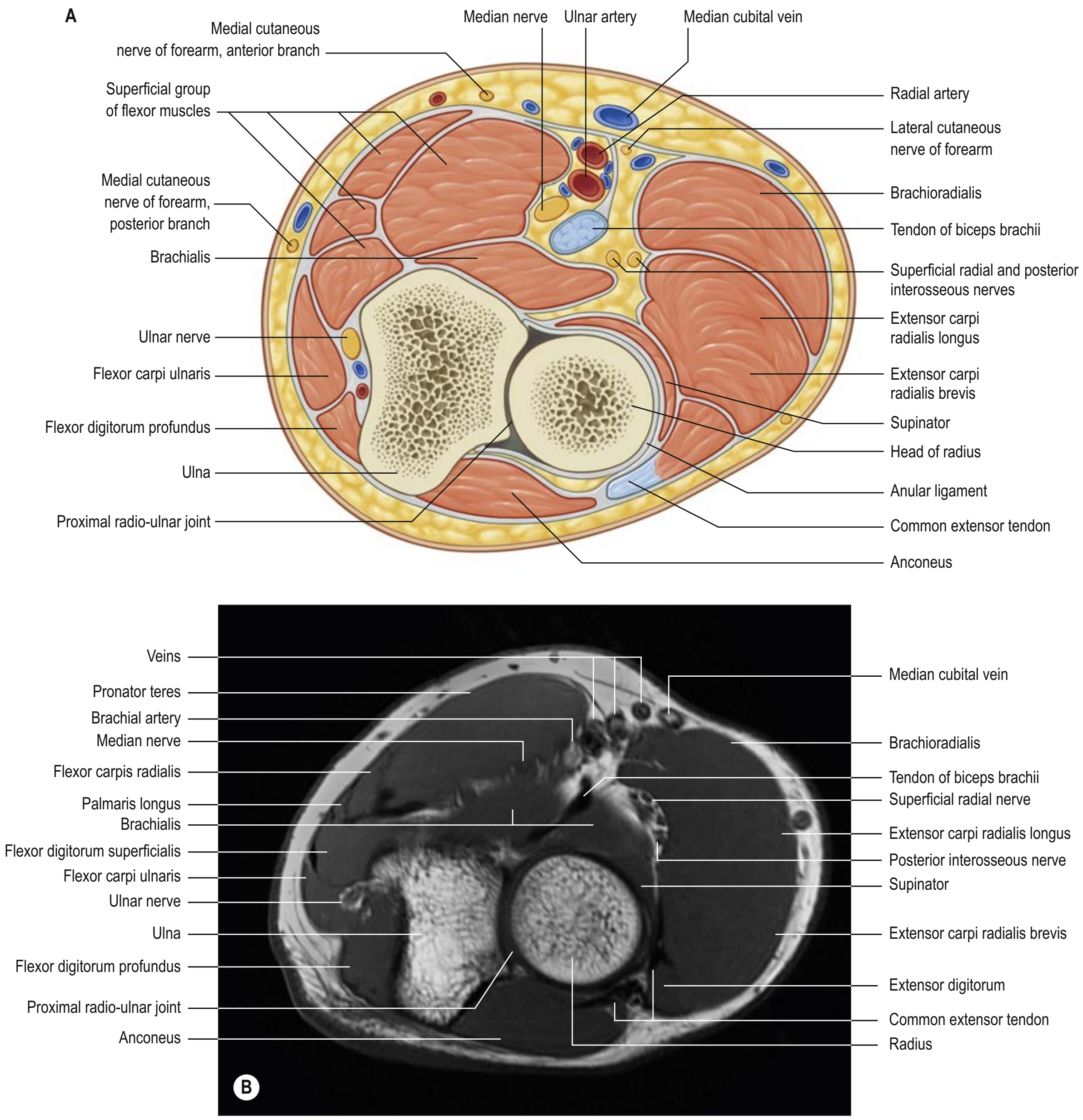
A
Medial cutaneous nerve of forearm, anterior branch
Median nerve
Ulnar artery
Median cubital vein
Superficial group of flexor muscles
Radial artery
Lateral cutaneous nerve of forearm
Medial cutaneous nerve of forearm, posterior branch
Brachioradialis
Tendon of biceps brachii
Brachialis
Superficial radial and posterior interosseous nerves
Ulnar nerve
Extensor carpi radialis longus
Flexor carpi ulnaris
Extensor carpi radialis brevis
Flexor digitorum profundus
Supinator
Head of radius
Ulna
Anular ligament
Proximal radio-ulnar joint
Common extensor tendon
Anconeus
Veins
Pronator teres
Brachial artery
Median nerve
Flexor carpis radialis
Palmaris longus
Brachialis
Flexor digitorum superficialis
Flexor carpi ulnaris
Ulnar nerve
Ulna
Flexor digitorum profundus
Proximal radio-ulnar joint
Anconeus
Median cubital vein
Brachioradialis
Tendon of biceps brachii
Superficial radial nerve
Extensor carpi radialis longus
Posterior interosseous nerve
Supinator
Extensor carpi radialis brevis
Extensor digitorum
Common extensor tendon
Radius
B

Fig. 50.17 The proximal left radio-ulnar joint. **A**, Transverse section. **B**, Axial T1-weighted MRI at the level of the proximal radio-ulnar joint.

radial head and holds it against the radial notch of the ulna. It is attached to the anterior margin of the notch. The ligament is wider posteriorly, where it may be composed of several bands. It is attached to a rough ridge at or behind the posterior margin of the notch. Some bands may diverge and attach superiorly to the lateral margin of the trochlear notch, or inferiorly to the supinator crest. Proximally, the anular ligament blends into the joint capsule, except posteriorly where the capsule is deep to the ligament. Distally, the anular ligament gives off a few fibres, which pass over the synovial membrane to attach to the radial neck. The superficial surface of the anular ligament blends into the radial collateral ligament and provides an attachment for a part of supinator. The deep surface of the anular ligament is lined with a thin layer of cartilage where it is in contact with the radial head. Distally, there is a synovial membrane that is reflected up on to the radial neck. The anconeus and the interosseous recurrent artery lie behind the ligament.

Quadrate ligament The quadrate ligament is a much thinner and more fibrous structure than the anular ligament. It runs between the radial neck and the upper part of the supinator fossa of the ulna, and is taut throughout pronation and supination. It lies over the synovial membrane on the distal surface of the joint.

Synovial membrane The synovial membrane of the proximal radio-ulnar joint is continuous with that of the elbow joint, forming one continuous synovial cavity. It attaches to the joint margins, lining the capsule and anular ligament. The quadrate ligament prevents herniation of the synovial membrane between the free edges of the anular ligament.

Vascular supply The vascular supply of the proximal radio-ulnar joint is derived from a rich periarticular anastomotic plexus (**Fig. 50.18**; see Fig. 50.19).

Innervation The proximal radio-ulnar joint is innervated by small branches arising from the musculocutaneous, median, radial and ulnar nerves.

Radio-ulnar syndesmoses

The radial and ulnar shafts are connected by two syndesmoses, an oblique cord and an interosseous membrane.

Oblique cord

The oblique cord is a small, inconstant, flat fascial band on the deep head of supinator (see Fig. 50.10). It extends from the lateral side of the ulnar tuberosity to the radius a little distal to its tuberosity. Its fibres are at right-angles to those in the interosseous membrane. Its functional significance is unclear.

Interosseous membrane

The interosseous membrane is a broad, thin, collagenous structure (see Fig. 50.10). Its fibres slant distomedially between the interosseous borders of the radius and ulna, and its distal part is attached to the posterior

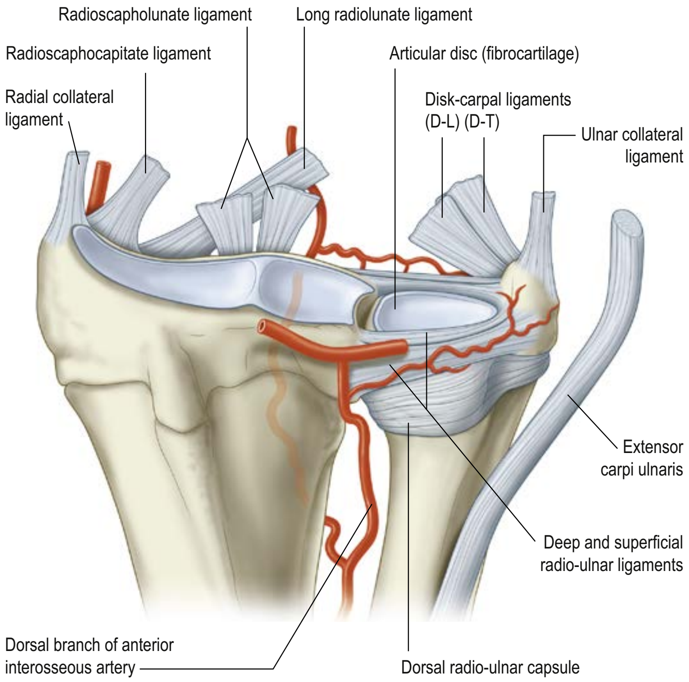
Radioscapholunate ligament
Long radiolunate ligament
Radioscaphocapitate ligament
Articular disc (fibrocartilage)
Radial collateral ligament
Disk-carpal ligaments (D-L) (D-T)
Ulnar collateral ligament
Extensor carpi ulnaris
Deep and superficial radio-ulnar ligaments
Dorsal branch of anterior interosseous artery
Dorsal radio-ulnar capsule

Fig. 50.18 The prime intrinsic stabilizer of the distal radio-ulnar joint is the triangular fibrocartilage. The triangular fibrocartilage complex consists of superficial and deep radio-ulnar fibres, the two disc carpal ligaments (disc–lunate (D–L) and disc–triquetral (D–T)), and the central articular disc. The articular disc is responsible for transferring load from the medial carpus to the pole of the distal ulna. The vascularized, peripheral radio-ulnar ligaments are nourished by dorsal and palmar branches of the posterior interosseous artery and are responsible for guiding the radiocarpal unit around the seat of the ulna. (Redrawn with permission from Kleinmann WB 2010 Stability of the distal radioulnar joint: biomechanics, pathophysiology, physical diagnosis and restoration of function. In: Slutsky DJ (ed) Principle and Practice of Wrist Surgery. Philadelphia: Saunders; Ch. 5, pp. 41–45.)

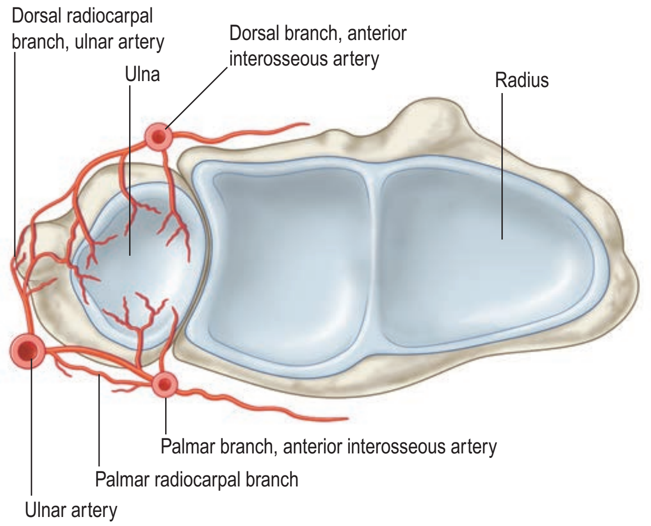
Dorsal radiocarpal branch, ulnar artery
Dorsal branch, anterior interosseous artery
Ulna
Radius
Palmar branch, anterior interosseous artery
Palmar radiocarpal branch
Ulnar artery

Fig. 50.19 The arterial anatomy of the triangular fibrocartilage complex. (Redrawn with permission from Thiru-Pathi RG, Ferlic DC, Clayton M et al 1986 Arterial anatomy of the triangular fibrocartilage of the wrist and its surgical significance. J Hand Surgery [Am] 11:258–63.)

division of the radial shaft. Two or three posterior bands occasionally descend distolaterally across the other fibres. The membrane is deficient proximally, starting 2 or 3 cm distal to the radial tuberosity, and broadest at midlevel. An oval aperture near its distal margin conducts the anterior interosseous vessels to the back of the forearm. The posterior interosseous vessels pass through a gap between its proximal border and the oblique cord.

The membrane provides attachments for the deep forearm muscles. Anteriorly, in its proximal three-quarters, it is related laterally to flexor pollicis longus and medially to flexor digitorum profundus; between them, it is related to the anterior interosseous vessels and nerve. In its distal quarter, it is related to pronator quadratus. Its posterior relations are supinator, abductor pollicis longus, extensors pollicis brevis, longus and indicis, and, near the carpus, the anterior interosseous artery and posterior interosseous nerve.

The interosseous membrane consists of several parts, the most important of which is the central band originally described by Hotchkiss et al (1989). This probably acts in conjunction with the radial head to restrain the radius from proximal migration and to stabilize the forearm. Previously described as being at its most taut in almost every position of rotation of the forearm, it now appears to maintain the same tension throughout pronation and supination. Noda et al (2009) have described four other subsidiary portions. The distal oblique band has fibres that arise from the ulna and incline distally and laterally; they are attached to the radius just proximal to the distal radio-ulnar joint and contribute to the anteroposterior stability of the joint.

Distal radio-ulnar joint

The distal radio-ulnar joint is a uniaxial pivot joint.

Articulating surfaces The articulating surfaces are between the convex distal head of the ulna and the concave ulnar notch of the radius; they are connected by an articular disc.

Fibrous capsule The fibrous capsule is thicker anteriorly and posteriorly, and more lax proximally.

Triangular fibrocartilage complex and distal radio-ulnar ligaments The triangular fibrocartilage complex (TFCC) is a ligamentous and cartilaginous structure that suspends the distal radius and ulnar carpus from the distal ulna. It stabilizes the ulnocarpal and radio-ulnar joints, transmits and distributes load from the carpus to the ulna, and facilitates complex movements at the wrist. By definition, it is made up of the triangular fibrocartilage proper (the articular disc), meniscus homologue (the ulnocarpal meniscus), ulnar collateral ligament, dorsal and palmar radio-ulnar ligaments, floor of extensor carpi ulnaris subsheath, and the ulnolunate and ulnotriquetral ligaments. The triangular fibrocartilage proper is a biconcave body composed of chondroid fibrocartilage that extends across the dome of the ulnar head, ranging in thickness between 2 and 5 mm. The meniscal homologue is a broad expansion of loose connective tissue that runs from the articular disc to the ulnar styloid and the surrounding joint capsule; it is not a major contributor to the structural integrity of the triangular fibrocartilage complex.

The triangular fibrocartilage complex is attached to the ulnar aspect of the lunate fossa of the radius. Medially, it is inserted into the head of the ulna and the base of the ulnar styloid. Here, it is joined by fibres from the ulnar part of the ulnar styloid (the ulnar collateral ligament); thus thickened, it attaches to the lunotriquetral interosseous ligament, triquetrum, hamate and base of the fifth metacarpal. A constant perforation just distal to the level of the ulnar styloid leads to the prestyloid recess. The dorsal and palmar (volar) aspects of the triangular fibrocartilage complex are thickened to form the dorsal and palmar radio-ulnar ligaments, which are attached to the dorsal and palmar ulnar corners of the distal radius and to the fovea of the ulnar head at the base of the ulnar styloid (Palmer and Werner 1981, Pacek and Buterbaugh 2015).

The triangular fibrocartilage complex receives its blood supply from the ulnar artery via its palmar and dorsal radiocarpal branches, the dorsal branch of the anterior interosseous artery and the palmar branch of the anterior interosseous artery. Only the outer 15–20% of the disc is vascularized; the rest is avascular (Thiru-Pathi et al 1986, Bednar et al 1991) (**Fig. 50.19**).

The triangular fibrocartilage complex acts as a cushion for the ulnar carpus, preventing ulnocarpal abutment and overloading of the ulna in ulnar deviation. It is a major stabilizer of the distal radio-ulnar joint. Degenerative perforation of the triangular fibrocartilage complex becomes more common with age and is a constant finding after the age of 50 years (Mikić 1978).

Synovial membrane The synovial membrane lines the capsule and forms a sacciform recess in front of the distal part of the interosseous membrane.

Vascular supply The arterial supply of the distal radio-ulnar joint is derived from the palmar and dorsal branches of the anterior interosseous artery, reinforced by the posterior interosseous and ulnar arteries.

Innervation The distal radio-ulnar joint is innervated by branches of the anterior and posterior interosseous nerves.

Movements at the humero-ulnar, humero-radial and proximal and distal radio-ulnar joints

The main movements that occur at the humero-ulnar, humero-radial and proximal and distal radio-ulnar joints are flexion, extension, supination and pronation.

Flexion and extension

The elbow joint has relatively stable semi-congruent articular surfaces that are assisted by strong static and dynamic stabilizers, and which allow a flexion–extension arc of approximately 150°. When the elbow is extended and supinated, the forearm forms a 'carrying angle' with the humerus of approximately 17°; the absolute angle varies from individual to individual. It exists because the medial edge of the trochlear projects distally by 6 mm and because the superior articular surface of the coronoid is oblique. The carrying angle is not present in flexion when the humerus and ulna are in the same plane. With the arm adducted and the elbow flexed, the little finger meets the clavicle. If the humerus is rotated laterally, the little finger reaches the anterior shoulder. Pronation of the extended forearm masks the carrying angle by lining up the arm, forearm and hand.

Accessory movements

Availatble with the *Gray's Anatomy* e-book

Pronation and supination

Movements at the humero-radial, proximal and distal radio-ulnar joints pronate and supinate the hand. In pronation, the radius turns anteromedially and obliquely across the ulna. Its proximal end remains lateral to the ulna while its distal end lies medially and the interosseous membrane becomes spiralled. In supination, the radius returns to its former position lateral and parallel to the ulna and the interosseous membrane becomes unspiralled. The hand can be turned through 140–150° with the elbow extended; this can be increased to nearly 360° by humeral rotation and movements of the scapula. Power is greater in supination, a fact that has affected the design of nuts, bolts and screws, which are tightened by supination in the right-handed.

Stability of the distal radio-ulnar joint

With the wrist in neutral extension and deviation, the main axis for transmission of force from the hand to the forearm passes through the head of the capitate, then through the scapholunate ligament and finally into the distal radius. Loading is transferred to the triangular fibrocartilage complex and distal ulna in ulnar deviation. The joint is stabilized by extrinsic and intrinsic structures.

Extrinsic stabilizers Extrinsic stabilizers include the tendon of extensor carpi ulnaris, pronator quadratus, the distal oblique band of the interosseous membrane and the sheath of the sixth dorsal compartment, which overlies extensor carpi ulnaris (Spinner and Kaplan 1970).

Intrinsic stabilizers Intrinsic stabilizers are stronger than extrinsic stabilizers and include the radio-ulnar capsule and the dorsal and palmar radio-ulnar ligaments. The dorsal and palmar radio-ulnar ligaments contain superficial and deep components. The superficial layers insert on to the ulnar styloid. The stronger, deep layers insert more laterally into the fovea adjacent to the articular surface of the pole of the distal ulna (Kleinmann 2010).

Muscles producing movement

Flexion. Movement is produced by brachialis, biceps brachii and brachioradialis. In slow flexion or its maintenance against gravity, brachialis and biceps are principally involved, even for light loads. With increasing speed and activity, brachioradialis is increasingly prominent; its attachments determine that it acts most effectively in mid-pronation. Against resistance, pronator teres, longus and brevis, flexors carpi radialis and ulnaris, and extensor carpi radialis may contribute.

Extension Movement is produced by triceps, anconeus and gravity.

Pronation Pronator quadratus is aided in rapid movement and against resistance by pronator teres. Gravity also assists.

Supination Movement is produced by supinator, in slow unresisted movement and extension, assisted by biceps in fast movements in flexion, especially when resisted.

MUSCLES OF THE FOREARM

There is some anatomical segregation by function of muscles that cross the elbow. Most of those that arise medially pass to the flexor aspect of the wrist, or stabilize or move the ulnar column of the carpus and the ulnar side of the hand. Those that arise laterally pass to the lateral column of the forearm and carpus, and to the extensor aspect of the wrist. The muscles that act on the thumb have a wide origin: the extensor and abductor muscles arise from the entire width of the interosseous membrane. Rotator muscles, such as supinator, pronator teres and pronator quadratus, pass between the radius and ulna, crossing the longitudinal axis of the forearm.

Anterior compartment

The anterior compartment contains the flexor muscles of the forearm. These are arranged in superficial and deep groups.

Superficial flexor compartment

Muscles of the superficial flexor compartment are pronator teres, flexor carpi radialis, palmaris longus, flexor digitorum superficialis and flexor carpi ulnaris.

Pronator teres

Attachments Pronator teres arises from two heads. The humeral origin of pronator teres is the larger and more superficial. It arises at the medial supracondylar ridge just proximal to the medial epicondyle from the common tendon of origin of the flexor muscles, from the intermuscular septum between it and flexor carpi radialis, and from the antebrachial fascia (see Fig. 50.6, **Figs 50.20–50.22**). The smaller ulnar head arises from the medial side of the coronoid process of the ulna, distal to the attachment of flexor digitorum superficialis, and joins the humeral head at an acute angle. This ulnar coronoid attachment may be absent in some individuals. The muscle passes obliquely across the forearm to end in a flat tendon that is attached to a rough area midway along the lateral surface of the radial shaft at the apex of its lateral curve (see Fig. 50.25). Accessory slips may arise from a supracondylar process of the humerus, if present, or from biceps, brachialis or the medial intermuscular septum.

Relations The median nerve usually enters the forearm between the two heads of pronator teres, separated from the ulnar artery by the ulnar head. The lateral border of pronator teres is the medial margin of the cubital fossa (see Fig. 48.53). Proximally, the medial border of pronator teres is related to the lateral aspect of flexor carpi radialis. Pronator teres is anterior to flexor digitorum superficialis.

Vascular supply The humeral head of pronator teres is supplied by the inferior ulnar collateral and anterior ulnar recurrent arteries. The ulnar head is supplied by the common interosseous artery, the mid portion of the muscle belly by direct branches from the ulnar artery, and the radial insertion by the radial artery.

Innervation Pronator teres is innervated by the median nerve, sixth and seventh cervical ventral rami.

Actions Pronator teres pronates the forearm by rotating the radius medially on the ulna. It is a weak flexor of the elbow joint.

Testing Pronator teres is tested by palpating its contracting fibres during pronation against resistance. The tendon of pronator teres is chiefly responsible for the symptoms of golfer's elbow or medial epicondylosis.

Flexor carpi radialis

Attachments Flexor carpi radialis arises from the common flexor origin on the medial epicondyle, the antebrachial fascia and from the adjacent intermuscular septa (see Fig. 49.11A). Its fusiform muscular belly converges in the mid-forearm into a long tendon that passes within a synovial sheath through a lateral canal, formed by the flexor retinaculum above and a groove on the trapezium beneath. It inserts on the palmar surface of the base of the second metacarpal and sends a slip to the third metacarpal. These distal attachments lie beneath the oblique head of adductor

The surface topography of the humero-ulnar joint permits some rotation of the ulna against the humerus. The radius acts as a mobile strut within the forearm, such that rotation of the distal radius around the ulna carries the radiocarpal joint, wrist and hand into pronation or supination. The medial side of the head of the radius is longer than the lateral side; this eccentric morphology causes a cam effect during rotation of the proximal radio-ulnar joint. The radius is suspended by the interosseous membrane from the ulna, which is the fixed structure in the forearm.

The interosseous membrane contributes to longitudinal stability by virtue of its oblique course from the radius proximally to the ulna distally. It appears to maintain the same tension throughout pronation and supination (Ekenstam et al 1984). If the membrane is disrupted, as in an Essex–Lopresti injury (fracture of the head of the radius, disruption of the interosseous membrane and dislocation of the distal radio-ulnar joint), the radius will migrate proximally; persistent radio-ulnar dissociation causes a complex instability of the forearm (Hotchkiss et al 1989). Correction of the fixed deformity of the forearm commonly seen in untreated cases of spastic cerebral palsy or birth lesions of the brachial plexus usually requires release of the membrane because it has become relatively shortened. Pronator quadratus and supinator protect the interosseous membrane, to some extent, during forced, rapid rotation of the forearm by ‘paying out’ eccentrically, thereby reducing the load applied across the membrane.

The elbow is stabilized by the intrinsic shape of the joint and by its ligaments and muscles. The trochlear pulley is deeply seated within the trochlear notch, while the olecranon provides anteroposterior stability. Anterior stability in the sagittal plane is enhanced by the joint capsule, biceps, brachialis and the bicipital aponeurosis; posterior stability is enhanced by the triceps tendon and aponeurosis.

The radial and ulnar collateral ligaments are key to stability in the coronal plane. Resistance to varus strain comes from the radial ligament complex, of which the posterior band is the most important. Resistance to valgus strain is provided by the ulnar collateral ligament complex, of which the anterior band is the most important. If the head of the radius is lost, an intact ulnar collateral ligament maintains stability of the elbow. If the ligament is disrupted, the ulna drifts into valgus, there is rotational instability and the trochlea is damaged. Stability of the radius is enhanced by anconeus and by the muscles arising from the lateral aspect of the distal humerus. Muscles that arise from the medial epicondyle contribute to stability of the ulna. Muscles that act across the elbow have a shunting effect, creating articular joint reaction compression forces that contribute to close-packing (the position of a joint in which the greatest stability is achieved for the least expended effort). The humero-ulnar joint is most closely packed and, therefore, most resistant to fatigue in flexion and supination.

The flexion–extension arc of the elbow is accompanied by some rotation; the ulna is slightly pronated in extension and supinated in flexion. In full extension, the radial head can be palpated posteriorly because the radial facet is larger than the capitulum. The excursion of the radial head in extension is limited by tension in the posterolateral ligament, by the muscles anterior to the joint and by the tip of the olecranon entering the olecranon fossa. In flexion, the rim of the radial head enters the radial fossa and the tip of the coronoid process enters the coronoid fossa. Flexion is principally limited by the apposition of soft tissues.

Accessory movements include anterior and posterior translation of the radial head on the ulnar radial notch, and of the ulnar head on the radial ulnar notch.

Accessory movements of the human elbow are minimal and facilitate the movements described above. The ulna rotates slightly at the elbow and allows a few degrees of abduction and adduction. The radial head exhibits a little anteroposterior translation on the capitulum when it moves on the ulnar radial notch and the anular ligament moves back and forth; this occurs maximally with the elbow in 90° of flexion.

Rotation of the forearm occurs between the head of the radius and the radial notch of the ulna proximally and the articulation of the head of the ulna and trochlear (sigmoid) notch. These proximal and distal radio-ulnar joints are pivot-type synovial joints; they act as a unit, permitting stable rotary motion (pronation 61–66°, supination 70–77°). During rotation, the distal radius moves around the head of the ulna. The axis for pronation and supination is often represented as a line through the centre of the radial head proximally and the ulnar attachment of the articular disc distally. This represents the axis of movement of the radius relative to the ulna but this does not remain stationary. The radial head rotates in the fibro-osseous ring; its distal lower end and articular disc swing round the head of the ulna. Rotation of the radial head occurs on the humeral capitulum. As the forearm moves from full pronation into supination, the ulna translocates medially by 9–10 mm, so that the axis of rotation shifts but still passes through the head of the ulna. In addition, the trochlear notch changes its position of contact with the ulnar head, lying dorsal proximally in pronation and palmar distally in supination. The distal end of the ulna is not stationary during these movements; it moves along a curved course, posterolaterally in pronation and anteromedially in supination. The axis of movement, as defined above, is therefore displaced laterally in pronation and medially in supination. Hence, the axis for pronation and supination of the forearm and hand passes between the bones at both the proximal and distal radio-ulnar joints when ulnar movement is marked, but through the centres of the radial head and ulnar styloid when it is minimal. The axis may be extended along any digit, depending on whether the distal end of the ulna is medially or laterally displaced. The hand will rotate further than the forearm because of the sliding–rotatory movement that occurs between the carpal bones and the bases of the metacarpals, and, to a very minor degree, at the radiocarpal joint.

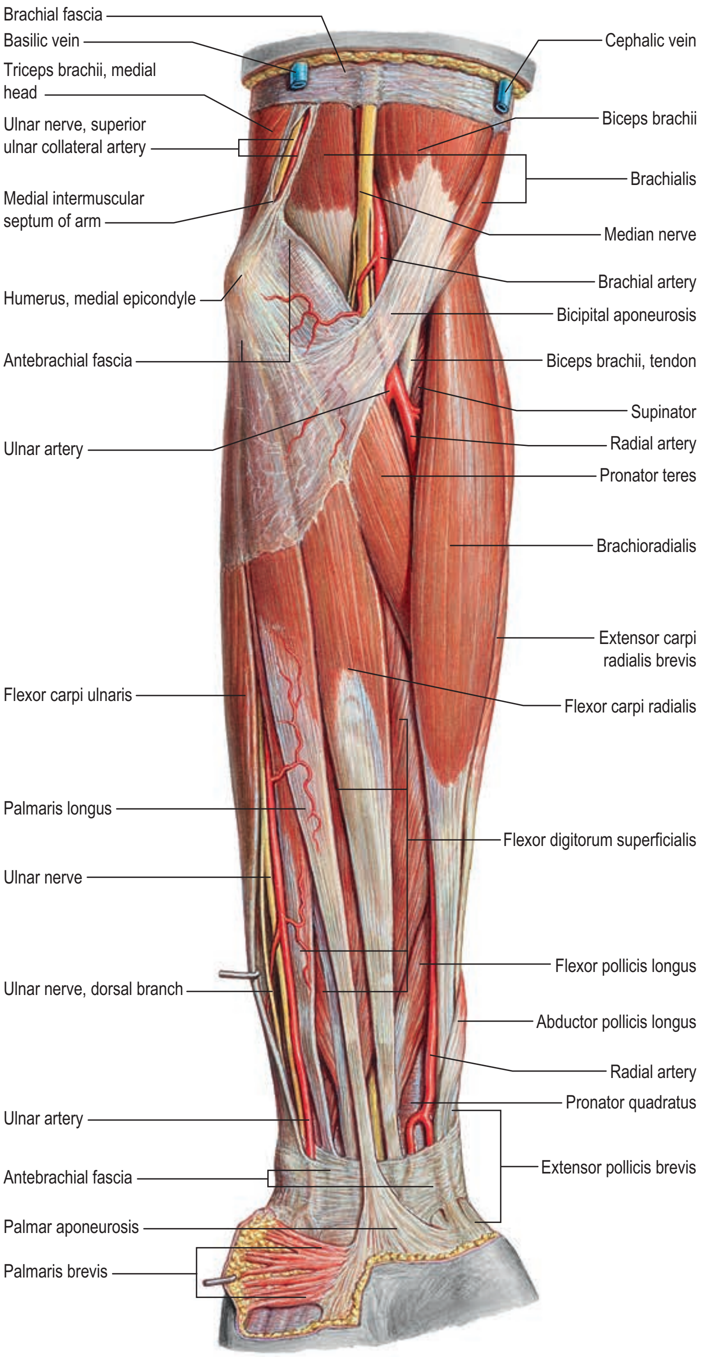
Brachial fascia
Basilic vein
Triceps brachii, medial head
Ulnar nerve, superior ulnar collateral artery
Medial intermuscular septum of arm
Humerus, medial epicondyle
Antebrachial fascia
Ulnar artery
Flexor carpi ulnaris
Palmaris longus
Ulnar nerve
Ulnar nerve, dorsal branch
Ulnar artery
Antebrachial fascia
Palmar aponeurosis
Palmaris brevis
Cephalic vein
Biceps brachii
Brachialis
Median nerve
Brachial artery
Bicipital aponeurosis
Biceps brachii, tendon
Supinator
Radial artery
Pronator teres
Brachioradialis
Extensor carpi radialis brevis
Flexor carpi radialis
Flexor digitorum superficilis
Flexor pollicis longus
Abductor pollicis longus
Radial artery
Pronator quadratus
Extensor pollicis brevis

Fig. 50.20 The superficial flexor muscles of the left forearm. (Sobotta Atlas of Human Anatomy © Elsevier GmbH, Urban & Fischer, Munich.)

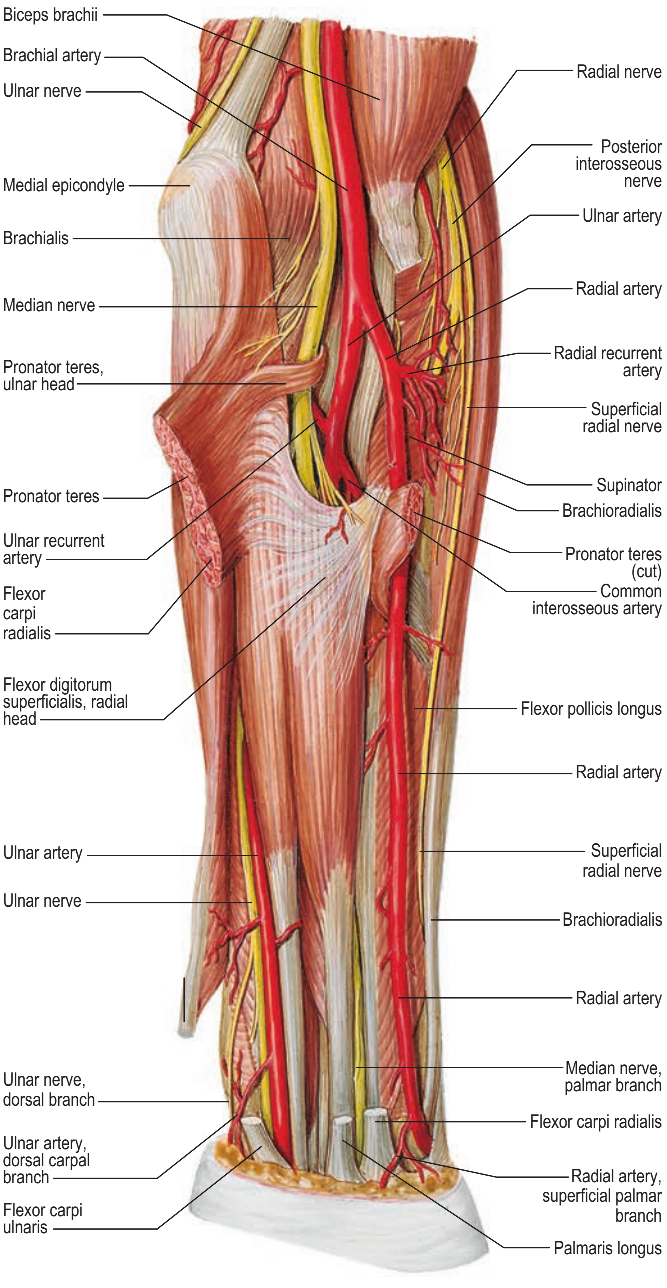
Biceps brachii
Brachial artery
Ulnar nerve
Medial epicondyle
Brachialis
Median nerve
Pronator teres, ulnar head
Pronator teres
Ulnar recurrent artery
Flexor carpi radialis
Flexor digitorum superficialis, radial head
Ulnar artery
Ulnar nerve
Ulnar nerve, dorsal branch
Ulnar artery, dorsal carpal branch
Flexor carpi ulnaris
Radial nerve
Posterior interosseous nerve
Ulnar artery
Radial artery
Radial recurrent artery
Superficial radial nerve
Supinator
Brachioradialis
Pronator teres (cut)
Common interosseous artery
Flexor pollicis longus
Radial artery
Superficial radial nerve
Brachioradialis
Radial artery
Median nerve, palmar branch
Flexor carpi radialis
Radial artery, superficial palmar branch
Palmaris longus

Fig. 50.21 The deep flexor muscles of the left forearm. (Sobotta Atlas of Human Anatomy © Elsevier GmbH, Urban & Fischer, Munich.)

pollicis. Rarely, the muscle may be absent. There may be accessory slips from the biceps tendon, bicipital aponeurosis, coronoid process or radius. Distally, it may also be attached to the flexor retinaculum, trapezium or fourth metacarpal.

Relations At its origin, flexor carpi radialis lies medial to pronator teres. In the lower part of the forearm, the radial artery lies between the tendon of flexor carpi radialis and the tendon of brachioradialis; the radial pulse may be palpated proximal to the wrist between these two tendons.

Vascular supply Flexor carpi radialis is supplied by a single dominant proximal pedicle and several distal minor pedicles. The dominant pedicle is formed by a branch that arises from either the anterior or the posterior ulnar recurrent artery. The posterior ulnar recurrent artery passes deep to pronator teres to enter the deep surface of flexor carpi radialis; from here, it divides into a small ascending branch and a larger descending branch. The distal minor pedicles supplying flexor carpi radialis are six to eight branches from the radial artery that enter the muscle on the anterolateral side.

Innervation Flexor carpi radialis is innervated by the median nerve, sixth and seventh cervical ventral rami.

Actions Flexor carpi radialis is a wrist flexor. It acts with flexor carpi ulnaris to effect balanced wrist flexion, and in concert with the radial extensors of the wrist to achieve balanced abduction of the hand.

Testing Flexor carpi radialis is tested by palpating its contracting fibres during flexion of the wrist against resistance.

Flexor digitorum superficialis

Attachments Flexor digitorum superficialis is the largest of the superficial flexors, and arises by two heads (see Figs 49.11A, 50.20–50.21). The humero-ulnar head arises from the medial epicondyle of the humerus via the common flexor origin, the anterior band of the ulnar collateral ligament, adjacent intermuscular septa, and from the medial side of the coronoid process proximal to the ulnar origin of pronator teres. The radial head, a thin sheet of muscle, arises from the anterior radial border between the radial tuberosity and the insertion of pronator teres. The median nerve and ulnar artery descend between the heads. The muscle usually separates into two strata, directed to digits two to five. The superficial stratum, joined laterally by the radial head, divides into two tendons for the middle and ring fingers. The deep stratum gives off a

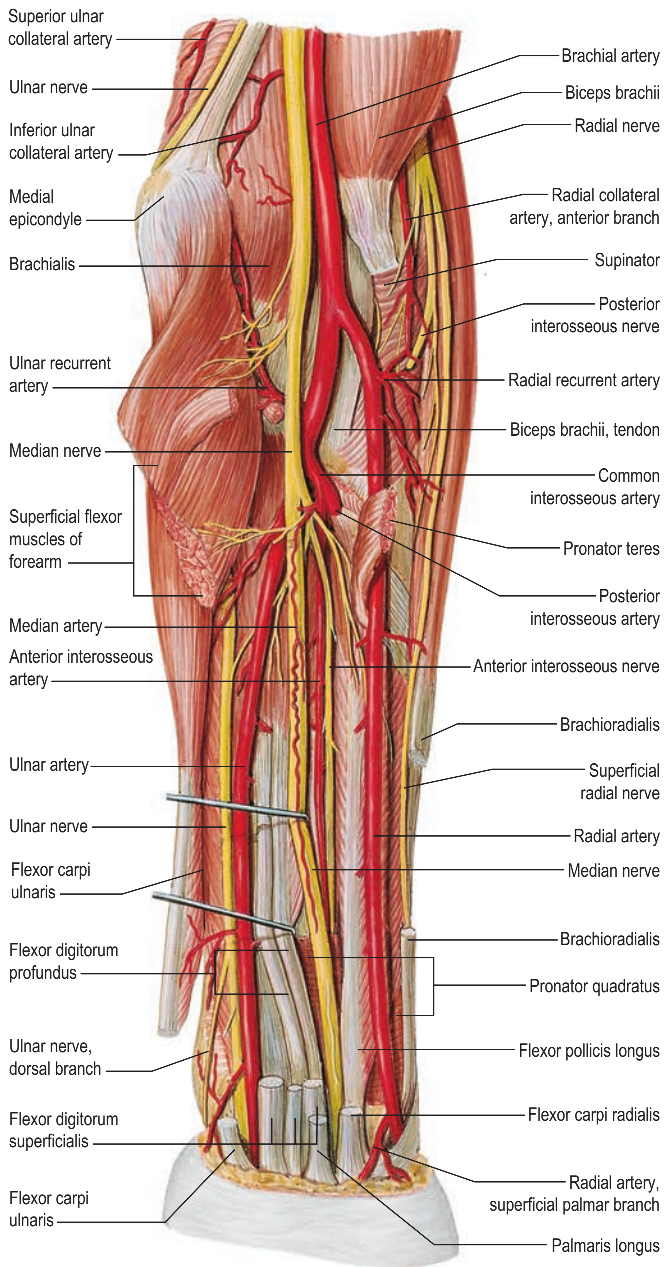
Superior ulnar collateral artery
Ulnar nerve
Inferior ulnar collateral artery
Medial epicondyle
Brachialis
Ulnar recurrent artery
Median nerve
Superficial flexor muscles of forearm
Median artery
Anterior interosseous artery
Ulnar artery
Ulnar nerve
Flexor carpi ulnaris
Flexor digitorum profundus
Ulnar nerve, dorsal branch
Flexor digitorum superficialis
Flexor carpi ulnaris
Brachial artery
Biceps brachii
Radial nerve
Radial collateral artery, anterior branch
Supinator
Posterior interosseous nerve
Radial recurrent artery
Biceps brachii, tendon
Common interosseous artery
Pronator teres
Posterior interosseous artery
Anterior interosseous nerve
Brachioradialis
Superficial radial nerve
Radial artery
Median nerve
Brachioradialis
Pronator quadratus
Flexor pollicis longus
Flexor carpi radialis
Radial artery, superficial palmar branch
Palmaris longus

Fig. 50.22 The deep flexor aspect of the left forearm. (Sobotta Atlas of Human Anatomy © Elsevier GmbH, Urban & Fischer, Munich.)

muscular slip to join the superficial fibres directed to the ring finger, and ends in two tendons for the index and little fingers. As the tendons pass behind the flexor retinaculum, they are arranged in pairs; the superficial pair passes to the middle and ring fingers, the deep pair to the index and little fingers. The four tendons diverge distal to the carpal tunnel. Each passes towards a finger superficial to the corresponding tendon of flexor digitorum profundus. The two tendons for each finger enter the digital flexor sheath at the metacarpophalangeal joint. The superficialis tendon splits into two bundles that pass around the profundus to lie posteriorly, and then reunite to insert into the anterior surface of the middle phalanx. Some fibres interchange from one bundle to another.

An intermediate tendon is always found in the central branching area of the muscle belly and is an important landmark in deep dissection; it may be confused with the median nerve. The radial head of flexor digitorum superficialis may be absent and the muscular slip from the deep stratum may provide most or all of the fibres acting on the index finger. The fibres associated with the little finger may be absent, in which case they are replaced by a separate slip from the ulna, flexor retinaculum or palmar fascia. Variations occur in the arrangement of the tendons.

Relations Flexor digitorum superficialis runs deep to pronator teres and flexor carpi radialis. The median nerve and ulnar artery descend between the heads of flexor digitorum superficialis, and the nerve continues distally deep to the muscle.

Vascular supply The humeral head of flexor digitorum superficialis is supplied by the anterior ulnar recurrent artery. The main body of the muscle is supplied on its anterior surface by three or four branches from both the ulnar and the radial arteries. The posterior surface is supplied by the ulnar artery and median artery, and the lateral surface by additional branches from the radial artery.

Innervation Flexor digitorum superficialis is innervated by the median nerve, eighth cervical ventral ramus and first thoracic ventral ramus.

Actions Flexor digitorum superficialis is a flexor of all the joints over which it passes, i.e. the wrist, metacarpophalangeal and proximal interphalangeal joints; its precise action depends on which other muscles are acting. It has independent muscle slips to all four fingers, and is therefore able to flex the proximal interphalangeal joints individually, unlike flexor digitorum profundus, which has a muscle group common to the middle, ring and little fingers.

Testing The independent action of flexor digitorum superficialis for a particular finger is tested by flexing that digit while holding the three other fingers in full extension. This eliminates any simultaneous contraction of the flexor digitorum profundus that might flex the digit.

Palmaris longus

Attachments Palmaris longus arises from the medial epicondyle of the humerus via the common flexor origin and from adjacent intermuscular septa and deep fascia. It is a slender, fusiform muscle that runs medial to flexor carpi radialis (see Figs 49.11A, 50.20, 50.32). It becomes tendinous in the mid-forearm, and the long tendon passes anterior (superficial) to the flexor retinaculum. A few fibres leave the tendon and interweave with the transverse fibres of the retinaculum but most of the tendon passes distally. As the tendon crosses the retinaculum, it broadens out to become a flat sheet that becomes incorporated into the palmar aponeurosis. Palmaris longus is occasionally absent on one or both sides.

Relations Palmaris longus runs distally, flanked by flexor carpi radialis and flexor carpi ulnaris, and superficial to flexor digitorum superficialis. The median nerve at the wrist lies partly under the cover of the tendon of palmaris longus and partly between the tendons of palmaris longus and flexor carpi radialis.

Vascular supply The muscle belly of palmaris longus is supplied by a small branch from the anterior ulnar recurrent artery. A contribution is sometimes made by the median artery, if this is well developed.

Innervation Palmaris longus is innervated by the median nerve, seventh and eighth cervical ventral rami.

Actions Palmaris longus is a weak wrist flexor. Through its insertion in the palmar aponeurosis, it also acts as an anchor for the skin and fascia of the hand against horizontal shearing forces.

Testing If the wrist is flexed against resistance, the taut tendon of palmaris longus will be seen in the midline of the flexor wrist crease as the tendon passes superficial to the flexor retinaculum. When testing palmaris longus, it helps to oppose the thumb to the middle fingertip at the same time as the wrist is flexed, in order to make palmaris stand out.

Flexor carpi ulnaris

Attachments Flexor carpi ulnaris is the most medial of the superficial forearm flexors (see Figs 50.20, 50.31–50.32). It arises by two heads, humeral and ulnar, connected by a tendinous arch (arcuate ligament of Osborne). The smaller humeral head arises from the medial epicondyle via the common flexor origin (see Fig. 49.11A). The ulnar head has an extensive origin from the medial margin of the olecranon and proximal two-thirds of the posterior border of the ulna (from an aponeurosis shared with extensor carpi ulnaris and flexor digitorum profundus) and from the intermuscular septum between it and flexor digitorum superficialis (see Fig. 50.6). Occasionally, there is a slip from the coronoid process. A thick tendon forms along its anterolateral border in its distal half. The tendon is attached to the pisiform, and from here it is prolonged to the hamate and fifth metacarpal by pisohamate and pisometacarpal ligaments. The attachment to the flexor retinaculum and the fourth or fifth metacarpal bones is sometimes substantial.

Relations Flexor carpi ulnaris is the most medial of the forearm flexors and forms the bulk of the soft tissue cover of the medial aspect of the ulna. The ulnar nerve and posterior ulnar recurrent artery pass under the tendinous arch between its humeral and ulnar heads. Ulnar vessels and nerve lie lateral to its tendon in the distal forearm.

Vascular supply The main arterial supply of flexor carpi ulnaris is derived from three pedicles. The proximal pedicle arises from a branch of the posterior ulnar recurrent artery as it passes between the humeral and ulnar heads. The middle pedicle arises from the ulnar artery and enters the muscle at the junction of the upper and middle thirds. The distal pedicles arise from the ulnar artery and enter the muscle at the musculotendinous junction. Flexor carpi ulnaris also receives a small supply near its origin from the inferior ulnar collateral artery.

Innervation Flexor carpi ulnaris is innervated by the ulnar nerve, seventh and eighth cervical ventral rami and first thoracic ventral ramus.

Actions Flexor carpi ulnaris is a powerful flexor and also adductor (ulnar deviation) of the wrist. When it acts with flexor carpi radialis, balanced wrist flexion is achieved. When it acts with extensor carpi ulnaris, balanced adduction occurs.

Testing Flexor carpi ulnaris is tested by palpating its tendon while the wrist is flexed against resistance, or by palpating the tendon while the patient abducts the little finger against resistance. The muscle synergistically stabilizes the pisiform, giving abductor digiti minimi a stable origin.

Deep flexor compartment

The muscles of the deep flexor compartment are flexor digitorum profundus, flexor pollicis longus and pronator quadratus (see Fig. 50.22).

Flexor digitorum profundus

Attachments Flexor digitorum profundus arises deep to the superficial flexors from the proximal three-quarters of the anterior and medial surfaces of the ulna (see Figs 50.5–50.6, 50.22). It embraces the attachment of brachialis above and extends distally almost to pronator quadratus. It also arises from a depression on the medial side of the coronoid process, from the proximal three-quarters of the posterior ulnar border by an aponeurosis that it shares with flexor and extensor carpi ulnaris, and from the anterior surface of the ulnar half of the interosseous membrane. The muscle ends in four tendons that run deep to the tendons of flexor digitorum superficialis and the flexor retinaculum. The part of the muscle that acts on the index finger is usually distinct throughout, while the tendons for the other fingers are interconnected by areolar tissue and tendinous slips as far as the palm. Anterior to their proximal phalanges, the tendons pass through the tendons of flexor digitorum superficialis to insert on the palmar surfaces of the bases of the distal phalanges. The tendons of the profundus undergo fascicular rearrangement as they pass through those of superficialis. Flexor digitorum profundus may be joined by accessory slips from the radius (which act on the index finger), flexor superficialis, flexor pollicis longus, the medial epicondyle or the coronoid process.

Relations Flexor digitorum profundus forms most of the surface elevation medial to the palpable posterior ulnar border. In the forearm, the median nerve runs on the anterior surface of its lateral aspect. In the palm, the lumbricals are attached to its tendons.

Vascular supply The origin of flexor digitorum profundus is supplied by the inferior ulnar collateral and ulnar recurrent arteries. The proximal part is supplied by one or two branches from either the ulnar or the common interosseous artery. The distal part is supplied by a series of branches from the ulnar artery, the anterior interosseous artery and the median artery.

Innervation The medial part of flexor digitorum profundus, i.e. the muscle bellies to the little and ring fingers, is innervated by the ulnar nerve. The lateral part, i.e. the muscle bellies to the middle and index fingers, is innervated by the anterior interosseous branch of the median nerve, eighth cervical ventral ramus and first thoracic ventral ramus.

Actions Flexor digitorum profundus flexes the distal interphalangeal joints of the fingers. It is also capable of flexing any or all of the joints over which it passes and therefore has a role in coordinated finger flexion. The index finger tendon is usually capable of independent function, whereas the other three work together.

Testing Flexor digitorum profundus is tested by flexing the distal interphalangeal joint while holding the proximal interphalangeal joint in extension.

Flexor pollicis longus

Attachments Flexor pollicis longus arises from the grooved anterior surface of the radius, and extends from below its tuberosity to the upper attachment of pronator quadratus (see Fig. 50.5, 50.21–50.22). It also arises from the adjacent interosseous membrane and, frequently, by a variable slip from the lateral, or more rarely the medial, border of the coronoid process, or from the medial epicondyle of the humerus. The muscle ends in a flattened tendon that passes behind the flexor retinaculum, between opponens pollicis and the oblique head of adductor pollicis, to enter a synovial sheath. It inserts on the palmar surface of the base of the distal phalanx of the thumb.

Flexor pollicis longus can sometimes be connected to flexor digitorum superficialis or profundus, or pronator teres. The interosseous attachment, and, indeed, the whole muscle, may be absent. Anomalous tendon slips from the flexor pollicis longus to flexor digitorum profundus are common.

Relations Flexor pollicis longus runs lateral to flexor digitorum profundus. The anterior interosseous nerve and vessels descend on the interosseous membrane between these muscles.

Vascular supply The medial half of flexor pollicis longus is supplied by the anterior interosseous artery. The lateral half is supplied by branches of the radial artery. The median artery may contribute if it is well developed.

Innervation Flexor pollicis longus is innervated by the anterior interosseous branch of the median nerve, seventh and eighth cervical ventral rami.

Actions Flexor pollicis longus principally flexes the phalanges of the thumb. It also flexes the carpometacarpal joint of the thumb, especially if the more distal joints are stiff or fused.

Testing Flexor pollicis longus is tested by flexing the interphalangeal joint of the thumb against resistance.

Pronator quadratus

Attachments Pronator quadratus is a flat, quadrilateral muscle that extends across the front of the distal parts of the radius and ulna (see Fig. 50.5). It arises from the oblique ridge on the anterior surface of the shaft of the ulna, the medial part of this surface and a strong aponeurosis that covers the medial third of the muscle. The fibres pass laterally and distally to the distal quarter of the anterior border and surface of the shaft of the radius (see Fig. 51.31). Deeper fibres insert into the triangular area above the ulnar notch of the radius.

Vascular supply Pronator quadratus receives its main arterial supply from the anterior interosseous artery as it passes through the interosseous membrane.

Innervation Pronator quadratus is innervated by the median nerve, seventh and eighth cervical ventral rami.

Actions Pronator quadratus is a pronator of the forearm and dynamic stabilizer of the distal radio-ulnar joint (DRUJ). The deeper fibres oppose separation of the distal ends of the radius and ulna when axial load is transmitted through the carpus.

Testing Pronator quadratus is tested by pronation of the forearm against resistance while the wrist finger flexors are relaxed. The simultaneous contraction of pronator teres makes it difficult to test the independent action of pronator quadratus.

Posterior compartment

The posterior compartment contains the extensor muscles of the forearm, brachioradialis and supinator. The superficial posterior muscles include anconeus, brachioradialis, extensor carpi radialis longus, extensor carpi radialis brevis, extensor digitorum, extensor digiti minimi and extensor carpi ulnaris. The deep posterior group of muscles includes supinator, abductor pollicis longus, extensor pollicis brevis, extensor pollicis longus and extensor indicis.

Superficial extensor compartment

Brachioradialis

Attachments Brachioradialis is the most superficial muscle along the radial side of the forearm and forms the lateral border of the cubital fossa (see Figs 50.22, 50.25). It arises from the proximal two-thirds of the lateral supracondylar ridge of the humerus and the anterior surface of the lateral intermuscular septum (see Figs 49.11A, 50.5). The muscle fibres end above mid-forearm level in a flat tendon that is inserted on the lateral side of the distal end of the radius, just proximal to the styloid process. This attachment may be more proximal; the muscle may fuse proximally with brachialis and the tendon may, occasionally, divide into two or three separately attached slips. In rare instances, it is double or absent.

Relations The radial nerve and the anastomosis between the profunda brachii artery and the radial recurrent artery lie in the groove between brachioradialis and brachialis, anterior to the lateral intermuscular septum. The tendon is crossed near its distal end by the tendons of abductor pollicis longus and extensor pollicis brevis. The radial artery is on its ulnar (medial) side. The superficial radial nerve emerges from between brachioradialis and extensor carpi radialis brevis to run superficially over the tendon of extensor carpi radialis brevis and extensor pollicis brevis, and then superficial to the extensor retinaculum.

Vascular supply Brachioradialis is supplied by branches of the radial recurrent artery that pierce the posteromedial surface of the muscle. It also receives branches from the radial collateral branch of the profunda brachii and directly from the radial artery in the distal part of the muscle.

Innervation Brachioradialis is innervated by the radial nerve, fifth and sixth cervical ventral rami.

Actions Brachioradialis is a powerful flexor of the elbow, acting most strongly with the forearm in mid-pronation. It is minimally active in slow flexion or with the forearm supine, but generates a powerful burst of activity in both flexion and extension when movement is rapid. Under these conditions, it develops a pronounced transarticular component of its force that helps to stabilize the elbow joint by balancing the centrifugal force of rapid swings in either direction.

Testing Brachioradialis can be seen and felt when the semi-pronated forearm is flexed against resistance.

Extensor carpi radialis longus

Attachments Extensor carpi radialis longus arises from the distal third of the lateral supracondylar ridge of the humerus and the front of the lateral intermuscular septum (see Fig. 49.11A). Some fibres join from the common tendon of origin of the forearm extensors. The muscle belly ends at the junction of the proximal and middle thirds of the forearm in a flat tendon that runs along the lateral surface of the radius, deep to abductor pollicis longus and extensor pollicis brevis. The tendon passes deep to the dorsal carpal ligament in a radial groove behind the styloid process alongside extensor carpi radialis brevis. Just before it is inserted on the radial side of the dorsal surface of the base of the second metacarpal, the tendon is crossed obliquely by the tendon of extensor pollicis longus. It may send slips to the first or third metacarpal bones and contributes to the intermetacarpal ligaments.

Relations Extensor carpi radialis longus runs alongside brachioradialis and is partly overlapped by it.

Vascular supply Extensor carpi radialis longus receives its principal arterial supply from a single branch of the radial recurrent artery. Additional blood supply comes from branches of the radial collateral branch of the profunda brachii and directly from the radial artery in the distal part of the muscle.

Innervation Extensor carpi radialis longus is innervated by the radial nerve, sixth and seventh cervical ventral rami.

Actions Extensor carpi radialis longus acts as an extensor and abductor of the wrist and midcarpal joints.

Testing The muscle belly and tendon of extensor carpi radialis longus can be palpated when the wrist is extended and abducted against resistance with the forearm pronated.

Extensor carpi radialis brevis

Attachments Extensor carpi radialis brevis arises from the lateral epicondyle of the humerus by a common tendon shared with extensor digitorum, extensor digiti minimi and extensor carpi ulnaris, the radial collateral ligament of the elbow joint, a strong aponeurosis that covers its surface, and adjacent intermuscular septa. The muscle belly ends at mid-forearm in a flat tendon that closely accompanies that of extensor carpi radialis longus to the wrist. The tendon passes under the extensor retinaculum, is crossed by the tendon of extensor pollicis longus, and is attached to the dorsal surface of the base of the third metacarpal on its radial side, distal to its styloid process, and on adjoining parts of the base of the second metacarpal. The tendons of both extensor carpi radialis longus and brevis share a common synovial sheath; they may split into slips that are variably attached to the second and third metacarpal bones. The muscles themselves may be united or may exchange muscular slips.

Relations Extensor carpi radialis brevis is shorter than extensor carpi radialis longus and is covered by it. The tendon passes deep to abductor pollicis longus and extensor pollicis brevis in the distal third of the forearm, then under the extensor retinaculum, where it lies in a shallow groove on the back of the radius, medial to the tendon of extensor carpi radialis longus, and separated from it by a low ridge.

Vascular supply Extensor carpi radialis brevis receives its arterial supply principally from two pedicles: a single branch from the radial recurrent artery, and a branch of the radial artery that arises about one-third of the way down the forearm. There is an additional blood supply proximally from branches from the radial collateral branch of the profunda brachii.

Innervation Extensor carpi radialis brevis is innervated by a branch from the radial nerve or from the posterior interosseous nerve, seventh and eighth cervical ventral rami. The branch to extensor carpi radialis brevis arises before the nerve enters the arcade of Frohse.

Actions Extensor carpi radialis brevis is the prime dorsiflexor of the wrist. It acts with extensor carpi radialis longus as an extensor and abductor of the wrist and mid-carpal joints. It acts in synergism with the finger flexors when making a fist.

Testing The muscle belly and tendon of extensor carpi radialis brevis can be palpated when the wrist is extended and abducted against resistance with the forearm pronated.

'Mobile wad' of Henry

Available with the *Gray's Anatomy* e-book

Extensor digitorum

Attachments. Extensor digitorum arises from the lateral epicondyle of the humerus via the common extensor tendon, the adjacent intermuscular septa and the antebrachial fascia (see Fig. 49.11A). The muscle belly divides in the distal third of the forearm into four tendons, which pass in a common synovial sheath with the tendon of extensor indicis through a tunnel under the extensor retinaculum. The tendons diverge on the dorsum of the hand, one to each finger. The tendon to the index finger is accompanied by extensor indicis, which lies ulnar (medial) to it. On the dorsum of the hand, adjacent tendons are linked by three variable intertendinous connections (juncturae tendinae), which are inclined distally and radially (see Figs 50.23, 51.11). The digital attachments enter a fibrous expansion on the dorsum of the proximal phalanges, to which lumbrical, interosseous and digital extensor tendons all contribute.

The tendons of extensor digitorum may be variably deficient. More commonly, they are doubled, or even tripled, in one or more digits: most often, the index finger or the middle finger. Occasionally, a slip of tendon passes to the thumb. The arrangement of the intertendinous connections on the dorsum of the hand is highly variable. The medial connection is strong and pulls the tendon of the little finger towards that of the ring finger, whereas the connection between the middle two tendons is weak and may be absent.

Relations The extensor tendon to the index finger lies radial (lateral) to the tendon of extensor indicis. The extensor tendon to the little finger lies radial (lateral) to the tendon of extensor digiti minimi.

Vascular supply The proximal third of extensor digitorum is supplied by branches from the radial recurrent artery, and the distal two-thirds are supplied by branches from the posterior interosseous artery. The very distal portion is supplied by a perforating branch from the anterior interosseous artery that passes through the interosseous membrane.

Innervation Extensor digitorum is innervated by the posterior interosseous nerve (seventh and eighth cervical ventral rami).

Actions Extensor digitorum can extend any or all of the joints over which it passes: wrist, metacarpophalangeal, and proximal and distal

Henry (1957) described a ‘mobile wad’ of three muscles, brachioradialis and the extensors carpi radialis longus and brevis, which are visible and palpable below the lateral epicondyle of the humerus, lying on the lateral aspect of the radius. The wad is tethered by a fan-shaped leash of vessels derived from the radial artery (the radial recurrent artery) that has to be released before the muscles can be fully mobilized. Its anterior and posterior margins are used to define the surgical approaches to the radius and to discover planes of cleavage. The anterior margin is used to define the anterior approach (of Henry) to the radius and can be extended down to the wrist at the level of the insertion of brachioradialis. This requires detachment of supinator from the radius, taking care not to damage the posterior interosseous nerve. More distally, pronator teres is released. This approach is particularly useful for plating fractures of the radius. The posterior margin is used to expose the posterior aspect of the forearm (posterior approach of Thompson) and, if need be, the posterior interosseous nerve, which, in any event, should be protected; unlike the anterior approach, this approach cannot be extended.

interphalangeal joints (the latter two via the extensor expansion of the digits). When acting on the metacarpophalangeal joints, extensor digitorum tends to spread the digits apart because of the different axes of the individual joints imposed by the transverse arch of the hand. The intertendinous bands stabilize the individual tendons as they cross the dorsum of the hand and permit some extension when a tendon has been divided in the metacarpal segment. The extent to which this occurs depends on the presence and orientation of the juncturae tendinae.

Testing The tendons of extensor digitorum can be readily felt, and usually seen, when the fingers are extended against resistance and the forearm is pronated.

Extensor digiti minimi

Attachments Extensor digiti minimi is medial to, and usually covered by, extensor digitorum; proximally, the bellies of these two muscles may be connected and indistinct from each other, whereas, in the mid-forearm, extensor digiti minimi is clearly discernible as a slender muscle (Fig. 50.23). It arises from the common extensor tendon by a thin, tendinous slip and adjacent intermuscular septa, and frequently has an additional origin from the antebrachial fascia. It forms a long tendon that constitutes the fifth dorsal compartment as it proceeds beneath the extensor retinaculum. Distal to the retinaculum, the tendon typically splits into two, and the lateral slip is joined by a tendon from extensor digitorum. All three tendons are attached to the dorsal digital expansion of the fifth digit; there may be a slip to the fourth digit. Extensor digiti minimi is rarely absent but, sometimes, it is fused with extensor digitorum.

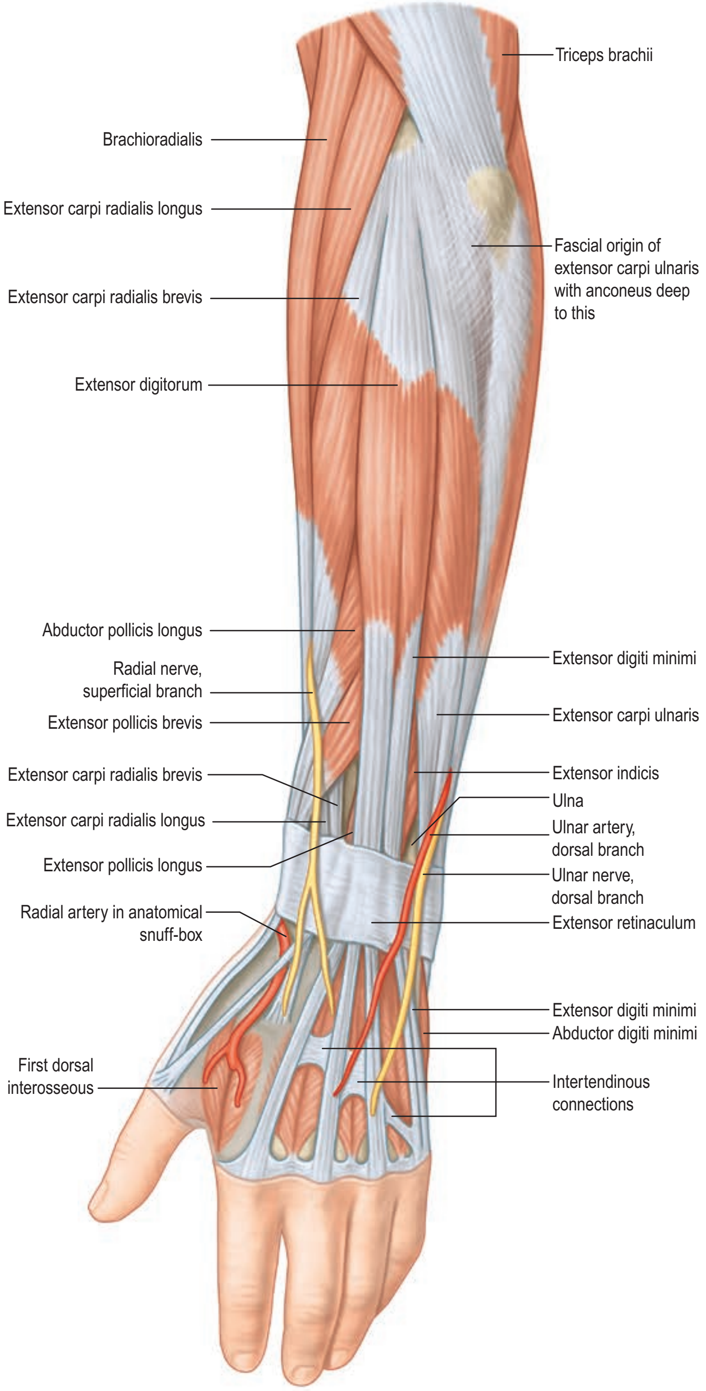
Triceps brachii
Brachioradialis
Extensor carpi radialis longus
Fascial origin of extensor carpi ulnaris with anconeus deep to this
Extensor carpi radialis brevis
Extensor digitorum
Abductor pollicis longus
Extensor digiti minimi
Radial nerve, superficial branch
Extensor carpi ulnaris
Extensor pollicis brevis
Extensor carpi radialis brevis
Extensor indicis
Ulna
Extensor carpi radialis longus
Ulnar artery, dorsal branch
Extensor pollicis longus
Ulnar nerve, dorsal branch
Radial artery in anatomical snuff-box
Extensor retinaculum
Extensor digiti minimi
Abductor digiti minimi
First dorsal interosseous
Intertendinous connections

Fig. 50.23 The superficial extensor muscles of the left forearm.

Relations The tendon of extensor digiti minimi lies ulnar (medial) to the common extensor tendon to the little finger. The dorsal branch of the ulnar artery and the dorsal branch of the ulnar nerve pass superficial to the extensor retinaculum and cross the tendon of extensor digiti minimi as it lies beneath the retinaculum.

Vascular supply Extensor digiti minimi is supplied by branches from the radial recurrent and posterior interosseous arteries, and by terminal branches from the anterior interosseous artery after it has pierced the interosseous membrane.

Innervation Extensor digiti minimi is innervated by the posterior interosseous nerve (seventh and eighth cervical ventral rami).

Actions Extensor digiti minimi can extend any of the joints of the little finger, or contribute to wrist extension. It permits extension of the little finger independently of the other digits, even in extremes of ulnar or radial wrist deviation.

Testing Extensor digiti minimi is tested by extending the little finger while holding the remaining fingers flexed at the metacarpophalangeal joints; this eliminates any simultaneous contraction of extensor digitorum.

Extensor carpi ulnaris

Attachments Extensor carpi ulnaris arises from the lateral epicondyle (where it forms the most medial part of the common extensor origin), the posterior border of the ulna (by an aponeurosis shared with flexor carpi ulnaris and flexor digitorum profundus) and overlying fascia (see Fig. 50.6). It runs between extensor digiti minimi and anconeus proximally, and extensor digiti minimi and flexor carpi ulnaris in the mid-forearm (see Figs 50.31–50.32). It forms a tendon in the distal third of the forearm that slides in a groove between the head and the styloid process of the ulna. It forms the content of the sixth dorsal compartment as it runs under the extensor retinaculum and is attached to a tubercle on the medial side of the base of the fifth metacarpal.

Vascular supply Proximally, extensor carpi ulnaris receives branches from the radial recurrent artery. Distally, it is supplied by several branches from the posterior interosseous artery.

Innervation Extensor carpi ulnaris is innervated by the posterior interosseous nerve (seventh and eighth cervical ventral rami).

Actions Extensor carpi ulnaris works synergistically with extensors carpi radialis longus and brevis and the digital flexors to effect balanced wrist extension, enabling a power grip with a clenched fist. It also acts with flexor carpi ulnaris to adduct the hand.

Testing The tendon can be felt lateral to the groove that overlies the posterior subcutaneous border of the ulna when the wrist is adducted against resistance.

Anconeus

Attachments Anconeus is a short, triangular muscle posterior to the elbow joint, partially and variably blended with triceps or extensor carpi ulnaris (Fig. 50.24). It arises by a separate tendon from the posterior surface of the lateral epicondyle of the humerus, proximal to the common extensor tendon. The tendon lies beneath the muscle belly of extensor carpi radialis longus. The muscle fibres run obliquely and medially towards the ulna, covering the posterior aspect of the anular ligament, and are attached to the lateral aspect of the olecranon and proximal quarter of the posterior surface of the shaft of the ulna.

An accessory muscle, anconeus epitrochlearis, may be present in up to one-third of individuals and has been reported to be an occasional cause of cubital tunnel syndrome (Grewal et al 2019).

Vascular supply Anconeus is supplied by branches of the posterior interosseous recurrent artery. A small number of musculocutaneous perforators reach the skin overlying the muscle.

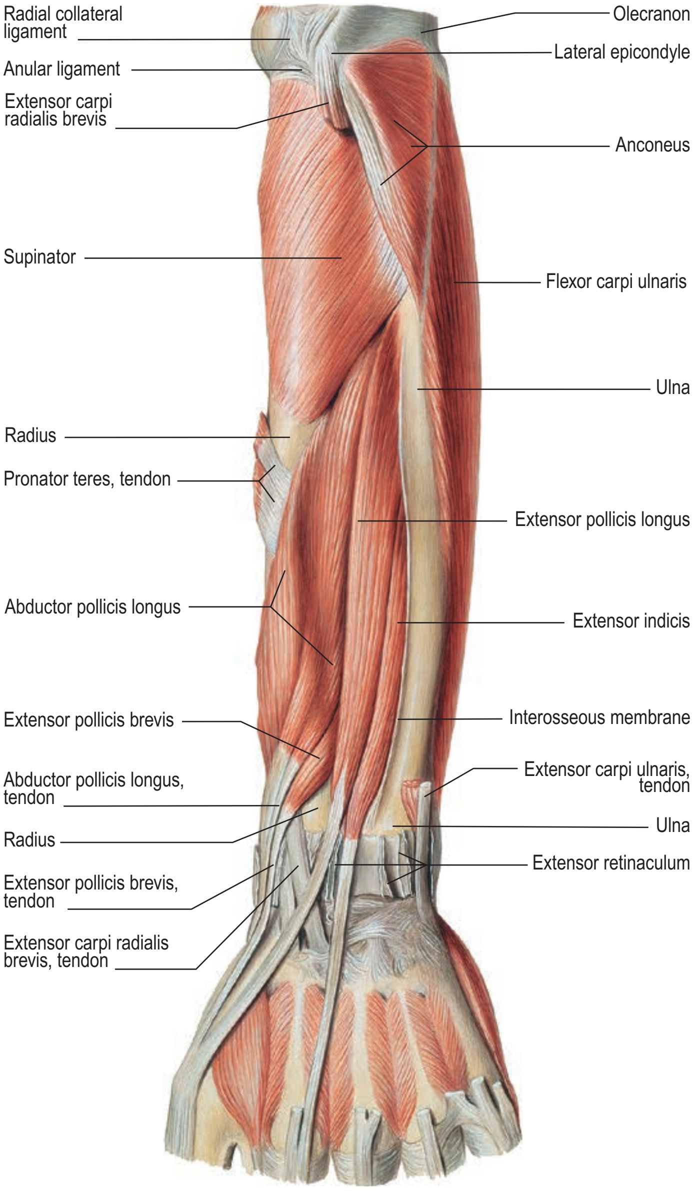

Fig. 50.24 The deep extensor muscles of the forearm. (Sobotta Atlas of Human Anatomy © Elsevier GmbH, Urban & Fischer, Munich.)

Innervation Anconeus is innervated by the radial nerve (sixth, seventh and eighth cervical ventral rami).

Actions Anconeus is an extensor of the elbow. Its principal function is not fully understood but it may control ulnar abduction in pronation, which is necessary if the forearm is to turn over the hand without translating it medially. In this way, a tool can be revolved 'on the spot' or it can be swept through an arc.

Deep extensor compartment

The five deep forearm extensor muscles are abductor pollicis longus, extensor pollicis longus and extensor pollicis brevis (all of which act on the thumb), extensor indicis and supinator. Apart from supinator, the other four deep forearm extensors all arise from the bones of the forearm and do not, therefore, act on the elbow.

Abductor pollicis longus

Attachments Abductor pollicis longus arises in part from the posterior surface of the shaft of the ulna, just distal to the insertion of anconeus, and from the adjoining interosseous membrane (see Fig. 50.6). The muscle runs obliquely in a lateral and distal direction from an apex formed by anconeus and supinator, and is joined by fibres that arise from the middle third of the posterior surface of the radius distal to the attachment of supinator (see Fig. 50.24). As it proceeds distally, abductor pollicis longus becomes more superficial in the forearm, where it is visible as an oblique elevation. The muscle fibres form a tendon just proximal to the wrist. The tendon runs in a groove on the lateral side of the distal end of the radius, accompanied by the tendon of extensor pollicis brevis. It runs under the extensor retinaculum in the first dorsal compartment. It usually splits into two slips; one is attached to the radial side of the first metacarpal base, and the other is attached to the trapezium. Slips from the tendon may continue into opponens pollicis or abductor pollicis brevis. Occasionally, the muscle itself may be wholly or partially divided.

Relations Abductor pollicis longus runs on the radial aspect of extensor pollicis longus. The posterior interosseous nerve runs over the belly of abductor pollicis longus with the accompanying posterior interosseous artery; the nerve runs to the border of abductor pollicis longus and then dives between the muscles bellies of abductor pollicis longus and extensor pollicis longus at the apex of their divergence.

Vascular supply Abductor pollicis longus is supplied proximally by a lateral branch from the posterior interosseous artery. Distally, it is supplied on the medial side by a perforating branch from the anterior interosseous artery.

Innervation Abductor pollicis longus is innervated by the posterior interosseous nerve (seventh and eighth cervical ventral rami).

Actions Abductor pollicis longus abducts the metacarpal of the thumb. It is the prime radial abductor of the thumb. It also acts to abduct the wrist. With abductor pollicis brevis, it effects palmar abduction.

Testing The tendon of abductor pollicis longus can be seen and felt at the radial aspect of the anatomical snuff-box when the thumb and wrist are abducted against resistance at the carpometacarpal joint.

Extensor pollicis longus

Attachments Extensor pollicis longus arises from the lateral part of the middle third of the posterior surface of the shaft of the ulna below abductor pollicis longus and from the adjacent interosseous membrane. It partly overlies the proximal attachment of the smaller extensor pollicis brevis (see Fig. 50.24). The tendon is formed just proximal to the wrist and passes through the third compartment of the extensor retinaculum in a narrow, oblique groove on the back of the distal end of the radius. It turns around a bony fulcrum, Lister's tubercle, which changes its line of pull from that of the forearm to that of the thumb, and is attached to the base of the distal phalanx of the thumb. The sides of the tendon are joined on the dorsum of the proximal phalanx by expansions from the tendon of abductor pollicis brevis laterally and from the first palmar interosseous and adductor pollicis medially.

Relations Extensor pollicis longus runs between abductor pollicis longus and extensor indicis in the forearm. The posterior interosseous artery runs over its muscle belly. After passing around Lister's tubercle, the tendon of extensor pollicis longus crosses the tendons of extensor carpi radialis brevis and longus obliquely.

Vascular supply Extensor pollicis longus is supplied on its superficial surface by branches from the posterior interosseous artery, and on its deep surface by perforating branches from the anterior interosseous artery.

Innervation Extensor pollicis longus is innervated by the posterior interosseous nerve (seventh and eighth cervical ventral rami).

Actions Extensor pollicis longus extends the distal phalanx of the thumb. Acting in association with extensor pollicis brevis and abductor pollicis longus, it extends the proximal phalanx and the metacarpal. In continued action, as a consequence of the obliquity of its tendon, extensor pollicis longus adducts the extended thumb and rotates it laterally. It is a weak extensor of the wrist.

Testing The tendon of extensor pollicis longus can be palpated at the ulnar border of the anatomical snuff-box when the thumb is extended at the interphalangeal joint against resistance. When the thumb is opposed and adducted, abductor pollicis brevis can extend the interphalangeal joint of the thumb, mimicking the action of extensor pollicis longus.

Extensor pollicis brevis

Attachments Extensor pollicis brevis arises from the posterior surface of the radius distal to abductor pollicis longus and from the adjacent interosseous membrane (see Fig. 50.6). It runs between abductor pollicis longus and extensor pollicis longus. The tendon is attached to the base of the proximal phalanx of the thumb and, commonly, has an additional attachment to the base of the distal phalanx, usually through a fasciculus that joins the tendon of extensor pollicis longus. Extensor pollicis brevis may be absent or fused completely with abductor pollicis longus.

Relations Extensor pollicis brevis is ulnar (medial) to, and closely connected with, abductor pollicis longus. In the distal forearm, the two muscles emerge between extensor carpi radialis brevis and extensor digitorum, and pass obliquely across the tendons of extensors carpi radialis brevis and longus (see Fig. 50.24). They cover the distal part of brachioradialis, and pass through the most lateral compartment of the extensor retinaculum in a single synovial sheath, sharing a groove in the distal radius. Ultimately, they cross, superficial to the radial styloid process and radial artery, to reach the dorsolateral base of the proximal phalanx of the thumb.

Vascular supply Extensor pollicis brevis is supplied from branches from the posterior interosseous artery, together with perforating branches from the anterior interosseous artery.

Innervation Extensor pollicis brevis is innervated by the posterior interosseous nerve (seventh and eighth cervical ventral rami).

Actions Extensor pollicis brevis extends the proximal phalanx and metacarpal of the thumb.

Testing The tendon of extensor pollicis brevis can be felt at the radial border of the anatomical snuff-box, lying medial to the tendon of abductor pollicis longus, when the metacarpophalangeal joint of the thumb is extended against resistance.

Extensor indicis

Attachments Extensor indicis is a narrow muscle that lies medial and parallel to extensor pollicis longus (see Fig. 50.24). It arises from the posterior surface of the ulna distal to extensor pollicis longus and the adjacent interosseous membrane. The tendon is formed just proximal to the wrist and passes under the extensor retinaculum in a common compartment with the tendons of extensor digitorum (see Fig. 51.11). Opposite the head of the second metacarpal, it joins the ulnar side of the tendon of extensor digitorum that serves the index finger. Extensor indicis occasionally sends accessory slips to the extensor tendons of other digits. Its tendon may be interrupted on the dorsum of the hand by an additional muscle belly (extensor indicis brevis manus) (Georgiev et al 2018).

Relations The posterior interosseous artery passes over the muscle belly of extensor indicis. On the dorsum of the hand, the tendon of extensor indicis lies on the ulnar aspect of the tendon of extensor digitorum to the index finger.

Vascular supply Extensor indicis is supplied on its superficial surface by branches from the posterior interosseous artery, and on its deep surface by perforating branches from the anterior interosseous artery.

Innervation Extensor indicis is innervated by the posterior interosseous nerve (seventh and eighth cervical ventral rami).

Actions Extensor indicis extends the index finger independently of the other digits. It is a weak extensor of the wrist.

Testing Extensor indicis is tested by extending the index finger while holding the remaining fingers flexed at the metacarpophalangeal joints in order to eliminate the effects of any simultaneous contraction of extensor digitorum.

Supinator

Attachments Supinator is a wide muscle that surrounds the proximal third of the radius. It has superficial and deep layers The two parts arise together, the superficial by tendinous fibres, and the deep by muscular fibres, from the lateral epicondyle of the humerus; the radial collateral ligament of the elbow joint; the anular ligament of the superior radio-ulnar joint; the supinator crest of the ulna and the posterior part of the triangular depression in front of it; and an aponeurosis that covers the muscle (see Figs 50.5–50.6; **Figs 50.25–50.26**). Supinator is attached distally to the lateral surface of the proximal third of the radius, down to the insertion of pronator teres. The radial attachment extends onto the anterior and posterior surfaces between the anterior oblique line and the fainter posterior oblique 'ridge'. Supinator is subject to frequent variation; small parts have acquired individual names, e.g. lateral and medial tensors of the anular ligament (Paraskevas and Ioannidis 2011).

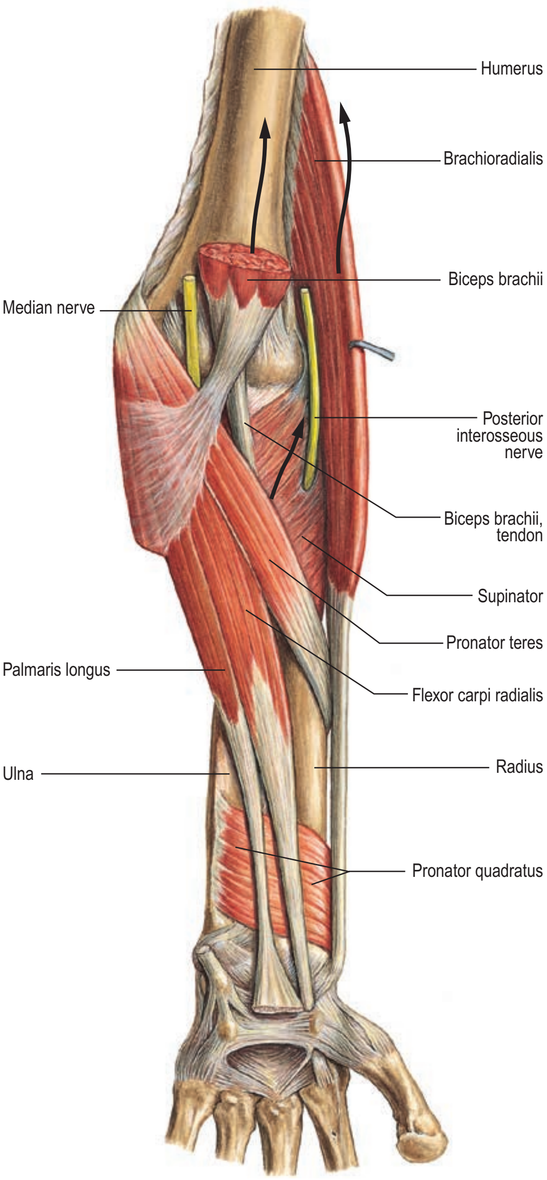

Fig. 50.25 The supinated forearm. (Sobotta Atlas of Human Anatomy © Elsevier GmbH, Urban & Fischer, Munich.)

Relations Supinator emerges under the lower border of anconeus and is related to abductor pollicis longus at its inferior medial border. Extensor carpi radialis brevis and longus pass over its radial aspect. The posterior interosseous nerve enters the forearm by passing between its superficial and deep heads.

Vascular supply The superficial part of supinator is supplied by branches from the radial recurrent artery. The deep part of supinator is supplied by branches from the posterior interosseous artery and the posterior interosseous recurrent artery.

Innervation Supinator is innervated by the posterior interosseous nerve (sixth and seventh cervical ventral rami).

Actions Supinator rotates the radius to bring the palm to face anteriorly. It acts alone in slow, unopposed supination, and together with biceps brachii in fast or forceful supination. An object, which potentially may be heavy, is often picked up with the forearm initially pronated. The more powerful supinator lifts the object against gravity; rotation is often combined with increasing elbow flexion in order to bring the object towards the eyes.

Testing Supinator lies too deep to be palpated. It may be assessed by supinating the forearm against resistance with the elbow extended, on the grounds that biceps brachii is inactive on supination when the elbow is fully extended.

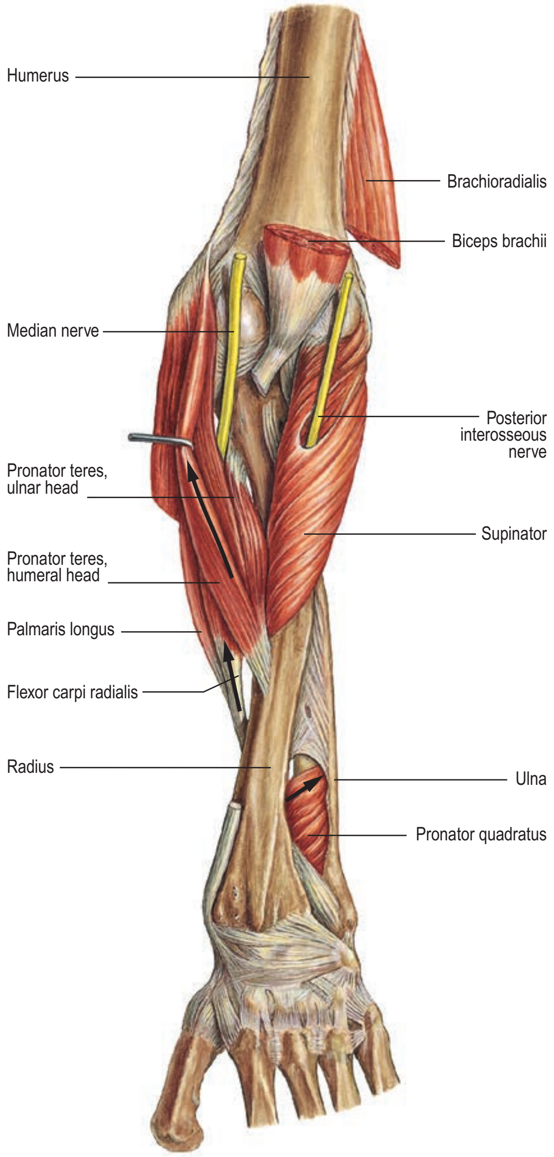
Humerus
Brachioradialis
Biceps brachii
Median nerve
Posterior interosseous nerve
Pronator teres, ulnar head
Supinator
Pronator teres, humeral head
Palmaris longus
Flexor carpi radialis
Radius
Ulna
Pronator quadratus

Fig. 50.26 The pronated forearm. (Sobotta Atlas of Human Anatomy © Elsevier GmbH, Urban & Fischer, Munich.)

Compartment syndrome of the forearm

Available with the *Gray's Anatomy* e-book

VASCULAR SUPPLY AND LYMPHATIC DRAINAGE

Arteries

Brachial artery

The brachial artery is medial in the arm but moves towards the midline, medial to the tendon of biceps brachii and deep to the bicipital aponeurosis. The latter separates the artery from the anterior structures, namely: the skin, superficial fascia and the median cubital vein. Posteriorly, brachialis separates it from the elbow joint. The median nerve passes close to the medial side of the artery. The artery divides into its terminal branches, the radial and ulnar arteries, at the level of the radial neck (Fig. 50.27).

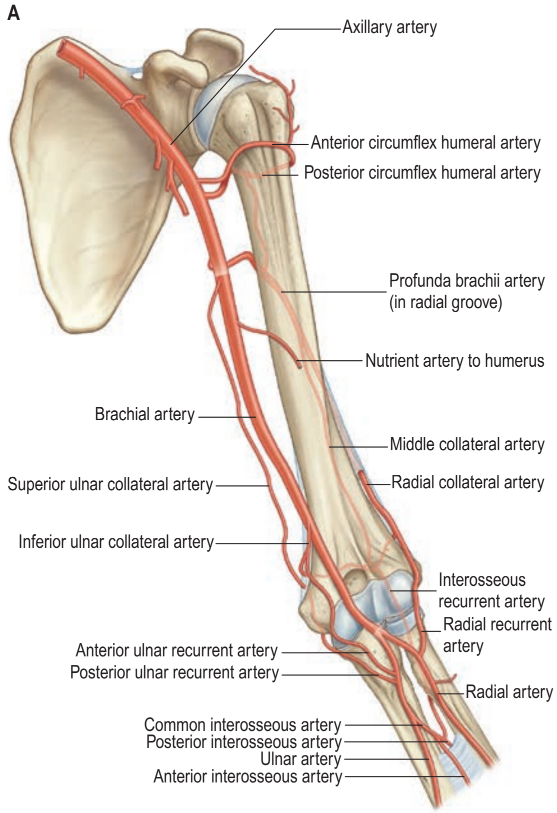
A
Axillary artery
Anterior circumflex humeral artery
Posterior circumflex humeral artery
Profunda brachii artery (in radial groove)
Nutrient artery to humerus
Brachial artery
Middle collateral artery
Superior ulnar collateral artery
Radial collateral artery
Inferior ulnar collateral artery
Interosseous recurrent artery
Radial recurrent artery
Anterior ulnar recurrent artery
Posterior ulnar recurrent artery
Radial artery
Common interosseous artery
Posterior interosseous artery
Ulnar artery
Anterior interosseous artery

Fig. 50.27 **A**, Arterial anastomoses around the left elbow joint, anterior aspect. (B, *continued online*)

Radial artery

The radial artery is smaller than the ulnar artery, yet appears a more direct continuation of the brachial artery (see Figs 50.21–50.22). It passes deep to brachioradialis and gives off the radial recurrent artery before continuing into the forearm. It descends along the lateral side of the forearm, accompanied by paired venae comitantes, from the medial side of the neck of the radius to the wrist. The artery is medial to the radial shaft proximally, and anterior to it distally. Proximally, it is overlapped anteriorly by the belly of brachioradialis, but elsewhere in its course it is covered only by the skin and superficial and deep fasciae. Its posterior relations in the forearm are, successively, the tendon of biceps, supinator, the distal attachment of pronator teres, the radial head of flexor digitorum superficialis, flexor pollicis longus, pronator quadratus and the lower end of the radius (where its pulsation is most accessible). Brachioradialis is lateral to the artery throughout its length. Pronator teres is medial to the proximal part of the artery, and the tendon of flexor carpi radialis is medial to the distal portion. The superficial radial nerve lies lateral to the middle third of the radial artery; multiple branches from the artery supply the nerve throughout its length.

The radial artery may occasionally arise from a continuation of a superficial brachial artery, or as a high proximal division of an otherwise normal brachial artery. It can give rise to the common interosseous artery.

Branches in the forearm

Radial recurrent artery The radial recurrent artery is given off by the radial artery just distal to the elbow joint (see Figs 50.21–50.22, 50.27). It passes between the superficial radial nerve and the posterior interosseous nerve before ascending beneath brachioradialis, anterior to supinator and brachialis. It supplies these muscles and then anastomoses with the radial collateral branch of the profunda brachii artery. The radial recurrent artery also gives branches to extensor carpi radialis longus, extensor digitorum, extensor digiti minimi and extensor carpi ulnaris. Its cutaneous branches are described on page 932.

Muscular branches Muscular branches are distributed to the muscles on the radial side of the forearm. Direct branches from the radial artery supply the radial insertion of pronator teres, the anterolateral aspect of flexor carpi radialis, the lateral surface of flexor digitorum superficialis, the lateral half of flexor pollicis longus, and the distal sections of extensor carpi radialis longus and extensor carpi radialis brevis.

Ulnar artery

The ulnar artery arises from the brachial artery just distal to the flexion crease of the elbow at the level of the radial neck, and reaches the medial side of the forearm in its upper third (see Figs 50.21–50.22). It is larger than the radial artery and is accompanied throughout its length by venae comitantes. In the forearm, the ulnar artery initially lies on brachialis

A compartment syndrome exists where increased pressure in an osseofascial compartment leads to decreased perfusion of the contents of the compartment. In the forearm, this commonly occurs as a result of trauma, external pressure, burns, arterial injury or post-ischaemic swelling. The resultant increase in interstitial pressure causes vascular occlusion and myoneural ischaemia. The patient presents with pain that is disproportionate to the severity of the injury and which is provoked or markedly increased by passive extension of the fingers. There may also be reduced sensation or paraesthesiae in the affected hand. If a compartment syndrome is suspected, compartment pressure measurements may be indicated, but, in unequivocal cases, the definitive treatment is emergency fasciotomies of the forearm. The absolute intracompartmental pressure threshold for decompression is the subject of debate: an absolute value of 30 mmHg is generally accepted, although some authorities prefer a figure that comes within 30 mmHg of diastolic pressure. The pressure in each compartment should be measured separately.

Incisions to decompress the flexor compartment (Ronel et al 2004) run from the medial epicondyle and curve down the anterior aspect of the forearm, ending on the radial side of flexor carpi ulnaris; from here, they may be extended distally to decompress the carpal tunnel, if necessary. The bicipital aponeurosis (lacertus fibrosus) is routinely released to decompress the median nerve. After retraction of the superficial flexors, the fascia over the deep muscles of the forearm may be incised over its full length. Both median and ulnar nerves should be inspected to ensure that their decompression is complete. The mobile wad and dorsal compartment are decompressed through a straight longitudinal incision that starts just distal to the lateral epicondyle; this is deepened through the plane between extensor digitorum and extensor carpi radialis brevis, and ends over the midline of the wrist. In both cases, the wounds are left open and dressed, and only closed when circumstances permit.

Failure to decompress a compartment syndrome promptly may lead to Volkmann's ischaemic contracture with severe loss of function in the affected forearm and hand. Subsequent amputation is not unknown.

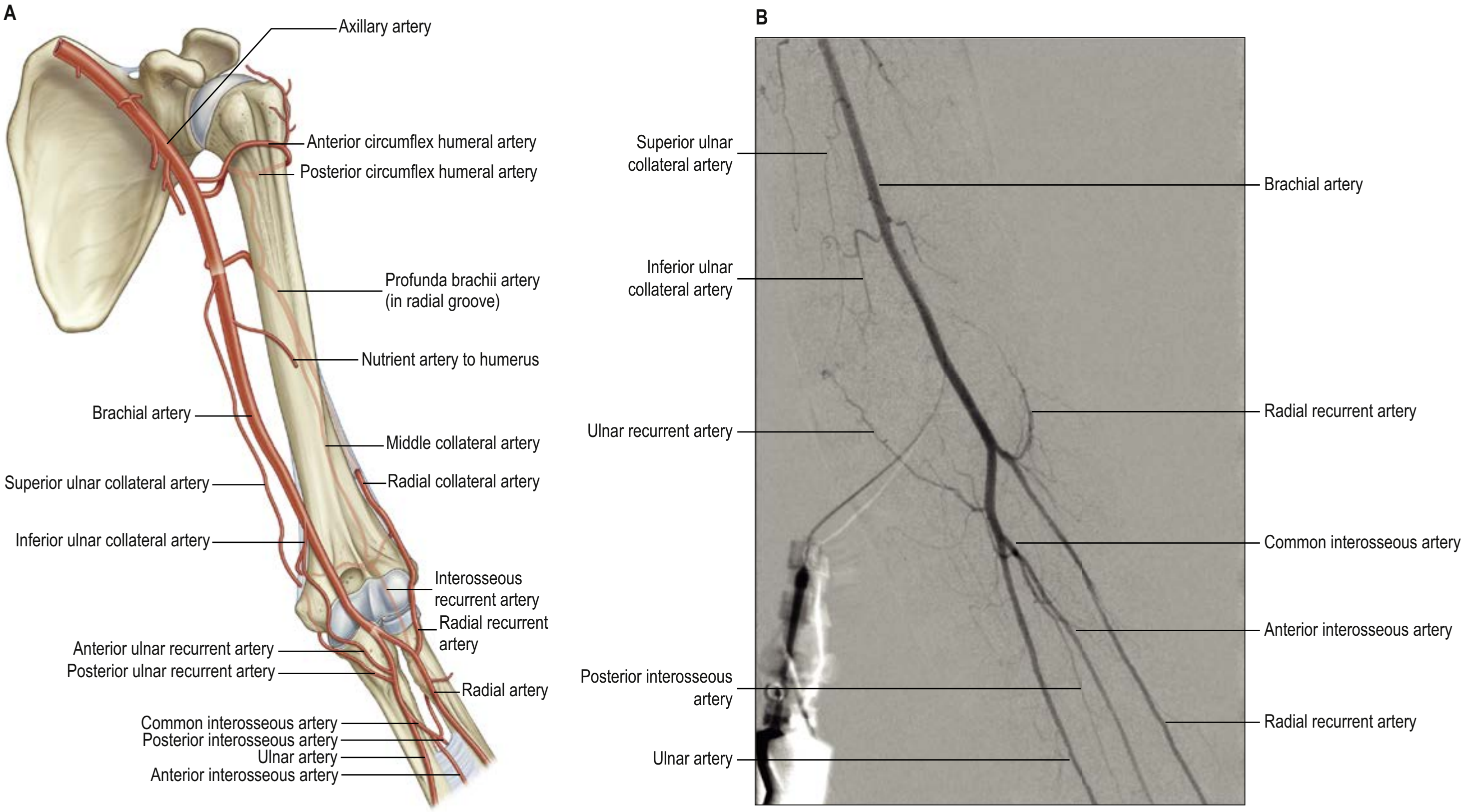
A
Axillary artery
Anterior circumflex humeral artery
Posterior circumflex humeral artery
Profunda brachii artery (in radial groove)
Nutrient artery to humerus
Brachial artery
Middle collateral artery
Radial collateral artery
Superior ulnar collateral artery
Inferior ulnar collateral artery
Interosseous recurrent artery
Radial recurrent artery
Anterior ulnar recurrent artery
Posterior ulnar recurrent artery
Radial artery
Common interosseous artery
Posterior interosseous artery
Ulnar artery
Anterior interosseous artery
B
Superior ulnar collateral artery
Brachial artery
Inferior ulnar collateral artery
Radial recurrent artery
Ulnar recurrent artery
Common interosseous artery
Anterior interosseous artery
Posterior interosseous artery
Radial recurrent artery
Ulnar artery

Fig. 50.27 **A**, Arterial anastomoses around the left elbow joint, anterior aspect. **B**, Digital subtraction angiogram of the left brachial to forearm arteries, injected via a catheter in the distal left brachial artery. The catheter and syringe filled with contrast medium (bottom left) cast a 'shadow' because they have moved between the initial subtraction mask and the acquisition run.

before passing deep to pronator teres, flexor carpi radialis, palmaris longus and flexor digitorum superficialis. It then lies on flexor digitorum profundus, between flexor carpi ulnaris and flexor digitorum superficialis, and is covered by the skin and superficial and deep fasciae. The artery crosses the flexor retinaculum, lateral to the ulnar nerve and pisiform bone, to enter the hand. The median nerve is a medial relation for approximately 2.5 cm distal to the elbow, and then crosses the artery, from which it is separated by the ulnar head of pronator teres. The ulnar nerve lies medial to the distal two-thirds of the artery, which supplies the nerve throughout its length; the palmar cutaneous branch of the ulnar nerve descends along the ulnar artery to reach the hand.

The ulnar artery may arise above the elbow, when it can lie superficial to the forearm flexors under the deep fascia; only rarely is it subcutaneous. When this occurs, the brachial artery supplies the common interosseous and the ulnar recurrent arteries.

Branches in the forearm

Anterior ulnar recurrent artery The anterior ulnar recurrent artery arises from the ulnar artery distal to the elbow and close to the origin of the ulnar artery itself. It ascends between brachialis and pronator teres, which it supplies, then anastomoses with the inferior ulnar collateral artery anterior to the medial epicondyle (see Fig. 50.27A). It limits distal extension of the medial Hotchkiss approach to the coronoid process.

Posterior ulnar recurrent artery The posterior ulnar recurrent artery arises from the ulnar artery distal to the anterior ulnar recurrent artery, passes dorsomedially between flexor digitorum profundus and flexor digitorum superficialis, and ascends between the posterior aspect of the medial epicondyle and the olecranon. It is deep to flexor carpi ulnaris, ascending between its heads with the ulnar nerve. It supplies flexor digitorum profundus, flexor digitorum superficialis, flexor carpi ulnaris, the ulnar nerve, underlying bone and the elbow joint, and anastomoses with the ulnar collateral artery and interosseous recurrent artery. The posterior ulnar recurrent artery and ulnar nerve are both vulnerable to injury behind the medial epicondyle (**Figs 50.28–50.29**).

Common interosseous artery The common interosseous artery is a short branch of the ulnar artery (see Figs 50.10, 50.22). It arises just distal to the radial tuberosity and passes back to the proximal border of the interosseous membrane, where it divides into the anterior and posterior interosseous arteries. Occasionally, the common interosseous artery is a branch of the radial artery.

Anterior interosseous artery The anterior interosseous artery arises from the common interosseous artery and descends on the anterior aspect of the interosseous membrane with the anterior interosseous branch of the median nerve (see Figs 50.10, 50.22, 50.27, 50.32). It is overlapped by contiguous sides of flexor digitorum profundus and flexor pollicis longus. Shortly after its origin, it usually gives off a slender median artery. This accompanies and supplies the median nerve as far as the palm, where it may join the superficial palmar arch or end as one or two palmar digital arteries. The median artery can also arise from the ulnar or the common interosseous artery. Muscular and nutrient branches from the anterior interosseous artery pierce the interosseous membrane to supply deep extensor muscles and the radius and ulna, respectively. A branch descends deep to pronator quadratus before piercing the interosseous membrane to join the anterior 'carpal' arch.

The anterior interosseous artery leaves the anterior compartment by piercing the interosseous membrane proximal to pronator quadratus. It anastomoses with the posterior interosseous artery in the posterior compartment of the forearm, and travels through a tunnel under the extensor retinaculum with the tendons of the digital extensors before joining the dorsal carpal arch. Three small cutaneous perforating branches supply the skin over the lower lateral border of the forearm.

Posterior interosseous artery The posterior interosseous artery arises from the common interosseous artery and is usually smaller than the anterior interosseous artery (see Figs 50.10, 50.27A). It passes dorsally between the oblique cord and proximal border of the interosseous membrane, and then between supinator and abductor pollicis longus. It descends deep in the groove between extensor carpi ulnaris and the extensor digiti minimi component of extensor digitorum. While in the groove, it gives rise to multiple muscular branches that supply these muscles and fasciocutaneous perforators that travel in the intermuscular septum between extensor carpi ulnaris and extensor digiti minimi. The posterior interosseous artery accompanies the deep branch of the radial nerve (posterior interosseous nerve) on abductor pollicis longus. Distally, it anastomoses with the terminal part of the anterior interosseous artery and the dorsal carpal arch.

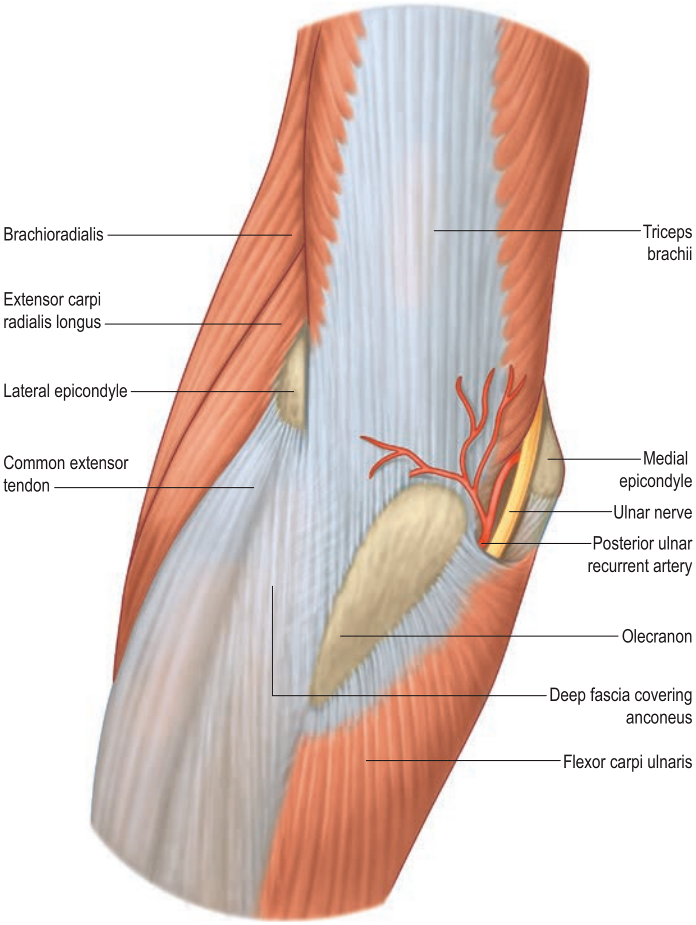
Brachioradialis
Extensor carpi radialis longus
Lateral epicondyle
Common extensor tendon
Triceps brachii
Medial epicondyle
Ulnar nerve
Posterior ulnar recurrent artery
Olecranon
Deep fascia covering anconeus
Flexor carpi ulnaris

Fig. 50.28 The posterior aspect of the left elbow: superficial structures.

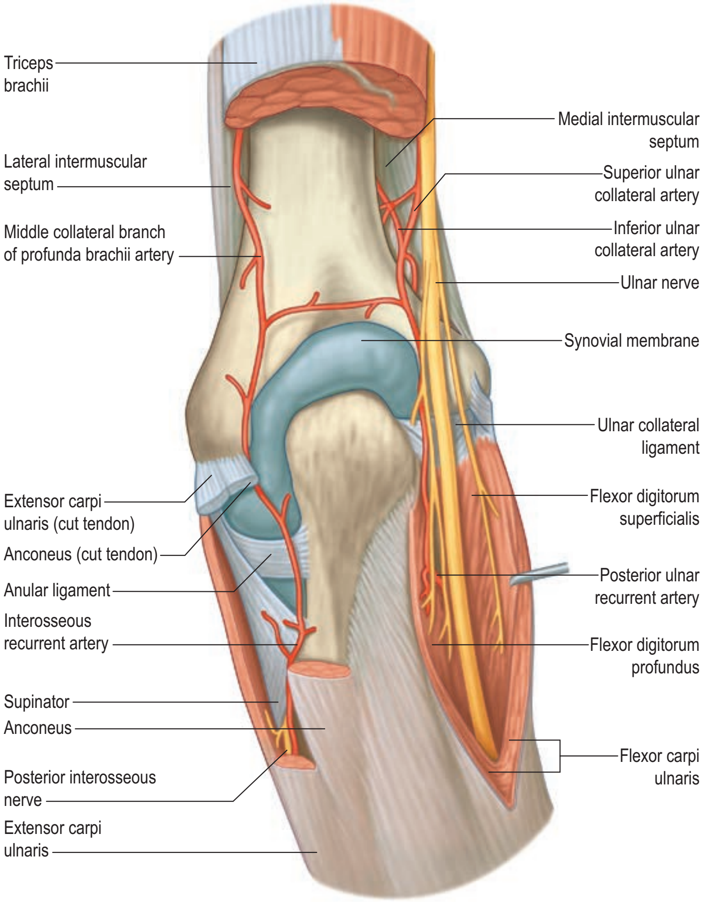
Triceps brachii
Lateral intermuscular septum
Middle collateral branch of profunda brachii artery
Extensor carpi ulnaris (cut tendon)
Anconeus (cut tendon)
Anular ligament
Interosseous recurrent artery
Supinator
Anconeus
Posterior interosseous nerve
Extensor carpi ulnaris
Medial intermuscular septum
Superior ulnar collateral artery
Inferior ulnar collateral artery
Ulnar nerve
Synovial membrane
Ulnar collateral ligament
Flexor digitorum superficialis
Posterior ulnar recurrent artery
Flexor digitorum profundus
Flexor carpi ulnaris

Fig. 50.29 The posterior aspect of the left elbow region: deep structures.

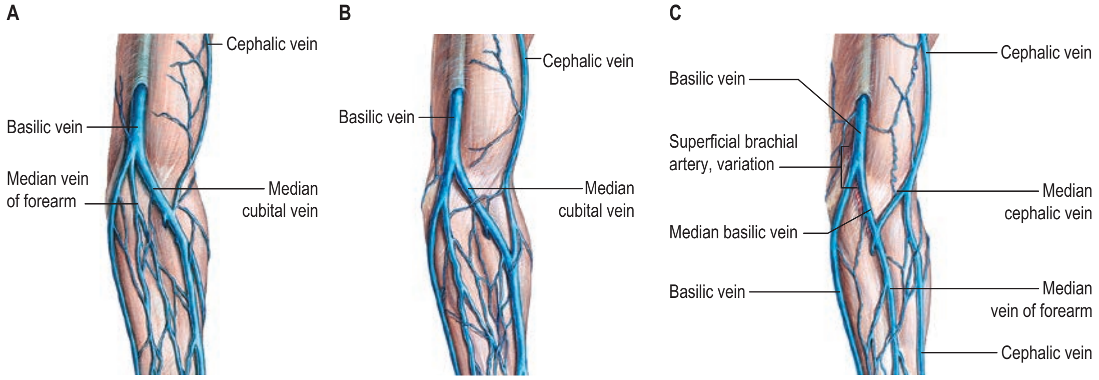

Fig. 50.30 A–C, Variations in the superficial veins of the left cubital fossa. (Sobotta Atlas of Human Anatomy © Elsevier GmbH, Urban & Fischer, Munich.)

Sometimes, the posterior interosseous artery disappears halfway down the forearm, in which case the anterior interosseous artery pierces the interosseous membrane more proximally to anastomose with it. Occasionally, the two vessels do not anastomose.

Posterior interosseous recurrent artery The posterior interosseous recurrent artery leaves the posterior interosseous artery near its origin and ascends between the lateral epicondyle and olecranon, either on or through supinator, and deep to anconeus. It anastomoses with the middle collateral branch of the profunda brachii artery, posterior ulnar recurrent artery and ulnar collateral artery. Occasionally, the artery is absent. Its cutaneous branches are described on page 932.

Collateral circulation at the elbow

The collateral circulation at the elbow is more robust than that at the knee. Alternative pathways include the profunda brachii artery, which accompanies the radial nerve through the lateral intermuscular septum to become the radial collateral artery. The superior ulnar collateral artery accompanies the ulnar nerve: in the adult, it may be as wide as 1.5 mm at its origin; hence its regular use as the artery to a free vascularized ulnar nerve graft. The inferior ulnar collateral artery is regularly seen during medial approaches to the elbow as a vessel that pierces the intermuscular septum to curl around the humerus between triceps and bone. On occasion, there is a substantial artery running with the median nerve. These vessels anastomose with recurrent branches from the ulnar and radial arteries to form a network that may maintain perfusion of the hand and the extensor muscles in cases where the brachial artery has been divided in the lower third of the arm (when there is no associated fracture or dislocation). Collateral circulation will diminish or cease altogether if the ulnar or radial nerve is entrapped within the fracture or compressed by haematoma (Blakey et al 2009, Birch 2011).

Veins

Deep veins

Venae comitantes run with the radial and ulnar arteries to drain the deep and superficial palmar venous arches, respectively. They unite near the elbow as paired brachial veins. The radial veins are smaller and receive the deep dorsal veins of the hand. The ulnar veins are larger and drain the deep palmar venous arch. They connect with superficial veins near the wrist and receive the venae comitantes of the anterior and posterior interosseous arteries near the elbow. A large branch connects them to the median cubital vein.

Superficial veins

Cephalic vein

The cephalic vein usually forms over the anatomical snuff-box on the radial side of the wrist from the radial end of the dorsal venous plexus (see Figs 48.4, 51.3). It curves proximally around the radial side of the forearm, receiving tributaries from both radial and ulnar aspects of the forearm. Distal to the elbow, a branch, the median cubital vein, diverges proximomedially to reach the basilic vein. The median cubital vein is joined by a branch from the deep veins (**Fig. 50.30**). The further course of the cephalic vein is described in Chapter 49 and Chapter 81.

Accessory cephalic vein The accessory cephalic vein may arise either from a dorsal forearm plexus or from the ulnar side of the dorsal venous network in the hand. It joins the cephalic vein distal to the elbow. A large oblique vein often connects the basilic and cephalic veins dorsally in the forearm.

Basilic vein

The basilic vein arises medially in the dorsal venous network of the hand (see Figs 48.4, 51.3). It ascends posteromedially in the forearm, inclining forwards to the anterior surface distal to the elbow, where it is joined by the median cubital vein. It then ascends superficially between biceps and pronator teres, and is crossed by filaments of the medial cutaneous nerve of the forearm that pass both superficial and deep to the vein. The basilic vein continues as the axillary vein from the lower border of teres major (Ch. 49 and Ch. 81).

Median vein

The median vein of the forearm drains the superficial palmar venous plexus and ascends through the anterior part of the forearm to join either the basilic or the median cubital vein (see Figs 49.34, 50.30). It may divide distal to the elbow to join both veins.

Lymphatic drainage

One or two supratrochlear nodes are superficial to the deep fascia proximal to the medial epicondyle and medial to the basilic vein; their efferents accompany the vein to join the deep lymph vessels. Small, isolated nodes sometimes occur along the radial, ulnar and interosseous vessels, in the cubital fossa near the bifurcation of the brachial artery, or in the arm medial to the brachial vessels.

Innervation

Median nerve

In the cubital fossa, the median nerve lies medial to the brachial artery, deep to the bicipital aponeurosis and anterior to brachialis. It usually enters the forearm between the heads of pronator teres, although, occasionally, it may pass posterior to both heads of the muscle, or it may pass through its humeral head (**Fig. 50.31**; see Figs 50.21–50.22). The nerve crosses to the lateral side of the ulnar artery, from which it is separated by the deep head of pronator teres, passes behind a tendinous bridge between the humero-ulnar and radial heads of flexor digitorum superficialis, and descends through the forearm posterior and adherent to flexor digitorum superficialis and anterior to flexor digitorum profundus. It is accompanied by the median branch of the anterior interosseous artery. The first branch of the median nerve to pronator teres arises 2–3 cm above the medial epicondyle. A second branch, or leash of branches, arises at the level of the tip of the medial epicondyle and innervates palmaris longus, flexor carpi radialis and flexor digitorum superficialis. About 5 cm proximal to the flexor retinaculum, the median nerve emerges from behind the lateral edge of flexor digitorum superficialis, and becomes superficial just proximal to the wrist. Here, it lies between the tendons of flexor digitorum superficialis and flexor carpi radialis, projecting laterally from beneath the tendon of palmaris longus. It then passes deep to the flexor retinaculum into the palm.

Branches in the forearm

Anterior interosseous nerve

The anterior interosseous nerve arises from the posterior aspect of the median nerve between the two heads of pronator teres, just distal to the branches to the superficial forearm flexors and proximal tendinous

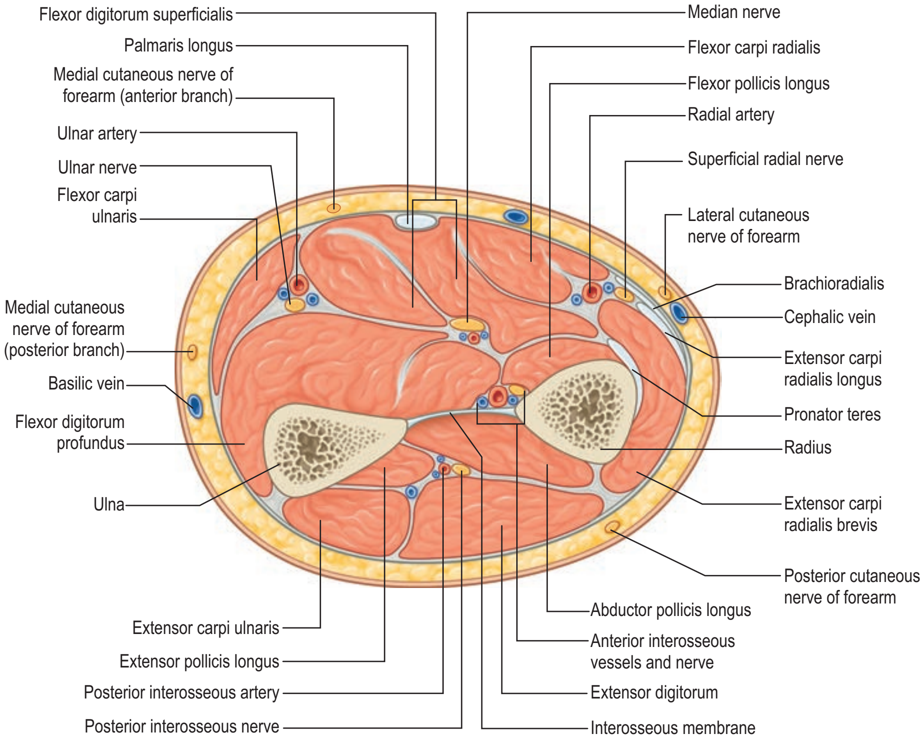
Flexor digitorum superficialis
Palmaris longus
Medial cutaneous nerve of forearm (anterior branch)
Ulnar artery
Ulnar nerve
Flexor carpi ulnaris
Medial cutaneous nerve of forearm (posterior branch)
Basilic vein
Flexor digitorum profundus
Ulna
Extensor carpi ulnaris
Extensor pollicis longus
Posterior interosseous artery
Posterior interosseous nerve
Median nerve
Flexor carpi radialis
Flexor pollicis longus
Radial artery
Superficial radial nerve
Lateral cutaneous nerve of forearm
Brachioradialis
Cephalic vein
Extensor carpi radialis longus
Pronator teres
Radius
Extensor carpi radialis brevis
Posterior cutaneous nerve of forearm
Abductor pollicis longus
Anterior interosseous vessels and nerve
Extensor digitorum
Interosseous membrane

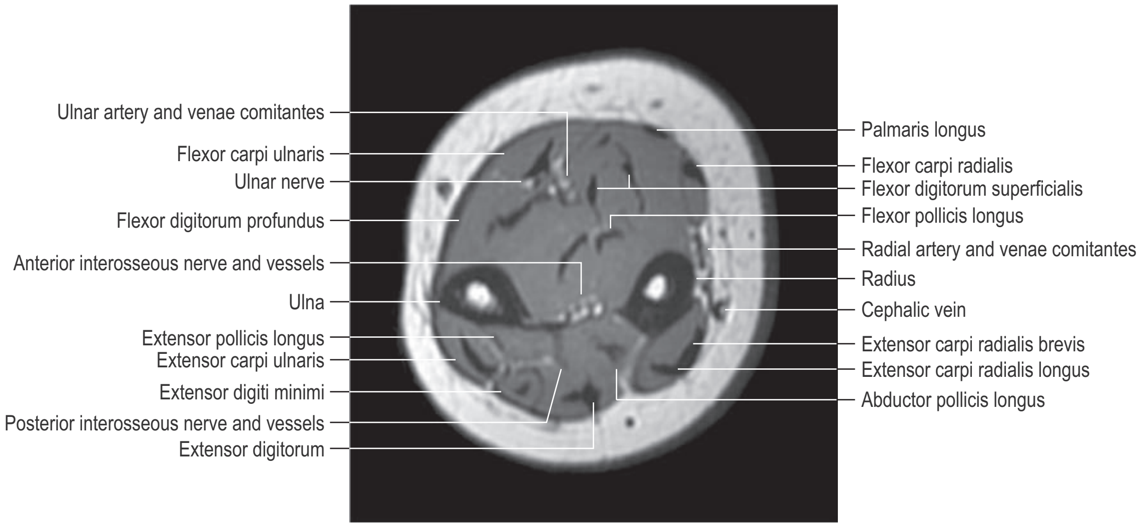
Ulnar artery and venae comitantes
Flexor carpi ulnaris
Ulnar nerve
Flexor digitorum profundus
Anterior interosseous nerve and vessels
Ulna
Extensor pollicis longus
Extensor carpi ulnaris
Extensor digiti minimi
Posterior interosseous nerve and vessels
Extensor digitorum
Palmaris longus
Flexor carpi radialis
Flexor digitorum superficialis
Flexor pollicis longus
Radial artery and venae comitantes
Radius
Cephalic vein
Extensor carpi radialis brevis
Extensor carpi radialis longus
Abductor pollicis longus

Fig. 50.32 **A**, Transverse section through the middle of the left forearm. **B**, Axial T1-weighted MRI at the mid-level of the supine forearm, oriented as in **A**.

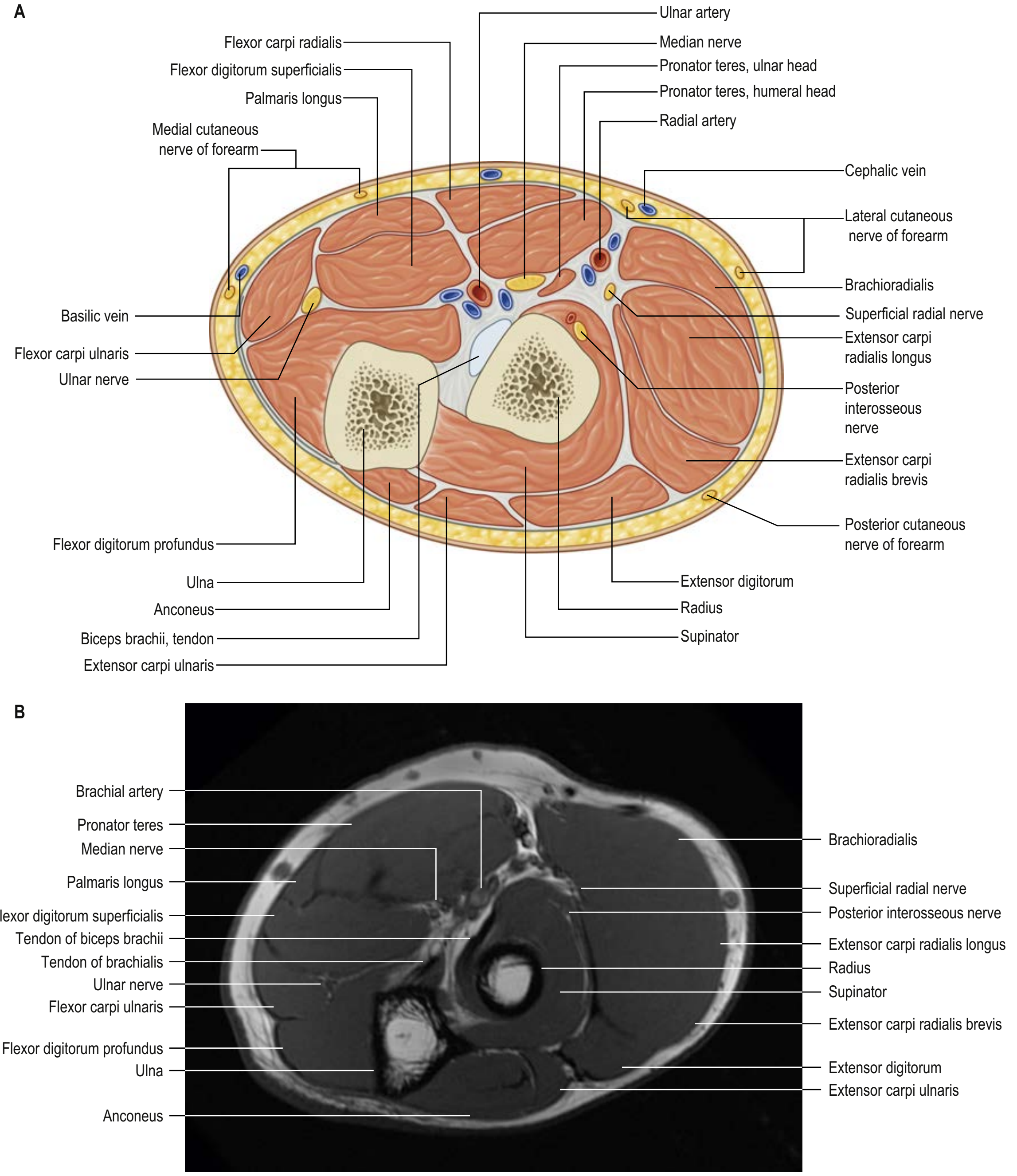
A
Ulnar artery
Flexor carpi radialis
Median nerve
Flexor digitorum superficialis
Pronator teres, ulnar head
Palmaris longus
Pronator teres, humeral head
Radial artery
Medial cutaneous nerve of forearm
Cephalic vein
Lateral cutaneous nerve of forearm
Brachioradialis
Basilic vein
Superficial radial nerve
Flexor carpi ulnaris
Extensor carpi radialis longus
Ulnar nerve
Posterior interosseous nerve
Extensor carpi radialis brevis
Posterior cutaneous nerve of forearm
Flexor digitorum profundus
Extensor digitorum
Ulna
Anconeus
Radius
Biceps brachii, tendon
Supinator
Extensor carpi ulnaris
B
Brachial artery
Pronator teres
Median nerve
Brachioradialis
Palmaris longus
Superficial radial nerve
Flexor digitorum superficialis
Posterior interosseous nerve
Tendon of biceps brachii
Extensor carpi radialis longus
Tendon of brachialis
Radius
Ulnar nerve
Supinator
Flexor carpi ulnaris
Extensor carpi radialis brevis
Flexor digitorum profundus
Extensor digitorum
Ulna
Extensor carpi ulnaris
Anconeus

Fig. 50.31 **A**, Transverse section through the left forearm at the level of the radial tuberosity: proximal aspect. **B**, Axial T1-weighted MRI through the left forearm at the level of the radial tuberosity, oriented as in **A**.

arch of flexor digitorum superficialis (see Figs 50.10, 50.22). It descends with the anterior interosseous artery anterior to the interosseous membrane, between and deep to flexor pollicis longus and flexor digitorum profundus (Fig. 50.32), supplying flexor pollicis longus and the lateral part of flexor digitorum profundus (to the index and middle fingers). Terminally, the anterior interosseous nerve lies posterior to pronator quadratus, which it supplies via its deep surface. It also supplies articular branches to the distal radio-ulnar, radiocarpal and carpal joints.

Palmar cutaneous branch

The palmar cutaneous branch starts about 3 cm proximal to the flexor retinaculum. It runs in a small tunnel in the sheath of flexor carpi radialis before piercing the deep fascia, where it divides into lateral branches that supply the thenar skin and connect with the lateral cutaneous nerve of the forearm. Medial branches supply the central palmar skin and connect with the palmar cutaneous branch of the ulnar nerve (see Figs 48.11, 50.21).

Muscular branches

Muscular branches are given off near the elbow to all the superficial flexor muscles except flexor carpi ulnaris. The branch to the part of flexor digitorum superficialis that serves the index finger is given off near the mid-forearm and may be derived from the anterior interosseous nerve. The median nerve is palpable in the anterior aspect of the elbow, deep to the bicipital aponeurosis. It is closely related to the brachial artery in the anterior aspect of the elbow, where it courses anterior to brachialis and medial to the artery.

Median nerve compression

The median nerve may be compressed at four sites in the elbow and forearm. The most proximal is the ligament of Struthers, where, if the median nerve is accompanied by the brachial artery, vascular symptoms and signs may also be present. More distally, it may become entrapped by a thickened bicipital aponeurosis. The other sites of compression are between the superficial and deep heads of pronator teres, and the proximal fibrous arch of flexor digitorum superficialis.

Martin–Gruber nerve connection.

Available with the *Gray's Anatomy* -book

Ulnar nerve

The ulnar nerve passes behind the medial epicondyle in a groove where it is easily palpable (see Figs 50.29, 48.12). It runs through the cubital tunnel, between the capsule of the humero-ulnar joint and the overlying arcuate ligament of Osborne joining the two heads of flexor carpi

Patients essentially present with one of two syndromes. The anterior interosseous nerve syndrome presents as a failure of pinch grip due to weakness of flexor pollicis longus and the radial portion of flexor digitorum profundus. This reduces the flexion power of the interphalangeal joint of the thumb and the distal interphalangeal joint of the index finger. The pronator syndrome presents with symptoms and signs that mimic carpal tunnel syndrome. Patients present with pain and altered sensation in the radial three and a half fingers of the hand that are aggravated by activity. However, a Tinel's sign will be positive over the proximal forearm, and sensation over the thenar eminence may be diminished, because the palmar cutaneous branch of the nerve arises above the carpal tunnel. The clinical presentation may vary in the presence of a Martin–Gruber anastomosis (Rodriguez-Niedenführ et al 2002).

Most patients will respond to non-operative treatment but those who fail to do so usually respond well to surgical decompression. Exploration and decompression should address all the potential areas of compression.

A motor communicating branch between the median and ulnar nerves in the forearm occurs in approximately one-quarter of patients. The most common variant has a branch passing from the anterior interosseous to the ulnar nerve. A number of patterns have been described where branches pass between flexors digitorum superficialis and profundus, deep to the ulnar artery, to join the ulnar nerve; such branches may explain the variations in innervation of the intrinsic muscles.

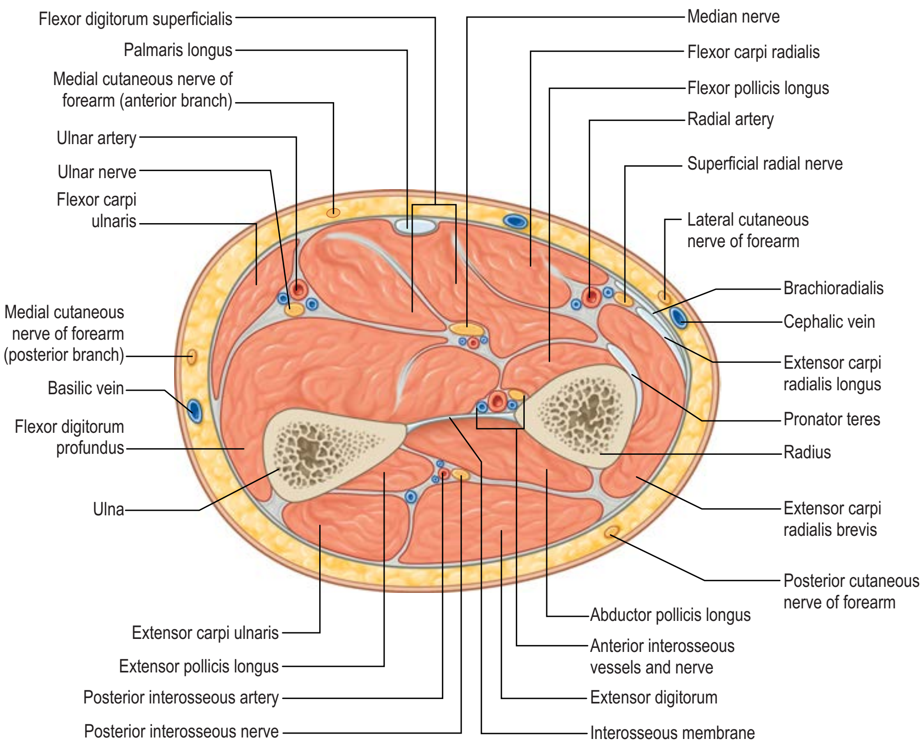
Flexor digitorum superficialis
Palmaris longus
Medial cutaneous nerve of forearm (anterior branch)
Ulnar artery
Ulnar nerve
Flexor carpi ulnaris
Medial cutaneous nerve of forearm (posterior branch)
Basilic vein
Flexor digitorum profundus
Ulna
Median nerve
Flexor carpi radialis
Flexor pollicis longus
Radial artery
Superficial radial nerve
Lateral cutaneous nerve of forearm
Brachioradialis
Cephalic vein
Extensor carpi radialis longus
Pronator teres
Radius
Extensor carpi radialis brevis
Posterior cutaneous nerve of forearm
Extensor carpi ulnaris
Extensor pollicis longus
Posterior interosseous artery
Posterior interosseous nerve
Abductor pollicis longus
Anterior interosseous vessels and nerve
Extensor digitorum
Interosseous membrane

Fig. 50.32 **A**, Transverse section through the middle of the left forearm. (B, *continued online*).

ulnaris. It gives off articular branches to the elbow as it lies between the medial epicondyle and the olecranon. In some individuals an accessory muscle, the anconeus epitrochlearis is found superficial to the cubital retinaculum connecting the medial epicondyle to the olecranon (Grewal et al 2019). The ulnar nerve enters the forearm between the two heads of flexor carpi ulnaris, which it supplies by two neurovascular pedicles, one arising just distal to the cubital tunnel and one in the forearm: it is superficial to the posterior and oblique parts of the ulnar collateral ligament and deep to the tough deep fascia of flexor carpi ulnaris (Osborne's fascia).

The ulnar nerve descends on the medial side of the forearm on flexor digitorum profundus (see Fig. 50.32). Proximally, it is covered by flexor carpi ulnaris; its distal half lies lateral to the muscle and is covered only by skin and fasciae. In the upper third of the forearm, the nerve is distant from the ulnar artery but, more distally, it comes to lie close to the medial side of the artery. About 5 cm proximal to the wrist, it gives off the dorsal cutaneous branch. At the wrist, the ulnar nerve passes under the superficial part of the flexor retinaculum (in Guyon's canal) and divides into superficial and deep branches (see Fig. 51.10).

Branches in the forearm

Muscular branches

There are two main muscular branches of the ulnar nerve in the forearm. They arise near the elbow and supply flexor carpi ulnaris and the medial half of flexor digitorum profundus.

Dorsal branch

The dorsal branch of the ulnar nerve continues distally and dorsally, deep to flexor carpi ulnaris. It perforates the deep fascia and descends along the medial side of the back of the wrist and hand. Its further course is described in Chapter 51 and Chapter 80.

Palmar cutaneous branch

The palmar cutaneous branch of the ulnar nerve arises in mid-forearm, descends on the ulnar artery, which it supplies, and then perforates the deep fascia. It communicates with the palmar branch of the median nerve and ends in the palmar skin. It sometimes supplies palmaris brevis. Its further course is described in Chapter 51 and Chapter 80.

Ulnar nerve compression

The ulnar nerve may be compressed by the arcade of Struthers at the level of the medial intermuscular septum; at the level of the flexor/pronator aponeurosis as it enters the forearm between the heads of flexor carpi ulnaris; or deep to the deep fascia of flexor carpi ulnaris which exhibits tough condensations extending up to 9 cm from the medial epicondyle (Siemionow et al 2007). The nerve is most often compressed at the level of the cubital tunnel by the Osborne's arcuate ligament; this is the most common nerve compression syndrome after that of the median nerve in the carpal tunnel.

Radial nerve

The radial nerve at the elbow lies in the deep groove between brachialis medially and brachioradialis and extensor carpi radialis longus laterally (see Fig. 50.21). The nerve to brachioradialis arises about three fingers'-breadths proximal to the lateral epicondyle; the nerve to extensor carpi radialis longus about one finger's-breadth more distal; and the nerve to extensor carpi radialis brevis about one finger's-breadth above the epicondyle. These branches arise from the main radial nerve as it runs between brachialis and brachioradialis. The nerve may be palpable at this level. The radial nerve divides into the posterior interosseous and superficial radial nerves anterior to the elbow at the level of the tip of the lateral epicondyle. Another branch to extensor carpi radialis brevis is usually given off here. There is some variation in the level at which branches of the radial nerve arise from the main trunk in different individuals. Branches to extensor carpi radialis brevis and supinator may arise from the main trunk of the radial nerve or from the proximal part of the posterior interosseous nerve, but almost invariably above the arcade of Frohse.

Branches in the forearm

Superficial radial nerve

The superficial radial nerve descends from the lateral epicondyle anterolaterally in the proximal two-thirds of the forearm, initially lying on supinator, lateral to the radial artery and behind brachioradialis. In the middle third of the forearm, it lies behind brachioradialis, close to the lateral side of the artery. It runs anterior to pronator teres, the radial head of flexor digitorum superficialis and flexor pollicis longus, and usually leaves the artery 7 cm proximal to the wrist and passes deep to the tendon of brachioradialis. It curves round the lateral side of the radius as it descends, pierces the deep fascia and divides into five, sometimes four, dorsal digital nerves. On the dorsum of the hand, it usually communicates with the posterior and lateral cutaneous nerves of the forearm.

Posterior interosseous nerve

The posterior interosseous nerve is the deep terminal branch of the radial nerve (see Figs 48.9, 50.21, 50.29). It reaches the back of the forearm by passing round the lateral aspect of the radius between the two heads of supinator (see Figs 50.25–50.26). It supplies supinator both before entering the muscle and as it passes through it. As it emerges from supinator posteriorly, the nerve gives off three short branches to

The cross-sectional area of the cubital tunnel has been shown to narrow by almost 55% in full flexion. Ultrasound studies have suggested that the ratio of the cross-sectional area of radial nerve: cubital tunnel is most strongly linked to reduced conduction velocity (Yoon et al 2007). Combining elbow flexion with direct pressure over the cubital tunnel for 60 seconds will elicit symptoms in most affected patients (Novak et al 1994). Other contributory factors are previous trauma, especially supracondylar and medial epicondyle fractures in childhood, valgus instability of the elbow in athletes involved in throwing sports, and degenerative disease.

The most reliable treatment for patients who fail to respond to non-surgical remedies is a simple release of the cubital tunnel. The release should be complete and include release of Osborne’s ligament and the deep fascia of flexor carpi ulnaris; care should be taken to avoid damage to branches of the medial cutaneous nerve of the forearm that usually cross the line of incision approximately 2 cm above the medial epicondyle and a mean 3.1 cm distal to the medial epicondyle in all patients (Lowe et al 2004). Anconeus epitrochlearis should be excised if present because it is a potential cause for recurrent symptoms. The ulnar nerve should not be circumferentially denuded of its retinaculum because this contains its intrinsic blood supply. Transposition of the nerve should be reserved for cases of persistent subluxation or of failure of a simple release to achieve symptomatic relief. This is relatively unusual and is said to occur in only 7% of cases.

The ulnar nerve is a mixed nerve and so patients may present with sensory or motor symptoms or a combination of the two, sometimes with additional physical signs of autonomic disturbance. There may be tenderness and a positive Tinel's sign over the nerve at the point of compression. Numbness and paraesthesiae occur early, followed, in more severe cases, by weakness of power grip and, ultimately, atrophy of the lumbricals and interossei with clawing of ring and little fingers.

extensor digitorum, extensor digiti minimi and extensor carpi ulnaris, and two longer branches, a medial branch to extensor pollicis longus and extensor indicis, and a lateral branch that supplies abductor pollicis longus and extensor pollicis brevis. The nerve at first lies between the superficial and deep extensor muscles, but at the distal border of extensor pollicis brevis, it passes deep to extensor pollicis longus and, diminished to a fine thread, descends on the interosseous membrane to the dorsum of the carpus. Filaments arising from its flattened termination supply the carpal ligaments and articulations. Articular branches from the posterior interosseous nerve supply carpal, distal radio-ulnar and some intercarpal and intermetacarpal joints. Digital branches supply the metacarpophalangeal and proximal interphalangeal joints.

The distal portion of the nerve lies in a separate fascial sheath in the radial, deep, aspect of the fourth dorsal compartment of the extensor retinaculum of the wrist, where it is located deep to extensor digitorum and extensor indicis.

Radial nerve compression

Radial nerve compression may occur at several sites in the elbow and forearm. The most proximal of these is within the radial tunnel, which starts where the deep branch of the radial nerve lies over the radiohumeral joint and ends at the point where the deep branch becomes the posterior interosseous nerve at the distal border of supinator. At the level of the radial head, the nerve may be compressed by fibrous bands. More distally, it has been suggested that branches of the radial recurrent artery may compress the posterior interosseous nerve. Other sites of compression are the tendinous edge of the deep surface of extensor carpi radialis brevis and the point at which the nerve passes under the arcade of Frohse and between the two heads of supinator. Rarely, the nerve can be compressed at the level of the distal border of supinator.

Lateral cutaneous nerve of the forearm

The lateral cutaneous nerve of the forearm is the cutaneous division of the musculocutaneous nerve. It lies between biceps brachii and brachialis, inclining from the medial to the lateral side, then passes through the cubital fossa lateral to the tendon of biceps brachii and deep to the cephalic vein and descends along the radial border of the forearm to the wrist (see Figs 49.33–49.34, 50.31–50.32). It supplies the skin of the anterolateral surface of the forearm (see Fig. 50.1) and connects with the posterior cutaneous nerve of the forearm and the terminal branch of the radial nerve by branches that pass around the radial border of the forearm. Its trunk gives rise to a slender recurrent branch that extends along the cephalic vein as far as the middle third of the upper arm, distributing filaments to the skin over the distal third of the anterolateral surface of the upper arm close to the vein. At the wrist joint, the lateral cutaneous nerve of the forearm is anterior to the radial artery. It gives off filaments that pierce the deep fascia and accompany the artery to the dorsum of the carpus. The nerve then passes to the base of the thenar eminence, where it ends in cutaneous rami, some of which connect with the terminal branch of the radial nerve and the palmar cutaneous branch of the median nerve.

Medial cutaneous nerve of the forearm

The medial cutaneous nerve of the forearm has already divided into anterior and posterior branches before it enters the forearm (see Figs 49.34, 50.31–50.32). The larger anterior branch usually passes anterior to, or occasionally behind, the median cubital vein, and descends anteromedially in the forearm to supply the skin as far as the wrist. It curves round to the dorsum of the forearm, descending on its medial border to the wrist, supplying the skin (see Fig. 50.1). It connects with the medial cutaneous nerve of the arm, the posterior cutaneous nerve of the forearm, and the dorsal branch of the ulnar nerve.

Posterior cutaneous nerve of the forearm

The posterior cutaneous nerve of the forearm passes along the dorsum of the forearm to the wrist (see Figs 49.34, 50.31–50.32). It supplies the central forearm skin along its course and, near its termination, joins the dorsal branches of the lateral cutaneous nerve of the forearm.

Nerve injuries at the elbow

Available with the *Gray's Anatomy* e-book

ANATOMICAL CONSIDERATIONS IN COMMON FOREARM AND ELBOW INJURIES

Available with the *Gray's Anatomy* e-book

Bonus e-book content

Fig. 50.13 E–G, Fluoroscopic and CT arthrograms of the elbow joint.

Fig. 50.27 B, Digital subtraction angiogram of the left brachial to forearm arteries.

Fig. 50.32 B, MRI at the mid-level of the supine forearm.

Fig. 50.33 Type 1 Monteggia fracture with anterior dislocation of the radial head.

Fig. 50.34 Galeazzi fracture-dislocation.

Fig. 50.35 Elbow dislocation.

Key reference

Birch R 2011 Surgical Disorders of the Peripheral Nerves, 2nd ed. London: Springer-Verlag.

An account of the current state-of-the-art practice of diagnosis and management of surgical lesions of the peripheral nerves, including the brachial plexus.

Patients present with one of two syndromes: the radial tunnel syndrome, in which the presentation is that of pain along the lateral border of the elbow and upper forearm (Roles and Maudsley 1972), or the posterior interosseous nerve syndrome, which presents with motor weakness in the distribution of the nerve particularly affecting the extensors digitorum and carpi ulnaris. Primary treatment is non-operative and involves the avoidance of activities that cause pain, aided by appropriate splintage. In resistant cases, surgical decompression may be necessary. A complete release of all potential areas of compression is essential.

The elbow is a notorious site for nerve injuries, especially in children. The close proximity of all the major nerve trunks to bone makes them vulnerable. The ulnar nerve is particularly at risk in elbow dislocation, especially when the medial epicondyle is displaced into the joint. All three nerves are at risk of displacement into a dislocated joint. The posterior interosseous and radial nerves are particularly at risk from a Monteggia fracture-dislocation. Any nerve may become entrapped within a fracture, e.g. the median nerve is often accompanied by the brachial artery in cases of supracondylar fracture. Pain that persists, or worsens, after reduction of a fracture suggests impending critical ischaemia, continuing irritation of the nerve, or both. The nerves are at risk during operations or other medical interventions, particularly so when normal anatomical planes are distorted by haematoma, fibrosis or bone fragments.

Fractures of the shaft of the radius and ulna are commonly displaced, reflecting not only the violence required to cause such injury but also the pull of the forearm muscles that may accentuate displacement of the fracture fragments. Open fractures or penetrating injuries to the forearm may be associated with nerve and vessel injury. Compartment syndrome can occur. Monitoring of compartment pressures and careful neurological examination are required.

Fracture-dislocations of the forearm

Monteggia, Galeazzi and Essex–Lopresti injuries are common combinations of high energy forearm fractures associated with accompanying soft tissue injury.

Monteggia fracture-dislocation

A Monteggia fracture-dislocation injury is a fracture of the proximal ulna with dislocation of the radial head. The interosseous membrane and the triangular fibrocartilage complex remain largely intact, which means that anatomical reduction of the ulnar fracture will usually restore congruity of the radiocapitellar and proximal radio-ulnar joints. The most common type of Monteggia fracture, type 1 (anterior dislocation), occurs when falling onto an outstretched arm hyperextends the elbow (**Fig. 50.33**). The forearm is in neutral to mid-pronation, biceps brachii resists the hyperextension, the anular and quadrate ligaments rupture under the bending force, and the radial head dislocates. Compressive load then transfers to the ulnar diaphysis, which fails in tension in an oblique fracture. Type II (posterior dislocation) involves longitudinal force directed up the forearm with the elbow in a flexed position. The ulnar cortex fails first before rupture of the ulnar collateral ligament complex and posterior dislocation of the radial head. Four subtypes of this injury pattern have been identified, based on the location and force direction through the ulnar fracture (Jupiter et al 1991). Type III Monteggia injuries result in lateral or anterolateral dislocation of the radial head, associated with a metaphysial fracture of the proximal ulna. Type IV Monteggia injuries result in an anterior dislocation of the radial head and a fracture through the proximal third of both the radius and the ulna. The mechanism of injury is similar to that seen in type I injuries but the anteriorly directed force of the distal ulnar fragment, combined with the biceps resistance force, causes a fracture through the proximal radius. There is poor inter-observer agreement in classifiying these injuries. It is most useful to consider them as apex anterior ulna fracture with an intact dislocated radial head, or apex posterior ulna fracture with a fractured radial head. The apex posterior injuries have a worse prognosis (Ring 2013).

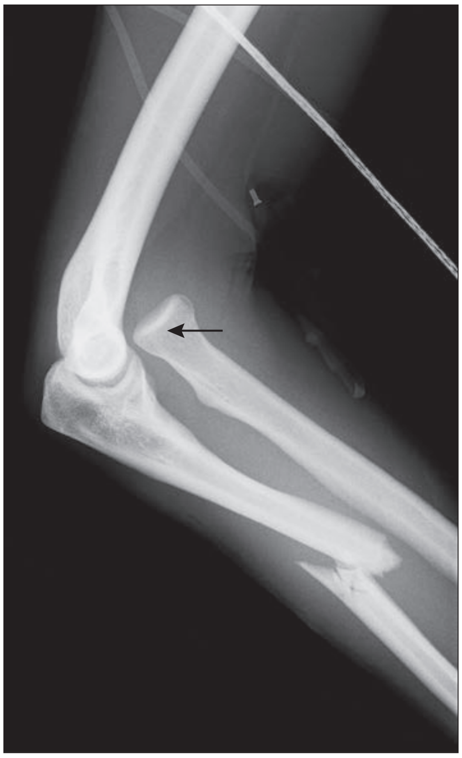

Fig. 50.33 Type 1 Monteggia fracture with anterior dislocation of the radial head (arrow).

Galeazzi fracture-dislocation

A Galeazzi injury is a fracture at the junction of the middle and distal thirds of the radius, associated with disruption of the distal radio-ulnar joint (**Fig. 50.34**). The injury occurs when the forearm is axially loaded and fully pronated. The radius fractures first, force transmission continues along the interosseous membrane to the distal ulna, the triangular fibrocartilage complex is disrupted and the ulnar head dislocates. The ulnar styloid can also be fractured in this injury (Galeazzi 1934).

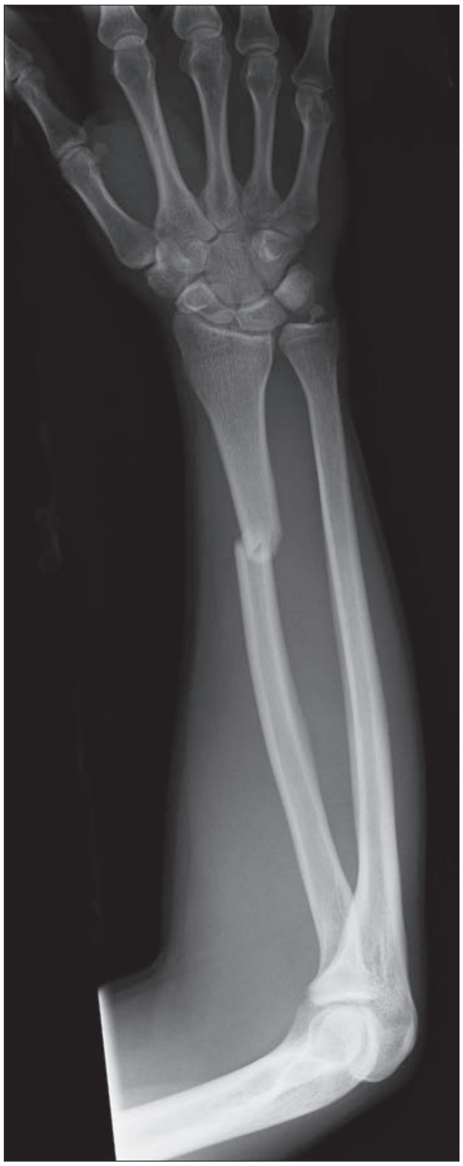

Fig. 50.34 Galeazzi fracture-dislocation.

Essex–Lopresti injury

Essex–Lopresti injury is a radio-ulnar dissociation injury, usually caused by a fall on to an outstretched hand that involves a fracture of the radial head, force transmission between the radius and ulna, and disruption of the central condensation of the interosseous membrane and the distal radio-ulnar joint. The radius migrates proximally relative to the ulna (Chow and Leung 2010).

Traumatic elbow instability

Posterolateral rotatory pattern instability and dislocation of the elbow, with or without associated fracture of the radial head and coronoid, are the three general patterns of traumatic elbow instability (Ring 2010). Posterolateral rotatory pattern instability is an injury of the capsule and ligaments that progresses from lateral to medial with a posterolateral rotatory mechanism (O'Driscoll et al 1992). It usually occurs as the result of a fall onto an outstretched hand that creates a valgus, axial posterolateral rotatory force. The ulna and forearm supinate away from the distal humerus and a posterior dislocation of the elbow occurs (**Fig. 50.35**). As the elbow dislocates posteriorly, the radial head and coronoid impact on the distal humerus, where either can fracture; the anterior band of the ulnar collateral ligament is the last structure to be disrupted. Varus posteromedial rotational pattern instability and anteromedial coronoid facet fractures occur when a fall on to an outstretched hand produces a varus, axial posteromedial force through the elbow. The anteromedial facet of the coronoid is fractured and the lateral ligament complex may be injured or the olecranon may be fractured. Anterior olecranon fracture-dislocations occur as a result of direct violence to the flexed elbow. The mechanism of posterior olecranon fracture dislocation is less certain; it occurs more commonly in osteopenic bone.

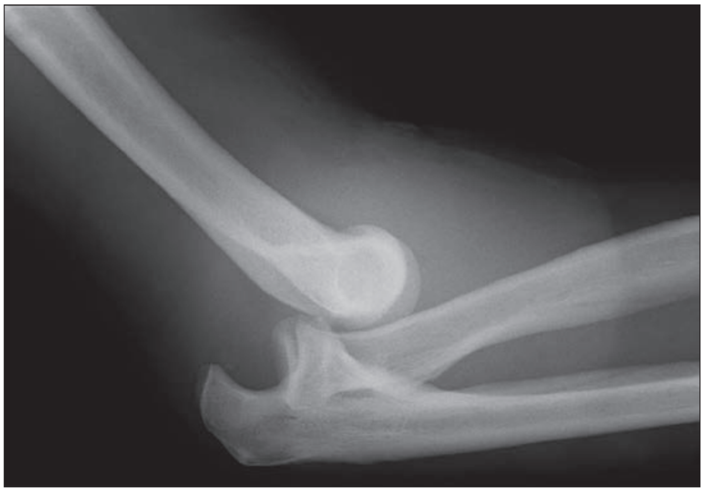

Fig. 50.35 Elbow dislocation.

References

Bednar MS, Arnoczky SP, Weiland AJ 1991 The microvasculature of the triangular fibrocartilage complex: its clinical significance. J Hand Surg [Am] 16:1101–5.

Birch R 2011 Surgical Disorders of the Peripheral Nerves, 2nd ed. London: Springer-Verlag.

An account of the current state-of-the-art practice of diagnosis and management of surgical lesions of the peripheral nerves, including the brachial plexus.

Blakey CM, Biant LC, Birch R 2009 Ischaemia and the pink, pulseless hand complicating supracondylar fractures of the humerus in childhood: long-term follow-up. J Bone Joint Surg Br 91:1487–92.

Camp CL, Jahandar H, Sinatro AM et al 2018 Quantitative anatomic analysis of the medial ulnar collateral ligament complex of the elbow. Orthop J Sports Med 6:2325967118762751.

Chow S-P, Leung F 2010 Radial and ulnar shaft fractures. In: Bucholz RW, Court-Brown CM, Heckman JD et al (eds) Rockwood and Green's Fractures in Adults, 7th ed. Philadelphia: Lippincott Williams & Wilkins; Ch. 31, pp. 881–904.

De Kesel R, Van Glabbeek F, Mugenzi D et al 2012 Innervation of the elbow joint: Is total denervation possible? A cadaveric anatomic study. Clin Anat 25:746–54.

Edwards DS, Arshad MS, Luokkala T et al 2018 The contribution of the posterolateral capsule to elbow joint stability: a cadaveric biomechanical investigation. J Shoulder Elbow Surg 27:1178–84.

Ekenstam FW, Palmer AK, Glisson RR 1984 The load on the radius and ulna in different positions of the wrist and forearm: a cadaver study. Acta Orthop Scand 55:363–5.

Galeazzi R 1934 Di una particolare sindrome traumatica dello scheletro dell'avambraccio. Atti Mem Soc Lomb Chir 2:12–15.

Georgiev GP, Tubbs RS, Iliev A et al 2018 Extensor indicis proprius muscle and its variants together with the extensor digitorum brevis manus muscle: a common classification. Clinical significance in hand and reconstructive surgery. Surg Radiol Anat 40:271–80.

Giannicola G, Sedati P, Cinotti G et al 2015 The ulnar greater sigmoid notch 'coverage angle': bone and cartilage contribution. Magnetic resonance imaging anatomic study on 78 elbows. J Shoulder Elbow Surg 24:1934–8.

Grewal SS, Collin P, Ishak B et al 2019 Innervation of the anconeus epitrochlearis muscle: MRI and cadaveric studies. Clin Anat 32:218–23.

Henry AK 1957 Extensile exposure, 2nd ed. Edinburgh: E and S Livingstone.

Hotchkiss RN, An K-N, Sowa DT et al 1989 An anatomic and mechanical study of the interosseous membrane of the forearm: pathomechanics of proximal migration of the radius. J Hand Surg [Am] 14A:256–61.

Jupiter JB, Leibovic SJ, Ribbans W et al 1991 The posteria Monteggia lesion. J Orthop Trauma 5:395–402.

Kleinmann WB 2010 Stability of the distal radioulnar joint: biomechanics, pathophysiology, physical diagnosis and restoration of function. In: Slutsky DJ (ed) Principle and Practice of Wrist Surgery. Philadelphia: Elsevier, Saunders; Ch. 5, pp. 41–5.

Lowe JB, Maggi SP, MacKinnon SE 2004 The position of the crossing branches of the medial antebrachial cutaneous nerve during cubital tunnel surgery in humans. Plast Reconstr Surg 114:692–6.

Macchi V, Tiengo C, Porzionato A et al 2014 The cubital tunnel: a radiologic and histotopographic study. J Anat 225:262–9.

Mikić ZD 1978 Age changes in the triangular fibrocartilage of the wrist joint. J Anat 126:367–84.

Noda K, Goto A, Murase T et al 2009 Interosseous membrane of the forearm: an anatomical study of ligament attachment locations. J Hand Surg [Am] 34A:415–22.

Novak CB, Lee GW, MacKinnon SE et al 1994 Provocative testing for cubital tunnel syndrome. J Hand Surg [Am] 19:817–20.

O'Driscoll SW, Morrey BF, Korinek S et al 1992 Elbow subluxation and dislocation. A spectrum of instability. Clin Orthop 280:186–97.

Pacek CA, Buterbaugh G 2015 Triangular fibrocartilage complex injuries. In: Miller MD, Thompson SR (eds) DeLee and Drez's Orthopaedic Sports Medicine, 4th ed. Philadelphia: Saunders; Ch. 76, pp. 875–83.

Palmer AK, Werner FW 1981 The triangular fibrocartilage complex of the wrist – anatomy and function. J Hand Surg [Am] 6:153–62.

Paraskevas GK, Ioannidis O 2011 Accessory muscles around the superior radioulnar joint: a morphological study. Ital J Anat Embryol 116:45–51.

Ring D 2010 Elbow fractures and dislocations. In: Bucholz RW, Court-Brown CM, Heckman JD et al (eds) Rockwood and Green's Fractures in Adults, 7th ed. Philadelphia: Lippincott Williams & Wilkins; Ch. 32, pp. 905–44.

Ring D 2013 Monteggia fractures. Orthop Clin North Am 44(1):59–66.

Rodriguez-Niedenführ M, Vazquez T, Parkin I et al 2002 Martin–Gruber anastomosis revisited. Clin Anat 15:129–34.

Roles NC, Maudsley RH 1972 Radial tunnel syndrome: resistant tennis elbow as a nerve entrapment. J Bone Joint Surg Br 54:499–508.

Ronel DN, Mtui E, Nolan WB 2004 Forearm compartment syndrome: anatomical analysis of surgical approaches to the deep space. Plast Reconstructr Surg 114:697–705.

Rouleau DM, Faber KJ, Athwal GS 2010 The proximal ulna dorsal angulation: a radiographic study. J Shoulder Elbow Surg 19:26–30.

Siemionow M, Agaoglu G, Hoffmann R 2007Anatomic characteristics of a fascia and its bands overlying the ulnar nerve in the proximal forearm: a cadaver study. J Hand Surg [Eur Vol] 32:302–7.

Spinner M, Kaplan EB 1970 Extensor carpi ulnaris: its relationship to stability of the distal radioulnar joint. Clin Orthop 68:124–8.

Thiru-Pathi RG, Ferlic DC, Clayton MI et al 1986 Arterial anatomy of the triangular fibrocartilage of the wrist and its surgical significance. J Hand Surg [Am] 11:258–63.

Yamaguchi K, Sweet FA, Bindra R et al 1997The extraosseous and intraosseous arterial anatomy of the adult elbow. J Bone Joint Surg Am 79:1653–62.

Yoon JS, Kim BJ, Kim SJ et al 2007 Ultrasonographic measurements in cubital tunnel syndrome. Muscle Nerve 36:853–55.

CHAPTER
51

Wrist and hand

SKIN AND SOFT TISSUES

Skin

Dorsal skin versus palmar skin

The dorsal skin is thin, mobile and frequently hirsute over the proximal phalanges and the ulnar aspect of the dorsum of the hand. The skin of the palm and the palmar surface of the digits is thick and hairless, with a well-defined stratum lucidum and a higher density of nerve endings and eccrine sweat glands, but no sebaceous glands. The skin on the dorsum is visible to others and has aesthetic relevance whereas the palmar skin has more functional relevance.

Skin creases and fingerprints

Flexure lines crease the skin of the flexor surfaces of the wrist and hand (**Fig. 51.1**) where they are anchored to the deep fascia. Less regular, mainly transverse, creases cross the dorsal aspect of the carpal, metacarpophalangeal and interphalangeal joints. The dorsal creases are more prominent in extension; the loose skin becomes stretched in flexion. (For a general review of 'skin lines', see Chapter 7.) Three anterior transverse lines usually cross the wrist. The proximal line marks the proximal limit of the flexor synovial sheaths, the intermediate line overlies the radiocarpal joint, and a distal line marks the proximal border of the flexor retinaculum.

In the palm, a curved radial longitudinal line bounds the thenar eminence, ending close to the distal wrist crease. Proximal and distal transverse lines ascend medially across the palm. The proximal line begins at the distal end of the thenar crease and runs obliquely to the middle of the hypothenar eminence across the shafts of the metacarpals. The distal palmar crease begins at or near the cleft between the index and middle finger, and curves across the palm over the necks of the metacarpals from the middle finger to little finger. In the ring and little finger the crease is just proximal to the underlying metacarpophalangeal joint.

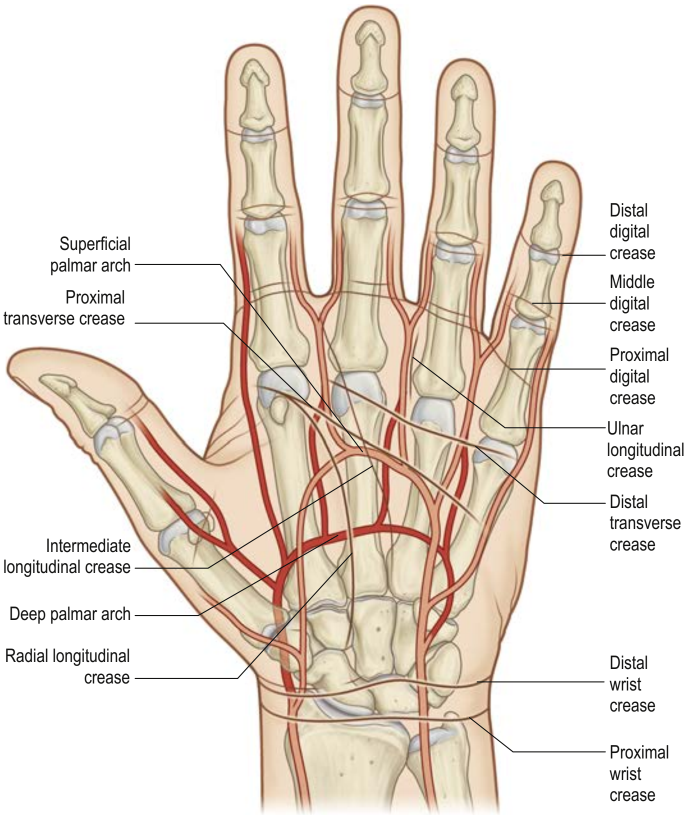

Fig. 51.1 The relation of the skin flexure lines and palmar arterial arches to the bones of the left hand. (Adapted from Drake RL, Vogl AW, Mitchell A (eds) Gray's Anatomy for Students, 2nd ed. Elsevier, Churchill Livingstone. Copyright 2010.)

The second to fifth digits have proximal, middle and distal sets of transverse lines. The proximal, often double, lies at the level of the distal margin of the webspace, approximately half way along the underlying proximal phalanx. The middle creases are usually double, the proximal line lying directly over the proximal interphalangeal joint. The distal lines are usually single, and lie proximal to the distal interphalangeal joints. The metacarpophalangeal joint of the thumb is crossed by a crease that starts on the radial side and ends in the web space level with the base of the proximal phalanx. There is a second, shorter, crease, usually 1 cm distal to this line. Two creases cross the interphalangeal joint of the thumb (see Fig. 51.1).

'Fingerprints' are striations that are unique to each individual and particularly well developed at sites of grip, namely the pulps of the fingers and thumb together with the base of the hypothenar eminence.

Cutaneous vascular supply

The skin of the palmar aspect of the wrist is supplied by branches from the superficial palmar branch of the radial artery, the ulnar artery and, occasionally, the median artery (**Fig. 51.2**). The skin over the thenar eminence is supplied by small perforating branches from the superficial palmar branch of the radial artery and the princeps pollicis. The skin over the hypothenar eminence is supplied by perforating branches from the ulnar artery, some of which pass through palmaris brevis. The rest of the palm is supplied by branches from the common palmar digital arteries that pierce the palmar aponeurosis, and branches from the radialis indicis artery. The palmar digital skin is supplied by branches from each digital artery. In the distal phalanx, the two digital arteries typically form an H-shaped anastomosis, from which cutaneous perforators fan out within the pulp. Deep digital veins accompanying the digital arteries are usually very small and frequently absent. Superficial palmar veins tend to pass dorsally and drain into the larger superficial dorsal venous system (**Fig. 51.3**).

The dorsal skin of the wrist is supplied by branches from an arterial plexus which lies over the extensor retinaculum and is formed by branches of the radial artery, including its dorsal carpal branch, the dorsal carpal branch of the ulnar artery, and the anterior and posterior interosseous arteries. The blood supply to the dorsum of the hand arises from longitudinal rows of four or five branches from each of the dorsal metacarpal arteries, which usually arise either directly from the radial artery or from the dorsal carpal arch. At the level of the neck of the metacarpals, where the second, third and fourth dorsal metacarpal arteries communicate with branches from the corresponding common palmar digital arteries, a large cutaneous perforating branch passes proximally to supply an area of skin as far as the dorsal aspect of the wrist.

The blood supply to the dorsum of the fingers arises proximally from the terminal branches of the dorsal metacarpal arteries, (supplying a region as far distally as the proximal interphalangeal joint) as well as from dorsal branches of the palmar digital arteries that are given off at the level of each phalanx (**Fig. 51.4**). At the level of the distal phalanx, the cutaneous supply comes from three dorsal arcades: a superficial arcade over the base of the distal phalanx, and two distal subungual arcades (**Fig. 51.5**). The skin of the dorsum of the thumb is supplied by longitudinal axial branches of the princeps pollicis and dorsal branches from the palmar digital arteries.

Degloving injuries of the hand and wrist

A degloving injury is one in which the skin is avulsed from its underlying structures, often leaving the entire musculoskeletal unit of the hand

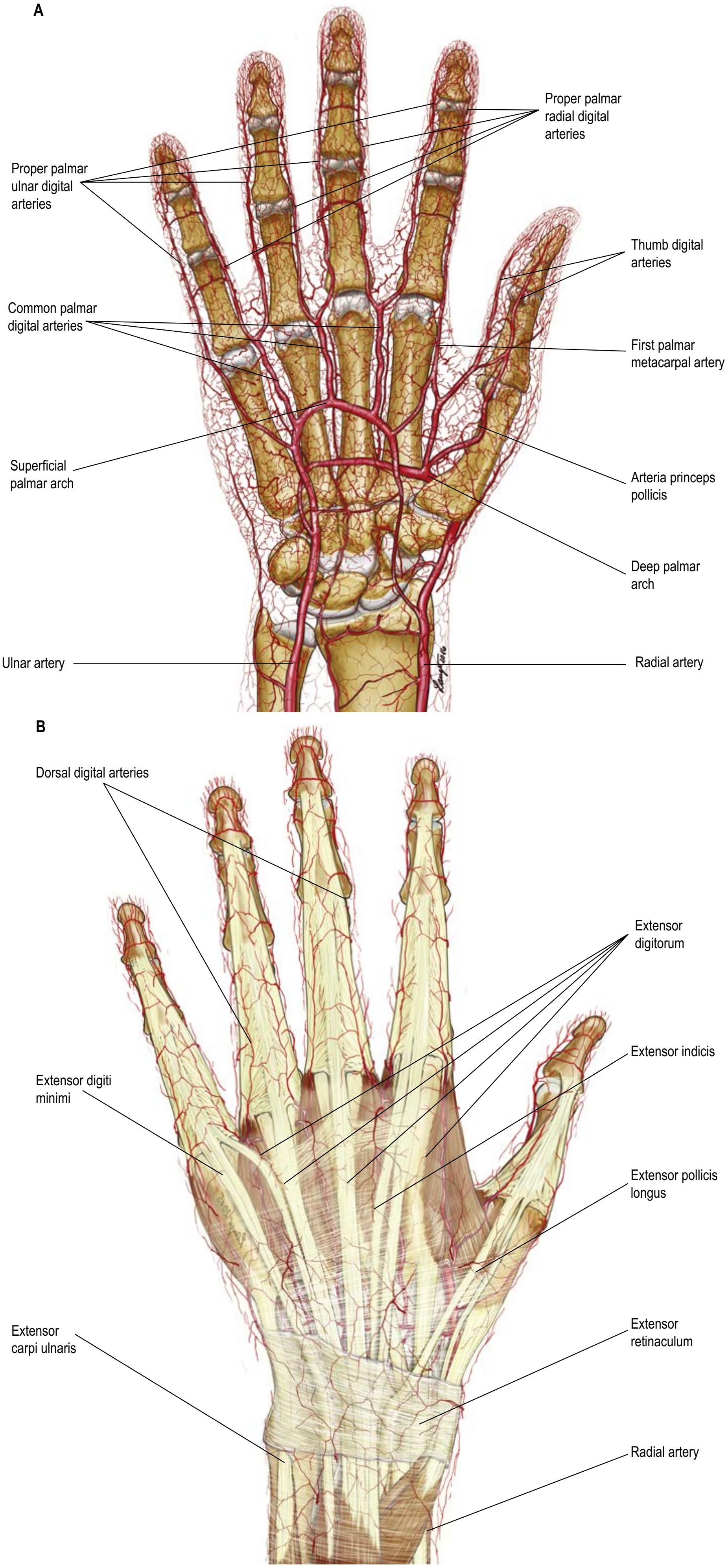
A
Proper palmar radial digital arteries
Proper palmar ulnar digital arteries
Thumb digital arteries
Common palmar digital arteries
First palmar metacarpal artery
Superficial palmar arch
Arteria princeps pollicis
Deep palmar arch
Ulnar artery
Radial artery
B
Dorsal digital arteries
Extensor digitorum
Extensor indicis
Extensor digiti minimi
Extensor pollicis longus
Extensor carpi ulnaris
Extensor retinaculum
Radial artery

Fig. 51.2 **A**, The blood supply to the palmar (volar) skin of the right wrist and hand. **B**, The blood supply to the dorsum of the left hand. (Copyright Martin Langer.)

Treatment of these injuries depends on their extent (Krishnamoorthy and Karthikeyan 2011). In complete avulsion, restoration of the tissue and microvascular anastomosis is called replantation. Where the skin remains attached but is devascularized, restoration of the blood supply by anastomosis is called revascularization. Because the traction injury may extend over a considerable distance, large sections of vessel may need to be excised: the judicious use of vein grafts is essential. If neither of these procedures is feasible, the avulsed skin may be defatted and reapplied to the affected part, where it effectively acts as a split skin graft. If none of these techniques is practicable, primary amputation may have to be considered. Subsequently, reconstruction may be by split-skin graft, skin/fasciocutaneous flap or free flap. The decision whether to reconstruct or to amputate is multifactorial and depends not just on the injury but on the medical, psychological and social situation of the patient.

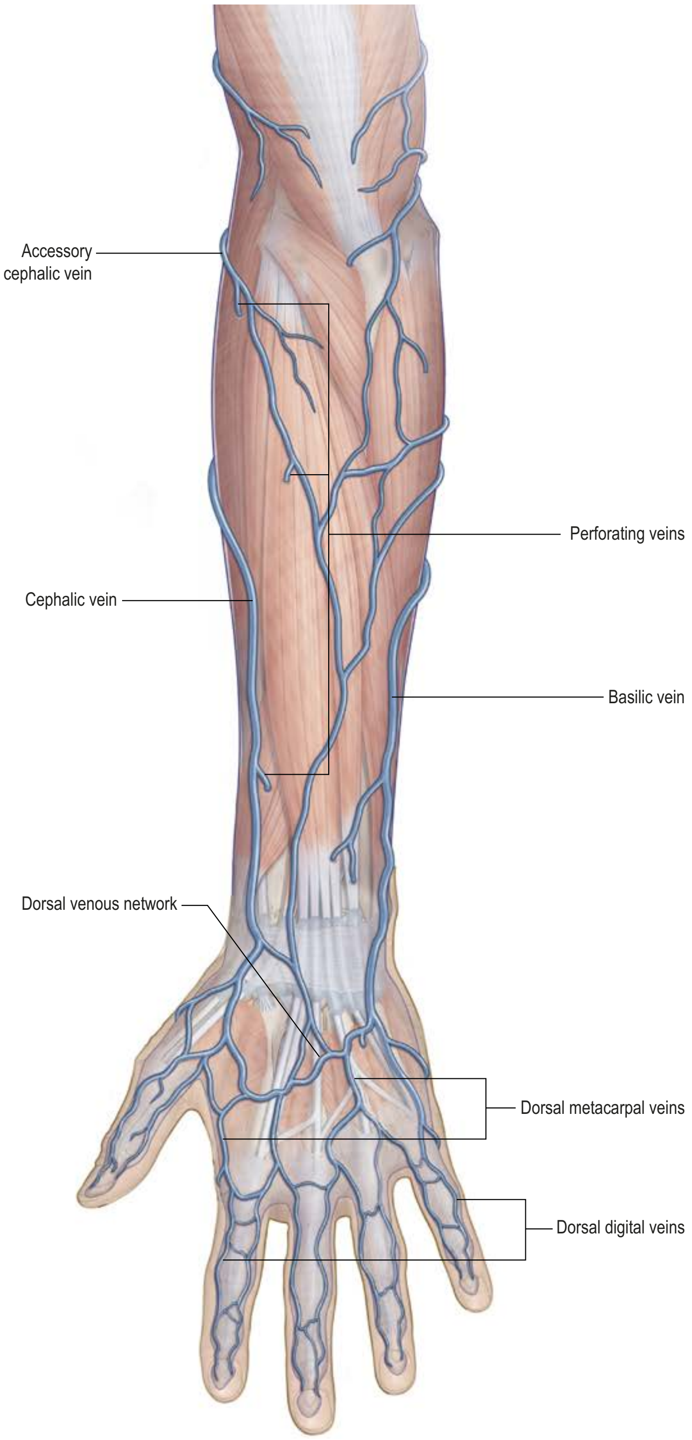
Accessory cephalic vein
Perforating veins
Cephalic vein
Basilic vein
Dorsal venous network
Dorsal metacarpal veins
Dorsal digital veins

Fig. 51.3 The veins of the dorsum of the hand. (Redrawn with permission from Drake RL, Vogl AW, Mitchell A et al (eds) Gray's Atlas of Anatomy. Elsevier, Churchill Livingstone. Copyright 2008.)

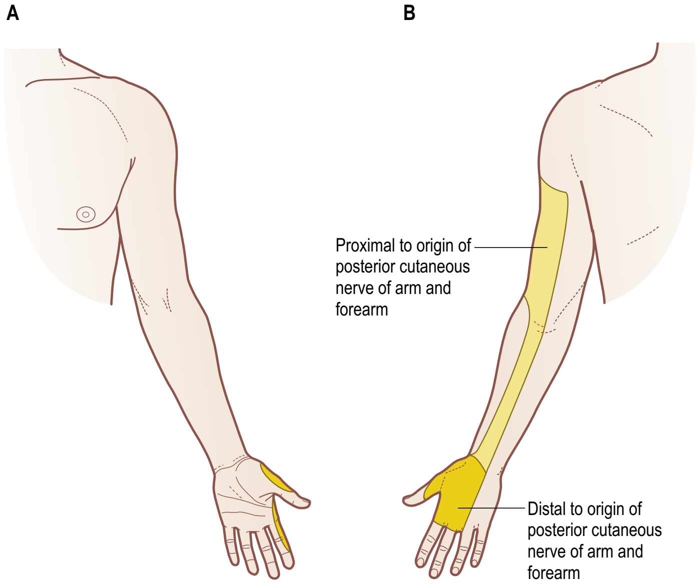
A
B
Proximal to origin of posterior cutaneous nerve of arm and forearm
Distal to origin of posterior cutaneous nerve of arm and forearm

Fig. 51.6 The approximate area of sensory loss or disturbance after complete interruption of the radial nerve. **A**, Anterior. **B**, Posterior. The area of sensory disturbance after high lesions is very variable.

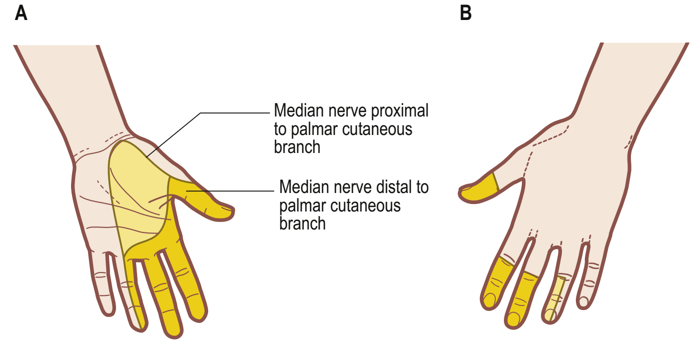
A
B
Median nerve proximal to palmar cutaneous branch
Median nerve distal to palmar cutaneous branch

Fig. 51.7 The approximate area of sensory loss or disturbance after complete interruption of the median nerve. **A**, Anterior. **B**, Posterior.

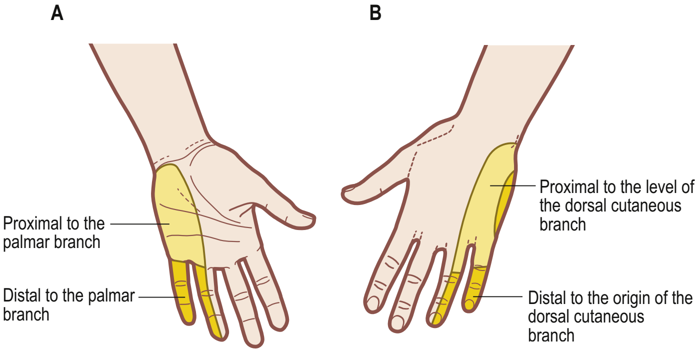
A
B
Proximal to the palmar branch
Distal to the palmar branch
Proximal to the level of the dorsal cutaneous branch
Distal to the origin of the dorsal cutaneous branch

Fig. 51.8 The approximate area of sensory loss or disturbance after complete interruption of the ulnar nerve. **A**, Anterior. **B**, Posterior.

intact, thereby permitting the patient to mobilize the 'naked' finger fully. These injuries occur as the result of a low velocity traction force being applied to the affected part. The plane of cleavage is through the subcutaneous tissues, leaving the underlying structures essentially intact. These injuries may occur if the hand is caught in industrial machinery, typically between rollers or in a conveyor belt.

The most common manifestation is the 'ring avulsion injury', when a ring is caught and the finger rapidly pulled away (Bamba et al 2018). The degloving may be complete or partial. Complete avulsion is rare, whereas avulsion of the skin of all or part of the finger is relatively common. Urbaniak et al (1981) grouped ring avulsion injuries into three classes: those in which the blood supply is intact (class I); those in which the blood supply is compromised (class II); and those in which digits are either completely degloved or amputated (class III). While these represent injuries of increasing severity, the avulsion force required to achieve them does not occur in a linear manner (Kupfer et al 1999). The longitudinal force applied to a finger causes a traction injury to the blood vessels, which may extend over a considerable distance. The crushing element of a degloving injury may cause skin necrosis and thrombosis of the underlying vessels (Brooks et al 2007).

Basic skin flaps in reconstruction

Available with the *Gray's Anatomy* e-book

Cutaneous innervation

The skin of the anterior aspect of the wrist is innervated by the terminal branches of the lateral and medial cutaneous nerves of the

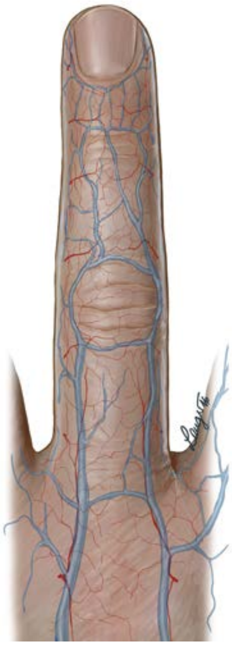

Fig. 51.4 Cutaneous arterial supply and venous drainage for the dorsum of the finger. (Copyright Martin Langer.)

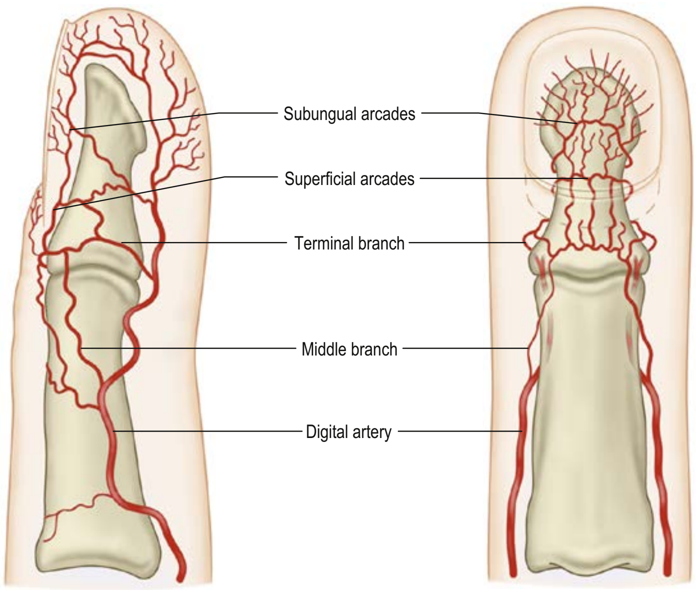

Fig. 51.5 Terminal vascular arcades over the distal phalanx. (With permission from Flint MH 1956 Some observations on the vascular supply of the nail bed and terminal segments of the fingers. BJPS 8:186–95.)

The pedicled groin flap used to be regarded as the workhorse flap for reconstruction of the hand. Swelling due to the dependent position of the hand, and the need for a second operation, coupled with the social stigma associated with the position of the hand, has led to it falling out of favour.

Regional and free flaps have gradually replaced the pedicled groin flap. Numerous different types of regional and free flaps have been used to cover soft tissue defects in the hand, based on the principle that the hand has a reliable vascular anatomy. The anatomical basis can be a named artery to which a free flap is attached (e.g. toe to thumb transfer), a naked vessel that can be rotated with a paddle of skin (e.g. the radial forearm and dorsal intermetacarpal artery flaps), or a skin flap based on a reliable subcutaneous blood supply (e.g. the cross-finger flap).

The radial forearm flap was originally described by surgeons from the Shenyang Military Hospital in 1978 and was consequently known as the 'Chinese flap'. It can be used as a free flap or as a reversed pedicled fasciocutaneous island flap to cover soft tissue defects of the ipsilateral hand. Its blood supply is based on septocutaneous perforators that arise from the distal part of the radial artery and supply the skin on the radial side of the lower forearm; these tend to become more sparse proximally. Venous drainage is by the venae comitantes and superficial subcutaneous veins.

The ulnar forearm flap is a fasciocutaneous flap based on the ulnar artery distal to its common interosseous branch. A variant on this flap based on the ascending branch of the dorsal ulnar artery was described by Becker and Gilbert (1988). It has the disadvantage of a short pedicle but is useful for achieving cover of defects of the proximal and ulnar side of the palm. For each of these flaps, the patency of the other vessel must be confirmed by the clinical 'Allen occlusive test' wherein both radial and ulnar arteries are occluded by digital pressure at the wrist then the ulnar or radial artery is released: perfusion of the hand indicates adequate residual flow in the other artery. This test is now supplemented by Doppler ultrasonography and angiography.

The posterior interosseous island flap, distally based on the dorsal carpal arterial arch via the anastomoses between the posterior and anterior interosseous arteries just lateral to the head of the ulna (Costa et al 2007), was introduced by Zancolli and Angrigiani in 1985 (Zancolli and Angrigiani 1988). Its principal advantages are that it spares both of the major arteries of the forearm and is a good match for the skin colour and texture of the dorsum of the hand. Care must be taken to avoid injury to the adjacent posterior interosseous nerve when harvesting the flap. Doppler studies should be carried out preoperatively to ensure the presence and positioning of the anastomoses between the posterior and anterior interosseous arteries. It has been claimed that most defects of the hand can be treated using this flap; its particular advantage is in the treatment of hand injuries with severe accompanying vascular damage.

The anatomical distribution of the first dorsal metacarpal artery allows a flap of skin over the dorsum of the proximal phalanx of the index finger to be raised on the artery and its accompanying venae comitantes. This flap is particularly useful under certain circumstances for reconstruction of the thumb following injury. The distribution of the second, third and fourth dorsal metacarpal arteries allows the surgical elevation of flaps of dorsal skin based either proximally, on the dorsal metacarpal arteries proper, or distally, on their direct cutaneous branches. These flaps may be used for reconstructing areas of missing tissue elsewhere in the hand. The dorsal cutaneous branch of the ulnar artery is constant and can support a flap of skin on the medial aspect of the distal forearm just proximal to the wrist; it is useful in the reconstruction of areas of missing skin in this region.

Anatomical studies that define the cutaneous vascularity of the hand provide the scientific foundations of new skin flap techniques. These can then be added to the surgeon's armamentarium when faced with soft tissue loss in the upper extremity (Moschella et al 1996, Moschella and Cordova 2006, Hierner et al 2016).

forearm. The skin of the palm is innervated by the palmar branches of the ulnar and median nerves. The skin of the radial aspect of the dorsum of the wrist and hand, as well as the dorsal aspect of the radial three and a half digits as far distally as the nail beds, is innervated by the dorsal digital nerves (the terminal branches of the radial nerve) (**Fig. 51.6**). The palmar skin of the thumb, index and middle fingers and the radial aspect of the ring finger is innervated by the median nerve, while that of the little finger and the ulnar side of the ring finger is innervated by the ulnar nerve (**Figs 51.7–51.8**). Between two and five dorsal digital nerves supply each digit. The skin of the ulnar aspect of the dorsum of the wrist and hand, and the dorsal aspect of the ulnar one and a half digits as far distally as the nail beds, is innervated by dorsal digital branches of the dorsal branch of the ulnar nerve. The skin of the dorsum of the middle and distal phalanges is innervated by dorsal branches of the palmar digital nerves (**Fig. 51.9**).

Nail apparatus

The nail apparatus is described in Chapter 7 (see Fig. 7.27) (Zook 1981).

It comprises the nail plate beneath which lie the germinal and sterile matrix. The tissue to the side of the nail plate is the paronychium. The nail is enveloped proximally by the nail fold, the roof of which is formed by skin and is known as the nail wall. The thin membrane beyond the roof onto the nail is the eponychium. The skin just beyond the nail plate is the hyponychium.

Soft tissues

Flexor retinaculum

The flexor retinaculum (see Fig. 51.27) is a strong, fibrous band that crosses the front of the carpus and converts its anterior concavity into the carpal tunnel which conveys the flexor tendons of the digits and the median nerve. The retinaculum is short and broad, measuring 2.5–3 cm in both dimensions. It is attached medially to the pisiform and the hook of the hamate. Laterally, it splits into superficial and deep laminae. The superficial lamina is attached to the tubercles of the scaphoid and trapezium. The deep lamina is attached to the medial lip of the groove on the trapezium. Together with this groove, the two laminae form a tunnel, lined by a synovial sheath, that contains the tendon of flexor carpi radialis. The retinaculum is crossed superficially by the ulnar vessels and nerve, immediately radial to the pisiform, and by the palmar cutaneous branches of the median and ulnar nerves (see Fig. 51.27). A slender band of fascia, the superficial part of the flexor retinaculum, bridges the ulnar neurovascular bundle and is attached to the radial side of the pisiform, forming a tunnel (Guyon's canal), which is the occasional site of ulnar nerve entrapment (**Fig. 51.10**). The tendons of palmaris longus and flexor carpi ulnaris are partly attached to the anterior surface of the retinaculum. Distally, some of the intrinsic muscles of the thumb and little finger are attached to the retinaculum. The retinaculum mimimizes the flexion torque that the long finger flexors transmit at the radiocarpal joint.

Guyon's canal Guyon's canal is a fibro-osseous canal, approximately 4 cm long in the adult, on the anteromedial aspect of the wrist (see Fig. 51.10). Its roof is formed by the superficial part of the flexor retinaculum and palmaris brevis. Its floor is formed by the transverse carpal and pisohamate ligaments and, more distally, by flexor digiti minimi. The ulnar side is bounded by flexor carpi ulnaris, the pisiform bone and abductor digiti minimi, and the radial side by the extrinsic flexor tendons, the transverse carpal ligament and the hook of the hamate. The fibrous arcade at the origin of the hypothenar muscles lies distally.

The canal transmits the ulnar nerve and artery, together with occasional venae comitantes. The ulnar nerve divides within it at the level of the hook of the hamate into a deep motor branch that passes deeply and radially around the medial and then the distal edge of the hook of hamate, and a superficial sensory branch that passes distally and ulnarwards. Depending on the site, motor, sensory or both components can be affected by compression: if the nerve is compressed proximally, both modalities will be affected, whereas, distal to the bifurcation, either the sensory or motor branch will be compromised.

Variations in the branching of the ulnar nerve may occur. The most common variant is its trifurcation into three branches (deep and two superficial) in about a third of cases, and varying innervation of the abductor digiti minimi.

Extensor retinaculum

The extensor retinaculum is a strong, fibrous band which extends obliquely across the back of the wrist (**Fig. 51.11**). It prevents 'bowstringing' of the long digital extensor tendons across the wrist joint, minimizing the torque that these tendons transmit to the radiocarpal joint as the fingers extend. It is attached laterally to the anterior border of the radius, then passes medially to blend into the fascia overlying the ulnar side of the distal forearm and carpus and into the anteromedial surfaces of the pisiform and triquetrum. As the retinaculum passes across the wrist, it is connected to vertical ridges that are attached to the back of the radius, creating separate compartments for abductor pollicis longus–extensor pollicis brevis, extensor carpi radialis longus–extensor carpi radialis brevis, extensor pollicis longus, extensor digitorum–extensor indicis, and extensor digiti minimi. Extensor carpi ulnaris has a separate sub-sheath attached only to the back of the head of the ulna (there would be no rotation if it were in continuity with the other extensors which are bound to the radius by the retinaculum).

Palmar fascial complex

The palmar fascia is a three-dimensional ligamentous system consisting of longitudinal, transverse and vertical fibres (**Fig. 51.12**).

Longitudinal fibre system

The longitudinal fibres run distally beyond the tendon of palmaris longus (if present) or the flexor retinaculum of the wrist (if palmaris longus is not present) to fan out across the whole width of the central third of the palm, producing four well-defined longitudinal bundles anterior to the metacarpals of the index, middle, ring and little fingers. This is known as the superficial palmar aponeurosis. A less well-defined bundle passes to the thumb. Distal to the transverse fibres of the palmar aponeurosis, the longitudinal fibres pass in three layers (McGrouther 1982). The most superficial longitudinal fibres (layer 1) are inserted superficially into the skin of the distal palm between the distal palmar crease and the proximal digital crease. Some superficial fibres pass distally into the palmar midline of the digit. Deeper longitudinal fibres (layer 2) pass deep to the natatory ligament and neurovascular bundles into the skin at the apex of the web space and into the fingers themselves, where they are continuous with Cleland's ligaments and the lateral digital sheet on either side. Deeper still, the longitudinal fibres in layer 3 perforate the deep transverse metacarpal ligament to pass around the sides of the metacarpophalangeal joint and attach to the metacarpal and proximal phalanx, and extensor tendon.

Transverse fibre system

The transverse fibre system consists of the superficial transverse metacarpal (natatory) ligament, the transverse fibres of the palmar aponeurosis and the deep transverse metacarpal ligament.

Superficial transverse metacarpal ligament (natatory ligament)

The fibres of the superficial transverse metacarpal ligament cross the apex of the web skin and extend into each digit to blend with the lateral digital sheet. They limit the separation of adjacent fingers and support the skin in the web space. Fibres on the ulnar side of the little finger surround the insertion of abductor digiti minimi. Fibres on the radial side of the index finger form the distal commissural ligament (of Grapow) which passes proximally to meet the fascia in front of the thumb metacarpal.

Transverse fibres of the palmar aponeurosis

The transverse fibres of the palmar aponeurosis (Skoog fibres) form the deepest layer of the palmar fascia. They lie proximal to the distal palmar crease in a band approximately 2 cm wide, interconnecting the anterior fibres of the flexor tendon sheaths with the fasciae over the thenar and hypothenar muscles. The extension to the first ray forms the proximal commissural ligament.

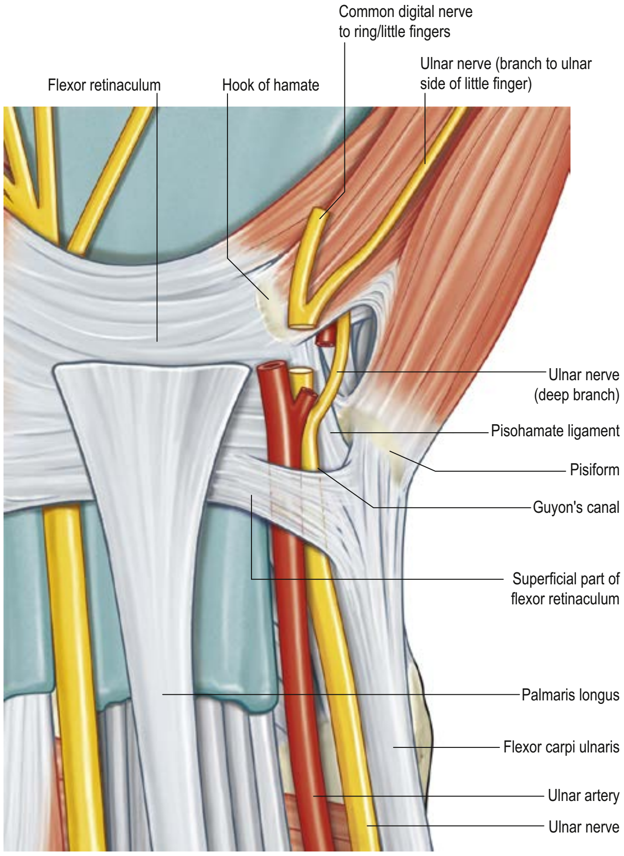
Common digital nerve to ring/little fingers
Flexor retinaculum
Hook of hamate
Ulnar nerve (branch to ulnar side of little finger)
Ulnar nerve (deep branch)
Pisohamate ligament
Pisiform
Guyon's canal
Superficial part of flexor retinaculum
Palmaris longus
Flexor carpi ulnaris
Ulnar artery
Ulnar nerve

Fig. 51.10 Guyon's canal (space) at the wrist. Note the possibilities of entrapment at, and distal to, the volar carpal ligament. (Courtesy of Rolfe Birch, all rights reserved. Published in Birch R, Surgical Disorders of the Peripheral Nerve, 2nd ed, 2011. London: Springer-Verlag.)

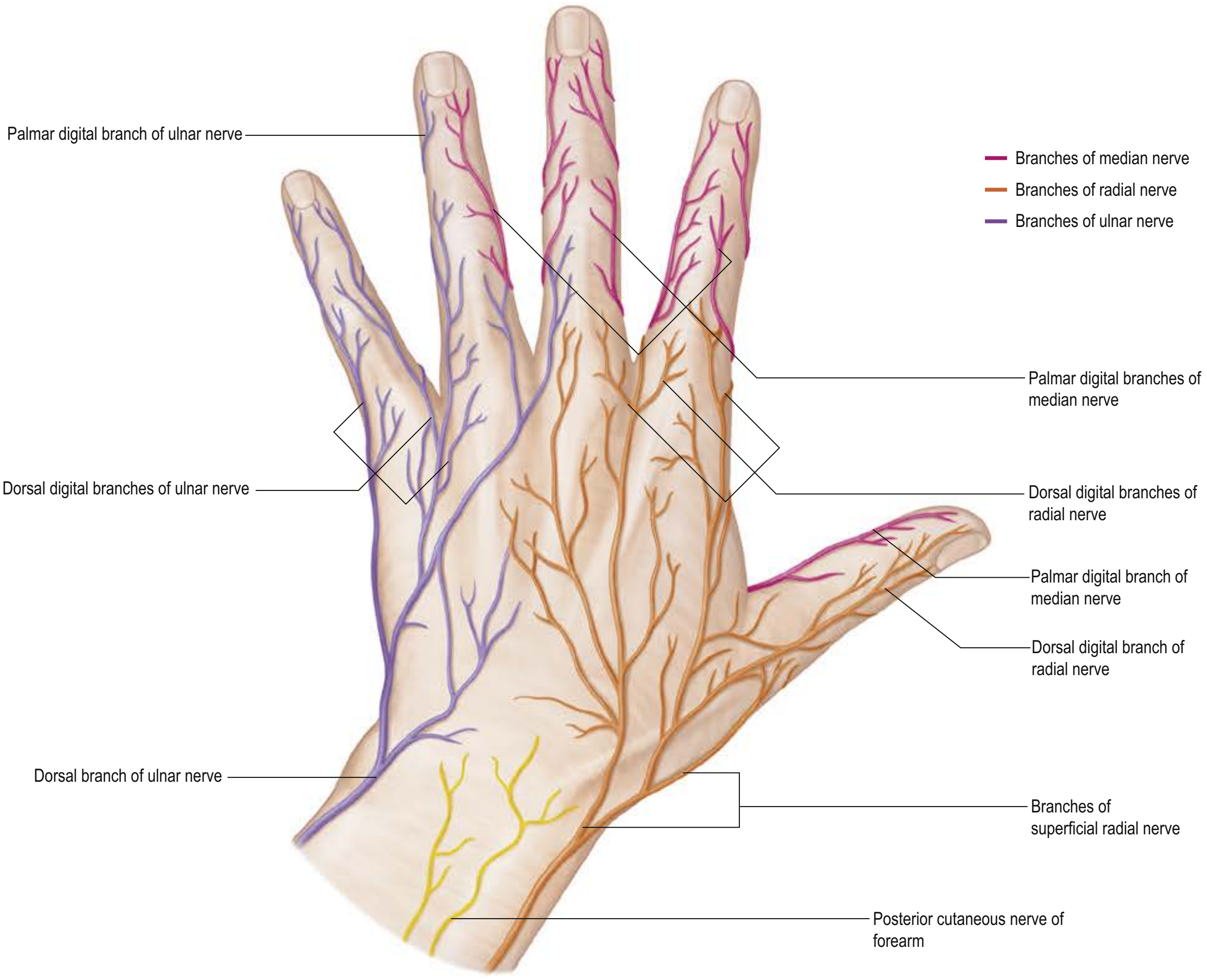
Palmar digital branch of ulnar nerve
Branches of median nerve
Branches of radial nerve
Branches of ulnar nerve
Palmar digital branches of median nerve
Dorsal digital branches of ulnar nerve
Dorsal digital branches of radial nerve
Palmar digital branch of median nerve
Dorsal digital branch of radial nerve
Dorsal branch of ulnar nerve
Branches of superficial radial nerve
Posterior cutaneous nerve of forearm

Fig. 51.9 The cutaneous nerves of the hand. Dorsal aspect.

Fig. 51.11 The synovial sheaths of the tendons on the extensor aspect of the left wrist. (Sobotta Atlas of Human Anatomy © Elsevier GmbH, Urban & Fischer, Munich.)

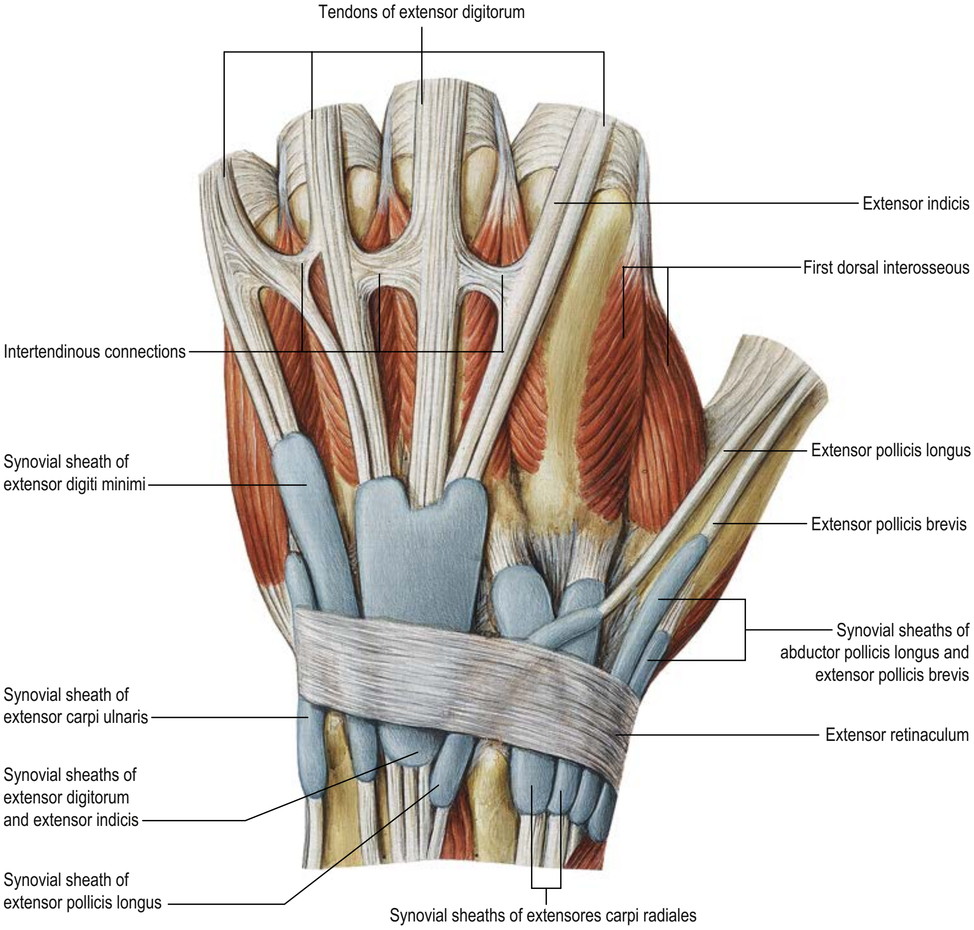
Tendons of extensor digitorum
Extensor indicis
First dorsal interosseous
Intertendinous connections
Extensor pollicis longus
Synovial sheath of extensor digiti minimi
Extensor pollicis brevis
Synovial sheaths of abductor pollicis longus and extensor pollicis brevis
Synovial sheath of extensor carpi ulnaris
Extensor retinaculum
Synovial sheaths of extensor digitorum and extensor indicis
Synovial sheath of extensor pollicis longus
Synovial sheaths of extensores carpi radiales

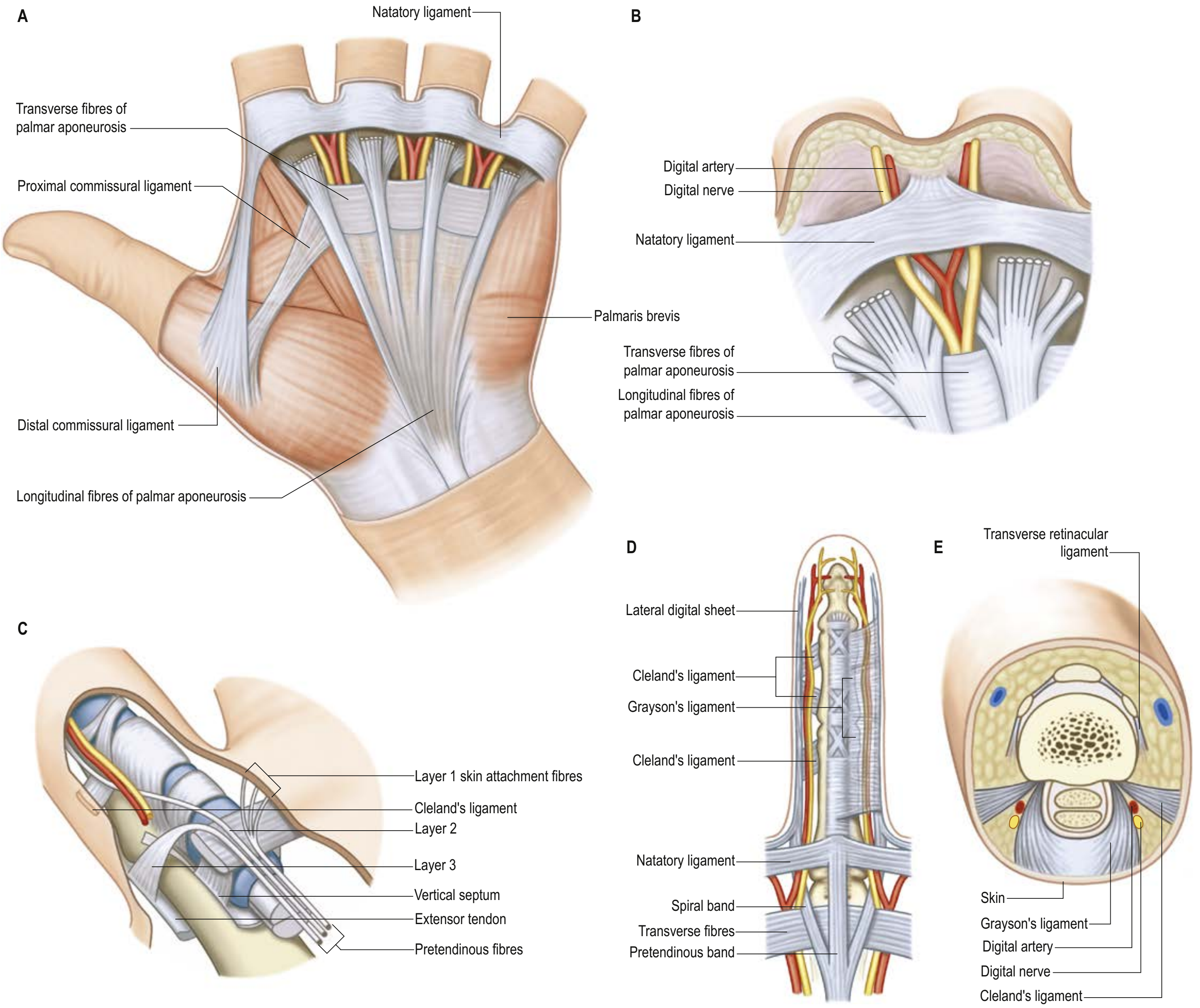
A
Natatory ligament
Transverse fibres of palmar aponeurosis
Proximal commissural ligament
Palmaris brevis
Distal commissural ligament
Longitudinal fibres of palmar aponeurosis
B
Digital artery
Digital nerve
Natatory ligament
Transverse fibres of palmar aponeurosis
Longitudinal fibres of palmar aponeurosis
C
Layer 1 skin attachment fibres
Cleland's ligament
Layer 2
Layer 3
Vertical septum
Extensor tendon
Pretendinous fibres
D
Lateral digital sheet
Cleland's ligament
Grayson's ligament
Cleland's ligament
Natatory ligament
Spiral band
Transverse fibres
Pretendinous band
E
Transverse retinacular ligament
Skin
Grayson's ligament
Digital artery
Digital nerve
Cleland's ligament

Fig. 51.12 The palmar aponeurosis and distal fascial complex. **A**, The palmar fascia. **B**, Structures at the web space. **C**, The fate of the distal longitudinal fibres. **D–E**, The normal digital fascia.

Deep transverse metacarpal ligament

The strong fibres of the deep transverse metacarpal ligament lie deep to the palmar aponeurosis and flexor sheaths, and are attached to the adjacent edges of the volar plates of the metacarpal heads of the little, ring, middle and index fingers. The ulnar edge of the little finger intermetacarpal ligament is attached to abductor digiti minimi; the radial edge of the index finger intermetacarpal ligament is attached to the first dorsal interosseous.

Vertical fibre system

The vertical fibres (of Grapow) are more delicate. They pass from the dermis, between the longitudinal and transverse fibres, to the fibrous flexor sheaths and the metacarpals. They are concentrated on either side of the palmar skin creases, as well as the thenar and hypothenar eminences. The vertical septa of Legueu and Juvara (Bilderback and Rayan 2004) pass from the transverse fibres of the palmar aponeurosis to the underlying deep transverse metacarpal ligament, forming compartments that contain the flexor tendons and the lumbricals and neurovascular bundles.

Digital fascial complex

The superficial fascia within a finger is fibrofatty in its palmar and dorsal aspects, but becomes condensed laterally into the lateral digital sheet. The flexor sheath is a well-defined thickening of the fascia (discussed in detail on page 975). Cleland's ligaments extend from the sides of the proximal interphalangeal joints, pass transversely and dorsal to the neurovascular bundles to insert into the lateral digital sheet (see Fig. 51.12D–E) (Zwanenburg et al 2014). Grayson's ligaments are more delicate and may even be discontinuous: they pass palmarwards from the lateral sides of the phalanges to pass over the midline of the flexor sheath to insert in the skin of the opposite side (see Fig. 51.12D–E). The retrovascular cord (of Thomine) is very flimsy in health. The oblique retinacular ligament (ORL) of Landsmeer (Adkinson et al 2014) is an inconsistent anatomical structure with tenuous fibres that connect the flexor sheath attachment to bone proximal to the proximal interphalangeal joint into the lateral band of the extensor tendon alongside the middle phalanx and into the base of the distal phalanx.

Functions of the fascia of the hand

The fascial continuum of the hand performs a number of different, but interrelated, functions, such as channelling structures in transit between the forearm and the digits transmitting loads; and anchoring, binding and tethering structures. It has a complex nerve supply suggesting a proprioceptive function (Stecco et al 2018).

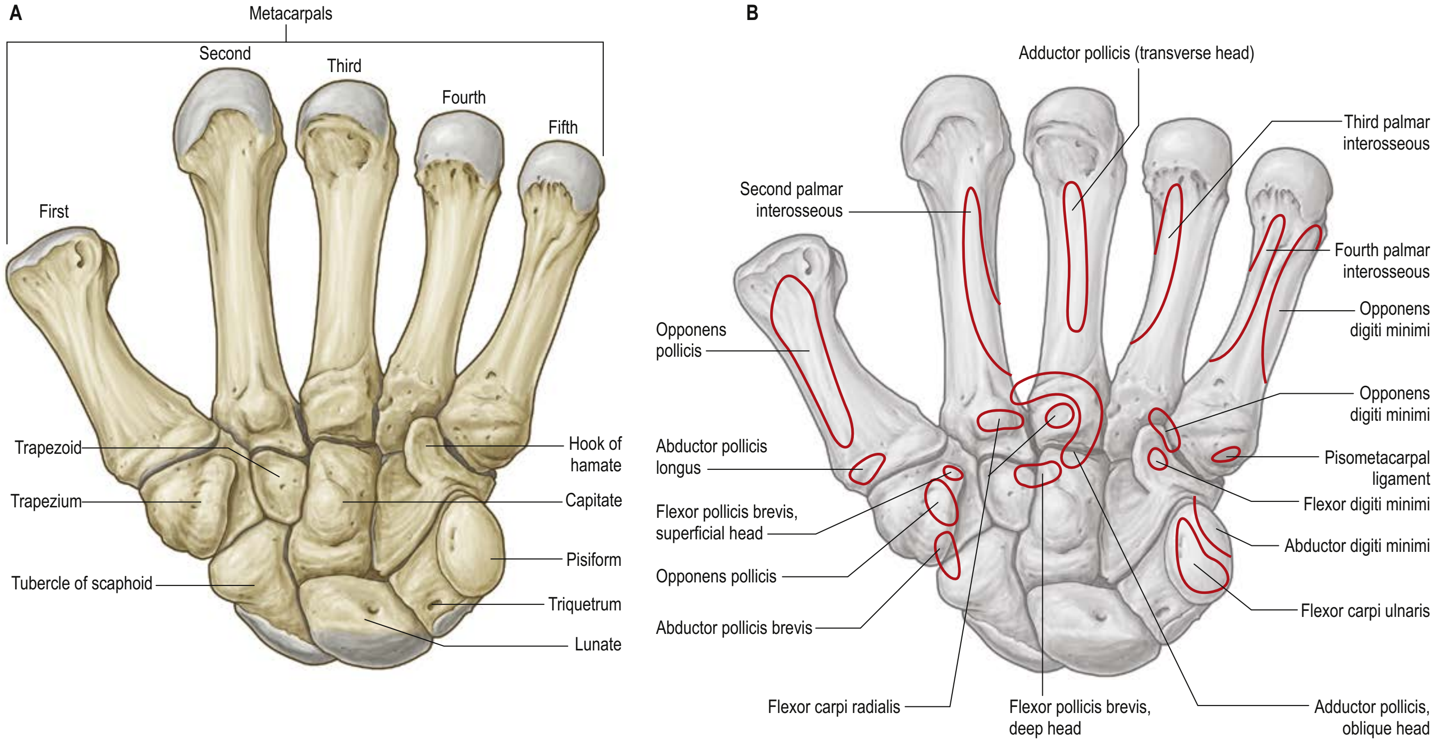
A
Metacarpals
Second
Third
Fourth
Fifth
First
Trapezoid
Trapezium
Tubercle of scaphoid
Hook of hamate
Capitate
Pisiform
Triquetrum
Lunate
B
Adductor pollicis (transverse head)
Third palmar interosseous
Second palmar interosseous
Fourth palmar interosseous
Opponens digiti minimi
Opponens pollicis
Opponens digiti minimi
Abductor pollicis longus
Pisometacarpal ligament
Flexor digiti minimi
Flexor pollicis brevis, superficial head
Abductor digiti minimi
Opponens pollicis
Flexor carpi ulnaris
Abductor pollicis brevis
Flexor carpi radialis
Flexor pollicis brevis, deep head
Adductor pollicis, oblique head

Fig. 51.13 **A**, The carpals and metacarpals of the left hand: palmar aspect. **B**, Sites of muscle attachments (except the dorsal interossei).

Channelling of structures in transit between forearm and digits

Available with the *Gray's Anatomy* e-book

Transmission of loads

Available with the *Gray's Anatomy* e-book

Anchorage

Available with the *Gray's Anatomy* e-book

Dupuytren's disease

Available with the *Gray's Anatomy* e-book

Digital and palmar spaces

There are many potential spaces within the hand, often with ill-defined margins. The nail fold is a 'U-shaped' space made up of the eponychium and the lateral nail fold. The pulp space in the apex and palmar pulp space of the fingertip are formed by the fibrous attachments of the distal phalanx to the digital pulp skin. The synovial flexor tendon sheaths are described on pages 975 and 976. The web space is bounded distally by the skin and natatory ligament, by the deep transverse metacarpal ligament posteriorly, and by the deep attachments of the palmar fascia, together with their lateral attachments to the tendon sheaths, proximally. The lumbrical canal transmits the lumbricals as they pass dorsally, palmar to the deep transverse metacarpal ligament and radial to the metacarpophalangeal joint; the interosseous canal transmits the interossei as they pass dorsal to the deep transverse metacarpal ligament to one side or other of the metacarpophalangeal joint. The deep palmar space is a complex, three-dimensional space, limited proximally by the carpal tunnel. It lies deep to the palmar aponeurosis, between the radial and ulnar condensations of vertical fibres that connect the palmar aponeurosis to the thenar and hypothenar eminences. Partitions that pass deeply from the longitudinal bands of the palmar aponeurosis form eight narrow compartments; four contain the digital flexor tendons and four contain the lumbricals and the neurovascular bundles.

Infections of the hand

Available with the *Gray's Anatomy* e-book

Compartment syndrome of the hand

Available with the *Gray's Anatomy* e-book

BONES

The skeleton of the hand comprises the carpus, metacarpus and the phalanges.

Carpus

The carpus contains eight bones: four each in proximal and distal rows (Figs 51.13–51.15). In radial to ulnar order, the scaphoid, lunate, triquetrum and pisiform make up the proximal row, and the trapezium, trapezoid, capitate and hamate make up the distal row. The pisiform articulates with the palmar surface of the triquetrum. The other three proximal bones form an arch that is convex proximally, and which articulates with the distal surface of the radius and central articular disc of the triangular fibrocartilage complex. The distal concavity of the arch articulates with the capitate and hamate.

The dorsal carpal surface is convex. The palmar surface forms a deeply concave carpal groove, accentuated by the palmar projection of the radial and ulnar borders. The ulnar projection is formed by the pisiform and the hook (hamulus) of the hamate. The pisiform is at the proximal border of the hypothenar eminence, on the ulnar side of the palm, and it is easily felt in front of the triquetrum. The hamulus is concave in a radial direction; its tip is palpable 2.5 cm distal and 1 cm radial to the pisiform, in line with the radial border of the ring finger. The radial border of the carpal groove is formed by the tubercles of the scaphoid and trapezium. The former is distal on the anterior scaphoid surface and palpable (sometimes also visible) as a small medial knob at the proximal border of the palmar thenar eminence, radial to the tendon of flexor carpi radialis. The tubercle of the trapezium is a vertically rounded ridge on the anterior surface of the bone, slightly hollow medially and just distal and radial to the scaphoid tubercle. The scaphoid can be moved passively into extension by direct backward pressure onto the scaphoid tubercle. The carpal groove is converted into an osseofibrous carpal tunnel by the flexor retinaculum which is attached to its margins: the tunnel transmits flexor tendons and the median nerve into the hand. The retinaculum strengthens the carpus and augments flexor efficiency. Ligaments are attached to the palmar and dorsal surfaces of all of the carpal bones, interconnecting the bones with each other and also to the radius, ulna and metacarpals.

Individual carpal bones

Scaphoid

The scaphoid is the largest element in the proximal carpal row (see Fig. 51.15A). It has a long axis that is distal, radial and palmar in

The vertical septa act as spacers between the tendons and neurovascular bundles of the individual digital rays. Where tendons change direction around a concave surface, the channels are thickened. The flexor tendon sheaths, flexor retinaculum and extensor retinaculum act as sheaths or pulleys to prevent bow-stringing of the tendons .

At points where compressive loading is applied to the hand, such as the finger pulp and palm, loculi of fat act as shock absorbers. The loculi are contained within defined fibrous boundaries, which means that the shape, but not the volume, of each loculus can change. The compliance or deformability of the boundaries determines the amount of shock absorption. The palm also contains much larger fibrous compartments between skin and skeleton that transmit muscles, tendons and other structures. The honeycomb pattern of these compartments constitutes the palmar shock absorption system. The soft, padded parts of the hand are able to conform to the contours of objects that are grasped which allows better interpretation of sensation and better grip. The hand must also resist tensile loading. Tendons and ligaments are particularly suitable for resisting such forces but many other parts of the fascial continuum, such as the anchorage system of the palm, also play a major role in resisting 'pulling' forces.

Whilst the thin hair-bearing skin on the dorsum has considerable excursion on flexion and extension, the thick palmar skin is retained by fascial ligaments that allow the hand to flex while retaining the skin in position. The palmar creases have been described as skin 'joints'. Fascial anchors may be vertical (perpendicular to the palm), as in the mid-palm, where scattered vertical fibres run from the dermis down into the depths of the hand; horizontal (in the plane of the palm); or oblique to the skin surface. As the hand grips an object, the skin creases constrain each intervening cushion of fat to provide a secure conforming grip; adhesion is further improved by sweating of the palmar skin.

The insertion of the longitudinal (pretendinous) fibres of the palmar aponeurosis is an example of a well-developed horizontal anchorage system. The most superficial longitudinal fibres insert into the dermis of the distal palm. This arrangement resists horizontal shearing force in gripping tasks, such as holding a hammer, where it prevents distal skin slippage or degloving of the palm during use. The characteristic blisters on the palms of those unaccustomed to such use map out the sites of the skin anchorage points. This anchorage system can be demonstrated by flexing the palm until the skin of the distal palm folds loosely. An attempt to pull the loose skin distally will reveal the anchoring longitudinal fibres of the palmar aponeurosis. Oblique anchors occur in the fingers where Cleland's ligaments tether the skin of the proximal and middle segments of the digits to the region of the proximal interphalangeal joints.

Binding

Transversely orientated fascial structures help to maintain the transverse arch of the hand by 'binding' the underlying skeletal structures or the tendon sheaths.

Limiting or tethering

Joint motion is limited not only by the action of its ligaments but also, in some cases, by skin tightness. Skin in the interdigital webs is reinforced by the natatory ligaments in the fingers and by the commissural ligament in the thumb, which resist stretch. The volar plates of the metacarpophalangeal and interphalangeal joints limit hyperextension. The deep transverse intermetacarpal ligaments prevent splaying (abduction from the axis of the third metacarpal).

Since the oblique retinacular ligament of Landsmeer runs from an attachment anterior to the axis of the proximal interphalangeal joint to an insertion posterior to the axis of the distal interphalangeal joint, it causes obligatory extension of the distal interphalangeal joint when the proximal interphalangeal joint extends – a 'tenodesis' effect.

Lubrication

There are many other gliding planes, e.g. between periosteum and the extensor apparatus, and between the extensor apparatus and the skin, on the dorsum of the digits. The flexor tendon sheaths are lined by synovium: the extensor tendons are also invested in a synovial gliding plane. Biomechanical studies of tendons gliding within their sheaths have emphasized the importance of avoiding extreme postures of a joint, which increase the friction between tendon and pulley, as well as the need to establish a smooth, well-lubricated tendon surface after repair. Increased friction within a tendon sheath may, in part, explain the cause of spontaneous rupture of extensor pollicis longus because the gliding resistance of the tendon has been shown to be significantly higher than that of other tendons (An 2007).

Vascular protection and pumping action

The blood vessels of the palm are surrounded by a cuff of tough fascia or by a fatty pad. When the hand is compressed, as in gripping, these relatively incompressible fascial structures protect the predominantly palmar arterial inflow into the hand to some extent. By contrast, large capacitance veins on the dorsum of the hand lie in gliding skin, surrounded by loose areolar tissue which allows the veins to dilate. However, when the hand grips firmly, the skin tightens, so expressing the venous blood.

Framework for muscle attachments

The fascial framework can be visualized as a harness by which muscles can act on the underlying skeleton: many of the small muscles of the hand are attached to it, at least in part. The metacarpophalangeal joint is moved by a ring of fascial and ligamentous structures that surrounds the joint and to which tendons are attached.

The cause of Dupuytren's disease remains unknown. Many theories have been postulated. Geographical variations in incidence suggest a genetic cause, but it is not a monoclonal process (Chansky et al 1999) and at least nine genetic loci have been implicated in its development (Dolmans et al 2011). Environmental risk factors include alcohol consumption, smoking, diabetes, manual work and vibration exposure, and possibly the ingestion of anticonvulsants (Descatha et al 2011). In the proliferative stage of the disease, there is considerable myofibroblast activity, which may be the result of upregulation of the musculo-aponeurotic fibrosarcoma oncogene homologue B (*MafB*), found in the diseased cord tissue (Lee et al 2006). Mechanical stimuli subsequently cause the alignment of myofibroblasts along the lines of traction, which are later replaced by collagen. These collagenous cords cause the flexion contractures that characterize the disease. Treatment of Dupuytren's disease includes suppressing myofibroblast turnover with radiotherapy; dividing the cord (fasciotomy) with a percutaneous needle or an enzyme (collagenase); surgically removing the cord (fasciectomy), which can include removal of the overlying involved skin (dermofasciectomy), and replacement with disease-free skin from elsewhere (skin autograft) .

The pattern of contracture is determined by the anatomy of the basic constituents of the palmar and digital fasciae. The physiological 'bands' formed by the healthy palmar fascia are replaced by pathological 'cords' of diseased tissue. The pretendinous bands that constitute the superficial layer (layer 1) of the palmar aponeurosis are most frequently involved. The development of nodules that tether the skin to the deep fascia usually precedes cord formation. Contracture of the pretendinous cords causes flexion of the metacarpophalangeal joints. Shortening of the vertical fibres causes skin pits. Involvement of the natatory ligament restricts abduction of the fingers. The transverse metacarpal fibres are never contracted and are a useful surgical landmark in the palm because the neurovascular bundle runs deep to them. The vertical fibres can become very thickened but do not contract: they form a dense barrier between the flexor tendons and the neurovascular bundle.

The pretendinous cord in the palm extends into a finger as a central cord that lies superficially in the midline. The lateral digital sheet gives rise to a lateral cord that is attached to the skin or flexor tendon sheath near Grayson's ligament, causing a flexion contracture of the proximal interphalangeal joint and, sometimes, displacing the digital neurovascular bundle medially. Spiral cords arise from the pretendinous band in layer 1 of the palmar fascia and pass deeper through layer 2 to become attached to the middle phalanx by Grayson's ligament. They are so named because they spiral round the neurovascular bundle, displacing it proximally, palmarwards and towards the midline as contracture increases, rendering it vulnerable to injury during fasciectomy (McFarlane 1974).

The ulnar side of the little finger often develops a dense cord (Barton's 'abductor cord') that runs from the medial edge of the insertion of abductor digiti minimi, through the lateral digital sheet and onto the anteromedial surface of the flexor sheath at the level of the A3 pulley. This causes a pronounced flexion contracture of the proximal interphalangeal joint and must be fully removed to achieve a successful and durable correction.

The distal interphalangeal joint is uncommonly involved because the palmar aponeurosis usually peters out beyond the sides of the middle phalanx. Nevertheless, a thin tight cord on one or other side of the digit can occur, causing a combined contracture of the proximal and distal interphalangeal joints. Distal interphalangeal joint hyperextension can occur in association with a severe prolonged contracture of the proximal interphalangeal joint, with secondary attrition of the central slip, soft tissue contractures and boutonnière deformity. Some authors have suggested that this deformity occurs because Dupuytren's disease affects the oblique retinacular ligament (Littler 1967).

The spaces of the hand form predictable sites of infection and also limit its spread. Infections in the digit can occur in the nail fold (paronychia); the distal pulp (a felon); and the flexor sheaths. The flexor synovial sheath of the thumb and the little finger often connect in the palm (see Fig. 51.27C) such that an infection in one can spread to the other causing a 'horseshoe abscess'. Deep infections in the palm are not usually confined to any particular space; the infection may be inoculated by direct penetration but more often occurs from a primary infection in the web space or flexor sheath.

An abscess in any of the digital or palmar spaces should always be drained. An understanding of the anatomy is crucial to successful surgical treatment. Incisions should, wherever possible, follow the line of the flexion creases and adhere to the principles of extensile exposure. A felon is drained with a midlateral incision or midline incision avoiding the neurovascular bundle and spreading apart the taut vertical septa. A web space infection is drained with a longitudinal incision that allows extensile exposure of the web space and the lumbrical-interosseous canals, also avoiding a web contracture that would follow a transverse incision. A thenar space abscess is drained through a palmar incision: the motor and palmar cutaneous branches of the median nerve are very vulnerable to iatrogenic damage (Birch 2011). The mid-palmar space is best approached through a combination of a transverse distal palmar incision with an oblique longitudinal extension (McDonald et al 2011), although alternative incisions can be employed, based on the location and size of the collection. Hypothenar space infections are very rare and tend to be confined by the hypothenar fascia, resulting in swelling of the ulnar side of the hand with some flexion and adduction of the little finger. These lesions are of less clinical consequence than other palmar collections because there is no direct communication with the two other major palmar spaces and hence the long flexors of the fingers and lumbricals are not involved. They may be drained by an incision along the ulnar border of the space without significant risk of damage to underlying structures. The flexor sheath is drained by a transverse or oblique incision over the flexion crease of the distal interphalangeal joint and another over the distal palmar (metacarpophalangeal) joint crease.

There are 10 identifiable muscle compartments in the hand: four contain each of the dorsal interossei; three contain the palmar interossei; three contain the thenar, hypothenar and adductor compartments. Any or all of these compartments may be injured by a rise in intracompartmental pressure caused by bleeding, blast, burn, crush, ischaemia–reperfusion and by injection, whether of therapeutic substances at low pressure or of industrial agents at high pressure. This rise in pressure prevents venous inflow then capillary (low pressure) inflow. Arterial (high pressure) inflow persists which causes yet more congestion; this compounds the rise in compartment pressure and the condition deteriorates. The tissues then become ischaemic, causing transient impairment then permanent necrosis. The hand will be extremely painful, usually with tingling and weakness due to nerve ischaemia. It becomes increasingly swollen. On examination, the tissues are tense; passive movement of the fingers is very painful due to stretching of the ischaemic muscles. There will be reduced sensitivity in the territory of the nerves passing through the compartment. Intra-compartmental pressure measurements should be taken; the means by which this is done is not critical (Ortiz and Berger 1998) but it should not delay emergency surgery if the diagnosis is reasonably suspected.

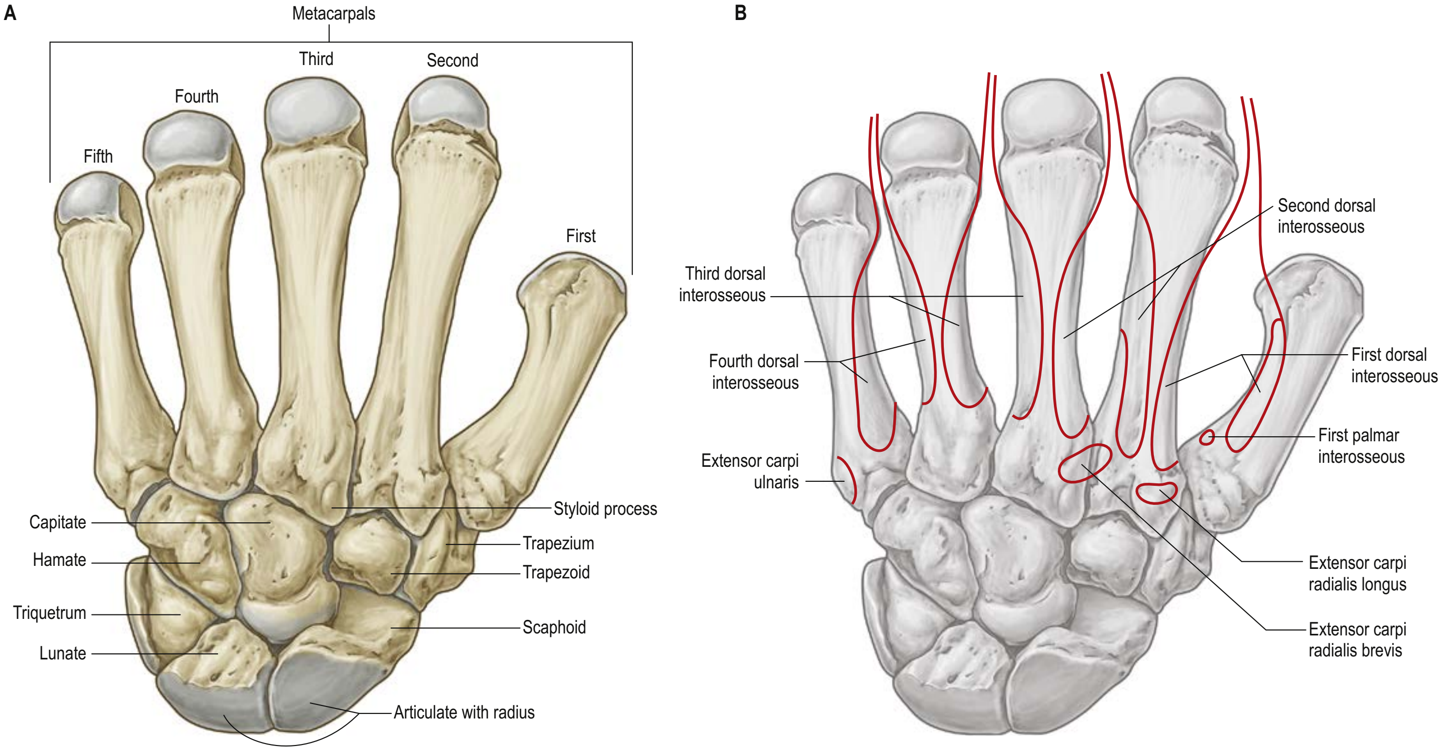
A
Metacarpals
Fifth
Fourth
Third
Second
First
Capitate
Hamate
Triquetrum
Lunate
Styloid process
Trapezium
Trapezoid
Scaphoid
Articulate with radius
B
Third dorsal interosseous
Fourth dorsal interosseous
Extensor carpi ulnaris
Second dorsal interosseous
First dorsal interosseous
First palmar interosseous
Extensor carpi radialis longus
Extensor carpi radialis brevis

Fig. 51.14 **A**, The carpals and metacarpals of the left hand: dorsal aspect. **B**, Sites of muscle attachments.

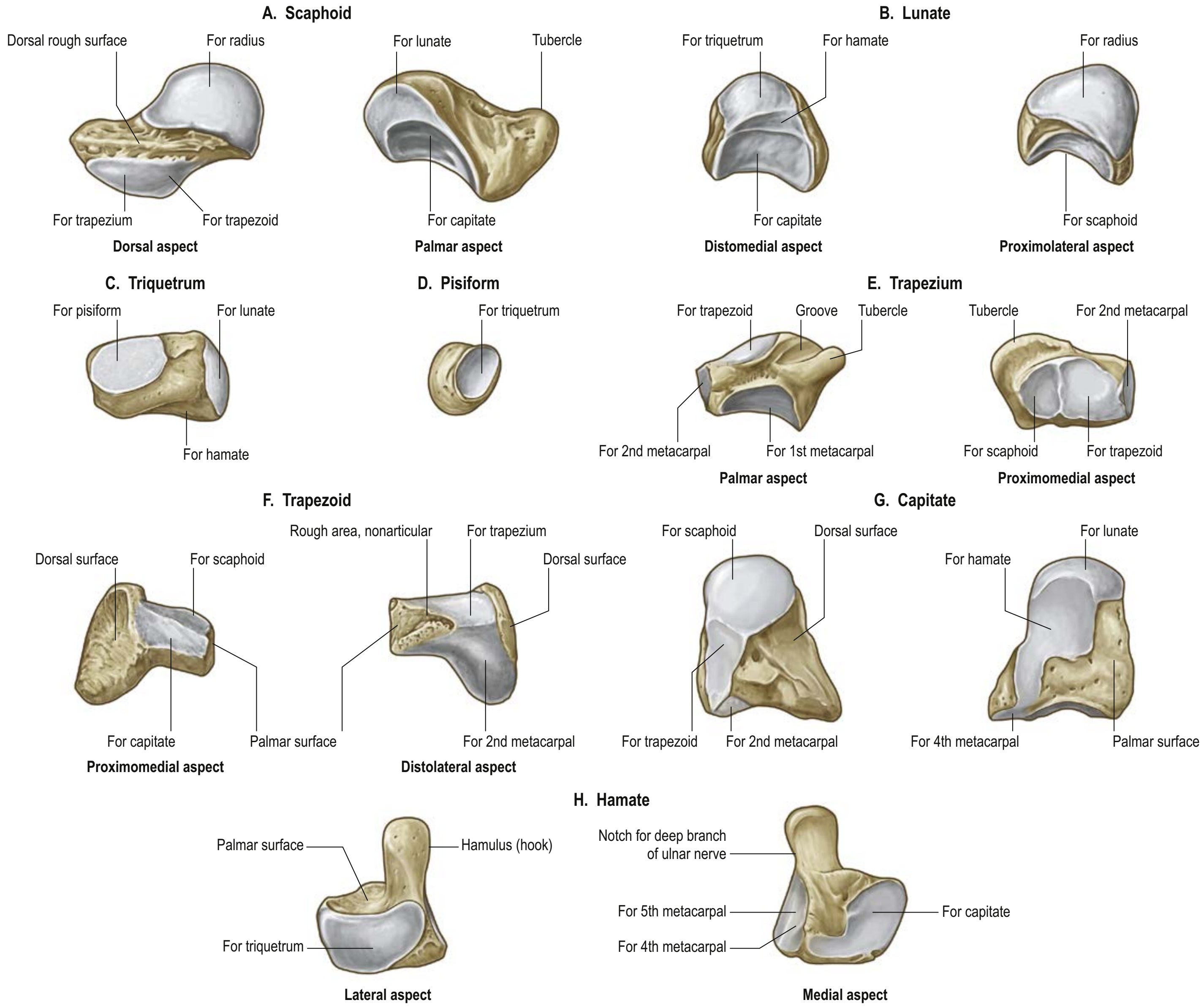
A. Scaphoid
Dorsal rough surface
For radius
For trapezium
For trapezoid
Dorsal aspect
For lunate
Tubercle
For capitate
Palmar aspect
B. Lunate
For triquetrum
For hamate
For capitate
Distomedial aspect
For radius
For scaphoid
Proximolateral aspect
C. Triquetrum
For pisiform
For lunate
For hamate
D. Pisiform
For triquetrum
E. Trapezium
For trapezoid
Groove
Tubercle
For 2nd metacarpal
For 1st metacarpal
Palmar aspect
Tubercle
For 2nd metacarpal
For scaphoid
For trapezoid
Proximomedial aspect
F. Trapezoid
Dorsal surface
For scaphoid
For capitate
Palmar surface
Proximomedial aspect
Rough area, nonarticular
For trapezium
Dorsal surface
For 2nd metacarpal
Distolateral aspect
G. Capitate
For scaphoid
Dorsal surface
For trapezoid
For 2nd metacarpal
For hamate
For lunate
For 4th metacarpal
Palmar surface
H. Hamate
Palmar surface
Hamulus (hook)
For triquetrum
Lateral aspect
Notch for deep branch of ulnar nerve
For 5th metacarpal
For 4th metacarpal
For capitate
Medial aspect

Fig. 51.15 Disarticulated carpal bones.

direction. A round tubercle on the distolateral part of its palmar surface is directed anterolaterally, and provides an attachment for the flexor retinaculum and abductor pollicis brevis; it is crossed by the tendon of flexor carpi radialis. The rough dorsal surface is slightly grooved, narrower than the palmar, and pierced by small nutrient foramina, which are often restricted to the distal half. The radial collateral ligament is attached to the lateral surface, which is also narrow and rough. The remaining 42% of the surfaces are all articular. The radial (proximal) surface is convex, proximal and directed proximolaterally; the lunate surface is flat and semilunar, and faces medially; the capitate surface is large, concave, distal and directed distomedially. The surface for the trapezium and trapezoid is continuous, convex and distal.

The blood supply of the scaphoid is derived from two sources (Gelberman and Menon 1980). Its dorsal ridge is penetrated by the dorsal scaphoid artery and by branches of the styloid artery. Its distal pole receives vessels from the palmar carpal artery or, in its absence, from branches of the superficial palmar artery (Oehmke et al 2009) or the first dorsal metacarpal artery. Variation in this pattern is not uncommon. The proximal pole is circumferentially devoid of periosteum and therefore has no arterial supply: it relies on intraosseous flow from the dorsal and distal supply, which is disrupted in a fracture through the waist of the scaphoid.

Scaphoid bone fractures

Available with the *Gray's Anatomy* e-book

Lunate

The lunate is approximately semilunar and articulates between the scaphoid and triquetrum in the proximal carpal row (see Fig. 51.15B). Its rough palmar surface, almost triangular, is larger and wider than the rough dorsal surface. Its smooth convex proximal surface articulates with the radius and the articular disc of the distal radio-ulnar joint. Its narrow lateral surface bears a flat semilunar facet for the scaphoid. The medial surface, which is almost square, articulates with the triquetrum and is separated from the distal surface by a curved ridge, usually somewhat concave for articulation with the edge of the hamate in adduction. The distal surface is deeply concave to fit the medial part of the head of the capitate. Its articulation with the hamate varies: in the type 1 lunate (35–55%) there is no articulation with the hamate, whereas in the type II lunate (45–65%), the medial facet articulates with the hamate (Viegas 1990). The blood supply relies on variable palmar (volar) and dorsal arteries that may or may not anastomose within the bone.

Kienböck's disease

Available with the *Gray's Anatomy* e-book

Triquetrum

The triquetrum is somewhat pyramidal. Its distal palmar surface bears an oval isolated facet for articulation with the pisiform. Its medial and dorsal surfaces are confluent (see Fig. 51.15C). The dorsal surface is marked by the strong ligamentous attachments of the ulnocarpal, dorsal intercarpal and radiolunate ligaments and is marked distally by the attachment of the ulnar collateral ligament, but is smooth proximally to match the articular disc of the triangular fibrocartilage complex. The lateral and distal, hamate, surface is concavo-convex, broad proximally and narrow distally. The lateral and proximal, lunate, surface is almost square.

Pisiform

The pisiform is a sesamoid bone within the tendon of flexor carpi ulnaris that increases the flexion torque applied by the muscle. It is shaped like a pea, with a distolateral long axis (see Fig. 51.15D). It bears a dorsal flat articular facet for the triquetrum. The tendon of flexor carpi ulnaris and its distal continuations, the pisometacarpal and pisohamate ligaments, are all attached to the palmar non-articular area. The deep motor branch of the ulnar nerve runs on its radial side.

Trapezium

The trapezium has a tubercle and groove on its rough palmar surface (see Fig. 51.15E). The tendon of flexor carpi radialis passes dorsomedial to the tubercle which acts as a pulley to prevent flexor carpi radialis from bowstringing palmarwards on flexion. Two layers of the flexor retinaculum are attached to its margins. The tubercle is obscured by the thenar muscles attached to it (opponens pollicis, flexor pollicis brevis and abductor pollicis brevis) (see Fig. 51.13B). The elongated, rough dorsal surface is related to the radial artery. The large lateral surface is rough for attachment of the radial collateral ligament and capsular ligament of the carpometacarpal joint of the thumb. A large sellar surface faces distolaterally and articulates with the base of the first metacarpal. Most distally, it projects between the bases of the first and second metacarpals and carries a small, quadrilateral, distomedially directed facet that articulates with the base of the second metacarpal. The large medial surface is gently concave for articulation with the trapezoid. The proximal surface is a small, slightly concave facet for articulation with the scaphoid. Its ridge, or 'summit', fits the concavity of the base of the first metacarpal, and extends in a palmar and lateral direction, at an angle of approximately 60° with the plane of the second and third metacarpals. Abduction and adduction occur in the plane of the ridge, which is shorter than the corresponding metacarpal groove. Their contours vary reciprocally: they are more curved near the base of the second metacarpal, whereas the radius of curvature is longer further away from this site. The two surfaces are not completely congruent, and the area of close contact probably moves towards the palm in adduction and dorsally in abduction. While the axis of flexion/extension passes through the trapezium, the axis for adduction/abduction is in the metacarpal base. Flexion is accompanied by medial rotation, and extension by lateral rotation.

Trapezoid

The trapezoid is small and irregular. It has a rough palmar surface that is narrower and smaller than its rough dorsal surface (see Fig. 51.15F). The distal surface, which articulates with the grooved base of the second metacarpal, is triangular, convex transversely and concave at right-angles to this. The medial surface articulates by a concave facet with the distal part of the capitate, the lateral surface articulates with the trapezium, and the proximal surface articulates with the scaphoid.

Capitate

The capitate is the central and largest carpal bone. It articulates with the base of the third metacarpal via its triangular distal concavo-convex surface (see Fig. 51.15G). Its lateral border is a concave strip for articulation with the medial side of the base of the second metacarpal. Its dorsomedial angle usually bears a facet for articulation with the base of the fourth metacarpal. The head projects into the concavity formed by the lunate and scaphoid, the proximal surface articulates with the lunate, and the lateral surface with the scaphoid. The facets for the scaphoid and trapezoid, though usually continuous on the distolateral surface, may be separated by a rough interval. The medial surface bears a large facet for articulation with the hamate, which is deeper proximally where it is partly non-articular. Palmar and dorsal surfaces are roughened for carpal ligaments, the dorsal being the larger.

Hamate

The hamate is cuneiform and bears an unciform hamulus (hook) that projects from the distal part of its rough palmar surface (see Fig. 51.15H). The hamulus is curved with a lateral concavity and its tip inclines laterally, contributing to the medial wall of the carpal tunnel. The tendon of flexor digitorum profundus to the little finger passes directly radial to the hamulus which acts as a pulley because the origin of this tendon is more radial than its insertion. The flexor retinaculum is attached to the apex of the hamulus. Distally, on the base of the hamulus, a slight transverse groove may be in contact with the terminal deep branch of the ulnar nerve. The remaining palmar surface, like the dorsal, is roughened for the attachment of ligaments. A faint ridge divides the distal surface into a smaller lateral facet that articulates with the base of the fourth metacarpal, and a medial facet for articulation with the base of the fifth. The proximal surface, the thin margin of the wedge, sometimes bears a narrow facet that contacts a reciprocal facet on the lunate. The medial surface is a broad strip, convex proximally, concave distally, that articulates with the triquetrum; distally, a narrow medial strip is non-articular. The lateral surface articulates with the capitate by a facet covering all but its distal palmar angle.

Ossification

Each carpal bone is ossified from one centre (**Fig. 51.16A–D**). Most are cartilaginous at birth, although ossification may have started in the capitate and hamate. The triquetrum begins to ossify in the third year and the lunate, scaphoid, trapezium and trapezoid begin to ossify in either the fourth year (females) or the fifth year (males). The pisiform begins to ossify in the ninth or tenth year (females) and in the twelfth year (males). The order varies according to sex, nutrition and, possibly, race. Occasionally, an os centrale occurs between the scaphoid, trapezoid and capitate bones and usually fuses with the scaphoid. Lunate and triquetral elements may occasionally fuse. Other fusions and accessory ossicles have also been described (Vaz and Trippia 2018).

Metacarpus

The metacarpus consists of five metacarpals, conventionally numbered in radio-ulnar order. These are small long bones, with a distal head, shaft and expanded base. The rounded heads articulate with the proximal phalanges. The articular surfaces of the head are convex, although less so transversely, and extend further on the palmar surfaces, especially at their margins. From a distal perspective the metacarpal head has a trapezoidal shape and is broader on its palmar aspect than its dorsal. The knuckles are produced by the metacarpal heads. The metacarpal bases articulate with the distal carpal row and with each other. The shafts have longitudinally concave palmar surfaces, which form hollows for the palmar muscles. Their dorsal surfaces bear a distal triangular area, which is continued proximally as a round ridge. These surfaces are palpable proximal to the knuckles.

The medial four metacarpals gently diverge proximodistally. The first metacarpal is more anterior and rotated medially on its axis through 90°, so that its morphologically dorsal surface is lateral, its radial border palmar, its palmar surface medial, and its ulnar border dorsal. Hence, the thumb flexes medially across the palm and can be rotated into opposition with each finger. Opposition is important in manual dexterity and depends on pronation of the thumb carpometacarpal joint and flexion-supination of the little finger carpometacarpal joint. When an object is grasped, the fingers and thumb encircle it from opposite sides, greatly increasing the power and precision of the grip.

Individual metacarpals

First metacarpal

The first metacarpal is shorter and thicker than the other metacarpals (Fig. 51.17A). Its dorsal (lateral) surface can be felt to face laterally; its long axis diverges distolaterally from its neighbour. The shaft is flattened, dorsally broad and transversely convex. The palmar (medial) surface is longitudinally concave and divided by a ridge into a larger lateral (anterior) and smaller medial (posterior) part. Opponens pollicis is attached to the radial border and adjoining palmar surface: the first dorsal interosseous muscle (radial head) is attached to its ulnar border and adjacent palmar surface. The base is concavo-convex and articulates with the trapezium. Abductor pollicis longus is attached on its lateral (palmar) side, the first palmar interosseous muscle to its ulnar side. The head is less convex than in other metacarpals and is transversely broad. Sesamoid bones glide on radial and ulnar articular eminences on its palmar aspect.

Second metacarpal

The second metacarpal has the longest shaft and largest base (Fig. 51.17B). The latter is grooved in a dorsopalmar direction for articulation with the trapezoid. Medial to the groove, a deep ridge articulates with the capitate; laterally, nearer the dorsal surface of the base, there is a quadrilateral facet for articulation with the trapezium, and just dorsal to this facet, a rough impression marks the attachment of extensor carpi radialis longus. On the palmar surface, a small tubercle or ridge receives flexor carpi radialis. The medial side of the base articulates with that of the third metacarpal by a long facet, centrally narrowed. The shaft is prismatic in section and longitudinally curved, convex dorsally, concave towards the palm. Its dorsal surface is distally broad but proximally narrows to a ridge that is covered by extensor tendons of the index finger. Its converging borders begin at the tubercles, one on each side of its head for the attachment of collateral ligaments. Proximally, the lateral surface inclines dorsally for the ulnar head of the first dorsal interosseous. The medial surface inclines similarly, and is divided by a faint ridge into a palmar strip for attachment of the second palmar interosseous, and a dorsal strip for attachment of the radial head of the second dorsal interosseous.

Third metacarpal

The third metacarpal has a short styloid process which projects proximally from the radial side of the dorsal surface (Fig. 51.17C). Its base articulates with the capitate by a facet which is anteriorly convex but dorsally concave where it invades the styloid process on the lateral aspect of its base. A strip-like facet, constricted centrally, articulates with the bases of the second metacarpal (laterally) and the fourth metacarpal (medially), the latter by two oval facets. The palmar facet may be absent: less frequently, the facets are connected proximally by a narrow bridge. The palmar surface of the base receives a slip from the tendon of flexor carpi radialis: extensor carpi radialis brevis is attached to its dorsal surface, beyond the styloid process. The shaft resembles that of the second metacarpal. The ulnar head of the second dorsal interosseous muscle is attached to its lateral surface; the radial head of the third dorsal interosseous is attached to its medial surface, and the transverse head of adductor pollicis to the intervening palmar ridge in its distal two-thirds. Its dorsal surface is covered by the extensor tendon.

Fourth metacarpal

The fourth metacarpal is shorter and thinner than the second and third (Fig. 51.17D). On its base, it displays two lateral oval facets for articulation with the base of the third metacarpal; the dorsal is usually larger and proximally in contact with the capitate. A single medial elongated facet is for articulation with the base of the fifth metacarpal. The quadrangular proximal surface articulates with the hamate; it is anteriorly convex and dorsally concave. The shaft is like the second, but a faint ridge on its lateral surface separates the attachments of the third palmar interosseous and the ulnar head of the third dorsal interosseous. The radial head of the fourth dorsal interosseous is attached to the medial surface.

Fifth metacarpal

The fifth metacarpal (Fig. 51.17E) differs in its medial basal surface, which is non-articular and bears a tubercle for extensor carpi ulnaris. The lateral basal surface is a facet, transversely concave, convex from palm to dorsum, for articulation with the hamate. A lateral strip articulates with the base of the fourth metacarpal. The shaft bears a triangular dorsal area that almost reaches the base; the lateral surface inclines dorsally only at its proximal end. Opponens digiti minimi is attached to the medial surface. The lateral surface is divided by a ridge, which is sometimes sharp, into a palmar strip for the attachment of the fourth palmar interosseous and a dorsal strip for the ulnar part of the fourth dorsal interosseous.

Ossification

Each metacarpal ossifies from a primary centre for the shaft and a secondary centre that is in the base of the first metacarpal and in the heads of the other four (Fig. 51.18).

Ossification begins in the midshaft about postmenstrual week 11. Centres for the second to fifth metacarpal heads appear in that order in the second year in females, and between 1½ to 2½ years in males. They unite with the shafts about the fifteenth or sixteenth year in females, and the eighteenth or nineteenth in males. The first metacarpal base begins to ossify late in the second year in females, early in the third year in males, uniting before the fifteenth year in females and seventeenth in males. Sometimes, the styloid process of the third metacarpal is a separate ossicle. The thumb metacarpal ossifies like a phalanx, and some authorities therefore consider that the thumb skeleton consists of three phalanges. Others believe that the distal phalanx represents fused middle and distal phalanges, a condition occasionally observed in the fifth toe. When the thumb has three phalanges, the metacarpal has a distal and a proximal epiphysis. It occasionally bifurcates distally. When it does, the medial branch has no distal epiphysis and bears two phalanges, while the lateral branch shows a distal epiphysis, and three phalanges. The existence of only a distal metacarpal epiphysis may be associated with a greater range of movement at the metacarpophalangeal joint. In the thumb, the carpometacarpal joint has the wider range, and the first metacarpal has a basal epiphysis. A distal epiphysis may appear in the first, and a proximal epiphysis in the second, metacarpal.

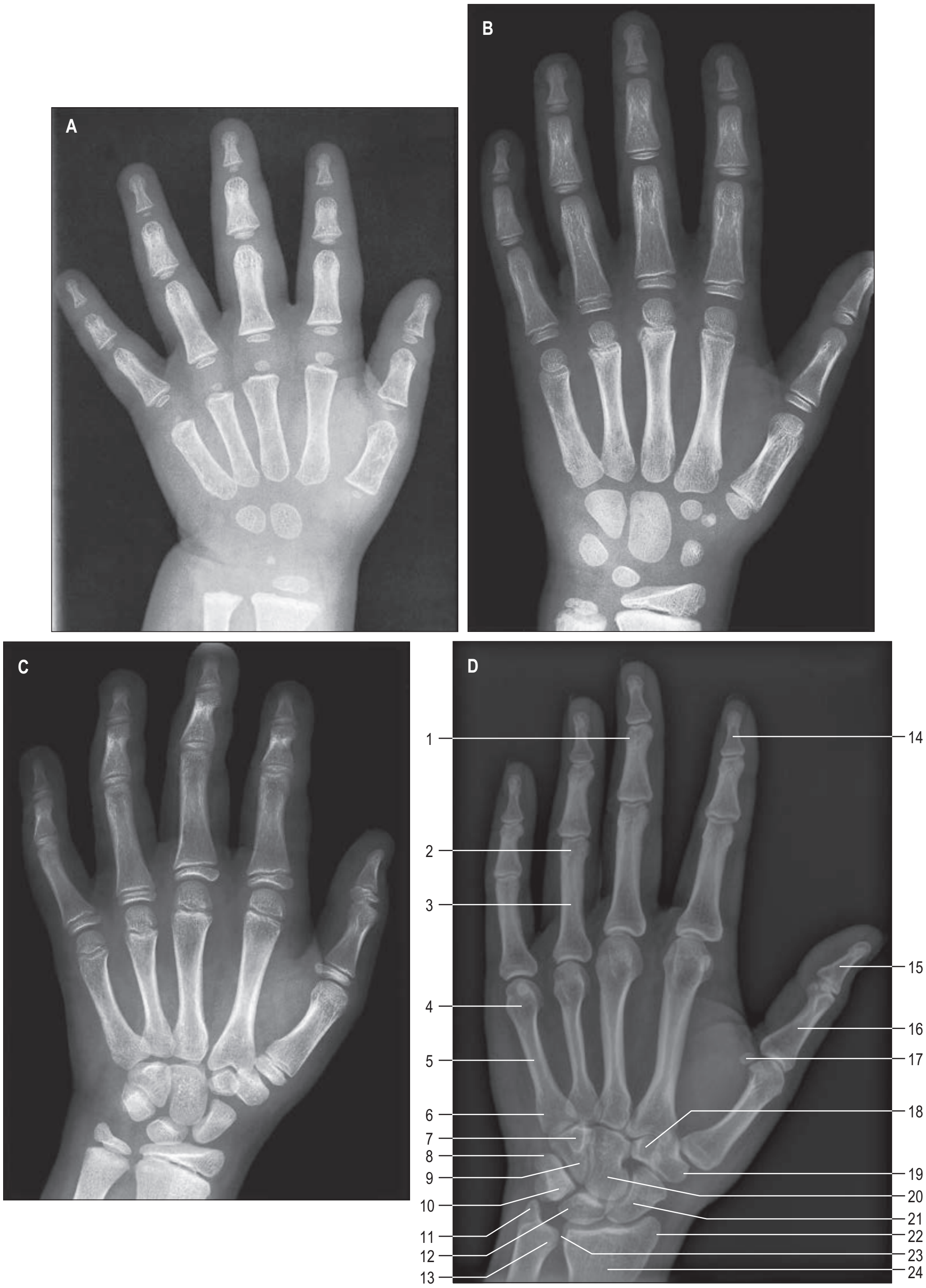

Fig. 51.16 A-D, Radiographs of hands illustrating maturing ossification from infant to adult, dorsopalmar projection. **A,** Male, 2½ years: note the early stages of ossification in the epiphyses at the proximal ends of the phalanges and first metacarpal; the distal ends of the remaining metacarpals and radius; and for the capitate, hamate and lunate. The centre for the lunate is typically preceded by the centre for the triquetrum. **B,** Male, 6½ years: note the more advanced state of the centres of ossification that are already visible in **A,** and the appearance of additional centres in the distal ulnar epiphysis and in the triquetrum, scaphoid, trapezium and trapezoid. **C,** Female, 11 years: compare the maturing ossification with that seen in **A** and **B**. Note the addition of the pisiform. **D,** Adult. Key: 1, head of middle phalanx of middle finger; 2, head of proximal phalanx of ring finger; 3, shaft of proximal phalanx of ring finger; 4, head of fifth metacarpal; 5, shaft of fifth metacarpal; 6, base of fifth metacarpal; 7, hook of hamate; 8, triquetrum; 9, hamate; 10, pisiform; 11, styloid process of ulna; 12, lunate; 13, head of ulna; 14, distal phalanx of index finger; 15, distal phalanx of thumb; 16, proximal phalanx of thumb; 17, sesamoid bone; 18, trapezoid; 19, trapezium; 20, capitate; 21, scaphoid; 22, styloid process of radius; 23, distal radio-ulnar joint; 24, radius.

The scaphoid is the most frequently fractured carpal bone (Kawamura and Chung 2008, Oka and Moritomo 2018), typically as a result of a fall on to the outstretched hand in a young adult male. The fracture most commonly occurs at the waist of the bone, probably because, on impact, the scaphoid folds into flexion over the taut radioscaphocapitate ligament. Distal tubercle fractures occur as a result of avulsions by the attached radial collateral ligament. Proximal fractures are the result of avulsion by the scapholunate ligament. Compson (1998), in a study of the true, rather than the radiological, anatomy of scaphoid fractures, identified three distinct fracture patterns: transverse through the 'surgical waist'; oblique (45° to the surgical waist) in the plane of the dorsal sulcus; and through the proximal pole. A fractured scaphoid is prone to non-union because of its anatomy. Since it is largely covered by articular cartilage, the surface area for arterial inflow is limited. There is no arterial inflow through the scapholunate ligament proximally; the blood supply enters distally, which means that a fracture through the waist or more proximally will cut off the blood supply to the proximal pole. However, it has been argued that an inadequate blood supply is unlikely to be the cause of scaphoid non-union after fracture (Oehmke et al 2009, Sendher and Ladd 2013).

Kienböck's disease, first described in 1910, is avascular necrosis of the lunate. Its aetiology remains unclear but is thought to be associated with an impaired arterial blood supply. Variations in the vascular anatomy may render an individual at increased risk of osteonecrosis. Up to eight small vessels usually enter both the dorsal and the palmar aspects of the bone, three on the dorsal surface and five on the palmar; they divide into smaller branches within the bone. Obstruction of the venous outflow may also lead to osteonecrosis. Extrinsic, nonvascular aetiological factors include trauma, steroid use and mechanical factors such as negative ulnar variance or variations in carpal osseous morphology that affect loading of the lunate.

While patients generally present with pain and stiffness of the wrist, these symptoms correlate poorly with the radiological findings and, indeed, patients may be asymptomatic. The natural history of the disease is variable; some progress and others do not. In the earliest stage, radiographs are normal and only an MRI can detect the disease. In later stages, the lunate becomes sclerotic and then collapses, the relative height of the lunate to the capitate diminishing from the usual ratio of 0.54. (For further reading, see Cross and Matullo (2014).)

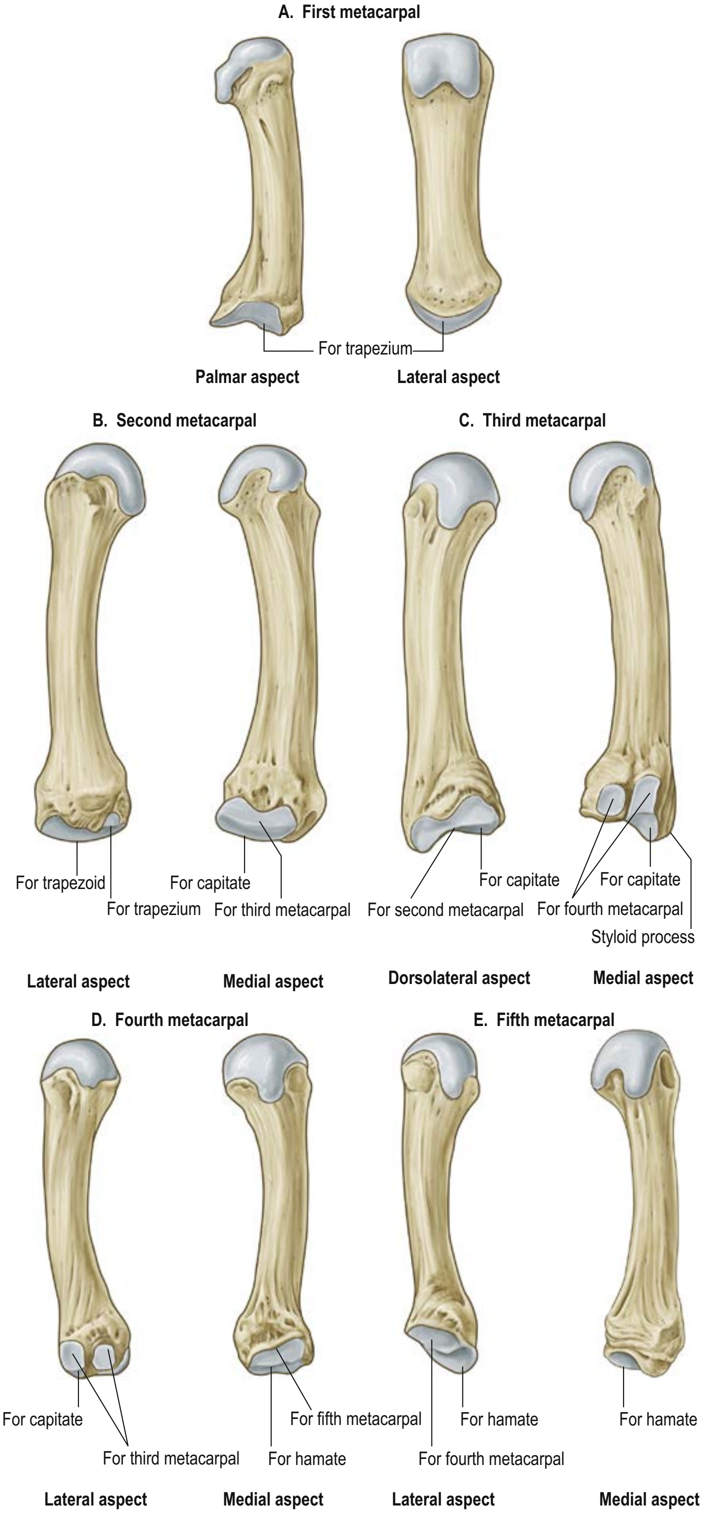
A. First metacarpal
For trapezium
Palmar aspect
Lateral aspect
B. Second metacarpal
C. Third metacarpal
For trapezoid
For capitate
For trapezium
For third metacarpal
For second metacarpal
For capitate
For capitate
For fourth metacarpal
Styloid process
Lateral aspect
Medial aspect
Dorsolateral aspect
Medial aspect
D. Fourth metacarpal
E. Fifth metacarpal
For capitate
For third metacarpal
For fifth metacarpal
For hamate
For hamate
For fourth metacarpal
For hamate
Lateral aspect
Medial aspect
Lateral aspect
Medial aspect

Fig. 51.17 Disarticulated metacarpal bones.

Phalanges

There are 14 phalanges, three in each finger and two in the thumb (see Fig. 51.18). Each has a head, shaft and proximal base. The shaft tapers distally, its dorsal surface transversely convex. The palmar surface is transversely flat but gently concave anteriorly in its long axis. The bases of the proximal phalanges carry concave, oval facets adapted to the metacarpal heads. Their own heads have a midline dorsal–palmar groove and encroach more on to the palmar surfaces. The bases of the middle phalanges carry two concave facets separated by a smooth ridge, conforming to the heads of the proximal phalanges and a dorsal lip to receive the central slip of the extensor tendon. The bases of the distal phalanges are adapted to the shallow midline groove of the middle phalangeal heads. A dorsal lip receives the conjoined extensor tendon and a palmar lip receives the flexor digitorum profundus tendon. The heads of the distal phalanges are non-articular and carry a rough, crescentic palmar tuberosity, to which the pulps of the fingertips are attached. The flatter dorsal surface is roughened to attach the nail matrix.

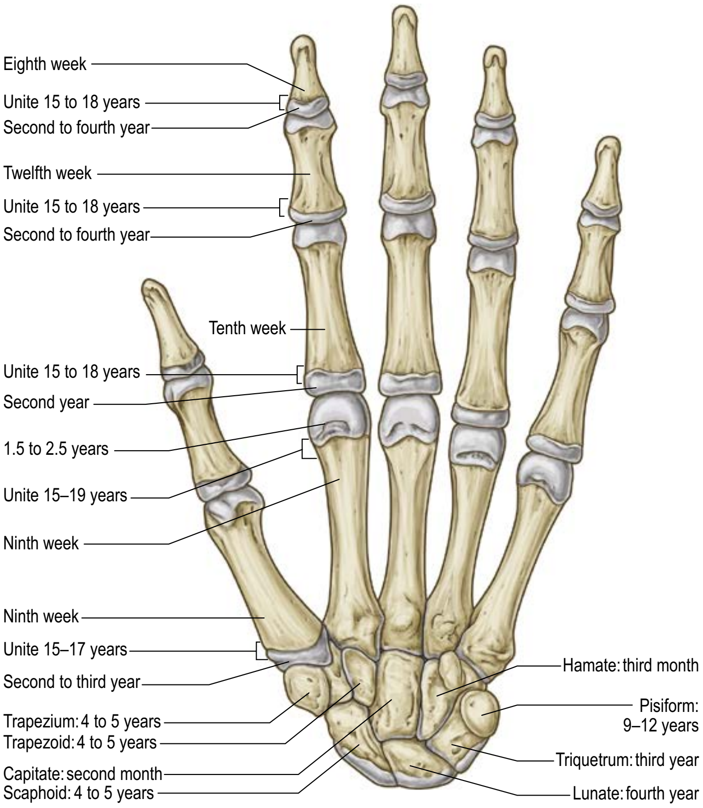
Eighth week
Unite 15 to 18 years
Second to fourth year
Twelfth week
Unite 15 to 18 years
Second to fourth year
Tenth week
Unite 15 to 18 years
Second year
1.5 to 2.5 years
Unite 15–19 years
Ninth week
Ninth week
Unite 15–17 years
Second to third year
Trapezium: 4 to 5 years
Trapezoid: 4 to 5 years
Capitate: second month
Scaphoid: 4 to 5 years
Hamate: third month
Pisiform: 9–12 years
Triquetrum: third year
Lunate: fourth year

Fig. 51.18 The approximate dates of ossification of the individual bones of the hand and their epiphyses.

Articular ligaments and numerous muscles are attached to the phalanges. The tendon of flexor digitorum profundus is attached to the palmar aspect of the base of the distal phalanx and the tendon of extensor digitorum to its dorsal surface. The tendon of flexor digitorum superficialis is attached to the anterolateral surface of the middle phalanx, and the central slip of the extensor mechanism into the base dorsally. The fibrous flexor sheath is attached to the sides of the proximal and middle phalanx. The dorsal interosseous is attached to the base of the proximal phalanx laterally or medially.

The phalanges of the little finger and the thumb differ. Abductor digiti minimi and flexor digiti minimi are attached to the medial side of the base of the proximal phalanx of the little finger. The tendon of extensor pollicis brevis is attached to the dorsolateral corner of the base of the proximal phalanx. The oblique and transverse heads of adductor pollicis, sometimes conjoined with the first palmar interosseous (medially), are attached to the anteromedial corner of the base of the proximal phalanx of the thumb.

Ossification

Phalanges are ossified from a primary centre for the shaft and a proximal epiphysial centre (see Fig. 51.18). Ossification begins prenatally in the shafts as follows: distal phalanges after postmenstrual week 10, proximal phalanges after postmenstrual weeks 11–12 and middle phalanges after postmenstrual week 14. Epiphysial centres appear in proximal phalanges early in the second year (females), or later in the same year (males), and in middle and distal phalanges in the second year (females), or third or fourth year (males). All epiphyses unite about the fifteenth to sixteenth year (females), and seventeenth to eighteenth year (males).

JOINTS

Radiocarpal joint

Articulating surfaces The radiocarpal joint is a synovial, biaxial and ellipsoid joint formed by articulation of the distal end of the radius and the articular disc of the triangular fibrocartilage (which overlies the ulnar head) with the scaphoid, lunate, triquetrum and their interposed ligaments (Figs 51.19–51.20). In the neutral position of the wrist, only the scaphoid and lunate are in contact with the radius and articular disc; the triquetrum comes into apposition with the disc only in full adduction of the wrist joint. The radial articular surface and distal discal surface form an almost elliptical, concave surface with a transverse long axis. The radial surface is bisected by an anteroposterior low ridge into two concavities to receive the reciprocal convex surface

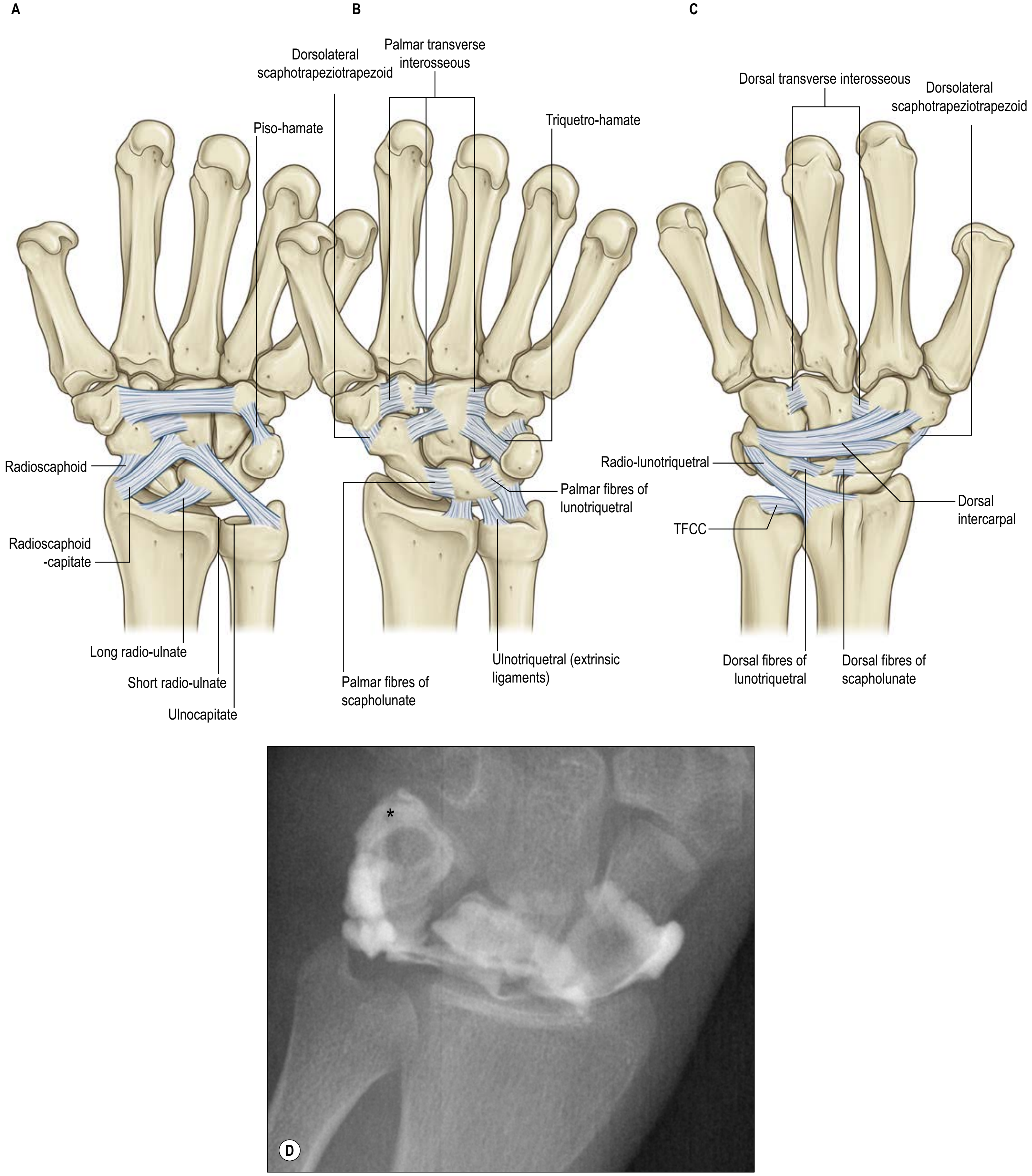
A
B
C
Dorsolateral scaphotrapeziotrapezoid
Palmar transverse interosseous
Piso-hamate
Triquetro-hamate
Dorsal transverse interosseous
Dorsolateral scaphotrapeziotrapezoid
Radioscaphoid
Radioscaphoid -capitate
Long radio-ulnate
Short radio-ulnate
Ulnocapitate
Palmar fibres of lunotriquetral
Palmar fibres of scapholunate
Ulnotriquetral (extrinsic ligaments)
Radio-lunotriquetral
TFCC
Dorsal intercarpal
Dorsal fibres of lunotriquetral
Dorsal fibres of scapholunate
*
D

Fig. 51.19 The joints and ligaments of the left wrist. **A**, Palmar aspect: extrinsic ligaments. **B**, Palmar aspect: intrinsic ligaments. **C**, Dorsal aspect. Key: TFCC, triangular fibrocartilage complex. **D**, A fluoroscopic arthrogram of the radiocarpal joint. Contrast medium (white) has been injected into the joint space from the dorsal aspect and has remained within the radiocarpal joint, indicating that the scapholunate ligament, lunotriquetral ligament, and triangular fibrocartilage disc are intact. Some normal extension is seen into the pisotriquetral recess at the ulnar aspect of the joint (*).

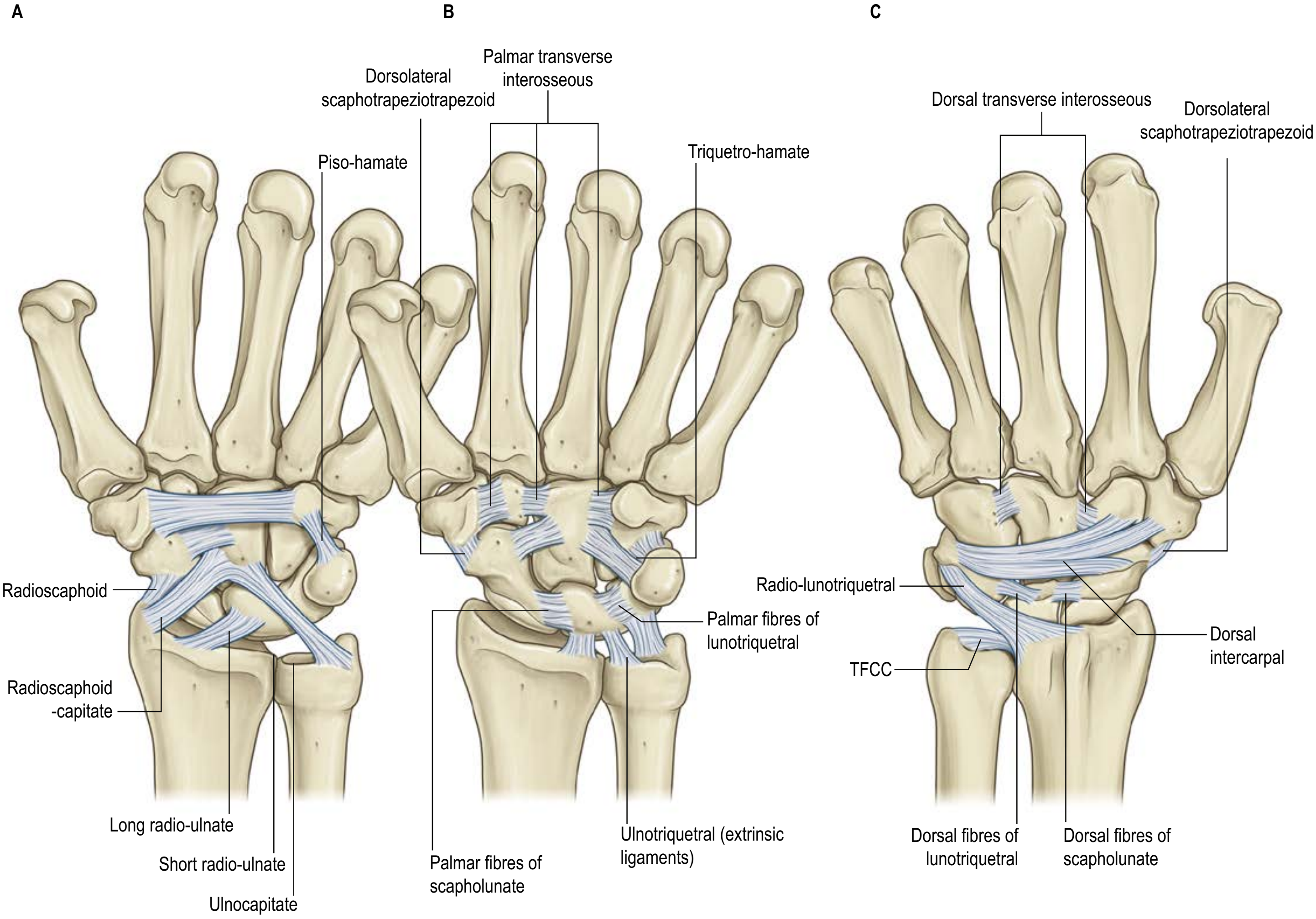
A
B
C
Palmar transverse interosseous
Dorsolateral scaphotrapeziotrapezoid
Piso-hamate
Triquetro-hamate
Dorsal transverse interosseous
Dorsolateral scaphotrapeziotrapezoid
Radioscaphoid
Radio-lunotriquetral
Palmar fibres of lunotriquetral
Dorsal intercarpal
TFCC
Radioscaphoid -capitate
Long radio-ulnate
Short radio-ulnate
Ulnocapitate
Palmar fibres of scapholunate
Ulnotriquetral (extrinsic ligaments)
Dorsal fibres of lunotriquetral
Dorsal fibres of scapholunate

Fig. 51.19 The joints and ligaments of the left wrist. **A**, Palmar aspect: extrinsic ligaments. **B**, Palmar aspect: intrinsic ligaments. **C**, Dorsal aspect. Key: TFCC, triangular fibrocartilage complex. (D, *continued online*)

of the scaphoid and lunate. The proximal articular surfaces of the scaphoid, lunate and triquetrum and their interosseous ligaments form a smooth convex surface that is received into the proximal concavity.

Fibrous capsule The fibrous capsule is an agglomeration of collagenous tissue which includes several more defined and thus named ligaments (see below). It is lined by a synovial membrane which is usually separate from that of the distal radio-ulnar and intercarpal joints. A prestyloid recess (recessus sacciformis) lies anteroradial to the styloid process of the ulna.

Synovial membrane The synovial membrane lines the fibrous capsule.

Muscles producing movement Movements accompany those of the intercarpal and midcarpal joints, and are described on page 969.

Carpal joints

The intercarpal joints connect the carpal bones. Their articular surfaces are saddle-shaped, flat, ellipsoid or spheroidal. The carpal bones are connected by an extensive array of ligaments, not all of which are specifically named. The flexor retinaculum is an accessory intercarpal ligament which connects the scaphoid and triquetrum to the hamate and pisiform.

Joints of the proximal carpal row

Joints of the proximal carpal row are between the scaphoid, lunate and triquetrum. In addition, the pisiform articulates with the palmar surface of the triquetrum at a small, oval, almost flat, synovial pisotriquetral joint. A thin capsule surrounds the joint. The synovial cavity is usually separate but may communicate with that of the radiocarpal joint.

Joints of the distal carpal row

Joints of the distal carpal row are between the trapezium, trapezoid, capitate and hamate. There is little movement at these joints.

Midcarpal joint

The midcarpal joint, between the scaphoid, lunate and triquetrum (proximally), and trapezium, trapezoid, capitate and hamate (distally), is a compound articulation that may be divided descriptively into medial and lateral parts. Throughout most of the medial compartment, the convexity formed by the head of the capitate and hamate articulates with a reciprocal concavity formed by the scaphoid, lunate and much of the triquetrum. However, most medially, the curvatures are reversed, forming a compound sellar joint. In the lateral compartment, the trapezium and trapezoid articulate with the scaphoid, forming a second planosellar compound articulation.

Carpal synovial membrane The extensive carpal synovial membrane lines an irregular articular cavity. Its proximal part is between the distal surfaces of the scaphoid, lunate and triquetrum, and the proximal surfaces of the distal carpal row. It has three distal prolongations between the four bones of the second row. The prolongation between the trapezium and trapezoid and/or between the trapezoid and capitate is often continuous with corresponding carpometacarpal joints, either from the second to the fifth, or from the second and third only. In the latter case, the joint between the hamate and fourth and fifth metacarpals has a separate synovial membrane. Synovial cavities of carpometacarpal joints are prolonged slightly between the metacarpal bases. The synovial joint between the pisiform and triquetrum is usually isolated.

Wrist ligaments

The distal radio-ulnar joint and triangular fibrocartilage complex are described on page 942.

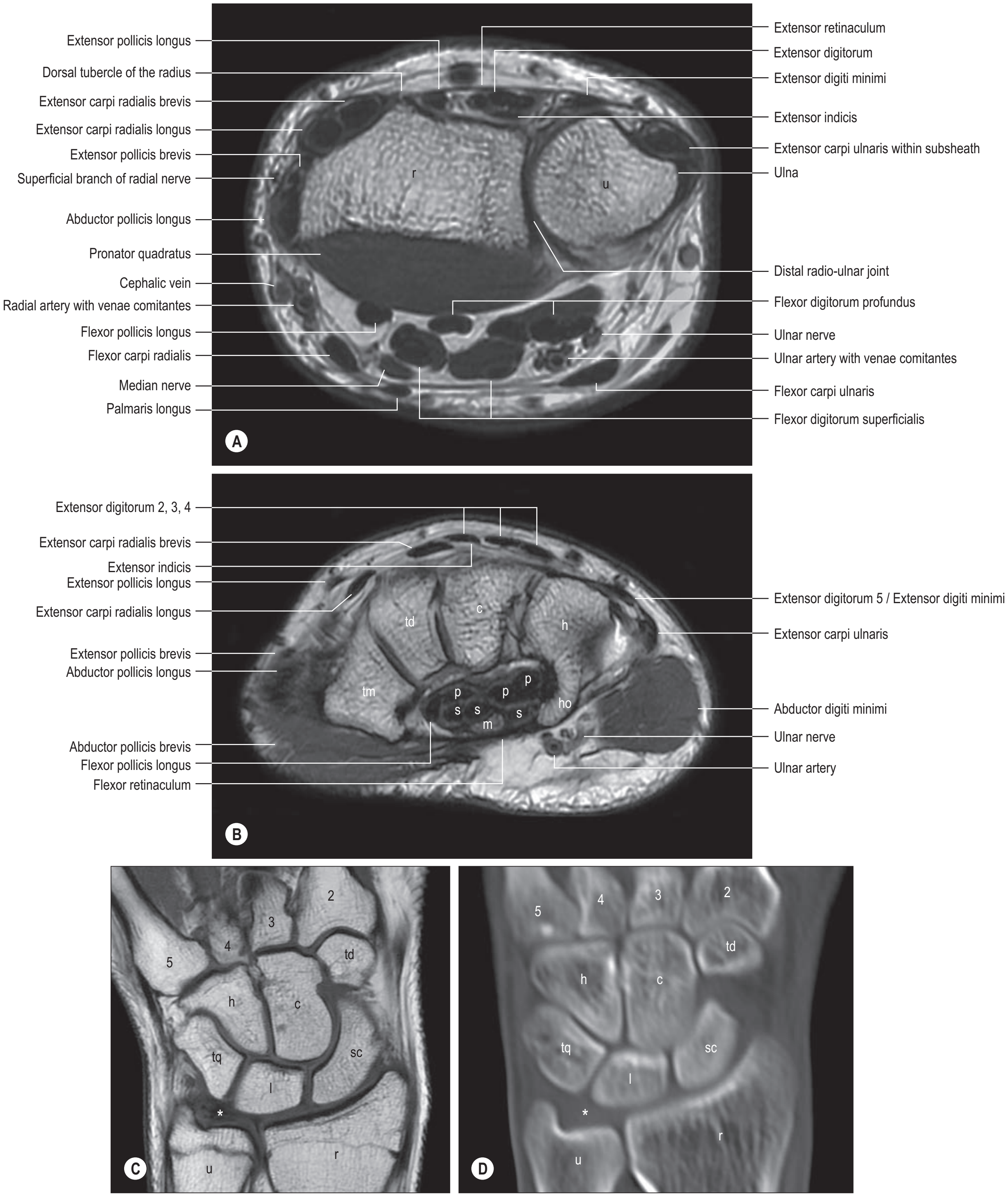
Extensor pollicis longus
Dorsal tubercle of the radius
Extensor carpi radialis brevis
Extensor carpi radialis longus
Extensor pollicis brevis
Superficial branch of radial nerve
Abductor pollicis longus
Pronator quadratus
Cephalic vein
Radial artery with venae comitantes
Flexor pollicis longus
Flexor carpi radialis
Median nerve
Palmaris longus
Extensor retinaculum
Extensor digitorum
Extensor digiti minimi
Extensor indicis
Extensor carpi ulnaris within subsheath
Ulna
Distal radio-ulnar joint
Flexor digitorum profundus
Ulnar nerve
Ulnar artery with venae comitantes
Flexor carpi ulnaris
Flexor digitorum superficialis
r
u
A
Extensor digitorum 2, 3, 4
Extensor carpi radialis brevis
Extensor indicis
Extensor pollicis longus
Extensor carpi radialis longus
Extensor pollicis brevis
Abductor pollicis longus
Abductor pollicis brevis
Flexor pollicis longus
Flexor retinaculum
Extensor digitorum 5 / Extensor digiti minimi
Extensor carpi ulnaris
Abductor digiti minimi
Ulnar nerve
Ulnar artery
td
c
h
tm
p
p
p
s
s
s
m
ho
B
2
3
4
5
td
h
c
tq
sc
l
*
r
u
C
5
4
3
2
td
h
c
tq
sc
l
*
r
u
D

Fig. 51.20 **A**–**B**, Axial T2-weighted MRI images of the prone wrist: **A**, at the level of the distal radio-ulnar joint; **B**, at the distal aspect of the carpal tunnel. **C**, Coronal T1-weighted MRI and **D** mean intensity projection CT slab, through the wrist of two different individuals. Key: r, radius; c, capitate; h, hamate; ho, hook of hamate; m, median nerve; p, flexor digitorum profundus; s, flexor digitorum superficialis; td, trapezoid; tm, trapezium; l, lunate, sc, scaphoid; tq, triquetrum; u, ulna; *, triangular fibrocartilagenous disc. The metacarpal bases are appropriately numbered.

The wrist ligaments can be divided into intra-articular and extra-articular ligaments. The intra-articular ligaments can be further divided into intrinsic and extrinsic ligaments. The *extra-articular* ligaments comprise the flexor retinaculum, extensor retinaculum and the pisohamate ligament. The *intrinsic* ligaments connect the bones within the carpus. The *extrinsic* ligaments are condensations of the joint capsule that connect the carpus to the forearm; they tend to be longer than the intrinsic ligaments and are approximately one-third as strong. The deeper surfaces of some of the extrinsic ligaments and the superficial surfaces of some of the intrinsic ligaments are identifiable at wrist arthroscopy.

Wrist ligaments are conventionally named for the bones to which they attach from proximal to distal and from radial to ulnar, e.g. the radioscaphocapitate ligament passes between the radius, scaphoid and capitate.

Extrinsic ligaments

The extrinsic ligaments are best considered as two distinct groups, palmar extrinsic carpal ligaments and the dorsal extrinsic carpal ligaments. These individual ligaments work together as a ligamentous complex with the intrinsics to stabilize the wrist.

Extrinsic palmar carpal ligaments

There are three palmar extrinsic ligaments which arise from the radius and three from the ulna. From radial to ulnar they are: the radioscaphocapitate (RSC), long radiolunate and short radiolunate (long and short

RL), ulnolunate (UL), ulnocapitate (UC) and ulnotriquetral UT (Berger 1997, Feipel and Rooze 1999).

When the synovial lining of the carpal tunnel is dissected away, two V-shaped ligamentous bands are visible with their apices lying distally (see Fig. 51.19A). This V-shaped ligamentous complex is termed the arcuate ligament. It is formed by the twin insertions of the radioscaphocapitate and ulnocapitate ligaments to the capitate in the distal carpal row.

Radioscaphocapitate ligament The radioscaphocapitate ligament originates from the radial styloid and the palmar lip of the radius, and has three parts. The radial part inserts onto the lateral aspect of the waist of the scaphoid (radioscaphoid ligament). The middle part continues as part of the distal 'V' and inserts onto the distal pole of the scaphoid. The ulnar part passes over the proximal pole of the scaphoid towards the mid-carpus to insert into the capitate, meeting with the fibres that originate from the ulnar side of the triangular fibrocartilage complex (ulnocapitate ligament) to form the arcuate ligament over the palmar aspect of the capitate. There is a discrete interval (the space of Poirier) between the inferior margin of the arcuate ligament and the palmar surface of the lunate. It is through this area of relative weakness that lunate dislocations may occur (Jones and Kakar 2012). The radioscaphocapitate ligament forms a fulcrum over which the scaphoid waist rotates in wrist movement.

Long radiolunate ligament The long radiolunate ligament (long RL) arises adjacent to the radioscaphocapitate ligament on the palmar lip of the radius, passes over and supports the proximal pole of the scaphoid, and inserts into the palmar surface of the lunate. It is discrete from the radioscaphocapitate ligament, from which it is separated by the interligamentous sulcus (see Video 51.1) continuous with the space of Poirier.

The long RL resists distal and ulnar translation of the lunate and is a current area of interest in the study of scapholunate instability.

Ligament of Testut The radioscapholunate ligament is covered by a thick synovial fold that is frequently referred to as the ligament of Testut. It is not a true ligament, more a conduit for nerves and blood vessels. It is a visible landmark during wrist arthroscopy connecting the anterior lip of the radius and the scapholunate interval.

Short radiolunate ligament The short radiolunate ligament arises from the palmar lip of the lunate fossa of the radius and passes directly to the radial border of the lunate just radial to the ulnolunate ligament.

Ulnolunate ligament The ulnolunate ligament originates from the palmar aspect of the triangular fibrocartilage complex (TFC) and inserts on to the palmar distal lip of the lunate adjacent to the short radiolunate ligament.

Ulnotriquetral ligament The ulnotriquetral ligament arises from the palmar aspect of the ulna, inserts into the medial aspect of the triquetrum, and continues distally to a further attachment to the medial aspect of the hamate.

Ulnocapitate ligament The ulnocapitate ligament passes from the ulnar fovea and proximal radio-ulnar ligament of the TFC and inserts into the ulnar border of the capitate. This ligament partially overlies the other ulnar carpal ligaments. Together they form the ulnar contributions to the arcuate ligament complex.

Extrinsic dorsal carpal ligaments

The dorsal wrist ligaments are comparatively thin and are reinforced by the floor and septa of the fibrous tunnels for the six dorsal compartments.

Dorsal radiolunotriquetral ligament The dorsal radiolunotriquetral ligament, also known as the dorsal radiocarpal (DRC) ligament, is the only dorsal ligament that attaches the radius to the carpus. It is formed of superficial and deep components. The superficial part connects the radius and triquetrum, and the deep part connects the radius, lunate and triquetrum. The wide superficial component arises from the dorsal margin of the distal radius and courses ulnarwards to insert on the dorsal edge of the triquetrum. The deep component takes a narrower origin from the ulnar aspect of the distal dorsal radius and passes in an ulnar direction to attach to part of the lunotriquetral articulation and the intrinsic lunotriquetral ligament.

Intrinsic ligaments

The intrinsic ligaments of the wrist are only attached to carpal bones (see Fig. 51.19A–C). They are stronger and shorter than the extrinsic ligaments and are connected with the extrinsic ligament complexes by interdigitating fibres. The intrinsic ligaments are subdivided into ligaments that connect the carpal bones of the proximal and distal rows, respectively, and ligaments that connect the rows by crossing over the midcarpal joint.

Proximal row interosseous ligaments The scapholunate ligament acts as the primary stabilizer of the scapholunate joint. In the sagittal plane, it is an approximate horseshoe-shape with palmar (volar), proximal and dorsal components.

The scapholunate ligament contains short transverse fibres that connect the dorsal aspect of the scaphoid to the lunate and more obliquely orientated fibres which connect the palmar aspects. The stronger and tighter dorsal component of the ligament acts as a hinge permitting just 20° of motion between the scaphoid and the lunate. The ligament continues in its proximal section as an interosseous membrane and is easily visualized from the radiocarpal joint at arthroscopy.

The lunotriquetral ligament has similar dorsal proximal and palmar (volar) components, but the fibres of the palmar component are the thickest and strongest. The interosseous membranous component of the scapholunate and lunotriquetral ligaments separate the midcarpal from the radiocarpal joint spaces. Leaking of dye from one of these joint spaces into the other during an arthrogram denotes a tear of one of these ligaments.

Distal row interosseous ligaments The strong interosseous ligaments of the distal row connect and stabilize the capitate, hamate, trapezium and trapezoid. They have superficial and deep components, and, unlike the ligaments of the proximal row, are seldom torn.

Palmar midcarpal ligaments The scaphotrapezial, the scaphotrapezoidal (STm) and the scaphocapitate ligaments constitute the scaphotrapeziotrapezoid ligament complex (STT). They serve to stabilize the triscaphe joint. The triquetrohamate ligament has both palmar (volar) and dorsal components and functions to resist flexion between the hamate and triquetrum. The triquetrocapitate ligament is a palmar (volar) structure that indirectly stabilizes the lunate through its contribution to the ulnar limb of the arcuate ligament.

Dorsal midcarpal ligaments The dorsal intercarpal ligament helps to stabilize the proximal carpal row. It consistently arises from the dorsal tubercle of the triquetrum. Its radial insertion is more variable but may include almost all the lunate and scaphoid, and about half of the trapezoid and trapezium. The ligament forms the floor of the fourth and fifth extensor compartments.

Arthroscopy of the wrist and hand

See **Video 51.1**.

Arthroscopy of the wrist joint allows inspection of articular surfaces and ligaments, identification of pathology and altered kinematics, and therapeutic manoeuvres using scissors, rongeurs, sutures and cautery. Wrist arthroscopy may be carried out through various anatomically defined 'portals' which allow access between the tendons and neurovascular structures into the midcarpal and radiocarpal joints.

Movements and loading of the wrist joint

Movements of the wrist (carpal kinematics)

See **Video 51.2**.

The wrist joint consists of a series of complex articulations between the eight carpal bones, the two forearm bones and the five metacarpals of the hand. The function of the wrist is to allow the hand to function independent of the position of forearm rotation. In order to do this, it needs to function as a universal joint. Our understanding of the exact mechanism by which it does this is developing as new techniques for imaging and tracking carpal movement become available. Despite the progress in imaging and kinematic measurement techniques, no past or present concept of carpal mechanics adequately explains the complex behaviour of the carpus (Rainbow et al 2015).

Flexion–extension The movements at the radiocarpal and intercarpal joints are considered together. The range of movement varies between individuals; the approximate ranges of active movement are flexion (85°), extension (85°), adduction (ulnar deviation) (45°), abduction (radial deviation) (15°). The range of flexion is greater at the radiocarpal joint, while in extension there is more movement at the midcarpal

Some portals are, as de Smet (2002) has described, 'frighteningly' close to key anatomical structures. Consequently, only the skin should be incised when establishing a portal, and the remaining dissection should be carried out with narrow blunt artery forceps to spread aside the neurovascular structures and tendons with subsequent penetration of the capsule using a blunt probe.

Dorsal radiocarpal portals The dorsal radiocarpal portals are named according to their relationship to the extensor tendon compartments (1–2, 3–4, 4–5, 6–R, 6–U) with 6–R and –U describing a portal radial or ulnar to the sixth compartment which transmits the extensor carpi ulnaris tendon. The 1–2 portal is usually avoided because of the proximity of the radial artery which lies just 3 mm (range 1–5 mm) radially: the branches of the superficial radial nerve are similarly adjacent (range 1–6 mm) (Abrams et al 1994). The 3–4 portal is normally used as the main viewing portal and the 4–5 or 6–R portal for instrumentation. The dorsal cutaneous branch of the ulnar nerve lies within 2.5 mm of the 6–R portal). The articular surfaces of the scaphoid and lunate are seen distally, linked by the scapholunate ligament. Proximally, the triangular fibrocartilage complex may be viewed.

Dorsal midcarpal portals The radial midcarpal portal (MCR) is used to view the scaphocapitate joint, scaphotrapezoid joint and scapholunate joint. The ulnar midcarpal portal (MCU) is used for viewing the hamate, triquetrum and lunotriquetral joint.

Volar portals Volar portals (radial, VR, midcarpal, VMC and ulnar, VU) are not commonly used because of their proximity to nerves and arteries. They allow a view of the dorsal capsule, the dorsal radiocarpal ligament and the palmar subregions of the scapholunate and lunotriquetral interosseous ligaments. Use of the volar radial portal carries with it the potential for damage to flexor carpi radialis, the palmar cutaneous branch of the median nerve and the lateral cutaneous nerve of the forearm, all of which can run close to, but not within 3 mm of, the portal. The volar ulnar portal lies more than 5 mm away from the ulnar neurovascular bundle, provided the entry point in the capsule is deep to the ulnar edge of the profundus tendons (Slutsky 2002).

The above description fits with the convenient consideration of wrist motion in the traditional orthogonal anatomical directions (flexion, extension, ulnar). However, in reality few if any functional tasks occur within these planes. Most day-to-day activities require simultaneous coupled movements. Fisk noted that many functional activities such as 'casting a fly, throwing a dart or conducting an orchestra' occur along an arc from extension and radial deviation to flexion and ulnar deviation (Fisk 1970). This observation led Palmer to coin the term 'dart thrower's motion' (Palmer 1985). During the 'dart-throwing' movement almost no movement occurs within the proximal row and the motion occurs almost entirely at the distal row of the carpus (Werner 2004). It is believed that this coupled wrist motion combined with an upright stance allowed early hominid species to begin using tools and throwing objects purposefully (Rohde et al 2010).

The lack of movement between the bones of the proximal carpal row during the dart thrower's movement has clinical implications for both surgical treatment of wrist arthritis and rehabilitation following injury or surgery of the proximal carpal row. Preservation of this oblique plane when carrying out a partial wrist fusion for arthritis potentially results in more natural wrist kinematics, as has been shown by the improved functional outcome in 3-corner fusion when compared to 4-corner fusion (Singh et al 2015). Traditionally, prolonged immobilization has been part of the routine rehabilitation of injuries or surgery to the proximal carpal row such as for fractures of the scaphoid and reconstruction of the scapholunate ligament. However, with the knowledge that the proximal row undergoes little movement during the dart thrower's movement it seems logical to allow early rehabilitation exercises provided they occur in this plane (Rohde et al 2010). Radiolunate fusion, a procedure used for conditions such as radiolunate arthritis and radiocarpal instability, incurs surprisingly little loss of functional wrist movement.

Movement of the carpus was originally quantified by measuring carpal bone length in static radiographs while the wrist was moved in orthogonal anatomical planes. From these observations two models emerged. Destot described a *row* or *rigid body* theory wherein the carpus was felt to move simply as proximal and distal rows (Destot 1926). According to this view, during the composite movement of wrist flexion and extension, approximately two-thirds of movement occurs at the radiocarpal joint and one-third at the midcarpal joint. Navarro described a model in which the carpus was believed to move in radial, central and ulnar *columns* more than it did in rows (Navarro 1921). This theory was modified (Taleisnik 1976) to incorporate the specific stabilizing role of the scaphoid as it bridges the proximal and distal rows. Further studies have suggested that carpal movement may display characteristics of both these models in varying proportions. The degree to which a wrist displays column-like or row-like behaviour depends on the bony architecture and ligamentous laxity (Craigen and Stanley 1995, Garcia-Elias 1995). An attempt to provide a unifying theory of carpal kinematics describes a stable central column with the triquetrum serving as an anchor to prevent ulnar translation, and the scaphoid functioning as a supporting lateral column (Sandow et al 2014). This concept of a central column based on the radiolunate articulation is at variance with other kinematic studies which have shown 60% load transmission through the radio-scaphoid joint (Ulrich et al 1999): the theory remains to be validated through a full range of motion, particularly within the dart thrower's plane (Rainbow et al 2015). With regards to carpal kinematics, it seems sage to recall the words of the statistician George Box, who said 'all models are wrong, but some are useful'.

Flexor carpi ulnaris is stronger than extensor carpi ulnaris, which, in turn, is stronger than extensors carpi radialis longus and brevis, and flexor carpi radialis. The other muscles are all weaker. It is for this reason that these muscles tend to be selected for the major tendon transfers around the wrist (Brand 1985). During flexion and extension, flexor carpi radialis, flexor carpi ulnaris and extensor carpi radialis brevis have a greater excursion than extensor carpi radialis longus and extensor carpi ulnaris. During radial and ulnar deviation, extensor carpi radialis longus and extensor carpi ulnaris have a greater excursion, whereas that of flexor carpi radialis is relatively small. The axes of rotation for flexion/extension and radial/ulnar deviation intersect at a point in the proximal part of the capitate bone. Flexor carpi radialis and flexor carpi ulnaris are most efficient in flexion, extensor carpi radialis brevis in extension, extensor carpi radialis longus in radial deviation and extensor carpi ulnaris in ulnar deviation.

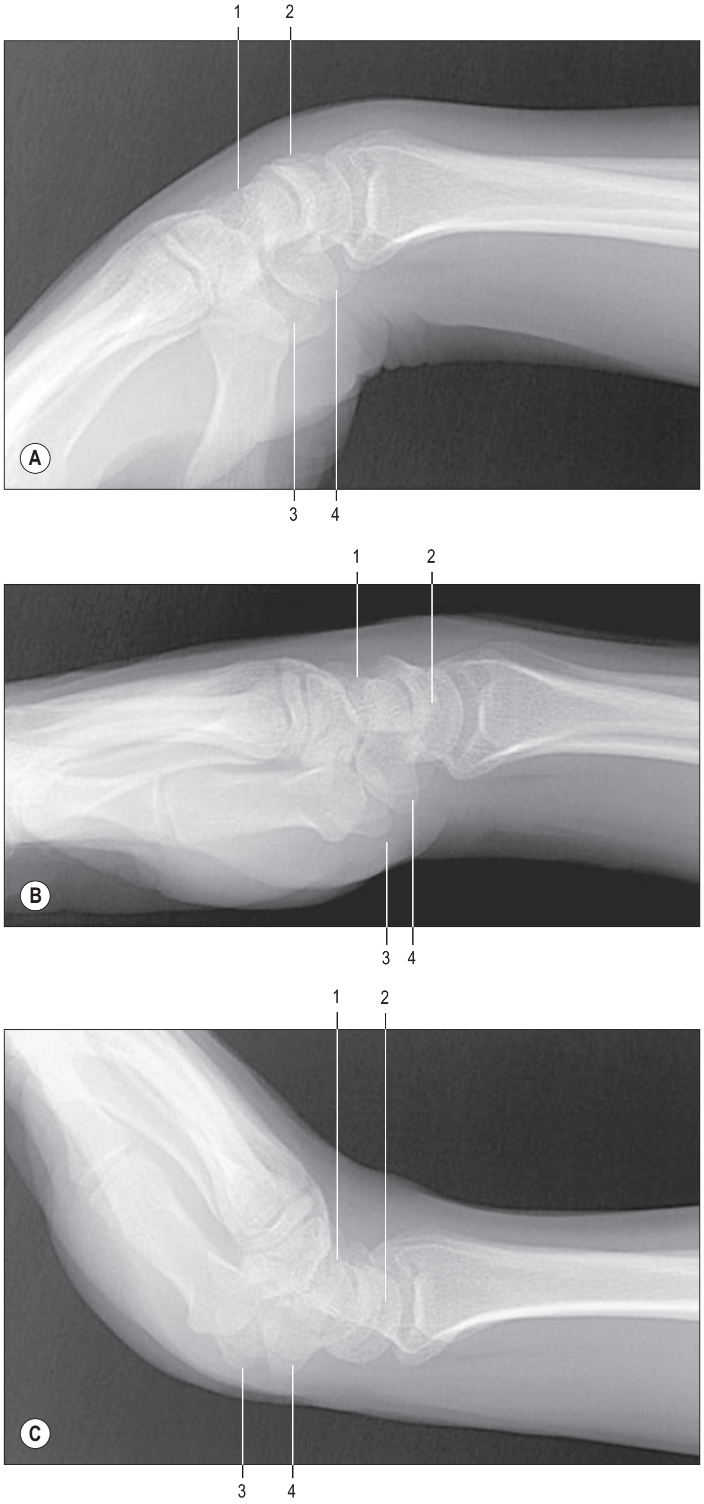

Fig. 51.21 **A**, A radiograph of the hand and wrist in full flexion: lateral aspect. Compare with **B**, and note the relative positions of the capitate and lunate, and the lunate and radius. **B**, A radiograph of the hand and wrist: lateral aspect. The long axes of the third metacarpal, capitate and lunate are, approximately, in line with the long axis of the radius. Note the relative positions of the capitate and lunate, and the lunate and radius. **C**, A radiograph of the hand and wrist in full extension: lateral aspect. Compare with **B** and note the alterations in the relative positions of the capitate and lunate, and the lunate and the radius. Key: 1, capitate; 2, lunate; 3, tubercle of the trapezium; 4, tubercle of the scaphoid.

joint (Fig. 51.21). Hence, the proximal surfaces extend further posteriorly on the lunate and scaphoid bones. These movements are influenced by antagonistic muscles, and therefore the range of flexion is perceptibly diminished when the fingers are flexed, due to increased tension in the extensors. Only when the joints are forced to the limits of flexion or extension with the digits relaxed are the dorsal or palmar ligaments fully stretched. During extension of the wrist, the distal carpal bones rotate into extension with slight radial deviation.

Adduction and abduction Most ulnar adduction occurs at the radiocarpal joint. The lunate articulates with both the radius and articular disc when the hand is in the midposition but, in adduction, it articulates solely with the radius, and the triquetrum now comes into contact with the articular disc (Fig. 51.22A). Much of the proximal articular surface of the scaphoid becomes subcapsular beneath the radial collateral ligament and forms a smooth, convex, palpable prominence in the floor of the 'anatomical snuff-box'. Radial abduction from the neutral position occurs at the midcarpal joint. A radiograph of the radially deviated hand shows that the capitate rotates round an anteroposterior axis so that its head passes medially and the hamate conforms to this; the distance between the lunate and the apex of the hamate is increased (Fig. 51.22B). The scaphoid rotates around a transverse axis, and its proximal articular surface moves ulnarwards so that the entire scaphoid now articulates solely with the radius. Movements are limited by the carpal collateral ligaments.

Dart thrower's motion

Available with the *Gray's Anatomy* e-book

Proximal and distal carpal row The proximal row (scaphoid, lunate and triquetrum) is an intercalated segment; no tendons insert onto the bones of the row. It is inherently unstable and controlled by specific retaining and gliding ligaments. Its relative position is determined by the dimensions of the space between the radius, triangular fibrocartilage complex and ulna on one side, and the rigid distal carpal row on the other. The proximal carpal row is subject to two opposing moments: the scaphoid straddles the proximal and distal rows and tends to rotate the proximal row into flexion under axial load and radial deviation. At the same time, there is a force tending to extend the proximal row, which is initiated by the distal row and transmitted via the midcarpal ligaments to the triquetrum. Stability of the midcarpal joint is thus ensured during both movement and loading. The distal carpal row (trapezium, trapezoid, capitate and hamate) can be regarded as one rigid structure. The scaphoid bridges the proximal and distal carpal rows and provides a functional couple between the two.

Muscles producing movements

Flexion Flexor carpi radialis, flexor carpi ulnaris and palmaris longus produce flexion, assisted by flexor digitorum superficialis, flexor digitorum profundus and flexor pollicis longus.

Extension Extensor carpi radialis longus, extensors carpi radialis brevis and ulnaris, assisted by extensors digitorum, digiti minimi, indicis and pollicis longus. With the forearm supinated, extensor carpi ulnaris is a pure extensor with no ulnar deviation moment.

Adduction (ulnar deviation) Flexor and extensor carpi ulnaris produce adduction. With the forearm pronated, extensor carpi ulnaris is a pure ulnar deviator with no extension moment.

Abduction (radial deviation) Flexor carpi radialis, extensors carpi radialis longus and brevis, with abductor pollicis longus and extensor pollicis brevis.

Loading of the wrist (carpal kinetics)

Axial loading, i.e. load or force applied along a line parallel to the long bones of the arm, occurs in clenching the fist. In most activities, loading is multiplanar with a combination of vectors of force. Grasping an object whilst lifting it against gravity with the elbow in flexion causes transverse and axial loading (Horii et al 1993).

Force transmission

Radiocarpal and ulnocarpal joints

The radiocarpal and ulnocarpal articulations involve the scaphoid and lunate fossae of the radius and the facet formed by the distal aspect of the triangular fibrocartilage complex. The scaphoid fossa contributes 43%, the lunate fossa 46% and the triangular fibrocartilage complex 11% of the total area of this articulating surface. Under resting conditions, about 20% of the surface area of the combined radiocarpal and ulnocarpal joint abuts the proximal carpal row. Greater contact is seen in forearm supination, radial deviation and dorsiflexion of the wrist. Lesser contact occurs in forearm pronation, ulnar deviation and palmar flexion of the wrist. Axial loading increases the contact area to a maximum of about 40%. Force across the joint also varies with the position of the forearm and the degree of wrist flexion. For a given load in wrist-neutral position, 50% of force passes across the scaphoid fossa,

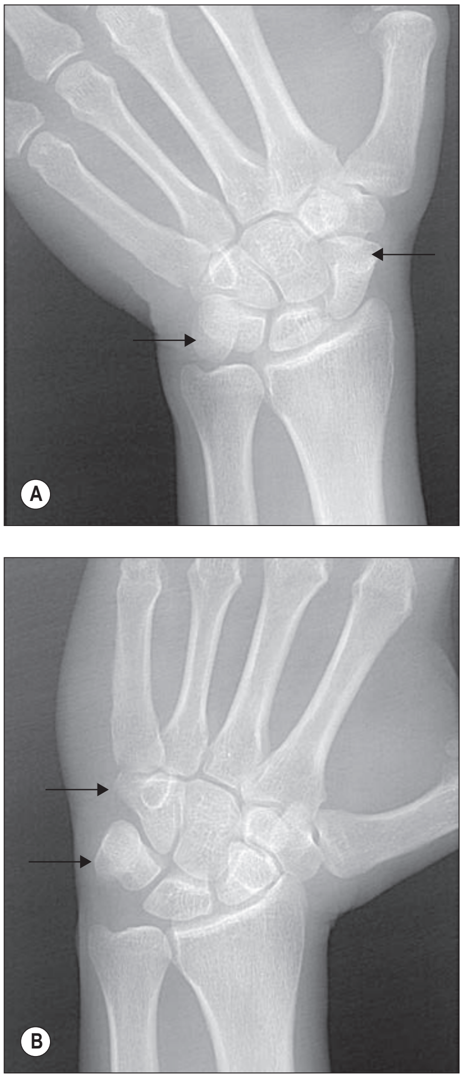

Fig. 51.22 **A**, A radiograph of the hand in full adduction (ulnar deviation): dorsopalmar projection. The arrows point to the scaphoid on the radial side and to the pisiform on the ulnar side. Compare with **B** and observe that the movements occur at both the radiocarpal and intercarpal joints. **B**, A radiograph of the same hand in full abduction (radial deviation). The arrows point to the hamate and pisiform. Compare with **A** and note that: the scaphoid and lunate have passed medially (ulnarly) so that the latter articulates to a large extent with the articular disc of the distal radio-ulnar joint; the pisiform is now widely separated from the styloid process of the ulna; the scaphoid, having rotated round a transverse axis, is much foreshortened; the apex of the hamate has been thrust away from the lunate by the rotation of the capitate around an anteroposterior axis; a gap has opened up between the distal portions of the hamate and triquetrum; and the long axes of the capitate and lunate are now almost in the same straight line.

35% through the lunate fossa and 15% across the triangular fibrocartilage complex. With a power grip, there is slight ulnar deviation and the proportion of force passing across the scaphoid and lunate fossae reverses.

Midcarpal joint

With the wrist in neutral position, 50–60% of a given load is transmitted from the distal row through the capitate to the scaphoid and lunate. Up to 30% of the load is transmitted via the scaphotrapeziotrapezoid joint and up to 20% via the hamate–triquetral joint.

Distal radio-ulnar joint (DRUJ)

See Chapter 50.

Power grip

In power grip, the wrist is positioned in mid-dorsiflexion and slight ulnar tilt. Force is transmitted from the hand and wrist via the radiocarpal joint and triangular fibrocartilage complex to both bones of the forearm, through the elbow joint to the humerus, and from there, via the glenohumeral joint, to the pectoral girdle. Dynamic muscle action accounts for transmission of a large part of the force; a smaller proportion is transmitted through the osseoligamentous structures. The distribution of force between the radius and ulna varies dynamically and depends on the absolute value of load, degree of forearm rotation and position of the carpus relative to the forearm.

Carpal instability

See **Video 51.3**.

The upper limb has evolved to facilitate the placing of the hand in space for prehension, but mobility of the hand on the forearm has evolved at the expense of stability. A wrist is said to be kinetically unstable when it cannot bear physiological loads without giving way or causing injury, and to be kinematically unstable when it exhibits sudden changes in carpal alignment during movement, manifest as a 'clunk' as one or more of the carpal bones move abnormally with respect to the others. Stability of the various joints, so that the bones maintain normal anatomical relations with respect to each other throughout the normal range of motion, is essential for physiological load transmission. Disruption of this complex system leads to pain, loss of function and, in time, degeneration of the articular surfaces.

Carpometacarpal joints

Carpometacarpal joint of the thumb

Articulating surfaces The carpometacarpal joint of the thumb (basal joint of the thumb) is a sellar joint between the first metacarpal base and trapezium. Its extensive articular surfaces and their topology ensure that the joint enjoys a wide mobility. Its curved saddle shape, as if designed for a 'scoliotic horse' (Kuczynski 1975), allows the metacarpal base to slide into flexion and pronation as the pulp of the thumb opposes the digits.

Ligaments The first metacarpal and trapezium are connected by lateral, anterior and posterior ligaments and a fibrous capsule. The broad lateral ligament runs from the lateral surface of the trapezium to the radial side of the metacarpal base. The palmar and dorsal ligaments are oblique bands that converge to the ulnar side of the metacarpal base from the palmar and dorsal surfaces of the trapezium, respectively.

Synovial membrane The synovial membrane lines the joint capsule and is separate from it.

Joint movements Except at its initiation, flexion is accompanied by pronation (medial rotation) of the thumb metacarpal, whilst pronation necessitates flexion. This linkage of movements is due largely to the shape of the articular surfaces and to the obliquity of the dorsal ligament (which, when taut, anchors the ulnar side of the metacarpal base while its radial side continues to move). Contraction of flexor pollicis brevis, assisted by opponens pollicis, produces medial rotation with flexion; combined with abduction, this opposes the thumb pulp to the pulps of the slightly flexed fingers. Full extension of the thumb metacarpal entails slight supination (lateral rotation), attributable to the saddle shape of the joint and to the action of the palmar ligament (similar to that of the dorsal ligament in flexion) (Edmunds 2011, Ladd et al 2013).

Muscles producing movements

Flexion Flexor pollicis brevis and opponens pollicis, aided by flexor pollicis longus which continues the flexion moment when the other joints of the thumb are flexed.

Extension Abductor pollicis longus and extensors pollicis brevis and longus.

Abduction Abductors pollicis brevis and longus.

Adduction Adductor pollicis and extensor pollicis longus.

Opposition Opposition describes the action of bringing the pulp of the thumb across the palm to appose the pulps of the digits. Abductor pollicis brevis abducts the thumb whilst opponens pollicis and flexor pollicis brevis simultaneously flex and pronate (medially rotate) the abducted thumb. Interpulpal pressure, generated by digital grasping, is increased by adductor pollicis and flexor pollicis longus.

Retroposition Retroposition describes elevating the pulp of the thumb into extension and ulnar adduction dorsal to the plane of the palm. Extensor pollicis longus uniquely provides this movement.

Some degree of carpal instability may occur as part of inherent hypermobility in affected individuals. More commonly it occurs after acute rupture or chronic attenuation of intrinsic and extrinsic carpal ligaments, which may be detected either clinically or radiologically as malalignment of the carpal bones. In clinical practice, certain patterns of instability predominate.

Garcia-Elias described a kinetic theory of carpal stability that states that the neutral posture of the lunate is preserved by balancing the flexion moment of the scaphoid with the extension moment of the triquetrum (Garcia-Elias 1997). When axially loaded, these rotational forces increase. If the interosseous scapholunate ligament is disrupted then the extension moment of the triquetrum remains unopposed leading to an extended position of the lunate. This is referred to as dorsal intercalated segment instability (DISI). In the absence of the luno-triquetral ligament the scaphoid flexion moment loses its antagonistic extension moment from the triquetrum and the lunate adopts a flexed posture: this is termed volar intercalated segment instability (VISI).

Circumduction Extensors, abductors, flexors and adductors acting consecutively in this, or reverse, order.

Second to fifth carpometacarpal joints

The second to fifth carpometacarpal joints are synovial ellipsoid joints between the carpus and second to fifth metacarpals. Although widely classed as plane, they have curved articular surfaces that are often of complex saddle shape. The bones are united by articular capsules and by dorsal, palmar and interosseous ligaments.

Ligaments The dorsal ligaments are the strongest, and connect the dorsal surfaces of the carpals and metacarpals. The second metacarpal has two ligaments, from the trapezium and trapezoid; the third has two, from the trapezoid and capitate; the fourth has two, from the capitate and hamate; and the fifth has a single band from the hamate, which is continuous with a similar palmar ligament, forming an incomplete capsule. The palmar ligaments are similar, except that the third metacarpal has three: a lateral from the trapezium, superficial to the tendon sheath of flexor carpi radialis, an intermediate from the capitate, and a medial from the hamate. The interosseous ligaments consist of two short, thick, fibrous bands. They are limited to one part of the carpometacarpal articulation and connect contiguous distal margins of the capitate and hamate with adjacent surfaces of the third and fourth metacarpals; they may be united proximally.

Synovial membranes The synovial membranes are often continuous with those of the intercarpal joints. Occasionally, the joint between the hamate and fourth and fifth metacarpals has a separate synovial cavity, bounded laterally by the medial interosseous ligament and its extensions to the palmar and dorsal parts of the capsule.

Muscles producing movements The second to fifth carpometacarpal joints exhibit an increasing range of movement, progressing from the radial to the ulnar side. Thus, there is little mobility at the base of the index ray but considerable mobility at the base of the small finger ray, which facilitates 'cupping' of the palm of the hand. Compressive forces between the metacarpals and the distal carpal row are estimated to be upwards of ten times the forces at the tips of the fingers during 'pinch' or 'chuck' grip.

Slight gliding movements are effected by the long flexor and extensor muscles of the digits.

Intermetacarpal joints

Articulating surfaces The second to fifth metacarpal bases articulate reciprocally by small cartilage-covered facets connected by dorsal, palmar and interosseous ligaments.

Fibrous capsule The intermetacarpal joints have fibrous capsules.

Ligaments The dorsal and palmar ligaments pass transversely from bone to bone. The interosseous ligaments connect contiguous surfaces just distal to their articular facets.

Synovial membranes The synovial membranes are continuous with those of the carpometacarpal articulations.

Movements at the carpometacarpal joints The fifth metacarpal is the most mobile and the second and third are the least mobile. These variations are easily demonstrated by opposing each digit to the thumb over the centre of the palm. While the majority of movement is in the thumb, the carpometacarpal joint of the little finger flexes, abducts and pronates (laterally rotates). Less movement occurs at the carpometacarpal joint of the ring finger and essentially none occurs at the middle and index (Tucker and Titley 2002).

Movements at the intermetacarpal joints Movements at the intermetacarpal articulations vary. There is very slight gliding movement in flexion–extension in the index–middle joint and slightly more glide in the middle–ring joint. There is more glide and some rotation during pronation and supination generated at the carpometacarpal joint in the ring–little joint and slight rotation in the little finger.

Muscles producing movements The extrinsic (i.e. forearm-derived) and intrinsic (i.e. palm-derived) flexors and extensors of the second to fifth digits move the carpometacarpal and intermetacarpal joints.

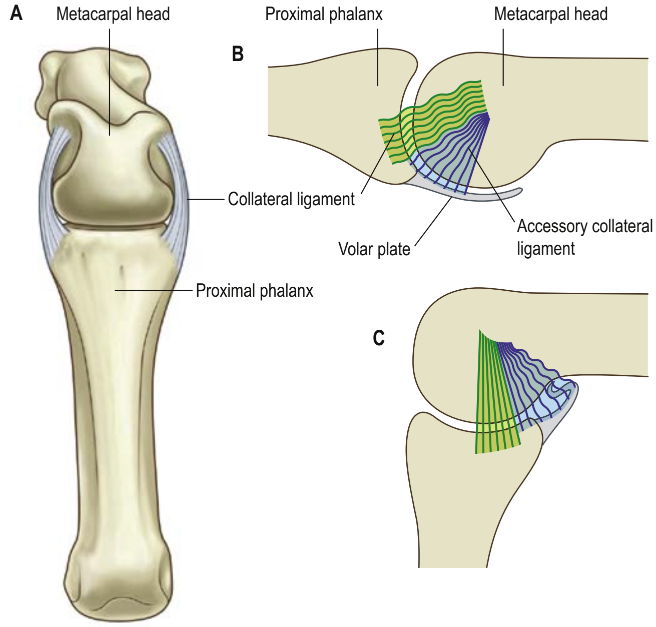

Fig. 51.23 The metacarpal head is narrower on its dorsal surface than its palmar surface (**A**), which means that the collateral ligament is loose in extension (**B**) but tight in flexion (**C**).

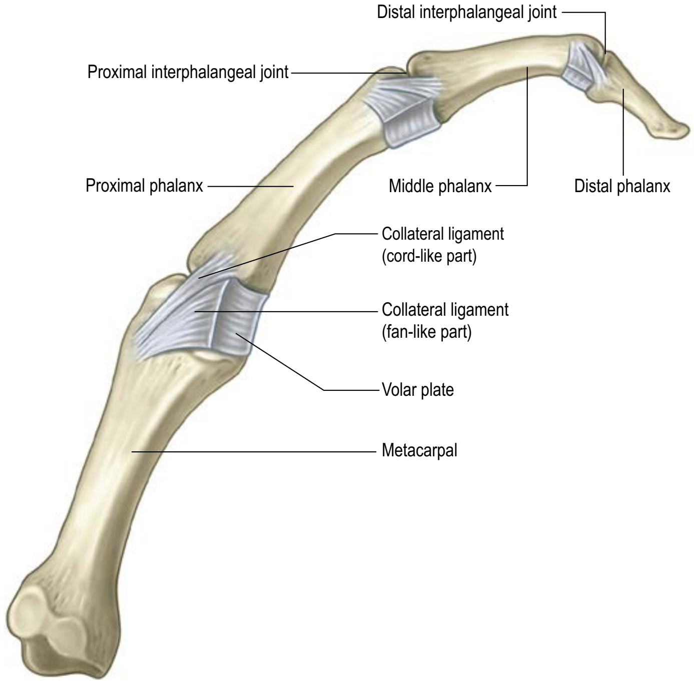
Distal interphalangeal joint
Proximal interphalangeal joint
Proximal phalanx
Middle phalanx
Distal phalanx
Collateral ligament (cord-like part)
Collateral ligament (fan-like part)
Volar plate
Metacarpal

Fig. 51.24 The metacarpophalangeal and digital joints of the left third finger: medial aspect.

Metacarpophalangeal joints

The metacarpal heads are incongruous with the shallow concavities on the phalangeal bases; they are not regularly convex but are partially divided on their palmar aspects and, thus, almost bicondylar. The dorsal width of the metacarpal head is about two-thirds of its palmar width, which means that the joint is lax in the coronal plane in extension yet taut in flexion (compared with the proximal interphalangeal joint which is taut throughout its range) (Fig. 51.23).

Fibrous capsule The metacarpophalangeal joints all have fibrous capsules.

Ligaments Each metacarpophalangeal joint has a palmar and two collateral ligaments.

Palmar ligaments The palmar ligaments (volar plates) are thick, dense and fibrocartilaginous. They are attached quite loosely to the metacarpal neck proximally and firmly to the base of the proximal phalanx distally (Fig. 51.24). The deep transverse metacarpal ligaments extend

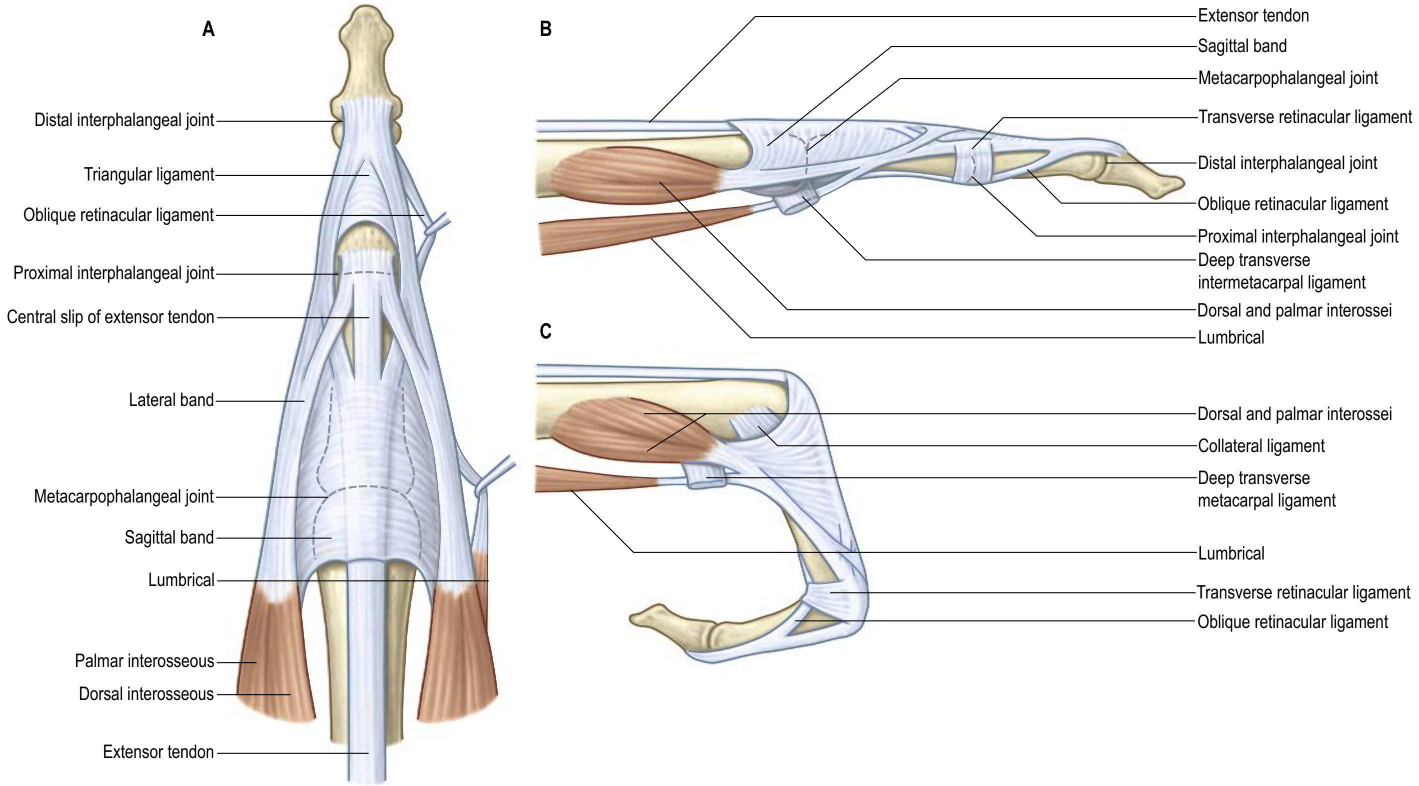
A
B
C
Distal interphalangeal joint
Triangular ligament
Oblique retinacular ligament
Proximal interphalangeal joint
Central slip of extensor tendon
Lateral band
Metacarpophalangeal joint
Sagittal band
Lumbrical
Palmar interosseous
Dorsal interosseous
Extensor tendon
Extensor tendon
Sagittal band
Metacarpophalangeal joint
Transverse retinacular ligament
Distal interphalangeal joint
Oblique retinacular ligament
Proximal interphalangeal joint
Deep transverse intermetacarpal ligament
Dorsal and palmar interossei
Lumbrical
Dorsal and palmar interossei
Collateral ligament
Deep transverse metacarpal ligament
Lumbrical
Transverse retinacular ligament
Oblique retinacular ligament

Fig. 51.25 The extensor mechanism of the finger. **A**, Dorsal view. **B**, Lateral view. **C**, Lateral view in flexion.

between the palmar plates from the ulnar side of the second metacarpal head to the radial side of the fifth metacarpal head. The collateral ligaments arise from the posterior tubercle on the lateral aspect of the metacarpal heads and insert into the palmar portion of the lateral aspect of the base of the proximal phalanges. The palmar aspects are grooved for the flexor tendons. The A1 component of the flexor tendon sheath is attached to the edge of the ligament and the associated attachment of the collateral ligament, but is not attached to the metacarpal. The deep surface of the volar plate increases the articular contact area for the metacarpal heads.

Deep transverse metacarpal ligaments The deep transverse metacarpal ligaments are three short, wide, flat bands that connect the palmar ligaments of the second to fifth metacarpophalangeal joints. They are related anteriorly to the lumbricals and digital vessels and nerves, and posteriorly to the interossei. The vertical fibres of the palmar aponeurosis (septa of Legueu and Juvara) join their palmar surfaces. On both sides of the third and fourth metacarpophalangeal joints, but only the ulnar side of the second and radial side of the fifth joints, the transverse (sagittal) bands of the extensor hood join the deep transverse metacarpal ligaments. The lumbricals and the phalangeal attachments of the dorsal interossei lie anterior to this band; the remaining attachments of the dorsal and palmar interossei are posterior to it (Fig. 51.25).

Collateral ligaments The collateral ligaments are attached proximally to the posterior tubercle and an adjacent pit on the side of the metacarpal neck. Two components pass distally. The more dorsal fibres form a cord-like band that is attached to the side of the palmar corner of the base of the proximal phalanx, blending with the insertion of the volar plate. The more palmar fibres spread distally and anteriorly to form a fan that can fold up like a concertina as the metacarpophalangeal joint flexes (see Fig. 51.23). The radial collateral ligament of the index finger is strongest because it must resist ulnar deviation when the thumb opposes the index finger. Because the metacarpal head is narrow dorsally and wider anteriorly, the collateral ligaments are tight only in full flexion but loose in extension.

Synovial membrane The metacarpophalangeal joints are lined by a synovial membrane.

Joint movements

Digits These include flexion, extension, adduction, abduction, circumduction and limited rotation. Rotation accompanies flexion–extension, e.g. when the finger flexes and rotates to place its tip near the centre of the palm. The range of rotation is frequently increased as a result of the resistance of a grasped object. Active flexion is 90° or more and is greater in the little finger than in the index. The range of extension depends on whether it is active or passive: the former is limited by the resistance of the antagonistic muscles, the latter is significantly greater because the volar plate offers little resistance. (This contrasts with the thumb–metacarpophalangeal joint and all the proximal interphalangeal joints, in which a rigid volar plate prevents hyperextension, so that passive and active extension are equal.) Passive extension is greater in the little finger than in the index. The range can be even greater in those with generally lax joints. The trapezoidal shape of the metacarpal heads means that the collateral ligament allows no ulnar or radial deviation of the proximal phalanx when the joint is fully flexed, but allows the fingers to move through about 20° in each direction when the joints are extended.

Slight supination (lateral rotation) accompanies digital flexion of the middle, ring and little fingers. Flexion of the index finger may be accompanied by little or no pronation. These movements allow the digits to cup around an object such that the thumb pulp can appose the middle–ring pulp as the sides of these touch each other whilst the edge of the index and little fingers touch the sides of the thumb pulp.

Thumb The metacarpophalangeal joint of the thumb has a flexion–extension range of approximately 60°, with minimal extension. The latter is prevented by a stout volar plate. There is minimal rotation and no abduction or adduction.

Accessory movements Anteroposterior translation of the phalanx on the metacarpal and distraction.

Muscles producing movements

Flexion In the fingers, flexion is produced by flexors digitorum superficialis and profundus, assisted by the lumbricals, interossei and flexor digiti minimi brevis (in the little finger). In the thumb, flexor pollicis longus flexes the thumb. Flexor pollicis brevis, abductor pollicis brevis and adductor pollicis flex the metacarpophalangeal joint through attachments to their respective tubercles at the anteromedial and anterolateral base of the proximal phalanx, and through the extensor hood overlying the dorsum of the base of the proximal phalanx.

Extension In the digits, extension is produced by extensor digitorum, assisted in the second and fifth digits by extensor indicis and extensor digiti minimi, respectively; in the thumb, extensors pollicis longus and brevis.

Adduction In extended fingers, adduction towards the middle finger is produced by the palmar interossei, enabled by a lax collateral ligament.

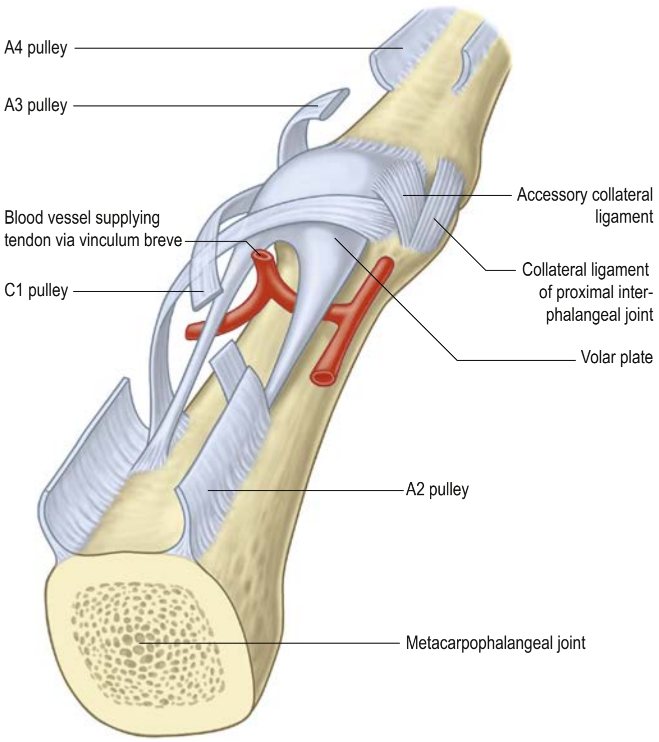
A4 pulley
A3 pulley
Blood vessel supplying tendon via vinculum breve
C1 pulley
Accessory collateral ligament
Collateral ligament of proximal interphalangeal joint
Volar plate
A2 pulley
Metacarpophalangeal joint

Fig. 51.26 The anatomy of the volar plate at a proximal interphalangeal joint. The blood vessel supplying the flexor tendons via the vincula brevum is shown; the mesentery forming the vinculum has been omitted.

In flexion, adduction is prevented by a taut collateral ligament. In the thumb, very limited metacarpophalangeal adduction is possible because of constraint by the radial collateral ligament.

Abduction In extended fingers, abduction from the axis of the middle finger is produced by the dorsal interossei and abductor digiti minimi. There is no abduction when the metacarpophalangeal joint is flexed because of tightening of the collateral ligament. When the fingers are flexed at the interphalangeal joints, active abduction at the metacarpophalangeal joints is possible. In the thumb, there is minimal or no abduction at the metacarpophalangeal joint because of the constraint of the ulnar collateral ligament. Abduction, if it occurs, is provided by abductor pollicis brevis.

Gamekeeper's thumb and skier's thumb

Available with the *Gray's Anatomy* e-book

Interphalangeal joints

The interphalangeal joints are uniaxial hinge joints.

Fibrous capsule Each interphalangeal joint has a fibrous capsule.

Ligaments The proximal interphalangeal joint is stable in all positions. Stability is conferred by a palmar ligament (the volar plate) and two collateral ligaments (**Fig. 51.26**; see Figs 51.23, 51.24) in addition to the flexor sheath, which is inserted not only into the side of the volar plate but also into the base and neck of the proximal phalanx, so conferring additional stability to the volar plate. There is a different arrangement in the metacarpophalangeal joint, where the sheath is inserted into the volar plate and the base of the proximal phalanx but not into the metacarpal.

Palmar ligament (volar plate) The volar plate of the proximal interphalangeal joint constitutes the floor of the interphalangeal joint. In the joint itself, the distal end of the volar plate is thickened laterally where it is firmly attached to the base of the middle phalanx at the position of the true attachment of the collateral ligament. Centrally, it is more delicate and blends with the volar periosteum of the middle phalanx. Proximally, the volar plate is also very delicate in its central portion, but it is thickened laterally to form the 'check rein ligaments' that are attached to the periosteum of the proximal phalanx, beyond the walls of the A2 pulley component of the fibrous flexor sheath. Nutrient branches of the digital arteries pass underneath these check ligaments to reach the vincula (see Fig. 51.26). The A3 pulley is attached to the edge of the volar plate, together with the accessory part of the collateral ligament.

Collateral ligaments The cord-like proper collateral ligaments pass from the dorsal half of the lateral aspect of the neck of the proximal phalanx to the lateral palmar corner of the base of the adjacent proximal phalanx, where they are incorporated into the insertion of the A3 pulley and volar plate. They remain taut throughout flexion and extension in contrast to the collateral ligaments of the metacarpophalangeal joint, which are taut in flexion but lax in extension. In the proximal interphalangeal joint, a fan-like accessory collateral ligament arises in continuity from the palmar edge of the main ligament and passes in a palmar direction to attach to the volar plate: it folds like a concertina on flexion. The accessory collateral ligament and check rein ligament are not found in the distal interphalangeal joint (Slattery et al 2014).

Synovial membrane Each interphalangeal joint has a synovial lining.

Factors maintaining stability Stability is conferred by the articular contours of the joint surfaces and the proper collateral ligaments (Allison 2005). The flexor and extensor tendons provide secondary stabilization. Stability against hyperextension of the proximal interphalangeal joint is enhanced by the three-dimensional box arrangement that is produced by the collateral ligament–volar plate complex.

Joint movements Flexion and extension are active movements at the interphalangeal joints. Their range is greater at the proximal joints. Flexion is considerable, whereas extension is limited by tension of the digital flexors and terminated by tension in the palmar ligaments. Flexion and extension are accompanied by slight rotation: during flexion, this turns the digital pulps into slight supination to face the opposed thumb: an opposite rotation occurs during extension.

Accessory movements Limited rotation, abduction, adduction and anteroposterior translation permit the fingers to adapt to the shapes of gripped objects and help to protect against stresses and strains.

Muscles producing movements
Flexion Flexion is produced by flexors digitorum superficialis and profundus at the proximal interphalangeal joints, flexor digitorum profundus at the distal interphalangeal joints and flexor pollicis longus at the interphalangeal joint of the thumb.

Extension Extension of the interphalangeal joint of the thumb is produced by extensor pollicis longus and by the combined pull of abductor pollicis brevis, flexor pollicis brevis and abductor pollicis through the extensor expansion (which simultaneously flexes the metacarpophalangeal joint). This supplementary action allows extension of the interphalangeal joint of the thumb even if extensor pollicis longus or the radial nerve are divided. Extension of the interphalangeal joints of the digits is achieved though the complex extensor mechanism with contributions from the central tendon (extensors digitorum, digiti minimi and indicis) and the lateral bands that draw from the lumbricals and interossei. Extension occurs simultaneously in both joints in digits 2–5. Simultaneous flexion at the metacarpophalangeal joints and extension at the interphalangeal joints of a digit are essential for the fine movements of writing, drawing, threading a needle, etc. The lumbricals and interossei are primary agents in flexing the metacarpophalangeal joints and also in extending the interphalangeal joints through their attachments to the dorsal digital expansions.

Mallet finger

Available with the *Gray's Anatomy* e-book

Swan neck deformity

Available with the Gray's Anatomy e-book

Boutonnière deformity

Available with the *Gray's Anatomy* e-book

Vascular supply of the joints of the wrist and hand

The radiocarpal joint is supplied by branches of the anterior interosseous artery, anterior and posterior carpal branches of the radial and ulnar arteries, palmar and dorsal metacarpal arteries, and recurrent rami of the deep palmar arch. The carpal joints are supplied by the posterior

The ulnar collateral ligament of the metacarpophalangeal joint of the thumb may be avulsed from its distal attachment to the base of the proximal phalanx by a combination of forced extension and radial deviation of the joint. Chronic attritional tears of this ligament are traditionally reported to occur in gamekeepers from wringing the necks of pheasants. Acute injuries typically occur in skiers who fall onto an outstretched hand while having the strap of a ski pole wrapped around the thumb, or if the thumb is caught in the snow (or the grid of an artificial slope). The ligament may be avulsed directly from the bone or with a pyramidal fragment of bone. The fragment also includes the insertion of the volar plate, flexor sheath and part of adductor pollicis. The ulnar collateral ligament is normally covered by the aponeurotic fibres of the tendon of adductor pollicis. Following avulsion, the proximal end can become superficially displaced around the proximal free edge of the aponeurotic insertion of adductor pollicis. This is termed a Stener lesion (Mattox et al 2015). The soft tissue interposition prevents the ends of the avulsed ligament from healing. The presence of a Stener lesion is indicated clinically if there is more than 30° of radial laxity when stressing the metacarpophalangeal joint in 40° of flexion. If the joint is assessed in extension, then the lateral fibres of the volar plate may contribute significantly to the lateral stability of the joint and give a false impression of stability. Surgical repair requires division of the aponeurotic fibres of adductor pollicis to expose the insertion, followed by reattachment of the avulsed ligament to its attachment in the anteromedial corner of the proximal phalanx. Postoperative rehabilitation requires early movement of the interphalangeal joint of the thumb, otherwise the adductor aponeurosis will adhere to the repair and prevent flexion of the tip. The ulnar collateral ligament is isometric, i.e. the same length in flexion and extension. Consequently, early movement of the metacarpophalangeal joint will prevent adherence of the repair to the side of the joint, which would otherwise limit movement.

The comparable injury to the radial collateral ligament is less common. It is caused by sudden, forced adduction of the metacarpophalangeal joint as the result of a fall or during ball games. The ligament may be ruptured in its mid-substance or avulsed from either bony attachment, usually the distal. A Stener lesion does not occur because the aponeurosis of abductor pollicis brevis is closely apposed to the joint and thus does not provide the space.

The oblique retinacular ligament of Landsmeer (see Fig. 51.25) runs from an attachment anterior to the axis of the proximal interphalangeal joint to an insertion posterior to the axis of the distal interphalangeal joint. This ligament is inconsistent (Adkinson et al 2014), but when present causes a dynamic tenodesis with obligatory extension of the distal interphalangeal joint when the proximal interphalangeal joint extends.

Mallet finger deformity is caused by laceration, traumatic rupture or an avulsion fracture of the distal extensor tendon to the terminal phalanx of the finger. It is usually caused by forced flexion of the distal phalanx of the finger or laceration of the tendon. A closed rupture is usually painless. The patient is unable to extend the distal interphalangeal joint actively, but it can be extended passively. As time passes, the residual extensor mechanism is pulled proximally by the intrinsic tone, which increases the torque across the dorsum of the interphalangeal joint, causing a secondary swan neck deformity.

Swan neck deformity is caused by hyperextension of the proximal interphalangeal joint, together with flexion of the distal interphalangeal joint and occurs as a result of an imbalance between the component parts of the extensor and flexor mechanism: it may be related to problems at the metacarpophalangeal, proximal interphalangeal and distal interphalangeal joints. The deformity can be caused by a number of factors: erosion of the volar plate of the proximal interphalangeal joint by synovitis, so that the joint can hyperextend; rupture of flexor digitorum superficialis from rheumatoid disease or laceration; intrinsic muscle tightness (spasm, ulnar drift, palmar subluxation of the proximal phalanx on the metacarpal head); mallet finger, where the extensor mechanism moves proximally because it is unconstrained by the distal insertion into the distal phalanx, conferring an increased extensor moment to the base of the middle phalanx.

A boutonnière deformity is a flexion deformity of the proximal interphalangeal joint with hyperextension of the distal interphalangeal joint. It reflects an imbalance between tension in the central slip and the lateral bands of the extensor mechanism following failure of the central slip. This can occur as a result of acute division or chronic attrition. Initially, the proximal interphalangeal joint still extends because the lateral bands are intact, but in time the dorsal triangular ligament becomes attenuated, allowing the lateral bands of the extensor tendon to migrate in a volar direction and the head of the proximal phalanx to migrate dorsally: the extensor mechanism then exerts a flexion force at the proximal interphalangeal joint. The terminal part of the extensor mechanism still runs dorsal to the axis of the distal interphalangeal joint but is relatively tightened due to anterior subluxation of the lateral bands, causing hyperextension at the distal interphalangeal joint. Initially, the deformity is passively correctable, but, with time, the soft tissues around the joint contract and a fixed deformity results.

carpal branches of the radial and ulnar arteries, and by the anterior interosseous artery. The carpometacarpal joint of the thumb receives its blood supply from the radial artery and its first dorsal metacarpal branch. The second to fifth carpometacarpal joints are supplied by the posterior carpal branches of the radial and ulnar arteries, by twigs from the anterior interosseous artery, and from the palmar digital arteries. The metacarpophalangeal joints receive their blood supply from the dorsal and palmar metacarpal arteries, the arteria princeps pollicis and the arteria radialis indicis. The interphalangeal joints are supplied by branches from the palmar digital arteries (see Fig. 51.2A).

Innervation of the joints of the wrist

The radiocarpal joint is innervated by the anterior interosseous nerve, posterior interosseous nerves and lateral antebrachial cutaneous nerves with contributions from the median, ulnar and radial nerves. The palmar cutaneous branch of the median nerve, the deep branch of the ulnar nerve, the superficial branch of the radial nerve and the dorsal branch of the ulnar nerve also innervate the capsule (Van de Pol et al 2006). The ulnar corner of the wrist and triangular cartilage is innervated by the dorsal cutaneous branch of the ulnar nerve, medial antebrachial cutaneous nerve and ulnar nerve. Occasionally it receives fibres from the anterior and posterior interosseous nerves (LaPorte et al 2014). These appear to be pure afferent nerves innervating mechanoreceptor endings (there are an average of 10 in each dorsal radiocarpal ligament) (Tomita et al 2007). Golgi organs, Pacinian corpuscles, Ruffini endings and free nerve endings are found in the palmar radiocarpal ligaments (Petrie et al 1997). The apparently uneven distribution of these receptors throughout the ligaments suggests as yet unspecified functional adaptations.

Innervation of the joints of each digit

The second to fifth carpometacarpal joints are innervated by branches of the ulnar nerve, the anterior interosseous nerve and the superficial radial and dorsal ulnar nerves. The metacarpophalangeal joints are innervated by twigs from the palmar digital branches of the median and ulnar nerve, the deep terminal branch of the ulnar nerve and the posterior interosseous nerve. The interphalangeal joints of the fingers are innervated by one branch, occasionally two, from the palmar digital branches of the median nerve (to the thumb, index, middle and ring fingers), and the ulnar nerve (to the ring and little fingers). The dorsal cutaneous nerves rarely provide innervation (Pastrana et al 2019).

Innervation of the joints of the thumb

The carpometacarpal joint of the thumb is innervated by branches from the lateral antebrachial cutaneous nerve, the palmar cutaneous branch of the median nerve and, less commonly, the superficial radial nerve (Tuffaha et al 2018). The interphalangeal joint of the thumb is innervated by a palmar capsular branch from the radial and ulnar digital nerve as well as a branch from each of the dorsal radial nerve terminal branches (Zaidenberg et al 2018).

Joint neurectomy

Available with the *Gray's Anatomy* e-book

MUSCLES

Extrinsic long flexors and extensors

The extrinsic long flexors and extensors are described on pages 942 to 950. The flexor and extensor retinacula are described on page 958.

Long flexor tendon apparatus

Flexor tendon sheaths

The fibrous sheaths of the flexor tendons are specialized parts of the palmar fascia. Each finger and the thumb have an osseo-aponeurotic tunnel that extends from the neck of the metacarpal to the distal phalanx. The proximal border is well defined, lying just beneath the distal palmar crease of the little, ring and middle fingers at the level of the neck of the metacarpal. The sheath consists of arcuate fibres that arch anteriorly over bone, tendons (where the sheath is required to be stiff) and the centres of joints (where a bucket-handle of arcuate fibres is a mechanically favourable arrangement). By contrast, where the sheath is required to fold to permit joint flexion, it consists of cruciate fibres. These fibrous sheaths are lined by a thin synovial membrane that provides a sealed lubrication system containing synovial fluid. The synovial membrane extends from the distal phalanx to mid-palm in the case of the index, middle and ring fingers, and further proximally in the case of the little finger (**Fig. 51.27C**). The sheaths around the thumb and little finger are continuous with the flexor sheaths in front of the wrist. The parietal synovial membrane is reflected on to the surface of the flexor tendon, forming a visceral synovium.

A standard nomenclature for the anular (A) and cruciform (C) pulleys is used. The usual pattern is as follows (**Fig. 51.27A–B**). The A1 pulley is situated anterior to the palmar cartilaginous plate of the metacarpophalangeal joint and may extend over the proximal part of the proximal phalanx. The A2 overlies the middle third of the proximal phalanx. It is the strongest pulley and arises from well-defined longitudinal ridges on the palmar aspect of the phalanx. Its distal edge is well developed. A pouch or recess of synovium extends superficial to the free edge of the pulley fibres so that the free edge forms a lip protruding into the synovial space. A3 is a narrow pulley lying palmar to the proximal interphalangeal joint. A4 overlies the middle third of the middle phalanx, and A5 overlies the distal interphalangeal joint. The cruciate fibres are numbered in a slightly different manner. C0 is palmar to the metacarpophalangeal joint. There are two cruciate zones, C1 and C2, at the proximal interphalangeal joint, and they lie just proximal and distal, respectively, to A3. At the distal interphalangeal joint, there is one pronounced cruciate system, C3, which lies between A4 and A5. Variations occur frequently. During flexion, the cruciate fibres become orientated more transversely in the digits, and the edges of adjacent anular pulleys approximate so that they form, in full flexion, a continuous tunnel of transversely orientated fibres. Surgically, the most important pulleys that prevent bowstringing of the flexor tendons are the A2 and A4 pulleys.

In the thumb, there are three constant pulleys: two anular and one oblique (**Fig. 51.28**). The A1 pulley is located at the metacarpophalangeal joint. The oblique pulley is located over the mid-portion of the proximal phalanx and its fibres pass from the ulnar aspect proximally to the radial aspect dorsally. The A2 pulley is thinner than the A1 pulley and is situated just proximal to the interphalangeal joint. The oblique pulley is the most important pulley in the thumb for maintaining the action of flexor pollicis longus.

Synovial sheaths of the carpal flexor tendons

Two synovial sheaths envelop the flexor tendons as they traverse the carpal tunnel: one for flexors digitorum superficialis and profundus, the other for flexor pollicis longus. These sheaths typically extend into the forearm for 2.5 cm proximal to the flexor retinaculum and, occasionally, communicate with each other deep to it. The sheath surrounding the tendons of the flexors digitorum reaches about halfway along the metacarpals, where it ends in blind diverticula around the tendons to the index, middle and ring fingers (see Fig. 51.27B). The sheath is prolonged around the tendons to the little finger and is usually continuous with their digital synovial sheath. The sheath of flexor pollicis longus, which is usually separate, is continued along the thumb as far as the insertion of the tendon (see Fig. 51.28).

Vincula

The phenomenon of tendon gliding within a fibrous sheath requires a very specialized arrangement of the vascular supply. Folds of synovial membrane, vincula brevia and longa, each containing a loose plexus of fascial fibres, carry blood vessels to the tendons at certain defined points (**Fig. 51.29**). Vincula brevia are attached to the deep surfaces of the tendons near to their insertions. There are two in each finger, one attaches flexor digitorum profundus to the region of the distal interphalangeal joint, and a more proximal vinculum lies deep to flexor digitorum superficialis at the proximal interphalangeal joint. Vincula longa are filiform: two are usually attached to each superficial tendon and one to each deep tendon.

Trigger finger

Available with the *Gray's Anatomy* e-book

Synovial sheaths of the carpal extensor tendons

Six tunnels deep to the extensor retinaculum transmit the extensor tendons, each containing a synovial sheath (**Fig. 51.30**). Each tunnel has an annotation from I to VI (1 to 6, first to sixth). The tendons of abductor pollicis longus and extensor pollicis brevis lie in a tunnel (compartment I) on the lateral side of the styloid process of the radius;

Precise knowledge of the nerve supply to the joints of the wrist and hand allows the surgeon to remove the afferent nerve supply in various conditions. This may effectively remove pain and avoid the alternative of joint excision, fusion or replacement, each of which has substantial disadvantages.

Trigger finger is a stenosing tenovaginosis of uncertain aetiology. The opening of the fibrous flexor sheaths of the fingers thickens to form a distinct palpable, often tender, nodule in the palm beneath the distal transverse palmar crease. This inhibits the normal excursion of the flexor tendons, causing the finger to lock down into flexion at all three joints. The corresponding extensor muscle is insufficiently powerful to extend the affected finger, so the patient does this passively, accompanied by a painful snap. As time passes the proximal interphalangeal joint develops a contracture. Treatment frequently requires corticosteroid injection or surgical division of the A1 pulley of the flexor sheath to relieve the stricture.

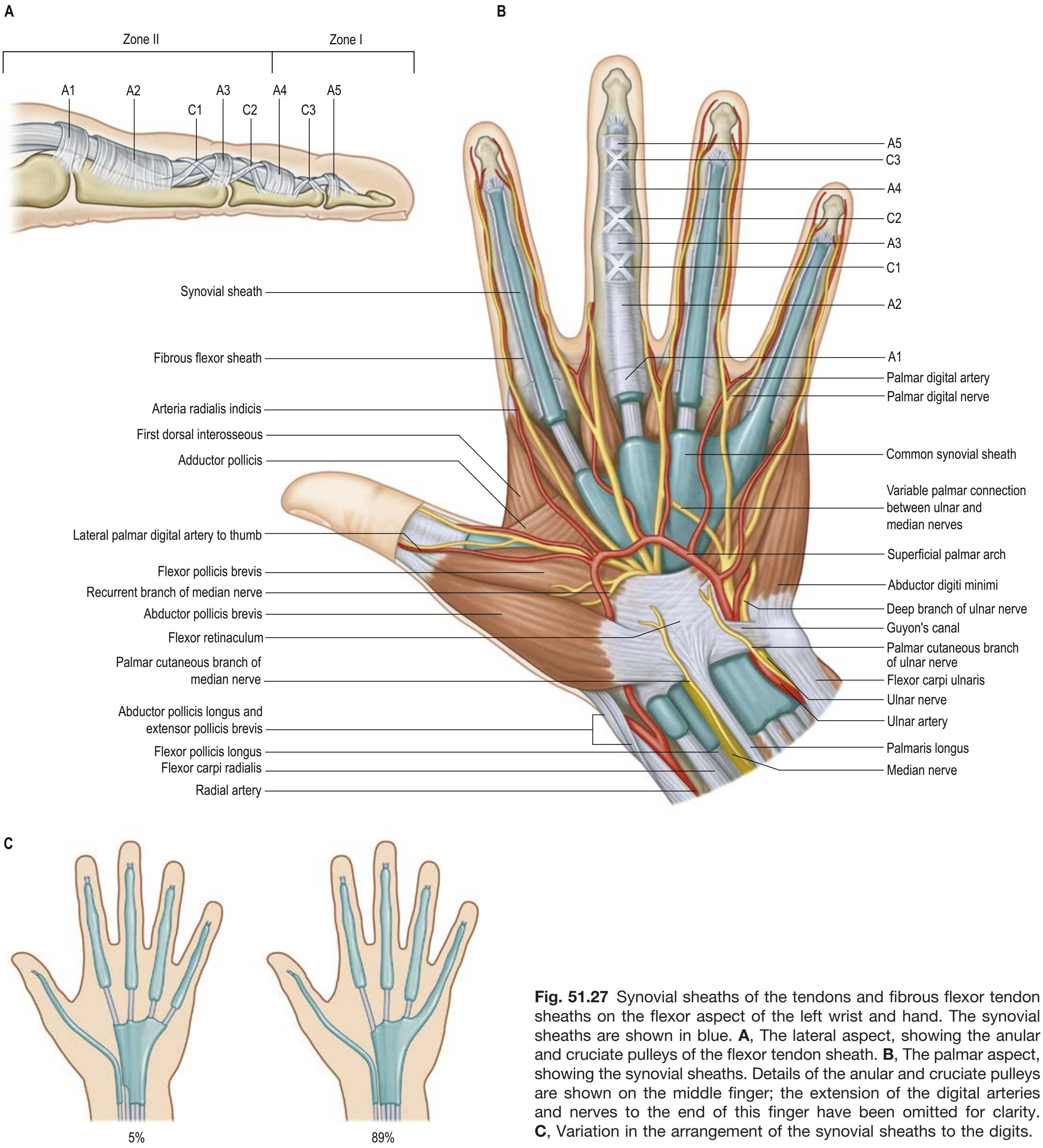
A
Zone II
Zone I
A1
A2
A3
A4
A5
C1
C2
C3
B
Synovial sheath
Fibrous flexor sheath
Arteria radialis indicis
First dorsal interosseous
Adductor pollicis
Lateral palmar digital artery to thumb
Flexor pollicis brevis
Recurrent branch of median nerve
Abductor pollicis brevis
Flexor retinaculum
Palmar cutaneous branch of median nerve
Abductor pollicis longus and extensor pollicis brevis
Flexor pollicis longus
Flexor carpi radialis
Radial artery
A5
C3
A4
C2
A3
C1
A2
A1
Palmar digital artery
Palmar digital nerve
Common synovial sheath
Variable palmar connection between ulnar and median nerves
Superficial palmar arch
Abductor digiti minimi
Deep branch of ulnar nerve
Guyon's canal
Palmar cutaneous branch of ulnar nerve
Flexor carpi ulnaris
Ulnar nerve
Ulnar artery
Palmaris longus
Median nerve
C
5%
89%

Fig. 51.27 Synovial sheaths of the tendons and fibrous flexor tendon sheaths on the flexor aspect of the left wrist and hand. The synovial sheaths are shown in blue. **A**, The lateral aspect, showing the anular and cruciate pulleys of the flexor tendon sheath. **B**, The palmar aspect, showing the synovial sheaths. Details of the anular and cruciate pulleys are shown on the middle finger; the extension of the digital arteries and nerves to the end of this finger have been omitted for clarity. **C**, Variation in the arrangement of the synovial sheaths to the digits.

there may be a separate synovial sheath for each, or the tendon of the abductor may be double. The floor of the sheath is formed by the insertion of brachioradialis. The tendons of extensors carpi radialis longus and brevis lie dorsomedial to the styloid process (compartment II); the tendon of extensor pollicis longus lies on the medial side of the dorsal (Lister's) tubercle of the radius (compartment III); the tendons of extensors digitorum and indicis lie in a tunnel on the medial side of the tubercle (compartment IV); the tendon of extensor digiti minimi lies dorsal to the distal radio-ulnar joint (compartment V); the tendon of extensor carpi ulnaris lies between the head and the styloid process of the ulna in a narrow groove (compartment VI). The tendon sheaths of abductor pollicis longus, extensors pollicis brevis and longus, extensors carpi radialis longus and brevis and extensor carpi ulnaris stop immediately proximal to the bases of the metacarpals, while those of extensors digitorum, indicis and digiti minimi are sometimes prolonged a little more distally along the metacarpus. The sheaths of compartments I–V are separated by vertical pillars that connect the dorsum of the distal radius and the extensor retinaculum. Compartment VI (containing extensor carpi ulnaris) has a separate subsheath that is not in continuity with the extensor retinaculum, an arrangement that allows rotation of the distal radio-ulnar joint that would not otherwise be possible if the rigid retinaculum linked compartments V and VI.

De Quervain's tenovaginitis

Available with the *Gray's Anatomy* e-book

De Quervain's tenovaginitis is a stenosing tenovaginosis of unknown aetiology that occurs in the first dorsal compartment at the level of the radial styloid. It involves the common extensor sheath containing the tendons of abductor pollicis longus and extensor pollicis brevis. There is palpable thickening of the tendon sheath with painful limitation of active extension and passive flexion of the thumb. Treatment may involve splinting, corticosteroid injection or surgery to divide the thickened sheath. The sheath is divided longitudinally along its dorsal attachment. This reduces the chance of 'bowstringing' of the abductor tendons on wrist flexion by retaining some pulley function. The surgeon must seek for a second and sometimes even third separate sheath within the first compartment. Care must be taken to avoid the immediately adjacent superficial radial nerve.

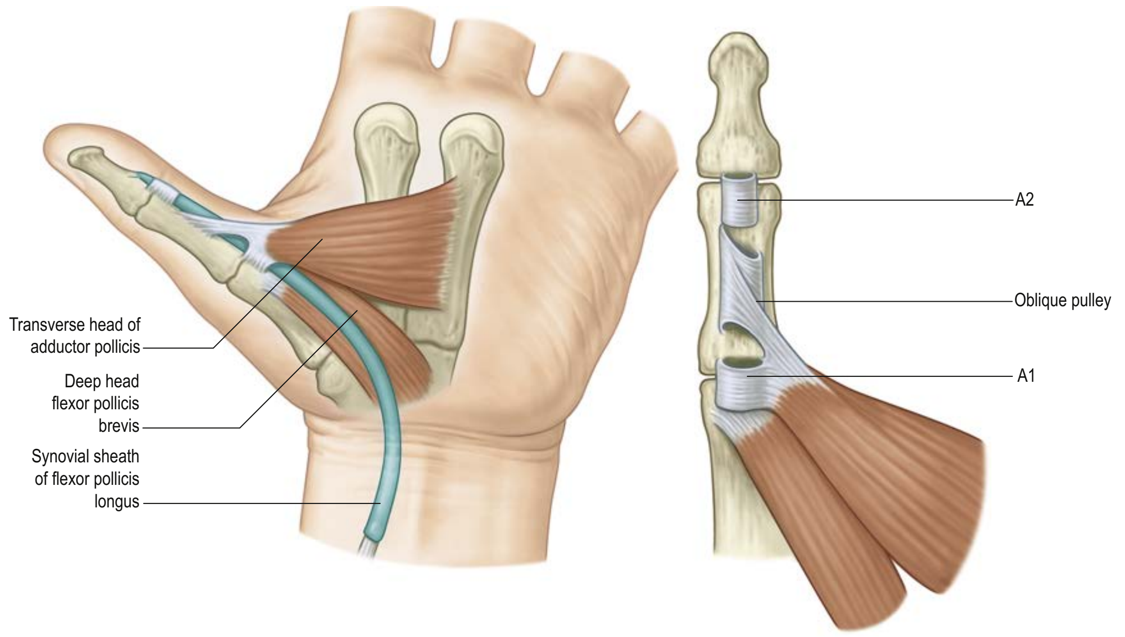
Transverse head of adductor pollicis
Deep head flexor pollicis brevis
Synovial sheath of flexor pollicis longus
A2
Oblique pulley
A1

Fig. 51.28 The flexor sheath of the left thumb, showing the anular and oblique pulleys. (From Doyle JR, Blythe WF 1977 Anatomy of the flexor tendon sheath and pulleys of the thumb. J Hand Surg Am 2:149–51. With permission from the American Society for Surgery of the Hand.)

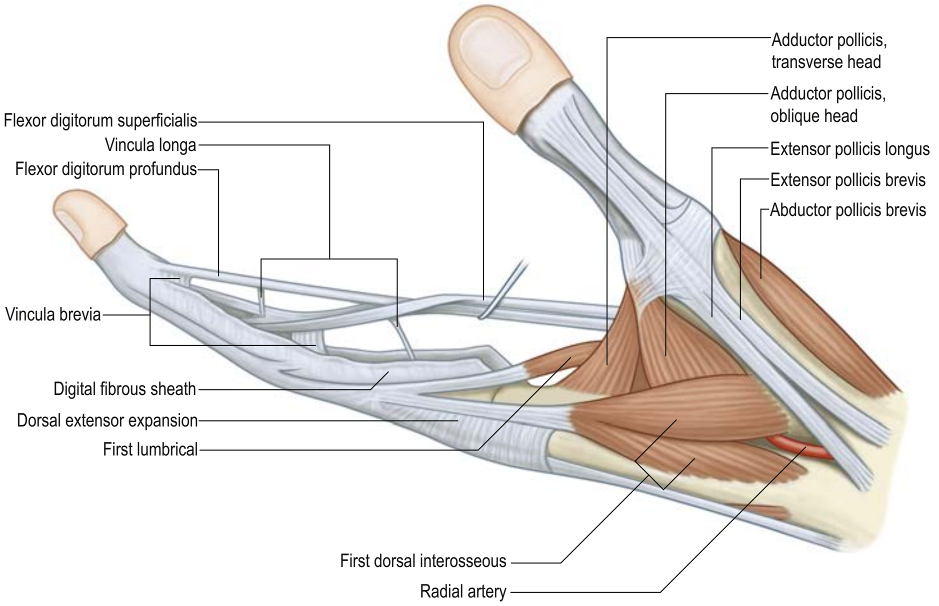
Flexor digitorum superficialis
Vincula longa
Flexor digitorum profundus
Vincula brevia
Digital fibrous sheath
Dorsal extensor expansion
First lumbrical
Adductor pollicis, transverse head
Adductor pollicis, oblique head
Extensor pollicis longus
Extensor pollicis brevis
Abductor pollicis brevis
First dorsal interosseous
Radial artery

Fig. 51.29 The tendons and vincula tendina of the index finger and the muscles in the first intermetacarpal space of the left hand: lateral aspect.

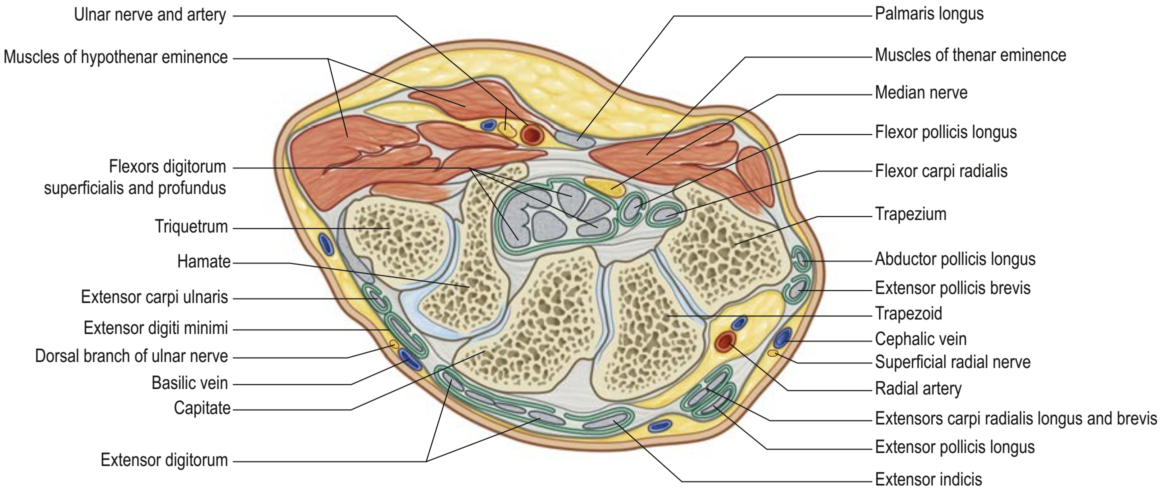
Ulnar nerve and artery
Muscles of hypothenar eminence
Flexors digitorum superficialis and profundus
Triquetrum
Hamate
Extensor carpi ulnaris
Extensor digiti minimi
Dorsal branch of ulnar nerve
Basilic vein
Capitate
Extensor digitorum
Palmaris longus
Muscles of thenar eminence
Median nerve
Flexor pollicis longus
Flexor carpi radialis
Trapezium
Abductor pollicis longus
Extensor pollicis brevis
Trapezoid
Cephalic vein
Superficial radial nerve
Radial artery
Extensors carpi radialis longus and brevis
Extensor pollicis longus
Extensor indicis

Fig. 51.30 A transverse section through the left wrist at the level of the distal row of the carpus, showing the muscle tendons (in grey) and their synovial sheaths (in green).

Extensor tendon apparatus

The extensor digitorum tendons emerge through the fourth dorsal compartment onto the dorsum of the hand, where they are joined together distally by a varying pattern of oblique interconnections, the juncturae tendinae. These typically pass in a distal direction from middle finger to index finger, and from ring finger to middle and little fingers. Proximal lacerations to the middle finger extensor tendon may result in only partial loss of extension because of these tendinous interconnections. There is considerable variability in the arrangement of the extensors over the back of the hand. There are usually two tendons to the middle and ring fingers, whereas the tendon to the little finger may be absent and replaced with a junctura tendinum from the ring finger.

At the level of the metacarpophalangeal joint, each extensor tendon is held in a central position over the dorsum of the joint by a flat, fibrous extensor expansion (see Fig. 51.25). The expansion extends on to the dorsum of the proximal phalanx of each digit, forming a movable hood that moves distally when the metacarpophalangeal joint is flexed, and proximally when it is extended. Each extensor tendon blends with the extensor expansion along its central axis and is separated from the metacarpophalangeal joint by a small bursa. The expansion is triangular in shape, with its base proximal. It receives the conjoined tendons of the interosseous and lumbrical muscles and is almost translucent between its margins and the tendon of extensor digitorum. Transverse fibres (the sagittal bands) pass to the volar plate and transverse metacarpal ligaments, separating the phalangeal attachment of the dorsal interosseous from the rest of the muscle, and the palmar interosseous from the lumbrical muscle. The margins of the extensor expansions are thickened on the radial side by the tendons of the lumbrical and interosseous muscles, and on the ulnar side either by the tendon of an interosseous alone or, in the case of the fifth digit, by abductor digiti minimi.

The tendons of the interossei join the extensor expansion at the level of the proximal portion of the proximal phalanx, while the tendons of the lumbricals join the extensor mechanism further distally at the mid-portion of the proximal phalanx. Their line of pull is anterior to the axis of rotation at the metacarpophalangeal joint, but dorsal to the axis of rotation at the proximal interphalangeal joint. The extensor mechanism trifurcates into a central slip and two lateral bands just proximal to the proximal interphalangeal joint. The central slip receives a contribution from the tendons of the lumbricals and interossei via the lateral bands. Similarly, some fibres from the central region pass to each lateral band, producing a criss-cross arrangement of fibres. The central slip attaches to the base of the middle phalanx, while the lateral bands continue distally; they eventually fuse together and insert into the distal phalanx. The tension in the central slip and the lateral bands varies as the finger moves between flexion and extension and plays a crucial role in coordinating synchronous activity between the proximal and distal interphalangeal joints.

The transverse and oblique retinacular ligaments of Landsmeer connect the fibrous flexor sheath to the extensor apparatus. The transverse retinacular ligament passes from the A3 pulley of the fibrous flexor sheath at the level of the proximal interphalangeal joint to the lateral border of the lateral extensor band. The oblique retinacular ligament lies deep to the transverse retinacular ligament. It originates from the lateral aspect of the proximal phalanx and flexor sheath (A2 pulley) and passes volar to the axis of rotation of the proximal interphalangeal joint, but in a dorsal and distal direction, to insert into the terminal extensor tendon.

Sagittal band movement

See **Video 51.4**.

Sagittal band injury

Available with the *Gray's Anatomy* e-book

Intrinsic muscles of the hand

The intrinsic muscles of the hand are organized into three groups plus a superficial muscle. The thenar muscles are flexor pollicis brevis, abductor pollicis brevis, opponens pollicis and adductor pollicis. The hypothenar muscles are abductor digiti minimi, flexor digiti minimi brevis and opponens digiti minimi. The interossei and lumbricals act on the fingers. Palmaris brevis is a superficial muscle that lies beneath the ulnar palmar skin.

Flexor pollicis brevis

Attachments Flexor pollicis brevis lies medial to abductor pollicis brevis (**Fig. 51.31**). It has superficial and deep parts. The superficial head arises from the distal border of the flexor retinaculum and the distal part of the tubercle of the trapezium, and passes along the radial side of the tendon of flexor pollicis longus. It is attached by a tendon that contains a sesamoid bone to the radial side of the base of the proximal phalanx of the thumb. The deep part arises from the trapezoid and capitate bones and from the palmar ligaments of the distal row of carpal bone, and passes deep to the tendon of flexor pollicis longus. It unites with the superficial head on the sesamoid bone and base of the first phalanx. The superficial head is frequently blended with opponens pollicis. The deep head varies considerably in size and may even be absent.

Relations Flexor pollicis brevis lies superficial in the thenar eminence and is distal to abductor pollicis brevis. It is crossed by the motor branch of the median nerve.

Actions Flexor pollicis brevis flexes the metacarpophalangeal joint.

Testing Flexor pollicis brevis is palpated whilst flexing the metacarpophalangeal joint, with the interphalangeal joint fully extended, to appose the pulp of the thumb against the pulp of the middle finger.

Abductor pollicis brevis

Attachments Abductor pollicis brevis is a thin, subcutaneous muscle in the proximolateral part of the thenar eminence (see Figs 51.13, 51.27). It arises mainly from the flexor retinaculum, but a few fibres spring from the tubercles of the scaphoid bone and trapezium and from the tendon of abductor pollicis longus. Its medial fibres are attached by a thin, flat tendon to the radial side of the base of the proximal phalanx of the thumb, and its lateral fibres join the dorsal digital expansion of the thumb. The muscle may receive accessory slips from the long and short extensors of the thumb, opponens pollicis, or the styloid process of the radius.

Relations Abductor pollicis brevis lies proximomedial to flexor pollicis brevis in the superficial part of the thenar eminence.

Actions Abductor pollicis brevis draws the thumb ventrally in a plane at right-angles to the palm of the hand (abduction).

Testing The subject abducts the thumb at right-angles to the palm against resistance; the muscle can be seen and felt.

Opponens pollicis

Attachments Opponens pollicis lies deep to abductor pollicis brevis (see Figs 51.13, 51.29, 51.31). It arises from the tubercle of the trapezium and the flexor retinaculum, and is attached to the whole length of the lateral border and the adjoining lateral half of the palmar surface of the metacarpal of the thumb. It does not insert into the proximal phalanx or the extensor expansion.

Relations Opponens pollicis lies deep between the other two muscles of the thenar eminence and is revealed only when they are retracted.

Actions Opponens pollicis flexes the metacarpal of the thumb and stabilizes the trapeziometacarpal joint.

Testing The subject touches the base of the little finger against resistance.

Adductor pollicis

Attachments Adductor pollicis arises by oblique and transverse heads (see Figs 51.13, 51.31). The oblique head is attached to the capitate bone, the bases of the second and third metacarpals, the palmar ligaments of the carpus, and the sheath of the tendon of flexor carpi radialis. Most of the fibres converge into a tendon (containing a sesamoid bone) that unites with the tendon of the transverse head and is attached to the ulnar side of the base of the proximal phalanx of the thumb. The most superficial fibres from the dorsal aspect pass into the medial side of the dorsal digital expansion of the thumb. The transverse head is the deepest of the muscles of the thumb; it is triangular and arises from the distal two-thirds of the palmar surface of the third metacarpal. The fibres converge to be attached, with the oblique head and the first palmar interosseous, to the base of the proximal phalanx of the thumb. The two parts of the adductor vary in relative size and degree of connection.

Injuries to the sagittal bands, from natural degeneration or a direct blow, can lead to subluxation of the extensor tendon. The radial sagittal band is usually affected. The tendon then passes anterior to the axis of the metacarpophalangeal joint, causing flexion and abduction of the proximal phalanx on the metacarpal. Secondary tightness of the opposite sagittal band and underlying collateral ligament promptly follows. Treatment involves immediate splinting to extend the metacarpophalangeal joint whilst keeping the proximal joint mobile. This reduces the sagittal band and allows healing. An alternative, particularly when there is secondary tightness of the opposite sagittal band, is surgical reconstruction.

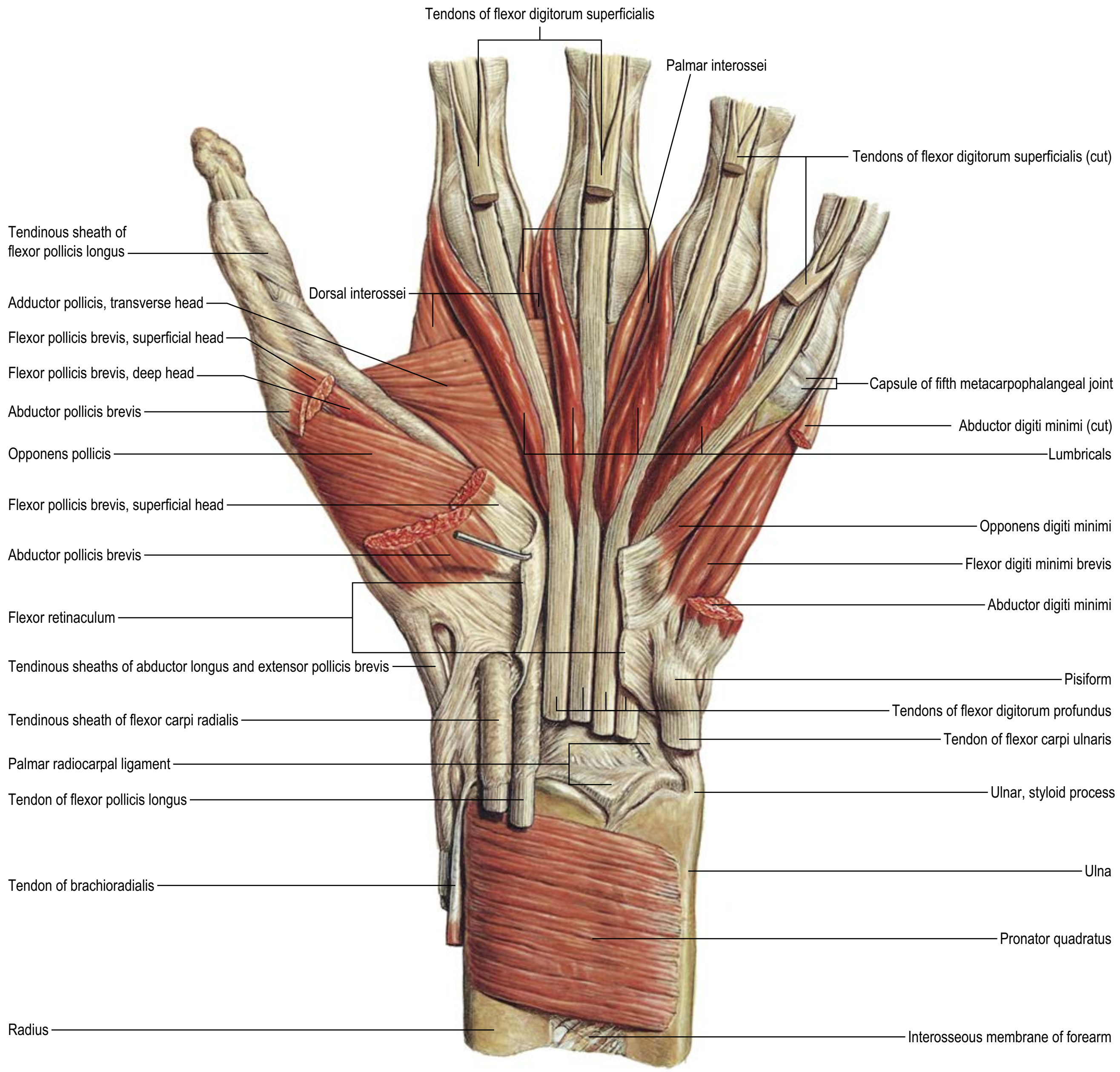
Tendons of flexor digitorum superficialis
Palmar interossei
Tendons of flexor digitorum superficialis (cut)
Tendinous sheath of flexor pollicis longus
Dorsal interossei
Adductor pollicis, transverse head
Flexor pollicis brevis, superficial head
Flexor pollicis brevis, deep head
Abductor pollicis brevis
Capsule of fifth metacarpophalangeal joint
Abductor digiti minimi (cut)
Opponens pollicis
Lumbricals
Flexor pollicis brevis, superficial head
Opponens digiti minimi
Abductor pollicis brevis
Flexor digiti minimi brevis
Abductor digiti minimi
Flexor retinaculum
Tendinous sheaths of abductor longus and extensor pollicis brevis
Pisiform
Tendinous sheath of flexor carpi radialis
Tendons of flexor digitorum profundus
Tendon of flexor carpi ulnaris
Palmar radiocarpal ligament
Tendon of flexor pollicis longus
Ulnar, styloid process
Tendon of brachioradialis
Ulna
Pronator quadratus
Radius
Interosseous membrane of forearm

Fig. 51.31 The muscles of the left hand. The deep layer is shown after cutting the flexor retinaculum and partial removal of several superficial muscles: palmar aspect. (Sobotta Atlas of Human Anatomy © Elsevier GmbH, Urban & Fischer, Munich.)

Relations The deep palmar arch and the deep branch of the ulnar nerve pass between the two heads of the muscle. Anteriorly, adductor pollicis is crossed by the flexor tendons of the index finger and their sheath and the first lumbrical, and is overlapped by flexor pollicis brevis. Posteriorly, it abuts against the first dorsal interosseous muscle: together, these muscles form the mass of the first web space of the hand.

Actions Adductor pollicis is the largest and most powerful of the intrinsic muscles and acts to approximate the thumb to the palm of the hand. It acts optimally when the abducted, rotated and flexed thumb is opposed to the fingers in gripping.

Testing The subject adducts the thumb at right-angles to the palm against resistance.

Abductor digiti minimi

Attachments Abductor digiti minimi arises from the pisiform bone, the tendon of flexor carpi ulnaris and the pisohamate ligament (see Figs 51.13, 51.27, 51.31). It ends in a flat tendon that divides into two slips: one is attached to the ulnar side of the base of the proximal phalanx of the little finger, and the other to the ulnar border of the dorsal digital expansion of extensor digiti minimi. The muscle may have two or three slips and may be fused with flexor digiti minimi brevis. An additional slip may arise from the flexor retinaculum, antebrachial fascia, or tendons of palmaris longus or flexor carpi ulnaris, and may be partly attached to the fifth metacarpal by a slip from the pisiform.

Relations Abductor digiti minimi lies along the ulnar border of flexor digiti minimi brevis and overlies opponens digiti minimi.

Actions Abductor digiti minimi abducts the little finger away from the fourth, e.g. in the habitual spreading of the digits when they are extended. Abduction is also possible when digits 2–4 are tightly adducted in flexion or extension.

Testing The little finger is abducted against resistance.

Flexor digiti minimi brevis

Attachments Flexor digiti minimi brevis arises from the convex surface of the hook of the hamate and the palmar surface of the flexor retinaculum, and inserts into the ulnar side of the base of the proximal phalanx of the little finger with abductor digiti minimi (see Fig. 51.31). It may be absent, or fused with the abductor, and it may attach to the distal end of the fifth metacarpal by a muscular slip.

Relations Flexor digiti minimi brevis lies lateral to the abductor. Its origin is separated from that of the abductor by the deep branches of the ulnar artery and nerve.

Actions Flexor digiti minimi brevis produces flexion of the little finger at its metacarpophalangeal joint, together with some lateral rotation.

Testing The subject flexes the metacarpophalangeal joint of the little finger against resistance with the interphalangeal joints in extension.

Opponens digiti minimi

Attachments Opponens digiti minimi is a triangular muscle lying under cover of the flexor and abductor (see Figs 51.13, 51.31). It arises from the convexity of the hook of the hamate and the contiguous portion of the flexor retinaculum, and inserts along the whole length of the ulnar margin of the fifth metacarpal and the adjacent palmar surface. The muscle is often divided into two lamellae by the deep branches of the ulnar artery and nerve. It blends to a variable degree with its neighbours.

Relations Opponens digiti minimi lies on the ulnar margin and adjacent palmar surface of the fifth metacarpal, overlapped by, and often partly fused with, the other two muscles of the hypothenar eminence.

Actions Opponens digiti minimi flexes the fifth metacarpal, drawing it forwards and rotating it laterally at the carpometacarpal joint; this deepens the hollow of the palm. These actions, together with flexion and some lateral rotation at the metacarpophalangeal and interphalangeal joints, bring the digit into opposition with the thumb.

Testing The subject opposes the tip of the little finger to the tip of the thumb with the interphalangeal joints of the little finger in extension.

Palmaris brevis

Attachments Palmaris brevis is a thin, quadrilateral muscle lying beneath the skin of the ulnar side of the palm (see Fig. 51.12A). It arises from the flexor retinaculum and the medial border of the central part of the palmar aponeurosis and is attached to the dermis on the ulnar border of the hand.

Relations Palmaris brevis is superficial to the ulnar artery and the superficial terminal branch of the ulnar nerve.

Actions Palmaris brevis wrinkles the skin on the ulnar side of the palm of the hand and deepens the hollow of the palm by accentuating the hypothenar eminence.

Testing The subject opposes the thumb to the little finger; the skin on the ulnar side of the palm is seen to pucker.

Interossei

The interossei occupy the intervals between the metacarpals and are divided into a palmar and a dorsal set.

Palmar interossei

Attachments Palmar interossei are smaller than dorsal interossei and lie on the palmar surfaces of the metacarpals rather than between them (**Fig. 51.32**; see Fig. 51.13). The middle finger has no palmar interosseous; the remaining digits have palmar interossei on their aspects that face the middle finger. The first is often rudimentary and is not described by all anatomists. When present, it arises from the ulnar side of the palmar surface of the base of the first metacarpal and the trapezium; it is inserted into the ulnar sesamoid and from here, it passes to the phalanx and, usually, also into the dorsal digital expansion. It may be considered to be the most lateral head of the oblique component of adductor pollicis. The second palmar interosseous arises from the ulnar side of the second metacarpal and is inserted into the same side of the digital expansion of the index finger. The third arises from the radial side of the fourth metacarpal and is inserted together with the third lumbrical. The fourth arises from the radial side of the fifth metacarpal and is attached with the fourth lumbrical and to the base of the proximal phalanx. The attachment of these muscles to the dorsal digital expansions (see Figs 51.25, 51.29) stabilizes the extensor tendons on the convex heads of the metacarpals during flexion and extension at the metacarpophalangeal joints. The interossei show little variation in their arrangement; occasionally they may be duplicated.

Relations The first palmar interosseous lies anterior to the lateral head of the first dorsal interosseous and is overlapped anteriorly by the oblique head of adductor pollicis that also crosses anterior to the second palmar interosseous. The third and fourth are overlapped by the long flexor tendons of the ring and little finger, respectively, within their flexor sheaths.

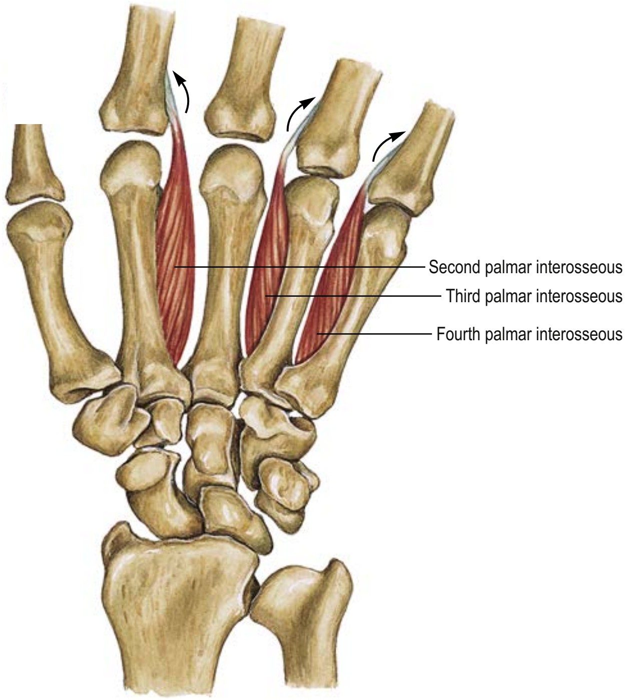
Second palmar interosseous
Third palmar interosseous
Fourth palmar interosseous

Fig. 51.32 The palmar interossei of the left hand: palmar aspect. Note that there is no first palmar interosseous in this specimen. (Sobotta Atlas of Human Anatomy © Elsevier GmbH, Urban & Fischer, Munich.)

Actions Palmar interossei adduct the fingers towards the longitudinal axis of the middle finger when the metacarpophalangeal joints are extended. This action is facilitated by the laxity of the collateral ligaments in extension (because the dorsal width of the metacarpal head is less than its palmar width). Interossei have a considerable cross-sectional area and, therefore, contribute significantly to metacarpophalangeal joint flexion and interphalangeal extension. When the interossei are paralysed, the grip strength of the hand is reduced and the arc of finger motion is abnormal, with a tendency for the fingers to claw. Each interosseous also rotates the digit at the metacarpophalangeal joint. Generally, this is not obvious because interossei act in pairs, but it may occur where one interosseous is deficient as a result of injury or congenital deformity.

Testing The subject adducts the index ring and little fingers against resistance.

Dorsal interossei

Attachments Dorsal interossei consist of four bipennate muscles, each arising from the adjacent sides of two metacarpals, but more extensively from the metacarpal of the finger into which the muscle passes (**Fig. 51.33**). They insert on the bases of the proximal phalanges and separately into the dorsal digital expansions (see Fig. 51.25). There is a narrow triangular interval between the double origin of each of these muscles; the radial artery passes through the first of these intervals, and a perforating branch from the deep palmar arch passes through each of the others. The first and largest muscle is sometimes called abductor indicis and is attached to the radial side of the proximal phalanx of the index finger and to the capsule of the adjoining metacarpophalangeal joint. The second and third are attached to the radial and ulnar sides of the middle finger, respectively. Whereas the second generally reaches the digital expansion and the proximal phalanx, the third usually extends only to the digital expansion. The fourth may be wholly attached to the digital expansion, but it often sends an additional slip to the proximal phalanx.

Relations The first dorsal interosseous abuts anteriorly with adductor pollicis. The other dorsal interossei occupy the spaces between the second and the fifth metacarpals.

Actions Dorsal interossei abduct and externally rotate the fingers away from the longitudinal axis of the middle finger. This allows cupping of

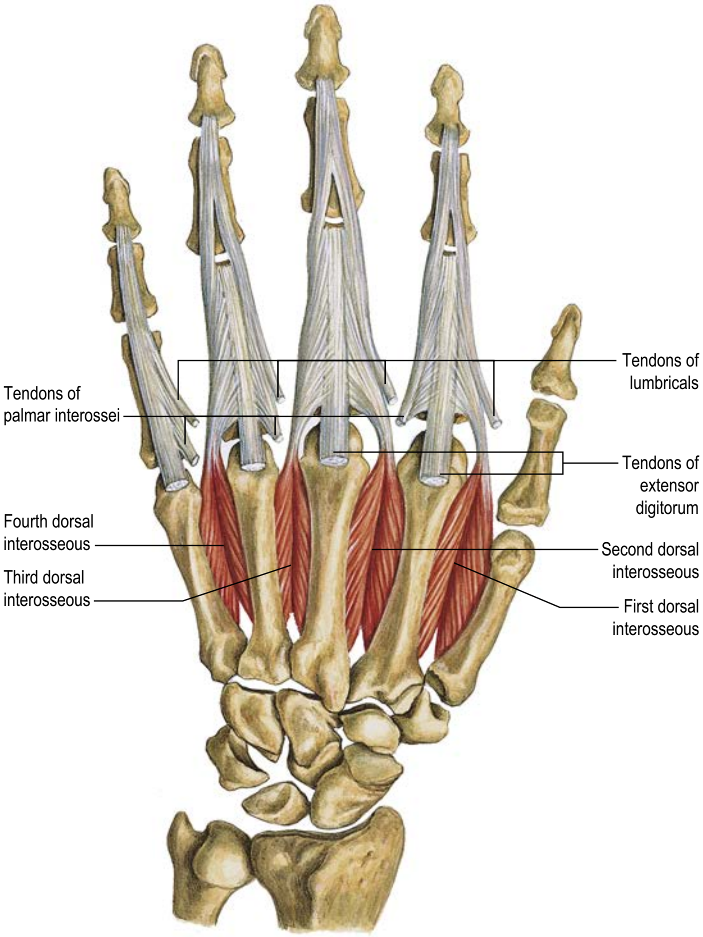
Tendons of palmar interossei
Tendons of lumbricals
Tendons of extensor digitorum
Fourth dorsal interosseous
Third dorsal interosseous
Second dorsal interosseous
First dorsal interosseous

Fig. 51.33 The dorsal interossei of the left hand: dorsal aspect. (Sobotta Atlas of Human Anatomy © Elsevier GmbH, Urban & Fischer, Munich.)

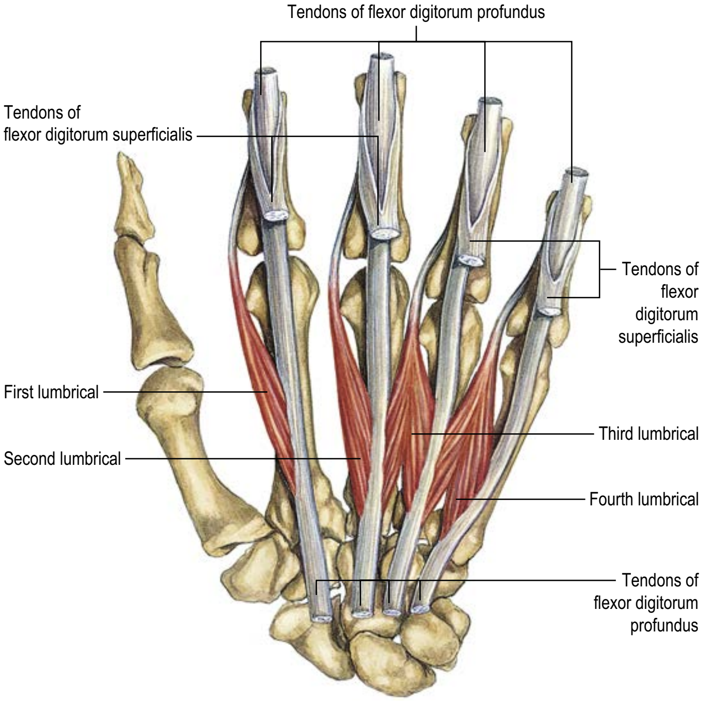
Tendons of flexor digitorum profundus
Tendons of flexor digitorum superficialis
Tendons of flexor digitorum superficialis
First lumbrical
Third lumbrical
Second lumbrical
Fourth lumbrical
Tendons of flexor digitorum profundus

Fig. 51.34 The lumbricals of the left hand: palmar aspect. (Sobotta Atlas of Human Anatomy © Elsevier GmbH, Urban & Fischer, Munich.)

the hand through the distal transverse metacarpal arch around an object such as a ball.

Testing The subject abducts the index, middle and ring fingers against resistance. The first dorsal interosseous is tested with the subject's fingers and palm flat on the table and the subject tries to abduct the index finger against the examiner's resistance. The muscle belly can be felt and seen.

Lumbricals

Attachments The four small lumbrical muscles arise from the tendons of flexor digitorum profundus (Fig. 51.34; see Fig. 51.31). The first and second are unipennate muscles and arise from the radial sides and palmar surfaces of the tendons of the index and middle fingers, respectively. The third arises from the adjacent sides of the tendons of the middle and ring fingers, and the fourth from the adjoining sides of the tendons of the ring and little fingers; both are bipennate muscles. Each passes to the radial side of the corresponding finger and is attached to the lateral margin of the dorsal digital expansion of extensor digitorum covering the dorsal surface of the finger. The lumbrical is distal to the interosseous and attached to the extensor retinaculum at a greater angle. Variations in the attachments of the lumbricals are common (Parminder 2013). Any of them may be unipennate or bipennate. When they are bipennate, the two heads arise from adjoining tendons of flexor digitorum profundus, and, in the case of the first lumbrical, from the tendon of flexor pollicis longus. Accessory lumbrical slips may be attached to an adjacent tendon of flexor digitorum superficialis.

Actions

See **Video 51.5**.

Lumbricals arise from flexor tendons and insert into the extensor apparatus. Since both attachments are mobile, they have the potential for producing movement at either. The action on the extensor apparatus extends both interphalangeal joints in a coordinated manner. The mode of action at the metacarpophalangeal joints is disputed, but if there is a flexor action, it is weaker than that of the interossei. Because of the more distal insertion into the expansion, the lumbricals can still extend the interphalangeal joints with the metacarpophalangeal joints flexed, whereas the interossei cannot. The effect on the flexor digitorum profundus attachment is to pull the tendon distally. The combined action on both origin and insertion is, therefore, to weaken the tone of flexor digitorum profundus and augment the extension tone. Pinching the index finger against the thumb without a lumbrical would result in a nail-to-nail contact; the addition of the lumbrical increases the interphalangeal joint extension and results in pulp-to-pulp pinch. Lumbricals contain many muscle spindles and have a long fibre length and it is therefore reasonable to assume that they play a role in proprioception.

The intrinsic muscles of the fingers, the interossei and lumbricals combined, have an important role in advancing metacarpophalangeal joint flexion yet inhibiting interphalangeal joint flexion when grip is initiated. This allows the fingers to form a hemisphere to hold an item such as a ball or a stick. In the absence of this accessory function, the long flexors would pull the interphalangeal joints into flexion too early which would hook the tips of the fingers and obstruct the space in front of the phalanges into which the ball would sit.

Testing Lumbricals cannot be tested in isolation but only as the lumbrical–interosseous muscle complex. The examiner asks the subject to hold the metacarpophalangeal joint of the finger in full flexion whilst fully extending the interphalangeal joints. An inability to do this causes the finger to assume a 'clawed' posture wherein the metacarpophalangeal joint extends and the interphalangeal joints flex. Tightness of the intrinsic muscles is assessed by the Bunnell test the metacarpophalangeal joint is held extended by the examiner and the proximal interphalangeal joint is passively flexed. An inability to flex the latter indicates that the intrinsic muscle is foreshortened.

Vascular supply to the intrinsic muscles of the hand

Flexor pollicis brevis is supplied by the superficial palmar branch of the radial artery, and branches from the princeps pollicis artery and radialis indicis artery. Abductor pollicis brevis is supplied by the superficial palmar branch of the radial artery and, often, by an independent branch directly from the radial artery lying on the radial aspect of the thumb. Opponens pollicis is supplied by the superficial palmar branch of the radial artery and by branches from the first palmar metacarpal artery (when present), arteria princeps pollicis, arteria radialis indicis and the deep palmar arch. Adductor pollicis is supplied by the arteria princeps pollicis and arteria radialis indicis (sometimes combined as the first palmar metacarpal artery) and by branches from the deep palmar arch. Abductor digiti minimi and flexor digiti minimi brevis are supplied by the deep palmar branch of the ulnar artery and branches from the ulnar end of the superficial palmar arch; the medial border of the little finger is supplied by the palmar digital artery. Opponens digiti minimi is supplied by the deep palmar branch of the ulnar artery and branches from the medial end of the deep palmar arch. Palmaris brevis is supplied by branches from the ulnar end of the superficial palmar arch. The palmar interossei are supplied by branches from the deep palmar arch, arteria princeps pollicis, arteria radialis indicis, palmar metacarpal arteries, proximal and distal perforating arteries, and common and proper digital (palmar) arteries. The dorsal interossei are supplied by the dorsal metacarpal arteries (first to fourth), palmar metacarpal arteries (second to fourth), radial artery (first), arteria princeps pollicis, arteria radialis indicis, three perforating branches from the deep palmar arch (proximal perforating arteries) and three distal perforating branches. Their tendons are supplied by branches from the common and proper palmar digital arteries and the dorsal digital arteries.

The first and second lumbricals are supplied by the first and second dorsal metacarpal and dorsal digital arteries. The third and fourth lumbricals are supplied by the second and third common palmar digital arteries, and the third and fourth dorsal digital arteries and their anastomoses with the palmar digital arteries.

Innervation of the intrinsic muscles of the hand

The superficial head of flexor pollicis brevis is usually innervated by the recurrent motor branch of the median nerve, and the deep head by the deep branch of the ulnar nerve; variation is common. Abductor pollicis brevis is innervated by the recurrent motor branch of the median nerve and is the only thenar muscle that is constantly supplied by the median nerve. Opponens pollicis is innervated by the lateral terminal branch of the median nerve and, commonly, by a branch of the deep terminal branch of the ulnar nerve. Adductor pollicis, abductor digiti minimi, flexor digiti minimi brevis, opponens digiti minimi and all the interossei are innervated by the deep branch of the ulnar nerve; the first dorsal interosseous and adductor pollicis are supplied by its most distal portion. Palmaris brevis is innervated by the superficial branch of the ulnar nerve. The first and second lumbricals are innervated by the median nerve, and the third and fourth lumbricals by the deep terminal branch of the ulnar nerve. The third lumbrical frequently receives a supply from the median nerve. The first and second lumbricals are, occasionally, innervated by the deep terminal branch of the ulnar nerve.

MOVEMENTS OF THE HAND

The apparently simple human functions of closing the hand to grasp an object, or opening the palm to release it, are, in reality, tasks of considerable mechanical complexity, requiring the simultaneous contraction of many individual muscles. The isolated action of a single muscle may be inferred from the positions of its origin and insertion, and the estimated line of action (usually, the centre line of the muscle) in relation to the axes of all the joints traversed by the muscle and its tendon. The limb can be regarded as a chain of joints crossed by muscles. If it is known which muscles are active, then the reason why one joint moves and others do not is a matter of simple mechanical relationships. For example, flexor pollicis longus is considered to have a major role as a flexor of the interphalangeal joint of the thumb. However, the position of its tendon relative to more proximal joints in the limb gives it the potential for producing flexion at the metacarpophalangeal joint and also at the trapeziometacarpal and wrist joints. In the living subject, the actual motion that takes place depends on which other muscle groups are acting as antagonists, and so the potential for movement must be considered for each joint in the chain in turn. Potential flexion at the wrist by flexor pollicis longus is generally balanced by wrist extensors and flexion at the trapeziometacarpal joint is balanced by abductor pollicis longus. Flexor pollicis longus will then have an action as a flexor of the metacarpophalangeal and interphalangeal joints only.

The factor that determines whether one or both of two joints will move is the turning moment at each. The greater the perpendicular distance from the line of muscle or tendon pull to the axis of the joint, the stronger is the turning effect of the muscle at the joint, but the smaller the range of joint motion that can be produced. In the case of flexor pollicis longus, the tendon is situated further from the axis of the metacarpophalangeal joint than from the axis of the interphalangeal joint; it will, therefore, tend to produce flexion preferentially at the metacarpophalangeal joint, unless that joint is restrained by extensor pollicis brevis. In this way, different postures of the thumb can be produced by the interplay of flexor and extensor forces. These simple guiding principles should provide an understanding of muscle action in the hand that is sufficient for most purposes.

In considering the role of a particular muscle, there is a tendency to concentrate on motion. Indeed, many muscles are named on the basis of the movements that they generate, although others, often those whose actions are the most difficult to interpret, are described according to their morphology or situation. A more important function may be the nature of the force generated. For example, although flexor pollicis longus flexes the thumb, a large range of flexion is actually required in only a few activities, such as grasping a narrow bar in the palm. In most pinch and manipulative tasks, the role of the thumb is to apply isometric force, which it does with such precision that it is possible to pick up an egg and neither crush nor drop it. Thus, for much of the time, flexor pollicis longus behaves as an extremely sophisticated mechanism for the application of force, in which contraction and proprioception are equally important.

The anatomical position of the hand (palm flat and pointing anteriorly, forearm supinated) is a convenient standard for studying structural relationships. The hand in the relaxed (anaesthetized) position adopts a posture of partial flexion and mid-supination/pronation (the reader can verify this by relaxing completely and observing forearm and hand position).

Special functions of the hand

Closing and opening the hand

Available with the *Gray's Anatomy* e-book

Movements of the thumb

Available with the *Gray's Anatomy* e-book

The paralysed hand

Available with the *Gray's Anatomy* e-book

VASCULAR SUPPLY

Arteries

Anastomoses occur between the radial and ulnar arteries at the wrist (via the palmar and dorsal carpal arches) and in the hand (via the superficial and deep palmar arches), and between their digital and metacarpal branches (**Figs 51.35, 51.36**) (Wong and Higgins 2015).

Radial artery

At the wrist, the radial artery passes on to the dorsal aspect of the carpus between the lateral carpal ligament and the tendons of abductor pollicis longus and extensor pollicis brevis (**Fig. 51.37**). It crosses the scaphoid bone and trapezium (in the anatomical snuff-box), where again, its pulsation is obvious; as it passes between the heads of the first dorsal interosseous, it is crossed by the tendon of extensor pollicis longus. Between the thumb extensors, it is crossed by the start of the cephalic vein and the branches of the radial nerve that pass to the thumb and index finger. Occasionally, it gives off a distal superficial dorsal branch that crosses the radial extensor tendons at the wrist, together with the superficial radial nerve. Branches of the lateral cutaneous nerve of the forearm run along its distal part as it curves round the carpus.

In the hand, the radial artery passes through the first interosseous space between the heads of the first dorsal interosseous and crosses the palm. At first, it lies deep to the oblique head of adductor pollicis and then passes between its oblique and transverse heads or through the transverse head. At the fifth metacarpal base, it anastomoses with the deep branch of the ulnar artery, completing the deep palmar arch (see Fig. 51.36).

Palmar carpal branch The palmar carpal branch arises near the distal border of pronator quadratus (see Fig. 50.9B). It crosses the anterior surface of the distal end of the radius, near the palmar carpal surface, and passes medially to anastomose behind the long flexor tendons with the palmar carpal branch of the ulnar artery. This transverse anastomosis is joined by longitudinal branches from the anterior interosseous artery and recurrent branches from the deep palmar arch, forming a cruciate palmar radiocarpal arch that supplies the carpal articulations and bones by descending branches.

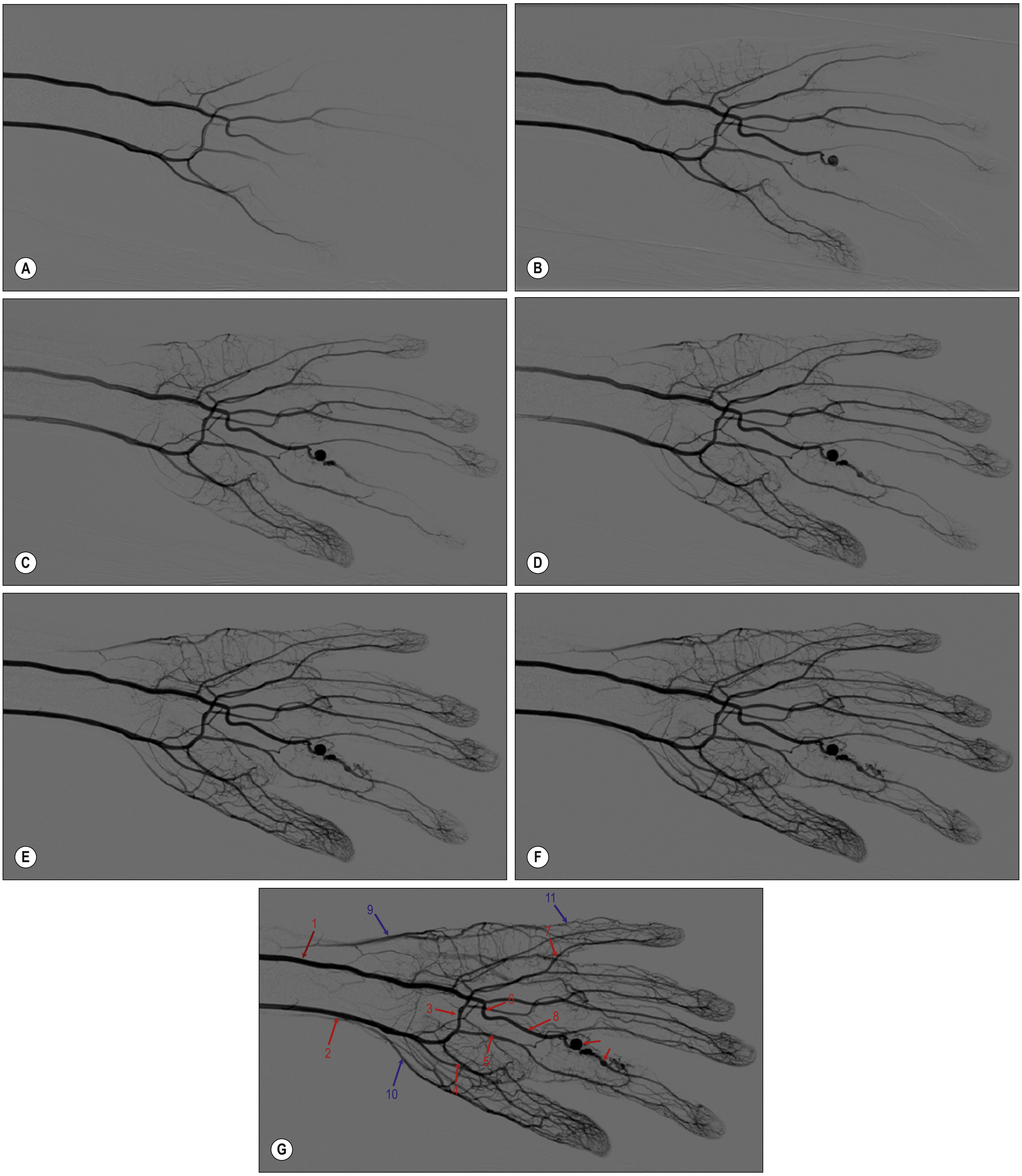

Fig. 51.35 A digital subtraction macroangiogram of the hand. Predominant phases. **A–B**, arterial phase; **C–D**, arteriolar phase; **E–F,** capillary phase; **G**, between capillary and venular phases. A small arterio-venous malformation shown on the index finger is suitable for radiologically guided embolization (unnumbered arrows). Key: 1, ulnar artery; 2, radial artery; 3, deep palmar arch; 4, princeps pollicis artery; 5, arteria radialis indicis; 6, superficial palmar arch (incomplete); 7, proper palmar digital artery (little finger); 8, common palmar digital artery; 9, basilic vein; 10, cephalic vein; 11, digital vein.

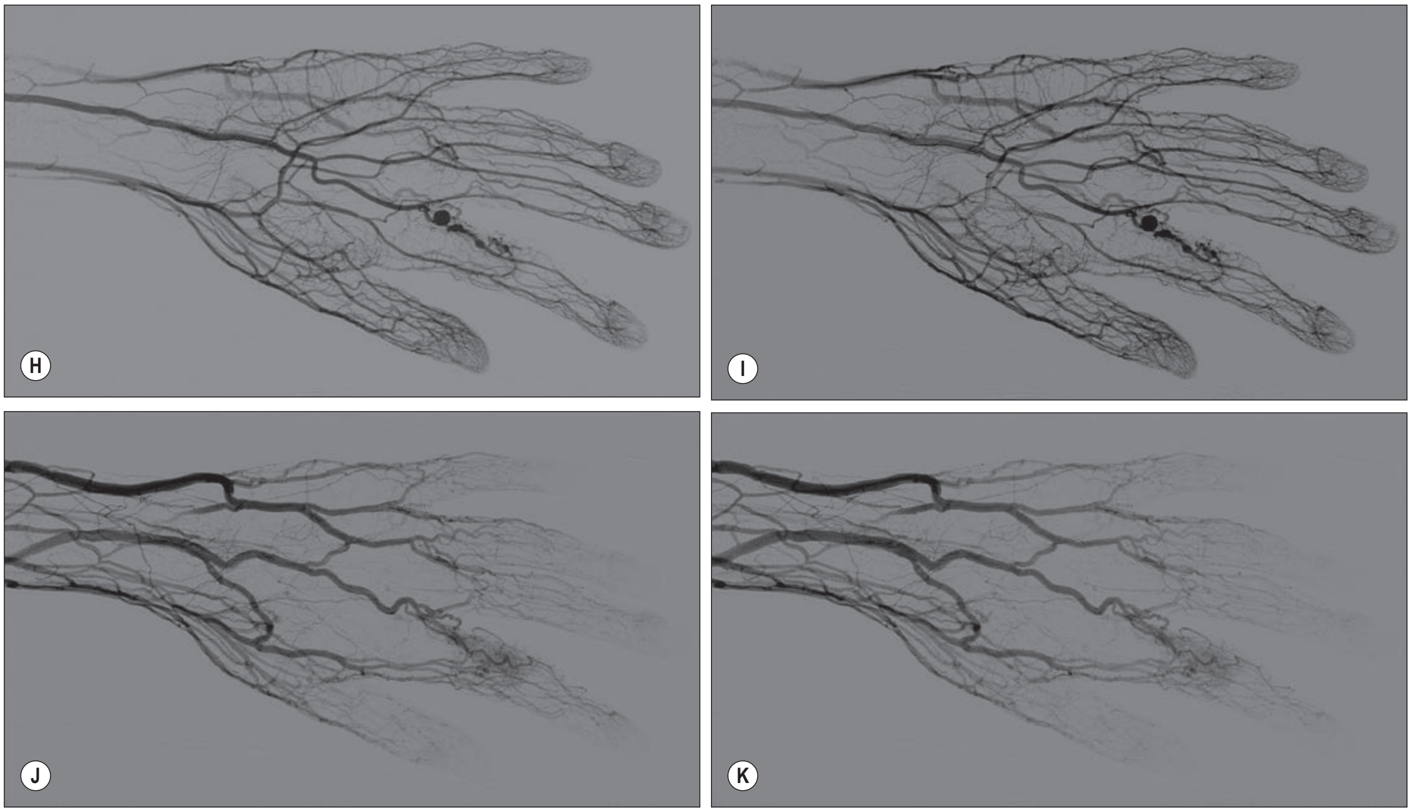

Fig. 51.35 cont'd, H–I, venular phase; **J–K**, venous phase.

Closing the hand

Whilst the fingers flex in gripping, grasping or making a fist, there are subtle differences in hand posture in these various activities. The basic mechanisms of hand closure will be described before special grips are considered.

As the digits flex, the wrist usually extends (dorsiflexes) at the same time. The involvement of the long digital flexors in this movement will be considered first, followed by an analysis of the role of the wrist.

Role of the long digital flexors

Flexor digitorum superficialis acts principally to flex the proximal interphalangeal joints, through its insertions into the middle phalanges. However, in each digit, it also has an action on the metacarpophalangeal joint because the tendon passes anterior to that joint. The muscle has the potential to produce flexion at the wrist for the same reason. The fact that each tendon arises from an individual muscle slip allows the clinician to test one finger at a time. The reader can verify this by attempting to flex each digit individually while using the other hand to keep the distal interphalangeal joints of the remaining fingers in extension. This test is frequently used in clinical practice and is useful for the middle and ring fingers, where flexion of one finger alone must be attributed to flexor digitorum superficialis. The index finger, however, has its own profundus musculotendinous unit and may, therefore, move independently under the action of this tendon. Many individuals cannot flex the proximal interphalangeal joint of the little finger alone, usually because of linkage between the tendons of the ring and little finger flexor digitorum superficialis, but occasionally because superficialis is deficient. Most individuals can flex the metacarpophalangeal joint of the little finger using flexor digiti minimi.

Flexor digitorum profundus is the only flexor of the distal interphalangeal joint. It also contributes, together with superficialis, to flexion at the proximal interphalangeal and metacarpophalangeal joints. These two long flexors (sometimes called extrinsic flexors because the muscle bellies are outside the hand) can be considered to act together to flex the fingers.

Role of the intrinsic muscles of the hand

The action of the long flexors alone would wind up the interphalangeal joints before the metacarpophalangeal joints, and the fingers would not move in a normal arc of flexion. This is precisely what happens in an ulnar nerve paralysis, in which the interossei and lumbricals are not functioning. These small (intrinsic) muscles have been described earlier in terms of their individual actions. For their role in coordinated activity, it is sufficient to appreciate that their contribution changes the arc produced by the long flexors, increasing flexion at the metacarpophalangeal joint and reducing flexion at the proximal and distal interphalangeal joints. All three joints are then angulated to the same degree and the fingers form a normal arc of flexion. As the finger flexes, the long extensor tendons (extensor digitorum, extensor indicis and extensor digiti minimi) aid the process by relaxing and allowing the extensor apparatus to glide distally on the dorsum of the phalanges.

Role of the wrist

As the fingers wind up to make a fist, the wrist tends to extend, particularly when force is applied. This extension has a marked effect on the excursion of the long flexor tendons. On its own, digital flexion requires the long tendons to move proximally in their sheaths and the flexor muscles in the forearm would shorten. The maximum excursion possible in flexor digitorum superficialis and flexor digitorum profundus is approximately 7 cm. Extension of the wrist tends to produce a lengthening of these muscles, which, in normal use, is almost enough to balance the shortening due to finger flexion; the net effect is a very slight shortening (approximately 1 cm) of the long flexors in the forearm. The wrist can, therefore, be seen as a mechanism for maximizing force because it allows the fingers to flex while maintaining the resting length of the extrinsic muscles near to the peak of the force–length curve. It is, of course, possible to wind up the fingers with the wrist held in a neutral position but the grip is somewhat weaker. With the wrist in full flexion, it is not possible to flex the fingers fully as there is insufficient excursion of the muscle unit.

Flexion of the fingers on gripping tends to result in a distal excursion of the long extensors. However, this tendency is counteracted by dorsiflexion of the wrist. The net effect is a very small proximal excursion of the long extensor tendons on gripping, mirroring the effect on the flexor surface. If the movement of the wrist is exaggerated so that the wrist is a little flexed on opening the hand, and fully dorsiflexed on closing it, the net excursion of long flexors and extensors is zero, i.e. this whole movement sequence can be completed with the forearm flexor and extensor muscles contracting isometrically.

The reader can observe the relationship between digits and wrist by performing the following manoeuvre. The wrist is held in a relaxed, mid-supinated position, with the elbow flexed at 90°. If the forearm is now rotated into pronation, the wrist will fall into flexion and the fingers will automatically extend. If the forearm is rotated into supination, the wrist will extend and the fingers flex. The finger movements compensate for the wrist movements and are entirely automatic; they are made without the need for any excursion of forearm flexor or extensor tendons. This test, the wrist tenodesis test, is a useful way of examining the limb for tendon injury. The pointing finger (which does not move with wrist motion) ‘points to’ a tendon injury.

Making a tight fist

It is possible to observe and to palpate the muscle groups that are active in making a tight fist. Flexor digitorum profundus and flexor digitorum superficialis are active, and flexor carpi ulnaris contracts strongly, as do the wrist extensors. Palpation of the long digital extensors on the dorsum of the wrist, the first dorsal interosseous in the thumb web, and of the other interossei and the thenar and hypothenar muscles, will confirm that all these muscles are contracting. As a firm fist is swung forwards in anger, brachioradialis stands out; at the moment of impact, virtually every muscle in the limb is active.

Role of the arches of the hand

The hand has *stable* elements and *mobile* elements (Tubiana et al 1996). The distal row of the carpus together with the second and third carpometacarpal joints are stable and rigid. The fourth and especially the fifth carpometacarpal joints, the thumb ray and the phalangeal joints are mobile. This allows the hand to form adaptable arches on gripping. The transverse carpal arch, formed by the carpal bones, is rigid. The metacarpal arch, between the metacarpal heads of the index and little finger, allows the ulnar side of the palm to curve into supination, by movement at the fourth and fifth carpometacarpal joints. The longitudinal arch, along the axis of a metacarpal and its phalanges, allows the finger to flex around an object. The thumb forms two important oblique arches, one between the tip of the thumb through the thumb–index web to the pulp of the index finger, the other from the pulp of the thumb, along the thumb ray, across the palm and along the front of the little finger to its pulp. As the fingers flex into the palm, the combined alignment and mobility of the involved joint surfaces bring all the finger tips to a focal point over the scaphoid tubercle. This also increases the security of grip of small items such as a golf ball.

Opening the hand

The hand is opened from its relaxed balanced posture, e.g. when stretching out to reach an object. This motion is made up of extension of the distal interphalangeal, proximal interphalangeal and metacarpophalangeal joints together with retroposition and extension of the thumb. As the fingers extend they tend to abduct and rotate outwards from the axis of the middle finger. The hand is provided with an ingenious mechanism that allows this to happen. The laws of mechanics would suggest that one motor would be required for every joint in a chain, together with some sort of controlling mechanism to ensure that the chain of joints moved together in a coordinated fashion. In the hand, this is achieved through an extensor apparatus that minimizes the number of motors required for movement by allowing the muscles to act on more than one joint, and by linking different levels in the mechanism so that the arc of motion is controlled.

The tendons of extensor digitorum run distally over the metacarpal heads, forming the major component of the extensor apparatus. Extensor digitorum has no insertion into the proximal phalanx and, therefore, exerts its extensor action on the metacarpophalangeal joint indirectly through more distal insertions. The first point of insertion is at the base of the middle phalanx (known as the ‘central slip’). Acting at this insertion alone, extensor digitorum can extend both metacarpophalangeal and proximal interphalangeal joints together. The interossei are also active in hand opening, since they extend both the proximal and interphalangeal joints through the lateral bands. There is, therefore, a range of possibilities. At one extreme, with no contribution from the interossei, the long extensor will exert all of its action at the metacarpophalangeal joint; this leads to full extension, and even hyperextension, while the proximal interphalangeal joint remains flexed (the typical ‘intrinsic minus’, or claw hand, of ulnar nerve paralysis). At the other extreme, when the intrinsics act strongly together with extensor digitorum, the proximal interphalangeal joint will extend completely while the metacarpophalangeal joint remains flexed (‘intrinsic plus’ hand). Thus, the hand possesses, in the proximal part of the extensor apparatus, a variable mechanism that allows different amounts of relative metacarpophalangeal or proximal interphalangeal joint motion.

In contrast, the more distal part of the extensor apparatus acts as an automatic or fixed mechanism that determines that the two interphalangeal joints, proximal and distal, will move together. The lateral slips of the extensor apparatus arise from extensor digitorum and pass distally on either side of the central slip and thus over the proximal interphalangeal joint; being further lateral, they are nearer the joint axis because the dorsal surface curves away on each side. A helpful analogy that has been suggested for this arrangement is to consider it as two pulleys of different size on one axle. The central slip can be regarded as a cord that passes over the larger wheel, and each lateral slip as a cord that passes over the smaller wheel. Since these latter pulleys are smaller, there is less longitudinal excursion for a given rotation of the wheel, and this allows some of the excursion to be used for another function, namely: extension at the distal joint. There is an additional mechanism by which the lateral slips move laterally during flexion of the proximal interphalangeal joint. The effect of this lateral movement is to reduce further the distance between the lateral slips and the joint axis, thereby reducing the amount of excursion at the proximal interphalangeal joint still more and allowing more excursion at the distal joint. When the hand flexes, this mechanical linkage system allows both interphalangeal joints to flex together in a coordinated way.

The extensor expansion also receives contributions from the interossei and lumbricals, which approach the digits from the webs and join the corresponding expansion in the proximal segment of the digit. These muscles can, therefore, act on the extensor apparatus at two levels: they can extend the proximal interphalangeal joint through fibres that radiate towards the central slip, and they can act on the distal interphalangeal joint through fibres that join the lateral slip.

The oblique retinacular ligament also passively aids synchronized extension by linking the terminal extensor fibres at the level of the distal interphalangeal joint with the flexor sheath just proximal to the proximal interphalangeal joint. This tightens with extension of the proximal interphalangeal joint causing obligatory passive extension of the distal interphalangeal joint. The presence of this structure can be confirmed by noting the marked resistance when passively flexing the distal joint with the proximal interphalangeal joint held passively extended, which resistance disappears if the proximal joint is flexed.

Apart from the components of the extensor expansion that are concerned with joint function, the whole structure requires additional anchorage (see Fig. 51.25). The transversely lying triangular ligament just distal to the insertion of the central slip prevents the lateral bands from subluxating too far outwards and palmarwards when the proximal interphalangeal joint flexes. Following a central slip rupture, this triangular ligament becomes attenuated, causing the lateral bands to slide outward and forwards until they pass anterior to the axis of the joint acting as flexor and causing the boutonnière deformity.

As the expansion glides backwards and forwards, the transverse fibres move like bucket handles. Smooth gliding layers are required under the expansion and retinacular ligaments to allow motion to occur without friction.

See **Video 51.6**.

The thumb does not easily assume the classical anatomical position. Therefore, the normal descriptive anatomical terms, i.e. anterior, posterior, medial and lateral, do not readily apply. The terms ‘palmar’, ‘dorsal’, ‘ulnar’ and ‘radial’ have been adopted in clinical practice.

An opposable thumb requires a different system of control from the other digits. Since the metacarpal is much more mobile than in the digits, muscles are needed to control the extra freedom of movement. The basic active movements are flexion–extension, abduction–adduction, rotation and circumduction. In the resting position of the first metacarpal, flexion and extension are parallel with the palmar plane, and abduction and adduction occur at right-angles to this.

Flexion and extension should be confined to motion at the interphalangeal or metacarpophalangeal joints). Palmar abduction (in which the first metacarpal moves away from the second at right-angles to the plane of the palm, and radial abduction in which the first metacarpal moves away from the second with the thumb in the plane of the palm, occur at the carpometacarpal joint. The opposite of radial abduction is ulnar adduction, or transpalmar adduction, in which the thumb crosses the palm towards its ulnar border. In clinical practice, the term adduction is generally used without qualification. Circumduction describes the angular motion of the first metacarpal, solely at the carpometacarpal joint, from a position of maximal radial abduction in the plane of the palm towards the ulnar border of the hand, maintaining the widest possible angle between the first and second metacarpals. Lateral inclinations of the first phalanx maximize the extent of excursion of the circumduction arc. Opposition is a composite position of the thumb (achieved by palmar abduction, flexion and pronation of the first metacarpal, with slight radial deviation and flexion of the metacarpophalangeal joint and slight flexion of the interphalangeal joint) such that the pulp of the thumb opposes the pulp of a digit with the nail of the thumb parallel to the palm (Bunnell 1938). Retroposition restores the hand from opposition, lifting the thumb backwards from the plane of the palm.

Rotary movements occur during circumduction. The simple angular movements described above combine with rotation about the long axis of the metacarpal shaft. In opposition, the shaft must rotate medially into pronation. In retroposition, the thumb must rotate laterally into supination. Axial rotation of the thumb metacarpal is produced by muscle activity (which moves the thumb through its arc of circumduction); the geometry of the articular surfaces of the trapeziometacarpal joint; and tensile forces in the ligaments (which combine with forces exerted by the muscles of opposition and retroposition to produce axial rotation). The stability of the first metacarpal is greatest after complete pronation in the position of full opposition, when the tension in the ligaments, muscular contraction and joint congruence combine to maximal effect.

Position of rest

The hand has a well-recognized position of rest, with the wrist in extension and the digits in some degree of flexion. The precise position of the thumb in the position of rest is variable. Typically, it is considered as the midpoint between maximal palmar abduction and maximal retroposition. In this position, the carpometacarpal joint lies at about 20° of radial abduction and 30° of palmar abduction; the metacarpophalangeal joint lies at about 40° of flexion and the interphalangeal joint at about 20° of flexion.

Grips

See **Video 51.7**.

From the position of rest, the tip of the thumb can approach the radial aspect of the fingers without incurring axial rotation because the palmar and dorsal trapeziometacarpal ligaments remain relaxed (see below). From different positions of the arc of circumduction, numerous different types of pinch grip are possible. In clinical practice, these have been classified into two main types: tip pinch and lateral (or key) pinch. Many forces contribute to these configurations.

The thumb is activated by monoarticular muscles (abductor pollicis longus and opponens pollicis), biarticular muscles (extensor pollicis brevis, adductor pollicis, abductor pollicis brevis and flexor pollicis brevis) and polyarticular muscles (extensor pollicis longus and flexor pollicis longus). It appears, however, that even a monoarticular muscle can change posture in all three joints by altering the overall balance of forces and it is, therefore, very difficult to attribute function to the individual intrinsic muscles. However, the thumb muscles do seem to provide two broad functions. They position the metacarpal, an activity automatically accompanied by rotation, and also control the axial stability of the skeleton of the thumb.

The thumb muscles may be classified into those used for retroposition, opposition and pinch grip.

Retroposition muscles

The muscles that bring about retroposition are extensor pollicis longus, extensor pollicis brevis and abductor pollicis longus. As the thumb moves into retroposition, automatic axial rotation produces supination of the first metacarpal. This is produced by the off-axis action of two parallel, but oppositely directed, forces: one exerted by extensors pollicis longus and brevis, and the other by abductor pollicis longus and the anterior oblique carpometacarpal ligament.

In the absence of extensor pollicis longus (from rupture, laceration or paralysis) the thumb cannot be retroposed. Only this muscle has the moment to elevate the thumb behind the plane of the palm.

Opposition muscles

A succession of activity occurs in the thenar muscles during the movement of opposition. Three subgroups of radial (abductor pollicis longus and extensor pollicis brevis), central (abductor pollicis brevis and opponens pollicis) and ulnar (flexor pollicis brevis) muscles are involved. These forces act simultaneously but with different intensities, depending on the situation of the thumb. As the thumb moves into opposition, there is automatic axial rotation of the first metacarpal shaft to produce pronation. This is produced by the paired action of oppositely directed forces: the opposition muscles provide one force, and the posterior oblique carpometacarpal ligament provides the other.

Pinch grip muscles

Pinch grip is mainly conferred by flexor pollicis longus and adductor pollicis. The former flexes the interphalangeal and metacarpophalangeal joints. The adductor pollicis adducts the thumb and, through the extensor expansion, counteracts excessive interphalangeal joint flexion from flexor pollicis longus. The proximal phalanx is stabilized from translating dorsally in pinch by the volar plate and by the extensor hood (which is actively contracted by the adductor pollicis and flexor pollicis brevis). The abductor pollicis longus also contracts firmly, locking the base of the metacarpal into a stable position of abduction and compression against the trapezium. The index finger is stabilized by the first dorsal interosseous which is, necessarily, the strongest of all the intrinsic muscles. With the index metacarpophalangeal joint fully flexed, the radial collateral ligament is taut and imparts additional static stability.

The wrist and hand may be paralysed by many conditions that affect the brain spinal cord, brachial plexus or peripheral nervous system. The aetiology can be traumatic, infective (such as poliomyelitis and leprosy), vascular, inflammatory or congenital. Each of these will cause different patterns of paralysis and contracture.

The main deformities from cerebral palsy are pronation of the forearm, flexion of the wrist and fingers, and flexion–adduction of the thumb (thumb in palm deformity). Flexion–adduction deformity of the thumb reflects an imbalance between its intrinsic and extrinsic musculature – principally powered by adductor pollicis, the first dorsal interosseous, flexor pollicis brevis and abductor pollicis brevis – which produces flexion, adduction and lateral rotation of the carpometacarpal joint, flexion and lateral rotation of the metacarpophalangeal joint and flexion of the interphalangeal joint. In an attempt to counteract this, the patient tends to hold the wrist in extreme flexion and ulnar deviation (Matev 1963). Surgery for the hand in cerebral palsy aims to optimize the ability to grasp and release objects and abduct the thumb to improve hand span. It is important to note that any procedure that improves one of these functions may well compromise the others.

In leprosy, the intrinsic muscles of the hand are paralysed. The metacarpophalangeal joints have no primary flexor but retain the powerful extensor digitorum. Extensor digitorum relies on a single muscle belly to extend the metacarpophalangeal joints and the proximal and the distal interphalangeal joints. In order to permit interphalangeal joint flexion with metacarpophalangeal joint extension (hook grip) there needs to be some 'slack' in the tendons distal to the metacarpophalangeal joints when extensor digitorum is contracted: the intrinsic muscles are responsible for trimming this slack in order to extend the interphalangeal joints fully. Absence of the intrinsic muscles results in four main disabilities: the fingers cannot be extended fully at the interphalangeal joints; abduction and adduction of the digits are lost; when grasping an object, flexion begins at the terminal joints, closing the fingers on themselves rather than on the palm; and the effective part of the finger becomes the tip and nail rather than the pulp (Brand 1958).

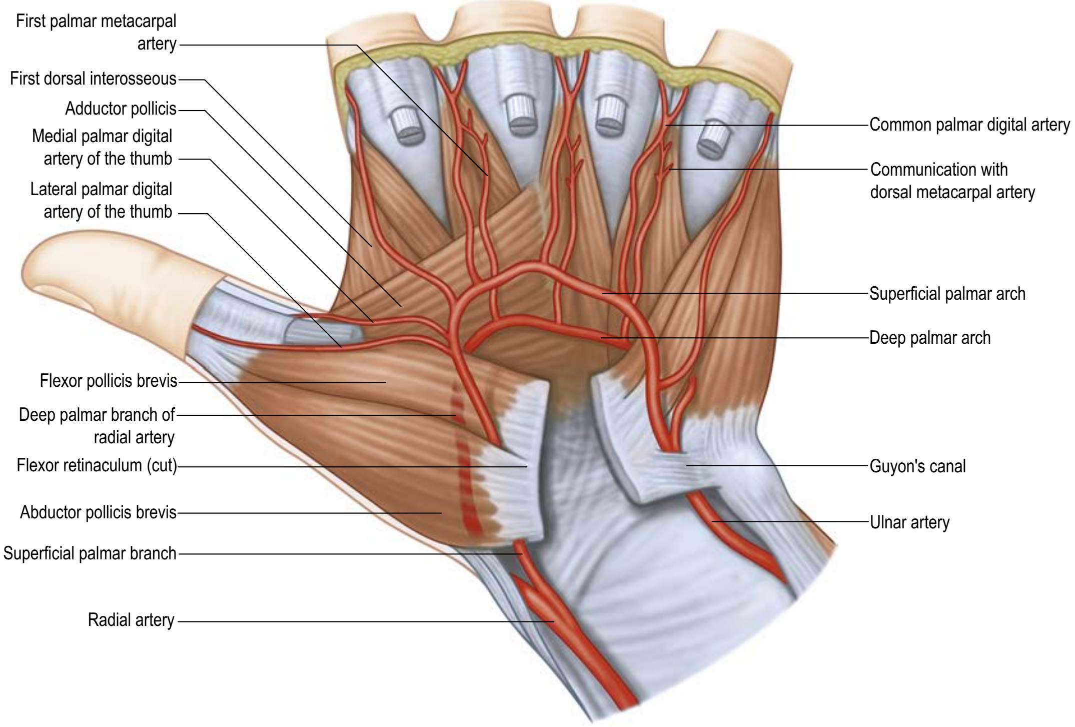
First palmar metacarpal artery
First dorsal interosseous
Adductor pollicis
Medial palmar digital artery of the thumb
Lateral palmar digital artery of the thumb
Flexor pollicis brevis
Deep palmar branch of radial artery
Flexor retinaculum (cut)
Abductor pollicis brevis
Superficial palmar branch
Radial artery
Common palmar digital artery
Communication with dorsal metacarpal artery
Superficial palmar arch
Deep palmar arch
Guyon's canal
Ulnar artery

Fig. 51.36 The deep palmar arch and its branches. Note that the palmar digital arteries to the thumb have a separate origin from the superficial palmar arch in this specimen (as sometimes occurs). The arteria princeps pollicis is absent in this specimen.

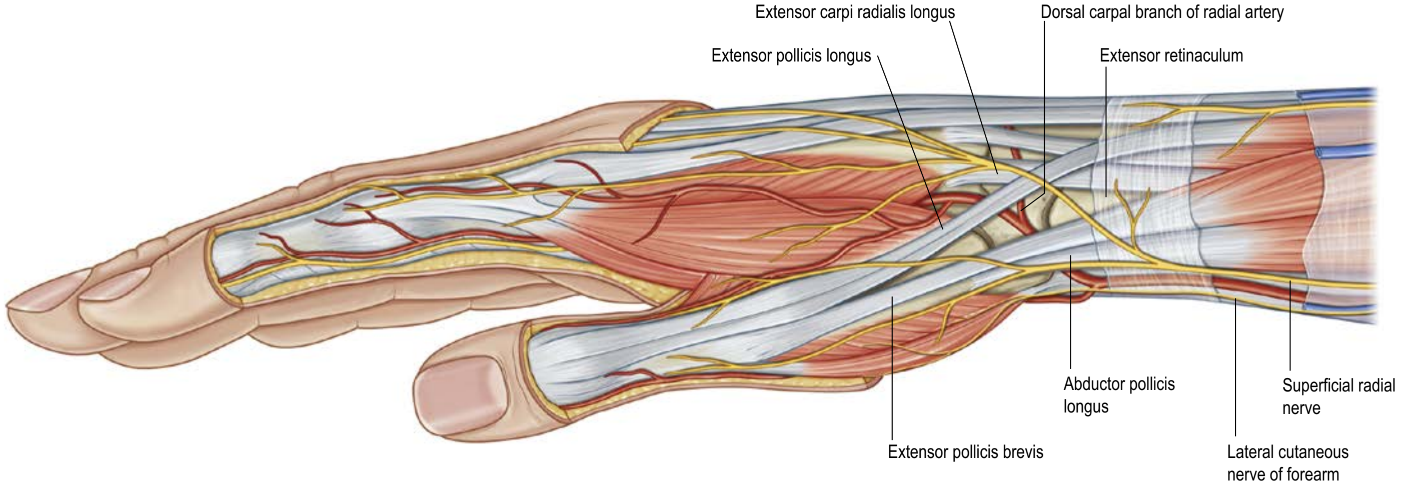
Extensor carpi radialis longus
Dorsal carpal branch of radial artery
Extensor pollicis longus
Extensor retinaculum
Abductor pollicis longus
Superficial radial nerve
Extensor pollicis brevis
Lateral cutaneous nerve of forearm

Fig. 51.37 The radial side of the hand. Note the course of the terminal branches of the superficial radial nerve and the lateral cutaneous nerve of the forearm. (Courtesy of Rolfe Birch, all rights reserved. Published in Birch R, Surgical Disorders of the Peripheral Nerve, 2nd ed. 2011. Springer-Verlag, London.)

Superficial palmar branch The superficial palmar branch arises from the radial artery just before it curves round the carpus. It passes through, and occasionally over, the thenar muscles, which it supplies, and usually anastomoses with the end of the ulnar artery to complete a superficial palmar arch (see Fig. 51.36). The superficial arch is complete in about 80% of cases (Zarzecki et al 2018).

Dorsal carpal branch The dorsal carpal branch arises deep to the tendons of the thumb extensors. It runs medially across the dorsal carpal surface under the tendons and anastomoses with the ulnar dorsal carpal branch, and also with the anterior and posterior interosseous arteries, to form a dorsal radiocarpal arch (see Figs 50.9A, 50.9C). The carpal arches are both close to bone and supply the distal epiphysial parts of the radius and ulna. Three dorsal metacarpal arteries descend from the dorsal intercarpal arch on the second to fourth dorsal interossei, and bifurcate into dorsal digital branches to supply the adjacent sides of all four fingers.

First dorsal metacarpal artery The first dorsal metacarpal artery arises from the radial artery just before it passes between the heads of the first dorsal interosseous. It divides, almost at once, into two branches that supply the adjacent sides of the thumb and index finger as far distally as the proximal interphalangeal joint. The radial side of the thumb receives a branch direct from the radial artery proper. In most cases, the first dorsal metacarpal artery follows a fascial course overlying the first dorsal interosseous and parallel to the second metacarpal. Occasionally, it may follow an intramuscular course. Distally, it anastomoses with the dorsal branches of the radiopalmar digital artery of the index finger over the proximal phalanx.

Second, third and fourth dorsal metacarpal arteries The second to fourth dorsal metacarpal arteries arise from the dorsal carpal arch. Near their origins, they anastomose with the deep palmar arch by proximal perforating arteries and, near their bifurcation, with dorsal perforating branches from the palmar metacarpal arteries that pass between the metacarpal necks. They also anastomose distally at the level of the web spaces with dorsal perforating branches from the palmar digital arteries from the superficial palmar arch. The third and fourth dorsal metacarpal arteries are much smaller than the first and second. Cutaneous branches from the dorsal metacarpal arteries supply the dorsal skin as far distally as the proximal interphalangeal joint. At the level of the neck of the second, third and fourth metacarpals, a direct cutaneous branch is given off that passes proximally and supplies an area of skin between the two adjacent metacarpals (see Fig. 51.2B).

Arteria princeps pollicis The arteria princeps pollicis (Miletin et al 2017) arises from the radial artery as it turns into the palm to form the deep palmar arch. It descends on the palmar aspect of the first metacarpal under the oblique head of adductor pollicis lateral to the first palmar interosseous. At the base of the proximal phalanx, deep to the tendon of flexor pollicis longus, the artery divides into two branches that appear between the medial and lateral attachments of the oblique head of adductor pollicis and run along both sides of the thumb. On the palmar surface of the distal phalanx, the branches form a pollicial arch that supplies the skin and subcutaneous tissue. The arteria princeps pollicis is the usual nutrient of supply to the first metacarpal.

Arteria radialis indicis The arteria radialis indicis is often a proximal branch of the arteria princeps pollicis, or may arise from the superficial arch or from the first dorsal metacarpal artery, or may combine with the arteria princeps pollicis to form the first palmar metacarpal artery. It descends between the first dorsal interosseous and transverse head of adductor pollicis, and runs along the lateral side of the index finger to its tip (see Fig. 51.36). It anastomoses with the index medial digital artery and with the arteria princeps pollicis and the superficial palmar arch at the distal border of the transverse head of adductor pollicis.

Deep palmar arch The deep palmar arch is formed by anastomosis of the end of the radial artery with the deep palmar branch of the ulnar artery (see Fig. 51.35G, 51.36). It crosses the bases of the metacarpals and interossei, covered by the oblique head of adductor pollicis, the tendons of the digital flexors and the lumbricals. In its concavity, running laterally, is the deep branch of the ulnar nerve. The deep palmar arch is incomplete in about 5% (Zarzecki et al 2018).

Palmar metacarpal artery The three palmar metacarpal arteries run distally from the convexity of the deep palmar arch on the interossei of the second to fourth spaces, and join the common digital branches of the superficial arch at the digital clefts (see Fig. 51.36). They supply nutrient branches to the medial four metacarpals.

Perforating branches Three perforating branches from the deep palmar arch cross the second to fourth interosseous spaces between the heads of the corresponding dorsal interossei and anastomose with the dorsal metacarpal arteries.

Recurrent branches Recurrent branches ascend proximally from the deep palmar arch anterior to the carpus to supply the carpal bones and intercarpal articulations. They end in the palmar carpal arch.

Ulnar artery

At the wrist, the ulnar artery (see Fig. 51.10) is covered by skin, fascia and palmaris brevis. It lies between the superficial and main parts of the flexor retinaculum, lateral to the ulnar nerve and pisiform.

Dorsal cutaneous branch A constant dorso-ulnar perforator vessel is given off distally. It arises 2–5 cm proximal to the pisiform and accompanies the dorsal cutaneous branch of the ulnar nerve. It emerges between flexor carpi ulnaris and extensor carpi ulnaris.

Palmar carpal branch The palmar carpal branch crosses the distal ulna deep to the tendons of flexor digitorum profundus and anastomoses with the palmar carpal branch of the radial artery to make a palmar radiocarpal arch.

Dorsal carpal branch The dorsal carpal branch arises just proximal to the pisiform. It curves deep to the tendon of flexor carpi ulnaris to reach the carpal dorsum, which it crosses laterally beneath the extensor tendons. It anastomoses with the dorsal carpal branch of the radial artery to complete the dorsal carpal arch. Near its origin, it sends a small digital branch along the ulnar side of the fifth metacarpal to supply the medial side of the dorsal surface of the fifth finger.

Deep palmar branch The deep palmar branch is often double. It passes between abductor and flexor digiti minimi, through or deep to opponens digiti minimi, and anastomoses with the radial artery, completing the deep palmar arch. The deep palmar branch accompanies the deep branch of the ulnar nerve.

Superficial palmar arch

The superficial palmar arch is an anastomosis fed mainly by the ulnar artery (see Figs 51.2A, 51.10, 51.36). The latter enters the palm with the ulnar nerve, anterior to the flexor retinaculum and lateral to the pisiform. It passes medial to the hook of the hamate, then curves laterally to form an arch that is convex distally and level with a transverse line through the distal border of the fully extended base of the thumb. About one-third of superficial palmar arches are formed by the ulnar artery alone, a further third are completed by the superficial palmar branch of the radial artery, and a third by the arteria radialis indicis, or a branch of either arteria princeps pollicis or the median artery. The superficial palmar arch is covered by palmaris brevis and the palmar aponeurosis, and it is superficial to flexor digiti minimi, branches of the median nerve and the tendons of the long flexors and the lumbricals.

Common and proper palmar digital arteries Three common palmar digital arteries arise from the convexity of the superficial palmar arch (see Figs 51.2A, 51.36). They pass distally on the second to fourth lumbricals, each joined by a corresponding palmar metacarpal artery from the deep palmar arch, and divide into two proper palmar digital arteries. These run along the contiguous sides of all four fingers, dorsal to the digital nerves, between Grayson's and Cleland's ligaments, anastomosing in the subcutaneous tissue of the fingertips and near the interphalangeal joints. Each digital artery has two dorsal branches that anastomose with the dorsal digital arteries and supply the soft parts dorsal to the middle and distal phalanges, including the matrices of the nails (see Fig. 51.2B). The palmar digital artery for the medial side of the little finger leaves the arch under palmaris brevis. Palmar digital arteries supply the metacarpophalangeal and interphalangeal joints and nutrient rami to the phalanges. They are the main digital supply because the dorsal digital arteries are minute. The origins of the palmar digital arteries of the thumb are quite variable. Both may arise from a single arteria princeps pollicis or they may arise separately from the superficial palmar arch. The ulnar digital artery may arise from the first dorsal metacarpal artery.

The terminal branches of the digital arteries contribute to a number of vascular arcades that provide a rich vascular supply for the distal elements of each digit (see Figs 51.2A, 51.5). Three distal phalangeal dorsal arterial arcades anastomose with each other and with those from the other side of the digit. The superficial arcade occurs at the level of the proximal nail fold and is supplied primarily by a dorsal branch from the palmar digital artery, which is given off at the level of the middle phalanx. The proximal subungual arcade is at the level of the lunula and is supplied by a terminal branch of the digital artery, which passes dorsally. The distal subungual arcade occurs more distally in the nail bed. It is supplied by a dorsal vessel that emerges from the point of confluence of the 'H'-shaped anastomosis between the terminal portions of both digital arteries, and passes from volar to dorsal aspect of the digit under the interosseous ligament connecting the proximal and distal parts of the distal phalanx.

Variations The ulnar and radial arteries to the hand may occasionally be supplemented by a median artery that contributes to, or supplies, the superficial palmar arch and by the anterior interosseous artery, which may make a contribution to the deep palmar arch. The median artery may persist in two different forms, palmar and antebrachial (Rodriguez-Niedenführ et al 1999). The palmar type arises from the junction of the ulnar artery and its common interosseous trunk; it is long and large, and reaches the palm, usually ending as the first or second common digital artery, or both. The antebrachial type is slender and short, usually arising from the anterior interosseous artery and finishing in the forearm. These variations are seen in about 20% of individuals and tend to be unilateral. Ulnar artery dominance in all digits is rare, complete radial artery dominance has been described in 28% of hands (Kleinert et al 1989).

Glomus tumours

Available with the *Gray's Anatomy* e-book

Veins

Superficial veins of the hand

Dorsal and palmar digital veins Dorsal digital veins pass along the sides of the fingers, joined by oblique branches (see Fig. 51.4). They unite from the adjacent sides of the digits into three dorsal metacarpal veins that form a dorsal venous network over the metacarpus (see Fig. 51.3). This is joined laterally by a dorsal digital vein from the radial side of the index finger and both dorsal digital veins of the thumb, and is prolonged proximally as the cephalic vein. Medially, a dorsal digital vein from the ulnar side of the little finger joins the network, which ultimately drains proximally into the basilic vein. A vein often connects

Glomus tumours are very painful tumours of the glomus bodies (small arteriovenous anastomoses involved in the regulation of peripheral skin temperature control (see Fig. 6.16)). They are often tiny and sometimes difficult to identify. These tumours typically occur in the proximal nail fold/subungual regions of the fingertips in association with the dorsal digital arterial arcades, although they can occur anywhere. They are diagnosed by exquisite point tenderness over the swelling, with reduction of tenderness when the finger is exsanguinated.

the central parts of the network to the cephalic vein near the mid-forearm. Palmar digital veins connect to their dorsal counterparts by oblique veins that pass between metacarpal heads. They also drain to a plexus superficial to the palmar aponeurosis, extending over both thenar and hypothenar regions. The venous drainage of the hand is predominantly dorsal: flexion and extension of the digits compresses the veins within the tight dorsal skin envelope, promoting venous return.

Deep veins of the hand

Superior and deep palmar venous arches Superficial and deep palmar venous arches accompany their arterial counterparts and receive correspondingly named tributaries; common palmar digital veins drain to the superficial arch and palmar metacarpal veins join the deep arch.

Palmar and dorsal metacarpal veins Deep veins accompanying the dorsal metacarpal arteries receive perforating tributaries from the palmar metacarpal veins and end in the radial veins and the dorsal venous network over the metacarpus. This network is joined laterally by a dorsal digital vein from the radial side of the index finger and by both digital veins of the thumb, and is prolonged proximally as the cephalic vein.

Cephalic vein The cephalic vein forms over the anatomical snuff-box from the radial extremity of the dorsal venous plexus and runs proximally over the distal lateral aspect of the radius, where it is easily visible. Its further course is described in Chapters 49, 50 and 81.

INNERVATION

Median nerve

The median nerve just proximal to the flexor retinaculum is lateral and superficial to the tendons of flexor digitorum superficialis and lies between the tendons of flexor carpi radialis and palmaris longus (see Fig. 51.30). It passes under the retinaculum in the 'carpal tunnel', where it may be compressed in carpal tunnel syndrome. Distal to the retinaculum, the nerve enlarges and flattens, and usually divides into five or six branches; the mode and level of division are variable. Within the carpal tunnel and hand, the median nerve has been shown to glide by up to 3 mm, depending on the position of the elbow and the attitude of the forearm in pronation or supination (Echigo et al 2008). The greatest longitudinal excursion of the median nerve (15.5 mm) is seen just proximal to the carpal tunnel; similar excursion of the ulnar nerve has been recorded as 14.8 mm in cadavers (Wilgis and Murphy 1986).

Muscular branch (motor or recurrent branch)

The muscular branch is short and thick, and arises from the lateral side of the nerve; it may be the first palmar branch or a terminal branch that arises level with the digital branches. It runs laterally, just distal to the flexor retinaculum and with a slight recurrent curve beneath the part of the palmar aponeurosis covering the thenar muscles (see Fig. 51.27B). It turns round the distal border of the retinaculum to lie superficial to flexor pollicis brevis, which it usually supplies, and either continues superficial to the muscle or traverses it. It gives a branch to abductor pollicis brevis that enters the medial edge of the muscle, and then passes deep to it to supply opponens pollicis, entering its medial edge. Its terminal part occasionally gives a branch to the first dorsal interosseous, and may be its sole or partial supply. The muscular branch may arise in the carpal tunnel and pierce the flexor retinaculum. Anomalies of the median nerve occur in approximately 10% of patients undergoing a carpal tunnel release. These branches usually arise from the ulnar side of the nerve and may be motor or sensory. (For further reading see Wynter and Dissabandara 2018.)

Palmar cutaneous nerve

This branch emerges from the radial side of the median nerve 3.5 cm to 6 cm proximal to the flexion increase of the wrist flexion. It runs distally alongside the ulnar edge of the sheath of flexor carpi radialis, radial and deep to palmaris longus to enter the palm either through or superficial to the flexor retinaculum (Fig. 51.27B). It usually ends in medial and lateral terminal branches to supply a patch of skin over and just beyond the anterior surface of the palm overlying the scaphoid tubercle and anterior aspect of the thumb carpometacarpal joint (Hobbs et al 1990, daSilva et al 1996).

Palmar digital branches

The median nerve usually divides into four or five digital branches. It often divides first into a lateral ramus, providing digital branches to the thumb and the radial side of the index finger, and a medial ramus, supplying digital branches to adjacent sides of the index, middle and ring fingers. Other modes of termination can occur.

Digital branches are commonly arranged as follows. They pass distally, deep to the superficial palmar arch and its digital vessels, at first anterior to the tendons of the long flexors. Two proper palmar digital nerves, sometimes from a common stem, pass to the sides of the thumb; the nerve supplying its radial side crosses in front of the tendon of flexor pollicis longus. The proper palmar digital nerve to the lateral side of the index finger also supplies the first lumbrical. Two common palmar digital nerves pass distally between the tendons of the long flexors. The lateral divides in the distal palm into two proper palmar digital nerves that traverse adjacent sides of the index and middle finger. The medial divides into two proper palmar digital nerves that supply adjacent sides of the middle and ring fingers. The lateral common digital nerve supplies the second lumbrical, and the medial receives a communicating twig from the common palmar digital branch of the ulnar nerve and may supply the third lumbrical. In the distal part of the palm, the digital arteries pass deeply between the divisions of the digital nerves; the nerves lie anterior to the arteries on the sides of the digits. The median nerve usually supplies palmar cutaneous digital branches to the radial three and a half digits (thumb, index, middle and the lateral side of the ring); sometimes, the radial side of the ring finger is supplied by the ulnar nerve. Occasionally, there is a communicating branch between the common digital nerve to the middle and ring fingers (derived from the median nerve) and the common digital nerve to the ring and little fingers (derived from the ulnar nerve); this may explain variations in sensory patterns that do not conform to the classic pattern.

The proper palmar digital nerves pass along the medial side of the index finger and both sides of the middle and the lateral side of the ring finger. They enter these digits in fat between slips of the palmar aponeurosis. Together with the lumbricals and palmar digital arteries, they pass dorsal to the superficial transverse metacarpal ligament and ventral to the deep transverse metacarpal ligament. In the digits, the nerves run distally beside the long flexor tendons (outside their fibrous sheaths), level with the anterior phalangeal surfaces and anterior to the digital arteries, between Grayson's and Cleland's ligaments. Each nerve gives off several branches to the skin on the front and sides of the digit and sends branches to the metacarpophalangeal and interphalangeal joints.

The digital nerves supply the fibrous sheaths of the long flexor tendons, blood vessels (vasomotor) and sweat glands (sudomotor). Distal to the base of the distal phalanx, each digital nerve gives off a branch that passes dorsally to the nail bed (see Fig. 51.9). The main nerve frequently trifurcates to supply the pulp and skin of the terminal part of the digit. Distal to the base of the proximal phalanx, each proper digital nerve also gives off a dorsal branch to supply the skin over the back of the middle and distal phalanges. The proper palmar digital nerves to the thumb and the lateral side of the index finger emerge with the tendons of the long flexors from under the lateral edge of the palmar aponeurosis. They are arranged in the digits as described above, except that, in the thumb, small distal branches supply the skin on the back of the distal phalanx only.

Other branches

In addition to the branches of the median nerve described above, variable vasomotor branches supply the radial and ulnar arteries and their branches. Some of the intercarpal, carpometacarpal and intermetacarpal joints are said to be supplied by the median nerve or its anterior interosseous branch; the precise details are uncertain.

Carpal tunnel syndrome

Carpal tunnel syndrome is the most common entrapment mononeuropathy. It is caused by compression of the median nerve as it passes through the fibro-osseous tunnel beneath the flexor retinaculum (see Fig. 51.38).

Carpal tunnel syndrome is usually idiopathic, however, certain diagnoses may predispose to the condition. The carpal tunnel may be narrowed by arthritic changes in the wrist joint, by thickening of the synovium (especially in rheumatoid disease), by soft tissue thickening, as may occur in myxoedema and acromegaly; it is associated with diabetes, oedema, obesity, pregnancy and vibration. The association with repetitive use and computing is controversial and has probably been overestimated. Normally, the median nerve slides smoothly in and out of the carpal tunnel during flexion and extension of the wrist, but when the nerve is compressed this sliding is restricted by traction which

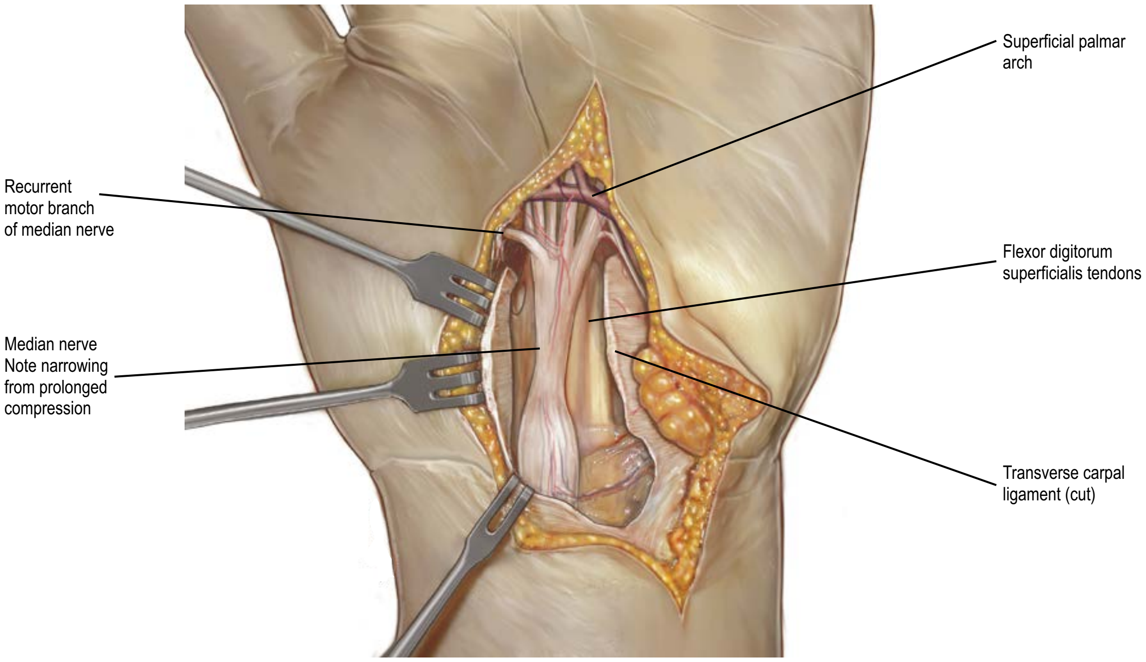
Superficial palmar arch
Recurrent motor branch of median nerve
Flexor digitorum superficialis tendons
Median nerve Note narrowing from prolonged compression
Transverse carpal ligament (cut)

Fig. 51.38 Carpal tunnel syndrome, left wrist, flexor aspect: the flexor retinaculum has been divided, exposing the median nerve. (Copyright Martin Langer.)

aggravates the conduction block. Typically, the syndrome produces painful paraesthesia and numbness in the thumb, index, middle and medial side of the ring fingers, which is worse at night and on manoeuvres such as holding a book or telephone. The palmar branch of the median nerve is spared because it does not pass through the carpal tunnel. With time, the compression leads to wasting and weakness of abductor pollicis brevis and loss of sweating in the cutaneous territory of the median nerve, sparing the patch overlying the scaphoid tubercle and palmar side of the carpometacarpal joint which is supplied by the palmar cutaneous nerve. Treatment depends on the cause. If present just at night, due to involuntary flexion of the wrist (which increase pressure in the carpal canal) then a splint may suffice. If the syndrome is of recent onset, especially in association with pregnancy or synovial thickening, then a steroid injection can be curative. For more persistent symptoms, and especially if there is evidence of axonal failure (numbness, loss of sweating, wasting of abductor pollicis brevis) then surgery is recommended. This involves dividing the flexor retinaculum (**Fig. 51.38**). The most common hazards of decompression are inadequate decompression because of failure to divide the most distal or most proximal part of the flexor retinaculum, damage to the motor branch causing weakness, or palmar cutaneous branch or one or more terminal sensory branches causing scar tenderness and a patch of numbness and damage to the superficial palmar arch causing a haematoma.

Anatomical anomalies of the median nerve in the carpal tunnel are very common (Henry et al 2015) and occur in up to 12% of hands. The most common are variations in the course of the recurrent motor branch in relation to the flexor retinaculum. These may be transligamentous (11.3%), subligamentous (13.5%%) or extraligamentous (75.2%). Damage may also occur to the palmar cutaneous branch of the median nerve and to the superficial connections between the median and ulnar nerves (Martin et al 1996) (the so-called Berrettini branch, division of which will leave the patient with numbness in the middle and ring fingers). Stancić et al (1999) noted that this connection was present in 81% of dissected hands and proposed that it should be regarded as a normal anatomical finding.

Median nerve division at the wrist

Median nerve division at the wrist leads to paralysis of the lumbricals to the index and middle fingers and of the thenar muscles (apart from flexor pollicis brevis and adductor pollicis), as well as loss of sensation to the thumb, index, middle and radial half of the ring fingers (see Fig. 51.7). The thenar muscles waste, and the adductor pollicis, which is no longer antagonized by flexor pollicis brevis and opponens pollicis, produces an adducted posture of the thumb. Division of the median nerve distal to the origin of its palmar cutaneous branch, which arises somewhere between 3.5 and 6 cm proximal to the proximal edge of the flexor retinaculum and the distal transverse wrist crease, will leave the branch intact to supply the skin over the thenar eminence and radial side of the proximal part of the hand. Careful clinical examination of the sensibility of the skin in this region should help to clarify the level of the lesion. High division of the nerve (Ch. 50) will, as with compressive lesions at this level, result in weakness of pronation of the forearm, radial flexion of the wrist and the lateral two fingers.

Ulnar nerve

At the wrist, the ulnar nerve passes under the superficial part of the flexor retinaculum (in Guyon's canal) with the ulnar artery, and divides into superficial and deep terminal branches (see Fig. 51.10).

Dorsal branch

The dorsal branch arises approximately 5 cm proximal to the wrist (see Fig. 50.9). It passes distally and dorsally, deep to flexor carpi ulnaris, perforates the deep fascia, descends along the medial side of the back of the wrist and hand, and then divides into two, or often three, dorsal digital nerves. The first supplies the medial side of the little finger; the second, the adjacent sides of the little and ring fingers; while the third, when present, supplies adjoining sides of the ring and middle fingers. The latter may be replaced, wholly or partially, by a branch of the radial nerve, which communicates with it on the dorsum of the hand (see Fig. 51.9). In the little finger, the dorsal digital nerves extend only to the base of the distal phalanx; in the ring finger, they extend only to the base of the middle phalanx. The most distal parts of the little finger and of the ulnar side of the ring finger are supplied by dorsal branches of the proper palmar digital branches of the ulnar nerve. The most distal part of the lateral side of the ring finger is supplied by dorsal branches of the proper palmar digital branch of the median nerve.

Superficial and deep terminal branches

Superficial terminal branch

The superficial terminal branch supplies palmaris brevis and the medial palmar skin. It divides into two palmar digital nerves. One supplies the medial side of the little finger. The other (a common palmar digital nerve) sends a branch to the median nerve and divides into two proper digital nerves to supply the adjoining sides of the little and ring fingers. The proper digital branches within the digit are distributed like those derived from the median nerve.

Deep terminal branch

The deep terminal branch accompanies the deep branch of the ulnar artery as it passes between abductor digiti minimi and flexor digiti minimi, and then perforates opponens digiti minimi to follow the deep palmar arch dorsal to the flexor tendons (see Fig. 51.27B). At its origin, it supplies the three short muscles of the little finger. As it crosses the hand, it supplies the interossei and the third and fourth lumbricals. It

The ulnar nerve can be compressed as it passes through Guyon's canal at the wrist.

Causes of compression at this site include a ganglion from the piso-triquetral joint, prolonged compression from a cyclist's handlebars, hook of hamate fracture, and proximity of aberrant or accessory muscles. The symptoms depend on the precise level at which the ulnar nerve and its branches are compressed. Altered sensation is noted in the palmar aspect of the little and ulnar half of the ring fingers; sensation on the ulnar aspect of the dorsum of the hand is normal due to preservation of the dorsal cutaneous branch. If the motor branch fibres are affected, there is weakness and wasting of the intrinsic muscles of the hand supplied by the ulnar nerve, with clawing posture in severe compression. Weakness of adductor pollicis and the first dorsal interosseous substantially degrades pinch strength: if a slip of paper is held in the key pinch position between the pulp of the thumb and the radial side of the index proximal interphalangeal joint, the tip of the thumb involuntarily flexes as flexor pollicis longus contracts to compensate for the absent adductor pollicis and first dorsal interosseous (Froment's sign).

Surgical treatment involves decompression of the nerve by division of the roof of Guyon's canal and removal of any causative lesion, such as a ganglion. Ulnar tunnel syndrome can be difficult to distinguish from more proximal causes of ulnar nerve compression, of which the most common is entrapment of the nerve in the cubital canal at the elbow. In this condition, sensory changes would include the dorso-ulnar aspect of the hand and motor changes would involve flexor carpi ulnaris and flexor digitorum profundus to the little and ring fingers. Clawing is less apparent with a more proximal failure of the ulnar nerve (the 'ulnar paradox') because flexor digitorum profundus also fails so there is less flexion force to expose the absent extensor moment of the paralysed intrinsics.

In the absence of obvious clinical indicators, an unpleasant tingling sensation (Tinel sign) over the site of compression, electrophysiological studies and MRI scans may aid diagnosis.

Ulnar nerve division at the wrist paralyses all the intrinsic muscles of the hand (apart from the radial two lumbricals, abductor pollicis brevis, and part of flexor pollicis brevis and opponens pollicis). The intrinsic muscle action of flexing the metacarpophalangeal joint and extending the interphalangeal joints is lost. The unopposed action of the long extensors and flexors of the fingers causes clawing, with extension of the metacarpophalangeal joints and flexion of the interphalangeal joints. (See section 'The paralysed hand' for explanation of why clawing occurs in the intrinsic minus hand.) The clawing is less intense in the index and middle fingers because their lumbricals are supplied by the median nerve.

There is sensory loss over the little finger and the ulnar half of the ring finger. The skin over the ulnar aspect of the dorsum of the hand is spared because the dorsal branch of the ulnar nerve is given off approximately 5 cm proximal to the wrist joint. A combined median and ulnar nerve palsy at the wrist results in a full claw hand with thenar and hypothenar flattening and thumb adduction and flexion (a simian hand).

The wrist joint is identified between the distal ends of the radius and ulna, and the proximal row of the carpus, on flexion and extension of the wrist. The line of the wrist joint corresponds to a line, convex superiorly, joining the radial and ulnar styloid processes. Its position is also marked by the proximal of the two transverse anterior wrist creases (see Fig. 48.54A). The radial styloid process normally sits 1 cm distal to the ulnar styloid process.

When the forearm is pronated, the head of the ulna forms a rounded surface elevation on the medial side of the posterior aspect of the wrist (see Figs 48.53C, 48.54B), and the ulnar styloid process projects distally from its posteromedial aspect. The radial styloid process projects inferiorly from the distal radius along the lateral aspect of the wrist. The posterior aspect of the lower end of the radius is partly obscured by the extensor tendons but is palpable. The prominent dorsal radial (Lister's) tubercle is both visible and palpable, and aligns with the web space between digits 2 and 3. The tendon of extensor pollicis longus in extensor compartment 3 sits medial to the tubercle, and the tendons of extensors carpi radialis longus and brevis sit lateral to the tubercle in compartment 2.

Four of the carpal bones are palpable. The pisiform is both visible and palpable on the palmar aspect of the medial wrist at the base of the hypothenar eminence. It is often overlain by the distal wrist crease. It can be moved over the articular surface of the triquetrum when the wrist is passively flexed. The hook of the hamate lies approximately 2.5 cm distal to the pisiform, in line with the ulnar border of the ring finger. It can be felt on deep palpation, and the superficial division of the ulnar nerve can be rolled from side to side over the tip of the hook. The tubercle of the scaphoid is situated at the base of the thenar eminence, in line with the tendon of flexor carpi radialis and, in many individuals, forms a small, visible elevation. Immediately distal to it, but covered by the muscles of the thenar eminence, the tubercle of the trapezium can be identified on deep palpation.

Proximal to the wrist creases, the prominent tendon of flexor carpi radialis can be seen and palpated when the wrist is flexed against resistance (see Fig. 48.54A). The radial artery lies on its lateral side and crosses the anterior margin of the expanded distal end of the radius, where it is palpable. It then passes posteriorly, deep to the tendons of abductor pollicis longus and extensor pollicis brevis, and enters the anatomical snuff-box, where its pulsations are palpable (see Fig. 48.54C).

Palpation lateral to flexor carpi radialis, 5–6 cm proximal to the wrist crease, reveals the muscle belly of flexor pollicis longus (flexing and extending the thumb will confirm that the examining finger is correctly placed). The area on the medial (ulnar) side of flexor carpi radialis tendon is packed with functionally important structures. The median nerve is either covered by, or situated just radial to, the tendon of palmaris longus. The latter can be identified by gently pinching the tips of the digits together and partially flexing the wrist (see Fig. 48.54A). Near to the wrist, the median nerve lies very close to the skin and can, therefore, be injured by relatively superficial lacerations. When palmaris longus is absent, only a thin covering of subcutaneous fat and deep fascia separate skin and nerve. The four tendons of flexor digitorum superficialis lie deep to the median nerve; the tendons to the middle and ring fingers lie anterior to those for the index and little fingers as they pass deep to the flexor retinaculum, and can be felt and usually seen to move during finger flexion/extension. Deeper still are the tendons of flexor digitorum profundus. The broad tendon of flexor carpi ulnaris is easily palpated passing to the pisiform on the ulnar side of the anterior wrist; the ulnar nerve, artery and venae comitantes lie along its lateral (radial) edge. Any sharp injury that cuts through the tendon usually has enough energy to sever the ulnar neurovascular bundle.

When the thumb is fully extended, the depression of the anatomical snuff-box is seen on the lateral aspect of the wrist immediately distal to the radial styloid process. The snuff-box is bounded on its anterolateral (radial) side by the tendons of abductor pollicis longus (laterally) and extensor pollicis brevis (immediately dorsomedial), and on its posteromedial/ulnar side by the tendon of extensor pollicis longus. Running a finger along extensor pollicis brevis enables palpation of the superficial radial nerve, which can be rolled from side to side on the tendon. The cephalic vein passes through the roof of the snuff-box, where it is visible and palpable, and the pulsation of the radial artery can be palpated deeply on its floor. Three bones are palpable distal to the radial styloid process along the floor of the anatomical snuff-box: the convex, ovoid proximal articular surface of the scaphoid (best palpated during alternating wrist abduction/adduction), the radial aspect of the trapezium and the expanded base of the first metacarpal. The first carpometacarpal joint forms a palpable depression distal to the trapezium.

The tendons located within the six extensor compartments of the wrist are subcutaneous and palpable (see Fig. 48.54B). Compartment I (containing abductor pollicis longus and extensor pollicis brevis) sits over the lateral radius. Regional tenderness to palpation occurs in de Quervain's tenosynovitis. Compartment II is bounded laterally by the radial styloid and medially by Lister's tubercle. The tendons of extensors carpi radialis longus and brevis in this compartment can be identified on the dorso-radial carpus when the fist is clenched and relaxed. Compartment III (containing extensor pollicis longus) is palpable to the medial side of Lister's tubercle: the tendon of extensor pollicis longus is palpable if the thumb pulp is actively retroposed behind the plane of the palm. Compartment IV (containing extensors digitorum and indicis) sits between the ulnar head and compartment III: the tendons of extensor digitorum are visible and palpable on the dorsum of the hand with the fingers fully extended. Compartment V (containing extensor digiti minimi) overlies the distal radio-ulnar joint. Compartment VI (containing extensor carpi ulnaris) overlies the dorso-ulnar corner of the ulnar head: the tendon of extensor carpi ulnaris is palpable distal to the ulnar styloid as it crosses the wrist, with the wrist in resisted extension and supination or pronation and adduction. The first dorsal interosseous forms a visible fleshy mass on the lateral part of the dorsal hand between the index finger and thumb, especially whilst abducting the index finger against resistance.

The palmar skin is marked by a number of creases but they are of little value as points of reference (see Fig. 51.1). Transverse skin creases cross the palmar aspect of the fingers in three places: the most proximal crease sits at the junction of the digit with the palm and lies approximately 2 cm distal to the metacarpophalangeal joint; the intermediate crease sits opposite the proximal interphalangeal joint; and the distal crease sits just proximal to the distal interphalangeal joint.

The first metacarpal is both visible and palpable on the dorsolateral hand; its dorsal aspect forms the lateral border of the hand. The fleshy elevation of the thenar eminence, produced by abductor and flexor pollicis brevis overlying opponens pollicis, is located on the lateral palm. The less prominent hypothenar eminence is located on the medial palm and is formed by the comparable muscles of the little finger. The medial aspect of the hypothenar eminence forms the medial border of the hand.

The dorsal aspects of the trapezium and of each of the metacarpals are partially palpable around the margins of the corresponding extensor tendons. The heads of the metacarpals form the prominences of the knuckles and are most obvious during digit flexion. On the dorsal hand, the metacarpophalangeal joint line forms a palpable depression either side of the digital extensor tendon: alternating digit flexion/extension aids identification. The joint can be aspirated/injected from this perspective. Palpation distal to the metacarpal head reveals the flared base of the corresponding proximal phalanx. The interphalangeal joints are palpable on the dorsal aspect of a flexed digit just distal to the prominences formed by the heads of the proximal and middle phalanges.

The flexor retinaculum, and therefore the surface position of the carpal tunnel, can be mapped according to its palpable bony attachments. Its distal border is concave inferiorly and is marked by a curved line that joins the tubercle of the trapezium to the hook of the hamate. Its proximal border is marked by a curved line, concave superiorly, which joins the tubercle of the scaphoid to the pisiform. Flexion of the wrist produces a number of transverse skin creases (usually two, sometimes three) at the wrist. The dominant, most distal, wrist crease normally sits distal to the lunate and overlies pisiform and the proximal edge of the flexor retinaculum. The carpal tunnel passes distal to this crease for 2.5–3 cm.

The position of the superficial palmar arterial arch is indicated by a horizontal line approximately 4 cm long, drawn at the level of the fully extended and partially abducted thumb. A horizontal line, approximately 4 cm long and running from a point just distal to the hook of the hamate, indicates the position of the deep palmar arterial arch, which is located approximately 1 cm proximal to the superficial arch. The digital neurovascular bundles pass along the medial and lateral sides of the dorsal and palmar (volar) surfaces of the digits, and can be anaesthetized in these positions via the web space.

ends by supplying adductor pollicis, the first dorsal interosseous and, usually, flexor pollicis brevis.

The medial part of flexor digitorum profundus is supplied by the ulnar nerve, as are the third and fourth lumbricals, which are connected with the tendons of this part of the muscle. Similarly, the lateral part of flexor digitorum profundus and the first and second lumbricals are supplied by the median nerve. The third lumbrical is often supplied by both nerves. The deep terminal branch gives branches to some intercarpal, carpometacarpal and intermetacarpal joints; precise details are uncertain. Vasomotor branches, arising in the forearm and hand, supply the ulnar and palmar arteries.

Ulnar nerve compression at the wrist

Available with the *Gray's Anatomy* e-book

Ulnar nerve division at the wrist

Available with the *Gray's Anatomy* e-book

Radial nerve

Branches of the superficial branch of the radial nerve reach the hand by curving around the wrist over the tendons of abductor pollicis longus and extensor pollicis brevis, and dividing into dorsal digital nerves (see Fig. 51.37). They usually communicate with the posterior and lateral cutaneous nerves of the forearm on the dorsum of the hand.

Dorsal digital nerves

There are usually four or five small dorsal digital nerves (see Fig. 51.9). The first supplies the skin of the radial side of the thumb and the adjoining thenar eminence, and communicates with branches of the lateral cutaneous nerve of the forearm. The second supplies the medial side of the thumb; the third, the lateral side of the index finger; the fourth, the adjoining sides of the index and middle fingers. The fifth communicates with a ramus of the dorsal branch of the ulnar nerve and supplies the adjoining sides of the middle and ring fingers, where it is frequently replaced by the dorsal branch of the ulnar nerve. The digital nerves of the thumb reach only to the root of the nail; those in the index finger, midway along the middle phalanx; and those to the middle and the lateral part of the ring finger may reach no further than the proximal interphalangeal joints. The remaining distal dorsal areas of the skin in these digits are typically supplied by palmar digital branches of the median and ulnar nerves. However, the superficial terminal branch of the radial nerve may supply the whole dorsum of the hand.

SURFACE ANATOMY OF THE WRIST AND HAND

See **Video 51.8** and **Video 51.9**.

Flexor/volar surface

Available with the *Gray's Anatomy* e-book

Anatomical snuff-box

Available with the *Gray's Anatomy* e-book

Extensor/dorsal surface

Available with the *Gray's Anatomy* e-book

Hand

Available with the *Gray's Anatomy* e-book

Bonus e-book content

Fig. 51.2 The blood supply to (**A**) the palmar (volar) skin of the right wrist and hand and (**B**) the dorsum of the left hand.

Fig. 51.10 Guyon's canal at the wrist.

Fig. 51.16 Dorsopalmar radiographs of the hand illustrating maturing ossification from infant to adult.

Fig. 51.19 D, A fluoroscopic arthrogram of the radiocarpal joint.

Fig. 51.35 A hand digital subtraction macroangiogram.

Fig. 51.38 Carpal tunnel syndrome.

Video 51.1 The arthroscopic anatomy of the radiocarpal joint.

Video 51.2 Movements of the wrist.

Video 51.3 Carpal mechanics and pathomechanics.

Video 51.4 Sagittal band function.

Video 51.5 Function of the intrinsic muscles of the hand.

Video 51.6 Movements of the thumb.

Video 51.7 Functional grips of the hand.

Video 51.8 Surface anatomy of the hand and wrist.

Video 51.9 Wrist block: surface anatomy.

Video 51.10 Wrist block: cadaveric anatomy.

Key references

Edmunds JO 2011 Current concepts of the anatomy of the thumb trapeziometacarpal joint. J Hand Surg Am 36:170–82.

Henry BM, Zwinczewska H, Roy J et al 2015 The prevalence of anatomical variations of the median nerve in the carpal tunnel: a systematic review and meta-analysis. PLoS One 10:e0136477.

Martin CH, Seiler JG 3rd, Lesesne JS 1996 The cutaneous innervation of the palm: an anatomic study of the ulnar and median nerves. J Hand Surg Am 21:634–8.

Miletin J, Sukop A, Baca V et al 2017 Arterial supply of the thumb: systematic review. Clin Anat 30:963–73.

Parminder K 2013 Morphological study of lumbricals – a cadaveric study. J Clin Diagn Res 7:1558–60.

Pastrana MJ, Zaidenberg EE, Palumbo D et al 2019 Innervation of the proximal interphalangeal joint: an anatomical study. J Hand Surg Am 44:422.

Rainbow MJ, Wolff AL, Crisco JJ et al 2015 Functional kinematics of the wrist. J Hand Surg Eur Vol 41(1):7–21.

Van de Pol GJ, Koudstaal MJ, Schuurman AH et al 2006 Innervation of the wrist joint and surgical perspectives of denervation. J Hand Surg Am 31:28–34.

Zarzecki MP, Popieluszko P, Zayachowski A et al 2018 The surgical anatomy of the superficial and deep palmar arches: a meta-analysis. J Plast Reconstr Aesthet Surg 71:1577–92.

Zwanenburg RL, Werker PMN, McGrouther DA 2014 The anatomy and function of Cleland's ligaments J Hand Surg Eur Vol 39:482–90.

References

Abrams RA, Petersen M, Botte MJ 1994 Arthroscopic portals of the wrist: an anatomic study. J Hand Surg Am 19:940–4.

Adkinson JM, Johnson SP, Chung KC 2014 The clinical implications of the oblique retinacular ligament. J Hand Surg Am 39:535–41.

Allison DM 2005 The anatomy of the collateral ligaments of the proximal interphalangeal joint. J Hand Surg Am 30:1026–31.

An KN 2007 Tendon excursion and gliding: clinical impacts from humble concept. J Biomech 40:713–18.

Bamba R, Malhotra G, Bueno RA Jr et al 2018 Ring avulsion injuries: a systematic review. Hand (N Y) 13:15–22.

Becker C, Gilbert A 1988 The ulnar flap – description and applications. Eur J Plast Surg 11:79–82.

Berger RA 1997 The ligaments of the wrist: a current overview of anatomy with considerations of their potential functions. Hand Clin 13:63–82.

Bilderback KK, Rayan GM 2004 The septa of Legueu and Juvara: an anatomic study. J Hand Surg Am 29:494–9.

Birch R 2011 Iatrogenous injuries. In: Surgical Disorders of the Peripheral Nerves, 2nd ed. London: Springer-Verlag; pp. 483–526.

Brand PW 1958 Paralytic claw hand. J Bone Joint Surg Br 40:618–32.

Brand PW 1985 Operations to restore muscle balance to the hand. In: Clinical Mechanics of the Hand. Mosby: St Louis.

Brooks D, Buntic RF, Kind GM et al 2007 Ring avulsion: injury pattern, treatment, and outcome. Clin Plast Surg 34:187–96.

Bunnell S 1938 Opposition of the thumb J Bone Joint Surg 20:269–84.

Chansky HA, Trumble TE, Conrad EU 3rd, et al 1999 Evidence for a polyclonal etiology of palmar fibromatosis. J Hand Surg Am 24(2):339–44.

Compson JP 1998 The anatomy of acute scaphoid fractures. J Bone Joint Surg Br 80:218–24.

Costa H, Pinto A, Zenha H 2007 The posterior interosseous flap – a prime technique in hand reconstruction: the experience of 100 anatomical dissections and 102 clinical cases. J Plast Reconstr Aesthet Surg 60:740–7.

Craigen MA, Stanley JK 1995 Wrist kinematics. Row, column or both? J Hand Surg Br 20(2):165–70.

Cross D, Matullo KS 2014 Kienböck disease. Orthop Clin North Am 45:141–52.

DaSilva MF, Moore DC, Weiss AP, et al 1996 Avoidance of transection of the palmar cutaneous branch of the median nerve in carpal tunnel release. J Hand Surg Am 21(4):644–50.

Descatha A, Jauffret P, Chastang JF et al 2011 Should we consider Dupuytren's contracture as work-related? A review and meta-analysis of an old debate. BMC Musculoskelet Disord 12:96.

de Smet L 2002 Pitfalls in wrist arthroscopy. Acta Orthop Belg 68:325–9.

Destot E 1926. The Classic: Injuries of the Wrist: A Radiological Study. New York, NY: Paul B. Hoeber.

Dolmans GH, Werker PM, Hennies HC 2011 Wnt signaling and Dupuytren's disease. N Engl J Med 365(4):307–17.

Echigo A, Aok M, Ishiai S et al 2008 The excursion of the median nerve during nerve gliding exercise: an observation with high-resolution ultrasonography. J Hand Ther 21:221–8.

Edmunds JO 2011 Current concepts of the anatomy of the thumb trapeziometacarpal joint. J Hand Surg Am 36:170–82.

Feipel V, Rooze M 1999 The capsular ligaments of the wrist: morphology, morphometry and clinical applications. Surg Radiol Anat 21:175–80.

Fisk GR 1970 Carpal instability and the fractured scaphoid. Ann R Coll Surg Engl 46:63–76.

Garcia-Elias M 1997 Kinetic analysis of carpal stability during grip. Hand Clinics 13(1):151–8.

Garcia-Elias M, Ribe M, Rodriguez J et al 1995 Influence of joint laxity on scaphoid kinematics. J Hand Surg Br 20(3):379–82.

Gelberman RH, Menon J 1980 The vascularity of the scaphoid bone. J Hand Surg Am 5:508–13.

Henry BM, Zwinczewska H, Roy J et al 2015 The prevalence of anatomical variations of the median nerve in the carpal tunnel: a systematic review and meta-analysis. PLoS One 10:e0136477.

Hierner R, Putz R, Bishop AT et al 2016 Flaps in Hand and Upper Limb Reconstruction: Surgical Anatomy, Operative Techniques and Differential Therapy. Elsevier.

Hobbs RA, Magnussen PA, Tonkin MA 1990 Palmar cutaneous branch of the median nerve. J Hand Surg Am 15(1):38–43.

Horii E, An K-N, Linscheid RL et al 1993 Excursion of prime wrist tendons. J Hand Surg Am 18A:83–90.

Jones DB Jr, Kakar S 2012 Perilunate dislocations and fracture dislocations. J Hand Surg Am 37:2168–73.

Kawamura K, Chung KC 2008 Treatment of scaphoid fractures and nonunions. J Hand Surg Am 33:988–97.

Kleinert JM, Fleming SG, Smith Abel C et al 1989 Radial and ulnar artery dominance in normal digits. J Hand Surg Am 14A:504–8.

Krishnamoorthy R, Karthikeyan G 2011 Degloving injuries of the hand. Indian J Plast Surg 44:227–36.

Kuczynski K 1975 The thumb and the saddle. Hand 7:120–2.

Kupfer DM, Eaton C, Swanson S et al 1999 Ring avulsion injuries: a biomechanical study. J Hand Surg Am 24:1249–53.

Ladd AL, Weiss AP, Crisco JJ et al 2013 The thumb carpometacarpal joint: anatomy, hormones, and biomechanics. Instr Course Lect 62:165–79.

LaPorte DM, Hashemi SS, Dellon A 2014 Sensory innervation of the triangular fibrocartilage complex: a cadaveric study. J Hand Surg Am 39:1122–4.

Lee LC, Zhang AY, Chong AK et al 2006 Expression of a novel gene, MafB, in Dupuytren's disease. J Hand Surg Am 31:211–18.

Littler JW 1967 The finger extensor mechanism. Surg Clin North Am 47(2):415–32.

McDonald LS, Bavaro MF, Hofmeister EP et al 2011 Hand infections. J Hand Surg Am 36A:1403–12.

McFarlane RM 1974 Patterns of the diseased fascia in the fingers in Dupuytren's contracture. Displacement of the neurovascular bundle. Plast Reconstr Surg 54:31–44.

McGrouther D 1982 The microanatomy of Dupuytren's contracture. Hand 14:215–36.

Martin CH, Seiler JG 3rd, Lesesne JS 1996 The cutaneous innervation of the palm: an anatomic study of the ulnar and median nerves. J Hand Surg Am 21:634–8.

Matev I 1963 Surgical treatment of spastic 'thumb-in-palm' deformity. J Bone Joint Surg Br 45:703–8.

Mattox R, Welk AB, Battaglia PJ et al 2015 Sonographic diagnosis of an acute Stener lesion: a case report. J Ultrasound 19:149–52.

Miletin J, Sukop A, Baca V et al 2017 Arterial supply of the thumb: systematic review. Clin Anat 30:963–73.

Moschella F, Cordova A 2006 Reverse homodigital dorsal radial flap of the thumb. Plast Reconstr Surg 117:920–6.

Moschella F, Cordova A, Pirrello R et al 1996 Anatomic basis for the dorsal radial flap of the thumb: clinical applications. Surgical and Radiologic Anatomy: SRA 18(3):179–81.

Navarro A 1921 Luxaciones del carpo. An Fac Med 6:113–41.

Oehmke MJ, Podranski T, Klaus R et al 2009 The blood supply of the scaphoid bone. J Hand Surg Eur Vol 34:351–7.

An anatomical study of 12 cadaver hands which demonstrates a variety of vascular anastomoses around the scaphoid. It notes that a dorsal approach to the scaphoid bone is possible as there is an available blood supply from the palmar circulation.

Oka K, Moritomo H 2018 Current management of scaphoid nonunion based on the biomechanical study. J Wrist Surg 7:94–100.

Ortiz JA Jr, Berger RA 1998 Compartment syndrome of the hand and wrist. Hand Clin 14:405–18.

Palmer AK, Werner FW, Murphy D et al 1985 Functional wrist motion: a biomechanical study. J Hand Surg Am 10(1):39–46.

Pan Y, Hung LK 2016 The course of the terminal posterior interosseous nerve and its relationship with wrist arthroscopy portals. J Wrist Surg 5:315–19.

Parminder K 2013 Morphological study of lumbricals- a cadaveric study. J Clin Diagn Res 7:1558–60.

Pastrana MJ, Zaidenberg EE, Palumbo D et al 2019 Innervation of the proximal interphalangeal joint: an anatomical study. J Hand Surg Am 44:422.

Petrie S, Collins J, Solomonow M et al 1997 Mechanoreceptors in the palmar wrist ligaments. J Bone Joint Surg Br 79:494–6.

Rainbow MJ, Wolff AL, Crisco JJ et al 2015 Functional kinematics of the wrist. J Hand Surg Eur Vol 41(1):7–21.

Rohde RS, Crisco JJ, Wolfe SW 2010 The advantage of throwing the first stone: how understanding the evolutionary demands of Homo sapiens is helping us understand carpal motion. J Am Acad Orthop Surg 18:51–8.

Rodriguez-Niedenführ M, Sanudo JR, Vazquez T et al 1999 Median artery revisited. J Anat 195:57–63.

Sandow MJ, Fisher TJ, Howard CQ et al 2014 Unifying model of carpal mechanics based on computationally derived isometric constraints and rules-based motion – the stable central column theory. J Hand Surg Eur Vol 39:353–63.

Sendher R, Ladd AL 2013 The scaphoid. Orthop Clin North Am 44:107–20.

Shyamalan G, Jordan RW, Kimani PK et al 2016 Assessment of the structures at risk during wrist arthroscopy: a cadaveric study and systematic review. J Hand Surg Eur Vol 41:852-8.

Singh HP, Dias JJ, Phadnis J et al 2015 Comparison of the clinical and functional outcomes following 3- and 4-corner fusions. J Hand Surg Am 40(6):1117–23.

Slattery D, Aland C, Durbridge G et al 2014 The connective tissue and ligaments of the distal interphalangeal joint: a review and investigation using ultra-high field 16.4 Tesla magnetic resonance imaging. J Hand Surg Eur Vol 39:398–404.

Slutsky DJ 2002 Volar portals in wrist arthroscopy. J Am Soc Surg Hand 2:225–32.

Stancić MF, Mićović V, Potocnjak M 1999 The anatomy of the Berrettini branch: implications for carpal tunnel release. J Neurosurg 91:1027–30.

Stecco C, Macchi V, Barbiieri A et al 2018 Hand fasciae innervation: the palmar aponeurosis. Clin Anat 31:1–4.

Taleisnik J 1976 The ligaments of the wrist. J Hand Surg Am 1:110–18.

Tomita K, Berger EJ, Berger RA et al 2007 Distribution of nerve endings in the human dorsal radiocarpal ligament. J Hand Surg Am 32A:466–73.

Tubiana R, Thomine J-M, Mackin E 1996 Examination of the hand and wrist. London: Martin Dunitz.

Tucker SC, Titley OG 2002 Metacarpal descent, definition and normal range. J Hand Surg Br 27:289–92.

Tuffaha SH, Quan A, Hashemi S 2018 Selective thumb carpometacarpal joint denervation for painful arthritis: clinical outcomes and cadaveric study. J Hand Surg Am 44(1):64.e1–64.e8.

Ulrich D, van Reitbergen B, LAib A et al 1999 Load transfer analysis of the distal radius from in-vivo high-resolution CT-imaging. J Biomechanics 32(8):821–8.

Urbaniak JR, Evans JP, Bright DS 1981 Microvascular management of ring avulsion injuries. J Hand Surg Am 6:25–30.

Van de Pol GJ, Koudstaal MJ, Schuurman AH et al 2006 Innervation of the wrist joint and surgical perspectives of denervation. J Hand Surg Am 31:28–34.

Vaz A, Trippia CR 2018 Small but troublesome: accessory ossicles with clinical significance. Radiol Bras 51:248–56.

Viegas SF 1990 The lunatohamate articulation of the midcarpal joint. Arthroscopy 6:5–10.

Wilgis ES, Murphy R 1986 The significance of longitudinal excursion in peripheral nerves. Hand Clin 2:761–6.

Wong VW, Higgins JP 2015 Interpretation of upper extremity arteriography vascular anatomy and pathology. Hand Clin 31:121–34.

Werner FW, Green JK, Short WH et al 2004 Scaphoid and lunate motion during a wrist dart throw motion. J Hand Surg Am 29(3):418–22.

Wynter S, Dissabandara L 2018 A comprehensive review of motor innervation of the hand: variations and clinical significance. Surg Radiol Anat 40:259–69.

Zaidenberg EE, Palumbo D, Martinez E et al 2018 Innervation of the interphalangeal joint of the thumb: anatomical study. J Hand Surg Eur Vol 43:631–4.

Zancolli EA, Angrigiani C 1988 Posterior interosseous island forearm flap. J Hand Surg Br 13:130.

Zarzecki MP, Popieluszko P, Zayachowski A et al 2018 The surgical anatomy of the superficial and deep palmar arches: a meta-analysis. J Plast Reconstr Aesthet Surg 71:1577–92.

Zook EG 1981 The perionychium: anatomy, physiology, and care of injuries. Clin Plast Surg 8:21–31.

Zwanenburg RL, Werker PMN, McGrouther DA 2014 The anatomy and function of Cleland's ligaments. J Hand Surg Eur Vol 39:482–90.

COMMENTARY

6.1

Nerve biomechanics

Kimberly S. Topp

Peripheral nerves are subject to physical forces as a result of body position and movement. Nonetheless, the biomechanical properties of these nerves permit continued electrical signalling when faced with reasonable physical demands. For example, when an individual moves from a standing to a sitting position, the sciatic nerve lengthens as it crosses the posterior aspect of the hip joint, its cross-sectional shape becomes elliptical and narrowed, and endoneurial fluid is forced proximally and distally away from the site of compression. The sciatic nerve glides proximally in the thigh towards the flexing hip joint and away from the knee joint (Topp and Boyd 2006).

When a nerve bed is elongated across a moving joint, the nerve is placed under longitudinal tension. The biomechanical response of that nerve may be documented in a load–elongation curve, measured in Newtons per millimetre (Haftek 1970). To enable comparisons to be made between nerves, the load–elongation curve may be translated into a stress–strain curve. Stress is defined as the intensity of force per unit cross-sectional area, and is reported in N/m^2 or MPa (Pascal). Strain is defined as the ratio of change in length to the original length, and is often reported as a percentage.

Three distinct regions are seen in nerve load–elongation or stress–strain curves (**Fig. 6.1.1**). In the initial 'toe' region of the curve, application of very little tensile load or stress results in significant elongation or strain. In the 'linear behaviour' region, there is a correlation between the applied load or stress and the elongation or strain. In the 'plastic' region of the curve, minimal load or stress results in mechanical failure and discontinuity of nerve structures.

Several structural features of peripheral nerves may be related to segments of the stress–strain curve, and these features may vary between nerves requiring functional adaptation. Nerve *in situ* is under tension: the transition between the 'toe' region and the 'linear behaviour' region of the curve corresponds roughly with the *in situ* strain (Kwan et al 1992).

The elasticity seen in the initial part of the stress–strain curve is due to structures that make up visible, periodic light–dark bands that were initially described by, and named after, Felix Fontana (Fontana 1781). These bands vary in their angulation, width, spacing and periodicity. Studies of rat sciatic nerve using Fourier analysis have shown a linear relationship between increasing nerve strain and decreasing band frequency and axonal undulations (Love et al 2013). *In vivo* microdissection studies coupled with computer modelling suggest that layers of perineurial cells are possibly responsible for the short-wavelength, large-amplitude bands and that wavy spiralling nerve fibres in the endoneurium are responsible for the long-wavelength, small-amplitude bands (Merolli et al 2012), the two patterns merging to form the visible bands of Fontana. In a recent study, however, the nerves of *Trembler-J* mice, a model of Charcot–Marie–Tooth disease, were found to have altered bands of Fontana, resulting solely from unusually long, sinuous axons moving out of phase (Power et al 2015). Increasing strain in the 'linear behaviour' region of the stress–strain curve causes the bands of Fontana to disappear (Pourmand et al 1994). An illustration of functional adaptation is seen in a study of nerves in the feeding pouch of the rorqual whale (Lillie et al 2017). These highly extensible nerves demonstrate straightening of nerve fibres and connective tissues internal to the thick epineurium at the transition from 'toe' region to 'linear behaviour' region of the stress–strain curve. Further lengthening is achieved through unfolding of the thick, elastin-laden epineurium, a feature that differs from other nerves in less mobile regions of this animal (Vogl et al 2017).

Anatomical features are also known to contribute to the 'linear behaviour' region of the stress–strain curve. The slope of this region is termed Young's modulus of elasticity, or stiffness in the case of the load–elongation curve. A steep slope indicates that the nerve is stiff: significant tensile force results in only a modest change in length. The modulus of elasticity or stiffness of an acellular nerve is comparable to that of fresh nerve, indicating that connective tissue fibres contribute to stiffness (Borschel et al 2003, Zilic et al 2016). Endoneurial fluid and the perineurial sheath that encloses the fluid compartment also contribute to stiffness. When a nerve is elongated, it undergoes transverse contraction (Walbeehm et al 2004): the reduction in cross-sectional area increases pressure in the endoneurial compartment and, consequently, stiffness of the nerve (Millesi et al 1995). As one might predict, nerve roots, which lack a perineurial sheath, demonstrate less stiffness than a peripheral nerve (Beel et al 1986). The differing biomechanical properties of nerve roots and nerves were investigated in a study of the neonatal brachial plexus (Singh et al 2018). There was less stiffness in the plexus roots, trunks and cords, compared to nerve branches or to the more frequently studied tibial nerve. External features, such as nerve branching, entering/exiting blood vessels, and paraneural tissue connections, resist elongation of the nerve in its nerve bed, and increase *in situ* nerve stiffness (Millesi et al 1995, Foran et al 2018).

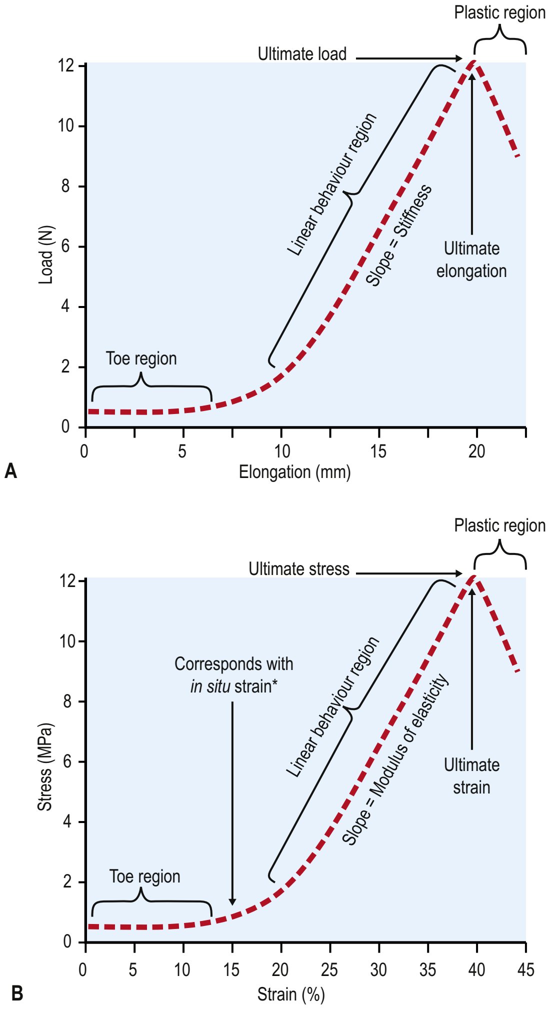

Fig. 6.1.1 Typical load–elongation (**A**) and stress–strain curves (**B**) for a peripheral nerve. The transition between the toe region and the linear region in the stress–strain curve (asterisk) has been shown to correspond approximately with the strain *in situ*. The slope of the stress–strain curve is called the modulus of elasticity and represents the stiffness of the nerve, as seen in the load–elongation curve. If the slope is steep, then the nerve has more stiffness and is less compliant to elongation. If the slope is less steep, then the nerve has less stiffness and is more compliant to elongation. Once the nerve has reached ultimate strain, the structural integrity of the nerve is overcome and the deformation is termed 'plastic' or 'permanent'. (From Topp KS, Boyd BS 2006 Structure and biomechanics of peripheral nerves: nerve responses to physical stresses and implications for physical therapist practice. Phys Ther 86:92–109.)

In the 'plastic' region of the stress–strain curve, increasing longitudinal stress causes non-recoverable elongation and structural integrity is lost. The force per unit cross-sectional area at the point of mechanical failure is termed ultimate stress and occurs at ultimate strain. At this point, a nerve behaves like a viscous material (Haftek 1970). The velocity and direction of the applied load influence the result: dynamic loads are more likely than quasistatic loads to result in nerve rupture (Mahan et al 2018). Additionally, nerve damage is more likely to occur at lower strains with forces applied along the long axis of the nerve when compared to forces applied orthogonally, and forces applied orthogonally result in rupture at nerve branch points (Mahan et al 2018). Along the stress–strain curve, structures within the nerve become impaired in a hierarchical fashion. With increasing tensile load, there is first sliding and loss of tenuous connections in the interface between the layer of inner perineurial cells and the sheath of outer perineurial cells and associated epineurial tissues (Tillett et al 2004, Georgeu et al 2005). With continued load, the core of nerve fibres and inner perineurial cell layers is disrupted and function is impaired or lost: ultimately, the sheath of outer perineurial and epineurial tissues ruptures. Given that acellular nerve is of significantly lower tensile strength and ultimate strain than fresh nerve (Borschel et al 2003), the perineurial cell layer should be appreciated for its ability to withstand stress. Although definitive anatomical studies are lacking, it is likely that microscopic disruptions of perineurial cell–cell connections occur with increasing stress along the 'linear behaviour' region of the stress–strain curve, long before ultimate strain is reached.

Nerve is best described as a viscoelastic tissue because its bio-mechanical properties are time-dependent. In response to fixed tension over time, nerve demonstrates creep or elongation (Grewal et al 1996). Slow elongation allows for higher ultimate strain (Haftek 1970, Rydevik et al 1990). When stretched to a fixed length over time, nerve exhibits stress relaxation or a reduction in tension (Wall et al 1991, Driscoll et al 2002).

Returning to the example of the sciatic nerve, during movement from standing to sitting, the nerve bed is elongated posterior to the hip as forward movement of the trunk causes flexion at the hip joint. The sciatic nerve is exposed to tensile load or stress with resultant elongation or strain, the magnitude of which is greatest near the moving joint. Adjusting to these forces, segments of the nerve converge towards the flexing hip joint, with minimal motion in distant segments (Topp and Boyd 2006). Endoneurial pressure resists transverse contraction. When the seated posture is assumed and maintained, the nerve undergoes stress-relaxation – until the next change in position.

References

Beel JA, Stodieck LS, Luttges MW 1986 Structural properties of spinal nerve root: biomechanics. Exp Neurol 91:30–40.

Borschel GH, Kia KF, Kuzon WM et al 2003 Mechanical properties of acellular peripheral nerve. J Surg Res 114:133–9.

Driscoll PJ, Glasby MA, Lawson GM 2002 An in vivo study of peripheral nerves in continuity: biomechanical and physiological responses to elongation. J Orthop Res 20:370–5.

Fontana F 1781 Traité sur le vénin de la vipere, sur les poisons américains, sur le laurier-cerise et sur quelques autres poisons végetaux. On y a joint des observations sur la structure primitive du corps animal. Différentes experiences sur la reproduction des nerfs et la description d'un nouveau canal de l'œil, vol. 2. Florence: Nyon L'Ainè.

Foran IM, Hussey V, Patel RA et al 2018 Native paraneurial tissue and paraneurial adhesions alter nerve strain distribution in rat sciatic nerves J Hand Surg 43:316–23.

Georgeu GA, Walbeehm ET, Tillett R et al 2005 Investigating the mechanical shear-plane between core and sheath elements. Cell Tissue Res 320:229–34.

Grewal R, Xu J, Sotereanos DG et al 1996 Biomechanical properties of peripheral nerves. Hand Clin 12:195–204.

Haftek J 1970 Stretch injury of peripheral nerve. Acute effects of stretching on rabbit nerve. J Bone Joint Surg 52:354–65.

Kwan MK, Wall EJ, Massie J et al 1992 Strain, stress and stretch of peripheral nerve. Rabbit experiments in vitro and in vivo. Acta Orthop Scand 63:267–72.

Lillie MA, Vogl AW, Gil KN et al 2017 Two levels of waviness are necessary to package the highly extensible nerves in rorqual whales. Curr Biol 27:673–79.

Love JM, Chuang T-H, Lieber RL et al 2013 Nerve strain correlates with structural changes quantified by Fourier analysis. Muscle Nerve 48:433–5.

Mahan MA, Yeoh S, Monson K et al 2018 Rapid stretch injury to peripheral nerves: biomechanical results. Neurosurgery 85(1):E137–E144.

Merolli A, Mingarelli L, Rochchi L 2012 A more detailed mechanism to explain the 'Bands of Fontana' in peripheral nerves. Muscle Nerve 46:540–7.

Millesi H, Zoch G, Reihsner R 1995 Mechanical properties of peripheral nerves. Clin Orthop Relat Res 314:76–83.

Pourmand R, Oches S, Jersild RA 1994 The relation of the beading of myelinated nerve fibers to the bands of Fontana. Neuroscience 61:373–80.

Power BJ, O'Reilly G, Murphy R et al 2015 Normal nerve striations are altered in the Trembler-J mouse, a model of Charcot–Marie–Tooth disease. Muscle Nerve 51:246–52.

Rydevik BL, Kwan MK, Myers RR et al 1990 An in vitro mechanical and histological study of acute stretching on rabbit tibial nerve. J Orthop Res 8:694–701.

Singh A, Shaji S, Delivoria-Papadopoulos M et al 2018 Biomechanical responses of neonatal brachial plexus to mechanic stretch. J Brachial Plex Peripher Nerve Inj 13:e8–e14.

Tillett RL, Afoke A, Hall SM et al 2004 Investigating mechanical behavior at a core–sheath interface in peripheral nerve. J Peripheral Nerv Sys 9:255–62.

Topp KS, Boyd BS 2006 Structure and biomechanics of peripheral nerves: nerve responses to physical stresses and implications for physical therapist practice. Phys Ther 86:92–109.

Vogl W, Petersen H, Adams A et al 2017 The functional anatomy of nerves innervating the ventral grooved blubber of fin whales (Balaenoptera Physalus). Anat Record 300:1963–72.

Walbeehm ET, Afoke A, de Wit T et al 2004 Mechanical functioning of peripheral nerves: linkage with the 'mushrooming' effect. Cell Tissue Res 316:115–21.

Wall EJ, Kwan MK, Rydevik BL et al 1991 Stress relaxation of a peripheral nerve. J Hand Surg Am 16:859–63.

Zilic L, Wilshaw S-P, Haycock JW 2016 Decellularisation and histological characterization of porcine peripheral nerves. Biotechnol Bioeng 112:2041–53.

COMMENTARY
6.2

The anatomy and variation of the coracoid attachment of the subclavius muscle and its relation to the clavi-coraco-axillary aponeurosis

Simon Lambert

The classic descriptions of the gross anatomy of the subclavius muscle in humans agree that it originates at the junction of the first rib and first costal cartilage immediately lateral to the costoclavicular ligament (Cave 1961), and inserts into the subclavian groove on the inferior surface of the clavicle, limited laterally by the conoid tubercle and terminating between the coracoclavicular ligaments. Additional, variable, insertions onto the coracoid process have also been noted. In one description, the lateral part of subclavius was separated into a superomedial part inserted, as usual, onto the inferior surface of the clavicle and an inferolateral part inserted onto the root of the coracoid process in 12 (16.8%) of 72 cases (Mori 1964). Several anatomical variations (largely duplications) have been reported (Le Double 1897, Georgiev and Jelev 2009, Ozcakar et al 2010, Yun et al 2018), of which the subclavius posticus appears to be the commonest (Cogar et al 2015). This aberrant muscle may play a role in more proximal neurogenic thoracic outlet syndromes (Hasan and Romeo 2001, Ozcakar et al 2010, Piyawinijwong and Sirisathira 2010, Muellner et al 2015), as well as being of relevance to cannulation of the subclavian vein (Kawagishi et al 2016) and venous occlusion syndromes (McCleery et al 1951, Lusskin et al 1967).

During a surgical anatomy programme conducted at the Division of Clinical and Functional Anatomy at the Medical University of Innsbruck in 2017 it was noted that, in many dissections, additional fibrous structures contiguous with, and extending from, the epimysial fascia of subclavius were inserted into the base, medial margin and tip of the coracoid process. This suggested, first, that anatomical variations of the insertion of subclavius onto the coracoid are more common than previously reported, and second, that the function of subclavius is more subtle than simply that of stabilizing the clavicle at the sternoclavicular joint (SCJ) as previously thought (Reis et al 1979).

In a series of subsequent dissections of 52 adult shoulders, the anatomy of the *origin* of subclavius was constant and there were no additional medial musculotendinous attachments. However, 23% of the specimens had some form of variation in the anatomy of the *muscular* part of subclavius. These included an *additional* muscular belly (i.e. a duplication rather than a substitution anomaly) inserting into the superior border of the scapula adjacent to the origin of omohyoid, consistent with the previously described subclavius posticus (two specimens); an additional muscular insertion to the clavicle (i.e. subclavius appeared to be bicipital) (seven specimens); the muscular part of subclavius extending directly to the body of the coracoid process; an additional muscular insertion at the base of the coracoid process; and an additional muscular insertion onto the glenohumeral joint capsule. Subclavius was perforated in one specimen by a venous plexus, but no other anomalies of the subclavian vein were noted in this, or other, cases.

Conversely, the anatomy of the coracoid *insertion* fibres was highly variable. Three shoulders did not have any extension to the coracoid process. In the other shoulders (94%) subclavius had a lateral extension that took one of three basic forms: a single strong cord-like band (37%); a planar twisted sheet-like structure attached along the medial side of the base of the coracoid process and extending to the body of the process, *discrete from the clavipectoral fascia* (32%); and a small, thin cord-like structure (24%). In two specimens, the cord-like structure was duplicated with one band passing deeply to the base of the coracoid process. The small fibrous extensions were often multiple, suggesting that they were a derivative form of a (perforated) planar sheet. Whatever their configuration, the fibrous structures comprised shiny, parallel-orientated fibres, resembling an aponeurosis.

There was a clear gender difference in the form of the aponeurosis, but no side difference. In male specimens there were thick cord-like structures in 14/24 (58%) dissections and a twisted sheet form in 11/24 (46%) dissections. In female specimens cord-like structures were present in 9/28 (32%), and a twisted sheet structure in 5/28 (18%).

The mean length of the insertion of subclavius into the subclavian groove was relatively constant, occupying, as a ratio of the clavicular length, approximately 38% (male) to 41% (female) of the inferior surface of the clavicle. However, there was a wide range of actual lengths of the insertion into the groove, varying up to 4.5 cm in total length. The form of the aponeurotic extension (robust cord, small cord, or twisted sheet) did not correlate with a particular range of lengths of the insertion of subclavius into the clavicle. The most lateral point of insertion of subclavius into the clavicle was further from the muscular origin the longer the overall clavicular insertion into the groove, but there was no correlation with the form of the aponeurotic extension: this also held true for the coracoid insertion of the aponeurosis (when one was present).

The nerve to subclavius was identified and dissected in 44 of 52 specimens, while the artery was seen in only 19 of 52 dissections. The nerve entered the muscle belly at a mean of 50% of the length of the muscle (from its origin) in the right specimens in females, and at a mean of 54% in the left specimens, while in the males the nerve entered the muscle at a mean of 59% of the muscle length on the right, and 54% on the left. These observations concur with those of Jeon et al (2018), where the artery to subclavius could be defined as it entered the muscle with the nerve.

The anatomy of subclavius and its *intrinsic* tendon structure have been elucidated by Cave and Warwick Brown (1952), who acknowledged the prior contribution of French anatomists to the description of the muscle and its relations. Their description corresponds to the structures seen in this series of dissections as the aponeurosis of extension of the subclavius fascia in its various forms, but discrete from the clavipectoral fascia. Testut (1904) illustrated the anatomy of subclavius in relation to the 'clavi-coraco-axillary aponeurosis'. A fascinating illustration in his text shows the tip of the coracoid process held within this extensive aponeurosis, which extended from the clavicle deep to pectoralis major to the upper part of the humerus, enveloping subclavius, pectoralis minor, coracobrachialis and the short head of biceps brachii from superiorly to inferolaterally. The coracoid process is thus suspended from the clavicle, and the trajectory of coracoid motion guided by the muscles enveloped by the clavipectoral fascia.

The strong cord-like form described here would appear to be an extension of the pars paramuscularis and forms a strong, concave inferior border to the musculo-aponeurotic structure bridging the first rib, the clavicle and the coracoid process. Importantly, this structure therefore bridges two joints (the sternoclavicular and scapulo- (acromio-) clavicular joints). The tendinous border is relatively inelastic, although deformable. This suggests that subclavius might actually function to pre-tension the pars paramuscularis and aponeurosis of extension, contributing to the control of the motion of the distal clavicle as an antagonist of the primary scapular motion muscles. A corollary to this suggestion is that the *functional* anatomy of subclavius might be better 'viewed' from the perspective of the clavicle (with the coracoid below it) rather than from the perspective of the observer (who sees the coracoid with the clavicle above it, and so presumes the function of subclavius is to limit movement at the sternoclavicular joint in relation to elevation, and pro-retraction, of the scapula). The nomenclature of the origin and insertion of subclavius persuades the observer that the muscle acts *on* the clavicle. However, the fact that the nerve to subclavius enters midway along its length *suggests* that the muscle contracts towards its centre. If this is so, then the muscle acts with the clavicle as its origin or base, and inserts onto its own robust tendinous border, attached medially to the first rib, and laterally to the coracoid and/or into the clavi-coraco-axillary aponeurosis in order to brace (pre-tension) the upper part of that aponeurosis during movement of the upper limb.

Subclavius and its lateral aponeurotic extension therefore form the superior element of a 'functional system' that contributes to the control of the position of the scapula in relation to the thorax (i.e. at the scapulothoracic 'joint') in a manner synonymous with all other articulations (i.e. there are at least two articulating surfaces whose relative movement is generated by muscular action, the range, arc and trajectory of which are determined by capsular or, in the case of the scapulothoracic joint, aponeurotic, restraints).

Our study in Innsbruck found the aponeurotic extension to be more common than previously documented (Mori 1964). If only the strong cord-like lateral fibrous extension is considered, then the frequency of that form in our series remains greater (35%) than previously described in a Japanese series (Mori 1964). We considered the twisted planar sheet-like aponeurosis, present in 31% of specimens, to be a variant (possibly an archetype) of this lateral extension, and not simply a fascial septum from the clavipectoral fascia. It is unclear why there should be a gender difference in the form of the lateral extension.

The function of subclavius in humans has been assumed to be that of stabilizing the sternoclavicular and acromioclavicular joints (Reis et al 1979). However, evidence suggests that muscle functions to regulate the output of kinetic energy in movement of the upper extremity rather than as a primary stabilizer of either the sternoclavicular or acromioclavicular joint. That the nerve to subclavius serves no other muscle suggests that subclavius has, or had, an important role in efficient brachiation, the modern equivalent being of overhead (sport-related) movements. Extending the muscle through a strong aponeurosis to the coracoid process (and so the scapula) would enhance this function.

Acknowledgement

The author is indebted to his co-workers at the Institute of Anatomy, University of Innsbruck, Austria for the completion of the work reported in this Commentary: Professor Erich Brenner, Dr Ulrich Crepaz-Egar, Dr Clemens Hengg, Dr Dominik Knierzinger, R Hoermann.

References

Cave AJ 1961 The nature and morphology of the costoclavicular ligament. J Anat 95:170–9.

Cave A, Warwick Brown R 1952 On the tendon of the subclavius muscle. J Bone Joint Surg Br 34:466–9.

Cogar AC, Johnsen PH, Potter HG et al 2015 Subclavius posticus: an anomalous muscle in association with suprascapular nerve compression in an athlete. Hand 10:76–9.

Georgiev GP, Jelev L 2009 Bilateral fibrous replacement of subclavius muscle in relation to nerve and artery compression of the upper limb. Int J Anat Var 2:57–9.

Hasan SS, Romeo AA 2001 Thoracic outlet syndrome secondary to an anomalous subclavius muscle. Orthopedics [Case Report Journal] 24:793–4.

Jeon A, Seo CM, Choi YJ et al 2018 Innervation of subclavius muscle: an anatomical study. Int J Morphol 36:817–20.

Kawagishi K, Tokumine J, Lefor AK 2016 Clinical study. The relationship of the subclavius muscle with relevance to venous cannulation below the clavicle. Anesthesiol Res Pract 2016:6249483.

Konstant W, Stern JT, Jr, Fleagle JG et al 1982 Function of the subclavius muscle in a nonhuman primate, the spider monkey (Ateles). Folia Primatol 38:170–82.

Le Double A-F 1897 Traité des variations du système musculaire de l'homme: et de leur signification au point de vue de l'anthropologie zoologique. Tome 1. Paris: Schleicher Frères; 1897.

Lusskin R, Weiss CA, Winer J 1967 The role of the subclavius muscle in the subclavian vein syndrome (costoclavicular syndrome) following fracture of the clavicle. A case report with a review of the pathophysiology of the costoclavicular space. Clin Orthop Relat Res 54:75–83.

McCleery RS, Kesterson JE, Kirtley JA et al 1951 Subclavius and anterior scalene muscle compression as a cause of intermittent obstruction of the subclavian vein. Ann Surg 133:588–602.

Mori M 1964 Statistics on the musculature of the Japanese. Okajimas Folia Anat Jpn 40:195–300.

Muellner J, Kaelin-Lang A, Pfeiffer O et al 2015 Neurogenic thoracic outlet syndrome due to subclavius posticus muscle with dynamic brachial plexus compression: a case report. BMC Res Notes 8:351.

Ozcakar L, Guney MS, Ozdag F et al 2010 A sledgehammer on the brachial plexus: thoracic outlet syndrome, subclavius posticus muscle, and traction in aggregate. Arch Phys Med Rehabil [Case Reports] 91:656–8.

Piyawinijwong S, Sirisathira N 2010 Supernumerary subclavius muscle in Thais: predisposing cause of thoracic outlet syndrome. J Med Assoc Thai 93:1065–9.

Reis FP, de Camargo AM, Vitti M et al 1979 Electromyographic study of the subclavius muscle. Acta Anat (Basel) 105:284–90.

Testut L 1904 Traite d'anatomie humaine, 5th ed. Paris: O. Doin.

Yun S, Park S, Kim CS 2018 Absence of the subclavius muscle with contralateral subclavius posticus muscle: first imaging report. Clin Imaging 49:54–7.

COMMENTARY
6.3

Instability of the shoulder – a neurological disease

Simon Lambert

This commentary addresses glenohumeral instability (GHI), although the analysis of stability and its perturbation, and the system of classification described, is applicable to all articulations in which the experience of symptomatic abnormal motion (the clinical syndrome of instability) is reported by a patient.

Stability: definition

Stability of any articulation (defined as asymptomatic normal mechanical behaviour at rest and in motion) depends on the retention of structural integrity, intact neural control systems (afferent, efferent and neuromuscular connectivity), and the absence of strain exceeding the yield point for the whole system. For the glenohumeral joint (GHJ) stability is therefore the product of a functionally (not necessarily anatomically) intact rotator cuff, competent capsular and labral structures, a sufficient surface arc (or surface area) of contact between humeral head and glenoid, and an intact neuromuscular system comprising central and peripheral connections, with functioning mechanoreceptors clustered in the capsule and labrum, and in the tendons of the rotator cuff (RC) and long head of biceps (LHBT).

The essence of stability and the stability equation

Motion about the centroid of rotation and ‘containment’ of the humeral head on the size-mismatched glenoid is the result of concavity compression, generated by the centralizing joint reaction force (CJRF) of the rotator cuff (including LHBT), and the generation of negative intra-articular pressure, facilitated by the conformity of the glenoid/labral surface. Rotator cuff competence is a function of centrally driven activation via feed-forward systems, and the strength and inertia of the cuff muscles. Shoulder joint position sense and motion are the products of right parietal cortical programming (the parietal reach region), and visual, vestibular and cervical afferent inputs: it appears that visual cues are more important than hand position in determining the control of shoulder motion. Maintenance of this activity is achieved through feedback mechanisms derived through mechanoreceptors in the capsular and labral structures, rotator cuff tendons and muscles, and the surfaces of the shoulder gliding planes (the acromio-coraco-deltoid-scapulothoracic space, and the glenohumeral joint space), and affected by the inertia of the rotator cuff tendino-fibrous ‘skeleton’ and muscles, and fascial and cutaneous afferents. The relationship between the dominant factors in creating stability in the GHJ can be illustrated by a simple diagram (**Fig. 6.3.1**), and described by an equation:

$$CJRF = RC^{a} + SAC^{b} + CLMNS^{c} + NS^{d}$$

(where *CJRF* is the centralizing joint reaction force, and the elements *RC* = rotator cuff, *SAC* = surface arc (area) of contact, *CLMNS* = capsulolabral mechano-nociceptive system, *NS* = central and peripheral neural control system elements, and a–d are factors describing the weight of each element in the overall mechanism of stability for that individual at a specific point in time).

The relative importance of each factor varies according to the individual case, but several points are common.

First, the anatomy of the rotator cuff is relatively invariant (although subscapularis can vary in the ‘height’ of its attachment to the lesser tuberosity). The number of muscle spindles (MS, predominantly *stretch* receptors) in rotator cuff muscles has been studied in marsupials and is approximately 1.5 times the number of Golgi tendon organs (GTO; predominantly *contraction* receptors) (Maass et al 2001a, 2001b). GTOs are situated predominantly in the musculotendinous junctions and at the regions of confluence between the tendon and capsule of the joint. Both muscle spindles and GTOs have large myelinated, fast conducting afferents. The GHJ will remain stable in the partial absence of medial capsulolabral structures (for instance after surgical release for frozen shoulder syndrome, or complete capsulotomy for total shoulder replacement), provided that the rotator cuff function is normal. Thus the dominant proprioceptive input for glenohumeral stability would appear to be from the muscles and the tendinous endoskeleton of the rotator cuff. The LHBT has a special role in linking rotator cuff activity, humeral head position and overall upper limb position, particularly in activities requiring optimal close-packing of the shoulder and elbow. Anomalies of the intra-articular tendon and isolated rupture of the tendon do not appear to contribute to humeral head instability, provided the closely associated components of the rotator cuff remain intact. By contrast, a rotator cuff rupture in an elderly patient presents as superior GHJ instability.

Second, the SAC can vary. Thus, segmental dysplasia of the glenoid, congenital glenoid version anomalies and humeral head defects (Broca or Hill–Sachs, and McLaughlin lesions) all contribute to a decrement in the SAC, which predisposes to failure of the CJRF vector to pass through the glenoid during all arcs of motion.

Third, the structure of the CLMNS can vary considerably. The labrum can be absent, hypoplastic, or dysplastic, and ligament anomalies are well recognized (and common) in subjects with no instability. The incidence of ligamentous anomalies in patients with atraumatic structural instability is the same as that in the general population: lax individuals do not appear to have a greater prevalence of anomalies of ligament morphology, although the molecular structure is clearly altered. The labrum contains numerous free nerve endings, with a frequency about ten times greater than any other corpuscular receptor type (Halata et al 1985), which are readily distorted by motion.

The number of corpuscular mechanoreceptors in the capsule of a marsupial is equivalent to that of muscle spindles, with about 87% being small lamellated corpuscles (rapid-response stretch signalling in a local region) having relatively smaller myelinated afferents than either MSs or GTOs. Pacinian corpuscles (rapid-response stretch signalling over a wider field) are found in the outer fibrous laminae of the capsule, predominantly in the axillary region, while Ruffini corpuscles, which are uncommon, are found in the dense fibrous layer of the capsule in the axilla, and the dermis of the skin. When articular afferents are stimulated in the cat shoulder there is a very short latency (3 ms) to contraction in biceps and deltoid, suggesting a monosynaptic reflex at spinal cord level (Knatt et al 1995). There therefore appears to exist a gradient of receptor speed, locality and density from within to without the joint. As is apparent from the preceding text, data is largely derived from non-human sources, but there is increasing clarity about the role of neural pathways in generating and maintaining shoulder joint stability (Myers and Lephart 2002). It is not known whether variations occur in the densities or function of mechanoreceptors in the capsule and labrum in patients with atraumatic structural and muscle-patterning.

Fourth, neural control systems are readily deranged, by central or peripheral neurological conditions: aberrant muscle activation or suppression contributes to GHJ instability (Gibson et al 2004), and diseases of the cerebellum and basal ganglia may present with shoulder instability, particularly of the scapulothoracic joint.

It is self-evident that we are not aware of our shoulder if it has not been injured or affected by a disease in some way, nor do we regard it during gestural and stereotactic activities. In other words, the presentation of our shoulder is unconscious: all activity is predicted, planned and executed without cognition. This lack of conscious awareness of the shoulder (or any other joint) seems likely to be a function of the entirety of the afferent data about the shoulder. Different combinations of afferent inputs must be produced during varying positions and actions involving the joint. However, providing the total afferent input remains within a range of normality for that joint at that particular time (as predicted by the purpose for which the joint action has been generated), there is no conscious awareness of the joint. If injured, there is awareness (i.e. a conscious, therefore cortical, event occurs, one usually signifying *potential* danger) and, if the injury is sufficient, what is clinically defined as ‘apprehension’ (i.e. a conscious, therefore cortical, event appreciated as a fear of *actual* danger) often accompanied by a reflex

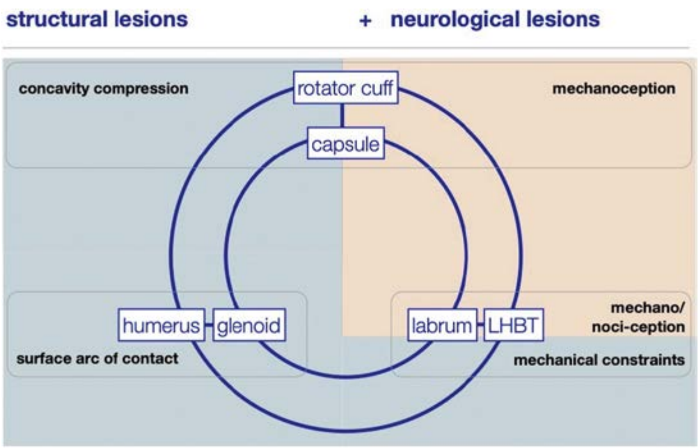

Fig. 6.3.1 Schematic of factors involved in generating stability in the glenohumeral joint. The inner (medial) system comprises the capsule, labrum and glenoid fossa, while the outer (lateral) system comprises the rotator cuff, long head of biceps tendon (LHBT) and the articular surface of the humerus. The LHBT forms a link between the two systems. All tissues contain mechanoceptors and nociceptors: the distribution of these in the human shoulder has been incompletely characterized. Key: grey indicates structural elements; ochre indicates non-structural (neural) elements.

activation of muscles of the shoulder girdle region. If the injury is more deleterious still, and tissue disruption of a critical ‘amount’ occurs, then pain will occur (in biological evolutionary terms, the incentive to remove oneself from the source of the injury). The central pathways of awareness, apprehension and pain are similar. The total afferent input from the shoulder joint has been changed in some way, and if there has been a disruption of tissues then that region of disruption will likely be de-afferented. A change in overall afferent input, either an absolute loss or an alteration in the ratio of inputs from the various sources, results in both cortical and spinal level reflex (protective) activity. Since the central nervous system works on the principle of inhibition, the ‘permission’ of spinal activity activating a shoulder girdle response (‘apprehension’) is produced by an inhibition of the normal inhibitory pathways of motor activation patterns. The individual becomes aware (now at cortical level) of actions, motions or positions of the arm in space which will both generate pain (through distortion of the injured afferent neural tissue) and unpleasant sensations perceived as potential or incipient displacement of the articular surfaces. Restoration of the afferent input, by the healing of the disrupted tissues (whether by natural means or by surgery) results in less pain and less apprehension. That some patients often remark that their shoulder ‘feels’ better immediately after restorative surgery (if undertaken soon after the injury) suggests that the afferent pathways from spinal level to cortical level remain intact and non-adapted. That other patients, also undergoing restorative surgery, particularly after recurrent episodes of dislocation or failed healing, take a long time to recover to the point of no apprehension suggests not only that re-afferentation is relatively less well organized and quantitatively diminished, but also that central re-adaptation has to occur. That rehabilitation programmes designed to restore stability take roughly the same period as programmes for integrating tendon transfers suggests similar central neural mechanisms are at work. Muscle-patterning instability, the so-called Stanmore type III instability (see below), is a large spectrum of disorders of shoulder stability, characterized by a lack of structural abnormalities, likely to be a failure (by inhibition) of the normal inhibitory pathways of muscle control.

The increased risk of a traumatic GHJ dislocation in the first-degree relatives of patients with traumatic (i.e. structural) GHJ instability suggests a predisposition to the condition, even where the structure of the joint was previously apparently normal. Whether this is located in the afferent, central, or efferent components of the neural control mechanisms is uncertain, but the part of the ‘system’ that could most readily be perturbed is the afferent, in terms of the number, density and distribution of mechanoreceptors.

Instability: a clinical definition

Instability is usefully defined as the condition of symptomatic abnormal motion of the joint. This universal definition combines the mechanistic view and the clinical perspective, and distinguishes the pathological state from the constitutional state of laxity, in which anatomical anomalies may exist, but do not necessarily cause impairment of function. Since it is a symptom, the term implies recognition (a cerebral cortical event) of the abnormal motion (a difference in position, motion direction or motion velocity has been identified by the patient): ‘instability’ cannot be determined by examining the shoulder under anaesthetic (EUA). Laxity (looseness) of the GHJ can be determined by EUA either by comparison of the perceived abnormal with the perceived normal side or by reference to what is considered a normal range of laxity for the population of which the patient is representative.

The relationship between the dominant factors in creating instability in the GHJ can be described by a second equation, derived from the first:

$$\text{Instability} = \left[RC^{a} + SAC^{b} + CLMNS^{c} + NS^{d}\right] P\,.\,t$$

where the elements *RC*, *SAC*, *CLMNS* and *NS* are as before (see above) and a–d are factors describing the weight of each element in the overall mechanism of instability for that individual at a specific point in time. *P* are patient-specific factors (occupational and sports, lifestyle, motivation in rehabilitation, etc.), and *t* represents the probability that pathology will evolve over time.

The pathologies causing instability comprise structural (*RC*, *SAC*) and non-structural (*NS*) elements. Many authors hold that the labrum has a structural role, particularly in anterior glenohumeral instability: by virtue of its content of noci-mechanoreceptor clusters and arborizations of free nerve endings, it clearly has a role in neural information loops and so also represents a non-structural stabilizing element. The structural elements may be developmentally abnormal, contain abnormal collagen, or acquire microtraumatic lesions over time (collectively defined as *atraumatic structural* elements) or damaged by extrinsic force (defined as *traumatic structural* elements). The non-structural elements can be developmentally abnormal (e.g. neuromuscular dyspraxias) or can be acquired over time as perturbations of neuromuscular control, particularly at periods of skeletal growth (**Fig. 6.3.2**).

The shoulder in hypermobility syndromes

Laxity (or ‘looseness’) is defined as asymptomatic motion in a shoulder through a range that would not be considered normal for the patient’s age or gender. Laxity varies with age. Adolescents have a greater overall range of motion than adults, and stiffness (reduced compliance of rotator cuff and capsular tissues) increases with age. Shoulder laxity can exist as part of the generalized benign hypermobility syndromes, or as part of an upper limb dominant form of hypermobility, or in isolation. In the latter form, if one shoulder alone is affected then congenital bony architectural anomalies should be considered, whereas if bilateral isolated shoulder hypermobility is present then soft tissue anomalies are more prevalent.

Appropriate laxity

Normal soft tissue laxity is influenced by many factors such as oestrogen levels, the state of hydration and training. Laxity is very useful in certain circumstances (for instance during childbirth), so selective biological advantage might be conferred on those who develop appropriate laxity. Similarly, degenerative arthritis is uncommon in those who have loose shoulders, unless there are associated morphological anomalies of the glenoid or proximal humerus or inappropriate operations have been performed.

Inappropriate laxity, energy expenditure and the rotator cuff

Much greater energy expenditure is required to maintain shoulder stability in hyperlax shoulders, which means that persistent laxity does not confer a selective biological advantage, except in those whose daily activities, including sport, require laxity for best performance (e.g. dancers and swimmers). These individuals must train consistently to protect their shoulder connective tissues from overload: the capacity of the rotator cuff to generate a centralizing joint reaction force (to keep the humeral articular surface on the glenoid) is much less at the extreme ranges of motion. The musculature of the rotator cuff is specifically organized from deep to superficial so that the shortest muscle fibres (the deepest fibres) take origin at the most lateral extent of their scapular attachment, and insert into the capsule of the shoulder. These fibres contribute most to the centralizing or stabilizing function. The most superficial muscle fibres take origin more medially on the scapula and insert into the humerus

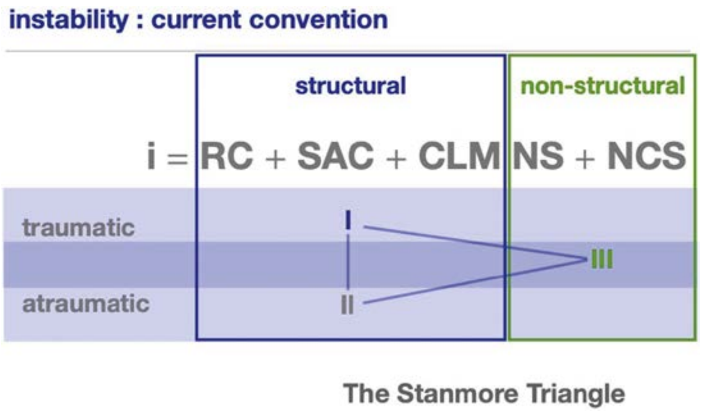

Fig. 6.3.2 Structural and non-structural elements of GHJ instability. These may be damaged (degenerative or traumatic, Stanmore type I), or underdeveloped (dysplastic or atraumatic, Stanmore type II). Note that 'non-structural' factors involved in generating instability may be damaged or dysplastic and are collectively brought under one group (Stanmore type III): this remains a weakness of the Stanmore system of classification of shoulder instability. Repeated 'sub-clinical' damage may occur, in structurally dysplastic or normal tissues, leading to instability through a mechanism involving repeated microtrauma. Abbreviations: CLMNS, capsulolabral mechano-nociceptive system; i, instability; NCS, central and peripheral neural control system elements; RC, rotator cuff; SAC, surface arc (area) of contact. (For further reading on the clinical syndromes of GHJ instability see Lambert 2007.)

lateral to the articular surface (on the tuberosities) through their tendons and by direct muscle insertions. These fibres contribute more to the initiation and control of motion of the shoulder. Each muscle fibre has a length at which it functions optimally and therefore each muscle, depending on the position of the shoulder, has a specific range of motion over which its constituent fibres contribute best to both stability and the control of motion. It follows that when the muscle fibres are at their shortest, at the extremes of range of motion, their effectiveness as both stabilizers and controllers of motion is suboptimal. At these positions the activity of the rotator cuff becomes very asymmetrical: the stability of the joint is less and the rapidity of response to motion diminished. Greater muscle bulk increases the inertia of the joint (its 'passive' resistance to displacement), so that training to increase muscle bulk will improve stability, but will conversely require greater energy expenditure. When training ceases, muscle tone diminishes and the joints are less protected. If, in addition, microtraumatic structural surface damage has occurred as a result of previous activity then the joint is at greater risk of degenerative change. The quality of proprioception is reduced in shoulders with hyperlaxity, instability and previous capsular trauma. Improvement in joint position and motion sense has been shown in trained shoulders, and after anterior capsular reconstruction in those with traumatic structural instability. It is not clear whether this is also the case for patients with atraumatic structural instability.

Group I (Traumatic structural instability)

The traumatic structural group includes the TUBS (Traumatic, Unilateral, Bankart lesion present [in the anterior instability type], Surgery usually indicated) group but also includes the posterior traumatic instability characterized by the McLaughlin or reversed Hill–Sachs lesion and posterior labral damage or locked posterior dislocation. Instability can thus be acute, recurrent or persistent (acute or chronic). Luxatio erecta is a specific version of anterior instability, usually of the more elderly, and may be associated with infraclavicular plexopathy, rotator cuff rupture and extensive bruising indicative of rupture of the humeral circumflex vessels. Surgical treatment is indicated for most patients in whom capsulolabral or rotator cuff disruption is evident: the choice and timing of open versus arthroscopic surgical techniques remains controversial.

Group II (Atraumatic structural instability)

In this group the incidence of ligamentous anomalies is the same as in the population of traumatic instabilities. The group contains the population defined as AMBRI (Atraumatic, often Multidirectional, often Bilateral, treated by Rehabilitation/physiotherapy). In the original definition of AMBRI, surgical treatment by inferior capsular shift is indicated if rehabilitation fails. However, this concept is flawed because some patients will possess some neuromuscular control aberration: surgery may fail because of the muscle-patterning behaviour (so-called type III instability) and patients may have a substantially greater probability of developing instability or post-capsulorrhaphy arthropathy if surgery is undertaken. The decision to operate should not be made on the basis of failed physiotherapy.

This group also contains a subgroup of individuals with benign hypermobility syndrome (of which Ehlers–Danlos syndrome is a variant), characterized by a Beighton score of greater than 5 out of a total possible 9 points. Hypermobility may be limited to the upper limbs. These patients may present with pain rather than overtly abnormal displacements and anterior atraumatic instability is less common than posterior atraumatic positional types. Posterior structural anomalies (including posterior glenoid dysplasia, excessive glenoid retroversion, glenoid hypoplasia, and medialized posterior capsular attachment) create an environment in which obligatory positional posterior displacement may occur during elevation of the arm in the sagittal plane. If abnormal, clinically obvious, muscle activation appears *at the onset* of this motion, then the diagnosis is modified to acknowledge the muscle-patterning: the case is group II/III (peripheral subtype). If the muscular activation occurs *during* the motion, and appears to be provoked by the position of the arm at the shoulder, then the diagnosis is still II/III but with the suffix (protective subtype). If there is no clinically or electrophysiologically proven aberrant muscle activation, then the condition is labelled II (positional subtype).

Scapular dyskinesis is common, and reflects the attempt by the scapular postural muscles to maintain scapulohumeral homeostasis. Serratus anterior can be suppressed in some cases: the aberrant muscle activity now affects the scapula primarily: this represents a scapulothoracic (STh) type III condition. Treatment consists of rehabilitation, avoidance of activities promoting the instability, pain management, and surgical intervention in selected cases. The variants of medially or laterally based inferior capsular shift with augmentation of dysplastic labral tissue are complemented in some cases of glenoid insufficiency by glenoid augmentation using autologous bone blocks (anteriorly and/or posteriorly), or glenoplasty (the Scott posterior glenoplasty, or posteroinferior segmental glenoplasty).

Group III (Muscle-patterning instability)

Muscle-patterning instability (MPI) consists of aberrant activation of large muscles identified by dynamic electromyography (latissimus dorsi, pectoralis major and anterior deltoid have been characterized thus far) and simultaneous suppression of the rotator cuff (infraspinatus has been characterized thus far: whether suppression of infraspinatus reflects suppression of the whole rotator cuff or specific suppression of infraspinatus is not yet clear). MPI can be clinically obvious, in polar group III, but may be occult, requiring dynamic electromyography (DEMG) for confirmation of the suspicion of the existence of MPI in the presentation (as in types II/III and III/II instabilities).

Demographic characteristics

Patients with abnormal muscular activation leading to 'pure' MPI appear to present in a trimodal distribution with peaks at 6, 14 and 20 years. The mean age at onset of symptoms is 14 years and the mean duration of symptoms before presentation is 8 years. In the under-10-year age group there are more girls (71% vs 47%), greater laxity (estimated with the Beighton score, 63% vs 29%), greater bilaterality (54% vs 42%) and fewer presenting with pain (17% vs 50%). As age increased, laxity decreased and pain increased. Bilaterality does not appear to be associated with gender, laxity or pain. Laxity is associated with gender but not pain or bilaterality. These observations suggest different aetiologies for the MPI in the three cohorts.

Bayley (2005) used DEMG in latissimus dorsi (LD), pectoralis major (PM), anterior deltoid (AD) and infraspinatus (IS) to evaluate the patterns of muscular activation in patients who clearly demonstrated, visibly or by palpation, apparently abnormal muscular activation immediately before and during dislocation of the glenohumeral joint in the outpatient clinic. These muscles were chosen because they were reliably accessible. Early pilot studies were expanded into a cohort study of over 1000 cases of GHI seen at the Royal National Orthopaedic Hospital, a tertiary referral centre, over a 22-year period (1981–2003), from which DEMG data were extracted. Muscle-patterning instability was diagnosed, clinically and/or electrophysiologically, in 494 shoulders of 386 patients (45% of the entire cohort of 1097 shoulders). In 44% the MP instability (MPI) affected both shoulders. The dominant arm was affected more often in right-handed patients, the non-dominant more often in left-handed patients. The central neurological basis for these differences remains obscure. There were 323 shoulders with 'pure' MPI; 161 shoulders presented a mixed picture of MPI in addition to either traumatic or atraumatic structural causes for the instability.

The value of recognizing this form of instability is considerable given the success of specialist physiotherapy using biofeedback techniques rather than conventional therapy for retraining abnormal muscle activity: 76% of patients had either no change or a deterioration in their condition with conventional therapy (including conventional strengthening exercises) compared with 61% of patients overall achieving improvement in their condition with specialist therapy. The incidence of iatropathic arthropathy increases with inappropriate surgery in those with type III instability, but has not been reported in patients with type III instability who did not undergo surgery.

Dynamic electromyography

Given the limitation that only four muscles have been studied in depth, the evidence strongly suggests that these, and perhaps other, muscles are implicated in many cases of instability. Inappropriate activity in PM, LD and AD, with suppression of IS, appear either singly or as couples in the generation of instability in the shoulder with and without capsular collagen insufficiency. Whether suppression of IS reflects specific inappropriate inactivity in IS alone or reflects abnormal activation of the rotator cuff as a whole remains unknown. DEMG provides additional information about abnormal muscle activation or suppression in subtle muscle-patterning instability in which clinical examination has a low specificity and sensitivity. DEMG was found to be most useful in patients presenting with pain, glenohumeral capsular insufficiency and occult muscle-patterning, categorized as the interpolar group II/III. Given that a chance of a successful outcome for rehabilitation of patients with MPI (symptoms abolished or controlled) was diminished five-fold for anterior and 10-fold for posterior instability after inappropriate surgery in patients with MPI, it is clear that the identification of this specific cohort is important. These patients contribute to the failures of the AMBRI group after rehabilitation (if MPI has not been recognized). It is noteworthy that the pathology is not defined by direction but rather that the direction of instability is determined by the pathology.

Rehabilitation is the first mode of treatment used for MPI: there is usually a change in aberrant muscle activity within 6 months. Therapy has to continue for at least two years, possibly for cortical re-imprinting to be re-established. There is a 25% recurrence rate within two years, needing 'top-up' therapy, including in-patient treatment in which a multidisciplinary approach is favoured. The value of specific suppression of specific muscles by injection of botulinum toxin is unclear.

Multidirectional instability (MDI)

MDI is not a diagnosis but a symptom. Multidirectional *laxity* is assessed by examination under anaesthesia (EUA). It may be difficult to determine if a lax shoulder is centralized during EUA. An individual shoulder may have the same pathology (i.e. group I, II or III pathology) causing instability in each of more than one direction, or more than one pathology (e.g. group I in one direction, and group II/III in the other direction), thus distinguishing 'group I' MDI from 'complex' MDI. The underlying diagnoses of the different directions of instability are distinguishable by the history, clinical observations, arthroscopy and/or magnetic resonance imaging with arthrography, supplemented by dynamic electro-myography (DEMG) where necessary. Each pathology is treated separately, with rehabilitation of MPI elements taking priority.

Summary

Functional disturbance within the neurological pathways that control joint stability appears to be a fundamental component of the pathologies that lead to instability. Current understanding of the afferent 'field' for stability in the shoulder is poor. Inferences from non-human experimental animal studies have been illuminating but it is unclear how accurately they reflect the human condition. The ascending pathways and spinal level reflexes needed to maintain shoulder stability in humans are even less well characterized. The subcortical and cortical mechanisms of control of shoulder (and other joint) motion are better understood as a result of experimental animal studies, but the interrelated mechanisms of joint position and motion awareness (proprioception), apprehension and pain await clarification.

Mechanical insufficiency in the anatomical structures that comprise the shoulder may lead to dysfunction that presents as the syndrome of instability. Given the variability of these anatomical structures, it seems reasonable to suggest that the overall afferent 'field' of the shoulder (from cutaneous to capsular and osseous mechanoceptors) exerts a more significant influence on joint stability or its perturbation. The neurological deficit consequent on structural damage or degeneration, or inherent in poorly developed tissues, may be more important, and the restoration of a neurologically healed shoulder may be a more logical goal than one which is structurally intact but neurologically incompetent.

References

Bayley JIL, Lewis A, Kitamura T 2005 The classification of shoulder instability. New light through old windows. Curr Orthop 8:97–108.

Gibson K, Growse A, Korda L et al 2004 The effectiveness of rehabilitation for nonoperative management of shoulder instability: a systematic review. J Hand Ther 17:229–42.

Halata Z, Rettig T, Schulze W 1985 The ultrastructure of sensory nerve endings in the human knee joint capsule. Anat Embryol 172:265–75.

Knatt T, Guanche C, Solomonow M et al 1995 The glenohumeral-biceps reflex in the feline. Clin Orthop 314:247–52.

Lambert S 2007 The classification of shoulder instability. In: Limb D, Hay S (eds) The Evidence for Orthopaedic Surgery. TFM Publishing Ltd; Ch. 8, pp. 99–108.

Maass S, Baumann KI, Halata K 2001a Topography of corpuscular mechanoreceptors in the shoulder joint region of Monodelphis domestica. Anat Rec 263:35–40.

Maass S, Baumann KI, Halata K 2001b Topography of muscle spindles and Golgi tendon organs in shoulder muscles on Monodelphis domestica. Ann Anat 183:237–42.

Myers JB, Lephart SM 2002 Sensorimotor deficits contributing to glenohumeral instability. Clin Orth 400:98–104.

CHAPTER

52

Thorax: overview and surface anatomy

The thorax is the upper part of the trunk. It consists of an external musculoskeletal cage, the thoracic wall and an internal cavity that contains the heart, lungs, oesophagus, trachea and main bronchi, thymus, vagus and phrenic nerves, sympathetic trunks and ganglia, thoracic duct, lymph nodes, and major systemic and pulmonary vasculature (**Fig. 52.1**). Superiorly, the thoracic cavity communicates with the neck and the upper limbs via the superior thoracic aperture. Inferiorly, it is separated from the abdominal cavity by the respiratory diaphragm. The thoracic cage offers protection to some of the superiorly located abdominal viscera: the majority of the liver lies inferior to the right dome (cupula) of the respiratory diaphragm; the stomach, spleen and left lobe of the liver lie inferior to the left dome of the diaphragm; and the posterior surfaces of the suprarenal glands and kidneys contact the anteroinferior surface of the lumbar part of the diaphragm.

MUSCULOSKELETAL FRAMEWORK

Bones and joints

The thoracic cage consists of 12 thoracic vertebrae and the intervening intervertebral discs, 12 pairs of ribs and their anteriorly located costal cartilages, and the sternum (**Fig. 52.2**). When articulated, they form an irregularly shaped osseocartilaginous frame (see Fig. 53.8). Laterally, the outer surface of the thoracic cage is convex and is formed by the ribs; anteriorly, it is slightly convex and is formed by the sternum and the distal parts of the ribs and their costal cartilages. The costal cartilages of the first seven pairs of ribs are connected to the sternum at the sternocostal joints, the costal cartilages of the eighth to tenth ribs usually join the inferior border of the superiorly located costal cartilage at the interchondral joints, and the eleventh and twelfth (sometimes the tenth) ribs and their cartilage are free (floating) at their anterior ends and project into the musculature of the abdominal wall. The posterolateral curvature of the ribs, from their head (vertebral end) to their angle (see Fig. 53.9), produces a deep internal groove, the paravertebral gutter, located on either side of the vertebral column. The ribs and costal cartilages are separated by intercostal spaces, which are deeper anteriorly and between the more superiorly located ribs. Each space is occupied by two or three layers of flat muscles and their aponeuroses (membranes), neurovascular bundles and lymphatic channels.

The superior thoracic aperture (thoracic inlet) typically measures 5 cm anteroposteriorly and 10 cm transversely (see Fig. 52.1). It is bounded by the body of the first thoracic vertebra posteriorly, the internal (medial) borders of the left and right first ribs, and the superior border (jugular notch) of the manubrium of the sternum anteriorly. It slopes anteriorly and inferiorly from the vertebral column, so that the apex of the lung is located in the inferior neck, above the level of the first rib and the medial one-third of the clavicle, and level with the body of the seventh cervical or first thoracic vertebra, or the intervening C7–T1 intervertebral disc; structures that pass between the thorax and the upper limb therefore pass over the first rib and the suprapleural membrane covering the pleurae and lung apex.

The inferior thoracic aperture (thoracic outlet) is bordered posteriorly by the body of the twelfth thoracic vertebra, posterolaterally by the twelfth rib and its costal cartilage and the distal end of the eleventh rib and its costal cartilage, anterolaterally by the cartilaginous ends of the seventh to tenth ribs (which unite and ascend as the costal arch or margin), and anteriorly by the xiphoid process of the sternum (see Fig. 52.2). In adults the dimension of the transverse plane of the aperture is larger than the sagittal plane, and the aperture slopes obliquely inferiorly and posteriorly towards the vertebral column, so that the thoracic cavity is deeper posteriorly than anteriorly.

The sternum is formed from three parts (manubrium, body and xiphoid process) that articulate at the manubriosternal and xiphisternal joints. The sternal plane passes horizontally through the manubriosternal joint (sternal angle, angle of Louis) at the level of the second costal cartilage anteriorly, intersecting the vertebral column posteriorly in a region that extends from the body of the fourth thoracic vertebra to the superior half of the body of the fifth thoracic vertebra (Mirjalili et al 2012a). The sternal plane separates the superior mediastinum from the inferior mediastinum and can be used as a reference plane to position intrathoracic mediastinal structures.

Muscles

Intrinsic and extrinsic muscles

The intrinsic muscles of the chest wall are the intercostal muscles, subcostalis, transversus thoracis, levatores costarum and serratus posterior superior and inferior (see Figs 46.71, 53.15). Transversus thoracis may mimic pleural thickening on CT imaging: the uncommon variants, sternalis and rectus thoracis bifurcalis, are important clinically because they may mimic a focal density in medial breast craniocaudal mammograms and may be encountered during reconstructive surgery of the breast and chest wall.

The intercostal muscles are arranged in consecutive layers in each intercostal space and are named according to their positional relationship to each other, i.e. external, internal and innermost (see Fig. 53.17). All the intrinsic muscles except levatores costarum are innervated

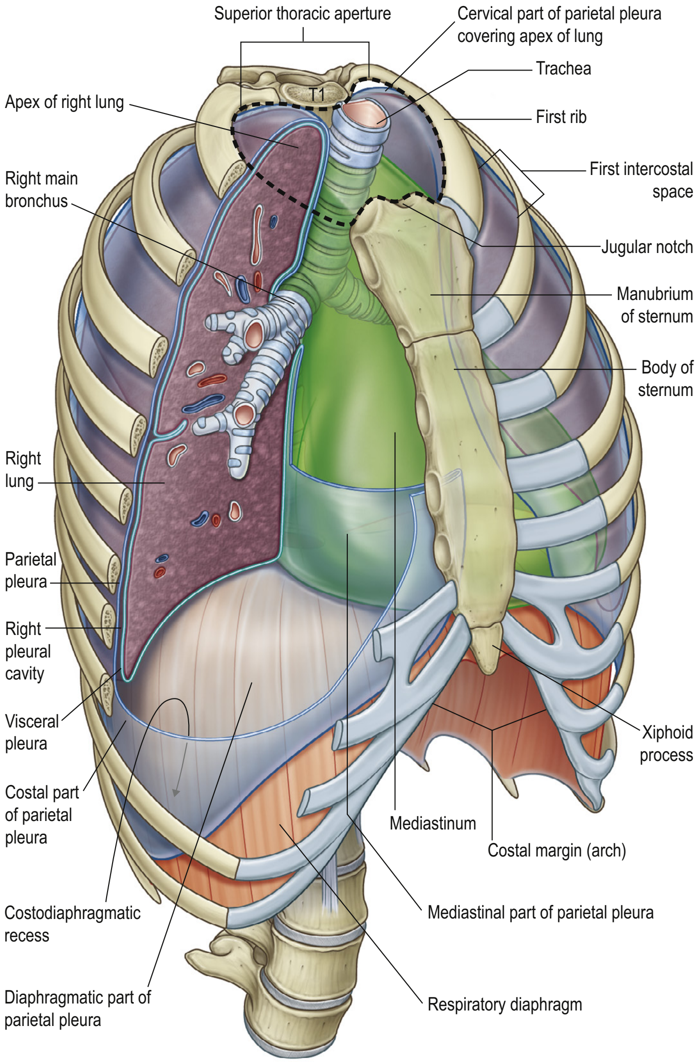

Fig. 52.1 The thoracic cage and thoracic cavity; showing the lungs, pleura, pleural cavity, diaphragm and mediastinum. (With permission from Drake RL, Vogl AW, Mitchell A et al (eds) Gray's Atlas of Anatomy, 2nd ed. Elsevier, Churchill Livingstone. Copyright 2015.)

The shape, dimensions and proportions of the thoracic cage vary between individuals, particularly with age and sex (Joshua et al 2014). In an adult, the dimensions of the thoracic cavity change continuously with the movements of the ribs and diaphragm during respiration (Ch. 55) and also with distension of the abdominal viscera and movement of the vertebral column. In a normal healthy adult, both the thoracic cage and abdominal wall move outwards on inspiration and inwards on expiration. Changes to this pattern, including paradoxical movements, may be seen in respiratory disease (Goldman 1982). Thoracic capacity is less in females than it is in males, both absolutely and proportionately; in the female, the sternum is normally shorter and the thoracic inlet more oblique.

In neonates and young infants, the thoracic cage has the shape of a truncated cone and is relatively round in cross-section, the ribs have an almost horizontal alignment, and the domes of the respiratory diaphragm and sternal ends of the clavicles sit in a more superior position than is the case in older children and adults (Openshaw et al 1984). Thoracic expansion is consequently limited and contributes little to breathing, which is reliant on the respiratory diaphragm. In a neonate, diaphragmatic contraction during inspiration pulls the thoracic cage inwards and moves the abdomen outwards, the thoraco-abdominal paradox. The neonatal thoracic wall is highly compliant and is easily deformed. By 2 years of age, as standing and walking begin, adult thoracic proportions and geometry have developed. These include downward sloping ribs, an oval cross-sectional shape to the thoracic cage, and a more inferior position of the domes of the respiratory diaphragm and the sternal ends of the clavicles (Openshaw et al 1984, Joshua et al 2014). This means that the thorax is able to move outwards during inspiration and the thoraco-abdominal paradox diminishes until it is no longer observed.

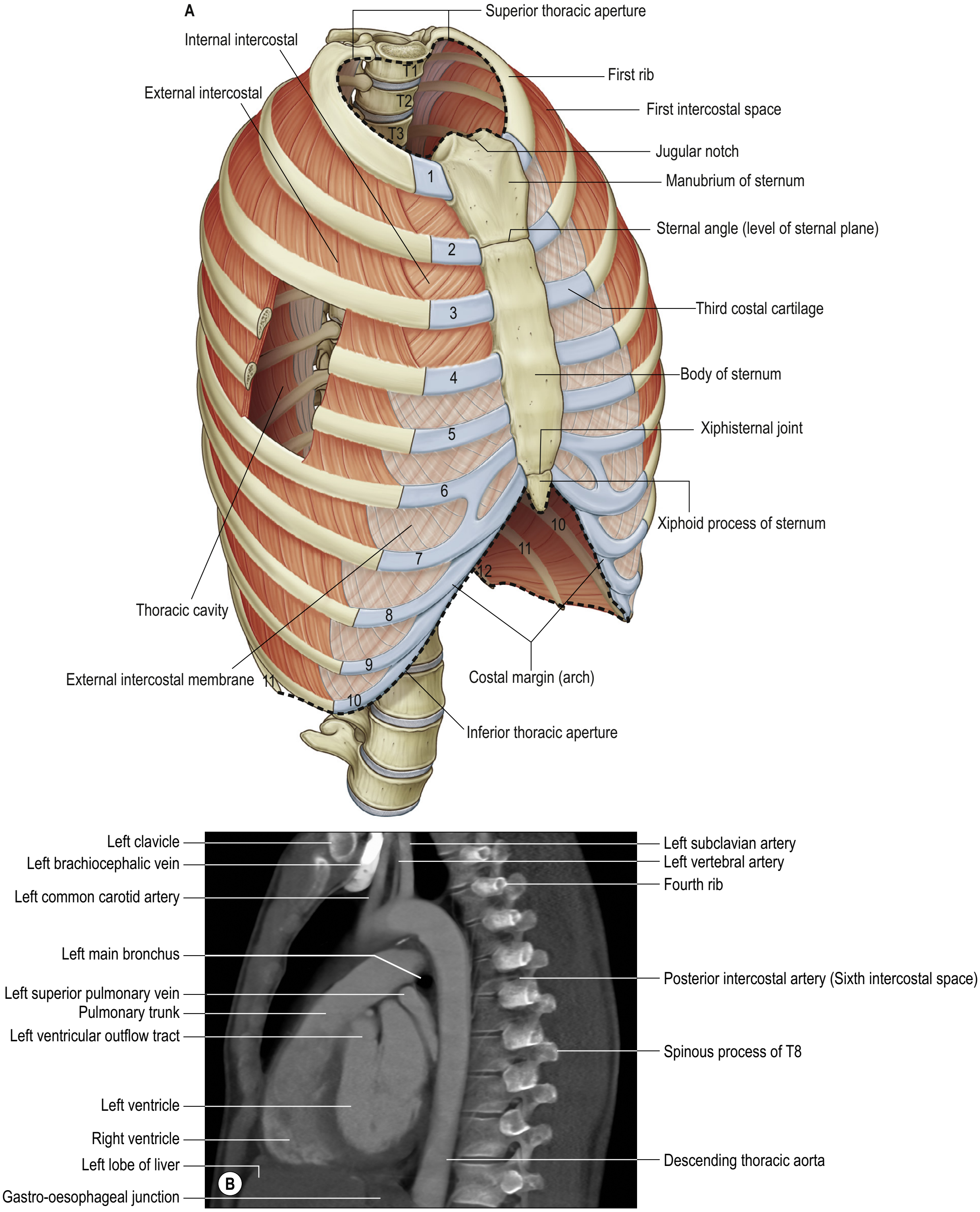
A
Superior thoracic aperture
Internal intercostal
External intercostal
T1
T2
T3
First rib
First intercostal space
Jugular notch
Manubrium of sternum
1
Sternal angle (level of sternal plane)
2
3
Third costal cartilage
4
Body of sternum
5
Xiphisternal joint
6
Xiphoid process of sternum
10
11
12
7
Thoracic cavity
8
9
Costal margin (arch)
External intercostal membrane
11
10
Inferior thoracic aperture
Left clavicle
Left brachiocephalic vein
Left common carotid artery
Left main bronchus
Left superior pulmonary vein
Pulmonary trunk
Left ventricular outflow tract
Left ventricle
Right ventricle
Left lobe of liver
Gastro-oesophageal junction
B
Left subclavian artery
Left vertebral artery
Fourth rib
Posterior intercostal artery (Sixth intercostal space)
Spinous process of T8
Descending thoracic aorta

Fig. 52.2 **A**, The musculoskeletal components of the thoracic wall showing the superior and inferior thoracic apertures. The costal cartilages and ribs are labelled accordingly 1–12. The first three thoracic vertebrae are labelled T1–T3. **B**, Left sagittal CT volume-rendered slab showing the left posterior intercostal arteries arising from the thoracic aorta. Note the origin of the left vertebral artery from the arch of the aorta (for a description of this variant, see Tardieu et al 2017). (A, With permission from Drake RL, Vogl AW, Mitchell A et al (eds) Gray's Atlas of Anatomy. Elsevier, Churchill Livingstone. Copyright 2015.)

segmentally by the intercostal nerves derived from the ventral rami of the thoracic nerves. Levatores costarum are innervated segmentally by lateral branches of the dorsal rami of the thoracic spinal nerves. The intrinsic muscles can elevate or depress a rib depending upon their location and are particularly active in forced (deep) breathing; some also help to stiffen the chest wall, thereby preventing paradoxical movement during inspiration and optimizing inspiratory/expiratory reserve volume.

The skeletal framework of the thoracic wall provides attachment sites for muscles associated functionally with the neck, back, upper limbs and abdomen. Some (e.g., scalenes, infrahyoid strap muscles, sternocleidomastoid, serratus anterior, pectoralis major and minor, external and internal abdominal obliques and rectus abdominis) may also function as accessory muscles of respiration; they are usually active only during forced breathing. Muscles with thoracic attachment are described in more detail in Chapters 35, 48 and 60.

Respiratory diaphragm

The respiratory diaphragm is a curved musculotendinous sheet attached to the circumference of the inferior thoracic aperture and the bodies of the superior two or three lumbar vertebrae. It forms the inferior boundary (floor) of the thoracic cavity and separates it from the abdominal cavity (Ch. 55). The diaphragm is relatively flat centrally, in the region inferior to the heart, and domed peripherally, rising higher on the right side than on the left, an asymmetry reflecting the differences in relative densities of the underlying abdominal viscera. From its most superior point on each side, the diaphragm slopes inferiorly to its peripheral costovertebral attachments. Posteriorly, the space between the diaphragm and the thoracic wall (costodiaphragmatic recess) is long and narrow. The position of the domes varies with body position; they are higher in the supine compared to the erect position. During quiet respiration in the erect position, diaphragmatic excursion is about 2 cm in both sexes, increasing to around 7 cm during deep breathing (Boussuges et al 2009); the range of excursion is often greater in men and may increase further whilst in the supine position (Takazakura et al 2004).

Diaphragmatic openings

The respiratory diaphragm is traversed by structures that pass between the thorax and abdomen, including the right and left vagus, phrenic, thoracic splanchnic and subcostal nerves, the thoracic duct, sympathetic trunks, right and left superior epigastric arteries (continuations of the internal thoracic arteries), and the azygos and hemiazygos veins. The inferior vena cava and oesophagus pass through the tendinous and muscular parts of the diaphragm, respectively (see Fig. 55.1). CT-based studies have shown the vertebral level at which they pass through the diaphragm is more inferior than reported conventionally.

THORACIC CAVITY

Fascia and spaces

The endothoracic fascia (parietal fascia of the thorax) is a mixture of tissue types including connective, adipose, lymphoid and smooth muscle. It lines the inner surface of the thoracic wall and the superior surface of the respiratory diaphragm, separating them from the respective region (part) of the parietal pleura. It is attached posteriorly to the periosteum of the thoracic vertebrae and becomes continuous with the thoracic prevertebral fascia; superiorly it forms the suprapleural membrane; inferiorly it is continuous with the endo-abdominal fascia via apertures in the respiratory diaphragm, e.g., the aortic hiatus (Dugan and Samson 1975).

Pleural cavities

The right and left pleural cavities are separate compartments within the thoracic cavity, located on either side of the mediastinum. Each surrounds a lung and its associated bronchial tree, vessels, nerves and lymphatics (Ch. 54). The walls are formed by a serous membrane, the pleura, arranged as a closed sac. Each cavity represents a potential space between the parietal and visceral pleura, two serous membranous layers that are continuous on the medial aspect of the lung root and pulmonary ligament at the pleural reflection. The outermost layer, the parietal pleura, lines the inner surface of the corresponding half of the thoracic wall, the superior surface of the ipsilateral hemidiaphragm and structures along the ipsilateral lateral side of the mediastinum. The parietal pleura covers part of the lung root, close to the hilum, then folds internally on itself to become continuous with the innermost layer, the visceral pleura, which adheres to the outer surface of the lobes of the lung, following the interlobar fissures. The two layers of pleura are in close contact throughout all phases of breathing, yet are able to slide freely over each other due to the presence of an intervening thin layer of serous fluid. The pleural cavity is maintained normally at a negative pressure by the inward elastic recoil of the lung and the outward pull of the thoracic wall. The lungs do not occupy the full extent of the pleural cavity during quiet breathing, but are free to move into recesses such as the costodiaphragmatic and costomediastinal recesses, during deep breathing.

Mediastinum

The mediastinum is a visceral compartment of the thoracic cavity, located within and adjacent to the median sagittal plane, between the right and left pleural cavities (see (Figs 52.1, 56.1): the mediastinal part of the parietal pleura forms its lateral boundaries. The mediastinum extends from the sternum anteriorly to the thoracic vertebral column posteriorly, and from the superior thoracic aperture superiorly to the respiratory diaphragm inferiorly. The sternal plane (which passes horizontally through the manubriosternal joint at the level of the second costal cartilage anteriorly, intersecting the vertebral column posteriorly in a region that extends from the body of the fourth thoracic vertebra to the superior half of the body of the fifth thoracic vertebra) is used to divide the mediastinum into superior and inferior parts. The sternal plane is sometimes defined as a fixed plane that passes from the manubriosternal joint to the most inferior part of the body of the fourth thoracic vertebra. Regional mediastinal content is reviewed in Ch. 56.

Superior mediastinum

Available with the *Gray's Anatomy* e-book

Inferior mediastinum

Available with the *Gray's Anatomy* e-book

VASCULAR SUPPLY AND LYMPHATIC DRAINAGE

Arteries

The skin of the thorax is supplied by direct cutaneous vessels and musculocutaneous perforators, which reach the skin primarily via the intercostal muscles, pectoralis major, latissimus dorsi and trapezius. The positions of the cutaneous vascular territories and their arterial supply guide the placement of free flap grafts for reconstructive surgery. Branches from the thoraco-acromial, lateral and superficial thoracic, internal thoracic, anterior and posterior intercostal, thoracodorsal, transverse cervical, dorsal scapular and circumflex scapular arteries are the major contributing vessels to the skin of the thoracic wall (see Figs 46.4, 53.1, 53.2).

The muscles of the thoracic wall receive their blood supply from the internal thoracic artery (either directly or via the musculophrenic artery), the supreme (highest) intercostal artery (from the costocervical trunk), the superior thoracic artery (from the axillary artery) and the descending thoracic aorta (via the posterior intercostal and subcostal arteries) (**Fig. 52.3**). The main anterior and posterior intercostal arteries pass around the superior aspect of each intercostal space, their anastomoses provide a potential route for collateral circulation in cases of aortic coarctation. Collateral branches of the intercostal arteries pass around the inferior aspect of each space. Additional contributions come from vessels that supply the proximal muscles of the upper limb, namely the suprascapular, superficial cervical, thoraco-acromial and subscapular arteries (see Fig. 46.4).

The detailed arterial supply of the thoracic viscera is described with the viscera.

Veins

The posterior intercostal veins and their collateral branches accompany their similarly named arterial counterparts in the superior and inferior aspect of each intercostal space (**Fig. 52.4**). The anterior intercostal veins are tributaries of the internal thoracic and musculophrenic veins; the internal thoracic veins drain into the ipsilateral brachiocephalic veins. The posterior intercostal veins drain directly or indirectly into the azygos vein on the right and the hemiazygos or accessory hemiazygos veins on the left. In some cases the veins from the upper two or three intercostal spaces on

More recent descriptions define the endothoracic fascia as the outermost connective tissue layer within the extrapleural space, a space situated between the parietal pleura and the inner surface of the thoracic wall and superior (thoracic) surface of the respiratory diaphragm (Santamarina et al 2017). The extrapleural space also contains a layer of adipose tissue in contact with the parietal pleura, loose connective tissue, vessels and lymphoid tissue. A range of pathologies may occur in this tissue plane, including liposarcoma, leiomyosarcoma, fibrosarcoma and lymphoma (Morelli et al 2007). An increased accumulation of extrapleural fat may be confused for pleural thickening on CT imaging (Im et al 1989).

The superficial subcutaneous fascia of the thorax, formed mainly by fat, is attached loosely to the skin and includes the breast tissue. Deeper fascial layers include those surrounding the muscles of the thoracic wall: some layers are dense and supportive, e.g. the clavipectoral fascia (Ch. 49) and the thoracolumbar fascia (Ch. 46).

The extrathoracic fascia is located posteriorly between the muscles that attach the scapula to the posterior thoracic wall and the underlying posterior thoracic wall (Latarjet and Juttin 1953). The extrafascial space is superficial to the extrathoracic fascia and is relatively sealed, whereas the subfascial space deep to the extrathoracic fascia communicates freely with the cervical region superiorly and with the lumbar region inferiorly.

The superior mediastinum lies between the manubrium of the sternum anteriorly and the anterior longitudinal ligament covering the bodies of the first four or five thoracic vertebrae and their intervening intervertebral discs posteriorly (depending upon the level at which the sternal plane intersects the vertebral column). It contains the lower ends of sternohyoid, sternothyroid and longus colli on each side; the aortic arch, brachiocephalic trunk and thoracic portions of the left common carotid and left subclavian arteries; the brachiocephalic veins and upper half of the superior vena cava; the supreme and superior intercostal veins; the vagus, cardiac, phrenic and left recurrent laryngeal nerves; and the trachea, oesophagus, thoracic duct, thymic remnants and lymph nodes (e.g. upper paratracheal, para-aortic, subaortic and prevascular nodes).

The inferior mediastinum, between the sternal plane and diaphragm, is divided into three parts: anterior, middle and posterior.

Anterior mediastinum The anterior mediastinum is primarily located on the left side where the point of reflection between the left costal and mediastinal part of the parietal pleura diverges from the median plane. It is bounded anteriorly by the sternum, laterally by the left and right mediastinal parietal pleura and posteriorly by the fibrous pericardium. It is approximately triangular in shape, being wider inferiorly, and may be absent above the level of the fourth costal cartilage if the left and right parietal pleural layers meet. Its anterior wall is formed mainly by the left transversus thoracis and the fifth to seventh left costal cartilages and intervening intercostal muscles. The anterior mediastinum contains loose areolar tissue, lymphatic vessels from the liver, thymic remnants (or fatty replacement), parasternal lymph nodes and mediastinal branches of the internal thoracic artery.

Middle mediastinum The middle mediastinum is the broadest part of the mediastinum. It contains the heart within the pericardial coverings and cavity; the ascending aorta; the inferior part of the superior vena cava with the azygos vein joining it; the tracheal bifurcation and right and left main bronchi; the pulmonary trunk dividing into the left and right pulmonary arteries; the right and left pulmonary veins (superior and inferior) and phrenic nerves; and hilar, subcarinal and lower paratracheal (tracheobronchial) lymph nodes.

Posterior mediastinum The posterior mediastinum is a relatively long and narrow space. It is bounded anteriorly by the fibrous pericardium, pulmonary vessels, tracheal bifurcation, left and right main bronchi and the posterior (or posterosuperior) surface of the respiratory diaphragm; posteriorly, depending on the level of the sternal plane, by the anterior longitudinal ligament covering the vertebral column from the bodies of the fourth or the superior half of the body of the fifth to the twelfth thoracic vertebrae and intervening intervertebral discs; and laterally by the mediastinal part of the parietal pleura. It contains multiple structures passing to/from the abdominal cavity and posterior thoracic wall including the descending thoracic aorta; the oesophagus and the anterior and posterior vagal trunks; the azygos venous system; the thoracic duct and lymph nodes (e.g., paraoesophageal and retrotracheal); the right and left sympathetic trunks and ganglia; and the left and right vagus nerves.

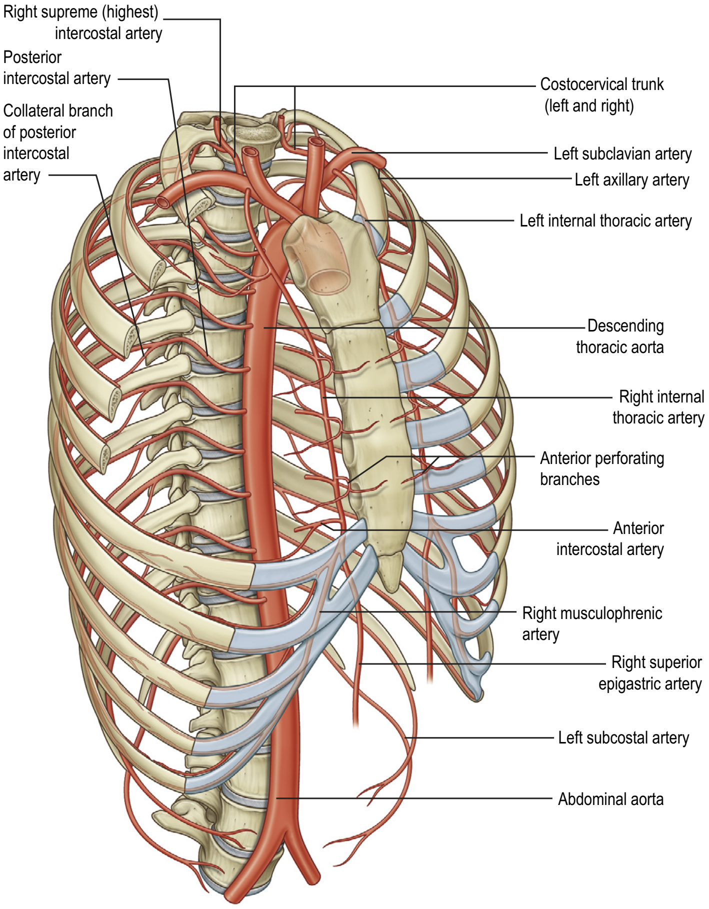
Right supreme (highest) intercostal artery
Posterior intercostal artery
Collateral branch of posterior intercostal artery
Costocervical trunk (left and right)
Left subclavian artery
Left axillary artery
Left internal thoracic artery
Descending thoracic aorta
Right internal thoracic artery
Anterior perforating branches
Anterior intercostal artery
Right musculophrenic artery
Right superior epigastric artery
Left subcostal artery
Abdominal aorta

Fig. 52.3 The thoracic and abdominal aorta, and the arteries of the thoracic wall (With permission from Drake RL, Vogl AW, Mitchell A et al (eds) Gray's Atlas of Anatomy, Elsevier, Churchill Livingstone. Copyright 2015.)

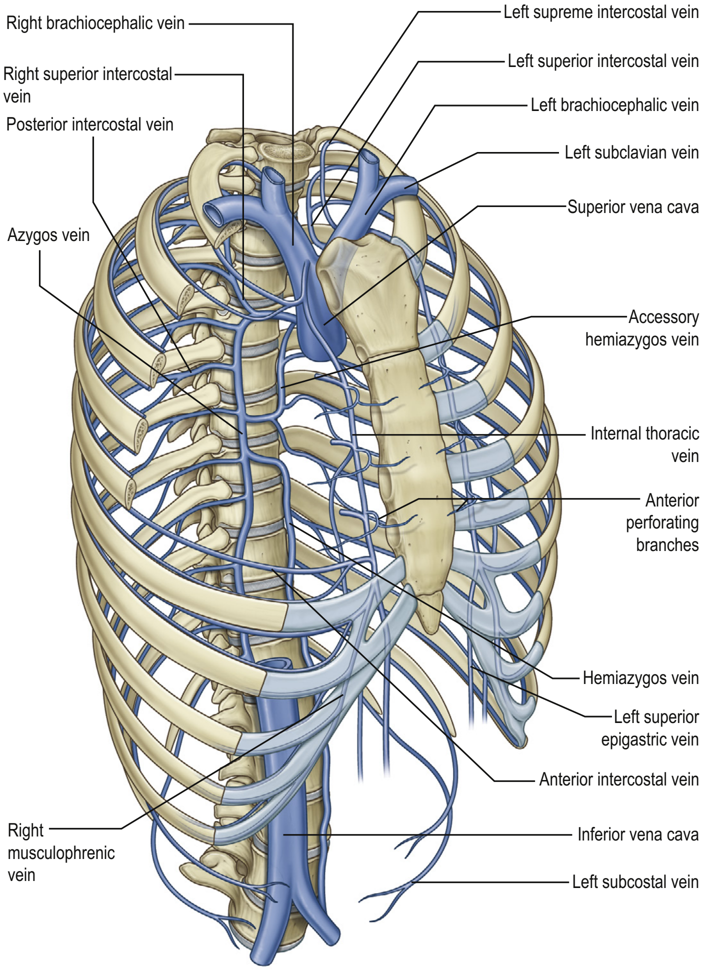
Right brachiocephalic vein
Right superior intercostal vein
Posterior intercostal vein
Azygos vein
Right musculophrenic vein
Left supreme intercostal vein
Left superior intercostal vein
Left brachiocephalic vein
Left subclavian vein
Superior vena cava
Accessory hemiazygos vein
Internal thoracic vein
Anterior perforating branches
Hemiazygos vein
Left superior epigastric vein
Anterior intercostal vein
Inferior vena cava
Left subcostal vein

Fig. 52.4 Veins of the thoracic wall and the azygos venous system. (With permission from Drake RL, Vogl AW, Mitchell A et al (eds) Gray's Atlas of Anatomy. Elsevier, Churchill Livingstone. Copyright 2015.)

the left join and drain directly into the left brachiocephalic vein. The azygos venous network shows great variation in its formation, origin, course, tributaries, anastomoses and termination (Loukas and Tubbs 2016) (see Figs 56.2–56.3).

Lymphatic drainage

Superficial lymphatic vessels of the thoracic wall ramify subcutaneously and converge on the axillary nodes (see Figs 46.5, 53.22), similarly lymphatic vessels from the breast tissue drain mainly to axillary nodes, with some passing initially to parasternal, interpectoral and supraclavicular nodes (see Fig. 53.24). The extent of drainage of the breast is of particular importance in metastatic breast cancer. Lymph vessels from deeper tissues of the thoracic walls drain mainly to the parasternal, intercostal and diaphragmatic nodes. Lymph from the thoracic viscera drains to consecutive node groups (stations) situated throughout the mediastinum (see Fig. 54.12).

INNERVATION

Thoracic spinal nerves

There are 12 pairs of thoracic spinal nerves. The ventral rami, unlike their cervical and lumbar counterparts, have retained a largely segmental distribution to the body wall (see Figs 24.10, 47.7, 53.3). The first to the eleventh intercostal nerves pass in the intercostal spaces between adjacent ribs, and the twelfth (subcostal nerve) passes inferior to the twelfth rib. Each is connected with an adjacent ganglion of the sympathetic trunk by pre- and postganglionic axons that form the white and grey rami communicantes, respectively (see Figs 24.13, 53.21). The majority of the intercostal nerves are distributed to the thoracic and, in the case of the more inferiorly located nerves, abdominal walls. The greater part of the first thoracic ventral ramus passes into the brachial plexus (see Fig. 48.6), together with variable proportions of the second and sometimes third thoracic ventral rami via the intercostobrachial nerves. The fourth to sixth intercostal nerves supply only the thoracic wall, whereas the seventh to eleventh nerves supply the thoracic and abdominal walls. The subcostal nerve is distributed to the abdominal wall and skin covering the superior part of the lateral aspect of the gluteal region and thigh. Communicating branches may link the intercostal nerves across the intercostal spaces posteriorly (see Fig. 56.6). The dorsal rami of the thoracic spinal nerves divide into medial and lateral branches that supply the intrinsic muscles of the back and the overlying postvertebral skin on a segmental basis (see Figs 46.3, 47.8).

The breast is mainly innervated by the anterior and lateral cutaneous branches of the fourth to sixth intercostal nerves. The nipple is innervated by a plexus formed primarily from cutaneous branches of the fourth intercostal nerve.

The supraclavicular branches of the cervical plexus (derived from the ventral ramus of the fourth cervical spinal nerve) innervate the skin over the clavicle and may communicate with the anterior cutaneous branches of the second thoracic ventral ramus.

Regional anaesthesia

Available with the *Gray's Anatomy* e-book

Autonomic innervation

The autonomic nervous system in the thorax consists of the left and right sympathetic trunks and left and right vagus nerves, and the cardiac, oesophageal and pulmonary plexuses (see Figs 56.6, 56.7).

Sympathetic trunks

The left and right thoracic sympathetic trunks and associated ganglia (commonly 11 in number) sit posterior to the costal part of the parietal pleura on either side of the vertebral column. The majority of the thoracic sympathetic ganglia lie anterior to the head of a rib; the first thoracic and inferior cervical ganglia are fused, and the inferior two or three thoracic ganglia are often located lateral to their correspondingly numbered vertebral bodies (see Fig. 56.6). A tumour of the superior

Regional anaesthesia may be used to alleviate the pain associated with rib fracture, thoracostomy, thoracotomy or breast surgery. Nerve blocks performed in the thoracic paravertebral space target the ventral rami of the thoracic spinal nerves (or the posterior intercostal nerves) as they travel through the fat-filled space (Bouman et al 2017). Various fascial plane blocks are used to target segmental and cutaneous branches of regional nerves as they pass through specific fascial planes or compartments (Elsharkawy et al 2018), for example, serratus anterior plane (Biswas et al 2018), pectoralis and serratus anterior plane (Pecs1 or Pecs2) and erector spinae plane blocks (Forero et al 2017). Anaesthetic agents are able to track through the fascial lined space or compartment into which they are injected: effective anaesthesia of multiple nerves can therefore be achieved via a single point of access.

pulmonary sulcus (apex of lung) may compress the ventral ramus of the first thoracic spinal nerve, the cervicothoracic ganglion or the sympathetic trunk (see Fig. 54.2) resulting in a loss of sympathetic innervation to the ipsilateral side of the head (Horner's syndrome) (Nikolaos et al 2014) and pain radiating to the medial aspect of the ipsilateral forearm (Bruzzi et al 2008).

Preganglionic sympathetic axons originate from neuronal somata in the intermediolateral nucleus (lateral horn) of the spinal cord from T1 to L2. They travel initially with the corresponding ventral roots (rami) and leave the latter as white rami communicantes to enter the adjacent sympathetic ganglion in the sympathetic trunk. Their targets vary; some synapse in the sympathetic ganglion that they enter, whereas others ascend or descend in the sympathetic trunk to synapse in cervical or lumbar ganglia, respectively. Many of the preganglionic axons that originate in the lower thoracic spinal segments (T5–T12) do not synapse locally but enter the abdominal cavity as the thoracic splanchnic nerves. These nerves pass through the posterior mediastinum and respiratory diaphragm to enter the abdominal cavity where they synapse either in prevertebral ganglia that surround the origin of the major visceral arteries arising from the abdominal aorta, e.g. the coeliac and superior mesenteric ganglia (Ch. 59), or around the medullary chromaffin cells of the suprarenal gland (Ch. 70). Axons destined for the cervical ganglia are mainly derived from preganglionic neurones in the first thoracic spinal nerve.

Vagus nerves in the thorax

Preganglionic parasympathetic axons arise from neuronal cell bodies in the dorsal motor nucleus of the vagus in the medulla oblongata. Those destined for the thoracic viscera travel in the pulmonary, cardiac and oesophageal branches of the vagus nerve (see Fig. 56.7) and synapse in minute ganglia in the walls of the target viscera. Axons travelling in cardiac branches join the cardiac plexuses and synapse in ganglia distributed over both atria, the interatrial septum and peri-nodal subepicardial tissue: when stimulated, they normally slow the cardiac cycle and constrict coronary arteries, although low level stimulation may increase heart rate (Ch. 57). Pulmonary branches contain axons that synapse in ganglia of the pulmonary plexuses; they are motor (broncho constrictor) to the circular non-striated muscle fibres of the bronchi and bronchioles, and secretomotor to the mucous glands of the respiratory epithelium.

Autonomic plexuses in the thorax

Cardiac plexus The cardiac plexus has a superficial component inferior to the aortic arch, lying between the arch and the pulmonary trunk, and a deep part between the aortic arch and tracheal bifurcation (Ch. 57, see Fig. 57.61).

Pulmonary plexus. The pulmonary plexuses are located both anterior and posterior to the hila of the lungs (Ch. 54 and see Fig. 56.7), and connect with the cardiac plexuses (Ch. 57).

Oesophageal plexus. The oesophageal plexus surrounds the oesophagus below the level of the hila of the lungs (Ch. 56, see Fig. 56.6).

SURFACE ANATOMY

Thoracic surface anatomy underpins proficient physical examination and clinical procedures such as thoracostomy, placing drains or catheters and siting surgical incisions. Previous cadaver-based descriptions of surface landmarks are now being revised based upon CT imaging of living subjects. These studies are demonstrating a wider range of variation in positional and surface anatomy than appears in the current anatomical literature (Hale et al 2010, Mirjalili et al 2012a, Keough et al 2016, Pak et al 2016, Shen et al 2016, Uzun et al 2016, Badshah et al 2017).

Skeletal landmarks

Anteriorly, the clavicle, sternoclavicular and acromioclavicular joints are palpable and visible in most individuals (**Fig. 52.5**). The sternum may be felt throughout its length in the midline; laterally it may be covered by pectoralis major. The jugular (suprasternal) notch is palpable in the midline at the superior border of the manubrium of the sternum and commonly sits horizontally level with the vertebral bodies of T2 or T3. The cartilaginous rings and lateral borders of the trachea are palpable immediately superior to the notch. The sternal angle (of Louis) is more pronounced in males than in females, and is palpable at the junction of the manubrium with the body of the sternum. It marks the level of the horizontal sternal plane and the medial ends of the second costal cartilages, and so offers a reference point at which to start counting ribs. In the majority of adults the sternal plane intersects the vertebral column in a region that extends from the vertebral body of T4 to the superior half of the vertebral body of T5. The xiphisternal joint and xiphoid process are palpable at the inferior end of the sternum; the joint usually lies at the level of the vertebral body of T9, although it may be slightly higher. The costal margin (arch) is palpable passing inferolaterally from either side of the xiphoid process of the sternum. Posteriorly, the free ends of the eleventh and twelfth ribs may be palpable. Tracing the twelfth rib superomedially aids identification of the spinous process of T12 (**Fig. 52.6**). In thin individuals, it is possible to palpate all ribs anteriorly, from the first to the costal margin, and laterally, from the fourth rib at the floor of the axilla to the costal margin. Posteriorly, the spinous processes of the thoracic vertebrae are palpable in the midline; the spinous process of T1 sits below that of C7 (vertebra prominens) and is often more prominent. The prominent and distinct angles of the ribs are palpable several centimetres lateral to the spinous processes of the vertebrae. The surface anatomy of the back is described in Chapter 46.

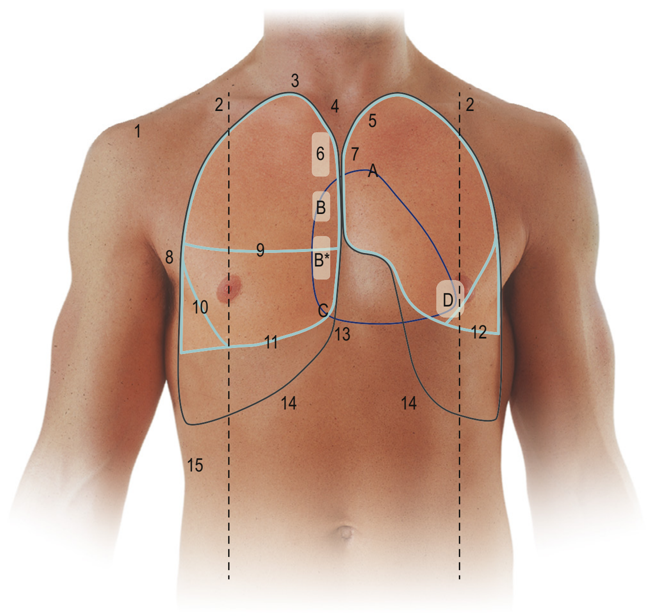

Fig. 52.5 Surface anatomy of the anterior thorax. Key: 1, right acromioclavicular joint; 2, clavicle and mid-clavicular line (dashed black); 3, apex of right lung, located posterior and 1–2 cm superior, to the medial one third of the clavicle; 4, jugular notch of the manubrium of sternum; 5, left sternoclavicular joint: marks the formation of the left brachiocephalic vein; 6, zone of formation of the superior vena cava: from the first to second costal cartilage level (white zone); 7, manubriosternal joint: marks the sternal plane and the second costal cartilage laterally; 8, pectoralis major and the anterior axillary fold; 9, horizontal fissure; 10, right oblique fissure; 11, lower anterior border of the right lung: typically, either at the sixth intercostal space or rib 7 in the mid-clavicular line; 12, lower anterior border of the left lung: typically, either at rib 5 or the fifth intercostal space in the mid-clavicular line; 13, xiphoid process; 14, costal margin (arch); 15, tenth costal cartilage; the lowest part of the costal margin. A–D and blue line: surface markings of the heart. A overlies the left second costal cartilage; B and B*, junction of superior vena cava with the right atrium; located posterior to the right third costal cartilage or intercostal space (white zone B) or posterior to the fourth to the fifth costal cartilage (white zone B*); C, right sixth costal cartilage; D, zone of location of the cardiac apex: commonly from the level of rib 5 to rib 6, and a mean of 8–9 cm from the midline.

Musculotendinous landmarks

In a lean, muscular subject, pectoralis major, the digitations of serratus anterior, latissimus dorsi, trapezius, external abdominal oblique and rectus abdominis are all visible and palpable. In females, the breasts may obscure part of the anterior thoracic wall.

The plexus has coronary, pulmonary, atrial and aortic extensions. The superficial (ventral) part is formed by the cardiac branch of the left superior cervical sympathetic ganglion and the inferior of the two cervical cardiac branches of the left vagus nerve. The deep (dorsal) part is formed by the cardiac branches of the cervical and upper thoracic sympathetic ganglia and of the vagus and recurrent laryngeal nerves. The only cardiac nerves that do not join it are those that join the superficial part of the plexus. Branches from the cardiac plexuses subsequently form the left and right coronary and atrial plexuses.

The posterior plexus provides the majority of the autonomic innervation to the lung and is formed by approximately 12 (range, 8–18) branches from the vagus nerve (Weijs et al 2015) and cardiac branches from the second to fifth (or sixth) thoracic sympathetic ganglia. The smaller anterior plexus is formed by 3 (range, 2–4) branches of the vagus nerve and cervical sympathetic cardiac nerves via the superficial and deep parts of the cardiac plexus. Branches of the recurrent laryngeal nerves form a plexus on the membranous posterior wall of the trachea; the plexus primarily innervates the trachea and proximal parts of the main bronchi, with branches to the oesophagus. Vagal nerve innervation is involved in the cough reflex, mucous production and control of bronchial diameter; inadvertent transection of the pulmonary vagal nerves during oesophagectomy may be related to the high incidence of postoperative pneumonia and pulmonary complications following oesophagectomy (Weijs et al 2017); preservation of vagal pulmonary branches is therefore desirable (Weijs et al 2016).

Preganglionic parasympathetic axons from the vagus and recurrent laryngeal nerves travel to ganglia in the oesophageal wall, either directly or through the oesophageal plexus and are motor to the smooth muscle in the lower oesophagus and secretomotor to mucous glands in the oesophageal mucosa. Vasomotor sympathetic axons arise from the first to sixth (sometimes fewer) thoracic segments of the spinal cord. Those passing from the more superior cord segments often synapse in the middle and inferior cervical sympathetic ganglia; their postganglionic axons are vasomotor to the vessels of the cervical and superior part of the thoracic oesophagus. Preganglionic axons from the fifth or sixth thoracic spinal cord segments pass directly to the oesophageal plexus or to the coeliac ganglion, where they synapse; postganglionic axons innervate the vessels of the distal oesophagus.

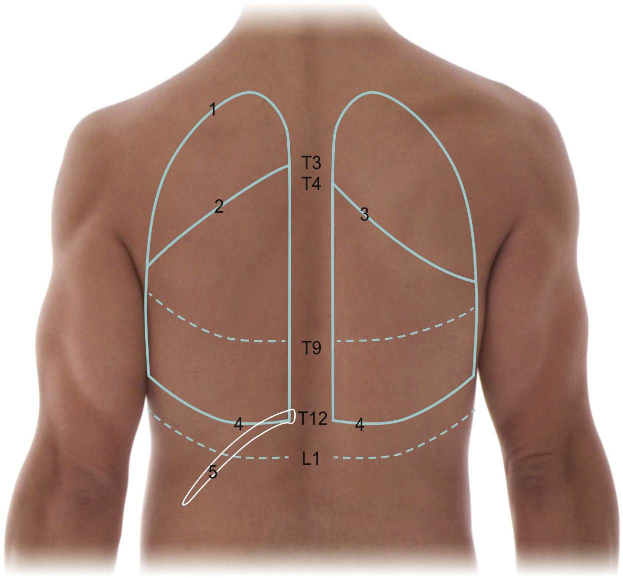

Fig. 52.6 Surface anatomy of the posterior thorax. The levels of the spinous processes of T3, T4, T9, T12 and L1 are indicated in the midline. Key: 1, border of the left lung; 2 and 3, oblique fissure of the lung: pass from the posterior part (neck) of rib 4 (level with the spinous process of T3) on the left side and the posterior part of rib 5 (level with the spinous process of T4) on the right side, to rib 6 in the mid-axillary line on both sides; 4, lower border of the lung, commonly located level with the vertebral body of T12, adjacent to the vertebral column at end tidal inspiration. Dashed blue lines indicate the range of levels for the lower border of the lung (from the vertebral bodies of T9 to L1); 5, rib 12: can be traced superomedially to aid identification of the spinous process of T12.

Breast

In females the base of the breast is relatively constant in position; it extends vertically from the second or third rib to the sixth rib, and the associated costal cartilage, and horizontally from the lateral sternal border medially to around the mid-axillary line laterally. The tail of the breast extends towards the axilla along the inferolateral border of pectoralis major (anterior axillary fold) (see Figs 53.22–53.23). In adult females, the location of the nipple is dependent on the size and shape of the breasts: the pigmented areola surrounding the nipple also varies in size. In adult males the nipple is often located either in the fourth intercostal space or over the fifth rib in the mid-clavicular line, approximately 20 cm from the jugular notch and 18 cm from the mid-clavicular point (Beckenstein et al 1996). The position of the nipple should never be relied upon for accurate landmarking.

Intrathoracic viscera

The sternal plane represents the inferior border of the superior mediastinum. It is typically described as marking the position of the tracheal bifurcation, the concavity of the aortic arch and the point where the azygos vein joins the superior vena cava. CT-based studies show these major structures are more commonly located below the sternal plane, from the level of the vertebral body of T5 to the vertebral body of T6 (Mirjalili et al 2012a) (**Fig. 52.7**; **Tables 52.1–52.2**): sometimes the aortic arch may be located in or above the sternal plane (Uzun et al 2016, Badshah et al 2017). The pulmonary trunk bifurcation is commonly located about 2–3 cm inferior to the level of the sternal plane, around the level of the vertebral body of T6 (Keough et al 2016, Pak et al 2016, Shen et al 2016, Uzun et al 2016); it may be located more often at a higher level in females.

Heart

The surface projection of the cardiac borders on to the anterior thoracic wall, between four landmark points, forms a trapezoid. The area of cardiac dullness may be mapped out via percussion. The description below applies to an average adult with a normal heart; this may be modified by age, sex, stature, ventilation, the position of the diaphragm, posture and pathology.

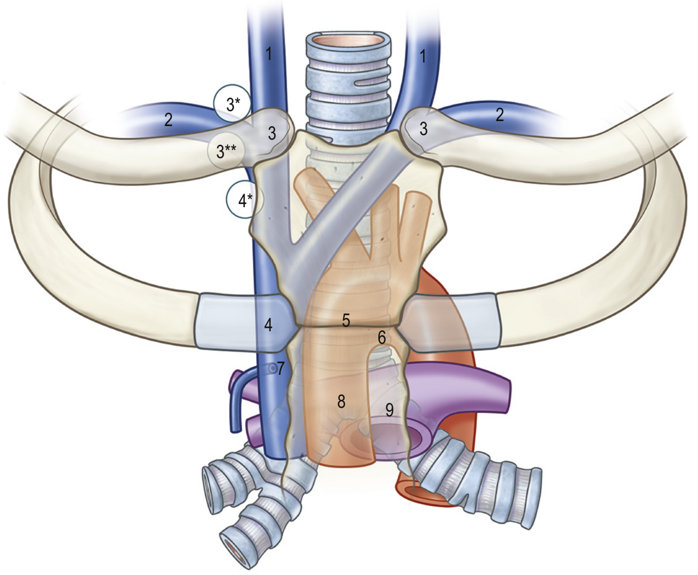

Fig. 52.7 Surface anatomy of the great vessels and tracheobronchial tree relative to bony landmarks. Key: 1, internal jugular vein; 2, subclavian vein; 3, formation of the brachiocephalic vein: commonly posterior to the sternoclavicular joint although this may vary with study population (e.g., 3* superolateral or 3** lateral to the sternoclavicular joint); 4, formation of the superior vena cava: commonly posterior to the right first or second costal cartilage or first intercostal space, although this position may vary with study population (e.g., 4*, posterior to the first costal cartilage); 5, manubriosternal joint (level of horizontal sternal plane); 6, concavity of the aortic arch, typically located inferior to the sternal plane, level with the vertebral body of T5; 7, azygos vein joining the superior vena cava, about 1 cm inferior to the sternal plane, level with the vertebral body of T5; 8, tracheal bifurcation, about 3 cm inferior to the sternal plane, level with the vertebral bodies of T5 or T6; 9, bifurcation of the pulmonary trunk, about 2–3 cm inferior to the sternal plane, level with the vertebral body of T6. (Redrawn with permission from Mirjalili S, Hale S, Buckenham T et al 2012 A reappraisal of adult thoracic surface anatomy. Clin Anat 25:827–34.)

The superior cardiac border is marked by a curved line joining the second left costal cartilage to the third right costal cartilage (each point about 1 cm lateral to the sternum) (see Fig. 52.5), the latter point representing the junction between the superior vena cava and right atrium. In some study populations this junction is located more commonly at the right third costal cartilage or third intercostal space level (Keough et al 2016, Pak et al 2016), whereas in others it is located at the fourth to the fifth right costal cartilage level (Mirjalili et al 2012a, Shen et al 2016). The right border is represented by a curved line joining the point marking the junction of the superior vena cava and right atrium with the sixth right costal cartilage, usually 1–2 cm lateral to the sternal edge. The inferior cardiac border runs leftwards from the sixth right costal cartilage to the cardiac apex, located approximately 8–9 cm lateral to the midline, commonly in the left fifth intercostal space or level with the fifth or sixth ribs (Mirjalili et al 2012a, Keough et al 2016, Pak et al 2016, Shen et al 2016), close to the mid-clavicular line. Clinicians vary considerably when locating the mid-clavicular line (Naylor et al 1987); a measurement from the midline is therefore preferred. The cardiac apex beat is usually palpable near the cardiac apex and represents the most inferolateral point at which cardiac pulsation is visible and palpable.

The left cardiac border gently curves superomedially from the cardiac apex to meet the second left costal cartilage approximately 1 cm from the left sternal edge. An oblique line joining the sternal end of the third left and sixth right costal cartilages represents the anterior part of the coronary (atrioventricular) sulcus, which separates the right atrium from the right ventricle. The projections of the cardiac valves, although in different planes, are sited along or close to this line (see Fig. 57.19). The orifice of the pulmonary valve is represented by an approximately horizontal 2.5 cm long line that lies over the superior border of the left third costal cartilage and the corresponding part of the left side of the sternum. The pulmonary trunk is delineated by two parallel lines drawn perpendicular to the ends of the pulmonary valve line, commonly up to the level of the left second intercostal space. The orifice of the aortic valve is located inferior and to the right of the orifice of the pulmonary valve, and is represented by a line approximately 2.5 cm long running inferolaterally and to the right from the medial end of the left third intercostal space. Two parallel lines, drawn perpendicular to the ends

TABLE 52.1 The level of key thoracic viscera relative to the sternal plane and vertebrae

	Mean position relative to sternal plane (range, cm)	Most common position/level (frequency % of 153 subjects studied)	Sex differences (95% CI)
Tracheal bifurcation	−3.1 cm (0 to −7.5)	T6 (46%) (range, inferior half of vertebral body of T4 to inferior half of vertebral body of T7)	1.3 cm higher in females (0.8–1.8 cm: p <0.001)
Aortic arch concavity	−1.1 cm (+2.8 to −4.8)	T5 (55%) (range, inferior half of vertebral body of T3 to inferior half of vertebral body of T6)	0.6 cm higher in females (0.1–1.1 cm: p = 0.01)
Azygos vein joining the superior vena cava	−2 cm (+1.3 to −6.4)	T5 (49%) (range, superior half of vertebral body of T4 to superior half of vertebral body of T7)	0.7 cm higher in females (0.3–1.2 cm: p = 0.001)
Pulmonary trunk bifurcation	Not reported	Superior half of vertebral body of T6 (28%) (range, T4–T5 to T7–T8 intervertebral discs)	No significant effect

Measurements relative to the sternal plane are shown as + (superior to the plane) and − (inferior to the plane).
Adapted from Mirjalili S, Hale S, Buckenham T et al 2012a A reappraisal of adult thoracic surface anatomy. Clin Anat 25:827–34.

TABLE 52.2 The level of key thoracic viscera relative to the sternal plane and vertebrae. A comparison of four study populations

	Study reference	Mean position relative to sternal plane (range, cm)	Most common position/level (frequency) (range)
Tracheal bifurcation	1	−3.1 cm (0 to −7.5)	T6 (46%) (range, inferior half of vertebral body of T4 to inferior half of vertebral body of T7)
	2	−2.3 cm (+2 to −6)	T5 (40%); T6 (35%) (range, superior half of vertebral body of T4 to superior half of vertebral body of T7)
	3	−1.4 cm	Not reported
	4	Not reported	T5 (45%) (range, T3–T4 intervertebral disc to vertebral body of T7)
Aortic arch concavity	1	−1.1 cm (+2.8 to −4.8)	T5 (55%) (range, inferior half of vertebral body of T3 to inferior half of vertebral body of T6)
	2	−0.4 cm (+2.7 to −3.2)	T5 (33%) (range, inferior half of T3 to superior half of vertebral body of T6)
	4	Not reported	T4 (58%) (range, vertebral bodies of T3–T5)
Azygos vein joining the superior vena cava	1	−2 cm (+1.3 to −6.4)	T5 (49%) (range, superior half of vertebral body of T4 to superior half of vertebral body of T7)
	2	−1.4 cm (+2.7 to −4.3)	T5 (47%) (range,T3–T4 to T6–T7 intervertebral discs)
	3	− 0.6 cm (Not reported)	Not reported
Pulmonary trunk bifurcation	1	Not reported	T6 (28%) (range, T4–T5 to T7–8 intervertebral discs)
	2	−2.8 cm (+0.9 to −5.6)	T6 (37%) (range, T4–T5 intervertebral disc to inferior half of vertebral body of T7)
	3	−2 cm (Not reported)	Not reported
	4	Not reported	T6 (42%) (range, vertebral bodies of T4–T8)

Measurements relative to the sternal plane are shown as + (superior to the plane) and − (inferior to the plane).
Adapted from (Study 1) Mirjalili S, Hale S, Buckenham T et al 2012a A reappraisal of adult thoracic surface anatomy. Clin Anat 25:827–34; (Study 2) Shen XH, Su BY, Liu JJ et al 2016 A reappraisal of adult thoracic and abdominal surface anatomy via CT scan in Chinese population. Clin Anat 29:165–74; (Study 3) Keough N, Mirjalili SA, Suleman FE et al 2016 The thoracic surface anatomy of adult black South Africans: a reappraisal from CT scans. Clin Anat 29:1018–24; (Study 4) Badshah M, Soames R, Ibrahim M et al 2017 Surface anatomy of major anatomical landmarks of the neck in an adult population: a CT evaluation of vertebral level. Clin Anat 30:781–7.

of the aortic valve line and slanting superolaterally towards the right side of the manubriosternal joint, delineate the location of the ascending aorta.

The orifice of the tricuspid valve is represented by a line approximately 4 cm long that starts near the midline just inferior to the level of the right fourth costal cartilage and passes down and slightly to the right. The centre of this line is level with the middle of the right fourth intercostal space. The orifice of the mitral valve is level with the left half of the sternum opposite the left fourth costal cartilage and is represented by a line approximately 3 cm long and descending to the right.

The direction of blood flow through a valve carries the valve sound with it, consequently the sites of cardiac valve auscultation do not correspond to the surface anatomy of the valves. Common sites at which to auscultate using a stethoscope are: the sternal end of the left second intercostal space (pulmonary area); the sternal end of the right second intercostal space (aortic area); near the cardiac apex in the fifth intercostal space (mitral area); and adjacent to the left lower sternal border, at the level of the fifth intercostal space (tricuspid area) (see Fig. 57.19).

Great vessels

Starting at the aortic valve (see above), the ascending aorta curves anteriorly, superiorly and to the right, and becomes the aortic arch posterior to the right half of the manubrium or the superior part of the right side of the sternal body, at the level of the right second costal cartilage or second intercostal space, respectively. The aortic arch lies mainly posterior to the manubrium of the sternum (see Fig. 52.7). The concavity of the arch is located commonly up to 1 cm inferior to the sternal plane (range, 2.7 cm superior to 4.8 cm inferior), approximately level with the superior half of the vertebral body of T5 (Mirjalili et al 2012a, Shen et al 2016), although it may be located in or superior to the sternal plane (Uzun et al 2016, Badshah et al 2017) (see Tables 52.1, 52.2). It then arches to the left within the superior mediastinum and descends such that the distal part of the arch protrudes just to the left of the manubrium around the level of the first intercostal space, where it is visible on thoracic X-ray (aortic knuckle). The brachiocephalic trunk arises approximately posterior to the centre point (or just to its left) of the manubrium and ascends toward the right sternoclavicular joint. The left and right brachiocephalic veins are commonly formed posterior to the sternoclavicular joints (Mirjalili et al 2012a); the right brachiocephalic vein descends almost vertically, whereas the left brachiocephalic vein passes inferiorly and to the right, posterior to the manubrium and across the midline. The position of formation of the brachiocephalic veins varies between study populations; for example, the right brachiocephalic vein may form lateral to the sternoclavicular joint (Shen et al 2016) or both brachiocephalic veins may form superolateral to the sternoclavicular joints (Keough et al 2016). According to conventional descriptions, the superior vena cava forms posterior to the right first costal cartilage. The majority of *in vivo* CT-based studies show it forms posterior to the right second costal cartilage or first intercostal space and the associated part of the manubrium (Mirjalili et al 2012a, Pak et al 2016, Shen et al 2016). The level of formation may be higher in females, children and younger adults, and in some adult study populations (Keough et al 2016). The position of the junction of the superior vena cava and right atrium is described above with the heart. The azygos vein joins the superior vena cava up to 2 cm inferior to the sternal plane at the level of the inferior part of the vertebral body of T5 (Mirjalili et al 2012a, Keough et al 2016, Shen et al 2016).

Lungs and pleural reflections

Anteriorly, the apex of the lung sits posterior, and up to 2 cm superior, to the medial one-third of the clavicle; posteriorly, it lies level with the vertebral body of C7 or T1, or the C7–T1 intervertebral disc (see Fig. 52.5). The surface markings of both the apex, costal surface and vertebral part of the lung correspond to those of the parietal pleura. Conventionally, the surface projection of the lower border of the lung is represented by a curved line that crosses the mid-clavicular line at the sixth rib, the mid-axillary line at the eighth rib, and is just lateral to the vertebral column at the tenth rib. CT data show this border, at the end of tidal inspiration, is located at the fifth rib or the fifth intercostal space on the left, or the sixth intercostal space or the seventh rib on the right, in the mid-clavicular line, and adjacent to the vertebral body of T12 posteriorly (range: vertebral bodies of T9–L1) (Mirjalili et al 2012a, Pak et al 2016, Shen et al 2016). In full expiration, the lower margin of the lung may rise 5 cm above the line of reflection of the parietal pleural within the costodiaphragmatic recess and may fully leave the retrosternal costomediastinal recess.

Trachea and bronchi

The trachea originates at the level of the inferior border of the cricoid cartilage, which usually sits at the level of the vertebral body of C7 (range, vertebral bodies of C5–T1) (Mirjalili et al 2012b). It passes inferiorly in the midline and bifurcates a mean of 1.4–3.1 cm inferior to the sternal plane, often level with the vertebral bodies of T5–T6 (Mirjalili et al 2012a, Shen et al 2016, Uzun et al 2016, Badshah et al 2017). The tracheal bifurcation may be more superior in location in females (Keough et al 2016). The trachea is palpable immediately superior to the jugular notch either by rolling one finger over its anterior surface or by defining its lateral borders with two fingers. A shift to one side indicates that the mediastinum has either been pulled over to that side by loss of lung volume, or pushed over by a pneumothorax or large pleural effusion. The level at which the trachea bifurcates appears to move inferiorly, on average, by a mean of 3 mm per decade.

Pulmonary fissures

The superior and inferior lobes of the left and right lung are normally separated by the oblique fissure; this is marked by a line that curves around the thoracic wall, from the posterior part (neck) of the fourth rib (level with the spinous process of T3) on the left side and the posterior part of the fifth rib (level with the spinous process of T4) on the right side, to the sixth rib in the mid-axillary line on both sides (Heřmanová et al 2012) (see Figs 52.5–52.6, 54.3). Continuing along the same trajectory of descent, the line marking the oblique fissure passes towards the inferior border of the lung near to the mid-clavicular line (i.e. 7–8 cm lateral to the anterior median plane), where it terminates. The lowest margin of the lung in the mid-clavicular line is located at the sixth intercostal space or the seventh rib on the right or at the fifth rib or the fifth intercostal space on the left (Mirjalili et al 2012a). As a convenient approximation, posteriorly the oblique fissure follows the medial border of the scapula when the upper limb is in full abduction. The left oblique fissure may be slightly more vertical than the right. The surface position of the pulmonary fissures show little change during inspiration and expiration (Heřmanová et al 2012).

The horizontal fissure lies between the superior and middle lobes of the right lung (see Figs 52.5, 54.3; **Fig. 52.8**). It extends from the right fourth costal cartilage at the right sternal border to intersect the oblique fissure, approximately in its middle one third. The right middle lobe may be projected on to the thoracic wall using three points: the fourth costal cartilage at the right sternal border (sternocostal joint), the fifth rib in the mid-axillary line and the sixth intercostal space or seventh rib in the mid-clavicular line. The superior lobe, and middle lobe on the right, lie anterior to the oblique fissure and are best examined from the anterior and lateral wall of the thorax. The inferior lobes lie posteriorly and should be examined via the posterior thoracic wall, below the level of the oblique fissure. The arrangement of the pulmonary fissures can vary widely (Wantanabe 2016).

Pleural margin and reflections

Starting in the midline at the sternal angle, the anterior line of reflection of the parietal pleura may be traced superiorly along a curved line that diverges from the midline and passes superiorly and laterally to the apex of the lung (see Fig. 52.5). The line lies 3–4 cm above the anterior end of the first rib; the surface marking is posterior, and up to 2 cm superior, to the medial one third (sternal end) of the clavicle. The right and left parietal pleurae are in contact retrosternally in the midline from the level of the second to the fourth costal cartilages, at which point they often diverge (see Fig. 53.4). Above this level and posterior to the manubrium the diverging lines of pleural reflection border a triangular shaped region which is occupied by the thymus, or its remnants. The pleura on the right descends almost vertically, often remaining near the midline, to the xiphoid process, whereas the pleura on the left deviates laterally by 3–5 cm and then passes inferolaterally to cross the anterior end of the sixth rib. This deviation produces an area, roughly triangular in shape (the pericardial triangle), between the heart and the sternum that is free of pleura; a needle puncture of the pericardium may be performed at this site and on the left lateral sternal edge with minimal risk of damaging the pleura.

The reflection of the parietal pleura (costal and diaphragmatic parts), forming the inferior limit of the costodiaphragmatic recess, may be followed around the chest wall along a line sitting just superior to the costal attachment of the respiratory diaphragm (see Fig. 52.1); passing from the sixth costal cartilage (sternocostal joint) lateral to the sternum, to the eighth rib in the mid-clavicular line, the tenth rib in the mid-axillary line and the twelfth rib, or just below, adjacent to the vertebral column. Viewed from posteriorly, the medial edges of the pleurae pass along a line joining the transverse processes of T12 to T2 on either side. The diaphragmatic part of the parietal pleura is fused to fascia on the superior (thoracic) surface of the respiratory diaphragm, with which it can be landmarked.

Respiratory diaphragm

The highest point of the dome of the respiratory diaphragm is commonly located level with the fifth intercostal space or the sixth rib on the right and the sixth rib or the sixth intercostal space on the left: these levels vary widely, from the fourth rib to the seventh intercostal space, and in some cases may even sit inferior to the costal margin (Mirjalili et al 2012a, Shen et al 2016). Conventionally, the inferior vena cava, oesophagus and descending thoracic aorta are said to traverse the respiratory diaphragm at the levels of the vertebral bodies of T8, T10 and T12, respectively. However, CT-based studies have shown that at end tidal inspiration, the inferior vena cava, oesophagus and aorta more commonly pass through the respiratory diaphragm at the levels of the vertebral bodies of T11 (sometimes T10) and T12, respectively (Mirjalili et al 2012a, Pak et al 2016, Shen et al 2016, Badshah et al 2017).

Paediatric thoracic surface anatomy

CT-based assessment of paediatric thoracic surface anatomy in subjects from birth to 12 years of age has shown that some structures are similar in position to those seen in adults, whereas others change position with increasing age (Tarr et al 2016, Fischer et al 2017).

Bonus e-book content

Fig. 52.2 **A**, The musculoskeletal components of the thoracic wall. **B**, Left sagittal CT volume-rendered slab showing the left posterior intercostal arteries.

Fig. 52.8 The relations of the pleura, lungs and pulmonary fissures to the thoracic cage.

Key references

Fischer NJ, Morreau J, Sugunesegran R et al 2017 A reappraisal of pediatric thoracic surface anatomy. Clin Anat 30:788–94.
This article compares thoracic surface and positional anatomy in living subjects from 0 to 12 years of age.

Hale SJ, Mirjalili SA, Stringer MD 2010 Inconsistencies in surface anatomy: the need for an evidence-based reappraisal. Clin Anat 23:922–93.
This article analyses the consistency of reporting of common surface anatomy landmarks and calls for an evidence-based reappraisal of clinically relevant surface projections.

Loukas M, Tubbs RS 2016 Adrenal, renal, gonadal, azygos, hemiazygos, lumbar, and ascending lumbar veins. In: Tubbs RS, Shoja MM, Loukas M (eds) Bergman's Comprehensive Encyclopedia of Human Anatomic Variation, 2nd ed. Hoboken: Wiley Blackwell; Ch. 69, pp. 890–3.
A description of the normal anatomy of the venous drainage of the posterior body wall with a comprehensive listing of the variations and developmental anomalies.

Mirjalili S, Hale S, Buckenham T et al 2012a A reappraisal of adult thoracic surface anatomy. Clin Anat 25:827–34.
An examination of key thoracic surface anatomical landmarks in vivo *using computed tomographic (CT) imaging.*

Wantanabe K 2016 Lungs. In: Tubbs RS, Shoja MM, Loukas M (eds) Bergman's Comprehensive Encyclopedia of Human Anatomic Variation, 2nd ed. Hoboken: Wiley Blackwell; Ch. 102, pp. 1216–33.
Describes morphological variations of normal and supernumerary lung fissures and pulmonary sequestrations. Supernumerary fissures (e.g. superior accessory fissure, medial basal fissure, left horizontal fissure and azygos fissure) do not exist normally and form supernumerary lobes. Pulmonary sequestrations (regions of lung parenchyma that do not have a normal connection to the tracheobronchial tree) have an anomalous systemic blood supply.

The sternal angle in the majority of children from birth to 12 years of age is located level with the vertebral body of T4 (range, inferior half of the vertebral body of T1 to the inferior half of the vertebral body of T5), and the sternal plane marks the level at which the azygos vein joins the superior vena cava. Relative to the sternal plane, the concavity of the aortic arch is located approximately 0–5 mm inferior and the bifurcation of the trachea and pulmonary artery are located approximately 10–15 mm inferior. The cardiac apex is located close to the mid-clavicular line from birth to 12 years of age; specifically, it is located approximately 4 cm (0–1 year of age), 5 cm (1–4 years of age) and 6 cm (4–12 years of age) to the left of the midline. The cardiac apex is typically located posterior to the fifth intercostal space (range, fourth intercostal space to the sixth rib) from birth to 4 years of age and posterior to the fourth intercostal space or the fifth rib from 4 to 12 years of age. The highest (most superior) part of the dome of the respiratory diaphragm is commonly located at the level of the fifth rib or the fifth intercostal space on the right and the sixth rib or the fifth intercostal space on the left; the left dome is slightly lower than the right, and both domes are flatter in children compared to adults. On average, the respiratory diaphragm is traversed by the inferior vena cava, oesophagus and descending thoracic aorta at the levels of the vertebral bodies of T9, T10 and T11, respectively, although some variability occurs. The apex of the lung is commonly situated posterior to the medial one third of the clavicle across all age groups, although it is sometimes located more laterally, i.e. posterior to the middle one third of the clavicle, in younger children.

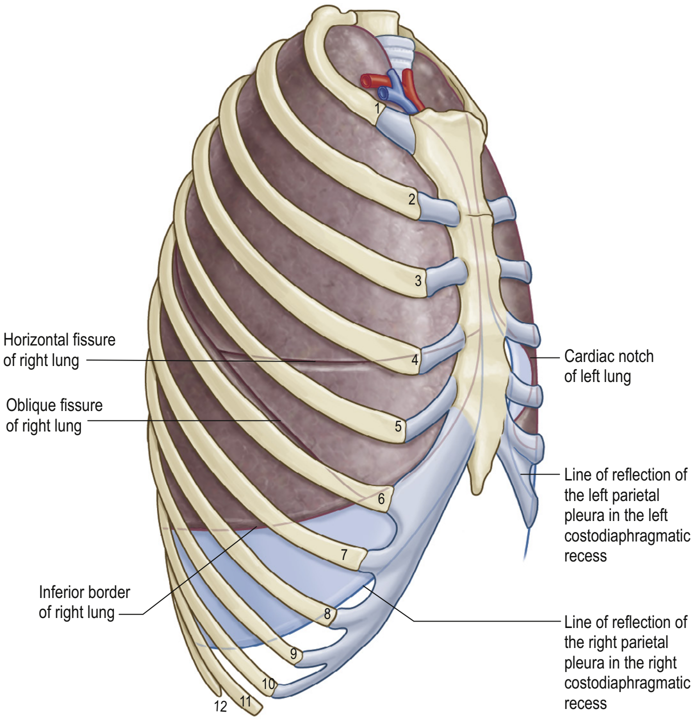
1
2
3
4
5
6
7
8
9
10
11
12
Horizontal fissure of right lung
Oblique fissure of right lung
Inferior border of right lung
Cardiac notch of left lung
Line of reflection of the left parietal pleura in the left costodiaphragmatic recess
Line of reflection of the right parietal pleura in the right costodiaphragmatic recess

Fig. 52.8 The relations of the pleura, lungs and pulmonary fissures to the thoracic cage (right anterolateral view).

The right and left brachiocephalic veins are formed posterior to the ipsilateral sternal head of the clavicle in the majority of children from birth to 11 years of age (Tarr et al 2016). The vertebral level of the formation of the superior vena cava and the junction between the superior vena cava and right atrium are variable in position (Fischer et al 2017). The superior vena cava forms most commonly posterior to the second right costal cartilage in children from 0–3 years of age, and moves superiorly to sit posterior to the right first costal cartilage or right first intercostal space during subsequent growth. The junction between the superior vena cava and right atrium is commonly located posterior to the right fourth costal cartilage in children from birth to 3 years of age, moving superiorly to sit posterior to the right third costal cartilage or right third intercostal space during subsequent growth in childhood. In adults the junction is commonly located posterior to the right fourth costal cartilage.

References

Badshah M, Soames R, Ibrahim M et al 2017 Surface anatomy of major anatomical landmarks of the neck in an adult population: a CT evaluation of vertebral level. Clin Anat 30:781–7.

Beckenstein MS, Windle BH, Stroup RT 1996 Anatomical parameters for nipple position and areolar diameter in males. Ann Plast Surg 36:33–6.

Biswas A, Castanov V, Li Z et al 2018 Serratus plane block: a cadaveric study to evaluate optimal injectate spread. Reg Anesth Pain Med 43:854–8.

Boussuges A, Gole Y, Blanc P 2009 Diaphragmatic motion studied by M-mode ultrasonography: methods, reproducibility, and normal values. Chest 135:391–400.

Bouman EAC, Sieben JM, Balthasar AJR et al 2017 Boundaries of the thoracic paravertebral space: potential risks and benefits of the thoracic paravertebral block from an anatomical perspective. Surg Radiol Anat 39:1117–25.

Bruzzi JF, Komaki R, Walsh GL et al 2008 Imaging of non-small cell lung cancer of the superior sulcus. Part 2: initial staging and assessment of resectability and therapeutic response. Radiographics 28:561–72.

Dugan DJ, Samson PC 1975 Surgical significance of the endothoracic fascia. The anatomic basis for empyemectomy and other extrapleural technics. Am J Surg 130:151–8.

Elsharkawy H, Maniker R, Bolash R et al 2018 Rhomboid intercostal and subserratus plane block: a cadaveric and clinical evaluation. Reg Anesth Pain Med. 43:745–51.

Fischer NJ, Morreau J, Sugunesegran R et al 2017 A reappraisal of pediatric thoracic surface anatomy. Clin Anat 30:788–94.

Compares thoracic surface and positional anatomy in living subjects from 0 to 12 years of age.

Forero M, Rajarathinam M, Adhikary S et al 2017 Erector spinae plane (ESP) block in the management of post thoracotomy pain syndrome: a case series. Scand J Pain 2017 17:325–9.

Goldman MD, 1982 Interpretation of thoracoabdominal movements during breathing. Clin Sci 62:7–11.

Hale SJ, Mirjalili SA, Stringer MD 2010 Inconsistencies in surface anatomy: the need for an evidence-based reappraisal. Clin Anat 23:922–93.

This article analyses the consistency of reporting of common surface anatomy landmarks and calls for an evidence-based reappraisal of clinically relevant surface projections.

Heřmanová Z, Ctvrtlík F, Heřman M 2012 Surface anatomy of the pulmonary fissures determined by high-resolution computed tomography. Clin Anat 25:835–43.

Im JG, Webb WR, Rosen A et al 1989 Costal pleura: appearances at high-resolution CT. Radiol 171:125–31.

Joshua A, Shetty L, Pare V et al 2014 Variations in the dimensions and shape of thoracic cage with aging: an anatomical review. Anat J Africa 3:346–55.

Keough N, Mirjalili SA, Suleman F et al 2016 The thoracic surface anatomy of adult black South Africans: a reappraisal from CT scans. Clin Anat 29:1018–24.

Latarjet M, Juttin P 1953 An anatomical and surgical study of the extra-thoracic fascia. Thorax 8:282–7.

Loukas M, Tubbs RS 2016 Adrenal, renal, gonadal, azygos, hemiazygos, lumbar, and ascending lumbar veins. In: Tubbs RS, Shoja MM, Loukas M (eds) Bergman's Comprehensive Encyclopedia of Human Anatomic Variation, 2nd ed. Hoboken: Wiley Blackwell; Ch. 69, pp. 890–3.

A description of the normal anatomy of the venous drainage of the posterior body wall with a comprehensive listing of the variations and developmental anomalies.

Mirjalili S, Hale S, Buckenham T et al 2012a A reappraisal of adult thoracic surface anatomy. Clin Anat 25:827–34.

An examination of key thoracic surface anatomical landmarks in vivo *using computed tomographic (CT) imaging.*

Mirjalili SA, McFadden SL, Buckenham T et al 2012b Vertebral levels of key landmarks in the neck. Clin Anat 25:851–7.

Morelli L, Pusiol T, Piscioli I 2007 Primary epithelioid leiomyosarcoma of the endothoracic fascia. Eur J Radiol Extra 61:45–48.

Naylor C, McCormack D, Sullivan S 1987 The midclavicular line: a wandering landmark. Canad Med Assoc J 136:48–50.

Nikolaos P, Vasilios L, Efstratios K et al 2014 Therapeutic modalities for Pancoast tumors. J Thorac Dis Suppl 1:S180–93.

Openshaw P, Edward S, Helms P 1984 Changes in rib cage geometry during childhood. Thorax 39:624–7.

Pak N, Patel SG, Hashemi Taheri AP et al 2016 A reappraisal of adult thoracic and abdominal surface anatomy in Iranians in vivo using computed tomography. Clin Anat 29:191–6.

Santamarina MG, Beddings I, Lermanda Holmgren GV et al 2017 Multidetector CT for evaluation of the extrapleural space. Radiographics 37:1352–70.

Shen XH, Su BY, Liu JJ et al 2016 A reappraisal of adult thoracic and abdominal surface anatomy via CT scan in Chinese population. Clin Anat 29:165–74.

Takazakura R, Takahashi M, Nitta N et al 2004 Diaphragmatic motion in the sitting and supine positions: healthy subject study using a vertically open magnetic resonance system. J Magn Reson Imaging 19:605–60.

Tardieu GG, Edwards B, Alonso F et al 2017 Aortic arch origin of the left vertebral artery: an anatomical and radiological study with significance for avoiding complications with anterior approaches to the cervical spine. Clin Anat 30:811–816.

Tarr GP, Pak N, Taghavi K et al 2016 Defining the surface anatomy of the central venous system in children. Clin Anat 29:157–64.

Uzun C, Atman ED, Ustuner E et al 2016 Surface anatomy and anatomical planes in the adult turkish population. Clin Anat 29:183–90.

Wantanabe K 2016 Lungs. In: Tubbs RS, Shoja MM, Loukas M (eds) Bergman's Comprehensive Encyclopedia of Human Anatomic Variation, 2nd ed. Hoboken: Wiley Blackwell; Ch. 102, pp. 1216–33.

Describes morphological variations of normal and supernumerary lung fissures and pulmonary sequestrations. Supernumerary fissures (e.g. superior accessory fissure, medial basal fissure, left horizontal fissure and azygos fissure) do not exist normally and form supernumerary lobes. Pulmonary sequestrations (regions of lung parenchyma that do not have a normal connection to the tracheobronchial tree) have an anomalous systemic blood supply.

Weijs TJ, Ruurda JP, Luyer MD et al 2015 Topography and extent of pulmonary vagus nerve supply with respect to transthoracic oesophagectomy. J Anat 227:431–9.

Weijs TJ, Ruurda JP, Luyer MD et al 2016 Preserving the pulmonary vagus nerve branches during thoracoscopic esophagectomy Surg Endosc 30:3816–22.

Weijs TJ, Ruurda JP, Luyer MDP et al 2017 New insights into the surgical anatomy of the esophagus. J Thorac Dis Suppl 8:S675–S680.

CHAPTER

53

Chest wall and breast

The chest wall surrounds the thoracic cavity. It is formed by: an osseocartilaginous frame consisting normally of 12 pairs of ribs, which articulate with the 12 thoracic vertebrae posteriorly and (except for the last two or three pairs of ribs) with the sternum anteriorly, via their costal cartilages; intrinsic muscles and muscles that connect the chest wall with the upper limb and the vertebral column; overlying skin, fasciae and breast tissue; and numerous blood and lymphatic vessels and nerves that supply the components of the musculoskeletal frame.

SKIN AND FASCIA

Skin

Vascular supply

Arteries

The skin of the thorax is supplied by a combination of direct cutaneous vessels and musculocutaneous perforators that reach the skin primarily via the intercostal muscles, pectoralis major, latissimus dorsi and trapezius. The major contributing vessels are branches from the thoraco-acromial, lateral thoracic, superficial thoracic and internal thoracic, anterior and posterior intercostal, thoracodorsal, transverse cervical, dorsal scapular and circumflex scapular arteries (**Figs 53.1–53.2**; see Fig. 46.4).

The anterior aspect of the thoracic skin is supplied by branches of the thoraco-acromial artery, the internal thoracic arteries, perforating branches from the intercostal arteries and branches from the lateral thoracic and superficial thoracic arteries. The thoraco-acromial artery supplies the skin primarily via musculocutaneous perforators from its pectoral branch that reach the skin through pectoralis major. Direct cutaneous branches also arise from the acromial and deltoid branches. The internal thoracic artery sends direct perforating branches to the skin covering the first (superior) six intercostal spaces and associated costal cartilages, accompanied by the cutaneous branches of the anterior intercostal nerves. The branches reach the skin after passing through pectoralis major and travelling laterally in the subcutaneous fat as direct cutaneous vessels. The right internal thoracic artery is normally larger than the left and the perforator in the second intercostal space is usually the largest. The lateral aspect of the thoracic skin is supplied by the lateral thoracic and superficial thoracic arteries, lateral cutaneous branches of the intercostal arteries, and musculocutaneous branches of the thoracodorsal artery (via latissimus dorsi). The lateral thoracic artery gives off direct cutaneous branches to the lateral chest wall in addition to musculocutaneous branches that pass through pectoralis major. The posterior aspect of the thoracic skin is supplied by the medial and lateral dorsal cutaneous branches of the posterior intercostal arteries (via erector spinae and latissimus dorsi) (see Fig. 53.18); musculocutaneous perforating branches from the superficial cervical, transverse cervical and dorsal scapular arteries (via trapezius); musculocutaneous perforating branches from the thoracodorsal artery and the intercostal arteries (via latissimus dorsi); and direct cutaneous branches from the circumflex scapular artery.

Veins

The intercostal veins accompany the similarly named arteries in the intercostal spaces (see Fig. 52.4). The small anterior intercostal veins are tributaries of the musculophrenic and internal thoracic veins, the latter draining into the ipsilateral brachiocephalic vein. The posterior intercostal veins drain directly or indirectly into the azygos vein on the right and the hemiazygos or accessory hemiazygos veins on the left. The azygos veins exhibit great variation in their origin, course, tributaries, anastomoses and termination (Ch. 56).

Lymphatic drainage

Superficial lymphatic vessels of the thoracic wall ramify subcutaneously and converge on the axillary nodes (see Figs 53.22, 53.24, 46.5 and Ch. 49). Lymph vessels from the deeper tissues of the thoracic walls drain mainly to the parasternal, intercostal and diaphragmatic lymph nodes.

Innervation

The skin of the thorax is supplied by cutaneous branches of cervical and thoracic spinal nerves in consecutive overlapping curved zones; the upper zones are almost horizontal and the lower curve obliquely inferiorly

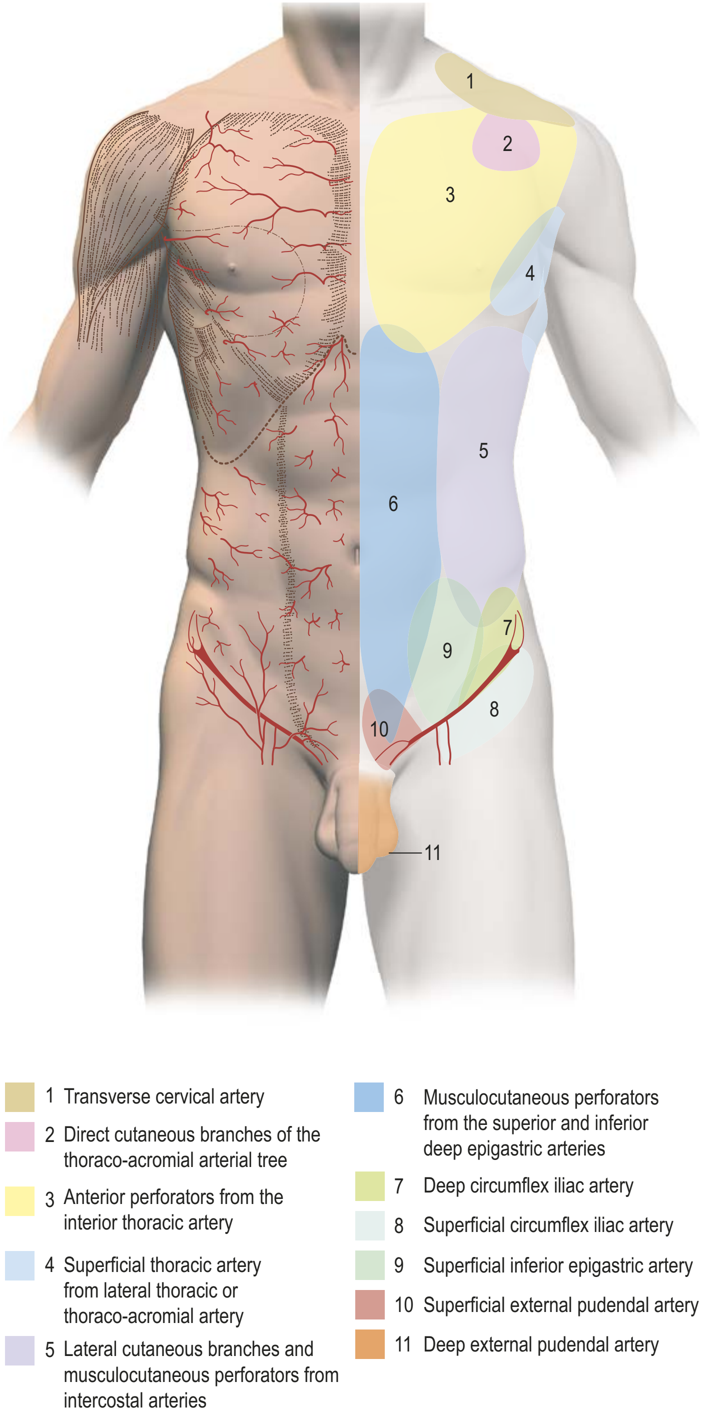
1
2
3
4
5
6
7
8
9
10
11
1 Transverse cervical artery
2 Direct cutaneous branches of the thoraco-acromial arterial tree
3 Anterior perforators from the interior thoracic artery
4 Superficial thoracic artery from lateral thoracic or thoraco-acromial artery
5 Lateral cutaneous branches and musculocutaneous perforators from intercostal arteries
6 Musculocutaneous perforators from the superior and inferior deep epigastric arteries
7 Deep circumflex iliac artery
8 Superficial circumflex iliac artery
9 Superficial inferior epigastric artery
10 Superficial external pudendal artery
11 Deep external pudendal artery

Fig. 53.1 Anatomical territories of cutaneous blood vessels on the anterior trunk. (With permission from Cormack GC, Lamberty BGH 1994 The Arterial Anatomy of Skin Flaps, 2nd ed. Edinburgh: Churchill Livingstone.)

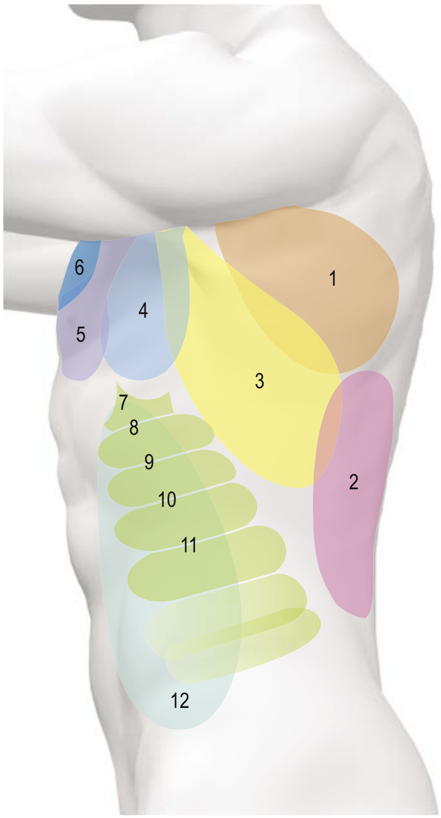

🟧	1	Circumflex scapular artery
🟪	2	Musculocutaneous perforators through latissimus dorsi from intercostal and lumbar arteries
🟨	3	Musculocutaneous perforators through latissimus dorsi from thoracodorsal artery
🟦	4	Cutaneous branches from thoracodorsal and lateral thoracic arteries
🟪	5	Thoraco-acromial arterial tree
🟦	6	Internal thoracic artery
🟩	7–11	Lateral cutaneous branches from intercostal arteries
⬜	12	Musculocutaneous perforators through external oblique from intercostal arteries

Fig. 53.2 Anatomical territories of cutaneous blood vessels on the lateral trunk. (With permission from Cormack GC, Lamberty BGH 1994 The Arterial Anatomy of Skin Flaps, 2nd ed. Edinburgh: Churchill Livingstone.)

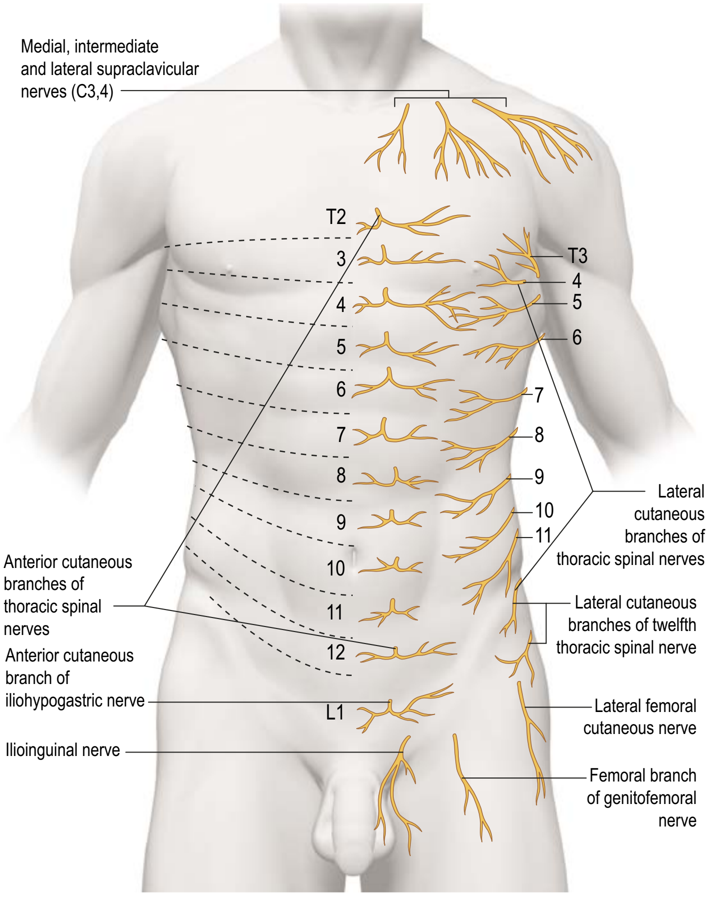
Medial, intermediate and lateral supraclavicular nerves (C3,4)
T2
3
4
5
6
7
8
9
10
11
12
L1
T3
4
5
6
7
8
9
10
11
Lateral cutaneous branches of thoracic spinal nerves
Anterior cutaneous branches of thoracic spinal nerves
Lateral cutaneous branches of twelfth thoracic spinal nerve
Anterior cutaneous branch of iliohypogastric nerve
Lateral femoral cutaneous nerve
Ilioinguinal nerve
Femoral branch of genitofemoral nerve

Fig. 53.3 The approximate segmental distribution of the cutaneous nerves on the anterior trunk. The contribution from the first thoracic spinal nerve is not shown and the considerable overlap that occurs between adjacent segments is not indicated.

around the thoracic wall as they pass to the anterior midline (median plane). On the upper anterior aspect of the thorax, the areas innervated by the ventral rami of the third and fourth cervical nerves adjoin those innervated by the ventral rami of the second (and sometimes first) thoracic spinal nerves because the intervening thoracic spinal nerves are distributed to the upper limb (Ladak et al 2014) (**Fig. 53.3**). There is a similar but less extensive 'gap' in innervation on the upper posterior thoracic wall (see Fig. 47.8). Most of the skin covering the posterior thorax is supplied by the dorsal rami of the thoracic spinal nerves.

The ventral rami of the first to the eleventh thoracic spinal nerves pass into the correspondingly numbered intercostal space, give off a lateral cutaneous branch distal to the angle of the rib (that then divides into anterior and posterior rami) and terminate near the sternum as an anterior cutaneous branch (that divides into medial and lateral branches) (see Fig. 53.21).

Branches of the supraclavicular nerves, which originate from the ventral rami of the third and fourth cervical spinal nerves, supply the skin in the upper pectoral region. Most of the ventral ramus of the first thoracic spinal nerve joins the brachial plexus, apart from a small inferior branch that becomes the first intercostal nerve. The lateral cutaneous branch of the second intercostal nerve (intercostobrachial nerve) supplies the skin of the axilla, lateral chest and medial arm. It courses as either a single trunk or in a bifurcating pattern (Henry et al 2017): its variability puts it at increased risk of injury during breast-related surgery, potentially resulting in postoperative pain and paraesthesia. The ventral rami of the seventh to eleventh thoracic spinal nerves supply the skin of the thoracic wall as they pass anteriorly and inferiorly; they continue beyond the costal cartilages to supply the skin and subcutaneous tissues of the abdominal wall (see Fig. 60.5). The skin of the abdomen at the level of the umbilicus is supplied by the ventral ramus of the tenth thoracic spinal nerve. The subcostal nerve (ventral ramus of twelfth thoracic spinal nerve) follows the inferior border of the twelfth rib and supplies the skin of the lower abdominal wall.

Fascia

Superficial fascia

The superficial fascia consists primarily of fat and is only loosely attached to the skin, an arrangement that allows movement of the underlying structures. Small blood vessels and nerves perforate the superficial fascia to supply the skin. The breast lies within the superficial fascia, apart from a superolateral extension that pierces the deep fascia to form the axillary process (tail, tail of Spence) in the female.

Deep fascia

Clavipectoral fascia

The clavipectoral fascia is the cranial continuation of the deep lamina of the pectoral fascia and the medial continuation of the parietal layer of the subscapular bursal fascia. It extends between the clavicle and pectoralis minor, surrounds subclavius and extends medially to the first rib. It is described in detail in Chapter 49.

BONE AND CARTILAGE

The 12 thoracic vertebrae and associated intervertebral discs are described in detail in Chapter 46.

Sternum

The sternum is an elongated, flattened bone that forms the middle portion of the anterior thoracic wall. It consists of three parts, namely (from cranial to caudal): manubrium, body and xiphoid process (**Figs 53.4–53.5**) and articulates with the clavicles at the sternoclavicular

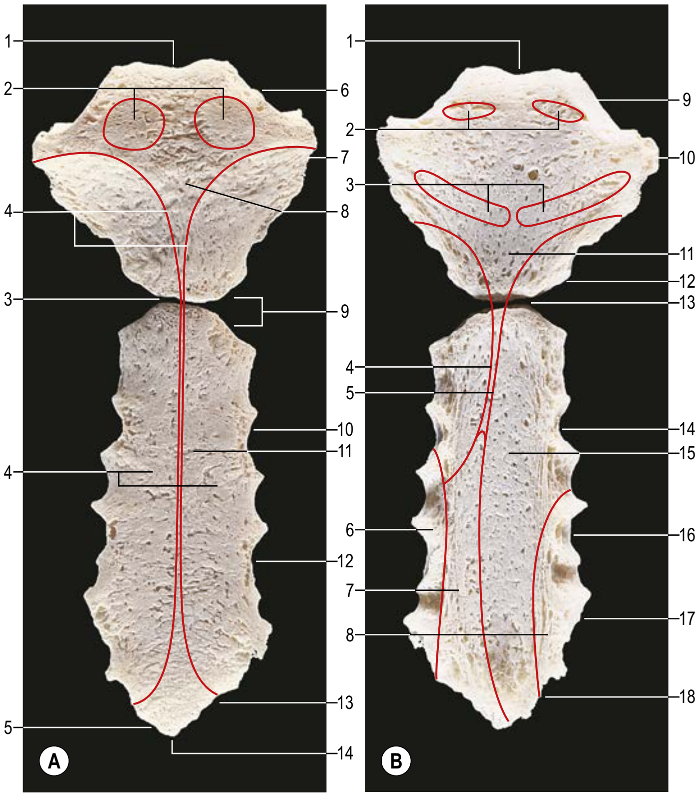

Fig. 53.4 The sternum, showing muscle attachments (red outline). **A**, Anterior aspect. Key: 1, jugular (suprasternal) notch; 2, attachment for sternocleidomastoid; 3, sternal angle and manubriosternal joint; 4, attachment for pectoralis major; 5, seventh costal notch; 6, clavicular notch; 7, first costal notch; 8, manubrium; 9, second costal notch; 10, third costal notch; 11, body of sternum; 12, fourth costal notch; 13, sixth costal notch; 14, xiphisternal joint. **B**, Posterior aspect. Key: 1, jugular notch; 2, attachment for sternohyoid; 3, attachment for sternothyroid; 4, edge of area covered by left pleura; 5, edge of area covered by right pleura; 6, attachment for transversus thoracis; 7, area in contact with pericardium; 8, attachment for transversus thoracis; 9, clavicular notch; 10, first costal notch; 11, manubrium; 12, second costal notch; 13, sternal angle and manubriosternal joint; 14, third costal notch; 15, body of sternum; 16, fourth costal notch; 17, fifth costal notch; 18, seventh costal notch.

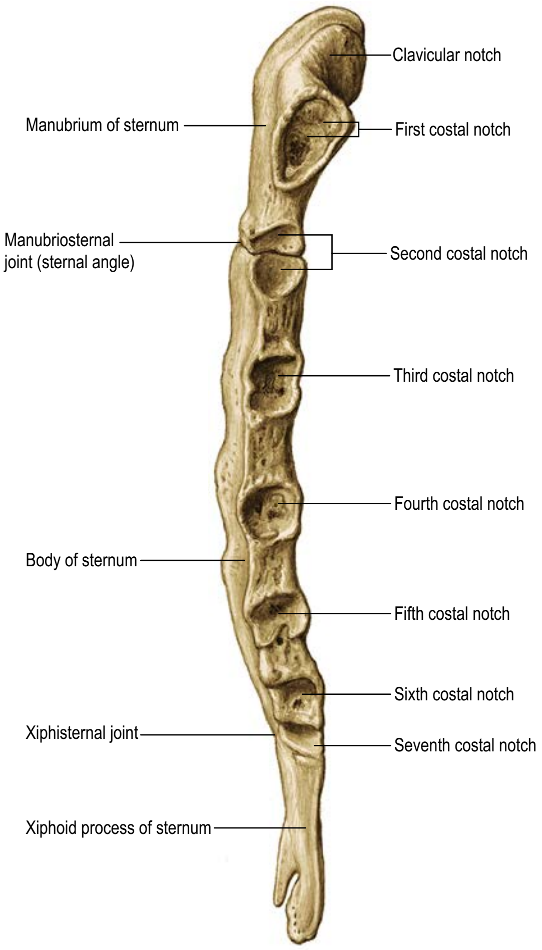

Fig. 53.5 The sternum, left lateral aspect. (Sobotta Atlas of Human Anatomy © Elsevier GmbH, Urban & Fischer, Munich.)

joints and with the cartilages of the first seven pairs of ribs at the costosternal joints. Until puberty, the body consists of four intersegmental sternebrae. The average length of the adult sternum is 16.5 cm in males and 15.0 cm in females: the ratio between the length of the sternal manubrium and body differs between males and females. Sternal growth may continue beyond the third decade and possibly throughout life.

The sternum projects (slopes) anteroinferiorly from the jugular notch. Viewed as a whole, and due to the angulation of the manubriosternal joint, the majority of the anterior surface of the sternum appears vertically convex and the posterior surface appears vertically concave. Inferiorly and proximal to the xiphoid process, the shape transitions to become vertically concave on both anterior and posterior surfaces. The geometry of the individual parts of the sternum vary with surface and region (Lindner et al 2017, Chakravarthi et al 2018). The manubrium is the broadest part, at its joints (articulations) with the first costal cartilages. It narrows at the manubriosternal joint, gradually widens to its joints with the fifth costal cartilages, and then narrows to the xiphoid process. The sternum contains highly vascular trabecular bone enclosed by a compact layer that is thickest in the manubrium between the clavicular notches. Centrally, the bone is relatively lightly constructed; the trabeculae are thicker and wider laterally. The medullary cavity contains haematopoietic bone marrow. The sternum and its component parts may be variable in morphology, joint alignment and fusion, and can contain clefts or foramen (Tubbs and Wantanabe 2016).

Manubrium of sternum

The jugular notch (superior border) of the manubrium of the sternum commonly aligns with the bodies of the second to third thoracic vertebrae, and the inferior border with the bodies of the fourth to fifth thoracic vertebrae at the manubriosternal joint. It has an average length of 5.1 cm and forms up to 35% of the total sternal length. It has a somewhat quadrangular shape, being broad and thick superiorly and narrowing inferiorly to its junction with the sternal body. The anterior and posterior surfaces are smooth in appearance. The anterior surface is transversely convex and vertically concave in shape, whereas the posterior surface is both transversely and vertically concave. The superior border is thick in the sagittal plane and bears the jugular (suprasternal) notch in the midline between the left and right clavicular notches. The clavicular notches are directed superiorly, posteriorly and laterally for articulation with the sternal articular surface of the clavicles. Fibres of the interclavicular ligament attach to the jugular notch. The inferior border is oval and rough and carries a thin layer of hyaline cartilage for articulation with the sternal body. The lateral borders are marked at the widest part of the manubrium by a depression for the first costal cartilage (first costal notch), and, inferior to this depression, by a small articular demifacet that articulates with part of the second costal cartilage. The narrow curved lateral border descends medially between these facets. There is little accessory movement at the manubriosternal joint, although pressure on either the sternal body or manubrium close to the joint will produce slight angling of the two sections, particularly in younger individuals.

Unlike all the other sternocostal joints, the joint between the manubrium and the first costal cartilage is a fibrous synarthrosis. It lies about 1 cm below and 1 cm lateral to the sternal (medial) end of the clavicle and is difficult to palpate.

Body of sternum

The body of the sternum is located level with the bodies of the fourth or fifth to the ninth thoracic vertebrae. It is longer, narrower and thinner than the manubrium, and is broadest at its junction with the fifth costal cartilages. The anterior surface is vertically convex and transversely varies from convex to concave depending upon region. It faces slightly superiorly and usually bears three variable transverse ridges that mark the levels of fusion of its four sternebrae (see Fig. 53.6B). Sternal foramina, of varying size, form and completeness, may occur in up to 10% of the population in the body of the sternum (Chakravarthi et al 2018). The posterior surface is vertically concave and transversely convex in shape and bears three transverse lines. The oval superior border articulates with the inferior border of the manubrium at the level of the manubriosternal joint (sternal angle) that commonly lies horizontally level with the inferior border of the body of the fourth thoracic vertebra, T4–T5 intervertebral disc or body of the fifth thoracic vertebra (the sternal plane), and is marked anteriorly and posteriorly by a transverse ridge and groove, respectively.

On each lateral border, at its superior angle and lateral to the manubriosternal joint, a small notch articulates with part of the second costal cartilage (see Figs 53.4–53.5). Inferiorly, four costal notches articulate with the third to sixth costal cartilages. The inferior angle bears a small facet, which, together with the xiphoid process, articulates with the seventh costal cartilage. Between these articular depressions are a series of curved bony edges that form the anterior limits of the associated intercostal spaces. The sternal body narrows from the fifth costal notch inferiorly to the xiphisternal joint, where it articulates with the xiphoid process.

Xiphoid process (xiphisternum)

The xiphoid process joins the inferior part of the sternal body at the xiphisternal joint, commonly level with the body of the ninth thoracic vertebra. It is the smallest and most variable part of the sternum, and may be broad and thin, pointed, bifid, triangular, perforated or curved (see Fig. 53.8). It sits in the epigastric region of the abdomen, therefore when elongated and curved anteriorly it may be mistaken for an epigastric mass, and when unusually long with a sharp bifid end it can damage the liver. The xiphoid process is cartilaginous during early life and is commonly ossified in adults. Costal notches located on the superolateral border, lateral to the xiphisternal joint, articulate with part of the seventh costal cartilages (see Fig. 53.5).

Muscle attachments The sternocostal head of pectoralis major and sternal head of sternocleidomastoid are attached to the anterior surface of the manubrium (see Fig. 53.4). Sternothyroid is attached to the posterior surface of the manubrium, opposite or just inferior to the first costal notch, and the most medial fibres of sternohyoid are attached superior to sternothyroid and level with the clavicular notch. The articular capsules of the sternocostal joints and sternocostal fibres of pectoralis major are attached to the anterior surface of the body of the sternum, and transversus thoracis (sternocostalis) is attached to the posterior surface. The external intercostal membranes are attached to the lateral borders of the body of the sternum between the costal notches. The most medial fibres of rectus abdominis and the aponeuroses of external and internal abdominal oblique are attached to the anterior surface of the xiphoid process. The linea alba is attached to its inferior end, and the aponeuroses of internal abdominal oblique and transversus abdominis are attached to its non-articular borders. Slips of the respiratory diaphragm are attached to its posterior surface, and posteriorly it is related to the liver.

Vascular supply The internal thoracic artery provides the main blood supply for the sternum via anterior and posterior networks of perforating arteries that directly penetrate the sternum at the level of each intercostal space. These networks are particularly well developed posteriorly and at the level of the fourth and fifth intercostal spaces.

The venous network is less developed. It is formed mainly by an inframedullary network of sinuses in the bone that drain via transcortical veins either into the peripheral sternal networks or the internal thoracic vein.

Innervation The manubrium is innervated by the anterior branch of the supraclavicular nerve and the anterior cutaneous branch of the first intercostal nerve, whereas the body of the sternum is innervated largely by anterior branches of the second to sixth intercostal nerves. The anterior (sternal) branch of the phrenic nerve arises within or immediately inferior to respiratory diaphragm and runs anteromedially to innervate the lower part of the body of the sternum and xiphoid process.

Ossification The sternum is formed by fusion of two cartilaginous sternal plates flanking the median plane. The arrangement and number of centres of ossification vary according to the level of completeness and time of fusion of the sternal plates, and according to the final width of the adult bone. Incomplete fusion leaves a sternal foramen (Tubbs and Wantanabe 2016). The manubrium is ossified from one to three centres that appear during postmenstrual weeks 17–20. The sternal body is formed from four sternebrae. The first and second sternebrae usually ossify from single centres that appear at about the same time (**Fig. 53.6A**). Centres in the third and fourth sternebrae are commonly paired, and appear during postmenstrual weeks 17–20 and 21–24, respectively; one of either pair may be delayed until after postmenstrual week 28, and the fourth sternebral centre may be absent. The xiphoid process begins to ossify in the third year or even later. In some sterna, all centres are single and median; in others, the manubrial centre is single and the sternebral centres are paired, symmetric or asymmetric. Union between the sternebral centres begins at puberty and proceeds from inferior to superior; by 25 years of age, they are all united (**Fig. 53.6B**).

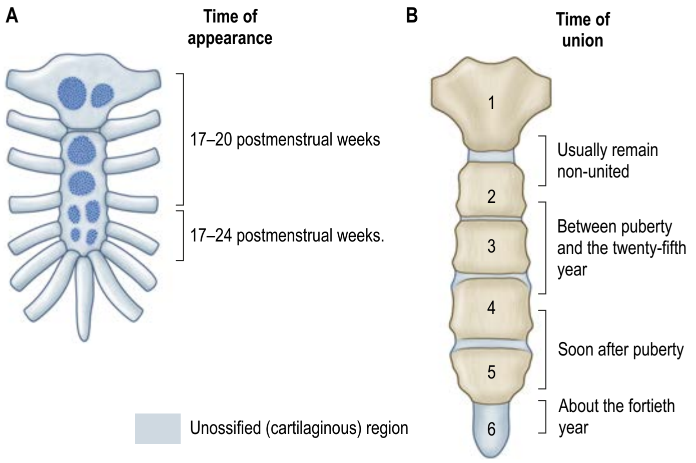
A
Time of appearance
17–20 postmenstrual weeks
17–24 postmenstrual weeks.
B
Time of union
1
2
3
4
5
6
Usually remain non-united
Between puberty and the twenty-fifth year
Soon after puberty
About the fortieth year
▢ Unossified (cartilaginous) region

Fig. 53.6 The ossification of the sternum. **A**, Before birth. **B**, After birth.

Suprasternal ossicles, paired or single, sometimes occur. They may fuse to the manubrium or articulate posteriorly at the lateral border of the jugular notch. When well formed, they are pyramidal with an articular base. The ossicles are cartilaginous at birth and ossify during adolescence.

Pectus excavatum and carinatum

Available with the *Gray's Anatomy* e-book

Clavicle

The clavicle is described in Chapter 49.

Ribs

The ribs are 12 pairs of curved bony arches with elastic properties (as measured by their stress–strain relationship) (**Fig. 53.8**). Each consists of a highly vascular trabecular bone containing large amounts of red marrow, enclosed in a thin layer of compact bone. The ribs articulate posteriorly with the thoracic vertebral column and form the greater part of the thoracic skeleton. Their number may be increased by cervical or lumbar ribs or reduced by the absence of the twelfth pair. The first seven 'true' ribs connect directly to the costal notches of the sternum by costal cartilages, whilst the remaining inferior five 'false' ribs either join the costal cartilage (ribs 8–10) located immediately superior, or 'float' free at their anterior ends as relatively small and delicate structures tipped with cartilage (ribs 11 and 12). The tenth rib may also float; the incidence varies from 35% to 70%, depending on ancestry. The ribs change in their width, height and angulation with growth and/or age (Openshaw et al 1984, Joshua et al 2014, Casha et al 2015).

The ribs are separated by the intercostal spaces, which are deeper anteriorly and between the more superiorly located ribs. The latter are less oblique than the inferiorly located ribs; obliquity is maximal at the ninth rib. The ribs increase in length up to the seventh and thereafter decrease in length. In general, they decrease in height or breadth from superior to inferior; the upper ten are at their highest/broadest at their anterior ends. The first two and the last three ribs have special features, whereas the remainder show a typical form.

Typical rib

A typical rib has a shaft with anterior and posterior ends (**Fig. 53.9**). The anterior costal end has a small concave depression for articulation with the lateral end of its cartilage. The shaft has an external convexity and is grooved internally near its inferior border, which is sharp, whereas its superior border is rounded. The posterior vertebral end has a head, neck and tubercle. The head presents two articular facets, separated by a transversely oriented crest. The inferior and larger facet articulates with the body of the correspondingly numbered vertebra, its crest attaches to the superiorly located intervertebral disc and the smaller superior facet articulates with the body of the vertebra above. The neck

Pectus excavatum is the most common congenital deformity of the anterior thoracic wall and is more common in males than females. It is a depression of the sternum and costal cartilage that is sometimes referred to as cobbler's chest, sunken chest, the crevasse or funnel chest. The lower (inferior) costal cartilages and the body of the sternum are depressed and there is some asymmetric curving of the ribs posteriorly. There is often an abnormal posture with dorsal lordosis, sometimes with developing scoliosis. The deformity is found either at birth (1 in 400 live births) or early in life; in the majority of cases, the condition is visible by 1 year of age but may not develop until puberty. The aetiology is unknown but some cases are associated with connective tissue diseases, such as Marfan syndrome.

The clinical significance of pectus excavatum may vary considerably (**Fig. 53.7**). Severe defects can lead to cardiopulmonary dysfunction, including changes in cardiac anatomy due to compression of the right ventricle and left atrium between the sternum and thoracic vertebral column. Almost all patients will have some degree of cosmetic concern, while back and chest pain may occur. Evaluation of the deformity demands careful symptom assessment in addition to baseline radiological investigations (chest radiograph and computed tomography (CT)). Where there are physiological restrictions, lung function tests, electrocardiograms (ECGs), echocardiograms and MR-based strain imaging form part of the assessment before specialist clinicians can determine the safety of surgical intervention (Lollert et al 2018). A classification system based on morphology using CT scanning has been proposed (Park et al 2004) and is useful for standardizing the results of surgical correction of the different subtypes.

Mild defects causing aesthetic concerns may be improved with customized silicone implants (Masson et al 1970) or with soft tissue reconstructive procedures (Raab et al 2009), to camouflage the concavity. More severe defects often require correction of the underlying skeletal deformity. Several techniques have been described. Open resection procedures were pioneered by Ravitch in the 1950s and subsequently minimally invasive techniques have gained in popularity (Ravitch 1955, Nuss et al 1988). With the development of three-dimensional (3D) printers, simulated surgeries can now be performed using patient-specific 3D chest wall models, allowing higher precision in bar placement and the number required for the best surgical outcome (Matsuo et al 2018). Additionally, 3D printing of titanium plate and polyethylene implants has allowed for advances in patient implant customization and an increase in optimal surgical outcomes (Lin et al 2018).

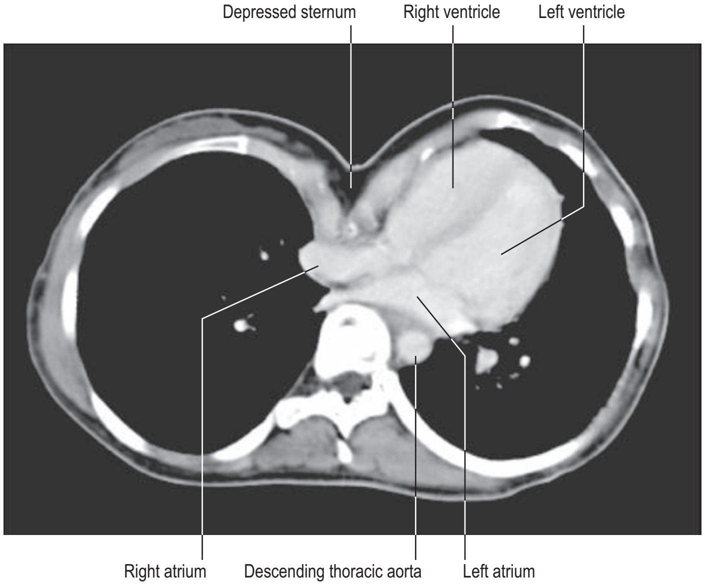

Fig. 53.7 Pectus excavatum (axial CT image), showing displacement and compression of mediastinal structures.

Pectus carinatum, often called 'pigeon chest', is an overgrowth of cartilage that causes the sternum to protrude forwards. It is less common than pectus excavatum, accounting for 5–20% of anterior thoracic wall deformities: a quarter of cases are familial. The condition may occur as a solitary congenital anomaly or in association with other genetic disorders. Although present in early childhood, pectus carinatum usually progresses during adolescence and then remains unchanged throughout adulthood. In recent years treatment has gravitated towards minimally invasive or noninvasive methods of applying external pressure to the anterior chest wall to depress the sternum (Wells and Coonar 2018). Pectus carinatum occurs in three different ways, most commonly in pubertal males aged 11–14 years undergoing a growth spurt. Some parents report that their child's pectus seemingly popped up 'overnight'. The second most common occurrence is from birth, when it is evident in newborns as a rounded chest, becoming more prominent as the child reaches 2 or 3 years old. The least common occurrence is as an acquired condition after open heart surgery, when healing has been aberrant. Pectus carinatum may be associated with Turner, Marfan, Ehlers–Danlos, Morquio's, Noonan's, Sly's or multiple lentigines syndromes, trisomies 18 or 21, homocystinuria, osteogenesis imperfecta or scoliosis.

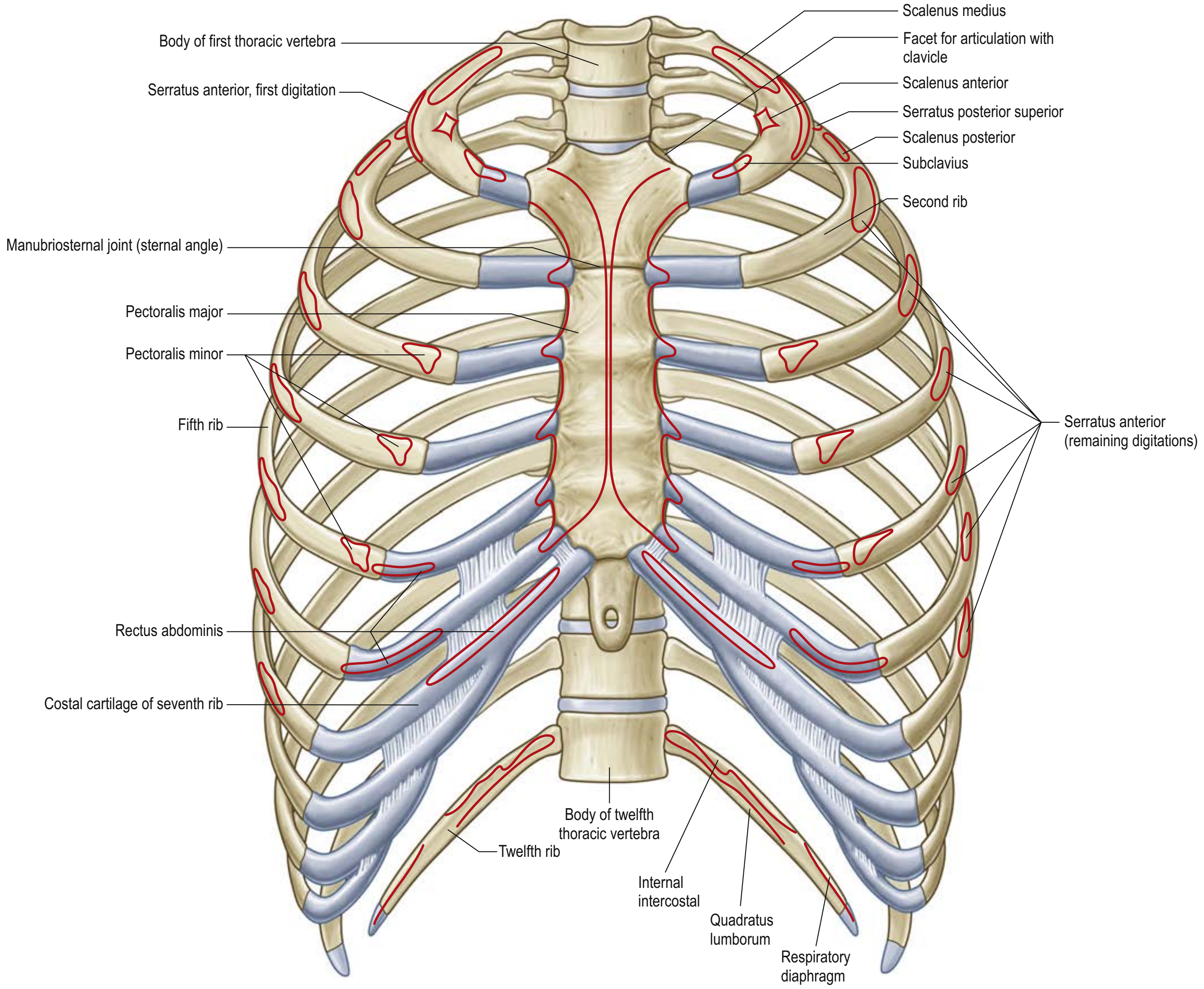
Body of first thoracic vertebra
Serratus anterior, first digitation
Manubriosternal joint (sternal angle)
Pectoralis major
Pectoralis minor
Fifth rib
Rectus abdominis
Costal cartilage of seventh rib
Twelfth rib
Body of twelfth thoracic vertebra
Internal intercostal
Quadratus lumborum
Respiratory diaphragm
Scalenus medius
Facet for articulation with clavicle
Scalenus anterior
Serratus posterior superior
Scalenus posterior
Subclavius
Second rib
Serratus anterior (remaining digitations)

Fig. 53.8 The skeleton of the thorax, anterior aspect, showing muscle attachments (red outline).

is the flat part distal to the head and anterior to the transverse process of the correspondingly numbered thoracic vertebra. It is oblique and faces anterosuperiorly. Its posteroinferior surface is rough and pierced by foramina. Its superior border is sharp and formed by the crest of the neck, and its inferior border is rounded. The tubercle is located posteriorly between the neck and angle of the rib and is more prominent in the superiorly located ribs. It is divided into a medial articular area that bears a small oval facet for the transverse process of the correspondingly numbered thoracic vertebra, and a roughened lateral non-articular area for ligamentous attachment. The shaft is thin and flat, with external and internal surfaces, and superior and inferior borders. It is curved, bent at the angle of the rib, about 5–6 cm lateral to the tubercle, and twisted about its long axis. The smooth internal surface of the rib is marked by the costal groove, bounded inferiorly by the inferior border and which houses the intercostal neurovascular bundle (see Fig. 53.17). The superior border of the costal groove continues posteriorly as the inferior border of the neck of the rib, but terminates anteriorly at the junction of the middle and anterior thirds of the shaft: the groove is often absent anterior to this junction

Attachments and relations A radiate ligament is attached along the anterior border of the head of the rib and an intra-articular ligament is attached along its crest (see Fig. 53.11). The anterior surface of the head is related to costal parietal pleura and, in the more inferior ribs, to the sympathetic trunk and ganglia. The anterior surface of the neck of the rib is divided by a faint transverse ridge, for attachment of the internal intercostal membrane, and is continuous with the inner lip of the superior border of the shaft. The area superior to the ridge, which is more or less triangular, is separated from the membrane by fatty tissue and the area inferior to the ridge is smooth and covered by costal parietal pleura. The posterior surface of the neck gives attachment to the costotransverse ligament and contains vascular foramina. The superior costotransverse ligament is attached to the crest on the neck of the rib that extends laterally into the outer lip of the superior border of the shaft. The rounded inferior border of the neck of the rib continues laterally into the superior border of the costal groove, and gives attachment to the internal intercostal membrane. The articular facet on the tubercles of the first to the sixth ribs is convex and faces posteromedially. In the subsequent three or four ribs it is almost flat, and faces inferiorly, posteriorly and slightly medially. The lateral costotransverse ligament is attached to the non-articular area.

The ridge on the external surface of the shaft (near to the angle of the rib) gives attachment to an upward continuation of the thoracolumbar fascia and lateral fibres of iliocostalis thoracis. From the second to the tenth ribs, the distance between angle and tubercle of the rib increases. Medial to the angle, the external surface gives attachment to levator costae and is covered by erector spinae. Near the sternal end of this surface, an indistinct oblique line, the anterior 'angle' of the rib, separates the attachments of external abdominal oblique and serratus anterior (or latissimus dorsi, in the case of the ninth and tenth ribs). The internal intercostal muscle is attached to the costal groove on the internal surface, and separates the intercostal neurovascular bundle from the bone of the rib. At its vertebral end, the costal groove faces inferiorly. The shaft of the rib broadens posteriorly near the angle, and the costal groove reaches its internal surface. The innermost intercostal muscle is attached to the superior border of the costal groove; this attachment occasionally extends to the anterior quarter of the rib. The external intercostal muscle is attached to the sharp inferior border of the rib. The superior border of the rib has two lips posteriorly, an inner and an outer lip. The internal intercostal muscles and the innermost intercostal muscles are attached to the inner lip and the external intercostal muscle is attached to the outer lip.

Vascular supply and innervation Typical ribs receive their blood supply anteriorly via branches from the internal thoracic artery (first six intercostal spaces) or musculophrenic artery (subsequent spaces), and

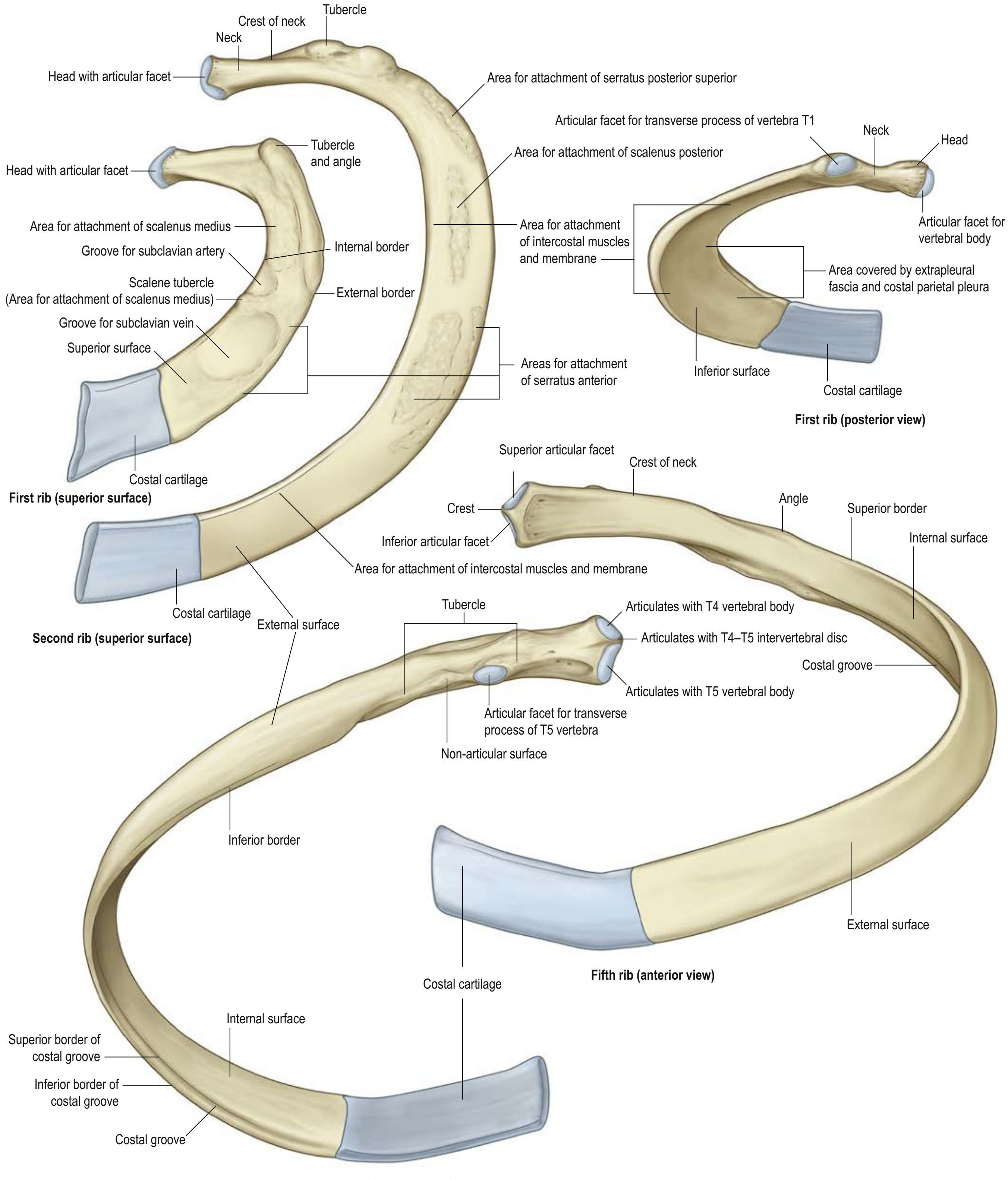
Tubercle
Crest of neck
Neck
Head with articular facet
Area for attachment of serratus posterior superior
Articular facet for transverse process of vertebra T1
Neck
Head
Tubercle and angle
Head with articular facet
Area for attachment of scalenus posterior
Area for attachment of scalenus medius
Groove for subclavian artery
Internal border
Area for attachment of intercostal muscles and membrane
Articular facet for vertebral body
Area covered by extrapleural fascia and costal parietal pleura
Scalene tubercle (Area for attachment of scalenus medius)
External border
Groove for subclavian vein
Superior surface
Areas for attachment of serratus anterior
Inferior surface
Costal cartilage
Costal cartilage
Superior articular facet
Crest of neck
Angle
Superior border
Crest
Internal surface
Inferior articular facet
Area for attachment of intercostal muscles and membrane
Costal cartilage
External surface
Tubercle
Articulates with T4 vertebral body
Articulates with T4–T5 intervertebral disc
Costal groove
Articulates with T5 vertebral body
Articular facet for transverse process of T5 vertebra
Non-articular surface
Inferior border
External surface
Costal cartilage
Internal surface
Superior border of costal groove
Inferior border of costal groove
Costal groove

First rib (superior surface)

First rib (posterior view)

Second rib (superior surface)

Fifth rib (anterior view)

Fith rib (posterior view)

Fig. 53.9 Surface features of the left first, second and fifth rib. (With permission from Drake RL, Vogl AW, Mitchell A et al (eds) Gray's Atlas of Anatomy. Elsevier, Churchill Livingstone. Copyright 2015.)

posteriorly from posterior intercostal arteries derived directly from the descending thoracic aorta. Venous drainage is into the corresponding intercostal vein and subsequently into the azygos system or the brachiocephalic vein (see Fig. 52.4). Typical ribs are innervated segmentally by branches from their corresponding intercostal nerves.

Variant and accessory ribs

Ribs may be asymmetric, absent, fused, intrathoracic or accessory (Tubbs and Wantanabe 2016). Accessory (supernumerary) ribs may be in a cervical or lumbar location, lumbar being the most common but least problematic.

First rib

The first rib is broad and flat, has superior and inferior surfaces and internal and external borders, and is the most acutely curved and shortest of all the ribs (see Fig. 53.9). It slopes obliquely anteroinferiorly towards its sternal end, which is larger than that of any other rib. The obliquity of the first rib means that the lung apex and covering pleura project superior to the superior thoracic aperture and into the neck.

The head of the first rib is small and round, bears an almost circular facet that articulates with the body of the first thoracic vertebra, and is turned slightly inferiorly relative to the tubercle of the rib. The neck of the rib is rounded and ascends posterolaterally, and the tubercle is wide and prominent and directed superiorly and posteriorly. Medially, an

Cervical ribs arise from the seventh cervical vertebra, occur in up to 1% of the population, and are thought to result from mutations of *HOX* genes (Chang et al 2013). Their size varies from a simple epiphysis on the transverse process of the seventh cervical vertebra to, more commonly, a structure with a head, neck and tubercle. When a shaft is present, it is of variable length and extends anterolaterally into the posterior triangle of the neck, where it may end freely or join the first rib or its costal cartilage, or even the manubrium of the sternum. Long cervical ribs have relations similar to those of the first thoracic rib: the brachial plexus (usually lower trunk) and subclavian vessels are superior and may become compressed in the narrow angle between the rib and scalenus anterior. This anatomical relationship means that cervical ribs may first be revealed by neurovascular symptoms (thoracic outlet syndrome, see Ch. 48) including ipsilateral limb pain, numbness, weakness or cold intolerance, particularly when the cervical rib puts pressure on the ventral rami of the eighth cervical and first thoracic spinal nerves. The symptoms resulting from a cervical rib are unrelated to the relative sizes of its constituent parts (specifically osseous vs fibrous). A cervical rib (pleurapophysis) may show synostosis or diarthrosis with either the anterior (parapophysial) or posterior (diapophysial) 'roots' of the transverse process of the seventh cervical vertebra or, more usually, with both.

oval facet articulates with the transverse process of the first thoracic vertebra. The angle and tubercle of the first rib normally coincide. The inferior surface of the flattened shaft of the rib is smooth whereas the superior surface is crossed obliquely by two shallow grooves, separated by a slight ridge that usually terminates at the scalene tubercle (a small pointed projection located on the internal border of the rib to which scalenus anterior is attached). The groove anterior to the scalene tubercle forms a bed for the subclavian vein, and the rough area between this and the first costal cartilage gives attachment to the costoclavicular ligament and, even more anteriorly, to subclavius (see Fig. 53.8). The subclavian artery and (usually) the lower trunk of the brachial plexus pass in the groove posterior to the scalene tubercle. Posterior to the scalene tubercle, scalenus medius is attached as far as the tubercle/angle of the rib.

The superior half of the smooth inferior surface is covered by endothoracic fascia and costal parietal pleura, the inferior half is an attachment point for the intercostal muscles and membranes. The external border is convex, thick posteriorly and thin anteriorly. It is covered posteriorly by scalenus posterior descending to the second rib. The first digitation of serratus anterior is, in part, attached to it, lateral to the groove for the subclavian vein. The internal border is concave and thin, and the scalene tubercle is near its midpoint. The suprapleural membrane (Sibson's fascia), covering the cervical parietal pleura and lung apex, is attached to the internal border (Ch. 54).

Vascular supply and innervation The first rib is supplied by the internal thoracic and supreme intercostal arteries, drained by the supreme intercostal vein and innervated by the first intercostal nerve.

Ossification The first rib has a primary ossification centre for the shaft, and secondary ossification centres for the head of the rib and the tubercle.

Second rib

The second rib is about twice the length of the first and has a similar curvature. The non-articular area of its tubercle is small. The angle of the rib is small and near the tubercle. The shaft is not twisted but at the tubercle is superiorly convex. The external surface of the shaft is convex and at around the midpoint is marked by a raised roughened prominence for the attachments of the inferior halves of the first and the second digitation of serratus anterior (see Figs 53.8–53.9). Passing anteriorly from the angle of the rib, a distinct midline ridge divides the external (upper) surface into outer and inner parts: scalenus posterior and serratus posterior superior are attached to the ridge and to the outer part. The internal surface of the shaft is smooth and concave, faces inferomedially and has a relatively short costal groove along the posterior part of its inferior border. The superior half of the internal surface is covered by endothoracic fascia and costal parietal pleura, and the inferior half is an attachment point for the intercostal muscles and membranes.

Vascular supply and innervation The second rib is supplied by the internal thoracic and supreme intercostal arteries, drained via the superior intercostal vein into the brachiocephalic vein, and by the anterior intercostal veins into the internal thoracic vein, and innervated by branches of the second intercostal nerve.

Ossification The second rib is ossified from a primary ossification centre for the shaft, which appears near the angle late in postmenstrual weeks 5–8. The secondary centres for the head and articular and non-articular parts of the tubercle appear around puberty, uniting to the shaft soon after the age of 20 years.

Tenth, eleventh and twelfth ribs

The tenth rib has a single facet on its head that articulates with the superior border of the body of the tenth thoracic vertebra near the pedicle, and may also articulate with the T9–T10 intervertebral disc. The costal cartilages of the ninth and tenth ribs may be united anteriorly by a fibrous joint, although in up to 70% of subjects the tenth rib may be free, in which case its end appears pointed like the eleventh and twelfth ribs.

The eleventh and twelfth ribs each have one large articular facet on their heads but no necks or tubercles. Their anterior ends are pointed and tipped with hyaline cartilage. The eleventh rib has a slight angle and shallow costal groove whereas the twelfth rib has neither, is much shorter and slopes cranially at its vertebral end. The internal surfaces of both ribs face slightly superiorly, this being more apparent in the twelfth.

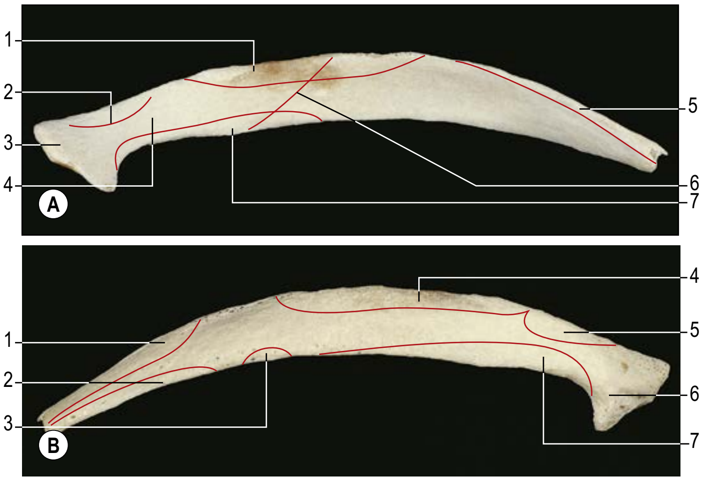

Fig. 53.10 The left twelfth rib, showing surface features, relations and muscle attachments (red outline). **A**, Internal (anterior) surface. Key: 1, attachment of internal intercostal muscle; 2, attachment of costotransverse ligament; 3, head of rib; 4, area covered by endothoracic fascia and costal part of parietal pleura; 5, attachment of respiratory diaphragm; 6, line of pleural reflection; 7, attachment of quadratus lumborum. **B**, External (posterior) surface. Key: 1, attachment of latissimus dorsi; 2, attachment of external abdominal oblique; 3, attachment of serratus posterior inferior; 4, attachment of external intercostal muscle; 5, attachment of levator costae; 6, head of rib; 7, attachment of erector spinae.

Numerous muscles and ligaments are attached to the twelfth rib (see Fig 53.8; **Fig. 53.10**). Quadratus lumborum and its anterior covering layer of thoracolumbar fascia are attached to the medial one-half to two-thirds of the inferior part of the anterior surface. The medial half of the internal surface is related to the costodiaphragmatic recess of the pleural cavity, approximately at the point where it is crossed by the lateral border of iliocostalis: the recess may extend inferior to the rib. The internal intercostal muscle (medially) and the respiratory diaphragm (laterally) are attached at or near the superior border. The inferior border and associated external surface give attachment to the middle layer of the thoracolumbar fascia and, lateral to quadratus lumborum, to the lateral arcuate ligament and posterior layer of the thoracolumbar fascia. The lumbocostal ligament is attached posteriorly, posterior to quadratus lumborum and normally close to the head of the twelfth rib (although it may extend more laterally): distally, the ligament is attached to the transverse processes of the first and second lumbar vertebrae and can be used to locate the subcostal nerve (Saker et al 2016). The lowest levator costae, longissimus thoracis and iliocostalis are all attached to the medial half of the external surface; serratus posterior inferior, latissimus dorsi and external abdominal oblique are attached to the lateral half of the external surface; the external intercostal muscle is attached along the central section of the superior part of the external surface. These attachments can vary; in particular, the attachments of the internal intercostal, levator costae and erector spinae merge and those of latissimus dorsi, the respiratory diaphragm and external abdominal oblique may reach the costal cartilage.

Vascular supply and innervation The tenth and eleventh ribs are supplied by the posterior intercostal arteries and by branches from the musculophrenic artery. The twelfth rib is supplied by the subcostal artery. Venous drainage is via the posterior intercostal and subcostal veins that drain into the azygos system and via the anterior intercostal veins (branches of the musculophrenic vein). The tenth and eleventh ribs are innervated by the corresponding intercostal nerve, and the twelfth rib is innervated by the subcostal nerve.

Ossification The tenth rib ossifies from a primary ossification centre in the shaft and secondary centres for the head and articular parts of the tubercle. The eleventh and twelfth ribs, without tubercles, both have two ossification centres.

Costal cartilages

The costal cartilages are the unossified anterior parts of the cartilaginous models from which the ribs develop. They are flat bars of hyaline cartilage that extend from the anterior ends of the ribs, and contribute greatly to thoracic mobility and elasticity (see Fig. 53.8). The upper seven pairs articulate with the sternum; the eighth to tenth articulate with the inferior border of the costal cartilage above; and the lowest two have free, pointed ends located within the soft tissue of the abdominal wall (see Figs 53.14, 53.15B). The costal cartilages increase in length from the first to the seventh, and then decrease to the twelfth. They diminish in breadth/height from first to last, as do the intercostal spaces. They are broad at their articulation with the ribs and taper as they pass anteriorly and toward the midline. The first and second are of even breadth and the sixth to eighth enlarge where their margins are in contact. The first descends a little, the second is horizontal and the third ascends slightly; the others are angulated and incline superomedially towards the sternum or cartilage above, in a plane slightly anterior to their ribs.

Each costal cartilage has two surfaces, borders and ends. The external (anterior/anterosuperior) surface is convex. The sternoclavicular articular disc, costoclavicular ligament and subclavius are all attached to the external surface of the first costal cartilage, pectoralis major is attached to the medial ends of the first six costal cartilages, rectus abdominis to the fifth to seventh and others, including the costal cartilages forming the costal arch (margin) offer attachment sites for the muscles of the anterior abdominal wall. The internal (posterior/posteroinferior) surface is concave. Sternothyroid is attached to the internal surface of the first costal cartilage, transversus thoracis is attached to the second to seventh costal cartilages, and transversus abdominis is attached to the seventh to twelfth costal cartilages. The internal intercostal muscles and external intercostal membranes are attached to the concave superior and convex inferior borders. At around the point (apex) of maximum convexity of the inferior border of the sixth (sometimes the fifth) to ninth costal cartilages an inferiorly facing oblong articular facet articulates with a superiorly facing articular facet on the superior border of the cartilage below via a synovial interchondral joint. The lateral end of each cartilage articulates with its corresponding rib. The medial end of the first cartilage articulates with the manubrium of the sternum; the medial ends of the six succeeding cartilages are round and articulate with shallow costal notches on the lateral margins of the body of the sternum (and the manubrium in the case of the second); those of the eighth to tenth are pointed and articulate with the costal cartilage above; and those of the eleventh and twelfth are pointed and free. With the exceptions of the fibrous synarthrosis between the first rib and sternum, and the costal cartilages of the ninth and tenth ribs, all the articulations are synovial. Costal cartilages may undergo calcification with age (Middleham et al 2015).

Rib fractures

Available with the *Gray's Anatomy* e-book

JOINTS

Manubriosternal joint

The manubriosternal joint lies between the manubrium and the body of the sternum approximately 7 cm below (inferior to) the jugular (suprasternal) notch of the manubrium. It is usually a symphysis but may be synovial, synchondrotic or synostotic. The bony surfaces are covered by hyaline cartilage and connected by a fibrocartilage that may ossify with increasing age. The central part of the disc is sometimes absorbed so that the joint appears synovial. Occasionally, in individuals over the age of 30 years, the manubrium appears to be joined to the body of the sternum by bone. However, the intervening cartilage may be only superficially ossified because ossification is not completed until late adult life. Early synostosis has been attributed to a persistent synchondrosis in place of a symphysis. In the newborn, union is by collagenous and elastic fibres, without chondrocytes.

Movements There is a small range of angulation between the longitudinal axes of the manubrium and the body of the sternum, and limited anteroposterior displacement. The powerful ligamentous attachments in this region mean that dislocation of the manubriosternal joint is rare, although it may be associated with high-energy trauma. Dislocation is most common when the joint is synovial, whereas synchondral and synosteal types typically fracture through the manubrium.

Xiphisternal joint

The joint between the xiphoid process and body of the sternum is a symphysis. It is usually transformed to a synostosis by the fortieth year but sometimes remains unchanged, even in older adults.

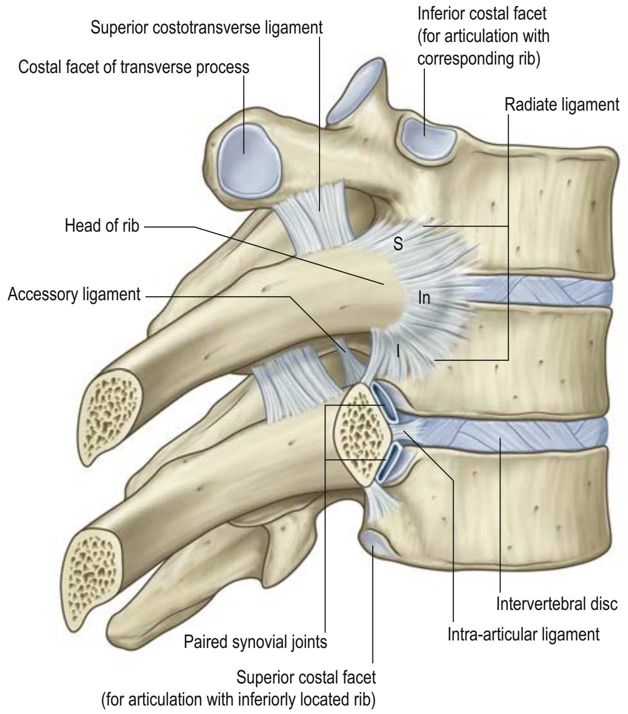
Superior costotransverse ligament
Inferior costal facet (for articulation with corresponding rib)
Costal facet of transverse process
Radiate ligament
Head of rib
S
Accessory ligament
In
I
Intervertebral disc
Paired synovial joints
Intra-articular ligament
Superior costal facet (for articulation with inferiorly located rib)

Fig. 53.11 Ligaments of the vertebral column and costovertebral joints, right lateral aspect. The anterior longitudinal ligament has been removed. The different fibre groups of the radiate ligament are shown. Abbreviations: S, superior fibres; In, intermediate fibres; I, inferior fibres. (With permission from Drake RL, Vogl AW, Mitchell A et al (eds) Gray's Atlas of Anatomy. Elsevier, Churchill Livingstone. Copyright 2015.)

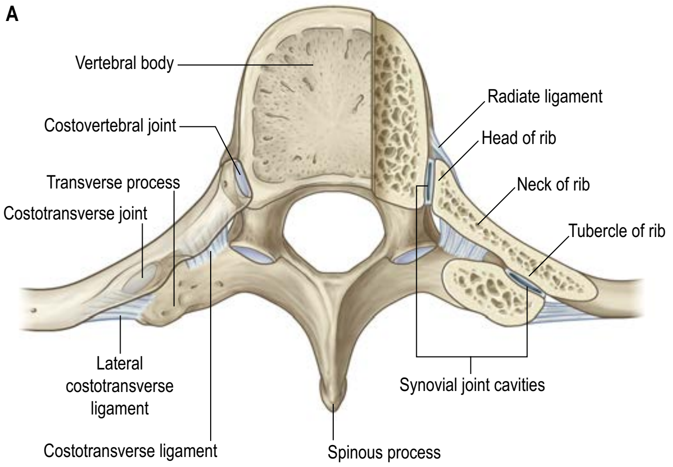

Fig. 53.12 A, Costovertebral and costotransverse joints, superior aspect. (B, *continued online*)

Sternoclavicular joint

The sternoclavicular joint is described in Chapter 49.

Costovertebral, sternocostal and interchondral joints

The heads of the ribs articulate with the bodies of the vertebrae at costovertebral joints; their necks and tubercles articulate with transverse processes at costotransverse joints.

Joints of the heads of the ribs

The head of a typical rib articulates with facets (often termed demifacets) on the margins of the bodies of adjacent thoracic vertebrae and with the intervening intervertebral disc (Figs 53.11–53.12). The first and tenth to twelfth ribs articulate with their corresponding vertebra alone by a simple synovial joint. For the second to ninth ribs, an intra-articular ligament bisects the joint, producing a double synovial compartment, so the joint is classified as both compound and complex. Often inaccurately described as a plane joint, the articular surfaces are

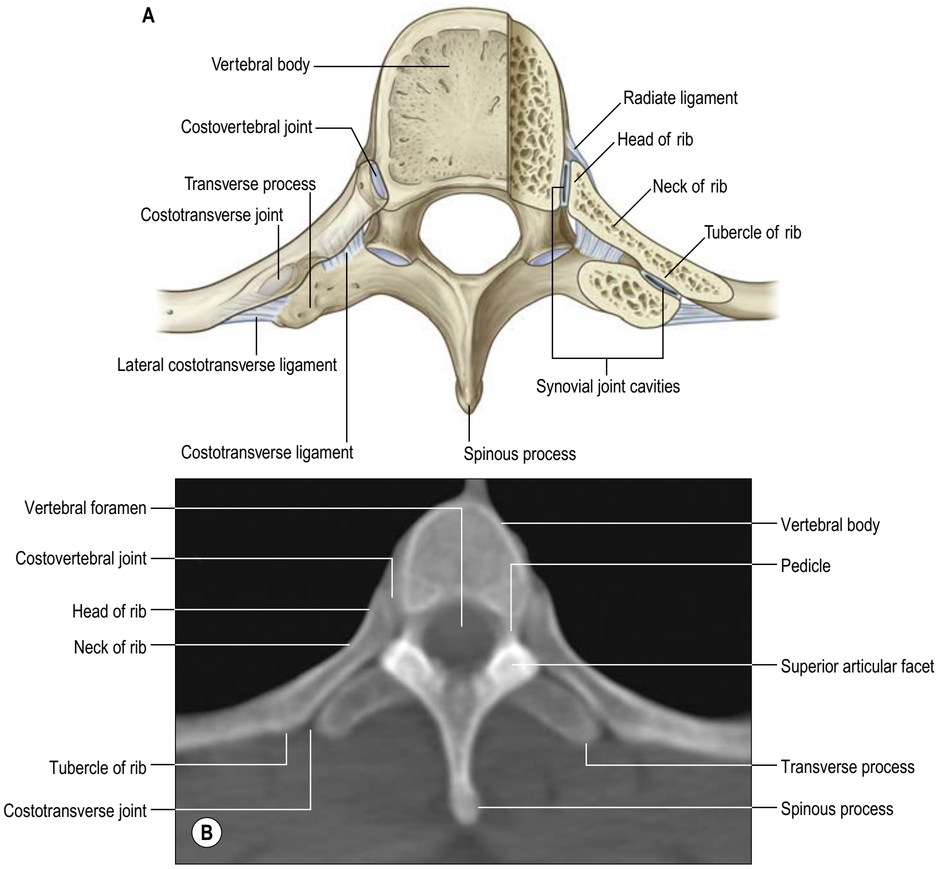
A
Vertebral body
Costovertebral joint
Transverse process
Costotransverse joint
Lateral costotransverse ligament
Costotransverse ligament
Spinous process
Radiate ligament
Head of rib
Neck of rib
Tubercle of rib
Synovial joint cavities
Vertebral foramen
Costovertebral joint
Head of rib
Neck of rib
Tubercle of rib
Costotransverse joint
B
Vertebral body
Pedicle
Superior articular facet
Transverse process
Spinous process

Fig. 53.12 **A**, Costovertebral and costotransverse joints, superior aspect. **B**, CT mean intensity projection slab through a typical rib and thoracic vertebra showing the typical arrangement of costotransverse and costovertebral joints. (A, Adapted from Drake RL, Vogl AW, Mitchell A et al (eds) Gray's Atlas of Anatomy. Elsevier, Churchill Livingstone. Copyright 2015.)

Despite their pliability, the ribs are much more frequently broken when compared to the sternum; the anterior and anterolateral portions of the middle to lower ribs are the most vulnerable. The elastic recoil of the ribs that articulate with and effectively suspend the sternum may explain the rarity of sternal fractures. Because traumatic stress is often the result of compression of the thorax, the usual site of fracture is just anterior to the angle of the rib, the weakest point of the bone, however direct impact may fracture a rib at any point. Nearly 10% of all patients admitted after blunt force thoracic trauma have one or more rib fractures. Morbidity and mortality increase as the number of fractured ribs increases (Tomas et al 2017): the ends of the broken bone may be driven inwards and potentially injure thoracic or upper abdominal viscera (Kasotakis et al 2017). The pain associated with rib fracture, particularly multiple rib fractures in older adults, can predispose to pneumonia by limiting normal airway protective mechanisms (e.g. cough).

slightly ovoid and the superior and inferior synovial articulations are obtusely angled to each other. The ligaments associated with the joints are capsular, radiate and intra-articular.

Fibrous capsule

A fibrous capsule connects the head of the rib to the circumference of the articular surface formed by an intervertebral disc and the demifacets of two adjacent vertebrae. Some of the superior fibres of the capsule traverse the intervertebral foramen to blend with the posterior aspect of the associated intervertebral disc. The posterior fibres are continuous with the costotransverse ligament.

Radiate ligaments

The radiate ligaments connect the anterior surface of the head of each rib, just distal to its articular surface, to the bodies of two articulating vertebrae and their intervening intervertebral disc. Superior fibres ascend to the body of the vertebra above, inferior fibres descend to the body of the vertebra below, and intermediate fibres, which are the shortest and least distinct, pass horizontally to the intervening intervertebral disc. The radiate ligament associated with the first rib is attached to the bodies of the seventh cervical and first thoracic vertebrae. The tenth to twelfth ribs articulate with single vertebral bodies and the radiate ligament is attached to the body of the corresponding vertebra and the body of the vertebra above.

Intra-articular ligament

The intra-articular ligament is a short flat band that joins the crest on the head of the rib, between the articular facets, to the intervertebral disc and so divides the synovial joint into two compartments. The ligament is absent from the first and tenth to twelfth costovertebral joints.

Costotransverse joints

The facet on the tubercle of a rib articulates with the costal facet on the transverse process of its corresponding vertebra (see Figs 53.11, 53.12). The eleventh and twelfth ribs lack this articulation. In the upper five or six joints, the articular surfaces are reciprocally curved; they are flatter in the joints located inferiorly (**Fig. 53.13**). The ligaments associated with the costotransverse joints are capsular, costotransverse, superior and lateral costotransverse, and accessory.

Fibrous capsule The fibrous capsule is thin, attached to articular peripheries and has a synovial lining.

Costotransverse ligament The costotransverse ligament fills the costotransverse foramen between the neck of a rib and the transverse process of its adjacent corresponding vertebra. Its numerous short fibres pass posteriorly from a rough area on the posterior surface of the neck of the rib to the anterior surface of the transverse process. A costotransverse ligament is rudimentary or absent in the eleventh and twelfth ribs.

Superior costotransverse ligament The superior costotransverse ligament has anterior and posterior layers. The anterior layer is attached between the crest on the neck of the rib and the inferior surface of the transverse process of the vertebra above, and blends laterally with the internal intercostal membrane; it is crossed by the intercostal vessels and nerve. The posterior layer is attached posteriorly on the neck of the rib, ascends posteromedially to the transverse process of the vertebra above, and blends laterally with the external intercostal muscle. The first rib has no superior costotransverse ligament. The inferior surface of the head, neck and sometimes the medial part of the shaft of the twelfth rib are connected to the transverse processes of the first and second lumbar vertebrae by the lumbocostal ligament.

Accessory ligament An accessory ligament is usually present. It lies medial to the superior costotransverse ligament, from which it is separated by the dorsal ramus of a thoracic spinal nerve and accompanying vessels. Its attachments are variable, but it usually passes from a depression medial to the tubercle of the rib to the inferior articular process and the base of the transverse process of the vertebra above.

Lateral costotransverse ligament The lateral costotransverse ligament is short, thick and strong. It passes obliquely from the apex of the transverse process of a vertebra to the rough non-articular part of the tubercle of the corresponding rib (see Figs 53.9, 53.12). The ligaments of the upper ribs appear to ascend from the transverse processes of the vertebrae, and are shorter and more oblique than those of the lower ribs, which appear to descend.

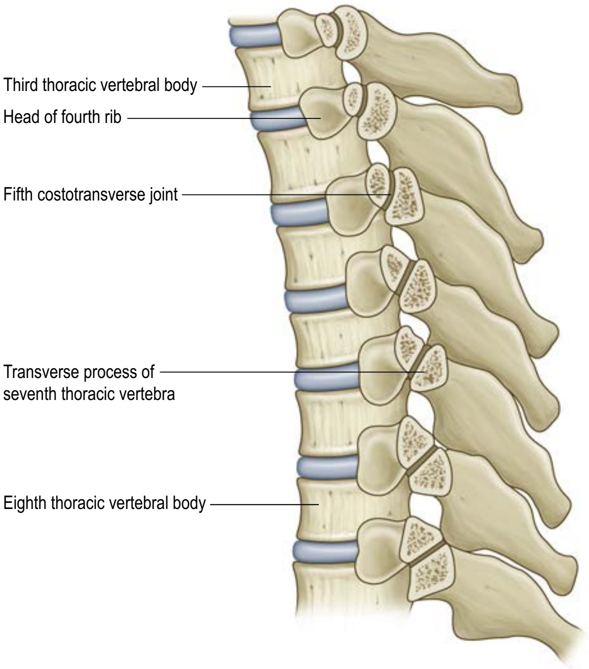
Third thoracic vertebral body
Head of fourth rib
Fifth costotransverse joint
Transverse process of seventh thoracic vertebra
Eighth thoracic vertebral body

Fig. 53.13 A section through the third to the ninth costotransverse joints. Note the concave facets on the superiorly located vertebral transverse processes and the less curved facets on the inferiorly located vertebral transverse processes.

Movements The strong, tight radiate and intra-articular ligaments attached to the head of a rib only permit slight gliding at the costovertebral joints. Strong ligaments bind the necks and tubercles of the ribs to the transverse processes of the vertebrae and limit movements at the costotransverse joints to slight gliding, guided by the shape and direction of the articular surfaces (see Fig. 53.13). The facets on the tubercles of the first six ribs are oval and vertically convex, and fit corresponding concavities on the anterior surfaces of the transverse processes of the vertebrae; up and down movements of tubercles consequently involve rotation of the costal necks about their long axes. The facets on the tubercles of the seventh to tenth ribs are almost flat and face posteriorly, inferiorly and medially; the opposing articular surfaces are located on the superior aspects of the transverse processes, which means that when these tubercles move superiorly, they also move posteromedially. Both the costovertebral and costotransverse joints move simultaneously and in the same directions; the neck of a rib therefore moves as if at a single joint in which the costovertebral and costotransverse joints form its ends.

The main movement of the neck of each of the first six ribs is one of rotation about its long axis (a slight superior–inferior movement is also seen): a downward rotation of its anterior surface is therefore associated with depression, and an upward rotation with elevation, of the shaft and anterior end of the rib. The shape of the costotransverse joint in the seventh to tenth ribs means that the neck of the rib ascends posteromedially or descends anterolaterally, increasing or decreasing the infrasternal angle, respectively; slight rotation accompanies these movements.

Sternocostal joints

The costal cartilages articulate with small concavities (costal notches) on the lateral sternal borders at the sternocostal joints (**Fig. 53.14**). The first sternocostal joint is an unusual type of synarthrosis (fibrous joint) and is often inaccurately called a synchondrosis. The second to seventh sternocostal joints are synovial, although articular cavities are often absent, particularly in the lower joints. Fibrocartilage covers the articular surfaces and also unites the costal cartilages and the sternum in those joints where cavities are absent. The seventh sternocostal joint may be synovial or symphysial. Ligaments associated with the joints include capsular, radiate sternocostal, intra-articular and costoxiphoid.

Fibrous capsules Fibrous capsules surround the second to seventh sternocostal joints. They are thin, blended with the sternocostal ligaments, and strengthened superiorly and inferiorly by fibres that connect the costal cartilages to the sternum.

Radiate sternocostal ligaments The radiate sternocostal ligaments are broad, thin bands that radiate from the anterior and posterior

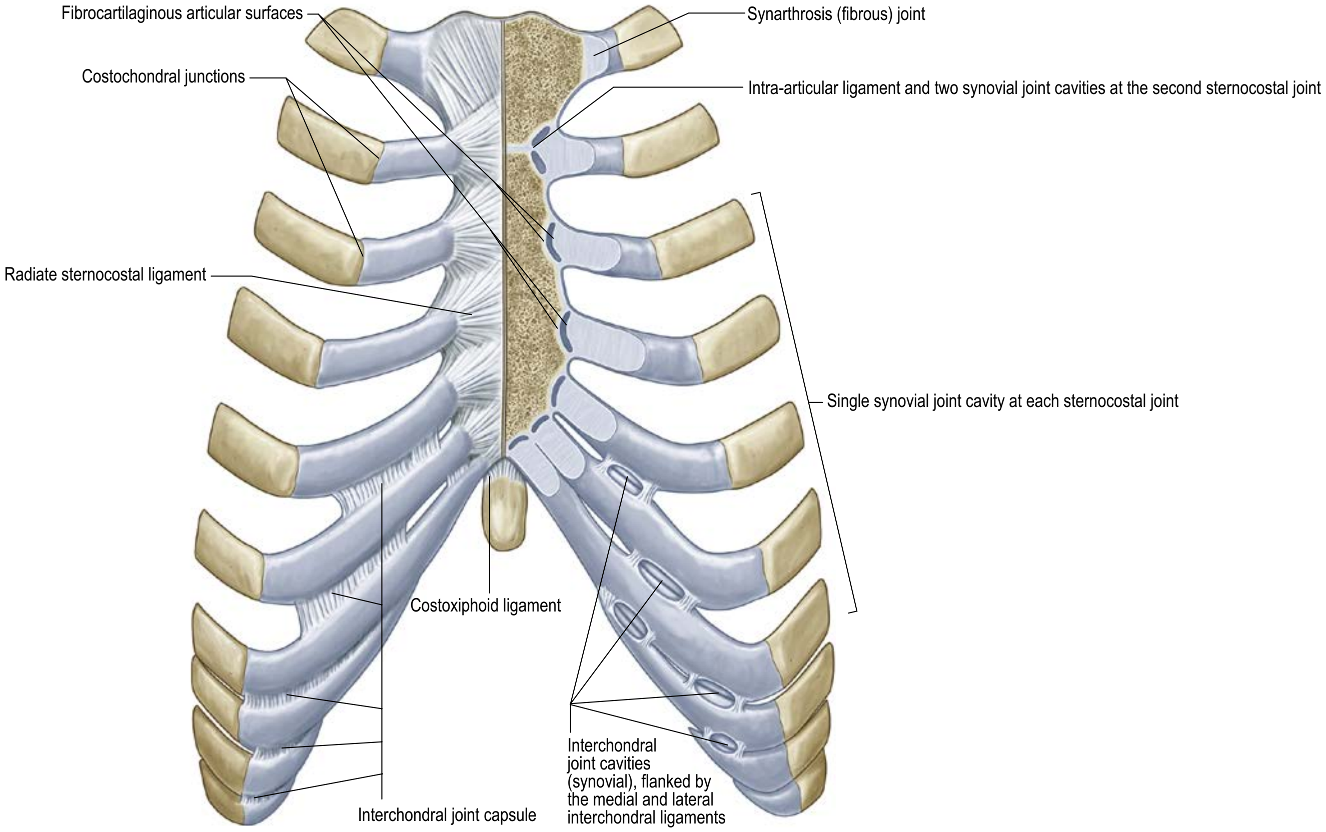
Fibrocartilaginous articular surfaces
Costochondral junctions
Radiate sternocostal ligament
Synarthrosis (fibrous) joint
Intra-articular ligament and two synovial joint cavities at the second sternocostal joint
Single synovial joint cavity at each sternocostal joint
Costoxiphoid ligament
Interchondral joint capsule
Interchondral joint cavities (synovial), flanked by the medial and lateral interchondral ligaments

Fig. 53.14 Sternocostal and interchondral joints, anterior aspect.

surfaces of the sternal ends of the costal cartilages of the true ribs to the adjacent corresponding sternal surfaces. Their superficial fibres intermingle with adjacent ligaments superiorly and inferiorly, with those of the contralateral side and with tendinous fibres of pectoralis major. Collectively, these tissues form a thick fibrous membrane around the sternum that is more apparent inferiorly.

Intra-articular ligaments Intra-articular ligaments are constant only between the second costal cartilages and the manubriosternal joint. The ligament associated with the second costal cartilage extends from the costal cartilage to the fibrocartilage uniting the manubrium and sternal body, and is therefore intra-articular. Occasionally, the third costal cartilage is connected with the first and second sternal segments (sternebrae) by a similar ligament. Fibrocartilaginous strands may occur in the third to seventh joints. Articular cavities may be absent at any age.

Costoxiphoid ligaments Costoxiphoid ligaments connect the anterior and posterior surfaces of the seventh (and sometimes sixth) costal cartilage to the same surfaces of the xiphoid process. They vary in length and breadth, and the posterior is less distinct.

Movements Small gliding movements, sufficient for ventilation, occur at the sternocostal joints.

Interchondral joints

Adjoining borders of the sixth to ninth costal cartilages articulate by apposition of small oblong facets. Each articulation is enclosed in a thin fibrous capsule, lined by synovial membrane, with lateral and medial interchondral ligaments. Sometimes the fifth cartilage articulates inferiorly with the sixth; this connection is usually formed by ligamentous fibres. Articulation between the ninth and tenth cartilages is never synovial, often fibrous and sometimes absent.

Costochondral junctions

When artificially separated from its rib, a costal cartilage has a rounded lateral end that fits a reciprocal depression in the rib. Periosteum and perichondrium are continuous across the costochondral junctions and the collagen of the osseous and cartilaginous matrices blend. No movement occurs at costochondral junctions. Costochondritis is a common condition of unknown aetiology that presents as pain and tenderness of the costochondral or sternocostal joints due to involvement of cutaneous intercostal nerve branches; a prevalence of 30% has been reported amongst patients presenting to an emergency department with chest pain (Gregory et al 2002).

MUSCLES

The intrinsic muscles of the chest wall are the intercostals, subcostales, transversus thoracis, levatores costarum, serratus posterior superior and inferior and, occasionally, sternalis (**Figs 53.15–53.16**). Scapular muscles and muscles connecting the upper limb, chest wall and vertebrae, i.e. trapezius, latissimus dorsi, rhomboids major and minor, levator scapulae, pectorales major and minor, and subclavius, are described in Chapter 49.

Intrinsic chest wall muscles

Intercostal muscles

The intercostal muscles are thin, consist of muscular and tendinous fibres and are arranged in layers within each intercostal space. Their names are derived from their positional relationship to each other, i.e. the external, internal and innermost intercostals (**Fig. 53.17**). There are 11 pairs of external and internal intercostal muscles, the innermost intercostal has a variable presence.

External intercostals

The external intercostal muscles pass between adjacent ribs, from the tubercle of the rib, where they blend with the posterior layer of the superior costotransverse ligaments, almost to the costal cartilage, where each continues forwards to the sternum as an aponeurotic layer, the external intercostal membrane (see Fig. 53.18). Each muscle passes from the inferior border of one rib to the superior border of the rib below; their fibres are angled obliquely inferiorly and laterally in the posterior part of an intercostal space, inferiorly and anteriorly in the lateral part of the space and inferiorly and medially in the anterior part of the space. They do not quite reach the anterior ends of the rib in the first two or three spaces, and they extend to the free ends of the costal cartilages in the tenth and eleventh spaces. The external intercostals are thicker than the internal intercostals.

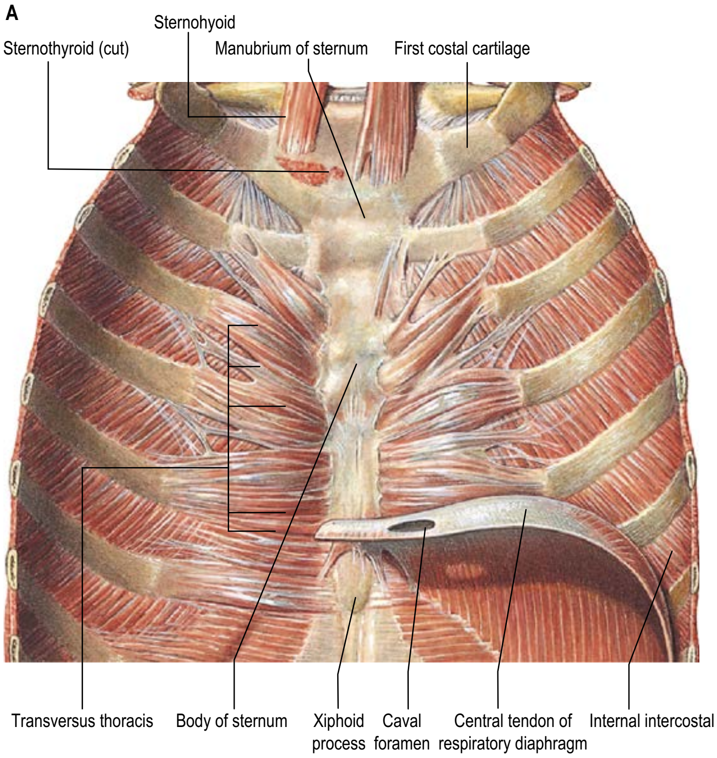
A
Sternohyoid
Sternothyroid (cut)
Manubrium of sternum
First costal cartilage
Transversus thoracis
Body of sternum
Xiphoid process
Caval foramen
Central tendon of respiratory diaphragm
Internal intercostal

Fig. 53.15 Muscles of the thoracic wall. **A**, The left transversus thoracis, exposed and viewed from its posterior aspect. The inferior part of transversus thoracis is in contact with the superior part of transversus abdominis in the interval between the sternal and costal origins of the respiratory diaphragm. (Sobotta Atlas of Human Anatomy © Elsevier GmbH, Urban & Fischer, Munich.) (B–D, *continued online*)

Innervation The external intercostals are innervated by the adjacent intercostal nerves.

Internal intercostals The internal intercostals pass between adjacent ribs, from the lateral border of the sternum or the anterior limits of the costal cartilages of the 'false' ribs, to the angle of the rib, where each is replaced by an aponeurotic layer, the internal intercostal membrane, that is continuous posteriorly with the anterior layer of a superior costotransverse ligament, and anteriorly with the fascia between the internal and external intercostal muscles. The muscle is thickest anteriorly, in its intercartilaginous or parasternal part. Each muscle descends from the floor of a costal groove and adjacent costal cartilage, and inserts into the superior border of the rib below; the muscle fibres are directed obliquely, nearly at right-angles to those of the external intercostal muscles.

Innervation The internal intercostals are supplied by the adjacent intercostal nerves.

Innermost intercostals

The innermost intercostals were once regarded as internal laminae of the internal intercostal muscles, especially since fibres in the two layers coincide in direction. Each muscle is attached to the internal aspects of two adjoining ribs. They are insignificant, and sometimes absent, in the upper intercostal spaces but become progressively more substantial in the lower spaces, typically extending through the middle two quarters of the intercostal spaces. Posteriorly, the innermost intercostals, in those spaces where they are well developed, may come together with the corresponding subcostales (see Fig. 53.15B). The innermost intercostals are related internally to the endothoracic fascia and costal parietal pleura, and externally to the intercostal nerves and vessels.

Innervation The innermost intercostals are innervated by the adjacent intercostal nerves.

Actions Contraction of the intercostal muscles during inspiration and expiration varies according to the intercostal space in which they are located and the position of the muscles within that space (Ch. 55). The intercostal muscles contribute to rigidity of the thoracic wall, helping to maximize inspiratory and expiratory volumes.

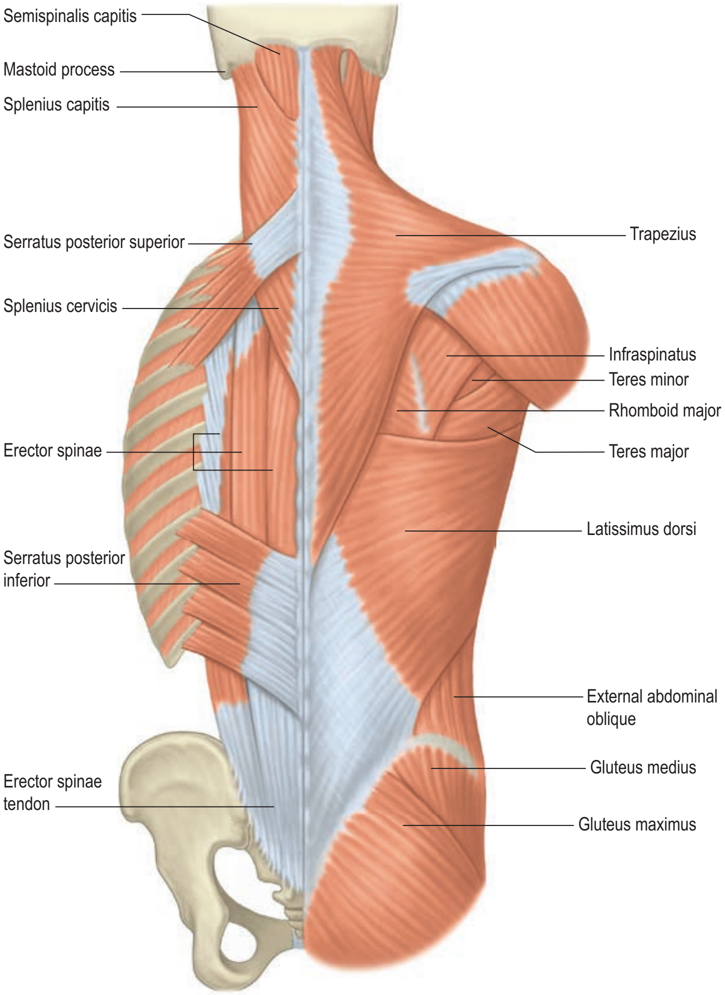
Semispinalis capitis
Mastoid process
Splenius capitis
Serratus posterior superior
Splenius cervicis
Trapezius
Infraspinatus
Teres minor
Rhomboid major
Teres major
Erector spinae
Latissimus dorsi
Serratus posterior inferior
External abdominal oblique
Gluteus medius
Erector spinae tendon
Gluteus maximus

Fig. 53.16 Superficial (extrinsic) muscles of the back.

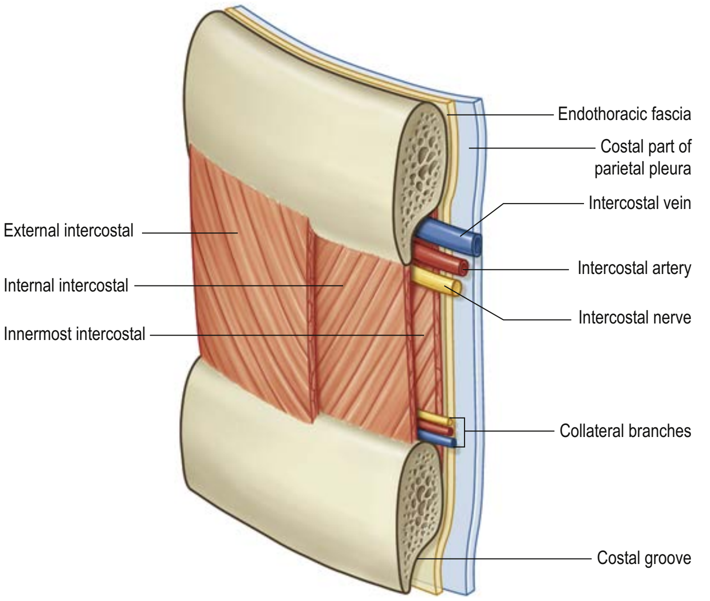
Endothoracic fascia
Costal part of parietal pleura
Intercostal vein
External intercostal
Intercostal artery
Internal intercostal
Intercostal nerve
Innermost intercostal
Collateral branches
Costal groove

Fig. 53.17 A right intercostal space, external aspect, showing the position of the intercostal vessels and nerve and their collateral branches relative to the intercostal muscles, and the position of the endothoracic fascia and costal parietal pleura.

Transversus thoracis

Transversus thoracis spreads over the internal surface of the anterior thoracic wall (see Fig. 53.15A). It arises from the inferior half to inferior third of the posterior surface of the sternum, the xiphoid process and the sternal ends of the fifth (sometimes fourth) to seventh costal cartilages. The fibres diverge as separate slips that pass superiorly and laterally to the inferior borders and internal surfaces of the costal cartilages

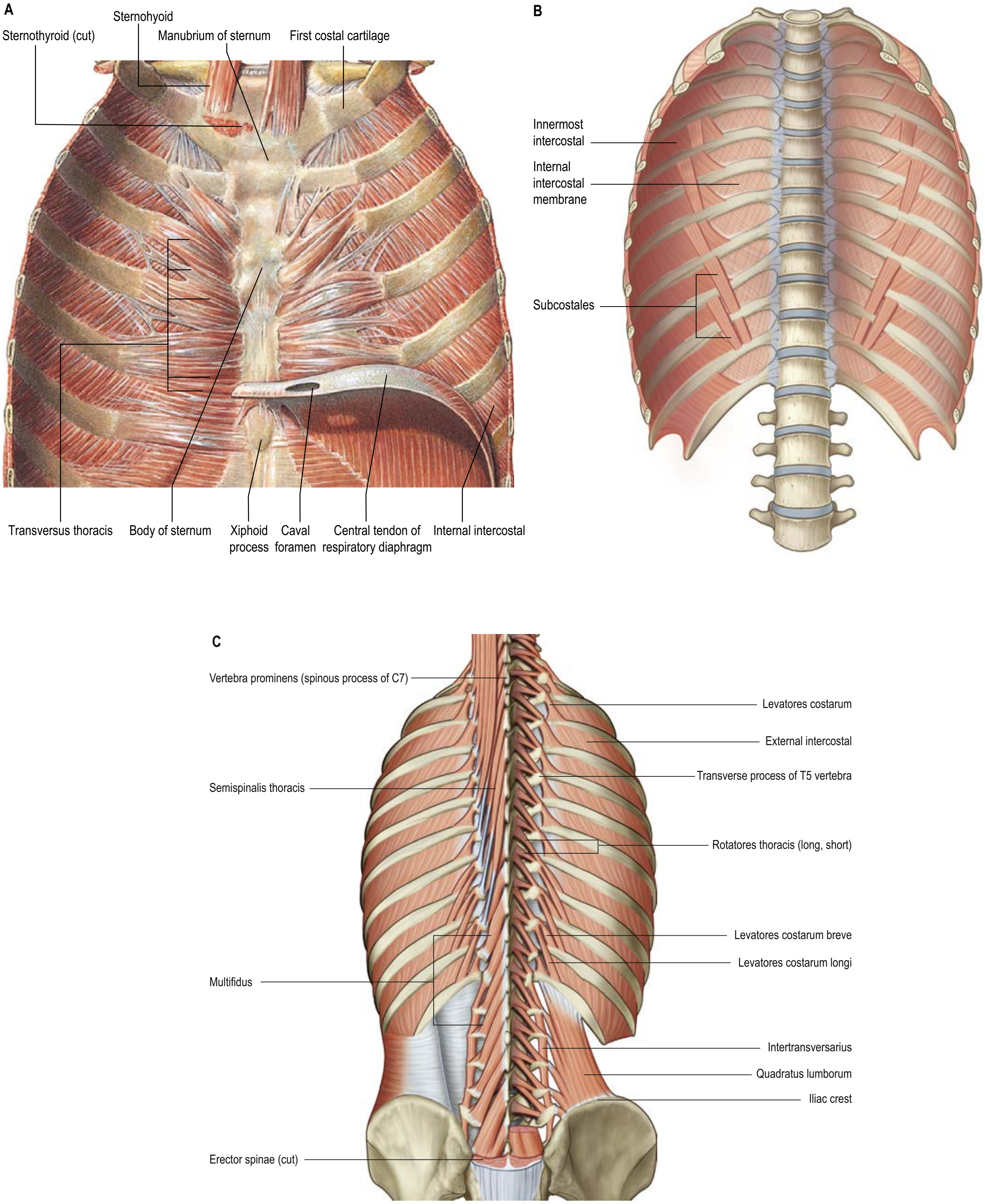
A
Sternohyoid
Sternothyroid (cut)
Manubrium of sternum
First costal cartilage
Transversus thoracis
Body of sternum
Xiphoid process
Caval foramen
Central tendon of respiratory diaphragm
Internal intercostal
B
Innermost intercostal
Internal intercostal membrane
Subcostales
C
Vertebra prominens (spinous process of C7)
Levatores costarum
External intercostal
Transverse process of T5 vertebra
Semispinalis thoracis
Rotatores thoracis (long, short)
Levatores costarum breve
Levatores costarum longi
Multifidus
Intertransversarius
Quadratus lumborum
Iliac crest
Erector spinae (cut)

Fig. 53.15 Muscles of the thoracic wall. **A**, The left transversus thoracis, exposed and viewed from its posterior aspect. The inferior part of transversus thoracis is in contact with the superior part of transversus abdominis in the interval between the sternal and costal origins of the respiratory diaphragm. **B**, Subcostales (internal surface of posterior thoracic wall). **C**, Levatores costarum (external surface of posterior thoracic wall). (A,D, Sobotta Atlas of Human Anatomy © Elsevier GmbH, Urban & Fischer, Munich. B,C, With permission from Drake RL, Vogl AW, Mitchell A et al (eds) Gray's Atlas of Anatomy, 2nd ed. Elsevier, Churchill Livingstone. Copyright 2015.)

Continued

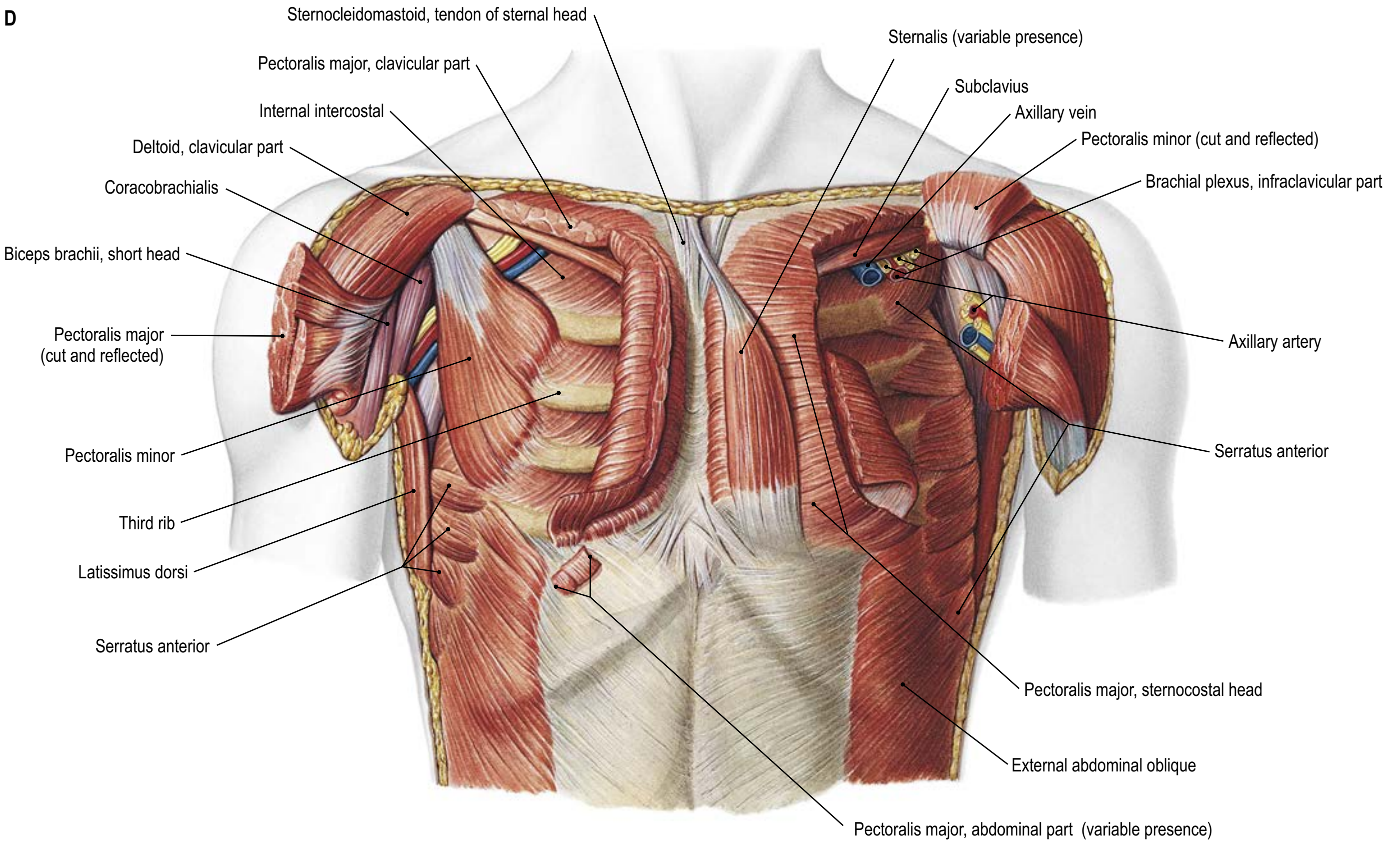
D
Sternocleidomastoid, tendon of sternal head
Sternalis (variable presence)
Pectoralis major, clavicular part
Subclavius
Internal intercostal
Axillary vein
Deltoid, clavicular part
Pectoralis minor (cut and reflected)
Coracobrachialis
Brachial plexus, infraclavicular part
Biceps brachii, short head
Pectoralis major
(cut and reflected)
Axillary artery
Pectoralis minor
Serratus anterior
Third rib
Latissimus dorsi
Serratus anterior
Pectoralis major, sternocostal head
External abdominal oblique
Pectoralis major, abdominal part (variable presence)

Fig. 53.15 D, Sternalis (external surface of anterior thoracic wall). (A,D, Sobotta Atlas of Human Anatomy © Elsevier GmbH, Urban & Fischer, Munich. B,C, With permission from Drake RL, Vogl AW, Mitchell A et al (eds) Gray's Atlas of Anatomy, 2nd ed. Elsevier, Churchill Livingstone. Copyright 2015.)

The use of pectoral nerve block (Pecs) and serratus anterior plane block (SAPB) to provide analgesia and anaesthesia to the anterior and anterolateral chest wall to manage postsurgical thoracic pain is well documented. These blocks alone are often insufficient to fully block the territory of the anterior cutaneous nerves that innervate the anterior chest wall in the sternal and medial breast/pectoral regions, and often leave a patient with postoperative residual pain. Recent advances in fascial plane blocks have enabled more effective delivery of analgesia to these regions (Piraccini et al 2018). In a parasternal intercostal nerve block (PSI), local anaesthetic is injected between the fascial planes of pectoralis major and the external intercostal muscle, blocking the anterior branches of the intercostal nerves. In a parasternal block (PSB) local anaesthetic is injected in the region between the fascial planes of pectoralis major and the internal intercostal muscles, blocking the anterior branches of the second to seventh thoracic intercostal nerves. In a transversus thoracis plane block (TTP), local anaesthetic is injected between the fascial planes of the internal intercostal muscles and transversus thoracis. Compared to Pecs and SAPB, the PSI, PSB and TTP fascial plane blocks have been shown to decrease postsurgical opioid consumption, and provide long-lasting pain relief, including in the anterior thoracic wall (Versyck et al 2017).

of the second to sixth ribs. The inferiormost fibres are horizontal and are contiguous with the superiormost fibres of transversus abdominis; the intermediate fibres are oblique; and the superiormost are almost vertical. Transversus thoracis varies in its attachments, between individuals and on opposite sides of the same individual. Similar in arrangement to the innermost intercostals and subcostales, transversus thoracis separates the intercostal neurovascular bundle (and also the internal thoracic artery and vein) from the costal part of the parietal pleura.

Innervation Transversus thoracis is innervated by the adjacent intercostal nerves.

Action Transversus thoracis depresses the costal cartilages to which it is attached.

Subcostales

Subcostales consist of muscular and aponeurotic fasciculi and are usually better developed in the lower (inferior) part of the internal surface of the posterior thoracic wall (see Fig. 53.15B). Each passes inferomedially from the internal surface of a rib, near its angle, to the internal surface of the second or third rib below (inferior). Their fibres run parallel to those of the internal intercostals and, like the innermost intercostals, they lie between the intercostal neurovasculature and the endothoracic fascia and costal part of the parietal pleura.

Innervation The subcostales are innervated by the adjacent intercostal nerves.

Action Subcostales depress the ribs.

Levatores costarum

Levatores costarum are strong bundles of muscle fibres located on the external surface of the thoracic wall that arise from the tips of the transverse processes of the seventh cervical and first to eleventh thoracic vertebrae (see Fig. 53.15C). They pass obliquely inferolaterally, parallel with the posterior borders of the external intercostal muscles. Each is attached to the superior border and external surface of the rib located immediately inferior to the vertebra from which it takes origin, between the tubercle and the angle of the rib (levatores costarum breve). Each of the four lower levatores costarum divides into two fasciculi; one is attached as already described, and the other descends to attach to the second rib inferior to its vertebral origin (levatores costarum longi).

Innervation Levatores costarum are innervated by the lateral branches of the dorsal rami of the corresponding cervical or thoracic spinal nerves (commonly C8–T11).

Action Levatores costarum elevate the ribs but their role and importance in ventilation is disputed. From their costal attachments they may assist in rotation and lateral flexion of the vertebral column.

Serratus posterior superior

Serratus posterior superior (see Fig. 53.16) is a thin quadrilateral muscle, located on the superior part of the posterior thoracic wall. It arises by a thin aponeurosis from the inferior part of the nuchal ligament, the spinous processes of the seventh cervical and first (superior) two or three thoracic vertebrae, and the associated supraspinous ligaments. It passes inferiorly and laterally and ends in four digitations attached to the superior borders and external surfaces of the second to fifth ribs, just lateral to their angles. It is superficial to the thoracic part of the thoracolumbar fascia and deep to rhomboid minor and major. The number of digitations can vary from three to six, and the muscle may be absent. Regional pain has been reported over the location of the muscle in myofascial pain syndromes.

Innervation Serratus posterior superior is innervated by the second to fifth intercostal nerves.

Action The attachments of serratus posterior superior indicate that it could elevate the ribs, although its role in ventilation in humans is uncertain. It may have a greater role in proprioception related to thoracic movement.

Serratus posterior inferior

Serratus posterior inferior (see Fig. 53.16) is a thin, irregularly quadrilateral muscle located on the posterior trunk at the junction of the thoracic and lumbar regions. It arises from the spinous processes of the last (inferior) two thoracic and first (superior) two or three lumbar vertebrae and the associated supraspinous ligaments by a thin aponeurosis that blends with the lumbar part of the thoracolumbar fascia. It passes superolaterally and its four digitations pass into the inferior borders and external surfaces of the last (inferior) four ribs, just lateral to their angles. There may be fewer than four digitations and, in rare cases, the entire muscle may be absent.

Innervation Serratus posterior inferior is innervated by ventral rami of the ninth to twelfth thoracic spinal nerves.

Action The attachments of serratus posterior inferior indicate that it could depress the ribs, although its role in ventilation in humans is uncertain. It may have a greater role in proprioception related to thoracic movement.

Sternalis

Sternalis is an anatomical variation well known to anatomists but relatively unknown to clinicians and surgeons (Snosek et al 2014) (see Fig. 53.15D). The muscle appears as a parasternal mass deep to the superficial fascia of the anterior thoracic wall and superficial to the pectoral fascia overlying pectoralis major. It may be a cord-like, flat band or irregular and flame-like in shape, it may present with a single, double or triple-bellied arrangement (Dudgeon et al 2017). It is almost twice as common unilaterally, and occurs more often on the right side. Various attachment sites have been described, including the sternum, inferior border of the clavicle, sternocleidomastoid fascia, pectoralis major, and the upper ribs and their costal cartilages, all superiorly, and the lower ribs and their costal cartilages, pectoralis major, the rectus sheath and the aponeurosis of external abdominal oblique, all inferiorly. Attachments may be contralateral and bilateral sternalis muscles may join. Most documented variants are innervated by either the medial pectoral nerve or an intercostal nerve. The muscle occurs in about 8% of the general population, but there is great variation both within and between different geographic populations (Snosek and Loukas 2016). Its superficial location makes it an ideal candidate for utilization as a muscular flap in plastic reconstruction of the head and neck region. For more extensive thoracic wall defect repairs, external abdominal oblique can be utilized as a muscular flap (Wang et al 2018).

Mechanism of thoracic cage movement

Breathing involves changing the thoracic volume by altering the vertical, transverse and anteroposterior dimensions of the thorax. The anatomy of breathing is considered in Chapter 55.

VASCULAR SUPPLY AND LYMPHATIC DRAINAGE OF THE CHEST WALL

Arteries

Muscles of the thoracic wall receive their blood supply from branches of the subclavian and axillary arteries and the descending thoracic aorta (see Fig. 52.3). Additional contributions come from vessels that supply the proximal muscles of the upper limb including the suprascapular, superficial cervical, thoraco-acromial, lateral thoracic and subscapular arteries.

Internal thoracic artery

The internal thoracic (mammary) artery arises inferiorly from the first part of the subclavian artery, approximately 2 cm superior to the sternal end of the clavicle and opposite the root of the thyrocervical trunk (see Fig. 52.3). It descends posterior to the first six costal cartilages and intervening intercostal spaces, about 1 cm lateral to the lateral sternal border and divides at the level of the sixth intercostal space into musculophrenic and superior epigastric branches. The superior epigastric artery is described in Chapter 60.

Both the right and left internal thoracic arteries are used as standard in coronary artery bypass grafting (CABG), reflecting successful long-term outcomes. Variations are rare; when present, however, they must be imaged prior to harvesting for CABG. Morphologically abnormal internal thoracic arteries have been shown to supply major parts of the gastrointestinal tract (Mashhour et al 2018).

Relations From its origin, the internal thoracic artery descends anteromedially, passing posterior to the sternal end of the clavicle, the internal jugular and brachiocephalic veins, and the first costal cartilage. As it enters the thoracic cavity, the phrenic nerve crosses it obliquely from its lateral side either superiorly or inferiorly (Ch. 55). The artery then descends

The aetiology is unknown: sternalis may be an example of a much larger group of variations, including pectoralis minimus, pectoralis tertius, infraclavicularis and chondroepitrochlearis, that are thought to be caused by a disturbance of the normal processes of pectoral muscle development. In rare cases sternalis can become symptomatic, causing painful soft tissue swelling in the parasternal region (Gruber et al 2016). The relationship of sternalis to pectoralis major may cause a diagnostic dilemma during breast surgery, mammography, computed tomography and magnetic resonance imaging scans because its appearance mimics tumour pathology of the region. The mammographic appearance of sternalis is variable. Typically visible in the medial aspect of the breast on a craniocaudal (CC) mammogram, it appears as a small soft tissue density or mass abutting the thoracic wall. Its margins and shape are variable. Sternalis is not usually seen on standard mediolateral oblique or mediolateral views.

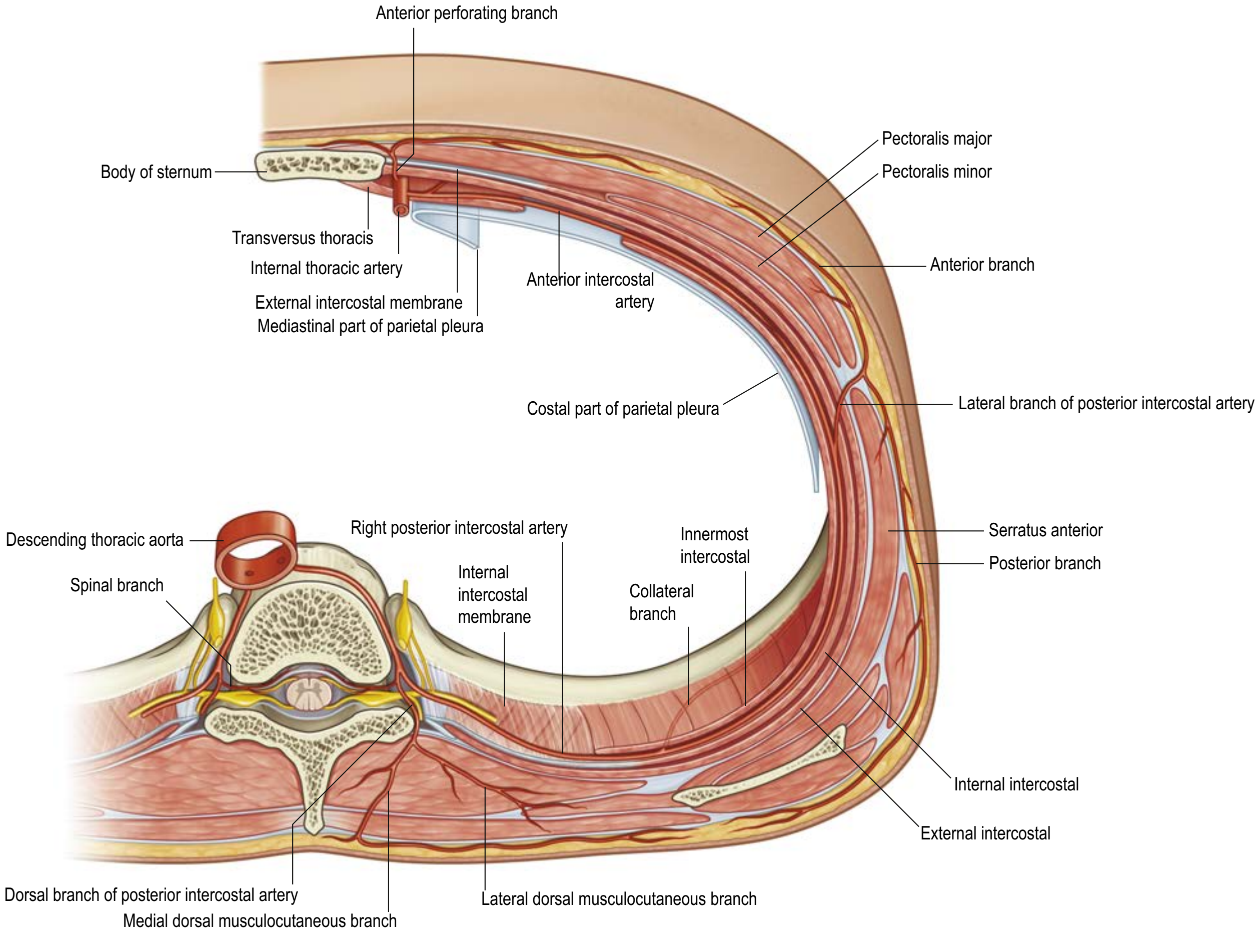
Anterior perforating branch
Body of sternum
Transversus thoracis
Internal thoracic artery
External intercostal membrane
Mediastinal part of parietal pleura
Anterior intercostal artery
Pectoralis major
Pectoralis minor
Anterior branch
Costal part of parietal pleura
Lateral branch of posterior intercostal artery
Descending thoracic aorta
Spinal branch
Right posterior intercostal artery
Internal intercostal membrane
Innermost intercostal
Collateral branch
Serratus anterior
Posterior branch
Internal intercostal
External intercostal
Dorsal branch of posterior intercostal artery
Medial dorsal musculocutaneous branch
Lateral dorsal musculocutaneous branch

Fig. 53.18 A transverse section through an intercostal space, showing the course and branching of a typical intercostal artery. Collateral branches are shown.

almost vertically to its bifurcation, lying anterior to transversus thoracis and posterior to the first six costal cartilages, internal intercostals and terminations of the first six intercostal nerves. Down to the second or third cartilage it is separated from the costal parietal pleura and its associated endothoracic fascia by a strong layer of fascia, and below this by transversus thoracis (see Fig. 53.18). The artery is accompanied by the parasternal lymph nodes (see Fig. 56.4A) and by venae comitantes that unite at about the third costal cartilage into a single vein medial to the artery. Its intermediate branches are sternal, anterior intercostal and perforating.

Sternal branches Sternal branches are distributed to transversus thoracis, the periosteum of the posterior sternal surface and the sternal red bone marrow. These branches, together with small branches of the pericardiacophrenic artery, anastomose with branches of the posterior intercostal and bronchial arteries to form a subpleural mediastinal plexus.

Anterior intercostal branches Anterior intercostal arteries are distributed to the first six intercostal spaces. They usually arise from the internal thoracic artery as single vessels that promptly divide into two branches (anterior and collateral intercostal arteries) that pass laterally along the superior and inferior borders of each space and anastomose with the posterior intercostal arteries and their collateral branches (Figs 53.17–53.18). Occasionally, separate branches of the anterior intercostal artery pass to the intercostal space located superiorly and/or inferiorly, or the two branches of an anterior intercostal artery may arise separately from the internal thoracic artery. At first, the arteries lie between the endothoracic fascia and associated costal parietal pleura posteriorly, and the internal intercostals anteriorly. As they pass posteriorly within a space they lie between the innermost and internal intercostals. They supply the intercostal muscles and send branches through them to the pectoral muscles, breast and skin.

Perforating branches Perforating branches traverse the first five or six intercostal spaces with the anterior cutaneous branches of the corresponding intercostal nerves. They pierce and supply pectoralis major, and then curve laterally to become cutaneous vessels that supply the skin (see Figs 53.18, 52.3). These cutaneous vessels provide the anatomical basis for surgically raising the deltopectoral skin flap that is used for reconstructing areas of missing tissue in the head and neck. The second to fourth branches supply the breast and become enlarged during lactation (see Fig. 53.22).

Musculophrenic artery The musculophrenic artery passes inferolaterally posterior to the seventh to ninth costal cartilages, close to the costal arch, then traverses the respiratory diaphragm and terminates near the eleventh (last) intercostal space (see Figs 52.3, 55.2). It anastomoses with the inferior phrenic and tenth and eleventh posterior intercostal arteries and ascending branches of the deep circumflex iliac arteries. Two anterior intercostal arteries branch from it for each of the seventh to ninth intercostal spaces, and are distributed similarly to their counterparts in other intercostal spaces. The musculophrenic artery also supplies the inferior part of the pericardium and the abdominal muscles.

Clinical significance of the internal thoracic artery

Available with the *Gray's Anatomy* e-book

Supreme intercostal artery

The supreme (highest) intercostal artery arises from the costocervical trunk. It descends between the parietal pleura (and its associated endothoracic fascia), and the neck of the first and second ribs, and anastomoses with the third posterior intercostal artery. As it crosses the neck of the first rib, it lies medial to the ventral ramus of the first thoracic spinal nerve, and lateral to the stellate ganglion (see Fig. 55.10). In the first intercostal space it gives off the first posterior intercostal artery, which has a similar distribution to the more inferiorly located posterior intercostal arteries. It descends to become the second posterior intercostal artery, usually also joining a branch from the third. The artery is not constant, and is more common on the right: when absent, it is replaced by a direct branch from the thoracic aorta.

Posterior intercostal arteries

There are usually nine pairs of posterior intercostal arteries. They arise from the posterior aspect of the descending thoracic aorta and are

The internal thoracic artery has a number of clinical uses but perhaps most significant is that it is the vessel of choice for coronary artery bypass grafting. It has become a commonly selected recipient vessel for free flap transfers to the chest wall, principally for breast reconstruction (Ninković et al 1995), and has largely superseded the thoracodorsal vessels for this purpose. It is routinely accessed by removing a portion of the third costal cartilage (**Fig. 53.19**), although some surgeons prefer to dissect the vessels between the ribs, with a rib-sparing approach (Parrett et al 2008, Malata et al 2011) or even utilizing the anterior perforating branches as they pierce pectoralis major (Park et al 2003, Munhoz et al 2004). The anterior perforating branches form the vascular pedicles for fasciocutaneous flaps raised from the anterior chest wall that have been used for many decades in head and neck reconstruction (Bakamjian et al 1971, Neligan et al 2007). The superior epigastric artery is the main vascular pedicle for the superiorly based rectus abdominis flap, a muscle or myocutaneous flap useful in breast, sternal and chest wall reconstruction (Hartrampf et al 1982). During CT-guided lung and mediastinal biopsies, the internal thoracic vessels must be avoided; exsanguination has been reported following Tru-Cut needle trauma: the approach must be at least 2 cm lateral to the sternal margin. The vessels are not seen easily on non-contrast fluoroscopic CT images.

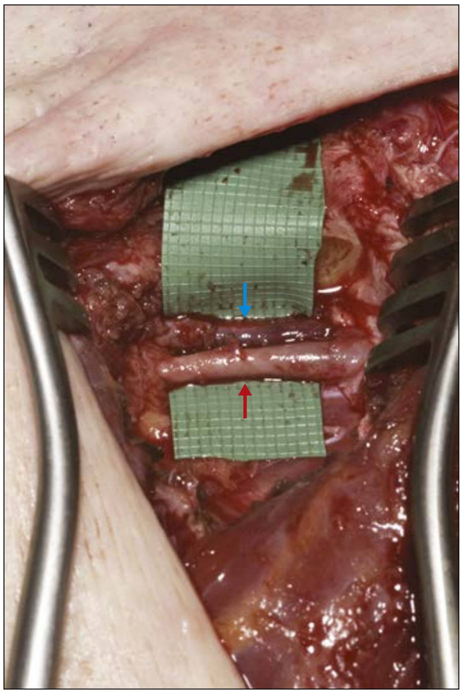

Fig. 53.19 The internal thoracic vessels prepared for micro-anastomosis beneath the third costal cartilage. The dissected internal thoracic artery (red arrow) and vein (blue arrow) are shown after removal of the right third costal cartilage. These vessels are divided to provide recipient blood supply for a free tissue transfer.

distributed to the third to eleventh intercostal spaces. The right posterior intercostal arteries are longer because the descending thoracic aorta deviates to the left (see Fig. 53.18): they cross the vertebral bodies posterior to the oesophagus, thoracic duct and azygos vein, and the parietal pleura covering the right lung. The left posterior intercostal arteries travel posteriorly across the vertebral bodies and are in contact with the parietal pleura covering the left lung; the first and second (branches of the supreme intercostal artery) are crossed by the left superior intercostal vein, and those located inferiorly are crossed by the hemiazygos and accessory hemiazygos veins. The sympathetic trunk and ganglia lie anterior to all of the arteries, and the thoracic splanchnic nerves are anterior to the more inferiorly located arteries.

Each artery crosses its intercostal space obliquely towards the angle of the rib above and continues forwards in its costal groove. It runs between the costal parietal pleura (and its associated endothoracic fascia), and the internal intercostal membrane as far as the angle of the rib, then passes between the internal and innermost intercostal muscles (see Fig. 53.17) and anastomoses with an anterior intercostal branch from either the internal thoracic or musculophrenic artery. Each artery is accompanied by a vein superiorly and a nerve inferiorly, except in the first three or four spaces, where the nerve is initially superior to the artery. The third posterior intercostal artery anastomoses with the supreme intercostal artery and may provide the major supply to the second intercostal space. The inferior two posterior intercostal arteries continue anteriorly into the abdominal wall, where they anastomose with the subcostal, superior epigastric and lumbar arteries (see Fig. 52.3). Each posterior intercostal artery has dorsal, collateral, muscular and cutaneous branches (see Fig. 53.18).

Dorsal branch Each dorsal branch passes posteriorly in the space between the necks of adjacent ribs (superiorly and inferiorly), the adjacent vertebral body (medially) and the superior costotransverse ligament (laterally) (see Fig. 53.11). Each dorsal branch gives off a spinal branch that enters the vertebral canal via the intervertebral foramen and supplies the vertebra, spinal cord and meninges, anastomosing with the spinal arteries located immediately superior, inferior and contralateral (see Fig. 53.18). It then divides into a medial and a lateral dorsal musculocutaneous branch; occasionally these arise separately from the posterior intercostal artery rather than from a common trunk. The medial branch crosses the transverse process of a vertebra with the medial branch of the dorsal ramus of a thoracic spinal nerve to supply spinalis, longissimus thoracis and an area of overlying skin. The lateral branch supplies longissimus thoracis and iliocostalis, and the medial aspects of latissimus dorsi and trapezius, in addition to an area of overlying skin (see Fig. 53.2).

Collateral intercostal branch A collateral intercostal branch arises near the angle of a rib and descends across the intercostal space to the superior border of the rib below, along which it courses to anastomose with its partner branch from the anterior intercostal branch of the internal thoracic or musculophrenic artery.

Muscular branches Muscular branches supply the intercostal and pectoral muscles and serratus anterior, and anastomose with the superior and lateral thoracic branches of the axillary artery. Mammary branches from the anterior intercostal vessels in the second to fourth spaces supply the pectoral muscles, breast tissue and covering skin, and enlarge during lactation.

Lateral cutaneous branch The lateral cutaneous branch arises in the posterior part of the intercostal space and travels anteriorly for a few centimetres with an accompanying vein and the lateral cutaneous branch of the accompanying intercostal nerve (see Fig. 53.21). This neurovascular bundle pierces the intercostal muscles and passes slightly inferiorly to emerge between the interdigitations of serratus anterior and external abdominal oblique. It divides into anterior and posterior branches that contribute to the blood supply of the skin of the lateral trunk (see Fig. 53.2); these vessels are less significant in the first three intercostal spaces.

Unnamed branches Unnamed branches supply tissues of the thoracic wall including the costal periosteum, bone and bone marrow of the ribs, tissues of the synovial and synarthrodial joints, and the parietal pleura and tissues of the extrapleural space.

Clinical significance of the posterior intercostal arteries

Available with the *Gray's Anatomy* e-book

Veins

Internal thoracic veins

The internal thoracic veins are formed by the union of the venae comitantes associated with the inferior half of the internal thoracic artery. Near the third costal cartilage, the veins unite and ascend medial to the artery to drain into the ipsilateral brachiocephalic vein. The internal thoracic veins have several valves. Their tributaries correspond to the branches of the internal thoracic artery and include the pericardiacophrenic veins, which run parallel to the phrenic nerves. The phrenic nerves are surrogate markers of the thymic border but are difficult to detect on CT: the pericardiacophrenic veins can therefore be used in their place as an important landmark when differentiating thymic versus non-thymic tumours (Ozawa et al 2018). The small anterior intercostal veins are tributaries of the internal thoracic and musculophrenic veins.

Left superior intercostal vein

The left superior intercostal vein drains the second and third (sometimes fourth) left posterior intercostal veins (see Fig. 56.7B). It ascends obliquely anteriorly across the left aspect of the aortic arch, lateral to the left vagus nerve and medial to the left phrenic nerve, to open into the left brachiocephalic vein. It usually receives the left bronchial veins and sometimes the left pericardiacophrenic vein, and connects inferiorly with the accessory hemiazygos vein. It may be seen on a chest X-ray as the 'aortic nipple', not to be confused with a small lung nodule.

Posterior intercostal veins

The eleven pairs of posterior intercostal veins accompany their respective arteries (see Fig. 52.4). Approaching the vertebral column, each vein receives a posterior tributary that returns blood from the dorsal musculature and skin and the external vertebral venous plexuses, and an intervertebral vein that drains the internal vertebral venous plexus. On both sides, the first posterior (supreme) intercostal vein ascends anterior to the neck of the first rib, then arches anteriorly, close to the lung apex to drain into the ipsilateral brachiocephalic or vertebral vein. On the right side, the second, third and often the fourth veins form a right superior intercostal vein that drains into the arch of the azygos vein. The more inferior intercostal spaces drain directly into the azygos vein. On the left side, the second, third and sometimes the fourth veins form a left superior intercostal vein. Veins from the fifth (sometimes fourth) to eighth intercostal spaces drain into the accessory hemiazygos vein, and veins from the ninth to the eleventh intercostal spaces drain into the hemiazygos vein; it should be remembered that the azygos system is highly variable.

Lymphatic drainage

Superficial lymphatic vessels of the thoracic wall ramify subcutaneously and converge on the axillary nodes (see Figs 53.22, 46.5). Those superficial to trapezius and latissimus dorsi unite to form up to twelve trunks that end in the subscapular (posterior axillary) nodes. Those in the pectoral region, including vessels from the skin covering the periphery of the breast and its subareolar plexus, run back, collecting those superficial to serratus anterior, to reach the pectoral (anterior axillary) nodes. Vessels near the lateral sternal margin pass between the costal cartilages to the parasternal nodes and anastomose across the sternum, providing a route for contralateral nodal spread in medially located breast carcinoma. A few vessels from the upper pectoral region ascend over the clavicle to the inferior deep cervical nodes. Lymph from the deeper tissues of the thoracic walls drains mainly to the parasternal, intercostal or diaphragmatic (phrenic) nodes.

Parasternal (internal thoracic) nodes

There are four or five parasternal nodes along each internal thoracic artery at the anterior ends of the intercostal spaces. They drain afferents from the breast, deeper structures of the supra-umbilical anterior abdominal wall, the superior hepatic surface (through a small anterior group of nodes posterior to the xiphoid process) and deeper parts of the anterior thoracic wall. Their efferents usually unite with those from the paratracheal (tracheobronchial) and brachiocephalic (prevascular)

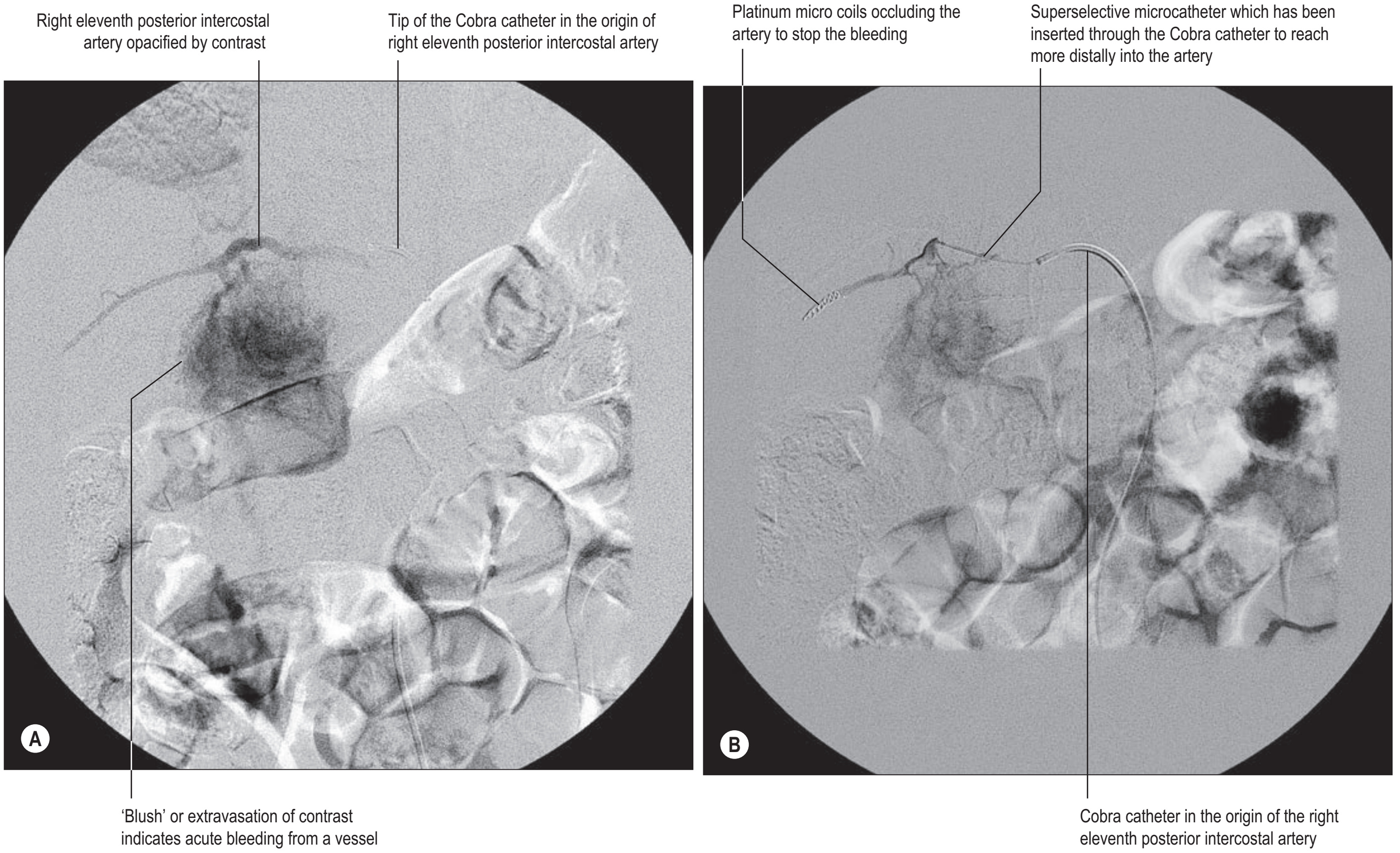
Right eleventh posterior intercostal artery opacified by contrast
Tip of the Cobra catheter in the origin of right eleventh posterior intercostal artery
Platinum micro coils occluding the artery to stop the bleeding
Superselective microcatheter which has been inserted through the Cobra catheter to reach more distally into the artery
A
B
'Blush' or extravasation of contrast indicates acute bleeding from a vessel
Cobra catheter in the origin of the right eleventh posterior intercostal artery

Fig. 53.20 A–B, Pre- and post-embolization images after selective catheterization of the right eleventh posterior intercostal artery.

Catheter embolization is an interventional radiology technique that can be used to block branches of the posterior intercostal arteries when they are bleeding, e.g. secondary to blunt trauma usually associated with rib fractures, or when there is an abnormality of the vertebra supplied by the dorsal branch of the posterior intercostal artery. In such cases, the posterior intercostal artery may be accessed by placing a catheter in the descending thoracic aorta, usually by puncturing the femoral artery in the femoral triangle. A smaller catheter (referred to as a superselective catheter) may then be placed in the posterior intercostal artery and embolic material (metallic coils or glue) is injected to block the artery. This can cause cessation of bleeding in cases of trauma and provide pain relief when, for example, the vertebral body is infiltrated with tumour (Fig. 53.20).

nodes to form the bronchomediastinal trunk (see Figs 54.12, 56.5). On either side, the bronchomediastinal trunk may either open directly into the jugulosubclavian junction; into either the internal jugular or subclavian vein near their junction; into the subclavian trunk; or into the lymphatic duct on the right or the thoracic duct on the left.

Intercostal nodes

Intercostal nodes occupy the intercostal spaces near the heads and necks of the ribs (see Fig. 56.4). They receive deep lymph vessels from the posterolateral aspects of the chest wall and breast, some of which are interrupted by small more laterally placed intercostal nodes. Efferent vessels from nodes in the lower intercostal spaces unite into a trunk that descends to the abdominal confluence of lymph trunks or to the thoracic duct. Efferent vessels from nodes in the left upper intercostal spaces end in the thoracic duct; those of the right upper intercostal spaces end in one of the right lymphatic trunks.

Diaphragmatic nodes

Located on the superior (thoracic) surface of the respiratory diaphragm, the diaphragmatic (phrenic) nodes are arranged in anterior, right lateral, left lateral and posterior groups (see Fig. 56.4A).

Anterior group The anterior group consists of two or three small nodes posterior to the base of the xiphoid process, draining the convex diaphragmatic surface of the liver, and one or two nodes on each side near the junction of the seventh rib and costal cartilage that receive anterior lymph vessels from the respiratory diaphragm. The anterior group drains to the parasternal nodes.

Lateral groups The lateral groups each contain two or three nodes and lie close to the point where the phrenic nerves enter the respiratory diaphragm. On the right, some nodes lie within the fibrous pericardium anterior to the intrathoracic part of the inferior vena cava. Their afferents drain the central part of the respiratory diaphragm; those on the right also drain the convex (diaphragmatic) surface of the liver, and their efferents pass to the para-oesophageal (posterior mediastinal), parasternal and brachiocephalic nodes.

Posterior group The posterior group consists of a few nodes that lie on the posterior aspect of the crura of the respiratory diaphragm and connect with the lateral and posterior aortic (prevertebral) and para-oesophageal (posterior mediastinal) nodes.

Lymphatic drainage of deeper tissues

Collecting vessels of the deeper thoracic tissues include lymphatics that drain the muscles attached to the ribs. Most end in axillary nodes but some from pectoralis major also drain to the parasternal nodes. Intercostal vessels drain the intercostal muscles, tissues of the extrapleural space (e.g. endothoracic fascia) and the costal parietal pleura; those from the anterior thoracic wall end in the parasternal nodes and their posterior counterparts drain to intercostal nodes.

Vessels from the respiratory diaphragm form a thoracic and an abdominal plexus, which anastomose freely, especially in areas covered by diaphragmatic parietal pleura and peritoneum, respectively. The thoracic plexus unites with lymph vessels draining the costal and mediastinal parts of the parietal pleura. Its efferents are: anterior, draining to the anterior diaphragmatic nodes near the junctions of the seventh rib and costal cartilage; middle, draining to nodes on the oesophagus (para-oesophageal) and around the intrathoracic part of the inferior vena cava (right lateral); and posterior, draining to nodes around the descending thoracic aorta at the point where it leaves the thorax. The abdominal plexus anastomoses with the hepatic lymphatics and peripherally with those of the subperitoneal tissue. Efferents from its right half pass to a group of nodes close to the right inferior phrenic artery, or in the right lateral aortic nodes. Those from the left half of the abdominal diaphragmatic plexus pass to the preaortic, lateral aortic and para-oesophageal nodes.

INNERVATION OF THE CHEST WALL

Thoracic ventral spinal rami

There are 12 pairs of ventral rami of the thoracic spinal nerves. The first 11 lie in the intercostal spaces, between the first to twelfth ribs (intercostal nerves) and the twelfth lies inferior to the twelfth rib (subcostal nerve). Each is connected with the adjacent sympathetic ganglion by grey and white rami communicantes; the grey ramus normally joins the nerve proximal to the point at which the white ramus leaves it (**Fig. 53.21**; see Fig. 56.6), although this pattern varies. Intercostal nerves are distributed primarily to the thoracic and abdominal walls. The first two nerves supply fibres to the upper limb in addition to their thoracic branches, the third to the sixth nerves supply only the thoracic wall, and the seventh to eleventh nerves supply both thoracic and abdominal walls. The twelfth (subcostal nerve) is distributed to the abdominal wall and skin covering the anterior aspect of the gluteal region. Communicating branches link the intercostal nerves posteriorly across the intercostal spaces (see Fig. 55.10), and the eighth to twelfth nerves communicate freely in the abdominal wall.

First to sixth thoracic ventral rami

The first thoracic ventral ramus divides unequally: a large branch ascends across the neck of the first rib, lateral to the supreme intercostal artery (see Fig. 55.10), to enter the brachial plexus, and a smaller branch (the first posterior intercostal nerve) runs in the first intercostal space and terminates as the anterior cutaneous branch. A lateral cutaneous branch pierces the chest wall anterior to serratus anterior and supplies the axillary skin; it may communicate with the intercostobrachial nerve and sometimes joins the medial cutaneous nerve of the arm. The first thoracic ventral ramus often receives a connecting branch from the second, which ascends anterior to the neck of the second rib.

The second to sixth thoracic ventral rami travel within their respective intercostal spaces inferior to the intercostal vessels (see Fig. 53.17). Posteriorly, they lie initially between the costal parietal pleura (and its associated endothoracic fascia), and the internal intercostal membrane, but more laterally they lie between the internal intercostals and subcostales and/or innermost intercostals. Near the sternum, they cross anterior to the internal thoracic vessels and transversus thoracis, pierce the internal intercostals, the external intercostal membrane and pectoralis major, and terminate as the anterior cutaneous branches of the intercostal nerves. The anterior cutaneous branch of the second intercostal nerve may be connected to the medial supraclavicular nerves of the cervical plexus. Branches from the sixth intercostal nerve supply abdominal skin immediately inferior to the apex of the costal arch (the infrasternal angle).

Branches Numerous slender muscular filaments supply the intercostals, serratus posterior superior and transversus thoracis. Anteriorly, some cross the costal cartilages to pass from one intercostal space to another. Each posterior intercostal nerve gives off a collateral and a lateral cutaneous branch before it reaches the angle of the adjoining ribs (see Fig. 53.21). The collateral branch follows the inferior border of the numerically corresponding intercostal space in the same intermuscular plane as the posterior intercostal nerve, which it may rejoin before it is distributed as an additional anterior cutaneous branch. The lateral cutaneous branch accompanies the main nerve for a short distance and then pierces the intercostal muscles obliquely. With the exception of the lateral cutaneous branches of the first and second intercostal nerves, each divides into anterior and posterior branches that subsequently pierce serratus anterior. The anterior branches pass anteriorly over the border of pectoralis major to supply the overlying skin; those from lateral branches of the fifth and sixth intercostal nerves also supply small motor branches to a variable number of upper digitations of external abdominal oblique. The posterior branches run posteriorly and supply the skin over the scapula and latissimus dorsi.

The lateral cutaneous branch of the second intercostal nerve is the intercostobrachial nerve (see Fig. 49.34). It crosses the axilla to reach the medial side of the arm and joins a branch of the medial cutaneous nerve of the arm. It then pierces the brachial (deep) fascia of the arm, and supplies the skin of the superior half of the posterior and medial aspects of the arm, communicating with the posterior brachial cutaneous branch of the radial nerve. Its size is in inverse proportion to the size of the medial cutaneous nerve of the arm. A second intercostobrachial nerve often branches from the anterior branch of the lateral cutaneous branch of the third intercostal nerve and sends fibres to the axilla and the medial side of the arm.

Seventh to eleventh thoracic ventral rami

The ventral rami of the seventh to eleventh thoracic spinal nerves follow a similar course to that described above for the ventral rami of the second to sixth thoracic spinal nerves. They continue anteriorly from

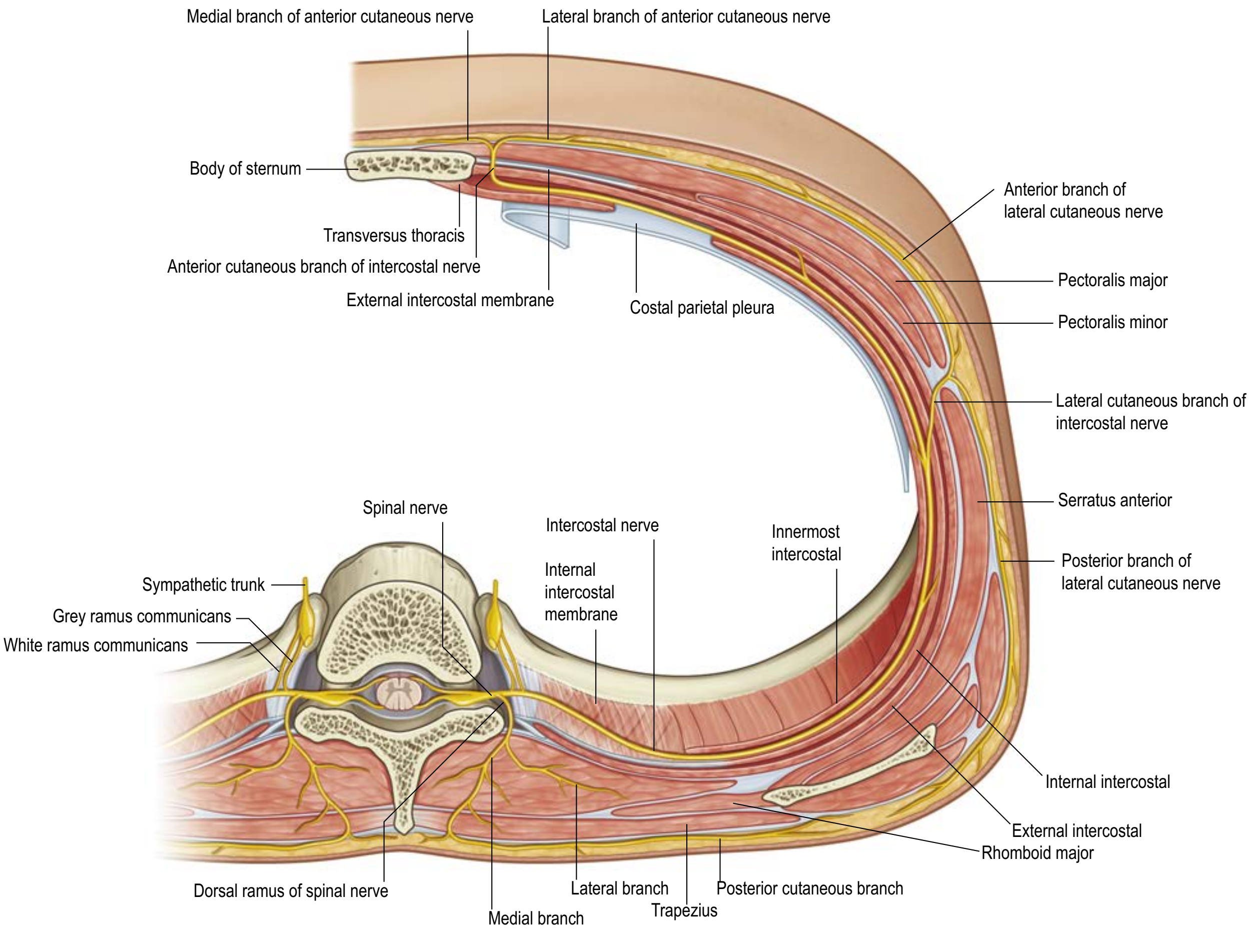
Medial branch of anterior cutaneous nerve
Lateral branch of anterior cutaneous nerve
Body of sternum
Transversus thoracis
Anterior cutaneous branch of intercostal nerve
External intercostal membrane
Costal parietal pleura
Anterior branch of lateral cutaneous nerve
Pectoralis major
Pectoralis minor
Lateral cutaneous branch of intercostal nerve
Serratus anterior
Posterior branch of lateral cutaneous nerve
Spinal nerve
Intercostal nerve
Innermost intercostal
Internal intercostal membrane
Sympathetic trunk
Grey ramus communicans
White ramus communicans
Internal intercostal
External intercostal
Rhomboid major
Dorsal ramus of spinal nerve
Lateral branch
Posterior cutaneous branch
Trapezius
Medial branch

Fig. 53.21 A transverse section through an intercostal space, showing the course and branching of a typical intercostal nerve.

the intercostal spaces into the abdominal wall and their further course is described in Chapter 60.

Lesions of the intercostal nerves

Available with the *Gray's Anatomy* e-book

Twelfth thoracic ventral ramus (subcostal nerve)

The ventral ramus of the twelfth thoracic spinal nerve (subcostal nerve) is larger than the others and gives a communicating branch (dorsolumbar nerve) to the ventral ramus of the first lumbar spinal nerve. As with the intercostal nerves, it gives off a collateral branch and then accompanies the subcostal vessels along the inferior border of the twelfth rib, passing posterior to the lateral arcuate ligament and kidney, and anterior to the superior part of quadratus lumborum. It perforates the aponeurosis of transversus abdominis to pass forwards between it and internal abdominal oblique. It is distributed in the same manner as the lower intercostal nerves. The subcostal nerve connects with the iliohypogastric nerve of the lumbar plexus and sends a branch to pyramidalis. Its lateral cutaneous branch pierces the internal and external abdominal oblique muscles and supplies the lowest slip of the latter. It usually descends over the iliac crest about 5 cm posterior to the anterior superior iliac spine (see Fig. 60.5) and is distributed to the skin covering the anterior aspect of the gluteal region; some nerve fibres may reach as low as the greater trochanter of the femur. A transversalis fascia plane (TFP) block can improve the coverage of proximal surgical incisions used in hip surgery, because both the inferior branches of the subcostal nerve and the iliohypogastric nerve are anaesthetized.

Thoracic dorsal spinal rami

The dorsal rami of the thoracic spinal nerves pass posteriorly close to the vertebral zygapophysial (facet) joints and divide into medial and lateral branches (see Figs 53.21, 47.10). Their course and distribution are reviewed in Chapter 47. Briefly, the medial branch emerges between the joint and the medial edge of the superior costotransverse ligament and intertransverse muscle. The lateral branch runs laterally in the interval between the ligament and the muscle before turning posteriorly and inferiorly at the level of the costotransverse joint.

The medial branches of the first to sixth thoracic dorsal rami subsequently pass between and supply semispinalis thoracis and multifidus, then pierce the rhomboids and trapezius and reach the skin near the vertebral spines (see Figs 53.15C, 53.16): they descend for some distance close to the vertebral spines before reaching the skin (see Fig. 47.8). The medial branches of the seventh to twelfth thoracic dorsal rami are distributed mainly to multifidus and longissimus thoracis and occasionally give fibres to the skin covering the median region of the back.

The lateral branches increase in size from superior to inferior and run through or deep to longissimus thoracis to the interval between it and iliocostalis cervicis, supplying these muscles and levatores costarum. A variable number of the lateral branches of the upper thoracic dorsal rami may supply the skin. The lower five or six lateral branches give off cutaneous branches that pierce serratus posterior inferior and latissimus dorsi in line with the angles of the ribs. The lateral cutaneous branches descend by as much as four ribs before they become superficial, e.g. the branch of the twelfth thoracic ramus reaches the skin only a few centimetres superior to the iliac crest.

BREAST

The breasts form a secondary sexual feature of females and the milk produced is a source of protection and nutrition for the neonate and infant. In young adult females, each breast is a rounded eminence largely lying within the superficial fascia covering parts of the anterior and lateral thoracic walls but spreading laterally to a variable extent toward the midaxillary line (**Figs 53.22–53.23**). Breast shape and size varies with genetics, race and dietary factors and on the age, parity and menopausal status of the individual. Breasts may be hemispherical, conical, variably pendulous, piriform or thin and flattened. In the adult female, the base of the breast (its deep attached surface) extends vertically from the second or third to the sixth rib/costal cartilage, and in the transverse plane from the lateral sternal border medially to the mid-axillary line laterally. The axillary process (tail or tail of Spence) of the breast is an extension of the superolateral quadrant towards the

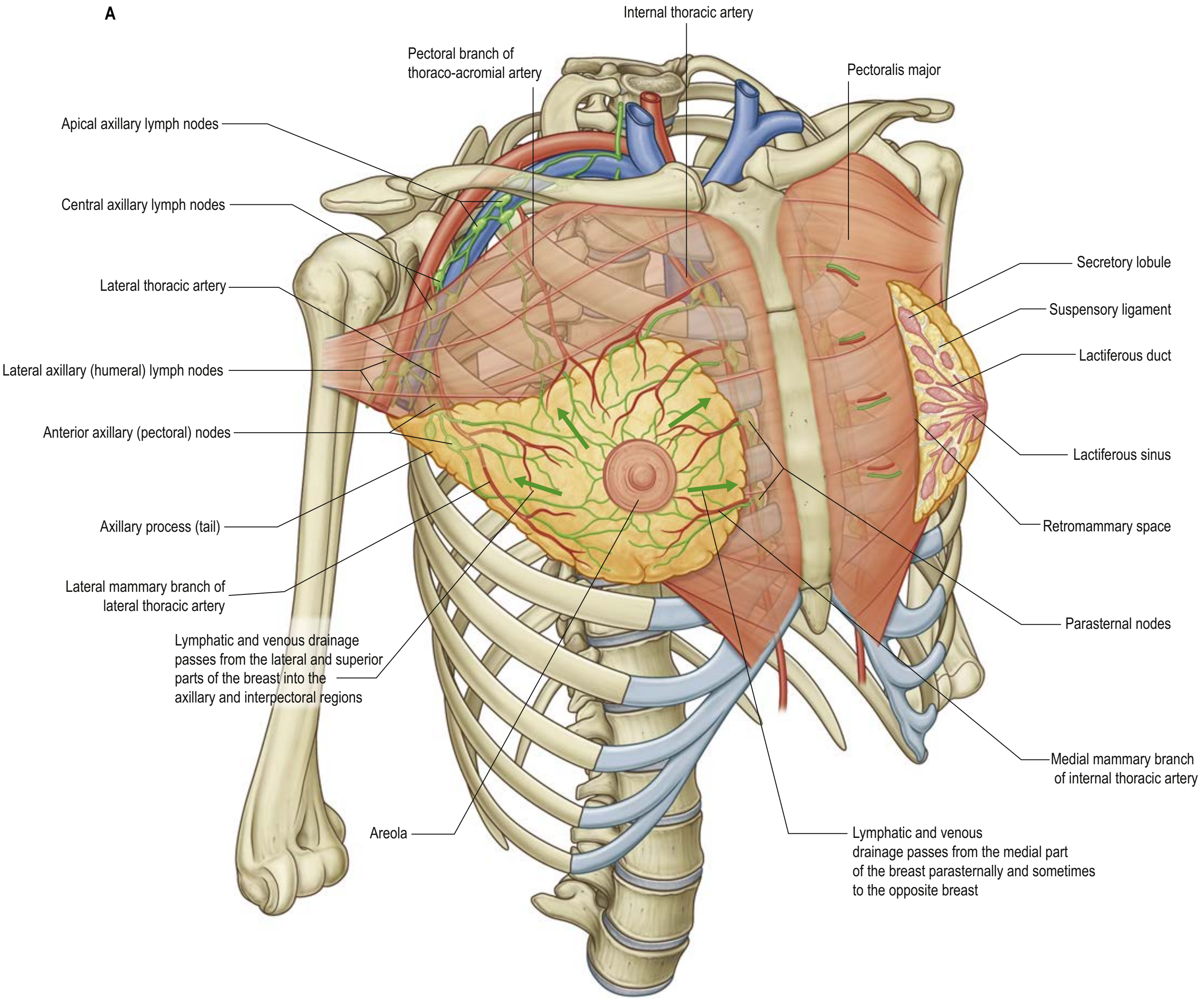
A
Internal thoracic artery
Pectoral branch of thoraco-acromial artery
Pectoralis major
Apical axillary lymph nodes
Central axillary lymph nodes
Lateral thoracic artery
Lateral axillary (humeral) lymph nodes
Anterior axillary (pectoral) nodes
Axillary process (tail)
Lateral mammary branch of lateral thoracic artery
Lymphatic and venous drainage passes from the lateral and superior parts of the breast into the axillary and interpectoral regions
Areola
Secretory lobule
Suspensory ligament
Lactiferous duct
Lactiferous sinus
Retromammary space
Parasternal nodes
Medial mammary branch of internal thoracic artery
Lymphatic and venous drainage passes from the medial part of the breast parasternally and sometimes to the opposite breast

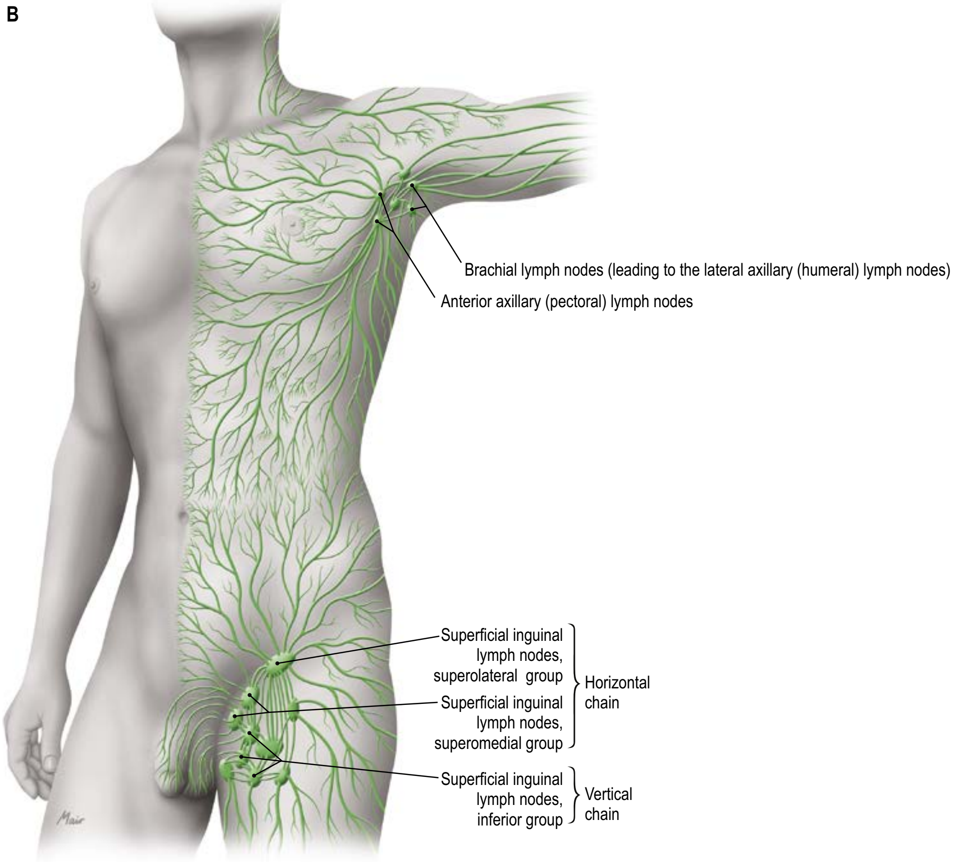
B
Brachial lymph nodes (leading to the lateral axillary (humeral) lymph nodes)
Anterior axillary (pectoral) lymph nodes
Superficial inguinal lymph nodes, superolateral group
Superficial inguinal lymph nodes, superomedial group
Horizontal chain
Superficial inguinal lymph nodes, inferior group
Vertical chain
Mair

Fig. 53.22 **A**, The location, relations, vascular supply and lymph drainage of the breast. **B**, Lymphatic drainage of the anterior thoracic and abdominal walls and skin of the breast. (A, With permission from Drake RL, Vogl AW, Mitchell A (eds) Gray's Anatomy for Students, 2nd ed. Elsevier, Churchill Livingstone. Copyright 2010.)

Slipping rib syndrome occurs with subluxation of the interchondral joints between the eighth to tenth rib costal cartilages. This may trap or impinge intercostal nerves, causing subsequent localized pain or referred abdominal pain (McMahon 2018). The dorsal cutaneous branch of an intercostal nerve can become entrapped as it penetrates the fascia of erector spinae, producing an area of numbness, usually with painful paraesthesia, that extends laterally from the posterior midline by about 10 cm, and is 10 cm in height (notalgia paraesthetica); the area between the medial border of the scapula and the spinous processes of the vertebrae is commonly affected. The anterior cutaneous branches of the intercostal nerves can also become entrapped as they penetrate the fascia of rectus abdominis, producing an area of numbness on the anterior abdominal wall, usually with painful paraesthesia, that extends from the anterior midline laterally by about 10 or 12 cm (rectus abdominis syndrome).

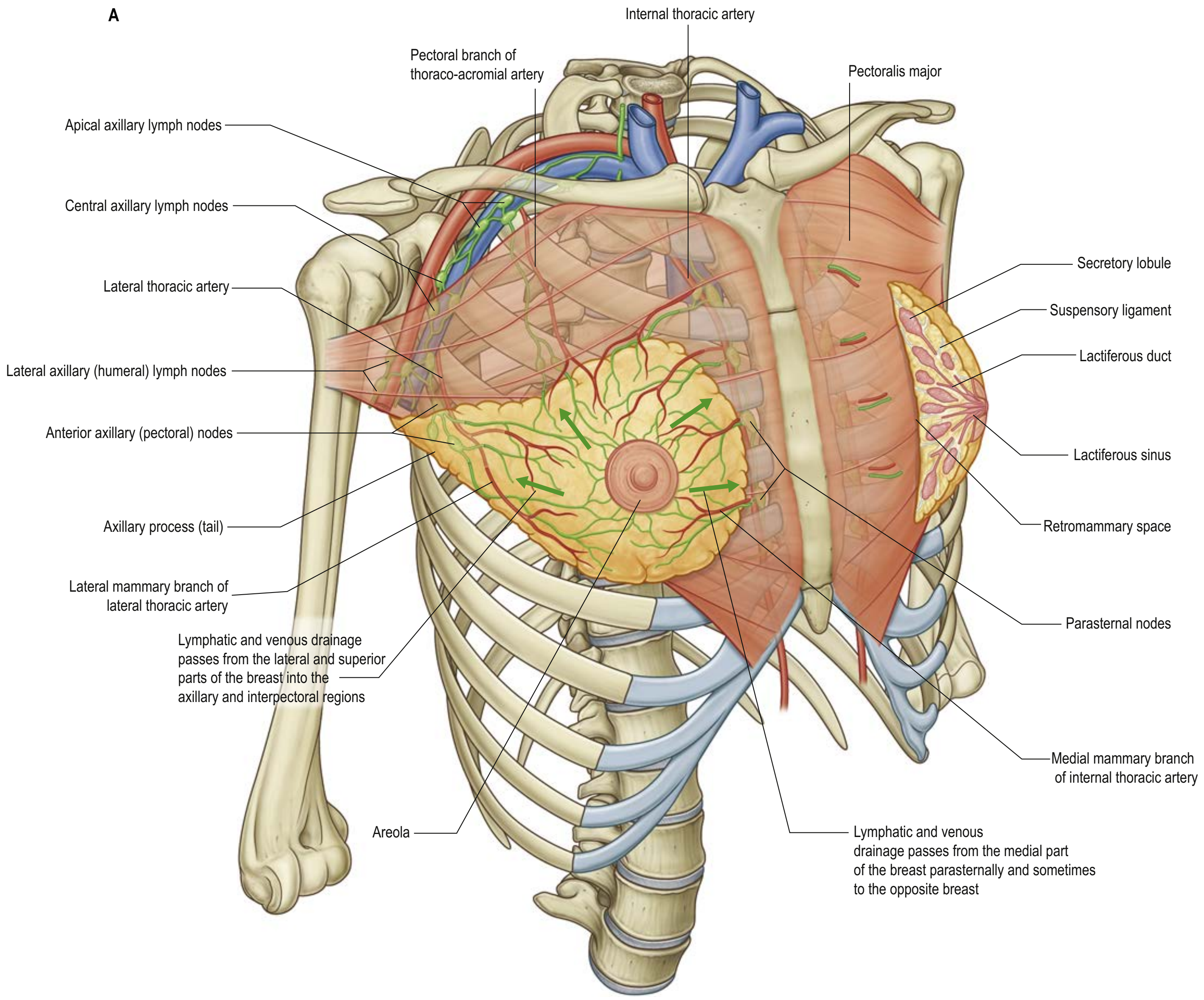
A
Internal thoracic artery
Pectoral branch of thoraco-acromial artery
Pectoralis major
Apical axillary lymph nodes
Central axillary lymph nodes
Lateral thoracic artery
Lateral axillary (humeral) lymph nodes
Anterior axillary (pectoral) nodes
Axillary process (tail)
Lateral mammary branch of lateral thoracic artery
Lymphatic and venous drainage passes from the lateral and superior parts of the breast into the axillary and interpectoral regions
Areola
Secretory lobule
Suspensory ligament
Lactiferous duct
Lactiferous sinus
Retromammary space
Parasternal nodes
Medial mammary branch of internal thoracic artery
Lymphatic and venous drainage passes from the medial part of the breast parasternally and sometimes to the opposite breast

Fig. 53.22 **A**, The location, relations, vascular supply and lymph drainage of the breast. (With permission from Drake RL, Vogl AW, Mitchell A (eds) Gray's Anatomy for Students, 2nd ed. Elsevier, Churchill Livingstone. Copyright 2010.) (B, *continued online*)

axilla along the inferolateral edge of pectoralis major; it may extend through the deep fascia toward the apex of the axilla.

Fascia

The complex fascial network that encases and shapes the breast has been variously described. According to Rehnke et al (2018), the glandular breast tissue is surrounded on its superficial and deep surfaces by anterior and posterior laminae, respectively, of superficial fascia and fat (see Fig. 53.23B). The fascial laminae and deep fascial system of the trunk interconnect around the perimeter of the breast via the circummammary ligament, a circular zone of adhesion traversed by nerves, blood vessels and lymphatic vessels. The breast lies on the deep pectoral fascia covering pectoralis major and serratus anterior superiorly, external abdominal oblique and its aponeurosis inferiorly as the latter forms the anterior wall of the rectus sheath, and the clavipectoral fascia laterally. Fibrous strands or sheets consisting of condensations of connective tissue extend between the posterior lamina of the superficial fascia and the dermis. These suspensory ligaments (retinacula or Cooper's ligaments) are often well developed in the superior parts of the breast and support the breast tissue, helping to minimize drooping. Loose connective tissue in the submammary space (between the posterior lamina of superficial fascia and the deep fascia of the trunk) allows the breast some degree of independent movement across the deep pectoral fascia. Advanced mammary carcinoma may cause tethering or fixation of the breast and its skin to the underlying musculature, resulting in indentation of the skin or breast movement upon contraction of pectoralis major. Occasionally, small projections of glandular tissue may pass through the deep fascia into the underlying muscle in normal subjects.

Nipple and areola

The nipple projects from the breast anteriorly (see Fig. 53.23). It may be cylindrical and rounded, hemispherical or flattened, depending on the effects of developmental, nervous or hormonal factors and external temperature on the erectile properties of the subareolar muscle of the nipple. The level of the nipple varies widely. In females, its site is dependent on the size and shape of the breasts; it often overlies the fourth intercostal space in prepubescent females. In the male, the nipple is usually sited in the fourth intercostal space in the mid-clavicular line, although this should not be relied upon when landmarking. In the young adult of either sex, the nipples are usually positioned 20–23 cm from the suprasternal notch in the mid-clavicular line and 19–23 cm apart in the horizontal plane. With increasing age, parity and weight, female breasts adopt an increasingly drooped shape and the position of the nipple descends to the level of the inframammary crease or below. In the nulliparous, the nipple is pink, light brown or darker, depending on the general melanization of the body. Occasionally, one or both nipples may not evert during prenatal development and remain permanently retracted (see below).

The skin covering the nipple and the surrounding areola (the disc of skin that circles the base of the nipple) has a convoluted surface. It contains numerous sweat and areolar (Montgomery's) glands that open directly onto the skin surface. The oily secretion of these specialized sebaceous glands acts as a protective lubricant and facilitates latching of the neonate during lactation; the glands are often visible in parous women, arranged circumferentially as small elevations, areolar (Montgomery's) tubercles, around the areola close to the margin. Other areolar glands, intermediate in structure between mammary and sweat glands, become enlarged in pregnancy and lactation as subcutaneous tubercles. The

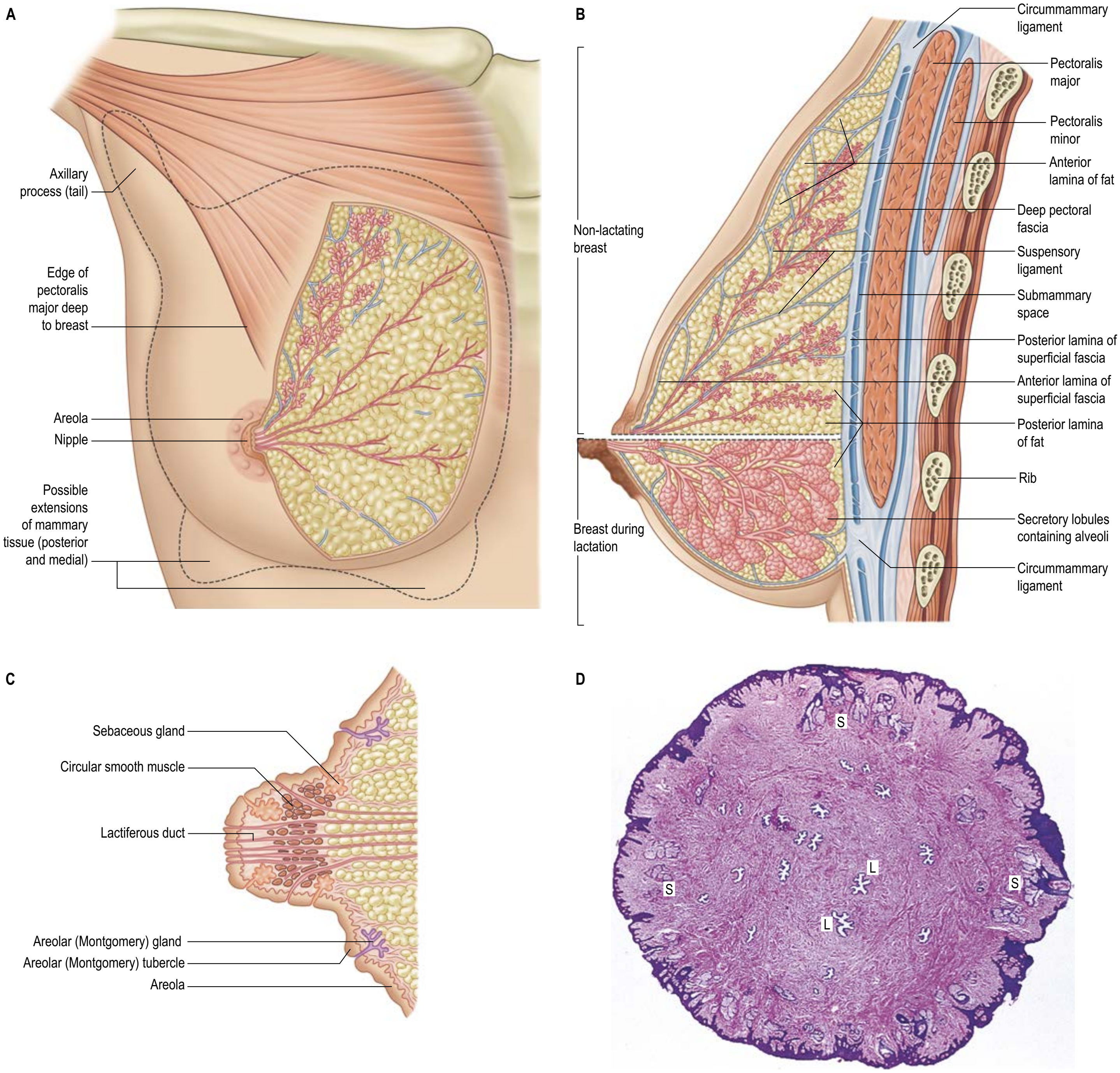
A
Axillary process (tail)
Edge of pectoralis major deep to breast
Areola
Nipple
Possible extensions of mammary tissue (posterior and medial)
B
Non-lactating breast
Breast during lactation
Circummammary ligament
Pectoralis major
Pectoralis minor
Anterior lamina of fat
Deep pectoral fascia
Suspensory ligament
Submammary space
Posterior lamina of superficial fascia
Anterior lamina of superficial fascia
Posterior lamina of fat
Rib
Secretory lobules containing alveoli
Circummammary ligament
C
Sebaceous gland
Circular smooth muscle
Lactiferous duct
Areolar (Montgomery) gland
Areolar (Montgomery) tubercle
Areola
D
S
S
S
L
L

Fig. 53.23 **A**, The structure of the breast. **B**, Fascia of the breast and changes in the breast during lactation. **C**, A section of the nipple. **D**, A cross-section of the nipple. There is a corrugated layer of stratified squamous keratinized epithelium over the nipple surface; 20 or more lactiferous ducts (L) open on to the surface; sebaceous glands (S) are deep to the epidermis. (D, With permission from Dr JB Kerr, Monash University, from Kerr JB 1999 Atlas of Functional Histology. London: Mosby.)

sebaceous glands of the areola are not usually associated with hair follicles although scattered hairs may be present at the areolar margin. The skin of the nipple and areola is rich in melanocytes and is therefore typically darker than the skin covering the remainder of the breast; the areola increases in size and further darkening occurs during the second month of pregnancy and subsequently persists to a variable degree.

Soft tissue

The breasts are normally composed of up to 20 discrete lobes that contain ductal-glandular tissue consisting of branching ducts and terminal secretory lobules in a connective tissue stroma (see Fig. 53.23). Each lobe is derived by branching from one central lactiferous duct in the nipple. The terminal duct lobular unit (TDLU or lobule) is the functional milk secretory component of the breast. Histological evidence suggests premalignant epithelial proliferations originate from the TDLU; alternatively, a predisposition to malignant transformation may be present throughout an individual lobe ('sick lobe' hypothesis), creating an impression of multifocality. Although lobes are usually described as discrete territories, they intertwine in three dimensions, merge at their edges and cannot be distinguished during surgery. The interlobular connective tissue stroma is dense and fibrocollagenous, whereas intralobular connective tissue has a loose texture that allows the rapid expansion of secretory tissue during pregnancy (see Figs 53.23B, 53.29B). Elsewhere in the normal breast, fibrous tissue surrounds the ductal glandular components and extends to the skin and nipple, assisting the mechanical coherence of the breast. The interlobular stroma contains variable amounts of adipose tissue, which is responsible for much of the increase in breast size at puberty.

Vascular supply and lymphatic drainage

Arteries

The breasts are supplied by branches of the axillary, internal thoracic and some anterior intercostal arteries. The axillary artery supplies blood via the superior thoracic artery (if present), the pectoral branches of the thoraco-acromial artery, the lateral thoracic artery (via

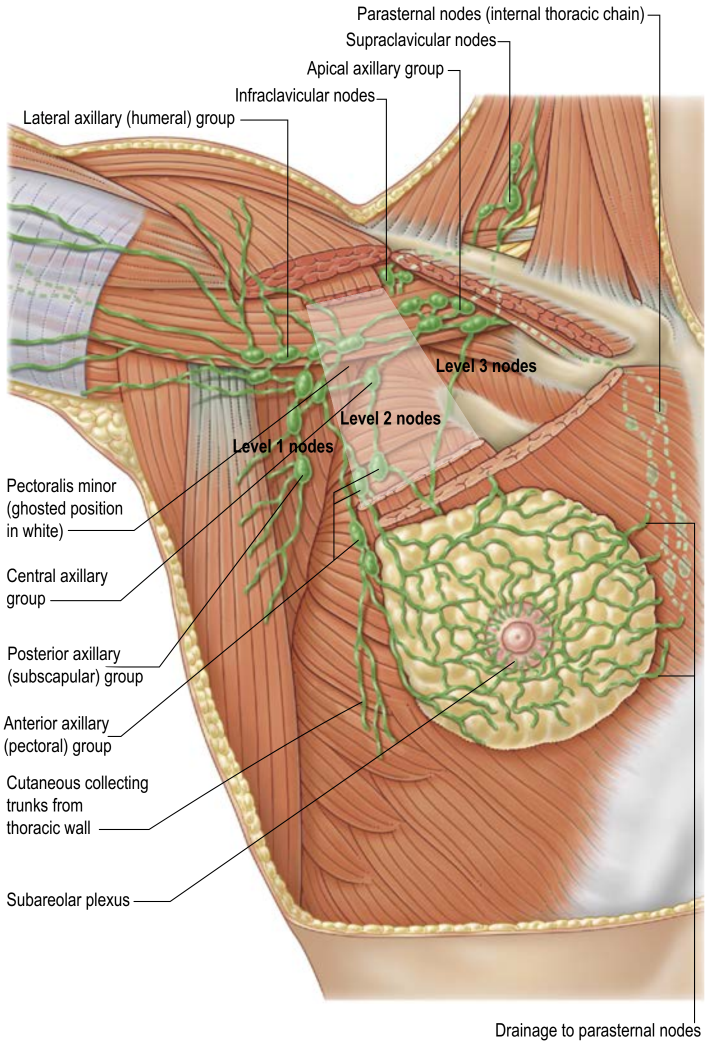
Parasternal nodes (internal thoracic chain)
Supraclavicular nodes
Apical axillary group
Infraclavicular nodes
Lateral axillary (humeral) group
Level 3 nodes
Level 2 nodes
Level 1 nodes
Pectoralis minor (ghosted position in white)
Central axillary group
Posterior axillary (subscapular) group
Anterior axillary (pectoral) group
Cutaneous collecting trunks from thoracic wall
Subareolar plexus
Drainage to parasternal nodes

Fig. 53.24 Lymph vessels of the breast and the draining axillary nodes (level 1–3 shown) and supraclavicular nodal groups.

lateral mammary branches that curve around the lateral border of pectoralis major to supply the lateral aspect of the breast) and the subscapular artery. The internal thoracic artery supplies medial mammary branches to the anteromedial part of the breast. The second to fourth anterior intercostal arteries may supply perforating branches more laterally in the anterior thorax. The second perforating artery is usually the largest and supplies the superior region of the breast, the nipple, areola and adjacent breast tissue. Arteries access the body of the breast tissue via circumferential connections between deep and superficial fasciae.

Veins

Blood drains from the circular venous plexus around the areola and from the glandular tissue of the breast into the axillary, internal thoracic and intercostal veins via veins that accompany the corresponding arteries. Individual variation is common.

Lymphatic drainage

The lymphatic drainage of the breast is of great clinical significance because metastatic dissemination occurs principally by the lymphatic routes (the breasts are the site of malignant change in as many as 1 in 8 women; Commentary 7.1). The dominant lymphatic drainage of the breast is derived from the dermal network (Fig. 53.24). Breast lymphatics branch extensively; the smallest valveless superficial lymph capillaries (20–70 μm diameter) drain into larger lymph pre-collecting vessels (~300 μm diameter) that contain valves and smooth muscle. These pre-collectors unite to form a subcutaneous network between skin and breast tissue and drain almost always to at least one sentinel node, usually near the lateral border of pectoralis minor (Suami et al 2008). Lymphatic blockage through tumour occlusion may therefore result in reverse flow through the lymphatic channels, resulting in oedema. The direction of lymphatic flow within the breast parallels the major venous tributaries and enters the regional lymph nodes via an extensive periductal and perilobular network of lymphatic channels. Most of these lymphatics drain into the axillary group of regional lymph nodes either directly or through the subareolar lymphatic plexus (see Fig. 49.48). Dermal lymphatics also penetrate pectoralis major to join channels that drain the deeper parenchymal tissues, and then follow the vascular channels to terminate in the regional lymph nodes below the level of the clavicle.

Lymphatics from the left breast ultimately terminate in the thoracic duct and, subsequently, the left subclavian vein. On the right, the lymphatics ultimately drain into the right subclavian vein near its junction with the internal jugular vein. Part of the medial sides of the breasts drain to the parasternal nodes, lying along the internal thoracic vessels. These may anastomose across the sternum, providing a route for contralateral nodal spread in medially located breast carcinoma. Parasternal nodes and vessels may drain inferiorly via the superior and inferior epigastric lymphatic routes to the superficial and deep inguinal nodes in the femoral triangle.

Axillary nodes receive more than 75% of the lymph from the breast. There are 20–40 axillary nodes, grouped somewhat artificially as anterior (pectoral), posterior (subscapular), lateral (humeral), central and apical. Surgically, the nodes are described in relation to pectoralis minor; those lying lateral or inferior to pectoralis minor are the low nodes (level 1), those lying posterior to pectoralis minor are the middle group (level 2), and those lying between the superomedial (upper) border of pectoralis minor and the inferior (lower) border of the clavicle are the upper or apical axillary nodes (level 3) (see Fig. 53.24). There may be one or two interpectoral (Rotter's) nodes lying between pectoralis minor and major. Efferent vessels may pass directly from the breast around the anterior axillary border and through the axillary fascia to the anterior axillary (pectoral) lymph nodes; some may pass directly to the posterior axillary (subscapular) nodes. A few vessels pass from the superior part of the breast to the apical axillary nodes, sometimes interrupted by the infraclavicular nodes or by small, inconstant, interpectoral nodes. Most of the remainder drain to parasternal nodes from the medial and lateral parts of the breast and accompany perforating branches of the internal thoracic artery. Lymphatic vessels occasionally follow lateral cutaneous branches of the posterior intercostal arteries to the intercostal nodes (see Fig. 56.4A).

Axillary surgery in breast cancer

Axillary lymph node dissection may be performed for diagnostic and therapeutic reasons. The presence of metastases within axillary lymph nodes has strong prognostic significance and may influence decisions on adjuvant therapy. Axillary lymph node dissection can lead to chronic postoperative problems such as pain, seroma formation, reduced mobility of the upper limb, impaired sensation and lymphoedema.

Lymphatic drainage in breast cancer and role of sentinel lymph node biopsy

Available with the *Gray's Anatomy* e-book

Innervation

Available with the *Gray's Anatomy* e-book

Ultrasound-guided peripheral nerve blocks in the management of breast pain

Available with the *Gray's Anatomy* e-book

Microstructure

The microstructure of breast tissue varies with age, time in the menstrual cycle, pregnancy and lactation. The following description relates to the mature, resting (non-lactating) breast. For most of their lengths, the ducts are lined by columnar epithelium (Fig. 53.25A–B). The bases of these cells are in close contact with numerous myoepithelial cells of ectodermal origin, similar to those of certain other glandular epithelia (see Figs 53.29A, 2.3, 2.4). Myoepithelial cells are so numerous that they form a distinct layer surrounding the ducts and presumptive alveoli, and give the epithelium a bilayer appearance.

Lactiferous ducts draining each lobe of the breast pass through the nipple and open on to its tip as up to 20 orifices. Close to their openings on the nipple, the stratified cuboidal epithelial lining of the lactiferous ducts is replaced by keratinized stratified squamous epithelium, continuous with the epidermis. Shed squames may

Nerves and lymph vessel in the axillary region must be considered as anatomical landmarks during surgery and carefully identified and preserved. Chronic neuropathic pain is a common consequence of surgery, with a prevalence of 25–60% (Jung et al 2003). Chronic pain exacerbates the stress associated with the already burdensome management of breast cancer and in many patients adversely impacts their daily life. Complete resection, stretch or compression of the lateral cutaneous branch of T2 (intercostobrachial nerve) may result in numbness or pain in the ipsilateral axilla, medial arm and upper anterior chest. Symptoms are more common and longer lasting when the origin of the nerve is injured as opposed to its peripheral branches (Jung et al 2003). Resection or compression of the long thoracic nerve, which passes inferior to the clavicle through the axillary sheath and then down the chest wall between the midaxillary and posterior axillary lines to innervate serratus anterior, can result in palsy (with scapular winging): shoulder pain may be exacerbated by shoulder instability and reduced abduction.

Lymphatic mapping with sentinel lymph node biopsy has become an important technique in the staging of patients with early breast cancer. Based upon the assumption that the majority of the lymphatic drainage of the breast occurs through the subareolar plexus (Suami et al 2009), a radiolabelled colloid is injected into either the subareolar tissue of the index quadrant of the breast or into the peritumoural and intradermal tissue overlying the primary breast cancer. At the time of surgery, a vital blue dye is injected after general anaesthesia is established. The combination of radioisotope and dye provides the most accurate means of localizing the sentinel node (Tanis et al 2001). The latter represents the first draining node within the axilla and is surgically removed for careful histopathological analysis to detect the presence of metastases. There is a 5–10% false-negative rate for this procedure that can be partly attributed to anatomical differences in lymphatic drainage (Tanis et al 2005, Suami et al 2008).

If the histopathological results prove negative, the morbidity associated with axillary dissection can be avoided. Where metastases to the axillary nodal group are found, axillary completion dissection or radiotherapy is offered. The majority of sentinel nodes are found in the low axilla (level 1) (see Fig. 53.24). Higher-level ‘skip’ nodes are involved in 5–10% of cases. Occasionally, the sentinel node is identified in an extra-axillary position, either within the breast parenchyma as an intramammary lymph node, or as a parasternal (internal thoracic) lymph node or in the lesser supraclavicular fossa.

The breast is innervated with sensory and sympathetic motor fibres by the anterior and lateral cutaneous branches of the fourth to sixth intercostal nerves. The nipple is supplied from the anterior branch of the lateral cutaneous branch of the fourth intercostal nerve, which forms an extensive plexus within the nipple, its fibres terminating close to the epithelium as free endings, Meissner corpuscles and Merkel disc endings. These are essential for signalling suckling to the central nervous system. Secretory activities of the gland are largely controlled by ovarian and neurohypophysial hormones rather than by efferent motor fibres. The areola has fewer sensory endings.

Regional anaesthesia is a valuable component of multimodal analgesia. Localized nerve blocks reduce both acute and chronic postsurgical pain, thereby enhancing recovery. Pectoral nerve blocks are attractive alternatives to paravertebral and thoracic epidural blocks for breast surgery due to their simplicity and minimal complications (Versyck et al 2017). The majority of pectoral (Pecs) blocks are performed under general anaesthetic and ultrasound guidance. The Pecs I block targets the medial and lateral pectoral nerves located in the fascial plane between pectoralis major and minor. The Pecs II block can be used in addition to Pecs I to extend coverage to the axilla and serratus anterior area by blocking the intercostobrachial nerve, the third to the sixth intercostal nerves (including their lateral cutaneous branches) and the long thoracic nerve. The anaesthetic agent is directed between pectoralis minor and serratus anterior, in the plane deep to the fascia covering serratus anterior. These blocks provide consistent effective regional analgesia, reducing postoperative pain and the need for opioid pain relief. Serratus blocks were developed to extend analgesia to the lateral thorax from the second to ninth intercostal nerves and have been used for both postsurgical breast and thoracotomy pain. Injection of local anaesthetic is directed both superficial and deep to serratus anterior: the spread of the anaesthetic in the fascial planes eliminates the need for multiple injections to target each intercostal nerve.

sometimes block the duct apertures in the non-pregnant breast. The ducts are slightly expanded at the base of the nipple, and there is considerable variation in duct diameter throughout the breast (Cooper 1840). The ductal system expands as it fills with milk during lactation, dilating even further to accommodate milk flow at milk ejection (Ramsay et al 2005). Each lactiferous duct is connected to a complex system of ducts and lobules, surrounded by connective tissue stroma, collectively forming a lobe of the breast (see Fig. 53.23B). Lobes vary in size, shape and depth. A single lobe may comprise from as little as 1% to as much as a 25% of the entire breast. Vestigial lobes have been identified and are composed of long ducts running deep into the breast with very few or no branches or glandular tissue. The presence of these lobes suggests a competitive process of ductal expansion and in part explains the observation of fewer functional lobes during lactation (Going and Moffat 2004). Whilst ducts can be intertwined, there is no evidence of anastomotic connections between lobes. Lobules consist of the portions of the glands that have secretory potential: their structure varies according to hormonal status. In the mature resting breast, each lobule consists of a cluster of blind-ended, branched ductules (**Fig. 53.25C**).

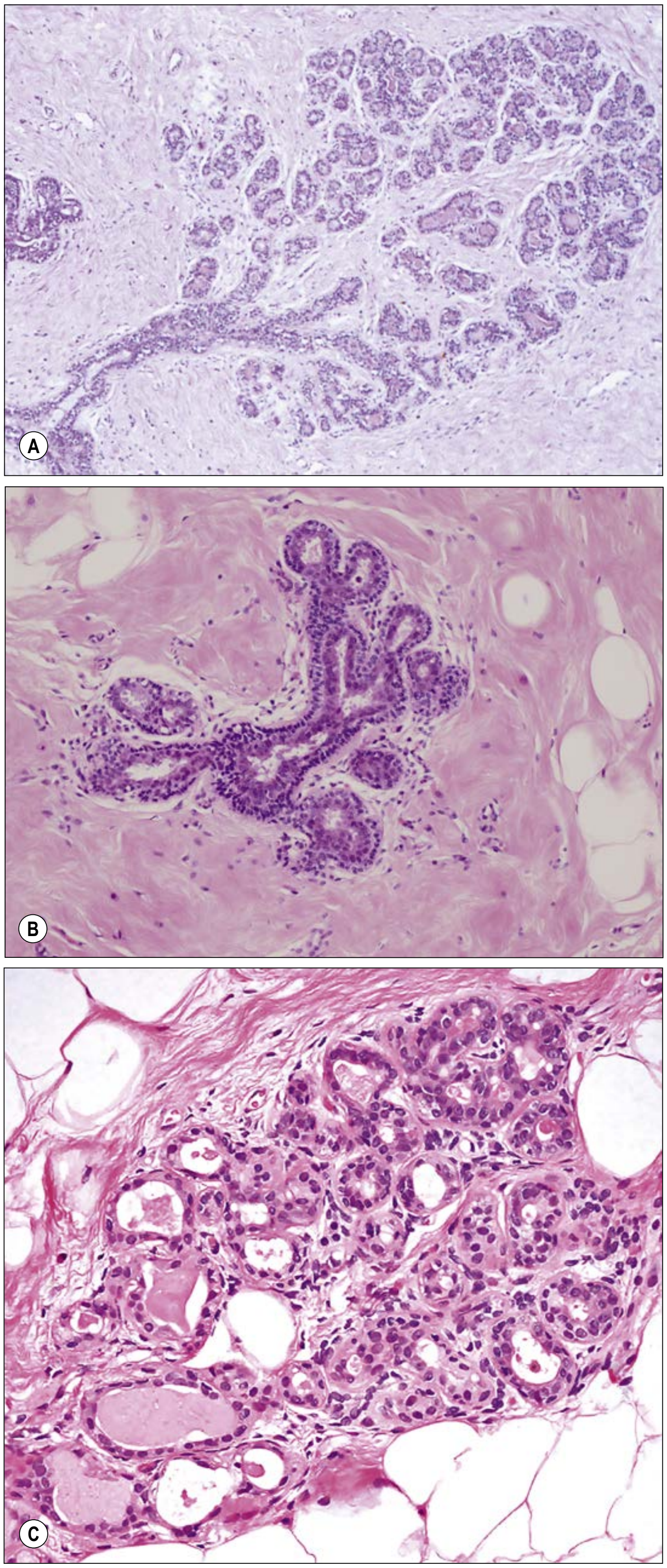

Fig. 53.25 **A**, A glandular lobule surrounded by collagenous interlobular connective tissue in the mature resting breast. A terminal duct (bottom left) branches extensively to terminate in rudimentary alveoli. **B**, Section through a large duct, surrounded by its smaller lobular branches, embedded in fibrocollagenous connective tissue. The ducts are lined by columnar epithelium enclosed by a prominent layer of myoepithelial cells, giving the appearance of a bilayered lining. **C**, Rudimentary alveoli shown at higher magnification, surrounded by fibrous and adipose connective tissue. (A, With permission from Young B, Heath JW 2000 Wheater's Functional Histology. Edinburgh: Churchill Livingstone. B, Courtesy of Mr Peter Helliwell, Department of Histopathology, Royal Cornwall Hospitals Trust, UK. C, Courtesy of Mr Peter Helliwell and the late Dr Joseph Mathew, Department of Histopathology, Royal Cornwall Hospitals Trust, UK.)

Internally, the nipple is composed mostly of collagenous dense connective tissue and contains numerous elastic fibres that wrinkle the overlying skin (see Fig. 53.23C–D). Deep to the nipple and areola, bundles of smooth muscle cells are arranged radially and circumferentially within the connective tissue and are thought to be remnants of the panniculus carnosus, a thin striated muscle layer attached to the deep surface of the skin, seen in other mammals. Their contraction, induced by cold or tactile stimuli (e.g. in suckling), causes erection of the nipple and wrinkling of the surrounding areola.

Development

The epithelial–mesenchymal interactions that give rise to the glandular tissue of the breast in both sexes can first be seen in Carnegie stages 16–17, when two ventral bands of thickened ectoderm, the mammary ridges (crests) or milk lines, extend from the axilla to the inguinal region (see Fig. 53.27). Invagination of the thoracic primary mammary buds as multiple longitudinal ducts occurs by stage 20, and the remaining mammary line involutes. Ductal epithelial branches subsequently develop, penetrating the mesenchyme at around stage 23.

The thoracic ectodermal ingrowths branch into 15–20 solid buds of ectoderm that will become the lactiferous ducts and their associated lobules and alveoli in the fully formed gland (**Fig. 53.26**). They are surrounded by somatopleuric mesenchyme that forms the connective tissue, fat and vasculature that is invaded by the nerves to the breast. Continued cell proliferation, elongation and further branching produce the alveoli and define the duct system. Nipple formation begins during stage 23, primitive ducts (mammary sprouts) develop from postmenstrual week 15, and canalization occurs at about postmenstrual week 24. During postmenstrual weeks 33–40, the ducts become canalized and the epidermis at the point of original development of the gland forms a small mammary pit, into which the lactiferous ducts open. Perinatally, the nipple is formed by mesenchymal proliferation. Should this process fail, the ducts open into shallow pits. Rarely, the nipple may not develop (athelia), an occurrence more commonly observed in accessory breast tissue.

Accessory breast tissue and nipples

Polymastia (supernumerary breasts) and polythelia (supernumerary nipples) may develop in males and females anywhere along the length of the mammary ridges (milk lines) (**Fig. 53.27**). Conversely, breast tissue may not develop at all (amastia), or there may be nipple development but no breast tissue (amazia). Supernumerary breast development occurs in most cases in the thoracic region, just inferior to the normal breast (90%), but may also occur in the axillary (5%) and abdominal regions (5%) and even on the medial thigh. Polythelia occurs along the same mammary line but no underlying glandular tissue develops. This condition is rare in females but is more common in males, in whom the accessory nipple may be mistaken for a mole.

Congenital inversion of nipple

Available with the *Gray's Anatomy* e-book

Under hormonal influence type 1 lobules (~11 alveolar buds) progress to type 2 (~47 alveolar buds) and type 3 lobules (~80 alveolar buds) that are larger in size consisting of a greater number of alveolar buds, reaching type 4 (the fully differentiated functional lobule) during lactation (Russo and Russo 2004). Greater numbers of type 1 lobules are observed in nulliparous women. However, in parous women with breast cancer more type 1 lobules and fewer type 3 lobules have been observed compared to parous women without breast cancer.

At birth the breasts have reached a similar developmental stage in both sexes, and the combination of fetal prolactin and maternal oestrogen may give rise to transient hyperplasia and neonatal galactorrhoea (the secretion of witch's milk). In males the breasts normally remain undeveloped whereas in females at puberty, in late pregnancy and during the period of lactation, they undergo further hormone-dependent developmental changes. The female breast is a unique organ in that it remains in a rudimentary (i.e. fetal) form until puberty, at which time its development continues under the influence of sex hormones. The adult form is reached in late adolescence, after which the breast is able to progress to a fully functioning milk-producing organ following pregnancy and childbirth. After the menopause the breast involutes into a predominantly fatty organ with reduced ductal-glandular parenchyma.

Congenital inversion of the nipples occurs rarely in the female population and is almost always bilateral. The majority of the cases are umbilicated, i.e. the nipple can be easily pulled forwards from its depressed position underneath the areolar surface. The condition is thought to be due to failure of proliferation of the mesenchymal tissue which then fails to push the nipple out. The remaining cases are due to invagination of the nipple. Apart from psychological implications, inversion of the nipple may cause recurrent mastitis and difficulty with breast feeding: the anomaly may be corrected surgically.

CHAPTER 53

Age-related changes

Prepuberty

The neonatal breast contains rudimentary lactiferous ducts but no alveoli. Until puberty, little branching of the ducts occurs, and any mammary enlargement is symmetric and reflects the growth of fibrous stroma and fat.

Puberty

In the postpubertal female the ducts elongate and become branched on stimulation by ovarian oestrogens. The ends of the branches form solid spheroidal masses of granular polyhedral cells, the potential alveoli. Oestrogens also promote adipocyte differentiation from mesenchymal cells in the interlobular stroma, and breast volume enlargement at puberty is mainly a consequence of lipid accumulation by these adipocytes.

From puberty onwards, externally recognizable breast development (thelarche) can be divided into five separate phases (Fig. 53.28): elevation of the breast bud (phase I); glandular subareolar tissue is present and both the nipple and breast project from the chest wall as a single mass (phase II); the areola increases in diameter and becomes pigmented, and there is proliferation of palpable breast tissue (phase

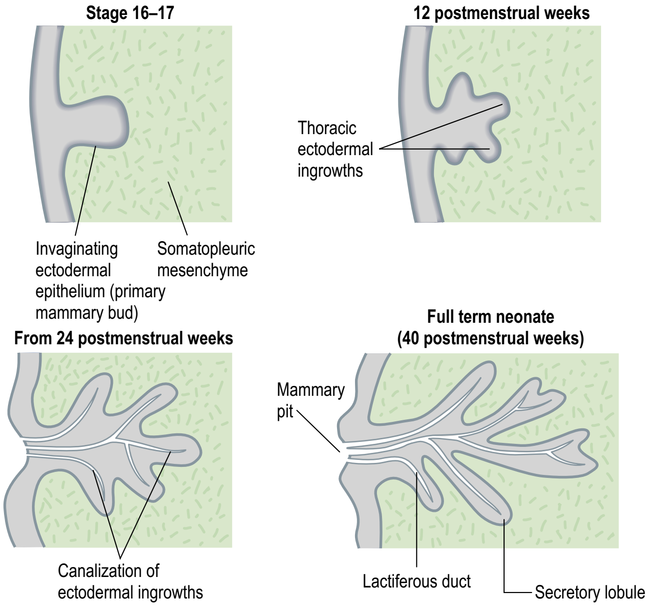
Stage 16–17
12 postmenstrual weeks
Thoracic ectodermal ingrowths
Invaginating ectodermal epithelium (primary mammary bud)
Somatopleuric mesenchyme
From 24 postmenstrual weeks
Full term neonate (40 postmenstrual weeks)
Mammary pit
Canalization of ectodermal ingrowths
Lactiferous duct
Secretory lobule

Fig. 53.26 Epithelial/mesenchymal interactions and growth of mammary lobules and ducts during development. (Embryonic stages 10–23 correlated to post fertilization days of development and postmenstrual weeks of pregnancy are shown in Fig. 23.3).

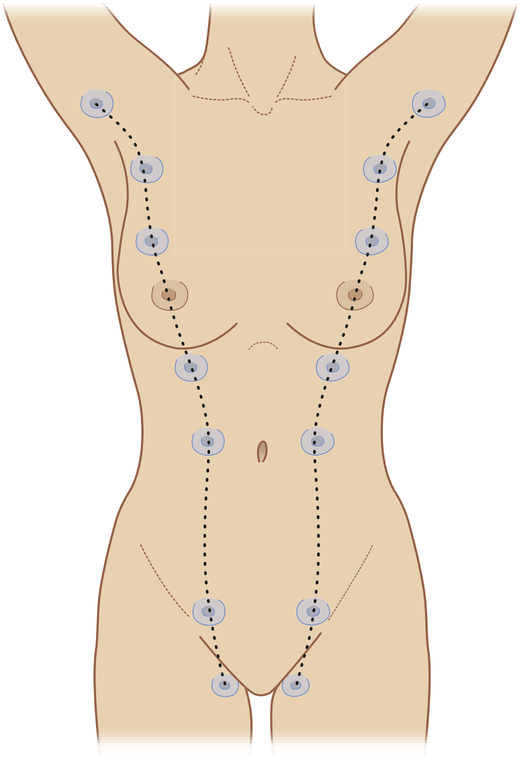

Fig. 53.27 The mammary ridges (milk lines) as potential sites for accessory nipples and breast tissue.

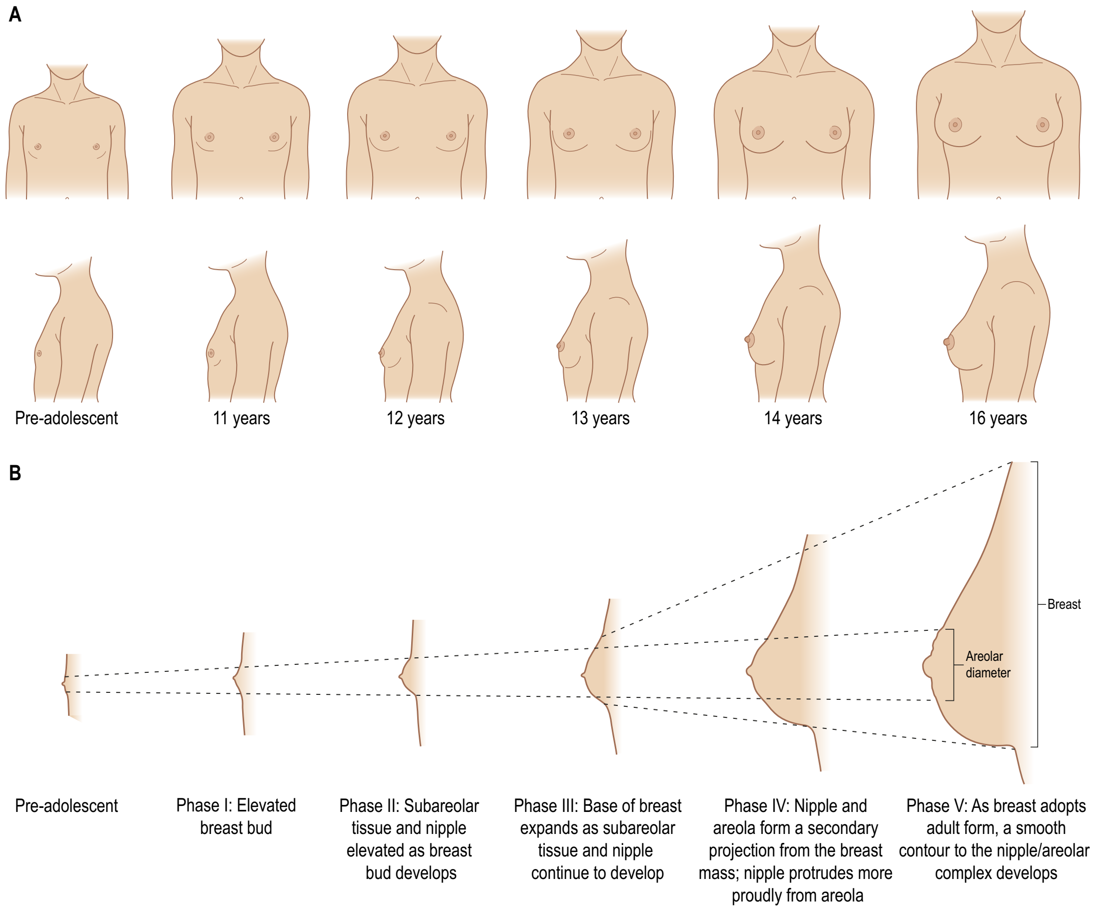
A
Pre-adolescent
11 years
12 years
13 years
14 years
16 years
B
Breast
Areolar diameter
Pre-adolescent
Phase I: Elevated breast bud
Phase II: Subareolar tissue and nipple elevated as breast bud develops
Phase III: Base of breast expands as subareolar tissue and nipple continue to develop
Phase IV: Nipple and areola form a secondary projection from the breast mass; nipple protrudes more proudly from areola
Phase V: As breast adopts adult form, a smooth contour to the nipple/areolar complex develops

Fig. 53.28 Pre- and post-pubertal development and structure of the female breast, demonstrating changes in the contour of the breast shown across 5 phases from 11 to 16 years of age.

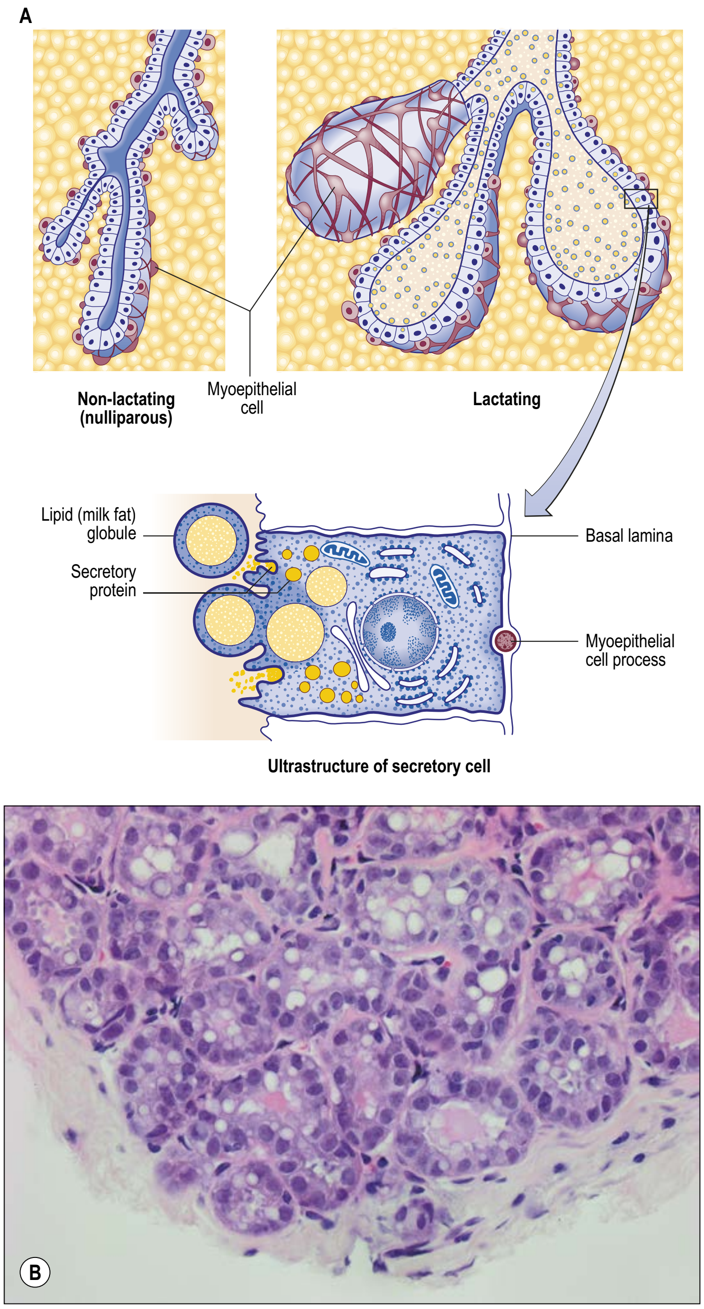

Fig. 53.29 The microstructure of breast epithelium. **A**, Note that the myoepithelial cell process is actually about half the relative size of that shown in the lower diagram. **B**, The peripheral part of a lactating breast lobule. The alveolar lumina contain milk secretion. Milk protein appears as eosinophilic material in the lumen and milk fat as pale cytoplasmic vacuoles in the secreted milk and in the alveolar epithelial cytoplasm. (B, Courtesy of Mr Peter Helliwell, Department of Histopathology, Royal Cornwall Hospitals Trust, UK)

III); further pigmentation and enlargement occur in the areola, so that the nipple and areola form a secondary mass anterior to the main part of the breast (phase IV); and a smooth contour to the breast develops (phase V).

Changes during the menstrual cycle

Changes occur in the breast tissues in the menstrual cycle. In the follicular phase (days 3–14) the stroma becomes less dense. Various changes, including luminal expansion, take place in the ducts, and there are occasional mitoses but no secretion. In the luteal phase (days 15–28) there is a progressive increase in stromal density and the ducts have an open lumen that contains secretion, associated with flattening of the epithelial cells. Cell proliferation is maximal on day 26 and thereafter the ductal system undergoes reduction; epithelial cell apoptosis is greatest on day 28 of the cycle. There are also changes in blood flow, greatest at mid-cycle, and an increase in the water content of the stroma in the second half of the menstrual cycle.

Postmenopausal

A decline in ovarian function triggers progressive atrophy of lobules and ducts after the menopause, and there is fatty replacement of glandular breast tissue. A few ducts and atrophic lobules may remain, the stroma becomes less cellular and collagenous fibres decrease. The amount of adipose tissue varies widely between individuals, as does the volume of glandular tissue, which is typically increased with the administration of hormone replacement therapy.

Changes associated with pregnancy and lactation

Pregnancy

As the output of oestrogen and progesterone, produced first by the corpus luteum and later by the placenta, increases during pregnancy, the intralobular ductal epithelium proliferates and the cells increase in size: the number and length of the ductal branches therefore increase. Alveoli develop at their termini and expand as their cells and lumina fill with newly synthesized and secreted milk. The myoepithelial cells, which are initially spindle-shaped, become highly branched stellate cells, especially around the alveoli. Adjacent myoepithelial cells intermesh to form a basket-like network around the alveoli and ducts, interposed between the basal lamina and the luminal cells (see Fig. 2.3). Their cytoplasm contains actin and myosin filaments, and they are contractile (see Fig. 2.4). Typically there is a concomitant reduction in adipose tissue in the stroma. The numbers of lymphocytes, including plasma cells, and eosinophils increase greatly. Blood flow through the breast increases to approximately double that of the non-pregnant state. Secretory activity in the alveolar cells rises progressively in the latter half of pregnancy. In late pregnancy, and for a few days after parturition, their product is different from later milk and is known as colostrum, characteristically low in lipid but rich in protein and immunoglobulins. Proliferation of the glandular breast parenchyma results in an overall increase in breast size through gestation.

Lactation

True milk secretion begins a few days after parturition as a result of a reduction in circulating oestrogen and progesterone, a change that appears to stimulate production of prolactin by the anterior lobe of the pituitary gland. Milk distends the alveoli so that the cells flatten as secretion increases (see Fig. 53.23B; **Fig. 53.29**). The alveolar cell cytoplasm accumulates membrane-bound granules of casein and other milk proteins and these are released from the apical plasma membrane by membrane fusion (merocrine secretion; see Fig. 2.6). Lipid vacuoles are formed directly in the apical cytoplasm as small lipid droplets that fuse with each other to create large ‘milk vacuoles’ up to 10 μm across. These are released as intact lipid droplets with a thin surround of apical plasma membrane and adjacent cytoplasm (apocrine secretion; see Fig. 2.6). Hormonal stimulation by oxytocin causes myoepithelial cells to contract and expel alveolar secretions into the ductal system in readiness for suckling. After the onset of lactation there is a gradual reduction in the numbers of lymphocytes and eosinophils in the stroma, although plasma cells continue to synthesize immunoglobulin A (IgA) for secretion into the milk. Alveolar cells take up IgA synthesized by adjacent plasma cells by endocytosis at their basal surfaces and secrete it apically, as dimers complexed to the epithelial secretory component.

Post lactation

Lactation may continue for several years. Whenever it finishes, the secretory tissue undergoes some involution but the ducts and alveoli never return completely to the pre-pregnant state. Two major processes are responsible for the regression of the alveolar–ductal system: a reduction in epithelial cell size and a reduction in cell numbers mediated via apoptosis. Gradually, the breast tissue reverts to its resting state. If another pregnancy occurs, the resting glandular tissue is reactivated and the process outlined above recurs. Up to the age of about 50 years, increasing amounts of elastic tissue tend to be laid down around vessels and ducts (elastosis), and in the stroma: elastosis does not normally continue into later life.

Mammary stem cells

Available with the *Gray's Anatomy* e-book

Postpartum mammary stem cells (MaSC) differ from other adult stem cells because they are likely to be involved in organ homeostasis and in postnatal development of the gland through each menstrual and reproductive cycle. Hormonal changes during puberty have been shown to drive ductal development through proliferation of MaSC in the terminal end buds (TEBs) in mice (Scheele et al 2017). TEBs consist of two layers, the cap cells that form the outer layer and differentiate into basal cells, and the body cells that form the inner layer and are precursors of luminal epithelial cells. TEBs are well characterized in rodents and are assumed to be analogous to terminal ductal lobular units (TDLUs) in humans, although their location at the periphery of ductal trees is the only confirmed shared feature.

Genetic lineage-tracing techniques in mice show that postpartum MaSC acting during puberty are unipotent (Davis et al 2016, Van Keymeulen et al 2017), although a small body of evidence suggests that some cells may also be bipotent or multipotent (Rios et al 2014, Wang et al 2018). It is currently unclear whether unipotent stem cells are the sole influential drivers of ductal elongation and alveologenesis during puberty in humans or during pregnancy in either humans or mice.

Together with unipotent stem cells responsible for the development and growth of the mammary epithelium, a population of cells may exist that act as multipotent stem cells under certain conditions (facultative or potential stem cells). These cells may be quiescent in the resting state and undetected by lineage tracing studies, and may only be recruited for regeneration in times of stress or exposure to a different microenvironment. Normal mammary cells may be transformed into bipotent stem cells when transplanted *ex vivo* into mice with cleared mammary fat pads (Stingl et al 2006).

Another unique population of cells seemingly involved in mammary gland remodelling are parity-induced mammary epithelial cells (PI-MEC): they have been identified in the ductal periphery and seemingly persist for multiple pregnancy–lactation cycles. PI-MECs only contribute to a luminal lineage that is hormone-receptor negative. The contribution of more than a single unipotent MaSC to the development of an alveolus during pregnancy or lactation confirms that a population of lineage-restricted MaSCs contribute to the functional mammary gland.

Rapid technological advances in the area of stem cell biology are providing a deeper understanding of stem cell dynamics integral to normal breast development and breast cancer (Lloyd-Lewis et al 2017). However, much of the research in mammary development is carried out in the mouse: species differences between mice and humans, particularly with respect to the architecture of the mammary gland, stroma and hormonal milieu, mean that experimental results should be interpreted with caution.

Histological changes are fibrosis and subsequent hyalinization. Ductal elements are usually present but lobular development is inconspicuous. The aetiology in the majority of cases is idiopathic. Broadly speaking, causes may be either physiological, reflecting imbalances of sex hormones in neonates, at puberty and in senescence, or pathological, reflecting hypogonadal or hyperoestrogenic states. Acquired causes include metabolic imbalances, endocrine and neoplastic conditions, and drug-induced gynaecomastia. In the adult male, unilateral gynaecomastia should be investigated to exclude male breast cancer.

Thoracocentesis is essential in the assessment of pleural effusion. A chest radiograph will confirm the location and extent of the effusion and clinical examination will identify the best position for aspiration, the posterior mid-scapular line being a common site. The skin of the desired intercostal space is cleaned and anaesthetized, and the aspiration needle is inserted at the inferior margin of the space because the main intercostal vessels run in the superior region of the space. After appropriate local analgesia has been applied, the needle is carefully advanced in a perpendicular direction through the fascial and muscular layers of the thoracic wall, until it passes through the parietal pleura and enters the pleural cavity (see Fig. 53.17). More complex or small effusions should be aspirated under ultrasound guidance.

Needle thoracocentesis is performed when a life-threatening tension pneumothorax is suspected. A needle is inserted into the second intercostal space in the mid-clavicular line on the affected side. A sudden escape of air is heard when the needle enters the parietal pleura. A thoracostomy followed by chest drain insertion must subsequently be performed within the revised triangle of safety after this procedure.

The site for thoracostomy and chest drain insertion is usually the fourth (ideally) or fifth intercostal space, between the mid and anterior axillary lines (revised triangle of safety). A thoracostomy is performed via a 2 cm horizontal skin incision, followed by blunt dissection (often using a clamp) through the subcutaneous tissues to the superior border of the inferior rib of the space, then through the intercostal muscles. The parietal pleura is penetrated with the tip of a clamp, and a gloved finger inserted into the pleural cavity to release pleural adhesions (pleural sweep). The chest drain tube is then inserted into the pleural cavity and attached to an underwater sealed container placed below the level of the lungs; the fluid level should rise and fall in the tube with ventilation.

Pericardiocentesis is performed to aspirate a pericardial effusion or, in an emergency, to decompress a cardiac tamponade, where pressure from blood in the pericardial space prevents the heart chambers from filling during the cardiac cycle, seriously impairing cardiac output. Rapid and extensive bleeds often clot and therefore limit the success of this procedure.

Pericardiocentesis is performed in either the fifth or sixth left intercostal space near the sternum (to avoid the more laterally located internal thoracic vessels) or 1–2 cm to the left of the angle between the junction of the xiphoid process and left costal arch. In the latter case, the needle is introduced and advanced at 45° to the skin, and directed superiorly and posteriorly towards the inferior angle of the left scapula until it enters the pericardial cavity.

Male breast

The male breast remains rudimentary throughout life. It is formed of small ducts (without lobules or alveoli) or solid cellular cords and a little supporting fibroadipose tissue (Ellis et al 1993). Slight temporary enlargement may occur in the newborn, reflecting the influence of maternal hormones, and again at puberty. The areola is well developed, although limited in area, and the nipple is relatively small. Normally the ducts do not extend beyond the areola in a male breast, although glandular tissue can be more extensive.

Gynaecomastia

Gynaecomastia is a benign proliferation of subareolar breast tissue in the male. It may be unilateral or bilateral and of varying severity (Simon et al 1973) and symptomatology. Pain or tenderness, thought to be due to accumulation of fluid in the glandular ducts, may be a presenting feature.

INTERVENTIONAL ACCESS TO THORACIC VISCERA

Thoracocentesis (pleural aspiration)

Available with the *Gray's Anatomy* e-book

Needle thoracocentesis

Available with the *Gray's Anatomy* e-book

Chest drain insertion

Available with the *Gray's Anatomy* e-book

Pericardiocentesis

Available with the *Gray's Anatomy* e-book

Thoracotomy incisions

Available with the *Gray's Anatomy* e-book

Sternotomy

Available with the *Gray's Anatomy* e-book

Axillary thoracotomy

Available with the *Gray's Anatomy* e-book

Thoracoscopic access

Available with the *Gray's Anatomy* e-book

Placement of electrocardiograph (ECG) leads

Available with the *Gray's Anatomy* e-book

Bonus e-book content

Fig. 53.7 Pectus excavatum (axial CT image).

Fig. 53.12 B, CT MIP slab through a typical rib and thoracic vertebra showing the costotransverse and costovertebral joints.

Fig. 53.15 B–D, Muscles of the thoracic wall.

Fig. 53.19 The internal thoracic vessels prepared for micro-anastomosis beneath the third costal cartilage.

Fig. 53.20 A–B, Pre- and post-embolization images after selective catheterization of the right eleventh posterior intercostal artery.

Fig. 53.22 B, Lymphatic drainage of the anterior thoracic and abdominal walls and skin of the breast.

Key references

Casha AR, Camilleri L, Manche A et al 2015 External rib structure can be predicted using mathematical models: an anatomical study with application to understanding fractures and intercostal muscle function. Clin Anat 28:512–19.

Chakravarthi KK, Siddaraju KS, Venumadhav N et al 2018 Anatomical and congenital variations of human dry sternum bone: its embryogenesis and clinical implications. Int J Res Med Sci 6:300–4.

Going JJ, Moffat DF 2004 Escaping from Flatland: clinical and biological aspects of human mammary duct anatomy in three dimensions. J Pathol 203:538–44.

Gregory PL, Biswas A, Batt ME 2002 Musculoskeletal problems of the chest wall in athletes. Sports Med 32:235–50.

Henry BM, Graves MJ, Pekala JR et al 2017 Origin, branching and communications of the intercostobrachial nerve: a meta-analysis with implications for mastectomy and axillary lymph node dissection in breast cancer. Cureus 9:e1101.

Versyck B, Geffen GV, Houwe PV 2017 Prospective double blind randomized placebo-controlled clinical trial of the pectoral nerves (Pecs) block type II. J Clin Anesth 40:46–50.

Thoracotomy incisions may be posterolateral or anterolateral, or involve a transverse thoracosternotomy.

Posterolateral incision A posterolateral incision is most commonly used in thoracic surgery for unilateral pulmonary resections, bullectomy, unilateral lung volume reduction surgery, chest wall resection and oesophageal surgery (Fry 2000). The patient is placed in a lateral decubitus position with adequate support of the elbow, axilla and knee with padding. The standard approach is via an incision from the anterior axillary line, which curves about 4 cm inferior to the inferior angle (tip) of the scapula and then vertically between the posterior midline and medial border of the scapula. The incision is usually extended to the level of the spine of the scapula. Overall, the incision forms an S-shape following the fifth intercostal space. The sixth or seventh intercostal space is used in oesophageal surgery.

The inferior portions of trapezius and latissimus dorsi are divided. Serratus anterior is retracted, and may be divided in a high (superior) thoracotomy. The costal muscle and pleura are dissected along the inferior margin of the intercostal space to avoid damaging the neurovascular bundle. The intercostal space should be spread slowly to avoid rib fracture: a small section of the posterior part of the rib may be removed to reduce the risk of fracture, particularly in patients older than 40 years. This technique provides good access to the thoracic contents; the main complication is postoperative pain as a consequence of intraoperative musculoskeletal traction, rib fracture and damage to the intercostal nerves.

Anterolateral incision The patient is placed in the supine position, with their arms by their sides. A roll is placed vertically under the back and hips in order to raise the operative side by approximately 45°. The incision is from the mid-axillary line over the fifth intercostal space along the inframammary skin fold, and curves superiorly parasternally. The pectoral muscles are divided, and subsequent access to the thorax is similar to that used in the posterolateral approach: access is limited, and may be improved by dividing costal cartilages.

'Clam shell' The transverse thoracosternotomy ('clam shell' incision) provides excellent exposure to both sides of the thoracic cavity and is therefore used in bilateral lung transplantation and in lung volume reduction surgery with bilateral lung resections. The patient is placed in the supine position with a roll vertically along the upper thoracic spine. Bilateral anterolateral incisions are made along the fifth intercostal space (or inframammary fold), and the sternum is transected. This allows the part of the thorax superior to the incision to be displaced upwards with a rib-spreader, hence the name 'clam shell'. The main disadvantage of the clam shell procedure is the need to transect the sternum; even after careful repair with sternal wires, there is a risk of sternal instability. This incision (in the fourth or fifth intercostal space) is also used for emergency access to the thorax in cases of loss of cardiac output from cardiac tamponade often resulting from penetrating trauma; spontaneous return of cardiac output may result from the rapid resolution of a tamponade and haemostasis.

Sternotomy is commonly needed in cardiac surgery. The patient is placed in the supine position with both arms extended by their side. A vertical incision is made in the midline (median plane) from the jugular (suprasternal) notch to a point just inferior to the xiphoid process, the tissues around the manubrium of the sternum and the xiphoid process are mobilized, and the pectoral fascia in the midline is incised. The sternum is divided equally and its two left and right halves retracted; it is subsequently closed using interosseous wire sutures.

The patient is placed in the lateral decubitus position, with arms abducted at 90° and supported on an arm rest. The incision is based along the desired intercostal space: for upper thoracic access, this is the second or third intercostal space. Latissimus dorsi is elevated and retracted, whereas serratus anterior is divided in the direction of its fibres. The anterior aspect of serratus anterior is divided to expose the intercostal muscles, which are divided in turn. Although the overall size of the incision is limited, it provides good access to the upper thorax. Postoperative pain is less than with some other approaches, but the long thoracic nerve may be damaged if serratus anterior is divided too posteriorly. The nerve is commonly located in the region between the mid and posterior axillary lines (Ebraheim et al 1998).

Occasionally, video-assisted thoracoscopic surgery is required to assess the mediastinum. The thoracoscope is usually introduced via the fifth intercostal space in the mid-clavicular line, with additional ports at the third and sixth intercostal spaces to assess the anterior mediastinum. To assess the posterior mediastinum, the thoracoscope is inserted into the seventh intercostal space in the mid-clavicular line.

The 12-lead ECG provides three-dimensional information on the electrical activity of the heart. The limb leads provide information about the electrical activity in the frontal plane and are placed on the left and right wrists and the left foot; the right foot acts as a neutral grounding point. The chest leads provide information about the electrical activity in the horizontal plane and are placed as follows: V1, right fourth intercostal space, parasternal position; V2, left fourth intercostal space, parasternal position; V3, midpoint of V2 and V4 on the left; V4, fifth intercostal space, mid-clavicular line on the left; V5, fifth intercostal space, anterior axillary line on the left; and V6, fifth intercostal space, mid-axillary line on the left.

References

Bakamjian VY, Long M, Rigg B 1971 Experience with the medially based deltopectoral flap in reconstructive surgery of the head and neck. Br J Plast Surg 24:174.

Casha AR, Camilleri L, Manche A et al 2015 External rib structure can be predicted using mathematical models: an anatomical study with application to understanding fractures and intercostal muscle function. Clin Anat 28:512–9.

Chakravarthi KK, Siddaraju KS, Venumadhav N et al 2018 Anatomical and congenital variations of human dry sternum bone: its embryogenesis and clinical implications. Int J Res Med Sci 6:300–4.

Chang KZ, Likes K, Davis K et al 2013 The significance of cervical ribs in thoracic outlet syndrome. J Vasc Surg 57:771–5.

Cooper AP 1840 On the Anatomy of the Breast. London: Longman, Orme, Green, Brown and Longmans.

Davis FM, Lloyd-Lewis B, Harris OB et al 2016 Single-cell lineage tracing in the mammary gland reveals stochastic clonal dispersion of stem/progenitor cell progeny. Nat Commun 25:13053.

Dudgeon SN, Marcotte KM, Fox GM et al 2017 A previously unclassified variant of sternalis muscle. Surg Radiol Anat 39:1417–9.

Ebraheim NA, Lu J, Porshinsky B et al 1998 Vulnerability of long thoracic nerve: an anatomic study. J Shoulder Elbow Surg 7:458–61.

Ellis H, Colborn GL, Skandalakis JE 1993 Surgical embryology and anatomy of the breast and its related anatomic structures. Surg Clin North Am 73:611–32.

Fry WA 2000 Thoracic incisions. In: Shields TW, LoCicero III J, Ponn RB (eds) General Thoracic Surgery, 5th ed. Philadelphia: Lippincott Williams & Wilkins; pp. 367–74.

Going JJ, Moffat DF 2004 Escaping from Flatland: clinical and biological aspects of human mammary duct anatomy in three dimensions. J Pathol 203:538–44.

Gregory PL, Biswas A, Batt ME 2002 Musculoskeletal problems of the chest wall in athletes. Sports Med 32:235–50.

Gruber L, Martinoli AS, Tagliafico J et al 2016 A rare case of a symptomatic sternalis muscle: ultrasonography and MRI correlation. Ultrasound International Open 2:E140–1.

Hartrampf CR, Scheflan M, Black PW 1982 Breast reconstruction with a transverse abdominal island flap. Plast Reconstr Surg 69:216–25.

Henry BM, Graves MJ, Pekala JR et al 2017 Origin, branching and communications of the intercostobrachial nerve: a meta-analysis with implications for mastectomy and axillary lymph node dissection in breast cancer. Cureus 9:e1101.

Joshua A, Shetty L, Pare V et al 2014 Variations in the dimensions and shape of thoracic cage with aging: an anatomical review. Anat J Africa 3(2):34–55.

Jung BF, Ahrendt GM, Oaklander AL et al 2003 Neuropathic pain following breast cancer surgery: proposed classification and research update. Pain 104:1–13.

Kasotakis G, Hasenboehler EA, Streib EW et al 2017 Operative fixation of rib fractures after blunt trauma: a practice management guideline from the Eastern Association for the surgery of trauma. J Trauma Acute Care Surg 82:618–26.

Ladak A, Tubbs RS, Spinner RJ 2014 Mapping sensory nerve communications between peripheral nerve territories. Clin Anat 27:681–90.

Lin WC, Lin KH, Huang HK et al 2018 Preoperative three-dimensional printing for surgical stabilization of rib fractures. J Med Sci 38:46–8.

Lindner J, Douglas L, Seligson D 2017 Orthopaedic anatomy of the sternum: a micro-CT study to guide the fixation of sternal fractures. Biol Eng Med 2:1–4.

Lloyd-Lewis B, Harris OB, Watson CJ et al 2017 Mammary stem cells: premise, properties and perspectives. Trends Cell Biology 27:556–67.

Lollert A, Emrich T, Eichstadt J et al 2018 Differences in myocardial strain between pectus excavatum patients and healthy subjects assessed by cardiac MRI: a pilot study. Eur Radiol 28:1276–84.

Malata CM, Moses M, Mickute Z et al 2011 Tips for successful microvascular abdominal flap breast reconstruction utilizing the 'total rib preservation' technique for internal mammary vessel exposure. Ann Plast Surg 66:36–42.

Masson JK, Payne WS, Gonzalez JB 1970 Pectus excavatum: use of preformed prosthesis for correction in the adult. Case report. Plast Reconstr Surg 46:399–402.

Mashhour A, Thabet A, Easo J et al 2018 The left internal thoracic artery supplying a major part of the gastrointestinal tract. J Thorac Cardiovasc Surg 155:e25–7.

Matsuo N, Matsumoto K, Taura Y et al 2018 Initial experience with a 3D printed model for preoperative simulation of the Nuss procedure for pectus excavatum. J Thorac Dis 10:E120.

McCraw JB, Dibbell DG, Carraway JH 1977 Clinical definition of independent myocutaneous vascular territories. Plast Reconstr Surg 60:341.

McMahon LE 2018 Slipping rib syndrome: a review of evaluation, diagnosis and treatment. Semin Pediatr Surg 27:183–8.

Middleham HP, Boyd LE, McDonald SW 2015 Sex determination from calcification of costal cartilages in a Scottish sample. Clin Anat 28:888–95.

Munhoz AM, Ishida LH, Montag E et al 2004 Perforator flap breast reconstruction using the internal mammary perforator branches as a recipient site: an anatomical and clinical analysis. Plast Reconstr Surg 114:62–8.

Neligan PC, Gullane PJ, Vesely M et al 2007 The internal mammary artery perforator flap: new variation on an old theme. Plast Reconstr Surg 119:891–3.

Nielsen TD, Moriggl B, Barckman J et al 2019 Cutaneous anaesthesia of hip surgery incisions with iliohypogastric and subcostal nerve blockade: a randomized trial. Acta Anaesthesiol Scand 63:101–10.

Ninković M, Anderl H, Hefel L et al 1995 Internal mammary vessels: a reliable recipient system for free flaps in breast reconstruction. Br J Plast Surg 48:533–9.

Nuss D, Kelly RE, Croitoru DP et al 1988 A 10 year review of a minimally invasive technique for the correction of pectus excavatum. J Paediatr Surg 33:545–52.

Ohgoshi Y, Ino K, Matsukawa M 2016 Ultrasound-guided parasternal intercostal nerve block. J Anesth 30:916.

Openshaw P, Edward S, Helms P 1984 Changes in rib cage geometry during childhood. Thorax 39:624–7.

Ozawa Y, Suzuki R, Hara M et al 2018 Identification of the pericardiacophrenic vein on CT. Cancer Imaging 18:1.

Park MC, Lee JH, Chung J et al 2003 Use of internal mammary vessel perforator as a recipient vessel for free TRAM breast reconstruction. Ann Plast Surg 50:132–7.

Park HJ, Lee SY, Lee CS et al 2004 The Nuss procedure for pectus excavatum: evolution of techniques and early results on 322 patients. Ann Thorac Surg 77:289.

Parrett BM, Caterson SA, Tobias AM et al 2008 The rib-sparing technique for internal mammary vessel exposure in microsurgical breast reconstruction. Ann Plast Surg 60:241–3.

Piraccini E, Biondi G, Byrne H et al 2018 Ultrasound guided transversus thoracic plane block, parasternal block and fascial planes hydrodissection for internal mammary post thoracotomy pain syndrome. Eur J Pain 22:1673–7.

Raab N, Holm-Muehlbauer C, Ninkovic M 2009 Free superficial epigastric artery flap for aesthetic correction of mild pectus excavatum. Plast Reconstr Surg 123:209e–11e.

Ramsay DT, Kent JC, Hartmann RA et al 2005 Anatomy of the lactating human breast redefined with ultrasound imaging. J Anat 206:6:525–34.

Ravitch MM 1955 The operative treatment of pectus excavatum. J S C Med Assoc 51:244–9.

Rehnke RD, Groening RM, Van Buskirk ER et al 2018 Anatomy of the superficial fascia system of the breast: a comprehensive theory of breast fascial anatomy. Plast Reconstr Surg 142:1135–44.

Rios AC, Fu NY, Lindeman GJ et al 2014 In situ identification of bipotent stem cells in the mammary gland. Nature 506:322–7.

Russo J, Russo IH 2004 Development of the human breast. Maturitas 49:2–15.

Saker E, Tardieu GG, Alonso F et al 2016 The forgotten lumbocostal ligament: anatomical study with application to thoracolumbar surgery. Cureus 8(12):e925.

Scheele CL, Hannezo E, Muraro MJ et al 2017 Identity and dynamics of mammary stem cells during branching morphogenesis. Nature 542:313–7.

Simon BE, Hoffman S, Khan S 1973 Classification and surgical correction of gynaecomastia. Plast Reconstr Surg 51:48.

Snosek M, Tubbs RS, Loukas M 2014 Sternalis muscle, what every anatomist and clinician should know. Clin Anat 27:866–84.

Snosek M, Loukas M 2016 Thoracic wall muscles. In: Tubbs RS, Shoja MM, Loukas M (eds) Bergman's Comprehensive Encyclopedia of Human Anatomic Variation, 2nd ed. Hoboken: Wiley Blackwell; Ch. 35, pp. 335–68.

Stingl J, Eirew P, Ricketson I et al 2006 Purification and unique properties of mammary epithelial stem cells. Nature 439:993–7.

Suami H, Pan WR, Mann GB et al 2008 The lymphatic anatomy of the breast and its implications for sentinel lymph node biopsy: a human cadaver study. Ann Surg Oncol 15:863–71.

Suami H, Pan WR, Taylor GI 2009 Historical review of breast lymphatic studies. Clin Anat 22:531–6.

Tanis PJ, Nieweg OE, Valdes Olmos RA et al 2001 Anatomy and physiology of lymphatic drainage of the breast from the perspective of sentinel node biopsy. J Am Coll Surg 192:399–409.

Tanis PJ, van Rijk MC, Nieweg OE 2005 The posterior lymphatic network of the breast rediscovered. J Surg Oncol 91:195–8.

Tomas X, Facenda C, Vaz N et al 2017 Thoracic wall trauma—misdiagnosed lesions on radiographs and usefulness of ultrasound, multidetector computed tomography and magnetic resonance imaging. Quant Imaging Med Surg 7:384–97.

Tubbs RS, Wantanabe K 2016 Ribs and sternum. In: Tubbs RS, Shoja MM, Loukas M (eds) Bergman's Comprehensive Encyclopedia of Human Anatomic Variation, 2nd ed. Hoboken: Wiley–Blackwell; Ch 11, pp. 76–81.

Van Keymeulen A, Fioramonti M, Centonze A et al 2017 Lineage-restricted mammary stem cells sustain the development, homeostasis, and regeneration of the estrogen receptor positive lineage. Cell Rep 20:1525–32.

Versyck B, Van Houwe P, van Geffen GJ et al 2017 A qualitative systematic review of the pectoral nerves block type I and II. Acta Anaesth Belg 68:49–62.

Wang C, Zhang R, Luo P et al 2018 Reconstruction of extensive thoracic wall defect using the external oblique myocutaneous flap: an analysis on 20 Chinese patients with locally advanced soft tissue sarcoma. J Surg Oncol 117:130–6.

Wells FC, Coonar AS 2018 Pectus carinatum. In: Thoracic Surgical Techniques. Cham: Springer International; Ch. 15, pp. 57–60.

CHAPTER
54

Pleura, lungs, trachea and bronchi

The lungs are the essential organs of respiration and are responsible for the exchange of oxygen and carbon dioxide in the blood. The functional anatomy of the thorax and respiratory diaphragm facilitates this complex process. Acting together, the muscles of respiration and the diaphragm increase the intrathoracic volume, creating a negative pressure within the pleural space that causes air influx and lung expansion (Ch. 55). The resultant reduction in intra-alveolar pressure prompts the flow of air down the pressure gradient, through the upper respiratory tract, trachea, bronchi and bronchioles, and finally into the alveoli, where gaseous exchange occurs. Conversely, a decrease in the intrathoracic volume increases intra-alveolar pressure, causing the expiration of air. The combined expiratory movements of the thorax and abdomen do not clear the lung of its gas with each breath; the presence of a large residual volume of gas minimizes the degree to which each new inspiration of air can affect the composition of gas in diffusion exchange with the blood (Lambertsen 1980). Besides efficient oxygen diffusion from alveolar air to blood, the lungs must also provide an inefficient carbon dioxide transfer, thus maintaining a stable carbon dioxide blood and tissue pressure, much higher (38–42 mmHg) than that in the atmosphere. Maintenance of critical homeostasis for carbon dioxide pressure is of greater importance than precise control of oxygen because so many essential electrical and metabolic functions depend on the hydrogen ion concentration $[H^+]$ of the fluids in which these functions are carried out.

The process of breathing exposes the lung to noxious agents, including gases, dust particles, bacteria and viruses, and to dehydration and temperature extremes. The mucous barrier (including its cellular and immunoglobulin factors), the mucociliary escalator, branching pattern of the airways and the cough reflex are all anatomical defences against these insults. Studies of trends of particle deposition in children and young adults have shown that pulmonary deposition fractions are highest in infants who are at greatest risk from exposure to airborne particulate matter (Asgharian et al 2004). Respiratory function may be compromised by either anatomical defects such as chest wall abnormalities, or by paralysis of respiratory muscles or regional pain. Similarly, ultrastructural abnormalities, such as ciliary dysfunction (as seen in Kartagener's syndrome), lead to recurrent respiratory infections and airway damage.

PLEURA

Each lung is covered by a double-layered serous membrane, the parietal and visceral pleura, arranged as a closed, invaginated sac. The visceral pleura adheres closely to the lung surface and follows the interlobar fissures, separately covering each lobe of the lung. In the region of the lung hilum, the visceral pleura lifts off the mediastinal surface of the lung, and continues along the lung root for a short distance before folding back (reflecting) on itself to continue as the mediastinal parietal pleura (**Fig. 54.1**). The parietal pleura covers the lateral mediastinal margins (forming its lateral boundary), most of the respiratory diaphragm and the corresponding half of the thoracic wall.

The pleural cavity represents the potential space between the parietal and visceral pleura. It incorporates an intervening thin film of pleural fluid that allows close sliding contact between the two layers during all phases of respiration. The pleural fluid has a high daily turnover: fluid is produced at 0.01–0.02 ml/kg/h and is continuously absorbed to maintain a pleural fluid level of 0.1–0.2 ml/kg. Fluid movement and absorption are supported by a balance between plasmatic and pleural (hydrostatic and oncotic) pressures and thoracic lymphatic drainage. Pleural effusions occur when the mechanisms that normally resorb the fluid are destabilized.

The negative pressure developed in the pleural cavity during inspiration is the result of the opposing outward pull of the chest wall and the inward elastic recoil of the lung. Any change in the elasticity of these structures or accumulation of fluid or air within the pleural cavity will alter respiratory activity either regionally or globally. Inter-regional disparities in ventilation normally exist as a result of local differences in thoracic expansion and position-related, gravity-dependent gradients in pleural pressure, and are reflected as regional inequalities in gas exchange.

The right and left pleural sacs are separate compartments. Their parietal layers touch posterior to the superior half of the body of the sternum at the anterior junction line (see Fig. 53.4B), and come close to each other, or may touch, posterior to the oesophagus and level with the bodies of the third to fifth thoracic vertebrae at the posterior junctional line. Both lines are visible on radiographs and/or cross-sectional imaging (see Fig. 56.20); changes in the appearance of either line can indicate pathology. More inferiorly, the descending aorta (on the left) and azygos vein (on the right) demarcate the medial extent of the posterior parts of the pleural sacs. Cardiac asymmetry dictates that the left pleural cavity may sometimes be smaller. Transudates accumulate earlier and more often within the larger right pleural cavity.

Some of the folded portions of the pleura at its sites of reflection or recess (e.g. retrosternal, interlobar fissures and the azygo-oesophageal recess), or regions of contact between the left and right pleural cavity (e.g. anterior/posterior junctional lines) are the only parts of normal pleura that can be visualized radiologically. Demonstration of significant pleural shadowing in any other region usually implies pathological pleural abnormality. At direct inspection of the pleural cavity, as during thoracoscopy, both the parietal and visceral pleura appear translucent; the underlying thoracic muscles and blood vessels are visible beneath the parietal pleura, and the lung and subpleural vascular network are visible beneath the visceral pleura, rendering the latter grey and variegated in appearance.

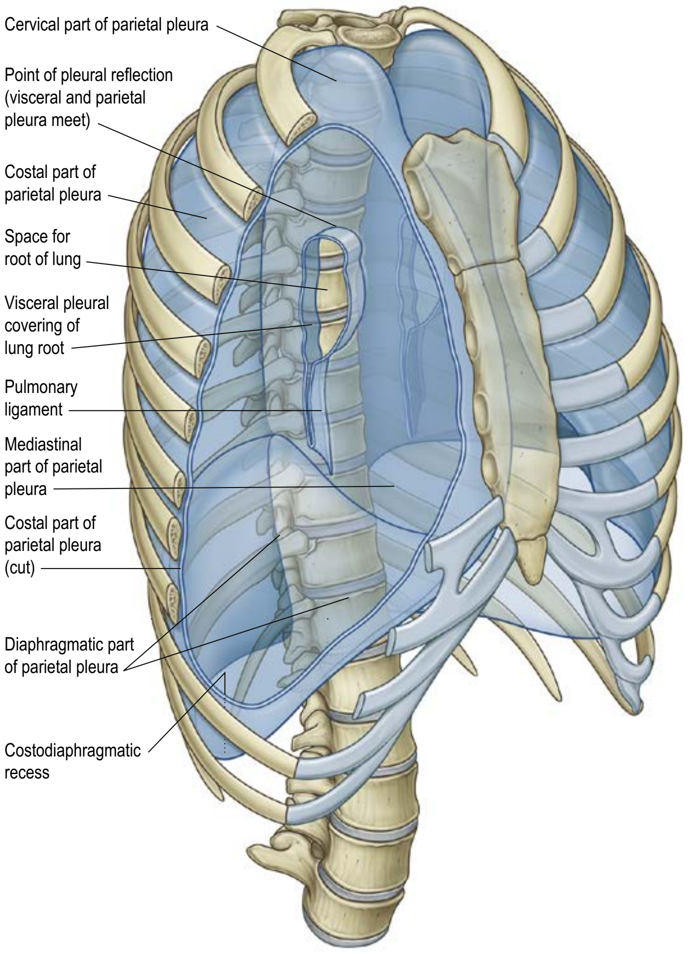
Cervical part of parietal pleura
Point of pleural reflection (visceral and parietal pleura meet)
Costal part of parietal pleura
Space for root of lung
Visceral pleural covering of lung root
Pulmonary ligament
Mediastinal part of parietal pleura
Costal part of parietal pleura (cut)
Diaphragmatic part of parietal pleura
Costodiaphragmatic recess

Fig. 54.1 Reflections and recesses of the parietal pleura. (Adapted with permission from Drake RL, Vogl AW, Mitchell A et al (eds) Gray's Atlas of Anatomy, 2nd ed. Elsevier, Churchill Livingstone. Copyright 2015.)

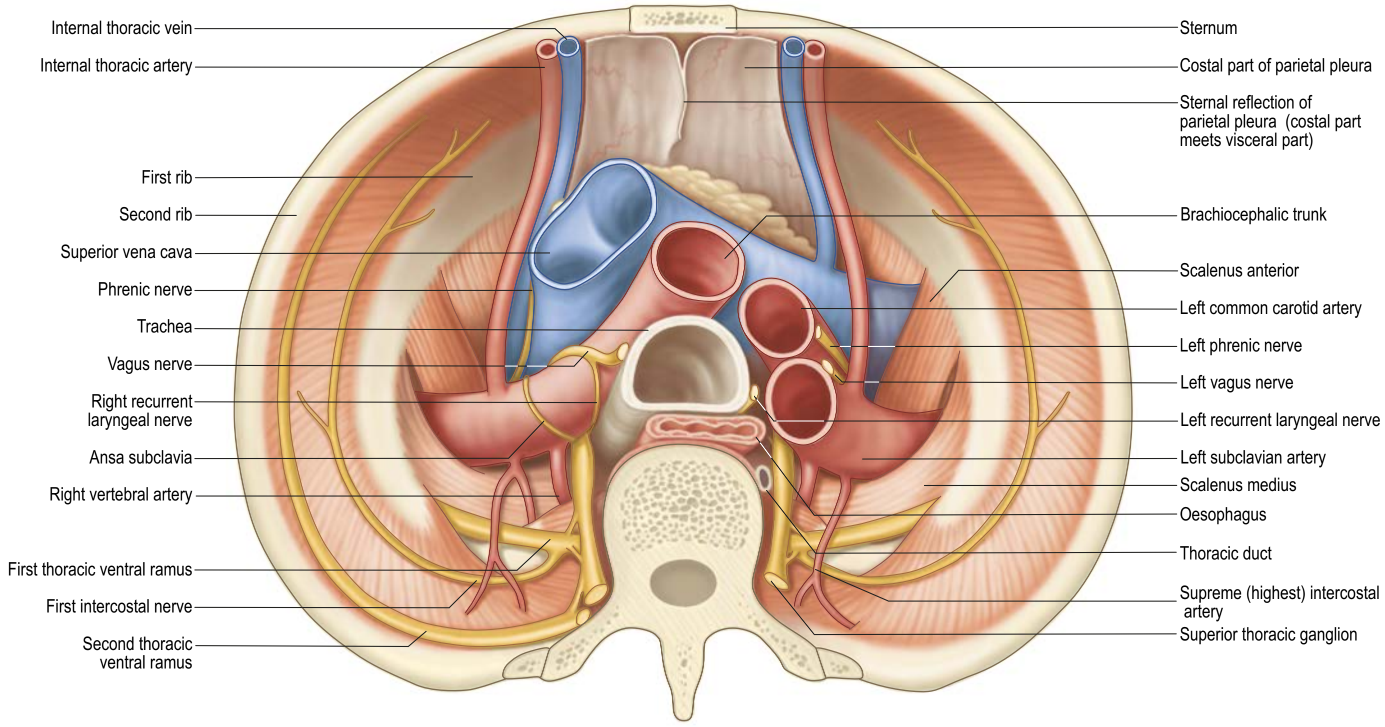
Internal thoracic vein
Internal thoracic artery
First rib
Second rib
Superior vena cava
Phrenic nerve
Trachea
Vagus nerve
Right recurrent laryngeal nerve
Ansa subclavia
Right vertebral artery
First thoracic ventral ramus
First intercostal nerve
Second thoracic ventral ramus
Sternum
Costal part of parietal pleura
Sternal reflection of parietal pleura (costal part meets visceral part)
Brachiocephalic trunk
Scalenus anterior
Left common carotid artery
Left phrenic nerve
Left vagus nerve
Left recurrent laryngeal nerve
Left subclavian artery
Scalenus medius
Oesophagus
Thoracic duct
Supreme (highest) intercostal artery
Superior thoracic ganglion

Fig. 54.2 An inferior view of structures related superiorly to the cervical pleura and suprapleural membrane (both have been removed).

Parietal pleura

Although continuous, different regions of parietal pleura are customarily distinguished by name according to the region they contact. The costal (costovertebral) part lines the internal surface of the thoracic wall and the lateral aspects of the vertebral bodies and intervening intervertebral discs; the diaphragmatic part covers the superior (thoracic) surface of the respiratory diaphragm; the cervical part (pleural dome) covers the inferior surface of the suprapleural membrane (in the region of the lung apex); and the mediastinal part covers the structures between the lungs and within the mediastinum, and forms the lateral border of the mediastinum. The surface markings of the parietal pleura are described in Chapter 52.

Costal part

The costal part of the parietal pleura lines the sternum, the lateral margins of the vertebral bodies and intervening intervertebral discs, the ribs and transversus thoracis and the intercostal muscles. External to the pleura, and located within the extrapleural space is the endothoracic fascia, a thin layer of loose connective tissue analogous to the transversalis fascia of the abdominal wall. Anteriorly, the costal pleura begins posterior to the sternum, where it is continuous with the mediastinal pleura along a line extending inferomedially, from posterior to the sternoclavicular joint to posterior to the sternal angle in the midline (see Fig. 53.4B). From here, the right and left costal pleurae descend in contact with each other to the level of the fourth costal cartilage and then diverge. On the right side, the pleura descends almost vertically to reach the posterior aspect of the xiphisternal joint, while on the left it diverges laterally and descends at a distance of 3–5 cm from the sternal margin to the anterior end of the sixth rib, forming the cardiac notch (pericardial triangle). On each side, the costal parietal pleura passes laterally, lining the internal surfaces of the costal cartilages, ribs, transversus thoracis and intercostal muscles. Posteriorly, it passes over the sympathetic trunk and its ganglia and splanchnic branches to reach the lateral sides of the vertebral bodies and intervertebral discs, where it again is continuous with the mediastinal pleura. Superior to the first rib, the costal pleura is continuous with the cervical pleura; inferiorly, it becomes continuous with the diaphragmatic pleura along a line that differs slightly on the two sides. On the right, the line of costodiaphragmatic reflection (junction) begins posterior to the xiphoid process, passes posterior to the seventh costal cartilage to reach the eighth rib in the midclavicular line and the tenth rib in the mid-axillary line, then the twelfth rib (approximately level with the superior border of the spinous process of the twelfth thoracic vertebra) adjacent to the vertebral column. On the left, the line initially follows the sixth costal cartilage but then follows a course similar to that on the right. In neonates and young children, the domes of the respiratory diaphragm are lower and flatter, reducing the angle of this point of reflection.

Diaphragmatic part

The diaphragmatic part of the parietal pleura covers most of the superior (thoracic) surface of the respiratory diaphragm where it is tightly attached to the phrenicopleural fascia, a continuation of the endothoracic fascia. It is continuous with the costal pleura around the periphery of the diaphragm, and within the costodiaphragmatic recess, and with the mediastinal pleura medially.

Cervical part

The cervical part of the parietal pleura is the continuation of the costal pleura over the apex of the lung and inferior to the suprapleural membrane, conforming tightly to both. It ascends medially from the internal border of the first rib to the apex of the lung, and then descends lateral to the trachea to become the mediastinal pleura. As a result of the obliquity of the first rib, the cervical pleura extends 3–4 cm superior to the first costal cartilage, up to or above the level of the neck of the first rib, reaching as high as the body of the seventh cervical vertebra (see Figs 54.1, 52.5). The cervical pleura is strengthened by the suprapleural membrane (Sibson's fascia), a thickening of the endothoracic fascia that is attached anteriorly to the internal border of the first rib and posteriorly to the anterior border of the transverse process of the seventh cervical vertebra. Scalenus minimus, when present, extends from the anterior border of the transverse process of the fifth, sixth and/or seventh cervical vertebra to the inner border of the first rib behind the subclavian groove, the cervical pleura and the suprapleural membrane (which it tenses). The cervical pleura and suprapleural membrane are related to the supraclavicular part of the brachial plexus, the stellate (cervicothoracic) ganglion and the vertebral vessels; the subclavian artery passes laterally in a groove located anterior to the most superior level of the membrane (**Fig. 54.2**).

Mediastinal part

The mediastinal part of the parietal pleura represents the lateral boundary of the mediastinum and forms a continuous covering above the level of the hilum of the lung, from the sternum anteriorly to the vertebral column posteriorly. On the right, it covers the right brachiocephalic vein, upper part of the superior vena cava, terminal part of the azygos vein, right phrenic and vagus nerves, trachea and oesophagus (see Figs 55.10A, 56.7A). On the left it covers the aortic arch, left phrenic and vagus nerves, left brachiocephalic and left superior intercostal veins,

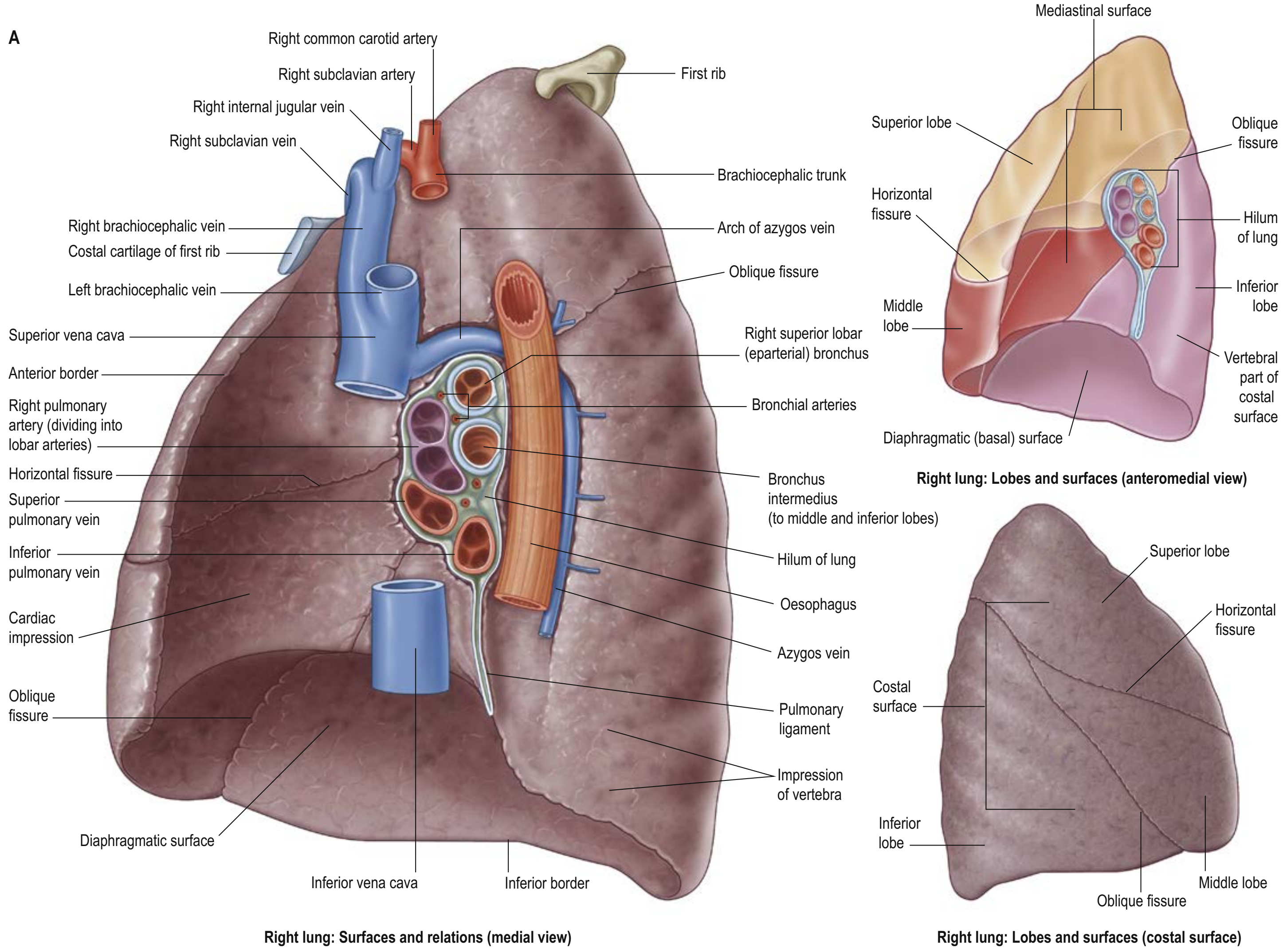
A
Right common carotid artery
Right subclavian artery
Right internal jugular vein
Right subclavian vein
First rib
Brachiocephalic trunk
Right brachiocephalic vein
Costal cartilage of first rib
Arch of azygos vein
Left brachiocephalic vein
Oblique fissure
Superior vena cava
Right superior lobar (eparterial) bronchus
Anterior border
Right pulmonary artery (dividing into lobar arteries)
Bronchial arteries
Horizontal fissure
Bronchus intermedius (to middle and inferior lobes)
Superior pulmonary vein
Inferior pulmonary vein
Hilum of lung
Oesophagus
Cardiac impression
Azygos vein
Oblique fissure
Pulmonary ligament
Impression of vertebra
Diaphragmatic surface
Inferior vena cava
Inferior border
Mediastinal surface
Superior lobe
Oblique fissure
Horizontal fissure
Hilum of lung
Inferior lobe
Middle lobe
Vertebral part of costal surface
Diaphragmatic (basal) surface
Superior lobe
Horizontal fissure
Costal surface
Inferior lobe
Middle lobe
Oblique fissure

Right lung: Surfaces and relations (medial view)

Right lung: Lobes and surfaces (anteromedial view)

Right lung: Lobes and surfaces (costal surface)

Fig. 54.3 The costal, mediastinal and diaphragmatic (basal) surfaces, and the mediastinal relations of the right (**A**) and left (**B**) lungs.

left common carotid and subclavian arteries, thoracic duct and oesophagus. At the root of the lung, it turns laterally to form a tube (sleeve) that encloses the structures passing to the lung hilum (see Fig. 54.1) and is continuous with the visceral pleura.

Visceral pleura

The visceral (pulmonary) part of the parietal pleura is adherent to the lung over all external surfaces, including those in the fissures, except at the hilum of the lung and along a line descending from this, that marks the formation and attachment of the pulmonary ligament (see Fig. 54.1; **Fig. 54.3**).

Pulmonary ligament

The pulmonary ligament, a thin almost vertically aligned double-layered fold of pleura, extends inferiorly from the region of the lung hilum and root. It passes between the mediastinal surface of the lung, where it joins the visceral pleura, and the lateral aspect of the mediastinum in the region of the oesophagus, where it joins the mediastinal part of the parietal pleura (see Figs 54.1, 54.3). It is continuous superiorly with the pleura around the lung hilum and root. Inferiorly, the two layers of pleura join, ending in a free sickle-shaped contour.

Parietal pleural recesses

The parietal pleura extends considerably beyond the inferior border of the lung but not as far as the attachment of the respiratory diaphragm, which means that the diaphragm is in contact with the costal cartilages and intercostal muscles below the line of pleural reflection from the thoracic wall to the diaphragm. In quiet inspiration, the inferior margin of the lung does not reach the point of parietal pleural reflection and the costal and diaphragmatic parts of the pleura are separated by a narrow slit, the costodiaphragmatic recess; the lower limit of the lung is normally about 5 cm superior to the lowest point of the recess. A similar costomediastinal recess exists between the mediastinum and the posterior surfaces of the sternum and costal cartilages, where the thin anterior margin of the lung projects toward the line of pleural reflection. The extent of this recess, the anterior costomediastinal line of pleural reflection, and the position of the anterior margin of the lung, exhibit individual variation.

The parietal pleural recesses allow the proportionate inspiratory expansion of the lungs with minimal friction. The same thin layer of pleural fluid within the recesses separates the costal and diaphragmatic parts of the parietal pleura during expiration, or the parietal pleura from the intervening visceral pleura during inspiration. Pleural adhesions and air or fluid accumulation limit this mechanism to a variable degree.

The inferior border of the costodiaphragmatic recess is an important consideration in surgical approaches to the kidney. The superior pole of the kidney crosses the twelfth rib and sometimes also the eleventh rib, which means that part of each kidney is associated with the parietal pleural reflection within the costodiaphragmatic recess. The parietal pleura may be damaged by flank incisions passing below the twelfth rib, but is more likely when rib resection is required during nephrectomy.

The aortico-oesophageal and azygo-oesophageal recesses project medially between the aorta and oesophagus on the left side and the azygos vein and oesophagus on the right side (see Fig. 56.7A).

Vascular supply and lymphatic drainage

The costal part of the parietal pleura is supplied by branches from the intercostal and internal thoracic arteries; the mediastinal part by

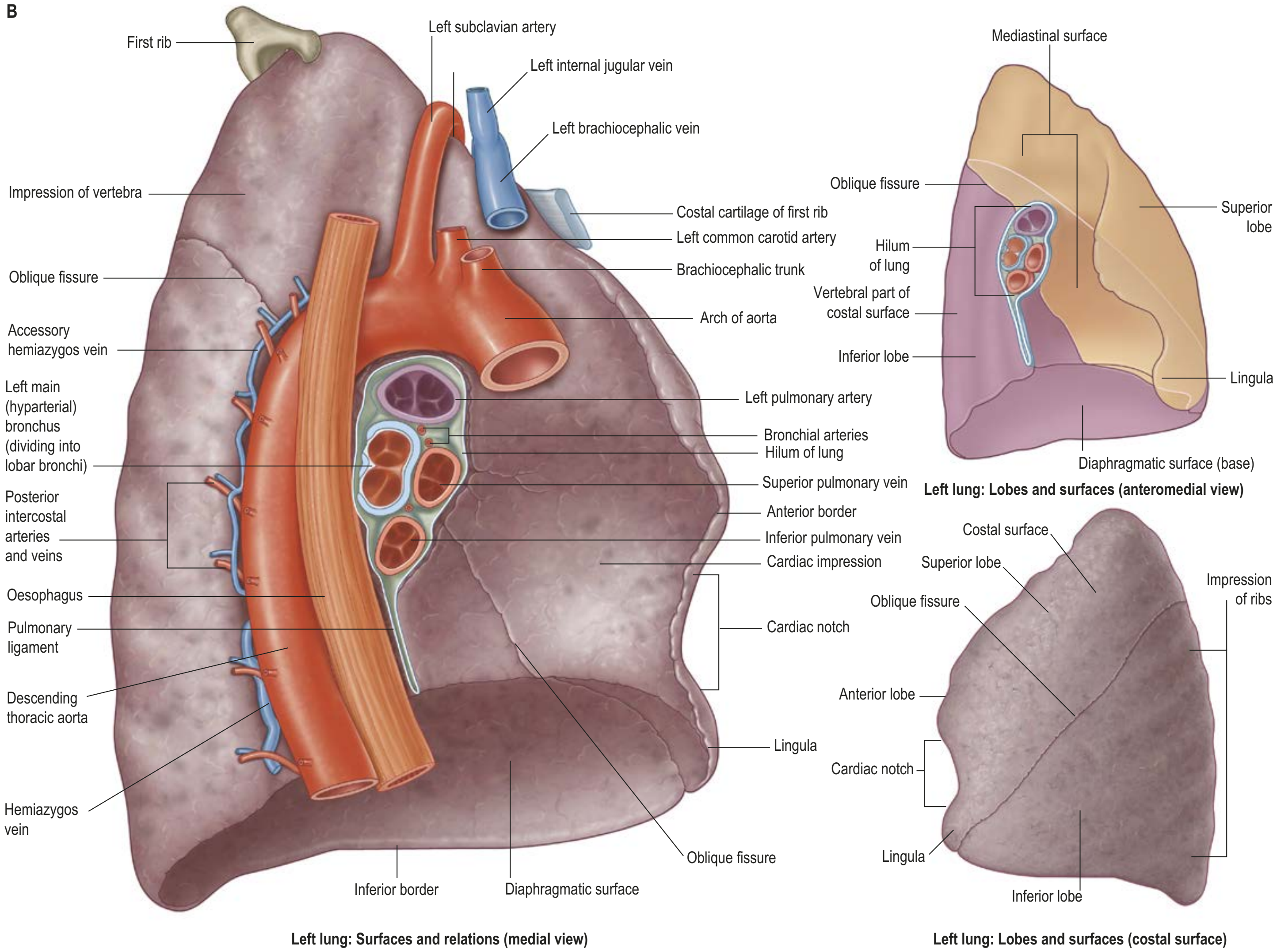
B
First rib
Left subclavian artery
Left internal jugular vein
Left brachiocephalic vein
Impression of vertebra
Costal cartilage of first rib
Left common carotid artery
Brachiocephalic trunk
Oblique fissure
Arch of aorta
Accessory hemiazygos vein
Left main (hyparterial) bronchus (dividing into lobar bronchi)
Left pulmonary artery
Bronchial arteries
Hilum of lung
Superior pulmonary vein
Posterior intercostal arteries and veins
Anterior border
Inferior pulmonary vein
Cardiac impression
Oesophagus
Cardiac notch
Pulmonary ligament
Descending thoracic aorta
Lingula
Hemiazygos vein
Oblique fissure
Inferior border
Diaphragmatic surface
Mediastinal surface
Oblique fissure
Superior lobe
Hilum of lung
Vertebral part of costal surface
Inferior lobe
Lingula
Diaphragmatic surface (base)
Costal surface
Superior lobe
Impression of ribs
Oblique fissure
Anterior lobe
Cardiac notch
Lingula
Inferior lobe

Left lung: Surfaces and relations (medial view)

Left lung: Lobes and surfaces (anteromedial view)

Left lung: Lobes and surfaces (costal surface)

Fig. 54.3 Continued.

branches from the bronchial, superior phrenic, internal thoracic and mediastinal arteries; the cervical part by branches from the subclavian artery; and the diaphragmatic part by the superficial part of the diaphragmatic microcirculation. Veins draining the parietal pleura join the thoracic wall veins, eventually draining into the superior vena cava mainly via the azygos system (see Fig. 56.2). Lymph from the costal part of the parietal pleura drains into the parasternal nodes anteriorly and intercostal nodes posteriorly, while that from the diaphragmatic pleura drains into the mediastinal, parasternal, para-aortic (phrenic) and coeliac nodes (see Figs 56.4A, 56.5).

The visceral pleura forms an integral part of the lung and, accordingly, its arterial supply and venous drainage are provided by the bronchial vessels. The bronchial arteries at the hilum form a circle, surrounding the main bronchus, and pleural branches from this anulus supply the visceral pleura covering the mediastinum, interlobar and apical surfaces of the lung, and part of the diaphragmatic (base) surface. The visceral pleura is drained by pulmonary veins, apart from an area around the hilum that drains into bronchial veins. The lymphatic drainage of the visceral pleura is initially via the subpleural lymphatic plexus. Lymph can pass via segmental or intersegmental lymphatic pathways, and sometimes via peribronchial lymphatic pathways; the exact pattern of drainage varies depending on lobe, segment, side and individual (Fourdrain et al 2018).

Innervation

The costal and peripheral regions of the diaphragmatic parietal pleurae are innervated by intercostal nerves. The mediastinal and central regions of the diaphragmatic parietal pleurae are innervated by the phrenic nerves (C3–C5). Irritation of the intercostal nerves causes pain that is referred to the similarly innervated part of the thoracic or abdominal wall, whereas irritation of the central diaphragmatic pleura causes pain that is referred to the lower neck and shoulder tip, i.e. to the C3 and C4 dermatomes of the affected side.

Pneumothorax

A breach of the parietal or visceral pleura (e.g. in chest wall injury) may lead to the accumulation of air within the pleural cavity (pneumothorax). Fluid (hydrothorax), blood (haemothorax) and, rarely, lymph (chylothorax) can also accumulate in this space. Pneumothoraces may occur spontaneously (rupture of emphysematous bullae, or subpleural 'blebs' typically in tall, asthenic males) or following rib fracture or penetrating trauma.

Microstructure

The smooth pleural surface consists of a single layer of flat mesothelial (serosal) cells separated from an underlying lamina propria of loose connective tissue by a basal lamina. Ultrastructurally, pleural and peritoneal mesothelial cells are similar in having a highly folded basal plasma membrane, in that their adjacent cell surfaces interdigitate and are joined by desmosomes, and in that their luminal surfaces bear numerous microvilli and some cilia. Cytoplasmic pinocytotic vesicles are common. The connective tissue covers the entire pulmonary surface; it extends from the hilum along the bronchial tree and accompanying blood vessels within the substance of the lung and divides the lung into numerous small polyhedral lobules, each of which receives a terminal bronchiole and arteriole, venules, lymphatics and nerves. Lobules vary in size; the superficial ones are the largest, visible as polygonal areas 5–15 mm across.

Occasionally, a valve-like effect occurs, so that air enters the pleural cavity during inspiration (due to the presence of a negative pressure) but cannot escape in expiration. This may result in a 'tension pneumothorax', which can be life-threatening and should be suspected whenever there are unilateral decreased breath sounds, hypotension, jugular venous distension and contralateral tracheal deviation (due to mediastinal shift). A tension pneumothorax requires immediate decompression. This may be carried out using a wide-bore needle; or a decompression cannula apparatus, inserted into the second intercostal space in the midclavicular line; or via a thoracostomy with an incision made through the fourth or fifth intercostal space between the anterior and mid-axillary lines followed by digital insertion to breach the parietal pleura and sweep away pleural adhesions (Fitzgerald et al 2008), followed by tube insertion for longer-term drainage.

Fluid collection in the pleural cavity may be due to congestive cardiac failure, hypoalbuminaemia or inflammatory, infective or neoplastic conditions. A developing pleural effusion causes obliteration of the costodiaphragmatic recess, where a lateral fluid meniscus is often visible from a non-loculated effusion on a frontal chest radiograph. Drainage of the fluid and subsequent analysis are required for diagnostic purposes. Where there is a collection of purulence (empyema) or blood, pleural cavity drainage is essential for therapeutic purposes. Ultrasonography is useful in assessing the size and characteristics of an effusion, such as the presence of loculation and debris and can demonstrate underlying consolidated lung. Computed tomography (CT) is used to assess the underlying lung parenchyma, endobronchium and mediastinal lymph nodes.

LUNGS

The lungs are the organs of respiration. They are situated on either side of the heart and other mediastinal structures and occupy most of the thoracic cavity. Each lung is free to move in its pleural cavity, except at the hilum and pulmonary ligament, where it is attached to the mediastinum. When removed from the thorax, a fresh normal lung is spongy, can float in water, and crepitates when handled because of the air within its alveoli. It is also highly elastic and so retracts on removal from the thorax. Its surface is smooth and shiny, and is divided by fine, dark lines into numerous small polyhedral lobules, each crossed by numerous finer lines, indicating the areas of contact between its most peripheral lobules and the visceral pleural surface.

In proportion to body stature, the lungs are heavier in males than in females (Thurlbeck 1982). At post mortem examination, the adult right lung usually weighs 340 g (142–835 g) in females and 445 g (185–967 g) in males; the adult left lung weighs 299 g (108–736 g) in females and 395 g (186–885 g) in males (Molina and DiMaio 2012, 2015). A fetal lung pair at 40 weeks post fertilization weighs 51 ± 16 g (Archie et al 2006). Lung volume, air volume and pulmonary tissue volume all increase linearly with body length (Rao et al 2010).

Pulmonary surface features

Each lung roughly resembles a halved cone and has an apex, base, distinct anterior and inferior borders and three outer facing surfaces (costal, diaphragmatic (base), mediastinal) (see Fig. 54.3). A posterior border is sometimes defined, although it is often rounded and relatively indistinct. During post mortem examination of preserved tissue each lung bears the impression of neighbouring structures that the lung was pressed against through the pleural coverings in life.

Apex

The apex, the rounded upper limit of the lung, extends above the superior thoracic aperture where it contacts the cervical pleura, and is covered in turn by the suprapleural membrane. As a consequence of the obliquity of the aperture, the apex rises 3–4 cm above the level of the first costal cartilage. The highest point of the apex is up to 2 cm above the medial third of the clavicle, at or above the neck of the first rib, and level with the body of the seventh cervical or first thoracic vertebra, or the intervening intervertebral disc; it sits in the root of the neck (see Fig. 35.18). Some consider the apex to be an intrathoracic structure when it does not rise above the neck of the first rib. The subclavian artery arches superolaterally over the suprapleural membrane and grooves the anterior surface of the membrane and lung apex just below its highest point, separating it from scalenus anterior (see Fig. 54.2). The cervicothoracic (stellate) sympathetic ganglion, ventral ramus of the first thoracic spinal nerve and supreme intercostal artery all lie posterior to the lung apex. Scalenus medius is lateral and the brachiocephalic trunk, right brachiocephalic vein and trachea are adjacent to the medial surface of the apex of the right lung. The left subclavian artery and left brachiocephalic vein are adjacent to the medial surface of the left lung apex.

Diaphragmatic surface (base)

The diaphragmatic surface (base) of the lung, when static, is semilunar and concave, moulded on the superior surface of the respiratory diaphragm, which separates each lung from the corresponding lobe of the liver, and the left lung from the gastric fundus and spleen. Since the respiratory diaphragm extends higher on the right than on the left, the concavity is deeper on the base of the right lung. Posterolaterally, the diaphragmatic surface has a more tapered shape that projects a little into the costodiaphragmatic recess. The change in diaphragmatic surface shape and relations is best viewed with inspiration/expiration radiographs, or with a ventilation CT series.

Costal surface

The costal surface of the lung is smooth and convex, and its shape is adapted to that of the thoracic wall, which is vertically deeper posteriorly. It is in contact with the costal pleura; in lung specimens that have been preserved *in situ*, this surface exhibits grooves that correspond with the overlying ribs, a situation similar to the hyperinflated lungs of patients with asthma. The vertebral part of the costal surface faces, and is impressed by, the anterolateral margins of the thoracic vertebrae and intervening intervertebral discs, posterior intercostal vessels and splanchnic nerves. Some consider the vertebral surface of the lung separate to the costal part.

Mediastinal surface

The mediastinal surface of the lung is deeply concave because it is adapted to the heart at the cardiac impression: the impression is much larger and deeper on the left lung where the heart projects more to the left of the median sagittal plane. The hilum of the lung, posterosuperior to this concavity, is the area where various structures of the lung root enter or leave the lung. The lung root and hilum are surrounded by a sleeve of pleura that extends inferiorly, posterior to the cardiac impression, as the pulmonary ligament. The mediastinal surface and vertebral part of the costal surface are sometimes collectively termed the medial surface (border) of the lung.

Other impressions on the lung surface

Cadaveric lungs that have been preserved *in situ* can show a number of other impressions that indicate their relations with surrounding structures, especially on the mediastinal surface (see Fig. 54.3). All these impressions reflect the intimate relationship between the lungs and adjacent mediastinal structures and offer a good perspective on surgical approaches or considerations, either from the anterior or posterior aspect of the corresponding pleural cavity.

Pulmonary borders

The inferior border of the lung is thin and sharp where the diaphragmatic and costal surfaces extend into the costodiaphragmatic recess and meet, and more rounded medially where the diaphragmatic and mediastinal surfaces meet (see Fig. 54.3). The surface anatomy of the inferior border of the lung is described in Chapter 52 (see Figs 52.5–52.6). The respiratory diaphragm rises more superiorly on the right to accommodate the liver, which means that the right lung is vertically shorter (by about 2–3 cm) than the left. However, cardiac asymmetry means that the right lung is broader, and has a greater capacity and weight than the left. Although not obvious, the posterior border separates the costal surface from the mediastinal surface and corresponds to the region of the lung adjacent to the heads of the ribs. It has no recognizable markings and is represented by a rounded region where the costal and vertebral surfaces of the lung meet. The thin, sharp, anterior border of the lung overlaps the pericardium (see Fig. 54.7). On the right it corresponds closely to the costomediastinal line of pleural reflection and is almost vertical. On the left it approaches the same line posterior to the sternum and superior to the fourth costal cartilage; inferior to this point it shows a variably shaped cardiac notch, the edge of which passes laterally for about 3.5 cm before curving inferomedially to the level of the sixth costal cartilage, about 4 cm from the midline. This region of the left lung does not reach the line of parietal pleural reflection (see Fig. 52.5) and so the fibrous pericardium is covered only by a double layer of parietal pleura (over the area of superficial cardiac dullness). Observations during surgery suggest that the line of pleural reflection, the anterior pulmonary margin and the costomediastinal pleural recess are all variable.

Pulmonary fissures and lobes

Left lung

The left lung is commonly divided into superior and inferior lobes by an oblique fissure that extends from the costal to the mediastinal surfaces, superior and inferior to the hilum (see Fig. 54.3B). When observing the surface of the lung, this fissure begins on the medial surface at the posterosuperior part of the hilum, near the pulmonary artery; ascends obliquely and posteriorly to cross the posterior border of the lung about 6 cm below the apex; next descends anteriorly across the costal surface, to reach the inferior border almost at its anterior limit; and finally ascends posteriorly on the mediastinal surface to the inferior part of the hilum. The surface and positional anatomy of the lung fissures is described in Chapter 52. The extent of completeness and/or orientation of the left oblique fissure is variable (Wantanabe 2016a); for example, the left oblique fissure is atypical (incomplete or absent) in 18% (Medlar 1947) to 73% (Yamashita 1978) of cases. The additional presence of a left horizontal fissure is a normal, occasional variant. Incomplete separation of the lobes and identification of the completeness of the fissures are important prior to lobectomy because individuals with incomplete fissures are more prone to develop postoperative air leaks and may require further procedures, such as stapling and pericardial sleeves.

The superior lobe lies anterosuperior to the oblique fissure and includes the apex, anterior border and much of the costal and most of the mediastinal surfaces of the lung. A small process, the lingula, is

On the mediastinal surface of the right lung (see Fig. 54.3A), the cardiac impression is related to the anterior surface of the right auricle, the anterolateral surface of the right atrium and partially to the anterior surface of the right ventricle. A wide groove ascends anterior to the hilum for the superior vena cava, the terminal portion of the right brachiocephalic vein and the right subclavian vein. Posteriorly, this groove is joined by a deep sulcus that arches forwards immediately superior to the hilum and is occupied by the azygos vein. The right side of the oesophagus makes a shallow vertical groove posterior to the hilum and the pulmonary ligament, and posterior to this is a vertical groove for the azygos vein. Towards the respiratory diaphragm it inclines left and leaves the right lung, and therefore does not reach the lower limit of this surface. Posteroinferiorly, the cardiac impression is confluent with a short, wide groove adapted to the inferior vena cava. Between the lung apex and the groove for the arch of the azygos vein, the trachea and right vagus nerve are close to the lung but do not mark it.

On the mediastinal surface of the left lung (see Fig. 54.3B), the cardiac impression is related to the anterolateral surface of the left ventricle and left auricle. The anterior surface of the conus arteriosus and adjoining part of the right ventricle are related to the lung as it ascends anterior to the hilum to accommodate the pulmonary trunk. A large groove arches over the hilum, and descends behind both it and the pulmonary ligament, corresponding to the aortic arch and descending thoracic aorta. From its summit, a narrower groove ascends to the apex for the left subclavian artery. Posterior to this, and superior to the aortic groove, the lung is impressed by the oesophagus (with potential contribution from the thoracic duct as it passes along the posterolateral surface of the oesophagus). Anterior to the groove for the subclavian artery there is a faint linear depression for the left brachiocephalic vein. Inferiorly, the oesophagus may create a groove posterior to the lower end of the pulmonary ligament.

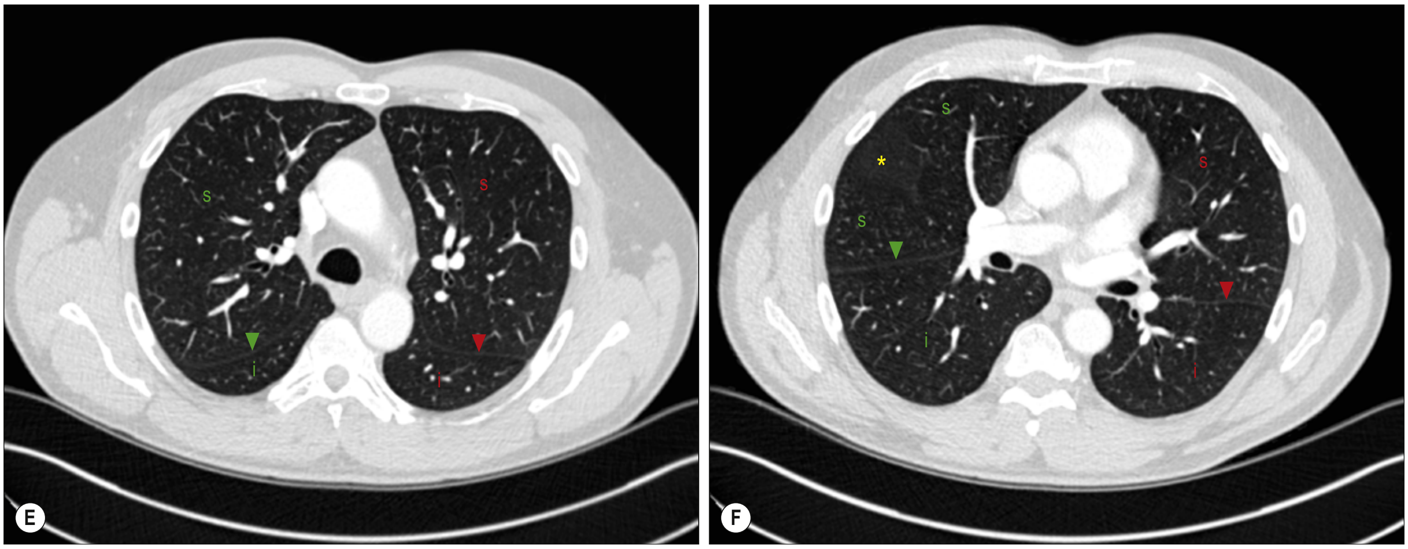

Fig. 54.4 E, Axial CT of the chest with intravenous contrast medium at the level of the lower trachea viewed with lung window settings, with arrowheads showing the right (green) and left (red) oblique fissures. Key: i, inferior lobe; s, superior lobe. **F**, Axial CT of the chest with intravenous contrast medium just inferior to the level of the carina viewed with lung window settings, with arrowheads marking the right (green) and left (red) oblique fissures and the yellow * marking the horizontal fissure in the plane of imaging. Key: i, inferior lobe; s, superior lobe. (A–D; G–J, *continued online*)

usually present at the inferior end of the cardiac notch. The larger inferior lobe lies posterior and inferior to the fissure and contributes almost the whole of the diaphragmatic surface, much of the costal surface and most of the posterior border and vertebral surface of the left lung.

Right lung

The right lung is divided commonly into superior, middle and inferior lobes by its oblique and horizontal fissures (see Fig. 54.3A). The oblique fissure separates the inferior from the superior and middle lobes, and although less vertical is similar in position on the lung surface to the left oblique fissure (described above). The surface and positional anatomy of the lung fissures is described in Chapter 52. On the surface of the lung, the right oblique fissure follows almost the same course as the left oblique fissure. A range of variation in the degree of completeness and/or orientation of the fissures is reported (Wantanabe 2016a). For example, the right oblique fissure is atypical (incomplete to absent) in 30% (Medlar 1947) to 71% (Yamashita 1978) of cases, whereas the right horizontal fissure is atypical in 62% (Medlar 1947) to 88% (Raasch et al 1982) of cases. The horizontal fissure is usually visible on a frontal chest radiograph and the oblique fissure is usually visible on a lateral radiograph and on a high-resolution CT scan as a curvilinear band passing from the lateral aspect of the costal surface to the hilum (**Fig. 54.4**). The smaller middle lobe is wedged between the superior and inferior lobes, and forms the inferior part of the anterior border, the anterior part of the inferior border and the associated part of the anteriorly located costal surface of the lung (see Fig. 54.7). The azygos vein may sometimes course in a more lateral position, within a four-layered pleural septum within the superior lobe, creating an 'azygos lobe'. This is not a true lobe, but a separated portion of the superior lobe that lacks its own bronchi, arteries or veins. The condition represents an incidental finding on chest radiographs or CT scans, with no associated morbidity; it may be confused with a pulmonary nodule, and loculated effusions may appear in the fissure. Accessory fissures may separate either the medial basal segment (Twining's line) or the superior segment from the remainder of the inferior lobe.

TRACHEA AND BRONCHI

Trachea

The adult trachea is a 10–11 cm long tube with cervical and thoracic parts. It is formed of cartilage and fibromuscular membrane and lined internally by mucosa. It descends from the cricoid cartilage of the larynx at the level of the body of the sixth (female) or seventh (male) cervical vertebra and divides into right and left main bronchi typically inferior to the sternal plane by 1–3 cm, and level with the body of the fifth or sixth thoracic vertebra or the T5–T6 intervertebral disc (see Fig. 52.7). It is located approximately in the midline sagittal plane but its point of bifurcation is usually a little to the right. In children less than 5 years of age a chest radiograph may demonstrate the trachea to appear to sharply deviate laterally to the right (buckle) at or just superior to the superior thoracic aperture and is considered a normal variant (Lee et al 2012). The variable position of the trachea in children makes it unreliable as an indicator of the presence of a right-sided aortic arch on a chest radiograph (Strife et al 1989).

The anterior and lateral surfaces of the trachea consist of 16–20 superimposed incomplete horseshoe-shaped 'rings' of hyaline cartilage and intervening anular ligaments formed from fibroelastic tissue that allows tracheal elongation during inspiration or neck movement (extension). During deep inspiration the tracheal bifurcation reaches the level of the body of the sixth thoracic vertebra. In children, the tracheal cartilages retain a high degree of elasticity that is often lost in adults: during full neck extension the length of the trachea increases by 0.95 ± 0.43 cm in a child (Jin-Hee et al 2005).

The posterior membranous wall is a flat, fibromuscular structure containing smooth muscle (trachealis). During the first postnatal year of life, tracheal diameter does not exceed 4 mm. Mean transverse diameter is greater than anteroposterior diameter up to the age of 6 years, after which the two diameters are nearly equal (Griscom and Wohl 1986). During later childhood, tracheal diameter in millimetres is approximately equal to age in years. The external transverse diameter is typically 2 cm in adult males and 1.5 cm in adult females. The lumen is about 12 mm in diameter in live adults but increases as a result of relaxation of the smooth muscle post mortem. The transverse shape of the lumen is variable, especially in the later decades of life, and it may be round, lunate or flattened. The trachea is funnel-shaped in neonates, when the upper end is wider than the lower end and gradually becomes cylindrical with increasing age. At bronchoscopy, the posterior membranous wall of the trachea bulges into the lumen and this is exaggerated during expiration and coughing. The distal end of the trachea is visible as a concave spur. A tracheal bronchus may occasionally arise, mainly from the right aspect of the trachea around 2 cm superior to the carina, as either a supernumerary lobar or apical bronchus, or a displaced apical or superior lobar (porcine) bronchus (Wantanabe 2016b). This occurs more commonly in males and may be associated with axial skeletal anomalies. A tracheal bronchus was noted in 2.4% of children undergoing bronchoscopy for respiratory symptoms (Wong et al 1999).

Relations of the cervical part of the trachea

Anterior relations

The cervical part of the trachea is covered anteriorly by skin and the intervening superficial and deep cervical fasciae, and the suprasternal space. It is crossed by the jugular venous arch and overlapped by sternohyoid and sternothyroid. The second to fourth tracheal cartilages are crossed by the isthmus of the thyroid gland, above which an anastomosis connects the two superior thyroid arteries; the pretracheal fascia, inferior thyroid veins, thymic remnants (in adults) and the thyroid ima artery (when present) are all anteroinferior. In children, the thymus (especially the left lobe) may extend anterior to the trachea to the level of the thyroid gland and the brachiocephalic trunk crosses obliquely in front of the trachea at, or a little above, the upper border of the manubrium; the left brachiocephalic vein may also rise a little above this level. An enlarged thyroid gland may cover the cervical part of the

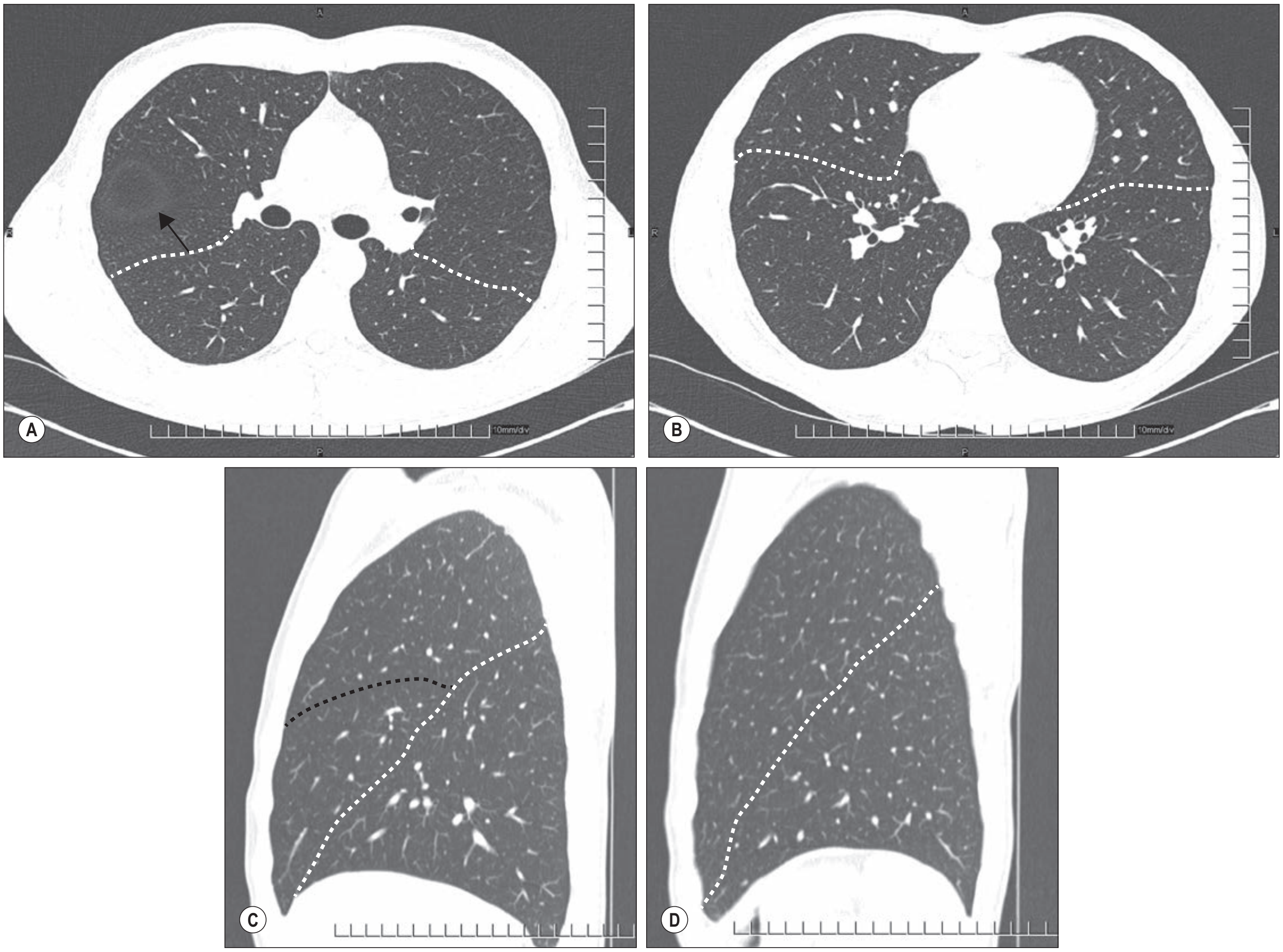

Fig. 54.4 **A**, An axial CT of the chest through the lungs inferior to the carina, demonstrating the left and right oblique fissures (white dashed lines). The circular avascular area anterior to the right oblique fissure and surrounded by a halo of white (arrow) is due to the horizontal fissure: in this individual the fissure is slightly domed and passes through the plane of the section. **B**, An axial section through the lungs at the mid-left atrial level, demonstrating the left and right oblique fissures (white dashed lines) as they pass more anteriorly and separate the inferior lobes from the superior (left lung) and middle (right lung) lobes. **C**, A sagittal section through the right lung, demonstrating the oblique (white dashed line) and horizontal fissures (black dashed line). **D**, A sagittal section through the left lung, demonstrating the oblique fissure (white dashed line).

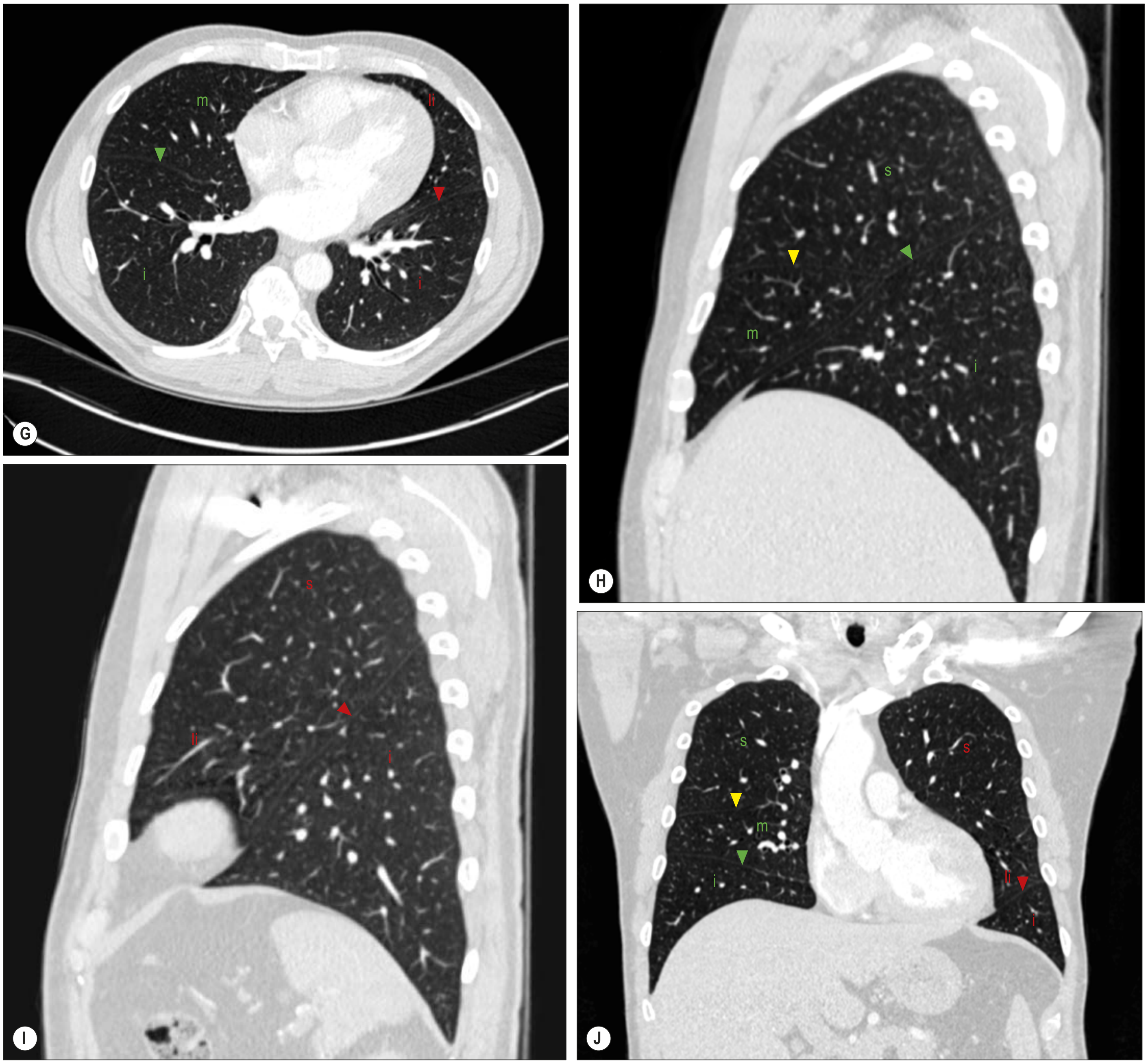

Fig. 54.4 cont'd **G,** Axial CT of the chest with intravenous contrast medium at the level of the left atrium viewed with lung window settings, with arrowheads marking the right (green) and left (red) oblique fissures. Key: li, lingula; i, inferior lobe; m, middle lobe. **H**, Right sagittal CT of the chest with intravenous contrast medium through the right lung viewed with lung window settings, with arrowheads marking the oblique fissure (green) and the horizontal fissure (yellow). Key: i, inferior lobe; m, middle lobe; s, superior lobe. **I**, Left sagittal CT of the chest with intravenous contrast medium through the left lung viewed with lung window settings, with the red arrowhead marking the oblique fissure. Key: li, lingula; i, inferior lobe; s, superior lobe. **J**, Coronal CT of the chest with intravenous contrast medium at the level of the aortic outflow tract and ascending aorta viewed with lung window settings, with the arrowheads marking the right (green) and left (red) oblique fissures, and the horizontal (yellow) fissure. Key: li, lingula; i, inferior lobe; m, middle lobe; s, superior lobe.

trachea and reach the superior mediastinum, usually anterior to the left brachiocephalic vein.

Obstruction of the upper airways, craniofacial trauma and neck cancers (especially laryngeal), in either the acute or the chronic setting, require a tracheostomy. This is the creation of a hole (stoma) in the anterior aspect of the trachea that can serve either independently or as a site for an indwelling tube allowing the spontaneous or mechanical ventilation of the patient. The procedure usually involves incising the second and third tracheal cartilages and may be performed surgically or percutaneously (Ciaglia et al 1985, Griggs et al 1990). Surgical approaches are via a horizontal or vertical incision, about 2–3 cm in length, made midway between the jugular (suprasternal) notch and the thyroid cartilage; platysma, sternohyoid and then sternothyroid are separated along the midline to expose the trachea. Alternatively, in some cases, particularly in an emergency, the lumen of the larynx can be accessed directly via incision of the cricothyroid membrane (cricothyroidotomy).

Posterior relations

The cervical part of the oesophagus is the main posterior relation of the cervical trachea, separating it from the vertebral column and the prevertebral fascia.

Lateral relations

The paired lobes of the thyroid gland, that commonly descend to the level of the fifth or sixth tracheal cartilage, and the common carotid and inferior thyroid arteries, are all lateral relations. The thyroid gland is covered in a fascial capsule, an extension of the pretracheal fascia. This capsule condenses posteriorly to form the suspensory ligament of the thyroid gland (Berry) which is connected firmly to the trachea at the posterior margin of the adjacent cartilage rings, and blends with the posterior membranous wall. The recurrent laryngeal nerves ascend on each side, in or near the tracheo-oesophageal groove. The posterior suspensory ligament and the nearby terminal branches of the inferior thyroid artery are important landmarks for intraoperative identification of the recurrent laryngeal nerve.

Relations of the thoracic part of the trachea

Anterior relations

As it descends through the superior mediastinum, the thoracic trachea lies posterior to the manubrium of the sternum, the inferior attachments of sternohyoid and sternothyroid the remnants of the thymus and the inferior thyroid veins. In children the thymus sits anterior to the trachea. The brachiocephalic trunk and left common carotid artery come to lie on the right and left of the trachea, respectively, as they diverge superiorly into the neck. Inferiorly, the aortic arch, brachiocephalic trunk, left common carotid artery, left brachiocephalic vein, deep part of the cardiac plexus and upper and lower pretracheal lymph nodes are all anterior to the trachea.

Posterior relations

The oesophagus, with its venous and neural plexuses, is posterior to the trachea and separates it from the vertebral column. The close relation of these two tubular structures forms a trachea–oesophageal groove on either side. The retrotracheal lymph nodes sit between the trachea and oesophagus from the superior thoracic aperture to the level of the carina of the trachea (see Fig. 54.12B).

Lateral relations

Laterally and on the right are the right lung with its pleural coverings and cavity, right vagus nerve, right brachiocephalic vein, superior vena cava and azygos vein. On the left are the arch of the aorta, left common carotid and left subclavian arteries. The left recurrent laryngeal nerve is initially situated between the trachea and aortic arch, and then lies within or just anterior to the tracheo-oesophageal groove.

The trachea and oesophagus can be compressed (or even eroded) by vascular rings resulting from abnormal formation of the aorta and its branches, such as a double aortic arch, right aortic arch, aberrant right subclavian artery, double ductus arteriosus or persistence of the fifth aortic arch (Ch. 20).

Right main bronchus and subdivisions

The right main (principal) bronchus is approximately 2.5 cm long, and is wider, shorter and more vertical than the left (**Figs 54.5–54.6**). These differences explain why inhaled foreign bodies enter the right main bronchus more often than the left. This is more common in children, who may present with breathlessness, unilateral wheeze or recurrent aspirations, and a chest radiograph may show air trapping in the affected lobe. The right main bronchus gives rise to its first branch, the superior lobar bronchus (or eparterial bronchus, since it arises superior to the pulmonary artery), then enters the right lung opposite the bodies of the fifth to the seventh thoracic vertebrae. The azygos vein arches over it to join the superior vena cava; the surface position of the junction (0.6–2 cm inferior to the sternal plane) is an approximate marker for the superior extent of the hilum of the lung (see Table 52.2). The right pulmonary artery lies at first inferior, then anterior to the right main bronchus (see Fig. 54.13). After giving off the superior lobar bronchus, which arises posterior or posterosuperior to the right pulmonary artery, the right main bronchus continues as the bronchus intermedius and crosses the posterior aspect of the artery, enters the pulmonary hilum posteroinferiorly, and divides into the middle and inferior lobar bronchi (or hyparterial bronchi, since they arise inferior to the pulmonary artery).

Normal variants in the bronchial anatomy are occasionally seen and consist of either displaced or supernumerary airways (Ghaye et al 2001), or bridging and braided bronchi (Wantanabe 2016a).

Right superior lobar bronchus

The right superior lobar bronchus arises from the lateral aspect of the main bronchus and runs superolaterally to enter the hilum of the lung. About 1 cm from its origin it divides into three segmental bronchi: apical, posterior and anterior.

Segmental bronchi

The apical segmental bronchus continues superolaterally towards the apex of the lung, which it supplies, and divides near its origin into apical and anterior branches. The posterior segmental bronchus serves the posteroinferior part of the superior lobe, passes posterolaterally and slightly superiorly, and soon divides into a lateral and a posterior branch. The anterior segmental bronchus runs anteroinferiorly to supply the remainder of the superior lobe and divides near its origin into a lateral and anterior branch of equal size.

Bronchus intermedius

The bronchus intermedius is the continuation of the right main bronchus distal to the branching of the right superior lobar bronchus. It courses in a similar direction to the right main bronchus, but with a slight rightward deviation. It is slightly flattened, typically 1 cm wide and 2.5 cm long, and gives rise to the right middle and lower lobar bronchi, and sometimes to an additional variant, the subsuperior segmental bronchus (see below).

Right middle lobar bronchus

The right middle lobar bronchus usually branches from the bronchus intermedius about 2 cm below the superior lobar bronchus and descends anterolaterally.

Segmental bronchi

The right middle lobar bronchus soon divides into lateral and medial segmental bronchi that are distributed to the homonymous segments of the middle lobe.

Right inferior lobar bronchus

The right inferior lobar bronchus is the continuation of the bronchus intermedius beyond the origin of the right middle lobar bronchus.

Segmental bronchus anatomy

At or a little below its origin from the bronchus intermedius, the right inferior lobar bronchus commonly gives off a large superior (apical) segmental bronchus posteriorly that runs to the upper part of the inferior lobe, and then divides into medial, superior and lateral branches; the medial and superior usually arise from a common stem. After giving off the superior segmental bronchus, the right inferior lobar bronchus descends posterolaterally. The medial basal segmental bronchus branches from its anteromedial aspect and runs inferomedially to serve a small region below the hilum. The inferior lobar bronchus continues inferolaterally and divides into an anterior basal segmental bronchus that descends anteriorly and a trunk that soon divides into a lateral basal segmental bronchus that descends laterally and a posterior basal segmental bronchus that descends posteriorly. In more than half of all right lungs, a subsuperior (subapical) segmental bronchus arises posteriorly

Anomalies include a common origin of the right superior and middle lobar bronchi; an accessory cardiac bronchus; a right lower lobar bronchus that may arise from the left main stem bronchus; and an oesophageal bronchus. These anatomical variants are largely asymptomatic, occasionally causing haemoptysis, recurrent infection and bronchiectasis. Congenital bronchial atresia is associated with a bronchocele and emphysematous changes in the peripheral lung fields (Wang et al 2012). Left bronchial isomerism, characterized by two hyparterial bronchi and two bilobed lungs, and right bronchial isomerism, characterized by two eparterial bronchi and two trilobed lungs, may be features of the heterotaxy syndrome, which may include congenital cardiac, liver, stomach, intestinal and splenic abnormalities (Wantanabe 2016a).

Lung lobation and the morphology of the tracheobronchial tree can predict the atrial situs. In *situs solitus*, the right main bronchus is short and eparterial (its branch for the right superior lobe lies over the second branch of the right pulmonary artery) and the left main bronchus is longer and hyparterial (it courses underneath the left pulmonary artery). A bilobed left lung and a trilobed right lung are typical in *situs solitus*. In *situs inversus*, there is a mirror imaging of the disposition seen in *situs solitus*. In *situs ambiguus*, the bronchi and lungs can display either a bilateral right morphology with bilateral trilobed lungs and bilateral eparterial bronchi (heterotaxy syndrome: incomplete or inappropriate lateralization of the thoracic and abdominal viscera, and asplenia) or a bilateral left morphology with bilateral bilobed lungs and bilateral hyparterial bronchi (heterotaxy syndrome and polysplenia) (Van Praagh et al 1992).

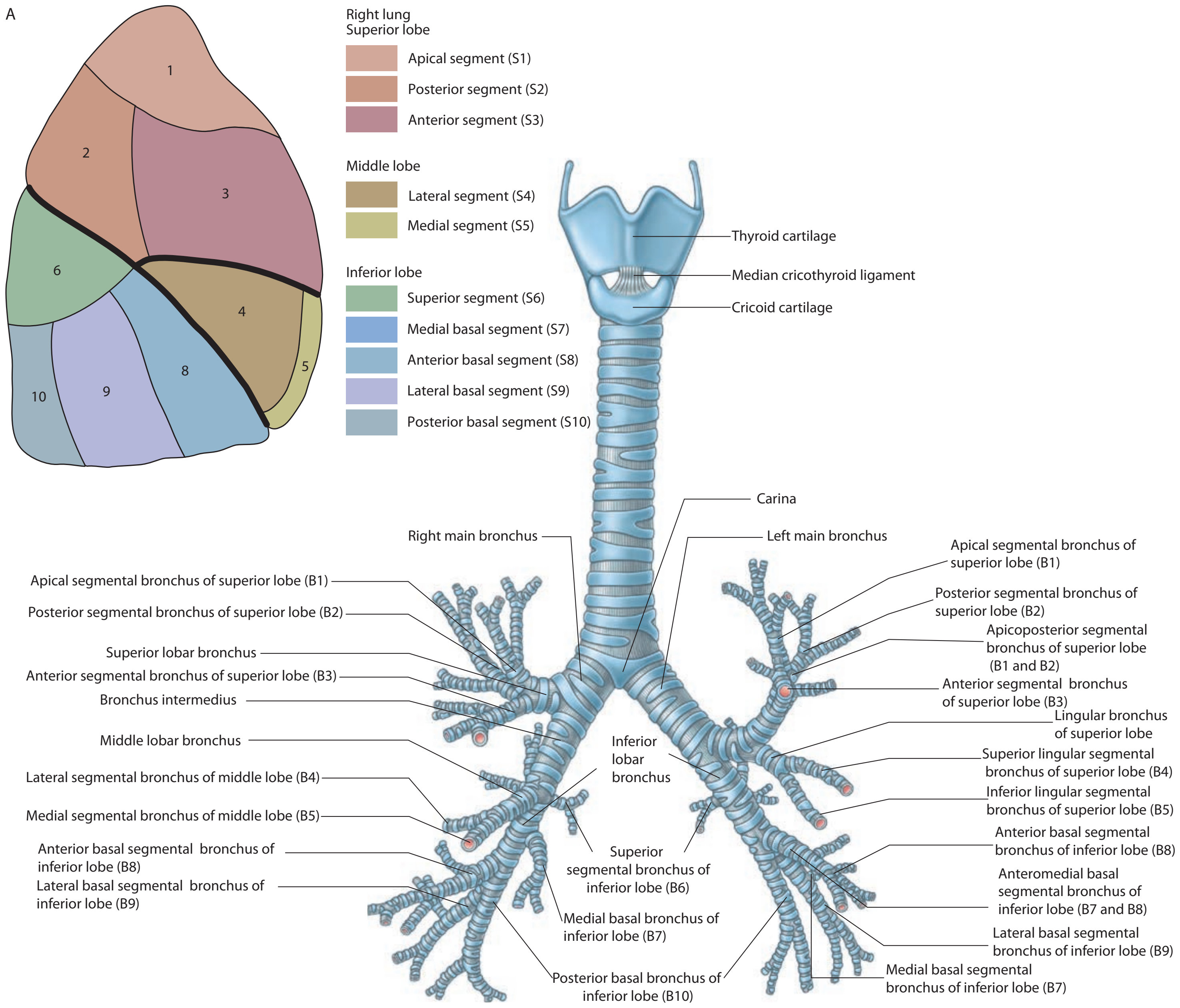
A
1
2
3
4
5
6
8
9
10
Right lung
Superior lobe
Apical segment (S1)
Posterior segment (S2)
Anterior segment (S3)
Middle lobe
Lateral segment (S4)
Medial segment (S5)
Inferior lobe
Superior segment (S6)
Medial basal segment (S7)
Anterior basal segment (S8)
Lateral basal segment (S9)
Posterior basal segment (S10)
Thyroid cartilage
Median cricothyroid ligament
Cricoid cartilage
Carina
Right main bronchus
Left main bronchus
Apical segmental bronchus of superior lobe (B1)
Posterior segmental bronchus of superior lobe (B2)
Superior lobar bronchus
Anterior segmental bronchus of superior lobe (B3)
Bronchus intermedius
Middle lobar bronchus
Lateral segmental bronchus of middle lobe (B4)
Medial segmental bronchus of middle lobe (B5)
Anterior basal segmental bronchus of inferior lobe (B8)
Lateral basal segmental bronchus of inferior lobe (B9)
Inferior lobar bronchus
Superior segmental bronchus of inferior lobe (B6)
Medial basal bronchus of inferior lobe (B7)
Posterior basal bronchus of inferior lobe (B10)
Apical segmental bronchus of superior lobe (B1)
Posterior segmental bronchus of superior lobe (B2)
Apicoposterior segmental bronchus of superior lobe (B1 and B2)
Anterior segmental bronchus of superior lobe (B3)
Lingular bronchus of superior lobe
Superior lingular segmental bronchus of superior lobe (B4)
Inferior lingular segmental bronchus of superior lobe (B5)
Anterior basal segmental bronchus of inferior lobe (B8)
Anteromedial basal segmental bronchus of inferior lobe (B7 and B8)
Lateral basal segmental bronchus of inferior lobe (B9)
Medial basal segmental bronchus of inferior lobe (B7)

Fig. 54.5 A, The cartilages of the larynx, trachea and bronchi (anterior view), and the bronchopulmonary segments on the costal surface of the right lung. The bronchopulmonary segment (S) and segmental bronchus (B) labels are shown in brackets. In the left lung, segments S1 and S2, and S7 and S8, may be fused. (Redrawn from an original figure drawn from a metal cast made by the late Lord Russell Brock, GKT School of Medicine, London.) (B, *continued online.*)

from the bronchus intermedius or the right inferior lobar bronchus 1–3 cm below the superior segmental bronchus and is distributed to the region of lung between the superior and posterior basal segments.

Left main bronchus and subdivisions

The left main (principal) bronchus is narrower, less vertical and twice as long (approximately 5 cm) as the right main bronchus (see Figs 54.5–54.6). Passing to the left, inferior to the aortic arch, it crosses anterior to the oesophagus, thoracic duct and descending thoracic aorta; the left pulmonary artery is at first anterior and then superior to it, at which point it may be termed the hyparterial bronchus. The left main bronchus enters the hilum of the left lung at the level of the bodies of the sixth to the seventh thoracic vertebrae and divides into the left superior and inferior lobar bronchi.

Left superior lobar bronchus

The left superior lobar bronchus arises from the anterolateral aspect of the left main bronchus. It curves laterally for a short distance and then divides into two branches (superior and inferior divisions). These branches are equivalent to the superior and middle lobar bronchial branches of the right main bronchus, except that the absence of a left middle lobe means that both are distributed to the left superior lobe.

Segmental bronchi

The superior division of the left superior lobar bronchus ascends 1 cm, gives off an anterior segmental bronchus and continues a further 1 cm as the apicoposterior segmental bronchus, which then divides into apical and posterior branches. The apical, posterior and anterior segmental bronchi are largely distributed as they are in the right superior lobe. The inferior division descends anterolaterally to the anteroinferior part of the left superior lobe (the lingula) and forms the lingular (common lingular) bronchus, which divides into superior and inferior lingular segmental bronchi. This is different from the pattern in the right middle lobe, where the corresponding distribution in the right middle lobe is to lateral and medial segments (see Fig. 54.7).

Left inferior lobar bronchus

The left inferior lobar bronchus descends posterolaterally and divides to supply the segmental territories of the left lung similar to those of the right lung.

Segmental bronchi

The superior (apical) segmental bronchus arises from the posterior surface of the inferior lobar bronchus posteriorly, about 1 cm from its origin. The anteromedial basal segmental bronchus arises anteriorly

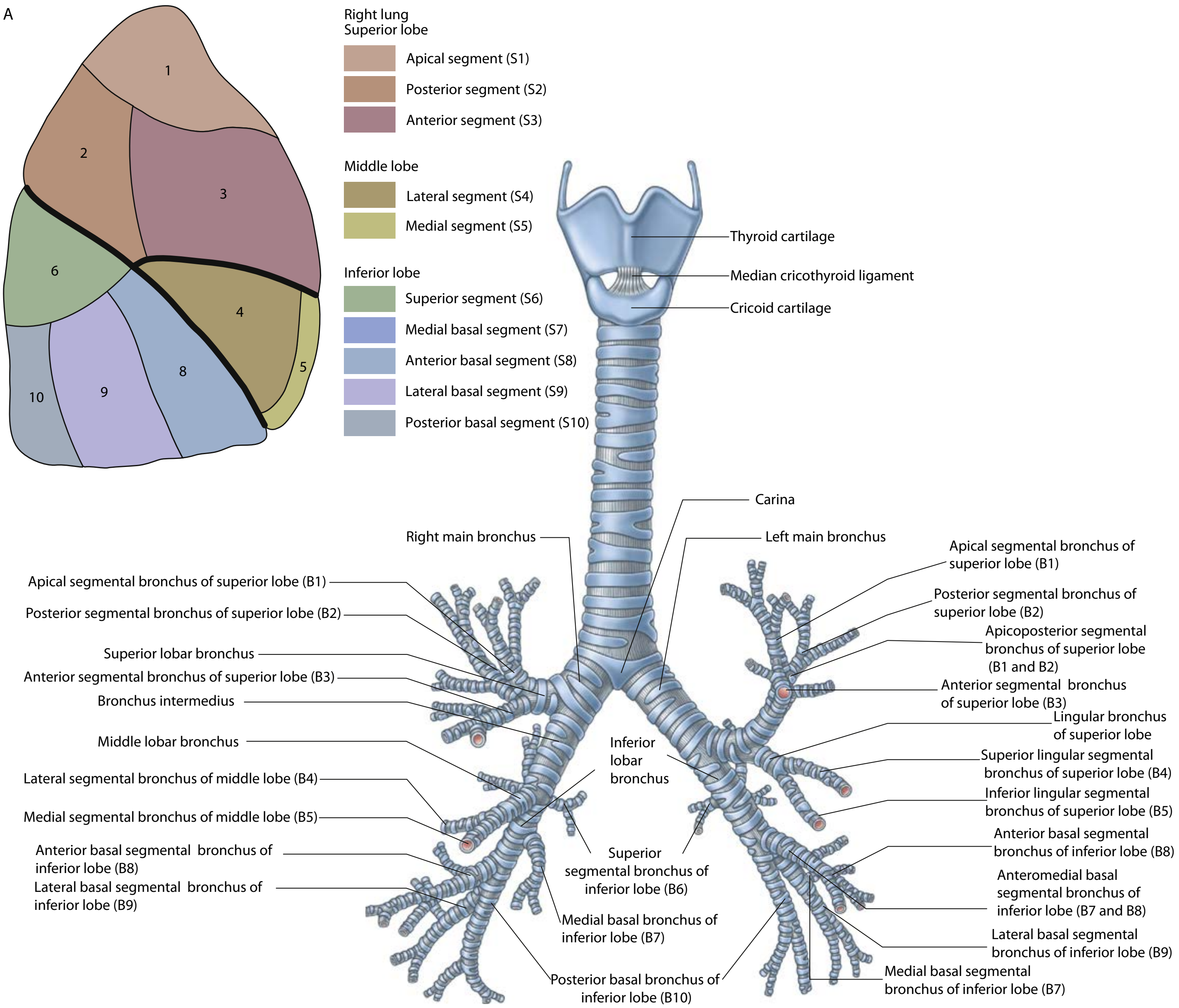
A
1
2
3
4
5
6
8
9
10
Right lung
Superior lobe
Apical segment (S1)
Posterior segment (S2)
Anterior segment (S3)
Middle lobe
Lateral segment (S4)
Medial segment (S5)
Inferior lobe
Superior segment (S6)
Medial basal segment (S7)
Anterior basal segment (S8)
Lateral basal segment (S9)
Posterior basal segment (S10)
Thyroid cartilage
Median cricothyroid ligament
Cricoid cartilage
Carina
Right main bronchus
Left main bronchus
Apical segmental bronchus of superior lobe (B1)
Posterior segmental bronchus of superior lobe (B2)
Superior lobar bronchus
Anterior segmental bronchus of superior lobe (B3)
Bronchus intermedius
Middle lobar bronchus
Lateral segmental bronchus of middle lobe (B4)
Medial segmental bronchus of middle lobe (B5)
Anterior basal segmental bronchus of inferior lobe (B8)
Lateral basal segmental bronchus of inferior lobe (B9)
Inferior lobar bronchus
Superior segmental bronchus of inferior lobe (B6)
Medial basal bronchus of inferior lobe (B7)
Posterior basal bronchus of inferior lobe (B10)
Apical segmental bronchus of superior lobe (B1)
Posterior segmental bronchus of superior lobe (B2)
Apicoposterior segmental bronchus of superior lobe (B1 and B2)
Anterior segmental bronchus of superior lobe (B3)
Lingular bronchus of superior lobe
Superior lingular segmental bronchus of superior lobe (B4)
Inferior lingular segmental bronchus of superior lobe (B5)
Anterior basal segmental bronchus of inferior lobe (B8)
Anteromedial basal segmental bronchus of inferior lobe (B7 and B8)
Lateral basal segmental bronchus of inferior lobe (B9)
Medial basal segmental bronchus of inferior lobe (B7)

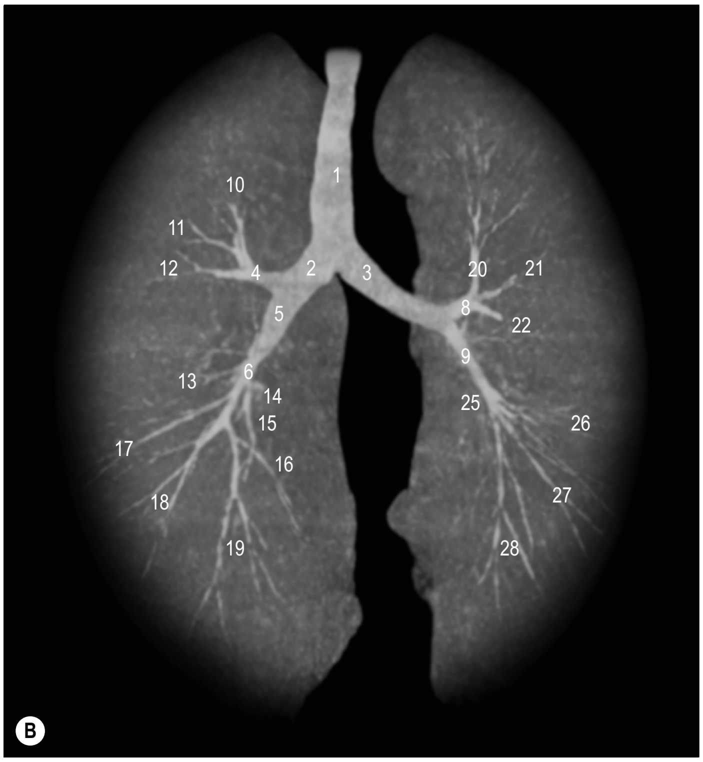
1
2
3
4
5
6
8
9
10
11
12
13
14
15
16
17
18
19
20
21
22
25
26
27
28
B

Fig. 54.5 **A,** The cartilages of the larynx, trachea and bronchi (anterior view), and the bronchopulmonary segments on the costal surface of the right lung. The bronchopulmonary segment (S) and segmental bronchus (B) labels are shown in brackets. In the left lung, segments S1 and S2, and S7 and S8, may be fused. **B,** Coronal minimum intensity projection from a CT of the chest showing the airways. The peripheries of the lungs have been cropped. Key: 1, trachea; 2, right main bronchus; 3, left main bronchus; 4, right superior lobar bronchus; 5, bronchus intermedius; 6, right inferior lobar bronchus; 7, middle lobar bronchus (see Fig. 54.6); 8, left superior lobar bronchus; 9, left inferior lobar bronchus; 10, apical segmental bronchus of the right superior lobe; 11, posterior segmental bronchus of the right superior lobe; 12, anterior segmental bronchus of the right superior lobe; 13, lateral segmental bronchus of the middle lobe; 14, medial segmental bronchus of the middle lobe; 15, superior (apical) segmental bronchus of the right inferior lobe; 16, medial basal segmental bronchus of the right inferior lobe; 17, anterior basal segmental bronchus of the right inferior lobe; 18, lateral basal segmental bronchus of the right inferior lobe; 19, posterior basal segmental bronchus of the right inferior lobe; 20, apicoposterior segmental bronchus of the left superior lobe; 21, anterior segmental bronchus of the left superior lobe; 22, lingular bronchus (to 23, superior and 24, inferior lingular segmental bronchi (see Fig. 54.6)); 25, superior (apical) segmental bronchus of the left inferior lobe; 26, anterior basal segmental bronchus of the left inferior lobe; 27, lateral basal segmental bronchus of the left inferior lobe; 28, posterior basal segmental bronchus of the left inferior lobe. (A, Redrawn from an original figure drawn from a metal cast made by the late Lord Russell Brock, GKT School of Medicine, London.)

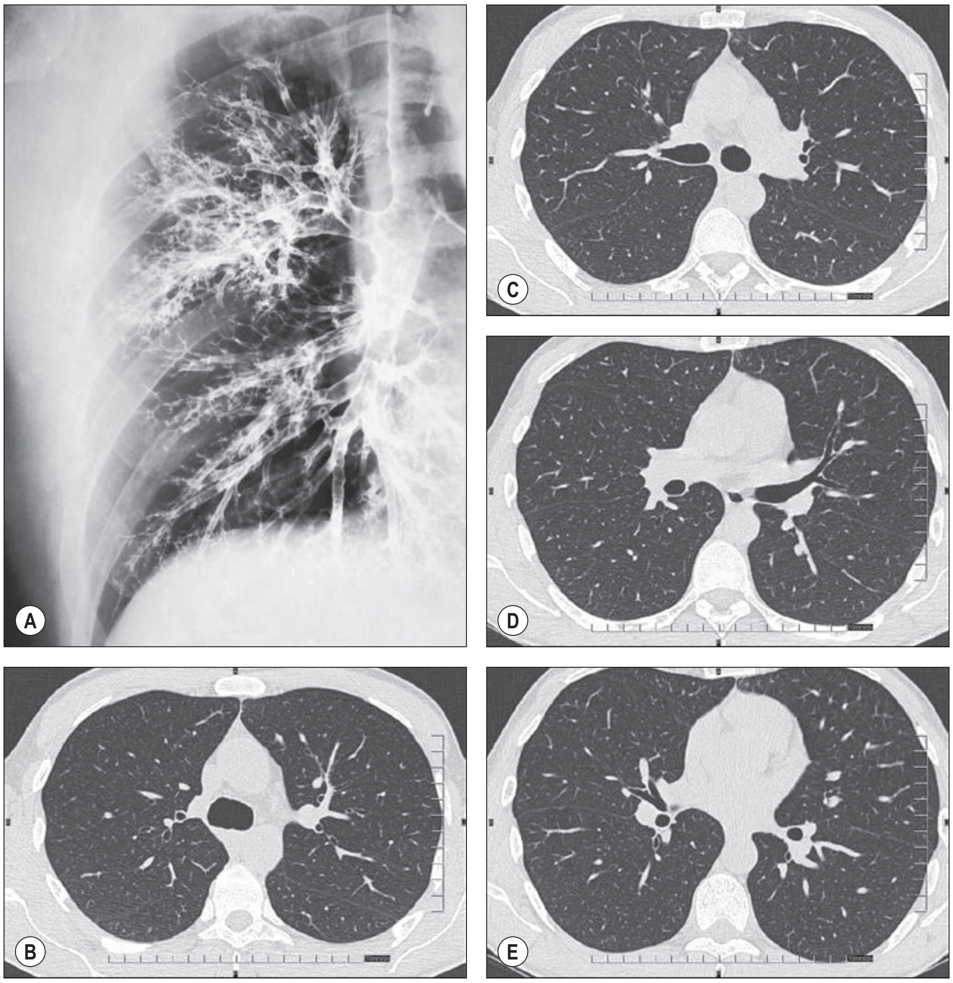

Fig. 54.6 A, A bronchogram showing the branching pattern of the trachea and bronchi of the right lung, in a slightly oblique, anteroposterior view. In this procedure, a radiopaque contrast medium has been introduced into the respiratory tract to coat the walls of the respiratory passages. For identification of the major branches, compare with Figs 54.5B, 54.13. **B–E,** Lung window CT images demonstrating branching of lobar and segmental bronchi from the level of the carina **(B)** to the bifurcation of the right middle lobar bronchus (E). (F–O, *continued online.*)

after a further 1–2 cm and branches into the anterior and medial basal segmental bronchi, and the continuing stem of the inferior lobar bronchus soon divides into lateral and posterior basal segmental bronchi. The anterior basal segmental bronchus is an occasional independent branch of the inferior lobar bronchus, and a subsuperior (subapical) segmental bronchus occasionally arises posteriorly from the left inferior lobar bronchus.

Bronchopulmonary segments

The left and right main bronchi divide into lobar bronchi that subsequently divide into segmental bronchi (see Fig. 54.5). A segmental bronchus supplies a structurally separate and functionally independent unit of lung tissue called a bronchopulmonary segment (**Figs 54.7–54.8**). Each segment is a separate respiratory unit that is surrounded by connective tissue that is continuous with the visceral pleura. The vascular and lymphatic arrangements of the segments are described on page 1030. The bronchopulmonary segments are named and numbered (S1–S10) according to their supplying segmental bronchus (B1–B10). Although a relatively common pattern of segmentation can be identified (**Table 54.1**), there is often variability in the number and arrangement of the segments (Wantanabe 2016a). The arrangement of bronchopulmonary segments permit the resection of abscesses and localized primary lung malignancy, whilst retaining the normal functioning parts of the lung.

Secondary pulmonary lobules

Progressive subdivisions of the bronchi occur within each bronchopulmonary segment, and the bronchi become increasingly narrow (see Fig. 54.11). All intrapulmonary bronchi are kept patent by cartilaginous plates that decline in size and number, and finally disappear when bronchi become bronchioles (less than 1 mm in diameter). The secondary lobule is the smallest macroscopic subsection of the peripheral lung and is bounded by connective tissue septa of uneven size and shape. It consists of three to six terminal bronchioles, the latter being the most peripheral bronchioles that do not have alveoli in their walls. Distal to each terminal bronchiole is an acinus, the functional unit of the lung for gas exchange. It consists of 3–4 orders of respiratory bronchioles, each leading to 3–8 orders of alveolar ducts: the walls of the ducts consist of alveolar sacs or the mouths of alveoli. The primary lobule is a subunit of the secondary pulmonary lobule and is the part of the lung distal to the respiratory bronchiole.

Cartilaginous support

The trachea and extrapulmonary bronchi contain a framework of incomplete rings of hyaline cartilage united by fibrous tissue and smooth muscle (**Fig. 54.9**). Intrapulmonary bronchi contain discontinuous plates or islands of hyaline cartilage in their walls (see Figs 54.5, 54.11).

Tracheal cartilages

Each of the 16–20 tracheal cartilages measures about 4 mm in height and 1 mm in thickness, appearing thicker in the middle part: the external surface is flat and the internal aspect is slightly convex. The cartilages encompass the anterior two-thirds of the trachea, the posterior third is the membranous (posterior) wall consisting of fibro-elastic and muscular tissue. Tracheal cartilage loses elasticity and calcifies in older age

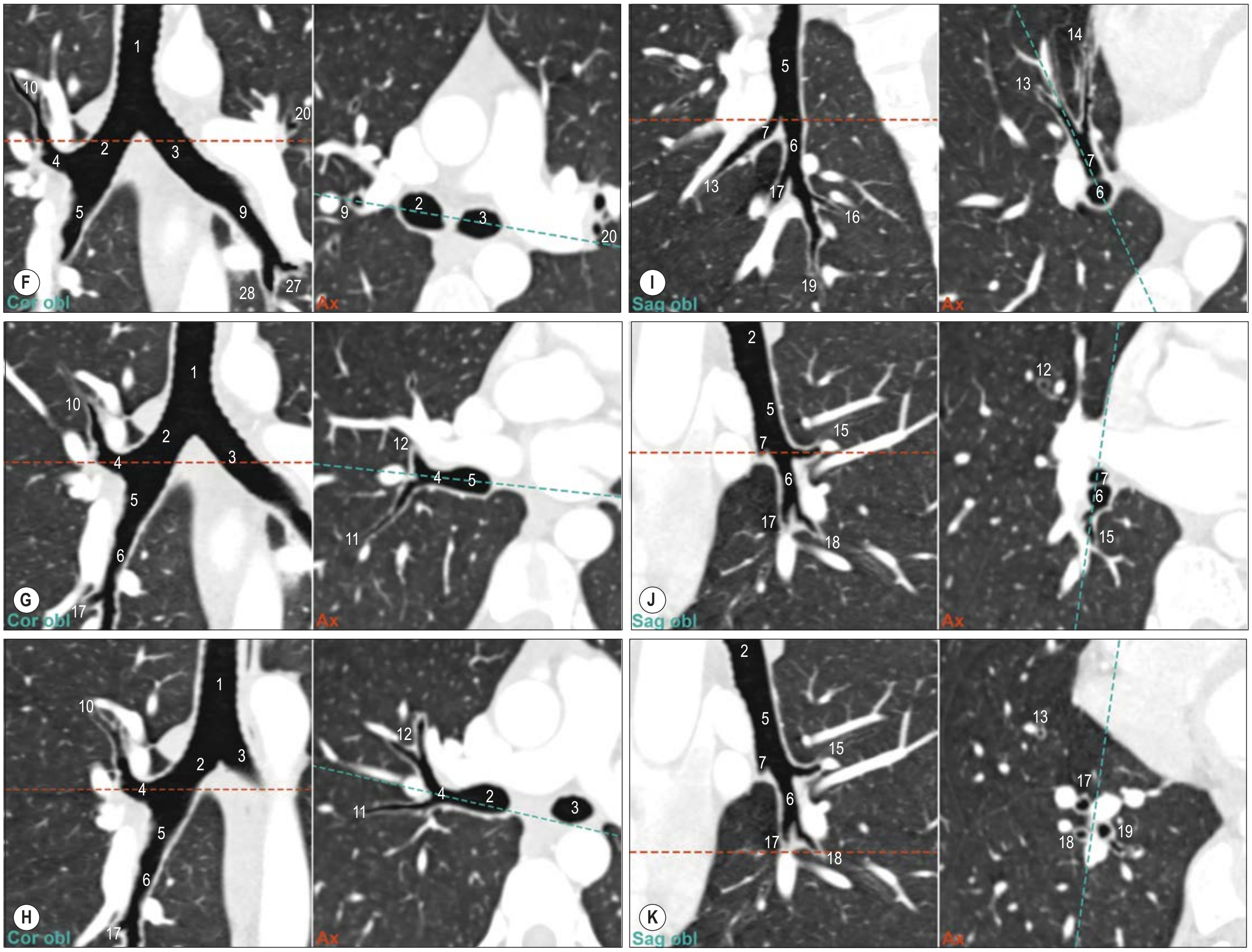
1
10
20
2
3
4
5
9
28
27
F
Cor obl
9
2
3
20
Ax
5
7
6
13
17
16
19
I
Sag obl
14
13
7
6
Ax
1
10
2
4
3
5
6
17
G
Cor obl
12
4
5
11
Ax
2
5
15
7
6
17
18
J
Sag obl
12
7
6
15
Ax
1
10
2
3
4
5
6
17
H
Cor obl
12
4
2
3
11
Ax
2
5
15
7
6
17
18
K
Sag obl
13
17
18
19
Ax

Fig. 54.6 A, A bronchogram showing the branching pattern of the trachea and bronchi of the right lung, in a slightly oblique, anteroposterior view. In this procedure, a radiopaque contrast medium has been introduced into the respiratory tract to coat the walls of the respiratory passages. For identification of the major branches, compare with Figs 54.5B, 54.13. **B–E**, Lung window CT images demonstrating branching of lobar and segmental bronchi from the level of the carina (**B**) to the bifurcation of the right middle lobar bronchus **(E). F–O**, Multiplanar reformat lung window CT images with planes selected specifically to highlight branching anatomy of the bronchial tree (Ax = axial, Sag = sagittal, Cor = coronal, obl = oblique; see Fig. 54.5B for the label key). **F**, At the carina. **G**, At the bronchus intermedius. **H**, At the right superior lobe bronchus. **I**, At the middle lobar bronchus. **J,** At the superior bronchus of the right inferior lobe. **K**, At the right inferior lobar bronchus.

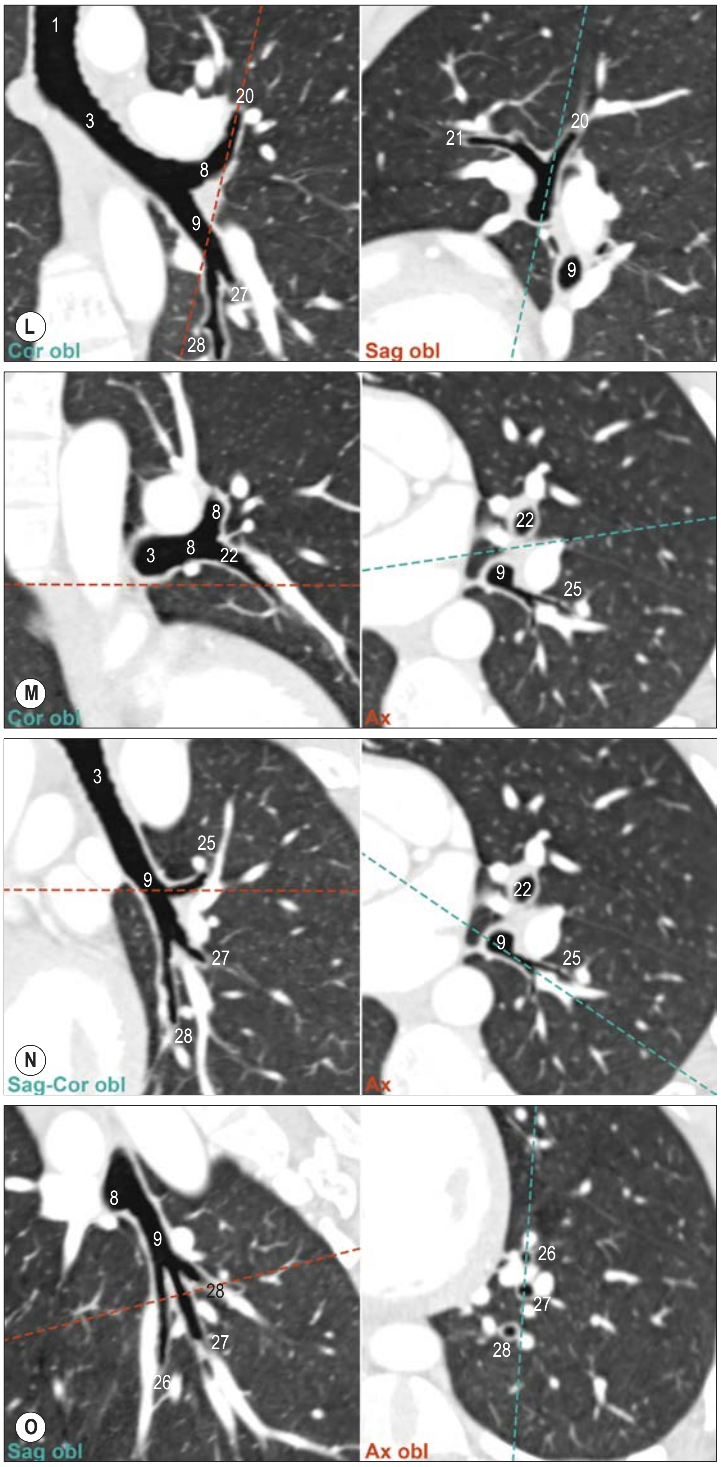
1
3
20
8
9
27
L
28
Cor obl
21
20
9
Sag obl
8
3
8
22
M
Cor obl
22
9
25
Ax
3
25
9
27
28
N
Sag-Cor obl
22
9
25
Ax
8
9
28
27
26
O
Sag obl
26
27
28
Ax obl

Fig. 54.6 cont'd **L**, At the left superior lobar bronchus. **M**, At the lingular bronchus. **N**, At the superior bronchus of the left inferior lobe. **O**, At the left inferior lobar bronchus.

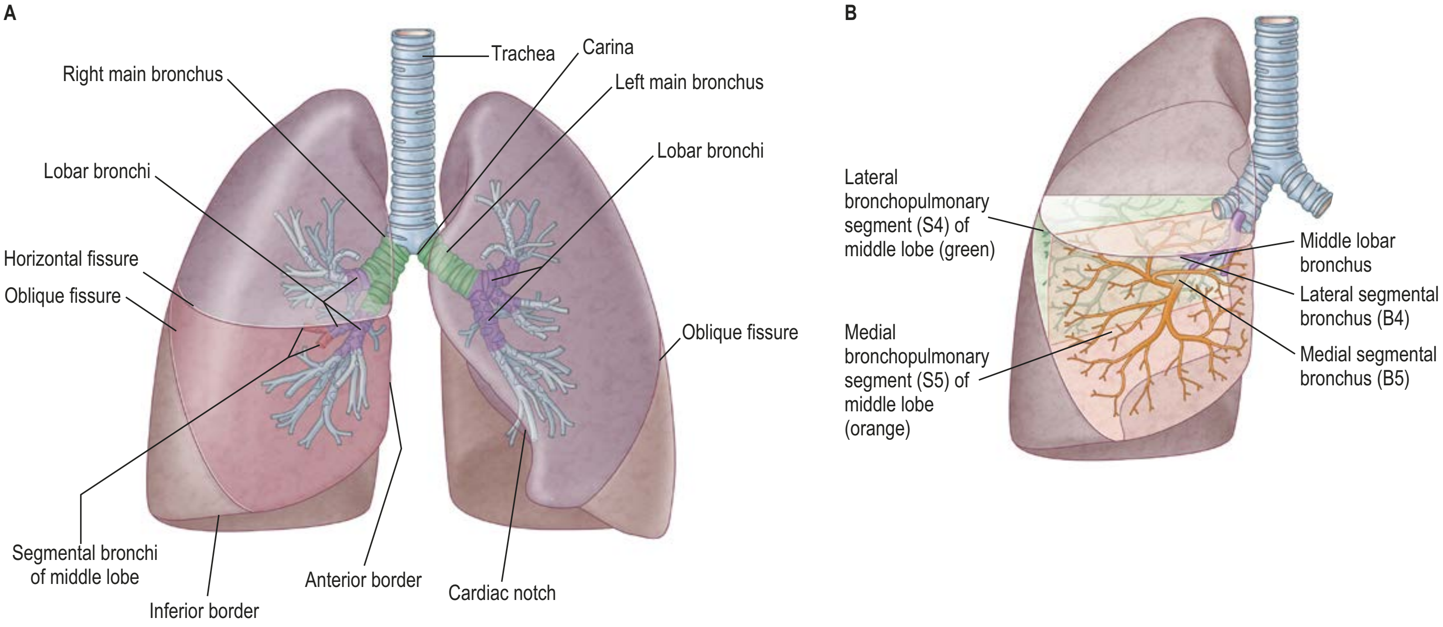
A
Right main bronchus
Trachea
Carina
Left main bronchus
Lobar bronchi
Lobar bronchi
Horizontal fissure
Oblique fissure
Oblique fissure
Segmental bronchi of middle lobe
Inferior border
Anterior border
Cardiac notch
B
Lateral bronchopulmonary segment (S4) of middle lobe (green)
Medial bronchopulmonary segment (S5) of middle lobe (orange)
Middle lobar bronchus
Lateral segmental bronchus (B4)
Medial segmental bronchus (B5)

Fig. 54.7 Lungs and bronchi (anterior view). The segmental bronchi and subsequent bronchial tree are projected onto the middle lobe of the right lung in different colours (compare with Fig. 54.8). (Sobotta Atlas of Human Anatomy © Elsevier GmbH, Urban & Fischer, Munich.)

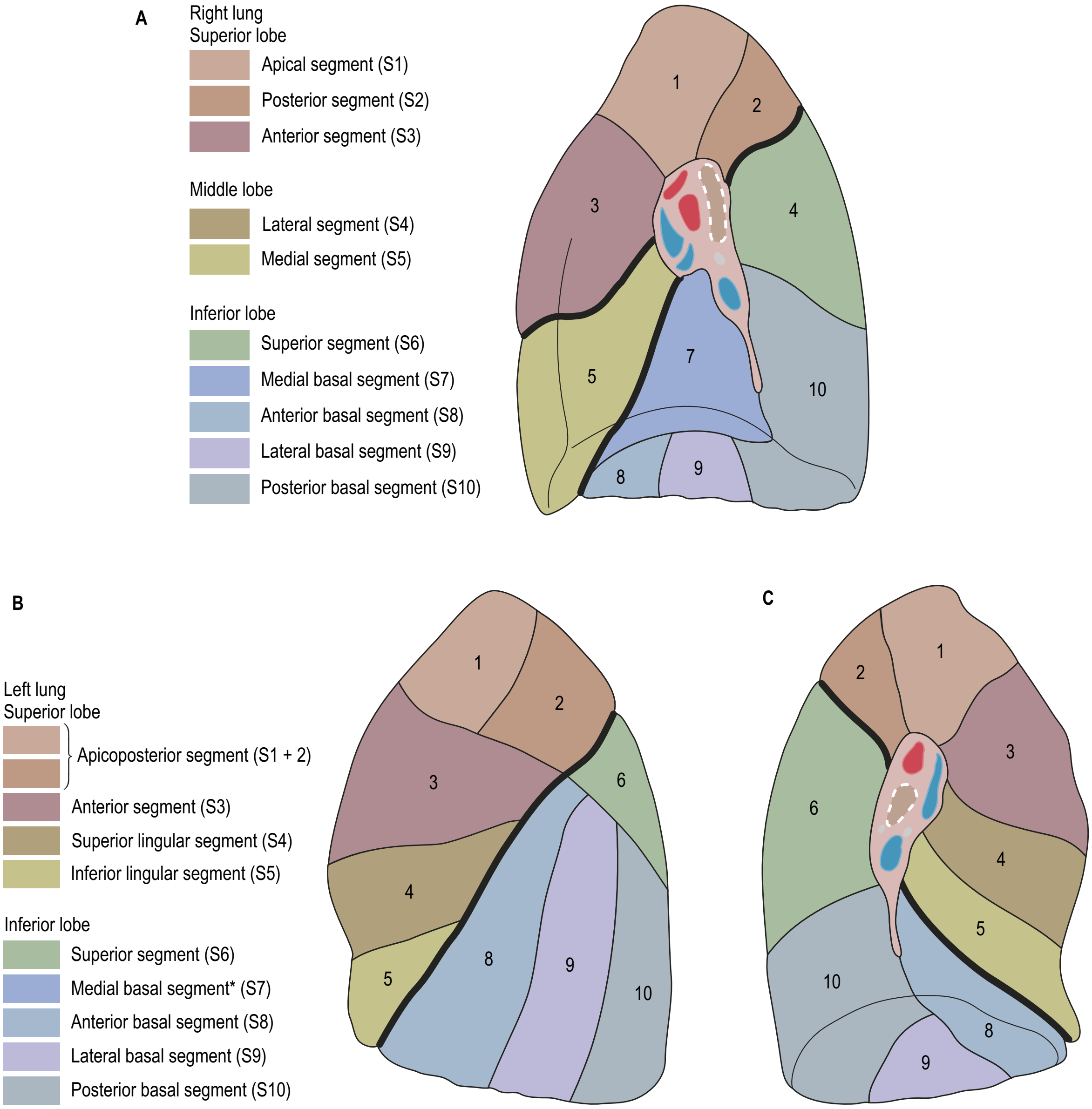
A
Right lung
Superior lobe
Apical segment (S1)
Posterior segment (S2)
Anterior segment (S3)
Middle lobe
Lateral segment (S4)
Medial segment (S5)
Inferior lobe
Superior segment (S6)
Medial basal segment (S7)
Anterior basal segment (S8)
Lateral basal segment (S9)
Posterior basal segment (S10)
1
2
3
4
5
7
10
8
9
B
Left lung
Superior lobe
Apicoposterior segment (S1 + 2)
Anterior segment (S3)
Superior lingular segment (S4)
Inferior lingular segment (S5)
Inferior lobe
Superior segment (S6)
Medial basal segment* (S7)
Anterior basal segment (S8)
Lateral basal segment (S9)
Posterior basal segment (S10)
1
2
3
6
4
8
9
5
10
C
2
1
3
6
4
5
10
8
9

Fig. 54.8 Bronchopulmonary segments of the right and left lungs, coloured to indicate the different territories. **A**, Right lung, mediastinal and diaphragmatic surfaces (see Fig. 54.5A for right lung lateral (costal) surface). **B**, Left lung, lateral (costal) surface. **C**, Left lung, mediastinal and diaphragmatic surfaces. *The medial basal segment (B7) may be fused with the anterior basal segment (B8). (Sobotta Atlas of Human Anatomy © Elsevier GmbH, Urban & Fischer, Munich.)

TABLE 54.1 Bronchopulmonary segments

	Right lung	Left lung
Superior lobe	S1, apical; S2, posterior; S3, anterior	S1, apical; S2, posterior; S3, anterior; S4, superior lingular; S5, inferior lingular; (S1 and S2 may be fused)
Middle lobe	S4, lateral; S5, medial	–
Inferior lobe	S6, superior (apical); S7, medial basal; S8, anterior basal; S9, lateral basal; S10, posterior basal	S6, superior (apical); S7, medial basal; S8, anterior basal; S9, lateral basal; S10, posterior basal; (S7 and S8 may be fused)

and adjacent cartilages may variously fuse. The first and the last two cartilages are more conspicuous, the first being the thickest (see Fig. 54.5) and the last merging into the incomplete rings at the origin of the left and right main bronchus. The tracheal bifurcation is marked by a cartilaginous spur, the carina.

Bronchial cartilages

Cartilaginous plates mainly surround the dorsal aspect of the lobar bronchi. They become more irregular and form progressively less of the bronchial walls in intrapulmonary bronchi and disappear in the bronchioles (see Fig. 54.11).

Vascular supply, lymphatic drainage and innervation

Trachea

The trachea is supplied mainly by branches of the inferior thyroid arteries, which anastomose with ascending branches of the bronchial arteries. Veins draining the trachea end in the inferior thyroid venous plexus. The lymph vessels pass to the pretracheal, retrotracheal and upper and lower paratracheal lymph nodes (Ch. 56, see Figs 54.12, 56.4A, Table 56.1).

Bronchi

Bronchial arteries

The bronchial arteries supply oxygenated blood and nutrition to the bronchi and connective tissue of the lungs and also supply the oesophagus (**Figs 54.10–54.11**). They are commonly derived from the proximal part of the descending thoracic aorta either directly or indirectly, travel and branch with the bronchi, and terminate around the level of the respiratory bronchioles. They anastomose with the branches of the pulmonary arteries, and together supply the visceral pleura of the lung.

Most commonly there is one right and two left bronchial arteries, although various combinations are possible, for example, two right and two left or two right and one left artery. The normal single right bronchial artery has a variable origin, usually arising as a common trunk with the right third posterior intercostal artery (a branch of the descending thoracic aorta), sometimes from the superior left bronchial artery or from various right intercostal arteries. There are normally two left bronchial arteries (superior and inferior) that branch separately from the descending thoracic aorta, although these may be singular and may also give rise to a right bronchial artery. Uncommon origins for the bronchial arteries include the abdominal aorta or the inferior phrenic, coronary, subclavian or internal thoracic arteries, or the brachiocephalic or thyrocervical trunks. A review of branching patterns and origins is presented by Akgun et al (2016).

The bronchial arteries accompany the bronchial tree and supply bronchial glands, the walls of the bronchi and larger pulmonary vessels. The bronchial branches form a capillary plexus in the muscular tunic of the air passages that supports a second mucosal plexus that communicates with branches of the pulmonary artery and drains into the pulmonary veins. Other arterial branches ramify in interlobular loose connective tissue and most end in either deep or superficial bronchial veins; some also ramify on the surface of the lung, forming subpleural capillary plexuses. The bronchopulmonary arterial anastomoses in the walls of the smaller bronchi and in the visceral pleura may be more numerous in the neonate and are subsequently obliterated.

In addition to the usual three main bronchial arteries, smaller bronchial branches arise from the descending thoracic aorta; some may travel through the pulmonary ligament and bleed during inferior lobectomy. The bronchial arteries are typically enlarged and tortuous in chronic pulmonary thromboembolic hypertension. They are not usually reconnected following lung transplantation. Aneurysms of a bronchial artery may mimic aortic aneurysms.

Bronchial veins

There are usually two bronchial veins on each side that drain blood from larger bronchi and hilar region structures. They form two distinct systems. Deep bronchial veins commence as intrapulmonary bronchiolar plexuses that communicate freely with the pulmonary veins and eventually join a single trunk that ends in a main pulmonary vein or in the left atrium. Superficial bronchial veins drain extrapulmonary bronchi, visceral pleura and the hilar lymph nodes. They also communicate with the pulmonary veins and end in the azygos vein on the right, and in the left superior intercostal or the accessory hemiazygos vein on the left. Much of the blood supplied by the bronchial arteries is returned via the pulmonary veins rather than the bronchial veins. The main bronchial arteries and veins run on the dorsal aspect of the extrapulmonary bronchi.

Lymphatic drainage

The pulmonary lymphatics originate in superficial and deep plexuses that start at the bronchioles: the walls of the alveoli and the alveolar ducts have no lymph vessels. The superficial plexus lies deep to the visceral pleura and its efferents pass around the margins of the lung and its fissures, eventually reaching the bronchopulmonary (hilar) nodes (**Fig. 54.12**). The deep lymphatics originate at bronchiolar level and follow the divisions of the bronchial tree and pulmonary vessels to the lung hilum, ending in the same nodes as the superficial plexus. In larger bronchi, the deep plexus has submucosal and peribronchial parts, but in smaller bronchi there is only a single plexus that extends to the bronchioles. Lymph node groups (stations) sit alongside the bronchi and are classified according to their location, specifically, subsegmental, segmental, lobar and hilar (Rusch et al 2009). Lymph from the hilar nodes drains into subcarinal (inferior tracheobronchial) and lower paratracheal (superior tracheobronchial) node groups.

Free anastomoses between the two superficial and deep plexuses are found only at the hilum and also peripherally, where small but dilatable channels connect superficial and deep lymphatic vessels: these connections direct lymph from the deep to the superficial channels when outflow from deep vessels is obstructed by pulmonary disease. There is a tendency for lymph vessels from the superior lobes to pass to the lower paratracheal (superior tracheobronchial) nodes, and those from the inferior lobes to pass to the subcarinal (inferior tracheobronchial) nodes. However, lymphatic vessels of adjoining lobes connect deep in the fissures which means that these connections are not exclusive. At the level of pulmonary lobation, the arrangement of lymphatic vessels follows the central artery of a lobule and its peripheral veins. Lymphoid aggregations, non-follicular in appearance, occur in peribronchial sites and in 'placoid' formations deep to the visceral pleura.

Innervation

The autonomic nervous system (either by direct axonal innervation or circulating neurotransmitter) controls many aspects of airway function, including regulation of airway smooth muscle tone, mucus secretion from submucosal glands and surface epithelial goblet cells, vascular permeability and blood flow (Belvisi 2002).

The trachea and bronchi are innervated by branches of the vagus nerves, recurrent laryngeal nerves and sympathetic trunks via the anterior and posterior pulmonary plexuses. The plexuses are interconnected and lie anterior and posterior to the structures of the lung root and hilum (see Figs 56.6–56.7, 57.61). The anterior plexus is small and is formed by branches from the vagus nerves and sympathetic cervical cardiac nerves via connections with the superficial cardiac plexus. The left and right posterior pulmonary plexuses are formed by the branches of the vagus nerves, and sympathetic cardiac branches from the second to fifth or sixth thoracic sympathetic ganglia. The left posterior plexus also receives branches from the left recurrent laryngeal nerve. Further details of the pulmonary plexuses are given in the description of the cardiac plexuses on page 1094. Branches of the plexuses enter the lung as networks that travel along successive branches of the bronchi and the pulmonary and bronchial vessels as far as the visceral pleura.

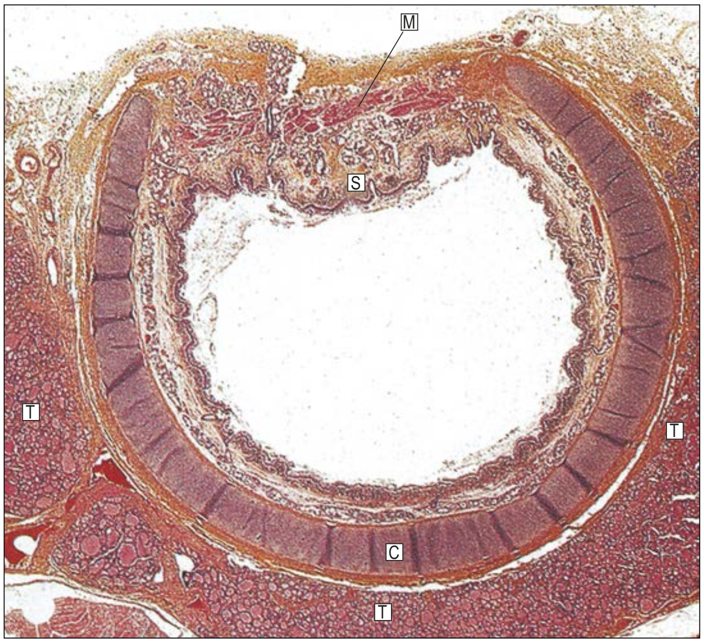

Fig. 54.9 A micrograph of the trachea of a child, sectioned transversely. An incomplete cartilage ring (C) is joined posteriorly by muscular tissue (M). Seromucous submucosal glands (S) are concentrated in this region and between adjacent cartilages. Note the thyroid gland tissue (T) surrounding the left, anterior and right sides of the trachea. (With permission from Stevens A, Lowe JS 1996 Human Histology, 2nd ed. London: Mosby.)

Some degree of mixing of blood between bronchial and pulmonary circulations and through small cardiac veins (venae cordis minimae or Thebesian veins) draining into the left ventricle normally occurs. A small degree of shunt, i.e. perfusion without ventilation, appears as normal and is usually 2–4%. Cardiac malformations with right-to-left flow, pulmonary arteriovenous malformations, congenital diaphragmatic herniae or pulmonary embolism cause more important shunting that is refractory to the administration of pure oxygen.

Efferent preganglionic parasympathetic nerves from the vagus nerve synapse on small ganglia within the walls of the tracheobronchial tree, likely acting as sites of integration and/or modulation of the input from extrinsic nerves or permitting local control of aspects of airway function by local reflex mechanisms. The predominant contractile innervation of airway smooth muscle is parasympathetic cholinergic, while the primary relaxant innervation of the airways is non-cholinergic (parasympathetic nerves containing nitric oxide synthase and vasoactive intestinal peptide). These parasympathetic nerves are anatomically and physiologically distinct and differentially regulated by reflexes. Stimulation of cholinergic nerves also results in mucus secretion and bronchial vasodilation. Sympathetic-adrenergic nerves play little, if any, role in directly regulating smooth muscle tone in the human airways, although they may control constriction of tracheobronchial blood vessels. Circulating noradrenaline (norepinephrine) can bring about bronchodilation through activation of β-adrenergic receptors in the airways. Extrapulmonary afferents may modulate neurally mediated regulation of airway smooth muscle tone (Canning and Fischer 2001).

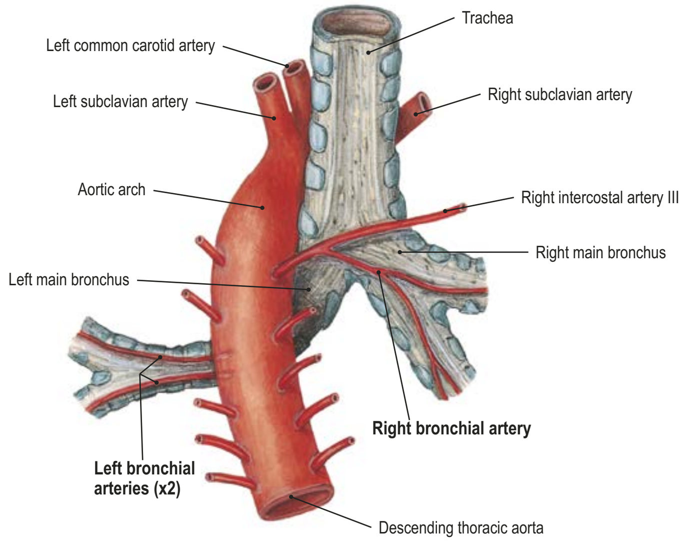

Fig. 54.10 The common pattern of origin of the bronchial arteries from the descending thoracic aorta (posterior view).

Lung root and hilum

The lung root connects the mediastinal surface of the lung to the heart and trachea, and is formed by a group of structures that enter or leave the lung hilum including the main bronchus, or its lobar branches, pulmonary artery, two pulmonary veins, bronchial vessels, a pulmonary autonomic plexus, lymph vessels, hilar (bronchopulmonary) lymph nodes and loose connective tissue, all enveloped by a double-layered sleeve of pleura (a visceral and a parietal layer) (see Figs 54.3, 54.13). The lung roots commonly lie opposite the bodies of the fifth to seventh thoracic vertebrae. The phrenic nerve, pericardiacophrenic vessels and anterior pulmonary plexus are common anterior relations of the left and right lung roots, the vagus nerve and posterior pulmonary plexus are common posterior relations and the pulmonary ligament is a common inferior relation.

Left hilum

The hilum of the left lung and the closely associated lung root are situated inferior to the aortic arch and anterior to the descending thoracic aorta. Usually, the order of structures at the hilum, from superior to inferior, is the pulmonary artery, left main (hyparterial) bronchus and inferior pulmonary vein (see Fig. 54.3B). The superior pulmonary vein is often the most anterior structure at the hilum, sitting anterior to the left main bronchus. The pulmonary artery is longer on the left side and may have branched before entering the hilum: each of its branches from the hilum to the oblique fissure must be identified in pulmonary resections.

Right hilum

The hilum of the right lung and the closely associated lung root are situated posterior to the superior vena cava and the fibrous pericardium covering the right atrium and inferior to the terminal (arching) part of the azygos vein. Usually the superior lobar (eparterial) bronchus is the most superior structure, with the bronchus intermedius located immediately inferior; the superior and inferior pulmonary veins are the most anterior (or anteroinferior) and inferior structures, respectively; and the pulmonary artery is anterior to the bronchi and may be either posterior and/or superior to the superior pulmonary vein (see Fig. 54.3A). One or two pulmonary arteries may be present at the hilum, depending on where the right pulmonary artery branches: when two are present their arrangement is commonly superior–inferior.

Pulmonary vascular supply and drainage

The lungs have two functionally distinct circulatory pathways. Pulmonary arteries convey systemic deoxygenated blood to the alveolar walls and pulmonary veins drain oxygenated blood back to the left atrium for systemic distribution by the left ventricle. The much smaller bronchial arteries, derived from the systemic circulation, provide oxygenated blood to lung tissues that do not have close access to atmospheric oxygen, i.e. those of the bronchi and larger bronchioles (see Fig. 54.10).

The pulmonary trunk bifurcates into right and left pulmonary arteries, each of which approaches the respective lung hilum via the lung root (**Fig. 54.13**). Each pulmonary artery divides into branches that accompany the segmental and subsegmental bronchi, mostly in a posterolateral position. The pulmonary capillaries form single-layered, thin-walled plexuses immediately outside the epithelium in the walls and septa of the alveoli and alveolar sacs (see Fig. 54.11). Pulmonary veins, two from each lung, drain the pulmonary capillaries; their rootlets coalesce into larger and more freely communicating veins that traverse the lung, for the most part independently of the pulmonary arteries and bronchi. Near the lung hilum, the pulmonary vessels accompany the main bronchial division, the veins lying anteromedial and the arteries posterolateral to the bronchi. This is not the case in the bronchopulmonary segments, where a segmental bronchus, its branches and associated arteries occupy a central position, whereas the many tributaries of the pulmonary veins run between segments, serving adjacent segments (which therefore drain into more than one vein). Some veins also lie beneath the visceral pleura, including the pleura in the interlobar fissures. It follows from this that a bronchopulmonary segment is not a complete vascular unit with an individual bronchus, artery and vein. During resection of segments, it is apparent that the planes between them are not avascular but are crossed by pulmonary veins and sometimes by branches of arteries. This relationship of bronchi, arteries and veins exhibits considerable variation, veins are the most variable and arteries are more variable than bronchi.

Pulmonary arteries

The right pulmonary artery divides into two large branches posterior to the superior vena cava, or immediately lateral to its right side (see Fig. 54.13). This intimate relationship facilitates the cavopulmonary anastomosis (the Glenn shunt) conceived to bypass the defective right heart chambers in various congenital cardiac disorders. A lymph node usually lies adjacent to the bifurcation. The smaller branch to the superior lobe usually divides again, supplying the majority of that lobe. The inferior branch descends anterior to the bronchus intermedius and posterior to the superior pulmonary vein. It provides a small recurrent branch to the superior lobe, and then, at the point where the horizontal fissure meets the oblique fissure, it gives off the branch to the middle lobe anteriorly, and a branch to the superior segment of the inferior lobe posteriorly. It then continues a short distance before dividing to supply the rest of the inferior lobe segments.

The left pulmonary artery emerges from under the concavity of the aortic arch and descends anterior to the descending thoracic aorta to enter the oblique fissure. The ligamentum arteriosum passes between the superior aspect of the left pulmonary artery and the proximal descending thoracic aorta; the aorta is relatively fixed in position by the ligament, and so may be ruptured in this region in cases of major trauma associated with rapid deceleration. The left recurrent laryngeal nerve branches from the left vagus nerve, passes inferior to the aortic arch to the left of the ligamentum arteriosum, and then courses superiorly posterior to the aortic arch; it is a close relation of the superior part of the left lung root and hilum, where it may be compressed or invaded by lung tumour. The branches of the left pulmonary artery are variable (Sivrikoz 2016). The first and largest branch is usually given off to the anterior segment of the left superior lobe. Before reaching the oblique fissure, the artery gives off a variable number of other branches to the superior lobe; it usually supplies a large branch to the superior segment of the inferior lobe as it enters the fissure. Lingular branches arise within the fissure, and the rest of the lower lobe is supplied by many varied branching patterns. It was a surgical aphorism of the late Lord Brock that when performing a left upper lobectomy, 'there was always one more branch of the pulmonary artery than you thought!'

Pulmonary sequestration

When a portion of lung exists without the appropriate bronchial and vascular connections, it is usually supplied by the systemic vasculature (descending thoracic or abdominal aorta or one of its branches) and drains into either the atria, superior vena cava or azygos venous system (Clements 1999) (**Figs 54.14–54.15**).

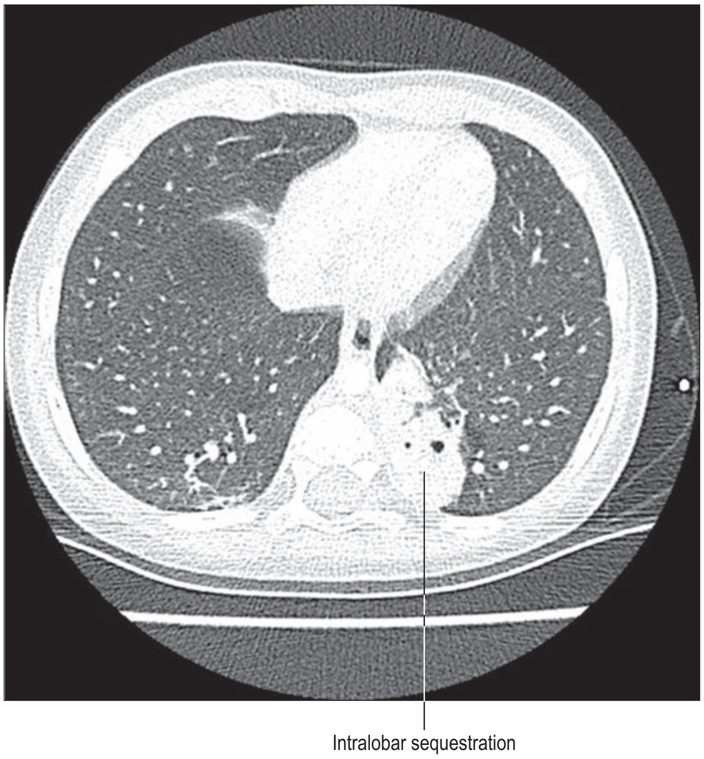

Fig. 54.14 A CT of the chest (lung windowed, axial view) showing an intralobar sequestration in the left inferior lobe of the lung in a 15-month-old girl. (Courtesy of Mr Hany Gabra and Mr Jonathan Goring, Great North Children's Hospital, Newcastle upon Tyne, UK.)

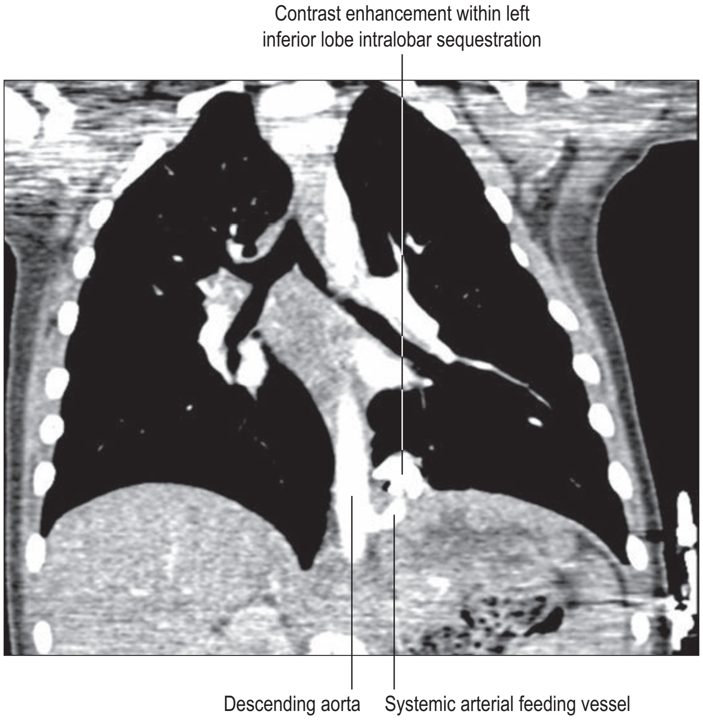
Contrast enhancement within left inferior lobe intralobar sequestration
Descending aorta
Systemic arterial feeding vessel

Fig. 54.15 A CT of the chest (coronal view) showing the systemic arterial blood supply from the abdominal aorta to an intralobar sequestration in the left inferior lobe of the lung in a 15-month-old girl. (Courtesy of Mr Hany Gabra and Mr Jonathan Goring, Great North Children's Hospital, Newcastle upon Tyne, UK.)

Unilateral absence of a pulmonary artery is a rare congenital anomaly characterized by normal lung volume and anatomy at birth. Revascularization before the age of 6 months avoids the development of lung hypoplasia (Alison et al 2011). The left pulmonary artery sling is a congenital anomaly where the left pulmonary artery arises from the right pulmonary artery, travels posteriorly over the right main bronchus and then passes between the trachea and oesophagus: it is associated with significant tracheobronchial stenosis (Zhong et al 2010).

Extralobar pulmonary sequestration segments are covered by visceral pleura and usually found below the left inferior lobe, whereas intralobar anomalies are usually embedded in normal lung, classically, in the posterior basal segment of the left inferior lobe. Extralobar pulmonary sequestration is normally asymptomatic but often associated with other congenital anomalies such as pulmonary hypoplasia, congenital diaphragmatic hernia, congenital cystic adenomatoid malformation and congenital heart disorders (Stocker et al 1978, Kravitz 1994). A fistula into the oesophagus may also develop. Consideration of differential diagnoses that include mediastinal or pulmonary tumours is mandatory.

A thrombus that has developed in the deep venous system (usually in the lower limb or pelvis) may embolize and travel in the right side of the circulation through the right atrium and right ventricle and lodge in the pulmonary vasculature. The clinical abnormalities observed depend on the size of the embolus and on the number and frequency of embolic episodes. Large emboli may lodge in branches of the main pulmonary artery and cause right ventricular dysfunction and hypoxia, representing a medical emergency. Smaller emboli may lodge in segmental pulmonary arteries and cause pleuritic chest pain, shortness of breath and haemoptysis, although the clinical picture is rarely pathognomonic. Pulmonary emboli cause a ventilation–perfusion ratio mismatch that can have serious physiological implications leading to a significant reduction in the oxygenation of blood. Ventilation–perfusion scans with radiolabelled xenon and technetium usually demonstrate segmental abnormalities in perfusion with normal ventilation in the corresponding regions. Pulmonary emboli may also be evaluated by contrast-enhanced spiral CT or pulmonary angiograms and appear as filling defects. Repetitive embolization may eventually lead to a dramatic reduction of the pulmonary vascular bed and chronic cor pulmonale. Thrombolysis, anticoagulation or inferior vena caval filters prevent progression or recurrence of embolism. A clot may also traverse a patent foramen ovale and lodge in the arterial system (paradoxical embolism), most severely in the cerebral circulation resulting in stroke (Kent and Thaler 2011).

The variable incorporation of the primitive pulmonary vein into the left atrium during development (Ch. 13) means that the number of main pulmonary veins may differ. Pulmonary vein atresia is a rare congenital anomaly (Kozak et al 2011). The left atrium is the heart chamber most posterior and median in position, and so the length of the left and right pulmonary veins is relatively equal, unlike the arteries and bronchi, where there are obvious left–right differences in length. The terminal parts of the pulmonary veins are surrounded by atrial myocardium; these areas represent potential accessory re-entrant circuits responsible for the initiation or maintenance of supraventricular tachycardias or atrial fibrillation and may be percutaneously ablated.

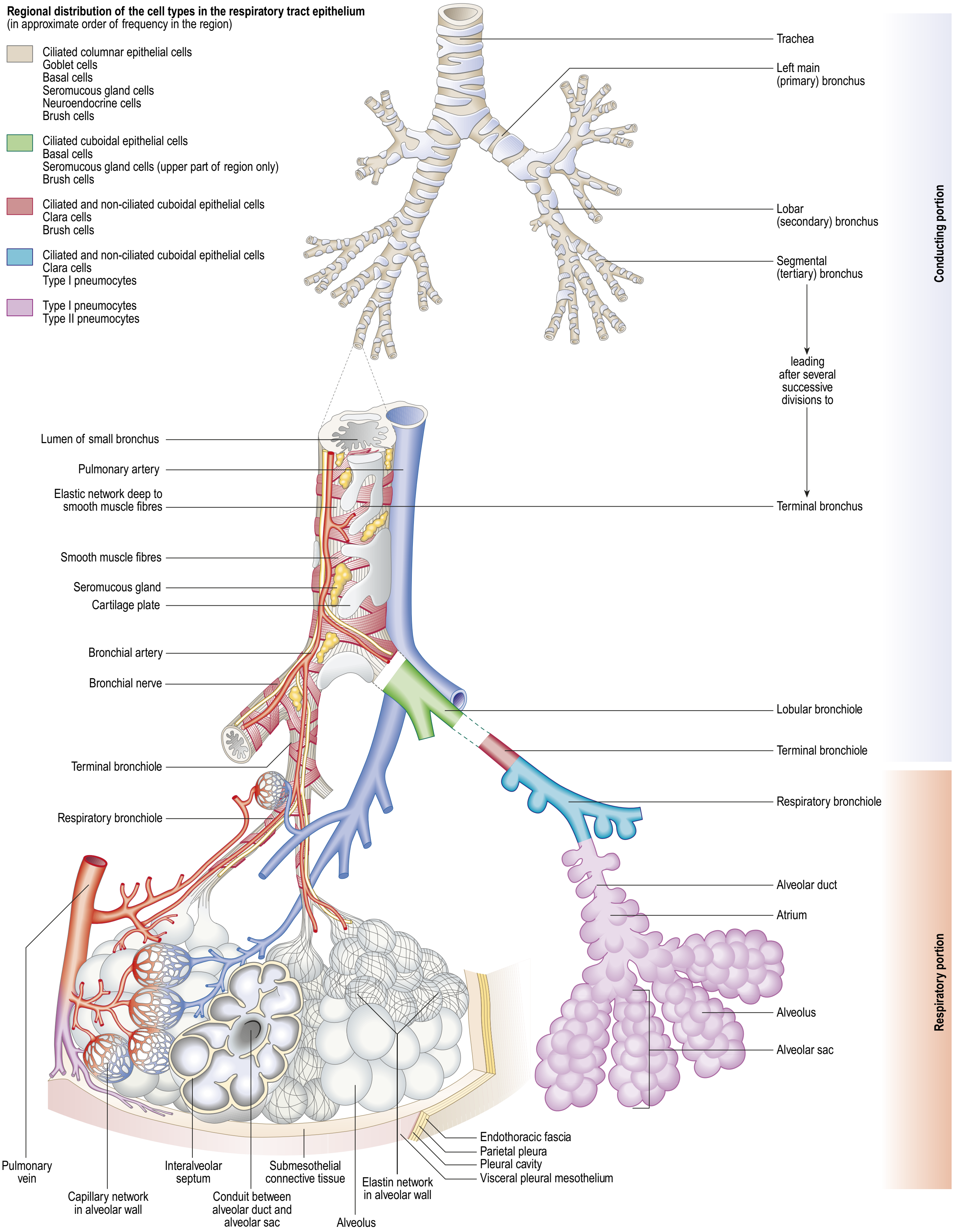
Regional distribution of the cell types in the respiratory tract epithelium
(in approximate order of frequency in the region)
⬜ Ciliated columnar epithelial cells
Goblet cells
Basal cells
Seromucous gland cells
Neuroendocrine cells
Brush cells
🟩 Ciliated cuboidal epithelial cells
Basal cells
Seromucous gland cells (upper part of region only)
Brush cells
🟥 Ciliated and non-ciliated cuboidal epithelial cells
Clara cells
Brush cells
🟦 Ciliated and non-ciliated cuboidal epithelial cells
Clara cells
Type I pneumocytes
🟪 Type I pneumocytes
Type II pneumocytes
Trachea
Left main (primary) bronchus
Lobar (secondary) bronchus
Segmental (tertiary) bronchus
leading after several successive divisions to
Terminal bronchus
Conducting portion
Lumen of small bronchus
Pulmonary artery
Elastic network deep to smooth muscle fibres
Smooth muscle fibres
Seromucous gland
Cartilage plate
Bronchial artery
Bronchial nerve
Terminal bronchiole
Respiratory bronchiole
Lobular bronchiole
Terminal bronchiole
Respiratory bronchiole
Alveolar duct
Atrium
Alveolus
Alveolar sac
Respiratory portion
Endothoracic fascia
Parietal pleura
Pleural cavity
Visceral pleural mesothelium
Pulmonary vein
Capillary network in alveolar wall
Interalveolar septum
Conduit between alveolar duct and alveolar sac
Submesothelial connective tissue
Alveolus
Elastin network in alveolar wall

Fig. 54.11 The respiratory tree and its arterial blood supply and venous drainage. The distribution of the different epithelial cells is shown. Blue is used for vessels that contain deoxygenated blood, and red for vessels that contain oxygenated blood. The deep lymphatic plexus (not shown) accompanies the bronchial artery and nerve to the bronchioles but does not reach the alveolar duct or beyond.

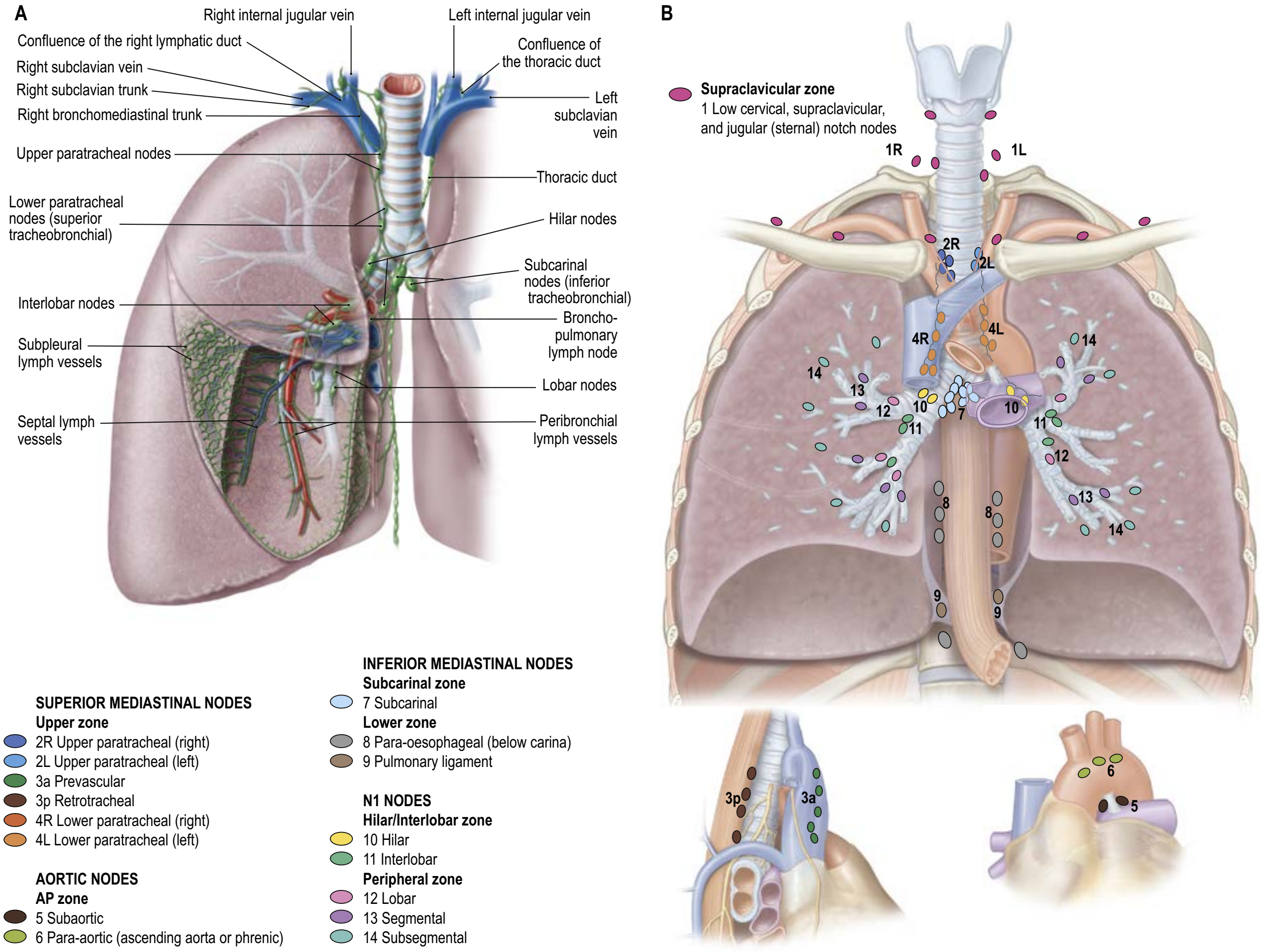
A
Right internal jugular vein
Left internal jugular vein
Confluence of the right lymphatic duct
Confluence of the thoracic duct
Right subclavian vein
Right subclavian trunk
Right bronchomediastinal trunk
Left subclavian vein
Upper paratracheal nodes
Thoracic duct
Lower paratracheal nodes (superior tracheobronchial)
Hilar nodes
Subcarinal nodes (inferior tracheobronchial)
Interlobar nodes
Broncho-pulmonary lymph node
Subpleural lymph vessels
Lobar nodes
Septal lymph vessels
Peribronchial lymph vessels
B
Supraclavicular zone
1 Low cervical, supraclavicular, and jugular (sternal) notch nodes
1R
1L
2R
2L
4R
4L
14
13
12
10
11
7
8
9
3p
3a
6
5
SUPERIOR MEDIASTINAL NODES
Upper zone
2R Upper paratracheal (right)
2L Upper paratracheal (left)
3a Prevascular
3p Retrotracheal
4R Lower paratracheal (right)
4L Lower paratracheal (left)
AORTIC NODES
AP zone
5 Subaortic
6 Para-aortic (ascending aorta or phrenic)
INFERIOR MEDIASTINAL NODES
Subcarinal zone
7 Subcarinal
Lower zone
8 Para-oesophageal (below carina)
9 Pulmonary ligament
N1 NODES
Hilar/Interlobar zone
10 Hilar
11 Interlobar
Peripheral zone
12 Lobar
13 Segmental
14 Subsegmental

Fig. 54.12 Lymphatic vessels, pathways and nodes (zones and stations) of the lung and tracheobronchial tree. **A**, The peribronchial and the subpleural and septal systems drain via different routes and converge in lymph nodes at the lung hilum. **B**, The lymph node groups of the lung, trachea and mediastinum, arranged as stations and zones. (Adapted from Rusch VW, Asamura H, Watanabe H et al 2009 The IASLC lung cancer staging project: a proposal for a new international lymph node map in the forthcoming seventh edition of the TNM classification for lung cancer. J Thorac Oncol 4(5):568–77.)

Pulmonary embolism and arteriography

Available with the *Gray's Anatomy* e-book

Pulmonary veins

There are usually four pulmonary veins, two from each lung. They originate from capillary networks in the alveolar walls and return oxygenated blood to the left atrium: they are devoid of valves. All the main tributaries of the pulmonary veins receive smaller tributaries, both intra- and intersegmental. By serial junctions, tributaries ultimately form a single lobar trunk (one for each lobe). Usually, there are three trunks in the right lung and two in the left: variations reflect the lobar arrangement of an individual. The right middle and superior lobar veins usually unite so that two veins, superior and inferior, leave each lung at the hilum: the superior pulmonary vein is anteroinferior to the pulmonary artery, and the inferior pulmonary vein is the most inferior hilar structure and is also slightly posterior (see Fig. 54.3). The right superior pulmonary vein is formed by the union of apical, anterior and posterior veins (draining the superior lobe) with a middle lobar vein formed by lateral and medial tributaries. The right inferior pulmonary vein is formed in the hilar region by the union of superior (apical) and common basal veins from the inferior lobe. The union of superior and inferior basal tributaries forms the common basal vein. Occasionally, the three right lobar veins remain separate. The right superior pulmonary vein passes posterior to the superior vena cava, and the inferior passes posterior to the right atrium.

The left superior pulmonary vein is formed by the union of apicoposterior, anterior and lingular veins. The left inferior pulmonary vein is formed by the union of the superior (apical) and common basal veins, the latter formed by the union of the superior and inferior basal veins. Both left superior and inferior pulmonary veins pass anterior to the descending thoracic aorta. Sometimes, the two left pulmonary veins form a single trunk, or they may be augmented by an accessory lobar vein from each lobe that unite to form a third left pulmonary vein.

The right and left pulmonary veins pass through the pericardia and open separately in the posterosuperior aspect of the left atrium (see Fig. 57.4B). Their terminations are separated medially by the oblique pericardial sinus, and laterally by smaller and variable pulmonary venous pericardial recesses that are directed superomedially.

Pulmonary defensive mechanisms

The respiratory tract presents a huge surface area that is vulnerable to desiccation, freezing, microbial invasion and the mechanical and chemical effects of inhaled particles. Inhaled air is humidified mainly in the upper respiratory tract, where it passes, with some turbulence, over the nasal and buccopharyngeal mucosae (Ch. 39). The secretions of the various glands of the tracheobronchial tree also help to prevent desiccation. Goblet cells secrete sulphated acid mucins; cells in mucous glands beneath the epithelial surface contain mainly carboxylated mucins, particularly those associated with sialic acid, although sulphated groups also occur; cells of serous glands contain neutral mucins. Goblet cells respond mainly to local irritation, while tubular glands, both mucous and serous, are predominantly under neural and hormonal control. Excessive or altered secretions may

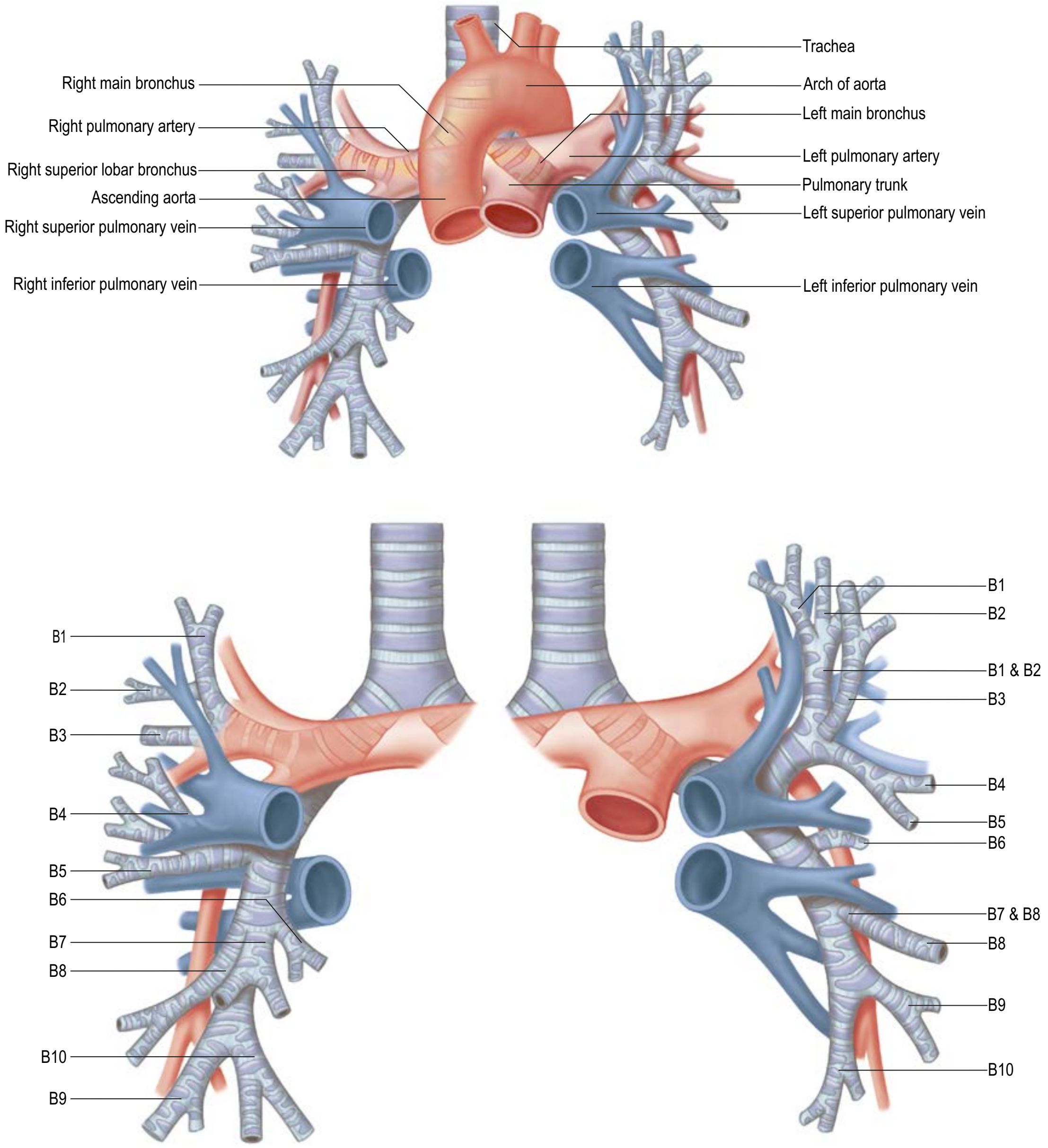
Right main bronchus
Right pulmonary artery
Right superior lobar bronchus
Ascending aorta
Right superior pulmonary vein
Right inferior pulmonary vein
Trachea
Arch of aorta
Left main bronchus
Left pulmonary artery
Pulmonary trunk
Left superior pulmonary vein
Left inferior pulmonary vein
B1
B2
B3
B4
B5
B6
B7
B8
B10
B9
B1
B2
B1 & B2
B3
B4
B5
B6
B7 & B8
B8
B9
B10

Fig. 54.13 The relationship between the central airways and the pulmonary vessels. The alphanumeric labels in the lower figure denote the numbers of the segmental bronchi supplying the corresponding bronchopulmonary segments.

obstruct the flow of air. Antibacterial and antiviral substances, e.g. lysozyme, IgA antibodies and possibly interferon, also appear in the secreted fluid.

Inhaled particles may be cleared by the cough reflex (see below) or removed via the mucociliary rejection current. Cilia sweep the fluid overlying the surfaces of bronchioles, bronchi and trachea upwards at 1 cm/min, and much of the inhaled matter trapped in the viscous fluid may be removed in this way. Particles small enough to reach the alveoli may be removed by alveolar phagocytes. Alveolar epithelium is continually replaced: the lifespan of alveolar squamous cells is approximately 3 weeks, and that of alveolar phagocytes is 4 days.

Numerous lymphoid nodules occur in the bronchial lining, providing foci for the production of lymphocytes and providing local immunological protection against infection both by cell-mediated (T-cell) activities, and by the production of immunoglobulins (mainly IgA) from B cells that are passed onto gland cells for secretion to the epithelial surface.

Anatomy of coughing

Under normal conditions, coughing is an important defensive reflex. It enhances clearance of secretions and particulates from the airways and protects from aspiration of foreign materials (occurring as a consequence of aspiration or inhalation of particulate matter, pathogens, accumulated secretions, postnasal drip, inflammation and mediators associated with inflammation). In some conditions coughing may become excessive, non-productive and potentially harmful to the airway mucosa.

The mechanical events of a cough can be divided into three phases. An initial deep inhalation generates the volume necessary for an effective cough and is followed by a compression phase, when forceful contraction of the muscles of the chest wall, respiratory diaphragm and abdominal wall against a closed glottis results in a rapid rise in intrathoracic pressure. Subsequent glottal opening causes a rapid peak expiratory airflow that dislodges and expels mucus from the airways and this forceful airway compression produces the coughing sound.

Rapidly adapting receptors (RAR)

Available with the *Gray's Anatomy* e-book

Slowly adapting stretch receptors (SAR)

Available with the *Gray's Anatomy* e-book

C fibres

Available with the *Gray's Anatomy* e-book

Bronchoscopy

Available with the *Gray's Anatomy* e-book

Microstructure of the conducting airways

The conducting airways are lined internally by a mucosa (see Fig. 2.16), and the epithelium lies on a thin connective tissue lamina propria. External to this is a submucosa, also composed of connective tissue that contains airway smooth muscle, glands, cartilage plates (depending on the level in the respiratory tree), vessels, lymphoid tissue and nerves. Cartilage is present from the trachea to the smallest bronchi but is absent (by definition) from bronchioles (see Fig. 54.9).

Epithelium

The epithelia of the trachea, bronchi and bronchioles are generally similar although the numbers of different cell types vary according to location. The extrapulmonary and larger intrapulmonary passages are lined with respiratory epithelium, which is pseudostratified and predominantly ciliated, and contains interspersed mucus-secreting goblet cells (see Fig. 2.2D). There are fewer cilia in terminal and respiratory bronchioles, and the cells are reduced in height to low columnar or cuboidal. The epithelium of smaller bronchi and bronchioles is folded into conspicuous longitudinal ridges that accommodate changes in luminal diameter (see Figs 54.11, 54.17). The epithelium in the respiratory bronchioles progressively reduces in height towards the alveoli, and is eventually composed of cuboidal, non-ciliated cells. Lateral pouches lined with squamous cells in the walls of the respiratory bronchioles provide an accessory respiratory surface.

Six distinct types of cell have been described in the conducting airways, namely: ciliated columnar, goblet, Clara, basal, brush and neuroendocrine (see Fig. 54.11). Lymphocytes and mast cells migrate into the epithelium from the underlying connective tissue.

Submucosal glands

Available with the *Gray's Anatomy* e-book

Connective tissue and muscle

Available with the *Gray's Anatomy* e-book

Microstructure of respiratory surfaces

Thin-walled respiratory surfaces (alveoli) are distributed as isolated patches within the walls of respiratory bronchioles and as tube-like alveolar ducts and balloon-like alveolar sacs that contain groups of adjacent alveoli (see Fig. 54.11).

Alveolar area

Each human lung contains approximately 300–500 million alveoli, giving a total surface area of 70–100 m^2. These values vary considerably between normal young individuals and the differences become more marked with age and as a consequence of degenerative changes. The number of alveoli increases from approximately 10 million at birth to the adult value, mainly in the first 8 years of life; thereafter, the increase in lung volume is achieved through augmentation of alveolar volume (Narayanan et al 2013). Their diameter when inflated varies with lung position, being greatest in superior regions because of the increased gravitational pressure at the lung base. Although the lung enlarges in all directions during inspiration, most of the change in volume appears to be due to the lengthening and expansion of the alveolar ducts and increase in the size of the openings into the air sacs, whereas the inspiratory change in the volume of the gas-conducting system is insignificant. The combined alveolar and capillary surface area for gaseous exchange is 60–80 m^2 surface and the capillary blood transit time at rest is 0.75 seconds, halving with exercise.

Alveolar structure

The alveoli are thin-walled pouches that lie in a delicate connective tissue containing a network of capillaries (**Figs 54.18–54.19**). Since the walls are extremely thin, they present a minimal barrier to gaseous exchange between the atmosphere and the blood in the capillaries. Adjacent alveoli are frequently in close contact, the intervening connective tissue forming the central part of an interalveolar septum. Alveolar macrophages are present within the alveolar lumen and migrate over the epithelial surface.

Interalveolar septum

The alveolar lining epithelium varies in thickness; extensive areas are as little as 0.05 µm thick (see Fig. 54.19). The epithelium lies on a basal lamina that is fused with the basal lamina surrounding the adjacent capillaries in the thin portions of a septum. The total barrier to diffusion between air and blood in these thin portions may be as little as 0.2 µm. The thick portions of a septum contain connective tissue elements, including elastic and collagen type III fibres, resident and migratory cells (see Fig. 54.18).

Alveolar epithelial cells (pneumocytes)

The alveolar epithelium is a mosaic of type I and II pneumocytes. Type I pneumocytes are simple squamous epithelial cells and form over 90% of the alveolar area. In histological sections they are characterized by the protrusion of their nuclei from the alveolar surface. Their basal laminae fuse with that of the adjacent capillary endothelium to form the thin portions of interalveolar septa. Their thin cytoplasm (0.05–0.2 µm) facilitates gaseous diffusion between the lumen of the alveolus and its capillaries. The edges of adjacent cells overlap and are joined by tight junctions, creating a strict diffusion barrier between the alveolar surface and underlying tissues. Together with a similar endothelial barrier, this arrangement limits the movement of fluid from blood and interstitial spaces into the alveolar lumen (the blood–air barrier). If damaged, type I pneumocytes, which do not divide, are replaced by type II pneumocytes, which proliferate and differentiate into type I pneumocytes.

The smaller type II cells are often more numerous than type I pneumocytes, but they contribute less than 10% of the alveolar surface area. In histological sections they are characterized by a brush-border projection from the alveolar surface. In the human lung, they are often associated with interalveolar pores of Kohn. Their cytoplasm contains numerous characteristic secretory lamellar bodies consisting of concentric whorls of phospholipid-rich membrane, the precursors of alveolar surfactant, which they can recycle (see Fig. 54.19C).

Interalveolar pores of Kohn

Interalveolar pores of Kohn are small pores lined by epithelium (usually type II pneumocytes), that cross interalveolar septa to link adjacent alveolar airspaces. Humans have up to seven pores per alveolus, ranging in size from 2 to 13 µm. These small passages may sustain the flow of air in the event of blockage of one of the alveolar ducts and also provide routes of migration for alveolar macrophages, bacteria and viruses.

Alveolar macrophages

Alveolar macrophages are derived from circulating monocyte precursors (see Fig. 4.12). They originate in haemopoietic tissue in the bone marrow, migrate into the alveolar lumen from adjacent blood vessels and connective tissue, and 'wander' about on the epithelial surfaces. They clear the respiratory spaces of inhaled particles that are small enough to reach the alveoli (hence their alternative name of 'dust cells'; see Fig. 4.13). Most of them migrate with their phagocytosed load to the bronchioles, where they are swept into the mucociliary rejection current and removed from the lung. Others migrate through the epithelium of the alveoli into the lymphatics that drain the connective tissue of the lung, and so pass into lymphoid tissue around the pulmonary lobules. Under normal conditions, alveolar macrophages have a granular cytoplasm because they contain phagocytosed particles; in smokers, the particles have a characteristic appearance and are called 'tar bodies'. When actively phagocytic, macrophages release proteases: if antiproteases such as α_1-antitrypsin that are normally present in the alveolar lining are deficient, macrophage activity may damage the lung. Alveolar macrophages are involved in the turnover of surfactant.

Alveolar macrophages can be recovered from sputum and are of diagnostic importance if they appear abnormal. For instance, whenever

Coughing is initiated when mechanically and chemically sensitive vagal afferents that innervate the airways from the upper respiratory tract to the terminal bronchioles and lung parenchyma are activated (Morice and Geppetti 2004, Canning et al 2014). Data from experimental studies suggest that the receptors innervated by these afferents may be broadly divided into three groups: slowly (SAR) and rapidly (RAR) adapting stretch receptors and bronchopulmonary unmyelinated C fibres (see below). The vagal afferents terminate centrally in largely non-overlapping regions of the caudal half of the nucleus tractus solitarius. Second-order neurones from this nucleus terminate on respiratory-related regions of the pons, medulla and spinal cord. Efferent impulses travel via the vagus, phrenic and spinal motor nerves to the inspiratory and expiratory muscles, larynx, respiratory diaphragm and abdominal wall muscles. Airway receptors in the external acoustic meatuses (external auditory canals), tympanic membranes, paranasal sinuses, pharynx, respiratory diaphragm, pleura, pericardium and stomach are probably mechanoreceptors, stimulated by triggers such as touch or displacement (Polverino et al 2012).

The specific pattern of a cough depends on the site and type of stimulation. Mechanical laryngeal stimulation results in immediate expiratory stimulation (sometimes termed the expiratory reflex), protecting the airway from aspiration; stimulation distal to the larynx causes a more prominent inspiratory phase to generate the airflow necessary to remove the stimulus.

During vigorous coughing, intrathoracic pressures may reach 300 mmHg (with an abrupt rise in pleural pressure from 6.5 to 13 kPa) and expiratory velocities approach 500 miles per hour (Ford et al 2007). While these pressures and velocities are responsible for the beneficial effects of cough on mucus clearance, they are also the cause of many of the complications of cough, including exhaustion, self-consciousness, insomnia, headache, dizziness, musculoskeletal pain, hoarseness, excessive perspiration, urinary incontinence and cough-induced multiple rib fractures.

Lesions that compress the upper airway, including arteriovenous malformations and retrotracheal masses, may present with chronic cough. Cough can also be a symptom of tracheobronchomalacia, which results from the loss of rigid support of the large airways and inspiratory collapse, usually seen in conjunction with obstructive lung disease in patients with a history of tobacco smoking. Chronic dry cough may be caused by irritation of the external acoustic meatus by impacted foreign bodies or cerumen (Jegoux et al 2002). The aetiology of the 'ear-cough' (otorespiratory reflex) is related to stimulation of the auricular branch of the vagus nerve (Arnold's nerve) (Feldman and Woodworth 1993). Holmes–Adie syndrome is a rare cause of coughing when autonomic dysfunction affects the vagus nerve. Patients present with anisocoria, abnormal deep tendon reflexes and patchy areas of hyperhidrosis or anhidrosis (Kimber et al 1998).

Differences among several sites from which cough stimuli can originate may result in variations in the sounds and patterns of coughing. Laryngeal stimulation produces a choking type of cough without a preceding inspiration. Inadequate mucociliary clearance mechanisms (as in bronchiectasis or cystic fibrosis) may produce a pattern of coughing with less violent acceleration of air and a sequence of interrupted expirations without any intervening inspiration.

Since cough is an important defensive reflex required to maintain the health of the lungs, individuals who do not cough effectively are at risk of atelectasis, recurrent pneumonia and chronic airways disease from aspiration and retention of secretions. Many disorders can impair the ability to cough effectively and this may result in persistent cough. The elderly, the newborn, lung transplant recipients and patients with paralysis or neuromuscular disorders have a poorly developed and/or compromised cough reflex and are rendered highly susceptible to infective and aspiration pneumonia (Polverino et al 2012). Patients with paralysis or neuromuscular disorders (including rib fractures) and chest wall anomalies may not generate the flows necessary for effective clearance of secretions due to defective 'pump' mechanisms. Individuals with reduced function of the abdominal wall musculature are particularly at risk of ineffective cough. Individuals with laryngeal disorders (e.g. vocal fold paresis or paralysis), including those with tracheostomies, may not achieve sufficient laryngeal closure to generate the increased intrathoracic pressures necessary for an effective cough.

RARs are dynamic receptors that respond to changes in airway mechanical properties (e.g. diameter, length and interstitial pressures). Functional studies of RARs suggest that they terminate within or beneath the epithelium mainly of the intrapulmonary airway (Widdicombe 2003). They may be differentiated from other airway afferents by their rapid adaptation (in 1–2 seconds) to sustained lung inflation (Schelegle and Green 2001). RARs are sporadically active throughout the respiratory cycle, activated by the dynamic mechanical forces that accompany lung inflation and deflation, and become more active as the rate and volume of lung inflation increase. Their activation initiates reflex bronchospasm and mucus secretion through parasympathetic pathways.

SARs are found mostly in alveoli and bronchioles. They are highly sensitive to the mechanical forces that act on the lung during breathing. Their activity increases during inspiration and peaks just prior to the initiation of expiration; they are thought to be the afferent fibres involved in the Hering–Breuer reflex, which terminates inspiration and initiates expiration when the lungs are adequately inflated. SARs appear to terminate primarily in the intrapulmonary airways. Their activation results in the central inhibition of respiration and the inhibition of the cholinergic drive to the airways, leading to decreased phrenic nerve activity and decreased airway smooth muscle tone (Canning et al 2001).

The majority of afferent nerves innervating the airways and lungs are unmyelinated C fibres, similar to the unmyelinated somatic sensory nerves that innervate the skin, skeletal muscle, joints and bones and that respond to noxious chemical and mechanical stimuli. In addition to their slow conduction velocity (<2 m/s), airway vagal afferent C fibres are distinguished from RARs and SARs by their relative insensitivity to mechanical stimulation and lung inflation. They are generally quiescent throughout the respiratory cycle (Lee and Pisarri 2001).

Bronchoscopy allows the direct visualization of the vocal folds (cords), trachea and major airways as far as the first division of the subsegmental airway. Occasionally, bronchoscopy can also provide some information about structures adjacent to the airways, e.g. significant subcarinal lymphadenopathy can cause splaying or widening of the carina. Bronchoscopy enables the acquisition of samples (e.g. bronchial lavage, bronchial brushings, bronchial and transbronchial biopsies); provides information about staging in lung cancer; facilitates therapeutic procedures (e.g. foreign body removal, ablation of tumours and insertion of airway stents). The information obtained by volume CT scanning can be reconstructed to provide three-dimensional images that can be used to create endobronchial views (virtual bronchoscopy, **Fig. 54.16**) or to demonstrate the pulmonary arteries.

Ciliated columnar cells

Ciliated columnar cells are the driving force of the mucociliary rejection current (escalator) in the bronchial tree. They vary from low to tall columnar, each cell has up to 300 cilia projecting from its apical surface. The cilia extend into a watery fluid secreted by serous cells of the submucosal glands, but their tips are in contact with a more superficial layer of thicker mucus secreted by surface goblet cells and mucous cells in the submucosal glands. The rate of ciliary beating is usually 12–16 per second; mechanical stimulation of the epithelial surface and inflammatory mediators increase the rate. In addition to tight junctions, which seal the apical intercellular space from the airway lumen, the ciliated cells are coupled by gap junctions that allow a change in rate of beating to spread from stimulated cells to their neighbours (probably via calcium signalling) so that their metachronal coordination remains intact. Primary ciliary dyskinesia is a ciliary abnormality inherited as an autosomal recessive disorder and may be a feature of Kartagener's syndrome (a combination of bronchiectasis, sinusitis and situs inversus).

Goblet cells

Goblet cells are present from the trachea (6000–7000 per mm^2) to the smaller bronchi but are normally absent from bronchioles. Their apical regions are full of large secretory vacuoles filled with mucinogen. When the epithelium is irritated, e.g. by tobacco smoke, the overall number of goblet cells increases, and they extend into the bronchioles.

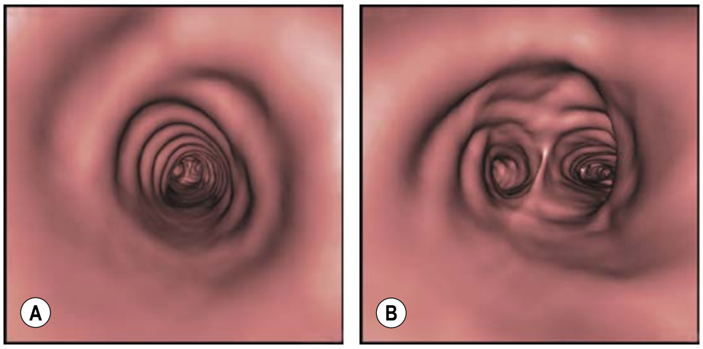

Fig. 54.16 A virtual CT bronchoscopic view obtained by planar reconstruction of spiral CT. **A**, Left main bronchus. **B**, Carina. (Courtesy of GE Medical Systems.)

Clara cells

Clara cells are cuboidal, non-ciliated cells with apices that bulge into each lumen. They contain numerous electron-dense secretory granules and lysosomes. Clara cells produce surfactant lipoprotein and thus share functional similarities with the type II alveolar cell of the pulmonary alveoli, although their secretory granules differ in structure and composition.

Basal cells

Basal cells are small, rounded cells that occur in parts of the airway lined by pseudostratified respiratory epithelium; they are mitotic stem cells for other epithelial cell types. Basal cells contact the basal lamina and are most frequent in the larger conducting passages.

Brush cells

Brush cells are slender, non-ciliated cells with characteristically long, stiff apical microvilli, hence their name. Although infrequent, they are present throughout all parts of the conducting airway passages, including the respiratory epithelium of the nasopharynx. They are in contact with afferent nerve fibres basally and are presumed to have a sensory receptor function.

Neuroendocrine cells

Neuroendocrine cells (dense-core, small granule or Kulchitsky cells) are found mainly in the basal part of the epithelium. They have a rounded shape and the cytoplasm basal to their nuclei contains numerous small, dense-cored vesicles, approximately 150 nm in diameter. They form part of the dispersed neuroendocrine system of amine precursor uptake and decarboxylation (APUD) cells (Ch. 3). Most numerous in fetal lungs, their number decreases dramatically after birth and there appears to be little further change in their frequency during adult life, although they may proliferate in certain pulmonary diseases.

Lymphocytes

T lymphocytes, derived from mucosa-associated lymphoid tissue (MALT), occur within the epithelium throughout the conducting airway tissues, particularly in the extrapulmonary portion. They are concerned with the immune surveillance of the epithelium. Clusters of lymphocytes sometimes lie beneath non-ciliated epithelial cells of the microfold (M-cell) type.

Mast cells

Mast cells are present within the basal regions of the epithelium. They resemble connective tissue mast cells, and their cytoplasmic histamine-containing granules are released in response to irritants, including inhaled allergens.

Tubuloacinar, seromucous glands are present in the submucosa of the trachea and bronchi and, to a lesser extent, in the larger bronchioles. They contain separate mucous and serous cells and are an important source of the mucus at the surface of the ciliated respiratory epithelium. Their secretions include mucins; bacteriostatic substances such as lysozyme and lactoferrin; secretory antibodies (immunoglobulin A (IgA)) produced by plasma cells in the submucosal connective tissue; and protease inhibitors (e.g. α_1-antitrypsin), important for neutralizing leukocyte-derived proteases in the respiratory tract, particularly elastase. Deficiency of α_1-antitrypsin causes chronic obstructive pulmonary disease, by inducing panacinar emphysema and bronchiectasis. The secretory acini and tubules are surrounded by myoepithelial cells innervated by autonomic axons.

Broad, longitudinal bands of elastin within the submucosa follow the course of the respiratory tree and connect with the elastin networks of the interalveolar septa (**Fig. 54.17**, see Fig. 54.11). This elastic framework is a vital mechanical element of the lung and is responsible for elastic recoil during expiration.

In the trachea and extrapulmonary bronchi, smooth muscle is mainly confined to the posterior, non-cartilaginous part of the tracheal tube (see Fig. 54.9). Along the entire intrapulmonary bronchial tree, smooth muscle forms two opposed helical tracts that become thinner and finally disappear at the level of the alveoli (see Fig. 54.11). The tone of these muscle fibres is under nervous and hormonal control; groups of muscle cells are coupled by gap junctions to spread excitation within fascicles. Muscle cell contraction narrows the airway, while relaxation permits bronchodilation. Some tone normally exists in the muscular bands, which relax slightly during inspiration and contract during expiration, so assisting the tidal flow of air. Abnormal contraction may be caused by circulating smooth muscle stimulants or by local release of excitants such as 5-HT (5-hydroxytryptamine, serotonin), histamine and leukotrienes, causing bronchospasm. Numerous mast cells are present in the connective tissue of the respiratory tree, especially towards the bronchioles.

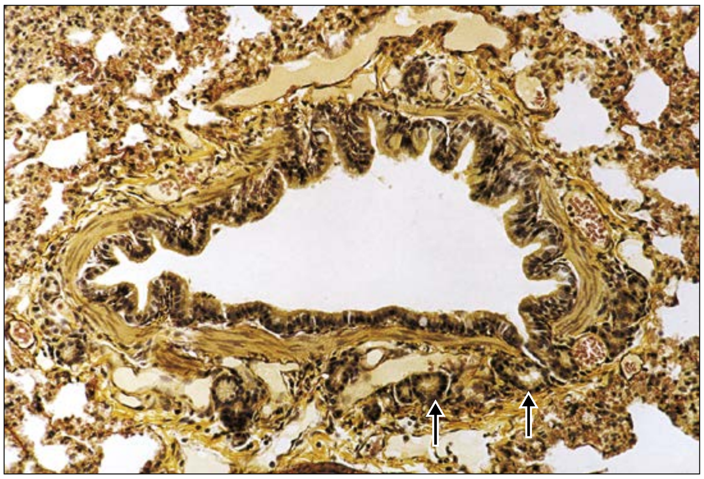

Fig. 54.17 A large bronchiole stained for elastin (black), showing smooth muscle in the bronchiolar wall and a few small seromucous glands (arrows).

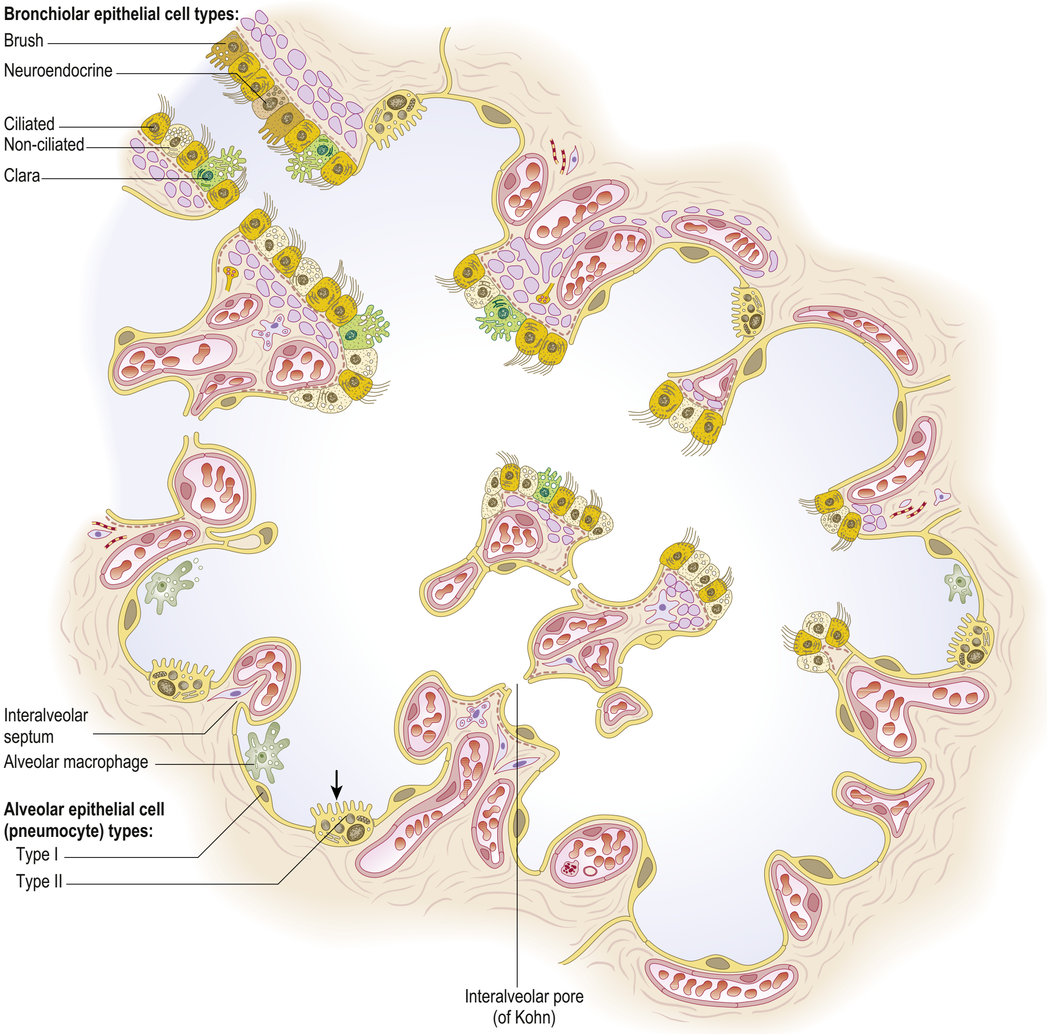
Bronchiolar epithelial cell types:
Brush
Neuroendocrine
Ciliated
Non-ciliated
Clara
Interalveolar septum
Alveolar macrophage
Alveolar epithelial cell (pneumocyte) types:
Type I
Type II
Interalveolar pore (of Kohn)

Fig. 54.18 The respiratory portion of the lung and its cell types. Type I pneumocytes have a large surface area and form much of the alveolar wall, but can be less numerous than type II pneumocytes, which have a larger, more distinct nucleus and protrude into the alveolar space (black arrow). The alveolar surface cytoplasm of each type II pneumocyte has clusters of surfactant-containing secretory vesicles, the release of which gives the cell membrane an irregular appearance histologically.

erythrocytes leak from pulmonary capillaries, the macrophages that engulf the extravasated cells become brick-red and are detectable in 'rusty' sputum. They are typical of congestive heart failure and often termed 'heart-failure cells'. Macrophages that migrate back into the connective tissue of the lung settle in patches that are visible beneath the visceral pleura, e.g. carbon-filled cells give the lungs a mottled appearance. However, if the inhaled particles are abrasive or chemically active, they may elude macrophage removal and damage the respiratory surface, producing fibrosis and a concomitant reduction in the respiratory area. This occurs in many industrial diseases, e.g. pneumoconiosis caused by coal dust, or asbestosis, where the long thin fibres of asbestos can cause considerable damage and may trigger fatal mesothelioma in the pleural lining.

Pulmonary surfactant

The alveolar surface is normally covered by a film of pulmonary surfactant, a complex mixture mainly of phospholipids (particularly dipalmitoylphosphatidylcholine and phosphatidylglycerol), with some protein and neutral lipid. Surfactant is stored in lamellar bodies and secreted in the form of tubular myelin (unrelated to myelin of the nervous system) by type II pneumocytes. It is recycled by type II pneumocytes or cleared (i.e. phagocytosed) by alveolar macrophages. Clara cells of the bronchiolar epithelium are thought to secrete surfactant of a different composition.

Surface tension at the alveolar surface is very high because the alveoli are minute and spherical, features that oppose expansion during inspiration and tend to collapse the alveoli in expiration. The detergent-like properties of pulmonary surfactant greatly reduce the surface tension and make ventilation of the alveoli much more efficient. As the volume of an alveolus alternatively increases and decreases, so does its surface area. With a fixed amount of surfactant in the alveolar film, the relative concentration of surfactant increases on exhalation. The fortunate result is a decrease in collapsing tendency as the alveolar volume decreases, stabilizing the alveolus and overcoming the tendency of small gas spaces to obliterate.

Bonus e-book content

Fig. 54.4 A–D, Axial and sagittal sections through the lungs, demonstrating the oblique and horizontal fissures. **G–J,** CTs of the chest with intravenous contrast medium viewed with lung window settings, demonstrating the oblique and horizontal fissures.

Fig. 54.5 B, Coronal MIP from a CT of the chest showing the airways.

Fig. 54.6 F–O, Multiplanar reformat lung window CT images with planes selected specifically to highlight branching anatomy of the bronchial tree.

Fig. 54.9 A micrograph of the trachea of a child, sectioned transversely.

Fig. 54.14 A CT of the chest (lung windowed, axial view) showing an intralobar sequestration in the left inferior lobe of the lung in a 15-month-old girl.

Fig. 54.15 A CT of the chest (coronal view) showing the systemic arterial blood supply from the abdominal aorta to an intralobar sequestration in the left inferior lobe of the lung in a 15-month-old girl.

Fig. 54.16 A virtual CT bronchoscopic view obtained by planar reconstruction of spiral CT.

Fig. 54.17 A large bronchiole stained for elastin.

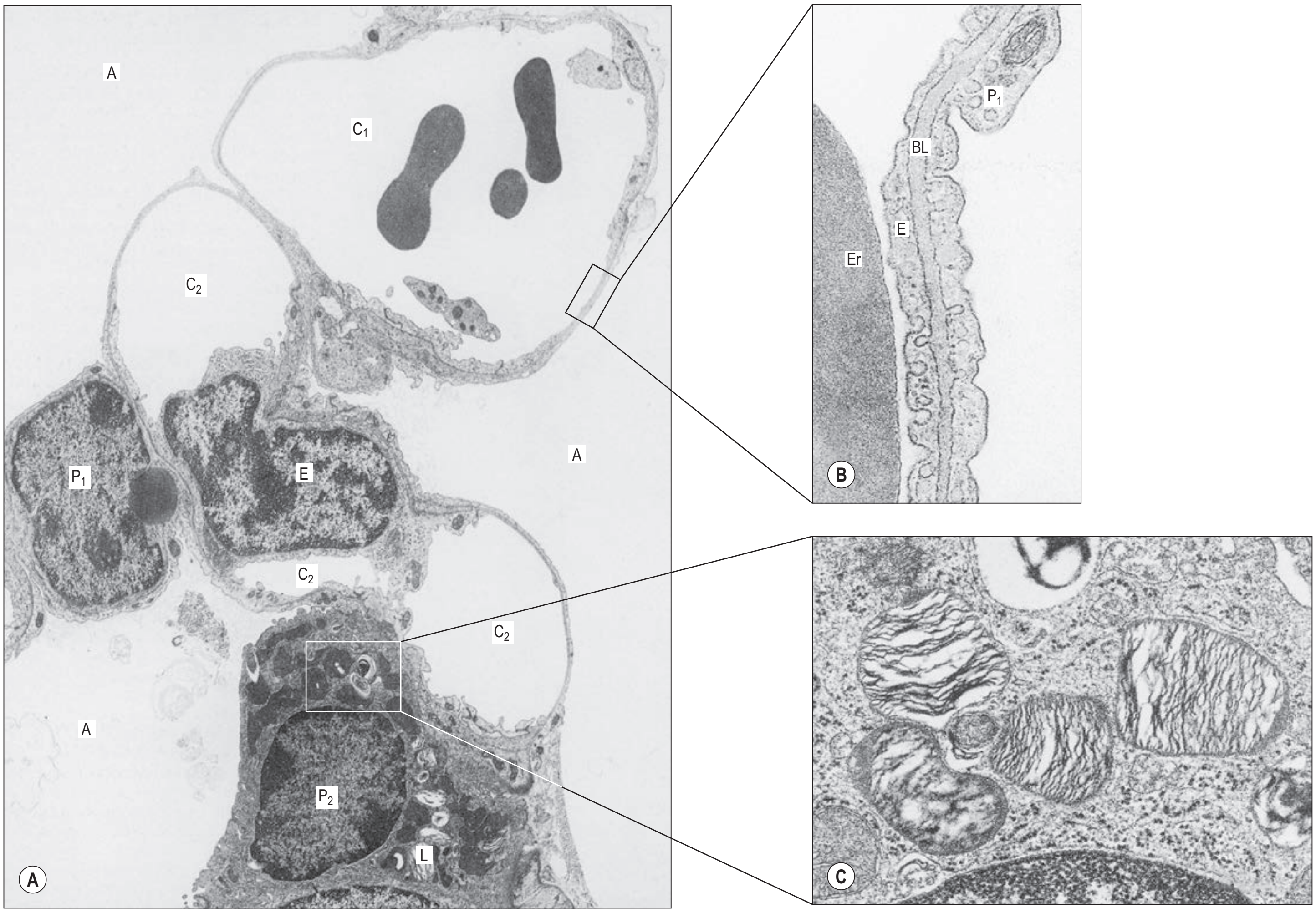

Fig. 54.19 **A**, An electron micrograph showing the septum between three adjacent alveoli (A). The septum contains two capillaries (C_1 and C_2) in section; the lower one is cut obliquely through the nucleus of an endothelial cell (E). Type I pneumocytes (P_1) line the alveolar airspaces except where a type II pneumocyte (P_2), with cytoplasmic lamellar bodies (L), intervenes. **B**, The thin portion of an interalveolar septum. Part of an erythrocyte (Er) is shown in the capillary lumen, lined by endothelium (E). The alveolar airspace (right) is lined by a type I pneumocyte (P_1). The two cells share a basal lamina (BL). **C**, Cytoplasmic lamellar bodies in a type II pneumocyte are composed mainly of phospholipids that contribute to the surfactant secreted by these pneumocytes and by Clara cells of the respiratory bronchioles. (With permission from Young B, Heath JW 2000 Wheater's Functional Histology. Edinburgh: Churchill Livingstone.)

Key references

Canning BJ, Fischer A 2001 Neural regulation of airway smooth muscle tone. Respir Physiol 125:113–27.

This article clarifies the effects of parasympathetic and sympathetic nerves on airway smooth muscle.

Rusch VW, Asamura H, Watanabe H et al 2009 The IASLC lung cancer staging project: a proposal for a new international lymph node map in the forthcoming seventh edition of the TNM classification for lung cancer. J Thorac Oncol 4:568–77.

A recommendation for a standardized grouping of lymph node stations together into 'zones' for consistency and the purposes of future survival analyses.

Wantanabe K 2016a Lungs. In: Tubbs RS, Shoja MM, Loukas M (eds) Bergman's Comprehensive Encyclopedia of Human Anatomic Variation, 2nd ed. Hoboken: Wiley Blackwell; Ch. 102, pp. 1216–33.

Wantanabe K 2016b Trachea. In: Tubbs RS, Shoja MM, Loukas M (eds) Bergman's Comprehensive Encyclopedia of Human Anatomic Variation, 2nd ed. Hoboken: Wiley Blackwell; Ch. 102, pp. 1212–16.

References

Akgun V, Hamcan S, Bozkurt Y et al 2016 Thoracic aorta. In: Tubbs RS, Shoja MM, Loukas M (eds) Bergman's Comprehensive Encyclopedia of Human Anatomic Variation, 2nd ed. Hoboken: Wiley Blackwell; Ch. 49, pp. 501–29.

Alison M, Garel L, Bigras JL et al 2011 Unilateral absence of pulmonary artery in children: bronchovascular anatomy, natural course and effect of treatment on lung growth. Pediatr Radiol 41:459–68.

Archie JG, Collins JS, Lebel RR 2006 Quantitative standards for fetal and neonatal autopsy. Am J Clin Pathol 126:256–65.

Asgharian B, Menache MG, Miller FJ 2004 Modeling age-related particle deposition in humans. J Aerosol Med 17:213–24.

Belvisi MG 2002 Overview of the innervation of the lung. Curr Opin Pharmacol 2:211–15.

Canning BJ, Fischer A 2001 Neural regulation of airway smooth muscle tone. Respir Physiol 125:113–27.

This article clarifies the effects of parasympathetic and sympathetic nerves on airway smooth muscle.

Canning BJ, Reynolds SM, Mazzone SB 2001 Multiple mechanisms of reflex bronchospasm in guinea pigs. J Appl Physiol 91:2642–53.

Canning BJ, Chang AB, Bolser DC et al 2014 Anatomy and neurophysiology of cough: CHEST Guideline and Expert Panel Report. Chest 146:1633–48.

Ciaglia P, Firsching R, Syniec C 1985 Elective percutaneous dilatational tracheostomy. A new simple bedside procedure; preliminary report. Chest 87:715–19.

Clements BS 1999 Congenital malformations of the lungs and airways. In: Taussig LM, Landau LI (eds) Pediatric Respiratory Medicine. St Louis: Mosby, p. 1106.

Feldman JI, Woodworth WF 1993 Cause for intractable chronic cough: Arnold's nerve. Arch Otolaryngol Head Neck Surg 119:1042.

Fitzgerald M, Mackenzie CF, Marasco S et al 2008 Pleural decompression and drainage during trauma reception and resuscitation. Injury 39:9–20.

Ford PA, Barnes PJ, Usmani OS 2007 Chronic cough and Holmes–Adie syndrome. Lancet 369:342.

Fourdrain A, Lafitte S, Iquille J et al 2018 Lymphatic drainage of lung segments in the visceral pleura: a cadaveric study. Surg Radiol Anat 40:15–19.

Ghaye B, Szapiro D, Fanchamps JM et al 2001 Congenital bronchial abnormalities revisited. Radiographics 21:105–19.

Griggs WM, Worthley LI, Gilligan JE et al 1990 A simple percutaneous tracheostomy technique. Surg Gynecol Obstet 170:543–5.

Griscom NT, Wohl ME 1986 Dimensions of the growing trachea related to age and gender. AJR Am J Roentgenol 146:233–7.

Jegoux F, Legent F, Beauvillain de Montreuil C 2002 Chronic cough and ear wax. Lancet 360:618.

Jin-Hee K, Ro YJ, Seong-Won M et al 2005 Elongation of the trachea during neck extension in children: implications of the safety of endotracheal tubes. Anesth Analg 101:974–7.

Kent DM, Thaler DE 2011 The Risk of Paradoxical Embolism (RoPE) study: developing risk models for application to ongoing randomized trials of percutaneous patent foramen ovale closure for cryptogenic stroke. Trials 12:185.

Kimber J, Mitchell D, Mathias CJ 1998 Chronic cough in the Holmes–Adie syndrome: association in 5 cases with autonomic dysfunction. J Neurol Neurosurg Psychiatry 65:583–6.

Kozak MF, Kozak AC, Souza AS et al 2011 Left pulmonary vein atresia: the contribution of multislice computed tomography. Pediatr Cardiol 32:108–10.

Kravitz RM 1994 Congenital malformations of the lung. Pediatr Clin North Am 41:453.

Lambertsen CJ 1980 The lungs: physical aspects of respiration. In: Mountcastle VB (ed) Medical Physiology, 14th ed. St Louis: CV Mosby; Ch. 67, pp. 1677–90.

Lee EY, Restrepo R, Dillman JR et al 2012 Imaging evaluation of pediatric trachea and bronchi: systematic review and updates. Semin Roentgenol 47:182–96.

Lee LY, Pisarri TE 2001 Afferent properties and reflex functions of bronchopulmonary C-fibres. Respir Physiol 125:47–65.

Medlar EM 1947 Variations in interlobar fissures. AJR Am J Roentgenol 57:723–5.

Molina K, DiMaio VJM 2012 Normal organ weights in men. Part II – The brain, lungs, liver, spleen and kidneys. Am J Forensic Med Pathol 33:368–72.

Molina K, DiMaio VJM 2015 Normal organ weights in women. Part II – The brain, lungs, liver, spleen and kidneys. Am J Forensic Med Pathol 36:182–7.

Morice AH, Geppetti P 2004 Cough. 5: The type 1 vanilloid receptor: a sensory receptor for cough. Thorax 59:257–8.

Narayanan M, Beardsmore CS, Owers-Bradley J et al 2013 Catch-up alveolarization in ex-preterm children: evidence from (3)He magnetic resonance. Am J Respir Crit Care Med 187:1104–9.

Polverino M, Polverino F, Fasolino M et al 2012 Anatomy and neuropathophysiology of the cough reflex arc. Multidiscip Respir Med 7:5.

Raasch BN, Carsky EW, Lane EJ et al 1982 Radiographic anatomy of the interlobar fissures: a study of 100 specimens. AJR Am J Roentgenol 138:1043–9.

Rao L, Tiller C, Coates C et al 2010 Lung growth in infants and toddlers assessed by multi-slice computed tomography. Acad Radiol 17:1128–35.

Rusch VW, Asamura H, Watanabe H et al 2009 The IASLC lung cancer staging project: a proposal for a new international lymph node map in the forthcoming seventh edition of the TNM classification for lung cancer. J Thorac Oncol 4:568–77.

A recommendation for a standardized grouping of lymph node stations together into 'zones' for consistency and the purposes of future survival analyses.

Schelegle ES, Green JF 2001 An overview of the anatomy and physiology of slowly adapting pulmonary stretch receptors. Respir Physiol 125:17–31.

Sivrikoz MC 2016 Pulmonary arteries. In: Tubbs RS, Shoja MM, Loukas M (eds) Bergman's Comprehensive Encyclopedia of Human Anatomic Variation, 2nd ed. Hoboken: Wiley Blackwell; Ch. 51, pp. 569–74.

Stocker JT, Drake RM, Madewell JE 1978 Cystic and congenital lung disease in the newborn. Perspect Pediatr Pathol 4:93.

Strife JL, Matsumoto J, Bisset GS 3rd et al 1989 The position of the trachea in infants and children with right aortic arch. Pediatr Radiol 19:226–9.

Thurlbeck WM 1982 Postnatal human lung growth. Thorax 37:564–71.

Van Praagh S, Santini F, Sanders SP 1992 Cardiac malpositions with special emphasis on visceral heterotaxy (asplenia and polysplenia syndromes). In: Fyler DC (ed) Nadas' Pediatric Cardiology. Philadelphia: Hanley & Belfus, pp. 589–608.

Wang Y, Dai W, Sun Y et al 2012 Congenital bronchial atresia: diagnosis and treatment. Int J Med Sci 9:207–12.

Wantanabe K 2016a Lungs. In: Tubbs RS, Shoja MM, Loukas M (eds) Bergman's Comprehensive Encyclopedia of Human Anatomic Variation, 2nd ed. Hoboken: Wiley Blackwell; Ch. 102, pp. 1216–33.

Wantanabe K 2016b Trachea. In: Tubbs RS, Shoja MM, Loukas M (eds) Bergman's Comprehensive Encyclopedia of Human Anatomic Variation, 2nd ed. Hoboken: Wiley Blackwell; Ch. 102, pp. 1212–16.

Widdicombe J 2003 Functional morphology and physiology of pulmonary rapidly adapting receptors (RARs). Anat Rec A Discov Mol Cell Evol Biol 270:2–10.

Wong KS, Lien R, Lin TY 1999 Clinical and computed tomographic features of tracheal bronchus in children. J Formos Med Assoc 98:646–8.

Yamashita H 1978 Roentgenologic anatomy of the lung. Tokyo: Igaku-Shoin, pp. 49–53.

Zhong YM, Jaffe RB, Zhu M et al 2010 CT assessment of tracheobronchial anomaly in left pulmonary artery sling. Pediatr Radiol 40:1755–62.

CHAPTER
55

Respiratory diaphragm and phrenic nerves

The respiratory diaphragm is a domed musculofibrous sheet, approximately 2–4 mm thick that separates the thoracic and abdominopelvic cavities (**Fig. 55.1**). The superior surface of the respiratory diaphragm is mainly convex and forms the floor of the thoracic cavity. It is covered by a layer of phrenicopleural fascia, a continuation of the endothoracic fascia, covered in turn by a layer of diaphragmatic parietal pleura, except in the region inferior to the heart, which is covered by a layer of parietal serous pericardium. The concave inferior surface of the respiratory diaphragm forms the roof of the abdominopelvic cavity and is mostly covered by a layer of diaphragmatic fascia, a continuation of the transversalis fascia, which is then covered by a layer of parietal peritoneum. The position of the domes or cupulae of the respiratory diaphragm is variable and may be altered by body position, ventilatory phase, thoracic cavity morphology, height and body mass. Conditions resulting in lung over-inflation, e.g. emphysema, cause diaphragmatic depression or flattening. Usually, after forced expiration, the right dome is level with the fourth costal cartilage anteriorly, whereas the left dome lies approximately one costal cartilage level lower. At end tidal inspiration in the supine position, the domes of the diaphragm descend to sit at the level of the fifth intercostal space anteriorly on the right and sixth rib on the left. On a posteroanterior (PA) chest radiograph at full inspiration, the highest point of the right hemidiaphragm is located at the anterior end of the sixth rib, or at the posterior end of the tenth rib; the left hemidiaphragm is normally 1.5–2.5 cm lower (see Fig. 56.17A). Unilateral paralysis may be seen as a raised hemidiaphragm on a chest radiograph, but this sign may be inconsistent.

In the erect position the amount of respiratory diaphragmatic excursion is approximately 1–2 cm during quiet breathing and 5–7 cm during deep breathing; all movements are slightly greater in males compared to females (Boussuges et al 2009, Jung et al 2014). The diaphragm lies more superiorly in the supine compared to the erect position. In the lateral decubitus position the lowermost gravity-dependent dome of the diaphragm sits at a higher level than the uppermost dome; this results in greater diaphragmatic muscle displacement, and therefore ventilation, on the gravity-dependent side (Froese 2006).

ATTACHMENTS AND COMPONENTS

The respiratory diaphragm consists of a central tendinous portion, the central tendon, and a muscular peripheral portion. The muscle fibres arise from the circumference of the inferior thoracic aperture and converge to an attachment to the central tendon; the posterior and lateral attachments are therefore located relatively inferior to the

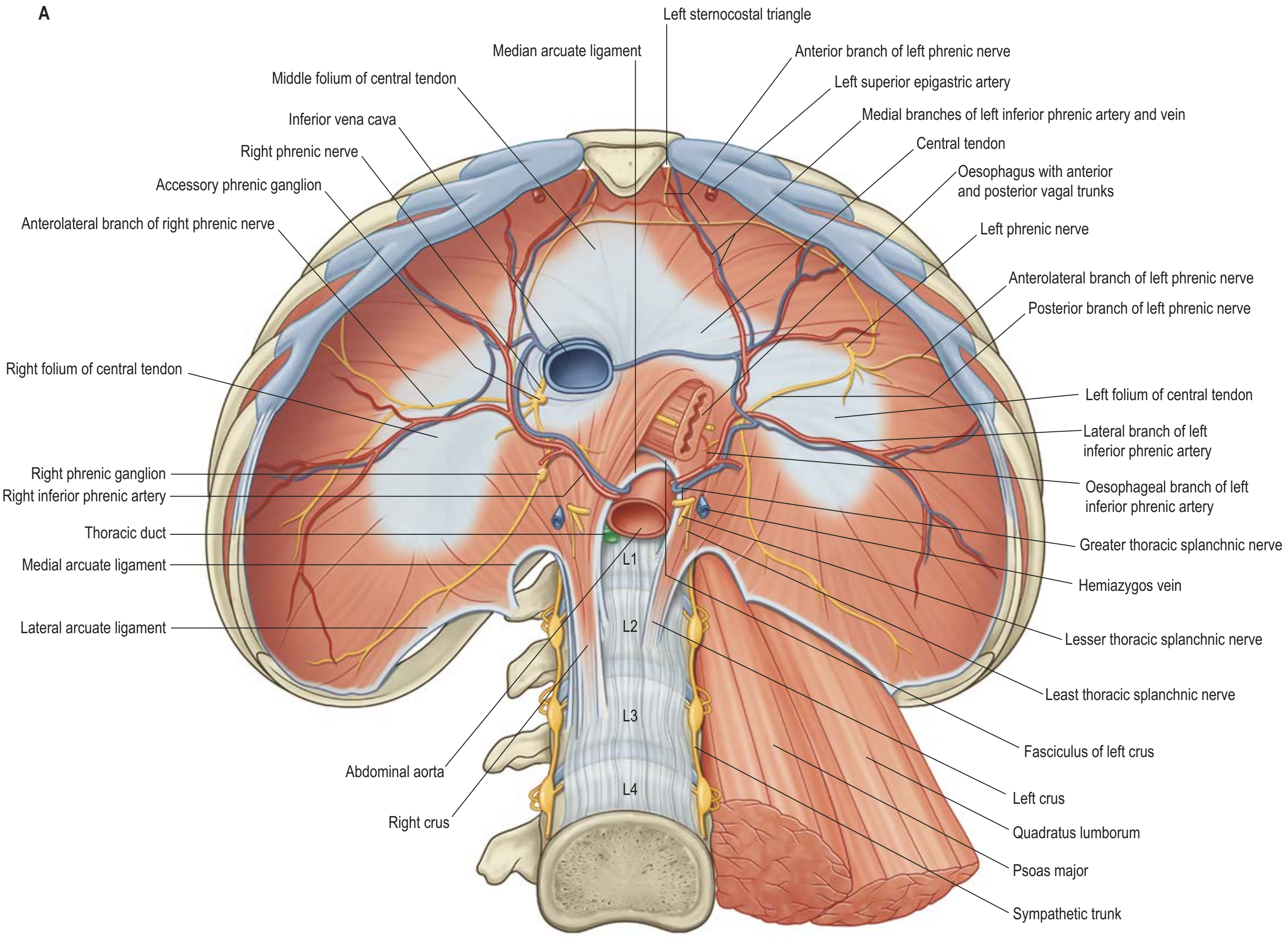
A
Left sternocostal triangle
Median arcuate ligament
Anterior branch of left phrenic nerve
Middle folium of central tendon
Left superior epigastric artery
Inferior vena cava
Medial branches of left inferior phrenic artery and vein
Right phrenic nerve
Central tendon
Accessory phrenic ganglion
Oesophagus with anterior and posterior vagal trunks
Anterolateral branch of right phrenic nerve
Left phrenic nerve
Anterolateral branch of left phrenic nerve
Posterior branch of left phrenic nerve
Right folium of central tendon
Left folium of central tendon
Lateral branch of left inferior phrenic artery
Right phrenic ganglion
Right inferior phrenic artery
Oesophageal branch of left inferior phrenic artery
Thoracic duct
Greater thoracic splanchnic nerve
Medial arcuate ligament
L1
Hemiazygos vein
Lateral arcuate ligament
L2
Lesser thoracic splanchnic nerve
Least thoracic splanchnic nerve
L3
Fasciculus of left crus
Abdominal aorta
L4
Left crus
Right crus
Quadratus lumborum
Psoas major
Sympathetic trunk

Fig. 55.1 A, Inferior view of the abdominal surface of the respiratory diaphragm.

Movement of the respiratory and pelvic diaphragms is often complementary. Magnetic resonance imaging has shown the respiratory and pelvic diaphragms to move symmetrically during normal respiration and other physiological processes: as the respiratory diaphragm descends during inspiration, the pelvic floor also descends in response to the change in intra-abdominal pressure. These changes assist with supporting the trunk and maintaining urinary continence during respiration and coughing (Talasz et al 2011).

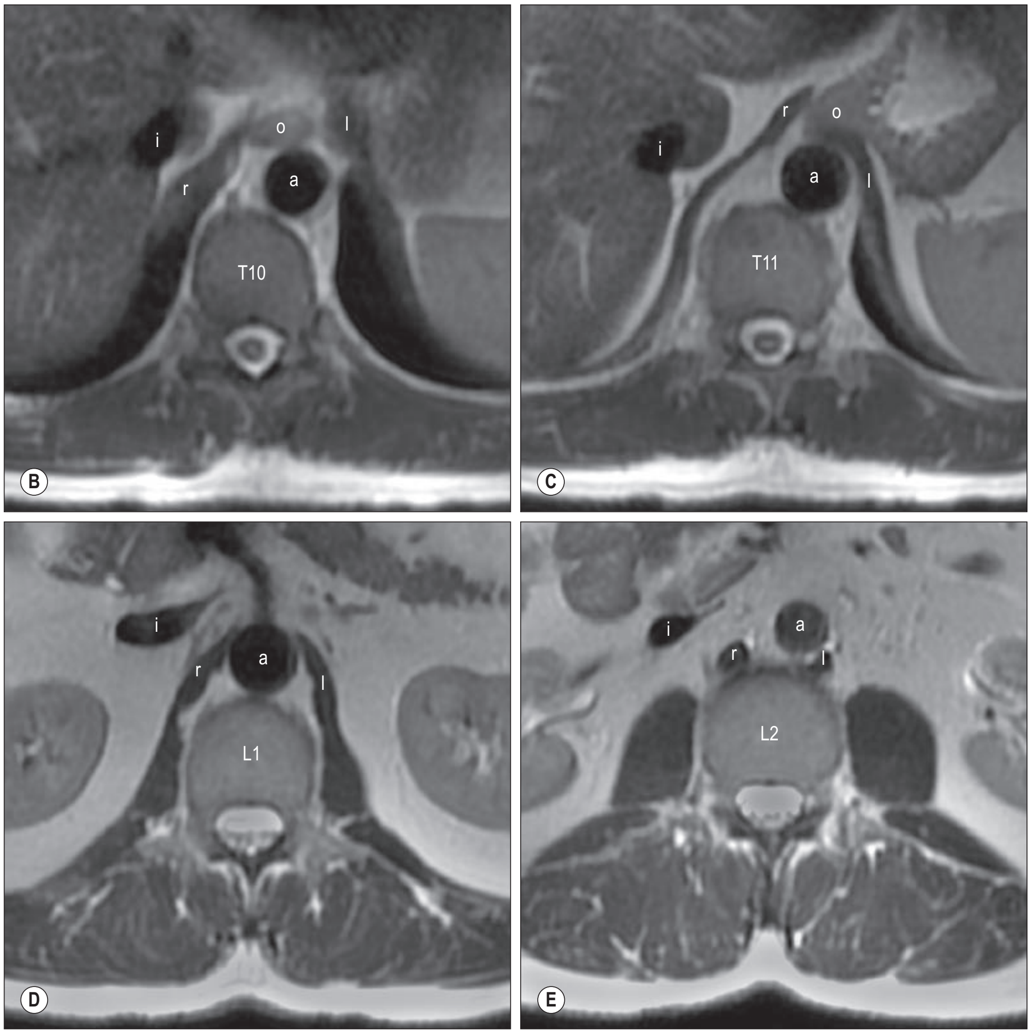

Fig. 55.1, cont'd B–E, Axial T2-weighted MRI images through the upper abdomen showing the posterior diaphragmatic attachments and hiatuses from superior to inferior. Key: a, aorta; i, inferior vena cava; l, left crus of respiratory diaphragm; o, oesophagus; r, right crus of respiratory diaphragm. (A, With permission from Drake RL, Vogl AW, Mitchell AWN (eds) Gray's Anatomy for Students, 3rd ed. Elsevier, Churchill Livingstone. Copyright 2015.)

anterior attachments (**Fig. 55.2**) (du Plessis et al 2015). The muscle can be considered in three parts, sternal, costal and lumbar. The sternal part is the smallest and varies in size and presence, it may be a broad and continuous band or may be absent (du Plessis et al 2015). It commonly arises as two muscular strips from the posterior surfaces of the rectus sheath and the xiphoid process, near its apex. On each side, the costal part arises from the internal surfaces and superior margins of the lower six costal cartilages and their adjoining ribs, and interdigitates with transversus abdominis (see Fig. 53.15A) (Sun et al 2016).

The lumbar part arises from two aponeurotic arches, the medial and lateral arcuate ligaments (Haller's or the lumbocostal arches), and asymmetrically from the more superiorly located lumbar vertebral bodies via the left and right crura. The medial arcuate ligament covers the upper part of psoas major. Medially, it is continuous with the lateral tendinous margin of the corresponding crus and is attached to the side of the first or second lumbar vertebral body. Laterally, it is fixed to the anterior aspect of the transverse process of the first lumbar vertebra. The lateral arcuate ligament covers and arches across quadratus lumborum, attaching medially to the anterior aspect of the transverse process of the first lumbar vertebra, and laterally to the inferior margin of the midpoint of the twelfth rib (Sun et al 2016).

The crura are tendinous at their attachments to the lumbar vertebrae and blend with the anterior longitudinal ligament (see Fig. 55.1). The broader and longer right crus arises from the anterolateral surfaces of the bodies and intervertebral discs of the superior three lumbar vertebrae. The left crus arises from the corresponding parts of the superior two lumbar vertebrae and intervertebral disc. The medial tendinous margins of the crura meet in the midline to form the median arcuate ligament, an often poorly defined tendinous arch that crosses anterior to the aorta at the level of the body of the twelfth thoracic vertebra (range, vertebral body of T10–L1). The crura vary greatly in length, thickness and the ratio of muscle to tendon (du Plessis et al 2015, Sun et al 2016).

The muscle fibres of the sternal, costal and lumbar parts of the respiratory diaphragm converge into the central tendon. Fibres from the xiphoid process are short, run almost horizontally and are occasionally aponeurotic. Fibres originating from the medial and lateral arcuate ligaments, and particularly the osteochondral surfaces of the ribs, are much longer. They arise almost vertically at first and then curve towards their central attachment. The right crus is commonly divided into three bundles of fibres (medial, middle and lateral), whereas the left crus is divided into two (medial and lateral) (Botros et al 1990). Muscle fibres from the crura diverge, the most lateral fibres pass more laterally as they ascend to the central tendon. Medial fibres of the right crus ascend and loop around the oesophagus where it passes through the diaphragm at the oesophageal hiatus; the more superficial fibres form the left margin, and the deeper fibres form the right margin of the hiatus. Multiple different patterns of crural muscle fibre arrangement may occur around the oesophageal hiatus (Loukas et al 2008a). Sometimes, a fleshy fasciculus from the medial side of the left crus crosses the aorta and runs obliquely through the fibres of the right crus towards the caval foramen; this fasciculus does not normally pass around the oesophageal hiatus on the right side.

The central tendon of the respiratory diaphragm is a thin but strong aponeurosis of closely interwoven fibres situated near the centre of the muscle. In the anteroposterior plane, it sits closer to the anterior thoracic wall, which means that the posterior muscle fibres are longer than the anterior fibres (**Fig. 55.3**). The central region of the central tendon lies immediately inferior to the pericardium, with which it partially blends. This region consists of four diagonal bands of fibres that fan out from a thick central node; from here, compressed tendinous strands decussate anterior to the oesophagus and to the left side of the inferior vena cava.

The central tendon is classically described as being trifoliate (cloverleaf) in shape, with middle, right and left folia. The middle folium projects anteriorly and is an equilateral triangle in shape, with the apex

The right and left sternocostal triangles (of Morgagni) are openings in the anterior part of the diaphragmatic muscle, between the sternal and costal parts (Downey 2011). They are covered by connective tissue and are the conduits by which the internal thoracic vessels access the anterior abdominal wall. A retrosternal (parasternal) hernia can pass through the triangles: it is more common on the right side and often congenital, which may reflect a deficit of muscle fibres in this region.

The lumbocostal triangle (of Bochdalek) represents a developmental defect resulting from an incomplete formation of the pleuroperitoneal membrane. When present, it is located in the posterolateral diaphragm between the lumbar and costal parts, superior to the lateral arcuate ligament. The lumbocostal triangle is devoid of muscle fibres, covered only by the diaphragmatic parietal pleura superiorly and parietal peritoneum inferiorly (Downey 2011), and is the most common route for congenital diaphragmatic herniation.

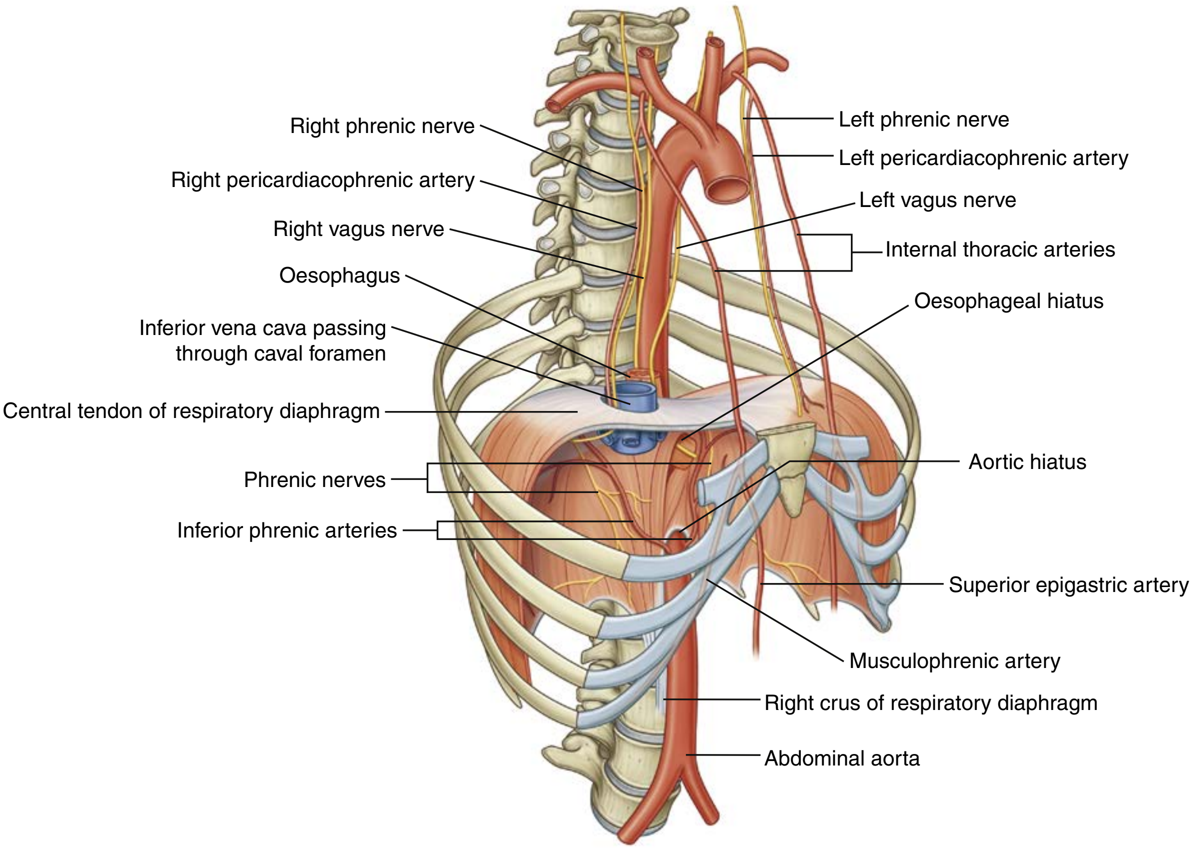
Right phrenic nerve
Right pericardiacophrenic artery
Right vagus nerve
Oesophagus
Inferior vena cava passing through caval foramen
Central tendon of respiratory diaphragm
Phrenic nerves
Inferior phrenic arteries
Left phrenic nerve
Left pericardiacophrenic artery
Left vagus nerve
Internal thoracic arteries
Oesophageal hiatus
Aortic hiatus
Superior epigastric artery
Musculophrenic artery
Right crus of respiratory diaphragm
Abdominal aorta

Fig. 55.2 The respiratory diaphragm with attachments, openings and arterial blood and nerve supply. (With permission from Drake RL, Vogl AW, Mitchell AWN (eds) Gray's Anatomy for Students, 3rd ed. Elsevier, Churchill Livingstone. Copyright 2015.)

directed towards the xiphoid process. The right and left folia are tongue-shaped and similar in length, although the left may be narrower; both curve posterolaterally to form a V-shape that spans the midline. The size and shape of the folia and the ratio of diaphragmatic muscle to tendon varies between individuals, the most common arrangement being a V-shaped central tendon and a 10–15% muscle to tendon ratio (du Plessis et al 2015). The muscle to tendon ratio can vary disproportionately, such that larger respiratory diaphragms may have a small central tendon, and smaller diaphragms may have a large central tendon and a relatively small amount of muscle.

PROFILE AND RELATIONS

The superior surface of the respiratory diaphragm is covered by three separate serous membranes. On each side, the diaphragmatic parietal pleura separates it from the base of the corresponding lung. Centrally, the parietal pericardium separates mainly the middle folium of the central tendon from the inferior surface of the heart. The middle folium is almost flat and extends more to the left than the right. From an anterior view, the smooth convex domes or cupulae of the left and right sides of the diaphragm rise above the middle folium: the right cupula is higher and slightly broader than the left. Most of the inferior surface of the diaphragm is covered by diaphragmatic fascia and parietal peritoneum. The right cupula conforms to the convex surface of the right lobe of the liver, right kidney and right suprarenal gland; the left cupula conforms to the surface of the left lobe of the liver, gastric fundus, spleen, left kidney and left suprarenal gland. Given the differences in their profiles and anatomical relationships, clinical descriptions of the respiratory diaphragm should always reference a specific side.

Ultrasound imaging Ultrasound examination of the posterior and lateral aspects of the respiratory diaphragm is best undertaken with the patient in the supine position, to limit veiling by other organs and reducing the risk of misdiagnosis due to underlying pulmonary pathologies. The respiratory diaphragm is typically identified by its curved morphology, deep location and specific echotexture. It is visualized as a thin, muscular hypoechoic line wedged between two hyperechoic layers consisting of parietal peritoneum and pleura (Fig. 55.4). During inspiration, the hypoechoic line thickens as the muscle contracts, making it more visible. An atrophic diaphragm may be suspected when the thickness of this line does not change during inspiration. The left side of the diaphragm often poses more of a challenge in visualization (Sarwal et al 2013).

OPENINGS

A number of structures pass between the thorax and abdomen via openings (apertures) in the respiratory diaphragm. There are three large openings, for the aorta, oesophagus and inferior vena cava, and a number of smaller openings (see Figs 55.1A, 55.3).

The aortic hiatus transmits the aorta, thoracic duct, lymphatic trunks from the lower posterior thoracic wall and, sometimes, the azygos and hemiazygos veins. It is the most posteroinferior of the openings, and is commonly found at the level of the superior half of the body of the twelfth thoracic vertebra (range, vertebral body of T10 to L1), slightly to the left of the midline. It is an osseo-aponeurotic opening bordered by the diaphragmatic crura laterally, the vertebral column and anterior longitudinal ligament posteriorly and the median arcuate ligament anteriorly; the aorta therefore normally passes posterior to the diaphragmatic musculature and as such is not affected by its contraction (Nason et al 2012). Occasionally, some tendinous fibres from the medial parts of the crura also pass posterior to the aorta, converting the osseo-aponeurotic hiatus into an aponeurotic fibrous ring.

The oesophageal hiatus transmits the oesophagus, anterior and posterior vagal trunks, gastric nerves, oesophageal branches of the left gastric vessels and lymphatic vessels. It is commonly located level with the inferior half of the body of the eleventh thoracic vertebra (range, vertebral body of T9 to L1–L2 intervertebral disc), anterosuperior to, and to the left of, the aortic hiatus. The elliptical hiatus has a slightly oblique long axis, and is bounded by muscle fibres that originate from the medial part of the right crus and cross the midline, forming a tunnel approximately 2.5 cm long that accommodates the distal part of the oesophagus. The outermost fibres run in a craniocaudal direction, and the innermost fibres are arranged circumferentially. There is no direct continuity between the oesophageal wall and the muscle around the oesophageal hiatus. The fascia on the inferior surface of the diaphragm, rich in elastic fibres, is continuous with the transversalis fascia and extends superiorly into the oesophageal hiatus in the shape of a flattened cone to blend with the oesophageal wall 2–3 cm superior to the gastro-oesophageal (squamocolumnar) junction. Some of its elastic fibres penetrate to the submucosa of the oesophagus. This

The diaphragm is connected to closely related organs by various connective tissue formations known as ligaments. Within the thoracic cavity, the inferior pulmonary ligament, a double-layered fold of parietal pleura, connects the inferior part of the hilum and root of the lung and the mediastinal surface of the inferior lobe of the lung to the diaphragm. The phrenico-oesophageal ligament, formed from peri-oesophageal areolar tissue, connects the diaphragm to the oesophagus as it passes through the oesophageal hiatus. Within the abdominopelvic cavity, a number of peritoneal formations form a series of supportive ligaments. The falciform ligament connects the anterior surface of the liver to the diaphragm and rectus sheath. The right and left coronary and triangular ligaments pass to the diaphragmatic surface of the liver forming the boundaries of the bare area of the liver. The phrenicosplenic and phrenicocolic ligaments connect the diaphragm to the spleen and splenic flexure of the colon, respectively. The suspensory muscle of the duodenum (ligament of Treitz) is formed from a series of muscular bands that originate from the left crus and connect to the duodenojejunal flexure (Bordoni and Zanier 2013).

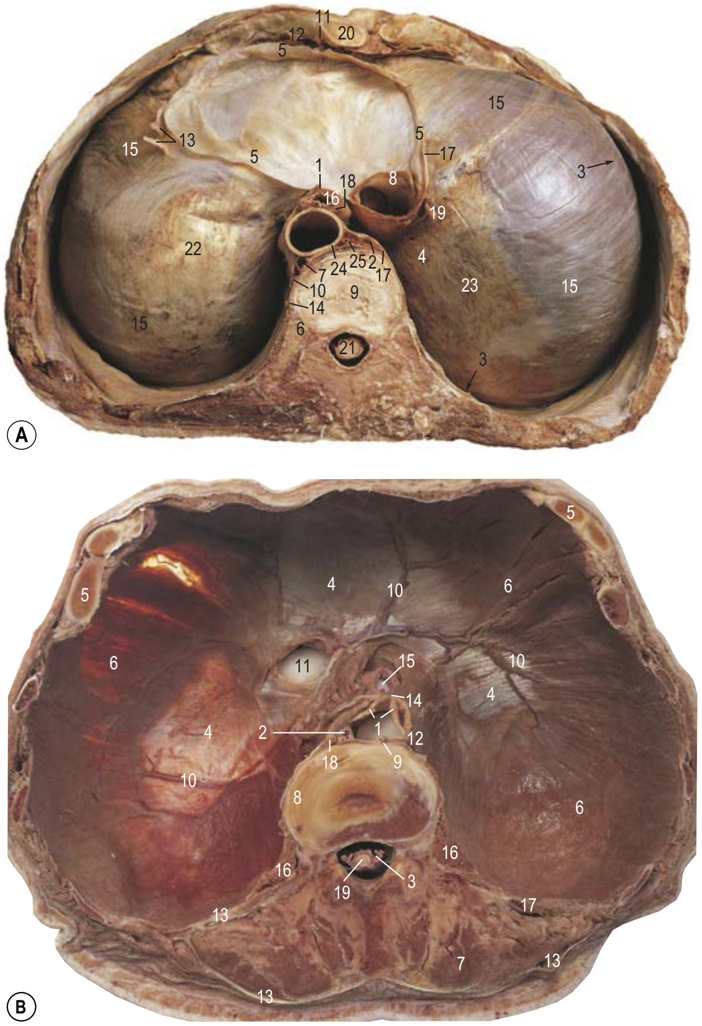

Fig. 55.3 Superior and inferior views of the respiratory diaphragm. **A**, Superior view showing the relationship between the central tendon and muscular components, and the prominent relationship between the diaphragm and the pericardium. Key: 1, anterior oesophageal plexus; 2, azygos vein; 3, costodiaphragmatic recess; 4, costomediastinal recess; 5, fibrous pericardium (cut edge); 6, head of left rib 9; 7, hemiazygos vein; 8, inferior vena cava; 9, intervertebral disc; 10, left greater thoracic splanchnic nerve; 11, left internal thoracic artery; 12, left musculophrenic artery; 13, branches of the left phrenic nerve; 14, left sympathetic trunk; 15, muscle of diaphragm; 16, oesophagus; 17, mediastinal parietal pleura (cut edge); 18, posterior oesophageal plexus; 19, right phrenic nerve; 20, seventh left costal cartilage; 21, spinal cord; 22, left folia of central tendon; 23, right folia of central tendon; 24, descending thoracic aorta; 25, thoracic duct. **B**, Inferior view showing muscular fibres attaching onto the central tendon, and associated openings and vasculature. Key: 1, abdominal aorta; 2, azygos vein; 3, cauda equina; 4, central tendon of the diaphragm; 5, costal cartilage (cut); 6, muscle of the diaphragm; 7, erector spinae muscle group; 8, L1–L2 intervertebral disc; 9, hemiazygos vein; 10, inferior phrenic vessels; 11, caval foramen; 12, left crus of respiratory diaphragm; 13, thoracolumbar fascia; 14, median arcuate ligament; 15, oesophagus (abdominal part); 16, psoas major; 17, quadratus lumborum; 18, right crus of respiratory diaphragm; 19, spinal cord. (With permission from Abrahams PH, Spratt JD, Loukas M et al (eds) McMinn and Abrahams' Clinical Atlas of Human Anatomy, 7th ed. Elsevier, Mosby. Copyright 2013.)

peri-oesophageal areolar tissue forms the phrenico-oesophageal ligament, that connects the oesophagus flexibly to the diaphragm, thus permitting freedom of movement during swallowing and ventilation while synchronously limiting superior oesophageal displacement.

The caval foramen transmits the inferior vena cava, which adheres to its margins, and branches of the right phrenic nerve (see Fig. 55.1A). It is the most superior of the three large openings, and lies approximately level with the superior part of the body of the eleventh thoracic vertebra (range, T8–T9 intervertebral disc to the body of the twelfth thoracic vertebra). Quadrilateral in shape with aponeurotic margins, it is located at the junction of the right folium of the central tendon with the central part. During inspiration, dilation of the caval foramen, combined with increased intra-abdominal pressure, increases cardiac venous return (Nason et al 2012).

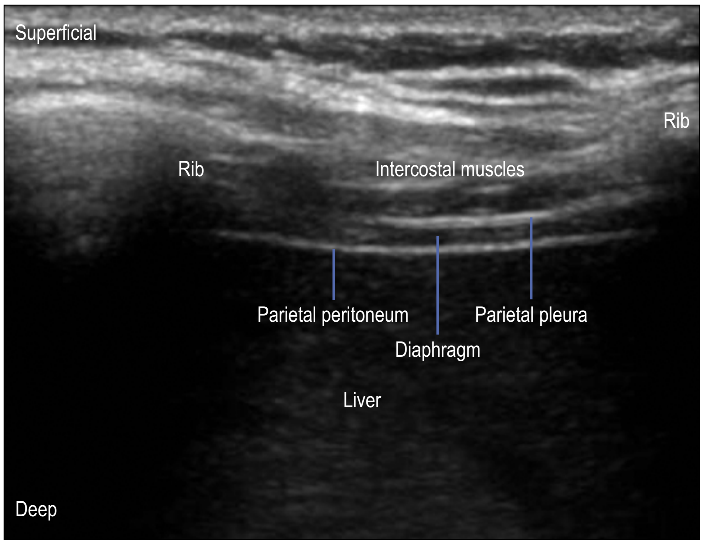

Fig. 55.4 Ultrasound of the respiratory diaphragm at the level of the eighth left intercostal space in the midaxillary line. The diaphragm is visualized as a hypoechoic (dark) line sitting between two hyperechoic (light) layers consisting of the parietal peritoneum and the parietal pleura. (With permission from Naicker J and van Tonder DJ, Department of Anatomy, University of Pretoria.)

Two smaller openings within each crus transmit the greater and lesser thoracic splanchnic nerves. The ganglionated sympathetic trunks usually enter the abdominal cavity posterior to the respiratory diaphragm, deep to the medial arcuate ligaments. There are frequently openings for small veins in the central tendon.

On each side of the respiratory diaphragm, small areas of muscle may be replaced by areolar tissue. The superior epigastric branch of the internal thoracic artery and some lymph vessels from the abdominal wall and convex surface of the liver pass through an area of areolar tissue covering the sternocostal triangle (between the sternal and costal attachments of the respiratory diaphragm). An inconstant area of areolar tissue between the costal attachment and the fibres that originate from the lateral arcuate ligament may be all that separates the diaphragmatic parietal pleura from the posterosuperior surface of the kidney. Additional smaller fascial spaces may be found throughout the lateral aspects of the domes of the diaphragm without evidence of vascular penetration. Although these spaces are found on both the left and right sides, they appear to be more numerous on the left (du Plessis et al 2015).

Oesophageal reflux Reflux of gastric contents into the oesophagus, with risk of pulmonary aspiration, is normally prevented by the specialized smooth muscle of the inferior oesophageal wall and the encircling crural muscle fibres forming a physiological barrier at the gastro-oesophageal junction. The diaphragm acts as a 'physiological' sphincter to prevent gastro-oesophageal reflux by constricting during inspiration (Nason et al 2012) (see also Ch. 63).

Hiatus hernia Deep inspiration followed by closure of the glottis and contraction of the muscles of the abdominal and thoracic walls provides additional power to all expulsive efforts including sneezing, coughing, laughing, crying, urination, defecation, vomiting and uterine fetal expulsion. The resulting increase in intra-abdominopelvic pressure can also be used to provide an anteriorly located pneumatic support to the vertebral column when lifting heavy objects. Repeated mechanical stress may eventually compromise the integrity of the oesophageal hiatus, leading to widening of the muscular hiatal tunnel. Concomitant laxity of the phrenico-oesophageal ligament allows the gastro-oesophageal junction to migrate into the posterior mediastinum, a condition that is normally termed a sliding (type I) hiatus hernia. Sliding hernias are typically acquired in the fifth decade of life, and are found in more than 50% of patients with gastro-oesophageal reflux. This reflux induces tonic contraction of the longitudinal oesophageal muscle, further exacerbating the hiatus hernia.

Congenital hernia Congenital respiratory diaphragmatic defects may cause abdominal organs, usually the stomach and/or the small bowel, colon, liver and spleen, to herniate through the diaphragm into the thoracic cavity; they are described in Chapter 20.

Herniation of the stomach into the thoracic cavity adjacent to the oesophagus is termed a para-oesophageal (type II) hiatus hernia. There are three distinct types: II, III and IV. Type II refers to a herniated stomach with normal positioning of the gastro-oesophageal junction. Type III, a 'mixed' hernia, refers to both a herniated stomach and a sliding-type hernia. Type IV refers to a hernia in which more than one-third of the stomach is herniated into the thoracic cavity. Para-oesophageal herniae can be diagnosed with barium swallow, CT or endoscopy (Daugherty et al 2017).

Eventration

Available with the *Gray's Anatomy* e-book

Diaphragmatic trauma

Available with the *Gray's Anatomy* e-book

Median arcuate ligament (Dunbar) syndrome

Available with the *Gray's Anatomy* e-book

VASCULAR SUPPLY AND LYMPHATIC DRAINAGE

Arteries

The rich arterial supply of the respiratory diaphragm is derived from anastomoses between the lower five intercostal and the subcostal arteries, the superior and inferior phrenic arteries and the pericardiacophrenic and musculophrenic arteries (Ch. 53).

Intercostal and subcostal arteries

The lower five intercostal and the subcostal arteries supply the costal margins of the respiratory diaphragm (Ch. 53).

Pericardiacophrenic and musculophrenic arteries

Available with the *Gray's Anatomy* e-book

Inferior phrenic arteries

The major arterial supply to the diaphragm is derived from the right and left inferior phrenic arteries, which usually arise either independently or as a common trunk from the coeliac trunk or the abdominal aorta (see Figs 55.1–55.2; **Fig. 55.5**). Less commonly, the right inferior phrenic artery arises from the right renal artery, the left gastric artery or the hepatic artery proper, and the left inferior phrenic artery arises from the left or right renal artery, the left gastric artery or the proper hepatic artery (Loukas et al 2005a, Tubbs et al 2016).

The arteries ascend anterolateral to the diaphragmatic crura, near the medial border of each suprarenal gland. The left inferior phrenic artery passes posterior to the oesophagus, and the right passes posterior to the inferior vena cava. Both arteries then run anteriorly; the left passes along the left side of the oesophageal hiatus and the right passes along the right side of the caval foramen. They both divide into medial and lateral branches near the posterior border of the central tendon. The medial branches curve anteriorly to anastomose with each other anterior to the central tendon, and with the musculophrenic and pericardiacophrenic arteries, when present. The lateral branches approach the thoracic wall and anastomose with the musculophrenic arteries and the lower posterior intercostal arteries. The left inferior phrenic artery sends ascending branches to the distal oesophagus, and the lateral branch of the right inferior phrenic artery supplies the inferior vena cava.

Superior phrenic arteries

The left and right superior phrenic arteries supply the superior surface of the diaphragm (**Figs 55.6–55.7**). They most commonly arise from either the descending thoracic aorta or the proximal segment of the tenth intercostal artery before it enters the intercostal space. The right artery (and less commonly the left) may arise from the distal segment of the tenth intercostal artery (Loukas et al 2007).

Veins

Phrenic veins

The superior surface of the respiratory diaphragm is drained by tributaries of the musculophrenic and pericardiacophrenic veins that run alongside the corresponding arteries. The inferior surface of the diaphragm is drained by tributaries of the right and left inferior phrenic veins that usually drain into the inferior vena cava inferior to the diaphragm (**Fig. 55.8** see Figs 55.1, 61.12). The right inferior phrenic vein may drain into the right hepatic vein or the inferior vena cava superior to the diaphragm; the left inferior phrenic vein may drain into the left suprarenal vein, the left renal vein, the left hepatic vein or, rarely, both the left suprarenal renal vein and the inferior vena cava (Loukas et al 2005b).

Lymphatic drainage

The respiratory diaphragm is drained by anterior, middle and posterior groups of lymph nodes that lie on its superior surface and that also drain the superior portion of the liver, the gastro-oesophageal junction and the inferior surface of the diaphragm. Lymph also drains anterosuperiorly to the parasternal and anterior mediastinal nodes, and posterosuperiorly to the posterior mediastinal and brachiocephalic nodes.

INNERVATION

The right and left phrenic nerves supply motor fibres to the muscle of the respiratory diaphragm and sensory fibres to the central parts of the diaphragm (C3, C4, C5) (**Fig. 55.9**). The lower six or seven intercostal nerves supply sensory fibres to the peripheral parts of the diaphragm. The fibres of the right crus of the diaphragm divide and pass to the right and left sides of the oesophagus and are innervated by both the right and left phrenic nerves.

Phrenic nerve

The left and right phrenic nerves are mixed somatic sensory and motor nerves that provide the sole motor supply to the respective hemidiaphragm. Each is derived mostly from the ipsilateral ventral ramus of the fourth cervical spinal nerve, with contributions from the ipsilateral

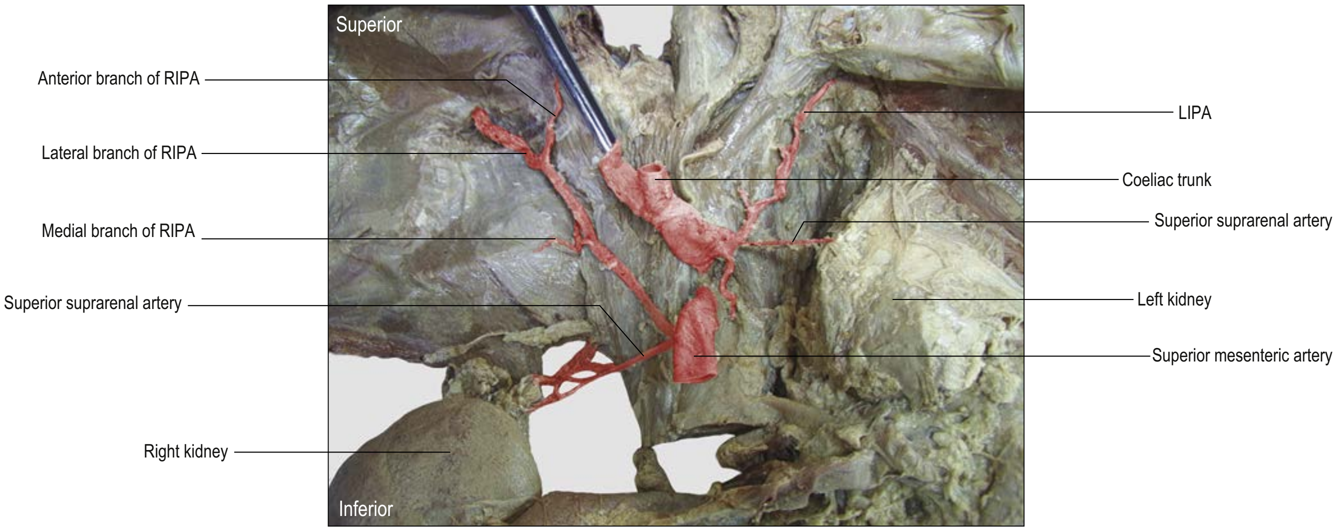

Fig. 55.5 A cadaveric dissection (anterior view) showing the origin and course of the right (RIPA) and left (LIPA) inferior phrenic arteries. The right inferior phrenic artery arises from the superior mesenteric artery (SMA), and the left inferior phrenic artery arises from the coeliac trunk. (With permission from Loukas M, Hullett J, Wagner T 2005 Clinical anatomy of the inferior phrenic artery. Clin Anat 18(5):357–65.)

Eventration is a focal bulge, usually located in the anteromedial segment of the muscular portion of the diaphragm. It is most often caused by a congenital thinning of the diaphragmatic muscle: such regions are covered by a thin fibroelastic connective tissue that stretches over time: eventration may be mistaken for a diaphragmatic hernia.

Eventration may be congenital or acquired as a result of pathological processes, including malignancy, trauma, infection and obesity. On X-ray imaging, the affected region appears as an elevated hump on a hemidiaphragm with an otherwise normal contour; there is often a sharp transition between the area of eventration and the surrounding normal diaphragm. The elevation becomes more pronounced with increased abdominal pressure and is typically found on the left; the affected part shows diminished or paradoxical movement during inspiratory 'sniff' testing while the posterior aspect of the ipsilateral dome acts normally (Nason et al 2012). Eventration and hemidiaphragmatic paralysis are differentiated by the amount of diaphragm involved: specifically, eventration involves only a part of a hemidiaphragm. Management is usually conservative but more aggressive treatment might be warranted should the patient become symptomatic, e.g. worsening dyspnoea, chronic atelectasis or recurrent pneumonia (Daugherty et al 2017).

Closed or penetrating thoraco-abdominal injuries may result in rupture or laceration of the diaphragm. With closed injuries and diaphragmatic rupture, abdominal contents may herniate into the thorax. CT imaging with planar reformation should be the primary mode of investigation (Shanmuganathan et al 2000): magnetic resonance imaging is usually performed when other imaging modalities have produced equivocal findings. Early operative repair is recommended because untreated cases may develop gastrointestinal obstruction or perforation. Patients with penetrating injuries may require additional assessment by thoracoscopy (Lowdermilk and Naunheim 2000).

In up to 25% of individuals, the median arcuate ligament lies inferior to its normal position, and anterior to the coeliac trunk. When this occurs, the coeliac trunk may become compressed and arch downward, leading to mesenteric angina and aneurysms in the pancreaticoduodenal arteries as a consequence of collateral flow. Most patients will present with postprandial pain, nausea and often vomiting, and many will avoid eating, resulting in significant weight loss. During expiration, concurrent movement of the abdominal aorta and the median arcuate ligament compresses the coeliac trunk; the position, angle and vertebral level of origin of the coeliac trunk are additional aetiological factors. Diagnosis is based mainly on the exclusion of other causes, e.g. compression of the vessel as a result of fibrotic or neoplastic changes in the sympathetic coeliac plexus and coeliac ganglion, as well as atherosclerotic changes in the coeliac trunk. Definitive diagnosis can only be made with multiple imaging modalities (Horton et al 2005).

The pericardiacophrenic and musculophrenic arteries originate from the internal thoracic artery (see Figs 55.2, 55.9): both are conventionally included in the description of the arterial supply of the diaphragm, but the extent to which these two arteries actually supply the diaphragm is uncertain. Studies have often failed to trace the phrenic branches of the pericardiacophrenic artery to the surface of the diaphragm, possibly because the vessels are too small to be detected angiographically (Loukas et al 2008b).

During liver resection, failure to control excessive bleeding from the hepatic veins impairs patient outcome and prognosis: correctly identifying and clamping the hepatic veins is therefore essential. The right inferior phrenic vein can be used to help to identify the hepatic veins because it usually drains into the inferior vena cava just cranial to the confluence of the hepatic veins into the inferior vena cava (see Fig. 55.8): tracing its course therefore allows a surgeon to visualize, encircle and clamp the hepatic veins prior to mobilization of the liver (Torzilli et al 2006).

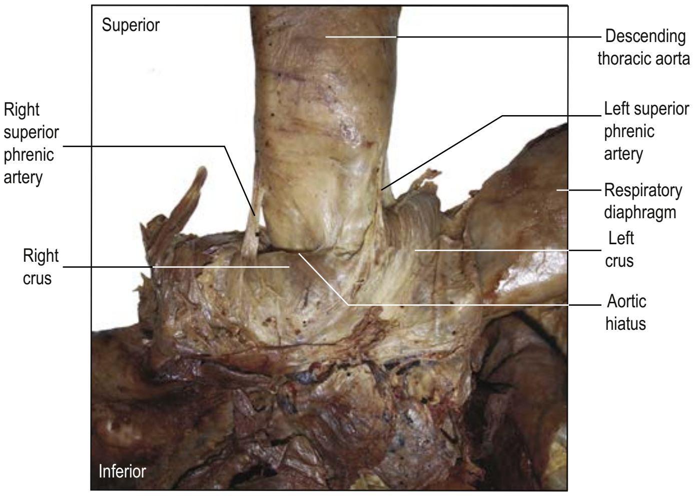
Superior
Descending thoracic aorta
Right superior phrenic artery
Left superior phrenic artery
Respiratory diaphragm
Left crus
Right crus
Aortic hiatus
Inferior

Fig. 55.6 A cadaveric dissection (anterior view) showing the origin of the right and left superior phrenic arteries from the descending thoracic aorta and supplying portions of the right and left diaphragmatic crura. (With permission from Loukas M, Louis RG Jr, Wartmann CT et al 2007 Superior phrenic artery: an anatomic study. Surg Radiol Anat 29(1):97–102.)

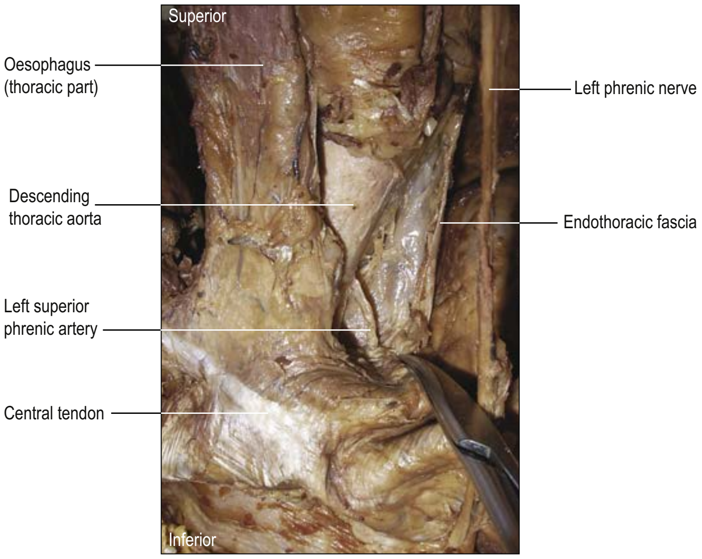
Superior
Oesophagus (thoracic part)
Left phrenic nerve
Descending thoracic aorta
Endothoracic fascia
Left superior phrenic artery
Central tendon
Inferior

Fig. 55.7 A cadaveric dissection (left lateral view) showing the left superior phrenic artery arising from the descending thoracic aorta. (With permission from Loukas M, Louis RG Jr, Wartmann CT et al 2007 Superior phrenic artery: an anatomic study. Surg Radiol Anat 29(1):97–102.)

ventral rami of the third and fifth cervical spinal nerves (see Figs 35.17–35.18). The course of the cervical part of the phrenic nerves is described on page 596 in Chapter 35. Within the thoracic cavity, the phrenic nerves descend anterior to the lung root and hilum, between the fibrous pericardium and mediastinal parietal pleura, accompanied by the pericardiacophrenic vessels. Each phrenic nerve supplies sensory branches to the mediastinal pleura, fibrous pericardium and parietal layer of serous pericardium. The right and left phrenic nerves differ in their intrathoracic relationships (Rajanna 1947).

Right phrenic nerve

The right phrenic nerve is shorter and more vertical than the left. At the root of the neck it is separated from the second part of the right subclavian artery by scalenus anterior (**Fig. 55.10A**). It then passes inferomedially through the superior thoracic aperture between the first part of the right subclavian artery and the right subclavian vein. Occasionally, the right or left phrenic nerves may pass anterior to, or through the anterior wall of, the respective subclavian vein (Paraskevas et al 2011). Around the level of the first rib or the first costal cartilage, the right phrenic nerve crosses the right internal thoracic artery either superiorly between the artery and the first rib, or inferiorly, pressed against the artery by the apex of the right lung and its covering pleura (Owens et al 1994). The nerve continues to descend, passing immediately lateral to the right brachiocephalic vein, the superior vena cava, the fibrous pericardium covering the right side of the right atrium and the inferior vena cava. It branches just superior to, or at the level of, the diaphragm.

Left phrenic nerve

At the root of the neck, the left phrenic nerve commonly leaves the medial border of scalenus anterior and passes anterior to the first part of the left subclavian artery and posterior to the left subclavian vein and the thoracic duct (**Fig. 55.10B**). Sometimes the right and left phrenic nerves are symmetric in their cervical course, in which case the left phrenic nerve is initially separated from the second part of the left subclavian artery by scalenus anterior. After passing through the superior thoracic aperture the left phrenic nerve crosses the left internal thoracic artery, most commonly superiorly, around the level of the first rib or the first costal cartilage (Owens et al 1994). It descends across the medial aspect of the apex of the left lung and its pleural covering to pass between the left common carotid and left subclavian arteries. The nerve then descends anteromedially and passes anterior and close to the left vagus nerve while in the region superior to the aortic arch and posterior to the left brachiocephalic vein. It continues inferiorly, passing anterior to the left superior intercostal vein, the aortic arch and the left lung root and hilum, after which it passes inferolaterally and to the left, over the fibrous pericardium covering the left atrium and left ventricle (see Fig. 55.9). As it passes over the fibrous pericardium, the left phrenic nerve is located more anterior than the right phrenic nerve and is therefore at greater risk of damage during the placement of surgical incisions to access the pericardial cavity.

Diaphragmatic relationships The right phrenic nerve passes through the central tendon of the respiratory diaphragm, either via the caval foramen or just lateral to it. The left phrenic nerve passes through the muscular part of the diaphragm anterior to the central tendon, just lateral to the fibrous pericardium covering the left pulmonary border of the heart, and posterior to the cardiac apex (see Fig. 55.9). At or slightly superior to the diaphragm each phrenic nerve supplies fine branches to the parietal pleura covering the central part of the respiratory diaphragm. Typically, the trunk of each nerve then divides into three branches (anterior or sternal, anterolateral and posterior) as it passes through the diaphragm (see Fig. 55.1A). The main branches may be submerged in diaphragmatic muscle or lie inferior to it. They supply motor fibres to the muscle and sensory fibres to the peritoneum and pleura covering the central part of the diaphragm. They also relay proprioceptive fibres from the musculature. The anterior (sternal) branch runs anteromedially towards the sternum and connects with its contralateral counterpart. The anterolateral branch runs to the lateral folia of the central tendon. The short posterior branch divides into a posterolateral ramus that passes posterior to the left or right folia of the central tendon and a posterior ramus that supplies the crura of the diaphragm. The posterolateral and posterior crural branches may arise separately from the phrenic nerve.

The phrenic nerves also relay proprioceptive information; the right phrenic nerve supplies the part of the right crus that lies to the right of the oesophagus, and the left phrenic nerve supplies the left crus and the part of the right crus that lies on the left of the oesophagus.

Phrenic ganglia The right phrenic nerve continues its course inferior to the diaphragm and frequently connects to the right phrenic ganglion. An additional, smaller, right accessory phrenic ganglion is sometimes located proximally along the phrenic nerve, close to its exit from the caval foramen (see **Fig. 55.1A**). The right phrenic ganglion has plexiform communications with the coeliac and aorticorenal ganglia and with the right suprarenal gland (**Fig. 55.11**). A left phrenic ganglion is less commonly seen; when present, it exhibits plexiform communications to several autonomic ganglia. Both phrenic nerves and ganglia are closely related to the diaphragmatic crura, therefore sutures for crural approximation in the repair of hiatal hernia must be placed superior to the ganglia in order to avoid iatrogenic injuries to the autonomic supply of the diaphragm and abdomen (Loukas et al 2016).

Lesions of the phrenic nerve An appreciation of the location of the main branches of the phrenic nerves is important to avoid iatrogenic surgical damage. Radial incisions in the diaphragm, passing from the costal margin toward the oesophageal hiatus, can lead to diaphragmatic paralysis, especially if made lateral to the point at which the phrenic nerve pierces the diaphragm, whereas thoraco-abdominal incisions in a circumferential manner in the periphery of the diaphragm do not involve any significant branches of the phrenic nerves and preserve diaphragmatic function. Similarly, incisions of the central part of the central tendon are relatively safe.

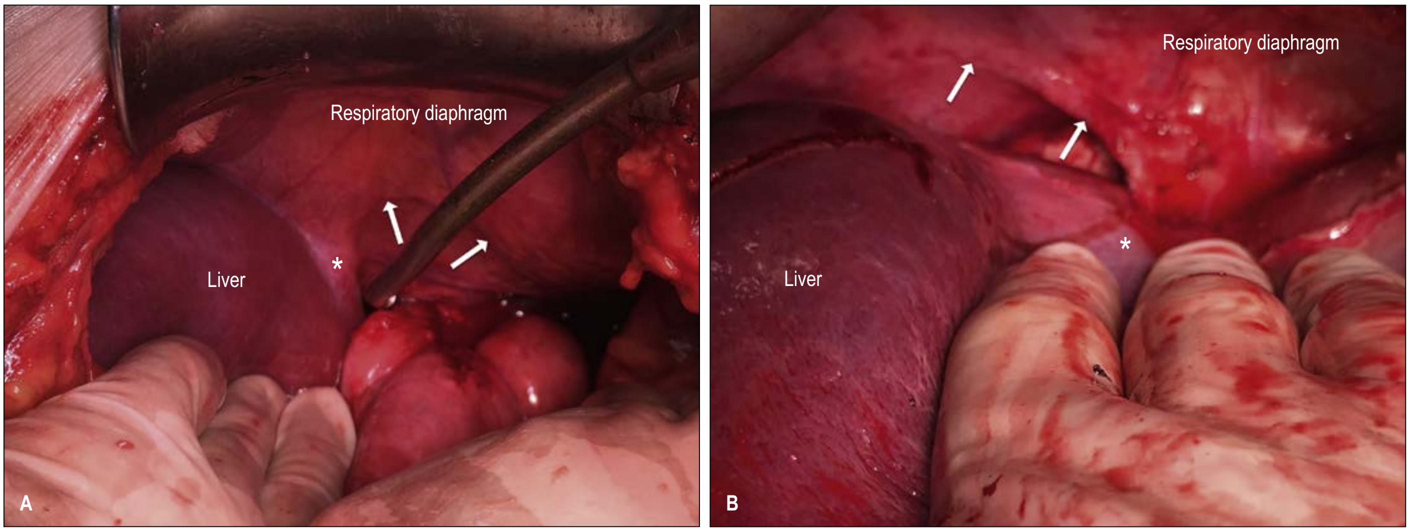

Fig. 55.8 Intraoperative inferior view of the respiratory diaphragm. With the liver retracted, the left inferior phrenic vein (**A**) and the right inferior phrenic vein (**B**) (both indicated by white arrows) can be used as landmarks, when followed to their terminations, to aid identification of the hepatic veins and inferior vena cava (*) during liver surgery. (Courtesy of Dr HJ Pretorius, Department of Surgery, Steve Biko Academic Hospital, Pretoria, South Africa.)

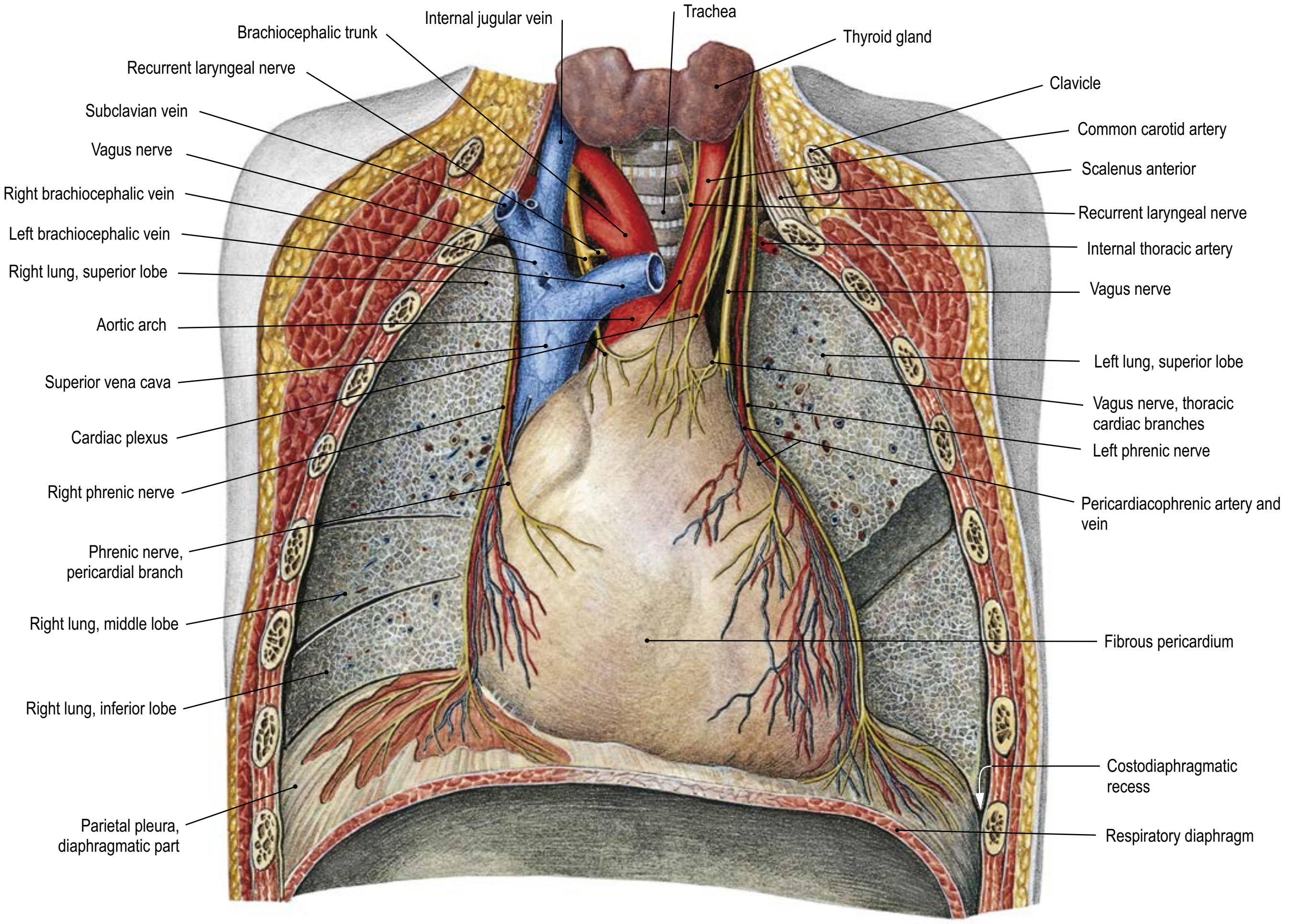
Brachiocephalic trunk
Internal jugular vein
Trachea
Thyroid gland
Recurrent laryngeal nerve
Clavicle
Subclavian vein
Common carotid artery
Vagus nerve
Scalenus anterior
Right brachiocephalic vein
Recurrent laryngeal nerve
Left brachiocephalic vein
Internal thoracic artery
Right lung, superior lobe
Vagus nerve
Aortic arch
Left lung, superior lobe
Superior vena cava
Vagus nerve, thoracic cardiac branches
Cardiac plexus
Left phrenic nerve
Right phrenic nerve
Pericardiacophrenic artery and vein
Phrenic nerve, pericardial branch
Right lung, middle lobe
Fibrous pericardium
Right lung, inferior lobe
Costodiaphragmatic recess
Parietal pleura, diaphragmatic part
Respiratory diaphragm

Fig. 55.9 The course and distribution of the right and left phrenic nerves within the thoracic cavity. (Sobotta Atlas of Human Anatomy © Elsevier GmbH, Urban & Fischer, Munich.)

Division of the phrenic nerve in the neck completely paralyses the corresponding half of the diaphragm, which subsequently atrophies. If an accessory phrenic nerve exists, section or crushing of the main nerve as it lies on scalenus anterior will not produce complete paralysis. The phrenic nerve may be involved in traumatic lesions of the upper brachial plexus. Cardiac surgery is one of the most common iatrogenic causes of phrenic nerve injury, especially when cold saline slush for myocardial preservation is instilled. The phrenic nerve may also be damaged during surgery for tumours of the lung or mediastinum, traumatic childbirth or radiation therapy, or by infections such as poliomyelitis (Nason et al 2012). Respiratory muscle weakness of rapid onset is a feature of Guillain–Barré syndrome.

Phrenic nerve damage leads to paradoxical movement of the diaphragm that is best observed fluoroscopically, with the patient first in the upright position (diaphragm unloaded), and then supine with a small weight on the abdomen (diaphragm loaded). Diaphragmatic paralysis can also be assessed by ultrasound examination, using an inhalation 'sniff' manoeuvre.

Referred pain Diaphragmatic irritation or pain is frequently felt at the tip of the shoulder, reflecting the common spinal nerve root origins of the phrenic and supraclavicular nerves (the ventral rami of the third and fourth cervical spinal nerves). It usually occurs when there is inflammation of the diaphragmatic parietal pleura, e.g. in basal pneumonia, pleural effusions, malignant disease, or irritation of the diaphragmatic parietal peritoneum, e.g. in pneumoperitoneum or subphrenic abscess, where involuntary diaphragmatic contraction (hiccups) may also occur.

Accessory phrenic nerve

The accessory phrenic nerve is described on page 596.

ANATOMY OF BREATHING

Breathing is a highly coordinated abdominal and thoracic process. The respiratory diaphragm is the main muscle of inspiration, responsible for approximately two-thirds of the volume of air intake during quiet breathing in healthy humans. Contraction of the external and internal intercostal muscles during inspiration and expiration varies with the superior-to-inferior position of an intercostal space and the position of the intercostal muscle within a given intercostal space. For example, the external intercostal muscles in the dorsal region of the more superiorly located intercostal spaces are mainly active during inspiration, whereas those in the ventral region of the more inferiorly located intercostal spaces are mainly active during expiration (De Troyer et al 2005).

Increasing the vertical, transverse and anteroposterior dimensions of the thoracic cavity increases the volume of the pleural cavity: the resulting decrease in pressure within the pleural cavity creates a pressure gradient that draws air at atmospheric pressure into the lungs. During expiration, the diaphragm relaxes and is moved superiorly by the intra-abdominal viscera and increased intra-abdominal pressure produced by contraction of the muscles of the anterior abdominal wall. Air is expelled from the lungs and the elastic recoil of the lung creates a subatmospheric pressure that returns the lateral and anteroposterior dimensions of the thorax to normal (De Troyer and Estenne 1988, Celli 1998). During inspiration, the most inferior ribs are fixed and contraction of the diaphragm draws the central tendon inferiorly, minimally altering diaphragmatic curvature. The cupulae of the diaphragm move inferiorly and slightly anteriorly, almost parallel to their original positions. The associated inferior displacement of the abdominal viscera is permitted by the extensibility of the abdominal wall, but the limit of this extensibility is soon reached. The central tendon, its further motion prevented by the abdominal viscera, becomes a fixed point from which the fibres of the diaphragm continue to contract. This causes the second

The ‘gold standard’ for assessment of phrenic nerve and diaphragm function is electrical or magnetic stimulation of the phrenic nerve with recording of the compound muscle action potential and/or the trans-diaphragmatic pressure. Electrical stimulation of the diaphragm, by ‘pacing’ of one or both phrenic nerves, has been used with some success in infants with congenital central alveolar hypoventilatory syndrome (‘Ondine’s curse’) and in patients with high cervical lesions of the spinal cord, where the diaphragm is paralysed but the lower motor neurones are intact. Electrodes are placed adjacent to the nerves, sometimes in the neck but more usually in the chest, and a ventilatory rhythm is established by stimuli delivered by an implanted device. As this is a non-physiological way of recruiting the muscle, the fibres must be ‘conditioned’ during the initial period of stimulation, so that they acquire the necessary resistance to fatigue.

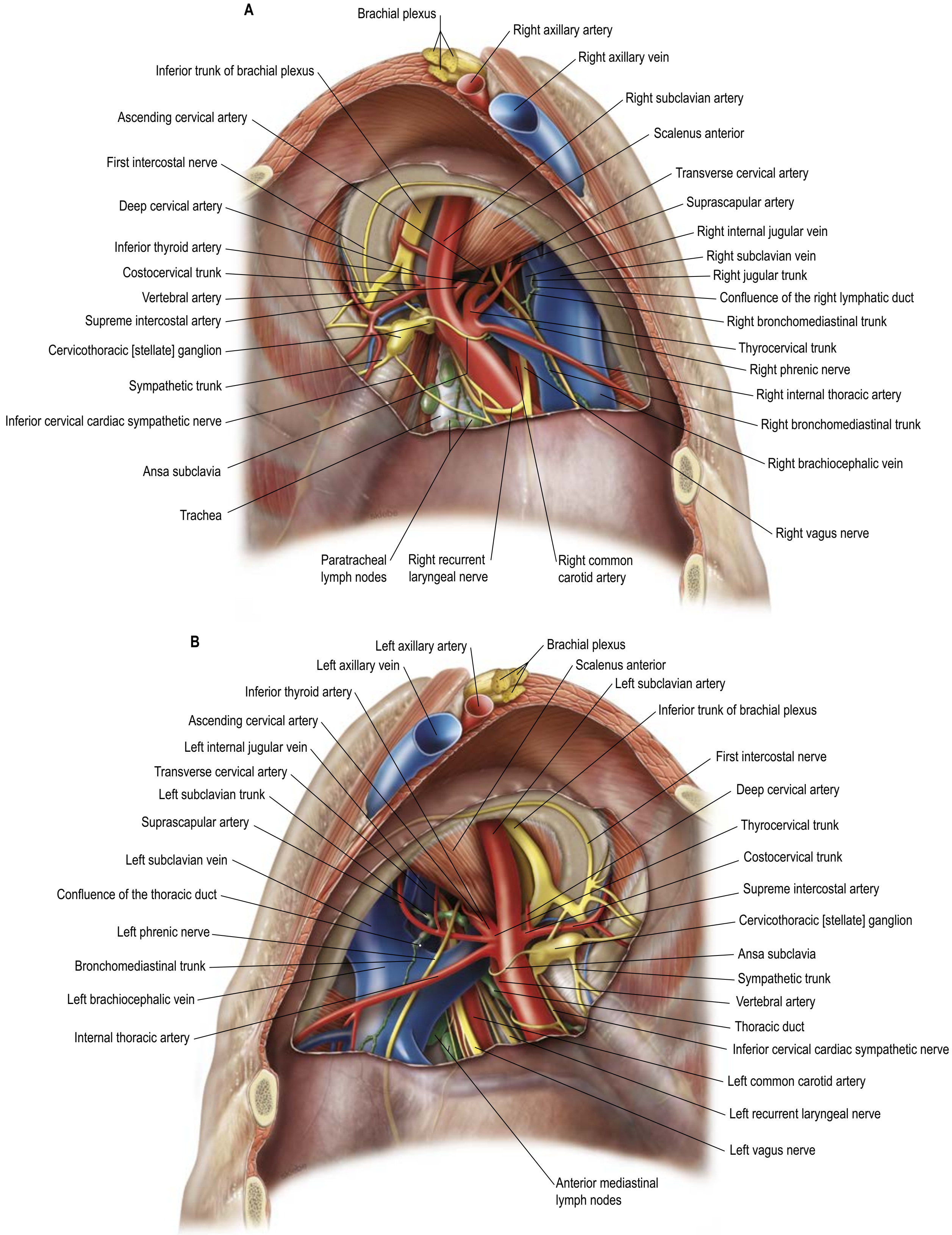
A
Brachial plexus
Right axillary artery
Right axillary vein
Inferior trunk of brachial plexus
Right subclavian artery
Ascending cervical artery
Scalenus anterior
First intercostal nerve
Transverse cervical artery
Deep cervical artery
Suprascapular artery
Right internal jugular vein
Inferior thyroid artery
Right subclavian vein
Costocervical trunk
Right jugular trunk
Vertebral artery
Confluence of the right lymphatic duct
Supreme intercostal artery
Right bronchomediastinal trunk
Cervicothoracic [stellate] ganglion
Thyrocervical trunk
Right phrenic nerve
Sympathetic trunk
Right internal thoracic artery
Inferior cervical cardiac sympathetic nerve
Right bronchomediastinal trunk
Ansa subclavia
Right brachiocephalic vein
Trachea
Right vagus nerve
Paratracheal lymph nodes
Right recurrent laryngeal nerve
Right common carotid artery
B
Left axillary artery
Brachial plexus
Left axillary vein
Scalenus anterior
Left subclavian artery
Inferior thyroid artery
Inferior trunk of brachial plexus
Ascending cervical artery
Left internal jugular vein
First intercostal nerve
Transverse cervical artery
Deep cervical artery
Left subclavian trunk
Suprascapular artery
Thyrocervical trunk
Left subclavian vein
Costocervical trunk
Supreme intercostal artery
Confluence of the thoracic duct
Cervicothoracic [stellate] ganglion
Left phrenic nerve
Ansa subclavia
Bronchomediastinal trunk
Sympathetic trunk
Left brachiocephalic vein
Vertebral artery
Internal thoracic artery
Thoracic duct
Inferior cervical cardiac sympathetic nerve
Left common carotid artery
Left recurrent laryngeal nerve
Left vagus nerve
Anterior mediastinal lymph nodes

Fig. 55.10 The course and anatomical relations of the phrenic nerves in the superior thoracic aperture and superior thorax. **A**, Right side showing the right phrenic nerve. **B**, Left side showing the left phrenic nerve. (Sobotta Atlas of Human Anatomy © Elsevier GmbH, Urban & Fischer, Munich.)

to tenth ribs to be elevated and the inferior portions of the ribs to be turned outwards as a result of direct transmission of pressure through the costal attachments of the diaphragm (zone of apposition) (Fig. 55.12). During inspiration, the bodies of the ribs move superiorly and laterally, increasing the transverse dimensions of the thoracic cavity in the same manner as a bucket handle swinging outwards. This effect is most evident in the seventh to tenth ribs. Movements at the costovertebral joints cause elevation of the anterior ends of the ribs that push the body of the sternum and the upper ribs anteriorly in a 'pump handle' movement; this effect is most evident in second to sixth ribs, and increases the anteroposterior dimension of the thorax. The right cupula of the diaphragm, which lies over the liver, has a greater resistance to overcome than the left, which lies over the stomach; consequently the right crus and the muscle fibres of the right side of the diaphragm are more substantial than those of the left. The balance between descent of the diaphragm, protrusion of the abdominal wall

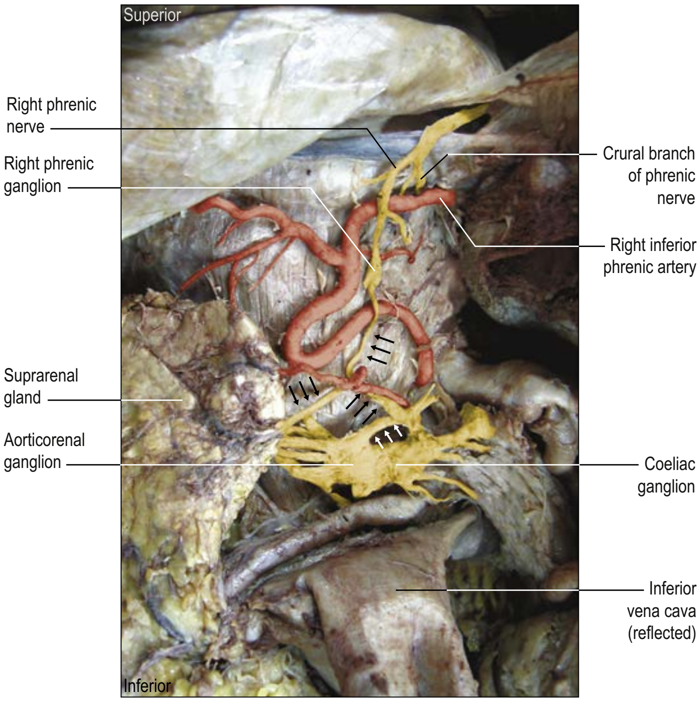

Fig. 55.11 A cadaveric dissection showing a right phrenic ganglion close to the right inferior phrenic artery and right diaphragmatic crus with plexiform communications to the coeliac ganglion, aorticorenal ganglion and suprarenal gland (arrows). The inferior vena cava has been reflected inferiorly. (With permission from Loukas M, Du Plessis M, Louis RG Jr et al 2016 The subdiaphragmatic part of the phrenic nerve – morphometry and connections to the autonomic ganglia. Clin Anat 29:120–8.)

('abdominal breathing') and elevation of the ribs ('thoracic breathing') varies between individuals and with the phase and depth of ventilation, the degree of distension of the stomach and intestines, and the size of the liver. The thoracic element is usually more evident in females, but increases in both sexes during deep inspiration.

The role of the abdominal wall in breathing is often underestimated. If the anterolateral abdominal wall connected the pelvic rim rigidly to the costal margins, inspiration would be impossible because the diaphragm could not descend (the abdominal contents would be incompressible), and the ribs could not rise (the connections to the pelvis would be inextensible). During normal breathing, the abdominal wall relaxes as the diaphragm contracts. It is possible to oppose this motion by tensing the abdomen, as in the 'beach posture' adopted to exaggerate the size of the chest. In this case, the abdominal contents fix the central tendon of the diaphragm, so that it raises the ribcage as it contracts, thus widening the gap between the ribs and the pelvic rim.

The ventilatory muscles must also work during sleep, when the pharyngeal muscles relax and upper airway resistance increases. In some individuals, particularly those with obesity, this relaxation can lead to periodic apnoea and marked hypoxia during sleep, implying that the pharyngeal muscles play an important ventilatory role in waking life. Although ventilatory muscles rarely tire in normal life, they do fatigue when placed under abnormal loads, e.g. in chronic obstructive pulmonary disease.

The primary role of the intercostal muscles is to stiffen the chest wall, preventing paradoxical motion during inspiratory diaphragmatic descent. This becomes most obvious immediately after high spinal cord injury, when there is flaccid paralysis of the entire trunk and only the diaphragm remains functional.

Bonus e-book content

Fig. 55.6 A cadaveric dissection (anterior view) showing the origin of the right and left superior phrenic arteries from the descending thoracic aorta and supplying portions of the right and left diaphragmatic crura.

Fig. 55.7 A cadaveric dissection (left lateral view) showing the left superior phrenic artery arising from the descending thoracic aorta.

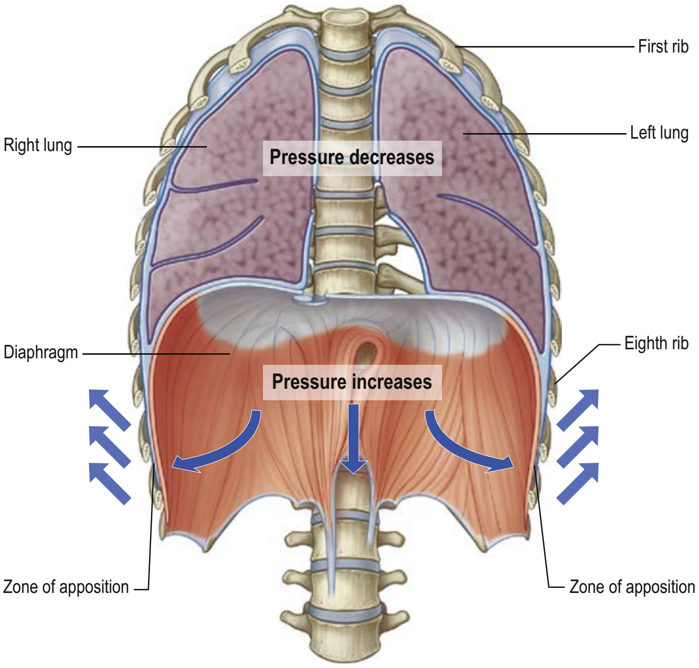

Fig. 55.12 Movements of the thoracic cage and respiratory diaphragm, and pressure changes within the thoracic and abdominal cavities during inspiration. (With permission from Drake RL, Vogl AW, Mitchell AWN (eds) Gray's Anatomy for Students, 3rd ed. Elsevier, Churchill Livingstone. Copyright 2015.)

Key references

De Troyer A, Kirkwood PA, Wilson TA 2005 Respiratory action of the intercostal muscles. Physiol Rev 85:717–56.

Du Plessis M, Ramai D, Shah S et al 2015 The clinical anatomy of the musculotendinous part of the diaphragm. Surg Radiol Anat 37:1013–20.

An article that describes the variations in the ratio between the surface area of the central tendon to the muscular region of the diaphragm, and defines a system for classification.

Froese AB 2006 Gravity, the belly, and the diaphragm: you can't ignore physics. Anesthesiol 104:193–6.

Loukas M, Wartmann CT, Tubbs RS et al 2008a Morphologic variation of the diaphragmatic crura: a correlation with pathologic process of the esophageal hiatus? Folia Morphol 67:273–9.

An article that describes the variable morphometry and muscle fibre arrangements of the diaphragmatic crura, and defines a 6-type classification system.

Owens WA, Gladstone DJ, Heylings DJ 1994 Surgical anatomy of the phrenic nerve and internal mammary artery. Ann Thorac Surg 58:843–4.

An observational study reporting the relationship of the left and right phrenic nerve with their respective internal thoracic arteries in the superior thoracic cavity.

The position of the respiratory diaphragm within the thoracic cavity varies with posture. It is highest (most superior) when the body is supine, when it performs the greatest range of ventilatory movements with normal breathing. When the body is erect, the diaphragm is located at a more inferior level and its ventilatory movements become smaller; when sitting, the diaphragm is at its most inferior level and its ventilatory movements are at their smallest. When the body is horizontal and on one side (lateral decubitus), the two halves of the diaphragm are positioned and move differently. The uppermost half sinks to a lower level than that seen when sitting, and moves little with ventilation. The lower half rises to a higher level in the thoracic cavity than it does even in the supine position, and its ventilatory excursions are considerably greater (Froese 2006). Changes in the position of the diaphragm with alterations in posture explain why patients with severe dyspnoea are most comfortable, and least short of breath, when sitting with the trunk upright.

In quiet breathing, the range of diaphragmatic excursion is about 1–2 cm, increasing to 5–7 cm during deep breathing (Boussuges et al 2009, Jung et al 2014). Following a forced inspiration, e.g. when breathing is partially obstructed, the right cupula of the diaphragm may descend to approximately the level of the body of the eleventh thoracic vertebra, while the left cupula may reach the level of the body of the twelfth thoracic vertebra. After forced expiration, the right cupula of the diaphragm is level anteriorly with the fourth costal cartilage, laterally with the fifth, sixth and seventh ribs, and posteriorly with the eighth rib; the left cupula is normally located more inferiorly by about one intercostal space, rib or costal cartilage.

The different pulmonary regions do not all move equally during ventilation. In quiet ventilation, the juxtahilar part of the lung moves minimally, the middle region moves only slightly and the superficial costal regions of the lung expand the most. The mediastinal surface, posterior border and apex move less because they are related to less movable structures. The diaphragmatic and costomediastinal regions expand most of all. Most of the volumetric change during ventilation occurs in the alveoli.

In a healthy adult with a vital capacity of 4.5 L, approximately 3 L is accounted for by diaphragmatic excursion. Immediately after high spinal cord injury, the vital capacity decreases to about 300 ml, even though the diaphragm is moving maximally, because the paradoxical incursion of the flaccid intercostal muscles results in a 2.7 L loss. After several weeks the paralysis usually becomes spastic, stiffening the chest wall, and the vital capacity increases towards its phrenic limit of about 3 litres. In the same way, high spinal cord injury reveals the role of the abdomen in inspiration and expiration. The abdominal musculature plays a major role in active expiration in humans. During the flaccid stage of high spinal cord paralysis, the only mechanisms available for returning the relaxed diaphragm into the thorax on expiration are passive recoil of the lungs and chest wall, and the weight of the abdominal viscera. The latter is the most important and operates only when an affected patient is lying down. If the patient is sat up or raised into an upright position, exhalation is impossible; trussing the abdomen with an elastic binder may be helpful. When the post injury paralysis becomes spastic, the stiff abdominal wall opposes inspiration.

References

Bordoni B, Zanier E 2013 Anatomic connection of the diaphragm: influence of respiration on the body system. J Multidiscip Healthc 6:281–91.

Botros KG, Bondok AA, Gabr OM et al 1990 Anatomical variations in the formation of the human oesophageal hiatus. Anat Anz 71:193–9.

Boussuges A, Gole Y, Blanc P 2009 Diaphragmatic motion studied by m-mode ultrasonography: methods, reproducibility, and normal values. Chest 135:391–400.

Celli B 1998 The diaphragm and respiratory muscles. Chest Surg Clin North Am 8:207–24.

Daugherty M, Kucera JN, Harvey M 2017 The pathological diaphragm. Contemp Diagn Radiol 40:1–7.

De Troyer A, Estenne M 1988 Functional anatomy of the respiratory muscles. Clin Chest Med 9:175–93.

De Troyer A, Kirkwood PA, Wilson TA 2005 Respiratory action of the intercostal muscles. Physiol Rev 85:717–56.

Downey R 2011 Anatomy of the normal diaphragm. Thorac Surg Clin 21:273–9.

Du Plessis M, Ramai D, Shah S et al 2015 The clinical anatomy of the musculotendinous part of the diaphragm. Surg Radiol Anat 37:1013–20.

An article that describes the variations in the ratio between the surface area of the central tendon to the muscular region of the diaphragm, and defines a system for classification.

Froese AB 2006 Gravity, the belly, and the diaphragm: you can't ignore physics. Anesthesiol 104:193–6.

Horton KM, Talamini MA, Fishman EK 2005 Median arcuate ligament syndrome: evaluation with CT angiography. RadioGraphics 25:1177–82.

Jung KJ, Park JY, Hwang DW et al 2014 Ultrasonographic diaphragmatic motion analysis and its correlation with pulmonary function in hemiplegic stroke patients Ann Rehabil Med 38:29–37.

Loukas M, Hullett J, Wagner T 2005a Clinical anatomy of the inferior phrenic artery. Clin Anat 18:357–65.

Loukas M, Louis RG Jr, Hullett J et al 2005b An anatomical classification of the variations of the inferior phrenic vein. Surg Radiol Anat 27:566–74.

Loukas M, Louis RG Jr, Wartmann CT et al 2007 Superior phrenic artery: an anatomic study. Surg Radiol Anat 29:97–102.

Loukas M, Wartmann CT, Tubbs RS et al 2008a Morphologic variation of the diaphragmatic crura: a correlation with pathologic process of the esophageal hiatus? Folia Morphol 67:273–9.

An article that describes the variable morphometry and muscle fibre arrangements of the diaphragmatic crura, and defines a 6-type classification system.

Loukas M, Diala el-Z, Tubbs RS et al 2008b A review of the distribution of the arterial and venous vasculature of the diaphragm and its clinical relevance. Folia Morphol (Warsz) 67:159–165.

Loukas M, Du Plessis M, Louis RG Jr et al 2016 The subdiaphragmatic part of the phrenic nerve – morphometry and connections to the autonomic ganglia. Clin Anat 29:120–8.

Lowdermilk GA, Naunheim KS 2000 Thoracoscopic evaluation and treatment of thoracic trauma. Surg Clin North Am 80:1535–42.

Nason LK, Walker CM, McNeeley MF et al 2012 Imaging of the diaphragm: anatomy and function. RadioGraphics 32:E51–E70.

Owens WA, Gladstone DJ, Heylings DJ 1994 Surgical anatomy of the phrenic nerve and internal mammary artery. Ann Thorac Surg 58:843–4.

Paraskevas GK, Raikos A, Chouliaras K et al 2011 Variable anatomical relationship of phrenic nerve and subclavian vein: clinical implication for subclavian vein catheterization. Br J Anaesth 106:348–51.

Rajanna MJ 1947 Anatomical and surgical considerations of the phrenic and accessory phrenic nerves. J Int Coll Surg 60:42–52.

Sarwal A, Walker FO, Cartwright MS 2013 Neuromuscular ultrasound for evaluation of the diaphragm. Muscle Nerve 47:319–29.

Shanmuganathan K, Killeen K, Mirvis SE et al 2000 Imaging of diaphragmatic injuries. J Thorac Imaging 15:104–11.

Sun J, Wang J, Luo T et al 2016 Surgical incision and approach in thoracolumbar extreme lateral interbody fusion surgery. Spine 41:E186–E190.

Talasz H, Kremser C, Kofler M et al 2011 Phase-locked parallel movement of diaphragm and pelvic floor during breathing and coughing – a dynamic MRI investigation in healthy females. Int Urogynecol J 22:61–8.

Torzilli G, Montorsi M, Palmisano A 2006 Right inferior phrenic vein indicating the right hepatic vein confluence into the inferior vena cava. Am J Surg 192:690–4.

Tubbs RS, Shoja MM, Loukas M (eds) 2016 Bergman's Comprehensive Encyclopaedia of Human Anatomic Variation. Hoboken: Wiley Blackwell.

CHAPTER

56

Mediastinum

The mediastinum is the visceral compartment between the two lungs and includes the mediastinal part of the parietal pleura. It is commonly defined as the region between the two pleural sacs, bounded laterally by the mediastinal parietal pleura, anteriorly by the sternum and posteriorly by the thoracic vertebral column, and extending vertically from the superior thoracic aperture (thoracic inlet) to the respiratory diaphragm (see Fig. 52.1). It communicates freely with the neck spaces and with the extraperitoneal, extrapleural and epidural spaces. Beyond each lung hilum, the mediastinum merges into the lung interstitium, incorporating the bronchial tree with its accompanying neurovascular bundles and the pulmonary vasculature.

The posterior mediastinal boundary is longer than the anterior as a result of the oblique orientation of the superior thoracic aperture and the posteroinferior curvature of the respiratory diaphragm. With respect to the median plane (midline), the mediastinum appears asymmetric.

The mediastinum is divided into superior and inferior mediastina by the sternal plane, which passes horizontally from the manubriosternal joint to intersect the vertebral column from the fourth to the superior half of the fifth thoracic vertebral body (Mirjalili et al 2012). This boundary is sometimes defined as a fixed plane passing from the manubriosternal joint to the inferior limit of the fourth thoracic vertebral body (**Fig. 56.1**). The inferior mediastinum is subdivided into anterior, middle and posterior parts.

Detailed accounts of mediastinal contents are included with descriptions of the respiratory viscera (Ch. 54), heart (Ch. 57) and great vessels (Ch. 58).

SUBDIVISIONS OF THE MEDIASTINUM

Superior mediastinum

The superior mediastinum lies between the manubrium of the sternum anteriorly and the bodies of the upper four or five thoracic vertebrae and the intervening intervertebral discs posteriorly. It is bounded laterally by the mediastinal parietal pleurae (see Fig. 56.1). The reflections of the left and right costal parietal pleura onto the superior mediastinum each follow a line that passes from the sternoclavicular joint in an inferomedial direction, to meet each other in the midline posterior to the sternal angle (see Fig. 53.4B). The resultant triangular space on the posterior surface of the manubrium of the sternum and between the lines of pleural reflection is occupied by the thymus or its remnants. The superior mediastinum contains the trachea, oesophagus, aortic arch, brachiocephalic trunk, left common carotid and subclavian arteries (the vertebral artery sometimes arises from the aortic arch between them), the internal thoracic arteries, the supreme intercostal, left superior intercostal, accessory hemiazygos, internal thoracic and inferior thyroid veins, and numerous lymph nodes, including those of the para-aortic, upper paratracheal, retrotracheal and prevascular groups (stations). Laterally, the superior mediastinal structures have the appearance of being 'shrink-wrapped' by the tightly applied mediastinal parietal pleura. The superior mediastinum transmits the sympathetic trunks, the sympathetic and parasympathetic cardiac nerves, the phrenic nerves laterally, the vagus nerves medially and the left recurrent laryngeal nerve. The terminal part of the thoracic duct emerges from the posterior aspect of the aortic arch and oesophagus, and passes superiorly between the left subclavian and left common carotid arteries to enter the neck (see Fig. 56.7B). The left and right brachiocephalic veins join to form the superior vena cava. The origins of sternothyroid and sternohyoid are attached to the posterior surface of the manubrium of the sternum. An enlarged thyroid gland may extend inferiorly between the manubrium and the brachiocephalic veins; its surgical excision requires care due to possible venous adherence. The origins of longus colli (inferior oblique and vertical intermediate portions) are the deepest contents of the superior mediastinum.

Inferior mediastinum

Anterior mediastinum

The anterior mediastinum lies between the sternal body and fibrous pericardium (see Fig. 56.1). It narrows above the level of the fourth

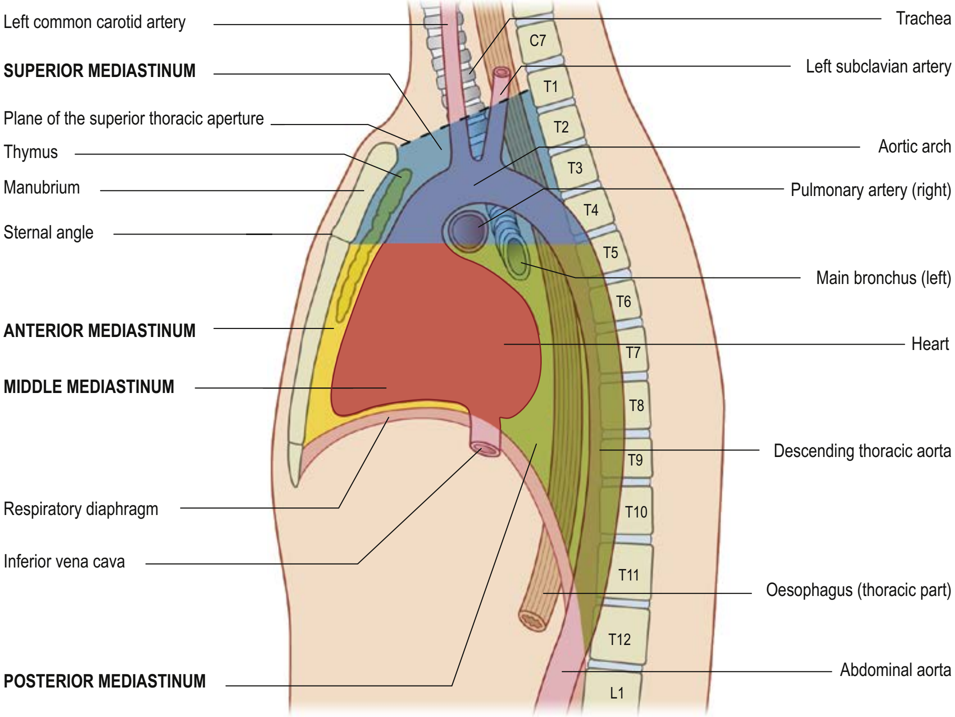

Fig. 56.1 Divisions of the mediastinum.

costal cartilages where the lines of pleural reflection converge (see Fig. 53.4B), and contains a variable amount of adipose tissue, loose connective tissue, sternopericardial ligaments, a few lymph nodes, the mediastinal branches of the internal thoracic artery, and sometimes part of the thymus gland or its remnants. The paired sternocostal triangles (of Morgagni) are openings between the sternal and costal attachments of the respiratory diaphragm: they are filled with areolar tissue and crossed by the superior epigastric vessels and by some lymph vessels from the abdominal wall and liver. A retrosternal hernia may pass through the triangles. The pericardium and the heart are routinely approached by either a complete or partial median sternotomy. The sternopericardial ligaments and the pleural reflections are easily separated by blunt dissection. In case of pericardial tamponade, the pericardial cavity can be drained through a left parasternal or subxiphoid approach, normally without entering the pleural cavity.

Middle mediastinum

The middle mediastinum is the broadest part of the inferior mediastinum (see Fig. 56.1) and contains the pericardia, heart and ascending aorta, the intrapericardial (inferior) half of the superior vena cava (receiving the azygos vein posteriorly), the tracheal bifurcation and main bronchi, the pulmonary trunk, right and left pulmonary arteries and veins, phrenic nerves, the deep part of the cardiac plexus and the subcarinal and lower paratracheal (tracheobronchial) lymph nodes. The short thoracic part of the inferior vena cava, both the extra- and intrapericardial segments, extends between the caval foramen of the respiratory diaphragm, through which it passes, and its termination in the right atrium. The structures forming the root of the lung converge at the hilum of the lung. The mediastinal part of the parietal pleura forms the lateral boundary of the middle mediastinum and is continuous with the visceral pleura at the level of the root of the lung and pulmonary ligament; the parietal pleura folds back (reflects) on itself to continue as the visceral pleura. The fibrous pericardium lies on, and is fused with, the middle folium of the central tendon of the respiratory diaphragm (see Fig. 55.3A).

Posterior mediastinum

The posterior mediastinum is the longest and narrowest part of the inferior mediastinum (see Fig. 56.1). It is bounded anteriorly by the tracheal bifurcation, fibrous pericardium and pulmonary vessels, and posteriorly by the bodies of the fourth or fifth to the twelfth thoracic vertebrae, and the intervening intervertebral discs. Numerous structures pass freely between the superior and posterior mediastina. The curved posterior third of the median (midline) region of the respiratory diaphragm constitutes the anteroinferior limit of the posterior mediastinum. Two pleural recesses, the aortico-oesophageal and azygo-oesophageal, project medially between the aorta and oesophagus on the left side and the azygos vein and oesophagus on the right side (see Fig. 56.7).

The posterior mediastinum contains the descending thoracic aorta (on the left side of the vertebral column), the oesophagus (median, but positioned anterior to the aorta inferiorly) and, more posteriorly, the azygos and hemiazygos venous systems, the thoracic duct, prevertebral and para-oesophageal lymph nodes, right and left sympathetic trunks and associated ganglia, and thoracic splanchnic nerves. The vagal trunks are located adjacent to the oesophagus; the anterior trunk is constituted mainly from the left vagus nerve and the posterior mainly from the right vagus nerve. The descending thoracic aorta gives off the intercostal arteries (see Fig. 52.3) and the largest anterior segmental medullary artery, the 'great radicular artery of Adamkiewicz' (Yoshioka et al 2003) (see Fig. 47.11).

There are communications between the posterior mediastinum and the abdomen either through, or posterior to, the respiratory diaphragm (Ch. 55). The oesophageal hiatus at the level of the body of the eleventh thoracic vertebra (conventionally reported as at the level of the body of the tenth thoracic vertebra), transmits the oesophagus, anterior and posterior vagal trunks, gastric nerves and oesophageal branches of the left gastric artery. The aortic hiatus at the level of the body of the twelfth thoracic vertebra transmits the aorta, thoracic duct and occasionally the azygos and hemiazygos vein. Apertures within the diaphragmatic crura transmit the thoracic splanchnic nerves; apertures deep to the medial arcuate ligament transmit the sympathetic trunks; minute openings in the central tendon of the respiratory diaphragm transmit small veins. All openings represent potential communication sites for suppurative or neoplastic processes.

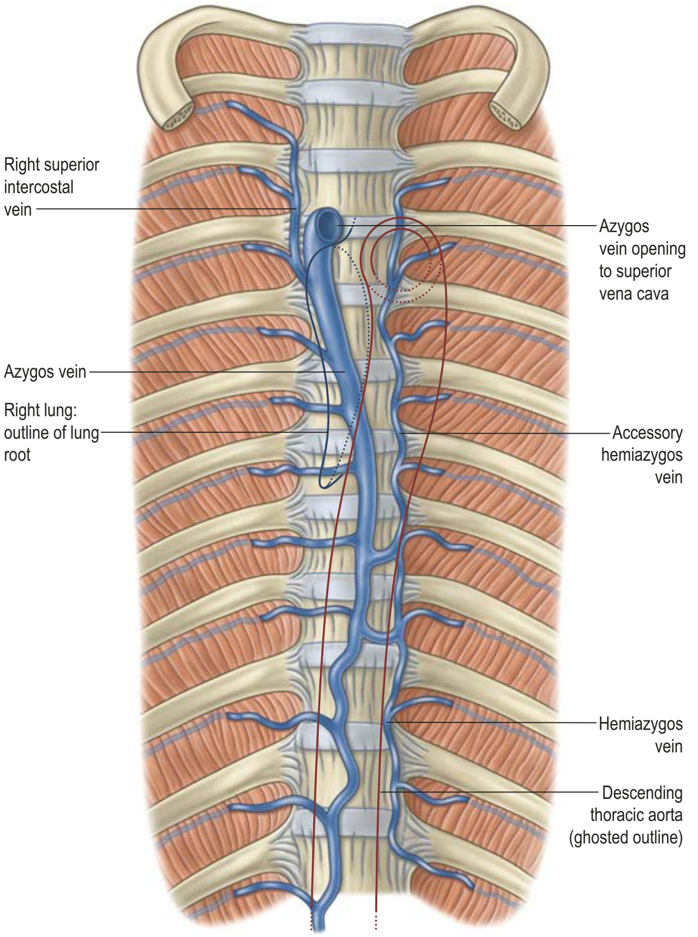
Right superior intercostal vein
Azygos vein opening to superior vena cava
Azygos vein
Right lung: outline of lung root
Accessory hemiazygos vein
Hemiazygos vein
Descending thoracic aorta (ghosted outline)

Fig. 56.2 A typical arrangement of the intrathoracic azygos, hemiazygos and accessory hemiazygos veins. Outlines of the root of the right lung and descending thoracic aorta are included for positional reference.

Mediastinal communications with the neck

Pathways exist between the oral cavity and the mediastinum via the parapharyngeal space and along other fascial planes/spaces of the neck. The parapharyngeal space is more likely to be infected than any of the other potential tissue spaces in the head and neck. It communicates with the retropharyngeal and pretracheal spaces, eventually reaching the superior mediastinum and then the inferior mediastinum (Chs 35, 37, 40). The planes between the buccopharyngeal, alar and prevertebral fasciae, the retropharyngeal and danger spaces, respectively, are a highway for the spread of air and gastric contents between the neck and mediastinum after oesophageal injury (Wind and Valentine 2013). The carotid sheath, containing the carotid arteries, internal jugular veins and vagus nerves, represents another potential route of communication.

Vascular supply and lymphatic drainage

The mediastinum contains the great vessels (ascending aorta, aortic arch and its branches, descending thoracic aorta, superior vena cava and the thoracic part of the inferior vena cava), the pulmonary arteries and veins, the internal thoracic and posterior intercostal arteries and veins, the azygos and hemiazygos venous systems, and the thoracic duct.

Great vessels of the superior mediastinum

The ascending aorta, aortic arch and its branches, descending thoracic aorta, pulmonary trunk and superior vena cava are described in Chapter 58.

Azygos venous system

Azygos vein

The azygos vein has a variable origin at or below the level of the renal veins (**Figs 56.2–56.3**; see Fig. 56.14B). When present, the azygos lumbar vein ascends anterior to the bodies of the upper lumbar vertebrae and passes either posterior to, or through, the right diaphragmatic

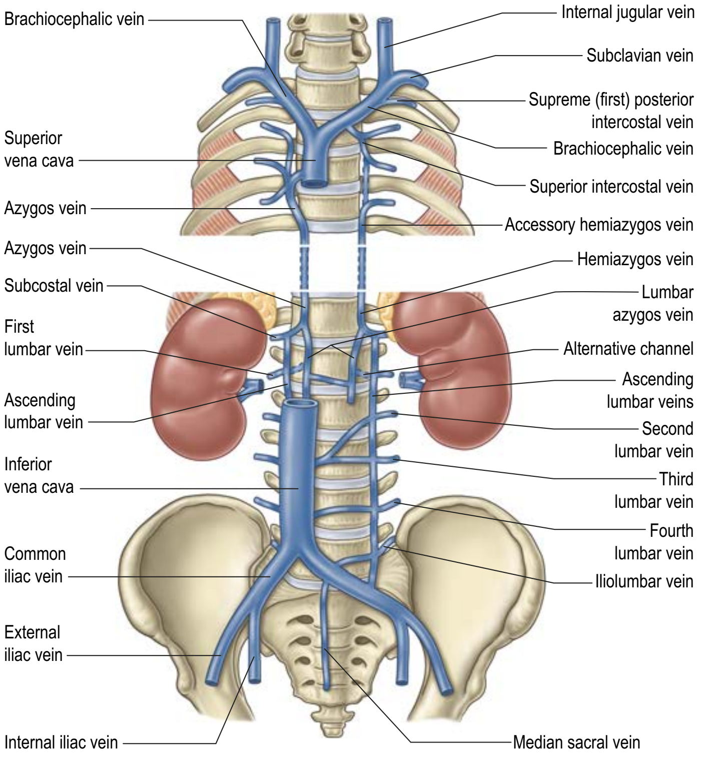

Fig. 56.3 The azygos venous system and its tributaries and connections.

crus or traverses the aortic hiatus to the right of the cisterna chyli. Anterior to the body of the twelfth thoracic vertebra, it is joined by a venous trunk, formed by the union of the right ascending lumbar and subcostal veins, to form the azygos vein. In the absence of a lumbar azygos vein, this common venous trunk continues as the azygos vein. The azygos vein passes to the right, posterior to the right crus of the respiratory diaphragm, and ascends in the posterior mediastinum to the level of the body of the fourth thoracic vertebra, where it arches anteriorly, superior to the right lung hilum and root, and joins the posterior aspect of the superior vena cava, just superior to the point where it passes into the pericardium.

In its course, the azygos vein lies anterior to the anterior longitudinal ligament covering the bodies of the lower eight thoracic vertebrae and the intervening intervertebral discs, and the right posterior intercostal arteries. Right lateral relations include the right sympathetic trunk and associated ganglia, the right greater thoracic splanchnic nerve, the right lung and parietal pleura. Left lateral relations include the thoracic duct, descending thoracic aorta and, where the vein arches anteriorly, the oesophagus, trachea and right vagus nerve. Aortic pulsations may assist venous return in the azygos and hemiazygos veins, although only a small and variable number of imperfect valves are present. Inferiorly, the azygos vein lies posterior to the oesophagus, from which it is separated by a right-sided pleural recess, the azygo-oesophageal recess. There are age-related differences in the appearance of the contour of this recess on computed tomography (CT); the recess is dextroconvex below the age of 6 years, non-concave (equally divided between straight and convex) between 6 and 12 years of age and concave, as seen in adults, after the age of 12 years of age (Miller et al 1993).

The major tributaries of the azygos vein are the right intercostal veins (excluding the right supreme (first) intercostal vein that drains into the right brachiocephalic vein), the right superior intercostal vein (usually formed by the union of the second to fourth intercostal veins), the right ascending lumbar and subcostal veins, mediastinal, oesophageal, superior phrenic, pericardial and right bronchial veins, and the hemiazygos and accessory hemiazygos veins.

Numerous anastomoses exist between the tributaries and the main trunks of the azygos, hemiazygos and accessory hemiazygos veins, the inferior vena cava and the vertebral venous plexuses. These allow for alternate drainage pathways in case of segmental agenesis ('interruption') or thrombosis of the inferior vena cava.

Hemiazygos vein

The hemiazygos vein represents the left-sided equivalent of the more inferior part of the azygos vein. It originates in a similar fashion, from the union of the left lumbar ascending and subcostal veins, but exhibits greater variability, and may also connect with the left renal vein via the equivalent of the lumbar azygos vein. The hemiazygos vein crosses the midline anterior to the body of the eighth or ninth thoracic vertebra, passing posterior to the descending thoracic aorta and oesophagus, and either anterior or posterior to the thoracic duct, to join the azygos vein (see Figs 56.2, 56.5B). It receives mediastinal, oesophageal and the ninth to eleventh left posterior intercostal veins.

Accessory hemiazygos vein

The accessory hemiazygos vein functions as the left-sided mirror image of the superior portion of the azygos vein. It drains the left fifth to eighth posterior intercostal veins and occasionally the left bronchial veins, and usually crosses the midline anterior to the body of the seventh thoracic vertebra to join the azygos vein. The supreme (first) left posterior intercostal vein drains directly into the left brachiocephalic vein, while the second to the fourth may connect indirectly to the accessory hemiazygos vein via the left superior intercostal vein (see Fig. 56.7). The accessory hemiazygos vein typically joins the azygos vein directly, but it can join the hemiazygos vein before draining into the azygos vein. One or more prevertebral transversal anastomoses can be present.

Variations of the azygos venous system

The origin, course, tributaries, anastomoses and termination of the azygos system of veins are all highly variable (Loukas and Tubbs 2016). The arrangement shown in **Fig. 56.2** represents the most common pattern with a right-sided azygos vein. The left-sided hemiazygos vein can be absent or underdeveloped, allowing direct drainage of the left intercostal veins into the azygos vein and/or the termination of the accessory hemiazygos vein into the left brachiocephalic vein either directly or by joining the left superior intercostal vein. In such cases, the azygos vein is located in a median position. In cases of common cardinal or anterior cardinal vein malformation, the azygos vein may enter the right atrium, right brachiocephalic vein or right subclavian vein rather than joining the superior vena cava.

Internal thoracic arteries and veins

The internal thoracic vessels are described in Chapter 53.

Pulmonary arteries and veins

The pulmonary vessels are described in Chapter 54.

Posterior intercostal arteries and veins

The posterior intercostal veins accompany their arteries in 11 pairs; they are described in Chapter 53.

Mediastinal lymph nodes

There are multiple groups of lymph nodes throughout the mediastinum. Conventionally they have been named according to the nearest mediastinal viscera or structure (which they often drain): parietal node groups drain the thoracic wall and visceral groups drain the thoracic viscera (**Fig. 56.4A**). However, this naming system implies that the mediastinal node groups are separate and distinct, whereas in reality they are part of a continuum. To better reflect their regional disposition, and for the purposes of cancer staging and management, mediastinal lymph node groups are best categorized into regional lymph node stations and zones (Rusch et al 2009) (see Fig. 54.12B, **Fig. 56.4B**, **Table 56.1**).

Pulmonary nodes within the lung parenchyma are continuous with the bronchopulmonary node groups (in order, these include subsegmental, segmental, lobar, interlobar and hilar nodes) (see Figs 56.4B, 54.12). Bronchopulmonary node groups are continuous with subcarinal (inferior tracheobronchial) nodes located inferior to the tracheal bifurcation and the lower paratracheal (superior tracheobronchial) nodes. In turn, these groups are continuous with the upper paratracheal groups of nodes that drain the lungs, bronchi, the thoracic part of the trachea, heart, pericardium and also receive efferent vessels from prevertebral nodes that receive lymph from the posterior respiratory diaphragm, thoracic oesophagus and intercostal lymph nodes. Efferent vessels ascend on the trachea to unite with efferents from the parasternal and brachiocephalic nodes to become the right and left bronchomediastinal trunks. The right trunk may occasionally join a right lymphatic duct or another right-sided lymph trunk, and the left trunk may join the thoracic duct, but usually they open independently in or near the ipsilateral junction of the internal jugular and subclavian vein (see Fig. 35.16).

Mediastinoscopy

Available with the *Gray's Anatomy* e-book

In congenital interruption of the inferior vena cava or acquired thrombosis, the azygos system provides an alternative pathway for venous drainage. A higher than usual azygos arch may travel over the apical region of the right superior lobe within an accessory azygos fissure, covered by four pleural layers (two parietal and two visceral), and isolate a portion of the superior lobe of the right lung medially: the 'azygos lobe' (Loukas and Tubbs 2016). If present, the azygos fissure can be identified on chest radiograph as a fine radiopaque line. The azygos vein located within the azygos fissure often presents as a lung 'pseudonodule' on a chest radiograph; it is typically comma-shaped and should not be confused with a more rounded appearance of early lung carcinoma or metastasis.

Metastatic involvement of mediastinal lymph nodes has important prognostic implications and influences the choice of treatment (Mountain and Dresler 1997, Rusch et al 2009). The staging system for lung cancer classifies node involvement using a nodal descriptor (N-'Stage'), where N0 indicates no regional lymph node metastases; N1 indicates involvement of ipsilateral peribronchial or hilar lymph nodes and intrapulmonary nodes; N2 indicates involvement of ipsilateral mediastinal and/or subcarinal nodes; and N3 indicates involvement of contralateral mediastinal or hilar nodes, and ipsilateral or contralateral scalene or supraclavicular nodes/scalene nodes (Goldstraw et al 2016, Chansky et al 2017, Lim et al 2018).

The decision to proceed with mediastinoscopic biopsy depends on whether suitable nodal stations (zones) seem involved on CT scanning and whether there is a history of prior neck and mediastinal surgical procedures. Complications of mediastinoscopy include haemorrhage, iatrogenic injury to the trachea or left recurrent laryngeal nerve and pneumothorax. Mediastinoscopy can be performed with video-assisted or direct optic visualization. A transverse incision is made at the level of the jugular (suprasternal) notch; sternohyoid and sternothyroid muscles within the superficial lamina of deep cervical fascia are retracted; the deep lamina of the deep cervical fascia is incised. The pretracheal plane is dissected and a space is created between the anterior aspect of the trachea and the brachiocephalic trunk inferior to the carina and along both sides of the trachea and main bronchi. This space facilitates biopsy of the upper paratracheal 2R and 2L stations, the right lower paratracheal 4R station and higher nodes from the left lower paratracheal 4L station superior to the aortic arch (see Fig. 54.12B; Table 56.1). The anterior part of subcarinal station 7 and bilateral hilar stations 10R and 10L may be accessible but are technically challenging. Lymph nodes can be sampled or removed entirely for histological evaluation.

The anterior part of the superior mediastinum is more difficult to assess by mediastinoscopy and usually requires an anterior mediastinotomy (Chamberlain procedure). This is performed to biopsy nodes from the more inferior aspect of the left lower paratracheal 4L station, subaortic station 5, para-aortic station 6 and subcarinal station 7, and also facilitates anterior mediastinal mass biopsy. Endobronchial ultrasound can be performed to biopsy lymph nodes in stations 1–4, 7 and 10–12, using fine needle aspiration through the tracheal or bronchial walls. In a similar way, transoesophageal ultrasound may help during biopsy of subcarinal station 7, para-oesophageal station 8 and pulmonary ligament station 9 nodes.

A video demonstrating lymph node dissection via mediastinoscopy can be seen in Rami-Porta (2012). A video demonstrating mediastinal lymph node dissection via tracheo-oesophageal mediastinoscopy can be seen in Turner (2010).

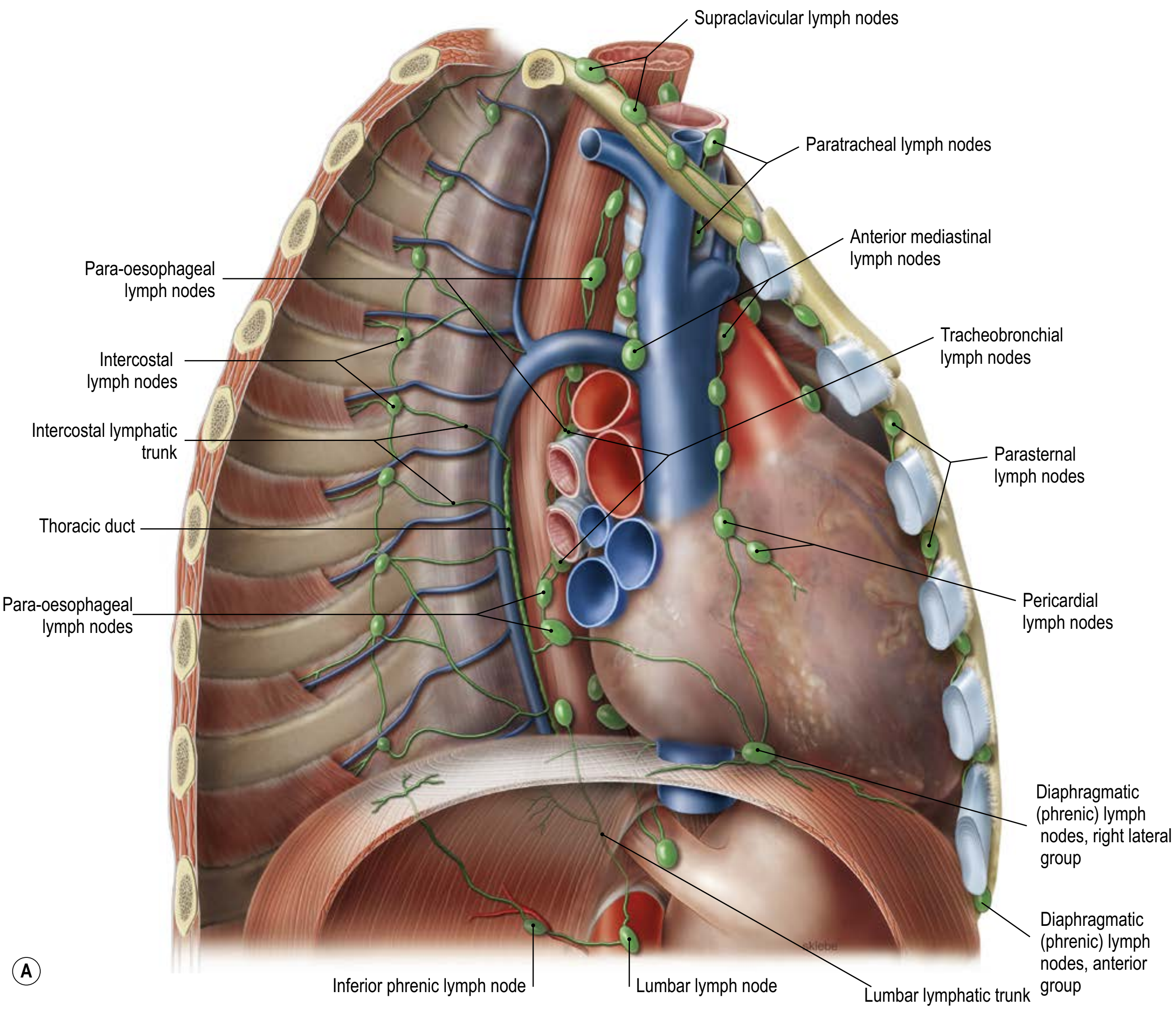
Supraclavicular lymph nodes
Paratracheal lymph nodes
Anterior mediastinal lymph nodes
Tracheobronchial lymph nodes
Parasternal lymph nodes
Pericardial lymph nodes
Diaphragmatic (phrenic) lymph nodes, right lateral group
Diaphragmatic (phrenic) lymph nodes, anterior group
Para-oesophageal lymph nodes
Intercostal lymph nodes
Intercostal lymphatic trunk
Thoracic duct
Para-oesophageal lymph nodes
A
Inferior phrenic lymph node
Lumbar lymph node
Lumbar lymphatic trunk

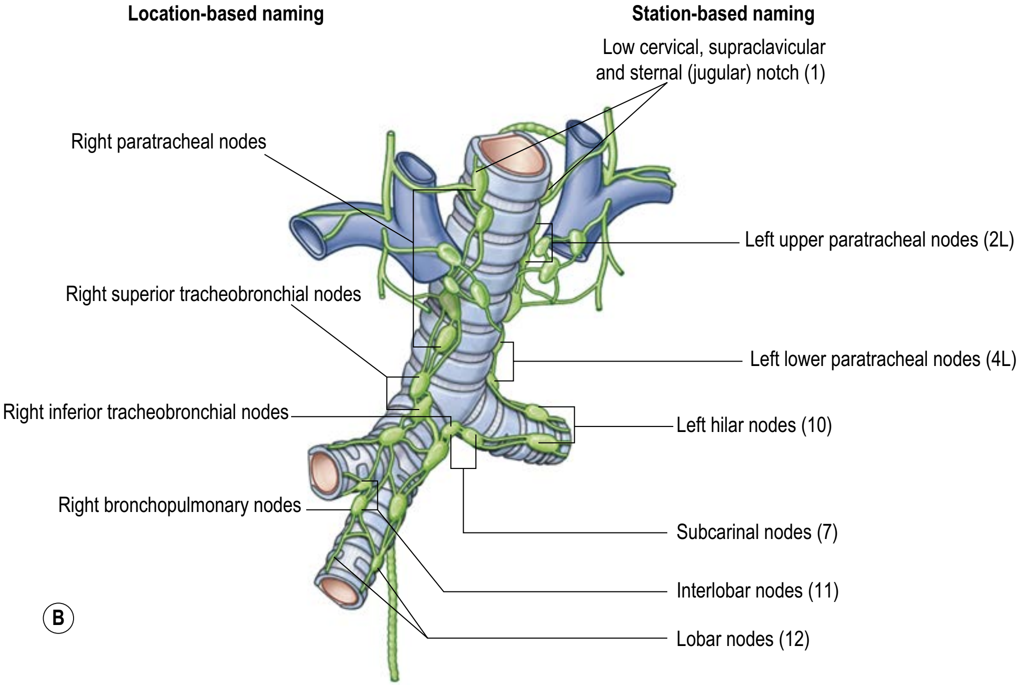
Location-based naming
Station-based naming
Low cervical, supraclavicular and sternal (jugular) notch (1)
Right paratracheal nodes
Left upper paratracheal nodes (2L)
Right superior tracheobronchial nodes
Left lower paratracheal nodes (4L)
Right inferior tracheobronchial nodes
Left hilar nodes (10)
Right bronchopulmonary nodes
Subcarinal nodes (7)
Interlobar nodes (11)
Lobar nodes (12)
B

Fig. 56.4 Mediastinal lymph node groups. **A**, The general disposition of the mediastinal lymph nodes, right lateral view. **B**, Lymph nodes and vessels of the tracheobronchial tree. Lymph node groups named according to their location are shown on the right side of the specimen and lymph node station-based names and numbers on the left side. (A, Sobotta Atlas of Human Anatomy © Elsevier GmbH, Urban & Fischer, Munich. B, Adapted with permission from Drake RL, Vogl AW, Mitchell A et al (eds) Gray's Atlas of Anatomy, 2nd ed. Elsevier, Churchill Livingstone. Copyright 2015.)

TABLE 56.1 Classification of regional mediastinal lymph nodes into regional lymph node stations/zones (for detail see Rusch et al 2009)

Nodes	Zone	Station	
	Supraclavicular	1	Low cervical, supraclavicular and sternal (jugular) notch
Superior mediastinal	Upper	2R	Upper paratracheal (right)
		2L	Upper paratracheal (left)
		3a	Prevascular
		3p	Retrotracheal
		4R	Lower paratracheal (right)
		4L	Lower paratracheal (left)
Aortic	Aorticopulmonary	5	Subaortic
		6	Para-aortic (ascending aorta or phrenic)
Inferior mediastinal	Subcarinal	7	Subcarinal
	Lower	8	Para-oesophageal (below carina)
		9	Pulmonary ligament
N1	Hilar/interlobar	10	Hilar
		11	Interlobar
	Peripheral	12	Lobar
		13	Segmental
		14	Subsegmental

THORACIC DUCT

The thoracic duct conveys the lymph from the majority of the entire body back to the venous circulation, except lymph from the right part of the head, neck and heart, right upper limb, parts of the left and right lung and part of the convex surface of the liver. It usually originates anterior to the body of the first or second lumbar vertebra, where the intestinal and two lumbar lymphatic trunks join to form the cisterna chyli. Both the thoracic duct and the cisterna chyli are variable in their origin, course and length; the latter is even more variable in width and shape than the thoracic duct (Song 2016). From the superior aspect of the cisterna chyli, the thoracic duct passes through the aortic hiatus and enters the posterior mediastinum, lying to the right of the midline, between the descending thoracic aorta and the azygos vein, up to the level of the body of the fifth or sixth thoracic vertebra, where it typically passes to the left, over the vertebral column and posterior to the oesophagus (see Fig. 56.7B). It may branch or even have duplicate trunks that eventually form a single thoracic duct (Song 2016). It continues superiorly, first posterior to the aortic arch adjacent to the left side of the oesophagus, then posterior to the left subclavian artery in the superior mediastinum. It subsequently arches over the left subclavian artery and descends anteriorly to empty into the venous circulation in the region of the left internal jugular and subclavian veins, either at their very confluence or in proximity, or sometimes into the left brachiocephalic vein (**Fig. 56.5**). In the space between longus colli, scalenus anterior and the suprapleural membrane, the duct usually arches 3–4 cm superior to the clavicle, crossing anterior to the vertebral vessels, the left sympathetic trunk, the vertebral sympathetic ganglion, the left thyrocervical trunk and the left phrenic nerve. The course and position of the thoracic duct determines the location of the effusion seen with duct injury or obstruction.

Two thoracic ducts are sometimes present within the mediastinum and may terminate in veins on their respective side of the body. Occasionally a single thoracic duct may empty into right-sided venous structures, a disposition that is more frequent in individuals with an aberrant right subclavian artery originating from the distal aortic arch and ascending posterior to the oesophagus.

The thoracic duct is commonly 36–45 cm in length, its external diameter varies according to region (Song 2016). When present as a single channel it is 5–8 mm in diameter at its origin, narrows to 2–3 mm at mid-thoracic level and then widens again at its termination: the diameter may fluctuate with lymph flow rate (Smith et al 2013). Alternatively, the thoracic duct may divide into two or three branches that eventually reunite or drain into both the left and right venous systems. The duct appears sinuous and has valves throughout its length; a bicuspid valve at its termination may prevent the backflow of blood. As it passes through the mediastinum, the thoracic duct also receives non-chylous lymph from tributaries that drain regions of the pulmonary parenchyma and parietal pleura. The sum of these sources accounts for a total lymphatic flow through the thoracic duct of 1500–2400 ml per day in proportion to the dietary intake of fat, particularly long-chain triglycerides.

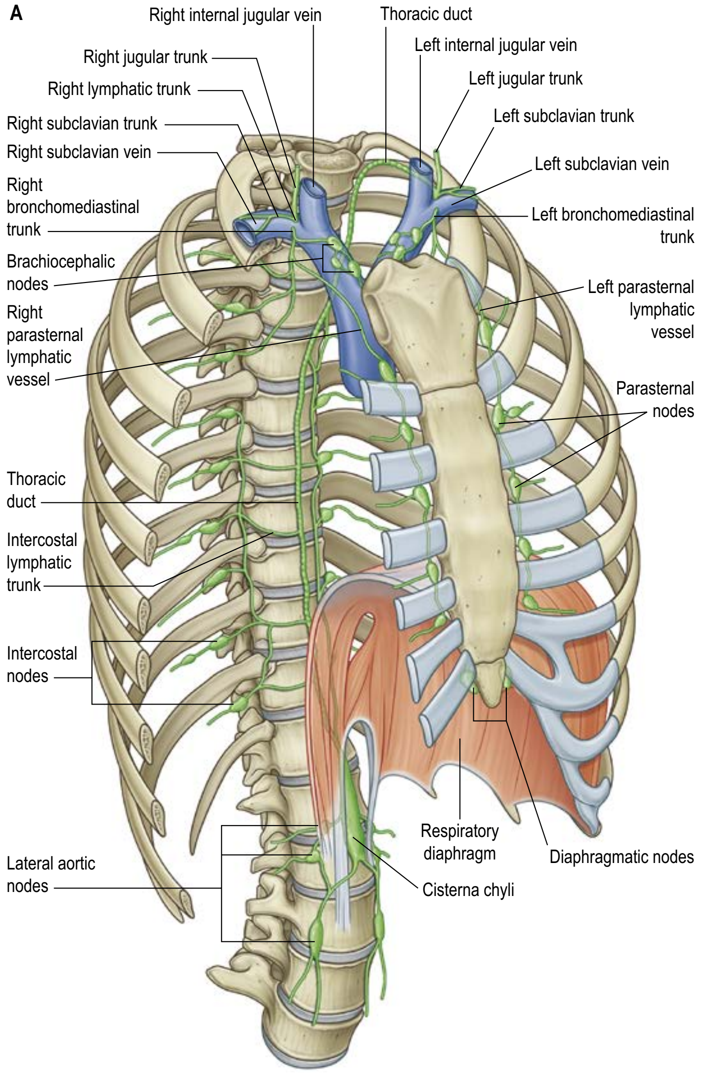

Fig. 56.5 The thoracic and right lymphatic ducts, and their tributaries. **A**, Major lymph nodes and vessels of the thoracic wall, and the termination of the lymphatic trunks. (B, *continued online*)

Tributaries of the thoracic duct

Some tributaries of the thoracic duct may terminate directly in the venous system. There are numerous anastomoses between visceral, parietal, limb and mammary lymphatics, as is apparent from observed multiple patterns of dissemination of cancer cells (see Figs 56.4–56.5). As well as the cisterna chyli and its tributaries, bilateral ascending lumbar lymphatic trunks from the upper lateral aortic (abdominal part) nodes pierce the corresponding diaphragmatic crus and eventually join the thoracic duct in the posterior mediastinum. The inferior six or seven intercostal lymphatic trunks from the corresponding bilateral intercostal nodes descend to terminate in the duct, either directly or by variable common trunks. The left upper intercostal lymphatics may join the cervical portion of the duct or the subclavian trunk. The left subclavian trunk usually joins the thoracic duct but may open independently into the left subclavian vein. These mediastinal trunks provide lymph drainage paths to the thoracic duct from the convex diaphragmatic aspect of the liver, the respiratory diaphragm, the pericardium, heart and oesophagus; many possess terminal bicuspid valves. The left bronchomediastinal trunk occasionally joins the thoracic duct but usually has an independent venous termination. The left jugular trunk usually joins the thoracic duct but may open independently into the left internal jugular vein (see Fig. 35.16).

Injury during oesophageal surgery

Available with the *Gray's Anatomy* e-book

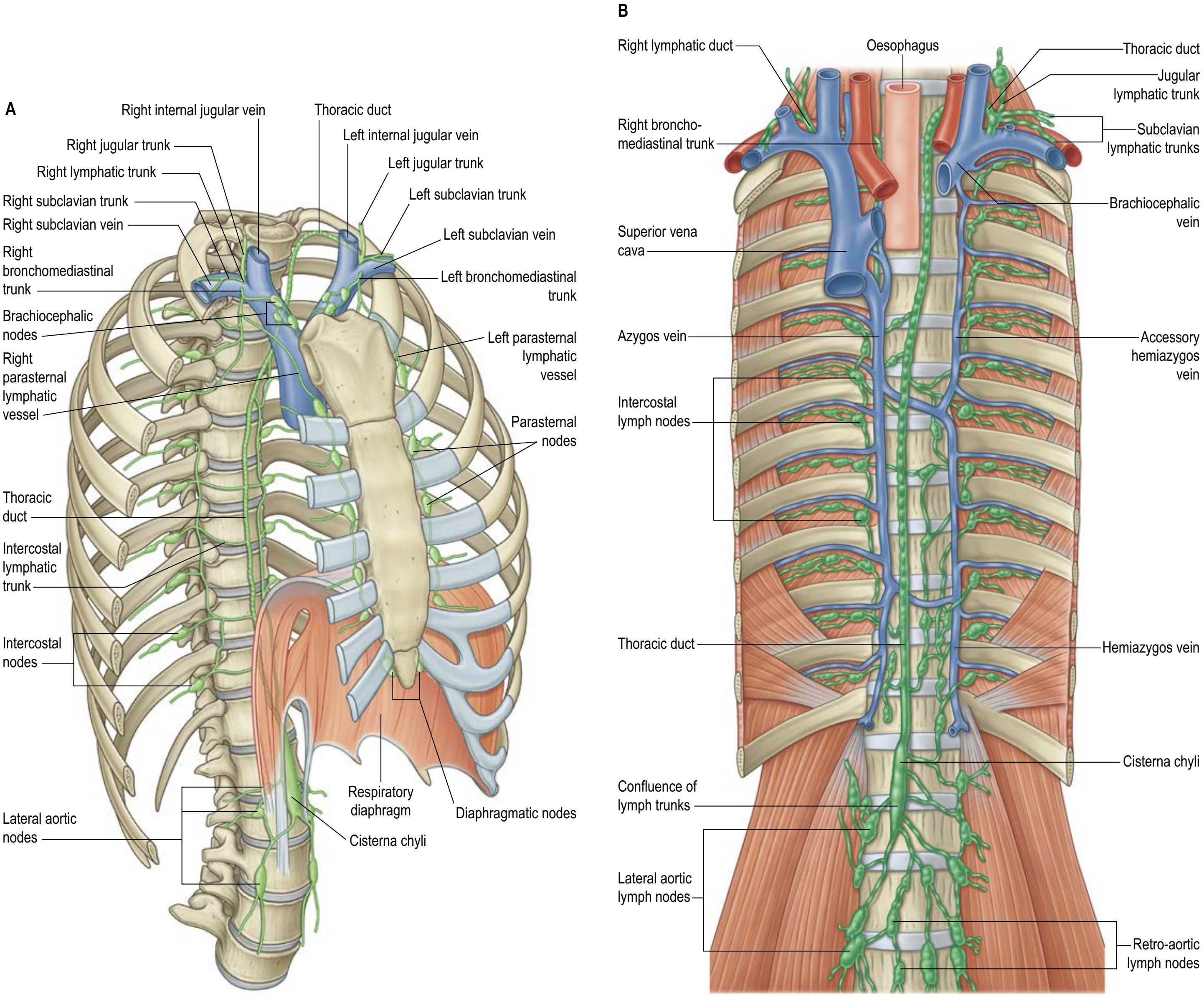
A
Right internal jugular vein
Thoracic duct
Left internal jugular vein
Right jugular trunk
Left jugular trunk
Right lymphatic trunk
Left subclavian trunk
Right subclavian trunk
Right subclavian vein
Left subclavian vein
Right bronchomediastinal trunk
Left bronchomediastinal trunk
Brachiocephalic nodes
Left parasternal lymphatic vessel
Right parasternal lymphatic vessel
Parasternal nodes
Thoracic duct
Intercostal lymphatic trunk
Intercostal nodes
Lateral aortic nodes
Respiratory diaphragm
Cisterna chyli
Diaphragmatic nodes
B
Right lymphatic duct
Oesophagus
Thoracic duct
Jugular lymphatic trunk
Right broncho-mediastinal trunk
Subclavian lymphatic trunks
Brachiocephalic vein
Superior vena cava
Azygos vein
Accessory hemiazygos vein
Intercostal lymph nodes
Thoracic duct
Hemiazygos vein
Cisterna chyli
Confluence of lymph trunks
Lateral aortic lymph nodes
Retro-aortic lymph nodes

Fig. 56.5 The thoracic and right lymphatic ducts, and their tributaries. **A**, Major lymph nodes and vessels of the thoracic wall, and the termination of the lymphatic trunks. **B**, Anterior view with the major proximal vascular relations *in situ*. Note that the accessory hemiazygos vein is crossing the median plane lower and the hemiazygos higher than typically found. (A, Adapted with permission from Drake RL, Vogl AW, Mitchell A et al (eds) Gray's Atlas of Anatomy, 2nd ed. Elsevier, Churchill Livingstone. Copyright 2015.)

The thoracic duct crosses the mediastinum at, or at about, the level of the body of the fifth thoracic vertebra which means that lymphatic injury or obstruction above or below this level results in a left- or right-sided pleural effusion (chylothorax), respectively (Doerr et al 2001). Anomalies and sites of injury to the duct are identified by lymphangiography, with or without post-procedure CT scanning, or lymphoscintigraphy. Lymphangiography is performed after bilateral localization of pedal lymphatics with a subcutaneous injection of methylene blue, followed by a minor surgical procedure to cannulate the lymphatic vessels, and injection of Lipiodol contrast agent. Conventional X-ray and CT imaging (without intravenous contrast) are then undertaken. Lymphangiography can identify areas of chyle leakage and lymphangiectasia in the majority of patients (Deso et al 2012).

Ligation of the thoracic duct via thoracoscopic surgery can be seen in Devulapalli (2016).

The variable origin, course and length of the thoracic duct, coupled with a failure to identify it during surgery, may lead to inadvertent incision or transection, particularly during trans-hiatal and thoracoscopic oesophageal surgery, with an incidence of 0.2–3% (Wemyss-Holden et al 2001). Thoracic duct laceration is a potentially life-threatening complication; mortality rates are higher with conservative management but remain elevated even after surgical ligation. Rupture of the thoracic duct leads to leakage of chyle, which is rich in lipid, protein, T lymphocytes (ranging from 400 to 6800 cells/μl), immunoglobulins and fat-soluble vitamins, and hence a progressive nutritional and immune deficit develops. Postoperative chylous effusions are usually the result of damage to ductal tributaries rather than to the duct itself, and are usually self-limiting. The greater incidence of injury with trans-hiatal resection may be attributable to shear forces exerted around the region of the duct during the mobilization of the distal oesophagus, whereas the limited field of view probably contributes to the greater incidence of thoracic duct injury during thoracoscopic surgery. Injury should be suspected in the postoperative period if there is either an enlarging mediastinal silhouette on serial chest radiographs or a significant drainage of milky looking fluid from chest or abdominal drains. An electrophoretic confirmation of the presence of chylomicrons in the pleural fluid is diagnostic amongst other tests. The thoracic duct may be injured during the left cervical approach for the exposure of the vertebral and subclavian arteries or the cervicothoracic (stellate) sympathetic ganglion. However, deliberate ligation of the duct at this level represents an accepted surgical manoeuvre with no particular consequences.

RIGHT LYMPHATIC TRUNK

The right lymphatic trunk has a variable anatomy (see Figs 56.5, 35.16). Its three main tributaries, the right jugular, subclavian and bronchomediastinal trunks, often empty separately into either the right internal jugular and/or subclavian veins. In up to 20% of individuals, they may aggregate to form the right lymphatic trunk that is usually 5–10 mm in length. The terminal portions of the right lymphatic trunk and of the thoracic duct are concealed by the scalene fat pad, rendering them more vulnerable during surgery.

AUTONOMIC NERVOUS SYSTEM

The thoracic autonomic nervous system consists of the right and left sympathetic trunks and associated ganglia, the vagus nerves, and the cardiac, pulmonary and oesophageal plexuses. The cardiac plexus is described in Chapter 57, the pulmonary plexus in Chapter 54, and the oesophageal plexus is described below.

Thoracic sympathetic trunk

The thoracic sympathetic trunks have ganglia that are almost equal in number to those of the thoracic spinal nerves (usually 11, occasionally 12, rarely 10 or 13), with which they are associated (**Figs 56.6–56.7**). Almost always, the first thoracic ganglion is fused with the inferior cervical ganglion, forming the cervicothoracic (stellate) ganglion; occasionally, the second thoracic ganglion is included in this fusion (Irwin et al 2016). The thoracic ganglia sit posterior to the costal part of the parietal pleura and except for the second and lowest two or three, they lie anterior to the heads of the ribs. The second thoracic sympathetic ganglion is commonly located in the second intercostal space, and the lowest two or three thoracic ganglia lie lateral to the bodies of the correspondingly numbered vertebrae. Inferiorly, the thoracic sympathetic trunks pass posterior to the medial arcuate ligament or through the ipsilateral diaphragmatic crus to become the lumbar sympathetic trunks.

The ganglia are relatively small and interconnected by intervening segments of the trunk. The classic description is that two or more rami communicantes, white (myelinated, preganglionic) and grey (unmyelinated, postganglionic), connect each ganglion with its corresponding spinal nerve, the white rami connecting with the spinal nerve distal to the grey. Variation in this pattern is common, especially at the upper thoracic levels and symmetry is rarely seen. Additional ascending and descending rami communicantes may emerge from the second (54% and 46%, respectively), third (6% and 25%) and fourth ganglia (5% and 8%) (Cho et al 2005). Occasionally, a grey and a white ramus fuse to form a 'mixed' ramus. An intrathoracic ramus may join the second intercostal nerve to the ventral ramus of the first thoracic spinal nerve proximal to the point where the latter sends a large branch to the brachial plexus (Kuntz 1927). This intrathoracic nerve of Kuntz is thought to carry sympathetic nerve fibres to the brachial plexus without passing through the sympathetic trunk and has been held responsible for the recurrence of symptoms following surgical sympathectomy. The anatomical variation exhibited by the rami communicantes and the location of the second sympathetic ganglion may also contribute to post-surgical symptom recurrence.

The medial branches from the upper five thoracic ganglia are very small and may supply nerve fibres in a retrograde manner to the thoracic parts of the aorta and its branches as they pass to the cardiac plexuses (Kawashima 2011). Rami of the second to fifth or sixth ganglia enter the posterior pulmonary plexus. Small branches from the pulmonary and cardiac nerves pass to the oesophagus and trachea. The larger medial branches from the lower seven ganglia supply the descending thoracic aorta and then unite to form the greater, lesser and least thoracic splanchnic nerves. The thoracic splanchnic nerves are variable in origin and presence (Irwin et al 2016); the greater thoracic splanchnic nerve is always present, the lesser is usually present and the least is often absent. A fourth (accessory) thoracic splanchnic nerve has been described.

The greater thoracic splanchnic nerve consists mainly of myelinated preganglionic efferent and visceral afferent nerve fibres. It is usually described as being formed by branches from the fifth to ninth or tenth thoracic sympathetic ganglia, but most commonly it originates from the seventh to the ninth thoracic sympathetic ganglia. Its roots vary in number from three to ten. It descends obliquely along the vertebral bodies and intervening intervertebral discs, sends branches to the descending thoracic aorta, and perforates the ipsilateral diaphragmatic crus to terminate mainly in the coeliac but also in the aorticorenal ganglion and suprarenal (adrenal) gland. A thoracic splanchnic ganglion is present on the nerve opposite the body of the eleventh or twelfth thoracic vertebra in most individuals. The lesser thoracic splanchnic nerve is formed commonly by rami of the ninth and tenth thoracic sympathetic ganglia (range, ninth to twelfth). It pierces the respiratory diaphragm with the greater thoracic splanchnic nerve, which it may join, and terminates in the aorticorenal ganglion. The least thoracic splanchnic nerve (or renal nerve) from the lowest thoracic sympathetic ganglion enters the abdomen with the sympathetic trunk and terminates in the renal plexus. Some nerve fibres from the greater thoracic splanchnic and vagus nerves form a fine web-like thoracic aortic plexus.

Thoracic sympathectomy

Endoscopic thoracic sympathectomy (ETS) is a surgical procedure used to relieve the symptoms of craniofacial, palmar or axillary hyperhidrosis, facial blushing and Raynaud's disease with digital ulcers.

Vagus nerve in the mediastinum

The vagus nerve contains branchiomotor, general visceral afferent and preganglionic parasympathetic nerve fibres. The proportion of efferent parasympathetic nerve fibres in the vagus nerve varies at different levels but is small relative to its sensory and sensorimotor content. The branchiomotor fibres arise from neurones in the nucleus ambiguus in the medulla oblongata and are distributed to the constrictor muscles of the pharynx and the intrinsic muscles of the larynx. The general visceral afferent fibres carry sensation from thoracic and abdominal viscera and from aortic arch baroreceptors and chemoreceptors and end in the caudal part of the nucleus solitarius of the medulla oblongata. The preganglionic parasympathetic nerves arise from cell bodies in the vagal dorsal nucleus in the medulla oblongata, travel in the nerve and in its pulmonary, cardiac, oesophageal, gastric and intestinal branches and synapse in minute ganglia in the visceral walls (see Fig. 56.6) (Mussa and Verberne 2013). Pulmonary branches contain axons that synapse in ganglia of the pulmonary plexuses: they are motor (bronchoconstrictor) to the circular non-striated muscle fibres of the bronchi and bronchioles (and therefore bring about bronchoconstriction), and secretomotor to the mucous glands of the respiratory epithelium. Cardiac branches join the cardiac plexuses and synapse in ganglia that are distributed freely over both atria in the subepicardial tissue. Postganglionic fibres are distributed to the atria and the atrioventricular bundle and are concentrated around the sinuatrial and, to a lesser extent, the atrioventricular nodes (Ch. 57). Cardiac branches slow the heart rate and diminish the force of contraction and may indirectly influence ventricular muscle via their effect on the atrioventricular node. The direct postganglionic parasympathetic innervation of the ventricles is sparse. The smaller branches of the coronary arteries are innervated mainly by parasympathetic vagal neurones, whereas the larger arteries are innervated mainly by sympathetic neurones.

Right vagus nerve

The right vagus nerve descends posterior to the right internal jugular vein in the neck and crosses anterior to the first part of the right subclavian artery to enter the thorax; the ansa subclavia is lateral, and the phrenic nerve is further lateral (see Fig. 55.10A). After giving off the right recurrent laryngeal nerve, it descends through the superior mediastinum, at first posterior to the right brachiocephalic vein, and then lateral to the trachea and posteromedial to the superior vena cava. Superiorly, the right mediastinal part of the parietal pleura and superior lobe of the right lung are lateral; inferiorly, the azygos vein and its arching terminal portion separate the right vagus nerve from the mediastinal parietal pleura (see Fig. 56.7A). The nerve next passes posterior to the right main bronchus and lies on the posterior aspect of the right lung root/hilum. Here, it gives off posterior bronchial branches that unite

ETS may be beneficial to ameliorate cerebral vascularization in patients with moyamoya disease and to treat migraine, hyperactive bronchial states, long QT syndrome, causalgic pain, erythromelalgia, Buerger's disease, Prinzmetal's angina, and chronic non-infectious rhinitis. ETS is also effective in frostbite injury, especially if performed within 36–72 hours of cold exposure.

The operation involves making tiny incisions posterior to the anterior axillary (pectoral) fold in the axilla, and insufflating a small amount of carbon dioxide into the thoracic cavity to allow access with a modified thoracoscope. In the treatment of facial blushing, it is sufficient to divide the nerve fibres that run superiorly from the second thoracic ganglion over the neck of the second rib, leaving the second ganglion almost intact. Treatment of palmar hyperhidrosis requires ablation thermocoagulation of the sympathetic trunk over the necks of the third and fourth ribs, taking care to avoid any spreading of thermal energy along the trunk in order to avoid damaging the more superior stellate ganglion (see Horner's syndrome below). The risk of compensatory sweating is greatly reduced, though not completely excluded, by limiting the number of ganglia treated to an absolute minimum. As an additional procedure, dividing the inconstant sympathetic pathways (nerve of Kuntz, ascending or descending additional rami communicantes) on the second, third and fourth ribs may improve surgical outcomes. The effect is immediately evident: the patient awakes from anaesthesia with dry, warm hands. In many cases, even hyperhidrosis of the feet improves, but the underlying anatomical and physiological mechanisms are not yet properly understood (Gofeld and Faclier 2006). Surgical complications are rare; Horner's syndrome is of most concern, and is caused by damage to the stellate ganglion and interruption of the sympathetic nerve fibres from the ventral rami of spinal nerves C8–T1 that ascend around the arteries supplying the head and neck (see Fig. 35.18). Side-effects include compensatory sweating (ranging from barely noticeable to profuse) in other locations of the body during exercise or from exposure to high temperatures in up to 70% of patients. Compensatory sweating is severe in 5% of patients, and may be more frequent in those with axillary hyperhidrosis when two more inferior ganglia have to be divided: for this reason, some surgeons do not now consider isolated axillary hyperhidrosis as an indication for this procedure. Gustatory or olfactory sweating may also occur in up to one-third of patients but is rarely considered a problem. Other documented side-effects are the inability to raise the heart rate during increased physical strain/load: in some cases, this has led to decreased ability to perform work and daily activities. Patients can also experience an uncomfortable sensation of not being able to control their body temperature.

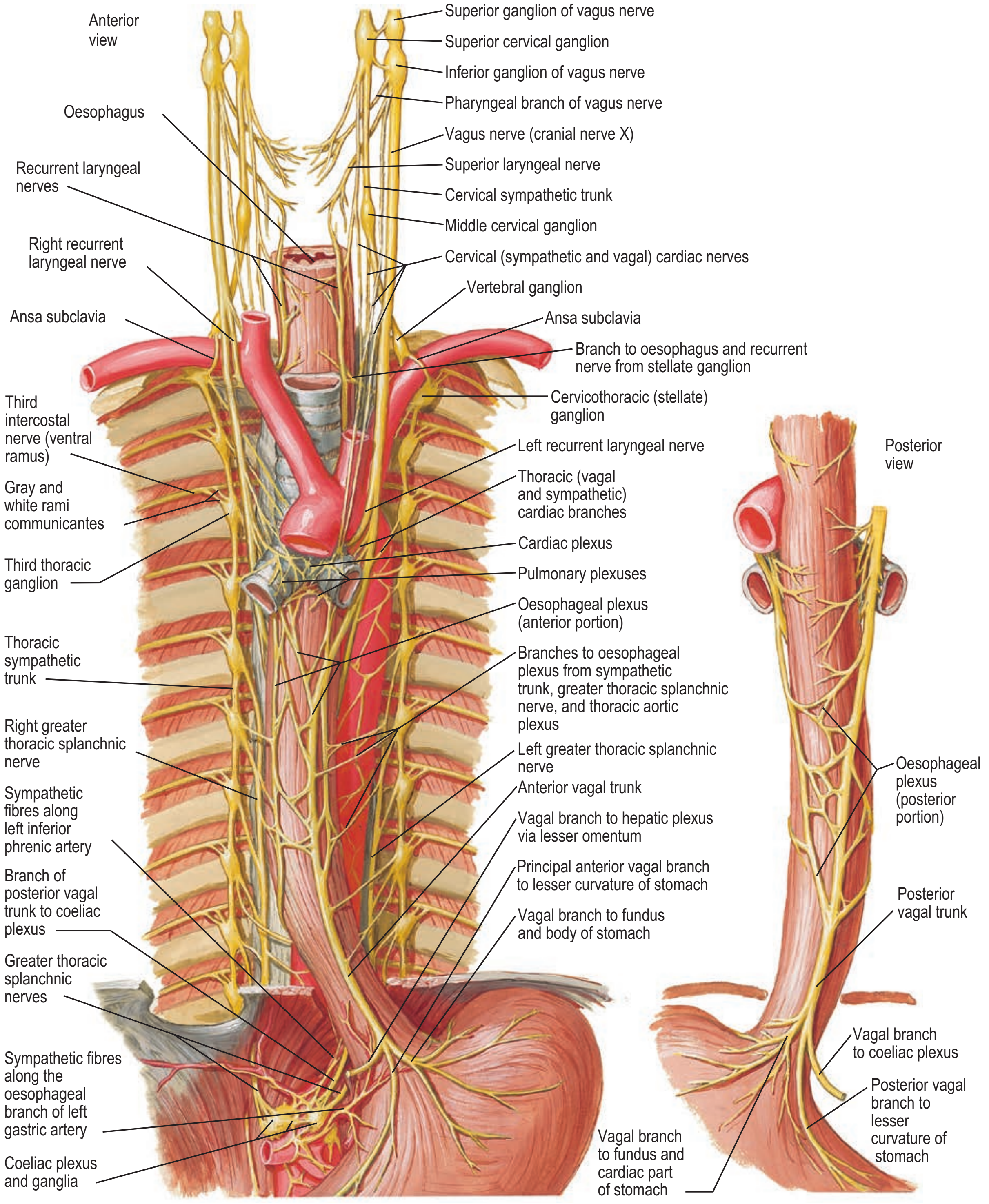
Anterior view
Oesophagus
Recurrent laryngeal nerves
Right recurrent laryngeal nerve
Ansa subclavia
Third intercostal nerve (ventral ramus)
Gray and white rami communicantes
Third thoracic ganglion
Thoracic sympathetic trunk
Right greater thoracic splanchnic nerve
Sympathetic fibres along left inferior phrenic artery
Branch of posterior vagal trunk to coeliac plexus
Greater thoracic splanchnic nerves
Sympathetic fibres along the oesophageal branch of left gastric artery
Coeliac plexus and ganglia
Superior ganglion of vagus nerve
Superior cervical ganglion
Inferior ganglion of vagus nerve
Pharyngeal branch of vagus nerve
Vagus nerve (cranial nerve X)
Superior laryngeal nerve
Cervical sympathetic trunk
Middle cervical ganglion
Cervical (sympathetic and vagal) cardiac nerves
Vertebral ganglion
Ansa subclavia
Branch to oesophagus and recurrent nerve from stellate ganglion
Cervicothoracic (stellate) ganglion
Left recurrent laryngeal nerve
Thoracic (vagal and sympathetic) cardiac branches
Cardiac plexus
Pulmonary plexuses
Oesophageal plexus (anterior portion)
Branches to oesophageal plexus from sympathetic trunk, greater thoracic splanchnic nerve, and thoracic aortic plexus
Left greater thoracic splanchnic nerve
Anterior vagal trunk
Vagal branch to hepatic plexus via lesser omentum
Principal anterior vagal branch to lesser curvature of stomach
Vagal branch to fundus and body of stomach
Vagal branch to fundus and cardiac part of stomach
Posterior view
Oesophageal plexus (posterior portion)
Posterior vagal trunk
Vagal branch to coeliac plexus
Posterior vagal branch to lesser curvature of stomach

Fig. 56.6 The thoracic autonomic nervous system. (Adapted with permission from Netter FH Atlas of Human Anatomy, 7th ed. Elsevier. Copyright 2019.)

with rami from the second to fifth/sixth thoracic sympathetic ganglia to form the right posterior pulmonary plexus. Two or three branches descend from the inferior part of this plexus on the posterior aspect of the oesophagus to join a left vagal branch and form the posterior oesophageal plexus. The posterior vagal trunk, containing nerve fibres from both vagus nerves, leaves the plexus and passes inferiorly on the posterior surface of the oesophagus, entering the abdomen by passing through the oesophageal hiatus in the respiratory diaphragm (see Fig. 55.6).

Left vagus nerve

The left vagus nerve enters the thorax posterior to the left brachiocephalic vein, between the left common carotid artery (anterior) and left subclavian artery (posterior) (see Fig. 55.10B). It descends through the superior mediastinum, crosses the left side of the aortic arch, gives off the left recurrent laryngeal nerve and then passes posterior to the left lung root/hilum (see Fig. 56.7B). Superior to the aortic arch, it is crossed anterolaterally by the left phrenic nerve, and on the aortic arch, it is crossed laterally by the left superior intercostal vein and sometimes by a continuation of the accessory hemiazygos vein. Posterior to the hilum of the left lung, the left vagus nerve gives off posterior bronchial branches that unite with rami of the second to fourth thoracic sympathetic ganglia to form the left posterior pulmonary plexus. Two or three branches descend anteriorly on the oesophagus and join with one or more rami from the right posterior pulmonary plexus to form the anterior oesophageal plexus. The anterior vagal trunk, containing nerve fibres from both vagus nerves, passes inferiorly on the anterior surface of the oesophagus and enters the abdomen through the oesophageal hiatus in the

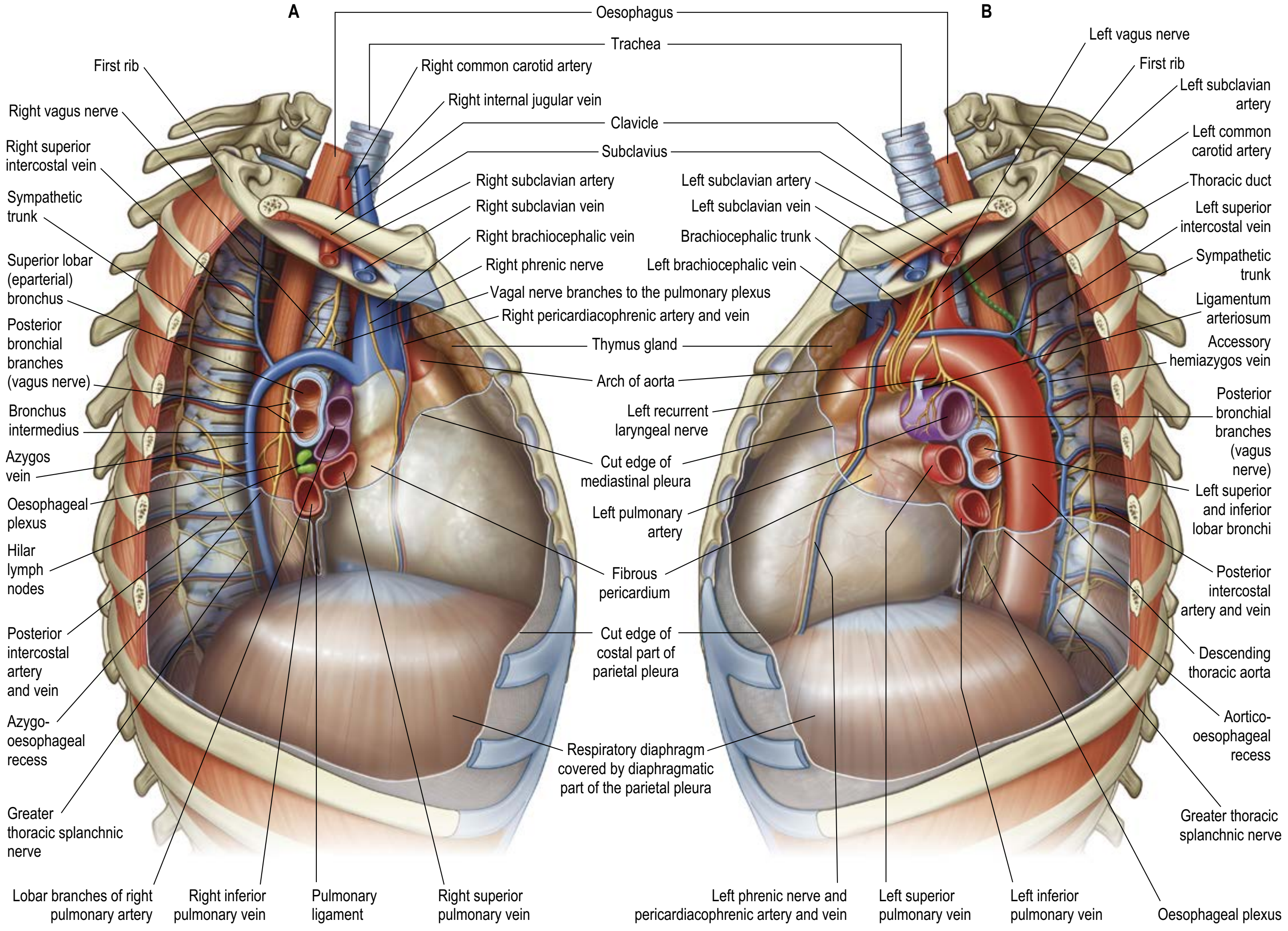
A
B
Oesophagus
Trachea
First rib
Right common carotid artery
Right internal jugular vein
Right vagus nerve
Clavicle
Right superior intercostal vein
Subclavius
Sympathetic trunk
Right subclavian artery
Right subclavian vein
Right brachiocephalic vein
Superior lobar (eparterial) bronchus
Right phrenic nerve
Vagal nerve branches to the pulmonary plexus
Right pericardiacophrenic artery and vein
Posterior bronchial branches (vagus nerve)
Thymus gland
Arch of aorta
Bronchus intermedius
Left recurrent laryngeal nerve
Azygos vein
Cut edge of mediastinal pleura
Oesophageal plexus
Left pulmonary artery
Hilar lymph nodes
Fibrous pericardium
Posterior intercostal artery and vein
Cut edge of costal part of parietal pleura
Azygo-oesophageal recess
Respiratory diaphragm covered by diaphragmatic part of the parietal pleura
Greater thoracic splanchnic nerve
Lobar branches of right pulmonary artery
Right inferior pulmonary vein
Pulmonary ligament
Right superior pulmonary vein
Left vagus nerve
First rib
Left subclavian artery
Left common carotid artery
Left subclavian artery
Thoracic duct
Left subclavian vein
Left superior intercostal vein
Brachiocephalic trunk
Left brachiocephalic vein
Sympathetic trunk
Ligamentum arteriosum
Accessory hemiazygos vein
Posterior bronchial branches (vagus nerve)
Left superior and inferior lobar bronchi
Posterior intercostal artery and vein
Descending thoracic aorta
Aortico-oesophageal recess
Greater thoracic splanchnic nerve
Left phrenic nerve and pericardiacophrenic artery and vein
Left superior pulmonary vein
Left inferior pulmonary vein
Oesophageal plexus

Fig. 56.7 The mediastinum. **A**, Right lateral aspect. **B**, Left lateral aspect. (Adapted with permission from Drake RL, Vogl AW, Mitchell A et al (eds) Gray's Atlas of Anatomy, 2nd ed. Elsevier, Churchill Livingstone. Copyright 2015.)

respiratory diaphragm (see Fig. 56.6). Numerous branches from the anterior vagal and left sympathetic trunks are distributed to the descending thoracic aorta. This pathway transmits the typical intense, excruciating pain of an intramural aortic haematoma from aortic dissection or laceration.

THYMUS

The thymus and the bone marrow are the two primary lymphoid organs. The thymus is an encapsulated soft organ that is typically bilobed; the two lobes are joined in the midline by connective tissue that merges with the capsule of each lobe (Figs 56.8–56.9). It can also be a single lobe, or tri-lobed, or X-shaped. Capsular tissue may have adhesions to the fibrous pericardium, which is thinner superiorly and so may easily tear or require a limited pericardotomy during thymectomy. The thymus is visible on CT and MRI just anterior to the ascending aorta and inferior to the left brachiocephalic vein. CT attenuation in younger individuals is homogeneous, being greater than that of the chest wall and cardiac muscles below the age of 1 year, and similar to that of these muscles after the age of 1 year (Sklair-Levy et al 2000): the decline in CT attenuation with age is secondary to fatty infiltration. The signal intensity with MRI on T2-weighted images is similar to or greater than that of adipose tissue.

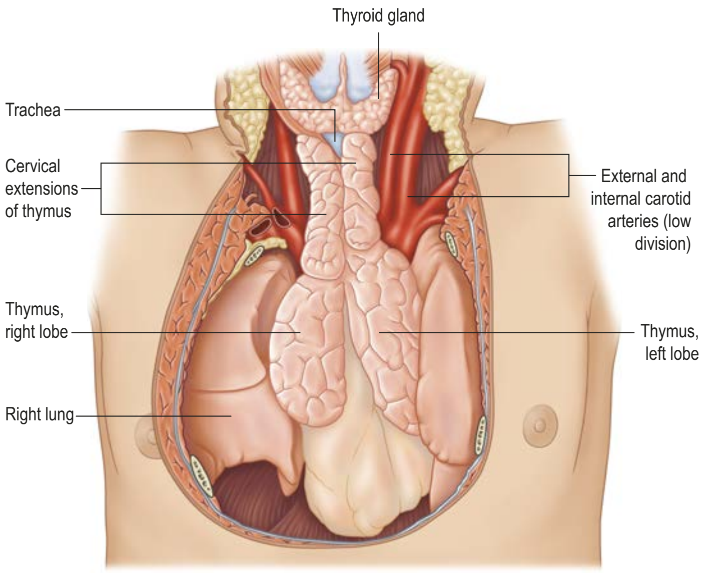
Thyroid gland
Trachea
Cervical extensions of thymus
External and internal carotid arteries (low division)
Thymus, right lobe
Thymus, left lobe
Right lung

Fig. 56.8 The neonatal thymus.

Relations

The thymus is largest in the early part of life, particularly around puberty, although it persists actively into old age despite considerable fibrofatty degeneration that sometimes obscures the existence of persistent thymic tissue. The greater part of the thymus lies in the anterior mediastinum and the anterior part of the superior mediastinum: its inferior aspect reaches the level of the fourth costal cartilages. In some children, the thymus has been described as encircling the left brachiocephalic vein (Han et al 1989). Superiorly, thymic extensions into the neck are common, reflecting its bilateral embryonic origins from the third pharyngeal pouch (see Fig. 17.19). The superior poles join at, and extend above, the level of the jugular notch of the manubrium of

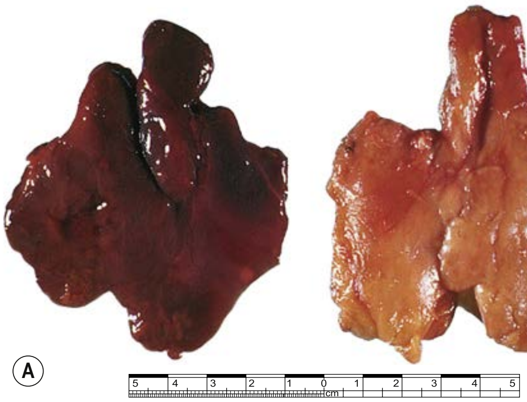

Fig. 56.9 **A**, A thymus from a 9-year-old female (left) and one from an 80-year-old male (right). Note the fibrofatty infiltration of the older thymus. (Courtesy of Professor M Kendall) (B–E, *continued online*.)

the sternum. The left pole usually extends higher and is seen first, sitting posterior to the infrahyoid muscles of the anterior neck during the initial stages of transcervical thymectomy. It sometimes reaches the inferior poles of the thyroid gland or even higher, and is connected to the thyroid gland by the thyrothymic ligament. Its shape conforms to that of adjacent structures. Inferiorly, the right lobe lies between the right side of the ascending aorta and the right lung, anterior to the superior cava. Anteriorly lie sternohyoid and sternothyroid muscles, superficial layer of deep cervical fascia, the manubrium of the sternum, the internal thoracic vessels and upper three costal cartilages. The mediastinal parts of the parietal pleurae lie laterally and the phrenic nerves can lie anterolateral and inferior; both structures can be injured during thymectomy. Posteriorly, the thymus is in contact with the vessels of the superior mediastinum (the left brachiocephalic vein and the inferior thyroid veins are usually partly embedded in the gland), the superior part of the thoracic trachea and the fibrous pericardium covering the anterior cardiac surface (right atrium and ventricle). Thoracic surgeons performing thymectomy must be aware of the anatomical variation in which the upper poles may lie posterior to the left brachiocephalic vein.

Additional thymic tissue is often found scattered around the thymus or in a range of ectopic locations: this is of importance when thymectomy is necessary (Jaretzki 1997, Varga 2016). The inferior parathyroid glands may be located within the thymus, reflecting their common origin from the third pharyngeal pouch. During development the thymus descends through the neck to the mediastinum and so ectopic thymic tissue/nodules may be found in a range of cervical or mediastinal locations, for example, lying near the trachea or oesophagus; within mediastinal adipose tissue; in the aorticopulmonary region; posterior to the brachiocephalic veins; posterior to the hyoid bone; rarely, near the carotid bifurcation/vessels. Ectopic intrathyroidal thymic tissue has been reported in children (Segni et al 2011).

Vascular supply and lymphatic drainage

Arteries

Thymic branches originating from the internal thoracic, inferior and sometimes superior, thyroid arteries supply the thymus and the surrounding mediastinal connective tissue. Since no definite hilum exists, the arterial branches travel either along the interlobar septa before entering the thymus at the junction of the cortex and medulla, or they reach the thymic tissue directly through the capsule.

Veins

Thymic veins drain to the left brachiocephalic, internal thoracic and inferior thyroid veins, and occasionally directly into the superior vena cava (see Fig. 58.1). One or more veins often emerge medially from each lobe of the thymus to form a common trunk that opens into the left brachiocephalic vein: they require careful ligation during thymectomy.

Lymphatic drainage

The thymus has no afferent lymphatics. Efferent lymphatics arise from the medulla and corticomedullary junction, drain through the extravascular spaces, accompany the supplying arteries and veins, and end in the brachiocephalic, paratracheal and subcarinal (tracheobronchial) and parasternal lymph nodes.

Innervation

The thymus is innervated from the sympathetic trunks via the cervicothoracic (stellate) ganglia or ansa subclavia and from the vagus nerves. Branches from the phrenic nerve and the inferior root of the ansa cervicalis are distributed mainly to the capsule. The two lobes are innervated separately through their dorsal, lateral and medial aspects. During development and before its descent into the thorax, the thymus is innervated by branches of the vagus nerves in the neck. After its descent, the thymus receives sympathetic innervation via nerve fibres that travel along the vessels that supply the gland: postganglionic sympathetic terminations branch radially and form a plexus with the vagal nerve fibres at the corticomedullary junction.

Microstructure

The thymus is responsible for the provision of thymus-processed (T) lymphocytes to the entire body, and provides a unique microenvironment in which thymocytes (T-cell precursors) undergo development, differentiation and clonal expansion to deliver the exquisitely specific T-cell response, simultaneously acquiring immune tolerance to the body's own components. These steps involve intimate interactions between thymocytes, mainly epithelial and antigen-presenting cells and biomolecular factors in the thymic environment. The thymus is also part of the neuroimmunological and neuroendocrine axes of the body, influenced by and influencing the products of these axes. Its activity therefore varies throughout life under the influence of different physiological states, disease conditions and chemical insults, such as hormones, drugs and pollutants. The thymus appears to be most active between the ages of 3 and 6 months, when the highest total number of thymocytes is present (Weerkamp et al 2005).

General architecture

It is useful to consider the embryological origins of the thymus in order to understand its cellular organization. It is derived from a number of sources, including epithelial derivatives of the third pharyngeal pouches, mesenchyme, haemolymphoid cells and vascular tissue. In section, the thymus can be seen to consist of an outer cortex of densely packed cortical thymocytes (T-cell precursors) and an inner medulla with fewer medullary thymocytes (**Fig. 56.10**). Both thymic lobes have a loose, fibrous connective tissue capsule, from which septa penetrate to the junction of the cortex and medulla, and partially separate the irregular lobules, which are each 0.5–2.0 mm in diameter (see Fig. 56.12). The connective tissue septa form a route of entry and exit for blood vessels and nerves, and carry efferent lymphatics. Most migrant cells enter or leave the thymus by this route. In each lobule, the cortex is composed of a superficial subcapsular cortex (a narrow band of cells immediately beneath the capsule) and a more extensive main cortex. The central medulla of both thymic lobes is continuous from one lobule to the next.

Epithelial framework

Unlike other lymphoid structures, in which the supportive framework is chiefly composed of reticular fibres, the thymus contains a network of interconnected epithelial reticular cells (see Fig. 56.10) that create an appropriate microenvironment, by cell-to-cell contact and the release of paracrine factors, in which thymocytes develop and mature into T lymphocyte cells. Although differing in morphology, all the epithelial reticular (nurse) cells of the thymus share a common origin from pharyngeal endoderm. They vary in size and shape, according to their positions within the thymus. Typically, they have pale, oval nuclei, an eosinophilic cytoplasm and intercellular desmosomal attachments. Intermediate filament bundles of cytokeratin lie within their cytoplasm. The subcapsular cells form a continuous external lining to the thymus, following its lobulated profile, ensheathing the

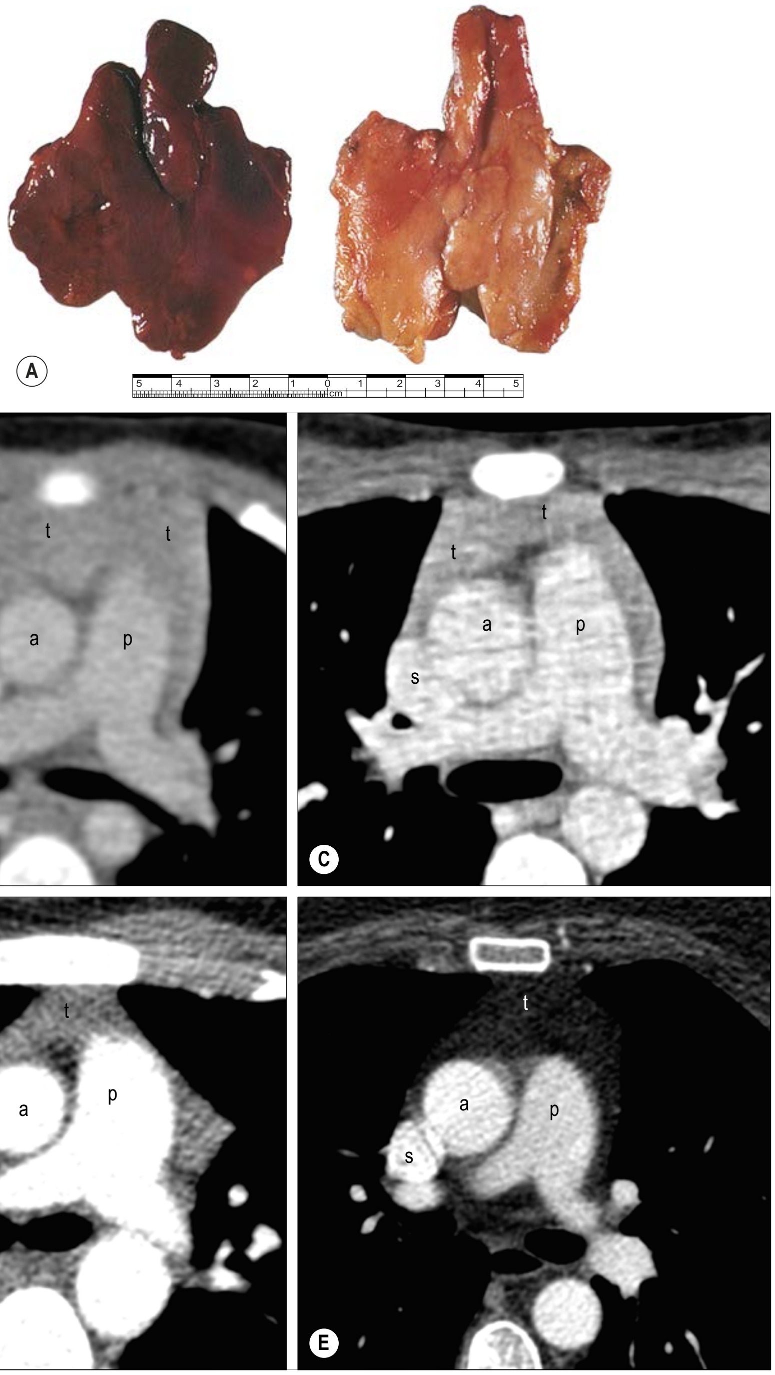

Fig. 56.9 **A**, Thymus glands from a 9-year-old female (left) and from an 80-year-old male (right). Note the fibrofatty infiltration of the older thymus. **B–E**, CT images of the chest with contrast medium showing the thymus in the anterior mediastinum in (**B**) a 10-month-old, (**C**) a 7-year-old, (**D**) a 17-year-old and (**E**) a 52-year-old. Notice how the thymus (t) reduces in volume relative to the great vessels with age (images are not to the same scale) and is then replaced by fatty material by late adulthood. Key: a, ascending aorta; p, pulmonary trunk; s, superior vena cava. (A, Courtesy of Professor M Kendall.)

The roles of the nervous system and other neuroendocrine elements in the overall biology of the thymus remain little understood. Many of the autonomic nerves most likely have a vasomotor effect, but other terminal branches (at least in rodents) ramify among the cells of the thymus, particularly the medulla, suggesting that they may have other roles. Innervation is complete by the onset of thymic function. The medulla contains a number of different types of non-lymphoid cells, including cells positive for vasoactive intestinal polypeptide and acetylcholinesterase, large non-myoid cells, and cells containing oxytocin, vasopressin and neurophysin, possibly of neural crest origin.

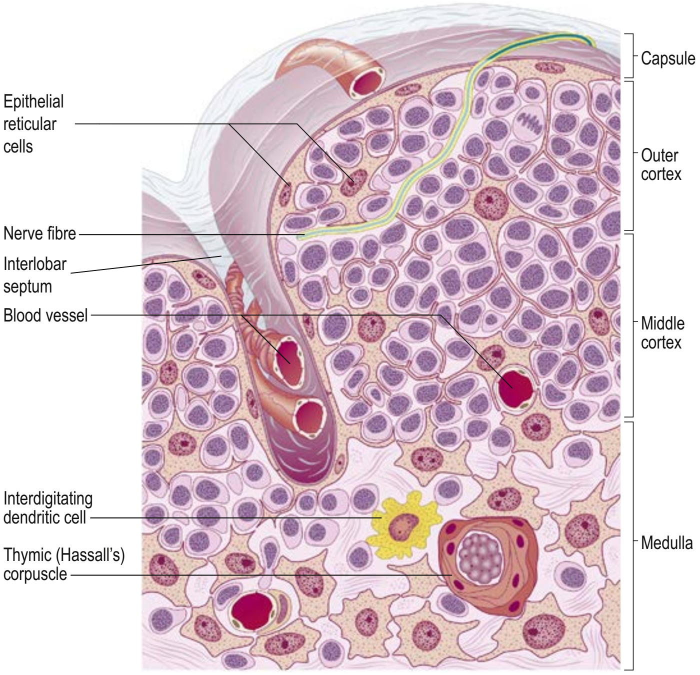
Capsule
Epithelial reticular cells
Outer cortex
Nerve fibre
Interlobar septum
Blood vessel
Middle cortex
Interdigitating dendritic cell
Medulla
Thymic (Hassall's) corpuscle

Fig. 56.10 Thymic structure and cellular organization, showing an interlobular septum, the cortical circulation and thymocytes within an epithelial framework.

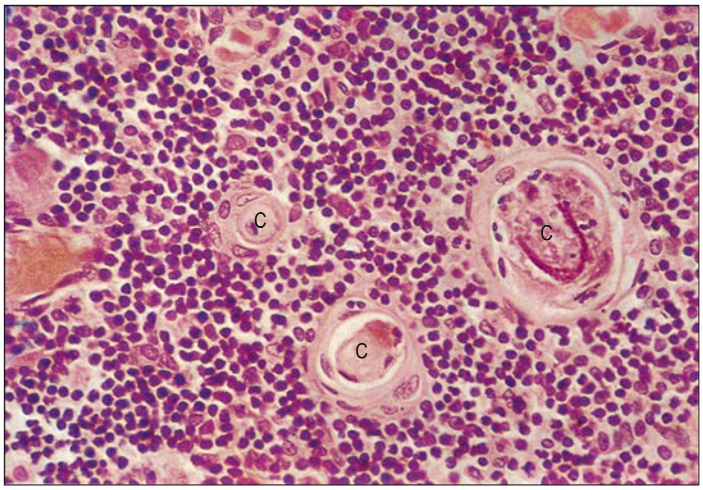

Fig. 56.11 The medulla of a neonatal thymus, showing three concentric thymic corpuscles (C) of varying degrees of maturity, surrounded by closely packed lymphocytes and a few epithelial reticular cells with larger nuclei.

penetrating vessels, and contributing to the blood–thymus barrier. Other cortical epithelial reticular cells form a loose mesh of long cytoplasmic processes, whereas medullary epithelial reticular cells tend to form more solid cords and thymic (Hassall's) corpuscles. Lymphocytes lie within the interstices of the mesh or between the cords. Large thymic epithelial reticular cells may be associated with around 50 or more thymocytes.

Thymic corpuscles are whorls of flattened, concentrically layered cells, 30–100 µm in diameter that characterize the thymic medulla (see Fig. 56.10; **Fig. 56.11**). Originating prenatally, and increasing in number throughout life, they perhaps remove dying thymocytes (their centres are eosinophilic and partly keratinized, and often contain cellular debris). Corpuscles with a similar appearance have been described in the palatine tonsil. For further reading, see Raica et al (2006), Asghar et al (2012).

Other non-lymphocytic thymic cells

The thymus also contains cells of the myeloid, fibroblastic and myoid lineages. Myeloid lineage cells include monocytes at the corticomedullary junction; mature macrophages throughout, but particularly in the cortex; and interdigitating dendritic (antigen-presenting) cells at the corticomedullary junction and in the medulla. Some dendritic cells are of lymphoid rather than myeloid origin (see Fig. 4.12). Fibroblasts are found in the capsule, perivascular spaces and medulla but are infrequent in the cortex, except in the involute thymus. Myoid cells, which are relatively rare, are situated mainly in the medulla and at the corticomedullary junction. They are large, rounded cells possessing a central nucleus surrounded by irregularly arranged bundles of myofilaments; their function is unknown, although it has been suggested that their contractions might aid the movement of lymphoid cells across or out of the thymus.

Thymocytes

The cortex is densely packed with small cortical thymocytes (presumptive T cells, see Ch. 4). They occupy the interstices of the epithelial reticulum, which they largely obscure in histological sections, and form 90% of the total weight of the neonatal thymus. A distinct subcapsular zone houses the thymic stem cells and lymphoblasts undergoing mitotic division. The first stem cells to enter the thymus in the embryo come from the yolk sac and liver during their haemopoietic phases. During later developmental periods, it is probable that all thymic lymphocytes originate in the bone marrow before passing in the blood stream to the thymus.

Thymocytes undergo mitosis in all cortical zones as the differentiating T cells mature, gradually moving deeper into the cortex (**Fig. 56.12**). The processes of thymocyte development and maturation to generate T cells depend on the microenvironment provided by epithelial cells, dendritic cells, macrophages and fibroblasts. T cells that either fail to recognize self-MHC (histocompatibility) molecules, or that recognize self-antigens, die by apoptosis in order to achieve functional immune reactivity and maintain self-tolerance, respectively. Over 95% of cortical thymocytes die within the thymus, and the surviving T cells migrate through the walls of high endothelial venules and efferent lymphatics to enter the circulation and populate secondary lymphoid tissues.

Microcirculation

Cortex

The pattern of blood flow differs in the cortex and medulla. Major blood vessels enter the gland at the corticomedullary junction and pass within each lobe, giving off small capillaries to the cortex and larger vessels to the medulla. Most cortical capillaries loop around at different depths in the cortex and join venules at the corticomedullary junction; some continue through the cortex and join larger capsular venules that leave the thymus. Sheaths of thymic epithelial reticular cells forming the blood–thymus barrier lie between the narrow perivascular space of the smaller cortical capillaries and cortical thymocytes (Henry et al 1992). This perivascular space sometimes contains pericytes and, rarely, neurones.

Medulla

Medullary blood vessels are not as well protected by epithelial cells, and those of the corticomedullary junction are only partially ensheathed, usually on their cortical aspect. Medullary vessels are variable in size and some have short lengths of cuboidal endothelium similar to those in lymph nodes and mucosa-associated lymphoid tissue (MALT).

Development

The embryology and prenatal development of the thymus are described in Chapter 17.

Thymic changes during postnatal life

At birth, the thymus is most often bilobar and is 4–6 cm long, 2.5–5 cm wide and 1 cm thick. The bulkiest part of the gland at this age is located immediately above the base of the heart where it covers the left and right phrenic nerves laterally: protection of these nerves is mandatory during paediatric cardiac surgery. The left lobe is longer and thicker than the right lobe in full-term neonates (Varga et al 2011). During childhood, the thymus narrows and lengthens and the cervical portion becomes less noticeable.

The thymus is largest relative to body mass at birth, weighing 10–15 g. It is typically larger in boys than girls at 6 months of age (Garly et al 2008). Studies of thymic mass after sudden death have recorded a wide variation at all ages, but the general pattern is that, after increasing

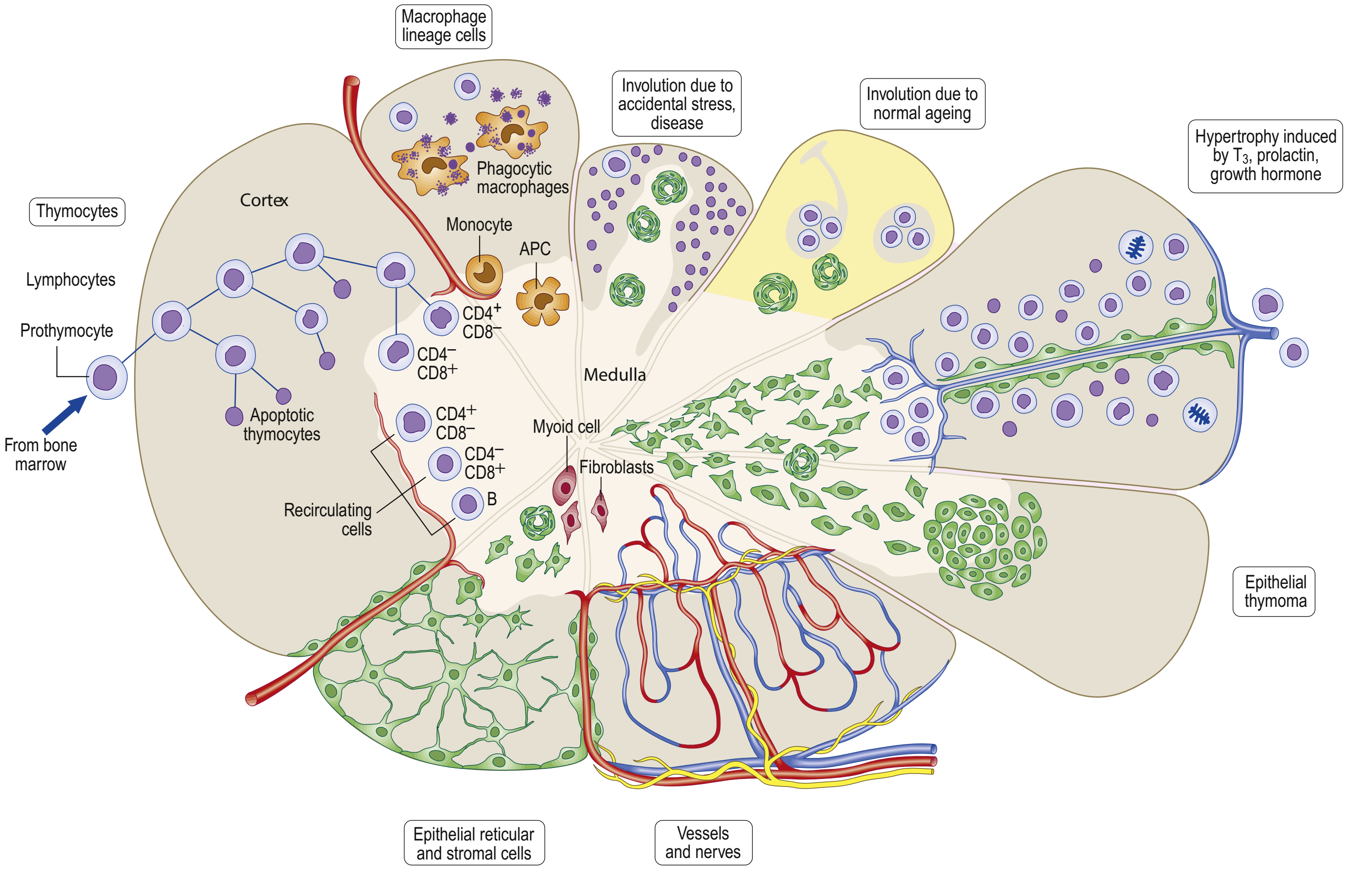

Fig. 56.12 The microscopic organization of the thymus at various stages of life and under different conditions. Abbreviations: APC, antigen-presenting cell; T_3, tri-iodothyronine hormone.

in the first year of life, the mean mass remains fairly constant at 20 g until the sixth decade, when a reduction occurs. At birth, individual adipocytes are present in connective tissue septa, and increased numbers are found within the cortex in the second and third decades of life. Fatty infiltration is usually complete by the fourth decade, when only the medulla and small patches of associated cortex are spared. This process is independent of body mass index (BMI).

In children, the gland is more pyramidal in shape and firmer than in later life, when the amount of lymphoid tissue is greatly reduced. In the fresh state, it is deep red, reflecting its rich vascularity (see Fig. 56.9). With age, it becomes thinner, greyer and increasingly infiltrated by yellow adipose tissue. Each of the two lobes is partially divided by the ingrowth of shallow septa, so that, superficially, the gland appears lobulated. As fatty atrophy proceeds, this lobulation becomes more distinct. In older adults the thymus may be distinguished from the surrounding mediastinal adipose tissue only by the presence of its capsule. However, even greatly atrophied glands usually contain perivascular areas of persistent lymphoid tissue. Thymocyte production and differentiation persist throughout life, and thymic T cells continue to populate peripheral lymphoid tissue, blood and lymph.

Congenital anomalies of the thymus

Undescended thymus, accessory thymic bodies and rare cysts of the third pharyngeal pouch are usually of no clinical significance in isolation. Patients with thymic agenesis, aplasia and hypoplasia, as in severe combined immune deficiency disease (SCID), have reduced lymphocyte numbers, and early death from infection is common. Most cases are familial, with autosomal recessive genes. Thymic aplasia is commonly associated with DiGeorge syndrome and deletion of chromosome 22q11.2 and is thought to be a consequence of insufficient neural crest cell migration into the third pharyngeal pouch. In young children, a large normal thymus may press on the trachea, causing episodes of ventilatory stridor. This condition must be differentiated from other congenital conditions such as vascular rings and slings that require surgical correction.

Thymectomy

Available with the *Gray's Anatomy* e-book

Thymoma and myasthenia gravis

Available with the *Gray's Anatomy* e-book

OESOPHAGUS

The oesophagus is a muscular tube, between 20 and 25 cm long in the adult (Kaisha Otsianyi et al 2011), that connects the pharynx to the stomach (see Figs 56.6, 56.16; **Figs 56.13–56.14**). It starts in the neck, level with the lower border of the cricoid cartilage (i.e. level with the body of the sixth cervical vertebra in females and the body of the seventh cervical vertebra in males). It descends largely anterior to the vertebral column through the superior and posterior mediastina, passes through the oesophageal hiatus in the respiratory diaphragm level with the superior half of the body of the eleventh thoracic vertebra (range, the body of the ninth thoracic vertebra to L1–L2 intervertebral disc) and ends at the gastric cardiac orifice, to the left of the midline, posterior to the left seventh costal cartilage and level with the body of the eleventh thoracic vertebra (range, superior half of the body of the tenth thoracic vertebra to L1–L2 intervertebral disc).

Generally vertical in its course, the oesophagus normally displays two shallow curves. Starting in the median plane, it inclines to the left as far as the inferior neck, gradually returns to the median plane near the body of the fifth thoracic vertebra, then deviates leftwards again at the body of the seventh thoracic vertebra before passing through the respiratory diaphragm. The oesophagus also deviates in the sagittal plane as it follows the cervicothoracic vertebral lordosis. Further inferiorly, it is pushed slightly to the right by the descending thoracic aorta before resuming its leftward course towards the oesophageal hiatus. It is the second narrowest part of the alimentary tract (the narrowest is the vermiform appendix) and is constricted at multiple points along its course, that are measured relative to the incisor teeth during oesophagoscopy. The constriction points are at its origin, where it is surrounded by cricopharyngeus (15 cm from the incisor teeth); where it is crossed anteriorly by the aortic arch (23 cm from the incisor teeth), and by the left main bronchus (28 cm from the incisor teeth); and as it passes through the respiratory diaphragm (40 cm from the incisor teeth). In

The thymus is essential for the normal development of lymphoid tissues during neonatal and early postnatal life. Thymectomy during this period results in hypoplasia of the peripheral lymphoid organs, wasting and an inability to mount an effective immune response, and is ultimately fatal. By the onset of puberty, when the main lymphoid tissues are fully developed, thymectomy is less debilitating, but effective responses to novel antigens are reduced.

Thymectomy is commonly performed for myasthenia gravis, usually after referral from a neurologist. The most beneficial effects of thymectomy are seen in myasthenic females who present with systemic muscular weakness; controversial operative groups include the elderly and those with isolated ocular symptoms.

Thymectomy is performed through a transcervical approach or a sternotomy, the choice of approach depending on the size and disposition of the diseased gland. The cervical approach involves a transverse incision that includes the sternal heads of both sternocleidomastoids, permitting good access to the substernal region (plane). Sternothyroid and sternohyoid are separated and the superior poles of the thymus are identified immediately deep to these muscles. A safe pre-thymic plane is created by blunt dissection just posterior to the sternum, facilitating subsequent mobilization of the gland. The mediastinal great vessels and the thymic vessels must be carefully identified. The thymic veins are selectively ligated and divided, especially those draining directly into the superior vena cava or the left brachiocephalic vein. The smaller arterial branches from the internal thoracic arteries are usually dealt with using electrocautery, care being taken to avoid injury to the phrenic nerves (patients are generally not given a paralytic agent during anaesthesia, so that the phrenic nerves can be identified intraoperatively). The thymus generally remains completely encapsulated and is separated without difficulty from the pericardium (occasionally, adhesions necessitate a limited pericardiectomy). Further inferiorly, a gentle push on the great vessels allows direct visualization into the interval between the aorta and pulmonary trunk to enable complete removal of the thymus in this vicinity. In most cases the thymus is removed completely with both upper and lower poles intact. Careful inspection of the remaining tissue in the mediastinum is performed to identify any possible anatomical anomalies that might result in retained thymic tissue after the operation. The most common anomaly is the unanticipated location of the upper poles of the thymus behind the left brachiocephalic vein. The interval between the aortic arch and pulmonary trunk is also a common location for thymic tissue and this area is sometimes difficult to expose with a transcervical approach. Any suspicious foci of adipose tissue in the mediastinum are removed, and, if necessary, sent for frozen section to ascertain whether or not they contain thymic tissue.

Thymic tumours may compress the trachea, oesophagus and large veins in the neck, causing hoarseness, cough, dysphagia and venous engorgement of the head and neck. Thymomas tend to have a heterogeneous signal intensity on MRI, often developing in one lobe of the thymus without affecting the other. Many affected patients also have myasthenia gravis or other autoimmune conditions. Myasthenia gravis, a chronic autoimmune disease of adults, presents as a diminution in power of repetitive contraction in certain voluntary muscles. Although there may be more than one condition with these signs, myasthenia gravis is essentially an autoimmune disease in which acetylcholine receptor proteins of neuromuscular junctions are attacked by autoantibodies. Muscles commonly involved are levator palpebrae superioris, leading to ptosis, and the extraocular muscles, leading to diplopia. Other muscles in the face, jaw, neck and limbs may be involved, and in severe cases, the ventilatory muscles are compromised. For further reading see Wolfe et al 2016.

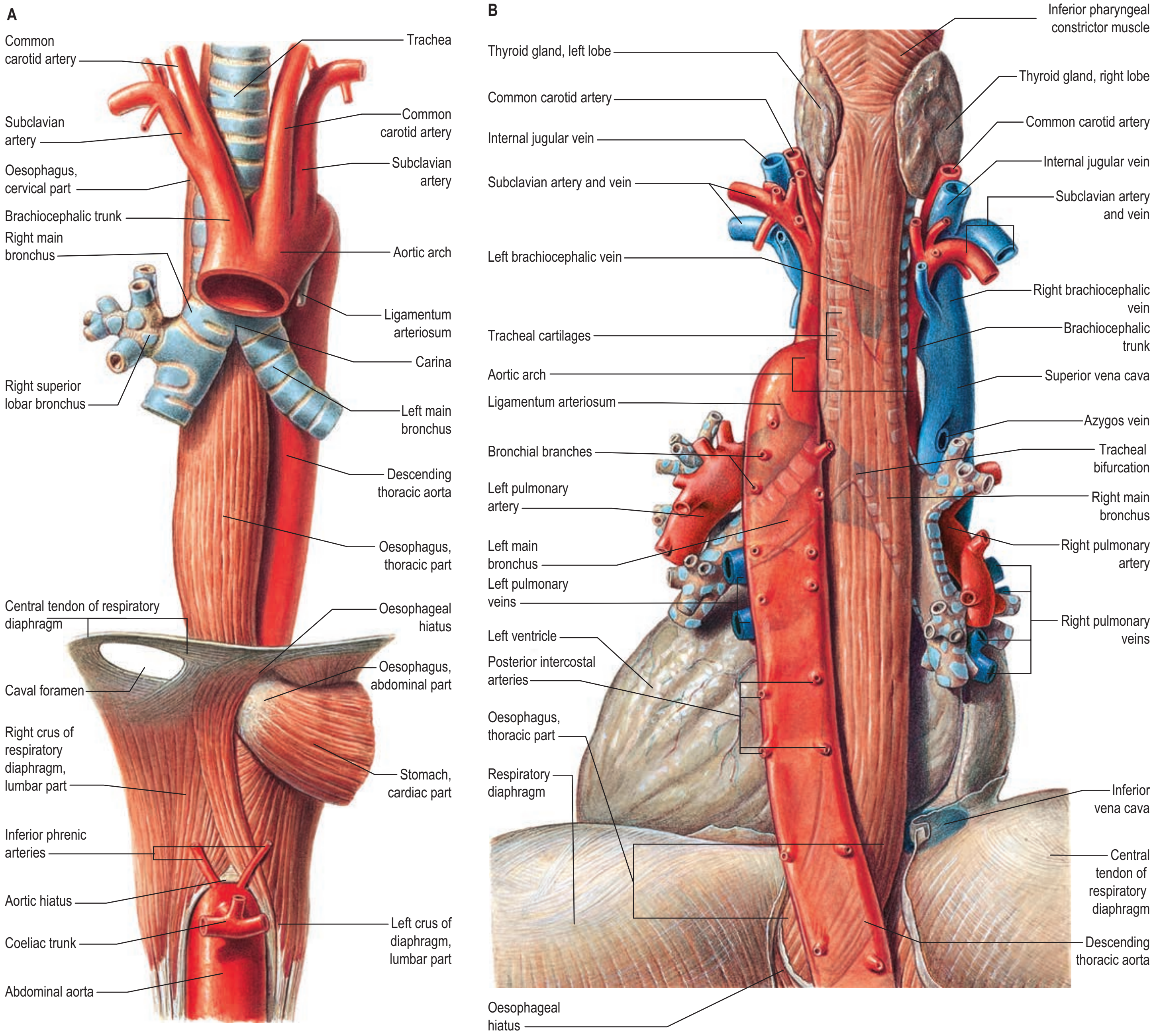
A
Common carotid artery
Subclavian artery
Oesophagus, cervical part
Brachiocephalic trunk
Right main bronchus
Right superior lobar bronchus
Central tendon of respiratory diaphragm
Caval foramen
Right crus of respiratory diaphragm, lumbar part
Inferior phrenic arteries
Aortic hiatus
Coeliac trunk
Abdominal aorta
Trachea
Common carotid artery
Subclavian artery
Aortic arch
Ligamentum arteriosum
Carina
Left main bronchus
Descending thoracic aorta
Oesophagus, thoracic part
Oesophageal hiatus
Oesophagus, abdominal part
Stomach, cardiac part
Left crus of diaphragm, lumbar part
B
Thyroid gland, left lobe
Common carotid artery
Internal jugular vein
Subclavian artery and vein
Left brachiocephalic vein
Tracheal cartilages
Aortic arch
Ligamentum arteriosum
Bronchial branches
Left pulmonary artery
Left main bronchus
Left pulmonary veins
Left ventricle
Posterior intercostal arteries
Oesophagus, thoracic part
Respiratory diaphragm
Oesophageal hiatus
Inferior pharyngeal constrictor muscle
Thyroid gland, right lobe
Common carotid artery
Internal jugular vein
Subclavian artery and vein
Right brachiocephalic vein
Brachiocephalic trunk
Superior vena cava
Azygos vein
Tracheal bifurcation
Right main bronchus
Right pulmonary artery
Right pulmonary veins
Inferior vena cava
Central tendon of respiratory diaphragm
Descending thoracic aorta

Fig. 56.13 The oesophagus and its mediastinal relations. **A**, Anterior view. **B**, Posterior view. (Sobotta Atlas of Human Anatomy © Elsevier GmbH, Urban & Fischer, Munich.)

children, the length of the oesophagus is best correlated with height (Yang et al 2005).

Cervical oesophagus

The cervical portion of the oesophagus is located posterior to the trachea, to which it is attached by loose connective tissue. The recurrent laryngeal nerves ascend on each side in or near the tracheo-oesophageal groove. Posteriorly are the vertebral column, longus colli, the anterior longitudinal ligament and the prevertebral layer of cervical fascia. Laterally, on each side, are the common carotid arteries and the posterior part of the thyroid gland. In the inferior neck, where the oesophagus deviates to the left, it sits closer to the left carotid sheath and thyroid gland than the right; the thoracic duct ascends for a short distance along its left side (see Figs 56.5B, 56.7B).

Thoracic oesophagus

The thoracic oesophagus (see Figs 56.13–56.14) is situated a little to the left of the midline in the superior mediastinum, between the trachea and the vertebral column. It passes posterior and to the right of the aortic arch to descend in the posterior mediastinum along the right side of the descending thoracic aorta. Inferiorly, as it inclines left, the thoracic oesophagus crosses anterior to the descending thoracic aorta and enters the abdomen through the respiratory diaphragm level with the superior half of the body of the eleventh thoracic vertebra (conventionally reported as level with the body of the tenth thoracic vertebra). As it descends, its immediate anterior relations successively are the trachea, tracheal bifurcation, right pulmonary artery, left main bronchus, fibrous pericardium (separating it from the left atrium) and the respiratory diaphragm. Posteriorly, it is related to the vertebral column, longus colli, right posterior intercostal arteries, thoracic duct, azygos vein and the terminal parts of the hemiazygos and accessory hemiazygos veins, and, near the diaphragm, the descending thoracic aorta. Two recesses in the pleural cavity track along the left and right sides of the oesophagus: the aortico-oesophageal recess lies on the left side between the oesophagus anteriorly and the descending thoracic aorta posteriorly and the azygo-oesophageal recess lies on the right side between the oesophagus anteriorly and the azygos vein and vertebral column posteriorly (see Fig. 56.7).

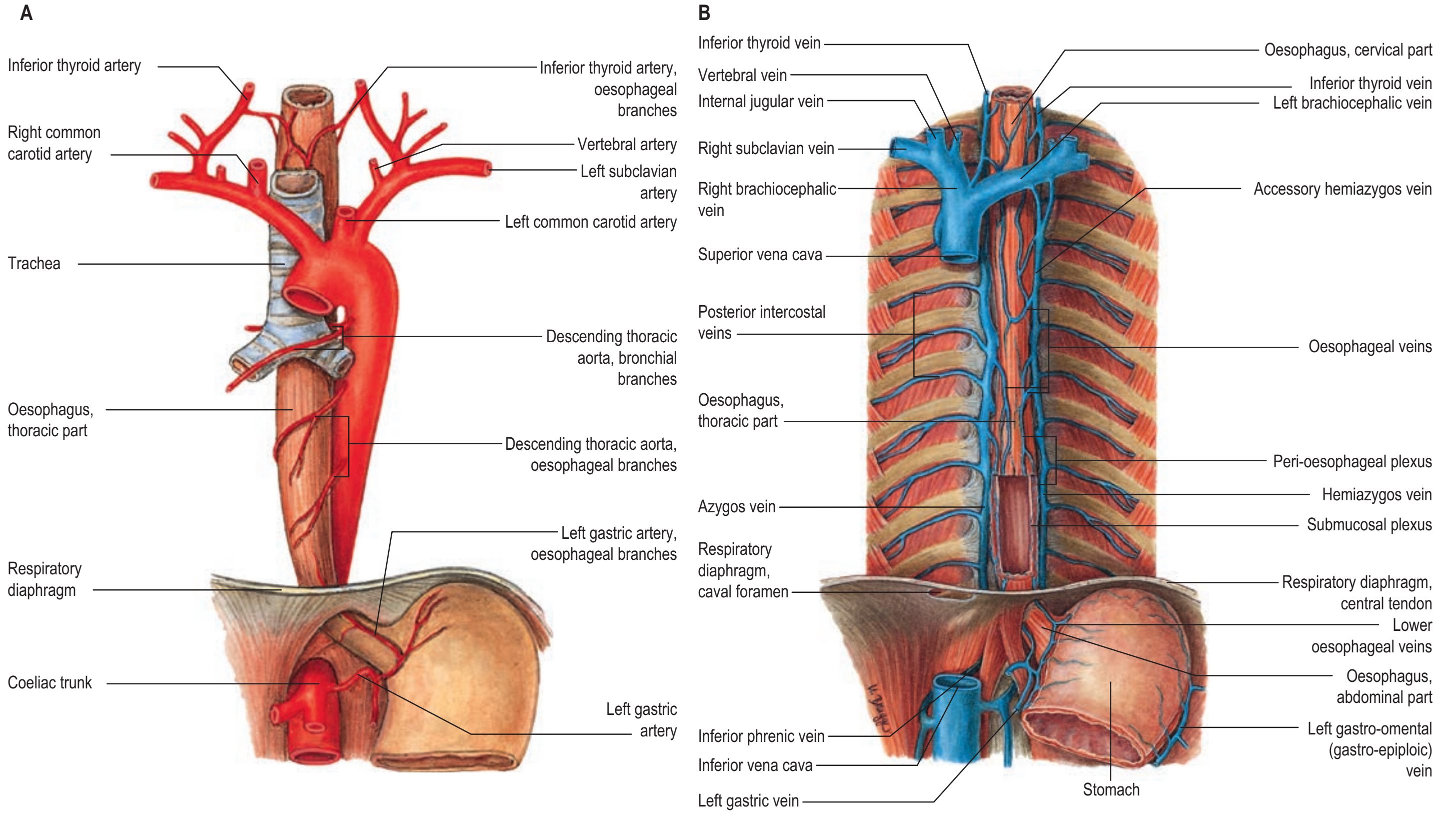
A
Inferior thyroid artery
Right common carotid artery
Trachea
Oesophagus, thoracic part
Respiratory diaphragm
Coeliac trunk
Inferior thyroid artery, oesophageal branches
Vertebral artery
Left subclavian artery
Left common carotid artery
Descending thoracic aorta, bronchial branches
Descending thoracic aorta, oesophageal branches
Left gastric artery, oesophageal branches
Left gastric artery
B
Inferior thyroid vein
Vertebral vein
Internal jugular vein
Right subclavian vein
Right brachiocephalic vein
Superior vena cava
Posterior intercostal veins
Oesophagus, thoracic part
Azygos vein
Respiratory diaphragm, caval foramen
Inferior phrenic vein
Inferior vena cava
Left gastric vein
Oesophagus, cervical part
Inferior thyroid vein
Left brachiocephalic vein
Accessory hemiazygos vein
Oesophageal veins
Peri-oesophageal plexus
Hemiazygos vein
Submucosal plexus
Respiratory diaphragm, central tendon
Lower oesophageal veins
Oesophagus, abdominal part
Left gastro-omental (gastro-epiploic) vein
Stomach

Fig. 56.14 The oesophagus, anterior view. **A**, Arterial blood supply. **B**, Venous drainage. (Sobotta Atlas of Human Anatomy © Elsevier GmbH, Urban & Fischer, Munich.)

In the superior mediastinum, left lateral relations include the terminal part of the aortic arch, left subclavian artery, thoracic duct, left mediastinal parietal pleura and the left recurrent laryngeal nerve. In the posterior mediastinum, left lateral relations include the descending thoracic aorta and, just before the oesophagus passes through the respiratory diaphragm, the left mediastinal parietal pleura. Right lateral relations include the right mediastinal parietal pleura and the azygos vein, as it arches anteriorly above the right main bronchus to join the superior vena cava. Inferior to the root of the lung, the vagus nerves descend in contact with the oesophagus, the right vagus becomes mainly posterior and the left vagus is anterior. The vagi subsequently unite to form a plexus around the oesophagus that gives origin inferiorly to the anterior and posterior vagal trunks (see Fig. 56.6). Low in the posterior mediastinum, the thoracic duct is posterior and to the right of the oesophagus, whereas at higher levels, the duct is posterior, crossing to the left of the oesophagus at about the level of the body of the fifth thoracic vertebra and then ascending on the left side of the oesophagus.

To the right of the oesophagus, just above the respiratory diaphragm, a small, serous infracardiac bursa may be present, representing the detached apex of the right pneumatoenteric recess.

The close relationship between the oesophagus, the heart and the thoracic aorta constitutes the anatomical basis of transoesophageal cardiovascular and aortic ultrasonography.

Vascular supply and lymphatic drainage

Arteries

The cervical oesophagus is supplied by the inferior thyroid artery and the thoracic oesophagus is supplied by bronchial and oesophageal branches of the descending thoracic aorta (see Fig. 56.14A). Four or five oesophageal branches arise from the anterior surface of the aorta and descend obliquely to the oesophagus, where they form a vascular chain that anastomoses above with the oesophageal branches of the inferior thyroid arteries, and below with ascending branches from the left inferior phrenic (see Fig. 56.13A) and left gastric arteries. Extensive devascularization of the oesophagus, as occurs in dissection of the descending thoracic aorta, may cause acute oesophageal necrosis (van der Wal-Visscher et al 2011).

Veins

Blood from the oesophagus drains into a superficial submucosal plexus (see Fig. 56.15A) that drains into a peri-oesophageal venous plexus from which the oesophageal veins arise. Veins from the thoracic oesophagus drain into the superior vena cava predominantly via the azygos venous system and, to a lesser extent, via the intercostal and bronchial veins (see Fig. 56.14B). Veins from the cervical oesophagus drain into the inferior thyroid veins.

The left gastric vein, which drains via the portal venous system, ascends along the lesser curvature of the stomach to the oesophageal opening in the respiratory diaphragm, where it receives several lower oesophageal veins: this is one of the sites of porto-caval (porto-systemic) venous anastomoses where variceal formation can occur in portal hypertension.

Oesophageal varices

Cirrhosis or fibrosis of the liver affects the vascular tree within the liver, resulting in a decrease of hepatic vascular compliance, and a likely increased vascular tone reflecting a reduction in endothelial vasodilators such as nitric oxide. The portal vascular resistance increases, leading to the formation of a collateral circulation. Porto-systemic shunting of blood occurs between the left gastric and lower oesophageal veins, largely as the result of the dilation of pre-existing channels.

Varices in the distal oesophagus are easily visible at endoscopy because they are situated superficially in the lamina propria. The blood from the superficial veins drains into a superficial venous plexus, then into a deeper intrinsic venous plexus and finally into the peri-oesophageal veins via perforating veins. Bidirectional flow is normally possible in this region, a phenomenon that accommodates pressure changes during breathing and Valsalva manoeuvres. However, in portal hypertension, the valves within the perforating vessels become incompetent and blood flow is retrograde, causing dilation (varices) of the deep intrinsic veins. The greater pressure within this region enlarges the varices, which may lead to rapid and life-threatening bleeding. Treatment is directed towards controlling the formation of a collateral circulation and the obliteration of varices that are susceptible to bleeding. This is achieved by paravariceal endoscopic injection of a sclerosant, causing obliteration of the varices as a result of thrombus formation. Fibrosis is also induced within the mucosa, which reduces the formation of new collateral vessels. Alternatively, rubber bands may be applied in an attempt to ligate the varices. Bleeding from varices is associated with a mortality rate of 25%, reflecting the problems of recurring hemorrhage and underlying comorbidity.

Lymphatic drainage

The oesophagus has an extensive, longitudinally continuous submucosal lymphatic system within which flow may be bidirectional: this is pertinent to lymphatic spread in oesophageal carcinoma. Efferent vessels from the cervical oesophagus drain to the deep cervical nodes either directly or through the paratracheal nodes. Vessels from the cervical oesophagus drain to para-oesophageal, deep cervical and supraclavicular nodes; those from the thoracic oesophagus drain directly to the thoracic duct or to paratracheal, retrotracheal, subcarinal and right recurrent laryngeal nodes; and those from the abdominal oesophagus drain to the nodes associated with the left gastric artery or other arteries originating from the coeliac trunk, including those associated with the lesser curvature of the stomach (Wang et al 2018).

Innervation

The upper oesophagus is supplied by the branches of the recurrent laryngeal nerve and by postganglionic sympathetic fibres that reach it by travelling along the inferior thyroid arteries. The lower oesophagus is supplied by the oesophageal plexus, a wide-meshed autonomic network that surrounds the oesophagus below the level of the roots of the lungs, and contains a mixture of parasympathetic and sympathetic nerve fibres (see Fig. 56.6).

Motor nerve fibres to the striated and smooth muscle of the oesophageal wall travel in the vagus nerve. Axons from branchiomotor neuronal cell bodies in the nucleus ambiguus travel via the recurrent laryngeal nerves and supply cricopharyngeus and the striated muscle of the upper third of the oesophagus. Axons from parasympathetic neuronal cell bodies in the dorsal nucleus of the vagus nerve pass through the oesophageal plexus and supply the smooth muscle that makes up the lower two-thirds of the oesophagus, after synapsing locally in the oesophageal wall. Other branches are given off by the vagus nerve as it travels through the mediastinum and pass directly to the oesophagus. The vagus also carries secretomotor fibres to mucous glands in the oesophageal mucosa and muscular and mucosal afferent (sensory) fibres that are thought to terminate mainly in the nucleus of the solitary tract.

Vasomotor sympathetic nerve fibres destined for the oesophagus arise from the upper 4–6 thoracic spinal nerves and associated spinal cord segments. Those from the upper thoracic ganglia pass to the middle and inferior cervical ganglia, where they synapse: postganglionic fibres innervate the vessels of the cervical and upper thoracic oesophagus. Those from the lower thoracic ganglia pass either directly to the oesophageal plexus or to the coeliac ganglion (via the greater thoracic splanchnic nerve), where they synapse: postganglionic fibres innervate the distal oesophagus. Visceral afferent fibres travel within the sympathetic nerve bundles to terminate within the upper thoracic spinal cord. This region of the spinal cord also receives visceral afferent fibres from the heart, which means that it is sometimes difficult to distinguish between pain of oesophageal and cardiac origin.

Microstructure

The tissues forming the thoracic oesophageal wall, from the lumen outwards, are the mucosa (consisting of epithelium, lamina propria and muscularis mucosae), submucosa, muscularis externa (consisting of inner circular and outer longitudinal muscle) and adventitia (**Fig. 56.15A**).

Mucosa

The mucosa is thick. At the gastro-oesophageal junction, a jagged boundary line separates the greyish-pink-coloured smooth oesophageal mucosa from the reddish-pink-coloured gastric mucosa, the latter covered by minute bulges and depressions. Throughout its length, the oesophageal lumen is marked by deep longitudinal grooves and ridges, which flatten (reduce) when the lumen is distended.

Epithelium

The epithelium is non-keratinized, stratified squamous and is continuous with that of the oropharynx. In humans this protective layer is 300–500 µm thick and is not affected by oesophageal distension. The boundary between the oesophageal epithelium and its lamina propria is distinct but markedly uneven because tall connective tissue papillae invaginate the epithelial base, helping to anchor the epithelium to underlying tissues (**Fig. 56.15B**). These papillae are permanent structures, are unaffected by oesophageal distension, and are rich in blood vessels and nerve fibres. At the base of the epithelium there is a basal lamina to which epithelial cells are attached by hemidesmosomes, an arrangement that also occurs in the oral mucosa.

Oesophageal epithelium is similar to other stratified squamous epithelia and so can be divided into a basal layer of proliferating cells, a parabasal layer of cells undergoing terminal differentiation and a flattened layer of superficial cells or squames that retain their nuclei. The most superficial strata of cells contain a few keratohyalin granules, in addition to keratin filaments. The epithelial cell population is constantly renewed by mitosis in the cuboidal basal and deepest parabasal cells: as the cells migrate towards the lumen, they become progressively polygonal and then more flattened and are eventually desquamated at the epithelial surface. This sequence of events normally takes 2–3 weeks, and is markedly slower than in the stomach and intestine.

The epithelium is an effective protection against mechanical injury during swallowing because of its thickness and the presence of mucus at its surface. However, protection is limited by repeated exposure to the strongly acidic, protease-rich secretions of the stomach, as occurs abnormally during reflux. Failure of the lower oesophageal sphincter allows reflux and results in ulceration and fibrosis, accompanied by dysphagia/odynophagia, with possible epithelial metaplasia (see Commentary 1.3) to a gastric-like mucosa (Barrett's mucosa), or to more overt neoplastic changes.

Dendritic cells Dendritic (Langerhans) cells are present in the oesophageal epithelium. They resemble those found in the epidermis and perform similar antigen-processing and antigen-presenting roles, that are important in immunostimulation of naïve T cells and mucosal defence (Ch. 4).

Lamina propria

The oesophageal lamina propria contains scattered groups of mucosa-associated lymphoid tissue (MALT), especially prominent near the gastro-oesophageal junction. Small tubular mucous glands occur in this region and also at the oesophago-pharyngeal junction.

Muscularis mucosae

The muscularis mucosae is composed mainly of longitudinal smooth muscle and forms a thin sheet near the epithelium, following its contours closely. It may be absent or represented only by sparse, scattered bundles at the pharyngeal end of the oesophagus, but becomes progressively thicker distally. The longitudinal orientation of its cells changes to a more plexiform arrangement near the gastro-oesophageal junction. The ducts of the oesophageal glands pierce the muscularis mucosae.

Submucosa

The submucosa loosely connects the mucosa and the muscularis externa, penetrating the longitudinal ridges of the oesophageal lumen. It contains larger blood vessels, nerves and mucous glands. Its elastic fibres aid closure of the oesophageal lumen after peristaltic dilation.

Oesophageal glands

Groups of small tubulo-acinar oesophageal glands lie mainly in the submucosa, each sending a single long duct through the intervening layers into the lumen. They are composed mostly of mucous cells; some serous cells that secrete lysozyme are also present. Close to the pharynx and stomach, the glands are simpler in form and restricted to the lamina propria of the mucosa (not the submucosa). The mucosal mucous glands of the abdominal oesophagus closely resemble the gastric cardiac glands, and are therefore named oesophageal cardiac glands.

Muscularis externa

The muscularis externa is up to 300 µm thick, and consists of an outer longitudinal and inner circular layer of muscle that is typical

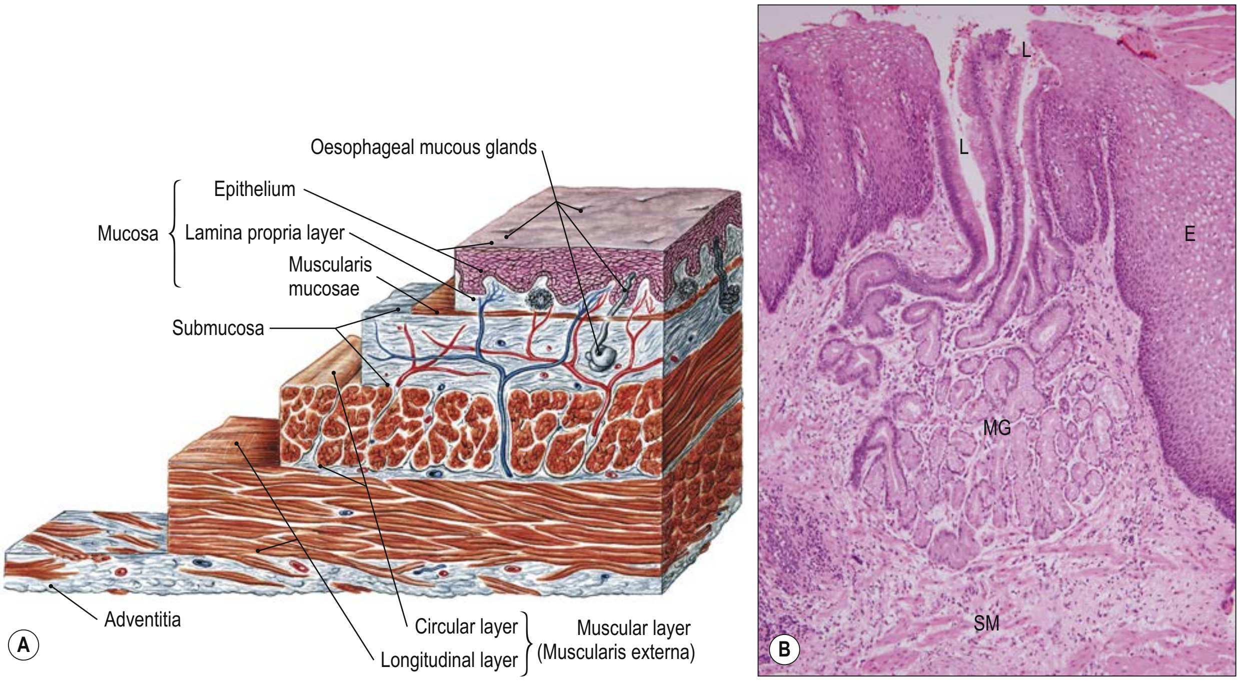

Fig. 56.15 Structure of the oesophageal wall. **A**, Main layers from the epithelium to the adventitia. **B**, Section through the wall of a human oesophagus, showing the superficial stratified squamous epithelium (E) lining the lumen (top), supported by a thin lamina propria and an indistinct muscularis mucosae at this level. The submucosa (SM) contains oesophageal mucous glands (MG, centre field) that secrete a thin mucus into the oesophageal lumen via a short duct. The duct has been sectioned through part of its wall in this specimen, so the duct lumen (L) appears duplicated. (Courtesy of Mr Peter Helliwell and the late Dr Joseph Mathew, Department of Histopathology, Royal Cornwall Hospitals Trust, UK.)

of the intestine. The thicker longitudinal layer exists as a continuous coat of fibres that extends almost the entire length of the oesophagus, except posterosuperiorly, 3–4 cm inferior to the cricoid cartilage, where it diverges as two fascicles that ascend obliquely and anteriorly, passing deep to the lower border of the inferior constrictor, and ending in a tendon that is attached superiorly to the posterior ridge of the cricoid lamina (**Fig. 56.16**). The V-shaped space between these fascicles is filled by the circular oesophageal muscle fibres, thinly covered inferiorly by decussating longitudinal fibres and superiorly by the cricopharyngeal part of the inferior constrictor.

In the upper third of the oesophagus, the muscularis externa is formed by skeletal muscle; in the middle third, smooth muscle fascicles intermingle with striated muscle; and the lower third contains only smooth muscle. This transition between striated and smooth muscle is reflected in the innervation pattern of the oesophagus.

Oesophageal diverticula

Portions of the oesophagus may expand secondary to increased intraluminal pressure, adhesion of nearby inflamed tissues, or muscle motility disorders. True oesophageal diverticula occur in two locations, either the subdiaphragmatic or parabronchial part of the oesophagus (Watanabe 2016). Superiorly, diverticula may form in the posterior wall of the distal laryngopharynx, through the interval between the inferior pharyngeal constrictor and cricopharyngeus (Zencker's diverticulum or pharyngeal pouch); it could be argued that they are not true oesophageal diverticula even though they are often classed as such.

Oesophagoscopy

Available with the *Gray's Anatomy* e-book

Transoesophageal ultrasound

Available with the *Gray's Anatomy* e-book

Oesophageal rupture

Available with the *Gray's Anatomy* e-book

Barium studies

Available with the *Gray's Anatomy* e-book

Development

The development of the oesophagus is described in Chapter 21.

Tracheo-oesophageal fistula

Tracheo-oesophageal fistula is described in Chapter 20.

Oesophageal sphincteric mechanisms

Radiological studies show that swallowed food stops momentarily in the gastric end of the oesophagus, before entering the stomach, suggesting the presence of a sphincter at this point. In the past, controversy surrounded the reason for this observation because only slight thickening of the muscle coat has been found in humans. There is now ample physiological and clinical evidence that closure depends on two major mechanisms. The more important of these is the lower oesophageal sphincter, a specialized zone of circular smooth muscle surrounding the oesophagus as it traverses the respiratory diaphragm and for much of its short abdominal course. This region of the oesophagus is maintained under tonic contraction, except during swallowing, when it relaxes briefly to admit ingesta to the stomach, and during vomiting. Intramural plexuses of the enteric nervous system and the neural release of nitric oxide contribute to its relaxation. The second mechanism is a functional external sphincter provided by the right crus of the respiratory diaphragm (see Fig. 55.1), which encircles the oesophagus as it passes into the abdomen and is attached to it by the phrenico-oesophageal ligament. Fluoroscopy, electromyography and manometry have shown that its muscular fibres contract around the oesophagus during inspiration and when

Accessory slips of smooth muscle sometimes pass between the oesophagus and left mediastinal parietal pleura (pleuro-oesophageal muscle) (Bilge et al 2013) or the left main bronchus (broncho-oesophageal muscle), trachea, fibrous pericardium or descending thoracic aorta (see Fig. 56.16). They may act to equilibrate the normal physiological changes in position, shape and dimensions of the various organs between which they extend during swallowing (Watanabe 2016). Superiorly, the circular muscle fibres blend posteriorly with the cricopharyngeal part of the inferior pharyngeal constrictor, and anteriorly, the uppermost fibres are attached to the lateral margins of the tendon of the two longitudinal muscle bundles (fasciculi) of the oesophagus. Inferiorly, the circular muscle fibres are continuous with the oblique layer of muscle fibres in the stomach wall.

Oesophagoscopy, a component of superior digestive endoscopic examination, may be indicated in patients with persistent non-cardiac chest pain, dysphagia, odynophagia (painful swallowing) or symptoms of reflux that include nocturnal cough. The endoscope is passed orally under direct vision with the patient in a lateral decubitus position, with or without sedation, and manoeuvred into the oesophageal inlet when the patient is asked to swallow; once through, the endoscope is advanced slowly under direct vision. The mucosa normally appears whitish-pink in colour, changing to red at the squamocolumnar junction (Z line) near the oesophageal hiatus in the respiratory diaphragm. Cranial displacement of the Z line by more than 2 cm is indicative of a hiatus hernia. There may be slight extrinsic compression by the aortic arch and the left main bronchus (see Fig. 56.19).

Endoscopic transoesophageal ultrasound permits assessment of the oesophageal wall and para-oesophageal structures, such as lymph nodes and the heart and thoracic aorta. Numerous surgical and percutaneous cardiovascular procedures are guided by transoesophageal echocardiography. The technique is more sensitive than CT in detecting mediastinal nodal metastases, allowing those less than 10 mm in size to be assessed. Normal lymph nodes cannot be identified easily by endoscopic ultrasound because they have the same echogenic characteristics as surrounding tissue; a hypoechoic or inhomogeneous echo portrayal on ultrasound is considered more suspicious of malignancy. Endoscopic ultrasound-guided fine needle aspiration allows accurate diagnosis for para-oesophageal nodes. Transbronchial fine needle aspiration is an alternative approach for sampling mediastinal or paratracheal nodes, guided by CT or positron emission tomography (PET) CT findings.

The majority of oesophageal ruptures are iatrogenic and occur during the instrumentation of the oesophagus during simple endoscopy, endoscopic intervention including dilation, and nasogastric tube placement. Other causes are barotrauma, foreign bodies and oesophageal carcinoma. Barotrauma occurs with intense retching and vomiting that may cause longitudinal tearing in the posterior wall of the thoracic oesophagus (Boerhaave's syndrome). Locations of oesophageal perforation are 60% thoracic, 25% cervical and 15% abdominal. Perforation in the cervical oesophagus occurs in the posterior wall, where it is at its thinnest, often corresponding to an area of mucosa with minimal muscular covering bordered by the pharyngeal inferior constrictor and cricopharyngeus (see Fig. 56.16). Mortality from oesophageal perforations is 20% and results from mediastinitis and necrotizing infection. Presenting symptoms include thoracic pain, odynophagia, haematemesis, subacute surgical emphysema, tachycardia, breathlessness and, in advanced cases, septic shock. Diagnosis and repair within 24 hours is associated with a better prognosis and a mortality rate of between 10% and 15%, whereas late diagnosis has a much greater mortality rate. For a perforation in the upper two-thirds of the thoracic oesophagus, a right thoracotomy in the fifth or sixth intercostal space is performed. The lower third of the oesophagus is approached through a left thoracotomy in the sixth or seventh intercostal space. The perforation is closed in layers after any necrotic tissue has been debrided.

A double-contrast barium swallow with fluoroscopy enables anatomical and functional assessment of the oesophagus (see Fig. 56.19). A standard examination involves the patient swallowing a barium solution and gas granules, and images are taken in the erect, supine and prone recumbent positions. The upright posture fully dilates the oesophagus and is useful in evaluating any constrictions. The narrow tubular lumen of the oesophagus is normally indented slightly by the aortic arch and the left main bronchus. The supine view allows better evaluation of any motor dysfunction and varices, and moving into the prone position provokes underlying gastro-oesophageal reflux. Both repeating single digital images and cine loops of fluoroscopy can be obtained. The fluoroscopic images demonstrate defective opening of the pharyngeal (upper) oesophageal sphincter and the nature of the contractions in the body of the oesophagus. The lower oesophageal sphincter can be assessed in achalasia. Other abnormalities, such as hiatal hernia and areas of narrowing or dilation of the oesophagus, can be demonstrated. Mucosal relief images are obtained once the bulk of the contrast media has passed into the stomach, and this provides fine mucosal detail. Cross-sectional imaging is usually used for the preoperative planning and staging of oesophageal tumours, and is of value in radiotherapy planning.

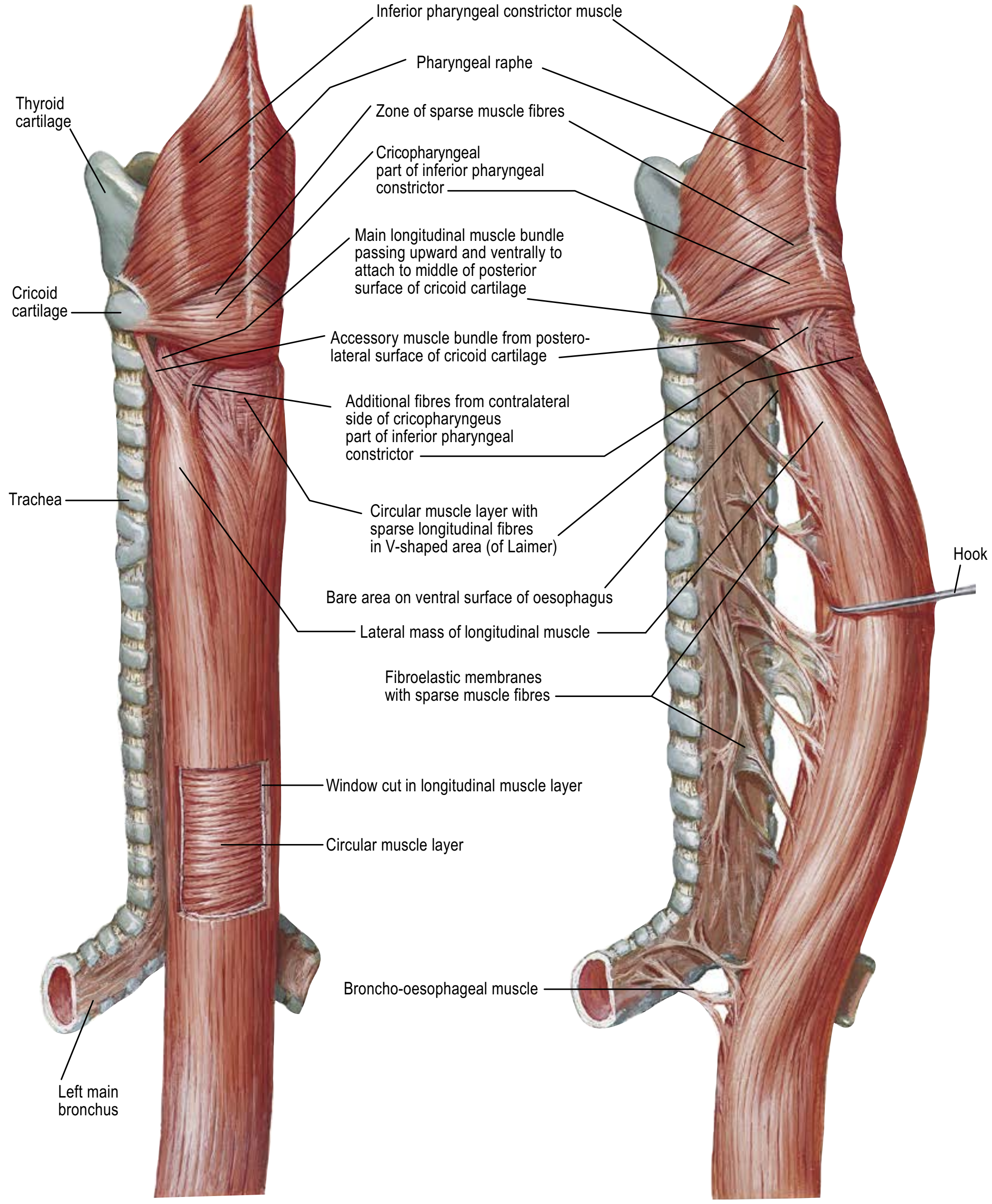
Inferior pharyngeal constrictor muscle
Pharyngeal raphe
Thyroid cartilage
Zone of sparse muscle fibres
Cricopharyngeal part of inferior pharyngeal constrictor
Main longitudinal muscle bundle passing upward and ventrally to attach to middle of posterior surface of cricoid cartilage
Cricoid cartilage
Accessory muscle bundle from postero-lateral surface of cricoid cartilage
Additional fibres from contralateral side of cricopharyngeus part of inferior pharyngeal constrictor
Trachea
Circular muscle layer with sparse longitudinal fibres in V-shaped area (of Laimer)
Hook
Bare area on ventral surface of oesophagus
Lateral mass of longitudinal muscle
Fibroelastic membranes with sparse muscle fibres
Window cut in longitudinal muscle layer
Circular muscle layer
Broncho-oesophageal muscle
Left main bronchus

Fig. 56.16 Musculature of the distal pharynx and oesophagus, showing accessory muscle bundles. (Adapted with permission from Netter FH Atlas of Human Anatomy, 7th ed. Elsevier. Copyright 2019.)

intra-abdominal pressure is increased, thus helping to prevent gastro-oesophageal reflux, even when the lower oesophageal sphincter is inhibited experimentally with atropine. The relative importance of these two agents in the prevention of oesophageal reflux is still a matter for debate. Clinically, there is a good correlation between this condition and lower oesophageal sphincter dysfunction in some cases, whereas in others failure of the respiratory diaphragmatic component, as seen in hiatus hernia, appears to be a major factor. The anatomical configuration of the gastro-oesophageal junction may also play some part in these processes.

Swallowing

The oesophageal phase of swallowing is described in Chapter 40.

Vomiting

In the initial phase of vomiting, the lower oesophageal sphincter and peri-oesophageal crural muscle fibres simultaneously relax and rapid diaphragmatic and abdominal muscular contraction commences, increasing intra-abdominal pressure.

Oesophageal dysmotility

Oesophageal dysmotility encompasses disorders of the upper and lower oesophageal sphincters (see gastro-oesophageal reflux in Chapter 63), congenital anomalies such as atresia, and achalasia. Upper oesophageal sphincter dysfunction is usually neurological; often brainstem disease impairs relaxation of cricopharyngeus with resultant dysphagia and aspiration as demonstrated by videofluoroscopy.

Achalasia of the cardia is a primary motor disorder of the oesophagus in which there is failure of relaxation of the lower oesophageal sphincter and loss of peristalsis in the oesophagus as a consequence of degeneration of myenteric plexus neurones. Dysphagia, regurgitation of undigested food and retrosternal chest pain result and a posteroanterior chest radiograph may show dilation of the oesophagus and retention of food products as a mottled, double-contoured mediastinal widening. Barium swallow shows a classic 'bird-beak' appearance as a result of failure of relaxation of the lower oesophageal sphincter and an absence of peristalsis. Oesophageal pressure manometry demonstrates absent or impaired relaxation of the lower oesophageal sphincter. Treatment options are endoscopic pneumatic balloon dilation or laparoscopic cardiomyotomy (Heller's myotomy). Alternatively, intrasphincteric injection of botulinum toxin may be offered in frail patients and confers lower morbidity and mortality.

Diffuse oesophageal spasm may present with dysphagia and chest pain. It is characterized by abnormal oesophageal contractions on barium swallow, and produces simultaneous segmental contractions that obliterate the oesophageal lumen to produce a 'corkscrew oesophagus'. Manometry also demonstrates these tetanic contractions. Non-specific oesophageal motility disorder occurs with ageing (presbyoesophagus) and is characterized by a decreased incidence of normal or even absent peristalsis after swallowing, often accompanied by repetitive tertiary contractions and failure of relaxation of the lower oesophageal sphincter. Oesophageal dysmotility is also seen in scleroderma and other connective tissue diseases where atrophic smooth muscle is replaced by fibrous tissue in the submucosa and lamina propria.

Gastro-oesophageal reflux

Gastro-oesophageal reflux is described in Chapter 63.

Hiatus hernia

Hiatus hernia is described in Chapter 55.

MEDIASTINAL IMAGING

Mediastinal structures may be viewed using X-ray, CT and MRI.

Normal mediastinal contours on a frontal chest radiograph

In the posteroanterior (PA) chest radiograph, the X-ray beam enters the posterior thoracic wall and exits the anterior thoracic wall during a full inspiratory breath-hold. The patient stands and flexes and partly abducts the arms over the radiographic detector; this protracts the scapulae and depresses the medial ends of the clavicles to clear the peripheral lung fields and lung apices, respectively. In this view, the heart and large blood vessels appear as the 'mediastinal silhouette' (**Fig. 56.17A**). Forming its left border, from superior to inferior, are the aortic arch ('aortic knuckle') sometimes with the left superior intercostal vein visible upon it ('aortic nipple'), left pulmonary artery and left ventricle. The descending thoracic aorta is projected as a continuous left paravertebral border to the respiratory diaphragm. The right border is delineated by structures containing deoxygenated blood: from superior to inferior are the right brachiocephalic vein, superior vena cava, right atrium and thoracic inferior vena cava. The right paratracheal stripe (up to 3 mm wide) is seen with the oval silhouette of the azygos vein arching anteriorly at its lower margin. In paediatric patients it is normal for the right lobe of the thymus to show as an opaque rightward triangular extension (thymic sail sign) (**Fig. 56.17B**). This appearance should not be confused with right upper lobe pneumonia.

An accessory lung fissure, the azygos fissure, is seen in 0.5% of posteroanterior chest radiographs, extending from the lung apex to the right tracheobronchial angle. The width of the azygos vein as it arches anteriorly to join the superior vena cava should be no more than 5 mm, but may measure up to 10 mm in the third trimester of pregnancy reflecting a physiological blood volume increase and the fact that flow through the inferior vena cava may be diminished as a result of compression by the uterus, with compensatory drainage through the azygos system. Congenital inferior vena cava interruption at the respiratory diaphragm or acquired inferior vena cava thrombosis also enlarge the azygos vein.

Dilation or displacement of any of these structures accentuates the normal bulges on the borders of the mediastinal silhouette; for example, an enlarged left auricle caused by mitral valve stenosis is seen between the left pulmonary artery and left ventricle. Pulmonary vessels associated with the roots of the lungs form the hilar contours. Superiorly, the anterior junctional line (representing the apposition of the left and right pleural cavities and lungs in the supracardiac region in the median plane), and inferiorly, the posterior junctional line (representing the apposition of the parietal pleura and pleural cavities posterior to the oesophagus), are sometimes visible. The azygo-oesophageal line (representing the medial border of the right lung in the azygo-oesophageal recess (see Fig. 56.7A)), can also sometimes be seen. The paraspinal lines are visible parallel to the right and left margins of the thoracic vertebral column.

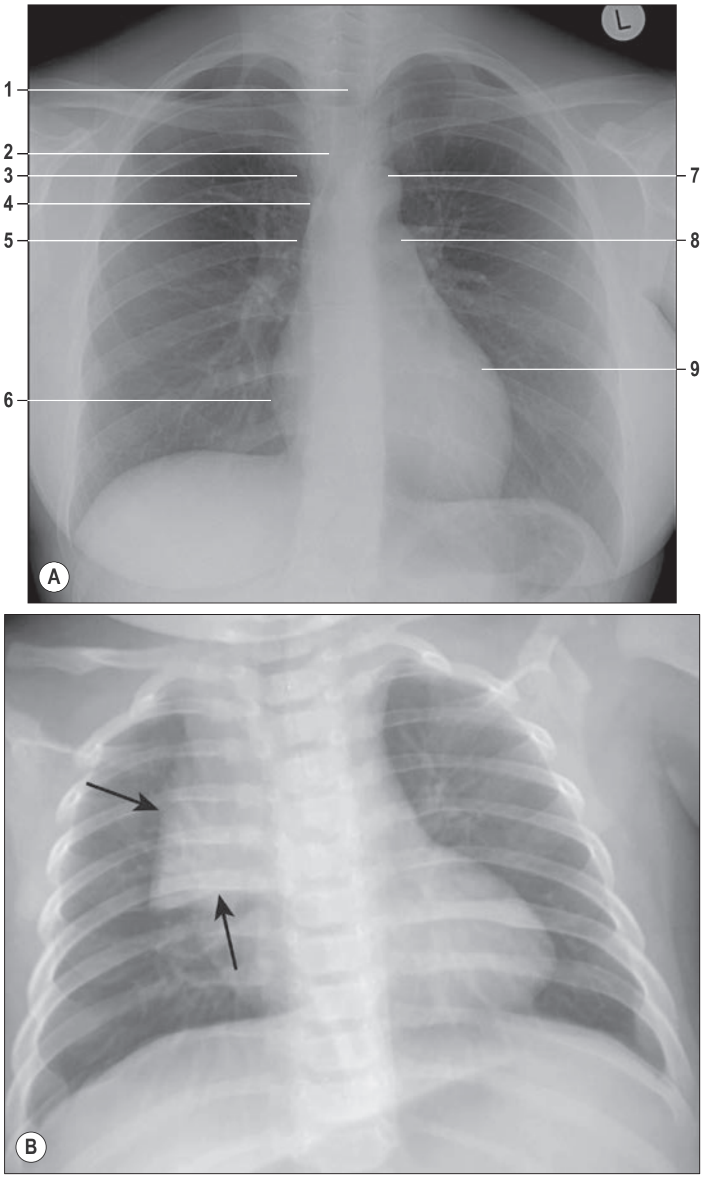

Fig. 56.17 Thoracic radiographs. **A**, A posteroanterior radiograph of an adult female thorax. Key: 1, trachea; 2, wall of right trachea (paratracheal stripe); 3, right brachiocephalic vein; 4, azygos vein; 5, superior vena cava; 6, right atrium (right pulmonary surface of the heart); 7, aortic arch; 8, left pulmonary artery; 9, left ventricle (left pulmonary surface of the heart). **B**, An anteroposterior radiograph of a paediatric thorax showing the normal 'thymic sail sign' (arrows). (With permission from Epelman M 2017 Fundamentals of Pediatric Imaging. Elsevier. Copyright 2017.)

Normal mediastinal contours on a lateral chest radiograph

On a lateral view, the cardiac silhouette in the middle mediastinum is seen above the anterior, horizontal part of the respiratory diaphragm (**Fig. 56.18**). The nomenclature of the cardiac chambers reflects their pre-rotational embryonic state: the right ventricle and left atrium form the anterior and posterior cardiac contours, respectively. Posteriorly, both the descending thoracic aorta and the oesophagus in the posterior mediastinum may be seen; the oesophagus can be visualized with swallowed air or barium on a chest radiograph or fluoroscopically in the barium swallow examination (**Fig. 56.19**). The compressive effect on the oesophagus of a dilated left atrium is readily identified during barium swallow. Superiorly, the less dense trachea and main bronchi are recognizable, the

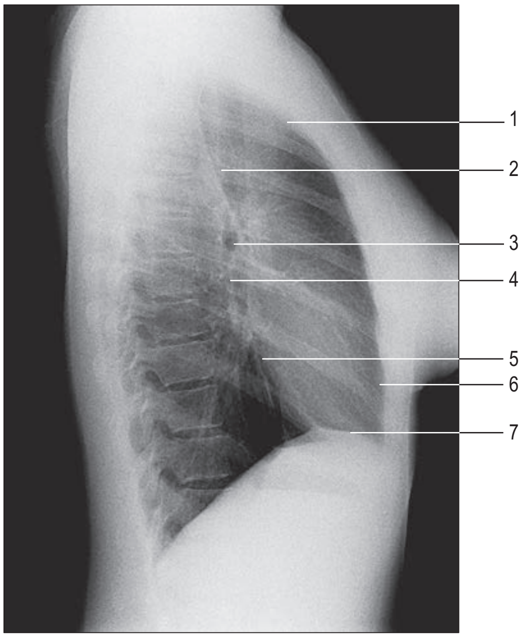

Fig. 56.18 A lateral radiograph of the adult female thorax. Key: 1, retrosternal line (fat); 2, posterior tracheal line; 3, right main bronchus; 4, bronchus intermedius; 5, left atrium; 6, right ventricle; 7, respiratory diaphragm (horizontal part).

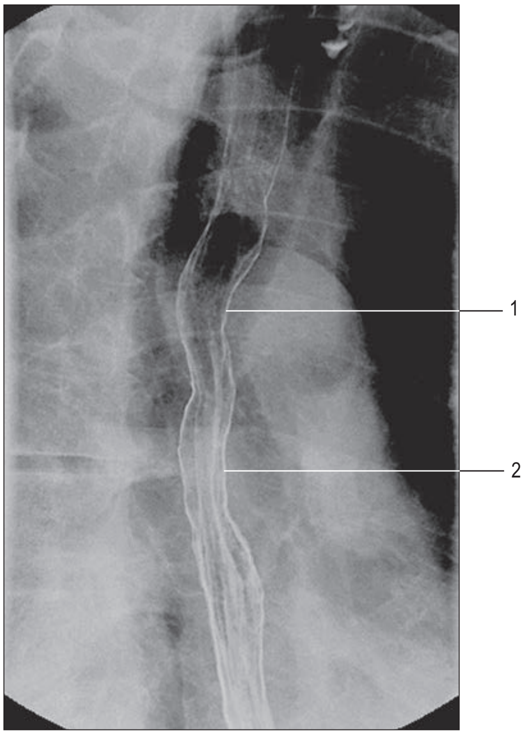

Fig. 56.19 An oblique radiograph of the thorax during barium swallow. Key: 1, indentation from aortic arch; 2, indentation from left main bronchus.

left main bronchus appearing almost circular, seen end-on due to its more horizontal orientation. The oesophagus is directly posterior to the trachea, and the adjacent anterior oesophageal and posterior tracheal walls appear as the posterior paratracheal line, seen in the majority of lateral radiographs and normally less than 5 mm wide.

The aortic arch and its main branches, anterior to the trachea, produce faint shadows in the superior mediastinum. The brachiocephalic veins are visible as an extrapleural bulge directly posterior to the manubrium. Retrosternal lung should always be seen; if it is absent, this raises a strong suspicion of a superior mediastinal tumour or lymphadenopathy. The thoracic part of the inferior vena cava is visible in the majority of patients as it drains into the right atrium.

CT and MRI of the mediastinal spaces

CT provides excellent mediastinal delineation (Figs 56.20–56.21), with intravenous contrast enhancement enabling normal anatomy to be distinguished from pathological lymph nodes and tumours. The hilar, pretracheal, subcarinal, right paratracheal, posterior tracheal and subaortic stations are common sites of lymph node metastases in lung cancer.

The pretracheal space, as seen on CT, is bordered by the trachea posteriorly, the superior vena cava and right brachiocephalic vein anteriorly, and the descending thoracic aorta and superior aortic recess of the transverse pericardial sinus to the left. The subaortic node station (located in the aortopulmonary window/interval) is located between the aortic arch superiorly, the left pulmonary artery inferiorly, the trachea medially and the left lung laterally. The right paratracheal space is between the right lung and the trachea on its anterolateral aspect; the posterior tracheal space is between the lung and the posterolateral aspect of the trachea; and the subcarinal space inferior to the carina is bounded by the main bronchi. On the right, the azygo-oesophageal recess (see Fig. 56.7A) is located posterior to the subcarinal space and on the left side is the oesophagus. All these areas are in direct continuity with each other and are inspected during transcervical mediastinoscopy.

The junctional areas are where the right and left lungs approach and often contact each other at the median plane. The anterior junction lies between the great vessels posteriorly, the posterior surface of the sternum and adjacent thoracic wall anteriorly, and the lungs laterally, specifically in the region where the left brachiocephalic vein, superiorly located mediastinal nodes, thymus and phrenic nerves are located. The posterior junction is an area posterior to the trachea and is where the pleurae-covered lungs appose. The paraspinal area (thoracic paravertebral space) lies between the lateral margins of the vertebral column and the pleurae covering the lungs and contains the intercostal vessels, the ganglionated sympathetic trunk and small lymph nodes surrounded by adipose tissue. The retrocrural space, between the diaphragmatic crura and vertebral bodies, is traversed by the descending thoracic aorta, azygos venous system, thoracic duct, intercostal arteries, sympathetic trunks and sympathetic thoracic splanchnic nerves.

Bonus e-book content

Fig. 56.5 The thoracic and right lymphatic ducts, and their tributaries.

Fig. 56.9 **B–E**, CT images of the chest with contrast medium showing the thymus in the anterior mediastinum at various ages.

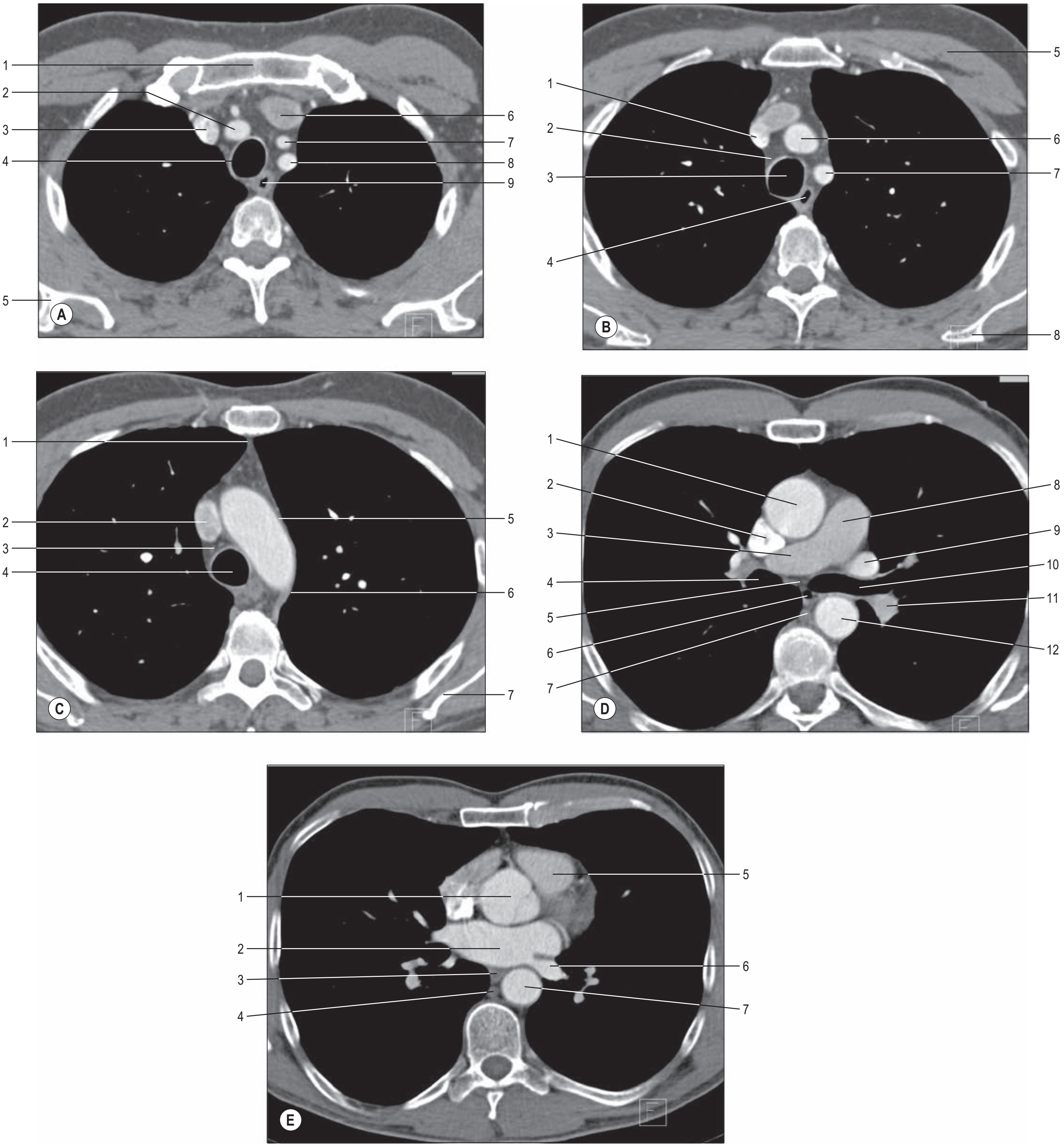

Fig. 56.20 Serial axial CT thoracic sections. **A**, At the level of the first costochondral junction. Key: 1, manubrium of the sternum; 2, brachiocephalic trunk; 3, right brachiocephalic vein; 4, trachea; 5, scapula; 6, left brachiocephalic vein; 7, left common carotid artery; 8, left subclavian artery; 9, oesophagus. **B**, At the level of the vertebral body of T3. Key: 1, superior vena cava formation; 2, pretracheal space; 3, trachea; 4, oesophagus; 5, pectoralis major; 6, left subclavian artery arising from brachiocephalic trunk (normal variant); 7, left subclavian artery; 8, scapula. **C**, At the level of the vertebral body of T4. Key: 1, anterior junction of parietal pleura; 2, superior vena cava; 3, pretracheal space; 4, trachea; 5, aortic arch; 6, oesophagus; 7, scapula. **D**, At the level of the vertebral body of T6. Key: 1, ascending aorta; 2, superior vena cava; 3, right pulmonary artery; 4, right main bronchus; 5, subcarinal space; 6, oesophagus; 7, azygos vein; 8, trunk of pulmonary artery; 9, left superior pulmonary vein; 10, left main bronchus; 11, inferior branch of the left pulmonary artery; 12, descending thoracic aorta. **E**, At the level of the vertebral body of T7. Key: 1, aortic root; 2, left atrium; 3, oesophagus; 4, azygos vein; 5, right ventricular outflow tract; 6, left inferior pulmonary vein; 7, descending thoracic aorta.

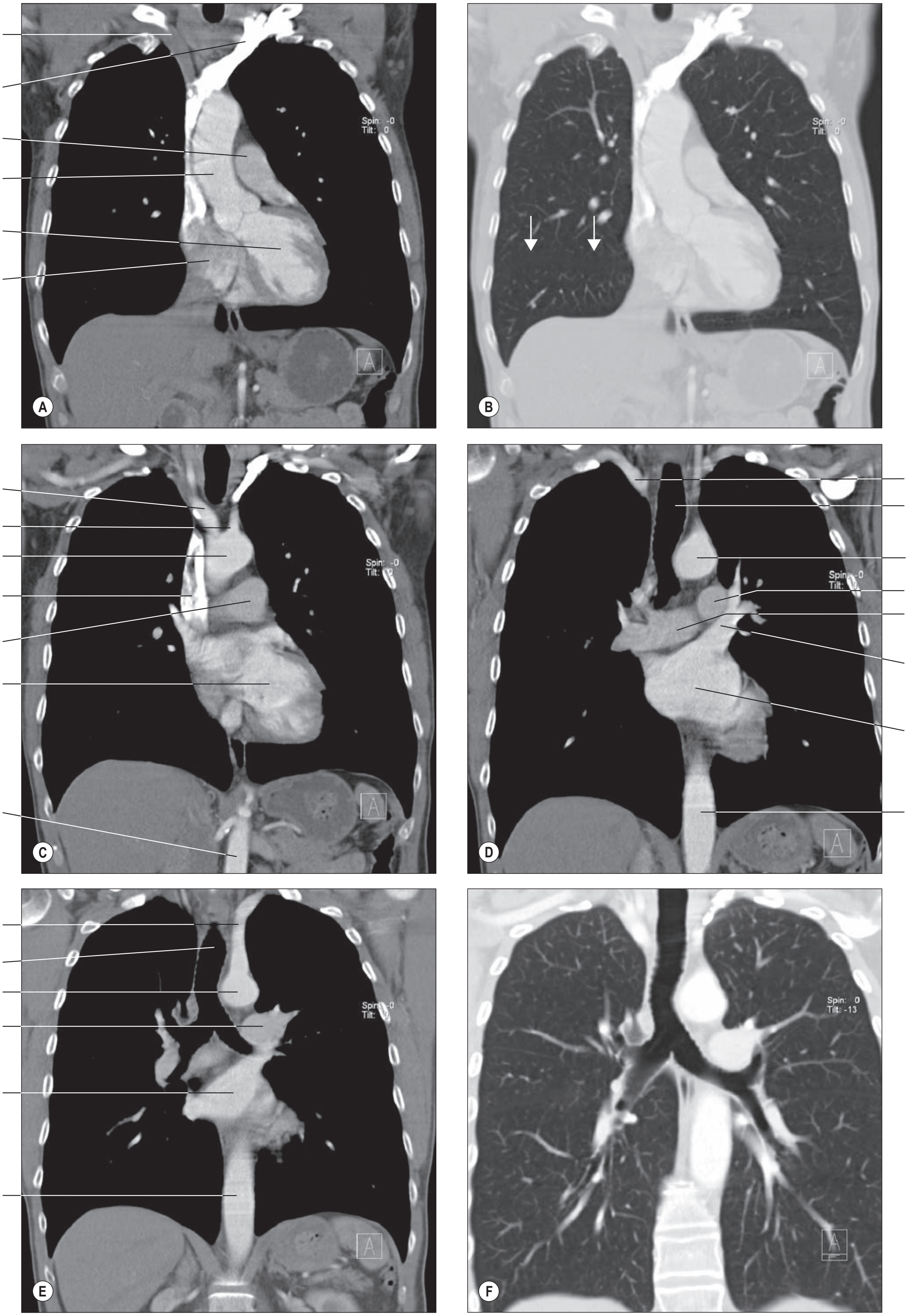
1
2
3
4
5
6
Spin: -0
Tilt: 0
A
Spin: -0
Tilt: 0
B
1
2
3
4
5
6
7
Spin: -0
Tilt: 0
C
1
2
3
4
5
6
7
8
Spin: -0
Tilt: 0
D
1
2
3
4
5
6
Spin: -0
Tilt: 0
E
Spin: 0
Tilt: -13
F

Fig. 56.21 Serial coronal thoracic CT sections. **A**, Key: 1, right brachiocephalic vein; 2, left brachiocephalic vein; 3, pulmonary trunk; 4, ascending aorta; 5, left ventricle; 6, right atrium. **B**, As **A**, but with lung window settings and showing the horizontal fissure (arrows). **C**, Key: 1, brachiocephalic trunk; 2, left common carotid artery; 3, aortic arch; 4, superior vena cava; 5, pulmonary trunk; 6, left ventricle; 7, abdominal aorta. **D**, Key: 1, right subclavian artery; 2, trachea; 3, aortic arch; 4, left pulmonary artery; 5, right pulmonary artery; 6, left superior pulmonary vein; 7, left atrium; 8, descending thoracic aorta. **E**, Key: 1, left subclavian artery; 2, trachea; 3, aortic arch; 4, left pulmonary artery; 5, left atrium; 6, descending thoracic aorta. **F**, As **E**, but with lung window settings.

Key references

Kawashima T 2011 Anatomy of the cardiac nervous system with clinical and comparative morphological implications. Anat Sci Int 86:30–49.

An exploration of the future implications of autonomic cardiac nervous system (ACNS) preservation in cardiovascular surgery.

Kuntz A 1927 Distribution of the sympathetic rami to the brachial plexus: its relation to sympathectomy affecting the upper extremity. Arch Surg 15:871–7.

A description of 'Kuntz's nerves'; intrathoracic somatic branches from the second thoracic spinal nerve which join the first thoracic spinal nerve without passing through the stellate ganglion, explaining the incomplete sympathetic blockade of the upper extremities in stellate ganglion blockade.

Loukas M, Tubbs RS 2016 Adrenal, renal, gonadal, azygos, hemiazygos, lumbar, and ascending lumbar veins. In: Tubbs RS, Shoja MM, Loukas M (eds) Bergman's Comprehensive Encyclopedia of Human Anatomic Variation, 2nd ed. Hoboken: Wiley Blackwell; Ch. 69, pp. 890–3.

A description of the normal anatomy of the venous drainage of the posterior body wall with a comprehensive listing of the variations and developmental anomalies.

Rusch VW, Asamura H, Watanabe H et al 2009 The IASLC lung cancer staging project: a proposal for a new international lymph node map in the forthcoming seventh edition of the TNM classification for lung cancer. J Thorac Oncol 4:568–77.

A recommendation for a standardized grouping of lymph node stations together into 'zones' for consistency and the purposes of future survival analyses.

Song Y-B 2016 Thoracic duct, chyle cistern and right lymphatic duct. In: Tubbs RS, Shoja MM, Loukas M (eds) Bergman's Comprehensive Encyclopedia of Human Anatomic Variation, 2nd ed. Hoboken: Wiley Blackwell; Ch. 75, pp. 921–34.

A description of the lymphatic passages of the abdominal and thoracic regions. Also includes a description of the variation in the length and pathway of the thoracic duct.

Varga I 2016 Thymus. In: Tubbs RS, Shoja MM, Loukas M (eds) Bergman's Comprehensive Encyclopedia of Human Anatomic Variation, 2nd ed. Hoboken: Wiley Blackwell; Ch. 73, pp. 914–18.

A description of the normal appearance of the thymus gland, morphological variations and the locations for ectopic thymic tissue.

Wang Y, Zhu L, Xia W et al 2018 Anatomy of lymphatic drainage of the esophagus and lymph node metastasis of thoracic esophageal cancer. Cancer Manag Res 10:6295–303.

A review of the various routes of lymphatic drainage of the oesophagus and lymph node metastasis rates to specific node groups.

Watanabe K 2016 Esophagus. In: Tubbs RS, Shoja MM, Loukas M (eds) Bergman's Comprehensive Encyclopedia of Human Anatomic Variation, 2nd ed. Hoboken: Wiley Blackwell; Ch. 105, pp. 1247–52.

A description of the oesophagus, its development, and the acquired or congenital anomalies that can affect the organ. Variations in oesophageal musculature are discussed.

Yang GS, Bishop WP, Smith BJ et al 2005 Radiographic and endoscopic measurements of esophageal length in pediatric patients. Ann Otol Rhinol Laryngol 114:587–92.

This article discusses the intersphincteric length of the oesophagus in a pediatric population, which best correlated with patient height and correlated less well with weight and age.

References

Asghar A, Syed YM, Nafis FA 2012 Polymorphism of Hassall's corpuscles in thymus of human fetuses. Int J Appl Basic Med Res 2:7–10.

Bilge O, Celik S, Aktug H.2013 The pleuro-esophageal muscle: a disregarded anatomical structure. Anat Sci Int.88:97–100.

Chansky K, Detterbeck FC, Nicholson AG et al 2017 The IASLC Lung Cancer Staging Project: External Validation of the Revision of the TNM Stage Groupings in the Eighth Edition of the TNM Classification of Lung Cancer. J Thorac Oncol 12:1109–21.

Cho HM, Lee DY, Sung SW 2005 Anatomical variations of rami communicantes in the upper thoracic sympathetic trunk. Eur J Cardiothorac Surg 27:320–4.

Deso S, Ludwig B, Kabutey NK et al 2012 Lymphangiography in the diagnosis and localization of various chyle leaks. Cardiovasc Intervent Radiol 35:117.

Devulapalli C, Anderson J, Llore NNP et al 2016 Thoracic duct ligation: right video-assisted thoracoscopic surgery approach. Op Tech Thor Cardiovasc Surg 21:152–9.

Doerr CH, Miller DL, Ryu JH 2001 Chylothorax. Semin Respir Crit Care Med 22:617.

Garly ML, Trautner SL, Marx C et al 2008 Thymus size at 6 months of age and subsequent child mortality. J Pediatr 153:683–8, 688.e1–3.

Gofeld M, Faclier G 2006 Bilateral pain relief after unilateral thoracic percutaneous sympathectomy. Can J Anaesth 53:258–62.

Goldstraw P, Chansky K, Crowley J et al 2016 The IASLC Lung Cancer Staging Project: Proposals for revision of the TNM stage groupings in the forthcoming (eighth) edition of the TNM classification for lung cancer. J Thorac Oncol 11:39–51.

Han BK, Babcock DS, Oestreich AE 1989 Normal thymus in infancy: sonographic characteristics. Radiology 170:471–4.

Henry L, Durrant TE, Anderson GJ 1992 Pericapillary collagen in the human thymus: implications for the concept of the 'blood–thymus' barrier. J Anat 181(Pt 1):39–46.

Irwin PA, Tubbs RI, Tubbs RS 2016 Autonomic nervous system. In: Tubbs RS, Shoja MM, Loukas M (eds) Bergman's Comprehensive Encyclopedia of Human Anatomic Variation, 2nd ed. Hoboken: Wiley Blackwell; Ch 88, pp. 1050–6.

Jaretzki III A 1997 Thymectomy for myasthenia gravis: analysis of the controversies regarding technique and result. Neurology 48 (Suppl 5):S52–-S63.

Kaisha Otsianyi W, Mutie T, Kioko HM 2011 The correlation of esophageal body length with measure of external body parameters. Int J Morphol 29:895–8.

Kawashima T 2011 Anatomy of the cardiac nervous system with clinical and comparative morphological implications. Anat Sci Int 86:30–49.

An exploration of the future implications of autonomic cardiac nervous system (ACNS) preservation in cardiovascular surgery.

Kuntz A 1927 Distribution of the sympathetic rami to the brachial plexus: its relation to sympathectomy affecting the upper extremity. Arch Surg 15:871–7.

A description of 'Kuntz's nerves'; intrathoracic somatic branches from the second thoracic spinal nerve which join the first thoracic spinal nerve without passing through the stellate ganglion, explaining the incomplete sympathetic blockade of the upper extremities in stellate ganglion blockade.

Lim W, Ridge CA, Nicholson AG et al 2018 The 8th lung cancer TNM classification and clinical staging system: review of the changes and clinical implications. Quant Imaging Med Surg 8:709–18.

Loukas M, Tubbs RS 2016 Adrenal, renal, gonadal, azygos, hemiazygos, lumbar, and ascending lumbar veins. In: Tubbs RS, Shoja MM, Loukas M (eds) Bergman's Comprehensive Encyclopedia of Human Anatomic Variation, 2nd ed. Hoboken: Wiley Blackwell; Ch. 69, pp. 890–3.

A description of the normal anatomy of the venous drainage of the posterior body wall with a comprehensive listing of the variations and developmental anomalies.

Manchanda S, Bhalla AS, Jana M et al 2017 Imaging of the pediatric thymus: clinicoradiologic approach. World J Clin Pediatr 6(1):10–23.

Miller FH, Fitzgerald SW, Donaldson JS 1993 CT of the azygoesophageal recess in infants and children. Radiographics 13:623–34.

Mirjalili S, Hale S, Buckenham T et al 2012 A reappraisal of adult thoracic surface anatomy. Clin Anat 25:827–34.

Mountain CF, Dresler CM 1997 Regional lymph node classification for lung cancer staging. Chest 111:1718–23.

Mussa BM, Verberne AJ 2013 The dorsal motor nucleus of the vagus and regulation of pancreatic secretory function. Exp Physiol 98:25–37.

Raica M, Encică S, Motoc A et al 2006 Structural heterogeneity and immunohistochemical profile of Hassall corpuscles in normal human thymus. Ann Anat 188:345–52.

Rami-Porta R, Call S 2012 Invasive staging of mediastinal lymph nodes: mediastinoscopy and remediastinoscopy. Thorac Surg Clin 22:177–89.

Rusch VW, Asamura H, Watanabe H et al 2009 The IASLC lung cancer staging project: a proposal for a new international lymph node map in the forthcoming seventh edition of the TNM classification for lung cancer. J Thorac Oncol 4:568–77.

A recommendation for a standardized grouping of lymph node stations together into 'zones' for consistency and the purposes of future survival analyses.

Segni M, di Nardo R, Pucarelli I et al 2011 Ectopic intrathyroidal thymus in children: a long-term follow-up study. Horm Res Paediatr 75:258–63.

Sklair-Levy M, Agid R, Sella T et al 2000 Age-related changes in CT attenuation of the thymus in children. Pediatr Radiol 30:566–9.

Smith ME, Riffat F, Jani P 2013 The surgical anatomy and clinical relevance of the neglected right lymphatic duct: review. J Laryngol Otol 127:128–33.

Song Y-B 2016 Thoracic duct, chyle cistern and right lymphatic duct. In: Tubbs RS, Shoja MM, Loukas M (eds) Bergman's Comprehensive Encyclopedia of Human Anatomic Variation, 2nd ed. Hoboken: Wiley Blackwell; Ch 75, pp. 921–34.

Turner BG, Gee DW, Cizginer S et al 2010 Endoscopic transesophageal mediastinal lymph node dissection and en bloc resection by using mediastinal and thoracic approaches (with video). Gastrointest Endosc 72:831–5.

van de Wal-Visscher E, Nieuwenhuijzen GA, van Sambeek MR et al 2011 Type B aortic dissection resulting in acute oesophageal necrosis. Ann Vasc Surg 25:837.

Varga I 2016 Thymus. In: Tubbs RS, Shoja MM, Loukas M (eds) Bergman's Comprehensive Encyclopedia of Human Anatomic Variation, 2nd ed. Hoboken: Wiley Blackwell; Ch. 73, pp. 914–18.

A description of the normal appearance of the thymus gland, morphological variations and the locations for ectopic thymic tissue.

Varga I, Uhrinova A, Toth F et al 2011 Assessment of the thymic morphometry using ultrasound in full-term newborns. Surg Radiol Anat 33:689–95.

Wang Y, Zhu L, Xia W et al 2018 Anatomy of lymphatic drainage of the esophagus and lymph node metastasis of thoracic esophageal cancer. Cancer Manag Res 10:6295–303.

A review of the various routes of lymphatic drainage of the oesophagus and lymph node metastasis rates to specific node groups.

Watanabe K 2016 Esophagus. In: Tubbs RS, Shoja MM, Loukas M (eds) Bergman's Comprehensive Encyclopedia of Human Anatomic Variation, 2nd ed. Hoboken: Wiley Blackwell; Ch. 105, pp. 1247–52.

A description of the oesophagus, its development, and the acquired or congenital anomalies that can affect the organ. Variations in oesophageal musculature are discussed.

Weerkamp F, de Haas EF, Naber BA et al 2005 Age-related changes in the cellular composition of the thymus in children. J Allergy Clin Immunol 115:834–40.

Wemyss-Holden SA, Launois B, Maddern GJ 2001 Management of thoracic duct injuries after oesophagectomy. Br J Surg 88:1442–8.

Wind GG, Valentine RJ 2013 Carotid arteries. In: Anatomic Exposures in Vascular Surgery. Philadelphia: Wolters Kluwer, Lippincott Williams & Wilkins; Ch. 1, pp. 23–50.

Wolfe GI, Kaminski HJ, Aban IB et al 2016 Randomized trial of thymectomy in myasthenia gravis. N Engl J Med 375:511–22. [Published correction appears in N Engl J Med 2017;376:2097. [Dosage error in article text].]

Yang GS, Bishop WP, Smith BJ et al 2005 Radiographic and endoscopic measurements of esophageal length in pediatric patients. Ann Otol Rhinol Laryngol 114:587–92.

This article discusses the intersphincteric length of the oesophagus in a pediatric population, which best correlated with patient height and correlated less well with weight and age.

Yoshioka K, Niinuma H, Ohira A et al 2003 MR angiography and CT angiography of the artery of Adamkiewicz: noninvasive preoperative assessment of thoracoabdominal aortic aneurysm. RadioGraphics 23:1215–25.

CHAPTER

57

Heart

PERICARDIUM

The pericardium contains the heart and the juxtacardiac parts of its great vessels (**Fig. 57.1**). It consists of two parts, the fibrous and the serous pericardia, arranged in three layers with a normal combined thickness of 1–2 mm, as seen on cross-sectional imaging (**Figs 57.2–57.3**). The fibrous pericardium is a closed sac made of tough connective tissue, completely surrounding but unattached to the heart (see Fig. 56.7). It develops through a sequential process of cavitation of the embryonic body wall by expansion of the secondary pleural cavity; its lateral walls are thus covered by the mediastinal part of the parietal pleura. The serous pericardium consists of two layers: the inner, visceral layer adheres to the heart and forms its outer, epicardial, covering and the outer, parietal layer adheres to the internal surface of the fibrous pericardium (Rodriguez and Tan 2017a). Except at their points of reflection, the two serous pericardial membranes are separated by a narrow space, the pericardial cavity, which contains a thin film of fluid that provides complete separation between the heart and its surroundings, allowing freedom of cardiac motion and shape change.

Many functions have been attributed to the pericardium. These include facilitating intrathoracic cardiac stability (via the sternopericardial ligaments and the fusion of the fibrous pericardium with the central diaphragmatic tendon and adventitia of the great vessels); reducing friction between the heart and the mediastinal structures; limiting cardiac distension and chamber dilation and so preventing hypertrophy; ensuring uniform cardiac distribution of pericardial cavity hydrostatic pressure, preventing ventriculoatrial regurgitations under increased ventricular end-diastolic pressure; forming a barrier to the spread of infection; facilitating atrial filling by promoting negative pericardial pressure during ventricular systole; and, in association with the pleural fluid, forming a system that automatically applies compensating hydrostatic pressures to the cardiac periphery when accelerating forces act.

Fibrous and serous pericardium

Fibrous pericardium

The fibrous pericardium is a roughly conical, compact, covering composed mainly of three collagen layers, cross-woven at 120° to each other; this arrangement limits stretch and ensures a physical barrier to disease. Three anchor points, superior, inferior and anterior, secure the pericardium and help maintain the normal intrathoracic cardiac disposition. The pericardium is continuous superiorly with the adventitia of the great vessels and the pretracheal fascia, inferiorly it is attached to the central diaphragmatic tendon and a small adjacent muscular area to its left, and anteriorly it is attached to the posterior sternal surface via the superior and inferior sternopericardial ligaments (the extent of these ligaments is variable, and the superior is often undetectable).

Anteriorly, the fibrous pericardium is almost completely separated from the thoracic wall by the costomediastinal recess of the parietal pleura and the lungs during inspiration (see Fig. 53.4B). However, in a small area posterior to the lower left half of the body of the sternum and the sternal ends of left fourth and fifth costal cartilages, the pericardium is in direct contact with the thoracic wall, and, until it regresses during early adulthood, the inferior extent of the thymus is anterior to the superior part of the pericardium. The main bronchi, oesophagus, descending thoracic aorta and posterior parts of the mediastinal surface of both lungs are all posterior relations. Laterally, the mediastinal parts of the parietal pleurae cover the mediastinal surfaces of the lungs. The phrenic nerve and pericardiacophrenic vasculature descend on each side between the fibrous pericardium and mediastinal part of the parietal pleura (see Fig. 56.7). Inferiorly, the pericardium is separated from the liver and gastric fundus by the respiratory diaphragm and the diaphragmatic fascia and parietal peritoneum covering its inferior (abdominal) surface. The ascending aorta, superior vena cava and the pulmonary arteries and veins all receive extensions of the fibrous pericardium; the inferior vena cava traverses the central tendon of the diaphragm and so has no such covering.

Serous pericardium

The serous pericardium forms the closed pericardial cavity (sac) within the fibrous pericardium. It has visceral and parietal layers. The parietal layer lines the internal surface of the fibrous pericardium. The visceral layer, or epicardium, covers the heart and great vessels, and at specific points folds back on itself (reflects) to become continuous with the parietal layer (see Fig. 57.1). The visceral layer of serous pericardium is a single layer composed of ciliated mesothelial cells supported on a thin subserosal layer of connective tissue rich in elastic fibres. The serosal cilia increase the surface area for fluid production and resorption, and reduce friction between the opposing pericardial layers. The visceral layer blends with interstitial myocardial tissue. The cardiac subserosal layer contains fat, especially along the ventricular side of the atrioventricular and interventricular sulci (grooves) and the inferior cardiac border. The main coronary vessels and their larger branches are embedded in this fat; the amount is related to the general extent of body fat and gradually increases with age. The anterior cardiophrenic angles typically possess increased epipericardial fat, which can be mistakenly identified as an abnormal mass on imaging (Rodriguez and Tan 2017b). The amount of epicardial adipose tissue may be a cardiometabolic risk factor, with increasing thickness linked to metabolic syndrome and diabetes mellitus. A significant correlation has been demonstrated between obesity in children and the thickness of this fat layer (Ozdemir et al 2010).

Pericardial reflections and sinuses The points of reflection of the serous pericardium around the great veins and arteries of the heart are arranged as two complex pericardial tubes that enclose the ascending aorta and pulmonary trunk and the venae cavae and four pulmonary veins. The perivenous tube is an inverted J in shape: the recess of its inner curve, located posterior to the left atrium and between the left and right superior pulmonary veins, is termed the oblique pericardial sinus. The transverse pericardial sinus is a passage between the two pericardial tubes (see Figs 57.1, 57.24): the ascending aorta and pulmonary trunk are anterior (**Fig. 57.4A,C**), and the atria and their great veins and the superior vena cava are posterior (**Fig. 57.4B,D**).

Pericardial cavity and fluid

The pericardial cavity is the space between the parietal and visceral layers of the serous pericardium. It surrounds the proximal part of the great vessels and the majority of the heart. Part of the cavity extends between the left atrium and descending thoracic aorta. The pericardial cavity in adult humans normally contains 20–60 ml (average 15–35 ml) of fluid (serous plasma ultrafiltrate) (Vogiatzidis et al 2015).

Vascular supply and lymphatic drainage

Approximately 80% of the pericardial blood supply is derived from the right and left internal thoracic arteries by way of the pericardiacophrenic arteries. Inferiorly, the pericardium is supplied by small branches from the intercostal and superior phrenic arteries. The posterior part of the pericardium is supplied from small mediastinal branches that are derived either directly from the descending thoracic aorta or from its oesophageal or bronchial branches. Venous drainage is through tributaries of the azygos venous system, internal thoracic and superior phrenic veins.

Cardiac lymphatics play a crucial role in cardiac function, such as maintaining fluid balance, removal of extravasated proteins and transport of immune cells (Vuorio et al 2016). The developed lymphatic network of the heart traverses all its layers, including those of the atria and ventricles and extends to the mitral valve. Most lymph drainage of the pericardium is to the thoracic and the right lymphatic ducts; upper

The arrangement of the oblique and transverse pericardial sinuses and of the main part of the pericardial cavity is influenced by the development of complex three-dimensional pericardial recesses between adjacent structures, grouped according to the position of their entrances (mouths) (see Fig. 57.1). The postcaval recess projects from the main pericardial cavity towards the left behind the atrial termination of the superior vena cava: it is limited superiorly by the right pulmonary artery and inferiorly by the right superior pulmonary vein, its entrance facing superolaterally and to the right. The right and left pulmonary venous recesses each project superomedially on the posterior surface of the left atrium, between the superior and inferior pulmonary veins on each side, indenting the side walls of the oblique pericardial sinus. The left pulmonary recess has an entrance under the fold of the oblique vein of the left atrium and passes to the left between the inferior aspect of the left pulmonary artery and the superior border of the left superior pulmonary vein. The right pulmonary recess lies between the inferior surface of the proximal part of the right pulmonary artery and the superior border of the left atrium. The superior aortic recess ascends from the transverse pericardial sinus, initially posterior to, and then to the right of, the ascending aorta, ending around the level of the sternal angle. The inferior aortic recess also extends from the transverse pericardial sinus, descending from a superiorly located entrance to run between the inferior part of the ascending aorta and the right atrium.

A triangular fold of serous pericardium reflected from the left pulmonary artery to the inferiorly located left superior pulmonary vein marks the site of the left common cardinal vein during development. It contains a fibrous ligament, a remnant of the left common cardinal vein (left duct of Cuvier) that is usually obliterated during development. This ligament descends anterior to the hilum of the left lung from the superior part of the left superior intercostal vein to the posterior surface of the left atrium, where it is continuous with the oblique vein of the left atrium. The left common cardinal vein may persist sometimes as a left superior vena cava: when present, it replaces the oblique vein of the left atrium and empties into the right atrium through the coronary sinus. When both common cardinal veins persist as a double superior vena cava, the transverse anastomosis between them that normally forms the left brachiocephalic vein may be small or absent. A left superior vena cava is normally joined by the left superior intercostal vein. Knowledge of these recesses and sinuses is important in the avoidance of misdiagnosis of lymphadenopathy or aortic dissection, and in surgical control of the great vessels.

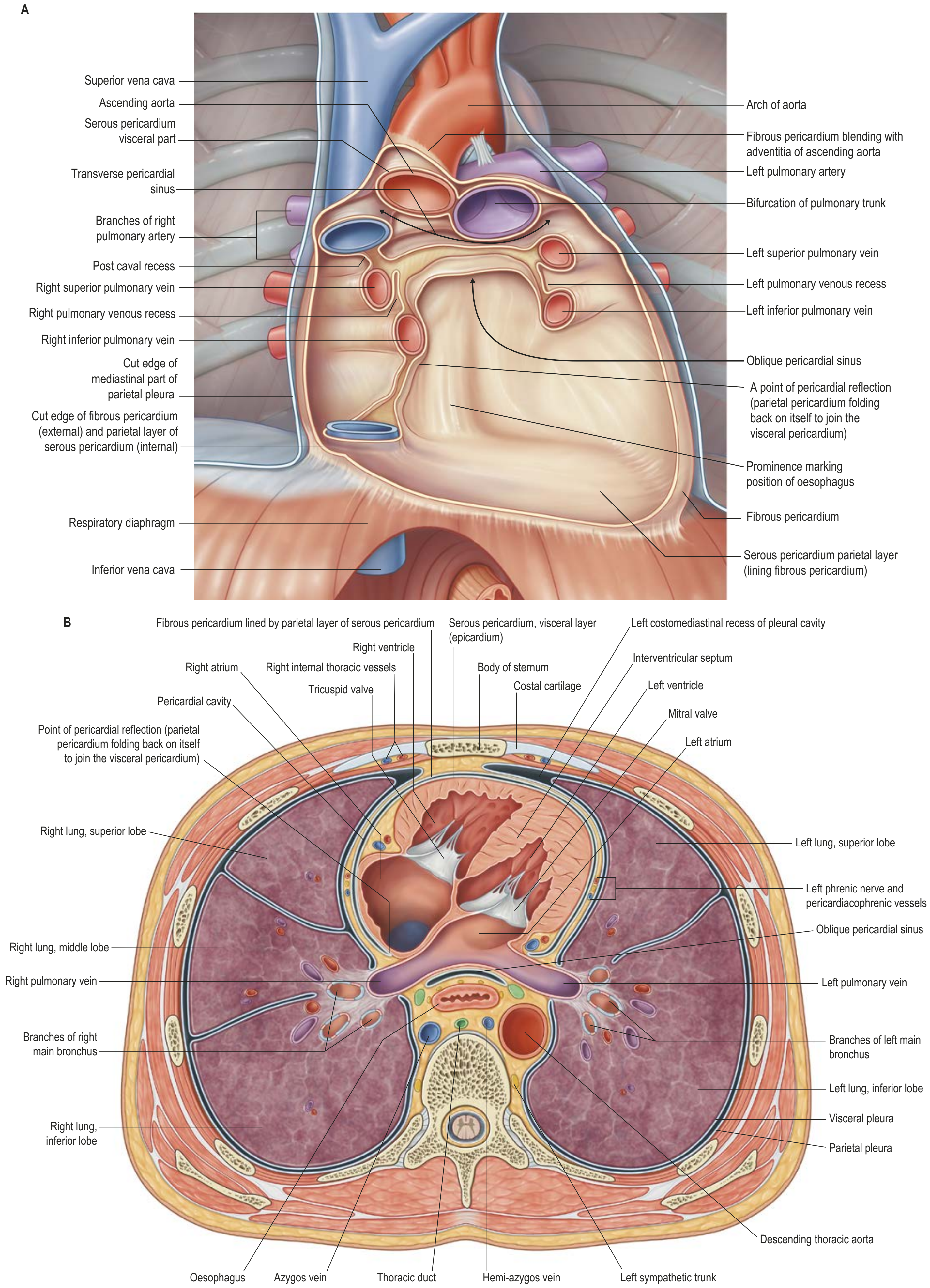
A
Superior vena cava
Ascending aorta
Serous pericardium visceral part
Transverse pericardial sinus
Branches of right pulmonary artery
Post caval recess
Right superior pulmonary vein
Right pulmonary venous recess
Right inferior pulmonary vein
Cut edge of mediastinal part of parietal pleura
Cut edge of fibrous pericardium (external) and parietal layer of serous pericardium (internal)
Respiratory diaphragm
Inferior vena cava
Arch of aorta
Fibrous pericardium blending with adventitia of ascending aorta
Left pulmonary artery
Bifurcation of pulmonary trunk
Left superior pulmonary vein
Left pulmonary venous recess
Left inferior pulmonary vein
Oblique pericardial sinus
A point of pericardial reflection (parietal pericardium folding back on itself to join the visceral pericardium)
Prominence marking position of oesophagus
Fibrous pericardium
Serous pericardium parietal layer (lining fibrous pericardium)
B
Fibrous pericardium lined by parietal layer of serous pericardium
Serous pericardium, visceral layer (epicardium)
Left costomediastinal recess of pleural cavity
Right ventricle
Interventricular septum
Right atrium
Right internal thoracic vessels
Body of sternum
Left ventricle
Tricuspid valve
Costal cartilage
Pericardial cavity
Mitral valve
Point of pericardial reflection (parietal pericardium folding back on itself to join the visceral pericardium)
Left atrium
Right lung, superior lobe
Left lung, superior lobe
Left phrenic nerve and pericardiacophrenic vessels
Oblique pericardial sinus
Right lung, middle lobe
Right pulmonary vein
Left pulmonary vein
Branches of right main bronchus
Branches of left main bronchus
Left lung, inferior lobe
Right lung, inferior lobe
Visceral pleura
Parietal pleura
Descending thoracic aorta
Oesophagus
Azygos vein
Thoracic duct
Hemi-azygos vein
Left sympathetic trunk

Fig. 57.1 Pericardial coverings, cavity, reflections and formations. **A**, Anterior view into the inner surface of the parietal layer of serous pericardium and the pericardial cavity, seen after cutting a window through the fibrous and parietal layer of serous pericardium, sectioning the large vessels at their cardiac origin and removing the heart. The positions of the oblique and transverse pericardial sinuses of the pericardial cavity are indicated. **B**, Transverse section through the thorax showing the heart, pericardial coverings and related viscera. (Adapted with permission from Drake RL, Vogl AW, Mitchell A et al (eds) Gray's Atlas of Anatomy, 2nd ed. Elsevier, Churchill Livingstone. Copyright 2015.)

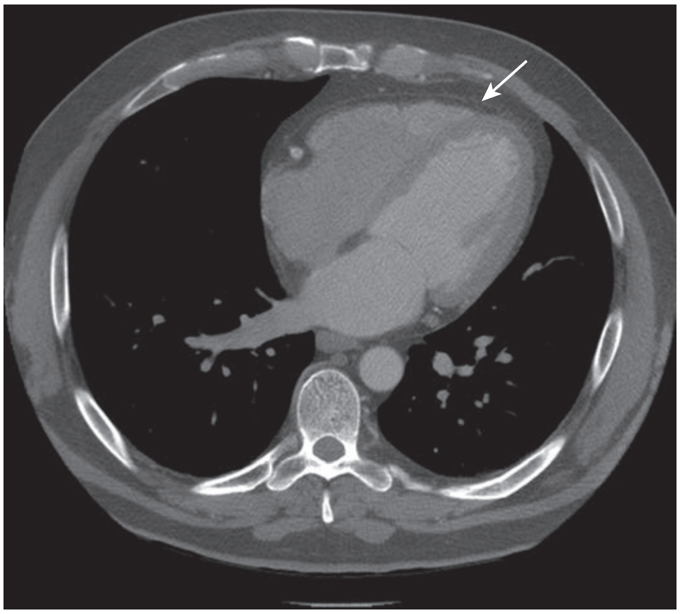

Fig. 57.2 The normal appearance of the pericardium on a contrast enhanced CT of a horizontal long axis view of the heart. The pericardium (white arrow) is a thin (1–3 mm) relatively dense curvilinear structure, anterior to the right ventricle where it is sandwiched between two less dense layers of fat. (With permission from Hutchison SJ 2009 Pericardial Diseases: Clinical Diagnostic Imaging Atlas. Elsevier.)

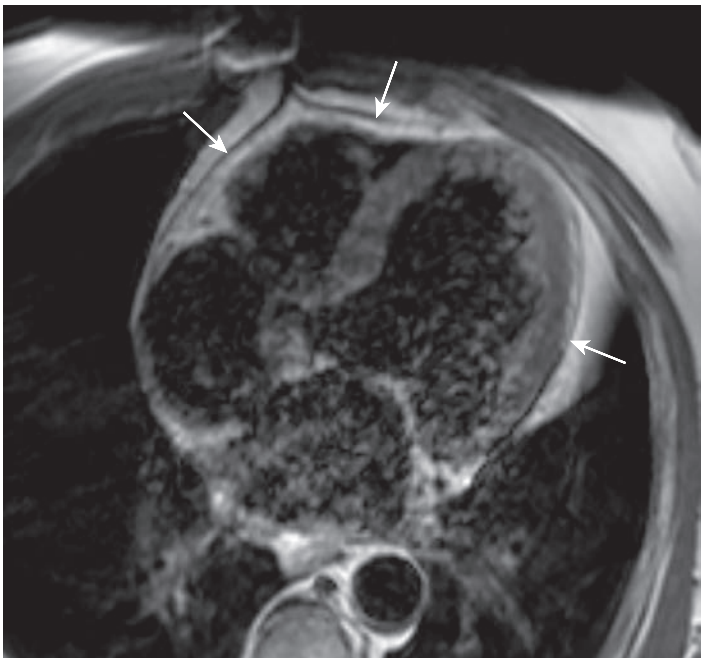

Fig. 57.3 The normal appearance of the pericardium on a T1-weighted four chamber view of the heart. The pericardium is a thin hypointense curvilinear structure (white arrows), that is best observed anterior to the right atrium and right ventricle where it is sandwiched between two hyperintense layers of fat. (With permission from Digumarthy SR, Abbara S, Chung JH 2020 Problem Solving In Chest Imaging. Elsevier).

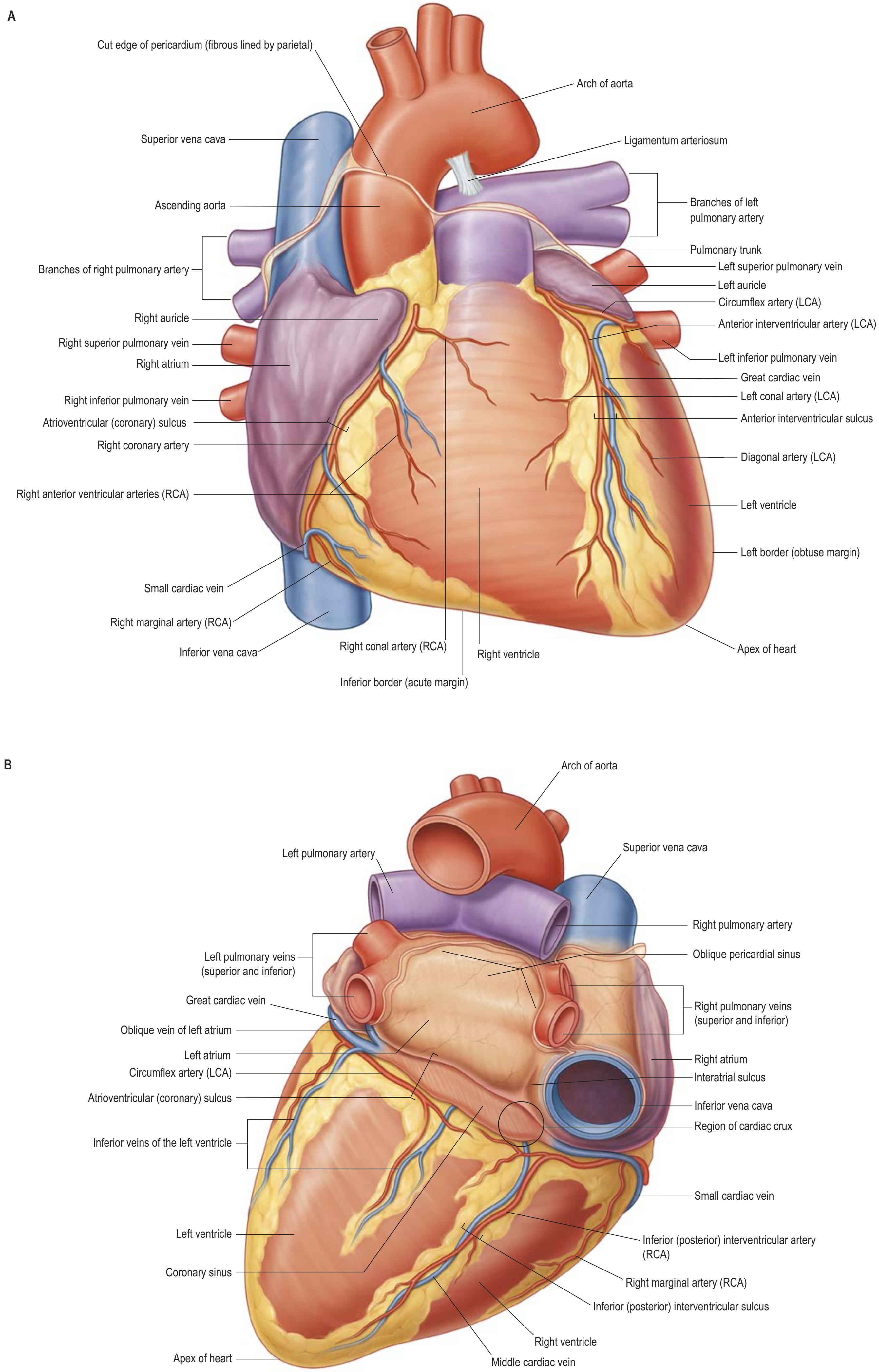

A
Cut edge of pericardium (fibrous lined by parietal)
Arch of aorta
Superior vena cava
Ligamentum arteriosum
Ascending aorta
Branches of left pulmonary artery
Pulmonary trunk
Branches of right pulmonary artery
Left superior pulmonary vein
Left auricle
Circumflex artery (LCA)
Right auricle
Anterior interventricular artery (LCA)
Right superior pulmonary vein
Right atrium
Left inferior pulmonary vein
Great cardiac vein
Right inferior pulmonary vein
Left conal artery (LCA)
Atrioventricular (coronary) sulcus
Anterior interventricular sulcus
Right coronary artery
Diagonal artery (LCA)
Right anterior ventricular arteries (RCA)
Left ventricle
Left border (obtuse margin)
Small cardiac vein
Right marginal artery (RCA)
Inferior vena cava
Right conal artery (RCA)
Right ventricle
Apex of heart
Inferior border (acute margin)
B
Arch of aorta
Left pulmonary artery
Superior vena cava
Right pulmonary artery
Oblique pericardial sinus
Left pulmonary veins (superior and inferior)
Great cardiac vein
Right pulmonary veins (superior and inferior)
Oblique vein of left atrium
Left atrium
Right atrium
Circumflex artery (LCA)
Interatrial sulcus
Atrioventricular (coronary) sulcus
Inferior vena cava
Region of cardiac crux
Inferior veins of the left ventricle
Small cardiac vein
Left ventricle
Inferior (posterior) interventricular artery (RCA)
Coronary sinus
Right marginal artery (RCA)
Inferior (posterior) interventricular sulcus
Right ventricle
Apex of heart
Middle cardiac vein

Fig. 57.4 The heart and great vessels. **A**, Anterior view. **B**, Inferior view. Abbreviations: RCA, branch of right coronary artery; LCA, branch of left coronary artery.

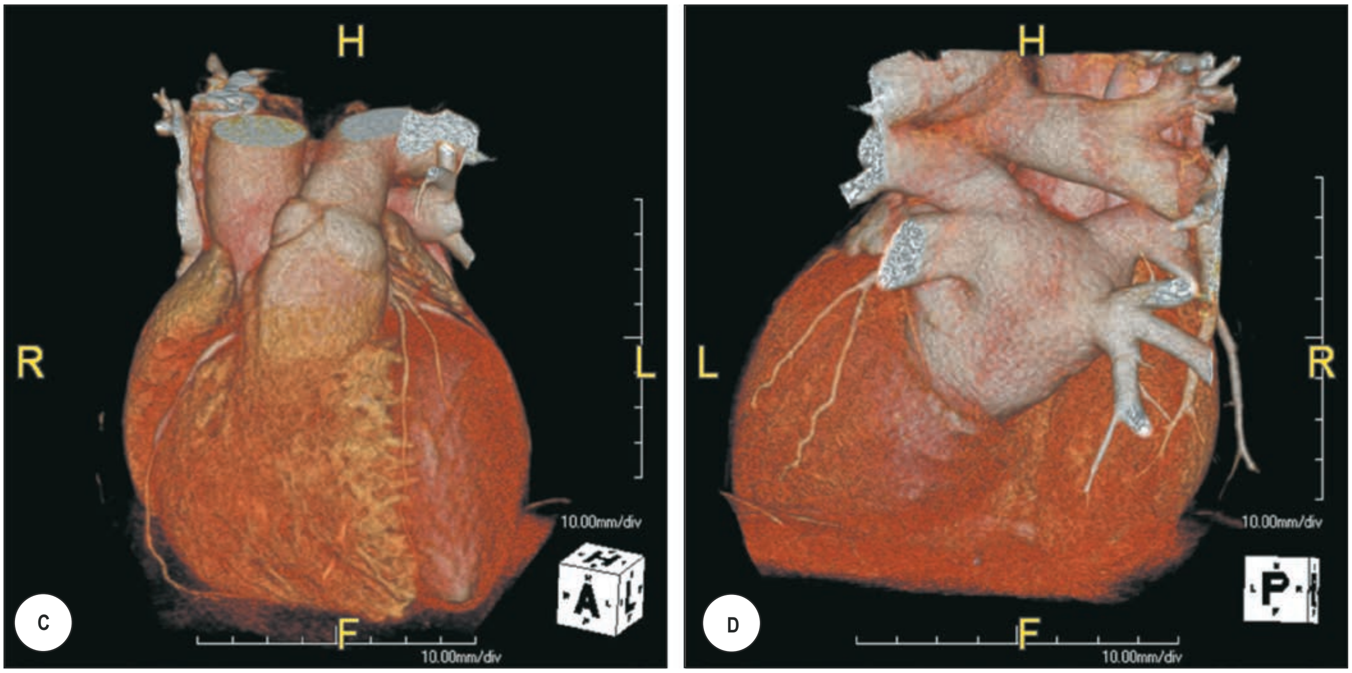
H
R
L
F
10.00mm/div
10.00mm/div
H
A
L
C
H
L
R
F
10.00mm/div
10.00mm/div
P
D

Fig. 57.4, cont'd C–D, Corresponding three-dimensional reconstructions from multislice computed tomography (CT) scanning.

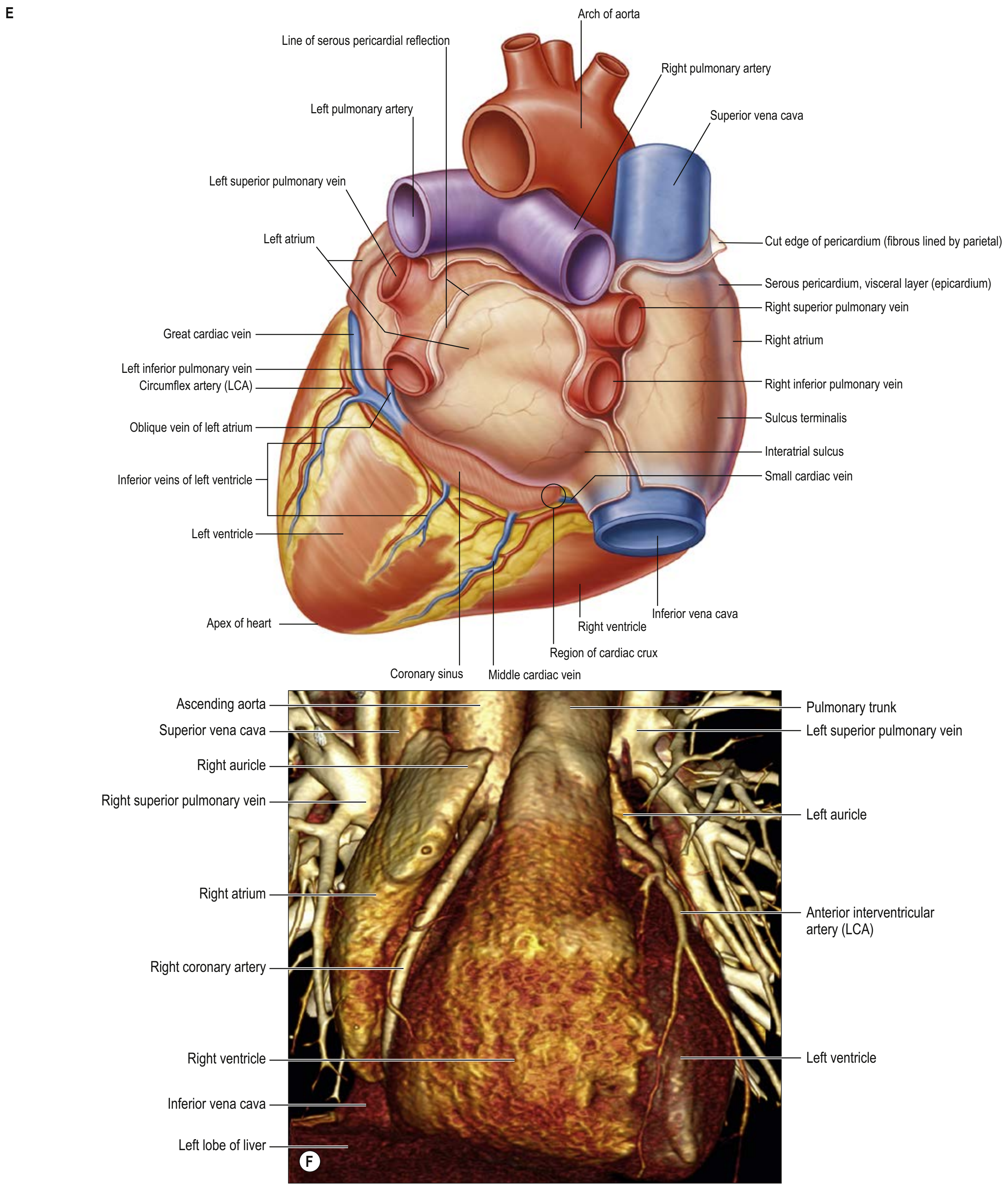
E
Arch of aorta
Line of serous pericardial reflection
Right pulmonary artery
Left pulmonary artery
Superior vena cava
Left superior pulmonary vein
Left atrium
Cut edge of pericardium (fibrous lined by parietal)
Serous pericardium, visceral layer (epicardium)
Right superior pulmonary vein
Great cardiac vein
Right atrium
Left inferior pulmonary vein
Circumflex artery (LCA)
Right inferior pulmonary vein
Oblique vein of left atrium
Sulcus terminalis
Interatrial sulcus
Inferior veins of left ventricle
Small cardiac vein
Left ventricle
Apex of heart
Inferior vena cava
Right ventricle
Region of cardiac crux
Coronary sinus
Middle cardiac vein
Ascending aorta
Pulmonary trunk
Superior vena cava
Left superior pulmonary vein
Right auricle
Right superior pulmonary vein
Left auricle
Right atrium
Anterior interventricular artery (LCA)
Right coronary artery
Right ventricle
Left ventricle
Inferior vena cava
Left lobe of liver
F

Fig. 57.4, cont'd **E**, Basal view. **F**, ECG-gated CT coronary angiogram of the heart and great vessels, anterior view. Note that this method of examination demonstrates contrast filling of the heart chambers and great vessels, and not cardiac muscle. Abbreviations: RCA, branch of right coronary artery; LCA, branch of left coronary artery. (A, B, E, Adapted with permission from Drake RL, Vogl AW, Mitchell A et al (eds) Gray's Atlas of Anatomy, 2nd ed. Elsevier, Churchill Livingstone. Copyright 2015.)

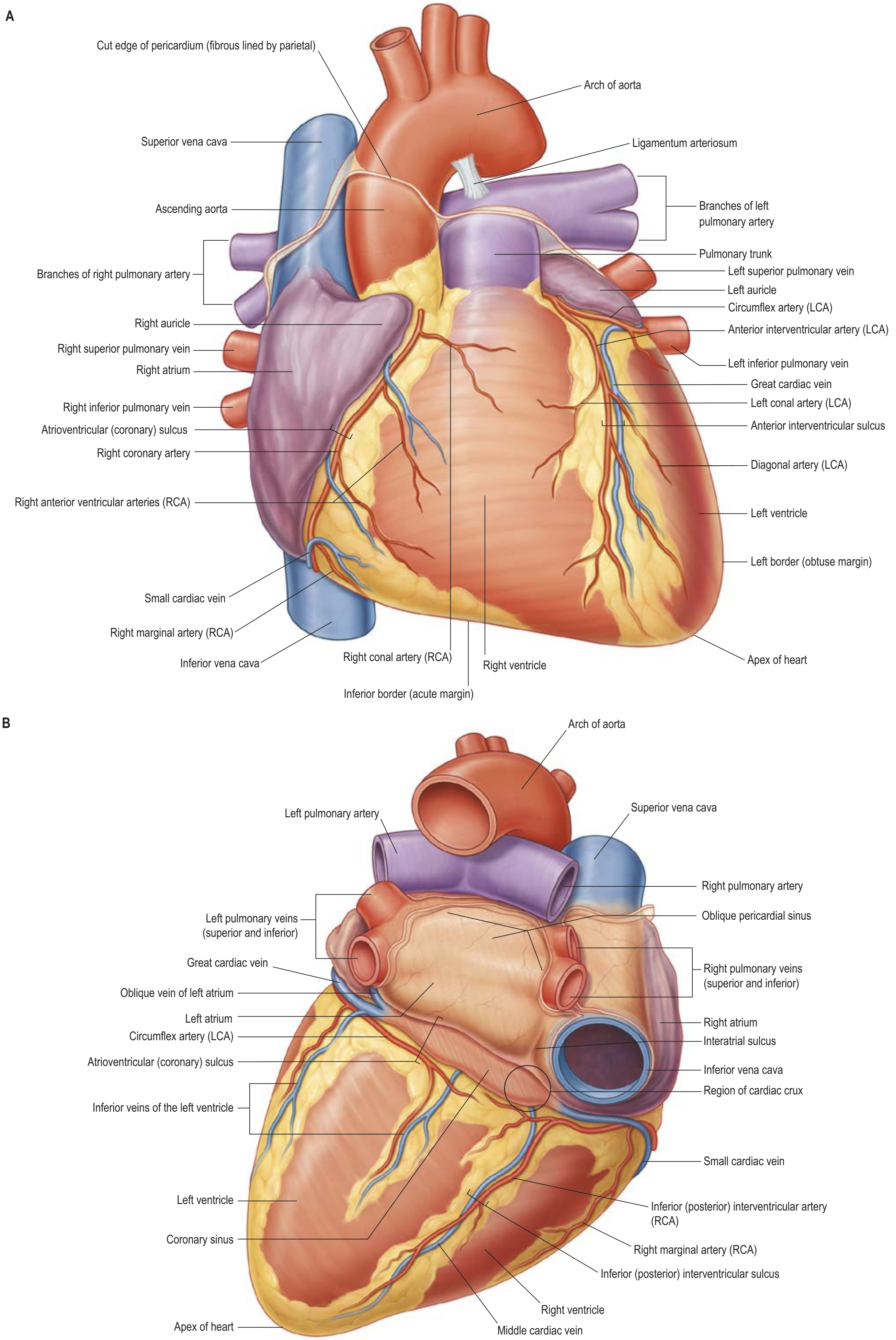
A
Cut edge of pericardium (fibrous lined by parietal)
Arch of aorta
Superior vena cava
Ligamentum arteriosum
Ascending aorta
Branches of left pulmonary artery
Branches of right pulmonary artery
Pulmonary trunk
Left superior pulmonary vein
Left auricle
Circumflex artery (LCA)
Right auricle
Anterior interventricular artery (LCA)
Right superior pulmonary vein
Left inferior pulmonary vein
Right atrium
Great cardiac vein
Right inferior pulmonary vein
Left conal artery (LCA)
Atrioventricular (coronary) sulcus
Anterior interventricular sulcus
Right coronary artery
Diagonal artery (LCA)
Right anterior ventricular arteries (RCA)
Left ventricle
Left border (obtuse margin)
Small cardiac vein
Right marginal artery (RCA)
Inferior vena cava
Right conal artery (RCA)
Right ventricle
Apex of heart
Inferior border (acute margin)
B
Arch of aorta
Left pulmonary artery
Superior vena cava
Right pulmonary artery
Oblique pericardial sinus
Left pulmonary veins (superior and inferior)
Great cardiac vein
Right pulmonary veins (superior and inferior)
Oblique vein of left atrium
Left atrium
Right atrium
Circumflex artery (LCA)
Interatrial sulcus
Atrioventricular (coronary) sulcus
Inferior vena cava
Region of cardiac crux
Inferior veins of the left ventricle
Small cardiac vein
Left ventricle
Inferior (posterior) interventricular artery (RCA)
Coronary sinus
Right marginal artery (RCA)
Inferior (posterior) interventricular sulcus
Right ventricle
Apex of heart
Middle cardiac vein

Fig. 57.4 The heart and great vessels. **A**, Anterior view. **B**, Inferior view. Abbreviations: RCA, branch of right coronary artery; LCA, branch of left coronary artery. (A, B, Adapted with permission from Drake RL, Vogl AW, Mitchell A et al (eds) Gray's Atlas of Anatomy, 2nd ed. Elsevier, Churchill Livingstone. Copyright 2015.) (C–F, *continued online*.)

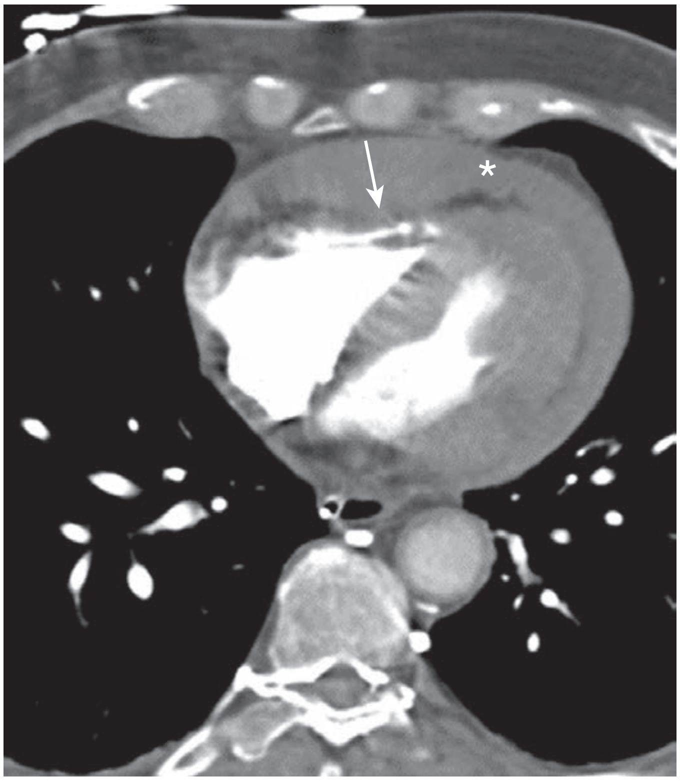

Fig. 57.5 Acute cardiac tamponade in a 22-year-old patient following a motor vehicle collision. Axial multidetector row CT images demonstrate an extensive high attenuation pericardial effusion indicative of haemopericardium (asterisk) and notching (partial collapse) of the anterior (sternocostal) wall of the right ventricle (arrow). (With permission from Raptis DA, Bhalla S 2018 Computed tomographic imaging of cardiac trauma. Radiologic Clinics of North America 57: 201–212.)

Cardiac tamponade is external compression of the heart, usually caused by accumulation of fluid in the pericardial cavity (pericardial effusion) (Fig. 57.5). This causes compression of the right atrium, reducing venous return and therefore reducing cardiac output. It may be secondary to trauma, proximal extension of a dissecting aortic aneurysm, cardiac surgery or central venous catheter insertion. A patient with cardiac tamponade will develop hypotension, chest tightness, dyspnoea and, possibly, a form of cardiogenic shock. The typical signs of a cardiac tamponade include three elements (Beck's triad): a small quiet heart (due to fluid within the pericardial cavity), falling atrial pressure (decreased stroke volume) and rising jugular venous pressure (impaired cardiac venous return). Emergency treatment involves first relieving the tamponade by percutaneous pericardial aspiration (pericardiocentesis), possibly followed by surgery to address the underlying cause. The volume of fluid may not be proportional to the degree of physiological circulatory impairment. A rapid increase in fluid volume within the pericardial cavity is more likely to cause cardiac tamponade than an increase that accumulates over a longer period of time. Echocardiography is an important tool for diagnosis and guiding subsequent percutaneous pericardial aspiration. Surgery is via a subxiphoid incision or a left anterior thoracotomy.

Pericardiocentesis is the aspiration of fluid from the pericardial cavity in cases of cardiac tamponade and for relief of symptomatic pericardial effusion. It can also be used for the diagnosis of neoplastic effusions and purulent pericarditis, and for introducing cytolytic agents into the pericardial cavity. Ultrasound-guided parasternal pericardiocentesis has become the preferred elective procedure. With acute traumatic cardiac tamponade, the subxiphoid approach is used; aspiration of as little as 10–20 ml of blood may greatly increase cardiac output. The parasternal approach with ultrasound guidance provides the most controlled approach to pericardiocentesis, and avoids injury to structures such as the respiratory diaphragm and phrenic nerve. Apical and abdominal approaches may also be used (Fig. 57.6). Pericardiocentesis is likely to be ineffective in cases of substantial haemorrhage into the pericardial cavity because of haemostasis and clot formation: in an emergency situation, a thoracotomy (often bilateral 'clamshell') and surgical opening of the pericardial cavity with clearance of the clot and occlusion of the source of the bleed can result in return of spontaneous circulation (ROSC).

Congenital anomalies of the pericardium include pericardial cysts and diverticula, and absence of the pericardium.

Pericardial cysts and diverticula

Pericardial cysts are congenital and form when a portion of pericardium is pinched off during early development. They are encapsulated with no pericardial communication, are most often incidental, and are located at the right cardiophrenic angle or sulcus, where they present as a well-defined ovoid expansion of the right inferolateral cardiac border on a chest X-ray; a thin-walled and sharply defined, usually round or elliptical, object with fluid attenuation on CT; and a homogeneous high signal object on fluid-sensitive MRI sequences (Fig. 57.7).

A pericardial diverticulum is a rare condition where a herniation through a defect in the parietal layer of serous pericardium communicates with the pericardial cavity. It typically occurs at the same place as a pericardial cyst and should be suspected when a complete wall cannot be identified in all parts of the mass (expansion).

Congenital absence of the pericardium

Congenital absence of the pericardium is rare: it encompasses defects ranging from a small foramen to absence of the entire fibrous sac. The majority of defects occur on the left side but can be located anywhere in the pericardium, and are three times more common in males. Failure of pericardial development may be a consequence of premature atrophy of the cardinal vein and hence poor nourishment of the left pleuropericardial membrane. The most common defect is complete absence of the left side of the pericardium. When this occurs, lung tissue is interposed between the pulmonary trunk and ascending aorta. Bulging of the left atrial auricle through the defect will cause ischaemic necrosis and compression of the left coronary artery, and a rotation of the heart to the left. Complete absence of the pericardium is usually asymptomatic. Partial defects may cause complications such as herniation of cardiac structures (Fig. 57.8).

Congenital pericardial defects are associated with other congenital abnormalities such as bronchogenic cysts, ventricular and atrial septal defects, patent ductus arteriosus, mitral stenosis, bicuspid aortic valve, pulmonary arteriovenous malformations, diaphragmatic hernia, midline closure defects or bronchopulmonary sequestration (Hutchison 2009). Pentalogy of Cantrell is a rare congenital abnormality consisting of absence of the diaphragmatic portion of the pericardium; midline closure defects, including sternal and abdominal wall defects; anterior diaphragmatic defect; and congenital heart defects.

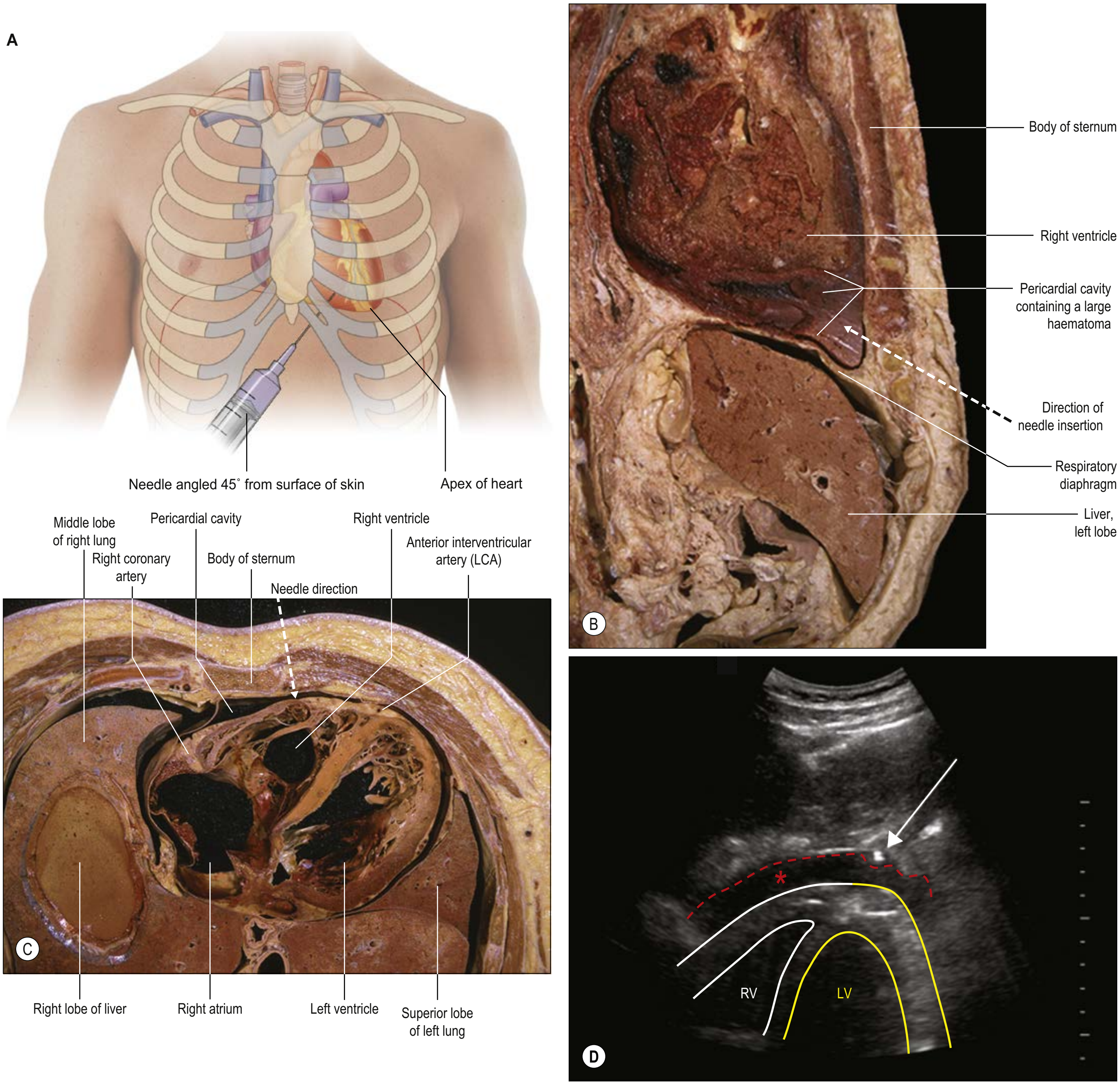
A
Needle angled 45˚ from surface of skin
Apex of heart
Middle lobe of right lung
Pericardial cavity
Right ventricle
Right coronary artery
Body of sternum
Anterior interventricular artery (LCA)
Needle direction
C
Right lobe of liver
Right atrium
Left ventricle
Superior lobe of left lung
Body of sternum
Right ventricle
Pericardial cavity containing a large haematoma
Direction of needle insertion
Respiratory diaphragm
Liver, left lobe
B
*
RV
LV
D

Fig. 57.6 **A**, The subxiphoid approach in pericardiocentesis. The needle is inserted into the angle between the xiphisternum and the left costal margin (arch) at about 45° to the anatomical transverse plane. **B**, A sagittal section in the median plane of a cadaver. The broken arrow shows the direction of the pericardiocentesis needle. **C**, An axial section through the lower part of the thorax to show the relationships of the pericardial cavity with adjacent structures. The broken arrow shows the direction of the pericardiocentesis needle. **D**, Bedside cardiac ultrasound performed in a 62-year-old man, demonstrating a large pericardial effusion consistent with cardiac tamponade (red asterisk). The broken red line shows the extended pericardial cavity. An 18-gauge 9 cm (3.5 inch) needle was attached to a 60 ml syringe and advanced between the xiphoid process and left costal margin at a 45° angle, directed towards the left shoulder (arrow). The white line demarcates the borders of the right ventricular wall (apical region) and right ventricular cavity (RV) at the cardiac apex; the yellow line depicts the left ventricular wall (apical region) and left ventricular cavity (LV). Abbreviation: LCA, branch of left coronary artery. (With permission from Loukas M, Walters A, Boon JM et al 2012 Pericardiocentesis: a clinical anatomy review. Clin Anat 25:872–81.)

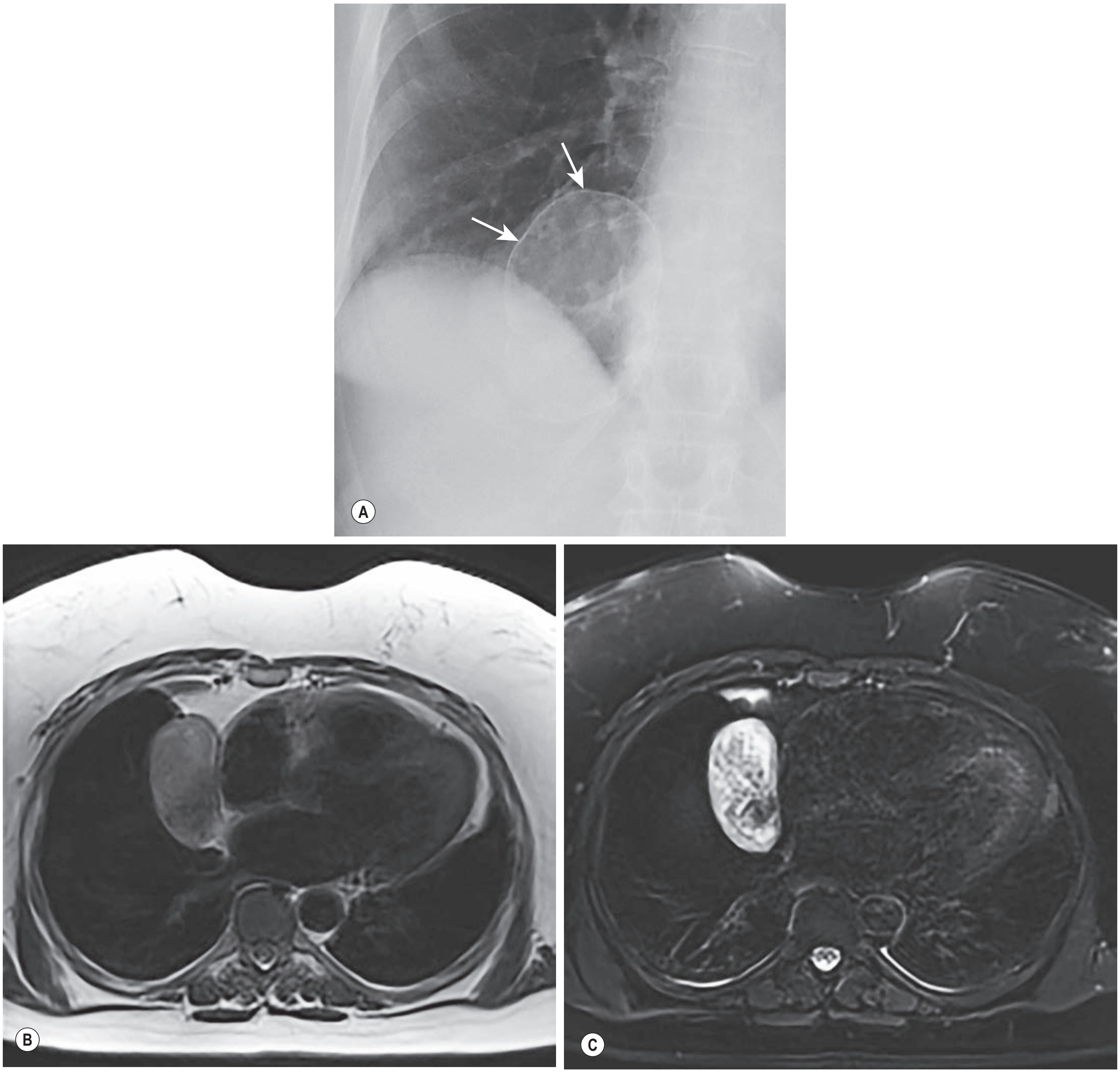

Fig. 57.7 TThe X-ray and MRI appearances of a pericardial cyst in two patients. Pericardial cysts most commonly occur on the right side and are asymptomatic. **A**, A posteroanterior (PA) chest X-ray showing a right-sided calcified pericardial cyst (white arrows). A rim-like calcification identifies the structure containing the calcification as cystic or saccular. **B, C,** MRI imaging (B, T2 weighted; C, T2 fat saturated) showing a fluid signal cystic lesion directly abutting the pericardium along the right pulmonary surface of the heart. (A, with permission from Herring W 2020 Recognizing abnormal calcifications and their causes. In: Learning Radiology: Recognizing the Basics. 4th ed. Elsevier.)

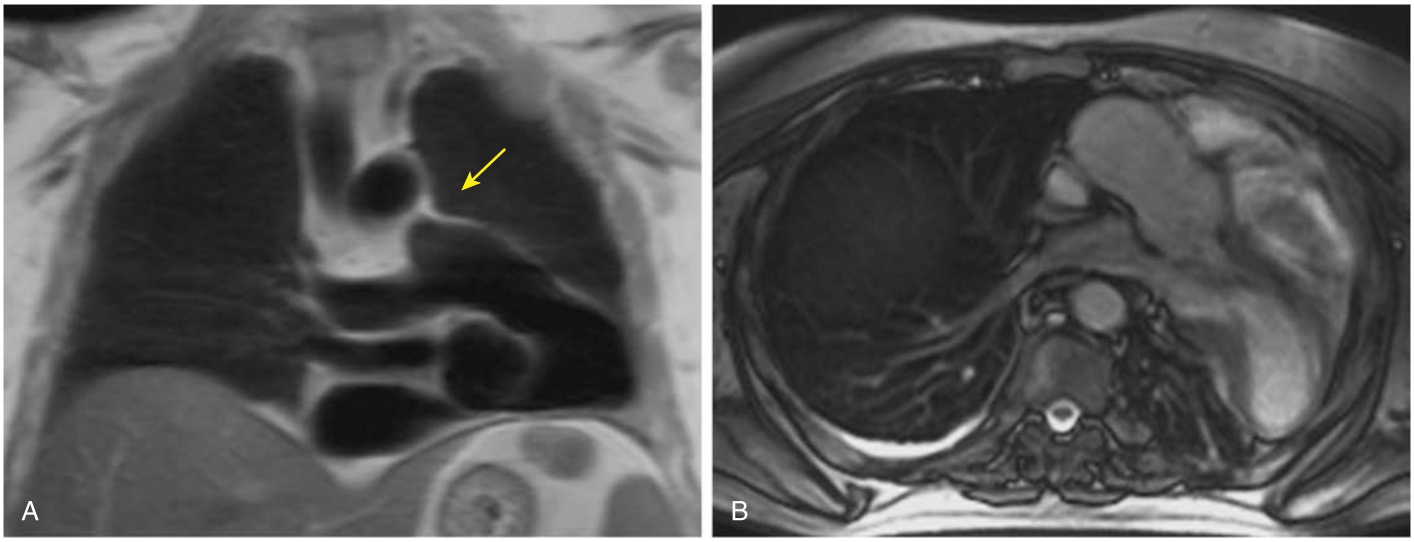

Fig. 57.8 Congenital absence of the pericardium. Coronal T1-weighted (**A**) and axial T2-weighted (**B**) cardiac magnetic resonance images showing pronounced left-sided rotation and displacement of the heart, filling the anterior portion of the left hemithorax. Pericardial absence can be difficult to visualize and is indicated by the abnormal location of the heart in the absence of other predisposing factors, and sometimes by the presence of lung tissue between the aortic arch and left atrium (yellow arrow). (With permission from Kim M-Y, Fairbairn T 2013 Complete congenital absence of the pericardium: an incidental finding. J Cardiol Cases 8: 148-150.)

mediastinal (e.g., para-aortic, subaortic, retrotracheal, prevascular) and parasternal internal thoracic lymph nodal groups also receive efferents (see Fig. 54.12B). There are two layers of pericardial lymphatic vessels, contacting and surrounding the parietal pericardium and also within the fat and loose areolar tissue. The anterior (sternocostal) part of the pericardium either drains laterally towards the phrenic nerves as they enter the diaphragm (lateral group of diaphragmatic nodes, superior phrenic nodes), or travels along the ventral border of the pericardium to enter the prepericardial lymph nodes located at the pericardio-diaphragmatic junction. Drainage from the lateral pericardium is more variable. Inferiorly, it drains towards the phrenic nerves and the pericardiacophrenic vessels as they reach the respiratory diaphragm, and includes the lateral pericardial nodes; superiorly, it drains into the tracheobronchial (subcarinal) and paratracheal lymph nodes. The posterior pericardium, including the posterior aspect of the associated dome of the respiratory diaphragm and extending as far as the pulmonary veins, drains superiorly to the superior and inferior tracheobronchial (upper and lower paratracheal, and subcarinal) lymph nodes. The portion of the pericardium that adheres to the diaphragm drains via short channels to the lymph nodes at the right border of the caval foramen in the central diaphragmatic tendon.

Lymphangiogenesis, the formation of new lymphatic vessels, is beneficial in delaying atherosclerotic plaque formation in coronary arteries. In patients with myocardial infarction, lymphangiogenesis is therapeutic during the healing process, reflecting its ability to reduce fluid retention and aid the clearance of inflammatory cells within the cardiac tissues.

Innervation

Pain from the parietal layer of serous pericardium is mainly transmitted by the left and right phrenic nerves. Pain from the visceral layer of serous pericardium is transmitted along visceral afferent fibres that travel via sympathetic nerves that arise from the cervical, upper thoracic and stellate ganglia and travel to the aortic and cardiac plexuses. The pericardium is also innervated by vagal fibres via the oesophageal plexus and left recurrent laryngeal nerve (see Fig. 57.61). Pericardial pain (somatic) is typically sharp, severe and substernal, often exacerbated when lying in the supine or left lateral position and relieved by leaning forwards; it occasionally radiates to the superior border of trapezius.

Cardiac tamponade

Available with the *Gray's Anatomy* e-book

Pericardiocentesis

Available with the *Gray's Anatomy* e-book

Congenital anomalies of the pericardium

Available with the *Gray's Anatomy* e-book

HEART

The heart has a complicated, spiral, three-dimensional structure that is markedly skewed (rotated) relative to the planes of the body. Historically, established anatomical orientation terms that have been applied to the heart were based on early embryological development before axial rotation of the heart tube (i.e. left and right sides). This, together with the traditional study of isolated whole or dissected hearts outside the body, hinders the intuitive understanding of the descriptive relations of *in vivo* and surface anatomy. The following description emphasizes such difficulties in order to circumvent certain misconceptions, before proceeding to an account of more detailed structure. The oblique position of the heart in the thorax may be conceptualized by comparing it to a deformed pyramid, with the base facing posteriorly and to the right, and the apex anteriorly and to the left. A line from the apex to the approximate centre of the base projected posterolaterally emerges near the right scapular line. Some surfaces of the cardiac 'pyramid' are flat and others relatively convex. The surfaces merge along rather ill-defined borders. Precise definitions of surfaces and intervening borders are therefore difficult. In the account that follows, terms from *Terminologia Anatomica* (2019) are used and more generally used terms from clinical practice are given as alternatives.

The heart is described as having a base and apex; its surfaces are designated as anterior (sternocostal), inferior (diaphragmatic), and right and left pulmonary (Fig. 57.9). Its borders are termed upper, inferior (acute margin or border), right and left (obtuse margin or border). The right pulmonary surface is sometimes referred to as a border, despite its extent. Although the heart is placed obliquely in the thorax, the atrial and ventricular septal structures are virtually in line, and inclined anteriorly and to the left at around 45° to the sagittal plane. The planes of the mitral and tricuspid valves are near vertical and not precisely co-planar; they are broadly at right-angles to the septal plane. The right atrium, therefore, is not only to the right, but also anterior and inferior to the left atrium, and it is partly anterior to the left ventricle. The right ventricle forms most of

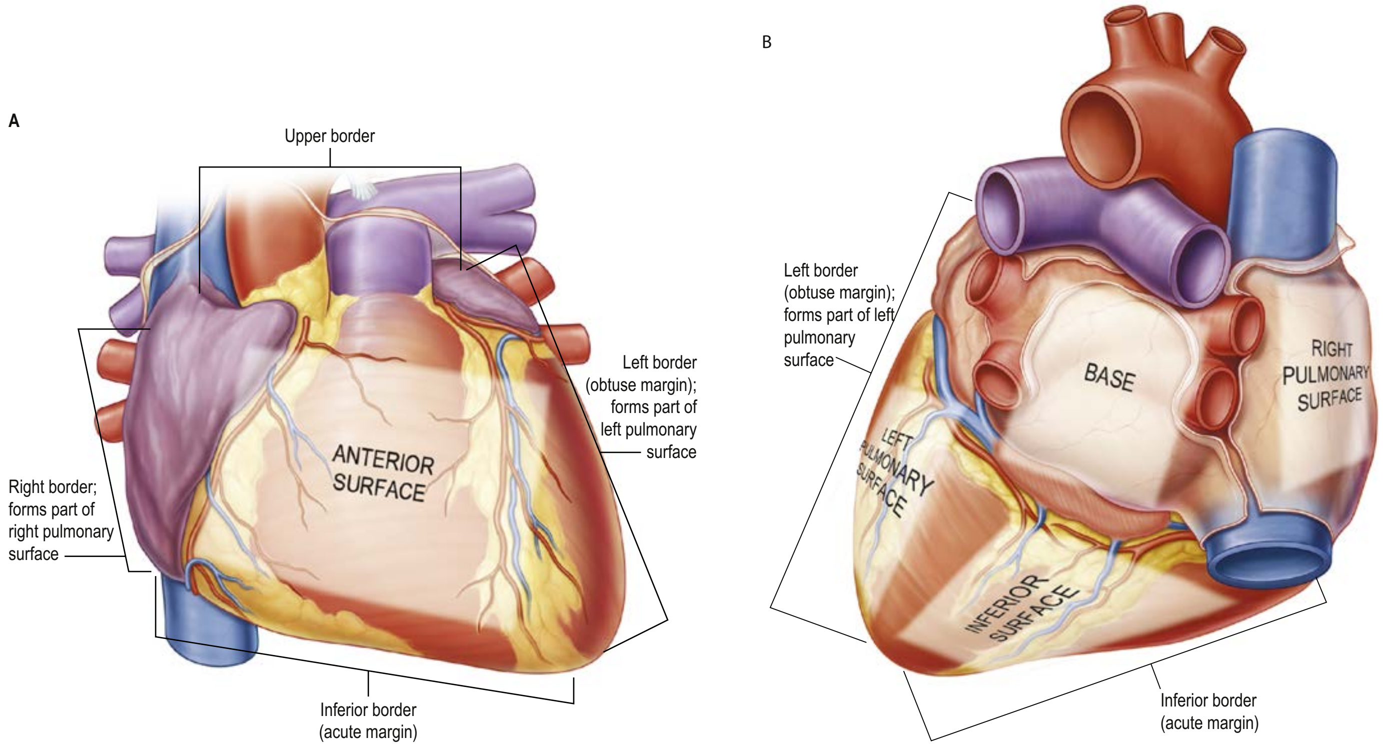
A
Upper border
Left border (obtuse margin); forms part of left pulmonary surface
ANTERIOR SURFACE
Right border; forms part of right pulmonary surface
Inferior border (acute margin)
B
Left border (obtuse margin); forms part of left pulmonary surface
BASE
RIGHT PULMONARY SURFACE
LEFT PULMONARY SURFACE
INFERIOR SURFACE
Inferior border (acute margin)

Fig. 57.9 The surfaces and borders of the heart. **A**, View of the anterior surface. **B**, View of the basal, inferior and pulmonary surfaces. (Adapted from Drake RL, Vogl AW, Mitchell A et al (eds) Gray's Atlas of Anatomy, 2nd ed. Elsevier, Churchill Livingstone. Copyright 2015.)

the anterior aspect of the ventricular mass (see Fig. 57.1B). Only its inferior end lies to the right of the left ventricle, while its upper extremity, supporting the pulmonary valve, is to the left of the left ventricle and superior to the level of the aortic valve (**Fig. 57.10**). The left atrium forms most of the posterior aspect of the heart, whereas the left ventricle is only prominent inferiorly, running along the left border to reach the cardiac apex. Each atrium is essentially to the right of and posterior to its respective ventricle. These general dispositions are of the greatest importance in planning or interpreting radiographs, CT and MRI studies, cardiac angiograms and echocardiograms (see Fig. 57.32).

The right heart (right-sided chambers), while forming the right border and pulmonary surface, follows a gentle curve and also covers most of the anterior aspect of the left heart (except for a left-sided strip of the left border that includes the cardiac apex). Thus, the right heart forms the largest part of the anterior surface, its outflow tract ascending until it terminates on the left side of the outflow tract from the left ventricle. The sites of the tricuspid and pulmonary valves are widely separated and on different planes, and the sectionally crescentic flat cavity of the right ventricle splays out between them (see Figs 57.18B, 57.27A). Conversely, the left heart (except the left-sided strip mentioned above) is largely posterior in position and, when viewed from the front (anteriorly), is obscured by the chambers of the right heart. The inlet to the left ventricle, which contains the mitral valve, is very close to its outlet (the aortic valve), the two being embraced by the wide tract linking the inlet and outlet parts of the right ventricle (see Fig. 57.36). The planes of the left ventricular orifices, although relatively inclined, are more nearly co-planar than those of the right (see Fig. 57.19). The left ventricular cavity is narrow and conical, and its tip sits within the cardiac apex.

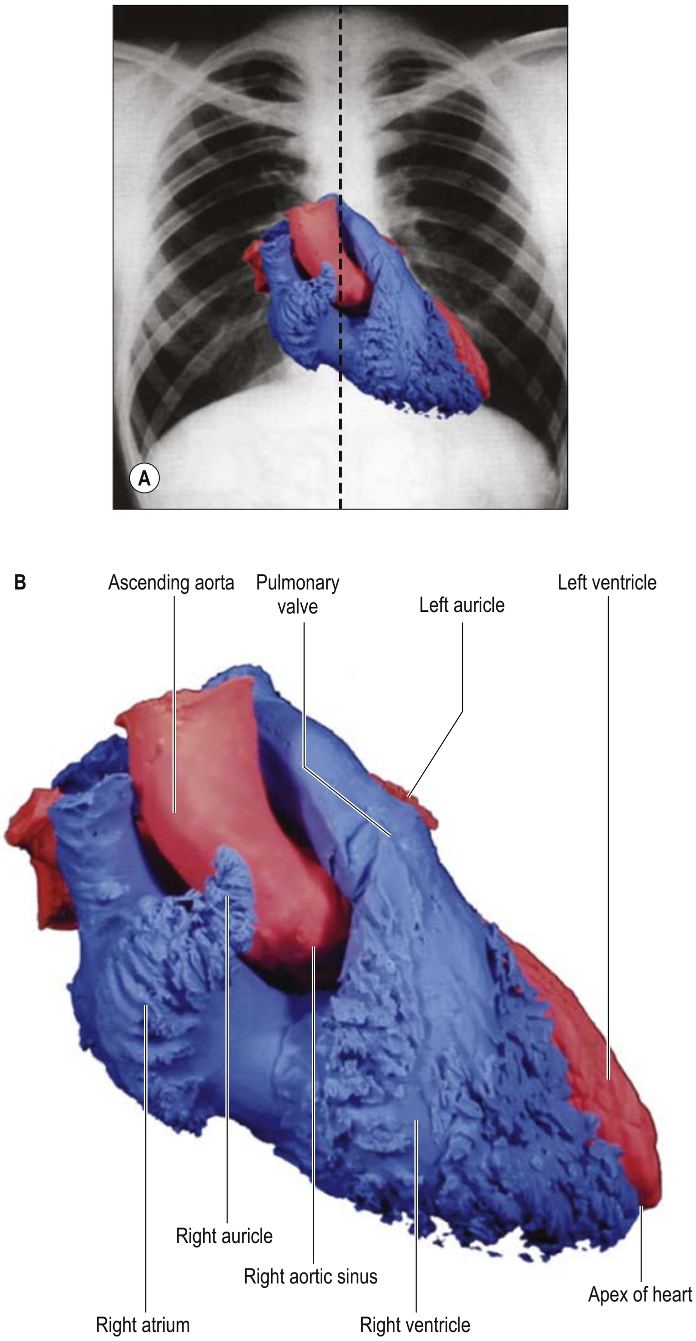

Fig. 57.10 A cast of the right (blue) and left (red) chambers of the heart. **A**, The cast superimposed on a normal posteroanterior (PA) chest radiograph. The black dashed line indicates the median plane. The long axis of the heart extends from the right shoulder towards the left hypochondrium. The adult heart is usually positioned within the mediastinum such that about one-third is to the right of the median plane and two-thirds to the left. **B**, The cast enlarged to show the chambers that form the various borders of the frontal cardiac silhouette. (With permission from Anderson R, Loukas M. 2009 The importance of attitudinally appropriate description of cardiac anatomy. Clin Anat 22:47–51.)

Structures within the heart should be described relative to the bodily coordinates rather than to the heart itself, i.e. they should be described like the rest of the body when viewed in the anatomical position: it is important to appreciate that the diaphragmatic surface is inferior, and the left atrium is posterior (**Fig. 57.11**).

General organization

The heart is a fused pair of valve-containing muscular pumps circulating blood in series through systemic (left heart) and pulmonary (right

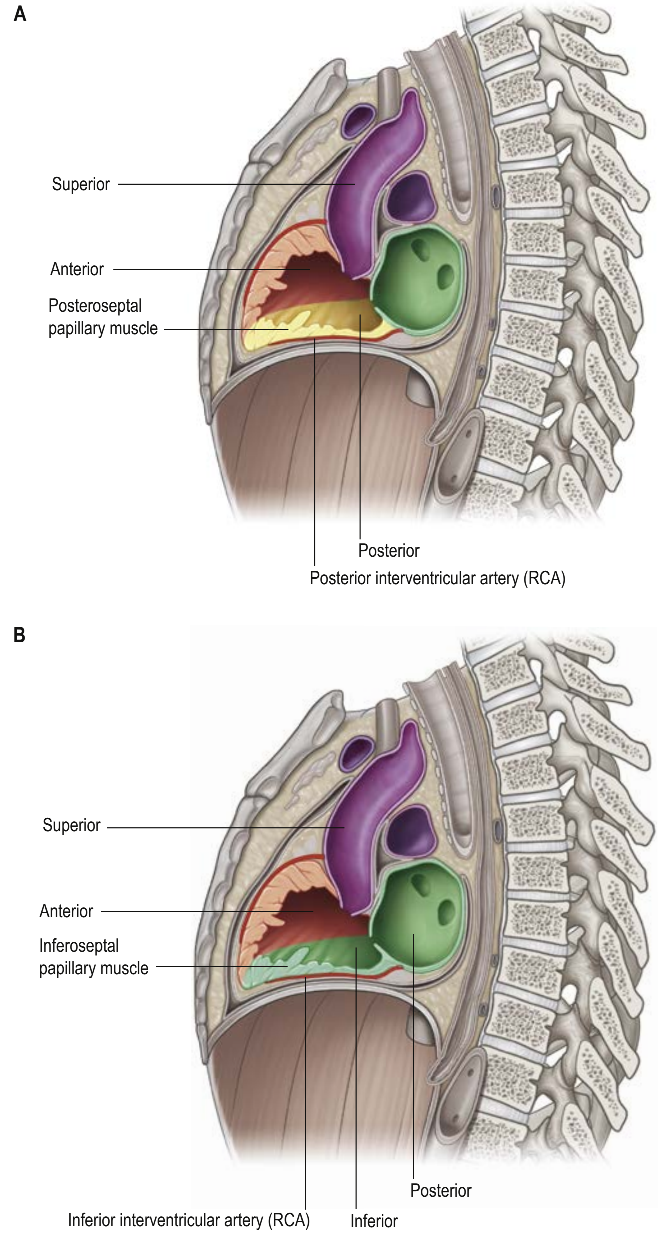
A
Superior
Anterior
Posteroseptal papillary muscle
Posterior
Posterior interventricular artery (RCA)
B
Superior
Anterior
Inferoseptal papillary muscle
Posterior
Inferior interventricular artery (RCA)
Inferior

Fig. 57.11 The fundamental differences between describing the heart according to (**A**) the conventional or (**B**) the attitudinally correct, orientation. Abbreviation: RCA, branch of right coronary artery. (With permission from Anderson R, Spicer D, Hlavacek A et al 2013 Describing the cardiac parts – attitudinally appropriate nomenclature. J Cardiovasc Transl Res 6:118–23.)

A typical example of not applying this concept is the posterior interventricular artery. In cardiological and older anatomical texts, this artery is described as being posterior and descending, whereas three-dimensional reconstruction of cross-sectional imaging of adults clearly demonstrates that the artery occupies the inferior interventricular sulcus on the inferior surface of the heart, and is not posterior to the anterior interventricular artery: it can be described as posterior and descending only when using the 'Valentine' position, with the heart removed from the body and positioned standing on its apex (Mori et al 2019). In life, the posterior interventricular sulcus is situated inferiorly rather than posteriorly: blockage of the inferior (posterior) interventricular artery can produce inferior myocardial infarction. Another example is the papillary muscles that support the leaflets of the mitral valve. These were conventionally described as being anterolateral and posteroseptal, reflecting the fact that the heart was placed on its apex (Valentine position) in order to describe its component parts. However, when examined in left anterior oblique orientation, the posteroseptal muscle is anterior and inferior to its partner, despite the fact that the latter is conventionally described as anterolateral (see Figs 57.4, 57.9, 57.10, 57.27A).

heart) circulations (see Fig. 57.4). The fibromuscular framework and conduction tissues of these physiologically separate pumps are structurally interwoven. Despite the functional disposition in series, the two pumps are topographically described in parallel. Of the four cardiac chambers, the two atria receive venous blood and serve as weakly contractile reservoirs for final filling of the two ventricles, which then provide the powerful expulsive contraction that forces blood into the main arterial trunks.

The right heart starts at the right atrium, which receives the superior and inferior venae cavae and the main myocardial venous inflow via the coronary sinus. The systemic venous blood traverses the right atrioventricular orifice, guarded by the tricuspid (right atrioventricular) valve, to enter the inlet part of the right ventricle. Contraction of the ventricle, particularly its apical trabecular part, closes the tricuspid valve and, with increasing pressure, ejects the blood through the muscular right ventricular outflow tract into the pulmonary trunk and then through the relatively low-resistance pulmonary vascular bed. Many structural features of the right heart, including its overall geometry, myocardial architecture and the construction and relative strengths of the tricuspid and pulmonary valves, accord with this low resistance and comparatively low changes in pressure.

The left heart starts at the left atrium, which receives all the pulmonary inflow of oxygenated blood and some coronary venous inflow. It contracts to fill the left ventricle through the left atrioventricular orifice, guarded by its mitral (left atrioventricular) valve. Left ventricular contraction rapidly increases the pressure in the apical trabecular part, closing the mitral valve and opening the aortic valve, enabling the ventricle to eject via the left ventricular outflow tract into the aortic sinuses, ascending aorta, and the entire systemic arterial tree, including the coronary arteries. This vast vascular bed presents a high peripheral resistance that, with large metabolic demands (especially the sustained requirements of the cerebral tissues), explains the relatively massive structural organization of the left heart. The ejection phase of the left ventricle is shorter than that of the right but its fluctuations in pressure are much greater. The heart is, therefore, a functionally and structurally asymmetric pair of combined pumps in which both ventricles are designed to deliver the same volume with each contraction into two very different resistive series circulations.

Cardiac size, shape and external features

The heart is a hollow, fibromuscular organ of a somewhat conical or pyramidal form, with a base, apex and a series of surfaces and borders (margins) (see Fig. 57.9). Enclosed in the pericardium, it occupies the middle mediastinum between the lungs and their pleural coverings (see Fig. 57.1). It is placed obliquely behind the body of the sternum, adjoining costal cartilages and ribs, and the intervening intercostal muscles. Approximately one-third of its mass lies to the right of the midline. An average adult heart is 12 cm from base to apex, 8–9 cm at its broadest transverse diameter and 6 cm from anterior to posterior. Its weight varies from 280 to 340 g (average 300 g) in males and from 230 to 280 g (average 250 g) in females. Cardiac weight is 0.45% of body weight in males and 0.40% in females. The difference in weight between males and females appears after the age of 12 years (Kortelainen 1997). Adult weight is achieved between the ages of 17 and 20 years. The heart reaches 50% of its adult dimensions at birth, 75% by 5 years and 90% by 12 years (Nidorf et al 1992).

Sulci on the cardiac surface

The division of the heart into four chambers produces boundaries that are visible externally as sulci (grooves). Some are deep and obvious and contain prominent structures. Others are less distinct or barely perceptible, and are sometimes obscured, in part, by the major structures that cross or traverse them.

The extensive interatrial sulcus (of Waterston) separates the two atria. The lateral limits are defined by the borders of the atria. The atrioventricular (coronary) sulcus separates the atria from the ventricles and contains the main parts of the right and circumflex coronary arteries. It descends obliquely to the right on the anterior (sternocostal) surface, separating the right atrium and its auricle (appendage) from the obliquely oriented right margin of the right ventricle and its conus arteriosus (infundibulum). Superiorly, it is obliterated by the crossing of the pulmonary trunk, and posterior to this, the ascending aorta from which the coronary arteries originate. Continuing to the left, the atrioventricular sulcus curves around the left border (obtuse margin) and descends to the right, separating the atrial base from the inferior surface of the ventricles (see Fig. 57.4). This inferior part of the atrioventricular sulcus then curves around the inferior border (acute margin) at its lower right end to become confluent with the anterior part of the sulcus. The inferior part of the sulcus sits slightly to the left of the anterior part. A section of the heart through the plane of the atrioventricular sulcus is at about 45° to the sagittal plane and at a variable angle to the transverse and coronal planes. It approximately traverses the lines of attachment of the atrioventricular valves and, even less precisely, those of the aortic and pulmonary valves. A line at right-angles to the centre of this plane will descend anteriorly and leftwards to the cardiac apex. Internally, the ventricles are separated by the interventricular septum; its margins correspond to the anterior and inferior interventricular sulci. The anterior sulcus, seen on the anterior cardiac surface, is near and almost parallel to the left border (obtuse margin). On the inferior surface, the inferior interventricular sulcus is closer to the midpoint of the ventricular mass. The interventricular sulci extend from the atrioventricular sulcus to the notch of the cardiac apex on the inferior border (acute margin), the latter a little to the right of the cardiac apex (see Fig. 57.24).

Cardiac base, apex, surfaces and borders

Posterior surface (base) of the heart The true cardiac base is somewhat quadrilateral, with curved lateral extensions (see Fig. 57.9). It faces posteriorly and to the right, separated from the bodies of the thoracic vertebrae (fifth to eighth when supine, sixth to ninth in the erect position) and their intervening intervertebral discs by the pericardium, right pulmonary veins, oesophagus, azygos venous system, thoracic duct and descending thoracic aorta. It is formed mainly by the left atrium, and only partly by the posterior part of the right atrium (see Fig. 57.4B). It extends superiorly to the bifurcation of the pulmonary trunk and inferiorly to the inferior part of the atrioventricular sulcus, which contains the coronary sinus and coronary arterial branches. It is limited to the right and left by the rounded surfaces of the corresponding atria. The junction of the atrioventricular, interatrial and inferior interventricular sulci is termed the cardiac crux. Two pulmonary veins on each side open into the left atrial part of the base, whereas the superior and the inferior venae cavae open into the respective parts of the right atrial basal region (see Fig. 57.4B). The area of the left atrial wall between the openings of right and left pulmonary veins forms the anterior wall of the oblique pericardial sinus (see Fig. 57.1). This description of the anatomical base reflects the usual position of the heart in the thorax. Some confusion is produced by other current usages of the term 'base', often applied to the segment of the atrioventricular and ventriculoarterial junctions seen after dissections through the atrioventricular sulcus. This area is better termed the base of the ventricles. In clinical practice, auscultation in or near the parasternal parts of the second intercostal spaces is often described as occurring at the 'clinical base', to make a distinction with the 'clinical apex'. Such descriptions, while less than perfect anatomically, are likely to persist.

Anatomical apex of the heart (cardiac apex) The apex of the conical left ventricle is directed anteroinferiorly and to the left and is overlapped by the left lung and its covering pleurae. The apex is located most commonly behind the fifth left rib, fifth left intercostal space or the sixth left rib, near or a little medial to the mid-clavicular line (a line located 8–9 cm lateral to the midline).

Anterior (sternocostal) surface of the heart Facing anteriorly and superiorly, the anterior surface has an acute rightward and a more gradual leftward convexity (see Fig. 57.1B; **Fig. 57.12**). It consists of an atrial region superior and to the right, and a ventricular region inferior and to the left of the atrioventricular sulcus. The atrial region is occupied almost entirely by the right atrium. The left atrium is largely hidden by the ascending aorta and pulmonary trunk: only a small part of the left atrial auricle projects forwards to the left of the pulmonary trunk. Of the ventricular region, about one-third is made up by the left and two-thirds by the right ventricle. The site of the interventricular septum between them is indicated by the anterior interventricular sulcus. The anterior surface is separated by the pericardium from the body of the sternum, the sternocostal muscles, the third to sixth costal cartilages and the intervening intercostal muscles. Because of the bulge of the heart to the left, more of this surface is behind the left costal cartilages than those on the right. It is also covered by the pleural membranes and the thin anterior borders of the lungs, except for a triangular area at the cardiac notch of the left lung. The lungs and their pleural coverings vary in their extent of cardiac overlap during breathing and between individuals.

Inferior (diaphragmatic) surface of the heart Largely horizontal, the inferior surface of the heart gently slopes anteroinferiorly towards

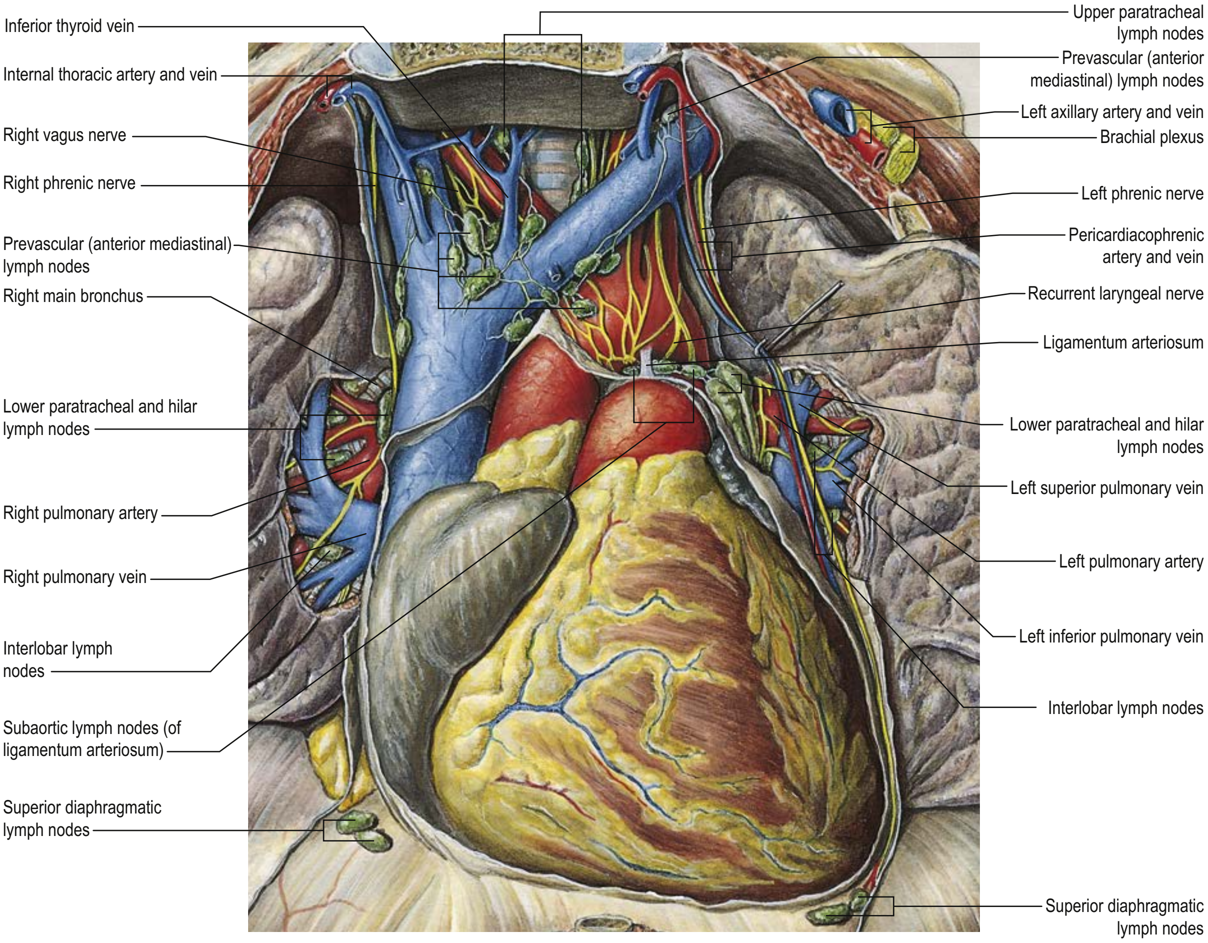
Inferior thyroid vein
Internal thoracic artery and vein
Right vagus nerve
Right phrenic nerve
Prevascular (anterior mediastinal) lymph nodes
Right main bronchus
Lower paratracheal and hilar lymph nodes
Right pulmonary artery
Right pulmonary vein
Interlobar lymph nodes
Subaortic lymph nodes (of ligamentum arteriosum)
Superior diaphragmatic lymph nodes
Upper paratracheal lymph nodes
Prevascular (anterior mediastinal) lymph nodes
Left axillary artery and vein
Brachial plexus
Left phrenic nerve
Pericardiacophrenic artery and vein
Recurrent laryngeal nerve
Ligamentum arteriosum
Lower paratracheal and hilar lymph nodes
Left superior pulmonary vein
Left pulmonary artery
Left inferior pulmonary vein
Interlobar lymph nodes
Superior diaphragmatic lymph nodes

Fig. 57.12 The heart, great vessels and the lungs *in situ*. The manubrium of the sternum has been retracted cranially, the thymus has been completely removed and the pericardium has been partially removed. The hilum of the lung has been dissected to expose the hilar, subaortic, para-aortic and hilar lymph nodes. (With permission from Waschke J, Paulsen F (eds) Sobotta Atlas of Human Anatomy, 15th ed. Elsevier, Urban & Fischer. Copyright 2013.)

the cardiac apex (see Figs 57.4B,D, 57.9). It is formed by the ventricles (primarily the left) and rests mainly on the central tendon but also, apically, on a small area of the left muscular part of the diaphragm. It is separated from the anatomical base of the heart by the atrioventricular sulcus, and is traversed obliquely by the inferior interventricular sulcus.

Left (pulmonary) surface of the heart Facing posterosuperiorly to the left, the left pulmonary surface consists almost entirely of the left border (obtuse margin) of the left ventricle; a small part of the left atrium and its auricle contribute superiorly. Convex and widest superiorly, where it is crossed by the atrioventricular sulcus, it narrows as it passes towards the cardiac apex. It is separated by the pericardium from the left phrenic nerve and pericardiacophrenic vasculature, and from the pleura covering the cardiac notch of the left lung.

Right (pulmonary) surface of the heart The right pulmonary surface is rounded and formed by the right atrial wall. It is separated by the pericardium from the pleura covering the mediastinal surface of the right lung, and from the right phrenic nerve and pericardiacophrenic vasculature. Its convexity merges inferiorly into the short intrathoracic part of the inferior vena cava and superiorly into the superior vena cava. The sulcus terminalis is a prominent landmark separating the systemic atrial venous sinus from the auricle; it curves approximately along the junction of the anterior and right surfaces, corresponding to the position of the crista terminalis.

Upper border of the heart The upper border is atrial, mainly the left atrium. Anterior to it are the ascending aorta and the pulmonary trunk (see Figs 57.1, 57.4B). At its right lateral extremity, the superior vena cava enters the right atrium.

Right border of the heart Corresponding to the right atrium, the profile of the right border is slightly convex to the right.

Inferior border of the heart Also known as the acute margin of the heart, the inferior border is sharp, thin and nearly horizontal. It extends from the inferior limit of the right border to the cardiac apex and is formed mainly by the right ventricle, with a small contribution from the left ventricle near the cardiac apex.

Left border of the heart Also known as the obtuse margin, the left border separates the anterior and left pulmonary surfaces. It is round and mainly formed by the left ventricle but, to a slight extent superiorly, is formed by the left atrial auricle. It descends obliquely, convex to the left, from the left atrial auricle to the cardiac apex.

Right atrium

General and external features

The right atrium is both anterior and to the right of the left atrium, and extends inferior to it (see Fig. 57.4A–D). Its walls form the right superior part of the anterior surface, the convex right (pulmonary) surface and a small part of the right side of the anatomical base. The superior vena cava opens into its roof, and the inferior vena cava into its inferoposterior part. The auricle is an extensive muscular pouch that projects anteriorly to overlap the right side of the ascending aorta: it is a broad, triangular, pyramidal structure and has a wide junction with the systemic venous part of the atrium. The junction between the venous part (sinus venosus) and the atrium proper is marked externally by the shallow sulcus terminalis running between the right sides of the openings of the two venae cavae. Internally, the sulcus terminalis corresponds to the crista terminalis, the site of origin of the extensive pectinate muscles that arise serially at right-angles from the crista and extend anterolaterally along the internal surface of the right atrial auricle. Posteriorly, the vertical interatrial sulcus passes inferiorly to the cardiac crux. Anteriorly, the right atrium is related to the anterior part of the mediastinal surface of the right lung, from which it is separated by pleura and pericardium. Laterally, the atrium is also related to the mediastinal surface of the right lung, but anterior to its hilum, and separated from the lung by the pleura, right phrenic nerve, pericardiacophrenic vessels and pericardium. Posteriorly and to the left, the interatrial septum and the surrounding infolded atrial walls separate the atria; this infolding is indicated by an extensive interatrial sulcus. Posteriorly and to the right are the right pulmonary veins. Medially are the ascending aorta and, to a limited extent, the pulmonary trunk and its bifurcation.

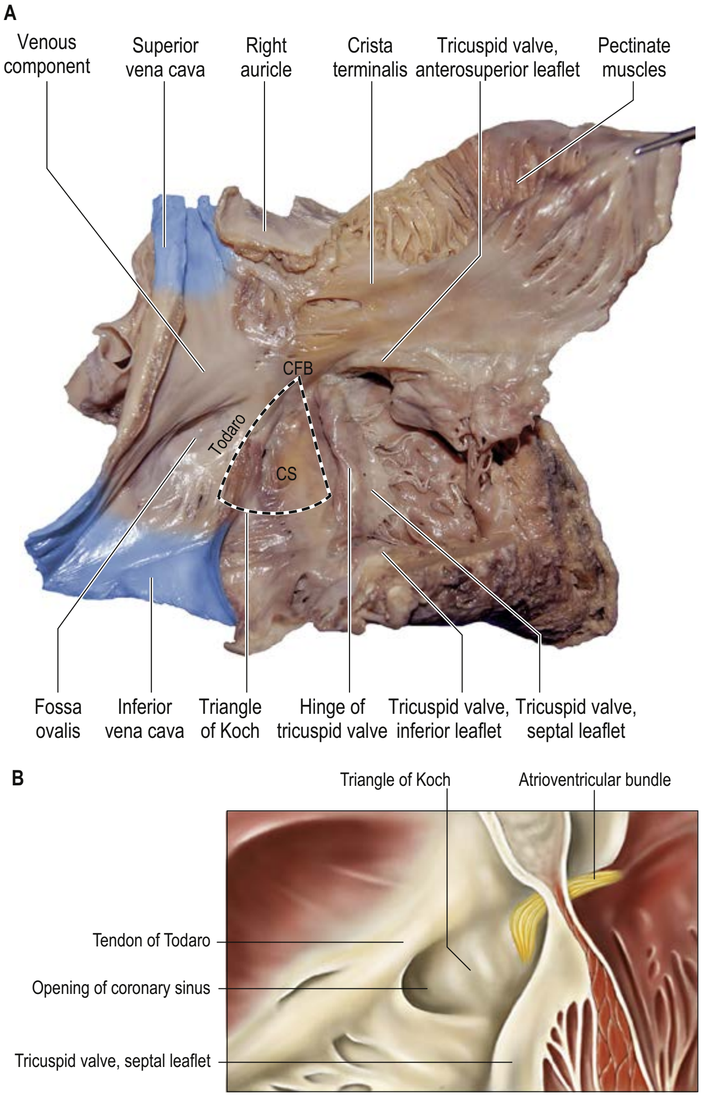

Fig. 57.14 **A**, The internal features of the right atrium. The superior and inferior venae cavae have been dissected, exposing the systemic venous part of the right atrium and the fossa ovalis. The dotted line indicates the triangle of Koch, demarcated by the opening of the coronary sinus (CS) and its valve (Thebesian valve); the anterior extension of the valve of the inferior vena cava (Eustachian), the tendon of Todaro (or tendon of the inferior pyramidal space), to the central fibrous body (CFB); and the septal leaflet of the tricuspid valve. **B**, The triangle of Koch marking the location of the atrioventricular node. (A, Image courtesy of Professor M Loukas.)

Internal features

The internal surface of the right atrium can be divided into three regions: the smooth-walled systemic venous part, located posteriorly, leads anteriorly to the vestibule of the tricuspid valve and to the atrial auricle (**Figs 57.13–57.14**). The wall of the vestibule is smooth but its junction with the auricle is ridged all around the atrioventricular junction by pectinate muscles. The smooth-walled systemic venous sinus receives the openings of the superior and inferior venae cavae and the coronary sinus.

The superior vena cava returns blood from the head, neck and upper limbs through an orifice that faces anteroinferiorly and has no valve; it also receives blood from the thoracic wall and the oesophagus via the azygos system (see Fig. 56.3).

The inferior vena cava is larger in diameter than the superior. It drains blood from all structures below and including the respiratory diaphragm into the lowest part of the atrium near the interatrial septum. Anterior to its orifice, and passing around its left margin toward the limbus (rim) of the fossa ovalis, is the flap-like valve of the inferior vena cava (Eustachian valve), a triangular fold of endocardium of varying size that encloses a few muscular fibres (see Fig. 57.13; **Fig. 57.15**). It is usually a fibrous or fibromuscular flap. When traced inferiorly, it forms the Eustachian ridge, and is continuous with the valve of the coronary sinus (Thebesian valve). The Eustachian ridge borders the coronary sinus and the fossa ovalis. The anterior extension of the valve of the inferior vena cava is seen as a fibrous strand, the tendon of Todaro (inferior pyramidal space), which forms part of the border of the

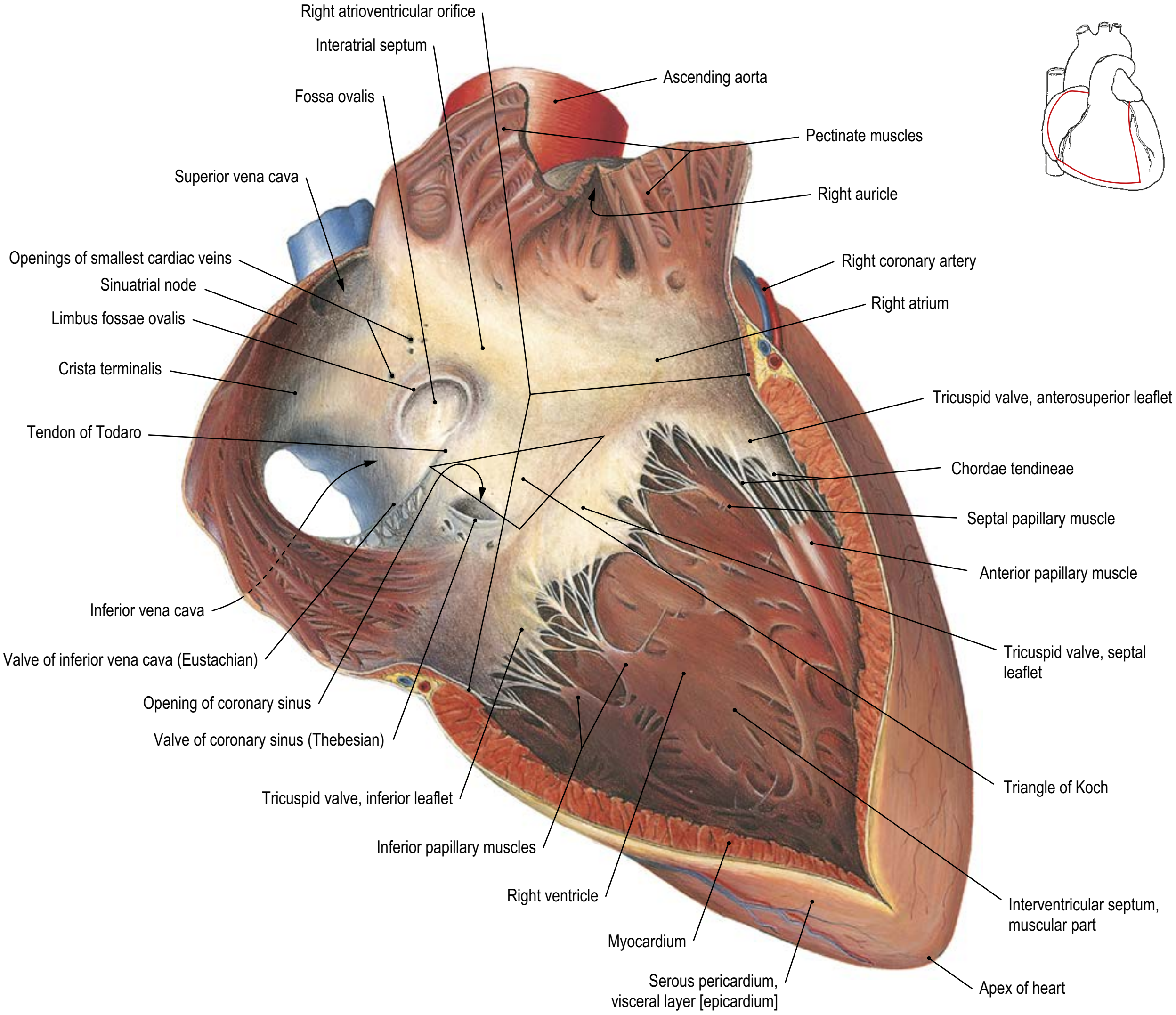
Right atrioventricular orifice
Interatrial septum
Fossa ovalis
Ascending aorta
Pectinate muscles
Superior vena cava
Right auricle
Openings of smallest cardiac veins
Sinuatrial node
Right coronary artery
Right atrium
Limbus fossae ovalis
Crista terminalis
Tricuspid valve, anterosuperior leaflet
Tendon of Todaro
Chordae tendineae
Septal papillary muscle
Anterior papillary muscle
Inferior vena cava
Tricuspid valve, septal leaflet
Valve of inferior vena cava (Eustachian)
Opening of coronary sinus
Valve of coronary sinus (Thebesian)
Triangle of Koch
Tricuspid valve, inferior leaflet
Inferior papillary muscles
Right ventricle
Interventricular septum, muscular part
Myocardium
Serous pericardium, visceral layer [epicardium]
Apex of heart

Fig. 57.13 The interior of the right atrium and ventricle revealed by cutting along the right and inferior borders and reflecting the anterior surface of the heart superiorly (With permission from Waschke J, Paulsen F (eds) Sobotta Atlas of Human Anatomy, 15th ed. Elsevier, Urban & Fischer. Copyright 2013.)

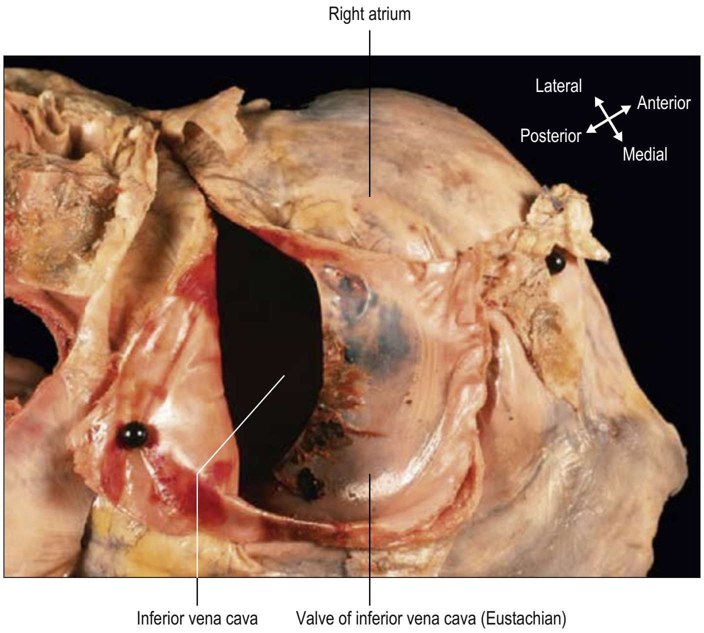
Right atrium
Lateral
Anterior
Posterior
Medial
Inferior vena cava
Valve of inferior vena cava (Eustachian)

Fig. 57.15 An inferior view of a cadaveric heart, demonstrating an unusually large valve of the inferior vena cava (Eustachian valve) occupying the majority of the lumen of the inferior vena cava. (With permission from Loukas M, Sullivan A, Tubbs R et al 2010. Chiari's network: review of the literature. Surg Radiol Anat 32:895–901.)

triangle of Koch, itself the anatomical landmark of the atrioventricular node. The lateral part of the valve of the inferior vena cava becomes continuous with the inferior end of the crista teminalis. The valve of the inferior vena cava is large during fetal life, when it serves to direct richly oxygenated blood (from the placenta) toward and through the foramen ovale of the interatrial septum and into the left atrium. The valve varies markedly in size in postnatal life, is sometimes cribriform or filamentous, and is often absent.

Occasionally, a reticulated network, Chiari's network, originates from the valve of the inferior vena cava and connects to different parts of the right atrium, including the coronary sinus. It is the result of incomplete resorption of the right valve of the embryonic sinus venosus (**Fig. 57.16**). Often clinically insignificant, Chiari's network has been associated with the pathogenesis of thromboembolic disease, endocarditis, arrhythmias, cardiac flow obstructions, heart murmurs, infective endocarditis, cardiac tumours and entrapment of catheters on percutaneous intervention.

The prominent sub-Thebesian recess is located anterior to the valve of the inferior vena cava and posteroinferior to the opening of the coronary sinus (see Fig. 57.18). The area extending from the valve of the inferior vena cava to the vestibule of the tricuspid valve, inferior to the opening of the coronary sinus (the cavotricuspid isthmus), is the target of catheter-directed ablation procedures, which are the treatment of choice for atrial flutter (Sánchez-Quintana et al 2013).

The coronary sinus opens into the systemic venous part of the right atrium between the orifice of the inferior vena cava, the fossa ovalis and the vestibule of the tricuspid valve (see Figs 57.13–57.14). It is often guarded by a thin, semicircular Thebesian valve (valve of the coronary sinus) that covers the lower part of the orifice. The upper limb of this valve joins the valve of the inferior vena cava and its muscular extension, the Eustachian ridge. It also joins a tendinous structure (tendon of Todaro or tendon of the inferior pyramidal space) running from this commissure into the sinus septum between the coronary sinus and the fossa ovalis. The tendon of Todaro runs forwards to insert into the central fibrous body and forms one of the borders of the triangle of Koch (triangle of the atrioventricular node). The opening of the coronary sinus forms a prominent landmark in the right atrium. The coronary sinus itself lies within the posterior and inferior parts of the atrioventricular sulcus (see Figs 57.4B,D,E) and is the conduit for the return of most of the venous blood from the heart, although some veins drain directly into the atrial chambers. The coronary sinus starts at the confluence of the oblique vein of the left atrium and the great cardiac vein, and receives the middle and small cardiac veins close to its junction with the right atrium. Several small venous openings, draining the smallest cardiac (Thebesian) veins, are found scattered around the atrial walls. They return a small fraction of blood from the heart, and are most numerous on the septal aspect. The anterior cardiac veins and, sometimes, the right marginal vein may enter the atrium through larger openings.

The right atrium and its auricle are separated from the systemic venous part by the crista terminalis, a smooth, C-shaped muscular ridge that originates from the upper part of the septal surface, passes anterior to the orifice of the superior vena cava and then skirts the right margin of the inner atrium to reach the right side of the orifice of the inferior vena cava. It marks the site of the right venous valve of the embryonic heart, corresponding externally to the sulcus terminalis. The sinu-atrial node is located in the superior part of the sulcus (groove), inferolateral to the orifice of the superior vena cava (see Fig. 57.13). The mean length of the crista terminalis is 51±9 mm and its thickness from epicardium to endocardium at the junction of the superior vena cava with the posterior atrial wall is 5.5 ±1.3 mm. The multiple raised parallel ridges of the pectinate muscles extend anterolaterally from the crista terminalis, reaching into the right auricle where they form several trabeculations. The largest and most prominent pectinate muscle, the taenia sagittalis (second crest or septum spurium), forms the bridge of the sulcus terminalis internally. The septal wall is dominated by the fossa ovalis, an oval depression superior and normally to the left of the orifice of the inferior vena cava. Its floor is the primary atrial septum (septum primum). The limbus (rim) of the fossa ovalis is prominent. Often said to represent the edge of the septum secundum, in reality the muscular borders of the fossa are no more than infoldings of the atrial walls, incorporating extracardiac adipose tissue. The limbus is most distinct anterosuperior to the fossa, and is usually deficient inferiorly. Some hearts display an excessive amount of extracardiac adipose tissue within the fold, markedly elevating the superior limbus of the fossa and forming the intervenous tubercle of Lower (interatrial fold of the inferior vena cava). A small slit-shaped passageway is sometimes found at the superior margin of the fossa ovalis. It ascends beneath the limbus, between it and the valve of the foramen ovale, to communicate with the left atrium, and represents failure of obliteration of the fetal foramen ovale, which remains patent or probe-patent in up to one-third of all normal hearts. Anteroinferiorly in the right atrium the large, oval vestibule leads to the right atrioventricular (tricuspid) orifice. A triangular zone, the triangle of Koch (triangle of the atrioventricular node), is present between the attachment of the septal leaflet of the tricuspid valve, the anteromedial margin of the opening of the coronary sinus (and its valve), and the palpable round, collagenous subendocardial tendon of Todaro (see Figs 57.13–57.14). Koch's triangle is a landmark of surgical importance since it contains the atrioventricular node and its atrial connections. Anterosuperior to the insertion of the tendon of Todaro, the septal wall is formed by the atrioventricular part of the membranous septum, which intervenes between the vestibule of the right atrium and the subaortic outlet of the left ventricle (**Fig. 57.17**). The bulging atrial wall anterosuperior to the membranous septum, the aortic mound (torus aorticus), marks the location of the non-adjacent aortic sinus with its enclosed aortic valvular leaflet.

Right ventricle

The right ventricle extends from the right atrioventricular (tricuspid) orifice nearly to the cardiac apex. It then ascends to the left to become the conus arteriosus (infundibulum) reaching the pulmonary orifice and supporting the leaflets of the pulmonary valve. Topographically, the ventricle possesses an inlet part that supports and surrounds the tricuspid (right atrioventricular) valve; a coarsely trabeculated apical part; and a muscular outlet (conus arteriosus or infundibulum) that surrounds the attachments of the pulmonary valve leaflets.

External features

The convex anterosuperior surface of the right ventricle makes up a large part of the anterior surface of the heart, and is separated from the thoracic wall by the fibrous and serous pericardium (see Figs 57.1B, 57.2–57.3). The left costomediastinal recess of parietal pleura and, to a lesser extent, the anterior border of the left lung are interposed superiorly and to the left. The inferior surface is flat and is related mainly (with the interposition of the serous pericardium) to the central tendon and a small adjoining muscular part of the respiratory diaphragm. The left and posterior wall is formed by the interventricular septum, slightly curved and bulging into the right ventricle so that, in sections across the cardiac axis, the outline of the right ventricle is crescentic (see Fig. 57.27). The wall of the right ventricle is relatively thin (3–5 mm), the ratio of the thickness of the right : left ventricular walls usually being 1 : 3.

Internal features

The inlet and outlet parts of the right ventricle, supporting and surrounding the leaflets of the tricuspid and pulmonary valves, respectively, are separated in the roof of the ventricle by the prominent supraventricular crest (**Fig. 57.18**). The crest is made up predominantly by the inner heart curvature, bounded on the epicardial aspect by the rightward margin of the transverse pericardial sinus. The crest is a thick, muscular, highly arched structure, extending obliquely anteriorly and to the right from a septal limb high on the interventricular septal wall to a mural or parietal limb on the anterolateral right ventricular wall. The posterolateral aspect of the crest provides the principal attachment for the anterosuperior leaflet of the tricuspid valve. The septal limb of the crest is embraced by the septal limbs of the septomarginal trabeculation (moderator band). The inlet and outlet parts of the ventricle extend apically into and from the prominent coarsely trabeculated part of the ventricle. The inlet part itself is also trabeculated, whereas the outlet part has predominantly smooth walls, albeit with septoparietal trabeculations anteriorly. The trabeculated appearance is produced by a myriad of endocardial lined, irregular muscular ridges and protrusions collectively known as trabeculae carneae. These protrusions and intervening grooves impart great variation in ventricular wall thickness; the protrusions vary in extent from slight ridges to trabeculations, fixed at both ends but otherwise free. Other conspicuous protrusions are the papillary muscles, which are inserted at one end on to the ventricular wall and are continuous at the other end with collagenous cords, the chordae tendineae (tendinous cords), inserted on the free edge of the tricuspid valvular leaflets. One protrusion in the right ventricle, the septomarginal trabecula, is particularly prominent, originating as one or more limbs from the upper two-thirds of the interventricular septum, from the supraventricular crest to the ventricular apex. Towards the ventricular apex, it supports the anterior papillary muscle of the tricuspid valve and, from this point, crosses to the parietal (anterior) wall of the ventricle. The septomarginal trabecula is often termed the moderator band, a name reflecting an earlier idea that it prevented overdistension of the

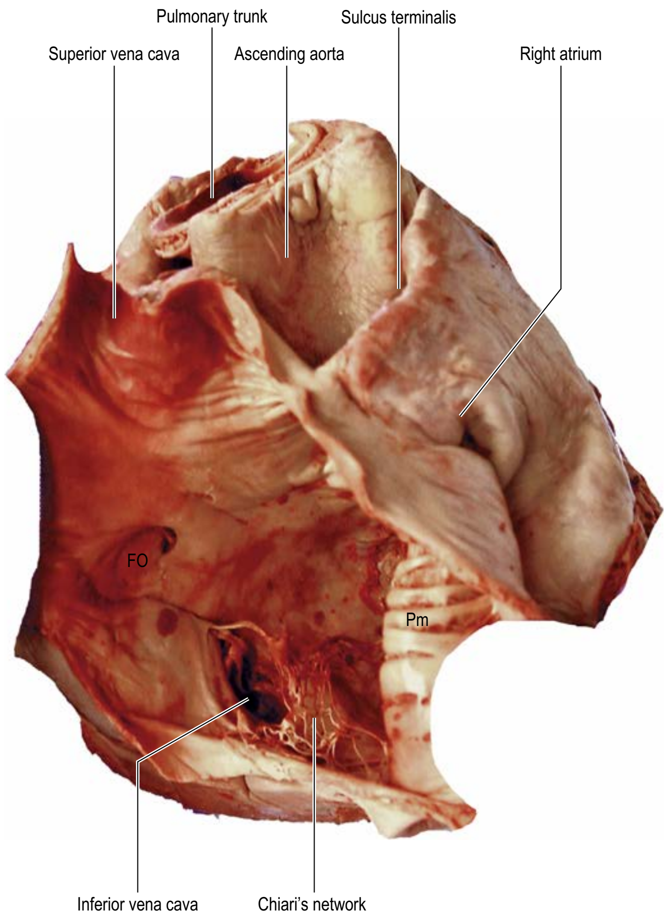
Pulmonary trunk
Sulcus terminalis
Superior vena cava
Ascending aorta
Right atrium
FO
Pm
Inferior vena cava
Chiari’s network

Fig. 57.16 Chiari’s network. There are multiple attachment sites around the opening of the inferior vena cava and inferiorly towards the coronary sinus (the reflected part of the right atrium covers the distal attachment to the coronary sinus). Abbreviations: FO, fossa ovalis; Pm, pectinate muscles. (With permission from Loukas M, Sullivan A, Tubbs R et al 2010. Chiari’s network: review of the literature. Surg Radiol Anat 32:895–901.)

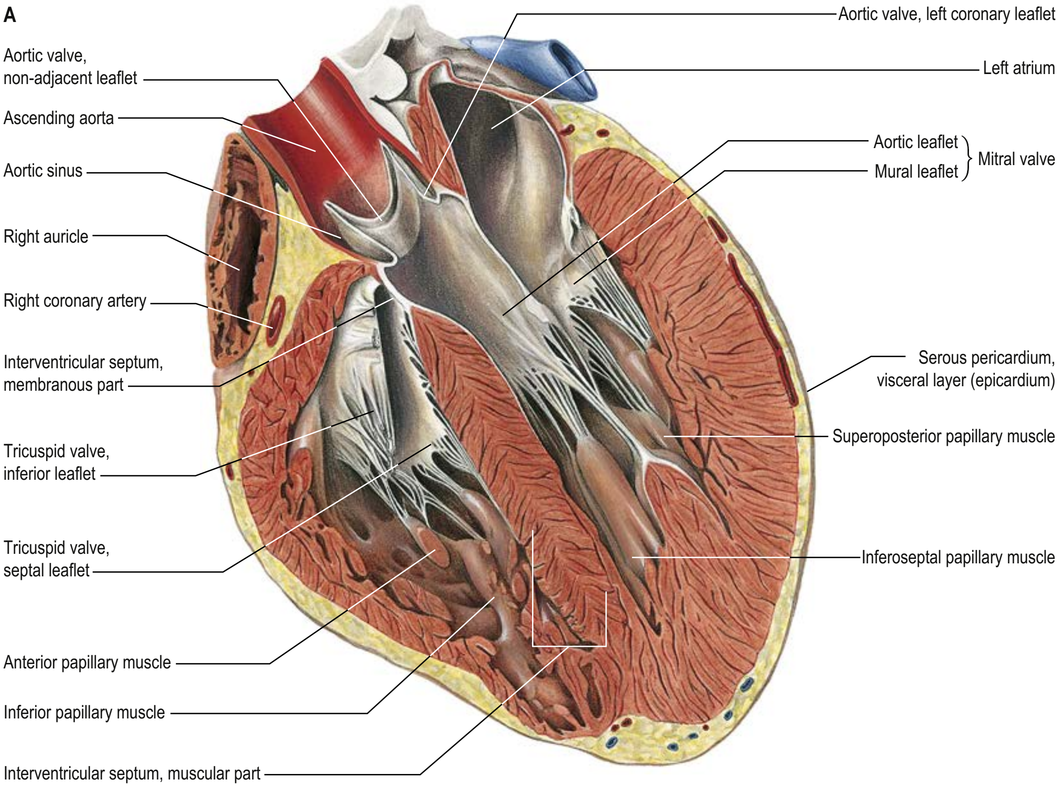
A
Aortic valve, non-adjacent leaflet
Ascending aorta
Aortic sinus
Right auricle
Right coronary artery
Interventricular septum, membranous part
Tricuspid valve, inferior leaflet
Tricuspid valve, septal leaflet
Anterior papillary muscle
Inferior papillary muscle
Interventricular septum, muscular part
Aortic valve, left coronary leaflet
Left atrium
Aortic leaflet
Mural leaflet
Mitral valve
Serous pericardium, visceral layer (epicardium)
Superoposterior papillary muscle
Inferoseptal papillary muscle

Fig. 57.17 A, A dissection opening the ventricles, viewed from a superolateral perspective. (With permission from Waschke J, Paulsen F (eds) Sobotta Atlas of Human Anatomy, 15th ed. Elsevier, Urban & Fischer. Copyright 2013.) (B, *continued online*)

ventricle. The role of the septomarginal trabecula as part of the conduction system of the heart involves carrying the right branch of the atrioventricular bundle, as conduction cardiomyocytes move towards the apex of the ventricle before entering the anterior papillary muscle. The septomarginal trabecula may be any combination of short or long and thick or thin: it is occasionally absent. A further series of prominent trabeculations, the septoparietal trabeculations, extend from the anterior surface of the septomarginal trabecula and run on to the parietal ventricular wall. The smooth-walled outflow tract (conus arteriosus or infundibulum), ascends to the left, superior to the septoparietal trabeculations and inferior to the arch of the supraventricular crest to the pulmonary orifice (Spicer and Anderson 2013).

Tricuspid (right atrioventricular) valve

The atrioventricular valvular complex of both ventricles consists of an orifice and its associated anulus, leaflets, supporting chordae tendineae of various types and papillary muscles. Harmonious interplay of these components, together with the myocardial mass, depends on the conduction tissues and mechanical cohesion provided by the cardiac skeleton. All parts change substantially in position, shape, angulation and dimensions during the cardiac cycle (see Fig. 57.20).

Tricuspid valvular orifice

The tricuspid valvular orifice is best seen from the right atrial aspect. It measures, on average, 11.4 cm in circumference in males and 10.8 cm in females. There is a clear line of transition from the atrial wall or interatrial septum to the lines of attachment of the valvular leaflets. Its margins are not precisely in a single plane. It is almost vertical but at 45° to the sagittal plane and slightly inclined to the vertical, such that it faces (on its ventricular aspect) anterolaterally to the left and somewhat inferiorly (**Fig. 57.19**). Roughly triangular, its margins are described as anterosuperior, inferior and septal, corresponding to the lines of attachment of the valvular leaflets. The connective tissues around the orifice of the atrioventricular valves separate the atrial and ventricular myocardial masses completely, except at the point of penetration of the atrioventricular bundle; they vary in density and disposition around the circumference of the valvular orifice. Extending from the right fibrous trigone of the central fibrous body is a pair of fila coronaria (curved, tapered, prong-like subendocardial tendons), which partly encircle the circumference of the right atrioventricular orifice (see Fig. 57.22). The latter is completed by more tenuous, deformable fibroblastic sulcal areolar tissue. Although the extent of cardiac fibrous tissue varies with sex and age, the tissue within the atrioventricular junction around the tricuspid orifice is always less robust than similar elements found at the attachments of the mitral valve. The topographical attachment of the free valvular leaflets in the tricuspid valve does not wholly correspond to the internal level of attachment of the fibrous core of the valvular leaflets to the junctional atrioventricular connective tissue. The line of attachment of the leaflets is best seen when the heart is examined grossly, and is more readily discerned clinically.

Tricuspid valvular leaflets

When they are closed, it is usually possible to distinguish the three leaflets in the tricuspid valve on the basis of the zones of apposition between them. The leaflets are located anterosuperiorly, septally and inferiorly, corresponding to the respectively named marginal sectors of the atrioventricular orifice (see Fig. 57.21A). The inferior leaflet is often described as being posterior, but when assessed in the attitudinally correct anatomical position, the leaflet is positioned inferiorly (Anderson and Loukas 2009). Each leaflet is a reduplication of endocardium enclosing a collagenous core, continuous on its free margin and ventricular aspect with diverging fascicles of chordae tendineae, and confluent with the anular connective tissue at the inserted margin.

In passing from the free margin to the inserted margin, all leaflets of the atrioventricular valves display rough, clear and basal zones. The rough zone is relatively thick, opaque and uneven on its ventricular aspect where most chordae tendineae are attached; its atrial aspect contacts the comparable surface of the adjacent leaflets during full valve closure. The clear zone is smooth and translucent, receives few chordae tendineae and has a thinner, fibrous core. The basal zone, extending 2–3 mm from the circumferential attachment (inserted margin) of the leaflets, is thicker (because of increased connective tissue), vascularized and innervated, and contains the insertions of the atrial myocardium. The anterosuperior leaflet is the largest part of the tricuspid valve and has a semicircular shape. It is attached mainly to the atrioventricular junction on the posterolateral aspect of the supraventricular crest, extending along its septal limb to the membranous septum ending at the anteroseptal commissure. One or more notches often indent its free margin. The attachment of the septal leaflet passes from the inferoseptal commissure on the inferior ventricular wall across the muscular septum, then angling across the membranous septum to the anteroseptal commissure. The septal leaflet defines one of the borders of the triangle of Koch, thereby aiding location of the atrioventricular node at the apex of this triangle, and ensuring avoidance during tricuspid valve surgery (see Figs 57.13–57.14, 57.22). The inferior leaflet is wholly mural in attachment and guards the inferior surface of the atrioventricular junction, its limits being the inferoseptal and anteroinferior commissures. The zone of apposition between the septal and the anterosuperior leaflets is supported by the septal papillary muscle of the conus arteriosus.

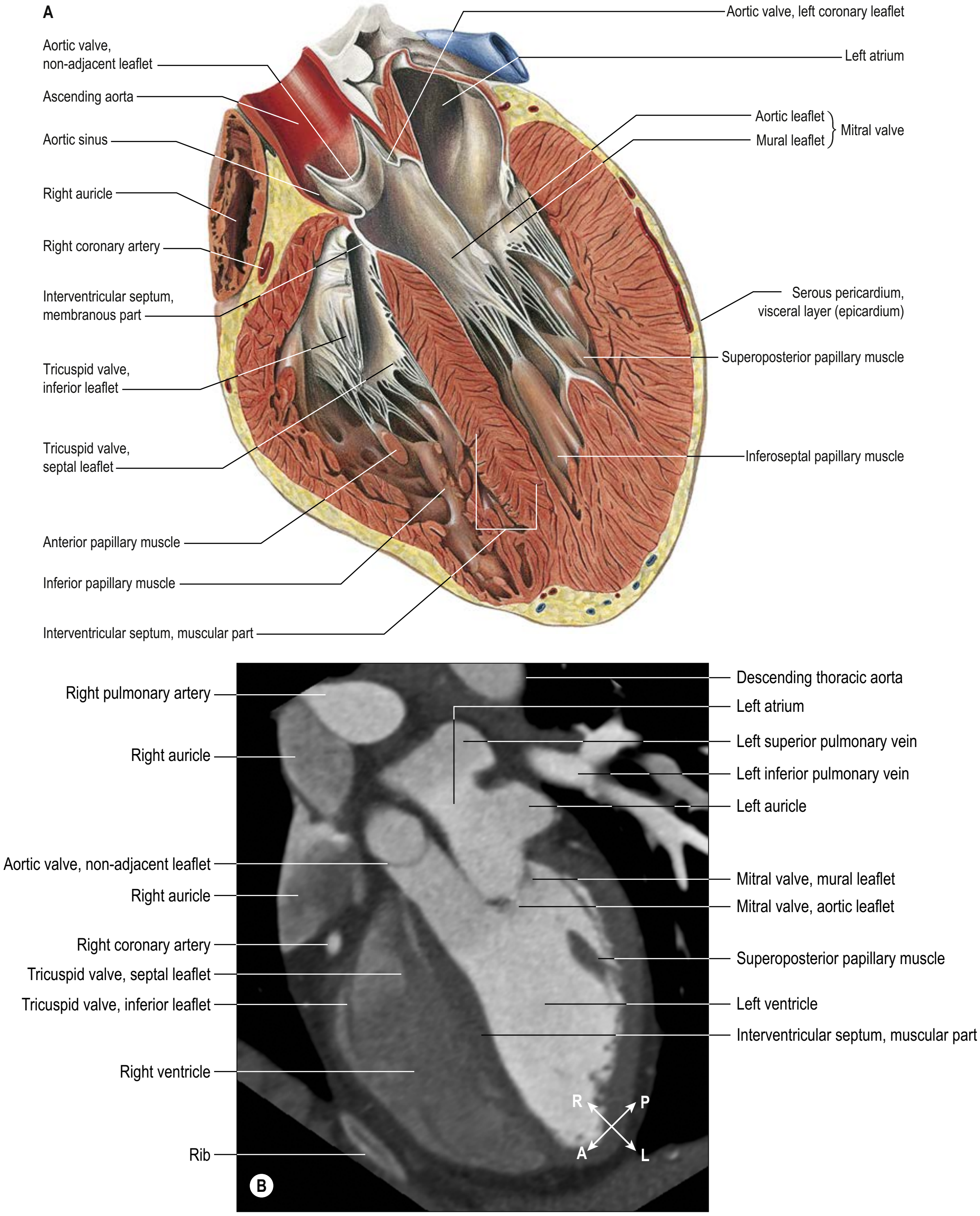
A
Aortic valve, non-adjacent leaflet
Ascending aorta
Aortic sinus
Right auricle
Right coronary artery
Interventricular septum, membranous part
Tricuspid valve, inferior leaflet
Tricuspid valve, septal leaflet
Anterior papillary muscle
Inferior papillary muscle
Interventricular septum, muscular part
Aortic valve, left coronary leaflet
Left atrium
Aortic leaflet
Mural leaflet
Mitral valve
Serous pericardium, visceral layer (epicardium)
Superoposterior papillary muscle
Inferoseptal papillary muscle
Right pulmonary artery
Right auricle
Aortic valve, non-adjacent leaflet
Right auricle
Right coronary artery
Tricuspid valve, septal leaflet
Tricuspid valve, inferior leaflet
Right ventricle
Rib
Descending thoracic aorta
Left atrium
Left superior pulmonary vein
Left inferior pulmonary vein
Left auricle
Mitral valve, mural leaflet
Mitral valve, aortic leaflet
Superoposterior papillary muscle
Left ventricle
Interventricular septum, muscular part
R
P
A
L
B

Fig. 57.17 **A**, A dissection opening the ventricles, viewed from a superolateral perspective. **B**, An ECG-gated CT coronary angiogram showing the ventricles from a superolateral perspective: note that this is a non-standard view. (A, With permission from Waschke J, Paulsen F (eds), Sobotta Atlas of Human Anatomy, 15th ed. Elsevier, Urban & Fischer. Copyright 2013.)

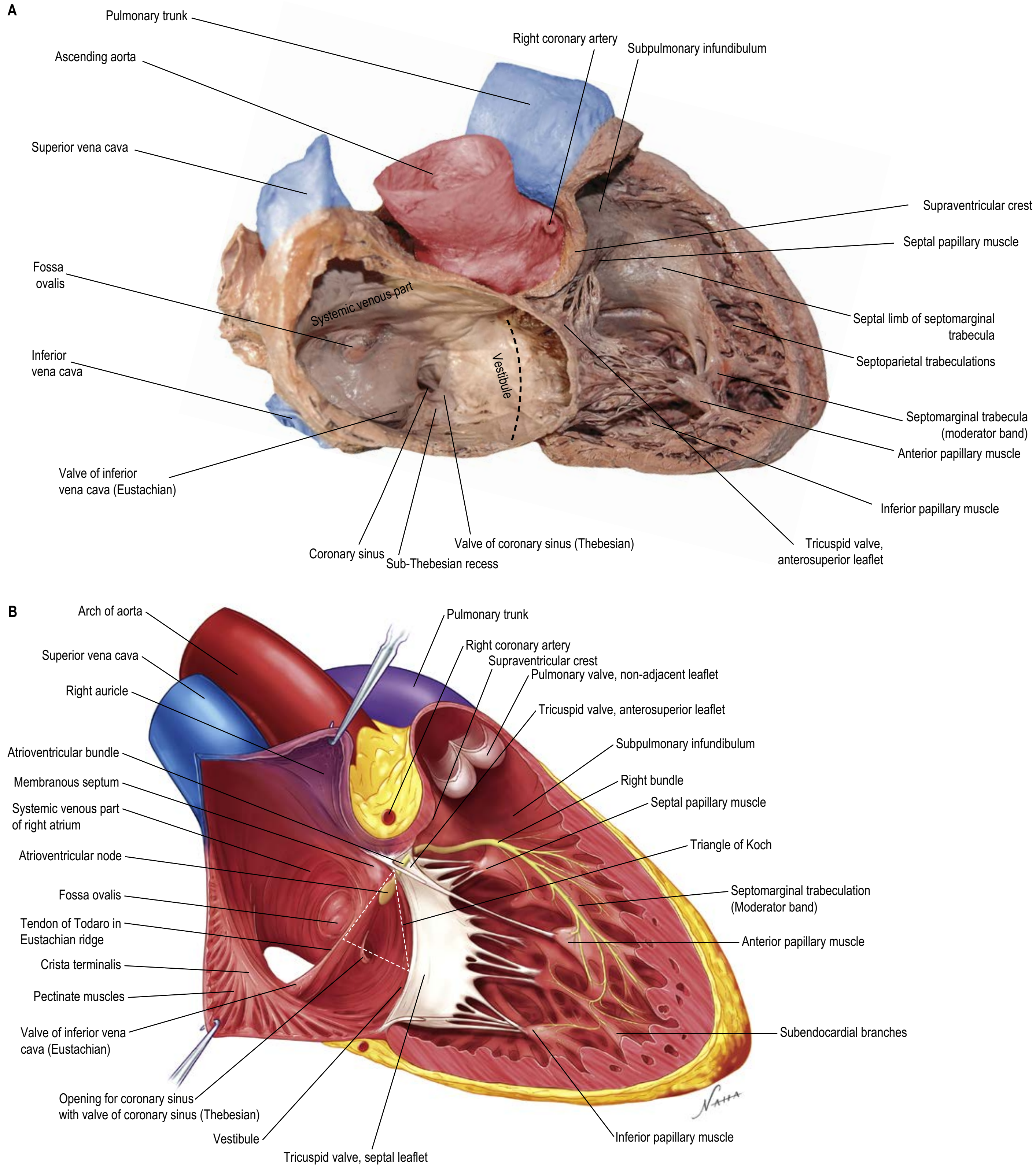
A
Pulmonary trunk
Right coronary artery
Subpulmonary infundibulum
Ascending aorta
Superior vena cava
Supraventricular crest
Septal papillary muscle
Fossa ovalis
Systemic venous part
Septal limb of septomarginal trabecula
Septoparietal trabeculations
Inferior vena cava
Vestibule
Septomarginal trabecula (moderator band)
Anterior papillary muscle
Valve of inferior vena cava (Eustachian)
Inferior papillary muscle
Valve of coronary sinus (Thebesian)
Tricuspid valve, anterosuperior leaflet
Coronary sinus
Sub-Thebesian recess
B
Arch of aorta
Pulmonary trunk
Superior vena cava
Right coronary artery
Supraventricular crest
Pulmonary valve, non-adjacent leaflet
Right auricle
Tricuspid valve, anterosuperior leaflet
Atrioventricular bundle
Subpulmonary infundibulum
Membranous septum
Right bundle
Systemic venous part of right atrium
Septal papillary muscle
Atrioventricular node
Triangle of Koch
Fossa ovalis
Septomarginal trabeculation (Moderator band)
Tendon of Todaro in Eustachian ridge
Anterior papillary muscle
Crista terminalis
Pectinate muscles
Valve of inferior vena cava (Eustachian)
Subendocardial branches
Opening for coronary sinus with valve of coronary sinus (Thebesian)
Vestibule
Inferior papillary muscle
Tricuspid valve, septal leaflet

Fig. 57.18 Internal features of the right atrium and ventricle shown (**A**) in a cadaveric heart and (**B**) an illustration showing the atrioventricular node, atrioventricular bundle and right bundle, viewed via a 'window dissection' (prepared by removing the anterosuperior wall of the right atrium and ventricle). The valve of the inferior vena cava (Eustachian) separates the inferior vena cava from the sub-Thebesian recess. The valve of the coronary sinus (Thebesian) guards the entry into the coronary sinus. The smooth circumferential area of atrial wall that surrounds the orifice of the tricuspid valve is the vestibule. Note the location of the supraventricular crest and septomarginal trabeculation. The body of the septomarginal trabeculation (moderator band) continues as a muscular band to the anterior papillary muscle and the parietal wall of the right ventricle. Conduction tissue accompanies fine trabeculae carneae and false chordae. (Image courtesy of Professor M Loukas.) See Fig. 57.36 for the left-sided conduction system.

Opening of the tricuspid valve

Despite its name, the tricuspid valve acts more like a bicuspid valve because its smallest septal leaflet is fixed between the atrial and ventricular septa. The remainder of the tricuspid anulus is muscular. The anulus of the tricuspid valve is less fibrous than the anulus of the mitral valve, which presumably accounts for the low occurrence of degenerative calcifications seen on the tricuspid valve (Saremi et al 2017). During diastole, the anulus dilates with right ventricular relaxation and the large anterosuperior and inferior leaflets move away from the plane of the anulus into the right ventricle. During systole, the anulus constricts as the right ventricle contracts and the two major leaflets move like sails about a relatively immobile septal leaflet and the septum itself (Fig. 57.20).

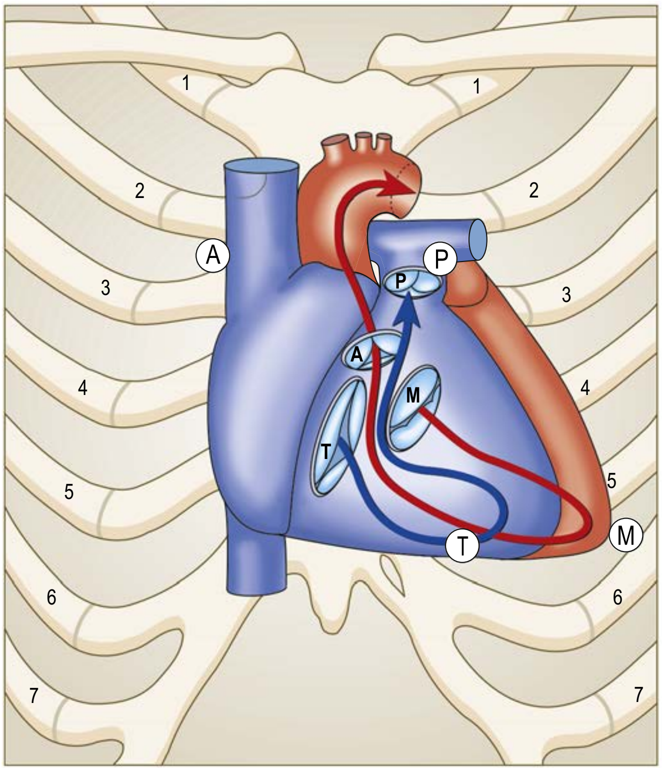

Fig. 57.19 The relationship between the anterior thoracic wall and valves of the heart. The right heart is blue, the blue arrow denotes the inflow and outflow channels of the right ventricle; the left heart is treated similarly in red. The positions, planes and relative sizes of the cardiac valves are shown. The position of the letters A, P, T and M (in a white circle) indicate the aortic, pulmonary, tricuspid and mitral auscultation areas of clinical practice, respectively. Note that, for the purpose of illustration, the orifices of the aortic, mitral and tricuspid valves are shown with some separation between them, whereas, in reality, the leaflets of the three valves are in fibrous continuity (see Fig. 57.22).

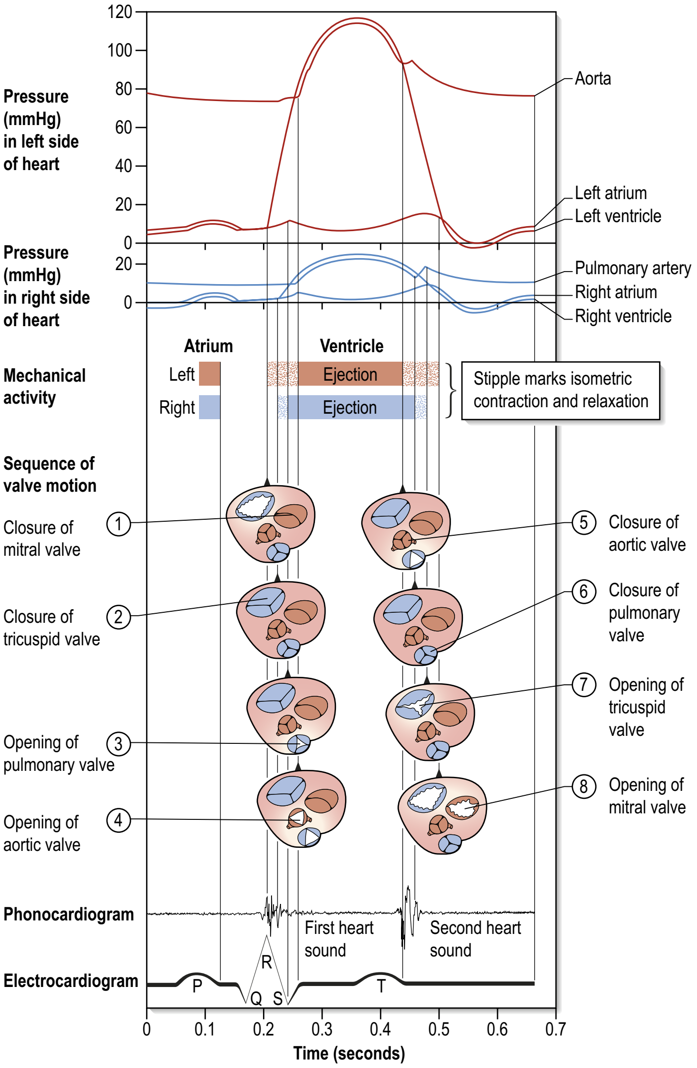

Fig. 57.20 A summary of some of the principal events that occur in the cardiac cycle. Systole begins at the onset of the first heart sound (see phonocardiogram) and ends at the onset of the second heart sound, when diastole begins, and this cycle repeats itself.

Tricuspid valvular chordae tendineae

The chordae tendineae are fibrous collagenous structures that support the leaflets of the atrioventricular valves. In about one-third of hearts, false chordae connect the papillary muscles to each other or to the ventricular wall or septum, or pass directly between points on the wall or septum, or both. Their numbers and dimensions in the right ventricle vary: approximately 40% of these false cords contain conduction cardiomyocytes.

The true chordae usually arise from small projections on the tips or margins of the apical third of papillary muscles, but may sometimes arise from the papillary muscle bases or directly from the ventricular walls and septum. They are attached to various parts of the ventricular aspects or the free margins of the valvular leaflets. True chordae are classified into first-, second- and third-order types, according to the distance of the attachment from the margins of the leaflets, but this classification has little functional or morphological merit. Fan-shaped chordae have a short stem from which branches radiate to attach to the free margins or ventricular aspect of the zones of apposition between leaflets and to the ends of adjacent leaflets. Rough-zone chordae arise from a single stem that usually splits into three parts that attach to the free margin, the ventricular aspect of the rough zone and to some intermediate points on the leaflet, respectively. Free-edge chordae are single, thread-like and often long, passing from either the apex or the base of a papillary muscle into a marginal attachment, usually near the midpoint of a leaflet or to one of the scallops on its free edge. Deep chordae pass beyond the free margins and, branching to various extents, reach the more peripheral rough zone or even the clear zone. Basal chordae are round or ribbon-like, long and slender, or short and muscular; they arise from the smooth or trabeculated ventricular wall and are attached to the inserted margin (basal part) of a leaflet.

Papillary muscles

The two major papillary muscles in the right ventricle are located in anterior and inferior positions. A third, smaller septal muscle lies medially, together with several smaller, variable muscles attached to the interventricular septum. The anterior papillary muscle is the largest, its base arising from the right anterolateral ventricular wall inferior to the anteroinferior commissure between the anterosuperior and inferior valvular leaflets, also blending with the right side of the septomarginal trabecula. The inferior papillary muscle, often bifid or trifid, arises from the myocardium inferior to the inferoseptal valvular commissure. The septal papillary muscle of the conus (muscle of Lancisi) is almost always present and is the most superior and largest of the small septal papillary muscles. It arises from the posterior septal limb of the septomarginal trabeculation and locates the right bundle branch within the right ventricle. All the major papillary muscles supply chordae to adjacent parts of the valvular leaflets they support (see Figs 57.17–57.18). A feature of the right ventricle is that the septal leaflet is tethered by individual chordae tendineae directly to the interventricular septum; such septal insertions are never seen in the left ventricle. When closed, the three leaflets fit snugly together, the pattern of the zones of apposition confirming the trifoliate arrangement of the tricuspid valve.

Pulmonary valve

The pulmonary valve, guarding the outflow from the right ventricle, sits at the top of the conus arteriosus (infundibulum) and is situated at some distance from the other three cardiac valves (see Fig. 57.19; **Figs 57.21–57.22**). Its plane of orientation faces superiorly to the left and slightly posteriorly. It has three semilunar leaflets, attached by convex edges partly to the infundibular wall of the right ventricle and partly to the origin of the pulmonary trunk. The line of attachments is curved, rising at the periphery of each leaflet near their zones of apposition (the commissures) and reaching the sinutubular junction of the pulmonary trunk, in a manner similar to that of the aortic valve (**Fig. 57.23**). Removal of the leaflets reveals that the fibrous semilunar attachments enclose three crescents of infundibular musculature within the pulmonary sinuses, whereas three roughly triangular segments of arterial wall are incorporated within the ventricular outflow tract beneath the apex of each commissure at the point of attachment. Thus there is no proper

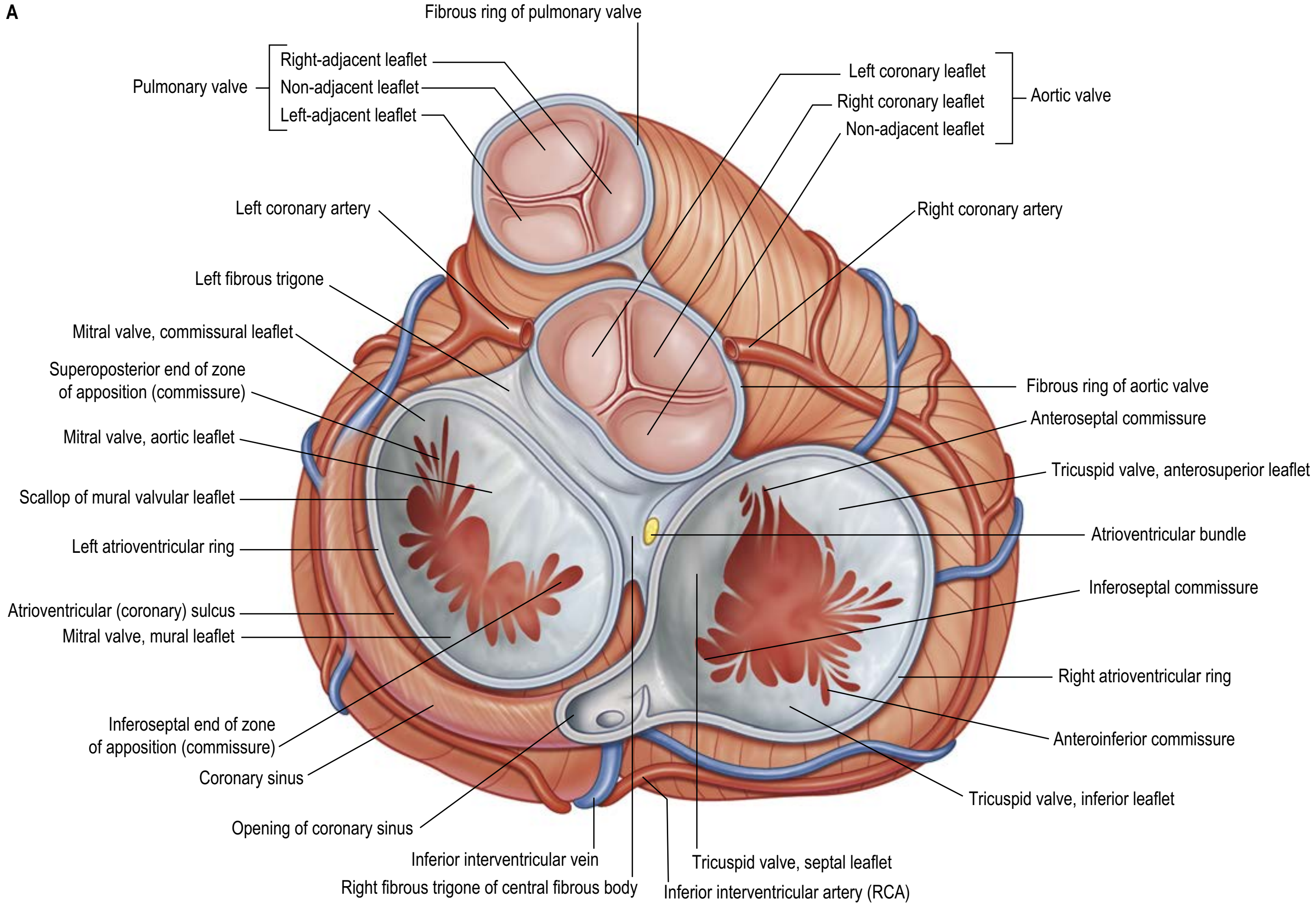
A
Fibrous ring of pulmonary valve
Pulmonary valve
Right-adjacent leaflet
Non-adjacent leaflet
Left-adjacent leaflet
Left coronary leaflet
Right coronary leaflet
Non-adjacent leaflet
Aortic valve
Left coronary artery
Right coronary artery
Left fibrous trigone
Mitral valve, commissural leaflet
Superoposterior end of zone of apposition (commissure)
Fibrous ring of aortic valve
Anteroseptal commissure
Mitral valve, aortic leaflet
Tricuspid valve, anterosuperior leaflet
Scallop of mural valvular leaflet
Atrioventricular bundle
Left atrioventricular ring
Inferoseptal commissure
Atrioventricular (coronary) sulcus
Mitral valve, mural leaflet
Right atrioventricular ring
Inferoseptal end of zone of apposition (commissure)
Anteroinferior commissure
Coronary sinus
Tricuspid valve, inferior leaflet
Opening of coronary sinus
Inferior interventricular vein
Tricuspid valve, septal leaflet
Right fibrous trigone of central fibrous body
Inferior interventricular artery (RCA)

Fig. 57.21 **A**, The atrioventricular valvular entrance (base) of the ventricles, after removal of the atria and the pericardium, exposing the coronary arteries and cardiac veins. Contrast the planes and positions of the aortic and pulmonary valves, and with Fig. 57.22. Abbreviations: RCA, branch of right coronary artery. (Adapted from Drake RL, Vogl AW, Mitchell A et al (eds) Gray's Atlas of Anatomy, 2nd ed. Elsevier, Churchill Livingstone. Copyright 2015.) (B, *continued online*)

circular 'anulus' supporting the leaflets of the valve, and the fibrous semilunar attachment is an essential requisite for snug closure of the nodules and lunules of the semilunar leaflets during ventricular diastole.

It is difficult to name the leaflets and corresponding sinuses of the pulmonary valve and trunk precisely according to the coordinates of the body because the valvular orifice is obliquely positioned. The convention of referring to the leaflets as anterior, posterior and septal is based on their fetal position: in the adult, the leaflets become anterior, right and left, respectively. Each leaflet is an endocardial fold with a variably developed intervening fibrous core that traverses both the free edge and the semilunar-shaped inserted margin. The latter is particularly thickened at its deepest central part (the nadir) of the base (inserted margin) of each leaflet, and therefore never forms a simple complete fibrous ring. The free margin of each leaflet contains a central localized collagenous thickening, the nodule of the semilunar leaflet (nodule of Arantius). Perforations within the leaflets close to the free margin and near the commissures are frequently present and are of no functional significance. Each semilunar leaflet is contained within one of the three sinuses of the pulmonary trunk.

Opening of the pulmonary valve

During diastole, all three leaflets of the pulmonary valve are tightly apposed (see Fig. 57.20). The pulmonary valve is difficult to visualize at echocardiography; atrial systole may help by causing a slight posterior movement of the valve leaflets. The pulmonary valve opens passively during ventricular systole and closes rapidly at the end of systole.

Left atrium

General, external and internal features

Although smaller in volume than the right, the left atrium has thicker walls (3 mm on average). It possesses a venous part that receives the right and left superior and inferior pulmonary veins, a vestibule and an auricle. Its cavity and walls are formed largely by the proximal parts of the primordial pulmonary veins that are incorporated into the atrial wall during development. The atrial auricle is a remnant of the initial atrial component of the primary heart tube (Ch. 13). The left atrium is roughly cuboidal, extending posterior to the right atrium and separated from it by the obliquely positioned interatrial septum. The right atrium is therefore anterolateral to the right part of the left atrium. The left part is covered anteriorly by the intraepicardial part of the pulmonary trunk and ascending aorta, and part of the intervening transverse pericardial sinus. Anteroinferiorly, and to the left, it adjoins the base of the left ventricle at the orifice of the mitral (left atrioventricular) valve. Its approximately quadrangular posterior wall forms most of the anatomical base of the heart, receives the terminations of (usually) two pulmonary veins from both the left and right lungs, and forms the anterior wall of the oblique pericardial sinus (see Fig. 57.1). This surface, with the atrial roof, ends on the right side at the shallow vertical interatrial sulcus that descends to the cardiac crux (see Figs 57.4B,E).

The left atrial auricle (appendage) is characteristically longer, narrower and more hooked than the right, and is a finger-like extension with more deeply indented margins (see Fig. 57.1; **Fig. 57.24**). It is constricted at its junction with the body of the atrium and all its contained pectinate muscles are smaller than their right-sided counterparts. The left atrium lacks a crista terminalis, and the muscle bundles in the auricle are arranged in a whorl-like fashion rather than being in an array. The tip of the auricle has a variable position, often lying over the pulmonary trunk and anterior interventricular branch of the left coronary artery, and pointing towards the ascending aorta. Its narrow morphology predisposes it to being a site for thrombus formation, especially in cases of atrial fibrillation.

The four pulmonary veins (left and right, superior and inferior) open into the superior part of the left and right posterolateral surfaces of the left atrium, two on each side (see Figs 57.1, 57.4B,E). This arrangement is present in 20–60% of studied subjects. Additional supernumerary or accessory pulmonary veins may be present (Hassani and Saremi 2017). A common variation includes the presence of a short or long left common venous trunk and multiple pulmonary veins on

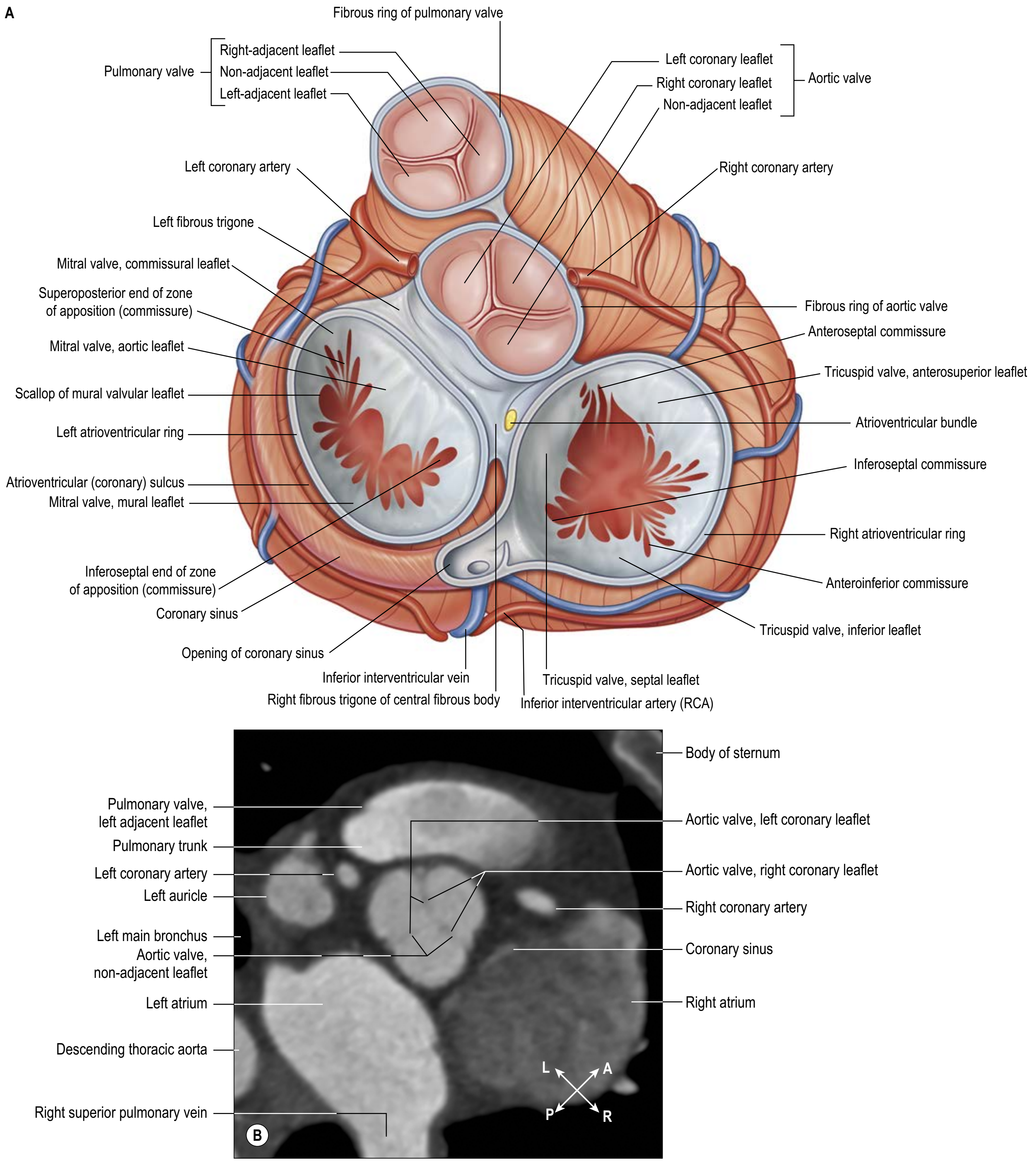
A
Fibrous ring of pulmonary valve
Pulmonary valve
Right-adjacent leaflet
Non-adjacent leaflet
Left-adjacent leaflet
Left coronary leaflet
Right coronary leaflet
Non-adjacent leaflet
Aortic valve
Left coronary artery
Right coronary artery
Left fibrous trigone
Mitral valve, commissural leaflet
Superoposterior end of zone of apposition (commissure)
Mitral valve, aortic leaflet
Scallop of mural valvular leaflet
Left atrioventricular ring
Atrioventricular (coronary) sulcus
Mitral valve, mural leaflet
Inferoseptal end of zone of apposition (commissure)
Coronary sinus
Opening of coronary sinus
Inferior interventricular vein
Right fibrous trigone of central fibrous body
Tricuspid valve, septal leaflet
Inferior interventricular artery (RCA)
Fibrous ring of aortic valve
Anteroseptal commissure
Tricuspid valve, anterosuperior leaflet
Atrioventricular bundle
Inferoseptal commissure
Right atrioventricular ring
Anteroinferior commissure
Tricuspid valve, inferior leaflet
B
Pulmonary valve, left adjacent leaflet
Pulmonary trunk
Left coronary artery
Left auricle
Left main bronchus
Aortic valve, non-adjacent leaflet
Left atrium
Descending thoracic aorta
Right superior pulmonary vein
Body of sternum
Aortic valve, left coronary leaflet
Aortic valve, right coronary leaflet
Right coronary artery
Coronary sinus
Right atrium
L
A
P
R

Fig. 57.21 **A**, The atrioventricular valvular entrance (base) of the ventricles, after removal of the atria and the pericardium, exposing the coronary arteries and cardiac veins. Contrast the planes and positions of the aortic and pulmonary valves, and with Fig. 57.22. Abbreviation: RCA, branch of right coronary artery. **B**, An ECG-gated CT coronary angiogram viewing the base of the ventricles: note that this is a non-standard view. (A, Adapted from Drake RL, Vogl AW, Mitchell A et al (eds) Gray's Atlas of Anatomy, 2nd ed. Elsevier, Churchill Livingstone. Copyright 2015.)

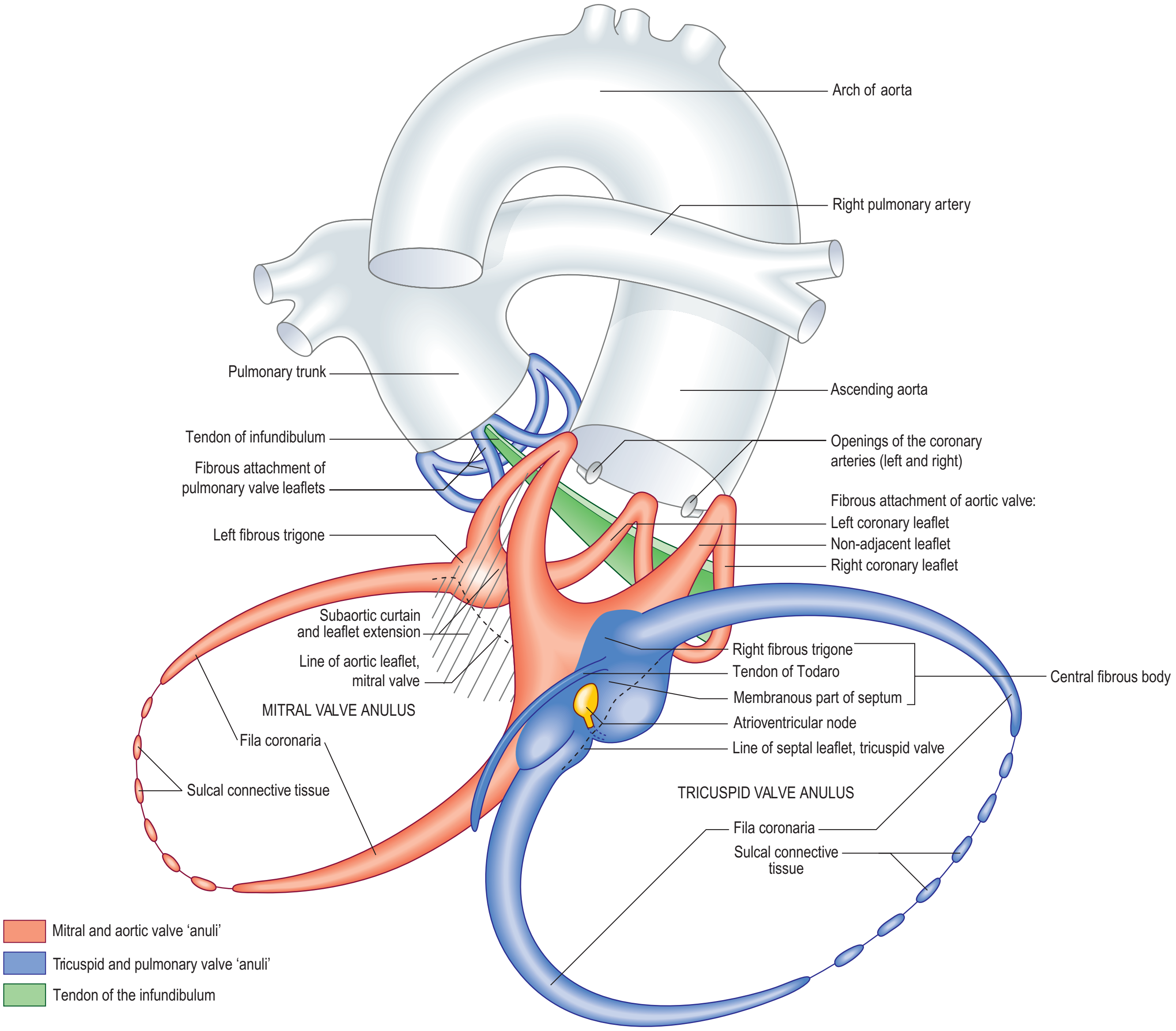
Arch of aorta
Right pulmonary artery
Pulmonary trunk
Ascending aorta
Tendon of infundibulum
Openings of the coronary arteries (left and right)
Fibrous attachment of pulmonary valve leaflets
Fibrous attachment of aortic valve:
Left coronary leaflet
Non-adjacent leaflet
Right coronary leaflet
Left fibrous trigone
Subaortic curtain and leaflet extension
Right fibrous trigone
Tendon of Todaro
Central fibrous body
Line of aortic leaflet, mitral valve
Membranous part of septum
Atrioventricular node
MITRAL VALVE ANULUS
Line of septal leaflet, tricuspid valve
Fila coronaria
Sulcal connective tissue
TRICUSPID VALVE ANULUS
Fila coronaria
Sulcal connective tissue
🟥 Mitral and aortic valve 'anuli'
🟦 Tricuspid and pulmonary valve 'anuli'
🟩 Tendon of the infundibulum

Fig. 57.22 Principal elements of the fibrous skeleton of the heart. For clarity, the view is from the right posterosuperior aspect. Perspective causes the pulmonary anulus to appear smaller than the aortic anulus, whereas, in fact, the reverse is the case. (Copyright of The Royal College of Surgeons of England. Reproduced with permission.)

the right (**Fig. 57.25**). The right superior and inferior pulmonary veins travel posterior to the respective vena cava. The orifices of the veins at their point of entry are smooth and oval. Interpulmonary ridges are usually present between ipsilateral orifices; the most prominent is located between the openings of the left auricle and left superior pulmonary vein. The ridges are infoldings of the left atrial wall and contain adipose tissue, atrial arteries and nerve bundles. At the site of the pericardial reflection, the atrial musculature extends into the pulmonary veins, forming myocardial sleeves that are thickest in the inferior wall of the superior pulmonary veins and the superior walls of the inferior pulmonary veins. They lie external to the venous tunica media and internal to the epicardium/adventitia. The myocardial sleeves, especially those of the superior veins, are often the site of focal electrical activity that initiates atrial fibrillation. Atrial myocardial bridges and crossing strands are often present, connecting the left superior and inferior pulmonary veins.

Several epicardial fat pads on the pulmonary venous part of the left atrium house the superior left, posterolateral, left inferior and posteromedial ganglionated cardiac intrinsic nerve plexuses (typically four). The smallest cardiac veins (venae cordis minimae) return blood directly from the myocardium to the left atrial cavity. The left atrial aspect of the interatrial septum has a characteristically rough appearance, bounded by a crescentic, superiorly concave ridge that marks the site of the fetal foramen ovale. The left-sided atrial septal pouch is a variant of the interatrial septum that carries a high association with cryptogenic strokes (Hołda and Koziej 2018). The vestibule is the smooth circumferential area of atrial wall that surrounds the orifice of the mitral valve (see Fig. 57.25; **Fig. 57.26**). The musculature that makes up the posteroinferior aspect of the left lateral wall of the atria, between the opening of the left inferior pulmonary vein or common left pulmonary vein, and the mitral valve anulus is known as the left atrial (mitral) isthmus. In this area, the vestibule of the left atrium directly faces the great cardiac vein, coronary sinus and the circumflex branch of the left coronary artery.

Left ventricle

General and external features

The left ventricle is constructed in accordance with its role as a powerful pump for the high-pressured systemic arterial circulation. Variously described as half-ellipsoid or cone-shaped, it is longer and narrower than the right ventricle, extending from its base in the plane of the atrioventricular sulcus to the cardiac apex. Its long axis descends anteriorly and to the left. In transverse section, at right-angles to the long axis, its cavity is oval or nearly circular, with walls three times thicker (8–12 mm) than those of the right ventricle (**Fig. 57.27**). It forms part of the anterior, left pulmonary and inferior cardiac surfaces. Except where obscured by the ascending aorta and pulmonary trunk, the base of the ventricular cone is superficially separated from the left atrium by part of the atrioventricular sulcus with the coronary sinus passing along its posterior and inferior aspect (see Fig. 57.4B,E). The anterior and inferior interventricular sulci indicate the lines of mural attachment of the ventricular septum and the limits of the ventricular territories. The anterior surface of the ventricle curves bluntly into its left pulmonary surface at the left border (obtuse margin) (see Figs 57.1B, 57.9).

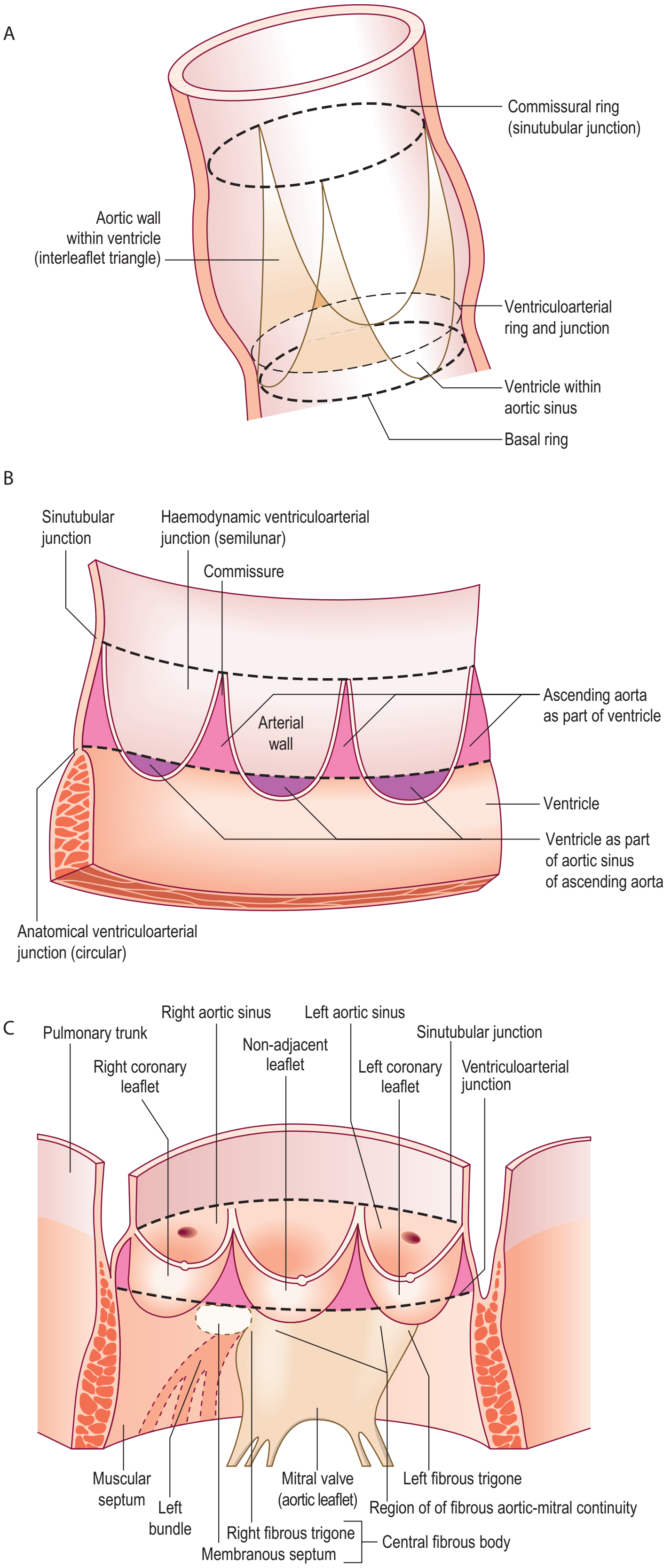
A
Commissural ring (sinutubular junction)
Aortic wall within ventricle (interleaflet triangle)
Ventriculoarterial ring and junction
Ventricle within aortic sinus
Basal ring
B
Sinutubular junction
Haemodynamic ventriculoarterial junction (semilunar)
Commissure
Arterial wall
Ascending aorta as part of ventricle
Ventricle
Ventricle as part of aortic sinus of ascending aorta
Anatomical ventriculoarterial junction (circular)
C
Right aortic sinus
Left aortic sinus
Pulmonary trunk
Non-adjacent leaflet
Sinutubular junction
Right coronary leaflet
Left coronary leaflet
Ventriculoarterial junction
Muscular septum
Left bundle
Mitral valve (aortic leaflet)
Left fibrous trigone
Region of of fibrous aortic-mitral continuity
Right fibrous trigone
Membranous septum
Central fibrous body

Fig. 57.23 **A**, The structure of the aortic root is best conceptualized in terms of a three-pronged coronet; there are at least three rings within this coronet but none supports the entirety of the attachments of the valvular leaflets (compare with **C**). **B**, The aortic valvular leaflets have been resected at their attachment to the aortic wall. Note the relationship of the leaflet insertions and the ventriculoarterial junction. **C**, The root of the aorta has been cut open and distended, in order to show the insertion of the semilunar leaflets. Note the zone of fibrous continuity between the leaflets of the aortic and mitral valves and their relationship to the fibrous trigones, and the semilunar attachment of the leaflets (compare with **B**). (Redrawn with permission, courtesy of Professor RH Anderson, Institute of Child Health, University College, London.)

The cross-sectional shape of the left ventricle changes from elliptical in the neonatal period to the round adult shape later in infancy (Azancot et al 1983). The effect of obesity on the heart is apparent as early as the second year of life. Obese children at 2 years of age may have a greater left ventricular mass compared with normal weight controls (de Jonge et al 2011).

Internal features

The left ventricle has an inlet part guarded by the mitral (left atrioventricular) valve, an outlet part guarded by the aortic valve and an apical trabecular part. The left atrioventricular orifice admits left atrial blood during diastole, the flow being directed towards the cardiac apex (**Fig. 57.28**; see Fig. 57.36). After closure of the mitral valvular leaflets and throughout the ejection phase of systole, blood is expelled from the cardiac apex through the aortic orifice. In contrast to the orifices within the right ventricle, those of the left ventricle are in close contact: fibrous continuity between leaflets of the aortic and mitral valves forms the subaortic curtain (see Fig. 57.22). The inlet and outlet turn sharply round this fibrous curtain (**Fig. 57.29**). The anteromedial wall is the muscular interventricular septum: its convexity completes the circular cross-section of the left ventricle (see Fig. 57.27). Towards the aortic orifice, the septum becomes the thin and collagenous membranous part of the interventricular septum, an oval or round area below and confluent with the right fibrous trigone (triangle) that separates the right and the non-adjacent leaflets of the aortic valve (see Figs 57.22, 57.30). Between the inferior limits of the free margins of the leaflets of the mitral valve and the ventricular apex, the muscular walls exhibit deeper, finer and more intricate trabeculae carneae (fine apical trabeculae carneae) than those of the right ventricle: they are more developed nearer the apex, and become smoother as the superior aspect of the interventricular septal surface is reached.

Hypertrophy of heart muscle

Available with the *Gray's Anatomy* e-book

Mitral (left atrioventricular) valve

The general description of the component parts of the tricuspid valve (see p. 1076) also applies to the mitral valve; it has an orifice with a supporting anulus, valvular leaflets and varying arrangements of chordae tendineae and papillary muscles.

Mitral valvular orifice

The mitral orifice, smaller than the tricuspid orifice, is a well-defined transitional zone between the left atrial wall and the inserted margin of the mitral valvular leaflet bases. It measures, on average, 9.0 cm in circumference in males and 7.2 cm in females. The approximately oval orifice is almost vertical and at 45° to the sagittal plane in diastole, but with a slight anterior tilt. Its ventricular aspect faces anterolaterally to the left and a little inferiorly towards the left ventricular apex (see Fig. 57.19). It is almost co-planar with the tricuspid orifice but posterosuperior to it, whereas it is posteroinferior and slightly to the left of the aortic orifice. The mitral, tricuspid and aortic orifices are intimately connected at the site of the central fibrous body (see Fig. 57.22). When the mitral valve leaflets close, they form a single zone of coaptation that should be termed the commissure: clinicians usually recognized the two ends of the zone as commissures. The anulus of the valve is not a simple fibrous ring but is made up of fibrocollagenous elements of varying consistency, from which the fibrous core of each leaflet take origin; the variable consistency is essential to allow the major changes in anular shape and dimensions during the cardiac cycle that are needed for optimal valvular efficiency. The area of the anulus increases linearly with body surface area in children and young adults (Poutanen et al 2006). The anulus is strongest at the internal aspects of the left and right fibrous trigones. Extending from these structures, the anterior and posterior fila coronaria (curved, tapered, fibrous, prong-like subendocardial tendons) partly encircle the orifice at the atrioventricular junction (see Fig. 57.22). Between the tips of the fila coronaria, the atrial and ventricular myocardial masses are separated by a more irregular sheet of deformable fibroelastic connective tissue. Spanning anteriorly between the fibrous trigones, the fibrous core of the central part of the aortic leaflet of the mitral valve is a continuation of the fibrous subaortic curtain that descends from the adjacent halves of the left and non-adjacent (non-coronary) valve leaflets (see Fig. 57.22, 57.29).

Mitral valvular leaflets

The mitral valvular leaflets have long been described as paired structures. The name 'bicuspid valve' is explicit but erroneous as a descriptor because the leaflets are not cuspid, or 'peaked', in form.

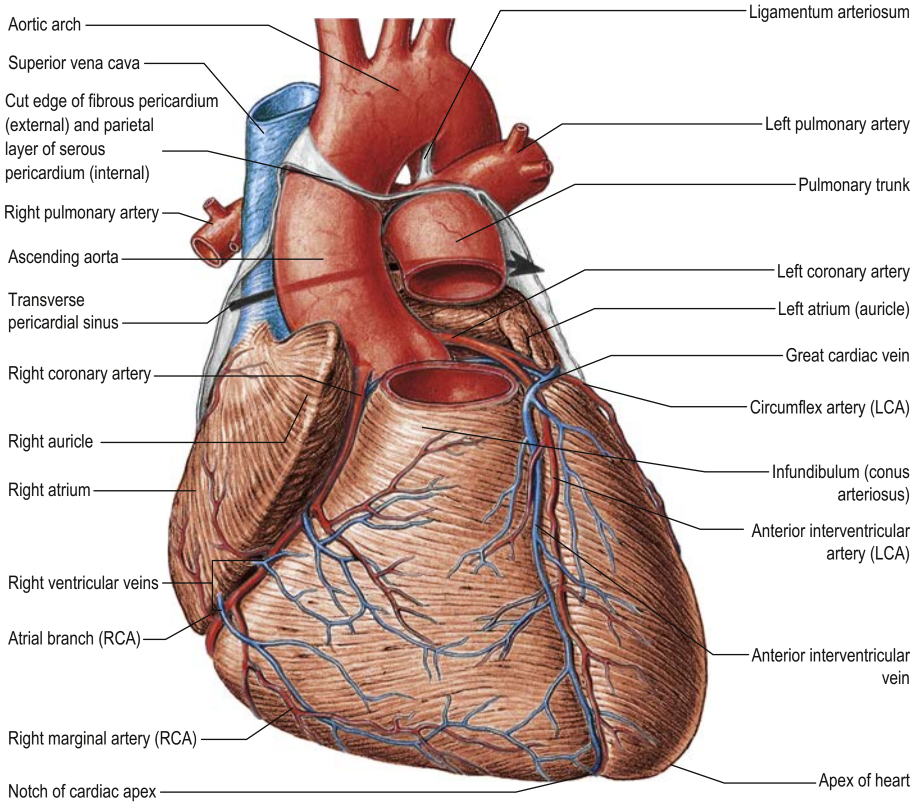
Aortic arch
Superior vena cava
Cut edge of fibrous pericardium (external) and parietal layer of serous pericardium (internal)
Right pulmonary artery
Ascending aorta
Transverse pericardial sinus
Right coronary artery
Right auricle
Right atrium
Right ventricular veins
Atrial branch (RCA)
Right marginal artery (RCA)
Notch of cardiac apex
Ligamentum arteriosum
Left pulmonary artery
Pulmonary trunk
Left coronary artery
Left atrium (auricle)
Great cardiac vein
Circumflex artery (LCA)
Infundibulum (conus arteriosus)
Anterior interventricular artery (LCA)
Anterior interventricular vein
Apex of heart

Fig. 57.24 The anterior (sternocostal) surface of the heart, with the initial part of the pulmonary trunk removed. Abbreviations: RCA, branch of right coronary artery; LCA, branch of left coronary artery. (With permission from Waschke J, Paulsen F (eds) Sobotta Atlas of Human Anatomy, 15th ed. Elsevier, Urban & Fischer. Copyright 2013.)

Hypertrophic cardiomyopathy is characterized by myocardial wall thickening, with a disproportionate thickening of the interventricular septum in comparison with the posterior wall. Echocardiography accurately assesses the degree of thickening and its effect on systolic function, such as dynamic left ventricular outflow obstruction, systolic anterior motion of the aortic leaflet of the mitral and mid-systolic closure of the aortic valve. There may also be a degree of diastolic dysfunction. Serial short-axis gradient echo MRI allows accurate measurement of wall thickness and is particularly useful in assessing apically confined hypertrophy. There are a number of histological changes, including cardiomyocytic disarray with replacement fibrosis and collagenous component expansion. Treatment is usually medical, except for refractory cases and when the left ventricular outflow tract obstruction has a gradient of greater than 50 mmHg. Ventricular septal myotomy and myectomy are performed in such cases. Catheter alcohol septal ablation has been introduced as a non-surgical alternative. A number of patients may also require implantation of cardiac defibrillators to prevent sudden cardiac death.

The heart of an athletic individual may physiologically hypertrophy but in a uniform fashion, and thickness decreases on deconditioning. In contrast, hypertrophic cardiomyopathy reveals asymmetric patterns of left ventricular hypertrophy, often with sharp segmental transitions, left atrial enlargement and unusual electrocardiographic patterns. There is an autosomal dominant inheritance pattern of abnormalities in genes coding for myocardial proteins associated with hypertrophic cardiomyopathy. Individuals with mutations of the β-MHC (major histocompatibility complex) gene usually develop the classic form of hypertrophy, whereas those with mutations of the cardiac troponin T gene generally have only mild or clinically undetectable hypertrophy. Rare forms of hypertrophy include localized left ventricular apical hypertrophy as a result of mutations of the cardiac troponin I gene, and isolated mid-cavity hypertrophy caused by mutations of cardiac actin and MLC (myosin light chain) genes.

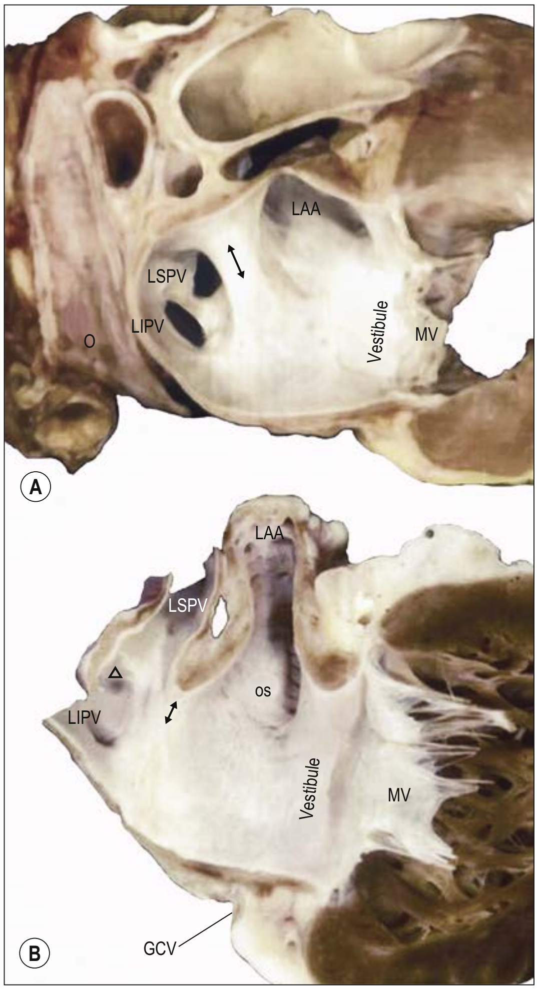

Fig. 57.25 Sagittal sections through a cadaveric heart showing the left side of the left atrium. **A**, The oesophagus (O) passing posterior to the posterior left atrial wall and a broad left-lateral ridge (double-headed arrow). The left superior (LSPV) and left inferior (LIPV) pulmonary veins enter the left atrium via a short common stem. Other abbreviations: LAA, left atrial auricle; MV, mitral valve. **B**, The section passes through the os (opening) of the left atrial auricle and the infolding of the ridge. The triangle indicates the carina or interpulmonary ridge between the left superior and inferior pulmonary veins. The great cardiac vein (GCV) runs inferior to the left atrial wall. (With permission from Ho SY, McCarthy KP, Faletra FF 2011 Anatomy of the left atrium for interventional echocardiography. Eur J Echocardiogr 12:11–15.)

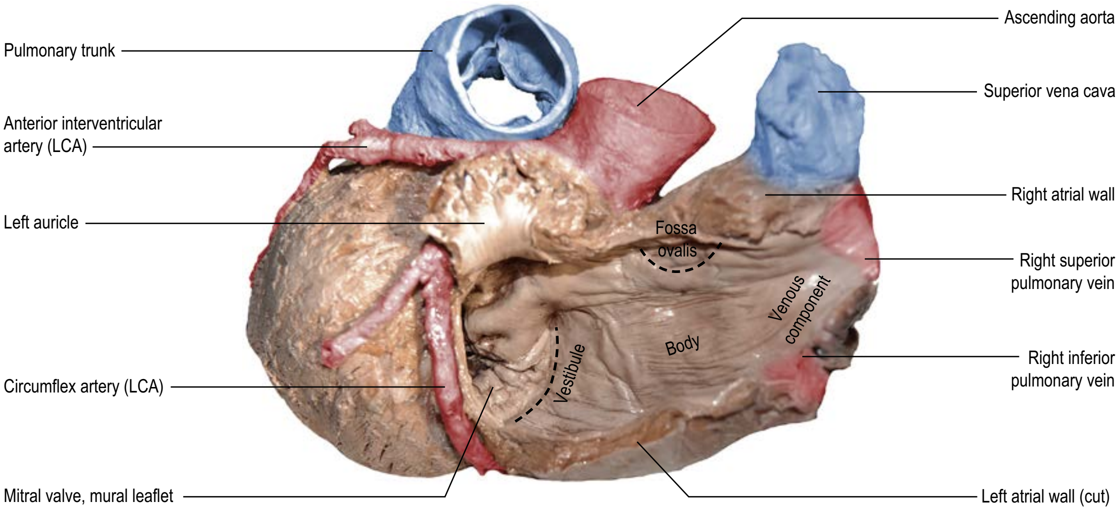
Pulmonary trunk
Anterior interventricular artery (LCA)
Left auricle
Circumflex artery (LCA)
Mitral valve, mural leaflet
Ascending aorta
Superior vena cava
Right atrial wall
Fossa ovalis
Right superior pulmonary vein
Venous component
Body
Vestibule
Right inferior pulmonary vein
Left atrial wall (cut)

Fig. 57.26 Posterior view into the left atrium following removal of the posterior left atrial wall in a cadaveric heart. The smooth-walled pulmonary vein-derived venous part of the left atrium is the most extensive. The septal aspect of the left atrium shows the crescentic line of the free edge of the valve of foramen ovale against the limbus (rim) of the fossa ovalis. The orifices of the right superior and inferior pulmonary veins are adjacent to the plane of the septal aspect of the left atrium. Abbreviation: LCA, branch of left coronary artery. (Image courtesy of Professor M Loukas.)

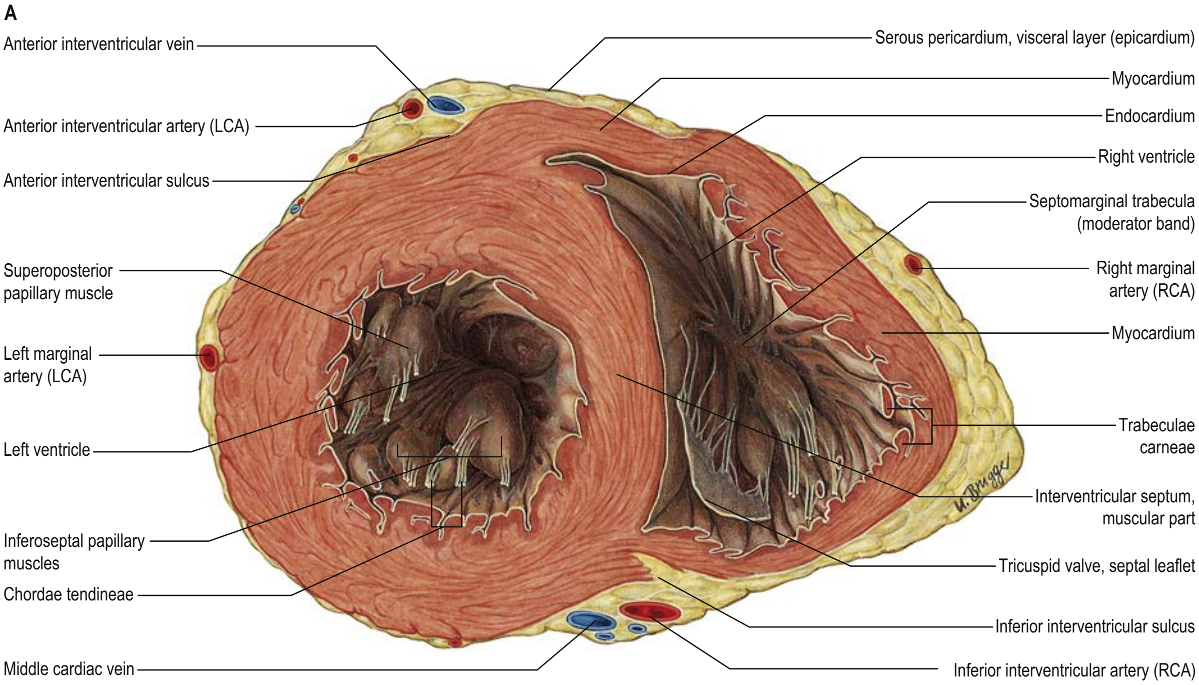
A
Anterior interventricular vein
Anterior interventricular artery (LCA)
Anterior interventricular sulcus
Superoposterior papillary muscle
Left marginal artery (LCA)
Left ventricle
Inferoseptal papillary muscles
Chordae tendineae
Middle cardiac vein
Serous pericardium, visceral layer (epicardium)
Myocardium
Endocardium
Right ventricle
Septomarginal trabecula (moderator band)
Right marginal artery (RCA)
Myocardium
Trabeculae carneae
Interventricular septum, muscular part
Tricuspid valve, septal leaflet
Inferior interventricular sulcus
Inferior interventricular artery (RCA)

Fig. 57.27 **A**, Left and right ventricles: cross-section perpendicular to the long axis of the heart. Abbreviations: RCA, branch of right coronary artery; LCA, branch of left coronary artery. (With permission from Waschke J, Paulsen F (eds) Sobotta Atlas of Human Anatomy, 15th ed. Elsevier, Urban & Fischer. Copyright 2013.) (B, *continued online*)

A small accessory (commissural) leaflet is almost always found between the two major leaflets (aortic and mural) and so the mitral valve is better described as a continuous veil that is attached around the entire circumference of the mitral orifice. The free edge of the mural and aortic leaflets normally bear several indentations that create a scalloped edge. Two indentations are sufficiently deep and regular to be defined as the ends of the solitary and oblique zone of apposition or the commissures of the valve. These inferoseptal (anteromedial) and superoposterior (posterolateral) extremities of the solitary zone of apposition may be regarded as two independent commissures.

The original designations of anterior and posterior for the valve leaflets are somewhat misleading because of the obliquity of the valve, and the terms aortic and mural leaflet, respectively, are now preferred. When the valve is laid open, the aortic leaflet (anterior, septal, 'greater' or anteromedial) is seen to guard one-third of the circumference of the orifice and to be semicircular or triangular, with few or no free marginal indentations or scallops. Its fibrous core (lamina fibrosa) is continuous on the outflow aspect, beyond the margins of the fibrous subaortic curtain, with the right and left fibrous trigones (see Figs 57.17, 57.21, 57.23C). Between the trigones, it is continuous with the fibrous subaortic curtain itself and, beyond the trigones, with the roots of the filia coronaria (see Fig. 57.22). The leaflet has a deep crescentic rough zone that receives various chordae tendineae. The ridge limiting the outer margin of the rough zone indicates the maximal extent of surface contact with the mural leaflet in full closure. A clear zone is seen between the rough zone and the valvular anulus; it is devoid of attachments of chordae, although its fibrous core carries extensions from chordae attached in the rough zone. The aortic leaflet has no basal zone and continues into the subaortic curtain. Hinging on its anular attachment, and continuous with the subaortic curtain, it is critically placed between the inlet and the outlet of the ventricle. During passive ventricular filling and atrial systole, its smooth atrial surface is important in directing a smooth flow of blood towards the body and apex of the ventricle. After the onset of ventricular systole and closure of the mitral valve, the ventricular aspect of its clear zone merges into the smooth surface of the subaortic curtain, which, with the remaining fibrous walls of the subvalvular aortic vestibule, forms the smooth boundaries of the outlet part of the ventricle.

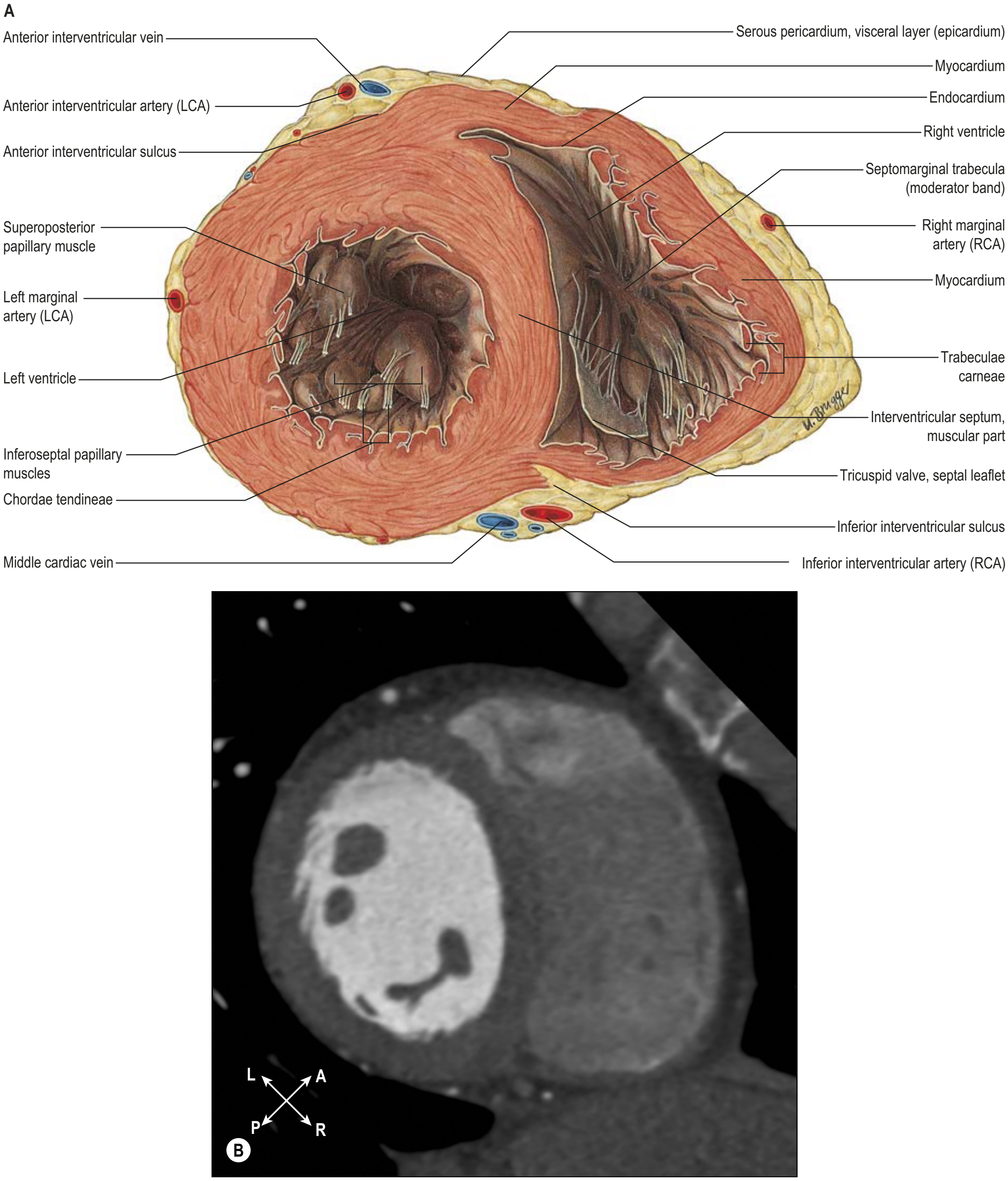
A
Anterior interventricular vein
Anterior interventricular artery (LCA)
Anterior interventricular sulcus
Superoposterior papillary muscle
Left marginal artery (LCA)
Left ventricle
Inferoseptal papillary muscles
Chordae tendineae
Middle cardiac vein
Serous pericardium, visceral layer (epicardium)
Myocardium
Endocardium
Right ventricle
Septomarginal trabecula (moderator band)
Right marginal artery (RCA)
Myocardium
Trabeculae carneae
Interventricular septum, muscular part
Tricuspid valve, septal leaflet
Inferior interventricular sulcus
Inferior interventricular artery (RCA)
L
A
P
R
B

Fig. 57.27 **A**, Left and right ventricles: cross-section perpendicular to the long axis of the heart. Abbreviations: RCA, branch of right coronary artery; LCA, branch of left coronary artery. **B**, An ECG-gated CT coronary angiogram cross-sectional view of the ventricles from the superior aspect for comparison. Note that this is a non-standard view. (With permission from Waschke J, Paulsen F (eds) Sobotta Atlas of Human Anatomy, 15th ed. Elsevier, Urban & Fischer. Copyright 2013.)

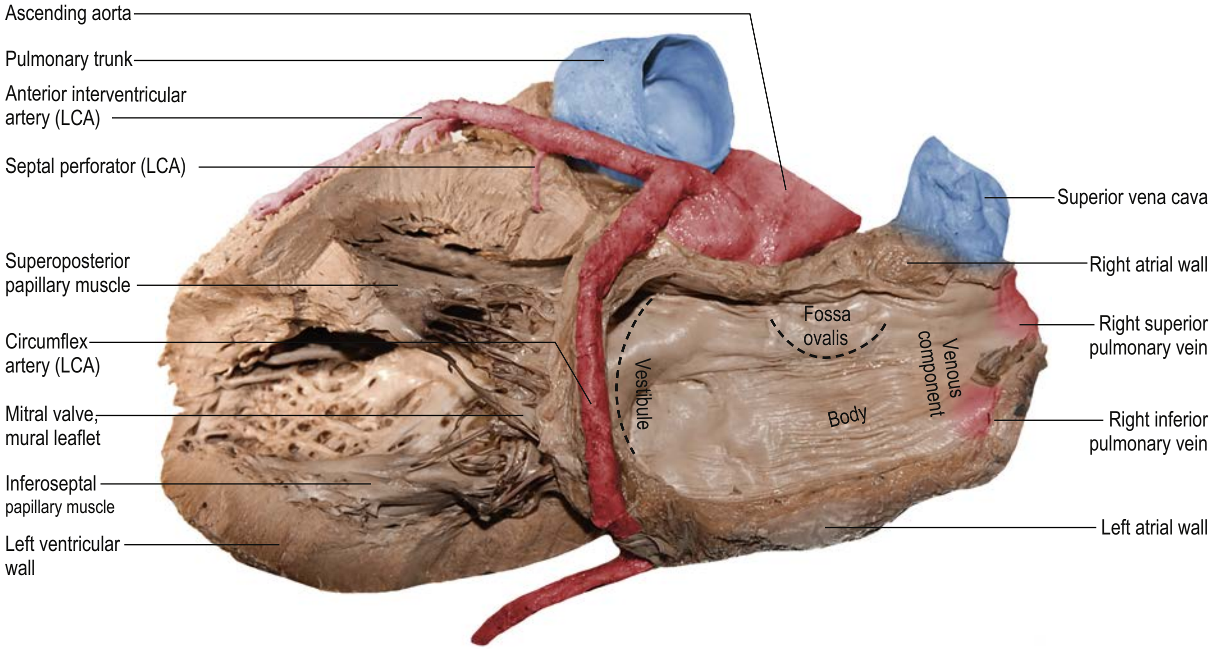
Ascending aorta
Pulmonary trunk
Anterior interventricular artery (LCA)
Septal perforator (LCA)
Superoposterior papillary muscle
Circumflex artery (LCA)
Mitral valve, mural leaflet
Inferoseptal papillary muscle
Left ventricular wall
Superior vena cava
Right atrial wall
Right superior pulmonary vein
Right inferior pulmonary vein
Left atrial wall
Fossa ovalis
Vestibule
Venous component
Body

Fig. 57.28 Interior of the left atria and ventricle in a cadaveric heart, exposing the papillary muscles of the ventricle. Note the thick wall of the left ventricle and the chordae tendineae of the mitral valve attaching to the papillary muscles. Abbreviation: LCA, branch of left coronary artery. Also see Fig. 57.36. (Image courtesy of Professor M Loukas.)

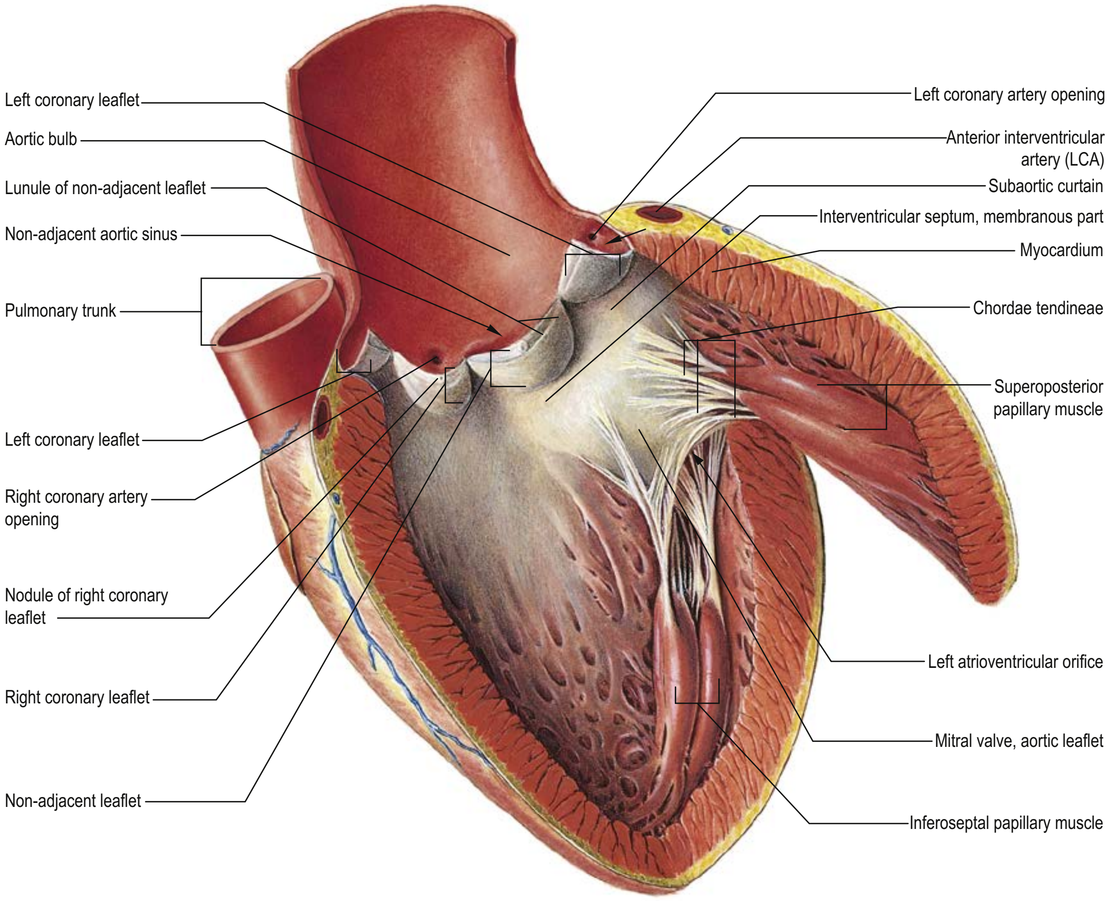
Left coronary leaflet
Aortic bulb
Lunule of non-adjacent leaflet
Non-adjacent aortic sinus
Pulmonary trunk
Left coronary leaflet
Right coronary artery opening
Nodule of right coronary leaflet
Right coronary leaflet
Non-adjacent leaflet
Left coronary artery opening
Anterior interventricular artery (LCA)
Subaortic curtain
Interventricular septum, membranous part
Myocardium
Chordae tendineae
Superoposterior papillary muscle
Left atrioventricular orifice
Mitral valve, aortic leaflet
Inferoseptal papillary muscle

Fig. 57.29 The aortic orifice opened to show the leaflets of the aortic valve, their nodules, lunules, commissures and the triple-scalloped line of their anular attachment. Also shown are the continuity of the subaortic curtain with connection to the aortic leaflet of the mitral valve, the openings of the left and right coronary arteries, and the spatial relationship of the aortic orifice to the pulmonary orifice and left ventricle. Abbreviation: LCA, branch of left coronary artery. (With permission from Waschke J, Paulsen F (eds) Sobotta Atlas of Human Anatomy, 15th ed. Elsevier, Urban & Fischer. Copyright 2013.)

The mural leaflet (posterior, ventricular, 'smaller' or posterolateral) usually has two or more minor indentations on its free margin that form scallops. Lack of definition of the major intervalvular commissures has led to disagreement and confusion concerning the territorial extent of this leaflet and the possible existence of accessory scallops. Examination of the valve in the closed position reveals that the mural leaflet may conveniently be regarded as comprising all the valvular tissue posterior to the inferoseptal (anterolateral) and superomedial (posteromedial) ends of the major zone of apposition with the aortic leaflet. Thus defined, it has a wider attachment to the anulus than does the aortic leaflet and guards two-thirds of the circumferential attachments. In most cases indentations usually divide the mural leaflet into

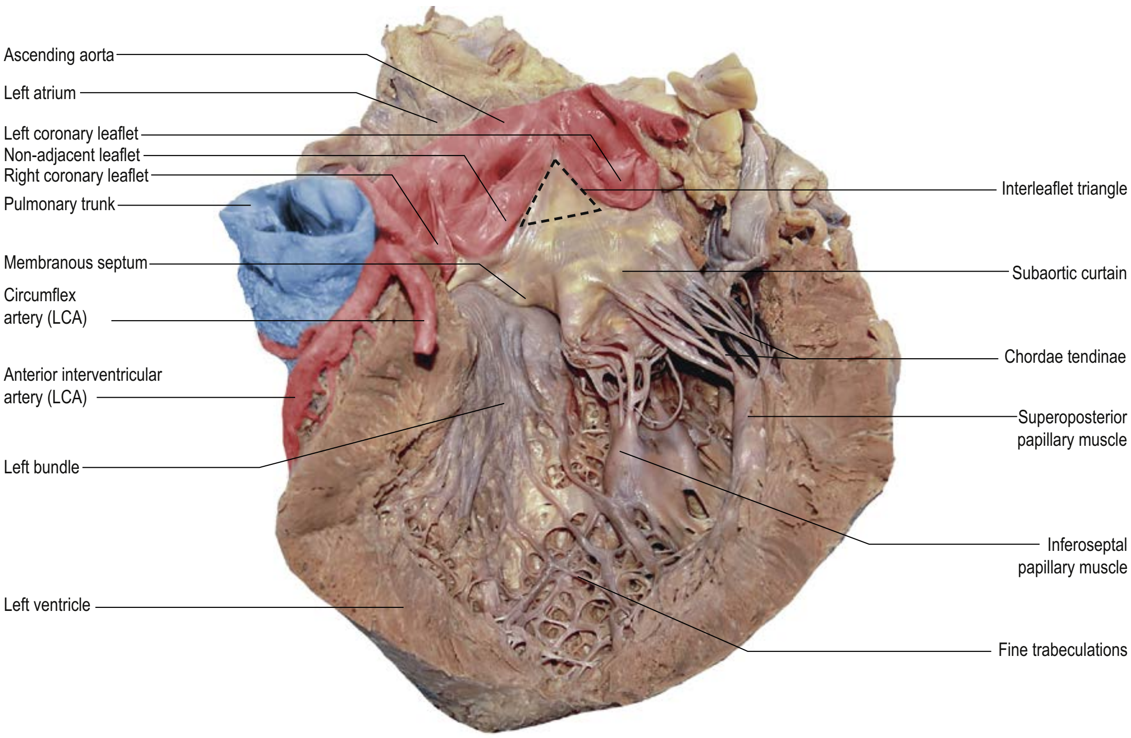

Fig. 57.30 Internal features of the left ventricle, aortic sinus and ascending aorta of a cadaveric heart. Transection of the aorta at the level of the sinutubular junction shows the closed leaflets of the aortic valve and the supporting sinuses named according to the origin of the coronary arteries (left coronary, right coronary and non-adjacent). However, these terms may be ambiguous if the coronary arteries arise in variable locations, whereas the terms of right, left and non-adjacent aortic sinus avoid this issue. Note the inter-leaflet triangles, membranous septum and fibrous continuity between the aorta and mitral valve. Abbreviation: LCA, branch of left coronary artery. (Image courtesy of Professor M Loukas.)

a relatively large middle scallop and smaller lateral and septal commissural scallops. Each scallop has a crescentic opaque rough zone, receiving on its ventricular aspect the attachments of the chordae that define the area of valvular apposition in full closure. From the rough zone to within 2–3 mm of its anular attachment, there is a membranous clear zone devoid of chordae. The basal 2–3 mm is thick and vascular, and receives basal chordae. The ratio of rough to clear zone in the aortic leaflet is 0.6 and in the middle scallop of the mural leaflet is 1.4. Much more of the mural leaflet is in apposition with the aortic leaflet during closure of the mitral valve.

Opening of the mitral valve

At the onset of diastole, opening is passive but rapid, the valvular leaflets parting and projecting into the ventricle as left atrial pressure exceeds left ventricular diastolic pressure (see Fig. 57.20). Passive ventricular filling proceeds as atrial blood pours to the apex, directed by the hanging aortic valvular leaflet. The leaflets begin to float passively together, hingeing on their anular attachments and partially occluding the ventricular inlet. Atrial systole now occurs, forcing blood apically and causing re-opening of the leaflets. As maximal filling is achieved, the leaflets again float rapidly together. Closure is followed by ventricular systole, which starts in the papillary muscles and continues rapidly as a general contraction of the walls and septum.

Mitral valvular chordae tendineae (tendinous cords)

The chordae tendineae of the mitral valve resemble those supporting the tricuspid valve (**Fig. 57.30**; see Fig. 57.29). False chordae are also irregularly distributed as in the right ventricle. They are single or multiple, thin, fibrous or fibromuscular structures that traverse the cavity of the left ventricle and have no connection with the valvular leaflets. They occur commonly in the left ventricle and often cross the subaortic outflow. Histologically, false chordae sometimes contain extensions from the ventricular conducting tissues; these left ventricular bands are often identified on echocardiography. It has been suggested that false chordae produce premature ventricular contractions and may be the cause of functional heart murmurs or innocent murmurs in children and young adults.

True mitral valve chordae may be divided into four types: interleaflet (commissural), rough zone (including the special strut chordae), cleft and basal chordae. Most true chordae divide into branches from a single stem soon after their origin from the apical third of a papillary muscle, or proceed as single chordae that each divide into several branches near their attachment. Basal chordae, in contrast, are solitary structures passing from the ventricular wall to the mural leaflet and are supported by their own miniature papillary muscles. There is such marked variation between the arrangement of the chordae (Gunnal et al 2015) that any detailed classification loses much of its clinical significance. Suffice it to say that, in the majority of hearts, the chordae support the free margins of the valvular leaflets, together with varying degrees of their ventricular aspects and bases, and there is some evidence to suggest that those leaflets with unsupported free edges become prone to prolapse in later life.

Papillary muscles

The two papillary muscles supporting the leaflets of the mitral valve vary in length and width, and may be bifid. The superoposterior muscle arises from the mural myocardium forming part of the anterior cardiac surface, and the inferoseptal muscle from the mural myocardium forming the inferior cardiac surface (see Figs 57.27, 57.28). Chordae tendineae arise mostly from the tip and apical third of each muscle but sometimes take origin near their base. The chordae from each papillary muscle diverge and are attached to corresponding areas of closure (apposition) on both valvular leaflets.

Aortic root

The aortic root, the anatomical bridge between the left ventricle and ascending aorta, consists of the aortic valvular leaflets supported by the aortic sinuses (of Valsalva), and the inter-leaflet triangles interposed between their basal attachments (inserted margin). As such, it is relatively long, but because of the semilunar attachment of the leaflets, it has no discrete proximal border. It is limited distally by the sinutubular junction, which is the only circular or anular structure located within the aortic root (see Figs 57.23, 57.30). The essential feature is the semilunar attachments of the valve leaflets; the lines of their point of hingeing cross the anatomical ventriculoarterial junction, marking a transition from the myocardium of the left ventricle to the fibroelastic tissue of the aortic sinuses (**Fig. 57.31**). The muscular portion of the aortic root is roughly half of its circumference. Descriptions of the aortic root over the years have included erroneous accounts of a valve anulus. Although echocardiographers used to describe this proximal

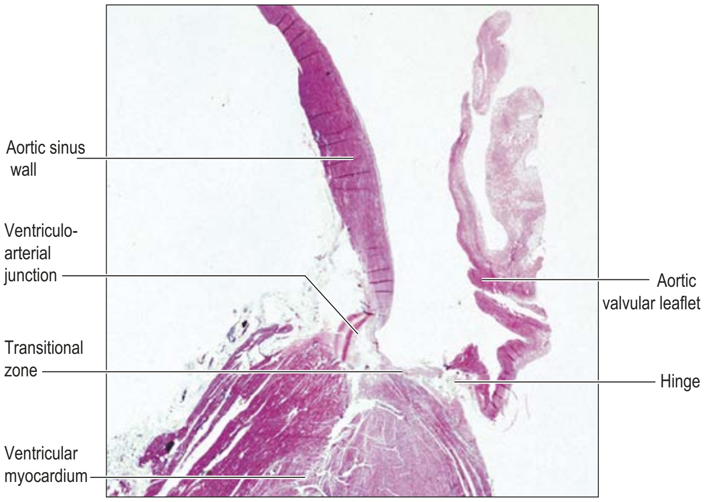

Fig. 57.31 A histological section through an aortic sinus demonstrating ventricular muscle supporting the transition from the fibroelastic wall of the sinus to the tissues of the valvular leaflet. The transitional area is anchored to the ventricular muscle. The hinge of the leaflet is located below the level of the ventriculoarterial junction. Importantly, there is no evidence of a ring-like structure in the form of an anulus supporting the hinge of the leaflet within the ventricle. The muscular tissue of the ventricle is stained pink; fibrous tissue, which would show up as a characteristic light colour with this stain, is absent. Haematoxylin and eosin stain. (Courtesy of Diane E Spicer.)

Coordinated contraction of the papillary muscles increases the tension in the chordae and promotes joining of the corresponding points on opposing leaflets, preventing their eversion. With general mural and septal excitation and contraction, left ventricular pressure increases rapidly. The leaflets 'balloon' towards the atrial cavity, and the atrial aspects of the rough zones come into maximal contact. Precise papillary contraction, and increasing tension in the chordae tendinae, continue to prevent valvular eversion and maintain valvular competence. The orifices and the leaflets of both the left and right atrioventricular valves undergo considerable changes in position, form and area during a cardiac cycle. Both valves move anteriorly and to the left during systole, and reverse their motion in diastole. The mitral valve reduces the area of its orifice (anulus) by as much as 40% during systole; its shape changes from circular to crescentic at the height of systole, the anular attachment of its aortic leaflet being the concavity of the crescent. The attachment of its mural leaflet, although remaining convex, contracts towards the anterior cardiac surface. The smooth left ventricular outflow tract (aortic vestibule) terminates at the leaflets of the aortic valve. Although stronger in construction, the aortic valve resembles the pulmonary valve (see Figs 57.21, 57.23, 57.29) in possessing three semilunar leaflets, supported within the three aortic sinuses (of Valsalva). Although the aortic valve, like the pulmonary valve, is often described as possessing an anulus in continuity with the fibrous skeleton, there is no complete collagenous ring that supports the attachments of the leaflets. As with the pulmonary valve, the anatomy of the aortic valve is dominated by the fibrous semilunar leaflet attachment (see Fig. 57.23C).

border in terms of an anulus, examination of cross-sections of the left ventricular outflow tract has never found any circular anatomical boundary or a distinct boundary of any kind (Loukas et al 2014a). There are at least two rings within the aortic root, attached in semilunar fashion from the sinutubular junction to a basal ventricular attachment, and neither serves to support the aortic valvular leaflets. Two of the leaflets are partially supported by muscle, and the third has an exclusively fibrous attachment. The root acts as a bridging structure not only anatomically, separating the myocardial and arterial parts of the left ventricular pathway, but also functionally because its proximal and distal parts can withstand considerable changes in ventricular and arterial pressures.

Aortic valve leaflets

Three sets of names are used to describe the aortic leaflets. Posterior, right and left refer to their embryonic positions before full cardiac rotation has occurred (Ch. 13). Names based on their approximate positions in maturity are anterior, left posterior and right posterior, respectively. Widespread clinical terminology, which links the leaflets and sinuses to the origins of the coronary arteries, has replaced anterior, left and right posterior leaflets with right coronary, left coronary and non-adjacent (non-coronary) leaflets, respectively. The non-coronary leaflet is more accurately termed the non-adjacent leaflet, since the associated aortic sinus may give rise (rarely) to a coronary artery that is consistently situated adjacent to the root of the pulmonary trunk. These clinical terms are preferable because they are simple and unambiguous.

The aortic valve leaflets are attached in part to the aortic wall and in part to adjacent supporting ventricular structures. The arrangement is more complicated than in the pulmonary valve because parts of the leaflets also take origin from the fibrous subaortic curtain, and are continuous with the aortic leaflet of the mitral valve (see Fig. 57.29). This fibrous area of continuity is thickened at its two ends to form the right and left fibrous trigones (see Figs 57.21, 57.22). The semilunar attachments of the aortic valve incorporate segments of ventricular tissue within the bases of two of the aortic sinuses that give rise to the coronary arteries. The aortic sinuses are named according to the aortic valvular leaflet with which they are associated (see Figs 57.23C, 57.29).

The semilunar attachments incorporate three triangular areas of aortic wall within the apex of the left ventricular outflow tract. They are interposed between the aortic sinuses and separate the cavity of the left ventricle from the pericardial cavity. Removal of the trigones in an otherwise intact heart is instructive in demonstrating the relationships of the aortic valve, which, justifiably, may be considered as the keystone of the heart. The first triangle, between the non-adjacent and left coronary leaflets, has a base continuous inferiorly with the fibrous subaortic curtain (see Figs 57.22, 57.30). The second triangle, between the right coronary and non-adjacent leaflets, has the membranous parts of the interventricular septum as its base. It faces the right ventricle, whereas its apex is directed towards the transverse pericardial sinus posterior to the origin of the right coronary artery. The third triangle, between the left and right coronary leaflets, has its base on the muscular interventricular septum and its apex directed to the plane of the space between the aortic wall and the free-standing sleeve of right ventricular infundibular musculature that supports the leaflets of the pulmonary valve. Although the basal attachments (inserted margins) of each aortic valvular leaflet are thickened and collagenous at their ventricular origins, the leaflets lack a continuous circular collagenous support and valvular function depends primarily upon the semilunar attachments of the leaflets.

The leaflets are endocardial folds with a central fibrous core covered by subendothelial fibroelastic tissue on its aortic and ventricular aspects. With the valve half open, each is equivalent to just greater than one-quarter of a sphere; an approximate hemisphere is completed when this is viewed in conjunction with the corresponding aortic sinus. Each leaflet has a thick basal border that is deeply concave on its aortic aspect, and a horizontal free margin that is only slightly thickened, except at its midpoint, where an aggregation of fibroelastic tissue on the ventricular aspect forms the nodule of the semilunar leaflet (Arantius). The nodule extends bilaterally along the central part of the inferior border of the lunule. The crescent-shaped zone of apposition (lunule), on the ventricular surface of the leaflet, extends along its free edge and up to one-third of its depth (see Fig. 57.29). Parts of the lunule are relatively thin and may be fenestrated, particularly in older adults; fenestrations are inconsequential if located above the line of valve closure. The aortic surface of each leaflet is rougher than its ventricular aspect.

Aortic sinuses (of Valsalva)

The three aortic sinuses (right, left and non-adjacent) are more prominent than those in the pulmonary trunk. The upper limit of each sinus reaches considerably beyond the level of the free border of each aortic valvular leaflet and forms a well-defined circumferential sinutubular ridge on the aortic inner surface, just above the aortic valvular leaflets (see Figs 57.23C, 57.29). Coronary arteries usually open near this ridge within the upper part of the sinus, but may be markedly variable in their origin. The walls of the sinuses are largely collagenous near the attachment of the leaflets but the amount of lamellated elastic tissue increases with distance from the region of attachment. At the midlevel of each sinus, its wall is about half the thickness of the supravalvular aortic wall and less than one-quarter of the thickness of the sinutubular ridge. At this level, the mean luminal diameter at the commencement of the aortic root is much larger than that of the ascending aorta; these details are functionally significant in the mechanism of aortic valvular motion. For example, a linear relationship between the diameter of the aortic sinus and the square root of body surface area has been described in children (Kaiser et al 2008).

Opening of the aortic valve

During diastole, the closed aortic valve supports an aortic column of blood at high but slowly diminishing pressure (see Fig. 57.20). Each sinus and its valvular leaflet form a hemispherical chamber. The three nodules of the semilunar leaflets are apposed and the free margins and lunular parts of the adjacent leaflets are tightly apposed on their ventricular aspects. From the aortic aspect, the closed valve is tiradiate, with three pairs of closely compressed lunules radiating from the nodules to their peripheral commissural attachments at the sinutubular junction (see Figs 57.21, 57.29). As ventricular systolic pressure increases, it exceeds aortic pressure and the valve is opened passively.

The fibrous wall of the sinuses nearest the aortic vestibule is almost inextensible but, more superiorly, the wall is fibroelastic. Under left ventricular ejection pressure, the radius of this region increases by about 16% in systole, as the commissures move apart to form a fully open triangular orifice. The free margins of the leaflets then become almost straight lines between their peripheral attachments. However, they do not flatten against the sinus walls, even at maximal systolic pressure, which is probably an important factor in their subsequent closure. During ejection, most blood enters the ascending aorta but some enters the sinuses, forming vortices that help to maintain the triangular mid-position of the leaflet during ventricular systole and also probably initiate their approximation at the end of systole. Tight and full closure occurs with the rapid decrease in ventricular pressure in diastole. Commissures narrow, nodules appose and the valve reassumes its triradiate form. Experiments indicate that 4% of ejected blood regurgitates through a valve with normal aortic sinuses, whereas 23% regurgitates through a valve without them. The normal structure of the aortic sinuses also promotes non-turbulent flow into the coronary arteries.

Echocardiography

Available with the *Gray's Anatomy* e-book

Connective tissue and fibrous skeleton of the heart

From epicardium to endocardium and from the orifices of the great veins to the roots of the arterial trunks, the intercellular spaces between contractile and conduction elements are permeated by connective tissue. The amount of connective tissue varies greatly in arrangement and form in different locations. Most of the fibrous tissue network of the heart is condensed at the atrioventricular junctions. The network assists in anchoring the valve leaflets to the ventricular masses and is crucial for the propagation of electrical conduction because it insulates the atrial chambers from the ventricular mass, other than at the site of the atrioventricular node. Over much of the heart, a fine layer of areolar tissue found beneath the mesothelium of the visceral part of the serous pericardium (epicardium) accumulates subepicardial fat, concentrated along the inferior border (acute margin), the atrioventricular and interventricular sulci, and their side channels. The coronary vessels and their main branches are embedded in this fat; the amount of fat increases with age. The endocardium also lies on a fine areolar tissue rich in elastic fibres. Fibrocellular components of these subepicardial and subendocardial

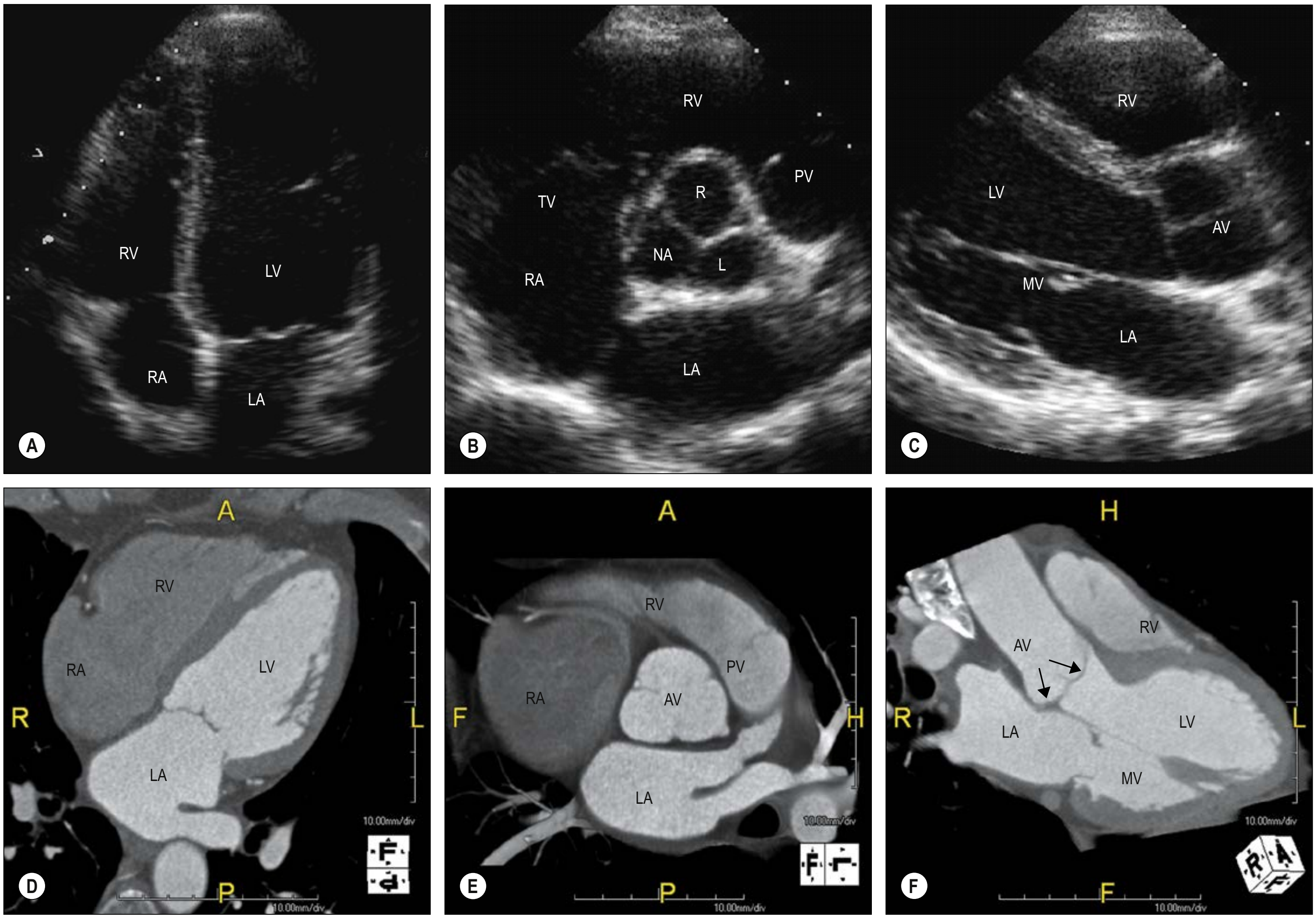

Fig. 57.32 Sectional cardiac anatomy shown by transthoracic echocardiography and CT. **A**, Four-chamber view. **B**, Short-axis view at aortic valve level. Note three aortic valvular leaflets (right, left and non-adjacent) and the central position of the aorta. **C**, Parasternal long-axis view. **D–F**, Corresponding images by CT. Note the different orientation compared with transthoracic echocardiography (looked at from below, foot to head). Abbreviations: A, anterior; AV, aortic valve; F, foot; H, head; L, left; LA, left atrium; LV, left ventricle; MV; mitral valve; NA, non-adjacent; P, posterior; PV, pulmonary valve; R, right; RA, right atrium; RV, right ventricle; TV, tricuspid valve. (Courtesy of Dr Konstantinos Dimopoulos, Royal Brompton and Chelsea and Westminster Hospitals, London.)

Echocardiography allows a detailed assessment of the functional anatomy of the heart. The gross anatomy of the heart can be evaluated by two-dimensional echocardiography in the parasternal, apical, suprasternal and subcostal positions (**Fig. 57.32**). The standardized planes used are long-axis, short-axis and four-chamber. The long-axis view is obtained by placing the ultrasound transducer in the left apicosternal position and provides detailed images of the left ventricle, ascending aorta, left atrium, and mitral and aortic valves (Fig. 57.32C). Angling the beam towards the right also allows assessment of the right atrium, right ventricle and tricuspid valves. Rotating the transducer by 90° in the clockwise direction produces the short-axis view, which allows assessment of the left ventricle, papillary muscles, chordae tendineae and mitral valve leaflets (Fig. 57.32B). The four-chamber view demonstrates the ventricles, atria, and mitral and tricuspid valves (Fig. 57.32A). Rotation of the transducer allows two-chamber views of the heart and more detailed assessment of the ascending aorta and aortic valve leaflets. Cardiac MRI and CT provide similar information on cardiac structure and function (see Figs 57.2, 57.35A–B), together with complementary information on great vessels (Fig. 57.32D–F) and other extracardiac intrathoracic structures.

layers blend on their mural aspects with the endomysial and perimysial connective tissue on the myocardium. Each cardiac myocyte is invested by a delicate endomysium composed of fine reticular, collagen and elastin fibres embedded in ground substance. This matrix is lacking only at desmosomal and gap junctional contacts of intercalated discs. Similar arrangements apply to ventricular conduction myocytes and their extensive working myocardial contacts. The connective tissue matrix itself is interconnected laterally to form bundles, strands or sheets of macroscopic proportions showing a complex geometric pattern. Surrounding and attaching to larger myocardial bundles are stronger perimysial condensations. The overall pattern is described in terms of struts and weaves. Despite its importance, the myocardial matrix cannot be grossly dissected.

Running at the ventricular base is a complex framework of dense collagen with membranous, tendinous and fibroareolar extensions, intimately related to atrioventricular valves and the aortic orifice. The structure as a whole is sufficiently distinct to be termed the fibrous skeleton of the heart. Although it is often stated that all four valves are contained within this skeleton, this is not the case. The leaflets of the pulmonary valve are supported on a free-standing sleeve of right ventricular infundibulum (conus arteriosus) that can easily be removed from the heart without disturbing either the fibrous skeleton or the left ventricle. Moreover, the fibrous skeleton of the heart does not incorporate the entirety of the atrioventricular and arterial anuli. Much of the insulation between the atrial and ventricular chambers is provided by the fibroadipose tissues within the atrioventricular sulci. There is some collagenous tissue in the mitral valvular anulus, but it is not always continuous with the fibrous structure. The tricuspid valvular anulus is almost exclusively composed of fibroadipose tissue. The only true fibrous part of the tricuspid anulus is where the valvular leaflets are attached to the central fibrous body (Saremi et al 2017). Another point of confusion is the idea that the fibrous skeleton provides the support for the cardiac valves. In reality, it is the overall structure of the atrioventricular junctions that supports the mitral and tricuspid valves, whereas the arterial valves are hinged within the valvular sinuses. The fibrous skeleton is strongest at the central fibrous body, which is the junction of the aortic, mitral and tricuspid valves (see Figs 57.21–57.22). Two pairs of curved, tapering, collagenous, fila coronaria extend from the central fibrous body. They are stronger on the left, where they pass partially around the mitral and tricuspid orifices. These orifices are almost co-planar and incline to face the cardiac apex. In contrast, the aortic valve faces superiorly, lying anterosuperior and to the right of the mitral orifice. Two of the leaflets of the aortic valve (left coronary and non-adjacent) are in fibrous continuity with the aortic leaflet of the mitral valve; this subaortic curtain is also an integral part of the fibrous skeleton (see Figs 57.21–57.23C). The two ends of the fibrous curtain are strengthened as the right and left fibrous trigones, which are the strongest parts of the skeleton. The right trigone and the membranous septum constitute the central fibrous body, which is penetrated by the atrioventricular bundle (His). The membranous septum is crossed on its right aspect by the attachment of the tricuspid valve leaflets, dividing the septum into atrioventricular and interventricular parts.

The aortic root is central within the fibrous skeleton and is often described in terms of an anulus integrated within the fibrous skeleton (Anderson et al 2013). However, as with the pulmonary valve, the structure of the aortic root corresponds to the triple fibrous semilunar attachments of its valvular leaflets. Within this complex circumferential zone, three crucially important triangular areas separate, on the ventricular aspect, the aortic sinuses that house the valvular leaflets (see Fig. 57.23). Collectively, the three interleaflet triangles can be conceptualized in terms of a three-pointed coronet; their triangular apices correspond to the tips of the valvular commissures and their walls, significantly thinner than those of the aortic sinuses, consist variously of collagen or admixed muscle strands and fibroelastic tissue. They form the subvalvular extensions of the aortic vestibule. The first triangle is the interval between the non-adjacent and left coronary sinuses/leaflets that is filled with the deformable subaortic curtain. The second triangle between the non-adjacent and right coronary sinuses/leaflets is continuous with the anterior surface of the membranous septum. The third triangle, between the two coronary aortic sinuses/leaflets, is filled with loose fibroelastic tissue and separates the extension of the subaortic root from the wall of the free-standing subpulmonary infundibulum. The pulmonary valve possesses no fibrous continuity with the other three valves; however, in few cases a small fibrous band, known as the tendon of the conus, extends between the aortic and pulmonary valvar sinuses (Saremi et al 2017). Previously this was thought to be the location of the tendon of the infundibulum (conal ligament) (Loukas et al 2007); in mouse hearts, the ligament is found at the level of the sinutubular junctions at the site of initial fusion of the distal outflow cushions. The line of proximal fusion is the longitudinal raphe sometimes seen in the muscular subpulmonary infundibulum.

Similar fibrous triangles separate the sinuses of the pulmonary trunk but they are significantly less robust. Use of the terms mitral and tricuspid anuli implies that the atrioventricular valves are supported by discrete circular fibrous rings, when, in reality, the valves are D-shaped structures integrally attached at the atrioventricular junctions. It is therefore inaccurate to consider these valvular orifices as circular. Rather, the straight edge of the ‘D’-shaped mitral valve represents a fibrous continuity between the aortic leaflet and the aortic root, and the remainder supports the mural leaflet. The straight edge of the ‘D’-shaped tricuspid valve represents the attachment of the septal leaflet, marking the inferior border of the triangle of Koch, and the remainder supports the anterosuperior and inferior leaflets. The attachments of the atrioventricular valves are not simple, rigid collagenous structures but dynamic, deformable lines that vary greatly at different peripheral points and change considerably with each phase of the cardiac cycle, and with increasing age. The tricuspid valvular leaflet attachments are even less robust than those of the mitral valve. At several sites, only fibroareolar tissue separates the atrial and ventricular muscular masses.

The fibroadipose tissue of the fibrous skeleton provides electrical insulation between the atrial and ventricular walls, ensuring electrophysiological discontinuity between the atrial and ventricular myocardial masses, with the atrioventricular conduction axis being the only muscular structure crossing the plane of insulation (Saremi et al 2017). It also provides direct attachment for the myocardium and for fibrous tissue throughout the heart as a support matrix for a three-dimensional meshwork of cardiomyocytes.

Arrangement of cardiomyocytes

Available with the *Gray's Anatomy* e-book

Congenital cardiac malformations

Congenital malformations of the heart are common and amount to about 25% of all congenital anomalies. Their incidence is estimated at 8 per 1000 live births, however, they are found in up to 2% of stillbirths. Only a small proportion of the anomalies are directly attributable to genetic or environmental factors and the majority are the result of multifactorial events.

Anomalies of cardiac position

Available with the *Gray's Anatomy* e-book

Acyanotic cardiac defects

Available with the *Gray's Anatomy* e-book

Cyanotic cardiac defects

Available with the *Gray's Anatomy* e-book

Conduction tissues

The cells of cardiac muscle differ from those of skeletal muscle in having the inherent ability to contract and relax spontaneously. This myogenic rhythm is shown by small pieces of cardiac tissue, and even isolated myocytes. Ventricular cells contract and relax at a lower frequency than atrial cells, but in the intact heart, both are synchronized to a more rapid rhythm, generated by pacemaker tissue in the sinuatrial and atrioventricular nodes and conveyed by a system of specialist conduction fibres in the atrioventricular conduction axis and the ventricular conducting pathways (Purkinje cells). For an account of excitation–contraction coupling in cardiac muscle, see Chapter 6.

The anatomical arrangement of these tissues is described in the context of the heart. Here, consideration is restricted to the cells that make up the impulse-generating and conduction system. All are modified cardiac cells. Three types within a continuum of morphology may be distinguished from normal working cells: nodal cells, transitional cells and Purkinje cardiomyocytes.

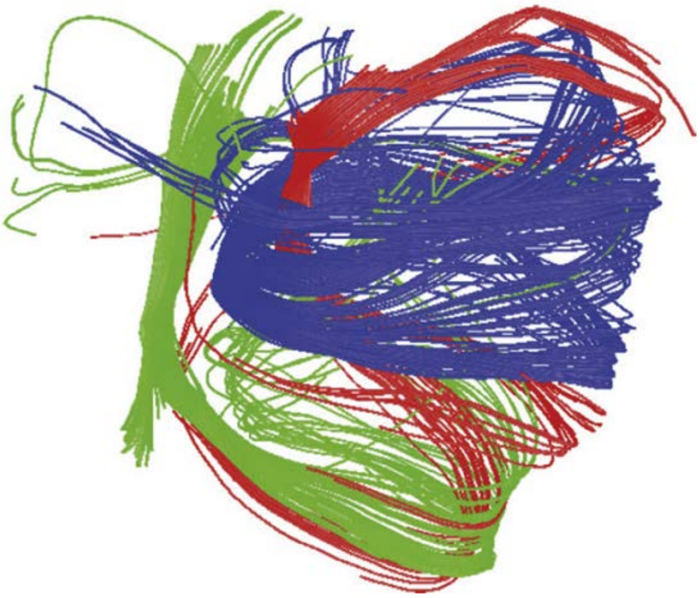

Fig. 57.33 Myocyte alignment in a cadaveric porcine heart acquired via diffusion tensor MRI and subsequent reconstruction. The tracks are created from the first eigenvectors and represent the alignment of the aggregated myocytes. This technique enables the identification of reproducible tracks, or pathways, through the myocardium that connect remote end and epicardial regions by means of simultaneous changes in helical and intrusion angles. (With permission from Anderson R, Smerup M, Sanchez-Quintana D et al 2009 The three-dimensional arrangement of the myocytes in the ventricular walls. Clin Anat 22:64–76.)

The microstructure of cardiac muscle is described in detail in Chapter 6. Diffusion tensor imaging, as well as microcomputed tomography, demonstrates the three-dimensional mesh of ventricular myocytes within a supporting matrix of fibrous tissue (Anderson et al 2018). One population is aligned so that the long axis of the aggregated cells is tangential to the epicardial and endocardial borders, albeit with marked variation in the angulation relative to the ventricular equator. Correlation with measurements taken using force probes shows that these myocytes produce the major unloading of the blood during ventricular systole. A second population is aligned at angles of up to 40° from the epicardium towards the endocardium and produces auxotonic forces during the cardiac cycle. Up to 40% of the cardiomyocyte chains in the ventricle are found to have a partially transmural alignment, which deviates from the prevailing tangential orientation of cardiomyocytes within the ventricles (Lunkenheimer et al 2018). The three-dimensional arrangement of the mesh as demonstrated in MRI of the porcine heart also mediates the realignment of cardiomyocytes that must take place during ventricular contraction and accounts for the extent of systolic mural thickening (**Fig. 57.33**).

The finding that the number of cardiomyocytes in the left ventricle increases between the first and the twentieth year of life suggests that children may be able to regenerate myocardium (Mollova et al 2013).

The most severe positional anomaly is an extrathoracic heart (ectopia cordis), where the heart usually projects to the surface through the lower thoracic and upper abdominal wall, remaining covered, in most instances, by the fibrous pericardium, and usually accompanied by herniation of the abdominal contents. A reversal in cardiac shape and position (mirror image) occurs predominantly in the right hemithorax (dextroposition). The cardiac apex may be directed to the right instead of the left (dextrocardia); this arrangement may be part of situs inversus, in which the heart, great vessels and thoraco-abdominal organs all occupy mirror-imaged positions. The heart may also be right-sided in Kartagener's syndrome (a subgroup of ciliary dyskinesias).

More usually, an abnormal location of the heart occurs in cases of isomerism, in which both sides of the thorax, including the main bronchi and the atrial auricles, retain features of either morphological right- or left-sidedness. Isomerism is also commonly associated with the anomalous arrangement of the abdominal organs: right isomerism with absence of the spleen (asplenia) and left isomerism with multiple spleens (polysplenia). Intracardiac anatomy in cases of isomerism is almost universally abnormal, and there are a range of heart defects (usually simpler in left and more complex in right isomerism).

These intrathoracic abnormal arrangements, with or without abdominal anomalies, often first manifest themselves incidentally following chest radiography. Reversal of normal anatomy has obvious clinical implications, a typical example being a patient with mirror-image arrangements and appendicitis, who presents with an acute left lower quadrant pain.

Most congenital heart anomalies can be detected during antenatal ultrasound screening (**Fig. 57.34**). Neonates with severe congenital heart disease may present with tachypnoea, difficulty in feeding, cyanosis and/or cardiovascular collapse, and there may be audible murmurs on auscultation. The vast majority of anomalies may be detected by postnatal echocardiography; in a very few cases, cardiac catheterization and direct measurements of pressure, oxygen saturations and angiography may be required.

Acyanotic cardiac defects are the result of either left-to-right cardiac shunting through heart defects (intra- or extracardiac) or of obstruction. Left-to-right shunting leads to an increased workload and stress on the heart and the lungs as a consequence of increased pulmonary blood flow and increased pulmonary venous return. Depending on the location of the shunt and the magnitude of left-to-right shunting, patients are at risk of developing pulmonary arterial hypertension unless timely corrective surgery is undertaken. Examples of defects leading to left-to-right shunting are simple atrial or ventricular septal defects or patent ductus arteriosus, or more complex atrioventricular septal defects, and/or a combination of any of these defects with abnormal atrioventricular or ventriculoarterial connections (e.g. a double-outlet right ventricle, where more than 50% of both the ascending aorta and the pulmonary trunk originate from the right ventricle). Obstructive lesions may involve the atrioventricular or arterial valves (e.g., stenosis), or narrow vessels (e.g., coarctation of the aorta or interrupted aortic arch). Depending on the level and severity of the obstruction, clinical presentations range from an asymptomatic heart murmur (common) to cardiovascular collapse (uncommon). Treatment in all cases is directed towards normalizing heart workload, systemic and pulmonary blood flow and cardiac output, and may be surgical and/or catheter-based.

Cyanotic cardiac defects may be attributable to a right-to-left intra- or extracardiac shunt or to a severe reduction in pulmonary blood flow. They may be caused by simple lesions such as severe pulmonary stenosis with an atrial septal defect and right-to-left shunting; Ebstein's malformation; moderate lesions, including Fallot's tetralogy, in which there is a ventricular septal defect, right ventricular outflow obstruction, right ventricular hypertrophy and an overriding aorta (the ascending aorta sits over an interventricular septal defect); or more complex lesions, including transposition of the great arteries (**Fig. 57.35**; Chs 13, 58), common arterial trunk and tricuspid and pulmonary atresia (often in the setting of hypoplastic right ventricle and functionally univentricular physiology). Totally anomalous pulmonary venous connection also results in cyanosis. Neonates with severe cyanotic congenital heart defects may be dependent on the patency of the ductus arteriosus; early diagnosis, treatment with intravenous prostaglandin infusion to delay ductus arteriosus closure and timely transfer to a tertiary centre for more definitive therapy is key to survival and good long-term outcomes. Major advances in the diagnosis and management of infants with congenital cardiac malformations in recent years have resulted in an increased number of adolescents and adults with palliated or repaired, but not cured, congenital heart disease. This is an area that poses multiple challenges to both cardiovascular and other medical disciplines.

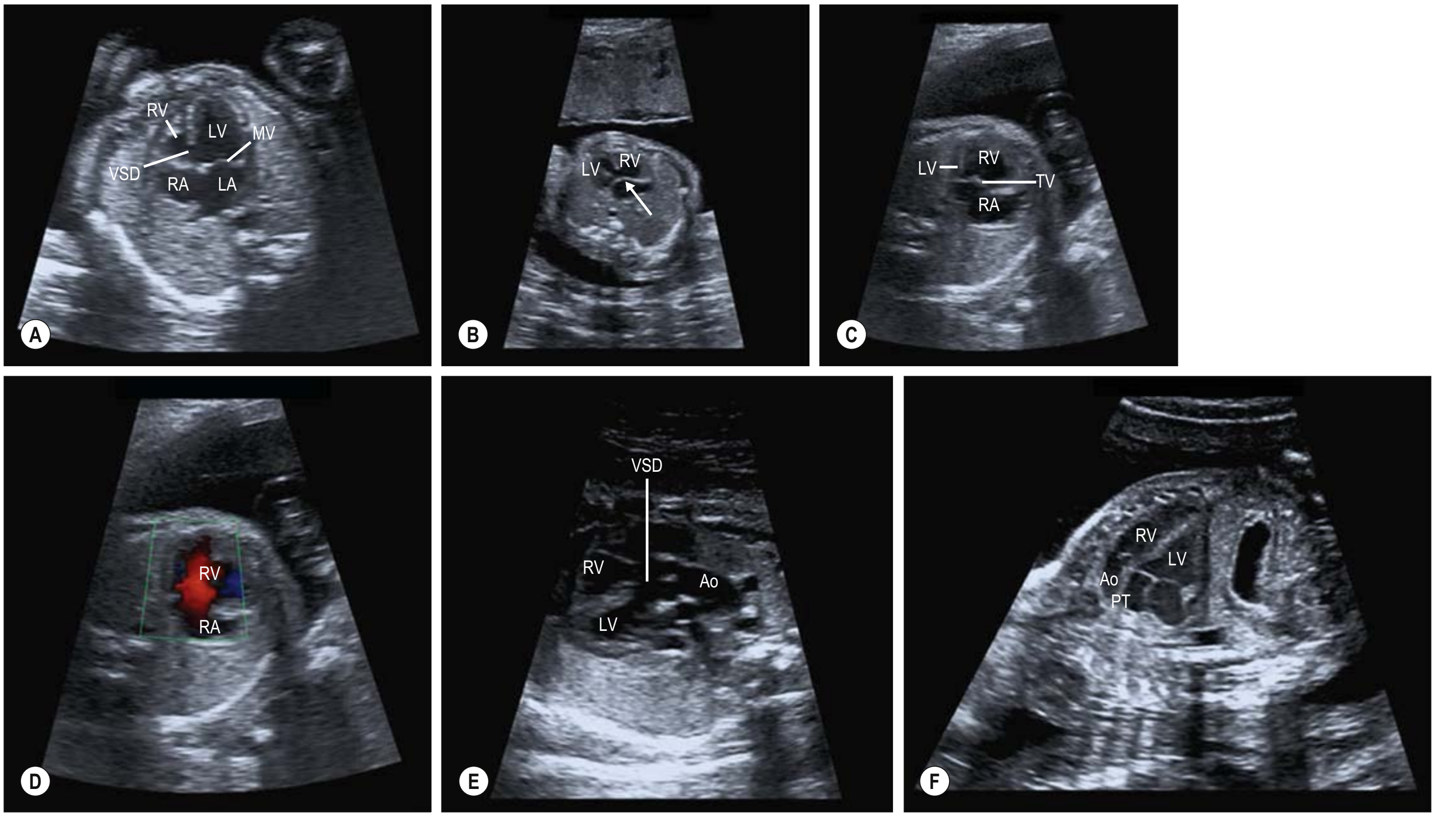

Fig. 57.34 Ultrasound imaging of fetal cardiac defects. **A**, Tricuspid atresia (postmenstrual week 21). A four-chamber view showing a large left ventricle and a hypoplastic right ventricle. The mitral valve is seen; no tricuspid valve is identified. There is an associated ventricular septal defect. **B**, An atrioventricular septal defect (postmenstrual week 20). A common atrioventricular valve (arrow) is associated with a defect in the atrioventricular septum. **C**, Hypoplastic left heart syndrome (postmenstrual week 32). This four-chamber view shows a large right atrium, right ventricle and tricuspid valve. There is a hypoplastic left ventricle; no mitral valve is identified. **D**, Hypoplastic left heart syndrome (postmenstrual week 32). This four-chamber view shows colour flow from right atrium to right ventricle across the tricuspid valve; no mitral valve is identified and there is no flow in the left side of the heart. **E**, Tetralogy of Fallot (postmenstrual week 33). The ascending aorta sits over (overrides) a ventricular septal defect. **F**, Transposition of the great arteries (vessels) (postmenstrual week 21). The ascending aorta and pulmonary trunk arise from the right ventricle and left ventricle, respectively, in a parallel orientation. Abbreviations: Ao, ascending aorta; LA, left atrium; LV, left ventricle; MV, mitral valve; PT, pulmonary trunk; RA, right atrium; RV, right ventricle; TV, tricuspid valve; VSD, ventricular septal defect. (Courtesy of Gurleen Sharland, Evelina London Children's Hospital.)

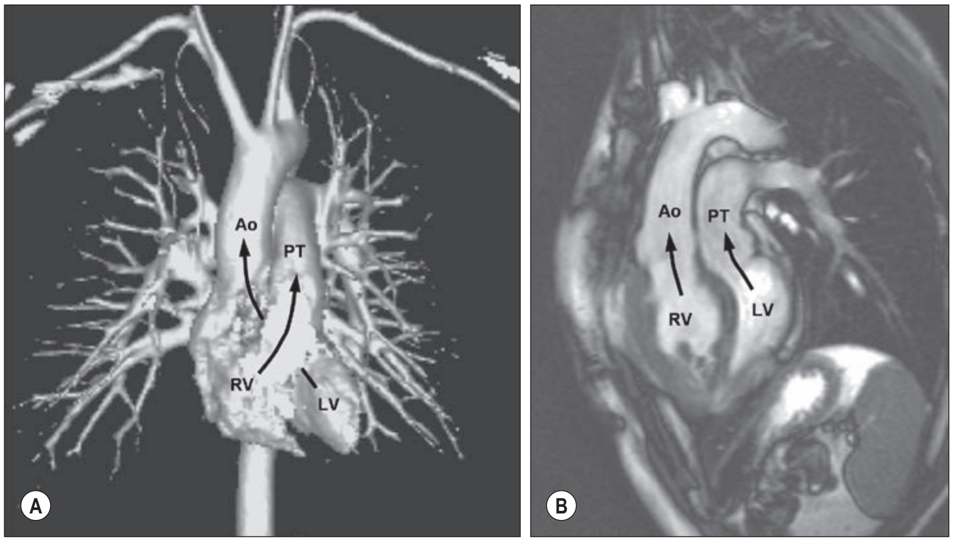

Fig. 57.35 Cardiac magnetic resonance angiography of a normal heart and a heart with transposition of the great vessels. **A**, Patient with a normal heart. Note the crossed relationship of the great arteries; the aorta arises from the left ventricle and runs to the right and posterior to the pulmonary trunk (at its origin) and towards the head. The pulmonary trunk arises from the right ventricle, anterior to the ascending aorta (at its origin), and crosses over and then runs to the left of the ascending aorta and then posteriorly towards the back (where it bifurcates into the right and left pulmonary arteries at the inferior surface (concavity) of the aortic arch). **B**, Patient with transposition of the great vessels (arteries). Note the parallel or side-by-side relationship of the great vessels and loss of their normal crossed relationship. The aorta runs anteriorly and arises from the right ventricle. The hypertrophied right ventricle supports the systemic circulation, and the ventricular septum bows from right to left. Abbreviations: Ao, ascending aorta; LV, left ventricle; PT, pulmonary trunk; RV, right ventricle. (Courtesy of Dr Philip Kilner, Royal Brompton Hospital, London.)

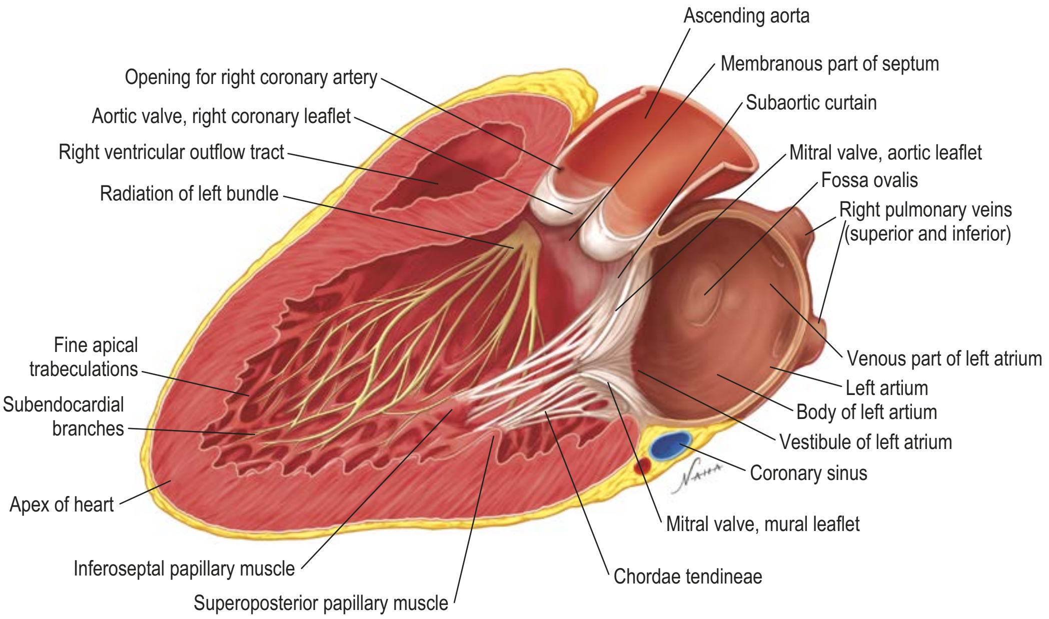
Ascending aorta
Membranous part of septum
Opening for right coronary artery
Subaortic curtain
Aortic valve, right coronary leaflet
Mitral valve, aortic leaflet
Right ventricular outflow tract
Fossa ovalis
Right pulmonary veins
(superior and inferior)
Radiation of left bundle
Fine apical
trabeculations
Venous part of left atrium
Left artium
Subendocardial
branches
Body of left artium
Vestibule of left atrium
Coronary sinus
Apex of heart
Mitral valve, mural leaflet
Inferoseptal papillary muscle
Chordae tendineae
Superoposterior papillary muscle

Fig. 57.36 Internal features and conduction system of the left side of the heart. Conduction tissue accompanies fine trabeculae carneae and false chordae. See Fig. 57.18B for the conduction system features in the right side of the heart. (Courtesy of Professor M Loukas.)

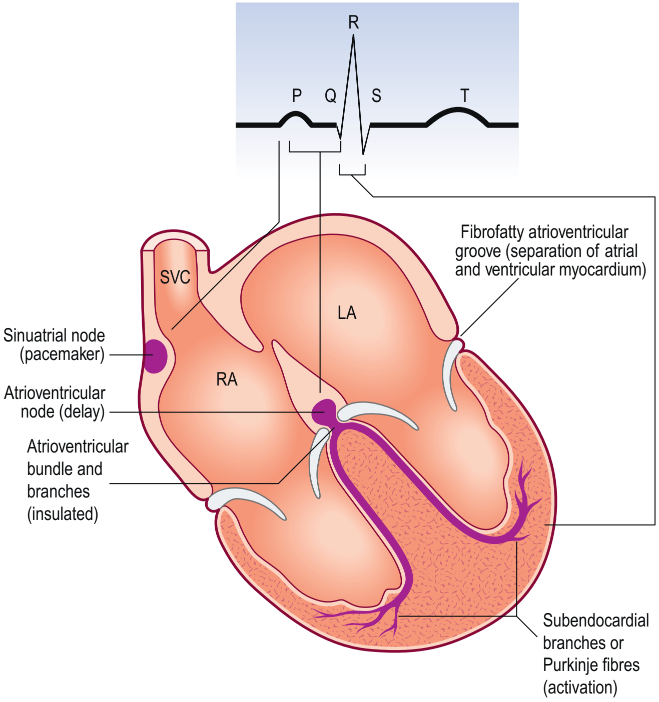
R
P
Q
S
T
Fibrofatty atrioventricular
groove (separation of atrial
and ventricular myocardium)
SVC
LA
Sinuatrial node
(pacemaker)
RA
Atrioventricular
node (delay)
Atrioventricular
bundle and
branches
(insulated)
Subendocardial
branches or
Purkinje fibres
(activation)

Fig. 57.37 The basic structure of the conduction system and its relationship with the electrocardiogram. Note the foramen ovale allowing for shunting *in utero* from the right atrium (RA) to the left atrium (LA). Other abbreviations: SVC, superior vena cava. (Redrawn by courtesy of Professor RH Anderson, Institute of Child Health, University College, London.)

Overview of the conduction system

Of all the cells in the heart, those of the sinuatrial node generate the most rapid rhythm, and therefore function as the cardiac pacemaker. The impulse, believed to be generated in the nodal cells, is transmitted over preferentially conducting pathways to right and left atria, and to the atrioventricular node. At the atrioventricular node, the impulse is delayed by 40 ms, allowing the atria to eject their contents fully before commencement of ventricular contraction, and also placing an upper limit on the frequency of signals that can be transmitted to the ventricles. The transitional cells interpose between the atrial cardiomyocytes and the nodal cells. There is no transition in humans between the node and the penetrating bundle, and the cells are virtually identical. Here they become continuous with cells of the ventricular system. Often described as Purkinje cells, these cells in the human heart are barely larger than working ventricular cardiomyocytes. Conduction of the impulse is rapid in the bundle and its branches (2–3 m/s, compared to 0.6 m/s in normal myocardium). The cardiac impulse therefore arrives at the cardiac apex before spreading through the ventricular walls, producing a properly coordinated ventricular ejection. The human heart beats ceaselessly at an average of 70 cycles every minute for many decades, maintaining perfusion of pulmonary and systemic tissues. The rate and stroke volume fluctuate in response to prevailing physiological demands. The principal events in a cardiac cycle (valvular, phonocardiogram, electrocardiogram, pressure and mechanical) are summarized in Fig. 57.20.

Cardiac efficiency depends on precise timing of the operation in interdependent structures. Passive diastolic filling of the atria and ventricles is followed by atrial systole, stimulated by discharge from the sinuatrial node, which completes ventricular filling. Excitation and contraction of the atria must be synchronous and finish before ventricular contraction; this is effected by a delay in the conduction of excitation from atria to ventricles. Thereafter, ventricular contraction proceeds in a precise manner. The atrioventricular valves are closed by ventricular systole, which must occur prior to closure; ventricular activation must therefore precede valvular closure, which spreads from the ventricular apices towards the outflow tracts and orifices.

Cardiac contraction originates unequivocally in specialized cardiomyocytes, but neural influences are important in adapting the intrinsic cardiac rhythm to functional demands from the entire body. All cardiomyocytes are excitable. They display autonomous rhythmic depolarization and repolarization of their cell membranes, conduction of waves of excitation via gap junctions to adjacent cardiomyocytes, and excitation–contraction coupling to their actomyosin complexes. These properties are developed to different degrees in different sites and in different types of cardiomyocyte (Ch. 6). The rate of depolarization and repolarization is slowest in the ventricular myocardium, intermediate in the atrial muscle, and fastest in the myocytes of the sinuatrial node. The latter override those generating slower rhythms and, in the normal heart, are the locus for the rhythmic initiation of cardiac cycles. Conversely, conduction velocity is slow in nodal myocytes, intermediate in the general population of working cardiac myocytes, and fastest in the myocytes of the ventricular conduction system.

The nodes and networks of the specialized myocardial cells constitute the cardiac conduction system (see Fig. 57.18B; **Figs 57.36–57.37**). The parts of this system are the sinuatrial and atrioventricular nodes, the atrioventricular bundle with its left and right bundle branches, and the subendocardial plexus of ventricular conduction cells (Purkinje cells). The main pacemaker rhythm of the heart (sinus rhythm) is generated within the system but is influenced by autonomic nerves. It is transmitted specifically from atria to ventricles via the atrioventricular node and bundle. The spread of excitation is very rapid but not instantaneous. Different parts of the ventricles are excited at slightly different times, with important functional consequences. Failure of the conduction system will not block cardiac contraction but the system will become poorly coordinated. The rhythm will be slower because it originates from a spontaneous (myogenic) activity in the working cardiac myocytes or in a subsidiary pacemaker in a more distal part of the diseased or disrupted conduction system. There are no specialized internodal and interatrial conduction pathways; the excitation emanating from the sinuatrial node spreads to the atrial musculature and to the atrioventricular node through ordinary working atrial myocardium. The geometric arrangement of fibres along well-organized atrial muscle bundles (e.g., the terminal crest, the limbus of the fossa ovalis and the interatrial (Bachmann's) bundle) provide a pathway for a marginally more rapid conduction than elsewhere within the atrium.

Sinuatrial node

In the majority of hearts, the sinuatrial node is a cigar-shaped structure, 8–25 mm long, located in the right atrium at the junction between the embryonic sinus venosus (venous) part and the primitive (proper) atrial part (see Figs 57.13, 57.37). In hearts over 65 years of age, a layer of connective or fatty tissue between the subendocardium and the body of the node may sometimes render it visible macroscopically. Extending on the right from the crest of the right auricle, the node typically courses posteroinferiorly into the upper part of the sulcus terminalis; in about 10% of hearts it extends in horseshoe fashion across the crest of the auricle. Nodal tissue does not occupy the full thickness of the right atrial wall from epicardium to endocardium, but is as a wedge of specialized subepicardial tissue within the sulcus terminalis. Its location is consistently marked by a large central artery originating equally from either the proximal part of the right coronary artery or the circumflex branch of the left coronary artery. Nodal cells are grouped circumferentially around the sinuatrial nodal artery, packed within a dense matrix of connective tissue as interlacing strands of myocytes. Histologically they are smaller, paler and more empty-looking than working atrial myocardial cells, being 5–10 µm in their greatest diameter, with a large central nucleus. Their pale appearance is attributable to the sparsity of organelles; myofibrils are few and irregularly arranged, and there is no proper sarcotubular system with little glycogen.

The sinuatrial node is described as having a head, body and tail, from which 5–8 short digitations of nodal tissue radiate towards the superior vena cava, subepicardium and crista terminalis, penetrating the working atrial myocardium (**Figs 57.38–57.39**). At the nodal periphery, nodal cells intermingle with slender, fusiform, transitional linking cells that are part of a heterogeneous cellular group intermediate in appearance between nodal cells and normal working atrial myocytes. The extent of nodal tissue can be mapped using molecular markers (Monfredi et al 2010). There are no autonomic ganglion cells within the node, although many border it anteriorly and posteriorly. Nerve fibres are present but do not appear to contact the nodal myocytes.

Paranodal area

A paranodal area within the crista terminalis, between the cells of the sinuatrial node and the working atrial cardiomyocytes, and possessing properties of both nodal and atrial tissues, has been identified (Molenaar et al 2011). Its precise function remains to be determined, but computer simulations suggest that it is an integral part of normal atrial activation and may play a role in pacemaking.

Internodal atrial myocardium

Specialized pathways have been alleged to connect the sinuatrial and atrioventricular nodes, but there is no evidence that tracts insulated from the working myocardium, as occurs in the ventricular conduction pathways, exist within the atrial walls. The impulse generated by the sinuatrial node is conducted more rapidly via the long axis of the atrial muscle bundles than it is transversely. The main pathways for conduction towards the atrioventricular node are the crista terminalis and the limbus of the fossa ovalis. Conduction to the left atrium is preferentially through the interatrial (Bachmann's) bundle; additional pathways occur through the limbus of the fossa ovalis and through the muscular connections between the walls of the coronary sinus and left atrium. During development, the walls of the sinus venosus (systemic venous part) are exclusively composed of primary myocardium. Although pathways within these walls may be identified in prenatal stages, primary myocardium is slowly conducting, which means that these pathways do not represent areas of preferentially rapid conduction.

Atrioventricular node

The atrioventricular node is an oblique, half-oval atrial structure, located within the atrial part of the muscular atrioventricular septum and separated from the ventricular musculature by the insulating tissues of the atrioventricular (coronary) sulcus (see Figs 57.18B, 57.21–57.22). Its anatomical landmarks are the boundaries of the triangle of Koch, specifically; the attachment of the septal leaflet of the tricuspid valve, the opening of the coronary sinus and the tendon of Todaro (inferior pyramidal space). The atrial aspect of the node is convex and overlain by atrial myocardium. Its left margin is concave and abuts on to the superior aspect of the central fibrous body. The basal end projects into the atrial muscle and the anteroinferior end enters the central fibrous body to become the penetrating atrioventricular bundle.

The node consists of both compact and transitional zones pervaded by an irregular collagenous reticulum that enmeshes the myocytes (**Fig. 57.40**). The compact zone consists of frequently stratified, interlocking nodal cells. Cells from the right and left atrial walls and the interatrial septum feed directly into the compact zone. The transitional zone envelops the compact portion of the node and consists of elongated transitional cells, intermediate in morphology and function between compact nodal cells and working atrial cardiomyocytes.

Extensions of nodal cardiomyocytes run in the direction of the coronary sinus along the tricuspid anulus (the putative slow pathway); in the anterior portion of the triangle of Koch near the compact portion of the atrioventricular node (the putative fast pathway); and in the direction of the mitral anulus (the left atrial extension) (Mani and Pavri 2014). In both sinuatrial and atrioventricular nodes, the intercellular contacts between nodal cells, and between nodal and transitional cells, are much less specialized than the intercalated discs between normal cardiac cells (Ch. 6). A sparsity of gap junctions is consistent with the absence from these areas of connexin-43 (a major protein component of mammalian gap junctions), and probably accounts for the observed difficulty in exciting these cells via adjacent cells. The atrioventricular delay may owe much to this relative non-excitability, which appears to disturb the spread of potential thereby delaying propagation; the narrow diameter of the transitional cells may also contribute to conduction delay.

The arterial supply to the atrioventricular node is from a characteristic vessel that originates from the dominant coronary artery at the cardiac crux. Autonomic ganglia are present between the node and the coronary sinus.

Atrioventricular bundle

The atrioventricular bundle (of His) is the direct continuation of the atrioventricular node and becomes oval, quadrangular or triangular in transverse sectional profile as it enters the central fibrous body (see Figs 57.18B, 57.36). It traverses the central fibrous body and branches into right and left bundles on the crest of the muscular interventricular septum; the branching tract is sandwiched between the muscular and the membranous parts of the septum.

The right bundle is a narrow, discrete, rounded group of fascicles that courses at first within the myocardium and then subendocardially towards the ventricular apex, entering the septomarginal trabeculation to reach the anterior papillary muscle. It has few branches to the ventricular walls in its septal course. At the origin of the anterior papillary muscle, it divides extensively into fine subendocardial fascicles that diverge, first embracing the papillary muscle, then recurving subendocardially for distribution to the remaining ventricular walls.

The left bundle and its subdivision show variability in position, size and structure (Cabrera et al 2020). The bundle commonly arises as numerous fine, intermingling fascicles that leave the left margin of the branching bundle through most of its course along the crest of the muscular interventricular septum, where it meets the membranous part of the septum. These fascicles form a flattened sheet down the smooth left ventricular septal surface that diverges apically and subendocardially across the left ventricular aspect of the interventricular septum, commonly (although not always) trifurcating into anterior, septal and posterior divisions (see Figs 57.23C, 57.30). Fine branches leave the sheets, forming subendocardial networks, which first surround the papillary muscles and then curve back subendocardially to be distributed to all parts of the ventricle. The principal branches of the bundle are insulated from the surrounding myocardium by sheaths of connective tissue.

Functional contacts between conduction and working ventricular myocytes become numerous only in the subendocardial terminal ramifications. Hence, papillary muscles contract first, followed by a wave of excitation and an ensuing contraction that travels from the apex of the ventricle to the arterial outflow tract. Because the network of conducting branches is subendocardial, muscular excitation proceeds from endocardium to epicardium.

Cardiac pacing

Available with the *Gray's Anatomy* e-book

Cardiac conduction studies

Available with the *Gray's Anatomy* e-book

Congenital conduction abnormalities

Available with the *Gray's Anatomy* e-book

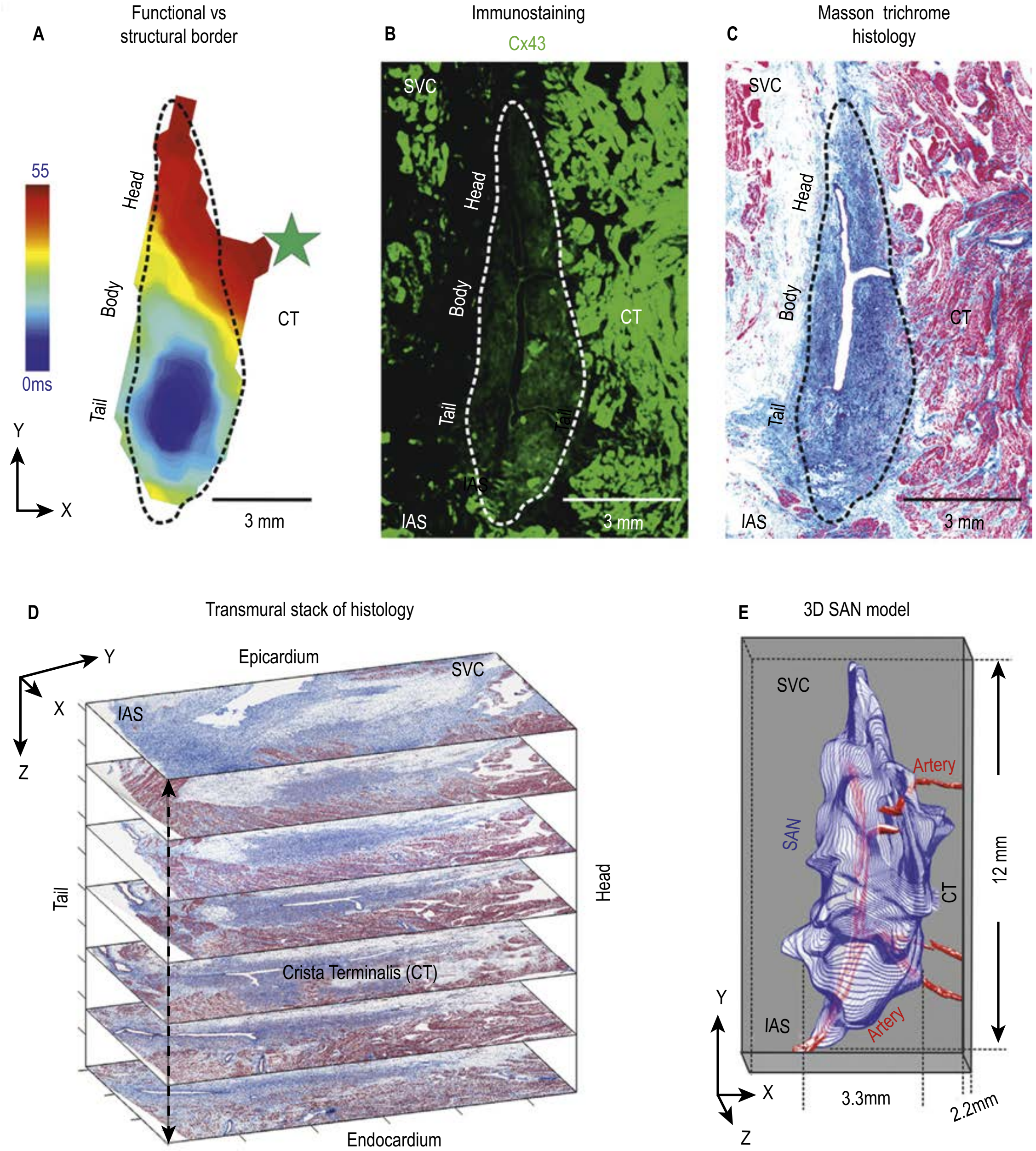

Fig. 57.38 Optical mapping, histology and three dimensional (3D) reconstruction of the sinuatrial node. **A**, Functional borders of the sinuatrial node determined by optical mapping, compared to the histologically determined structural border (dashed line). Green star indicates a conduction pathway (digitation) from the sinuatrial node to the atrial myocardium, one of the initial sites of atrial myocardial excitation (an atrial breakthrough point). **B**, Borders of the sinuatrial node determined by immunostaining for the expression of connexin-43 in the atrial myocardium. **C**, Dense fibrous tissue (stained blue using Masson's trichrome) within the sinoatrial node. **D**, Serial sequential sections through the sinuatrial node from epicardium to endocardium. **E**, 3D reconstruction of serial histological sections of the sinuatrial node (blue) and associated arteries (red). Abbreviations: CT, crista terminalis; IAS, interatrial septum; SAN, sinuatrial node; SVC, superior vena cava. (With permission from Csepe TA, Zhao J, Hansen BJ et al 2016 Human sinoatrial node structure: 3D microanatomy of sinoatrial conduction pathways. Prog Biophys Mol Biol 120:164–178.)

Immunohistochemical staining of the developing heart indicates that the precursors of the atrioventricular conduction system arise from a ring of slow conducting primary myocardium within the atrioventricular junction and outflow tracts (see Fig. 13.11). The definitive atrioventricular node forms in the dorsal part of the interventricular ring and is continuous with the first part of the atrioventricular bundle; the segment of the interventricular ring that encircles the developing left ventricular outflow tract involutes. As the ventricles grow and expand on each side of the muscular ventricular septum, cells on the dorsal part of the crest and on the luminal surface of the septum differentiate into the fast-conducting Purkinje fibres and bundle branches of the atrioventricular bundle. The ventral parts largely disappear, the persisting segment within the ventricles extends along the septum beyond the branching atrioventricular bundle and forms a dead-end tract.

Wolff–Parkinson–White syndrome is caused by abnormal small strands of otherwise unremarkable ventricular myocardium that run through the insulating fibroareolar tissue of the atrioventricular sulcus, connecting the atrial and ventricular myocardial masses at some point around the atrioventricular junctions.

Temporary pacing wires are usually inserted by cannulation of either the internal jugular or subclavian veins; the latter approach carries a slightly greater risk of a pneumothorax because of the proximity of the pleural membranes, pleural cavity and lung. Other potential risks are brachial plexus injury if the entry site is too posterior, and thoracic duct injury if the left subclavian vein is cannulated. The most common location for permanent pacemaker devices is subcutaneously on the anterior thoracic wall. Access to the chambers and endocardium of the right heart is gained via the cephalic vein within the deltopectoral groove.

Intracardiac electrocardiography and electrophysiology are used to assess cardiac conduction and rhythm abnormalities. A catheter is inserted via the femoral, subclavian or internal jugular veins using a guidewire technique. Fluoroscopy, echocardiography and, more recently, cardiac magnetic resonance are used to guide accurate placement of the catheters to the appropriate position. The sites of study are the high right atrium (for assessing the atrioventricular bundle and right bundle branch) and the coronary sinus (for evaluating atrioventricular junctional arrhythmias and accessory pathways). The multipolar electrodes provide detailed electro-anatomical mapping of the sequence of excitation from the atria, atrioventricular junction and ventricles. The origin of supraventricular arrhythmias, ventricular tachycardias, accessory conduction pathways and re-entrant pathways can be identified and used to guide radiofrequency ablation.

In the past, there was an anatomical basis for the majority of presenting congenital conduction abnormalities: they were the product of either accessory pathways or conduction tissue dysgenesis at any point from the atrioventricular node to the atrioventricular bundle. Today, conduction abnormalities are increasingly likely to relate to long-standing haemodynamic problems and/or the effects of previous surgery for patients with congenital heart defects. This reflects the fact that, although surgery for most of these defects has been available for the past four decades, surgery itself has not been curative; more often than not, patients develop conduction abnormalities and arrhythmia from surgical scars that cause haemodynamic problems such as chamber dilation and/or hypertrophy. Occasionally, conduction abnormalities are caused by tumours such as multifocal Purkinje cell tumours, or benign congenital polycystic tumours of the atrioventricular node.

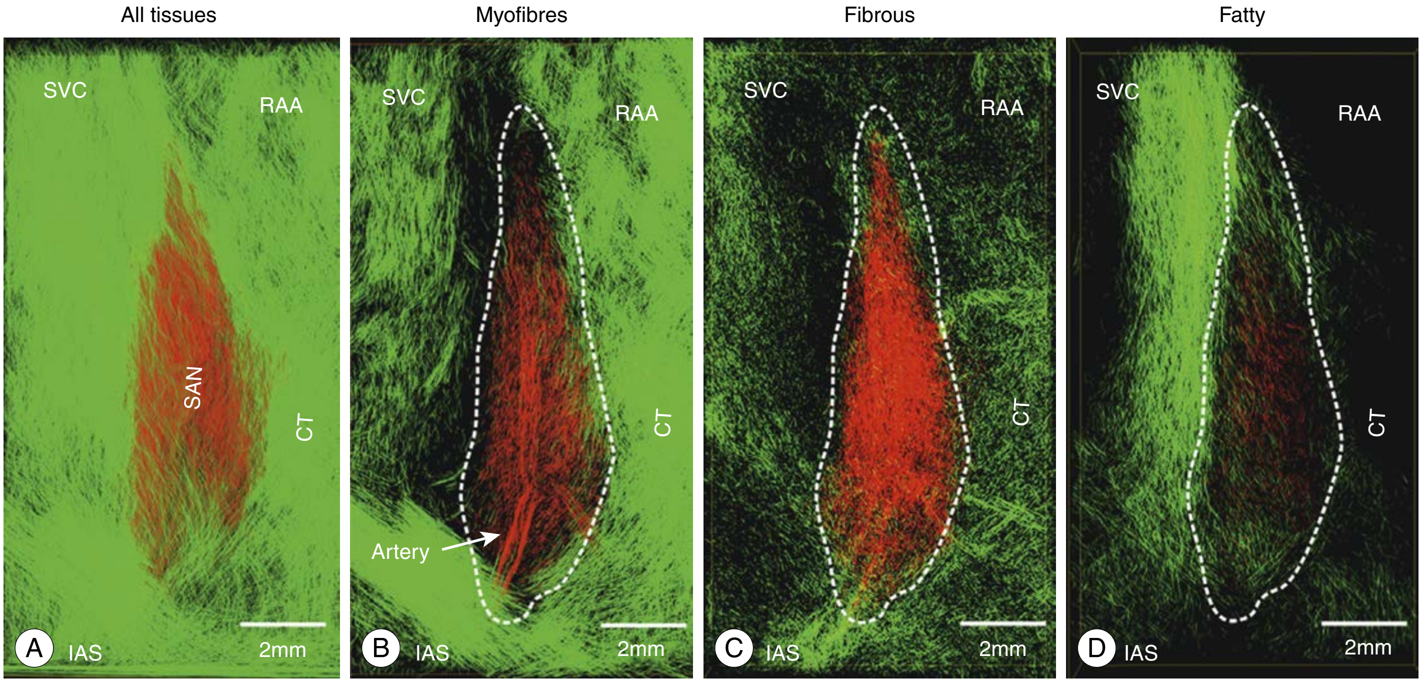
All tissues
Myofibres
Fibrous
Fatty
SVC
RAA
SAN
CT
IAS
2mm
Artery
A
B
C
D

Fig. 57.39 Differential tissue composition of the sinuatrial node (red, surrounded by white dashed line) and surrounding atrial tissue (green) shown using three-dimensional (3D) computational modelling of stained sequential histological sections. **A**, A fibre tracking approach with seeding in different textures shows all tissue types (myofibres, fibrous and fatty) overlaid. **B**, Myofibres and sinuatrial arteries. **C**, Fibrous tissue. **D**, Fatty tissue. Abbreviations: CT, crista terminalis; IAS, interatrial septum; RAA, right atrial auricle; SAN, sinuatrial node; SVC, superior vena cava. (With permission from Csepe TA, Zhao J, Hansen BJ et al 2016 Human sinoatrial node structure: 3D microanatomy of sinoatrial conduction pathways. Prog Biophys Mol Biol 120:164–178.)

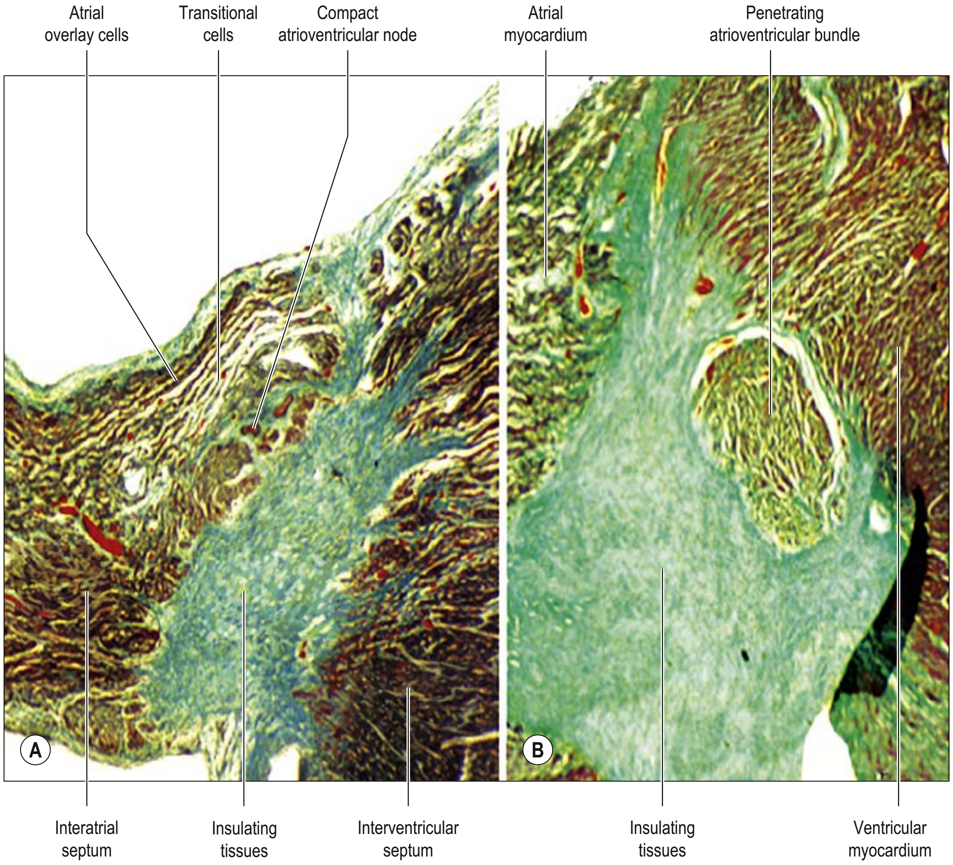
Atrial overlay cells
Transitional cells
Compact atrioventricular node
Atrial myocardium
Penetrating atrioventricular bundle
A
B
Interatrial septum
Insulating tissues
Interventricular septum
Insulating tissues
Ventricular myocardium

Fig. 57.40 Histological sections showing the features of **(A)** the atrioventricular node and **(B)** the penetrating atrioventricular bundle. Trichrome method, fibrous tissue stained green. (With permission from Anderson RH, Boyett MR, Dobrzynski H et al 2013a. The anatomy of the conduction system: implications for the clinical cardiologist. J Cardiovasc Transl Res 6:187–96.)

Vascular supply and lymphatic drainage

Coronary arteries

The right coronary artery arises from the right aortic sinus and the left coronary artery from the left aortic sinus of the proximal ascending aorta (see Figs 57.21, 57.23; **Fig. 57.41**); the level of the opening of each artery is variable. The two arteries form an oblique inverted crown (hence their name) within the atrioventricular sulcus. They also form a variable and often insignificant anastomosis (in the non-pathological state) via marginal and interventricular loops that intersect at the cardiac apex. The main arteries and major branches are usually subepicardial, but those in the atrioventricular and interventricular sulci are often deeply sited, and occasionally hidden by or embedded in overlapping myocardium (myocardial bridging) (see Fig. 57.53). The left or right coronary artery is classed as being dominant if it gives off the inferior interventricular branch, which supplies the inferior part of the ventricular septum and often part of the inferolateral wall of the left ventricle. The right coronary artery is dominant in around 60% of hearts. Anastomoses between right and left coronary arteries are abundant in the fetus but are much reduced by one year of age. Anastomoses providing collateral circulation may become prominent in conditions of chronic hypoxia and in coronary artery disease. An additional collateral circulation is provided by small branches from mediastinal, pericardial and bronchial vessels.

Normal coronary arterial calibre, based on arterial casts or angiogram measurements, ranges between 1.5 and 5.5 mm. The calibre of the left origin exceeds the right in 60% of hearts, the right being larger in 17%, and both vessels being of approximately equal calibre in 23%. The external diameter of the left coronary artery increases from 2.1 mm at the age of 1 year to 3.3 mm at the age of 15 years (Pesonen et al 1991) and the diameters of the coronary arteries may increase up to the 30th year. A significant association has been found between the diameters of the right and left coronary arteries at 0 (birth), 1 and 6 months of age and birth weight, height and body surface area (Karagol et al 2012).

A wide range of coronary artery anomalies or variants may occur, and are categorized according to the origin (connection), course, area of termination of the artery, or the presence of anastomoses, bridging, fistula or atresia (Muresian 2016) (Commentary 7.2).

Right coronary artery

The right coronary artery arises from the right aortic sinus; its opening is usually below the sinutubular junction (see Fig. 57.23). The artery is usually single, although up to four openings have been observed, reflecting the independent origins of the conal, sinuatrial nodal and ventricular arteries (**Figs 57.42–57.43**). The right coronary artery passes at first anteriorly and slightly to the right between the right atrial auricle and pulmonary trunk. On reaching the atrioventricular sulcus, it descends almost vertically to the right side of the inferior cardiac border, curving around it into the inferior part of the sulcus in which it passes towards the cardiac crux (the junction of the atrioventricular, interatrial and interventricular sulci) (see Fig. 57.4B). The artery ends a little to the left of the crux, often by anastomosing with the circumflex branch of the left coronary artery. The right coronary artery may end near the right cardiac border, between this and the crux, or more often it reaches the left border, replacing the more distal part of the circumflex artery. Its branches supply the right and variable parts of the left chambers and atrioventricular septum. Usually, the first branch is the conal branch of the right coronary artery (Loukas et al 2014b). This vessel arises independently from the right aortic sinus in approximately 33% of hearts and is sometimes termed the third coronary artery, but this is an inappropriate term because a similarly named vessel arises from the left coronary circulation. The conal branch of the right coronary artery branches anteroinferiorly over the conus arteriosus (infundibulum) and over the superior aspect of the right ventricle, sometimes anastomosing with a similar branch from the anterior interventricular (left anterior descending) artery to form Vieussens arterial ring, an inconstant anastomosis around the right ventricular outflow tract that may provide an important collateral circulation in cases of arterial occlusion (**Figs 57.44–57.45**) (Loukas et al 2009).

The first segment of the right coronary artery (between its origin and the right side of the inferior cardiac margin) gives off anterior atrial and ventricular branches that diverge widely. The ventricular arteries arise at almost 90° from the right coronary artery, an arrangement that is in marked contrast to the more acutely angled origins of the ventricular branches of the left coronary artery. The anterior ventricular branches, usually two or three, ramify towards the cardiac apex, but they rarely reach the apex unless the right marginal artery is included within this group. The right marginal artery is greater in calibre than the other anterior ventricular arteries and reaches the cardiac apex in most hearts. When it is very large, there may be no additional anterior ventricular branch. Two, sometimes three, small inferior ventricular branches, arise from the second segment of the right coronary artery between the right side of the inferior cardiac margin and cardiac crux to supply the inferior aspect of the right ventricle. Their size is inversely proportional to that of the right marginal artery, which usually extends to the inferior cardiac surface. On approaching the cardiac crux, the right coronary artery normally produces up to three inferior interventricular branches (occasionally none). The actual inferior interventricular artery sits within the interventricular sulcus, and may be flanked either to the right or left, or on both sides, by these parallel branches. When these flanking vessels exist, branches of the inferior interventricular artery are small and sparse. The inferior interventricular artery is occasionally replaced by a branch of the left coronary artery. Although the atrial branches of the right coronary artery are sometimes described as part of anterior, lateral (right or marginal) and posterior groups, they are usually small single vessels, 1 mm in diameter (**Figs 57.46–57.48**). The right anterior and lateral branches (occasionally double, and very rarely triple) mainly supply the right atrium. The posterior branch is usually single and supplies both atria.

The artery of the sinuatrial node is an atrial branch distributed largely to right atrial myocardium. Its origin is variable: most commonly, it arises as the first atrial branch of the right coronary artery, less often from its right lateral atrial branch, and least often from its inferior atrioventricular part. It may sometimes originate from the circumflex branch of the left coronary artery. It usually passes posteriorly in the groove between the right atrial auricle and ascending aorta, and branches around the junction of the superior vena cava and right atrium, typically as an arterial loop from which small branches supply the right atrium. A large branch, the ramus cristae terminalis, traverses and supplies the sinuatrial node: it would seem more appropriate to name this branch the nodal artery, given that the vessel currently bearing this name is predominantly atrial in distribution.

Interventricular septal branches of the right coronary artery are relatively short and leave the inferior interventricular branch to perforate and supply the inferior part (about one-third) of the interventricular septum. They are numerous but do not usually reach the apical region of the septum. The largest interventricular septal artery, usually the first branch, commonly arises from the inverted loop said to characterize the right coronary artery at the crux and it almost always supplies the atrioventricular node. Small, recurrent atrioventricular branches originate from the ventricular branches of the right coronary artery as they cross the atrioventricular sulcus and supply adjacent atrial myocardium.

Left coronary artery

The left coronary artery is usually larger in calibre than the right. It supplies a greater volume of myocardium, including almost all of the left ventricle and atrium, and most of the interventricular septum (see Fig. 57.42; **Figs 57.49–57.51**). In hearts with right dominance, the right coronary artery supplies a variable amount of the inferior region of the left ventricle (see Fig. 57.41A–C).

The left coronary artery arises from the left aortic sinus. The opening of the artery sometimes lies inferior to the margin of the valve leaflets and may be double, usually leading into the circumflex and anterior interventricular (left anterior descending) branches of the left coronary artery. Its initial portion, between its opening and first branches, varies in length from a few millimetres to a few centimetres. The artery lies between the pulmonary trunk and the left atrial auricle, emerging into the atrioventricular sulcus, where it turns left. This part is loosely embedded in subepicardial fat and usually has no branches, but may give off a small atrial branch and, rarely, the sinuatrial nodal artery. Upon reaching the atrioventricular sulcus, the left coronary artery divides into its two main branches: the circumflex and anterior interventricular arteries.

The anterior interventricular artery is commonly described as the continuation of the left coronary artery. It descends obliquely forwards and to the left in the interventricular sulcus (**Fig. 57.52**), sometimes deeply embedded in or crossed by myocardial tissue (myocardial bridges), and by the great cardiac vein and its tributaries.

Almost invariably, the anterior interventricular artery reaches the cardiac apex, where it terminates in around 33% of hearts. More frequently, it curves around the notch of the cardiac apex into the inferior interventricular sulcus and passes one-third to one-half of the way along its length, meeting the terminal parts of the inferior interventricular branches of the right coronary artery.

The anterior interventricular artery gives off right and left anterior ventricular and interventricular septal branches, and a variable number

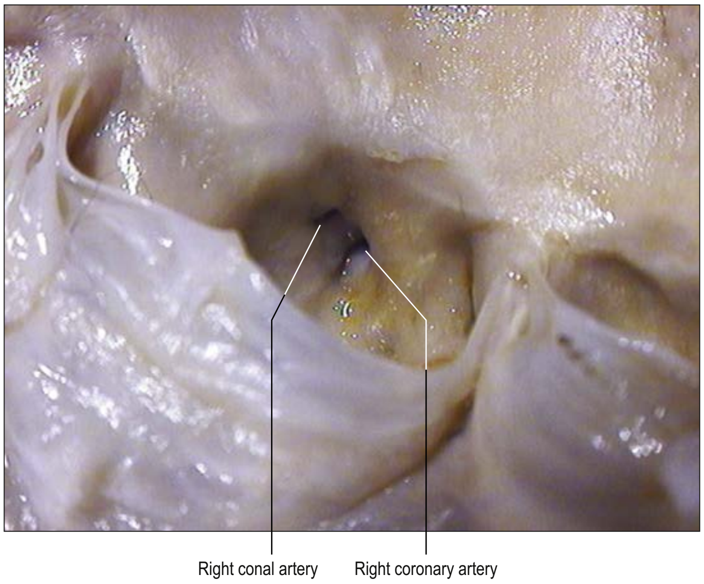

Fig. 57.43 The right coronary sinus, revealing the openings of both a right coronary artery and a right conal artery. (With permission from Loukas M, Sharma A, Blaak C 2013 The clinical anatomy of the coronary arteries. J Cardiovasc Transl Res 6:197–207.)

Congenital anomalies of the coronary arteries are found rarely in children. The two most common anomalies are coronary arteriovenous fistula and anomalous left coronary artery arising from the pulmonary trunk (Uysal et al 2014). Other congenital anomalies include ectopic origin of circumflex artery (normally a branch of the left coronary artery) from right coronary artery, single coronary artery arising from right aortic sinus, ectopic right coronary artery arising from the left aortic sinus, left or right coronary artery arising from the ascending aorta (Clemente et al 2010).

Myocardial bridges are reported to have a frequency varying from 0.5 to 40% when identified clinically and from 15 to 85% when found at autopsy (**Fig. 57.53**). The wide variation in frequency indicates that many bridges may be asymptomatic during life. The major clinical conditions produced by a myocardial bridge are cardiac ischaemia, atherosclerosis and sudden cardiac death. The incidence of atherosclerosis is increased when the right coronary artery is bridged. Although a relationship between myocardial bridges and sudden cardiac death has not been established, autopsy series have shown histological evidence of otherwise unexplained ischaemia in individuals with myocardial bridges; many died during exercise and had no other risk factors for coronary arterial disease.

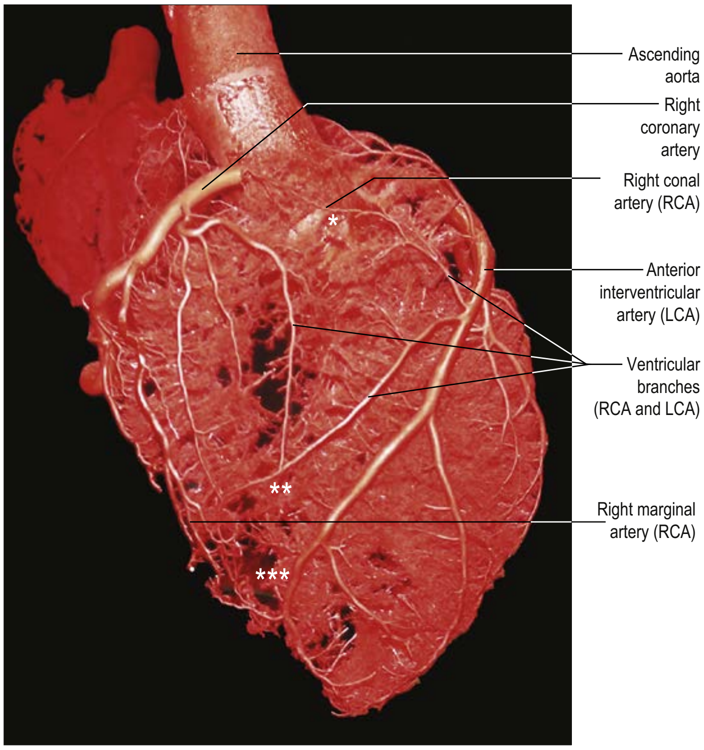
Ascending aorta
Right coronary artery
Right conal artery (RCA)
Anterior interventricular artery (LCA)
Ventricular branches (RCA and LCA)
Right marginal artery (RCA)
*
**
***

Fig. 57.44 A variation of the arterial ring (arterial circle or anulus) of Vieussens (*). This corrosion cast specimen shows the right conal artery, a branch of the right coronary artery, anastomosing with a proximal ventricular branch of the anterior interventricular artery. A second anastomosis (**) occurs between the ventricular branches of the right coronary and anterior interventricular arteries. Close to the apex, a third anastomosis (***) appears between the distal part of the anterior interventricular artery and branches of the marginal branch of the right coronary artery. Abbreviations: RCA, branch of right coronary artery; LCA, branch of left coronary artery. (With permission from Loukas M, Bilinsky S, Bilinsky E et al 2009 The clinical anatomy of the coronary collateral circulation. Clin Anat 22:146–60.)

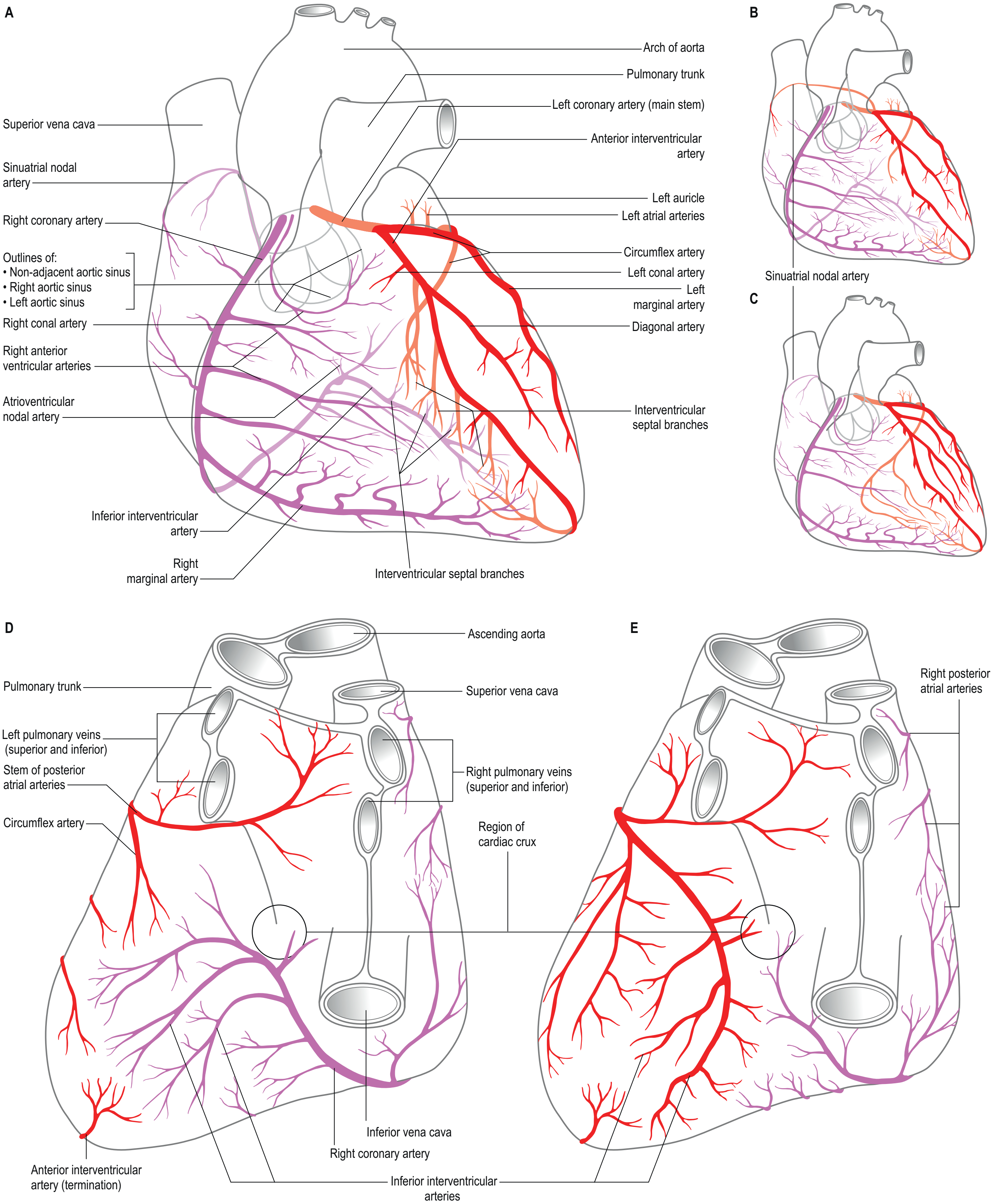
A
Arch of aorta
Pulmonary trunk
Left coronary artery (main stem)
Anterior interventricular artery
Superior vena cava
Sinuatrial nodal artery
Left auricle
Left atrial arteries
Right coronary artery
Circumflex artery
Outlines of:
• Non-adjacent aortic sinus
• Right aortic sinus
• Left aortic sinus
Left conal artery
Left marginal artery
Right conal artery
Diagonal artery
Right anterior ventricular arteries
Atrioventricular nodal artery
Interventricular septal branches
Inferior interventricular artery
Right marginal artery
Interventricular septal branches
B
Sinuatrial nodal artery
C
D
Ascending aorta
Pulmonary trunk
Superior vena cava
Left pulmonary veins (superior and inferior)
Stem of posterior atrial arteries
Right pulmonary veins (superior and inferior)
Circumflex artery
Region of cardiac crux
Inferior vena cava
Right coronary artery
Anterior interventricular artery (termination)
Inferior interventricular arteries
E
Right posterior atrial arteries

Fig. 57.41 Anterior and posteroinferior views of the coronary arterial system, with the principal variations. The right coronary arterial tree is shown in purple, the left in red. **A–C** (anterior view) show the posterior and inferior distribution in a paler shade. **A**, The most common arrangement. **B**, A common variation in the origin of the sinuatrial nodal artery. **C**, An example of left coronary artery dominance, also showing an uncommon origin of the sinuatrial nodal artery. **D–E** (posteroinferior view) show the right coronary arterial tree in purple and the left in red. **D**, An example of the more normal distribution in right coronary artery dominance. **E**, A less common form of left dominance. In views **D** and **E** the inferior (diaphragmatic) surface of the ventricular part of the heart has been artificially displaced and foreshortened to clarify the details of the inferior distribution of the coronary arteries.

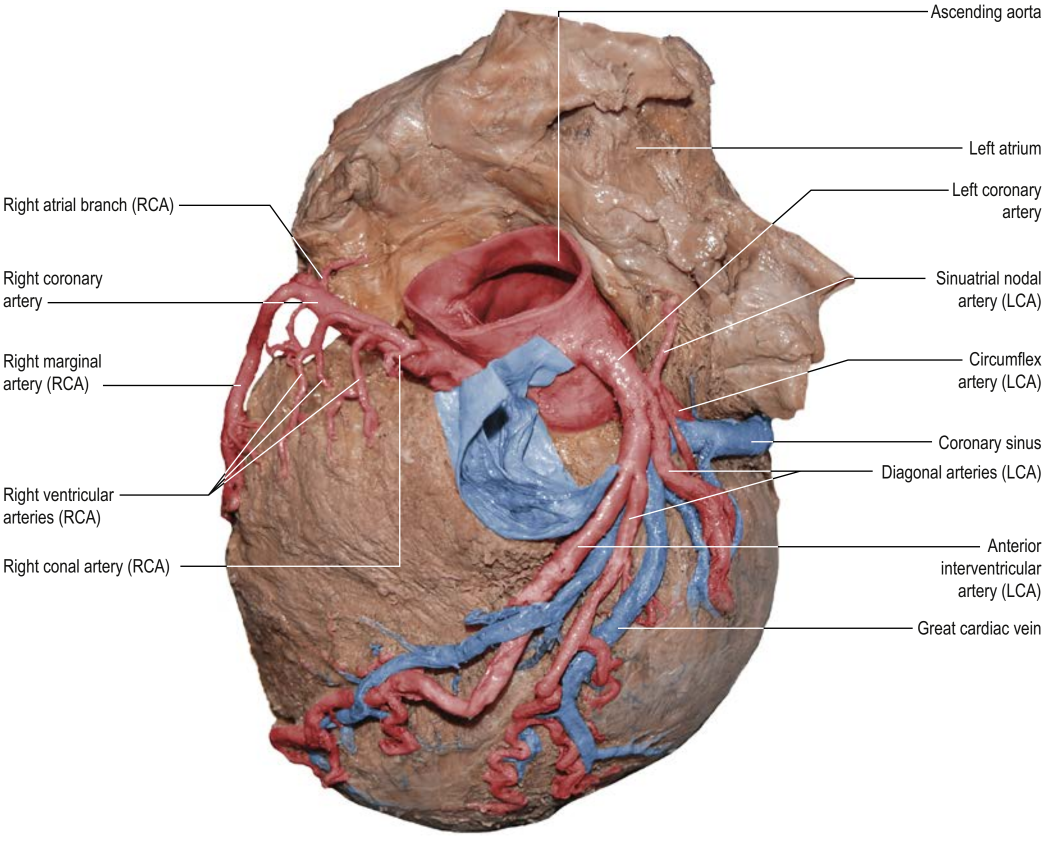

Fig. 57.42 A dissection of a cadaveric heart in which both coronary arteries have been exposed to reveal their branches to the right and left ventricles, respectively. Note how the great cardiac vein is intertwined around the anterior interventricular artery. Abbreviations: RCA, branch of right coronary artery; LCA, branch of left coronary artery. (Image courtesy of Professor M Loukas.)

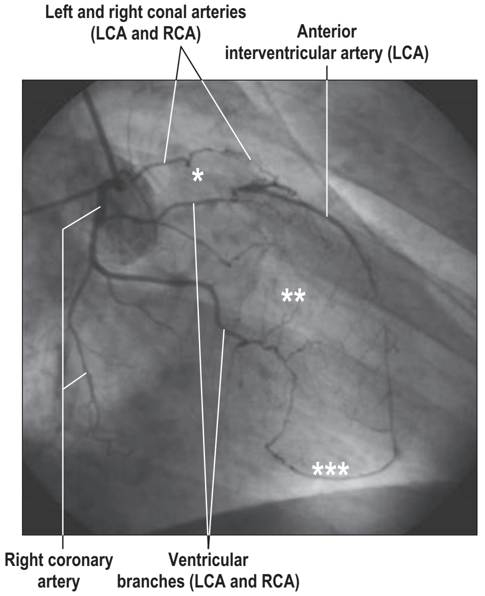
Left and right conal arteries (LCA and RCA)
Anterior interventricular artery (LCA)
*
**
***
Right coronary artery
Ventricular branches (LCA and RCA)

Fig. 57.45 A right coronary artery angiogram demonstrating three collateral arterial anastomoses. Across the area of the subpulmonary conus arteriosus, the right conal artery, a branch of the right coronary artery, anastomoses with the left conal artery, a branch of the anterior interventricular artery, to form the arterial ring of (arterial circle or anulus) of Vieussens (*). Ventricular branches of the right coronary artery anastomose with the proximal (**) and distal portions (***) of the anterior interventricular artery, forming two additional collateral pathways. As a result, there is contrast medium in the anterior interventricular artery. Abbreviations: RCA, branch of right coronary artery; LCA, branch of left coronary artery. (With permission from Loukas M, Bilinsky S, Bilinsky E et al 2009 The clinical anatomy of the coronary collateral circulation. Clin Anat 22:146–60.)

of corresponding posterior branches. Anterior right ventricular branches are small and rarely number more than one or two; the right ventricle is supplied almost entirely by the right coronary artery. Up to nine large left anterior ventricular arteries branch at acute angles from the anterior interventricular artery, crossing the anterior aspect of the left ventricle diagonally, with the largest reaching the rounded left (obtuse) cardiac border. One, termed the left diagonal artery, often dominates, sometimes arising separately from the left coronary artery, which then ends by trifurcation. It is reported in at least 33–50% of hearts, and may be doubled in around 20%. A small left conal artery frequently leaves the anterior interventricular artery near its origin, and anastomoses on the conus arteriosus with its counterpart from the right coronary artery and with the vasa vasorum of the pulmonary trunk and ascending aorta. The interventricular septal branches leave the anterior interventricular artery almost perpendicularly, and pass posteroinferiorly within the septum, usually supplying its anterior two-thirds. The first interventricular septal artery usually supplies the atrioventricular bundle at the point of its division into right and left bundles. Small inferiorly located interventricular septal branches from the same source supply the inferior third of the septum for a variable distance from the cardiac apex (Loukas et al 2009).

The circumflex branch of the left coronary artery, comparable to the anterior interventricular artery in calibre, curves leftwards in the atrioventricular sulcus, and continues around the left cardiac border into the posterior and then inferior part of the sulcus, terminating to the left of the cardiac crux in most hearts, although sometimes continuing as the inferior interventricular artery. Proximally, the left atrial auricle usually overlaps it. A large ventricular branch, the left marginal artery, normally arises from the left circumflex artery at a 90° angle and branches over the rounded left border, supplying much of the adjacent left ventricle, typically to its apex. Smaller anterior and inferior branches of the circumflex artery also supply the left ventricle. Anterior ventricular branches (from one to five, commonly two or three) course parallel to the diagonal artery when it is present, and replace it when it is absent. Inferior ventricular branches are smaller and fewer because the left ventricle is partly supplied by the inferior interventricular branch of the right coronary artery. When this artery is small or absent, it is accompanied or replaced by often doubled or tripled interventricular continuations of the circumflex artery.

The artery to the sinuatrial node is often derived from the first 1–2 cm of the circumflex artery after its origin from the left coronary artery (anterior circumflex segment) and less often from the remaining length of the circumflex artery. It passes over and supplies the left atrium, encircles the superior vena cava (similar to a right coronary sinuatrial nodal branch) and sends a large branch through the node; despite its name, it is predominantly atrial in distribution. The artery to the atrioventricular node, sometimes the terminal branch of the circumflex artery (20%), arises near the cardiac crux. When this occurs, the circumflex artery usually gives off the inferior interventricular artery, an example of left dominance.

Coronary arterial distribution

Details of coronary arterial distribution should be integrated into a concept of total cardiac supply. Most commonly, the right coronary artery supplies all of the right ventricle (except a narrow strip to the right of the anterior interventricular sulcus); a variable part of the

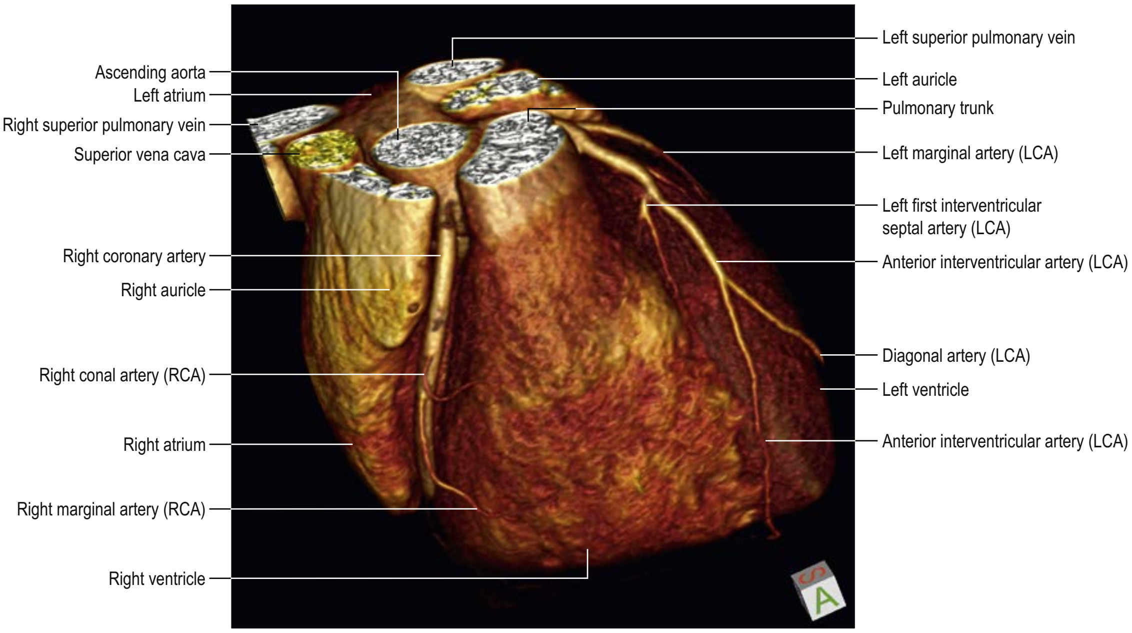
Ascending aorta
Left atrium
Right superior pulmonary vein
Superior vena cava
Right coronary artery
Right auricle
Right conal artery (RCA)
Right atrium
Right marginal artery (RCA)
Right ventricle
Left superior pulmonary vein
Left auricle
Pulmonary trunk
Left marginal artery (LCA)
Left first interventricular septal artery (LCA)
Anterior interventricular artery (LCA)
Diagonal artery (LCA)
Left ventricle
Anterior interventricular artery (LCA)
S
A

Fig. 57.46 ECG-gated volume-rendered CT coronary angiogram in a superior anterior oblique view of the heart. Abbreviations: RCA, branch of right coronary artery; LCA, branch of left coronary artery.

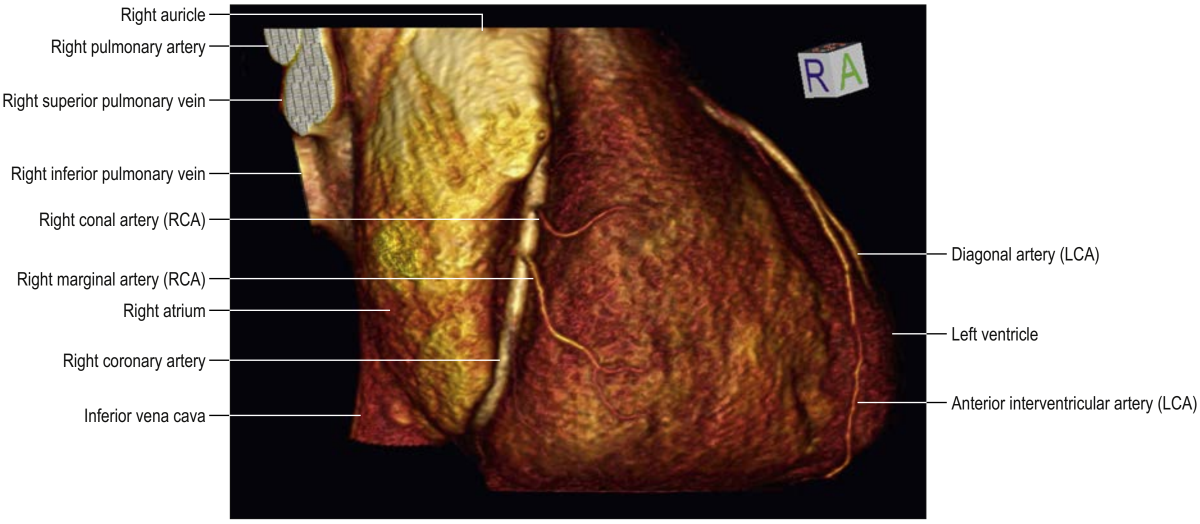
Right auricle
Right pulmonary artery
Right superior pulmonary vein
Right inferior pulmonary vein
Right conal artery (RCA)
Right marginal artery (RCA)
Right atrium
Right coronary artery
Inferior vena cava
R A
Diagonal artery (LCA)
Left ventricle
Anterior interventricular artery (LCA)

Fig. 57.47 ECG-gated volume-rendered CT coronary angiogram in a right anterior oblique view of the heart. Abbreviations: RCA, branch of right coronary artery; LCA, branch of left coronary artery.

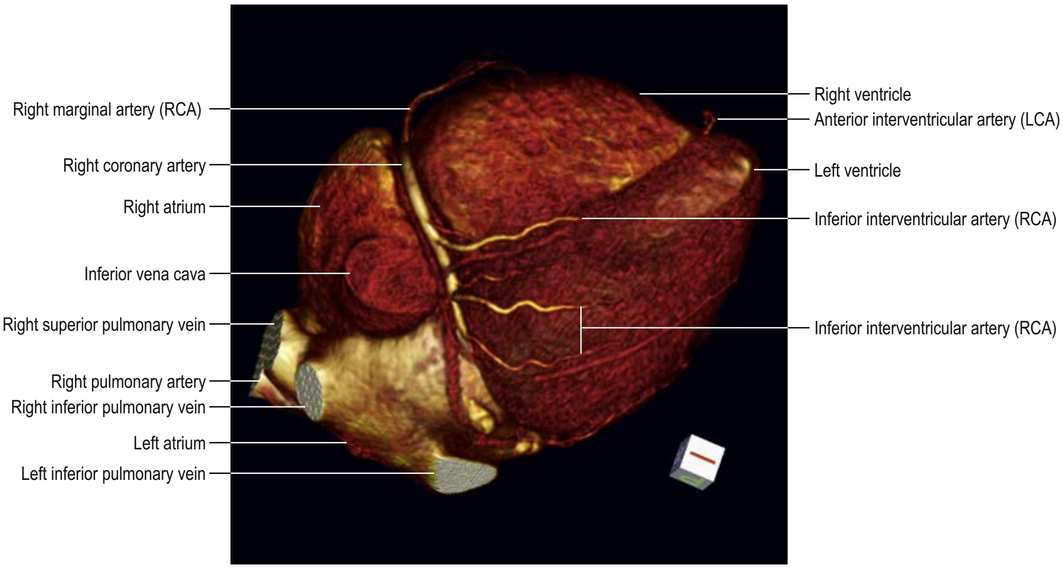
Right marginal artery (RCA)
Right coronary artery
Right atrium
Inferior vena cava
Right superior pulmonary vein
Right pulmonary artery
Right inferior pulmonary vein
Left atrium
Left inferior pulmonary vein
Right ventricle
Anterior interventricular artery (LCA)
Left ventricle
Inferior interventricular artery (RCA)
Inferior interventricular artery (RCA)

Fig. 57.48 ECG-gated volume-rendered CT coronary angiogram in an inferior oblique view of the heart. Abbreviations: RCA, branch of right coronary artery; LCA, branch of left coronary artery.

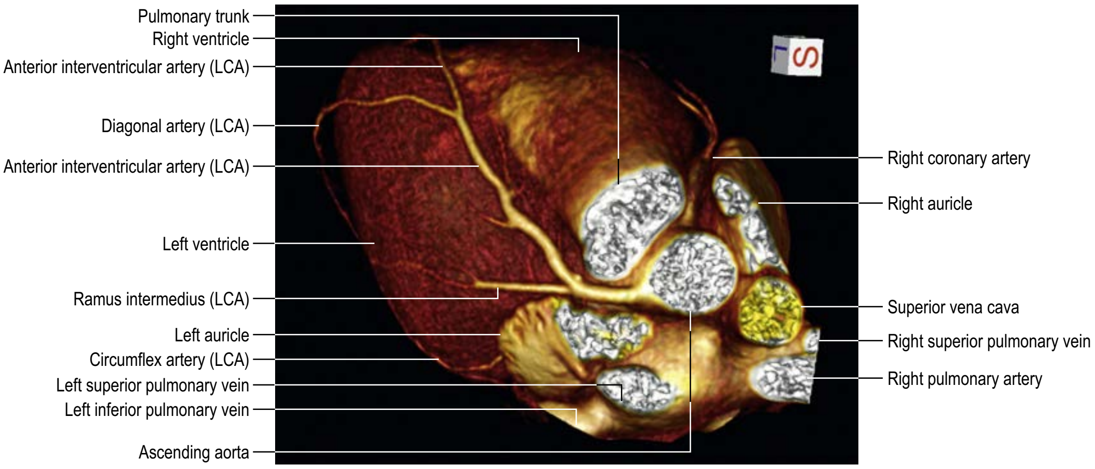
Pulmonary trunk
Right ventricle
Anterior interventricular artery (LCA)
Diagonal artery (LCA)
Anterior interventricular artery (LCA)
Left ventricle
Ramus intermedius (LCA)
Left auricle
Circumflex artery (LCA)
Left superior pulmonary vein
Left inferior pulmonary vein
Ascending aorta
S
L
Right coronary artery
Right auricle
Superior vena cava
Right superior pulmonary vein
Right pulmonary artery

Fig. 57.49 ECG-gated volume-rendered CT coronary angiogram in a left superior oblique view of the heart. Abbreviation: LCA, branch of left coronary artery.

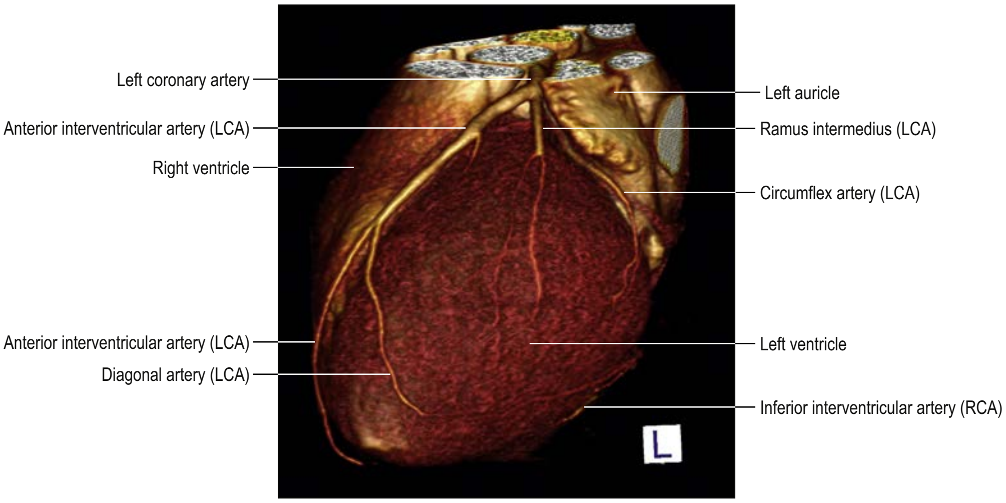
Left coronary artery
Anterior interventricular artery (LCA)
Right ventricle
Anterior interventricular artery (LCA)
Diagonal artery (LCA)
Left auricle
Ramus intermedius (LCA)
Circumflex artery (LCA)
Left ventricle
Inferior interventricular artery (RCA)
L

Fig. 57.50 ECG-gated volume-rendered CT coronary angiogram in a left view of the heart. Abbreviations: RCA, branch of right coronary artery; LCA, branch of left coronary artery.

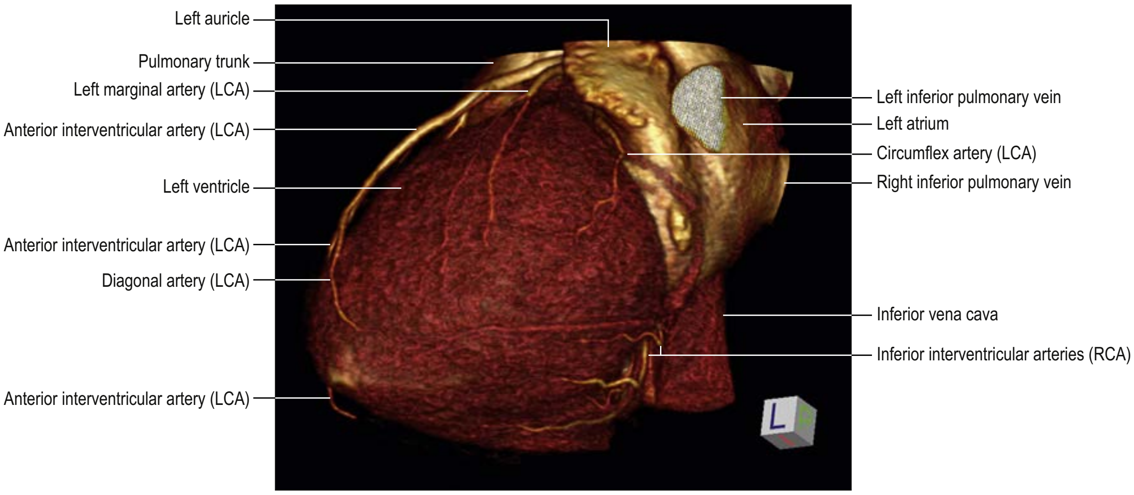
Left auricle
Pulmonary trunk
Left marginal artery (LCA)
Anterior interventricular artery (LCA)
Left ventricle
Anterior interventricular artery (LCA)
Diagonal artery (LCA)
Anterior interventricular artery (LCA)
Left inferior pulmonary vein
Left atrium
Circumflex artery (LCA)
Right inferior pulmonary vein
Inferior vena cava
Inferior interventricular arteries (RCA)
L

Fig. 57.51 ECG-gated volume-rendered CT coronary angiogram in a left posterior oblique view of the heart. Abbreviations: RCA, branch of right coronary artery; LCA, branch of left coronary artery.

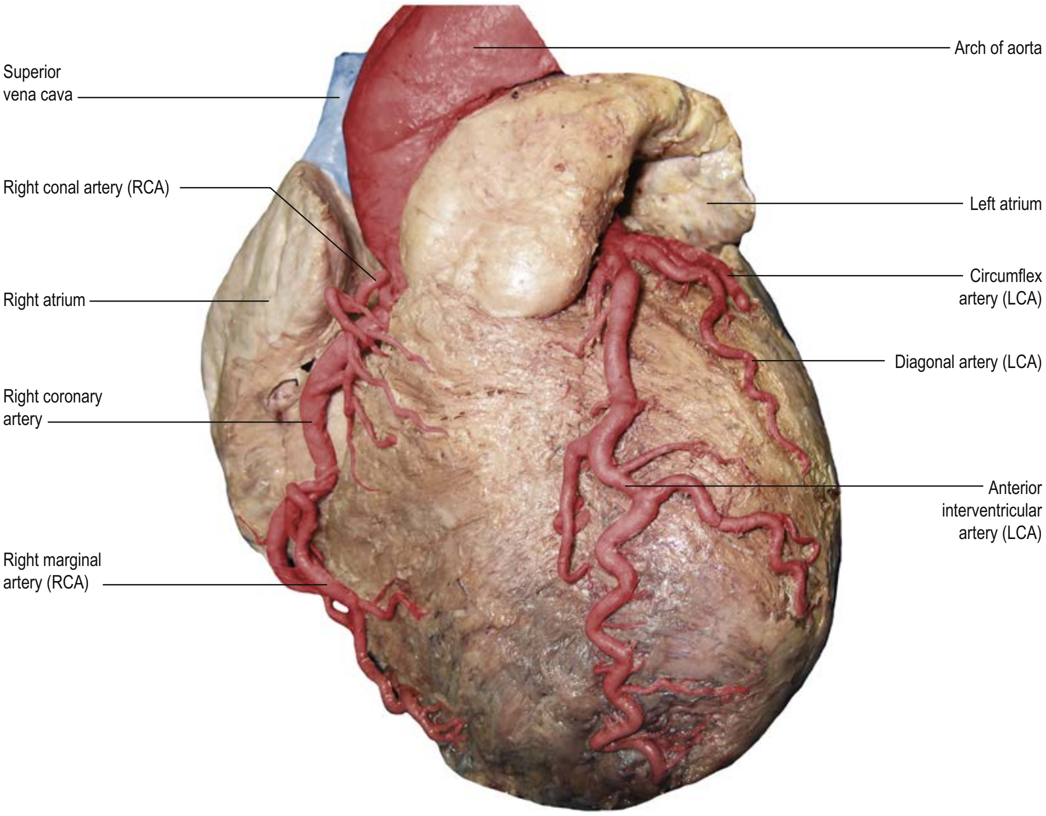

Fig. 57.52 The course of the left coronary artery and its branches, shown on a dissected cadaveric heart. Abbreviations: RCA, branch of right coronary artery; LCA, branch of left coronary artery. (With permission from Loukas M, Sharma A, Blaak C 2013 The clinical anatomy of the coronary arteries. J Cardiovasc Transl Res 6:197–207.)

inferior aspect of the left ventricle; the inferior one-third of the interventricular septum; the right atrium and part of the left atrium; the conduction system as far as the proximal parts of the right and left bundles (branches of the atrioventricular bundle). Left coronary artery distribution is reciprocal and includes most of the left ventricle; a narrow strip of right ventricle; the anterior two-thirds of the interventricular septum; most of the left atrium. Variations in the coronary arterial system mainly affect the inferior aspect of the ventricles and reflect the relative dominance of coronary arterial supply (see Fig. 57.41). The term dominance is misleading because the left artery almost always supplies a greater volume of tissue than the right. In right dominance, the inferior interventricular artery is derived from the right coronary artery, and in left dominance it is derived from the left coronary artery. In the balanced pattern of supply, branches of both the left and right coronary arteries run in or near the inferior interventricular sulcus.

Less is known about variations in atrial supply because the small vessels involved are not easily preserved in the corrosion casts that are used for analysis. In more than 50% of individuals, the right atrium is supplied by the right coronary artery alone. More than 62% of left atria are supplied mainly by the left coronary artery, 27% by the right coronary artery (in each group a small accessory supply from the other coronary artery exists) and 11% are supplied almost equally by both arteries. Arterial supply to the sinuatrial and atrioventricular nodes also varies: the sinuatrial node is supplied more often by the right coronary artery and fewer than 10% of sinuatrial nodes receive a bilateral supply. The atrioventricular node is usually supplied by the right coronary artery.

Coronary anastomoses

Available with the *Gray's Anatomy* e-book

Extracardiac anastomoses

Extracardiac anastomoses connect various coronary arterial branches with other intrathoracic vessels, most commonly involving the bronchial and internal thoracic arteries (**Fig. 57.54**). To a much lesser degree, anastomoses between coronary arteries and pericardiacophrenic branches of the internal thoracic, anterior mediastinal, intercostal and oesophageal arteries also exist.

Coronary angiography

Available with the *Gray's Anatomy* e-book

Coronary revascularization

Available with the *Gray's Anatomy* e-book

Coronary artery fistula

A coronary artery fistula is an abnormal connection that directly links one or more coronary arteries to a heart chamber or to major thoracic vessels without an interposed capillary bed.

Cardiac veins

The cardiac venous system is divided into two major parts. The greater system consists of large vessels that lie within the subepicardial myocardium and drain most of the outer myocardium. These veins extend over the myocardial surface and do not adhere to topographical borders, although the larger collecting vessels lie within the interventricular sulci before draining into the coronary sinus (see Fig. 57.4; **Fig. 57.59**). The intercommunicating parts of this system are the coronary sinus and its tributaries, the anterior cardiac venous system, and the ventricular septal and atrial veins. The coronary sinus and its tributaries return blood to the right atrium from the entire heart (including its septa), except for the anterior region of the right ventricle and small, variable parts of both atria and the left ventricle. The anterior cardiac veins drain an anterior region of the right ventricle; this expands to include a region around the right cardiac border when the right marginal vein joins this group.

The smaller system functions primarily to return venous blood from the inner myocardial walls into the right atrium and ventricle and, to a lesser extent, into the left atrium and sometimes the left ventricle. It contains the smallest cardiac (Thebesian) veins that drain the subendocardial myocardium either directly, via connecting intramural arteries and veins, or indirectly, via subendocardial sinusoidal spaces.

Variation in cardiac veins Attempts to categorize variations in cardiac venous circulation into types have not produced any accepted pattern. The coronary sinus may receive all the cardiac veins, except the smallest (Thebesian) veins, including the anterior cardiac veins, which may be reduced by diversion into the small cardiac vein and then to the coronary sinus.

Coronary sinus

Most cardiac veins drain into the wide coronary sinus, 2 or 3 cm long, lying in the inferior atrioventricular (coronary) sulcus between the left atrium and ventricle (see Fig. 57.4B,E). The sinus opens into the right atrium between the opening of the inferior vena cava and the right atrioventricular orifice. The opening may be guarded by the valve of the coronary sinus (Thebesian valve), a fold of endocardium (see Fig. 57.13); the fold may be absent or may cover completely the opening of the sinus. The tributaries of the coronary sinus are the great, small and middle cardiac veins, the inferior vein of the left ventricle and the oblique vein of the left atrium; all except the oblique vein have valves

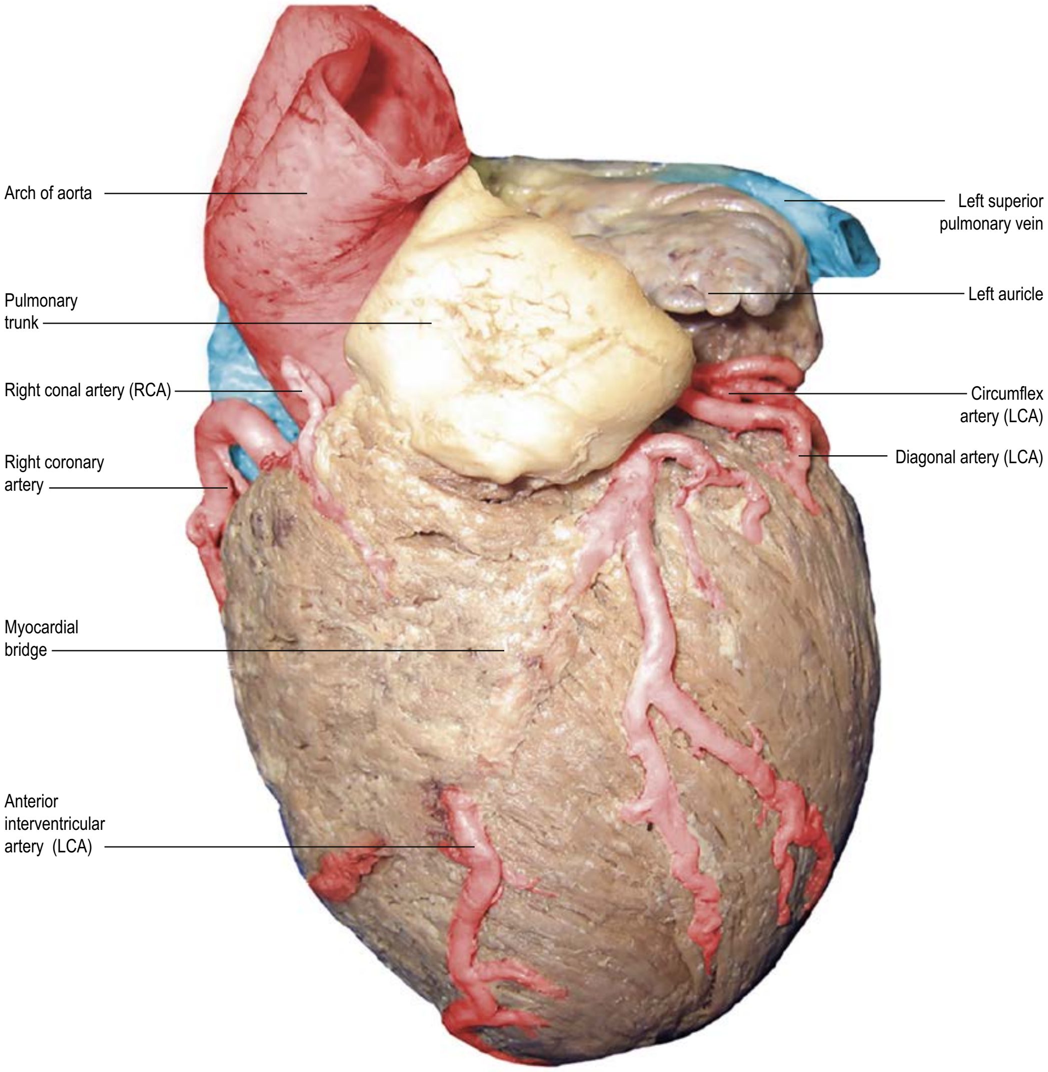

Fig. 57.53 A myocardial bridge covering a large part of the anterior interventricular artery, shown on a dissected cadaveric heart. Abbreviations: RCA, branch of right coronary artery; LCA, branch of left coronary artery. (Image courtesy of Professor M Loukas.)

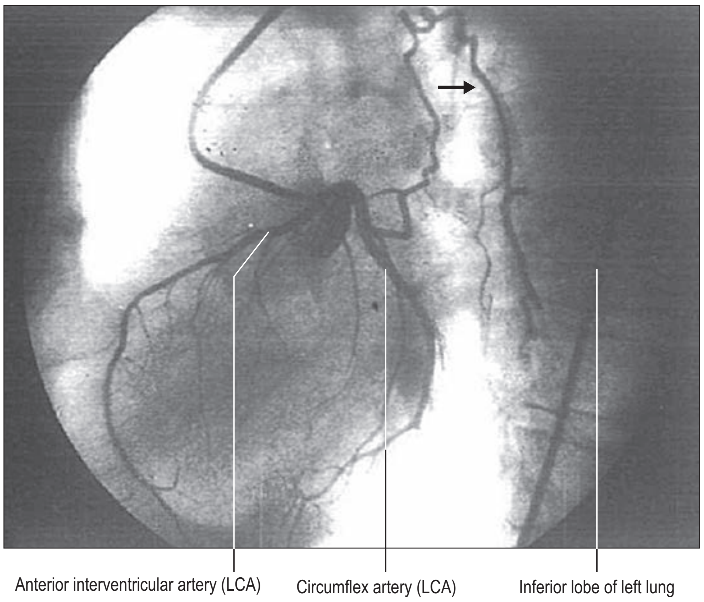
Anterior interventricular artery (LCA)
Circumflex artery (LCA)
Inferior lobe of left lung

Fig. 57.54 A left coronary angiogram in left lateral projection, showing a large, tortuous vessel (arrow) arising from the proximal part of the circumflex branch of the left coronary artery and anastomosing with the bronchial artery, which continues to supply the inferior lobe of the left lung. Abbreviations: LCA, branch of left coronary artery. (With permission from Stefas L, Assayag P, Aubry P et al 1990 Coronary to bronchial artery anastomosis with bronchial steal syndrome demonstrated by thallium-201 myocardial tomoscintigraphy. Eur Heart J 11:275–9.)

Uncommonly, variants of coronary arteries may be present and are the second most common cause of sudden cardiac death in young athletes. Anomalous origins of the coronary artery, particularly from the contralateral aortic sinus, are the variant that is most commonly associated with sudden cardiac death. Other anomalies include left coronary artery origin from the pulmonary trunk, coronary fistula and left main stem atresia (Kastellanos et al 2018).

The cardiac collateral circulation represents a built-in system for coronary arterial bypass. The first few centimetres of the main stems of the left and right coronary arteries are devoid of anastomotic branches. Collateral channels are abundant further distally, exhibiting variable calibres and occupying numerous locations, allowing for bidirectional flow between most arteries. Approximately 30 different sites of collateral extramural vessels have been described, the most frequent being at the cardiac apex; the anterior aspect of the right ventricle; the inferior aspect of the left ventricle; the cardiac crux; the interatrial and interventricular sulci; between the sinuatrial nodal and other atrial vessels (see Figs 57.44–57.45). Anastomoses between branches of the coronary arteries, both subepicardial and myocardial, and between these arteries and extracardiac vessels (see Fig. 57.54) are of great clinical importance. Clinical studies suggest that anastomoses cannot rapidly provide collateral routes sufficient to circumvent sudden coronary obstruction. Nevertheless, it has long been established that anastomoses do occur, particularly between fine subepicardial branches, and they may increase during the life of an individual by both angiogenesis and arteriogenesis. The Vieussens arterial ring is a collateral vessel that crosses the conus arteriosus inferior to the pulmonary trunk, and provides an anastomosis between the conal branches of the right coronary artery and the anterior interventricular artery. The artery to the sinuatrial node commonly provides a communication between the proximal parts of the left and right coronary arteries. The apical collateral artery joins the interventricular arteries. The frequent enlargement of the first

TABLE 57.1 **Patterns of cardiac collateral arteries**

Grade	Description
0	Total absence of any collateral arteries
1	Poorly developed collateral arteries with no prominent distal channel visualized by angiography
2	Presence of moderate collateral arteries providing faint but delayed opacification of a prominent distal channel
3	Good collateral arteries giving clear opacification of a prominent distal channel
4	Excellent collateralization giving full and brisk opacification of prominent distal vessels

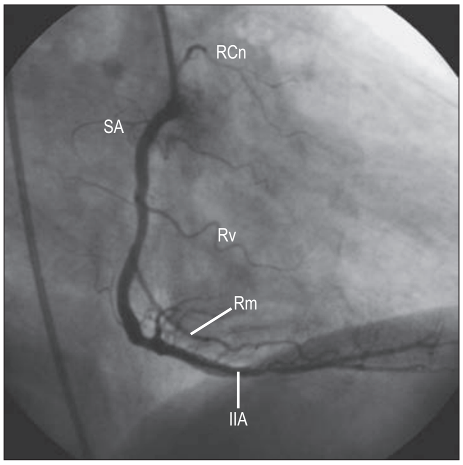

Fig. 57.55 A right coronary angiogram showing several branches of the right coronary artery. Abbreviations: RCn, right conal artery; IIA, inferior interventricular artery; Rm, marginal branch of right coronary artery; Rv, right ventricular branch; SA, sinuatrial nodal artery. (Courtesy of Professor M Loukas.)

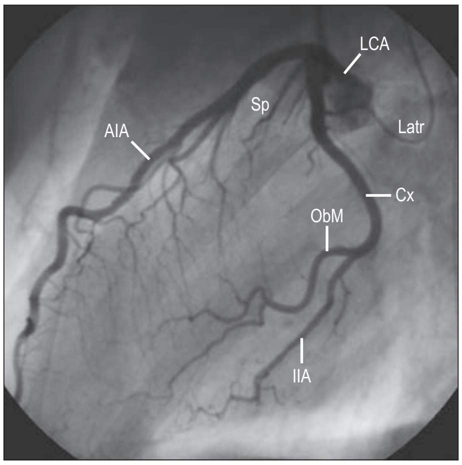

Fig. 57.56 A left coronary angiogram showing several branches of the left coronary artery (LCA). Other abbreviations: AIA, anterior interventricular artery; Latr, left atrial branch; Cx, circumflex artery; ObM, obtuse marginal (left border); IIA, inferior interventricular artery; Sp, interventricular septal artery. (Courtesy of Professor M Loukas.)

interventricular septal branch of the anterior interventricular artery, Kugel's anastomotic artery (arteria anastomotica auricularis magna), has been described as running between the proximal parts of the coronary arteries along the anterosuperior margin of the fossa ovalis to anastomose with the distal part of the right coronary artery. Clinical imaging (catheter angiography and colour Doppler ultrasound) has led to the development of a grading system to describe the overall pattern of cardiac collateral arteries (Table 57.1).

The posterior pericardium also receives a direct supply from the bronchial arteries: extracardiac coronary anastomoses involving bronchial arteries are typically found at the pericardial reflections, such as the points of entry of the superior and inferior venae cavae. The most common anastomoses are with the circumflex branch of the left coronary artery via the posterior pericardial reflections and reflect the close proximity of the bronchial arteries within the root of the lung. In pathological conditions, notably those resulting in pericardial adhesions, it is also possible for extracardiac anastomoses to develop through trans-pericardial vascularization. Extracardiac communications also exist with coronary atrial branches, especially the sinuatrial nodal artery. The effectiveness of any of these connections as collateral routes in coronary occlusion is not well quantified. Coronary arteriovenous anastomoses and numerous connections between the coronary circulation and cardiac cavities, producing so-called 'myocardial sinusoids' and 'arterioluminal vessels', have been reported, but their importance in coronary disease remains uncertain.

Coronary angiography may be performed by introducing a catheter through the femoral, radial or brachial artery. The femoral artery is punctured with a needle 3 cm below the inguinal ligament while the lower limb is held adducted and slightly externally rotated. The exact position is guided by palpation of the femoral arterial pulse, and the needle is inserted at an angle of 45° to the artery. After arterial puncture, a fine guidewire is inserted through the needle and fed into the artery. The catheter is then inserted over the guidewire and passed through the external and common iliac arteries into the abdominal aorta, then through the descending thoracic aorta, aortic arch and ascending aorta. The brachial or radial artery may be used for percutaneous access to the circulation. Once the catheter is located in the ascending aorta, a variety of guidewires may be used to enter the coronary vessels for selective arteriography and interventions. Angiography is performed with standard high osmolality contrast medium and cine-angiography. In selected patients, new-generation, low osmolality contrast medium may be used. All the coronary arteries are catheterized and visualized in a variety of views to obtain a full evaluation of their anatomy and to determine the location and degree of any stenosis (Figs 57.55–57.56). The opening of the left coronary artery arises from the left aortic sinus and is best viewed in the direct frontal and left anterior oblique projections. The right anterior oblique view is useful in demonstrating the diagonal and anterior interventricular branches of the left coronary artery. The right coronary artery originates from the right aortic sinus and is usually visualized in the right anterior oblique view. Pressure and oxygen saturations can be measured via the catheter; changes in pressure across valves allow the degree of stenosis to be measured. Coronary blood flow and relative flow reserve can also be calculated. Significant stenosis may be treated initially by balloon angioplasty followed by stent insertion. The balloon exerts pressure against the plaque in the arterial wall, fracturing and splitting the plaque. The splinting effect of the plaque and elastic recoil are reduced, resulting in an increase in the arterial lumen. Stent insertion reduces the rate of re-stenosis.

Atherosclerosis causing more than 60% stenosis of the terminal diameter of the coronary arteries is likely to cause significant reduction in myocardial perfusion. Patients with high-grade lesions, left main stem coronary artery or triple-vessel disease with impaired left ventricular function are usually considered for coronary artery bypass grafting. The common grafts that are used are the internal thoracic (mammary) and radial arteries. The left internal thoracic artery and radial artery grafts have a greater patency rate than saphenous vein grafts. Approximately 15% of saphenous vein grafts occlude in 1 year and, from then on, at an annual rate of 1–2% in the first 6 years and 4% thereafter; between 40% and 50% of saphenous vein grafts have occluded by 10 years, whereas only about 10% of left internal thoracic or radial artery grafts will have occluded over this time. The common surgical approach is via a midline sternotomy (Ch. 53). If the internal thoracic artery is used as a donor graft, it is divided distally (maintaining its proximal origin from the subclavian artery) and anastomosed to the coronary artery distal to the stenosis. If radial artery grafts are used, they must bridge the stenosis via both proximal and distal anastomoses. In selected cases, minimally invasive direct coronary artery bypass grafting is performed, but the approach is dependent on the vessel being grafted. The anterior approach, via a mini-thoracotomy through the left fourth intercostal space, is used for grafting the left anterior interventricular and diagonal arteries. The anterolateral approach, via an incision in the left third intercostal space from the mid-clavicular to anterior axillary lines, is used for grafting early marginal branches of the circumflex branch of the left coronary artery. The lateral approach, via a lateral thoracotomy measuring only 10 cm in size through the left fifth or sixth intercostal spaces, allows grafting of the circumflex vessels. Extrathoracic approaches that are occasionally used include the subxiphoid approach for the distal part of the right coronary artery and inferior interventricular artery. The vast majority of patients are treated with stent placement (Fig. 57.57). Port access surgery allows for full revascularization with cardiopulmonary bypass and obviates the need for midline sternotomy.

Coronary artery fistulae are rare (Fig. 57.58); those that arise from a coronary artery and then terminate in a chamber of the heart are known as coronary cameral fistulae, while those terminating in a vein are coronary arteriovenous fistulae. Fistulae may be congenital or may develop later in life. Congenital fistulae are more common and account for 50% of paediatric coronary vascular aberrations: they are believed to be derived from the smallest cardiac (Thebesian) veins. Acquired coronary artery fistulae are most commonly iatrogenic in aetiology but may also occur after traumatic injury. The most commonly seen are of the coronary cameral type, from the right coronary artery into the right side of the heart.

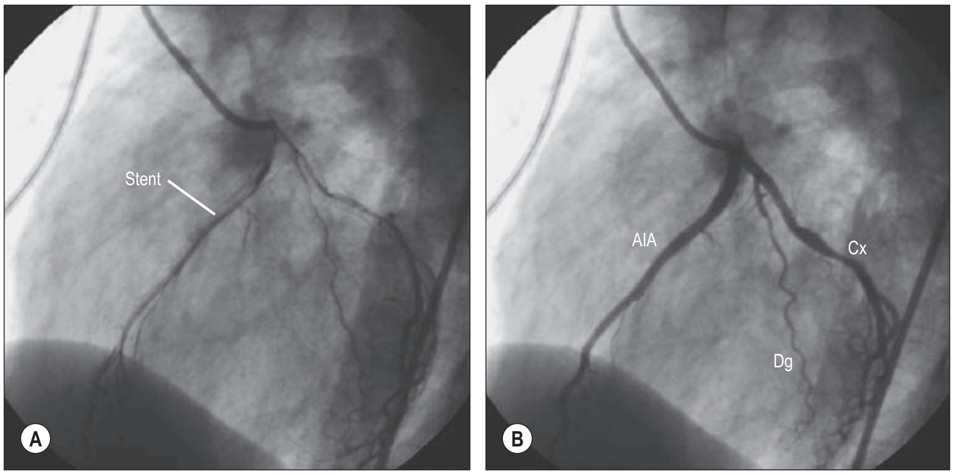

Fig. 57.57 A left coronary angiogram showing: **A**, A stent placement within the anterior interventricular artery; **B**, After stent placement (and once the contrast medium has filled the coronary arterial tree), the anterior interventricular artery shows no evidence of stenosis. Abbreviations: AIA, anterior interventricular artery; Dg, diagonal branch; Cx, circumflex artery. (Courtesy of Professor M Loukas.)

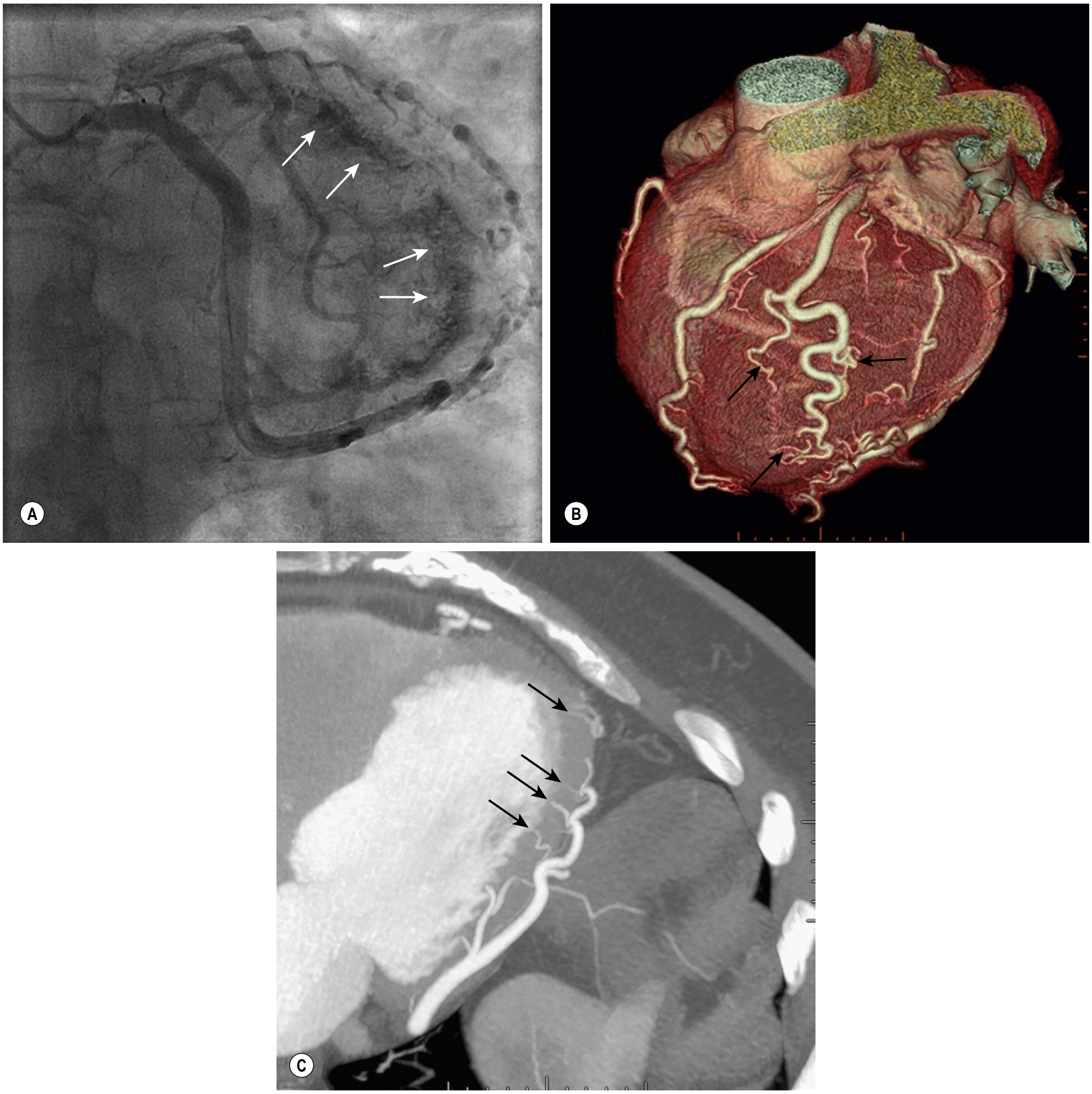

Fig. 57.58 A–C. A coronary artery (cameral) fistula. **A**, A left coronary angiogram showing a semicircular blush of contrast in the left ventricular chamber (white arrows) associated with the presence of fistulae. **B**, Volume-rendered CT coronary artery angiogram with semi-transparent cardiac chambers showing distal tortuous branches (black arrows) of a large left diagonal artery passing into the left ventricular chamber. **C**, A double oblique 15 mm maximum intensity projection image taken parallel to the distal part of the circumflex branch of the left coronary artery, showing fistulae (black arrows) connecting directly with the left ventricular chamber. (With permission from Mitchell GR, Morgan-Hughes G, Roobottom C 2010 Coronary arterial microfistulae: a CT coronary angiography perspective. J Cardiovasc Comput Tomog 4:279–80.)

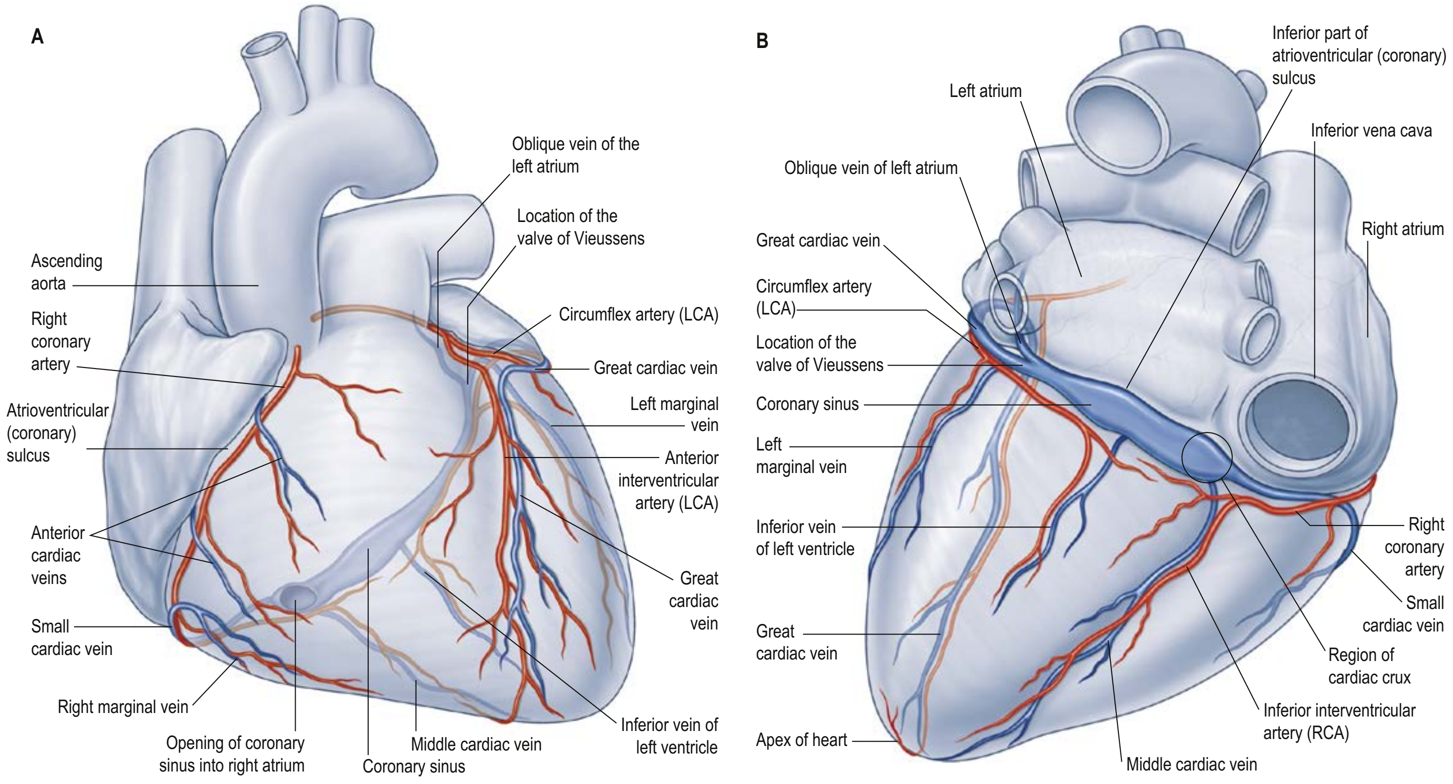
A
Oblique vein of the left atrium
Location of the valve of Vieussens
Ascending aorta
Right coronary artery
Circumflex artery (LCA)
Great cardiac vein
Left marginal vein
Atrioventricular (coronary) sulcus
Anterior interventricular artery (LCA)
Anterior cardiac veins
Great cardiac vein
Small cardiac vein
Right marginal vein
Opening of coronary sinus into right atrium
Middle cardiac vein
Coronary sinus
Inferior vein of left ventricle
B
Left atrium
Inferior part of atrioventricular (coronary) sulcus
Inferior vena cava
Oblique vein of left atrium
Right atrium
Great cardiac vein
Circumflex artery (LCA)
Location of the valve of Vieussens
Coronary sinus
Left marginal vein
Inferior vein of left ventricle
Right coronary artery
Small cardiac vein
Great cardiac vein
Region of cardiac crux
Inferior interventricular artery (RCA)
Apex of heart
Middle cardiac vein

Fig. 57.59 The cardiac veins. **A**, Anterior view. **B**, Posteroinferior view. Abbreviations: RCA, branch of right coronary artery; LCA, branch of left coronary artery. (Adapted with permission from Drake RL, Vogl AW, Mitchell A et al (eds) Gray's Atlas of Anatomy, 2nd ed. Elsevier, Churchill Livingstone. Copyright 2015.) (C, *continued online*)

at their openings. Isolated absence of the coronary sinus has been reported, with coronary venous drainage into the pulmonary trunk (Ogawa et al 2013).

Great cardiac vein The great cardiac vein begins at the cardiac apex, and ascends in the anterior interventricular sulcus to the atrioventricular sulcus, which it follows, passing to the left and posteriorly to enter the coronary sinus at its origin. It receives tributaries from the left atrium and both ventricles, including the large left marginal vein that ascends the left (obtuse) border of the heart. It usually courses superior to the arterial branches. The valve of Vieussens normally sits at the opening of the great cardiac vein at its junction with the oblique vein of the left atrium (this junction often representing the start of the coronary sinus); smaller diminutive valves may occur. The valve of Vieussens can impede the passage of a catheter into the great cardiac vein.

Small cardiac vein The small cardiac vein lies in the anterior part of the inferior atrioventricular sulcus between the right atrium and ventricle, receiving blood from the inferior parts of each chamber and opening into the atrial end of the coronary sinus. The right marginal vein passes right, along (or near) the inferior cardiac border. It sometimes joins the small cardiac vein in the atrioventricular sulcus, although typically opens directly into the right atrium.

Middle cardiac vein The middle cardiac vein begins at the cardiac apex and runs posteriorly in the inferior interventricular sulcus to end in the coronary sinus near its atrial termination. The vein is also described as meeting the great cardiac vein at the cardiac apex, and so forming, with the coronary sinus, a complete venous circle.

Inferior vein of the left ventricle The inferior vein of the left ventricle (previously named the posterior vein of the left ventricle) lies on the inferior surface of the left ventricle, a little to the left of the middle cardiac vein. It usually opens into the middle of the coronary sinus, but may sometimes empty into the great cardiac vein. Rarely, the inferior vein of the left ventricle is absent, in which case the left marginal vein drains most of the left ventricular wall.

Oblique vein of the left atrium The diminutive oblique vein of the left atrium descends obliquely on the posterior aspect of the left atrium to join the coronary sinus. Its junction with the great cardiac vein marks the start of the coronary sinus and, often, the location of the valve of Vieussens. It is continuous above with the ligament of the left superior vena cava.

Left marginal vein

The left (obtuse) marginal vein courses over or near the left border of the heart, draining much of the left ventricular myocardium. It runs superficial to the marginal branch of the left coronary artery and usually drains into the great cardiac vein, although it may sometimes drain directly into the coronary sinus.

Anterior cardiac veins

The anterior cardiac veins drain the anterior part of the right ventricle. Usually two or three, and up to five, they ascend in subepicardial tissue to cross the anterior part of the atrioventricular sulcus, passing deep or superficial to the right coronary artery. They drain into the right atrium, near the atrioventricular sulcus, separately or in variable combinations, or may open into a subendocardial collecting channel.

Right marginal vein

The right marginal vein courses along the inferior (acute) border of the heart, draining adjacent parts of the right ventricle, and usually opens separately into the right atrium, although it may join the anterior cardiac veins or, less often, the coronary sinus. It is often grouped with the small cardiac veins, but it is larger in calibre, being comparable to or even wider than the anterior cardiac veins.

Smallest cardiac veins

The smallest cardiac (venae cordis minimae, Thebesian) veins open directly into all heart chambers. Their numbers and size are highly variable: vessels up to 2 mm in diameter open into the right atrium and vessels as small as 0.5 mm in diameter open into the right ventricle, all with valveless openings. Numerous smallest cardiac veins have been identified in the right atrium and ventricle but they are rarely found in the left side. Four types of smallest cardiac veins have been described. Venoluminal veins drain directly into the cardiac chambers; venosinusoidal veins drain into subendocardial sinusoids (which, in turn, drain into the cardiac chambers); arterioluminal veins connect small arteries and arterioles directly with the cardiac chambers; and arteriosinusoidal veins connect thin arteries or arterioles with subendocardial sinusoidal spaces.

Cardiac venous anastomoses

Widespread anastomoses occur at all levels of the cardiac venous circulation, on a scale exceeding that of the arteries and amounting to a venous plexus. Not only are adjacent veins often connected, but connections also exist between tributaries of the coronary sinus and those of the anterior cardiac veins. Abundant anastomoses occur at

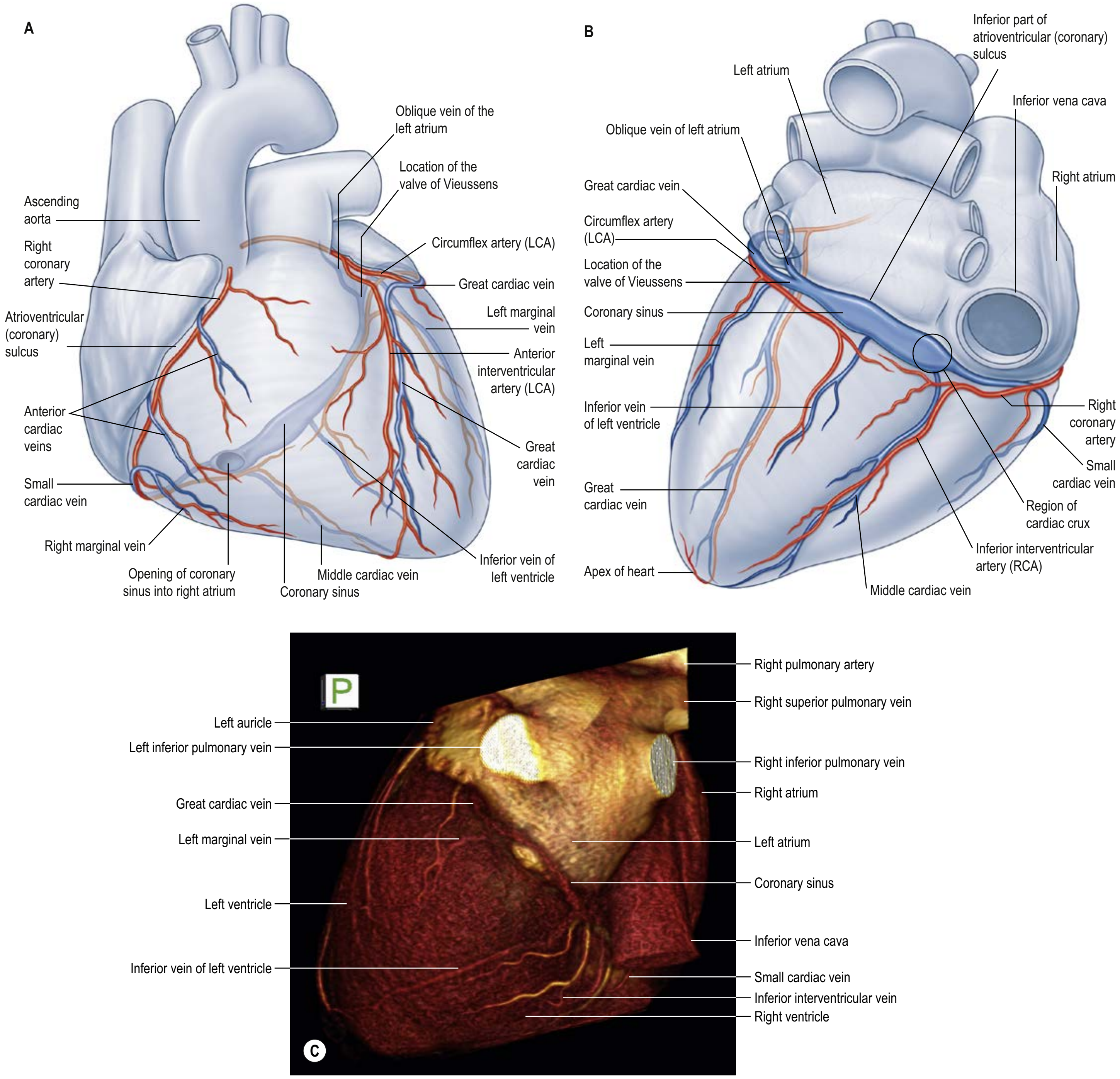
A
Oblique vein of the left atrium
Location of the valve of Vieussens
Ascending aorta
Right coronary artery
Circumflex artery (LCA)
Great cardiac vein
Left marginal vein
Atrioventricular (coronary) sulcus
Anterior interventricular artery (LCA)
Anterior cardiac veins
Great cardiac vein
Small cardiac vein
Right marginal vein
Opening of coronary sinus into right atrium
Coronary sinus
Middle cardiac vein
Inferior vein of left ventricle
B
Inferior part of atrioventricular (coronary) sulcus
Left atrium
Inferior vena cava
Oblique vein of left atrium
Great cardiac vein
Right atrium
Circumflex artery (LCA)
Location of the valve of Vieussens
Coronary sinus
Left marginal vein
Inferior vein of left ventricle
Right coronary artery
Small cardiac vein
Great cardiac vein
Region of cardiac crux
Inferior interventricular artery (RCA)
Apex of heart
Middle cardiac vein
P
Right pulmonary artery
Right superior pulmonary vein
Left auricle
Left inferior pulmonary vein
Right inferior pulmonary vein
Right atrium
Great cardiac vein
Left marginal vein
Left atrium
Coronary sinus
Left ventricle
Inferior vena cava
Inferior vein of left ventricle
Small cardiac vein
Inferior interventricular vein
Right ventricle
C

Fig. 57.59 The cardiac veins. **A**, Anterior view. **B**, Posteroinferior view. **C**, ECG-gated volume-rendered CT coronary angiogram in a posterior view of the heart showing the cardiac veins. Abbreviations: RCA, branch of right coronary artery; LCA, branch of left coronary artery. (A, B, Adapted with permission from Drake RL, Vogl AW, Mitchell A et al (eds) Gray's Atlas of Anatomy, 2nd ed. Elsevier, Churchill Livingstone. Copyright 2015.)

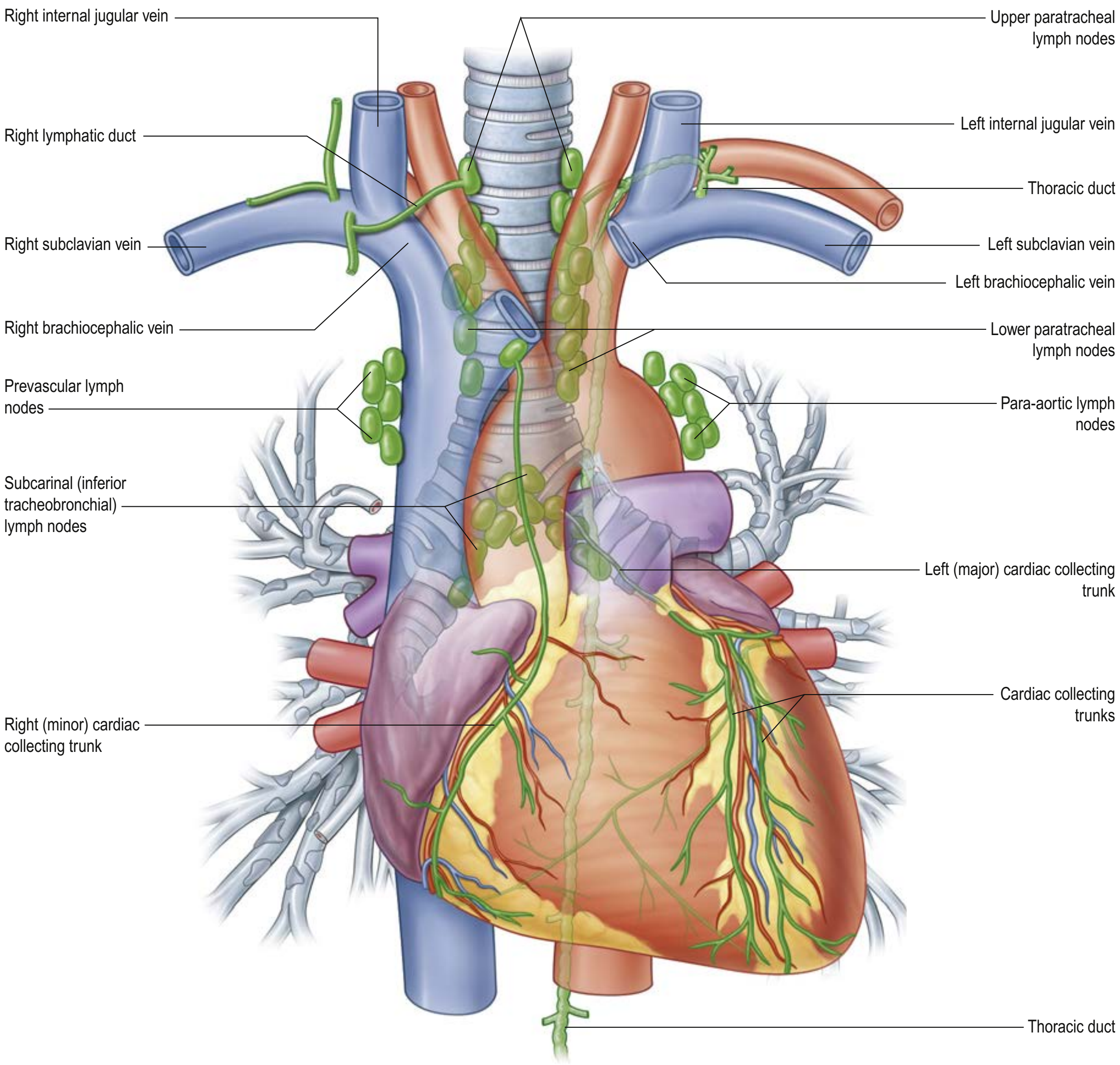
Right internal jugular vein
Upper paratracheal lymph nodes
Right lymphatic duct
Left internal jugular vein
Thoracic duct
Right subclavian vein
Left subclavian vein
Left brachiocephalic vein
Right brachiocephalic vein
Lower paratracheal lymph nodes
Prevascular lymph nodes
Para-aortic lymph nodes
Subcarinal (inferior tracheobronchial) lymph nodes
Left (major) cardiac collecting trunk
Cardiac collecting trunks
Right (minor) cardiac collecting trunk
Thoracic duct

Fig. 57.60 The cardiac lymphatic system. (Adapted from from Loukas M, Shah S, Bhusnurmath S et al 2013 A general outline of the cardiac lymphatic system. In: Karunamuni G (ed) The Cardiac Lymphatic System. Springer Nature.)

the cardiac apex and its anterior and inferior aspects. Like the coronary arteries, cardiac veins are connected with extracardiac vessels, particularly the vasa vasorum of the large vessels that are continuous with the heart.

Lymphatic drainage of the heart

Cardiac lymphatic vessels form subendocardial, myocardial and subepicardial plexuses that play essential roles in myocardial fluid and immune cell homeostasis (Brakenhielm and Alitalo 2019). The valved lymphatic subepicardial precollector channels display very few lymphatic smooth muscle cells: lymph propulsion from the heart is largely dependent upon the rate and force of cardiac contractions and the duration of diastole, and passes from the subendocardial to the subepicardial plexuses. Efferent vessels from the subepicardial plexuses form the left (major) and right (minor) cardiac collecting trunks: their number, arrangement, course and destination and the terminology used to described them vary (e.g. Loukas et al 2013; Ratajska et al 2014). Generally, two or three left-sided trunks ascend the anterior interventricular sulcus, receiving vessels from both ventricles. On reaching the atrioventricular sulcus, they are joined by a large vessel from the inferior surface of the left ventricle that first ascends in the inferior interventricular sulcus and then turns along the atrioventricular sulcus. The vessel formed by this union, the left cardiac collecting trunk, ascends between the pulmonary trunk and the left atrium and usually ends in a subcarinal (inferior tracheobronchial) node. The right cardiac collecting trunk receives efferents from the right atrium and the right border and inferior surface of the right ventricle. It ascends in the atrioventricular sulcus, near the right coronary artery, and then anterior to the ascending aorta, and ends in a brachiocephalic or prevascular node, usually on the left (**Fig. 57.60**) (Loukas et al 2011).

Innervation

Initiation of the cardiac cycle is myogenic, originating in the sinuatrial node. It is harmonized in rate, force and output by autonomic nerves that innervate the sinuatrial nodal tissue and its digitations, coronary vessels and the working atrial and ventricular musculature. During development the autonomic cardiac neurones originate from cells of the neural crest, neurotrophic factors from nearby vasculature assist in the development and maintenance of these neurones (Hasan 2013). All cardiac branches of the vagus nerves (parasympathetic) and sympathetic trunk (except the cardiac branch of the superior cervical sympathetic ganglion, which is entirely efferent) contain both afferent and efferent fibres.

Sympathetic cardiac innervation

The postganglionic sympathetic fibres that modulate efferent neural responses to the cardiac tissues and cardiac function originate in the cervicothoracic (stellate) ganglion, with contributions from the cervical, vertebral and upper thoracic ganglia. The ganglia receive preganglionic sympathetic input from neurones originating in the intermediolateral column (nucleus) of the upper thoracic spinal cord (Goldberger et al 2019). Efferent postganglionic fibres pass to the cardiac plexus as the cervical and thoracic cardiac nerves (Kawashima 2005), and then travel with the coronary vasculature towards the endocardium. When stimulated, they release noradrenaline (norepinephrine) that activates beta-adrenergic receptors in the cardiac tissue (Linz et al 2014). The resultant effect is an increase in conduction speed in the atrioventricular node as well as increased heart rate and force of cardiac muscular contractions. Sympathetic innervation increases heart rate and dilates the coronary arteries, whereas parasympathetic vagal innervation has the opposite effect.

Baroreceptors (mechanoreceptors) located in the adventitia of the aortic wall and carotid sinus detect intra-arterial pressure changes. Afferent

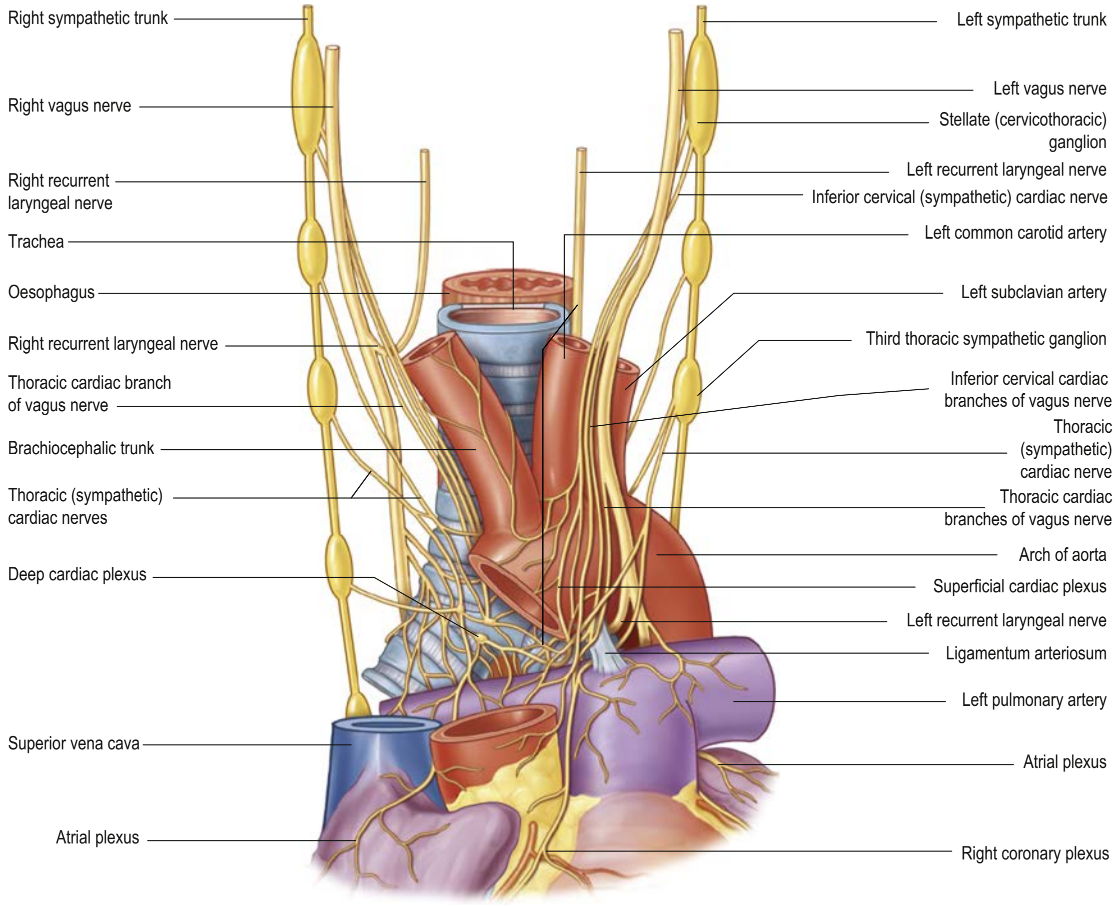
Right sympathetic trunk
Right vagus nerve
Right recurrent laryngeal nerve
Trachea
Oesophagus
Right recurrent laryngeal nerve
Thoracic cardiac branch of vagus nerve
Brachiocephalic trunk
Thoracic (sympathetic) cardiac nerves
Deep cardiac plexus
Superior vena cava
Atrial plexus
Left sympathetic trunk
Left vagus nerve
Stellate (cervicothoracic) ganglion
Left recurrent laryngeal nerve
Inferior cervical (sympathetic) cardiac nerve
Left common carotid artery
Left subclavian artery
Third thoracic sympathetic ganglion
Inferior cervical cardiac branches of vagus nerve
Thoracic (sympathetic) cardiac nerve
Thoracic cardiac branches of vagus nerve
Arch of aorta
Superficial cardiac plexus
Left recurrent laryngeal nerve
Ligamentum arteriosum
Left pulmonary artery
Atrial plexus
Right coronary plexus

Fig. 57.61 The cardiac plexus and its source from the cervical branches of the vagus nerves and sympathetic trunks. Also seen are its extensions to the pulmonary, atrial and coronary plexuses. Note the numerous junctions between sympathetic and parasympathetic (vagal) branches that form the plexus.

input passes to the nuclei of the solitary tract in the medulla oblongata (Ch. 28) which in turn regulates sympathetic and parasympathetic output to the heart and modulates heart rate and blood pressure (Goldberger et al 2019). Evidence suggests that in addition to 'flight and fight' responses the sympathetic nervous system maintains cardiac function in resting states via specific neuro-cardiac junctions, such as the interface between sympathetic motor neurones and cardiomyocytes (Zaglia and Mongillo 2017). The sympathetic nervous system is overly active in patients with heart failure and certain therapies targeting this pathway have reduced mortality rates. Imaging of cardiac sympathetic innervation is important to determine prognosis of these treatments (Kobayashi et al 2017). For further reading see Chapter 6 and Coote and Chauhan (2016) and Jamali et al (2017).

Parasympathetic cardiac innervation

Parasympathetic innervation mainly slows heart rate and constricts the coronary arteries. Its effects are mediated by the cardiac branches of the vagus nerve, which divide into superior and inferior branches before entering the heart through the cardiac plexus (Goldberger et al 2019). Parasympathetic innervation of the cardiac musculature is mediated by cholinergic muscarinic receptors that function dissimilarly to those of the sympathetic adrenergic beta receptors (Linz et al 2014). Experimental evidence suggests that groups of vagal preganglionic neurones originating in the nucleus ambiguus and dorsal vagal nucleus control the heart rate and atrioventricular conductance (via their innervation of nodal tissue) and modulate the contractility and excitability of the ventricular myocardium (Gourine et al 2016).

Preganglionic cardiac parasympathetic axons arising from either the dorsal vagal nucleus or the nucleus ambiguus run in cervical cardiac branches of the vagus nerve to synapse in the cardiac plexuses and atrial walls. Intrinsic cardiac neurones are limited to the atria and interatrial septum, and are most numerous in the subepicardial connective tissue near the sinuatrial and atrioventricular nodes. There is evidence that these intrinsic ganglia are not simple nicotinic relays but may act as sites for integration of extrinsic nervous inputs and form complex circuits for the local neuronal control of the heart and perhaps even local reflexes. Postganglionic neurones distributed within discrete fat pads on the atrial surface can mediate cardiac function. The ganglion cells in a fat pad adjacent to the epicardium of the right pulmonary veins selectively mediate negative chronotropic effects whereas ganglion cells in a fat pad at the junction between the inferior aspect of the right atrium and the inferior vena cava mediate the slowing of atrioventricular conduction (Sánchez-Quintana et al 2014).

Cardiac plexus

Nearing the heart, the autonomic nerves form a mixed cardiac plexus, usually described in terms of a superficial part inferior to the aortic arch, lying between the arch and the right pulmonary artery, and a deep part between the aortic arch and the tracheal bifurcation. The cardiac plexus is also described with reference to regional names for its coronary, pulmonary, atrial and aortic extensions (**Fig. 57.61**). Ganglion cells are largely confined to the atrial tissues, with a preponderance adjacent to the sinuatrial node, but some may also be found within the heart along the branches of the plexuses. Their axons are considered to be largely, if not exclusively, postganglionic parasympathetic. Cholinergic and adrenergic fibres, arising in or passing through the cardiac plexus, are distributed most profusely to the sinuatrial and atrioventricular nodes; the supply to the atrial and ventricular myocardium is much less dense. Adrenergic fibres supply the coronary arteries and cardiac veins. Rich plexuses of nerves containing cholinesterase, adrenergic transmitters and other peptides, e.g. neuropeptide Y, are found in the subendocardial regions of all chambers and within the valvular leaflets.

Superficial (ventral) part of the cardiac plexus The superficial part of the cardiac plexus lies inferior to the aortic arch and anterior to the right pulmonary artery. It is formed by the cardiac branch of the left superior cervical sympathetic ganglion and the inferior of the two cervical cardiac branches of the left vagus nerve. A small cardiac ganglion is usually present in this plexus immediately below the aortic arch, to the right of the ligamentum arteriosum. This part of the cardiac plexus has connections with the deep part, the right coronary plexus and the left anterior pulmonary plexus.

Deep (dorsal) part of the cardiac plexus The deep part of the cardiac plexus lies anterior to the tracheal bifurcation, superior to the point of division of the pulmonary trunk and posterior to the aortic arch. It is formed by the cardiac branches of the cervical and upper thoracic sympathetic ganglia, the vagus and recurrent laryngeal nerves. The only cardiac nerves that do not join it are those that join the superficial part of the plexus. The deep plexus consists of right and left halves, the right typically surrounding the brachiocephalic trunk, and the left surrounding the aortic arch. The more dorsal (deep) aspect is larger than its more ventral (superficial) aspect on both sides. Branches from the right half of the deep part of the cardiac plexus pass both anterior and posterior to the right pulmonary artery. Fibres passing anterior to the pulmonary artery are more numerous; they supply a few filaments to the right anterior pulmonary plexus before continuing onwards to form part of the right coronary plexus. Fibres passing posterior to the pulmonary artery supply a few filaments to the right atrium and then continue into the left coronary plexus. The left half of the deep part of the cardiac plexus is connected to the superficial part; it supplies filaments to the left atrium and left anterior pulmonary plexus, and forms much of the left coronary plexus.

Left coronary plexus The left coronary plexus is larger than the right and is formed mainly by the prolongation of the left half of the deep part of the cardiac plexus and a few fibres from the right half. It accompanies the left coronary artery to supply the left atrium and ventricle.

Right coronary plexus The right coronary plexus is formed from both superficial and deep parts of the cardiac plexus. It accompanies the right coronary artery to supply the right atrium and ventricle.

Atrial plexuses The atrial plexuses are derivatives of the right and left continuations of the cardiac plexus along the coronary arteries. Their fibres are distributed to the corresponding atria, overlapping those from the coronary plexuses.

Intrinsic cardiac nervous system

In addition to the peripheral autonomic innervation, the heart has an intrinsic nervous system, the ganglionic plexus, which regulates heart rate, atrial and ventricular refractoriness and contractility, and coronary blood flow. Ganglia of the plexus receive an extrinsic innervation and interact with the myocardium through various neurotransmitters. The intrinsic cardiac nervous system is a complex of distinct subplexuses located on the superior and posterior surfaces of the right and left atria, and the inferior and lateral aspects of the posterior surface of the left atrium and left pulmonary vein (Sánchez-Quintana et al 2014). It has been implicated in the pathophysiology of several conditions, including arrhythmias, heart failure and myocardial infarction (Wake and Brack 2016). Atrial fibrillation is initiated and maintained by the autonomic nervous system and may be corrected by transection of the parasympathetic and sympathetic afferent and efferent fibres in the ganglionated plexus in the epicardial fat pads through catheter ablation (Hanna and Shivkumar 2018).

Bonus e-book content

Fig. 57.2 The normal appearance of the pericardium on a contrast enhanced CT of a horizontal long axis view of the heart.

Fig. 57.3 Normal pericardium. A T1-weighted four chamber view of the heart.

Fig. 57.4 C–D, Corresponding three-dimensional reconstructions from multislice computed tomography (CT) scanning. **E**, Basal (posterior) view of the heart and great vessels. **F,** CT coronary angiogram of the heart and great vessel, anterior view.

Fig. 57.5 Acute cardiac tamponade.

Fig. 57.6 Subxiphoid pericardiocentesis, and cardiac ultrasound demonstrating a large pericardial effusion consistent with cardiac tamponade.

Fig. 57.7 The X-ray and MRI appearances of a pericardial cyst.

Fig. 57.8 Congenital absence of the pericardium.

Fig. 57.12 The heart, great vessels and the lungs *in situ.*

Fig. 57.13 The interior of the right atrium and ventricle.

Fig. 57.15 An unusually large valve of the inferior vena cava.

Fig. 57.16 Chiari's network.

Fig. 57.17 B, A coronary angiogram showing the ventricles from a superolateral perspective.

Fig. 57.21 B, A coronary angiogram viewing the base of the ventricles from posteriorly.

Fig. 57.24 The anterior (sternocostal) surface of the heart.

Fig. 57.25 Sagittal sections through a cadaveric heart showing the left side of the left atrium.

Fig. 57.27 B, A coronary angiogram cross-section view of the ventricles from the superior aspect.

Fig. 57.31 A histological section through an aortic sinus.

Fig. 57.32 Sectional cardiac anatomy shown by transthoracic echocardiography and CT.

Fig. 57.33 Myocyte alignment in a cadaveric porcine heart.

Fig. 57.34 Ultrasound imaging of fetal cardiac defects.

Fig. 57.35 Cardiac magnetic resonance angiography of a normal heart and a heart with transposition of the great vessels (arteries).

Fig. 57.38 Measurements of the width, height and relative position of the sinuatrial node.

Fig. 57.39 Histological sections of the sinuatrial nodal body.

Fig. 57.40 Histological sections showing the features of the atrioventricular node and the penetrating atrioventricular bundle.

Fig. 57.43 The right coronary sinus, revealing the openings of both a right coronary artery and a right conal artery.

Fig. 57.44 A variation of the arterial ring of Vieussens.

Fig. 57.46–57.49 CT anatomy of the right and/or left coronary arteries and their branches.

Fig. 57.50–57.51 Volume-rendered CT images of the anterior interventricular and circumflex branches of the left coronary arteries.

Fig. 57.53 A myocardial bridge covering a large part of the anterior interventricular artery.

Fig. 57.54 A left coronary angiogram showing a tortuous variant branch supplying the inferior lobe of the left lung.

Fig. 57.55–57.56 Right and left, respectively, coronary angiograms.

Fig. 57.57 A left coronary angiogram showing the placement of a stent within the anterior interventricular artery and the vessel following stent placement.

Fig. 57.58 A coronary artery (cameral) fistula.

Fig. 57.59 C, CT coronary angiogram in a posterior view of the heart showing the cardiac veins.

Table 57.1 Patterns of cardiac collateral arteries.

Key references

Anderson RH, Loukas M 2009 The importance of attitudinally appropriate description of cardiac anatomy. Clin Anat 22:47–51.

Anderson RH, Spicer DE, Hlavacek AM et al 2013 Wilcox's Surgical Anatomy of the Heart, 4th ed. Cambridge: Cambridge University Press.

Loukas M, Abel N, Tubbs RS et al 2011 The cardiac lymphatic system. Clin Anat 24:684–91.

Loukas M, Bilinsky E, Bilinsky S et al 2014a The anatomy of the aortic root. Clin Anat 27:748–56.

Muresian H 2016 Coronary arteries. In Tubbs RS, Shoja MM, Loukas M Bergman's comprehensive encyclopedia of human anatomic variation, 2nd ed. Hoboken: Wiley–Blackwell; Ch. 50, pp. 530–68.

Sánchez-Quintana D, Pizarro G, López-Mínguez JR et al 2013 Standardized review of atrial anatomy for cardiac electrophysiologists. J Cardiovasc Transl Res 6:124–44.

References

Anderson RH, Loukas M 2009 The importance of attitudinally appropriate description of cardiac anatomy. Clin Anat 22:47–51.

Anderson RH, Spicer DE, Hlavacek AM et al 2013 Wilcox's Surgical Anatomy of the Heart, 4th ed. Cambridge: Cambridge University Press.

Anderson RH, Agger P, Stephenson RS 2018 The incorrect notion of the 'unique myocardial band'. Eur J Cardiothorac Surg 54:612.

Azancot A, Caudell TP, Allen HD et al 1983 Analysis of ventricular shape by echocardiography in normal fetuses, newborns, and infants. Circulation 68:1201–11.

Brakenhielm E, Alitalo K 2019 Cardiac lymphatics in health and disease. Nature Rev Cardiol 16:56–68.

Cabrera J-A, Porta-Sanchex A, Tung R et al 2020 Tracking down the anatomy of the left bundle to optimise left bundle branch pacing. JACC: Case Reports 2:750–755.

Clemente A, Del Borrello M, Greco P et al 2010 Anomalous origin of the coronary arteries in children: diagnostic role of three-dimensional coronary MR angiography. Clin Imaging 34:337–43.

Coote JH, Chauhan RA 2016 The sympathetic innervation of the heart: important news insights. Auton Neurosci 199:17–23.

de Jonge LL, van Osch-Gevers L, Willemsen SP et al 2011 Growth, obesity, and cardiac structures in early childhood: the Generation R study. Hypertension 57:934–40.

Goldberger JJ, Arora R, Buckley U et al 2019 Autonomic nervous system dysfunction: JACC Focus Seminar. J Am Coll Cardiol 2019 73:1189–206.

Gourine AV, Machhada A, Trapp S et al 2016 Cardiac vagal preganglionic neurones: an update. Auton Neurosci 199:24–8.

Gunnal SA, Wabale RN, Farooqui MS 2015. Morphological study of chordae tendinae in human cadaveric hearts. Heart Views 16:1–12.

Hanna P, Shivkumar K 2018. Targeting the cardiac ganglionated plexi for atrial fibrillation: modulate or destroy? JACC Clin Electrophysiol 4:1359–61.

Hasan W 2013 Autonomic cardiac innervation: development and adult plasticity. Organogenesis 9:176–93.

Hassani C, Saremi F 2017 Comprehensive cross-sectional imaging of the pulmonary veins. Radiographics 37:1928–54.

Hołda MK, Koziej M 2018 Left-sided atrial septal pouch as a risk factor of cryptogenic stroke: a systematic review and meta-analysis. Cerebrovasc Dis 46:223–9.

Hutchison SJ 2009 Pericardial diseases: clinical diagnostic imaging atlas. Philadelphia: Saunders; pp. 8–15.

Jamali HK, Waqar F, Gerson MC 2017 Cardiac autonomic innervation. J Nucl Cardiol 24:1558–70.

Kaiser T, Kellenberger CJ, Albisetti M et al 2008 Normal values for aortic diameters in children and adolescents – assessment in vivo by contrast-enhanced CMR-angiography. J Cardiovasc Magn Reson 10:56.

Karagol BS, Orun UA, Zenciroglu A et al 2012 The diameter of coronary arteries in healthy newborns at birth, 1 and 6 months of ages. J Matern Fetal Neonatal Med 25:2729–34.

Kastellanos S, Aznaouridis K, Vlachopoulos C et al 2018. Overview of coronary artery variants, aberrations and anomalies. World J Cardiol 10:127–40.

Kawashima T 2005 The autonomic nervous system of the human heart with special reference to its origin, course, and peripheral distribution. Anat Embryol 209:425–438.

Kobayashi R, Chen X, Werner RA et al 2017 New horizons in cardiac innervation imaging: introduction of novel 18F-labeled PET tracers. Eur J Nucl Med Mol Imaging 44:2302–9.

Kortelainen ML 1997 Adiposity, cardiac size and precursors of coronary atherosclerosis in 5 to 15-year-old children: a retrospective study of 210 violent deaths. Int J Obes Relat Metab Disord 21:691–7.

Linz D, Ukena C, Mahfoud F et al 2014 Atrial autonomic innervation: a target for interventional antiarrhythmic therapy? J Am Coll Cardiol 63:215–24.

Loukas M, Tubbs RS, Bright JL et al 2007 The anatomy of the tendon of the infundibulum revisited. Folia Morphol (Warsz) 66:33–8.

Loukas M, Groat C, Khangura R et al 2009 The normal and abnormal anatomy of the coronary arteries. Clin Anat 22:114–28.

Loukas M, Abel N, Tubbs RS et al 2011 The cardiac lymphatic system. Clin Anat 24:684–91.

Loukas M, Shah S, Bhusnurmath S et al 2013 A general outline of the cardiac lymphatic system. In: The Cardiac Lymphatic System: An Overview. (Karunamuni G ed). Chapter 1: 3–16. Springer New York.

Loukas M, Bilinsky E, Bilinsky S et al 2014a The anatomy of the aortic root. Clin Anat 27:748–56.

Loukas M, Patel S, Cesmebasi A et al 2014b The clinical anatomy of the conal artery. Clin Anat 29:371–9.

Lunkenheimer PP, Niederer P, Stephenson RS et al 2018 What is the clinical significance of the ventricular mural antagonism? Eur J Cardiothoracic Surg 53:714–23.

Mani BC, Pavri BB 2014 Dual atrioventricular nodal pathways physiology: a review of relevant anatomy, electrophysiology, and electrocardiographic manifestations. Indian Pacing Electrophysiol J 14:12–25.

Molenaar P, Anderson R, Sharma V et al 2011 Computer three-dimensional anatomical reconstruction of the human sinus node and a novel paranodal area. Anat Rec (Hoboken) 294:970–9.

Mollova M, Bersell K, Walsh S et al 2013 Cardiomyocyte proliferation contributes to heart growth in young humans. Proc Nat Acad Sci U S A 110:1446–51.

Monfredi O, Dobrzynski H, Mondal T et al 2010 The anatomy and physiology of the sinoatrial node – a contemporary review. Pacing Clin Electrophysiol 33:1392–406.

Mori S, Tretter JT, Spicer DE et al 2019 What is the real cardiac anatomy? Clin Anat 32:288–309.

Muresian H 2016 Coronary arteries. In Tubbs RS, Shoja MM, Loukas M Bergman's comprehensive encyclopedia of human anatomic variation, 2nd ed. Hoboken: Wiley–Blackwell; Ch. 50, pp. 530–68.

Nidorf SM, Picard MH, Triulzi MO et al 1992 New perspectives in the assessment of cardiac chamber dimensions during development and adulthood. J Am Coll Cardiol 19:983–8.

Ogawa K, Hishitani T, Hoshino K 2013 Absence of the coronary sinus with coronary venous drainage into the main pulmonary artery. Cardiol Young 23:759–62.

Ozdemir O, Hizli S, Abaci A et al 2010 Echocardiographic measurement of epicardial adipose tissue in obese children. Pediatr Cardiol 31:853–60.

Pesonen E, Hirvonen J, Karkola K et al 1991 Dimensions of the coronary arteries in children. Ann Med 23:85–8.

Poutanen T, Tikanoja T, Sairanen H et al 2006 Normal mitral and aortic valve areas assessed by three- and two-dimensional echocardiography in 168 children and young adults. Pediatr Cardiol 27:217–25.

Ratajska A, Gula G, Flaht-Zabost A et al 2014 Comparative and developmental anatomy of cardiac lymphatics. Sci World J 2014: https://doi.org/10.1155/2014/183170.

Rodriguez ER, Tan CD 2017a Structure and anatomy of the human pericardium. Prog Cardiovasc Dis 59:327–40.

Rodriguez ER, Tan CD 2017b Structure of the human pericardium and responses to pathologic processes. Am Coll Cardiol 59(4):327–40.

Sánchez-Quintana D, Pizarro G, López-Mínguez JR et al 2013 Standardized review of atrial anatomy for cardiac electrophysiologists. J Cardiovasc Transl Res 6:124–44.

Sánchez-Quintana D, López-Mínguez JR, Macías Y et al 2014 Left atrial anatomy relevant to cather ablation. Cardiol Res Pract 2014:289720.

Saremi F, Sánchez-Quintana D, Mori S et al 2017 Fibrous skeleton of the heart: anatomic overview and evaluation of pathologic condition with CT and MR imaging. Radiographics 37:1330–51.

Spicer DE, Anderson RH 2013 Methodological review of ventricular anatomy – the basis for understanding congenital cardiac malformations. J Cardiovasc Transl Res 6:145–54.

Uysal F, Bostan OM, Semizel E et al 2014 Congenital anomalies of coronary arteries in children: the evaluation of 22 patients. Pediat Cardiol 35:778–84.

Vuorio T, Tirronen A, Yla-Herttuala S 2016 Cardiac lymphatics – a new avenue for therapeutics? Trends Endocrinol Metabol 28:2327–37.

Vogiatzidis K, Zarogiannis SG, Aidonidis I et al 2015 Physiology of pericardial fluid production and drainage. Front Physiol 6:62.

Wake E, Brack K 2016 Characterization of the intrinsic cardiac nervous system. Auton Neurosci 199:3–16.

Zaglia T, Mongillo M 2017 Cardiac sympathetic innervation, from a different point of (re)view. J Physiol 595:3919–30.

CHAPTER
58

Great vessels

MAJOR BLOOD VESSELS

The major blood vessels of the thorax include the pulmonary trunk, the thoracic aorta and its branches, and the superior and inferior venae cavae and their tributaries (Fig. 58.1).

Arteries

Pulmonary trunk

The pulmonary trunk conveys deoxygenated blood from the right ventricle to the lungs (see Figs 57.4, 57.10). About 5 cm in length and 3 cm in diameter, it is the most anterior of the cardiac vessels and arises from the pulmonary anulus surrounding the subpulmonary conus arteriosus (infundibulum) at the base of the right ventricle, superior and to the left of the supraventricular crest. The pulmonary trunk inclines posterosuperiorly and divides into right and left pulmonary arteries, of almost equal size, at the level of the body of the sixth thoracic vertebra (range, bodies of the fourth to the eighth thoracic vertebrae), 2–3 cm inferior to the sternal plane (horizontal plane through the sternal angle) and inferior to the aortic arch to the left of the midline (see Tables 52.1–52.2). The bifurcation of the pulmonary trunk commonly lies anteroinferior and to the left of the tracheal bifurcation and the associated subcarinal (inferior tracheobronchial) lymph nodes and deep cardiac plexus. In the fetus, at the level of the tracheal bifurcation, the left pulmonary artery is connected to the aortic arch by the ductus arteriosus, the obliterated remnant of which forms the ligamentum arteriosum in the adult (Ch. 13).

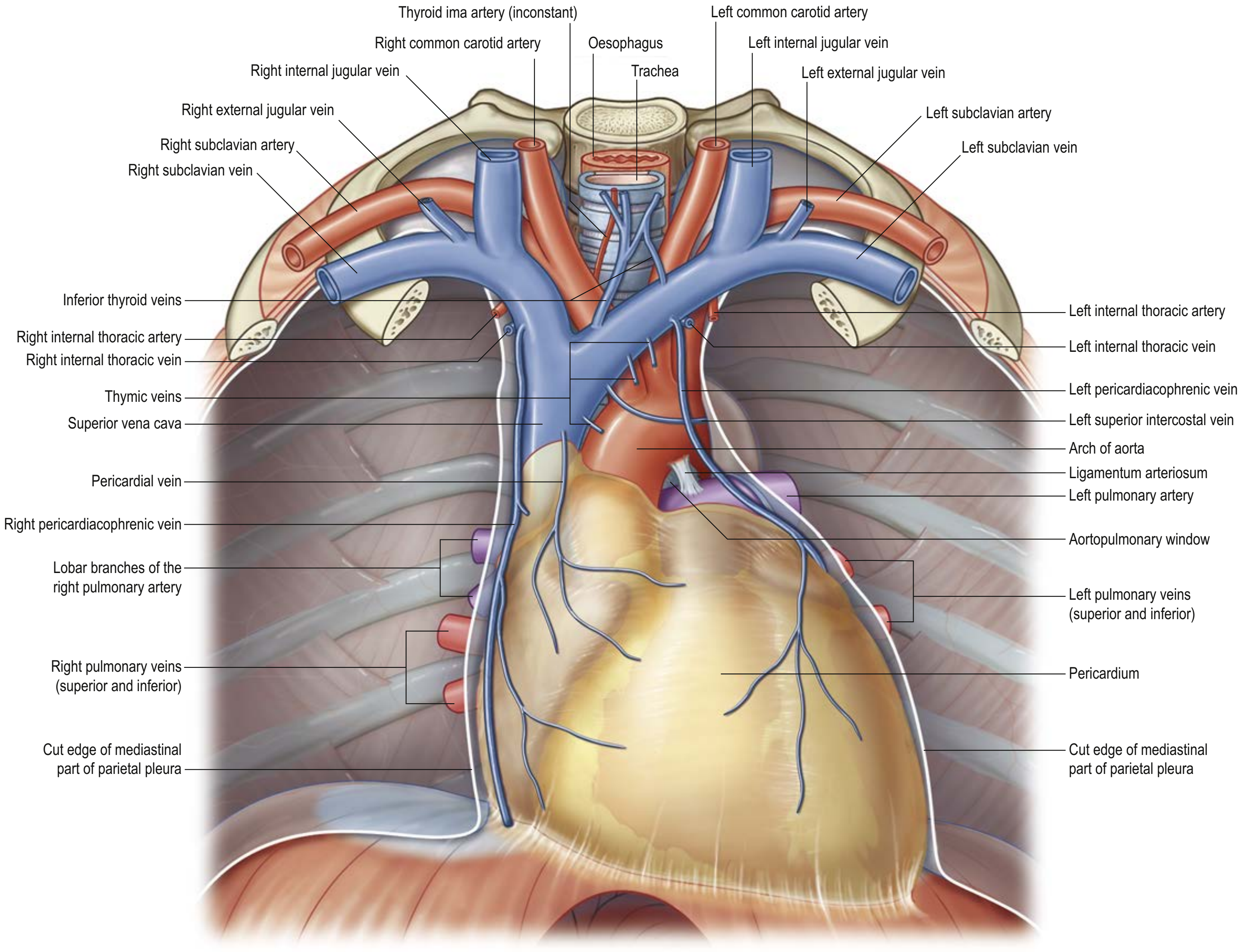
Thyroid ima artery (inconstant)
Left common carotid artery
Right common carotid artery
Oesophagus
Left internal jugular vein
Right internal jugular vein
Trachea
Left external jugular vein
Right external jugular vein
Left subclavian artery
Right subclavian artery
Left subclavian vein
Right subclavian vein
Inferior thyroid veins
Right internal thoracic artery
Right internal thoracic vein
Thymic veins
Superior vena cava
Pericardial vein
Right pericardiacophrenic vein
Lobar branches of the right pulmonary artery
Right pulmonary veins (superior and inferior)
Cut edge of mediastinal part of parietal pleura
Left internal thoracic artery
Left internal thoracic vein
Left pericardiacophrenic vein
Left superior intercostal vein
Arch of aorta
Ligamentum arteriosum
Left pulmonary artery
Aortopulmonary window
Left pulmonary veins (superior and inferior)
Pericardium
Cut edge of mediastinal part of parietal pleura

Fig. 58.1 The arteries and veins (great vessels) of the mediastinum and their branches/tributaries. (Adapted from Drake RL, Vogl AW, Mitchell A et al Gray's Atlas of Anatomy, 2nd ed. Elsevier, Churchill Livingstone. Copyright 2015.)

Relations The pulmonary trunk is located entirely within the pericardium, enclosed with the ascending aorta in a common sheath of the visceral layer of serous pericardium (see Figs 57.1, 58.1). The fibrous pericardium gradually blends with and disappears within the adventitia of the pulmonary arteries. Anteriorly, it is separated from the sternal end of the left second intercostal space, and/or the third costal cartilage, by the pericardium, pleura, left lung and the superior part of transversus thoracis. Posterior relations of the proximal part near to its origin are the ascending aorta and left coronary artery, and superiorly, the left atrium. Moving superiorly, the ascending aorta spirals around the pulmonary trunk and comes to lie to the right of its more superior part. The atrial auricles and left and right coronary arteries lie on each side of its origin. The superficial cardiac plexus lies between the branching of the pulmonary trunk and the aortic arch (see Fig. 57.61). The tracheal bifurcation and subcarinal lymph nodes are superior and to the right (see Fig. 52.7).

Variations and congenital anomalies The pulmonary trunk is a relatively constant structure and there are minimal variations in healthy individuals. Congenital anomalies include pulmonary atresia and truncus arteriosus (common truncus).

Right and left pulmonary arteries

The pulmonary arteries are described in Chapter 54.

Thoracic aorta

Ascending aorta

The ascending aorta is typically about 5 cm in length. It originates at the base of the left ventricle, commonly level with the inferior border of the third left costal cartilage, and initially ascends whilst curving anteriorly and to the right. It passes from posterior to the left half of the sternum to become the aortic arch posterior to the right half of the inferior part of the manubrium of the sternum, or the manubriosternal joint (level with the right second costal cartilage), or the superior part of the right side of the sternal body (level with the right second intercostal space). In children, the diameter of the thoracic aorta correlates most closely with body surface area (Kervancioglu et al 2006, Kaiser et al 2008).

Relations The ascending aorta lies within the fibrous pericardium, enclosed in a tube of visceral serous pericardium together with the pulmonary trunk (see Figs 58.1, 57.1, 57.4). The conus arteriosus of the right ventricle, initial segment of the pulmonary trunk and right auricle are anterior to its lower part. Superiorly, it is separated from the sternum by the pericardium, the pleura and the anterior border of the right lung, loose areolar tissue and the thymus or its remnants. The left atrium, right pulmonary artery and right main bronchus are posterior. The superior vena cava (also partly posterior) and the right atrium are to the right. The left atrium and, more superiorly, the pulmonary trunk are to the left. At least two para-aortic bodies (aortopulmonary paraganglia) lie between the ascending aorta and the pulmonary trunk. Relative to the ascending aorta, the inferior para-aortic body is located on its anterior surface near to the heart, and the middle para-aortic body is located on its right side.

The aortopulmonary window is a space between the pulmonary trunk and aortic arch, bordered by the ascending aorta anteriorly, the descending aorta posteriorly, the mediastinal part of the parietal pleura laterally and the left main bronchus medially (Deutsch and Savides 2005) (see Fig. 58.1; **Fig. 58.4**). It contains lymph nodes, fatty tissue, the ligamentum arteriosum, the superficial cardiac plexus, cardiac nerves and the left recurrent laryngeal nerve.

Aortic arch

The aortic arch continues from the ascending aorta and lies mainly within the superior mediastinum (see Fig. 57.4A–C). Its origin, slightly to the right of the midline, is level typically with either the right first intercostal space, the second costal cartilage or the second intercostal space. The arch initially ascends obliquely and posteriorly to the left over the anterior surface of the trachea, and then posteriorly across its left side. It ascends superiorly to the midlevel of the manubrium of the sternum, and curves around the hilum of the left lung. Posteriorly it descends to the left of the body of the fourth thoracic vertebra: at around the level of the sternal plane, posterior to the second left sternocostal joint, it continues as the descending thoracic aorta. The concavity of the aortic arch may lie superior, on or inferior to the sternal plane: most commonly it is inferior to the plane (see Fig. 52.7, Tables 52.1–52.2).

The shadow of the aortic arch is easily identified in frontal chest radiographs, where it is seen as a rounded leftward projection (aortic knuckle) to the left of the manubrium of the sternum (see Fig. 56.17). The shadow of the adjacent left superior intercostal vein crossing its left side, from posterior to anterior, may form an additional small rounded shadow termed the 'aortic nipple'. The aortic arch is best visualized in left anterior oblique views on angiography and with equivalent computed tomography (CT) reconstruction planes, when the pulmonary trunk and its left branch will be seen inferiorly occupying the concavity of the arch.

The concavity of the aortic arch is the upper curved limit through which structures gain access to, or leave, the hilum of the left lung. The diameter of the aortic arch initially matches that of the ascending aorta but is significantly reduced distal to the origin of the three large branches to the head, neck and upper limbs. The aortic isthmus, a small stricture at the border of the aortic arch with the descending thoracic aorta, may be followed by a dilation; in the fetus, the isthmus lies between the origin of the left subclavian artery and the opening of the ductus arteriosus (Ch. 13).

Relations The left mediastinal part of the parietal pleura is located anterior and to the left of the aortic arch. Deep to the pleura, the arch is crossed, in anteroposterior order, by the left phrenic nerve, left lower cervical cardiac branch of the vagus nerve, left superior cervical cardiac branch(es) of the sympathetic trunk, the left thoracic cardiac branches of the vagus nerve, and the left vagus nerve (see Figs 56.6, 56.7B, 57.61). As the latter crosses the aortic arch, its recurrent laryngeal branch hooks inferior to the vessel, to the left posterior aspect of the ligamentum arteriosum, and then ascends on the right of the aortic arch. The left superior intercostal vein ascends obliquely anteriorly on the arch, anterolateral to the left vagus nerve and posteromedial to the left phrenic nerve and pericardiacophrenic vessels. The left lung and pleura separate all these structures from the thoracic wall. Posterior and to the right are the trachea and the deep cardiac plexus, the left recurrent laryngeal nerve, the oesophagus, thoracic duct and vertebral column. Superiorly, the brachiocephalic trunk, left common carotid and left subclavian arteries arise from its convexity (from right to left), and are crossed anteriorly near their origins by the left brachiocephalic vein. The branching of the pulmonary trunk (into pulmonary arteries), left main bronchus, ligamentum arteriosum, superficial cardiac plexus and the left recurrent laryngeal nerve are typically inferior.

Pneumomediastinum and aortic nipple

Available with the *Gray's Anatomy* e-book

Variations of the aortic arch The most superior level of the aortic arch is typically about 2.5 cm inferior to the jugular notch, although this may vary. It is located more superiorly, closer to the jugular notch, in infants and again in senescence when it is a result of vascular ectasia.

In a right-sided aortic arch, the aorta curves over the hilum of the right lung and descends to the right of the vertebral column: this is usually associated with transposition of the thoraco-abdominal viscera (situs inversus) (Akgun et al 2016). Less often, after arching over the hilum of the right lung, the descending thoracic aorta may pass posterior to the oesophagus to gain a left-sided position, and this is not accompanied by visceral transposition. The presence of a right-sided aortic arch is of relevance when planning the repair of oesophageal atresia in neonates.

The aorta may divide into ascending and descending trunks, the former dividing into three branches to supply the head and upper limbs. Alternatively, it may divide near its origin, producing a double aortic arch; the two branches soon reunite and the oesophagus and trachea usually pass through the interval between them. Entrapment of the oesophagus and/or trachea by a double aortic arch, or by aberrant great vessels (arteries), is referred to as a vascular ring.

Branches and variations From right to left, the brachiocephalic trunk, left common carotid and left subclavian arteries arise from the convex aspect of the aortic arch (see Figs 58.1, 57.4,). These vessels may branch from the beginning of the aortic arch or the superior part of the ascending aorta. The distance between their origins varies, the most frequent being apposition of the left common carotid artery to the brachiocephalic trunk. Multiple variants of their branching pattern have been observed; other branches may arise from the aortic arch, including the inferior thyroid, thyroidea ima, thymic, left coronary and bronchial arteries (Akgun et al 2016). The left vertebral artery may arise between the left common carotid and the left subclavian arteries (see Fig. 52.5B).

The coronary arteries usually originate from the aortic sinuses, but occasionally may arise from ectopic locations. Most commonly, an ectopic left coronary artery arises from the pulmonary trunk or one of its branches (Anomalous Left Coronary Artery from the Pulmonary Artery (ALCAPA) or Bland–White–Garland syndrome) (Fig. 58.2; Commentary 7.2). This potentially fatal condition requires urgent surgical correction because the myocardium is supplied with deoxygenated pulmonary blood instead of systemic blood (Loukas et al 2009). Infantile symptoms include pallor, fatigue, irritability, weak cry, cough, dyspnoea, and signs of ischaemia and cardiac failure precipitated during or after feeding, or during defecation or crying. The electrocardiogram may reveal deep narrow Q waves, left ventricular hypertrophy and left axis deviation. Radiologically, cardiomegaly is present with left ventricular and left atrial enlargement. Colour flow imaging can identify the anomalous origin of the left coronary artery. The pulmonary trunk may also give rise to the right coronary artery, the anterior interventricular branch of the left coronary artery, or even both coronary arteries. Typically, there is an extensive development of collateral vessels in the heart (Fig. 58.3).

Pulmonary atresia is caused by a complete obstruction of pulmonary outflow and may be due to an absence or defect of the pulmonary valvular leaflets. It is associated with a blind-ending pulmonary trunk that causes right ventricular hypoplasia. Reduced flow may render the pulmonary trunk atretic, small or even normal in size, making diagnosis challenging. A diminished pulmonary flow is supplied through a patent ductus arteriosus (Smith and McKay 2004), and a concomitant ventricular septal defect may permit outflow from the right ventricle. Surgical repair is necessary to allow adequate oxygenation of blood throughout the body.

In truncus arteriosus (common truncus), a single common arterial trunk exits the heart and subsequently divides into the pulmonary trunk and the ascending aorta. Early neonatal life is possible because there is usually a coexisting ventricular septal defect; expedited surgical repair is necessary to avoid congestive heart failure, failure to thrive and death.

Pneumomediastinum is an overarching term that describes the presence of air in the mediastinum. It may arise from a wide range of pathological conditions or physiological states, e.g. penetrating trauma, ruptured major airways or oesophagus, hyperventilation or distressed ventilation such as acute asthma, periparturition or diabetic ketoacidosis.

The aortic nipple is the radiographic term used to describe a lateral nipple-like projection located on the aortic knuckle. It corresponds to the end-on appearance of the left superior intercostal vein coursing anteriorly and is not observed in all individuals. It may be mistaken radiologically for lymphadenopathy or an intrapulmonary nodule or neoplasm. Despite their relative independence, the aortic nipple is defined by new contours in cases of pneumomediastinum, taking on an 'inverted aortic nipple' appearance (Fig. 58.5). In this position, the inverted aortic nipple

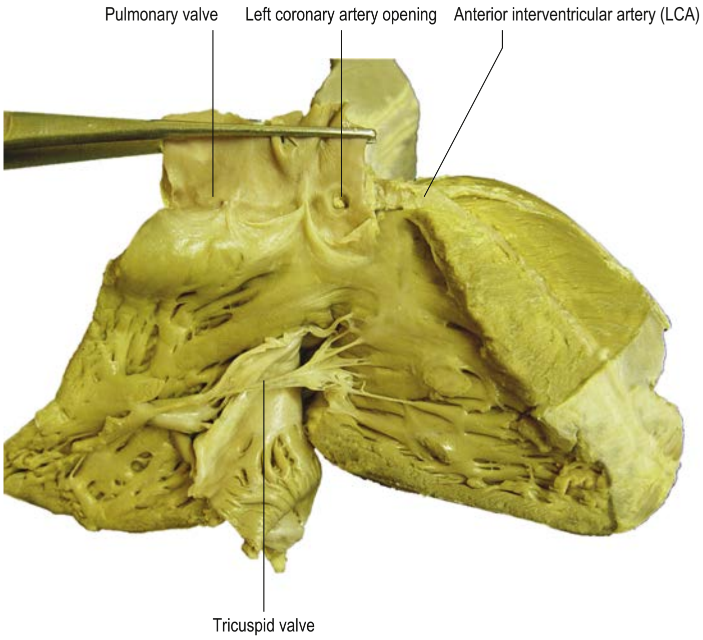
Pulmonary valve
Left coronary artery opening
Anterior interventricular artery (LCA)
Tricuspid valve

Fig. 58.2 A case of a left coronary artery arising from the pulmonary trunk (Bland–White–Garland syndrome). (Courtesy of Professor M Loukas. With permission from Loukas M, Groat C, Khangura R et al 2009 The normal and abnormal anatomy of the coronary arteries. Clin Anat 22:114–28.)

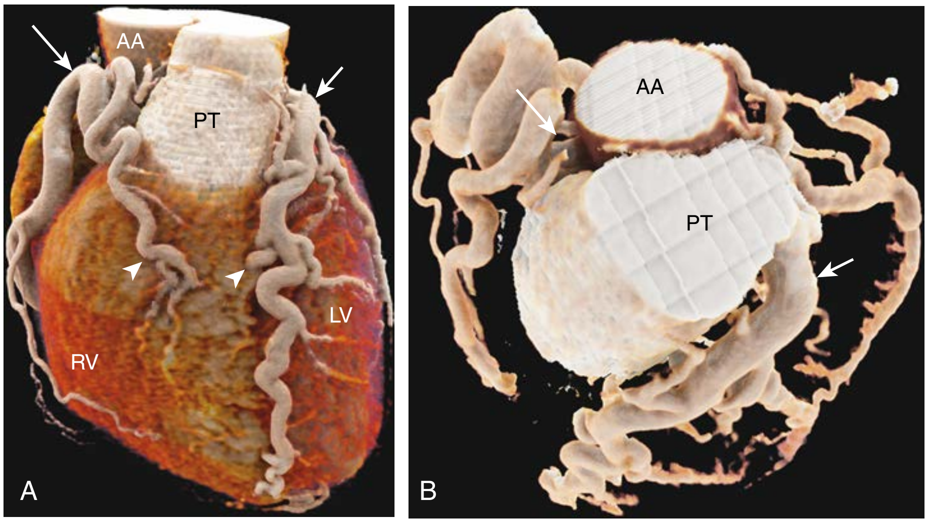

Fig. 58.3 A-G, Anomalous left coronary artery from the pulmonary artery (ALCAPA), also known as Bland–White–Garland syndrome, in an adult male. **A**, Anterior oblique volume rendered (VR) image shows dilated right (long arrow) and left (short arrow) coronary arteries with extensive hypertrophied collateral vessels (arrow heads). **B**, Top-down VR image shows a conventional origin of the right coronary artery (long arrow) from the ascending aorta and an aberrant origin of the left coronary artery from the pulmonary trunk (short arrow). **C**, Right lateral oblique view shows a large right coronary artery (long arrow) with dilated branches including a large conal branch (arrow head). **D**, Left lateral view shows the aberrant origin of the left coronary artery from the pulmonary trunk (short arrow) and dilated dilated anterior interventricular (white arrow head), circumflex arteries (black arrow head) and associated branch vessels. **E**, Anterior oblique VR image shows coronary arteries with heart chambers removed. Note the dilated right (long arrow) and left (short arrow) coronary arteries with extensive hypertrophied collateral vessels (arrow heads). **F**, Anterior oblique VR image of coronary arteries and myocardium shows dilated right (long arrow) and left (short arrow) coronary arteries and an extensive collateral supplying the left ventricle and interventricular septum (arrow heads). **G**, Inferior view showing large right coronary artery (long arrow) with multiple large collateral vessels supplying the inferior left ventricle (arrow heads). Abbreviations. AA, ascending aorta; PT, pulmonary artery; RA, right atrium; RV, right ventricle; LA, left atrium; LV, left ventricle.

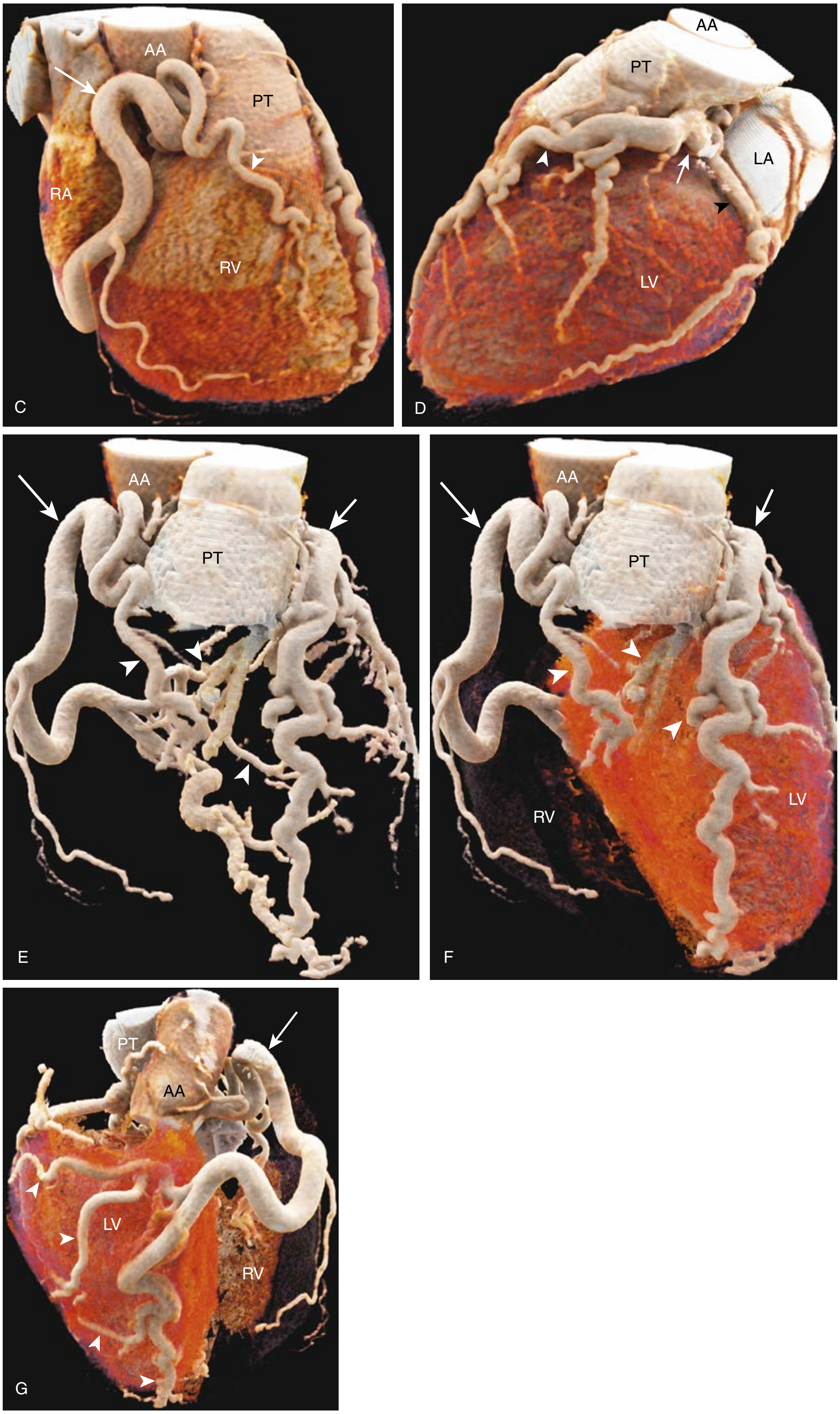
AA
PT
RA
RV
C
AA
PT
LA
LV
D
AA
PT
E
AA
PT
RV
LV
F
PT
AA
LV
RV
G

Fig. 58.3 cont'd

may facilitate radiographic discrimination of pneumomediastinum from similar conditions. The presence of a particularly prominent aortic nipple has also been shown to precede pathological conditions such as venous obstruction in the superior and inferior venae cavae or left brachiocephalic vein, and has been identified in conditions where venous flow through the left superior intercostal vein is increased (e.g. portal venous hypertension and certain congenital venous anomalies).

There are several variants of this arrangement. The most common are: when a right-sided aortic arch and the upper part of the descending thoracic aorta pass anterior to the oesophagus and trachea, and the ductus arteriosus passes posterior to the oesophagus into an aortic diverticulum; a right-sided aortic arch and the upper part of the descending thoracic aorta pass anteriorly, and the ductus arteriosus is inserted into the left subclavian artery arising as a fourth branch from the aortic arch; a left-sided descending thoracic aorta is attached to a left-sided ductus arteriosus anterior to the oesophagus, and a right-sided aortic arch passes posteriorly; the right superior part of the descending thoracic aorta wraps around the oesophagus and the ductus arteriosus is right-sided; the right upper part of the aorta wraps around the oesophagus and the ductus arteriosus is left-sided (Akgun et al 2016).

The left common carotid artery may arise from the brachiocephalic trunk, when it is known as a bovine arch (7%), although this does not represent the morphology seen in bovines. Rarely, the left common carotid and subclavian arteries may arise from a left brachiocephalic trunk or from the right common carotid artery, with the right subclavian artery arising separately (Akgun et al 2016). The right common carotid and subclavian arteries may arise separately, in which case the right subclavian artery often branches from the left part of the aortic arch distal to the left subclavian artery, and usually passes posterior to the oesophagus as an aberrant right subclavian artery (sometimes referred to as a lusoria artery). A diverticular outpouching (diverticulum of Kommerell) may be present at the origin of an aberrant left or right subclavian artery from a right or left aortic arch, respectively (**Fig. 58.6**). It can become aneurysmal and cause fatal haemorrhage during endoscopy and can form a vascular ring around the oesophagus and trachea, presenting in the neonate as a feeding disorder with failure to thrive.

Rare avian forms of branching have been reported. For example, the right common carotid and right subclavian arteries arise from the aortic arch, and the left common carotid and left subclavian arteries arise from the descending thoracic aorta (Akgun et al 2016). Alternatively, two common arterial trunks arise from the aortic arch, the right trunk branching into the left and right common carotid arteries, and the left trunk branching into the left and right subclavian arteries. Another rare order of the branching from the aortic arch is (from right to left): the right subclavian artery, left subclavian artery, followed by the right common carotid and left common carotid arteries, the latter two arising close together and almost forming a common carotid trunk.

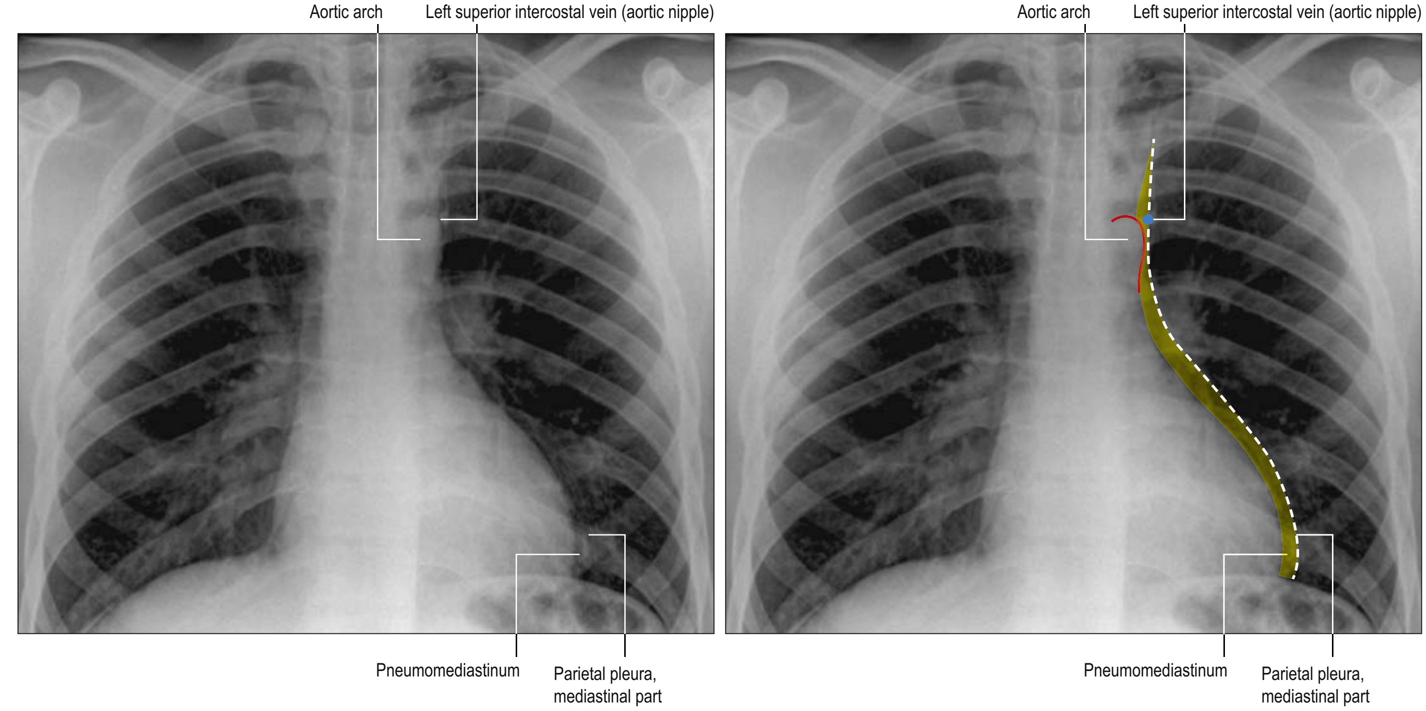
Aortic arch
Left superior intercostal vein (aortic nipple)
Aortic arch
Left superior intercostal vein (aortic nipple)
Pneumomediastinum
Parietal pleura, mediastinal part
Pneumomediastinum
Parietal pleura, mediastinal part

Fig. 58.5 A posteroanterior (PA) chest radiograph, showing the 'aortic nipple' appearance of the left superior intercostal vein (green dot) in a patient with pneumomediastinum. (Courtesy of Professor M Loukas. With permission from Walters A, Cassidy L, Muhleman M et al 2013 Pneumomediastinum and the aortic nipple: the clinical relevance of the left superior intercostal vein. Clin Anat 27:757–63.)

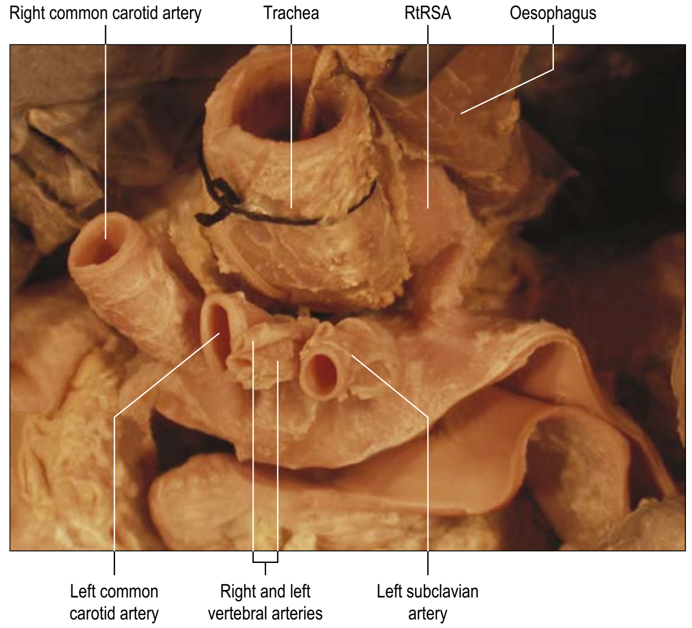
Right common carotid artery
Trachea
RtRSA
Oesophagus
Left common carotid artery
Right and left vertebral arteries
Left subclavian artery

Fig. 58.6 A dissection showing a left aortic arch that gives rise to a common vertebral trunk (seen branching into the right and left vertebral arteries) and a retrotracheal aberrant right subclavian artery (RtRSA), also known as a lusoria artery. (Courtesy of Professor M Loukas with permission from Loukas M, Louis RG Jr, Gaspard J et al 2006 A retrotracheal right subclavian artery in association with a vertebral artery and thyroidea ima. Folia Morphol (Warsz) 65:236–41.)

The aortic arch may curve posterior to the oesophagus and trachea, instead of passing anteriorly, and may show variation in its branching. For example, another rare avian form reported is with both carotid arteries originating from the same common trunk, and a left subclavian artery originating from the aortic arch, while the right subclavian artery arises from the descending thoracic aorta. One or more of the ductus arteriosi may remain patent.

Very rarely, the external and internal carotid arteries arise separately from the aortic arch and the common carotid artery is absent on one or both sides, or both carotid arteries and one or both vertebral arteries can be separate branches. When a right aortic arch and descending thoracic aorta occur, the arrangement of its three branches is reversed and the common carotid arteries may have a single trunk. Other arteries may branch from it; most commonly, these are one or both bronchial arteries and the thyroidea ima artery.

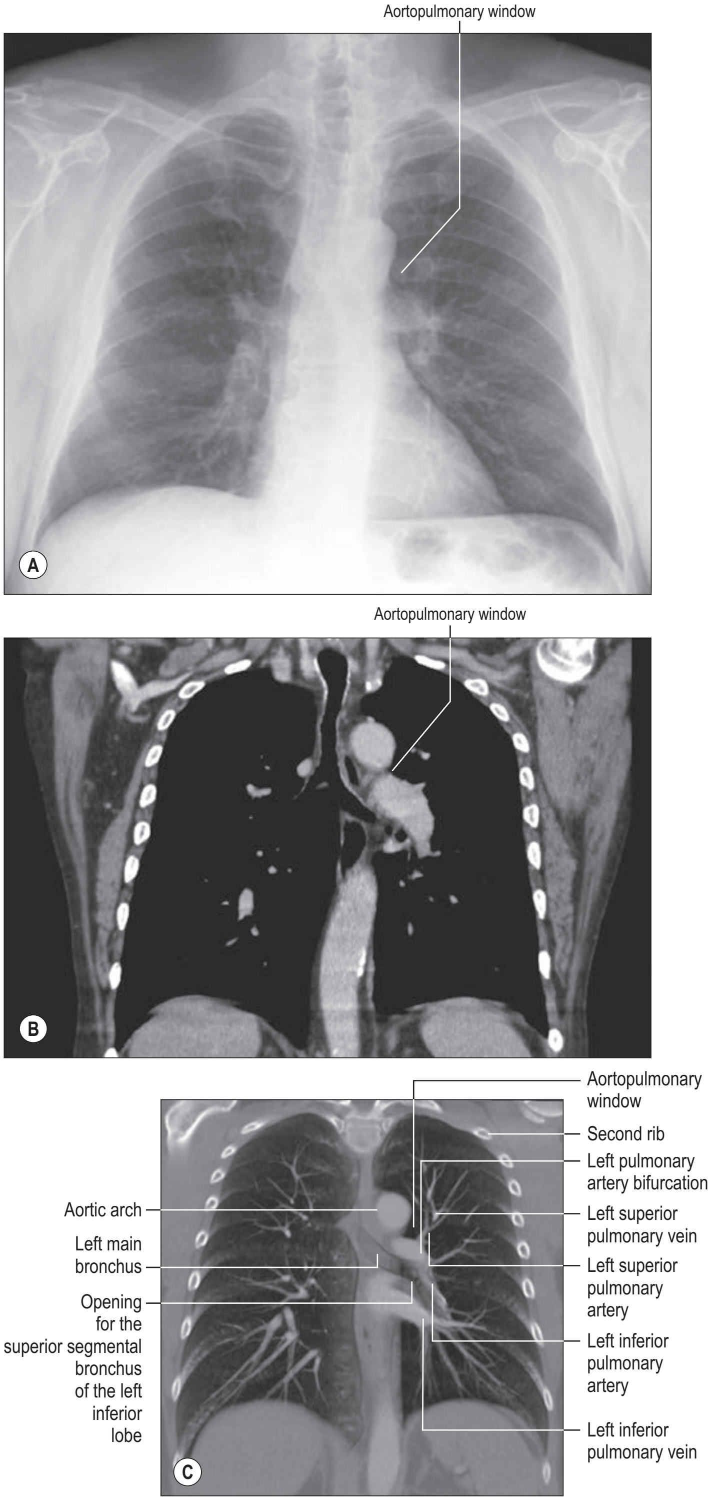
Aortopulmonary window
A
Aortopulmonary window
B
Aortopulmonary window
Second rib
Left pulmonary artery bifurcation
Aortic arch
Left superior pulmonary vein
Left main bronchus
Left superior pulmonary artery
Opening for the superior segmental bronchus of the left inferior lobe
Left inferior pulmonary artery
Left inferior pulmonary vein
C

Fig. 58.4 The aortopulmonary window. **A**, A posteroanterior chest radiograph. **B**, A coronal CT scan reconstruction. **C,** A coronal volume-rendered slab of a CT pulmonary angiogram through the posterior chest showing the aortopulmonary window and surrounding structures.

Coarctation of the thoracic aorta The aortic lumen is occasionally partly or completely obliterated, either above (preductal or infantile type), opposite or just beyond (postductal or adult type), the entry of the ductus arteriosus. In the preductal type, the length of coarctation is variable, aortic arch hypoplasia is common and the left subclavian and even the brachiocephalic trunk may be involved. Severe forms of infantile coarctation and its extreme form (aortic interruption) may be patent ductus arteriosus-dependent, as there is no time for effective collateral circulation to develop. Prostaglandin infusion prior to transfer, and surgery at a tertiary centre, often provide a good mid- to long-term outlook for such infants.

The postductal type of coarctation has been attributed to abnormal extension of tissue of the ductus arteriosus into the aortic wall, stenosing both vessels as the duct contracts after birth. This form may permit years of normal life, allowing the development of an extensive collateral circulation to the aorta distal to the stenosis (Figs 58.7–58.8). High vascularity of the thoracic wall is important and clinically characteristic. Many arteries that arise indirectly from the aorta proximal to the region of coarctation anastomose with vessels that are connected to the aorta distal to the region of coarctation; these vessels form a bypass route and become greatly enlarged. Thus, in the thoracic wall, the thoraco-acromial, lateral thoracic and subscapular arteries (from the axillary artery), the suprascapular artery (from the subclavian artery) and the supreme intercostal artery (from the costocervical trunk) anastomose with other posterior intercostal arteries and the internal thoracic artery and its terminal branches (e.g. the musculophrenic artery) anastomose with many of the posterior intercostal arteries and the inferior epigastric arteries (from the external iliac artery). Posterior intercostal arteries are always involved, and enlargement of their dorsal branches may eventually groove (notch) the inferior margins of the ribs. The radiographic shadow of an enlarged left subclavian artery is also increased. Enlargement of the scapular vessels and anastomoses may lead to widespread interscapular pulsation which is palpated easily with the palm of the hand, and is sometimes heard on auscultation.

Aortic aneurysm formation

Available with the *Gray's Anatomy* e-book

Aortic dissection

Available with the *Gray's Anatomy* e-book

Para-aortic bodies

Para-aortic bodies (aortopulmonary paraganglia) belong to the branchiomeric category of paraganglia. They are chemoreceptors and respond to changes in arterial gas concentrations such as lowered pO_2, increased pCO_2 and increased hydrogen ion concentration. These microscopic structures occur in several locations within the thorax. Coronary paraganglia lie between the ascending aorta and pulmonary trunk, either anteriorly or posteriorly, adjacent to the proximal aorta (aortic root); pulmonary paraganglia lie in the groove between the ductus arteriosus and the pulmonary trunk; subclavian–supra-aortic paraganglia lie between either the right subclavian and right common carotid arteries, or the left subclavian and left common carotid arteries, or caudal to the left subclavian artery, adjacent to the aortic arch.

Rarely, tumours may arise within the para-aortic bodies (e.g. mediastinal paragangliomas that originate in the pulmonary trunk and aortic arch). Generally, these tumours are asymptomatic and are discovered incidentally, but they may occasionally lead to feelings of pressure and hoarseness (Rooke et al 2007).

Brachiocephalic trunk (brachiocephalic artery)

The brachiocephalic trunk, the largest diameter branch of the aortic arch, is 4–5 cm in length (see Figs 58.1, 57.4A–B). It arises from the convexity of the aortic arch posterior to the centre of the manubrium of the sternum, and ascends posterolaterally to the right, initially located anterior to the trachea, then on its right. It divides into the right common carotid and right subclavian arteries level with the superior border of the right sternoclavicular joint, or immediately superior to it. The brachiocephalic trunk and left common carotid artery may share a common origin (Osborn 1998).

Relations The anterior surface of the brachiocephalic trunk is separated from the manubrium of the sternum by sternohyoid and sternothyroid, thymic remnants, the left brachiocephalic and right inferior thyroid veins (crossing its root), and sometimes by the right cardiac branches (cervical and/or thoracic) of the vagus nerve. Posterior relations are the trachea (inferiorly) and the right mediastinal part of the parietal pleura (superiorly). The right vagus nerve is posterolateral (superiorly) and lateral to the trachea (inferiorly) (see Fig. 56.7A). On its right side are the right brachiocephalic vein and the upper part of the superior vena cava and mediastinal part of the parietal pleura, and on its left side are thymic remnants, the origin of the left common carotid artery, the inferior thyroid veins, the thyroidea ima artery (if present) and the trachea (superiorly).

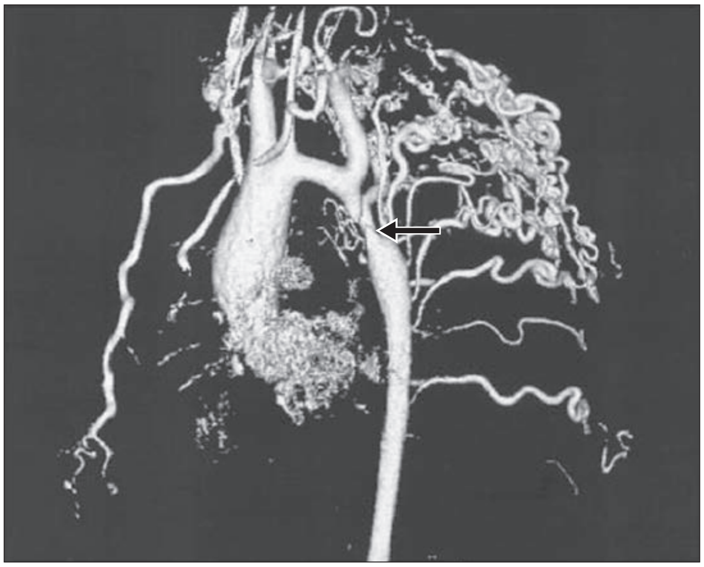

Fig. 58.7 A cardiac magnetic resonance (MR) angiogram showing three-dimensional reconstruction of a native aortic coarctation (arrow) in an adult with extensive collateral flow. Note the marked dilation of the left subclavian artery, supplying most of the collateral vessels, and mild hypoplasia of the aortic arch. (Courtesy of Dr Raad Mohiaddin, Royal Brompton Hospital, London.)

Degeneration of the aortic tunica media and intimal dissection play a major role in the pathogenesis of aneurysms affecting the ascending aorta and aortic arch. Smooth muscle cells are lost and elastic fibres degenerate, producing cystic spaces in the media that then fill with mucoid material. The loss of these structural cells leads to weakening of the wall with progressive dilation. Ageing and hypertension are major predisposing factors to cystic medial degeneration and there is a strong link with cigarette smoking. Thoracic aortic aneurysms are categorized by their location. A particular pattern of aortic root involvement, anulo-aortic ectasia, is seen in Marfan syndrome (Baliga et al 2007). Descending aortic aneurysms are generally caused by atherosclerosis (90%) and the remainder result from mycotic disease or trauma.

Associations also exist between thoracic aortic aneurysm and other connective tissue diseases such as homocysteinuria and Ehlers–Danlos syndrome. A genetic relation is seen in familial thoracic aortic aneurysm syndrome (Baliga et al 2007). Rarely, aneurysms may occur as a result of Takayasu's arteritis, or infections within the aortic wall. Some aortic aneurysms are incidental findings on chest films or CT studies. Symptomatic cases present with breathlessness, unbearable chest and back pain, hoarse voice, cough and haemoptysis. Early diastolic murmurs caused by aortic regurgitation may be audible. Repair is carried out in patients with symptoms or fusiform dilation measuring more than 5 cm in diameter. Aneurysms may also occur in an aberrant right subclavian artery and may involve the diverticulum of Kommerell, leading to dysphagia and even tracheal compression. Inadvertent rupture may occur during endoscopy because of the retro-oesophageal location.

Aortic dissection occurs as a result of degeneration of the tunica media of the aortic wall and is associated with senescence, persistent hypertension or collagen vascular diseases such as Marfan syndrome. Many patients with aortic dissection have a pre-existing aneurysm. Other associations include aortic coarctation, Turner syndrome, cocaine abuse (<1%) and trauma during surgical procedures. There is a higher prevalence in males than females, but after 75 years of age there is no sex difference in prevalence (Baliga et al 2007). In a classic aortic dissection, an intimal tear may occur, producing a split into the tunica media that creates a false lumen (Fig. 58.9). If another tear occurs, connection can be made once again with the true lumen (double-barrel aorta). Additional aetiopathologies include penetrating atherosclerotic ulceration, where an atherosclerotic plaque ruptures into the aortic tunica media, and aortic intramural haematoma, where the vasa vasorum haemorrhage into the wall of the aorta (Baliga et al 2007).

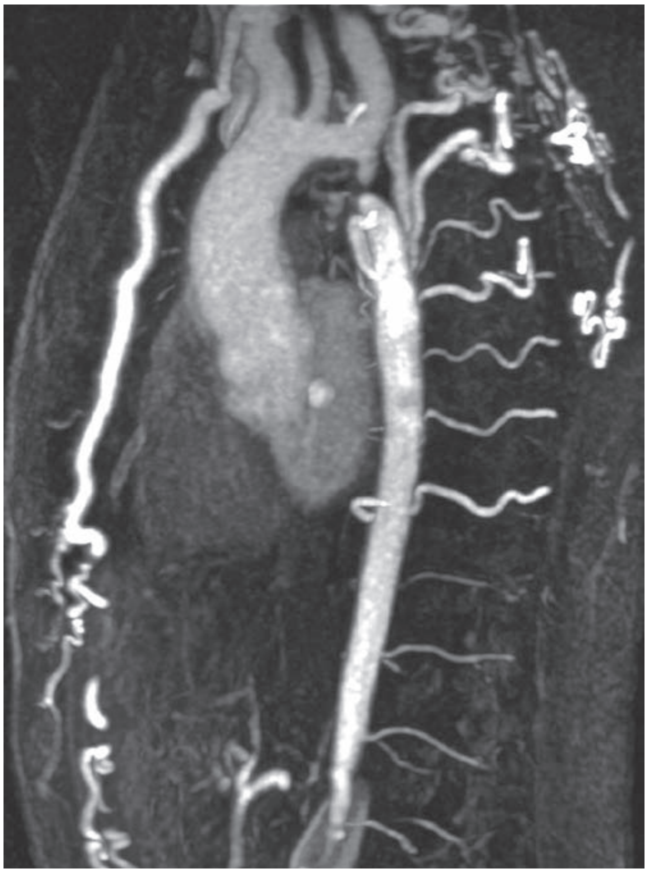

Fig. 58.8 MRA (sagittal oblique reconstruction) of a patient presenting with hypertension and femoral delay. There is a coarctation of the aorta just beyond the left subclavian artery and an extensive collateral circulation through intercostal and internal thoracic arteries. (With permission from Fattoni R, Lovato L 2015. The thoracic aorta: diagnostic aspects. In Grainger and Allison's Diagnostic Radiology. 553-590.)

Aortic dissections are classified as types I, II, IIIa and IIIb (DeBakey classification), or types A and B (Stanford classification). Dissections that include the aorta proximal to the left subclavian artery, with or without distal extension, are classified as type I, II or A. Type I involves up to the entire aorta (ascending, arch and descending), whereas type II involves the ascending aorta only. Dissections that are distal to the left subclavian artery are classified as type IIIa (extend to the respiratory diaphragm), IIIb (extend below the respiratory diaphragm) or B. These cases present acutely with severe retrosternal, neck or interscapular chest pain. Depending on the extent of the dissection, they may be associated with neurological signs, diarrhoea or leg weakness. Extension into the pericardium causes cardiac tamponade and circulatory collapse. Diagnosis is established by echocardiography and on contrast-enhanced CT or magnetic resonance imaging (MRI). Medical management is possible for descending aortic dissections, while surgical repair is essential for ascending aortic or aortic arch dissection.

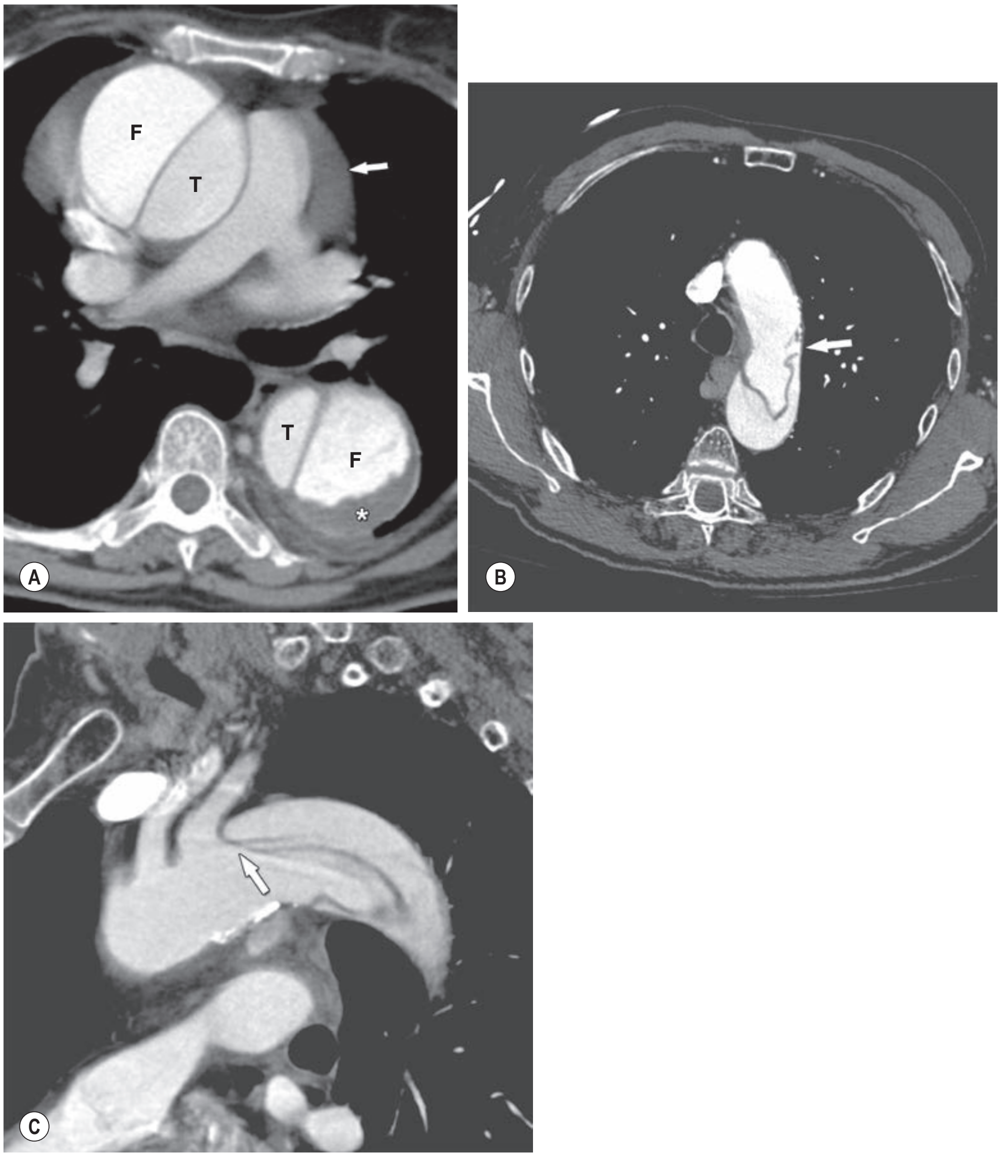

Fig. 58.9 A-C. Contrast enhanced CT images of thoracic aortic dissection, showing a double barrelled aortic lumen with true (T) and false (F) lumen. **A**, Stanford type A (axial section) aortic dissection including both the ascending aorta and descending thoracic aorta. A pericardial effusion (white arrow) is also present. **B**, Stanford type B aortic dissection (axial sections) showing the intimal defect (white arrow) and opening between the true and false lumina. **C**, Stanford type B aortic dissection (sagittal oblique section) showing the dissection flap (white arrow) originating immediately distal to the origin of the left subclavian artery. (With permission from Salgado R, Habets J, Budde RPJ 2015. Diseases of the thoracic aorta and pulmonary arteries. In Advanced Cardiac Imaging (Nieman K, Gaemperle O, Lancellotti P et al eds) Chapter 20, 661-705. Woodhead Publishing Series in Biomaterial, Elsevier.)

Branches The brachiocephalic trunk usually has only terminal branches, the right common carotid and right subclavian arteries. A thymic or bronchial branch, or a thyroidea ima artery (occasionally), can arise from it (see Fig. 58.1). The thyroidea ima artery is a small and inconstant artery that may arise from the aortic arch, brachiocephalic trunk, common carotid, subclavian, pericardiacophrenic or internal thoracic arteries; most commonly it arises from right-sided vessels (Tunali 2016, Yalcin 2016). It ascends on the trachea to the thyroid isthmus, where it terminates.

Descending thoracic aorta

The descending thoracic aorta is located within the posterior mediastinum (see Figs 52.3, 56.1, 56.6–56.7B, 56.13–56.14A, 56.20D–E). It is continuous with the aortic arch, beginning level with the lower border of the body of the fourth thoracic vertebra (typically at the sternal plane, although the level of this plane may vary), and ending anterior to the lower border of the body of the twelfth thoracic vertebra at the aortic hiatus, through which it passes. It is to the left of the vertebral column at its origin, and reaches the midline (median plane), anterior to the vertebral bodies, as it descends.

Relations Anterior to the descending thoracic aorta, from superior to inferior, are the hilum of the left lung, the pericardium separating it from the left atrium, the oesophagus and the lumbar part of the respiratory diaphragm. The vertebral column and accessory hemiazygos (superiorly) and hemiazygos (inferiorly) veins are posterior. To the right is the thoracic duct and the azygos vein, and inferiorly, to both the left and right sides, are the pleura-covered parts of the mediastinal surfaces of the respective lungs. The oesophagus with its associated plexus of nerves is closely related to the descending thoracic aorta: it is located to the right of the descending aorta in the upper thorax, anterior to it in the lower thorax, and anterolaterally to the left at the level of the respiratory diaphragm. Occasionally, the descending thoracic aorta traverses the respiratory diaphragm to the left and posterior to the oesophagus (Berdjas and Turina 2011).

Branches

The descending thoracic aorta provides visceral branches to the pericardium, lungs, bronchi and oesophagus, and parietal branches to the thoracic wall and vertebral column.

Pericardial branches A variable number of small vessels are distributed to the posterior aspect of the pericardium.

Bronchial arteries Bronchial arteries vary in number, size and origin. There is usually only one right bronchial artery that commonly arises from the right third posterior intercostal artery, but it may arise from the superior left bronchial artery, or various right posterior intercostal arteries. It runs posterior to the right main bronchus. The left bronchial arteries, usually two, arise from the descending thoracic aorta, near the body of the fifth or sixth thoracic vertebra, and run posterior to the left main bronchus. The bronchial arteries supply the pulmonary areolar tissue, bronchopulmonary lymph nodes, pericardium, visceral pleura and thoracic oesophagus (Ch. 54).

Oesophageal branches Two or three oesophageal arteries that arise either anteriorly or from the right side of the descending thoracic aorta supply the distal thoracic oesophagus (Norton et al 2008).

Mediastinal branches Numerous small vessels supply lymph nodes and areolar tissue in the posterior mediastinum.

Superior phrenic branches Superior phrenic arteries arise from the distal descending thoracic aorta and are distributed posteriorly to the superior (thoracic) surface of the respiratory diaphragm, anastomosing with the musculophrenic and pericardiacophrenic arteries (see Fig. 55.6).

Posterior intercostal arteries The posterior intercostal arteries and their branches are described in Chapter 53.

Subcostal arteries The subcostal arteries are the last paired branches of the descending thoracic aorta, arising in series with the posterior intercostal arteries and inferior to the twelfth ribs. Each runs laterally, anterior to the body of the twelfth thoracic vertebra and posterior to the thoracic splanchnic nerves, sympathetic trunk, costal part of the parietal pleura and lumbar part of the respiratory diaphragm. The right subcostal artery is also posterior to the thoracic duct and azygos vein, while the left is posterior to the hemiazygos vein. Each artery enters the abdomen at the lower border of the twelfth rib, accompanied by the twelfth thoracic (subcostal) nerve, lying posterior to the lateral arcuate ligament and kidney, and anterior to quadratus lumborum. The right artery courses posterior to the ascending colon, and the left courses posterior to the descending colon. The subcostal arteries pierce the aponeurosis of transversus abdominis to become more superficial, and continue toward the anterior midline in the plane between transversus abdominis and internal abdominal oblique; they anastomose with the superior epigastric, lower posterior intercostal and lumbar arteries. Each has a dorsal branch, distributed like those of the posterior intercostal arteries.

Aberrant artery (right dorsal aorta vestige) A small artery sometimes leaves the descending thoracic aorta from its right side near the origin of the right bronchial artery. It ascends to the right behind the trachea and oesophagus and may anastomose with the right supreme intercostal artery.

Aortic rupture in trauma Rupture of the ascending aorta is usually associated with a high immediate mortality (Baliga et al 2007). Blunt aortic rupture commonly occurs in road traffic accidents and has a 20% survival rate. There is usually a transverse tear involving the tunica intima and tunica media of the aortic wall; systemic circulatory pressure may cause the formation of a false aneurysm. Rupture of the isthmus region of the descending thoracic aorta is more common, probably because it marks the junction between the mobile and fixed parts of the aorta. Other sites include the ascending aorta proximal to the origin of the brachiocephalic trunk, the aortic arch and the abdominal aorta. Rupture is likely to be the result of a number of factors, including torsion, shear and stretching forces, possibly compounded by hydrostatic pressure.

Aortic atherosclerosis or calcification Echocardiography, particularly transoesophageal, allows detailed assessment of proximal aortic atherosclerosis implicated in systemic embolic events and strokes, and the extent of turbulent flow. MRI can allow accurate assessment of the composition and size of atherosclerotic plaques and flow dynamics, permitting assessment of the risk of plaque rupture and thrombus formation.

Subclavian arteries

Right subclavian artery

The right subclavian artery arises from the brachiocephalic trunk either posterior to the right sternoclavicular joint or immediately superior to it (level with the body of the second thoracic vertebra or T1–T2 intervertebral disc (Badshah et al 2017)) (see Fig. 52.3). It ascends superolaterally to the level of the first rib, where it is located posterior to both the sternal end of the clavicle and scalenus anterior; it has a minimal intrathoracic presence. The vessel then passes inferolaterally across the superior surface of the first rib, and at the external border of the rib becomes the right axillary artery (see Fig. 48.3).

Left subclavian artery

In the majority of individuals the left subclavian artery originates independently from the aortic arch after the origins of the brachiocephalic and left common carotid arteries (see Fig. 57.4). It ascends into the neck posterior to scalenus anterior, then passes inferolaterally towards the external border of the first rib, where it becomes the left axillary artery. A common origin occasionally exists between the left subclavian and vertebral arteries. Bilateral brachiocephalic trunks are rare: each divides into common carotid and subclavian arteries.

Relations In the thorax the left subclavian artery is related anteriorly to the left common carotid artery and left brachiocephalic vein (and sometimes the inferior thyroid vein), from which it is separated by the left vagus, cardiac and phrenic nerves (see Figs 56.6–56.7, 57.12). Sternothyroid and sternohyoid lie between the vessel and the upper left aspect of the posterior surface of the manubrium of the sternum.

The mediastinal surface of the left lung and parietal pleura are lateral, and also encroach on its anterior and posterior surfaces. The trachea, left recurrent laryngeal nerve, oesophagus and thoracic duct are medial. When located immediately lateral to the oesophagus, the thoracic duct and longus colli are posterior.

Common carotid arteries

The right and left common carotid arteries differ in their length and origin. The right is exclusively cervical and arises from the brachiocephalic trunk posterior to the superior part of the right sternoclavicular joint, or immediately superior to the joint. The left originates directly from the aortic arch immediately posterolateral to the brachiocephalic trunk and therefore has both thoracic and cervical parts. The origin of the arteries may be variable; for example, both common carotid arteries may emerge from the brachiocephalic trunk (Panagouli et al 2018), separately from the aorta or from a common trunk (Akgun et al 2016).

Right common carotid artery

The right common carotid artery and its relations are described in Chapter 35.

Left common carotid artery

The left common carotid artery (see Figs 58.1, 35.8) ascends and enters the neck by passing through the superior thoracic aperture, posterior to the left sternoclavicular joint. Its thoracic part is 2.0–2.5 cm long. It lies initially anterior to the trachea, and moves to its left side as it ascends. The cervical course of the artery is described in Chapter 35.

Relations Sternohyoid and sternothyroid, the parietal pleura and the mediastinal surface of the left lung, the left brachiocephalic vein and the thymic remnants are anterior and separate the left common carotid artery from the manubrium of the sternum (Fig. 58.1). The trachea, left subclavian artery, left border of the oesophagus, left recurrent laryngeal nerve and thoracic duct are posterior. To the right are the inferior part of the brachiocephalic trunk and the trachea, inferior thyroid veins and thymic remains. To the left are the left vagus and phrenic nerves, and the parietal pleura and the mediastinal surface of the left lung.

Veins

Brachiocephalic veins

The right and left internal jugular and subclavian veins join to form the right and left brachiocephalic veins, respectively. The right and left brachiocephalic veins join to form the superior vena cava (see Figs 35.14, 52.5, 52.7, 57.12).

Right brachiocephalic vein

The right brachiocephalic vein is about 2.5 cm long. It is commonly formed posterior to the right sternoclavicular joint, although this may vary with study population (see Fig. 52.7). It descends almost vertically to join the left brachiocephalic vein, forming the superior vena cava posterior to the right second costal cartilage or first intercostal space and the associated part of the sternum. It is located anterolateral to the brachiocephalic trunk and right vagus nerve; the right pleura, phrenic nerve and internal thoracic artery are initially posterolateral, becoming lateral inferiorly (see Figs 35.14, 55.10A, 56.7A). Its tributaries are the right vertebral, right internal thoracic and right inferior thyroid veins, and sometimes the right supreme intercostal (first right posterior intercostal) vein.

Left brachiocephalic vein

The left brachiocephalic vein is about 6 cm long. It arises posterior to the left sternoclavicular joint, although this may vary with study population (see Fig. 52.7). It initially sits anterior to the cervical part of the parietal pleura, then descends obliquely and to the right, posterior to the superior half of the manubrium of the sternum, reaching the right second costal cartilage or first intercostal space and the associated part of the sternum where it joins the right brachiocephalic vein to form the superior vena cava (see Figs 58.1, 35.14, 57.12). It is separated from the left sternoclavicular joint and manubrium by sternohyoid and sternothyroid, the thymus or its remnants, and areolar tissue. Near its junction with the right brachiocephalic vein it is partly covered by the mediastinal part of the right parietal pleura. It crosses anterior to the left internal thoracic, left subclavian, left common carotid and brachiocephalic arteries, the left phrenic and left vagus nerves, and the trachea (see Fig. 55.10B). The aortic arch is normally inferior to it. Its tributaries are the left vertebral, left internal thoracic, left inferior thyroid and left superior intercostal veins, and sometimes the left supreme intercostal (first left posterior intercostal), thymic and left pericardiacophrenic veins.

In children, the length and diameter of the left brachiocephalic vein are closely related to height; the diameter reaches adult dimensions at around 10–12 years of age (**Figs 58.10–58.11**)(Sanjeev and Karpawich 2006).

Superior vena cava

The superior vena cava returns blood to the heart from the tissues above the respiratory diaphragm. It is approximately 7 cm in length and is formed by the junction of the left and right brachiocephalic veins. According to conventional anatomical descriptions, the superior vena cava forms posterior to the right first costal cartilage. However, the majority of *in vivo* CT-based studies show that it forms posterior to the right second costal cartilage or first intercostal space and the associated part of the sternum. It descends vertically, being slightly convex to the right, and drains into the right atrium either posterior to the right third costal cartilage, or the third intercostal space, or the region posterior to the right fourth to fifth costal cartilages (see Fig. 52.5). Its inferior half is within the fibrous pericardium and it is covered anterolaterally by the visceral layer of serous pericardium (from which the retrocaval recess projects) (see Figs 57.1, 57.4A–B, 57.12). In children the length and diameter of the superior vena cava are closely related to height; the diameter reaches adult dimensions at around 10–12 years of age (see Figs 58.10–58.11) (Sanjeev and Karpawich 2006). The superior vena cava is valveless.

Relations The mediastinal surface of the right lung and parietal pleura are anterior, lateral and posterolateral, and the pericardium intervenes inferiorly; anteriorly these structures separate the superior vena cava from the right internal thoracic artery, transversus thoracis and the associated region of the anterior thoracic wall (see Figs 55.10A, 56.7A). The trachea and right vagus nerve are located posteromedially, and the hilum of the right lung is posterior. The right phrenic nerve is an immediate right lateral relation, the brachiocephalic trunk and ascending aorta sit to the left of the superior part, and the aorta sits anteromedial to the inferior part, of the superior vena cava (see Fig. 57.4A).

Tributaries Tributaries of the superior vena cava are the azygos vein and small veins from the pericardium and other mediastinal structures, e.g. the thymus (see Figs 56.7A, 58.1).

Superior vena cava obstruction Superior vena cava obstruction is characterized by headaches, facial and neck venous congestion, and oedema, reflecting impaired venous drainage of the head, neck and upper limbs, and of the collateral circulation, resulting in chest wall telangiectasia. Several of the symptoms may subside with recumbency, or may be aggravated by standing up (erect posture). The obstruction may be either partial or complete, and may occur suddenly or gradually. It is usually caused by mediastinally invasive right upper lobe primary bronchogenic carcinoma, metastatic involvement of the right paratracheal lymph nodes or non-Hodgkin lymphoma.

Haemorrhagic intrathoracic goitre, mediastinitis (either benign, malignant or fibrous), mediastinal haematoma, constrictive pericarditis, mediastinal cyst, thrombosis of the superior vena cava and sarcoidosis are less common aetiologies. Radiographic findings might include widening of the upper mediastinum on the frontal view or obliteration of the retrosternal space on the lateral view. Other correlative findings may include pulmonary or mediastinal masses, lymphadenopathy, an enlarged or obliterated azygos venous system, pleural effusion or rib notching. This is usually considered to be an oncological emergency and symptoms are often completely and promptly relieved by insertion of a vascular stent via the femoral vein or by radiotherapy to the affected region after a tissue diagnosis is established.

Variations of the brachiocephalic veins and superior vena cava The left and right brachiocephalic veins may enter the right atrium separately, the right vein descending like a normal superior vena cava. During embryological development, if the cardinal vein does not obliterate, it will persist as a left-sided superior vena cava. A left superior vena cava may have a slender connection with the right superior vena cava and subsequently cross the left side of the aortic arch to pass anterior to the hilum of the left lung before turning to enter the right atrium. It replaces the oblique vein of the left atrium (of Marshall) and coronary sinus, and receives all the normal tributaries of the coronary sinus. Other variations include drainage of the hemiazygos vein directly into the persistent left superior vena cava (Liu et al 2019). The left brachiocephalic vein sometimes projects above the manubrium (more frequently in childhood) and crosses the midline superior to the jugular notch, immediately anterior to the trachea. A left-sided superior vena cava may cause difficulties when placing a cardiac catheter, pacing or defibrillating electrodes because the angle between the left superior vena cava and the left subclavian vein is more acute than that normally found between the left subclavian and left brachiocephalic vein. Its calibre may also be smaller than that of the right. Even if insertion of a catheter into a left superior vena cava is possible, the angle at which the catheter enters the right atrium causes difficulty when attempting to place it into the right ventricle and pulmonary trunk; this generally leaves the catheter tip against the coronary sinus, making it difficult to obtain blood samples. In the majority of cases of persistent left superior venae cava, blood drains into the right atrium via the coronary sinus. When this does not happen, the coronary sinus is absent, and the persistent left superior vena cava drains directly into the right atrium. Cyanosis reflects a persistent right-to-left shunt and affected individuals have a higher risk for paradoxical embolism. Radiographically, there is a paramediastinal bulge anterior to the aortic arch. Electrocardiograms show a left P-wave axis. Diagnosis can be confirmed by cardiac catheterization and angiography. Persistent left superior vena cava may be associated with extracardiac conditions such as VACTERL association (vertebral defects, anal atresia, cardiac malformations, tracheo-oesophageal fistula with oesophageal atresia, radial and renal dysplasia, and limb anomalies); trisomy 21; 22q11; CHARGE association (coloboma, heart defects, choanal atresia, mental retardation, genital and ear anomalies); and 45 XO karyotype (Turner syndrome).

If the superior vena cava is duplicated, the right superior vena cava may drain into the right atrium and the left superior vena cava into the left atrium. Although double superior vena cava is largely asymptomatic, it is usually (along with a sole left-sided superior vena cava) associated with congenital cardiac anomalies, such as pulmonary stenosis, coarctation of the aorta, tetralogy of Fallot and atrial septal defects.

Inferior vena cava

The inferior vena cava returns blood to the heart from infradiaphragmatic tissues. It passes through the caval foramen of the respiratory diaphragm between the right folia and central area of the central tendon of the diaphragm at the level of the superior half of the body of the eleventh thoracic vertebra (see Fig. 55.1), and drains into the inferoposterior part of the right atrium (see Fig. 57.4B). The thoracic part is short, and is partly within and partly outside the pericardial sac. The extrapericardial part is separated from the mediastinal part of the parietal pleura and right lung by the right phrenic nerve and associated pericardiacophrenic vessels, and the intrapericardial part is covered, except posteriorly, by the visceral layer of serous pericardium (see Fig. 57.4E). The abdominal course of the inferior vena cava is described in Chapter 61.

Collateral venous channels In obstruction of the superior part of the inferior vena cava, the azygos and hemiazygos veins and vertebral venous plexuses are the main collateral channels that maintain venous circulation. They connect the superior and inferior venae cavae and communicate with the common iliac vein via the ascending lumbar veins and with multiple tributaries of the inferior vena cava.

Variations The inferior vena cava may be congenitally interrupted, duplicated, left-sided or even absent.

Bonus e-book content

Fig. 58.2 A case of a left coronary artery arising from the pulmonary trunk (Bland–White–Garland syndrome).

Fig. 58.3 Anomalous left coronary artery from the pulmonary artery (ALCAPA), also known as Bland–White–Garland syndrome, in an adult male

Fig. 58.5 A posteroanterior (PA) chest radiograph showing the 'aortic nipple' appearance of the left superior intercostal vein in a patient with pneumomediastinum.

Fig. 58.6 A dissection showing a left aortic arch that gives rise to a common vertebral trunk and a retrotracheal aberrant right subclavian artery, also known as a lusoria artery.

Fig. 58.7 A cardiac magnetic resonance angiogram showing three-dimensional reconstruction of a native aortic coarctation in an adult with extensive collateral flow.

Fig. 58.8 MRA showing coarctation of the aorta just beyond the left subclavian artery and an extensive collateral circulation through intercostal and internal thoracic arteries.

Fig. 58.9 Contrast enhanced CT images of thoracic aortic dissection.

Fig. 58.10 Sites of measurement of the left brachiocephalic vein and superior vena cava in children from 0 to 12 years of age at angiography.

Fig. 58.11 Diameters of the distal brachiocephalic vein (left), mid-brachiocephalic vein (left), brachiocephalic–superior vena cava junction and mid-superior vena cava in children from 0 to 12 years of age.

Key references

Akgun V, Hamcan S, Bozkurt Y et al 2016 Thoracic aorta. In: Tubbs RS, Shoja MM, Loukas M Bergman's Comprehensive Encyclopedia of Human Anatomic Variation, 2nd ed. Hoboken: Wiley–Blackwell; Ch. 49, pp. 501–29.

Badshah M, Soames R, Ibrahim M et al 2017 Surface anatomy of major anatomical landmarks of the neck in an adult population: a CT evaluation of vertebral level. Clin Anat 30(6):781–7.

Loukas M, Groat C, Khangura R et al 2009 The normal and abnormal anatomy of the coronary arteries. Clin Anat 22:114–28.

Spratt J 2016 Inferior vena cava, portal and hepatic venous systems. In: Tubbs RS, Shoja MM, Loukas M Bergman's Comprehensive Encyclopedia of Human Anatomic Variation, 2nd ed. Hoboken: Wiley–Blackwell; Ch. 68, pp. 877–89.

Tunali S 2016 Subclavian artery. In: Tubbs RS, Shoja MM, Loukas M Bergman's Comprehensive Encyclopedia of Human Anatomic Variation, 2nd ed. Hoboken: Wiley–Blackwell; Ch. 52, pp. 575–82.

Yalcin B 2016 Thyroid gland. In: Tubbs RS, Shoja MM, Loukas M Bergman's Comprehensive Encyclopedia of Human Anatomic Variation, 2nd ed. Hoboken: Wiley–Blackwell; Ch. 99, pp. 1189–204.

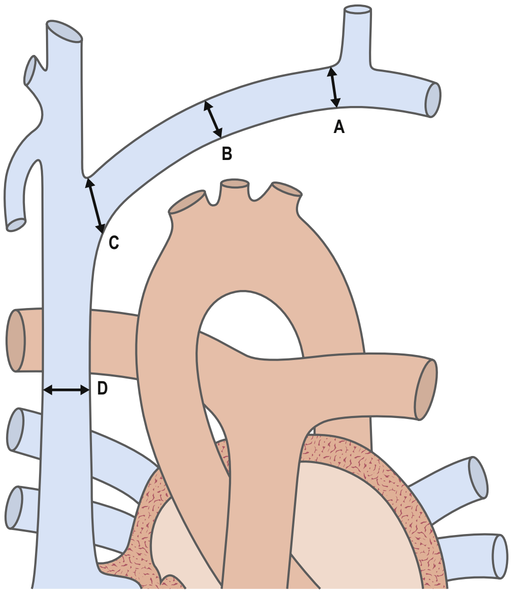

Fig. 58.10 Sites of measurement of the left brachiocephalic vein and superior vena cava in children from 0 to 12 years of age at angiography. Key: A, distal brachiocephalic vein; B, mid-brachiocephalic vein; C, brachiocephalic–superior vena cava junction; D, mid-superior vena cava. (Redrawn with permission from Sanjeev S, Karpawich PP 2006 Superior vena cava and innominate vein dimensions in growing children: an aid for interventional devices and transvenous leads. Pediatr Cardiol 27(4):414–19.)

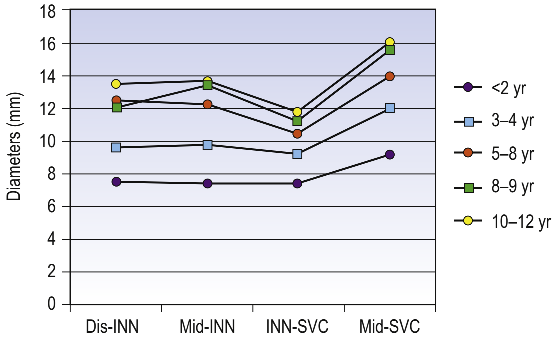

Fig. 58.11 Diameters of the distal brachiocephalic vein (dis-INN), mid-brachiocephalic vein (mid-INN), brachiocephalic–superior vena cava junction (INN-SVC) and mid-superior vena cava (mid-SVC) in children from 0 to 12 years of age. (Redrawn with permission from Sanjeev S, Karpawich PP 2006 Superior vena cava and innominate vein dimensions in growing children: an aid for interventional devices and transvenous leads. Pediatr Cardiol 27(4):414–19.)

Embryologically, if the right subcardinal vein fails to anastomose with the hepatic sinusoids, the hepatic segment of the inferior vena cava fails to develop. When this occurs, the hemiazygos or azygos veins, both of which originate from the cranial supracardinal veins, return blood to the heart. Azygos continuation of the inferior vena cava, characterized by a prominent azygos vein, is a variant that the paediatric surgeon should be aware of when undertaking repair of oesophageal atresia and tracheo-oesophageal atresia in neonates. The azygos vein, which is commonly ligated and divided during this procedure, should be spared because ligation of this vessel in neonates with azygos continuation of the inferior vena cava leads to intraoperative circulatory collapse and death. Double inferior vena cava (right side usually dominant) is a result of the persistence of all or any segments of the subcardinal veins. One of the most common variations is a left-sided inferior vena cava, which is formed if the right supracardinal vein regresses and the left supracardinal vein persists (Spratt 2016). There may also be a duplication of the inferior vena cava, which typically occurs inferior to the level of the renal veins, and is the result of persistence of the left lumbar and thoracic supracardinal veins and left suprasubcardinal anastomosis as well as malformation of the right subcardinal–hepatic anastomosis. Abnormalities associated with duplication of the inferior vena cava include congenital heart disease, congenital absence of the right kidney, cloacal extrophy, renal ectopia with abdominal aneurysm, right retrocaval ureter, left retrocaval ureter and congenital absence of the iliac anastomosis, abnormal left upper limb drainage and transcaval ureter.

In situs inversus with dextrocardia, the inferior vena cava passes inferiorly along the left side instead of the right. In situs inversus with levocardia, the inferior vena cava remains on the right side. In situs ambiguus (heterotaxy) the major organs are arranged ambiguously within the body. Prominent azygos veins with interrupted inferior vena cava are associated with heterotaxy (Punn and Olson 2010). Situs ambiguus with polysplenia is associated with an absence of parts of the inferior vena cava on the right side (with continuation through the azygos or hemiazygos vein), transposition of the inferior vena cava to the left side, or duplication of the inferior vena cava with one on the right and one on the left. Situs inversus with asplenia is similar to that of polysplenia, in that the inferior vena cava may be absent with azygos continuation or with the inferior vena cava to the left of the midline. In situs inversus totalis, transposition of the inferior vena cava consists of a right-sided inferior vena cava. The inferior vena cava may have an abnormally high insertion into the right atrium.

Scimitar syndrome, a form of anomalous pulmonary venous drainage, occurs when there is an abnormal connection between the right pulmonary vein(s) and the inferior vena cava. This often involves hypoplasia of the pulmonary veins and the pulmonary trunk and arteries, as well as abnormal ipsilateral lung parenchyma. This creates a left-to-right shunt and increases the risk of right ventricular failure as a result of ventricular hypertrophy. Typical symptoms include respiratory insufficiency such as recurrent respiratory infections, heart failure, or pulmonary hypertension.

Congenital agenesis of the inferior vena cava may occur and may be completely asymptomatic because venous drainage of the lower limbs occurs through anastomosed channels of the azygos and hemiazygos veins. However, this condition may be associated with a higher risk for deep vein thrombosis.

References

Akgun V, Hamcan S, Bozkurt Y et al 2016 Thoracic aorta. In: Tubbs RS, Shoja MM, Loukas M Bergman's Comprehensive Encyclopedia of Human Anatomic Variation, 2nd ed. Hoboken: Wiley–Blackwell; Ch. 49, pp. 501–29.

Badshah M, Soames R, Ibrahim M et al 2017 Surface anatomy of major anatomical landmarks of the neck in an adult population: a CT evaluation of vertebral level. Clin Anat 30(6):781–7.

Baliga RR, Neinaber CA, Isselbacher EM et al 2007 Aortic Dissection and Related Syndromes. Ann Arbor, MI: Springer.

Berdjas D, Turina MI 2011 Operative Anatomy of the Heart. Berlin: Springer.

Deutsch J, Savides TJ 2005 Normal Thoracic Anatomy in Digital Human Anatomy and Endoscopic Ultrasonography. Hamilton, ON: BC Decker.

Kaiser T, Kellenberger CJ, Albisetti M et al 2008 Normal values for aortic diameters in children and adolescents – assessment in vivo by contrast-enhanced CMR-angiography. J Cardiovasc Magn Reson 10:56.

Kervancioglu P, Kervancioglu M, Tuncer CM 2006 Echocardiographic study of aortic root diameter in healthy children. Saudi Med J 27:27–30.

Liu F, Ruze A, Amuti S et al 2019 A rare variation of the hemiazygos vein draining into the persistent left superior vena cava. Anat Sci Int 94(3):269–73.

Loukas M, Groat C, Khangura R et al 2009 The normal and abnormal anatomy of the coronary arteries. Clin Anat 22:114–28.

Norton JA, Barie PS, Bollinger RR et al 2008 Surgery: Basic Science and Clinical Evidence, 2nd ed. New York: Springer.

Osborn AG 1998 Diagnostic Cerebral Angiography. Philadelphia: Lippincott, Williams & Wilkins.

Panagouli E, Tsoucalas G, Papaioannou T et al 2018 Right and left common carotid arteries arising from the brachiocephalic, a rare variation of the aortic arch. Anat Cell Biol 51(3):215–17.

Punn R, Olson I 2010 Anomalies associated with a prominent azygos vein on echocardiography in the pediatric population. J Am Soc Echocardiogr 23:282–5.

Rooke TW, Sullivan TM, Jaff MR 2007 Unusual Vascular Diseases in Vascular Medicine and Endovascular Interventions. Columbia, MD: Blackwell Futura, pp. 134–5.

Sanjeev S, Karpawich PP 2006 Superior vena cava and innominate vein dimensions in growing children: an aid for interventional devices and transvenous leads. Pediatr Cardiol 27:414–19.

Smith A, McKay R 2004 A Practical Atlas of Congenital Heart Disease. London: Springer.

Spratt J 2016 Inferior vena cava, portal and hepatic venous systems. In: Tubbs RS, Shoja MM, Loukas M Bergman's Comprehensive Encyclopedia of Human Anatomic Variation, 2nd ed. Hoboken: Wiley–Blackwell; Ch. 68, pp. 877–89.

Tunali S 2016 Subclavian artery. In: Tubbs RS, Shoja MM, Loukas M Bergman's Comprehensive Encyclopedia of Human Anatomic Variation, 2nd ed. Hoboken: Wiley–Blackwell; Ch. 52, pp. 575–82.

Yalcin B 2016 Thyroid gland. In: Tubbs RS, Shoja MM, Loukas M Bergman's Comprehensive Encyclopedia of Human Anatomic Variation, 2nd ed. Hoboken: Wiley–Blackwell; Ch. 99, pp. 1189–204.

COMMENTARY

7.1

Breast cancer

Donna Geddes, James Going

Breast cancer is a common disease, particularly in postmenopausal women (Fentiman 1993). Each year, in the United Kingdom, there are approximately 40,000 new cases diagnosed and 14,000 deaths. Male breast cancers constitute up to 1% of all mammary malignancies and may include tissue beyond the areolar boundary.

Breast cancers arise within the epithelia of lobules or ducts. As they increase in size and become invasive, they often lead to a fibrous stromal tissue reaction. Breast lumps may be classified as benign or malignant masses. More advanced malignant breast lumps (carcinomas) may have the clinical signs of infiltrating adjacent structures, leading to a hard and irregular mass with skin-tethering, muscle fixation, skin infiltration or oedema of the overlying skin (*peau d'orange*). Standard radiological imaging investigations of the breast include mammography and ultrasonography. Mammography is useful in detecting the presence of malignant masses as a stellate opacity with architectural distortion of the surrounding parenchyma. Preinvasive breast cancer, e.g. ductal carcinoma *in situ*, may appear as microcalcifications on the mammogram. An ultrasound scan of the breast is helpful to distinguish solid from cystic (fluid-filled) masses, and can also aid in the distinction of breast cancer from benign lumps by the different attenuation characteristics of the ultrasound waves and blood-flow patterns. Ultrasound may also be useful in guiding core biopsy.

A strong association between increased mammographic breast density and risk of breast cancer has been shown repeatedly. Breast density is assessed by mammograms where the appearance of the fibroglandular tissue is dense or white and the adipose tissue is less dense or grey. The fibroglandular tissue is comprised of epithelial cells, fibroblasts and connective tissue. Several scales of categorization of breast density have been devised. Wolfe was the first to introduce mammographic categorization of four mammographic patterns (Wolfe et al 1976a,1976b). Since then, in an effort to increase reproducibility of assessment of mammographic density, a number of methods have been devised comprising five or six categories. By the 1990s computerized measurements of mammograms were developed to calculate both total and percentage mammographic density. The computerized method has also been shown to be predictive of breast cancer risk. In general, there is high reproducibility and consistency between the scales, especially identification of women with high mammographic density (Garrido-Estepa et al 2010). Mammographic density appears to be influenced by a number of factors, including somatotype, BMI at 18 years of age, history of biopsy-confirmed benign breast disease (for both pre- and postmenopausal women) and hormone replacement therapy. It should be noted that premenopausal women's breasts are more mammographically dense due to the increased fraction of glandular and collagenous tissue present prior to postmenopausal involution. Given that the majority of breast malignancies are also radio-dense, this limits the effectiveness (as measured by the reduction in breast cancer mortality) of mammographic screening in premenopausal women. Breast cancer rates increase in 40- to 49-year-old women compared to those less than 40 years of age. These statistics may prompt clinicians to consider screening high-risk women and also incorporate supplementary imaging such as ultrasound or magnetic resonance imaging in those with high breast density.

Magnetic resonance imaging (MRI) is useful in diagnosis, particularly in women with younger, denser breasts, achieving higher sensitivity of breast cancer detection but with lower specificity. A cytological diagnosis of a breast lump can be achieved using fine-needle aspiration (FNA) to evaluate the cellular component of a lump. FNA is also useful to drain symptomatic breast cysts. A wide-bore needle biopsy is a procedure performed under local anaesthetic to obtain several pieces of specimen for a histological diagnosis with the tissue architecture maintained. This permits distinction between *in situ* and invasive cancer, and provides an indication of tumour subtype by evaluation of the pathological characteristics. Vacuum-assisted mammotome biopsies based on the wide-bore needle enable some benign and indeterminate lesions to be excised for full histological analysis and, in some patients, can avoid the need for conventional open surgery.

If a breast lump has to be surgically removed, the incision should be based, whenever possible, in the relaxed skin tension lines, for the best cosmetic results. In women with sizeable malignant lesions in whom breast conservation surgery is to be attempted, the skin incision should be planned with consideration of the possible requirement for a subsequent mastectomy if the margins of excision are incompletely excised by pathological criteria (Swanson et al 2002). Most women with single breast cancers of up to 4 cm in diameter are treated by breast conservation rather than mastectomy. This is a combination of surgery (tumour excision and sentinel node biopsy or clearance) together with external beam radiotherapy to minimize the risk of local recurrence. Patients with larger tumours are likely to be treated by mastectomy with axillary lymph node clearance. Neo-adjuvant endocrine or chemotherapy treatment prior to surgery may improve operability to allow breast conservation surgery of larger tumours.

During axillary dissection to clear the axillary lymph nodes, the long thoracic nerve (to serratus anterior), the thoracodorsal vessels, the thoracodorsal nerve (to latissimus dorsi), and the medial and lateral pectoral nerves are all identified and carefully preserved. The boundaries of the axillary dissection are the long thoracic nerve medially, the thoracodorsal vascular pedicle laterally and the axillary vein superiorly. The posterior limit of the dissection is the anterior (ventral) surface of subscapularis. The superomedial limit of a level 1 axillary dissection extends to the lateral (inferolateral) border of pectoralis minor at the apex of the axilla; a level 2 dissection extends to the medial (superomedial) border of pectoralis minor; and a level 3 dissection extends beyond the medial border until it reaches the point where the axilla is limited by the first rib (the latter is easily distinguished by its flat superior surface, easily palpable at surgery). Failure to preserve the long thoracic nerve will result in lifting of the medial border of the scapula (winging) from the posterior thoracic wall and a reduced scapula protraction. The intercostobrachial nerve is often sacrificed in an axillary lymph node clearance operation, and this may result in anaesthesia of a narrow strip of skin along the upper medial border of the ipsilateral arm.

Molecular breast cancer signatures

Mammary cell markers distinguish luminal from basal cells in the human breast. CK7, CK18 and Claudin-4 are expressed in luminal cells but not myopepithelial cells. CD10, SMA and p63 are expressed in myoepithelial cells but not luminal cells (Santagata and Ince 2014). Steroid hormone receptors are used in the classification of breast carcinomas. It remains clinically useful to classify carcinomas by the presence of the oestrogen receptor (ER+), progesterone receptor (PR+) and human epidermal growth factor receptor 2 (HER2+). Carcinomas not expressing any of these markers are referred to as triple-negative cancers (ER/PR/HER2−). Carcinomas expressing ER and PR are likely to respond to ER antagonists or aromatase inhibitors, blocking peripheral oestrogen production.

More recently, technological advances, including gene expression microarrays and next-generation sequencing, have emphasized the diversity and heterogeneity of breast cancer and greatly expanded knowledge of breast cancer biology. Breast cancer is driven by alterations in DNA and epigenetic changes that activate or suppress growth genes and high-throughput technologies have led to a more detailed identification of an array of subtypes that allow more targeted treatment of the cancer. For example, multiple genes can be tested that allow discrimination of luminal ER-positive tumours into subgroups that have better or worse prognosis. Similarly, basal-like cancers are typically triple-negative (although not all triple-negative breast cancers are basal-like) and display upregulation of basal cell genes. Basal-like cancers can be divided into four subtypes. One subtype, in particular, shows upregulation of androgen receptor and has a relatively good prognosis (Provenzano et al 2018). Using a combination or both clinical variables and molecular subtyping is more predictive than any single measure alone (Malhotra 2010).

Reconstructive surgery for breast cancer disease

Breast reconstruction may be performed at the time of mastectomy for breast cancer, or at a later stage (Serletti and Moran 2000). During a mastectomy where an immediate breast reconstruction is planned, the glandular breast tissue is removed either through a conventional mastectomy skin incision or in association with preservation of the native breast skin (skin-sparing mastectomy). Patient selection is important to minimize the risk of breast cancer recurrence in the skin of the reconstructed breast mound or associated lymph nodes. In an implant-based immediate breast reconstruction, a tissue expander is placed beneath the musculofascial plane consisting of pectoralis major, in continuity laterally under serratus anterior with the intervening fascia, and the abdominal fascia inferiorly. The lower fibres of the attachment of pectoralis major to the sixth rib need to be detached, otherwise the implant will be placed too high on the chest wall. The tissue expander has to stretch the potential space below this musculofascial plane to match the space created by the removed breast beneath the subcutaneous plane and the deep fascia overlying pectoralis major. The tissue expander is subsequently replaced by a silicone or saline breast implant.

The skin and volume component of the breast can also be replaced by the latissimus dorsi musculocutaneous flap, with or without an underlying silicone or saline breast implant. Latissimus dorsi and an overlying paddle of skin are raised on its dominant vascular pedicle: namely, the thoracodorsal vessels, which enter the muscle on its deep surface and send perforating branches through the muscle to the overlying skin. The flap is transferred in an arc from the posterior to the anterior thorax and fashioned to make a new breast. An implant may be required to provide additional volume replacement, in which case it is placed beneath the flap. The donor site defect on the back is directly sutured. In selected cases, this flap can be raised with additional superficial fascia and fat, to avoid the need for a silicone implant. This is known as the extended or autologous latissimus dorsi flap.

Women with a suitable abdominal panniculus may have breast reconstruction utilizing this tissue. Historically, this was achieved with a pedicled transverse rectus abdominis musculocutaneous (TRAM) flap based on the superior epigastric artery, where the skin and fat of the lower abdomen, attached to the rectus muscle, are transposed into the breast defect and shaped into a breast reconstruction.

The development of microvascular techniques over the past 30 years has seen an increase in the popularity of free tissue transfers, based on the inferior epigastric artery (often termed by surgeons the deep inferior epigastric artery), including muscle-sparing (MS-)TRAM flaps and deep inferior epigastric artery perforator (DIEP) flaps. These flaps require dissection of the blood vessels within rectus abdominis, rather than sacrifice of the entire muscle, and this aims to reduce donor site morbidity, including hernias and bulging. Radiological investigations (CT angiograms, MRI and duplex) are used to determine the calibre and position of cutaneous perforator vessels within these flaps to improve the accuracy of dissection and enhance surgical outcome (**Fig. 7.1.1**). Free TRAM and DIEP flap vessels are anastomosed to recipient vessels in the thoracic region; the internal thoracic or the thoracodorsal artery are used most frequently for this purpose.

Breast reconstruction using an autologous method, such as the extended latissimus dorsi, free MS-TRAM and DIEP flap, avoids the need for a silicone implant and has advantages in terms of producing a more natural appearance and achieving greater longevity of results. Free tissue transfers for breast reconstruction are also performed using buttock tissue (superior and inferior gluteal artery perforator flaps) and thigh tissue (transverse upper gracilis and anterolateral thigh flaps).

Breast reconstruction using autologous tissue

One of the earliest recorded breast reconstructions using latissimus dorsi, based on the thoracodorsal pedicle, was published by Tansini in 1906. The flap incorporated superficial fascia and a skin paddle attached to the muscle, and was used to replace part of the breast skin envelope that had been removed during the mastectomy. This form of breast reconstruction inexplicably fell out of regular use until the 1970s, when there was renewed interest in the latissimus dorsi musculocutaneous flap combined with silicone breast implants (Bostwick et al 1977, Schneider et al 1978) and improved definitions of the vascular supply and territory of the flap (McCraw et al 1977, Maxwell et al 1979).

Later in the twentieth century, further developments of this most versatile flap meant that breast reconstruction could be performed without a silicone implant. The so-called 'extended' flap (Hokin and Silfverskiold 1987) used autologous tissues exclusively; it was designed to satisfy an increasing demand for breast reconstruction in an era when silicone implants were under scrutiny because of safety fears and proposed links with autoimmune diseases. Further developments to maximize the volume available for autologous reconstructions of small to medium-sized breasts included harvesting larger skin paddles from the back and burying them beneath the breast skin envelope after de-epithelializing their surface (Papp et al 1988), and inclusion of additional fat pads in the back to increase flap volume (Delay et al 1998).

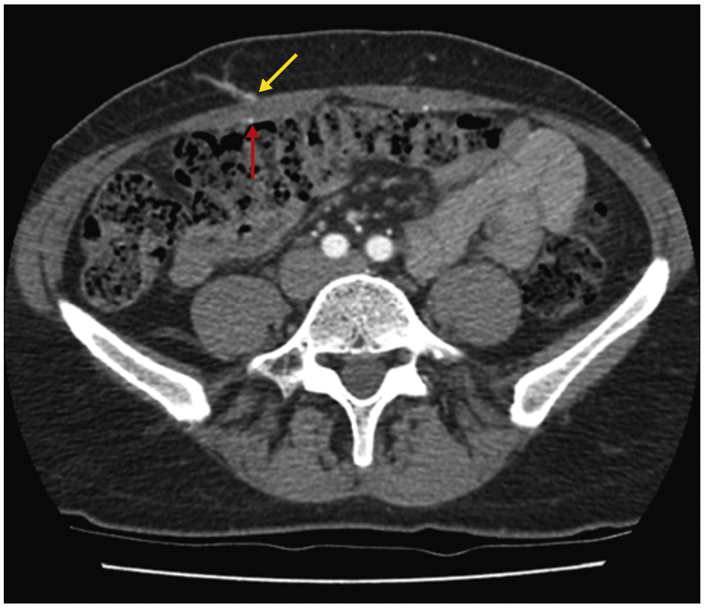

Fig. 7.1.1 A CT angiogram showing the deep inferior epigastric artery (red arrow) and a cutaneous perforating vessel (yellow arrow) emerging from the rectus sheath for MS-TRAM and DIEP flap reconstruction.

Despite the enhancements to the latissimus dorsi flap, the lower abdominal region provides a plentiful and more reliable source of tissue for reconstructive surgeons and also avoids the sometimes troublesome and often unsightly dorsal donor site wound. DIEP or MS-TRAM flaps are generally considered the first choice for breast reconstruction when the tissues are adequate.

The first description of lower abdominal tissues being used as a free flap appeared in 1979 (Holmstrom 1979), although at this time the pedicled TRAM flap was a far more popular choice for reconstruction. This was mainly because microvascular techniques were still in development and the required instruments and microscopes were not widely available. However, over the years, it became possible to achieve excellent, reliable results without the problems of fat necrosis and abdominal wall weakness associated with the pedicled version (Grotting et al 1989, Arnez et al 1991, Schusterman et al 1994). The TRAM flap particularly lends itself to microsurgical transfer on account of the characteristics of the supplying vessels (the inferior epigastric artery is 2.5–3 mm in diameter and its venae comitantes are 3 mm in diameter); the length of the pedicle (frequently up to 15 cm); and the large surface area of skin supplied by these vessels (see Fig. 53.1).

Further developments in dissection techniques, combined with a desire to reduce donor site morbidity, led to the first description of a 'perforator' flap based on the same vessels (Allen and Treece 1994). This is the DIEP flap, which captures the same soft tissue area of the abdomen for reconstruction, but attempts to avoid injury to rectus abdominis by dissecting the perforating vessels through the muscle rather than by sacrificing it. Some authors have identified fewer donor site bulges and herniae with DIEP flaps compared with TRAM flaps (Blondeel et al 1997), and it is for this reason that DIEP flaps are the preferred choice, if possible. However, the perforating vessels are not always anatomically favourable for allowing safe harvest of the flap. Many clinicians have adopted radiological studies (CT angiogram, duplex or MR angiogram) to determine the calibre and position of the vessels preoperatively for more accurate surgical planning (see Fig. 7.1.1).

References

Allen RJ, Treece P 1994 Deep inferior epigastric perforator flap for breast reconstruction. Ann Plast Surg 32:32–38.

Arnez ZM, Bajec J, Bardsley AF et al 1991 Experience with 50 free TRAM flap breast reconstructions. Plast Reconstr Surg 87:470–478.

Blondeel PN, Vanderstraeten GG, Monstrey SJ et al 1997 The donor site morbidity of free DIEP flaps and free TRAM flaps for breast reconstruction. Br J Plast Surg 50:322–330.

Bostwick J, Vasconez LO, Jurkiewicz MJ 1977 Breast reconstruction after a radical mastectomy. Plast Reconstr Surg 61:682–693.

Delay E, Gounot N, Bouillot A et al 1998 Autologous latissimus breast reconstruction: a 3 year clinical experience with 100 patients. Plast Reconstr Surg 102:1461–1478.

Fentiman IS 1993 Detection and Treatment of Early Breast Cancer. London: Martin Dunitz.

Garrido-Estepa M, Ruiz-Perales F, Miranda J et al 2010 Evaluation of mammographic density patterns: reproducibility and concordance among scales. BMC Cancer 10:485.

Grotting JC, Urist MM, Maddox WA et al 1989 Conventional TRAM flap versus free microsurgical TRAM flap for immediate breast reconstruction. Plast Reconstr Surg 83:828–841.

Hokin JA, Silfverskiold KL 1987 Breast reconstruction without an implant: results and complications using an extended latissimus dorsi flap. Plast Reconstr Surg 79:58–66.

Holmstrom H 1979 The free abdominoplasty flap and its use in breast reconstruction. Scand J Plast Reconstr Surg 13:423–427.

Malhotra GK, Zhao X, Band H et al 2010 Histological, molecular and functional subtypes of breast cancers. Cancer Biol Ther 10:955–60.

Maxwell GP, McGibbon BM, Hoopes JE 1979 Vascular considerations in the use of a latissimus dorsi myocutaneous flap after a mastectomy with an axillary dissection. Plast Reconstr Surg 64:771–780.

McCraw JB, Dibbell DG, Carraway JH 1977 Clinical definition of independent myocutaneous vascular territories. Plast Reconstr Surg 60:341–352.

Papp C, Zanon E, McCraw J 1988 Breast volume replacement using the de-epithelialised latissimus dorsi myocutaneous flap. Eur J Plast Surg 11:120–125.

Provenzano E, Ulaner GA, Chin SF 2018 Molecular classification of breast cancer. PET Clinics 13:325–38.

Santagata S, Ince TA 2014 Normal cell phenotypes of breast epithelial cells provide the foundation of a breast cancer taxonomy. Expert Rev Anticancer Ther 14:1385–9.

Schneider WJ, Hill HL, Brown RG 1978 Latissimus dorsi myocutaneous flap for breast reconstruction. Br J Plast Surg 30:277–281.

Schusterman MA, Kroll SS, Miller MJ et al 1994 The free transverse rectus abdominis musculocutaneous flap for breast reconstruction: one center's experience with 211 consecutive cases. Ann Plast Surg 32:234–241.

Serletti JM, Moran SL 2000 Microvascular reconstruction of the breast. Semin Surg Oncol 19:264–71.

Swanson GP, Rynearson K, Symmonds R 2002 Significance of margins of excision on breast cancer recurrence. Am J Clin Oncol 25:438–41.

Tansini I 1906 Sopra il mio nuovo processo di amputazione della mamella. Riforma Medica (Palermo, Napoli) 12:757.

Wolfe JN 1976a Risk for breast cancer development determined by mammographic parenchymal pattern. Cancer 37:2486–92.

Wolfe JN 1976b Breast patterns as an index of risk for developing breast cancer. AJR Am J Roentgenol 126:1130–7.

COMMENTARY

7.2

Computed tomography coronary angiography (CTCA) of anomalous coronary vasculature

Julia Sun, Jonathan Weir-McCall

Invasive coronary angiography has long been used to map coronary arterial anatomy and associated disease. In this procedure, a contrast agent is instilled into a coronary artery via a catheter inserted into the opening (ostium) of that artery within an aortic sinus. The fluoroscopic images that are acquired have a high spatial and temporal resolution and are of benefit in patient diagnosis and treatment, but they are two-dimensional (2D). In marked contrast, computed tomography (CT) is a non-invasive imaging modality that can demonstrate the anatomy and relations of a region of interest in 3D.

Despite the benefits afforded by CT, the cross-sectional imaging community used to regard the heart as an 'object of mystery' because of the rapidity of its movements and the limited speed of the available technology. Recent advances in the temporal resolution of CT scanners and associated radiation dose have enabled the development of computed tomography coronary angiography (CTCA), which is able to capture motion-free, essentially 'freeze-frame', 3D images of the heart and coronary vasculature. Image quality can still be adversely affected by the presence of a tachycardia: in such cases image quality can be enhanced using a pharmacological intervention to reduce heart rate or by timing (gating) scans to end diastole or end systole, when the coronary arteries and associated cardiac structures show the least movement. The simplicity of image capture and quality improves as technology develops: the latest generation of CT scanners are now fast enough to acquire diagnostic images even in patients with tachycardia (Agliata et al 2019).

After volumetric dataset acquisition using CTCA, post-processing with 3D reconstruction tools such as volume rendering and multiplanar reformatting enables visualization of the course, origin and anatomical relationships of the coronary arteries to neighbouring structures in a level of detail unmatched by other modalities. A relatively new post-processing technique, cinematic rendering, provides striking photorealistic images from CTCA datasets (Dappa et al 2016). While standard volume rendering is able to demonstrate anatomy and anatomical relationships in three dimensions, the overall quality achieved with cinematic rendering is much higher (see Commentary I.4 and Fig. 7.2.7C–D for a comparison of standard 3D volume rendering of the coronary arteries with cinematic rendering).

Classification of coronary artery anomalies

While there is no universal definition for the division between coronary artery variants and anomalies, a simple, robust and commonly used threshold defines variants as differences occurring in >1% of the population, and anomalies as differences occurring in ≤1% of the population (Angelini 2002, 2007). Variants and anomalies may be asymptomatic and only of relevance during cardiac surgery or may cause chest pain, shortness of breath, or serious cardiovascular sequelae (Levin et al 1978, Frescura et al 1998). Coronary artery anomalies can be grouped into three broad categories: anomaly of origin and course; anomaly of intrinsic anatomy (absence, atresia or duplication); and anomaly of termination. Some anomalies are asymptomatic and discovered incidentally, whereas others require treatment for symptomatic relief or to ensure continued cardiac function. CTCA is an important clinical tool for the diagnosis and detailed mapping of anomalies and the addition of photorealistic cinematic rendering further enhances its quality and utility for surgical and procedural planning and research, especially in cases of complex aberrant anatomy.

An exhaustive list of all the documented coronary anomalies is not possible in a single article. The cases in this commentary demonstrate a mixture of both the most common and most serious anomalies and have been selected to highlight the sometimes extreme deviations from normal coronary artery anatomy that can occur. Many permit survival to adulthood, and although extremely rare, the physician should be aware of their existence in clinical practice.

Anomalies of origin and course

Anomalies of coronary artery origin and course are the most commonly encountered of the three categories of anomalous vessels. The left coronary artery, anterior interventricular branch or circumflex branch of the left coronary artery, or the right coronary artery, can all arise from ectopic positions, which include a non-conventional aortic sinus, the ascending aorta, pulmonary trunk or other coronary arteries. The proximal part of an anomalous coronary artery follows one of five paths (pre-pulmonic, retro-aortic, inter-arterial, trans-septal or retro-cardiac) to access its more usual distal course and designated perfusion territory (Fig. 7.2.1). The pre-pulmonic and retro-aortic paths pass anterior to the pulmonary trunk and posterior to the ascending aorta, respectively, whereas the inter-arterial path passes between the ascending aorta and pulmonary trunk. The trans-septal path is subpulmonic, traversing anteriorly and inferiorly through the myocardium of the interventricular septum; the retro-cardiac path passes around the heart within the atrioventricular (coronary) sulcus (Kim et al 2006).

Depending on their location and initial path, a proportion of anomalous coronary arteries are associated with functional ischaemia and are the second most common cause of sudden cardiac death among young athletes (Basso et al 2000). Anomalous vessels taking the inter-arterial path are most frequently associated with sudden cardiac death, perhaps due to the exercise-related expansion of the ascending aorta and pulmonary trunk and the consequent increase in angulation and decrease in luminal diameter of the anomalous vessel (Angelini et al 2006) (Fig. 7.2.2). Sudden cardiac death is more likely with an inter-arterial anomalous left coronary artery or anterior interventricular artery because of the larger volume of subtended myocardium at risk during an associated cardiac event (Moustafa et al 2008). Other paths are not commonly associated with haemodynamic compromise because they are not associated with luminal narrowing (Fig. 7.2.3), but their location may complicate surgery.

Single coronary artery

A single coronary artery is an anomaly in which only one coronary artery arises from an aortic sinus and supplies the entire heart (Fig. 7.2.4). A range of permutations of origin, course and distribution may occur, some of which can be classified into predefined groups (Lipton et al 1979). The left or right coronary artery may be singular and perfuse the entire heart, or the left coronary artery may arise ectopically from a relatively normal right coronary artery or *vice versa*. The proximal part of the ectopic artery may follow one of the five paths previously described to reach its normal course and territory (see Fig. 7.2.1). A single coronary artery may be associated with other congenital cardiac anomalies such as transposition of the great vessels, coronary artery fistulae, bicuspid aortic valve and the tetralogy of Fallot. The direction of blood flow in cases of a single coronary artery is normally anterograde or centrifugal (from larger central vessels to smaller peripheral vessels), whereas in left coronary artery atresia the direction of blood flow is partially retrograde or centripetal (from the smaller peripheral collateral vessels to one or more of the main left-sided arteries) (Musiani et al 1997). The vascular supply of the left ventricle when there is a single coronary artery is much better developed than it is in left coronary artery atresia, where the collateral vessels supplying the left ventricle are small (see Fig. 7.2.6).

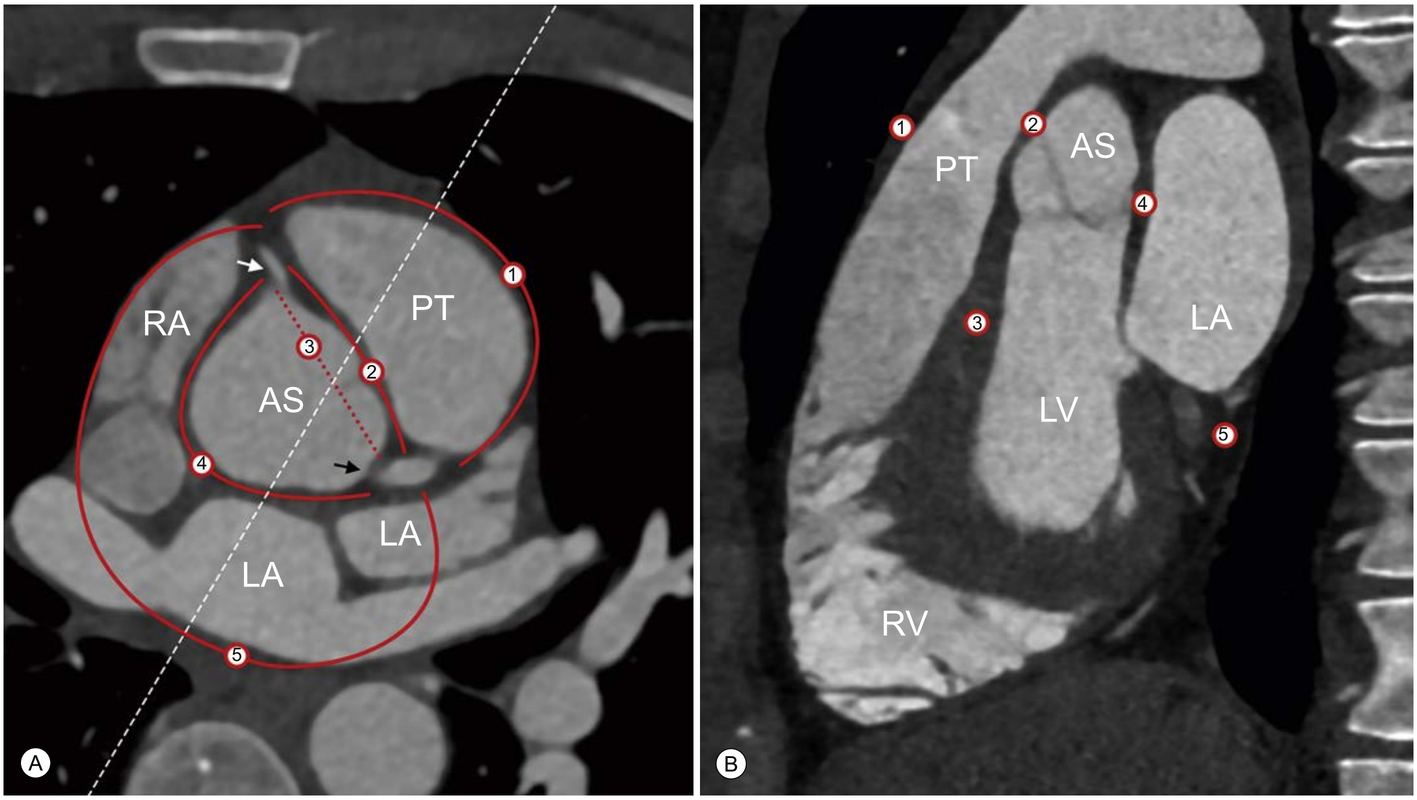

Fig. 7.2.1 CTCA showing the five paths along which the proximal part of an anomalous coronary artery may travel. The numbers 1–5 correspond to the five paths: 1, pre-pulmonic; 2, inter-arterial; 3, trans-septal; 4, retro-aortic; 5, retro-cardiac. **A**, Axial image at the level of the pulmonary trunk and origin of the left (black arrow) and right (white arrow) coronary arteries. The five paths are indicated by red lines. **B**, Sagittal oblique image (corresponding to the dashed white line in **A**) showing the position of the five paths relative to the great vessels and heart. Abbreviations: AS, aortic sinus; LA, left atrium; LV, left ventricle; PT, pulmonary trunk; RA, right atrium; RV, right ventricle.

Anomalous origins from the pulmonary trunk

Anomalous coronary artery origin from the pulmonary trunk is one of the more haemodynamically significant coronary artery anomalies (Fig. 7.2.5). Either the left or right coronary artery or, uncommonly, both arteries may be involved. Cases where both coronary arteries arise from the pulmonary trunk are unlikely to survive beyond the first month of life without surgical intervention.

Anomalous origin of the right coronary artery from the pulmonary trunk (ARCAPA) and anomalous origin of left coronary artery from the pulmonary trunk/artery (ALCAPA or Bland–White–Garland syndrome) are rare (Pfannschmidt et al 1992, Williams et al 2006). ARCAPA is usually asymptomatic with no evidence of myocardial ischaemia. ALCAPA is of little relevance *in utero* where systemic (aortic) and pulmonary arterial pressures are equal, so that antero-grade flow to the heart of similarly oxygenated blood occurs through both left and right coronary arteries. After birth, closure of the ductus arteriosus and a fall in pulmonary vascular resistance reduces pulmonary arterial pressure, which results in retrograde flow through the left coronary artery. Adequate perfusion of the territory of the left coronary artery becomes reliant on the development of a collateral circulation from the right coronary artery, which consequently dilates to accommodate the increased blood flow. The majority of patients with ALCAPA die during their first year of life, but occasionally patients with well-established collateral vessels may present later in life and are classified as having 'adult type' ALCAPA (Wesselhoeft et al 1968).

Anomalies of intrinsic anatomy

Hypoplasia or atresia of the ostium of a coronary artery within the aortic sinus can obstruct that artery at or near its origin and can result in a collateral circulation from the functional (normal) coronary artery developing to supply the affected territory (Fig. 7.2.6). Coronary ostial atresia is often associated with ischaemic manifestations (Musiani et al 1997). When the left coronary artery is affected, right-to-left collateralization occurs during the later stages of development, and is often insufficient to meet the oxygen requirements of the left ventricular myocardium. Atresia of the ostium or proximal part of a coronary artery may be accompanied or replaced by a fibrous connection spanning the gap between the aortic sinus and a more distal functional part of the affected coronary artery. The fibrous connection can pull on its points of attachment causing a focal distortion that may be visible as a beak-like projection on imaging. Single coronary artery anomalies are not characterized by a focal distortion of adjacent vessel walls because their developmental origin is different and no such fibrous remnant exists.

Anomalies of termination

An anomalous termination occurs when a coronary artery drains directly or via branches into a cardiac chamber, great vessel or other vascular structure, rather than into a capillary bed of the heart. Reported sites of abnormal termination include the right and left atria and ventricles, coronary venous system, pulmonary arteries and pulmonary veins. Fistulae terminating in the right heart chambers, pulmonary trunk or pulmonary arteries are the most common (Fig. 7.2.7). Depending on the position of origin and the vessel or chamber of termination, the affected vessel may become dilated or tortuous in response to increased blood flow and aneurysms may form (Fig. 7.2.8).

While most instances of coronary artery fistulae are congenital, some result from iatrogenic injury, infection or inflammatory disease. Larger coronary artery fistulae with significant intra-cardiac shunts are rare in adults: most are detected and repaired during childhood (Gowda et al 2006). Many are asymptomatic and identified incidentally on coronary angiography (Wilde and Watt 1980). Although the degree of left-to-right shunting of blood is usually very small and of little consequence, the presence of large or multiple left-to-right shunts could result in a right ventricular volume overload (Rittenhouse et al 1975). Multiple fistulae may form a complex network of shunts. A careful interrogation of conventional CTCA images can help identify fistulae within a tangled network of collateral vessels, some of which may initially be hidden from view on the 3D rendered images (Fig. 7.2.9): cinematic rendering can aid this task by depicting a more recognizable model of complex aberrant anatomy. The presence of fistulae can complicate surgical approaches to the heart; exact mapping of their anatomy and relations is required in such cases.

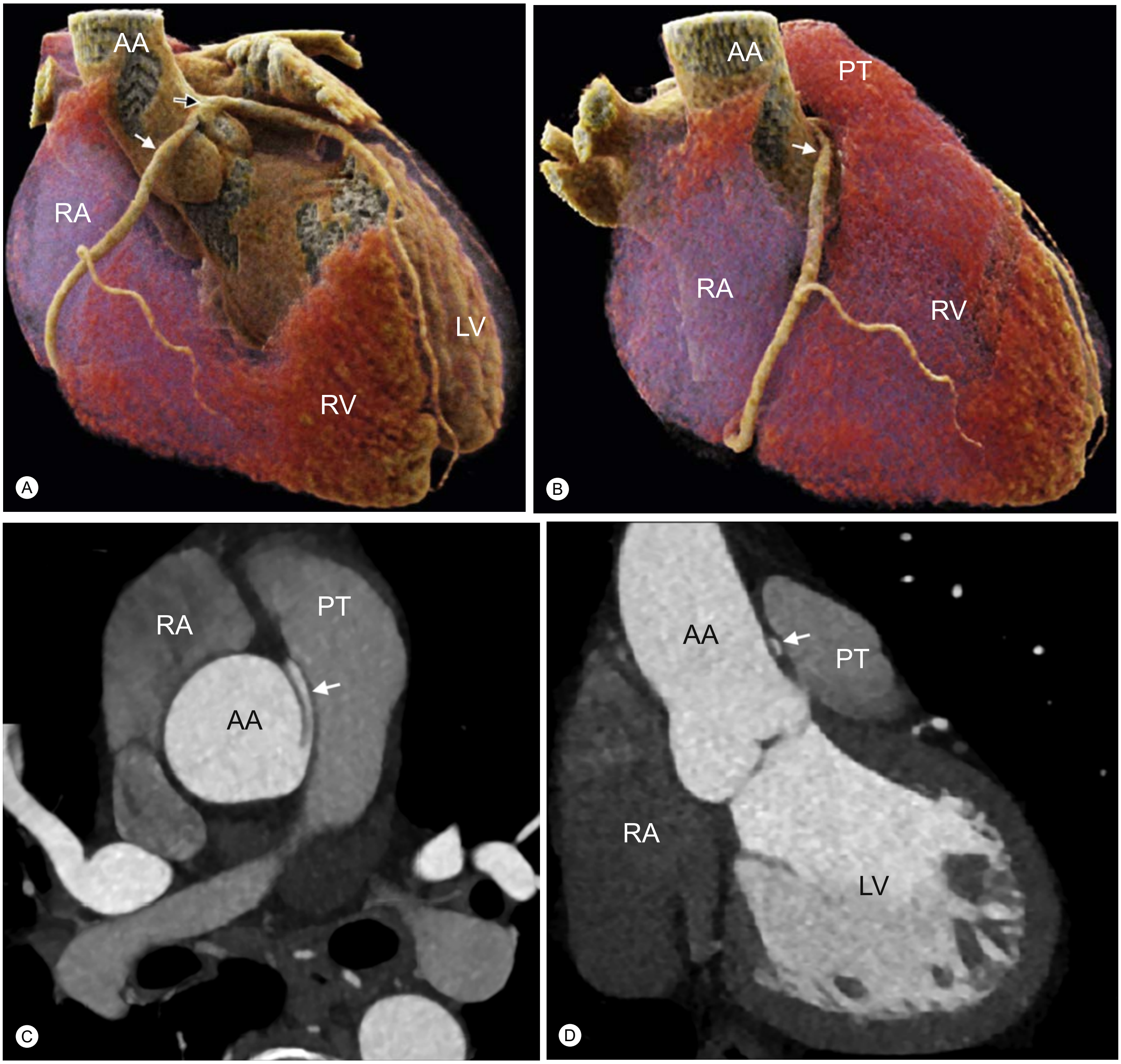

Fig. 7.2.2 CTCA showing an anomalous origin of the right coronary artery from the left aortic sinus and the inter-arterial course of its proximal part. **A**, Cinematic rendered image showing an anterior view with the right ventricle and pulmonary trunk removed to show the anomalous origin of the right coronary artery (white arrow) from the left aortic sinus adjacent to the left coronary artery (black arrow). **B**, Cinematic rendered image showing an anterior view of the right coronary artery (white arrow), with its proximal part passing through the interval between the ascending aorta and pulmonary trunk (inter-arterial path). **C**, Axial image showing the origin and proximal part (white arrow) of the right coronary artery passing between the ascending aorta and pulmonary trunk. **D**, Sagittal oblique image showing compression (note the oval-shaped lumen) of the inter-arterial part of the right coronary artery (white arrow). Abbreviations: AA, ascending aorta; LV, left ventricle; PT, pulmonary trunk; RA, right atrium; RV, right ventricle.

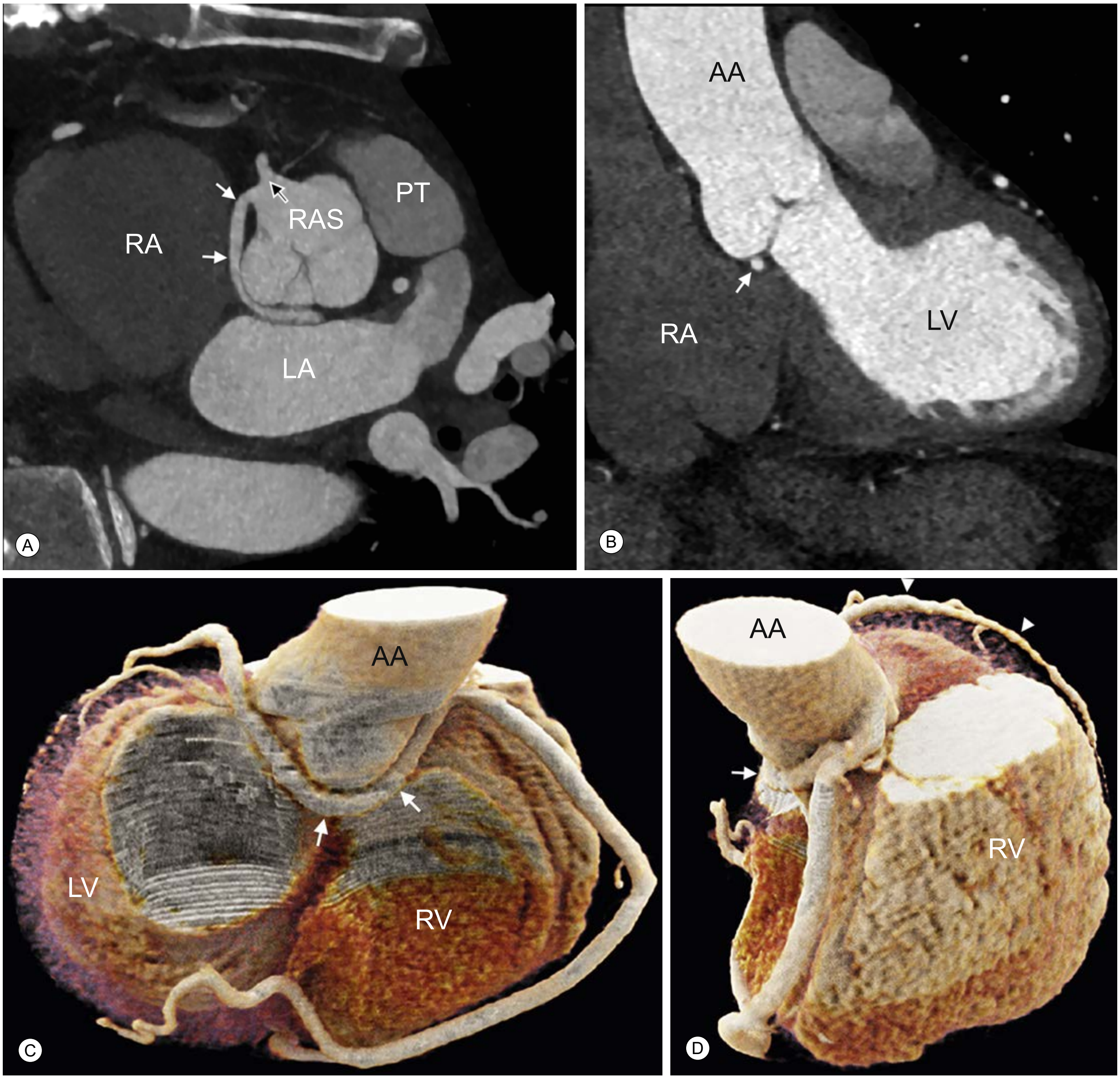

Fig. 7.2.3 CTCA showing an anomalous origin of the anterior interventricular artery and the retro-aortic course (posterior to the ascending aorta and anterior to the left atrium) of its proximal part. **A**, Axial image showing the anterior interventricular branch of the left coronary artery (white arrows) originating from the right aortic sinus, adjacent to a normal right coronary artery (black arrow), and the retro-aortic path of its proximal part. **B**, Sagittal oblique image showing the anterior interventricular artery passing posteriorly to take a retro-aortic path (white arrow). Note the relatively rounded lumen of the coronary artery indicating an absence of compression. **C** and **D**, Cinematic rendered images showing right posterolateral (**C**) and right anterolateral (**D**) views with both atria removed to reveal the retro-aortic course of the anterior interventricular artery (white arrows) and the conventional position of its more distal part in the anterior interventricular sulcus (white arrowheads). Abbreviations: AA, ascending aorta; LV, left ventricle; PT, pulmonary trunk; RA, right atrium; RAS, right aortic sinus; RV, right ventricle.

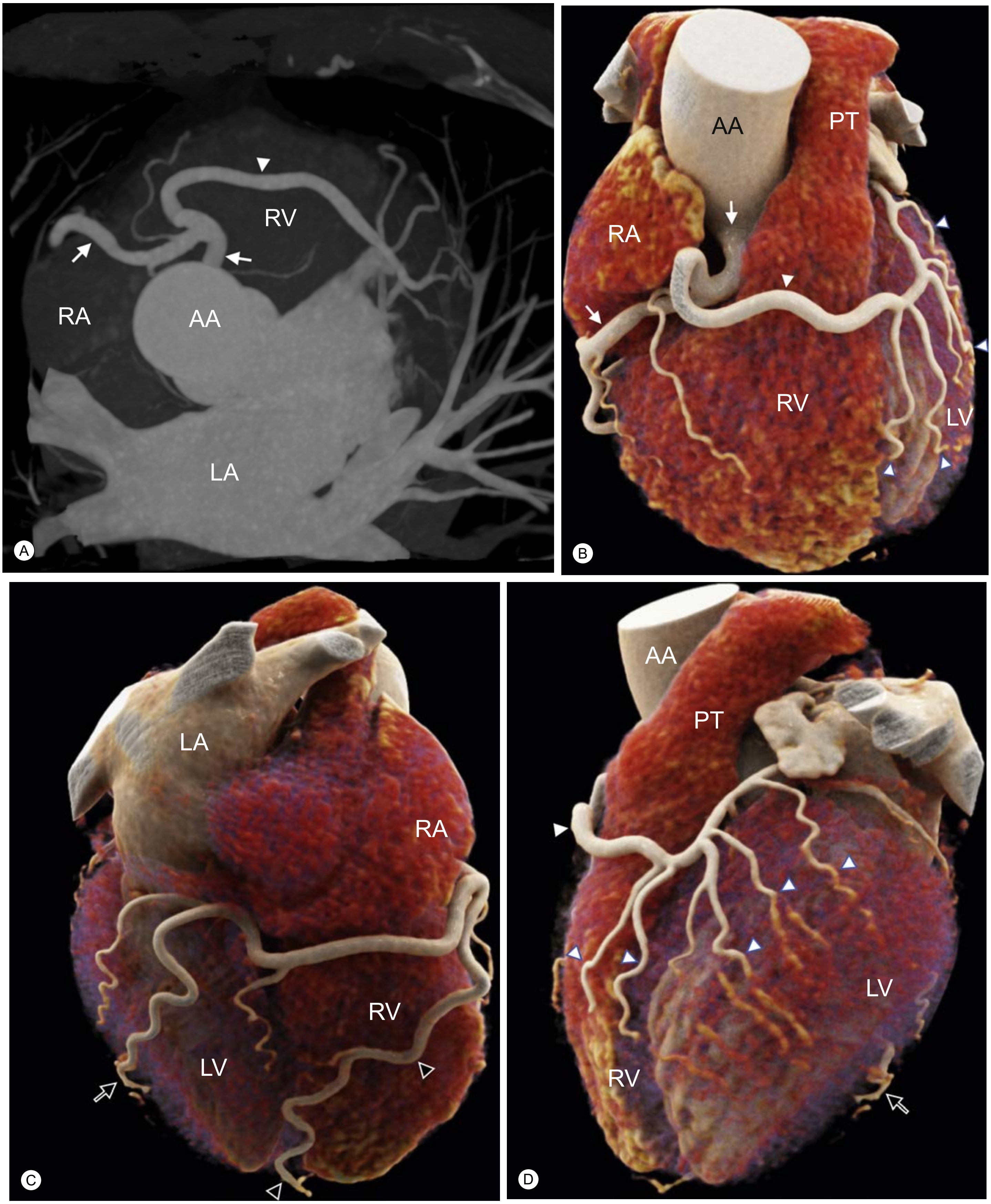

Fig. 7.2.4 CTCA showing a single right coronary artery (white arrows) arising from the right aortic sinus, with a dilated conal branch (white arrowheads) passing over the conus arteriosus to perfuse the left ventricle (white arrowheads with blue outline). The normal left coronary arterial system is absent. **A**, Maximum intensity projection (MIP) axial image at the level of the aortic sinuses. **B–D**, Cinematic rendered images showing right anterior (**B**), inferior (**C**) and left anterior (pulmonary surface) (**D**) views of the distribution of the single right coronary artery. The right coronary artery gives rise to a large inferior interventricular branch (black arrowheads) and a large posterolateral branch to the inferior and pulmonary surfaces of the left ventricle (black arrows), and multiple branches (arising from the conal branch) to the left pulmonary surface of the left ventricle (white arrowheads with blue outline). Abbreviations: AA, ascending aorta; LA, left atrium; LV, left ventricle; PT, pulmonary trunk; RA, right atrium; RV, right ventricle.

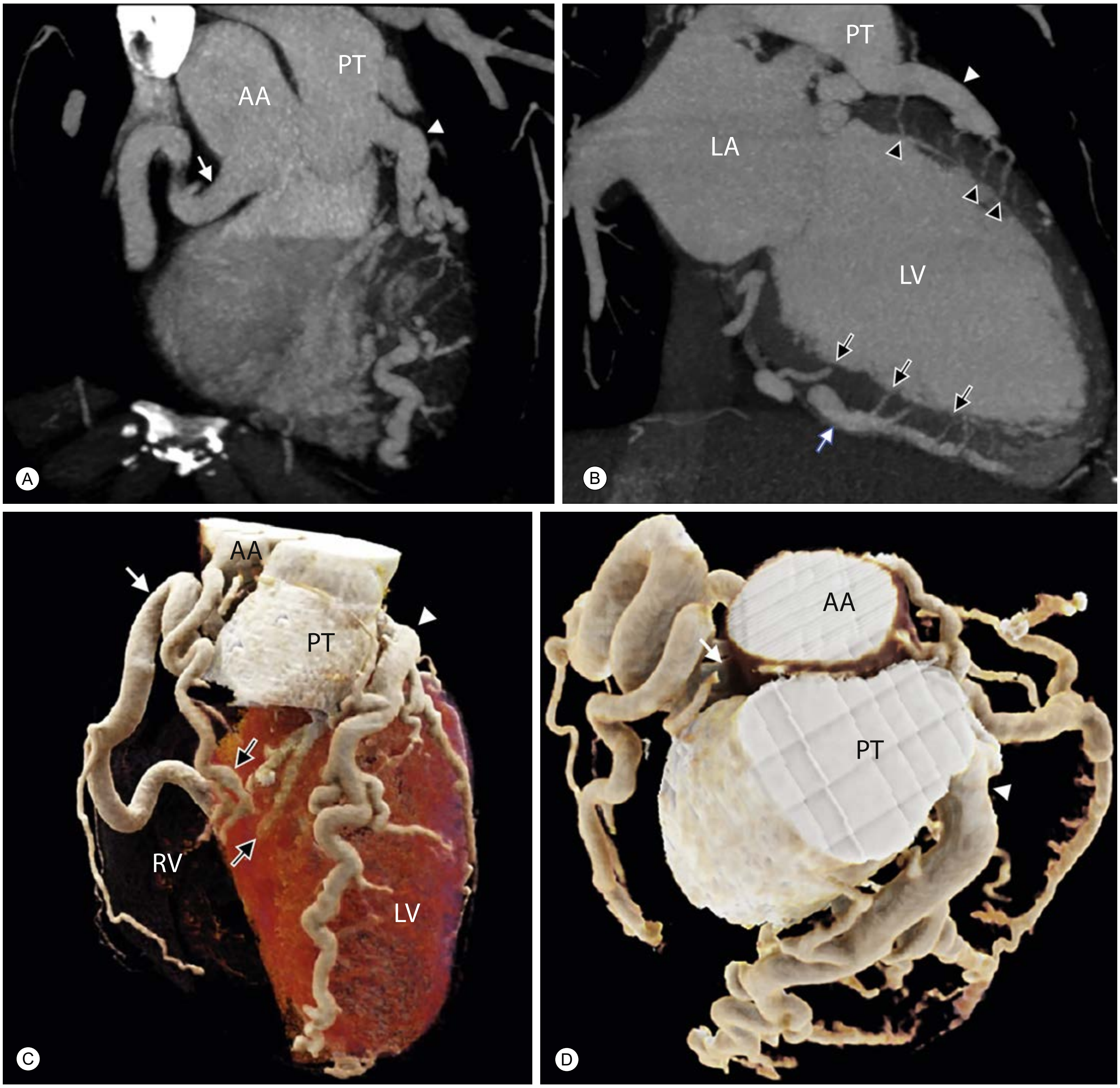

Fig. 7.2.5 CTCA showing an anomalous origin of the left coronary artery from the pulmonary trunk/artery (ALCAPA or Bland–Garland–White syndrome) in an adult male. The left and right coronary arteries are indicated by a white arrowhead and arrow, respectively. **A**, Maximum intensity projection (MIP) coronal image through the ascending aorta and pulmonary trunk showing a dilated right coronary artery arising from the right aortic sinus and a left coronary artery arising from the pulmonary trunk. **B**, Two-chamber long axis MIP view of the left atrium and left ventricle showing multiple enlarged collateral vessels (black arrows) branching from the inferior interventricular branch of the right coronary artery (white arrow with blue outline) to supply the inferior wall of the left ventricle. Enlarged collateral vessels from the anterior part of the left ventricular wall (black arrowheads) join and drain into the left coronary artery, which is continuous with the pulmonary trunk. **C**, Cinematic rendered image showing a left anterior view of the relationship between the coronary arteries and the left ventricular myocardium. Extensive hypertrophied collateral vessels (black arrows) supply the interventricular septum. The right ventricle is transparent. **D**, Top-down cinematic rendered image of the coronary arterial system with other cardiac anatomy removed. Abbreviations: AA, ascending aorta; LA, left atrium; LV, left ventricle; PT, pulmonary trunk; RV, right ventricle.

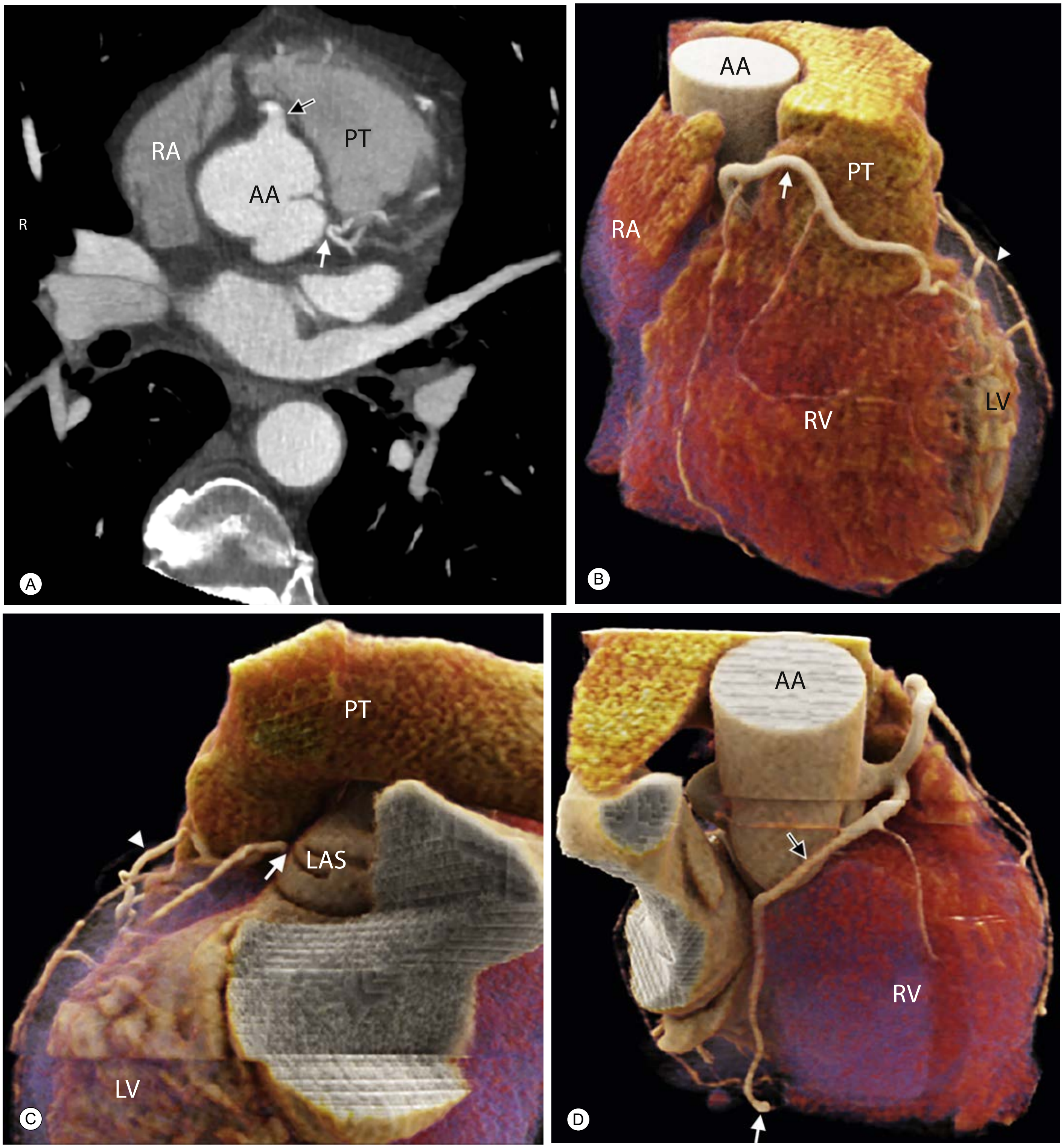

Fig. 7.2.6 CTCA showing atresia of the ostium (opening) of the left coronary artery. **A**, Axial image at level of the aortic sinuses showing a normal right coronary artery origin (black arrow) and atresia of the left coronary artery origin with no visible connection between the left aortic sinus and the small anterior interventricular artery (white arrow). **B–D**, Cinematic rendered images. **B**, Anterior view showing a dilated conal branch of the right coronary artery (white arrow) connecting to, and supplying the territory of, the anterior interventricular branch of the left coronary artery (white arrowhead). The coronary arteries supplying the left ventricular wall are small in calibre and insufficient to meet increases in myocardial demand. **C**, Close up of a posterior view with the left atrium partially removed showing a small anterior interventricular artery (white arrowhead) and a gap (white arrow) at the normal site of origin of the proximal left coronary artery from the left aortic sinus. **D**, Right lateral (pulmonary surface) view with both atria removed showing a vessel branching from the right coronary artery and taking a retro-aortic route (black arrow) to become continuous with the inferior interventricular artery (white arrow). Abbreviations: AA, ascending aorta; LAS, left aortic sinus; LV, left ventricle; PT, pulmonary trunk; RA, right atrium; RV, right ventricle.

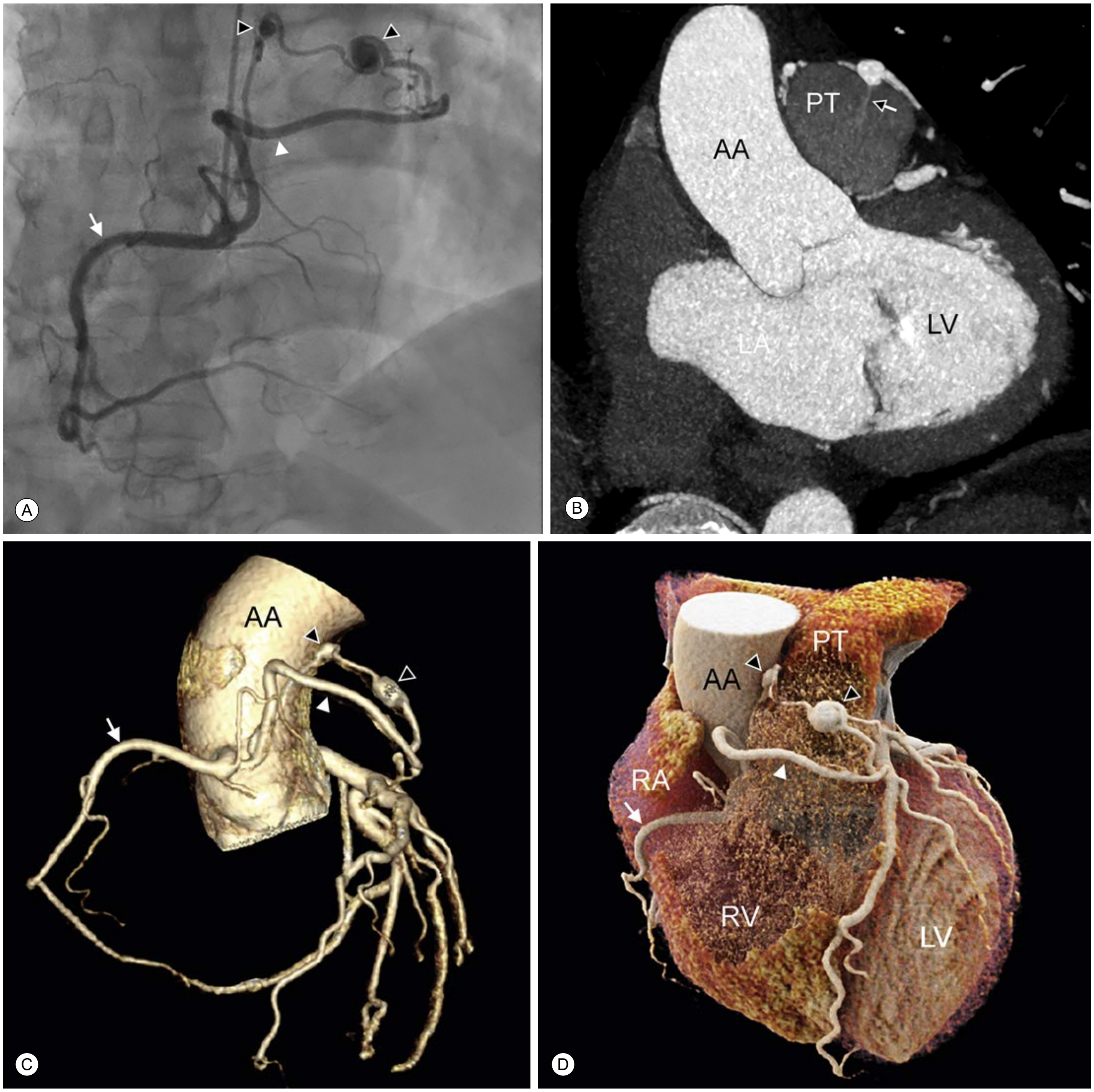

Fig. 7.2.7 A coronary artery fistula between the right coronary artery and the pulmonary trunk. **A**, Fluoroscopic image of a conventional invasive coronary artery angiogram showing an incidental finding of an aberrant vessel (white arrowhead) arising from the right coronary artery (white arrow). The aberrant vessel is wrapped around the pulmonary trunk and has two small aneurysms (black arrowheads). **B**, CTCA showing an oblique image centred on the larger of the two aneurysms. A tiny jet of contrast agent (black arrow) can be seen passing through a fistula between the aneurysm and pulmonary trunk. **C** and **D**, show similar lateral views of the heart enabling a comparison of 3D real time volumetric rendering (**C**) and cinematic rendering (**D**) of the coronary arterial system. Note the enhanced quality achieved using cinematic rendering. Abbreviations: AA, ascending aorta; LV, left ventricle; PT, pulmonary trunk; RA, right atrium; RV, right ventricle.

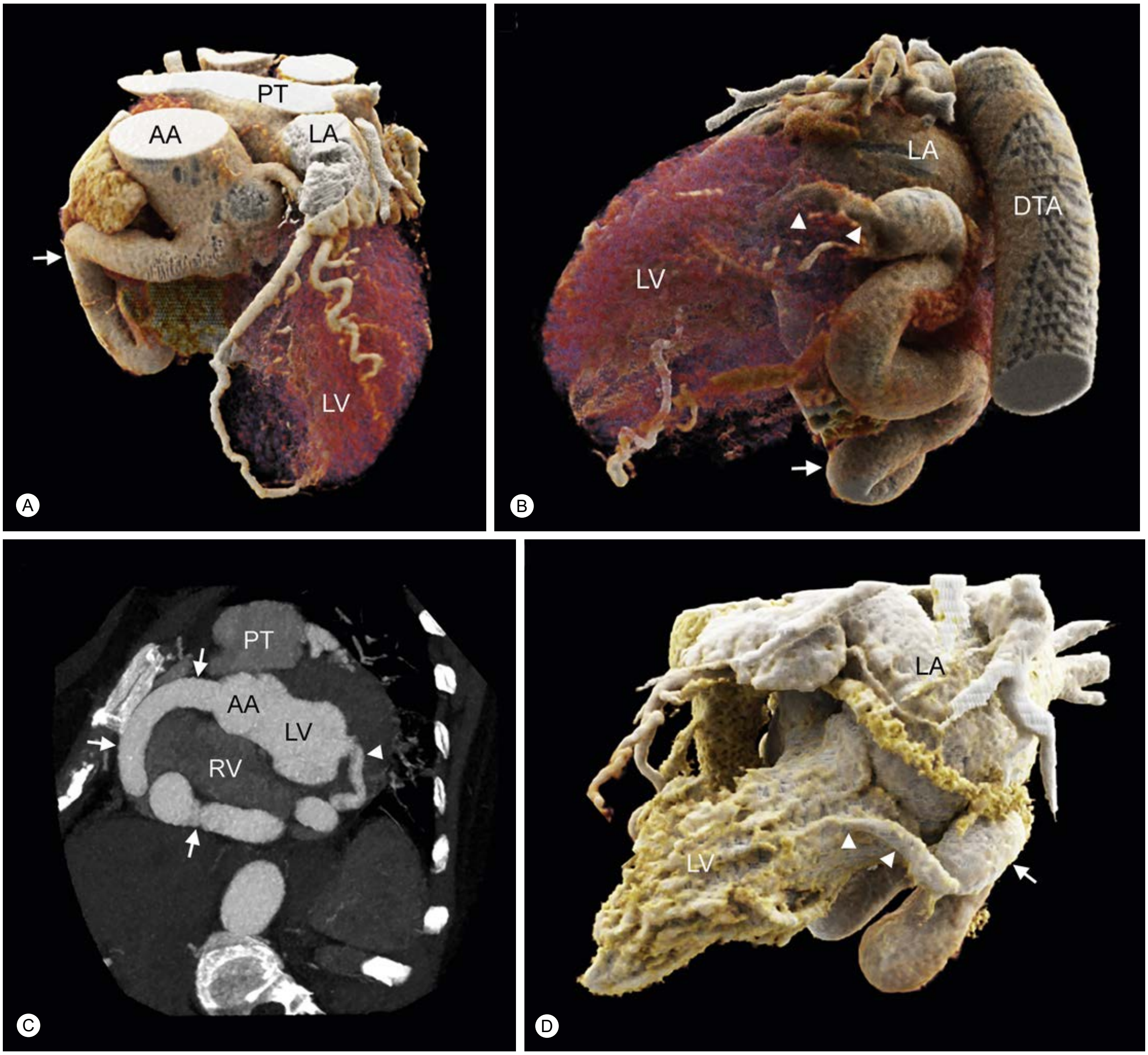

Fig. 7.2.8 CTCA of a coronary artery fistula showing the right coronary artery (white arrow) terminating in the left ventricle (white arrowhead). Cinematic rendered images showing **A**, left anterior and **B**, left inferolateral views of the course of the dilated right coronary artery as it travels around the atrioventricular (coronary) sulcus and enters the left ventricle through its inferior wall. **C**, Maximum intensity projection image showing an oblique view of a dilated right coronary artery passing from its origin to its insertion into the left ventricular chamber. **D**, Cinematic rendered image showing a left inferolateral view of the blood (contrast agent) within the cardiac chambers and coronary arteries: the myocardium has been removed. This image type provides a better visualization of the continuity of flow between the right coronary artery and left ventricle. Abbreviations: AA, ascending aorta; DTA, descending thoracic aorta; LA, left atrium; LV, left ventricle; PT, pulmonary trunk; RV, right ventricle.

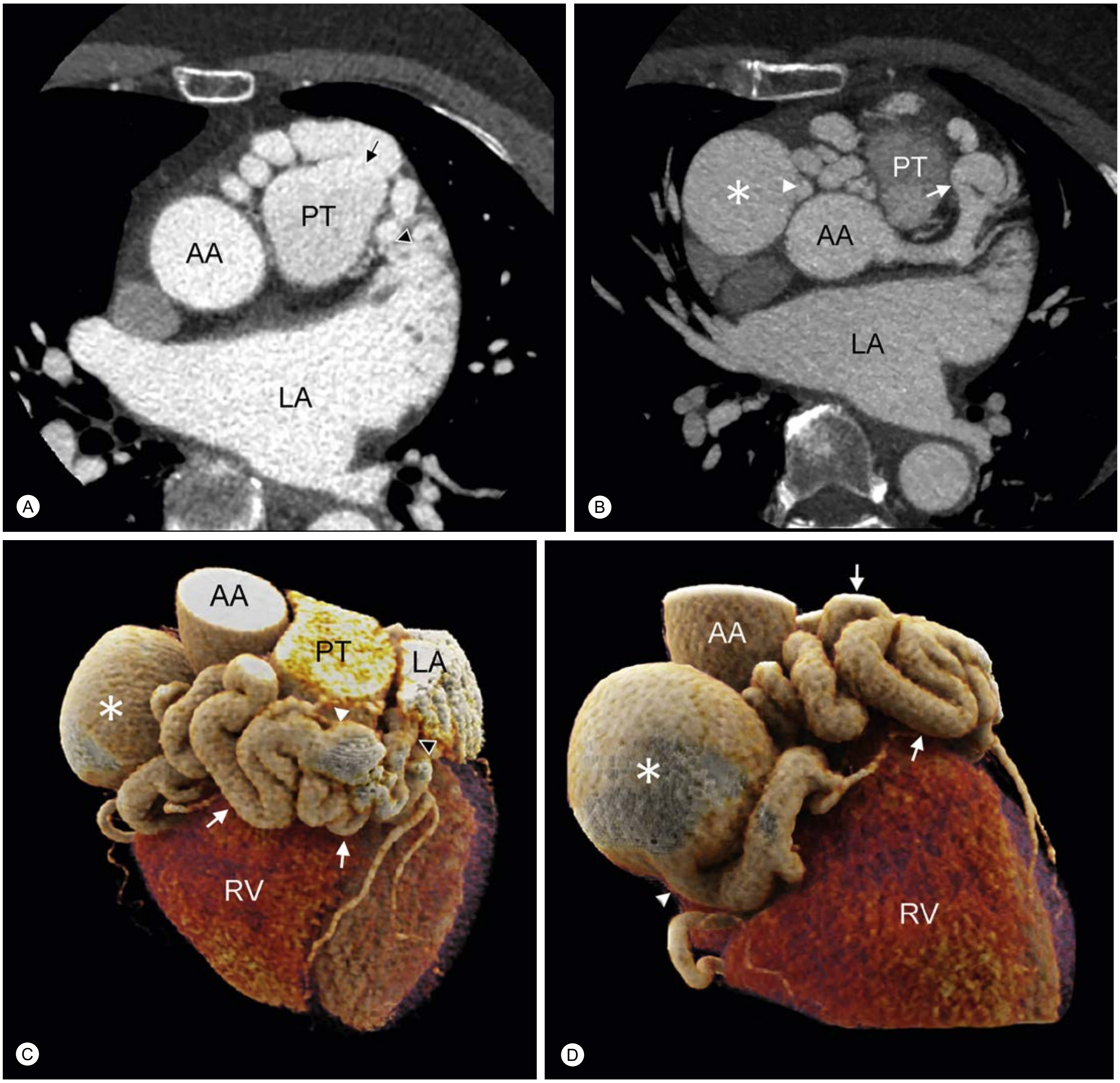

Fig. 7.2.9 CTCA showing complex coronary artery fistulae. **A**, Axial image at the level of the pulmonary trunk showing a complex network of dilated collateral coronary vessels with connections to the pulmonary trunk (black arrow) and left atrial auricle (black arrowhead). **B**, Axial image at the level of the aortic sinuses showing involvement of the anterior interventricular branch of the left coronary artery (white arrow), further complicated by an aneurysm of the right coronary artery (*) which also communicates with the collateral coronary vessels (white arrowhead). **C**, Cinematic rendered image showing an anterior view of the collateral vessels (white arrows) surrounding and in communication with the pulmonary trunk (white arrowhead) and left atrial auricle (black arrowhead). The aneurysm of the right coronary artery is again visible (*). **D**, Cinematic rendered image showing a posterior view of the right coronary artery aneurysm (*) in connection with a dilated right coronary artery (white arrow head). The superior connection with the collateral coronary vessels (white arrows at top of image) is hidden from view. Abbreviations: AA, ascending aorta; LA, left atrium; PT, pulmonary trunk; RV, right ventricle.

References

Agliata G, Schicchi N, Agostini A et al 2019 Radiation exposure related to cardiovascular CT examination: comparison between conventional 64-MDCT and third-generation dual-source MDCT. Radiol Med 124:753–61.

Angelini P 2002 Coronary artery anomalies – current clinical issues: definitions, classification, incidence, clinical relevance, and treatment guidelines. Texas Heart Inst J 29:271–8.

Angelini P 2007 Coronary artery anomalies. Circulation 115:1296–305.

Angelini P, Walmsley RP, Libreros A et al 2006 Symptomatic anomalous origination of the left coronary artery from the opposite sinus of Valsalva: clinical presentations, diagnosis, and surgical repair. Texas Heart Inst J 33:171–9.

Basso C, Maron BJ, Corrado D et al 2000 Clinical profile of congenital coronary artery anomalies with origin from the wrong aortic sinus leading to sudden death in young competitive athletes. J Am Coll Cardiol 35:1493–501.

Dappa E, Higashigaito K, Fornaro J et al 2016 Cinematic rendering – an alternative to volume rendering for 3D computed tomography imaging. Insights Imaging 7:849–56.

Frescura C, Basso C, Thiene G et al 1998 Anomalous origin of coronary arteries and risk of sudden death: A study based on an autopsy population of congenital heart disease. Hum Pathol 29:689–95.

Gowda RM, Vasavada BC, Khan IA 2006 Coronary artery fistulas: clinical and therapeutic considerations. Int J Cardiol 107:7–10.

Kim SY, Seo JB, Do K-H et al 2006 Coronary artery anomalies: classification and ECG-gated multi–detector row CT findings with angiographic correlation. RadioGraphics 26:317–33.

Levin DC, Fellows KE, Abrams HL 1978 Hemodynamically significant primary anomalies of the coronary arteries. Angiographic aspects. Circulation 58:25–34.

Lipton MJ, Barry WH, Obrez I et al 1979 Isolated single coronary artery: diagnosis, angiographic classification, and clinical significance. Radiology 130:39–47.

Moustafa SE, Zehr K, Mookadam M et al 2008 Anomalous interarterial left coronary artery: An evidence based systematic overview. Int J Cardiol 126:13–20.

Musiani A, Cernigliaro C, Sansa M et al 1997 Left main coronary artery atresia: Literature review and therapeutical considerations. Eur J Cardiothoracic Surg 11:505–14.

Pfannschmidt J, Ruskowski H, de Vivie E 1992 Das Bland-White-Garland-Syndrom (BWGS). Klin Pädiatrie 204:328–34.

Rittenhouse EA, Doty DB, Ehrenhaft JL 1975 Congenital coronary artery—cardiac chamber fistula. Ann Thorac Surg 20:468–85.

Wesselhoeft H, Fawcett JS, Johnson AL 1968 Anomalous origin of the left coronary artery from the pulmonary trunk. Circulation 38:403–25.

Wilde P, Watt I 1980 Congenital coronary artery fistulae: Six new cases with a collective review. Clin Radiol 31:301–11.

Williams IA, Gersony WM, Hellenbrand WE 2006 Anomalous right coronary artery arising from the pulmonary artery: A report of 7 cases and a review of the literature. Am Heart J 152:1004.e9–17.

CHAPTER

59

Abdomen and pelvis: overview and surface anatomy

GENERAL STRUCTURE AND FUNCTION OF THE ABDOMINOPELVIC CAVITY

Although often considered separately, the abdomen and pelvis form the largest continuous visceral cavity in the body. Together, they provide multiple vital functions including: housing and protection of the digestive and urinary tracts and of the internal reproductive organs; a conduit for neurovascular communication between the thorax and lower limb; support and attachment for the external genitalia; access to and from the internal reproductive organs and urinary tract; assistance with physiological functions such as respiration, defecation and micturition; support for the vertebral column in weight-bearing, maintenance of posture and movement; and, in females, the ability to support gestation.

Musculoskeletal framework of the abdomen and pelvis

The walls of the abdominopelvic cavity consist of five lumbar vertebrae and their intervening intervertebral discs (lying in the posterior midline); the muscles of the anterior abdominal wall lying anteriorly (rectus abdominis) and anterolaterally (transversus abdominis, internal abdominal oblique and external abdominal oblique); the muscles of the posterior abdominal wall (psoas major, quadratus lumborum and the respiratory diaphragm); the bony 'basin' formed by the walls of the greater and lesser pelves; the muscles of the pelvic diaphragm and perineum lying inferiorly; and the respiratory diaphragm lying superiorly (Fig. 59.1). In addition, the superior aspect of the abdominal cavity gains protection from the inferior six ribs and their cartilages, even though these structures are technically part of the thoracic wall.

The muscles of the abdominal wall are important for movement of the trunk (flexion, extension and rotation). The anterolateral muscles in particular provide assistance with rotation of the thorax in relation to the pelvis (or vice versa if the thorax is fixed).

The abdominal cavity is somewhat kidney-shaped in horizontal cross-section owing to the posterior indentation of the vertebral column. In standing, the linea terminalis lies at an angle of about 55° to the horizontal such that the anterior superior iliac spines and pubic tubercles are in approximately the same coronal plane. The mean angle between the superior border of the first segment of the sacrum and the horizontal plane is about 40–45° (Woon et al 2013).

Thoracoabdominal interface

The respiratory diaphragm (diaphragm, thoracic diaphragm) constitutes the interface between the thoracic and abdominal cavities (Ch. 55). There are three principal pathways between the two cavities across the respiratory diaphragm: the caval foramen in the central tendon transmits the inferior vena cava and right phrenic nerve; the oesophageal hiatus, encircled by the right crus of the respiratory diaphragm, transmits the oesophagus, vagal trunks and vessels; and the aortic hiatus, posterior to the median arcuate ligament, transmits the aorta, thoracic duct and, usually, the azygos vein. The hemiazygos vein usually enters the thorax through the left crus of the respiratory diaphragm. Other lymphatics from the abdomen drain to the thorax alongside the inferior vena cava and via small vessels passing through and around the respiratory diaphragm. Thoracic splanchnic nerves reach the abdomen through the crura of the respiratory diaphragm and posterior to the medial arcuate ligaments, and the left phrenic nerve pierces the left side of the respiratory diaphragm. The subcostal vessels pass into the abdomen posterior to the lateral arcuate ligaments of the respiratory diaphragm. Anteriorly, the superior epigastric vessels pass between the costal and xiphoid process attachments, i.e. sternocostal foramen of the respiratory diaphragm. Neurovascular structures also cross between the thorax and abdomen within the subcutaneous tissues.

Pelvis–lower limb interface

The pelvis forms an integral part of the bony structure of both the abdominopelvic cavity and the lower limbs. It transmits the weight of the upright body and provides a stable platform for movement of the hip joint and bipedal locomotion. Its bony surfaces provide attachment sites for the muscles of the buttock and thigh (Ch. 77), the pelvic diaphragm and perineal membrane, the abdominal wall and lower back. The pelvis also transmits the neurovascular structures that supply the lower limb. There are four principal pathways between the pelvis and lower limb: the interval deep to the inguinal ligament anterior to the superior ramus of the pubis and ilium, which transmits the femoral neurovascular structures and lymphatics; the greater and lesser sciatic foramina, which transmit the gluteal vessels and nerves, sciatic nerve and internal pudendal vessels and pudendal nerve; and the obturator foramen, which transmits the obturator nerve, vessels and lymphatics. Autonomic nerves travel with the arterial supply to the lower limb and with the branches of the sacral plexus. Neurovascular structures also cross between the lower limb and pelvis within the subcutaneous tissues.

GENERAL ARRANGEMENT OF ABDOMINOPELVIC AUTONOMIC NERVES

What follows is a brief overview of the autonomic nervous system in the abdominopelvic region; descriptions of the neurovascular supply to individual organs are given in the relevant chapters. The autonomic supply to the abdominal and pelvic viscera is via the abdominopelvic part of the sympathetic trunk and the greater, lesser and least thoracic splanchnic nerves (sympathetic), and the vagus and pelvic splanchnic nerves (parasympathetic). There are numerous interconnections between plexuses and ganglia, particularly in the major plexuses around the abdominal aorta; hence, the descriptions tend to be simplifications based on the 'main' supply to each organ (Fig. 59.2). Details of the terminations of these fibres are given in the description of the general microstructure of the wall of the hollow viscera.

As a general rule, sympathetic neurones from the abdominopelvic autonomic plexuses inhibit visceral smooth muscle motility and glandular secretions, induce sphincter contraction and cause vasoconstriction. Parasympathetic stimulation leads to opposing effects. Visceral afferents also pass through these autonomic plexuses.

Sympathetic innervation

The cell bodies of neurones of the sympathetic supply of the abdomen and pelvis lie in the intermediolateral grey matter of the first to the twelfth thoracic and the first two lumbar spinal segments. Myelinated axons from these neurones travel in the ventral ramus of the spinal nerve of the same segmental level, leaving it via a white ramus communicans to enter a thoracic or lumbar ganglion. Visceral branches can exit at the same level or ascend or descend several levels in the sympathetic trunk before exiting; they leave the ganglia without synapsing and pass medially, giving rise to the paired greater, lesser and least thoracic splanchnic nerves and to the lumbar and sacral splanchnic nerves. Axons destined to supply somatic structures synapse in the sympathetic ganglion of the same level, and postganglionic, unmyelinated axons leave the ganglion as one or more grey rami communicantes to enter the spinal nerve of the same segmental level.

Greater thoracic splanchnic nerve

On each side, the greater thoracic splanchnic nerve is derived from the medial branches of the fifth to ninth thoracic ganglia. It gives off branches to the descending thoracic aorta and enters the abdomen through the fibres of the ipsilateral crus of the respiratory diaphragm, on which it descends anteroinferiorly. The main trunk of the nerve enters the superior aspect of the coeliac ganglion, where most of the

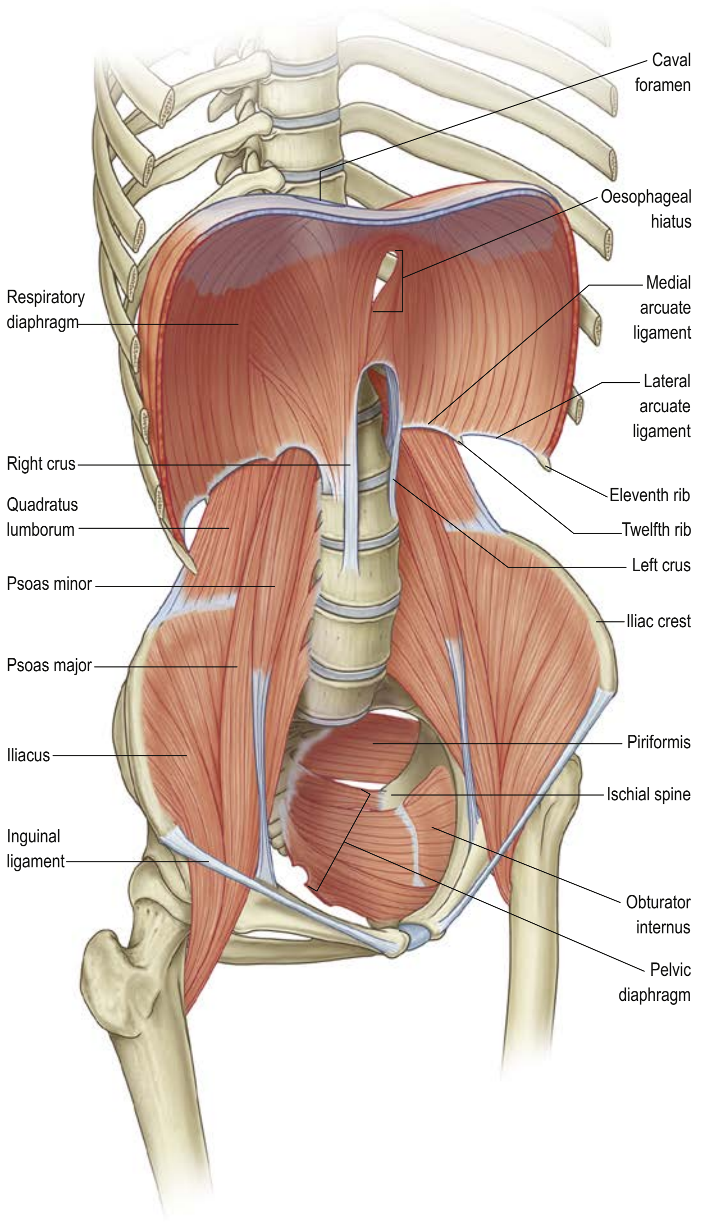
Caval foramen
Oesophageal hiatus
Medial arcuate ligament
Lateral arcuate ligament
Respiratory diaphragm
Right crus
Quadratus lumborum
Psoas minor
Psoas major
Iliacus
Inguinal ligament
Eleventh rib
Twelfth rib
Left crus
Iliac crest
Piriformis
Ischial spine
Obturator internus
Pelvic diaphragm

Fig. 59.1 The bony and muscular structures making up the abdominopelvic cavity. The anterolateral abdominal muscles have been removed for clarity.

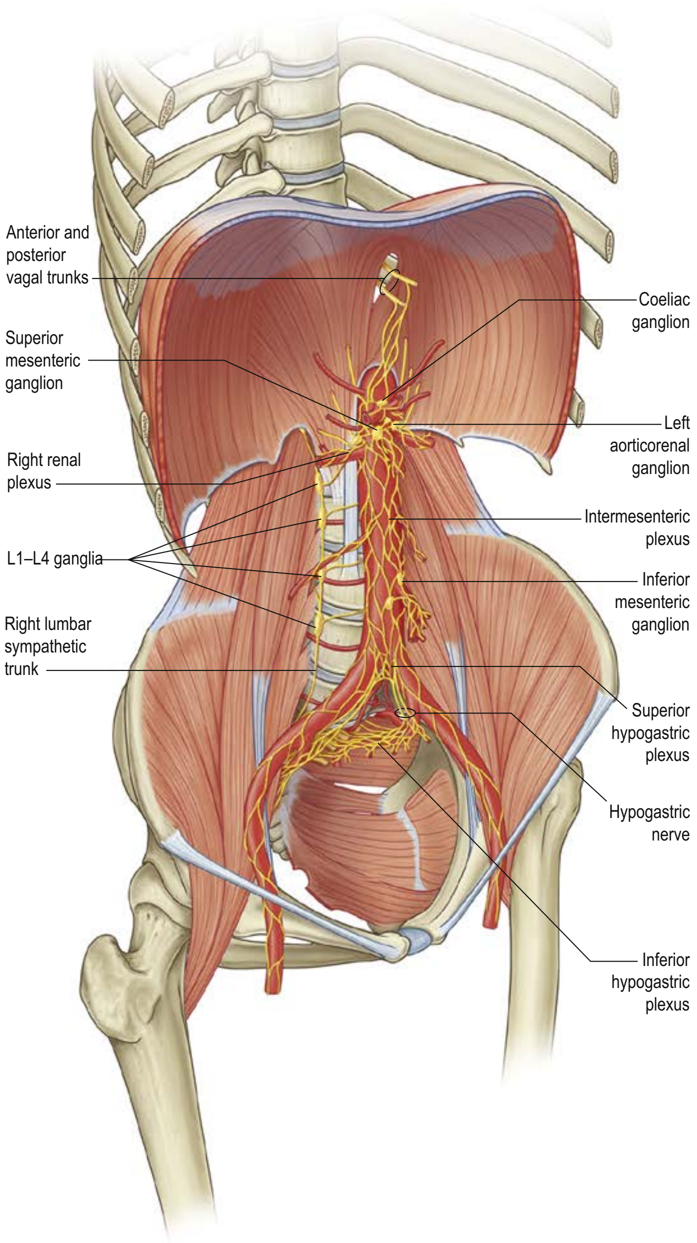
Anterior and posterior vagal trunks
Superior mesenteric ganglion
Right renal plexus
L1–L4 ganglia
Right lumbar sympathetic trunk
Coeliac ganglion
Left aorticorenal ganglion
Intermesenteric plexus
Inferior mesenteric ganglion
Superior hypogastric plexus
Hypogastric nerve
Inferior hypogastric plexus

Fig. 59.2 The overall arrangement of the autonomic plexuses of the abdominal and pelvic viscera. The major ganglia are indicated and note their associated plexuses.

preganglionic fibres synapse (but not those destined for the medulla of the suprarenal gland).

Lesser thoracic splanchnic nerve

On each side, the lesser thoracic splanchnic nerve is derived from the medial branches of the tenth and eleventh (or ninth and tenth) thoracic ganglia. It enters the abdomen running through the most inferior fibres of the ipsilateral crus of the respiratory diaphragm or under the medial arcuate ligament, and then lies on the crus as it runs anteroinferiorly. The trunk of the nerve joins the aorticorenal ganglion and may give branches to the lateral aspect of the coeliac ganglion. It occasionally joins the greater and least thoracic splanchnic nerves as a single splanchnic nerve.

Least thoracic splanchnic nerve

On each side, the least thoracic splanchnic nerve is derived from the medial branches of the eleventh and/or twelfth thoracic ganglion. It enters the abdomen medial to the sympathetic trunk under the medial arcuate ligament of the respiratory diaphragm and runs inferiorly to join the renal plexus. The trunk of the nerve enters the aorticorenal ganglion and may give branches to the lateral aspect of the coeliac ganglion. It is sometimes part of the lesser thoracic splanchnic nerve, when it forms a twig that enters the renal plexus just below the aorticorenal ganglion.

The thoracic splanchnic nerves show considerable individual variation in their origin and distribution (Loukas et al 2010). For example, the greater thoracic splanchnic nerve can receive a contribution from the fourth or tenth thoracic ganglion of the sympathetic trunk or originate only from the sixth to ninth ganglia.

Lumbar sympathetic system

The lumbar part of each sympathetic trunk usually contains four ganglia lying on the anterolateral aspects of the lumbar vertebrae along the medial margin of psoas major (see Figs 59.2–59.4, 61.15) (Murata et al 2003). Superiorly, it is continuous with the thoracic part of the sympathetic trunk posterior to the medial arcuate ligament. Inferiorly, it passes posterior to the common iliac vessels and is continuous with the sacral part of the sympathetic trunk. On the right side, it lies posterior to the inferior vena cava; on the left, it is posterior to the lateral aortic nodes. It is anterior to most of the lumbar vessels but may pass posterior to some lumbar veins.

On each side, the first, second and sometimes the third lumbar ventral rami are connected to the lumbar part of the sympathetic trunk by white rami communicantes. All lumbar ventral rami are joined near their origins by long, slender, grey rami communicantes from the four lumbar ganglia. Their arrangement is irregular: one ganglion can give rami to two or three lumbar ventral rami, one lumbar ventral ramus can receive rami from two ganglia, or grey rami can leave the sympathetic trunk between ganglia (Murata et al 2003).

Somatic and vascular branches

Sympathetic nerve branches accompany the lumbar arteries round the sides of the vertebral bodies, medial to the fibrous arches to which psoas major is attached, to provide sympathetic innervation to the segmental distribution of the lumbar arteries. Branches from the lumbar ganglia innervate the abdominal aorta and common, external and internal iliac arteries, forming delicate nerve plexuses that extend along the vessels. Other postganglionic sympathetic nerves to vessels and skin travel with somatic nerves. Thus, the femoral nerve carries vasoconstrictor sympathetic nerves to the femoral artery and its branches in the thigh, as well as sympathetic fibres in its cutaneous branches. Postganglionic fibres travelling with the obturator nerve supply the obturator artery and a variable patch of skin of the medial thigh. Sympathetic denervation of vessels in the lower limb can occur by removing or ablating the proximal three lumbar ganglia and intervening parts of the sympathetic trunk; this procedure can be useful for treating some varieties of vascular insufficiency of the lower limb.

Lumbar splanchnic nerves

Four lumbar splanchnic nerves pass as medial branches from the ganglia to join the coeliac, inferior mesenteric and superior hypogastric plexuses (see Fig. 59.4). The first lumbar splanchnic nerve, from the first ganglion of the lumbar part of the sympathetic trunk, gives branches to the coeliac, renal and inferior mesenteric plexuses. The second lumbar splanchnic nerve joins the inferior part of the intermesenteric or inferior mesenteric plexus. The third lumbar splanchnic nerve arises from the third or fourth ganglion and joins the superior hypogastric plexus. The fourth lumbar splanchnic nerve from the lowest ganglion joins the distal part of the superior hypogastric plexus, or the hypogastric nerve. It is important to note that lumbar splanchnic nerves contribute to the superior and inferior hypogastric plexuses and therefore to the innervation of the neck of the urinary bladder, ductus deferens and prostate, among other structures. Injury to these nerves, e.g. during aortoiliac surgery, can result in sexual dysfunction.

Pelvic sympathetic system

The sacral part of the sympathetic trunk usually consists of four or five ganglia located medial or anterior to the anterior sacral foramina posterior to the presacral fascia (Oh et al 2004). Occasionally, one or two coccygeal ganglia are present. The sacral part of the sympathetic trunk is continuous above with the lumbar part of the sympathetic trunk, and preganglionic fibres descend from the distal lumbar spinal cord segments via this route. The first sacral ganglion is the largest. Ganglia become progressively smaller in the caudal direction (Blaszczyk 1981). The sacral sympathetic trunk is often asymmetric, with absent or fused ganglia, and cross-communications between sides are frequent. Each ganglion sends at least one grey ramus communicans to its adjacent spinal nerve but up to 11 such branches from a single ganglion have been reported (Potts 1925).

The sacral part of the sympathetic trunk converges caudally to form a solitary retroperitoneal structure, the ganglion impar (ganglion of Walther), which lies at a variable level between the sacrococcygeal joint and the apex of the coccyx; it is occasionally paired, unilateral or absent (Oh et al 2004). It conveys sympathetic fibres to and nociceptive afferents from the perineum and terminal urogenital regions. Anaesthetic blockade of the ganglion impar can be used to treat intractable perineal pain carried by visceral afferent fibres in patients with pelvic cancers (Toshniwal et al 2007).

Somatic and vascular branches

Grey rami communicantes containing postganglionic sympathetic nerves pass from the pelvic sympathetic ganglia to the sacral and coccygeal spinal nerves. There are no white rami communicantes at this level. The postganglionic fibres are distributed via the sacral and coccygeal plexuses (Woon and Stringer 2014). Thus, sympathetic fibres in the tibial nerve are conveyed to the popliteal artery and its branches in the leg and foot, whilst those in the pudendal and superior and inferior gluteal nerves accompany these arteries to the perineum and buttocks, respectively. Small branches also travel with the median and lateral sacral arteries.

Sacral splanchnic nerves

Sacral splanchnic nerves pass directly from the ganglia of the sacral part of the sympathetic trunk to the inferior hypogastric plexus and, from there, to pelvic viscera; they usually arise from the first two sacral ganglia.

Parasympathetic innervation

The parasympathetic neurones innervating the abdomen and pelvis lie either in the posterior nucleus of the vagus nerve or in the intermediolateral grey matter of the second, third and fourth sacral spinal cord segments. Traditionally, the vagus nerves have been said to supply parasympathetic innervation to the abdominal viscera as far as the distal transverse colon, i.e. they supply derivatives of the foregut and midgut. Derivatives of the hindgut are supplied by parasympathetic fibres travelling via the pelvic splanchnic nerves (see below); the overlap between these two supplies is variable. The vagal trunks are derived from the oesophageal plexus and enter the abdomen via the oesophageal hiatus, closely related to the anterior and posterior walls of the abdominal part of the oesophagus (see Fig. 56.6). The anterior vagal trunk is mostly derived from the left vagus nerve and the posterior vagal trunk from the right vagus nerve. The nerves supply the abdominal part of the oesophagus and stomach directly. The anterior vagal trunk gives off a hepatic branch, which innervates the liver and its vasculature, including the gallbladder and bile ducts, and the other structures in the free edge of the lesser omentum (hepatoduodenal ligament). The posterior vagal trunk supplies branches to the coeliac plexus; these fibres frequently constitute the largest portion of the fibres contributing to the plexus. They arise directly from the posterior vagal trunk and from its gastric branch, and run posterior to the peritoneum, deep to the posterior wall of the superior part of the omental bursa, to reach the coeliac plexus. Their synaptic relays with postganglionic neurones are situated in the myenteric (Auerbach's) and submucosal (Meissner's) plexuses in the wall of the hollow viscera (see below).

Pelvic splanchnic nerves

Pelvic splanchnic nerves to the pelvic viscera travel in the ventral rami of the second, third and fourth sacral spinal nerves. They leave the nerves as they exit the anterior sacral foramina and pass in the presacral tissue as a fine network of branches that are distributed to three principal destinations. Most pass anterolaterally into the network of nerves that form the inferior hypogastric plexus; from there, they pass to the pelvic viscera. Some join directly with the hypogastric nerves and ascend out of the pelvis as far as the superior hypogastric plexus; from there they are distributed with branches of the inferior mesenteric artery (Ch. 65). A few run superolaterally in the presacral fascia, over the linea terminalis anterior to the left iliac vessels, and pass directly into the tissue of the retroperitoneum toward the sigmoid and descending colons. The pelvic splanchnic nerves are motor to the smooth muscle of the derivatives of the hindgut and wall of the urinary bladder, supply vasodilator fibres to the erectile tissues of the penis and clitoris, and are secretomotor to the derivatives of the hindgut.

An experimental study of the differential expression of transcription factors in embryonic mice argued that thoracic and sacral pools of preganglionic neurones share a common sympathetic identity and that the sacral autonomic outflow should therefore be regarded as sympathetic (Espinosa-Medina et al 2016). This controversial view has been challenged (Horn 2018).

Abdominopelvic autonomic plexuses and ganglia

The abdominopelvic autonomic plexuses are somewhat variable and often fuse or are closely interrelated. The following descriptions encompass their main features (**Figs 59.3–59.4**).

Coeliac plexus

The coeliac plexus is located at the level of the twelfth thoracic and first lumbar vertebrae. It is a dense network that unites the coeliac ganglia, and surrounds the coeliac trunk and the proximal superior mesenteric artery. It is posterior to the stomach and omental bursa and anterior to the crura of the respiratory diaphragm and the beginning of the abdominal aorta, and lies medial to the suprarenal glands. The plexus and ganglia receive the greater and lesser thoracic splanchnic nerves and branches from the vagal trunks. The plexus is in continuity with small branches along adjacent arteries and is connected to the phrenic, splenic, hepatic, superior mesenteric, suprarenal, renal and ovarian/testicular plexuses. Visceral afferent fibres in the coeliac plexus convey pain and other sensations from proximal abdominal viscera. Anaesthesia or ablation of these nerves (coeliac plexus blockade) is sometimes undertaken to treat medically intractable pain from pancreatic disorders.

Coeliac and aorticorenal ganglia

The coeliac ganglia are irregular neural masses, measuring approximately 2 cm across, located between the origin of the coeliac trunk and superior mesenteric artery, medial to the suprarenal glands and anterior to the crura of the respiratory diaphragm (Zhang et al 2006). They vary in number, size, shape and precise location; there are often two, one on each side. The right ganglion is frequently posterior to the inferior vena cava, and the left ganglion often lies posterior to the origin of the splenic artery. The ipsilateral greater thoracic splanchnic nerve joins the superior part of each ganglion and the lesser thoracic splanchnic nerve joins the inferior part. The most inferior part of each ganglion usually forms a distinct

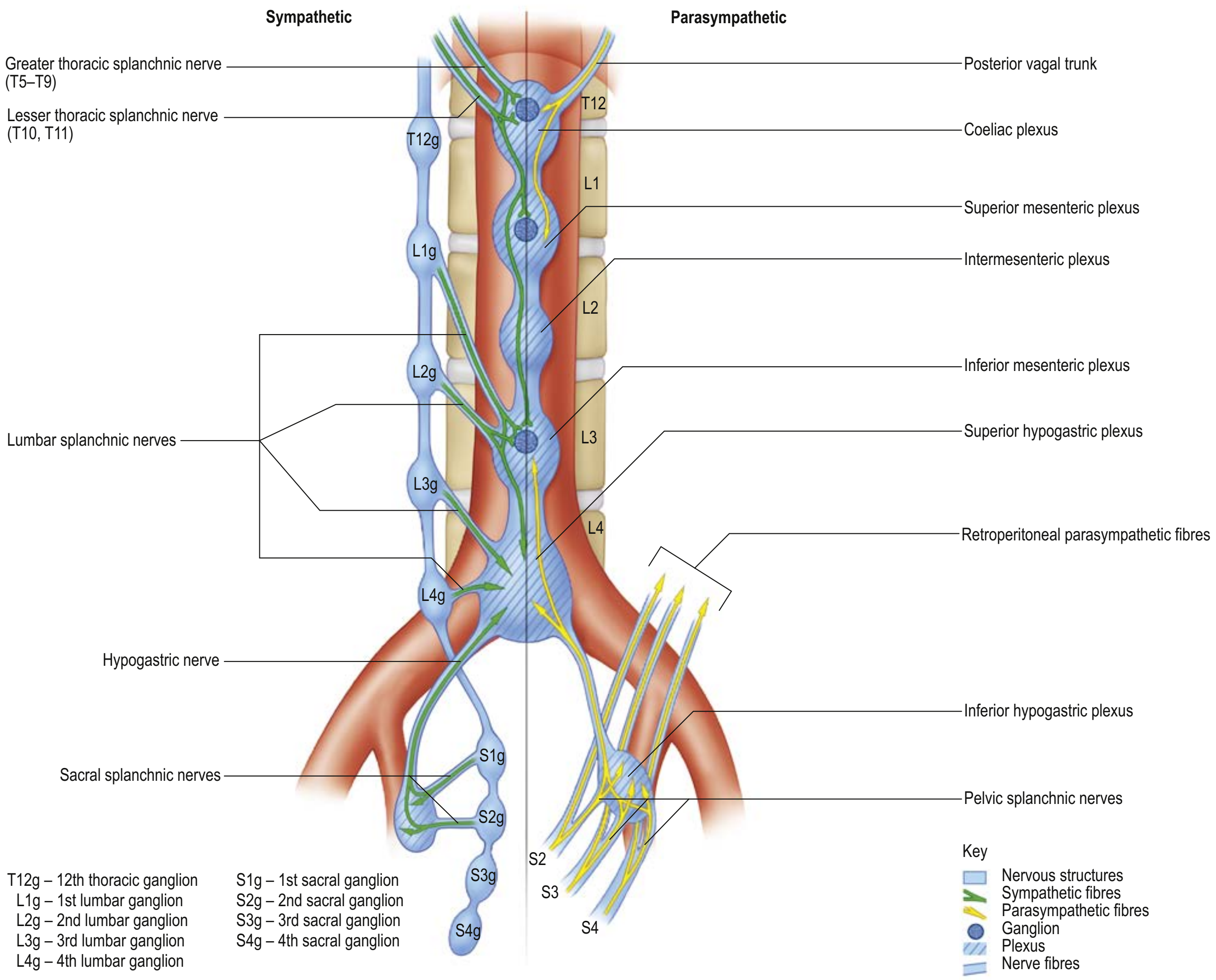
Sympathetic
Parasympathetic
Greater thoracic splanchnic nerve (T5–T9)
Lesser thoracic splanchnic nerve (T10, T11)
T12g
L1g
L2g
L3g
L4g
Lumbar splanchnic nerves
Hypogastric nerve
Sacral splanchnic nerves
S1g
S2g
S3g
S4g
T12
L1
L2
L3
L4
S2
S3
S4
Posterior vagal trunk
Coeliac plexus
Superior mesenteric plexus
Intermesenteric plexus
Inferior mesenteric plexus
Superior hypogastric plexus
Retroperitoneal parasympathetic fibres
Inferior hypogastric plexus
Pelvic splanchnic nerves
T12g – 12th thoracic ganglion
L1g – 1st lumbar ganglion
L2g – 2nd lumbar ganglion
L3g – 3rd lumbar ganglion
L4g – 4th lumbar ganglion
S1g – 1st sacral ganglion
S2g – 2nd sacral ganglion
S3g – 3rd sacral ganglion
S4g – 4th sacral ganglion
Key
Nervous structures
Sympathetic fibres
Parasympathetic fibres
Ganglion
Plexus
Nerve fibres

Fig. 59.3 The autonomic plexuses innervating the abdominal and pelvic viscera: schematic diagram.

subdivision, the aorticorenal ganglion, which receives the ipsilateral lesser splanchnic nerve and gives origin to most of the renal plexus.

Phrenic plexus

The phrenic plexus is a periarterial extension of the coeliac plexus around the right inferior phrenic artery, adjacent to the right crus of the respiratory diaphragm (Rusu 2006). It contains one or two phrenic ganglia and a definable nerve trunk that connects the coeliac plexus and phrenic nerve: the phrenic ganglion is probably sympathetic (Tubbs et al 2008). The phrenic plexus supplies branches to the suprarenal glands and the respiratory diaphragm.

Superior mesenteric plexus and ganglion

The superior mesenteric plexus lies in the pre-aortic connective tissue posterior to the pancreas, around the origin of the superior mesenteric artery. It is an inferior continuation of the coeliac plexus and includes branches from the posterior vagal trunk and coeliac plexus. Its branches accompany the superior mesenteric artery and its branches. The superior mesenteric ganglion lies superiorly in the plexus, usually above the origin of the superior mesenteric artery.

Intermesenteric plexus

Like other parts of the abdominal aortic autonomic plexus, the intermesenteric plexus is not a discrete structure but is part of a continuous periarterial nerve plexus connected to the ovarian/testicular, inferior mesenteric, iliac and superior hypogastric plexuses. It lies on the lateral and anterior aspects of the aorta, between the origins of the superior and inferior mesenteric arteries, and consists of numerous fine, interconnected nerve fibres and a few ganglia continuous superiorly with the superior mesenteric plexus and inferiorly with the superior hypogastric plexus. It is not well characterized but receives parasympathetic and sympathetic branches from the coeliac plexus and additional sympathetic contributions from the first and second lumbar splanchnic nerves.

Inferior mesenteric plexus

The inferior mesenteric plexus lies around the origin of the inferior mesenteric artery and is distributed along its branches. It is formed predominantly from the aortic plexus, supplemented by sympathetic fibres from the first and second lumbar splanchnic nerves and ascending pelvic parasympathetic fibres from the inferior hypogastric plexus (via the hypogastric nerves and superior hypogastric plexus). Disruption of the inferior mesenteric plexus alone rarely causes clinically significant disturbances of autonomic function.

Superior hypogastric plexus

The superior hypogastric plexus lies anterior to the aortic bifurcation, the left common iliac vein, median sacral vessels, fifth lumbar vertebral body and promontory of the sacrum, and between the common iliac arteries. It lies within extraperitoneal connective tissue in the midline, extending a little to the left. The breadth of the plexus and its constituent nerves varies; appearances range from a reticular-like arrangement to a band-like structure or one or two distinct nerve trunks (Paraskevas et al 2008). The medial attachment of the sigmoid mesocolon and superior limit of the mesorectum lie anterior to the distal part of the plexus, separated from it by a thin layer of loose connective tissue. The plexus is formed by branches from three main sources: the abdominal aortic plexus (sympathetic and parasympathetic), lumbar splanchnic nerves (sympathetic) and pelvic splanchnic nerves (parasympathetic), which ascend from the inferior hypogastric plexus via the right and left hypogastric nerves (Kraima et al 2015). Visceral sensory fibres also pass through the plexus. The hypogastric nerves lie in loose connective tissue just posterolateral to the proximal mesorectum and pass over the linea terminalis medial to the internal iliac vessels. The superior hypogastric plexus conveys branches to the inferior mesenteric plexus and to the ureteric, ovarian/testicular and common iliac nerve plexuses; additional small branches turn abruptly forwards into the proximal mesorectum to travel with the superior anorectal artery.

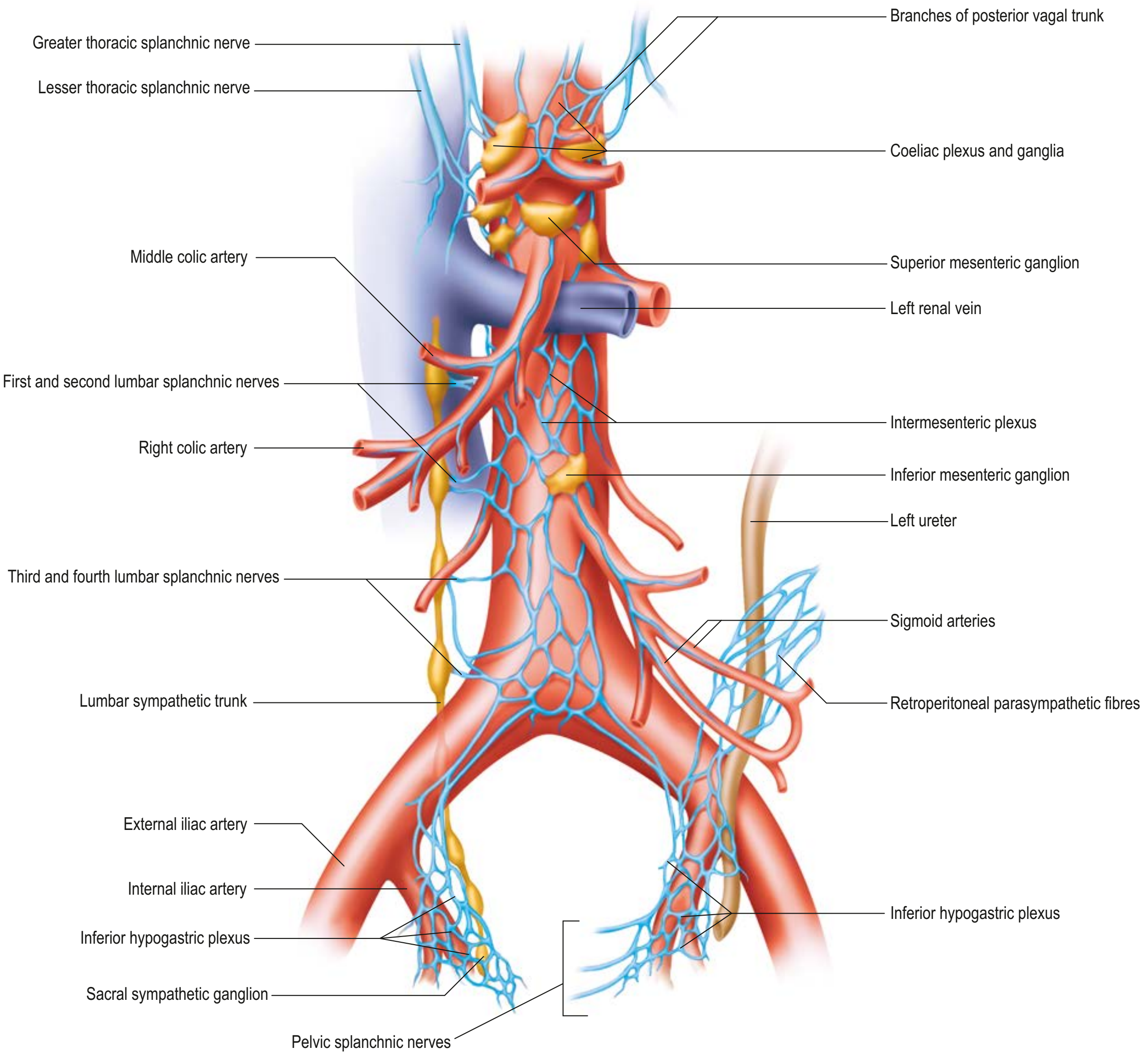
Greater thoracic splanchnic nerve
Lesser thoracic splanchnic nerve
Middle colic artery
First and second lumbar splanchnic nerves
Right colic artery
Third and fourth lumbar splanchnic nerves
Lumbar sympathetic trunk
External iliac artery
Internal iliac artery
Inferior hypogastric plexus
Sacral sympathetic ganglion
Pelvic splanchnic nerves
Branches of posterior vagal trunk
Coeliac plexus and ganglia
Superior mesenteric ganglion
Left renal vein
Intermesenteric plexus
Inferior mesenteric ganglion
Left ureter
Sigmoid arteries
Retroperitoneal parasympathetic fibres
Inferior hypogastric plexus

Fig. 59.4 The major autonomic plexuses of the abdomen and pelvis.

Inferior hypogastric plexus

The inferior hypogastric plexus lies in the thin extraperitoneal connective tissue on the pelvic side wall anterolateral to the mesorectum. The internal iliac vessels and the attachments of levator ani and obturator internus lie laterally, and the superior vesical and occluded part of the umbilical arteries superiorly. In males the inferior hypogastric plexus lies posterolaterally on either side of the seminal glands, prostate and the fundus of the urinary bladder (Röthlisberger et al 2018): the point where the ductus deferens crosses the ureter provides an approximate guide to the superior limit of the plexus (Mauroy et al 2003). The proximal border of the plexus lies beneath the peritoneum of the rectovesical pouch and is in contact with the lateral aspect of the fundus of the urinary bladder. The anterior border reaches the posterior aspect of the prostate; at its inferior limit, the cavernous nerves of the penis pass forwards to reach the posterolateral aspect of the prostate (see Fig. 73.8). In females, each plexus lies lateral to the cervix of the uterus, vaginal fornix and the fundus of the urinary bladder, often extending into the broad ligament of the uterus: the proximal limit of the plexus corresponds approximately to the level where the uterine artery crosses the ureter (Azaïs et al 2013).

The inferior hypogastric plexus is formed mainly from pelvic splanchnic (parasympathetic) and sacral splanchnic (sympathetic) branches; a smaller contribution is derived from sympathetic fibres (from the inferior lumbar ganglia) that descend into the plexus from the superior hypogastric plexus via the hypogastric nerves. It gives origin to a complex network of small pelvic branches that supply the pelvic viscera either directly or indirectly via periarterial plexuses. The branches of the inferior hypogastric plexus supply the ductus deferens, seminal glands, prostate, bulbo-urethral glands and penis in males; the ovary, uterine tubes, uterus, cervix of the uterus and vagina in females; and the urinary bladder and distal ureter in both sexes. The plexus plays a key role in continence and sexual function.

Hypogastric nerves The hypogastric nerves are usually paired nerve bundles but can consist instead of multiple filaments. They contain sympathetic fibres (mostly descending from the superior hypogastric plexus) and parasympathetic fibres (ascending from the inferior hypogastric plexus). The nerves run between the superior and inferior hypogastric plexuses on each side posterior to the presacral fascia medial to the internal iliac vessels and lateral to the anterior sacral foramina.

Other autonomic plexuses and ganglia

Additional plexuses are described for abdominopelvic viscera, such as the hepatic and ovarian/testicular plexuses. Each plexus tends to lie around the main arterial supply to the named organ, receive both sympathetic and parasympathetic fibres from one or more of the major autonomic plexuses, and contain at least one ganglion. Thus, autonomic ganglia supplying the testis are found around the origin of the testicular arteries from the abdominal aorta and have connections with the renal and intermesenteric plexuses and the first and second lumbar splanchnic nerves (Motoc et al 2010).

Para-aortic bodies

The para-aortic bodies (also known as paraganglia or, collectively, as the organ of Zuckerkandl) are collections of neural crest-derived chromaffin tissue found in close relation to the abdominal aortic plexus. They are relatively large in the fetus, reach a maximum size at around 3 years of age, and have usually regressed by adulthood. They are most commonly found as a pair of bodies lying anterolateral to the abdominal aorta in the region of the inferior mesenteric and superior hypogastric plexuses, but multiple smaller collections may be present. Occasionally they are found as high as the coeliac plexus or as low as the inferior hypogastric plexus in the pelvis, or can be close to the ganglia of the lumbar part of the sympathetic trunk. Rarely, scattered cells that persist into adulthood can be the sites of paraganglioma (Subramanian and Maker 2006).

GENERAL ARRANGEMENT OF ABDOMINOPELVIC VASCULAR SUPPLY

The major vessels that occupy the peritoneal cavity and pelvis not only supply the viscera, retroperitoneal structures and much of the bony and soft tissue walls, but also course through the cavities en route to supplying the lower limbs. From the caval foramen and aortic hiatus in the respiratory diaphragm, the inferior vena cava and abdominal aorta follow the general parabolic shape of the lumbar spine (**Figs 59.5–59.6**).The individual parts of the aortoiliac and iliocaval systems are described in the relevant chapters.

Arterial supply to the gastrointestinal tract

The arterial supply to the gastrointestinal tract is derived from the large unpaired branches of the aorta, e.g. coeliac trunk, superior and inferior mesenteric arteries. Major variants in the origin of these arteries are uncommon (Ch. 61). Accessory or replaced branches to the abdominal viscera are more common. The inferior mesenteric artery almost always arises separately but replaced, accessory or anastomotic vessels can arise from the proximal superior mesenteric artery or its branches (Tubbs et al 2016).

The coeliac trunk and its branches supply foregut derivatives that extend from the distal oesophagus to the mid part of the descending part of the duodenum, together with associated viscera (e.g. liver, spleen and pancreas). The superior mesenteric artery supplies derivatives of the midgut, which extends from the mid descending duodenum to the distal third of the transverse colon (including jejunum, ileum, caecum, appendix, and ascending and transverse colons). The inferior mesenteric artery supplies the derivatives of the hindgut that extend from the distal transverse colon to the proximal anal canal. Even in the absence of accessory arteries, there are numerous anastomoses among these vascular territories. For example, anastomoses around the head of the pancreas and the duodenum are formed between the anterior and posterior superior pancreaticoduodenal arteries and the anterior and posterior inferior pancreaticoduodenal arteries, and between the posterior superior pancreaticoduodenal artery and jejunal arteries (Ch. 68). Anastomoses between the territories of the superior and inferior mesenteric arteries are less numerous; the most consistent is the marginal artery (Ch. 65).

Hepatic portal venous system

All portal venous systems connect two capillary beds. The hepatic portal system connects the capillary bed of the abdominal and pelvic parts of the gastrointestinal tract, from the abdominal part of the oesophagus to the distal anal canal, together with all derived organs other than the liver (i.e. the pancreas, gallbladder and spleen) and the hepatic sinusoidal 'capillary' bed (**Fig. 59.7**). The intrahepatic hepatic portal vein ramifies and ends in the hepatic sinusoids: blood drains from the sinusoids into central veins that converge to form the hepatic veins which drain into the inferior vena cava (Ch. 66). In fetal and early postnatal life, valves are demonstrable in tributaries of the hepatic

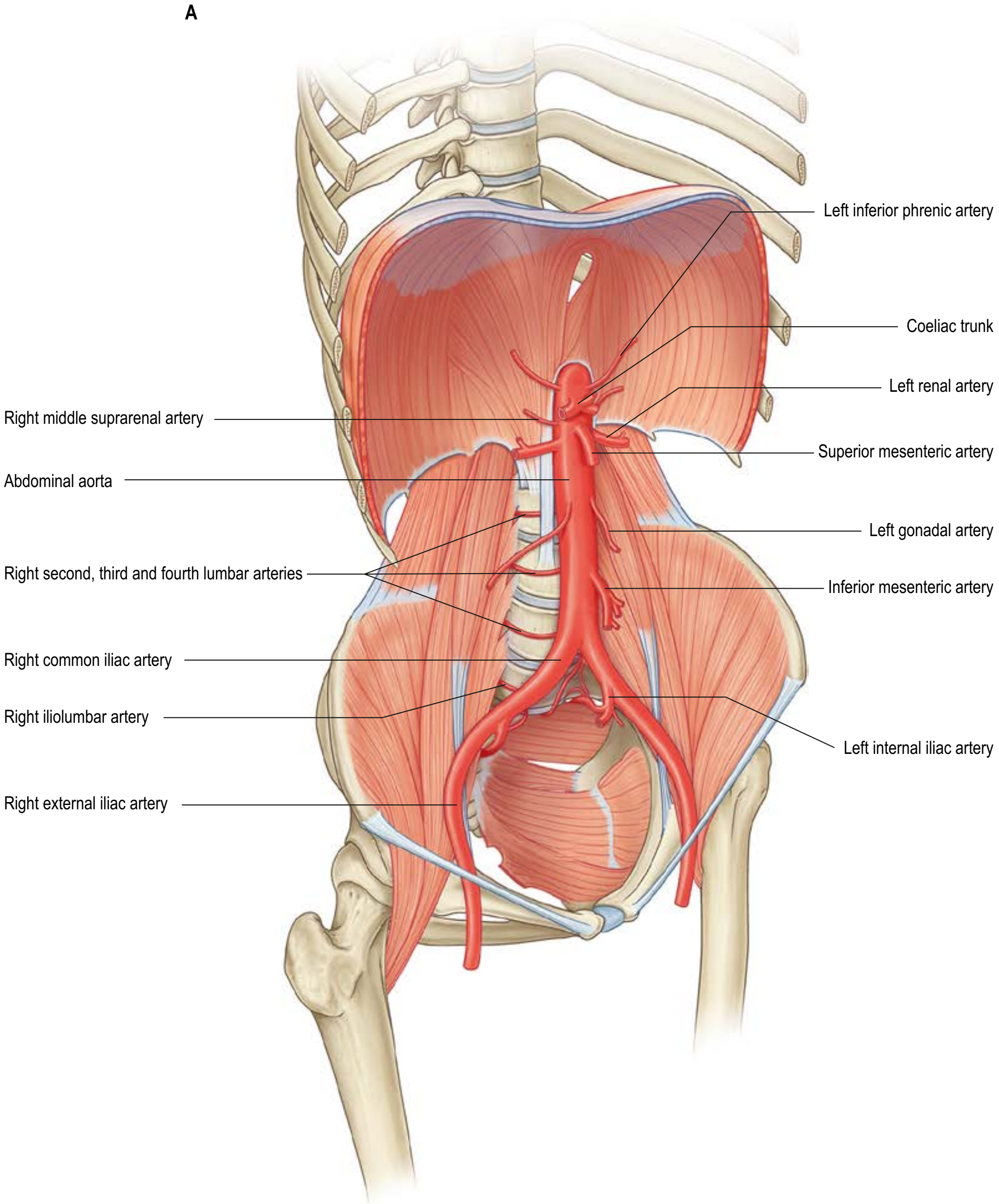
A
Left inferior phrenic artery
Coeliac trunk
Left renal artery
Superior mesenteric artery
Left gonadal artery
Inferior mesenteric artery
Left internal iliac artery
Right middle suprarenal artery
Abdominal aorta
Right second, third and fourth lumbar arteries
Right common iliac artery
Right iliolumbar artery
Right external iliac artery

Fig. 59.5 A, The abdominal aorta and its major branches in the abdomen and pelvis. (B, *continued online*)

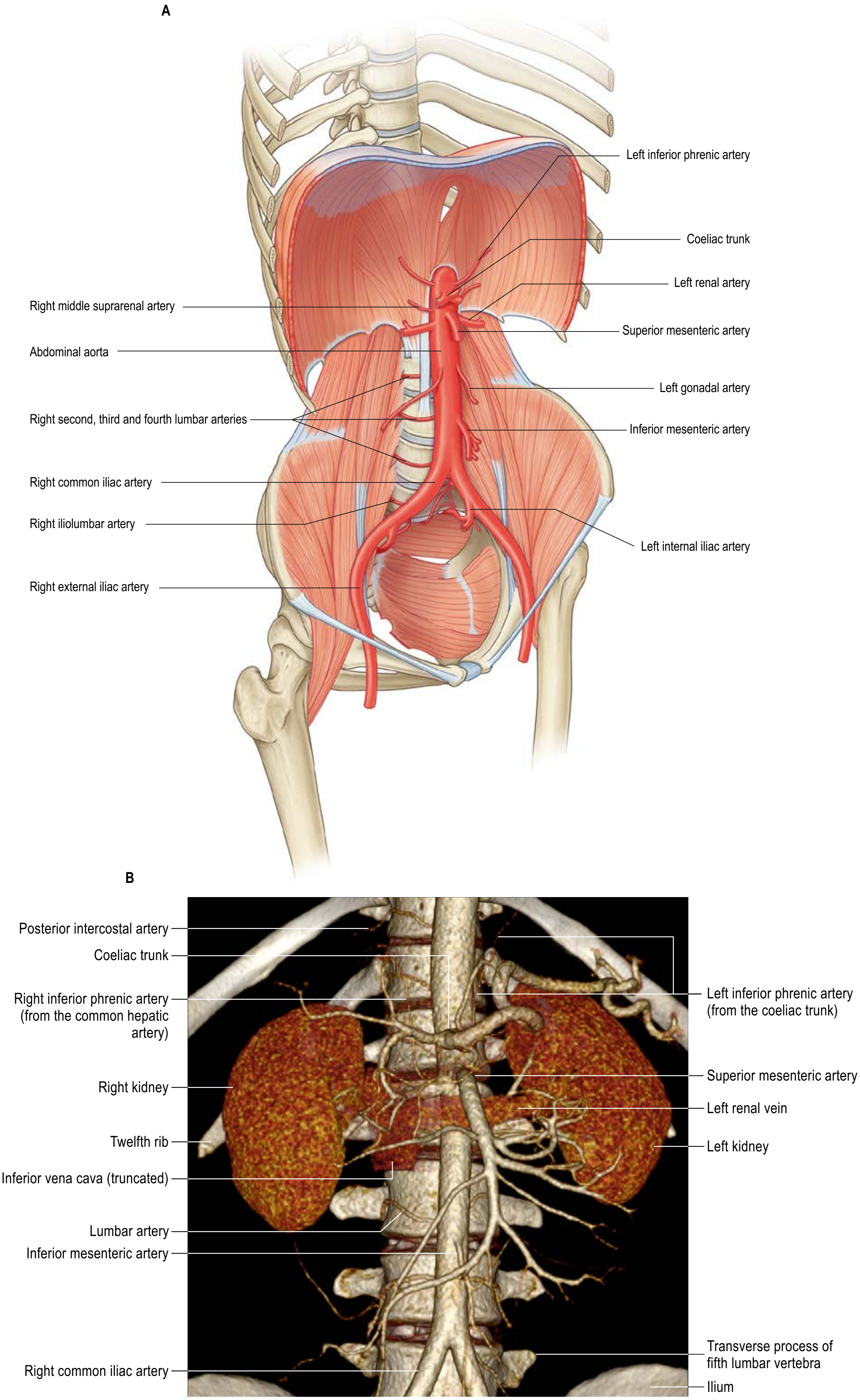
A
Left inferior phrenic artery
Coeliac trunk
Left renal artery
Right middle suprarenal artery
Superior mesenteric artery
Abdominal aorta
Left gonadal artery
Right second, third and fourth lumbar arteries
Inferior mesenteric artery
Right common iliac artery
Right iliolumbar artery
Left internal iliac artery
Right external iliac artery
B
Posterior intercostal artery
Coeliac trunk
Right inferior phrenic artery (from the common hepatic artery)
Left inferior phrenic artery (from the coeliac trunk)
Superior mesenteric artery
Right kidney
Left renal vein
Twelfth rib
Left kidney
Inferior vena cava (truncated)
Lumbar artery
Inferior mesenteric artery
Transverse process of fifth lumbar vertebra
Right common iliac artery
Ilium

Fig. 59.5 A, The abdominal aorta and its major branches in the abdomen and pelvis. **B,** Volume-rendered CT angiogram of the abdominal aorta, frontal view. The renal arteries are obscured by the overlying renal veins and the gonadal arteries are too small to be seen.

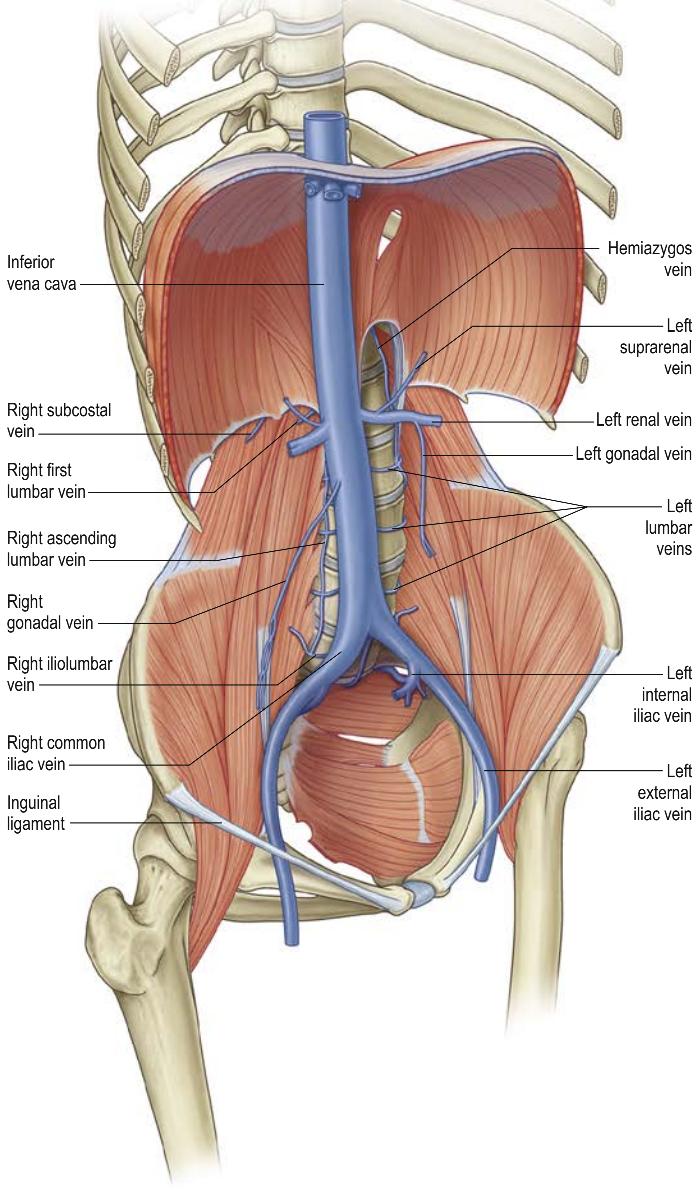
Inferior vena cava
Hemiazygos vein
Left suprarenal vein
Right subcostal vein
Left renal vein
Left gonadal vein
Right first lumbar vein
Left lumbar veins
Right ascending lumbar vein
Right gonadal vein
Right iliolumbar vein
Left internal iliac vein
Right common iliac vein
Left external iliac vein
Inguinal ligament

Fig. 59.6 The inferior vena cava and its major tributaries in the abdomen and pelvis.

portal vein but they usually atrophy with further maturation. There are no valves in the hepatic portal vein in adults.

Hepatic portal vein

The hepatic portal vein is formed from the convergence of the superior mesenteric and splenic veins posterior to the neck of the pancreas at the level of the first lumbar intervertebral disc (in the transpyloric plane) (see Fig. 59.7). It is approximately 8 cm long in the adult and ascends obliquely to the right posterior to the first part of the duodenum, the bile duct and gastroduodenal artery; at this point, it is directly anterior to the inferior vena cava. It enters the right border of the lesser omentum (i.e. hepatoduodenal ligament) and ascends anterior to the omental foramen to reach the right end of the porta hepatis, where it divides into right and left main branches, which accompany the corresponding branches of the hepatic artery into the liver. In the lesser omentum, the hepatic portal vein lies posterior to both the bile duct and the hepatic artery. It is surrounded by the hepatic plexus and accompanied by lymphatics and some lymph nodes.

Tributaries of the hepatic portal vein

The main extrahepatic tributaries of the hepatic portal vein are the left gastric vein and the posterior superior pancreaticoduodenal vein (Ch. 66). Within the liver, the left branch receives the remnant of the umbilical vein via the round ligament of the liver. Collateral pathways between the hepatic portal vein and the systemic venous system can become engorged (varices) as a result of portal hypertension which is most commonly due to cirrhosis of the liver (Pillai et al 2015).

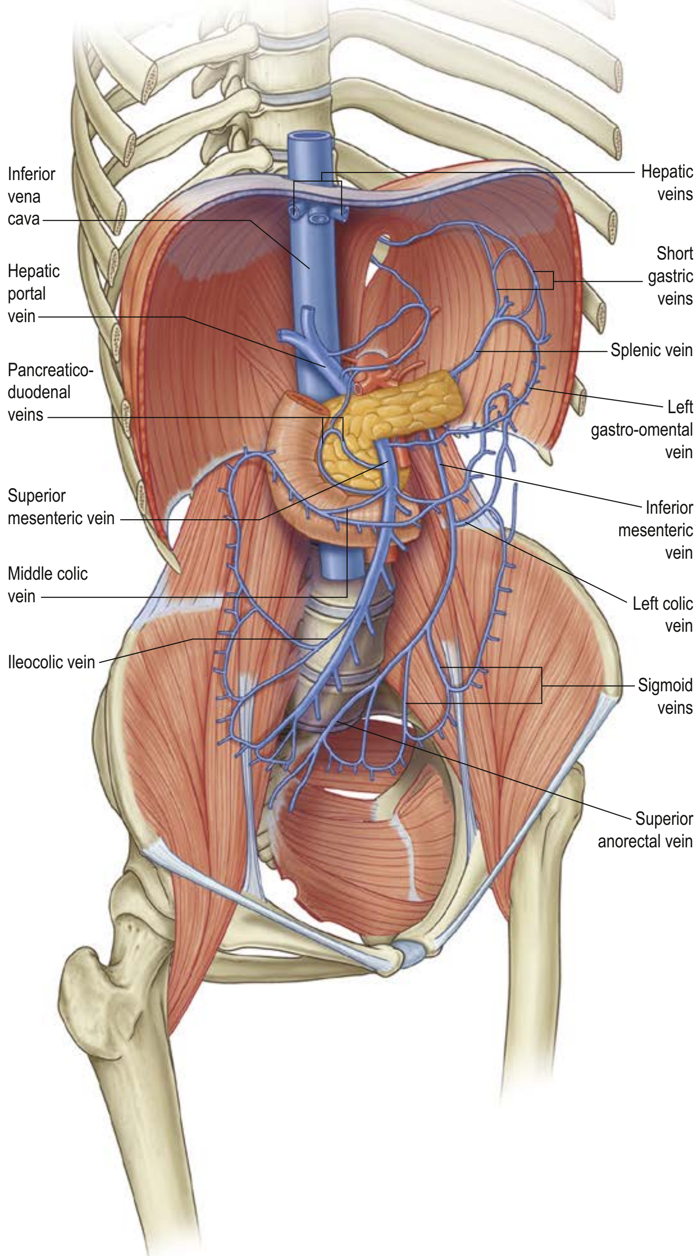
Inferior vena cava
Hepatic veins
Short gastric veins
Hepatic portal vein
Splenic vein
Pancreatico-duodenal veins
Left gastro-omental vein
Superior mesenteric vein
Inferior mesenteric vein
Middle colic vein
Left colic vein
Ileocolic vein
Sigmoid veins
Superior anorectal vein

Fig. 59.7 The overall arrangement of the hepatic portal venous system draining various abdominal viscera.

GENERAL MICROSTRUCTURE OF THE WALL OF THE GASTROINTESTINAL TRACT

The wall of the gastrointestinal tract displays a common structural plan that is modified regionally to take account of local functional differences. The general microstructure is best appreciated by reference to the development of the gut (Ch. 21). Much of the alimentary canal originates as a tube of endoderm enclosed in splanchnopleuric mesoderm. Its external surface faces the embryonic coelom, and the endodermal lining forms the epithelium of the canal and also the secretory and ductal cells of various glands that secrete into the lumen, including the pancreas and liver. The splanchnopleuric mesoderm forms the connective tissue, muscle layers, blood vessels and lymphatics of the wall, and its external surface becomes the visceral mesothelium or serosa. There is no serosa surrounding the cervical and thoracic portions of the oesophagus, or below the point where the derivatives of the hindgut traverse the pelvic diaphragm; in these sites the digestive tract is surrounded by connective tissue adventitia. Neural elements invade the gut from neural crest tissue (Ch. 14). The smooth muscle of the muscularis externa layers of the digestive tract is supplemented with striated muscle at its beginning (from the pharyngeal arches) and end.

The mature wall of hollow abdominal viscera has four main layers: mucosa, submucosa, muscularis externa and serosa (Fig. 59.8). The mucosa (mucous membrane) is the innermost layer and is subdivided into a lining epithelium, an underlying lamina propria (a layer of loose connective tissue, where simple glands may also be found) and a thin layer of smooth muscle, the muscularis mucosae. The submucosa is a strong and highly vascularized layer of connective tissue, which, in some regions, contains glands with ducts to the luminal surface. The muscularis externa consists of inner circular and outer longitudinal layers of smooth muscle; an incomplete oblique muscle layer is present only in the stomach. The external surface is bounded by serosa or adventitia, depending on its position within the body.

Mucosa

Epithelium

The epithelium is the site of secretion and absorption and provides a defence against various threats, including microorganisms. Its protective function against mechanical, thermal and chemical injury is particularly evident in the oesophagus and anal canal, where it is thick, stratified and covered in mucus, which serves as a protective lubricant. At other sites the epithelium lining the gastrointestinal tract is single-layered, and either cuboidal (in glands) or columnar. It contains cells modified for absorption as well as various types of secretory cell.

The barrier function and selectivity of absorption depend on tight junctions over the entire epithelium. The surface area of the lumen available for secretion or absorption is increased by mucosal folds, crypts, villi and glands (see Fig. 59.8). Microvilli on the surfaces of individual absorptive cells amplify the area of apical plasma membrane in contact with the contents of the gastrointestinal tract. Some glands lie in the lamina propria and some in the submucosa; others (the liver and pancreas) are totally external to the wall of the gut. All of these glands drain into the lumen of the gastrointestinal tract. The epithelium also contains scattered neuroendocrine (enteroendocrine) cells.

Lamina propria

The lamina propria consists of compact connective tissue, often rich in elastin fibres, which supports the surface epithelium and contains

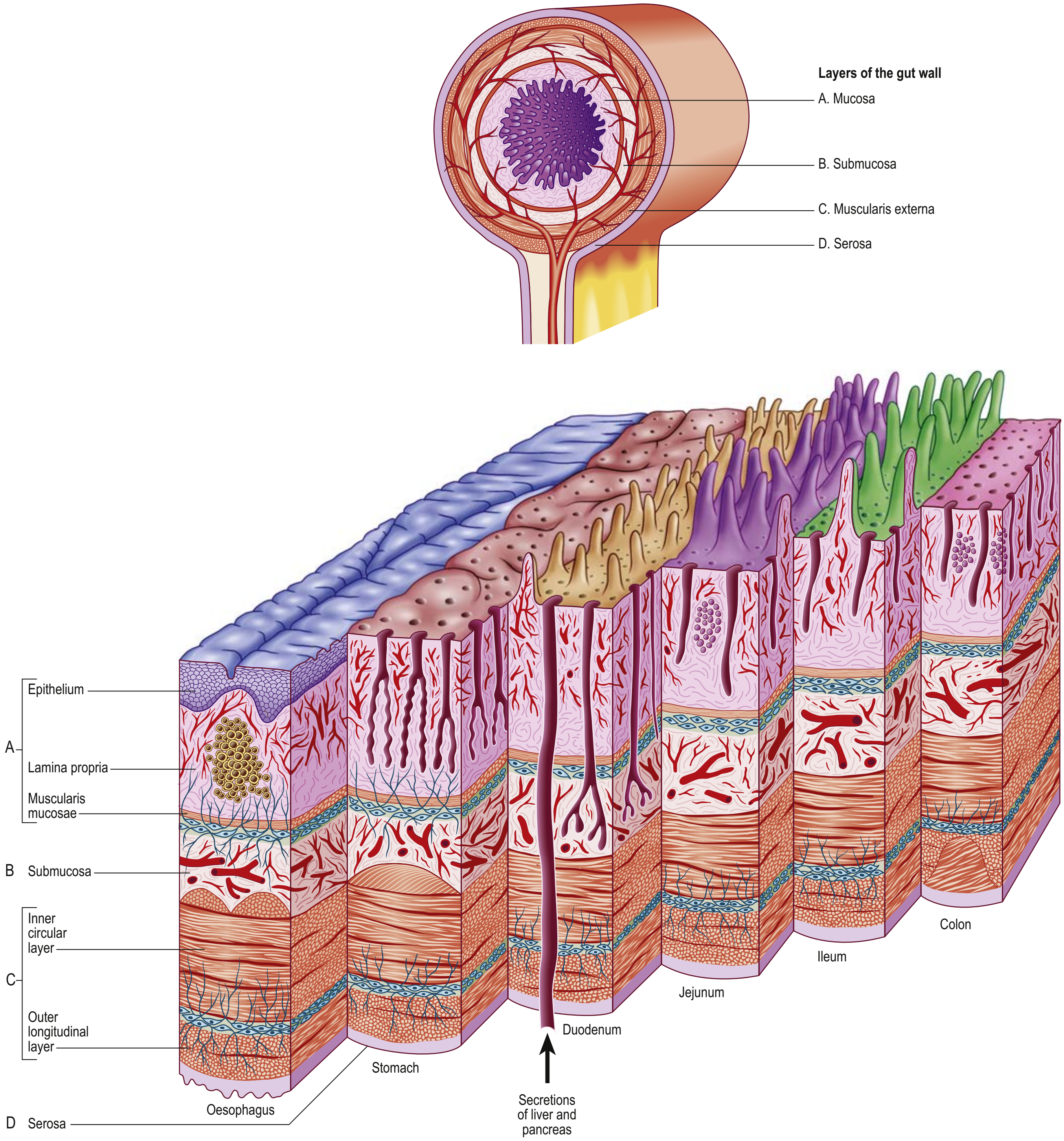
Layers of the gut wall
A. Mucosa
B. Submucosa
C. Musculoris externa
D. Serosa
Epithelium
A
Lamina propria
Muscularis mucosae
B Submucosa
Inner circular layer
C
Outer longitudinal layer
D Serosa
Oesophagus
Stomach
Duodenum
Secretions of liver and pancreas
Jejunum
Ileum
Colon

Fig. 59.8 The general arrangement of the digestive tract to show the layers of its walls at various levels.

nutrient vessels and lymphatics. Lymphoid follicles are present in many regions of the gastrointestinal tract, most notably in aggregated lymphoid nodules, particularly in the distal small intestine, e.g. Peyer's patches. Cells within the lamina propria are the source of growth factors that regulate cell turnover, differentiation and repair in the overlying epithelium.

Muscularis mucosae

The muscularis mucosae is particularly well developed in the oesophagus and the large intestine, especially in the terminal part of the rectum. In addition, single muscle cells originating from the muscularis mucosae are found inside the villi or between the tubular glands of the stomach and large intestine. By its contraction, the muscularis mucosae can alter the surface configuration of the mucosa locally, allowing it to adapt to the shapes and mechanical forces imposed by the contents of the lumen, and in the intestinal villi, promoting vascular exchange and lymphatic drainage.

Submucosa

The submucosa contains large bundles of collagen and is the strongest layer of the wall of the gastrointestinal tract. However, it is also pliable and deformable, and can therefore adjust to changes in the length and diameter of the wall of the hollow viscus. Its contained arterial network is relatively dense and supplies both the mucosa and the muscle coat. The submucosa extends into the rugae of the gastric wall, the plicae circulares (valves of Kerckring) of the small intestine (but not the villi), and the folds that project into the lumen of the colon and rectum.

Muscularis externa

The muscularis externa usually consists of distinct inner circular and outer longitudinal layers that create waves of peristalsis responsible for the movement of ingested material through the lumen of the hollow viscus. In the stomach, where movements are more complex, there is an incomplete oblique layer of muscle, internal to the other two layers. The circular muscle layer is thicker than the longitudinal muscle except in the colon, where the longitudinal muscle is condensed into three bands (taeniae coli).

The muscularis externa is composed almost exclusively of smooth muscle, except in the proximal oesophagus, where smooth muscle blends with striated muscle. Although the proximal oesophageal musculature resembles that of the pharynx, it is entirely under involuntary control. For most of its length, the smooth muscle of the wall of the gastrointestinal tract consists of ill-defined bundles of cells, typically visceral in type and somewhat larger than vascular smooth muscle cells. They are approximately 500 μm long, regardless of body size, and are electrically and mechanically coupled. Their fasciculi lack a perimysium but have sharp boundaries.

The arrangement of the musculature allows a segment of the gastrointestinal tract to undergo extensive changes in diameter (to virtual occlusion of the lumen) and length, although elongation is limited by the mesenteries. The coordinated activity of the two muscle layers produces a characteristic motor behaviour that is mainly propulsive and directed aborally (peristalsis), combined with a non-propulsive motor activity that either mixes the luminal contents, as occurs in the stomach, or partitions them, as occurs at the pyloric sphincter. The muscle maintains a constant volume, so that shortening of a segment of the wall of the hollow viscus is accompanied by thickening of the muscle layer.

Intestinal smooth muscle exhibits variable and changing degrees of contraction on which rhythmic (or phasic) contractions are superimposed. Slow waves of rhythmic electrical activity, driven by changes in membrane potentials in pacemaker cells (interstitial cells), spread throughout the thickness of the circular and longitudinal smooth muscle coats. After spreading circumferentially, slow waves can move in either oral or anal directions, causing segmental contraction. The distances of propagation and the patterns of this spontaneous activity differ among areas of the intestine. Neural regulation of slow and phasic contractions involves excitatory and inhibitory transmitters that are released from the myenteric plexus. This motor control is closely coordinated with mucosal absorption and secretion, and is mediated via intrinsic nerves in the submucous plexus. The peristaltic reflex occurs during passage of luminal contents down the intestine. It involves ascending contraction and descending relaxation; the sensory limb is mediated by sensory neurones that respond to either mucosal stimulation (intrinsic primary afferents) or muscle stretch (extrinsic afferents).

Interstitial cells

Interstitial cells of Cajal (ICCs) are found throughout the length of the gastrointestinal tract, where they lie in close contact with nerve terminals; they have numerous gap junctions with each other and with smooth muscle cells. Distinct networks are found in the myenteric plexus between the circular and longitudinal muscles. Looser arrangements exist within the individual muscle layers and the submucosa of the wall of the hollow viscera, and isolated or small groups of ICCs are also found in the subserosal region. ICCs originate from mesenchymal cells and resemble smooth muscle cells but have fewer contractile elements and their intermediate filaments contain vimentin rather than desmin. They are involved in generating pacemaker signals, propagating electrical slow wave activity, neuromuscular transmission, and mechanosensation (Sanders et al 2014). Defective ICC function has been implicated in a wide range of gastrointestinal motility disorders (Al-Shboul 2013) and in the development of gastrointestinal stromal tumours (Roggin and Posner 2012).

Cells with a similar morphology have been found in association with smooth muscle at many other sites such as the urethra, ductus deferens, prostate, urinary bladder, corpus cavernosum, ureter, uterine tube and uterus. They may act as electrical pacemakers in the urethra and ureter but their role at other sites is less certain (Drumm et al 2014).

Serosa and adventitia

A layer of connective tissue of variable thickness lies external to the muscularis externa. In many places it contains adipose tissue. Where the hollow viscera are covered by visceral peritoneum the external layer is a serosa, consisting of mesothelium overlying a thin layer of connective tissue. In extraperitoneal regions the surfaces of the gastrointestinal tract in contact with the peritoneum are covered by serosa, while other parts are covered by connective tissue that blends with the surrounding fasciae and is referred to as an adventitia.

Vascular plexuses

Vascular plexuses are present at various levels of the wall, especially in the submucosa and mucosa; they connect with vessels that supply the surrounding tissues or those entering through the mesentery, and accompany the ducts of outlying glands.

Innervation

The wall of the hollow viscera is densely innervated by both the enteric nervous system (intrinsic control) and the autonomic nervous system (extrinsic control). The latter is not essential for function, as evidenced by intestinal activity after transplantation of the extrinsically denervated part of the gastrointestinal tract. In contrast, neuropathies affecting the enteric nervous system, such as Hirschsprung's disease, are potentially life-threatening. For a detailed description of the enteric nervous system, see Furness et al (2014).

Extrinsic innervation

Extrinsic innervation of the gastrointestinal tract is from sympathetic, parasympathetic and visceral sensory nerves. The cell bodies of preganglionic parasympathetic axons are found in the dorsal nucleus of the vagus nerve in the medulla oblongata and in the second to fourth sacral segments of the spinal cord. Their main targets in the wall of the hollow viscera are the enteric neurones of the myenteric plexus. The vagus nerve plays a major role in oesophageal propulsion, gastric acid secretion and emptying of the stomach, gallbladder contraction and pancreatic exocrine secretion. Pelvic splanchnic nerves innervate the distal colon and rectum. Sympathetic neurones have their preganglionic cell bodies in the intermediolateral grey matter (lamina VII) of the thoracolumbar segments of the spinal cord; those destined for the smooth muscle of the wall of the hollow viscera mostly pass through the sympathetic trunk without synapsing and relay in prevertebral ganglia (coeliac, mesenteric and pelvic), whereas those mediating vasoconstriction synapse in the sympathetic trunk or prevertebral ganglia. Postganglionic sympathetic fibres are distributed with the branches of the coeliac trunk and mesenteric arteries to three principal targets: the myenteric and submucosal ganglia (causing inhibition), blood vessels (inducing vasoconstriction) and sphincter muscles (inducing contraction).

Visceral sensory fibres are distributed throughout the layers of the walls of the hollow viscera. They respond to various stimuli including excessive muscular contraction or distension, ischaemia and inflammation; their cell bodies are located in the inferior ganglion of the vagus nerve and in thoracic and lumbosacral spinal ganglia (visceral afferent fibres that run with sympathetic efferent fibres). Their central projections reach the brain stem and spinal cord, respectively. Sensory fibres in the vagus nerve are more numerous in the derivatives of the foregut than those of the derivatives of the midgut and are concerned with physiological responses such as satiety, whereas pain and discomfort are mediated by spinal pathways.

Intrinsic innervation

The intrinsic innervation of the gastrointestinal tract is derived from enteric neurones distributed throughout its wall in thousands of small ganglia, each consisting of neuronal cell bodies supported by enteric glial cells; it is estimated that there are between 200 and 600 million neurones in the human enteric nervous system. Enteric neurones are derived from neural crest cells and innervate the hollow viscera from oesophagus to anus, together with the pancreas and bile ducts.

Most of the enteric neurones in the wall of the gastrointestinal tract are found in two ganglionated plexuses (**Fig. 59.9**). The most extensive of these is the myenteric (Auerbach's) plexus, which consists of a network of nerve fibres and small ganglia lying between the circular and longitudinal layers of the muscularis externa. It runs in continuity from the oesophagus to the anus. The submucosal (Meissner's) plexus has outer and inner components and is present throughout the intestines but is absent or minimal in the oesophagus and stomach (Nagy and Goldstein 2017).

Interconnecting, non-ganglionated nerve plexuses lie at various levels in the wall of the gastrointestinal tract, including the lamina propria (mucosal plexus); at the interface between the submucosa and muscularis externa; between the circular and longitudinal muscles (the non-ganglionated part of the myenteric plexus); and within the serosa.

Individual enteric neurones function in one of several ways: as afferent (sensory) nerves responding to mechanical and chemical stimuli; as efferent (motor) nerves innervating epithelial cells (influencing absorption, secretion and/or the release of hormones), smooth muscle (excitatory or inhibitory), arterioles (vasoconstriction or vasodilatation) and lymphoid tissue; or as interneurones that relay and integrate signals. Collectively, they are involved in a hierarchy of enteric reflexes that include local reflexes within the wall of the hollow viscera; reflexes mediated through prevertebral ganglia; and reflexes mediated through the central nervous system (the gut–brain axis). The functions of enteric neurones can be further modulated by local environmental factors, e.g. enteric glia, gut microbiota and feeding state, and by general factors in the host, e.g. the immune system, stress and disease (Brierley and Linden 2014). Pathological states become manifest by abnormal secretion, impaired absorption, disordered gastrointestinal motility and pain.

SURFACE ANATOMY OF THE ABDOMEN AND PELVIS

Abdominal planes and regions

For descriptive purposes, the abdomen can be divided into regions using a combination of horizontal and vertical planes that are based on skeletal landmarks. Cross-sectional imaging-based studies in adults have enabled traditional descriptions of abdominal surface anatomy to be validated or updated. The extent to which these surface projections can be extrapolated to neonates, infants and children is uncertain; some differences are inevitable given their different visceral and body proportions (Stringer and Mirjalili 2017). In this chapter, descriptions of the surface projections and vertebral level correlations with the positions of abdominal structures refer to the arrangement most commonly seen in adults. However, it is important to note that there is considerable inter-individual variation in surface anatomy, compounded by potential variations related to age, sex, posture, respiration, body shape and body mass (Mirjalili and Stringer 2012).

Vertical lines and planes

The midline (or median plane) passes through the xiphoid process and the pubic symphysis. There are two paramedian lines, left and right, passing from the midclavicular point to a point midway between the anterior superior iliac spine and the pubic symphysis (**Fig. 59.10A**). In the upper abdomen, this line approximates to the lateral border of rectus abdominis.

Horizontal lines and planes

Several horizontal reference planes have been defined but, with modern cross-sectional imaging, their clinical utility for positioning abdominal viscera has become limited. Nevertheless, they provide a guide as to the approximate relative positions of abdominal viscera with respect to vertebral levels and bony surface landmarks.

The xiphisternal joint most often lies in the same horizontal (axial) plane as the vertebral body of T9 (Mirjalili et al 2012b).

The transpyloric plane lies midway between the jugular (suprasternal) notch of the manubrium and the superior border of the pubic symphysis. This corresponds to a plane approximately midway between the xiphisternal joint and the umbilicus, or slightly below. In most individuals the plane intersects either the inferior half of the vertebral body of L1, the L1–L2 intervertebral disc, or the superior half of the vertebral body of L2 (range, inferior half of the vertebral body of T12 to inferior half of the vertebral body of L2); it sits more superiorly in males (range, inferior half of the vertebral body of L1 to L1–L2 intervertebral disc) than in

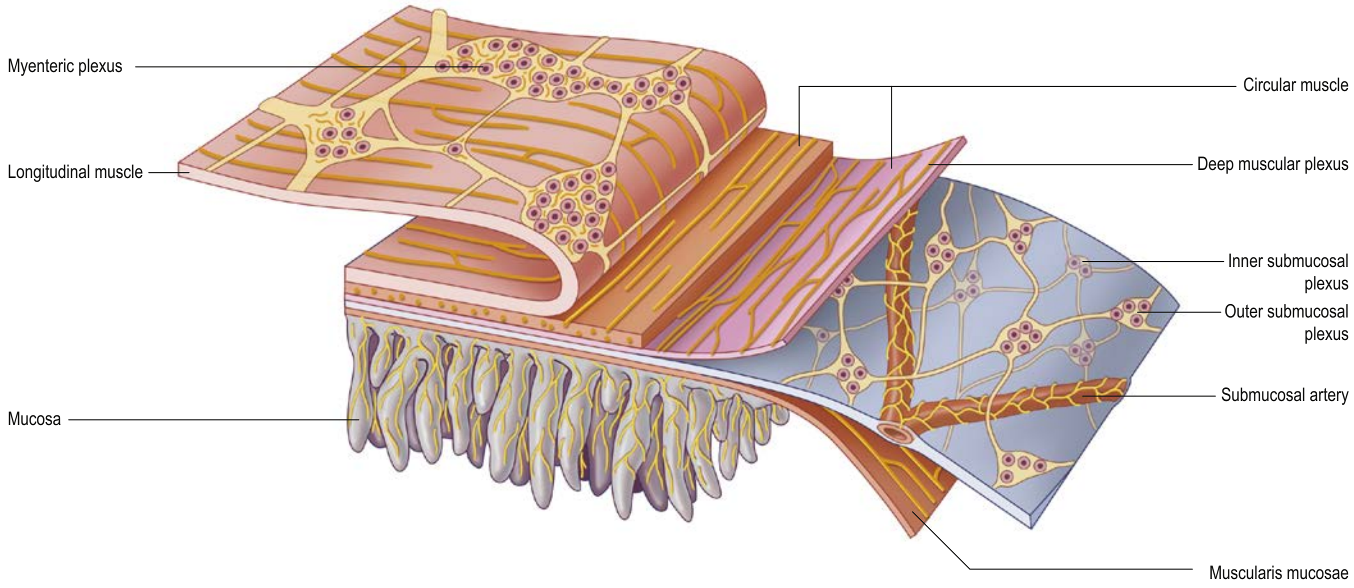

Fig. 59.9 The organization of the enteric nervous system in the small intestine. There are two ganglionated plexuses: the myenteric plexus between the longitudinal and circular layers of the external musculature, and the submucosal plexus (SMP), which has outer and inner components. Nerve fibre bundles connect the ganglia and form plexuses innervating the longitudinal muscle, circular muscle, muscularis mucosae, intrinsic arteries and mucosa. Axons of extrinsic origin also run in these nerve fibre bundles. There are also innervations of gastroenteropancreatic (GEP) endocrine cells and gut-associated lymphoid tissue (GALT), which are not shown here. (Redrawn from Furness JB. The enteric nervous system and neurogastroenterology. Nat Rev Gastroenterol Hepatol 2012;9:286–294. Reprinted with permission from Nature Publishing Group.)

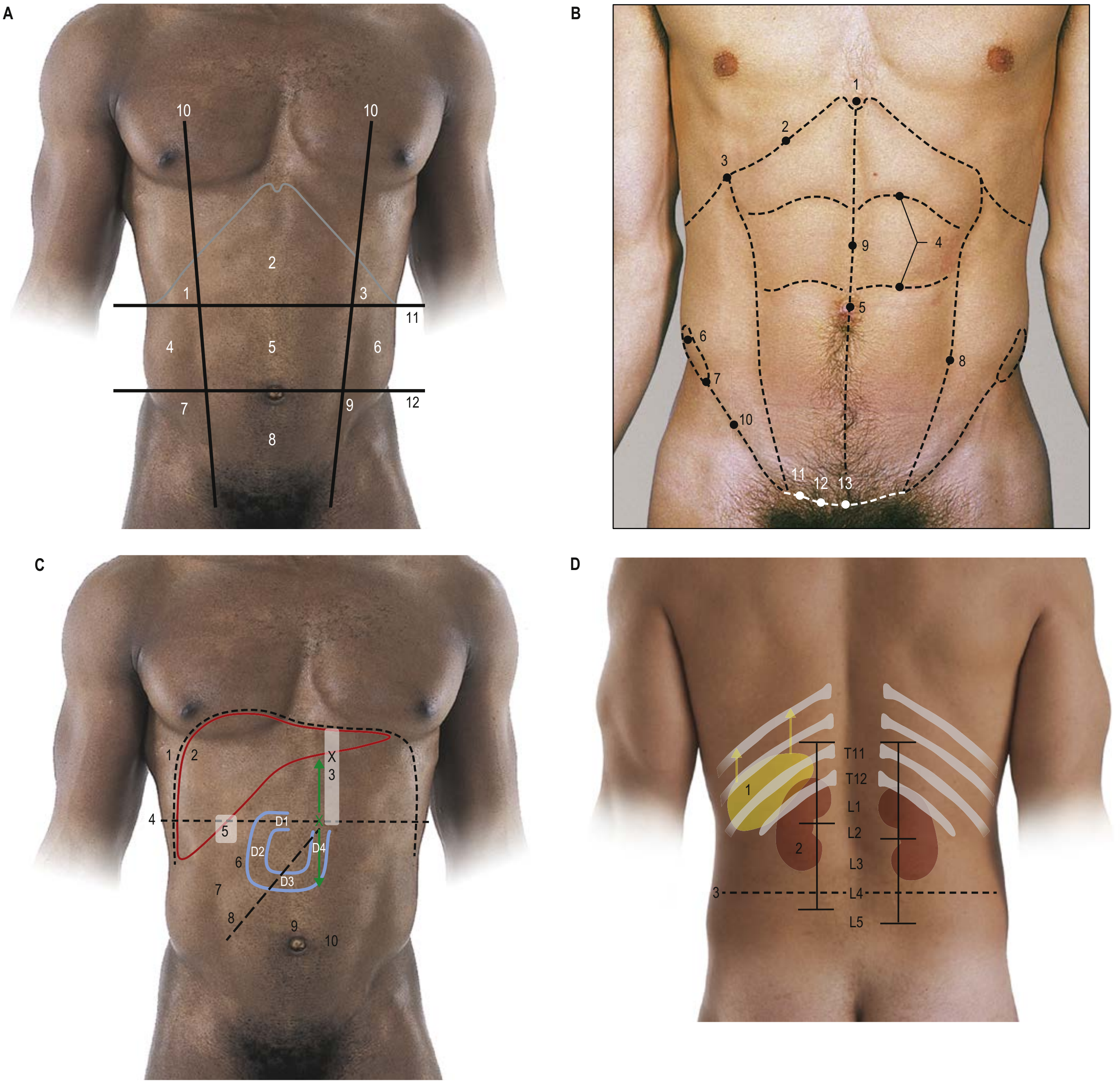

Fig. 59.10 **A**, Nine regions of the anterior abdominal wall. Key: 1, right hypochondriac region; 2, epigastric region; 3, left hypochondriac region; 4, right lateral region; 5, umbilical region; 6, left lateral region; 7, right inguinal region; 8, hypogastric region; 9, left inguinal region; 10, paramedian (midclavicular to midinguinal) line; 11, subcostal plane; 12, intertubercular plane. **B**, Anterior abdominal wall landmarks. Key: 1, xiphoid process; 2, costal margin (arch); 3, tip of the ninth costal cartilage; 4, tendinous intersections of rectus abdominis; 5, umbilicus; 6, iliac crest; 7, anterior superior iliac spine; 8, linea semilunaris; 9, linea alba; 10, inguinal ligament; 11, pubic tubercle; 12, pubic crest; 13, pubic symphysis. **C**, The surface projection of the abdominal viscera. Key: 1, respiratory diaphragm position (black dashed line): superior-most aspect on the right level with fifth intercostal space and superior most aspect of left level with the sixth rib; 2, liver: mapped between three points: right sixth rib/intercostal space midclavicular line, left fifth intercostal space/sixth rib midclavicular line and right tenth costal cartilage midaxillary line; 3, zone of gastro-oesophageal junction position (white): mainly located (black X) posterior to left seventh costal cartilage, level with the vertebral body of T11; 4, transpyloric plane; 5, region of fundus of gallbladder position (white), usually on or below the transpyloric plane; 6, duodenum: four parts marked D1–D4; 7, semilunar line; 8, position of mesentery of the small intestine; 9, linea alba; 10, tendinous intersection of rectus abdominis; X, (green) duodenojejunal flexure at L1, arrows show range of locations (inferior half of the vertebral body of T11 to superior half of the vertebral body of L3). **D**, The surface position of the spleen and kidneys. Key: 1, spleen: sits deep to tenth to twelfth ribs with its long axis aligned with the eleventh rib (yellow arrows show range of locations); 2, kidney (black lines shown range of positions of the superior and inferior poles, and the common position of the hilum); 3, supracristal plane. (D, Derived with permission from Mirjalili SA, McFadden SL, Buckenham T et al 2012b A reappraisal of adult abdominal surface anatomy. Clin Anat 25:844–50.)

females (inferior half of the vertebral body of L2) (Mirjalili et al 2012a, Uzun et al 2016). Anteriorly, it intersects the costal margin (arch) at the ninth costal cartilage, where the semilunar line crosses, and where a distinct 'step' may be palpable. The following structures lie approximately within the transpyloric plane (Mirjalili et al 2012a, 2012b): the origin of the superior mesenteric artery; the origin of the hepatic portal vein (from the confluence of the superior mesenteric and splenic veins posterior to the neck of the pancreas); the hilum of the left kidney (the hilum of the right kidney may be slightly more inferior); the origin of the renal arteries; the level of the duodenojejunal flexure; and the termination (conus medullaris) of the spinal cord (Nasr 2017). The pylorus may be found in the transpyloric plane but is not a constant feature.

The subcostal plane is defined by a line that joins the lowest point of the costal arch on each side (usually, the tenth costal cartilage); it most commonly intersects the vertebral body of L2 (range, T12–L1 intervertebral disc to superior half of the vertebral body of L3) (Mirjalili et al 2012a, Uzun et al 2016).

The supracristal plane (Tuffier's line) joins the most superior point of the iliac crest on each side. It serves as a useful landmark for the aortic bifurcation and when a lumbar puncture or spinal injection is performed, and usually lies at the level of the vertebral body or the spinous process of L4 or the L4–L5 intervertebral disc (Fig. 76.19) (Mirjalili et al 2012a, Pak et al 2016, Shen et al 2016, Uzun et al 2016).

The intertubercular plane joins the iliac tubercles and commonly lies at the level of the vertebral body of L5, near its proximal border. It is an approximate landmark for the origin of the inferior vena cava from the confluence of the left and right common iliac veins.

The plane of the pubic crest is in line with the superior border of the pubic symphysis. In supine individuals, this plane frequently intersects the head of the femur and the most inferior part of the coccyx (Mirjalili et al 2012a, Uzun et al 2016), but there are variations relating to the degree of lumbar lordosis, sacral inclination and pelvic tilt.

Abdominal regions

The abdomen can be divided into nine regions using the subcostal and intertubercular planes, and left and right midclavicular lines. Alternatively, the midclavicular line may be substituted for the paramedian plane, as defined previously (see Fig 59.10A). The nine regions are used in clinical practice for descriptive localization of a patient's pain or tenderness, or the position of a mass, and can be used to reference the position of abdominal viscera. From superior to inferior, the nine regions are: the epigastric region, flanked by the right and left hypochondriac regions; the umbilical region, flanked by the right and left lateral (flank) regions; and the hypogastric region, flanked by the right and left inguinal regions. In practice, these regions are often loosely defined without strict reference to their boundaries. An alternative system of description involves dividing the abdomen into quadrants using the median plane and a horizontal line passing through the umbilicus.

Anterior abdominal wall

Skeletal landmarks

The superior boundary of the anterior abdominal wall is formed by several clear landmarks (**Fig. 59.10B–C**). The xiphoid process is palpable inferior to the body of the sternum, in the midline. From here, the left and right costal arches can be felt passing inferolaterally from the seventh costal cartilage at the xiphisternal joint to the tenth costal cartilage. The distal border of the ninth costal cartilage can usually be defined as a distinct 'step' along the costal arch. The inferior part of the costal arch lies in the midaxillary line and is formed by the inferior margin of the tenth costal cartilage. Further palpation may reveal the distal ends of the eleventh and twelfth ribs, although these may be difficult to feel in the obese or if the ribs are short.

The inferior boundary of the anterior abdominal wall is formed, from lateral to medial, by the iliac crest, which descends to the anterior superior iliac spine; the inguinal ligament, which runs inferomedially to the pubic tubercle; and the pubic crest, which extends from the pubic tubercle laterally to the pubic symphysis in the midline. The pubic tubercle is palpable on the anterosuperior surface of the pubic bone approximately 2 cm lateral to the midline. The prominent tendon of adductor longus (best felt with the hip flexed, abducted and laterally rotated) attaches to the body of the pubis directly below the pubic tubercle, and can therefore be used to verify the position of the pubic tubercle.

The posterolateral boundary of the anterior abdominal wall is the midaxillary line.

Soft tissue landmarks

Umbilicus

The umbilicus is an obvious landmark with a relatively inconstant position. In the supine adult, it usually lies level with the vertebral body of L4 (range, L2–L3 intervertebral disc to superior half of the vertebral body of S1) (Mirjalili et al 2012b, Shen et al 2016). The umbilicus can lie at a more inferior level in children and the obese, and in adults in the erect position or with a distended anterior abdominal wall.

Rectus abdominis

In a thin, muscular individual, the tendinous intersections of rectus abdominis may be visible, especially when the muscle is tensed by lifting the head against resistance or by sitting up; the tendinous intersections are usually situated at the level of the umbilicus, the level of the xiphoid process and midway between these two points (see Fig. 59.10B–C).

Linea alba

The linea alba is usually visible only in thin, muscular individuals in the median plane. It is wider and more obvious above the umbilicus, and is less visible below this level (Ch. 60) (see Figs 59.10B–C, Fig. 60.2).

Semilunar line

The semilunar (Spigelian) line lies along the lateral margin of the rectus sheath and is visible as a shallow, curved groove in muscular individuals, particularly when the abdominal muscles are tensed, e.g. by sitting up from the lying position (Fig. 59.10B–C). It passes from the ninth costal cartilage to the pubic tubercle.

Midinguinal point

The midinguinal point is at the midpoint of a line between the pubic symphysis and the anterior superior iliac spine. In adults, it is the approximate surface marking of the femoral artery (located just inferior to the inguinal ligament) and the deep inguinal ring (located just superior to the inguinal ligament) (Hale et al 2010).

Inferior epigastric artery

The inferior epigastric artery lies along the medial border of the deep inguinal ring immediately above the inguinal ligament. Up to the level of the umbilicus, it follows a course that lies approximately 40% of the distance between the midline and a sagittal plane running through the anterior superior iliac spine (Epstein et al 2004). The surface anatomy of the artery is particularly important in laparoscopic surgery because trocar insertion may injure the vessel, causing a rectus sheath haematoma or intra-abdominal bleeding. The artery can be avoided if a trocar is inserted at least two-thirds of the distance along a horizontal line between the midline and a sagittal plane passing through the anterior superior iliac spine.

Superficial reflexes

Cremasteric reflex

Stroking the skin of the medial side of the thigh evokes a reflex contraction of cremaster, which elevates the ipsilateral testis. The reflex is mediated by the genitofemoral nerve (L1 and L2 ventral rami), although the afferent arc of the reflex may be via sensory fibres in the ilio-inguinal nerve. The reflex is usually absent if there is torsion of a testis.

Superficial abdominal reflex

Gently stroking each of the four quadrants of the anterior abdominal wall normally elicits a visible contraction of the ipsilateral abdominal wall muscles. Historically the reflex was used to help localize lesions in the spinal cord such as syringomyelia but is now of limited clinical significance because of the availability of neuroimaging and the difficulties of eliciting the reflex in multiparous women, the elderly and the obese (Fujimori et al 2010, Gosavi and Lo 2014).

Intra-abdominal viscera and respiratory diaphragm

The surface markings of the intra-abdominal viscera are variable and depend on age, sex, body habitus, nutritional state, phase of ventilation, body position and pathology. The availability of cross-sectional and ultrasound medical imaging of the abdominal viscera has reduced the need to rely on surface anatomy alone in clinical practice. Nevertheless, a sound knowledge of surface anatomy helps guide proficient physical and ultrasound-based examinations, invasive procedures such as lumbar puncture, and surgical approaches. The following descriptions should be regarded as the most common approximate markings in a healthy supine adult (Fig. 59.10C). The spinous processes of the lumbar vertebrae can be used to locate vertebral levels, the inferior part of the spinous process normally marking the level of the inferior part of the correspondingly numbered vertebral body or the intervertebral disc below.

Respiratory diaphragm

In the supine position at end-tidal inspiration the most superior part of the respiratory diaphragm is most frequently located level with the fifth intercostal space in the midclavicular line on the right and the sixth rib in the midclavicular line on the left, and ranges from the fourth intercostal space to below the costal arch (Mirjalili et al 2012c, Shen et al 2016) (Fig. 59.10C) (see Ch. 55 for further discussion of the respiratory diaphragm). These levels are approximate, not only because of individual variation but also because respiratory diaphragmatic excursion in the erect position during quiet breathing is about 1–2 cm and increases to about 5–7 cm during deep breathing (Jung et al 2014, Boussuges et al 2009). The highest part of the respiratory diaphragm may reach as high as the fourth rib on maximal expiration.

Stomach

The gastro-oesophageal junction lies to the left of the midline, posterior to the left seventh costal cartilage, at the level of the vertebral body of T11 (range, superior half of the vertebral body of T10 to L1–L2 intervertebral disc), the level being more inferior in females and more superior in the obese (Mirjalili et al 2012b) (see Fig. 59.10C). The stomach lies in a curve normally within the left hypochondriac and epigastric regions, although it may lie as distally as the umbilical or hypogastric regions when distended. The epigastric region is the usual place to auscultate for a 'succussion splash' caused by gastric outlet obstruction or stasis, and is also the region in infants where a thickened pylorus, e.g. hypertrophic pyloric stenosis, is palpable.

Duodenum

The superior (first) part of the duodenum sits in, and sometimes ascends above, the transpyloric plane (vertebral body of L1); the descending (second) part usually lies just to the right of the midline, alongside the vertebral bodies of L2 and L3; the horizontal (third) part usually crosses the midline at the level of the vertebral body of L3; and the ascending (fourth) part ascends to the left of the vertebral body of L2, reaching the transpyloric plane in the region of the inferior half of the vertebral body of L1 (see Fig. 59.10C). The duodenojejunal flexure commonly sits level with the vertebral body of L1 (range, lower half of the vertebral body of T11 to superior half of the vertebral body of L3) (Mirjalili et al 2012b). In children from 0 to 11 years of age the duodenojejunal flexure is also commonly located level with the vertebral body of L1 (range, level with the vertebral bodies of T11 to L3) (Koch et al 2016), which is of clinical importance when assessing for duodenal or gut tube malrotation.

Small intestine and its mesentery

The attachment of the mesentery of the small intestine to the posterior abdominal wall passes obliquely inferiorly to the right, from a point just to the left of the vertebral body of L1 (the transpyloric plane) in men and the vertebral body of L2 (the subcostal plane) in women, towards the right iliac fossa.

Appendix

The appendix is located in the right lower quadrant of the abdomen but is highly variable in its length and position. Studies analysing barium enemas in supine adults have shown the position of the proximal appendix to be variably located and rarely precisely at McBurney's point (a point two-thirds of the way along a line drawn to join the anterior superior iliac spine to the umbilicus) (Naraynsingh et al 2002).

Liver

At the end of normal tidal inspiration, the inferior border of the liver extends along a line that passes from the right tenth costal cartilage in the midaxillary line to the left fifth intercostal space/sixth rib in the midclavicular line (see Fig. 59.10C). It may be palpable inferior to the costal arch in healthy adults on deep inspiration, especially near the median plane. The superior border of the liver follows a line that passes from the right fifth rib or intercostal space in the midclavicular line to the left fifth intercostal space or sixth rib in the midclavicular line, and can be mapped with the curved contour of the respiratory diaphragm (Mirjalili et al 2012c). This border curves slightly downwards at its centre and crosses the midline posterior to the xiphisternal joint. The right border of the liver is curved to the right and joins the superior and inferior right limits. The superior border of the liver can be defined by dullness to percussion when compared with the resonance of the lungs above.

Gallbladder

The fundus of the gallbladder is commonly identified in the transpyloric plane near the junction of the semilunar line with the costal arch (see Fig. 59.10C). Recent data have shown that the fundus of the gallbladder lies in the transpyloric plane in approximately one-third of supine individuals and below that plane in most others (Mirjalili et al 2012b, Uzun et al 2016).

Spleen

The spleen is traditionally described as sitting on the left posterolateral abdominal wall deep to the ninth to eleventh ribs. Recent data from supine individuals show that the spleen sits deep to the tenth to the twelfth ribs in 50% of subjects and deep to the ninth to eleventh ribs in 25%, with its long axis aligning most closely with either the eleventh or tenth rib, respectively (Mirjalili et al 2012b, Shen et al 2016, Pak et al 2016). It passes anterior to the midaxillary line in most subjects (**Fig. 59.10D**). The spleen extends from a point about 5 cm to the left of the midline at the level of the spinous process of T11 and extends about 3 cm anterior to the midaxillary line. In children the spleen is often in a more superior location, with its long axis aligning with the ninth or tenth rib (Subramaniam et al 2016).

Retroperitoneal viscera

The surface projections of the retroperitoneal viscera are reasonably reliable and may be used to guide clinical examination or identification of structures on radiological images.

Pancreas

The surface projection of the head of the pancreas lies within the concavity of the duodenum on the right side of the vertebral body of L2; the neck lies in the transpyloric plane, level with the L1-L2 intervertebral disc; the body passes obliquely superolaterally to the left towards the spleen; and the tail lies slightly above the transpyloric plane.

Kidney

On average, the right kidney lies 2 cm lower than the left, although the left kidney can sit lower than the right in about 10% of cases (Mirjalili et al 2012b). The vertebral limits of the left kidney are between the vertebral bodies of T12 and L3 or L4, while those for the right kidney are between the vertebral bodies of L1 and L4 (range, superior half of the vertebral body of T11 to inferior half of the vertebral body of L5) (see Fig. 59.10D). The superior poles of both kidneys lie anterior to the twelfth rib, and may also lie anterior to the eleventh rib in 30% (left) and 10% (right) of subjects. In adults in the supine position at end-tidal inspiration, the centres of the hila of the kidneys most commonly lie level with the L1-L2 intervertebral disc or the vertebral body of L2: the hilum of the right kidney is slightly lower than the hilum of the left kidney (Pak et al 2016, Shen et al 2016, Uzun et al 2016). It is important to note that both kidneys move vertically by a mean of approximately 2 cm during deep respiration and both can descend by several centimetres when moving from lying to standing (Schwartz et al 1994, Reiff et al 1999).

The inferior pole of the normal right kidney may occasionally be felt in thin individuals by bimanual palpation via the renal angle (twelfth rib and lateral border of erector spinae) on full inspiration. The centre of the hilum of the kidney is approximately 6 cm from the midline in males and 5 cm in females.

Ureter

The ureter descends on either side, about 5 or 6 cm from the midline, from approximately the level of the transpyloric plane (range, inferior half of the vertebral body of L1 to superior half of the vertebral body of L2): this origin is slightly lower on the right. Each ureter passes downwards just medial to the tips of the transverse processes of the lumbar vertebrae and, in the pelvis, curves medially to enter the fundus of the urinary bladder.

Abdominal aorta and branches

The abdominal aorta begins at the level of the vertebral body of T12 near the midline. It descends and bifurcates at the vertebral body of L4 (range, inferior half of the vertebral body of L3 to inferior half of the vertebral body of L5), usually just to the left of the midline and up to 3 cm caudal to the umbilicus (Mirjalili et al 2012b, Pak et al 2016, Shen et al 2016, Uzun et al 2016). The aortic bifurcation is also most commonly located level with the vertebral body of L4 in children from 0 to 11 years of age (Subramaniam et al 2016). The position of the aortic bifurcation is moved slightly proximally with an increased lumbar lordosis (Moussallem et al 2012). The pulsations of the abdominal aorta can be felt in a supine individual of lower body mass by pressing firmly and deeply in the midline, thereby compressing the aorta on to the bodies of the lumbar vertebrae.

Unpaired visceral arteries

The coeliac trunk arises from the abdominal aorta immediately after it enters the abdomen at the level of the vertebral body of T12; the superior mesenteric artery arises most commonly at the level of the vertebral body of L1, close to the transpyloric plane; and the inferior mesenteric

The length of the normal adult kidney, measured along its long axis, is approximately 11.5 cm in males and 11.0 cm in females (Hale et al 2010); the left kidney is a few millimetres longer than the right (Cheong et al 2007, Glodny et al 2009). There is a small reduction in kidney length beyond 50 years of age (Glodny et al 2009). Each kidney is approximately 5–6 cm wide. Both its longitudinal and transverse axes are slightly oblique, such that the superior pole of each kidney is nearer the midline and the hilum is more anterior than the lateral surface.

artery usually arises at the level of the vertebral body of L3 (Mirjalili et al 2012b, Pak et al 2016, Shen et al 2016, Uzun et al 2016). The level of origin of each of these arteries is similar in children from 0 to 11 years of age (Subramaniam et al 2016).

Renal arteries

The left and right renal arteries most commonly arise level with the inferior half of the vertebral body of L1, approximately in the transpyloric plane (range, inferior half of the vertebral body of L1 to the superior half of the vertebral body of L2) (Mirjalili et al 2012b, Pak et al 2016, Shen et al 2016). Similar observations have been made in children aged 0–11 years (Subramaniam et al 2016).

Iliac arteries

The surface projection of the common iliac artery corresponds to the superior third of a broad line, slightly convex laterally, joining the aortic bifurcation (see above) to a point midway between the anterior superior iliac spine and the pubic symphysis. The external iliac artery corresponds to the inferior two-thirds of this line.

Inferior vena cava

The inferior vena cava most commonly forms level with the vertebral body of L5 in the intertubercular plane (range, superior half of the vertebral body of L4 to the superior half of the vertebral body of S1) to the right of the midline (Mirjalili et al 2012b, Pak et al 2016, Shen et al 2016). It forms level with the vertebral body of L4 in children aged 0–3 years, and level with the vertebral body of L5 in children aged 4–11 years (Subramaniam et al 2016). The inferior vena cava was traditionally thought to leave the abdomen through the caval foramen of the respiratory diaphragm at the level of the vertebral body of T8. In some individuals this may hold true (Keough et al 2016), however more commonly, the caval foramen is located between the levels of the vertebral bodies of T10 and T11 (Mirjalili et al 2012b, Shen et al 2016, Pak et al 2016).

Pelvis

The posterior superior iliac spines lie commonly at the level of the vertebral body of S2 (range, the L5–S1 interspinous space to the spinous process of S3 along the median sacral crest) (McGaugh et al 2007); some individuals have a depression or dimple (sacroiliac fovea) in the overlying skin. This palpable bony landmark corresponds approximately to the termination of the spinal dural sac (Nasr 2017) and the middle of the sacroiliac joint. The second dorsal sacral foramen lies approximately 2–3 cm medial to the posterior superior iliac spine on each side at an angle of 45° (McGrath and Stringer 2011). The latter is potentially useful for locating the branches of the sacral dorsal rami in the treatment of medically refractory sacroiliac pain.

Sciatic nerve

The sciatic nerve leaves the pelvis approximately one-third of the way along a line between the posterior superior iliac spine and the ischial tuberosity and enters the thigh approximately half way between the greater trochanter of the femur and the ischial tuberosity (see Fig. 76.19) (Currin et al 2014). In children from 0 to 11 years of age, the sciatic nerve is located within the middle third of two reference lines; a line joining the posterior superior iliac spine to the ischial tuberosity, and a line joining the greater trochanter to the ischial tuberosity (Selkirk et al 2016).

Other surface landmarks for pelvic structures are described in Chapter 76.

COMMON CLINICAL PROCEDURES

Pneumoperitoneum for laparoscopy

A pneumoperitoneum is frequently established by accessing the peritoneal cavity just below the umbilicus. An incision through the linea alba allows access to the peritoneum at a point where there is relatively little extraperitoneal fat. Additional working ports are inserted through the anterior abdominal wall, avoiding major vessels such as the inferior epigastric artery.

Surgical incisions

Most surgical incisions are sited according to surgical imperatives rather than anatomical constraints. Access to the peritoneal cavity is usually gained by dividing or splitting muscles. Common approaches include the midline incision through the relatively avascular linea alba, the transverse suprapubic (Pfannenstiel) incision for pelvic procedures, and, in infants and children, the upper abdominal transverse incision. In recent years, progressively more abdominal surgery has been performed using laparoscopic procedures (minimally invasive or 'keyhole' surgery) utilizing, for example, the umbilicus.

Intestinal stomas (ileostomy, colostomy)

When possible, intestinal stomas are usually formed through transrectus (rectus abdominis) incisions. A cruciate incision is made in the anterior layer of the rectus sheath and the muscle fibres are split, avoiding injury to the epigastric vessels. This incision offers the advantage that fibres of rectus abdominis support the stoma, providing a dynamic, contractile surround that tends to reduce the risk of herniation occurring around the stoma.

Suprapubic catheterization

The urinary bladder can be accessed for short- or long-term catheterization through the anterior abdominal wall. As the urinary bladder fills, its superior aspect rises above the pubis and can be relatively easily accessed by a midline transcutaneous puncture through the most distal part of the linea alba.

Endoscopic surgery

Endoscopic surgery is a broad term that encompasses all types of surgery performed using flexible or rigid fibre-optic endoscopes inserted through natural body orifices or small surgical incisions. It overlaps with the field of minimally invasive surgery. The aim is to minimize or eliminate external incisions and hasten the patient's recovery, whilst providing optimum treatment of the pathology with an acceptably low risk of complications. In the abdomen and pelvis it includes therapeutic procedures performed using an endoscope inserted via the mouth (gastroscope or duodenoscope), anus (proctoscope, sigmoidoscope or colonoscope), urethra (cystoscope or ureteroscope) or vagina, or via small surgical incisions in the anterior or posterior abdominal wall (laparoscope and other endoscopic systems).

A refinement of the technique is natural orifice transluminal endoscopic surgery, in which abdominal operations are performed using an endoscope inserted through a natural orifice (e.g. mouth, anus, urethra) and then through an incision in the viscus that has been entered (e.g. stomach, urinary bladder, vagina). For example, pelvic and intra-abdominal contents can be accessed through the vagina via the recto-uterine pouch. Hysterectomy, oophorectomy, pelvic organ prolapse repair and incontinence surgery are commonly performed using transvaginal techniques. This approach avoids the morbidity of abdominal incision but there are risks of sciatic, femoral and common fibular nerve injury from prolonged surgery in the lithotomy position.

A further development of endoscopic minimally invasive surgery has been the introduction of robotically assisted surgery, which allows the surgeon to manipulate precision instruments from a console remote from the patient whilst viewing the operative field in three dimensions. The procedure is becoming increasingly common in procedures such as prostatectomy.

Bonus e-book content

Fig. 59.5 B, Volume-rendered CT angiogram of the abdominal aorta.

Video 59.1 Dissection of the posterior abdominal wall.

Video 59.2 Dissection of the lumbosacral junction.

Key references

Furness JB, Callaghan BP, Rivera LR et al 2014 The enteric nervous system and gastrointestinal innervation: integrated local and central control. Adv Exp Med Biol 817:39–71.

A comprehensive review of gastrointestinal innervation and the complexities of the enteric nervous system.

Kraima AC, van Schaik J, Susan S et al 2015 New insights in the neuroanatomy of the human adult superior hypogastric plexus and hypogastric nerves. Auton Neurosci 189:60–7.

A cadaveric study that found parasympathetic fibres in the superior hypogastric plexus based on immunohistochemistry.

Loukas M, Klaassen Z, Merbs W et al 2010 A review of the thoracic splanchnic nerves and celiac ganglia. Clin Anat 23:512–22.

A critical review of the thoracic splanchnic nerves.

Mirjalili SA, Stringer MD 2012 The need for an evidence-based reappraisal of surface anatomy. Clin Anat 25:816–8.

This issue of the journal Clinical Anatomy in which this article is found features several original articles reappraising surface anatomy of the trunk using cross-sectional CT imaging in supine adults. These articles provide a more evidence-based approach to key surface anatomy landmarks in the chest, abdomen and pelvis.

Pillai AK, Andring B, Patel A et al 2015 Portal hypertension: a review of portosystemic collateral pathways and endovascular interventions. Clin Radiol 70:1047–59.

A review of the pathophysiology, anatomy and imaging of spontaneous portosystemic collaterals and the clinical manifestations of portal hypertension.

Tubbs RS, Shoja MM, Loukas M 2016 Bergman's Comprehensive Encyclopedia of Human Anatomic Variation. Hoboken: Wiley Blackwell.

This book is an invaluable source of detailed, evidence-based information about anatomical variations.

References

Al-Shboul OA 2013 The importance of interstitial cells of Cajal in the gastrointestinal tract. Saudi J Gastroenterol 19:3–15.

Azaïs H, Collinet P, Delmas V et al 2013 Uterosacral ligament and hypogastric nerve anatomical relationship. Application to deep endometriotic nodules surgery. Gynecol Obstet Fertil 41:179–83.

Blaszczyk B 1981 Variation of ganglia of the pelvic segment of the sympathetic trunk in human fetuses. Folia Morphol (Warsz) 39:313–26.

Boussuges A, Gole Y, Blanc P 2009 Diaphragmatic motion studied by m-mode ultrasonography: methods, reproducibility, and normal values. Chest 135:391–400.

Brierley SM, Linden DR 2014 Neuroplasticity and dysfunction after gastrointestinal inflammation. Nat Rev Gastroenterol Hepatol 11:611–27.

Cheong B, Muthupillai R, Rubin MF et al 2007 Normal values for renal length and volume as measured by magnetic resonance imaging. Clin J Am Soc Nephrol 2:38–45.

Currin SS, Mirjalili SA, Meikle G et al 2014 Revisiting the surface anatomy of the sciatic nerve in the gluteal region. Clin Anat 28:144–9.

Drumm BT, Koh SD, Andersson KE 2014 Calcium signalling in Cajal-like interstitial cells of the lower urinary tract. Nat Rev Urol 11:555–64.

Epstein J, Arora A, Ellis H 2004 Surface anatomy of the inferior epigastric artery in relation to laparoscopic injury. Clin Anat 17:400–8.

Espinosa-Medina I, Saha O, Boismoreau F et al 2016 The sacral autonomic outflow is sympathetic. Science 354:893–7.

Fujimori T, Iwasaki M, Nagamoto Y et al 2010 The utility of superficial abdominal reflex in the initial diagnosis of scoliosis: a retrospective review of clinical characteristics of scoliosis with syringomyelia. Scoliosis 5. doi: 10.1186/1748-7161-5-17.

Furness JB, Callaghan BP, Rivera LR et al 2014 The enteric nervous system and gastrointestinal innervation: integrated local and central control. Adv Exp Med Biol 817:39–71.

A comprehensive review of gastrointestinal innervation and the complexities of the enteric nervous system.

Glodny B, Unterholzner V, Taferner V et al 2009 Normal kidney size and its influencing factors – a 64-slice MDCT study of 1.040 asymptomatic patients. BMC Urol 9:1–19.

Gosavi TD, Lo YL 2014 Images in clinical medicine. Superficial abdominal reflex. N Engl J Med. 2014 370(18).

Hale SJ, Mirjalili SA, Stringer MD 2010 Inconsistencies in surface anatomy: the need for an evidence-based reappraisal. Clin Anat 23:922–93.

Horn JP 2018 The sacral autonomic outflow is parasympathetic: Langley got it right. Clin Auton Res 28:181–5.

Jung KJ, Park JY, Hwang DW et al 2014 Ultrasonographic diaphragmatic motion analysis and its correlation with pulmonary function in hemiplegic stroke patients Ann Rehabil Med 38:29–37.

Keough N, Mirjalili SA, Suleman FE et al 2016 The thoracic surface anatomy of adult black South Africans: a reappraisal from CT scans. Clin Anat 29:1018–24.

Koch C, Taghavi K, Hamill J et al 2016 Redefining the projectional and clinical anatomy of the duodenojejunal flexure in children. Clin Anat 29:175–82.

Kraima AC, van Schaik J, Susan S et al 2015 New insights in the neuroanatomy of the human adult superior hypogastric plexus and hypogastric nerves. Auton Neurosci 189:60–7.

A cadaveric study that found parasympathetic fibres in the superior hypogastric plexus based on immunohistochemistry.

Loukas M, Klaassen Z, Merbs W et al 2010 A review of the thoracic splanchnic nerves and celiac ganglia. Clin Anat 23:512–22.

A critical review of the thoracic splanchnic nerves.

Mauroy B, Demondion X, Drizenko A et al 2003 The inferior hypogastric plexus (pelvic plexus): its importance in neural preservation techniques. Surg Radiol Anat 25:6–15.

McGaugh JM, Brismee JM, Dedrick GS et al 2007 Comparing the anatomical consistency of the posterior superior iliac spine to the iliac crest as reference landmarks for the lumbopelvic spine: a retrospective radiological study. Clin Anat 20:819–25.

McGrath MC, Stringer MD 2011 Bony landmarks in the sacral region: the posterior superior iliac spine and the second dorsal sacral foramina: a potential guide for sonography. Surg Radiol Anat 33:279–86.

Mirjalili SA, Stringer MD 2012 The need for an evidence-based reappraisal of surface anatomy. Clin Anat 25:816–8.

This issue of the journal Clinical Anatomy features several original articles reappraising surface anatomy of the trunk using cross-sectional CT imaging in supine adults. These articles provide a more evidence-based approach to key surface anatomy landmarks in the chest, abdomen and pelvis.

Mirjalili SA, McFadden SL, Buckenham T et al 2012a Anatomical planes: are we teaching accurate surface anatomy? Clin Anat 25:819–26.

Mirjalili SA, McFadden SL, Buckenham T et al 2012b A reappraisal of adult abdominal surface anatomy. Clin Anat 25:844–50.

Mirjalili S, Hale S, Buckenham T et al 2012c A reappraisal of adult thoracic surface anatomy. Clin Anat 25:827–34.

Motoc A, Rusu MC, Jianu AM 2010 The spermatic ganglion in humans: an anatomical update. Rom J Morphol Embryol 51:719–23.

Moussallem CD, Abou Hamad I, El-Yahchouchi CA et al 2012 Relationship of the lumbar lordosis angle to the abdominal aortic bifurcation and inferior vena cava confluence levels. Clin Anat 25:866–71.

Murata Y, Takahashi K, Yamagata M et al 2003 Variations in the number and position of human lumbar sympathetic ganglia and rami communicantes. Clin Anat 16:108–13.

Nagy N, Goldstein AM 2017 Enteric nervous system development: a crest cell's journey from neural tube to colon. Semin Cell Dev Biol 66:94–106.

Naraynsingh V, Ramdass MJ, Singh J et al 2002 McBurney's point: are we missing it? Surg Radiol Anat 24:363–5.

Nasr AY 2017 Clinical relevance of conus medullaris and dural sac termination level with special reference to sacral hiatus apex: anatomical and MRI radiologic study. Anat Sci Int 92:456–7.

Oh CS, Chung IH, Ji HJ et al 2004 Clinical implications of topographic anatomy on the ganglion impar. Anesthesiology 101:249–50.

Pak N, Patel SG, Hashemi Taheri AP et al 2016 A reappraisal of adult thoracic and abdominal surface anatomy in Iranians in vivo using computed tomography. Clin Anat 29:191–6.

Paraskevas G, Tsitsopoulos P, Papaziogas B et al 2008 Variability in superior hypogastric plexus morphology and its clinical applications: a cadaveric study. Surg Radiol Anat 30:481–8.

Pillai AK, Andring B, Patel A et al 2015 Portal hypertension: a review of portosystemic collateral pathways and endovascular interventions. Clin Radiol 70:1047–59.

A review of the pathophysiology, anatomy and imaging of spontaneous portosystemic collaterals and the clinical manifestations of portal hypertension.

Potts TK 1925 The main peripheral connections of the human sympathetic nervous system. J Anat 59:129–35.

Reiff JE, Werner-Wasik M, Valicenti RK et al 1999 Changes in the size and location of kidneys from the supine to standing positions and the implications for block placement during total body irradiation. Int J Radiat Oncol Biol Phys 45:447–9.

Roggin KK, Posner MC 2012 Modern treatment of gastric gastrointestinal stromal tumors. World J Gastroenterol 18:6720–8.

Röthlisberger R, Aurore V, Boemke S et al 2018 The anatomy of the male inferior hypogastric plexus: What should we know for nerve sparing surgery. Clin Anat 31:788–96.

Rusu MC 2006 Considerations on the phrenic ganglia. Ann Anat 188:85–92.

Sanders KM, Ward SM, Koh SD 2014 Interstitial cells: regulators of smooth muscle function. Physiol Rev 94:859–907.

Schwartz LH, Richaud J, Buffat L et al 1994 Kidney mobility during respiration. Radiother Oncol 32:84–6.

Selkirk GD, Mclaughlin AC, Mirjalili SA 2016 Revisiting the surface anatomy of the sciatic nerve in the gluteal region in children using computed tomography. Clin Anat 29:211–6.

Shen XH, Su BY, Liu JJ et al 2016 Reappraisal of adult thoracic and abdominal surface anatomy via CT scan in Chinese population. Clin Anat 29:165-74.

Stringer MD, Mirjalili SA 2017 Clinical anatomy of the newborn. In: Puri P (ed) Newborn Surgery, 4th ed. London: Taylor & Francis Group, pp. 28–39.

Subramanian A, Maker VK 2006 Organs of Zuckerkandl: their surgical significance and a review of a century of literature. Am J Surg 192:224–34.

Subramaniam H, Taghavi K, Mirjalili SA 2016 A reappraisal of pediatric abdominal surface anatomy utilizing in vivo cross–sectional imaging. Clin Anat 29:197–203.

Toshniwal GR, Dureja GP, Prashanth SM 2007 Trans-sacrococcygeal approach to ganglion impar block for management of chronic perineal pain: a prospective observational study. Pain Physician 10:661–6.

Tubbs RS, Stetler W, Kelly DR et al 2008 Immunohistochemical study of the phrenic ganglion. Anat Sci Int 83:159–61.

Tubbs RS, Shoja MM, Loukas M 2016 Bergman's Comprehensive Encyclopedia of Human Anatomic Variation. Hoboken: Wiley Blackwell.

This book is an invaluable source of detailed, evidence-based information about anatomical variations.

Uzun C, Atman ED, Ustuner E et al 2016 Surface anatomy and anatomical planes in the adult Turkish population. Clin Anat 29:183–90.

Woon JT, Perumal V, Maigne JY et al 2013 CT morphology and morphometry of the normal adult coccyx. Eur Spine J 22:863–70.

Woon JT, Stringer MD 2014 Redefining the coccygeal plexus. Clin Anat 27:254–60.

Zhang XM, Zhao QH, Zeng NL et al 2006 The celiac ganglia: anatomic study using MRI in cadavers. Am J Roentgenol 186:1520–3.

CHAPTER
60

Anterior abdominal wall

The anterior abdominal wall constitutes a curved hexagonal area defined superiorly by the costal arches (margins) and xiphisternal junction, laterally by the mid-axillary line, and inferiorly by an imaginary line running along the iliac crests, inguinal ligament and pubic symphysis. It is continuous with the posterior abdominal wall and paravertebral tissues, forming a flexible sheet of skin, muscle and connective tissue across the anterior and lateral aspects of the abdomen. It is also contiguous with the respiratory diaphragm and with the bony and myofascial structures of the thorax. These tissues form the complex structures of the myopectineal orifice and the inguinal canal, which connect the peritoneal cavity to the scrotum in males or to the labia majora in females. The anterior abdominal wall maintains the shape of the abdomen and aids in numerous physiological functions. However, its dysfunction is equally notable, as hernia repair remains the single most common type of operation performed by general surgeons.

SKIN AND SOFT TISSUE

The integument of the anterior abdominal wall comprises skin, soft tissues, lymphatic and vascular structures, and segmental nerves. The outer layer is formed from the skin and subcutaneous fat. The skin is non-specialized and variably hirsute, depending on sex and ancestry. All postpubertal individuals have some extension of the pubic hair on to the skin of the anterior abdominal wall, though this is commonly most pronounced in males, where the hair can extend to the umbilicus in a triangular pattern. The subcutaneous fat of the abdominal wall is highly variable in thickness, depending in part on sex and caloric intake.

Soft tissue

Superficial fascia

The superficial fascia of the abdominal wall lies between the dermis and the muscles, and is conventionally divided into a superficial fatty layer (Camper's fascia) and a membranous layer (Scarpa's fascia) deeper to this. In reality there are three layers, with a further layer of adipose tissue deep to the membranous layer (i.e. deep fatty layer) (Lancerotto et al 2011). These three layers are particularly well defined in the child; the membranous layer remains well defined in adults. Lying within the superficial fascial planes are adipose tissue, blood vessels, lymphatics, nerves and, in the inguinal region, superficial inguinal nodes.

Superficial fatty layer

The superficial fatty layer contains a variable amount of fat that is partitioned by fibrous septa connecting the dermis with the deeper membranous layer. Inferiorly it is continuous with the superficial fascia of the thigh, and medially it is continuous over the linea alba. In males this layer continues over the external genitalia, where it becomes thin and pale red and contains very little adipose tissue. In the scrotum it also contains the smooth muscle fibres of dartos. In females it continues from the hypogastric region of the abdomen into the labia majora and perineum.

Membranous layer

The membranous layer is a variably developed entity composed of connective tissue and elastic fibres. In the adult its thickness varies over the anterior abdominal wall, becoming thinner in the proximal abdomen (Lancerotto et al 2011). Measured histologically, it is between 0.5 and 1 mm thick but it appears thicker on computed tomography (Chopra et al 2011, Lancerotto et al 2011). It is loosely connected to the underlying aponeurosis of external abdominal oblique and the rectus sheath by oblique fibrous septa. Superiorly, it is continuous with the superficial fascia over the remainder of the trunk. In the midline it is adherent to the linea alba and pubic symphysis. Inferiorly, it fuses with the iliac crest, and extends superficial to the inguinal ligament and fuses with the fascia lata at the inguinal crease. In males it extends onto the dorsum of the penis, forming the fundiform ligament of the penis, and onto the scrotum where it becomes continuous with the membranous layer of the superficial fascia of the perineum (Colles' fascia). In females it continues into the labia majora and is continuous with the superficial fascia of the perineum.

In boys the testis can frequently be retracted out of the scrotum into the loose areolar tissue between the membranous layer of superficial fascia over the inguinal canal and the aponeurosis of external abdominal oblique.

Deep fatty layer

The thickness of the deep fatty layer is more variable than the superficial fatty layer. It is thin or absent where the membranous layer fuses with bony prominences and the linea alba, and can become markedly thick in some morbidly obese individuals. Its adipocytes show different metabolic activities from those in the superficial fatty layer (Chopra et al 2011). Liposuction preferentially removes this layer of fat with relative preservation of the superficial fatty layer in order to avoid skin dimpling and other skin contour irregularities (Markman and Barton 1987).

Transversalis fascia

The transversalis fascia is a thin layer of connective tissue lying between the deep surface of transversus abdominis and the extraperitoneal fat. It is part of the general layer of thin fascia between the peritoneum and the abdominal wall. Posteriorly, it fuses with the anterior layer of the thoracolumbar fascia; anteriorly, it forms a continuous sheet. Superiorly, it blends with the fascia covering the inferior surface of respiratory diaphragm. Inferiorly, it is continuous with the iliac and pelvic parietal fasciae. It is attached to the iliac crest between the origins of transversus abdominis and iliacus, and to the posterior margin of the inguinal ligament as a discrete thickening known as the iliopubic tract (Teoh et al 1999); it consists of transverse fibres that fan out laterally towards the anterior superior iliac spine to blend with the iliopsoas fascia and run medially to the pubic bone. The iliopubic tract is a landmark structure during laparoscopic inguinal hernia repair, although it is often incorrectly described as the inguinal ligament. Medial to the femoral sheath the transveralis fascia is fused to the pubis behind the conjoint aponeurosis (conjoint 'tendon'). An inferior extension of the fascia forms the anterior part of the femoral sheath. A further thickening of the transversalis fascia, the interfoveolar ligament, runs inferior to the inguinal ligament at the medial margin of the deep inguinal ring; it may contain muscle fibres.

The transversalis fascia continues as the internal spermatic fascia over the structures that pass through the deep inguinal ring (the testicular vessels and ductus deferens in males and the round ligament of the uterus in females).

Extraperitoneal connective tissue

The extraperitoneal connective tissue lying between the peritoneum and the fasciae lining the abdominal and pelvic cavities contains a variable amount of fat. This adipose tissue is the most common content of small congenital umbilical and epigastric hernias (see below). The fat is especially abundant on the posterior wall of the abdomen around the kidneys but scanty proximal to the iliac crest and in much of the pelvis. The inferior epigastric vessels themselves are contained within an envelope of fat as they travel from the external iliac vessels to rectus abdominis. This fat pad serves as an anatomical landmark during various types of abdominal hernia repairs. An abundance of fat in the extraperitoneal space also enables a peritoneal flap to be created easily: such a flap can be used to cover mesh during hernia surgery (a so-called extraperitoneal or 'pre-peritoneal' hernia repair). Areas with little fat, where the peritoneum and transversalis fascia are in direct contact with one another, are difficult to separate, commonly resulting in rents in the peritoneum that must be carefully repaired.

Vascular supply and lymphatic drainage

Understanding the blood supply of the anterior abdominal wall is critical when planning incisions, creating lipocutaneous or myofascial flaps or reconstructing the abdominal wall during ventral hernia repair (**Fig. 60.1**).

Superior epigastric artery and veins

The superior epigastric artery is a terminal branch of the internal thoracic artery. It arises at the level of the sixth costal cartilage and descends between the costal and sternal parts of the diaphragm, accompanied by two or more veins that drain to the internal thoracic vein (see Fig. 60.1; **Fig. 60.2**). The vessels pass anterior to the distal fibres of transversus thoracis and the proximal fibres of transversus abdominis before entering the rectus sheath, where they run inferiorly behind rectus abdominis. They anastomose with the inferior epigastric arteries within rectus abdominis in one of several potential branching patterns (Rozen et al 2008).

Vascular branches supply rectus abdominis itself and perforate the anterior layer of the rectus sheath to supply the abdominal skin and subcutaneous fat. These vessels generally penetrate rectus abdominis within a 10 cm circle around the umbilicus and are referred to clinically as ‘periumbilical perforator’ vessels. A branch given off in the proximal rectus sheath passes anterior to the xiphoid process of the sternum and anastomoses with a corresponding contralateral branch. This vessel can give rise to bleeding during surgical incisions that extend up to and alongside the xiphoid process. The superior epigastric artery also gives small branches to the anterior part of the diaphragm. On the right, small branches reach the falciform ligament, where they anastomose with branches from the hepatic artery.

Inferior epigastric artery and veins

The inferior epigastric artery (often referred to as the deep inferior epigastric artery in clinical practice in order to distinguish it from the superficial (inferior) epigastric artery) originates from the medial aspect of the external iliac artery just proximal to where the vessels pass deep to the inguinal ligament (see Figs 60.1–60.2; **Fig. 60.3**). Its accompanying veins, usually two, unite to form a single vein that drains into the external iliac vein (Rozen et al 2009). The vessel curves forwards in the extraperitoneal tissue and ascends obliquely along the medial margin of the deep inguinal ring. It lies posterior to the spermatic cord, separated from it by the transversalis fascia. It pierces the transversalis fascia and enters the posterior layer of the rectus sheath by passing anterior to the arcuate line.

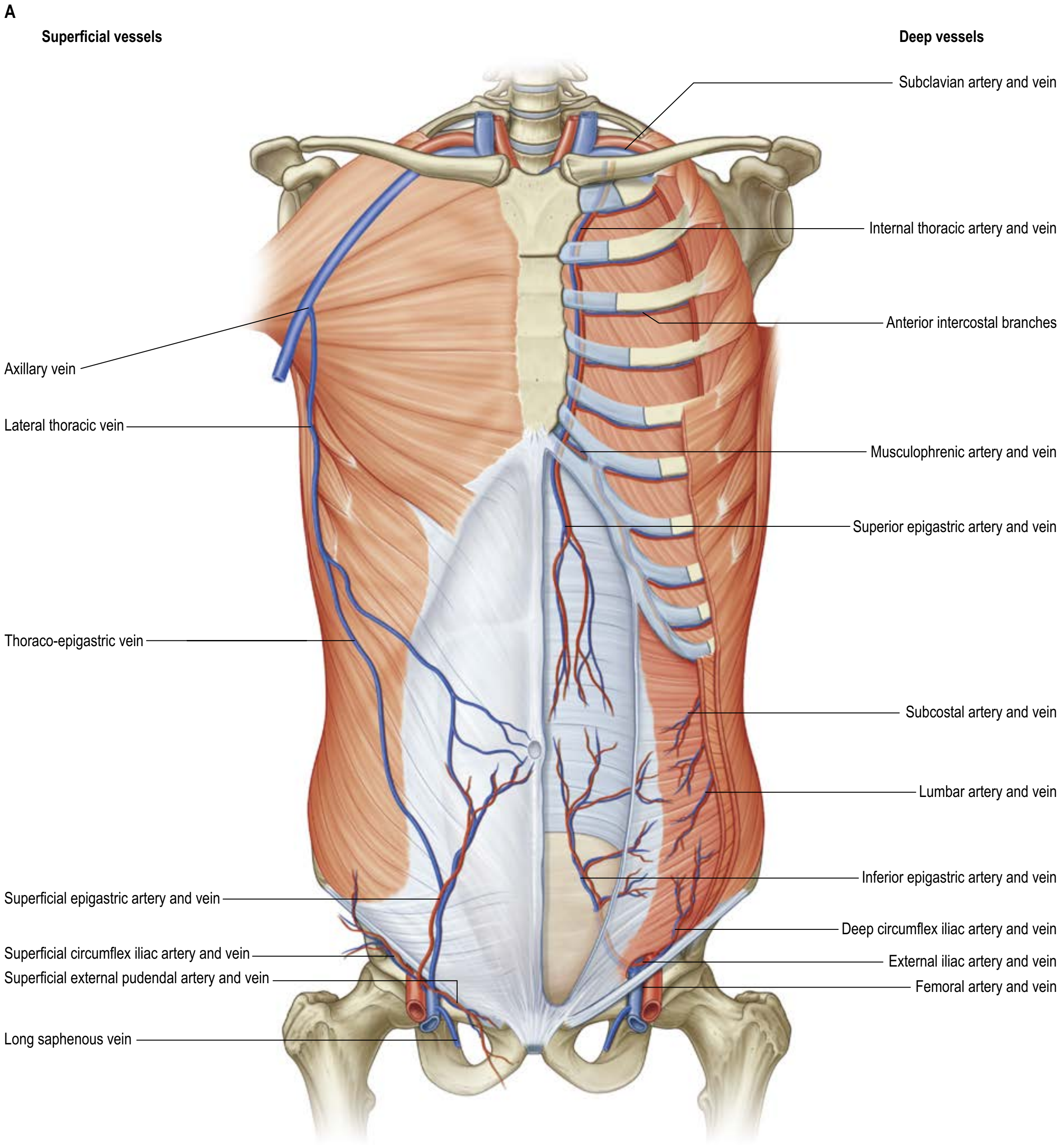
A
Superficial vessels
Deep vessels
Subclavian artery and vein
Internal thoracic artery and vein
Anterior intercostal branches
Axillary vein
Lateral thoracic vein
Musculophrenic artery and vein
Superior epigastric artery and vein
Thoraco-epigastric vein
Subcostal artery and vein
Lumbar artery and vein
Inferior epigastric artery and vein
Superficial epigastric artery and vein
Deep circumflex iliac artery and vein
Superficial circumflex iliac artery and vein
External iliac artery and vein
Superficial external pudendal artery and vein
Femoral artery and vein
Long saphenous vein

Fig. 60.1 **A**, The blood supply of the anterior abdominal wall. The left rectus abdominis has been removed to show the superior and inferior epigastric vessels. (B, *continued online*)

Surgical zones have been defined to better understand this vascular distribution. **Zone 1** is the central proximal abdomen. Superiorly, it receives blood supply from the superior epigastric artery, a branch of the internal thoracic artery. Inferiorly it is supplied by the inferior epigastric artery, a branch of the external iliac artery. As the superior and inferior epigastric arteries run posterior to rectus abdominis they supply musculocutaneous perforating vessels (the so-called periumbilical perforator vessels) to the overlying tissues. The superior and inferior epigastric arteries converge in the proximal umbilical region. **Zone 2** encompasses the hypogastric region distal to the arcuate line (semicircular line of Douglas). The area is supplied medially by superficial and deep branches of the inferior epigastric artery. Laterally, the blood supply arises from the superficial circumflex iliac artery as a branch of the femoral artery. **Zone 3** is the area proximal to the arcuate line and lateral to the semilunar line (linea semilunaris). It is perfused inferiorly by the deep circumflex iliac artery and superiorly by the musculophrenic artery, a branch of the internal thoracic artery.

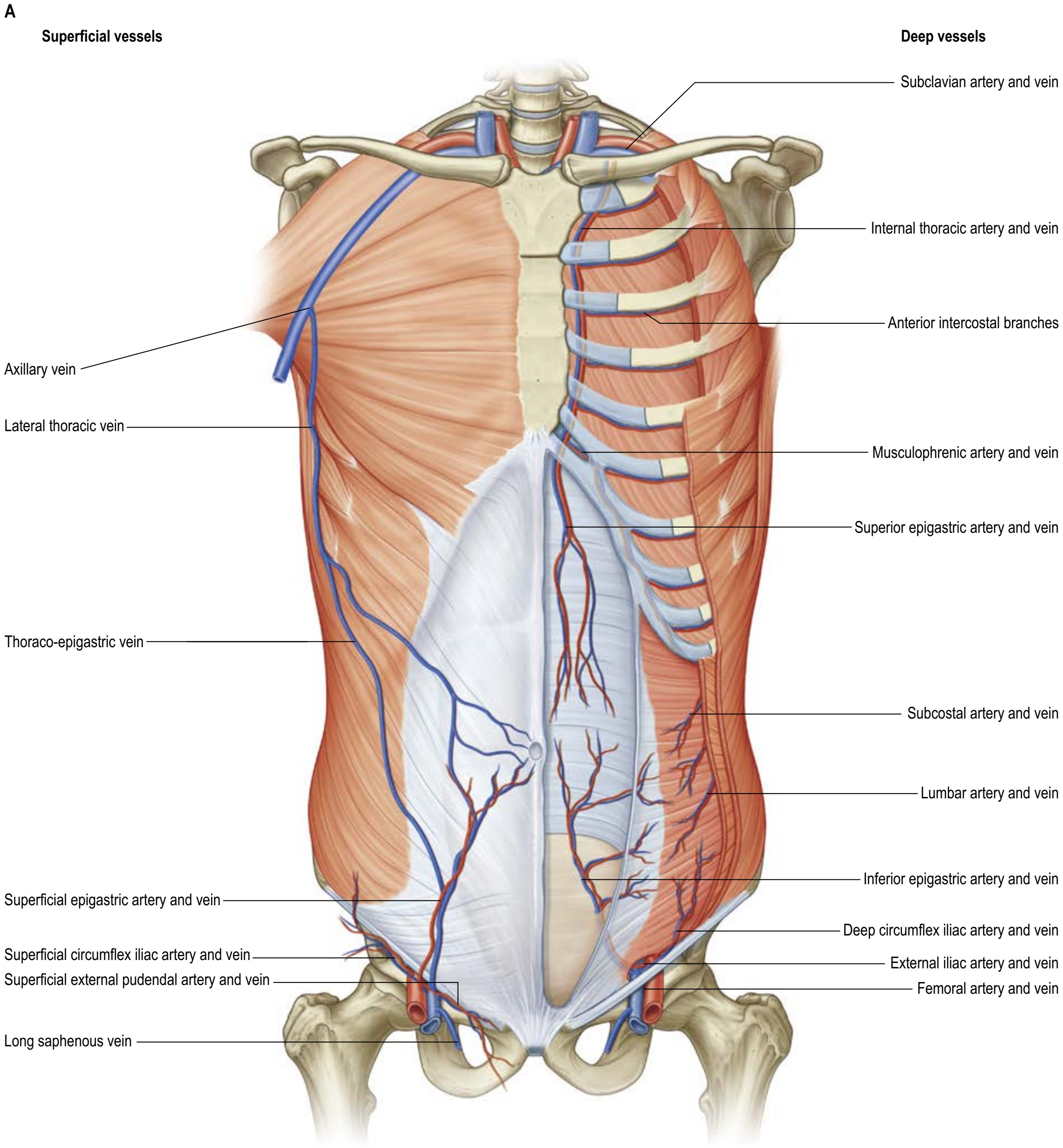
A
Superficial vessels
Deep vessels
Subclavian artery and vein
Internal thoracic artery and vein
Anterior intercostal branches
Axillary vein
Lateral thoracic vein
Musculophrenic artery and vein
Superior epigastric artery and vein
Thoraco-epigastric vein
Subcostal artery and vein
Lumbar artery and vein
Inferior epigastric artery and vein
Superficial epigastric artery and vein
Deep circumflex iliac artery and vein
Superficial circumflex iliac artery and vein
External iliac artery and vein
Superficial external pudendal artery and vein
Femoral artery and vein
Long saphenous vein

Fig. 60.1 **A**, The blood supply of the anterior abdominal wall. The left rectus abdominis has been removed to show the superior and inferior epigastric vessels.

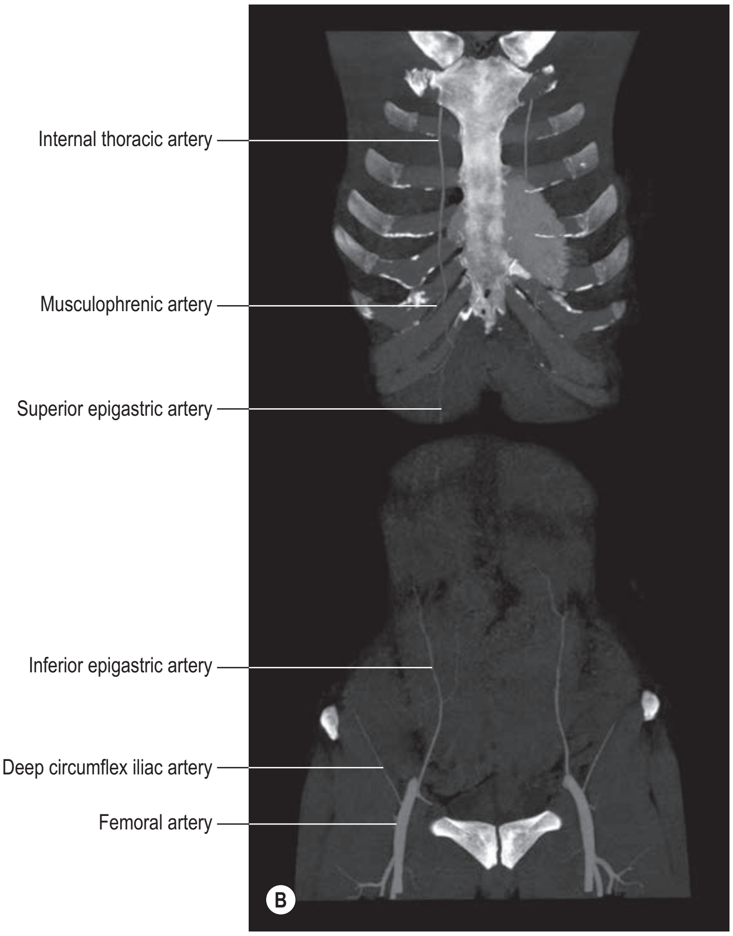
Internal thoracic artery
Musculophrenic artery
Superior epigastric artery
Inferior epigastric artery
Deep circumflex iliac artery
Femoral artery
B

Fig. 60.1 cont'd B, Maximum intensity projection (MIP) coronal reconstruction slabs from a CT aortogram through the arterial supply of the upper and lower anterior abdominal walls. The sections are slightly oblique to each other in their coronal plane, and have been stitched together in order to show these vessels simultaneously.

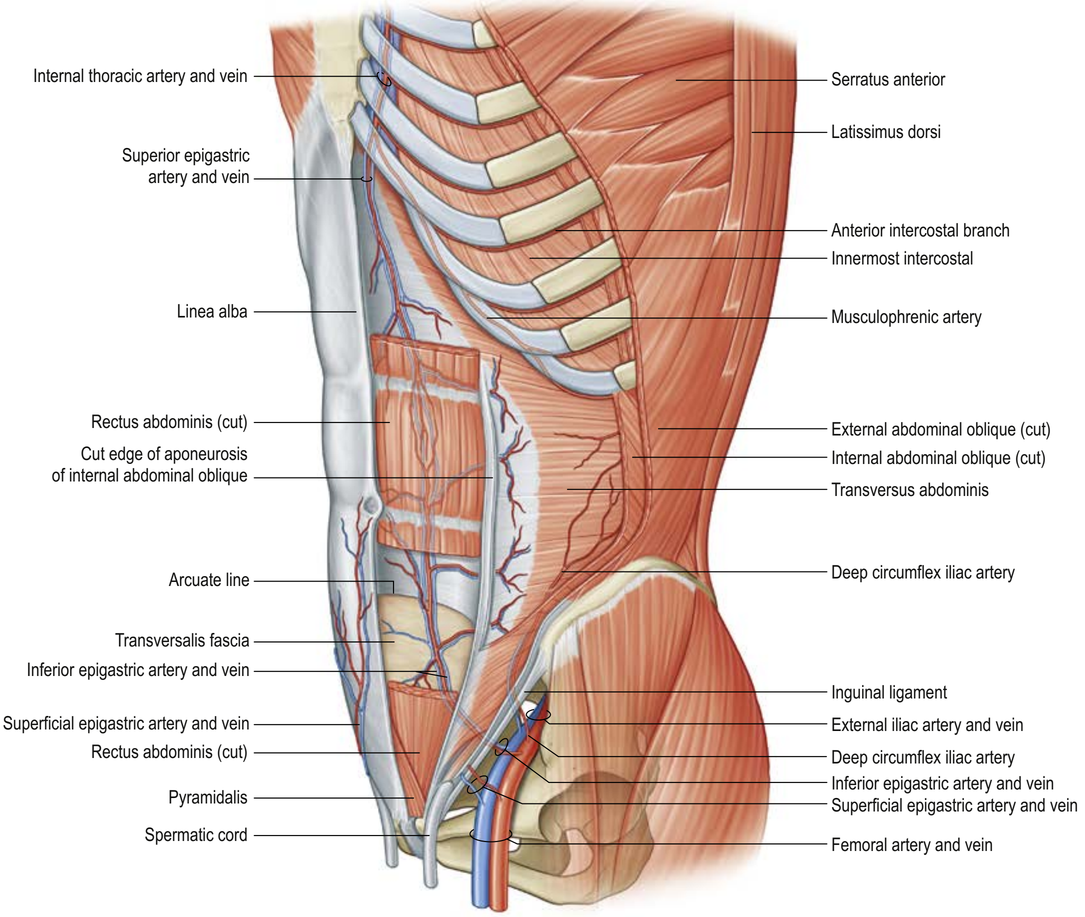
Internal thoracic artery and vein
Superior epigastric artery and vein
Linea alba
Rectus abdominis (cut)
Cut edge of aponeurosis of internal abdominal oblique
Arcuate line
Transversalis fascia
Inferior epigastric artery and vein
Superficial epigastric artery and vein
Rectus abdominis (cut)
Pyramidalis
Spermatic cord
Serratus anterior
Latissimus dorsi
Anterior intercostal branch
Innermost intercostal
Musculophrenic artery
External abdominal oblique (cut)
Internal abdominal oblique (cut)
Transversus abdominis
Deep circumflex iliac artery
Inguinal ligament
External iliac artery and vein
Deep circumflex iliac artery
Inferior epigastric artery and vein
Superficial epigastric artery and vein
Femoral artery and vein

Fig. 60.2 The muscles and arterial supply of the anterolateral abdominal wall. Portions of the left rectus abdominis have been removed to show the superior and inferior epigastric vessels.

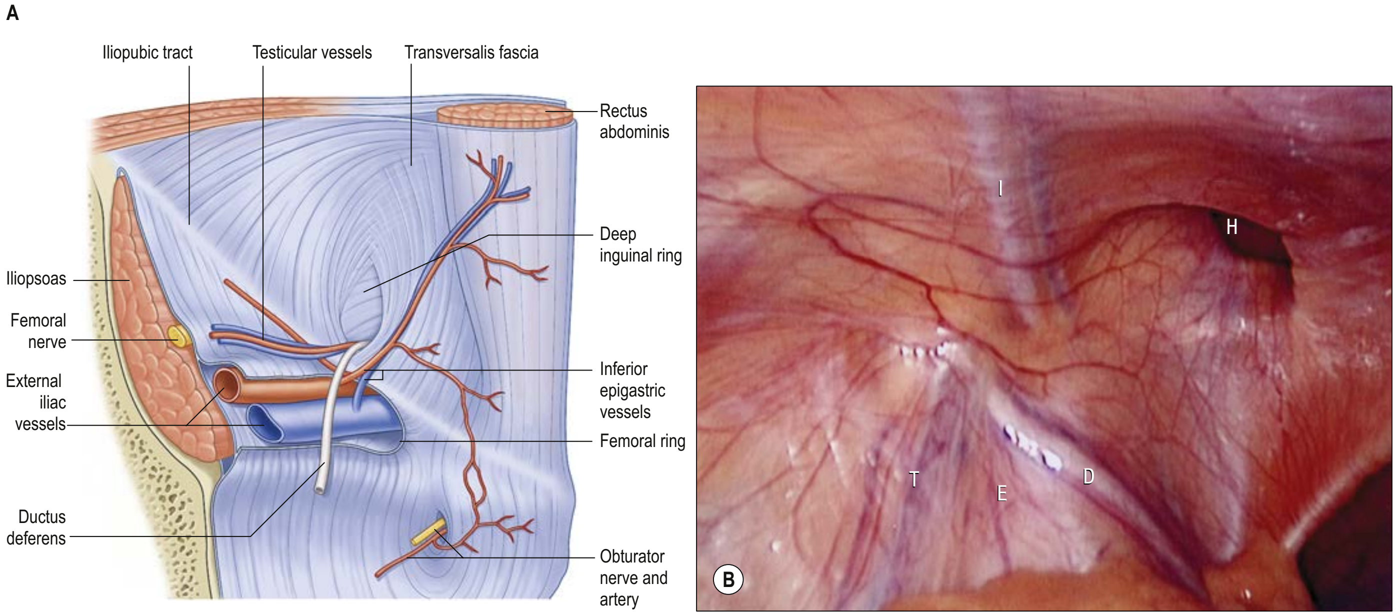
A
Iliopubic tract
Testicular vessels
Transversalis fascia
Rectus abdominis
Deep inguinal ring
Iliopsoas
Femoral nerve
External iliac vessels
Inferior epigastric vessels
Femoral ring
Ductus deferens
Obturator nerve and artery
I
H
T
E
D
B

Fig. 60.3 **A**, The deep aspect of the distal part of the anterior abdominal wall of the left side. The femoral and deep inguinal rings are displayed, together with the vessels and other structures in relation to them and also the opening into the obturator canal. **B**, A laparoscopic view showing the parietal peritoneum covering the area. Abbreviations: D, ductus deferens; E, external iliac vessels; H, orifice of direct inguinal hernia; I, inferior epigastric vessels; T, testicular vessels. (B, With permission from Drake RL, Vogl AW, Mitchell A (eds) Gray's Anatomy for Students, 2nd ed. Elsevier, Churchill Livingstone. Copyright 2010.) (C, *continued online*)

In this part of its course it is visible through the parietal peritoneum of the anterior abdominal wall and with this covering forms the lateral umbilical fold. Disruption of the artery by surgical incisions (e.g. insertion of laparoscopic ports, surgical tacks or abdominal drains) can cause a haematoma, which can expand to considerable size because there is no adjacent tissue against which the bleeding can be tamponaded.

The inferior epigastric arteries ascend and anastomose with their superior counterparts as a single vessel in only about 30% of cases (El-Mrakby and Milner 2002). Branching into two vessels before anastomosing is the most common pattern, accounting for almost 60%, with a trifurcation in the remainder. The inferior epigastric arteries have an average diameter of approximately 3 mm at their origin, compared to an average diameter of 1.6 mm at the origin of the superior epigastric arteries, presumably explaining why the inferior epigastric arteries provide the 'dominant' blood supply to rectus abdominis. Preliminary ligation of the inferior epigastric artery is often performed when preparing a myocutaneous flap from the mid or lower rectus abdominis based on the superior epigastric artery; this encourages augmentation of the superior epigastric arterial supply.

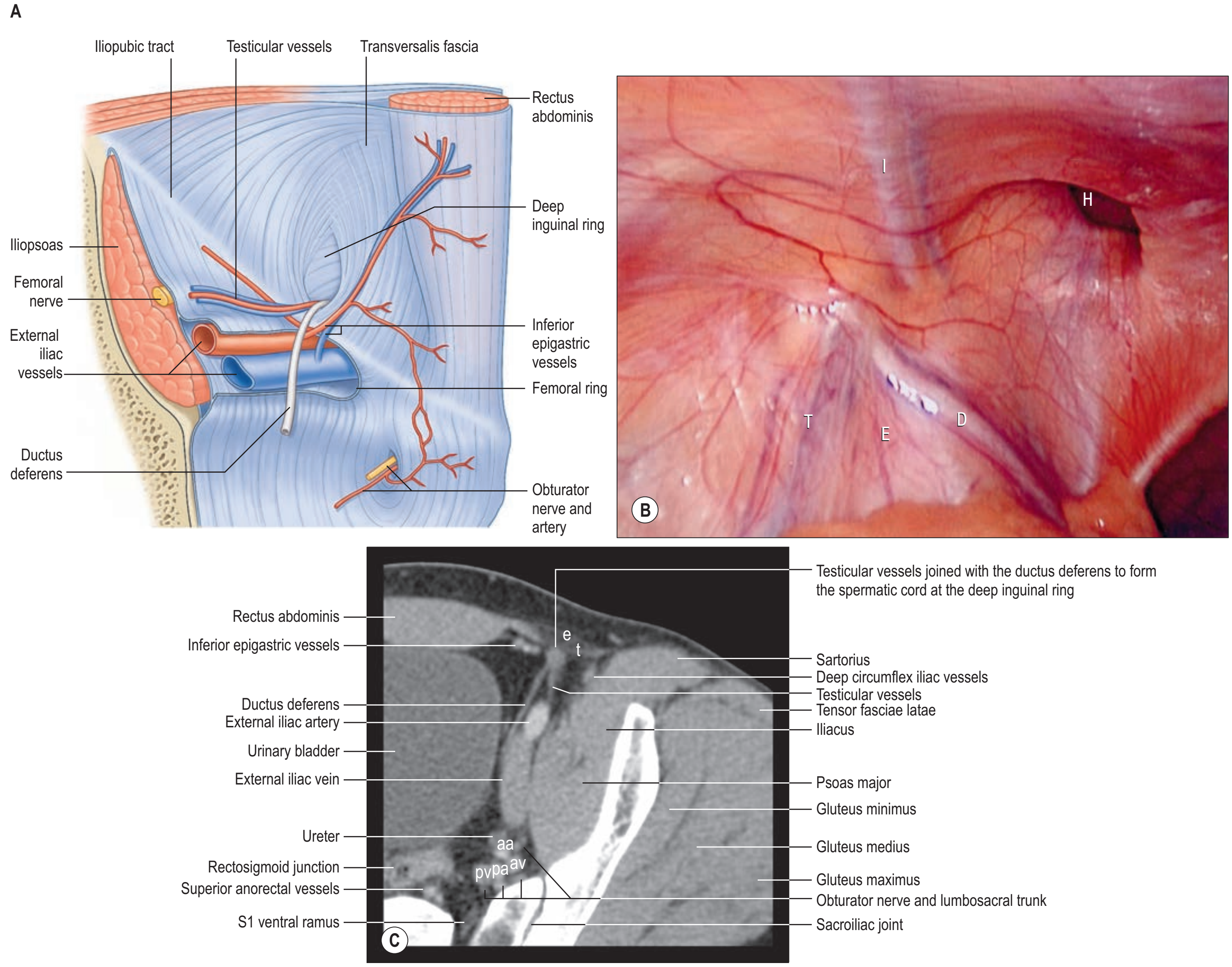
A
Iliopubic tract
Testicular vessels
Transversalis fascia
Rectus abdominis
Deep inguinal ring
Iliopsoas
Femoral nerve
External iliac vessels
Inferior epigastric vessels
Femoral ring
Ductus deferens
Obturator nerve and artery
B
I
H
T
E
D
C
Testicular vessels joined with the ductus deferens to form the spermatic cord at the deep inguinal ring
Rectus abdominis
Inferior epigastric vessels
e
t
Sartorius
Deep circumflex iliac vessels
Testicular vessels
Ductus deferens
External iliac artery
Tensor fasciae latae
Iliacus
Urinary bladder
External iliac vein
Psoas major
Gluteus minimus
Ureter
aa
Gluteus medius
Rectosigmoid junction
pv pa av
Gluteus maximus
Superior anorectal vessels
Obturator nerve and lumbosacral trunk
S1 ventral ramus
Sacroiliac joint

Fig. 60.3 **A**, The deep aspect of the distal part of the anterior abdominal wall of the left side. The femoral and deep inguinal rings are displayed, together with the vessels and other structures in relation to them and also the opening into the obturator canal. **B**, A laparoscopic view showing the parietal peritoneum covering the area. Abbreviations: D, ductus deferens; E, external iliac vessels; H, orifice of direct inguinal hernia; I, inferior epigastric vessels; T, testicular vessels. **C**, Slightly oblique axial CT with intravenous contrast medium showing the ductus deferens joining the testicular vessels at the deep inguinal ring to form the spermatic cord. Key: aa, anterior division of the internal iliac artery; av, anterior division of the internal iliac vein; e, external abdominal oblique fascia; pa, posterior division of the internal iliac artery; pv, posterior division of the internal iliac vein; t, transversalis fascia. (B, With permission from Drake RL, Vogl AW, Mitchell A (eds) Gray's Anatomy for Students, 2nd ed. Elsevier, Churchill Livingstone. Copyright 2010.)

Branches of the inferior epigastric artery anastomose with branches of the superior epigastric artery within rectus abdominis at a variable level proximal to the umbilicus (Rozen et al 2008). Other branches anastomose with terminal branches of the distal five posterior intercostal, subcostal and lumbar arteries at the lateral border of the rectus sheath. Inferolaterally, branches anastomose with the deep circumflex iliac artery.

The ductus (vas) deferens in males or the round ligament of the uterus in females pass medially after hooking around the inferior epigastric artery at the deep inguinal ring. The inferior epigastric vessels form the lateral border of the inguinal triangle (Hesselbach's triangle). The boundaries of this anatomical region are seen during laparoscopic inguinal hernia repair: the inferior border of the triangle is formed by the iliopubic tract/inguinal ligament and the medial border by the lateral margin of rectus abdominis. Hernias occurring within the triangle are termed direct inguinal hernias.

The inferior epigastric artery also gives off the cremasteric artery, a pubic branch and muscular and cutaneous branches. The cremasteric artery accompanies the spermatic cord in males, supplies cremaster and other coverings of the cord and anastomoses with the testicular artery. In females the artery is small and accompanies the round ligament of the uterus. A pubic branch, near the femoral ring, descends posterior to the pubis and anastomoses with the pubic branch of the obturator artery. The pubic branch of the inferior epigastric artery can be larger than the obturator artery and supply most of the territory of the obturator artery in the thigh, in which case it is referred to as the aberrant obturator artery (Pai et al 2009). It lies close to the medial border of the femoral ring and can be injured during medial dissection of the ring in femoral hernia repair, laparoscopic inguinal hernia repair, or with pelvic fractures. Muscular branches supply the abdominal muscles and peritoneum and anastomose with the circumflex iliac and lumbar arteries. Cutaneous branches arise within rectus abdominis, and perforate the aponeurosis of external abdominal oblique to supply the overlying skin. They anastomose with branches of the superficial epigastric artery, contributing to the 'periumbilical perforator vessels'. These perforating vessels have been mapped in detail because they are particularly important in creating large lipocutaneous flaps on the abdominal wall: if this requires ligation of these vessels, the flap is at risk of necrosis (Rozen et al 2008).

Occasionally, the inferior epigastric artery arises from the femoral artery. It then ascends anterior to the femoral vein, passing deep to the inguinal ligament and into the abdominal cavity before following its usual abdominal course. Rarely it arises from the external iliac artery in common with an aberrant obturator artery or from the obturator artery itself.

The superior and inferior epigastric arteries are important sources of collateral blood flow between the internal thoracic artery, the external iliac artery and the lumbar vessels when aortic blood flow is compromised. Additionally, small tributaries of the inferior epigastric vein draining the skin around the umbilicus anastomose with terminal branches of the umbilical vein that drain into the liver via the falciform ligament. These portosystemic communications can dilate substantially in patients with portal hypertension, resulting in portal venous blood draining into the systemic circulation via the inferior epigastric veins. Back pressure to the level of the skin leads to a pattern of dilated, serpiginous superficial veins radiating out from the umbilicus, referred to as the 'caput medusae'.

Posterior intercostal, subcostal and lumbar arteries

In the paraspinal region, the tenth and eleventh posterior intercostal arteries, the subcostal artery and the lumbar arteries all pierce the posterior aponeurosis of transversus abdominis to enter the neurovascular plane of the abdominal wall running between transversus abdominis and internal abdominal oblique (**Fig. 60.4**). The arteries on either side run forwards, giving off muscular branches to the overlying internal and external abdominal obliques, before anastomosing with lateral branches of the superior and inferior epigastric arteries at the lateral border of the rectus sheath, just medial to the semilunar line (see Fig. 60.4). The location of these arteries is of clinical importance when myofascial flaps are created during anterior abdominal wall reconstruction, not because

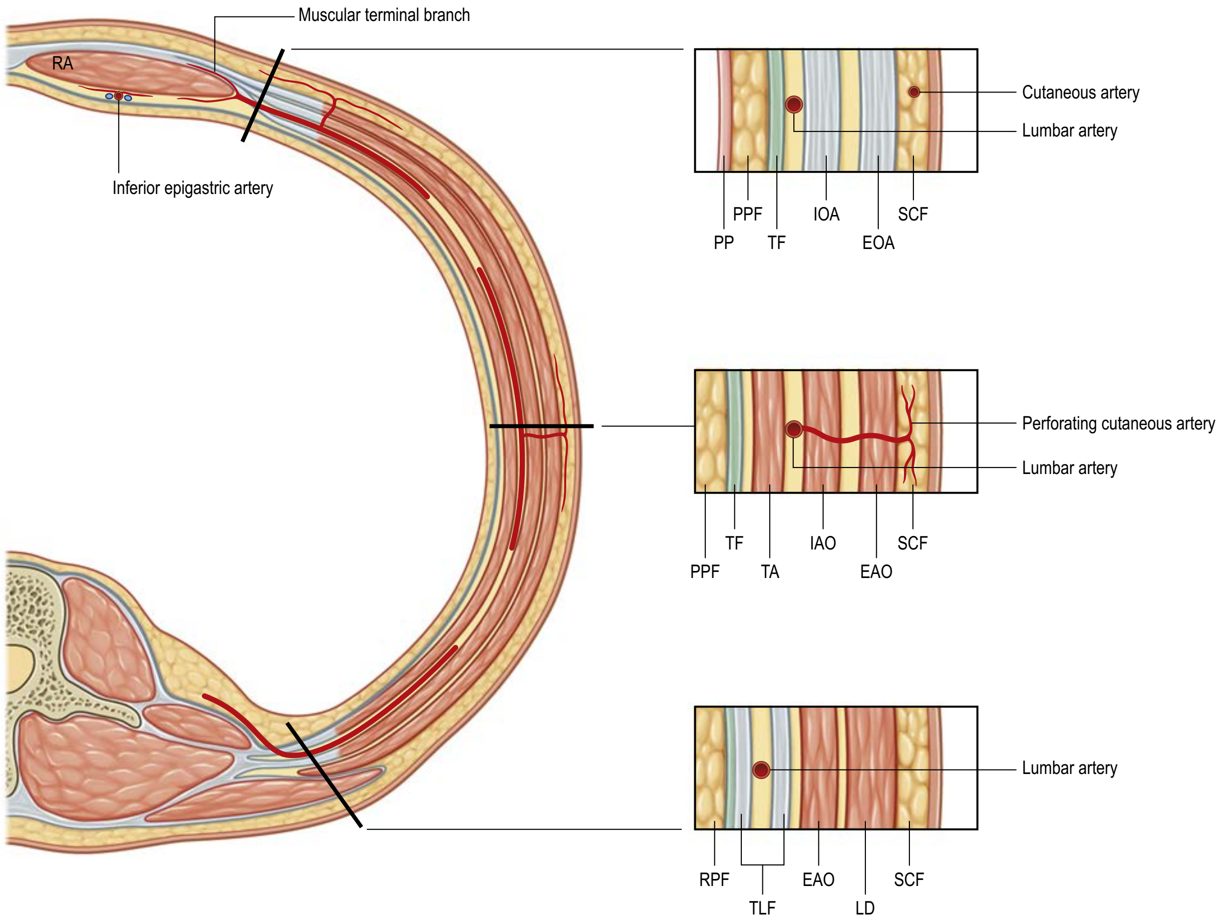

EAO	External abdominal oblique	PP	Parietal peritoneum	SCF	Subcutaneous fat
EOA	External abdominal oblique aponeurosis	PPF	Preperitoneal fat	TA	Transversus abdominis
IAO	Internal abdominal oblique	RA	Rectus abdominis	TF	Transversalis fascia
IOA	Internal abdominal oblique aponeurosis	RPF	Retroperitoneal fat	TLF	Thoracolumbar fascia
LD	Latissimus dorsi				

Fig. 60.4 The arrangement of the anterolateral abdominal wall vessels at the level of the mid-abdomen.

of their vascular contributions but because of their accompanying nerves, which innervate rectus abdominis. Division of these nerves can result in a segmental denervation of portions of rectus abdominis and/or the lateral anterior abdominal wall musculature. Perforating vessels run vertically through the myofascial planes to supply the overlying skin and subcutaneous tissue. A small contribution to the supply of the distal abdominal muscles comes from branches of the deep circumflex iliac arteries.

The anterior abdominal wall is also supplied by branches of the femoral artery: namely, the superficial epigastric, superficial circumflex iliac and superficial external pudendal arteries, and by the deep circumflex iliac artery arising from the external iliac artery (see Fig. 76.4A).

Lymphatic drainage

The highest concentration of lymphatic vessels in the anterior abdominal wall is found in the dermis (Friedman et al 2015). Lymphatic vessels from the lumbar and gluteal regions run with the superficial circumflex iliac vessels, and those from the abdominal skin distal to the umbilicus run with the superficial epigastric vessels. Both drain into the superficial inguinal nodes. Lymphatic vessels from the proximal umbilical region drain to axillary and parasternal nodes. Enlargement of a lymph node in the umbilical region is rare but can herald an abdominal or pelvic malignancy.

The deep lymphatic vessels accompany the deeper arteries. Laterally, they run either with the lumbar arteries to drain into the lateral aortic nodes, or with the posterior intercostal and subcostal arteries to nodes in the posterior mediastinum. Lymphatics in the proximal anterior abdominal wall run with the superior epigastric vessels to parasternal nodes while those in the distal abdominal wall run with the deep circumflex iliac and inferior epigastric arteries to external iliac nodes. For further reading, see Tourani et al (2013).

Segmental nerves

The ventral rami of the sixth to eleventh intercostal nerves, the subcostal nerve (twelfth thoracic) and first lumbar nerve (iliohypogastric and ilio-inguinal nerves) innervate the muscles and skin of the anterior abdominal wall (Rozen et al 2008). The seventh to the twelfth thoracic ventral rami continue anteriorly into the abdominal wall (**Fig. 60.5**). Approaching the costal arch, the seventh to tenth intercostal nerves curve medially across the deep surface of the costal cartilages between the digitations of the respiratory diaphragm and transversus abdominis. The subcostal nerve often gives a branch to the first lumbar ventral ramus (dorsolumbar nerve), and in these cases therefore contributes to the lumbar plexus (Ch. 61). It accompanies the subcostal vessels along the inferior border of the twelfth rib, passing posterior to the lateral arcuate ligament and kidney, and anterior to the proximal part of quadratus lumborum.

All these segmental nerves run anteriorly within a thin layer of fascia in the neurovascular plane between transversus abdominis and internal abdominal oblique, where they branch and interconnect with adjacent nerves and give off branches to the lateral musculature (Rozen et al 2008). Cutaneous branches supply the skin of the lateral and anterior abdominal walls. The nerves enter the rectus sheath at its lateral margin by penetrating the posterior lamina of internal abdominal oblique and penetrating rectus abdominis on its posterior aspect. Here they give off muscular branches to rectus abdominis, transversus abdominis and pyramidalis, and cutaneous branches that pierce the anterior layer of the rectus sheath to supply overlying skin.

The ninth intercostal nerve supplies skin proximal to the umbilicus, the tenth intercostal nerve supplies skin that consistently includes the umbilicus, and the eleventh intercostal nerve supplies skin distal to the umbilicus (see Fig. 24.10; **Fig. 60.5**). The subcostal nerve supplies the skin over the anterior gluteal region just distal to the iliac crest and the skin of the distal abdomen and inguinal region (overlapping with the L1 dermatome in this

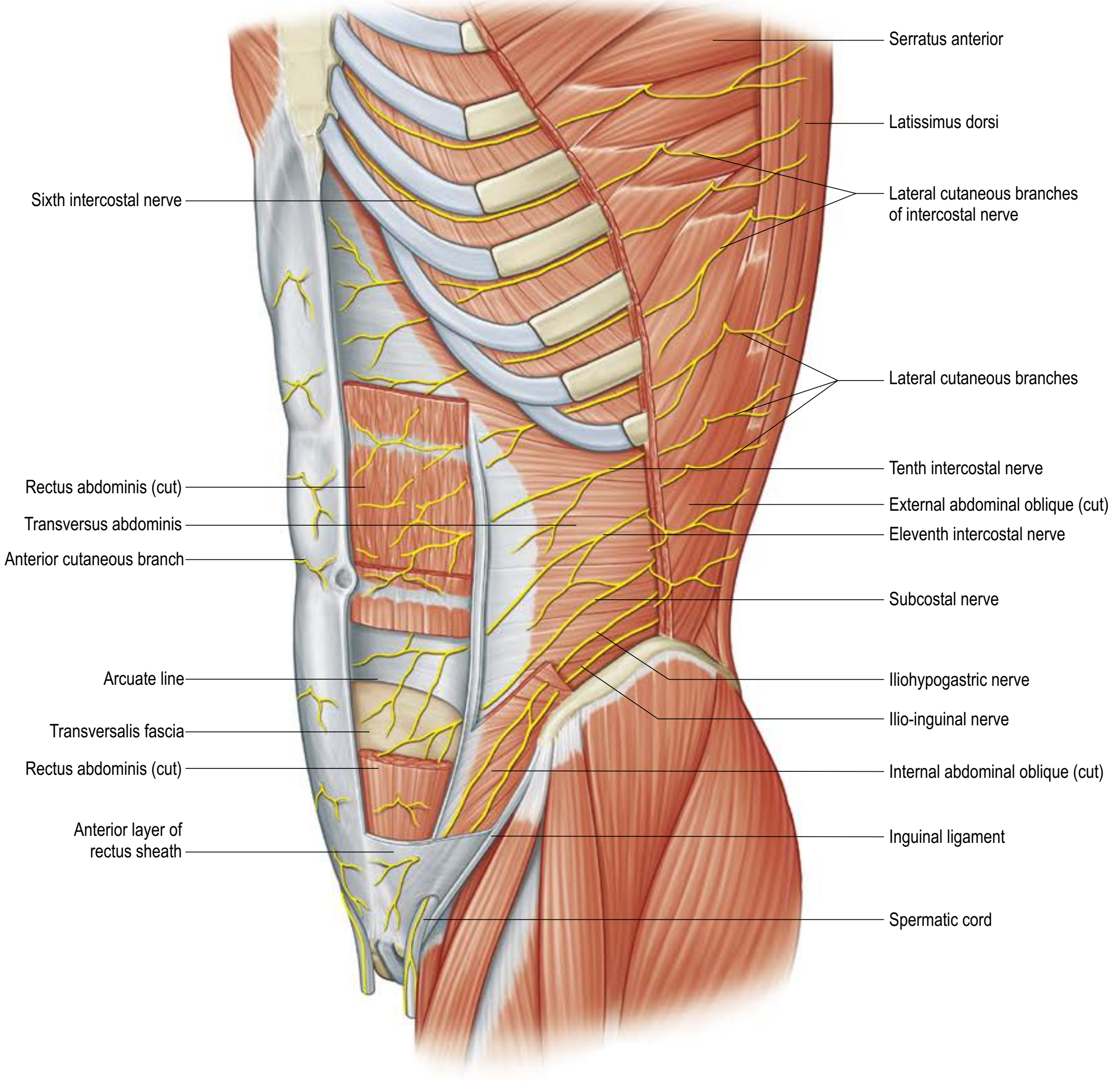
Sixth intercostal nerve
Rectus abdominis (cut)
Transversus abdominis
Anterior cutaneous branch
Arcuate line
Transversalis fascia
Rectus abdominis (cut)
Anterior layer of rectus sheath
Serratus anterior
Latissimus dorsi
Lateral cutaneous branches of intercostal nerve
Lateral cutaneous branches
Tenth intercostal nerve
External abdominal oblique (cut)
Eleventh intercostal nerve
Subcostal nerve
Iliohypogastric nerve
Ilio-inguinal nerve
Internal abdominal oblique (cut)
Inguinal ligament
Spermatic cord

Fig. 60.5 The cutaneous branches of the distal intercostal and lumbar nerves. Portions of the muscles of the anterior abdominal wall have been removed, including most of the anterior layer of the rectus sheath and parts of rectus abdominis.

region) (Lee et al 2008). A typical dermatome map of the anterior abdominal wall is shown in Fig. 24.10. The inferior intercostal nerves and subcostal nerve also provide sensory fibres to the costal parts of the diaphragm and parietal peritoneum.

MUSCLES

Anterolateral muscles of the abdomen

Rectus abdominis, external and internal abdominal obliques, transversus abdominis and pyramidalis constitute the anterolateral abdominal musculature. They act together to perform a range of functions, some of which involve the generation of positive pressure within one or more body cavities. Although many of these activities can occur with no 'forced assistance', exhalation, defecation and micturition can be aided by the generation of positive intra-abdominal pressure. Parturition, coughing and vomiting always require such positive pressure. Under resting conditions, the tone developed within the muscles provides support for the abdominal viscera and retains the normal contour of the abdomen. The consequences of diminished muscular support can be seen in patients who have massive anterior abdominal wall hernias or congenital conditions such as 'prune belly syndrome' where there is deficiency or absence of these muscles.

Active contraction of the muscles is important for maintaining abdominal wall tone. The compression of the abdominal cavity required to increase intra-abdominal pressure is mainly effected by contraction of the respiratory diaphragm. The pelvic girdle, lumbar vertebrae and distal thorax provide rigidity to parts of the abdominal wall. During the generation of positive intra-abdominal pressure, the abdominal muscles hold the abdominal wall in a relatively fixed position rather than generating pressure directly: because most of the abdominal wall is muscular, the anterolateral abdominal wall muscles must contract synchronously to prevent displacement of the viscera.

The anterolateral abdominal muscles contribute little to the movements of the trunk during normal sitting and standing: these movements are controlled predominantly by the muscles of the back. However, movements of the trunk against resistance or when an individual is supine require the anterolateral abdominal muscles. Rectus abdominis is the most important in these situations, producing flexion of the trunk. If the pelvic girdle is fixed, the trunk is flexed. With a fixed thorax, contraction of rectus abdominis causes the pelvis to tilt and lift. Lateral flexion and rotation of the trunk against resistance is provided by unilateral contraction of external and internal abdominal obliques and transversus abdominis.

Rectus abdominis

Rectus abdominis is a paired, long, strap-like muscle that extends along the entire length of the anterior abdominal wall on either side of the linea alba (**Fig. 60.8**). It varies widely in width and thickness from individual to individual but is generally widest in the proximal abdomen. The muscle fibres of rectus abdominis are usually interrupted by one to four fibrous bands (three being the most common) or tendinous intersections, which pass transversely or obliquely across the muscle. One is usually situated at the level of the umbilicus, another opposite the free end of the xiphoid process and the third about midway between the other two. They are rarely full-thickness and usually extend only half-way through the anterior thickness of the muscle, fusing with the fibres of the anterior layer of the rectus sheath. Occasionally, one or two incomplete intersections are present distal to the umbilicus. The intersections may represent the myosepta delineating the myotomes that form the muscle (Rai et al 2018).

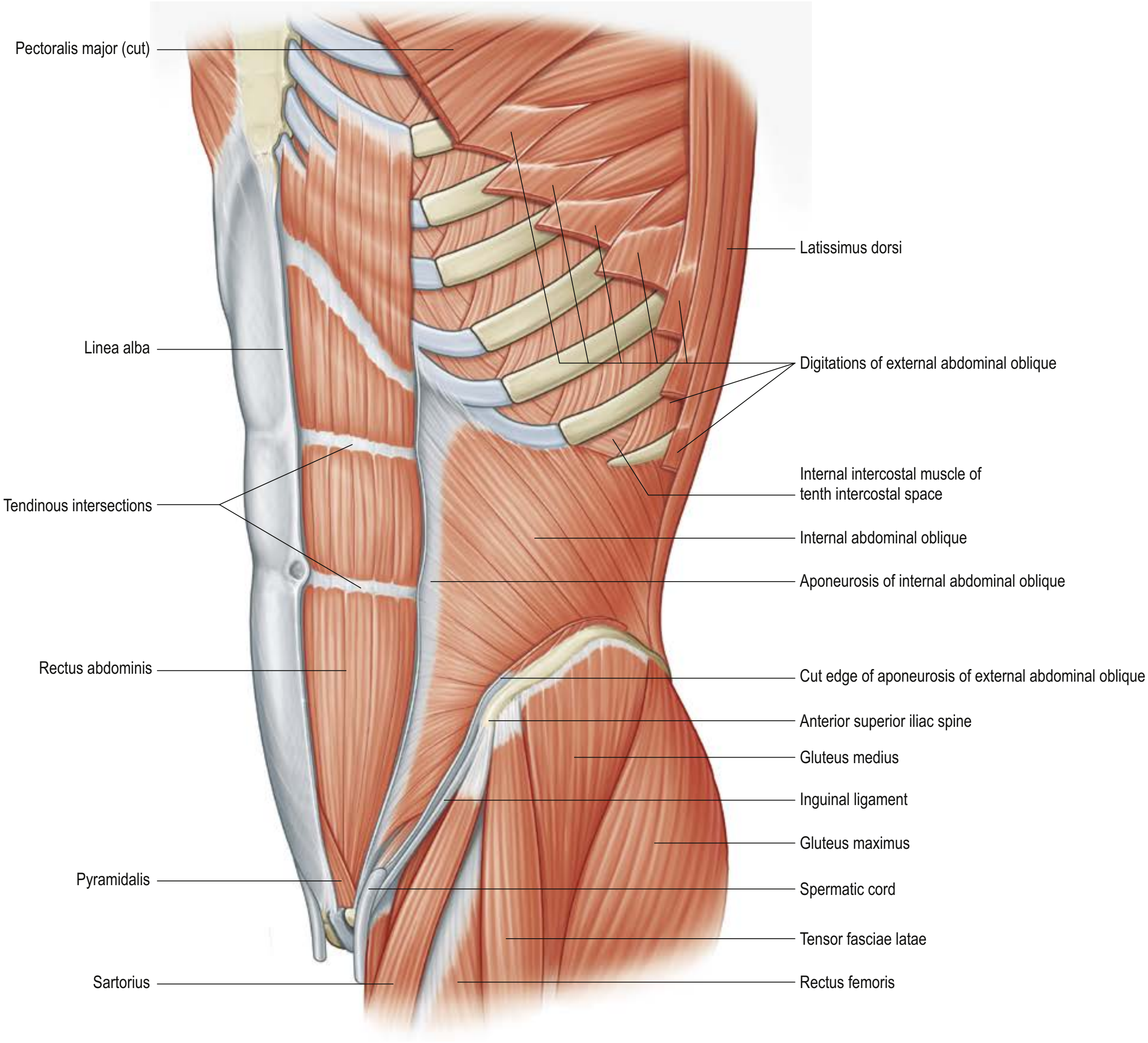
Pectoralis major (cut)
Latissimus dorsi
Linea alba
Digitations of external abdominal oblique
Internal intercostal muscle of tenth intercostal space
Tendinous intersections
Internal abdominal oblique
Aponeurosis of internal abdominal oblique
Rectus abdominis
Cut edge of aponeurosis of external abdominal oblique
Anterior superior iliac spine
Gluteus medius
Inguinal ligament
Gluteus maximus
Pyramidalis
Spermatic cord
Tensor fasciae latae
Sartorius
Rectus femoris

Fig. 60.8 Muscles of the left side of the trunk. External abdominal oblique has been removed to show internal abdominal oblique, but its digitations from the ribs have been preserved. The anterior layer of the rectus sheath has been removed.

The anterolateral abdominal wall muscles are innervated by several segmental nerves and injury to a single nerve rarely causes a clinically detectable loss of muscle tone. The overlap between sequential dermatomes means that significant cutaneous anaesthesia and muscle denervation are appreciated only after at least two sequential nerves have been surgically sectioned (Fig. 60.6).

The transversus abdominis plane (TAP) blockade is a regional anaesthetic technique for abdominal surgery. It involves delivery of analgesic medication between internal abdominal oblique and transversus abdominis, thus providing local anaesthesia to the skin, muscles of the anterior abdominal wall and the parietal peritoneum, while avoiding the epidural-associated risks of central nervous system depression, urinary bladder retention, hypotension, or epidural catheter dislodgement. In abdominal surgeries, TAP blockade has been shown to reduce overall narcotic use (and narcotic-associated side effects), improve overall pain relief and reduce hospital length of stay.

TAP blockade can be performed 'blind'(using anatomical landmarks and feeling a blunt needle 'pop' through myofascial planes) by using real-time sonography to visualize an appropriately positioned needle tip, or by direct visualization of a needle entering the correct plane with subsequent bulging of transversus abdominis as fluid enters this plane (Fig. 60.7).

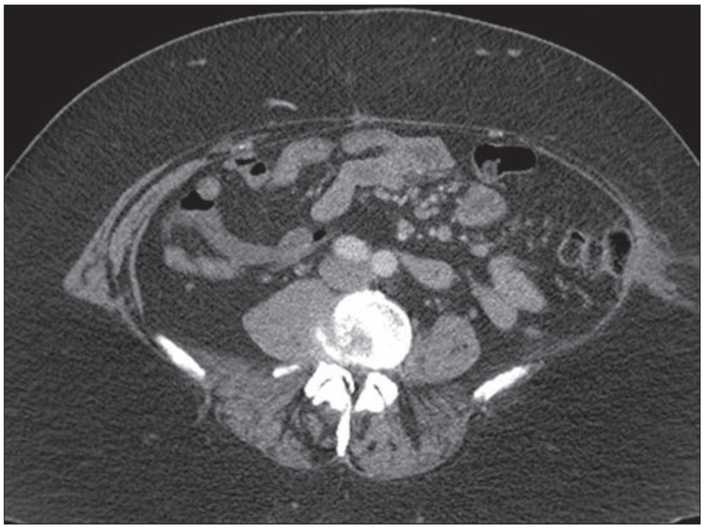

Fig. 60.6 Denervation loss of the entire left abdominal wall (rectus abdominis, external abdominal oblique, internal abdominal oblique and transversus abdominis) as a result of a traumatic flank injury. Note the loss of muscle mass and bulging on the left compared to the normal (contralateral) right side.

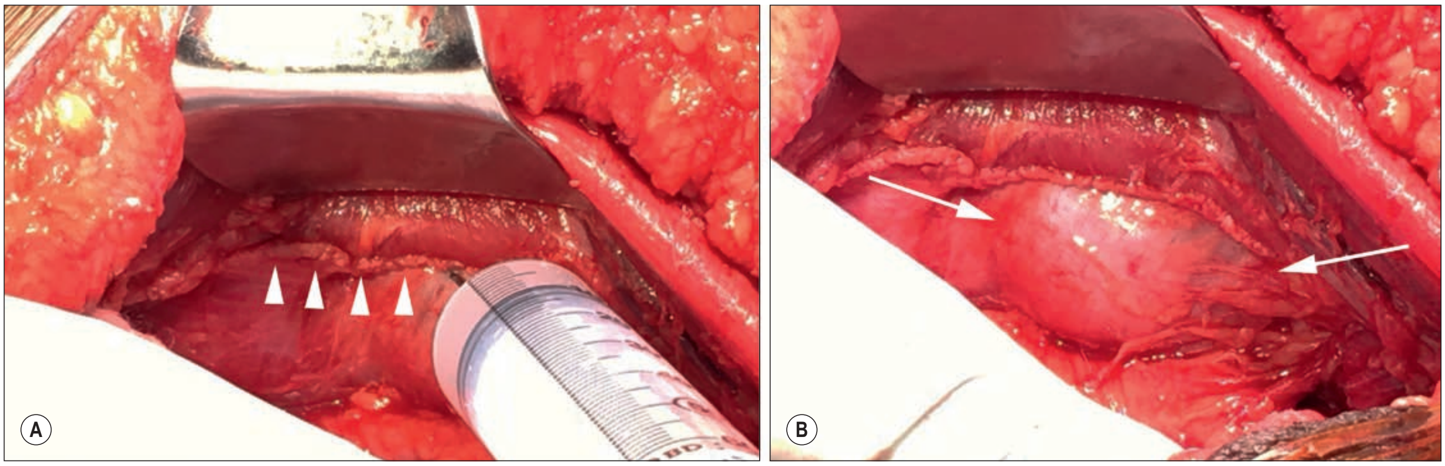

Fig. 60.7 Direct visualization of a transversus abdominis plane block. **A**, An anaesthetic, liposomal bupivacaine, is delivered into the intramuscular plane immediately adjacent to the cut edge of transversus abdominis (arrowheads). **B**, Correct placement is visually confirmed by identifying posterior bulging of the muscle belly as it is displaced by the injected bolus (arrows).

The medial border of each rectus abdominis abuts the linea alba. Its lateral border is sometimes visible on the surface of the anterior abdominal wall as a gently curved groove, the semilunar line, which extends from the tip of the ninth costal cartilage to the pubic tubercle. In a muscular individual it is readily visible, even when the muscle is not actively contracting, but in many obese and non-obese individuals it can be completely obscured.

Attachments Rectus abdominis arises by two tendons. The larger, lateral tendon is attached to the pubic crest and can extend beyond the pubic tubercle to the pecten pubis. The medial tendon interlaces with the contralateral muscle and blends with ligamentous fibres covering the front of the pubic symphysis. Additional fibres may arise from the distal part of the linea alba. The pubic attachment of the tendon of rectus abdominis and the anterior layer of the rectus sheath run over the anterior surface of the pubic symphysis and become continuous with the attachments of gracilis and adductor longus (Norton-Old et al 2013). Superiorly, rectus abdominis is attached by three slips of muscle to the fifth, sixth and seventh costal cartilages. The most lateral fibres are usually attached to the anterior end of the fifth rib; occasionally this slip is absent or it extends to the third and fourth ribs. The most medial fibres are occasionally connected to the adjacent ligaments of the costosternal joint and the side of the xiphoid process.

Vascular supply Rectus abdominis is supplied principally by the superior and inferior epigastric arteries, the latter being the dominant supply. Small terminal branches from the distal three posterior intercostal arteries, the subcostal artery, the lumbar arteries and the deep circumflex iliac artery can contribute, particularly at the lateral edges and the distal parts of the muscle, where they anastomose with small lateral branches of the epigastric arteries. Rectus abdominis provides a reliable and versatile myocutaneous flap, either pedicled or free, because of the excellent vascularity provided by the epigastric vessels and because the muscle belly can be separated from its surrounding sheath.

Innervation Rectus abdominis is innervated segmentally by the terminal branches of the ventral rami of the distal six or seven thoracic spinal nerves (Stecco et al 2017). It can also receive a branch from the ilio-inguinal nerve (Rozen et al 2008).

Actions Rectus abdominis contributes to flexion of the trunk and the maintenance of abdominal wall tone required during straining.

Rectus sheath

Rectus abdominis on each side is enclosed by a fibrous sheath (**Figs 60.9–60.12**). The anterior layer of the rectus sheath extends the entire length of the muscle and fuses with periosteum and ligaments at sites of the muscle's attachments. The posterior layer of the rectus sheath is complete behind the proximal two-thirds of the muscle but absent distal to this level, which corresponds to approximately one-third of the distance between the umbilicus and the pubis (Loukas et al 2008). The termination of the posterior layer of the rectus sheath is usually gradual but can be abrupt and marked by a clearly visible curved horizontal line known as the arcuate line.

The rectus sheath is formed from the aponeuroses of external and internal abdominal oblique and transversus abdominis. Each aponeurosis is bilaminar; the fibres from all three anterior leaves run obliquely upwards, whereas the posterior leaves run obliquely downwards at right angles to the anterior leaves. Proximal to the arcuate line, the anterior layer of the rectus sheath is composed of both leaves of the aponeurosis of external abdominal oblique and the anterior leaf of the aponeurosis of internal abdominal oblique fused together. The posterior layer of the rectus sheath is composed of the posterior leaf of the aponeurosis of internal abdominal oblique and both leaves of the aponeurosis of transversus abdominis. Thus, both the anterior and posterior layers of the rectus sheath consist of three layers of fibres, the middle layer running at right-angles to the other two. Distal to the arcuate line, all three aponeuroses from external and internal abdominal oblique and transversus abdominis pass into the anterior layer of the rectus sheath leaving only the transversalis fascia, extraperitoneal tissues (fat and connective tissue) and the parietal peritoneum to cover the posterior aspect of rectus abdominis (see Fig. 60.9).

At the midline, the anterior and posterior layers of the rectus sheath are closely approximated. Fibres from each layer decussate to the opposite side of the sheath, forming a continuous aponeurosis with the contralateral muscles; they also decussate anteroposteriorly, crossing from the anterior layer of the rectus sheath to the posterior layer of the rectus sheath. The dense fibrous line caused by this decussation is called the linea alba. External and internal abdominal oblique and transversus abdominis can therefore be regarded as digastric muscles with a central tendon comprising the linea alba (Rizk 1980). The decussating fibres at the linea alba can be used to identify the midline during surgical incisions.

Linea alba and umbilicus

The linea alba is a tendinous raphe extending from the xiphoid process to the pubic symphysis and pubic crest. It lies between the left and right rectus abdominis and is formed by the interlacing and decussating aponeurotic fibres of external and internal abdominal oblique and transversus abdominis. At its distal end, the linea alba has two attachments to the pubis: superficial fibres are attached to the pubic symphysis, and deeper fibres form a triangular lamella that is attached behind rectus abdominis to the posterior surface of both pubic crests

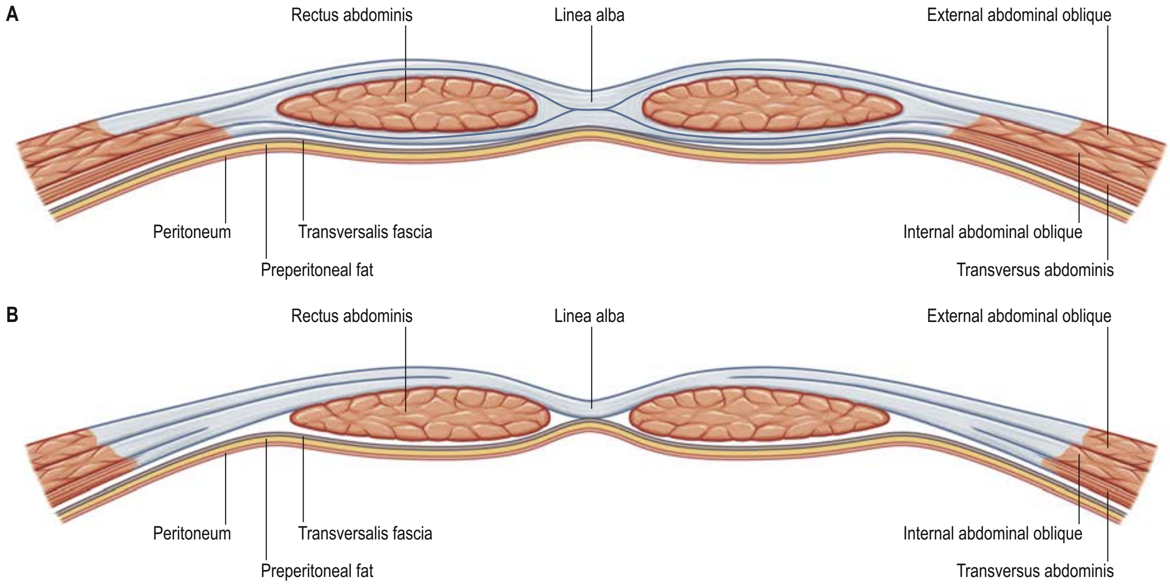

Fig. 60.9 Transverse sections through the anterior abdominal wall. **A**, Immediately proximal to the umbilicus. **B**, Distal to the arcuate line. The bilaminar nature of each muscular aponeurosis is difficult to illustrate in cross-section. The fibres appear to fuse into a single sheet during formation of the rectus sheath. Note that rectus abdominis is supported directly by the transversalis fascia distal to the arcuate line. (C–D, *continued online*)

Without vascular division (a pedicled flap), the proximal half of the muscle can be used for breast reconstruction; the distal half can be transposed to the inguinal region or proximal thigh or rotated on its distal attachments into the perineum for reconstruction after radical pelvic and perineal resections. Because the inferior epigastric vessels are sufficiently large, the distal portion of rectus abdominis can be harvested as a free flap. The vessels are ligated at their junction with the external iliac vessels and are taken together with the distal portion of rectus abdominis. The overlying fascia, adipose tissue and skin can be taken as part of the flap as necessary to manage the soft tissue defect. The free flap is then revascularized by creating anastomoses between the epigastric vessels and the vessels near the defect that is being managed by placement of the flap.

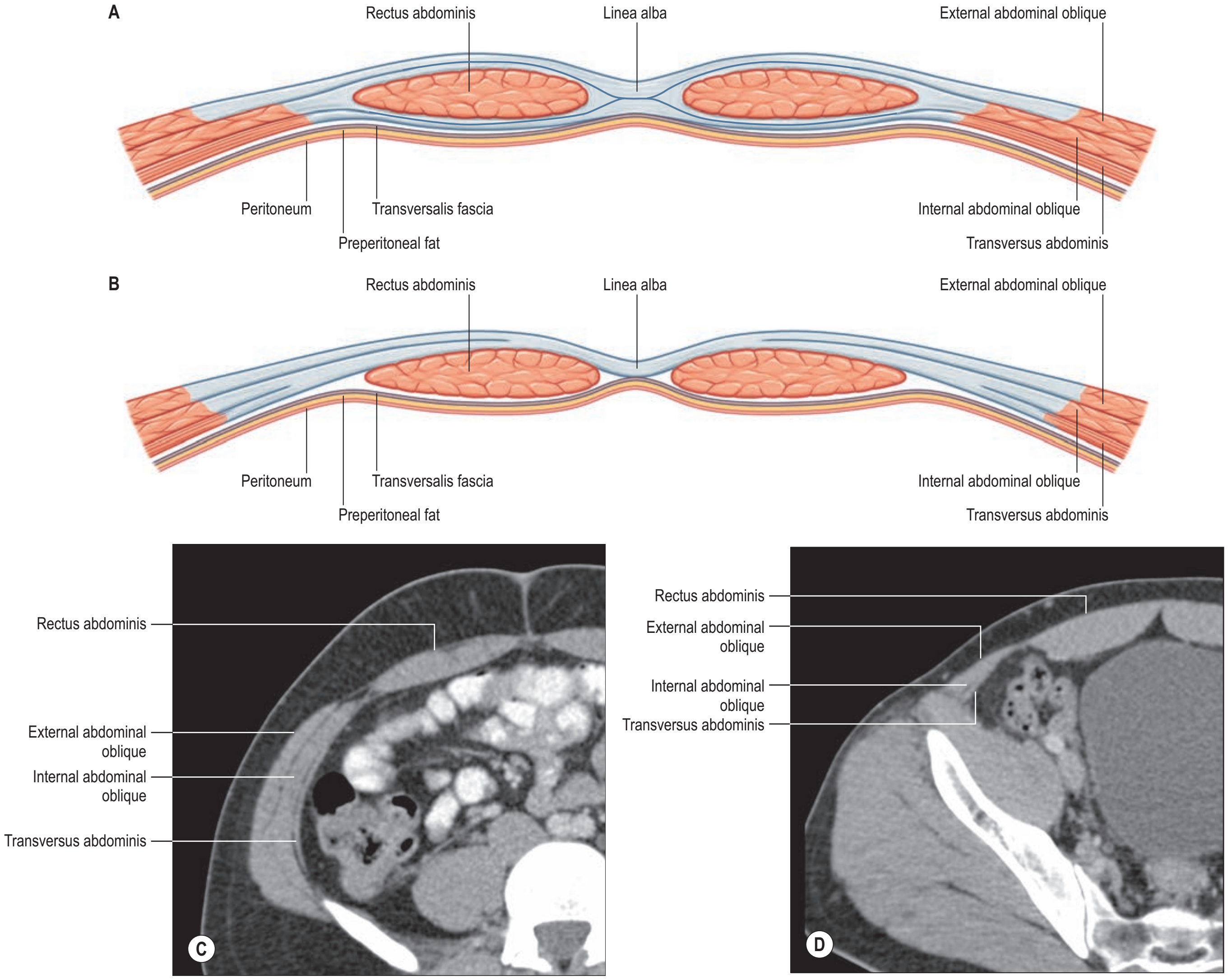
A
Rectus abdominis
Linea alba
External abdominal oblique
Peritoneum
Transversalis fascia
Preperitoneal fat
Internal abdominal oblique
Transversus abdominis
B
Rectus abdominis
Linea alba
External abdominal oblique
Peritoneum
Transversalis fascia
Preperitoneal fat
Internal abdominal oblique
Transversus abdominis
Rectus abdominis
External abdominal oblique
Internal abdominal oblique
Transversus abdominis
C
Rectus abdominis
External abdominal oblique
Internal abdominal oblique
Transversus abdominis
D

Fig. 60.9 Transverse sections through the anterior abdominal wall. **A**, Immediately proximal to the umbilicus. **B**, Distal to the arcuate line. The bilaminar nature of each muscular aponeurosis is difficult to illustrate in cross-section. The fibres appear to fuse into a single sheet during formation of the rectus sheath. Note that rectus abdominis is supported directly by the transversalis fascia distal to the arcuate line. **C–D**, CT of the abdomen and pelvis with intravenous and oral contrast medium (within small bowel loops) showing the muscle and aponeurotic layers of the anterior abdominal wall above (**C**) and below (**D**) the arcuate line. Note how the aponeurosis of internal oblique splits either side of rectus abdominis in **D**.

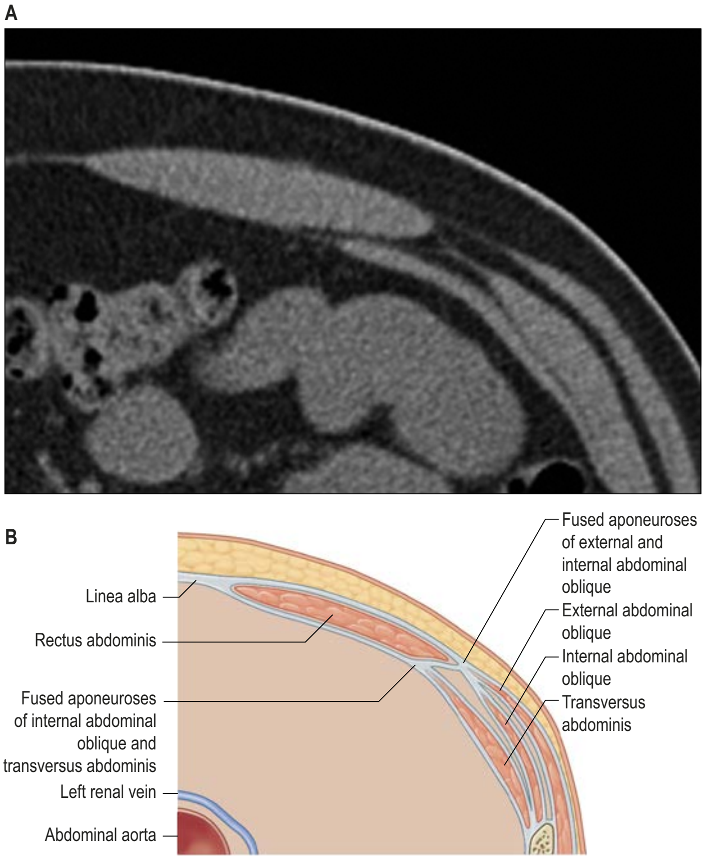
A
B
Linea alba
Rectus abdominis
Fused aponeuroses of internal abdominal oblique and transversus abdominis
Left renal vein
Abdominal aorta
Fused aponeuroses of external and internal abdominal oblique
External abdominal oblique
Internal abdominal oblique
Transversus abdominis

Fig. 60.10 The rectus sheath. CT (**A**) and diagram (**B**) of the anterior abdominal wall, demonstrating the formation of the rectus sheath proximal to the umbilicus. The anterior layer of the rectus sheath is composed of both leaves of the aponeurosis of external abdominal oblique and the anterior leaf of the aponeurosis of internal abdominal oblique, fused together. The posterior layer of the rectus sheath is composed of the posterior leaf of the aponeurosis of internal abdominal oblique and both leaves of the aponeurosis of transversus abdominis.

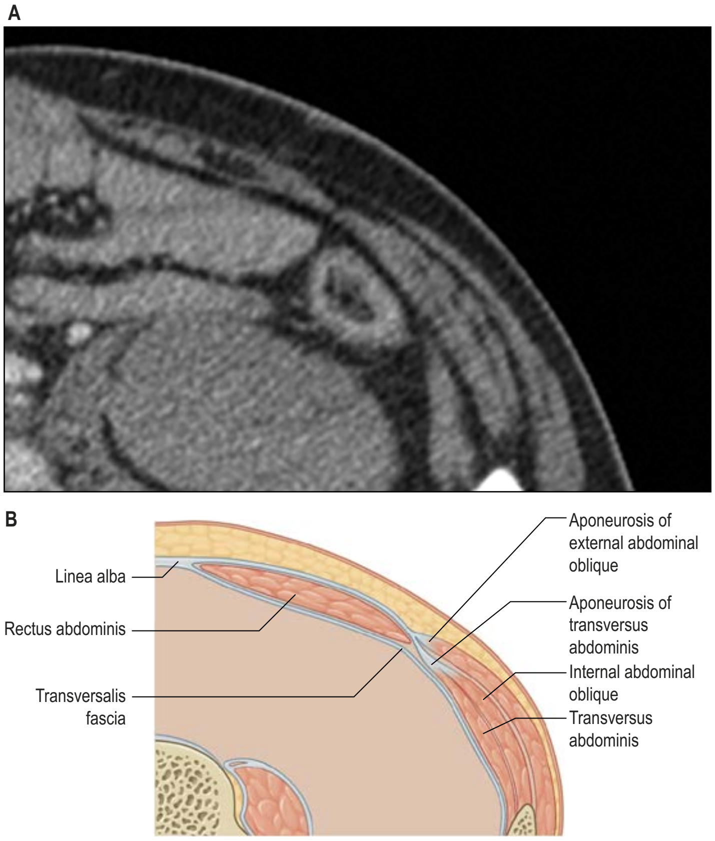
A
B
Linea alba
Rectus abdominis
Transversalis fascia
Aponeurosis of external abdominal oblique
Aponeurosis of transversus abdominis
Internal abdominal oblique
Transversus abdominis

Fig. 60.11 The rectus sheath. CT (**A**) and diagram (**B**) of the anterior abdominal wall, demonstrating the formation of the rectus sheath distal to the umbilicus. The posterior layer of the rectus sheath is replaced by the transversalis fascia and extraperitoneal connective tissue.

(adminiculum lineae albae). The pyramidalis is attached to the suprapubic part of the linea alba. The linea alba is visible externally in those who are lean and muscular as a shallow midline groove in the anterior abdominal wall. Its width varies along its length: it is wider superior to the umbilicus than inferior to it and generally widest at the level of the umbilicus (Rath et al 1996). It is wider and thinner in women, in adults aged over 50 years and in obese individuals and multiparous women (Naraynsingh et al 2012). Its tensile strength is proportional to its thickness and density (Korenkov et al 2001). The linea alba is relatively bloodless but it is crossed superficially from side to side by a few small blood vessels.

The umbilicus is a fibrous cicatrix that lies just distal to the midpoint of the linea alba and is covered by an adherent area of skin. It consists of skin, a fibrous layer (representing the area of fusion between the round ligament of the liver, the median umbilical ligament and two medial umbilical ligaments), the transversalis fascia, the umbilical fascia surrounding the urachal remnant, and peritoneum (Fathi et al 2012). Its appearance and position are variable (Fathi et al 2012). In adults, it tends to lie at a relatively more distal position with advancing age, in men and in individuals with a higher body mass index.

In the fetus the umbilicus transmits the umbilical vessels, urachus and, up to the third month of gestation, the vitelline or yolk stalk. It closes a few days after birth, but the vestiges of the vessels and urachus remain attached to its deep surface. The remnant of the embryonic left umbilical vein forms the round ligament of the liver. The obliterated umbilical arteries form the medial umbilical ligaments on the deep surface of the anterior abdominal wall: when covered with parietal peritoneum they form the medial umbilical folds. The partially obliterated remains of the urachus persist as the median umbilical ligament: when covered with parietal peritoneum, it forms the median umbilical fold. Both congenital and acquired umbilical hernias are common; most childhood umbilical hernias close spontaneously and do not require surgical repair. The umbilicus is the most common site for laparoscopic access to the peritoneal cavity.

Divarication of the left and right rectus abdominis

The linea alba can thin and widen in the upper abdomen, most commonly as a result of pregnancy, obesity or chronic straining (Akram and Matzen 2014). Abdominal viscera protrude beneath the thinned tissue as a broad, lenticular, midline bulge, particularly when intra-abdominal pressure is raised, and the left and right rectus abdominis become widely separated or divaricated. This state is not true herniation because all the layers of the anterior abdominal wall in the region are intact. Divarication (or diastasis of the rectus muscles) is generally considered a cosmetic issue alone, but can be associated with true hernias of the abdominal wall, most commonly at the umbilicus. Surgical correction of this issue requires suture plication (performed either anterior or posteriorly to rectus abdominis) of the thinned linea alba with or without the addition of mesh for support.

Pyramidalis

Pyramidalis is a triangular muscle that lies anterior to the distal part of rectus abdominis within the rectus sheath. It varies considerably in size, and can be larger on one side than on the other. It may be absent on one or both sides (in as many as 20% of individuals) or, rarely, can be duplicated. Pyramidalis is generally rudimentary in humans and is of little clinical or surgical relevance.

Attachments Pyramidalis is attached by tendinous fibres to the anterosuperior margin of the pubis and to ligamentous fibres anterior to the pubic symphysis. The muscle becomes smaller as it runs upwards and ends in a pointed apex that is attached medially to the linea alba: this attachment often lies midway between the umbilicus and pubis, but can lie higher.

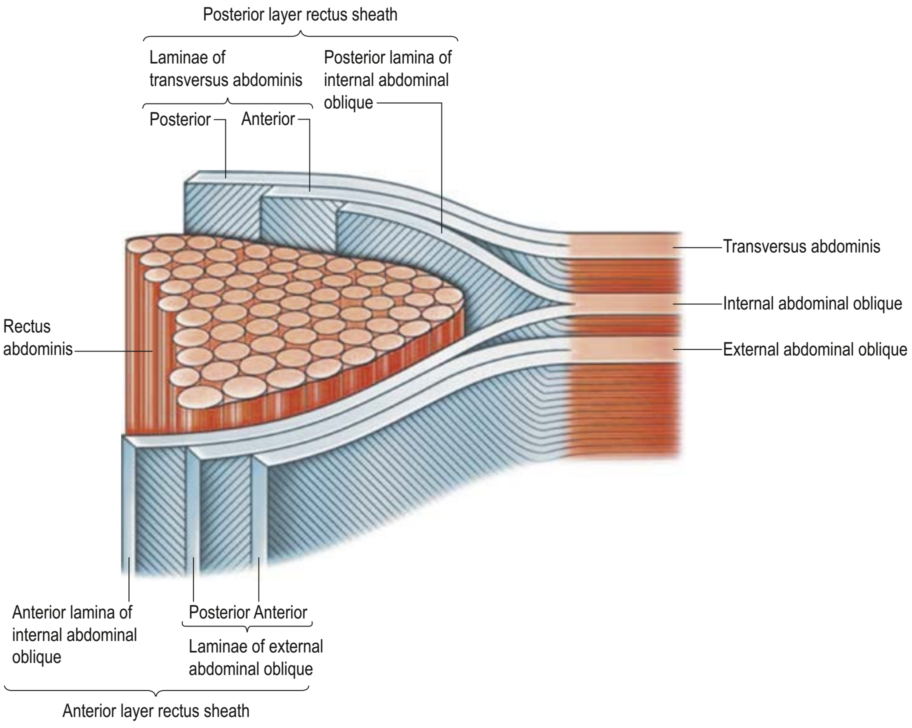
Posterior layer rectus sheath
Laminae of transversus abdominis
Posterior lamina of internal abdominal oblique
Posterior
Anterior
Transversus abdominis
Internal abdominal oblique
External abdominal oblique
Rectus abdominis
Anterior lamina of internal abdominal oblique
Posterior Anterior
Laminae of external abdominal oblique
Anterior layer rectus sheath

Fig. 60.12 The concept of bilaminar aponeuroses of external and internal abdominal oblique and transversus abdominis. Note that the fibres of the superficial and deep laminae are approximately at right-angles; decussations occur as part of the linea alba.

Vascular supply Pyramidalis is supplied by branches of the inferior epigastric artery. A small artery frequently crosses the midline posterior to the belly of the muscle to anastomose with the contralateral vessel.

Innervation Pyramidalis can be innervated via the ventral rami of the twelfth thoracic, first lumbar or second lumbar spinal nerves: fibres travel in anterior cutaneous branches of the subcostal nerve, the ilio-inguinal nerve or the genital branch of the genitofemoral nerve (Tokita 2006).

Actions Pyramidalis contributes to tensing the distal linea alba but is of doubtful physiological significance.

External abdominal oblique

Attachments External abdominal oblique is the largest and most superficial of the three anterolateral abdominal muscles (Fig. 60.13). It curves around the lateral and anterior parts of the abdomen and is attached to the external surfaces and inferior borders of the distal eight ribs. The attachments rapidly become muscular and interdigitate with the distal fibres of serratus anterior and latissimus dorsi along an imaginary oblique line that extends downwards and backwards. The proximal attachments are close to the costal cartilages of the corresponding ribs, the middle ones arise from the ribs at some distance from their cartilages, and the most distal are close to the distal end of the twelfth rib. The fibres of external abdominal oblique diverge as they pass to their distal attachments. Those from the distal two ribs pass nearly vertically downwards and attach to the anterior half or more of the outer lip of the iliac crest. The middle and upper fibres pass downwards and forwards, and end in the anterior aponeurosis, the fibres of which cross the midline. The junction between muscle and aponeurosis extends along an imaginary vertical line from the ninth costal cartilage to just distal to the level of the umbilicus; muscle fibres do not usually descend beyond an imaginary line from the anterior superior iliac spine to the umbilicus.

The inguinal ligament is formed by the inferior margin of the aponeurosis of external abdominal oblique extending between the anterior superior iliac spine and the pubic tubercle. The fibres of the aponeurosis of external abdominal oblique are not parallel to the long axis of the inguinal ligament; they approach the ligament obliquely at an angle of 10–20° and then turn medially to run along the ligament to reach the pubic tubercle (Lytle 1974). The deepest fibres of the aponeurosis spread out posteromedially to insert into the pecten pubis.

The proximal and distal rib attachments of the muscle can be absent. Digitations or even the entire muscle can be duplicated. The proximal attachments of the muscle are sometimes continuous with pectoralis major or serratus anterior.

Vascular supply External abdominal oblique is mainly supplied by branches from the distal posterior intercostal and subcostal arteries proximally and the deep circumflex iliac artery distally. There are additional smaller contributions (Schlenz et al 1999).

Innervation External abdominal oblique is innervated by the ventral rami of the distal six thoracic spinal nerves via the terminal branches of the distal five intercostal nerves and the subcostal nerve.

Actions External abdominal oblique contributes to the maintenance of abdominal tone, increasing intra-abdominal pressure, and lateral flexion of the trunk against resistance.

Inguinal ligament

The inguinal ligament is the thick distal border of the aponeurosis of external abdominal oblique that stretches between the anterior superior iliac spine and the pubic tubercle. Its medial half is curled in on itself, forming the gutter-like ‘floor’ of the inguinal canal (sometimes referred to surgically as the ‘shelving edge’). The ligament is not exactly linear but has an inferior and an anterior convexity. At its distal border it is fused with the fascia lata. Laterally it is fused with the iliopsoas fascia (Lytle 1974). At the medial end of the inguinal ligament, near its site of attachment to the pubic tubercle, some of its fibres extend posteriorly and laterally to attach to the pecten pubis, forming the triangular, shelf-like lacunar ligament. Other fibres pass upwards and medially behind the superficial inguinal ring and external abdominal oblique aponeurosis to join the rectus sheath and linea alba; these constitute the reflected part of the inguinal ligament (Tubbs et al 2009). Fibres from both sides decussate in the linea alba.

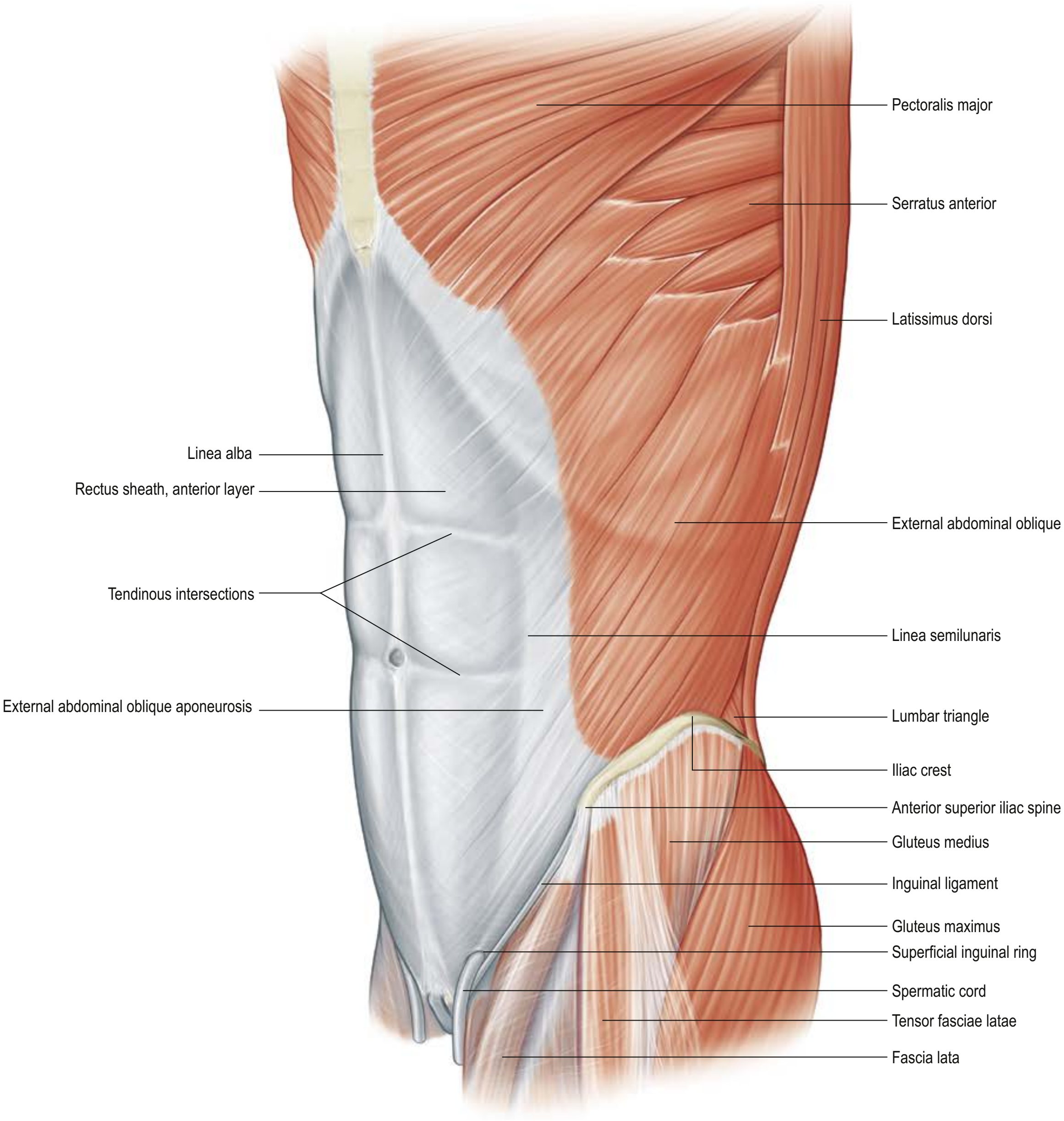
Pectoralis major
Serratus anterior
Latissimus dorsi
Linea alba
Rectus sheath, anterior layer
External abdominal oblique
Tendinous intersections
Linea semilunaris
External abdominal oblique aponeurosis
Lumbar triangle
Iliac crest
Anterior superior iliac spine
Gluteus medius
Inguinal ligament
Gluteus maximus
Superficial inguinal ring
Spermatic cord
Tensor fasciae latae
Fascia lata

Fig. 60.13 The left anterolateral abdominal wall muscles.

Internal abdominal oblique

Attachments Internal abdominal oblique lies deep to external abdominal oblique for most of its course (see Fig. 60.8). It is thinner and less bulky than external abdominal oblique. Its fibres are traditionally stated to arise from the lateral two-thirds of the inguinal ligament but in fact they arise from the corresponding length of a slightly deeper structure known as the iliopectineal arch (Acland 2008), a thickened band of iliopsoas fascia that passes downwards and medially from the anterior superior iliac spine to the iliopubic eminence of the pubis. Further laterally, internal abdominal oblique is attached to the anterior two-thirds of the iliac crest deep to the attachment of external abdominal oblique. Posteriorly, some fibres are attached to the thoracolumbar fascia. The fibres originating from the posterior end of the iliac attachment pass obliquely upwards and are attached to the inferior borders and tips of the distal three or four ribs and their cartilages. Here, the attachments merge with those of internal intercostal. The fibres from the anterior end of the iliac crest diverge and end in the anterior aponeurosis, which gradually broadens in a distal to proximal direction. The most proximal part of the aponeurosis is attached to the cartilages of the seventh to ninth ribs. The fibres that originate adjacent to the inguinal ligament arch downwards and medially across the spermatic cord in the male and the round ligament of the uterus in the female. They become tendinous, fuse with the corresponding part of the aponeurosis of transversus abdominis, and attach to the pubic crest and medial part of the pecten pubis, forming the conjoint aponeurosis.

Vascular supply Internal abdominal oblique is mainly supplied by branches from the distal posterior intercostal and subcostal arteries, the inferior epigastric artery and the deep circumflex iliac artery. There are several smaller contributions (Yang et al 2003).

Innervation Internal abdominal oblique is innervated by the ventral rami of the distal six thoracic spinal nerves via the terminal branches of the distal five intercostal nerves and the subcostal nerve. In addition, it receives a small contribution derived from the ventral ramus of the first lumbar spinal nerve via the iliohypogastric and ilio-inguinal nerves.

Actions Internal abdominal oblique contributes to the maintenance of abdominal tone, increasing intra-abdominal pressure, and lateral flexion of the trunk against resistance.

Although thinner and less bulky than external abdominal oblique, the muscle undergoes compensatory hypertrophy following surgical release of the external abdominal oblique aponeurosis from its insertion on the anterior layer of the rectus sheath. This operation, a so-called anterior component separation myofascial release, is often performed as part of a complex hernia repair.

Transversus abdominis

Attachments Transversus abdominis is the deepest of the anterolateral abdominal muscles (Fig. 60.14). It is attached to the iliopectineal arch deep to the lateral third of the inguinal ligament, the anterior two-thirds of the inner lip of the anterior part of the iliac crest, the

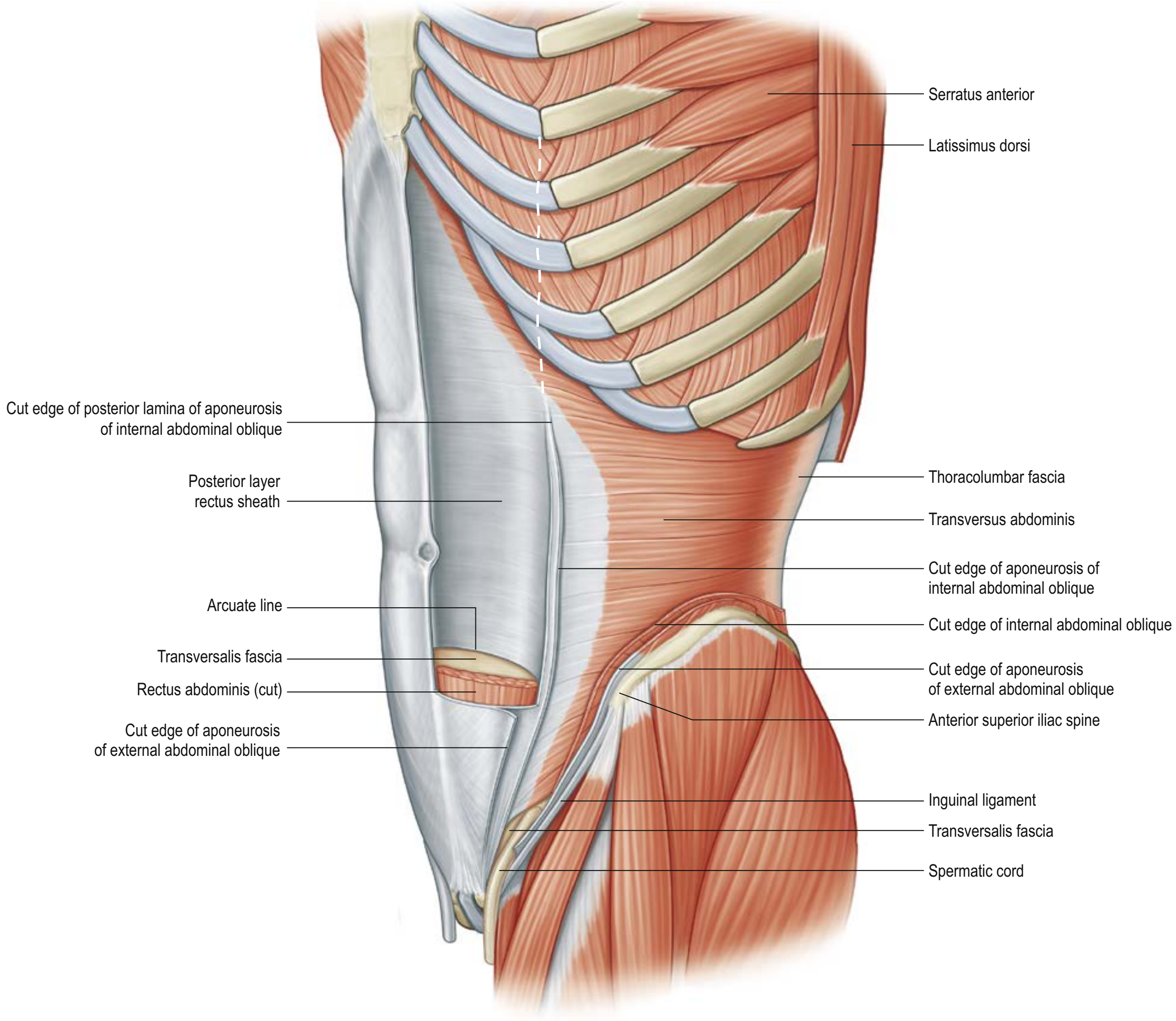
Serratus anterior
Latissimus dorsi
Cut edge of posterior lamina of aponeurosis of internal abdominal oblique
Posterior layer rectus sheath
Thoracolumbar fascia
Transversus abdominis
Cut edge of aponeurosis of internal abdominal oblique
Arcuate line
Cut edge of internal abdominal oblique
Transversalis fascia
Cut edge of aponeurosis of external abdominal oblique
Rectus abdominis (cut)
Anterior superior iliac spine
Cut edge of aponeurosis of external abdominal oblique
Inguinal ligament
Transversalis fascia
Spermatic cord

Fig. 60.14 Left transversus abdominis. The aponeurosis of transversus abdominis fuses into the posterior layer of the rectus sheath proximal to the arcuate line. The position of the lateral border of rectus abdominis is shown by the dotted white line.

thoracolumbar fascia between the iliac crest and the twelfth rib, and the internal aspects of the distal six costal cartilages. The costal attachments interdigitate with those of the respiratory diaphragm. The muscle ends anteriorly in an aponeurosis; the distal fibres of the aponeurosis curve downwards and medially, together with those of the aponeurosis of internal abdominal oblique, and insert into the pubic crest and pecten pubis to form the conjoint aponeurosis. A few muscle fibres may run from the distal border of transversus abdominis to the inguinal ligament and reinforce the interfoveolar ligament (see above). The remainder of the aponeurosis passes medially and the fibres decussate at, and blend with, the linea alba. The proximal costal and anterior iliac fibres of transversus abdominis are short and the thoracolumbar fibres are the longest. Near the xiphoid process, the aponeurosis is formed only a few centimetres from the linea alba and so the muscular part of transversus abdominis extends behind rectus abdominis into the posterior layer of the rectus sheath. The medial edge of the muscle, at the origin of the aponeurosis, curves downwards and laterally, and is furthest from the lateral edge of the rectus sheath at the level of the umbilicus. It then curves downwards and medially towards the superficial inguinal ring giving the muscle belly its characteristic half-hourglass shape.

Occasional defects in the distal muscular and aponeurotic parts of both internal abdominal oblique and transversus abdominis result in intermuscular hernia formation (lateral ventral or Spigelian hernia). The two muscles are sometimes fused and, rarely, transversus abdominis is absent (Saga and Takahashi 2016).

Vascular supply Transversus abdominis is supplied by branches from the distal posterior intercostal and subcostal arteries, the superior and inferior epigastric arteries, the superficial and deep circumflex iliac arteries and the lumbar arteries.

Innervation Transversus abdominis is innervated by the ventral rami of the distal six thoracic and first lumbar spinal nerves via the terminal branches of the distal five intercostal nerves, the subcostal nerve and the iliohypogastric and ilio-inguinal nerves.

Actions Transversus abdominis contributes mainly to the maintenance of abdominal tone and increasing intra-abdominal pressure.

Conjoint aponeurosis

The conventional description of a conjoined or conjoint tendon has been challenged since the 1940s, when the alternative term conjoined aponeurosis was proposed on the grounds that it more properly described the distal union of internal abdominal oblique and transversus abdominis (Chandler and Schadewald 1944). A local thickening in the conjoined aponeurosis that might be called a conjoint tendon occurs rarely. (For a review of the literature associated with Henle's ligament, falx inguinalis, conjoined tendon, conjoined area, conjoint tendon and conjoint area, see Gnanadev et al (2018).)

The conjoint aponeurosis is formed from the distal fibres of internal abdominal oblique and the distal part of the aponeurosis of transversus abdominis. It is attached to the pubic crest and extends to a variable extent along the pecten pubis (see Fig. 60.18). It descends behind the superficial inguinal ring and acts to strengthen the medial portion of the posterior wall of the inguinal canal. Medially, the proximal fibres of the aponeurosis fuse with the anterior layer of the rectus sheath, and laterally, some fibres can blend with the interfoveolar ligament.

Cremaster

Attachments Cremaster consists of loosely arranged muscle fasciculi lying along the spermatic cord or round ligament of the uterus. It is

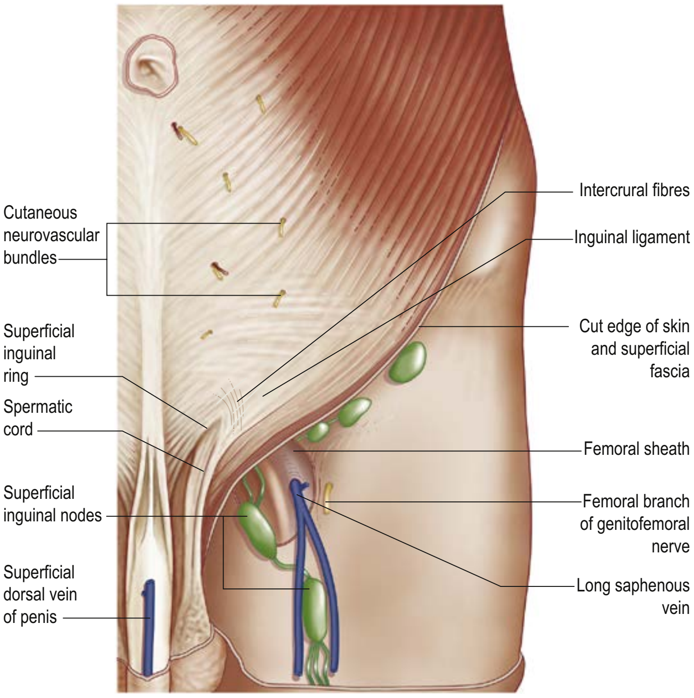
Cutaneous neurovascular bundles
Superficial inguinal ring
Spermatic cord
Superficial inguinal nodes
Superficial dorsal vein of penis
Intercrural fibres
Inguinal ligament
Cut edge of skin and superficial fascia
Femoral sheath
Femoral branch of genitofemoral nerve
Long saphenous vein

Fig. 60.15 Superficial structures of the inguinal region and distal part of the anterior abdominal wall on the left side.

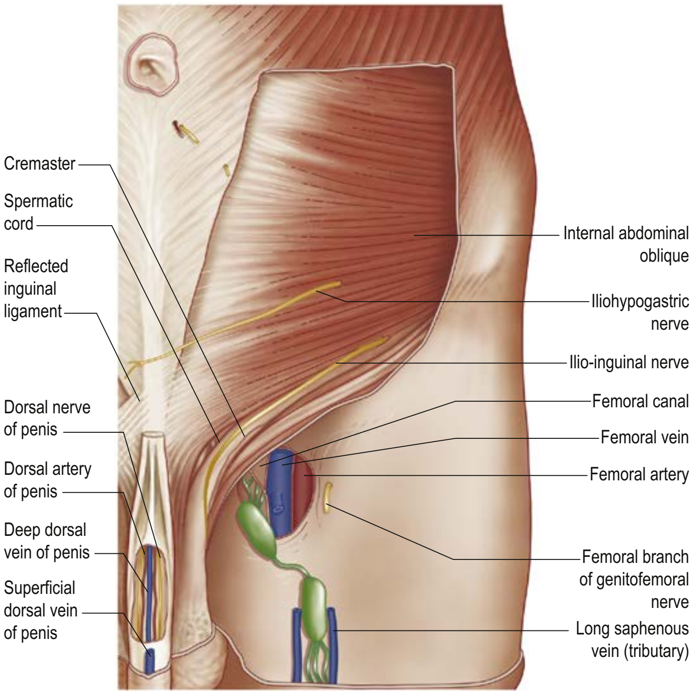
Cremaster
Spermatic cord
Reflected inguinal ligament
Dorsal nerve of penis
Dorsal artery of penis
Deep dorsal vein of penis
Superficial dorsal vein of penis
Internal abdominal oblique
Iliohypogastric nerve
Ilio-inguinal nerve
Femoral canal
Femoral vein
Femoral artery
Femoral branch of genitofemoral nerve
Long saphenous vein (tributary)

Fig. 60.16 Dissection of the regions shown in Fig. 60.15, with part of external abdominal oblique removed.

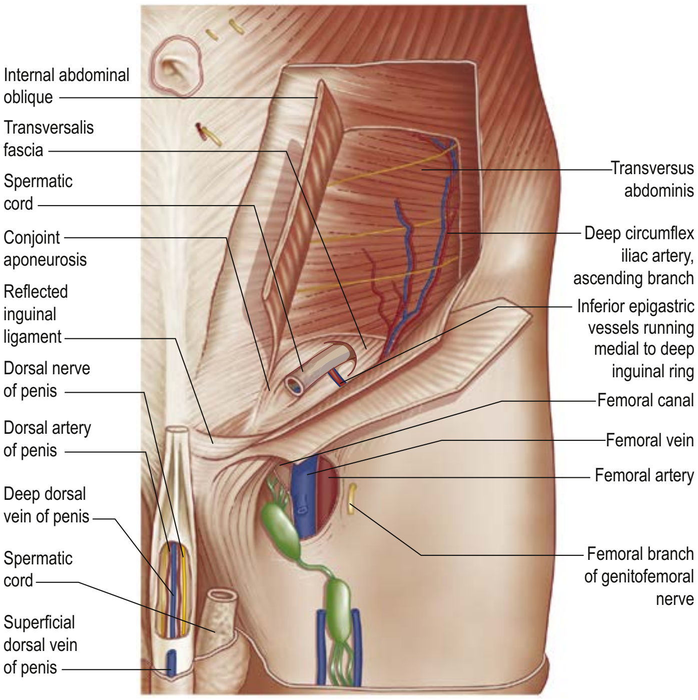
Internal abdominal oblique
Transversalis fascia
Spermatic cord
Conjoint aponeurosis
Reflected inguinal ligament
Dorsal nerve of penis
Dorsal artery of penis
Deep dorsal vein of penis
Spermatic cord
Superficial dorsal vein of penis
Transversus abdominis
Deep circumflex iliac artery, ascending branch
Inferior epigastric vessels running medial to deep inguinal ring
Femoral canal
Femoral vein
Femoral artery
Femoral branch of genitofemoral nerve

Fig. 60.17 Dissection of the inguinal region and distal part of the anterior abdominal wall on the left side, with parts of external and internal abdominal oblique removed.

variable in thickness but thickest in young males. Together with connective tissue, it forms an incomplete coating around the spermatic cord known as the cremasteric fascia, which extends down around the testis deep to the external spermatic fascia. The muscle consists of a lateral part that arises mainly from the inferomedial border of internal abdominal oblique and transversus abdominis but also has attachments to the middle of the inguinal ligament, and a medial part attached to the pubic tubercle, lateral pubic crest and the distal border of transversus abdominis; this part is variably developed and can be absent (Shafik 1977). The longitudinal muscle fibres spread out over the spermatic cord as it approaches the superficial inguinal ring. Cremaster is composed of both striated and smooth muscle fibre bundles (Schwarz and Hirtler 2017).

Vascular supply Cremaster is supplied by the cremasteric artery, a branch of the inferior epigastric artery.

Innervation Cremaster is innervated by the genital branch of the genitofemoral nerve, derived from the first and second lumbar spinal nerves.

Actions Cremaster pulls the testis up towards the superficial inguinal ring. Although it contains striated muscle fibres, it is not usually under voluntary control. Stroking the skin of the medial side of the thigh evokes a reflex contraction of the muscle, the cremasteric reflex, which is most pronounced in boys and may be a protective reflex. Cremaster could also be involved in testicular thermoregulation since it is activated by the cold.

Inguinal canal

The inguinal canal is a natural passageway between the muscle layers of the anterior abdominal wall in the inguinal region (Lytle 1979) (**Figs 60.15–60.17**; see Figs 74.15–74.16). Its size and form vary with age, and although it is present in both sexes it is best developed in males. The canal is an oblique tunnel with deep and superficial openings or rings. It transmits the spermatic cord in males, the round ligament of the uterus in females, and the ilio-inguinal nerve and genital branch of the genitofemoral nerve in both sexes.

Superficial inguinal ring

The superficial inguinal ring is a hiatus in the aponeurosis of external abdominal oblique, just proximal and lateral to the pubic crest. The ring is actually triangular, its apex pointing laterally towards the anterior superior iliac spine. Although it varies in size it does not usually extend laterally beyond the medial third of the inguinal ligament. It is smaller in females. The base of the triangular opening lies along the pubic crest and its sides are the lateral and medial crura of the opening in the aponeurosis. The lateral crus is stronger and is attached to the pubic tubercle. The medial crus is thinner and its fibres attach to the front of the pubic symphysis and interlace with contralateral fibres. A few intercrural fibres arch proximal to the apex of the superficial inguinal ring (see Fig. 60.15). Some fibres from the aponeurosis of external abdominal oblique and its overlying fascia continue downwards from the medial crus over the spermatic cord, and form the delicate external spermatic fascia; consequently, the superficial 'ring' appears less of a discrete opening.

Deep inguinal ring

The deep inguinal ring is an opening in the transversalis fascia, approximately midway between the anterior superior iliac spine and the pubic symphysis, and about 1 cm proximal to the inguinal ligament (Hale et al 2010). It is oval with a roughly vertical long axis. Its size varies among individuals but it is usually 1–2 cm wide in adults and larger in males. It is related superiorly to the arched distal margin of transversus abdominis and medially to the interfoveolar ligament (see Fig. 60.18). The inferior epigastric vessels run in the medial border of the deep inguinal ring. Traction on the fascial ring exerted by contraction of

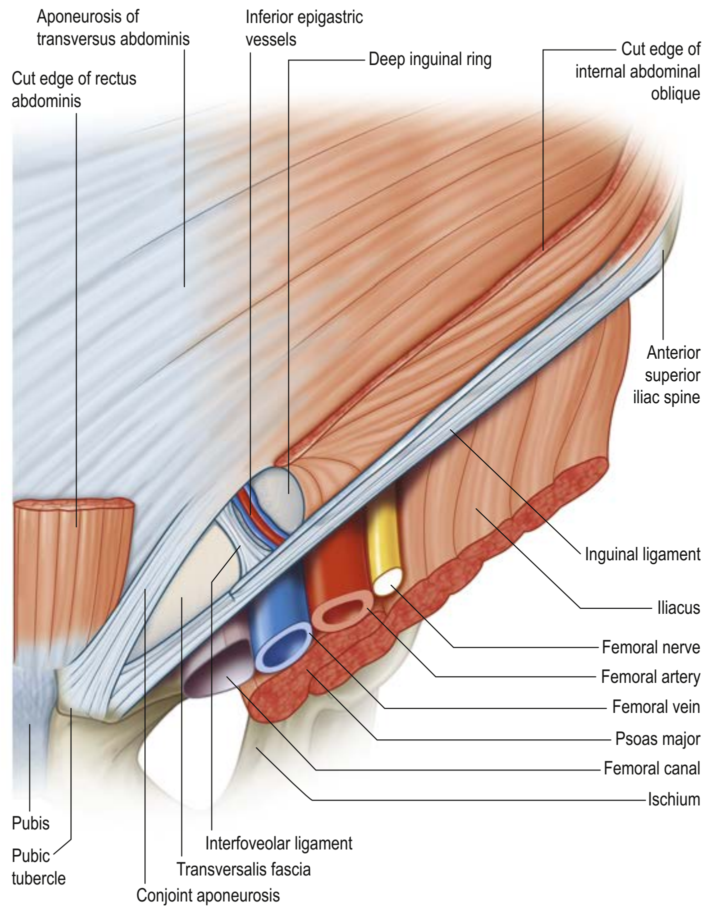

Fig. 60.18 Deep structures of the inguinal canal. The aponeurosis of external abdominal oblique has been removed. For clarity, the fibres of internal abdominal oblique and rectus abdominis have been divided, and the structures passing postero-inferiorly to the inguinal ligament have been excluded.

internal abdominal oblique can narrow the opening when intra-abdominal pressure is increased.

Boundaries

The inguinal canal slants obliquely downwards and medially, parallel to and just proximal to the medial part of the inguinal ligament. It extends from the deep to the superficial inguinal rings; its length depends on the age of the individual, but in adults it is 3–6 cm. The canal is bounded anteriorly by skin, superficial fascia and the aponeurosis of external abdominal oblique. In its lateral third the anterior wall is reinforced by the muscular fibres of internal abdominal oblique. Posteriorly, the reflected inguinal ligament, the conjoint aponeurosis and the transversalis fascia separate it from extraperitoneal connective tissue and peritoneum. Superiorly, the arched fibres of internal abdominal oblique and transversus abdominis form the conjoint aponeurosis medially. Inferiorly, the transversalis fascia unites with the inguinal ligament; the lacunar ligament lies at the medial end.

In the newborn the deep and superficial inguinal rings are nearly superimposed and the inguinal canal is extremely short, only about 1 cm long (Parnis et al 1997). As a child grows, the anterior abdominal wall muscles develop further, causing the rings to separate and the inguinal canal to lengthen. The canal becomes progressively more oblique, so by adulthood it has separate anterior and posterior walls. As the arched fibres of internal abdominal oblique and transversus abdominis contract, they straighten and move closer to the inguinal ligament. This motion serves as a protective mechanism against hernia formation, the so-called 'shutter' effect. At the superficial inguinal ring and the medial end of the anterior wall of the inguinal canal, where the canal is weakest, the posterior wall is strengthened by the conjoint aponeurosis and reflected inguinal ligament. Increases in intra-abdominal pressure transmitted to the posterior wall of the canal are resisted by contraction of the three anterolateral abdominal wall muscles. The fibres of internal abdominal oblique and transversus abdominis, which form the conjoint aponeurosis, are constantly active in standing; this activity increases during episodes of increased intra-abdominal pressure.

Lacunar ligament

The lacunar ligament is a triangular band of fibrous tissue lying mainly posterior to the medial end of the inguinal ligament. It measures approximately 2 cm from base to apex and is a little larger in males. It is formed by fibres of the medial end of the inguinal ligament and fibres from the fascia lata that join the medial end of the inguinal ligament distally (Lytle 1974). The fibres of the inguinal ligament run posteriorly and laterally to the medial end of the pecten pubis and are continuous with the fascia associated with pectineus. They form a near-horizontal, triangular sheet with a curved lateral border that forms the medial border of the femoral canal. The apex of the triangle is attached to the pubic tubercle. A strong fibrous band, the pectineal ligament (Cooper's ligament), extends laterally along the pecten pubis from the attachment of the lacunar ligament (Faure et al 2001).

Relations

The inferior epigastric vessels are important medial relations of the deep inguinal ring (**Fig. 60.18**). They lie on the transversalis fascia as they ascend obliquely behind the conjoint aponeurosis to enter the rectus sheath. The inguinal triangle is an important clinical landmark related to the posterior wall of the inguinal canal and is best appreciated by examining the inguinal canal region from within the abdomen (see Fig. 60.3). The triangle is bounded inferiorly by the medial third of the iliopubic tract, medially by the distal lateral border of rectus abdominis, and laterally by the inferior epigastric vessels.

Myofascial flaps and component separation

Available with the *Gray's Anatomy* e-book

HERNIAS OF THE ANTERIOR ABDOMINAL WALL

A wide range of spontaneously occurring anterior abdominal wall hernias has been described, including inguinal, femoral, umbilical, epigastric and Spigelian (Larson and Farley 2002, Dabbas et al 2011, Novitsky 2016). These hernias occur at areas of intrinsic weakness in the layers of the abdominal wall, whereas incisional hernias are a common postoperative complication of surgery and can occur at any location in the abdominal wall.

Hernias of the myopectineal orifice

The myopectineal orifice (of Fruchaud) (see Fig. 60.3) is the surgical name given to the inferomedial aspect of the anterior abdominal wall. It encompavsses the deep inguinal ring, the inguinal triangle and the portal inferior to the inguinal ligament that transmits femoral neurovascular structures (Wolloscheck and Konerding 2009). The inguinal ligament travels diagonally through the myopectineal orifice dividing it into two parts. Although the myofascial anatomy is arranged to support these areas of weakness (e.g. the deep inguinal ring, the superficial inguinal ring, the femoral canal and the inguinal triangle), the region is a common site of herniation, particularly in males. Such hernias are described by their origin within the pelvic cavity into inguinal hernias (direct and indirect) or femoral hernias (**Fig. 60.19**).

Indirect inguinal hernia

An indirect inguinal hernia arises through the deep inguinal ring lateral to the inferior epigastric vessels (see Fig. 60.19A). Many indirect hernias are related to the abnormal persistence of a patent processus vaginalis, a tube-like extension of peritoneum through the inguinal canal that is present during normal development and normally becomes occluded soon after birth. Others are acquired as a result of progressive weakening of the posterior wall of the inguinal canal in the region of the deep inguinal ring. The hernia can pass through the deep inguinal ring or expand the deep inguinal ring such that it is no longer a clear entity. Small indirect hernias lie distal and lateral to the fibres of the conjoint aponeurosis, but larger hernias often distort and thin the tendon superiorly. Small indirect hernias that do not protrude beyond the inguinal canal are covered by the same inner layers as the spermatic cord: namely, the internal spermatic fascia and cremaster. If the hernia extends through the superficial inguinal ring, it is also covered by the external spermatic fascia. In hernias related to a persistent fully patent processus vaginalis, the hernia contents can descend as far as the tunica vaginalis anterior to the testis. In many individuals with a partial or fully patent processus vaginalis, an indirect hernia manifests during childhood; but an actual hernia into the potential sac may not develop until adult life, often as a consequence of increased intra-abdominal pressure or sudden muscular strain.

The goal of repairing massive midline ventral hernias lies in re-approximation of the linea alba, thereby restoring anatomy and maximizing the physiological potential of the anterior abdominal wall. However, large fascial defects often will not permit primary re-approximation without undue tension. Many techniques have been developed that use the layered nature of the abdominal wall musculature, allowing additional mobiliztion of the fascial edges by 'releasing' incisions in myofascial layers (Rosen 2017). These repairs are often reinforced with synthetic or bioprosthetic mesh applied in various ways: onlay (superficial to the superficial fascia), sublay (within the myofascial layers or placed in an extraperitoneal position) or underlay (deep to the peritoneum and exposed to intra-abdominal contents).

Anterior component separation, originally described by Ramirez in 1990, refers to bilateral release of the external abdominal oblique muscles, which potentially can provide up to 10 cm, 20 cm and 8 cm of medial mobilization at the proximal, mid and distal abdomen, respectively (Ramirez et al 1990). This mobilization permits midline approximation of rectus muscles and creates a large pocket for the onlay placement of mesh. A disadvantage of this technique is that in order to access and isolate external abdominal oblique lateral to the semilunar line from a midline incision, large subcutaneous flaps must be raised. This necessitates ligation of perforating vessels that supply the overlying subcutaneous tissue, rendering the flaps vulnerable to ischaemia, necrosis and infection. In an attempt to overcome this limitation, methods of external abdominal oblique release have been developed to preserve the periumbilical perforating vessels that traverse rectus abdominis and the anterior layer of the rectus sheath. Endoscopic techniques access the same myofascial layer through smaller, lateral incisions, while perforating-sparing open techniques create a subcutaneous tunnel proximal and distal to the umbilicus that is connected laterally (thus preserving all the blood supply that enters the abdominal wall near the umbilicus). While reducing the likelihood of wound necrosis and infection, these methods also reduce the maximum medial advancement by 1–2 cm on each side and do not create the large pocket necessary for onlay placement of mesh. When the release of external abdominal oblique is insufficient, an additional 2–4 cm of fascial advancement can be gained by simultaneous release of the posterior layer of the rectus sheath. A posterior layer of the rectus sheath release can also be added to create a pocket deep to rectus abdominis for the sublay placement of mesh, which for a variety of reasons could be preferable to onlay placement of mesh.

The posterior layer of the rectus sheath can be incised independently of external abdominal oblique release, allowing access to the retromuscular space and providing several other options for medial advancement. The traditional Rives–Stoppa–Wantz technique, developed during the 1970s, involves incising the posterior layer of the rectus sheath just lateral to the linea alba, allowing a retromuscular dissection to the lateral edge of the rectus sheath. If this does not gain sufficient medial advancement, further extension can be obtained by release of transversus abdominis (Novitsky et al 2012). The posterior layer of the rectus sheath can again be incised 1–2 cm medial to the semilunar line, safely preserving the laterally perforating neurovascular bundles. The division of the posterior lamella of internal abdominal oblique exposes the underlying transversus abdominis muscle belly. Delicate transection of this muscle at its most medial insertion allows access to a plane deep to transversus abdominis and superficial to the transversalis fascia, extraperitoneal fat and peritoneum. This plane of dissection can be extended laterally to psoas major, inferiorly to the retropubic space (of Retzius), and superiorly beneath the respiratory diaphragm.

The same extraperitoneal plane can be entered directly at the linea alba. While this allows for lateral dissection, it does not provide the benefit of any fascial advancement/release. Moreover, the peritoneum is exceptionally thin and can be particularly adherent to the transversalis fascia. As a result, holes are created in predictable locations during an extraperitoneal hernia repair (such as at the costal arch and at the semilunar line at the level of the umbilicus).

In addition to the medial mobilization of fascia aided by myofascial flap component separations, these myofascial planes allow for mesh reinforcement with extensive overlap of the hernia defect. They also prevent mesh exposure to intra-abdominal contents (Heller et al 2012). Multiple other component separation operations have been described, several of which necessitate division of the neurovascular bundles that enter rectus abdominis laterally. While affording medial tissue advancement and wide mesh overlap, these operations result in denervation of rectus abdominis and can lead to abdominal wall dysfunction.

Incorrectly performed component separation procedures can result in unintended complete division of the semilunar line. This devastating complication results in iatrogenic hernias lateral to rectus that can extend from the costal arch to the inguinal ligament. Options for repairing these defects are limited, which makes a robust knowledge of abdominal wall anatomy critical for the surgeon performing such operations.

Indirect inguinal hernias are present in as many as 3–5% of full-term infants and upwards of 30% of premature babies. They are more common on the right (60%) than the left (25%) and less commonly bilateral (15%). They can go unnoticed at the time of birth, but become apparent as a bulge in the inguinal region noticed when the baby is crying.

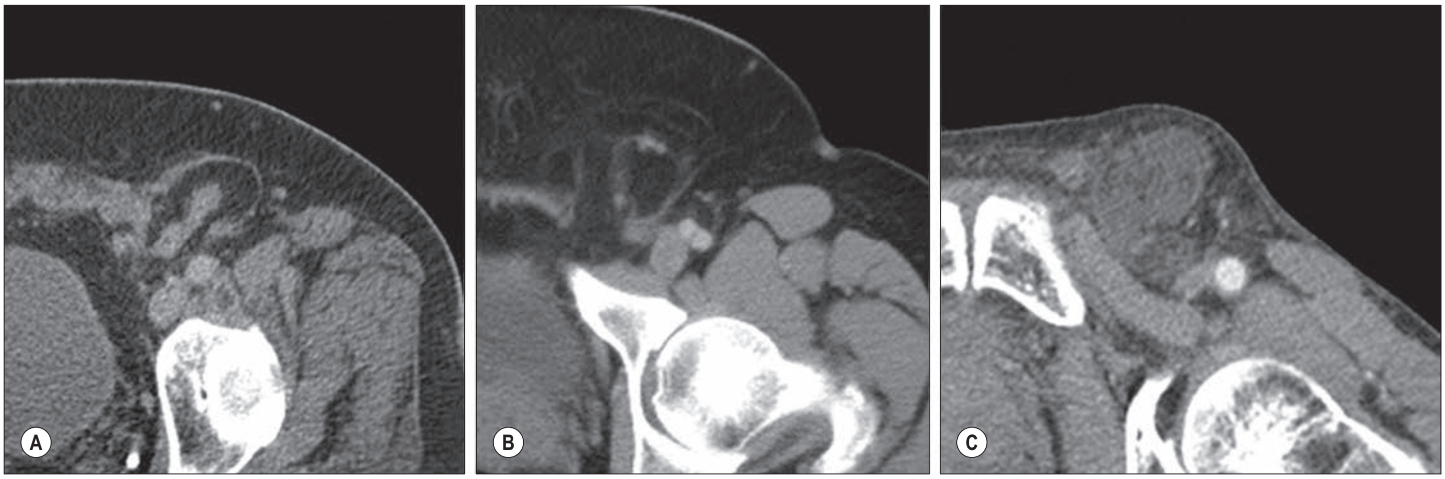

Fig. 60.19 CT of hernias of the myopectineal orifice. **A**, Indirect hernia occurring lateral to the inferior epigastric vessels containing part of the sigmoid colon. **B**, Direct inguinal hernia occurring medial to the inferior epigastric vessels containing extraperitoneal fat. **C**, Incarcerated femoral hernia occurring medial to the femoral vein and containing ischaemic omental fat.

Direct inguinal hernia

A direct inguinal hernia arises medial to the inferior epigastric vessels, within the inguinal triangle (see Fig. 60.19B). Direct hernias are caused by an acquired weakness of the posterior wall of the inguinal canal (see Fig. 60.3B); as they enlarge, they frequently extend through the anterior wall of the inguinal canal or superficial inguinal ring, becoming covered by the external spermatic fascia in the process. A direct inguinal hernia can closely resemble an indirect hernia and can be difficult to distinguish on physical examination.

Clinical features of inguinal hernias

Available with the *Gray's Anatomy* e-book

Femoral hernia

The femoral sheath is continuous with the transversalis fascia anteriorly and the iliopsoas fascia posteriorly. The medial compartment of the sheath is the femoral canal, which typically contains lymphatics embedded in loose adipose connective tissue. The opening of this canal is the femoral ring, bounded anteriorly by the inguinal ligament, posteriorly by the pectineal ligament, medially by the crescentic lateral margin of the lacunar ligament and laterally by the femoral vein. A femoral hernia protrudes through the femoral ring, which is normally closed by a femoral septum of extraperitoneal tissue and is therefore a site of potential weakness: variations in the attachment of the lacunar ligament can also contribute to hernia formation.

Umbilical hernia

Umbilical defects arise from a failure of closure of the umbilical ring after return of the herniated midgut loop into the embryo. The most common variety of umbilical hernia is caused by a weakness of the umbilical scar tissue and is often seen in babies, especially those of African descent. Unlike inguinal hernias in infants, which require surgical repair, the vast majority of umbilical hernias will eventually close spontaneously during early childhood. Most umbilical hernias in adults are acquired as a result of stretching the supporting umbilical fascia (Fig. 60.20), commonly as a result of obesity and chronically increased intra-abdominal pressure (e.g. multiple pregnancies or ascites). The most extreme variety of umbilical hernia is known as an omphalocele or exomphalos, a congenital anomaly in which abdominal viscera, covered by a membrane, protrude through a wide umbilical defect (Fig. 60.21).

Epigastric hernia

Epigastric hernias arise from defects caused by incomplete fusion of the bilateral fibres that decussate to form the linea alba and represent 2–3% of all abdominal wall hernias. They are generally small (often too small to palpate) and asymptomatic, although they can be a source of pain and discomfort if extraperitoneal fat becomes trapped in the defect (Fig. 60.22).

Spigelian hernia

A Spigelian hernia is a protrusion of extraperitoneal fat or a peritoneal sac through a congenital or acquired defect in the abdominal wall in the region of the intersection of the semilunar line with the arcuate line (Larson and Farley 2002, Skandalakis et al 2006). Distal to this level, the aponeuroses of external and internal abdominal oblique and transversus abdominis all pass anterior to rectus abdominis and the posterior layer of the rectus sheath ends. A Spigelian hernia is an interstitial (or intraparietal) hernia in that the hernia passes through a defect in the aponeuroses of transversus abdominis and internal abdominal oblique but remains deep to the overlying aponeurosis of external abdominal oblique (Fig. 60.23). Because external abdominal oblique is intact, the fascial defect cannot be palpated on physical examination, often leading to a delay in diagnosis.

Incisional hernia

Incisional hernias comprise as many as 20% of all anterior abdominal wall hernias. They arise as a postoperative complication of abdominal incisions as a result of technical failures, wound infection and patient-related factors such as obesity, smoking, medical comorbidities and old age (Carlson et al 1995). Incisional hernias range in size from a few millimetres (hernias related to laparoscopic port site incisions) to massive defects that contain most of the abdominal contents and include a large fascial defect (Fig. 60.24).

Parastomal hernia

Available with the *Gray's Anatomy* e-book

Bonus e-book content

Fig. 60.1 B, MIP coronal reconstruction slabs: CT aortogram through the upper and lower anterior abdominal wall arterial supply.

Fig. 60.3 C, Slightly oblique axial CT with intravenous contrast medium shows the ductus deferens joining the testicular vessels at the deep inguinal ring.

Fig. 60.6 Denervation loss of the entire left abdominal wall.

Fig. 60.7 Direct visualization of a transversus abdominis plane block.

Fig. 60.9 C–D, Transverse sections through the anterior abdominal wall. CT of the abdomen and pelvis with intravenous and oral contrast medium.

Fig. 60.19 CT, hernias of the myopectineal orifice.

Fig. 60.20 CT, umbilical hernia in the setting of obesity.

Fig. 60.21 Paediatric umbilical defects.

Fig. 60.22 CT, small symptomatic epigastric hernia containing inflamed extraperitoneal fat.

Fig. 60.23 CT, Spigelian hernia with bowel obstruction.

Fig. 60.24 CT, massive incisional hernia with loss of abdominal domain.

Fig. 60.25 CT, parastomal hernia.

Video 60.1 Dissection of the anterior abdominal wall.

Key references

Carlson MA, Ludwig KA, Condon RE 1995 Ventral hernia and other complications of 1,000 midline incisions. South Med J 88:450–3.

A summary of the outcomes in 1079 consecutive clean or clean-contaminated midline abdominal incisions after both elective and emergency operations done between 1984 and 1991.

Cassar K, Munro A 2002 Surgical treatment of incisional hernia. Br J Surg 89:534–45.

A review that compares the long-term recurrence rates of open primary repair with open mesh and laparoscopic repair, citing the inadequacy of open primary repair.

El-Mrakby HH, Milner RH 2002 The vascular anatomy of the lower anterior abdominal wall: a microdissection study on the deep inferior epigastric vessels and the perforator branches. Plast Reconstr Surg 109:539–43; discussion 44–7.

An account of how the inferior epigastric artery provides the main blood supply to the distal abdominal wall. Microdissection of the artery, its main branches and the perforator vessels was undertaken in 20 cadavers and the findings summarized.

Friedman T, Coon D, Kanbour-Shakir A 2015 Defining the lymphatic system of the anterior abdominal wall: an anatomical study. Plast Reconstr Surg 135:1027–32.

A histological study that found that the lymphatic vessels of the anterior abdominal wall travel primarily in the dermis.

Novitsky YW, Elliott HL, Orenstein SB et al 2012 Transversus abdominis muscle release: a novel approach to posterior component separation during complex abdominal wall reconstruction. Am J Surg 204:709–16.

A description of the novel technique for posterior component separation, which was associated with a low perioperative morbidity and a low recurrence rate. Overall, transversus abdominis release could be an important addition to the armamentarium of surgeons undertaking major abdominal wall reconstructions.

Indirect inguinal hernias descend from lateral to medial, following the path of the inguinal canal, whereas direct inguinal hernias tend to protrude more directly anteriorly. With the hernia reduced, pressure applied over the region of the deep inguinal ring can prevent the appearance of an indirect hernia on standing or straining, but even so, distinguishing an indirect from a direct inguinal hernia by physical examination alone is not reliable (Ralphs et al 1980, Tromp et al 2014). Direct hernias are more likely to have a wide neck, making strangulation less likely.

In females, the femoral ring is relatively wider and it changes during pregnancy, which helps to explain why femoral hernias account for about 20% of all inguinal hernias in females but less than 1% of inguinal hernias in males (Whalen et al 2011). The ring also widens with advancing age, which is one reason why femoral hernias are more common in older females. Nevertheless, inguinal hernias remain the most common hernias in females and the elderly, despite a higher prevalence of femoral hernias in this patient demographic.

When a tongue of omentum or a loop of intestine bulges through the ring, it pushes out a hernia sac of peritoneum that is covered by extraperitoneal tissue (the femoral septum) and descends within the femoral canal to the saphenous opening (see Fig. 60.19C). It is prevented from descending further by the configuration of the femoral sheath and by the attachment of fascia to the inferior horn of the saphenous opening. The hernia sac can turn anteriorly, stretching the cribriform fascia and curving upwards over the inguinal ligament within the subcutaneous tissues. While in the canal, the hernia is usually small because it is contained by the surrounding tissues, but it enlarges as it expands into the subcutaneous tissues.

The small size and anatomical location of femoral hernias explains why they can easily be missed on physical examination, particularly in obese individuals. They are also much more prone to strangulation than inguinal hernias (Whalen et al 2011). The site of strangulation varies: it can be at the neck of the hernia sac, at the saphenous opening, or at the junction of the falciform margin of the saphenous opening with the free edge of the lacunar ligament. If the lacunar ligament must be divided to widen the neck of the hernia and to permit reduction of the herniated contents, care must be taken to avoid or control an aberrant obturator artery (see above).

The pubic tubercle can be a useful landmark during attempts to distinguish an inguinal from a femoral hernia: a femoral hernia lies distal and lateral to this landmark, whereas an inguinal hernia is proximal to it. However, clinical differentiation of inguinal region hernias can be relatively unreliable (Hair et al 2001), prompting the use of radiological imaging in suspected cases (Whalen et al 2011).

There is currently little consensus among surgeons as to the optimum method of repairing incisional hernias: numerous techniques have been described (Cassar and Munro 2002). Repairs can be conducted open, laparoscopically or robotically. They may or may not involve the use of mesh (of which there are hundreds of varieties), which can be placed in multiple locations among the layers of the abdominal wall. They can involve separating myofascial or lipocutaneous flaps to effect a repair. Needless to say, an understanding of abdominal wall anatomy is paramount in providing a durable repair without compromising physiological function.

Parastomal hernias are a sub-class of incisional hernias. When the gastrointestinal or urinary systems are no longer able to remain in continuity (for any number of reasons), a loop of intestine is delivered through rectus abdominis to serve as a conduit for stool or urine. When this myofascial trephine expands it can permit the omentum, a loop of intestine, or the stoma loop itself to herniate into the subcutaneous tissues (**Fig. 60.25**). Parastomal hernias are exceptionally common, occurring in up to 50% of all patients with an ostomy, and are often found in association with midline incisional hernias. They represent an extraordinarily challenging clinical problem because the ostomy loop of intestine and the myofascial orifice defect must remain at the conclusion of the repair. This has implications for mesh configuration, mesh interaction with the intestine, the risk of mesh infection and the likelihood of hernia recurrence.

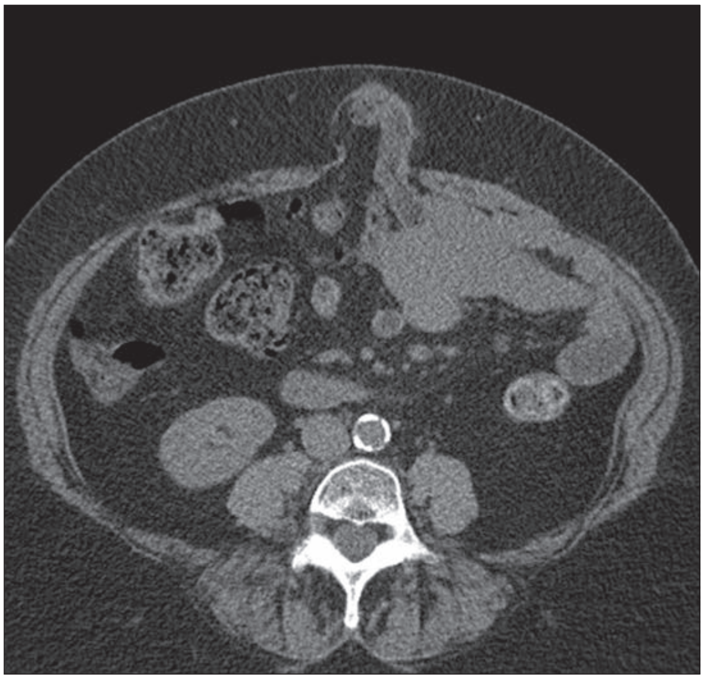

Fig. 60.20 CT of an umbilical hernia occurring in the setting of obesity. The hernia contains a non-obstructed segment of small intestine.

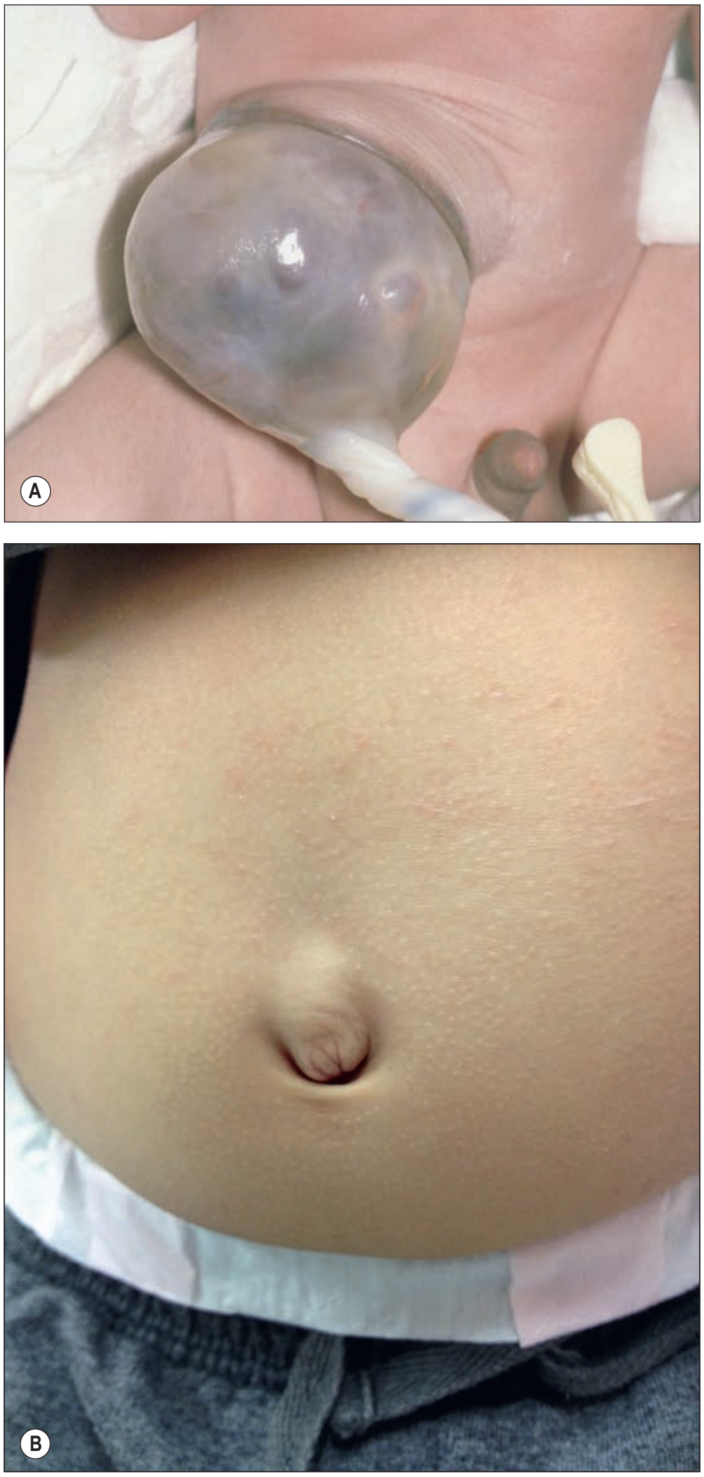

Fig. 60.21 Paediatric umbilical defects. **A**, A neonatal exomphalos. **B**, A persistent umbilical hernia in a child. (A, B, Courtesy of Professor Mark Stringer.)

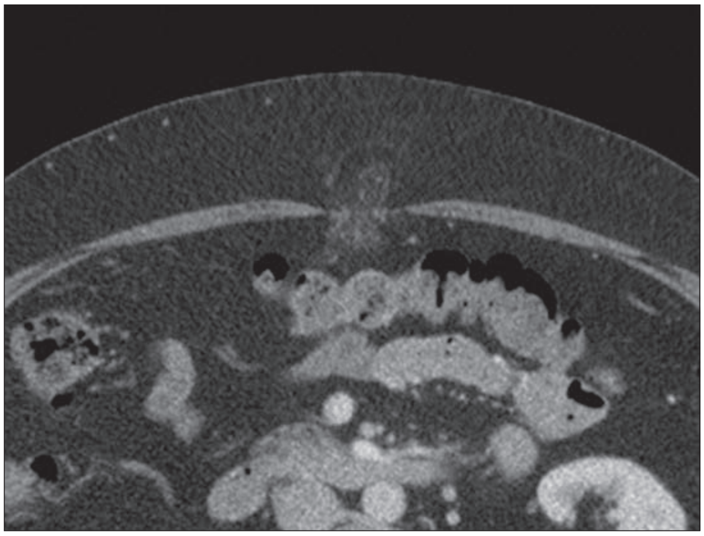

Fig. 60.22 CT of a small, symptomatic epigastric hernia containing inflamed extraperitoneal fat.

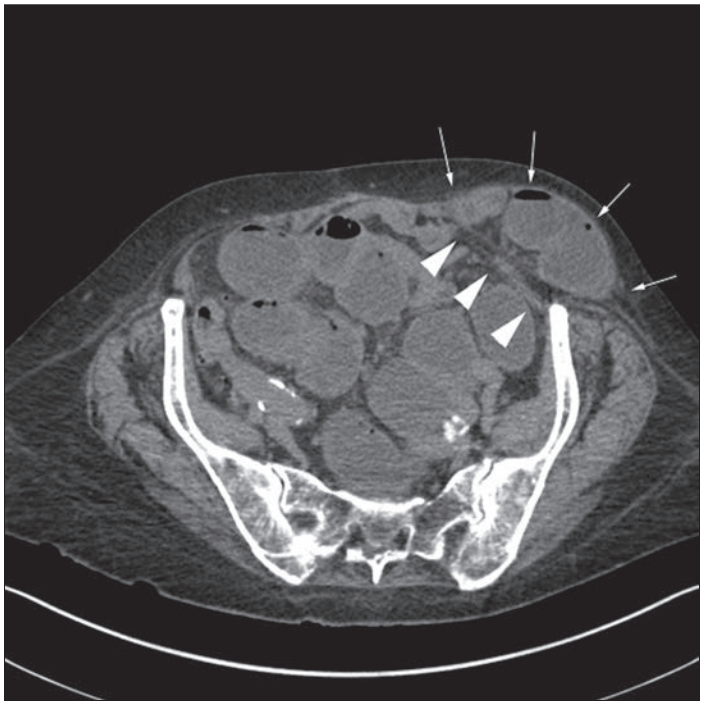

Fig. 60.23 CT of a Spigelian hernia with bowel obstruction. A part of the small intestine is present deep to the intact aponeurosis of external abdominal oblique (arrows) but has herniated superficial to internal abdominal oblique and transversus abdominis (arrowheads) through a more inferior defect.

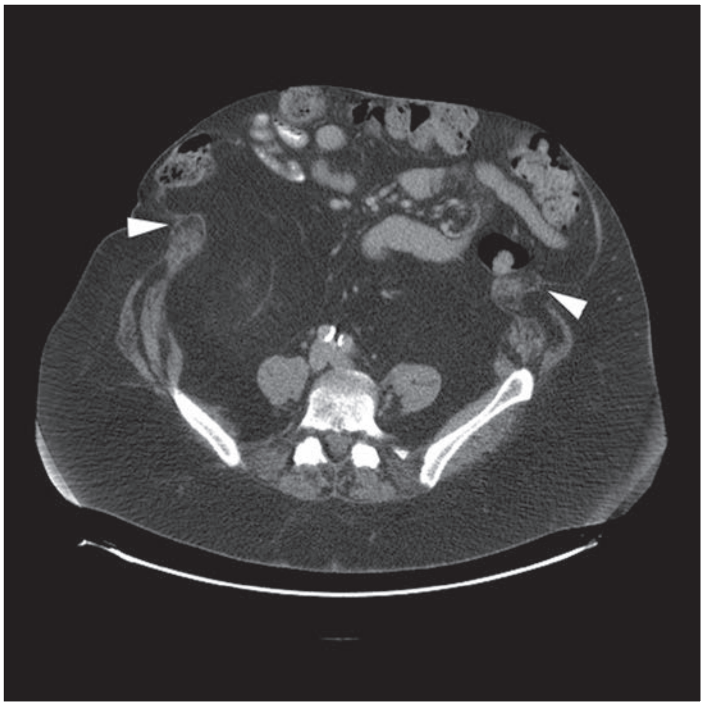

Fig. 60.24 CT of a massive incisional hernia with loss of abdominal domain. The defect between rectus abdominis (arrowheads) can be seen. Most of the small and large intestines are out of the abdominal cavity, with only retroperitoneal fat still within the confines of the abdomen.

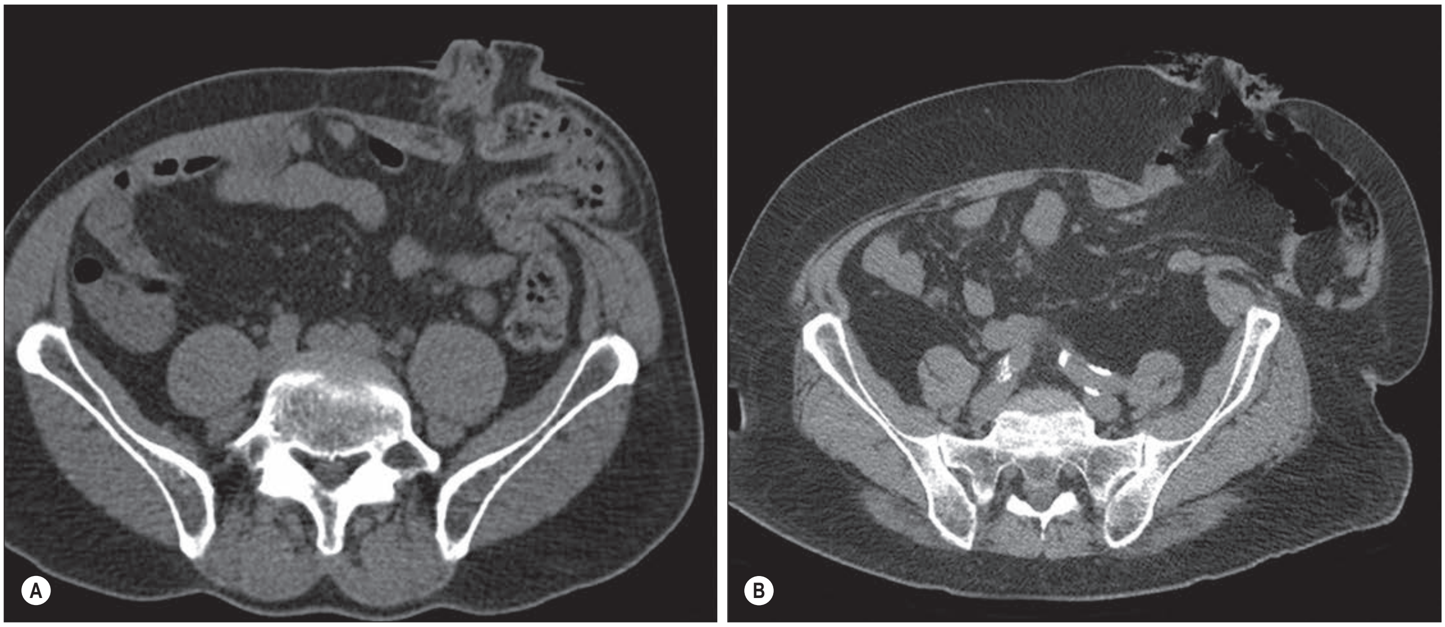

Fig. 60.25 CT of a parastomal hernia. **A**, Colostomy bowel loop herniating into the subcutaneous tissues. **B**, Ileostomy defect containing multiple loops of small intestine herniating through a defect in rectus abdominis.

Novitsky YW. 2016 Hernia Surgery Current Principles. New York: Springer.

This text summarizes the types and incidence of hernias of the abdominal wall and describes operative repairs, their outcomes and complications.

Rai R, Azih LC, Iwanaga J et al 2018 Tendinous inscriptions of the rectus abdominis: a comprehensive review. Cureus 10:1–12.

Ramirez OM, Ruas E, Dellon AL 1990 'Components separation' method for closure of abdominal wall defects: an anatomic and clinical study. Plast Reconstr Surg 86:519–26.

Closure of large abdominal wall defects usually requires the transposition of remote myocutaneous flaps or free-tissue transfers. The purpose of this study was to determine if separation of the muscle components of the abdominal wall would allow each unit to be mobilized over a greater distance than is possible by mobilization of the entire abdominal wall as a block.

Rosen MJ 2017 Atlas of Abdominal Wall Reconstruction, 2nd ed. Philadelphia: Elsevier.

A text that summarizes the relevant anatomy of the abdominal wall, relating this to techniques for abdominal wall reconstructions.

References

Acland RD 2008 The inguinal ligament and its lateral attachments: correcting an anatomical error. Clin Anat 21:55–61.

Akram J, Matzen SH 2014 Rectus abdominis diastasis. J Plast Surg Hand Surg 48:163–9.

Carlson MA, Ludwig KA, Condon RE 1995 Ventral hernia and other complications of 1,000 midline incisions. South Med J 88:450–3.

A summary of the outcomes in 1079 consecutive clean or clean-contaminated midline abdominal incisions after both elective and emergency operations done between 1984 and 1991.

Cassar K, Munro A 2002 Surgical treatment of incisional hernia. Br J Surg 89:534–45.

A review that compares the long-term recurrence rates of open primary repair with open mesh and laparoscopic repair, citing the inadequacy of open primary repair.

Chandler S, Schadewald M 1944 Studies on the inguinal region. 1. The conjoined aponeurosis versus the conjoined tendon. Anat Rec 89: 339–43.

Chopra J, Rani A, Rani A et al 2011 Re-evaluation of superficial fascia of anterior abdominal wall: a computed tomographic study. Surg Radiol Anat 33:843–9.

Dabbas N, Adams K, Pearson K et al 2011 Frequency of abdominal wall hernias: is classical teaching out of date? JRSM Short Rep 2:5.

El-Mrakby HH, Milner RH 2002 The vascular anatomy of the lower anterior abdominal wall: a microdissection study on the deep inferior epigastric vessels and the perforator branches. Plast Reconstr Surg 109:539–43; discussion 44–7.

An account of how the deep inferior epigastric artery provides the main blood supply to the distal anterior abdominal wall. Microdissection of the artery, its main branches and the perforator vessels was undertaken in 20 cadavers and the findings summarized.

Fathi AH, Soltanian H, Saber AA 2012 Surgical anatomy and morphologic variations of umbilical structures. Am Surg 78:540–4.

Faure JP, Hauet T, Scepi M et al 2001 The pectineal ligament: anatomical study and surgical applications. Surg Radiol Anat 23:237–42.

Friedman T, Coon D, Kanbour-Shakir A 2015 Defining the lymphatic system of the anterior abdominal wall: an anatomical study. Plast Reconstr Surg 135:1027–32.

A histological study that found that the lymphatic vessels of the anterior abdominal wall travel primarily in the dermis.

Gnanadev R, Iwanaga J, Oskouian RJ et al 2018 Henle's ligament: a comprehensive review of its anatomy and terminology over almost one and a half centuries. Cureus 10:1–8.

Hair A, Paterson C, O'Dwyer PJ 2001 Diagnosis of a femoral hernia in the elective setting. J R Coll Surg Edinb 46:117–18.

Hale SJ, Mirjalili SA, Stringer MD 2010 Inconsistencies in surface anatomy: the need for an evidence-based reappraisal. Clin Anat 23:922–30.

Heller L, McNichols CH, Ramirez OM 2012 Component separations. Semin Plast Surg 26:25–8.

A description of how, since its original description, the components separation technique underwent multiple modifications with the ultimate goal of decreasing the morbidity associated with the traditional procedure. The extensive subcutaneous lateral dissection had been associated with ischaemia of the midline skin edges, wound dehiscence, infection and seroma. Although the current trend is to proceed with minimally invasive component separation and to reinforce the fascia with mesh, the basic principles of the techniques, as described by Ramirez et al in 1990, have not changed over the years.

Korenkov M, Beckers A, Koebke J et al 2001 Biomechanical and morphological types of the linea alba and its possible role in the pathogenesis of midline incisional hernia. Eur J Surg 167:909–14.

Lancerotto L, Stecco C, Macchi V et al 2011 Layers of the abdominal wall: anatomical investigation of subcutaneous tissue and superficial fascia. Surg Radiol Anat 33:835–42.

Larson DW, Farley DR 2002 Spigelian hernias: repair and outcome for 81 patients. World J Surg 26:1277–81.

An account of Spigelian hernia, a rare partial abdominal wall defect. The frequent lack of physical findings, along with vague associated abdominal complaints, makes the diagnosis elusive. Patients from the Mayo Clinic were reviewed retrospectively to find all patients who had undergone surgical repair of a Spigelian hernia from 1976 to 1997.

Lee MW, McPhee RW, Stringer MD 2008 An evidence-based approach to human dermatomes. Clin Anat 21:363–73.

Loukas M, Myers C, Shah R et al 2008 Arcuate line of the rectus sheath: clinical approach. Anat Sci Int 83:140–4.

Lytle WJ 1974 The inguinal and lacunar ligaments. J Anat 118:241–51.

Lytle WJ 1979 Inguinal anatomy. J Anat 128:581–94.

Markman B, Barton FE 1987 Anatomy of the subcutaneous tissue of the trunk and lower extremity. Plast Reconstr Surg 80:248–54.

Naraynsingh V, Maharaj R, Dan D et al 2012 Strong linea alba: myth or reality? Med Hypotheses 78:291–2.

Norton-Old KJ, Schache AG, Barker PJ et al 2013 Anatomical and mechanical relationship between the proximal attachment of adductor longus and the distal rectus sheath. Clin Anat 26:522–30.

Novitsky YW, Elliott HL, Orenstein SB et al 2012 Transversus abdominis muscle release: a novel approach to posterior component separation during complex abdominal wall reconstruction. Am J Surg 204:709–16.

A description of the novel technique for posterior component separation, which was associated with low perioperative morbidity and low recurrence rate. Overall, transversus abdominis release could be an important addition to the armamentarium of surgeons undertaking major abdominal wall reconstructions.

Novitsky YW 2016 Hernia Surgery Current Principles. New York: Springer.

This text summarizes hernias of the abdominal wall and describes operative repairs, their outcomes and complications.

Pai MM, Krishnamurthy A, Prabhu LV et al 2009 Variability in the origin of the obturator artery. Clinics (São Paulo) 64:897–901.

Parnis SJ, Roberts JP, Hutson JM 1997 Anatomical landmarks of the inguinal canal in prepubescent children. Aust N Z J Surg 67:335–7.

Rai R, Azih LC, Iwanaga J et al 2018 Tendinous inscriptions of the rectus abdominis: a comprehensive review. Cureus 10:1–12.

Ralphs DN, Brain AJ, Grundy DJ et al 1980 How accurately can direct and indirect inguinal hernias be distinguished? Br Med J 280:1039–40.

Ramirez OM, Ruas E, Dellon AL 1990 'Components separation' method for closure of abdominal wall defects: an anatomic and clinical study. Plast Reconstr Surg 86:519–26.

Closure of large abdominal wall defects usually requires the transposition of remote myocutaneous flaps or free-tissue transfers. The purpose of this study was to determine if separation of the muscle components of the abdominal wall would allow each unit to be mobilized over a greater distance than is possible by mobilization of the entire abdominal wall as a block.

Rath AM, Attali P, Dumas JL et al 1996 The abdominal linea alba: an anatomo-radiologic and biomechanical study. Surg Radiol Anat 18:281–8.

Rizk NN 1980 A new description of the anterior abdominal wall in man and mammals. J Anat 131:373–85.

Rosen MJ 2017 Atlas of Abdominal Wall Reconstruction, 2nd ed. Philadelphia: Elsevier.

A text that summarizes the relevant anatomy of the abdominal wall, relating this to techniques for abdominal wall reconstructions.

Rozen WM, Ashton MW, Taylor GI 2008 Reviewing the vascular supply of the anterior abdominal wall: redefining anatomy for increasingly refined surgery. Clin Anat 21:89–98.

Rozen WM, Pan WR, Le Roux CM et al 2009 The venous anatomy of the anterior abdominal wall: an anatomical and clinical study. Plast Reconstr Surg 124:848–53.

Saga T, Takahashi N 2016 Abdominal wall muscles. In: Tubbs RS, Shoja MM, Loukas M (eds) Bergman's Comprehensive Encyclopedia of Human Anatomic Variation. Hoboken: Wiley Blackwell; Ch. 36, pp. 369–80.

Schlenz I, Burggasser G, Kuzbari R et al 1999 External oblique abdominal muscle: a new look on its blood supply and innervation. Anat Rec 255:388–95.

Schwarz GM, Hirtler L 2017 The cremasteric reflex and its muscle – a paragon of ongoing scientific discussion: a systematic review. Clin Anat 30:498–507.

Shafik A 1977 The cremasteric muscle. In: Johnson AD, Gomes WR (eds) The Testis. New York: Academic Press.

Skandalakis PN, Zoras O, Skandalakis JE et al 2006 Spigelian hernia: surgical anatomy, embryology, and technique of repair. Am Surg 72:42–8.

Stecco C, Azzena GP, Macchi V et al 2017 Rectus abdominis muscle innervation: an anatomical study with surgical implications in diep flap harvesting. Surg Radiol Anat 40:865–72.

Teoh LS, Hingston G, Al-Ali S et al 1999 The iliopubic tract: an important anatomical landmark in surgery. J Anat 194:137–41.

Tokita K 2006 Anatomical significance of the nerve to the pyramidalis muscle: a morphological study. Anat Sci Int 81:210–24.

Tourani SS, Taylor GI, Ashton MW 2013 Anatomy of the superficial lymphatics of the abdominal wall and the upper thigh and its implications in lymphatic microsurgery. J Plast Reconstr Aesthet Surg 66:1390–5.

Tromp WG, van den Heuvel B, Dwars BJ 2014 A new accurate method of physical examination for differentiation of inguinal hernia types. Surg Endosc 28:1460–4.

Tubbs RS, McDaniel JG, Burns AM et al 2009 Anatomy of the reflected ligament of the inguinal region. Rom J Morphol Embryol 50:689–91.

Whalen HR, Kidd GA, O'Dwyer PJ 2011 Femoral hernias. BMJ 343:d7668.

Wolloscheck T, Konerding MA 2009 Dimensions of the myopectineal orifice: a human cadaver study. Hernia 13:639–42.

Yang D, Morris SF, Geddes CR et al 2003 Neurovascular territories of the external and internal abdominal oblique muscles. Plast Reconstr Surg 112:1591–5.

CHAPTER

61

Posterior abdominal wall and retroperitoneum

DEFINITIONS, BOUNDARIES AND CONTENTS

The posterior abdominal wall has no agreed uniform definition. It is the posterior boundary of the abdominal cavity, and in common with the anterior and lateral abdominal walls, it is composed of several layers (skin, superficial fascia, muscle, extraperitoneal fat/fascia and parietal peritoneum). The vertebral column and paravertebral muscles are part of the posterior abdominal wall, but are usually discussed as part of the back. The posterior abdominal wall is continuous with the posterior thoracic wall at the posterior attachment of the respiratory diaphragm, with the posterior wall of the pelvis inferiorly, and with the anterolateral abdominal wall laterally.

The retroperitoneum is nestled between the posterior abdominal wall and its lining layer of posterior parietal peritoneum. Inferiorly and laterally, it is continuous with the extraperitoneal connective tissues lining the pelvis and anterolateral abdominal wall, respectively. The posterior border of the retroperitoneum is variably defined, depending on whether psoas major and quadratus lumborum are regarded as its contents or boundaries. Advances in cross-sectional imaging techniques have improved our understanding of the anatomy of the retroperitoneum but terminology is not standardized with regard to its components. Terms such as spaces, compartments, subcompartments, recesses and domains have been used to describe the whole and parts of this region.

The retroperitoneum houses parts of the gut tube in whole or in part, namely the duodenum, and the ascending and descending colons, and their vessels and nerves; and the pancreas, kidneys, ureters and suprarenal glands and their vessels and nerves. The mesentery of the small intestine, transverse and sigmoid colons and the ligaments of the liver and spleen all arise from the posterior parietal peritoneum as it covers the posterior abdominal wall. The retroperitoneum also contains the abdominal aorta and its branches; the inferior vena cava and its tributaries; the origins of the azygos and hemiazygos veins; the pre- and lateral aortic nodes, the cisterna chyli and the origin of the thoracic duct; the diaphragmatic crura; the lumbar plexus and lumbosacral trunk; and the autonomic plexuses of the abdomen.

SKIN AND SOFT TISSUES

The skin of the posterior abdominal wall is supplied by musculocutaneous branches of the lumbar arteries and veins, and is innervated by the dorsal rami of the lower thoracic and lumbar spinal nerves. The cutaneous distribution of the dorsal rami of the fourth and fifth lumbar spinal nerves is variable and controversial (Lee et al 2008).

Various fascial and connective tissues within the retroperitoneum have been defined and used to divide this region into smaller parts: the boundaries of these smaller parts are not universally agreed and clinical observations often do not support the described anatomical margins (Dodds et al 1986).

Thoracolumbar fascia

The thoracolumbar fascia is a complex arrangement of multilayered fascial planes and aponeurotic sheets that separates the paraspinal muscles from the muscles of the posterior abdominal wall (quadratus lumborum and psoas major) (Willard et al 2012) (**Figs 61.1–61.3**; see Fig. 46.6). It is most prominent at the caudal end of the lumbar spine where layers of aponeurotic tissue unite and blend to form a thickened brace between the two posterior superior iliac spines and extend caudally to reach the ischial tuberosities. The thoracolumbar fascia is described in detail in Chapter 46.

Iliopsoas fascia

Psoas fascia

The anterior surface of psoas major is covered by a relatively dense layer of fascia. Medially, this fascia is continuous with the attachments of the muscle to the transverse processes and bodies of the lumbar vertebrae. Laterally, it blends with the fascia over quadratus lumborum superiorly and is continuous with the iliac fascia inferiorly. Superiorly, it merges with the medial arcuate ligament; inferiorly, it extends into the thigh around the tendon of iliopsoas. The psoas fascia separates the anterior surface of the muscle and the lumbar plexus within it from the retroperitoneal structures lying anteriorly. An abscess within psoas major, which can arise by haematogenous seeding or by direct extension of infection from adjacent structures, e.g. the spine, kidneys or colon, often tracks along the muscle within the fascia.

Iliac fascia

The iliac fascia overlies iliacus. Superiorly and laterally it is attached to the inner aspect of the iliac crest, and medially it blends with the anterior layer of the thoracolumbar fascia over quadratus lumborum and with the psoas fascia. Inferiorly and laterally it continues into the thigh to fuse with the femoral sheath, while medially it is attached to the periosteum of the ilium and iliopubic eminence near the linea terminalis. Both the femoral nerve and lateral femoral cutaneous nerve lie under the iliac fascia in the pelvis, where they can be targeted for image-guided anaesthetic nerve blockade (Hebbard et al 2011).

Visceral fasciae

The organization of the retroperitoneum is most easily conceptualized in terms of subsections rather than delineation by fasciae (Dodds et al 1986). The fasciae bounding these parts are variable and difficult to see on cross-sectional imaging. Moreover, clinical observations of the spread of pathological fluids and air often do not match anatomically defined fascial boundaries.

The fascial layers located between the parietal peritoneum lining the posterior abdominal wall and quadratus lumborum have been described in confusing eponymous terms in the literature. Different authors have used the same eponym for different fasciae; different eponyms have been used to refer to the same fascia. For example, 'Gerota's fascia' has been used to denote the entire renal fascia or to its anterior or posterior layers (Chesbrough et al 1989). 'Toldt's fascia' has been used to denote the fusion fascia behind the ascending or descending colon (Culligan et al 2013), or the posterior layer of renal fascia, or the fusion fascia posterior to the tail of the pancreas (Kimura et al 2010). 'Zuckerkandl's fascia' has been used to refer to the posterior or anterior layers of renal fascia (Chesbrough et al 1989). 'Treitz's fascia' has been used to describe the fusion fascia behind the head of the pancreas (Kimura et al 2010). The concept of 'fusion fascia' describes a retroperitoneal fascia formed by the fusion of an embryonic mesentery with the anterior wall of the embryonic retroperitoneum (Hikspoors et al 2019). It is an avascular layer that allows a dissection plane to be developed and also limits the spread of disease. Many of these fasciae and the subsections they create are not recognized in *Terminologia Anatomica* but are well established in the clinical literature and are discussed below.

Traditional teaching of the retroperitoneum divides it into the anterior and posterior pararenal spaces and the perirenal space. The anterior pararenal space lies between the parietal peritoneum lining the posterior abdominal wall and the anterior layer of renal fascia. This oversimplification fails to explain all patterns of disease containment or spread (Dodds et al 1986). The smallest set of divisions within the retroperitoneum sufficient to explain most such phenomena is as follows. Some of the spaces are illustrated in the context of clinical disease in **Figs 61.4-61.6**.

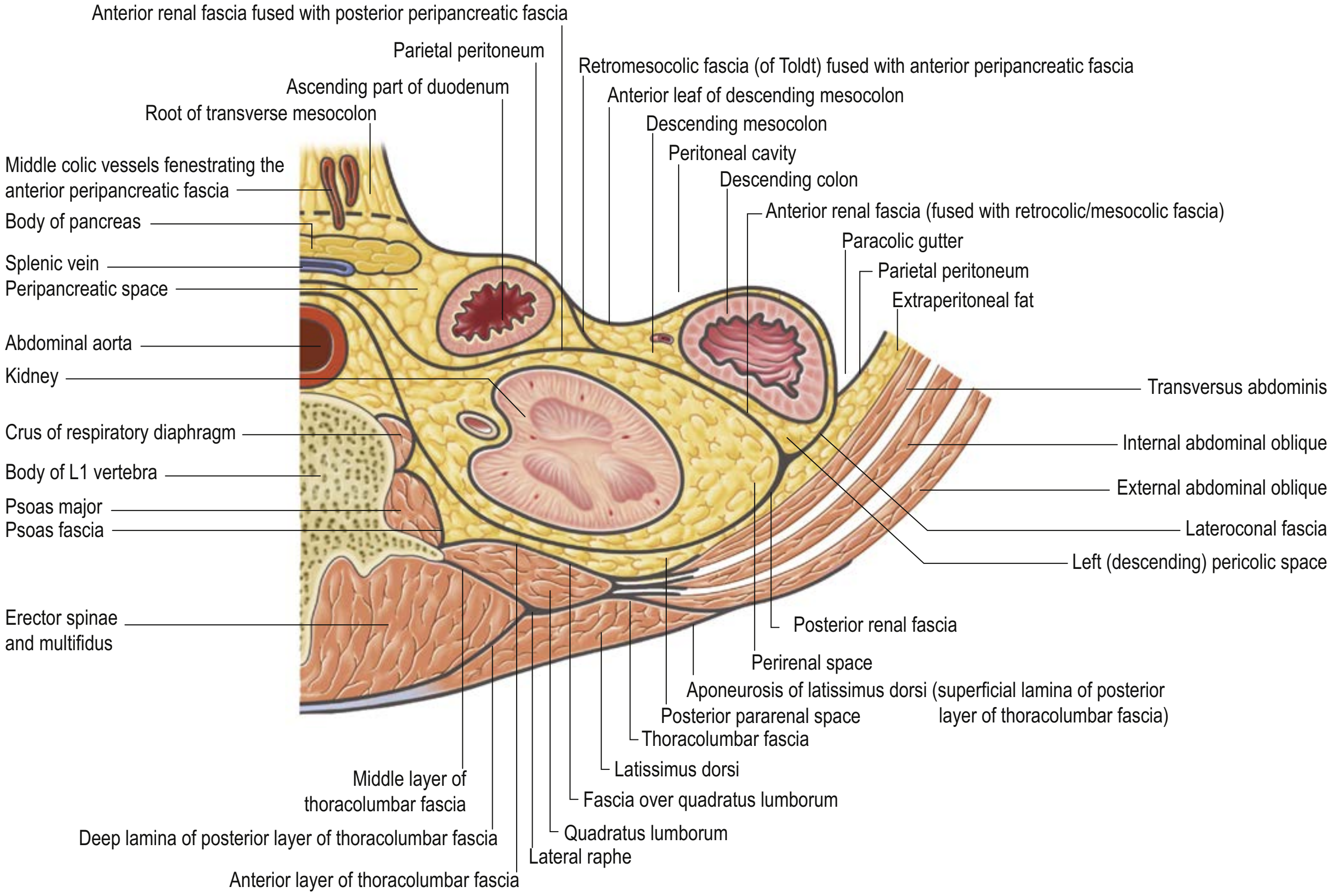
Anterior renal fascia fused with posterior peripancreatic fascia
Parietal peritoneum
Ascending part of duodenum
Root of transverse mesocolon
Retromesocolic fascia (of Toldt) fused with anterior peripancreatic fascia
Anterior leaf of descending mesocolon
Descending mesocolon
Peritoneal cavity
Descending colon
Anterior renal fascia (fused with retrocolic/mesocolic fascia)
Paracolic gutter
Parietal peritoneum
Extraperitoneal fat
Middle colic vessels fenestrating the anterior peripancreatic fascia
Body of pancreas
Splenic vein
Peripancreatic space
Abdominal aorta
Kidney
Crus of respiratory diaphragm
Body of L1 vertebra
Psoas major
Psoas fascia
Erector spinae and multifidus
Transversus abdominis
Internal abdominal oblique
External abdominal oblique
Lateroconal fascia
Left (descending) pericolic space
Posterior renal fascia
Perirenal space
Aponeurosis of latissimus dorsi (superficial lamina of posterior layer of thoracolumbar fascia)
Posterior pararenal space
Thoracolumbar fascia
Latissimus dorsi
Fascia over quadratus lumborum
Quadratus lumborum
Lateral raphe
Middle layer of thoracolumbar fascia
Deep lamina of posterior layer of thoracolumbar fascia
Anterior layer of thoracolumbar fascia

Fig. 61.1 Anatomy of the upper retroperitoneum (left side). A transverse section at approximately the level of the first lumbar vertebra, showing the location and relationships of the peripancreatic space.

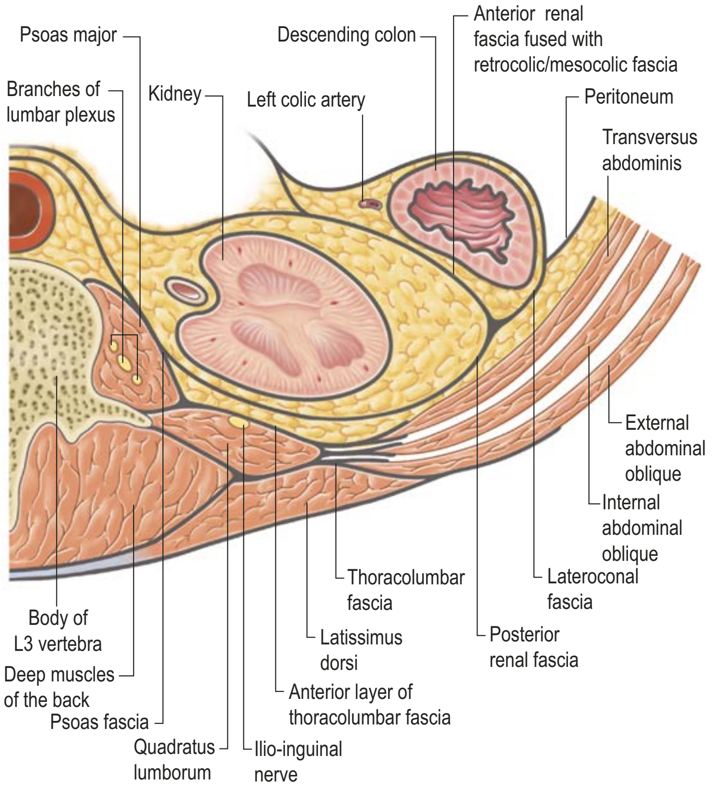
Psoas major
Branches of lumbar plexus
Kidney
Descending colon
Left colic artery
Anterior renal fascia fused with retrocolic/mesocolic fascia
Peritoneum
Transversus abdominis
External abdominal oblique
Internal abdominal oblique
Lateroconal fascia
Posterior renal fascia
Thoracolumbar fascia
Latissimus dorsi
Anterior layer of thoracolumbar fascia
Ilio-inguinal nerve
Quadratus lumborum
Psoas fascia
Deep muscles of the back
Body of L3 vertebra

Fig. 61.2 Anatomy of the mid-retroperitoneum (left side). A transverse section at approximately the level of the third lumbar vertebra, showing the location and relationships of the perirenal space.

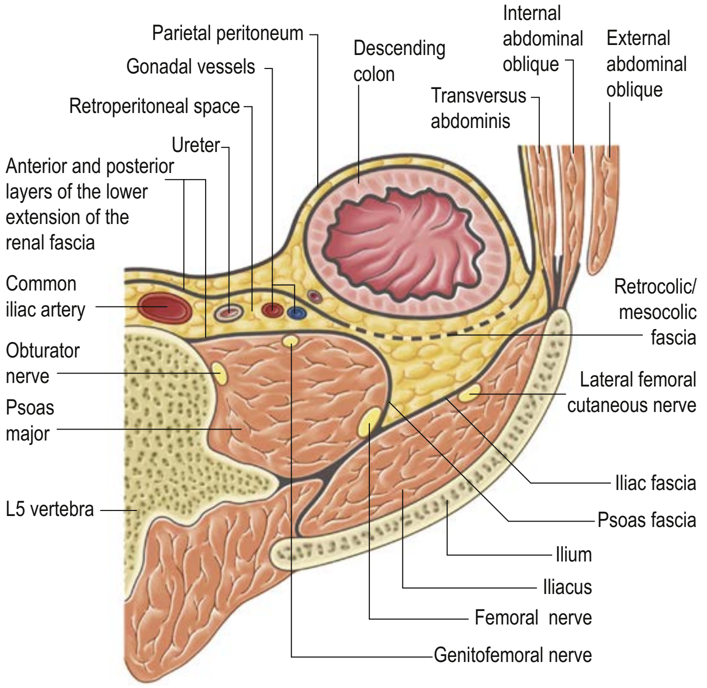
Parietal peritoneum
Gonadal vessels
Retroperitoneal space
Ureter
Anterior and posterior layers of the lower extension of the renal fascia
Descending colon
Internal abdominal oblique
Transversus abdominis
External abdominal oblique
Common iliac artery
Obturator nerve
Psoas major
L5 vertebra
Retrocolic/ mesocolic fascia
Lateral femoral cutaneous nerve
Iliac fascia
Psoas fascia
Ilium
Iliacus
Femoral nerve
Genitofemoral nerve

Fig. 61.3 Anatomy of the lower retroperitoneum (left side). A transverse section at approximately the L4 vertebral level, showing the location and relationships of the pericolic space.

Perirenal space

The paired perirenal spaces are bounded by the renal fascia, which envelops the kidney and suprarenal gland on each side. The renal fascia is traditionally described as having anterior and posterior layers which are continuous with each other laterally (see Figs 61.1–61.3 and Chapter 72). It can usually be identified on cross-sectional radiological imaging as a thin layer surrounding the kidney and suprarenal gland, separated from the fibrous capsule of the kidney by a variable amount of perirenal fat. Inferiorly, the perirenal space continues distally around the ureter but becomes progressively narrower and may or may not extend into the pelvis posterior to the posterior parietal peritoneum lining. Medially, the two perirenal spaces may interconnect anterior to the abdominal aorta and inferior vena cava (Kneeland et al 1987). The existence of a fascial partition separating the kidney and ipsilateral suprarenal gland within the envelope of renal fascia is controversial (Amin et al 1976).

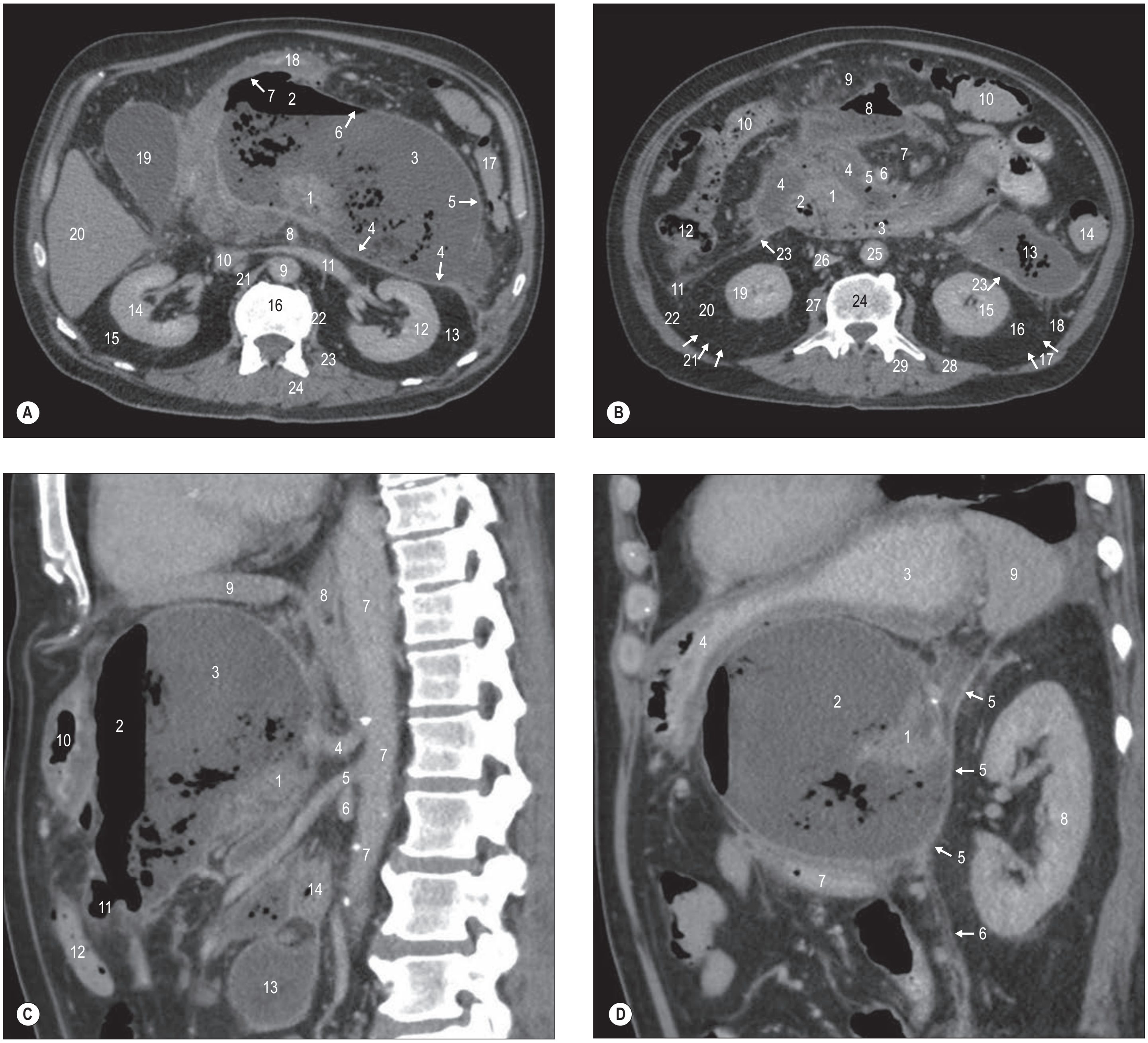

Fig. 61.4 A 58-year-old male with chronic pancreatitis and a peripancreatic pseudocyst. Oral and intravenous contrast-enhanced CT (axial and sagittal planes). The pseudocyst, containing air and fluid, has expanded the peripancreatic space. The fusion fasciae forming the boundaries of the peripancreatic space are thickened through chronic inflammation and are easily visible. **A**, A transverse section at the level of the body of the second lumbar vertebra. Key: 1, neck of pancreas; 2, air in anterior part of collection (outlining peripancreatic space); 3, fluid and debris in posterior (dependent) part of collection (outlining peripancreatic space); 4, retropancreatic fusion fascia; 5, anterior peripancreatic fascia fused to right leaf of left mesocolon; 6, anterior peripancreatic fascia deep to left mesocolon and collapsed omental bursa; 7, anterior peripancreatic fascia fused to peritoneum of omental bursa; 8, superior mesenteric artery; 9, abdominal aorta; 10, inferior vena cava; 11, left renal vein; 12, left kidney; 13, left perirenal space (not distinguishable from left posterior pararenal space); 14, right kidney; 15, right perirenal space (not distinguishable from right posterior pararenal space); 16, upper L2 vertebral body; 17, left colic flexure; 18, stomach (elevated and compressed by collection); 19, gallbladder; 20, right lobe of liver (segments 5 and 6); 21, right crus of respiratory diaphragm; 22, origin of left psoas major; 23, left quadratus lumborum; 24, left erector spinae. **B**, A transverse section at the level of the body of the fourth lumbar vertebra. Key: 1, inferior part of body and uncinate process of pancreas; 2, distal descending part of duodenum; 3, horizontal part of duodenum; 4, peripancreatic space collection (around and anterior to pancreas and duodenum); 5, superior mesenteric vein; 6, superior mesenteric artery; 7, mesentery of small intestine; 8, part of collection dissecting into transverse mesocolon; 9, transverse mesocolon (fused to greater omentum); 10, transverse colon; 11, collection dissecting behind ascending colon; 12, ascending colon; 13, collection (with air) dissecting behind descending colon; 14, descending colon; 15, left kidney; 16, left perirenal space; 17, left posterior layer of renal fascia (normal thickness, therefore faint); 18, left posterior pararenal space; 19, right kidney; 20, right perirenal space; 21, right posterior layer of renal fascia; 22, right posterior pararenal space; 23, anterior pararenal fascia (thickened through chronic inflammation); 24, superior L4 vertebral body; 25, abdominal aorta; 26, inferior vena cava; 27, right psoas major; 28, left quadratus lumborum; 29, left erector spinae. **C**, A mid-sagittal section. Key: 1, neck of pancreas; 2, air in anterior part of collection; 3, fluid in posterior part of collection; 4, coeliac trunk; 5, superior mesenteric artery; 6, left renal vein; 7, abdominal aorta; 8, diaphragmatic crura; 9, left lobe of liver; 10, antrum of stomach (collapsed); 11, part of collection dissecting into transverse mesocolon; 12, transverse colon; 13, part of collection dissecting into mesentery of small intestines; 14, horizontal part of duodenum. **D**, A left sagittal section through left hilum of the kidney. Key: 1, body of pancreas; 2, fluid collection; 3, fundus of stomach (containing oral contrast); 4, body of stomach (containing oral contrast and displaced); 5, left anterior layer of renal fascia fused with retropancreatic fascia; 6, left anterior layer of renal fascia fused with right leaf of left mesocolon (fusion fascia of Toldt); 7, ascending part of duodenum; 8, left kidney; 9, spleen.

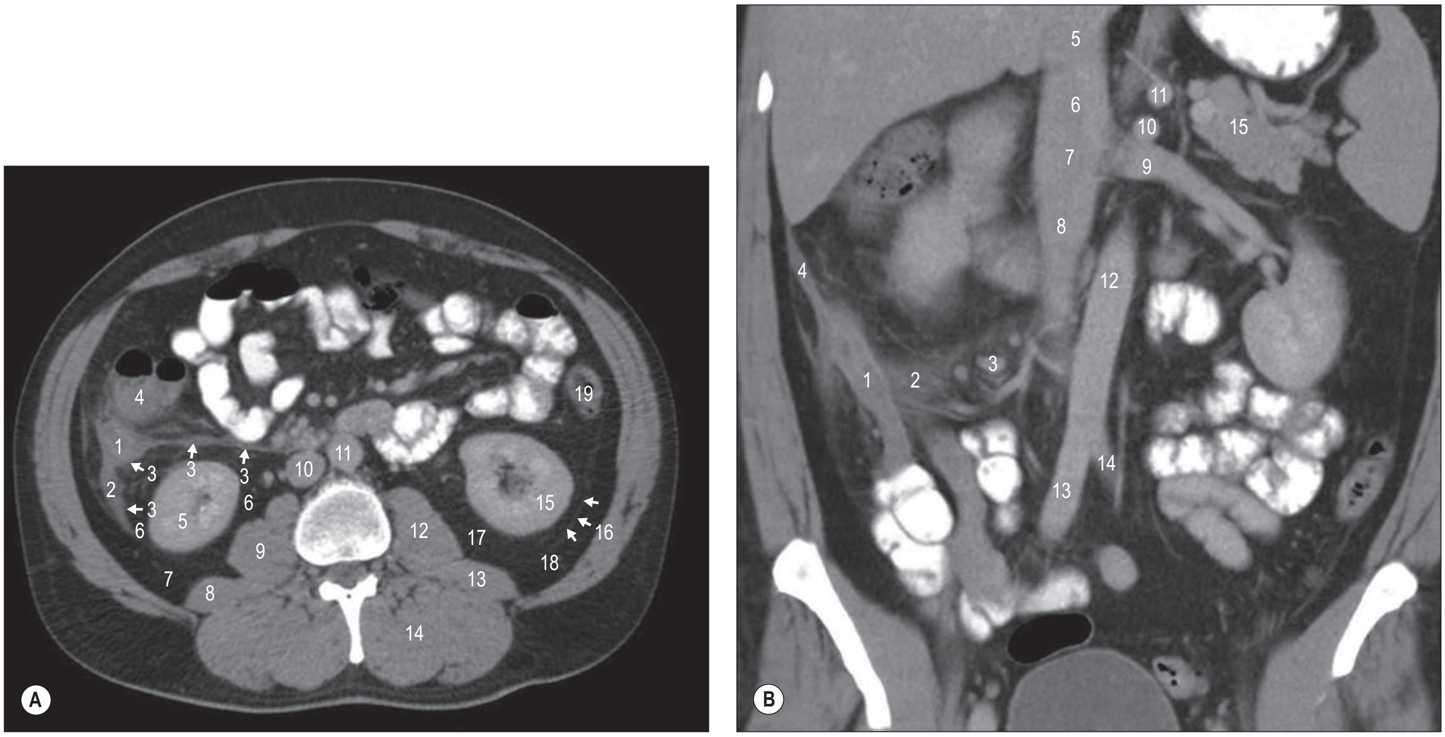

Fig. 61.5 A 43-year-old male with subacute retrocaecal appendicitis. Inflammatory fluid in the right pericolic space. The fused right anterior layer of renal fascia and right mesocolon (the fusion fascia of Toldt) are visible. **A**, A transverse section through the appendix. Key: 1, thickened and inflamed retrocaecal appendix; 2, inflammatory fluid tracking posteriorly in right pericolic space, anterior to right perirenal space; 3, anterior layer of renal fascia (fused with retrocolic/mesocolic) fascia; 4, caecum/ascending colon; 5, right kidney; 6, right perirenal space; 7, right posterior pararenal space (the posterior layer of renal fascia is difficult to identify); 8, right quadratus lumborum; 9, right psoas major; 10, inferior vena cava; 11, abdominal aorta; 12, left psoas major; 13, left quadratus lumborum; 14, left erector spinae; 15, left kidney parenchyma; 16, left posterior layer of renal fascia; 17, left perirenal space; 18, left posterior pararenal space; 19, descending colon. **B**, A coronal section through the appendix. Key: 1, thickened and inflamed retrocaecal appendix; 2, inflammatory fluid and oedema extending along right mesocolon towards root of mesentery; 3, enlarged inflamed right ileocolic node; 4, inflammatory fluid tracking in right mesocolon; 5, inferior vena cava – retrohepatic segment; 6, inferior vena cava – infrahepatic segment; 7, inferior vena cava – renal segment; 8, inferior vena cava – infrarenal segment; 9, left renal vein; 10, superior mesenteric artery; 11, coeliac trunk; 12, abdominal aorta; 13, right common iliac artery; 14, left common iliac artery; 15, tail of pancreas.

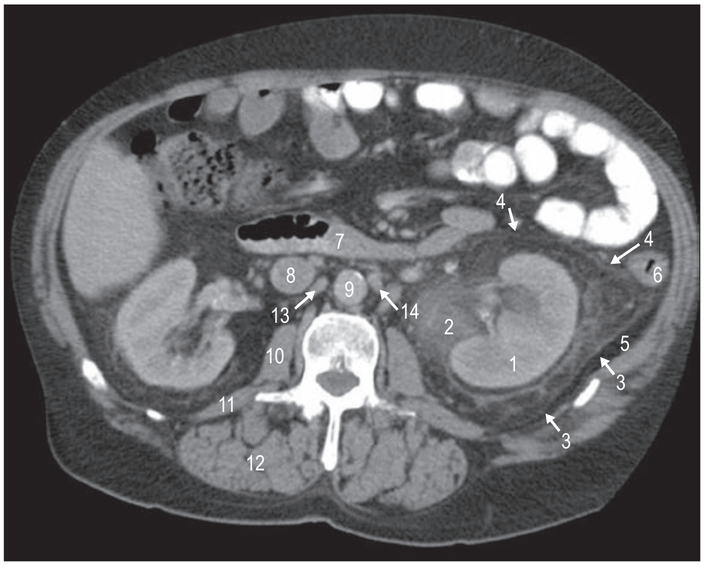

Fig. 61.6 A 61-year-old male with mid-ureteric calculus causing high-grade obstruction of the left ureter and extravasation of urine from the left renal hilum. Oral and intravenous contrast-enhanced CT. A transverse section through the left renal hilum (the calculus is inferior to the plane of this section). Key: 1, left kidney; 2, extravasated urine in left perirenal space; 3, posterior layer of renal fascia; 4, anterior layer of renal fascia; 5, left posterior pararenal space; 6, descending colon; 7, horizontal part of duodenum; 8, inferior vena cava; 9, abdominal aorta; 10, right psoas major; 11, right quadratus lumborum; 12, right erector spinae; 13, lumbar node (borderline enlarged); 14, left lateral aortic nodes (borderline enlarged).

Anterior and posterior pararenal spaces

The anterior pararenal space (an oversimplification) refers to the region between the anterior layer of renal fascia and the parietal peritoneum lining the posterior abdominal wall. On the right, it contains the descending (second) part of the duodenum and the ascending colon, and on the left, the ascending (fourth) part of the duodenum and the descending colon.

The posterior pararenal space lies between the posterior layer of renal fascia anteriorly and the thoracolumbar and psoas fasciae posteriorly. It contains a variable amount of fat. Laterally it is continuous with the extraperitoneal fat of the anterolateral abdominal wall, and inferiorly with the retroperitoneal fat overlying iliacus and the pelvic wall, and the fat around the urinary bladder (Coffin et al 2015).

When the ascending or descending colon is retrorenal (an anatomical variant), these structures and pericolic space lie in a groove between the posterior layer of renal fascia and the posterior pararenal space.

Peripancreatic space

The peripancreatic space contains the duodenum and pancreas, the origins of the superior mesenteric vessels and the retroperitoneal segments of the bile duct, hepatic portal vein and hepatic artery. The posterior boundary is a fusion fascia formed by fusion of the embryonic duodenal mesentery to the anterior wall of the embryonic retroperitoneum (Dodds et al 1986). This fascia is termed the 'retropancreatic' or 'retropancreaticoduodenal' fascia in the imaging literature, and 'fusion fascia of Treitz' in the surgical literature (Kimura et al 2010). It forms a relatively avascular dissection plane that is used to mobilize the duodenum and head of the pancreas.

The lateral extent of the peripancreatic space is variable; it lies posterior to the ascending and descending colons and anterior to the perirenal space (see Fig. 61.1). At the tail of the pancreas, the peripancreatic space lies in continuity with the splenorenal ligament. Anteriorly, it is in continuity with the transverse mesocolon and mesentery of the small intestine. Consequently, peripancreatic fluid collections can extend into both mesenteries and extend posterior to the ascending and descending colons but do not usually cross into the perirenal and pericolic spaces.

Pericolic spaces

The ascending and descending pericolic spaces are the narrow regions surrounding the respective parts of the colon and are continuous medially with the mesocolon (see Figs 61.1–61.3). The pericolic spaces contain a variable amount of fat and are limited anteriorly, superiorly and laterally by the serosa of the colon. Inferiorly, they are continuous with the retroperitoneum of the iliac fossae. Posteriorly, each pericolic space is limited by a fusion fascia formed by the right leaf of the embryonic mesocolon fusing to the left leaf of the embryonic duodenal mesentery and anterior wall of the embryonic retroperitoneum further laterally (Dodds et al 1986). This retrocolic fascia (of Toldt) (Culligan et al 2013, Culligan et al 2014) forms the classic avascular plane of dissection when a hemicolectomy is performed. Its plane is entered by incising the junction of the serosa of the colon with the parietal peritoneum at the white line (of Toldt) in the paracolic gutter. Radiologically, the retrocolic fascia may be indistinguishable from the anterior layer of renal fascia when lateral to the duodenum and pancreas. Variation in colonic retroperitonealization can produce a free mesocolic pedicle (most commonly seen at the caecum).

Lateroconal fascia

The lateroconal fascia was originally defined as the fascial layer extending from the junction of the anterior and posterior layers of renal fascia to the parietal peritoneum in the paracolic gutter (Congdon and Edson 1941). It is better understood as the lateral extension of the retrocolic fusion fascia that blends with the parietal peritoneum (see Figs 61.1–61.3).

BONES

The posterior abdominal wall is supported by the vertebral column and pelvic girdle. The individual bones are the last two ribs, the twelfth thoracic and five lumbar vertebrae, and the sacrum and ilium, together with their interconnecting ligaments.

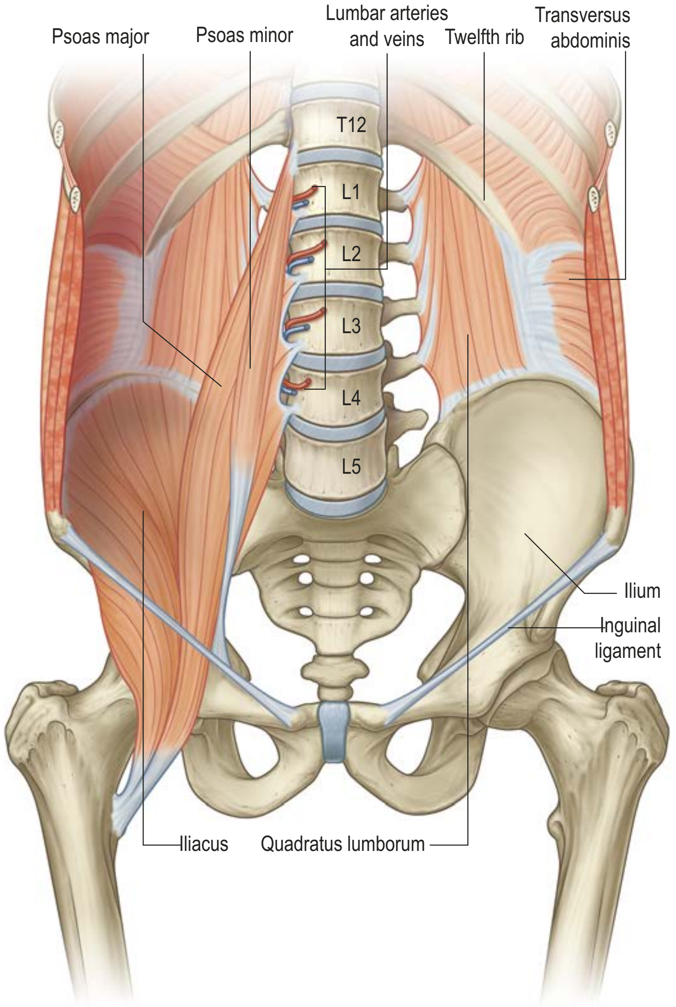

Fig. 61.7 Bones and muscles of the posterior abdominal wall. Left psoas major and the diaphragm have been removed. (Adapted from Drake RL, Vogl AW, Mitchell A (eds) Gray's Anatomy for Students, 2nd ed. Elsevier, Churchill Livingstone. Copyright 2010.)

MUSCLES

Most of the muscles of the posterior abdominal wall are functionally part of the pelvic girdle/lower limb or vertebral column. They provide the surface against which the neurovascular and visceral structures of the retroperitoneum lie (**Fig. 61.7**; see Fig. 61.15).

Quadratus lumborum

Quadratus lumborum is an irregularly shaped rectangular muscle, broader at its inferior attachment than superiorly.

Attachments The inferior attachment is by aponeurotic fibres to the iliac crest over an area 5–7 cm lateral to the distal end of the transverse process of the fourth lumbar vertebra and/or the iliolumbar ligament. Fascicles pass from the iliac crest to be attached superiorly to either the anteroinferior surface of the twelfth rib (iliocostal), or the distal ends of the transverse processes of the upper four lumbar vertebrae (iliolumbar), or the lateral surface of the twelfth thoracic vertebra (iliothoracic). Some fascicles may pass from the lumbar transverse processes to the twelfth rib (lumbocostal). Fascicles vary in number and size but typically are arranged in three layers. The anterior layer consists primarily of iliocostal and iliothoracic fascicles, the middle layer consists primarily of lumbocostal fascicles, and the posterior layer consists primarily of iliocostal fascicles laterally and iliolumbar fascicles medially (Phillips et al 2008).

Relations Anteriorly are the colon (ascending on the right, descending on the left), kidney, psoas major and minor (when present), and diaphragm. The subcostal, iliohypogastric and ilio-inguinal nerves lie on the fascia anterior to the muscle, bound down to it by the medial continuation of the transversalis fascia.

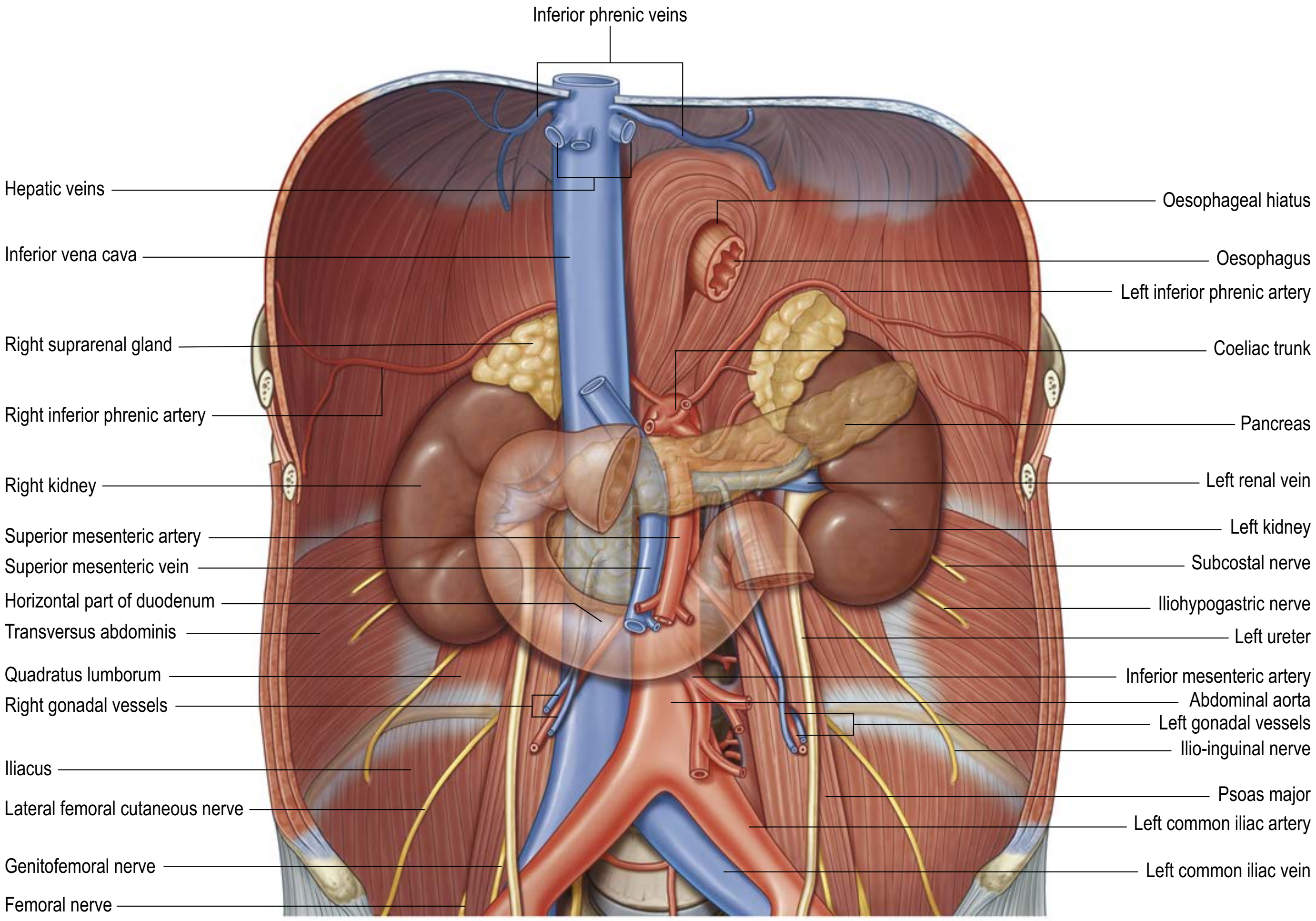
Inferior phrenic veins
Hepatic veins
Inferior vena cava
Right suprarenal gland
Right inferior phrenic artery
Right kidney
Superior mesenteric artery
Superior mesenteric vein
Horizontal part of duodenum
Transversus abdominis
Quadratus lumborum
Right gonadal vessels
Iliacus
Lateral femoral cutaneous nerve
Genitofemoral nerve
Femoral nerve
Oesophageal hiatus
Oesophagus
Left inferior phrenic artery
Coeliac trunk
Pancreas
Left renal vein
Left kidney
Subcostal nerve
Iliohypogastric nerve
Left ureter
Inferior mesenteric artery
Abdominal aorta
Left gonadal vessels
Ilio-inguinal nerve
Psoas major
Left common iliac artery
Left common iliac vein

Fig. 61.8 The abdominal aorta and inferior vena cava and their branches. The fasciae, lymphatics and connective tissues have been removed for clarity.

Vascular supply Quadratus lumborum is supplied by branches of the lumbar arteries, the arteriae lumbales imae from the median sacral artery, the lumbar branch of the iliolumbar artery, and branches of the subcostal artery.

Innervation Quadratus lumborum is innervated by the ventral rami of the twelfth thoracic and upper three or four lumbar spinal nerves.

Actions The iliocostal fascicles of quadratus lumborum fix the twelfth rib, helping to stabilize the lower attachments of the respiratory diaphragm during inspiration. The actions of the iliolumbar fascicles are less clear: their contribution to lateral flexion or extension are reported to be weak (Phillips et al 2008, Park et al 2012). Quadratus lumborum is reported to undergo considerable hypertrophy in some sporting activities (Ranson et al 2008).

Psoas major, psoas minor and iliacus

Psoas major and iliacus are functionally important in the lower limb and are described together with psoas minor in Chapter 77.

Posterior abdominal wall hernias

In the absence of a previous surgical incision, visceral herniation through the posterior abdominal wall is rare because the muscular and fascial layers usually protect against protrusion. However, the posterior free border of external abdominal oblique, the inferior free border of latissimus dorsi and the iliac crest delimit the inferior lumbar triangle (of Petit), an area of potential weakness through which a lumbar hernia may develop (see Fig 60.13) (Stamatiou et al 2009).

VASCULAR SUPPLY AND LYMPHATIC DRAINAGE

Abdominal aorta

The abdominal aorta begins at the aortic hiatus of the respiratory diaphragm anterior to the twelfth thoracic vertebra. It descends anterior to the lumbar vertebrae and bifurcates into two common iliac arteries anterior to the fourth lumbar vertebra or the intervertebral disc between the fourth and fifth lumbar vertebrae, slightly to the left of the midline (Mirjalili et al 2012a, 2012b, Moussallem et al 2012) (**Figs 61.8–61.11**). The angle of bifurcation is very variable (Moussallem et al 2012). The mean adult diameter of the aorta inferior to the origin of the renal arteries measured by computed tomography is 19–21 mm (males) and 16–18 mm (females) (Rogers et al 2013), but there are ethnic variations (Jasper et al 2014). Measured by ultrasound, equivalent values are 20±2.5 mm (males) and 17±1.5 mm (females) (Needleman 2006). The mean calibre of the abdominal aorta decreases slightly from proximal to distal. With advancing age, there is a progressive increase in abdominal aortic diameter in both sexes and the tapering becomes more pronounced (Fleischmann et al 2001). In the elderly, the abdominal aorta frequently becomes ectatic and tortuous, changing the angle and position of the bifurcation and rotating the origins of the major branches.

Relations

The proximal abdominal aorta is directly related anteriorly to the coeliac trunk and its branches, autonomic nerve plexuses and lymphatics. Inferior to the coeliac trunk, the superior mesenteric artery leaves the aorta and descends anterior to the left renal vein. The body of the pancreas is anterior to these vessels; the splenic vein is on its posterior surface and extends obliquely up and to the left. Further anteriorly, the omental bursa separates the proximal abdominal aorta from the lesser omentum, stomach and left lobe of the liver. Inferior to the pancreas, the horizontal part of the duodenum crosses the aorta anteriorly.

The twelfth thoracic vertebra, the upper four lumbar vertebrae, intervening intervertebral discs and the anterior longitudinal ligament lie posterior to the abdominal aorta. Lumbar arteries arise from its posterior aspect, and the third and fourth (and sometimes the second) left lumbar veins cross posterior to it to reach the inferior vena cava. The abdominal aorta can overlap the medial border of psoas major on the left.

On the right, the abdominal aorta is related superiorly to the cisterna chyli and thoracic duct, the azygos vein and the right crus of the respiratory diaphragm, which overlaps and separates it from the inferior vena cava and right coeliac ganglion. Below the second lumbar vertebra it is

Approximately 80% of abdominal aortic aneurysms occur in the aorta inferior to the origin of the renal arteries. Males with atherosclerosis are most at risk of developing the condition, particularly from the sixth decade onwards (Takayama and Yamanouchi 2013). The high mortality risk from spontaneous rupture has prompted the development of ultrasound screening programmes to detect aneurysms and repair them electively. Overall, surgery is performed in patients with an aneurysm greater than 5.0 cm (females) and 5.5 cm (males) in diameter (Groeneveld et al 2018). Repair is most commonly performed by open surgery or endovascular stenting (endovascular aneurysm repair).

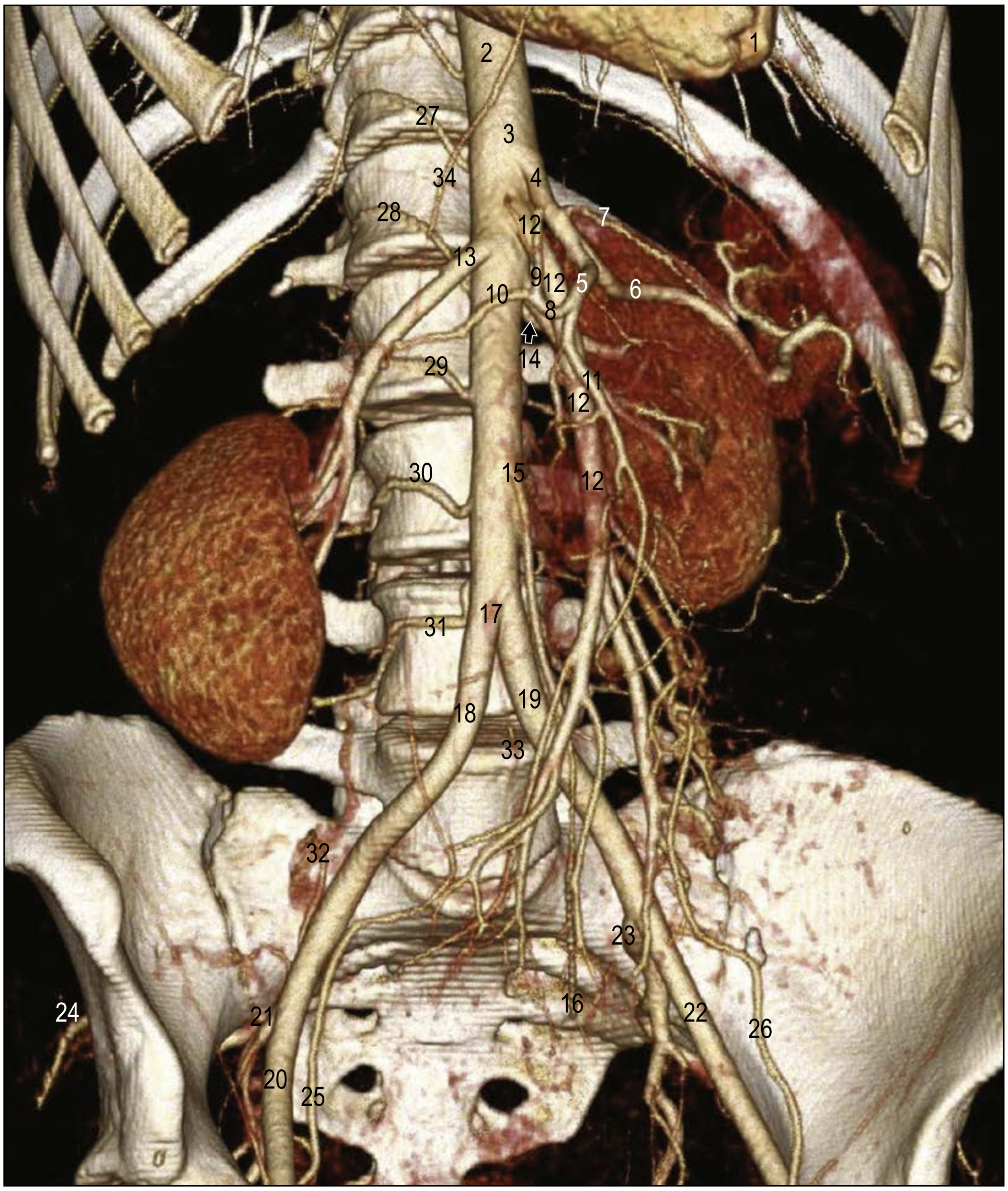

Fig. 61.10 The abdominal aorta and its branches. A 36-year-old female investigated by CT aortogram for possible Marfan's aortic dissection; only the normal abdominal aorta part of the dataset is shown in this three-dimensional reconstruction. Surface shaded display. Key: 1, apex of left ventricle; 2, distal thoracic aorta; 3, approximate position of aortic hiatus; 4, coeliac trunk; 5, common hepatic artery; 6, splenic artery; 7, left gastric artery; 8, proper hepatic artery; 9, left hepatic artery; 10, right hepatic artery; 11, gastroduodenal artery; 12, superior mesenteric artery; 13, right renal artery; 14, left renal artery partly obscured by proper hepatic artery lying more superficial (with arrow); 15, inferior mesenteric artery; 16, superior rectal artery; 17, aortic bifurcation anterior to the fourth lumbar vertebra; 18, right common iliac artery; 19, left common iliac artery; 20, right external iliac artery; 21, right internal iliac artery; 22, left external iliac artery; 23, left internal iliac artery; 24, right superior gluteal artery; 25, right inferior epigastric artery; 26, left inferior epigastric artery; 27, right subcostal artery; 28, right first lumbar artery; 29, right second lumbar artery; 30, right third lumbar artery; 31, right fourth lumbar artery; 32, right iliolumbar artery; 33, median sacral artery; 34, right superior epigastric artery (continuing from right internal thoracic artery). Note the low-lying right kidney.

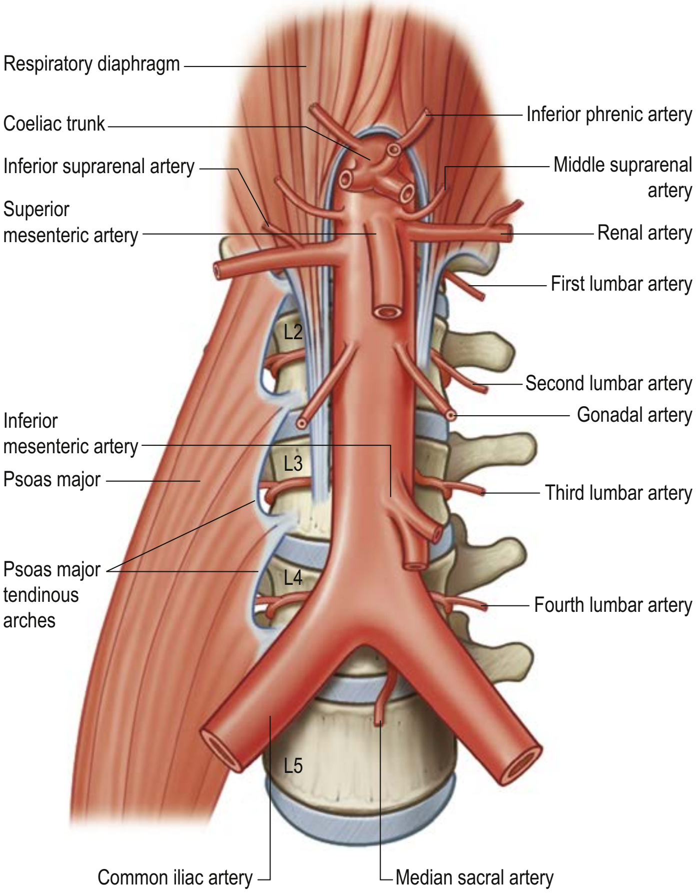

Fig. 61.9 The branches of the abdominal aorta.

closely applied to the left side of the inferior vena cava. This close relationship allows a fistula to develop between the aorta and adjacent inferior vena cava, a rare complication of aneurysmal disease or trauma. On the left, the aorta is related superiorly to the left crus of the respiratory diaphragm and left coeliac ganglion. Level with the second lumbar vertebra, it is related to the ascending part of the duodenum, the left sympathetic trunk and the inferior mesenteric vein.

Branches

The branches of the abdominal aorta are described as anterior, lateral and dorsal (see Fig. 61.9). The anterior (unpaired) and lateral (paired) branches are distributed to the viscera, while the dorsal branches supply the body wall, vertebral column and the vertebral canal and its contents. The aorta terminates by dividing into the right and left common iliac arteries.

Anterior group

Coeliac trunk

The coeliac trunk is the first anterior branch and arises just inferior to the aortic hiatus, usually at the level of the vertebral body of the twelfth thoracic vertebra. It is 1–3 cm long and passes almost horizontally anteriorly and slightly to the right superior to the body of the pancreas and splenic vein. In most individuals it trifurcates into the left gastric, common hepatic and splenic arteries. Variations occur and include a separate origin of the left gastric artery from the abdominal aorta, one or both inferior phrenic arteries arising from the coeliac trunk, and the superior mesenteric artery or one or more of its branches arising in common with the coeliac trunk (Panagouli et al 2013). Anterior to the coeliac trunk lies the omental bursa. The coeliac plexus surrounds the coeliac trunk, sending extensions along its branches. On the right lie the right coeliac ganglion, right crus of the respiratory diaphragm and the caudate lobe of the liver. To the left lie the left coeliac ganglion, left crus of the respiratory diaphragm and the cardia of the stomach. Rarely, the coeliac trunk can be compressed by the median arcuate ligament (Dunbar syndrome), resulting in visceral ischaemia and abdominal pain (Ho et al 2017).

Superior mesenteric artery

The superior mesenteric artery originates from the aorta approximately 1–2 cm below the coeliac trunk, at the level of the body of the first lumbar vertebra (Mirjalili et al 2012b) (Chs 64, 65). It lies posterior to the body of the pancreas and splenic vein and is separated from the aorta by the left renal vein. It passes anteriorly and inferiorly, anterior to the uncinate process of the pancreas and the horizontal (third) part of the duodenum, to enter the root of the mesentery of the small intestines and supply derivatives of the midgut. Numerous anatomical variants have been described (Tubbs et al 2016), the most common being an accessory or replaced right hepatic artery arising near the origin of the superior mesenteric artery. Present in about 15% of individuals, the accessory or replaced right hepatic artery courses posterior to the hepatic portal vein and ascends posterolateral to the bile duct (Winston et al 2007).

Inferior mesenteric artery

The inferior mesenteric artery is smaller than the superior mesenteric artery. It arises from the anterior or left anterolateral aspect of the abdominal aorta at about the level of the body of the third lumbar vertebra, 3-4 cm proximal to the aortic bifurcation and posterior to the inferior border of the horizontal part of the duodenum (Ch. 65).

Lateral group

Suprarenal artery

The right and left middle suprarenal arteries arise from each side of the abdominal aorta, level with the superior mesenteric artery. Each passes laterally over the crus of the respiratory diaphragm to the suprarenal gland, where it anastomoses with the suprarenal branches of the ipsilateral inferior phrenic and renal arteries (Toni et al 1988) (Ch. 70). The right middle suprarenal artery passes posterior to the inferior vena cava near the right coeliac ganglion. The left middle suprarenal artery passes close to the left coeliac ganglion, splenic artery and the superior border of the pancreas.

Renal artery

The renal arteries are two of the largest branches of the abdominal aorta and arise laterally just inferior to the origin of the superior mesenteric artery at about the level of the body of the first lumbar vertebra (Mirjalili et al 2012b) (Ch. 72). When the arteries arise at different cranio-caudal levels, the right ostium is usually superior to the left. The right renal artery is longer and passes posterior to the inferior vena cava, right renal vein, head of the pancreas and descending part of the duodenum. The left renal artery passes behind the left renal vein, the body of the pancreas and the splenic vein. Variations in the number, origin, course and branching patterns of the renal arteries are common.

Gonadal artery

The gonadal arteries (ovarian or testicular) are two long, slender vessels that arise from the aorta a little inferior to the renal arteries. Each passes inferolaterally deep to the posterior parietal peritoneum covering psoas major to supply the ipsilateral gonad (Chs 74, 75). One or both gonadal arteries can arise from a renal artery or be double.

Dorsal group

Inferior phrenic arteries

The inferior phrenic arteries usually arise either from the aorta, just superior to the level of the coeliac trunk, or directly from the coeliac trunk; occasionally, they originate from the renal artery (Loukas et al 2005a, Gwon et al 2007). They contribute to the arterial supply of the respiratory diaphragm. Each artery ascends laterally, anterior to the crus of the respiratory diaphragm, near the medial border of the ipsilateral suprarenal gland and then divides into an ascending and a descending branch. The left ascending branch passes behind the oesophagus and runs anteriorly on the left side of the oesophageal hiatus, where it bifurcates; one branch curves anteriorly to anastomose with its counterpart anterior to the central tendon of the respiratory diaphragm and the other approaches the thoracic wall to anastomose with the musculophrenic and pericardiacophrenic arteries. The right ascending branch passes posterior to the inferior vena cava and then bifurcates; one branch runs anteriorly on the right side of the caval foramen before anastomosing with its counterpart anterior to the central tendon of the respiratory diaphragm, and the other passes laterally on the inferior surface of the respiratory diaphragm. The descending branches on each side supply the respiratory diaphragm and anastomose with the lower posterior intercostal and musculophrenic arteries. Each inferior phrenic artery gives off two or three small superior suprarenal arteries. The abdominal part of the oesophagus, fibrous capsule of the liver and the superior border of the spleen may also receive small arterial twigs from this vessel.

The inferior phrenic artery may be a source of significant collateral blood flow to large hepatocellular cancers and is sometimes specifically

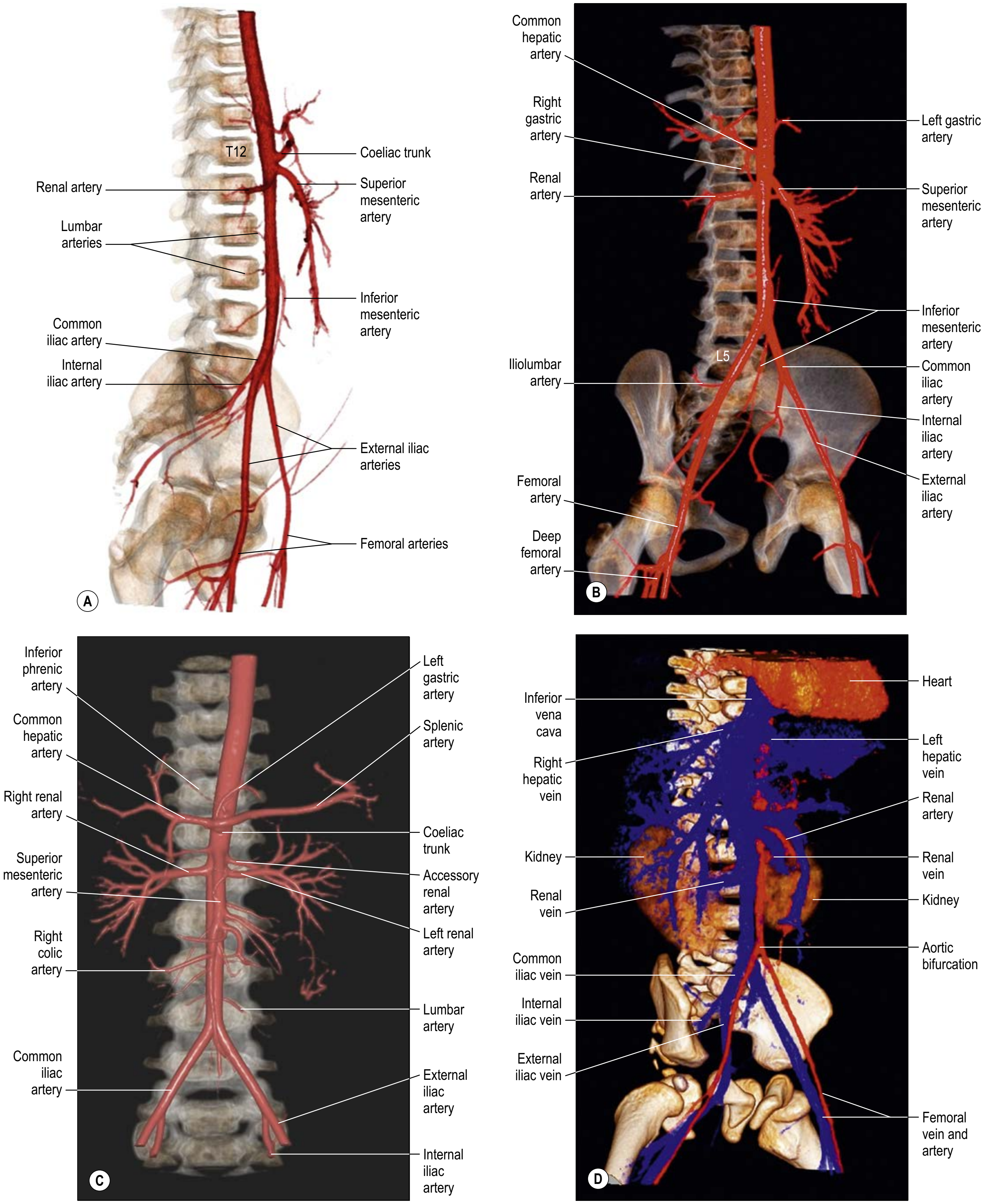
T12
Renal artery
Lumbar arteries
Common iliac artery
Internal iliac artery
Coeliac trunk
Superior mesenteric artery
Inferior mesenteric artery
External iliac arteries
Femoral arteries
A
Common hepatic artery
Right gastric artery
Renal artery
Iliolumbar artery
Femoral artery
Deep femoral artery
L5
Left gastric artery
Superior mesenteric artery
Inferior mesenteric artery
Common iliac artery
Internal iliac artery
External iliac artery
B
Inferior phrenic artery
Common hepatic artery
Right renal artery
Superior mesenteric artery
Right colic artery
Common iliac artery
Left gastric artery
Splenic artery
Coeliac trunk
Accessory renal artery
Left renal artery
Lumbar artery
External iliac artery
Internal iliac artery
C
Inferior vena cava
Right hepatic vein
Kidney
Renal vein
Common iliac vein
Internal iliac vein
External iliac vein
Heart
Left hepatic vein
Renal artery
Renal vein
Kidney
Aortic bifurcation
Femoral vein and artery
D

Fig. 61.11 Volume-rendered abdominal angiograms from paediatric patients. **A,** Oblique/lateral view demonstrating major branches of the aorta. T12, body of twelfth thoracic vertebra. **B,** Anterolateral view of patient seen in **A,** better illustrating the renal artery and branches of the coeliac trunk. **C,** An accessory renal artery. **A,** The aorta and inferior vena cava and its branches, anterolateral view. (Courtesy of Jon C Betts Jr, Children's of Alabama, Birmingham, AL, USA.)

Continued

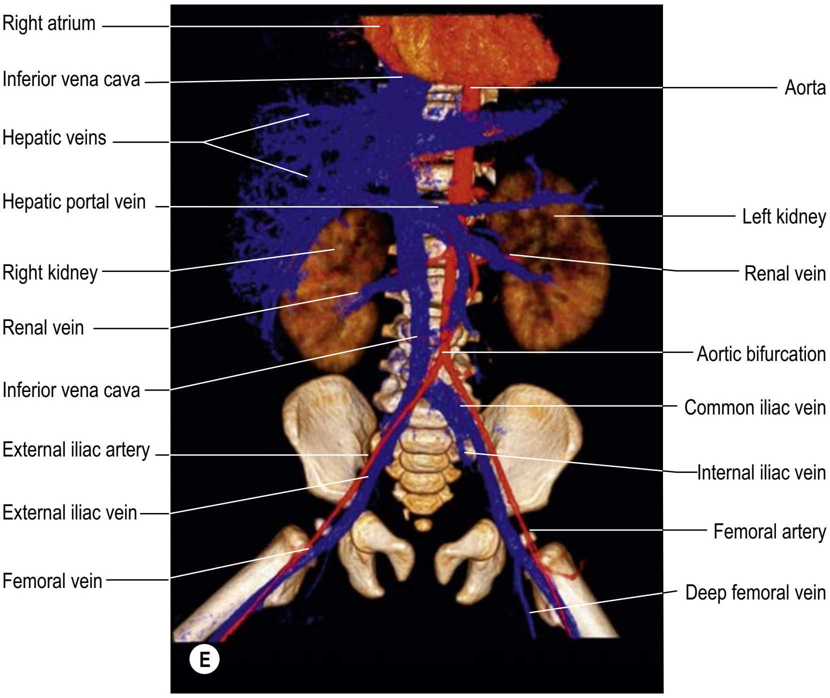

Fig. 61.11 cont'd E, Anterior view of patient seen in **D**. The hepatic portal vein is truncated at its origin at the confluence of the superior mesenteric and splenic veins (unlabelled). Note the unfused segments of the sacrum and juvenile forms of the hip and parts of the pelvic girdle. (Courtesy of Jon C Betts Jr, Children's of Alabama, Birmingham, AL, USA.)

occluded, along with the relevant hepatic artery, when such tumours are treated by arterial embolization.

Lumbar arteries

There are usually four lumbar arteries on each side, in series with the posterior intercostal arteries. They arise from the posterolateral aspect of the abdominal aorta, opposite the lumbar vertebrae. A fifth, smaller, pair occasionally arises from the median sacral artery, but lumbar branches of the iliolumbar arteries often take their place. The lumbar arteries run posterolaterally on the first to the fourth lumbar vertebral bodies, passing behind the sympathetic trunk and tendinous arches formed by the attachments of psoas major to the vertebral bodies. The right lumbar arteries pass posterior to the inferior vena cava. The superior two right lumbar arteries and the first left lumbar artery lie behind the corresponding crus of the respiratory diaphragm. Just beyond the intervertebral foramina, each lumbar artery divides into a medial branch, which gives off spinal and ganglionic branches; a middle branch, from which dorsal and anastomotic branches arise; and a lateral branch, which supplies the abdominal wall (Arslan et al 2011). Of particular importance is the spinal branch known as the great radicular artery (artery of Adamkiewicz), which frequently originates from an upper lumbar artery, particularly on the left side (Biglioli et al 2004) (Ch. 47). Injury to this vessel, e.g. during thoracoabdominal aortic surgery, can cause spinal cord infarction.

The lateral branch of each lumbar artery runs posterior to psoas major and the lumbar plexus, then across the anterior surface of quadratus lumborum, before piercing the posterior aspect of transversus abdominis to run forwards between it and internal abdominal oblique. Perforating branches pass posteriorly to supply the muscles and skin of the posterior abdominal wall (Kiil et al 2009). The lumbar arteries anastomose with one another and the lower posterior intercostal, subcostal, iliolumbar, deep circumflex iliac and inferior epigastric arteries.

The dorsal branch of each lumbar artery passes backwards between the adjacent transverse processes to supply the back muscles, vertebrae and their joints and the skin of the back.

Median sacral artery

The median sacral artery is a small branch that usually arises from the posterior aspect of the aorta a little above its bifurcation. It descends close to the midline, anterior to the fourth and fifth lumbar vertebrae, sacrum and coccyx. At the level of the fifth lumbar vertebra it is crossed by the left common iliac vein and often gives off a small lumbar artery (arteriae lumbales imae), whose small branches reach the anus and rectum via the anococcygeal ligament. Anterior to the fifth lumbar vertebra, the median sacral artery anastomoses with a lumbar branch of the iliolumbar artery. Anterior to the sacrum, it anastomoses with the lateral sacral arteries and sends branches into the anterior sacral foramina.

Inferior vena cava

The inferior vena cava (Figs 61.12–61.13) conveys blood to the right atrium from almost all of the structures inferior to the respiratory diaphragm. Most of its course is within the abdomen, but a small segment lies within the pericardium in the thoracic cavity.

The inferior vena cava is formed by the junction of the left and right common iliac veins anterior to the fifth lumbar vertebral body, about 1 cm to the right of the midline. It ascends anterior to the vertebral column, to the right of the aorta, and lies in a deep groove on the posterior surface of the liver, sometimes completely surrounded by liver tissue. It traverses the central tendon of the respiratory diaphragm and passes through the fibrous pericardium and a posterior inflection of the serous pericardium to open into the posteroinferior part of the right atrium. Its abdominal portion is devoid of valves. The inferior vena cava can be encircled and controlled between the renal veins inferiorly and the hepatic veins superiorly, e.g. during operations on a renal cell carcinoma extending into the inferior vena cava.

Relations of the abdominal part of the inferior vena cava

The inferior vena cava lies behind the parietal peritoneum lining the posterior abdominal wall. At its origin it is related anteriorly to the right common iliac artery. From below upwards, its anterior surface is crossed obliquely by the root of the mesentery of the small intestine and its contained vessels and nerves, the right gonadal artery and the horizontal part of the duodenum. Further cranially, it lies posterior to the head of the pancreas and superior (first) part of the duodenum, separated from those structures by the bile duct and hepatic portal vein. Superior to the duodenum, its anterior surface is covered by the parietal peritoneum lining the posterior abdominal wall, which forms the posterior wall of the omental foramen and separates the inferior vena cava from the right free border of the lesser omentum, i.e. the hepatoduodenal ligament and its contents. Superior to this, it is intimately related to the liver anteriorly.

The posterior relations of the inferior vena cava include the lower three lumbar vertebral bodies and their intervertebral discs, the anterior longitudinal ligament, sympathetic trunk, right third and fourth lumbar arteries, and psoas major on the right. Superior to these structures, it is

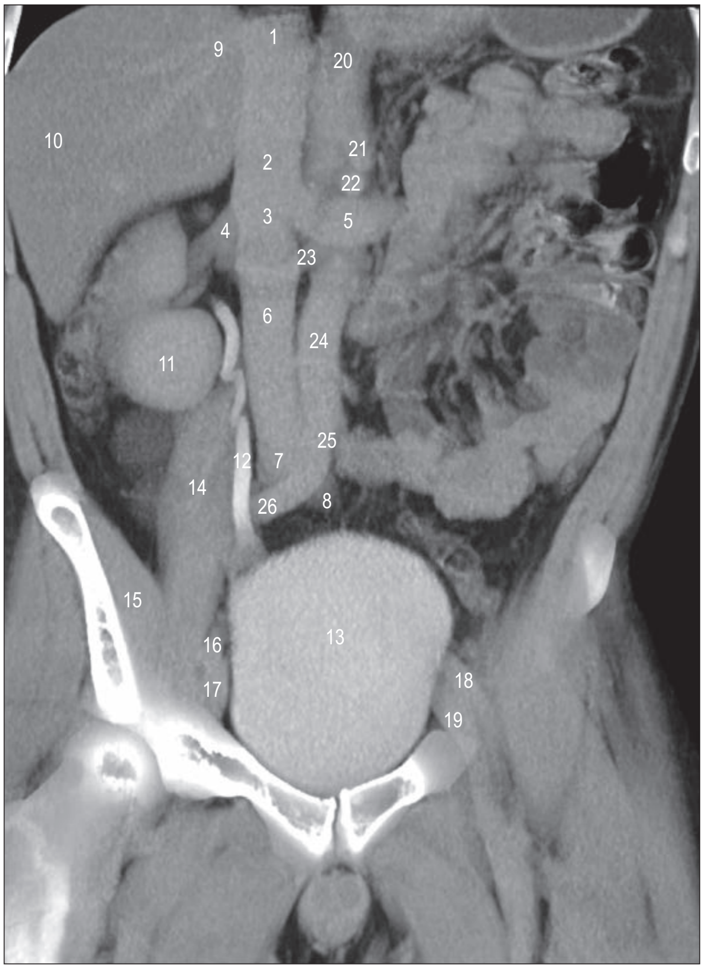

Fig. 61.13 A 41-year-old male investigated for microscopic haematuria. CT intravenous urogram. Normal study. Late phase acquisition. Oblique coronal, mid-abdominal 15 mm slab, maximal intensity projection (MIP) reformats. Key: 1, inferior vena cava, hepatic segment; 2, inferior vena cava, infrahepatic segment; 3, inferior vena cava, renal segment; 4, right renal vein; 5, left renal vein crossing anterior to the aorta; 6, inferior vena cava, infrarenal segment; 7, inferior vena cava, confluence (partly obscured by right common iliac artery); 8, left common iliac vein (coursing posteriorly out of slab; right common iliac vein obscured); 9, right hepatic vein joining inferior vena cava; 10, liver; 11, right kidney inferior pole parenchyma; 12, right ureter (with excreted contrast); 13, urinary bladder (with excreted contrast); 14, right psoas major; 15, right iliacus; 16, right external iliac artery; 17, right external iliac vein; 18, left external iliac artery; 19, left external iliac vein; 20, distal thoracic aorta; 21, coeliac trunk; 22, superior mesenteric artery; 23, right renal artery passing posterior to the inferior vena cava; 24, aorta, infrarenal segment; 25, aortic bifurcation (partly obscured); 26, right common iliac artery (left common iliac artery courses posteriorly out of slab).

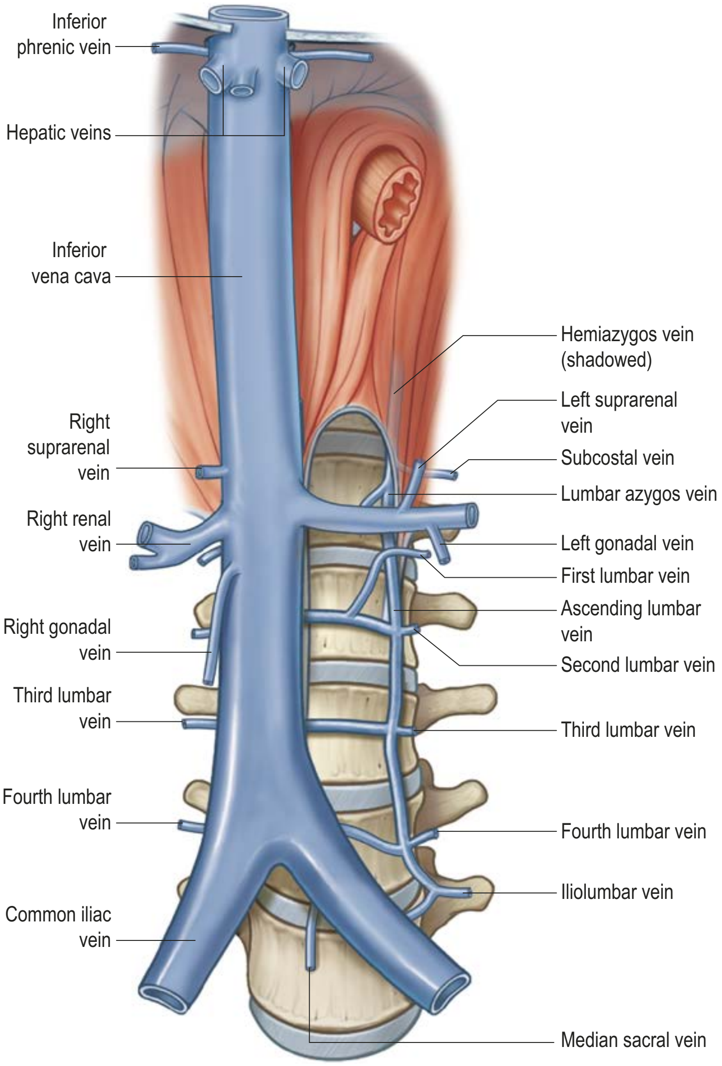

Fig. 61.12 Tributaries of the inferior vena cava emphasizing the left lumbar veins and their interconnections.

related posteriorly to the right renal and middle suprarenal arteries, the medial part of the right suprarenal gland, the right coeliac ganglion and the right inferior phrenic arteries.

The right ureter, medial border of the right kidney, descending part of the duodenum and the right lobe of the liver are all lateral to the right side of the inferior vena cava. The abdominal aorta, right crus of the respiratory diaphragm and the caudate lobe of the liver are on its left side.

The normal diameter of an adult inferior vena cava is up to 30 mm (Moeller and Reif 2000); its cross-sectional shape and calibre reflect the degree of venous filling. Anatomical variants, related to its complex embryogenesis (Ch. 13), are well described. Among these are a double inferior vena cava (the left-sided vessel usually joins the left renal vein); azygos continuation of the inferior vena cava; a left-sided inferior vena cava (which may exist in isolation or as part of situs inversus) (Ang et al 2013, Spentzouris et al 2014).

Tributaries

The inferior vena cava usually receives the common iliac veins at its origin and the lumbar, right gonadal, renal, right suprarenal, hepatic and inferior phrenic veins throughout its course (see Fig. 61.12).

Lumbar veins

Four pairs of lumbar veins collect blood from the territories supplied by the corresponding lumbar arteries, including the posterior, lateral and anterior abdominal walls. These branches anastomose posteriorly with tributaries of the azygos and hemiazygos veins, and anteriorly with branches of the epigastric, circumflex iliac and lateral thoracic veins. These superficial anastomoses provide alternative routes of venous drainage from the pelvis and lower limbs to the heart when the inferior vena cava is obstructed. The lumbar veins communicate with the external and internal vertebral venous plexuses, providing an additional collateral pathway for venous return.

The paired longitudinal ascending lumbar veins connect the individual ipsilateral lumbar veins. The third and fourth lumbar veins usually pass anteriorly on the sides of the corresponding vertebral bodies to enter the posterior aspect of the inferior vena cava; the left lumbar veins pass posterior to the abdominal aorta and are therefore longer. The first and second lumbar veins are much more variable and may drain into the inferior vena cava or the ascending lumbar, lumbar azygos or renal veins (on the left); they are often connected to each other. The first lumbar vein often passes inferiorly to join the second lumbar vein or, less commonly, drains either directly into the ascending lumbar vein or passes anteriorly over the body of the first lumbar vertebra to join the lumbar azygos vein. The second lumbar vein may join the inferior vena cava at or near the level of the renal veins or, less commonly, join the third lumbar or ascending lumbar vein.

Ascending lumbar veins

The paired ascending lumbar veins run medial to psoas major and connect the ipsilateral common iliac, iliolumbar and lumbar veins. The ascending lumbar vein is variable in its course and connections; rarely, the whole vein or a segment is absent on one side (Lolis et al 2011). It commonly joins the subcostal vein to form the azygos vein on the right and the hemiazygos on the left. The azygos and hemiazygos veins run anteriorly over the body of the twelfth thoracic vertebra and pass deep to or through the right and left crura of the respiratory diaphragm, respectively, into the thoracic cavity (Ch. 56). The ascending lumbar vein is usually joined by a small vein, the lumbar azygos vein, from the back of the inferior vena cava or left renal vein. Sometimes, the ascending lumbar vein ends in the first lumbar vein, which then joins the lumbar azygos vein at the level of the first lumbar vertebra. Blood can flow in either direction in the ascending lumbar veins (Morita et al 2007).

Gonadal veins

The right gonadal vein enters the inferior vena cava directly on its right anterolateral aspect at an acute angle about 2 cm inferior to the left renal vein in adults; occasionally, it drains into the right renal vein (Tubbs et al 2016). The left gonadal vein terminates in the left renal vein. Both veins may be replaced by multiple vessels in the lower abdomen and sometimes remain double as far as their termination. Of the two gonadal veins, the left is more prone to develop venous incompetence.

Renal veins

The renal veins are large-calibre vessels that lie anterior to the renal arteries and open into the inferior vena cava almost at right angles (Ch. 72). The left is three times longer than the right (approximately 7.5 cm and 2.5 cm, respectively), and lies on the posterior abdominal wall posterior to the splenic vein and body of the pancreas. It passes to the right in the angle between the abdominal aorta posteriorly and the superior mesenteric artery anteriorly and empties into the inferior vena cava. Occasionally, the left renal vein or an accessory left renal vein is retro-aortic. The right renal vein lies posterior to the descending part of the duodenum and sometimes to the lateral part of the head of the pancreas.

Suprarenal vein

Most commonly, a single vein drains each suprarenal gland (Ch. 70). The short right suprarenal vein drains directly into the inferior vena cava at the level of the twelfth thoracic vertebra; the longer left vein usually joins the left renal vein and may receive the left inferior phrenic vein. Numerous anatomical variations of this vein have been described (Cesmebasi et al 2014).

Inferior phrenic veins

The inferior phrenic veins usually originate on the superior surface of the respiratory diaphragm but run mostly on its inferior surface to drain into the posterolateral aspect of the inferior vena cava. Both veins receive several diaphragmatic tributaries. The left vein runs to the left of the oesophageal hiatus, whereas the right courses to the right of the caval foramen; each receives a venous tributary from the oesophagus (Loukas et al 2005b). The left inferior phrenic vein frequently communicates with the left gastric vein and may therefore become prominent in portal hypertension. Both inferior phrenic veins usually drain directly into the inferior vena cava just inferior to the respiratory diaphragm, sometimes joining anteriorly to form a short common trunk. The right occasionally drains into the right hepatic vein or inferior vena cava superior to the respiratory diaphragm, whereas the left frequently drains into the left suprarenal, left renal or left hepatic vein.

Collaterals developing as a result of occlusion of the inferior vena cava

Obstruction of the inferior vena cava from thrombosis, embolism, extrinsic compression (e.g. tumour or pregnancy) or intrinsic disease results in the development of an extensive venous collateral circulation via tributaries that ultimately connect to the superior vena cava. These include the azygos–hemiazygos venous system, the vertebral venous plexuses and the superficial veins of the thoracic and abdominal walls. The lumbar veins contribute significantly to these pathways (Golub et al 1992).

Lymphatic drainage

Lymph from the skin and subcutaneous tissues of the abdominal wall drains via small calibre superficial lymphatics to axillary and inguinal nodes (Tourani et al 2013). The midline and the level of the umbilicus form inconstant and variable watershed boundaries for these drainage territories. Lymphatics from the deeper layers of the body wall and the abdominal and pelvic viscera drain almost exclusively to the cisterna chyli and thoracic duct. The former drains via ipsilateral nodes in the retroperitoneum concentrated around the external iliac and common iliac vessels and along the lateral aspects of the aorta and inferior vena cava. There is considerable overlap between the lymphatic drainage of individual viscera. At certain sites there is a cranio-caudal sequence of lymph nodes, e.g. lateral aortic nodes; and parasternal and inferior epigastric nodes. Some lymphatic drainage from the bare area of the liver occurs directly across the respiratory diaphragm to the thoracic cavity.

The paired viscera of the retroperitoneum drain to lateral aortic nodes around the origin of their arterial supply. Thus, the kidneys and suprarenal glands drain to nodes around the hilum of the kidney and to lateral aortic nodes around the origin of the renal arteries (first and second lumbar vertebral levels). The testes drain to lateral aortic and lateral, precaval and retrocaval nodes (approximately second lumbar vertebral level); the pattern of lymphatic spread from a testicular malignancy suggests that lymph from the left testis drains to left lateral aortic nodes en route to the cisterna chyli, whereas lymph from the right testis drains to right and then left lateral aortic nodes before reaching the cisterna chyli. Lymph from the ovary may drain via lymphatics in the broad ligament of the uterus and round ligament of the uterus to internal iliac and inguinal nodes, respectively. Lymphatic drainage of the ureters is less well defined but follows a regional pattern to nearby nodes.

The lymphatic drainage of the retroperitoneal colon and rectum is described in Chapter 65. The pancreas drains to numerous pancreatic nodes (Ch. 68) and to nodes between the hepatic portal vein and inferior vena cava (clinically referred to as portacaval nodes), splenic, superior mesenteric and coeliac nodes. The lymphatic drainage of the duodenum is not well described but the lymphatics generally drain to nodes related to local arteries (Ch. 64). Whilst the clinical pattern of nodal metastases usually reflects normal lymphatic drainage pathways, lymphatic obstruction may lead to metastases at unusual nodal sites.

Cisterna chyli and abdominal lymph trunks

The abdominal origin of the thoracic duct usually lies to the right of the midline at the level of the body of the twelfth thoracic vertebra or the intervertebral disc between the twelfth thoracic and first lumbar vertebrae. It receives almost all the lymph from below the respiratory diaphragm via the cisterna chyli, a localized saccular or fusiform lymphatic dilation formed most commonly by the union of the intestinal trunk and the left lumbar trunk (Phang et al 2014). The cisterna chyli is approximately 1 cm wide and 2 cm long in the cadaver (Loukas et al 2007): studies using magnetic resonance imaging (MRI) *in vivo* have shown that it expands considerably during movement from supine to sitting and again from sitting to standing (Niggemann et al 2010).

The formation of the cisterna chyli is variable and it may be absent. When present, it usually lies anterior to the first and second lumbar vertebrae, posterior to the right crus of the respiratory diaphragm and to the right of the abdominal aorta, but it may be located at a more proximal vertebral level (**Fig. 61.14**). The most common configuration, found in approximately two-thirds of individuals, is a single structure formed from the union of the intestinal trunk and the left (or, less commonly, the right) lumbar trunk (Loukas et al 2007). In most other individuals it is formed by the confluence of the intestinal and both lumbar trunks, with additional small branches from intercostal lymphatics (intercostal trunks) and retro-aortic nodes (Skandalakis et al 2004). The proximal two right lumbar arteries and the right lumbar azygos vein lie between the cisterna chyli and the vertebral column.

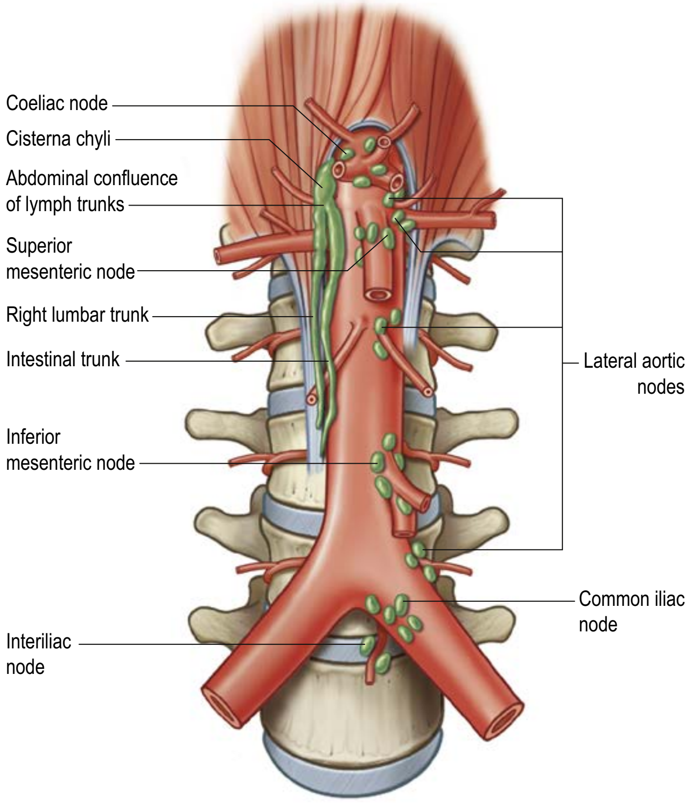

Fig. 61.14 Abdominal nodes emphasizing the main pre-aortic groups. Only the left-sided lateral aortic nodes are shown, for clarity. NB: the cisterna chyli is more commonly formed by the intestinal trunk and the left lumbar trunk (rather than the right lumbar trunk shown in this diagram).

The paired lumbar trunks are formed by lymphatic vessels draining lateral aortic nodes. The intestinal trunk (which may be double) receives vessels draining from coeliac, superior and inferior mesenteric nodes that collectively drain the entire abdominal gastrointestinal tract down to the anal canal. The thoracic duct leaves the superior end of the cisterna chyli and passes through the aortic hiatus of the respiratory diaphragm posterolateral to the right side of the aorta. Its thoracic continuation is described in Chapter 56.

The major lymphatic vessels adjacent to the abdominal aorta are at risk of injury during surgical procedures that involve peri-aortic dissection and/or lymphadenectomy. Injury to these lymphatic vessels or their obstruction by malignant disease can cause leakage of lymph manifesting as chylous ascites or chylothorax.

Retroperitoneal lymph node groups

The lymphatic drainage of the rectum, colon, stomach, pancreas, oesophagus and other organs is often described in terms of lymph node stations and levels of dissection that relate to the management of malignant disease. The terminology and classification of retroperitoneal lymph nodes are based on their location. In classic anatomical descriptions, the lymph nodes of the retroperitoneum around the abdominal aorta are grouped into pre-aortic, lateral and retro-aortic nodes, but adjacent nodal groups merge into one another with no clear demarcating boundaries. Normal lymph node dimensions are very variable. Cross-sectional imaging frequently uses 10 mm as an approximate measurement for the upper limit of normal lymph node dimensions in the adult (Moeller and Reif 2000): some normal retroperitoneal nodes such as the portacaval nodes are typically larger.

Pre-aortic nodes

Pre-aortic nodes drain the gastrointestinal viscera including the pancreas, liver and spleen. They lie anterior to the aorta clustered around its anterior unpaired visceral branches and can be subdivided into coeliac, superior mesenteric and inferior mesenteric nodes. Their efferent lymphatics contribute to the formation of the intestinal lymph trunk.

Coeliac nodes

Coeliac nodes drain lymph from nodes around the stomach, splenic hilum, porta hepatis, cystic duct, lesser omentum, portacaval nodes,

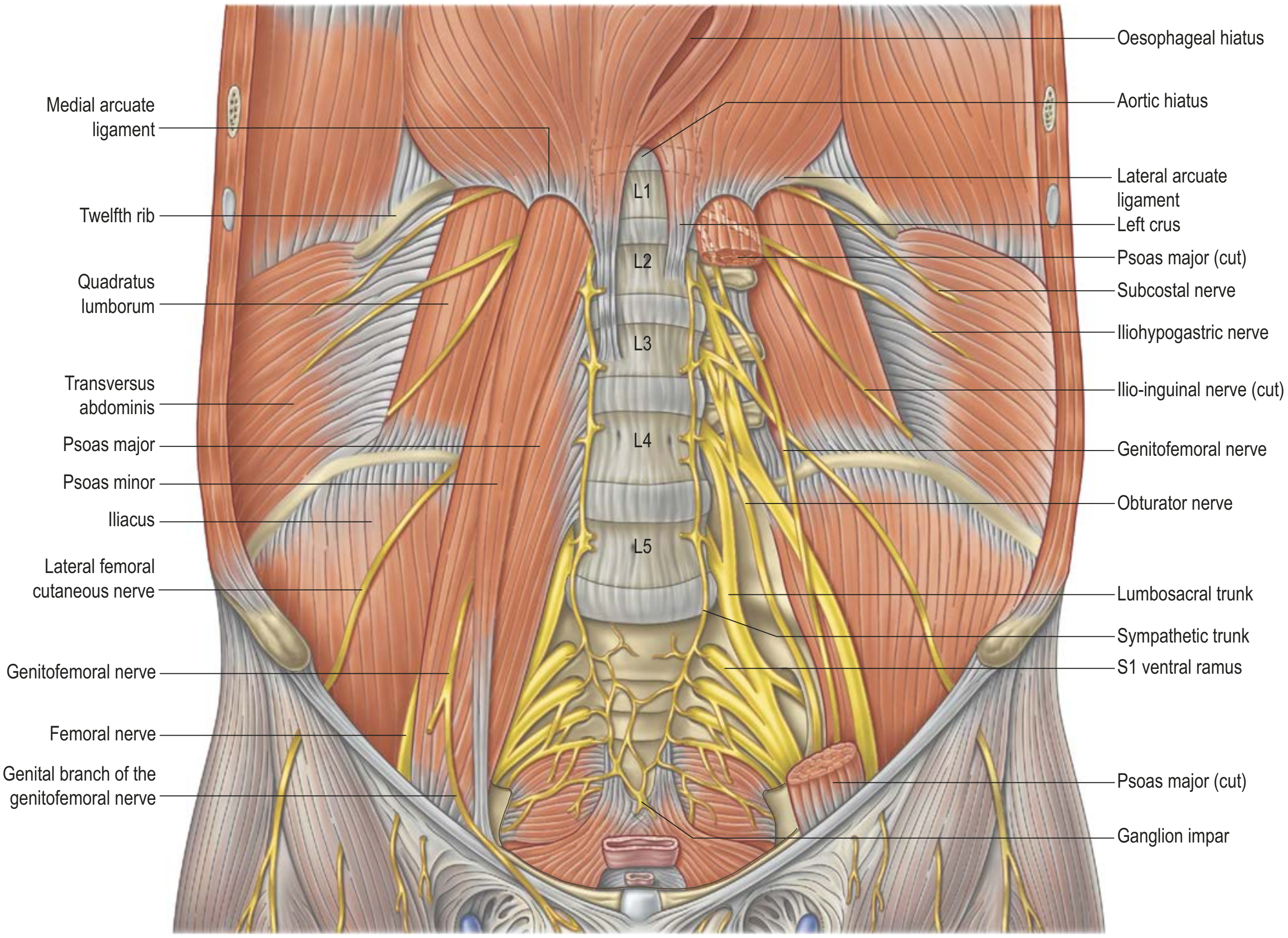
Medial arcuate ligament
Twelfth rib
Quadratus lumborum
Transversus abdominis
Psoas major
Psoas minor
Iliacus
Lateral femoral cutaneous nerve
Genitofemoral nerve
Femoral nerve
Genital branch of the genitofemoral nerve
L1
L2
L3
L4
L5
Oesophageal hiatus
Aortic hiatus
Lateral arcuate ligament
Left crus
Psoas major (cut)
Subcostal nerve
Iliohypogastric nerve
Ilio-inguinal nerve (cut)
Genitofemoral nerve
Obturator nerve
Lumbosacral trunk
Sympathetic trunk
S1 ventral ramus
Psoas major (cut)
Ganglion impar

Fig. 61.15 Muscles and nerves of the posterior abdominal wall. Psoas major on the left has been removed to expose the ventral rami contributing to the lumbar plexus and quadratus lumborum.

pancreatic nodes and pancreaticoduodenal nodes. They also receive lymph from superior and inferior mesenteric nodes and their efferent lymphatics drain to the intestinal trunks.

Superior mesenteric nodes

Superior mesenteric nodes share an extensive overlap with the drainage territory of coeliac nodes, with subsidiary nodal groups that include pancreatic, pancreaticoduodenal, portacaval, ileocolic, mesenteric and inferior mesenteric nodes. Efferent lymphatics drain to the intestinal trunks either directly or via coeliac nodes.

Inferior mesenteric nodes

Inferior mesenteric nodes such as the superior rectal nodes drain lymph from derivatives of the hindgut, including the distal transverse, descending and sigmoid colons, and the rectum.

Lateral aortic groups

Lateral aortic (para-aortic) nodes lie on either side of the abdominal aorta and inferior vena cava anterior to the medial margins of psoas major, the crura of the respiratory diaphragm and the sympathetic trunks. Constituent nodal groups that are recognized clinically include the retrocrural (posterior to the diaphragmatic crura at the aortic hiatus); left and right hilar (of the kidney); aortocaval, lateral caval, retrocaval and precaval groups. Retro-aortic nodes are sometimes included within the lateral aortic group. The latter drain into the paired intestinal trunks that terminate directly or indirectly in the cisterna chyli and thoracic duct. There are lymphatic connections between lateral aortic, pre-aortic, retro-aortic and contralateral lateral aortic nodes. The lateral aortic nodes drain the deep layers of the body wall, the retroperitoneal paired viscera (including the gonads) and tributaries from the iliac nodes. Lymph from the right ovary or testis drains via lymphatics travelling with the gonadal vessels to the right lateral aortic and pre-aortic nodes at the level of the second lumbar vertebra, whereas lymph from the left ovary or testis drains to the left lateral aortic nodes just inferior to the left renal vein (Morton and Thomas 2008, Paño et al 2011).

Iliac nodes

Paired iliac nodes are distributed around the common, external and internal iliac arteries and veins. Constituent groups include the common iliac, external iliac, internal iliac and obturator nodes. The latter are located near the obturator foramen and, together with the iliac nodes, are a common site of lymph node metastasis in prostate cancer. 'Pelvic side-wall' nodes, lying adjacent to the ilium but not associated with a large artery or vein, are also described in the clinical literature. The iliac nodes drain the pelvic viscera and walls, except for the ovaries and those parts of the rectum drained by superior anorectal nodes. They also drain lymph from the inguinal nodes and lower limbs.

INNERVATION

The posterior abdominal wall contains the lumbar plexus and numerous autonomic plexuses and ganglia that lie close to the abdominal aorta and its branches (Figs 61.15–61.16).

Lumbar plexus

The lumbar ventral rami pass laterally into the posterior part of psoas major, anterior to the transverse processes of the lumbar vertebrae (Moro et al 2003, Benglis et al 2009). The first four lumbar ventral rami, usually together with a contribution from the twelfth thoracic ventral ramus, form the lumbar plexus. Although there are many variations, the most common arrangement of the plexus is described here (Tubbs et al 2018).

The first lumbar ventral ramus is often joined by a branch from the twelfth thoracic ventral ramus, and these contribute to the formation of the iliohypogastric and ilio-inguinal nerves, which run laterally on the posterior abdominal wall. A branch from the first lumbar ventral ramus unites with a branch from the second lumbar ventral ramus to form the genitofemoral nerve. The second, third and most of the fourth lumbar ventral rami divide into ventral and dorsal

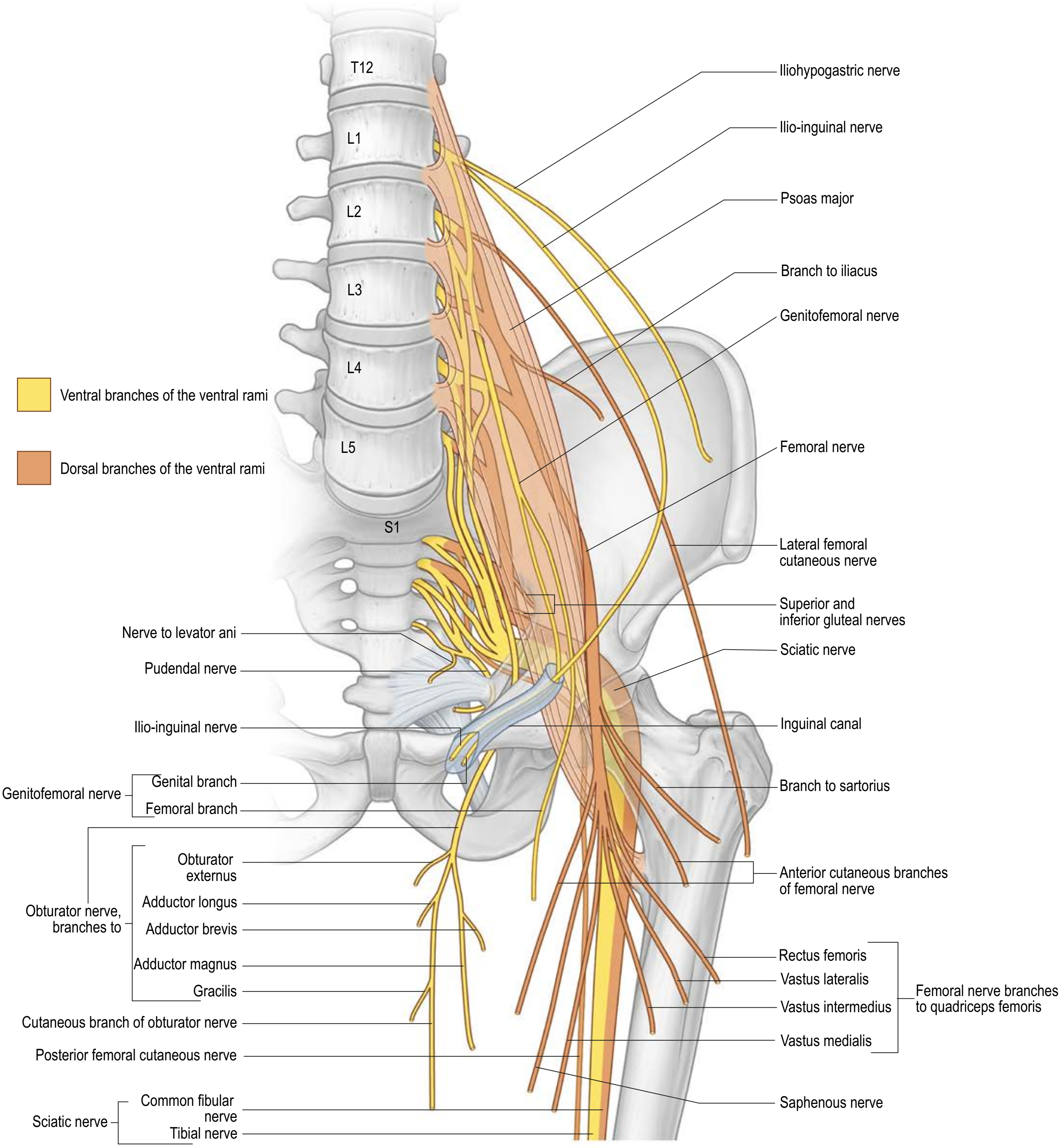
T12
L1
L2
L3
L4
L5
S1
Ventral branches of the ventral rami
Dorsal branches of the ventral rami
Iliohypogastric nerve
Ilio-inguinal nerve
Psoas major
Branch to iliacus
Genitofemoral nerve
Femoral nerve
Lateral femoral cutaneous nerve
Superior and inferior gluteal nerves
Sciatic nerve
Inguinal canal
Branch to sartorius
Anterior cutaneous branches of femoral nerve
Rectus femoris
Vastus lateralis
Vastus intermedius
Vastus medialis
Femoral nerve branches to quadriceps femoris
Saphenous nerve
Nerve to levator ani
Pudendal nerve
Ilio-inguinal nerve
Genitofemoral nerve
Genital branch
Femoral branch
Obturator nerve, branches to
Obturator externus
Adductor longus
Adductor brevis
Adductor magnus
Gracilis
Cutaneous branch of obturator nerve
Posterior femoral cutaneous nerve
Sciatic nerve
Common fibular nerve
Tibial nerve

Fig. 61.16 The lumbar plexus and its branches.

divisions; the ventral divisions unite to form the obturator nerve, while most of the nerve fibres in the dorsal divisions form the femoral nerve. The remaining fibres from the fourth lumbar ventral ramus join the fifth lumbar ventral ramus to form the lumbosacral trunk, which descends to join the sacral plexus. Branches from the dorsal divisions of the second and third lumbar ventral rami unite to form the lateral femoral cutaneous nerve. The accessory obturator nerve, when present, usually arises from the third and fourth ventral rami. The lumbar plexus is supplied by branches from the lumbar vessels that supply psoas major.

The division of constituent ventral rami into ventral and dorsal branches is not as clear in the lumbar and sacral plexuses as it is in the brachial plexus. Lateral cutaneous branches of the twelfth thoracic and first lumbar ventral rami are drawn into the gluteal skin, but otherwise these nerves are similar to intercostal nerves. The second lumbar ventral ramus is more complex. It contributes substantially to the femoral and obturator nerves, and also has an anterior terminal branch (the genital branch of the genitofemoral) and a lateral cutaneous branch that contributes to the lateral femoral cutaneous nerve and the femoral branch of the genitofemoral nerve. Anterior terminal branches of the third to fifth lumbar and first sacral ventral rami are suppressed, but the corresponding branches of the second and third sacral ventral rami supply the perineal skin.

The furcal nerve is an independent nerve with its own ventral and dorsal rootlets most commonly arising alongside the fourth lumbar spinal nerve. Its branches contribute to the femoral and obturator nerves arising from the lumbar plexus and to the lumbosacral trunk (Harshavardhana and Dabke 2014). The term ‘furcal’ refers to its forked nature, since it links the lumbar and sacral plexuses. Occasionally, the furcal nerve arises at the level of either the third or the fifth lumbar spinal nerves, in which case the sacral plexus is considered prefixed or postfixed, respectively.

Inflammatory processes, such as retrocaecal appendicitis on the right and diverticular abscess on the left, can occur in the posterior abdominal wall in the tissues immediately anterior to psoas major. These may irritate one or more branches of the lumbar plexus, causing pain or sensory disturbance in the distribution of the affected nerves, e.g. the skin of the thigh, hip or buttock.

Muscular branches

Small branches from the lumbar ventral rami supply adjacent muscles such as psoas major and quadratus lumborum (Mahan et al 2017).

Iliohypogastric nerve

Distribution

The iliohypogastric nerve usually originates from the first lumbar ventral ramus but may arise wholly or in part from the twelfth thoracic ventral ramus (Klaassen et al 2011). It emerges from the upper lateral border of psoas major and crosses obliquely posterior to the inferior pole of the kidney on the anterior surface of quadratus lumborum. Above the iliac crest, it enters the posterior part of transversus abdominis and then runs anteriorly between transversus abdominis and internal abdominal oblique, which it supplies. It gives off a lateral cutaneous branch that pierces internal and external abdominal oblique above the iliac crest and supplies the posterolateral gluteal skin. It continues forwards, pierces internal abdominal oblique approximately 3 cm medial and 1 cm inferior to the anterior superior iliac spine (in adults), and then penetrates the external abdominal oblique aponeurosis approximately 3 cm above and medial to the superficial inguinal ring to supply the skin of the hypogastric region. The iliohypogastric nerve frequently connects with the ilio-inguinal nerve and less commonly with the subcostal nerve. Motor branches of the iliohypogastric nerve innervate transversus abdominis and internal abdominal oblique. Cutaneous branches innervate the skin of the posterolateral gluteal and hypogastric regions.

Injury

The iliohypogastric nerve is occasionally injured by a surgical incision in the right inguinal region, e.g. during an inguinal hernia repair, open appendicectomy or abdominal wall trocar placement, but there is rarely any noticeable sensory loss because the skin of the hypogastric region is innervated from several sources. Division of the iliohypogastric nerve above the anterior superior iliac spine may weaken the posterior wall of the inguinal canal and predispose to formation of a direct inguinal hernia.

Ilio-inguinal nerve

Distribution

The ilio-inguinal nerve usually originates from the first lumbar ventral ramus but may receive a contribution from the twelfth thoracic or second lumbar ventral rami (Klaassen et al 2011). It emerges from the lateral border of psoas major, with or just inferior to the iliohypogastric nerve, passes obliquely across the anterior aspect of quadratus lumborum and the superior part of iliacus and enters transversus abdominis about 3 cm medial and 4 cm inferior to the anterior superior iliac spine (in the adult); at this site, it is readily blocked by local anaesthetic. In this region, a branch may connect with the iliohypogastric or lateral femoral cutaneous nerve. It pierces internal abdominal oblique more inferiorly, supplies it, and then traverses the remainder of the inguinal canal superficial to the spermatic cord or round ligament of the uterus. It emerges with the spermatic cord from the superficial inguinal ring and divides into terminal cutaneous branches.

Numerous anatomical variations have been described (Al-dabbagh 2002, Ndiaye et al 2007). The ilio-inguinal and genitofemoral nerves may interconnect within the inguinal canal, so that each innervates the skin of the genitalia to a variable extent (Rab et al 2001, Cesmebasi et al 2015). The ilio-inguinal nerve may pierce the aponeurosis of external abdominal oblique proximal to the superficial inguinal ring or divide into terminal branches within the inguinal canal. It may form a common trunk with the iliohypogastric nerve as far as the midpoint of the inguinal canal or may be very small or absent, in which case the iliohypogastric nerve and genital branch of the genitofemoral nerve supply its territory. Rarely it arises as a branch of the genitofemoral nerve. Motor branches of the ilio-inguinal nerve supply transversus abdominis and internal abdominal oblique; the fibres are given off before the nerve enters the lateral aspect of the inguinal canal. Sensory branches innervate the skin of the proximal medial thigh and the skin over the root of the penis and proximal part of the scrotum in males (anterior scrotal nerve), or the skin covering the mons pubis and the adjoining labium majus in females (anterior labial nerve).

Injury

The ilio-inguinal nerve may be injured or entrapped during inguinal surgery, particularly for inguinal hernia repair, leading to sensory disturbances including pain from the external genitalia and proximal medial thigh (Ndiaye et al 2007).

Genitofemoral nerve

Distribution

The genitofemoral nerve originates from the first and second lumbar ventral rami and is formed within the substance of psoas major. It descends obliquely anteriorly through the muscle to emerge on its anterior surface nearer the medial border, opposite the third or fourth lumbar vertebra (Moro et al 2003). It then descends deep to the posterior parietal peritoneum overlying psoas major, crosses obliquely posterior to the ureter, and divides into genital and femoral branches; it may divide close to its origin such that its branches emerge separately from psoas major. The genital branch crosses the distal part of the external iliac artery, enters the inguinal canal through the deep ring and accompanies the spermatic cord or round ligament of the uterus. It exits the superficial inguinal ring, usually posterior to the spermatic cord or round ligament of the uterus, and supplies cremaster and the skin of the external genitalia. The femoral branch descends lateral to the external iliac artery before crossing the deep circumflex iliac artery to pass deep to the inguinal ligament (occasionally, through it) (Rab et al 2001) and enter the femoral sheath lateral to the femoral artery. It pierces the anterior aspect of the femoral sheath and fascia lata and supplies the skin over the proximal part of the femoral triangle. It may connect with the lateral femoral cutaneous nerve and anterior femoral cutaneous branches of the femoral nerve. Motor branches of the genitofemoral nerve innervate cremaster via its genital branch. Sensory fibres travelling in the genital branch innervate the skin of the scrotum in males and of the mons pubis and labium majus in females; there is considerable variability and overlap with the cutaneous distribution of the ilio-inguinal nerve (Cesmebasi et al 2015).

Injury

The genital branch of the genitofemoral nerve may be injured during inguinal hernia repair (open or laparoscopic), leading to neuralgia (Cesmebasi et al 2015).

Femoral nerve

The femoral nerve descends through psoas major and emerges on or deep to its lateral border, about 4 cm above the inguinal ligament (Moore and Stringer 2011). It passes between psoas major and iliacus deep to the iliac fascia and lies lateral to the femoral artery and sheath as it runs posterior to the inguinal ligament into the thigh. It gives off motor branches that supply iliacus, pectineus, sartorius and quadriceps femoris; articular branches to the hip, knee and ankle joints; branches to the femoral artery; cutaneous branches that supply the majority of the skin covering the anterior thigh, medial leg and medial foot (see Fig. 61.16). Injury to the femoral nerve may result in loss of sensation and paraesthesias within its cutaneous distribution, as well as difficulty ambulating, especially descending stairs. The further course and distribution of the femoral nerve are described in Chapter 77.

Lateral femoral cutaneous nerve

The lateral femoral cutaneous nerve (lateral cutaneous nerve of the thigh) is usually derived from the second and third lumbar ventral rami, but variable contributions from the first to the third lumbar ventral rami have been described (de Ridder et al 1999). The nerve emerges from the posterolateral border of psoas major and crosses iliacus obliquely, running towards the anterior superior iliac spine. It supplies sensory fibres to the parietal peritoneum in the iliac fossa. On the right, the nerve passes posterolateral to the caecum, from which it is separated by the iliac fascia and peritoneum; on the left, it passes posterior to the inferior part of the descending colon. Both nerves usually pass posterior to the inguinal ligament about 1–2 cm medial to the anterior superior iliac spine; occasionally they pass through or, rarely, anterior to the ligament (Tubbs et al 2016). A separate fascial canal for this nerve has been described (Hanna 2017). Occasionally, the nerve lies anterior or superior to the anterior superior iliac spine as it enters the thigh. In the thigh, the lateral femoral cutaneous nerve usually passes anterior or lateral to sartorius but may pierce the muscle. Its further course and distribution are described in (Chapter 77).

Obturator nerve

The obturator nerve is formed within the substance of psoas major to emerge from its posteromedial border near the fifth lumbar vertebra (Kirchmair et al 2008). It passes posterior to the common iliac vessels and lateral to the internal iliac vessels, descends on the lateral wall of the pelvis attached to the obturator fascia, and lies anterosuperior to the obturator vessels before running into the obturator canal to enter the thigh. The obturator nerve is said to have no branches in the abdomen or pelvis, although it has been reported to send articular branches to the anterior aspect of the sacroiliac joint. Its sensory branches innervate the hip and knee joints, and a small, variable patch of skin on the proximal medial thigh, and its motor branches innervate obturator externus, adductor longus, adductor brevis, adductor magnus, gracilis and sometimes pectineus (see Fig. 61.16) (Tubbs et al 2016).

Compression of the obturator nerve, e.g. by an obturator hernia, may result in weakness of the muscles of the adductor compartment of the thigh and pain and paraesthesias along the medial thigh, inferiorly to the knee (Howship-Romberg sign). The further course and distribution are described in Chapter 77.

Accessory obturator nerve

The accessory obturator nerve is sometimes present, more often on the left (Turgut et al 2017), and is usually formed by the third and fourth lumbar ventral rami. It emerges from the medial border of psoas major, lateral to the obturator nerve, and runs over the superior pubic ramus posterior to pectineus, where it gives off branches to the muscle and sometimes to the hip joint; it may join with the anterior branch of the obturator nerve (Ch. 77).

Lumbar sympathetic system

The lumbar part of each sympathetic trunk usually contains four interconnected ganglia lying in extraperitoneal connective tissue on the anterolateral aspects of the lumbar vertebrae along the medial margin of psoas major (see Fig. 61.10). Superiorly, it is continuous with the thoracic part of the sympathetic trunk posterior to the medial arcuate ligament at the level of the first and second lumbar vertebrae (Feigl et al 2011). Inferiorly, it passes posterior to the common iliac vessels and is continuous with the sacral part of the sympathetic trunk. On the right side, it lies posterior to the inferior vena cava; on the left, it is posterior to the lateral aortic nodes. It is anterior to most of the lumbar vessels but may pass behind some lumbar veins.

The first, second, and sometimes the third, lumbar ventral rami are each connected to the lumbar part of the sympathetic trunk by a white ramus communicans. All lumbar ventral rami are joined near their origins by long, slender grey rami communicantes from the four lumbar ganglia. Their arrangement is irregular: one ganglion may give rami to two or three lumbar ventral rami; one lumbar ventral ramus may receive rami from two ganglia; grey rami communicantes may leave the sympathetic trunk between ganglia (Murata et al 2003).

The lumbar sympathetic trunks are vulnerable during retroperitoneal lymph node dissection: their injury can impair emission of seminal fluid and lead to retrograde ejaculation.

Lumbar parasympathetic system

The parasympathetic supply to the abdominal viscera is provided by the vagus nerve to the coeliac and superior mesenteric plexuses, and by pelvic splanchnic nerves that are distributed through the inferior hypogastric and inferior mesenteric plexuses to derivatives of the hindgut (Ch. 59).

Para-aortic bodies

The para-aortic bodies (also known as paraganglia or, collectively, as the organ of Zuckerkandl), are collections of neural crest-derived chromaffin tissue closely related to the aortic autonomic plexuses. They are relatively large in the fetus, where they may have a role in maintaining blood pressure by catecholamine secretion. They reach a maximum size at around 3 years of age and have normally regressed by adulthood. They are usually found as paired structures lying anterolateral to the abdominal aorta in the region of the inferior mesenteric and superior hypogastric plexuses, but multiple smaller collections may be present. Occasionally they are found as far proximally as the coeliac plexus or as far distally as the inferior hypogastric plexus, or they may be closely applied to the ganglia of the lumbar part of the sympathetic trunk. Scattered cells that persist into adulthood may, rarely, be the sites of paraganglioma (Pacak and Tella 2018).

Bonus e-book content

Fig. 61.4 A 58-year-old male with chronic pancreatitis and a peripancreatic pseudocyst.

Fig. 61.5 A 43-year-old male with subacute retrocaecal appendicitis.

Fig. 61.6 A 61-year-old male with mid-ureteric calculus causing high-grade obstruction of the left ureter and extravasation of urine from the left hilum of the kidney.

Fig. 61.10 The abdominal aorta and its branches.

Fig. 61.13 A 41-year-old male investigated for microscopic haematuria.

Key references

Culligan K, Remzi FH, Soop M et al 2013 Review of nomenclature in colonic surgery – proposal of a standardised nomenclature based on mesocolic anatomy. Surgeon 11:1–5.
A review making sense of mesocolic anatomy based on findings from modern investigative techniques.

Dodds WJ, Darweesh RMA, Lawson TL et al 1986 The retroperitoneal spaces revisited. AJR Am J Roentgenol 147:1155–61.
An important radiological perspective on the retroperitoneal 'spaces'.

Hikspoors JPJM, Kruepunga N, Mommen GMC et al 2019 The development of the dorsal mesentery in human embryos and fetuses. Semin Cell Dev Biol 92:18–26.
This is one of a series of papers in an issue of Seminars in Cell and Developmental Biology *that focus on aspects of mesenteric organogenesis. Other papers address mesenteric anatomy and development; mesenteric contributions to abdominal organogenesis; processes underpinning mesenteric development.*

Klaassen Z, Marshall E, Tubbs RS et al 2011 Anatomy of the ilioinguinal and iliohypogastric nerves with observations of their spinal nerve contributions. Clin Anat 24:454–61.
Together with Ndiaye et al 2007, these two papers provide a useful description of the anatomy of the ilio-inguinal and iliohypogastric nerves and underline the importance of the ilio-inguinal nerve in clinical practice.

Loukas M, Wartmann CT, Louis RG Jr et al 2007 Cisterna chyli: a detailed anatomic investigation. Clin Anat 20:683–8.
This article revises traditional concepts about the cisterna chyli and its formation.

Mirjalili SA, McFadden SL, Buckenham T et al 2012b A reappraisal of adult abdominal surface anatomy. Clin Anat 25:844–50.
A paper that challenges some traditional surface anatomical landmarks by investigating results from analysis of CT images in living supine adults.

Ndiaye A, Diop M, Ndoye JM et al 2007 Anatomical basis of neuropathies and damage to the ilioinguinal nerve during repairs of groin hernias (about 100 dissections). Surg Radiol Anat 29:675–81.
Together with Klaassen et al 2011, these two papers provide a useful description of the anatomy of the ilio-inguinal and iliohypogastric nerves and underline the importance of the ilioinguinal nerve in clinical practice.

Tubbs RS, Shoja M, Loukas M 2016 Bergman's Comprehensive Encyclopedia of Human Anatomic Variation. Hoboken: Wiley Blackwell.
A textbook dedicated to detailing the anatomical variations found in man.

Tubbs RS, Loukas M, Hanna AS et al 2018 Surgical Anatomy of the Lumbar Plexus. New York: Thieme.
This book reviews the detailed anatomy and surgical implications of the lumbar plexus and its branches.

Willard FH, Vleeming A, Schuenke MD et al 2012 The thoracolumbar fascia: anatomy, function and clinical considerations. J Anat 221:507–36.
An evidence-based review of the complex and clinically important thoracolumbar fascia.

References

Al-dabbagh AK 2002 Anatomical variations of the inguinal nerves and risks of injury in 110 hernia repairs. Surg Radiol Anat 24:102–7.

Amin M, Blandford AT, Polk HC Jr 1976 Renal fascia of Gerota. Urology 7:1–3.

Ang WC, Doyle T, Stringer MD 2013 Left-sided and duplicate inferior vena cava: a case series and review. Clin Anat 26:990–1001.

Arslan M, Comert A, Acar HI et al 2011 Surgical view of the lumbar arteries and their branches: an anatomical study. Neurosurgery 68:16–22.

Benglis DM, Vanni S, Levi AD 2009 An anatomical study of the lumbosacral plexus as related to the minimally invasive transpsoas approach to the lumbar spine. J Neurosurg Spine 10:139–44.

Biglioli P, Roberto M, Cannata A et al 2004 Upper and lower spinal cord blood supply: the continuity of the anterior spinal artery and the relevance of the lumbar arteries. J Thorac Cardiovasc Surg 127:1188–92.

Cesmebasi A, Du Plessis M, Iannatuono M et al 2014 A review of the anatomy and clinical significance of adrenal veins. Clin Anat 27:1253–63.

Cesmebasi A, Yadav A, Gielecki J et al 2015 Genitofemoral neuralgia: a review. Clin Anat 28:128–35.

Chesbrough RM, Burkhard TK, Martinez AJ et al 1989 Gerota versus Zuckerkandl: the renal fascia revisited. Radiology 173:845–6.

Coffin A, Boulay-Coletta I, Sebbag-Sfez D et al 2015 Radioanatomy of the retroperitoneal space. Diagn Intern Imaging 96:171–86.

Congdon ED, Edson JN 1941 The cone of renal fascia in the adult white male. Anat Rec 80:289–313.

Culligan K, Remzi FH, Soop M et al 2013 Review of nomenclature in colonic surgery – proposal of a standardised nomenclature based on mesocolic anatomy. Surgeon 11:1–5.

A review making sense of mesocolic anatomy based on findings from modern investigative techniques.

Culligan K, Walsh S, Dunne C et al 2014 The mesocolon: a histological and electron microscopic characterization of the mesenteric attachment of the colon prior to and after surgical mobilization. Ann Surg 260:1048–56.

de Ridder VA, de Lange S, Popta JV 1999 Anatomical variations of the lateral femoral cutaneous nerve and the consequences for surgery. J Orthop Trauma 13:207–11.

Dodds WJ, Darweesh RM, Lawson TL et al 1986 The retroperitoneal spaces revisited. AJR Am J Roentgenol 147:1155–61.

An important radiological perspective on the retroperitoneal 'spaces'.

Feigl GC, Kastner M, Ulz H et al 2011 Topography of the lumbar sympathetic trunk in normal lumbar spines and spines with spondylophytes. Br J Anaesth 106:260–5.

Fleischmann D, Hastie TJ, Dannegger FC et al 2001 Quantitative determination of age-related geometric changes in the normal abdominal aorta. J Vasc Surg 33:97–105.

Golub RM, Parsons RE, Sigel B et al 1992 A review of venous collaterals in inferior vena cava obstruction. Clin Anat 5:441–51.

Groeneveld ME, Meekel JP, Rubinstein SM et al 2018 Systematic review of circulating, biomechanical, and genetic markers for the prediction of abdominal aortic aneurysm growth and rupture. J Am Heart Assoc 7:e007791.

Gwon DI, Ko GY, Yoon HK et al 2007 Inferior phrenic artery: anatomy, variations, pathologic conditions, and interventional management. Radiographics 27:687–705.

Hanna A 2017 The lateral femoral cutaneous nerve canal. J Neurosurg 126:972–78.

Harshavardhana NS, Dabke HV 2014 The furcal nerve revisited. Orthop Rev (Pavia) 6:5428.

Hebbard P, Ivanusic J, Sha S 2011 Ultrasound-guided supra-inguinal fascia iliaca block: a cadaveric evaluation of a novel approach. Anaesthesia 66:300–5.

Hikspoors JPJM, Kruepunga N, Mommen GMC et al 2019 The development of the dorsal mesentery in human embryos and fetuses. Semin Cell Dev Biol 92:18–26.

This is one of a series of papers in an issue of Seminars in Cell and Developmental Biology *that focus on aspects of mesenteric organogenesis. Other papers address mesenteric anatomy and development; mesenteric contributions to abdominal organogenesis; processes underpinning mesenteric development.*

Ho KKF, Walker P, Smithers BM et al 2017 Outcome predictors in median arcuate ligament syndrome. J Vasc Surg 65:1745–52.

Jasper A, Harshe G, Keshava SN et al 2014 Evaluation of normal abdominal aortic diameters in the Indian population using computed tomography. J Postgrad Med 60:57–60.

Kiil BJ, Rozen WM, Pan WR et al 2009 The lumbar artery perforators: a cadaveric and clinical anatomical study. Plast Reconstr Surg 123:1229–38.

Kimura W, Yano M, Sugawara S et al 2010 Spleen-preserving distal pancreatectomy with conservation of the splenic artery and vein: techniques and its significance. J Hepatobiliary Pancreat Sci 17:813–23.

Kirchmair L, Lirk P, Colvin J et al 2008 Lumbar plexus and psoas major muscle: not always as expected. Reg Anesth Pain Med 33:109–14.

Klaassen Z, Marshall E, Tubbs RS et al 2011 Anatomy of the ilioinguinal and iliohypogastric nerves with observations of their spinal nerve contributions. Clin Anat 24:454–61.

Together with Ndiaye et al 2007, these two papers provide a useful description of the anatomy of the ilio-inguinal and iliohypogastric nerves and underline the importance of the ilio-inguinal nerve in clinical practice.

Kneeland JB, Auh YH, Rubenstein WA et al 1987 Perirenal spaces: CT evidence for communication across the midline. Radiology 164:657–64.

Lee MW, McPhee RW, Stringer MD 2008 An evidence-based approach to human dermatomes. Clin Anat 21:363–73.

Lolis E, Panagouli E, Venieratos D 2011 Study of the ascending lumbar and iliolumbar veins: surgical anatomy, clinical implications and review of the literature. Ann Anat 193:516–29.

Loukas M, Hullett J, Wagner T 2005a Clinical anatomy of the inferior phrenic artery. Clin Anat 18:357–65.

Loukas M, Louis RG Jr, Hullett J et al 2005b An anatomical classification of the variations of the inferior phrenic vein. Surg Radiol Anat 27:566–74.

Loukas M, Wartmann CT, Louis RG Jr et al 2007 Cisterna chyli: a detailed anatomic investigation. Clin Anat 20:683–8.

This article revises traditional concepts about the cisterna chyli and its formation.

Mahan MA, Sanders LE, Guan J et al 2017 Anatomy of psoas muscle innervation: cadaveric study. Clin Anat 30:479–86.

Mirjalili SA, Hale SJ, Buckenham T et al 2012a A reappraisal of adult thoracic surface anatomy. Clin Anat 25:827–34.

Mirjalili SA, McFadden SL, Buckenham T et al 2012b A reappraisal of adult abdominal surface anatomy. Clin Anat 25:844–50.

A paper that challenges some traditional surface anatomical landmarks by investigating results from analysis of CT images in living supine adults.

Moeller TB, Reif E 2000 Normal Findings in CT and MRI. New York: Thieme.

Moore AE, Stringer MD 2011 Iatrogenic femoral nerve injury: a systematic review. Surg Radiol Anat 33:649–58.

Morita S, Kimura T, Masukawa A et al 2007 Flow direction of ascending lumbar veins on magnetic resonance angiography and venography: would 'descending lumbar veins' be a more precise name physiologically? Abdom Imaging 32:749–53.

Moro T, Kikuchi S, Konno S et al 2003 An anatomic study of the lumbar plexus with respect to retroperitoneal endoscopic surgery. Spine (Phila Pa 1976) 28:423–8.

Morton GC, Thomas GM 2008 Testis. In: Halperin EC, Perez C, Brady LW (eds) Perez and Brady's Principles and Practice of Radiation Oncology, 5th ed. Wolters Kluwer.

Moussallem CD, Abou Hamad I, El-Yahchouchi CA et al 2012 Relationship of the lumbar lordosis angle to the abdominal aortic bifurcation and inferior vena cava confluence levels. Clin Anat 25:866–71.

Murata Y, Takahashi K, Yamagata M et al 2003 Variations in the number and position of human lumbar sympathetic ganglia and rami communicantes. Clin Anat 16:108–13.

Ndiaye A, Diop M, Ndoye JM et al 2007 Anatomical basis of neuropathies and damage to the ilioinguinal nerve during repairs of groin hernias (about 100 dissections). Surg Radiol Anat 29:675–81.

Together with Klaassen et al 2011, these two papers provide a useful description of the anatomy of the ilio-inguinal and iliohypogastric nerves and underline the importance of the ilio-inguinal nerve in clinical practice.

Needleman L 2006 Measurements of the abdominal aorta. In: Goldberg BB, McGahan JP (eds) Atlas of Ultrasound Measurements, 2nd ed. Boston: Elsevier, Mosby.

Niggemann P, Förg A, Grosskurth D et al 2010 Postural effect on the size of the cisterna chyli. Lymphat Res Biol 8:193–7.

Pacak K, Tella SH 2018 Pheochromocytoma and paraganglioma. In: Degroot LJ, Chrousos G, Dungan K et al (eds) Endotext [Internet]. https://www.ncbi.nlm.nih.gov/books/NBK481899/.

Panagouli E, Venieratos D, Lolis E et al 2013 Variations in the anatomy of the celiac trunk: a systematic review and clinical implications. Ann Anat 195:501–11.

Paño B, Sebastià C, Buñesch L et al 2011 Pathways of lymphatic spread in male urogenital pelvic malignancies. Radiographics 31:135–60.

Park RJ, Tsao H, Cresswell AG et al 2012 Differential activity of regions of the psoas major and quadratus lumborum during submaximal isometric trunk efforts. J Orthop Res 30:311–18.

Phang K, Bowman M, Phillips A et al 2014 Review of thoracic duct anatomical variations and clinical implications. Clin Anat 27:637–44.

Phillips S, Mercer S, Bogduk N 2008 Anatomy and biomechanics of quadratus lumborum. Proc Inst Mech Eng H 222:151–9.

Rab M, Ebmer J, Dellon AL 2001 Anatomic variability of the ilioinguinal and genitofemoral nerve: implications for the treatment of groin pain. Plast Reconstr Surg 108:1618–23.

Ranson C, Burnett A, O'Sullivan P et al 2008 The lumbar paraspinal muscle morphometry of fast bowlers in cricket. Clin J Sport Med 18:31–7.

Rogers IS, Massaro JM, Truong QA et al 2013 Distribution, determinants, and normal reference values of thoracic and abdominal aortic diameters by computed tomography (from the Framingham Heart Study). Am J Cardiol 111:1510–16.

Skandalakis JE, Coborn, GL, Weidman, TA et al 2004 Lymphatic system. In: Skandalakis JE (ed in chief) Skandalakis' Surgical Anatomy. Athens: Paschalidis Medical Publications. Ch. 29; pp. 1641–59.

Spentzouris G, Zandian A, Cesmebasi A et al 2014 The clinical anatomy of the inferior vena cava: a review of common congenital anomalies and considerations for clinicians. Clin Anat 27:1234–43.

Stamatiou D, Skandalakis JE, Skandalakis LJ et al 2009 Lumbar hernia: surgical anatomy, embryology, and technique of repair. Am Surg 75:202–7.

Takayama T, Yamanouchi D 2013 Aneurysmal disease: the abdominal aorta. Surg Clin North Am 93:877–91.

Toni R, Mosca S, Favero L et al 1988 Clinical anatomy of the suprarenal arteries: a quantitative approach by aortography. Surg Radiol Anat 10:297–302.

Tourani SS, Taylor GI, Ashton MW 2013 Anatomy of the superficial lymphatics of the abdominal wall and the upper thigh and its implications in lymphatic microsurgery. J Plast Reconstr Aesthet Surg 66:1390–5.

Tubbs RS, Shoja M, Loukas M 2016 Bergman's Comprehensive Encyclopedia of Human Anatomic Variation. Hoboken: Wiley Blackwell.

A textbook dedicated to detailing the anatomical variations found in man.

Tubbs RS, Loukas M, Hanna AS et al 2018 Surgical Anatomy of the Lumbar Plexus. New York: Thieme.

This book reviews the detailed anatomy and surgical implications of the lumbar plexus and its branches.

Turgut M, Protas M, Gardner B et al 2017 The accessory obturator nerve: an anatomical study with literature analysis. Anatomy 11: 121–127.

Willard FH, Vleeming A, Schuenke MD et al 2012 The thoracolumbar fascia: anatomy, function and clinical considerations. J Anat 221:507–36.

An evidence-based review of the complex and clinically important thoracolumbar fascia.

Winston CB, Lee NA, Jarnagin WR et al 2007 CT angiography for delineation of celiac and superior mesenteric artery variants in patients undergoing hepatobiliary and pancreatic surgery. AJR Am J Roentgenol 189:W13–19.

CHAPTER
62

Peritoneum, mesentery and peritoneal cavity

The peritoneum is the largest serous membrane in the body. In males the peritoneum forms a closed sac, but in females it is open at the abdominal ostia of the uterine tubes. Its smooth appearance is unremarkable, but its conformation varies. Directly beneath the single layer of mesothelium is a well-developed basement membrane, outside which is a rich lymphatic plexus. Microscopic mesothelial pores or peritoneal stomata are distributed throughout the peritoneum but particularly on the undersurface of the respiratory diaphragm and anterior abdominal wall (Wassilev et al 1998). At the peritoneal stomata the mesothelium is close to underlying lymphatic endothelial cells and there is no intervening basement membrane. Both peritoneal stomata and sites of macrophage and lymphoid aggregates ('milky spots') in the omenta contribute to peritoneal fluid absorption, and their occlusion by malignant cells can result in ascites (diZerega and Rodgers 1992, Hagiwara et al 1994). Neighbouring mesothelial cells are joined by junctional complexes but permit macrophages to pass. Some regions of the submesothelial connective tissue also contain macrophages, lymphocytes and adipocytes.

The normal pressure within the peritoneal cavity is about 2–10 mmHg (higher in pregnant and obese individuals) (Sanchez et al 2001). It can be measured directly using a catheter inserted into the abdomen, or indirectly by monitoring the pressure in the urinary bladder or stomach. The pressure inside the abdomen can increase after trauma as a result of the accumulation of blood, fluid or oedema, leading to 'abdominal compartment syndrome'. In such patients, monitoring of intra-abdominal pressure can identify major increases (above about 25 mmHg) that could jeopardize blood flow to vital organs and dictate the need for urgent decompression.

PERITONEAL FLUID

The peritoneal cavity lies between the parietal peritoneum, which lines the abdominal walls, the visceral peritoneum (covering abdominal viscera and mesentery) and the peritoneal reflection. It contains a small amount of peritoneal fluid, rarely more than 5 ml in healthy males and postmenopausal females (Yoshikawa et al 2013). Up to 25 ml of fluid can be present in healthy young females, depending on the phase of the menstrual cycle (Koninckx et al 1980). The fluid allows the viscera covered with peritoneum, i.e. intermesenteric, to glide freely within the peritoneal cavity. Normal peritoneal fluid contains water, proteins (less than 30 g per litre), electrolytes and solutes derived from interstitial fluid in the adjacent tissues and from plasma in local capillaries. It also contains a few cells, including desquamated mesothelium, nomadic peritoneal macrophages, mast cells, fibroblasts, lymphocytes and other leukocytes. Macrophages migrate freely between the peritoneal cavity and the surrounding connective tissue. In females, blood or fluid can enter the peritoneal cavity from a ruptured ovarian follicle or from the retrograde flow of menstrual fluid along the uterine tubes (which can cause endometriosis). Under normal circumstances, the peritoneal cavity contains no air.

The peritoneum and its fluid have important defensive properties (Autio 1964). Peritoneal fluid flows in a predominantly clockwise direction around the peritoneal cavity and gravitates to dependent sites within the cavity: diaphragmatic respiratory movements, negative intrathoracic pressure and intestinal peristalsis encourage flow from the pelvis to the subphrenic regions, even when the individual is erect (Meyers et al 1987, Meyers 1994). Fluid preferentially ascends from the inferior abdomen and pelvis to the right subhepatic and subphrenic spaces via the right paracolic gutter (deeper than the left paracolic gutter in the supine position and there is no phrenicocolic ligament or reflection to obstruct flow) (Meyers 1973). Passage across the midline to the left subphrenic space is prevented by the falciform ligament. Malignant cells can become trapped within peritoneal recesses or in the milky spots of the greater omentum, where they proliferate and produce visible and palpable tumour deposits. These sites must be deliberately examined during searches for peritoneal metastases (Zonca et al 2008). Gross infiltration of the omentum by cancer is often referred to as an 'omental cake'. The movement of peritoneal fluid explains the presence of disease at sites such as the undersurface of the right half of the respiratory diaphragm and the pelvic pouches. An example is Fitz–Hugh–Curtis syndrome, in which organisms causing gonorrhoea or chlamydia organisms enter the peritoneal cavity through the uterine tubes and are transported in the peritoneal fluid to the right upper quadrant, where they cause perihepatic inflammation. Disruption of the integrity of the peritoneum by percutaneous puncture, laparoscopy or open surgery profoundly affects its defensive function and can create 'sticky' sites where pathogens or malignant cells can settle and proliferate.

Rarely there are direct communications (pleuroperitoneal fenestrae) between the peritoneal and pleural cavities (Simmons and Mir 1989, Pestieau et al 2000).

PERITONEAL ATTACHMENTS

The parietal peritoneum is attached to the muscular layers of the abdominal wall by extraperitoneal connective tissue. It detaches from the abdominal wall to continue as the visceral peritoneum of nearby viscera (including the mesentery). The region of detachment is referred to as the peritoneal reflection (**Fig. 62.1A**). The parietal peritoneum is only loosely attached around the urinary bladder and rectum so as to accommodate alterations in their size, whereas it adheres firmly to the inferior surface of the respiratory diaphragm and linea alba. The extraperitoneal tissue over the posterior abdominal wall frequently contains large amounts of fat, especially in obese males. Visceral peritoneum adheres firmly to the underlying viscera, often blends with connective tissue in the wall of the organ and rarely contains loose connective or adipose tissue.

GENERAL ARRANGEMENT OF THE PERITONEUM

The gastrointestinal tract develops as a single tube suspended in the abdominal cavity by ventral and dorsal regions of the mesentery (Ch. 21). The mesentery is derived from the dorsal and ventral mesenteries. The rotation and subsequent attachment of parts of the gastrointestinal tract to the posterior abdominal wall create the impression that these structures are retroperitoneal. However, it is now acknowledged that the mesentery is continuous and that all regions of the intestine are centrally connected via the attached mesentery (Byrnes et al 2019a–2019d) (see Fig. 62.1A). The intestines can be divided into attached and non-attached regions. Attached regions include the duodenum, ascending and descending colons and the rectum. Non-attached regions include the stomach, small intestine, and the transverse and sigmoid colon.

The mesentery is continuous from the gastro-oesophageal to the anorectal junctions (Byrnes et al 2019a–2019d). All abdominal digestive organs are continuous with a region of the mesenteric frame. Some regions (the greater and lesser omenta) differ considerably in appearance from others, including the mesocolon and mesosigmoid (sigmoid mesocolon). Where the parietal peritoneum detaches from the abdominal wall as the peritoneal reflection, and extends to adjacent viscera such as the liver, it is often termed a 'ligament'. The mesentery contains neurovascular bundles and lymphatic **vessels** that supply digestive system organs. In individuals with obesity, extensive adipose tissue within the mesentery can obscure neurovascular bundles. In contrast, in the very young, elderly or malnourished, the mesentery lacks adipose tissue and neurovascular bundles are more obvious within 'mesenteric pedicles' that are routinely used as anatomical landmarks to guide abdominal surgeons.

The surfaces of viscera attached to the mesentery contribute to the visceral component of the peritoneal landscape. The latter is often subdivided into potential 'spaces' where fluids such as blood or purulence can accumulate under pathological conditions.

Surgical planes are defined by anatomical structures

Abdominal surgeons rigorously follow an anatomical roadmap when conducting resections, in order to minimize blood loss and trauma to tissues. The map is created by the mesentery and its continuity with abdominal digestive organs, and the surrounding peritoneal reflection. The surgeon incises the peritoneum to access the plane between the mesentery and underlying fascia (**Fig. 62.1B**). When the intact mesentery has been detached from the fascia back to the midline, it can be disconnected by dividing major vascular trunks. These activities are repeated at all levels from the oesophagus to the rectum and are based on the anatomical foundation provided by the mesentery and associated peritoneum (**Figs 62.2-62.4**).

Peritoneum of the upper abdomen

The abdominal part of the oesophagus, stomach, liver and spleen all lie within a region that runs from the posterior to the anterior abdominal walls and is broadly termed the mesogastrium (Coakley and Hricak 1999). Its attachments are divisible into regions such as the falciform ligament, coronary ligament, lesser omentum (hepatogastric and hepatoduodenal ligaments), greater omentum (including the gastrocolic ligament), gastrosplenic ligament, splenorenal ligament and phrenicocolic ligament (see Fig. 62.1A; **Fig. 62.5**).

Falciform ligament

The falciform ligament is a thin anteroposterior double fold of peritoneum that represents an anterior portion of the mesentery connecting the liver to the posterior aspect of the anterior abdominal wall. It extends inferiorly to the level of the umbilicus and superiorly it narrows to a depth of 1–2 cm as the distance between the liver and anterior abdominal wall decreases. Its two peritoneal layers separate to enclose the liver, to which it adheres firmly. Superiorly, the two peritoneal layers are continuous with the parietal peritoneum on the undersurface of the respiratory diaphragm, from which they are reflected laterally to form the superior layer of the coronary ligament of the liver on the right and the left triangular ligament of the liver on the left. The inferior aspect of the falciform ligament forms a free border, where the two peritoneal layers are continuous with each other as they enclose the round ligament of the liver (ligamentum teres hepatis), a remnant of the umbilical vein. Because the peritoneum of the falciform ligament is continuous with that covering the posterior abdominal wall and with the parietal peritoneum of the anterior abdominal wall, blood from a retroperitoneal haemorrhage (commonly, acute haemorrhagic pancreatitis) can track beneath the peritoneum and appear as haemorrhagic discoloration around the umbilicus (Cullen's sign). The blood-tinged fluid reaches the peri-umbilical region via the lesser omentum and the falciform ligament.

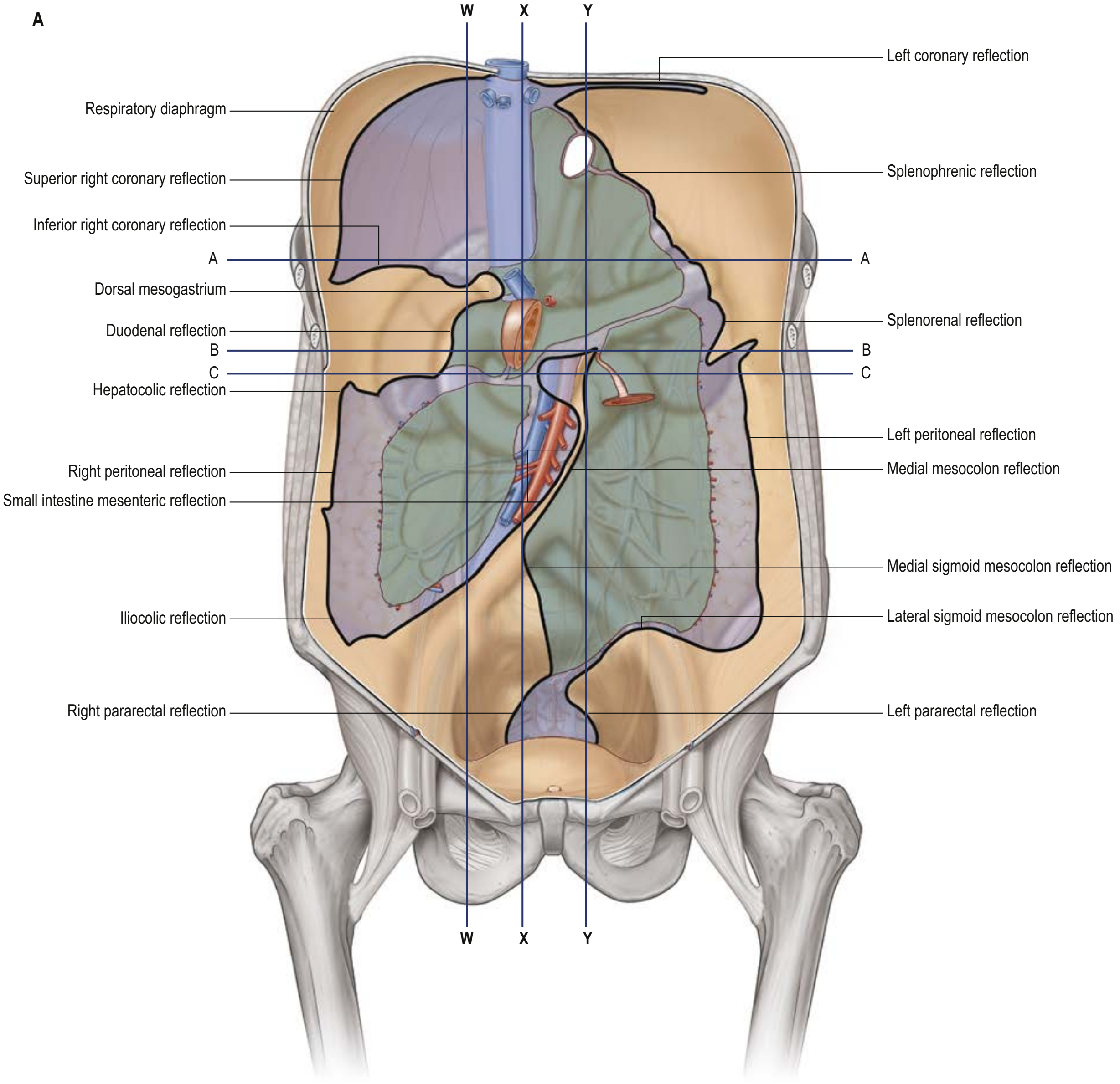
A
W
X
Y
Respiratory diaphragm
Superior right coronary reflection
Inferior right coronary reflection
A
Dorsal mesogastrium
Duodenal reflection
B
C
Hepatocolic reflection
Right peritoneal reflection
Small intestine mesenteric reflection
Iliocolic reflection
Right pararectal reflection
Left coronary reflection
Splenophrenic reflection
A
Splenorenal reflection
B
C
Left peritoneal reflection
Medial mesocolon reflection
Medial sigmoid mesocolon reflection
Lateral sigmoid mesocolon reflection
Left pararectal reflection
W
X
Y

Fig. 62.1 **A**, The posterior abdominal wall, showing the lines of peritoneal reflection, after removal of the liver, spleen, stomach, jejunum, ileum, caecum, transverse colon and sigmoid colon. The various sessile organs can be seen through the posterior wall of the parietal peritoneum. Note the ascending and descending colons, duodenum, kidneys, suprarenal glands, pancreas and inferior vena cava. Line W–W represents the plane of Fig. 62.2. Line X–X represents the plane of Fig. 62.3. Line Y–Y represents the plane of Fig. 62.4. Line A–A represents the plane of Fig. 62.5A. Line B–B represents the plane of Fig. 62.5B. Line C–C represents the plane of Fig. 62.5C. *Continued*

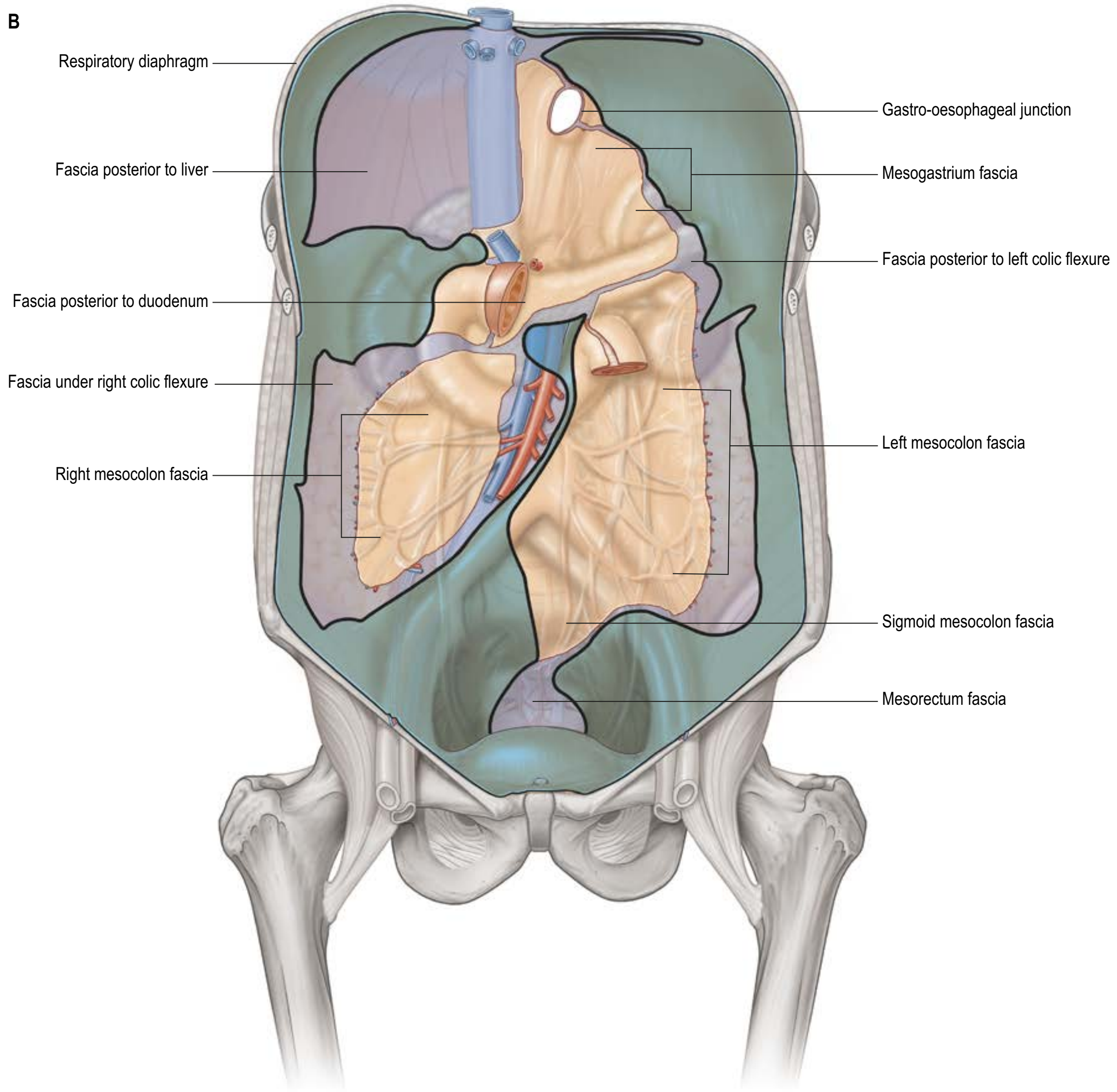
B
Respiratory diaphragm
Fascia posterior to liver
Fascia posterior to duodenum
Fascia under right colic flexure
Right mesocolon fascia
Gastro-oesophageal junction
Mesogastrium fascia
Fascia posterior to left colic flexure
Left mesocolon fascia
Sigmoid mesocolon fascia
Mesorectum fascia

Fig. 62.1 cont'd B, Regions of fascial attachment of various abdominal organs.

Peritoneal and mesenteric connections of the liver

The liver is almost completely covered in visceral peritoneum, and only the 'bare area' posteriorly is directly apposed to the right half of the respiratory diaphragm. Peritoneal ligaments (also referred to as peritoneal reflections) and regions of mesentery run from the liver to the surrounding viscera and to the abdominal wall and respiratory diaphragm (see Figs 62.1A, 62.2); they are described in detail in Chapter 66.

The coronary ligament is formed by the reflection of the peritoneum from the respiratory diaphragm onto the superior and posterior surfaces of the right lobe of the liver. Between the two layers of this ligament, a large triangular area, the bare area of the liver, is devoid of peritoneal covering. Here, the liver is connected to, but separated from, the respiratory diaphragm by a thin layer of areolar tissue. On the right, the two layers of the coronary ligament converge laterally to form the right triangular ligament. On the left, the two layers of peritoneal reflection fuse to form the left triangular ligament. The superior layer of the coronary ligament is reflected superiorly onto the undersurface of the diaphragm and inferiorly onto the right and superior surfaces of the liver. The inferior layer of the coronary ligament is reflected inferiorly from the posterior surface of the liver onto the posterior abdominal wall, where it is continuous with the parietal peritoneum overlying the right kidney, and continues to the superior (first) part of the duodenum and right colic flexure (see Fig. 62.3). Medially, it passes in front of a short segment of the inferior vena cava lying between the superior part of the duodenum inferiorly and the caudate process of the liver superiorly, forming the posterior wall of the omental foramen. It continues to the left as the peritoneum overlying the anterior surface of the dorsal mesogastrium, turns anteriorly and continues as the undersurface of the greater omentum.

The peritoneal recess between the inferior surface of the liver and the colic component of the right colic flexure is known as the hepatorenal recess (pouch of Morison) (Stringer 2009). In the supine position, this is the most dependent part of the peritoneal cavity in the upper abdomen and is a site toward which fluid or peritoneal metastases can gravitate.

The right triangular ligament is a short, V-shaped fold at the right lateral limit of the bare area of the liver where the two layers of the coronary ligament converge. As it is reflected onto the abdominal wall it is continuous with the parietal peritoneum of the right posterolateral abdominal wall. Surgical division of the right triangular and coronary ligaments allows the right lobe of the liver to be retracted anteriorly, exposing the lateral aspect of the inferior vena cava posterior to the liver.

The left triangular ligament is a double layer of peritoneum that extends for a variable distance over the superior border of the left lobe of the liver. Medially, the anterior leaf is continuous with the left layer (or left surface) of the falciform ligament, while the posterior leaf is continuous with the lesser omentum. The left triangular ligament lies anterior to the abdominal part of the oesophagus, the superior limits of the lesser omentum, and part of the fundus of the stomach. It is continuous with the parietal peritoneum lining the undersurface of the left side of the respiratory diaphragm, which is continuous with the parietal peritoneum lining the posterior abdominal wall. Division of the left triangular ligament allows the left lobe of the liver to be mobilized; the ligament is an important stabilizing factor for the left lobe after excision of the right lobe of the liver.

Lesser omentum

The lesser omentum is a region of mesentery derived from the ventral mesogastrium. Formed by two layers of peritoneum separated by a variable amount of connective tissue and fat, it runs between the inferior, visceral surface of the liver and the abdominal part of the oesophagus, stomach, pylorus and superior part of the duodenum. Superiorly, its attachment to the inferior surface of the liver forms an L shape. The

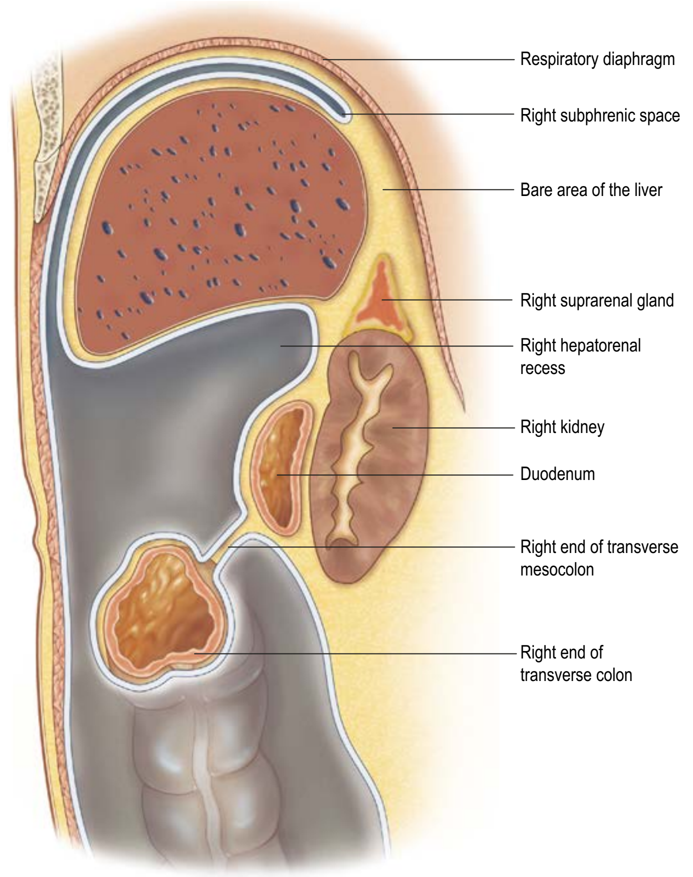
Respiratory diaphragm
Right subphrenic space
Bare area of the liver
Right suprarenal gland
Right hepatorenal recess
Right kidney
Duodenum
Right end of transverse mesocolon
Right end of transverse colon

Fig. 62.2 A sagittal section through the abdomen to the right of the omental foramen along the line of W–W in Fig. 62.1.

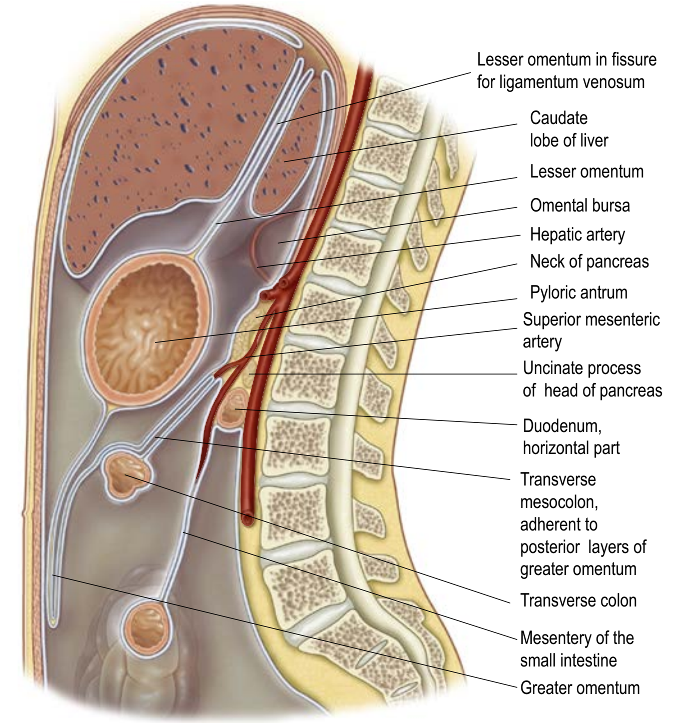
Lesser omentum in fissure for ligamentum venosum
Caudate lobe of liver
Lesser omentum
Omental bursa
Hepatic artery
Neck of pancreas
Pyloric antrum
Superior mesenteric artery
Uncinate process of head of pancreas
Duodenum, horizontal part
Transverse mesocolon, adherent to posterior layers of greater omentum
Transverse colon
Mesentery of the small intestine
Greater omentum

Fig. 62.4 A sagittal section through the abdomen, approximately in the median plane. Compare with Fig. 62.1. The section cuts the posterior abdominal wall along the line Y–Y in Fig. 62.1. The peritoneal cavity is shown by blue shading; the peritoneum and its cut edges are in pale blue.

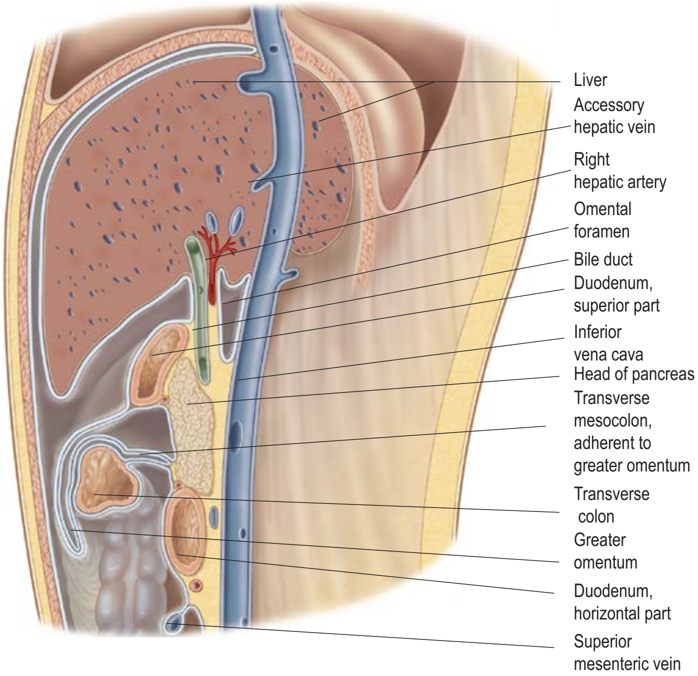
Liver
Accessory hepatic vein
Right hepatic artery
Omental foramen
Bile duct
Duodenum, superior part
Inferior vena cava
Head of pancreas
Transverse mesocolon, adherent to greater omentum
Transverse colon
Greater omentum
Duodenum, horizontal part
Superior mesenteric vein

Fig. 62.3 A section through the superior part of the abdominal cavity, along the line X–X in Fig. 62.1. The boundaries of the omental foramen are shown and a small recess of the omental bursa is displayed anterior to the head of the pancreas. Note that the transverse colon and its mesocolon adhere to the posterior two layers of the greater omentum. Four peritoneal layers contribute to the formation of the greater omentum.

vertical component of the L shape is formed by the fissure for the ligamentum venosum, and inferiorly, the attachment turns horizontally to complete the L in the porta hepatis. The part of the lesser omentum running between the liver and the stomach is the hepatogastric ligament and the part between the liver and duodenum is the hepatoduodenal ligament. The right and left gastric vessels, branches of the vagal trunks and lymph nodes are contained within the two layers of the hepatogastric ligament close to its attachment to the stomach. An accessory or replaced left hepatic artery is sometimes present. The anterior layer of the lesser omentum descends from the fissure for the ligamentum venosum on to the anterior surface of the abdominal part of the oesophagus, stomach and duodenum. The posterior layer descends from the fissure and runs on to the posterior surface and pylorus of the stomach: it forms part of the anterior surface of the omental bursa (see Fig. 62.4). At the lesser curvature of the stomach, the peritoneal layers of the lesser omentum become continuous with the visceral peritoneum covering the anterior and posterior surfaces of the stomach.

The free right lateral border of the lesser omentum (i.e. the hepatoduodenal ligament) is thickened to form a mesenteric pedicle that extends from the porta hepatis to the junction between the superior and descending (second) parts of the duodenum. It forms the anterior boundary of the omental foramen and contains the hepatic portal vein (posteriorly), the bile duct (anteriorly to the right) and proper hepatic artery (anteriorly to the left) (see Figs 62.3, 62.5B), together with lymphatic vessels, lymph nodes and hepatic autonomic nerves. An accessory or replaced right hepatic artery sometimes arises from the superior mesenteric artery in the free edge of the lesser omentum, usually running posterior to the hepatic portal vein. Often the free margin of the lesser omentum extends to the right as the cystoduodenal ligament that contains the gallbladder, cystic artery and duct and lymph nodes (Ashaolu et al 2011). This is of considerable clinical significance: this mesenteric appendage must be visualized in order to remove the gallbladder safely (i.e. cholecystectomy). The hepatoduodenal ligament continues distally posterior to the superior part of the duodenum and merges with the mesentery of the duodenum.

The superior border of the lesser omentum is short and runs over the inferior surface of the respiratory diaphragm between the liver and the medial aspect of the abdominal part of the oesophagus. The lesser omentum is thinner in this region and contains a variable amount of connective tissue, especially fat. It has a translucent appearance where it is thinnest, a feature that guides surgeons in identifying regions that can be divided safely.

Greater omentum

The greater omentum is the largest peritoneal fold and hangs inferiorly from the greater curvature of the stomach. When the undisturbed abdomen is opened, the greater omentum is frequently draped over the superior abdominal organs, but often not in the even distribution shown in many illustrations. It is usually thin but always contains some adipose tissue and is a common site for storage of fat in obese individuals, particularly males (Coulier 2009). The greater omentum is a double sheet: each sheet consists of two layers of peritoneum separated by a small amount of connective tissue. The two sheets are folded back on themselves and adhere firmly to each other inferior to the transverse colon. Above this level the anterior sheet separates from the posterior sheet and is attached to the greater curvature of the stomach (see Fig. 62.4); this supracolic part of the greater omentum is known as the gastrocolic ligament. The most anterior layer of peritoneum of the greater omentum is continuous with the visceral peritoneum over the anterior surface of the stomach and duodenum. The anterior sheet descends from the greater curvature of the stomach and superior part of the duodenum for a variable distance into the peritoneal cavity and then turns sharply backwards on itself to ascend as the posterior sheet. The posterior sheet is extremely thin where it attaches to the transverse colon and superior surface of the transverse mesocolon. It extends cephalad, attached to (but not fused with) the superior surface of the transverse mesocolon, until it reaches the inferior border of the body and head of the pancreas (see Figs 62.4, 62.5C). At the pancreas the anterior layer envelops the pancreas and continues cephalad as the dorsal mesogastrium (see above). During surgery, the transverse mesocolon and greater omentum are separated by dividing through the posterior layer of the greater omentum, where this first attaches to the transverse colon. Alternatively, surgeons frequently divide directly through the greater omentum at the level where it approaches the greater curvature of the stomach. These activities are essential for gaining entry into the omental bursa.

On the left side of the abdomen, the greater omentum is attached to the gastrosplenic ligament or the peritoneal reflection in this region; on the right side, it extends to the beginning of the duodenum (see Fig. 62.4). A region of peritoneal reflection, the hepatocolic ligament, always extends from the inferior surface of the right lobe of the liver to the right colic flexure. The right border of the greater omentum usually adheres to the anterior surface of this region of reflection and thereafter to the right colic flexure and superior part of the ascending colon. In individuals, with obesity the right border of the greater omentum often extends laterally to adhere to the lateral border of the ascending colon and its associated region of peritoneal reflection (Jackson's membrane). Less commonly, the left border of the greater omentum adheres to the anterior surface of the descending colon.

The greater omentum has a rich blood supply derived from the right and left gastro-omental (gastro-epiploic) vessels that run between the two peritoneal layers of the anterior sheet of greater omentum, close to the greater curvature of the stomach. These vessels give off numerous omental branches that run the length of the omentum. Microscopic capillary convolutions, sometimes termed 'omental glomeruli', lie directly beneath the mesothelium of the greater omentum. They are surrounded by aggregations of macrophages and lymphocytes (milky spots) that drain into lymphatic vessels (Shimotsuma et al 1993); the macrophages form clusters near the mesothelial surface, while B and T lymphocytes are grouped around vessels. The fenestrated endothelium lining the omental glomeruli and the mesothelium overlying the milky spots form sites of leukocyte migration and peritoneal fluid absorption (Platell et al 2000). The number and size of milky spots increase when there is peritoneal inflammation, highlighting their defensive role.

The greater omentum serves several important functions. It is highly mobile and frequently adheres to inflamed viscera or foreign bodies within the abdominal cavity. This can limit the spread of infection, as in the walling-off of acute appendicitis, and promote haemostasis. However, it can also block peritoneal drains and catheters (such that omentectomy is sometimes performed when intraperitoneal catheters are placed). It absorbs peritoneal fluid. It contains macrophages and lymphoid tissue capable of destroying pathogens; for example, macrophages and neutrophils readily migrate from the greater omentum into the peritoneal cavity when there is peritonitis. It promotes neovascularization of the structures to which it adheres and thus promotes healing of ischaemic tissues and supports splenic autotransplantation (Ch. 69).

The remarkable capacity of the greater omentum to participate in reparative processes is highlighted by its use as an omental pedicle flap or free flap in reconstructive surgery: it has been used to support closure of gastrointestinal perforations, fill 'dead space' after surgical excision of pathology, and cover wound defects. A greater omental pedicle or free flap based on the right gastro-omental vessels can be mobilized by dividing the gastric branches of these vessels close to the surface of the stomach and the left gastro-omental vessels near their origin.

Peritoneal connections of the spleen

The peritoneal connections of the spleen anchor it in the left upper quadrant of the abdomen. Although they are called ligaments, they are regions of peritoneal reflection from the parietal peritoneum of the left upper quadrant to the spleen. They include the gastrosplenic, splenorenal and phrenicocolic ligaments. The gastrosplenic ligament runs between the greater curvature of the stomach and the splenic hilum, and is the cephalad continuation of the greater omentum. The peritoneal layers of the gastrosplenic ligament separate to enclose the spleen. The outer layer then detaches from the spleen to form the splenorenal and phrenicocolic ligaments that continue posteriorly as the dorsal mesogastrium, forming the posterior wall of the omental bursa. The splenorenal ligament extends from the spleen to the posterior abdominal wall and the phrenicocolic ligament connects the left colic flexure to the respiratory diaphragm.

The splenorenal ligament (see Figs 62.1, 62.5B) is continuous medially with the peritoneum of the posterior wall of the omental bursa over the left kidney and runs up to the splenic hilum, where it is continuous with the posterior layer of the gastrosplenic ligament. The posterior layer of the splenorenal ligament is continuous laterally with the peritoneum over the inferior surface of the respiratory diaphragm and runs onto the splenic surface over the renal impression. The splenic vessels lie between the layers of the splenorenal ligament; the tail of the pancreas is usually present in its inferior portion.

As the gastrosplenic ligament is a cephalad extension of the greater omentum, it also consists of two layers of peritoneum (see Fig. 62.5B). The posterior layer is continuous with the peritoneum of the splenic hilum and the peritoneum over the posterior surface of the stomach. This layer continues medially as the anterior surface of the dorsal mesogastrium. The anterior layer is continuous with the peritoneum reflected off the gastric impression of the spleen and with the peritoneum over the anterior surface of the stomach. The short gastric and left gastro-omental branches of the splenic artery, with their corresponding veins, pass between the layers of the gastrosplenic ligament.

The phrenicocolic ligament is a region of peritoneal reflection extending from the colic component of the left colic flexure to the adjacent parietal peritoneum. Medially, it is attached to the left border of the greater omentum. Inferiorly, it continues as the left lateral reflection. Superiorly, it continues as the splenorenal ligament or region of reflection.

Undue traction on the peritoneal attachments of the spleen at surgery can cause a capsular tear and serious bleeding. A clear understanding of peritoneal anatomy in this region is therefore essential for the surgeon. Downward traction on the phrenicocolic ligament during mobilization of the left colic flexure is particularly hazardous; medial traction on the greater omentum can also injure the spleen if the omentum adheres to the fibrous capsule of the spleen. Unfortunately, surgical trauma is the main cause for splenectomy.

Peritoneum of the lower abdomen

The posterior surface of the inferior anterior abdominal wall is lined by parietal peritoneum, which extends from the linea alba centrally to the lateral paracolic gutters, where it is reflected over the front and sides of the ascending colon on the right and the descending colons on the left (see Fig. 62.5C). The ascending and descending colons are now regarded as having attached regions of mesentery (i.e. the right and left mesocolon respectively). The surface of the viscus is considered to be lined by visceral peritoneum that is continuous with the parietal peritoneum at regions of peritoneal reflection. In keeping with this, the parietal peritoneum is reflected onto the small intestine mesentery where this approaches the posterior abdominal wall, and continues laterally as the right mesocolon. The anatomical organization of the small and large intestines and associated mesentery explain the organization of their surrounding peritoneal reflection at all levels from the duodenojejunal flexure to the mesorectum.

Transverse mesocolon

The mesentery of the transverse colon is a region of the mesentery associated with the large intestine that suspends the transverse colon in the peritoneal cavity. The transverse mesocolon attaches centrally and obliquely from the anterior aspect of the descending part of the duodenum, over the head and neck of the pancreas superior to the duodenojejunal junction, and over the superior pole of the left kidney to the left colic flexure (see Figs 62.2–62.4). It contains the middle colic vessels and their branches, together with autonomic nerves from the aortic plexus, lymphatic vessels and lymph nodes. Near the left colic flexure, the ascending branch of the left colic artery terminates within the transverse mesocolon. Its two peritoneal layers pass to the posterior surface of the transverse colon, where they separate to invest it. In between the flexures, the superior layer of mesocolic peritoneum is attached to the

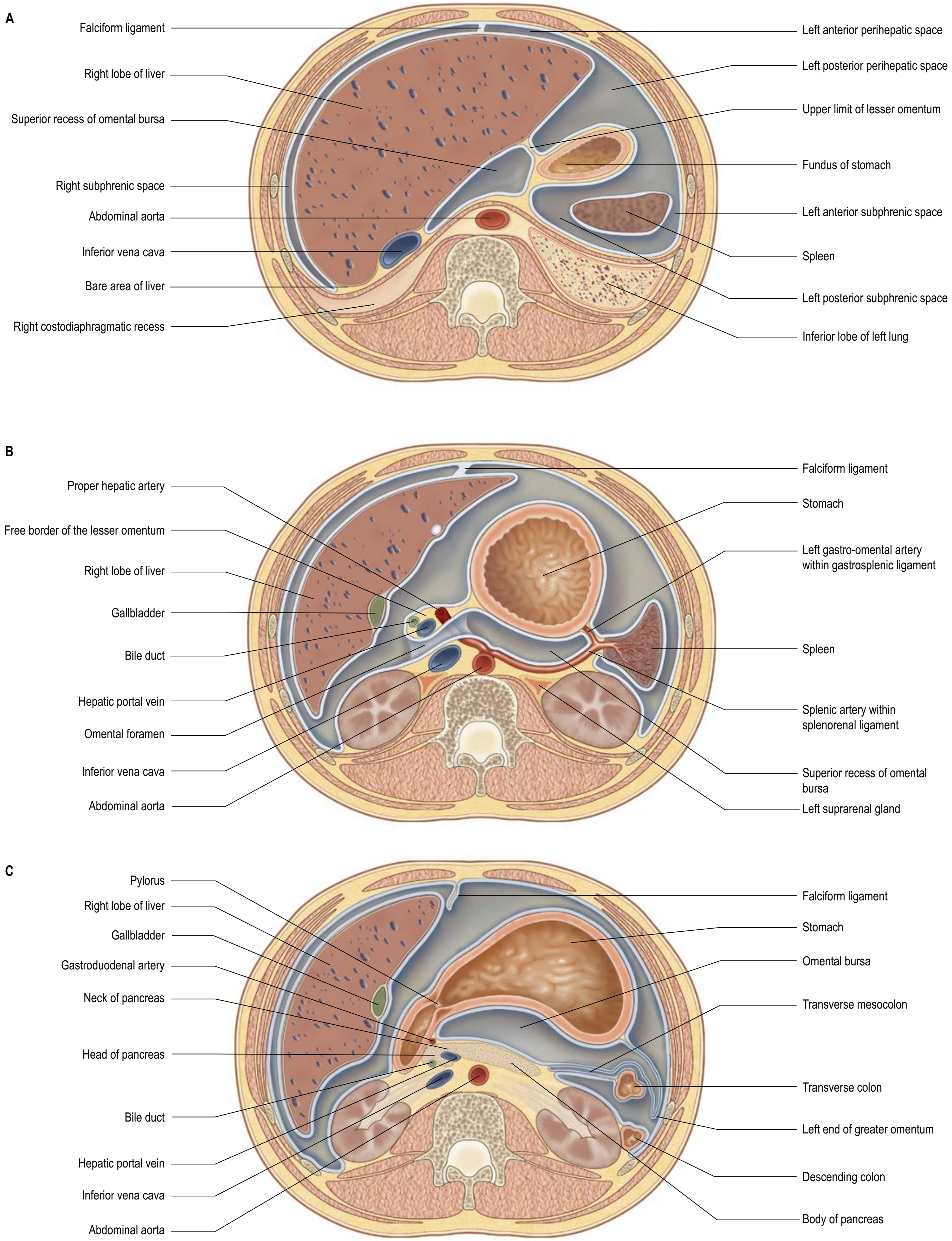
A
Falciform ligament
Right lobe of liver
Superior recess of omental bursa
Right subphrenic space
Abdominal aorta
Inferior vena cava
Bare area of liver
Right costodiaphragmatic recess
Left anterior perihepatic space
Left posterior perihepatic space
Upper limit of lesser omentum
Fundus of stomach
Left anterior subphrenic space
Spleen
Left posterior subphrenic space
Inferior lobe of left lung
B
Proper hepatic artery
Free border of the lesser omentum
Right lobe of liver
Gallbladder
Bile duct
Hepatic portal vein
Omental foramen
Inferior vena cava
Abdominal aorta
Falciform ligament
Stomach
Left gastro-omental artery within gastrosplenic ligament
Spleen
Splenic artery within splenorenal ligament
Superior recess of omental bursa
Left suprarenal gland
C
Pylorus
Right lobe of liver
Gallbladder
Gastroduodenal artery
Neck of pancreas
Head of pancreas
Bile duct
Hepatic portal vein
Inferior vena cava
Abdominal aorta
Falciform ligament
Stomach
Omental bursa
Transverse mesocolon
Transverse colon
Left end of greater omentum
Descending colon
Body of pancreas

Fig. 62.5 Transverse sections through the abdomen viewed from below. The peritoneal cavity is shown by blue shading; the peritoneum and its cut edges are in pale blue. **A**, At the approximate level of the line A–A in Fig. 62.1. The line passes through the bare area of the liver at the superior end of the lesser omentum. The parts of the left subphrenic space are clearly seen, although they are continuous with each other. **B**, At the approximate level of line B–B in Fig. 62.1. **C**, Approximately at the level of the line C–C in Fig. 62.1.

posterior layer of the greater omentum (see Fig. 62.4). The inferior layer of peritoneum is continuous with the anterior surface of the mesentery of the small intestine and right mesocolon in the midline and to the right, and with the anterior surface of the left mesocolon to the left. The transverse and right mesocolon and the mesentery of the small intestine converge centrally to form a region of considerable technical and pathological importance that contains the superior mesenteric artery and vein.

Mesentery of the small intestine

The mesentery of the small intestine is formed from two layers of peritoneum (anterosuperior and posteroinferior) that fan out towards an intestinal margin from a diagonal origin running across the posterior abdominal wall from the duodenojejunal flexure to the ileocaecal junction (see Fig. 62.1A). It continues as the right mesocolon, and where it does so it is attached to the posterior abdominal wall, although the attachment of mesentery to posterior abdominal wall is obscured by the peritoneal reflection at this level. The mesentery of the small intestine and the right and transverse mesocolon converge on a central region that is more appropriately termed the root of the mesentery. Jejunal and ileal branches of the superior mesenteric vessels, nerves related to the superior mesenteric plexus, lymphatic vessels and regional lymph nodes, all lie in the adipose tissue of the mesentery of the small intestine. The length and mobility of this mesentery can make it difficult to determine the site and orientation of a loop of small intestine through a small surgical incision. Tracing the continuity of a peritoneal layer of mesentery onto the posterior abdominal wall can be useful for orientating an isolated loop if the duodenojejunal flexure or ileocaecal junction is not readily accessible.

Right mesocolon

The right mesocolon is a continuation of the mesentery of the small intestine. It is apposed to the posterior abdominal wall from which it is separated by a fascial layer. Laterally it is directly connected to the caecum and ascending colon. It continues as the hepatic component of the transverse mesocolon. Where the small intestinal region of the mesentery continues as the right mesocolon, a mesothelial bridge (reflection) between the visceral peritoneum of the mesentery and the parietal peritoneum of the posterior abdominal wall is an important anatomical landmark defining the medial boundary of the right mesocolon (Byrnes et al 2019a–2019d).

Meso-appendix

The mesentery of the appendix, the meso-appendix, arises from the posterior surface of the mesentery in the ileocaecal region. It attaches to the appendix along its length, but it can end just short of the distal end of the appendix. It encloses the blood vessels, nerves and lymph vessels of the appendix and usually contains a lymph node. A fold of peritoneum is sometimes observed between the terminal ileum and the anterior layer of the meso-appendix (the 'bloodless fold of Treves'). The position of the meso-appendix is of considerable clinical importance. As it arises from the posterior surface of the main body of the mesentery, the appendix frequently takes up a retrocaecal position. Its positioning in this location means that appendicitis is often a difficult diagnosis, and that the appendix and meso-appendix can be difficult to expose and divide during surgery.

Left mesocolon

The left mesocolon is the region of mesocolon between the transverse mesocolon proximally and the sigmoid mesocolon distally. It is apposed to the posterior abdominal wall from which it is separated by a fascial layer. A mesothelial bridge (reflection) occurs at the medial boundary of the left mesocolon and links the parietal peritoneum of the posterior abdominal wall with the visceral peritoneum of the left mesocolon. The left mesocolon is directly connected to the medial border of the descending colon and is the distal continuation of the splenic component of the transverse mesocolon.

Sigmoid mesocolon

The sigmoid mesocolon (mesosigmoid) is the distal continuation of the left mesocolon (see Fig. 62.1A). At the rectosigmoid junction it continues distally into the pelvis as the mesorectum. Medially, it is attached to the posterior abdominal wall. Laterally, this region separates from the posterior abdominal wall as the mobile region of the sigmoid mesocolon. The medial and lateral boundaries of the attached region of sigmoid mesocolon are obscured from direct visualization by the peritoneal reflection at this level. Bands of peritoneum can run from the proximal sigmoid colon to the abdominal wall in the left iliac fossa: they are congenital adhesions that are often mistaken for the peritoneal reflection at this level. The sigmoid mesocolon contains the inferior mesenteric artery and the superior anorectal artery (i.e. the continuation of the inferior mesenteric artery). Sigmoid arteries arise primarily from the inferior mesenteric artery and travel in the sigmoid mesocolon to the sigmoid colon.

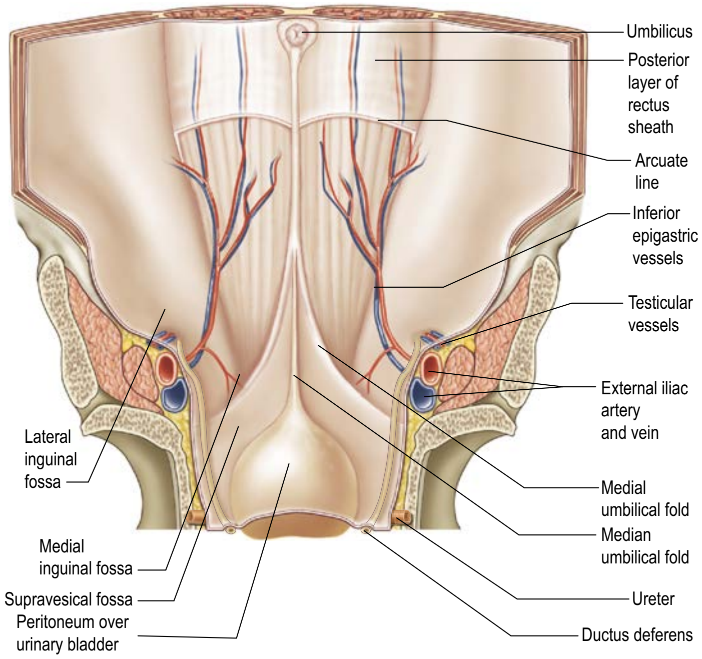

Fig. 62.6 The infra-umbilical part of the male anterior abdominal wall: posterior surface, with the peritoneum *in situ*.

Peritoneum of the inferior anterior abdominal wall

The peritoneum of the inferior anterior abdominal wall is raised into five folds (sometimes referred to as 'ligaments') that diverge as they descend from the umbilicus. They are the median, right and left medial, and right and left lateral, umbilical folds (**Fig. 62.6**; see Figs 73.5, 73.6). The median umbilical fold extends from the umbilicus to the apex of the bladder and contains the urachus or its remnant. The medial umbilical fold overlies the obliterated umbilical artery. The lateral umbilical fold covers the inferior epigastric vessels inferior to their entry into the rectus sheath. The supravesical fossa lies between the medial and median umbilical folds on each side of the midline. The medial and lateral inguinal fossae lie on either side of a lateral umbilical fold. The lateral inguinal fossa overlies the deep inguinal ring, and the medial inguinal fossa overlies the femoral ring (Healy and Reznek 1999).

Peritoneum of the pelvis

The parietal peritoneum of the abdominal wall is continuous with the parietal peritoneum that lines the side walls of the pelvis. The arrangement of the pelvic visceral peritoneum differs between the sexes.

Peritoneum of the male pelvis

In males, peritoneum is reflected off the pelvic side walls and on to the rectum and mesorectum. These are the pararectal regions of the reflection and are surgically important because they must be divided to access the plane between the mesorectum and underlying fascia. They coalesce anteriorly in the distal pelvis to form the anterior reflection. A gulley, the rectovesical pouch, is created by the organization of the peritoneum at this level. The urinary bladder, seminal glands and ductus deferens are positioned deep to the anterior region of peritoneum. The peritoneum covering the posterosuperior surface of the urinary bladder forms a paravesical fossa on each side that is limited laterally by a ridge of peritoneum containing the ductus deferens (**Fig. 62.7**); the depths of the paravesical fossae depend on the volume of urine in the bladder. When the urinary bladder is empty, a transverse vesical fold is sometimes visible at laparoscopy; its medial portion overlies the superior

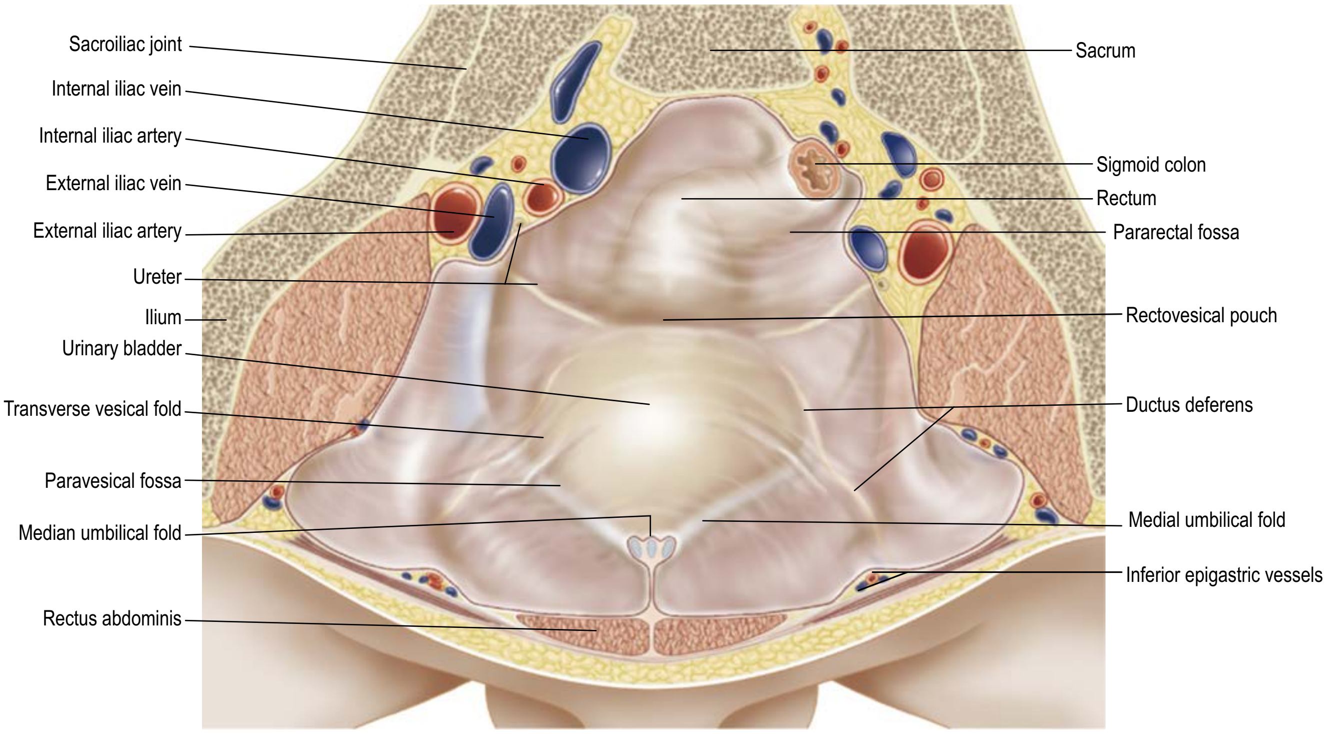
Sacroiliac joint
Internal iliac vein
Internal iliac artery
External iliac vein
External iliac artery
Ureter
Ilium
Urinary bladder
Transverse vesical fold
Paravesical fossa
Median umbilical fold
Rectus abdominis
Sacrum
Sigmoid colon
Rectum
Pararectal fossa
Rectovesical pouch
Ductus deferens
Medial umbilical fold
Inferior epigastric vessels

Fig. 62.7 The peritoneum of the male pelvis: anterosuperior view. Note that the ureter, urinary bladder, rectum and ductus deferens are all deep to the peritoneum.

vesical artery or arteries (Boaz et al 2011). The ureters and internal iliac vessels can cause slight elevations in the peritoneum between the paravesical and pararectal fossae. The median umbilical fold extends superiorly from the apex of the bladder on the posterior surface of the inferior anterior abdominal wall to the umbilicus: when the urinary bladder distends, the overlying peritoneum is lifted so that part of the underlying surface of the bladder comes into direct contact with the anterior abdominal wall.

Peritoneum of the female pelvis

In females, peritoneum covers the anterolateral surface of the proximal rectum and mesorectum, as it does in males, but it descends further over the anterior surface of the rectum. The pararectal and paravesical fossae are limited laterally by the peritoneum that covers the uterosacral ligaments and round ligaments of the uterus, respectively (see Figs 75.11B, 75.18). The presence of the uterus and vagina means that there are two pelvic pouches instead of the single rectovesical pouch seen in males. The peritoneum from the rectum is reflected anteriorly on to the posterior surface of the posterior part of the vaginal fornix and the uterus, forming the recto-uterine pouch (of Douglas). The depth of the pouch, i.e. the extent to which it descends on the posterior surface of the vagina, is variable (Baessler and Schuessler 2000). The peritoneum covers the fundus and body of the uterus, descending on its anterior surface as far as the junction of the body and cervix, and from there it is reflected forwards on to the posterosuperior surface of the urinary bladder, forming a shallow vesico-uterine pouch. As in males, the peritoneum over the urinary bladder is reflected on to the posterior surface of the inferior anterior abdominal wall. Recto-uterine folds containing the uterosacral ligaments pass posteriorly from the sides of the cervix of the uterus to the sacrum, running lateral to the rectum.

Peritoneum is also reflected from the anterior and posterior uterine surfaces to the lateral pelvic walls as the broad ligament of the uterus (see Fig. 75.18). This consists of anterior and posterior layers that are continuous at the superior border of the ligament. The broad ligament contains the uterine tubes in its free superior peritoneum and it merges with the pelvic parietal peritoneum at its base. The ovarian fossa is a shallow depression in the peritoneal lining of the lateral pelvic wall between the peritoneal ridges formed by the occluded part of the umbilical arteries anteriorly, the ureter posteriorly, and the external iliac vessels above; it lies posterior to the lateral attachment of the broad ligament of the uterus and usually contains the ovary in nulliparous females.

Vascular and lymphatic drainage

Parietal and visceral peritonea develop from the somatopleural and splanchnopleural layers, respectively, of the lateral plate mesoderm. Parietal peritoneum is supplied by the somatic blood vessels of the abdominal and pelvic walls, and its lymphatics join vessels in the body wall and drain to parietal nodes. Visceral peritoneum is best considered as an integral part of the viscus it covers; its blood supply and lymphatic drainage therefore correspond to those of the associated viscus. The region between, i.e. the peritoneal reflection, represents a transitional zone in terms of the origins of its vascular and lymphatic drainage and innervation.

Innervation

The parietal peritoneum is innervated by somatic efferent and afferent nerves that also supply the muscles and skin of the overlying body wall. The visceral peritoneum is innervated by afferent nerves that travel with the autonomic supply in the mesentery to the underlying viscera. Sensations arising from pathologies that affect the parietal or visceral peritoneum reflect these different patterns of innervation. Well-localized pain is elicited by mechanical, thermal or chemical stimulation of nociceptors in the parietal peritoneum; the pain is usually limited to the affected region. Somatic nerves that innervate the parietal peritoneum also supply the corresponding segmental skin and muscles: when the parietal peritoneum is irritated there is local reflex muscle contraction, resulting in clinical signs of guarding or even rigidity of the anterior abdominal wall. The parietal peritoneum covering the respiratory diaphragm is supplied centrally by afferent fibres from the phrenic nerves and peripherally by the inferior intercostal nerves and subcostal nerves: peripheral irritation of the diaphragm can therefore result in pain localized in the distribution of the inferior thoracic spinal nerves, while central irritation causes referred pain in the cutaneous distribution of the third to fifth cervical spinal nerves (the shoulder region). The innervation of the parietal peritoneum of the lesser pelvis is poorly documented.

Irritation or stretching of the visceral peritoneum causes poorly localized discomfort. The sensation of pain is referred to a diffuse area of the abdominal wall. Discomfort from structures derived from the foregut is felt in the epigastric region; that from structures derived from the midgut in the umbilical region; and that from structures derived from the hindgut in the hypogastric region. None of these sensations is significantly lateralized. Pain from the pancreas, gallbladder and small intestine can radiate to the back. Stretching or irritation of the visceral peritoneum can also elicit profound reflex vasomotor and cardiac changes mediated by autonomic nerves, including a vasovagal response. This is of considerable clinical relevance. Painful responses to manipulation of the parietal peritoneum can be abolished by local or regional anaesthesia. In marked contrast, the direct central connections of visceral afferents, particularly via the vagus nerve, mean that stretching the visceral peritoneum can have profound effects, including acute haemodynamic instability, despite local or regional (including spinal) anaesthesia.

GENERAL ARRANGEMENT OF THE PERITONEAL CAVITY

The peritoneum is organized into parietal and visceral parts and intervening areas of reflection (where the parietal peritoneum is reflected onto adjacent viscera with which it merges). Together, these form the peritoneal cavity. The region of the cavity that is attached to the lateral and anterior abdominal wall is relatively featureless. In contrast, while the contour of the reflection and visceral peritoneum appears more complex, it is explained by the shape of the underlying digestive system organs, including the mesentery. The cavity can be subdivided into the greater sac and the omental bursa. The greater sac is the main peritoneal cavity surrounding most of the abdominal and pelvic viscera. The omental bursa is a substantial diverticulum of the dorsal mesentery at this level and is situated posterior to the stomach and lesser omentum. The greater sac and omental bursa communicate via the omental foramen.

For clinical purposes, the peritoneal cavity can be divided into several ‘spaces’ (see below); pathological processes are often contained within these spaces and their anatomy can influence diagnosis and treatment. It has also been divided into two regions separated by the transverse mesocolon: the supramesocolic (often simply called supracolic) region superior to the transverse mesocolon and the infracolic region inferior to the transverse mesocolon. It should be noted that this classification is little used in current clinical practice.

Supramesocolic region

Available with the *Gray’s Anatomy* e-book

Right subphrenic space

The right subphrenic space lies between the respiratory diaphragm and the anterior, superior and right lateral surfaces of the right lobe of the liver. It is bounded on the left by the falciform ligament and posteriorly by the superior layer of the coronary ligament (see Fig. 62.3).

Hepatorenal recess (right subhepatic space)

The hepatorenal recess (right subhepatic space) lies between the inferior surface of the right lobe of the liver and the superior pole of the right kidney. It is bounded superiorly by the inferior layer of the coronary ligament, laterally by the right lateral abdominal wall, posteriorly by the anterior surface of the superior pole of the right kidney, and inferomedially by the right colic flexure, transverse mesocolon, descending part of the duodenum and part of the head of the pancreas. In the supine position, the hepatorenal recess is more dependent than the right paracolic gutter. Pathological fluid collections can develop at this site.

Omental bursa

The omental bursa is a cavity lined with peritoneum and connected to the main peritoneal cavity (greater sac) by the omental foramen (of Winslow). It develops under the left half of the respiratory diaphragm, providing a mesenteric platform into which the stomach, spleen and pancreas can emerge. It has posterior and anterior walls and superior, inferior, right and left borders. The bursa varies in size according to the volume of the viscera making up its walls, and it can be partially obliterated by natural adhesions between its anterior and posterior walls.

The anterior wall of the omental bursa consists of the posterior peritoneal layer of the lesser omentum, the peritoneum over the posterior wall of the stomach and superior part of the duodenum, and the posterior superior part of the anterior layer of the greater omentum (see above) (see Fig. 62.4). At its right border, the anterior wall is mostly formed by the lesser omentum, but towards the left, the lesser omentum becomes progressively shorter and more of the anterior wall is formed by the posterior surface of the stomach and greater omentum. The spleen is positioned at the left lateral extent of the bursa.

The greater omentum curves posterolaterally at the lateral border of the bursa and is continuous posteriorly with the posterior wall of the bursa, which is the dorsal mesogastrium, and is attached to the posterior abdominal wall under the left half of the respiratory diaphragm. The body of the pancreas is located in the inferior part of the posterior wall. The posterior wall detaches at the inferior margin of the pancreas to continue distally over the superior surface of the transverse mesocolon. It detaches from the transverse colon to continue as the greater omentum (see Fig. 62.4).

The inferior phrenic, splenic, left gastric and common hepatic arteries are located in the mesentery of the omental bursa: they use the frame of the bursa to travel to their target organs. The superior border of the omental bursa is narrow and lies between the right side of the abdominal part of the oesophagus and the superior end of the fissure for the ligamentum venosum and is sometimes referred to as the superior recess of the omental bursa. Here, the peritoneum of the posterior wall of the omental bursa is reflected anteriorly from the respiratory diaphragm to join the posterior layer of the lesser omentum.

The right border of the omental bursa is where the peritoneum overlying the head and neck of the pancreas is reflected onto the inferior aspect of the superior part of the duodenum. The line of this reflection ascends to the left, along the medial side of the gastroduodenal artery. Near the superior border of the duodenum, the right border of the omental bursa joins the inferior aspect of the omental foramen round the proper hepatic artery. The omental foramen therefore interrupts the right border. Superior to the omental foramen, the right border is formed by the peritoneal reflection from the respiratory diaphragm to the right margin of the caudate lobe of the liver, which then crosses the inferior vena cava. The left border of the omental bursa runs from the left end of the transverse mesocolon and is mostly formed by the inner peritoneal layers of the splenorenal and gastrosplenic ligaments. The region of the omental bursa between the splenorenal and gastrosplenic ligaments is referred to as the splenic recess. Superior to the spleen, the two ligaments merge to form the short gastrophrenic ligament, which passes anteriorly from the respiratory diaphragm to the posterior aspect of the fundus of the stomach and forms part of the superior left border of the omental bursa. The two layers of the gastrophrenic ligament diverge near the abdominal part of the oesophagus, leaving part of the posterior surface of the stomach devoid of peritoneum. The left gastric artery runs forwards here into the lesser omentum.

The omental bursa is indented by a crescentic mesenteric arch that runs from the superior border of the neck of the pancreas to the superior part of the lesser curvature of the stomach: it is variously described but commonly known as the gastropancreatic fold. The superior part of this arch contains the left gastric artery as it runs from the coeliac trunk to the lesser curvature of the stomach. The inferior part contains the common hepatic artery as it runs from the coeliac trunk to the lesser omentum. When the arch is prominent, it divides the omental bursa into a smaller superior and a larger inferior recess. The superior recess lies posterior to the lesser omentum and encloses the caudate lobe of the liver; it extends superiorly into the fissure for the ligamentum venosum and lies adjacent to the right crus of the respiratory diaphragm posteriorly. The inferior recess of the omental bursa lies between the stomach and pancreas, and is contained within the double sheet of greater omentum.

Acute pancreatitis is probably the most common cause of a fluid collection within the omental bursa (or just posterior to its posterior wall). Bleeding from trauma or a ruptured aneurysm of the splenic artery and perforation of a posterior gastric ulcer are other causes of omental bursa fluid collections.

Omental foramen

The omental foramen is a short, vertical slit, about 3 cm in height in adults, posterior to the free right border of the lesser omentum, and is the entrance to the omental bursa from the greater sac. The hepatoduodenal ligament, the thickened free right margin of the lesser omentum that extends between the porta hepatis above and the superior border of the superior part of the duodenum below, forms the anterior boundary of the omental foramen. Within this free border lie the bile duct (anteriorly on the right), the proper hepatic artery (anteriorly on the left) and the hepatic portal vein (posteriorly), together with nerves and lymphatics. Rapid control of the proper hepatic artery and hepatic portal vein can be exerted by compression of the free edge of the lesser omentum (a 'Pringle' manoeuvre), which is a potentially useful technique during surgery. Superiorly, the peritoneum of the posterior layer of the hepatoduodenal ligament runs over the caudate process of the liver, forming the roof of the omental foramen. This layer of peritoneum is then reflected onto the inferior vena cava, forming the posterior border of the foramen. The floor of the foramen is formed by the peritoneal reflection overlying the superior border of the superior part of the duodenum as it runs anteriorly, superior to the head of the pancreas. A narrow passage, the vestibule of the omental bursa, can be formed to the left of the foramen between the caudate process superiorly and the superior part of the duodenum inferiorly. To the right, the rim of the foramen is continuous with the peritoneum of the greater sac. The anterior and posterior walls of the foramen are normally apposed, which partly explains why patients can develop large fluid collections isolated to the greater sac or omental bursa (Shrestha et al 2010).

Left subphrenic space

The left subphrenic space lies between the respiratory diaphragm, the anterior and superior surfaces of the left lobe of the liver, the anterosuperior surface of the stomach and the diaphragmatic surface of the spleen. To the right it is bounded by the falciform ligament. It is expanded in the absence of the spleen and is a common site for fluid collection after splenectomy. The left subphrenic space is substantially larger than the right and can be divided into a left perihepatic space and anterior and posterior subphrenic spaces, all of which are in continuity in the absence of disease. The definitions of the boundaries of these spaces vary.

The left anterior subphrenic space is large and lies between the superior and anterolateral surfaces of the spleen and the respiratory diaphragm. Inferiorly and medially, this space is bounded by the phrenicocolic and splenorenal regions of peritoneal reflection and the gastrosplenic ligament. The left subphrenic space is a relatively common site of fluid collection after upper abdominal surgery, particularly surgery involving the spleen or adjacent pancreas. The left posterior subphrenic space is small and lies between the fundus of the stomach and the diaphragm superior to the origin of the splenorenal region of peritoneal reflection.

The left perihepatic space is sometimes subdivided into anterior and posterior spaces. The left anterior perihepatic space lies between the anterosuperior surface of the left lobe of the liver and the respiratory diaphragm. The left posterior perihepatic space, also known as the gastrohepatic recess, lies inferior to the left lobe of the liver. It extends into the fissure for the ligamentum venosum on the right. Posteriorly, it is separated from the superior recess of the omental bursa by the lesser omentum.

Extraperitoneal subphrenic spaces

There are two potential subphrenic spaces that actually lie outside the peritoneum but are clinically relevant because they can be sites of fluid accumulation. The right extraperitoneal space is bounded by the two layers of the coronary ligament, the bare area of the liver and the inferior surface of the right half of the respiratory diaphragm. The left extraperitoneal space lies anterior to the left suprarenal gland and superior pole of the left kidney.

Inframesocolic region

The inframesocolic region (also called the infracolic region) lies inferior to the transverse mesocolon and transverse colon and is divided into two unequal spaces by the mobile region of the mesentery of the small intestine. It contains the right and left paracolic gutters lateral to the ascending and descending colons, respectively.

The supramesocolic region lies between the respiratory diaphragm and the transverse mesocolon and can be arbitrarily divided into right and left supramesocolic spaces. The right supramesocolic space can be subdivided into the right subphrenic space, the right subhepatic space and the omental bursa. The left supramesocolic space can be divided into the left subphrenic space and the left perihepatic space. These ‘spaces’ usually communicate but can nevertheless be sites of localized fluid collection.

Right and left infracolic spaces

Available with the *Gray's Anatomy* e-book

Paracolic gutters

The right and left paracolic gutters are peritoneal depressions on the posterior abdominal wall alongside the ascending and descending colons, respectively. The principal paracolic gutter lies lateral to the colon on each side. The right paracolic gutter runs from the superolateral aspect of the right colic flexure down the lateral aspect of the ascending colon and caecum and is continuous with the peritoneum of the pelvic cavity inferiorly. Superiorly, it is continuous with the hepatorenal recess and with the omental bursa through the omental foramen. Bile, purulence, blood or other fluids can run along the gutter and collect in sites distant to the viscus of origin. In supine patients, infected fluid from the right iliac fossa can ascend in the gutter to the right subphrenic space. In erect or semi-recumbent positions, fluid from the stomach, duodenum or gallbladder can run down the gutter to collect in the right iliac fossa (mimicking acute appendicitis) or pelvis to form an abscess. The right paracolic gutter is deeper than the left, which could explain why subphrenic collections are more common on the right.

Recesses of the peritoneal cavity

Peritoneal fossae or recesses are difficult to standardize, so they are less discussed in the literature than they were in the past. However, these recesses are occasionally sites of internal herniation. If a loop of intestine becomes trapped in a fossa or recess, it can become obstructed or strangulated from constriction at the entrance to the recess. The contents of the peritoneal fold forming the fossa/recess must be considered when such a hernia is repaired.

Duodenal recesses

Available with the *Gray's Anatomy* e-book

Caecal recesses

Available with the *Gray's Anatomy* e-book

Intersigmoid recess

Available with the *Gray's Anatomy* e-book

Internal hernias

Available with the *Gray's Anatomy* e-book

Additional clinical aspects of the peritoneal cavity

Peritoneal fluid collections

Fluid collections frequently develop within the peritoneal cavity in response to a wide range of pathological processes. In the absence of inflammation, peritoneal adhesions or previous surgery, serous fluid tends to be distributed widely between the peritoneal spaces. Simple ascites can therefore be drained freely from any convenient dependent part of the peritoneal cavity; drainage is most commonly performed by blind puncture or ultrasound-guided insertion of a catheter into the inferior left or right paracolic gutters. The mobility of the small intestine makes iatrogenic injury during this procedure very unlikely.

Fluid collections caused by inflammatory processes are often much thicker because they contain purulence, fibrin or blood. Furthermore, they are usually associated with peritoneal adhesions arising from peritoneal inflammation. These factors predispose to the formation of localized fluid collections that can become walled-off as the inflammatory process progresses. Any region of the peritoneum can develop a localized collection, but the subphrenic and subhepatic spaces and pelvic pouches are the most common sites because they are well defined by the peritoneal folds and viscera that form their boundaries and they are the most dependent regions within the peritoneal cavity.

Surgical access to the peritoneum is less often needed today because advances in radiologically guided percutaneous drainage using fluoroscopy, ultrasound, computed tomography (CT) or magnetic resonance imaging (MRI) offer reliable and versatile methods for accessing the peritoneum, including relatively inaccessible subhepatic, perihepatic or intermesenteric collections. Posterolateral approaches or approaches through the greater sciatic foramen can be used to access the retroperitoneum or pelvis, respectively. Occasionally, a surgical approach is required, for example, a subcostal or lateral intercostal incision to drain a subphrenic abscess or an inguinal incision to drain a pelvic abscess.

Peritoneal dialysis

The mean surface area of the peritoneum in the adult female has been estimated to be about $1.4\,\text{m}^2$ (the visceral peritoneum accounting for about 80% of the total) (Albanese et al 2009). Mesothelium resembles vascular endothelium in that it allows the passage of ions and small molecules. Normally, the volume of fluid transmitted by peritoneal surfaces is small, but large volumes can be instilled into the peritoneal cavity and then siphoned out, using the peritoneum as a dialysing membrane, for example to support individuals with acute or chronic renal failure.

Ventriculoperitoneal shunts

The absorptive capabilities of the peritoneum can be exploited to absorb excess transitional fluids from several sites in the body. The most common of these is the absorption of cerebrospinal fluid in patients with hydrocephalus, diverted into the peritoneal cavity using a shunt (a fine catheter) from the cerebral ventricles. The catheter placed within the peritoneal cavity is connected to a one-way valve placed over the skull so that reflux of peritoneal fluid into the cerebral ventricles is prevented. The cerebrospinal fluid is continuously absorbed by the peritoneum, maintaining normal pressure within the ventricles.

Intraperitoneal cancer chemotherapy

In patients with peritoneal metastases, attempts to optimize the benefits of cytoreductive surgery can involve the administration of chemotherapeutic agents (diluted in large volumes of fluid) directly into the peritoneal cavity. The peritoneum can be accessed via an intraperitoneal catheter connected to a subcutaneous port or by repeated paracentesis. The infused chemotherapeutic agents can be retained locally for longer than systemically administered agents. Targeting drugs to the peritoneal space can improve the results of treatment if complete tumour resection is not possible.

Bonus e-book content

Fig. 62.7 The peritoneum of the male pelvis: anterosuperior view.

Video 62.1 Dissection of the peritoneal cavity.

Key references

Byrnes KG, McDermott KW, Coffey JC (eds) 2019a Mesenteric organogenesis. Semin Cell Dev Biol 92:1–138.

"Mesenteric Organogenesis" is the title of a special issue of Seminars in Cell and Developmental Biology. *It contains 12 review articles that address mesenteric anatomy and development, processes underpinning mesenteric development, and mesenteric contributions to abdominal organogenesis.*

diZerega GS, Rodgers KE 1992 The Peritoneum. New York: Springer-Verlag.

A text dedicated to the peritoneum, including its function and composition.

Healy JC, Reznek RH 1999 The anterior abdominal wall and peritoneum. In: Butler P, Mitchell A, Ellis H (eds) Applied Radiological Anatomy. Cambridge: Cambridge University Press, pp. 189–200.

A demonstration of the imaging anatomy of the peritoneal spaces and reflections using cross-sectional imaging.

Platell C, Cooper D, Papadimitriou JM et al 2000 The omentum. World J Gastroenterol 6:169–76.

A comprehensive review of the greater omentum.

The right and left infracolic spaces are conceptual zones without defined anatomical boundaries and are little referenced in current clinical practice. The right space is the region of the peritoneal cavity inferior to the transverse mesocolon and lateral to the right side of the mobile region of the mesentery of the small intestine. The left space is the corresponding space on the opposite side of the mobile region of the mesentery of the small intestine.

There can be several folds of peritoneum around the ascending (fourth) part of the duodenum and the duodenojejunal junction. They form a number of named recesses, which are highly variable in anatomical organization, and that arise after the duodenojejunal junction (and associated mesentery) adopts a final position *in utero*. Although it has been suggested that these recesses are sites of internal herniation, this is extremely rare (Zonca et al 2008).

Superior duodenal recess

The superior duodenal recess is occasionally present, often in association with an inferior duodenal recess. It lies directly to the left of the ascending part of the duodenum, adjacent to the second lumbar vertebra, and posterior to a crescentic superior duodenal fold of peritoneum. This fold has a semilunar free inferior margin that merges laterally with the peritoneum overlying the left kidney. The inferior mesenteric vein lies within the left mesocolon and is positioned close to the recess (when present).

Inferior duodenal recess

The inferior duodenal recess is usually present, often in association with a superior recess, with which it can share an orifice. It lies to the left of the ascending part of the duodenum, adjacent to the third lumbar vertebra, posterior to an avascular, triangular inferior duodenal fold, which has a sharp superior edge. It usually admits one or two fingertips and extends inferiorly, sometimes posterior to the ascending part of the duodenum and to the left, anterior to the ascending branch of the left colic artery and the inferior mesenteric vein.

Paraduodenal recess

The paraduodenal recess can occur in conjunction with superior and inferior duodenal recesses. It lies a little to the left and slightly posterior to the ascending part of the duodenum, posterior to a falciform fold of peritoneum. The free right edge of this fold contains the inferior mesenteric vein and ascending branch of the left colic artery, and is part of the left mesocolon. Herniation here is extremely rare (Khan et al 1998).

Retroduodenal recess

The retroduodenal recess is the largest of the duodenal recesses but is rarely present. It lies posterior to the horizontal and ascending parts of the duodenum and anterior to the abdominal aorta, is up to 10 cm deep, and has a wide orifice flanked by duodeno-parietal peritoneal regions of reflection. The recess arises because the confluence between the mesentery of the small intestine and right mesocolon has failed to attach to the posterior abdominal wall and incomplete attachment creates the impression of a recess.

Duodenojejunal recess

The duodenojejunal or mesocolic recess occurs in a minority of adults; when present, it is almost never associated with other duodenal recesses. It is approximately 3 cm deep and lies to the left of the abdominal aorta, between the duodenojejunal junction and the central region of the mesentery. It is bounded superiorly by the pancreas, on the left by the kidney, and inferiorly by the left renal vein. Its circular opening lies between two peritoneal folds and faces inferiorly and to the right.

Mesentericoparietal recess

The mesentericoparietal recess or fossa is rarely present. It lies just inferior to the horizontal part of the duodenum and invaginates the superior part of the mesentery of the small intestine towards the right. Its orifice is large and faces to the left, posterior to a fold of mesentery raised by the superior mesenteric artery. This recess is the site of the rare 'right paraduodenal hernia'.

Folding of the peritoneal reflection at the ileocaecal level generates a variety of recesses that have the potential to become sites of internal herniation (Rivkind et al 1986). Paracaecal recesses are common sites for abscess formation after acute appendicitis.

Superior ileocaecal recess

The superior ileocaecal recess is usually best developed in children and is often absent in the aged or obese. It is a narrow slit bounded anteriorly by a vascular fold of peritoneum containing the anterior caecal vessels, posteriorly by the ileal mesentery, inferiorly by the terminal ileum and on the right by the ileocaecal junction. Its orifice opens to the left.

Inferior ileocaecal recess

The inferior ileocaecal recess is similarly well developed in the young but frequently obliterated by fat in adults. It is formed by the ileocaecal fold, which extends from the antero-inferior aspect of the terminal ileum to the anterior aspect of the meso-appendix (or to the appendix or caecum). It is also known as the 'bloodless fold of Treves', although it sometimes contains blood vessels that bleed if divided during surgery. If inflamed, especially when the appendix and its mesentery are retrocaecal, it can be mistaken for the meso-appendix. The recess is bounded anteriorly by the ileocaecal fold, superiorly by the terminal ileum and associated mesentery, to the right by the caecum, and posteriorly by the superior part of the meso-appendix. Its orifice opens inferiorly and to the left.

Retrocaecal recess

The retrocaecal recess lies posterior to the caecum. It ascends posterior to the ascending colon to a variable extent, often being large enough to admit an entire finger. It is bounded anteriorly by the caecum (and sometimes the ascending colon), posteriorly by the parietal peritoneum, and on each side by caecal folds (parietocolic folds) passing from the caecum to the posterior abdominal wall. The appendix frequently occupies this retrocaecal recess. There can also be one or more shallow paracaecal or paracolic recesses: they are simply depressions within the right paracolic gutter and are not sites of internal herniation.

The intersigmoid recess is present in fetal life and infancy but often subsequently disappears. It lies lateral to the mobile region of the sigmoid mesocolon, between it and the parietal peritoneum of the left iliac fossa. As these structures are its anatomical determinants, it is highly variable in appearance.

An internal hernia is a protrusion of a viscus through a normal or abnormal aperture (which includes a surgically created opening) within the confines of the abdominal cavity (Martin et al 2006). It is possible for any of the peritoneal recesses, foramina or cul-de-sacs described in this chapter to be associated with the development of an internal hernia; but with a clinically apparent internal hernia, the relevant peritoneal recess is usually enlarged and its aperture narrower than normal. Although they are rare, the most common sites for internal hernia (in the absence of adhesions) are the paraduodenal recess, followed by the recesses around the caecum and omental foramen.

References

Albanese AM, Albanese EF, Mino JH et al 2009 Peritoneal surface area: measurements of 40 structures covered by peritoneum: correlation between total peritoneal surface area and the surface calculated by formulas. Surg Radiol Anat 31:369–77.

Ashaolu JO, Ukwenya VO, Adenowo TK 2011 Cystoduodenal ligament as an abnormal fold and the accompanying anatomical and clinical implications. Surg Radiol Anat 33:171–4.

Autio V 1964 The spread of intraperitoneal infection. Acta Chir Scand Suppl 36:5–31.

Baessler K, Schuessler B 2000 The depth of the pouch of Douglas in nulliparous and parous women without genital prolapse and in patients with genital prolapse. Am J Obstet Gynecol 182:540–4.

Boaz NT, Martin AH, Thompson K et al 2011 Structure and functional significance of the transverse vesical fold. Clin Anat 24:62–9.

Byrnes KG, McDermott KW, Coffey JC (eds) 2019a Mesenteric organogenesis. Semin Cell Dev Biol 92:1–138.

Byrnes KG, McDermott K, Coffey JC 2019b Development of mesenteric tissues. Semin Cell Dev Biol 92:55–62.

Byrnes KG, Walsh D, Dockery P et al 2019c Anatomy of the mesentery:current understanding and mechanisms of attachment. Semin Cell Dev 92:12–17.

Byrnes KG, Walsh D, Lewton-Brain P, McDermott K et al 2019d Anatomy of the mesentery: historical development and recent advances. Semin Cell Dev Biol 92:4–11.

Coakley FV, Hricak H 1999 Imaging of peritoneal and mesenteric disease: key concepts for the clinical radiologist. Clin Radiol 54:563–74.

An explanation of the complex anatomy of the upper abdominal peritoneal fold suspending the stomach, liver and spleen.

Coulier B 2009 64-row MDCT review of anatomic features and variations of the normal greater omentum. Surg Radiol Anat 31:489–500.

diZerega GS, Rodgers KE 1992 The Peritoneum. New York: Springer-Verlag.

A text dedicated to the peritoneum, including its function and composition.

Hagiwara A, Takahashi T, Sawai T et al 1994 Milky spots as the implantation site for malignant cells in peritoneal dissemination in mice. Cancer Res 54:687–92.

Healy JC, Reznek RH 1999 The anterior abdominal wall and peritoneum. In: Butler P, Mitchell A, Ellis H (eds) Applied Radiological Anatomy. Cambridge: Cambridge University Press, pp. 189–200.

A demonstration of the imaging anatomy of the peritoneal spaces and reflections using cross-sectional imaging.

Khan MA, Lo AY, VandeMaele DM 1998 Paraduodenal hernia. Am Surg 64:1218–22.

Koninckx PR, Renaer M, Brosens IA 1980 Origin of peritoneal fluid in women: an ovarian exudation product. Br J Obstet Gynaecol 87:177–83.

Martin LC, Merkle EM, Thompson WM 2006 Review of internal hernias: radiographic and clinical findings. AJR Am J Roentgenol 186:703–17.

Meyers MA 1973 Distribution of intra-abdominal malignant seeding: dependency on dynamics of flow of ascitic fluid. Am J Roentgenol Radium Ther Nucl Med 119:198–206.

Meyers M 1994 Dynamic Radiology of the Abdomen: Normal and Pathologic Anatomy. New York: Springer.

Meyers MA, Oliphant M, Berne AS et al 1987 The peritoneal ligaments and mesenteries: pathways of intraabdominal spread of disease. Radiology 163:593–604.

A systematic application of anatomic and dynamic principles to the understanding and diagnosis of intra-abdominal disease.

Pestieau SR, Wolk R, Sugarbaker PH 2000 Congenital pleuroperitoneal communication in a patient with pseudomyxoma peritonei. J Surg Oncol 73:174–8.

Platell C, Cooper D, Papadimitriou JM et al 2000 The omentum. World J Gastroenterol 6:169–76.

A comprehensive review of the greater omentum.

Rivkind AI, Shiloni E, Muggia-Sullam M et al 1986 Paracecal hernia: a cause of intestinal obstruction. Dis Colon Rectum 29:752–4.

Sanchez NC, Tenofsky PL, Dort JM et al 2001 What is normal intra-abdominal pressure? Am Surg 67:243–8.

Shimotsuma M, Shields JW, Simpson-Morgan MW et al 1993 Morphophysiological function and role of omental milky spots as omentum-associated lymphoid tissue (OALT) in the peritoneal cavity. Lymphology 26:90–101.

Shrestha BM, Brown PW, Wilkie ME et al 2010 The anatomy and pathology of the lesser sac: implications for peritoneal dialysis. Perit Dial Int 30:496–501.

Simmons LE, Mir AR 1989 A review of management of pleuroperitoneal communication in five CAPD patients. Adv Perit Dial 5:81-3.

Stringer MD 2009 Eponyms in Surgery and Anatomy of the Liver, Bile Ducts and Pancreas. London: Royal Society of Medicine Press.

A short reference book that contains information and illustrations relating to the original descriptions and the authors of many of the eponyms cited in this chapter (e.g. Cullen, Winslow, Morison).

Wassilev W, Wedel T, Michailova K et al 1998 A scanning electron microscopy study of peritoneal stomata in different peritoneal regions. Ann Anat 180:137–43.

Yoshikawa T, Hayashi N, Maeda E et al 2013 Peritoneal fluid accumulation in healthy men and postmenopausal women: evaluation on pelvic MRI. AJR Am J Roentgenol 200:1181–5.

Zonca P, Maly T, Mole DJ et al 2008 Treitz's hernia. Hernia 2:531–4.

Further reading

Blackburn SC, Stanton MP 2014 Anatomy and physiology of the peritoneum. Semin Pediatr Surg 23:326-30.

Coffey JC, O'Leary DP 2016 The mesentery: structure, function, and role in disease. Lancet Gastroenterol Hepatol 1:238–47.

Coffey JC, Culligan K, Walsh LG et al 2016 An appraisal of the computed axial tomographic appearance of the human mesentery based on mesentericcontiguity from the duodenojejunal flexure to the mesorectal level. Eur Radiol 26:714–21.

Culligan K, Coffey JC, Kiran RP et al 2012 The mesocolon: a prospective observational study. Colorectal Dis 14:421–8.

Feldberg MA, van Leeuwen MS 1990 The properitoneal fat pad associated with the falciform ligament. Imaging of extent and clinical relevance. Surg Radiol Anat 12:193–202.

Harrison OJ, Sharma RD, Niayesh MH 2011 Early intervention in intersigmoid hernia may prevent bowel resection – a case report. Int J Surg Case Rep 2:282–4.

Hikspoors JPJM, Kruepunga N, Mommen GMC et al 2019 The development of the dorsal mesentery in human embryos and fetuses. Semin Cell Dev Biol 92:18–26.

van Baal JO, van de Vijver KK, Nieuwland R et al 2017 The histopathology and pathophysiology of the peritoneum. Tissue Cell 49: 95–105.

CHAPTER
63

Abdominal oesophagus and stomach

ABDOMINAL PART OF THE OESOPHAGUS

The abdominal part of the oesophagus is 1–2.5 cm long, lies to the left of the midline and is slightly broader at the cardiac orifice than at the oesophageal hiatus, which lies at the level of the eleventh thoracic vertebra (Mirjalili et al 2012). It runs obliquely to the left and slightly posteriorly and ends at the gastro-oesophageal junction, where it is continuous with the cardiac orifice of the stomach. Its anterior wall is effectively longer than its posterior wall because of the obliquity of the diaphragmatic crura. The abdominal part of the oesophagus lies posterior to the left lobe of the liver and anterior to the left crus of the respiratory diaphragm, the left inferior phrenic vessels and the left greater and lesser thoracic splanchnic nerves. Its surface is covered by a thin layer of connective tissue and visceral peritoneum that contains the anterior and posterior vagus nerves and the oesophageal branches of the left gastric vessels. The anterior and posterior vagal trunks can be single or composed of multiple trunks (Jackson 1949); the anterior vagal trunk is closely applied to the anterior outer surface of the longitudinal muscle coat of the oesophagus lying in the 2 o'clock position. It is often a thread-like nerve and difficult to visualize. It is imperative that the surgeon appreciates the position of the anterior vagal trunk to avoid injury leading to gastroparesis during a cardiomyotomy or fundoplication. The posterior vagal trunk is a more substantial structure that usually lies within loose connective tissue immediately posterior and to the right of the oesophagus, making its identification during surgery somewhat easier. However, the position of the trunk can vary; it can lie anywhere on the right side of the oeosphagus. Again it is imperative that the surgeon identify the nerve at fundoplication to avoid injury or incorporation into the wrap. Unlike the more proximal parts of the oesophagus, the muscular wall of the abdominal part of the oesophagus is composed entirely of smooth muscle.

The abdominal part of the oesophagus is effectively tethered to the margins of the oesophageal hiatus by the phrenico-oesophageal ligament and probably acts to limit upward and downward mobility of the oesophagus within the oesophageal hiatus (Kwok et al 1999, Apaydin et al 2008). The importance of this anchor function has been recognized in more recent times by surgeons performing fundoplications, many of whom now reconstruct the ligament with sutures between the left lateral oesophagus and the left crus (**Fig. 63.1**). The ligament is formed by two circumferential layers of elastin- and collagen-rich connective tissue containing smooth muscle fibres. The distal layer is an extension of the transversalis fascia inferior to the respiratory diaphragm; it is thin and only loosely attached to the oesophagus. The proximal layer is continuous with the endothoracic fascia superior to the respiratory diaphragm; it is thicker, contains more elastin than its inferior counterpart, and runs cranially and obliquely to fuse firmly with the wall of the oesophagus. A variable amount of adipose tissue lies in the triangular interval between the two layers of the ligament. In the elderly, the ligament tends to become attenuated: it loses collagen fibres and contains more adipose tissue. The phrenico-oesophageal ligament is denser anteriorly where it bridges between the outer layer of the oesophageal wall and the arching fibres of the crura of the diaphragm. Identification of the phrenico-oesophageal ligament on the thinner portion of the left crus is the gateway to safe mobilization of the oesophagus during surgery: once it is breached, the oesophagus can be easily mobilized and the aorta viewed posteriorly.

The peritoneal reflection posterior to the abdominal part of the oesophagus is short and continues directly on to the posterior surface of the fundus of the stomach; it is sometimes referred to as the gastrophrenic ligament. It encloses the oesophageal branches of the left gastric vessels and the coeliac branches of the posterior vagal trunk and can thus be considered to form an extremely short, wide mesentery to the abdominal part of the oesophagus. In adults, a fat pad is sometimes visible beneath the peritoneum over the anterior surface of the gastro-oesophageal junction and can be a useful surgical marker of the gastro-oesophageal junction.

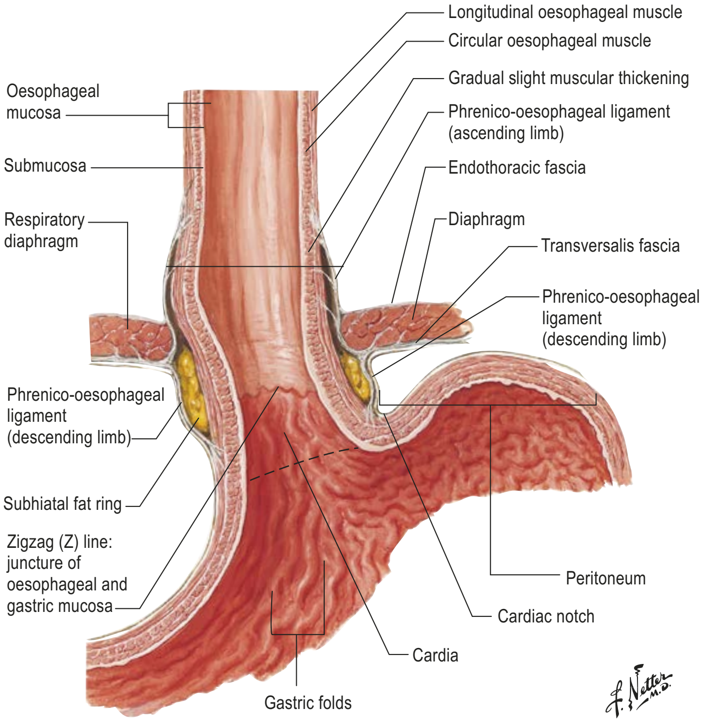
Longitudinal oesophageal muscle
Circular oesophageal muscle
Oesophageal mucosa
Gradual slight muscular thickening
Phrenico-oesophageal ligament (ascending limb)
Submucosa
Endothoracic fascia
Respiratory diaphragm
Diaphragm
Transversalis fascia
Phrenico-oesophageal ligament (descending limb)
Phrenico-oesophageal ligament (descending limb)
Subhiatal fat ring
Zigzag (Z) line: juncture of oesophageal and gastric mucosa
Peritoneum
Cardiac notch
Cardia
Gastric folds
F. Netter M.D.

Fig. 63.1 **A**, The anatomical structures around the abdominal part of the oesophagus. (Reprinted from Netter Anatomy Illustration Collection, © Elsevier Inc. All Rights Reserved.) (B–E, *continued online*)

Hiatal hernia

Available with the *Gray's Anatomy* e-book

Vascular supply and lymphatic drainage

Arteries

The abdominal part of the oesophagus is supplied by numerous oesophageal branches of the left gastric artery that ascend beneath the visceral peritoneum to supply perforating branches to the intramural and submucosal plexuses. The posterior surface usually receives an additional blood supply via branches of the upper short gastric arteries, reinforced by terminal arteries from the oesophageal branches of the descending thoracic aorta and occasionally an ascending branch of the posterior gastric artery (Liebermann-Meffert et al 1987).

Veins

Mucosal and submucosal veins drain via plexuses to the left gastric and upper short gastric veins in the abdomen and to the azygos/hemiazygos system of veins in the thorax. The distal oesophagus is an important site of porto-systemic anastomosis where oesophageal varices develop in portal hypertension (see below).

Lymphatic drainage

The lymphatics of the oesophagus are concentrated into submucosal and intermuscular plexuses. Both of these plexuses receive lymph from all layers of the oesophageal wall (Kuge et al 2003, Rice et at 2016). Terminology is not straightforward. In general, lymphatic drainage from the oesophagus communicates with nodes in the adventitia, para-oesophageal nodes or the thoracic duct directly (Wang et al 2018). However, the lymphatics of the distal third of the oesophagus do not

Fig. 63.1 A–E, The anatomical structures around the abdominal part of the oesophagus. **B–C**, Coronal CT.

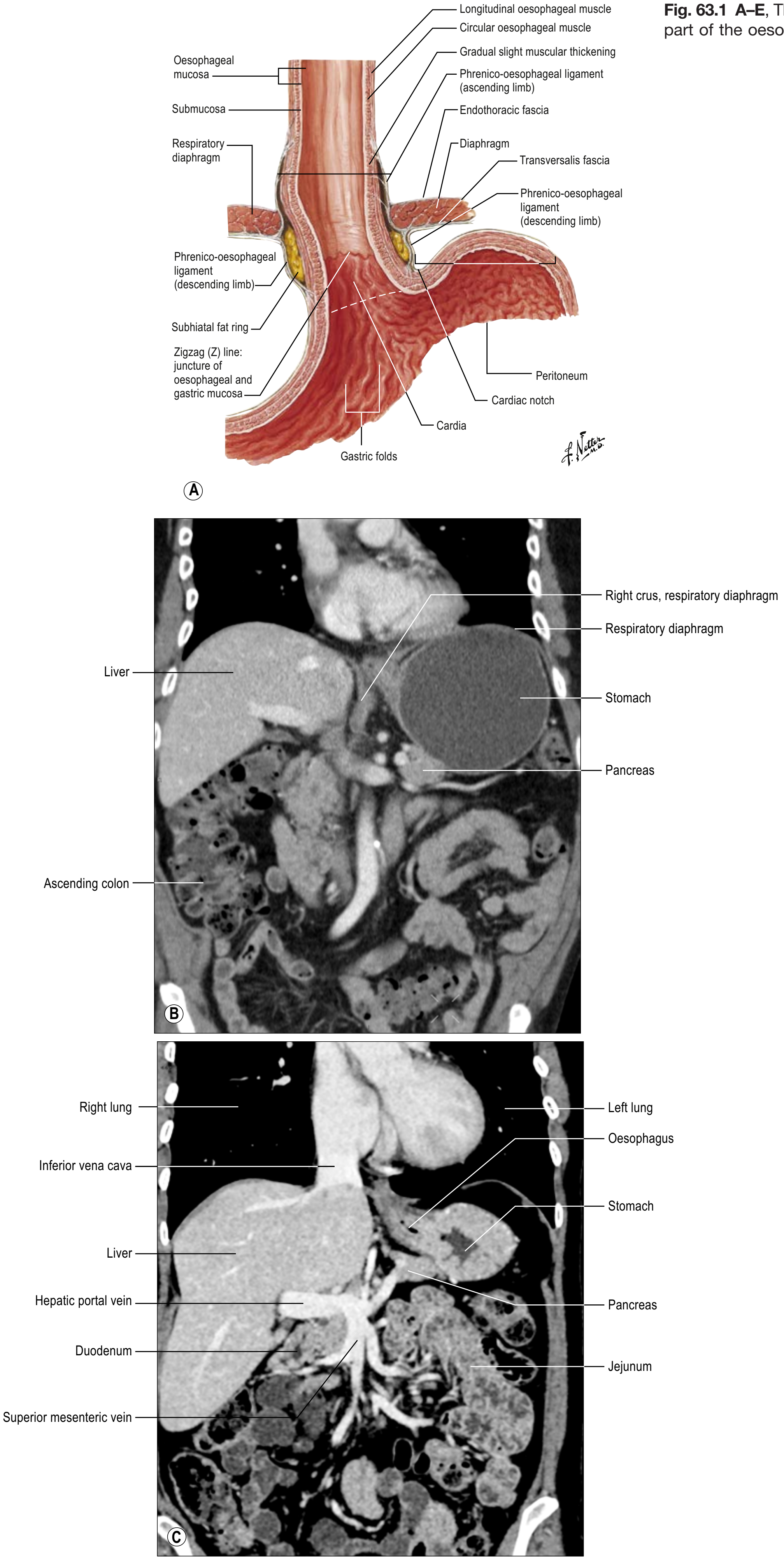
Longitudinal oesophageal muscle
Circular oesophageal muscle
Gradual slight muscular thickening
Phrenico-oesophageal ligament (ascending limb)
Endothoracic fascia
Diaphragm
Transversalis fascia
Phrenico-oesophageal ligament (descending limb)
Oesophageal mucosa
Submucosa
Respiratory diaphragm
Phrenico-oesophageal ligament (descending limb)
Subhiatal fat ring
Zigzag (Z) line: juncture of oesophageal and gastric mucosa
Gastric folds
Cardia
Cardiac notch
Peritoneum
F. Netter M.D.
A
Right crus, respiratory diaphragm
Respiratory diaphragm
Liver
Stomach
Pancreas
Ascending colon
B
Right lung
Left lung
Oesophagus
Inferior vena cava
Stomach
Liver
Hepatic portal vein
Pancreas
Duodenum
Jejunum
Superior mesenteric vein
C

Continued

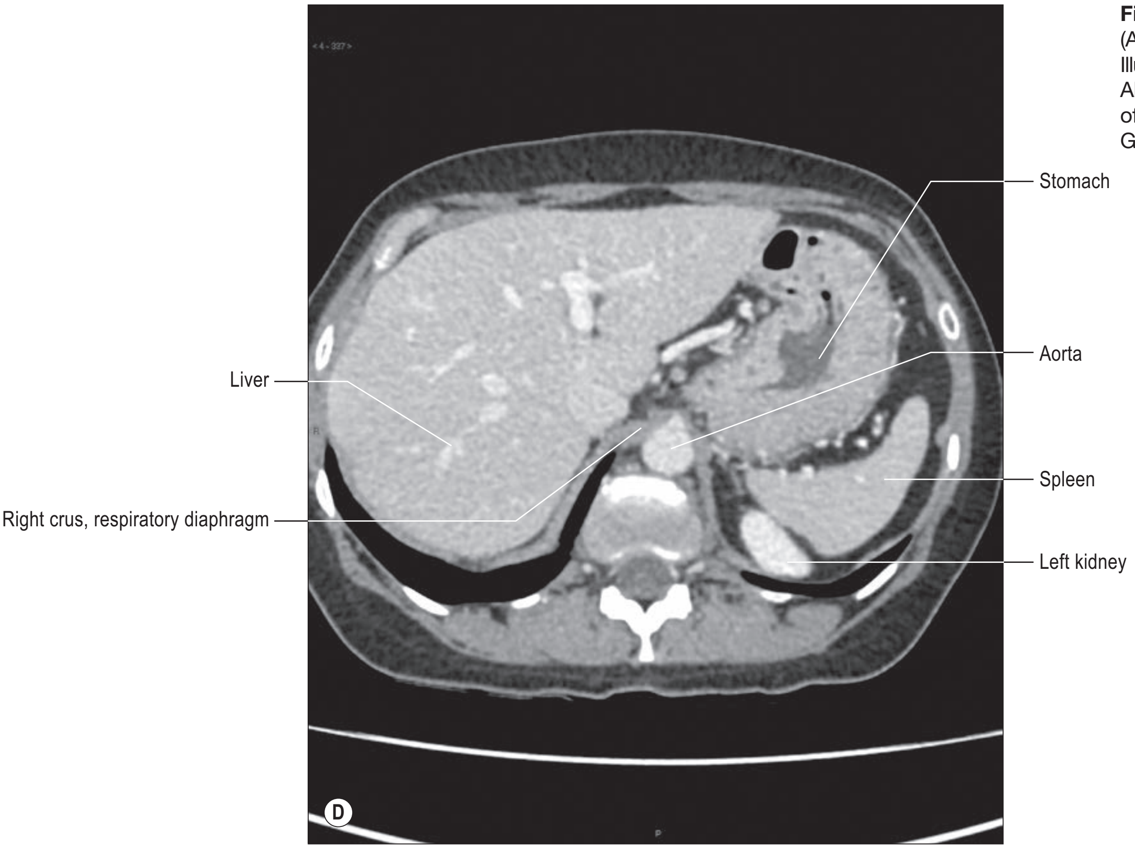

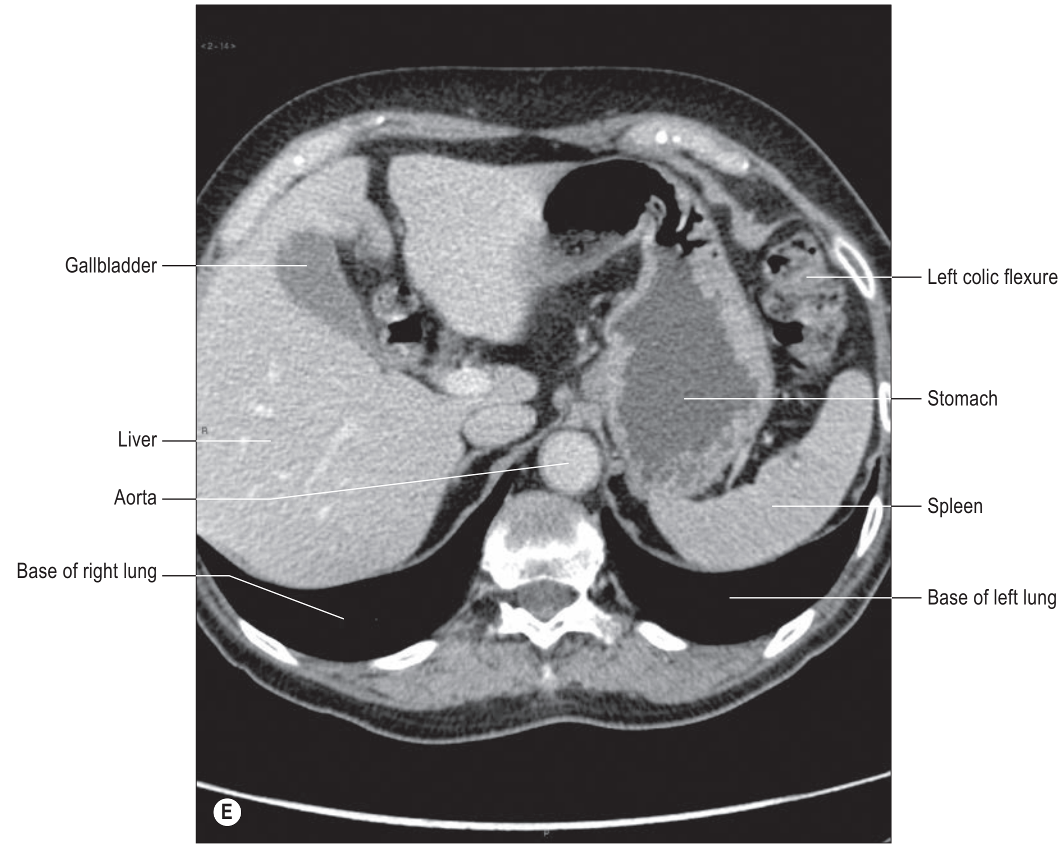

Fig. 63.1, cont'd D–E, Axial CT. (A, Reprinted from Netter Anatomy Illustration Collection, © Elsevier Inc. All Rights Reserved. B–E, Courtesy of Dr Stuart Ballantyne, Gartnavel General Hospital, Glasgow.

Hiatal hernia is a relatively common condition involving expansion of the oesophageal hiatus and herniation of the stomach through the respiratory diaphragm into the thorax. It is more common in elderly and obese individuals. There are two types of hiatal hernia: the sliding type accounts for at least 90%, and the para-oesophageal or mixed type makes up the remainder (Roman and Kahrilas 2014). In a sliding hiatal hernia the abdominal part of the oesophagus and cardia of the stomach traverse the oesophageal hiatus. In contrast, with a para-oesophageal hiatal hernia the abdominal part of the oesophagus and pylorus lie beneath the diaphragm and a varying portion of the stomach passes through the hiatus. On occasion, the entire stomach can rotate, forming an 'upside-down stomach' with the stomach twisted around its axis. It is important that endoscopists appreciate the anatomical differences between the two herniae in order to distinguish correctly between them. A hiatal hernia can be asymptomatic or associated with symptoms of gastro-oesophageal reflux. Para-oesophageal hiatal hernias can cause obstruction and/or ischaemia of the herniated part of the stomach. Treatment of a symptomatic sliding hiatal hernia is directed at managing associated gastro-oesophageal reflux. If suppression of acid production by medication fails, the patient may require anti-reflux surgery. This has traditionally consisted of a fundoplication, but a small flexible band of interlinked titanium beads with magnetic cores applied around the lower oesophageal sphincter is increasingly becoming the first line in the surgical management of medically recalcitrant gastro-oesophageal reflux.

drain to para-oesophageal nodes of the same level but distally to the left gastric nodes and nodes around the cardia, and then to coeliac nodes (Tachimori 2017). Therefore, cancer of the lower thoracic oesophagus tends to metastasize to nodes of the upper abdominal area (Tamaki et al 2012).

Innervation

The oesophagus has a well-developed intrinsic nervous system consisting of a ganglionated myenteric plexus and a sparsely ganglionated submucosal plexus, modulated by extrinsic autonomic nerves. Parasympathetic innervation of the abdominal part of the oesophagus is derived directly from the oesophageal plexus and, to a lesser extent, from the anterior and posterior vagal trunks. These nerves are motor to the distal oesophagus and both stimulatory and inhibitory to the lower oesophageal sphincter, maintaining basal tone and coordinating distal oesophageal peristalsis with relaxation of the sphincter during swallowing (the latter being mediated by intrinsic nitrergic inhibitory neurones under vagus nerve control). Sympathetic supply to the distal oesophagus originates from the fifth to twelfth thoracic spinal segments mainly via the greater and lesser thoracic splanchnic nerves and the coeliac plexus. Nociceptive signals are conveyed by afferent nerves accompanying sympathetic nerves and by vagus nerve afferents, which are also involved in mechanosensory signalling (Neuhuber et al 2006).

STOMACH

The stomach is the widest part of the alimentary tract and lies between the oesophagus and the duodenum. It performs numerous functions, including the temporary storage of ingested nutrients, mechanical breakdown of solid food, chemical digestion of proteins, regulation of the passage of chyme into the duodenum, secretion of intrinsic factor for vitamin B_{12} absorption, secretion of gut hormones and secretion of acid to aid digestion (including the absorption of iron). It is also important in microbial defence.

The stomach is situated in the upper abdomen, extending from the left upper quadrant downwards, forwards and to the right, lying in the left hypochondriac, epigastric and umbilical regions. It occupies a recess beneath the respiratory diaphragm and anterior abdominal wall bounded by the upper abdominal viscera on either side. Its mean capacity increases from approximately 20–30 ml at birth to approximately 1000–1500 ml in adults. The peritoneal surface of the stomach is interrupted by the attachments of the greater and lesser omenta, which define the greater and lesser curvatures and separate the anterior and posterior surfaces.

Parts of the stomach

For descriptive purposes, the stomach can be divided into fundus, body, pyloric antrum and pylorus by artificial lines drawn on its external surface (**Fig. 63.2**). The internal appearance and microstructure of these regions vary. The fundus is dome-shaped and projects above and to the left of the oesophageal opening (cardiac orifice) to lie in contact with the left side of the respiratory diaphragm; it lies above a horizontal line drawn from the cardiac notch to the greater curvature. The body extends from the fundus to the angular incisure, a constant external notch at the lower end of the lesser curvature. The cardia is the region of the stomach adjacent to the oesophageal opening. A line drawn from the angular incisure to an inconstant indentation on the greater curvature defines the lower boundary of the body. The pyloric antrum extends from this line to where the stomach narrows to become the pyloric canal (1–2 cm long), which terminates at the pyloric orifice (Didio and Anderson 1968).

Gastric relations

Gastric curvatures

Lesser curvature

The lesser curvature extends between the cardiac and pyloric orifices and forms the medial border of the stomach. It descends from the medial side of the oesophagus in front of the decussating fibres of the right crus of the respiratory diaphragm, curves downwards and to the right, and lies anterior to the superior border of the pancreas (**Fig. 63.3**). It ends at the pylorus, just to the right of the midline. In the most dependent part there is typically a notch, the angular incisure; the position and appearance of the incisure vary with gastric distension. The lesser omentum is attached to the lesser curvature and contains the right and left gastric vessels.

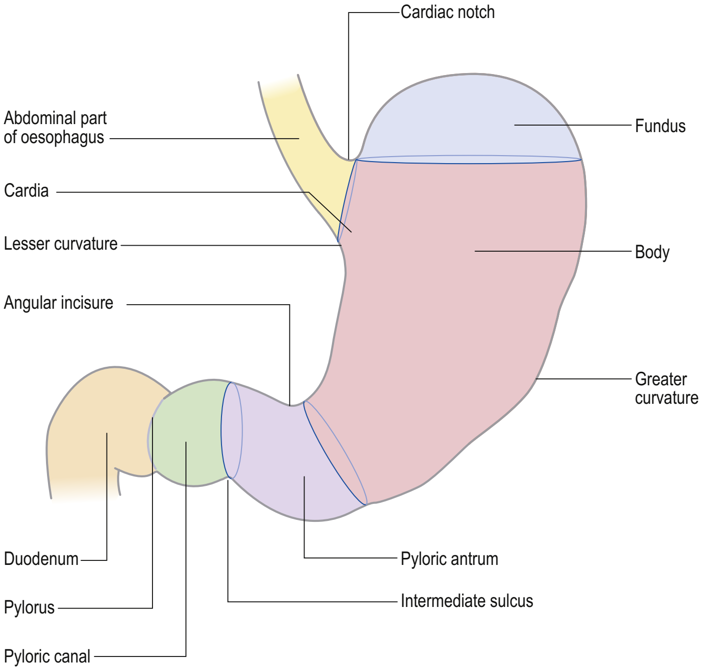

Fig. 63.2 The parts of the stomach.

Greater curvature

The greater curvature is two to three times longer than the lesser curvature (Csendes and Burgos 2005). It starts from the cardiac notch, formed between the lateral border of the abdominal part of the oesophagus and the fundus of the stomach, and arches upwards, posterolaterally and to the left. Its highest convexity, the apex of the fundus, is approximately level with the left sixth rib anteriorly but varies among individuals and during respiration (Mirjalili et al 2012). From this point, it sweeps inferiorly and anteriorly, slightly convex to the left, almost as far as the tenth costal cartilage in the supine position, where it turns medially to end at the pylorus in the transpyloric plane at the lower border of the first lumbar vertebra. There is frequently a groove, the intermediate sulcus, in the curvature close to the pyloric canal. The start of the greater curvature is covered by peritoneum, which continues over the anterior surface of the stomach. Laterally, the greater curvature gives attachment to the gastrosplenic ligament and, below this, to the greater omentum, which contains the gastro-omental (gastro-epiploic) vessels. The gastrosplenic ligament and the greater omentum, together with the gastrophrenic and splenorenal ligaments, are continuous derivatives of the original dorsal mesogastrium; their names merely indicate regions of the same continuous sheet of peritoneum and its associated connective tissue.

Gastric volvulus

Available with the *Gray's Anatomy* e-book

Gastric surfaces

When the stomach is empty and contracted, the anterior and posterior surfaces tend to face superiorly and inferiorly; but as the stomach distends, they face progressively more anteriorly and posteriorly (**Fig. 63.4**).

Anterior surface

The entire anterior surface of the stomach is covered by peritoneum. The lateral part of the anterior surface lies posterior to the left costal arch in contact with the respiratory diaphragm, which separates it from the left parietal pleura, the base of the left lung, the pericardium and the left seventh to ninth ribs and costal cartilages (**Fig. 63.5**). It also lies posterior to the costal attachments of the proximal fibres of transversus abdominis. The superior left part of this surface curves posteriorly and lies in contact with the visceral surface of the spleen. The right half of the anterior surface is related superiorly to the left lobe of the liver and inferiorly to the anterior abdominal wall, through which it can be accessed by a needle for placement of a gastrostomy tube (see below). When the stomach is empty, the transverse colon can lie adjacent to the anterior surface.

Gastric volvulus is much less common than volvulus of either the sigmoid colon or the caecum. It occurs when the stomach rotates abnormally and may be organo-axial or mesentero-axial. In organo-axial volvulus, the axis of rotation runs from below the cardiac orifice to the pylorus: the pyloric antrum, body and fundus rotate upwards such that the greater curvature comes to lie above the lesser curvature. In mesentero-axial volvulus, rotation occurs about an axis drawn 'across' the body of the stomach, usually just above the angular incisure. This type of volvulus is perpendicular to the axis of organo-axial volvulus. The distal body and pyloric antrum rotate anteriorly, superiorly and laterally while the upper body and fundus rotate posteriorly, medially and inferiorly. Although it is relatively mobile within the upper abdomen, the stomach is normally tethered at the gastro-oesophageal junction and the pylorus; to the spleen by the gastrosplenic ligament; and to the liver by the hepatogastric ligament. The attachment to the transverse colon via the gastrocolic ligament also restrains the stomach but this is the most mobile attachment. For either type of gastric volvulus to occur, some or all of these points of tethering must be loosened either by previous surgical division or by chronic lengthening and laxity of their connective tissue. Organo-axial volvulus is more common because the lesser omentum, and gastrosplenic and gastrocolic ligaments are more likely to undergo chronic lengthening by traction than the other attachments of the stomach. Mesentero-axial volvulus requires the gastro-oesophageal junction and pylorus to be sufficiently mobile so as to come into close approximation, which is much less common. Despite the rich arterial supply to the stomach, either type of volvulus can cause a strangulating obstruction.

Provided the detorted stomach is viable, gastric volvulus is typically managed by fixation of the anterior surface of the stomach to the anterior abdominal wall ('gastropexy') (García et al 2013): the recurrence rate is very high. An alternative is to insert one or more percutaneous endoscopic gastrostomy (PEG) tubes to fix the stomach to the anterior abdominal wall, a manoeuvre that is particularly useful in the unfit patient when a lengthy surgical procedure is contraindicated. Gastric volvulus of the organo-axial type is frequently associated with a para-oesophageal hiatal hernia that must also be repaired. This surgery can usually be carried out laparoscopically and most surgeons would advocate performing a combination of a hiatal repair, fundoplication with or without a gastropexy.

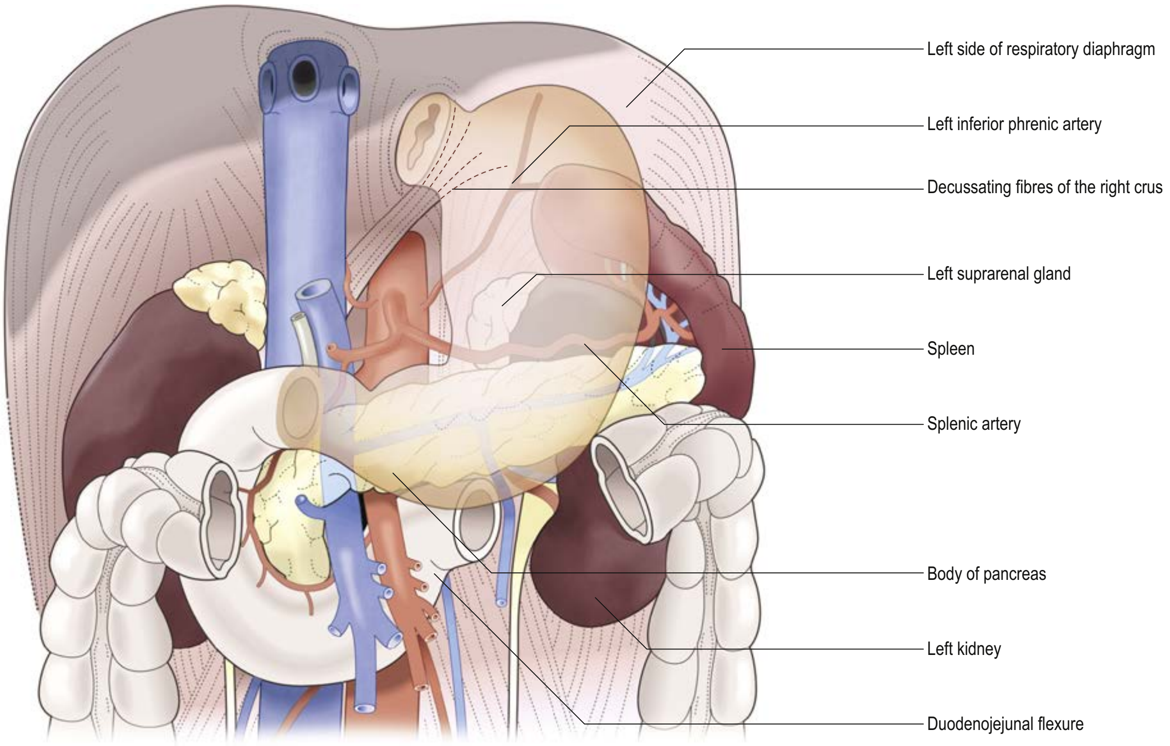
Left side of respiratory diaphragm
Left inferior phrenic artery
Decussating fibres of the right crus
Left suprarenal gland
Spleen
Splenic artery
Body of pancreas
Left kidney
Duodenojejunal flexure

Fig. 63.3 The posterior relations of the stomach.

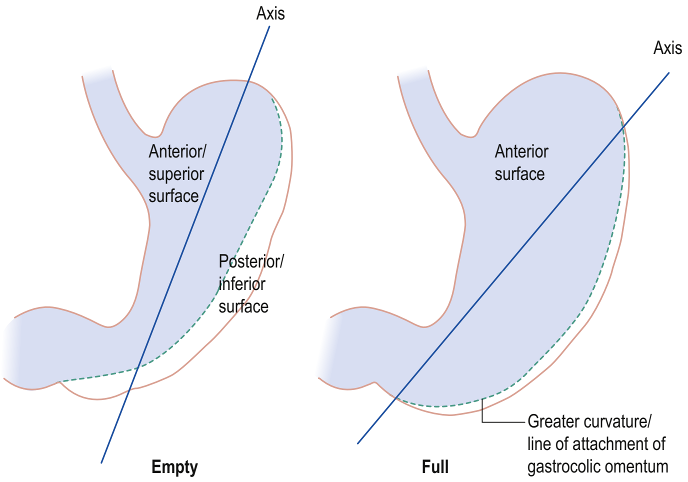
Axis
Anterior/
superior
surface
Posterior/
inferior
surface
Empty
Axis
Anterior
surface
Full
Greater curvature/
line of attachment of
gastrocolic omentum

Fig. 63.4 Axes of the empty and full stomach. As the stomach distends, the greater curvature 'rolls' downwards and the anterosuperior surface comes to lie almost completely vertical as the anterior surface.

Posterior surface

The posterior surface is covered by peritoneum except near the cardiac orifice, where a small, triangular area contacts the left crus of the respiratory diaphragm and sometimes the left suprarenal gland. The left gastric vessels reach the lesser curvature at the right extremity of this bare area. The gastrophrenic ligament passes from the lateral aspect of this bare area to the inferior surface of the respiratory diaphragm. The posterior surface of the stomach lies anterior to the left crus and inferior fibres of the diaphragm, the left inferior phrenic vessels, the left suprarenal gland, the superior pole of the left kidney, the splenic artery, the anterior surface of the pancreas and the superior layer of the transverse mesocolon (see Fig. 63.3). Together, these form the shallow stomach bed, which is separated from the stomach by the omental bursa (over which the stomach slides as it distends). The upper left part of the posterior surface curves anterolaterally and lies in contact with the visceral surface of the spleen. The transverse mesocolon separates the stomach from the duodenojejunal flexure and proximal jejunum.

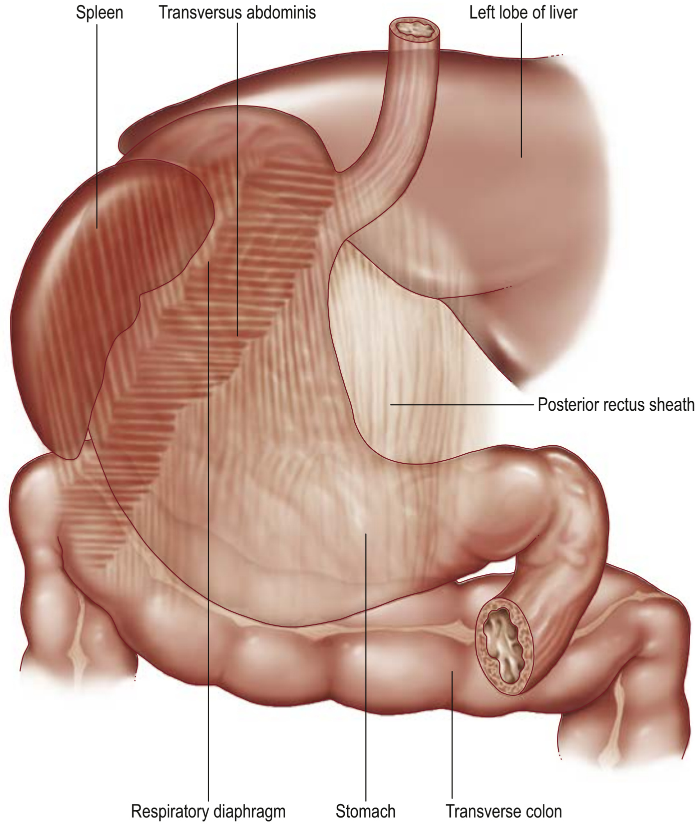
Spleen
Transversus abdominis
Left lobe of liver
Posterior rectus sheath
Respiratory diaphragm
Stomach
Transverse colon

Fig. 63.5 Anterior relations of the stomach, viewed from behind. The fibres of the respiratory diaphragm (oblique), transversus abdominis (transverse) and rectus abdominis (vertical) can be seen through the outlines of the stomach and its visceral relations.

Gastric orifices

Cardiac orifice and gastro-oesophageal junction

The oesophagus opens into the stomach at the cardiac orifice (see Fig. 63.1). This is usually situated to the left of the midline behind the seventh costal cartilage at the level of the eleventh thoracic vertebra (Mirjalili et al 2012). It is, on average, about 40 cm from the incisor teeth in the adult. The right side of the abdominal part of the oesophagus is continuous with the lesser curvature and the left side with the greater curvature.

Internally, the transition between the oesophagus and stomach is difficult to define because gastric fundal mucosal folds extend a variable distance up the abdominal part of the oesophagus. For practical purposes, the gastro-oesophageal junction is usually identified by a circumferential

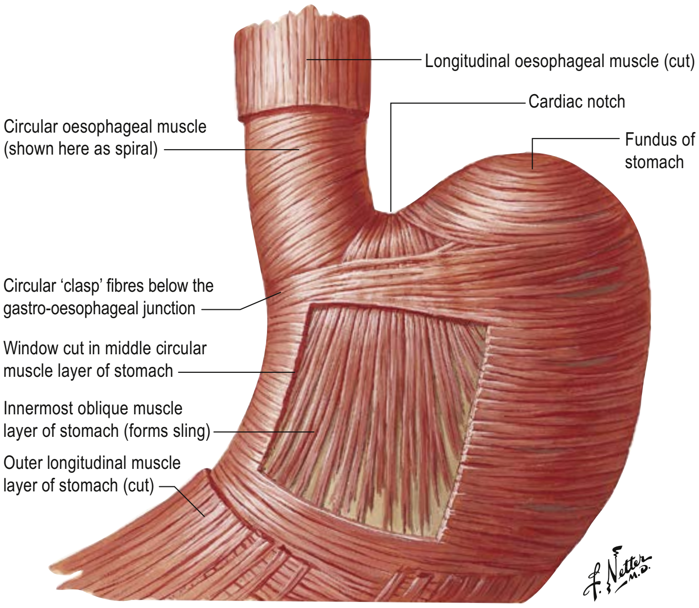
Longitudinal oesophageal muscle (cut)
Cardiac notch
Circular oesophageal muscle (shown here as spiral)
Fundus of stomach
Circular 'clasp' fibres below the gastro-oesophageal junction
Window cut in middle circular muscle layer of stomach
Innermost oblique muscle layer of stomach (forms sling)
Outer longitudinal muscle layer of stomach (cut)
F. Netter M.D.

Fig. 63.6 Detail of the arrangements of the muscle layers of the oesophageal and gastric walls. (Reproduced and modified from Netter Anatomy Illustration Collection, © Elsevier Inc. All Rights Reserved.)

'zigzag' line ('Z line') between the pale pink oesophageal squamous epithelium above and the red columnar epithelium below. In the healthy oesophagus, the Z line is located at the proximal extent of the gastric mucosal folds. When metaplastic columnar epithelium extends above the gastric folds into the distal oesophagus, it is regarded as pathological and termed Barrett's oesophagus. A sliding hiatal hernia with or without Barrett's oesophagus can make endoscopic identification of the gastro-oesophageal junction particularly difficult.

Externally, a fat pad is often present in adults beneath the peritoneum over the anterior surface of the gastro-oesophageal junction. The junction is also demarcated by a sling of longitudinal and oblique gastric muscle fibres that forms a loop on the superior, left, side of the gastro-oesophageal junction between the oesophagus and the stomach.

Lower oesophageal sphincter and gastro-oesophageal reflux

At rest, there is a pressure gradient across the gastro-oesophageal junction, reflecting the negative intrathoracic pressure transmitted to the thoracic oesophagus and the positive intra-abdominal pressure transmitted to the stomach (augmented by any contraction of the stomach). Several anatomical and physiological factors normally prevent gastro-oesophageal reflux. The two major antireflux mechanisms are the tonically contracted, specialized, thickened intrinsic circular smooth muscle of the distal oesophagus, which is reinforced by the extrinsic encircling fibres of the right crus of the respiratory diaphragm. Together, these exert a radial pressure on the lower 2–4 cm of oesophagus, creating an effective high-pressure zone (HPZ) that can be measured by electromyography or manometry (Paterson 2001, Mittal and Goyal 2006, Hershcovici et al 2011). The description of the intrinsic muscles of the lower oesophageal sphincter can be refined further to include clasp-like semicircular smooth muscle fibres on the right side of the oesophagus and sling-like oblique gastric muscle fibres on the left side (Stein et al 1995, Preiksaitis and Diamant 1997). The distribution of these muscle fibres corresponds to the anatomical and functional asymmetry of the HPZ.

At and just below the level of entry of the abdominal part of the oesophagus into the stomach, the circular fibres of the intermediate layer of the muscularis externa lying over the upper lesser curvature are particularly pronounced; they are sometimes referred to as 'clasp' fibres and exert fairly constant myogenic tone (**Fig. 63.6**). Since the oesophagus passes obliquely into the stomach, the tone in the clasp fibres rises with increasing gastric distension and these fibres can act to draw the anterior and posterior surfaces together, increasing the tone at the gastro-oesophageal junction and contributing to the HPZ. There are also several minor antireflux factors: the folds of gastric mucosa present at the gastro-oesophageal junction form a mucosal rosette that helps to create a fluid- and gas-tight seal from the basal tonic contraction of the muscular wall of the distal oesophagus; the angle of the cardiac orifice (angle of His), formed in part by the pull of the oblique fibres of the innermost layer of gastric smooth muscle, thereby constituting a type of 'flap valve'; and the length of the abdominal part of the oesophagus, which is buttressed externally by pads of adipose tissue at and distal to the level of the oesophageal hiatus. These anatomical and physiological features are collectively referred to as the lower oesophageal sphincter. The oesophageal part of the lower oesophageal sphincter is controlled by the intramural plexuses of the enteric nervous system; activation of inhibitory neurones releasing nitric oxide leads to relaxation of the sphincter. Muscle tone is reduced in advance of the oesophageal peristaltic wave during swallowing and raised again after the food bolus has passed. During inspiration, the greater negative intrathoracic pressure increases the gastro-oesophageal pressure gradient, but this is offset by increased pressure in the HPZ from contraction of the peri-oesophageal fibres of the right crus of the respiratory diaphragm. Activation of the crura slightly before the rest of the respiratory diaphragm facilitates this antireflux mechanism.

Barrett's oesophagus

Available with the *Gray's Anatomy* e-book

Pyloric orifice

The pyloric orifice is the opening from the stomach into the duodenum. When the body is supine and the stomach empty, it typically lies 1–2 cm to the right of the midline in the transpyloric plane, which passes through the lower border of the body of the first lumbar vertebra. The pyloric sphincter is formed by a circumferential thickening of circular muscle interlaced with connective tissue septa and some longitudinal muscle fibres, and is palpably thicker than the adjacent stomach and duodenum. The circular pyloric constriction on the surface of the stomach usually indicates the location of the pyloric sphincter, and may be marked by a prepyloric vein (of Mayo) that crosses the anterior surface in a caudal direction.

Gastric form and internal appearances

Numerous factors influence both the form and the position of the stomach, including the posture and build of the individual, the extent to which the stomach is filled, the position of the surrounding viscera, and the tone of the abdominal wall and gastric musculature. The empty stomach is most commonly J-shaped; the fundus usually contains air; and in the erect posture, the pylorus descends to the level of the second or third lumbar vertebra. The lowest part of the pyloric antrum can lie distal to the level of the umbilicus, and the overall axis of the organ is slightly inclined from the vertical (**Fig. 63.7**). In short, obese individuals the axis of the stomach lies more towards the horizontal with a 'steer-horn' shape.

The extent of filling mainly affects the shape and position of the body of the stomach. As the stomach fills it expands forwards and downwards, but when the colon or small intestine are distended the fundus enlarges towards the liver and the respiratory diaphragm. As stomach capacity increases, the pylorus is displaced to the right and the axis of the whole organ lies in a more oblique direction (see Fig. 63.4).

Internal appearances

During endoscopic examination (**Fig. 63.8**) the stomach is typically at least partially distended by air. The cardiac orifice and the lowest portion of the abdominal part of the oesophagus viewed from above are typically closed at rest by tonic contraction of the lower oesophageal sphincter. The transition between the pale pink squamous epithelium of the oesophagus and the red columnar epithelium of the stomach, the 'Z line', is usually clearly visible at the proximal extent of the gastric mucosal folds (Silverstein and Tytgat 1991). Viewed retrogradely from within the distended stomach, the cardiac orifice lies medial to the fundus, with a mucosal fold between the two corresponding to the acute angle at this orifice. The mucosa also appears slightly thickened, forming part of the 'mucosal rosette' that lines the orifice and contributes to its closure (see above).

In the partially distended stomach, the mucosa of the body and to a lesser extent the fundus is thrown into longitudinal folds (gastric folds or rugae) (see Fig. 63.7). These are most obvious on the anterolateral, lateral and posterolateral parts of the stomach towards the greater curvature. The smoother mucosa along the lesser curvature forms a 'gastric canal' or '*magenstrasse*' that enables liquids entering the stomach to be fast-tracked to the pylorus (see Fig. 63.8).

The gastric areas within the pyloric antrum are small undulations of the mucosal surface that give a subtle cobblestone-type appearance on double contrast barium meal examination (see Fig. 63.7) (Mackintosh and Kreel 1977). The few folds present in the pyloric antrum when the stomach is relaxed disappear with distension. The pyloric antrum adjacent to the pyloric canal, the prepyloric antrum, Reflux of gastric contents into the distal oesophagus as a result of transient relaxation of the lower oesophageal sphincter occurs as a normal daily event in most individuals. Prolonged episodes of acid reflux as a result of a weak lower oesophageal sphincter or sliding hiatal hernia can cause oesophagitis and its associated complications. Surgical procedures to prevent abnormal reflux are aimed at restoring a normal length of intra-abdominal oesophagus, repairing any hiatal hernia and increasing the pressure surrounding the intra-abdominal part of the oesophagus. This last is usually achieved by wrapping the fundus of the stomach around the intra-abdominal part of the oesophagus (fundoplication).

The converse type of lower oesophageal sphincter dysfunction occurs in achalasia, which is characterized by reduced or absent ganglion cells in the myenteric plexus of the distal oesophagus and gastro-oesophageal junction. The loss of inhibitory neurones at this site leads to impaired relaxation of the lower oesophageal sphincter on swallowing, causing dysphagia: oesophageal contraction becomes disorganized, resulting in proximal oesophageal dilatation. Classically, achalasia is characterized by a ‘bird’s beak’ appearance on a barium swallow examination. The dilated oesophagus tapers sharply distally, there is poor oesophageal emptying and a non-relaxing lower oesophageal sphincter. Oesophageal manometry reveals aperistalsis of the oesophagus and a high pressure non-relaxing lower oesophageal sphincter. The main treatment options include surgical myotomy (Heller’s cardiomyotomy), balloon dilatation or botulinum toxin injection, all of which address the hypertonic muscle fibres at the distal end of the oesophagus. Peroral endoscopic myotomy (POEM) has been described as an alternative intervention (Schlottmann and Patti 2018).

Barrett’s oesophagus can be defined as a change in the epithelium of the oesophagus in which any portion of the normal squamous epithelium lining has been pathologically replaced by a metaplastic ‘intestinalized’ columnar epithelium (see Commentary 1.3). There is a strong association between gastro-oesophageal reflux and the development of Barrett’s oesophagus, which is also seen more commonly in Caucasian males and obese patients. The abnormal intestinal metaplasia can extend for a variable length proximally from the gastro-oesophageal junction, and associated macroscopic mucosal changes can be seen on endoscopy. The Prague classification is used to document the nature of the Barrett’s oesophagus accurately in terms of its circumferential and maximal extents above the gastro-oesophageal junction. Barrett’s oesophagus is recognized as the most important precursor lesion for oesophageal adenocarcinoma (Naini et al 2016)

Infantile hypertrophic pyloric stenosis is due to idiopathic hypertrophy of the circular muscle of the pylorus and causes gastric outlet obstruction in early infancy. It is readily treated by dividing the thickened pyloric muscle (pyloromyotomy) without dividing the pyloric gastric mucosa. Division of the vagal innervation to the pylorus can result in a functional gastric outlet obstruction or delayed gastric emptying; both common sequelae of gastric mobilization and oesophagectomy. To counter this possibility, a pyloroplasty can be fashioned involving full division of the anterior pyloric wall and reconstruction in the counter direction to promote drainage. Historically, pyloroplasty was performed to promote gastric drainage when vagotomy was used to treat peptic ulceration.

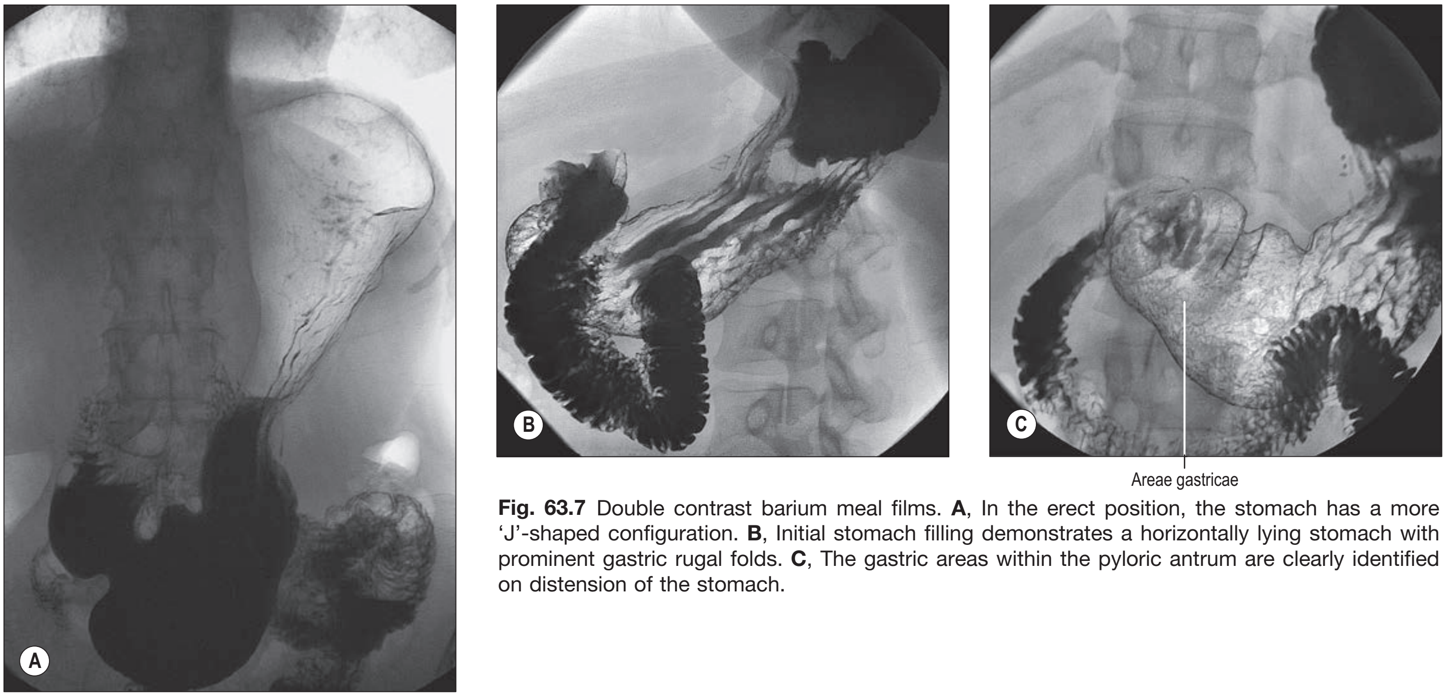

Fig. 63.7 Double contrast barium meal films. **A**, In the erect position, the stomach has a more 'J'-shaped configuration. **B**, Initial stomach filling demonstrates a horizontally lying stomach with prominent gastric rugal folds. **C**, The gastric areas within the pyloric antrum are clearly identified on distension of the stomach.

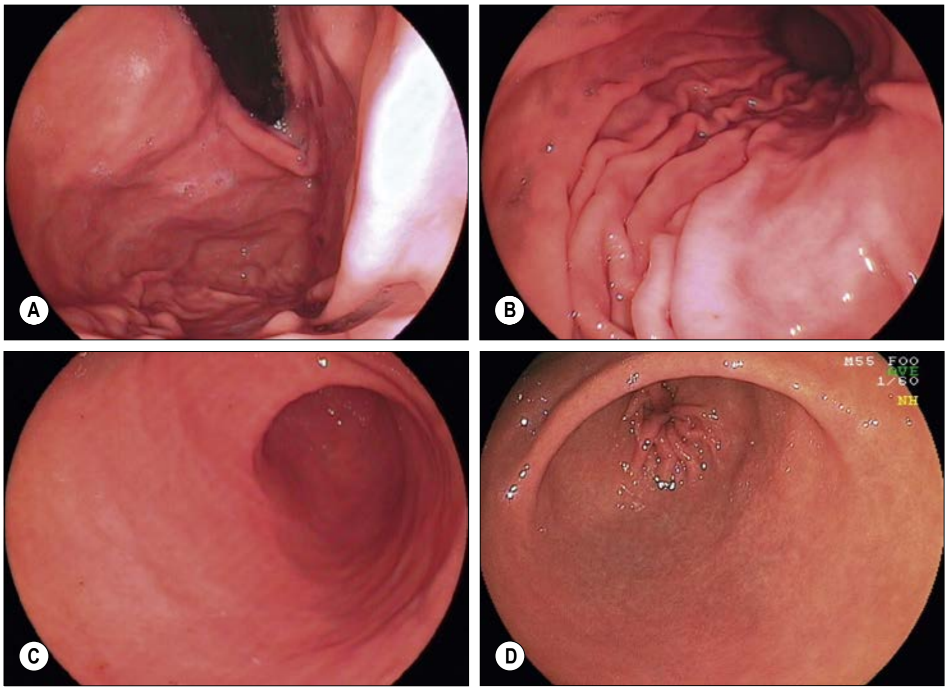

Fig. 63.8 Endoscopic appearances of the stomach. **A**, The cardiac orifice and fundus from below, showing the pronounced lateral mucosal fold at the cardiac orifice. **B**, The body and greater curvature, showing mucosal folds ('*magenstrasse*'). **C**, The pyloric antrum, showing the internal appearance of the angular incisura. **D**, The prepyloric antrum and opening of the pyloric canal.

has a smooth mucosal surface that culminates in a slight puckering of the mucosa at the pyloric orifice caused by contraction of the pyloric sphincter.

Gastrostomy

Available with the *Gray's Anatomy* e-book

Vascular supply and lymphatic drainage

Arteries

The arterial supply to the stomach comes predominantly from the coeliac trunk, although there are intramural anastomoses with arteries of other origins at the two ends of the stomach (Figs 63.9–63.11).The left gastric artery usually arises directly from the coeliac trunk. The short gastric arteries, left gastro-omental artery and, when present, the posterior gastric artery are branches of the splenic artery. The right gastric artery and right gastro-omental artery usually arise from the proper hepatic artery and the gastroduodenal artery, respectively.

Left gastric artery

The left gastric artery is the smallest branch of the coeliac trunk. It ascends to the left of the midline and crosses over the distal end of the left crus of the respiratory diaphragm beneath a fold of peritoneum in the upper posterior wall of the omental bursa (the gastropancreatic fold). Here, it lies adjacent to the left inferior phrenic artery and medial or anterior to the left suprarenal gland. It runs forwards into the superior portion of the lesser omentum adjacent to the proximal end of the lesser curvature, and then it turns anteroinferiorly to run along the lesser curvature between the two peritoneal leaves of the lesser omentum. At the highest point of its course it gives off one or more oesophageal branches. In its course along the lesser curvature it gives off multiple branches that run on to the anterior and posterior surfaces of the

Since the inferior half of the anterior surface of the stomach lies adjacent to the anterior abdominal wall in the left upper quadrant, it can be readily accessed to form a gastrostomy. The mobility of the stomach means that it can be approximated to the parietal peritoneum on the proximal anterior abdominal wall and a communication can then be established between the lumen of the stomach and the skin surface. This is commonly undertaken by percutaneous puncture of the stomach guided by an endoscope within the gastric lumen, and is termed a percutaneous endoscopic gastrostomy (PEG). Other versions include a radiologically inserted gastrostomy (RIG) and either open or laparoscopic insertion of a gastrostomy tube that can then be used for feeding or drug administration. Caution is needed to avoid inadvertent transfixion of the transverse colon, which may be interposed between the stomach and anterior abdominal wall.

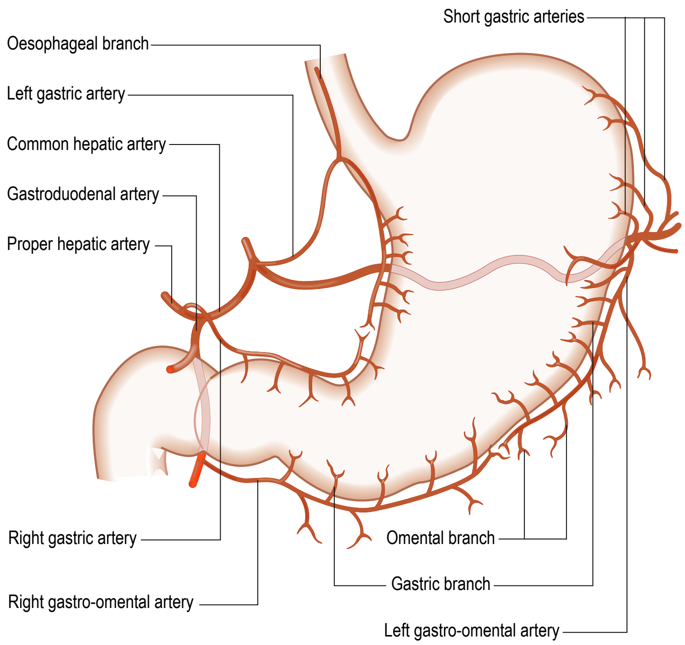

Fig. 63.9 The arterial supply of the stomach. A posterior gastric artery is not shown in this illustration.

stomach, after which it anastomoses with the right gastric artery in the region of the angular incisure.

Rarely, the left gastric artery (replaced or accessory) arises from the common hepatic or left hepatic arteries, or directly from the abdominal aorta (Panagouli et al 2013). The most common of these variations is an origin from the left hepatic artery, when the left gastric artery passes between the peritoneal layers of the proximal lesser omentum to reach the lesser curvature of the stomach. However, a replaced/accessory left hepatic artery arising from the left gastric artery is more common than a replaced/accessory left gastric artery origin.

Short gastric arteries

For practical purposes, the short gastric arteries can be defined as those arteries arising above the level of the splenic artery and supplying the fundus of the stomach on its greater curvature. The short gastric arteries vary in number, commonly between five and seven. They arise from the splenic artery or its terminal divisions, or from the proximal left gastro-omental artery, and pass between the layers of the gastrosplenic ligament to supply the fundus of the stomach and cardiac orifice. They anastomose with branches of the left gastric and left gastro-omental arteries. Rarely, an accessory left gastric artery arises with these vessels from the distal splenic artery.

Left gastro-omental artery

The left gastro-omental artery is the largest branch of the splenic artery. It arises near the splenic hilum and runs anteroinferiorly between the layers of the gastrosplenic ligament into the proximal gastrocolic part (gastrocolic ligament) of the greater omentum. Here, it descends between the layers of peritoneum close to the greater curvature and often anastomoses with the right gastro-omental artery. It gives off gastric branches to the fundus of the stomach through the gastrosplenic ligament, and to the body of the stomach through the gastrocolic ligament. These are necessarily longer than the gastric branches of the right gastro-omental artery and can be up to 8 cm long. Omental branches arise along the course of the vessel and descend between the layers of the greater omentum. A particularly large omental branch commonly originates close to the origin of the left gastro-omental artery, descends in the lateral portion of the greater omentum and provides a large arterial supply to this part.

Posterior gastric artery

A posterior gastric artery supplying the posterior wall of the upper part of the body of the stomach is commonly present but there has been a lack of consensus regarding its origin, course and distribution. When present, it usually arises from the splenic artery (typically from its midsection) posterior to the body of the stomach (see Fig. 63.11) and ascends behind the peritoneum of the omental bursa towards the fundus to reach the posterior surface of the stomach. It can also arise from the left gastric artery or coeliac trunk (Loukas et al 2007).

Right gastric artery

The right gastric artery is a relatively small artery that usually arises from the proper hepatic artery and runs forwards into the lesser omentum just above the superior part of the duodenum. It then travels within the lesser omentum along the lesser curvature of the stomach, giving off multiple branches to the anterior and posterior surfaces of the stomach, before anastomosing with the left gastric artery. Less commonly, the right gastric artery arises from the common hepatic, left hepatic or gastroduodenal arteries (Tubbs et al 2016).

Right gastro-omental artery

The right gastro-omental artery usually originates from the gastroduodenal artery behind the superior part of the duodenum, anterior to the head of the pancreas. It passes inferiorly towards the midline just below the pylorus and then runs laterally along the greater curvature between the layers of the greater omentum about 1–2 cm from the greater curvature of the stomach. It ends by anastomosing with the left gastro-omental artery (although this anastomosis is variably developed (Ndoye et al 2006) and can be absent). The right gastro-omental artery gives off gastric branches that ascend onto the anterior and posterior surfaces of the pyloric antrum and distal body of the stomach, omental branches that descend into the greater omentum, and duodenal branches that contribute to the supply of the inferior aspect of the superior part of the duodenum (Settembre et al 2018). The course of the right gastro-omental artery can vary: it can pass down into the greater omentum before arching back towards the greater curvature; it is important that the surgeon appreciates this anatomical variation if relying on the right gastro-omental artery to supply a surgically fashioned gastric conduit during reconstruction following oesophagectomy.

Arterial anastomoses of the stomach

The major named vessels supplying the stomach form extensive arterial anastomoses throughout the wall of the stomach but particularly in the submucosa. The rich arterial supply to the stomach ensures that the high mucosal blood flow required for physiological functioning is maintained even if one or more vessels become occluded: the stomach shows considerable resistance to ischaemia, even when multiple arterial supplies are lost.

Oesophageal arteries originating from the descending thoracic aorta anastomose with vessels supplying the fundus of the stomach in the region of the cardiac orifice. At the pyloric orifice, the extensive network of vessels supplying the duodenum allows for some anastomosis between branches of the superior mesenteric artery and pyloric vessels derived from arteries arising from the coeliac trunk. The right and left gastro-omental arteries and left and right gastric arteries anastomose along the greater and lesser curvatures, respectively. The short gastric and left gastric arteries anastomose in the fundus. The pyloric arteries are branches of the right gastric and right gastro-omental arteries. They pierce the duodenal wall around its entire circumference just distal to the pyloric sphincter and reach the submucosa. Here, they divide into two or three rami that run towards the stomach in the submucosa of the pyloric canal and terminate in the mucosa of the pyloric antrum (**Fig. 63.12**) (Piasecki 1974). The pyloric arteries anastomose with submucosal arteries in the duodenum and pyloric antrum close to their origin and termination, respectively. The pyloric sphincter is supplied by gastric and pyloric arteries via branches that leave their parent vessels in the subserosal and submucosal levels to penetrate the pyloric sphincter.

The extensive arterial anastomoses in the stomach wall allow the surgeon to run a gastric conduit off just the right gastro-omental and right gastric arteries, thereby providing reconstructive options following oesophagectomy: the blood supply can be sufficient to anastomose the gastric conduit as far proximally as the cervical part of the oesophagus.

Dieulafoy lesions

Abnormalities of the intramural vascularity of the stomach are a rare cause of acute upper gastrointestinal haemorrhage. The so-called ‘Dieulafoy’ lesion consists of an abnormally large artery that penetrates the muscular coat of the stomach, runs a tortuous course in the submucosa, and protrudes through a small mucosal defect where it is vulnerable to rupture: it occurs most often near the lesser curvature within a few centimetres of the gastro-oesophageal junction (Baxter and Aly 2010). The vessel can usually be clipped endoscopically, but if this fails, under-running of the vessel at open surgery may be required.

Veins

The veins draining the stomach ultimately empty into the hepatic portal vein. A rich submucosal and intramural venous network gives rise to veins

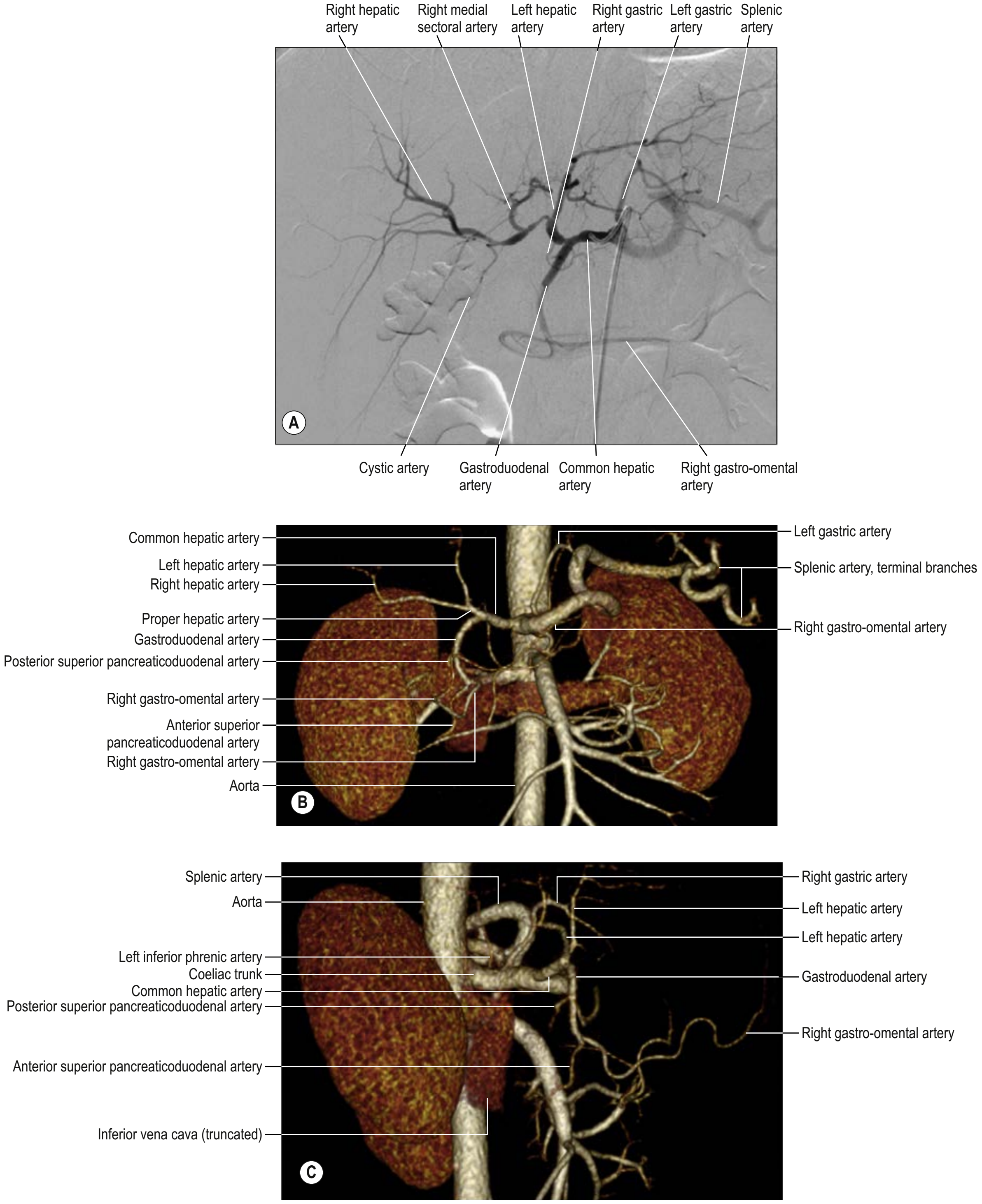
Right hepatic artery
Right medial sectoral artery
Left hepatic artery
Right gastric artery
Left gastric artery
Splenic artery
A
Cystic artery
Gastroduodenal artery
Common hepatic artery
Right gastro-omental artery
Common hepatic artery
Left hepatic artery
Right hepatic artery
Proper hepatic artery
Gastroduodenal artery
Posterior superior pancreaticoduodenal artery
Right gastro-omental artery
Anterior superior pancreaticoduodenal artery
Right gastro-omental artery
Aorta
B
Left gastric artery
Splenic artery, terminal branches
Right gastro-omental artery
Splenic artery
Aorta
Left inferior phrenic artery
Coeliac trunk
Common hepatic artery
Posterior superior pancreaticoduodenal artery
Anterior superior pancreaticoduodenal artery
Inferior vena cava (truncated)
C
Right gastric artery
Left hepatic artery
Left hepatic artery
Gastroduodenal artery
Right gastro-omental artery

Fig. 63.10 The coeliac trunk and its branches. **A**, Digital subtraction angiogram. **B–C**, Volume-rendered CT angiograms of the abdominal aorta: frontal view (**B**) and right lateral view (**C**). (A, Courtesy of Dr James McCall, Chelsea & Westminster Hospital, London.) (D–F, *continued online*)

that usually accompany the corresponding named arteries and drain into either the splenic or superior mesenteric veins, although some pass directly into the hepatic portal vein. The course and distribution of the veins is highly variable even up to the level of the major named vessels.

Short gastric veins

Three to five short gastric veins drain the fundus and the upper part of the greater curvature of the stomach into the splenic vein or one of its large tributaries: they travel within the gastrosplenic ligament (Power et al 2001).

Left gastro-omental vein

The left gastro-omental (gastro-epiploic) vein drains both the anterior and posterior surfaces of the body of the stomach and the adjacent greater omentum via multiple tributaries. It runs superolaterally along the greater curvature, between the layers of the gastrocolic ligament, and drains into the splenic vein within the gastrosplenic ligament.

Right gastro-omental vein

The right gastro-omental (gastro-epiploic) vein drains the greater omentum, distal body and pyloric antrum. It runs medially along the greater curvature in the upper part of the gastrocolic omentum. Just proximal to the pylorus, it passes posteriorly to drain into the superior mesenteric vein posterior to the neck of the pancreas. The right gastro-omental vein can receive the right colic vein (forming a 'gastrocolic trunk') and/or the superior pancreaticoduodenal vein close to its entry into the superior mesenteric vein (Yamaguchi et al 2002, Stefura et al 2018).

Left gastric vein

The left gastric vein drains the proximal body and fundus of the stomach. It ascends along the lesser curvature to the gastro-oesophageal junction, where it receives several distal oesophageal veins. It then curves posteriorly and medially behind the posterior wall of the omental bursa. It usually passes anterior or posterior to the common hepatic artery and drains into the hepatic portal vein at the level of the proximal border of the superior part of the duodenum (which corresponds to 1–2 cm from

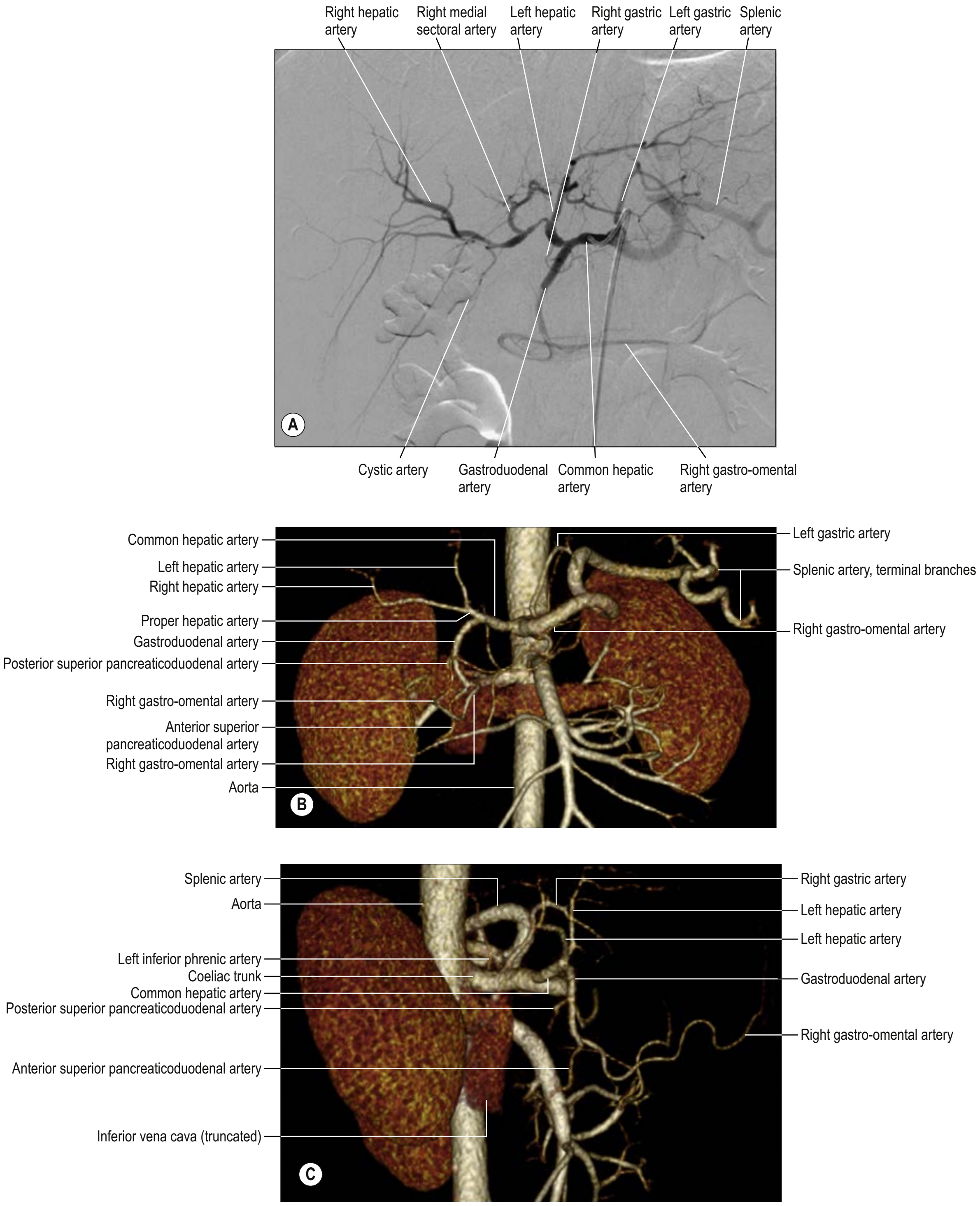
Right hepatic artery
Right medial sectoral artery
Left hepatic artery
Right gastric artery
Left gastric artery
Splenic artery
A
Cystic artery
Gastroduodenal artery
Common hepatic artery
Right gastro-omental artery
Common hepatic artery
Left hepatic artery
Right hepatic artery
Proper hepatic artery
Gastroduodenal artery
Posterior superior pancreaticoduodenal artery
Right gastro-omental artery
Anterior superior pancreaticoduodenal artery
Right gastro-omental artery
Aorta
B
Left gastric artery
Splenic artery, terminal branches
Right gastro-omental artery
Splenic artery
Aorta
Left inferior phrenic artery
Coeliac trunk
Common hepatic artery
Posterior superior pancreaticoduodenal artery
Anterior superior pancreaticoduodenal artery
Inferior vena cava (truncated)
C
Right gastric artery
Left hepatic artery
Left hepatic artery
Gastroduodenal artery
Right gastro-omental artery

Fig. 63.10 The coeliac trunk and its branches. **A**, Digital subtraction angiogram. **B–C**, Volume-rendered CT angiograms of the abdominal aorta: frontal view (**B**) and right lateral view (**C**).

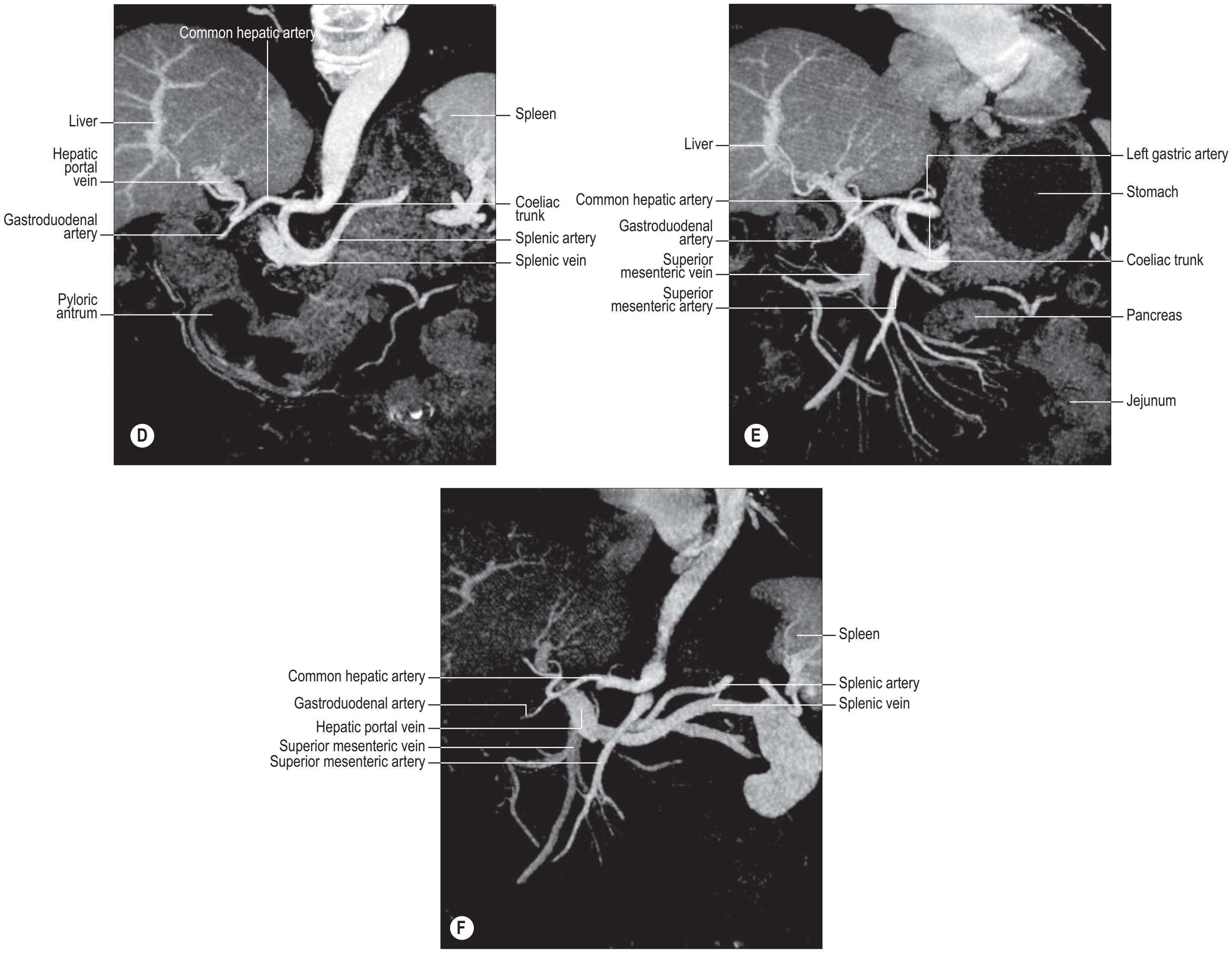
Common hepatic artery
Liver
Hepatic portal vein
Gastroduodenal artery
Pyloric antrum
Spleen
Coeliac trunk
Splenic artery
Splenic vein
D
Liver
Common hepatic artery
Gastroduodenal artery
Superior mesenteric vein
Superior mesenteric artery
Left gastric artery
Stomach
Coeliac trunk
Pancreas
Jejunum
E
Common hepatic artery
Gastroduodenal artery
Hepatic portal vein
Superior mesenteric vein
Superior mesenteric artery
Spleen
Splenic artery
Splenic vein
F

Fig. 63.10, cont'd D-F, Coronal CT angiograms showing the blood supply of the stomach and neighbouring organs. (A, Courtesy of Dr James McCall, Chelsea & Westminster Hospital, London. D–F, Courtesy of Dr Stuart Ballantyne, Gartnavel General Hospital, Glasgow)

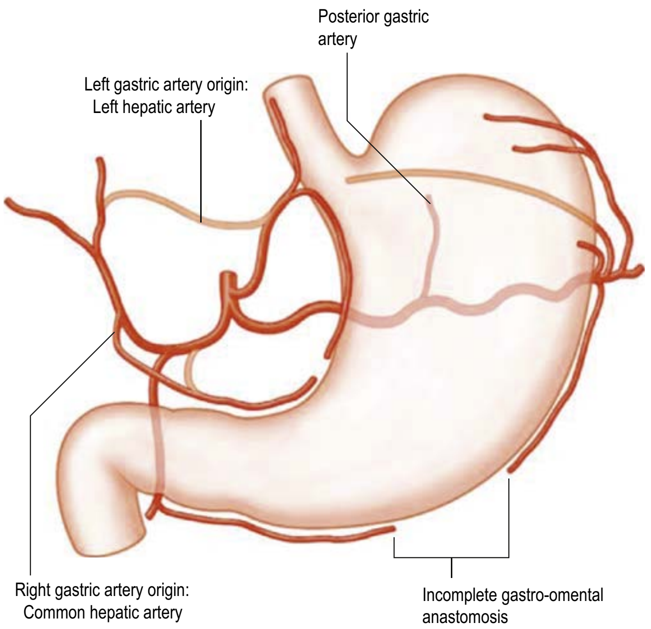
Posterior gastric artery
Left gastric artery origin: Left hepatic artery
Right gastric artery origin: Common hepatic artery
Incomplete gastro-omental anastomosis

Fig. 63.11 Principal variations in the arterial supply of the stomach. Accessory vessels or possible replaced origins of vessels are shown in pale pink.

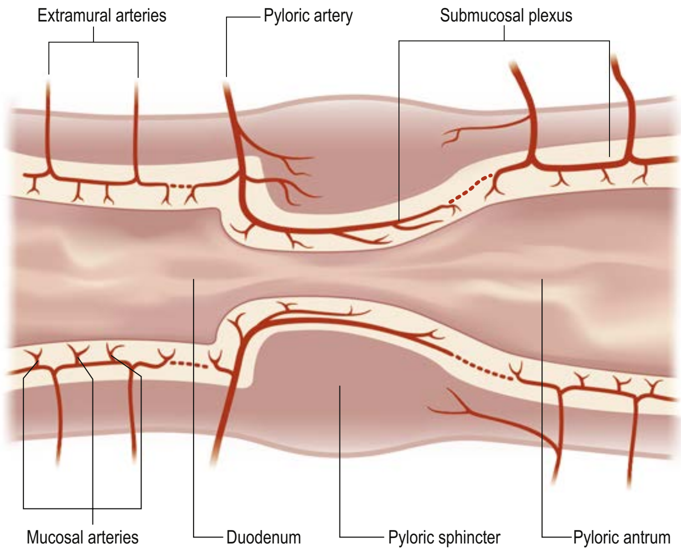

Fig. 63.12 The blood supply to the stomach and the proximal duodenum: a scheme of arterial arrangements at the gastroduodenal junction. Dotted lines indicate sites where the submucous plexus may be non-continuous. Shaded areas represent the muscular layer of the visceral wall. (Redrawn courtesy of C Piasecki, Department of Anatomy, Royal Free Hospital School of Medicine, London, and the Journal of Anatomy.)

the origin of the portal vein) (Rebibo et al 2012). In up to one-third of individuals, it passes anterior or posterior to the common hepatic artery but terminates in the splenic vein. On rare occasions, it drains into the left branch of the hepatic portal vein within the liver (Ohkubo 2000), a variant that may be clinically important in portal hypertension. Knowledge of these venous variations is important during lymphadenectomy for gastric cancer to avoid unexpected venous bleeding.

Right gastric vein

The right gastric vein is typically small and runs along the medial end of the lesser curvature, passing under the peritoneum as it is reflected from the posterior aspect of the pylorus and superior part of the duodenum on to the posterior wall of the omental bursa. It drains directly into the hepatic portal vein at the level of the superior part of the duodenum. It receives the prepyloric vein as it ascends anterior to the pylorus at the level of the pyloric orifice. Rarely, the right gastric vein drains directly into a branch of the hepatic portal vein within the liver.

Posterior gastric veins

One or more distinct posterior gastric veins can be present, draining the middle of the posterior surface of the stomach into the splenic vein: they can become particularly prominent in portal hypertension (Kimura et al 1990).

Oesophageal and gastric varices

Blood from the oesophageal mucosa normally drains into a submucosal venous plexus, then into a deeper intrinsic venous plexus and finally into oesophageal veins via perforating veins. In the abdominal part of the oesophagus, the perforating veins drain into tributaries of the left gastric vein, whereas in the distal thoracic part of the oesophagus, they drain into tributaries of the azygos and hemiazygos venous systems. Bidirectional flow is possible in this region and accommodates pressure changes during breathing and Valsalva manoeuvres.

Oesophageal and gastric varices are abnormally dilated veins that occur in the submucosal plexus of the distal oesophagus and fundus of the stomach when portal venous pressure is chronically elevated (typically greater than 15 mmHg). This can arise as a consequence of liver fibrosis or cirrhosis, or hepatic portal vein thrombosis, or from a variety of other causes. Portal hypertension leads to the recanalization of occluded embryonic venous channels connecting tributaries of the portal system and the systemic venous circulation (e.g. the round ligament of the liver), and progressive dilation of small, naturally occurring venous anastomoses between portal and systemic venous tributaries (Paquet 2000). The raised pressure causes the valves within these veins to become incompetent, permitting retrograde flow and the development of varices. Varices in the distal oesophagus are readily visible at endoscopy because they are situated superficially and protrude into the lumen of the oesophagus (Fig. 63.13); they are vulnerable to rupture and are a source of major gastro-intestinal bleeding. Gastric varices can also be present on the inferior aspect of the cardiac orifice. Isolated gastric varices can also develop as a result of splenic vein thrombosis. The close anatomical relationship between the splenic vein and the pancreas means that inflammation or cancers of the pancreas can result in the formation of a thrombus in the splenic vein. Because the short gastric veins drain into the splenic vein, thrombosis of that vein will result in increased pressure and engorgement, leading to varices in the fundus of the stomach.

Lymphatic drainage

The stomach has a rich network of lymphatics that connect with lymphatics draining other viscera within the proximal abdomen. At the gastro-oesophageal junction the lymphatics are continuous with those draining the distal oesophagus; in the region of the pylorus they are continuous with those draining the duodenum and pancreas. In general, lymphatics follow the course of the arteries supplying the stomach. However, many separate groups of nodes are now recognized (Fig. 63.14) and their relationship to the specific regions and vascular territories of the stomach is of great importance during resection of the stomach, particularly for malignancy. Pancreatic and hepatic lymphatics are significant in draining the stomach during disease.

Gastrectomy and gastric lymphadenectomy

Surgery for gastro-oesophageal malignancy involves various degrees of radical resection of lymph nodes that drain the tumour. Locoregional lymphatic spread can occur in the absence of haematogenous spread and gastric cancer can therefore remain a localized disease, even when lymph nodes are involved (Brierley et al 2017). Hence, gastrectomy with meticulous lymphadenectomy can be curative in a proportion of patients with gastric cancer and lymph node involvement.

The extent of potential/actual lymph node involvement by the tumour is classified as N1 (locoregional nodes specific to the tumour site); N2 (regional and major named vessel nodes draining the tumour); and N3 (wider-draining nodes, including lateral aortic nodes). Gastrectomies can be classified according to the node groups excised with the tumour: D1 (removal of the affected portion of the stomach and *en bloc* resection of N1 nodes); D2 (total gastrectomy, including all N1 and N2 nodes); and D3 (total gastrectomy plus extensive lymphadenectomy that includes the associated proximal abdominal lymph nodes: namely, pancreatic, superior mesenteric, coeliac, hepatic and middle colic) (Japanese Gastric Cancer Association 2011).

Innervation

The stomach is innervated by sympathetic and parasympathetic nerves. A variety of neurotransmitters have been identified within the pyloric sphincter, including acetylcholine, nitric oxide, enkephalins and vasoactive intestinal polypeptide. Inhibition of the pyloric sphincter is mediated by nitrergic fibres whilst basal tone is mostly cholinergic (although it should be noted that many other factors, including acid and luminal

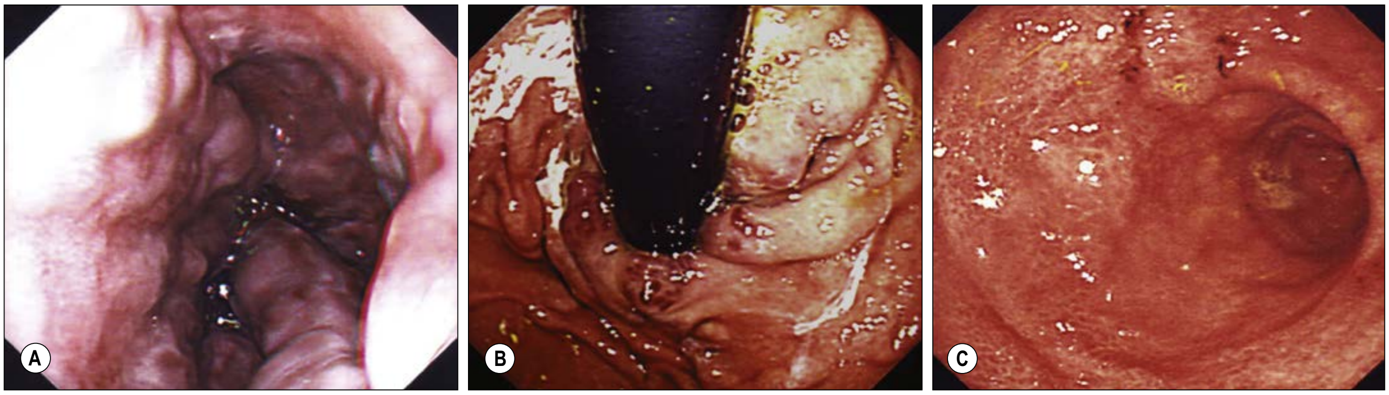

Fig. 63.13 The endoscopic appearance of oesophageal and gastric varices in portal hypertension. **A**, Oesophageal varices. **B**, Fundal varices seen from within the stomach after retroflexion of the gastroscope. **C**, Portal gastropathy (pyloric antrum) due to venous congestion of the gastric mucosa.

Continued

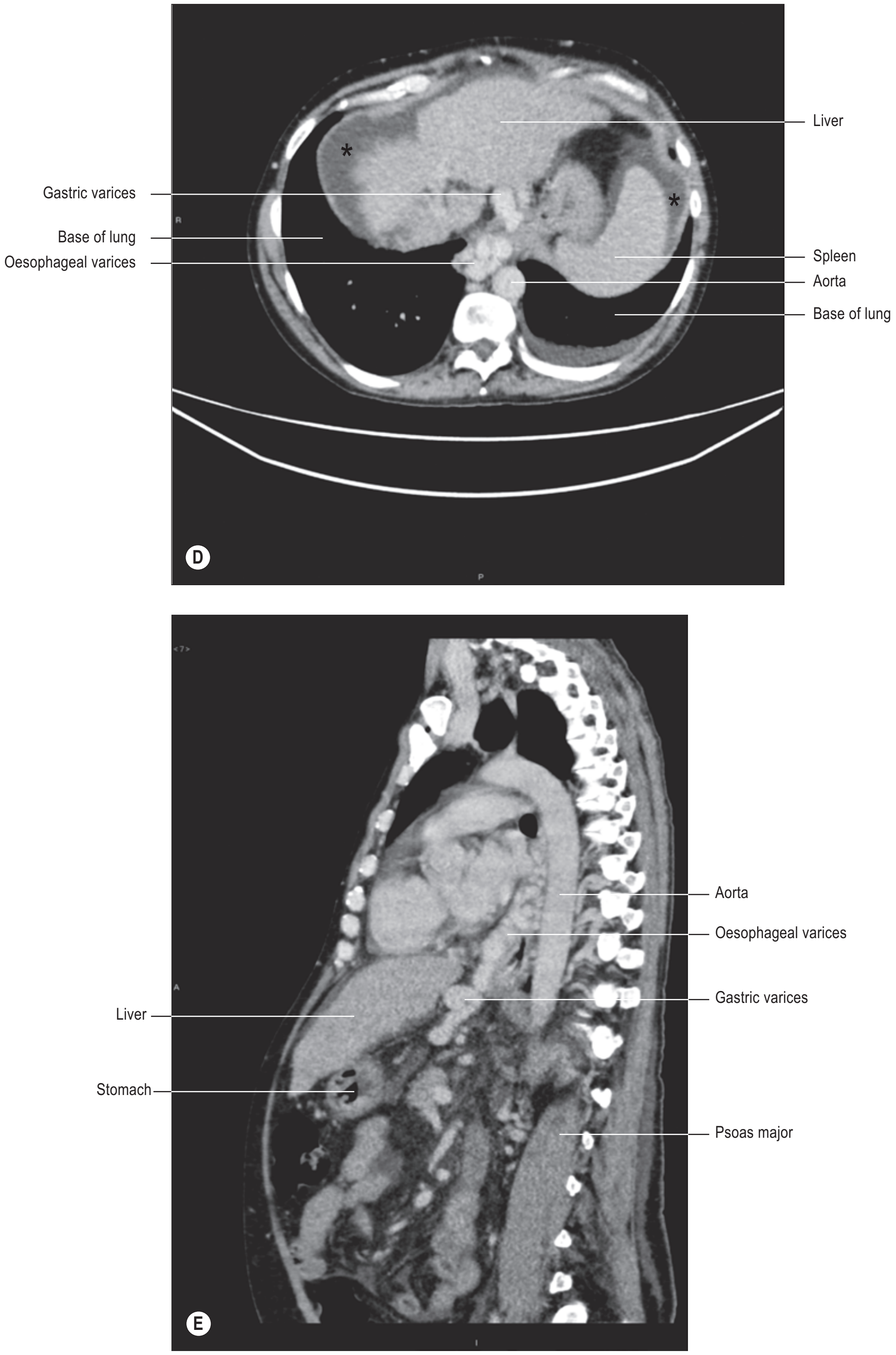
Liver
Gastric varices
*
*
Base of lung
Oesophageal varices
Spleen
Aorta
Base of lung
D
Aorta
Oesophageal varices
Gastric varices
Liver
Stomach
Psoas major
E

Fig. 63.13, cont'd D, Axial CT: note the cirrhotic liver and surrounding ascites (*), that is also seen around the spleen. **E**, Sagittal CT. (A–C, Courtesy of Professor Mark Stringer. D–E, Courtesy of Dr Stuart Ballantyne, Gartnavel General Hospital, Glasgow.)

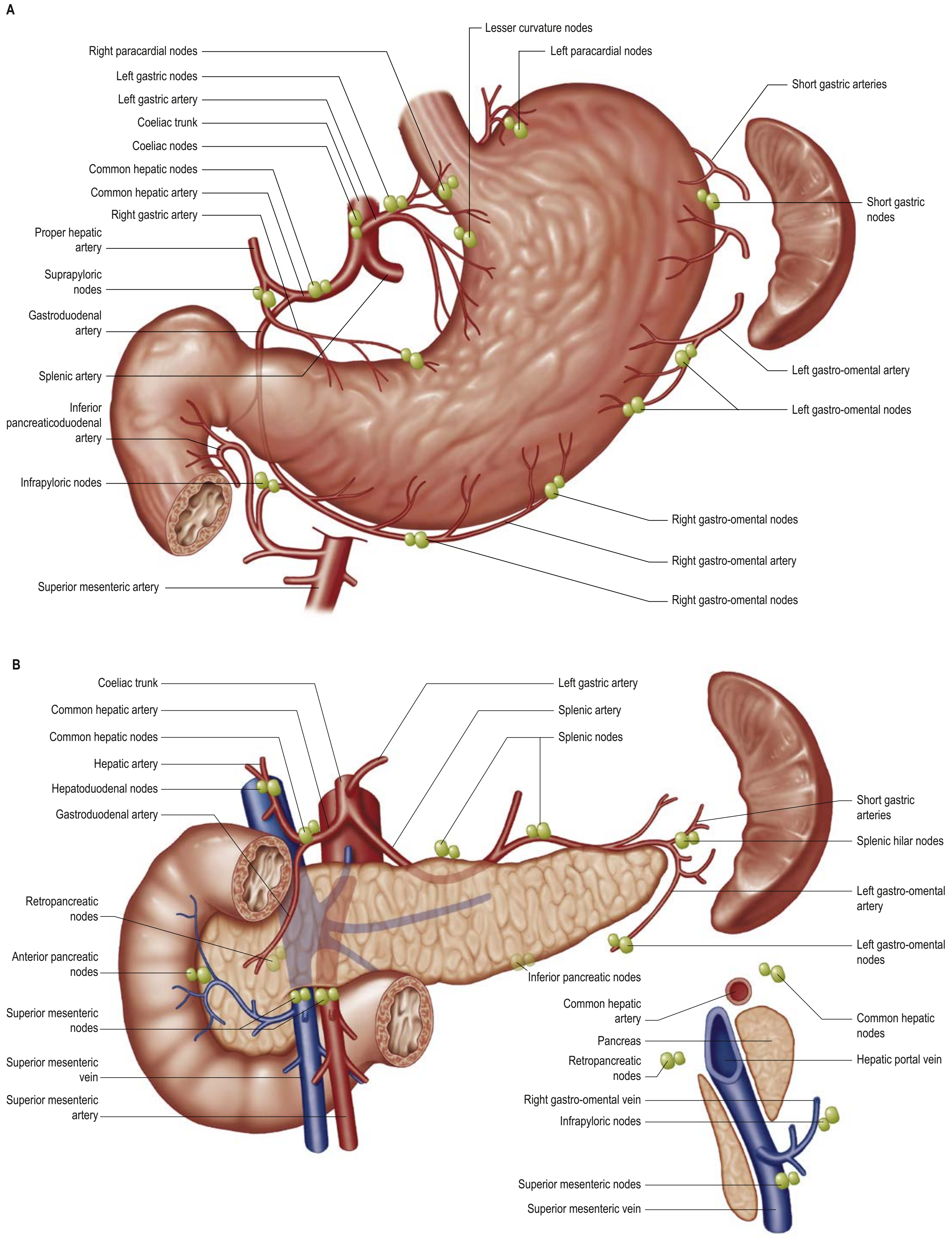
A
Lesser curvature nodes
Right paracardial nodes
Left paracardial nodes
Left gastric nodes
Left gastric artery
Short gastric arteries
Coeliac trunk
Coeliac nodes
Common hepatic nodes
Short gastric nodes
Common hepatic artery
Right gastric artery
Proper hepatic artery
Suprapyloric nodes
Gastroduodenal artery
Splenic artery
Left gastro-omental artery
Left gastro-omental nodes
Inferior pancreaticoduodenal artery
Infrapyloric nodes
Right gastro-omental nodes
Right gastro-omental artery
Superior mesenteric artery
Right gastro-omental nodes
B
Coeliac trunk
Left gastric artery
Common hepatic artery
Splenic artery
Common hepatic nodes
Splenic nodes
Hepatic artery
Hepatoduodenal nodes
Short gastric arteries
Gastroduodenal artery
Splenic hilar nodes
Left gastro-omental artery
Retropancreatic nodes
Left gastro-omental nodes
Anterior pancreatic nodes
Inferior pancreatic nodes
Common hepatic artery
Superior mesenteric nodes
Common hepatic nodes
Pancreas
Hepatic portal vein
Retropancreatic nodes
Superior mesenteric vein
Right gastro-omental vein
Superior mesenteric artery
Infrapyloric nodes
Superior mesenteric nodes
Superior mesenteric vein

Fig. 63.14 The main lymph node stations of the stomach (**A**) and upper abdominal viscera (**B**). The sagittal relationships of the lymph node groups around the neck of the pancreas are shown bottom right. The lateral aortic nodes are among the most proximal lymph nodes for these viscera but have been removed for clarity.

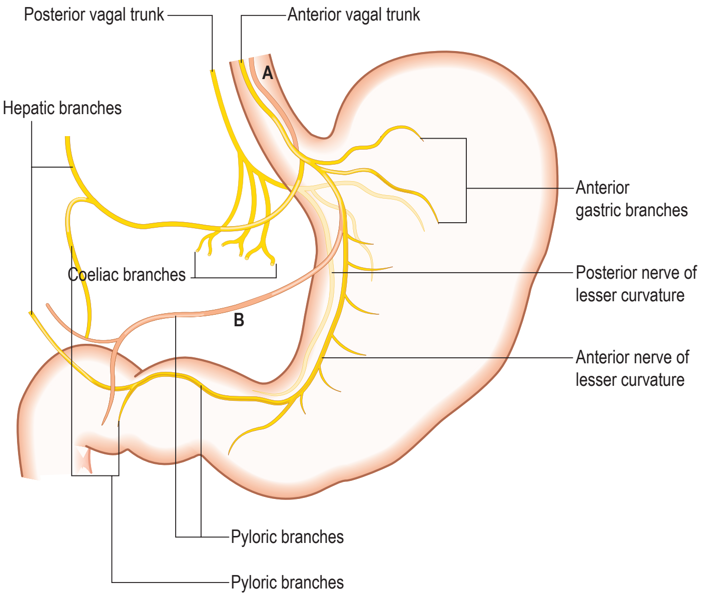

Fig. 63.15 The distribution of the vagal trunks to the stomach. The two most common variations in the anterior vagal trunk are shown in pink. Key: A, multiple main trunks; B, low origin of the hepatic/pyloric branch lying close to the lesser curvature.

nutrients, influence pyloric sphincter contraction; Ramkumar and Schulze (2005)).

Sympathetic innervation

The sympathetic supply to the stomach originates from the fifth to twelfth thoracic spinal cord segments and is mainly distributed via the greater and lesser thoracic splanchnic nerves and the coeliac plexus. Peri-arterial plexuses form along the arteries arising from the coeliac trunk. Additional innervation comes from fibres of the hepatic plexus, which pass to the proximal body and fundus via the lesser omentum and by direct branches from the greater thoracic splanchnic nerves.

Sympathetic activity causes vasoconstriction, inhibits gastric motility and constricts the pylorus.

Parasympathetic innervation

The parasympathetic supply to the stomach is from the vagus nerves (**Fig. 63.15**). The anterior vagal trunk (formed mainly from fibres from the left vagus nerve within the oesophageal plexus) is often double or even triple and supplies filaments to the cardiac orifice. The nerve is closely applied to the anterior surface of the outer muscle of the abdominal part of the oesophagus and usually divides near the gastro-oesophageal junction into gastric, pyloric and hepatic branches (Jackson 1949). The proximal gastric branches radiate on the anterior surface of the proximal body and fundus of the stomach but the main gastric branch (also known as the anterior nerve of the lesser curvature or greater anterior gastric nerve) lies in the lesser omentum near the lesser curvature. It supplies branches to the body and pyloric antrum and usually terminates near the angular incisure in a crow's foot type of pattern (Shanthi and Sudhayesshayyan 2011). The hepatic branch runs almost transversely between the peritoneal layers of the lesser omentum towards its free edge to reach the porta hepatis, where hepatic branches ramify. From here, some fibres descend adjacent to the common hepatic artery and its branches to supply the pylorus, duodenum and pancreas. An additional pyloric branch often arises from the main gastric branch during its course; this runs inferomedially to the pyloric antrum, where it gives off branches to the pylorus before running superiorly to contribute to the hepatic plexus. Variations in the main gastric branch include accessory pyloric branches and high and low courses of the hepatic and pyloric branches in the lesser omentum.

The posterior vagal trunk usually lies within loose connective tissue immediately posterior and to the right of the oesophagus. It divides into gastric branches and one or more coeliac branches. Gastric branches run posterior to the cardiac orifice and body of the stomach and extend to the proximal pyloric antrum, but do not normally reach the pyloric sphincter. The largest gastric branch (also known as the posterior nerve of the lesser curvature or the greater posterior gastric nerve) descends posteriorly near the lesser curvature. The coeliac branch arises from the posterior vagal trunk and carries most of the fibres contributing to the coeliac plexus. One or two small hepatic branches can also originate from the coeliac branch of the nerve.

The parasympathetic nerve supply is secretomotor to the gastric mucosa and motor to the gastric musculature. It is responsible for coordinated relaxation of the pyloric sphincter during gastric emptying. However, most fibres within the vagus nerves are afferent and convey gut sensation, including fullness, nausea and probably pain.

Referred pain

Pain sensation from the stomach is poorly localized and, in common with other structures of foregut derivation, is referred to the epigastric region. Pain arising from the gastro-oesophageal junction is commonly referred to the distal retrosternal and subxiphoid areas.

Microstructure

The gastric wall consists of the major layers found elsewhere in the gut, i.e. mucosa, submucosa, muscularis externa and serosa, together with gastric vessels and nerves (**Figs 63.16–63.17**). The microstructure reflects the functions of the stomach as an expandable muscular sac lined by secretory epithelium, although there are local structural and functional variations in this pattern.

Mucosa

The mucosa is a thick layer with a soft, smooth surface that is mostly reddish brown in life but pink in the region of the pylorus. In the contracted stomach, the mucosa is folded into numerous folds (gastric folds) most of which are longitudinal. They are most marked towards the pylorus and along the greater curvature. The gastric folds represent large furrows in the submucosal connective tissue (see below) rather than variations in the thickness of the mucosa covering them, and they are obliterated when the stomach is distended. As elsewhere in the gut, the mucosa is composed of a surface epithelium, lamina propria and muscularis mucosae.

Epithelium

When viewed microscopically at low magnification, the internal surface of the stomach wall appears honeycombed by small, irregular gastric pits: there are approximately 60–100 gastric pits per square millimetre of mucosa, each pit having a diameter of approximately 70 µm and a depth of about 0.2 mm (Lillibridge 1964) (see Figs 63.16–63.17). The base of each gastric pit receives several long, tubular gastric glands that extend deep into the lamina propria as far as the muscularis mucosae. Simple columnar mucus-secreting epithelium covers the entire luminal surface, including the gastric pits, and comprises a continuous layer of surface mucous cells that release gastric mucus from their apical surfaces to form a thick, protective, lubricant layer over the gastric lining. This epithelium commences abruptly at the Z line at the cardiac orifice, where there is a sudden transition from oesophageal stratified squamous epithelium.

Gastric glands

Although all gastric glands are tubular, they vary in form and cellular composition in different parts of the stomach (**Fig. 63.18**). They can be divided into three groups: cardiac, principal and pyloric. The most highly specialized are the principal glands.

Principal gastric glands

The principal glands are found in the body and fundus of the stomach, three to seven opening into each gastric pit. Their junction with the base of the pit is the isthmus; immediately basal to this is the neck; and the remainder is the base. The walls of the gland contain at least five distinct cell types: chief, parietal, mucous neck, stem and neuroendocrine.

Chief (peptic) cells (see Fig. 63.16) are the source of the digestive enzymes pepsin and lipase. They are usually basal in position and cuboidal in shape, and their nuclei are rounded and euchromatic. They contain secretory zymogen granules and their abundant cytoplasmic RNA renders them strongly basophilic. Parietal (oxyntic) cells are the source of gastric acid and of intrinsic factor, a glycoprotein necessary for the absorption of vitamin B_{12}. They are large, oval and strongly eosinophilic and have centrally placed nuclei.

Parietal cells occur intermittently along the walls of the more apical half of the gland but can reach as far as the isthmus; they bulge laterally into the surrounding connective tissue. They have a unique ultrastructure related to their ability to secrete hydrochloric acid. The luminal side of the cell is deeply invaginated to form a series of blind-ended channels (canaliculi) that bear numerous irregular microvilli covered by a plasma membrane rich in H^+/K^+ ATPase antiporter channels. The latter actively secrete hydrogen ions into the lumen; chloride ions

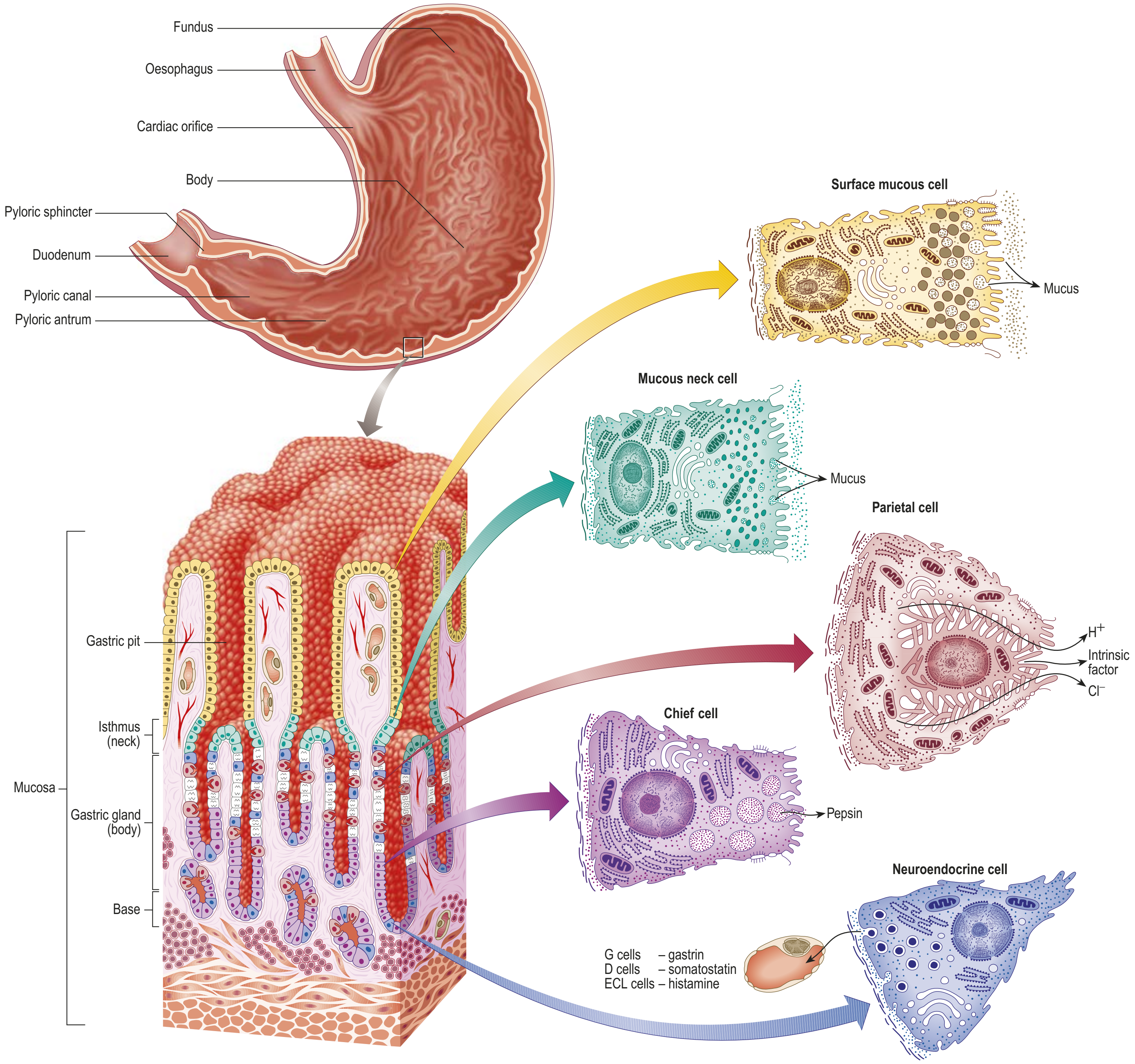

Fig. 63.16 Principal regions of the interior of the stomach and the microstructure of tissues and cells within its wall. Undifferentiated, dividing cells are shown in white. Abbreviations: ECL, enterochromaffin-like.

follow along the electrochemical gradient. The mitochondria-rich cytoplasm facing these channels contains a tubulo-vesicular system of abundant fine membranous tubules directed towards the canalicular surface. The precise structure of the cell varies with its secretory phase: when stimulated, the number and surface area of microvilli increases up to five-fold, probably as a result of the rapid fusion of the tubulo-vesicular system with the plasma membrane. This process is reversed at the end of stimulated secretion, when the excess membrane retreats back into the tubulo-alveolar system and microvilli are lost.

Mucous neck cells are numerous at the necks of the glands and are scattered along the walls of the more basal regions. They are typical mucus-secreting cells, displaying apical secretory vesicles containing mucins and basally displaced nuclei; their products are distinct histochemically from those of the superficial mucous cells.

Stem cells are relatively undifferentiated mitotic cells from which the other types of gland cell are derived. They are relatively few in number and are situated in the isthmus of the gland and the bases of the gastric pits. Stem cells are columnar and possess a few short apical microvilli. They periodically undergo mitosis; their progeny migrate either apically, to differentiate into new surface mucous cells, or basally, to form mucous neck, parietal, chief or neuroendocrine cells. All of these cells have a limited lifespan, especially the mucus-secreting types, so they are continually replaced. The typical replacement period for surface mucous cells is three days, and that for mucous neck cells is one week. Other cell types appear to live much longer.

Neuroendocrine (enteroendocrine) cells occur in all types of gastric gland but more frequently in the body and fundus of the stomach. They are situated mainly in the deeper parts of the glands, among the chief cells. They are basally situated, pleomorphic cells and display irregular nuclei surrounded by granular cytoplasm that contains clusters of large (0.3 µm) secretory granules. Neuroendocrine cells synthesize a number of biogenic amines and polypeptides that are important in the control of gut motility and glandular secretion. They are part of the system of dispersed neuroendocrine cells (Ch. 3). In the stomach they include gastrin-producing G cells; somatostatin-producing D cells; histamine-producing ECL (enterochromaffin-like) cells; serotonin-producing enterochromaffin cells; and ghrelin-producing P/D(1)-type endocrine cells (Sakata and Sakai 2010).

Cardiac glands

Cardiac glands are confined to a small area near the cardiac orifice; some are simple tubular glands, others are compound branched tubular glands. Mucus-secreting cells predominate; parietal and chief cells are present but sparse.

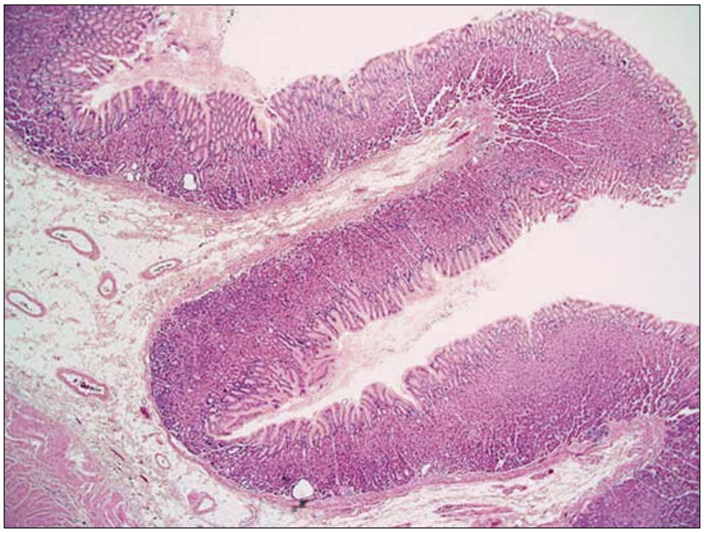

Fig. 63.17 A low-power micrograph showing the stomach wall, thrown into gastric folds that are visible macroscopically. The surface epithelium is infolded microscopically to form gastric pits. Gastric glands extend through the thickness of the mucosal lamina propria and open into the bases of the gastric pits. A muscularis mucosae layer and submucosa follow the contours of the gastric folds. Part of the external muscularis layers is seen below left. (Courtesy of Mr Peter Helliwell and the late Dr Joseph Mathew, Department of Histopathology, Royal Cornwall Hospitals Trust, UK.)

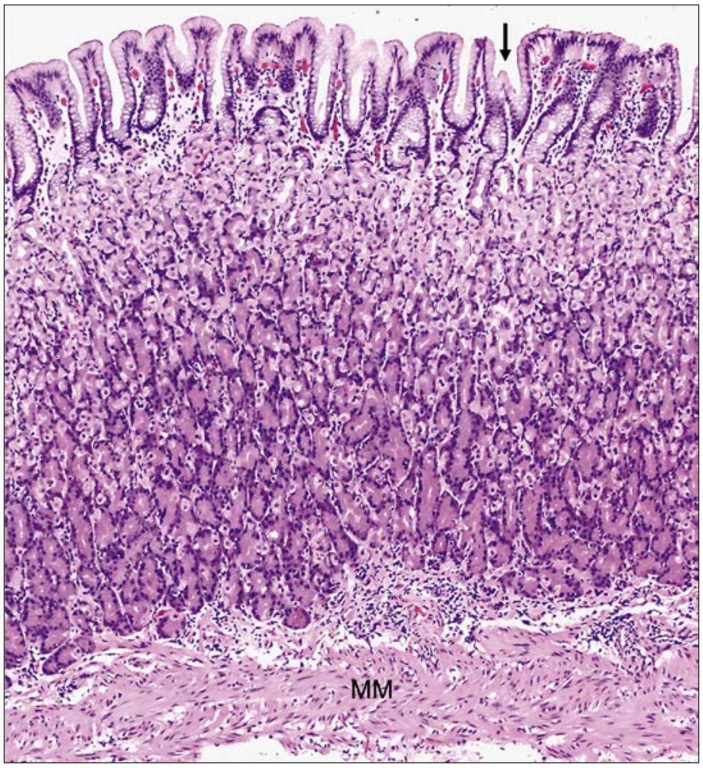

Fig. 63.18 A micrograph showing gastric glands in the mucosa of the wall of the stomach. Pale-staining surface mucous cells and mucous cells lining the gastric pits (arrow) are shown in the upper field. Tubular glands open into gastric pits and are lined by mucous neck cells, with parietal cells, chief cells, stem cells and neuroendocrine cells at deeper levels (not readily distinguishable at this magnification). Note the muscularis mucosae (MM), with the submucosa below. (Courtesy of Mr Peter Helliwell and the late Dr Joseph Mathew, Department of Histopathology, Royal Cornwall Hospitals Trust, UK.)

Pyloric glands

Pyloric glands empty via groups of two or three short, convoluted tubes into the bases of the deep gastric pits of the pyloric antrum; the pits occupy about two-thirds of the mucosal depth. The glands are populated mainly by mucus-secreting cells but they also contain neuroendocrine cells, especially G cells, which secrete gastrin when activated by appropriate mechanical stimulation (causing increased gastric motility and secretion of gastric juices). Although parietal and chief cells are scarce, parietal cells are always present in both fetal and postnatal pyloric glands. They can also appear in the duodenal mucosa, proximally near the pylorus, in adult tissue.

Lamina propria

The lamina propria forms a connective tissue framework between the glands. It contains small masses of lymphoid tissue, gastric lymphatic follicles, which resemble solitary intestinal follicles (especially in early life). It also contains a complex periglandular vascular plexus involved in maintaining the mucosal environment, e.g. the removal of bicarbonate produced in the tissues as a counterpart to acid secretion, and neural plexuses rich in both sensory and motor terminals.

Muscularis mucosae

The muscularis mucosae is a thin layer of smooth muscle fibres lying external to the layer of glands, arranged as continuous inner circular and outer longitudinal layers and a discontinuous external circular layer. The inner layer sends strands of smooth muscle cells between the glands; their contraction probably assists in emptying into the gastric pits.

Submucosa

The submucosa is a variable layer of loose connective tissue. It contains thick bundles of collagen, numerous elastin fibres, blood vessels and nervous plexuses, including the ganglionated submucosal (Meissner's) plexus.

Muscularis externa

The muscularis externa is a thick muscle coat immediately under the serosa, with which it is closely connected by subserous loose connective tissue. From innermost outwards it contains oblique, circular and longitudinal layers of smooth muscle fibres (see Fig. 63.6). The layers are variably developed in different regions of the stomach and not easily separated. Clasp-like semicircular smooth muscle fibres are present on the right side of the oesophagus and sling-like oblique gastric muscle fibres on the left side; the latter radiate horizontally towards the greater curvature and maintain the angle between the oesophagus and stomach. The circular muscle layer is thicker in the distal pyloric antrum, where it forms the pyloric sphincter. The outer longitudinal layer is most pronounced in the proximal two-thirds of the stomach.

The muscularis externa enables the stomach to produce churning movements that mix food with the gastric secretions. When the muscles contract they reduce the volume of the stomach and throw the mucosa into longitudinal folds, i.e. gastric folds (see above). Muscle activity is controlled by a network of unmyelinated autonomic nerve fibres and their ganglia, which lie between the muscle layers in the myenteric (Auerbach's) plexus.

Interstitial cells of Cajal

As in smooth muscle elsewhere in the gut, interstitial cells of Cajal are present within the submucosa and muscular layers of the stomach. These spindle-shaped cells contact nerve fibres and form gap junctions with smooth muscle cells, consistent with their role in modulating motor neurotransmission. Interstitial cells of Cajal are involved in generating rhythmic gastric slow-wave contractions and are important in gastric motility. They have been implicated in the pathogenesis of gastric motility disorders such as diabetic gastric paresis (Negreanu et al 2008) and in the development of gastrointestinal stromal tumours (GISTs) (Roggin and Posner 2012). These are uncommon mesenchymal tumours that usually develop in a submucosal location and exhibit a spectrum of clinical behaviour from benign to malignant based upon size and mitotic rate. Surgical resection is usually indicated for localized tumours greater than 2 cm in diameter.

Serosa or visceral peritoneum

The serosa is an extension of the visceral peritoneum. It covers the entire surface of the stomach other than along the attachments of the greater and lesser omenta to the greater and lesser curvatures, respectively, where the peritoneal layers are separated by vessels and nerves, and over a small posterosuperior area near the cardiac orifice, where the stomach contacts the respiratory diaphragm at the reflections of the gastrophrenic and left gastropancreatic folds.

Endoscopic mucosal resection and submucosal dissection

Endoscopic mucosal resection (EMR) is a technique that can be applied in the oesophagus and stomach in order to excise dysplastic lesions or early cancers that remain confined to the mucosa (Pech et al 2008). EMR is a misnomer since the technique involves resection of both the mucosa and submucosa. This is a safe and effective technique for removing superficial lesions within the upper gastrointestinal tract. The resected specimen can then be assessed histologically. This is important for early oesophageal adenocarcinoma since EMR can be curative for a T1a cancer (which is confined to the mucosa) as the risk of lymph node metastasis is very low, in contrast to a T1b cancer invading the submucosa, when the risk of lymph node metastasis is much greater (various studies show 10–40%) so alternative treatment is required, such as formal surgical resection (oesophagectomy or gastrectomy) and lymphadenectomy (Ancona 2008, Dubecz et al 2015). EMR is limited to small superficial lesions up to about 20 mm. Endomucosal-submucosal dissection (ESD) has recently become available through the development of small knives that can be used down the endoscope allowing en bloc resection of larger lesions.

GASTRIC MOTILITY

In simple terms, the proximal region of the stomach (fundus and proximal body) functions mostly as a temporary storage compartment, regulating intragastric pressure and the onward passage of chyme into the distal stomach. Proximal gastric tone decreases with swallowing (receptive relaxation) and in response to gastric distension (gastric accommodation). Its activity is modulated by enterogastric reflexes (e.g. acid, protein or fat in the duodenum inhibits proximal gastric muscle contraction) and gut hormones (e.g. cholecystokinin, gastrin, glucagon and vasoactive intestinal polypeptide). The vagus nerve plays a key role in these reflexes. In contrast to this activity, the muscle of the distal region of the stomach exhibits strong phasic contractions that increase in amplitude towards the pylorus; these occur about three times per minute and act to grind the food mechanically and propel it towards the pylorus. Solid material lags behind liquids, and when the contents of the pyloric antrum reach the contracted pylorus, only the liquid and small particulate solids can be expelled into the duodenum; larger solid matter is retropulsed back into the stomach for further breakdown (Patrick and Epstein 2008).

Bonus e-book content

Fig. 63.1 B-E, The anatomical structures around the abdominal part of the oesophagus. **B–C**, Coronal CT. **D–E**, Axial CT.

Fig 63.10 D-F, Coronal CT angiograms: blood supply of the stomach and neighbouring organs.

Fig 63.13 Oesophageal and gastric varices in portal hypertension. **A–C**, Endoscopic appearance. **D**, Axial CT. **E**, Sagittal CT.

Key references

García RM, Tomás NP, Pozo CD et al 2013 Laparoscopic treatment of acute gastric volvulus. Cir Esp 91:189–93.

A case series that included 10 patients with acute gastric volvulus treated by laparoscopic gastropexy. The technique was shown to be safe and effective in the emergency setting.

Japanese Gastric Cancer Association 2011 Japanese Classification of Gastric Carcinoma – 3rd English edition. Gastric Cancer 14:101–12.

A detailed, widely accepted description of the lymph node fields of the proximal abdominal viscera, particularly in relation to malignancy.

Mittal RK, Goyal RK 2006 Sphincter mechanisms at the lower end of the esophagus. Part 1 Oral cavity, pharynx and esophagus. GI Motility online. doi:10.1038/gimo14.

A review that discusses the principal anatomical mechanisms that prevent reflux at the gastro-oesophageal junction and explains how failure of one or more of these can lead to progressive gastro-oesophageal reflux disease.

Paquet KJ 2000 Causes and pathomechanisms of oesophageal varices development. Med Sci Monit 6:915–28.

An explanation of how chronic liver diseases cause a pathological increase in portal vein pressure, leading to the development of portosystemic venous collaterals, including oesophageal varices. This article reviews the pathogenesis, diagnosis and treatment of oesophageal varices.

Paterson WG 2001 The normal anti-reflux mechanism. Chest Surg Clin North Am 11:473–83.

An article that describes the normal mechanisms that prevent reflux of gastric contents into the oesophagus, including the resting tone of the lower oesophageal sphincter, the mechanical effect of the crural sling, and the specialized anatomy of the proximal stomach.

Pech O, Behrens A, May A et al 2008 Long-term results and risk factor analysis for recurrence after curative endoscopic therapy in 349 patients with high-grade intraepithelial neoplasia and mucosal adenocarcinoma in Barrett's oesophagus. Gut 57:1200–6.

A paper showing that endoscopic therapy (endoscopic resection and photodynamic therapy) was safe and highly effective at treating patients with high-grade dysplasia and intramucosal (T1a) cancer associated with Barrett's oesophagus.

Silverstein FE, Tytgat GNJ 1991 Atlas of Gastrointestinal Endoscopy, 2nd ed. New York: Gower Medical Publishing.

A pictorial atlas that includes over 900 endoscopic images along the entire length of the gastrointestinal tract. The accompanying text discusses normal and abnormal features and therapeutic techniques.

Tubbs RS, Shoja M, Loukas M 2016 Bergman's Comprehensive Encyclopedia of Human Anatomic Variation. Hoboken: Wiley Blackwell.

A textbook dedicated to detailing the anatomical variations found in man.

References

Ancona E, Rampado S, Cassaro M et al 2008 Prediction of lymph node status in superficial esophageal carcinoma. Ann Surg Oncol 15:3278–88.

A study reporting that intramucosal cancers and those invading the upper third of the submucosa are associated with significantly fewer nodal metastases than tumours invading deeper into the submucosa. This demonstrated the potential for endoscopic treatment of superficial lesions and the need for oesophagectomy and lymphadenectomy where there is invasion beyond the upper third of the submucosa.

Apaydin N, Uz A, Evirgen O et al 2008 The phrenico-esophageal ligament: an anatomical study. Surg Radiol Anat 30:29–36.

Baxter M, Aly EH 2010 Dieulafoy's lesion: current trends in diagnosis and management. Ann R Coll Surg Engl 92:548–54.

Brierley JD, Gospodarowicz MK, Wittekind C (eds) 2017 TNM Classification of Malignant Tumours, 8th ed. Hoboken: Wiley Blackwell.

Csendes A, Burgos AM 2005 Size, volume and weight of the stomach in patients with morbid obesity compared to controls. Obes Surg 15:1133–6.

Didio LJ, Anderson MC 1968 The 'Sphincters' of the Digestive System. Baltimore: Williams & Wilkins.

Dubecz A, Kern M, Solymosi N et al 2015 Predictors of lymph node metastasis in surgically resected T1 esophageal cancer. Ann Thorac Surg 99:1879–85.

García RM, Tomás NP, Pozo CD et al 2013 Laparoscopic treatment of acute gastric volvulus. Cir Esp 91:189–93.

A case series that included 10 patients with acute gastric volvulus treated by laparoscopic gastropexy. The technique was shown to be safe and effective in the emergency setting.

Hershcovici T, Mashimo H, Fass R 2011 The lower esophageal sphincter. Neurogastroenterol Motil 23:819–30.

Jackson RG 1949 Anatomy of the vagus nerves in the region of the lower esophagus and the stomach. Anat Rec 103:1–18.

Japanese Gastric Cancer Association 2011 Japanese Classification of Gastric Carcinoma – 3rd English edition. Gastric Cancer 14:101–12.

A detailed, widely accepted description of the lymph node fields of the upper abdominal viscera, particularly in relation to malignancy.

Kimura K, Ohto M, Matsutani S et al 1990 Relative frequencies of portosystemic pathways and renal shunt formation through the 'posterior' gastric vein: portographic study in 460 patients. Hepatology 12:725–8.

Kuge K, Murakami G, Mizobuchi S et al 2003 Submucosal territory of the direct lymphatic drainage system to the thoracic duct in the human esophagus. J Thorac Cardiovasc Surg 125:1343–9.

Kwok H, Marriz Y, Al-Ali S et al 1999 Phrenoesophageal ligament revisited. Clin Anat 12:164–70.

Liebermann-Meffert D, Lüscher U, Neff U et al 1987 Esophagectomy without thoracotomy: is there a risk of intramediastinal bleeding? A study on blood supply of the esophagus. Ann Surg 206:184–92.

Lillibridge CB 1964 The fine structure of the normal human gastric mucosa. Gastroenterology 47:269–90.

Loukas M, Wartmann CT, Louis RG Jr et al 2007 The clinical anatomy of the posterior gastric artery revisited. Surg Radiol Anat 29:361–6.

Mackintosh CE, Kreel L 1977 Anatomy and radiology of the areae gastricae. Gut 18:855–64.

Mirjalili SA, Hale SJ, Buckenham T et al 2012 A reappraisal of adult thoracic surface anatomy. Clin Anat 25:827–34.

Mittal RK, Goyal RK 2006 Sphincter mechanisms at the lower end of the esophagus. Part 1 Oral cavity, pharynx and esophagus. GI Motility online doi: 10.1038/gimo14.

A review article that discusses the principal anatomical mechanisms that prevent reflux at the gastro-oesophageal junction and explains how failure of one or more of these can lead to progressive gastro-oesophageal reflux disease.

Naini BV, Souza RF, Odze RD 2016 Barrett's esophagus: a comprehensive and contemporary review for pathologists. Am J Surg Pathol 40:e45–e66.

Ndoye JM, Dia A, Ndiaye A et al 2006 Arteriography of three models of gastric oesophagoplasty: the whole stomach, a wide gastric tube and a narrow gastric tube. Surg Radiol Anat 28:429–37.

Negreanu LM, Assor P, Mateescu B et al 2008 Interstitial cells of Cajal in the gut – a gastroenterologist's point of view. World J Gastroenterol 14:6285–8.

Neuhuber WL, Raab M, Berthoud HR et al 2006 Innervation of the mammalian esophagus. Adv Anat Embryol Cell Biol 185:1–73.

Ohkubo M 2000 Aberrant left gastric vein directly draining into the liver. Clin Anat 13:134–7.

Panagouli E, Venieratos D, Lolis E et al 2013 Variations in the anatomy of the celiac trunk: a systematic review and clinical implications. Ann Anat 195:501–11.

Paquet KJ 2000 Causes and pathomechanisms of oesophageal varices development. Med Sci Monit 6:915–28.

An explanation of how chronic liver diseases cause a pathological increase in portal pressure leading to the development of portosystemic collaterals, including oesophageal varices. This article reviews the pathogenesis, diagnosis and treatment of oesophageal varices.

Paterson WG 2001 The normal anti-reflux mechanism. Chest Surg Clin North Am 11:473–83.

An article that describes the normal mechanisms that prevent reflux of gastric contents into the oesophagus, including the resting tone of the lower oesophageal sphincter, the mechanical effect of the crural sling, and the specialized anatomy of the proximal stomach.

Patrick A, Epstein O 2008 Review article: gastroparesis. Aliment Pharmacol Ther 27:724–40.

Pech O, Behrens A, May A et al 2008 Long-term results and risk factor analysis for recurrence after curative endoscopic therapy in 349 patients with high-grade intraepithelial neoplasia and mucosal adenocarcinoma in Barrett's oesophagus. Gut 57:1200–6.

A paper showing that endoscopic therapy (endoscopic resection and photodynamic therapy) was safe and highly effective at treating patients with high-grade dysplasia and intramucosal (T1a) cancer associated with Barrett's oesophagus.

Piasecki C 1974 Blood supply to the human gastroduodenal mucosa with special reference to the ulcer-bearing areas. J Anat 118:295–335.

Power D, Forshaw M, Birch J et al 2001 The distribution and clinical anatomy of the short gastric veins. Internet J Surg 3:1–3.

Preiksaitis HG, Diamant NE 1997 Regional differences in cholinergic activity of muscle fibers from the human gastroesophageal junction. Am J Physiol 272:G1321–7.

Ramkumar D, Schulze KS 2005 The pylorus. Neurogastroenterol Motil 17(Suppl 1):22–30.

Rebibo L, Chivot C, Fuks D et al 2012 Three-dimensional computed tomography analysis of the left gastric vein in a pancreatectomy. HPB (Oxford) 14:414–21.

Rice TW, Ishwaran H, Ferguson MK et al 2016 Cancer of the esophagus and esophagogastric junction: an eighth edition staging primer. J Thorac Oncol 12:36–42.

Roggin KK, Posner MC 2012 Modern treatment of gastric gastrointestinal stromal tumors. World J Gastroenterol 18:6720–8.

Roman S, Kahrilas PJ 2014 The diagnosis and management of hiatal hernia. BMJ 349:g6154.

Sakata I, Sakai T 2010 Ghrelin cells in the gastrointestinal tract. Int J Pept 2010. pii: 945056. doi: 10.1155/2010/945056.

Schlottmann F, Patti MG 2018 Laparoscopic Heller myotomy versus per oral endoscopic myotomy: evidence-based approach to the treatment of esophageal achalasia. Am Surg 84:496–500.

Settembre N, Labrousse M, Magnan PE et al 2018 Surgical anatomy of the right gastro-omental artery: a study on 100 cadaver dissections. Surg Radiol Anat 40:415–22.

Shanthi KC, Sudhayesshayyan D 2011 Branching pattern of the anterior nerve of Latarjet and its clinical significance. J Clin Diagn Res 5:980–3.

Silverstein FE, Tytgat GNJ 1991 Atlas of Gastrointestinal Endoscopy, 2nd ed. New York: Gower Medical Publishing.

A pictorial atlas that includes over 900 endoscopic images along the entire length of the gastrointestinal tract. The accompanying text discusses normal and abnormal features and therapeutic techniques.

Stefura T, Kacprzyk A, Droś J et al 2018 The venous trunk of Henle (gastrocolic trunk): a systematic review and meta-analysis of its prevalence, dimensions, and tributary variations. Clin Anat 31:1109–21.

Stein HJ, Liebermann-Meffert D, DeMeester TR et al 1995 Three-dimensional pressure image and muscular structure of the human lower esophageal sphincter. Surgery 117:692–8.

Tachimori Y 2017 Pattern of lymph node metastases of squamous cell esophageal cancer based on the anatomical lymphatic drainage system: efficacy of lymph node dissection according to tumor location. J Thorac Dis 9:S724–S730.

Tamaki Y, Sasaki R, Ejima Y et al 2012 Efficacy of intraoperative radiotherapy targeted to the abdominal lymph node area in patients with esophageal carcinoma. J Rad Res 53:882–91.

Tubbs RS, Shoja M, Loukas M 2016 Bergman's Comprehensive Encyclopedia of Human Anatomic Variation. Hoboken: Wiley Blackwell.

A textbook dedicated to detailing the anatomical variations found in man.

Wang Y, Zhu L, Xia W et al 2018 Anatomy of lymphatic drainage of the esophagus and lymph node metastasis of thoracic esophageal cancer. Cancer Manag Res 10:6295–303.

Yamaguchi S, Kuroyanagi H, Milson JW et al 2002 Venous anatomy of the right colon: precise structure of the major veins and gastrocolic trunk in 58 cadavers. Dis Colon Rectum 45:1337–40.

CHAPTER

64

Small intestine

OVERVIEW

The small intestine consists of the duodenum, jejunum and ileum. It extends from the pylorus to the ileocaecal junction and has a mean length of 5 metres (3–8.5 metres) when measured intraoperatively in adults (Teitelbaum et al 2013). The duodenum extends from the stomach to the duodenojejunal junction, marked by the suspensory ligament of the duodenum (ligament of Treitz). There is no clear boundary between the jejunum and ileum, but there is a gradual transition in morphology from the proximal to distal ends of the small intestine. The distal 30 cm or so of the ileum is often referred to as the terminal ileum: it has some specialized physiological functions.

The duodenum is in the proximal abdomen and is mostly retroperitoneal. The jejunum and ileum occupy the central and distal parts of the abdominal cavity and usually lie within the boundary formed by the colon. The small intestine is attached to the anterior wall of the retroperitoneum by a mesentery that allows the intestinal loops to be relatively mobile. In the supine position, loops of jejunum can be found anterior to the transverse colon, stomach and lesser omentum, whereas in the erect position, loops of ileum can descend into the pelvis anterior to the rectum. The greater omentum covers the proximal jejunum and ileum to a variable extent. The jejunum and ileum are covered by visceral peritoneum on all but their mesenteric borders, where the peritoneum is reflected to enclose the adipose tissue of the mesentery. The small intestine mesentery abuts about 20% of the circumference of the muscular wall of the ileum and somewhat less of the jejunum.

DUODENUM

The adult duodenum is approximately 25 cm long and is the shortest, widest and most predictably located part of the small intestine. The proximal 2.5 cm is intraperitoneal and the remainder is retroperitoneal. The duodenum forms an elongated 'C' shape that lies between the level of the first and third lumbar vertebrae in the supine position (Kellogg 1933). The inferior 'limb' of the C extends further to the left of the midline than the superior limb. The head of the pancreas lies within the concavity of the duodenum, which is 'draped' over the prominence formed by the lumbar spine; the duodenum therefore curves in an anteroposterior direction as well as forming a 'C' shape. The duodenum lies entirely proximal to the level of the umbilicus. It is described as having four parts (**Fig. 64.1**).

Superior part

The superior (first) part is the most mobile part of the duodenum and is about 5 cm long. It starts at the termination of the pylorus of the stomach and ends at the superior duodenal flexure. The proximal 2.5 cm is intraperitoneal. The distal 2.5 cm is covered by peritoneum on its anterior and superior surfaces and forms the inferior boundary of the omental foramen (of Winslow). The lesser omentum is attached to its superior border and the greater omentum to its inferior border. The first 2–3 cm of the duodenum is lined by relatively smooth mucosa and readily distends on insufflation during endoscopy. This part is frequently referred to as the duodenal bulb (duodenal cap). Beyond the duodenal bulb, the internal appearance is characterized by circular folds of mucosa that remain pronounced, even during endoscopic insufflation (**Fig. 64.2**). During contrast radiology, the duodenal bulb shows a few longitudinal folds continuous with the pylorus (Mather Cordiner and Calthrop 1936) and appears triangular; it is often visible on plain radiographs of the abdomen as an isolated air shadow to the right of the first or second lumbar vertebra. The superior part of the duodenum passes superiorly, posteriorly and laterally before curving sharply inferiorly at the superior duodenal flexure. This portion transitions to a retroperitoneal position where peritoneum only covers its anterior aspect. The section from the duodenal bulb to the superior duodenal flexure lies posterior and inferior to the quadrate lobe of the liver.

The superior part of the duodenum lies anterior to the gastroduodenal artery, bile duct and hepatic portal vein and anterosuperior to the head and neck of the pancreas. The gastroduodenal artery lies immediately posterior to the posterior wall of the duodenum; a penetrating peptic ulcer on the posterior wall can erode into the gastroduodenal artery or one of its branches and cause dramatic haemorrhage. A penetrating peptic ulcer on the anterior wall can perforate into the peritoneal cavity, causing peritonitis because the anterior surface of the superior part of the duodenum is covered only by peritoneum.

Lymph nodes near the common hepatic and hepatoduodenal arteries lie close to the superior part of the duodenum (see Fig. 63.14B). They can be visualized using endoscopic ultrasound and sampled using a fine needle under endoscopic ultrasound guidance. The nodes are important in the staging of gastric, pancreatic or bile duct tumours, or identifying metastases from other solid tumours of the abdominal cavity. The proximity of the bile duct to the superior part of the duodenum enables endoscopic ultrasound examination of the distal bile duct and surgical anastomosis between bile duct and duodenum (choledochoduodenostomy) when required.

Descending part

The descending (second) part of the duodenum is approximately 8 cm long. It starts at the superior duodenal flexure and runs inferiorly in a gentle curve, convex to the right side of the vertebral column and extending to the inferior border of the third lumbar vertebral body. It then turns sharply medially at the inferior duodenal flexure, which marks its junction with the horizontal (third) part of the duodenum. The descending part of the duodenum is covered by peritoneum only on its proximal anterior surface. It lies posterior to the gallbladder and the right lobe of the liver at its start and is crossed anteriorly by the transverse colon. The right end of the gastrocolic ligament and the origin of the transverse mesocolon are attached to the anterior surface of the duodenum by loose connective tissue. The connective tissue and vessels forming the mesentery of the superior aspect of the ascending colon and right colic flexure are loosely attached to its anterior surface, inferior to the attachment of the transverse mesocolon. This part of the duodenum is at risk of iatrogenic injury during surgical mobilization of the ascending colon and right colic flexure.

The descending part of the duodenum lies anterior to the hilum of the right kidney, the right renal vessels, the lateral edge of the inferior vena cava and right psoas major (see Fig. 64.1C). The head of the pancreas and the bile duct are medial and the right colic flexure is cephalad and lateral. Part of the head of the pancreas is sometimes embedded in the medial duodenal wall, and pancreatic 'rests' in the duodenal wall can produce small filling defects on contrast radiology. The internal appearance is similar to that of the distal portion of the superior part of the duodenum, with pronounced mucosal folds (**Fig. 64.3**). The bile duct and pancreatic duct (of Wirsung) enter the medial wall, where they usually unite to form a common channel, which frequently contains a dilated segment known as the hepatopancreatic ampulla (of Vater) (Ch. 68). The narrow distal end of this channel opens on the summit of the major duodenal papilla, a mucosal elevation situated on the posteromedial wall of the descending part of the duodenum, 8–10 cm distal to the pylorus. A duodenal mucosal fold often partially encircles the major papilla, forming a hood (Horiguchi and Kamisawa 2010) (see Fig. 64.3). A second, accessory pancreatic duct (of Santorini) is sometimes present and usually opens about 2 cm proximal to the major duodenal papilla on the minor duodenal papilla (Kamisawa et al 2010, Suda 2010).

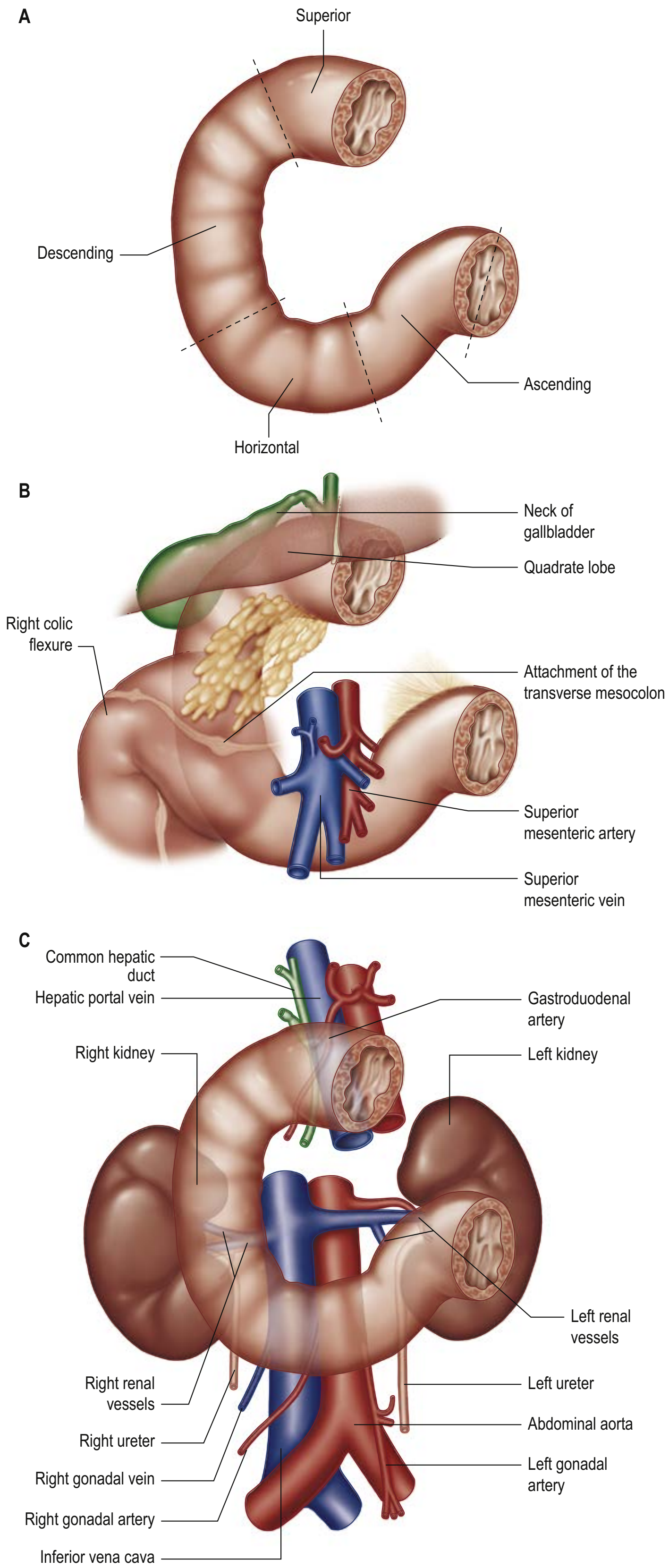
A
Superior
Descending
Ascending
Horizontal
B
Neck of gallbladder
Quadrate lobe
Right colic flexure
Attachment of the transverse mesocolon
Superior mesenteric artery
Superior mesenteric vein
C
Common hepatic duct
Hepatic portal vein
Gastroduodenal artery
Right kidney
Left kidney
Left renal vessels
Right renal vessels
Left ureter
Right ureter
Abdominal aorta
Right gonadal vein
Left gonadal artery
Right gonadal artery
Inferior vena cava

Fig. 64.1 **A**, The four parts of the duodenum. **B**, Anterior relations of the duodenum. **C**, Posterior relations of the duodenum.

Duodenal diverticula

Available with the *Gray's Anatomy* e-book

Kocher manoeuvre to expose the posterior aspect of the head of the pancreas

Available with the *Gray's Anatomy* e-book

Horizontal part

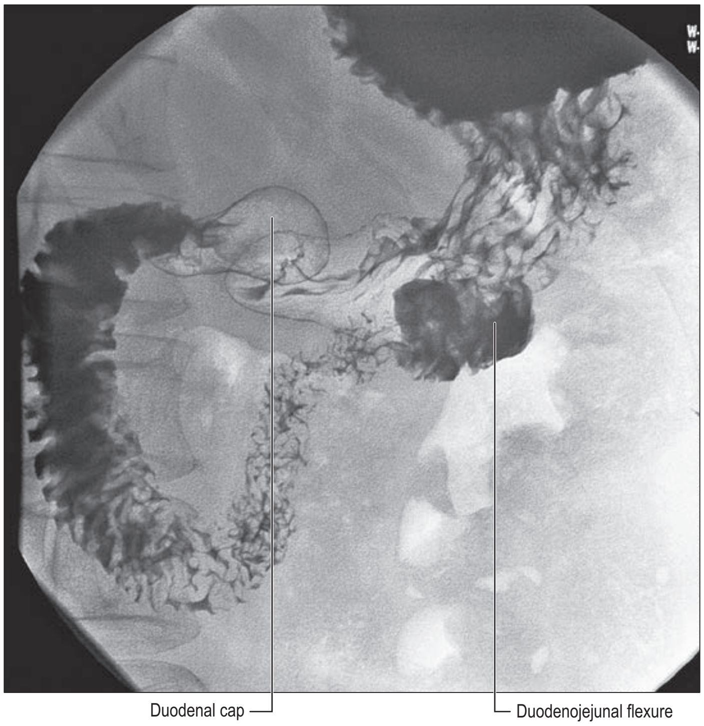
Duodenal cap
Duodenojejunal flexure

Fig. 64.2 The contrast radiographic appearance of the duodenum showing a distended duodenal bulb (duodenal cap) and the remainder of the duodenum up to the duodenojejunal flexure.

The horizontal (third) part of the duodenum starts at the inferior duodenal flexure and is approximately 10 cm long. It runs from the right side of the inferior border of the third lumbar vertebra and passes to the left and slightly superiorly, anterior to the inferior vena cava and abdominal aorta, becoming continuous with the ascending part of the duodenum (see Fig. 64.1C). It lies posterior to the transverse mesocolon and is crossed anteriorly by the origin of the mesentery of the small intestine and the superior mesenteric vessels. The inferior portion of its anterior aspect is covered by peritoneum, reflected anteriorly to form the posterior layer of the root of the mesentery of the small intestine. The anterior surface of its left end, close to the junction with the ascending (fourth) part, is also covered by peritoneum.

The horizontal part of the duodenum lies anterior to the right ureter, right psoas major, right gonadal vessels, inferior vena cava and abdominal aorta (at the origin of the inferior mesenteric artery), and inferior to the head of the pancreas. Anteroinferiorly, loops of jejunum lie in the right and left infracolic compartments. The middle of the horizontal part lies in the angle between the superior mesenteric artery anteriorly and the abdominal aorta posteriorly. Loss of perivascular adipose tissue can cause narrowing of this angle and is a rare cause of duodenal obstruction, known as superior mesenteric artery syndrome (Merrett et al 2009).

Ascending part

The ascending (fourth) part of the duodenum is 2.5 cm long. It starts just to the left of the abdominal aorta, runs superiorly and laterally to the level of the superior border of the second lumbar vertebra, then turns sharply anteroinferiorly at the duodenojejunal flexure to become continuous with the jejunum. The inferior mesenteric vein lies either posterior to the duodenojejunal flexure or at its lateral margin, deep to a peritoneal fold: the duodenojejunal flexure is a useful landmark for locating the inferior mesenteric vein radiologically or surgically. The abdominal aorta, left sympathetic trunk, left psoas major, left renal and left gonadal vessels all lie posterior, the left kidney and left ureter lie posterolateral, and the transverse colon and mesocolon are anterior, separating it from the stomach (see Fig. 61.8). The inferior border of the body of the pancreas is superior. The peritoneum of the root of the mesentery of the small intestine descends over its anterior surface.

At its left lateral limit, the ascending part of the duodenum becomes progressively invested in peritoneum such that the duodenojejunal flexure is suspended from the anterior wall of the retroperitoneum by a double fold of peritoneum, the suspensory ligament of the duodenum. This has two parts: the first part may contain skeletal muscle fibres and runs from the right crus of the diaphragm to connective tissue around the coeliac trunk, and the second part contains smooth muscle and descends from connective tissue around the coeliac trunk to the

The duodenum is the most common site for a diverticulum in the small intestine. Diverticula are usually solitary and can be congenital (containing all layers of the duodenal wall) or acquired (protrusion of the mucosa and submucosa through a defect in the muscular coat of the intestinal wall). They are typically located on the medial wall of the descending part of the duodenum, intimately related to the head of the pancreas: the major duodenal papilla is frequently found either on the mucosal fold at the mouth of a diverticulum or arising from the mucosa within it. Diverticula can complicate the interpretation of contrast radiographs of the duodenum or biliary system, and can cause difficulties during attempted endoscopic cannulation of the major duodenal papilla. Most are asymptomatic but they can be complicated by bleeding, inflammation, perforation and, occasionally, pancreatitis or biliary complications (Fotiades et al 2005).

The Kocher manoeuvre is used to expose retroperitoneal structures, such as an injury to the inferior vena cava, or the hilum of the kidney or the head of the pancreas, especially as an early step in a pancreaticoduodenectomy operation. The manoeuvre describes the division of the posterior and lateral attachments of the descending portion of the duodenum to allow medial rotation and reflection of the duodenum and head of the pancreas. The inferior vena cava is identified posterior to the horizontal portion of the duodenum and the attachments posterior to the duodenum, medial to the right ureter and anterior to the inferior vena cava, are divided. This is carried cephalad along the lateral aspect of the descending part of the duodenum. The right renal vein and right gonadal vein are often visualized during this manoeuvre. A complete Kocher manoeuvre is carried to the lateral edge of the abdominal aorta, allowing full inspection of the inferior vena cava and the superior mesenteric artery.

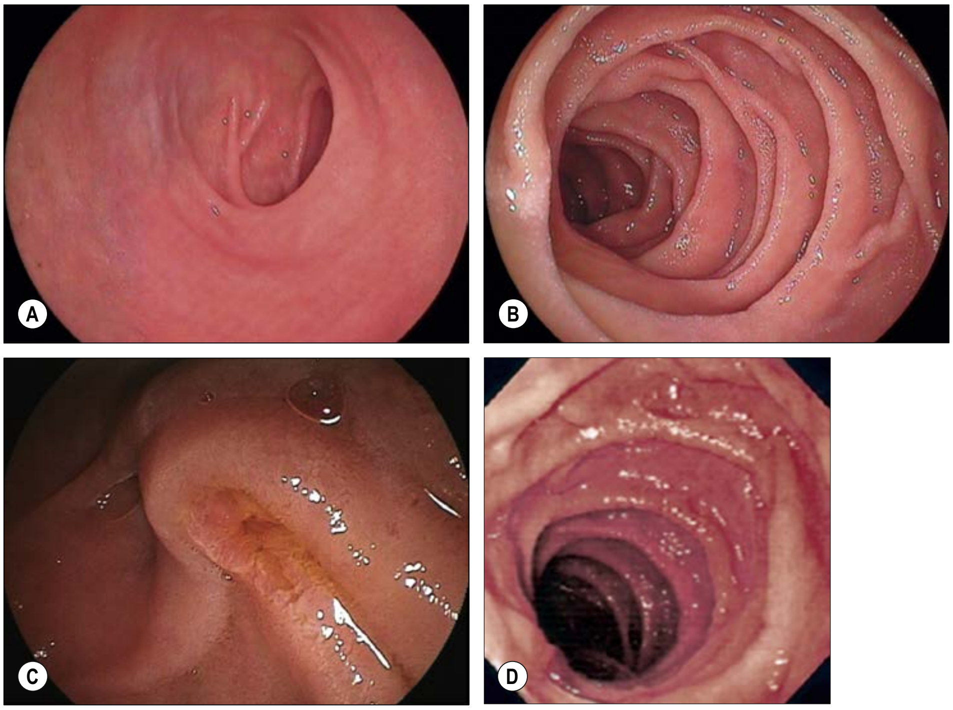

Fig. 64.3 The endoscopic appearance of the duodenum. **A**, Duodenal bulb. **B**, Descending part, showing the pronounced, 'branched' mucosal folds. **C**, Major duodenal papilla. **D**, Horizontal part.

duodenum, passing posterior to the pancreas anterior to the left renal vein. The ligament is often absent or rudimentary in adults and its function is unknown (Kim et al 2008). Its length determines the location of the duodenojejunal junction. A short, narrow suspensory ligament causes the ascending part of the duodenum to take a commonly depicted course cephalad prior to the sharp inferior turn to the jejunum, whereas a broad, flat ligament makes this angle less acute. The suspensory ligament of the duodenum is avascular. The vascular supply to the ascending part of the duodenum enters its wall from the posteromedial aspect.

The duodenojejunal flexure and the suspensory ligament of the duodenum are important landmarks in the radiological and surgical diagnosis of incomplete rotation and malrotation of the small intestine (Ch. 21). For many small intestine resection operations, distance is measured from the suspensory ligament of the duodenum.

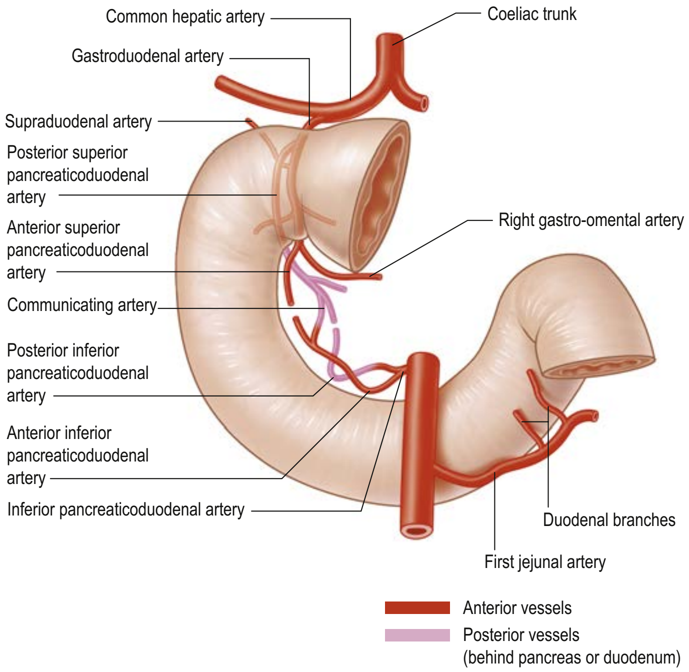
Common hepatic artery
Coeliac trunk
Gastroduodenal artery
Supraduodenal artery
Posterior superior pancreaticoduodenal artery
Anterior superior pancreaticoduodenal artery
Right gastro-omental artery
Communicating artery
Posterior inferior pancreaticoduodenal artery
Anterior inferior pancreaticoduodenal artery
Inferior pancreaticoduodenal artery
Duodenal branches
First jejunal artery
🟥 Anterior vessels
▨ Posterior vessels (behind pancreas or duodenum)

Fig. 64.4 The arterial supply of the duodenum. Only representative branches of the small vessels, which can be multiple, are shown.

Vascular supply and lymphatic drainage

Arteries

The main vessels supplying the duodenum are the superior and inferior pancreaticoduodenal arteries. The superior and descending parts of the duodenum also receive contributions from other sources including the right gastric, supraduodenal, right gastro-omental, common hepatic and gastroduodenal arteries (**Fig. 64.4**). Branches of the superior pancreaticoduodenal artery may contribute to the supply of the pyloric canal, anastomosing to a minor extent with the gastric arteries within the muscular layer of the junction between the pylorus and duodenum. Because of this robust vascular supply, ischaemia of the duodenum is a rare clinical finding and is often a bellwether of severe and generalized circulatory compromise.

Gastroduodenal artery

The gastroduodenal artery usually arises from the common hepatic artery posterior or superior to the superior part of the duodenum. It descends posterior to the retroperitoneal portion of the superior part of the duodenum to the left of the bile duct. At the inferior border of the superior part of the duodenum it is commonly described as dividing into the right gastro-omental and superior pancreaticoduodenal arteries, but this anatomical arrangement is rare (Bradley 1973, Bertelli et al 1995, Bertelli et al 1996) and its usual branching pattern is as follows. As it descends posterior to the superior part of the duodenum it usually gives off the posterior superior pancreaticoduodenal artery, several retroduodenal branches that supply the superior part and the proximal portion of the descending part of the duodenum, and a supraduodenal artery that supplies the anterosuperior part of the proximal duodenum (Bianchi and Albanèse 1989). As the gastroduodenal artery emerges inferior to the superior part of the duodenum it usually gives off the right gastro-omental artery and several pyloric branches. It then descends on the anterior surface of the pancreas, where it divides into the anterior superior pancreaticoduodenal artery and pancreatic branches. Although the gastroduodenal artery usually branches from the common hepatic artery, it occasionally originates from other sources including the coeliac trunk, the superior mesenteric artery, as a trifurcation with the right and left hepatic arteries, or from the right or left hepatic artery. The gastroduodenal artery or one of its branches can be a source of haemorrhage from a penetrating posterior duodenal ulcer (see above) or a site of aneurysm or pseudoaneurysm formation, and for these reasons, it is an important vessel for interventional radiologists.

Superior pancreaticoduodenal arteries

There are usually two superior pancreaticoduodenal arteries: posterior and anterior. The posterior superior pancreaticoduodenal artery is usually a separate branch of the gastroduodenal artery and is given off posterior to the superior border of the superior part of the duodenum. It descends to the right, anterior to the hepatic portal vein and bile duct, where the latter lies posterior to the superior part of the duodenum. It then spirals around the right side of the bile duct to run posterior to the head of the pancreas, crosses posterior to the pancreatic segment of the bile duct (which is embedded, to a variable degree, in the head of the pancreas), and anastomoses with the posterior inferior pancreaticoduodenal artery (Bertelli et al 1996). The posterior superior pancreaticoduodenal artery supplies branches to the head of the pancreas, the superior and descending parts of the duodenum, and several branches to the distal part of the bile duct.

The anterior superior pancreaticoduodenal artery is usually a terminal branch of the gastroduodenal artery and descends in the anterior groove between the descending part of the duodenum and the head of the pancreas or on the anterior surface of the pancreas parallel to the groove (Bertelli et al 1995). It supplies branches to the superior and descending parts of the duodenum and to the head of the pancreas, and then passes posteriorly to anastomose with the anterior inferior pancreaticoduodenal artery.

Inferior pancreaticoduodenal artery

The inferior pancreaticoduodenal artery usually arises from the superior mesenteric artery or its first jejunal branch near the superior border of the horizontal part of the duodenum (Bertelli et al 1996). It crosses posterior to the superior mesenteric vein and passes posterior to the uncinate process of the pancreas, where it divides into the anterior and posterior pancreaticoduodenal arteries. The anterior pancreaticoduodenal artery passes to the right, immediately inferior and then anterior to the inferior border of the head of the pancreas, and runs superiorly to anastomose with the anterior superior pancreaticoduodenal artery. The posterior branch runs posteriorly to the right posterior to the head of the pancreas and anastomoses with the posterior superior pancreaticoduodenal artery (Bertelli et al 1997). Both branches supply the head of the pancreas, its uncinate process, and the superior and descending parts of the duodenum. Occasionally, the anterior and posterior pancreaticoduodenal arteries arise separately from the superior mesenteric or first jejunal artery.

Jejunal artery branches

Branches from the first jejunal branch of the superior mesenteric artery supply the ascending part of the duodenum and frequently anastomose with a terminal branch of the anterior superior pancreaticoduodenal artery. The ascending part of the duodenum therefore receives a potential collateral supply from the coeliac trunk and superior mesenteric artery, which means that it is not commonly affected by ischaemia.

Veins

Submucosal and intramural veins give rise to small veins that accompany the corresponding named arteries. The venous anatomy of this region is variable and not well characterized. The superior pancreaticoduodenal vein runs superiorly on the posterior surface of the head of the pancreas, posterior to the distal bile duct, and usually drains into the hepatic portal vein. The inferior pancreaticoduodenal vein runs inferiorly and usually drains into the superior mesenteric vein or its first jejunal tributary. Small veins from the superior part and the superior aspect of the descending part of the duodenum drain directly into the hepatic portal vein, and veins from the horizontal and ascending parts can drain directly into the superior mesenteric vein. Numerous small anastomoses are present between veins of the descending and horizontal parts of the duodenum and retroperitoneal veins (Murakami et al 1999).

Lymphatic drainage

Duodenal lymphatics run to nodes associated with the superior and inferior pancreaticoduodenal arteries, and from there to nodes related to the common hepatic and superior mesenteric arteries and coeliac trunk and to nodes in supra- and infra-pyloric positions and within the hepatoduodenal ligament. Lymphatic drainage to lateral aortic nodes has also been described (Hirai et al 2001).

Duodenal feeding

Available with the *Gray's Anatomy* e-book

Innervation

The duodenum is innervated by both parasympathetic and sympathetic neurones.

Preganglionic sympathetic neurones have their cell bodies in the intermediolateral grey matter in the fifth to the twelfth thoracic spinal cord segments. Their fibres travel via the greater and lesser thoracic splanchnic nerves to the coeliac plexus and synapse in the coeliac and superior mesenteric ganglia; postganglionic axons are distributed to the duodenal wall via peri-arterial plexuses on the branches of the coeliac trunk and superior mesenteric artery. The sympathetic nerves are vasoconstrictor to the duodenal vasculature and inhibitory to duodenal musculature.

The preganglionic parasympathetic supply is carried by vagal fibres that travel from the coeliac plexus and synapse on neurones in the duodenal wall. The parasympathetic supply is secretomotor to the duodenal mucosa and motor to the duodenal musculature.

Referred pain

In common with other structures derived from the foregut, pain arising from the proximal duodenum is poorly localized and referred to the epigastric region. It is mediated by afferent fibres that accompany the sympathetic neurones.

JEJUNUM

The jejunum has an external diameter of about 4 cm and an internal diameter of about 3 cm. It has a thicker wall than the ileum and a rich arterial blood supply. The circular folds (plicae circulares) (see below) are most pronounced in the proximal jejunum, where they are more numerous and deeper than elsewhere in the small intestine (**Figs 64.5–64.6**). They frequently 'branch' around the lumen and can appear to be stacked on top of each other, giving the jejunum a characteristic appearance during single contrast radiography (see Fig. 64.6), computed tomography enterography (**Fig. 64.7A**) or magnetic resonance (MR) enterography (**Fig. 64.7B**). The circular folds are also clearly visible by capsule endoscopy, in which images of the small intestine are transmitted wirelessly from a small swallowed camera the size of a pill (**Fig. 64.8**).

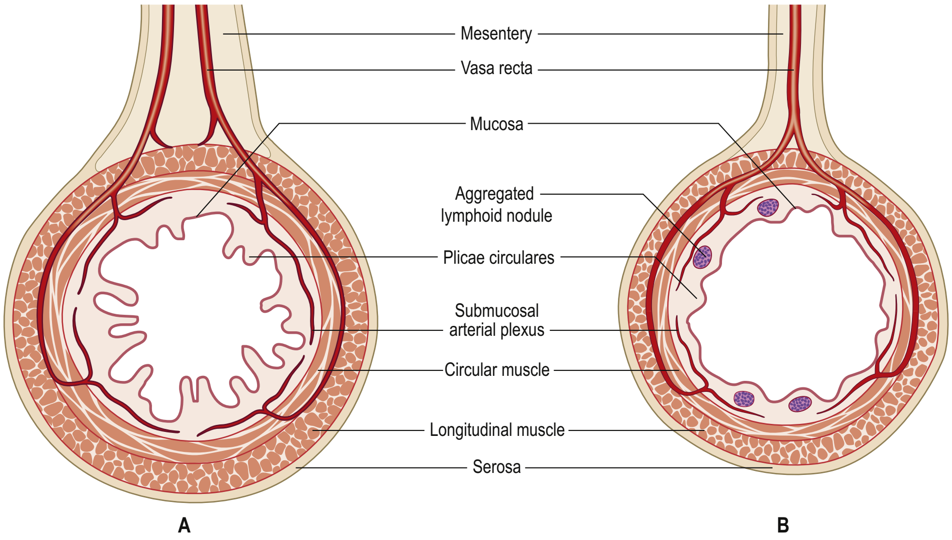

Fig. 64.5 Typical cross-sections through the proximal jejunum (**A**) and terminal ileum (**B**). The mesenteric attachment is wider in the jejunum and two leaves of vessels enter the intestinal wall. The latter is also thicker in the jejunum.

When gastric emptying is functionally impaired – as, for example, in gastroparesis – nutrition can be delivered directly into the duodenum or jejunum via a nasal transpyloric feeding tube.

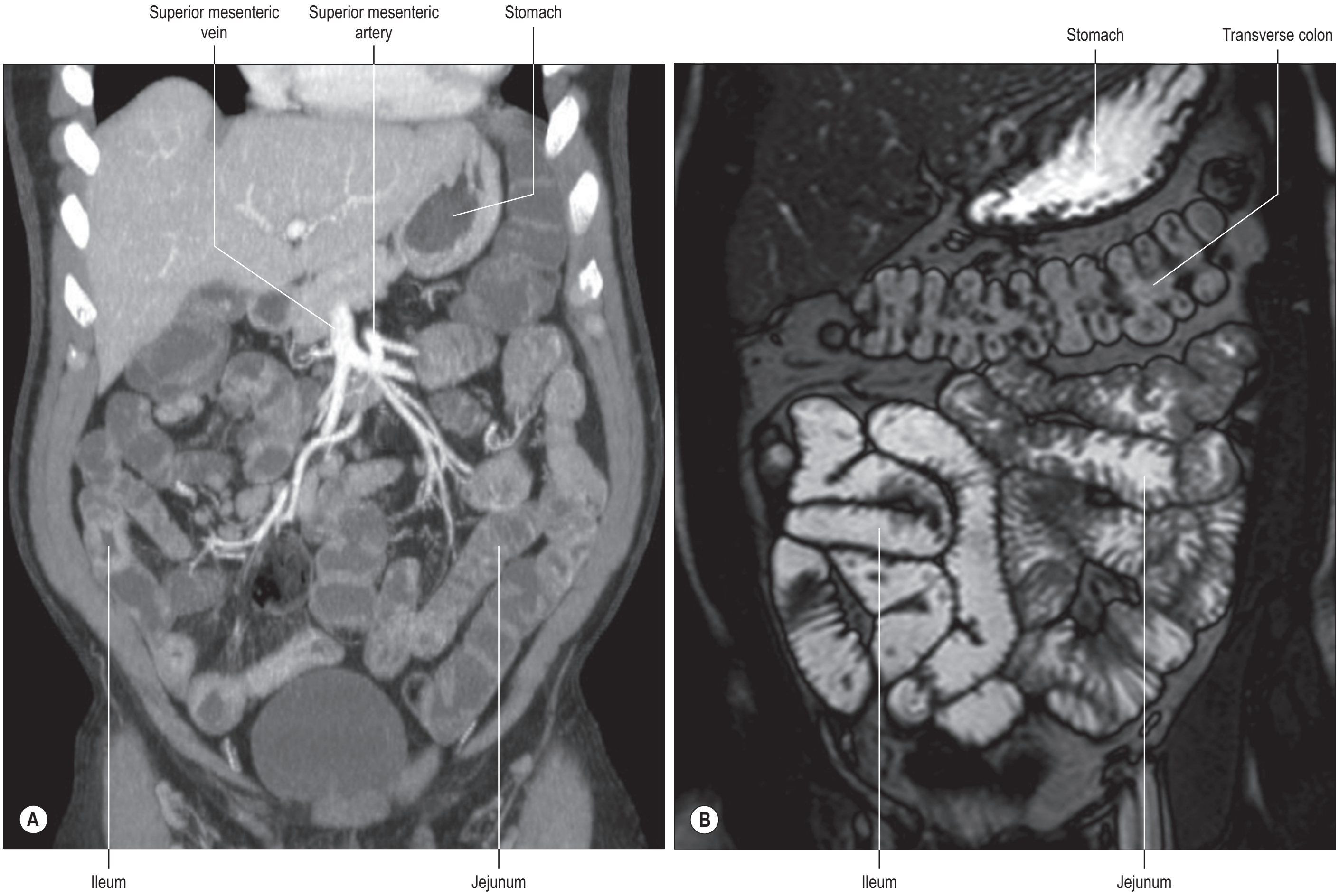
Superior mesenteric vein
Superior mesenteric artery
Stomach
Stomach
Transverse colon
A
B
Ileum
Jejunum
Ileum
Jejunum

Fig. 64.7 **A**, Computed tomography enterography. Coronal image showing small intestinal loops and superior mesenteric vessels. **B**, Magnetic resonance (MR) enterography. Coronal image showing the small intestine and transverse colon.

In the supine position, the jejunum usually occupies the proximal left infracolic compartment, extending distally to the umbilical region. The first one or two loops often occupy a recess between the left part of the transverse mesocolon and the left kidney. On supine radiological examination, the jejunal loops are characteristically situated in the proximal abdomen, to the left of the midline, whereas the ileal loops tend to lie in the inferior right part of the abdomen and pelvis. This distribution can be reversed in small intestine obstruction owing to rotation of the dilated intestine around its mesenteric attachment.

Jejunal feeding

Available with the *Gray's Anatomy* e-book

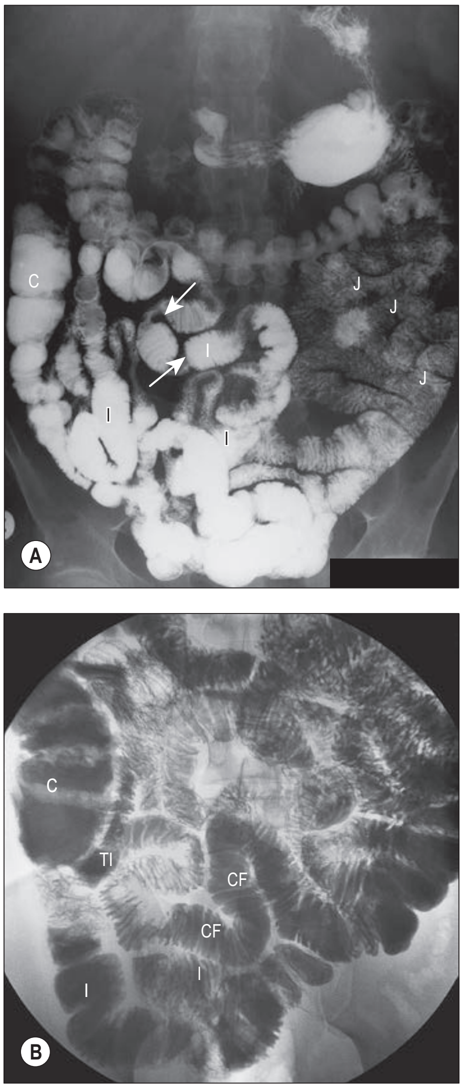

Fig. 64.6 Barium studies of the jejunum and ileum. **A**, Barium follow-through. The feathery appearance of the small intestine is due to the circular folds and is most prominent in the jejunum. The constrictions (arrows) are the result of peristalsis. **B**, Small intestine enteroclysis. The circular folds are clearly demonstrated by this technique. Abbreviations: C, caecum; I, ileum; J, jejunum; CF, circular folds; TI, terminal part of ileum.

ILEUM

The ileum has an external diameter of about 3 cm, an internal diameter of about 2.5 cm and tends to have a thinner wall than the jejunum (see Fig. 64.5B). The circular folds become progressively less obvious in the distal ileum; they tend to be single and flatter (see Figs 64.6–64.7; **Fig. 64.9**). The mucosa of the terminal ileum immediately proximal to the ileocaecal junction can appear almost flat at endoscopy, although the villi can be seen when viewed at near focus (see Fig. 64.9) and at capsule endoscopy (see Fig. 64.8).

In the supine position, the ileum lies mainly in the hypogastric region and right inguinal region. The terminal ileum frequently lies in the pelvis, from where it ascends over the right psoas major and right iliac vessels and ends by opening at the ileocaecal junction in the right inguinal region.

Anatomical differences between the jejunum and ileum

While there is no clear boundary between the jejunum (the proximal two-fifths of the small intestine beyond the duodenum) and the ileum (the distal three-fifths), there are general anatomical differences between those regions. The wall of the jejunum is thicker and more vascular, has a greater number of more prominent circular folds, and contains less lymphoid tissue than the ileum. There are also differences between the mesenteric vessels in the jejunum and ileum (Conley et al 2010). The jejunal mesentery, measured from the superior mesenteric artery to the mesenteric border of the intestine, is shorter than the ileal mesentery, and the jejunal arteries are slightly larger than their ileal counterparts. The jejunum typically contains 1–3 tiers of vascular arcades, whereas there are often 2–6 tiers in the ileum (**Fig. 64.10**). The straight arteries (vasa recta) in the ileum are more numerous, shorter and narrower than in the jejunum. The jejunal and ileal arteries, arcades and straight arteries are muscular arteries capable of influencing blood flow, which can range between 10% and 35% of cardiac output (Rosenblum et al 1997).

Solitary lymphoid nodules are scattered throughout the small intestinal mucosa but are most numerous in the distal ileum. Aggregated lymphoid nodules, Peyer's patches, are circular or oval masses containing 5–260 follicles. They vary in size, shape and distribution, most measuring 2–8 cm and visible macroscopically as dome-like elevations, usually along the antimesenteric border of the intestine. They are rarely present in the duodenum; small, circular, few in number and impalpable in the distal jejunum; and larger, more numerous and often palpable in the ileum (particularly in the terminal 25 cm; Van Kruiningen et al 2002). Intestinal villi are small or absent over the larger lymphoid nodules. Aggregated lymphoid nodules are most prominent in early childhood and, when enlarged in viral infections, may form the apex of an intussusception. They become less prominent around puberty and become fewer during adult life (Cornes 1965a, 1965b).

Ileal diverticulum

Available with the *Gray's Anatomy* e-book

Jejunostomy and ileostomy

Available with the *Gray's Anatomy* e-book

Short bowel syndrome

Available with the *Gray's Anatomy* e-book

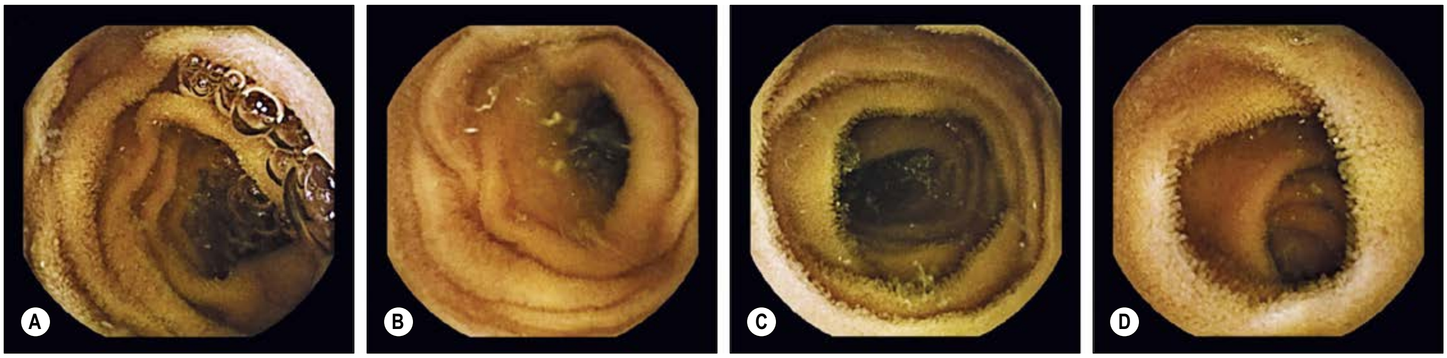

Fig. 64.8 The small intestine visualized by capsule endoscopy (PillCam®). **A**, The proximal jejunum at 1 h 34 min. **B**, The distal jejunum at 1 h 51 min. **C**, The proximal ileum at 2 h 25 min. **D**, The distal ileum at 3 h 34 min. Note the presence of circular folds and visible intestinal villi. (Courtesy of Simon Gabe.)

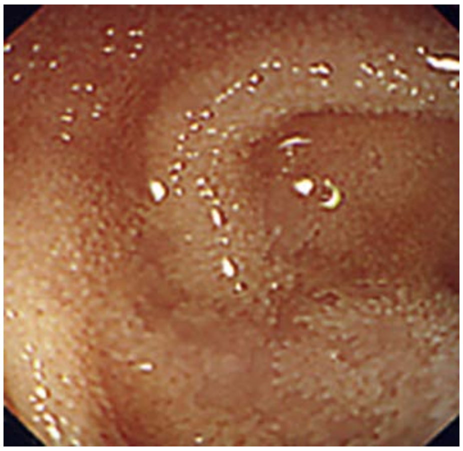

Fig. 64.9 The endoscopic appearance of the terminal ileum.

In patients with a functioning intestine who cannot tolerate adequate oral or intragastric feeding, jejunal feeding is often the preferred option. Enteral feeding is associated with fewer complications than parenteral (intravenous) nutrition: it maintains the integrity of the gut mucosa (thereby reducing bacterial translocation from the gut lumen), decreases the likelihood of aspiration from gastro-oesophageal reflux, is less of a stimulus for pancreaticobiliary secretion, and mitigates the need for central venous access and its accompanying risks. Jejunal feeds can be delivered via a nasojejunal or gastrojejunal tube or directly into the jejunum; gastrojejunal and jejunal tubes can be inserted endoscopically, radiologically or surgically. The distal end of the feeding tube must lie beyond the duodenojejunal flexure to prevent reflux of feeding into the duodenum and stomach.

A rare congenital ileal diverticulum (Meckel's diverticulum) represents the remnant of the proximal part of the omphalo-enteric duct (vitello-intestinal duct, yolk stalk). It projects from the antimesenteric border of the terminal ileum and is commonly located between 50–100 cm from the ileocaecal junction. It is variable in length (usually 2–5 cm in adults) and often possesses a short 'mesentery' of adipose tissue containing an omphalomesenteric artery (vitelline artery), from the termination of the superior mesenteric artery, that extends from the ileal mesentery to its base (**Fig. 64.11**). The lumen of the diverticulum usually has a calibre similar to that of the ileum. The tip is normally free but occasionally it is connected to the anterior abdominal wall near the umbilicus by a fibrous band. The mucosa is typically ileal, but small heterotopic areas of gastric body type epithelium, pancreatic, colonic or other tissues can also occur in the wall of a diverticulum. Unopposed acid secretion by heterotopic gastric body type epithelium can cause ulceration and bleeding in the adjacent normal ileal mucosa. Diverticular inflammation can mimic acute appendicitis: because the congenital ileal diverticulum and the appendix are both derived from the midgut, pain from either structure is referred to the periumbilical region. Rarer complications of a congenital ileal diverticulum include intestinal obstruction, intussusception, perforation, calculi and tumours (Sagar et al 2006, Uppal et al 2011).

In clinical practice, a stoma is a surgically created opening from a hollow viscus to the skin, classified according to its location. An intestinal stoma can be either an end stoma, in which only the proximal end of the divided intestine is anastomosed to the skin, or a loop stoma, in which both the proximal and distal ends of the intestines are exteriorized on the surface (**Fig. 64.12**). The volume output of a jejunostomy is greater than that of an ileostomy, less solid in character, and more likely to result in excessive fluid, electrolyte and nutrient losses.

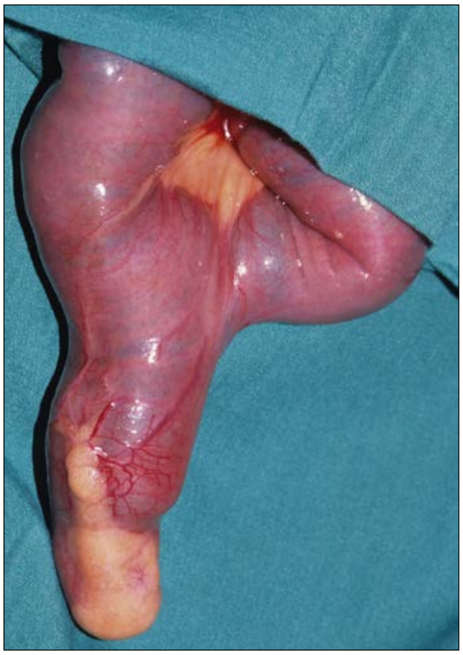

Fig. 64.11 A congenital ileal diverticulum (Meckel's diverticulum) containing ectopic mucosa at its tip. (Courtesy of Professor Mark Stringer, Christchurch Hospital, New Zealand.)

The mean length of the small intestine, measured from the duodenojejunal flexure to the ileocaecal junction *in vivo*, is about 5 m but can range from 3 to 8.5 m (Teitelbaum et al 2013). Males have a longer small intestine than females, and height is positively associated with the length of the small intestine (Teitelbaum et al 2013). Short bowel syndrome results from surgical resection, congenital deficiency or disease-associated loss of absorption, and is characterized by the inability to maintain protein-energy, fluid, electrolyte or micronutrient balances on a conventionally accepted normal diet (O'Keefe et al 2006). If untreated, short bowel syndrome leads to dehydration, malnutrition and weight loss. Adults with the greatest risk of developing intestinal failure fall into three groups: those with an end-jejunostomy and <100 cm of residual small intestine; those with a jejunocolic anastomosis and <50 cm residual small intestine; and those with a jejunoileal anastomosis and <35 cm of residual small intestine (despite the presence of an ileocaecal junction and colon) (Nightingale and Woodward 2006, Jeppesen 2013).

After surgical resection the remaining small intestine undergoes an adaptive process that involves morphological and functional changes: it dilates and intestinal villus height and intestinal gland depth increase, thereby expanding the absorptive surface area. Adaptation begins soon after intestinal resection and can continue for up to two years (Jeppesen and Mortensen 2002). The ability of the proximal and distal small intestine to adapt differ. The likelihood of regaining intestinal autonomy is greatest in patients with a retained segment of ileum and colon in continuity, in contrast to patients with a residual duodenojejunal segment and an end-jejunostomy (Jeppesen 2013). Many patients with short bowel syndrome are maintained on parenteral nutrition for lengthy periods.

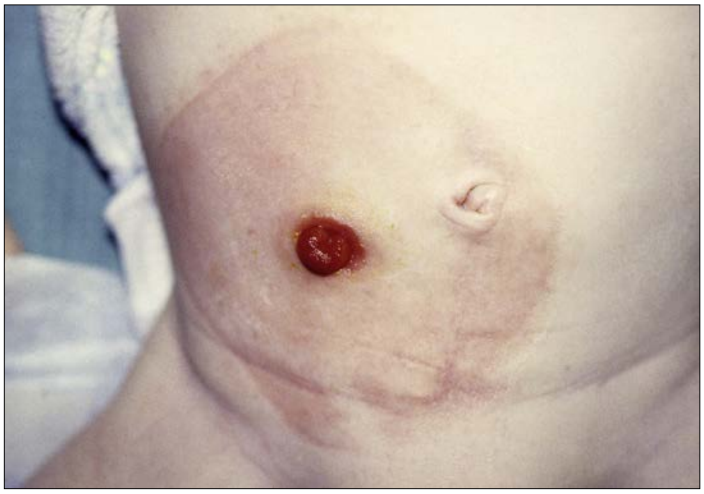

Fig. 64.12 A temporary loop ileostomy in an infant. The skin marking around the stoma is from the stoma bag adhesive. (Courtesy of Professor Mark Stringer, Christchurch Hospital, New Zealand.)

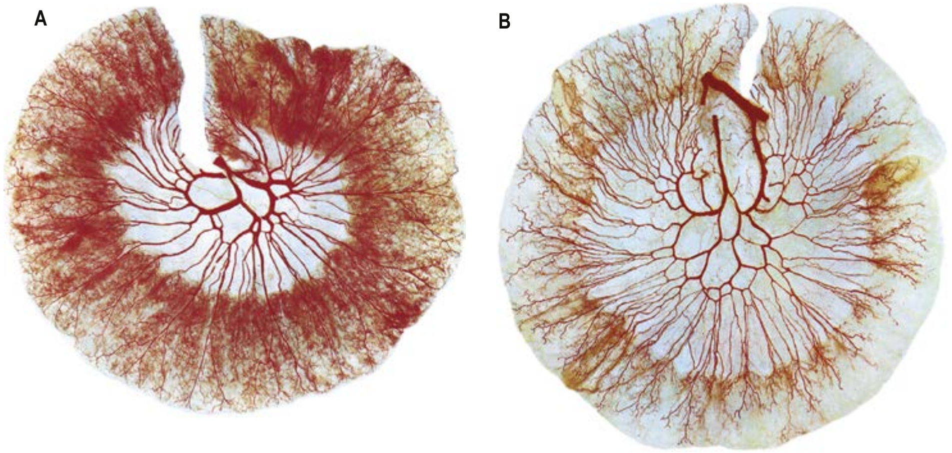

Fig. 64.10 Specimens of the jejunum (**A**) and ileum (**B**) from a cadaver where the superior mesenteric artery was injected with red-coloured gelatin before fixation. Subsequently, the specimens were dehydrated and then cleared in benzene, followed by methyl salicylate. The largest vessels present are the jejunal and ileal branches of the superior mesenteric artery and these are succeeded by anastomotic arterial arcades, which are relatively few in number (1–3) in the jejunum, becoming more numerous (2–6) in the ileum. From the arcades, straight arteries pass towards the gut wall; frequently, successive straight arteries are distributed to opposite sides of the gut. Note the denser vascularity of the jejunal wall. (Specimens prepared by MCE Hutchinson; photographs by Kevin Fitzpatrick on behalf of GKT School of Medicine, London.)

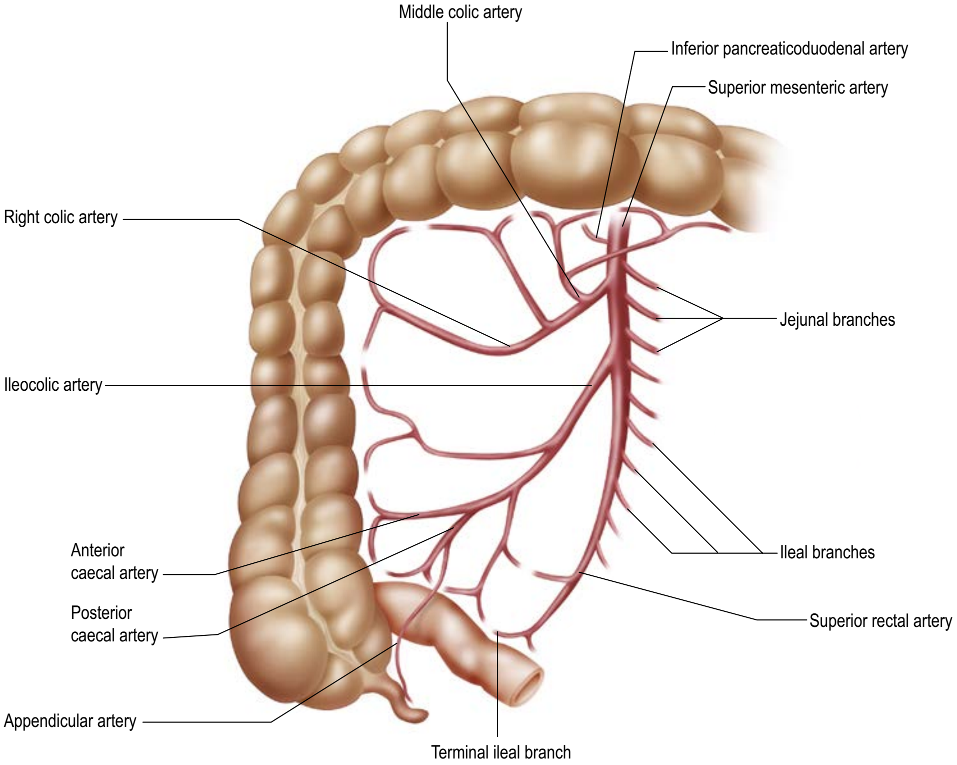

Fig. 64.13 The superior mesenteric artery and its branches. The outlines of representative ileum, appendix, caecum, ascending and transverse colons are shown for reference. Only the origin of jejunal and ileal branches is shown. For details of arcades, see Fig. 64.10.

Small intestinal transplantation

Available with the *Gray's Anatomy* e-book

Vascular supply and lymphatic drainage

Arteries

Branches from the superior mesenteric artery supply the jejunum and ileum. The arteries divide as they approach the mesenteric border of the intestine (see Fig. 64.5), giving off numerous branches that extend between the muscular layers before forming a submucosal arterial plexus that supplies the mucosa. Although there is a rich anastomotic network of arteries within the intestinal mesentery, there are few anastomoses between the terminal branches close to the intestinal wall. The intramural and submucosal arterial networks consist of small-calibre vessels only. Consequently, division or occlusion of several consecutive straight arteries can produce segmental ischaemia of the intestine, while division of more proximal arterial branches in the small intestine mesentery might not cause ischaemia because of collateral flow through vascular arcades.

Superior mesenteric artery

The superior mesenteric artery originates from the abdominal aorta 1 cm inferior to the coeliac trunk, at the level of the inferior border of the first lumbar vertebra in the transpyloric plane (**Figs 64.13–64.15**). The angle of its origin from the aorta is acute (mean value 45°, range 38–60° and greater in individuals with a greater body mass index; Ozkurt et al 2007). Among the major branches of the descending aorta, the superior mesenteric artery typically has the most acute take-off angle. The result is less turbulent flow, which makes embolic events more likely than in the other visceral arterial branches of the abdominal aorta. The acuteness of the angle between the aorta and superior mesenteric artery can make intravascular cannulation via the transfemoral route somewhat difficult. The artery is usually surrounded by fat, lymphatics and neural tissue at its origin, which helps to increase the angle and the distance between it and the aorta, thereby preventing compression of the duodenum where it is crossed by the artery. The artery descends anterior to the uncinate process of the pancreas and the horizontal part of the duodenum and posterior to the splenic vein and the body of the pancreas. The left renal vein lies posterior to it and separates it from the aorta (see Fig. 64.15B). Within the small intestine mesentery, the superior mesenteric artery crosses anterior to the inferior vena cava, right ureter and right psoas major. Its calibre progressively decreases as successive branches are given off to the jejunum and ileum, and its terminal branch anastomoses with the termination of the ileocolic artery.

The superior mesenteric artery usually gives off the inferior pancreaticoduodenal, middle colic, right colic and ileocolic arteries from its right side, and jejunal and ileal arteries from its left side. Its jejunal and ileal arteries form vascular arcades within the small intestine mesentery. The last of these arcades forms an irregular and incomplete marginal artery (of Drummond) of the small intestine. Straight arteries are given off from the most distal arcades and pass directly to the small intestine.

Anatomical variations in the origin and branching pattern of the superior mesenteric artery are well described (Winston et al 2007, Horton and Fishman 2010) (see also Ch. 65). It can be the source of

Small intestine transplantation has become a standard clinical procedure for selected patients with intestinal failure (Abu-Elmagd et al 2009). Intestinal failure can result from an inadequate surface area for nutrient absorption, as in short bowel syndrome, or dysmotility of the stomach or small intestine. The small intestine can be transplanted in isolation or along with the liver and/or other abdominal organs such as the pancreas (multivisceral transplant). Postoperatively, patients are recommenced on parenteral nutrition, and enteral feeding is started via a feeding jejunostomy once intestinal motility has returned. Protein is delivered as peptides and fats as medium-chain triglycerides, which are absorbed directly into the mesenteric veins and not via the lymphatics (divided when the graft is taken from the donor and not anastomosed to recipient lymphatics). Parenteral nutrition can usually be discontinued 3–6 weeks after small intestine transplantation but may continue to be used to supplement enteral feeding when stoma losses are large.

Intestinal dysmotility is common after intestinal transplantation. There is no extrinsic nerve supply to the graft but intrinsic small intestine motility usually recovers within 48–72 hours after transplantation (Gunning and Friend 1998). Adequate gastric emptying is often delayed for several weeks, despite pyloroplasty and the administration of drugs to enhance gastric motility. Reinnervation of the allograft via its vascular pedicle is slow (Walther et al 2013). Intestinal motility is also affected by any inflammatory response caused by rejection. Denervation and division of the lymphatic drainage of the intestinal allograft do not appear to impair long-term function seriously. In animal models, lymphatic drainage is re-established within 21–28 days, which is consistent with observations in patients (Kocandrle et al 1966).

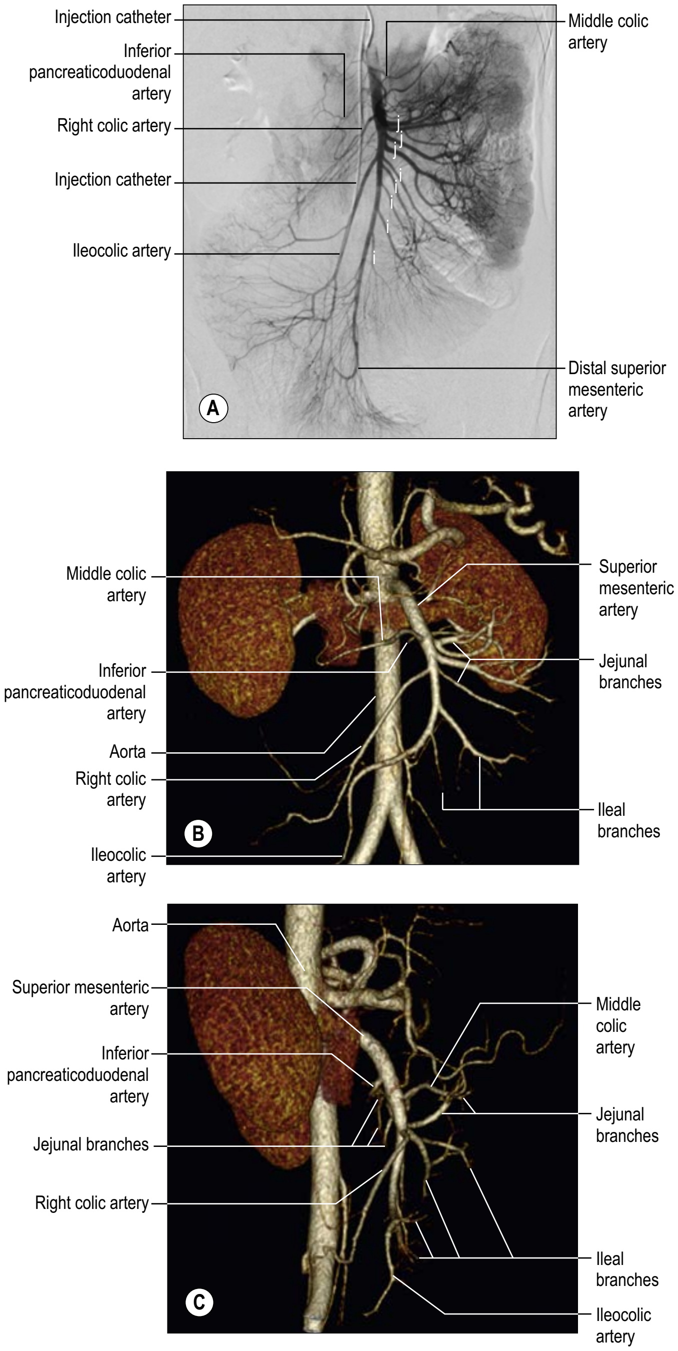

Fig. 64.14 The superior mesenteric artery and its branches. **A**, Digital subtraction angiogram. **B**–**C**, Volume-rendered CT angiograms: slightly oblique frontal view (**B**), right lateral view (**C**). Key: i, ileal branches; j, jejunal branches.

the common hepatic, gastroduodenal, accessory or replaced right hepatic, accessory pancreatic, splenic or rarely the inferior mesenteric artery. Also rare is a superior mesenteric artery arising from a common coeliacomesenteric trunk (Rountas et al 2013).

The remnant of the omphalomesenteric artery (vitelline artery) (the embryonic artery that originally connected the intestinal circulation to the yolk sac) is usually obliterated; when present, it forms the artery supplying a congenital ileal diverticulum. It is occasionally represented in the mesentery by a fibrous strand from the termination of the superior mesenteric artery to the ileum.

Surgical exposure of the superior mesenteric artery

Available with the *Gray's Anatomy* e-book

Jejunal branches Usually, 4–6 jejunal branches arise from the left side of the proximal portion of the superior mesenteric artery (see Figs 64.13–64.14). They are distributed to the jejunum via 1–3 tiers of arterial arcades, the most distal of which gives rise to straight arteries. The latter run almost parallel in the mesentery before being distributed alternately to either side of the small intestine, forming two distinct 'leaves' of vessels within the mesentery separated by a relatively avascular plane (see Fig. 64.5A).This vascular arrangement allows a dilated segment of small intestine to be bisected longitudinally and tubularized to double its length, a potentially useful technique for achieving small intestine lengthening in short bowel syndrome (Bianchi 1984). Small twigs from the jejunal arteries supply regional mesenteric nodes.

Ileal branches Ileal branches are more numerous (around 8–12) and slightly smaller in calibre than jejunal branches. They arise from the left and anterior aspects of the superior mesenteric artery. The length of the mesentery from the superior mesenteric artery to the mesenteric border of the intestine is greater in the ileum, and so the branches form between two and six arcades before giving rise to multiple straight arteries that run directly towards the ileal wall (see Fig. 64.10B). These branches run parallel in the mesentery and are distributed to both aspects of the ileum. They are shorter and thinner than their jejunal counterparts, particularly in the distal ileum, and do not form such distinct parallel 'leaves' of vessels. The terminal ileal arcades are supplied by the ileal branch of the ileocolic artery and the last ileal branch of the superior mesenteric artery (see Fig. 64.13). Few other vessels connect the ileocolic and superior mesenteric artery territories, and this makes surgical dissection of the ileocolic artery up to its origin relatively simple.

Veins

Superior mesenteric vein

The superior mesenteric vein drains the small intestine, caecum, ascending and transverse colons, and parts of the stomach and greater omentum (**Fig. 64.16**; see Fig. 59.7). It is formed in the mesentery of the small intestine by the union of tributaries from the terminal ileum, caecum and appendix. It ascends in the mesentery to the right of the superior mesenteric artery, passing anterior to the right ureter, inferior vena cava, horizontal part of the duodenum and uncinate process of the pancreas. It joins the splenic vein posterior to the neck of the pancreas in the transpyloric plane (inferior border of L1 vertebra) to form the hepatic portal vein.

The superior mesenteric vein receives jejunal, ileal, ileocolic, right colic, middle colic, right gastro-omental and inferior pancreaticoduodenal veins. A major proximal jejunal branch usually runs transversely posterior to the superior mesenteric artery to enter the right posterolateral aspect of the superior mesenteric vein (Kim et al 2007). The right colic vein is highly variable. When present, it can drain directly into the superior mesenteric vein or join the right gastro-omental or inferior pancreaticoduodenal vein to form a 'gastrocolic trunk', which then drains into the superior mesenteric vein (Yamaguchi et al 2002). Although the inferior mesenteric vein usually drains into the splenic vein, it can join the superior mesenteric vein directly or its confluence with the splenic vein (Graf et al 1997).

Lymphatic drainage

The lymphatic system of the small intestine regulates tissue fluid homeostasis, participates in immune surveillance, and transports dietary fat and fat-soluble vitamins from the gut lumen. It is organized into two networks. First, lacteals from the villi drain into a plexus of lymphatics in the submucosa and are joined by vessels from lymph spaces at the bases of solitary lymphoid follicles; these lymphatic vessels have few if any valves. Second, a coarse plexus of lymphatics also runs in the muscularis externa between the two muscle layers. The submucosal and muscular networks share few connections but both communicate freely with larger valved collecting lymphatics at the mesenteric border of the small intestine (Miller et al 2010). Mesenteric lymphatics pass between the layers of the mesentery and drain via a series of mesenteric nodes concentrated around the regional mesenteric vessels. Individual segments of small intestine have a relatively wide field of lymphatic drainage, which makes radical surgical resection of draining lymph nodes difficult if the blood supply to the remaining unaffected small intestine is to be preserved. Mesenteric nodes drain into superior mesenteric nodes around the proximal part of the superior mesenteric artery.

Innervation

The jejunum and ileum are innervated by parasympathetic and sympathetic fibres via the superior mesenteric plexus (see Figs 59.2–59.4). Preganglionic sympathetic axons originate from neurones in the intermediolateral grey matter of the mid-thoracic spinal cord segments and travel in the greater and lesser thoracic splanchnic nerves to the coeliac and superior mesenteric ganglia, where they synapse. Postganglionic axons accompany the superior mesenteric artery into the mesentery and are distributed along branches of the artery. The sympathetic nerves are vasoconstrictor to the vasculature and inhibitory to the musculature of the jejunum and ileum. Sympathetic neurotransmitters also have an

The superior mesenteric artery can be exposed through transperitoneal or retroperitoneal approaches. For a retroperitoneal approach, a left flank incision is used and the superior mesenteric artery is exposed at the base from the left lateral aspect. From the transperitoneal approach the superior mesenteric artery can be accessed through the omental bursa with medial visceral rotation. These exposures are important for either gaining control of a bleeding distal vessel, or more often to expose the superior mesenteric artery for bypass or embolectomy in the setting of intestinal ischaemia.

Retroperitoneal flank approach to expose the superior mesenteric artery

The patient is typically positioned in a modified right lateral decubitus position for this approach. In this position, the shoulders lie at an angle to the operating table with the left upper limb supported on an arm board, but the pelvis is maintained in a position with as much posterior rotation as possible. An incision can be made in the ninth, tenth or eleventh intercostal space extending posteriorly to the mid-axillary line and anteriorly to the lateral edge of rectus abdominis. The incision can be extended in either direction to provide additional exposure. External and internal intercostal are divided, as well as transversus abdominis. Intercostal muscles are divided over the top of the corresponding rib and the thorax can then be entered. Often the respiratory diaphragm must be divided as well. Anteriorly, blunt dissection is typically used to elevate the peritoneum off posterior muscles and the thoracolumbar fascia. The colon, spleen and tail of the pancreas are reflected anteriorly. The plane can be developed posterior to the kidney. The left lateral edge of the abdominal aorta is identified and the superior mesenteric artery can be visualized from the left lateral aspect as well.

Transperitoneal approaches to expose the superior mesenteric artery

A number of different incisions can be used to gain access to the peritoneal cavity, though a vertical midline incision is probably the most common. There are three approaches, with specific exposure determined by which aspect of the superior mesenteric artery needs to be exposed.

Transperitoneal omental bursa approach

The left lobe of the liver is reflected anteriorly. With leftward retraction on the stomach, the hepatogastric ligament can be divided either superior or inferior to the left gastric artery. Dissection of the muscular fibres of the left crus of the respiratory diaphragm will expose the anterior surface of the abdominal aorta. Typically, the coeliac artery is encountered first, overlaid with decussating muscle fibres and the nerves of the coeliac plexus. Large lymphatic channels can also be encountered. Inferior retraction of the body of the pancreas will expose the first few centimetres of the superior mesenteric artery.

Transperitoneal approach with medial visceral rotation

A full left medial visceral rotation (Mattox manoeuvre) provides exposure to the entire abdominal aorta and proximal visceral vessels. The lateral peritoneal reflection of the descending colon is divided and extended superiorly, curving towards the aortic hiatus. A retroperitoneal plane is developed as the colon, spleen and the tail of the pancreas are rotated to the right. The left crus of the respiratory diaphragm may need to be divided to expose the anterior aspect of the abdominal aorta, depending on its inferior extent. The kidney is generally left in position, which provides broad exposure to the origin of the proximal superior mesenteric artery.

Inframesocolic approach

The transverse colon is reflected superiorly to expose the root of the mesentery, while the jejunum and ileum are reflected inferiorly and to the right. The superior mesenteric artery can typically be palpated. A transverse incision made to the right of the suspensory ligament of the duodenum, and inferior to the pancreas, will typically expose both the superior mesenteric artery and vein. Typically, the middle colic artery and the first jejunal branch of the superior mesenteric artery are also visualized, but access to the origin of the superior mesenteric artery might be limited.

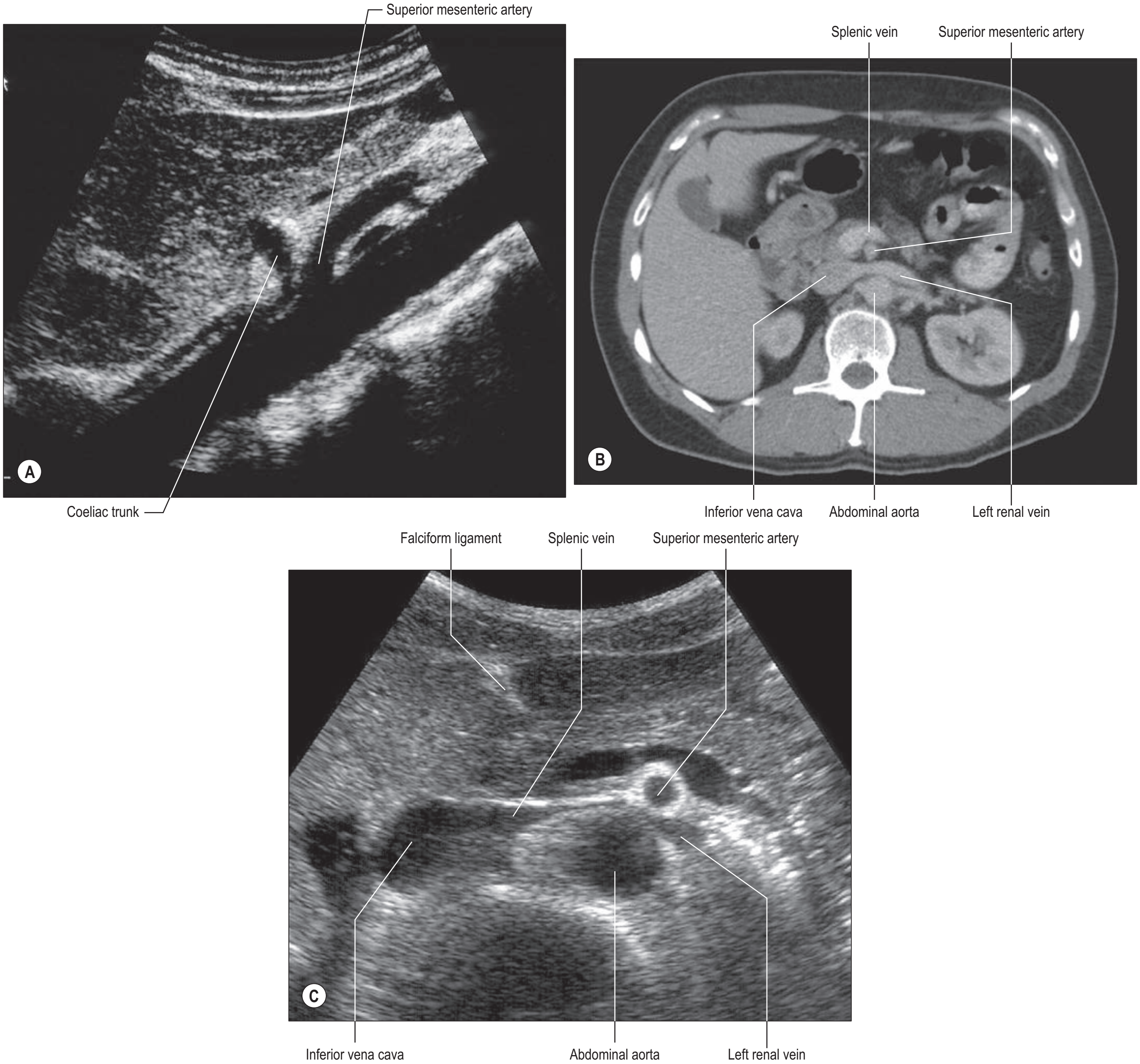
Superior mesenteric artery
Coeliac trunk
A
Splenic vein
Superior mesenteric artery
B
Inferior vena cava
Abdominal aorta
Left renal vein
Falciform ligament
Splenic vein
Superior mesenteric artery
C
Inferior vena cava
Abdominal aorta
Left renal vein

Fig. 64.15 **A**, An ultrasound image through the origin of the superior mesenteric artery, sagittal plane. **B**, Axial CT in an adult demonstrating the relationship of the superior mesenteric artery to the left renal vein. **C**, An axial ultrasound image showing the superior mesenteric artery and the splenic vein. (A–C, Courtesy of Professor Mark Stringer, Christchurch Hospital, New Zealand.)

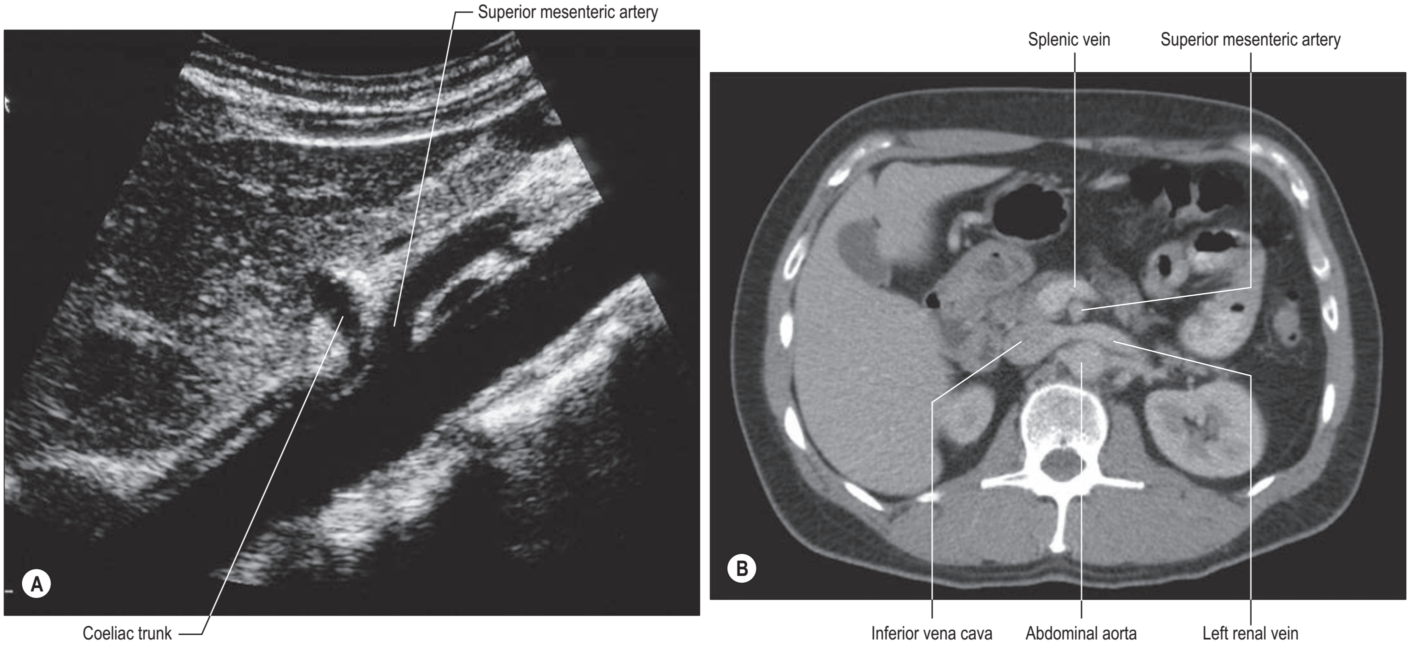

Fig. 64.15 **A**, An ultrasound image through the origin of the superior mesenteric artery, sagittal plane. **B**, Axial CT in an adult demonstrating the relationship of the superior mesenteric artery to the left renal vein. (Courtesy of Professor Mark Stringer, Christchurch Hospital, New Zealand.) (C, *continued online*)

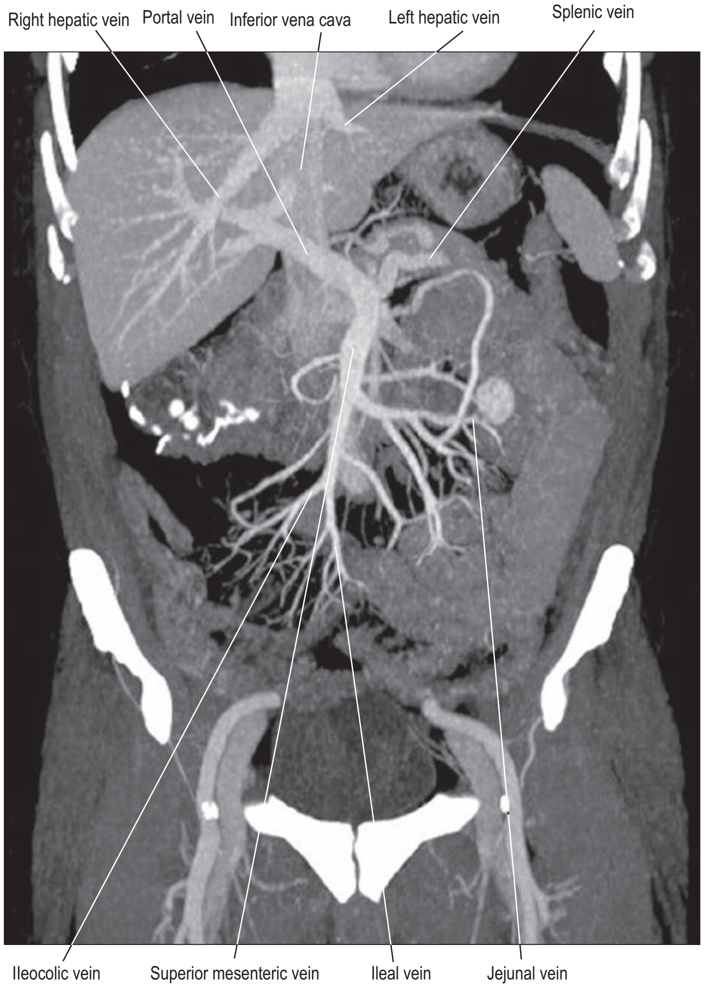

Fig. 64.16 The superior mesenteric vein and its branches. CT venogram, coronal plane. (Courtesy of Dr Nasir Khan, Chelsea and Westminster Hospital, London.)

immunomodulatory role by influencing mucosa-associated lymphoid tissue (Straub et al 2006). Preganglionic parasympathetic axons travel in the vagus nerves and are secretomotor to the mucosa and motor to the smooth muscle of the jejunum and ileum. Visceral afferents from the small intestine, conveying pain and other gut sensations, travel with the splanchnic and vagus nerves.

Referred pain

In common with other structures derived from the midgut, the visceral sensation of pain arising from the jejunum or ileum is poorly localized and is usually referred to the periumbilical region.

SMALL INTESTINE PHYSIOLOGY

Fluids and electrolytes

Available with the *Gray's Anatomy* e-book

Nutrients

Available with the *Gray's Anatomy* e-book

Motility

Available with the *Gray's Anatomy* e-book

MICROSTRUCTURE

The small intestinal wall is composed of mucosa, submucosa, muscularis externa and serosa or adventitia (see Fig. 59.8). The mucosa is thick and very vascular in the proximal small intestine but thinner and less vascular distally. In places, it is ridged by the underlying submucosa to form circular folds, which protrude into the lumen; mucosal finger- or leaf-like intestinal villi cover the whole surface (Fig. 64.17). There are numerous simple, tubular intestinal glands between the bases of the villi, and additional duodenal submucosal glands (see Fig. 59.8). The submucosa contains aggregated lymphoid nodules, most numerous in the ileum.

Circular folds

Except in the superior (first) part of the duodenum, large circular folds of mucosa (plicae circulares, valvulae conniventes, valves of Kerckring) project into the lumen of the small intestine, orientated either transversely or slightly obliquely to its long axis (see Figs 64.8, 64.17; Fig. 64.18). Unlike gastric folds, they do not disappear during distension of the intestine. Most extend round half or two-thirds of the luminal circumference, some are complete circles, some bifurcate and join adjacent circular folds, while others are spiral and extend one or more times round the lumen. Larger circular folds are up to 8 mm deep but most are smaller than this, and larger folds often alternate with smaller ones. Circular folds begin to appear 2.5–5 cm beyond the pylorus and are

The principal functions of the small intestine are fluid and electrolyte haemostasis, digestion and absorption of nutrients, immunoregulation and secretion of hormones. The absorptive capacity of the small intestine is greatly enhanced by the circular folds, intestinal villi and microvilli, which increase its surface area by factors of approximately 2, 7 and 13, respectively (Helander and Fändriks 2014), yielding a total estimated surface area of almost 30 m^2.

The secretion and absorption of electrolytes and fluid are two essential functions of the small intestinal epithelium. In healthy adults, the gastrointestinal tract is capable of secreting 8–10 litres of fluid per day in addition to the 1.5–2 litres ingested each day. To reduce this volume to the typical ileocaecal daily flow of approximately 2 litres per day, the small intestinal epithelium has a large number of transport molecules and regulatory proteins. Net fluid movement across the gastrointestinal epithelium is primarily the result of the active transport of sodium, chloride and bicarbonate ions. The jejunum can only absorb sodium across a small sodium gradient and therefore does not normally absorb salt and water, but secretes it into the lumen. Most fluid and electrolyte absorption occurs in the ileum, which is able to absorb across a larger sodium gradient (Nightingale and Spiller 2001): proximal small intestine fistulae or surgical jejunostomies therefore have a higher volume output with greater electrolyte losses than more distal stomata.

The mucosal brush border has an abundance of enzymes and pumps on its surface. Examples include the sodium-dependent glucose transporter protein (SGLT1) and the fructose transporter protein (GLUT5). Oligosaccharides are broken down to monosaccharides by enzymes at the brush border of the small intestine before being transported across the mucosa. A deficiency of lactase on the mucosal brush border is relatively common and results in lactose intolerance. Proteins are broken down into single amino acids and small peptides. The peptidase gradient across the microvillus brush border increases along the length of the small intestine, suggesting that amino acids are absorbed more distally than carbohydrates. Dietary fats are emulsified by biliary secretions and then broken down by pancreatic lipase into free fatty acids and phospholipids, which form micelles. The lipid components are then absorbed within the distal small intestine and converted into chylomicrons in the enterocytes before being secreted into the lymphatic system. Minerals such as calcium, magnesium, phosphorus and iron, and the water- and fat-soluble vitamins, are predominantly absorbed in the duodenum and proximal jejunum (Farrell 2002, Malik and Westergaard 2002). Vitamin B_{12} is absorbed in the terminal ileum after binding to intrinsic factor released by gastric parietal cells. Bile is largely composed of bile acid salts conjugated to taurine or glycine. These salts are deconjugated by bacteria in the ileum to either a free acid or a secondary bile acid. The free acids are reabsorbed by passive transport in the jejunum and ileum. The terminal ileum has an active sodium cotransporter that scavenges conjugated bile acids. Reabsorbed bile acids enter the portal circulation and are returned to the liver for re-secretion.

The motility of the small intestine differs depending on whether the individual is fasting or postprandial. In the fasting state, the smooth muscle of the small intestine exhibits cyclical myoelectrical activity, the so-called migrating motor complex (MMC). The frequency of these slow waves is regulated by interstitial cells of Cajal and is about 11/minute in the jejunum, decreasing along the length of the small intestine to 7–8/minute in the ileum (Husebye 1999). When slow waves are amplified beyond a threshold by neural, endocrine or paracrine stimulation, action potentials are generated, resulting in smooth muscle contraction. This spreads circumferentially at first and then propagates along the entire circumference of the intestine in an aboral direction, causing a ring-like contraction of the circular smooth muscle that progresses distally along the small intestine (about 10% of contractions reaching the ileum).

The MMC consists of three phases: phase I is a period of quiescence, phase II is composed of irregular contractions and phase III is a short burst of phasic contractions at the maximum frequency of the slow waves for that part of the intestine. The velocity of migration is 5–10 cm/minute in the jejunum, decreasing gradually along the small intestine to about 1 cm/minute in the ileum. The MMC requires an intact enteric nervous system and does not depend on extrinsic innervation. Consequently, MMCs are present in transplanted (denervated) small intestine. However, there is evidence that extrinsic innervation modulates the MMC. For example, sleep causes the almost complete disappearance of phase II. Phase III activity normally recovers in the proximal small intestine within a few hours of major abdominal surgery, although the pressure wave amplitude is temporarily reduced. Somatostatin and opioids decrease phase II activity. After a meal, the cyclical fasting activity is abolished for several hours and replaced by irregular contractions that consist of both segmental ‘stationary’ contractions and propulsive contractions (Barnert 2007).

Assessment of small intestine motility can complement detailed microscopic examination of full-thickness biopsy specimens of the intestine when conditions associated with intestinal dysmotility are characterized, helping to distinguish intestinal neuropathy from visceral myopathy. Wireless motility capsules are also finding increasing use. These devices are pill-shaped and can be either swallowed or placed into the stomach with an endoscope. Sensors for pH, pressure and temperature record measurements and send these wirelessly to an external recording device. Based on the patterns of these pH, temperature and pressure curves, gastric emptying, small intestine transit and colonic transit times are easily decipherable.

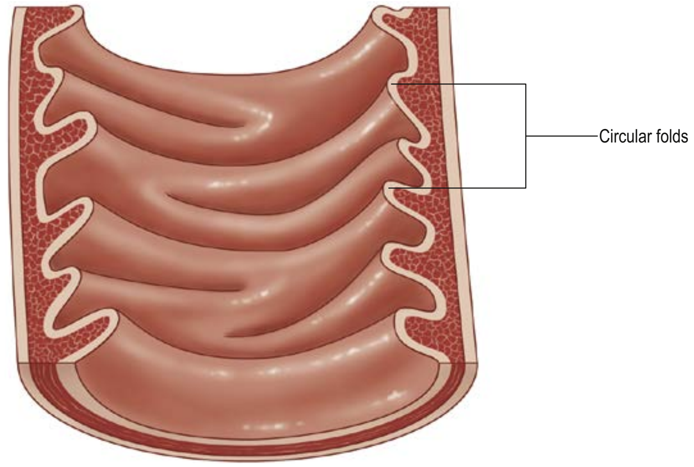

Fig. 64.17 The internal aspect of a representative sample of the proximal jejunum, showing circular folds.

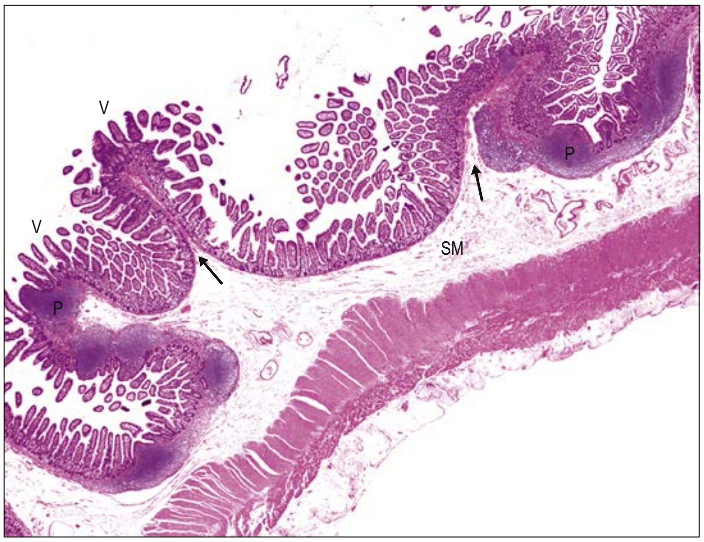

Fig. 64.18 A low-power micrograph showing several circular folds (arrows) in the wall of the ileum. The folds are covered with villi (V) projecting into the lumen, and the submucosa (SM) extends into the core of each fold. Circular (innermost) and longitudinal smooth muscle layers form the underlying muscularis externa. Large masses of aggregated lymphoid nodules (Peyer's patches, P) lie in the mucosa. (Courtesy of Mr Peter Helliwell and the late Dr Joseph Mathew, Department of Histopathology, Royal Cornwall Hospitals Trust, UK.)

relatively large and close together in the distal duodenum and proximal jejunum. Beyond this point, they diminish in size and disappear almost completely in the terminal ileum, which therefore has a relatively thin wall. The circular folds increase the absorptive surface area and enhance mechanical segmentation in the small intestine. They are visible at endoscopy (see Fig. 64.3), during small intestine contrast studies (see Fig. 64.6), and sometimes on plain radiographs.

Intestinal villi

Intestinal villi are highly vascular projections of the mucosal surface, just visible to the naked eye (see Fig. 64.18; **Figs 64.19–64.21**). They cover the entire small intestinal mucosa, increase the surface area of the lumen about seven-fold (Helander and Fändriks 2014), and give it a velvety texture. Villi are large and numerous in the duodenum and jejunum but smaller and fewer in the ileum. In the superior part of the duodenum they appear as broad ridges, become tall and foliate in the distal duodenum and proximal jejunum, and then gradually shorten to a finger-like form in the distal jejunum and ileum. Villi range from 10 to 40 per mm^2 in density and from 0.5 to 1.0 mm in height (see Fig. 64.19). Infoldings of the mucosa dip down from the bases of the villi for a short distance into the lamina propria: these intestinal glands (crypts of Lieberkühn) are most prominent in the proximal small intestine (see Fig. 64.20).

Mucosa

The mucosa consists of epithelium, lamina propria and muscularis mucosae.

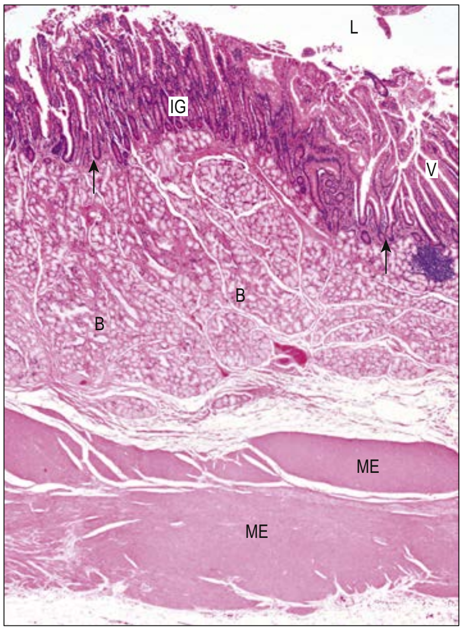

Fig. 64.19 A low-power micrograph showing the wall of the duodenum, with villi (V) projecting into the lumen (L); intestinal glands (IG) in the mucosa, seen mainly in transverse section; muscularis mucosae (arrows); submucosal seromucous glands (B); and muscularis externa (ME). (Courtesy of Mr Peter Helliwell and the late Dr Joseph Mathew, Department of Histopathology, Royal Cornwall Hospitals Trust, UK.)

Epithelium

A single-layered epithelium covers the intestinal villi (see Figs 64.20, 2.2C) and also lines the intestinal glands that open between the bases of villi. Two types of cell, enterocytes and goblet cells, cover the surfaces of the villi. Microfold cells (M cells) are restricted to the dome epithelium that covers localized accumulations of lymphoid tissue. All three cell types contact and adhere basally to a basal lamina, and all are derived from a common stem cell in the intestinal glands.

Enterocytes Enterocytes are columnar absorptive cells, approximately 20 μm tall, and are the most numerous cell type in the small intestinal lining. They are responsible for nutrient absorption: their surfaces bear up to 3000 microvilli, greatly increasing the surface area for absorption (Marsh and Swift 1969). Collectively, microvilli are visible by light microscopy as a 1 μm thick brush border (microvillous border or striated border): individual microvilli can be resolved only by electron microscopy. Enterocyte nuclei are elongated vertically, mainly euchromatic and located just below the centre of the cell.

The apical cell surface is resistant to protease attack because microvilli possess a specialized glycoprotein-rich surface coat (glycocalyx; see Fig. 1.26). Together with an overlying layer of mucus (Johansson et al 2011), this glycocalyx protects the epithelium against pancreatic enzymes in the intestinal lumen. The cell coat also contains a number of digestive enzymes as integral membrane proteins, including enzymes that degrade disaccharides and oligopeptides prior to absorption.

The luminal surface is an important barrier to diffusion. Nutrients generally have to pass through enterocytes (transcellular absorption) before they reach the underlying lamina propria and its blood vessels and lymphatics (central lymphatic vessels or lacteals). Classical epithelial junctional complexes encircle the apical plasma membranes of adjacent enterocytes, their tight junctions forming an effective barrier to non-selective diffusion between the gut lumen and the body as a whole. The lateral plasma membranes of enterocytes are highly folded and interdigitate to form complex intercellular boundaries that are anchored periodically by desmosomes and that make contact at gap junctions. The lateral intercellular space expands during active absorption; by supplementing transport across the basal cell surface it is an additional conduit for the passage of fluids with nutrients and other solutes to the vessels of the lamina propria.

After differentiation, enterocytes have a lifespan of about five days. Their position on the intestinal villus wall reflects their stage in the life cycle. They undergo programmed, apoptotic cell death and are shed from the tips of the villi. They are replaced at the bases of the villi by stem cell mitosis. Enterocytes located in the bases of the intestinal villi have a mainly secretory role, contributing more to absorption as they migrate towards the lumen.

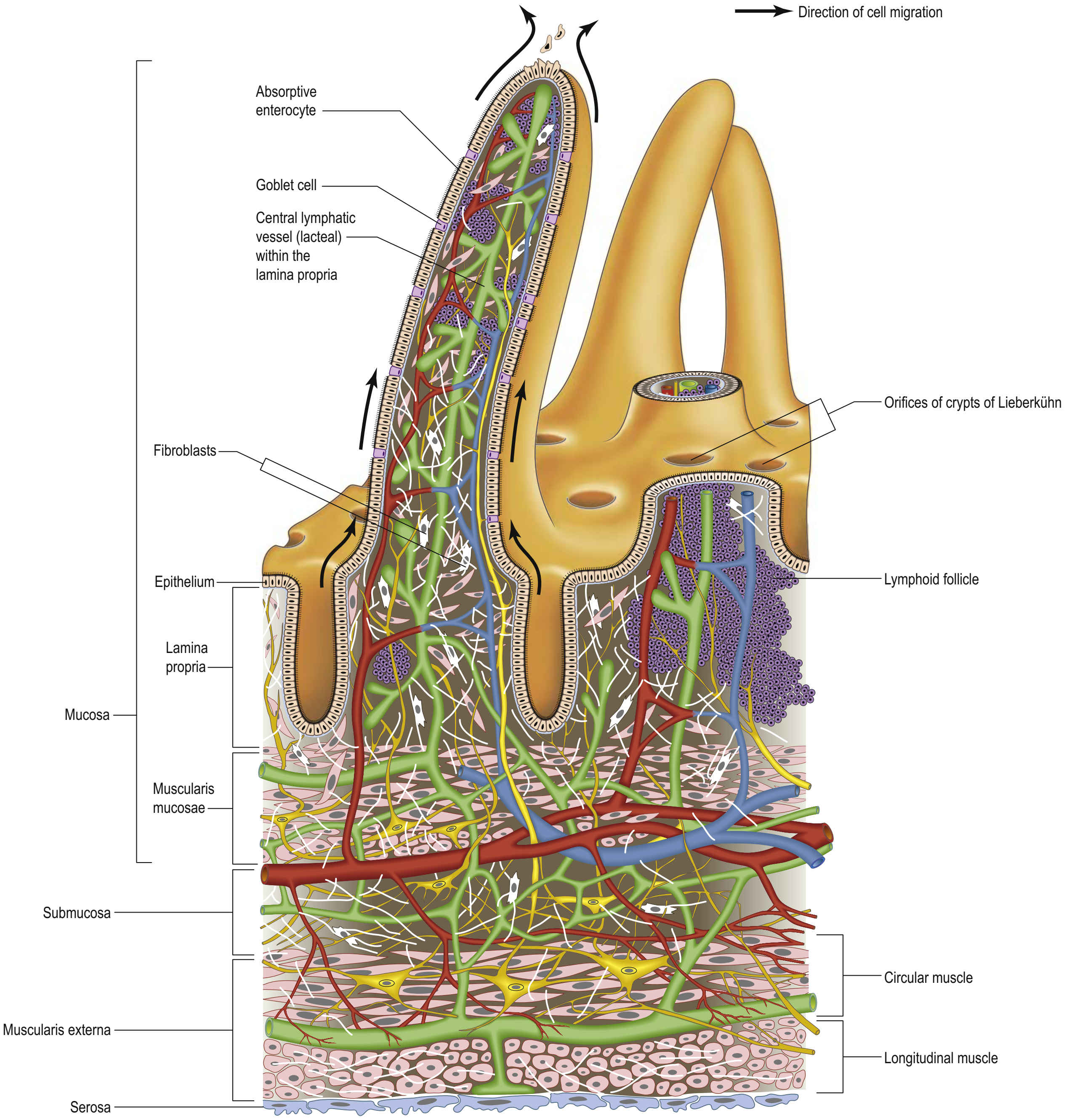
Direction of cell migration
Absorptive enterocyte
Goblet cell
Central lymphatic vessel (lacteal) within the lamina propria
Orifices of crypts of Lieberkühn
Fibroblasts
Epithelium
Lymphoid follicle
Lamina propria
Mucosa
Muscularis mucosae
Submucosa
Circular muscle
Muscularis externa
Longitudinal muscle
Serosa

Fig. 64.20 The architecture of an intestinal villus. The various layers and cells are not drawn to scale.

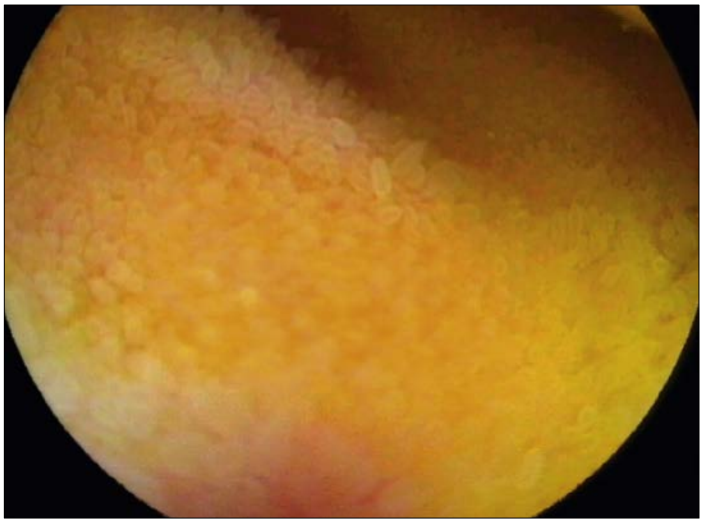

Fig. 64.21 The endoscopic appearance of the terminal villi (magnified).

Goblet cells Goblet cells increase in number from the duodenum to their highest density in the terminal ileum. They have elongated basal nuclei, an apical region containing many membrane-bound mucinogen granules, and apical surfaces that bear a few short microvilli. Goblet cell mucins contribute to protection against microorganisms and toxins in the gut lumen, and also provide lubrication and mechanical protection from the intestinal contents.

Microfold (M) cells Microfold cells are present where the epithelium covers lymphoid aggregates in the intestinal wall. They are cuboidal or flattened and have long, widely spaced microfolds rather than microvilli on their apical surfaces. They sample luminal antigens by endocytosis and transport antigens to lymphocytes lying within intercellular pockets formed by deep invaginations of the M-cell basolateral plasma membranes. (See Chapter 4 for details of antigen processing and presentation.)

Lymphocytes Intraepithelial lymphocytes are found in close association with M cells and also between the basolateral regions of enterocytes and goblet cells. They are migratory cells derived from the underlying lymphoid tissue and constitute an important means of immune defence.

Intestinal glands

Intestinal glands (intestinal crypts, crypts of Lieberkühn) are tubular pits that open into the lumen throughout the intestinal mucosa via

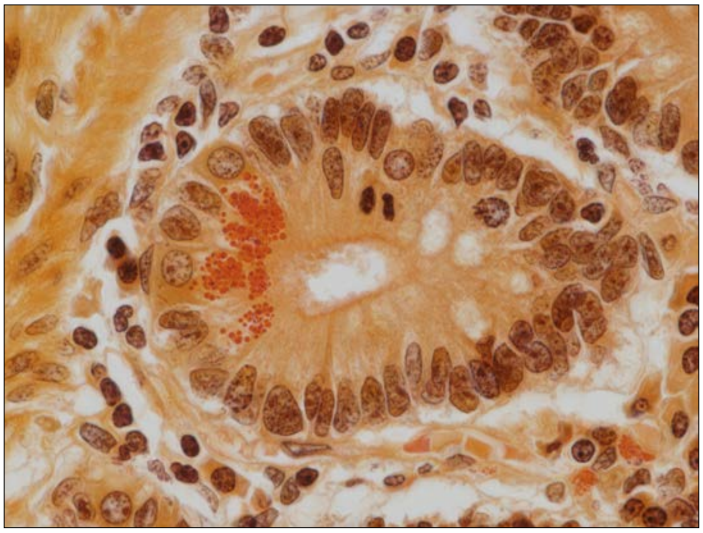

Fig. 64.22 Transverse section through a crypt in the ileum, lined by columnar epithelial cells with vertically elongated nuclei (a mitotic figure is seen in the upper field). Paneth cells with round nuclei and orange-stained secretory granules in their apical cytoplasm are seen on the left. Lendrum's phloxine–tartrazine stain. (Courtesy of Mr Peter Helliwell and the late Dr Joseph Mathew, Department of Histopathology, Royal Cornwall Hospitals Trust, UK.)

small circular apertures between the bases of the villi (see Fig. 64.20). Their thin walls are composed of columnar enterocytes supplemented by mucous cells of the duodenal submucosa, Paneth cells, stem cells and neuroendocrine cells. They are separated by a basal lamina from a rich capillary plexus within the lamina propria.

Enterocytes Enterocytes in the intestinal glands secrete ions and alkaline fluid to dilute chyme and aid absorption by structurally similar cells that cover the villi.

Mucous cells The mucous cells of the duodenal submucosa in the intestinal glands are similar to the goblet cells of the villi.

Paneth cells Paneth cells are highly specialized epithelial cells of the small intestine, involved in the coordination of many physiological functions. They were first identified more than a century ago on the basis of their readily discernible secretory acidophilic granules that stain strongly with eosin or phosphotungstic acid-haematoxylin (**Fig. 64.22**). Paneth cells are numerous in the deeper parts of the intestinal glands. They synthesize and secrete lysozyme, a highly specific antibacterial enzyme, other defensive proteins (alpha-defensins), tumour necrosis factor alpha (TNF-α), and phospholipase A that help to protect the luminal surface. These antimicrobial molecules are key mediators of host–microbe interactions, including maintaining the homeostatic balance with colonizing microbiota and providing innate immune protection from enteric pathogens (Clevers and Bevins 2013). Paneth cells secrete factors that help sustain and modulate epithelial stem and progenitor cells in the intestinal glands.

Stem cells Stem cells occur in a zone just above the basal region of the intestinal glands. Lineage tracing has demonstrated that Lgr5^{hi} crypt base columnar stem cells generate all cell types of the small intestinal epithelium (Barker et al 2007, Clevers 2013). These cells divide rapidly in the intestinal gland compartment directly above the Paneth cells. Their progeny (transit-amplifying cells) move upwards from this compartment onto the surfaces of the intestinal villi while differentiating into goblet cells, tuft cells, neuroendocrine cells and enterocytes. An individual cell takes only 4–5 days to reach the tip of an intestinal villus and undergo apoptosis. Paneth cells escape this upward flow and migrate downwards to settle at the bases of the intestinal glands, where they can remain for one month or more (Clevers and Bevins 2013). Stem cell daughter cells and young transit-amplifying cells retain their plasticity and can revert back to stem cells if an intestinal gland is injured and existing stem cells are lost.

Neuroendocrine cells Several types of neuroendocrine cell are scattered among the walls of the intestinal glands and less commonly over the intestinal villi. They can all be identified by their clear cytoplasm and round nucleus. They secrete bioactive peptides such as gastrin, cholecystokinin and secretin basally into the surrounding lamina propria. Eleven distinct subpopulations of neuroendocrine cells have been described, distributed throughout the gastrointestinal tract, each producing unique signalling molecules. Intestinal gland neuroendocrine cells are derived from stem cells, that also give rise to enterocytes and other epithelial elements (Posovszky 2017).

Lamina propria

The lamina propria is composed of connective tissue and provides mechanical support for the epithelium. It has a rich vascular plexus, receives nutrients absorbed by the enterocytes, and forms the cores of the intestinal villi. It contains lymphoid tissue, fibroblasts and connective tissue extracellular matrix fibres, smooth muscle cells, eosinophils, macrophages, mast cells, capillaries, lymphatic vessels and unmyelinated nerves. Plasma cells are numerous. Lymphocytes may be clustered in solitary or aggregated follicles, some of which extend through the muscularis mucosae into the submucosa.

Villus core

Each intestinal villus has a core of delicate connective tissue that contains a large, blind-ending lymphatic vessel or lacteal (so called because of its milky content of suspended chylomicrons, the droplets of apoprotein–lipid complex elaborated by enterocytes from absorbed dietary fats). The core also contains blood vessels, nerves and smooth muscle cells derived from fine extensions of the muscularis mucosae. Each lacteal, usually single but occasionally double, starts in a closed dilated extremity near the tip of an intestinal villus and extends through the core to the base of the villus, where it joins a narrower lymphatic plexus in the deeper lamina propria. Its wall is a single layer of endothelial cells. Smooth muscle cells surround the lacteal throughout each villus, and their contraction propels its contents into the underlying lymphatic plexus. Capillaries within the core are lined by fenestrated endothelium to facilitate the rapid intake of nutrients that diffuse from the covering absorptive epithelium.

Mucosa-associated lymphoid tissue

Mucosa-associated lymphoid tissue (MALT; Ch. 4) consists of lymphoid follicles covered by follicle-associated intestinal epithelium that includes scattered M cells. MALT is found mainly in the lamina propria but sometimes expands into the submucosa; it is the source of B and T lymphocytes and other related cells involved in the immune defence of the gut wall. MALT produces immunoglobulin A (IgA), the most abundant immunoglobulin in the body and the major class of antibody secreted by the gut mucosa. IgA regulates the composition, geographical distribution and function of bacterial communities along the gastrointestinal tract via T cell dependent and independent pathways and has also been implicated in autoimmune and inflammatory conditions of the gut.

Like other masses of MALT (except lymph nodes), solitary and aggregated lymphoid follicles are most prominent around the age of puberty, after which they decrease in number and size, although many persist into old age. For further details of intestinal MALT and its function, including aggregated lymphoid nodules, see Didierlaurent et al (2005).

Muscularis mucosae

The muscularis mucosae forms the base of the mucosa and has external longitudinal and internal circular layers of smooth muscle cells. It follows the surface profiles of the circular folds and sends fine fascicles of smooth muscle cells into the cores of the villi.

Submucosa

The submucosa is composed of loose connective tissue and contains blood vessels, lymphatics and nerves. Its ridged elevations form the cores of the circular folds. The geometry of its collagen and elastin fibres permits the considerable changes in transverse and longitudinal dimensions that accompany peristalsis whilst still providing adequate support, elasticity and strength. The submucosa is an important histological landmark in the pathological staging for some gastrointestinal malignancies.

Submucosal glands

Submucosal glands (Brunner's glands) are limited to the submucosa of the duodenum (see Fig. 64.19). Their ducts traverse the muscularis mucosae to enter the bases of the intestinal glands. They are largest and most numerous near the pylorus and form an almost complete layer in the proximal half of the descending part of the duodenum; thereafter, they gradually diminish in number and disappear at the duodenojejunal junction. They are small, branched tubuloacinar glands; each has several secretory acini lined by low columnar epithelial cells, which produce an alkaline (pH 9) mucoid secretion that effectively neutralizes acidic chyme from the stomach. Many neuroendocrine cells are present among the acinar cells.

Muscularis externa

The muscularis externa, sometimes known as muscularis propria, consists of a thin external longitudinal layer and a thick internal circular layer of smooth muscle cells. It is thicker in the proximal small intestine and is mainly responsible for the differential appearance of the proximal jejunum and distal ileum on computed tomography.

Interstitial cells of Cajal

Interstitial cells of Cajal (ICC) are found throughout the gastrointestinal tract, lying in close contact with nerve terminals (Farrugia 2008). They originate from mesenchymal cells and can be considered as specialized smooth muscle cells. However, whereas smooth muscle cells develop an extensive array of contractile elements, ICC are fusiform cells with a large oval nucleus, sparse cytoplasm, dendritic-like processes, few contractile elements, an abundance of endoplasmic reticula and mitochondria, and characteristic sets of channels in their membranes, including CD117, a tyrosine kinase receptor (Mostafa et al 2010). ICC contact each other and neighbouring smooth muscle cells via gap junctions. They form distinct networks in the myenteric plexus between the circular and longitudinal muscle layers: looser arrangements occur within the individual muscle layers and the submucosa of the gut. Isolated or small groups of ICC are also found in connective tissue septa and the subserosal layer. ICC are involved in generating pacemaker signals, propagating electrical slow wave activity, neuromuscular transmission, and mechanosensation (Sanders et al 2014): defective ICC function has been implicated in a wide range of intestinal motility disorders (Al-Shboul 2013).

Serosa

The serosa is visceral peritoneum. It consists of a subserosal layer of loose connective tissue covered by mesothelium. Serosa covers most of the muscularis externa, with the exception of the parts adjacent to mesenteric adipose tissue and the retroperitoneal portions of the duodenum, both of which are covered mainly by connective tissue.

Bonus e-book content

Fig. 64.7 **A–B**, CT and MRI enterography.

Fig. 64.9 The endoscopic appearance of the terminal ileum.

Fig. 64.11 A congenital ileal diverticulum (Meckel's diverticulum).

Fig. 64.12 A temporary loop ileostomy in an infant.

Fig. 64.15 **C** An axial ultrasound image showing the superior mesenteric artery and the splenic vein.

Key references

Kellogg EL 1933. The Duodenum: Its Structure and Function, Its Diseases and Their Medical and Surgical Treatment. New York: Paul B Hoeber Inc.

A classic textbook devoted to the duodenum.

Sanders KM, Ward SM, Koh SD 2014 Interstitial cells: regulators of smooth muscle function. Physiol Rev 94:859–907.

A review of the structural, functional and molecular features of interstitial cells of Cajal and their importance in smooth muscle function.

Teitelbaum EN, Vaziri K, Zettervall S et al 2013 Intraoperative small bowel length measurements and analysis of demographic predictors of increased length. Clin Anat 26:827–32.

Information on small bowel length in living adults, which varies with sex, height and age.

References

Abu-Elmagd KM, Costa G, Bond GJ et al 2009 Five hundred intestinal and multivisceral transplantations at a single center: major advances with new challenges. Ann Surg 250:567–81.

Al-Shboul OA 2013 The importance of interstitial cells of Cajal in the gastrointestinal tract. Saudi J Gastroenterol 19:3–15.

Barker N, van Es JH, Kuipers J et al 2007 Identification of stem cells in small intestine and colon by marker gene Lgr5. Nature 449:1003–7.

Barnert J 2007 Motility and transit in the small bowel. Current Topics in Neurogastroenterology: Proceedings of the 2nd International Symposium of Neurogastroenterology. Cluj Napoca, Romania: Editura Medicală Universitară 'Iuliu Hațieganu'.

Bertelli E, Di Gregorio F, Bertelli L et al 1995 The arterial blood supply of the pancreas: a review. I. The superior pancreaticoduodenal and the anterior superior pancreaticoduodenal arteries. An anatomical and radiological study. Surg Radiol Anat 17:97–106.

Bertelli E, Di Gregorio F, Bertelli L et al 1996 The arterial blood supply of the pancreas: a review. II. The posterior superior pancreaticoduodenal artery. An anatomical and radiological study. Surg Radiol Anat 18:1–9.

Bertelli E, Di Gregorio F, Bertelli L et al 1997 The arterial blood supply of the pancreas: a review. IV. The anterior inferior and posterior pancreaticoduodenal aa., and minor sources of blood supply for the head of the pancreas. An anatomical review and radiologic study. Surg Radiol Anat 19:203–12.

Bianchi A 1984 Intestinal lengthening: an experimental and clinical review. J R Soc Med 77(Suppl 3):35–41.

Bianchi HF, Albanèse EF 1989 The supraduodenal artery. Surg Radiol Anat 11:37–40.

Bradley RL 1973 Surgical anatomy of the gastroduodenal artery. Int Surg 58:393–6.

Clevers HC, Bevins CL 2013 Paneth cells: maestros of the small intestinal crypts. Annu Rev Physiol 75:289–311.

Clevers H 2013 The intestinal crypt, a prototype stem cell compartment. Cell 154:274–84.

Conley D, Hurst PR, Stringer MD 2010 An investigation of human jejunal and ileal arteries. Anat Sci Int 85:23–30.

Cornes JS 1965a Number, size, and distribution of Peyer's patches in the human small intestine. Gut 6:225–29.

Cornes JS 1965b Number, size, and distribution of Peyer's patches in the human small intestine. Part II: The effect of age on Peyer's patches. Gut 6:230–3.

Didierlaurent A, Simonet M, Sirard JC 2005 Innate and acquired plasticity of the intestinal immune system. Cell Mol Life Sci 62:1285–7.

Farrell JJ 2002 Digestion and absorption of nutrients and vitamins. In: Feldman M, Friedman LS, Sleisenger MH (eds) Gastrointestinal and Liver Disease, 7th ed. Philadelphia: Saunders, pp. 1715–50.

Farrugia G 2008 Interstitial cells of Cajal in health and disease. Neurogastroenterol Motil 20(Suppl 1):54–63.

Fotiades CI, Kouerinis IA, Papandreou I et al 2005 Current diagnostic and treatment aspects of duodenal diverticula: report of two polar cases and review of the literature. Ann Gastroenterol 18:441–4.

Graf O, Boland GW, Kaufman JA et al 1997 Anatomic variants of mesenteric veins: depiction with helical CT venography. AJR Am J Roentgenol 168:1209–13.

Gunning KEJ, Friend PJ 1998 Intestinal transplantation. In: Klinck JR, Lindop MJ (eds) Anaesthesia and Intensive Care for Organ Transplantation. London: Chapman & Hall Medical, pp. 297–309.

Helander HF, Fändriks L 2014 Surface area of the digestive tract – revisited. Scand J Gastroenterol 49:681–9.

Hirai I, Murakami G, Kimura W et al 2001 Long descending lymphatic pathway from the pancreaticoduodenal region to the para-aortic nodes: its laterality and topographical relationship with the celiac plexus. Okajimas Folia Anat Jpn 77:189–99.

Horiguchi S, Kamisawa T 2010 Major duodenal papilla and its normal anatomy. Dig Surg 27:90–3.

Horton KM, Fishman EK 2010 CT angiography of the mesenteric circulation. Radiol Clin North Am 48:331–45.

Husebye E 1999 The patterns of small bowel motility: physiology and implications in organic disease and functional disorders. Neurogastroenterol Motil 11:141–61.

Jeppesen PB 2013 Short bowel syndrome – characterisation of an orphan condition with many phenotypes. Expert Opinion Orphan Drugs 1:515–25.

Jeppesen PB, Mortensen PB 2002 Enhancing bowel adaptation in short bowel syndrome. Curr Gastroenterol Rep 4:338–47.

Johansson ME, Ambort D, Pelaseyed T et al 2011 Composition and functional role of the mucus layers in the intestine. Cell Mol Life Sci 68:3635–41.

Kamisawa T, Takuma K, Tabata T et al 2010 Clinical implications of accessory pancreatic duct. World J Gastroenterol 16:4499–503.

Kellogg EL 1933 The Duodenum: Its Structure and Function, Its Diseases and Their Medical and Surgical Treatment. New York: Paul B Hoeber Inc.

A classic textbook devoted to the duodenum.

Kim HJ, Ko YT, Lim JW et al 2007 Radiologic anatomy of the superior mesenteric vein and branching patterns of the first jejunal trunk: evaluation using multi-detector row CT venography. Surg Radiol Anat 29:67–75.

Kim SK, Cho CD, Wojtowycz AR 2008 The ligament of Treitz (the suspensory ligament of the duodenum): anatomic and radiographic correlation. Abdom Imaging 33:395–7.

Kocandrle V, Houttuin E, Prohaska JV 1966 Regeneration of the lymphatics after autotransplantation and homotransplantation of the entire small intestine. Surg Gynecol Obstet 122:587–92.

Malik A, Westergaard H 2002 Short bowel syndrome. In: Feldman M, Friedman LS, Sleisenger MH (eds) Gastrointestinal and Liver Disease, 7th ed. Philadelphia: Elsevier, Saunders, pp. 1807–16.

Marsh MN, Swift JA 1969 A study of the small intestinal mucosa using the scanning electron microscope. Gut 10:940–9.

Mather Cordiner GR, Calthrop GT 1936 The radiography of the duodenal cap. Br J Surg 23:700–15.

Merrett ND, Wilson RB, Cosman P et al 2009 Superior mesenteric artery syndrome: diagnosis and treatment strategies. J Gastrointest Surg 13:287–92.

Miller MJ, McDole JR, Newberry RD 2010 Microanatomy of the intestinal lymphatic system. Ann N Y Acad Sci 1207(Suppl 1):E21–E28.

Mostafa RM, Moustafa YM, Hamdy H 2010 Interstitial cells of Cajal, the maestro in health and disease. World J Gastroenterol 16:3239–48.

Murakami G, Hirata K, Takamuro T et al 1999 Vascular anatomy of the pancreaticoduodenal region: a review. J Hepatobiliary Pancreat Surg 6:55–68.

Nightingale J, Spiller R 2001 Normal intestinal anatomy and physiology. In: Nightingale J (ed), Intestinal Failure. London: Greenwich Medical Media, pp. 17–36.

Nightingale J, Woodward JM 2006 Guidelines for management of patients with a short bowel. Gut 55:1–12.

O'Keefe SJ, Buchman AL, Fishbein TM et al 2006 Short bowel syndrome and intestinal failure: consensus definitions and overview. Clin Gastroenterol Hepatol 4:6–10.

Ozkurt H, Cenker MM, Bas N et al 2007 Measurement of the distance and angle between the aorta and superior mesenteric artery: normal values in different BMI categories. Surg Radiol Anat 29:595–9.

Posovszky C 2017 Development and anatomy of the enteroendocrine system in humans. Endocr Dev 32:20–37.

Rosenblum JD, Boyle CM, Schwartz LB 1997 The mesenteric circulation. Surg Clin North Am 77:289–306.

Rountas CH, Fanariotis M, Vlychou M et al 2013 Celiomesenteric trunk demonstrated by multi-detector computed tomography angiography: two cases of a rare vascular variation. Folia Morphol (Warsz) 72:171–5.

Sagar J, Kumar V, Shah DK 2006 Meckel's diverticulum: a systematic review. J R Soc Med 99:501–5.

Sanders KM, Ward SM, Koh SD 2014 Interstitial cells: regulators of smooth muscle function. Physiol Rev 94:859–907.

A review of the structural, functional and molecular features of interstitial cells of Cajal and their importance in smooth muscle function.

Straub RH, Wiest R, Strauch UG et al 2006 The role of the sympathetic nervous system in intestinal inflammation. Gut 55:1640–9.

Suda K 2010 Histopathology of the minor duodenal papilla. Dig Surg 27:137–9.

Teitelbaum EN, Vaziri K, Zettervall S et al 2013 Intraoperative small bowel length measurements and analysis of demographic predictors of increased length. Clin Anat 26:827–32.

Information on small bowel length in living adults, which varies with sex, height and age.

Uppal K, Tubbs RS, Matusz P et al 2011 Meckel's diverticulum: a review. Clin Anat 24:416–22.

Van Kruiningen HJ, West AB, Freda BJ et al 2002 Distribution of Peyer's patches in the distal ileum. Inflamm Bowel Dis 8:180–5.

Walther A, Coots A, Nathan J et al 2013 Physiology of the small intestine after resection and transplant. Curr Opin Gastroenterol 29:153–8.

Winston CB, Lee NA, Jarnagin WR et al 2007 CT angiography for delineation of celiac and superior mesenteric artery variants in patients undergoing hepatobiliary and pancreatic surgery. AJR Am J Roentgenol 188:W13–19.

Yamaguchi S, Kuroyanagi H, Milson JW et al 2002 Venous anatomy of the right colon: precise structure of the major veins and gastrocolic trunk in 58 cadavers. Dis Colon Rectum 45:1337–40.

CHAPTER
65

Large intestine

The large intestine extends from the ileocaecal junction to the anus (**Fig. 65.1**). It begins as the caecum and vermiform appendix, which are usually located in the right iliac fossa. The ascending colon passes superiorly in the right lateral region to the right hypochondriac region, where it bends to the left to form the right colic flexure and become the transverse colon. This loops across the abdomen with an anteroinferior convexity until it reaches the left hypochondriac region, where it curves inferiorly to form the left colic flexure (**Fig. 65.2**). From there, it descends in the left lateral region as the descending colon before continuing as the sigmoid colon in the left iliac region. The sigmoid colon descends into the lesser pelvis and becomes the rectum anterior to the third sacral vertebra. The rectum transitions to the anal canal at the level of the pelvic diaphragm. Embryologically, the large intestine is formed from the distal midgut, all of the hindgut and the anal pit (proctodeum) (Ch. 22 and Figs 22.4, 22.7E). Knowledge of the development of the large intestine not only helps to explain its anatomy, relations (including peritoneal attachments) and neurovascular supply, but is also fundamental to understanding congenital large intestine disorders such as anorectal malformations and malrotation of the gut.

In the adult, the large intestine is approximately 1–1.5 m long *in vivo*, although there is considerable individual variation. It differs from the small intestine in several ways: it has a greater calibre; for much of its course it is more fixed in position; the outer longitudinal muscle layer of the colon is concentrated into three longitudinal bands, taeniae coli; small fatty projections, omental appendices, are scattered over its free surface (although these tend to be absent from the caecum, appendix and rectum); and the colonic wall is puckered into haustra, visible on plain radiographs as incomplete septations arising from the wall of the intestine (**Fig. 65.3**; see Fig. 65.2). Its calibre is greatest near the caecum, gradually diminishes towards the sigmoid colon, and then increases again in the rectum, where the distal third is dilated to form the rectal ampulla. The mean internal diameter of the large intestine is 4.8 cm (Helander and Fändriks 2014).

During development, the large intestine is temporarily suspended by a midline dorsal mesentery. However, after rotation of the gut *in utero*, large portions of it come to lie adherent to the retroperitoneum, while other segments remain suspended by a mesentery within the abdominal cavity, i.e. an intermesenteric position. The mesenteries of the colon consist of two layers of visceral peritoneum enclosing adipose and connective tissues and surrounding vessels, nerves and lymphatics that run forward from retroperitoneal structures. The caecum may be firmly adherent to the retroperitoneum but is frequently suspended by a short mesentery, especially in infants. The ascending colon is usually adherent to the retroperitoneum, while the transverse colon is suspended by a mesocolon and is freely mobile within the upper abdomen. The left and right colic flexures may have a short mesentery. The descending colon is adherent to the retroperitoneum, usually down to the level of the iliac crest, and the sigmoid colon has a mesentery of variable length. The sigmoid mesentery shortens as it approaches the pelvis and practically disappears at the level of the rectosigmoid junction. The proximal third of the rectum is covered by peritoneum on its anterior and lateral aspects, and the middle third by peritoneum on its anterior aspect only; the distal third is below the peritoneum.

The microstructure of the large intestine corresponds to the general pattern of the gut wall, comprising a mucous membrane consisting of epithelium, lamina propria and muscularis mucosae, surrounded by inner circular and outer longitudinal layers of smooth muscle and a serosa (see Figs 65.3, 65.50, 65.51). The mucosa also contains scattered neuroendocrine cells derived from the amine precursor uptake and decarboxylation (APUD) cell lineage; these cells produce amines and/or peptides, which act as hormones or neurotransmitters. Unlike the small intestine, the mucosa of the large intestine lacks villi, and the intestinal glands contain a high proportion of goblet (mucin-secreting) cells. In the appendix, the intestinal glands are sparse and numerous lymphoid follicles are found in the mucosa and submucosa. Although it is not a vital organ, the primary function of the colon is transmission and elimination of intestinal contents, but it also has important absorptive and secretory roles. The large intestine has its own intrinsic (enteric) nerve supply, the activity of which is modulated by extrinsic innervation.

External appearance

The haustra of the colon are frequently absent in the caecum and often relatively sparse in the ascending and proximal transverse colon. They become more pronounced beyond the middle of the transverse colon. The sigmoid colon often has marked haustra. Omental appendices are small, fat-filled pouches of peritoneum that project from the external surface of the colon and are supplied by blood vessels that perforate its wall. There are few, if any, omental appendices on the serosal surface of the caecum, and only a limited number scattered along the ascending colon. They are more common over the distal colon and particularly numerous on the surface of the sigmoid colon, where they can be large in the obese individual. The rectum has no omental appendices.

The three taeniae coli are located in fairly constant positions beneath the serosa of the colon, except in the transverse colon. They are found on the antimesenteric aspect of the colon directly opposite the mesentery (free taenia), posterolaterally (omental taenia) and posteromedially (mesocolic taenia) midway between the free taenia and the mesentery (see Fig. 65.3). In the ascending and descending colon, the omental taeniae are often hidden by the peritoneal reflection on to the colonic wall. In the transverse colon, the taeniae are rotated as a consequence of the dependent position of this segment of colon, so anterior becomes inferior, posteromedial becomes posterior, and posterolateral becomes superior. The width of the taeniae coli remains fairly constant throughout the colon but they broaden out in the distal part of the sigmoid colon and gradually merge to form a complete longitudinal muscle layer around the rectum, which therefore has no external haustra.

Internal appearance

The haustra of the colon represent sites where the mucosa and submucosa of the colonic wall are infolded; these folds partially span the lumen of the colon but never form a complete circumferential ring. The pattern of haustra and appearance of the colonic mucosa help the clinician appreciate the level reached during flexible endoscopic examinations of the colon (Silverstein and Tytgat 1991). In the caecum, the three taeniae coli converge to form a characteristic 'trefoil' pattern on the caecal wall (**Fig. 65.4**). The distal caecum is usually devoid of haustra, although a spiral mucosal pattern is often seen in the region of the orifice of the appendix (**Fig. 65.5**). The ileal orifice can be identified as a thickened fold (**Fig. 65.6**) and can be cannulated endoscopically to examine the terminal ileum. In the distal caecum and ascending colon, the haustra can extend across one-third of the lumen. In the transverse colon, the haustra often confer a triangular appearance to the cross-section of the lumen when it is viewed along its axis at colonoscopy (**Fig. 65.7**). The haustra of the descending and sigmoid colon tend to be thicker and shorter, producing a more circular lumen cross-section (**Figs 65.8–65.9**). The wall of the colon is thinnest in the region of the caecum and ascending colon, where it is at risk of perforation during therapeutic endoscopic procedures. The overall luminal diameter is often smallest in the descending colon. The tortuosity of the sigmoid colon means that shorter lengths of it are visible during endoscopy than elsewhere in the colon. The haustra of the rectum usually form consistent and recognizable transverse rectal folds (spiral valves of Houston) and the submucosal vessels tend to be more pronounced than in the colon (**Fig. 65.10**). Most patients are found to have two or three folds and these are useful landmarks for planning rectal surgery (Abramson 1978). Distinct veins are usually visible during endoscopy, and are most marked above the anorectal junction.

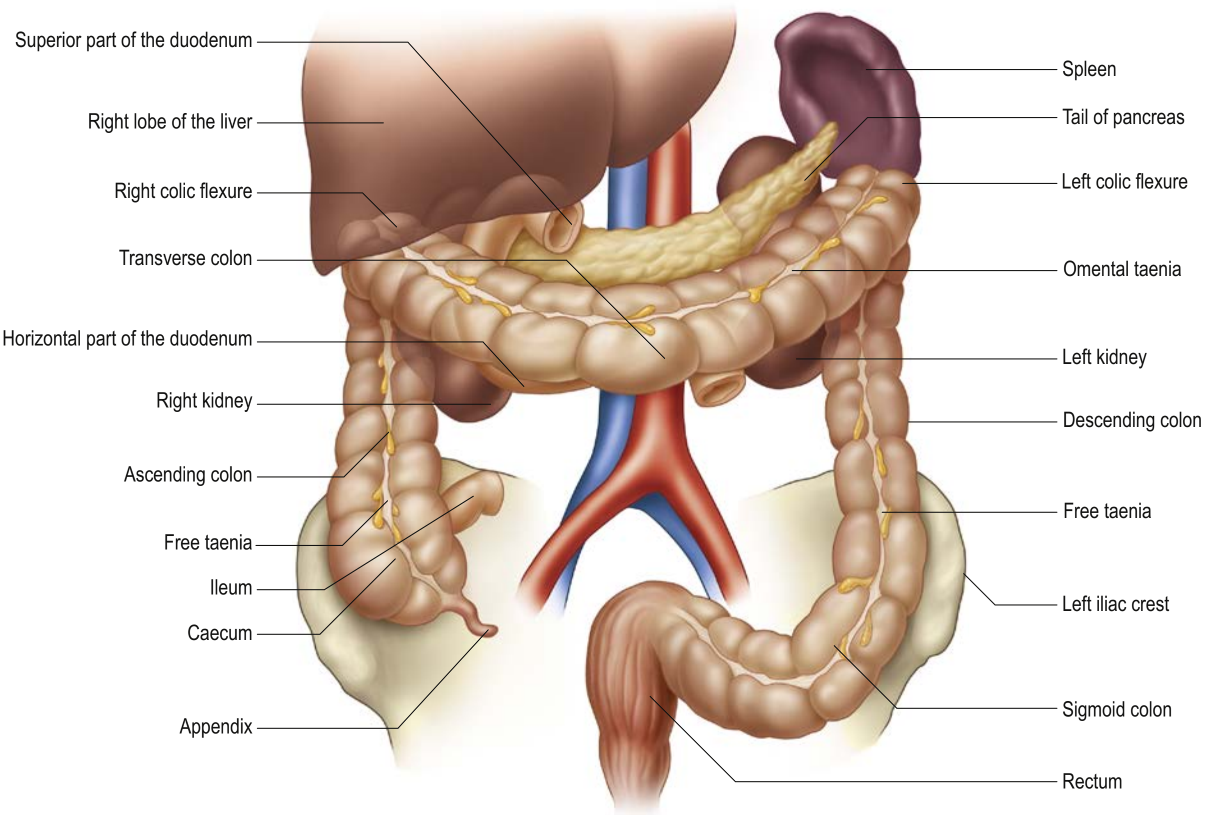
Superior part of the duodenum
Right lobe of the liver
Right colic flexure
Transverse colon
Horizontal part of the duodenum
Right kidney
Ascending colon
Free taenia
Ileum
Caecum
Appendix
Spleen
Tail of pancreas
Left colic flexure
Omental taenia
Left kidney
Descending colon
Free taenia
Left iliac crest
Sigmoid colon
Rectum

Fig. 65.1 An overview of the colon and its relations.

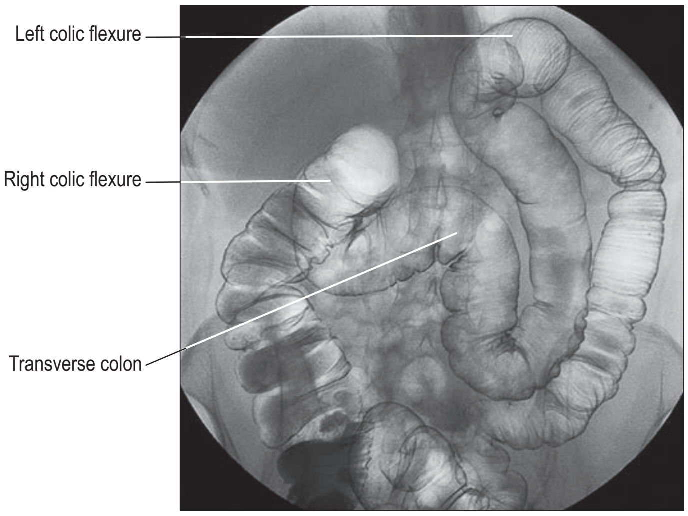
Left colic flexure
Right colic flexure
Transverse colon

Fig. 65.2 The appearance of the colon on double contrast barium enema examination, demonstrating the transverse colon and left and right colic flexures.

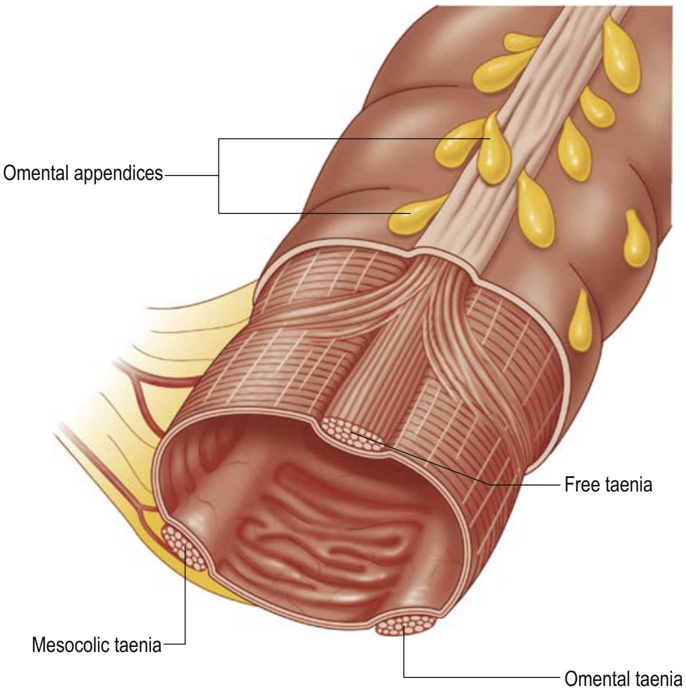
Omental appendices
Free taenia
Mesocolic taenia
Omental taenia

Fig. 65.3 Layers of the colonic wall.

Radiological appearances

Cross-sectional imaging of the colon can be performed with computed tomography (CT) and magnetic resonance imaging (MRI). On axial images, the colon may be filled with particulate faeces and flatus (Fig. 65.11). The wall in normal individuals is thin. The caecum and ascending colon often contain faecal residue. The transverse colon may contain faeces or flatus and lies in a variable position, suspended by its mesentery. The descending colon lies in the retroperitoneum on the left and seldom contains much faecal residue. The volume data sets produced by multislice CT can generate virtual colonoscopic mucosal images of the distended and cleaned colon, and surface-rendered images of the internal surface of the colon (Fenlon 2002).

Vascular supply and lymphatic drainage

Arteries

The arterial supply of the large intestine is derived from both the superior and the inferior mesenteric arteries (Fig. 65.12) (Jackson 1999). The caecum, appendix, ascending colon and proximal two-thirds of the transverse colon (derived from the midgut) are supplied from ileocolic, right colic and middle colic arteries, branches of the superior mesenteric

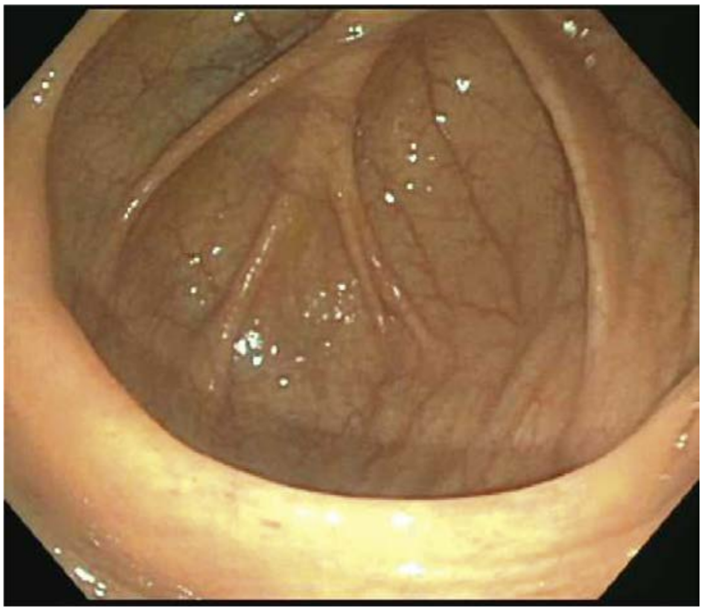

Fig. 65.4 The endoscopic appearance of the caecum. The characteristic trefoil appearance of the confluence of the three taeniae is usually obvious. The ileocaecal junction can be seen in the lower half proximal to the confluence. (Courtesy Dr Jasneet Singh Bhullar, University of Pittsburgh Medical Center, Williamsport, PA.)

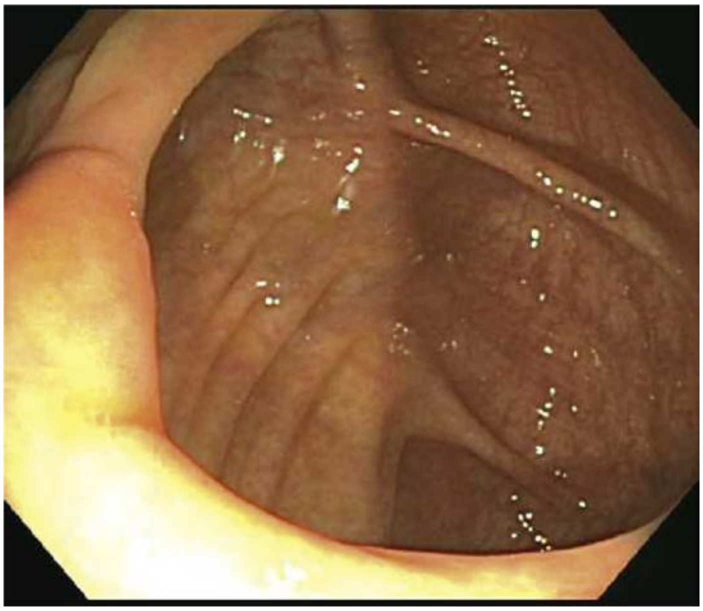

Fig. 65.6 The endoscopic appearance of the ascending colon showing the ileocaecal junction. (Courtesy Dr Kunal Kochar, Advocate Lutheran General Hospital, Park Ridge, IL.)

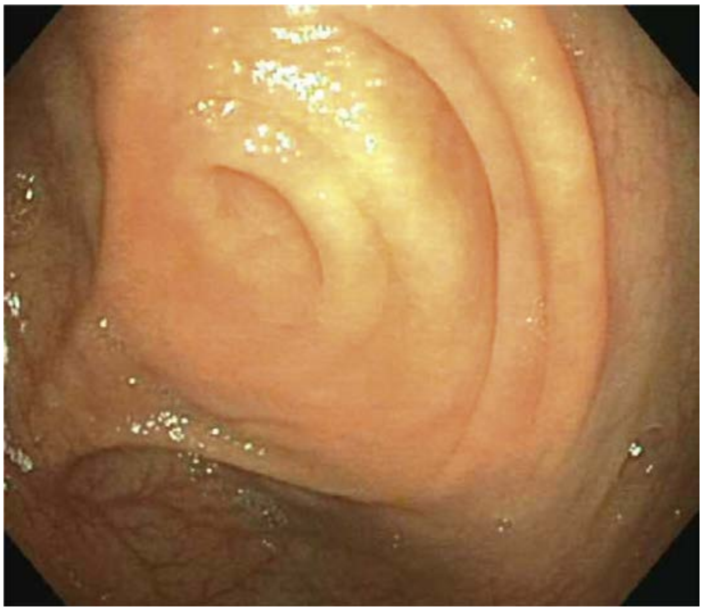

Fig. 65.5 The endoscopic appearance of the orifice of the appendix, seen as a slit-like depression near the centre of this view of the distal caecum. The orifice may vary from a small depression to an obvious luminal structure. (Courtesy Dr Jasneet Singh Bhullar, University of Pittsburgh Medical Center, Williamsport, PA.)

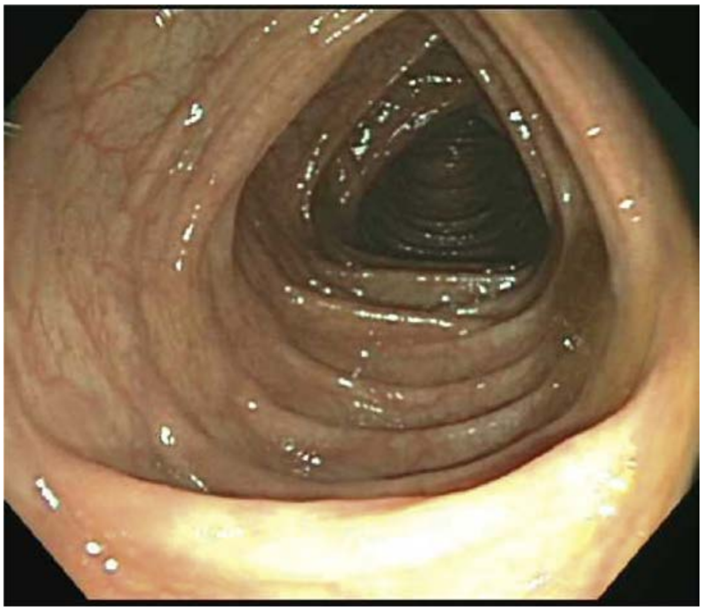

Fig. 65.7 The endoscopic appearance of the transverse colon: note the characteristic triangular appearance of the haustra when viewed collectively (see also Fig. 65.11C). (Courtesy Dr Jasneet Singh Bhullar, University of Pittsburgh Medical Center, Williamsport, PA.)

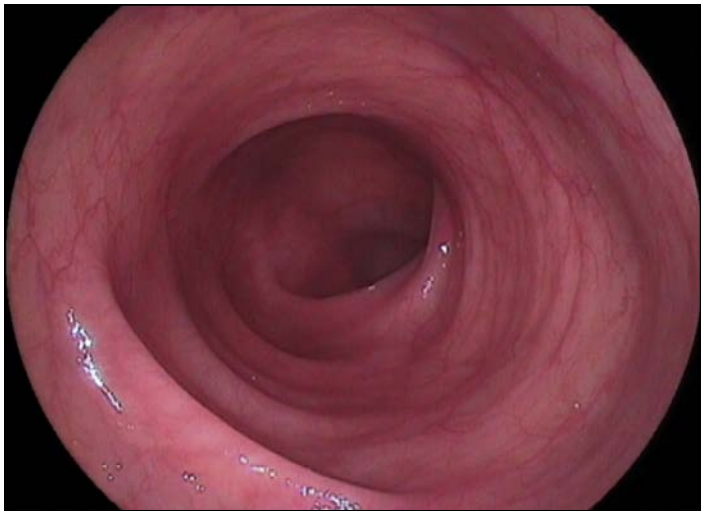

Fig. 65.8 The endoscopic appearance of the descending colon: its lumen tends to look rather more featureless than the more proximal colon.

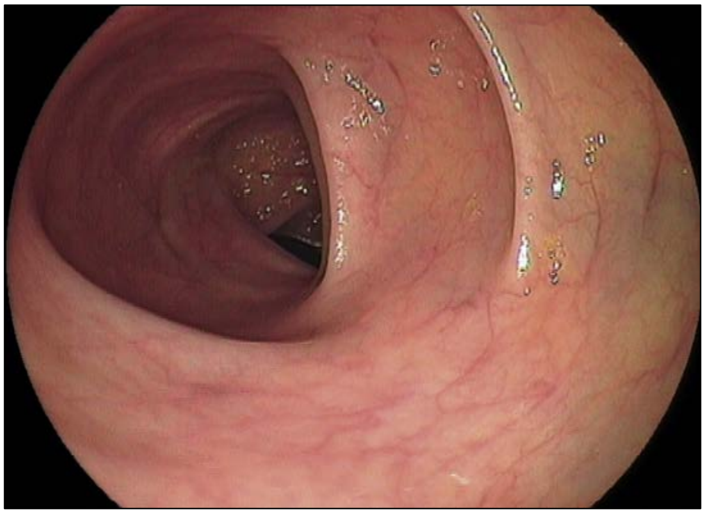

Fig. 65.9 The endoscopic appearance of the sigmoid colon; note the characteristic multiple large mucosal folds.

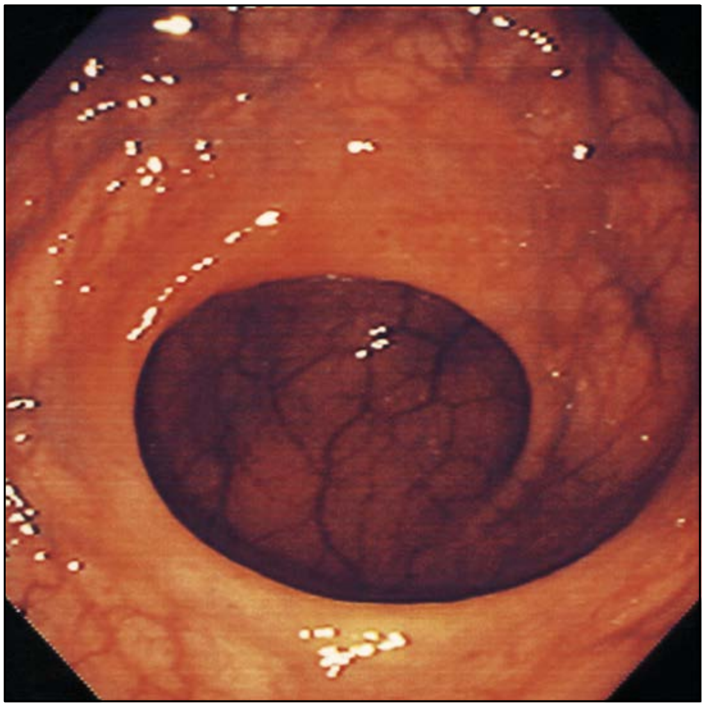

Fig. 65.10 The endoscopic appearance of the rectum: note the large transverse folds, with little else in the way of mucosal folds, which characterize the rectum. Prominent submucosal vessels are often seen, particularly in the distal third.

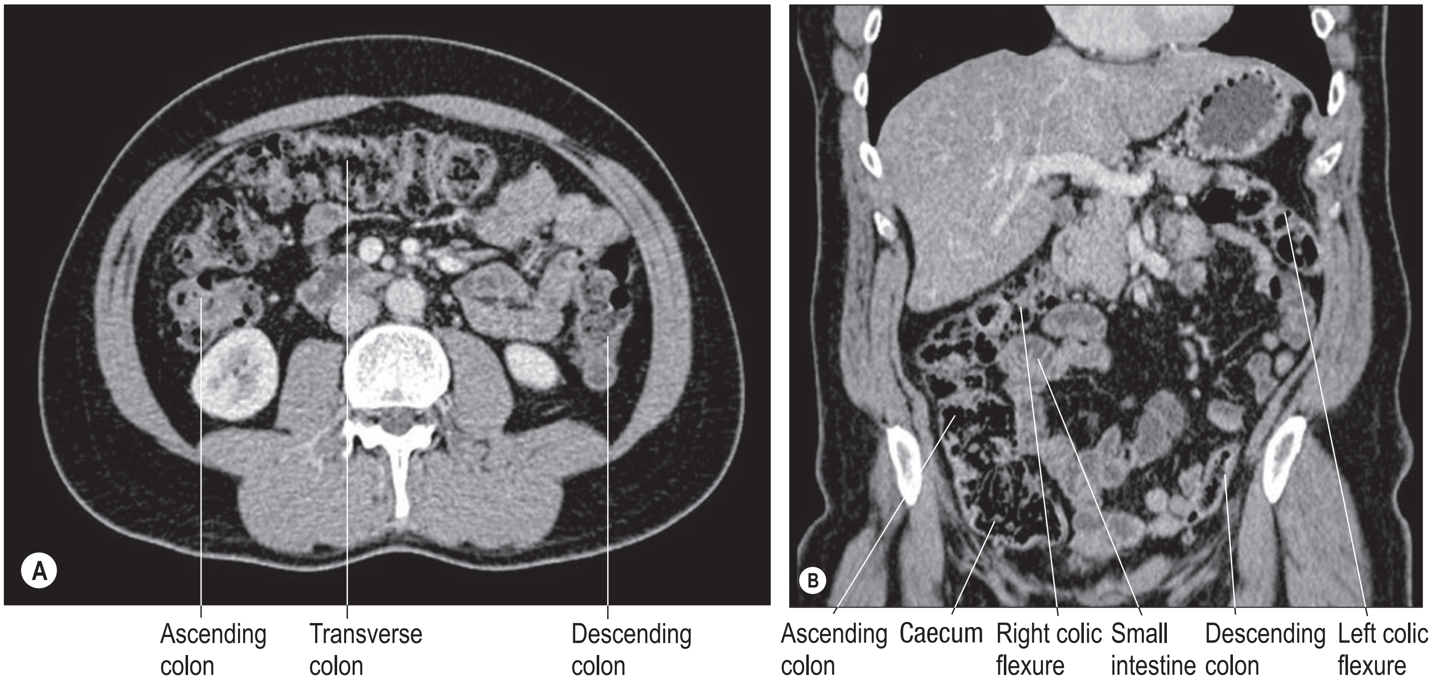
A
B
Ascending colon
Transverse colon
Descending colon
Ascending colon
Caecum
Right colic flexure
Small intestine
Descending colon
Left colic flexure

Fig. 65.11 The appearance of the colon on multislice computed tomographic examination. **A**, Axial CT. **B**, Coronal reformat showing normal calibre and distribution of the abdominal colon (ascending, transverse and descending). (A, B, Courtesy of Dr Louise Moore, Chelsea and Westminster Hospital.) (C,D *continued online*)

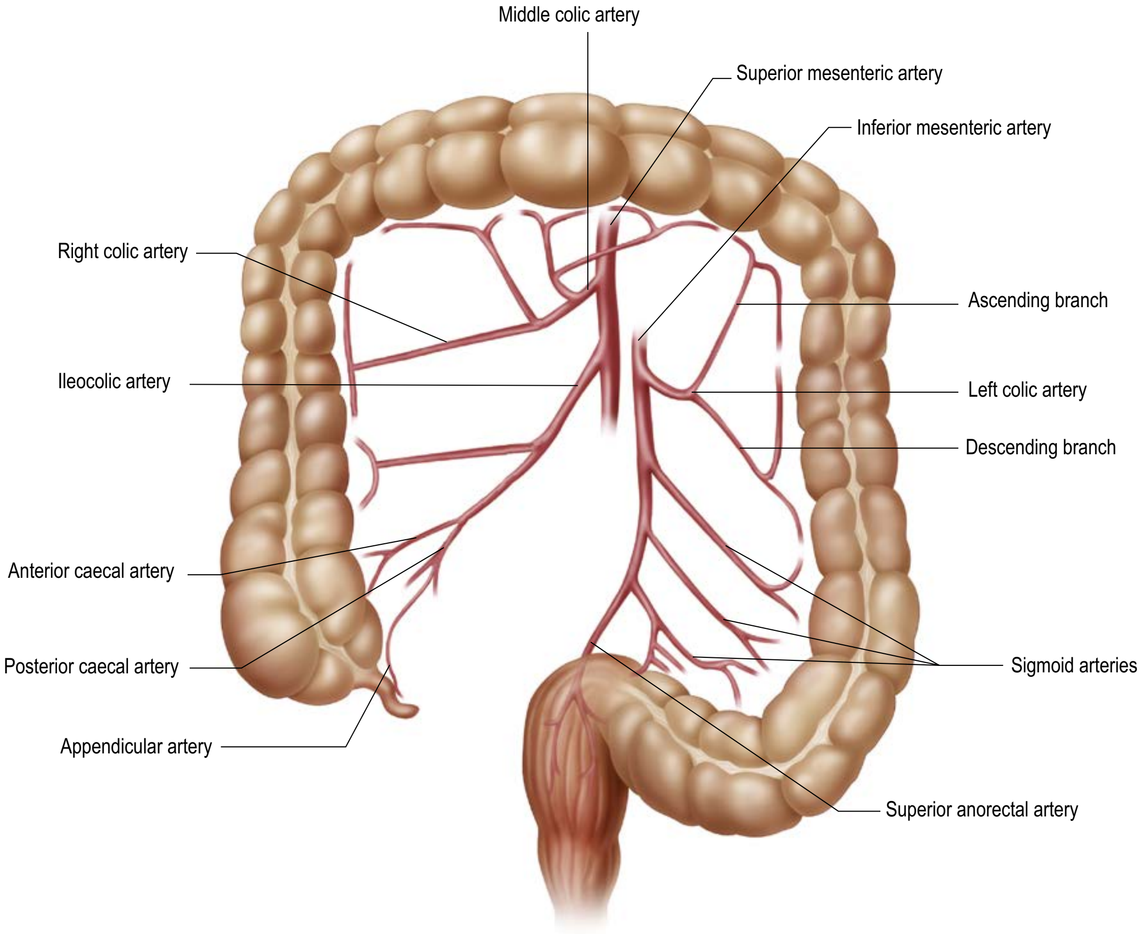
Middle colic artery
Superior mesenteric artery
Inferior mesenteric artery
Right colic artery
Ascending branch
Ileocolic artery
Left colic artery
Descending branch
Anterior caecal artery
Posterior caecal artery
Sigmoid arteries
Appendicular artery
Superior anorectal artery

Fig. 65.12 The main branches of the superior and inferior mesenteric arteries.

artery. The distal third of the transverse colon, descending and sigmoid colon, rectum and proximal anal canal (hindgut derivatives) are supplied predominantly from the inferior mesenteric artery via the left colic, sigmoid and superior rectal arteries, with a small contribution from branches of the internal iliac artery (the middle and inferior anorectal arteries).

The arteries of the midgut- and hindgut-derived intestine contribute to an anastomotic vessel, the marginal artery (of Drummond), which runs in the mesentery along the inner margin of the colon and gives off short terminal branches to the wall of the intestine. These divide into vasa brevia, which pass directly through the muscular layer of the colonic wall, and vasa longa, which travel through the subserosa for a short distance before running through the circular muscle, giving off branches to the omental appendices (Fig. 65.13). The marginal artery is formed by the main branches and arcades arising from the ileocolic, right colic, middle colic and left colic arteries. It is most apparent in the ascending, transverse and descending colons (Fig. 65.14) but poorly developed in the sigmoid

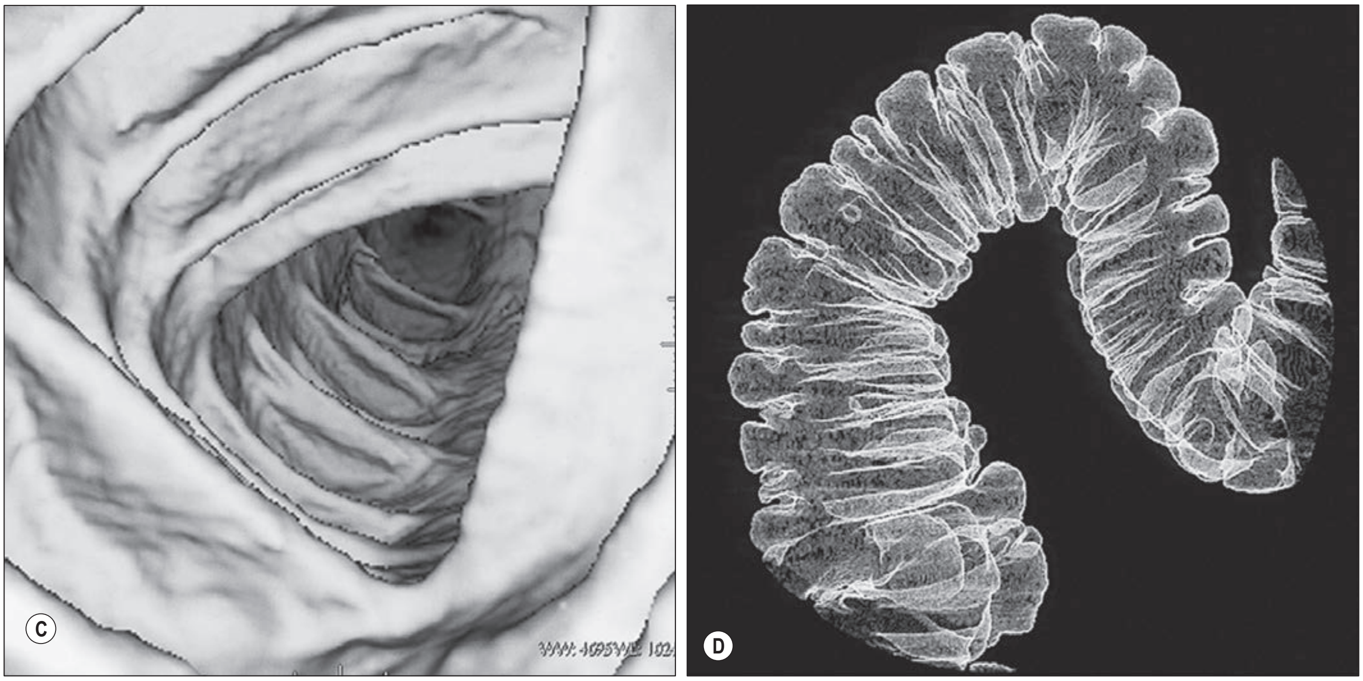

Fig. 65.11 **C**, Volume rendering of the colonic wall using the axial data set to produce virtual colonoscopic views, showing the triangular lumen of the transverse colon. **D**, Volume rendering of the air-filled colon using the axial data set to give an image similar to a double contrast barium enema, demonstrating haustra. (C, D, Courtesy of GE Worldwide Medical Systems.)

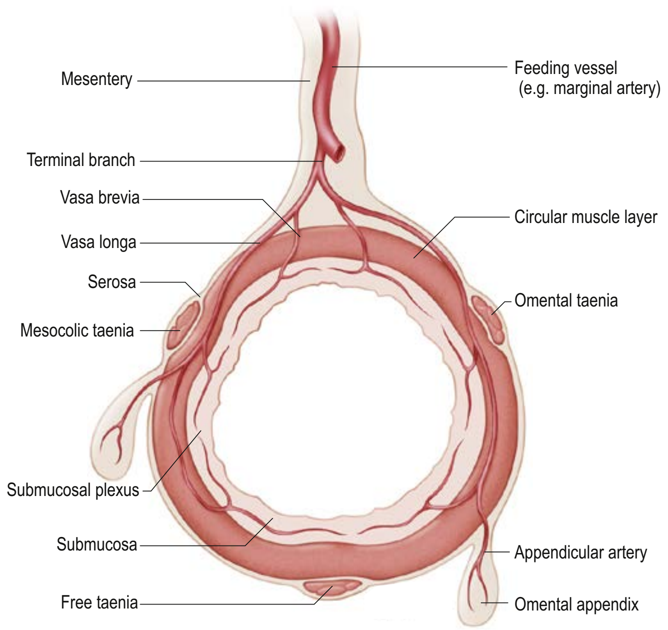

Fig. 65.13 The typical pericolic arrangement of the arterial vasculature.

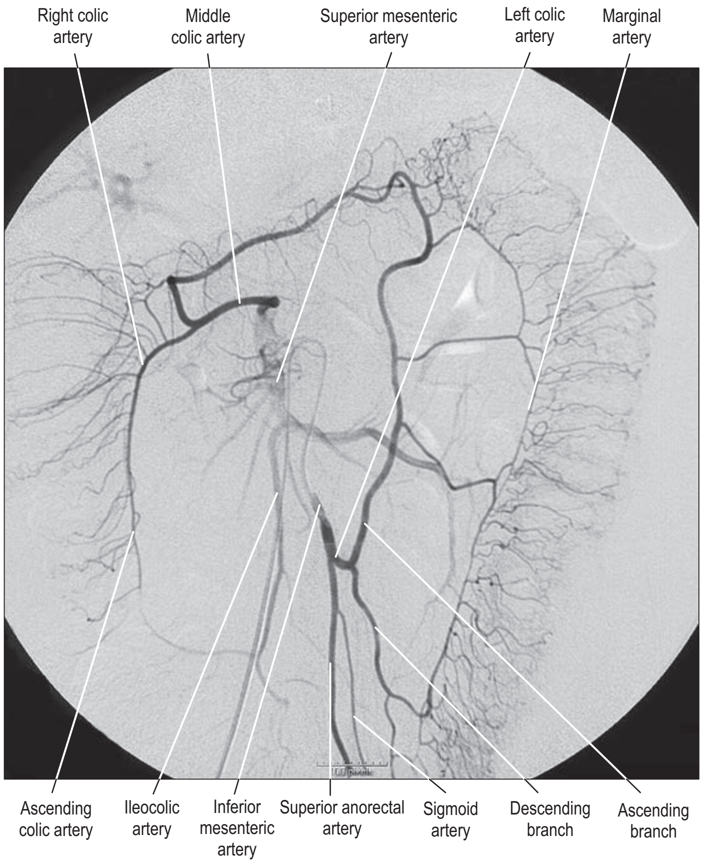

Fig. 65.14 The marginal artery running parallel to the colon and providing an anastomosis between the branches of the superior mesenteric artery supplying the right side of the colon and the branches of the inferior mesenteric artery supplying the left side of the colon (digital subtraction arteriogram). (Courtesy of Dr J Jackson, Hammersmith Hospital, London.)

colon. The marginal artery in the region of the left colic flexure can be absent or too narrow to be of functional significance. Nevertheless, it can dilate considerably when one of the main visceral arteries is compromised since it then provides a collateral arterial supply to the colon. The most susceptible part of the chain of anastomosing vessels is at the junction of midgut- and hindgut-derived intestine in the distal transverse colon near the left colic flexure. However, the arterial supply to this region may be augmented by an inner arterial arc (of Riolan), which runs a meandering course in the colonic mesentery between the main trunk of the middle colic artery and the ascending branch of the left colic artery (Fisher and Fry 1987, Gourley and Gering 2005). When present, this vessel is usually only prominent when there is occlusion of the superior or inferior mesenteric artery.

Colonic vascular occlusion

The marginal artery of the colon can become massively dilated when there is chronic stenosis or occlusion of the superior or inferior mesenteric artery. The latter may occur, for example, in association with an abdominal aortic aneurysm, when the descending colon remains viable because the marginal artery continues to receive an adequate blood supply from left branches of the middle colic artery and the sigmoid colon gains its blood supply from the middle anorectal and inferior anorectal arteries. When colonic ischaemia does occur, it is usually maximal in the region of the left colic flexure and proximal descending colon because this segment is farthest from the collateral arterial supplies. Occlusion of the common iliac arteries can also result in dilation of the marginal and inferior mesenteric arteries, which become an important collateral supply to the lower limbs via dilated middle anorectal arteries commonly arising from either the internal pudendal or inferior gluteal artery (Bilhim et al 2013).

Veins

The venous drainage of the large intestine is primarily into the hepatic portal vein via the superior mesenteric and inferior mesenteric veins, although some drainage from the rectum occurs via middle anorectal veins into the internal iliac veins, and inferior anorectal veins into the internal pudendal veins. Those parts of the colon derived from the midgut (caecum, appendix, ascending colon and proximal two-thirds of the transverse colon) drain into colic branches of the superior mesenteric vein, while hindgut derivatives (distal third of the transverse colon, descending and sigmoid colon, rectum and proximal anal canal) drain into the inferior mesenteric vein (**Fig. 65.15**).

Lymphatic drainage

Lymph drainage from the large intestine follows the course of the arteries. Thus, lymphatic vessels of the caecum and the ascending and proximal transverse colon drain ultimately into lymph nodes related to the superior mesenteric artery, while those of the distal transverse colon, descending colon, sigmoid colon and rectum drain into nodes following the course of the inferior mesenteric artery (**Fig. 65.16**). In cases where the distal transverse colon or left colic flexure is predominantly supplied by vessels from the middle colic artery, most of the lymphatic drainage of this area may be to superior mesenteric nodes.

Colic nodes

Lymph nodes related to the colon form four groups: epicolic, paracolic, intermediate colic and preterminal colic. Epicolic nodes are minute whitish nodules on the serosal surface of the colon, sometimes within the omental appendices. Paracolic nodes lie along the medial borders of the ascending and descending colon and along the mesenteric borders of the transverse and sigmoid colon. Intermediate colic nodes lie along the named colic vessels (the ileocolic, right colic, middle colic, left colic, sigmoid and superior rectal arteries). Preterminal colic nodes lie along the main trunks of the superior and inferior mesenteric arteries and drain into pre-aortic nodes at the origin of these vessels.

Ascending mesocolic nodes are significantly larger than sigmoid mesocolic ones; this is relevant to lymph node retrieval and examination after resection for colonic cancer (Ahmadi et al 2015).

Radical lymphadenectomy during resection of colorectal cancer requires removal of the highest possible lymph nodes draining the region of colon in which the tumour is located. In cases of cancer of the rectum or sigmoid colon, this usually involves excision of the preterminal colic nodes along the inferior mesenteric artery with ligation of the artery at its root or just below the origin of the left colic artery. At least 12 lymph nodes must be excised in an oncologically resected partial colectomy for cancer.

MIDGUT-DERIVED PART OF THE LARGE INTESTINE

Caecum

This blind pouch, approximately 6 cm long, lies below the level of the ileocaecal junction (**Fig. 65.17**), anterior to the right iliac and psoas fasciae, with the lateral femoral cutaneous nerve interposed. The caecum

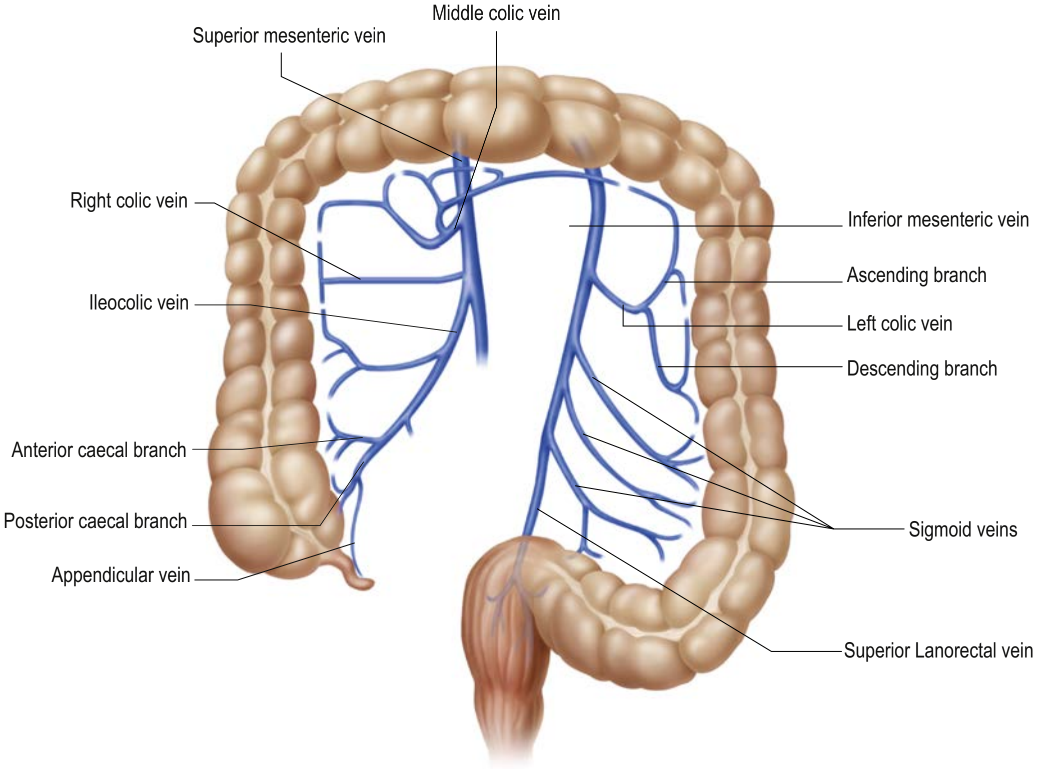
Middle colic vein
Superior mesenteric vein
Right colic vein
Ileocolic vein
Anterior caecal branch
Posterior caecal branch
Appendicular vein
Inferior mesenteric vein
Ascending branch
Left colic vein
Descending branch
Sigmoid veins
Superior Lanorectal vein

Fig. 65.15 The main branches of the superior and inferior mesenteric veins.

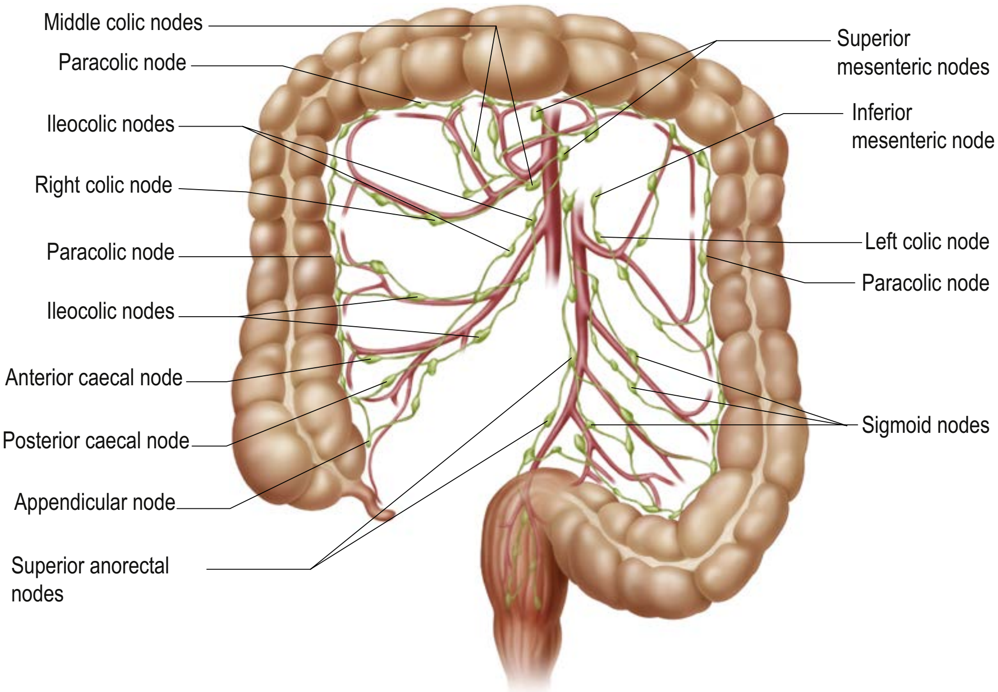
Middle colic nodes
Paracolic node
Ileocolic nodes
Right colic node
Paracolic node
Ileocolic nodes
Anterior caecal node
Posterior caecal node
Appendicular node
Superior anorectal nodes
Superior mesenteric nodes
Inferior mesenteric node
Left colic node
Paracolic node
Sigmoid nodes

Fig. 65.16 The lymph vessels and nodes draining the large intestine.

usually lies adjacent to the anterior abdominal wall unless the greater omentum or loops of small intestine are interposed. It is often completely covered by peritoneum, which is reflected posteriorly and inferiorly to the floor of the right iliac fossa. The three taeniae coli lie anteriorly, posteromedially and posterolaterally and converge on the base of the appendix. During childhood, the lateral wall of the caecum outgrows the medial wall such that the orifice of the appendix, which is originally at the distal caecum, usually comes to lie slightly posteromedially.

Fluid and electrolyte reabsorption by the large intestine begins in the caecum but occurs mostly in the ascending and transverse colon. The distensible 'sac-like' morphology of the caecum allows large volumes of semi-liquid chyme from the small intestine to be stored. Its relatively large diameter makes it liable to distension with increased intracolonic pressure and it is the region of the large intestine at greatest risk of perforation secondary to colonic distension (from obstruction or other pathology).

Ileocaecal junction

The terminal ileum joins the posteromedial aspect of the large intestine at the junction of the caecum and colon, where it projects into the lumen of the large intestine as the ileal papilla (Fig. 65.18A). This projection consists of two lips and its precise shape and form varies from slit-like to an oval mucosal rosette, depending, in part, on the state of contraction or distension of the caecum. The ileocolic lip is approximately horizontal and is at the junction between the ileum and colon; the ileocaecal lip is longer and more concave, and is at the junction between the ileum and caecum. At their bases, the lips fuse and continue as the frenulum of the ileal orifice.

The ileal papilla is formed by the mucosa, submucosa and external muscle layers of the ileum, continuing through the wall of the large intestine and combining with corresponding layers from the caecum inferiorly and the colon superiorly (Fig. 65.18B). Its internal surface is lined by small intestinal mucosa and its large intestine surface is covered by large intestine mucosa; these epithelial surfaces meet near the tip of the ileal papilla. A localized thickening of the muscle at the base of the ileal papilla is consistent with physiological data that suggest the presence of an intrinsic anatomical sphincter (Pollard et al 2012). In addition, the bilabial configuration of the ileal papilla could confer a valvular function. The ileocaecal junction performs several roles: it provides partial mechanical and functional separation of the luminal environments of the small and large intestine, which differ in composition, pH and bacterial content; it impedes reflux from the colon; and it helps to regulate antegrade small intestine transit.

Caecal volvulus

If the caecum and ascending colon are attached to the posterior abdominal wall by a narrow mesentery, the ileocaecal region is at risk of twisting about its mesenteric pedicle, creating a caecal volvulus. In such cases, the caecum becomes markedly distended because of the strangulating closed loop intestinal obstruction that develops. Non-anatomical factors such as caecal distension can also contribute to the pathogenesis of caecal volvulus (Madiba and Thomson 2002, Tannouri et al 2017).

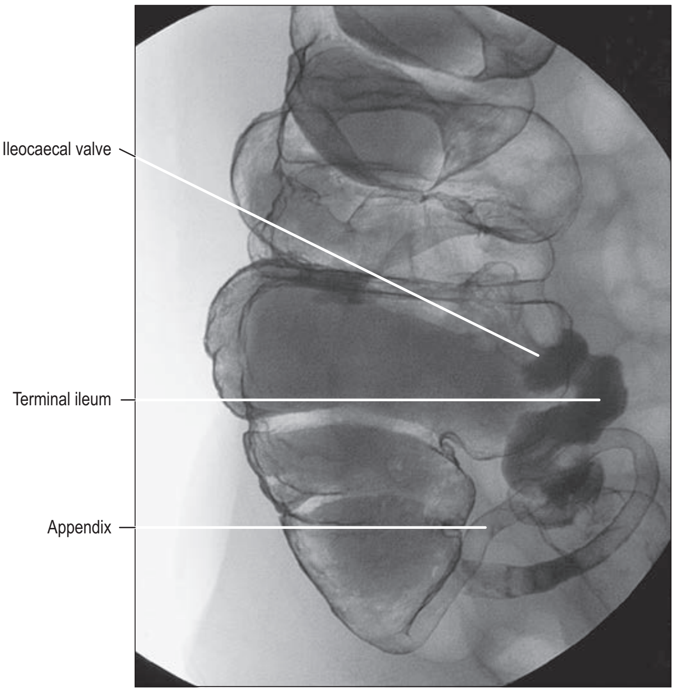

Fig. 65.17 The caecum and ileocaecal junction, double contrast barium enema appearance.

Appendix

The appendix is a narrow, blind-ending tube, usually 6–10 cm long in the adult. It joins the posteromedial wall of the caecum below the ileocaecal junction. The appendix grows in length and diameter during early childhood, reaching almost mature dimensions by about three years of age (Searle et al 2013). It usually lies in the right iliac fossa but its distal end may occupy one of several positions (Fig. 65.19) (Buschard and Kjaeldgaard 1973). In clinical practice, the tip is most commonly retrocaecal or retrocolic (behind the caecum or proximal ascending colon, respectively, anterior to iliacus and psoas major), or pelvic (when the appendix descends over the linea terminalis, close to the right uterine tube and ovary in females). Other positions include subcaecal, and pre- or post-ileal (anterior or posterior to the terminal ileum, respectively), especially when a long meso-appendix allows greater mobility. The surface marking for the base of the appendix has traditionally been described by McBurney's point (two-thirds of the way along a line between the umbilicus and right anterior superior iliac spine) but its position is variable and is affected by posture, caecal distension and other factors (Hale et al 2010).

The appendix has a continuous outer layer of longitudinal muscle formed by the coalescence of the three taeniae coli. Its lumen is irregularly narrowed by submucosal lymphoid tissue. The meso-appendix is a triangular mesentery running between the terminal ileum and appendix; it contains a variable amount of fat and frequently ends short of the distal end of the appendix. A fold of peritoneum runs between the terminal ileum and the anterior layer of the meso-appendix (the 'bloodless fold of Treves'), and another fold of peritoneum containing the anterior caecal vessels extends from the terminal ileal mesentery to the anterior wall of the caecum (and contains the anterior caecal artery). The luminal orifice is sometimes partially covered by a mucosal fold forming an asymmetric 'valve' (see Fig. 65.5). The lumen can be widely patent in early childhood but is often partially or wholly obliterated in the elderly. Agenesis and duplication of the appendix are exceptionally rare (Barlow et al 2013, Tubbs et al 2016).

Microstructure

The layers of the wall of the appendix are similar to those of the large intestine in general but with some notable differences. The serosa forms a complete covering, except along the mesenteric attachment. The outer longitudinal muscle is a complete layer of uniform thickness, except in a few small areas where the muscularis externa is deficient, allowing the serosa to come into contact with the submucosa.

Microscopic examination of the appendix reveals the epithelial layer, prominent lymphoid tissue of the mucosa, and the underlying submucosa, muscularis propria, serosa and subserosal connective tissue. The conspicuous (and often confluent) lymphoid aggregates are a characteristic feature of the appendix that can involve both the mucosa and the submucosa (Fig. 65.20). The mucosa is covered by columnar epithelium, which contains M cells where it overlies the mucosal lymphoid tissue. Intestinal glands are similar to those of the colon but are fewer and less densely packed. They penetrate deep into the lamina propria. The submucosal lymphoid tissue frequently exhibits germinal centres within its follicles, indicative of B cell activation. Lymphoid follicles are absent at birth but accumulate during the first 10 years of life to become

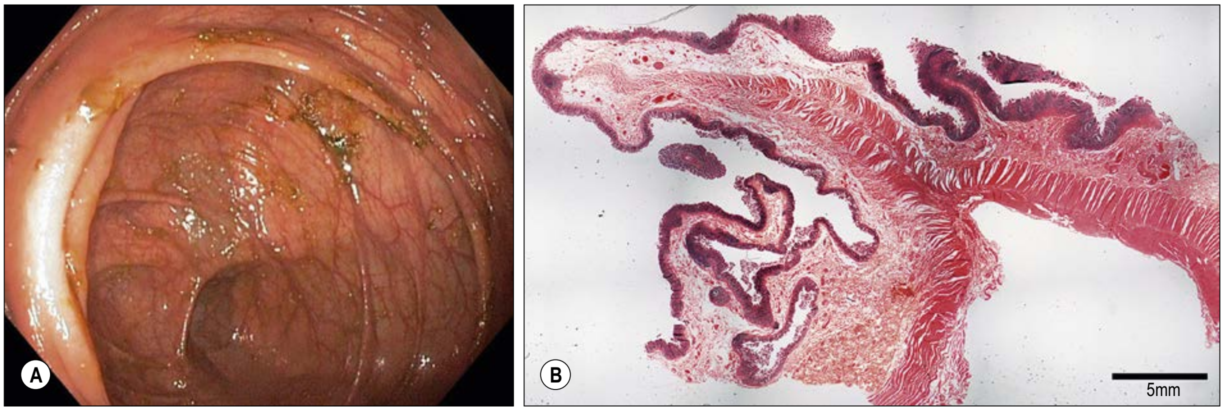

Fig. 65.18 **A**, The endoscopic appearance of the ileal papilla, which appears as a bilabial structure on the left of this view of the distal caecum. **B**, A photomicrograph showing a longitudinal section through the ileocaecal lip of the ileal papilla (haematoxylin and eosin); the ileal mucosa is visible superiorly. (A, Courtesy of Dr Michael Schultz. B, Courtesy of Drs Matthew Pollard and Mark Stringer.)

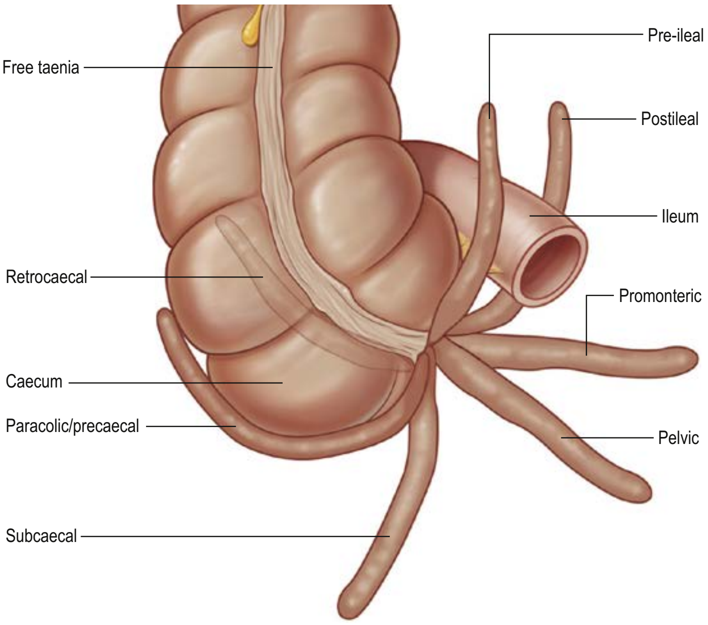

Fig. 65.19 The major positions of the appendix encountered at surgery or post mortem.

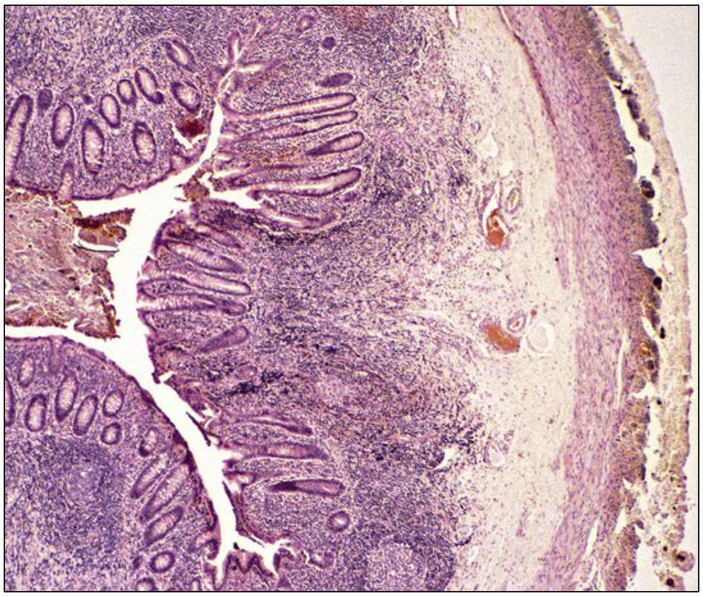

Fig. 65.20 A low-power micrograph of the appendix in transverse section, showing part of its circumference and a faecal pellet lodged in its lumen. Lymphoid tissue (basophilic staining) occupies much of the mucosa between crypts, and part of the submucosa. The muscularis externa and outermost serosal layer are seen at the right of the field.

prominent. In adults, the lymphoid follicles gradually atrophy; in the elderly, the lumen of the appendix can be partially obliterated by fibrous tissue (Barlow et al 2013).

Acute appendicitis

Acute appendicitis can develop if the lumen is obstructed by inspissated material, a faecolith (appendicolith) or lymphoid swelling. This can lead to suppuration, infarction and necrosis. Appendicoliths are more common in children than adults but their prevalence is variable, reflecting differences among populations, definitions and methods of detection. In one radiographic study of normal appendices removed incidentally at surgery or at autopsy, calcified faecoliths were identified in 2.7% (Felson 1949). The increased size of the appendicular orifice in early childhood and the decreased size of the lumen in the elderly could explain why acute appendicitis is less common in these age groups. Low suspicion can lead to delayed diagnosis in the elderly resulting in higher morbidity and mortality (Bhullar et al 2014). Although the appendix is well supplied by arterial anastomoses at its base, the appendicular artery is an end artery; its close proximity to the wall of the appendix makes it susceptible to thrombosis during acute appendicitis, which explains the high frequency of gangrenous perforation seen in the disease.

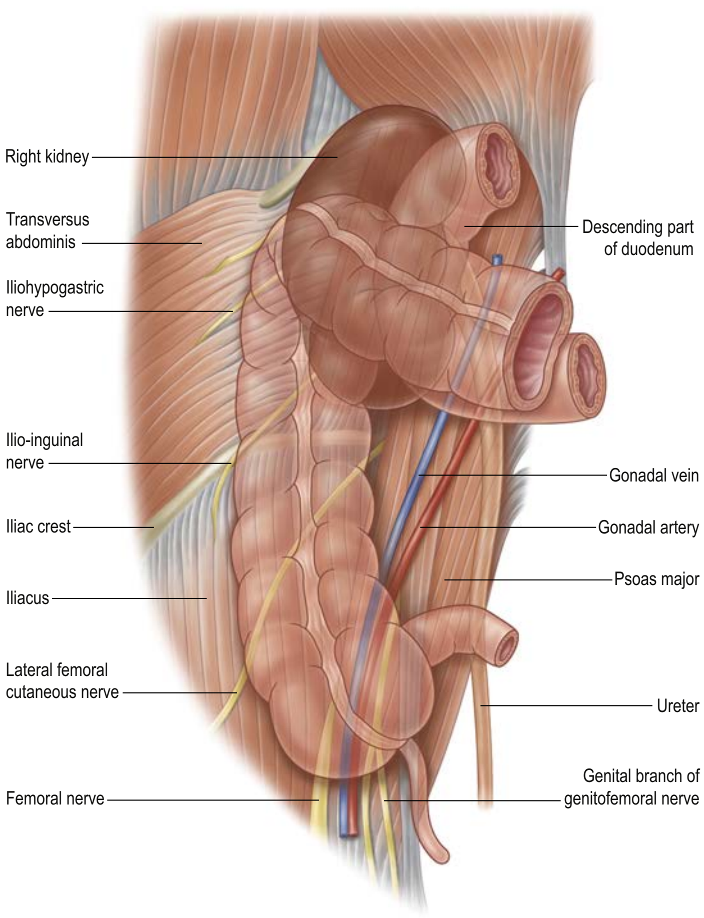

Fig. 65.21 Posterior relations of the ascending colon.

Visceral afferent fibres within adjacent nerves are responsible for the initial symptoms of acute appendicitis (colicky pain with or without emesis) that are caused by distension and inflammation of the appendix. Abdominal pain from appendicitis is poorly localized initially and referred to the umbilical region of the abdomen, consistent with the midgut derivation of the appendix. It is not until parietal peritoneum adjacent to the appendix becomes involved in the inflammatory process that somatic nociceptors are stimulated, resulting in localization of pain to the right iliac fossa. Removal of the appendix is not in itself associated with any discernible long-term sequelae but this does not mean it is an entirely vestigial organ. There is some evidence that it acts as a reservoir for normal gut flora, enabling the large intestine flora to recover more rapidly after severe gastroenteritis (Randal Bollinger et al 2007).

Ascending colon

The ascending colon is 15–20 cm long and passes upwards from the ileocaecal junction to the right colic flexure, separated posteriorly by loose connective tissue from the iliac fascia, iliolumbar ligament, quadratus lumborum, transversus abdominis and the renal fascia anterior and inferolateral to the right kidney. The lateral femoral cutaneous nerve, usually the fourth lumbar artery, and sometimes the ilio-inguinal and iliohypogastric nerves lie posteriorly as they cross quadratus lumborum (Fig. 65.21). Both the lateral and anterior surfaces of the ascending colon are covered by peritoneum which is composed of two layers of mesothelium containing fat embedded within a connective tissue lattice, vessels and nerves; it is attached to the retroperitoneum via a layer of connective tissue (Coffey 2013, Culligan et al 2014) known as Toldt's fascia, which forms the plane of dissection when a right hemicolectomy is performed.

Right colic flexure

The right colic flexure, forming the junction between the ascending and transverse colon, is variable in position and has a less acute angle than the left colic flexure. It overlies the anterior surface of the inferior pole

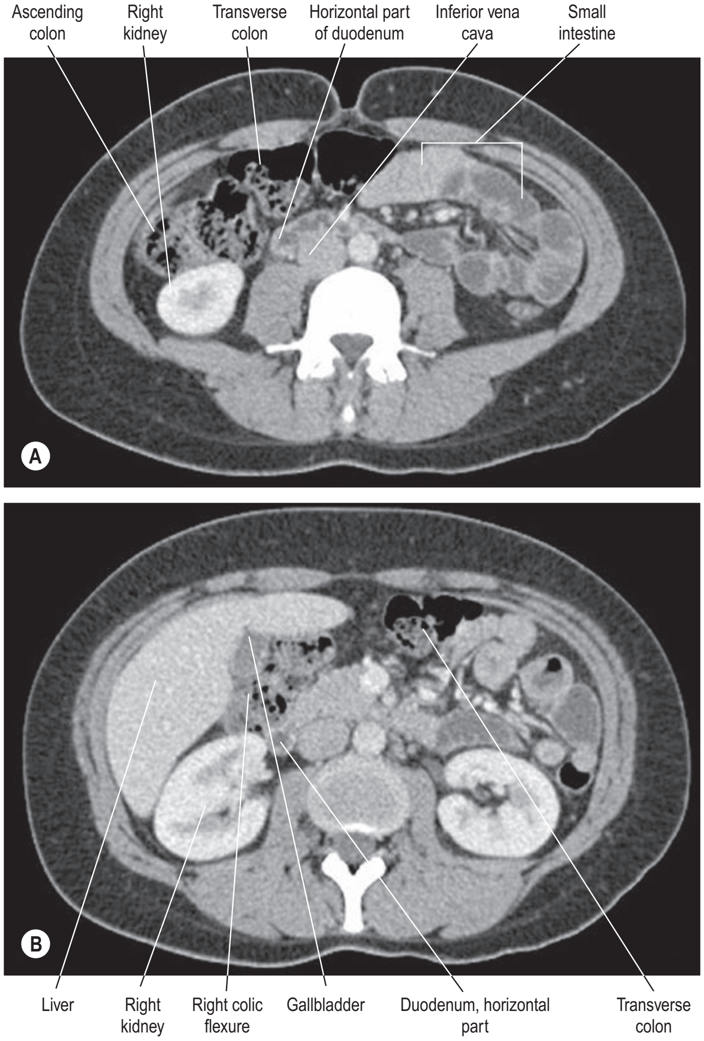

Fig. 65.22 Axial CT of the ascending colon obtained (**A**) at the level of the mid ascending colon and (**B**) at the level of the right colic flexure, showing the relationship of the ascending colon and right colic flexure to the right lobe of the liver, the right kidney, the descending part of the duodenum and the gallbladder. (Courtesy of Dr Louise Moore, Chelsea and Westminster Hospital, London.)

of the right kidney, abutting the inferior surface of the right lobe of the liver above (see Fig. 65.21; **Fig. 65.22B**), the descending part of the duodenum medially, and the fundus of the gallbladder anteromedially. The posterior aspect of the right colic flexure is not covered by peritoneum and is in direct contact with renal fascia. The greater omentum often extends from its attachment to the transverse colon on to the right colic flexure.

Transverse colon

The transverse colon is highly variable in both length (approximately 50 cm on average) and the extent to which it hangs down anterior to the small intestine between sites of attachment at the right and left colic flexures. The greater curvature of the stomach and the gastrocolic ligament, which fuses with the transverse colon anteriorly and continues inferiorly as the greater omentum, are superior. The transverse colon is suspended by the transverse mesocolon, which is attached from the inferior pole of the right kidney, across the descending part of the duodenum and pancreas, to the superior pole of the left kidney. The left colic flexure lies at a more superior level than the right colic flexure, often abutting the spleen under the lower ribs. Because of the disposition of the transverse colon and the more posteriorly sited flexures, the free taenia of the ascending and descending colon is positioned inferiorly. The transverse mesocolon affords considerable mobility to the transverse colon. Occasionally, the colon is interposed between the liver and the diaphragm, when it can be mistaken for free intraperitoneal flatus on imaging; when this is associated with gastrointestinal symptoms it is referred to as Chilaiditi's syndrome (Murphy et al 2000).

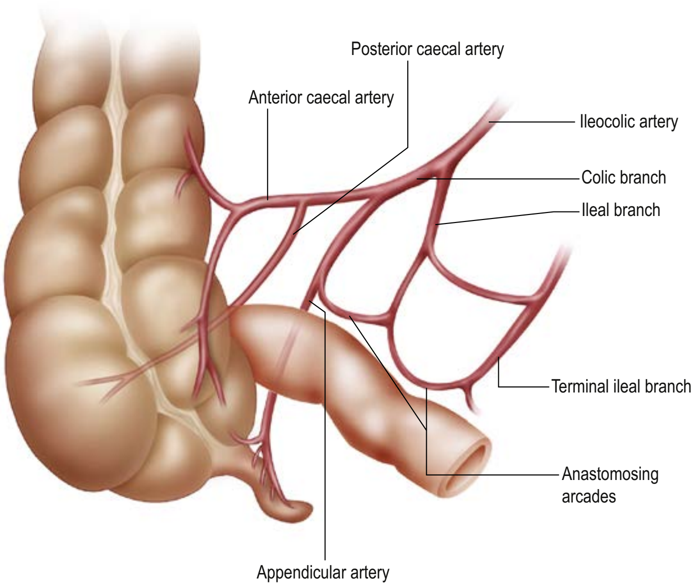

Fig. 65.23 The arteries of the caecum, appendix and ascending colon.

Vascular supply and lymphatic drainage of the midgut-derived large intestine

Arteries

Superior mesenteric artery

The artery of the midgut is the superior mesenteric artery, which arises from the anterior surface of the aorta at the level of the lower border of the body of the first lumbar vertebra. It runs steeply downwards, posterior to the splenic vein and body of the pancreas, with the superior mesenteric vein on its right, and directly anterior to the left renal vein, the uncinate process of the pancreas and the horizontal part of the duodenum. It then enters the root of the mesentery of the small intestine and passes obliquely downwards and to the right, giving off several branches to the large intestine.

Ileocolic artery

The ileocolic artery arises from the superior mesenteric artery near the root of the mesentery of the small intestine, descending within that mesentery to the right towards the caecum, and crossing anterior to the right ureter, gonadal vessels and psoas major. It usually divides into superior and inferior branches, the superior branch running up along the left side of the ascending colon to anastomose with the right colic artery (or right branch of the middle colic artery) (Veeresh et al 2012). The inferior branch runs to the ileocaecal junction and divides into anterior and posterior caecal arteries, the appendicular artery and an ileal branch that passes to the left in the ileal mesentery to anastomose with a terminal ileal branch of the superior mesenteric artery (**Fig. 65.23**). The latter therefore provides a collateral arterial supply to the caecum. The ileocolic artery provides the major arterial supply to the caecum; traction on the caecum in the direction of the anterior superior iliac spine will cause the artery to tent up the mesentery, allowing the vessel to be easily identified.

The appendicular artery usually arises directly from the ileocolic artery and descends posterior to the terminal ileum to enter the meso-appendix a short distance from the base of the appendix (see Fig. 65.23). Here, it gives off a recurrent branch that anastomoses at the proximal appendix with a branch of the posterior caecal artery. The appendicular artery approaches the distal end of the organ, at first near to and then in the edge of the meso-appendix. Its terminal part lies on the wall of the appendix and can become thrombosed in appendicitis, resulting in distal gangrene or necrosis. Less commonly, the appendicular artery arises from the posterior caecal artery or an ileal artery (Ouattara et al 2007) (see Fig. 65.12). Accessory appendicular arteries are common; two or more arteries may supply the appendix.

Right colic artery

The right colic artery is relatively small and variable in its anatomy (Batra et al 2013, Haywood et al 2017). It usually arises as a common trunk with the middle colic artery, but can originate directly from the superior mesenteric artery or from the ileocolic artery (when it is referred to as an accessory right colic artery) (**Fig. 65.24**). It passes to the right, across the right psoas major and quadratus lumborum,

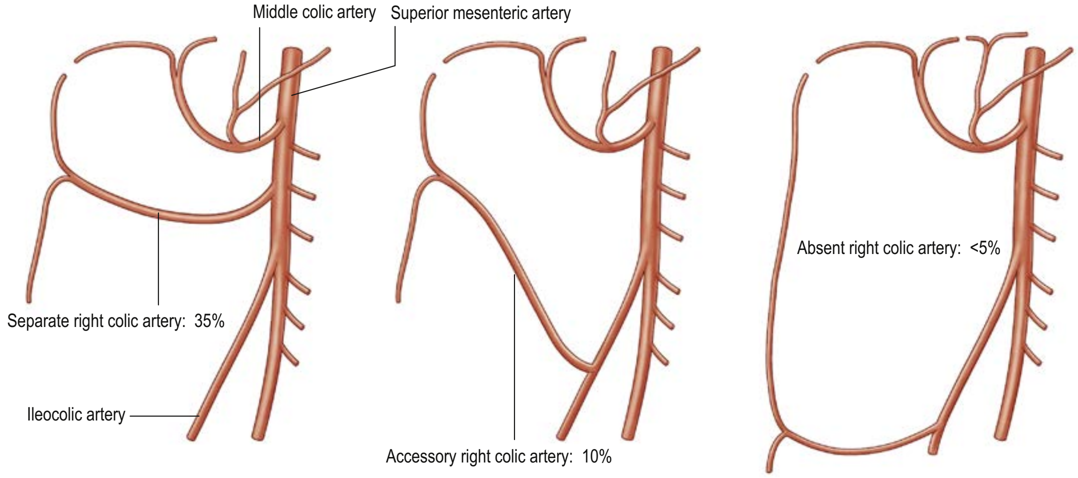
Middle colic artery
Superior mesenteric artery
Separate right colic artery: 35%
Ileocolic artery
Accessory right colic artery: 10%
Absent right colic artery: <5%

Fig. 65.24 Anatomical variants of the right colic artery.

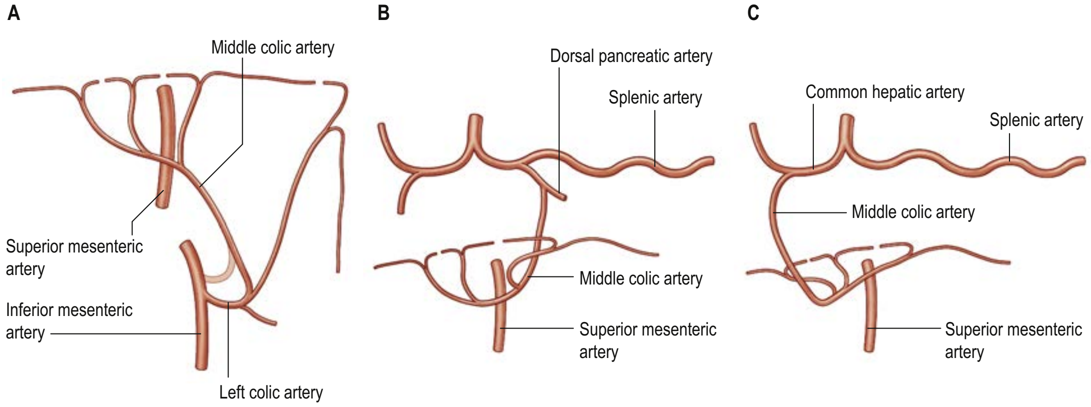

Fig. 65.25 Variants in the origin of the middle colic artery; only replaced arteries have been illustrated for simplicity. Accessory arteries are more common than completely replaced arteries. **A**, The left colic artery or inferior mesenteric artery. **B**, The dorsal pancreatic artery. **C**, The common hepatic artery. Each variant accounts for fewer than 5% of cases.

crossing the right gonadal vessels and ureter. Near the left side of the ascending colon it divides into a descending branch, which runs down to anastomose with the superior branch of the ileocolic artery, and an ascending branch, which passes up across the inferior pole of the right kidney to the right colic flexure, where it anastomoses with a branch of the middle colic artery. Together, these anastomoses form the marginal artery at the right colic flexure.

Middle colic artery

The middle colic artery arises from the right side of the superior mesenteric artery, either separately or in common with the right colic artery, just inferior to the neck of the pancreas, and passes anteriorly and superiorly within the transverse mesocolon, just to the right of the midline. As it approaches the colon, it usually divides into right and left branches. The right branch anastomoses with the ascending branch of the right colic artery. The left branch supplies the terminal part of midgut derivatives and anastomoses with a branch of the left colic artery near the left colic flexure. The marginal artery thus formed lies a few centimetres from the mesenteric edge of the transverse colon. Sometimes, the middle colic artery divides into three or more branches within the transverse mesocolon, in which case the most lateral branches form the arterial anastomoses. An accessory, or rarely a replaced, middle colic artery can arise directly from the abdominal aorta (Yoshida et al 1993), dorsal pancreatic, hepatic, inferior mesenteric or left colic arteries (**Fig. 65.25**). In addition, an accessory middle colic artery is occasionally found arising from the superior mesenteric artery proximal to the origin of the actual middle colic artery (Turmezei and Cockburn 2009).

Veins

All the branches of the superior mesenteric artery are accompanied by correspondingly named veins. These tributaries drain into the superior mesenteric vein, which ascends to the right of the artery, crossing the horizontal part of the duodenum and uncinate process of the pancreas. Behind the neck of the pancreas, at the level of the transpyloric plane (the inferior border of the body of the first lumbar vertebra), it joins the splenic vein to form the hepatic portal vein, which ascends behind the superior part of the duodenum to reach the liver. The right colic vein is highly variable: it can drain either directly into the superior mesenteric vein, or into the right gastro-omental or inferior pancreaticoduodenal veins to form a 'gastrocolic trunk' that drains into the superior mesenteric vein, or it can be entirely absent (Yamaguchi et al 2002, Stefura et al 2018). Several tributaries draining into one or more middle colic veins are highly variable in extent and position. The middle colic veins drain either into the superior mesenteric vein, just before its junction with the splenic vein, or directly into the hepatic portal vein. The appendicular vein usually joins the caecal vein to become the ileocolic vein; infection from the appendix can therefore be carried directly to the liver via the hepatic portal vein.

Lymphatic drainage

Lymphatic vessels originate from both anterior and posterior aspects of the colon. Lymph drainage from midgut derivatives follows the course of the superior mesenteric artery. Thus, lymph from the caecum and appendix drains to nodes associated with the ileocolic artery, and lymph from the distal ascending colon and right colic flexure drains to nodes along the right colic artery (see Fig. 65.16). When the distal transverse colon and left colic flexure are predominantly supplied by the middle colic artery, lymph drainage of this segment is also largely to superior mesenteric nodes. Lymphatic vessels in the appendix are numerous and combine to form vessels that ascend in the meso-appendix, occasionally interrupted by one or more nodes. They unite to form three or four larger vessels that anastomose with lymphatic vessels draining the ascending colon into ileocolic nodes.

HINDGUT-DERIVED REGION OF LARGE INTESTINE

Left colic flexure

The left colic flexure marks the junction between the transverse and descending colons and lies in the left hypochondriac region, anterior to the tail of the pancreas and the left kidney (**Fig. 65.26**). Its position

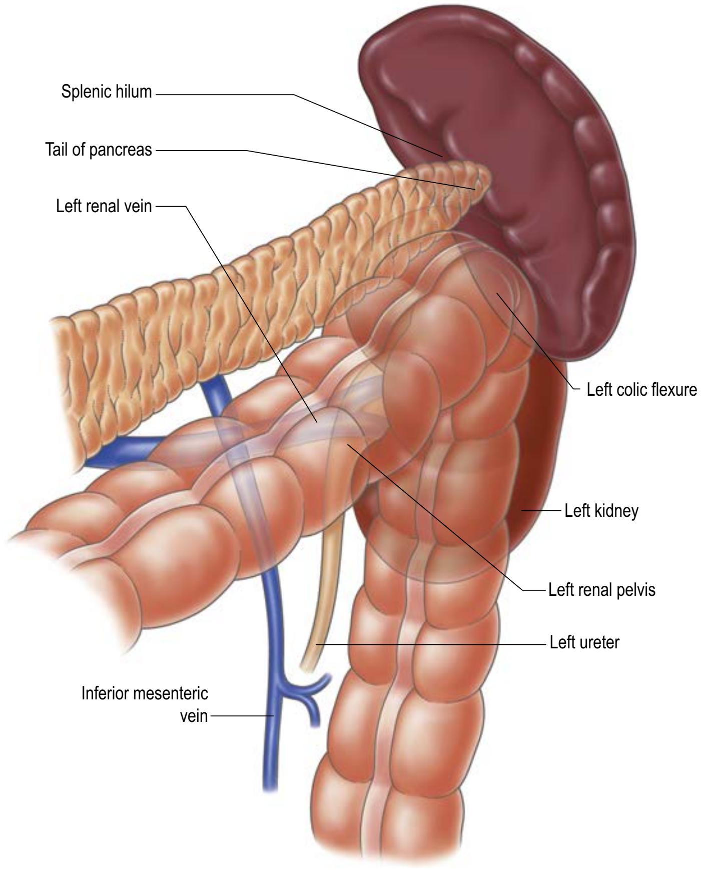
Splenic hilum
Tail of pancreas
Left renal vein
Left colic flexure
Left kidney
Left renal pelvis
Left ureter
Inferior mesenteric vein

Fig. 65.26 Relations of the left colic flexure.

with respect to the spleen is variable: it usually lies inferomedial to the anterior extremity, forming the colic impression, but it can lie anterior to the splenic hilum or even a little above. The left colic flexure is often attached to the splenic capsule by a peritoneal ligament and inadvertent downward traction on the flexure during surgery can tear the capsule. The phrenicocolic ligament attaches the left colic flexure to the respiratory diaphragm below the anterior extremity of the spleen at about the level of the tenth rib. The left colic flexure lies more superiorly and posteriorly than the right colic flexure and often adopts a very acute angle such that the distal transverse colon overlaps the proximal descending colon; there may be peritoneal and omental adhesions between the two structures.

Descending colon

The descending colon is 25–30 cm long and descends from the left colic flexure in the left hypochondriac region to the level of the iliac crest, where it curves medially anterior to iliacus to transition to the sigmoid colon. In most individuals it is retroperitoneal, covered anteriorly and on both sides by peritoneum, but it is occasionally more mobile, being suspended from the posterior abdominal wall by a short mesocolon (Saunders et al 1995). Its lateral peritoneal reflection in the left paracolic gutter is marked by a white line (of Toldt). The posterior surface of the descending colon is separated by a layer of loose connective tissue from the anterior layer of renal fascia inferolateral to the left kidney, transversus abdominis, quadratus lumborum, iliacus and the lateral margin of psoas major (Fig. 65.27). The subcostal vessels and nerve, iliohypogastric, ilio-inguinal, lateral femoral cutaneous, femoral and genitofemoral nerves, and, usually, the fourth lumbar artery also lie posteriorly, and loops of jejunum are anterior. The descending colon is narrower and more deeply placed than the ascending colon. Omental appendices are more common in this part of the colon.

Sigmoid colon

The sigmoid colon runs from the greater pelvis to the beginning of the rectum at the level of the third sacral vertebra. It is usually suspended from the posterior abdominal and pelvic walls by a fan-shaped sigmoid mesocolon, but may be tethered by congenital adhesions to the parietal peritoneum over iliacus. Consequently, its length and position are highly variable. It usually lies within the pelvic cavity anterior to the rectum on the peritoneum covering the urinary bladder (and uterus in the female). It is usually completely invested in peritoneum. The root of the sigmoid mesocolon has an inverted V-shaped attachment; the right limb of this inverted 'V' ascends from a point anterior to the third sacral vertebra to the bifurcation of the left common iliac vessels (crossed by the left ureter) and descends from this point along the external iliac vessels.

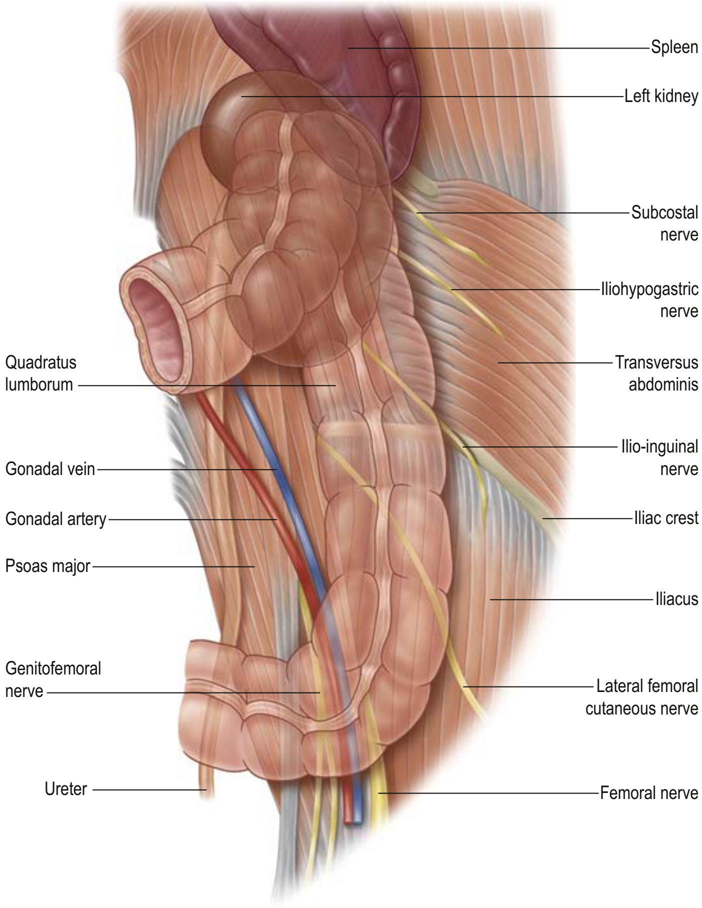
Spleen
Left kidney
Subcostal nerve
Iliohypogastric nerve
Quadratus lumborum
Transversus abdominis
Ilio-inguinal nerve
Gonadal vein
Gonadal artery
Iliac crest
Psoas major
Iliacus
Genitofemoral nerve
Lateral femoral cutaneous nerve
Ureter
Femoral nerve

Fig. 65.27 Posterior relations of the descending colon.

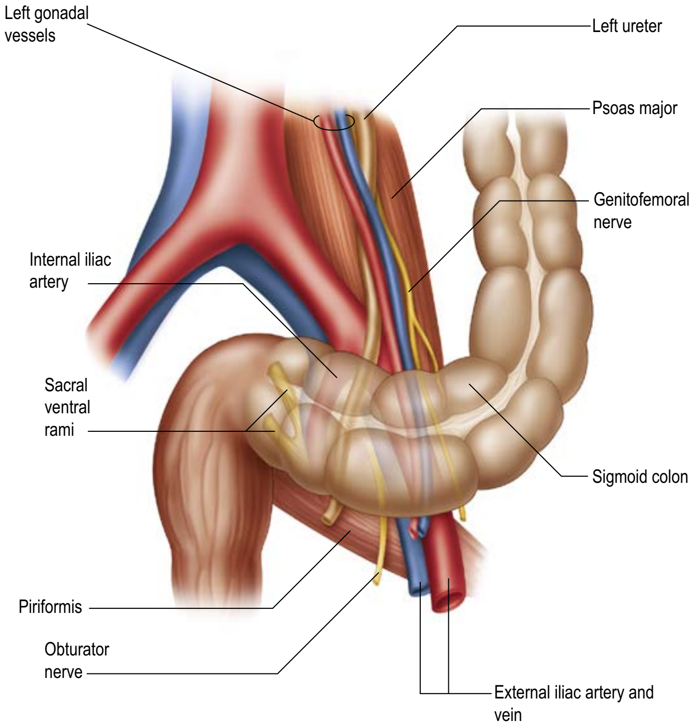
Left gonadal vessels
Left ureter
Psoas major
Genitofemoral nerve
Internal iliac artery
Sacral ventral rami
Sigmoid colon
Piriformis
Obturator nerve
External iliac artery and vein

Fig. 65.28 Posterior relations of the sigmoid colon.

Between the fixed junctions with the descending colon and rectum, the relations of the sigmoid colon are quite variable (**Fig. 65.28**). Laterally lie the left external iliac vessels, the obturator nerve, ovary or ductus deferens, and the lateral pelvic wall; posteriorly lie the left external and internal iliac and gonadal vessels, ureter, piriformis and the sacral plexus; anteroinferiorly lie the urinary bladder in males, or the uterus and urinary bladder in females; superiorly and to the right, the sigmoid colon is in contact with loops of the ileum. The gonadal vessels and ureter lie in a distinct fascial plane, which is the inferior extension of the renal fascia and is separate from the sigmoid mesocolon. This plane can be recognized and separated during surgical resection of the sigmoid mesocolon. The taeniae coli of the sigmoid colon are wider than elsewhere in the colon, and coalesce at its distal end to form a complete circumferential longitudinal muscle layer. Omental appendices are particularly prominent in the sigmoid colon.

The position and shape of the sigmoid colon depend on its length (which increases with age) and mobility; the length of the sigmoid mesocolon (usually longer in males); and the degree of distension of the colon, rectum, urinary bladder and uterus. The length of the sigmoid colon and its mesosigmoid differ among ethnic groups (Alatise et al 2013).

Sigmoid volvulus Rotation or volvulus of the sigmoid colon can occur around its mesenteric attachment. Volvulus is more likely when the sigmoid colon is longer and its mesosgimoid is longer and wider (Akinkuotu et al 2011). It does not occur when the sigmoid colon and its mesocolon are short. The anatomical features predisposing to sigmoid volvulus are most commonly found in sub-Saharan Africans and chronically institutionalized patients.

Diverticular disease Acquired diverticula commonly occur in the sigmoid colon, particularly in Western populations. Most patients with diverticular disease are asymptomatic, 10–25% progress to diverticulitis, and 10–15% of those develop complications (Kaushik et al 2016). These diverticula frequently develop in parallel rows between the mesenteric taenia coli and the two antimesenteric taeniae where the colonic wall is weaker; at this site the outer longitudinal muscle is deficient and the circular muscle is traversed by arteries supplying the submucosal vascular plexus (Slack 1962). However, the predilection to diverticula in the sigmoid colon probably relates to causative factors rather than intrinsic differences in the structure of this segment of the colon. In contrast, congenital diverticula can occur at any site in the colon (**Fig. 65.29**) and are often found along the mesenteric border.

Mesocolon

The mesocolon extends along the entire length of the colon and is continuous with the small intestine mesentery proximally and the mesorectum distally. The mesocolon consists of fat embedded within a connective tissue lattice and sandwiched between two layers of mesothelium; it also contains nerves, blood and lymphatic vessels, and lymph nodes. A layer of loose connective tissue, known as Toldt's fascia, lies immediately posterior to the mesocolon (Culligan et al 2014). Complete excision of the relevant segment of mesocolon by dissecting within or posterior to the plane of Toldt's fascia has been shown to improve survival in colon cancer (Søndenaa et al 2014).

Rectum

The rectum is continuous with the sigmoid colon at the level of the third sacral vertebra and ends as it passes through the pelvic diaphragm (the pubo-analis (puborectalis) part of levator ani) (**Fig. 65.30**), where it is continuous with the anal canal. It descends within the concavity of the sacrum and coccyx, at first running posteriorly and then curving anteriorly. The junction between the anteriorly directed distal rectum and the posteriorly directed anal canal is the anorectal flexure, which is maintained by pubo-analis. This is 2–3 cm anterior to and slightly below the tip of the coccyx, level with the apex of the prostate in males. The rectum also deviates in three lateral curves: upper, convex to the right; middle (the most prominent), convex to the left; and lower, convex to the right. Both ends of the rectum are in the median plane.

Although variable in absolute length, the rectum is often defined in clinical practice as extending approximately 15 cm above the anal orifice. Its proximal diameter is similar to that of the sigmoid colon, but more distally it becomes dilated as the rectal ampulla. Unlike the sigmoid colon, the rectum has no haustra, omental appendices or taeniae coli. The taeniae merge a few centimetres above the rectosigmoid junction, initially forming wide anterior and posterior muscular bands; these then fuse to form a continuous outer layer of longitudinal muscle investing the entire length of the rectum. At the rectal ampulla, a few longitudinal muscle fibres pass forwards from the anterior rectal wall to the perineal body and urethra (recto-urethralis).

The proximal third of the rectum is covered by peritoneum on its anterior and lateral aspects, and the middle third by peritoneum on its anterior aspect only; the distal third is below the peritoneum. The peritoneum is reflected anteriorly on to the urinary bladder in males to form the rectovesical pouch, or on to the posterior part of the vaginal fornix in females to form the recto-uterine pouch (of Douglas). The level of this reflection is more superior in males. In male neonates, the peritoneum extends on the anterior rectal wall as far as the inferior limit of the prostate. Superiorly, it is firmly attached to the muscle layer of the sigmoid colon by fibrous connective tissue, but as it descends on to the rectum it is more loosely attached by fatty connective tissue, which allows considerable expansion of the proximal half of the rectum.

When the rectum is empty, the mucosa has several longitudinal folds in its inferior part, which become effaced during distension. The rectum commonly has two to three permanent semilunar transverse rectal folds (although the number can vary), which are most marked in rectal distension (see Fig. 65.10) (Abramson 1978). Two types of transverse rectal folds have been recognized. One consists of the mucosa, the circular muscle layer and part of the longitudinal muscle, and is marked externally by an indentation. The other is devoid of longitudinal muscle and has no external marking. When three transverse rectal folds are found, the most superior fold at the beginning of the rectum can be on either the left or the right and it occasionally encircles the rectal lumen. The middle fold is largest and most constant and lies immediately superior to the rectal ampulla, projecting from the anterior and right wall just below the level of the anterior peritoneal reflection; the circular muscle is particularly prominent in this fold. The inferior fold is on the left and is the most variable. Although the function of these structures is unknown, some have opined that they might retard faecal passage allowing for distinction between faeces and flatus (Shafik et al 2001).

Relations Posterior to the rectum and mesorectum, separated by the presacral fascia, are the lower three sacral vertebrae, coccyx, median and lateral sacral vessels, and the most distal portion of the sacral part of the sympathetic trunk. Laterally, the proximal rectum is related to the sigmoid colon and/or small intestine, while below the peritoneal reflection lie levator ani, obturator internus, the obturator nerve and vessels, ureters, the inferior hypogastric plexus, internal iliac vessels, piriformis and the sacral plexus. Anteriorly, the rectum is related to the sigmoid colon and/or small intestine in both sexes, and the fundus of the urinary bladder, seminal glands, ductus deferens, terminal parts of the ureters, and the prostate in males (see Figs 65.34, 74.17). In females, the cervix/body of the uterus and vagina are anterior, the latter separated from the rectum by a rectovaginal septum. In postmenopausal females, and after childbirth, the connective tissue of the rectovaginal septum can atrophy or become thinned, reducing the support of the anterior rectal and posterior vaginal walls.

Mesorectum and rectal fasciae

The mesorectum is the distal continuation of the mesosigmoid. It encases the proximal rectum posterolaterally and the distal rectum circumferentially and tapers towards the anorectal junction (**Figs 65.31–65.36**). It contains adipose connective tissue, the superior anorectal artery and its branches, the superior anorectal vein and its tributaries and lymphatic vessels and nodes. It is much bulkier posteriorly and is enclosed by mesorectal fascia, a distinct layer of connective tissue that is also called the fascia propria of the rectum and that separates the mesorectum from the bony pelvis (see Figs 65.31, 65.32). This fascia limits the mesorectum posteriorly and lies anterior to the presacral fascia (of Waldeyer), separated by a so-called retrorectal 'space'. The rectum and mesorectal fascia are connected to the parietal fascia of the pelvis by two 'lateral ligaments' and one posterior ligament, the rectosacral fascia (Gaudio et al 2010). The latter is a thin layer of connective tissue that passes obliquely downwards from the presacral fascia to fuse with the mesorectal fascia posterior to the rectum 3–5 cm above the anorectal junction (García-Armengol et al 2008). The mesorectal fascia is surrounded by a thin and relatively avascular layer of loose areolar tissue, which separates

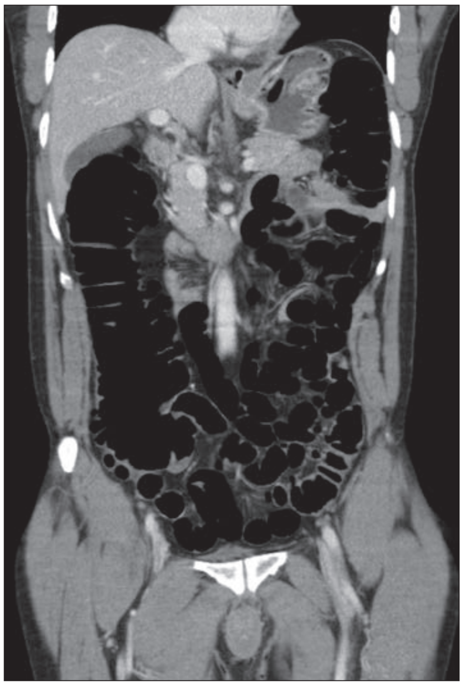

Fig. 65.29 CT (coronal reformat) showing diverticulosis of both the ascending and sigmoid colons. (Courtesy of Dr Kamini Patel, Homerton Hospital, London.)

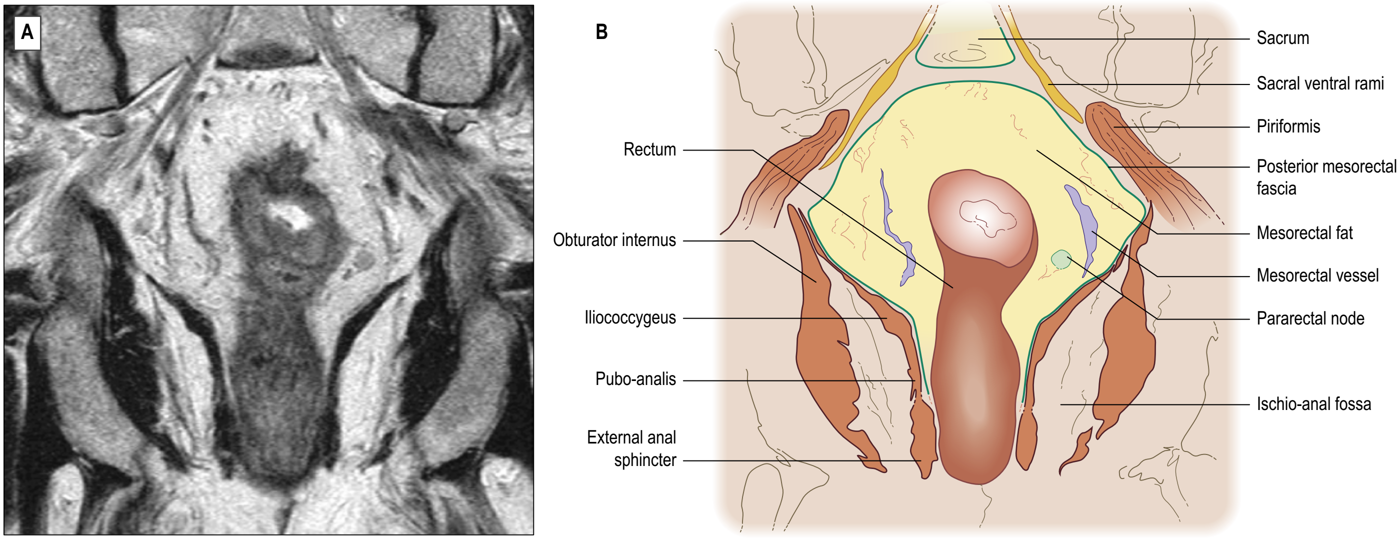
A
B
Sacrum
Sacral ventral rami
Piriformis
Posterior mesorectal fascia
Mesorectal fat
Mesorectal vessel
Pararectal node
Ischio-anal fossa
Rectum
Obturator internus
Iliococcygeus
Pubo-analis
External anal sphincter

Fig. 65.30 **A**, A coronal T2-weighted MRI of the rectum in a female. **B**, A line diagram illustrating the main features in **A**.

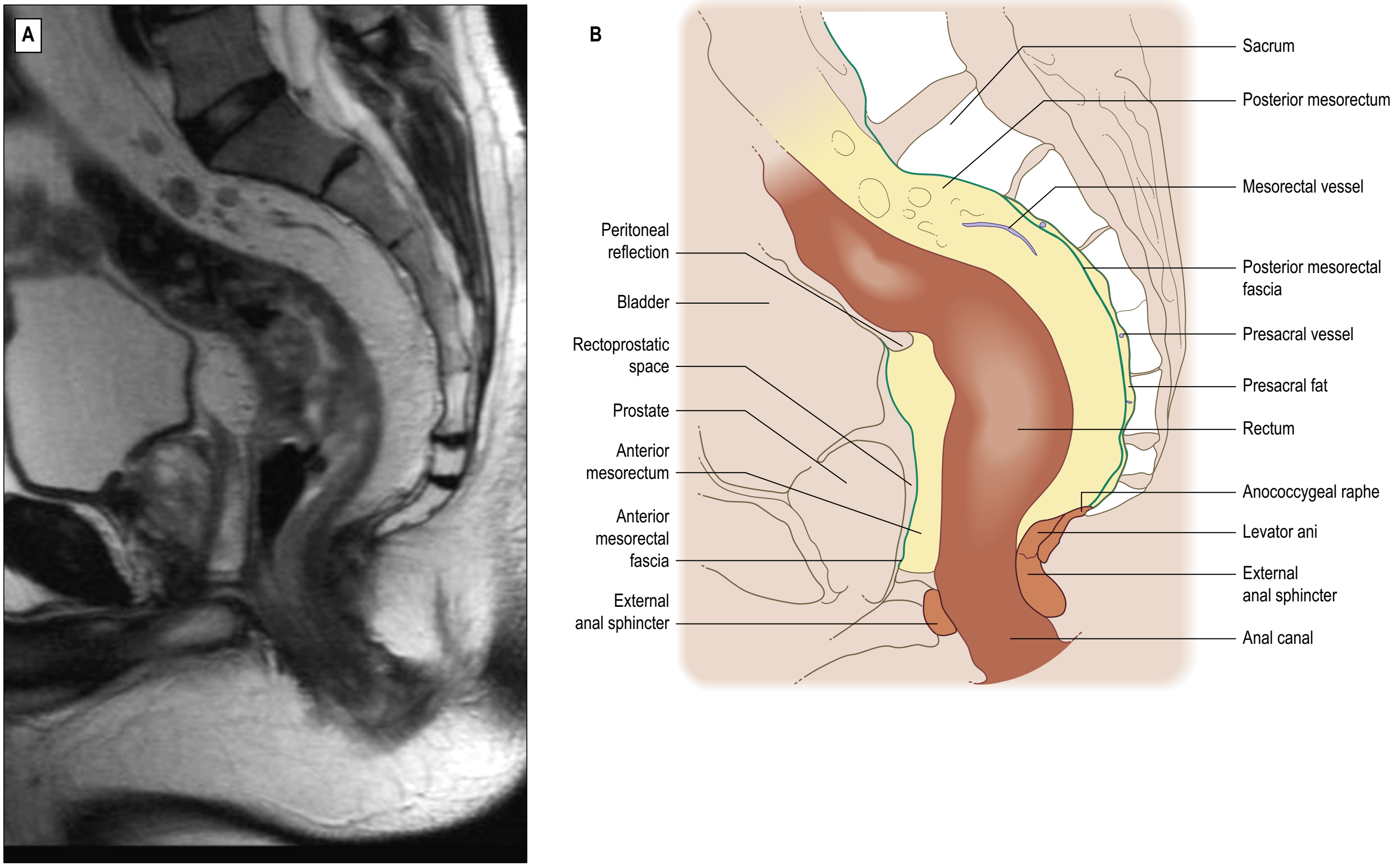
A
B
Peritoneal reflection
Bladder
Rectoprostatic space
Prostate
Anterior mesorectum
Anterior mesorectal fascia
External anal sphincter
Sacrum
Posterior mesorectum
Mesorectal vessel
Posterior mesorectal fascia
Presacral vessel
Presacral fat
Rectum
Anococcygeal raphe
Levator ani
External anal sphincter
Anal canal

Fig. 65.31 **A**, A sagittal T2-weighted MRI of the rectum in a male. **B**, A line diagram illustrating the main features in **A**.

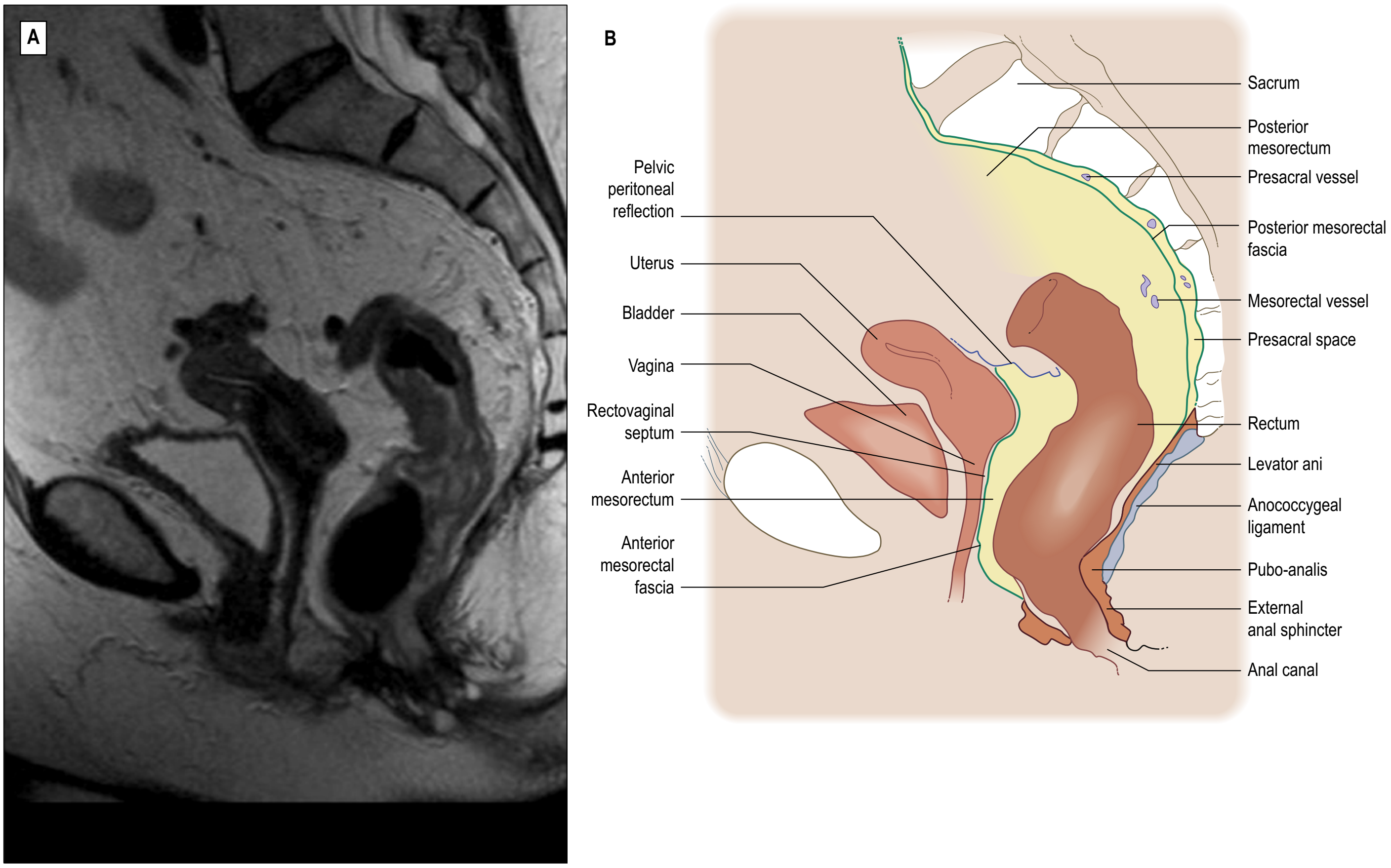
A
B
Pelvic peritoneal reflection
Uterus
Bladder
Vagina
Rectovaginal septum
Anterior mesorectum
Anterior mesorectal fascia
Sacrum
Posterior mesorectum
Presacral vessel
Posterior mesorectal fascia
Mesorectal vessel
Presacral space
Rectum
Levator ani
Anococcygeal ligament
Pubo-analis
External anal sphincter
Anal canal

Fig. 65.32 **A**, A sagittal T2-weighted MRI of the rectum in a female. **B**, A line diagram illustrating the main features in **A**.

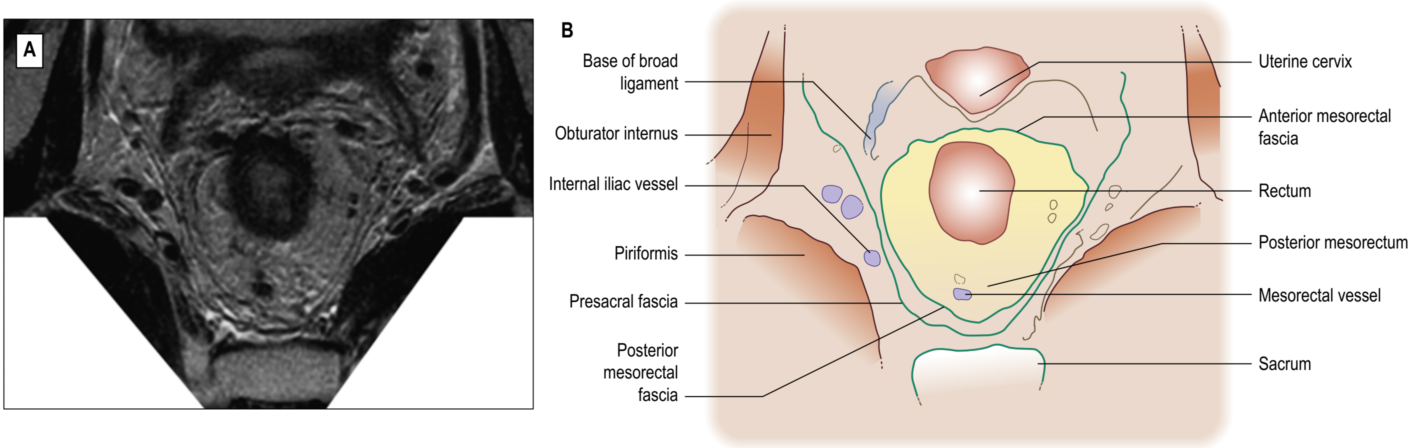
A
B
Base of broad ligament
Obturator internus
Internal iliac vessel
Piriformis
Presacral fascia
Posterior mesorectal fascia
Uterine cervix
Anterior mesorectal fascia
Rectum
Posterior mesorectum
Mesorectal vessel
Sacrum

Fig. 65.33 **A**, An axial T2-weighted MRI of the proximal rectum in a female. **B**, A line diagram illustrating the main features in **A**.

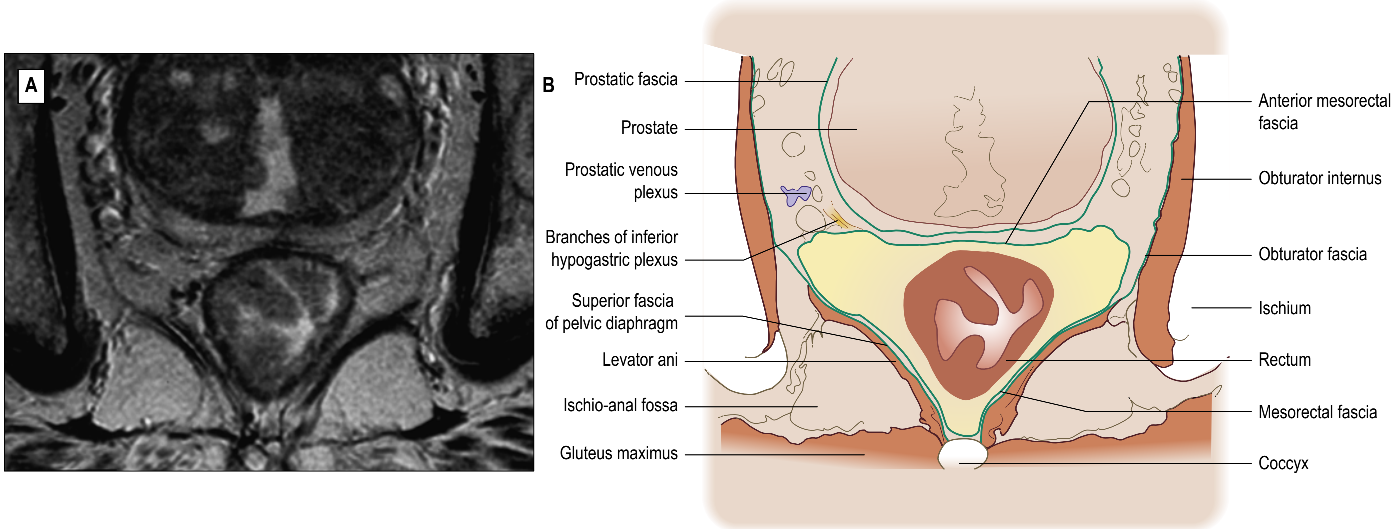
A
B
Prostatic fascia
Prostate
Prostatic venous plexus
Branches of inferior hypogastric plexus
Superior fascia of pelvic diaphragm
Levator ani
Ischio-anal fossa
Gluteus maximus
Anterior mesorectal fascia
Obturator internus
Obturator fascia
Ischium
Rectum
Mesorectal fascia
Coccyx

Fig. 65.34 **A**, An axial T2-weighted MRI of the mid rectum below the peritoneal reflection in a male. **B**, A line diagram illustrating the main features in **A**.

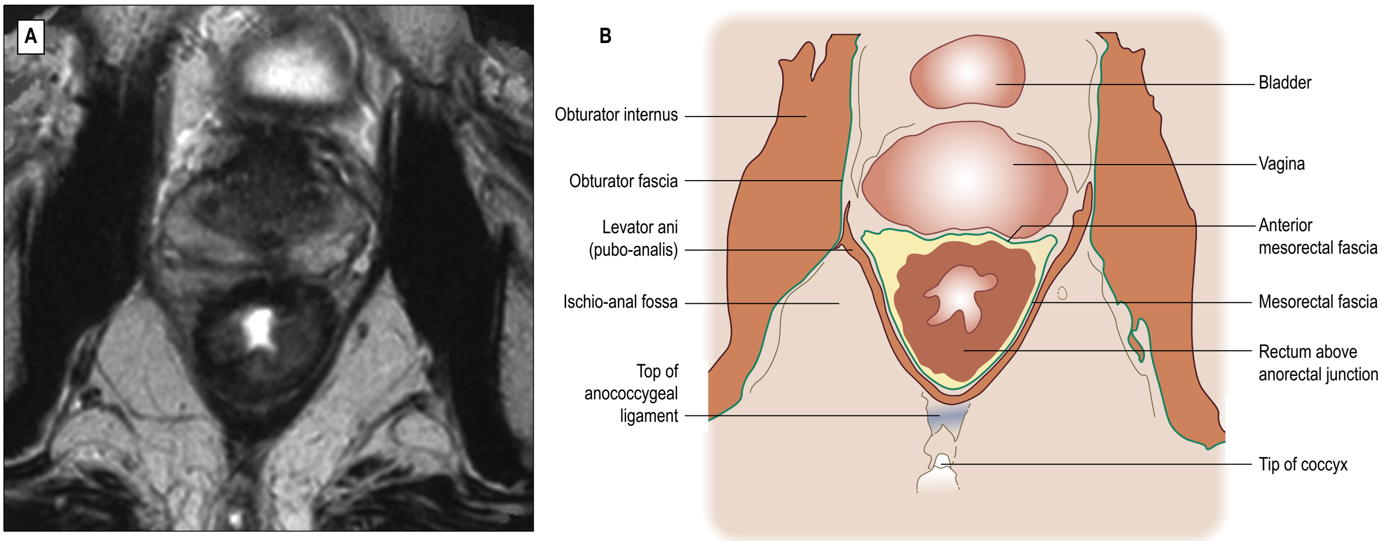
A
B
Obturator internus
Obturator fascia
Levator ani (pubo-analis)
Ischio-anal fossa
Top of anococcygeal ligament
Bladder
Vagina
Anterior mesorectal fascia
Mesorectal fascia
Rectum above anorectal junction
Tip of coccyx

Fig. 65.35 **A**, An axial T2-weighted MRI of the distal rectum below the peritoneal reflection in a female. **B**, A line diagram illustrating the main features in **A**.

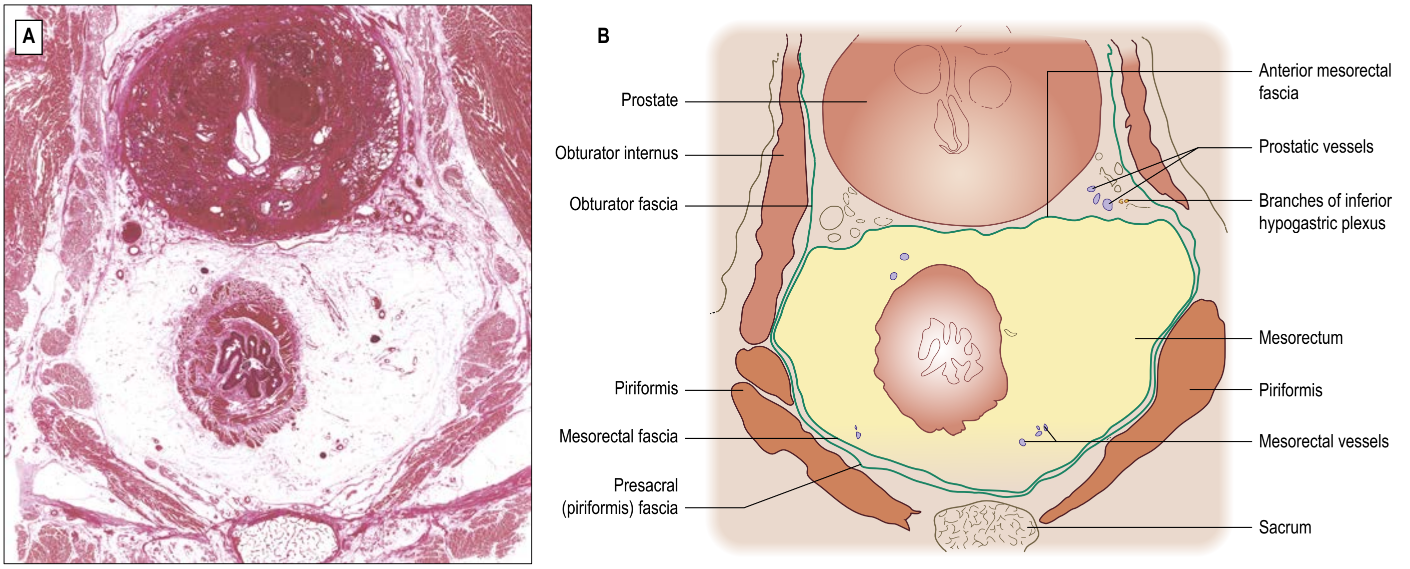
A
B
Prostate
Obturator internus
Obturator fascia
Piriformis
Mesorectal fascia
Presacral (piriformis) fascia
Anterior mesorectal fascia
Prostatic vessels
Branches of inferior hypogastric plexus
Mesorectum
Piriformis
Mesorectal vessels
Sacrum

Fig. 65.36 **A**, A light microscope transverse section of the mid rectum (male, cadaveric specimen). **B**, A line diagram illustrating the main features in **A**.

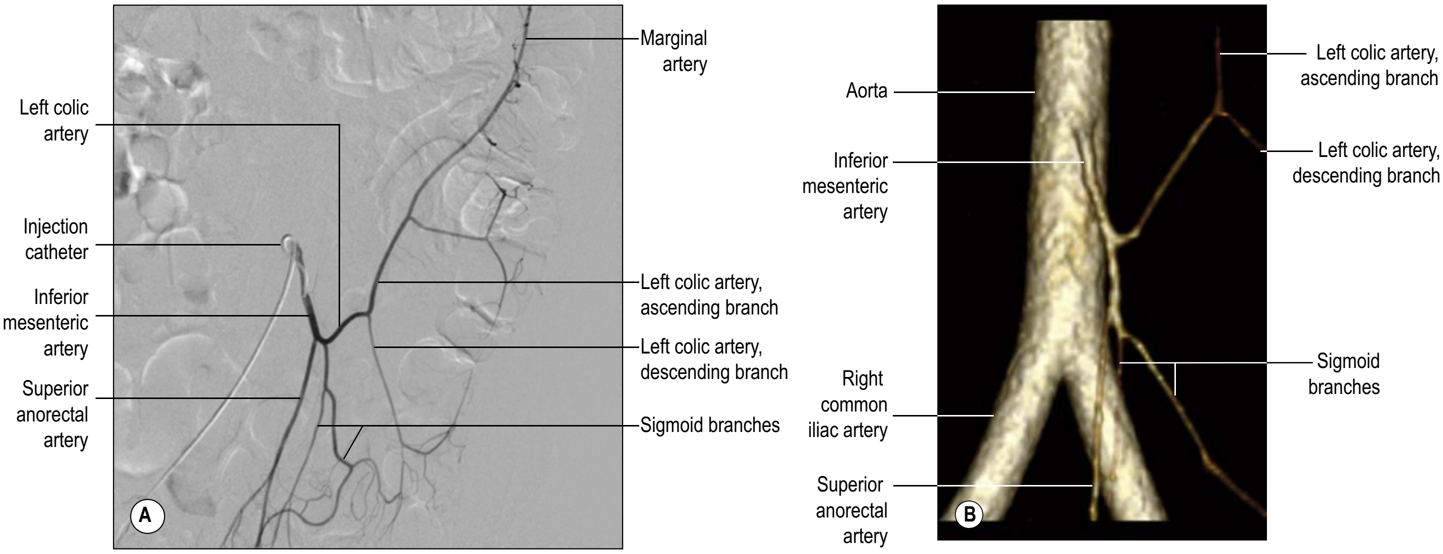
Left colic artery
Injection catheter
Inferior mesenteric artery
Superior anorectal artery
Marginal artery
Left colic artery, ascending branch
Left colic artery, descending branch
Sigmoid branches
A
Aorta
Inferior mesenteric artery
Right common iliac artery
Superior anorectal artery
Left colic artery, ascending branch
Left colic artery, descending branch
Sigmoid branches
B

Fig. 65.37 **A**, Digital subtraction angiogram of the inferior mesenteric artery. **B**, Volume-rendered CT angiogram of the aorta, frontal view of the inferior mesenteric artery and its branches.

In prolapse of the rectum involving all layers of the rectal wall, the mid and proximal rectum descend towards the pelvic diaphragm on straining. Descent occurs within the lumen of the rectum as a form of intussusception, and could be a consequence of the large diameter of the rectal ampulla and relative fixation of the anal canal. The loose adipose tissue of the upper mesorectum and the 'lateral ligaments' offer only limited resistance against rectal descent. It is common for the region around the anus and rectum bound by levator ani to be chronically enlarged in patients suffering from recurrent rectal prolapse, but this is probably a consequence rather than a cause of the prolapse. In females, the recto-uterine pouch also descends with the anterior rectal wall.

When the rectovaginal septum is grossly effaced, especially in postmenopausal females, the pressure of defecation can cause bulging of the rectal wall into the posterior vagina and, in extreme cases, through the vaginal orifice. Weakness of the pelvic diaphragm contributes to the prolapse by allowing the perineum to descend during straining.

An important concept in the surgical treatment of adenocarcinoma of the rectum is the need to excise the rectum in continuity with the mesorectum and its contained lymph nodes in order to avoid local tumour recurrence (Heald et al 1982). In total mesorectal excision, the posterolateral plane of dissection is outside the mesorectal fascia but anterior to the presacral fascia and its underlying venous plexus. Laterally, the plane is interrupted only by small branches of the middle anorectal vessels; anteriorly, it merges with the rectovesical or rectovaginal septum. The inferior hypogastric plexus is closely related to the plane of dissection laterally; these nerves must be preserved to retain urinary bladder and sexual function. Total mesorectal excision involves complete excision of the rectum down to the level of the pelvic diaphragm, where the pubo-analis component of levator ani merges with the deep component of the external anal sphincter. Superiorly, the inferior mesenteric artery is ligated near its origin.

In abdominoperineal excision of the rectum, it should be noted that the mesorectum becomes extremely thin at the point where the rectum passes through levator ani. To achieve adequate surgical margins, the plane of dissection is through the ischio-anal fossa and levator ani outside pubo-analis and into the mesorectal plane well above the pelvic diaphragm.

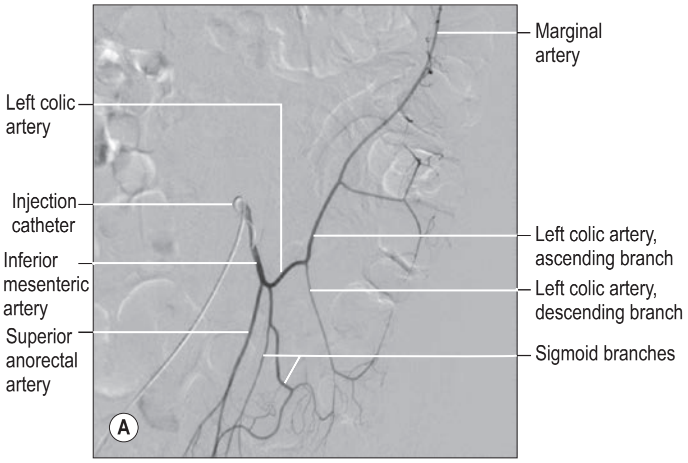
Marginal artery
Left colic artery
Injection catheter
Inferior mesenteric artery
Superior anorectal artery
Left colic artery, ascending branch
Left colic artery, descending branch
Sigmoid branches
A

Fig. 65.37 **A**, Digital subtraction angiogram of the inferior mesenteric artery. (B, *continued online*)

it from the posterior and lateral walls of the true pelvis. Superiorly, the mesorectal fascia blends with the connective tissue bounding the mesosigmoid. Laterally, it extends around the rectum and mesorectum, and becomes contiguous anteriorly with a denser condensation of fascia, Denonvilliers' fascia. A number of terms are used interchangeably for the fascia in this region, thus, for example, this fascia is also known as the rectovesical septum in males although it extends caudal to the urinary bladder and is particularly dense posterior to the prostate and seminal glands (prostato-seminal fascia); it lies immediately anterior to the mesorectal fascia, to which it may be fused (Lindsey et al 2000). It appears that there is no clearly identified membranous layer consistent with Denonvilliers' fascia between the posterior vaginal and the anterior rectal walls (Zhang et al 2016).

The mesorectal fascia is visible by CT, MRI and dissection (Bissett et al 2001). On MRI, the mesorectum appears as a fat-filled envelope containing blood vessels and lymph nodes; small nerves are not visible but interlacing connective tissue strands can be seen. The mesorectal fascia is recognizable on axial MRI as a low-signal layer surrounding the mesorectum, corresponding to a distinct condensation of fascia seen on histological sections (Brown et al 1999). Identification of this layer in patients with a malignant rectal tumour can help predict the success of surgical resection. Branches of the inferior hypogastric plexus and middle anorectal vessels enter the mesorectum anterolaterally: they are ensheathed by fascia and are sometimes referred to collectively as the 'lateral rectal ligaments'. The number and calibre of the middle anorectal vessels are highly variable; they can be very small or even absent (Sato and Sato 1991). The 'lateral ligaments' are not clearly seen on MRI or CT, and only appear as an identifiable structure with surgical traction on the rectum. The fascia of the 'ligaments' is flimsy and probably contributes little to support of the rectum. Parietal fascia covers levator ani and the muscles of the side wall of the pelvis, and is continuous posteriorly with the presacral fascia.

Rectal prolapse

Available with the *Gray's Anatomy* e-book

Rectocele

Available with the *Gray's Anatomy* e-book

Rectal cancer

Available with the *Gray's Anatomy* e-book

Vascular supply and lymphatic drainage of the hindgut-derived intestine

Arteries

Inferior mesenteric artery

The artery of the hindgut-derived gut is the inferior mesenteric artery (Figs 65.37–65.39), which arises from the anterior or left anterolateral aspect of the aorta behind the inferior border of the horizontal (third) part of the duodenum 3–4 cm above the aortic bifurcation, at the level of the third lumbar vertebra. It runs obliquely down to the linea terminalis (pelvic brim) initially anterior to and then to the left of the abdominal aorta. It gives off the left colic and sigmoid arteries and crosses the origin of the left common iliac artery medial to the ureter, with the inferior mesenteric vein lying between. Beyond the linea terminalis it continues in the root of the sigmoid mesocolon as the superior anorectal artery.

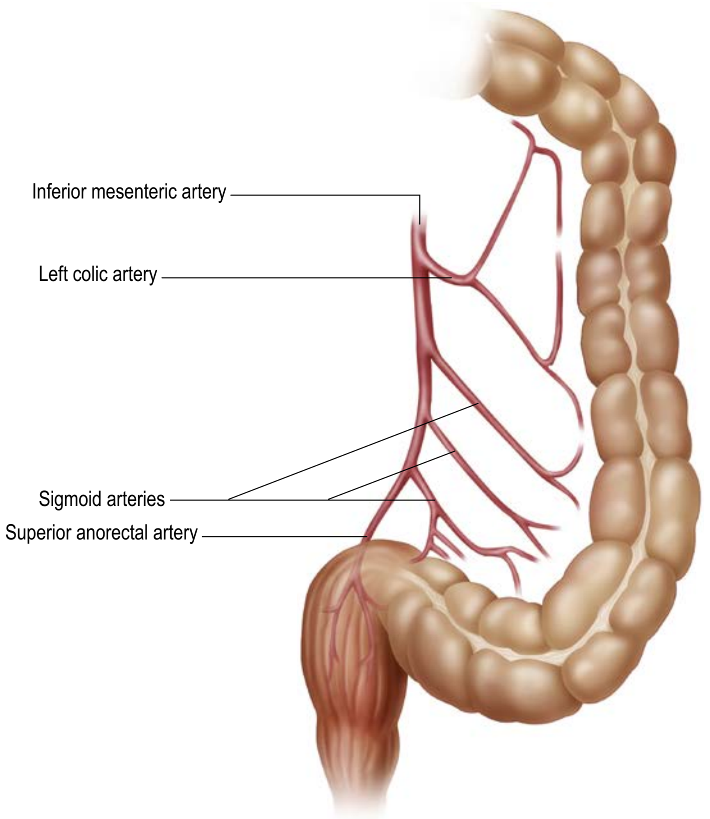

Fig. 65.38 The inferior mesenteric artery.

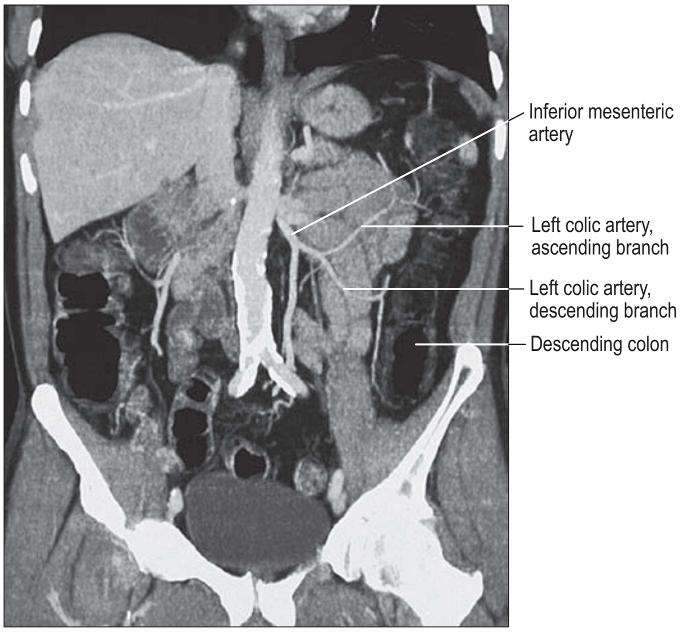
Inferior mesenteric artery
Left colic artery, ascending branch
Left colic artery, descending branch
Descending colon

Fig. 65.39 Coronal reformat CT of the vascular supply of the descending colon from the inferior mesenteric artery via the ascending and descending branches of the left colic artery. (Courtesy of Dr Louise Moore, Chelsea and Westminster Hospital, London.)

Left colic artery

The left colic artery usually arises from the inferior mesenteric artery shortly after its origin, ascends within the left colic mesentery and divides into an ascending and a descending branch (see Figs 65.38–65.39). The ascending branch passes upwards across the left psoas major, gonadal vessels, ureter and left kidney, and is crossed by the inferior mesenteric vein; its terminal branches anastomose with those of the left branch of the middle colic artery within the

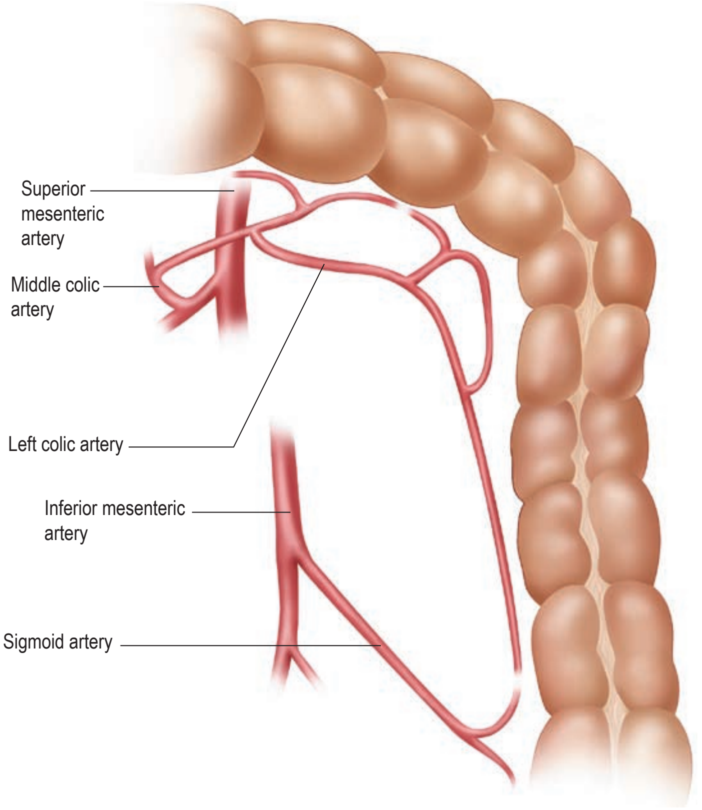

Fig. 65.40 A replaced left colic artery arising from the middle colic artery.

transverse mesocolon. The descending branch passes laterally and inferiorly and anastomoses with branches from the ascending branch and the most proximal sigmoid artery to form part of the marginal artery. The arterial arcades thus formed supply the distal third of the transverse and the descending colons. The left colic artery can originate from or in common with a sigmoid artery (Murono et al 2015). Occasionally, an accessory, or rarely, a replaced, left colic artery originates from the trunk of the superior mesenteric artery or its middle colic or first jejunal artery (**Fig. 65.40**). When present, it runs laterally in the upper left colic mesentery just inferior to the duodenojejunal flexure to supply the proximal descending colon, and forms all or part of the marginal artery in the region of the distal transverse colon. The left colic artery can itself give rise to an accessory left middle colic artery. Occasionally it gives rise to a branch shortly after its origin, which ascends in the mesentery and anastomoses directly with a similar descending branch of the left branch of the middle colic artery (the so-called arc of Riolan; van Gulik and Schoots 2005).

The dominant arterial supply of the left colic flexure is usually from the left colic artery but can be from the left branch of the middle colic artery. The marginal artery in this region may be absent or small, but it can enlarge considerably if the inferior mesenteric artery is stenosed or occluded.

Sigmoid arteries

The inferior mesenteric artery gives rise to between two and five sigmoid arteries, which descend obliquely in the sigmoid mesocolon anterior to the left psoas major, ureter and gonadal vessels. They supply the distal descending colon and sigmoid colon and anastomose superiorly with the left colic artery and inferiorly with the superior anorectal artery. Unlike the arrangement in the small intestine, arterial arcades do not form until the arteries are close to the wall of the colon, when small branches arise to supply the sigmoid colon directly. A true marginal artery is less obvious in the sigmoid colon. There is often a significant interval in the mesentery between the highest sigmoid artery and the descending branch of the left colic artery; this forms a useful guide to the arterial territories during surgical dissection.

Vascular ligation in left colonic resections

During resection of the distal descending and sigmoid colon, ligation of the inferior mesenteric artery close to its origin preserves the bifurcation of the left colic artery and helps to maintain the arterial supply to the proximal descending colon via the anastomosis between the left branch of the middle colic artery and the ascending branch of the left colic artery. Ligation of the left colic artery close to its bifurcation can interfere with this supply and render the proximal descending colon ischaemic. Similarly, if the inferior mesenteric vein is ligated, then the bifurcation of the left colic vein forms the route of venous drainage from the proximal descending colon to the middle colic vein.

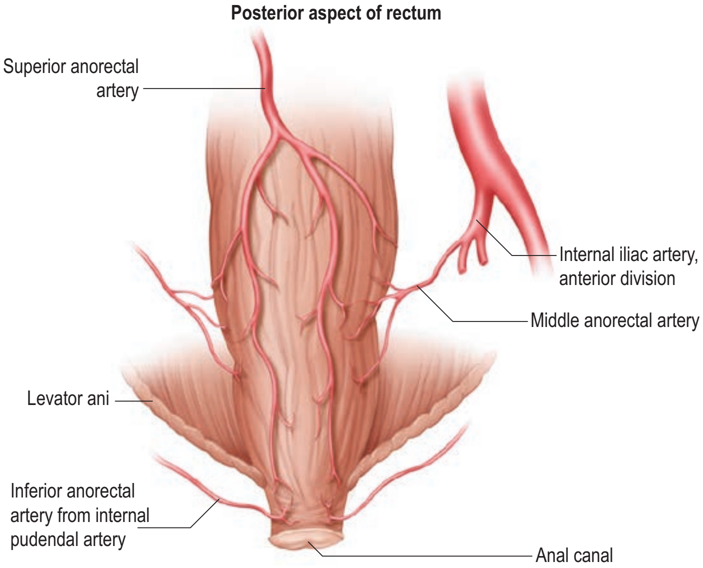
Posterior aspect of rectum
Superior anorectal artery
Internal iliac artery, anterior division
Middle anorectal artery
Levator ani
Inferior anorectal artery from internal pudendal artery
Anal canal

Fig. 65.41 The arterial supply of the rectum.

Superior anorectal artery

The principal arterial supply to the upper two-thirds of the rectum is via the superior anorectal artery (**Fig. 65.41**). The inferior mesenteric artery crosses the left common iliac vessels medial to the ureter and descends in the medial limb of the sigmoid mesocolon, straddled by the hypogastric nerves on either side. As it crosses the linea terminalis it becomes the superior anorectal artery. At the level of the third sacral vertebra, where the rectum begins, the artery enters the proximal mesorectum in the midline and divides into two branches that descend, initially posterolaterally and then on each side of the rectum. Terminal branches pierce the rectal wall and anastomose with branches of the middle anorectal and inferior anorectal arteries within the rectal submucosa.

Middle and inferior anorectal arteries

The middle anorectal arteries, when present, arise from the internal pudendal, inferior gluteal, internal iliac arteries and less frequently from other internal iliac artery branches (DiDio et al 1986, Bilhim et al 2013). When present, they enter the mesorectum anterolaterally in the 'lateral ligaments' and provide some additional supply to the middle third of the rectum. The inferior anorectal arteries are terminal branches of the internal pudendal arteries. They cross the ischio-anal fossa to enter the proximal anal canal laterally and supply the internal and external anal sphincters, the anal canal and peri-anal skin. Ascending branches supply the distal third of the rectum, anastomosing with terminal branches of the superior anorectal artery in the rectal submucosa. The rectum also rarely receives a small arterial supply from the median sacral artery via a branch that enters posteriorly at the level of the anorectal junction (Young 1897).

Veins

Inferior mesenteric vein

The inferior mesenteric vein drains the rectum and the sigmoid, descending and distal transverse colon (see Fig. 65.15; **Fig. 65.42**). It begins as the continuation of the superior anorectal vein from the rectal plexus, through which it connects with the middle anorectal and inferior anorectal veins. The inferior mesenteric vein lies to the left of the inferior mesenteric artery in the retroperitoneum and ascends anterior to the left psoas major and left ureter; it may cross the gonadal vessels or ascend medial to them. It lies just lateral or occasionally posterior to the duodenojejunal flexure, where it can be located intraoperatively. The inferior mesenteric vein receives the superior anorectal vein, several sigmoid veins and the left colic vein. It usually passes posterior to the inferior border of the body of the pancreas and anterior to the left renal

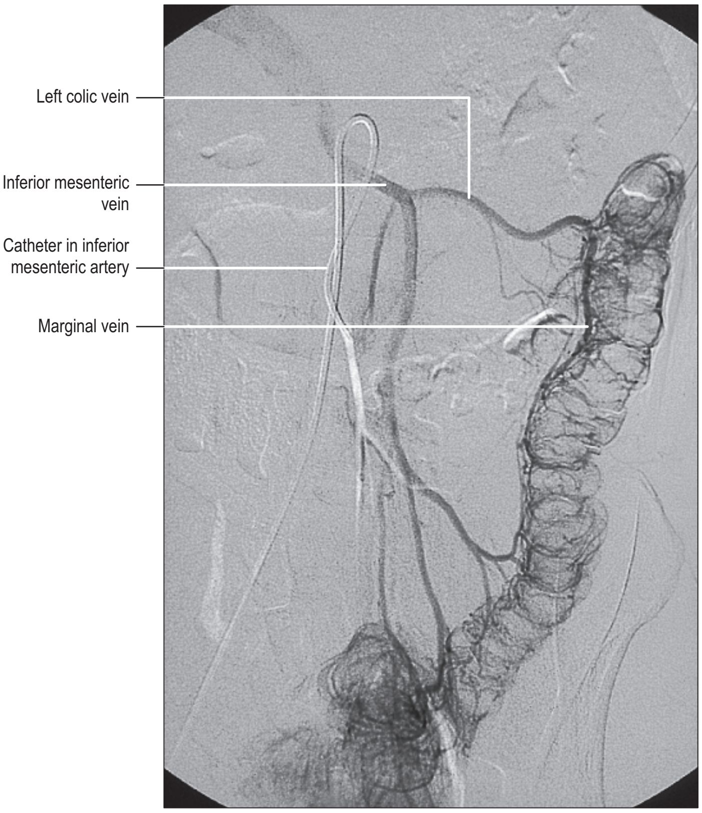

Fig. 65.42 The inferior mesenteric vein and its tributaries, digital subtraction arteriogram. (Courtesy of Dr Adam Mitchell, Charing Cross Hospital, London.)

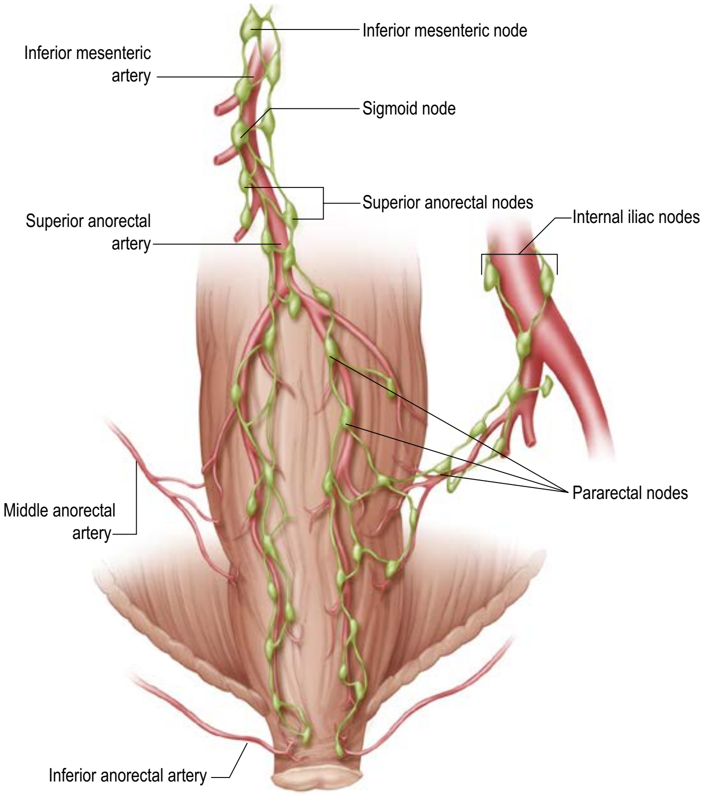

Fig. 65.43 Lymph nodes of the rectum and proximal anal canal (posterior view).

vein to drain into the splenic vein, but it can also drain into the confluence of the splenic and superior mesenteric veins or directly into the superior mesenteric vein (Graf et al 1997).

Rectal venous plexus

The rectal venous plexus surrounds the rectum and connects anteriorly with the vesical plexus in males or the uterine and vaginal venous plexuses in females. It consists of internal veins beneath the mucosa of the rectum and proximal anal canal, and external veins lying outside the muscular wall. The proximal two-thirds of the rectum and the internal part of the rectal venous plexus drain mainly to the superior anorectal vein and, from there, to the inferior mesenteric vein; the middle third of the rectum drains via one or more middle anorectal veins into the internal iliac vein; and the distal third of the rectum and anal canal drains via inferior anorectal veins into the internal pudendal veins. The rectal venous plexus is therefore a site of communication between the hepatic portal and systemic venous systems.

Superior anorectal vein

Venous tributaries from the rectal venous plexus ascend in the rectal submucosa and pierce the rectal wall to form the superior anorectal vein. This runs in the proximal mesorectum and root of the sigmoid mesocolon to the left of the superior anorectal artery, crossing the linea terminalis and left common iliac vessels to form the inferior mesenteric vein (see Fig. 65.44).

Left colic vein

The left colic vein is formed from several tributaries, including ascending and descending branches that correspond to the similarly named arteries. The left colic vein usually lies superior to its corresponding artery, and has a shorter course because the inferior mesenteric vein lies lateral to the inferior mesenteric artery (see Fig. 65.42). Occasionally there are two left colic veins that both drain into the inferior mesenteric vein (Tubbs et al 2016).

Lymphatic drainage

Small lymphoid aggregates measuring no more than a few millimetres are occasionally visible on the surface of the large intestine (epicolic and epirectal nodes). Lymph from the descending colon drains to paracolic nodes in the mesentery adjacent to the colon and from there to intermediate nodes along the left colic artery (Jamieson and Dobson 1909). Lymphatics from the sigmoid colon follow a similar pathway from paracolic to intermediate nodes in the sigmoid mesocolon. Intramural lymph from the rectum and anal canal above the pectinate line drains predominantly to pararectal nodes in the adipose tissue of the mesorectum and then along lymphatics accompanying the superior anorectal artery (Fig. 65.43). These intermediate nodes then drain to lymph nodes along the inferior mesenteric artery and from there to pre-aortic nodes. Some lymphatics from the distal rectum travel with the middle and inferior anorectal arteries to internal iliac nodes and along the median sacral artery to sacral nodes. The clinical significance of such drainage for the spread of malignancy from the distal rectum is debated (Bell et al 2009).

Innervation of the large intestine

The innervation of the large intestine is complex and includes the enteric nervous system (made up of motor neurones, intrinsic sensory neurones and interneurones lying within the wall of the gut); the autonomic nervous system (sympathetic and parasympathetic innervation); and extrinsic sensory innervation (visceral afferents) (Brookes et al 2009).

The enteric nervous system consists of ganglionated nerve plexuses lying in the submucosa (Meissner's plexus) and between the longitudinal and circular smooth muscle layers (Auerbach's myenteric plexus). Collectively, these nerves are concerned with control of mucosal functions (secretion, blood flow) and the propulsion of luminal contents by rhythmic and synchronized contractions. Motor neurones can be inhibitory or excitatory. Intrinsic sensory neurones are activated by mechanical stimuli such as stretch and muscle tension, and by chemical stimuli released by neuroendocrine cells in the wall of the gut (see Fig. 3.28). Sensory neurones project locally on to myenteric interneurones and motor neurones, allowing reflex activity to spread along the gut. Interstitial cells of Cajal are present within the submucous and myenteric neural plexuses. In summary, they act as a link between smooth muscle cells and extrinsic neurones, and are responsible for the intrinsic pacemaker activity of the gut; their activity is modulated by external autonomic nerves.

The large intestine is richly innervated by sympathetic neurones that originate either directly from the sympathetic trunk or indirectly via the aortic plexus; the former are mostly involved in the control of blood flow (vasoconstriction), while the latter also influence the secretory activity and motility of the gut. The cell bodies of preganglionic sympathetic fibres supplying the midgut-derived intestine are found in the intermediolateral nuclei of the fifth to the twelfth thoracic spinal segments and those of the hindgut-derived intestine in the intermediolateral nuclei of the first and second lumbar spinal segments. Postganglionic sympathetic neurones from both sources release noradrenaline (norepinephrine), causing presynaptic inhibition within enteric circuits, slowing gut motility and driving contraction of sphincters, e.g. internal anal sphincter. Sympathetic supply to the midgut-derived intestine is conveyed to the coeliac and superior mesenteric plexuses via the greater and lesser thoracic splanchnic nerves; postganglionic axons are distributed with branches of the superior mesenteric artery. Sympathetic supply to the hindgut-derived intestine is conveyed via the lumbar splanchnic nerves that synapse in the abdominal aortic and inferior mesenteric plexuses, and via sacral splanchnic nerves that synapse in the superior and inferior hypogastric plexuses; postganglionic fibres are distributed with branches of the inferior mesenteric artery and are inhibitory to smooth muscle of the hindgut-derived colon.

The midgut-derived intestine receives its parasympathetic innervation from the vagus nerve, via the coeliac and superior mesenteric plexuses, whereas the hindgut-derived intestine receives its parasympathetic innervation from the pelvic splanchnic nerves. The cell bodies of the pelvic splanchnic nerves are located in the second to fourth sacral spinal cord segments, the sacral parasympathetic nucleus. These parasympathetic fibres enter the inferior hypogastric plexus, where some synapse. From here, some pass directly to the rectum and other pelvic viscera while others ascend by one of two routes: either within the hypogastric nerves to the superior hypogastric plexus to be distributed along branches of the inferior mesenteric artery, or by passing directly through the retroperitoneal tissues to reach the left colic flexure and the descending and sigmoid colon. Most preganglionic parasympathetic neurones synapse in intramural plexuses in the gut wall; from there, postganglionic neurones innervate the glands (secretomotor) and muscle (motor) of the large intestine. Parasympathetic stimulation is integral to colonic propulsion and defecation and to relaxation of the internal anal sphincter.

Visceral afferent impulses mediating sensations of distension and spasm from the midgut-derived intestine travel with the vagus nerve while the hindgut-derived intestine is innervated by afferent neurones with cell bodies in the lumbar (mostly L2 and L3) and sacral (mostly S1 and S2) dorsal root ganglia and these travel alongside autonomic nerves (Brookes et al 2009). Visceral afferent innervation of intramural colonic blood vessels probably conveys the sensation of colonic distension (Song et al 2009), while visceral afferents in the rectum convey the sensation of rectal filling and are involved in reflex propulsive activity.

Motor function of the large intestine

Healthy colorectal function includes absorption of water and sodium from the intestinal lumen, net antegrade propulsion of intestinal contents at an adequate rate, and temporary faecal storage. Colonic motor activity is greatest during the day and increases on waking and after meals. It is characterized by sustained tonic contractions and brief phasic contractions. Phasic contractions are subdivided according to whether or not they propagate along the colon. Non-propagating contractions are associated with segmental mixing of luminal contents, whereas propagated sequences can be retrograde or antegrade. In the normal colon, antegrade activity is more frequent than retrograde sequences, which are seen more in the proximal colon. High-amplitude propagated contractions occur in adults 4–6 times per day, originate anywhere in the colon (but mostly proximally), and migrate for a variable distance distally (Narducci et al 1987, Bharucha 2012). They are often associated with defecation or passing flatus. The sigmoid colon exhibits cyclical bursts of motor activity, which may be important in modulating the delivery of faeces to the rectum. A high-pressure zone with unique contractile properties in response to sigmoid colon and rectal distension or contraction has been demonstrated in the distal sigmoid colon (the so-called rectosigmoid sphincter; Shafik et al 2003). Rectal motor activity is characterized by motor complexes that can be triggered by propagating contractions from the proximal colon and by the delivery of faeces or flatus from the sigmoid colon. However, since their propagation is frequently retrograde, it has been suggested that they help to keep the rectum empty, thereby preventing the untimely delivery of colonic contents.

ANAL CANAL

Although often defined differently between anatomists and clinicians, the anal canal begins at the pelvic diaphragm and ends at the anal orifice (Figs 65.44–65.46) (Lee and Kim 2018). It is directed posteriorly because the sling-like pubo-analis pulls the rectum anteriorly to create the anorectal flexure. The anal canal lies 2–3 cm anterior and slightly inferior to the tip of the coccyx, opposite the apex of the prostate in males. At the anal orifice, the squamous epithelium lining the distal anal canal becomes continuous with the skin of the perineum. The area of pigmentation of skin around the anal orifice corresponds approximately to the extent of the external anal sphincter. The anal orifice can be difficult to identify, particularly in males in whom the perineum can 'funnel' upwards into the distal anal canal, but the characteristic puckering of the skin formed by the penetrating fibres of the conjoint longitudinal muscle of the anal canal provides a useful landmark. Such penetrating fibres have been termed corrugator cutis ani.

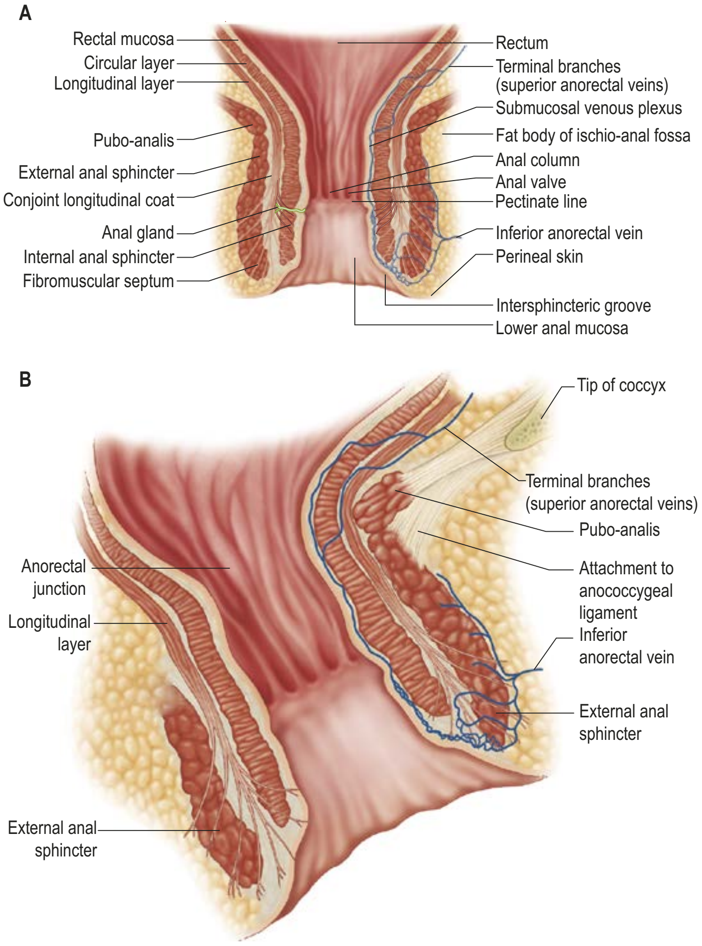

Fig. 65.44 A, A coronal section through the anal canal; glandular and vascular structures are shown unilaterally for clarity. **B**, A sagittal section through the anal canal; the anal canal is angled posteriorly and so anterior sphincteric structures appear to be lower than posterior structures. The glandular, vascular and fibromuscular structures have been omitted for clarity. (C, *continued online*)

The anal canal consists of an inner epithelial lining, a vascular subepithelium, the internal and external anal sphincters, fibromuscular supporting tissue, and dense neuronal networks of autonomic and somatic origin. Functionally, it represents a zone of high pressure. It is 2–5 cm long in adults; the anterior wall is slightly shorter than the posterior. It is usually shorter in females. At rest, it forms an oval or triradiate slit in the anteroposterior plane rather than a truly circular canal. The arrangement of the external anal sphincter and its attachments to the perineal body and coccyx create sites of maximum pressure in the anterior and posterior midline of the canal.

Anteriorly, the middle third of the anal canal is attached by dense connective tissue to the perineal body, which separates it from the membranous urethra in males and from the distal vagina in females. Laterally and posteriorly, the anal canal is surrounded by the loose adipose tissue of the ischio-anal fossae; this arrangement allows the canal to expand but offers a potential pathway for the spread of perianal sepsis. Posteriorly, it is attached to the coccyx via the anococcygeal ligament, a midline connective tissue band containing smooth and skeletal muscle fibres that runs between the posterior aspect of the middle region of the external anal sphincter and the coccyx. The anococcygeal ligament is traditionally regarded as lying just inferior to the midline raphe of levator ani but its relationship to the raphe is more complex (Kinugasa et al 2011). Kinugasa et al (2012) hypothesized that the classically described anococcygeal raphe is in fact, simply a superficial part of the anococcygeal ligament.

The ischial spines can be palpated laterally by an examining finger in the proximal anal canal. The pudendal nerves pass over the attachment of the sacrospinous ligament onto the ischial spine and pudendal nerve motor terminal latency can be measured digitally using a modified electrode worn on the examining glove.

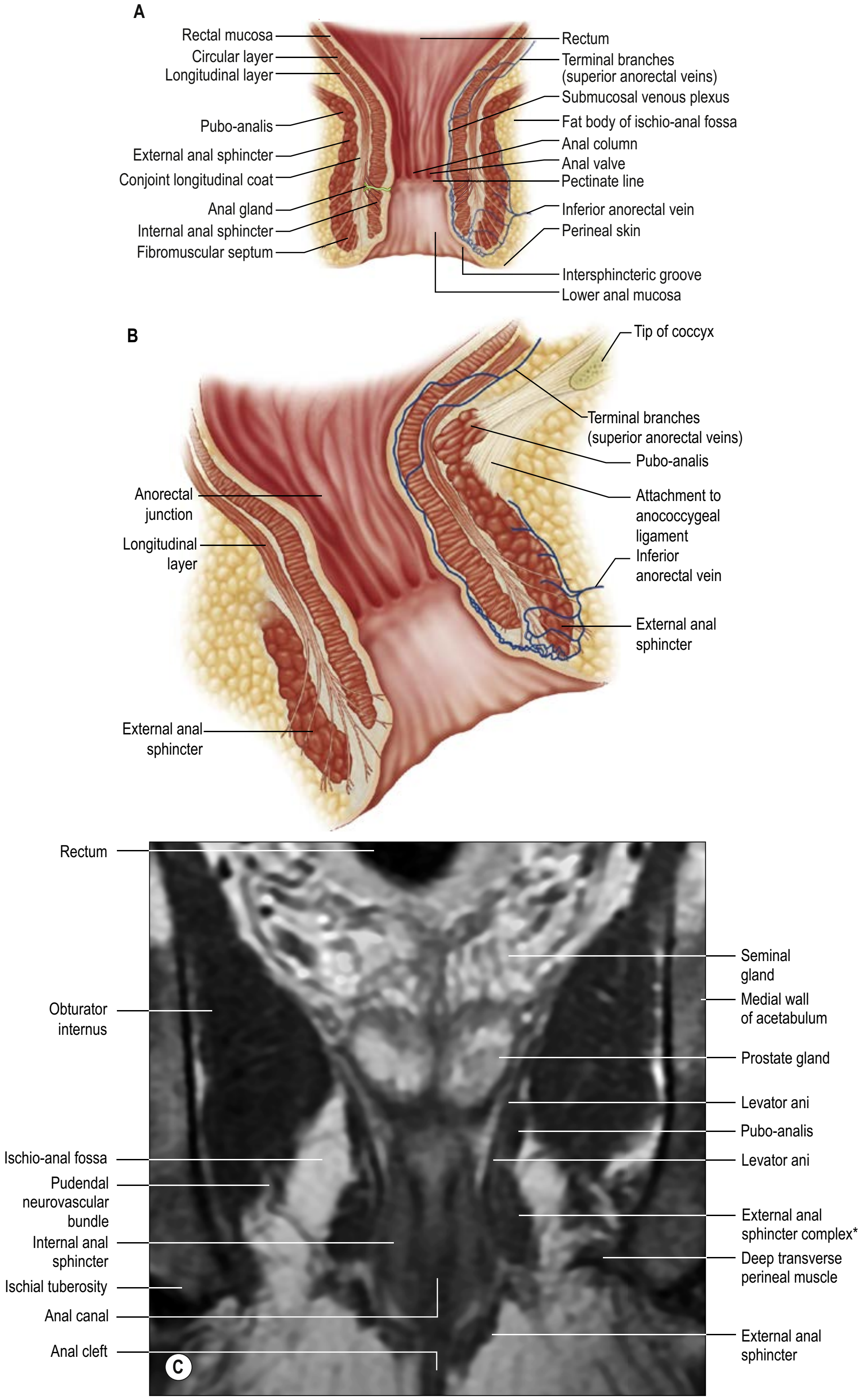
A
Rectal mucosa
Circular layer
Longitudinal layer
Pubo-analis
External anal sphincter
Conjoint longitudinal coat
Anal gland
Internal anal sphincter
Fibromuscular septum
Rectum
Terminal branches (superior anorectal veins)
Submucosal venous plexus
Fat body of ischio-anal fossa
Anal column
Anal valve
Pectinate line
Inferior anorectal vein
Perineal skin
Intersphincteric groove
Lower anal mucosa
B
Tip of coccyx
Terminal branches (superior anorectal veins)
Pubo-analis
Attachment to anococcygeal ligament
Inferior anorectal vein
External anal sphincter
Anorectal junction
Longitudinal layer
External anal sphincter
Rectum
Obturator internus
Ischio-anal fossa
Pudendal neurovascular bundle
Internal anal sphincter
Ischial tuberosity
Anal canal
Anal cleft
C
Seminal gland
Medial wall of acetabulum
Prostate gland
Levator ani
Pubo-analis
Levator ani
External anal sphincter complex*
Deep transverse perineal muscle
External anal sphincter

Fig. 65.44 **A**, A coronal section through the anal canal; glandular and vascular structures are shown unilaterally for clarity. **B**, A sagittal section through the anal canal; the anal canal is angled posteriorly and so anterior sphincteric structures appear to be lower than posterior structures. The glandular, vascular and fibromuscular structures have been omitted for clarity. **C**, Coronal T2-weighted MRI of the anal canal. *The external anal sphincter 'complex' here is used as a term for the muscle fibres of inferior pubo-analis and superior external anal sphincter, which are indistinguishable.

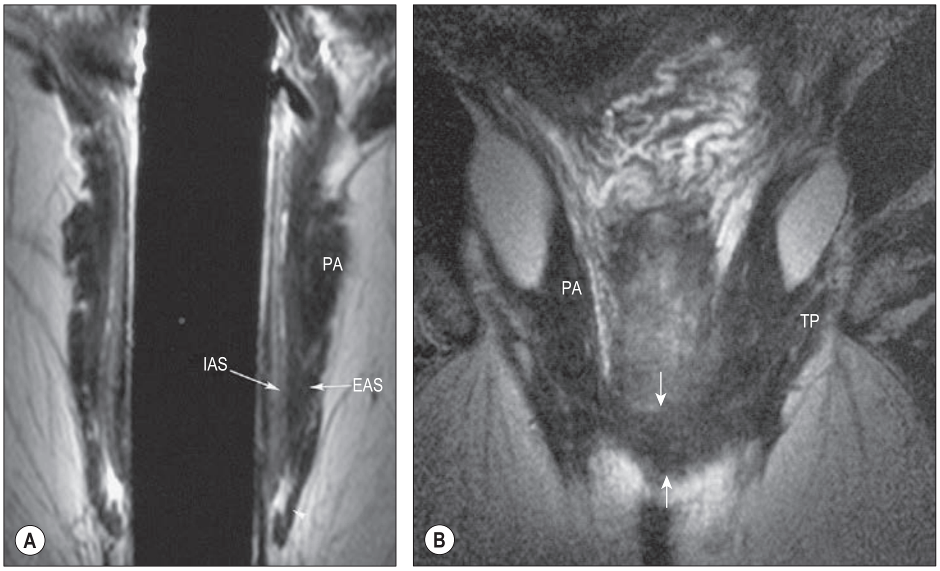

Fig. 65.45 **A**, A mid-coronal MRI endocoil image of the anal canal. **B**, An anterior coronal MRI endocoil section in a female showing superficial transverse perineal (TP) joining the external anal sphincter anteriorly (between arrows). Other abbreviations: EAS, external anal sphincter; IAS, internal anal sphincter; PA, pubo-analis.

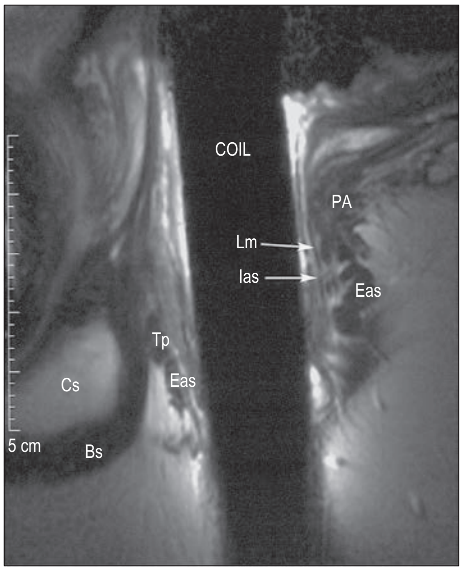

Fig. 65.46 MRI endocoil mid-sagittal view of the anal canal in a male. Abbreviations: Bs, bulbospongiosus; Cs, corpus spongiosum; Eas, external anal sphincter; Ias, internal anal sphincter; Lm, longitudinal muscle; PA, pubo-analis; Tp, superficial transverse perineal.

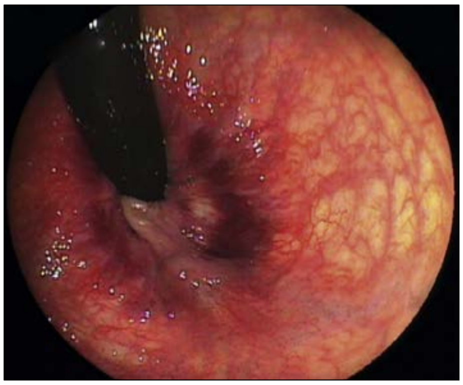

Fig. 65.47 The endoscopic appearance of the anorectal junction viewed internally from above. The endoscope is visible in the upper left corner of the image.

Lining of the anal canal

The proximal part of the anal canal is lined by reddish columnar epithelium similar to that of the rectum; it contains secretory and absorptive cells with numerous tubular intestinal glands. Distally, the epithelium becomes cuboidal and darker just above the level of the anal valves (**Fig. 65.47**). The subepithelial tissues are mobile and relatively distensible and contain submucosal arterial and venous plexuses.

In the mid anal canal there are 6–10 vertical mucosal folds, the anal columns (of Morgagni). These are better defined in children than in adults. They frequently contain a terminal branch of the superior anorectal artery and vein, supplemented to a variable degree by middle and inferior anorectal vessels (Thomson 1975). Dilated submucosal veins in the proximal anal canal form an internal rectal plexus. Tiny arteriovenous connections to these dilated submucosal veins give the blood within them a higher oxygen tension and therefore a redder colour than normal venous blood. The submucosal vessels are most prominent in the left-lateral, right-posterior and right-anterior quadrants of the wall of the canal (approximately 3, 7 and 9 o'clock when viewed in the lithotomy position); here, the subepithelial tissues are expanded into three 'anal cushions'. Although variable in number and position, these help to seal the anal canal and contribute to the maintenance of continence to flatus and fluid. The anal cushions are important in the pathogenesis of haemorrhoids. The distal ends of the columns form small crescentic folds, called anal valves, between which lie small recesses known as anal sinuses. The anal valves and sinuses together form the scalloped pectinate line, which is firmly anchored to submucosal connective tissue. Anal glands open into small depressions, anal crypts (sinuses), in the anal valves. The glands are branched and lined by stratified columnar epithelium. Cystic dilations in the intestinal glands can extend through the internal anal sphincter and even into the external anal sphincter (Seow-Choen and Ho 1994).

The epithelium below the pectinate line is smooth and typically shows an abrupt transition to parchment-coloured, non-keratinized, stratified squamous epithelium, which lacks sweat and sebaceous glands and hair follicles but contains numerous somatic sensory nerve endings conveying sensations of touch, pain and temperature (Duthie and Gairns 1960). It extends down to the intersphincteric groove, a palpable depression at the distal border of the internal anal sphincter. Distal to the intersphincteric groove, the anal canal is lined by hair-bearing, keratinizing, stratified squamous epithelium, which is continuous with the perianal skin. Dilated veins in the subepithelial tissue below the pectinate line contribute to an external rectal plexus (see Fig. 65.44); this can be seen on clinical examination as a circumferential ring at the anal orifice if the subject is asked to bear down.

The junction between the columnar epithelium above and the squamous epithelium below is referred to as the anal pecten. It is variable in length and position but often extends about 1 cm proximal to the pectinate line (Fenger 1987). There are nerve endings including thermoreceptors in the submucosa around the proximal anal transition zone; they probably play a role in continence by providing a highly specialized 'sampling' mechanism to identify the contents of the distal rectum when the proximal anal canal relaxes (Kadam-Halani et al 2018).

The well-defined muscularis mucosae of the rectum continues into the proximal anal canal. Some fibres from the conjoint longitudinal muscle of the anal canal traverse the internal anal sphincter and turn cranially to merge with the muscularis mucosae, forming the submucosal muscle of the anal canal (also called the musculus submucosae ani, or musculus canalis ani, or Treitz's muscle). Attachments of the longitudinal fibres to the submucosal muscle of the anal canal are particularly dense at the pectinate line (the mucosal suspensory ligament (of Parks)), causing the mucosa to be tethered more firmly at this level and approximately marking the watershed between the hepatic portal and systemic venous drainage of the rectal plexuses. The attachments of fibres from the longitudinal muscle layer, the muscularis mucosae of the anal canal, also create 'spaces' within the submucosa: a proximal submucous space, a marginal space extending from the pectinate line to the intersphincteric groove, and a perianal space distally.

Muscles of the anal canal

The anal canal is surrounded by internal and external anal sphincters, separated by the conjoint longitudinal muscle layer, the whole arrangement being named the anal sphincter complex (**Figs 65.48–65.49**) (Al-Ali et al 2009). The anatomy of this region has been clarified in recent years using endoanal sonography and MRI.

Internal anal sphincter

The internal anal sphincter is the specialized, thickened terminal part of the inner circular muscle of the large intestine. It is thicker in males and in patients with chronic constipation. The muscle fibre arrangement is not truly circular, but rather a tight spiral that shortens and widens with relaxation. It commences at the anorectal junction and ends proximal to the anal orifice; its distal border is palpable at the intersphincteric groove. It is traversed by fibres passing medially from the conjoint longitudinal muscle into the submucosa.

The internal anal sphincter is tonically contracted at rest but it relaxes as a consequence of reflex activity, predominantly during defecation. Transient relaxation of the upper internal anal sphincter occurs in response to rectal distension (the recto-anal inhibitory reflex) and postprandial rectal contractions (the sampling reflex). Relaxation allows the distal rectal contents to pass into the proximal anal canal, enabling their physical nature to be consciously or subconsciously perceived; this is accompanied by sustained contraction of the distal internal anal sphincter and contraction of the external anal sphincter to maintain continence. The recto-anal inhibitory reflex is primarily mediated by the enteric nervous system, although spinal pathways could modulate it. It is absent in patients with Hirschsprung's disease.

Vascular supply and innervation

The internal anal sphincter is supplied by terminal branches of the superior rectal and inferior anorectal vessels and innervated extrinsically by autonomic nerves. Sympathetic fibres originate in the L1 and L2 parts of the spinal cord and parasympathetic fibres in the S2 to S4 parts of the spinal cord, both being distributed via the inferior hypogastric plexus. Stimulation of cholinergic muscarinic receptors (parasympathetic) causes internal anal sphincter relaxation and longitudinal anal muscle contraction, while α-adrenergic receptor stimulation (sympathetic) causes both the internal anal sphincter and longitudinal muscle to contract. Activation of nitrergic nerves also mediates internal anal sphincter relaxation and is the rationale for using topical nitroglycerine and other drugs that promote nitric oxide for treating pathological conditions associated with increased resting anal tone.

Conjoint longitudinal muscle

The conjoint longitudinal muscle of the anal canal is a direct continuation of the outer longitudinal smooth muscle of the rectum, descending between the internal and external anal sphincters, and augmented in its proximal part by striated muscle fibres from the medial aspect of levator ani (Lunniss and Phillips 1992). It is particularly prominent in the fetus, where it is actually thicker than the internal anal sphincter. With advancing age, there is gradual replacement of muscle by connective tissue, so the layer becomes thin in the elderly and few muscle fibres are seen in its distal part. As it passes down the anal canal, muscle fibres peel off in three directions: internally, through the internal anal sphincter to reach the anal submucosa; inferiorly, through the striated muscle of the distal and subcutaneous part of the external anal sphincter to insert into the perianal skin (some of these fibres, e.g. corrugator cutis ani encircling the anal orifice); and outwards, through the upper part of the external anal sphincter (see Fig. 65.44). The most inferior fibres create a honeycomb arrangement in the subcutaneous fat and separate a superficial perianal space from the deeper ischio-anal fossa. Additional ramifications of this muscle beyond the external anal sphincter have been described, emphasizing its central role in anorectal stability (Courtney 1950).

The conjoint longitudinal muscle is innervated by autonomic nerves that share their origin with those supplying the internal anal sphincter. Its contraction during defecation shortens and widens the anal canal and everts the anal orifice. The muscle degenerates and is gradually replaced by connective tissue with age (Haas et al 1984). Its extensions provide pathways for the spread and containment of infection.

External anal sphincter

The external anal sphincter forms the bulk of the anal sphincter complex. It is an oval tube of striated muscle composed mostly of type I slow twitch muscle fibres adapted for prolonged contraction. It is shorter and thinner in females (Rociu et al 2000). The historical concept of the muscle having three parts (deep, superficial and subcutaneous) is no longer valid, but proximal (deep) and distal (superficial or subcutaneous) parts are still described by some authors. The superior part surrounds the internal anal sphincter while the inferior part encircles the anal canal inferior to the internal anal sphincter (Fritsch et al 2002, Al-Ali et al 2009).

The external anal sphincter is attached to the anococcygeal ligament posteriorly and to the perineal body anteriorly; some muscle fibres on each side of the sphincter decussate to form a commissure in the anterior and posterior midline. The most proximal fibres blend with the inferior medial fibres of pubo-analis and attach to the anococcygeal raphe posteriorly and superficial transverse perineal muscle anteriorly. The distal part of the external anal sphincter extends below the internal anal sphincter and is traversed by the terminal fibres of the conjoint longitudinal muscle (see above). Anteriorly, it is attached to bulbospongiosus and bulbocavernosus (Shafik et al 2007). Like levator ani and the internal anal sphincter, the external anal sphincter is tonically contracted at rest (the postural reflex).

Vascular supply and innervation

The external anal sphincter is supplied by the inferior anorectal vessels with a small contribution from the median sacral artery. It is innervated bilaterally by the inferior anal nerve from the pudendal nerve (containing contributions from the second, third and fourth sacral ventral rami). The pudendal nerve also carries afferent fibres from the lining of the anal canal and perianal skin. The proximal external anal sphincter may also receive motor fibres from the nerve to levator ani, which is derived from the ventral rami of predominantly the third through fifth sacral spinal nerves (Loukas et al 2016).

Intersphincteric space and anal glands

The intersphincteric 'space' is a potential space between the conjoint longitudinal muscle layer and the external anal sphincter. It can be entered surgically to provide access in a variety of operations (e.g. intersphincteric excision of the rectum and intersphincteric approaches to fistulae). Within the space lie the anal glands, the source of most anal fistulae (Parks 1961). There is an average of 12 anal glands within the adult anal canal, evenly distributed around the circumference. Their function is unknown, but they secrete mucin (different in composition from that secreted by rectal mucosa) and they communicate with the anal lumen via ducts (lined by epithelium similar to that of the anal pecten), which cross the internal anal sphincter to open at the level of the anal valves immediately above the pectinate line (Seow-Choen and Ho 1994). Retrograde passage of bacteria from the anal canal to the gland is understood to cause infection; inflammatory occlusion of the duct prevents spontaneous drainage back into the anal canal. Sepsis can then spread along different routes to cause abscesses and fistulae within various spaces (Parks et al 1976). High trans-sphincteric fistulae involving the proximal two-thirds of the external anal sphincter remain a surgical challenge because division of muscle involving more than one-third of the sphincter can result in incontinence (Subhas et al 2012).

Vascular supply and lymphatic drainage of the anus

Arteries

The anal canal is supplied by terminal branches of the superior anorectal artery and the inferior anorectal artery from the internal pudendal artery, together with a small contribution from the median sacral artery. The arterial supply to the epithelium of the distal anal canal in the midline, particularly posteriorly, is relatively deficient (Klosterhalfen et al 1989); it is further diminished if the internal anal sphincter is hypertonic (Schouten et al 1996). The epithelium is more firmly tethered to underlying structures in the midline, which may also be a focal point of pressure in the anal canal. Collectively, these factors are thought to predispose to the occurrence of acute and chronic anal fissures, which are most commonly found in the midline, especially posteriorly.

Veins

The venous drainage of the anal canal parallels the arterial supply. The proximal canal is drained predominantly by the superior anorectal veins, tributaries of the inferior mesenteric vein; some blood returns to the internal iliac veins via the middle anorectal veins. The distal part of

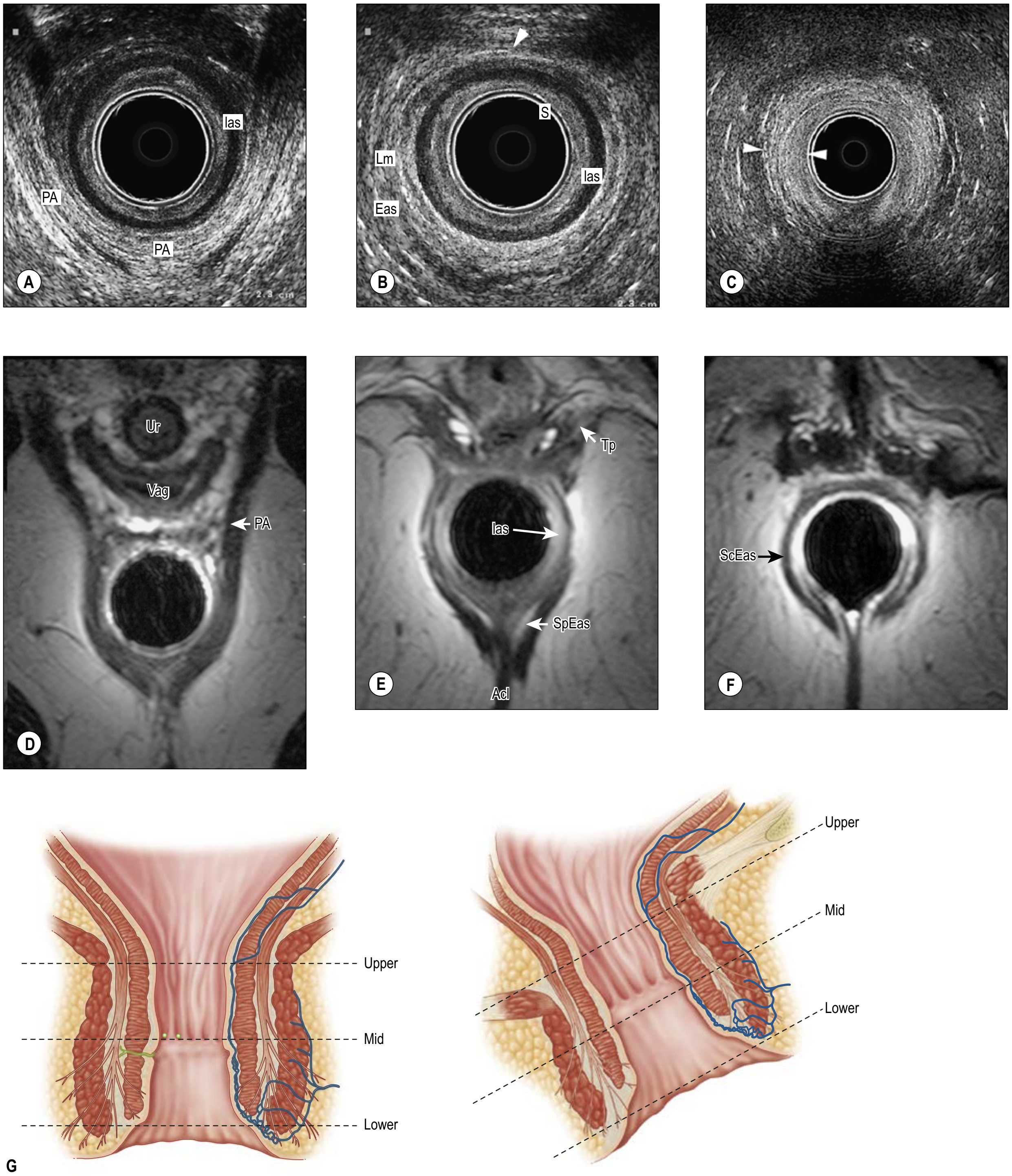

Fig. 65.48 **A–C**, Axial views of the anal canal at three levels on endoanal ultrasound in a female. The endoanal ultrasound probe is the central black structure. **A**, The proximal part of the anal canal. The 'U' shape of pubo-analis is visible. **B**, The middle part of the anal canal. The external anal sphincter is now a complete ring anteriorly (arrowhead). **C**, The distal part of the anal canal. Below the termination of the internal anal sphincter, the longitudinal layer extends through the subcutaneous external anal sphincter (between arrowheads). **D–F**, MRI of the anal canal. **D**, At proximal anal canal level, the sling of pubo-analis extends anteriorly to the pubic bones. **E**, At mid anal canal level, the superficial transverse perineii fuse into the external anal sphincter anteriorly. The distal part of the external anal sphincter is attached either side of the anococcygeal ligament. **F**, The distal anal canal level, below the internal anal sphincter. **G**, A key for levels of the anal canal. Abbreviations: Acl, anococcygeal ligament; Eas, external anal sphincter; Ias, internal anal sphincter; Lm, longitudinal muscle; PA, pubo-analis; S, subepithelial tissues; ScEas, subcutaneous (lower) part of the external anal sphincter; SpEas, superficial (middle) external anal sphincter; Tp, transverse perineii; Ur, urethra; Vag, vagina.

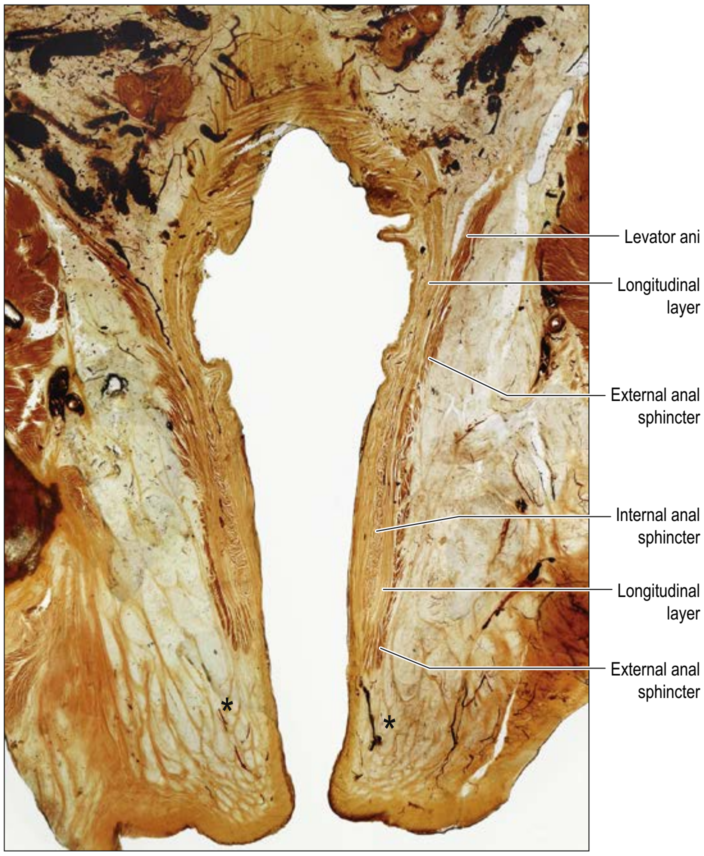
Levator ani
Longitudinal layer
External anal sphincter
Internal anal sphincter
Longitudinal layer
External anal sphincter
*
*

Fig. 65.49 A transilluminated 2.5 mm thick coronal section of a male pelvis processed for epoxy resin E12 sheet plastination, showing the entire length of the anal canal and its muscular layers: namely, the external anal sphincter, conjoint longitudinal muscle and internal anal sphincter. Note the continuity of the external anal sphincter with levator ani superiorly, consisting of two parts, upper and lower. The proximal part of the conjoint longitudinal muscle is continuous with the longitudinal muscular layer of the rectum and, inferiorly, its fibres traverse the lower part of the external anal sphincter to blend with or form fibro-fatty, honeycomb-like compartments around the peri-anal region (asterisks). The internal anal sphincter ends above the lower part of the external anal sphincter. (Courtesy of Dr Saad Al-Ali, with permission from Al-Ali S, Blyth P, Beatty S et al (2009) Correlation between gross anatomical topography, sectional sheet plastination, microscopic anatomy and endoanal sonography of the anal sphincter complex in human males. J Anat 215:212–20.)

the anal canal, including the external rectal plexus, drains via the inferior anorectal veins of the internal pudendal vein into the internal iliac vein.

Haemorrhoids

Available with the *Gray's Anatomy* e-book

Lymphatic drainage

Lymph from the proximal anal canal drains cranially into the submucosal and intramural lymphatics of the rectum. Lymphatics around pubo-analis drain to internal iliac nodes. Lymph from the distal anal canal and external anal sphincter drains to inguinal nodes. This pattern of drainage is particularly relevant to the lymphatic spread of malignant tumours from the distal rectum and anal canal. Blockage of lymph drainage along normal routes can lead to unusual patterns of dissemination.

Defecation

Defecation is the act of voiding stool from the anus and involves the coordinated function of the colon and rectum, pelvic diaphragm and anal sphincters. It is influenced by multiple factors including colonic transit, stool volume and consistency, posture, age, sex, psychology and behaviour, culture and lifestyle (Palit et al 2012). Social behaviour entrains defecation to occur at a time of convenience rather than simply in response to a defecatory urge. The urge to defecate is preceded by high-amplitude propagated contractions in the colon, which result in the antegrade propulsion of intraluminal contents to the rectum; these contractions increase in frequency and intensity just before expulsion. The response to rectal filling involves intact afferent fibres travelling from the rectum, reflex rectal contractions and normal rectal wall biomechanics. The rectum acts as a reservoir and is able to relax to accommodate faecal material and flatus (adaptive relaxation). Periodic sampling within the proximal anal canal helps to determine the nature of the rectal content. If the defecatory urge is inconvenient, pubo-analis and the external anal sphincter, which are tonically contracted at rest, can be further contracted voluntarily to move stool back up from the distal rectum. If the defecatory urge is associated with a conscious decision to evacuate, distal progression of colonic high-amplitude propagating complexes, rectal contractions, raised intra-abdominal pressure from voluntary straining (the efficiency of which is influenced by posture) and relaxation of pubo-analis (which straightens the anorectal flexure) and the anal sphincters all combine to enable defecation. Relaxation of the internal anal sphincter is a reflex response to rectal distension, whereas relaxation of the external anal sphincter is voluntary. During defecation, contraction of the conjoint longitudinal muscle shortens and opens the anal canal and flattens the anal cushions. Rectal contents and a variable quantity of colonic contents are evacuated. After defecation, the external anal sphincter contracts (the closing reflex), the internal anal sphincter gradually recovers its resting tone and the postural reflex is reactivated. The conjoint longitudinal muscle relaxes, permitting the anal canal to elongate and the anal cushions to re-expand.

Problems with defecation can result from impaired colonic transit or from various functional or mechanical rectal disorders (Lunniss et al 2009). Functional causes include inadequate or ineffective expulsive effort, paradoxical contraction of the pelvic diaphragm and external anal sphincter (dyssynergia) and lack of normal sensation (rectal hyposensitivity). Mechanical causes include impedance to evacuation when straining (rectal intussusception, obstructing masses or anal stenosis), misdirection of force vectors during straining (rectocele), or dissipation of evacuatory forces (ballooning perineum).

Anal continence and incontinence

As long as anal pressure exceeds rectal pressure, faecal continence will be maintained. Anal resting tone is derived mainly from sympathetically mediated tonic contraction of the internal anal sphincter, augmented by contraction of the external anal sphincter. Anal continence involves central, spinal and peripheral pathways, somatic, autonomic and enteric nerves, intact sacral sensorimotor reflexes, and structurally and functionally intact smooth and striated musculature.

Sphincteric causes of faecal incontinence can be structural (disruption or atrophy of part of the sphincter musculature) or neuropathic (injury to the nerve supply to the sphincters), or a combination of both. The most common causes of sphincter disruption are obstetric injury,

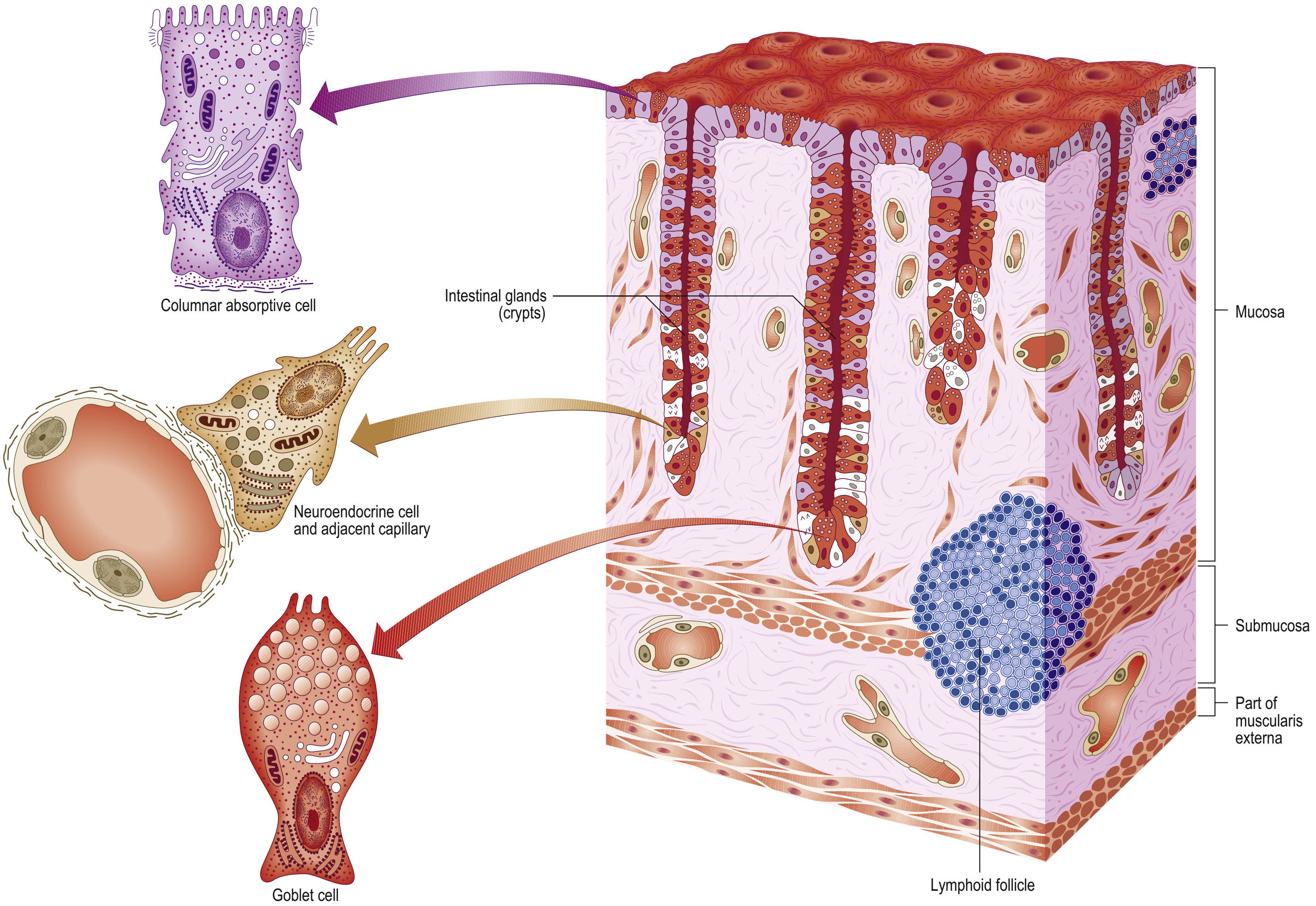
Columnar absorptive cell
Intestinal glands (crypts)
Mucosa
Neuroendocrine cell and adjacent capillary
Submucosa
Part of muscularis externa
Lymphoid follicle
Goblet cell

Fig. 65.50 The microstructure of the colonic wall and its epithelial cells. Note the aggregations of lymphocytes (blue) and undifferentiated epithelial cells (white).

‘Haemorrhoids’ refer to the abnormal downward displacement of anal cushions, which are prominences of anal mucosa formed by loose connective tissue, smooth muscle, and arteries and veins. Around 5% of the general population has haemorrhoidal disease to some extent (Randhawa et al 2015). Haemorrhoids are associated with laxity of the anal canal submucosa and enlargement of the terminal branches of the superior anorectal artery supplying the anal cushions.

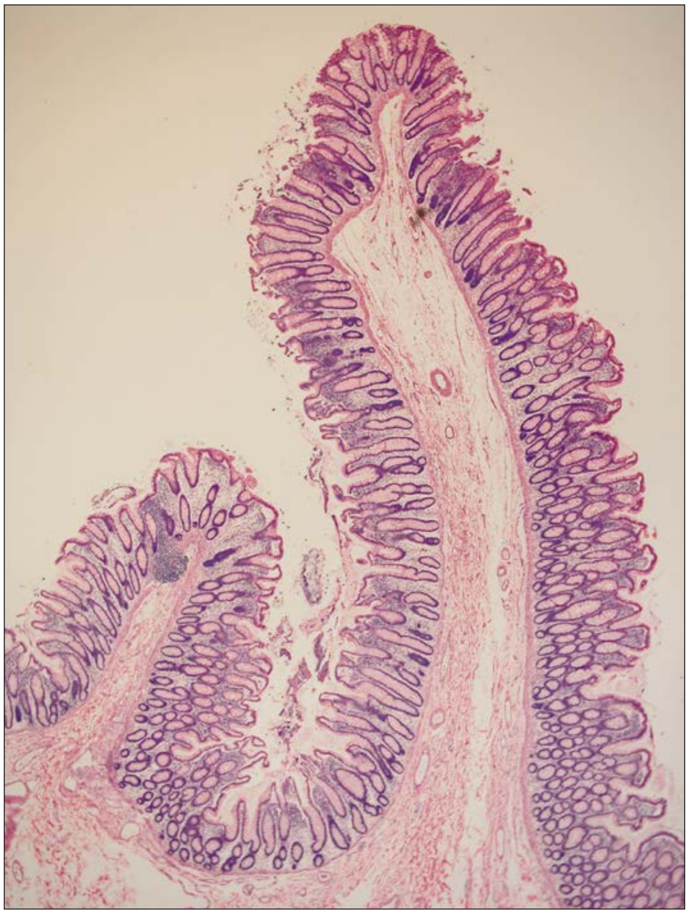

Fig. 65.51 A low-power view of the large intestine showing macroscopic folds of the mucosa and submucosa due to contraction of the external musculature. The surface epithelium receives the secretions of tubular glands in the lamina propria. They are supported by a well-defined muscularis mucosae, seen as a thin pink layer of smooth muscle separating the mucosa from the submucosa; the latter extends into the macroscopic folds. The muscularis externa lies beneath (not shown). (Courtesy of Mr Peter Helliwell and the late Dr Joseph Mathew, Department of Histopathology, Royal Cornwall Hospitals Trust, UK.)

anal surgery (for haemorrhoids, fistulae or fissures) and trauma. Pudendal neuropathy is most commonly associated with childbirth (prolonged second stage of labour) and chronic straining.

Although the anus constitutes the final barrier to faecal incontinence, factors operating proximal to the anal sphincters, such as the rate at which the stool is delivered to the rectum, rectal sensation and compliance, and adaptive relaxation, are also essential for maintaining faecal continence. Even if the sphincter mechanisms are structurally and functionally intact, faecal incontinence can occur, e.g. in diarrhoeal states or conditions where there is loss of rectal reservoir function (Scott and Lunniss 2007). Conversely, chronic rectal distension with retained faeces can result in passive (overflow) leakage, e.g. because the recto-anal inhibitory reflex is persistently activated, producing a chronically relaxed internal anal sphincter, and/or rectal sensation is blunted, causing diminished conscious contraction of the external anal sphincter.

MICROSTRUCTURE OF THE LARGE INTESTINE

The submucosal and muscularis layers of tissue in the large intestinal wall (Fig. 65.50) resemble those in the small intestine, whereas the mucosal layer differs in that that villi and circular folds are absent and the intestinal glands are longer and predominantly mucus-secreting. The microscopic structure of the colonic wall (Fig. 65.51) shows the characteristic four layers, mucosa, submucosa, muscular layer and serosa.

Mucosa

The mucosa is pale, smooth and, in the colon, raised into numerous crescent-shaped folds between the sacculi. It is thicker, darker, more vascular and more loosely attached to the submucosa in the rectum.

Epithelium

The luminal surface of all but the anorectal junction is lined by columnar cells, mucous (goblet) cells and occasional microfold (M) cells that are restricted to the epithelium overlying lymphoid follicles.

Columnar (absorptive) cells Columnar (absorptive) cells are the most numerous of the epithelial cell types. Although there is some variation in their structure, they all bear apical microvilli that are shorter and less regular than those on enterocytes in the small intestine. Typical junctional complexes around their apices limit extracellular diffusion from the lumen across the intestine wall.

Mucous (goblet) cells Mucous cells have a structure similar to those of the small intestine but are more numerous. They are outnumbered by absorptive cells for most of the length of the colon but they are equally frequent towards the rectum, where their numbers increase.

Microfold (M) cells Microfold cells overlie mucosal lymphoid tissue and are similar to those of the small intestine.

Intestinal glands

Intestinal glands are narrow, perpendicular tubular glands; they are longer, more numerous and more closely spaced than those of the small intestine. Their orifices lend a cribriform appearance to the mucosa in surface view. The glands are lined by low columnar epithelial cells, mainly goblet cells, augmented by columnar absorptive cells and neuroendocrine cells. The latter are situated mainly at the bases of the glands and secrete basally into the lamina propria. In general, the glands lack Paneth cells, although some may be present in the caecum. Stem cells located at or near the bases of the intestinal glands are the source of the other epithelial cell types in the large intestine. They provide cells that migrate towards the luminal surface of the intestine; their progeny differentiate, undergo apoptosis and are shed after approximately five days.

Lamina propria

The lamina propria is composed of connective tissue that supports the epithelium, forming a specialized periglandular myofibroblast sheath around each intestinal gland. Solitary lymphoid follicles within the lamina propria, similar to those of the small intestine, are most abundant in the caecum, appendix and rectum, but are also found scattered along the rest of the large intestine; efferent lymphatic vessels originate within them. Lymphatic vessels are absent from the intercryptal lamina propria.

Muscularis mucosae

The muscularis mucosae of the large intestine is essentially similar to that of the small intestine.

Submucosa

The submucosa of the large intestine is similar to that of the small intestine.

Muscularis externa

The muscularis externa has outer longitudinal and inner circular layers of smooth muscle, as elsewhere in the intestinal tract. The longitudinal muscle fibres form a continuous layer aggregated into macroscopically visible longitudinal bands or taeniae coli (see Figs 65.3 and 65.13). Between the taeniae coli the longitudinal muscle layer is much thinner, less than half the thickness of the circular muscle layer. The circular muscle fibres form a thin layer over the caecum and colon, a thicker layer in the walls of the rectum and the internal anal sphincter in the anal canal. Fascicles are exchanged between circular and longitudinal muscle layers, especially near the taeniae coli: deviation of longitudinal muscle fibres from the taeniae coli to the circular muscle layer could in some instances explain the haustra of the colon.

Serosa

The serosa or visceral peritoneum is variable in extent. Small, fat-filled omental appendices are most numerous on the sigmoid and transverse colons but generally absent from the rectum.

Bonus e-book content

Fig. 65.4 The endoscopic appearance of the caecum.

Fig. 65.5 The endoscopic appearance of the orifice of the appendix.

Fig. 65.6 The endoscopic appearance of the ascending colon showing the ileocaecal junction.

Fig. 65.7 The endoscopic appearance of the transverse colon.

Fig. 65.8 The endoscopic appearance of the descending colon: its lumen tends to look rather more featureless than the more proximal colon.

Fig. 65.9 The endoscopic appearance of the sigmoid colon; note the characteristic multiple large mucosal folds.

Fig. 65.10 The endoscopic appearance of the rectum: note the large transverse folds, with little else in the way of mucosal folds, which characterize the rectum. Prominent submucosal vessels are often seen, particularly in the distal third.

Fig. 65.11 **C**, Volume rendering of the colonic wall using the axial data set to produce virtual colonoscopic views, showing the triangular lumen of the transverse colon. **D**, Volume rendering of the air-filled colon using the axial data set to give an image similar to a double contrast barium enema, demonstrating haustra.

Fig. 65.29 Coronal CT showing diverticulosis of both the ascending and sigmoid colons.

Fig. 65.30 A coronal T2-weighted MRI, female rectum, plus a line diagram.

Fig. 65.31 A sagittal T2-weighted MRI, male rectum, plus a line diagram.

Fig. 65.32 A sagittal T2-weighted MRI, female rectum, plus a line diagram.

Fig. 65.33 An axial T2-weighted MRI, female proximal rectum, plus a line diagram.

Fig. 65.34 An axial T2-weighted MRI, male mid rectum below the peritoneal reflection, plus a line diagram.

Fig. 65.35 An axial T2-weighted MRI, female distal rectum below the peritoneal reflection, plus a line diagram.

Fig. 65.36 A light microscope transverse section, male, mid rectum (cadaveric specimen), plus a line diagram.

Fig. 65.37 **B**, Volume-rendered CT angiogram of the aorta, frontal view of the inferior mesenteric artery and its branches.

Fig. 65.44 **C**, A coronal T2-weighted MRI of the anal canal.

Fig. 65.48 Axial views of the female anal canal at three levels on endoanal ultrasound.

Fig. 65.49 A transilluminated 2.5 mm thick coronal section of a male pelvis processed for epoxy resin E12 sheet plastination, showing the entire length of the anal canal.

Key references

Barlow A, Muhleman M, Gielecki J et al 2013 The vermiform appendix: a review. Clin Anat 26: 833–42.

Brookes SJ, Dinning PG, Gladman MA 2009 Neuroanatomy and physiology of colorectal function and defecation: from basic science to human clinical studies. Neurogastroenterol Motil 21: 9–19.

A contemporary review of the neuroanatomy and physiology of colorectal motor function.

Fenlon HM 2002 Virtual colonoscopy. Br J Surg 89:1–3.

A description and review of the use of multislice CT to image the colon.

Fisher DF Jr, Fry WJ 1987 Collateral mesenteric circulation. Surg Gynecol Obstet 164:487–92.

A review of collateral mesenteric circulations that develop during disease processes.

Heald RJ, Husband EM, Ryall RDH 1982 The mesorectum in rectal cancer surgery: the clue to pelvic recurrence? Br J Surg 69:613–16.

The original description of the mesorectal plane and its relevance to the surgical excision of rectal tumours.

Kadam-Halani PK, Arya LA, Andy UU 2018 Clinical anatomy of fecal incontinence in women. Clin Anat 30:901–11.

Lee JM, Kim NK 2018 Essential anatomy of the anorectum for colorectal surgeons focused on the gross anatomy and histologic findings. Ann Coloproctol 34:59–71.

Lunniss PJ, Gladman MA, Benninga MA et al 2009 Pathophysiology of evacuation disorders. Neurogastroenterol Motil 21:31–40.

A review of the spectrum and classification of rectal evacuatory disorders.

Palit S, Lunniss PJ, Scott SM 2012 The physiology of human defecation. Dig Dis Sci 57:1445–64.

A detailed review of contemporary understanding of the normal physiology of defecation.

Tubbs RS, Shoja MM, Loukas M 2016 Bergman's Encyclopedia of Human Anatomic Variation. Hoboken: Wiley Blackwell.

A textbook dedicated to detailing the anatomical variations found in man.

References

Abramson DJ 1978 The valves of Houston in adults. Am J Surg 136:334–6.

Ahmadi O, McCall JL, Stringer MD 2015 Mesocolic lymph node number, size, and density: an anatomical study. Dis Colon Rectum 58:726–35.

Akinkuotu A, Samuel JC, Msiska N et al 2011 The role of the anatomy of the sigmoid colon in developing sigmoid volvulus: a case-control study. Clin Anat 24:634–7.

Al-Ali S, Blyth P, Beatty S et al 2009 Correlation between gross anatomical topography, sectional sheet plastination, microscopic anatomy and endoanal sonography of the anal sphincter complex in human males. J Anat 215:212–20.

Alatise OI, Ojo O, Nwoha P et al 2013 The role of the anatomy of the sigmoid colon in developing sigmoid volvulus: a cross-sectional study. Surg Radiol Anat 35:249–57.

Barlow A, Muhleman M, Gielecki J et al 2013 The vermiform appendix: a review. Clin Anat 26: 833–42.

Batra A, Kaur J, Parihar D et al 2013 Variations in origin of right colic artery supplying the colon. CIBTech J Surg 2:14–20.

Bell S, Sasaki J, Sinclair G et al 2009 Understanding the anatomy of lymphatic drainage and the use of blue-dye mapping to determine the extent of lymphadenectomy in rectal cancer surgery: unresolved issues. Colorectal Dis 11:443–9.

Bharucha AE 2012 High amplitude propagated contractions. Neurogastroenterol Motil 24:977–82.

Bhullar JS, Chaudhary S, Cozakov Y et al 2014 Acute appendicitis in the elderly: diagnosis and management still a challenge. Am Surg 80: E295–E297.

Bilhim T, Pereira JA, Tinto HR et al 2013 Middle rectal artery: myth or reality? Retrospective study with CT angiography and digital subtraction angiography. Surg Radiol Anat 35:517–22.

Bissett IP, Fernando CC, Hough DM et al 2001 Identification of the fascia propria by magnetic resonance imaging and its relevance to preoperative assessment of rectal cancer. Dis Colon Rectum 44:259–65.

Brookes SJ, Dinning PG, Gladman MA 2009 Neuroanatomy and physiology of colorectal function and defecation: from basic science to human clinical studies. Neurogastroenterol Motil 21: 9–19.

A contemporary review of the neuroanatomy and physiology of colorectal motor function.

Brown G, Richards CJ, Newcombe RG et al 1999 Rectal carcinoma: thin-section MR imaging for staging in 28 patients. Radiology 211:215–22.

Buschard K, Kjaeldgaard A 1973 Investigations and analysis of the positions, fixation, length and embryology of the vermiform appendix. Acta Chir Scand 139:293–8.

Coffey JC 2013 Surgical anatomy and anatomic surgery – clinical and scientific mutualism. Surgeon 11:177–82.

Courtney H 1950 Anatomy of the pelvic diaphragm and anorectal musculature as related to sphincter preservation in anorectal surgery. Am J Surg 79:155–73.

Culligan K, Walsh S, Dunne C et al 2014 The mesocolon: a histological and electron microscopic characterization of the mesenteric attachment of the colon prior to and after surgical mobilization. Ann Surg 260:1048–56.

DiDio LJ, Diaz-Franco C, Schemainda R et al 1986 Morphology of the middle rectal arteries: a study of 30 cadaveric dissections. Surg Radiol Anat 8:229–36.

Duthie HL, Gairns FW 1960 Sensory nerve-endings and sensation in the anal region of man. Br J Surg 47:585–95.

Felson B 1949 Appendiceal calculi: incidence and clinical significance. Surgery 25:734–37.

Fenger C 1987 The anal transitional zone. Acta Pathol Microbiol Immunol Scand Suppl 289:1–42.

Fenlon HM 2002 Virtual colonoscopy. Br J Surg 89:1–3.

A description and review of the use of multislice CT to image the colon.

Fisher DF Jr, Fry WJ 1987 Collateral mesenteric circulation. Surg Gynecol Obstet 164:487–92.

A review of collateral mesenteric circulations that develop during disease processes.

Fritsch H, Brenner E, Lienemann A et al 2002 Anal sphincter complex: reinterpreted morphology and its clinical relevance. Dis Colon Rectum 45:188–94.

García-Armengol J, García-Botello S, Martínez-Soriano F et al 2008 Review of the anatomic concepts in relation to the retrorectal space and endopelvic fascia: Waldeyer's fascia and the rectosacral fascia. Colorectal Dis 10:298–302.

Gaudio E, Riva A, Franchitto A et al 2010 The fascial structures of the rectum and the 'so-called mesorectum': an anatomical or a terminological controversy? Surg Radiol Anat 32:189–90.

Gourley EJ, Gering SA 2005 The meandering mesenteric artery: a historic review and surgical implications. Dis Colon Rectum 48:996–1000.

Graf O, Boland GW, Kaufman JA et al 1997 Anatomic variants of mesenteric veins: depiction with helical CT venography. AJR Am J Roentgenol 168:1209–13.

Haas PA, Fox TA Jr, Haas GP 1984 The pathogenesis of hemorrhoids. Dis Colon Rectum 27:442–50.

Hale SJ, Mirjalili SA, Stringer MD 2010 Inconsistencies in surface anatomy: the need for an evidence-based reappraisal. Clin Anat 23:922–30.

Haywood M, Molyneux C, Mahadevan V et al 2017 Right colic artery anatomy: a systematic review of cadaveric studies. Tech Coloproctol 21:937–43.

Heald RJ, Husband EM, Ryall RDH 1982 The mesorectum in rectal cancer surgery: the clue to pelvic recurrence? Br J Surg 69:613–16.

The original description of the mesorectal plane and its relevance to the surgical excision of rectal tumours.

Helander HF, Fändriks L 2014 Surface area of the digestive tract – revisited. Scand J Gastroenterol 49:681–9.

Jackson JE 1999 Vascular anatomy of the gastrointestinal tract. In: Butler P, Mitchell AWM, Ellis H (eds) Applied Radiological Anatomy. Cambridge: Cambridge University Press.

Jamieson JK, Dobson JF 1909 The lymphatics of the colon. Ann Surg 50:1077–90.

Kadam-Halani PK, Arya LA, Andy UU 2018 Clinical anatomy of fecal incontinence in women. Clin Anat 30:901–11.

Kaushik M, Bhullar JS, Bindroo S et al 2016 Minimally invasive management of complicated diverticular disease: current status and review of literature. Dig Dis Sci 61:663–72.

Kinugasa Y, Arakawa T, Abe S et al 2011 Anatomical reevaluation of the anococcygeal ligament and its surgical relevance. Dis Colon Rectum 54:232–7.

Kinugasa Y, Arakawa T, Abe H et al 2012 Anococcygeal raphe revisited: a histological study using mid-term human foetuses and elderly cadavers. Yonsei Med J 53:849–55.

Klosterhalfen B, Vogel P, Rixen H et al 1989 Topography of the inferior rectal artery: a possible cause of chronic primary anal fissure. Dis Colon Rectum 32:43–52.

A detailed postmortem angiographic study demonstrating the arrangement of anal arterial supply.

Lee JM, Kim NK 2018 Essential anatomy of the anorectum for colorectal surgeons focused on the gross anatomy and histologic findings. Ann Coloproctol 34:59–71.

Lindsey I, Guy RJ, Warren BF et al 2000 Anatomy of Denonvilliers' fascia and pelvic nerves, impotence, and implications for the colorectal surgeon. Br J Surg 87:1288–99.

Loukas M, Joseph S, Etienne D et al 2016 Topography and landmarks for the nerve supply to the levator ani and its relevance to pelvic floor pathologies. Clin Anat 29:516–23.

Lunniss PJ, Gladman MA, Benninga MA et al 2009 Pathophysiology of evacuation disorders. Neurogastroenterol Motil 21:31–40.

A review of the spectrum and classification of rectal evacuatory disorders.

Lunniss PJ, Phillips RK 1992 Anatomy and function of the anal longitudinal muscle. Br J Surg 79:882–4.

Madiba TE, Thomson SR 2002 The management of cecal volvulus. Dis Colon Rectum 45:264–7.

Murono K, Kawai K, Kazama S et al 2015 Anatomy of the inferior mesenteric artery evaluated using 3-dimensional CT angiography. Dis Colon Rectum 58:214–9.

Murphy JM, Maibaum A, Alexander G et al 2000 Chilaiditi's syndrome and obesity. Clin Anat 13:181–4.

Narducci F, Bassotti G, Gaburri M et al 1987 Twenty four hour manometric recording of colonic motor activity in healthy man. Gut 28:17–25.

Ouattara D, Kipré YZ, Broalet E et al 2007 Classification of the terminal arterial vascularization of the appendix with a view to its use in reconstructive microsurgery. Surg Radiol Anat 29:635–41.

Palit S, Lunniss PJ, Scott SM 2012 The physiology of human defecation. Dig Dis Sci 57:1445–64.

A detailed review of contemporary understanding of the normal physiology of defecation.

Parks AG 1961 The pathogenesis and treatment of fistula in ano. Br Med J 1:463–9.

An early, full description of the relationship between the anatomy of anal glands and cryptoglandular sepsis.

Parks AG, Gordon PH, Hardcastle JD 1976 A classification of fistula-in-ano. Br J Surg 63:1–12.

Pollard MF, Thompson-Fawcett MW, Stringer MD 2012 The human ileocaecal junction: anatomical evidence of a sphincter. Surg Radiol Anat 34:21–9.

Randal Bollinger R, Barbas AS, Bush EL et al 2007 Biofilms in the large bowel suggest an apparent function of the human vermiform appendix. J Theor Biol 249:826–31.

Randhawa S, Bhullar JS, Rana G et al 2015 Necrotizing fasciitis – a sinister complication of hemorrhoidectomy. Int J Colorectal Dis 30: 851–2.

Rociu E, Stoker J, Eijkemans MJ et al 2000 Normal anal sphincter anatomy and age- and sex-related variations at high-spatial-resolution endoanal MR imaging. Radiology 217:395–401.

Sato K, Sato T 1991 The vascular and neuronal composition of the lateral ligament of the rectum and the rectosacral fascia. Surg Radiol Anat 13:17–22.

Saunders BP, Phillips RK, Williams CB 1995 Intraoperative measurement of colonic anatomy and attachments with relevance to colonoscopy. Br J Surg 82:1491–3.

Schouten WR, Briel JW, Auwerda JJ et al 1996 Anal fissure: new concepts in pathogenesis and treatment. Scand J Gastroenterol Suppl 218:78–81.

Scott SM, Lunniss PJ 2007 Risk factors in faecal incontinence In: Ratto C, Doglietto GB (eds) Fecal Incontinence. Diagnosis and Treatment. London: Springer, pp. 43–66.

A review of both congenital and acquired risk factors in faecal incontinence with descriptions of the underlying pathophysiologies.

Searle AR, Ismail KA, Macgregor D et al 2013 Changes in the length and diameter of the normal appendix throughout childhood. J Pediatr Surg 48:1535–9.

Seow-Choen F, Ho JM 1994 Histoanatomy of anal glands. Dis Colon Rectum 37:1215–18.

Shafik A, Doss S, Ali YA et al 2001 Transverse rectal folds of rectum: anatomic study and clinical implications. Clin Anat 14:196–203.

Shafik A, Asaad S, Doss S 2003 Identification of a sphincter at the sigmoidorectal canal in humans: histomorphologic and morphometric studies. Clin Anat 16:138–43.

Shafik A, Shafik IA, el-Sibai O et al 2007 Physioanatomical relationship of the external anal sphincter to the bulbocavernosus muscle in the female. Int Urogynecol J Pelvic Floor Dysfunct 18:851–6.

Silverstein FE, Tytgat GNJ 1991 Atlas of Gastrointestinal Endoscopy, 2nd ed. London: Gower Medical.

Slack WW 1962 The anatomy, pathology and some clinical features of diverticulitis of the colon. Br J Surg 50:185–90.

Søndenaa K, Quirke P, Hohenberger W et al 2014 The rationale behind complete mesocolic excision (CME) and a central vascular ligation for colon cancer in open and laparoscopic surgery: proceedings of a consensus conference. Int J Colorectal Dis 29:419–28.

Song XY, Chen BN, Zagorodnyuk VP et al 2009 Identification of medium/high threshold extrinsic mechanosensitive afferent nerves to the gastrointestinal tract. Gastroenterology 137:274–84.

Stefura T, Kacprzyk A, Droś J et al 2018 The venous trunk of Henle (gastrocolic trunk): a systematic review and meta-analysis of its prevalence, dimensions, and tributary variations. Clin Anat 31:1109–21.

Subhas G, Bhullar JS, Al-Omari A et al 2012 Setons in the treatment of anal fistula: review of variations in materials and techniques. Dig Surg 29:292–300.

Tannouri S, Hendi A, Gilje E et al 2017 Pediatric colonic volvulus: a single-institution experience and review. J Pediatr Surg 52:1062–66.

Thomson WH 1975 The nature of haemorrhoids. Br J Surg 62:542–52.

An anatomical and clinical study directed at understanding the nature of haemorrhoids.

Tubbs RS, Shoja MM, Loukas M 2016 Bergman's Encyclopedia of Human Anatomic Variation. Hoboken: Wiley Blackwell.

A textbook dedicated to detailing the anatomical variations found in man.

Turmezei TD, Cockburn JF 2009 Digital subtraction angiography of the superior mesenteric artery: identifying arterial branches. Clin Anat 22:777–9.

van Gulik TM, Schoots I 2005 Anastomosis of Riolan revisited: the meandering mesenteric artery. Arch Surg 140:1225–9.

Veeresh H, Halasagi SS, Shakuntala RP et al 2012 A study of arterial supply of caecum in humans. J Evol Med Dent Sci 1:811–6.

Yamaguchi S, Kuroyanagi H, Milson JW et al 2002 Venous anatomy of the right colon: precise structure of the major veins and gastrocolic trunk in 58 cadavers. Dis Colon Rectum 45:1337–40.

Yoshida T, Suzuki S, Sato T 1993 Middle mesenteric artery: an anomalous origin of a middle colic artery. Surg Radiol Anat 15:361–3.

Young AH 1897 Abnormalities of the middle sacral artery, and their morphological significance. J Anat Physiol 31:169–75.

Zhang M, Kaw A, Chapuis PH et al 2016 Does Denonvilliers' fascia exist in women? Am J Obstet Gynecol 214:663–4.

CHAPTER

66

Liver

The liver is the largest of the abdominal viscera, occupying a substantial portion of the upper abdominal cavity. It occupies most of the right hypochondriac and epigastric regions and frequently extends into the left hypochondriac region as far as the left anterior axillary line (Fig. 66.1). As the body grows from infancy to adulthood, the liver rapidly increases in size. This period of growth reaches a plateau around 18 years and is followed by a gradual decrease in liver weight from middle age. The ratio of liver to body weight decreases with growth from infancy to adulthood. The liver weight is 4–5% of body weight in infancy and decreases to approximately 2% in adulthood. The size of the liver also differs between the sexes (being smaller in females) and body size (enlarging with fat deposition in obese individuals). It has an overall wedge shape, in part determined by the form of the upper abdominal cavity into which it grows. The narrow end of the wedge lies towards the left hypochondriac region and the anterior edge points anteriorly and inferiorly. The superior and right lateral aspects are shaped by the anterolateral abdominal and thoracic walls, and by the respiratory diaphragm. The inferior aspect is shaped by the adjacent viscera. The fibrous capsule of the capsule is no longer considered important in maintaining the shape of the liver; it allows expansion when the liver hypertrophies in response to disease, surgical resection or contralateral embolization of the hepatic portal vein or hepatic artery.

The liver is reddish-brown in colour. It assumes a more yellowish tinge with increasing fat (steatosis) and the edges become more rounded. These changes occur commonly in individuals who are obese and/or drink an excessive amount of alcohol. The liver gains a bluish tinge with venous outflow obstruction (Budd–Chiari syndrome) or congestive heart failure. The texture of the organ is usually soft to firm, though this depends partly on the volume of blood it contains and on its content of adipose and fibrous connective tissues.

The liver performs a wide range of metabolic activities required for homeostasis, nutrition and immune defence. For example, it is important for the removal and breakdown of toxic or potentially toxic materials from the blood; the regulation of blood glucose and lipids; the storage of certain vitamins, iron and other micronutrients; the synthesis of proteins and clotting factors; the metabolism of amino acids; and bile production. It is involved in a plethora of other biochemical reactions. Since most of these processes are exothermic, a substantial part of the thermal energy production of the body, especially at rest, is provided by the liver. The liver is populated by phagocytic macrophages, components of the mononuclear phagocyte system capable of removing particulates from the blood stream. It is an important site of haemopoiesis in the fetus; extramedullary haemopoiesis in the setting of haematological disease.

An account of the more common eponyms relating to the anatomy and surgery of the liver is provided in Stringer (2009).

Surfaces of the liver

The liver is usually described as having superior, anterior, right, posterior and inferior surfaces with a distinct inferior border (Figs 66.2–66.3). However, the superior, anterior and right surfaces are continuous and no definable borders separate them. It is more appropriate to group them as the diaphragmatic surface, which is mostly separated from the inferior, or visceral, surface by a narrow inferior border. At the infrasternal angle, the inferior border is adjacent to the anterior abdominal wall and accessible to physical examination by percussion, but not usually palpable except on deep inspiration. In the midline, the inferior border of the liver is near the transpyloric plane. In women and children the border often projects a little inferior to the right costal arch (margin).

Superior surface The superior surface is the largest and lies immediately below the respiratory diaphragm, separated from it by peritoneum, except for a small triangular area where the two layers of the falciform ligament diverge. Most of the superior surface lies beneath the right superior aspect of the respiratory diaphragm, but there is a shallow cardiac impression centrally that corresponds to the position of the heart above the central tendon of the diaphragm. The left side of the superior surface lies beneath part of the left side of the diaphragm.

Anterior surface The anterior surface is approximately triangular and convex and is covered by peritoneum, except at the attachment of the

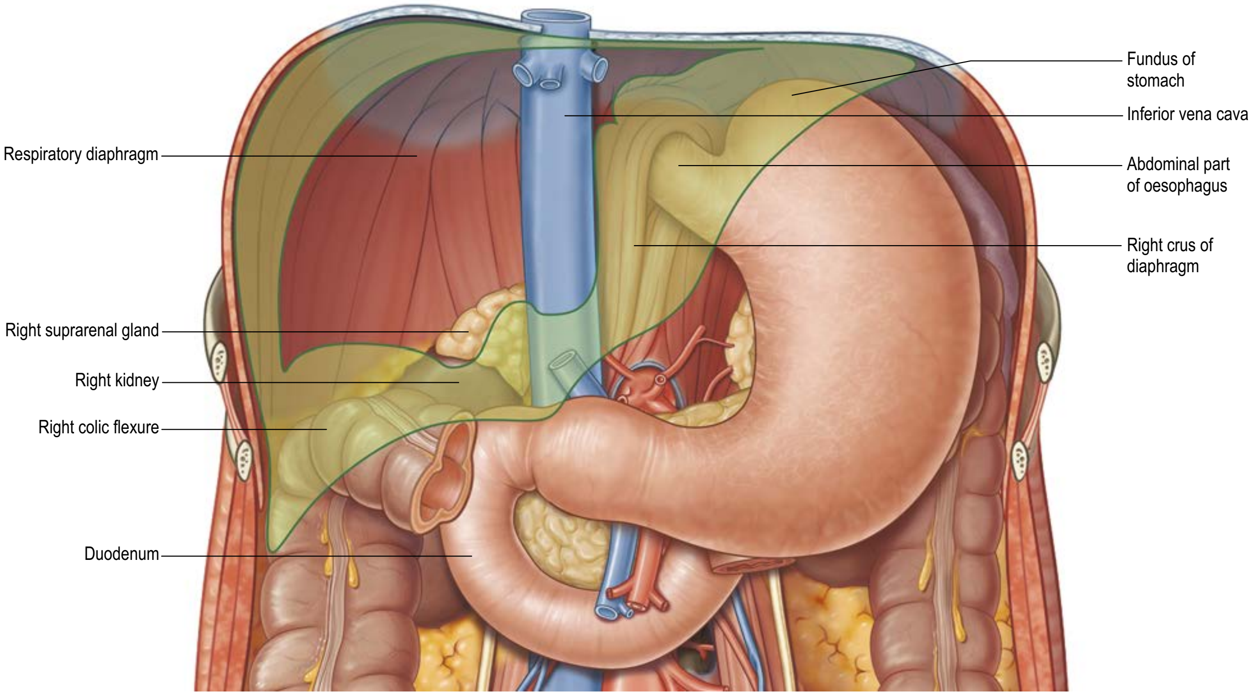

Fig. 66.1 The ‘bed’ of the liver. The outline of the liver is shaded green. The bare area of the liver is unshaded.

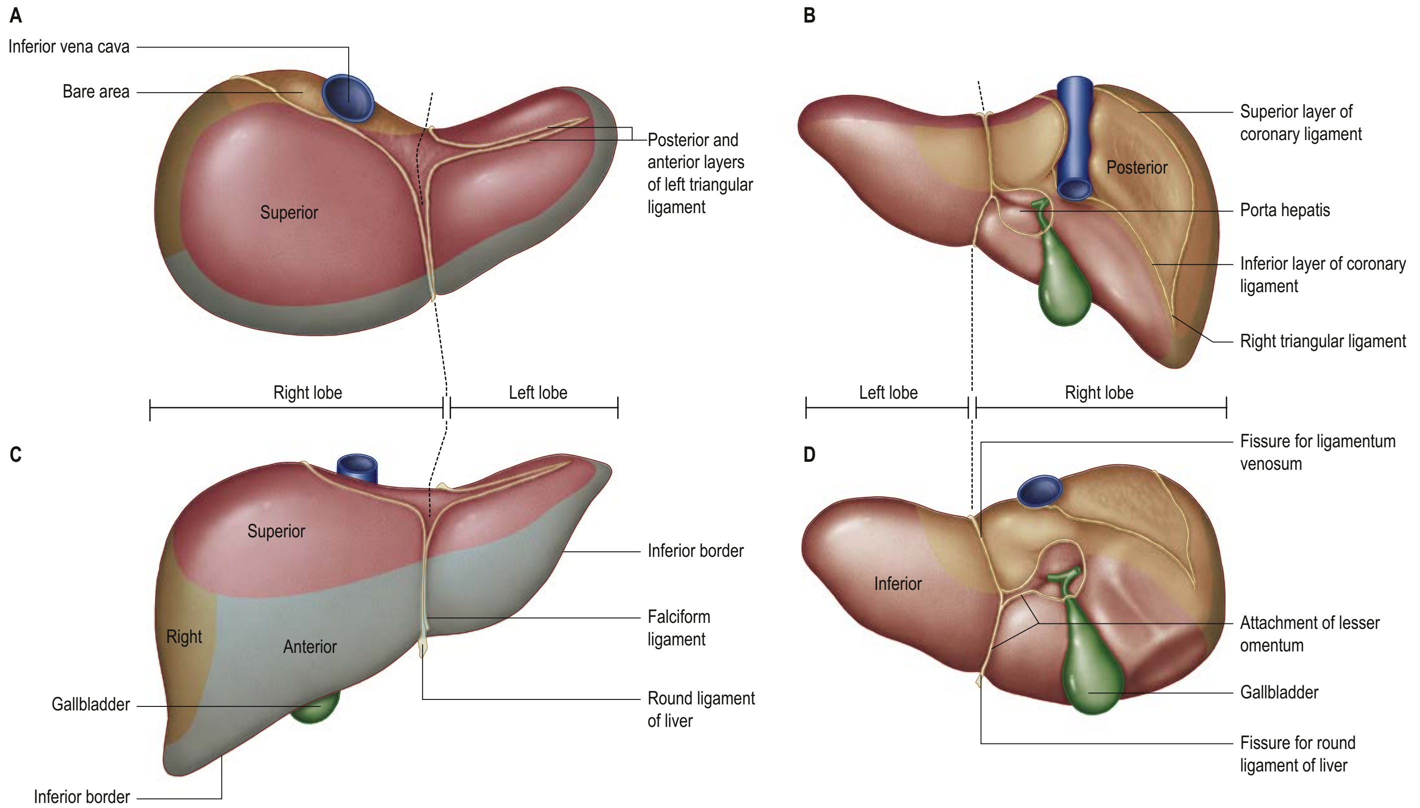
A
Inferior vena cava
Bare area
Superior
Posterior and anterior layers of left triangular ligament
B
Superior layer of coronary ligament
Posterior
Porta hepatis
Inferior layer of coronary ligament
Right triangular ligament
Right lobe
Left lobe
Left lobe
Right lobe
C
Superior
Inferior border
Falciform ligament
Right
Anterior
Round ligament of liver
Gallbladder
Inferior border
D
Fissure for ligamentum venosum
Inferior
Attachment of lesser omentum
Gallbladder
Fissure for round ligament of liver

Fig. 66.2 The surfaces and external features of the liver. **A**, Superior view. **B**, Posterior view. **C**, Anterior view. **D**, Inferior view.

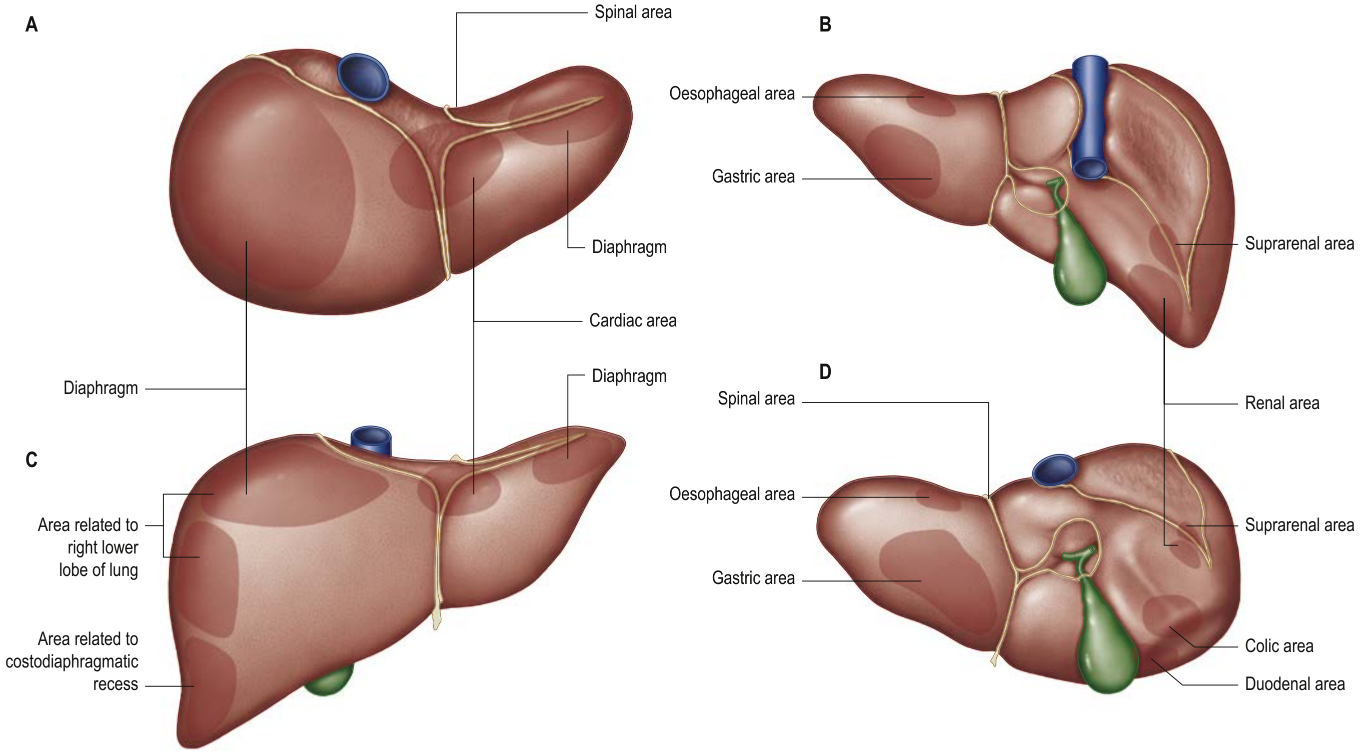
A
Spinal area
Diaphragm
Cardiac area
Diaphragm
Diaphragm
B
Oesophageal area
Gastric area
Suprarenal area
Renal area
C
Area related to right lower lobe of lung
Area related to costodiaphragmatic recess
D
Spinal area
Oesophageal area
Gastric area
Suprarenal area
Colic area
Duodenal area

Fig. 66.3 Relations of the liver. **A**, Superior view. **B**, Posterior view. **C**, Anterior view. **D**, Inferior view.

falciform ligament. Much of it is in contact with the anterior attachment of the respiratory diaphragm. On the right, the diaphragm separates it from the pleura and the sixth to the tenth ribs and costal cartilages, and on the left, from the seventh and eighth costal cartilages.

Right surface The right surface is covered by peritoneum and lies adjacent to the right superior aspect of the respiratory diaphragm, which separates it from the right lung and pleura and the seventh to the eleventh ribs. The right lung and basal pleura lie superior and lateral to its proximal third, between the diaphragm and the seventh and eighth ribs. The diaphragm, the costodiaphragmatic recess lined by pleura, and the ninth and tenth ribs lie lateral to the middle and lower thirds of the right surface. Lateral to the lower third, the diaphragm and thoracic wall are in direct contact. Rarely, the right colic flexure and proximal transverse colon lie on a long mesentery over the right, anterior and superior surfaces of the liver; this can lead to misdiagnosis of pneumoperitoneum on a radiograph or very rarely cause symptoms (Chilaiditi's syndrome) (Ch. 65).

Posterior surface The posterior surface is convex, wide on the right but narrow on the left. A median concavity corresponds to the forward convexity of the vertebral column close to the attachment of the ligamentum venosum. Much of the posterior surface is attached to the respiratory diaphragm by loose connective tissue, forming the triangular 'bare area'. The inferior vena cava lies in a groove or tunnel in the medial end of the bare area. To the left of the groove for the inferior vena cava, the posterior surface of the liver is formed by the caudate lobe and is covered by a layer of peritoneum continuous with that of the inferior layer of the coronary ligament and the layers of the lesser omentum. The caudate lobe is related to the diaphragmatic crura and the right inferior phrenic artery superior to the aortic hiatus, and is separated by these structures from the descending thoracic aorta.

The fissure for the ligamentum venosum separates the caudate lobe from the left lobe. It cuts deeply in front of the caudate lobe and contains the two layers of the lesser omentum. The posterior surface of the left lobe bears a shallow impression near the superior end of the fissure for the ligamentum venosum that is caused by the abdominal part of the oesophagus. The posterior surface of the left lobe to the left of this oesophageal impression is related to the fundus of the stomach. Together, these posterior relations make up what is sometimes referred to as the 'bed' of the liver (see Fig. 66.1).

Inferior surface The inferior surface is bounded by the inferior edge of the liver. It blends with the posterior surface in the region of the origin of the lesser omentum, the porta hepatis and the inferior layer of the coronary ligament, and is marked near the midline by a sharp fissure that contains the round ligament of the liver (ligamentum teres hepatis; the obliterated fetal left umbilical vein). The gallbladder usually lies in a shallow fossa of variable depth: it can have a short mesentery or be completely intrahepatic. The quadrate lobe lies between the fissure for the round ligament of the liver and the gallbladder.

The inferior surface of the left lobe is related inferiorly to the fundus of the stomach and the superior aspect of the lesser omentum. The quadrate lobe lies adjacent to the pylorus, the superior part of the duodenum and the inferior part of the lesser omentum. Occasionally, the transverse colon lies between the duodenum and the quadrate lobe. To the right of the gallbladder, the inferior surface is related to the right flexure of the colon, the right suprarenal gland and right kidney, and the superior part of the duodenum (see Fig. 66.1).

Supports of the liver

Available with the *Gray's Anatomy* e-book

Gross anatomical lobes

Historically, the liver has been divided on the basis of its external appearance into right, left, caudate and quadrate lobes, defined in part by peritoneal ligamentous attachments. Additional liver lobes have been reported but are rare.

Right lobe The right lobe is the largest in volume and contributes to all surfaces of the liver. It is divided from the left lobe by the falciform ligament anteriorly and superiorly and by the ligamentum venosum and fissure for the round ligament of the liver inferiorly. On the inferior surface, to the right of the grooves formed by the round ligament of the liver and ligamentum venosum, the porta hepatis separates two prominences: the caudate lobe lies posterior and the quadrate lobe lies anterior. The gallbladder lies in a shallow fossa on the inferior surface of the liver between the quadrate lobe on the left and the right lobe on the right.

Left lobe The left lobe is the smaller of the two main lobes, though it is nearly as large as the right lobe in young children. It lies to the left of the falciform ligament with no subdivisions. It is substantially thinner than the right lobe, having a thin apex that points into the left upper quadrant.

Quadrate lobe The quadrate lobe is visible as a prominence on the inferior surface of the liver to the right of the groove formed by the round ligament of the liver. Although it is anatomically part of the right lobe, its vascular inflow is from the left branch of the hepatic portal vein and left hepatic artery and its biliary outflow is to the left hepatic duct. It lies anterior to the porta hepatis and is bounded by the fossa of the gallbladder to the right, a short portion of the inferior border anteriorly, the fissure for the round ligament of the liver to the left, and the porta hepatis posteriorly. Like the caudate lobe, its morphology varies among individuals (Joshi et al 2009).

Caudate lobe The caudate lobe is visible as a prominence on the inferior and posterior surfaces to the right of the groove formed by the ligamentum venosum: it lies posterior to the porta hepatis and the hepatogastric ligament. To its right is the groove for the inferior vena cava. Above, it continues into the superior surface on the right of the superior end of the fissure for the ligamentum venosum. In gross anatomical descriptions, this lobe is said to arise from the right lobe but it is functionally separate.

Functional anatomical divisions

Current understanding of the functional anatomy of the liver is based on Couinaud's division of the liver into eight functional segments (subsequently nine, then later revised back to eight), based on the distribution of portal venous branches in the parenchyma (Couinaud 1957). Understanding the intrahepatic biliary anatomy, especially of the right ductal system, was enhanced by contributions from Hjortsjö (1951) and Healey and Schroy (1953), who used the biliary system as the main guide for division of the liver (**Fig. 66.4**). All models use the branching pattern of either the portal and hepatic veins (the 'French' model) or the bile ducts (the 'American' model) as segmentation criteria, but differ in their nomenclature (Terminology Committee of the International Hepato-Pancreato-Biliary Association 2000, Strasberg 2005, Bismuth 2013, Strasberg and Phillips 2013, Makuuchi 2013, Majno et al 2014, Hikspoors et al 2017).

The liver is divided into four portal sectors (right anterior, right posterior, left medial and left lateral) by the four main branches of the hepatic portal vein. The three main hepatic veins lie between these sectors as intersectoral veins. The intersectoral planes are also called portal fissures (or scissures). Each sector is subdivided into segments (usually two) on the basis of their supply by tertiary divisions of the perivascular fibrous capsules (Glissonian sheaths) (see below).

Fissures and sulci of the liver

Knowledge of the fissures of the liver is essential for understanding liver surgery. Three major portal fissures, main, left and right portal fissures, not visible on the surface, run through the liver parenchyma and contain the three main hepatic veins. Three minor fissures, umbilical, venous and fissure of Gans (Rouvière's sulcus, incisura hepatis dextra) are visible as physical clefts in the liver surface. Accessory fissures are rare. However, diaphragmatic sulci are seen in approximately 40% of livers and usually on the superior surface of the right lobe (Macchi et al 2003).

Main portal fissure The main portal fissure (Cantlie's line) extends from the midpoint of the fossa of the gallbladder at the inferior margin of the liver back to the midpoint of the inferior vena cava. It contains the middle hepatic vein and separates the liver into right and left hemilivers. Segments V and VIII lie immediately to the right, and segment IV immediately to the left, of the main portal fissure.

Left portal fissure The left portal fissure divides the left hemiliver into left medial and left lateral sectors. It extends from the midpoint of the inferior edge of the liver between the falciform ligament and the left triangular ligament to the point that marks the confluence of the left and middle hepatic veins. It contains the left hepatic vein and separates the left medial (anterior) and left lateral (posterior) sectors; segment III lies immediately anteriorly and segment II posteriorly.

Right portal fissure The right portal fissure divides the right hemiliver into right posterior and right anterior sectors. The plane of the right portal fissure is the most variable of the portal fissures: it runs approximately diagonally through the anatomical right lobe from the lateral end of the inferior border to the termination of the right hepatic vein. The portal fissure divides the right anterior sector (segments V and VIII) from the right posterior sector (segments VI and VII) and contains the right hepatic vein. It traverses the thickest portion of liver parenchyma that is commonly transected during liver resection.

Umbilical fissure The umbilical fissure (fissure for the round ligament of the liver) separates segments II and III from segment IV and contains a major branch of the left hepatic vein (the umbilical fissure vein). It is marked anteriorly by the attachment of the falciform ligament and inferiorly by the round ligament of the liver, where it may be

The liver is stabilized and maintained in its position in the right upper quadrant of the abdomen by both static and dynamic factors. A three-tier classification of supporting structures has been proposed: the suspensory attachments of the inferior vena cava, hepatic veins, and coronary and triangular ligaments to the posterior abdominal wall (primary factors); the support provided by the right kidney, right colic flexure and duodenopancreatic complex (secondary factors); and the attachment of the falciform ligament to the anterior abdominal wall and respiratory diaphragm (tertiary factors) (Flament et al 1982). The surgical implications of these different factors are important for understanding the pathophysiology of blunt liver trauma and the stability of transplanted liver grafts. The inferior vena cava and the hepatic veins, especially the right hepatic vein, appear to be the most important anatomical structures supporting the bulk of the liver. Other factors that influence the position of the liver within the abdominal cavity include positive intra-abdominal pressure and the movement of the diaphragm during respiration.

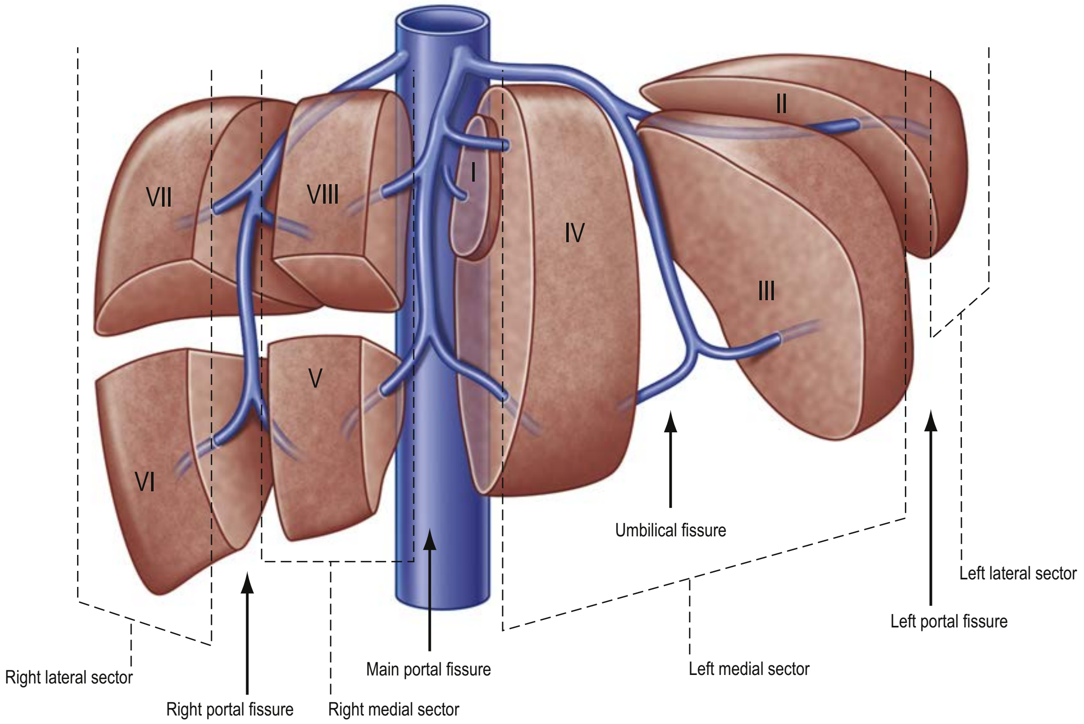

Fig. 66.4 The fissures and sectors of the liver. (Right lateral = right posterior; right medial = right anterior.)

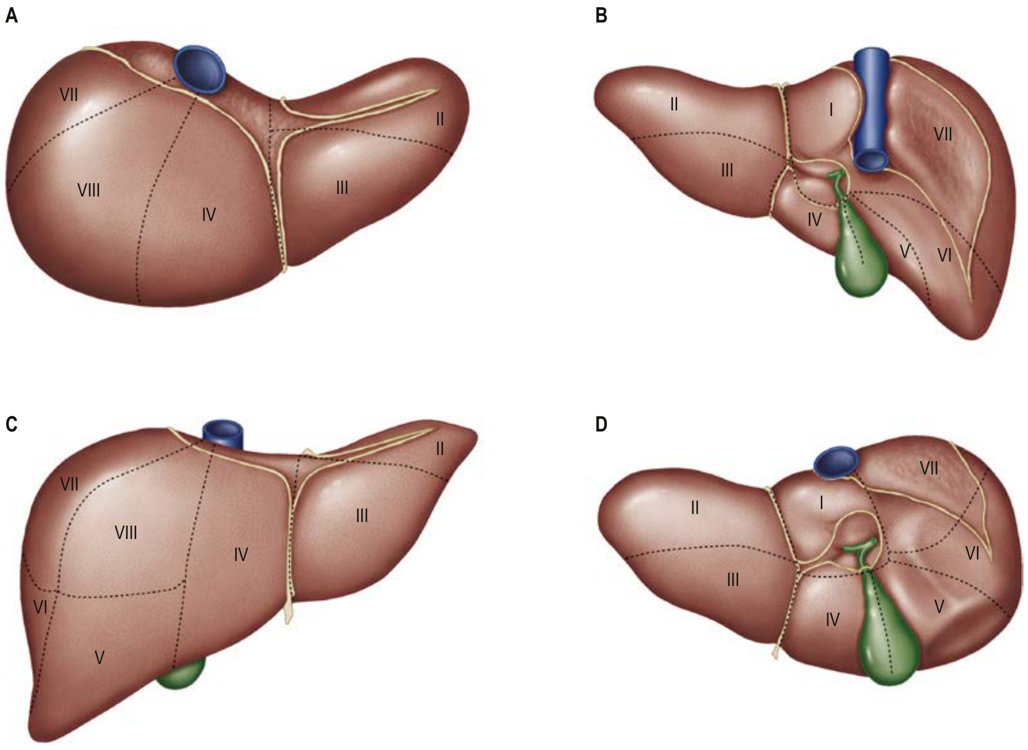

Fig. 66.5 Segments of the liver (after Couinaud). **A**, Superior view. **B**, Posterior view. **C**, Anterior view. **D**, Inferior view. The segments are usually referred to by number (name): I (caudate); II (left lateral superior); III (left medial inferior); IV (left medial superior) (sometimes subdivided into superior and inferior parts); V (right medial inferior); VI (right lateral inferior); VII (right lateral superior); VIII (right medial superior).

covered by a bridge of liver tissue extending between segments III and IV. When present, this bridge is usually avascular and can be divided safely with diathermy during surgery. The umbilical fissure also contains the umbilical portion of the left branch of the hepatic portal vein, segmental bile ducts converging to form the left hepatic duct, and the terminal branches of the left hepatic artery. The umbilical portion of the left branch of the hepatic portal vein offers direct surgical access to the left branch of the hepatic portal vein during surgery for cholangiocarcinoma of the porta hepatis and in operations to restore intrahepatic portal blood flow after hepatic portal vein occlusion. Knowledge of the arrangement of the vascular and biliary structures within the umbilical fissure is also essential when the liver is split for an adult and paediatric recipient and for live donor liver transplantation for a child recipient.

Venous fissure The fissure for the ligamentum venosum (venous fissure) is directly continuous with the umbilical fissure on the undersurface of the liver. It contains the ligamentum venosum (the obliterated ductus venosus) and lies between the caudate lobe and segment II.

Fissure of Gans The fissure of Gans (Rouvière's sulcus) lies on the undersurface of the right lobe of the liver posterior to the fossa of the gallbladder and anterior to segment I. It occurs in over 80% of normal livers, often marks the variable site of division of the portal pedicle to the right posterior sector and is a useful landmark during laparoscopic cholecystectomy (Singh and Prasad 2017, Lockhart and Singh-Ranger 2018).

Sectors and segments of the liver

Sectors

Each sector of the liver contains between one and three segments: the right posterior sector contains segments VI and VII; the right anterior sector contains segments V and VIII; the left medial sector contains segment IV (and part of I); the left lateral sector contains segments II and III (**Fig. 66.5**). The segments are numbered clockwise from below, starting with segment I and ending with segment VIII (see Figs 66.4–66.5; **Fig. 66.6**).

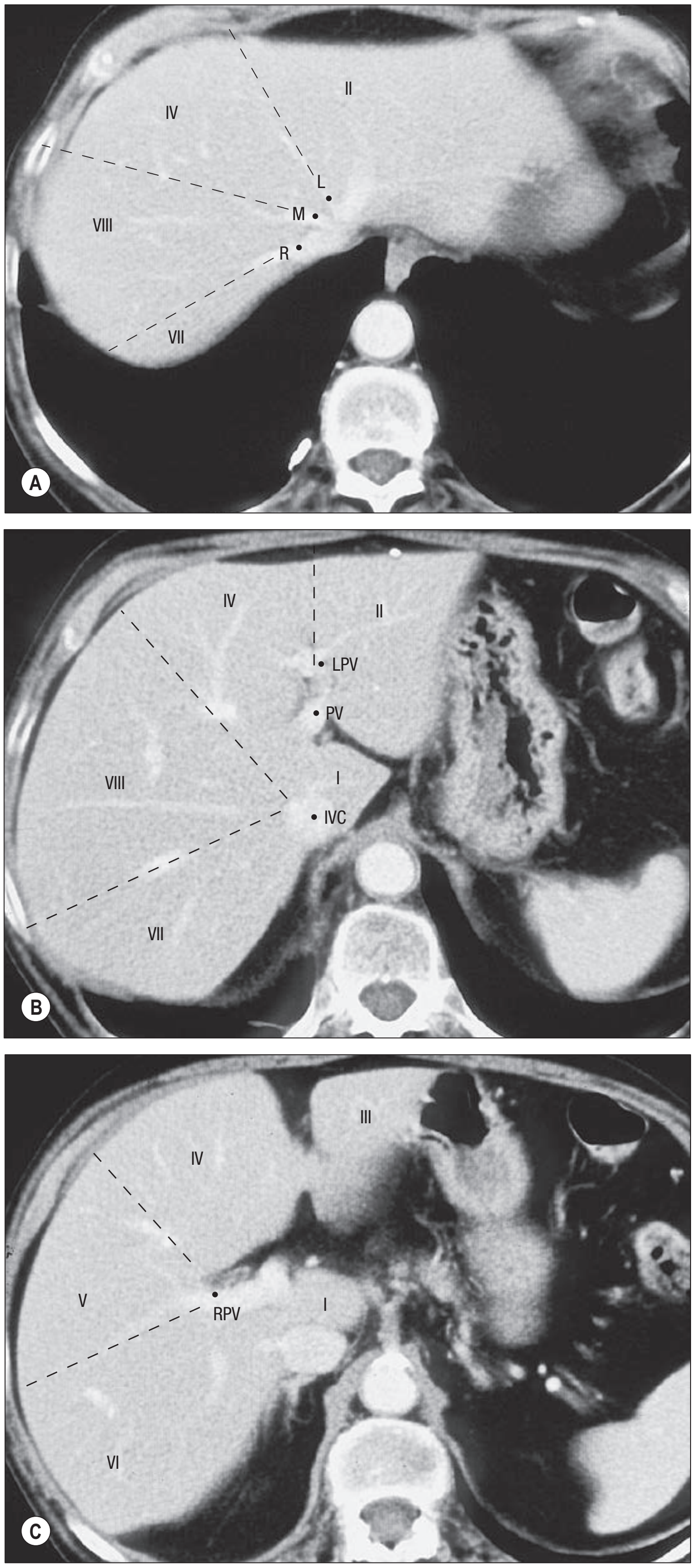

Fig. 66.6 Segments of the liver seen on axial computed tomography (CT). **A**, A contrast enhanced CT shows the left (L), middle (M) and right (R) hepatic veins at the superior aspect of the liver, marking the left, main and right portal fissures. **B**, Inferior to this, the caudate lobe (segment I) lies between the inferior vena cava (IVC) and the portal vein (PV). The left branch of the hepatic portal vein (LPV) separates segment II superiorly from segment III inferiorly. **C**, The right branch of the hepatic portal vein (RPV) divides segments V and VI inferiorly from segments VII and VIII superiorly (**B**).

Segment I Segment I corresponds to the anatomical caudate lobe and additional adjacent parenchyma supplied by branches of the hepatic portal vein at the porta hepatis and arterial branches that arise from the left and/or the right hepatic arteries. Segment I lies posterior to segment IV; the caudate process extends to the left, posterior to the hepatogastric ligament. The segment straddles the inferior vena cava, with its left half directly adjacent to segment II and its right half wrapped to a variable extent around the retrohepatic portion of the inferior vena cava. The segment that wraps around the inferior vena cava most often includes a larger vein that drains directly into the inferior vena cava. In the European literature, segment I is subdivided into three parts, the caudate process, caudate lobe (Spiegel's lobe) and paracaval portion; right and left subdivisions are recognized in Asia. The perivascular fibrous capsules to segment I arise from both right and left main capsules, which means that the segment receives vessels from both the left and right branches of the hepatic portal vein and hepatic arteries. The venous drainage of the caudate lobe is directly into the inferior vena cava by multiple small tributaries that usually arise from the lower third of the segment, occasionally from the middle third, but rarely from the upper third. The bile ducts draining the segment are closely related to the confluence of the right and left hepatic ducts (Ch. 67), such that excision of bile duct tumours affecting the porta hepatis of the liver usually requires removal of segment I.

Segment II Segment II lies posterolateral to the left portal fissure, often has only one perivascular fibrous capsule, and drains into the left hepatic vein. Rarely, a separate vein drains directly into the inferior vena cava.

Segment III Segment III lies between the umbilical fissure and the left portal fissure. It is supplied by one to three perivascular fibrous capsules and drains into the left hepatic vein: the veins of the falciform ligament can provide an alternative drainage route. Very rarely, the segment drains to the middle hepatic vein; when this occurs, reconstruction is required following a right hepatectomy involving resection of the middle hepatic vein and in split liver transplantation (Dar et al 2008).

Segment IV Segment IV lies between the umbilical fissure and the main portal fissure, immediately anterior to segment I. It is supplied by three to five perivascular fibrous capsules, most of which arise in the umbilical fissure; their origins are often close to the fibrous capsules that supply segments II and III. Occasionally, segment IV is supplied by branches from the main left pedicle. Segment IV is typically divided into IVa superiorly and IVb inferiorly by two separate perivascular fibrous capsules. This subdivision is relevant to transverse hepatectomy, in which segments IVb, V and VI are removed along a transverse portal plane (Sugarbaker 1990). Segment IV usually drains into the middle hepatic vein, but it can also drain into the left hepatic vein through veins of the falciform ligament.

Segment V Segment V is the inferior segment of the right anterior sector and lies between the middle and the right hepatic veins. Its size is variable, as are the number of perivascular fibrous capsules that supply it from the right anterior capsule. Venous drainage is usually into the right and middle hepatic veins but can be directly into the inferior vena cava via an inferior right hepatic vein.

Segment VI Segment VI forms the inferior part of the right posterior sector, which is posterior to the right portal fissure. It is often supplied by two to three branches from the right posterior perivascular fibrous capsule. Occasionally, the perivascular fibrous capsule to segment VI arises directly from the right pedicle. Venous drainage is normally into the right hepatic vein but, as in segment V, can be directly into the inferior vena cava via an inferior right hepatic vein.

Segment VII Segment VII forms the superior part of the right posterior sector and lies posterior to the right hepatic vein. The sheath to segment VII is often single. The venous drainage is into the right hepatic vein; occasionally, the segment drains directly into the inferior vena cava.

Segment VIII Segment VIII is the superior part of the right anterior sector. The right anterior sectoral sheath ends in segment VIII and supplies it, after giving off branches to segment V. Venous drainage is to the right and middle hepatic veins.

Peritoneal attachments and ligaments of the liver

The liver is attached to the anterior abdominal wall, diaphragm and other viscera by several peritoneal ligaments.

Falciform ligament and round ligament of the liver

The liver is attached to the anterior abdominal wall by the falciform ligament, derived from the ventral mesogastrium in the embryo. The two layers of this ligament pass posteriorly and slightly to the right from the posterior surface of the anterior abdominal wall and the undersurface of the diaphragm in the midline, and are attached to the anterior and superior surfaces of the liver. On the most superior surface, the right leaf runs laterally and is continuous with the superior layer of the coronary ligament. The left layer of the falciform ligament turns medially and is continuous with the anterior layer of the left triangular ligament. The round ligament of the liver is the obliterated remnant of the left umbilical vein of the fetus; it runs in the inferior free border of the falciform ligament and continues into a fissure on the inferior surface of the liver. In fetal life, the left umbilical vein opens into the left branch of the hepatic portal vein and usually becomes obliterated soon after birth. However, it sometimes remains partially patent such that it can be dissected at the umbilicus, dilated and used to access the left branch of the hepatic portal vein in some individuals. Typically, the round ligament of the liver reopens in the setting of portal hypertension caused by cirrhosis of the liver, and it can become a sizeable collateral channel to the anterior abdominal wall.

The round ligament of the liver is important in abdominal surgery for several reasons. It is often divided in upper abdominal surgery to optimize access to the upper abdominal viscera or as the first step in mobilizing the liver. It is vascularized by numerous small arterial branches (mainly from the artery to segment IV) that anastomose with branches of the superior epigastric artery; it is therefore important to ligate or coagulate the ligament during its division. The round ligament of the liver is a guide to the segment III hepatic duct in hepaticojejunostomy formation, and to the left branch of the hepatic portal vein lying in the umbilical fissure during mesenterico-portal vein bypass (Vellar et al 1998, di Francesco et al 2014).

Coronary ligament

The coronary ligament is formed by the reflection of the peritoneum from the respiratory diaphragm onto the superior and posterior surfaces of the right lobe of the liver. A large triangular area of liver devoid of peritoneal covering, the so-called 'bare area', lies between the two layers of the coronary ligament. Here, the liver is attached to the diaphragm by loose connective tissue that is continuous inferiorly with the 'anterior pararenal space'. On the right, the two layers of the coronary ligament converge laterally to form the right triangular ligament. On the left, the two layers become closely applied and form the left triangular ligament. The superior layer of the coronary ligament is reflected superiorly onto the inferior surface of the respiratory diaphragm and inferiorly onto the right and superior surfaces of the liver. The inferior layer of the coronary ligament is reflected inferiorly over the right suprarenal gland and right kidney and superiorly onto the inferior surface of the liver. Surgical division of the right triangular and coronary ligaments allows the right lobe of the liver to be rotated anteriorly and to the left to expose the lateral aspect of the inferior vena cava posterior to the liver.

Triangular ligaments

The left triangular ligament is a double layer of peritoneum that extends for a variable length over the superior border of the left lobe of the liver. Medially, the anterior leaf is continuous with the left layer of the falciform ligament, and the posterior layer is continuous with the left layer of the lesser omentum. The left triangular ligament lies in front of the abdominal part of the oesophagus and part of the fundus of the stomach: its division allows the left lobe of the liver to be mobilized for exposure of the abdominal part of the oesophagus and crura of the respiratory diaphragm. However, the left triangular ligament is also an important stabilizing factor for the left lobe after excision of the right lobe of the liver: its division destabilizes the left lobe so that it can rotate and displace into the space created under the right half of the diaphragm, compromising the venous outflow of the left lobe and/or portal venous inflow to the left lobe, with consequent liver dysfunction. If the left triangular ligament is divided, the left lobe should be stabilized by reattaching the falciform ligament to the anterior abdominal wall.

The right triangular ligament is a short structure that lies at the right lateral limit of the 'bare area' of the liver and represents the convergence laterally of the two layers of the coronary ligament.

Lesser omentum

The lesser omentum is a double layer of peritoneum that extends from the lesser curvature of the stomach and proximal duodenum to the inferior surface of the liver. Its free margin contains the portal triad (Ch. 62). Its attachment to the inferior surface of the liver is L-shaped. The vertical component follows the line of the fissure for the ligamentum venosum, the fibrous remnant of the ductus venosus. More inferiorly, the attachment runs horizontally to complete the L-shape in the porta hepatis. At its superior end, the left layer of the lesser omentum is continuous with the posterior layer of the left triangular ligament, and the right layer is continuous with the coronary ligament as it encloses the inferior vena cava. At its inferior end, the two layers of the lesser omentum diverge to surround the structures of the porta hepatis. A thin, fibrous condensation of fascia usually runs from the medial end of the porta hepatis into the fissure for the round ligament of the liver. This fascial condensation is continuous with the lower border of the falciform ligament where the round ligament of the liver re-emerges at the inferior border of the liver. Care should be taken when dividing the lesser omentum because it may contain a replaced or accessory left hepatic artery; when present, this invariably extends to the liver at the base of the umbilical fissure and can be identified by a pulsation in the lesser omentum close to that fissure.

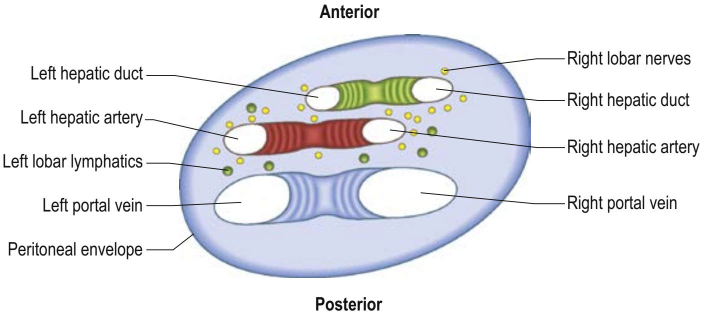

Fig. 66.7 A cross-section of the structures at the porta hepatis viewed from above.

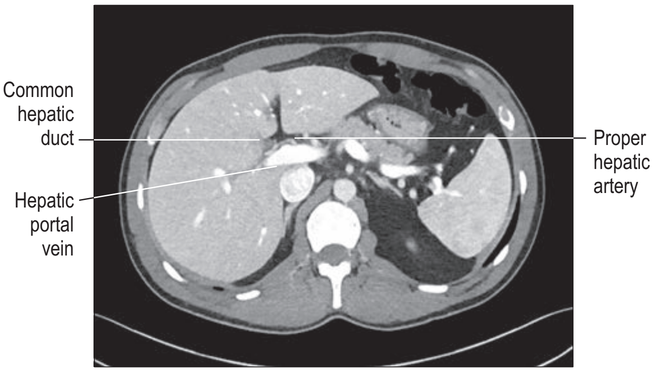

Fig. 66.8 An axial CT of the porta hepatis. The hepatic ducts lie anteriorly, the hepatic portal vein posteriorly and the hepatic artery between the two.

Ligamentum venosum

The ligamentum venosum represents the obliterated venous connection that existed in the fetus between the left branch of the hepatic portal vein and the termination of the left hepatic vein (the ductus venosus). It is used as a guide to gain control of the left hepatic vein outside the liver during surgery. By dividing the ligament close to its insertion into the left hepatic vein and retracting it laterally, the angle between the left and the middle hepatic veins can be accessed.

This manoeuvre can be helpful in left liver resection with preservation of the caudate lobe, but if the caudate lobe is to be removed, the left hepatic vein (or more usually the confluence of the left and middle hepatic veins with the inferior vena cava) can be approached more posteriorly without division of the ligamentum venosum.

Porta hepatis, hepatoduodenal ligament and hilar plate

The porta hepatis is a deep transverse fissure on the inferior surface of the liver, between the quadrate lobe anteriorly and the caudate process posteriorly. It contains the hepatic portal vein, hepatic artery and hepatic nervous plexuses as they ascend into the parenchyma of the liver, and the right and left hepatic ducts and some lymph vessels that emerge from the liver. The hepatic ducts usually lie anterior to the hepatic portal vein and its branches, and the hepatic artery with its branches lies between the two (**Figs 66.7–66.8**). However, the right hepatic artery sometimes lies anterior to the common hepatic duct, a variation that is important during bile duct reconstruction by hepaticojejunostomy (Michels 1966). All these structures are enveloped within a sheath of loose connective tissue (perivascular fibrous capsule) that surrounds the vessels and bile ducts as they course through the liver parenchyma and is continuous with the fibrous capsule. The dense aggregation of vessels, supporting connective tissue and liver parenchyma just superior to the porta hepatis is often referred to as the 'hilar plate' of the liver (Kawarada et al 2000). Understanding the concept of the hilar plate is important in surgical approaches to the hilar structures, and division or lowering of the hilar plate is essential for optimum surgical access to the left hepatic duct.

The hepatic artery, bile duct and hepatic portal vein extend between the porta hepatis and the superior border of the duodenum in the free edge of the hepatoduodenal ligament, which forms the anterior boundary of the omental foramen (of Winslow). Rapid control of the vessels entering the porta hepatis (the hepatic pedicle) can be obtained by compressing them in the free edge of the lesser omentum (a 'Pringle' manoeuvre); this is conveniently done by dividing the lesser omentum immediately to the left of these structures and passing a tape around them through the omental foramen.

The left hepatic duct is extrahepatic as it descends obliquely along the undersurface of segment IV (the quadrate lobe) to the confluence of the hepatic ducts. Access to this extrahepatic segment of the left hepatic duct is particularly useful during a biliary-enteric bypass procedure to treat a stricture of the hepatic duct confluence. The right hepatic duct is more intrahepatic and extension of a hepaticojejunal anastomosis on to the right hepatic duct necessitates incision of the liver in the fossa for the gallbladder.

Perivascular fibrous capsules

The fibrous capsule of the liver (Glisson's capsule) becomes condensed as the perivascular fibrous capsules (Glissonian sheaths) around the branches of the portal triad structures as they enter the liver and subdivide into segmental branches (Kuntz and Kuntz 2008). Thus, each bile duct, hepatic artery and hepatic portal vein is surrounded by a single fibrous capsule. Within each capsule, the hepatic portal vein is surrounded by loose areolar connective tissue, making dissection of the hepatic portal vein relatively easy. The fibrous tissue around the bile ducts and hepatic artery is tougher so dissection of these structures is more difficult. This capsular arrangement facilitates surgical control of the right and left vasculobiliary pedicles of the liver, as well as sectoral and segmental divisions in complex liver resections (Yamamoto et al 2012).

Vascular supply and lymphatic drainage

The hepatic artery, hepatic portal vein and hepatic veins supply or drain the liver. The portal vein and hepatic artery ascend in the lesser omentum to the porta hepatis, where each usually bifurcates. The common hepatic duct and lymphatic vessels descend from the porta hepatis alongside the hepatic portal vein and hepatic artery (see Fig. 66.8). The hepatic veins leave the liver via its posterior surface and run directly into the inferior vena cava.

Hepatic artery

During fetal and early postnatal life the common hepatic artery is the largest branch of the coeliac trunk, whereas in adults it is intermediate in size between the left gastric and splenic arteries. The common hepatic artery (**Fig. 66.9**) gives off the right gastric and gastroduodenal arteries (**Fig. 66.9A**). After originating from the coeliac trunk, it passes anteriorly and laterally, above the superior border of the pancreas, to the superior aspect of the first part of the duodenum. It is subdivided into the common hepatic artery, from the coeliac trunk to the origin of the gastroduodenal artery, and the proper hepatic artery, from that point to its bifurcation. Both parts ascend anterior to the hepatic portal vein and medial to the bile duct within the free margin of the hepatoduodenal ligament in the anterior wall of the omental foramen. The left and right hepatic arteries arise at a variable level

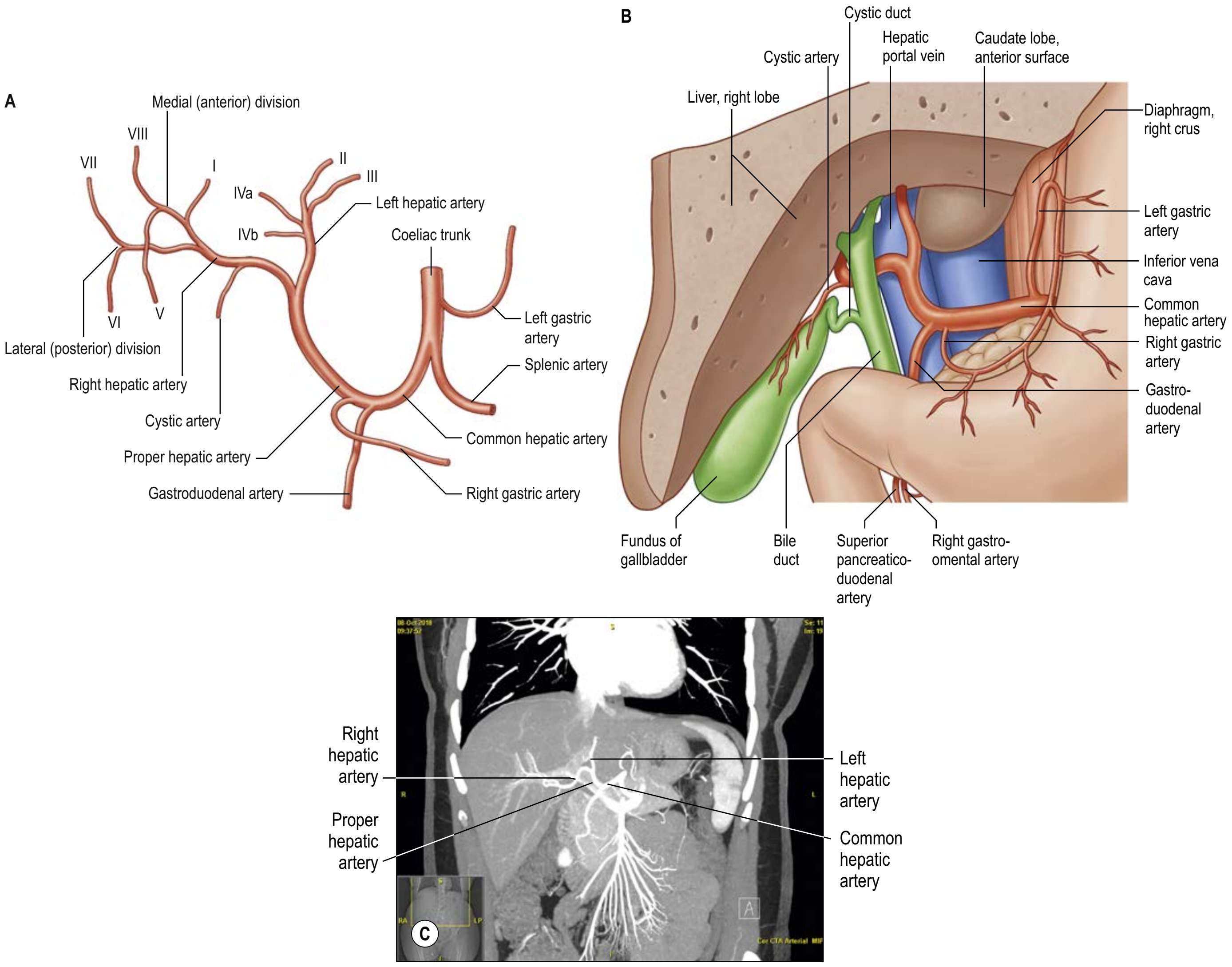
A
Medial (anterior) division
VIII
VII
I
II
III
IVa
IVb
Left hepatic artery
Coeliac trunk
VI
V
Lateral (posterior) division
Right hepatic artery
Cystic artery
Proper hepatic artery
Gastroduodenal artery
Left gastric artery
Splenic artery
Common hepatic artery
Right gastric artery
B
Cystic duct
Hepatic portal vein
Caudate lobe, anterior surface
Cystic artery
Liver, right lobe
Diaphragm, right crus
Left gastric artery
Inferior vena cava
Common hepatic artery
Right gastric artery
Gastro-duodenal artery
Fundus of gallbladder
Bile duct
Superior pancreatico-duodenal artery
Right gastro-omental artery
Right hepatic artery
Proper hepatic artery
Left hepatic artery
Common hepatic artery
C

Fig. 66.9 The hepatic artery. **A**, Branches. **B**, Usual relations of the hepatic artery, bile duct and hepatic portal vein to each other in the lesser omentum: anterior aspect, portion of the liver removed. Note that the left gastric artery more commonly arises from the coeliac trunk. **C**, CT showing hepatic artery anatomy. (D, *continued online*)

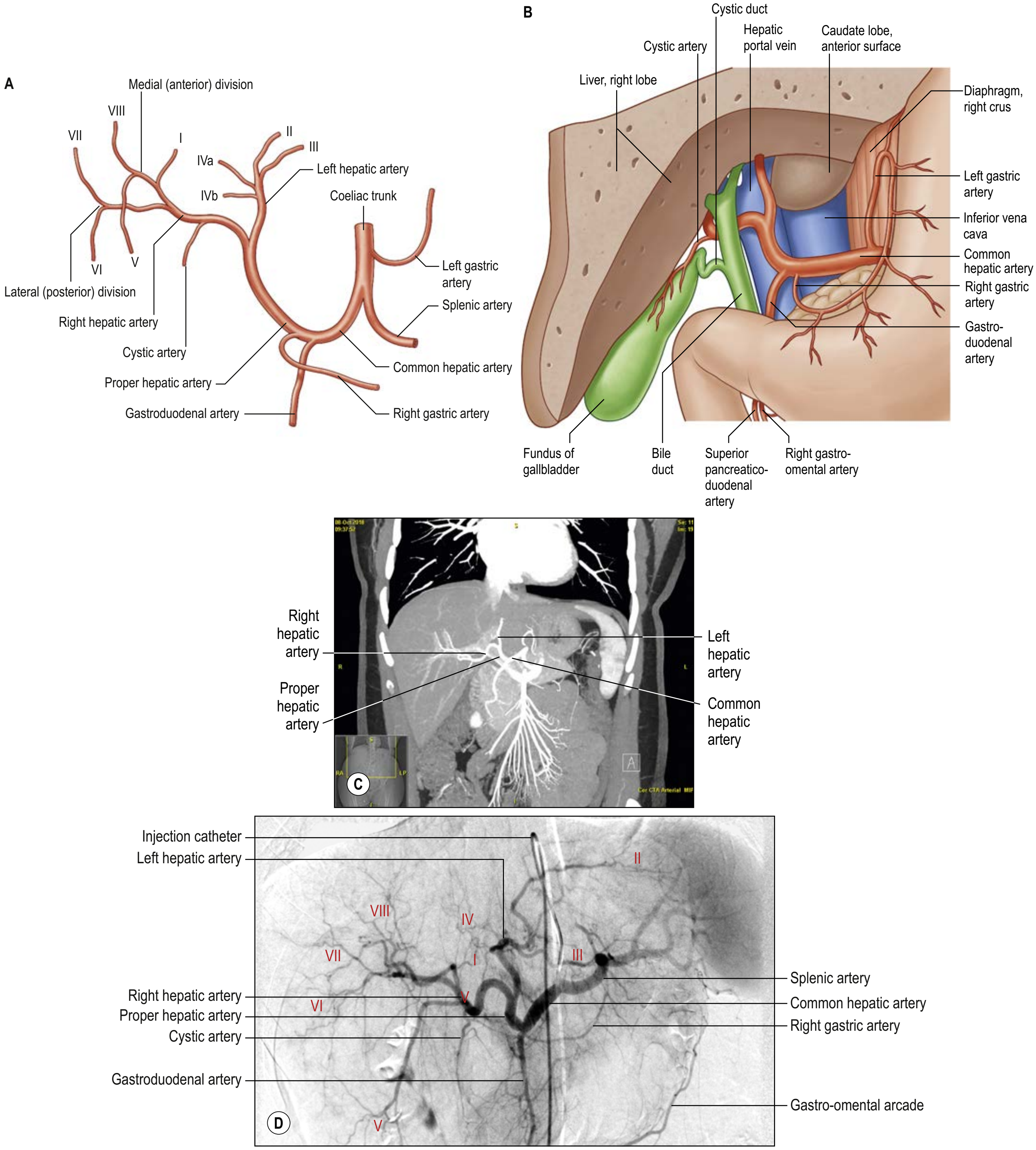
A
Medial (anterior) division
VIII
VII
I
II
III
IVa
IVb
Left hepatic artery
Coeliac trunk
V
VI
Lateral (posterior) division
Left gastric artery
Splenic artery
Right hepatic artery
Cystic artery
Common hepatic artery
Proper hepatic artery
Gastroduodenal artery
Right gastric artery
B
Cystic duct
Hepatic portal vein
Caudate lobe, anterior surface
Cystic artery
Liver, right lobe
Diaphragm, right crus
Left gastric artery
Inferior vena cava
Common hepatic artery
Right gastric artery
Gastro-duodenal artery
Fundus of gallbladder
Bile duct
Superior pancreatico-duodenal artery
Right gastro-omental artery
Right hepatic artery
Proper hepatic artery
Left hepatic artery
Common hepatic artery
C
Injection catheter
Left hepatic artery
II
VIII
IV
VII
I
III
VI
V
Right hepatic artery
Proper hepatic artery
Cystic artery
Gastroduodenal artery
Splenic artery
Common hepatic artery
Right gastric artery
Gastro-omental arcade
D
V

Fig. 66.9 The hepatic artery. **A**, Branches. **B**, Usual relations of the hepatic artery, bile duct and hepatic portal vein to each other in the lesser omentum: anterior aspect, portion of the liver removed. Note that the left gastric artery more commonly arises from the coeliac trunk. **C**, CT showing hepatic artery anatomy. **D**, Digital subtraction angiogram of the coeliac trunk showing the hepatic arterial tree; note that the left gastric artery has not filled.

below the porta hepatis. The right hepatic artery typically crosses posterior (occasionally anterior) to the common hepatic duct (**Fig. 66.9B**). Its usual course is toward the common hepatic duct: it bends inferiorly before crossing posterior to the duct and then bends back up toward the right hepatic duct lateral to the common hepatic duct and hepatic portal vein. Its close proximity to the bifurcation of the bile duct means that it is often involved or encased by bile duct cancers that arise at the bifurcation (hilar cholangiocarcinoma). The right hepatic artery is more frequently involved than the left hepatic artery in bile duct cancers of the porta hepatis. Occasionally, the right hepatic artery crosses anterior to the common hepatic duct and is more vulnerable to injury during biliary surgery. It almost always divides into an anterior branch supplying segments V and VIII and a posterior branch supplying segments VI and VII. The anterior division also often supplies a branch to segment I and the gallbladder. The proper hepatic artery sometimes divides at a more proximal level close to its origin; occasionally it divides distally, well to the left of the porta hepatis. The main significance of a proximal division is that the right hepatic artery can pass posterior to the hepatic portal vein (Launois and Jamieson 1993). The segmental arteries of the liver are macroscopically end arteries, although some collateral circulation occurs between segments via fine terminal branches.

Anatomical variants of the normal arrangement of the hepatic arteries are found in about one-third of individuals and are important to recognize because they are relevant to surgical and interventional radiological procedures (Michels 1966, Covey et al 2002, López-Andújar et al 2007, Saba and Mallarini 2011). An artery that supplies a part of the liver in addition to the normal artery supplying that part is defined as an accessory artery. A replaced hepatic artery is an artery that does not originate from an orthodox position and provides the sole supply to that part of the liver.

The most common anatomical variants are a replaced or accessory left hepatic artery that arises from the left gastric artery, or a replaced or accessory right hepatic artery that arises from the superior mesenteric artery, both occurring in 10–20% of individuals.

Variations in the intrahepatic arteries are common and can be important surgically. For example, the segment IV artery most commonly arises from the left hepatic artery, but in up to 30% of cases it arises from the right hepatic artery or the proper hepatic artery (Onishi et al 2000). The segment IV artery never arises to the right of the common hepatic duct, which means that if the right hepatic artery is divided to the right of the common hepatic duct, the arterial supply to segment IV is not endangered. Failure to recognize this variation can compromise the blood supply to segment IV following right hepatectomy, and it is especially important during right liver donation for live donor liver transplantation.

Veins

The liver has two venous systems. The portal venous system conveys blood from the majority of the gastrointestinal tract and its associated organs to the liver. The hepatic venous system drains blood from the liver parenchyma into the inferior vena cava.

Hepatic portal vein

The hepatic portal vein is formed posterior to the neck of the pancreas, usually from the convergence of the superior mesenteric and splenic veins (**Fig. 66.12**; see also Fig. 59.7). Its origin lies in the transpyloric plane between the inferior border of the body of the first lumbar vertebra and the superior border of the body of the second lumbar vertebra (Mirjalili et al 2012). The hepatic portal vein is approximately 8 cm long and ascends obliquely to the right, posterior to the superior (first) part of the duodenum, bile duct and gastroduodenal artery, and anterior to the inferior vena cava. It enters the hepatoduodenal ligament and ascends anterior to the omental foramen to reach the right end of the porta hepatis, where it divides into right and left main branches that enter the liver. In the lesser omentum, the hepatic portal vein lies posterior to both the bile duct and the hepatic artery. It is surrounded by the hepatic nervous plexus and accompanied by numerous lymphatics and some lymph nodes. The hepatic portal vein contains smooth muscle in its wall and, in experimental animals at least, has well-developed spontaneous contractions with frequencies between 0.01 and 1 Hz (Burt 2003). It is typically valveless.

The main extrahepatic tributaries of the hepatic portal vein are the left gastric vein, which ends in the left margin of the hepatic portal vein, and the posterior superior pancreaticoduodenal vein near the head of the pancreas. The hepatic portal vein divides into right and left branches at the porta hepatis of the liver (**Fig. 66.13**). The left branch of the hepatic portal vein has a longer extrahepatic course (4–5 cm) than the right branch of the hepatic portal vein, tends to lie more horizontally, and is often smaller in calibre. The horizontal portion runs along the inferior surface of segment IV and invariably gives branches to segment I and sometimes to segment IV. The left branch of the hepatic portal vein continues within the liver, giving off a segment II branch laterally before taking a more anterior and vertical course in the umbilical fissure, where it gives off branches to segments III and IV and receives the obliterated left umbilical vein (round ligament of the liver). Most of the portal venous supply to segment IV comes from the left branch of the hepatic portal vein and only occasionally from either the right branch of the hepatic portal vein or its branches to segments V or VIII. The right branch of the hepatic portal vein is only 2–3 cm in length and usually divides into a right medial (anterior) sectoral division supplying segments V and VIII, and a right lateral (posterior) sectoral division supplying segments VI and VII. The medial division can give a branch to segment I.

Hepatic portal vein variations usually involve the right branch (Covey et al 2004). When this branch is absent (10–15% of livers), the hepatic portal vein usually trifurcates into left portal, right anterior and right posterior sectoral veins. Absence of the right branch of the hepatic portal vein might be considered as a relative contraindication for split liver and live donor liver transplantations because this variation is often associated with a similar variation in biliary anatomy. The right anterior sectoral portal vein can arise from the hepatic portal vein, or the right posterior sectoral portal vein can originate from the left branch of the hepatic portal vein, variations that are important to remember during left-sided liver resection. When the bifurcation of the hepatic portal vein is absent, the hepatic portal vein enters the liver, giving off the right sectoral branches, and then turns left to supply the left lobe, a variation that presents an added complexity in major liver surgery (Chaib 2009).

Porto-systemic shunts

Increased pressure within the portal venous system can result in dilation of portal venous tributaries and reversed flow at sites of porto-systemic anastomoses. Common sites of porto-systemic shunts are listed in **Table 66.1**, and see also Sharma and Rameshbabu (2012).

Hepatic veins

The liver drains by three major hepatic veins into the suprahepatic part of the inferior vena cava and via numerous minor hepatic veins that drain into the retrohepatic inferior vena cava. The adult retrohepatic inferior vena cava is 6–7 cm long and is surrounded to a variable extent by segment I (Camargo et al 1996). The three major veins are located between the four sectors of the liver (see Fig. 66.6A; **Figs 66.14–66.15**). Thus, the right hepatic vein lies between the right anterior and posterior sectors, the middle hepatic vein lies between the right and left hemilivers, and the left hepatic vein lies between the left medial and lateral sectors. During hepatic resection, the surgeon should transect the liver parenchyma slightly to the left or right of the particular fissure that is being opened to avoid the main trunk of a hepatic vein.

Right hepatic vein

The right hepatic vein is the longest and largest hepatic vein. It is usually single, but occasionally remains as two trunks until it terminates by draining into the inferior vena cava. It runs in the right portal fissure between the right medial and lateral sectors. It drains the whole of segments VI and VII and variable proportions of segments V and VIII, depending on the extent to which these segments drain into the middle hepatic vein. The right hepatic vein is formed anteriorly near the inferior border of the liver and lies in a coronal plane through most of its course. It drains into the inferior vena cava near the superior border of the caudate lobe. Of the three major hepatic veins, the right hepatic vein is most variable in calibre, reflecting the variable contribution of the middle hepatic vein to the drainage of segments V and VIII and the existence of an accessory right inferior (30%) and/or middle hepatic vein (10%) (Fang et al 2012). The hepatic venous anatomy is particularly important in right lobe living donation and can be assessed preoperatively by computed tomography (CT) or magnetic resonance imaging (MRI), and/or by intraoperative ultrasound.

Middle hepatic vein

The middle hepatic vein lies in the main portal fissure between the right and left hemilivers. It usually joins the left hepatic vein and terminates in the inferior vena cava as a short common trunk; it ends as a single trunk in the inferior vena cava in fewer than 10% of individuals. The middle hepatic vein drains the central part of the liver and receives constant tributaries from segments IV, V and VIII. The vein from segment IV lies in a sagittal plane and enters the middle hepatic vein on its left side. The vein from segment VIII runs transversely into the right side of the middle hepatic vein and is sometimes large enough to be mistaken for the middle hepatic vein. Anteriorly, the middle hepatic vein drains some of segment V; the calibres of the tributaries draining segments V and VIII are variable. Intrahepatic venous anastomoses between the middle and right hepatic veins, particularly in segment VIII, have been reported in up to one-third of adult livers (Hribernik and Trotovšek 2014).

A replaced proper hepatic artery can arise from the superior mesenteric artery (**Fig. 66.10**) and can be suspected at surgery by a relatively superficial hepatic portal vein (reflecting the absence of a hepatic artery that would normally ascend in front of the vein). More commonly, a replaced or accessory right hepatic artery arises from the superior mesenteric artery (see Fig. 66.10; **Fig. 66.11**). In such cases, the variant artery runs in the lesser omentum posterior to the hepatic portal vein and bile duct and can usually be identified at surgery by palpable pulsation posterior to the hepatic portal vein. An accessory right hepatic artery can be injured during resection of the pancreatic head because it lies close to the hepatic portal vein. Occasionally, a replaced or accessory left hepatic artery arises from the left gastric artery, entering the liver through the umbilical fissure; this artery provides a source of collateral supply in cases where the arteries at the porta hepatis are occluded, but it can also be injured during mobilization of the stomach as it lies in the superior portion of the lesser omentum. Rarely, an accessory left or right hepatic artery arises from the gastroduodenal artery or directly from the aorta. The presence of replaced arteries can be life-saving in patients with bile duct cancer; because they are further away from the bile duct they tend to be spared from infiltration by the cancer, making excision of the tumour feasible. Knowledge of these variations is also essential when whole and split liver transplantation is performed, and their presence often requires reconstruction.

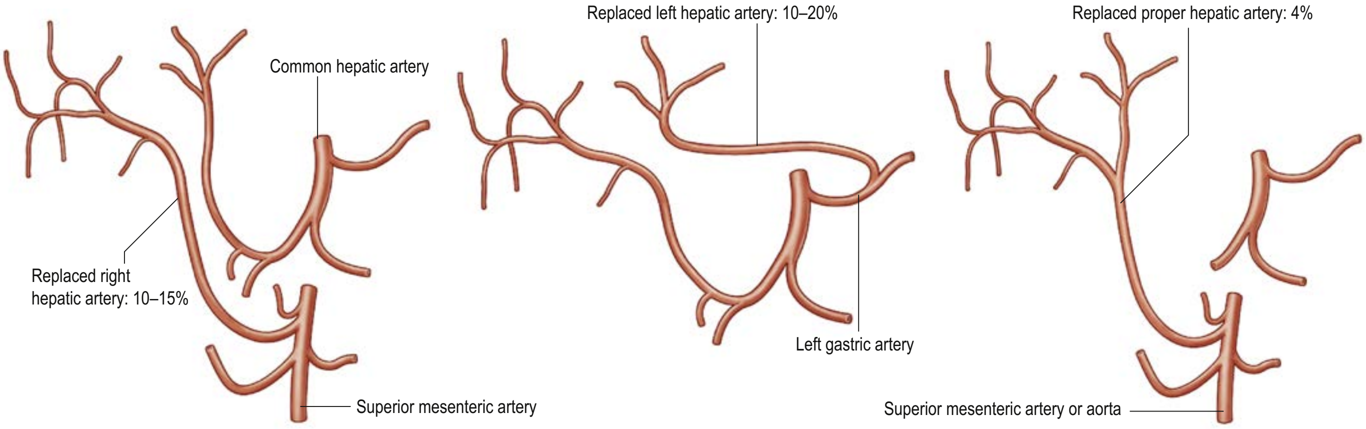
Replaced left hepatic artery: 10–20%
Replaced proper hepatic artery: 4%
Common hepatic artery
Replaced right hepatic artery: 10–15%
Left gastric artery
Superior mesenteric artery
Superior mesenteric artery or aorta

Fig. 66.10 Common hepatic artery variants.

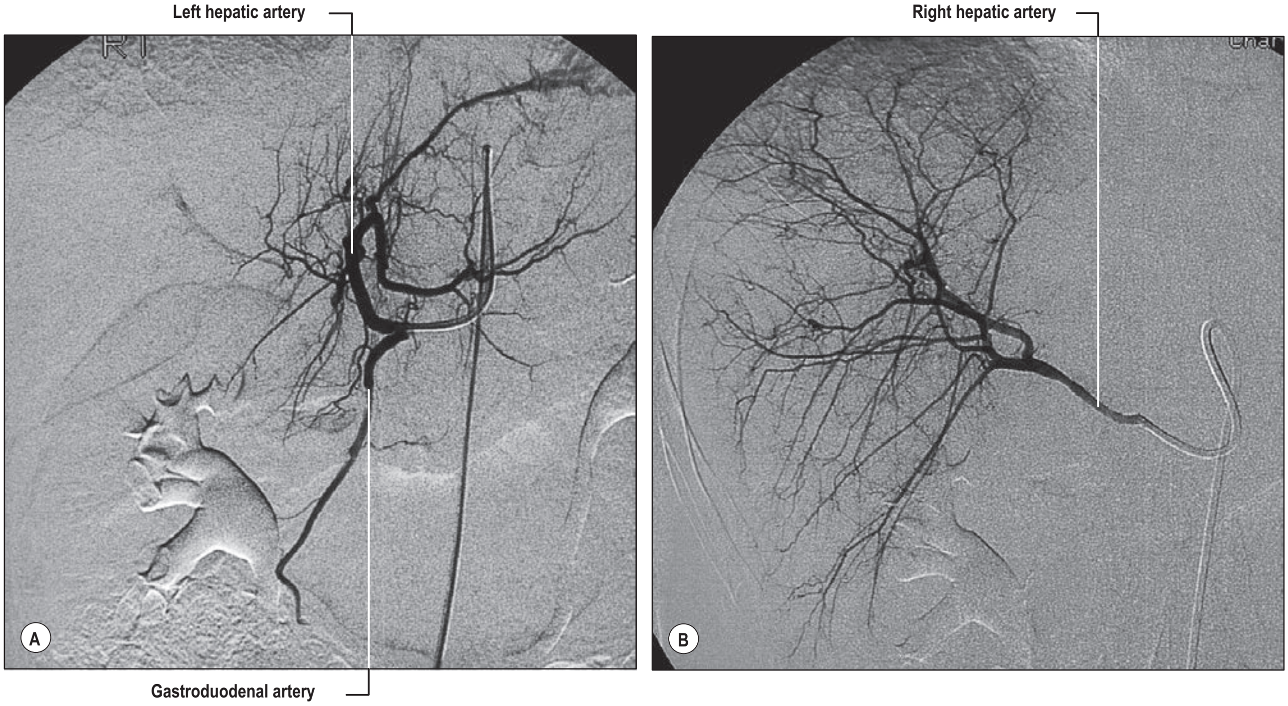
Left hepatic artery
Right hepatic artery
A
B
Gastroduodenal artery

Fig. 66.11 Hepatic arteriograms. **A**, A selective hepatic arteriogram shows normal left hepatic artery branches and small right hepatic artery branches. **B**, The right hepatic artery arises from the origin of the superior mesenteric artery.

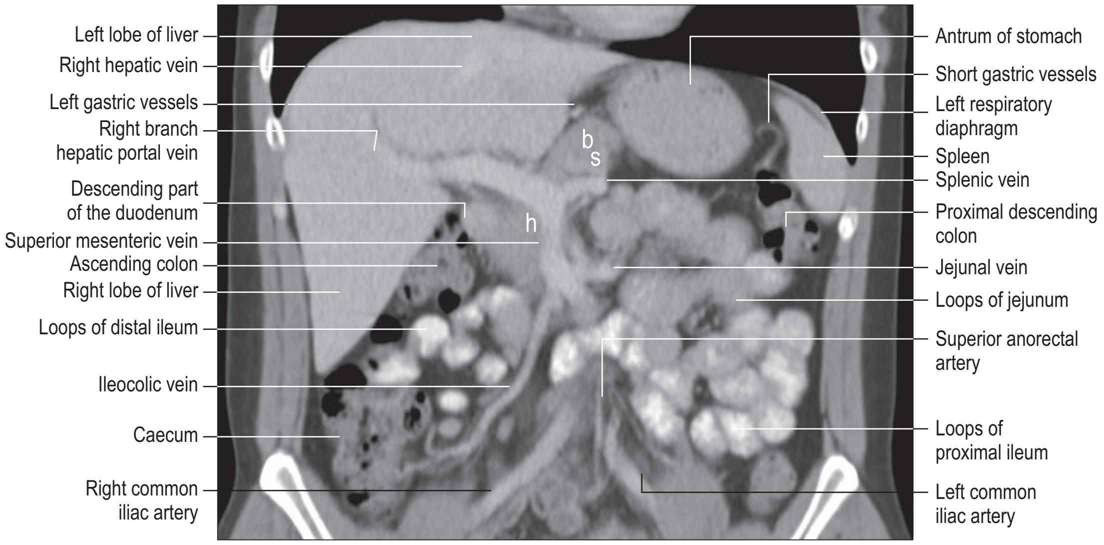
Left lobe of liver
Right hepatic vein
Left gastric vessels
Right branch hepatic portal vein
Descending part of the duodenum
Superior mesenteric vein
Ascending colon
Right lobe of liver
Loops of distal ileum
Ileocolic vein
Caecum
Right common iliac artery
b
s
h
Antrum of stomach
Short gastric vessels
Left respiratory diaphragm
Spleen
Splenic vein
Proximal descending colon
Jejunal vein
Loops of jejunum
Superior anorectal artery
Loops of proximal ileum
Left common iliac artery

Fig. 66.12 Coronal CT of the abdomen and pelvis with intravenous and oral contrast medium showing the superior mesenteric and portal veins. Abbreviations: b, body of pancreas; h, head of pancreas; s, splenic artery.

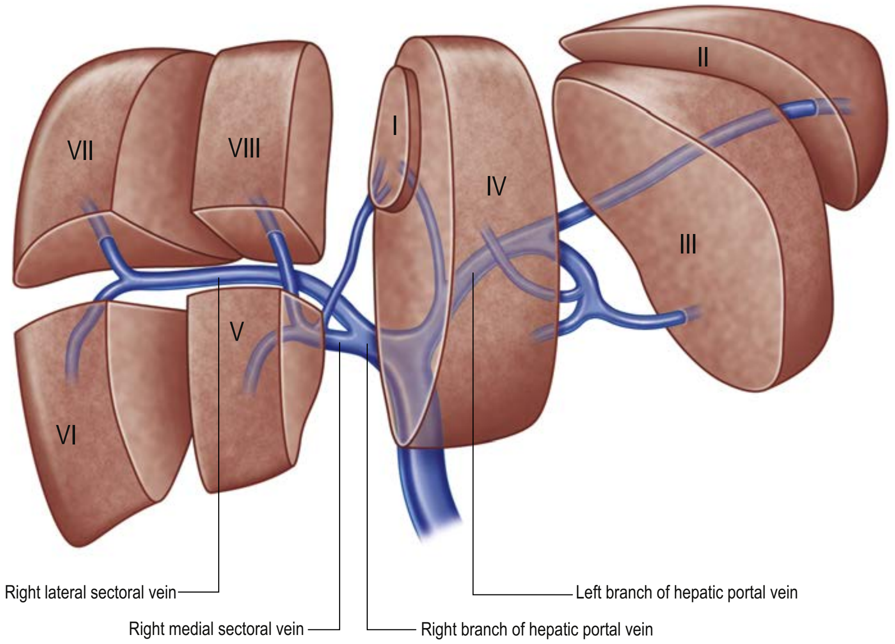
VII
VIII
I
II
IV
III
V
VI
Right lateral sectoral vein
Right medial sectoral vein
Right branch of hepatic portal vein
Left branch of hepatic portal vein

Fig. 66.13 The hepatic portal vein and its intrahepatic branches. (Right lateral = right posterior; right medial = right anterior.)

TABLE 66.1 Common sites of porto-systemic anastomoses in portal hypertension and associated clinical implications

Hepatic portal vein tributaries	Systemic veins	Clinical presentations
Left gastric vein	Distal oesophageal veins draining into azygos and hemiazygos veins	Oesophageal and gastric varices
Superior anorectal veins	Middle and inferior anorectal veins draining into internal iliac and internal pudendal veins	Rectal varices
Persistent tributaries of left branch of hepatic portal vein in round ligament of the liver	Periumbilical branches of epigastric and intercostal veins	‘Caput medusae’
Tributaries of right branch of hepatic portal vein overlying ‘bare area’ of liver	Retroperitoneal veins draining into azygos, hemiazygos, lumbar, intercostal and inferior phrenic veins	Dilated retroperitoneal veins at risk during surgery or interventional procedures
Omental and colonic veins near right and left colic flexures	Retroperitoneal veins near right and left colic flexures	Can be problematic during surgery

Left hepatic vein

The left hepatic vein lies between the left medial and left lateral sectors of the liver and drains segments II, III and occasionally IV. Small veins draining segment II and occasionally the superior part of segment IV, can drain directly into the inferior vena cava. The umbilical fissure vein, a major tributary of the left hepatic vein, usually runs between segments III and IV and contributes to their drainage. Occasionally, the vein draining segment III ends separately in the confluence of the left and middle hepatic veins. These variations in venous drainage are significant in split liver transplantation and live donor liver transplantation.

Minor hepatic veins

Segment I veins, ranging in number from one to five, drain directly into the inferior vena cava. Since this segment has a venous drainage independent of the rest of the liver, segment I often continues to drain effectively and undergoes compensatory hypertrophy in patients with Budd–Chiari syndrome, where the major hepatic veins are obstructed. There can be an accessory inferior or middle right hepatic vein, and several smaller ‘retrohepatic’ veins that drain the right lobe directly into the inferior vena cava. When present, these veins are surgically important, especially if they exceed 5 mm in diameter. They drain segments V and VI independently of the three major hepatic veins, which means that a tumour involving the latter can be resected safely as long as venous drainage from the accessory veins is preserved. In live donor and split liver transplantations, larger accessory veins must be individually anastomosed to the recipient inferior vena cava to ensure adequate venous drainage.

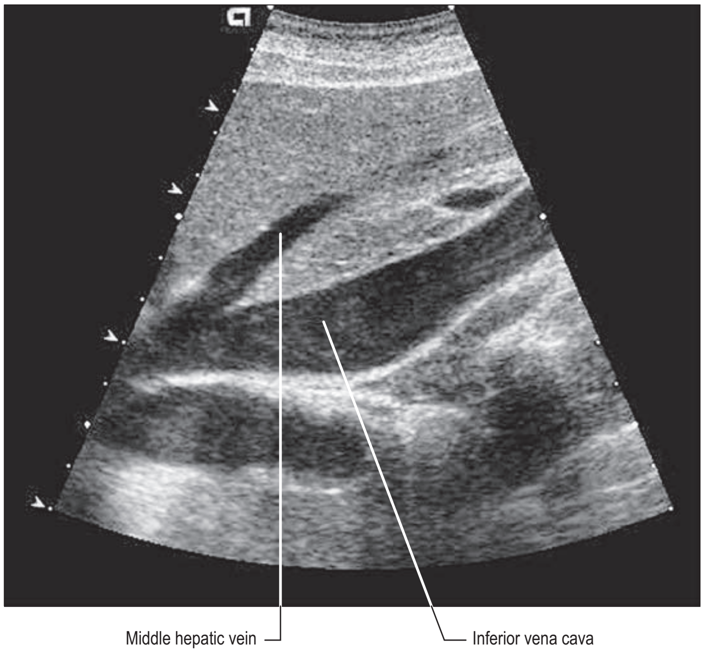

Fig. 66.14 Ultrasound of the liver in the sagittal plane. The middle hepatic vein is seen draining into the inferior vena cava.

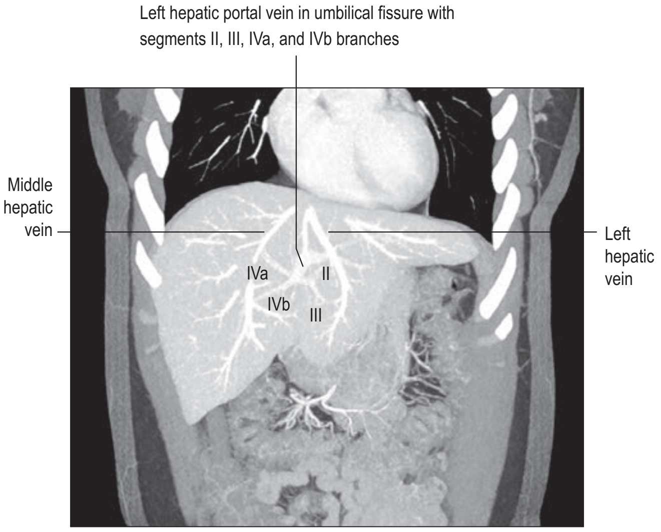
Left hepatic portal vein in umbilical fissure with segments II, III, IVa, and IVb branches
Middle hepatic vein
Left hepatic vein
IVa
II
IVb
III

Fig. 66.15 CT showing relations between the left and middle hepatic veins and the left branch of the hepatic portal vein (with segments II, III, IVa and IVb branches).

Transjugular intrahepatic porto-systemic shunt (TIPS) procedure for portal hypertension

Available with the *Gray's Anatomy* e-book

Lymphatic drainage

Lymph from the liver is rich in protein and is mostly a product of the hepatic sinusoids (Ohtani and Ohtani 2008). It passes via deep and superficial pathways to nodes superior and inferior to the respiratory diaphragm (Trutmann and Sasse 1994). Obstruction of hepatic venous drainage increases the flow of lymph in the thoracic duct.

Superficial hepatic lymphatics

Superficial lymphatics run in subserosal areolar tissue over the surface of the liver and drain in four directions. Lymphatics from most of the posterior surface, including the caudate lobe, drain into nodes alongside the inferior vena cava; a few lymphatics from the posterior surface of the left lobe pass towards the oesophageal hiatus and nodes around the cardia of the stomach. Lymphatics in the coronary and right triangular ligaments can pass directly to the thoracic duct. Lymphatics from most of the inferior, anterior and superior surfaces drain into hepatic nodes at the porta hepatis. A few lymphatics from the right superior surface accompany the inferior phrenic artery across the right crus of the respiratory diaphragm to drain into coeliac nodes.

Deep hepatic lymphatics

Fine lymphatics within the portal triads and around interlobular veins merge to form larger vessels. Some ascend through the parenchyma to pass through the caval foramen of the respiratory diaphragm and drain into nodes located in the inferior mediastinum, but most drain to lymph nodes at the porta hepatis.

Innervation

The parenchyma of the liver is supplied by nerves arising from the hepatic plexus that all enter the liver at the porta hepatis. Some nerve fibres also appear to arise from the right phrenic nerve and this might be the basis of referred shoulder pain in patients with biliary colic (Skandalakis et al 2004). The fibrous capsule of the liver is supplied by fine branches of the inferior intercostal nerves that also supply the parietal peritoneum, particularly around the 'bare area' and superior surface of the liver: distension or disruption of the fibrous capsule causes well-localized sharp pain.

Hepatic plexus

The hepatic plexus receives preganglionic parasympathetic fibres from the anterior and, to a lesser extent, the posterior vagal trunk, and postganglionic sympathetic fibres via the coeliac and superior mesenteric plexuses. Nerve fibres accompany the branches of the portal triad into the liver, penetrating as far as the hepatocytes. Aminergic, cholinergic, peptidergic and nitrergic nerve fibres have been identified and appear to be involved in hepatic metabolism and the control of sinusoidal blood flow (McCuskey 2004): the transplanted, denervated liver indicates that this role is not essential. Multiple fine branches from the plexus supply the extrahepatic bile ducts and gallbladder; parasympathetic fibres are motor to the smooth muscle of the bile ducts and gallbladder and inhibitory to the sphincter of the bile duct. Branches from the plexus also run inferiorly with the right gastric artery to contribute to the supply of the pylorus; with the gastroduodenal artery and its branches to reach the pylorus, proximal duodenum and pancreas; and with the right gastro-omental (gastro-epiploic) artery to provide a small contribution to the nerve supply of the stomach.

Referred pain

Pain arising from the parenchyma of the liver is poorly localized. In common with other structures of foregut origin, pain is referred to the epigastric region. Stretch or irritation of the fibrous capsule of the liver by inflammation or neoplasia produces well-localized 'somatic' pain. Pathology involving the diaphragmatic surface of the liver can be referred via the phrenic nerve to the right shoulder region (C3, C4, C5 dermatomes).

Microstructure

The liver is essentially an epithelial-mesenchymal outgrowth of the caudal part of the foregut, with which it remains connected via the biliary tree (Ch. 59). Most of the surface of the liver is covered by a typical serosa, the visceral peritoneum. Beneath this, and enclosing the whole organ, is a thin (50–100 μm) capsule of connective tissue, from which extensions pass into the liver as septa and trabeculae. Branches of the hepatic artery and hepatic portal vein, together with bile ductules and ducts, run within these connective tissue trabeculae (portal tracts). The combination of two types of blood vessel and a bile duct is termed a portal triad, and is usually accompanied by one or more lymphatic vessels and nerves (**Fig. 66.16**).

The liver parenchyma consists of a complex network of epithelial cells, supported by connective tissue and perfused by a rich blood supply from the portal vein and hepatic artery. The epithelial cells, hepatocytes, carry out the major metabolic activities, but additional cell types have storage, phagocytic and mechanically supportive functions. In the mature liver, hepatocytes are arranged mainly in plates (or cords when seen in two-dimensional sections) that are usually only one cell thick, separated by venous sinusoids that anastomose with each other via gaps in the plates (**Fig. 66.17**).

Bile is secreted by hepatocytes and is collected in a network of minute channels (canaliculi) between adjacent hepatocyte plasma membranes. Hepatocytes can therefore be regarded as exocrine cells, secreting bile into the gastrointestinal tract via the extrahepatic bile ducts. Their other metabolic functions involve complex biochemical exchanges with the blood.

The fetal liver is a major haemopoietic organ; erythrocytes, leukocytes and platelets develop from mesenchyme covering the sinusoidal endothelium.

In cases of extreme chronic portal hypertension a large calibre anastomosis between the portal and systemic circulations can be created within the liver parenchyma by inserting a stent between a large hepatic portal vein and a hepatic vein within the liver. The stent is introduced through a catheter inserted into the internal jugular vein and guided into the liver under radiological control (Siramolpiwat 2014). This large shunt relieves the severe portal hypertension but tends to worsen hepatic encephalopathy.

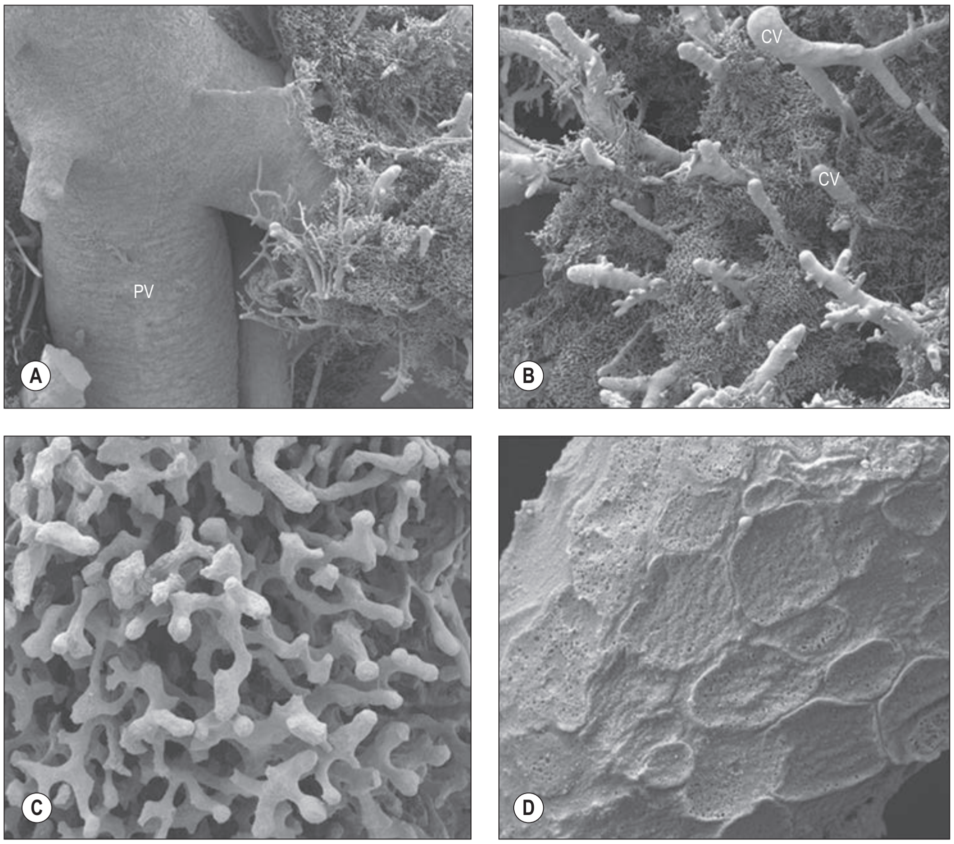

Fig. 66.17 Scanning electron micrographs of a resin corrosion cast of the liver demonstrating the three-dimensional arrangement of the hepatic sinusoids. **A**, A hepatic portal vein (PV) branch within a portal triad ×33 100 μm. **B**, Sinusoids and central veins (CV) ×37 100 μm. **C**, A sinusoidal network ×330 10 μm. **D**, Sinusoidal endothelial cells ×7000 1 μm. (Courtesy of Professor Greg Jones, University of Otago, New Zealand).

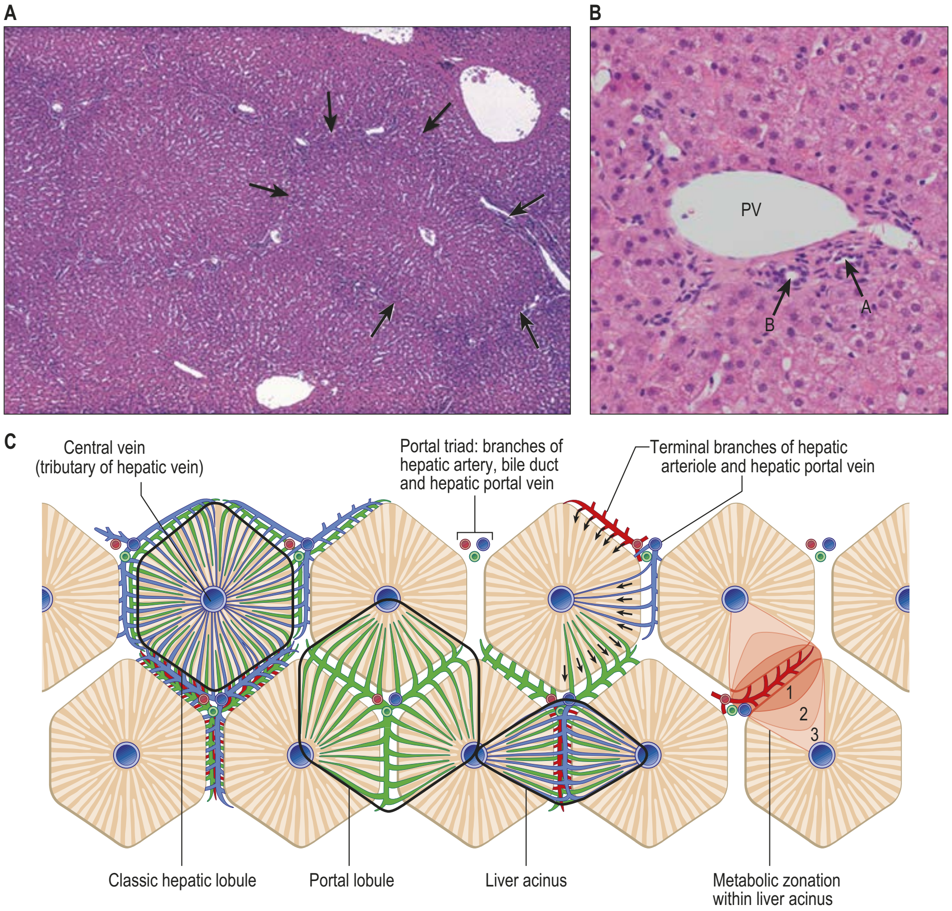
A
B
PV
B
A
C
Central vein
(tributary of hepatic vein)
Portal triad: branches of hepatic artery, bile duct and hepatic portal vein
Terminal branches of hepatic arteriole and hepatic portal vein
1
2
3
Classic hepatic lobule
Portal lobule
Liver acinus
Metabolic zonation within liver acinus

Fig. 66.16 The structural organization of the liver. **A**, Lobules bordered by delicate connective tissue septa (arrows) in which run branches of the hepatic portal vein, hepatic artery and bile duct, grouped as portal triads. A central vein drains each lobule. **B**, A portal triad containing branches of the hepatic portal vein (PV; generally the largest profile), the hepatic artery (A) and a bile duct (B), with typical round epithelial nuclei. Other small bile ductule and arteriolar branches are also visible. **C**, A functional view, in which the territories of the hepatic lobules are shown as regular hexagons (unlike their real appearance, which is highly variable). Functionally, the liver microarchitecture is better considered in terms of acini extending between adjacent central venules and divided into three zones as shown. (A, With permission from Dr JB Kerr, Monash University, from Kerr JB 1999 Atlas of Functional Histology. London: Mosby. B, Courtesy of Mr Peter Helliwell and the late Dr Joseph Mathew, Department of Histopathology, Royal Cornwall Hospitals Trust, UK.)

Lobulation of the liver

The structural unit of the liver is the lobule: a roughly hexagonal arrangement of plates of hepatocytes, separated by intervening sinusoids that radiate outwards from a central vein, with portal triads at the vertices of each hexagon (**Fig. 66.18**; see Fig. 66.16). The central veins drain into the hepatic veins. In some species the classic lobular units are delimited microscopically by distinct connective tissue septa. However, the lobular organization of the human liver is not immediately evident in histological sections; the lobules do not have distinct boundaries, and connective tissue is sparse. The plates do not pass straight to the periphery of a lobule like the spokes of a wheel but run irregularly as they anastomose and branch.

Detailed studies of human liver, using three dimensional reconstruction and morphometric analyses combined with histopathological observations, have revealed a highly ordered arrangement of functional units, the liver acini. Each acinus is an approximately ovoid mass of tissue, orientated around the terminal branches of a hepatic arteriole and portal venule, with its long axis defined by two adjacent central veins. It includes the hepatic tissue served by these afferent vessels and is bounded by adjacent acini. Acinar functional heterogeneity is related to blood supply, thus the functional capacities of hepatocytes in a periportal zone (zone 1) differ from those in an intermediate zone (zone 2) or in a perivenous (pericentral or centrilobular) zone (zone 3) (Kietzmann 2017) (see Fig. 66.16C).

The acinar definition of hepatic microarchitecture has clarified the interpretation of liver histopathology, particularly in relation to zones of hypoxic damage, glycogen deposition and removal, and toxic injury, all of which are related to the direction of blood flow.

Blood supply

Preterminal hepatic arterioles within the acini convey arterial blood to the sinusoids, mostly via a fine capillary plexus that drains to branches of the hepatic portal vein. A small proportion of arterial blood passes directly to the hepatic sinusoids, bypassing these capillary plexuses. Sinusoids thus contain mixed venous and arterial blood. Central veins from adjacent lobules form interlobular veins that unite as hepatic veins and drain to the inferior vena cava.

Hepatic plates (cords)

The endothelium of the sinusoids is fenestrated and lacks a continuous basal lamina, enabling the endothelial cells to act as a dynamic blood filter (Fraser et al 1995). The sinusoids are separated from the plates of hepatocytes by a narrow gap, the perisinusoidal space (of Disse), that is normally 0.2–0.5 µm wide but which distends in hypoxic states. The space contains interstitial fluid, the microvilli of adjacent hepatocytes, hepatic stellate cells, fine collagen fibres (mostly type III with some types I and IV), and occasional non-myelinated nerve terminals.

A network of minute, interconnecting biliary canaliculi (approximately 1 µm in diameter) runs between the hepatic plates. The canaliculi are formed by the apposed plasma membranes of adjacent hepatocytes, sealed by tight junctions that isolate the canalicular lumen (and bile) from adjacent intercellular space. Canaliculi conduct bile to the bile canals (of Hering), trough-like structures lined by cholangiocytes and hepatocytes within the liver lobules. Each canal collects bile from multiple canaliculi and empties into a bile ductule (lined by cholangiocytes) that drains into an interlobular bile duct within the portal tracts (Roskams et al 2004, Saxena and Theise 2004). The flow of bile is thus towards the periphery of the lobule, in the opposite direction to the centripetal blood flow.

Cells of the liver

Resident cells of the liver include hepatocytes, hepatic stellate cells (perisinusoidal cells; fat-storing cells; cells of Ito), sinusoidal endothelial cells, stellate macrophages (Kupffer cells), the epithelial cells of the biliary tree (cholangiocytes), hepatic stem cells, hepatic natural killer lymphocytes (pit cells) and connective tissue cells of the capsule and portal tracts (see Fig. 66.16B).

Hepatocytes About 80% of the volume of the liver and 60% of its cellular population is made up of hepatocytes (parenchymal cells) (see Fig. 66.18). They are polyhedral, with 5–12 sides, and measure 20–30 µm across. The nuclei are round, euchromatic and often tetraploid, polyploid or multiple, with two or more in each cell. The cytoplasm typically contains a considerable amount of rough and smooth endoplasmic reticulum, many mitochondria, lysosomes and well-developed Golgi apparatus, all features indicating high metabolic activity. Glycogen granules and lipid vacuoles are usually prominent. Numerous large peroxisomes and vacuoles containing enzymes, e.g. urease in distinctive crystalline forms, indicate the complex metabolism of these cells. Their role in iron metabolism is reflected by the presence of storage vacuoles containing crystals of ferritin and haemosiderin.

The cell surface facing the sinusoids exhibits numerous microvilli, approximately 0.5 µm long, creating a large surface area (approximately

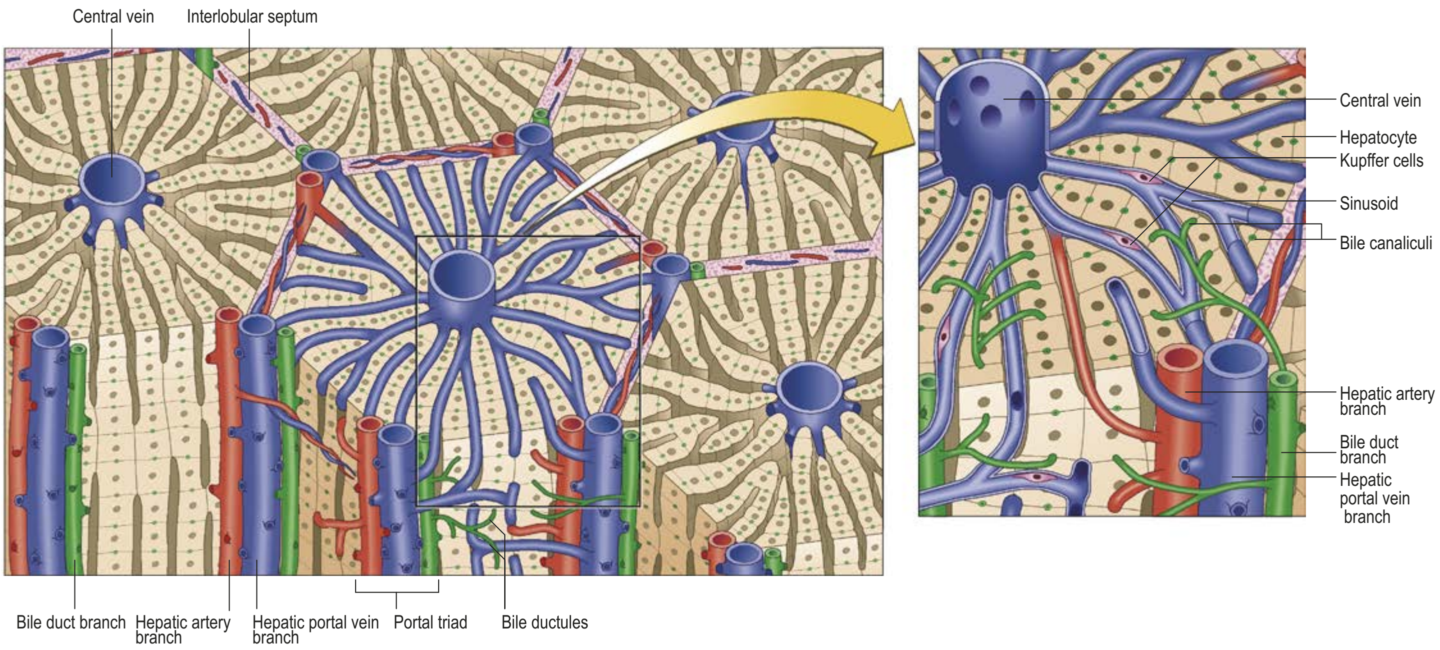

Fig. 66.18 Hepatic microstructure: sinusoidal endothelial cells are not shown.

70% of the hepatocyte surface) exposed to blood plasma. Elsewhere, hepatocytes are linked by numerous gap junctions and desmosomes. The lateral plasma membranes of adjacent hepatocytes form microscopic channels, bile canaliculi, which are specialized regions of intercellular space formed by apposing grooves in the membranes and sealed from extraneous interstitial space by tight junctions. Four types of transmembrane molecules (occludins, claudins, junctional adhesion molecules and Coxsackie virus and adenovirus receptors) constitute the core units of the functional protein complexes of the tight junctions (Lee 2012) (see Fig. 1.27). Individual tight junction complexes, either alone or in combination, are involved in signalling pathways in health and disease. Numerous membrane-bound exocytotic vesicles cluster near the lumina of the canaliculi because the secretion of bile is targeted at the canalicular plasma membrane. The tight junctions surrounding the biliary canaliculi prevent bile from entering the interstitial fluid or blood plasma, thereby creating a blood–bile barrier.

Hepatic stellate cells Hepatic stellate cells are much less numerous than hepatocytes. They lie within the perisinusoidal space between the sinusoids and the hepatocyte plates. Irregular in outline, they are characterized by numerous cytoplasmic lipid droplets in which the fat-soluble vitamin A is stored. They secrete most of the intralobular matrix components, including collagen type III (reticular) fibres and are a significant source of growth factors involved in liver homeostasis and regeneration. They play a major role in pathological processes (Yin et al 2013). In response to liver injury hepatic stellate cells become activated and predominantly myofibroblast-like. They are responsible for the replacement of damaged hepatocytes with collagenous scar tissue, hepatic fibrosis, seen initially in zone 3 around central veins. Fibrosis can progress to cirrhosis, where the parenchymal architecture and pattern of blood flow within the liver are both destroyed, with major systemic consequences.

Sinusoidal endothelial cells Hepatic venous sinusoids are generally wider than blood capillaries and are lined by a thin but highly fenestrated endothelium that lacks a complete basal lamina. The endothelial cells are typically flattened, each with a central nucleus, and are joined to each other by junctional complexes. The fenestrae are grouped in clusters with a mean diameter of 100 nm, allowing plasma direct access to the basal plasma membranes of hepatocytes. Their cytoplasm contains numerous transcytotic vesicles.

Stellate macrophages Stellate macrophages (Kupffer cells) of the liver are derived from circulating blood monocytes and originate in the bone marrow. They are long-term hepatic residents and lie within the sinusoidal lumina attached to the endothelial surface. They can be found in both the centrilobular and periportal zones but are typically more concentrated in the periportal zones: their function and structures differ depending on their location. They form the largest population of the mononuclear phagocyte system responsible for removing cellular and microbial debris from the circulation and for secreting cytokines involved in defence: they have been implicated in the pathogenesis of various hepatic diseases, including endotoxin tolerance, liver transplantation, nonalcoholic fatty liver disease, and alcoholic liver disease (Li et al 2017). They remove aged and damaged red blood cells from the hepatic circulation, a function normally shared with the spleen but fulfilled entirely by the liver after splenectomy.

Hepatic stem cells Hepatic stem cells are undifferentiated, pluripotent cells and are understood to reside around the bile canals; they are derived from the ductal plate in fetal livers. Their progeny are small epithelial cells (8–18 µm) with large oval nuclei and scanty cytoplasm, expressing both biliary epithelial and hepatocyte markers (Roskams et al 2010).

Bonus e-book content

Fig. 66.9 D, Digital subtraction angiogram of the coeliac trunk showing the hepatic arterial tree.

Fig. 66.10 Common hepatic artery variants.

Fig. 66.11 Hepatic arteriograms.

Fig. 66.17 Scanning electron micrographs of a resin corrosion cast of the liver.

Key references

Bismuth H 2013 Revisiting liver anatomy and terminology of hepatectomies. Ann Surg 257:383–6.
Couinaud C 1957 Le Foie: études anatomiques et chirurgicales. Paris: Masson.
Couinaud's original descriptive studies of liver segmentation.
Healey JE, Schroy PC 1953 Anatomy of the biliary ducts within the human liver: analysis of the prevailing pattern of branchings and the major variations of the biliary ducts. Arch Surg 66:599–616.
Launois B, Jamieson GG 1993 Modern Operative Techniques in Liver Surgery. Clinical Surgery International 18. Edinburgh: Churchill Livingstone.
Makuuchi M 2013 Could we or should we replace the conventional nomenclature of liver resections? Ann Surg 237:387–9.
Skandalakis JE, Coborn GL, Weidman TA et al 2004 Liver. In: Skandalakis JE (ed) Skandalakis' Surgical Anatomy. Athens: Paschalidis Medical Publications; Ch. 19, pp. 1005–92.
Terminology Committee of the International Hepato-Pancreato-Biliary Association 2000 The Brisbane 2000 Terminology of Liver Anatomy and Resections. HPB 2:333–9.

References

Bismuth H 2013 Revisiting liver anatomy and terminology of hepatectomies. Ann Surg 257:383–6.

Burt RP 2003 Phasic contractions of the rat portal vein depend on intracellular Ca^{2+} release stimulated by depolarization. Am J Physiol Heart Circ Physiol 284:H1808–17.

Camargo AM, Teixeira GG, Ortale JR 1996 Anatomy of the ostia venae hepaticae and the retrohepatic segment of the inferior vena cava. J Anat 188:59–64.

Couinaud C 1957 Le Foie: études anatomiques et chirurgicales. Paris: Masson.

Couinaud's original descriptive studies of liver segmentation.

Chaib E 2009 Absence of bifurcation of the portal vein. Surg Radiol Anat 31:389–92.

Covey AM, Brody LA, Maluccio MA et al 2002 Variant hepatic arterial anatomy revisited: digital subtraction angiography performed in 600 patients. Radiology 224:542–7.

Covey AM, Brody LA, Getrajdman GI et al 2004 Incidence, patterns, and clinical relevance of variant portal vein anatomy. AJR Am J Roentgenol 183:1055–64.

Dar FS, Faraj W, Heaton ND et al 2008 Variation in the venous drainage of left lateral segment liver graft requiring reconstruction of segment III vein with donor iliac artery. Liver Transplant 14:576–9.

di Francesco F, Grimaldi C, de Ville de Goyet J 2014 Meso-Rex bypass – a procedure to cure prehepatic portal hypertension: the insight and the inside. J Am Coll Surg 218:e23–36.

Fang CH, You JH, Lau WY et al 2012 Anatomical variations of hepatic veins: three-dimensional computed tomography scans of 200 subjects. World J Surg 36:120–4.

Flament JB, Delattre JF, Hidden G 1982 The mechanisms responsible for stabilising the liver. Anat Clin 4:125–35.

Fraser R, Dobbs BR, Rogers GW 1995 Lipoproteins and the liver sieve: the role of the fenestrated sinusoidal endothelium in lipoprotein metabolism, atherosclerosis, and cirrhosis. Hepatology 21:863–74.

Healey JE, Schroy PC 1953 Anatomy of the biliary ducts within the human liver: analysis of the prevailing pattern of branchings and the major variations of the biliary ducts. Arch Surg 66:599–616.

Hikspoors JPJM, Peeters MMJP, Kruepunga N et al 2017 Human liver segments: role of cryptic liver lobes and vascular physiology in the development of liver veins and left-right asymmetry. Sci Rep 7:17109.

Hjortsjö CH 1951 The topography of the intrahepatic duct systems. Acta Anat (Basel) 11:599–615.

Hribernik M, Trotovšek B 2014 Intrahepatic venous anastomoses with a focus on the middle hepatic vein anastomoses in normal human livers: anatomical study on liver corrosion casts. Surg Radiol Anat 36:231–7.

Joshi SD, Joshi SS, Athavale SA 2009 Some interesting observations on the surface features of the liver and their clinical implications. Singapore Med J 50:715–9.

Kawarada Y, Das BC, Taoka H 2000 Anatomy of the hepatic hilar area: the plate system. J Hepatobiliary Pancreat Surg 7:580–6.

Kietzmann T 2017 Metabolic zonation of the liver: the oxygen gradient revisited. Redox Biol 11:622–30.

Kuntz E, Kuntz HD 2008 Hepatology Textbook and Atlas, 3rd ed. Heidelberg: Springer.

Launois B, Jamieson GG 1993 Modern Operative Techniques in Liver Surgery. Clinical Surgery International 18. Edinburgh: Churchill Livingstone.

Lee NP 2012 The blood–biliary barrier, tight junctions and human liver diseases. Adv Exp Med Biol 763:171–85.

Li P, He K, Li J et al 2017 The role of Kupffer cells in hepatic diseases. Mol Immunol 85:222–9.

Lockhart S, Singh-Ranger G 2018 Rouvière's sulcus-aspects of incorporating this valuable sign for laparoscopic cholecystectomy. Asian J Surg 41:1–3.

López-Andújar R, Moya A, Montalvá E et al 2007 Lessons learned from anatomic variants of the hepatic artery in 1,081 transplanted livers. Liver Transpl 13:1401–4.

McCuskey RS 2004 Anatomy of efferent hepatic nerves. Anat Rec A Discov Mol Cell Evol Biol 280:821–6.

Macchi V, Feltrin G, Parenti A et al 2003 Diaphragmatic sulci and portal fissures. J Anat 202:303–8.

Majno P, Mentha G, Toso C et al 2014 Anatomy of the liver: an outline with three levels of complexity – a further step towards tailored territorial liver resections. J Hepatol 60:654–62.

Makuuchi M 2013 Could we or should we replace the conventional nomenclature of liver resections? Ann Surg 237:387–9.

Michels NA 1966 Newer anatomy of the liver and its variant blood supply and collateral circulation. Am J Surg 112:337–47.

Mirjalili SA, McFadden SL, Buckenham T et al 2012 Anatomical planes: are we teaching accurate surface anatomy? Clin Anat 25:819–26.

Ohtani O, Ohtani Y 2008 Lymph circulation in the liver. Anat Rec 291:643–52.

Onishi H, Kawarada Y, Das BC et al 2000 Surgical anatomy of the medial segment (S4) of the liver with special reference to bile ducts and vessels. Hepatogastroenterology 47:143–50.

Roskams T, Katoonizadeh A, Komuta M 2010 Hepatic progenitor cells: an update. Clin Liver Dis 14:705–18.

Roskams TA, Theise ND, Balabaud C et al 2004 Nomenclature of the finer branches of the biliary tree: canals, ductules, and ductular reactions in human livers. Hepatology 39:1739–45.

Saba L, Mallarini G 2011 Anatomic variations of arterial liver vascularization: an analysis by using MDCTA. Surg Radiol Anat 33:559–68.

Saxena R, Theise N 2004 Canals of Hering: recent insights and current knowledge. Semin Liver Dis 24:43–8.

Sharma M, Rameshbabu CS 2012 Collateral pathways in portal hypertension. J Clin Exp Hepatol 2:338–52.

Singh M, Prasad N 2017 The anatomy of Rouvière's sulcus as seen during laparoscopic cholecystectomy: a proposed classification. J Minim Access Surg. 13:89–95.

Siramolpiwat S 2014 Transjugular intrahepatic portosystemic shunts and portal hypertension-related complications. World J Gastroenterol 20:16996–7010.

Skandalakis JE, Coborn GL, Weidman TA et al 2004 Liver. In: Skandalakis JE (ed) Skandalakis' Surgical Anatomy. Athens: Paschalidis Medical Publications; Ch. 19, pp. 1005–92.

Strasberg SM 2005 Nomenclature of hepatic anatomy and resections: a review of the Brisbane 2000 system. J Hepatobiliary Pancreat Surg 12:351–5.

Strasberg SM, Phillips C 2013 Use and dissemination of the Brisbane 2000 nomenclature of liver anatomy and resections. Ann Surg 257:377–82.

Stringer MD 2009 Eponyms in Surgery and Anatomy of the Liver, Bile Ducts and Pancreas. London: Royal Society of Medicine.

A concise illustrated account of the derivation of and individuals behind the more common eponyms associated with liver anatomy and surgery.

Sugarbaker PH 1990 En bloc resection of hepatic segments 4B, 5 and 6 by transverse hepatectomy. Surg Gynecol Obstet 170:250–2.

Terminology Committee of the International Hepato-Pancreato-Biliary Association 2000 The Brisbane 2000 Terminology of Liver Anatomy and Resections. HPB 2:333–9.

Trutmann M, Sasse D 1994 The lymphatics of the liver. Anat Embryol (Berl) 190:201–9.

Vellar ID, Banting SW, Hardy KJ 1998 The anatomical basis for segment III cholangiojejunostomy with analysis of 13 cases. Aust NZ J Surg 68:498–503.

Yamamoto M, Katagiri S, Ariizumi S et al 2012 Glissonean pedicle transection method for liver surgery (with video). J Hepatobiliary Pancreat Sci 19:3–8.

Yin C, Evason KJ, Asahina K et al 2013 Hepatic stellate cells in liver development, regeneration, and cancer. J Clin Invest 123:1902–10.

Further reading

Abdel-Misih SRZ, Bloomston M 2010 Liver anatomy. Surg Clin North Am 90:643–53.

Bismuth H 1982 Surgical anatomy and anatomical surgery of the liver. World J Surg 6:5–9.

Castaing D 2008 Surgical anatomy of the biliary tract. HPB 10:72–6.

Gillard JH, Patel MC, Abrahams PH et al 1998 Riedel's lobe of the liver: fact or fiction? Clin Anat 11:47–9.

Goldsmith NA, Woodburne RT 1957 Surgical anatomy pertaining to liver resection. Surg Gynecol Obstet 195:310–8.

Mavrides E, Moscoso G, Carvalho JS et al 2001 The anatomy of the umbilical, portal and hepatic venous systems in the human fetus at 14–19 weeks of gestation. Ultrasound Obstet Gynecol 18:598–604.

Rex H 1888 Beiträge zur Morphologie der Säugerleber. Morph Jahrb 14:517–616.

Takasaki K, Koabayashi S, Tanaka S et al 1986 Highly selected hepatic resection by Glissonian sheath-binding method. Dig Surg 3:121 (abstract).

CHAPTER

67

Gallbladder and biliary tree

The biliary tree comprises the system of ducts that collect and deliver bile from the liver to the descending (second) part of the duodenum. It is conventionally divided into intrahepatic and extrahepatic biliary trees. The intrahepatic ducts are formed from bile ductules that join to form segmental ducts. These merge to form right and left hepatic ducts close to the porta hepatis. The extrahepatic biliary tree comprises the extrahepatic segments of the right and left hepatic ducts, the common hepatic duct, the cystic duct and gallbladder, and the bile duct (**Fig. 67.1**).

GALLBLADDER

The gallbladder is a pear-shaped, blind-ending diverticulum attached to the bile duct by the cystic duct (**Fig. 67.2**). It stores and concentrates bile. In life it is grey–blue in colour and is usually firmly attached by connective tissue to the inferior surface of the right lobe of the liver, between segments IV and V at the lower limit of the principal plane. In the adult the gallbladder is between 7 and 10 cm long, with a resting volume of about 25 ml and a capacity of up to 50 ml (Di Ciaula et al 2012). It usually lies in a shallow fossa (fossa for the gallbladder) on the visceral surface of the right lobe of the liver, covered by peritoneum continued from the surface of the liver. This attachment can vary widely. Rarely, the gallbladder is almost completely buried within the liver (intrahepatic gallbladder; Guiteau et al 2009), or suspended from the liver by a mesentery (when it is at risk of torsion; Gupta et al 2009), or connected to the duodenum by a variant component of the lesser omentum, the cystoduodenal ligament (which has been found in up to 35% of dissections; Ashaolu et al 2015).

The gallbladder is described as having a fundus, body, infundibulum and neck. The neck lies at the medial end, close to the porta hepatis, and almost always has a short peritoneal attachment (see above) (mesentery) to the liver, which usually contains the cystic artery. The mucosa at the medial end of the neck is obliquely ridged, forming a crescentic fold that is continuous with the spirally arranged mucosal folds in the cystic duct (Dasgupta and Stringer 2005). The neck usually lies anterior to the descending part of the duodenum. The body of the gallbladder normally lies in contact with the visceral surface of the liver. The body lies anterior to the descending part of the duodenum and the proximal end of the transverse colon. The bulbous fundus lies at the lateral end of the body and usually projects past the inferior border of the liver to a variable extent. Here it frequently lies in contact with the anterior abdominal wall deep to the ninth costal cartilage, where the lateral edge of the right rectus abdominis crosses the costal arch. This is where enlargement of the gallbladder is best sought on clinical examination. The fundus commonly lies adjacent to the transverse colon. The infundibulum is a tapered and sometimes angulated part of the gallbladder between the body and neck of the gallbladder.

The gallbladder varies in size and shape. The fundus can be elongated and highly mobile. Rarely it is folded back on the body of the gallbladder, the so-called Phrygian cap; on ultrasound, this can be wrongly interpreted as an apparent septum within an otherwise normal gallbladder. Other anatomical variants of the gallbladder include duplication, with or without a double cystic duct; agenesis; internal septation; and an ectopic location (most commonly left-sided) (Gross 1936, Faure et al 2008, Tubbs et al 2016). Although rare, these congenital anatomical variations are particularly important if the patient requires surgery for gallbladder or gallstone disease (Lamah et al 2001, Chowbey et al 2004, Singh et al 2006, Castorina et al 2014).

Hartmann's pouch

Available with the *Gray's Anatomy* e-book

INTRAHEPATIC BILIARY TREE

Segmental and sectoral ducts

The segmental ducts of the left part of the liver have a relatively constant pattern, although more than one segmental duct can drain each particular segment. The left hepatic duct is formed by the union of segments II and III ducts, most often deep to or to the left of the umbilical part of the left branch of the hepatic portal vein (see Fig. 67.1). The biliary drainage of segment IV is more variable but is usually by a single duct into the left hepatic duct. The right hepatic duct is formed by the union of the right anterior (medial) and posterior (lateral) sectoral ducts. The right anterior (medial) sectoral bile duct drains segments V and VIII, and the right posterior (lateral) sectoral duct drains segments VI and VII. The right posterior sectoral duct usually curves around the posterior aspect of the right anterior duct before fusing with its medial aspect; this is known as Hjortsjö's crook and is an important technical consideration when the liver is resected (**Fig. 67.3**). The right posterior sectoral duct (and associated blood vessels) is frequently located in Rouvière's sulcus (see below), which is a reasonably constant cleft 2–3 cm in length on the liver surface to the right of the porta hepatis anterior to the caudate lobe. An average of three small ducts drain the caudate lobe (segment I) at the hilar plate; the right-sided duct usually drains to the right hepatic duct or the posterior sectoral branch whereas the left-sided duct frequently crosses over to drain into the right posterior sectoral duct (Makki et al 2018).

The right hepatic duct and its branches are more often subject to variation than the left ductal system (Cucchetti et al 2011, Chaib et al 2014). These variations have been classified into seven main types (**Table 67.1**, **Fig. 67.4**) (Yoshida et al 1996), although additional very rare variants have also been described (Nayman et al 2016, Stringer 2016). Left intrahepatic ductal variations mostly relate to the drainage pattern of segment IV; this segmental bile duct usually drains into the left hepatic duct but in some cases it opens into a segment II or III bile duct, the right anterior sectoral duct, or even the common hepatic duct (Chaib et al 2014).

EXTRAHEPATIC BILIARY TREE

Cystic duct

The cystic duct drains the gallbladder into the bile duct. In adults it is usually 2–4 cm long and has a luminal diameter of 2–3 mm (Dasgupta and Stringer 2005). Occasionally it is very short, which makes its division during cholecystectomy potentially hazardous. It passes posteriorly and medially from the neck of the gallbladder, often in a tortuous fashion, to unite with the common hepatic duct and form the bile duct. The anatomy of the junction between the cystic duct and common hepatic duct is variable (see Fig. 67.4). In most individuals the cystic duct joins the middle third of the combined lengths of the common hepatic and bile ducts (Shaw et al 1993), but it can also drain into the distal bile duct ('low insertion') or into a more proximal duct such as the proximal common hepatic duct or right hepatic duct. It usually joins the right lateral aspect of the common hepatic duct but can merge medially, anteriorly or posteriorly; and it usually forms an oblique angle with the common hepatic duct but can spiral around it or run parallel to it in the hepatoduodenal ligament for a variable distance before merging (Lamah et al 2001, Onder et al 2013, Stringer 2016) (**Fig. 67.8**). Irrespective of the site or type of union, the terminal part of the cystic duct is frequently fused to the common hepatic duct for a variable distance.

An oblique groove on the inferior surface of the liver posterior to the fossa for the gallbladder is present in 70–80% of livers. It is variously known as the fissure of Gans, Rouvière's sulcus or the incisura hepatis dextra (Ch. 66). It overlies the division of the right posterior (lateral) portal pedicle, where it gives off the inferior segment VI branch. It has been increasingly recognized as a useful anatomical landmark during hepatic resection and in laparoscopic cholecystectomy (since the cystic duct and artery lie anterosuperior to the sulcus while the bile duct lies posteroinferior) (Dahmane et al 2013).

A pouch-like structure (Hartmann's pouch) may occasionally project from the neck of the gallbladder at its junction with the body of the gallbladder (Davies and Harding 1942, Anandhi and Alagavenkatesan 2018). It is thought to be produced by adhesions between the neck of the gallbladder and the cystic duct: once these adhesions are separated and the cystic duct is mobilized, Hartmann's pouch disappears. A significant association between the presence of a Hartmann's pouch and gallstones has been reported, but the aetiology is unclear (Skandalakis et al 2004, van Eijck et al 2007).

A small, rare bile duct known as a subvesical duct from segment V of the liver can traverse the fossa for the gallbladder and join the right hepatic duct or its anterior sectoral branch or the common hepatic duct (Schnelldorfer and Sarr 2012). This duct is important because it can be injured during cholecystectomy, causing a postoperative bile leak (Spanos and Syrakos 2006). These ducts are more likely to be injured if the gallbladder is not dissected close to its wall. A subvesical duct may also drain directly into the gallbladder (cholecystohepatic duct) or cystic duct (cystohepatic duct) and should not be confused with a hepatocystic duct (which is present when the bile duct is absent and both hepatic ducts drain directly into the gallbladder, which in turn drains via the cystic duct into the duodenum) (Losanoff et al 2002) (**Figs 67.5-67.7**).

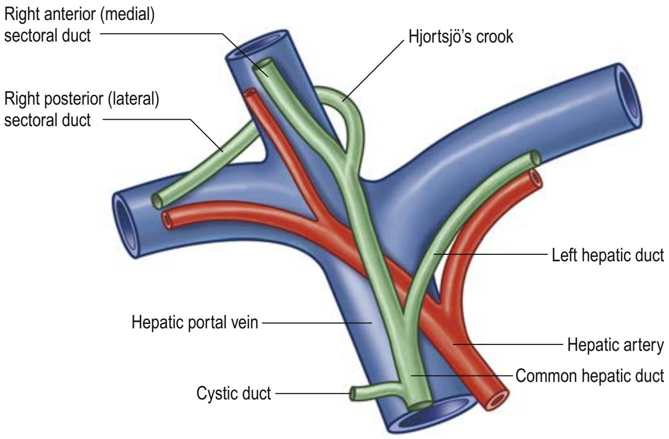

Fig. 67.3 Hjortsö's crook. The right posterior (lateral) sectoral bile duct usually hooks around the right anterior (medial) sectoral pedicle, rendering it vulnerable to injury when an extended left hepatectomy is performed that includes segments V and VIII of the liver (left trisectionectomy).

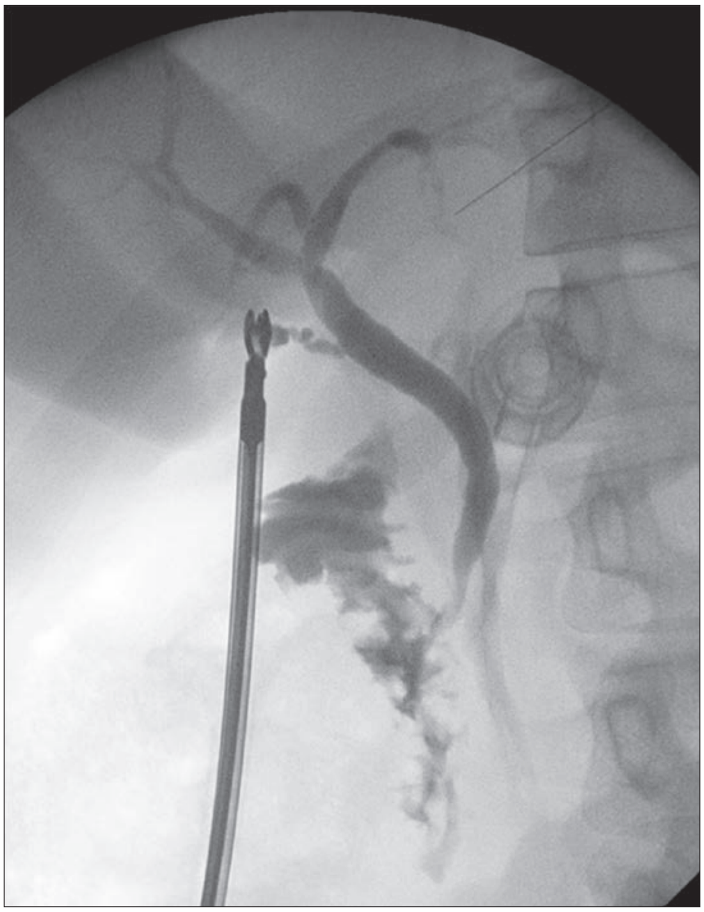

Fig. 67.5 Operative cholangiogram showing a trifurcation pattern of intrahepatic duct union (type 2). An endoscopic clamp/catheter is occluding the cystic duct. (Courtesy of Dr Scott Diamond, Surgeon, Wellington, New Zealand.)

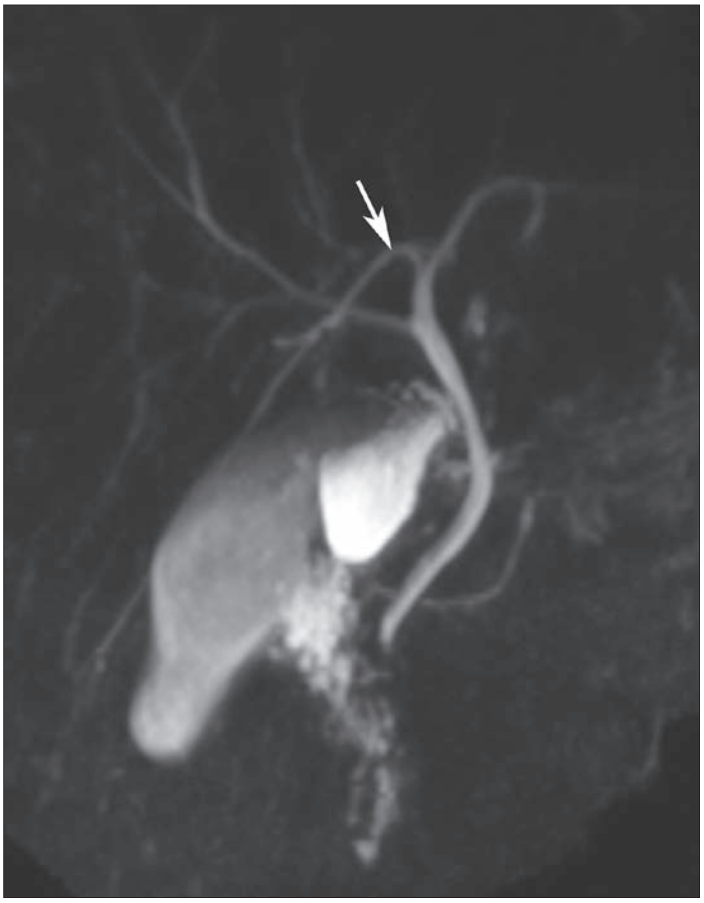

Fig. 67.6 Magnetic resonance cholangiopancreatogram showing the right posterior sectoral duct (arrow) draining into the left hepatic duct (type 3 intrahepatic duct drainage pattern). (Courtesy of Dr Matthew MacKay, Radiologist, Wellington, New Zealand.)

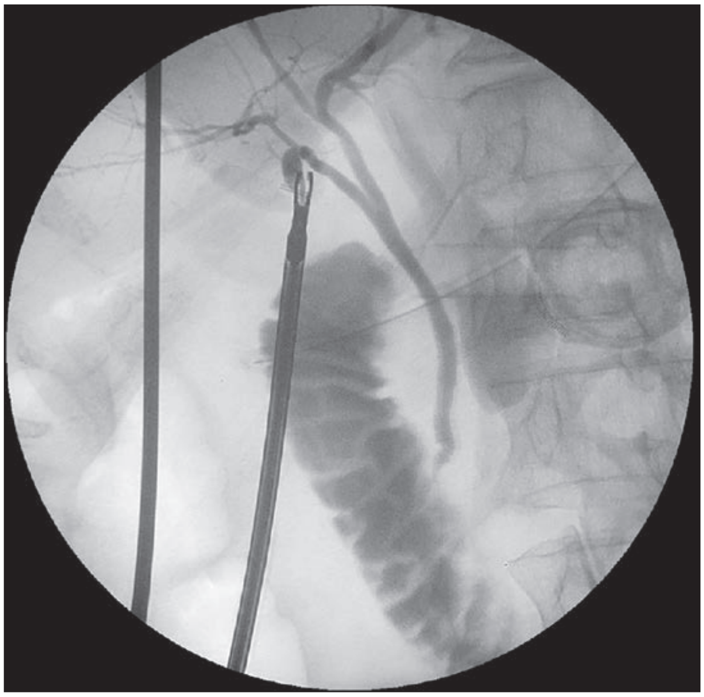

Fig. 67.7 Cystohepatic duct. Operative cholangiogram showing a posterior sectoral duct draining into the cystic duct. Also known as a 'cystohepatic duct' this is one of the rare variants referred to in Table 67.1. (With permission from Brown AW, Wilson RB 2018 Legacy of Le Quesne: operative cholangiography in the modern era. Aust NZ J Surg 88(9):819–20.)

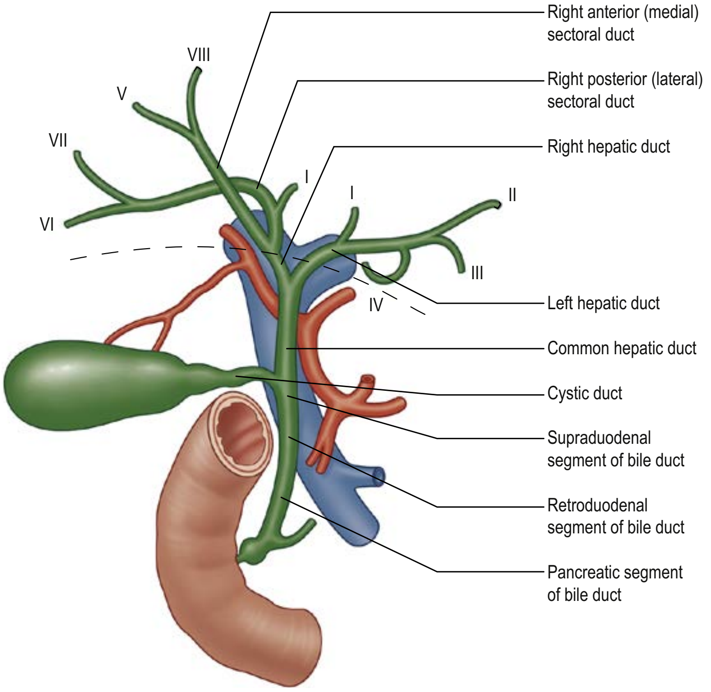
Right anterior (medial) sectoral duct
Right posterior (lateral) sectoral duct
Right hepatic duct
Left hepatic duct
Common hepatic duct
Cystic duct
Supraduodenal segment of bile duct
Retroduodenal segment of bile duct
Pancreatic segment of bile duct
VIII
V
VII
VI
I
I
II
III
IV

Fig. 67.1 The overall arrangement of the intrahepatic and extrahepatic biliary tree. The segmental ducts often branch just before they enter the main ducts, or are multiple as they enter the main ducts, but for clarity are shown here as single ducts. Note that segment I often drains via both right and left hepatic ducts. The level of the liver at the porta hepatis is shown by the dashed line.

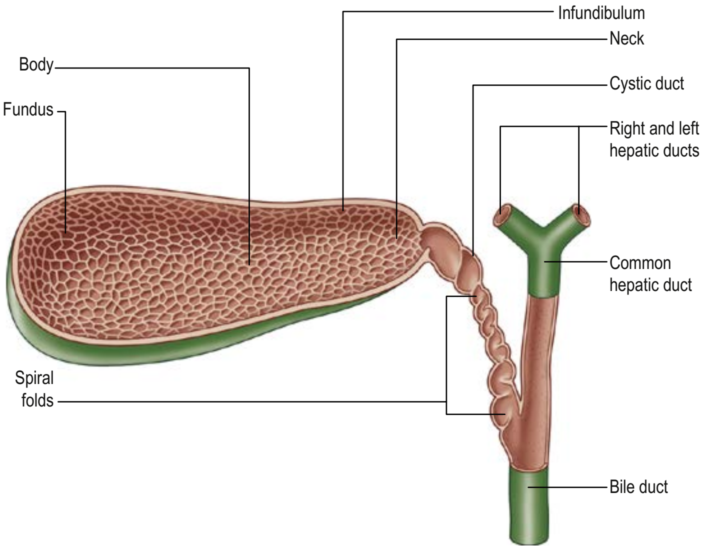

Fig. 67.2 The interior of the gallbladder and bile ducts.

TABLE 67.1 Major variations of the intrahepatic duct drainage patterns

Type	Approximate % of population	Description
1	60*	'Normal' anatomy
2	10–15	No right hepatic duct. The common hepatic duct is formed by the union of right anterior sectoral, right posterior sectoral and left hepatic ducts (trifurcation pattern)
3	10–15	One of the right sectoral ducts (more often the posterior) joins the left hepatic duct
4	5–10	Low drainage of one of the right sectoral ducts (more often the posterior) into the common hepatic duct
Rare	<10	The segment V duct or the right posterior sectoral duct drains into the cystic duct or gallbladder

Data from Cucchetti et al 2011, Chaib et al 2014, Gupta et al 2016, Nayman et al 2016.

*This figure is higher in males and lower in females, who are more likely to have variant intrahepatic bile duct anatomy. NB The percentages of different types vary among populations.

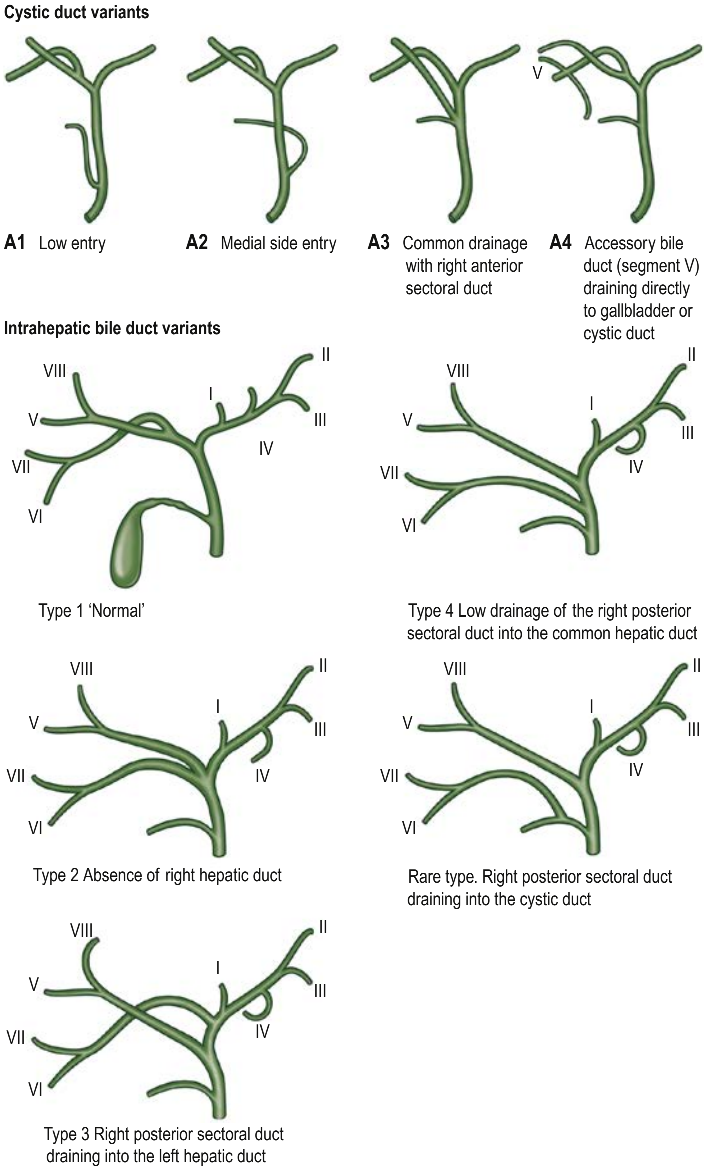

Cystic duct variants

A1 Low entry **A2** Medial side entry **A3** Common drainage with right anterior sectoral duct **A4** Accessory bile duct (segment V) draining directly to gallbladder or cystic duct

Intrahepatic bile duct variants

Type 1 'Normal'

Type 4 Low drainage of the right posterior sectoral duct into the common hepatic duct

Type 2 Absence of right hepatic duct

Rare type. Right posterior sectoral duct draining into the cystic duct

Type 3 Right posterior sectoral duct draining into the left hepatic duct

Fig. 67.4 Variations in the anatomy of the cystic and intrahepatic bile ducts. The cystic duct variations are labelled A1–A4 and the intrahepatic bile duct variations as types 1–4 (see Table 67.1). In the type 2 pattern, the right sectoral ducts may have a short extrahepatic segment.

Rarely, the cystic duct is double or absent (when the gallbladder drains directly into the bile duct), or receives an anomalous hepatic duct from segment V of the liver. These variations in cystic duct anatomy are of considerable importance during surgical excision of the gallbladder (cholecystectomy). The cystic duct must be identified passing to the neck of the gallbladder and must be occluded some distance away from the bile duct to prevent injury to the latter (Fig. 67.8). A preliminary operative cholangiogram is essential if the anatomy is unclear or anomalous.

The mucosa of the cystic duct has 2–10 crescentic folds that project into the lumen and form a spiral; these are continuous with those in the neck of the gallbladder. The function of these spiral folds (of Heister) is unknown but they could help to preserve the patency of this narrow, tortuous duct rather than regulate the flow of bile, as is commonly stated (Dasgupta and Stringer 2005).

Hepatic ducts

The right and left hepatic ducts emerge from the liver and unite near the right end of the porta hepatis to form the common hepatic duct. The extrahepatic segment of the right hepatic duct is short (0.5–2.0 cm in adults) and nearly vertical, while the left hepatic duct is longer (1.5–3.5 cm) and more horizontal, and lies along the inferior border of segment IV of the liver. The accessibility of the extrahepatic segment of the left hepatic duct is exploited when performing a surgical biliary bypass in patients with benign extrahepatic biliary duct strictures (Myburgh 1993).

In adults, the common hepatic duct descends approximately 3 cm before being joined obliquely on its right by the cystic duct to form the

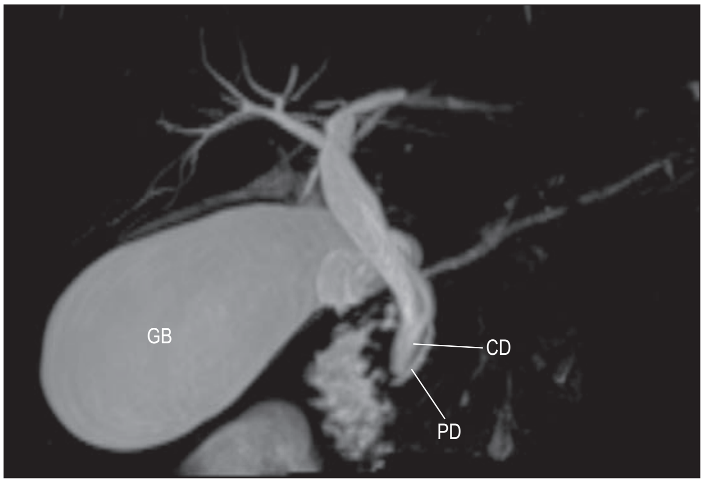

Fig. 67.8 Magnetic resonance cholangiopancreatogram showing a low medial union between the cystic duct (CD) and the distal bile duct. Other abbreviations: PD, pancreatic duct; GB, gallbladder. (Courtesy of Dr Matthew MacKay, Radiologist, Wellington, New Zealand.)

bile duct. The common hepatic duct lies to the right of the hepatic artery and anterior to the hepatic portal vein in the hepatoduodenal ligament. In healthy adults the luminal diameter of the common hepatic duct, as measured by ultrasound, is less than 5 mm.

Bile duct

The bile duct is formed near the porta hepatis by the junction of the cystic and common hepatic ducts (**Figs 67.9–67.10**). In adults, it is usually between 6 and 8 cm long and its luminal diameter, as measured by ultrasound, is no more than 7 mm (Perret et al 2000); the diameter increases slightly with advancing age from a mean of 3.6 mm below 60 years to a mean of 4 mm after 80 years. The bile duct can be divided into supraduodenal, retroduodenal and pancreatic segments. The supraduodenal segment descends posteriorly and slightly to the left, anterior to the omental foramen and inferior vena cava, in the hepatoduodenal ligament, where it lies anterior and to the right of the hepatic portal vein and to the right of the hepatic artery. This part of the bile duct is the most accessible at surgery. The retroduodenal segment lies behind the superior part of the duodenum with the gastroduodenal artery on its left. The pancreatic segment runs in a groove on the posterior surface of the head of the pancreas, embedded in the gland to a variable degree; it lies up to 2 cm away from the medial wall of the descending part of the duodenum and anterior to the right renal vein. The pancreatic segment of the bile duct typically has a tapered appearance (see Fig. 67.9; **Fig. 67.11**). The posterior superior pancreaticoduodenal artery, a branch of the gastroduodenal artery, descends anterior to the retroduodenal segment of the bile duct (at the superior border of the pancreas) before spiralling around the right side of the bile duct to reach the posterior surface of the head of the pancreas (Bertelli et al 1996).

Hepatopancreatic ampulla

As it descends behind the head of the pancreas medial to the descending part of the duodenum, the bile duct approaches the right end of the pancreatic duct. The two ducts usually enter the duodenal wall together in a Y configuration to form a 2–10 mm long common channel (Flati et al 1994). This common channel often contains a dilation known as the hepatopancreatic ampulla (of Vater) and it opens via a single orifice on to the medial wall of the descending part of the duodenum at the major duodenal papilla (see Fig. 67.9B). In clinical practice, the whole region is often termed the pancreaticobiliary junction. Occasionally, the bile duct and pancreatic duct unite outside the duodenal wall to form an abnormally long common channel or the two ducts are separated by a septum or drain into the duodenum separately (Kamisawa and Okamoto 2008).

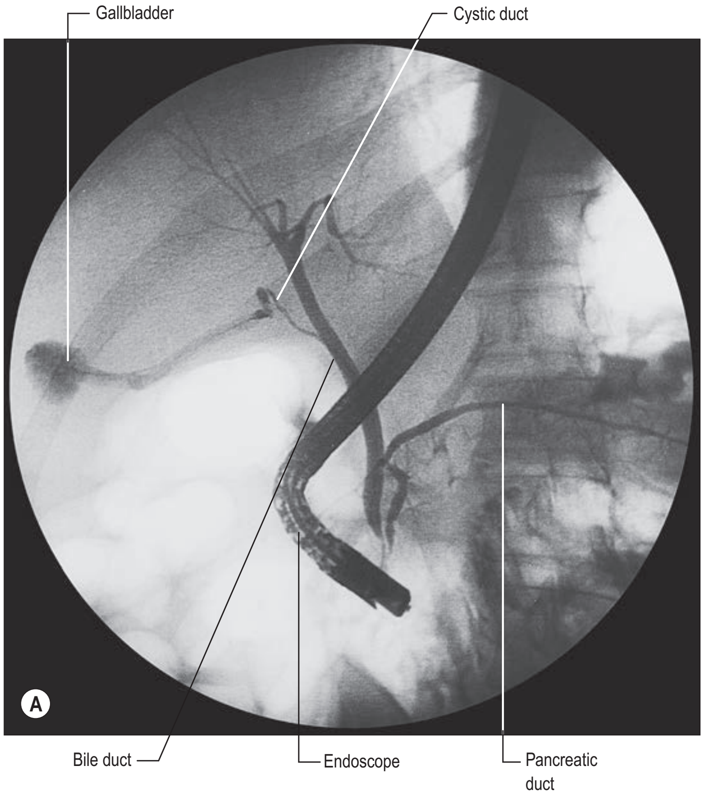

Fig. 67.9 A, An endoscopic retrograde cholangiopancreatogram. (B, *continued online*)

The mucosa of the terminal 5–10 mm of the bile and pancreatic ducts has a complex arrangement of circumferentially arranged folds (Purvis et al 2013) (**Fig. 67.12**). Their distribution and orientation impede reflux of duodenal contents into the bile and pancreatic ducts, and they sometimes cause difficulty cannulating the major duodenal papilla during endoscopic retrograde cholangiopancreatography (ERCP).

A complex arrangement of smooth muscle with prominent circular fibres surrounds the distal bile duct as the sphincter of the bile duct and the sphincter of the ampulla (sphincter of Oddi); to a lesser extent, it also surrounds the terminal part of the pancreatic duct as the sphincter of the pancreatic duct (Boyden 1957, Didio and Anderson 1968, Ironside et al 2019). The whole sphincter muscle complex lies mostly within the wall of the duodenum and, in adults, is approximately 15–20 mm long; it contains a high pressure zone that can be detected by manometry (Habib et al 1988, Teilum 1991). The smooth muscle of the sphincter of the ampulla is developmentally and anatomically distinct from the adjacent duodenal muscle. The sphincter regulates the flow of bile and pancreatic secretions into the duodenum and impedes reflux of duodenal contents into the ductal system (Guelrud et al 1990); it is inhibited by cholecystokinin (CCK), which not only relaxes the sphincter but also causes gallbladder contraction (Woods et al 2005). Division of the upper part of the sphincter of the ampulla (sphincterotomy) can be required to allow access to the bile duct during ERCP.

The pancreaticobiliary junction is clinically important because it can be affected by various congenital and acquired disorders. An anomalous union between the bile and pancreatic ducts, particularly one resulting in an abnormally long common channel, can be associated with congenital bile duct dilation, recurrent pancreatitis and/or gallbladder cancer (Kimura et al 1985, Misra and Dwivedi 1990, Stringer 2018). Acquired pathology in this region also includes gallstone obstruction and periampullary tumours.

Cystohepatic triangle

The triangular region formed between the cystic duct, the common hepatic duct and the inferior surface of the liver is the cystohepatic (hepatobiliary) triangle (**Fig. 67.13**). It is often mistakenly referred to as Calot's triangle, which is an isosceles triangle based on the common hepatic duct, with the cystic artery and cystic duct forming its sides (Stringer 2009). The cystohepatic triangle is bridged by the double layer of peritoneum that forms the short and variable mesentery of the cystic duct. Between these two layers there is a variable amount of adipose and connective tissues, lymphatics, the cystic node, autonomic nerves and usually the cystic artery as it travels from the right hepatic artery to the gallbladder. Occasionally there is also an accessory cystic duct located in the triangle (see above). Understanding the variations in biliary and arterial anatomy as they relate to the triangle is of considerable importance during excision of the gallbladder in order to avoid injury to the common hepatic or bile duct or right hepatic artery (Suzuki et al 2000, Talpur et al 2010).

Gallstones

Available with the *Gray's Anatomy* e-book

Endoscopic cholangiopancreatography

Available with the *Gray's Anatomy* e-book

Biliary drainage

Available with the *Gray's Anatomy* e-book

VASCULAR SUPPLY AND LYMPHATIC DRAINAGE

Cystic artery

The cystic artery usually (approximately 80%) arises from the right hepatic artery (**Fig. 67.14**, but see Fig. 67.15) and most often passes posterior to the common hepatic duct within the cystohepatic triangle, Gallstones are relatively common and usually form in the gallbladder. Gallbladder contraction can move a gallstone towards the narrow cystic duct, where it can cause obstruction and pain (biliary colic). If the stone continues to occlude the cystic duct, it will lead to inflammation of the gallbladder (acute cholecystitis) or a sterile distension of the gallbladder (mucocele); providing the gallbladder has not been inflamed previously, it will be non-fibrotic and distensible, and the fundus often becomes palpable below the costal arch. A gallstone lodged in the cystic duct or neck of the gallbladder can also produce an inflammatory swelling that compresses the common hepatic duct, resulting in partial obstruction to the flow of bile and the development of jaundice (the so-called 'Mirizzi syndrome'; Stringer 2009). If the gallstone passes through the cystic duct, it can become impacted in the distal bile duct or at the pancreaticobiliary junction, causing obstructive jaundice, cholangitis and/or acute pancreatitis.

The bile duct and/or pancreatic duct can be accessed endoscopically from the duodenum for diagnostic cholangiography and/or pancreatography, and for therapeutic interventions such as the relief of biliary obstruction by insertion of an internal stent. The acute angle between the distal bile duct and pancreatic duct can make direct cannulation of the bile duct difficult. In such cases, the superior part of the major duodenal papilla can be incised (pre-cut sphincterotomy) to facilitate cannulation of the bile duct. This incision, and the more extensive sphincterotomy that is sometimes needed to release an impacted gallstone (Sakai et al 2012), is occasionally complicated by arterial bleeding. The risk can be reduced by making the incision in the 10–11 o'clock region of the sphincter (Mirjalili and Stringer 2011). Endoscopic sphincterotomy can result in uncontrolled reflux of duodenal contents into the distal bile duct and ascending biliary infection.

The proximity of the fundus of the gallbladder to the anterior abdominal wall facilitates ultrasound-guided percutaneous drainage of a distended, obstructed gallbladder. Because the cystic duct has a small calibre and spiral folds, drainage of the gallbladder is rarely sufficient to decompress the biliary tree when the bile duct is obstructed. In such cases, temporary or permanent biliary drainage can be achieved by the endoscopic insertion of a biliary stent through the obstruction via the major duodenal papilla, surgical bile diversion, or percutaneous transhepatic drainage. The last-named involves image-guided puncture of a dilated intrahepatic bile duct and the insertion of an external drain or an internal stent through the biliary obstruction.

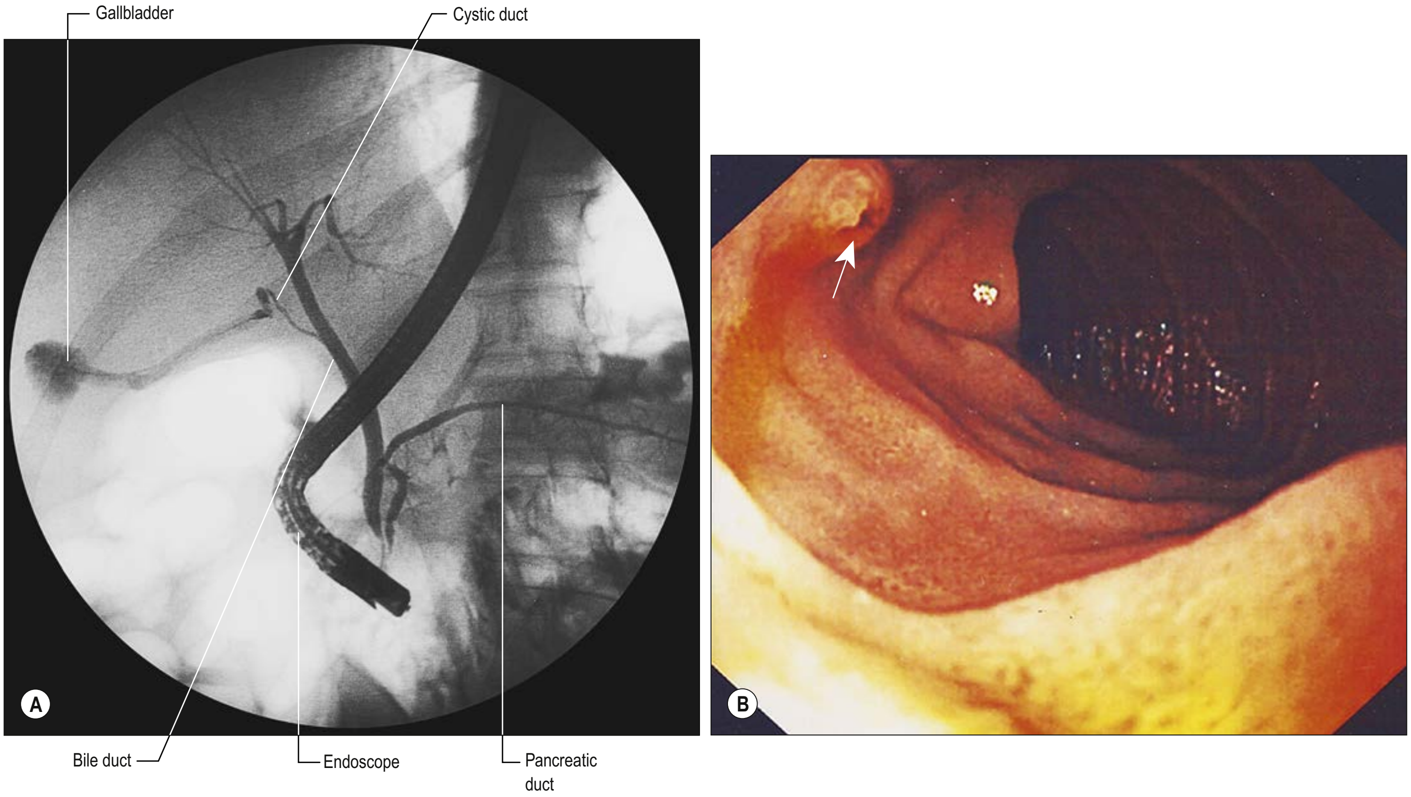

Fig. 67.9 **A**, An endoscopic retrograde cholangiopancreatogram. **B**, Endoscopic image of the major duodenal papilla (arrow) on the medial wall of the descending duodenum.

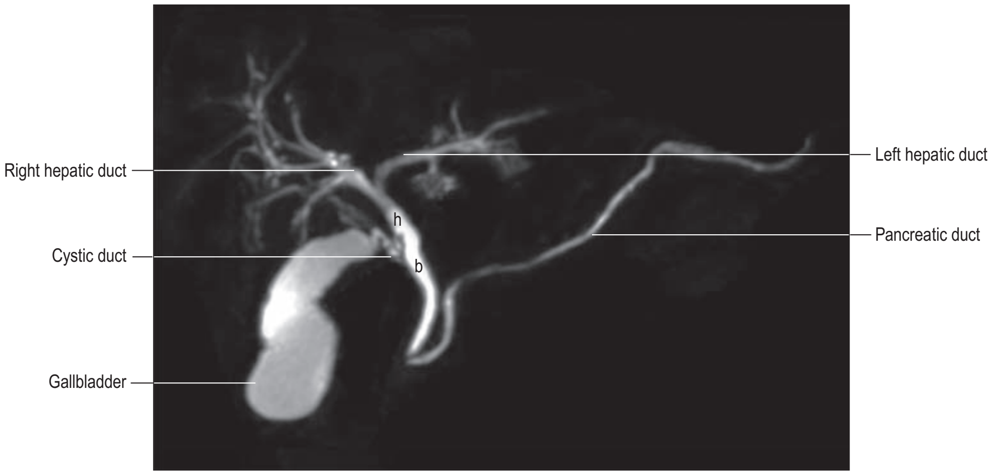

Fig. 67.10 Maximal intensity projection from a magnetic resonance cholangiopancreaticogram. Abbreviations: b, bile duct; h, common hepatic duct.

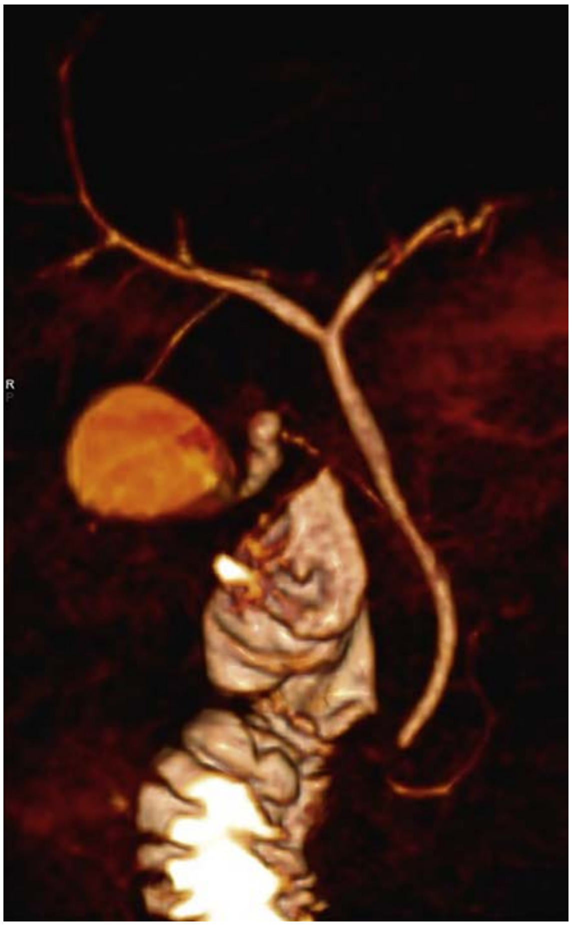

Fig. 67.11 Magnetic resonance cholangiopancreatogram of a normal biliary tree from a 23-year-old male undergoing investigation in preparation for living donor liver transplantation. (Courtesy of Dr Ashley Guthrie, Leeds, UK.)

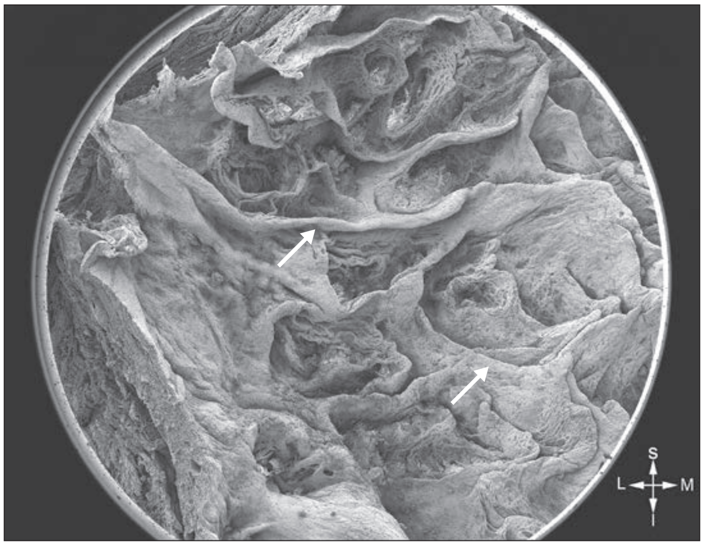

Fig. 67.12 A scanning electron micrograph showing mucosal folds (arrows) lining the wall of the hepatopancreatic ampulla. Abbreviations: I, inferior; L, lateral; M, medial; S, superior.

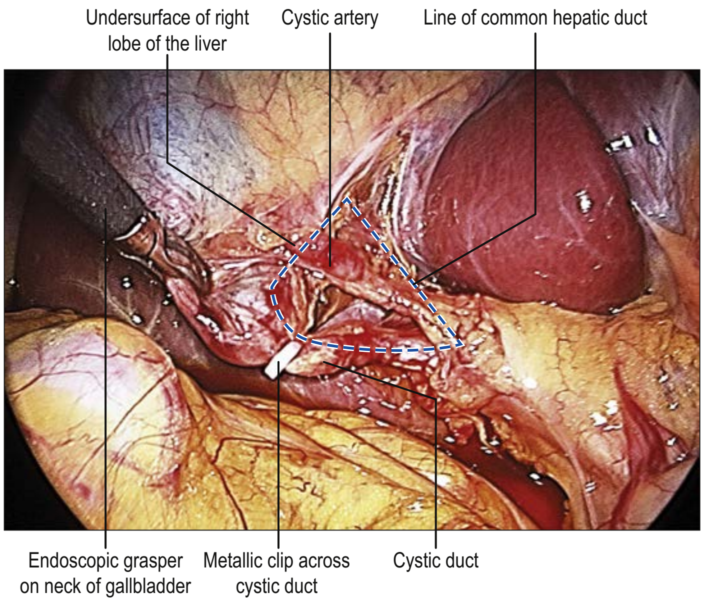
Undersurface of right lobe of the liver
Cystic artery
Line of common hepatic duct
Endoscopic grasper on neck of gallbladder
Metallic clip across cystic duct
Cystic duct

Fig. 67.13 A view of the cystohepatic triangle (dashed line) at laparoscopic cholecystectomy. In this patient, the cystic artery can be seen crossing the triangle superficially en route to the gallbladder. (Courtesy of Richard Flint, Christchurch Hospital.)

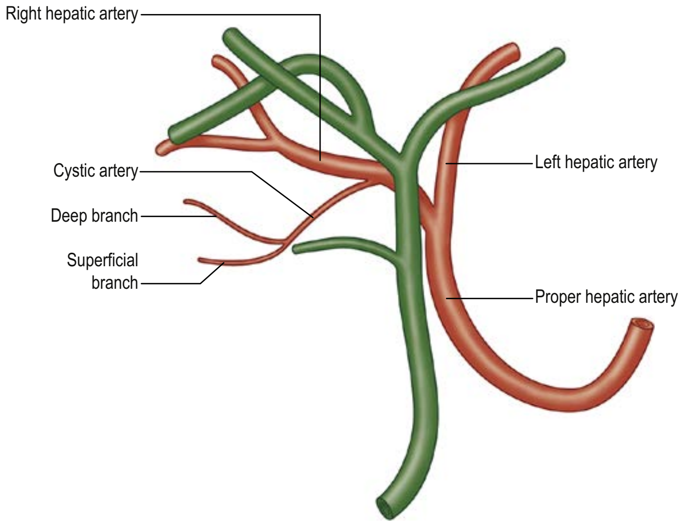

Fig. 67.14 Normal anatomy of the cystic artery.

where it lies superior to the cystic duct (Andall et al 2016). On reaching the superior aspect of the neck of the gallbladder it divides into superficial and deep branches that anastomose over the surface of the body and fundus. The cystic artery is usually less than 3 mm in diameter; a larger artery in the cystohepatic triangle is more likely to be the right hepatic artery. While the cystic artery usually traverses the cystohepatic triangle it may lie outside when it passes anterior, posterior or inferior to the cystic duct (Xia et al 2015).

The origin of the cystic artery is variable (**Fig. 67.15**). The most common variant is an origin from the proper hepatic artery, when it often crosses anterior to the bile or common hepatic ducts to reach the gallbladder. Rarely it arises from the coeliac trunk or left hepatic, gastroduodenal, superior pancreaticoduodenal, right gastric, or superior mesenteric arteries; in these cases, the cystic artery might not traverse the cystohepatic triangle. The cystic artery frequently bifurcates close to its origin, giving rise to two vessels. Alternatively, an accessory cystic artery can arise from the proper hepatic artery or one of its branches. If the right hepatic artery passes anterior to the bile or hepatic duct the cystic artery is short. Small arterial branches from segment IV or V of the liver can contribute to the supply of the body of the gallbladder, particularly when it is substantially intrahepatic; these help to protect the gallbladder from ischaemic necrosis if inflammation results in thrombosis of the cystic artery.

The cystic artery also gives rise to multiple fine branches that contribute to the blood supply of the extrahepatic bile ducts.

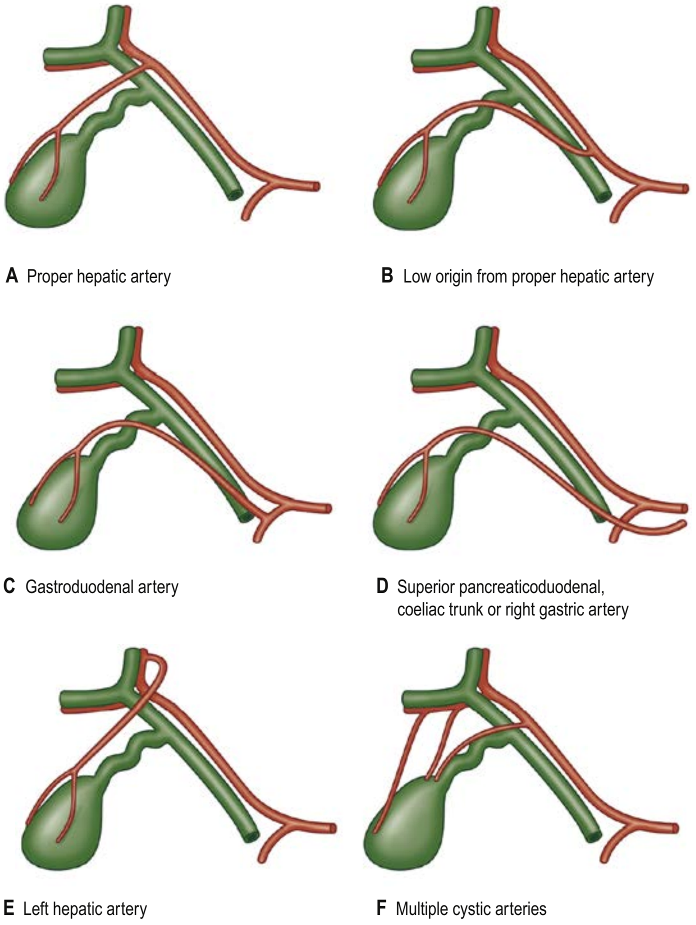
A Proper hepatic artery
B Low origin from proper hepatic artery
C Gastroduodenal artery
D Superior pancreaticoduodenal, coeliac trunk or right gastric artery
E Left hepatic artery
F Multiple cystic arteries

Fig. 67.15 Variant anatomy of the cystic artery.

Ductal arteries

The bile and hepatic ducts are supplied by a fine network of arteries arising from several sources. The bile duct is frequently supplied by 2–4 small-calibre arteries that form a long, tortuous, anastomotic network along its length; these narrow vessels tend to be concentrated at the 3 and 9 o'clock positions around the circumference of the duct (Northover and Terblanche 1979). The network is fed by arteries from the right hepatic artery above, reinforced by fine branches from the cystic artery. Branches from three main arterial sources often supply the bile duct from below: the posterior superior pancreaticoduodenal artery, the retroduodenal artery (both of which originate from the gastroduodenal artery and cross anterior to the retroduodenal segment of the bile duct), and a retroportal artery arising from the superior mesenteric artery or coeliac trunk and passing to the right on the posterior surface of the hepatic portal vein and anastomosing with the right hepatic or retroduodenal arteries (Northover and Terblanche 1979, Chen et al 1999). The supraduodenal segment of the bile duct is less well vascularized than the retroduodenal and pancreatic segments, and excessive dissection of this segment can result in an ischaemic bile duct stricture.

The extrahepatic right and left hepatic ducts are supplied by a fine network of arteries that arise from the right and left hepatic arteries and form an anastomotic plexus within the connective tissue of the hilar plate (Kawarada et al 2000, Castaing 2008). The intrahepatic ducts are supplied by segmental branches of the hepatic artery arising within the Glissonian sheaths (Stapleton et al 1998, Vellar 1999). These form a microvascular network around the ducts that drains into intrahepatic portal venules. The dependence of the intrahepatic bile ducts on their hepatic arterial blood supply is well recognized in liver transplantation since hepatic artery thrombosis can lead to diffuse intrahepatic biliary strictures despite preservation of portal venous blood flow.

Cystic veins

The venous drainage of the gallbladder is rarely by a single cystic vein and there are usually multiple small veins. Those arising from the superior surface of the body and neck lie in loose connective tissue between the gallbladder and liver and drain into the branches of the hepatic portal vein within the liver. The remainder of the organ drains by one or two small cystic veins into either branches of the hepatic portal vein within the liver or portal venous tributaries draining the hepatic ducts and proximal bile duct (Sugita et al 2000). Only rarely does a single or double cystic vein drain directly into the right branch of the hepatic portal vein. A fine venous plexus on the surface of the common hepatic and bile ducts communicates laterally with so-called marginal veins that drain inferiorly to the posterior superior pancreaticoduodenal vein and superiorly primarily into the hepatic portal vein (Vellar 2001).

Lymphatic drainage

Lymph from the gallbladder and cystic duct drains via several pathways: to the cystic node, which usually lies above the cystic duct in the cystohepatic triangle, and from there via nodes in the hepatoduodenal ligament and along the common hepatic artery to coeliac nodes; via lymphatics that descend along the bile duct to the superior retropancreaticoduodenal nodes (which communicate with lateral aortic nodes); and directly to superior mesenteric nodes (Sato et al 2013). Lymphatics on the deep aspect of the gallbladder connect directly with intrahepatic lymph vessels.

Lymphatic vessels accompanying the hepatic ducts and proximal bile duct drain to hepatic nodes at the porta hepatis and then via lymph nodes in the hepatoduodenal ligament to coeliac nodes. Lymphatics from the distal bile duct also drain to the latter but some pass directly to pancreatic and superior mesenteric nodes.

INNERVATION

The gallbladder and the extrahepatic biliary tree are innervated by branches from the hepatic plexus. The gallbladder contracts in response to cholecystokinin (CCK) and parasympathetic (vagus nerve) stimulation. Postganglionic sympathetic nerve fibres from the coeliac and superior mesenteric ganglia are inhibitory to gallbladder smooth muscle. Sympathetic afferents from the gallbladder convey pain sensation; they travel with the greater and lesser thoracic splanchnic nerves and have their cell bodies in the T7–T9 spinal cord segments. Pain from the gallbladder is referred to the right hypochondriac and epigastric regions and can radiate around the back inferior to the right scapula. As the phrenic nerves and especially the right phrenic nerve extend onto the gallbladder, these might be involved in such pain (Yi et al 2007). Inflammation of the parietal peritoneum overlying the gallbladder produces localized right upper quadrant pain. Diverse neurotransmitters have been identified within intrinsic neurones of the gallbladder (Balemba et al 2004).

The bile duct and smooth muscle of the hepatopancreatic ampulla are also innervated by the vagus nerves, either directly or via the hepatic plexus, and by sympathetic nerves.

MICROSTRUCTURE

Gallbladder

The fundus of the gallbladder is completely covered by a serosa, and the inferior surfaces and sides of the body and neck of the gallbladder are usually covered by a serosa. If the gallbladder has a mesentery, the serosa extends around the sides of the body and neck onto the superior surface and continues into the serosa of the mesentery, whereas the serosa is limited to the inferior surfaces only if the gallbladder is intrahepatic. Beneath the serosa is subserous loose connective and adipose tissue. The microstructure of the wall of the gallbladder generally resembles that of the small intestine. The mucosa is yellowish-brown and elevated into minute folds (rugae) with a honeycomb appearance (see Fig. 67.2). In section, projections of the mucosa into the gallbladder lumen resemble intestinal villi, but they are not fixed structures and the surface flattens as the gallbladder fills with bile. The epithelium is a single layer of columnar absorptive cells with apical microvilli; basally, the spaces between epithelial cells are dilated by resorbed fluid, as bile is concentrated (**Fig. 67.16**). There are no goblet cells in the epithelium. The epithelial cells actively absorb water and solutes from the bile and concentrate it up to ten-fold. Many capillaries and lymphatic vessels lie beneath the basal lamina. The thin fibromuscular layer is composed of collagenous tissue and smooth muscle cells arranged loosely in longitudinal, circular and oblique bundles.

Mesentery of the gallbladder

Available with the *Gray's Anatomy* e-book

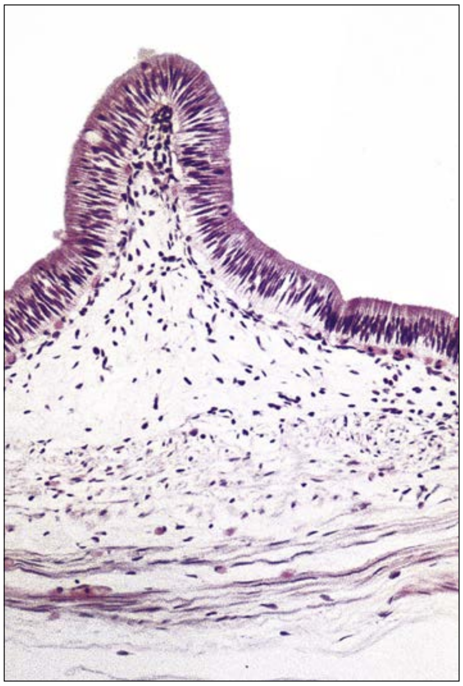

Fig. 67.16 A low-power micrograph showing the gallbladder wall, with a mucosal projection that flattens in the full gallbladder, and the thin muscular layer.

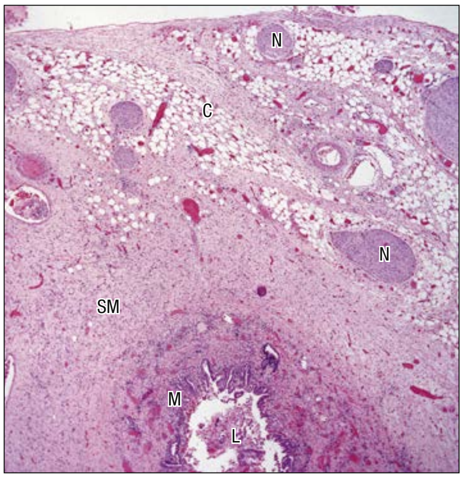

Fig. 67.17 A low-power micrograph showing the structure of a human bile duct. L, lumen; M, mucosal lining; SM, smooth muscle coat; C, outer connective tissue; N, nerve fibre bundles. (Courtesy of Mr Peter Helliwell and the late Dr Joseph Mathew, Department of Histopathology, Royal Cornwall Hospitals Trust, UK.)

Bile ducts

The walls of the large biliary ducts consist of external fibrous and internal mucosal layers (**Fig. 67.17**). The outer layer is fibrous connective tissue containing a variable number of longitudinal, oblique and circular smooth muscle cells. The mucosa is continuous with that in the hepatic ducts, gallbladder and duodenum. The epithelium is columnar and there are numerous tubulo-alveolar (or tubulo-acinar) mucosal glands in the duct walls.

Expulsion of gallbladder contents is under neuroendocrine control. Fat in the duodenum causes the release of CCK by intestinal neuroendocrine cells, which stimulates the gallbladder to contract because muscle cells in its walls bear surface CCK receptors. When the pressure exceeds 100 mm H_2O of bile, the sphincter of the ampulla relaxes and bile enters the descending part of the duodenum. The termination of the united bile and pancreatic ducts is packed with villous, valvular folds of mucosa that contain muscle cells in their connective tissue cores. Contraction is thought to result in retraction and clumping of these folds, thus preventing reflux of duodenal contents and controlling the exit of bile.

A mesentery of the gallbladder is an anatomical variant where either the gallbladder or the cystic duct and artery have a mesentery that allows the gallbladder to hang freely from the undersurface of the liver (the so-called mobile or floating gallbladder). The presence of a mesentery may predispose to torsion (volvulus) of the gallbladder with resultant vascular compromise (Gross 1936, Stieber and Bauer 1983, Shaikh et al 2005).

Bonus e-book content

Fig. 67.3 Hjortsö's crook.

Fig. 67.5 Operative cholangiogram: trifurcation pattern of intrahepatic duct union (type 2).

Fig. 67.6 MR cholangiopancreatogram: type 3 intrahepatic duct drainage pattern.

Fig. 67.7 Cystohepatic duct.

Fig. 67.8 MR cholangiopancreatogram: low medial union between cystic and distal bile ducts.

Fig. 67.9 **B**, Endoscopic image: major duodenal papilla, descending part of the duodenum.

Fig. 67.10 Maximal intensity projection from a magnetic resonance cholangiopancreaticogram.

Fig. 67.11 MR cholangiopancreatogram: normal biliary tree.

Fig. 67.12 Scanning electron micrograph: wall of the hepatopancreatic ampulla.

Key references

Andall RG, Matusz P, du Plessis M et al 2016 The clinical anatomy of cystic artery variations: a review of over 9800 cases. Surg Radiol Anat 38:529–39.

This article describes common and clinically important variations in the course of the cystic artery. The hepatobiliary surgeon needs to be aware of these variants in order to avoid iatrogenic injury to biliary ducts or aberrant vessels.

Castaing D 2008 Surgical anatomy of the biliary tract. HPB 10:72–6.

An overview of the surgical anatomy of the bile ducts, including the anatomy of the biliary confluence, and the blood supply and lymphatics of the biliary tract.

Cucchetti A, Peri E, Cescon M et al 2011 Anatomic variations of intrahepatic bile ducts in a European series and meta-analysis of the literature. J Gastrointest Surg 15:623–30.

An analysis of 200 cholangiograms from liver donors, coupled with a detailed literature review exploring intrahepatic bile duct anatomy in different ethnic groups.

Dasgupta D, Stringer MD 2005 Cystic duct and Heister's 'valves'. Clin Anat 18:81–7.

A review of cystic duct anatomy and the significance of its spiral mucosal folds.

Gross R 1936 Congenital anomalies of the gallbladder. A review of one hundred and forty eight cases with a report of double gall-bladder. Arch Surg 32:131–62.

A seminal paper on congenital anomalies of the gallbladder.

Nayman A, Özbek O, Erol S et al 2016 Magnetic resonance cholangiopancreatography evaluation of intrahepatic bile duct variations with updated classification. Diagn Interv Radiol 22:489–94

An analysis of intrahepatic biliary variants in 2143 Turkish patients examined using magnetic resonance cholangiopancreatography (MRCP).

Stringer MD 2009 Eponyms in Surgery and Anatomy of the Liver, Bile Ducts and Pancreas. London: Royal Society of Medicine Press.

A short reference book that contains illustrated accounts of the original descriptions of eponyms cited in this chapter, along with a brief biography of the person after whom the structure is named.

Suzuki M, Akaishi S, Rikiyama T et al 2000 Laparoscopic cholecystectomy, Calot's triangle, and variations in cystic arterial supply. Surg Endosc 14:141–4.

An article that documents a consecutive series of 244 laparoscopic cholecystectomies, in which the cystic artery was not present in the hepatocystic triangle in 11%, and a further 7% of patients had an accessory cystic artery or other arterial variants.

Talpur KA, Laghari AA, Yousfani SA et al 2010 Anatomical variations and congenital anomalies of extrahepatic biliary system encountered during laparoscopic cholecystectomy. J Pak Med Assoc 60:89–93.

An analysis of anatomical variants encountered in 300 adults undergoing cholecystectomy for gallstone disease. Variants were recorded in 20% of patients and predominantly involved the cystic artery (11%), cystic duct (4%), right hepatic artery (3%) and gallbladder (2%).

Tubbs RS, Shoja MM, Loukas M 2016 Bergman's Comprehensive Encyclopedia of Human Anatomic Variation. Hoboken: Wiley.

A definitive reference text on human anatomical variation. Variant biliary anatomy is present in 20–40% of individuals.

References

Anandhi PG, Alagavenkatesan VN 2018 Anatomical variations in the extra-hepatic biliary system: a cross sectional study. Int J Res Med Sci 6:1342–47.

Andall RG, Matusz P, du Plessis M et al 2016 The clinical anatomy of cystic artery variations: a review of over 9800 cases. Surg Radiol Anat 38:529–39.

This article describes common and clinically important variations in the course of the cystic artery. The hepatobiliary surgeon needs to be aware of these variants in order to avoid iatrogenic injury to biliary ducts or aberrant vessels.

Ashaolu JO, Olayinka J, Ukwenya VO 2015 The prevalence and classification of the cystoduodenal ligament. Anat Res Int 2015:742621. doi: 10.1155/2015/742621.

Balemba OB, Salter MJ, Mawe GM 2004 Innervation of the extrahepatic biliary tract. Anat Rec A Discov Mol Cell Evol Biol 280:836–47.

Bertelli E, Di Gregorio F, Bertelli L et al 1996 The arterial blood supply of the pancreas: a review. II. The posterior superior pancreaticoduodenal artery. An anatomical and radiological study. Surg Radiol Anat 18:1–9.

Boyden EA 1957 The anatomy of the choledochoduodenal junction in man. Surg Gynecol Obstet 104:640–52.

Castaing D 2008 Surgical anatomy of the biliary tract. HPB 10:72–6.

An overview of the surgical anatomy of the bile ducts, including the anatomy of the biliary confluence, and the blood supply and lymphatics of the biliary tract.

Castorina S, Scilletta R, Domergue J 2014 Gallbladder agenesis: laparoscopic views of a significant diagnostic challenge. Surg Radiol Anat 36:619–20.

Chaib E, Kanas AF, Galvão FH et al 2014 Bile duct confluence: anatomic variations and its classification. Surg Radiol Anat 36:105–9.

Chen WJ, Ying DJ, Liu ZJ et al 1999 Analysis of the arterial supply of the extrahepatic bile ducts and its clinical significance. Clin Anat 12:245–9.

Chowbey PK, Wadhwa A, Sharma A et al 2004 Ectopic gallbladder: laparoscopic cholecystectomy. Surg Laparosc Endosc Percutan Tech 14:26–8.

Cucchetti A, Peri E, Cescon M et al 2011 Anatomic variations of intrahepatic bile ducts in a European series and meta-analysis of the literature. J Gastrointest Surg 15:623–30.

An analysis of 200 cholangiograms from liver donors, coupled with a detailed literature review exploring intrahepatic bile duct anatomy in different ethnic groups.

Dahmane R, Morjane A, Starc A 2013 Anatomy and surgical relevance of Rouvière's sulcus. Scientific World J 2013:254287. doi: 10.1155/2013/254287.

Dasgupta D, Stringer MD 2005 Cystic duct and Heister's 'valves'. Clin Anat 18:81–7.

A review of cystic duct anatomy and the significance of its spiral mucosal folds.

Davies F, Harding HE 1942 The pouch of Hartmann. Lancet 1:193–5.

Di Ciaula A, Wang DQ, Portincasa P 2012 Gallbladder and gastric motility in obese newborns, pre-adolescents and adults. J Gastroenterol Hepatol 27:1298–305.

Didio JA, Anderson MC 1968 Biliary and Pancreatic Ducts: The 'Sphincters' of the Digestive System. Baltimore: Williams & Wilkins, pp. 129–51.

Faure JP, Doucet C, Scepi M et al 2008 Abnormalities of the gallbladder, clinical effects. Surg Radiol Anat 30:285–90.

Flati G, Flati D, Porowska B et al 1994 Surgical anatomy of the papilla of Vater and the biliopancreatic ducts. Am Surg 60:712–8.

Gross R 1936 Congenital anomalies of the gallbladder. A review of one hundred and forty eight cases with a report of double gall-bladder. Arch Surg 32:131–62.

A seminal paper on congenital anomalies of the gallbladder.

Guelrud M, Mendoza S, Rossiter G et al 1990 Sphincter of Oddi manometry in healthy volunteers. Dig Dis Sci 35:38–46.

Guiteau JJ, Fisher M, Cotton RT et al 2009 Intrahepatic gallbladder. J Am Coll Surg 209:672.

Gupta A, Rai P, Singh V et al 2016 Intrahepatic biliary duct branching patterns, cystic duct anomalies, and pancreas divisum in a tertiary referral center: a magnetic resonance cholangiopancreaticographic study. Ind J Gastroenterol 35:379–384.

Gupta V, Singh V, Sewkani A et al 2009 Torsion of gall bladder, a rare entity: a case report and review article. Cases J 2:193.

Habib FI, Corazziari E, Biliotti D et al 1988 Manometric measurement of human sphincter of Oddi length. Gut 29:121–5.

Ironside N, Wang X, Purvis N, et al 2019 The 3-D muscular structure of the human pancreaticobiliary junction. Eur J Anat 23:253–9.

Kamisawa T, Okamoto A 2008 Pancreatographic investigation of pancreatic duct system and pancreaticobiliary malformation. J Anat 212:125–34.

Kawarada Y, Das BC, Taoka H 2000 Anatomy of the hepatic hilar area: the plate system. J Hepatobiliary Pancreat Surg 7:580–6.

Kimura K, Ohto M, Saisho H et al 1985 Association of gallbladder carcinoma and anomalous pancreaticobiliary ductal union. Gastroenterol 89:1258–65.

Lamah M, Karanjia ND, Dickson GH 2001 Anatomical variations of the extrahepatic biliary tree: review of the world literature. Clin Anat 14:167–72.

A literature review of anatomical variations affecting the extrahepatic bile ducts.

Losanoff JE, Jones JW, Richman BW et al 2002 Hepaticocystic duct: a rare anomaly of the extrahepatic biliary system. Clin Anat 15:314–15.

Makki K, Chorasiya V, Srivastava A et al 2018 Analysis of caudate lobe biliary anatomy and its implications in living donor liver transplantation – a single centre prospective study. Transpl Int 31:1041–9.

Mirjalili SA, Stringer MD 2011 The arterial supply of the major duodenal papilla and its relevance to endoscopic sphincterotomy. Endoscopy 43:307–11.

Misra SP, Dwivedi M 1990 Pancreaticobiliary ductal union. Gut 31:1144–9.

Myburgh JA 1993 The Hepp–Couinaud approach to strictures of the bile ducts. I. Injuries, choledochal cysts, and pancreatitis. Ann Surg 218:615–20.

Nayman A, Özbek O, Erol S et al 2016 Magnetic resonance cholangiopancreatography evaluation of intrahepatic bile duct variations with updated classification. Diagn Interv Radiol 22:489–94.

An analysis of intrahepatic biliary variants in 2143 Turkish patients examined using magnetic resonance cholangiopancreatography (MRCP).

Northover JM, Terblanche J 1979 A new look at the arterial supply of the bile duct in man and its surgical implications. Br J Surg 66:379–84.

Onder H, Ozdemir MS, Tekbaş G et al 2013 3-T MRI of the biliary tract variations. Surg Radiol Anat 35:161–7.

Perret RS, Sloop GD, Borne JA 2000 Bile duct measurements in an elderly population. J Ultrasound Med 19:727–30.

Purvis NS, Mirjalili SA, Stringer MD 2013 The mucosal folds at the pancreaticobiliary junction. Surg Radiol Anat 35:943–50.

Sato T, Ito M, Sakamoto H 2013 Pictorial dissection review of the lymphatic pathways from the gallbladder to the abdominal para-aortic lymph nodes and their relationships to the surrounding structures. Surg Radiol Anat 35:615–21.

Schnelldorfer T, Sarr MG 2012 What is the duct of Luschka? A systematic review. J Gastrointest Surg 16:656–62.

Shaikh AA, Charles A, Domingo S et al 2005 Gallbladder volvulus: report of two original cases and review of the literature. Am Surg 71:87–9.

Shaw MJ, Dorsher PJ, Vennes JA 1993 Cystic duct anatomy: an endoscopic perspective. Am J Gastroenterol 88:2102–6.

Singh B, Ramsaroop L, Allopi L et al 2006 Duplicate gallbladder: an unusual case report. Surg Radiol Anat 28:654–7.

Skandalakis JE, Coborn GL, Weidman TA et al 2004 Extrahepatic biliary tract and gallbladder. In: Skandalakis JE (ed) Skandalakis' Surgical Anatomy. Athens: Paschalidis Medical Publications; Ch. 20, pp. 1095–150.

Spanos CP, Syrakos T 2006 Bile leaks from the duct of Luschka (subvesical duct): a review. Langenbecks Arch Surg 391:441–7.

Stapleton GN, Hickman R, Terblanche J 1998 Blood supply of the right and left hepatic ducts. Br J Surg 85:202–7.

Stieber AC, Bauer JJ 1983 Volvulus of the gallbladder. Am J Gastroenterol 78:96–8.

Stringer MD 2009 Eponyms in Surgery and Anatomy of the Liver, Bile Ducts and Pancreas. London: Royal Society of Medicine Press.

A short reference book that contains illustrated accounts of the original descriptions of eponyms cited in this chapter, along with a brief biography of the person after whom the structure is named.

Stringer MD 2016 Gallbladder and extrahepatic bile ducts. In: Tubbs RS, Shoja MM, Loukas M. Bergman's Comprehensive Encyclopedia of Human Anatomic Variation. Hoboken: J Wiley. Ch 107, pp. 1261–71.

A definitive reference text on human anatomical variation. Variant biliary anatomy is present in 20–40% of individuals.

Stringer MD 2018 Choledochal cysts. In Barreto SG and Windsor JA (eds) Surgical Diseases of the Pancreas and Biliary Tree. Springer Nature, Singapore Pte Ltd. pp. 121–47.

Sugita M, Ryu M, Satake M et al 2000 Intrahepatic inflow areas of the drainage vein of the gallbladder: analysis by angio-CT. Surgery 128:417–21.

Suzuki M, Akaishi S, Rikiyama T et al 2000 Laparoscopic cholecystectomy, Calot's triangle, and variations in cystic arterial supply. Surg Endosc 14:141–4.

An article that documents a consecutive series of 244 laparoscopic cholecystectomies, in which the cystic artery was not present in the hepatocystic triangle in 11%, and a further 7% of patients had an accessory cystic artery or other arterial variants.

Talpur KA, Laghari AA, Yousfani SA et al 2010 Anatomical variations and congenital anomalies of extrahepatic biliary system encountered during laparoscopic cholecystectomy. J Pak Med Assoc 60:89–93.

An analysis of anatomical variants encountered in 300 adults undergoing cholecystectomy for gallstone disease. Variants were recorded in 20% of patients and predominantly involved the cystic artery (11%), cystic duct (4%), right hepatic artery (3%) and gallbladder (2%). Anatomical variants were associated with a slightly increased incidence of postoperative morbidity.

Teilum D 1991 In vitro measurement of the length of the sphincter of Oddi. Endoscopy 23:114–6.

van Eijck FC, van Veen RN, Kleinrensink GJ et al 2007 Hartmann's gallbladder pouch revisited 60 years later. Surg Endosc 21:1122–5.

Vellar ID 1999 The blood supply of the biliary ductal system and its relevance to vasculobiliary injuries following cholecystectomy. Aust N Z J Surg 69:816–20.

Vellar ID 2001 Preliminary study of the anatomy of the venous drainage of the intrahepatic and extrahepatic bile ducts and its relevance to the practice of hepatobiliary surgery. ANZ J Surg 71:418–22.

Woods CM, Mawe GM, Toouli J et al 2005 The sphincter of Oddi: understanding its control and function. Neurogastroenterol Motil 17:31–40.

Xia J, Zhang Z, He Y et al 2015 Assessment and classification of cystic arteries with 64-detector row computed tomography before laparoscopic cholecystectomy. Surg Radiol Anat 37:1027–34.

Yoshida J, Chijiiwa K, Yamaguchi K et al 1996 Practical classification of the branching types of the biliary tree: an analysis of 1,094 consecutive direct cholangiograms. J Am Coll Surg 182:37–40.

Yi SQ, Ohta T, Tsuchida A et al 2007 Surgical anatomy of innervation of the gallbladder in humans and *Suncus murinus* with special reference to morphological understanding of gallstone formation after gastrectomy. World J Gastroenterol 13:2066–71.

CHAPTER

68

Pancreas

The pancreas is one of the largest digestive glands. Its primary function is exocrine, secreting enzymes involved in the digestion of lipids, carbohydrates and proteins. It has an additional endocrine function derived from clusters of cells scattered throughout the gland, which take part in glucose homeostasis and the control of upper gastrointestinal tract motility and function.

The healthy pancreas is yellow, with a soft to firm consistency and a lobulated surface. Its texture (hard or soft) has important implications for pancreatic surgery: the harder the gland, the lower the rate of leakage of pancreatic fluid after a pancreatic reconstruction procedure.

The pancreas is divided into a head, neck, body and tail (**Figs 68.1–68.3A**). The head of the pancreas usually has a distinct uncinate process. In adults, the pancreas is between 12 and 15 cm long and is shaped like a flattened 'tongue' of tissue lying in the retroperitoneum, thicker at its medial end (head) and thinner towards the lateral end (tail). The head lies within the curve of the duodenum and the remainder of the gland extends transversely and slightly cranially across the retroperitoneum and posterior to the stomach to the splenic hilum. It is 'draped' over the inferior vena cava, the hepatic portal vein/superior mesenteric vein and splenic vessels. In adults it has an average volume of 70–80 cm^3, although this varies considerably among individuals (with a range of 40–170 cm^3) and tends to be greater in males (Djuric-Stefanovic et al 2012). Pancreatic volume increases with age, reaching a peak during the fourth decade. From about 60 years of age the gland atrophies and adipose connective tissue replaces exocrine tissue (Saisho et al 2007, Caglar et al 2012). Pancreatic diameters tend to be smaller in patients with diabetes mellitus (DeSouza et al 2018).

The anterior (ventral) surface of the pancreas is covered by parietal peritoneum and its inferior border abuts the root of the transverse mesocolon. A loose connective tissue layer immediately posterior to the pancreas (sometimes known as the fusion fascia of Treitz in the region of the head of the pancreas and as the fusion fascia of Toldt in the region of the body and tail) contains vessels that supply the gland (Kimura 2000).

Head

The head of the pancreas lies to the right of the midline, anterior and to the right of the vertebral column, within the curve of the duodenum. This is the thickest and broadest part of the pancreas but it is still flattened in the anteroposterior plane. Superiorly, it lies adjacent to the superior part of the duodenum; however, close to the pylorus, where the duodenum is on a short mesentery, the superior part of the head is overlapped anteriorly by the duodenum. The duodenal border of the head is flattened, slightly concave and adherent to the descending part of the duodenum, particularly around the hepatopancreatic ampulla. The superior and inferior pancreaticoduodenal arcades supply the head of the pancreas. The inferior border of the head of the pancreas lies superior to the horizontal part of the duodenum and is continuous with the uncinate process. The anterior surface of the head is covered by peritoneum and abuts the transverse mesocolon (**Fig. 68.3B**). Posteriorly, the bile duct is partially embedded within the head of the gland just proximal to its junction with the pancreatic duct near the major duodenal papilla (Burgard et al 1991, Nagai 2003). The posterior surface of the head of the pancreas lies anterior to the inferior vena cava at the level of the termination of the right gonadal vein. Near the midline, the head continues as the neck.

Uncinate process

The uncinate process is a hook-shaped continuation of the inferomedial part of the head of the pancreas. Embryologically, it is separate from the rest of the gland. It extends medially anterior to the abdominal aorta and superior to the horizontal part of the duodenum, which can be obstructed by a pancreatic tumour at this site. On sagittal cross-sectional imaging, the left renal vein, the uncinate process and the horizontal part of duodenum can be seen lying between the superior mesenteric artery anteriorly and the abdominal aorta posteriorly.

Neck

The neck of the pancreas is approximately 2 cm wide and connects the head to the body. It is often the most anterior part of the gland and can be defined as that part of the pancreas lying anterior to the formation of the hepatic portal vein (usually the union of the superior mesenteric and splenic veins) (**Fig. 68.4D–E**). This relationship is crucial for the evaluation of pancreatic cancer because malignant involvement of the hepatic portal vein may have to be considered when the cancer is resected. Encasement of the superior mesenteric artery running posterior to the head of the pancreas is usually considered a contraindication to resection. The superior mesenteric and hepatic portal veins groove the posterior aspect of the neck. The inferior mesenteric vein joins the confluence of the superior mesenteric and splenic veins in one-third of individuals (Kimura 2000; see Fig. 68.7). The anterior surface of the neck of the pancreas is covered by peritoneum and lies inferior to the pylorus. The anterior superior pancreaticoduodenal branch of the gastroduodenal artery runs through the pancreas at the junction of the head and neck.

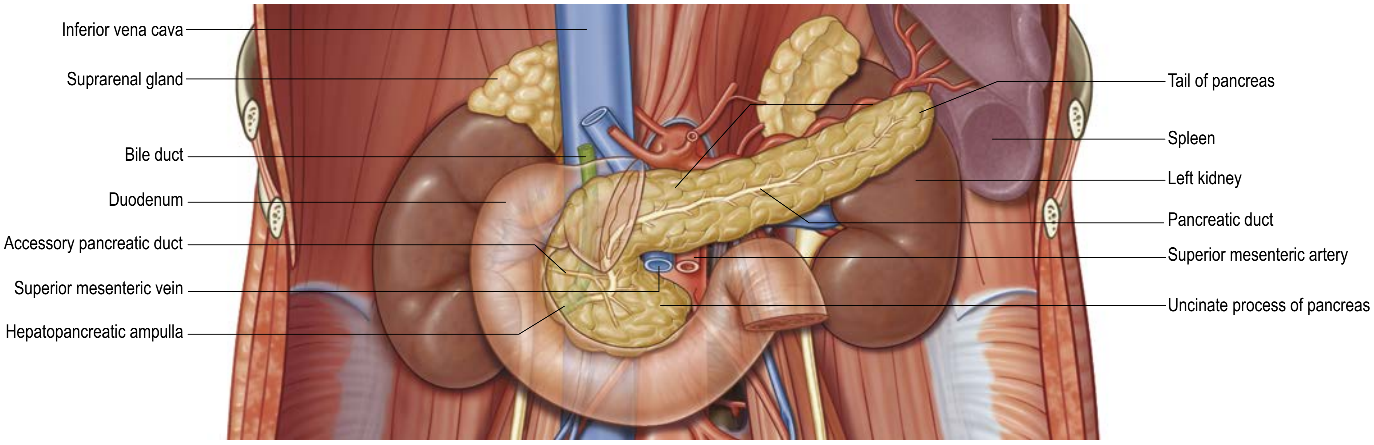

Fig. 68.1 The relations of the pancreas.

Body

The body of the pancreas is the longest part of the gland and runs from the neck to the tail, becoming progressively thinner. It is slightly triangular in cross-section and has anterior and posterior surfaces and superior and inferior borders. It lies to the left of the superior mesenteric vessels.

Anterior surface The anterior surface is covered by peritoneum, which is reflected anteroinferiorly from the surface of the pancreas to be continuous with the posterior layer of the greater omentum and the transverse mesocolon (see Fig. 62.3). The two layers of the transverse mesocolon diverge along this surface (see Fig. 68.3B). Above the attachment of the transverse mesocolon, the anterior surface of the pancreas is separated from the stomach by the omental bursa.

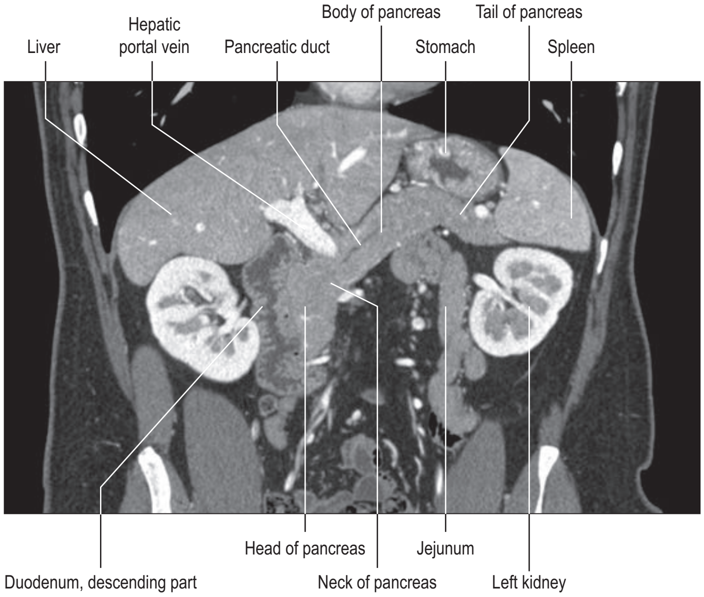
Liver
Hepatic portal vein
Pancreatic duct
Body of pancreas
Stomach
Tail of pancreas
Spleen
Duodenum, descending part
Head of pancreas
Neck of pancreas
Jejunum
Left kidney

Fig. 68.2 A coronal reformat CT of the pancreas showing its relations in the upper abdomen. (Courtesy of the Department of Radiology, Global Hospital, Chennai, India.)

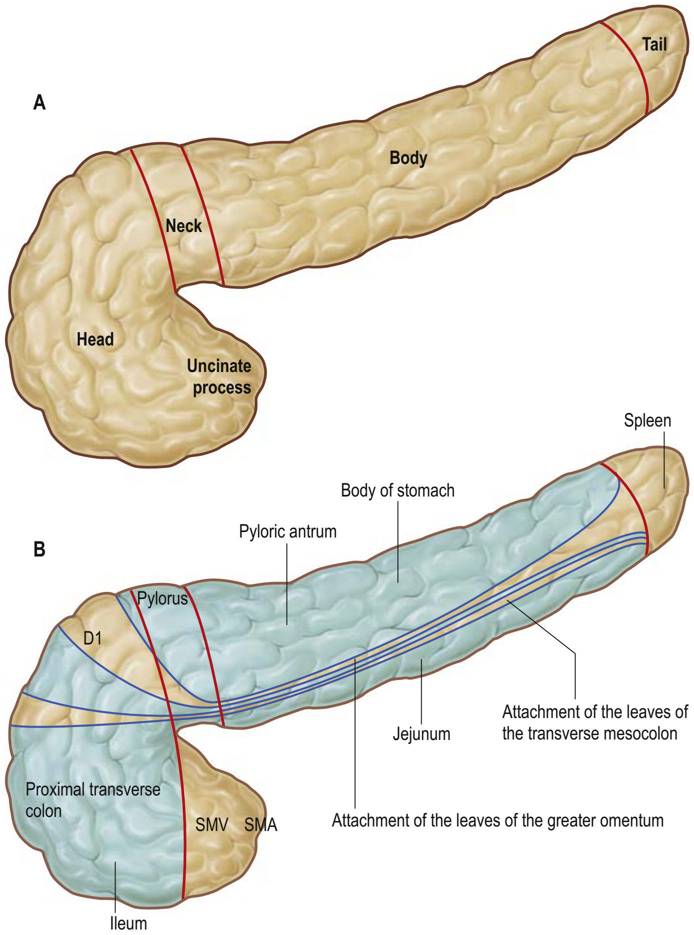
A
Tail
Body
Neck
Head
Uncinate process
B
Spleen
Body of stomach
Pyloric antrum
Pylorus
D1
Attachment of the leaves of the transverse mesocolon
Jejunum
Proximal transverse colon
SMV
SMA
Attachment of the leaves of the greater omentum
Ileum

Fig. 68.3 **A**, The regions and anterior surfaces and borders of the pancreas. **B**, The anterior relations of the pancreas. Areas covered in peritoneum are shown in blue. The spleen lies anterior to the anterior leaf of the splenorenal ligament and not in direct contact with the pancreas. Abbreviations: D1, superior (first) part of the duodenum; SMA, superior mesenteric artery; SMV, superior mesenteric vein.

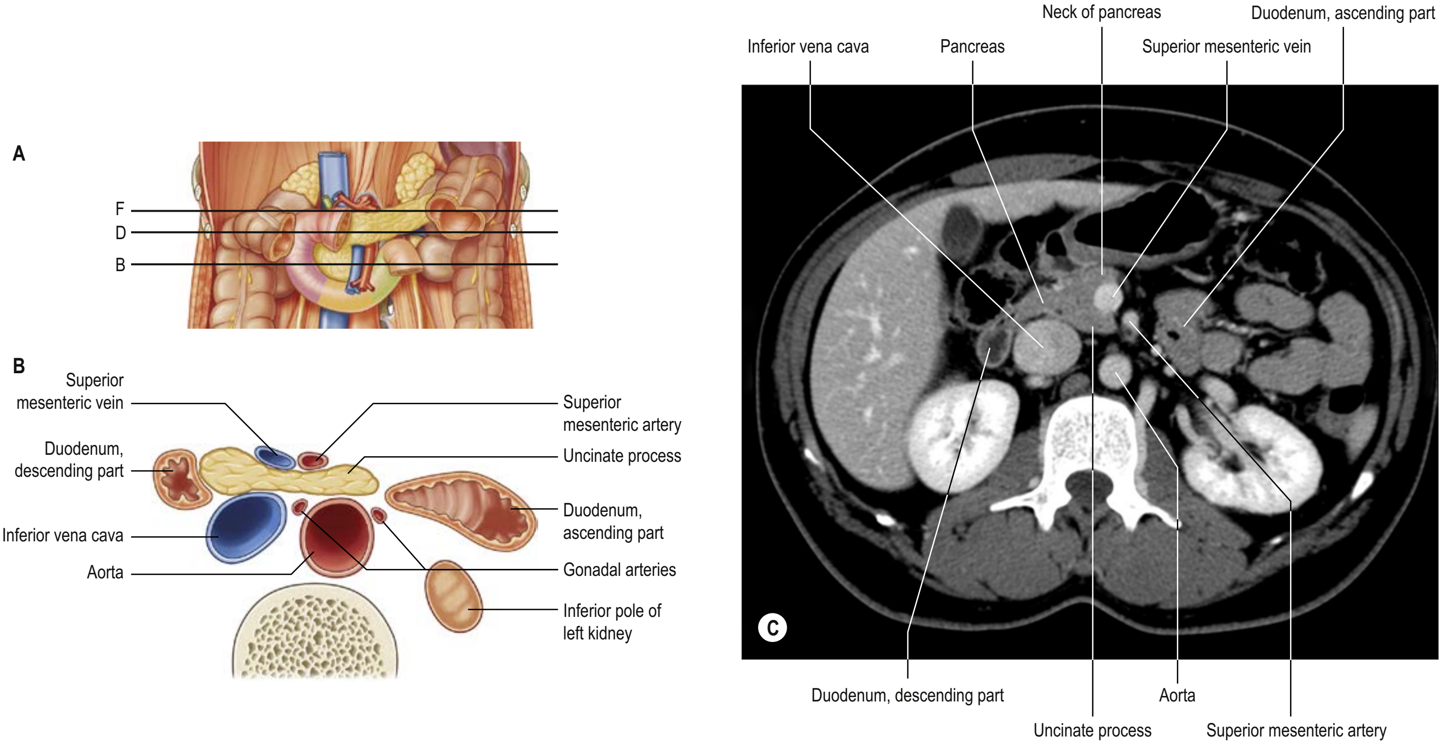
A
F
D
B
B
Superior mesenteric vein
Duodenum, descending part
Inferior vena cava
Aorta
Superior mesenteric artery
Uncinate process
Duodenum, ascending part
Gonadal arteries
Inferior pole of left kidney
Inferior vena cava
Pancreas
Neck of pancreas
Superior mesenteric vein
Duodenum, ascending part
C
Duodenum, descending part
Uncinate process
Aorta
Superior mesenteric artery

Fig. 68.4 **A**, The posterior relations of the pancreas, with planes of section labelled as shown in **B**, **D** and **F**. **B**, Diagrammatic cross-section taken at the mid level of the uncinate process, and equivalent CT axial image (**C**).

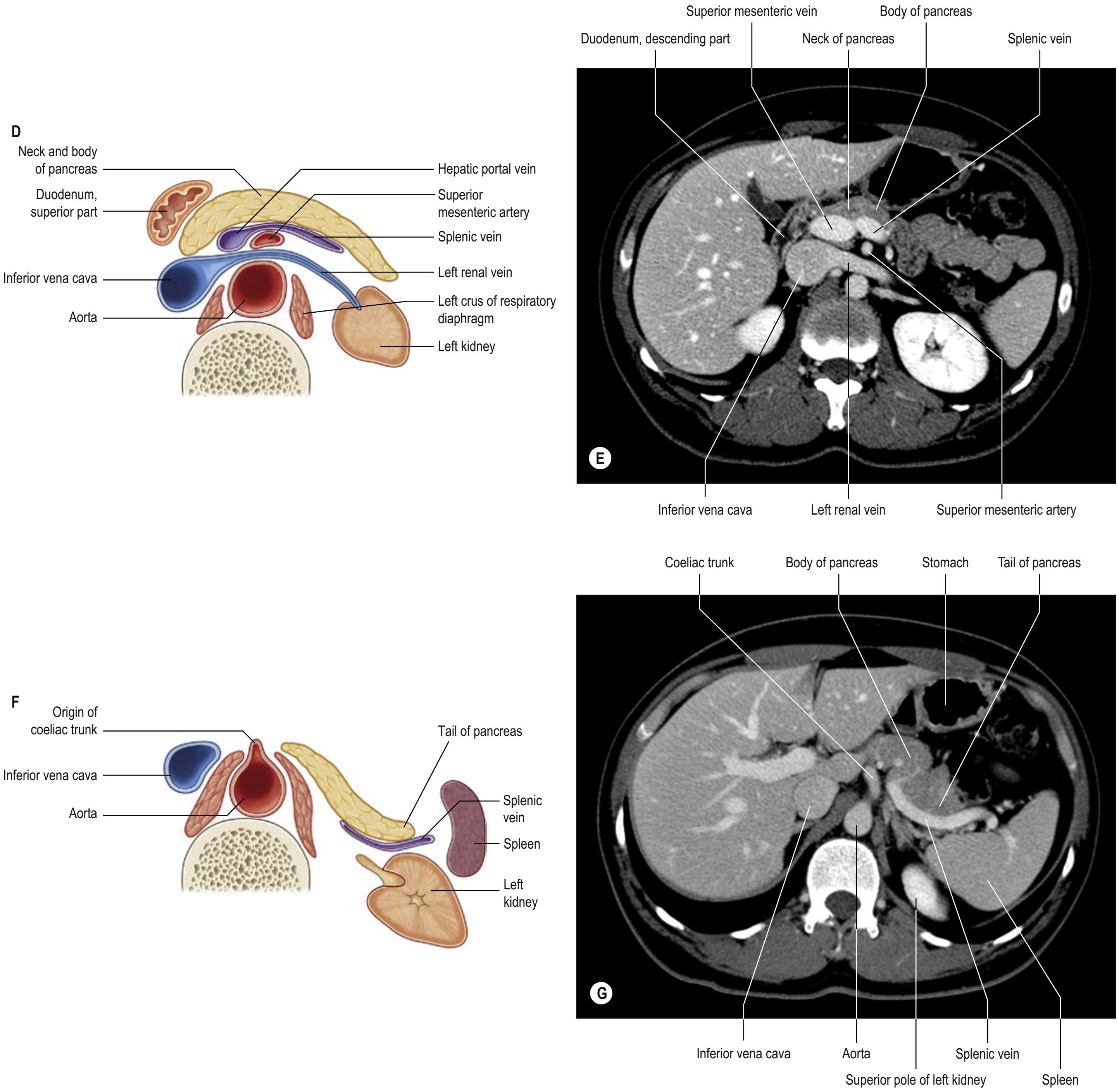
D
Neck and body of pancreas
Duodenum, superior part
Inferior vena cava
Aorta
Hepatic portal vein
Superior mesenteric artery
Splenic vein
Left renal vein
Left crus of respiratory diaphragm
Left kidney
Superior mesenteric vein
Body of pancreas
Duodenum, descending part
Neck of pancreas
Splenic vein
E
Inferior vena cava
Left renal vein
Superior mesenteric artery
F
Origin of coeliac trunk
Inferior vena cava
Aorta
Tail of pancreas
Splenic vein
Spleen
Left kidney
Coeliac trunk
Body of pancreas
Stomach
Tail of pancreas
G
Inferior vena cava
Aorta
Splenic vein
Superior pole of left kidney
Spleen

Fig. 68.4, cont'd Diagrammatic cross-sections and equivalent CT axial image taken at the head and neck **(D–E)**, and tail **(F–G)** of the pancreas.

Posterior surface The posterior surface of the pancreas is devoid of peritoneum. It lies on the fusion fascia of Toldt anterior to the abdominal aorta and the origin of the superior mesenteric artery, the left crus of the diaphragm, the left suprarenal gland, the superior pole of the left kidney surrounded by renal fascia, and the left renal vein (Kimura 2000; see Figs 68.1, 68.4A–G). The splenic vein runs from left to right directly on this surface of the gland and indents it to a variable extent, ranging from a shallow groove to nearly a tunnel.

Superior border To the right, the superior border of the body of the pancreas is rounded, but it becomes narrower and sharper to the left. An omental eminence usually projects from the right end of the superior border above the level of the lesser curvature of the stomach. The superior border lies anterior to the coeliac trunk and its branches, the common hepatic and splenic arteries: the common hepatic artery runs to the right just superior to the gland, and the splenic artery passes tortuously to the left, projecting above the superior border at several points.

Inferior border At the medial end of the inferior border of the neck of the pancreas, the superior mesenteric vessels travel posterior to the gland. Laterally, the inferior mesenteric vein runs posterior to the inferior border to join the splenic vein or the confluence of the splenic and superior mesenteric veins. This is a useful site for identification of the inferior mesenteric vein on computed tomography (CT) and during resection of the descending colon. The superior mesenteric artery lies medial to the superior mesenteric vein and is a critical structure that must be identified when the pancreas is divided between its head and neck during a pancreaticoduodenectomy (Whipple procedure).

Tail

The tail of the pancreas is the narrowest, most left-lateral portion of the gland and is continuous with the body. It is between 1.5 and 3.5 cm long in adults and lies between the splenorenal ligament and the splenic hilum. It either terminates at the base of the splenorenal ligament or extends into the splenic hilum, where it is at risk of injury during a splenectomy when the splenic vessels are divided. The splenic artery and its branches, and the splenic vein and its tributaries, lie posterior to the tail (see Fig. 68.4F–G).

Pancreatic ducts

The exocrine pancreatic tissue drains into multiple small lobular ducts. There are several anatomical variations of the ducts draining the pancreas. The most common variation is a single pancreatic duct and a single accessory duct (**Fig. 68.5**) that reflects the embryological development of the dorsal and ventral pancreatic ducts (see Figs 21.3–21.4). The pancreatic duct (of Wirsung) usually runs through the gland slightly diagonally from left to right, from a more inferior location in the head to a more superior location. Its size varies, which has significant implications for pancreatic surgery when a reconstruction is planned. The duct is formed by the junction of several lobular (secondary) ducts in the tail. It increases in calibre within the body of the pancreas as it receives further lobular ducts that join almost at right-angles to its long axis, forming a herringbone pattern. It can often be visualized on ultrasonography, measuring approximately 3 mm in diameter in the head, 2 mm in the body and 1 mm in the tail; the calibre of the duct increases from about the fifth decade onwards (Glaser et al 1987). As it reaches the neck of the gland, the pancreatic duct runs inferiorly and posteriorly towards the bile duct, which descends through the head of the pancreas. The two ducts unite and enter the wall of the descending part of the duodenum obliquely; a dilation, the hepatopancreatic ampulla (of Vater) is sometimes found at this union. The terminal part of the pancreatic duct contains a few mucosal folds that impede reflux of pancreatic juice (Purvis et al 2013). The length of the common pancreaticobiliary channel is variable and measures up to 5–7 mm in most individuals (Horaguchi et al 2014). An abnormally long common channel can occur in isolation or with congenital choledochal dilation and is associated with pancreaticobiliary reflux and an increased risk of biliary tract cancer (Kamisawa et al 2010a).

The accessory pancreatic duct (of Santorini) drains the superior part of the anterior portion of the head of the pancreas. Much smaller in calibre than the pancreatic duct, it is formed within the head of the pancreas from several lobular ducts and usually communicates with the pancreatic duct near the neck of the gland or near its first inferior branch (Kamisawa 2004, Kamisawa and Okamoto 2008). The accessory duct usually opens onto a small, rounded minor duodenal papilla that lies about 2 cm proximal to the major duodenal papilla (see Fig. 68.5A). If the duodenal end of the accessory duct fails to develop, the lobular ducts drain via small channel(s) into the pancreatic duct (Hernandez-Jover et al 2011). The anatomy of the pancreatic duct and accessory pancreatic duct can vary, reflecting variations in the development and fusion of the dorsal and ventral pancreatic ducts.

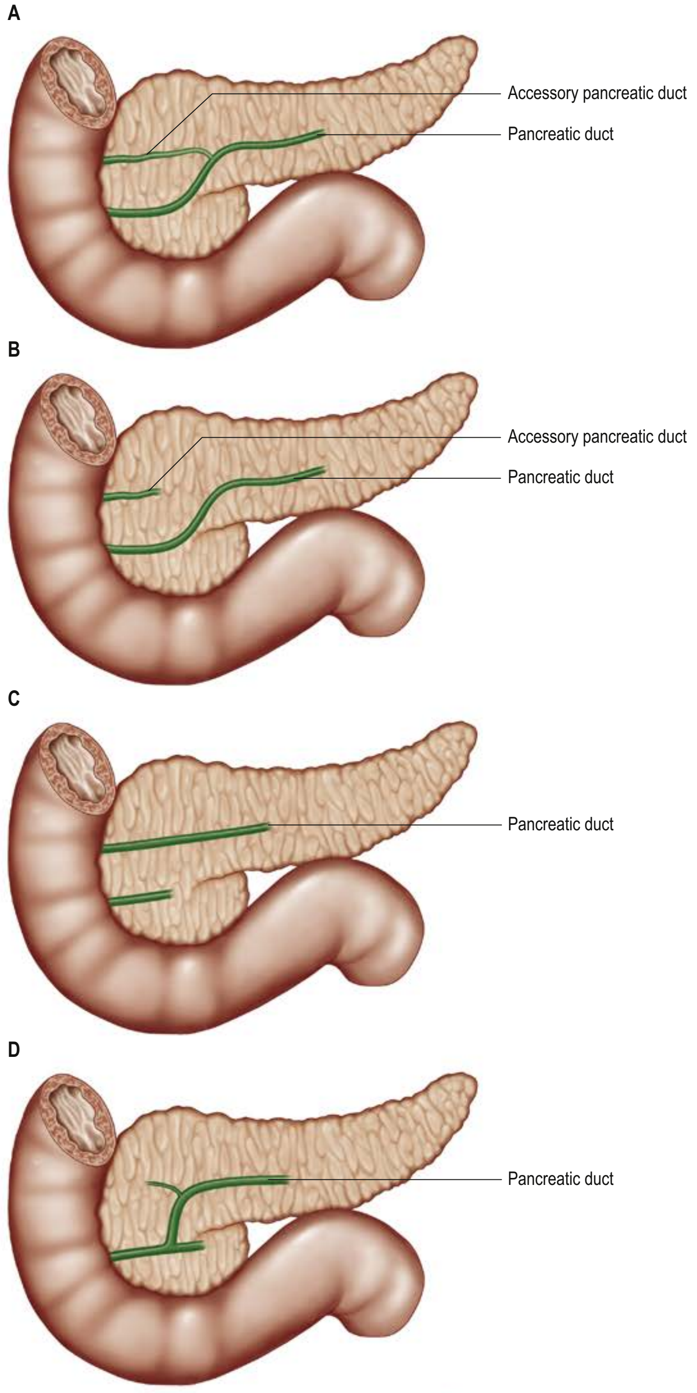

Fig. 68.5 The normal and variant ductal anatomy of the pancreas. **A**, Normal. The pancreatic duct is formed by fusion of the dorsal and ventral bud ducts, and communicates with the accessory pancreatic duct. **B**, Normal. There is no communication between the pancreatic duct and a normally positioned accessory duct. **C**, Pancreas divisum. Most of the pancreas drains via a dominant dorsal duct that enters the duodenum at the minor duodenal papilla. A short ventral duct is seen draining, along with the bile duct, into the major duodenal papilla. **D**, Absence of accessory duct. (E–G, *continued online*)

Vascular supply and lymphatic drainage

Arteries

The pancreas has a rich arterial supply from branches of the coeliac trunk and superior mesenteric artery (**Figs 68.6A–C**; see also Fig. 64.4). The head of the pancreas and adjoining duodenum are supplied mainly by four arteries: anterior and posterior superior pancreaticoduodenal arteries via the gastroduodenal artery from the coeliac trunk, and anterior and posterior inferior pancreaticoduodenal arteries via the inferior pancreaticoduodenal artery from the superior mesenteric artery. The two anterior arteries supply the anterior aspects of the duodenum, head of the pancreas, and uncinate process, and join to form the anterior pancreaticoduodenal arcade. The two posterior arteries supply the posterior (dorsal) aspect of the head of the pancreas, adjacent duodenum and distal bile duct, and can join to form a posterior pancreaticoduodenal arcade.

The body and tail of the pancreas are supplied by multiple small direct branches from the splenic artery, including the dorsal pancreatic artery. Small arteries characteristically run along the superior and inferior borders of the gland, lying either in a deep groove or within the gland. They are fed along their length by the pancreaticoduodenal and splenic arteries. When the pancreas is transected during pancreatic surgery, bleeding from these vessels is avoided by ligating the superior and inferior borders of the pancreas using transfixion sutures prior to transection.

Posterior superior pancreaticoduodenal artery

The posterior superior pancreaticoduodenal artery usually arises as the first branch of the gastroduodenal artery at the superior edge of the superior (first) part of the duodenum. It runs to the right, anterior to the supraduodenal segment of the bile duct, before spiralling posteriorly around the pancreatic segment of the bile duct and descending on the posterior surface of the head of the pancreas. It gives branches to the duodenum, head of the pancreas, and bile duct before anastomosing with the posterior inferior pancreaticoduodenal artery to form the posterior pancreaticoduodenal arcade. The posterior superior pancreaticoduodenal artery can also give origin to the retroduodenal and supraduodenal arteries that supply the duodenum (Bertelli et al 1996a). The spiral course of the posterior superior pancreaticoduodenal artery reflects its embryonic development: it is the artery to the anterior aspect of the ventral pancreatic bud and the bile duct that subsequently rotate clockwise posterior to the duodenum and dorsal pancreatic bud (Bertelli et al 1997).

Anterior superior pancreaticoduodenal artery

The anterior superior pancreaticoduodenal artery usually arises as the smaller terminal branch of the gastroduodenal artery, together with the right gastro-omental artery. It originates posterior to the superior portion

Patients who develop acute pancreatitis are more likely to have a poorly developed minor duodenal papilla: if this were not so, the patent accessory duct system could act as a secondary drainage mechanism for the main ductal system and thus prevent the elevation of intraductal pressure likely to cause acute pancreatitis (Kamisawa et al 2010b). One clinically important variation is pancreas divisum, which is seen in 5–10% of individuals (Rana et al 2012; see Fig. 68.5C,G). In this condition, normal duct fusion fails and the accessory pancreatic duct drains the entire pancreas, except that part of the head that develops from the ventral bud, via the minor duodenal papilla. The relatively small size of the minor duodenal papilla could impair pancreatic drainage, leading to recurrent pancreatitis.

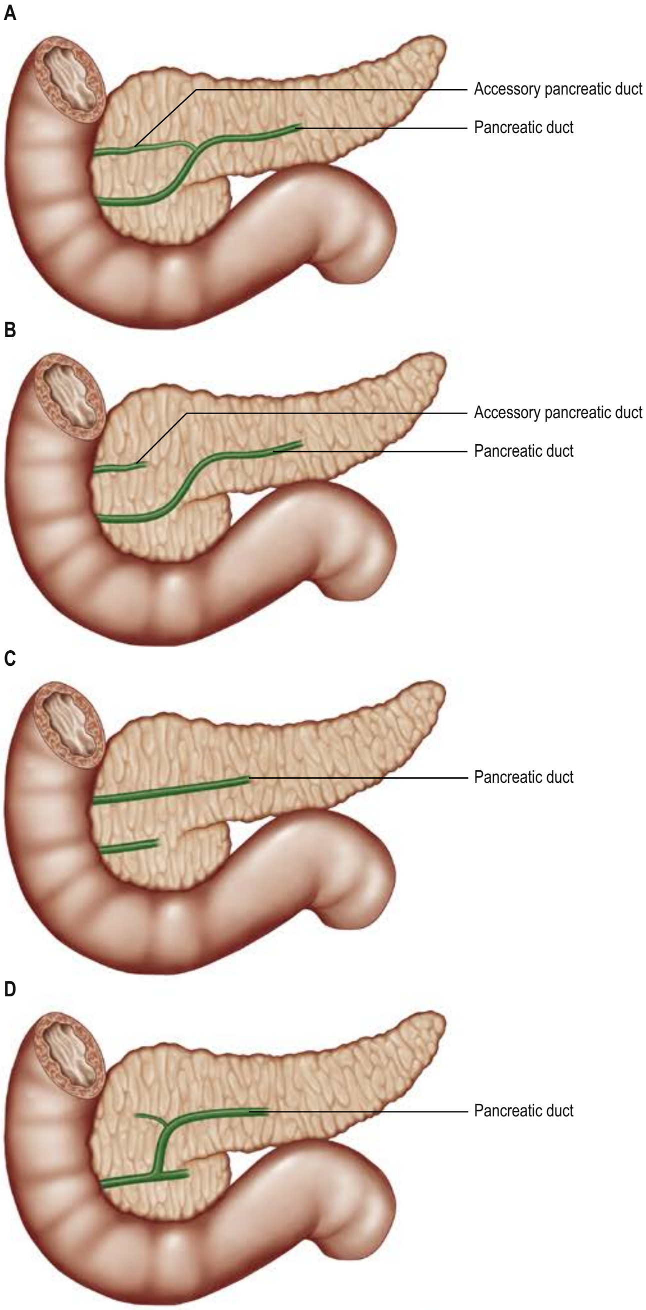
A
Accessory pancreatic duct
Pancreatic duct
B
Accessory pancreatic duct
Pancreatic duct
C
Pancreatic duct
D
Pancreatic duct

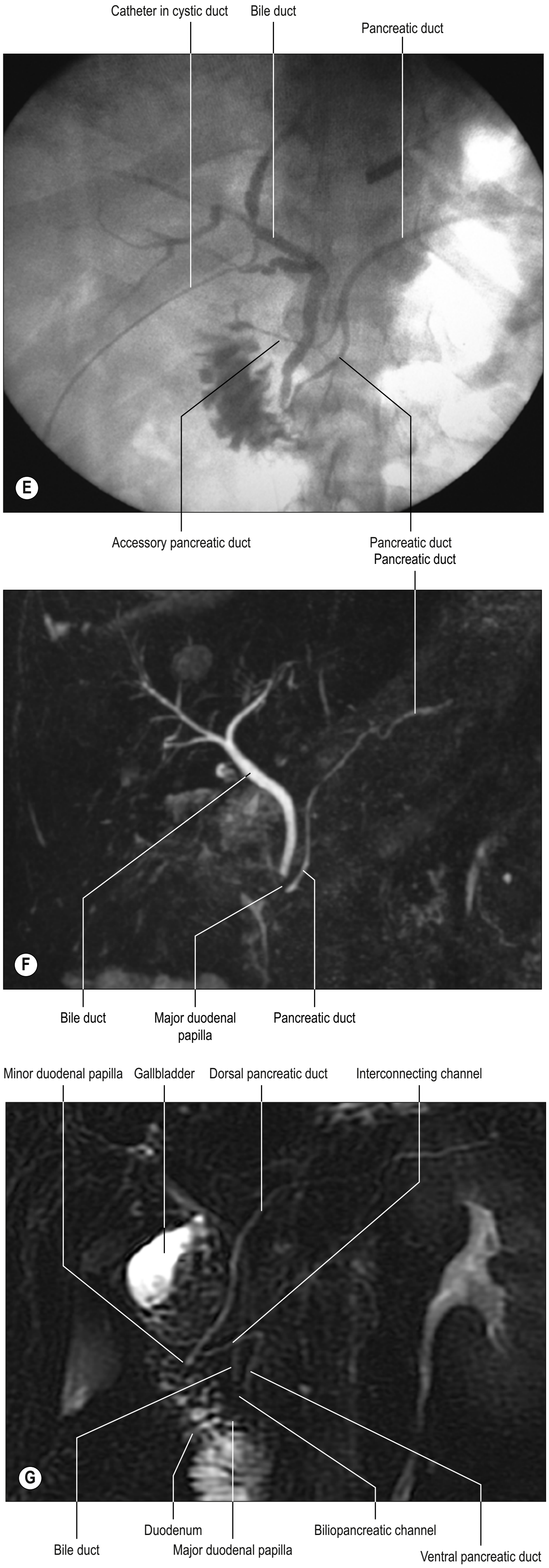
Catheter in cystic duct
Bile duct
Pancreatic duct
E
Accessory pancreatic duct
Pancreatic duct
Pancreatic duct
F
Bile duct
Major duodenal papilla
Pancreatic duct
Minor duodenal papilla
Gallbladder
Dorsal pancreatic duct
Interconnecting channel
G
Bile duct
Duodenum
Major duodenal papilla
Biliopancreatic channel
Ventral pancreatic duct

Fig. 68.5 The normal and variant ductal anatomy of the pancreas. **A**, Normal. The pancreatic duct is formed by fusion of the dorsal and ventral bud ducts, and communicates with the accessory pancreatic duct. **B**, Normal. There is no communication between the pancreatic duct and a normally positioned accessory duct. **C**, Pancreas divisum. Most of the pancreas drains via a dominant dorsal duct that enters the duodenum at the minor duodenal papilla. A short ventral duct is seen draining, along with the bile duct, into the major duodenal papilla. **D**, Absence of accessory duct. **E**, Intraoperative cholangiogram visualizing the pancreatic duct opening into the duodenum through the major duodenal papilla, the accessory duct opening through the minor duodenal papilla and its communicating branch. **F**, Normal magnetic resonance cholangiopancreatogram (MRCP). The dorsal duct joins with the distal ventral duct in the head of the pancreas. **G**, Pancreas divisum. MRCP reconstruction shows that the dorsal duct is dominant and enters the duodenum at the minor duodenal papilla. A short ventral pancreatic duct is seen draining with the bile duct into the major duodenal papilla. (E–G, Courtesy of Mohamed Rela, Global Hospitals, Chennai, India.)

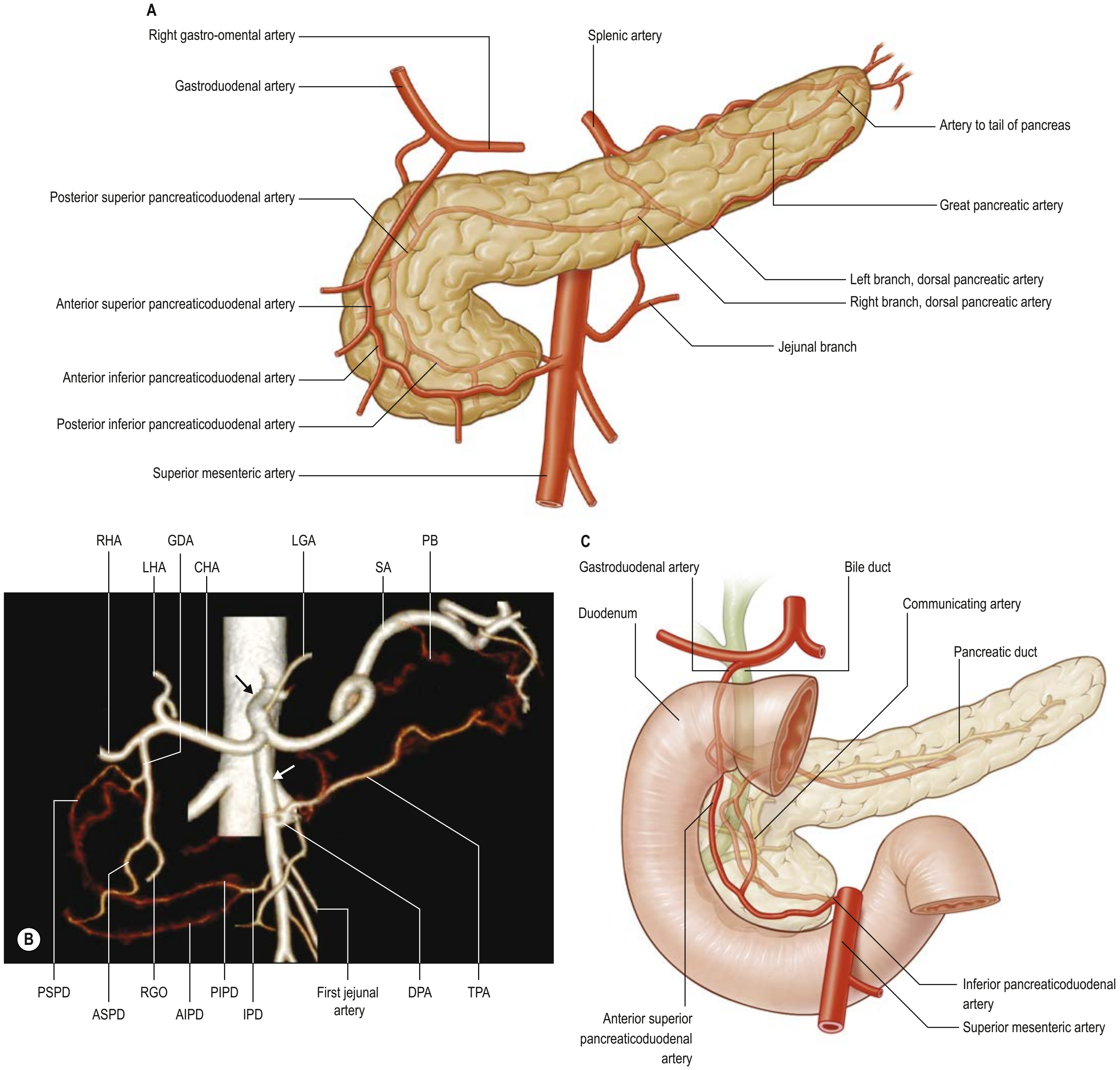
A
Right gastro-omental artery
Gastroduodenal artery
Posterior superior pancreaticoduodenal artery
Anterior superior pancreaticoduodenal artery
Anterior inferior pancreaticoduodenal artery
Posterior inferior pancreaticoduodenal artery
Superior mesenteric artery
Splenic artery
Artery to tail of pancreas
Great pancreatic artery
Left branch, dorsal pancreatic artery
Right branch, dorsal pancreatic artery
Jejunal branch
RHA
GDA
LGA
PB
LHA
CHA
SA
B
PSPD
ASPD
RGO
AIPD
PIPD
IPD
First jejunal artery
DPA
TPA
C
Gastroduodenal artery
Bile duct
Duodenum
Communicating artery
Pancreatic duct
Inferior pancreaticoduodenal artery
Superior mesenteric artery
Anterior superior pancreaticoduodenal artery

Fig. 68.6 **A**, The arterial supply of the pancreas. **B**, A CT angiographic reconstruction. The black arrow points to the coeliac trunk, and the white arrow points to the superior mesenteric artery. Anastomotic arcades, both anterior and posterior, can be seen coursing around the head of the pancreas. The body and tail of the pancreas are supplied by multiple pancreatic branches (PB) from the splenic artery and the dorsal pancreatic artery (DPA), which, in this example, arises from the superior mesenteric artery, and gives origin to the inferior (transverse) pancreatic artery (TPA). Other abbreviations: AIPD, anterior inferior pancreaticoduodenal artery; ASPD, anterior superior pancreaticoduodenal artery; CHA, common hepatic artery; GDA, gastroduodenal artery; IPD, inferior pancreaticoduodenal artery; LGA, left gastric artery; LHA, left hepatic artery; PIPD, posterior inferior pancreaticoduodenal artery; PSPD, posterior superior pancreaticoduodenal artery; RGO, right gastro-omental artery; RHA, right hepatic artery; SA, splenic artery. **C**, The anterior and posterior pancreaticoduodenal arterial arcades and a typical communicating artery. (Adapted with permission from Mirjalili SA, Stringer MD 2011 The arterial supply of the major duodenal papilla and its relevance to endoscopic sphincterotomy. Endoscopy 43(4):307–11.)

of the duodenum and runs inferiorly on the anterior aspect of the head of the pancreas at a variable distance medial to the groove between the descending duodenum and head of the pancreas. It passes inferiorly around the right or inferior border of the head of the pancreas, often piercing the gland to reach the posterior surface of the uncinate process, where it joins the anterior inferior pancreaticoduodenal artery to form the anterior pancreaticoduodenal arcade (Bertelli et al 1995).

Inferior pancreaticoduodenal artery

An inferior pancreaticoduodenal artery is present in most individuals. It usually arises either directly from the superior mesenteric artery at the inferior border of the pancreas or as a common vessel with the first jejunal artery (a pancreaticoduodenojejunal trunk) from the posterior or left aspect of the superior mesenteric artery (Bertelli et al 1996b, Horiguchi et al 2008). It runs to the right, posterior to the superior mesenteric vein, to reach the posterior surface of the uncinate process, where it divides into anterior and posterior inferior pancreaticoduodenal arteries. When it arises as a pancreaticoduodenojejunal trunk, the artery gives off a jejunal branch and then runs posterior to both the superior mesenteric artery and vein before dividing into its terminal branches. The inferior pancreaticoduodenal artery is at risk of bleeding during the retroperitoneal dissection of a Whipple procedure. Occasionally, it is absent and the anterior and posterior inferior pancreaticoduodenal arteries arise separately from the superior mesenteric artery.

The smaller anterior inferior pancreaticoduodenal artery runs to the right on the posterior surface of the uncinate process to join the anterior superior pancreaticoduodenal artery and form the anterior pancreaticoduodenal arcade. The larger posterior inferior pancreaticoduodenal artery runs on the posterior surface of the head of the pancreas, parallel and superior to the anterior inferior pancreaticoduodenal artery and joins the posterior superior pancreaticoduodenal artery to form the posterior pancreaticoduodenal arcade (Bertelli et al 1997).

Communicating arteries

Multiple small arteries run between the anterior and posterior pancreaticoduodenal arcades, either via the pancreaticoduodenal groove or through the substance of the gland. The largest and most consistent of these is the communicating artery (sometimes known as the middle pancreaticoduodenal arcade) that passes between the pancreatic duct and accessory pancreatic duct and connects the anterior pancreaticoduodenal arterial arcade and the posterior superior pancreaticoduodenal artery (Yamaguchi et al 2001; see Fig. 68.6C). This artery gives rise to most of the small arteries that supply the major duodenal papilla (Mirjalili and Stringer 2011).

Other arterial arcades in the head of the pancreas

Kirk's arcade is formed by a right branch of the dorsal pancreatic artery that emerges on to the anterior surface of the head of the gland and anastomoses with a branch of either the gastroduodenal artery or the anterior pancreaticoduodenal arcade (Woodburne and Olsen 1951). It supplies the anterior surface of the head and neck of the gland.

Splenic artery

The splenic artery arises from the coeliac trunk and runs posterior to the superior border of the pancreas to the splenic hilum (see Fig. 68.6A). It gives off multiple small branches along its course that penetrate and supply the pancreas, including the dorsal pancreatic artery; the great pancreatic artery, arising approximately two-thirds of the way along the gland; and the artery to the tail of the pancreas, arising near the tail. These branches lie on or within the posterior aspect of the gland and often anastomose with the inferior pancreatic artery. Anatomical variations are not unusual, and the dorsal, great or inferior pancreatic arteries can be dominant in any one individual (Wu et al 2011).

Dorsal pancreatic artery

The dorsal pancreatic artery commonly arises from the initial 2 cm of the splenic artery, although it can also take origin from the common hepatic or superior mesenteric arteries or the coeliac trunk (Horiguchi et al 2008). It is short and gives off numerous branches, including a terminal left branch near the inferior border of the gland. Several right-sided branches run to the head of the pancreas, passing either posterior or anterior to the superior mesenteric vein to supply the posterior or anterior surface of the head of the pancreas, respectively; they anastomose with arteries of the pancreaticoduodenal arcade (Tsutsumi et al 2014). The terminal left branch anastomoses with the inferior pancreatic artery.

The length and course of the dorsal pancreatic artery depend primarily on its site of origin. When it arises from the splenic artery, common hepatic artery or coeliac trunk, it runs inferiorly on the posterior surface of the pancreas, whereas if it arises from the superior mesenteric artery, it runs superiorly. These variations should be taken into account during organ procurement because injury to the dorsal pancreatic artery, including at its origin, can jeopardize the pancreatic graft as a result of inadequate perfusion of the tail of the pancreas (Baranski et al 2016). The artery uniformly terminates near the inferior border of the pancreas close to the confluence of the splenic and superior mesenteric veins (Bertelli et al 1998).

Inferior pancreatic artery

The inferior (transverse) pancreatic artery commonly originates from the left terminal branch of the dorsal pancreatic artery. It runs to the left on the posterior surface of the gland close to its inferior border, gives multiple branches to the body and tail, and anastomoses with other pancreatic branches of the splenic artery. Occasionally, the inferior pancreatic artery originates from the gastroduodenal artery or the anterior superior pancreaticoduodenal artery, crossing the anterior surface of the head of the pancreas to reach the inferior border of the neck of the gland and then the tail. In such cases it may be the dominant artery to the body of the pancreas, and its injury or deliberate ligation during pancreaticoduodenectomy can cause ischaemia of the pancreas.

Arterial segmentation of the pancreas

Available with the *Gray's Anatomy* e-book

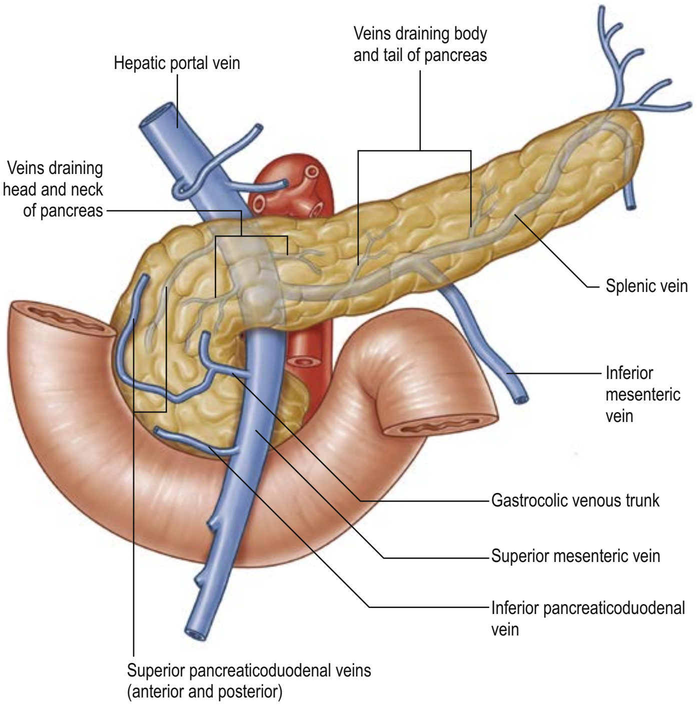
Hepatic portal vein
Veins draining body and tail of pancreas
Veins draining head and neck of pancreas
Splenic vein
Inferior mesenteric vein
Gastrocolic venous trunk
Superior mesenteric vein
Inferior pancreaticoduodenal vein
Superior pancreaticoduodenal veins (anterior and posterior)

Fig. 68.7 Venous drainage of the pancreas. (Adapted from Drake RL, Vogl AW, Mitchell A (eds) Gray's Anatomy for Students, 2nd ed. Elsevier, Churchill Livingstone. Copyright 2010.)

Veins

Multiple veins drain the pancreas into the hepatic portal, superior mesenteric and splenic veins (Mourad et al 1994; **Fig. 68.7**). Although variations are common, the anterior superior pancreaticoduodenal vein typically joins either the confluence of the right gastro-omental and right colic veins (the gastrocolic trunk of Henle) or the right gastro-omental vein alone, to drain into the superior mesenteric vein at the inferior border of the neck of the pancreas (Mourad et al 1994, Lange et al 2000). The posterior superior pancreaticoduodenal vein drains cranially into the hepatic portal vein. Both anterior and posterior inferior pancreaticoduodenal veins usually drain directly into the posterior aspect of the superior mesenteric vein inferior to the uncinate process. These veins can be a major source of blood loss when the uncinate process is dissected off the superior mesenteric vein during a pancreaticoduodenectomy procedure. In most individuals the first and second jejunal veins form a single vein known as the first jejunal trunk that drains into the superior mesenteric vein (Ishikawa et al 2017). Veins from the body and tail of the gland drain directly into the splenic vein. An inferior (transverse) pancreatic vein sometimes runs along the inferior border of the pancreas to join the inferior mesenteric vein. A few pancreatic veins communicate with systemic veins in the retroperitoneum (veins of Retzius) and can form retroperitoneal varices in patients with portal hypertension.

Lymphatic drainage

The lymphatic drainage of the pancreas is extensive (see Fig. 63.14B), which partly explains the poor prognosis of individuals with pancreatic cancer. Lymphatic vessels start within the interlobular septa within the gland and join to form larger lymphatic vessels that follow the paths of local arteries (Deki and Sato 1988, O'Morchoe 1997). Lymphatics from the tail and body of the pancreas drain mostly into nodes along the splenic artery and inferior border of the gland, and from there to pre-aortic nodes between the coeliac trunk and superior mesenteric artery. Lymphatics from the neck and head drain more widely into nodes along the pancreaticoduodenal, superior mesenteric and hepatic arteries, and ultimately into pre-aortic nodes (Donatini and Hidden 1992, Cesmebasi et al 2015). There is no evidence of lymphatic channels within the pancreatic islets.

Innervation

The pancreas is innervated by extra- and intra-pancreatic plexuses of autonomic nerves (Love et al 2007, Zuo et al 2012). Preganglionic vagal efferents with cell bodies in the posterior nucleus of the vagus nerve reach the pancreas via hepatic, gastric and coeliac branches of the vagus nerve.

The pancreas can be divided into two arterial 'segments' separated by a relatively avascular plane. There is disagreement about the definition of these segments. One view is that they are separated by a plane passing to the left of the superior mesenteric artery, such that the head and neck are supplied by branches of the gastroduodenal and superior mesenteric arteries and the body and tail are supplied by branches of the splenic artery (Busnardo et al 1988). An alternative view holds that the anterior segment consists of the superior part of the pancreatic head, neck, body and tail (derived from the dorsal pancreatic bud), and the posterior segment consists of the inferior part of the head and the uncinate process (derived from the ventral pancreatic bud) (Sakamoto et al 2000). In both schemes, the pancreatic duct crosses between the segments. Currently, segmental anatomy is of limited practical surgical significance.

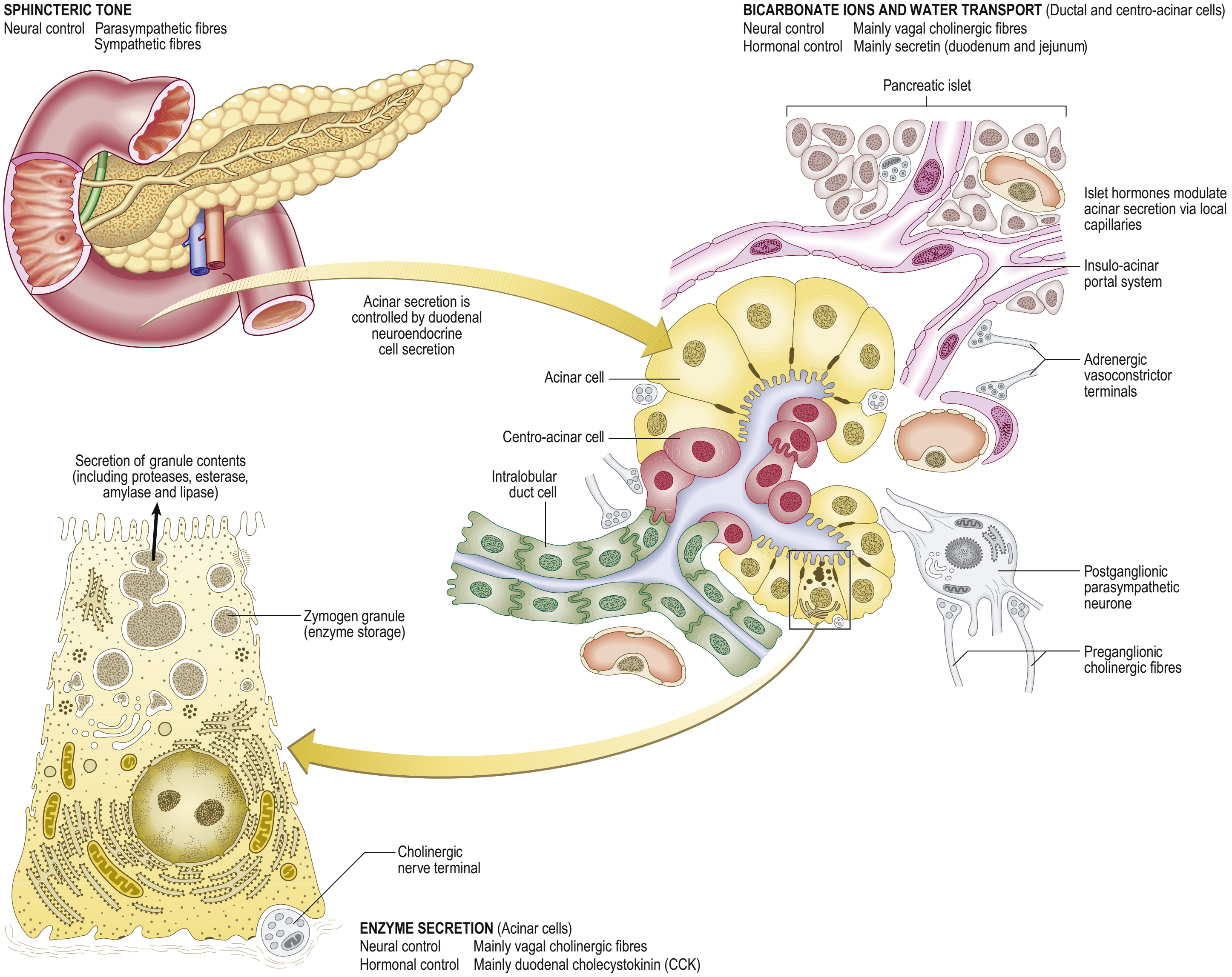
SPHINCTERIC TONE
Neural control Parasympathetic fibres
Sympathetic fibres
BICARBONATE IONS AND WATER TRANSPORT (Ductal and centro-acinar cells)
Neural control Mainly vagal cholinergic fibres
Hormonal control Mainly secretin (duodenum and jejunum)
Pancreatic islet
Islet hormones modulate acinar secretion via local capillaries
Insulo-acinar portal system
Adrenergic vasoconstrictor terminals
Acinar secretion is controlled by duodenal neuroendocrine cell secretion
Acinar cell
Centro-acinar cell
Intralobular duct cell
Secretion of granule contents (including proteases, esterase, amylase and lipase)
Zymogen granule (enzyme storage)
Postganglionic parasympathetic neurone
Preganglionic cholinergic fibres
Cholinergic nerve terminal
ENZYME SECRETION (Acinar cells)
Neural control Mainly vagal cholinergic fibres
Hormonal control Mainly duodenal cholecystokinin (CCK)

Fig. 68.8 The microstructure of the exocrine pancreas and the mechanisms by which its secretion is controlled. Pancreatic stellate cells (see text) are not shown.

They synapse with postganglionic parasympathetic pancreatic neurones that are distributed singly or clustered in ganglia in the interlobular connective tissue, lobules and islets. Postganglionic fibres ramify in the interacinar spaces and supply acinar cells and islets, modulating both exocrine and endocrine secretion (see Fig. 68.10). They reach the islets via the blood vessels: in marked contrast to mouse pancreas (widely used in experimental models analysing pancreatic function), relatively few parasympathetic axons terminate in the human endocrine pancreas (Pénicaud 2017) and endocrine cells of the human islet do not appear to be directly innervated (Rodriguez-Diaz et al 2012). Postganglionic parasympathetic neurones are also contacted by enteric neurones from the stomach and duodenum, sympathetic efferents and other pancreatic neurones and a network of interstitial cells (of Cajal) provides an additional link between autonomic nerves and pancreatic acini.

The cell bodies of preganglionic sympathetic nerves are located in the intermediolateral nuclei of the spinal cord (T6–T12); their axons travel in the thoracic splanchnic nerves and synapse in the coeliac and superior mesenteric ganglia. Postganglionic sympathetic nerves innervate the smooth muscle cells of vessels and ducts within the pancreas, causing vasoconstriction and inhibiting exocrine secretion.

Visceral afferents, travelling via parasympathetic and sympathetic routes, convey sensory information from the pancreas via the inferior (nodose) ganglion of the vagus nerve (terminating in the solitary tract), and via the coeliac plexus and greater thoracic splanchnic nerves (terminating in the dorsal horn of the spinal cord, T5–T9).

Extrapancreatic nerve plexuses are particularly abundant in the head and neck of the pancreas, where two plexuses have been identified (Yoshioka and Wakabayashi 1958). Pancreatic head plexus I originates from the coeliac ganglia and plexus and travels on the posterior surface of the head of the pancreas and along the medial margin of the uncinate process. Pancreatic head plexus II originates from the superior mesenteric ganglion and plexus and travels along the inferior pancreaticoduodenal artery on the uncinate process (Mochizuki et al 2010, Zuo et al 2012, Isaji et al 2018).

Perineural invasion is relatively common in pancreatic cancer and not only adversely affects prognosis, but may also be a factor in the pain associated with this disease (Bapat et al 2011).

Referred pain

Pain arising in the pancreas is poorly localized. Inflammatory or cancerous processes arising from the gland rapidly involve the tissues of the retroperitoneum that are innervated by somatic nerves and pain is localized to the lower thoracic spine, consequently patients complain of low back pain. Intractable pain from chronic pancreatitis or inoperable pancreatic tumours can be controlled by thermal or chemical ablation of the coeliac plexus.

Microstructure

The pancreas is composed of exocrine and endocrine tissues. The main tissue mass, forming 98% of the pancreas, is exocrine; the pancreatic islets that form the endocrine component are embedded in it (Figs 68.8–68.10).

Exocrine pancreas

The exocrine pancreas is a branched acinar gland (see Fig. 2.6) surrounded and incompletely lobulated by delicate loose connective tissue. Individual acini are composed of roughly spherical clusters of pyramidal cells that secrete digestive enzymes. A narrow intralobular duct lined by flattened or cuboidal centro-acinar cells originates from

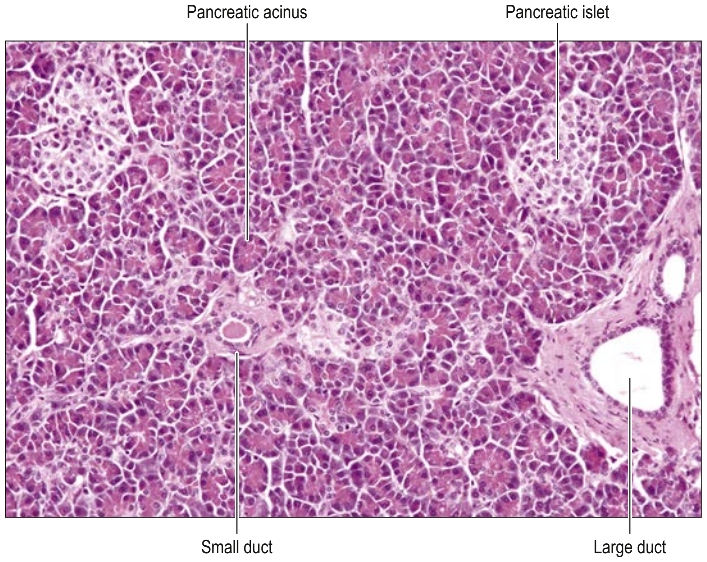
Pancreatic acinus
Pancreatic islet
Small duct
Large duct

Fig. 68.9 Microstructure of the pancreas. The exocrine tissue consists of acini with pyramid-shaped columnar cells arranged in spherical clusters. Acinar secretions drain into intralobular ducts, which, in turn, join larger interlobular ducts, present in interlobular septa containing blood vessels. Interspersed between the acini are islets of Langerhans, which appear as clusters of pale-staining cells surrounded by a network of capillaries, seen as narrow clear spaces. Adipocytes are also sometimes present. Haematoxylin and eosin. (Courtesy of Dr Mukul Vij, Global Hospital, Chennai, India.)

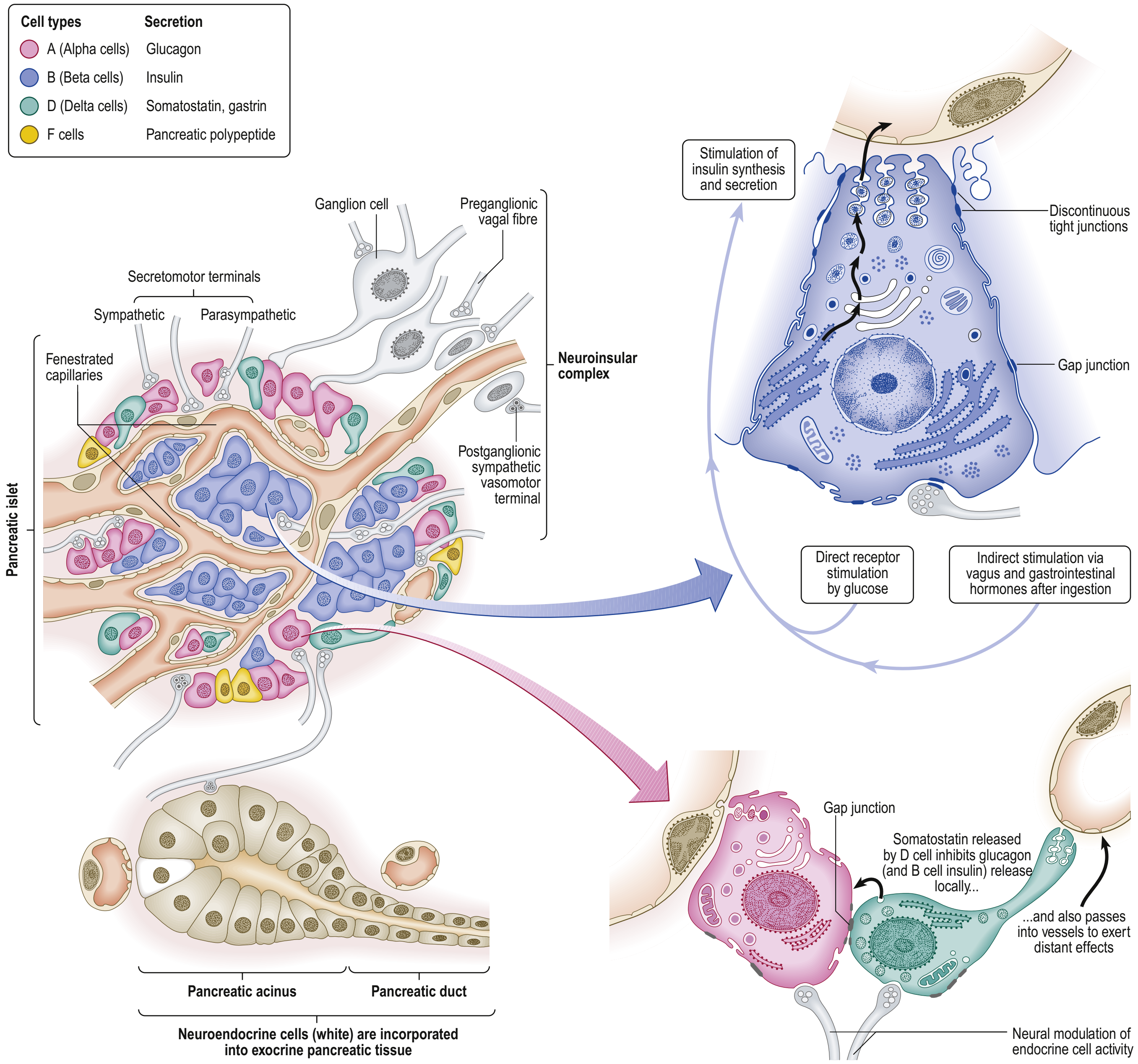

Cell types	Secretion
● A (Alpha cells)	Glucagon
● B (Beta cells)	Insulin
● D (Delta cells)	Somatostatin, gastrin
● F cells	Pancreatic polypeptide

Ganglion cell
Preganglionic vagal fibre
Secretomotor terminals
Sympathetic
Parasympathetic
Fenestrated capillaries
Neuroinsular complex
Postganglionic sympathetic vasomotor terminal
Pancreatic islet
Pancreatic acinus
Pancreatic duct
Neuroendocrine cells (white) are incorporated into exocrine pancreatic tissue
Stimulation of insulin synthesis and secretion
Discontinuous tight junctions
Gap junction
Direct receptor stimulation by glucose
Indirect stimulation via vagus and gastrointestinal hormones after ingestion
Gap junction
Somatostatin released by D cell inhibits glucagon (and B cell insulin) release locally...
...and also passes into vessels to exert distant effects
Neural modulation of endocrine cell activity

Fig. 68.10 The microstructure and control of function of the endocrine pancreas.

within each secretory acinus. Intralobular ducts, which release bicarbonate ions and water into their lumina, unite to form larger interlobular ducts lined by taller cuboidal and eventually columnar epithelium. The latter are surrounded by connective tissue septa containing smooth muscle, autonomic nerves and adipose tissue. Neuroendocrine cells are present among the columnar ductal cells, and mast cells are numerous in the surrounding connective tissue. A network of intralobular arteries, arterioles and capillaries forms around the terminal ducts, acini and the richly vascularized endocrine islets (Love et al 2007).

Acinar cells Acinar cells have a basal nucleus surrounded by abundant basophilic rough endoplasmic reticulum and an apical region containing dense eosinophilic secretory zymogen granules. A prominent supranuclear Golgi complex is associated with large, membrane-bound granules containing the protein constituents of pancreatic secretion, including enzymes that are only active after release. Ganglionic neurones and cords of undifferentiated epithelial cells are also found within the acini. The structure of the exocrine pancreas and its functional regulation are summarized in Fig. 68.8.

Stellate cells Pancreatic stellate cells are myofibroblast-like cells distributed in the exocrine part of the pancreas, mainly in the peri-acinar space, where their long cytoplasmic processes encircle the base of the acinus, and in perivascular and periductal regions of the pancreas. They are usually in a quiescent state but have been implicated in the pathogenesis of chronic pancreatitis and pancreatic cancer when activated (Omary et al 2007, Masamune and Shimosegawa 2013).

Endocrine pancreas

Pancreatic islets (of Langerhans) constitute the endocrine component of the pancreas. The human pancreas can contain more than a million islets distributed throughout the gland but most numerous in the tail. Each islet consists of a highly vascularized cluster of polyhedral cells arranged in a trabecular pattern, closely approximated to a dense network of fenestrated capillaries that enables substrates to be transported bidirectionally between the islet cells and the circulation (In't Veld and Marichal 2010). Islets are innervated by autonomic nerve fibres that travel with the blood vessels and end blindly in the pericapillary spaces. True synaptic contact between these nerve fibres and islet cells has not been demonstrated, although it has been suggested that they have a role in islet function (Rodriguez-Diaz et al 2012). Specialized staining techniques are necessary to distinguish various islet cells, designated alpha, beta, delta, epsilon and pancreatic polypeptide (PP) or F cells. Beta cells secrete insulin and are the most abundant cell type (nearly 50% in human islets); alpha cells secrete glucagon (30–40%). Delta cells and PP cells are less common and secrete somatostatin and pancreatic polypeptide, respectively. Epsilon cells secrete ghrelin. Unlike murine islets, where beta cells form the core and are surrounded by alpha cells, human islets show no cell-type-specific localization. The various cell types are uniformly distributed along the microvasculature and have extensive interlinkages with other islet cells. Their general organization is shown in Fig. 68.10.

Acute pancreatitis

Available with the *Gray's Anatomy* e-book

Chronic pancreatitis

Available with the *Gray's Anatomy* e-book

Pancreatic tumours

Available with the *Gray's Anatomy* e-book

Pancreatic transplantation

Available with the *Gray's Anatomy* e-book

Bonus e-book content

Fig. 68.5 E, Intraoperative cholangiogram. **F**, Normal magnetic resonance cholangiopancreatogram (MRCP). **G**, Pancreas divisum.

Key references

Busnardo AC, DiDio LJ, Thomford NR 1988 Anatomicosurgical segments of the human pancreas. Surg Radiol Anat 10:77–82.
A description explaining the segmental vascularity of the pancreas and the watershed area near the neck of the pancreas.

Cesmebasi A, Malefant J, Patel SD et al 2015 The surgical anatomy of the lymphatic system of the pancreas. Clin Anat 28:527–37.
A review of the literature describing the lymphatics of the pancreas, pancreatic pathologies and the available imaging methodologies that are used to study the pancreatic lymphatics.

DeSouza SV, Yoon HD, Singh RG et al 2018 Quantitative determination of pancreas size using anatomical landmarks and its clinical relevance: a systematic literature review. Clin Anat 31:913–26.
Alterations in the size of the pancreas are clinically relevant in diseases of both the endocrine and exocrine pancreas. This paper is a systematic literature review documenting the methodology used and quantitative data obtained in studies of the size of the pancreas.

In't Veld P, Marichal M 2010 Microscopic anatomy of the human islet of Langerhans. Adv Exp Med Biol 654:1–19.
A detailed description of the human islet of Langerhans.

Kamisawa T, Okamoto A 2008 Pancreatographic investigation of pancreatic duct system and pancreaticobiliary malformation. J Anat 212:125–34.
A review of the pancreatic ductal system.

Kimura W 2000 Surgical anatomy of the pancreas for limited resection. J Hepatobil Pancreat Surg 7:473–9.
A beautifully illustrated description of the surgical anatomy of the pancreas.

Kimura W, Nagai H 1995 Study of surgical anatomy for duodenum-preserving resection of the head of the pancreas. Ann Surg 221:359–63.
A detailed description of the vascular anatomy of the head of the pancreas and duodenum.

Nagai H 2003 Configurational anatomy of the pancreas: its surgical relevance from ontogenetic and comparative-anatomical viewpoints. J Hepatobil Pancreat Surg 10:48–56.
A well-illustrated description of the arrangement of vascular and other structures around the duodenum and head of pancreas, with explanations based on the embryological development of the pancreas, foregut and midgut.

Woodburne RT, Olsen LL 1951 The arteries of the pancreas. Anat Rec 111:255–70.
One of the earliest comprehensive reviews of pancreatic arterial anatomy.

Acute inflammation of the pancreas can result from a variety of pancreatic insults, including gallstone obstruction of the hepatopancreatic ampulla, causing reflux of bile and pancreatic fluid into the pancreatic duct. This precipitates intraparenchymal activation of inactive digestive enzymes, leading to cell injury, an inflammatory cascade and destruction of pancreatic tissue.

The regional anatomy of the pancreas explains most of the clinical complications of acute pancreatitis. Irritation of the stomach contributes to gastric stasis and emesis inflammation of the superior mesenteric plexus can contribute to paralytic ileus; vascular inflammation can cause superior mesenteric or hepatic portal vein thrombosis, arterial bleeding or pseudoaneurysms and ischaemia of the transverse colon. Haemorrhaged blood can accumulate in the retroperitoneal tissues around the pancreas and track laterally to the flanks (Grey Turner's sign), inferiorly to the inguinal ligaments (Fox's sign), or via the lesser omentum and bare area of the liver to the falciform ligament and the skin around the umbilicus (Cullen's sign), manifesting as diffuse bruising.

Acute peripancreatic fluid collections frequently resolve spontaneously as the inflammation in the pancreas subsides. Accumulation of fluid anterior to the pancreas, just deep to the posterior wall of the omental bursa, can result in a 'pseudocyst' containing amylase-rich fluid and debris but lacking a true epithelial lining (Banks et al 2013). A large pseudocyst bulges anteriorly into the omental bursa in contact with the posterior wall of the stomach, lesser omentum and gastrosplenic ligament. If it does not resolve spontaneously, the pseudocyst can be drained internally through the posterior wall of the stomach by endoscopic or open surgery, or externally by means of a percutaneous drain inserted under radiological guidance.

Sustained injury to the pancreas can result in permanent damage, leading to parenchymal fibrosis and calcification within the parenchyma and the pancreatic ducts. This often causes chronic pain, diabetes mellitus and pancreatic exocrine insufficiency with steatorrhoea and malnutrition. Fibrosis can involve the bile duct in the head of the pancreas, leading to obstructive jaundice, and/or the splenic vein, causing splenic vein thrombosis and 'left-sided' portal hypertension.

Most pancreatic tumours are ductal adenocarcinomas derived from exocrine ductal epithelium. Up to two-thirds of such tumours are located in the head of the pancreas and often obstruct the pancreatic segment of the bile duct early in the course of disease, leading to obstructive jaundice. The appearance of a dilated bile duct and pancreatic duct on cross-sectional imaging (the 'double duct' sign) is characteristic of tumours of the head of the pancreas. Advanced tumours can invade the adjacent duodenum, causing obstruction of the gastric outlet and/or the hepatic portal or superior mesenteric veins posterior to the neck of the pancreas. A tumour in the body or tail of the gland often grows to a large size before presenting as an abdominal mass or with back pain and weight loss (Yeo et al 2002). Tumours of the uncinate process can cause early involvement of the superior mesenteric vessels and duodenum (O'Sullivan et al 2009). Peripancreatic and pre-aortic nodes can be involved, together with hepatic nodes, in tumours of the head of the pancreas, and nodes of the splenic hilum can be involved in tumours of the tail of the pancreas.

Surgery for tumours of the head of the pancreas usually involves combined resection of the head and duodenum (pancreaticoduodenectomy) as a consequence of their shared blood supply. The resectability of the tumour depends on the presence and extent of major vascular involvement, particularly the hepatic portal vein and superior mesenteric vessels. An accessory or replaced right hepatic artery running cranially on the posterior surface of the head of the pancreas and posterior to the supraduodenal segment of the bile duct is at risk of injury during such procedures (Turrini et al 2010). Recognition of this variation and preservation of the artery are essential to maintain the arterial supply to the right lobe of the liver. In distal or total pancreatectomy, spleen-preserving resections are generally undertaken if the underlying pathology does not involve the splenic vein lying in the groove on the posterior surface of the gland, taking care to control the multiple small pancreatic venous tributaries. In duodenum-preserving resection of the head of the pancreas, which is sometimes undertaken for chronic pancreatitis and benign pancreatic tumours, preservation of an adequate duodenal blood supply from the pancreaticoduodenal arterial arcades is important (Kimura and Nagai 1995). Stenosis of the coeliac trunk is common in elderly individuals with atherosclerosis. Here, the arterial blood supply to the liver is provided by the superior mesenteric artery through hypertrophied arteries of the anterior and posterior pancreaticoduodenal arcades. Care should be taken to avoid ligation of these branches during pancreatic surgery because this could cause hepatic ischaemia.

The pancreas is usually transplanted together with the kidney (a simultaneous pancreas–kidney transplant) in patients with end-stage renal disease caused by diabetes mellitus. In selected patients, the pancreas alone can be transplanted to treat poor glycaemic control and hypoglycaemia unawareness (White et al 2009).

The donor pancreas is recovered from a deceased donor, usually as part of a multi-organ recovery procedure. The entire pancreas and the duodenal C loop (attached to the head of the pancreas) and spleen (closely related to the tail of the pancreas) are recovered to prevent injury to the vascular arcades in the pancreaticoduodenal groove and minimize handling of the pancreas during organ recovery (Abu-Elmagd et al 2000). The arterial supply for the donor pancreas is based on the splenic artery and the superior mesenteric artery, both of which are carefully preserved during the donor operation and reconstructed to a Y-shaped deceased donor iliac artery graft to enable a single arterial anastomosis to be performed in the recipient. The venous drainage is through the hepatic portal vein. The donor pancreas is implanted in the pelvis and the reconstructed artery is anastomosed to the external iliac artery. The hepatic portal vein of the graft can be anastomosed to either an iliac vein or the superior mesenteric vein of the recipient: there is no evidence to support the superiority of one technique over the other (Bazerbachi et al 2012). Drainage of the exocrine pancreatic secretions is into the ileum through a duodeno-ileal anastomosis or into the recipient urinary bladder through a duodeno-cystic anastomosis. Complications of the procedure result mainly from injury sustained by the donor pancreas during the organ recovery, storage and transplantation process, and include graft pancreatitis and graft necrosis leading to bleeding, thrombosis of vascular anastomoses and sepsis (Delis et al 2004, Troppmann 2010). In most patients, pancreas transplantation provides the potential for an insulin-free life and retards the development of diabetes-related complications (Gruessner et al 2012).

References

Abu-Elmagd K, Fung J, Bueno J et al 2000 Logistics and technique for procurement of intestinal, pancreatic, and hepatic grafts from the same donor. Ann Surg 232:680–7.

Banks PA, Bollen TL, Dervenis C et al 2013 Classification of acute pancreatitis–2012: revision of the Atlanta classification and definitions by international consensus. Gut 62:102–11.

Bapat AA, Hostetter G, Von Hoff DD et al 2011 Perineural invasion and associated pain in pancreatic cancer. Nat Rev Cancer 11:695–707.

Baranski AG, Lam HD, Braat AE et al 2016 The dorsal pancreatic artery in pancreas procurement and transplantation: anatomical considerations and potential implications. Clin Transplant 30:1360–4.

Bazerbachi F, Selzner M, Marquez MA et al 2012 Portal venous versus systemic venous drainage of pancreas grafts: impact on long-term results. Am J Transplant 12:226–32.

Bertelli E, Di Gregorio F, Bertelli L et al 1995 The arterial blood supply of the pancreas: a review. I. The superior pancreaticoduodenal and the anterior superior pancreaticoduodenal arteries: an anatomical and radiological study. Surg Radiol Anat 17:97–106.

Bertelli E, Di Gregorio F, Bertelli L et al 1996a The arterial blood supply of the pancreas: a review. II. The posterior superior pancreaticoduodenal artery: an anatomical and radiological study. Surg Radiol Anat 18:1–9.

Bertelli E, Di Gregorio F, Bertelli L et al 1996b The arterial blood supply of the pancreas: a review. III. The inferior pancreaticoduodenal artery: an anatomical review and a radiological study. Surg Radiol Anat 18:67–74.

Bertelli E, Di Gregorio F, Bertelli L et al 1997 The arterial blood supply of the pancreas: a review. IV. The anterior inferior and posterior pancreaticoduodenal aa., and minor sources of blood supply for the head of the pancreas: an anatomical review and radiologic study. Surg Radiol Anat 19:203–12.

Bertelli E, Di Gregorio F, Mosca S et al 1998 The arterial blood supply of the pancreas: a review. V. The dorsal pancreatic artery: an anatomic review and a radiologic study. Surg Radiol Anat 20:445–452.

Burgard G, Gilly F, Braillon G et al 1991 Anatomic basis of the surgical approach to the retropancreatic common bile duct. Surg Radiol Anat 13:352–3.

Busnardo AC, DiDio LJ, Thomford NR 1988 Anatomicosurgical segments of the human pancreas. Surg Radiol Anat 10:77–82.

A description explaining the segmental vascularity of the pancreas and the watershed area near the neck of the pancreas.

Caglar V, Songur A, Yagmurca M et al 2012 Age-related volumetric changes in pancreas: a stereological study on computed tomography. Surg Radiol Anat 34:935–41.

Cesmebasi A, Malefant J, Patel SD et al 2015 The surgical anatomy of the lymphatic system of the pancreas. Clin Anat 28:527–37.

A review of the literature describing the lymphatics of the pancreas, pancreatic pathologies and the available imaging methodologies that are used to study the pancreatic lymphatics.

Deki H, Sato T 1988 An anatomic study of the peripancreatic lymphatics. Surg Radiol Anat 10:121–35.

Delis S, Dervenis C, Bramis J et al 2004 Vascular complications of pancreas transplantation. Pancreas 28:413–20.

DeSouza SV, Yoon HD, Singh RG et al 2018 Quantitative determination of pancreas size using anatomical landmarks and its clinical relevance: a systematic literature review. Clin Anat 31:913–26.

Alterations in the size of the pancreas are clinically relevant in diseases of both the endocrine and exocrine pancreas. This paper is a systematic literature review documenting the methodology used and quantitative data obtained in studies of the size of the pancreas.

Djuric-Stefanovic A, Masulovic D, Kostic J et al 2012 CT volumetry of normal pancreas: correlation with the pancreatic diameters measurable by the cross-sectional imaging, and relationship with the gender, age, and body constitution. Surg Radiol Anat 34:811–17.

Donatini B, Hidden G 1992 Routes of lymphatic drainage from the pancreas: a suggested segmentation. Surg Radiol Anat 14:35–42.

Glaser J, Hogemann B, Krummenerl T et al 1987 Sonographic imaging of the pancreatic duct: new diagnostic possibilities using secretin stimulation. Dig Dis Sci 32:1075–81.

Gruessner AC, Sutherland DE, Gruessner RW 2012 Long-term outcome after pancreas transplantation. Curr Opin Organ Transplant 17:100–5.

Hernandez-Jover D, Pernas JC, Gonzalez-Ceballos S et al 2011 Pancreatoduodenal junction: review of anatomy and pathologic conditions. J Gastrointest Surg 15:1269–81.

Horiguchi A, Ishihara S, Ito M et al 2008 Multislice CT study of pancreatic head arterial dominance. J Hepatobil Pancreat Surg 15:322–6.

Horaguchi J, Fujita N, Kamisawa T et al 2014 Pancreatobiliary reflux in individuals with a normal pancreaticobiliary junction: a prospective multicenter study. J Gastroenterol 49:875–81.

In't Veld P, Marichal M 2010 Microscopic anatomy of the human islet of Langerhans. Adv Exp Med Biol 654:1–19.

A detailed description of the human islet of Langerhans.

Isaji S, Murata Y, Kishiwada M 2018 New Japanese classification of pancreatic cancer. In: Neoptolemos J, Urrutia R, Abbruzzese J (eds) Pancreatic Cancer. New York: Springer.

Ishikawa Y, Ban D, Matsumura S et al 2017 Surgical pitfalls of jejunal vein anatomy in pancreaticoduodenectomy. J Hepatobiliary Pancreat Sci 24:394–400.

Kamisawa T 2004 Clinical significance of the minor duodenal papilla and accessory pancreatic duct. J Gastroenterol 39:605–15.

Kamisawa T, Okamoto A 2008 Pancreatographic investigation of pancreatic duct system and pancreaticobiliary malformation. J Anat 212:125–34.

A review of the pancreatic ductal system.

Kamisawa T, Suyama M, Fujita N et al 2010a Pancreatobiliary reflux and the length of a common channel. J Hepatobil Pancreat Surg 17:865–70.

Kamisawa T, Takuma K, Tabata T et al 2010b Clinical implications of accessory pancreatic duct. World J Gastroenterol 16:4499–503.

Kimura W 2000 Surgical anatomy of the pancreas for limited resection. J Hepatobil Pancreat Surg 7:473–9.

A beautifully illustrated description of the surgical anatomy of the pancreas.

Kimura W, Nagai H 1995 Study of surgical anatomy for duodenum-preserving resection of the head of the pancreas. Ann Surg 221:359–63.

A detailed description of the vascular anatomy of the head of the pancreas and duodenum.

Lange JF, Koppert S, van Eyck CH et al 2000 The gastrocolic trunk of Henle in pancreatic surgery: an anatomo-clinical study. J Hepatobil Pancreat Surg 7:401–3.

Love JA, Yi E, Smith TG 2007 Autonomic pathways regulating pancreatic exocrine secretion. Auton Neurosci 133:19–34.

Masamune A, Shimosegawa T 2013 Pancreatic stellate cells–multi-functional cells in the pancreas. Pancreatology 13:102–5.

Mirjalili SA, Stringer MD 2011 The arterial supply of the major duodenal papilla and its relevance to endoscopic sphincterotomy. Endoscopy 43:307–11.

Mochizuki K, Gabata T, Kozaka K et al 2010 MDCT findings of extrapancreatic nerve plexus invasion by pancreas head carcinoma: correlation with en bloc pathological specimens and diagnostic accuracy. Eur Radiol 20:1757–67.

Mourad N, Zhang J, Rath AM et al 1994 The venous drainage of the pancreas. Surg Radiol Anat 16:37–45.

Nagai H 2003 Configurational anatomy of the pancreas: its surgical relevance from ontogenetic and comparative-anatomical viewpoints. J Hepatobil Pancreat Surg 10:48–56.

A well-illustrated description of the arrangement of vascular and other structures around the duodenum and head of the pancreas, with explanations based on the embryological development of the pancreas, foregut and midgut.

Omary MB, Lugea A, Lowe AW et al 2007 The pancreatic stellate cell: a star on the rise in pancreatic diseases. J Clin Invest 117:50–9.

A detailed review of the pancreatic acinar cell, which is the focus of research into its possible role in a multitude of pancreatic disorders.

O'Morchoe CC 1997 Lymphatic system of the pancreas. Microsc Res Tech 37:456–77.

O'Sullivan AW, Heaton N, Rela M 2009 Cancer of the uncinate process of the pancreas: surgical anatomy and clinicopathological features. Hepatobiliary Pancreat Dis Int 8:569–74.

Pénicaud L 2017 Autonomic nervous system and pancreatic islet blood flow. Biochimie 143:29–32.

Purvis NS, Mirjalili SA, Stringer MD 2013 The mucosal folds at the pancreaticobiliary junction. Surg Radiol Anat 35:943–50.

Rana SS, Gonen C, Vilmann P 2012 Endoscopic ultrasound and pancreas divisum. JOP 13:252–7.

Rodriguez-Diaz R, Speier S, Molano RD et al 2012 Noninvasive in vivo model demonstrating the effects of autonomic innervation on pancreatic islet function. Proc Natl Acad Sci U S A 109:21456–61.

Saisho Y, Butler AE, Meier JJ et al 2007 Pancreas volumes in humans from birth to age one hundred taking into account sex, obesity, and presence of type-2 diabetes. Clin Anat 20:933–42.

A description of pancreatic volumes and the ratio of parenchymal and adipose components in humans, with an account of how it changes with age and sex.

Sakamoto Y, Nagai M, Tanaka N et al 2000 Anatomical segmentectomy of the head of the pancreas along the embryological fusion plane: a feasible procedure? Surgery 128:822–31.

Troppmann C 2010 Complications after pancreas transplantation. Curr Opin Organ Transplant 15:112–18.

Tsutsumi M, Arakawa T, Terashima T et al 2014 Morphological analysis of the branches of the dorsal pancreatic artery and their clinical significance. Clin Anat 27:645–52.

Turrini O, Wiebke EA, Delpero JR et al 2010 Preservation of replaced or accessory right hepatic artery during pancreaticoduodenectomy for adenocarcinoma: impact on margin status and survival. J Gastrointest Surg 14:1813–9.

White SA, Shaw JA, Sutherland DE 2009 Pancreas transplantation. Lancet 373:1808–17.

Woodburne RT, Olsen LL 1951 The arteries of the pancreas. Anat Rec 111:255–70.

One of the earliest comprehensive reviews of pancreatic arterial anatomy.

Wu ZX, Yang XZ, Cai JQ et al 2011 Digital subtraction angiography and computed tomography angiography of predominant artery feeding pancreatic body and tail. Diabetes Technol Ther 13:537–41.

Yamaguchi H, Wakiguchi S, Murakami G et al 2001 Blood supply to the duodenal papilla and the communicating artery between the anterior and posterior pancreaticoduodenal arterial arcades. J Hepatobil Pancreat Surg 8:238–44.

Yeo TP, Hruban RH, Leach SD et al 2002 Pancreatic cancer. Curr Probl Cancer 26:176–275.

Yoshioka H, Wakabayashi T 1958 Therapeutic neurotomy on head of pancreas for relief of pain due to chronic pancreatitis. Arch Surg 76: 546–54.

Zuo HD, Zhang XM, Li CJ et al 2012 CT and MR imaging patterns for pancreatic carcinoma invading the extrapancreatic neural plexus (Part I): anatomy, imaging of the extrapancreatic nerve. World J Radiol 4:36–43.

CHAPTER

69

Spleen

The spleen is a large, encapsulated, complex mass of vascular and lymphoid tissues situated in the upper left quadrant of the abdominal cavity between the fundus of the stomach and the respiratory diaphragm. It is mainly concerned with phagocytosis and immune responses but is also important in immunological defence, metabolism and maintenance of circulating blood elements (Steiniger 2015, Tarantino et al 2013; **Table 69.1**). In the fetus, the spleen is a major site of haemopoiesis and can resume this role postnatally in certain pathological conditions (Üngör et al 2007). However, it is not essential for life; if the spleen is removed, many of its functions can be assumed by the liver and other tissues of the mononuclear phagocytic system.

Gross anatomy

The size and weight of the spleen vary with age and sex, and can also vary slightly in the same individual under different conditions. The adult spleen is usually 9–14 cm long, 6–8 cm wide and 3–5 cm thick. It reaches its largest dimension in puberty and diminishes in size thereafter (DeLand 1970, Sprogøe-Jakobsen and Sprogøe-Jakobsen 1997). Although its weight increases during puberty, it is comparatively largest in the young child and tends to diminish in size and weight in old age (Skandalakis et al 1993, Üngör et al 2007, Coquet et al 2010). The average weight of an adult spleen depends on the volume of blood it contains; emptied of blood it weighs between 70 and 120 g, whereas *in vivo* its weight ranges from 150 to 350 g (Nakamura et al 1989, Skandalakis et al 1993, Petroianu 2011).

TABLE 69.1 Summary of splenic functions

General functions	Specific functions
Haematological and immunological	Haemopoiesis
	Maturation of blood elements
	Immunoglobulin activation
	Recirculation of T and B lymphocytes
Production	Leukocytes
	Peptides
	Immunoglobulins (mainly IgM)
	Opsonins
	Tuftsin
	Properdin
	Complement factors
	Stem cells
Storage	Leukocytes, e.g. monocytes, B and T lymphocytes
	Platelets
	All metals
Clearance	Microorganisms
	Parasites
	Circulating antigens
	Altered circulating cells
	Circulating foreign bodies
Synthesis	Precursor of hepatic functions
Metabolism	Lipids
	Cholesterol
	Bilirubin
	Amino acids
Control	Bone marrow
	Mononuclear phagocytic function
	Somatic growth

The shape of the spleen is also variable: it is mostly determined by its relations to neighbouring structures during development and often appears as a slightly curved wedge. The superolateral aspect is covered by the respiratory diaphragm and the inferomedial aspect mostly by the neighbouring stomach, left kidney and left colic flexure. In the fetus, the spleen is lobulated (Ch. 21); the adult spleen usually retains a notch(es) on its superior border, although additional surface notches can persist (Mikhail et al 1979). In a study of 113 post mortem, i.e. unfixed, specimens, Parsons (1901) observed 1–7 splenic notches in over 90% of specimens; two notches were the most common finding and the majority were located on the superior border of the spleen.

A splenic lobule that fails to coalesce with the developing spleen can persist as an accessory (supernumerary) spleen. This fully functional island of splenic tissue is found in approximately 14% of individuals and may be located in any part of the abdomen, or even outside it, but is most commonly present near the splenic hilum within the gastrosplenic ligament or greater omentum (Faller 1985, Vikse et al 2017; **Fig. 69.1**). Other anatomical variations of the spleen include asplenia, hyposplenia, and splenogonadal and splenopancreatic fusions.

A normal adult spleen is not palpable on abdominal examination and has to triple in size before it becomes palpable below the left costal arch (Mikhail et al 1979). In supine healthy adults it is most frequently located between the tenth and twelfth ribs, with its long axis along the eleventh rib (Gupta et al 1976, Mirjalili et al 2012).

Relations

The spleen has superolateral diaphragmatic and inferomedial visceral surfaces (**Fig. 69.2**), superior and inferior borders, and anterior and posterior extremities. The convex, smooth diaphragmatic surface faces mostly superiorly and laterally. The diaphragmatic surface is separated from the left costodiaphragmatic recess, lower lobe of the left lung and the left tenth to twelfth ribs by the underside of the respiratory diaphragm (**Figs 69.3–69.4**).

The visceral surface is irregular, faces inferomedially towards the abdominal cavity and is marked by gastric, renal and colic impressions. A pancreatic impression is sometimes present. Michels (1942) found that the tail of the pancreas contacts the spleen in approximately one-third of individuals. The gastric impression faces anteromedially and is broad and concave where the spleen lies adjacent to the posterior aspect of the fundus, upper body and upper greater curvature of the stomach. It is separated from the stomach by a peritoneal recess, limited by the gastrosplenic ligament. The renal impression is slightly concave and lies on the posteroinferior part of the visceral surface, separated from the gastric impression above by a ridge of splenic tissue and the splenic hilum. It faces inferomedially and slightly backwards and is related to the upper lateral area of the anterior surface of the left kidney and sometimes to the superior border of the left suprarenal gland. The colic impression is usually flat; it lies at the anterior extremity of the spleen and is related to the left colic flexure and the phrenicocolic ligament. The splenic hilum is a long fissure pierced by the splenic vessels, nerves and lymphatics, and lies on the visceral surface closer to the inferior border.

The superior border separates the diaphragmatic surface from the gastric impression and is usually convex. The inferior border separates the renal impression from the diaphragmatic surface and is more rounded and blunt than the superior border. The posterior extremity usually faces the vertebral column. The anterior extremity is longer and less angulated than the posterior extremity and connects the superior and inferior borders anteriorly; it is related to the colic impression and often lies adjacent to the left colic flexure and phrenicocolic ligament.

The anterior extremity of the spleen is particularly at risk of injury from blunt abdominal trauma or during surgical procedures on the stomach, tail of the pancreas, left kidney, left suprarenal gland and

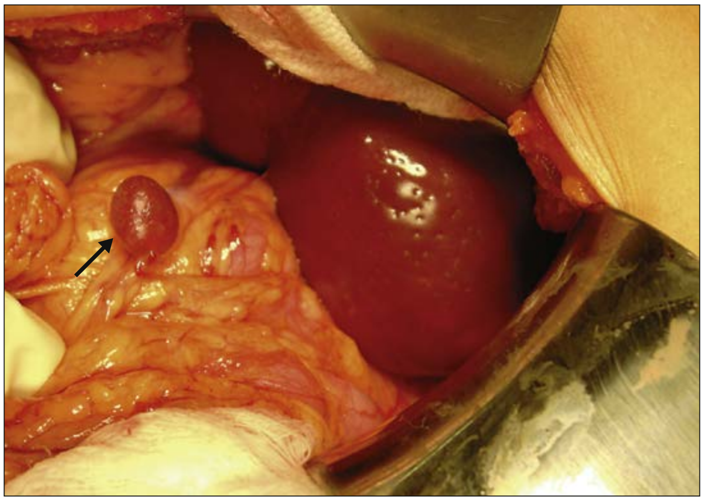

Fig. 69.1 A supernumerary spleen located in the greater omentum (arrow). Supernumerary spleens are usually isolated and may be connected to the spleen or splenic pedicle by thin vessels.

The most common clinical manifestations of splenic disorders are splenomegaly and a decrease in the number of cellular elements in the blood (cytopenias). The most serious long-term consequence of removal of the spleen is severe sepsis. One study of children who underwent splenectomy found that 7% were hospitalized for sepsis and 38% of these occurred within the first year following the procedure (Madenci et al 2018).

Spleens in men are proportionally heavier than those in women. In pathological conditions, the spleen may expand and retain blood; weights rarely exceed 700 g, but gigantic spleens exceeding 10 kg have been reported (DeLand 1970, Skandalakis et al 1993, Sprogøe-Jakobsen and Sprogøe-Jakobsen 1997). Splenomegaly compresses and displaces adjacent organs, causing abdominal discomfort, dyspepsia, respiratory restriction and difficulty walking (Coetzee 1982, Petroianu 2011).

colon. Excessive traction of the stomach, transverse colon or greater omentum can tear the splenic fibrous capsule and superficial parenchyma by way of their peritoneal attachments, causing bleeding that can be difficult to control (Merchea et al 2012).

Splenic ligaments

The spleen develops between the two leaves of the dorsal mesogastrium (see Figs 21.6–21.7) and so it is almost entirely invested in visceral peritoneum that is firmly adherent to its fibrous capsule (Üngör et al 2007). The dorsal mesogastric attachments persist as peritoneal ligaments. The superior part of the splenic hilum is connected to the stomach via the gastrosplenic ligament, and to the posterior abdominal wall by a variably developed phrenicosplenic ligament. A presplenic fold connecting the spleen to the stomach is sometimes seen anterior to the gastrosplenic ligament and may contain the left gastro-omental (gastro-epiploic) vessels (Skandalakis et al 2004). The inferior part of the splenic hilum is further connected to the posterior abdominal wall by the splenorenal ligament and to the left colic flexure by the splenocolic ligament. A spleno-omental fold may connect the spleen to the greater omentum: this is known as the ‘criminal’ fold of Morgenstern because careless surgical traction on it can traumatize the spleen (Skandalakis et al 2004). Each of these ligaments is made up of two layers of peritoneum containing fat, blood and lymphatic vessels and nerves. The phrenicosplenic ligament runs between the spleen and the peritoneum covering the undersurface of the respiratory diaphragm. The anterior layer of the splenorenal ligament is continuous with the

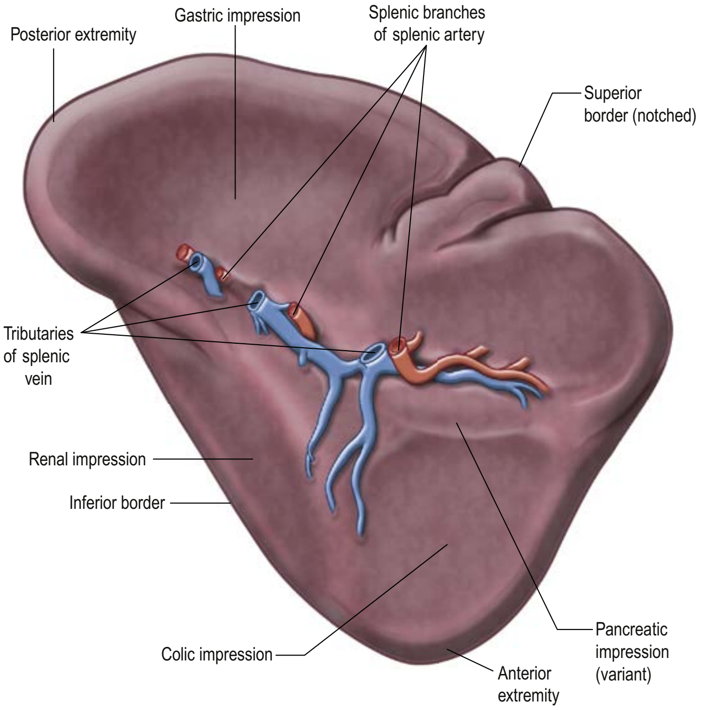
Posterior extremity
Gastric impression
Splenic branches of splenic artery
Superior border (notched)
Tributaries of splenic vein
Renal impression
Inferior border
Colic impression
Anterior extremity
Pancreatic impression (variant)

Fig. 69.2 The visceral surface of the spleen.

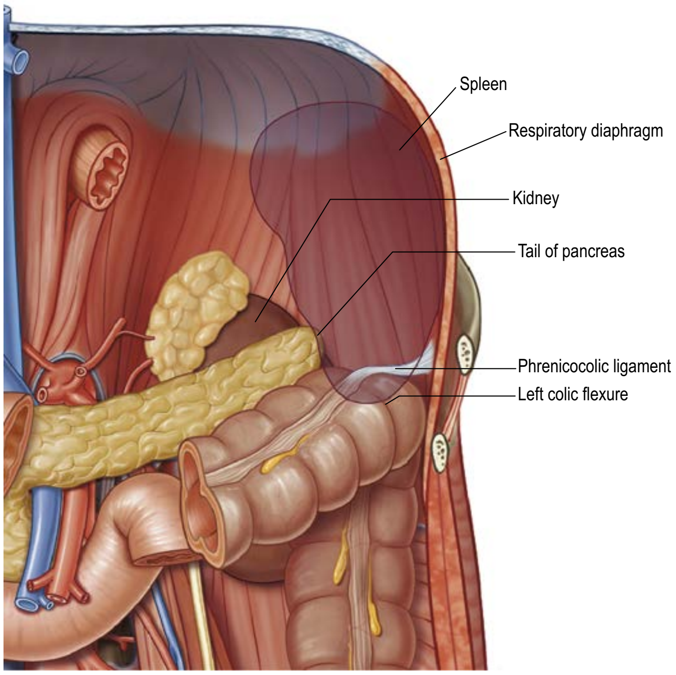
Spleen
Respiratory diaphragm
Kidney
Tail of pancreas
Phrenicocolic ligament
Left colic flexure

Fig. 69.3 The posterior relations of the spleen. (Adapted from Drake RL, Vogl AW, Mitchell A (eds) Gray’s Anatomy for Students, 2nd ed. Elsevier, Churchill Livingstone. Copyright 2010.)

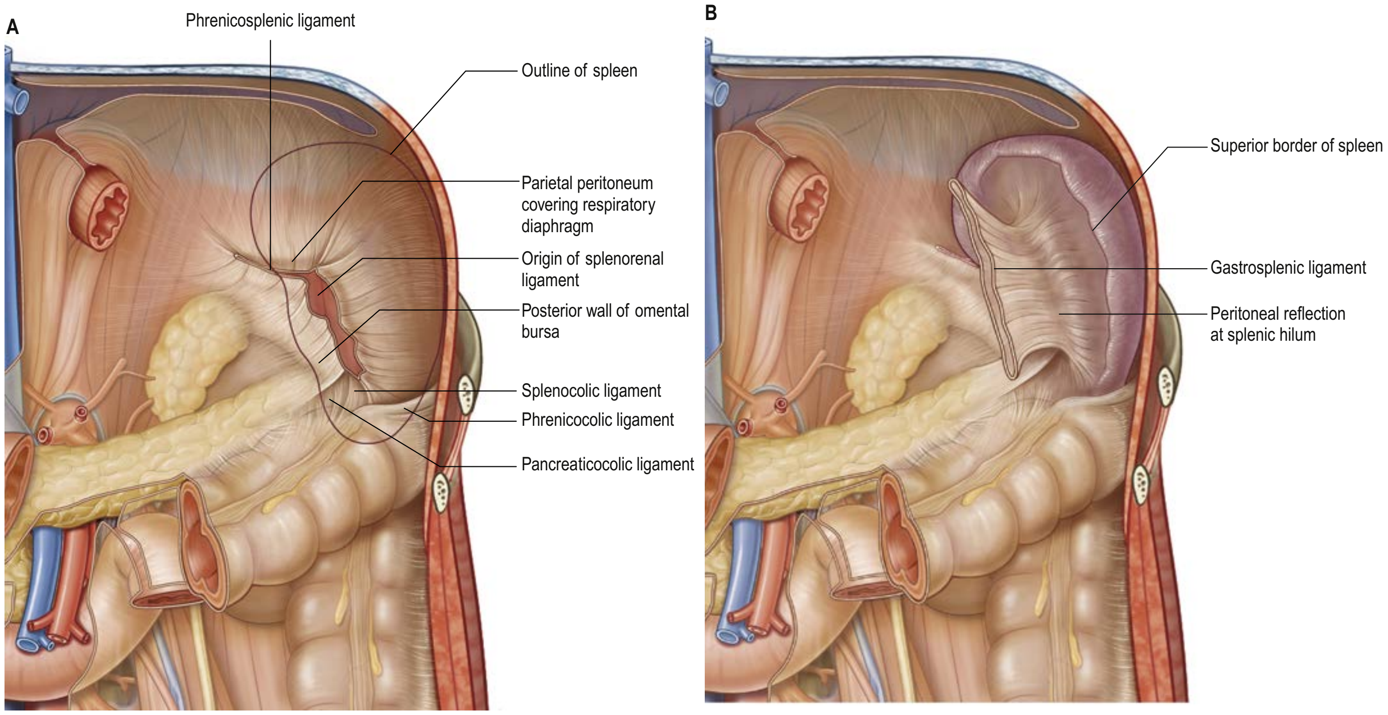
A
Phrenicosplenic ligament
Outline of spleen
Parietal peritoneum covering respiratory diaphragm
Origin of splenorenal ligament
Posterior wall of omental bursa
Splenocolic ligament
Phrenicocolic ligament
Pancreaticocolic ligament
B
Superior border of spleen
Gastrosplenic ligament
Peritoneal reflection at splenic hilum

Fig. 69.4 The peritoneal connections of the spleen. **A**, The posterior peritoneal connections, seen as if the spleen has been removed, with the folds fixed in their ‘normal’ positions. **B**, The anterior peritoneal connections, seen with the spleen in place, as if the stomach and greater omentum have been removed, with the folds fixed in their ‘normal’ positions. (Adapted from Drake RL, Vogl AW, Mitchell A (eds) Gray’s Anatomy for Students, 2nd ed. Elsevier, Churchill Livingstone. Copyright 2010.)

peritoneum of the posterior wall of the omental bursa over the left kidney, and with the posterior layer of the gastrosplenic ligament at the splenic hilum. The posterior layer of the splenorenal ligament is continuous with the peritoneum over the inferior surface of the respiratory diaphragm and anterior surface of the left kidney. The terminal portions of the splenic artery and vein, and, more inferiorly, the tail of the pancreas, lie between the two peritoneal layers of the splenorenal ligament. The tail of the pancreas can be injured during dissection when ligating and dividing the splenic vessels, resulting in bleeding, local pancreatitis and pancreatic fistula formation (Skandalakis et al 1993).

The gastrosplenic ligament is continuous with the fibrous capsule of the spleen, the serosa of the stomach and the greater omentum. It contains the short gastric artery and its branches and the left gastro-omental artery, all of which arise from the splenic artery, together with their corresponding veins. During splenectomy or mobilization of the fundus of the stomach, the short gastric vessels must not be ligated too close to the stomach because there is a risk of local gastric necrosis, perforation and their consequences.

The phrenicocolic ligament connects the left colic flexure to the respiratory diaphragm and runs inferior and lateral to the anterior extremity of the spleen (see Fig. 69.4). It is continuous with the peritoneum of the left lateral end of the transverse mesocolon at the end of the tail of pancreas, and the splenorenal ligament at the splenic hilum (Merchea et al 2012, Skandalakis et al 1993). When the phrenicocolic ligament is being divided, particularly when electrocautery is used, the colon is at risk of injury.

Mobile spleen

Available with the *Gray's Anatomy* e-book

Vascular supply and lymphatic drainage

Arteries

The spleen is supplied by the splenic artery, one of the most tortuous arteries in the body (**Fig. 69.5**, see Figs 63.10, 63.14B, 69.6). The reason for the tortuosity, which can become more pronounced with advancing age, is not understood, although there have been several proposals (Cortés and Pellico 1988, García-Porrero and Lemes 1988, Borley et al 1995, Sylvester et al 1995, Liu et al 1996, Pandey et al 2004). The splenic artery almost always arises from the coeliac trunk, in common with the left gastric and common hepatic arteries. However, it can originate from the common hepatic artery or the left gastric artery, or, rarely, directly from the abdominal aorta either in isolation or as a splenomesenteric trunk (Tubbs et al 2016).

From its origin, the artery runs a little way inferiorly before turning to the left behind the stomach to run horizontally posterior to the superior border of the body and tail of the pancreas. Multiple loops or even coils of the artery appear above the superior border of the pancreas (McFee et al 1995, Pandey et al 2004). The splenic artery courses anterior to the left kidney and left suprarenal gland and runs in the splenorenal ligament behind or above the tail of the pancreas. In its course it gives off numerous branches to the pancreas (dorsal pancreatic, great pancreatic artery, and artery to the tail of the pancreas) and, near its termination, it gives off the short gastric arteries and the left gastro-omental artery (Skandalakis et al 1993). Additional variant branches include a posterior gastric artery and small retroperitoneal branches.

The splenic artery is 8–32 cm long and its calibre usually exceeds that of the common hepatic and left gastric arteries, ranging from 3 to 12 mm. Splenic arterial blood flow is approximately 3 ml/sec/100 g, corresponding to approximately 7% of cardiac output (Trubel et al 1985, Cortés and Pellico 1988, García-Porrero and Lemes 1988, Nakamura et al 1989, Skandalakis et al 1993, Pandey et al 2004).

The splenic artery usually divides into two, or occasionally three, branches before entering the splenic hilum. The superior and inferior branches are sometimes known as superior and inferior polar arteries; as they enter the hilum they divide into four or five segmental arteries, each of which supplies a segment of splenic tissue. There is relatively little arterial collateral circulation between segments, which means that occlusion of a segmental vessel often leads to infarction of part of the spleen. Segmental arteries divide within the splenic trabeculae, becoming trabecular arteries. These leave the trabeculae and give rise to central arterioles that are surrounded by thick lymphoid sheaths of white pulp. Central arterioles ramify into several penicillar arterioles that feed the sinusoids of the red pulp. There is considerable communication among arterioles (Mikhail et al 1979, García-Porrero and Lemes 1988, Trubel et al 1988, Sow et al 1991, Liu et al 1996).

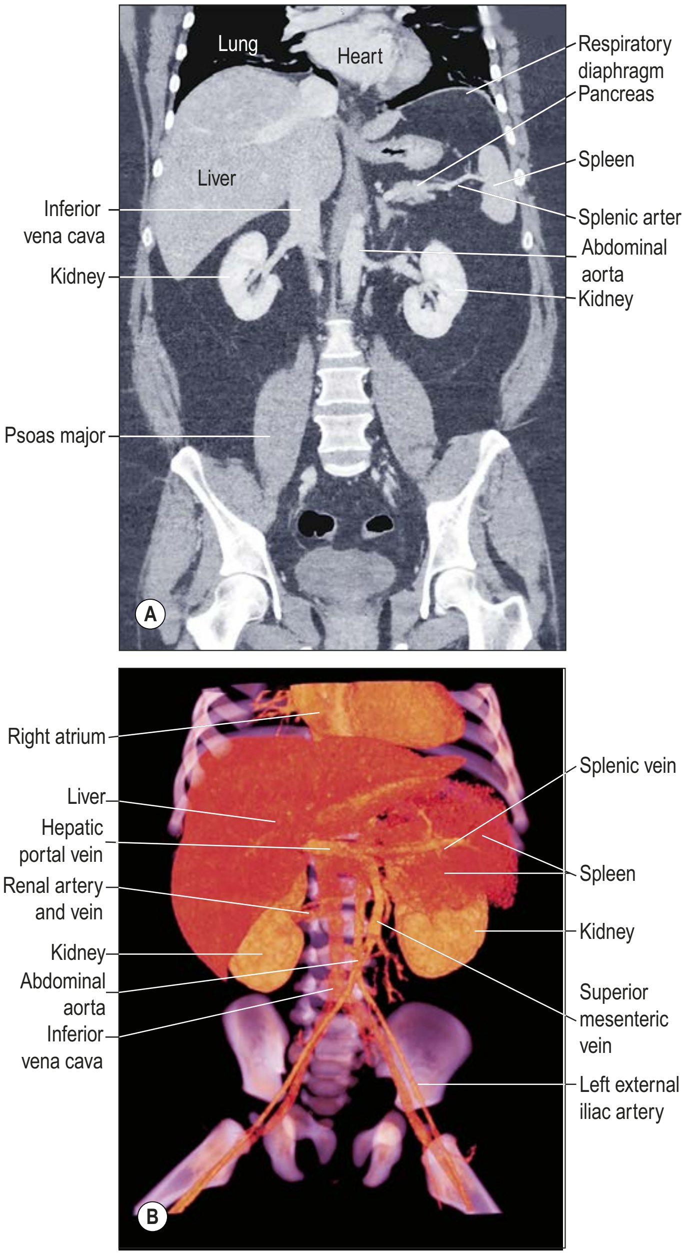

Fig. 69.5 **A**, Coronal MRI of an adult female: note the spleen and splenic artery. **B**, Volume-rendered abdominal angiogram from a paediatric patient showing the spleen and splenic vein. Note the unfused segments of the sacrum and juvenile forms of the hip and parts of the pelvic girdle. (Courtesy of Jon C Betts Jr, Children's of Alabama, Birmingham, AL, USA.)

The short gastric arteries in the gastrosplenic ligament provide an additional arterial supply to the posterior extremity of the spleen that is distinct from the splenic hilar vessels. These short gastric vessels connect the posterior extremity of the spleen to the fundus of the stomach and preserve the viability of this region of the spleen after surgical ligation of the splenic pedicle (Skandalakis et al 1993).

Veins

Blood from the spleen is collected by trabecular veins that join to form the segmental veins draining individual splenic segments. In general, there are no anastomoses between intrasegmental venous tributaries. The segmental veins join to form two (superior and inferior) or three (superior, middle and inferior) 'lobar' veins that emerge from the length of the splenic hilum and unite to form the splenic vein within the splenorenal ligament (see Fig. 69.2). Communicating veins may interconnect lobar veins (Par et al 1965, DeLand 1970, Gupta et al 1980, Sow et al 1991, Liu et al 1996).

The splenic vein most commonly runs posterior to the splenic artery and tail and body of the pancreas (Skandalakis et al 2004) (see Figs 68.4D–G, 69.5, 69.6) (Par et al 1965, Gürleyik et al 2000). It crosses the posterior abdominal wall anterior to the left kidney and abdominal aorta, separated from the left sympathetic trunk and left crus of the respiratory diaphragm by the left renal vessels, and from the abdominal aorta by the

Operating on a normal-sized spleen is a relatively straightforward procedure for most surgeons. Mobilization of the spleen requires division of the phrenicocolic, gastrosplenic and phrenicosplenic ligaments. Undue traction on the phrenicocolic ligament during mobilization of the left colic flexure can tear the splenic fibrous capsule, causing bleeding: this is less likely if the phrenicocolic ligament is retracted laterally rather than inferiorly and medially (Merchea et al 2012). The diaphragmatic surface of the spleen is occasionally adherent to the peritoneum on the undersurface of the respiratory diaphragm: adhesions can be a consequence of inflammation of the spleen or may be congenital (Skandalakis et al 1993, Petroianu 2011).

The peritoneal ligaments associated with the spleen vary in length; longer ligaments, especially the splenorenal ligament, afford the spleen greater mobility, and can stretch its vascular pedicle. While this facilitates surgical mobilization, it can render the spleen more susceptible to injury from shear forces during trauma.

A floating or wandering spleen is characterized by excessive mobility and migration of the spleen outside the left hypochondriac region. In such cases, the spleen can undergo torsion or cause urinary bladder or rectal symptoms from local pressure; imaging usually confirms the diagnosis. If surgical treatment is necessary, the spleen is freed from local adhesions and returned to the left hypochondriac region, the surgeon shortening and suturing its ligaments to the respiratory diaphragm (McFee et al 1995, Petroianu 2011).

superior mesenteric artery and left renal vein (Par et al 1965, Gupta et al 1976, Gupta et al 1980, Liu et al 1996). It ends posterior to the neck of the pancreas, where it joins the superior mesenteric vein to form the hepatic portal vein. Along its course it receives the short gastric veins, left gastro-omental veins, pancreatic veins, posterior gastric vein, left gastric vein and inferior mesenteric veins (the latter two do so in approximately 30% of individuals (Gerber et al 1951)). Anastomoses between the splenic vein and left renal vein have been reported, particularly in cases of portal hypertension (Bowdler 2002). Approximately 60% of hepatic portal vein blood flow is derived from the gut and the remainder from the spleen and pancreas (Par et al 1965, Gupta et al 1980, Dawson et al 1986, Oguro et al 1993, Liu et al 1996, Gürleyik et al 2000). Obstruction of the hepatic portal or splenic veins can lead to reversed venous flow through the splenic vein and its tributaries, resulting in splenomegaly and widespread varices (Re et al 1985, Skandalakis et al 1993, Petroianu 2011).

Lymphatic drainage

The lymphatic drainage of the spleen begins with the peri-arteriolar lymphoid sheaths (PALS) in the white pulp. The lymphatic vessels run toward the splenic hilum along trabecular arteries in the trabeculae, and then flow into the lymph nodes at the hilum. The lymphatic vessels from the subcapsular plexus also flow to the lymph nodes at the splenic hilum (**Fig. 69.6**). From there lymph drains to superior pancreatic, inferior pancreatic and pancreaticoduodenal nodes, and from there to coeliac nodes and the cisterna chyli (Bowdler 2002). There are no lymphatic vessels in the red pulp.

In malignant neoplasms of the greater curvature of the stomach, pancreas or distal transverse colon, it may be necessary to remove the spleen and tail of the pancreas to achieve a radical resection. In leukaemias and lymphomas, lymphadenopathy of splenic nodes and splenomegaly may be found during staging investigations (Petroianu 2011).

Innervation

The spleen is innervated by both components of the autonomic nervous system; the sympathetic supply is dominant. Postganglionic sympathetic nerves from the coeliac plexus travel with the splenic vessels. They innervate arteries at least to the trabecular level and have the potential to influence blood flow within the human spleen (Kudoh et al 1979). Parasympathetic nerves from the posterior vagal trunk may travel with the splenic vessels to the spleen, but this innervation has been questioned (Skandalakis et al 2004, Martelli et al 2014, Jung et al 2017). In contrast to some animals, the motor innervation of the human splenic fibrous capsule is largely vestigial: the fibrous capsule contains minimal quantities of smooth muscle and therefore does not contract. However, the fibrous capsule and parenchyma are innervated by sensory fibres that convey pain. Mild to moderate splenomegaly is often painless but splenic inflammation from infection, infarction,

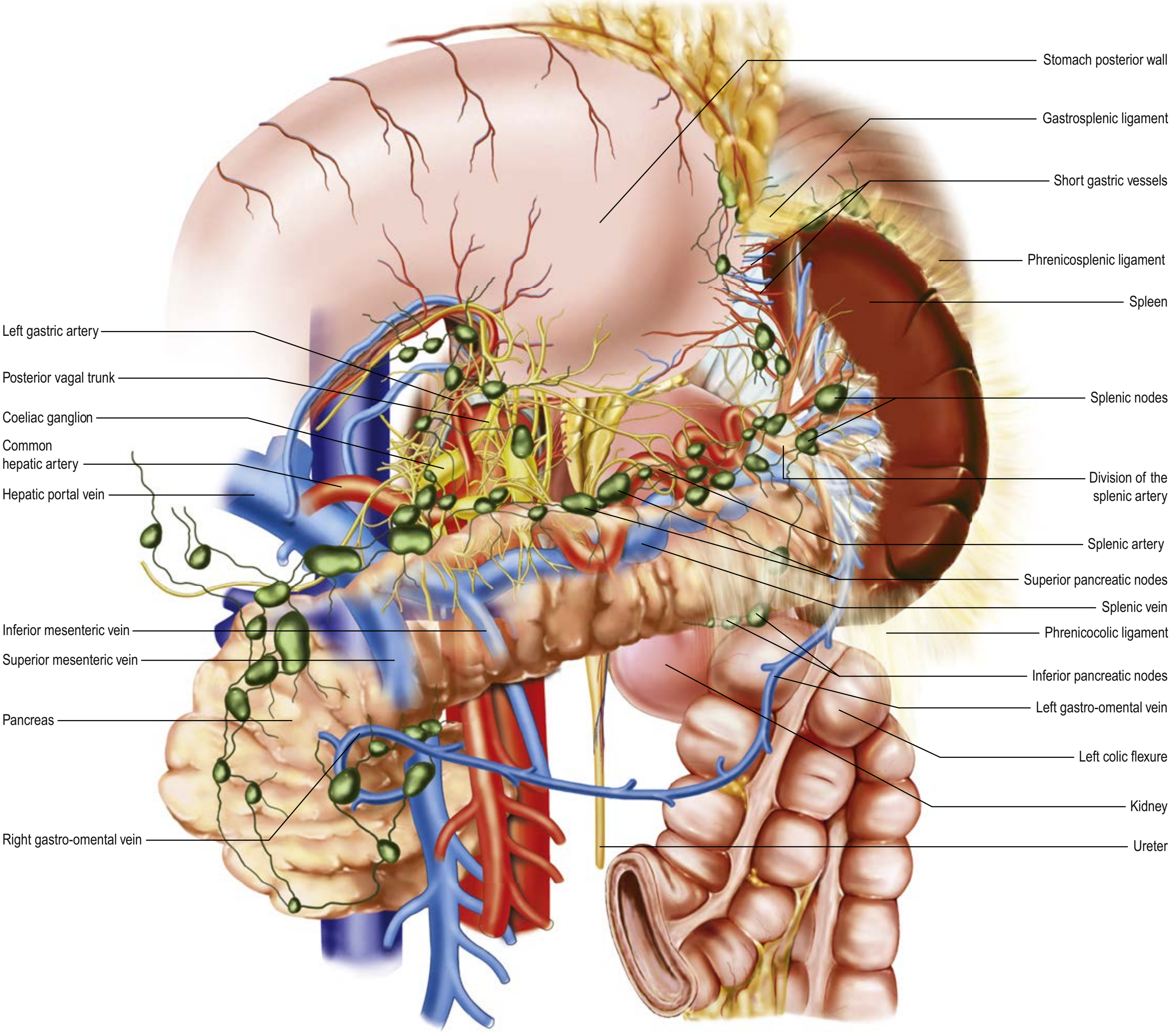
Stomach posterior wall
Gastrosplenic ligament
Short gastric vessels
Phrenicosplenic ligament
Spleen
Left gastric artery
Posterior vagal trunk
Coeliac ganglion
Common hepatic artery
Hepatic portal vein
Splenic nodes
Division of the splenic artery
Splenic artery
Superior pancreatic nodes
Splenic vein
Inferior mesenteric vein
Superior mesenteric vein
Phrenicocolic ligament
Inferior pancreatic nodes
Left gastro-omental vein
Pancreas
Left colic flexure
Kidney
Right gastro-omental vein
Ureter

Fig. 69.6 The lymph nodes related to the spleen. The pancreas has been rendered partially transparent to visualise the major blood vessels lying posteriorly. The greater curvature of the stomach has been reflected superiorly to expose its posterior surface and the posterior wall of the omental bursa has been removed. (Courtesy of Dr Andy Petroianu and Dr Iriam Starling.)

sickle cell disease, splenic artery embolization or abrupt distension of the fibrous capsule (e.g. haematoma) can cause severe pain, intensified by inflammation of the overlying parietal peritoneum. Referred pain from the splenic parenchyma is poorly localized to the epigastric region.

Microstructure

The spleen contains the largest single mass of lymphoid tissue in the body in direct continuity with the circulation. Splenic parenchyma is divided into two principal regions, white pulp and red pulp, named according to the appearance of the cut surface of a fresh spleen (**Fig. 69.7**). The microstructure of the spleen has been studied in many animals, most extensively in rats, mice and humans. However, species-specific differences have caused some terminological confusion when describing what are probably functionally equivalent zones: for example, the human spleen does not appear to contain large marginal or perimarginal sinuses or ellipsoids (although macrophage-sheathed capillaries may be equivalent to ellipsoids), and the so-called marginal zones (a B-cell compartment between red and white pulps) are arranged differently in rodent and human spleens. In humans, white pulp contains accumulations of T and B lymphocytes in periarteriolar lymphatic sheaths (PALS) and lymphatic follicles. Red pulp is a loose connective tissue containing many different types of blood cell, arterioles and macrophage sheathed capillaries, the latter consisting mainly of endothelial cells, pericytes, CD271$^+$ stromal capillary sheath cells of varying phenotype (CD271 is the low affinity nerve growth factor receptor p75), CD68$^+$CD163$^-$ macrophages and recirculating B lymphocytes (Steiniger 2015).

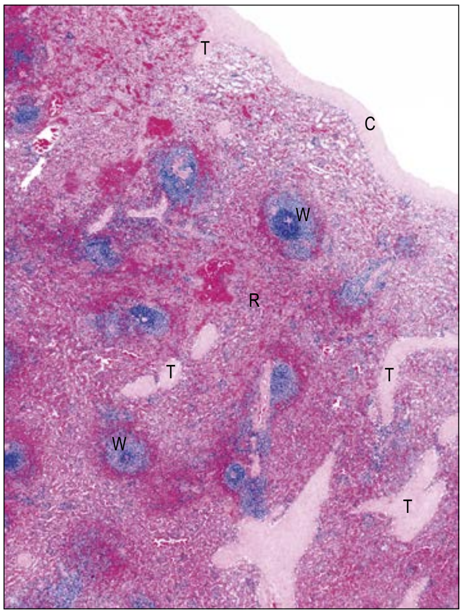

Fig. 69.7 A section through the spleen. White pulp (W) is present as ovoid areas of basophilic tissue. Red pulp (R) lies between white pulp tissue and consists of splenic sinusoids and intervening cellular cords. Part of the fibrous capsule (C) is seen top right, from which trabeculae (T) extend into the splenic tissue. (Courtesy of Mr Peter Helliwell and the late Dr Joseph Mathew, Department of Histopathology, Royal Cornwall Hospitals Trust, UK.)

Fibrous framework

The serosa of the peritoneum covers the entire spleen, except at its hilum and where the peritoneal ligaments are attached. The connective tissue fibrous capsule, deep to the serosa, is approximately 1.5 mm thick and contains abundant type I collagen fibres and some elastin fibres. It consists of an outer and inner lamina in which the directions of the collagen fibres differ, so increasing its strength. Numerous trabeculae extend from the fibrous capsule into the substance of the spleen, where they branch to form a connective tissue scaffold (Faller 1985, Scothorne 1985). The largest trabeculae enter at the splenic hilum and divide into branches in the splenic pulp, providing conduits for the splenic vessels and nerves (see Fig. 69.9). Within the spleen, these branches become continuous with a delicate network of type III (reticular) collagen fibres that pervades both the red and white pulps and is maintained by fibroblasts within its interstices (Gupta et al 1976, Scothorne 1985, Krieken and Velde 1988).

White pulp

The white pulp in an adult human spleen accounts for up to 20% of the total splenic volume. Spherical lymphoid follicles form the major compartment. Branches of the splenic artery radiate out into the parenchyma from the splenic hilum, ramifying within the trabeculae. In their terminal few millimetres, their connective tissue adventitia is replaced by a sheath of T lymphocytes, the peri-arteriolar lymphoid sheath (PALS) (**Figs 69.8–69.9**). This is expanded in places by aggregations of B lymphocytes, lymphoid follicles measuring 0.25–1 mm in diameter and visible to the naked eye on the freshly cut surface of the spleen as white semi-opaque dots, in contrast to the surrounding deep reddish purple of the red pulp. Follicles are usually situated near the terminal branches of arterioles and typically protrude to one side of a vessel, which consequently appears to be eccentrically placed within the follicle. Arterioles branch laterally within follicles to form a series of parallel terminal arterioles, the penicillar (follicular) arterioles (Scothorne 1985, Krieken and Velde 1988; see Fig. 69.9).

Follicles are centres of lymphocyte aggregation and proliferation. After antigenic stimulation they become sites of intensive B cell proliferation, developing germinal centres similar to those found in lymph nodes; antigen presentation by follicular dendritic cells is involved in this process. Germinal centres regress when the stimulus abates. Follicles tend to atrophy with advancing age and may be absent in the very elderly (Scothorne 1985, Krieken and Velde 1988).

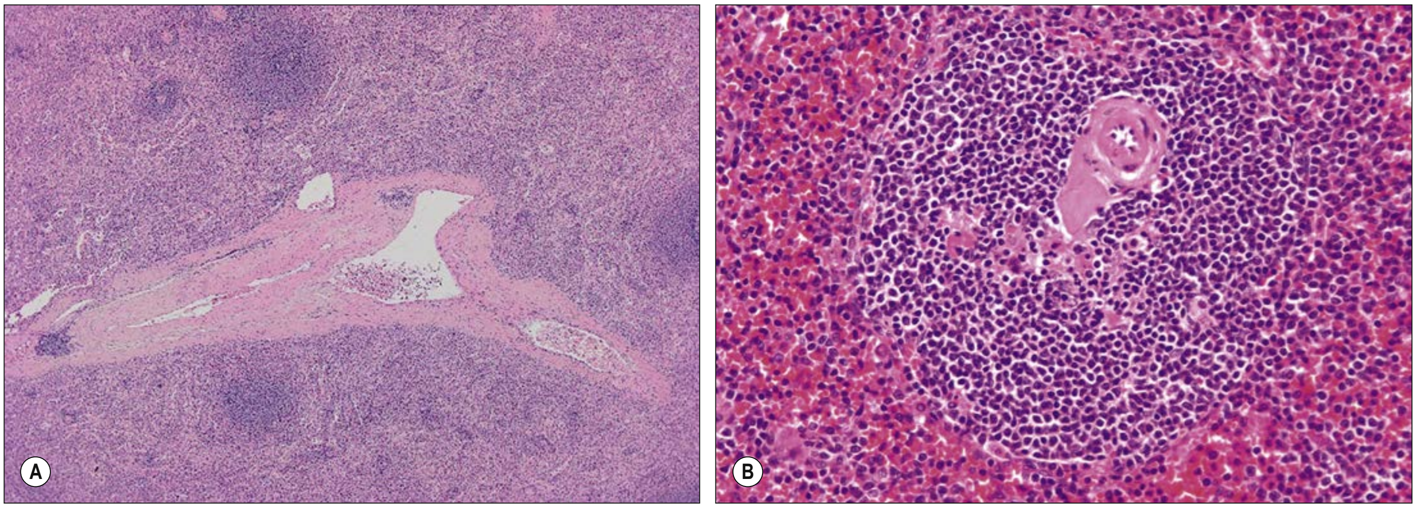

Fig. 69.8 **A**, Human spleen, showing a connective tissue trabeculum (centre field) enclosing several profiles of splenic arterioles and venules, surrounded by red pulp. Embedded in the red pulp are several white pulp follicles, seen as islands of basophilic tissue. **B**, High-power view of spleen, showing a white pulp follicle (centre) with an eccentrically placed follicular arteriole surrounded by a peri-arteriolar lymphoid sheath. Red pulp lies around the follicle. (Courtesy of Mr Peter Helliwell, Department of Histopathology, Royal Cornwall Hospitals Trust, UK.)

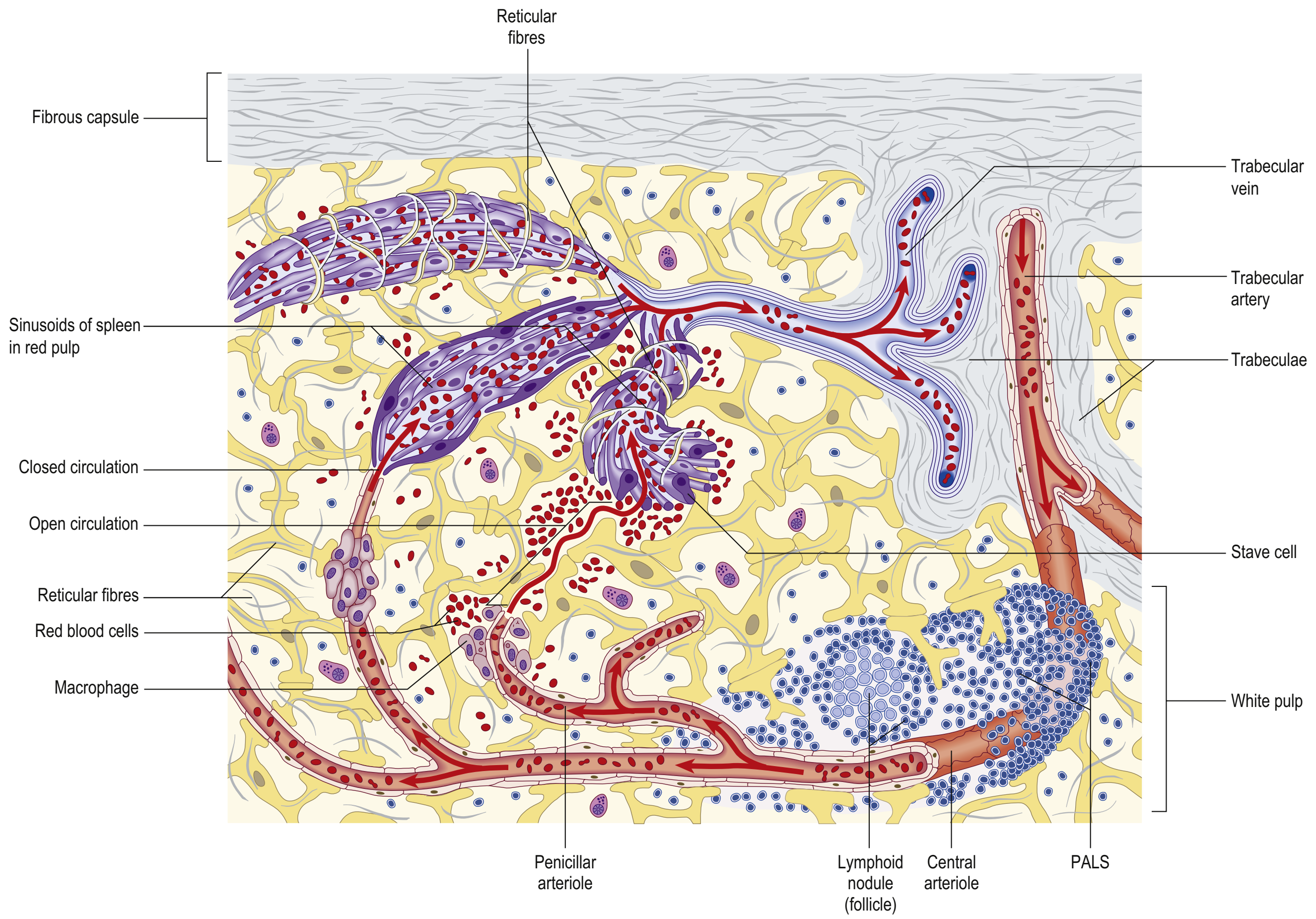

Fig. 69.9 The main features of splenic structure, not to scale. The fibrous capsule, trabeculae, reticular fibres and cells, the peri-arteriolar lymphoid sheaths and follicles (white pulp), and the cellular cords and venous sinusoids of the red pulp are shown. The 'open' and 'closed' theories of splenic circulation are illustrated: it is likely that most of the circulation is of the open form. The venous sinusoids are lined by specialized endothelial 'stave' cells; the intercellular gaps of these have been over-emphasized for clarity.

Red pulp

The red pulp constitutes approximately 75% of the total splenic volume and is a unique filtration device that enables the spleen to clear particulate material from the blood as it perfuses the organ (Scothorne 1985, Krieken and Velde 1988, Mishra 2016; see Fig. 69.7). It contains large numbers of venous sinusoids that ultimately drain into tributaries of the splenic vein. The sinusoids are separated from each other by a fibrocellular network of small bundles of collagen fibres, the reticulum, numerous reticular fibroblasts and splenic macrophages. Seen in two dimensions, these intersinusoidal regions appear as strips of tissue, the splenic cords (cords of Billroth; pulpar strands) (see Fig. 69.9), whereas in reality they form a three-dimensional continuum around the venous spaces (Chen 1978, Weiss 1983, Scothorne 1985, Krieken and Velde 1988).

Venous sinusoids are elongated ovoid vessels, approximately 50 µm in diameter, supported externally by circumferential and longitudinal reticular fibres and lined by a characteristic, discontinuous endothelium that is unique to the spleen. The long, narrow endothelial cells are aligned with the long axes of the sinusoids; previously called stave cells because of their resemblance to the planks in a barrel, they are now often called rod- or rib-shaped cells (see Fig. 69.9). These cells are attached to their neighbours at intervals along their length by short stretches of intercellular junctions that alternate with intercellular slits that allow blood cells to squeeze into the lumen of the sinusoid from the surrounding splenic cords (Pivkin et al 2016). A discontinuous basal lamina is present on the abluminal aspect of the sinus.

Large, stellate fibroblasts, reticular cells, lie around the sinusoids. They synthesize the matrix components of the reticulum, including collagen and proteoglycans, and their cytoplasmic processes help to compartmentalize the reticular space. Blood from the open ends of the capillaries that originate from penicillar arterioles percolates through the reticular spaces within the splenic cords. Macrophages in the reticular spaces remove blood-borne particulate material, including ageing and damaged erythrocytes. If the number of damaged erythrocytes increases, the reticular cells proliferate and the red pulp expands, causing the spleen to enlarge (Kudoh et al 1979, Scothorne 1985).

Perifollicular zone

The perifollicular zone lies between the follicular marginal zone and the red pulp: it is the site where blood is delivered into the red pulp and where many lymphocytes leave the circulation to migrate to their respective T and B lymphocyte aggregations in the white pulp (Steiniger et al 2001). These lymphocytes are more loosely arranged than they are in the white pulp, and are held in a dense network of reticular fibres and cells.

Splenic microcirculation

Segmental splenic arteries ramify in the trabeculae as trabecular arteries which taper to become central arterioles that pass through the white pulp and give off penicillar arterioles. These leave the white pulp and traverse the perifollicular zone to enter the red pulp, where the capillaries and sinuses at the end of the arterial tree and the beginning of the venous part of the circulation, respectively, are not connected so that blood flows in spaces delimited by fibroblasts rather than endothelial cells (Gupta et al 1976, Scothorne 1985, García-Porrero and Lemes 1988, Steiniger 2015, Steiniger et al 2018). Evidence supports a predominantly 'open' splenic circulation in humans, in which blood empties into and percolates slowly through the reticular tissue of the splenic cords before re-entering the vascular lumen through slits in the walls of the venous sinusoids (Chen 1978, Cavalli et al 1982, Pivkin et al 2016). From the venous sinusoids, blood collects in venules that unite to form small veins that run within the trabeculae and drain into segmental splenic veins (Chen 1978, Cavalli et al 1982, Scothorne 1985, Petroianu 2011).

Whether there is an alternative, 'closed' route in which blood enters the venous sinusoids directly from arterioles and capillaries in the perifollicular zone is unclear: it has been suggested that there is a totally open circulation system in the human spleen (Steiniger et al 2015). Either way, the blood is exposed to macrophages and the filtering mechanism of the spleen responsible for removing abnormal and effete cells, blood cell particles, bacteria, parasites and foreign antigens.

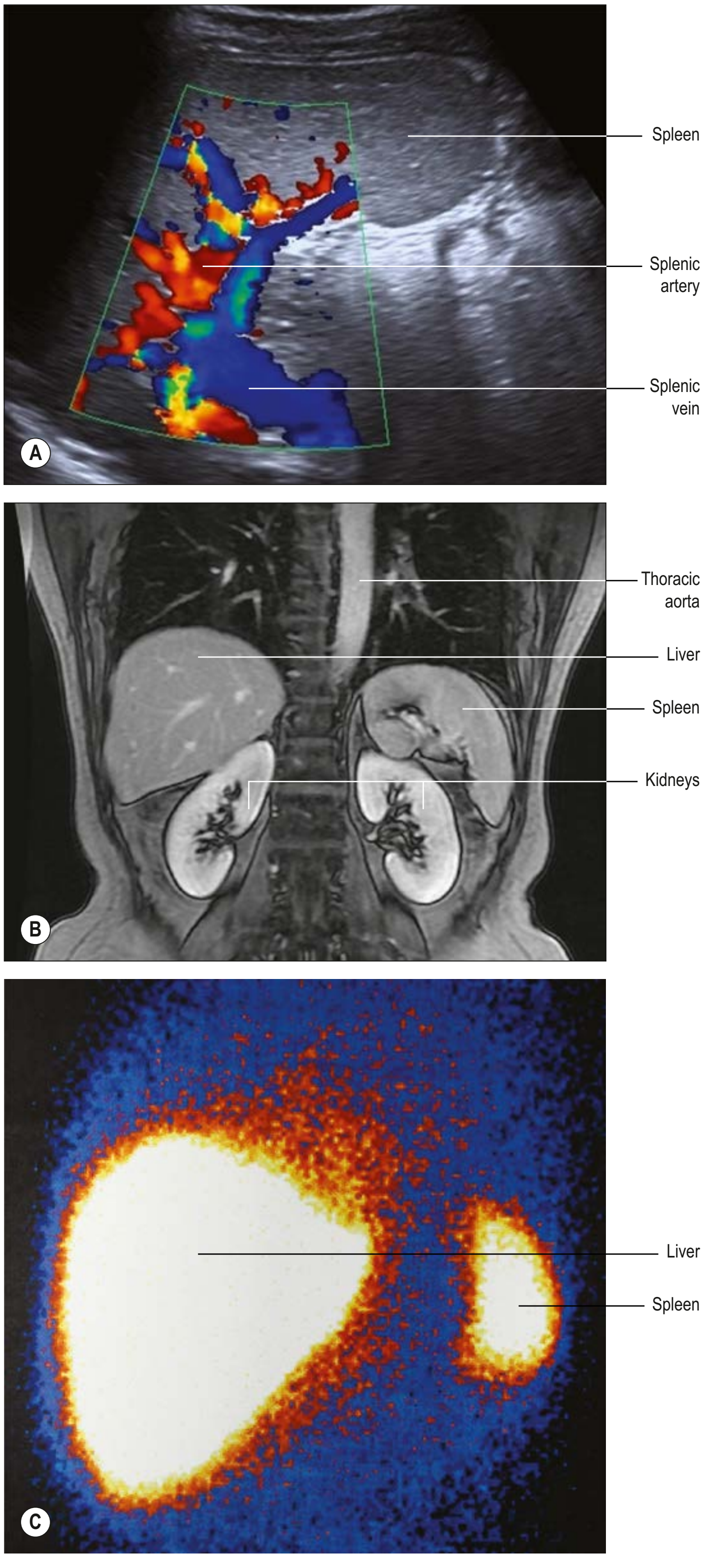

Fig. 69.10 Splenic imaging. **A**, Ultrasound with colour Doppler. **B**, Magnetic resonance image. **C**, A radioisotope scan (^{99m}Tc sulphur colloid).

Imaging

Imaging modalities used to observe the spleen include ultrasound (US), computed tomography (CT), magnetic resonance imaging (MRI), arteriography, splenoportography and scintigraphy (Buntain et al 1988, Nakamura et al 1989, Merran et al 2007, Xu et al 2009, Omar and Freeman 2016) (**Fig. 69.10**, see Fig. 69.5). Cross-sectional imaging is particularly useful for assessing tumours and infiltrations of the spleen. Percutaneous drainage of splenic and perisplenic fluid collections is routinely performed under image guidance, and percutaneous splenic biopsy is being increasingly used in diagnosis. Arteriography is essential for selective embolization and the insertion of an arterial stent to treat splenic artery aneurysms. Scintigraphy can be used to investigate splenic phagocytic function by quantifying the uptake of radioactive labelled agents (e.g. ^{99m}Technetium sulphur colloid or heat-damaged erythrocytes) (Hermann and Winkel 1977, Merran et al 2007, Xu et al 2009, Petroianu 2011).

Splenomegaly

Available with the *Gray's Anatomy* e-book

Splenic trauma

Available with the *Gray's Anatomy* e-book

Splenectomy

Available with the *Gray's Anatomy* e-book

Bonus e-book content

Fig. 69.1 A supernumerary spleen located in the greater omentum.

Fig. 69.11 Examples of different pathologies causing splenomegaly.

Fig. 69.12 Splenic trauma.

Key references

Bowdler AJ (ed) 2002 The Complete Spleen: Structure, Function, and Clinical Disorders. Totowa: Humana Press.

A revised and updated edition of Professor Anthony Bowdler's classic work, with an emphasis on splenic microvasculature, splenic functions as part of the immune system, and splenic pathologies and their management.

Coetzee T 1982 Clinical anatomy and physiology of the spleen. South Afr Med J 61:737–46.

A classic reference paper on splenic anatomy and physiology.

García-Porrero JA, Lemes A 1988 Arterial segmentation and subsegmentation in the human spleen. Acta Anat 131:276–83.

A detailed description of the relation between the arterial distribution and spleen segmentation.

Liu DL, Xia S, Xu W et al 1996 Anatomy of vasculature of 850 spleen specimens and its application in partial splenectomy. Surgery 119:27–33.

A detailed description of the vascular anatomy of the spleen and its role in surgical procedures.

Parsons FG 1901 Notches and fissures of the spleen. J Anat Physiol 35:416–27.

A sentinel paper describing the notches and fissures seen on the surface of the spleen.

Skandalakis PN, Colborn GL, Skandalakis LJ et al 1993 The surgical anatomy of the spleen. Surg Clin North Am 73:747–68.

One of the most complete descriptions of splenic anatomy.

Steiniger BS 2015 Human spleen microanatomy: why mice do not suffice. Immunology 145:334–46.

A detailed review of current knowledge regarding the microanatomy of the spleen in humans with comparative anatomy.

Tubbs RS, Shoja MM, Loukas M 2016 Bergman's Comprehensive Encyclopedia of Human Anatomic Variation. Hoboken: Wiley Blackwell.

A textbook dedicated to detailing the anatomical variations found in man.

Vikse J, Sanna B, Henry BM et al 2017 The prevalence and morphometry of an accessory spleen: a meta-analysis and systematic review of 22,487 patients. Int J Surg 45:18–28.

A meta-analysis of data documenting the prevalence, number, location and morphometry of accessory spleens.

The numerous causes of splenomegaly can be classified broadly into haematological (e.g. lymphoproliferative, myeloproliferative, erythrocyte disorders); vascular (e.g. portal hypertension); infectious (e.g. viral, bacterial, other); autoimmune; and infiltrative (e.g. storage disorders and tumours) (Cavalli et al 1982, Re et al 1985, Petroianu 1988, 2011; **Fig. 69.11**).

The spleen is one of the most frequently injured organs during blunt abdominal trauma (**Fig. 69.12**). It is particularly prone to injury during rapid deceleration or compression, and its peritoneal ligaments render it vulnerable to shearing injuries of the parenchyma and splenic vessels. Irritation of the respiratory diaphragm from splenic haemorrhage with resultant referred left shoulder pain is known as Kehr's sign. Fractures of the lower left ribs can be associated with blunt injuries and can lacerate the spleen (Buntain et al 1988). Traction on peritoneal ligaments or adhesions can lead to inadvertent tears of the splenic capsule during surgical procedures such as mobilization of the left colic flexure.

Contrast-enhanced CT imaging is particularly useful for assessing splenic trauma. Most splenic injuries from blunt abdominal trauma are successfully treated by conservative management. Extensive burst injuries with persistent bleeding or major injuries to the hilar vessels may require splenectomy but various repair techniques are available. With hilar injuries, a subtotal splenectomy, preserving the short gastric vessels and posterior extremity only, is one option. Minor intraoperative capsular tears can be controlled by the application of topical haemostatic agents and sutures, although direct suture repair is challenging because the splenic pulp is fragile. Arteriography and embolization are additional techniques that can be used to control bleeding or treat vascular lesions (Petroianu 2011).

Most surgical procedures performed on the spleen should start with ligation of the splenic artery at the superior border of the tail of the pancreas. This can be difficult in patients with portal hypertension, splenic artery aneurysm, retroperitoneal fibrosis, regional lymphadenopathy or inflammatory conditions. After splenic artery ligation, the spleen becomes softer because most of its contained blood returns to the circulation. Despite the interruption of splenic artery inflow, the posterior extremity of the spleen continues to be perfused by the short gastric arteries, and the anterior extremity may be supplied retrogradely via the left gastro-omental artery. Ligation and division of the splenic vein should be the last step before removal of the spleen to maximize autotransfusion of blood from the spleen (Petroianu et al 1989, Sow et al 1991, Skandalakis et al 1993, Petroianu and Petroianu 1994, Liu et al 1996, Petroianu 2011).

In partial or subtotal splenectomy, the vessels that supply the part of the spleen to be removed are ligated and divided close to the organ. The devascularized region turns dark blue, demarcating it from the residual viable splenic tissue; the organ is then divided in this plane (Sow et al 1991, Petroianu and Petroianu 1994, Liu et al 1996, Christo and DiDio 1997, Gürleyik et al 2000). Wedge excision leaves two flaps of splenic fibrous capsule that can be sutured or stapled to cover the remaining raw parenchyma, after suture of any visible bleeding vessels (Petroianu 1988, 1993, 2011; **Fig. 69.12B**).

If total splenectomy is required to treat splenic trauma, autotransplantation of splenic tissue into the greater omentum or mesentery of the intestines can preserve useful splenic function. Approximately 20% of the original splenic mass needs to be transplanted and venous drainage of this tissue must be to the hepatic portal venous system to maintain the metabolic and immunological functions of the splenic tissue (Oguro et al 1993, Petroianu 2011).

Total splenectomy has numerous potential consequences. Intraoperatively, bleeding or injury to the pancreas, stomach or colon can occur, while early postoperative complications include left-sided basal pulmonary atelectasis and pleural effusion; abscess in the subphrenic space; transient leukocytosis and thrombocytosis with the risk of thrombotic complications. As mentioned earlier, there is an increased risk of infection (especially from encapsulated bacteria), which can be fatal (Petroianu 2011).

Conservative management of splenic trauma and partial splenectomy now enables splenic function to be preserved in situations where splenectomy would once have been routinely performed. Furthermore, most surgical procedures on the spleen can now be performed laparoscopically, which readily affords inspection of the spleen from multiple perspectives (Sow et al 1991, Poulin and Thibaut 1993).

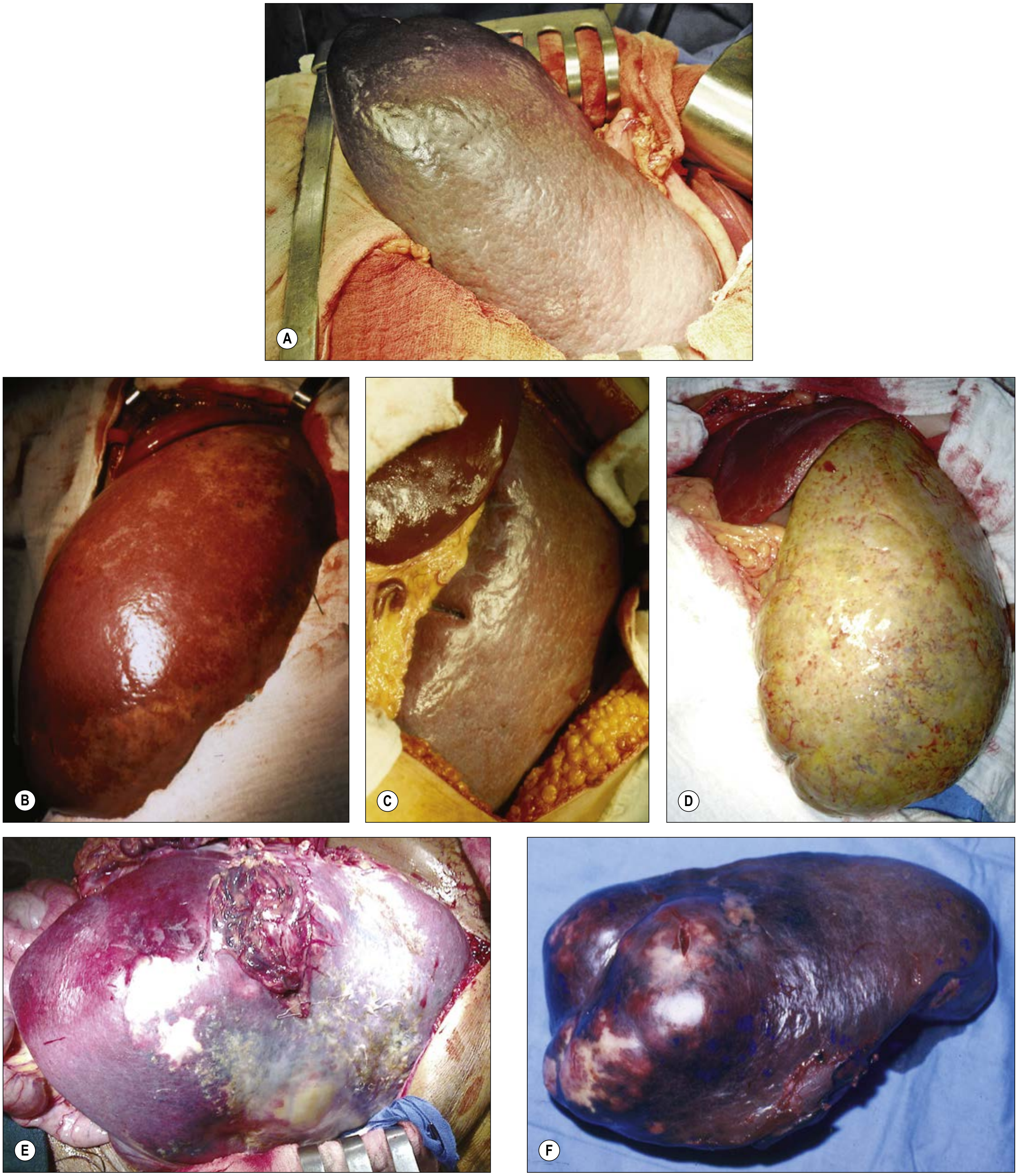

Fig. 69.11 Examples of different pathologies causing splenomegaly. **A**, Portal hypertension. **B**, Gaucher's disease. **C**, Myelofibrosis. **D**, Thalassaemia. **E**, Sarcoma. **F**, Lymphoma.

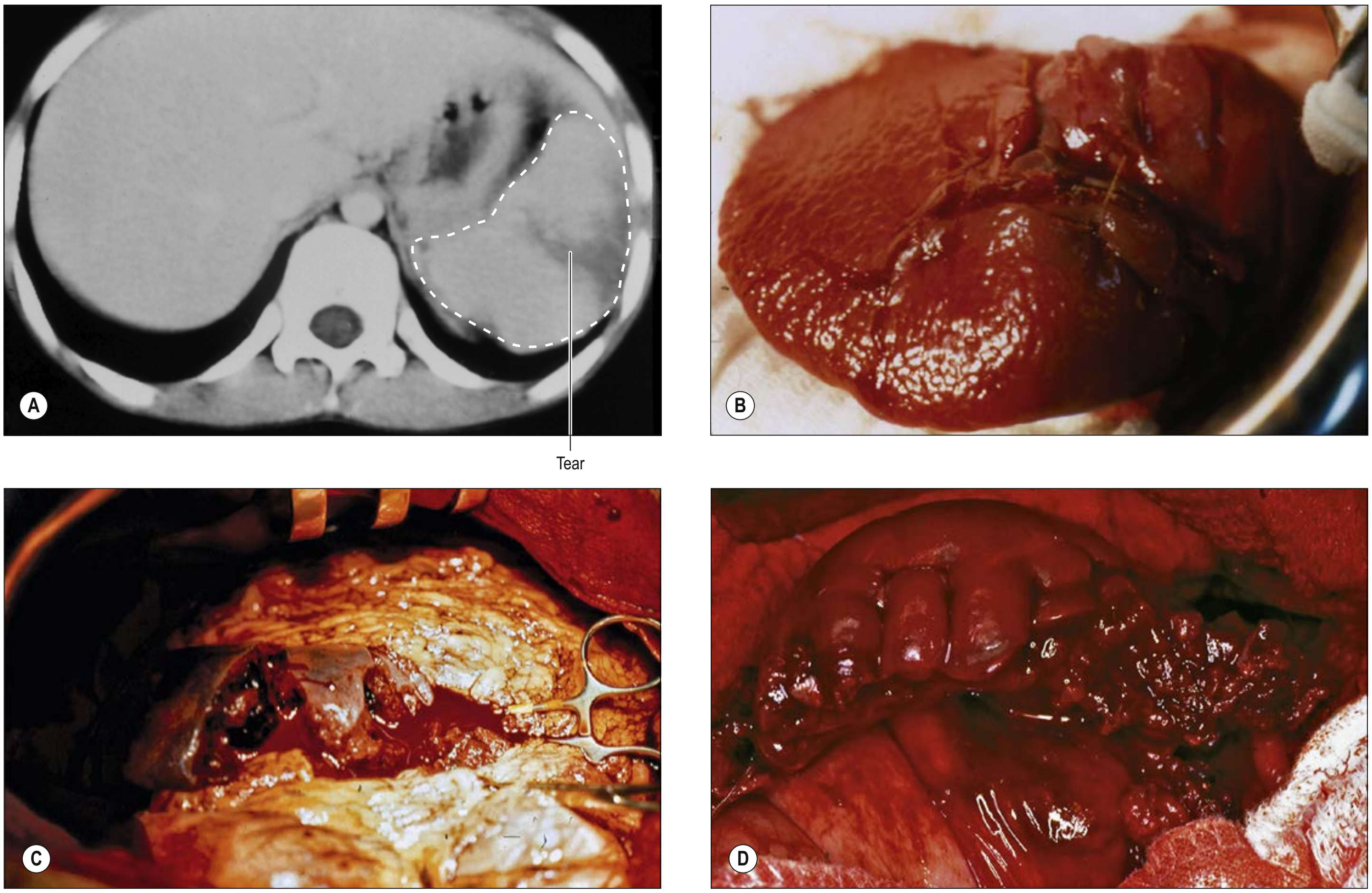

Fig. 69.12 Splenic trauma. **A**, CT showing multiple splenic tears. **B**, Suture repair of a ruptured spleen. **C**, Complete splenic rupture. The splenic hilum has been clamped to control bleeding. **D**, Subtotal splenectomy after treatment of the patient illustrated in **C**.

References

Borley NR, McFarlane JM, Ellis H 1995 A comparative study of the tortuosity of the splenic artery. Clin Anat 8:219–21.

Bowdler AJ (ed) 2002 The Complete Spleen: Structure, Function, and Clinical Disorders. Totowa: Humana Press.

A revised and updated edition of Professor Anthony Bowdler's classic work, with an emphasis on splenic microvasculature, splenic functions as part of the immune system, and splenic pathologies and their management.

Buntain WL, Gould HR, Maull KI 1988 Predictability of splenic salvage by computed tomography. J Trauma 28:24–34.

Cavalli G, Re G, Casali AM et al 1982 The microvascular architecture of spleen in congestive splenomegaly. Pathol Res Pract 174:131–46.

Chen L-T 1978 Microcirculation of the spleen. Science 201:157–9.

Christo MC, DiDio LJ 1997 Anatomical and surgical aspects of splenic segmentectomies. Ann Anat 179:461–74.

Coetzee T 1982 Clinical anatomy and physiology of the spleen. South Afr Med J 61:737–46.

A classic reference paper on splenic anatomy and physiology.

Coquet B, Sandoz B, Savoie PH et al 2010 Anthropometric characterization of spleen in children. Surg Radiol Anat 32:25–30.

Cortés JA, Pellico LG 1988 Arterial segmentation in the spleen. Surg Radiol Anat 10:323–32.

Dawson DL, Molina ME, Conner CES 1986 Venous segmentation of the human spleen. Am Surg 52:253–6.

DeLand FH 1970 Normal spleen size. Radiology 97:589–92.

Faller A 1985 Splenic architecture reflected in the connective tissue structure of the human spleen. Experientia 41:164–7.

García-Porrero JA, Lemes A 1988 Arterial segmentation and subsegmentation in the human spleen. Acta Anat 131:276–83.

A detailed description of the relation between the arterial distribution and spleen segmentation.

Gerber AB, Lev M, Goldberg SL 1951 The surgical anatomy of the splenic vein. Am J Surg 82:339–43.

Gupta CD, Gupta SC, Arora AK et al 1976 Vascular segments in the human spleen. J Anat 121:613–6.

Gupta SB, Gupta SC, Gupta CD 1980 Venous segments in the human spleen. Indian J Med Res 72:465–9.

Gürleyik E, Gürleyik G, Bingöl K et al 2000 Perfusion and functional anatomy of the splenic remnant supplied by short gastric vessels. Excerpta Med 179:490–3.

Hermann HJ, Winkel K 1977 Scintigraphy of the spleen. Lymphology 10:115–9.

Jung W, Levesque JP, Ruitenberg MJ 2017 It takes nerve to fight back: the significance of neural innervation of the bone marrow and spleen for immune function. Semin Cell Dev Biol 61:60–70.

Krieken JH, Velde J 1988 Normal histology of the human spleen. Am J Surg Pathol 12:777–85.

Kudoh G, Hoshi K, Murakami T 1979 Fluorescence microscopic and enzyme histochemical studies of the innervation of the human spleen. Arch Histol Jpn 42:169–80.

Liu DL, Xia S, Xu W et al 1996 Anatomy of vasculature of 850 spleen specimens and its application in partial splenectomy. Surgery 119:27–33.

A detailed description of the vascular anatomy of the spleen and its role in surgical procedures.

McFee RB, Musacchio T, Gorgescu D et al 1995 Wandering spleen with torsion in a geriatric patient. Dig Dis Sci 40:2656–9.

Madenci AL, Armstrong LB, Kwon NK et al 2018 Incidence and risk factors for sepsis after childhood splenectomy. J Pediatr Surg 54:1445–48.

Martelli D, McKinley MJ, McAllen RM 2014 The cholinergic anti-inflammatory pathway: a critical review. Auton Neurosci 182:65–9.

Merchea A, Dozois EJ, Wang JK et al 2012 Anatomic mechanisms for splenic injury during colorectal surgery. Clin Anat 25:212–7.

Merran S, Cohen PK, Servois V 2007 Scanographie de la rate: anatomie normale, variantes et pièges. J Radiol 88:549–58.

Michels NA 1942 The variational anatomy of the spleen and splenic artery. Am J Anat 70:21–72.

Mikhail Y, Kamel R, Nawar NN et al 1979 Observations on the mode of termination and parenchymal distribution of the splenic artery with evidence of splenic lobation and segmentation. J Anat 128:253–8.

Mirjalili SA, McFadden SL, Buckenham T et al 2012 A reappraisal of adult abdominal surface anatomy. Clin Anat 25:844–50.

Mishra PK 2016 Textbook of Surgical Gastroenterology, volume 2. New Delhi: Jaypee Brothers Medical Publishers.

Nakamura T, Moriyasu F, Ban N et al 1989 Quantitative measurement of abdominal arterial blood flow using image-directed Doppler ultrasonography. J Clin Ultrasound 17:261–8.

Oguro A, Taniguchi H, Koyama H et al 1993 Relationship between liver function and splenic blood flow. Ann Nucl Med 7:251–5.

Omar A, Freeman S 2016 Contrast-enhanced ultrasound of the spleen. Ultrasound. 24:41–9.

Pandey SK, Bhattacharya S, Mishra RN et al 2004 Anatomical variations of the splenic artery and its clinical implications. Clin Anat 17:497–502.

Par MM, Barry P, Autissier JM et al 1965 Considérations sur la morphologie de la veine splénique et de ses affluents. Soc Nac Med 1:539–47.

Parsons FG 1901 Notches and fissures of the spleen. J Anat Physiol 35: 416–27.

A seminal paper describing the notches and fissures seen on the surface of the spleen.

Petroianu A 1988 Treatment of portal hypertension by subtotal splenectomy and central splenorenal shunt. Postgrad Med J 64:38–41.

Petroianu A 1993 Subtotal splenectomy and portal variceal disconnection in the treatment of portal hypertension. Can J Surg 36:251–4.

Petroianu A 2011 The Spleen. London: Bentham Science.

Petroianu A, Ferreira VL, Barbosa AJ 1989 Morphology and viability of the spleen after subtotal splenectomy. Brazil J Med Biol Res 22:491–495.

Petroianu A, Petroianu S 1994 Anatomy of gastrosplenic vessels in patients with schistosomal portal hypertension. Clin Anat 7:80–3.

Pivkin IV, Peng Z, Karniadakis GE et al 2016 Biomechanics of red blood cells in human spleen. Proc Natl Acad Sci U S A 113:7804–9.

Poulin EC, Thibaut C 1993 The anatomical basis for laparoscopic splenectomy. Can J Surg 36:484–8.

Re G, Casali A, Cavalli D et al 1985 Morphological bases of splenic circulation in congestive splenomegaly. Haematologica 70:283–90.

Scothorne RJ 1985 The spleen: structure and function. Histopathology 9:663–9.

Skandalakis PN, Colborn GL, Skandalakis LJ et al 1993 The surgical anatomy of the spleen. Surg Clin North Am 73:747–68.

One of the most complete descriptions of splenic anatomy.

Skandalakis JE, Coborn GL, Weidman TA et al 2004 Spleen. In: Skandalakis JE (ed.) Skandalakis' Surgical Anatomy. Athens: Paschalidis Medical Publications; Ch. 22, pp. 1231–87.

Sow ML, Dia A, Ouedraogo T 1991 Anatomic basis for conservative surgery of the spleen. Surg Radiol Anat 13:81–7.

Sprogøe-Jakobsen S, Sprogøe-Jakobsen U 1997 The weight of normal spleen. Forensic Sci Int 88:215–23.

Steiniger BS 2015 Human spleen microanatomy: why mice do not suffice. Immunology 145:334–46.

A detailed review of current knowledge regarding the microanatomy of the spleen in humans with comparative anatomy.

Steiniger B, Barth P, Hellinger A 2001 The perifollicular and marginal zones of the human splenic white pulp. Am J Pathol 159:501–12.

Steiniger BS, Ulrich C, Berthold M et al 2018 Capillary networks and follicular marginal zones in human spleens. Three-dimensional models based on immunostained serial sections. PLoS One 13:e0191019.

Sylvester PA, Stewart R, Ellis H 1995 Tortuosity of the human splenic artery. Clin Anat 8:214–8.

A description of the tortuosity of the splenic artery, demonstrating its importance in anatomical and surgical approaches.

Tarantino G, Scalera A, Finelli C 2013 Liver-spleen axis: intersection between immunity, infections and metabolism. World J Gastroenterol 19:3534–42.

Trubel W, Turkof E, Rokitansky A et al 1985 Incidence, anatomy and territories supplied by the posterior gastric artery. Acta Anat 124:26–30.

Trubel W, Rokitansky A, Turkof E et al 1988 Correlations between posterior gastric artery and superior polar artery in human anatomy. Anat Anz 167:219–23.

Tubbs RS, Shoja MM, Loukas M 2016 Bergman's Comprehensive Encyclopedia of Human Anatomic Variation. Hoboken: Wiley Blackwell.

A textbook dedicated to detailing the anatomical variations found in man.

Üngör B, Malas MA, Sulak O et al 2007 Development of spleen during fetal period. Surg Radiol Anat 29:543–50.

Vikse J, Sanna B, Henry BM et al 2017 The prevalence and morphometry of an accessory spleen: a meta-analysis and systematic review of 22,487 patients. Int J Surg 45:18–28.

A meta-analysis of data documenting the prevalence, number, location and morphometry of accessory spleens.

Weiss L 1983 The red pulp of the spleen. Clin Haematol 12:375–93.

Xu WL, Li SL, Wang Y et al 2009 Role of color Doppler flow imaging in applicable anatomy of spleen vessels. World J Gastroenterol 15:607–11.

CHAPTER

70

Suprarenal gland

The suprarenal (adrenal) glands lie immediately superior and slightly anterior to the superior pole of each kidney (see Figs 72.5, 61.8). The glands are golden yellow in colour and are enclosed within the renal fascia, where they are separated from the kidneys by a small amount of loose connective tissue. Each gland possesses two functionally and structurally distinct areas: an outer cortex and an inner medulla derived from mesoderm and neural crest cells, respectively.

Macroscopically, the glands are slightly different in external appearance (**Fig. 70.1**). The right suprarenal gland is pyramidal in shape and has two well-developed lower projections (limbs), giving a cross-sectional appearance similar to a three-pointed star. The left is more semilunar in shape, flattened in the anteroposterior plane, and marginally larger than the right. The bulk of the right suprarenal gland sits on the superior pole of the right kidney and the bulk of the left suprarenal gland lies on the anteromedial aspect of the superior pole of the left kidney.

The dimensions of the suprarenal glands in adults have been measured *in vivo* from axial computed tomography (CT) (Vincent et al 1994). The mean maximum width of the suprarenal gland is approximately 50 mm, and the mean width of each limb of the gland (medial and lateral) is approximately 30-40 mm (Carsin-Vu et al 2016). No individual limb should measure more than 5 mm in transverse section. In adults, each suprarenal gland weighs approximately 5 g (the medulla contributes about one-tenth of the total weight) and has a volume of approximately 3–6 cm^3 (Wang et al 2013).

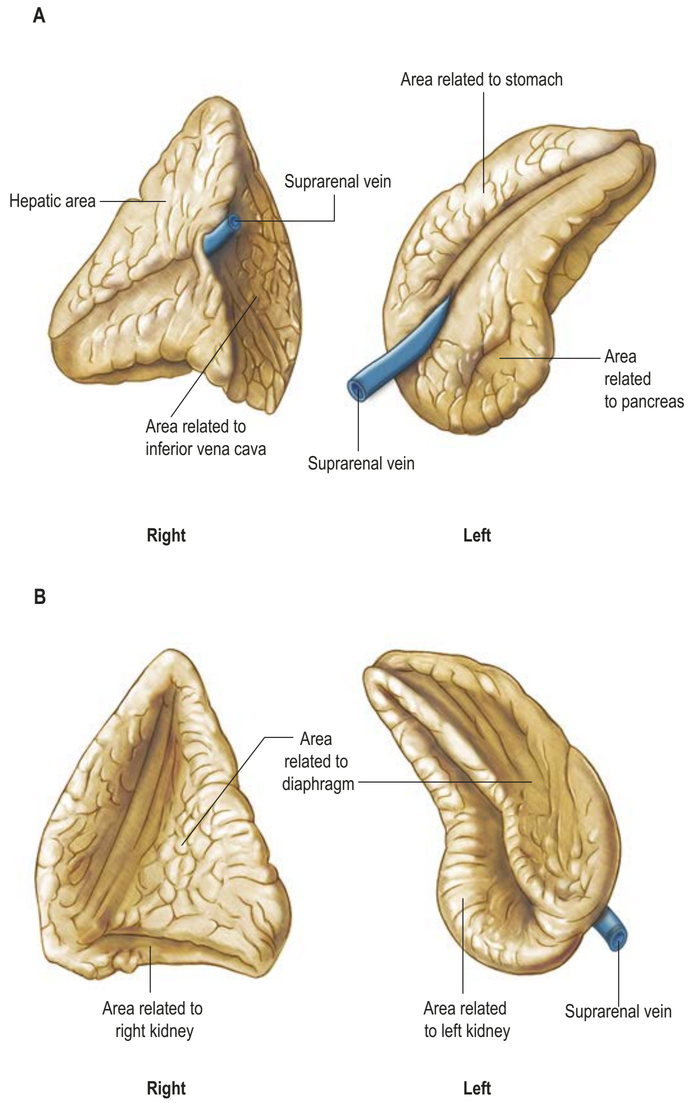

Fig. 70.1 The suprarenal glands. **A**, Anterior aspect. **B**, Posterior aspect.

At birth, the suprarenal glands are proportionately larger and are approximately one-third the size of the ipsilateral kidney. The cortex of each gland is expanded by a well-developed inner 'fetal zone', responsible for producing dehydroepiandrosterone (DHEA), the substrate for placental oestrogen in the fetus. The suprarenal cortex, specifically the fetal zone, shrinks immediately after birth and the medulla grows comparatively little. By the end of the second postnatal month, the weight of the suprarenal gland has decreased by more than 50%. The glands begin to grow again by the end of the second year of life and regain their weight at birth by puberty. There is little further weight increase in adult life.

Small accessory nodules composed mainly of cortical tissue, also known as 'adrenal rests', can occur in the areolar tissue near the suprarenal glands. They are also occasionally found in the spermatic cord, epididymis or testis (Altin et al 1992) and the ovary or broad ligament of the uterus. Ectopic suprarenal gland tissue can cause diagnostic confusion and is rarely the site of neoplastic change.

Right suprarenal gland

The right suprarenal gland lies posterior to the inferior vena cava, separated from it by only a thin layer of renal fascia and connective tissue. It also lies posterior to the right lobe of the liver and anterior to the right crus of the respiratory diaphragm and superior pole of the right kidney (**Fig. 70.2**). The renal surface of the right suprarenal gland overlaps the anterosuperior aspect of the superior pole of the right kidney, the two lower projections (limbs) of the gland straddling the kidney. The anterior surface has two distinct facets: a narrow medial facet that lies posterior to the inferior vena cava and a triangular lateral facet that lies in contact with the bare area of the liver. The most inferior part of the anterior surface may be covered by the peritoneal reflection of the coronary ligament, which also represents the upper aspect of the hepatorenal recess. Here, the gland lies posterior to the lateral border of the descending part of the duodenum. Below the superior border, near the anterior surface of the gland, the right suprarenal vein emerges from the hilum to join the inferior vena cava. This vein is short, which makes surgical resection of the gland or mobilization of the inferior vena cava potentially hazardous. It can be inadvertently avulsed from the inferior vena cava during surgery or, occasionally, by high-energy deceleration injuries. The posterior surface of the gland is divided into upper and lower areas by a curved transverse ridge. The larger upper area is slightly convex and abuts the respiratory diaphragm, whereas the smaller lower area is concave and lies in contact with the superior aspect of the superior pole of the right kidney. The medial border of the gland is thin and lies lateral to the right coeliac ganglion and the right inferior phrenic artery where the artery runs over the right crus of the respiratory diaphragm.

Left suprarenal gland

The left suprarenal gland lies close to the left crus of the respiratory diaphragm (Fig. 70.2). Its medial aspect is convex longitudinally, whereas the lateral aspect is concave because it is moulded by the medial surface of the superior pole of the left kidney. The superior border is sharply defined while the renal surface is more rounded. The upper part of the anterior surface is covered by the peritoneum of the posterior wall of the omental bursa, which separates it from the stomach and sometimes from the inferior border of the spleen. A small lower part of the anterior surface is not covered by peritoneum and lies adjacent to the pancreas and splenic artery. The hilum faces inferiorly from the lower part of the medial aspect. The left suprarenal vein emerges from the hilum and runs inferomedially to join the left renal vein. The posterior surface of the gland is divided by a ridge into a lateral area adjoining the kidney and a smaller medial area that lies in contact with the left crus of the respiratory diaphragm. The medial border lies lateral

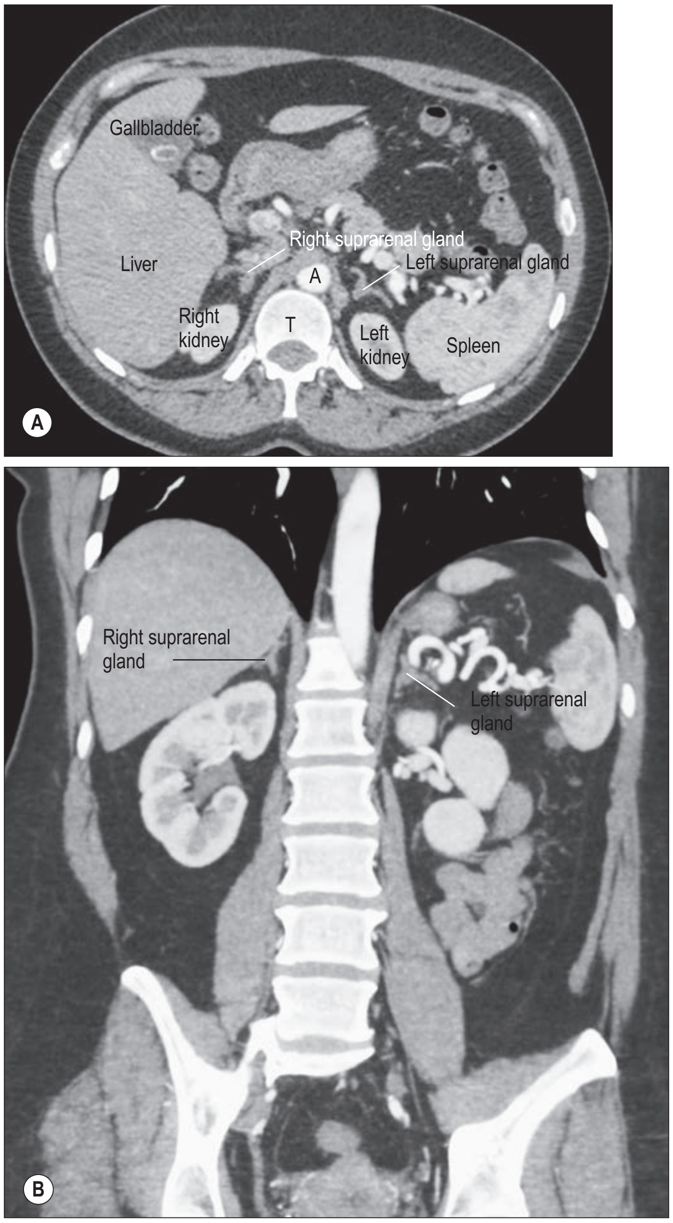

Fig. 70.2 Computed tomography (CT) of the suprarenal glands. **A**, Axial contrasted abdominal CT. **B**, Coronal contrasted abdominal CT. Abbreviations. A, aorta. T, thoracic vertebral body. (Courtesy of Dr R Shane Tubbs, Tulane University School of Medicine, New Orleans, LA, USA.)

to the left coeliac ganglion and the left inferior phrenic and left gastric arteries, which ascend on the left crus of the diaphragm.

Vascular supply and lymphatic drainage

Arteries

The suprarenal glands have one of the highest arterial flow rates per gram of tissue (up to 5 ml/g/min) (Williams and Leggett 1989). Each gland is supplied by superior, middle and inferior suprarenal arteries, the main branches of which can be multiple (Fig. 70.3). These vessels ramify over the capsule before penetrating the gland to form a subcapsular arterial plexus, from which fenestrated sinusoids pass around clustered glomerulosa cells and between the columns of the zona fasciculata to a deep plexus in the zona reticularis. Venules from this plexus pass between medullary chromaffin cells to the central vein, which they enter between prominent bundles of smooth muscle fibres. Some relatively large arteries bypass this indirect route and pass directly to the medulla (Fig. 70.4). The arterial supply of the suprarenal gland is prone to considerable variation (Manso and DiDio 2000, Dutta 2010) and only the more common variants will be described here.

Superior suprarenal arteries

The superior suprarenal artery usually arises from the ipsilateral inferior phrenic artery and passes to the gland as four or five small branches. It occasionally arises from the abdominal aorta.

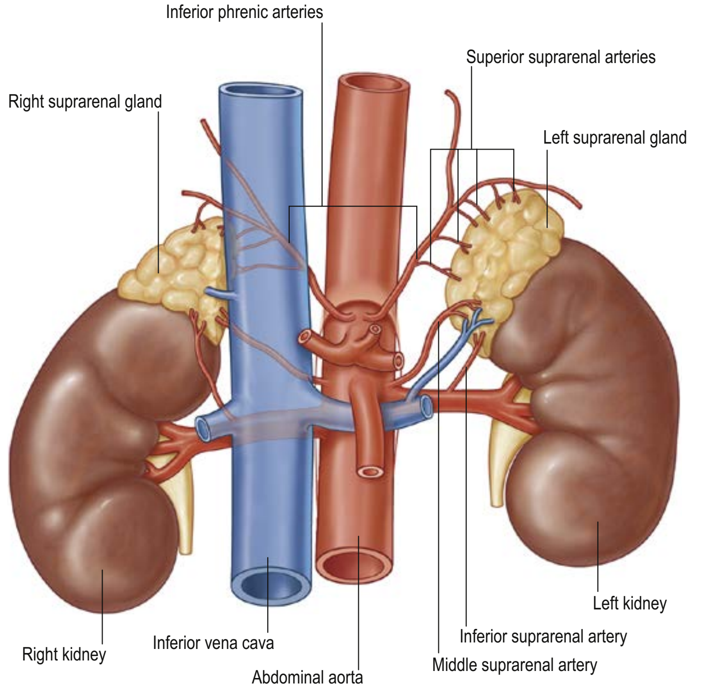

Fig. 70.3 The arterial supply and venous drainage of the suprarenal glands. (With permission from Drake RL, Vogl AW, Mitchell A (eds) Gray's Anatomy for Students, 2nd ed. Elsevier, Churchill Livingstone. Copyright 2010.)

Middle suprarenal arteries

The middle suprarenal artery is usually single, but can be multiple or absent. It often arises from the lateral aspect of the abdominal aorta at around the level of the superior mesenteric artery and ascends slightly over the crura of the respiratory diaphragm to anastomose with the other suprarenal arteries on the surface of the suprarenal gland. The right middle suprarenal artery passes behind the inferior vena cava close to the right coeliac ganglion, whereas the left middle suprarenal artery passes close to the left coeliac ganglion, splenic artery and the superior border of the pancreas. The middle suprarenal artery can originate from either the ipsilateral inferior phrenic or renal artery.

Inferior suprarenal arteries

The inferior suprarenal arteries often contribute most of the arterial supply to the suprarenal gland. One or two arteries usually arise from the ipsilateral renal artery, but the inferior suprarenal arteries can originate from either the abdominal aorta or the ipsilateral gonadal artery.

Veins

The central vein emerges from the hilum of the suprarenal gland to form the suprarenal vein, which is usually single (Dobbie and Symington 1966). The right vein is very short and passes directly and horizontally into the posterior aspect of the inferior vena cava. An accessory right suprarenal vein is occasionally present and runs from the hilum superomedially to join the inferior vena cava above the right suprarenal vein. The short course renders the right suprarenal vein(s) vulnerable to injury or even avulsion from the inferior vena cava during surgery if undue traction is applied. The left suprarenal vein is longer and descends medially, anterolateral to the left coeliac ganglion, then passes posterior to the body of the pancreas. This vessel usually drains into the left renal vein and may receive the left inferior phrenic vein (Loukas et al 2005). Since the venous drainage from each suprarenal gland is usually via a single vein, infarction of the gland is more likely to be caused by injury to a suprarenal vein than to one of the suprarenal arteries.

Understanding the variant venous anatomy of the suprarenal gland is important to preclude haemorrhage during adrenalectomy. Cadaveric studies have shown little variation in suprarenal venous anatomy but suggest that variants are more common on the right (Cesmebasi et al 2014). However, a large surgical series of patients undergoing laparoscopic removal of the suprarenal gland found that 13% had variant venous anatomy for this structure (Scholten et al 2013). Common variants included an absent main suprarenal vein, accessory suprarenal veins, a branch to the inferior phrenic vein, and draining to the right hepatic vein on the right or, on the left, to the inferior vena cava.

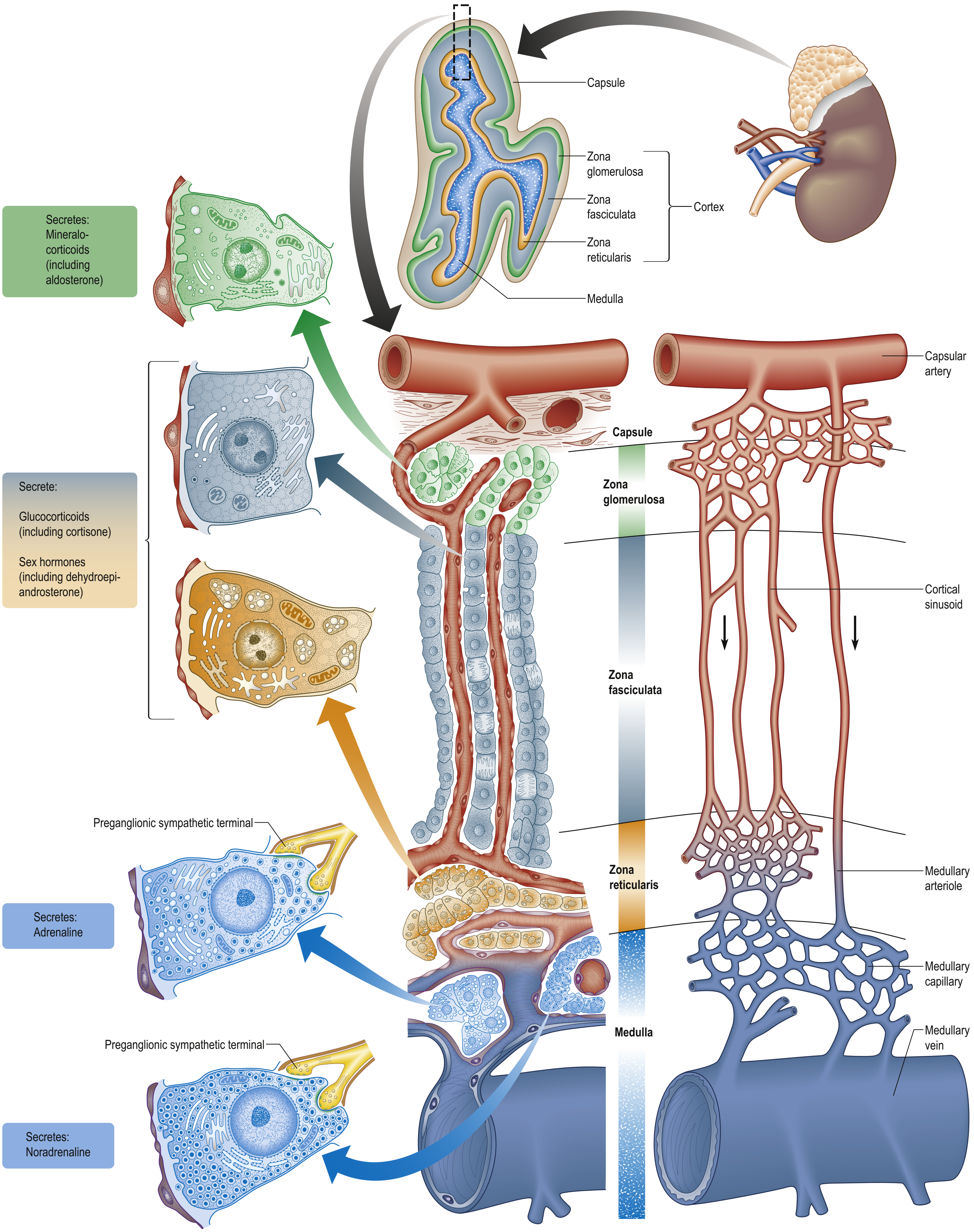
Capsule
Zona
glomerulosa
Zona
fasciculata
Zona
reticularis
Cortex
Medulla
Secretes:
Mineralo-
corticoids
(including
aldosterone)
Secrete:
Glucocorticoids
(including cortisone)
Sex hormones
(including dehydroepi-
androsterone)
Capsular
artery
Capsule
Zona
glomerulosa
Cortical
sinusoid
Zona
fasciculata
Preganglionic sympathetic terminal
Zona
reticularis
Medullary
arteriole
Secretes:
Adrenaline
Medullary
capillary
Medulla
Medullary
vein
Preganglionic sympathetic terminal
Secretes:
Noradrenaline

Fig. 70.4 The gross sectional appearance, microstructure, vasculature and ultrastructure of the suprarenal gland. Brief functional summaries are included.

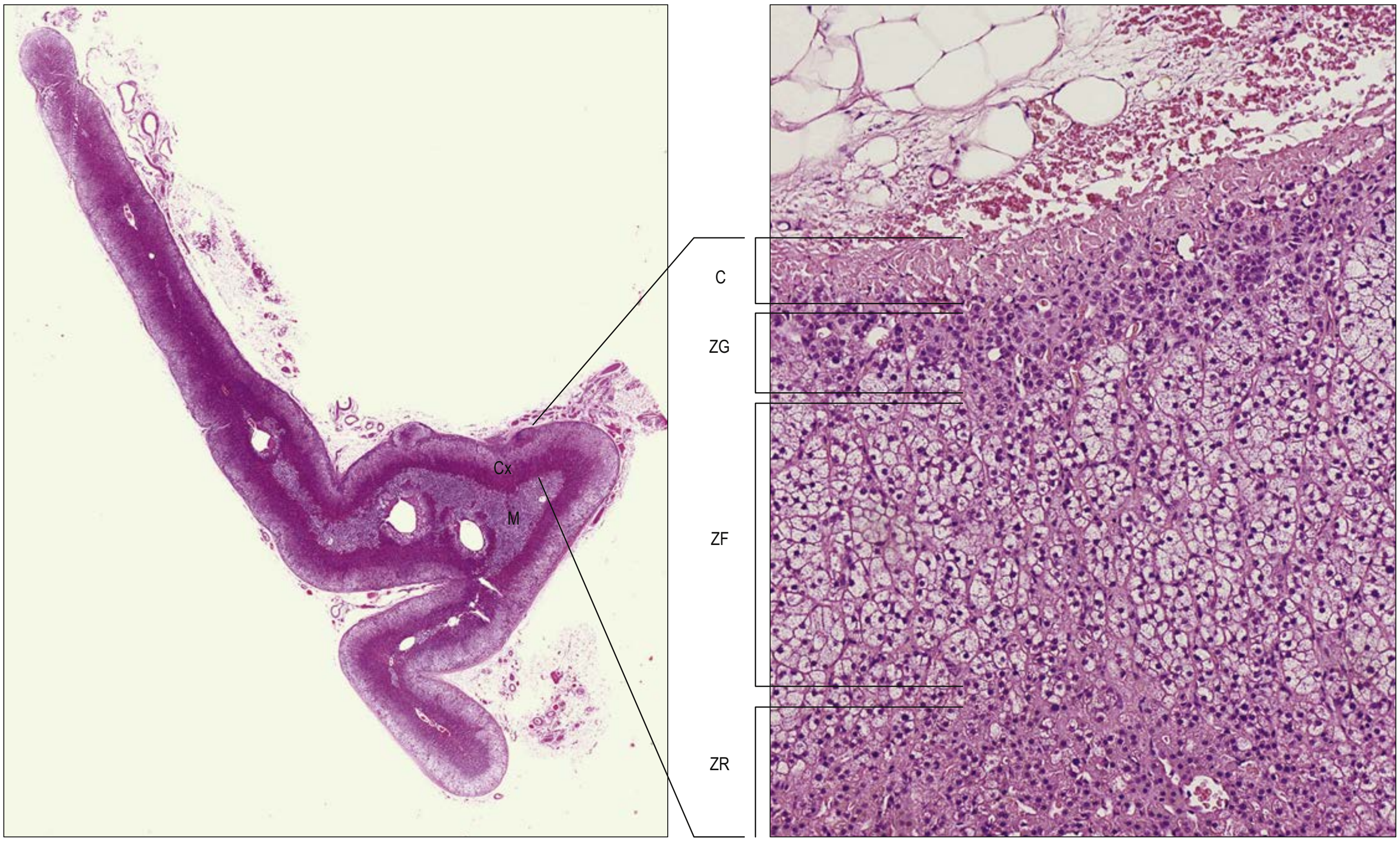

Fig. 70.5 A cross-section through an adult suprarenal gland showing the cortex (Cx) and highly vascular medulla (M). The cortex is shown at higher magnification to demonstrate the capsule (C), the zona glomerulosa (ZG), zona fasciculata (ZF) and zona reticularis (ZR). The boundaries between zones are indistinct and variable. (Courtesy of Mr Peter Helliwell and the late Dr Joseph Mathew, Department of Histopathology, Royal Cornwall Hospitals Trust, UK.)

Lymphatic drainage

Lymphatic vessels within the capsule of the suprarenal gland communicate with subcapsular lymphatics that drain medially to lumbar nodes (Merklin 1966, Skandalakis et al 2004). A few capsular lymphatics communicate with lymph vessels that pass through the respiratory diaphragm (Tokiwa et al 1993).

Innervation

Relative to its size, the suprarenal gland has a greater autonomic nerve supply than any other organ. The nerves are distributed throughout the gland, including around blood vessels, where they act to regulate blood flow; in the medulla, where they stimulate the release of catecholamines from chromaffin cells; in the cortex, where they can influence steroid hormone production (Tóth et al 1997). A suprarenal plexus lies between the medial aspect of each gland and the coeliac and aorticorenal ganglia. Cholinergic preganglionic sympathetic fibres travelling mainly in the greater thoracic splanchnic nerves reach the plexus and synapse on clusters of large medullary chromaffin cells. The precise spinal level of origin of these preganglionic fibres is uncertain and some may also travel in the lesser and least thoracic splanchnic nerves: cadaveric dissection studies in humans, both adult and fetal, have revealed significant differences not only in the origin and number of the splanchnic nerve rami but also in the communications between them (Naidoo et al 2001, Yang et al 2008, Loukas et al 2010). A smaller proportion of postganglionic sympathetic nerve fibres innervate cortical blood vessels. Other nerve fibres containing a variety of neurotransmitters have been identified within the suprarenal cortex and could be involved in modulating steroid hormone secretion (Li et al 1999). Experimental tracing studies in rats, guinea-pigs and marmosets found that the cell bodies of afferent nerve fibres arising in the suprarenal medulla were almost all located in dorsal root ganglia, and, less often, in the nodose ganglia of the vagus nerves (Coupland 1989, Parker et al 1993).

Microstructure and function

In section, the suprarenal glands have an outer cortex, which is yellowish in colour and forms the main mass. The suprarenal glands also have a thin medulla, forming about one-tenth of the gland, which is dark red or greyish depending on its content of blood (see Fig. 70.4; **Fig. 70.5**). The medulla is completely enclosed by cortex except at the hilum. The gland has a thick collagenous capsule from which trabeculae extend deep into the cortex. The capsule contains a rich arterial plexus that supplies branches to the suprarenal gland.

Suprarenal cortex

The suprarenal cortex is composed of a zona glomerulosa, zona fasciculata and zona reticularis (see Fig. 70.5). The outer, subcapsular, zona glomerulosa consists of a narrow region of small polyhedral cells arranged in rounded clusters. These cells have deeply staining nuclei and a basophilic cytoplasm containing a few lipid droplets. Ultrastructurally, they each have an abundant smooth endoplasmic reticulum that is typical of steroid-synthesizing cells. The broader, intermediate, zona fasciculata consists of large polyhedral basophilic cells arranged in straight columns, two cells wide, separated by parallel fenestrated venous sinusoids. These cells each contain many lipid droplets and large amounts of smooth endoplasmic reticulum. The innermost part of the cortex, the zona reticularis, consists of branching interconnected columns of rounded cells, each with a cytoplasm containing smooth endoplasmic reticulum, numerous lysosomes, and aggregates of brown lipofuscin pigment that accumulate with age.

Cortical cells produce several hormones: cells in the zona glomerulosa produce mineralocorticoids, e.g. aldosterone, which regulates electrolyte and water balance; cells in the zona fasciculata produce hormones maintaining carbohydrate balance, e.g. the glucocorticoid cortisol (hydrocortisone); and cells in the zona reticularis produce sex hormones, e.g. progesterone, oestrogens and androgens. The suprarenal cortex is essential for life and complete bilateral removal is lethal without replacement therapy.

Suprarenal medulla

The suprarenal medulla is composed of groups and columns of chromaffin cells (phaeochromocytes), separated by wide venous sinusoids and supported by a network of reticular fibres. Medullary chromaffin cells, so called from their colour reaction to dichromate fixatives, form part of the neuroendocrine system and are functionally equivalent to postganglionic sympathetic neurones. These cells store the catecholamines noradrenaline (norepinephrine) and adrenaline (epinephrine) and release them into the medullary venous plexus. Release is under preganglionic sympathetic control and is mediated by the sympathetic neurones that occur either singly or in small groups in the medulla.

Most medullary chromaffin cells synthesize adrenaline and store it in small granules with a dense core. The less numerous noradrenaline-secreting cells have larger granules with a dense eccentric core. Some cells synthesize both hormones. Chromogranin proteins package catecholamines within the granules, which also contain encephalins, opiate-like proteins that have endogenous analgesic effects under some circumstances. All of the cells are large, with large nuclei and basophilic, faintly granular cytoplasm. They form single rows along the venous sinusoids. Sympathetic axon terminals synapse with the medullary chromaffin cells on the surfaces that face away from the sinusoids.

The sinusoids are lined by a fenestrated endothelium and drain to the central vein and suprarenal vein. Under normal circumstances, little adrenaline or noradrenaline is released. Secretion of these substances increases in response to fear, anger or stress. Unlike the cortex, the suprarenal medulla is not essential for life.

Neoplastic lesions of the suprarenal glands

Available with the *Gray's Anatomy* e-book

Suprarenal gland excision

Available with the *Gray's Anatomy* e-book

Key references

Cesmebasi A, Du Plessis M Iannatuono M et al 2014 A review of the anatomy and clinical significance of adrenal veins. Clin Anat 27:1253–63.

A review of the surgical anatomy of the suprarenal (adrenal) veins, including their development.

Manso JC, DiDio LJ 2000 Anatomical variations of the human suprarenal arteries. Ann Anat 182:483–8.

A study of vascular corrosion casts, demonstrating anatomical variations of the arterial supply to the suprarenal gland.

Scholten A, Cisco RM, Vriens MR et al 2013 Variant adrenal venous anatomy in 546 laparoscopic adrenalectomies. JAMA Surg 148:378–83.

A study of the types and frequency of adrenal vein variants: a higher probability of adrenal vein variants should be anticipated when operating on phaeochromocytomas and larger adrenal tumours.

Skandalakis JE, Coborn GL, Weidman TA et al 2004 Adrenal (suprarenal) glands. In: Skandalakis JE (ed) Surgical Anatomy. Athens: Paschalidis Medical Publications; Ch.27, pp. 1541–66.

A comprehensive chapter on the surgical anatomy of the suprarenal (adrenal) glands.

Several neoplastic lesions can be encountered arising from the suprarenal glands, including adenomas, phaeochromocytomas, myelolipomas, oncocytomas, cysts, adrenocortical carcinomas (ACC), and metastases from other malignancies. Many of these lesions require surgical resection, and therefore a firm understanding of suprarenal gland anatomy is critical for their successful treatment. In this section the most common and clinically relevant lesions of the suprarenal gland are reviewed.

Adenomas

Adenomas most commonly arise from the zona glomerulosa or the zona fasciculata of the suprarenal cortex. Up to 10% of incidentally detected suprarenal gland adenomas are functional and autonomously produce hormones (Mantero et al 1997). These lesions, which are composed of lipid-rich cells, commonly show low attenuation (less than 10 Hounsfield units) on unenhanced computed tomography (CT) (Young 2007, Johnson et al 2009). Alternatively, suprarenal adenomas can be detected on CT by their characteristic high degree of washout (greater than 60%) on delayed phase imaging performed 10–15 minutes after contrast administration. Suprarenal adenomas can also be reliably detected on chemical shift magnetic resonance imaging (MRI).

Functional adenomas arising from the zona glomerulosa cause a symptom complex known as Conn's syndrome. This syndrome is characterized by hypertension, hypokalaemia and metabolic alkalosis. Bilateral adrenal hyperplasia can cause identical symptoms and must be distinguished from an aldosterone-producing adenoma, as the treatment of hyperplasia is medical with aldosterone-blocking medications, such as spironolactone, whereas aldosterone-producing adenomas require surgical excision. The two conditions can typically be differentiated on the basis of imaging findings or with selective suprarenal vein sampling, which is indicated in elderly patients who are prone to equivocal imaging findings that can lead to incorrect lateralization of the source of mineralocorticoid excess. Primary hyperaldosteronism is diagnosed by measuring morning plasma aldosterone and renin levels (Fassnacht et al 2016). A high ratio between the two hormones (typically defined as an aldosterone:renin ratio greater than 20) is indicative of disorders of aldosterone excess. Some recommend a salt loading test as further confirmation of the diagnosis.

Adenomas arising from the zona fasciculata can result in cortisol excess or what is known as Cushing's syndrome. This syndrome is clinically characterized by central obesity, increased adiposity/rounding of the face (moon face), fat deposition between the shoulders (buffalo hump), hypertension, glucose intolerance, fatigue, abdominal striae and easy bruising. Functional adenomas causing cortisol excess also require surgical excision.

An autonomous cortisol-producing adenoma is diagnosed after observing an elevated cortisol level on an overnight 1 mg dexamethasone suppression test (Fassnacht et al 2016). This finding can be confirmed with the late-night salivary cortisol test or with a 24-hour urinary cortisol level. Other conditions that cause cortisol excess include exogenous steroid use, pituitary gland adenomas (also known as Cushing's disease), adrenocortical carcinoma (ACC) and paraneoplastic syndromes. None of these alternative causes of cortisol excess will show suppression on the overnight 1 mg dexamethasone suppression test. However, Cushing's disease will show suppression with a higher 2 mg dose of dexamethasone. Through a combination of imaging findings and metabolic testing, the precise cause of cortisol excess can typically be identified and addressed.

While rare, adenomas can also arise from the zona reticularis. These tumours can lead to excess production of sex hormones leading to virilization in women and feminization in men. Because of the rarity of these lesions, metabolic testing for sex hormones is not indicated in asymptomatic patients who present with an incidentally detected suprarenal gland tumour. However, it is worth noting that ACCs commonly present with symptoms of excess sex steroid production and patients presenting with related symptoms should be evaluated with an eye for this potentially aggressive malignancy.

Phaeochromocytomas

Phaeochromocytomas are catecholamine-producing tumours that arise from the medulla of the suprarenal glands. They are most commonly sporadic and unilateral; however, several hereditary syndromes can give rise to multifocal lesions. Syndromes associated with the development of phaeochromocytomas include von Hippel–Lindau disease, neuro fibromatosis type 1, succinate dehydrogenase deficiency, and multiple endocrine neoplasia 2A and 2B.

Phaeochromocytomas commonly result in symptoms of catecholamine excess, including hypertension, tachycardia, headache and hyperhidrosis. On CT, phaeochromocytomas are highly vascular and typically display delayed contrast washout (Young 2007). On T2-weighted MRI, these lesions are markedly hyperintense and display the characteristic 'light bulb sign'. Phaeochromocytomas have the potential for metastatic spread, which can be assessed with contrast-enhanced cross-sectional imaging (CT or MRI), or functional imaging with either ^{131}I-metaiodobenzylguanidine single-photon imaging or 2-deoxy-2-[^{18}F]fluoro-D-glucose positron emission tomography.

The presence of a phaeochromocytoma is confirmed with metabolic testing for plasma-free metanephrines or urinary fractionated metanephrines (Fassnacht et al 2016). Phaeochromocytomas require surgical resection with adrenalectomy. Prior to surgery, alpha-adrenergic blockade, most commonly with phenoxybenzamine, is needed to prevent an intraoperative hypertensive crisis.

Myelolipomas

Myelolipomas are benign non-metabolically active tumours of the suprarenal gland that are composed of trilineage haemopoietic precursor cells and mature fat. These lesions can be distinguished on CT from other suprarenal masses by the finding of large areas of macroscopic fat with negative Hounsfield units. Myelolipomas are most commonly asymptomatic and do not require treatment or follow-up imaging. Treatment in the form of surgical resection is only indicated for symptom management.

Adrenocortical carcinoma (ACC)

ACC is a rare primary malignancy of the suprarenal gland. Most cases of ACC are sporadic, unilateral and present at an advanced stage. Upwards of 50% of ACCs have hypersecretion of one or more of the cortical suprarenal gland hormones (Terzolo et al 2007). ACCs tend to be larger than other suprarenal gland tumours, with an average size of approximately 10 cm at presentation (Gröndal et al 1990). It is estimated that 10–20% of all suprarenal gland tumours greater than 4 cm are ACCs, so surgical resection should be considered for tumours meeting this size cut-off that are otherwise without the imaging hallmarks of a benign tumour (Young 2007, Azoury et al 2017). On CT imaging, ACCs tend to have irregular borders, calcifications and areas of necrosis. Additionally, extension into adjacent organs or the inferior vena cava is common.

Surgical excision is the mainstay of treatment for ACC. *En bloc* resection of the tumour and any involved organs should performed. A regional lymphadenectomy is also commonly performed for the purposes of disease control and tumour staging. Surgical resection is indicated for patients with localized and locally advanced disease. For patients with metastatic disease, primary tumour resection is indicated to alleviate symptoms. This is typically performed in combination with metastasectomy. Following surgical resection, consideration should be given to administration of adjuvant mitotane, a derivative of the insecticide dichlorodiphenyltrichloroethane (DDT), which inhibits steroidogenesis and remains the first line agent for metastatic ACC (Fassnacht et al 2018). The prognosis of ACC is quite poor, with 5-year survival rates often reported as less than 50% (Kim et al 2016).

Other metastases

The suprarenal glands are a common site for metastases from other malignancies. One study found that in patients with a history of a previous malignancy, approximately 50% of newly discovered suprarenal gland lesions were metastatic (Lenert et al 2001). Tumours that commonly metastasize to the suprarenal glands include melanoma, renal cell carcinoma, lung cancers and breast cancer. Metastatic lesions can be distinguished from primary lesions of the suprarenal gland through a combination of clinical history, imaging findings (lesions will be greater than 10 Hounsfield units on non-contrasted CT and will enhance) and percutaneous biopsy. Depending on the underlying malignancy and extent of metastatic spread, some metastases can be treated with surgical resection while others require systemic therapy.

One or both of the suprarenal glands may be removed using 'open surgery', which remains the standard of care for patients with ACC who require *en bloc* resection of their tumour. For other lesions of the suprarenal gland requiring surgery, minimally invasive techniques are now generally preferred. The original laparoscopic approaches for removal of the suprarenal gland were described during the 1990s and have since been adopted throughout most of the world (Gagner et al 1992, Mercan et al 1995). Both the open and minimally invasive techniques for removal of the suprarenal gland can be performed via a transabdominal or retroperitoneal approach. The retroperitoneal approach offers the advantage of remaining outside the abdominal cavity and so avoids encountering adhesions and potentially causing iatrogenic injury to other organs. Advantages of the transabdominal approach include a larger working space and more familiar anatomical relations. Ultimately, the choice of surgical technique is dictated by a combination of surgeon experience and patient-specific factors.

References

Altin MA, Gündo H, Aksoy F 1992 Adrenal rests in the inguinal region in children. Pediatr Surg Int 7:446–8.

Azoury SC, Nagarajan N, Young A et al 2017 Computed tomography in the management of adrenal tumors: does size still matter? J Comput Assist Tomogr 41:628–32.

Carsin-Vu A, Oubaya N, Mulé S et al 2016 MDCT linear and volumetric analysis of adrenal glands: normative data and multiparametric assessment. Eur Radiol 26:2494–501.

Cesmebasi A, Du Plessis M, Iannatuono M et al 2014 A review of the anatomy and clinical significance of adrenal veins. Clin Anat 27:1253–63.

A review of the surgical anatomy of the suprarenal veins, including their development.

Coupland RE, Parker TL, Kesse WK et al 1989 The innervation of the adrenal gland. III. Vagal innervation. J Anat 163:173–81.

Dobbie JW, Symington T 1966 The human adrenal gland with special reference to the vasculature. J Endocrinol 34:479–89.

Dutta S 2010 Suprarenal gland – arterial supply: an embryological basis and applied importance. Rom J Morphol Embryol 51:137–40.

Fassnacht M, Arlt W, Bancos I et al 2016 Management of adrenal incidentalomas: European Society of Endocrinology Clinical Practice Guideline in collaboration with the European Network for the Study of Adrenal Tumors. Eur J Endocrinol 175:G1–G34.

Guideline on the work-up and management of suprarenal incidentalomas.

Fassnacht M, Dekkers OM, Else T et al 2018 European Society of Endocrinology Clinical Practice Guidelines on the management of adrenocortical carcinoma in adults, in collaboration with the European Network for the Study of Adrenal Tumors. Eur J Endocrinol 179:G1–G46.

Guideline on the management of adrenocortical carcinoma.

Gagner M, Lacroix A, Bolte E 1992 Laparoscopic adrenalectomy in Cushing's syndrome and pheochromocytoma. N Engl J Med 327:1033.

Gröndal S, Cedermark B, Eriksson B et al 1990 Adrenocortical carcinoma. A retrospective study of a rare tumor with a poor prognosis. Eur J Surg Oncol 16:500–6.

Johnson PT, Horton KM, Fishman EK 2009 Adrenal imaging with multidetector CT: evidence-based protocol optimization and interpretative practice. Radiographics 29:1319–31.

Kim Y, Margonis GA, Prescott JD et al 2016 Nomograms to predict recurrence-free and overall survival after curative resection of adrenocortical carcinoma. JAMA Surg 151:365–73.

Lenert JT, Barnett CC Jr, Kudelka AP et al 2001 Evaluation and surgical resection of adrenal masses in patients with a history of extra-adrenal malignancy. Surgery 130:1060–7.

Li Q, Johansson H, Grimelius L 1999 Innervation of human adrenal gland and adrenal cortical lesions. Virchows Arch 435:580–9.

Loukas M, Louis RG Jr, Hullett J et al 2005 An anatomical classification of the variations of the inferior phrenic vein. Surg Radiol Anat 27: 566–74.

Loukas M, Klaassen Z, Merbs W et al 2010 A review of the thoracic splanchnic nerves and celiac ganglia. Clin Anat 23:512–22.

Manso JC, DiDio LJ 2000 Anatomical variations of the human suprarenal arteries. Ann Anat 182:483–8.

A study of vascular corrosion casts, demonstrating anatomical variations of the arterial supply to the suprarenal gland.

Mantero F, Masini AM, Opocher G et al 1997 Adrenal incidentaloma: an overview of hormonal data from the National Italian Study Group. Horm Res 47:284–9.

Mercan S, Seven R, Ozarmagan S et al 1995 Endoscopic retroperitoneal adrenalectomy. Surgery 118:1071–5.

Merklin RJ 1966 Suprarenal gland lymphatic drainage. Am J Anat 119:359–74.

Naidoo N, Partab P, Pather N et al 2001 Thoracic splanchnic nerves: implications for splanchnic denervation. J Anat 199:585–90.

Parker TL, Kesse WK, Mohamed AA et al 1993 The innervation of the mammalian adrenal gland. J Anat 183: 265–76.

Scholten A, Cisco RM, Vriens MR et al 2013 Variant adrenal venous anatomy in 546 laparoscopic adrenalectomies. JAMA Surg 148:378–83.

A study of the types and frequency of adrenal vein variants: a higher probability of adrenal vein variants should be anticipated when operating on phaeochromocytomas and larger adrenal tumours.

Skandalakis JE, Coborn GL, Weidman TA et al 2004 Adrenal (suprarenal) glands. In: Skandalakis JE (ed) Surgical Anatomy. Athens: Paschalidis Medical Publications; Ch.27, pp. 1541–66.

A comprehensive chapter on the surgical anatomy of the suprarenal glands.

Terzolo M, Angeli A, Fassnacht M et al 2007 Adjuvant mitotane treatment for adrenocortical carcinoma. N Engl J Med 356:2372–80.

Tokiwa K, Nakamura K, Ogita S et al 1993 Lymphatic drainage of adrenal neuroblastoma. J Pediatr Surg 28:927–9.

Tóth IE, Vizi ES, Hinson JP et al 1997 Innervation of the adrenal cortex, its physiological relevance, with primary focus on the noradrenergic transmission. Microsc Res Tech 36:534–45.

Vincent JM, Morrison ID, Armstrong P et al 1994 The size of normal adrenal glands on computed tomography. Clin Radiol 49:453–5.

Wang X, Jin ZY, Xue HD et al 2013 Evaluation of normal adrenal gland volume by 64-slice CT. Chin Med Sci J 27:220–4.

Williams LR, Leggett RW 1989 Reference values for resting blood flow to organs of man. Clin Phys Physiol Meas 10:187–217.

Yang HJ, Gil YC, Lee WJ 2008 Anatomy of thoracic splanchnic nerves for surgical resection. Clin Anat 21:171–7.

Young WF Jr 2007 The incidentally discovered adrenal mass. N Engl J Med. 356: 601–10.

A review of the imaging and metabolic work-up of suprarenal masses.

CHAPTER 71

Lesser pelvis and perineum

LESSER PELVIS

The lesser pelvis is a bowl-shaped structure formed from the sacrum, pubis, ilium, ischium, the ligaments that interconnect these bones, and the muscles that line their inner surfaces. It begins at the level of the plane passing through the promontory of the sacrum, the arcuate line of the ilium, the pecten pubis and the posterior surface of the pubic crest. This plane, or 'inlet', lies at an angle of between 35° and 50° up from the horizontal; the bony structures above it are sometimes referred to as the greater pelvis. They form part of the walls of the lower abdomen. In children, the width of the pelvic inlet is an age-independent predictor of chest width and thoracic dimensions (Emans et al 2005). The ischiopubic synchondrosis is the temporary cartilage formed between the pubis and ischium prior to the completion of ossification around 12 years of age (Herneth et al 2000). The 'outlet' of the lesser pelvis is formed by the ischiopubic rami, ischial tuberosities, sacrotuberous ligaments and distal sacrum. The bones surround a central pelvic canal that forms an anteriorly concave curve (the curve of Carus); in the female, it constitutes the birth canal. The topography of the bony and ligamentous pelvis is considered in full detail in Chapter 77.

Muscles and fasciae

Pelvic muscles

The muscles arising within the pelvis form two groups. Piriformis and obturator internus form part of the walls of the pelvis and are considered primarily as muscles of the lower limb (Fig. 71.1). Levator ani and ischiococcygeus form the pelvic diaphragm and delineate the inferior limit of the lesser pelvis (Fig. 71.2). The fasciae investing the muscles are continuous with visceral pelvic fascia superiorly, perineal fascia inferiorly and obturator fascia laterally.

Piriformis

Piriformis forms part of the posterolateral wall of the lesser pelvis and is attached to the anterior surface of the sacrum, the gluteal surface of the ilium near the posterior inferior iliac spine, the capsule of the adjacent sacroiliac joint and, sometimes, to the superior part of the pelvic surface of the sacrotuberous ligament. It passes out of the pelvis through the greater sciatic foramen superior to the sacrospinous ligament. Within the pelvis, the posterior surface of this muscle lies against the sacrum, and its anterior surface is related to the rectum (especially on the left), the sacral plexus and branches of the internal iliac vessels. Piriformis is described in more detail in Chapter 77.

Obturator internus

Obturator internus and its fascia form part of the anterolateral wall of the lesser pelvis. These attach to the structures surrounding the obturator foramen, ischiopubic ramus, the pelvic surface of the hip bone inferior and posterior to the linea terminalis, and the superior part of the greater sciatic foramen. These structures are also attached to the medial part of the pelvic surface of the obturator membrane. Specialized portions of the obturator fascia give attachment to some of the fibres of levator ani (tendinous arch of levator ani), so that only the superior portion of obturator internus can be seen from above. The inferior portion forms part of the boundaries of the ischio-anal fossa. In the male, the superior portion lies lateral to the urinary bladder, the obturator and vesical vessels, and the obturator nerve. In the female, the attachments of the broad ligament of the uterus, the distal end of the uterine tubes and the uterine vessels also lie medial to obturator internus and its fascia.

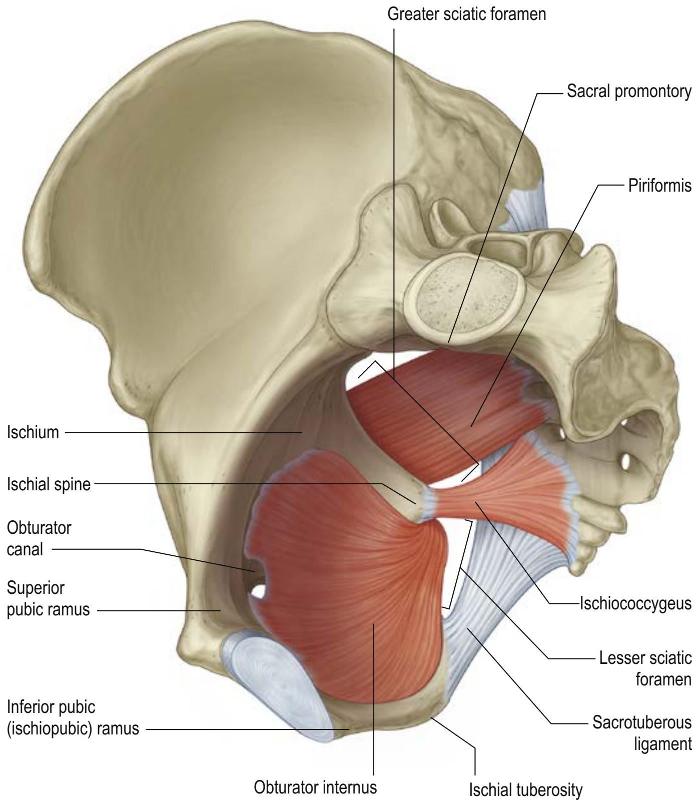

Fig. 71.1 Piriformis, obturator internus and the ligaments of the pelvis. Those muscles relating only to the pelvis or perineum have been omitted for clarity. (Adapted with permission from Drake RL, Vogl AW, Mitchell A (eds), Gray's Anatomy for Students, 2nd ed. Elsevier, Churchill Livingstone. Copyright 2010.)

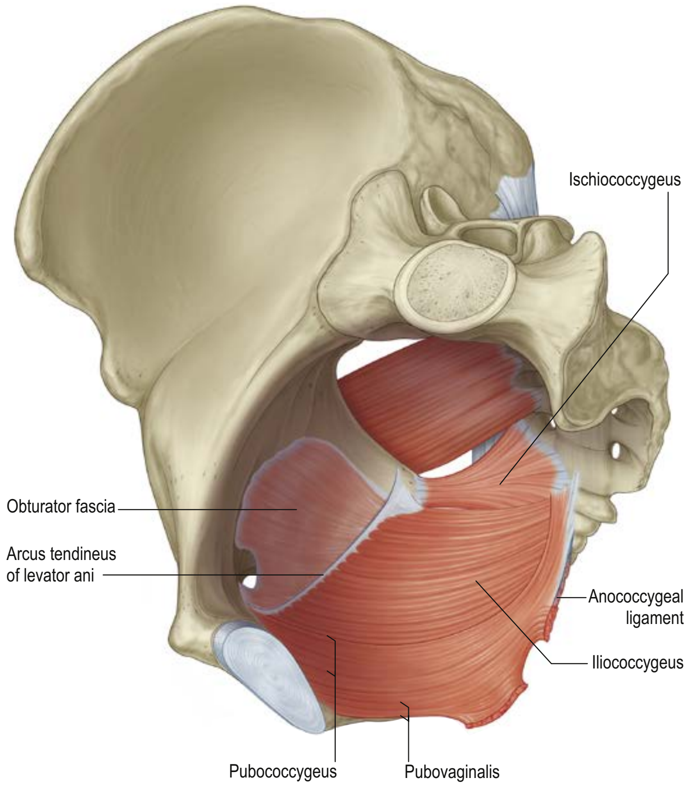

Fig. 71.2 Muscles of the female pelvis. The superior gluteal and obturator vessels and nerves, and the pelvic viscera, have been omitted for clarity. (Adapted with permission from Drake RL, Vogl AW, Mitchell A (eds) Gray's Anatomy for Students, 2nd ed. Elsevier, Churchill Livingstone. Copyright 2010.)

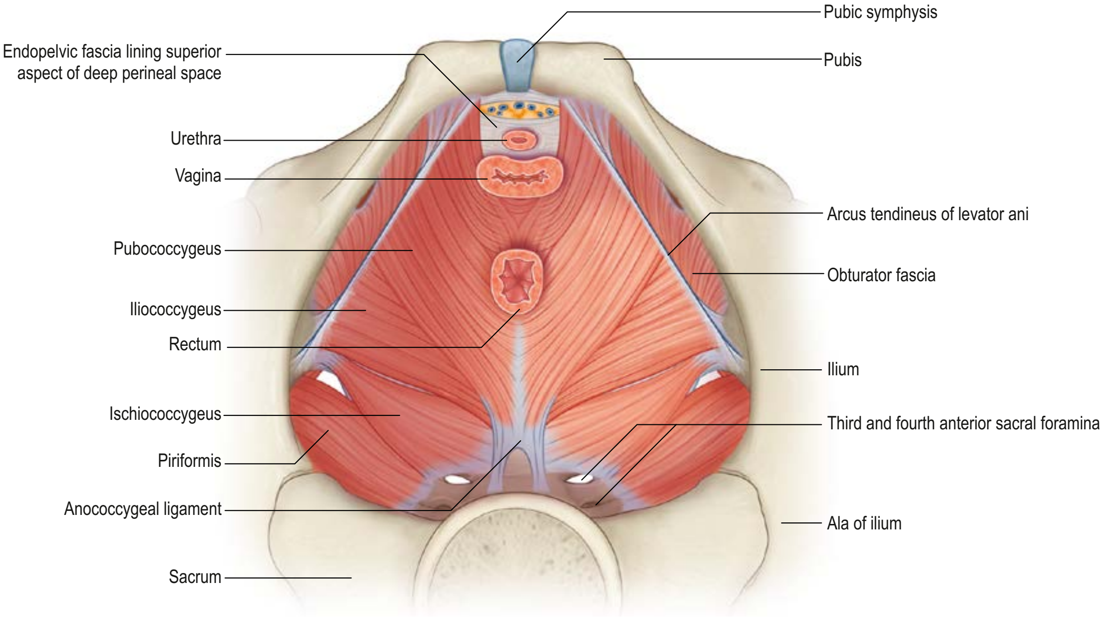

Fig. 71.3 Muscles of the female pelvis viewed from above. The anorectal junction, vagina and urethra have been divided at the level of the pelvic diaphragm.

Levator ani (pubococcygeus, iliococcygeus and pubo-analis)

Levator ani is a broad muscular sheet of variable thickness attached to the internal surface of the pelvis. It forms a large portion of the pelvic diaphragm (**Fig. 71.3**) (Lawson 1974a, Roberts et al 1988, Wendell-Smith and Wilson 1991). The muscle is subdivided into named portions according to their attachments and the pelvic viscera to which they are related (pubococcygeus, iliococcygeus and pubo-analis). These parts are often referred to as separate muscles but the boundaries between them cannot easily be distinguished; moreover, they perform many similar physiological functions. Pubococcygeus is often subdivided into separate parts according to the pelvic viscera to which each part relates (e.g. puboprostaticus, pubovaginalis). Levator ani arises from each side of the walls of the pelvis along the condensation of the obturator fascia (the tendinous arch of levator ani). Fibres from ischiococcygeus attach to the sacrum and coccyx but the remaining parts of the muscle converge in the midline. Fibres from iliococcygeus join via a partly fibrous intersection and form the iliococcygeal raphe posterior to the anorectal junction. Closer to the anorectal junction, and elsewhere in the pelvic diaphragm, the fibres are nearly continuous with those of the opposite side, such that the muscle forms a sling (iliococcygeus and pubo-analis).

Attachments The attachments for pubococcygeus, iliococcygeus and pubo-analis are as follows.

Pubococcygeus Pubococcygeus originates from the posterior aspect of the body of the pubis and passes posteriorly almost horizontally. Its most medial fibres run directly lateral to the urethra and its sphincter as it passes through the pelvic diaphragm; here, the muscle is correctly called puboperinealis, although it is often referred to as pubo-urethralis because of its juxtaposition to the proximal half of the urethra in both sexes, however, no direct connection with the urethra is present. In males, some of these fibres lie lateral and inferior to the prostate and are referred to as puboprostaticus. In females, fibres run further back and attach to the lateral walls of the vagina, where they are referred to as pubovaginalis. In both sexes, fibres from this part of pubococcygeus attach to the perineal body; a few elements also attach to the anorectal junction. Some fibres decussate and blend with the longitudinal rectal muscle and fascial elements to contribute to the conjoint longitudinal coat of the anal canal. Behind the rectum, other fibres of pubococcygeus form a tendinous intersection as part of the anococcygeal raphe.

Iliococcygeus Iliococcygeus is attached to the inner surface of the ischial spine inferior and anterior to the attachment of ischiococcygeus, and also to the tendinous arch of levator ani as far anteriorly as the obturator canal (see Fig. 71.2). The most posterior fibres are attached to the apex of the sacrum and coccyx, but the majority join fibres from the contralateral side to form a raphe that is effectively continuous with the fibroelastic anococcygeal ligament, which is closely applied to its inferior surface; some muscle fibres may attach into the ligament. The raphe provides a strong attachment for the pelvic diaphragm posteriorly and must be divided to allow wide excisions of the anorectal canal to be performed during abdominoperineal excisions for malignancy. An accessory slip sometimes arises from the most posterior part and is referred to as iliosacralis.

Pubo-analis Pubo-analis lies lateral to pubococcygeus and cannot be seen from inside the pelvis. It originates from the inner surface of the ischiopubic rami immediately adjacent to, and sometimes partly arising from, the perineal membrane. Its fibres pass lateral to those of iliococcygeus and pubococcygeus to decussate posterior to the rectum at the anorectal junction. The border between pubo-analis and some fibres of the external anal sphincter is indistinct.

Ischiococcygeus Ischiococcygeus lies posterosuperior to and is contiguous with levator ani. It arises as a triangular musculotendinous sheet with its apex attached to the pelvic surface and tip of the ischial spine, and its base attached to the lateral margins of the coccyx and the fifth sacral vertebral segment. Ischiococcygeus is rarely absent, but can be almost completely tendinous rather than muscular. It lies on the pelvic aspect of the sacrospinous ligament and can be fused with it, particularly if it is mostly tendinous. The sacrospinous ligament may represent either a degenerate part or an aponeurosis of the muscle, since muscle and ligament are coextensive.

Relations The superior, pelvic surface of levator ani is separated only by fascia (superior pelvic diaphragmatic, visceral and extraperitoneal) from the urinary bladder, prostate or uterus and vagina, rectum and peritoneum. Its inferior, perineal surface forms the medial wall of the ischio-anal fossa and the superior wall of the anterior recess of the fossa, both being covered by the inferior fascia of the pelvic diaphragm. The posterior border is separated from the coccyx by areolar tissue. The medial borders of the two levator muscles and the inferior ischiopubic rami border the levator hiatus, through which pass the urethra, vagina (in the female) and anus. In the female, that portion of the hiatus that lies anterior to the perineal body is referred to as the urogenital hiatus.

Vascular supply Levator ani is supplied by branches of the inferior gluteal, inferior vesical and internal pudendal arteries.

Innervation The nerves to levator ani originate mainly from the third and fourth sacral ventral (anterior) rami, with lesser contributions from the second sacral ventral ramus. These nerves enter the pelvis just above ischiococcygeus, sometimes piercing it, to pass along the anterior surface of ischiococcygeus and pubococcygeus, supplying these muscles and sending fibres to pubo-analis (Roberts and Krishingner 1967, Sato 1980). The pudendal nerve can also supply pubococcygeus from its lateral surface through its inferior anal and perineal branches.

Actions Pubococcygeus and pubo-analis pull the pelvic and perineal structures anteriorly and superiorly, occluding the levator hiatus. In the female, this action occludes the vagina and prevents prolapse of the pelvic organs through the urogenital hiatus. The constant baseline activity of levator ani is similar to that of the external anal sphincter, modulated to adjust to the loads placed on them. The action of pubo-analis and pubococcygeus also reinforces the external anal sphincter and helps to create the anorectal angle. Iliococcygeus and to a lesser extent the less muscular ischiococcygeus form a relatively horizontal diaphragm, especially in the posterior half of the pelvis, that assists pubo-analis in achieving bowel and bladder continence.

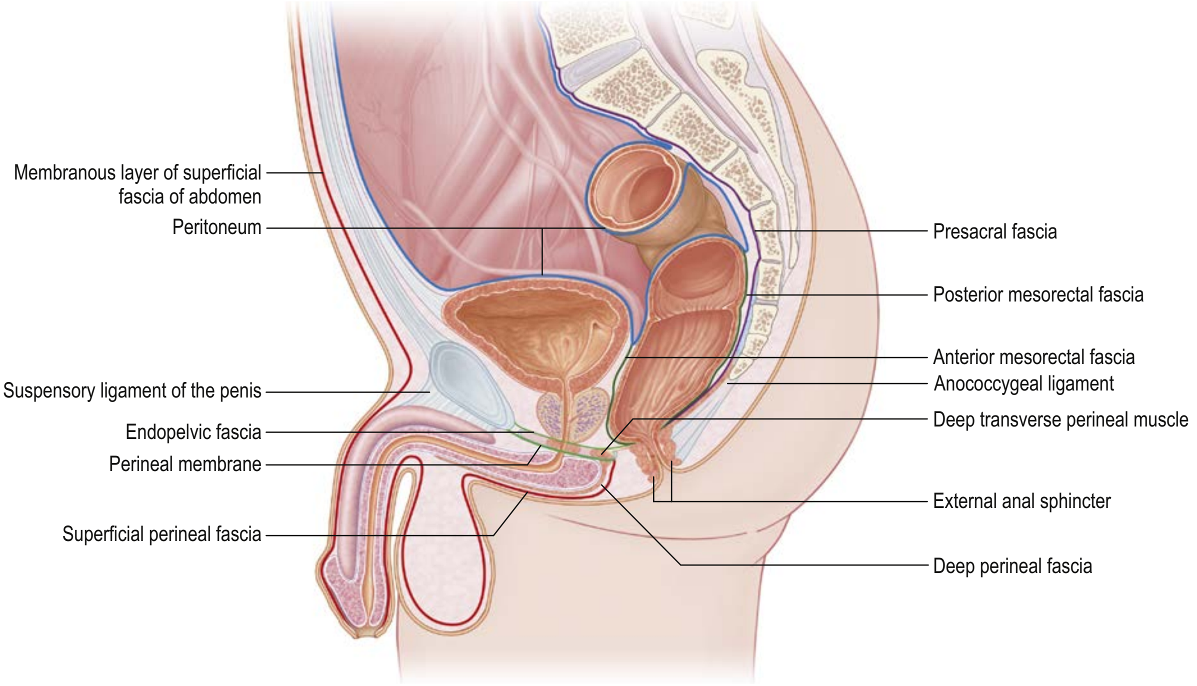
Membranous layer of superficial fascia of abdomen
Peritoneum
Suspensory ligament of the penis
Endopelvic fascia
Perineal membrane
Superficial perineal fascia
Presacral fascia
Posterior mesorectal fascia
Anterior mesorectal fascia
Anococcygeal ligament
Deep transverse perineal muscle
External anal sphincter
Deep perineal fascia

Fig. 71.4 Fasciae of the male pelvis and perineum: median sagittal section. The visceral parietal fasciae have been omitted for clarity.

Levator ani must relax appropriately to permit expulsion of urine and, particularly, faeces; it contracts with the abdominal muscles and the respiratory diaphragm to raise intra-abdominal pressure. It forms much of the muscular pelvic diaphragm, which supports the pelvic viscera. Like the respiratory diaphragm, but unlike the abdominal muscles, levator ani is also active in the inspiratory phase of quiet respiration. In pregnancy, the shape of the pelvic diaphragm can help to direct the fetal head into the anteroposterior diameter of the pelvic outlet.

Pelvic fasciae

It is convenient to divide the pelvic fasciae into the parietal pelvic fascia, which forms the coverings of the pelvic muscles, and the visceral pelvic fascia, which forms the coverings of the pelvic organs and their neurovascular supply (Fig. 71.4).

Parietal pelvic fascia

The parietal pelvic fascia consists of the obturator fascia, piriformis fascia, superior fascia over the pelvic diaphragm and the presacral fascia.

Obturator fascia

The parietal pelvic fascia on the pelvic (medial) surface of obturator internus is well differentiated. In humans, anterior to the lateral attachment of the pelvic organs, a portion of it is derived from the degenerated superior portion of the attachment of levator ani. It is connected to the posterior part of the arcuate line of the ilium and is continuous with iliac fascia. Anterior to this, as it follows the line of origin of obturator internus, it is gradually separated from the attachment of the iliac fascia and a portion of the periosteum of the ilium and pubis spans between them. It arches below the obturator vessels and nerve, investing the obturator canal, and is attached anteriorly to the posterior aspect of the pubis. Behind the obturator canal, the fascia is markedly aponeurotic and gives a firm attachment to the iliococcygeus, usually called the tendinous arch of levator ani (see Figs 71.3, 71.14–71.15). Superior to the attachment of levator ani, the fascia is thin and effectively comprises only the epimysium of the muscle and overlying connective tissue; posteriorly, it forms part of the lateral wall of the ischio-anal fossa in the perineum; anteriorly, it merges with the fasciae of the muscles of the deep perineal space, which is continuous with the ischio-anal fossa. The obturator fascia is continuous with the periosteum of the hip bone and piriformis fascia.

Fascia over piriformis

The fascia over the internal surface of piriformis is very thin and fuses with the periosteum on the anterior sacrum at the margins of the anterior sacral foramina. It ensheathes the ventral rami that emerge from these foramina so that the nerves are often described as lying behind the fascia. The internal iliac vessels lie in front of the piriformis fascia and their branches draw out sheaths of the fascia and extraperitoneal tissue into the gluteal region, superior and inferior to piriformis.

Fascia over levator ani

Both surfaces of levator ani have a fascial covering: the combination of the two fascial layers and the intervening muscle is called the pelvic diaphragm. On the inferior surface, the fascia is continuous with the obturator fascia below the tendinous arch of levator ani laterally. It covers the medial wall of the ischio-anal fossa and blends below with fasciae on the external urethral sphincter and the external anal sphincter. The superior fascia of the pelvic diaphragm is markedly thicker than the inferior fascia and is attached anteriorly to the posterior aspect of the body of the pubis, approximately 2 cm superior to its inferior border. It extends laterally across the superior pubic ramus, blending with the obturator fascia and continuing along an irregular line to the ischial spine. It is continuous posteriorly with the piriformis fascia and the anterior sacrococcygeal ligament. Medially, the superior fascia of the pelvic diaphragm blends with the visceral pelvic fascia to contribute to the endopelvic fascia.

Tendinous arch of the pelvic fascia

Low on the superomedial aspect of the superior fascia of the pelvic diaphragm, a thick white band of condensed connective tissue extends from the inferior part of the pubic symphysis to the superior margin of the ischial spine. It provides attachment for the condensations of visceral pelvic fasciae that provide support to the urethra and urinary bladder, and to the vagina in females (see below).

Presacral fascia

The presacral fascia forms a hammock-like structure behind the posterior portion of the mesorectal fascia. Laterally, it extends to the origin of the piriformis fascia and the superior fascia of the pelvic diaphragm, with which it blends; more inferiorly, it extends between the white line of the parietal pelvic fascia on either side. Inferiorly, it extends to the anorectal junction, where it fuses with the posterior aspect of the mesorectal fascia and the iliococcygeal raphe at the level of the anorectal junction. Superiorly, it can be traced to the origin of the superior hypogastric plexus, where it thins progressively over the sacral promontory and becomes continuous with the retroperitoneal tissues. The right and left hypogastric nerves and inferior hypogastric plexuses lie on its surface. It forms a distinct layer that can be seen both on magnetic resonance imaging (MRI) of the pelvis and during surgery. The presacral fascia provides an important landmark because extension of rectal tumours through it significantly reduces the possibility of curative resectional surgery. Dissection in the plane posterior to the fascia can result in bleeding from the presacral veins. The adventitia of the veins is partly attached to the posterior surface of the fascia, which means that the haemorrhage can be severe (because the veins are unable to contract properly). The presacral fascia is a useful structure to which the rectum can be sutured during rectopexy for rectal prolapse.

Visceral pelvic fascia

The urogenital organs in both sexes are connected bilaterally to the pelvic walls by neurovascular mesenteric condensations ensheathed by a meshwork of loose connective and adipose tissues and lying above the perineal membrane (Ricci et al 1947, Campbell 1950, Range and Woodburne 1964, Roberts et al 1964, Reiffstuhl 1982). The lateral attachments of the pelvic organs to the pelvic side walls are referred to as the endopelvic fascia. Considered as a unit, the connections provide a conduit for neurovascular elements passing from the pelvic side wall to the organs and serve as attachments that help to retain the pelvic organs in place, playing an important role in preventing pelvic organ prolapse in females (DeLancey 1992). They are associated with loose connective tissue that extends to the midline, separating the bladder from the vagina and the vagina from the rectum in the female, and separating the bladder, prostate and seminal glands from the rectum in the male. The fasciae contain different amounts of connective tissue and smooth muscle: where they are either unusually dense or form visible ridges, they are called 'ligaments' (e.g. cardinal ligament, uterosacral ligament). Clinically, these lateral attachments are often referred to as visceral 'ligaments', but they are quite unlike the bands of dense, regular connective tissue that typify skeletal ligaments. Their lateral attachments sweep off the pelvic walls, arising from the superior fascia over levator ani and from part of the piriformis fascia more superiorly and posteriorly. The ligaments passing to the urinary bladder in the male, or the bladder and proximal vagina and uterus in the female, are relatively long, but these lateral connections become shorter towards the pelvic outlet, until at the level of the perineal membrane there is a direct connection between the organs and the pelvic walls.

In the female, the cardinal ligament surrounds the uterovaginal junction and extends distally to mid-vagina, where the vagina has a more direct lateral attachment at the tendinous arch of the pelvic fascia. The portions that attach to the uterus and vagina are sometimes called the parametrium and paracolpium, respectively. Further accounts of the paravisceral portions of the visceral pelvic fascia are given in the chapters describing the organs to which the fascia relates. The uterosacral ligament is a visible fold of tissue flanking the rectum as it descends posterior to the cervix in the female. It contains a considerable amount of smooth muscle near its attachment to the cervix and some of the pelvic autonomic nerves. A similar vesicosacral fold is present in the male.

Approximately 1 cm above the inferior border of the pubis and 1 cm lateral to the midline, a band of dense pelvic connective tissue, the anterior end of the tendinous arch of the pelvic fascia, is attached to either the paravaginal (female) or the prostatic (male) tissues. This band extends on the inner surface of levator ani and joins the tendinous arch of levator ani to the ischium, just above the ischial spine. The attachment of the paravaginal tissue to the pubis is sometimes called the pubo-urethral ligament, a misnomer because it is not attached to the urethra. The attachment of the anterior vaginal wall to the tendinous arch of the pelvic fascia, the paravaginal attachment, helps to provide support to the vagina, urethra and urinary bladder.

There is much less condensation of connective tissue around the rectum. A layer presumed to be a peritoneal fusion fascia is described between the rectum and either the seminal glands in the male or the vagina in the female (the rectovesical septum or rectovaginal septum, respectively): it is not connected to the rectum. The connective tissue over the longitudinal muscles of the rectum is thickened just superior to the point where it traverses levator ani and fuses with the endopelvic fascia and the anococcygeal ligament, forming a structure that is sometimes referred to as a rectosacral ligament.

Vascular supply and lymphatic drainage

The lesser pelvis contains the internal iliac arteries and veins, and the lymphatics that drain most of the pelvic viscera. The common and external iliac vessels and the lymphatics that drain the lower limb lie along the linea terminalis and in the lower retroperitoneum, but are conveniently discussed together with the vessels of the lesser pelvis. There is remarkable variation in the terminal branching pattern for the iliac vessels and no two individuals have quite the same anatomy. However, there are general patterns, and the following description will consider the common pattern.

Arteries

Common iliac artery

The abdominal aorta bifurcates into the right and left common iliac arteries anterolateral to the left side of the body of the fourth lumbar vertebra (Roberts and Krishingner 1967). These arteries diverge as they descend and they divide at the level of the sacroliac joint into external and internal iliac arteries. The external iliac artery is the principal artery of the lower limb. The internal iliac artery provides the principal supply to the walls and viscera of the pelvis, the perineum and the gluteal region.

Right common iliac artery The right common iliac artery is approximately 5 cm long. It passes obliquely across part of the bodies of the fourth and the fifth lumbar vertebrae, and is crossed anteriorly by the sympathetic rami to the pelvic plexus and, at its division into internal and external iliac arteries, by the ureter. It is covered by the parietal peritoneum, which separates it from the small intestine. Posteriorly, it is separated from the bodies of the fourth and fifth lumbar vertebrae and the intervening intervertebral disc by the right sympathetic trunk, the terminal parts of the common iliac veins and the start of the inferior vena cava, the obturator nerve, lumbosacral trunk and iliolumbar artery. Laterally, the inferior vena cava and the right common iliac vein lie superiorly and the right psoas major lies inferiorly. The left common iliac vein is medial to the proximal part of the right common iliac artery.

Left common iliac artery The left common iliac artery is shorter than the right and is approximately 4 cm long. Lying anteriorly are branches of the sympathetic trunk that contribute to the superior hypogastric plexus, the superior anorectal artery and, at its terminal bifurcation, the ureter. The sympathetic trunk, the bodies of the fourth and fifth lumbar vertebrae and the intervening intervertebral disc, the obturator nerve, lumbosacral trunk and iliolumbar artery are all posterior. The left common iliac vein is posteromedial and the left psoas major is lateral.

Branches In addition to the external iliac and internal iliac branches, each common iliac artery also gives small branches to the peritoneum, psoas major, ureter, adjacent nerves and surrounding areolar tissue. The common iliac artery occasionally gives rise to the iliolumbar artery and accessory or replaced renal arteries if the kidney is low-lying.

Internal iliac artery

Each internal iliac artery is approximately 4 cm long and begins at the common iliac bifurcation, level with the lumbosacral intervertebral disc and anterior to the sacroiliac joint (**Figs 71.5–71.6**). It descends posteriorly to the superior margin of the greater sciatic foramen, where it divides into an anterior division, which continues in the same line towards the ischial spine, and a posterior division, which passes back to the greater sciatic foramen. The anterior division primarily supplies the pelvic organs, while the posterior division primarily supplies muscles in the hip and back. The ureter and, in females, the ovary and distal end of the uterine tube, are anterior to the artery. The internal iliac vein, lumbosacral trunk and sacroiliac joint are posterior. Laterally are the external iliac vein, between the artery and psoas major, and the obturator nerve lying inferior to the vein. Medially, the parietal peritoneum and tributaries of the internal iliac vein separate the artery from the terminal ileum on the right and the sigmoid colon on the left. For details of the considerable variation in the anatomy of the internal iliac artery see Tubbs et al (2016).

In the fetus, the internal iliac artery is twice the size of the external iliac artery and is the direct continuation of the common iliac artery. The main trunk ascends on the anterior abdominal wall to the umbilicus, converging on the contralateral artery, and the two arteries run through the umbilicus to enter the umbilical cord as the umbilical arteries. At birth, when placental circulation ceases, only the pelvic segment remains patent as the internal iliac artery and part of the superior vesical artery and the remainder becomes a fibrous medial umbilical ligament. Persistence of the umbilical artery has been described and can cause extrinsic obstruction of the distal ureter (Gupta et al 1999). In males, the patent part (commonly, the superior vesical artery) usually gives off the artery to the ductus deferens.

Posterior division branches

The branches of the posterior division of the internal iliac artery are the iliolumbar, lateral sacral and superior gluteal arteries.

Iliolumbar artery The iliolumbar artery is the first branch of the posterior division of the internal iliac artery and ascends laterally anterior to the sacroiliac joint and lumbosacral trunk. It lies posterior to the obturator nerve and external iliac vessels, and reaches the medial border of psoas major, dividing behind it into the lumbar and iliac branches. The lumbar branch supplies psoas major and quadratus lumborum, and anastomoses with the fourth lumbar artery. It sends a small spinal branch through the intervertebral foramen between the fifth lumbar and first sacral vertebrae to supply radicular branches to the cauda equina. The iliac branch supplies iliacus; between the muscle and bone it anastomoses with the iliac branches of the obturator artery. A large nutrient branch enters an oblique canal in the ilium. Other branches run around the iliac crest, contribute to the supply of gluteal and abdominal muscles, and anastomose with the superior gluteal, circumflex iliac and lateral circumflex femoral arteries (see Fig. 76.4).

Lateral sacral arteries The lateral sacral arteries are usually double. If they are single, they soon divide into superior and inferior branches.

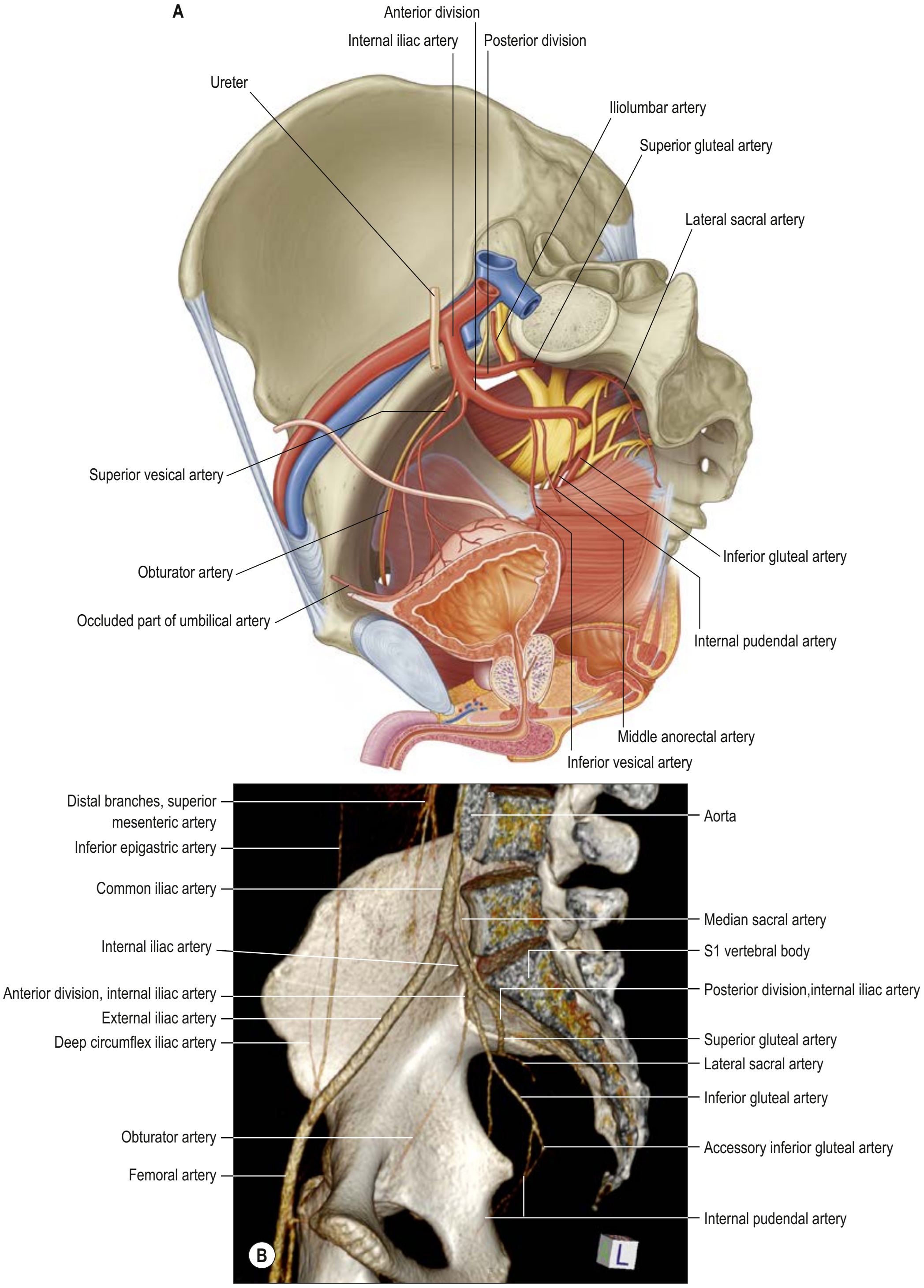
A
Anterior division
Internal iliac artery
Posterior division
Ureter
Iliolumbar artery
Superior gluteal artery
Lateral sacral artery
Superior vesical artery
Obturator artery
Occluded part of umbilical artery
Inferior gluteal artery
Internal pudendal artery
Middle anorectal artery
Inferior vesical artery
Distal branches, superior mesenteric artery
Inferior epigastric artery
Common iliac artery
Internal iliac artery
Anterior division, internal iliac artery
External iliac artery
Deep circumflex iliac artery
Obturator artery
Femoral artery
Aorta
Median sacral artery
S1 vertebral body
Posterior division,internal iliac artery
Superior gluteal artery
Lateral sacral artery
Inferior gluteal artery
Accessory inferior gluteal artery
Internal pudendal artery
B
L

Fig. 71.5 **A**, Arteries of the male pelvis. **B**, Volume-rendered CT angiogram of a male pelvis. Left anterior oblique view of the right hemipelvis showing branches of the internal iliac artery. The vesical and middle anorectal branches of the anterior division are too small to be visualized.

The superior and larger branch passes medially into the first or second anterior sacral foramen, supplies the sacrum and contents of the sacral canal, and then leaves the sacrum via the corresponding posterior foramen to supply the skin and muscles posterior to the sacrum. The inferior branch crosses obliquely anterior to piriformis and the sacral anterior rami, and then descends lateral to the sympathetic trunk to anastomose with its fellow and the median sacral artery anterior to the coccyx. Its branches enter the anterior sacral foramina and are distributed in the same way as the branches of the superior artery.

Superior gluteal artery The superior gluteal artery is the largest branch of the internal iliac artery and effectively forms the main continuation of its posterior division. It runs posteriorly between the lumbosacral trunk and the first sacral ventral ramus, or between the first and second sacral ventral rami, and then turns slightly inferiorly, leaving the pelvis via the greater sciatic foramen above piriformis and dividing into superficial and deep branches. In the pelvis, it supplies piriformis, obturator internus and a nutrient artery to the ilium. The superficial branch enters the deep surface of gluteus maximus. Its numerous branches supply the muscle and anastomose with the inferior gluteal branches (see Fig. 77.47), while others perforate the tendinous medial attachment of the muscle to supply the skin over the sacrum, where they anastomose with the posterior branches of the lateral sacral arteries. The deep branch of the superior gluteal artery passes between gluteus medius and the ilium, soon dividing into superior and inferior branches. The superior branch skirts the superior border of gluteus minimus to the anterior superior iliac spine and anastomoses with the deep circumflex iliac artery and the ascending branch of the lateral circumflex femoral artery. The inferior branch runs through gluteus minimus obliquely, supplies it and gluteus medius, and anastomoses with the lateral circumflex femoral artery. A branch enters the trochanteric fossa to join the inferior gluteal artery and ascending branch of the medial circumflex femoral artery; other branches run through gluteus minimus to supply the hip joint.

The superior gluteal artery occasionally arises directly from the internal iliac artery with the inferior gluteal artery and sometimes from the internal pudendal artery.

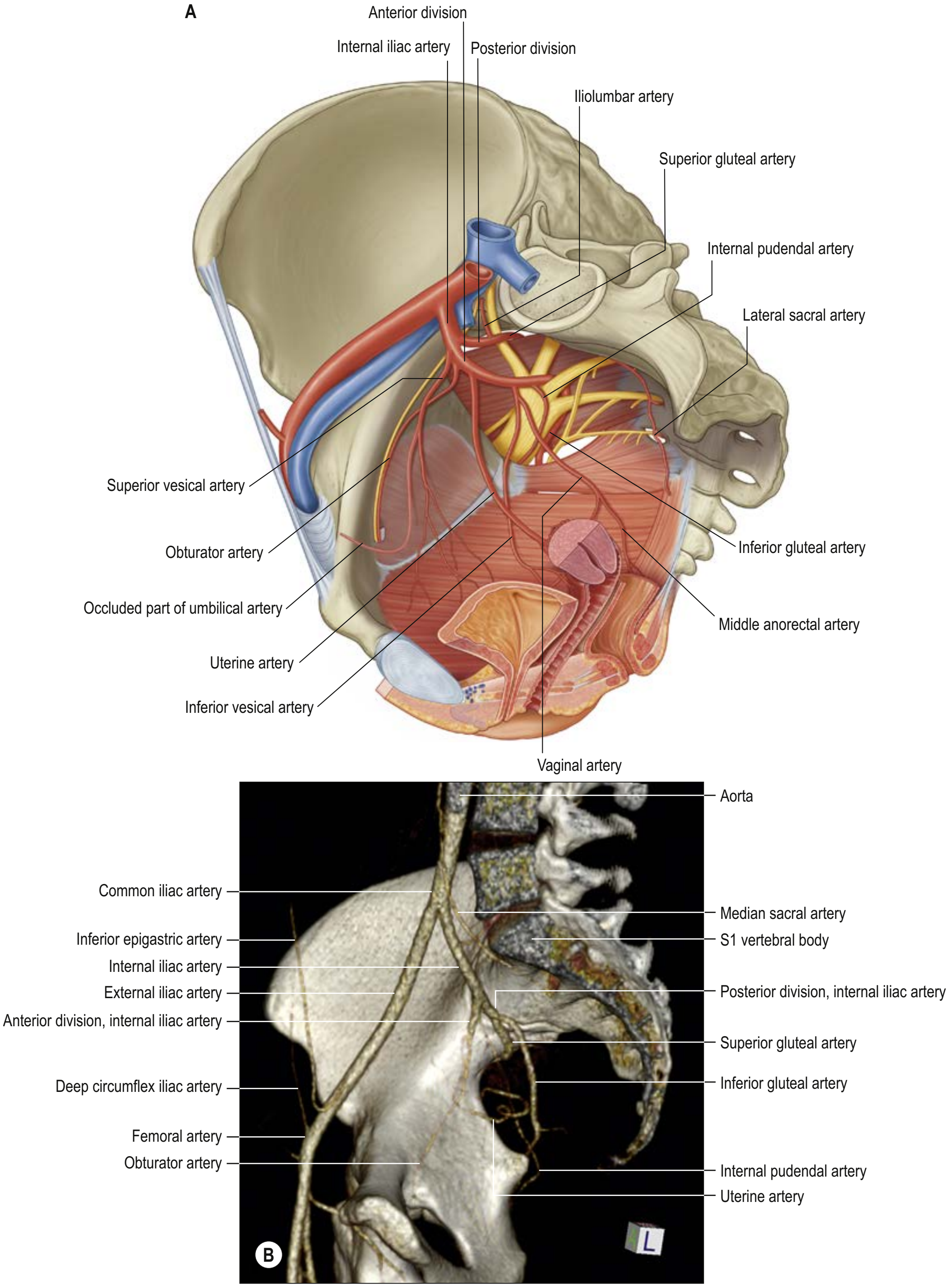
A
Anterior division
Internal iliac artery
Posterior division
Iliolumbar artery
Superior gluteal artery
Internal pudendal artery
Lateral sacral artery
Superior vesical artery
Obturator artery
Occluded part of umbilical artery
Uterine artery
Inferior vesical artery
Inferior gluteal artery
Middle anorectal artery
Vaginal artery
Aorta
Common iliac artery
Median sacral artery
S1 vertebral body
Inferior epigastric artery
Internal iliac artery
External iliac artery
Posterior division, internal iliac artery
Anterior division, internal iliac artery
Superior gluteal artery
Deep circumflex iliac artery
Inferior gluteal artery
Femoral artery
Obturator artery
Internal pudendal artery
Uterine artery
L
B

Fig. 71.6 A, Arteries of the female pelvis. **B**, Volume-rendered CT angiogram of a female pelvis. Left anterior oblique view of the right hemipelvis showing branches of the internal iliac artery. The vesical and inferior anorectal branches of the anterior division are too small to be visualized. Note that the middle gluteal artery arises from the posterior division as a variant.

Anterior division branches

The branches of the anterior division of the internal iliac artery are the superior and inferior vesical, middle anorectal, vaginal, obturator, uterine, internal pudendal and inferior gluteal arteries (see Fig. 71.6). There is significant variation in the branching patterns of the anterior division and therefore only the general principles will be considered here.

Superior vesical artery The superior vesical artery is the first large branch of the anterior division. It lies on the lateral wall of the pelvis, just inferior to the linea terminalis, and runs anteroinferiorly, medial to the periosteum of the posterior surface of the pubis. It supplies the distal end of the ureter, the urinary bladder, the proximal end of the ductus deferens and the seminal glands. It also gives origin to the umbilical artery in the fetus, which remains as a fibrous cord – the medial umbilical ligament – in the adult. This vessel occasionally remains patent as a small artery supplying the umbilicus.

Inferior vesical artery The inferior vesical artery sometimes arises as a common branch with the middle anorectal artery. It supplies the urinary bladder, prostate, seminal glands and ductus deferens in the male, and the urinary bladder in the female, where it is often replaced by the vaginal artery. De Treigny et al (2017) identified this vessel in roughly one half of females.

Middle anorectal artery The middle anorectal artery runs into the lateral fascial coverings of the mesorectum. It often consists of multiple branches, can be small, and occasionally arises either close to or in common with the origin of the inferior vesical artery in males.

Vaginal artery In females, the vaginal artery sometimes replaces the inferior vesical artery. It can arise from the uterine artery close to its origin as either a single vessel or multiple branches.

Obturator artery The obturator artery usually arises from the anterior division of the internal iliac artery, but it may also arise as a common branch with the iliolumbar or superior gluteal arteries, or from the external iliac artery as a separate branch or with the inferior epigastric artery (Pai et al 2009). It runs anteroinferiorly on the lateral pelvic wall to the upper part of the obturator foramen. In the pelvis, it is related laterally to the obturator fascia and is crossed on its medial aspect by the ureter and, in the male, by the ductus deferens. The obturator nerve is superior to the artery, the obturator vein inferior to it. The obturator artery provides iliac branches to the iliac fossa that supply the underlying bone and iliacus and anastomose with the iliolumbar artery. It gives off a branch that runs medially to the urinary bladder and sometimes replaces the inferior vesical artery. In the female, the ovary lies medial to the obturator artery. A pubic branch usually arises just before the obturator artery leaves the pelvis and ascends over the pubis to anastomose with the contralateral artery and the pubic branch of the inferior epigastric artery.

The obturator artery leaves the pelvis via the obturator canal. It divides into anterior and posterior branches that encircle the obturator foramen between obturator externus and the obturator membrane. The anterior branch curves anteriorly on the membrane and then inferiorly along its anterior margin to supply branches to obturator externus, pectineus, adductors longus, brevis and magnus and gracilis. It anastomoses with the posterior branch and the medial circumflex femoral artery. The posterior branch follows the posterior margin of the obturator foramen, turning anteriorly on the ischial part to anastomose with the anterior branch. It supplies the muscles attached to the ischial tuberosity and anastomoses with the inferior gluteal artery. An acetabular branch enters the hip joint at the acetabular notch, ramifies in the fat of the acetabular fossa and sends a branch along the ligament of the head of the femur.

The obturator artery is occasionally replaced by an enlarged pubic branch of the inferior epigastric artery that descends almost vertically to the obturator foramen. It usually lies near the external iliac vein, lateral to the femoral ring, and is rarely injured during inguinal or femoral hernia surgery. It may curve along the edge of the lacunar ligament, partly encircling the neck of a hernia sac, and can be cut inadvertently during enlargement of the femoral ring in reducing a femoral hernia.

Uterine artery The uterine artery is large. It usually arises inferior to the obturator artery on the lateral wall of the pelvis, running inferomedially within the cardinal ligament. It may arise directly from the internal iliac artery, the superior gluteal artery, obturator artery or from a common trunk with the internal pudendal artery (Chantalat et al 2014).

Internal pudendal artery (pelvic portion) The internal pudendal artery is the smaller terminal branch of the anterior division of the internal iliac artery. Close to its origin it crosses anterior to piriformis, the sacral plexus and the inferior gluteal artery. It descends laterally to the inferior aspect of the greater sciatic foramen, where it leaves the pelvis between piriformis and ischiococcygeus and enters the gluteal region (see Fig. 75.3B). It next curves around the posterior aspect of the ischial spine and enters the ischio-anal fossa via the lesser sciatic foramen. This course effectively allows the nerve to wrap around the posterior limit of levator ani at its attachment to the ischial spine. Posterior to the ischial spine the artery is covered by gluteus maximus, the pudendal nerve is medial and the nerve to obturator internus is lateral. The artery passes through the ischio-anal fossa in the pudendal canal (Alcock's canal) in the fascia covering obturator internus, giving off the inferior anorectal artery early in its course through the fossa (see Fig. 71.12). It gives off several muscular branches in the pelvis and the gluteal region to supply adjacent muscles and nerves.

Inferior gluteal artery The inferior gluteal artery is the larger terminal branch of the anterior division of the internal iliac artery. It descends posteriorly, anterior to the sacral plexus and piriformis but posterior to the internal pudendal artery. It passes between either the first and second, or the second and third, sacral ventral rami, then between piriformis and ischiococcygeus, before running through the inferior aspect of the greater sciatic foramen to reach the gluteal region. It next runs inferiorly with the sciatic and posterior femoral cutaneous nerves, deep to gluteus maximus and between the greater trochanter and ischial tuberosity, and continues down the thigh, supplying the skin and anastomosing with branches of the perforating arteries. The inferior gluteal and internal pudendal arteries often arise as a common stem from the internal iliac artery, sometimes with the superior gluteal artery. In the pelvis, the inferior gluteal artery gives branches to piriformis, ischiococcygeus and iliococcygeus, and occasionally gives rise to the middle anorectal artery. It can supply vessels to the seminal glands and prostate.

External iliac artery

The external iliac arteries are larger than the internal iliac arteries (see Figs 71.5–71.6). Each artery descends laterally along the medial border of psoas major, from the common iliac bifurcation to a point midway between the anterior superior iliac spine and the pubic symphysis, and enters the thigh posterior to the inguinal ligament to become the femoral artery.

The parietal peritoneum and extraperitoneal tissues separate the right external iliac artery from the terminal ileum and, usually, the appendix, and the left external iliac artery from the sigmoid colon and coils of small intestine anteromedially. The external iliac artery can be crossed at its origin by the ureter and it is subsequently crossed by the gonadal vessels, the genital branch of the genitofemoral nerve, the deep circumflex iliac vein, and the ductus deferens or round ligament of the uterus. Posteriorly, the artery is separated from the medial border of psoas major by the iliac fascia. The external iliac vein lies partly posterior to its upper part but is more medial below. Laterally, it is related to psoas major, which is covered by the iliac and psoas fasciae. Numerous lymph vessels and nodes lie on its anterior and lateral aspects. The external iliac artery primarily supplies the lower limb and as such has few branches in the pelvis. It gives off very small vessels to psoas major and neighbouring lymph nodes, but has no other branches until it gives off the deep circumflex iliac and inferior epigastric arteries, near to where it passes deep to the inguinal ligament.

Deep circumflex iliac artery The deep circumflex iliac artery branches laterally from the external iliac artery almost opposite the origin of the inferior epigastric artery (see Fig. 76.4). It ascends and runs laterally to the anterior superior iliac spine deep to the inguinal ligament in a sheath formed by the union of the transversalis and iliac fasciae. There, it anastomoses with the ascending branch of the lateral circumflex femoral artery, pierces the transversalis fascia and skirts the inner lip of the iliac crest. About halfway along the iliac crest, it runs through transversus abdominis, and then between transversus abdominis and internal abdominal oblique, to anastomose with the iliolumbar and superior gluteal arteries. It gives off a large ascending branch at the anterior superior iliac spine that runs between internal abdominal oblique and transversus abdominis, supplies both muscles, and anastomoses with the lumbar and inferior epigastric arteries.

Inferior epigastric artery The inferior epigastric artery originates from the external iliac artery posterior to the inguinal ligament. It curves forwards in the anterior extraperitoneal tissue, ascends obliquely along the medial margin of the deep inguinal ring and continues as an artery of the anterior abdominal wall.

Veins

The lesser pelvis contains a large number of veins that drain the pelvic walls and most of the viscera contained within the lesser pelvis, and also carry venous blood from the gluteal region, hip and thigh. The external iliac veins, which lie close to the linea terminalis, carry the venous drainage from most of the lower limb. The major veins draining the pelvis frequently follow their named arterial counterparts, while the small tributaries exhibit considerable inter-individual variation.

Common iliac vein

The common iliac vein is formed by the union of the external and internal iliac veins, anterior to the sacroiliac joints (see Fig. 76.8). It ascends obliquely to end at the right side of the fifth lumbar vertebra, uniting at an acute angle with the contralateral vessel to form the inferior vena cava. The right common iliac vein is shorter and more nearly vertical, lying posterior and then lateral to its artery; the right obturator nerve passes posteriorly. The left common iliac vein is longer and more oblique and lies first medial, then posterior, to its artery. It is crossed anteriorly by the attachment of the sigmoid mesocolon and superior anorectal vessels. Each vein receives iliolumbar and, sometimes, lateral sacral veins. The left common iliac vein usually drains the median sacral vein. There are no valves in these veins.

The left common iliac vein occasionally ascends to the left of the aorta to the level of the kidney, where it receives the left renal vein and then crosses anterior to the aorta to join the inferior vena cava; this vessel represents the persistent caudal half of the left postcardinal or supracardinal vein.

Median sacral veins The right and left median sacral veins accompany the corresponding arteries anterior to the sacrum, where they unite to form a single vein that usually ends in the left common iliac vein, but sometimes ends at the common iliac junction.

Internal pudendal veins The internal pudendal veins are venae comitantes of the internal pudendal artery and unite as a single vessel that drains into the internal iliac vein. They receive veins from the inferior anorectal veins and either the bulb of the penis and scrotum, or the clitoris and labia.

Internal iliac vein

The internal iliac vein is formed by the convergence of several veins above the greater sciatic foramen. It does not have the predictable trunks and branches of the internal iliac artery but its tributaries drain the same territories. It ascends posteromedial to the internal iliac artery to join

The anteroposterior diameters of the common, external and internal iliac arteries are strongly correlated to body surface area (BSA) in children, in contrast to adults, where the relation is inconsistent. Vessel diameters measured by ultrasonography are significantly larger in boys than in girls. The relationship between vessel diameters and BSA is shown in Fig. 71.7 (Munk et al 2002).

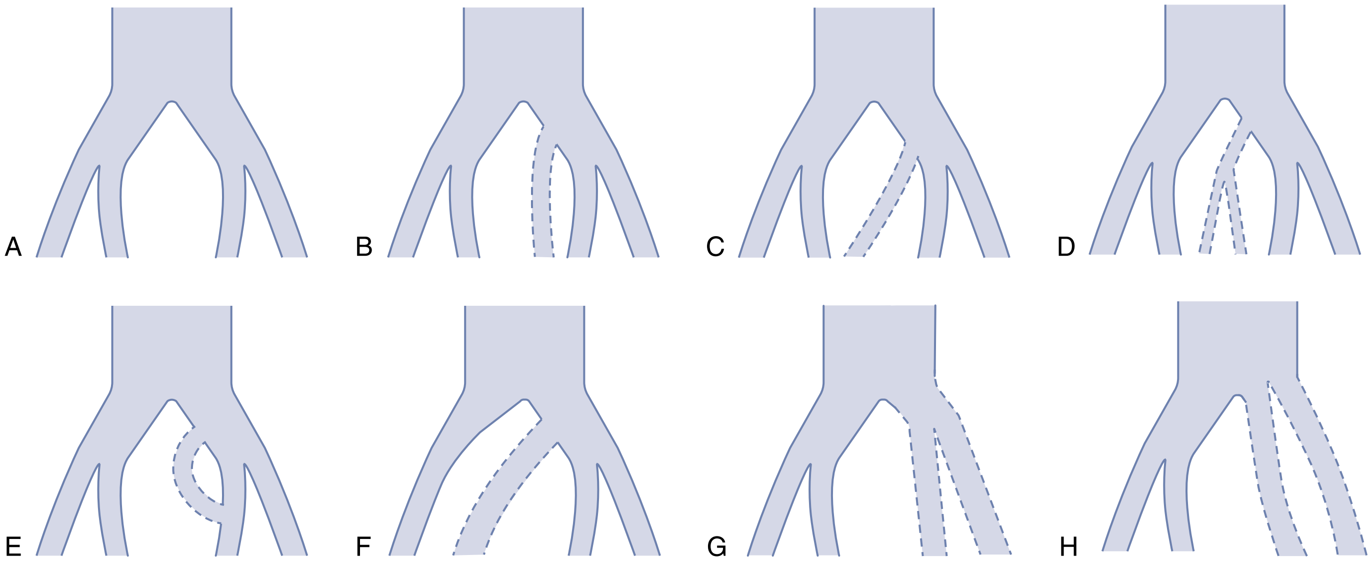

Fig. 71.7 The relations between anteroposterior diameters of the right common, internal and external iliac arteries and body surface area (BSA) in boys and girls between the ages of 1 and 16 years. (Redrawn from DePietro DM, Carlon T, Trerotola SO, Sudheendra D. Endovascular Treatment of an Anatomically Complex Iliac Lesion and a Review of Variant Iliac Venous Anatomy. J Vasc Interv Radiol. 2020;31(2):260–264.)

the external iliac vein, forming the common iliac vein at the linea terminalis, anterior to the lower part of the sacroiliac joint. It is covered anteromedially by parietal peritoneum. Its tributaries are the gluteal, internal pudendal and obturator veins, which originate outside the pelvis; the lateral sacral veins, which run from the anterior surface of the sacrum; and the middle anorectal, vesical, uterine and vaginal veins, which originate in the venous plexuses of the pelvic viscera (**Fig. 71.8**).

The venous drainage of the leg can be blocked by thrombosis involving the external iliac systems and the inferior vena cava. Under these circumstances, the pelvic veins, particularly the internal iliac tributaries, enlarge and provide a major avenue of venous return from the femoral system. Surgical interference with these veins can seriously compromise venous drainage and precipitate oedema of one or both lower limbs.

Superior gluteal veins The superior gluteal veins are the venae comitantes of the superior gluteal artery. They receive tributaries that correspond to the branches of the superior gluteal artery and enter the pelvis via the greater sciatic foramen, superior to piriformis. They join the internal iliac vein, frequently as a single trunk.

Inferior gluteal veins The inferior gluteal veins are venae comitantes of the inferior gluteal artery. They begin proximally and posteriorly in the thigh, where they anastomose with the medial circumflex femoral and first perforating veins, and they enter the pelvis low in the greater sciatic foramen, joining to form a vessel that opens into the distal part of the internal iliac vein. The inferior gluteal and superficial gluteal veins connect by perforating veins (Doyle 1970). The gluteal veins probably have a venous 'pumping' role, and provide collaterals between the femoral and internal iliac veins.

Obturator vein The obturator vein begins in the proximal adductor region and enters the pelvis via the obturator foramen. It runs posteriorly and superiorly on the lateral pelvic wall below the obturator artery and between the ureter and internal iliac artery, and ends in the internal iliac vein. It is sometimes replaced by an enlarged pubic vein that joins the external iliac or the inferior epigastric veins (Sanna et al 2018).

Lateral sacral veins The lateral sacral veins accompany the lateral sacral arteries and are interconnected by a sacral venous plexus.

Middle anorectal vein The middle anorectal vein begins in the anorectal venous plexus and drains the rectum and mesorectum. Variable in size, it runs laterally on the pelvic surface of levator ani to end in the internal iliac vein. The middle anorectal vein often receives tributaries from the urinary bladder and either the prostate and seminal gland or the posterior aspect of the vagina.

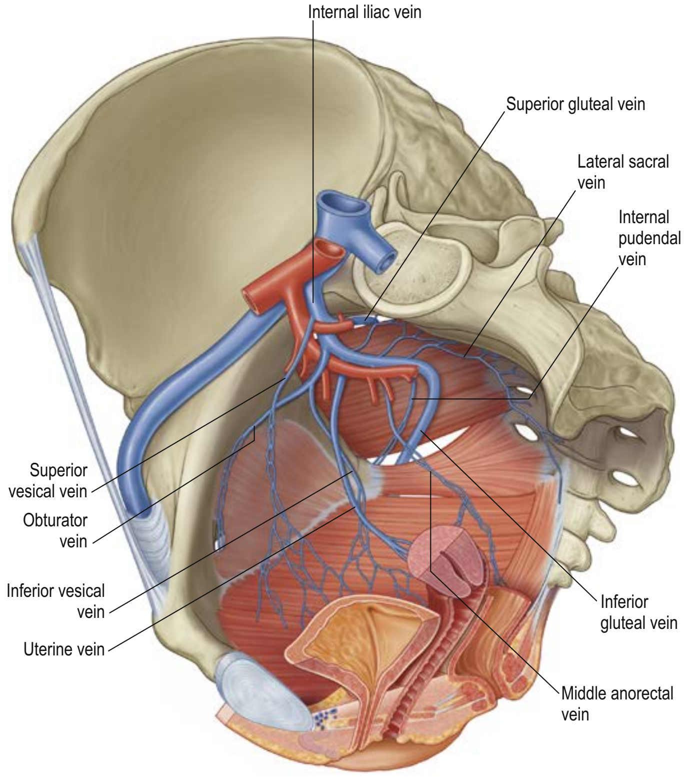

Fig. 71.8 Veins of the female pelvis.

External iliac vein

The external iliac vein is the proximal continuation of the femoral vein (see Figs 76.8, 77.49). It begins posterior to the inguinal ligament, ascends along the linea terminalis and ends anterior to the sacroiliac joint by joining the internal iliac vein to form the common iliac vein. On the right it lies medial to the external iliac artery, gradually inclining behind it as it ascends. On the left it is wholly medial. Disease of the external iliac artery can cause it to adhere closely to the vein at the point where it is in contact, and, particularly on the right side, the walls of the vessels can become fused, making dissection hazardous. The external iliac vein is crossed medially by the ureter and internal iliac artery and by the ductus deferens (males) or the round ligament of the uterus and ovarian vessels (females). Psoas major lies laterally, except where the artery intervenes. The vein is usually valveless but sometimes contains a single valve. Its tributaries are the inferior epigastric, deep circumflex iliac and pubic veins. Agenesis of the external iliac vein has been reported in association with Klippel–Trenaunay syndrome (Doğan et al 2003).

Inferior epigastric vein One or two inferior epigastric veins accompany the inferior epigastric artery and drain into the external iliac vein just proximal to the inguinal ligament.

Deep circumflex iliac vein The deep circumflex iliac vein is formed from venae comitantes of the corresponding artery. It joins the external iliac vein a little above the inferior epigastric vein after crossing anterior to the external iliac artery.

Pubic vein The pubic vein connects the external iliac and obturator veins. It ascends on the pelvic surface of the pubis with the pubic branch of the inferior epigastric artery and occasionally replaces the normal obturator vein.

Lymphatic drainage

The lymph nodes in the pelvis are grouped around the common, external iliac and internal iliac vessels and are named accordingly (Nesselrod 1936).

Common iliac nodes

The common iliac nodes drain both internal and external iliac nodes and therefore receive the entire lymphatic drainage of the lower limb. They usually lie in medial, lateral and anterior chains around the common iliac artery, the lateral chain constituting the main route. One or two nodes lie inferior to the aortic bifurcation and anterior to the fifth lumbar vertebra or sacral promontory. The common iliac nodes drain to the lateral aortic nodes.

External iliac nodes

The external iliac nodes usually form three subgroups, lateral, medial and anterior to the external iliac vessels (see Fig. 75.3B). The medial nodes are considered the main channel of drainage, collecting lymph from the lower limb via the inguinal nodes, the deeper layers of the infra-umbilical abdominal wall, the medial compartment of the thigh, the glans penis or clitoris, the membranous urethra, prostate, fundus of the bladder, cervix of the uterus and proximal vagina. Their efferents pass to the common iliac nodes.

Inferior epigastric and circumflex iliac nodes The inferior epigastric and circumflex iliac nodes are associated with their similarly named vessels and drain the corresponding areas to the external iliac nodes.

Internal iliac nodes

The internal iliac nodes surround the branches of the internal iliac vessels. They receive afferents from most of the pelvic viscera (with the exception of the gonads and most of the rectum), the deeper parts of the perineum and the gluteal and posterior thigh muscles, and drain to the common iliac nodes. The individual groups are considered in the description of the viscera. There are frequent connections between the right and left groups, particularly when they lie close to the anterior and posterior midlines (**Fig. 71.9**).

Innervation

The pelvis contains the lumbosacral trunk, the sacral and coccygeal plexuses and the pelvic parts of the sympathetic and parasympathetic systems. Collectively, these nerves carry the somatic and autonomic innervation to most of the pelvic organs, and to the muscles of the pelvic diaphragm and perineum, the gluteal region and the lower limb.

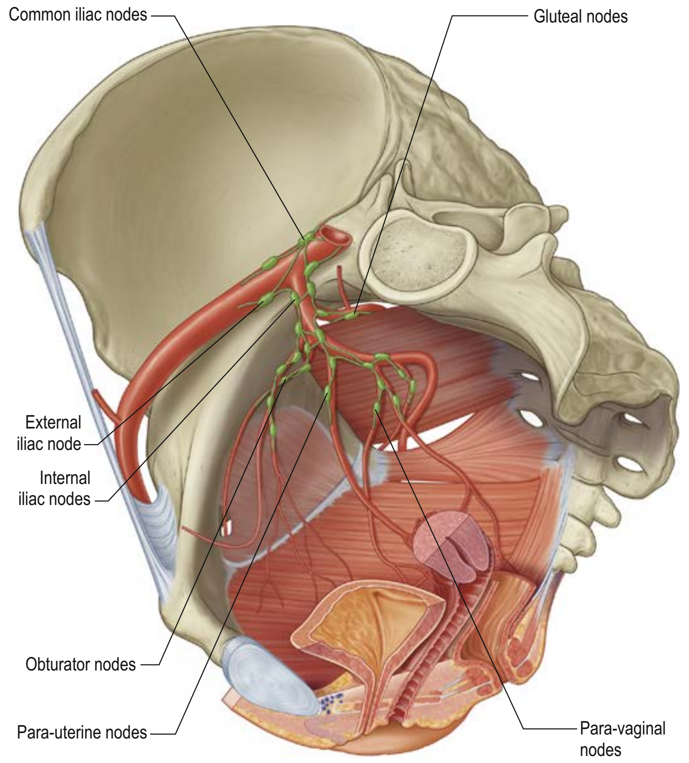
Common iliac nodes
Gluteal nodes
External iliac node
Internal iliac nodes
Obturator nodes
Para-uterine nodes
Para-vaginal nodes

Fig. 71.9 Lymphatic drainage of the female pelvis and urinary bladder.

The ventral rami of the sacral and coccygeal spinal nerves form the sacral and coccygeal plexuses (Fig. 71.10). The upper four sacral ventral rami enter the pelvis via the anterior sacral foramina, the fifth enters between the sacrum and coccyx, and the ventral ramus of the coccygeal nerve curves anteriorly and inferior to the rudimentary transverse process of the first coccygeal segment. The first and second sacral ventral rami are large, the third to fifth diminish progressively in size, and the coccygeal ventral ramus is the smallest. Each receives a grey ramus communicans from a corresponding sympathetic ganglion. Preganglionic parasympathetic fibres leave the second to fourth sacral ventral rami as the pelvic splanchnic nerves and continue to minute ganglia in the walls of the pelvic viscera.

Lumbosacral trunk and sacral plexus

The sacral plexus is formed by the lumbosacral trunk, the first to third sacral ventral rami, and part of the fourth sacral ventral ramus (the remainder of the fourth sacral ventral ramus joins the coccygeal plexus).

The lumbar part of the lumbosacral trunk contains part of the fourth and all of the fifth lumbar ventral rami; it appears at the medial margin of psoas major and descends over the linea terminalis, at first medial to and then distally crossing anterior to the sacroiliac joint, to join the first sacral ventral ramus. The greater parts of the second and third sacral rami converge on the inferomedial aspect of the lumbosacral trunk in the greater sciatic foramen to form the sciatic nerve. The ventral and dorsal divisions of the nerves do not separate physically from each other but their fibres remain separate within the rami; the ventral and dorsal divisions of each contributing root join within the sciatic nerve. The fibres of the dorsal divisions will go on to form the common fibular nerve, and the fibres of the ventral division form the tibial nerve. Occasionally, the sciatic nerve divides into common fibular and tibial nerves inside the pelvis; when this occurs, the common fibular nerve usually runs through piriformis.

The sacral plexus lies against the posterior pelvic wall anterior to piriformis, posterior to the internal iliac vessels and ureter, and posterior to the sigmoid colon on the left. The superior gluteal vessels run either between the lumbosacral trunk and first sacral ventral ramus, or between the first and second sacral anterior rami, while the inferior gluteal vessels lie between either the first and second, or the second and third, sacral ventral rami.

The sacral plexus is not commonly involved in malignant tumours of the pelvis because it lies behind the relatively dense presacral fascia, which resists all but locally very advanced malignant infiltration. When it occurs, there is intractable pain in the distribution of the branches of the plexus, which can be very difficult to treat. The plexus can also be involved in reticuloses or be affected by plexiform neuromas.

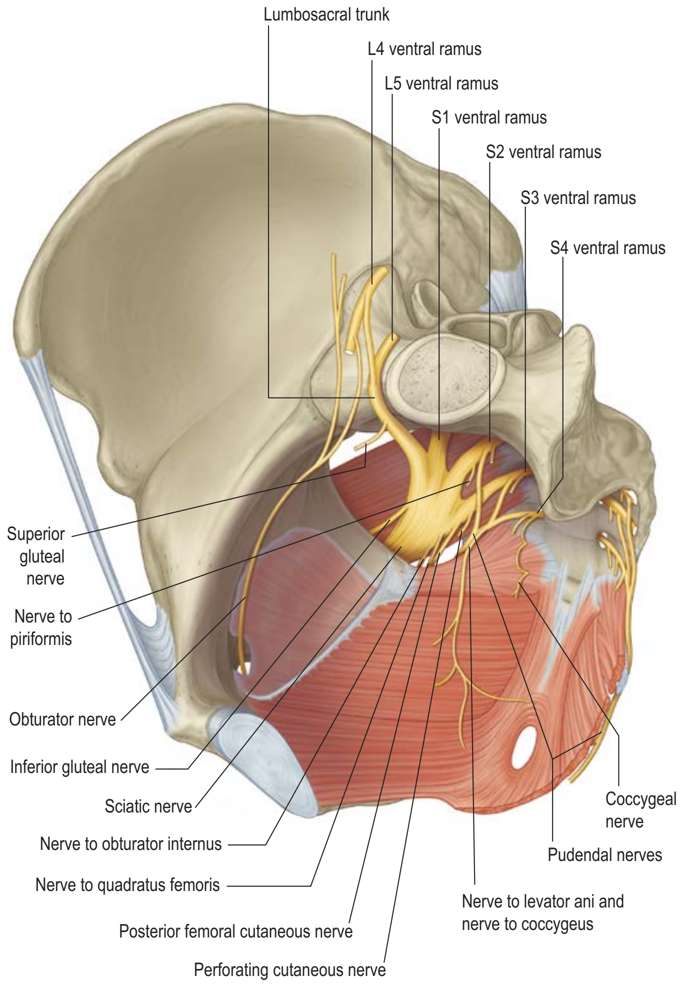
Lumbosacral trunk
L4 ventral ramus
L5 ventral ramus
S1 ventral ramus
S2 ventral ramus
S3 ventral ramus
S4 ventral ramus
Superior gluteal nerve
Nerve to piriformis
Obturator nerve
Inferior gluteal nerve
Sciatic nerve
Nerve to obturator internus
Nerve to quadratus femoris
Posterior femoral cutaneous nerve
Perforating cutaneous nerve
Coccygeal nerve
Pudendal nerves
Nerve to levator ani and nerve to coccygeus

Fig. 71.10 The lumbosacral plexus in the pelvis.

TABLE 71.1 Branches of the sacral plexus

Nerve	Ventral divisions	Dorsal divisions
Nerve to quadratus femoris	L4, L5, S1	
Nerve to obturator internus	L5, S1, S2	
Nerve to piriformis		S1, S2 and direct branches from superior gluteal nerve
Superior gluteal nerve		L4, L5, S1
Inferior gluteal nerve		L5, S1, S2
Posterior femoral cutaneous nerve	S2, S3	S1, S2
Tibial nerve (sciatic nerve)	L4, L5, S1, S2, S3	
Common fibular nerve (sciatic nerve)		L4, L5, S1, S2
Perforating cutaneous nerve		S2, S3
Pudendal nerve	S2, S3, S4	
Nerves to levator ani	S4	

Branches of the sacral plexus

The branches of the sacral plexus are shown in **Table 71.1**.

The course and distribution of most of these branches are covered fully in Section 9 and in Chapter 80.

Pudendal nerve (in the pelvis)

The pudendal nerve arises from the ventral divisions of the second, third and fourth sacral ventral rami and is formed just above the superior border of the sacrotuberous ligament and the upper fibres of ischiococcygeus (Klink 1953, Sato 1980). It leaves the pelvis via the greater sciatic foramen between piriformis and ischiococcygeus (see Fig. 71.10), enters the gluteal region and passes dorsal to the sacrospinous ligament, close to its attachment to the ischial spine, where it lies medial to the internal pudendal vessels. It accompanies the internal pudendal artery through the lesser sciatic foramen into the pudendal canal on the lateral wall of the ischio-anal fossa. In the posterior part of the canal, it gives rise to the inferior anal and perineal nerves; the dorsal nerve of the penis or clitoris continues anteriorly from this origin.

Sacral visceral branches

Visceral branches, the pelvic splanchnic nerves, arise from the second to fourth sacral ventral rami and innervate the pelvic viscera.

Sacral muscular branches

Several muscular branches arise from the fourth sacral ventral ramus to supply the superior surface of levator ani and the upper part of the external anal sphincter. The branches to levator ani enter the superior surface of the muscle. The branch to the external anal sphincter (also referred to as the perineal branch of the fourth sacral nerve) reaches the ischio-anal fossa by running either through ischiococcygeus or between ischiococcygeus and iliococcygeus: it also supplies the skin between the anus and coccyx.

Coccygeal plexus

The coccygeal plexus is formed by a small descending branch from the fourth sacral ventral ramus and by the fifth sacral and coccygeal ventral rami. The fifth sacral ventral ramus emerges from the sacral hiatus, curves round the lateral margin of the sacrum inferior to its cornu, and pierces ischiococcygeus inferiorly to reach its pelvic surface. Here it is joined by a descending branch of the fourth sacral ventral ramus; the small trunk so formed descends on the pelvic surface of ischiococcygeus, joins the minute coccygeal ventral ramus that emerges from the sacral hiatus, and curves round the lateral coccygeal margin, piercing ischiococcygeus to reach the pelvis. The small trunk that is formed in this way is the coccygeal plexus. Anococcygeal nerves arise from it and form a few fine filaments that pierce the sacrotuberous ligament to supply the adjacent skin.

Pelvic part of the sympathetic system

The pelvic sympathetic trunk lies in the extraperitoneal tissue, anterior to the sacrum beneath the presacral fascia (Fig. 71.11), and supplies the pelvic organs and vascular system. It lies medial or anterior to the anterior sacral foramina and has four or five interconnected ganglia. Superiorly, it is continuous with the lumbar sympathetic trunk. The right and left trunks converge distal to the most inferior ganglia and unite in the small ganglion impar anterior to the coccyx. Grey rami communicantes pass from the ganglia to sacral and coccygeal spinal nerves; there are no white rami communicantes. Medial branches connect across the midline, and twigs from the first two ganglia join the inferior hypogastric plexus or the hypogastric nerve. Other branches form a plexus on the median sacral artery.

Vascular branches

Preganglionic fibres for the vessels supplying the pelvis and lower limb are derived from the lower three thoracic and upper two or three lumbar spinal cord segments. They reach the lower thoracic and upper lumbar ganglia through white rami communicantes and descend through the sympathetic trunk to synapse in the lumbar ganglia. Postganglionic fibres pass from these ganglia via grey rami communicantes to the second, third and fourth lumbar ventral rami and then to the femoral nerve, which carries them to the femoral artery and its branches. Some fibres descend through the lumbar ganglia to synapse in the upper two or three sacral ganglia, from which postganglionic axons pass through grey rami communicantes to the roots of the sacral plexus. Those in the pudendal and superior and inferior gluteal nerves accompany the arteries of the same name to the gluteal and perineal tissues; branches can also supply the pelvic nodes. Those joining the tibial nerve are carried to the popliteal artery and are distributed via its branches to the leg and foot.

Sympathetic denervation of vessels in the lower limb is used, rarely, for treating vascular insufficiency of the lower limb; it can be effected by removing or ablating the upper three lumbar sympathetic ganglia and the intervening parts of the sympathetic trunk.

PERINEUM

Anal and urogenital triangles

The perineum is an approximately diamond-shaped region that lies inferior to levator ani, between the medial aspects of the thighs and anterior to the sacrum and coccyx. It is usually described as if from the position of an individual lying supine with the hips abducted and partially flexed. The surface projection of the perineum and the form of the skin covering it vary considerably, depending on the position of the thighs, whereas the deep tissues themselves occupy relatively fixed positions. The perineum is bounded anteriorly by the pubic symphysis and its inferior pubic ligament, posteriorly by the coccyx, anterolaterally by the ischiopubic rami and the ischial tuberosities, and posterolaterally by the sacrotuberous

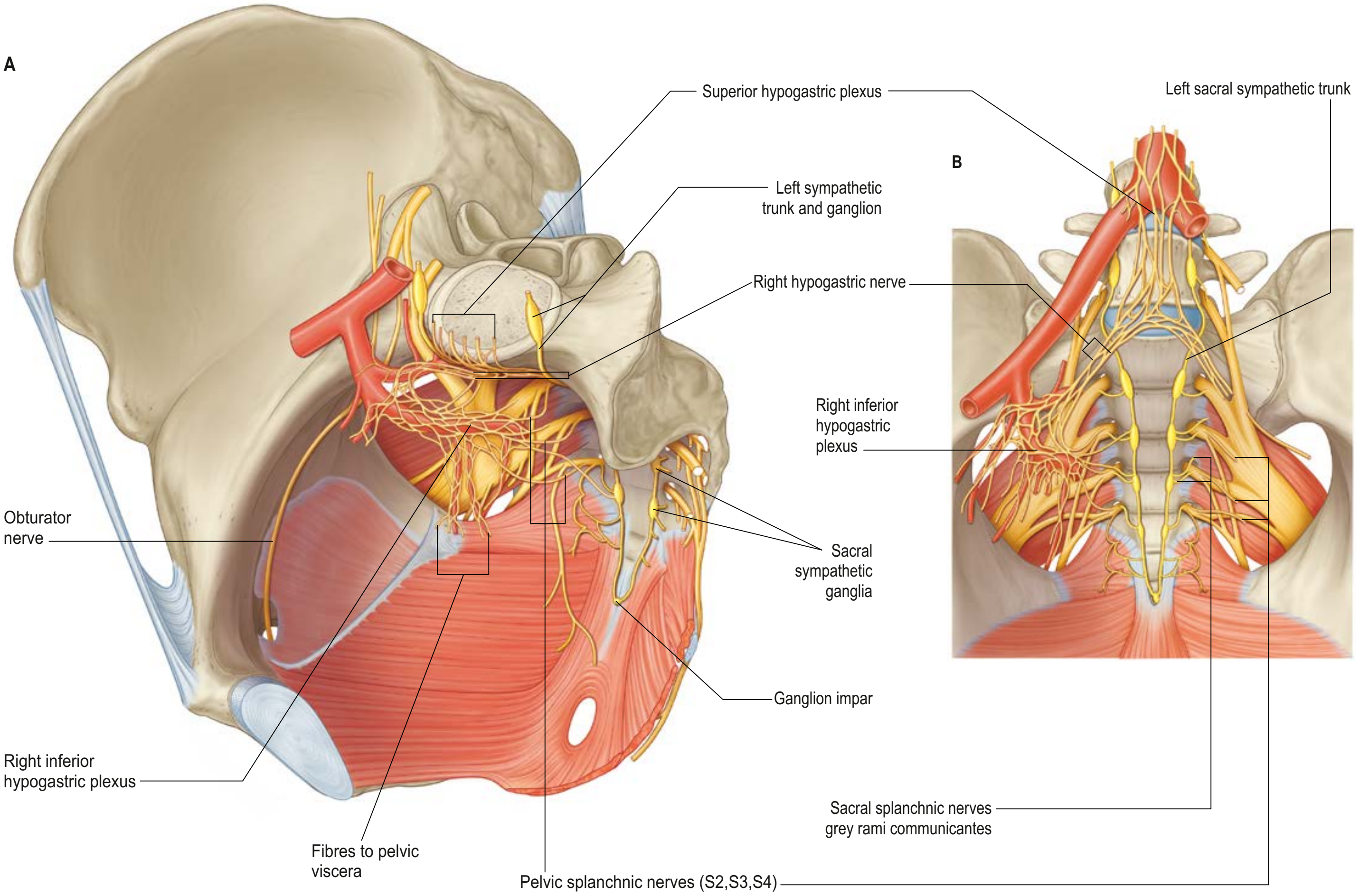
A
B
Superior hypogastric plexus
Left sacral sympathetic trunk
Left sympathetic trunk and ganglion
Right hypogastric nerve
Right inferior hypogastric plexus
Obturator nerve
Sacral sympathetic ganglia
Ganglion impar
Right inferior hypogastric plexus
Sacral splanchnic nerves grey rami communicantes
Fibres to pelvic viscera
Pelvic splanchnic nerves (S2,S3,S4)

Fig. 71.11 Autonomic nerves of the pelvis.

ligaments. The deep limit of the perineum is the inferior surface of the pelvic diaphragm. The superficial limit is the skin that is continuous with the skin over the medial aspect of the thighs and the lower abdominal wall. An arbitrary line joining the ischial tuberosities (the inter-ischial line) divides the perineum into an anterior urogenital triangle and a posterior anal triangle. The urogenital triangle faces inferiorly and anteriorly, whereas the anal triangle faces inferiorly and posteriorly at an approximate angle of 120° from the plane of the urogenital triangle.

The male urogenital triangle contains the root of the penis (**Fig. 71.12**) (Ch. 74), and the female urogenital triangle contains the mons pubis, the labia majora and minora, the clitoris, the vaginal orifice and the external urethral orifice (Ch. 75).

Anal triangle

The structure of the anal triangle is similar in males and females, the main difference being that in females the wider transverse dimension of the triangle is associated with giving birth. The anal triangle is lined by superficial and deep fasciae and contains the anal canal and its sphincters, and the ischio-anal fossa and its contained nerves and vessels.

Superficial fascia of the anal triangle

The superficial fascia (subcutaneous tissue) of the region is thin and is continuous with the superficial/subcutaneous fascia of the skin of the perineum, thighs and buttocks.

Deep fascia of the anal triangle

The deep fascia lines the inferior surface of levator ani and is continuous at its lateral origin with the fascia over obturator internus below the attachment of levator ani. It lines the proximal portion of the ischio-anal fossa and its lateral walls.

Ischio-anal fossa

The ischio-anal fossa is an approximately horseshoe-shaped region filling most of the anal triangle. It is filled with loose adipose tissue and blood vessels and nerves (see Fig. 71.12). The 'arms' of the horseshoe are triangular in cross-section because levator ani slopes medially from its lateral pelvic origin towards the anorectal junction (see Fig. 65.44). The anal canal and its sphincters lie in the centre of the horseshoe. Above them, the medial limit of the fossa is formed by the deep fascia over levator ani. The outer boundary of the fossa is formed anterolaterally by the fascia over obturator internus and the periosteum of the ischial tuberosities. Posterolaterally, the outer boundary is formed by the inferior border of gluteus maximus and the sacrotuberous ligament.

An anterior recess of the ischio-anal fossa lies cranial to the perineal membrane and transverse perineal muscles and extends anteriorly as far as the posterior surface of the pubis, below the attachment of levator ani. Posteriorly, the fossa contains the attachment of the external anal sphincter to the distal end of the coccyx; above and below this, the adipose tissue of the fossa is uninterrupted across the midline. These continuations of the ischio-anal fossa allow infections, tumours and fluid collections within them to enlarge relatively freely to the side of the anal canal, and also to spread with little resistance to the contralateral side and deep to the perineal membrane. The internal pudendal vessels and accompanying nerves lie in the lateral wall of the ischio-anal fossa, enclosed in fascia forming the pudendal canal. The inferior anorectal vessels and nerves cross the fossa from the pudendal canal and often branch within it.

The ischio-anal fossa is an important surgical plane during resections of the anal canal and anorectal junction for malignancy. It provides an easy, relatively bloodless, plane of dissection that encompasses all of the muscular structures of the anal canal and leads to the inferior surface of levator ani.

External anal sphincter

The external anal sphincter is a band of striated muscle that surrounds the most inferior part of the anal canal (Oh and Kark 1972, Lawson 1974b, Dalley 1987). The most superior fibres blend with the most inferior fibres of pubo-analis; the two are seen to be contiguous on endoanal ultrasound and MRI. Anteriorly, some of these upper fibres decussate into the superficial transverse perineal muscles. Posteriorly, fibres are attached to the anococcygeal raphe. Most of the middle fibres of the external anal sphincter surround the distal part of the internal sphincter, and are attached anteriorly in the perineal body and posteriorly to the coccyx via the anococcygeal ligament. Some fibres from each side of the sphincter decussate in these areas to form a sort of commissure in the anterior and posterior midline. The anterior and posterior attachments of the external anal sphincter give the muscular tube an oval profile lying anteroposteriorly. A subcutaneous portion encircles the anal verge and creates the radial skin creases surrounding the anus. The lower fibres lie below the level of the internal anal sphincter and are separated from the lowest anal epithelium by submucosa. The thickness of the external anal sphincter is positively correlated with age in children (de la Portilla and López-Alonso 2009, Rehman et al 2011) and negatively correlated with age in males (Rociu et al 2000).

Anococcygeal ligament and iliococcygeal raphe

The anococcygeal ligament is a musculotendinous structure running between the external anal sphincter and the coccyx. The iliococcygeal raphe (the decussation of the posterior fibres of iliococcygeus) lies just superior

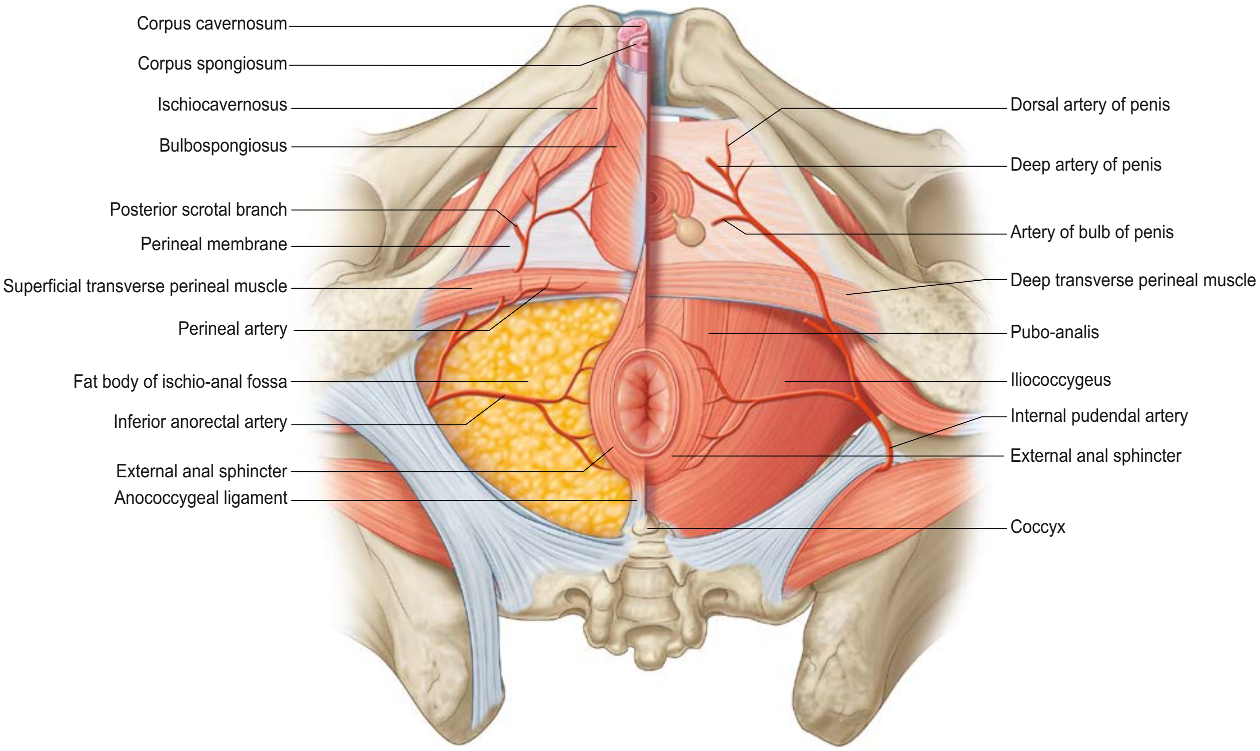

Fig. 71.12 Muscles and fasciae of the male perineum. On the left side of the figure, only the skin and superficial fascia of the perineum have been removed. The posterior scrotal branch of the perineal artery has been shown as it runs anteriorly into the scrotal tissues. On the right side, the corpora cavernosa and corpus spongiosum and their associated muscles, the superficial perineal muscles and perineal membrane have been removed to reveal the underlying deep muscles and arteries of the perineum. All veins and nerves have been omitted for clarity.

to the anococcygeal ligament and is separated from the rectum by presacral fascia: these structures are often referred to as the postanal plate. Division of the anococcygeal raphe can cause descent of the anal canal and a lowering of the posterior part of the anal triangle, but does not demonstrably interfere with the process of defecation (Kinugasa et al 2012).

Urogenital triangle

The urogenital triangle is bounded posteriorly by the inter-ischial line, which usually overlies the posterior border of the transverse perineal muscles. Anteriorly and laterally, it is bounded deeply by the pubic symphysis and ischiopubic rami. In males, the urogenital triangle extends superficially to encompass the scrotum and the root of the penis. In females, it extends to the lower limit of the labia and mons pubis. The urogenital triangle is divided into two parts by a strong perineal membrane: the deep perineal space lies superior to the membrane and the superficial perineal space lies inferior to it.

The female urogenital triangle includes muscles, fasciae, erectile structures and spaces similar to those in the male. There are some differences in size and disposition reflecting the presence of the vagina and female external genitalia.

Deep perineal space

Perineal membrane

It was once thought that the anterior pelvic outlet was spanned by a triangular, trilaminar, musculofascial structure, the urogenital diaphragm, that consisted of urogenital sphincter muscles sandwiched between two layers of fascia and connected to the perineal body, the periosteum of the ischiopubic rami and the inferior pubic ligament of the pubis, and perforated by the urethra and vagina. Oelrich introduced the alternative term 'perineal membrane' (Oelrich 1983). Detailed histological examination of serial cross-sections now supports the concept of the perineal membrane as part of a larger interconnected support apparatus with distinct posterior and anterior portions that are intimately connected with levator ani. The posterior portion is related to the support of the perineal body and lateral vaginal wall by its attachment to the ischiopubic ramus, and the anterior portion is contiguous with the urethral supportive apparatus (Stein and DeLancey 2008). The perineal membrane is particularly thick where it is attached to the inferior pubic ligament, and is here referred to as the transverse perineal ligament. The posterior border of the perineal membrane is continuous with the deep part of the perineal body at its posterior margin and is continuous with the fascia over the superficial transverse perineal muscles.

In the male, the perineal membrane is crossed by the urethra, which traverses it 2–3 cm behind the inferior border of the pubic symphysis; the vessels and nerves to the root of the penis; the ducts of the bulbourethral glands; the deep dorsal vessels and dorsal nerves of the penis, behind the pubic arch in the midline; and the posterior scrotal vessels and nerves, anterior to the transverse perinei.

In the female, the perineal membrane is divided almost into two halves by the vagina and urethra, such that it forms a triangle on each side of these structures. The lateral margins of the vagina are attached to the perineal membrane at the level of the hymenal ring, and levator ani lies on its cranial surface. The ducts of the greater vestibular glands (Bartholin's glands) are at this level in the posterior lateral vaginal orifice. The deep dorsal vessels and dorsal nerves of the clitoris lie within its fibres.

Urethral sphincter mechanism

The urethral sphincter mechanism consists of both striated and smooth muscle sphincters (Oelrich 1980, 1983, Huisman 1983). The striated urogenital sphincter has an upper circular element that surrounds the urethra in the female and the apex of the prostate in the male, between the neck of the bladder and perineal membrane. In the female, at the level of the perineal membrane, it extends laterally outside the urethra in two arch-shaped bands, compressor urethrae and sphincter urethrovaginalis, which lie on the cranial surface of the perineal membrane (**Fig. 71.13**). Compressor urethrae follows the pubic arch and is attached to connective tissue in this area near the inner surface of the ischiopubic ramus. Sphincter urethrovaginalis extends caudally to surround the lateral margin of the vaginal wall. In the male, these lateral extensions are not well developed and the sphincter in this area primarily encircles the membranous urethra, forming a robust constrictor at this level. The smooth muscle sphincter consists of circularly orientated smooth muscle cells that lie between the striated sphincter and the longitudinal smooth muscle and urethral lumen and is not well developed. In children, the inner diameter of the urethral sphincter increases with age: a cutoff value of 3 mm has been reported to predict detrusor–sphincter incoordination (Kakizaki et al 2003).

Innervation The urethral sphincter mechanism extends from the perineum through the urogenital hiatus into the pelvic cavity. It is probably innervated via the perineal branch of the pudendal nerve from below, and direct branches from the sacral plexus and the pelvic splanchnic nerves from above: all of these nerves originate in the second, third and fourth sacral spinal segments.

Actions Urinary incontinence mainly affects females and is more common after vaginal deliveries. Continence is maintained by an elegantly orchestrated system of muscles and connective tissues that involves the urethral sphincters and the tissues that support them. The urethral sphincter mechanism compresses the mid-urethra in females and the membranous urethra in males, particularly when the bladder contains urine. Its location around the region of highest urethral closing pressure suggests it is important in urinary continence. At rest, activity

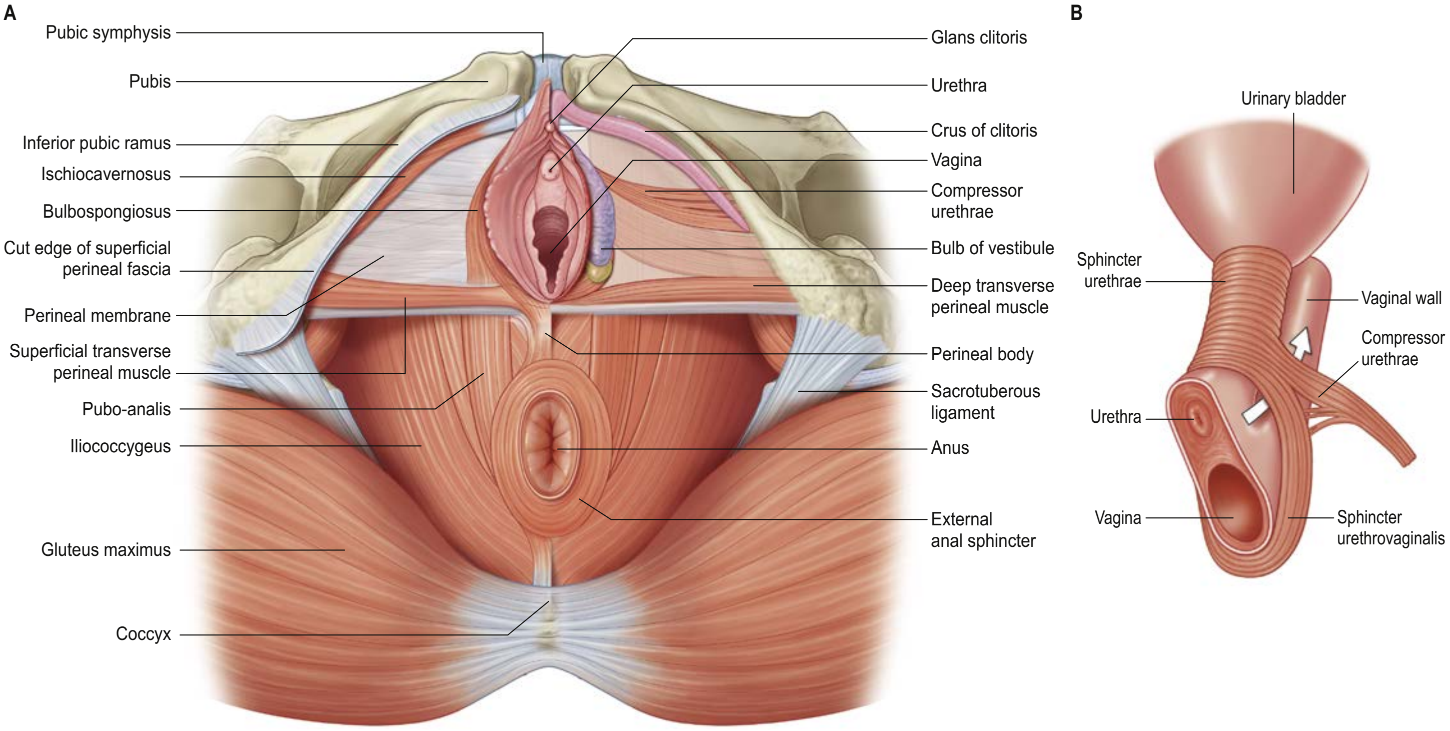

Fig. 71.13 Muscles of the female perineum. **A**, On the right side, the membranous layer of superficial fascia has been removed (note the cut edge). On the left side, superficial perineal muscles and overlying fascia have been removed to show the deep perineal muscles. **B**, The continuity of the deep perineal muscles with sphincter urethrae.

of both the smooth and striated sphincters contributes to this closure and, during times of increased need, voluntary contraction of the striated sphincter augments this closure. In the distal portion of the urethra, where it is adjacent to the perineal membrane, arch-shaped components of the striated sphincter (compressor urethrae and sphincter urethrovaginalis) pass between the urethra and pubis, and contraction compresses the lumen until it is closed. All muscles are relaxed during micturition to aid voiding: striated muscle contraction can help to expel the final drops of urine or semen from the proximal spongy urethra in the male.

During increases in abdominal pressure that occur, for example, during a cough, urinary bladder pressure rises above the urethral closure pressure that normally keeps the lumen of the urethra closed. In this situation, the urethral closure pressures that prevent urine leakage rise because the urethra is compressed against the fascial tissues that lie between it and the vaginal wall. If this layer is stable and unyielding, the urethra can be compressed closed against it, but if it is not well supported, this mechanism is less effective and leakage can occur (DeLancey 1994). Overall urinary continence during such events is a combination of sphincter contraction and pressure transmission with the former being the predominant factor (DeLancey et al 2008).

Superficial and deep perineal fasciae

Superficial perineal fascia

The superficial perineal fascia (Colles' fascia) forms a clear, surgically recognizable, subcutaneous plane of the anterior perineum (Tobin and Benjamin 1949). It is firmly attached posteriorly to the fascia over the superficial transverse perineal muscles and the posterior limit of the perineal membrane. Laterally, it is attached to the margins of the ischiopubic rami as far posteriorly as the ischial tuberosities. From here, it runs more superficially to the skin of the urogenital triangle, lining the skin of the external genitalia; in the male, it is also continuous with the fascial layer in the skin of the scrotum that contains the dartos muscle. In females, the fascia follows the same limits but is much less extensive in the labia majora. This layer runs anteriorly and superiorly into the skin of the lower abdominal wall where it is continuous with the membranous fascia (Scarpa's fascia). English-speaking anatomists refer to these tissue layers as a 'superficial fascia' but this is a misnomer; more accurately, they constitute the membranous layer of subcutaneous tissue.

Deep perineal fascia

The deep perineal fascia is a layer of fascia that overlies the superficial muscles of the perineum (bulbospongiosus, ischiocavernosus, superficial transverse perineal muscle). It is, in effect, the investing fascia of these muscles and, as such, is firmly attached to the borders of the muscles at their attachments to the ischiopubic rami, posterior margin of the perineal membrane and perineal body. Anteriorly, it fuses with the suspensory ligament of the penis or clitoris, and the fasciae of external abdominal oblique and the rectus sheath.

Subcutaneous and superficial perineal spaces

Subcutaneous perineal space

The subcutaneous perineal space lies between the deep and the superficial perineal fasciae. Under normal circumstances, these two layers are only separated by relatively thin subcutaneous connective tissue; the skin of the anterior perineum and external genitalia is relatively mobile over the deeper structures. However, this space is capable of expanding considerably in the presence of fluid accumulation; blood, urine or fluid collecting in the superficial perineal space following trauma or surgery on the urogenital triangle will spread throughout the tissues of the triangle, including the scrotum or labia majora, but cannot pass posteriorly into the anal triangle or laterally into the medial thigh because of the firm tethering of the posterior attachments of the subcutaneous fascia. Since the superficial perineal fascia is continuous with the fascia of the anterior abdominal wall, fluid, blood or purulence can also track freely between the subcutaneous tissues of the anterior abdominal wall and the subcutaneous perineal space (e.g. postsurgical haematomas of the abdominal wall readily cause discoloration of the perineal and genital skin).

Superficial perineal space

The superficial perineal space lies below the perineal membrane and is limited superficially by the deep perineal fascia (**Fig. 71.14**). It contains the corpora cavernosa and corpus spongiosum, ischiocavernosus, bulbospongiosus and the superficial transverse perineal muscles, and branches of the internal pudendal vessels and pudendal nerves. In the female, it is crossed by the urethra and vagina and contains the clitoris. In the male, it contains the spongy urethra as it runs in the root of the penis. It is a fully confined space: injuries to the contents of the space (such as bleeding into the urethra in the root of the penis) do not communicate with the subcutaneous or deep spaces unless the fascial coverings are also lacerated or breached.

Perineal body

The perineal body is an aggregation of fibromuscular tissue located in the midline at the junction between the anal and urogenital triangles, just anterior to the external anal sphincter (Oh and Kark 1973). It is attached to many structures in both the deep and superficial perineal spaces. Posteriorly, it merges with fibres from the external anal sphincter and the conjoint longitudinal coat. Superiorly, it is continuous with the rectovesical or rectovaginal septum, including fibres from levator ani (pubo-analis or pubovaginalis). Anteriorly, it receives a contribution from the deep and superficial transverse perineal muscles and bulbospongiosus (see Figs 71.4, 71.13). The perineal body is continuous with the perineal membrane and the superficial perineal fascia. Since the latter runs forwards into the skin of the perineum, the perineal body is tethered to the skin of the central perineum, which is often puckered

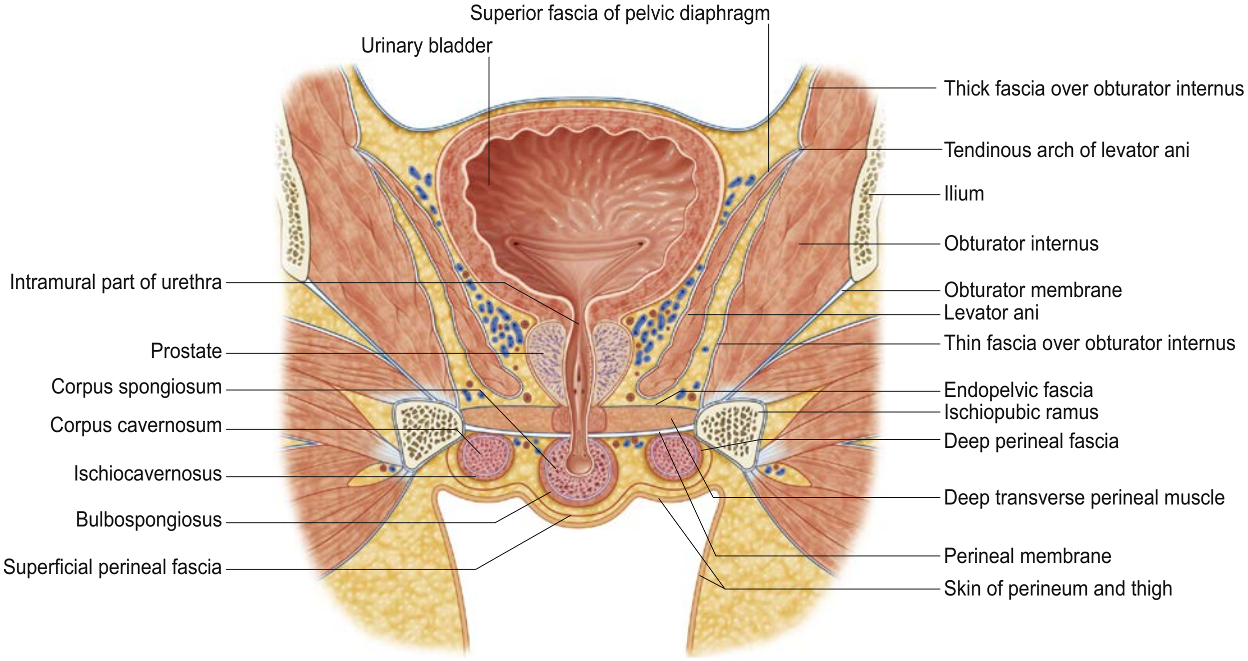
Superior fascia of pelvic diaphragm
Urinary bladder
Thick fascia over obturator internus
Tendinous arch of levator ani
Ilium
Obturator internus
Intramural part of urethra
Obturator membrane
Levator ani
Thin fascia over obturator internus
Prostate
Corpus spongiosum
Endopelvic fascia
Ischiopubic ramus
Corpus cavernosum
Deep perineal fascia
Ischiocavernosus
Deep transverse perineal muscle
Bulbospongiosus
Perineal membrane
Superficial perineal fascia
Skin of perineum and thigh

Fig. 71.14 Muscles and fasciae of the male perineum: coronal view. The section passes through the bulb of the penis at the level of the urethra. The deep perineal space is continuous with the ischio-anal fossa posteriorly. The visceral and parietal fasciae have been omitted for clarity. The pelvic fascia over the 'pelvic' aspect of the deep transverse perineal muscle is very thin and does not form a distinct layer: in places it blends with the parietal pelvic fascia over the inferior aspect of levator ani.

over it. In males, this is continuous with the raphe of the scrotum. In females, the perineal body lies directly posterior to, and is attached to, the posterior commissure of the labia majora and the vaginal orifice.

Spontaneous lacerations of the perineal body sustained during vaginal childbirth are often associated with injury to the anterior fibres of the external anal sphincter. The deliberate division of the perineal body to facilitate delivery (episiotomy) is sometimes angled laterally to avoid such sphincteric injuries. The perineal body is often used to position radiological markers in the assessment of pelvic diaphragm dysfunction.

Perineal muscles

Superficial transverse perineal muscles

The superficial transverse perineal muscles are narrow strips of muscle that run more or less transversely across the superficial perineal space anterior to the anus, from the medial and anterior aspects of the ischial tuberosities to the perineal body (see Fig. 71.13). A few fibres can also pass into the ipsilateral bulbospongiosus or external anal sphincter. They are occasionally small or even absent.

Bulbospongiosus

Bulbospongiosus differs between the sexes. In the male, it lies in the midline, anterior to the perineal body (see Fig. 71.12). It consists of two symmetric parts united by a median fibrous raphe. The fibres attach to the perineal body, in which they decussate, and to the superficial transverse perinei and the external anal sphincter; they diverge like the sides of a feather from the median raphe. A thin layer of posterior fibres joins the posterior portion of the perineal membrane. Most of the middle fibres encircle the bulb of the penis and adjacent corpus spongiosum, and attach to an aponeurosis on the dorsal surfaces. The anterior fibres spread out over the sides of the corpora cavernosa, ending partly in them, anterior to ischiocavernosus, and partly in a tendinous expansion that covers the dorsal vessels of the penis. In the female, bulbospongiosus also attaches to the perineal body, but the muscle on each side is separate and covers the superficial parts of the bulbs of the vestibule and greater vestibular glands (see Fig. 71.13). Fibres run anteriorly on either side of the vagina to attach to the corpora cavernosa of the clitoris, and a few fibres cross over the dorsum of the body of the clitoris.

Actions In the male, bulbospongiosus helps to empty the urethra of urine after the urinary bladder has emptied. It can assist in the final stage of erection as the middle fibres compress the erectile tissue of the bulb of the penis and the anterior fibres contribute by compressing the deep dorsal vein of the penis. It contracts six or seven times during ejaculation, assisting in the expulsion of semen. In the female, bulbospongiosus acts to constrict the vaginal orifice and express the secretions of the greater vestibular glands. Anterior fibres contribute to tumescence of the clitoris by compressing its deep dorsal vein.

Ischiocavernosus

In the male, ischiocavernosus covers the crus of the penis. It is attached by tendinous and muscular slips to the medial aspect of the ischial tuberosity posteriorly, and to the ischial ramus on both sides of the crus (see Fig. 71.12). These fibres end in an aponeurosis that is attached to the sides and undersurface of the crus of the penis. In the female, ischiocavernosus is related to the crus of the clitoris but is otherwise similar to the corresponding muscle in the male (**Figs 71.15–71.16**).

Actions Ischiocavernosus compresses the crus of the penis and can help to maintain penile erection. The two muscles form the urogenital triangle with the superficial transverse perineal muscles posteriorly. When contracted, the two ischiocavernosi act together to stabilize the erect penis. In the female, ischiocavernosus can help to promote tumescence of the clitoris.

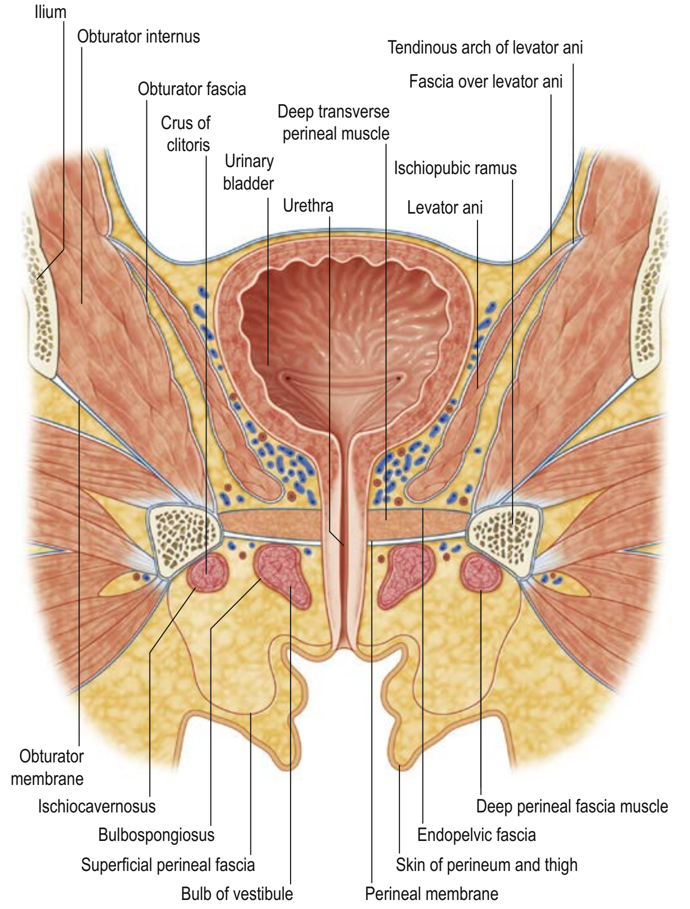
Ilium
Obturator internus
Tendinous arch of levator ani
Obturator fascia
Fascia over levator ani
Crus of clitoris
Deep transverse perineal muscle
Urinary bladder
Ischiopubic ramus
Urethra
Levator ani
Obturator membrane
Ischiocavernosus
Deep perineal fascia muscle
Bulbospongiosus
Endopelvic fascia
Superficial perineal fascia
Skin of perineum and thigh
Bulb of vestibule
Perineal membrane

Fig. 71.15 Muscles and fasciae of the female perineum – coronal view. The section passes through the bulb of the vestibule at the level of the urethra. The deep perineal space is continuous with the ischio-anal fossa posteriorly. The visceral and parietal fasciae have been omitted for clarity. The pelvic fascia over the 'pelvic' aspect of the deep transverse perineal muscles is very thin and does not form a distinct layer: in places it blends with the parietal pelvic fascia over the inferior aspect of levator ani.

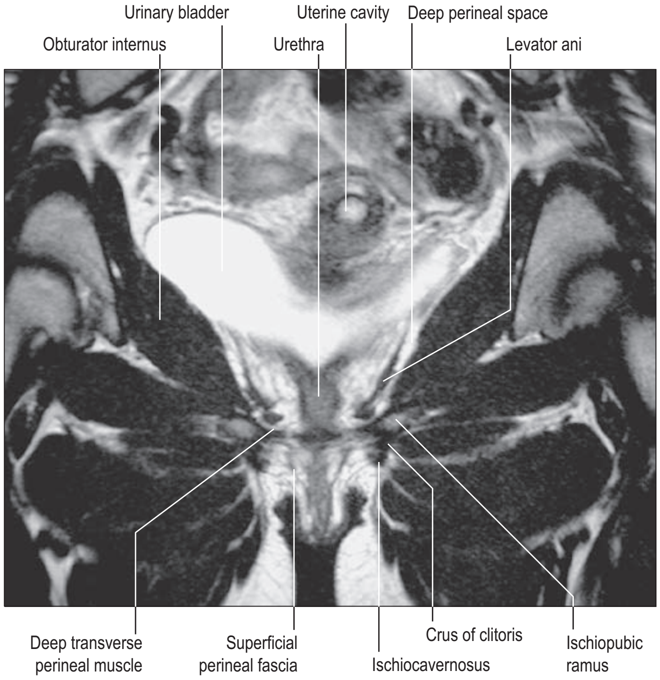
Urinary bladder
Uterine cavity
Deep perineal space
Obturator internus
Urethra
Levator ani
Deep transverse perineal muscle
Superficial perineal fascia
Crus of clitoris
Ischiocavernosus
Ischiopubic ramus

Fig. 71.16 Muscles and fasciae of the female perineum: coronal T2-weighted MRI. (Courtesy of Dr J Lee and Ms K Wimpey, Chelsea and Westminster Hospital, London.)

Vascular supply and lymphatic drainage

Arteries

Internal pudendal artery (in the perineum)

The internal pudendal artery enters the perineum around the posterior aspect of the ischial spine and runs on the lateral wall of the ischio-anal fossa in the pudendal canal with the internal pudendal veins and the pudendal nerve. The canal lies about 4 cm superior to the inferior limit of the ischial tuberosity and is formed by connective tissue binding the internal pudendal vessels and pudendal nerve to the medial surface of the fascia covering obturator internus. As the artery approaches the margin of the ischial ramus, it proceeds superficial or deep to the perineal membrane, along the medial margin of the inferior pubic ramus, en route to its target structures.

In the male, the internal pudendal artery distal to the perineal artery gives a branch to the bulb of the penis before it divides into the deep and dorsal arteries of the penis (see Fig. 71.12). The artery to the bulb of the penis supplies the corpus spongiosum, and the deep artery of the penis supplies the corpus cavernosum on each side. The dorsal artery runs on the dorsal aspect of the penis and supplies circumflex branches to the corpora cavernosa and corpus spongiosum that end by anastomosing near the corona of the glans and supplying the glans and prepuce of the penis.

In the female, a similar branch of the internal pudendal artery is distributed to the corpus spongiosum and vagina. The deep arteries supply the corpora cavernosa of the clitoris; the dorsal arteries supply the glans and prepuce of the clitoris.

Branches of the internal pudendal artery are sometimes derived from an accessory pudendal artery, which is usually a branch of the internal pudendal artery before its exit from the pelvis.

Inferior anorectal artery

The inferior anorectal artery arises just after the internal pudendal artery enters the pudendal canal on the lateral wall of the ischio-anal fossa. It runs anteromedially through the adipose tissue of the ischio-anal fossa to reach the external anal sphincter and it often branches before reaching the sphincter. During dissections of the anal canal, particularly during perineal excisions of the anus or rectum, the inferior anorectal vessels are encountered in the ischio-anal fossa and must be ligated before division; otherwise they tend to retract laterally, where they can cause troublesome bleeding.

Perineal artery

The perineal artery is a branch of the internal pudendal artery that arises near the anterior end of the pudendal canal and runs through the perineal membrane. In the male, it approaches the scrotum in the superficial perineal space, between bulbospongiosus and ischiocavernosus (see Fig. 74.24). A small transverse branch passes medially, inferior to the superficial transverse perineal muscle, to anastomose with the contralateral artery and with the posterior scrotal and inferior anorectal arteries. It supplies the transverse perinei, the perineal body and the posterior attachment of the bulb of the penis. The posterior scrotal arteries are usually terminal branches of the perineal artery but can also arise from its transverse branch. They are distributed to the scrotal skin and dartos in the male and supply the perineal muscles. In the female, the perineal artery runs an almost identical course to that in the male and gives off posterior labial branches (see Fig. 75.4).

Veins

Internal pudendal veins

The internal pudendal veins are venae comitantes of the internal pudendal artery and unite as a single vessel ending in the internal iliac vein. The perineal tributaries receive veins from the bulb of the penis and the scrotum, or the clitoris and labia, and the inferior anorectal veins join towards the posterior end of the pudendal canal.

Lymphatic drainage

The lymphatics from the skin of the penis and scrotum, or skin of the clitoris and labia, drain together with lymphatics from the perineal skin to the superficial inguinal nodes, and from there to the deep inguinal nodes. The corpora cavernosa and corpus spongiosum of the penis or clitoris drain directly to the deep inguinal nodes (see Fig. 76.10).

Innervation

Pudendal nerve (in the perineum)

The pudendal nerve gives rise to the inferior anal and perineal nerves and to the dorsal nerves of the penis or clitoris. The course of its branches parallels the pudendal vessels (see Figs 74.24, 75.4). The pudendal nerve occupies a constant position over the ischial spine. It can be 'blocked' by infiltration with a local anaesthetic applied via a needle passed through the lateral wall of the vagina to anaesthetize the perineal and anal skin. It can also be palpated over the ischial spine through the lateral wall of the rectum.

Inferior anal nerve

The inferior anal (rectal) nerve runs either through the medial wall of the pudendal canal with the inferior anorectal vessels, or behind the sacrospinous ligament directly from the fourth sacral ventral ramus without passing through the pudendal canal (Maldonado et al 2015), or occasionally it arises directly from the sacral plexus and crosses the sacrospinous ligament or rejoins the pudendal nerve. The nerve crosses the ischio-anal fossa to supply the external anal sphincter, the lining of the distal part of the anal canal and the skin around the anus. It frequently breaks into terminal branches before reaching the lateral border of the external anal sphincter. Its cutaneous branches distributed around the anus overlap the branches of the perineal branch of the posterior femoral cutaneous nerve and of the posterior scrotal or labial nerves. In females, the inferior anal nerve can supply sensory branches to the distal part of the vagina.

Perineal nerve

The perineal nerve is the inferior and larger terminal branch of the pudendal nerve in the pudendal canal. It runs anteriorly, inferior to the internal pudendal artery and accompanies the perineal artery, dividing into posterior scrotal or posterior labial and muscular branches. The posterior scrotal or labial nerves are usually double; they have medial and lateral branches that run over the perineal membrane and pass anteriorly in the lateral part of the urogenital triangle with the posterior scrotal or posterior labial branches of the perineal artery. They supply the skin of the scrotum or labia majora, respectively, overlapping the distribution of the perineal branch of the posterior femoral cutaneous nerve and inferior anal nerve. In females, the posterior labial branches also supply sensory fibres to the skin of the distal vagina.

Muscular branches arise directly from the pudendal nerve to supply the superficial transverse perineal muscles, bulbospongiosus, ischiocavernosus, external urethral sphincter and the anterior parts of the external anal sphincter and levator ani. In males, the branch to bulbospongiosus pierces this muscle to supply the corpus spongiosum penis, and ends in the urethral mucosa.

Dorsal nerve of the penis or clitoris

The dorsal nerve of the penis or clitoris runs anteriorly above the internal pudendal artery along the ischiopubic ramus, deep to the perineal membrane. It supplies the corpus cavernosum and accompanies the dorsal artery of the penis or clitoris between the layers of the suspensory ligament of the penis or clitoris. The dorsal nerve of the penis runs on the dorsum of the penis to end in the glans penis.

Bonus e-book content

Fig. 71.7 The relations between anteroposterior diameters of the right common, internal and external iliac arteries and body surface area in boys and girls between the ages of 1 and 16 years.

Video 71.1 Dissection of the sacral plexus.

Key references

Dalley AF 1987 The riddle of the sphincters. Am Surg 53:298–306.
A review of the anatomy of the external anal sphincter that brings clarity to the discussion of controversial and competing concepts.

Huisman AB 1983 Aspects on the anatomy of the female urethra with special relation to urinary continence. Contrib Gynecol Obstet 10:1–31.
A detailed and comprehensive account of the anatomy of the urethra based on histological examination.

Lawson JO 1974a Pelvic anatomy. I. Pelvic floor muscles. Ann R Coll Surg Engl 54:244–52.
An objective evaluation of the anatomy of levator ani based on serial histological sections.

Oelrich TM 1980 The urethral sphincter muscle in the male. Am J Anat 158:229–46.
See comments for Oelrich 1983.

Oelrich TM 1983 The striated urogenital sphincter muscle in the female. Anat Rec 205:223–32.
This study, along with its companion article concerning the male urethral sphincter anatomy, dispelled the longstanding errors surrounding a 'urogenital diaphragm' and corrected the anatomy of the urethral sphincter.

Reiffenstuhl G 1982 The clinical significance of the connective tissue planes and spaces. Clin Obstet Gynecol 25:811–20.
The complex 3-dimensional network of the pelvic connective tissues has been confusing to many; this clearly illustrated article shows the different elements of the pelvic fasciae.

Tubbs RS, Shoja M, Loukas M 2016 Bergman's Comprehensive Encyclopedia of Human Anatomic Variation. Hoboken: Wiley Blackwell.
A textbook dedicated to detailing the anatomical variations found in man.

References

Campbell RM 1950 The anatomy and histology of the sacrouterine ligaments. Am J Obstet Gynecol 59:1–12.

Chantalat E, Merigo, O, Chaynes P et al 2014 Radiological anatomical study of the origin of the uterine artery. Surg Radiol Anat 36:1093–9.

Dalley AF 1987 The riddle of the sphincters. Am Surg 53:298–306.

A review of the anatomy of the external anal sphincter that brings clarity to the discussion of controversial and competing concepts.

DeLancey JO 1992 Anatomic aspects of vaginal eversion after hysterectomy. Am J Obstet Gynecol 166:1717–24.

DeLancey JO 1994 Structural support of the urethra as it relates to stress urinary incontinence: the hammock hypothesis. Am J Obstet Gynecol 170:1713–23.

DeLancey JO, Trowbridge ER, Miller JM et al 2008 Stress urinary incontinence: relative importance of urethral support and urethral closure pressure. J Urol 179:2286–90.

de la Portilla F, López-Alonso M 2009 Endosonography of the anal canal: findings in children. Dis Colon Rectum 52:711–4.

de Treigny OM, Roumiguie M, Deudon R et al 2017 Anatomical study of the inferior vesical artery: is it specific to the male sex? Surg Radiol Anat 39:961–5.

Doğan R, Doğan OF, Oç M et al 2003 A rare vascular malformation, Klippel–Trenaunay syndrome. Report of a case with deep vein agenesis and review of the literature. J Cardiovasc Surg 44:95–100.

Doyle JF 1970 The perforating veins of the gluteus maximus. Ir J Med Sci 3:285–8.

Emans JB, Ciarlo M, Callahan M et al 2005 Prediction of thoracic dimensions and spine length based on individual pelvic dimensions in children and adolescents: an age-independent, individualized standard for evaluation of outcome in early onset spinal deformity. Spine 30:2824–9.

Gupta NP, Kumar M, Karan SC et al 1999 Lower ureteral obstruction due to a persistent umbilical artery. Urol Int 63:249–51.

Herneth AM, Trattnig S, Bader TR et al 2000 MR imaging of the ischiopubic synchondrosis. Magn Reson Imaging 18:519–24.

Huisman AB 1983 Aspects on the anatomy of the female urethra with special relation to urinary continence. Contrib Gynecol Obstet 10:1–31.

A detailed and comprehensive account of the anatomy of the urethra based on histological examination.

Kakizaki H, Moriya K, Ameda K et al 2003 Diameter of the external urethral sphincter as a predictor of detrusor–sphincter incoordination in children: comparative study of voiding cystourethrography. J Urol 169:655–8.

Kinugasa Y, Arakawa T, Abe H et al 2012 Anococcygeal raphe revisited: a histological study using mid-term human foetuses and elderly cadavers. Yonsei Med J 53:849–55.

Klink EW 1953 Perineal nerve block: an anatomic and clinical study in the female. Obstet Gynecol 1:137–46.

Lawson JO 1974a Pelvic anatomy. I. Pelvic floor muscles. Ann R Coll Surg Engl 54:244–52.

An objective evaluation of the anatomy of levator ani based on serial histological sections.

Lawson JO 1974b Pelvic anatomy. II. Anal canal and associated sphincters. Ann R Coll Surg Engl 54:288–300.

Maldonado PA, Chin K, Garcia AA et al 2015 Anatomic variations of pudendal nerve within pelvis and pudendal canal: clinical applications. Am Obstet Gynecol 213:727.e1–6.

Munk A, Darge K, Wiesel M et al 2002 Diameter of the infrarenal aorta and the iliac arteries in children: ultrasound measurements. Transplantation 73:631–5.

Nesselrod JP 1936 An anatomic restudy of the pelvic lymphatics. Ann Surg 104:905–16.

An account of the importance of the pelvic lymphatic system in tumour spread and treatment that provides an accurate description of its component parts.

Oelrich TM 1980 The urethral sphincter muscle in the male. Am J Anat 158:229–46.

See comments for Oelrich 1983.

Oelrich TM 1983 The striated urogenital sphincter muscle in the female. Anat Rec 205:223–32.

This study, along with its companion article concerning the male urethral sphincter anatomy, dispelled the longstanding errors surrounding a 'urogenital diaphragm' and corrected the anatomy of the urethral sphincter.

Oh C, Kark AE 1972 Anatomy of the external anal sphincter. Br J Surg 59:717–23.

Oh C, Kark AE 1973 Anatomy of the perineal body. Dis Colon Rectum 16:444–54

Pai MM, Krishnamurthy A, Prabhu L et al 2009 Variability in the origin of the obturator artery. Clinics (Sao Paulo) 64:897–901.

Range RL, Woodburne RT 1964 The gross and microscopic anatomy of the transverse cervical ligaments. Am J Obstet Gynecol 90:460–7.

Rehman Y, Stensrud KJ, Morkrid L et al 2011 Endosonographic evaluation of anal sphincters in healthy children. J Pediatr Surg 46:1587–92.

Reiffenstuhl G 1982 The clinical significance of the connective tissue planes and spaces. Clin Obstet Gynecol 25:811–20.

The complex 3-dimensional network of the pelvic connective tissues has been confusing to many; this clearly illustrated article shows the different elements of the pelvic fasciae.

Ricci JV, Lisa JR, Thom CH et al 1947 The relationship of the vagina to adjacent organs in reconstructive surgery. Am J Surg 74:387–410.

A great deal has been written about the 'fascia' of the female pelvis as it relates to the problem of pelvic organ prolapse. Ricci's approach, using whole-pelvic cross-sectional anatomy, brings clarity to this discussion.

Roberts WH, Krishingner GL 1967 Comparative study of human internal iliac artery based on Adachi classification. Anat Rec 158:191–6.

A description of the variation in the anatomy of the internal iliac artery.

Roberts WH, Habenicht J, Krishingner G 1964 The pelvic and perineal fasciae and their neural and vascular relationships. Anat Rec 149:707–20

Roberts WH, Harrison CW, Mitchell DA et al 1988 The levator ani muscle and the nerve supply of its puborectalis component. Clin Anat 1:267–83.

Rociu E, Stoker J, Eijkemans MJ et al 2000 Normal anal sphincter anatomy and age-and sex-related variations at high-spatial-resolution endoanal MR imaging. Radiology 217:395–401.

Sanna B, Henry BM, Vikse J et al 2018 The prevalence and morphology of the corona mortis (crown of death): a meta-analysis with implications in abdominal wall and pelvic surgery. Injury 49:302–8.

Sato K 1980 Amorphological analysis of the nerve supply of the sphincter ani externus, levator ani and coccygeus. Kaibogaku Zasshi 55:187–223.

Stein TA, DeLancey JO 2008 Structure of the perineal membrane in females: gross and microscopic anatomy. Obstet Gynecol 111:686–93.

Tobin CE, Benjamin JA 1949 Anatomic and clinical re-evaluation of Camper's, Scarpa's and Colles' fasciae. Surg Gynecol Obstet 88:545–59.

A description of the anatomy of Camper's, Scarpa's and Colles' fasciae that clarifies understanding of these structures, which are often poorly described or incorrectly illustrated.

Tubbs RS, Shoja M, Loukas M 2016 Bergman's Comprehensive Encyclopedia of Human Anatomic Variation. Hoboken: Wiley Blackwell.

A textbook dedicated to detailing the anatomical variations found in man.

Wendell-Smith CP, Wilson PM 1991 The vulva, vagina and urethra and the musculature of the pelvic floor. In: Philipp E, Setchell M, Ginsburg J (eds) Scientific Foundations of Obstetrics and Gynaecology. Oxford: Butterworth–Heinemann, pp. 84–100.

CHAPTER
72

Kidney and ureter

KIDNEY

The kidneys excrete end products of metabolism and excess water. These actions are essential for the control of concentrations of various substances in the body, maintaining electrolyte and water balance approximately constant in the tissue fluids. The kidneys also have endocrine functions, producing and releasing erythropoietin, which affects red blood cell formation; renin, which influences blood pressure; 1,25-dihydroxycholecalciferol (the metabolically active form of vitamin D), which is involved in the control of calcium absorption and mineral metabolism; and other soluble factors with metabolic actions.

In the fresh state the kidneys are reddish-brown. They are retroperitoneal, located on either side of the vertebral column, and are surrounded by adipose tissue. Superiorly the kidneys are level with the upper border of the twelfth thoracic vertebra on the left and the first lumbar vertebra on the right, and inferiorly, with the third or fourth lumbar vertebra on the left and the fourth lumbar vertebra on the right (Mirjalili et al 2012). The right is usually slightly inferior to the left, reflecting its relationship to the liver. The left is a little longer and narrower than the right and lies nearer the median plane (**Fig. 72.1**). The long axis of each kidney is directed inferolaterally and the transverse axis posteromedially, which means that the anterior and posterior aspects usually described are, in fact, anterolateral and posteromedial. An appreciation of this orientation is important in percutaneous and endo-urological renal surgery.

In adults, each kidney is typically 11 cm in length, 6 cm in width and 3 cm in anteroposterior dimension. The left kidney may be 1.5 cm longer than the right; it is rare for the right kidney to be more than 1 cm longer than the left. The average weight is 150 g in men and 135 g in women. In thin individuals with a lax abdominal wall, the lower pole of the right kidney can just be felt in full inspiration by bimanual physical examination of the abdomen, but this is unusual. In the fetus and the newborn, the kidney normally has 12 lobules; in the adult, these lobules are fused to present a smooth surface, although any remaining traces of lobulation can mimic a renal mass on radiological imaging.

Absent and ectopic kidneys A single absent kidney, resulting from the failure of the metanephrogenic blastema to join a ureteric bud (metanephric diverticulum) on the affected side, is seen in one in 1200 individuals. There are no clinical sequelae, but the ipsilateral ductus deferens and/or epididymis can also be absent and there may be other congenital anomalies, including imperforate anus, cardiac valvular anomalies and oesophageal atresia. A single kidney often shows

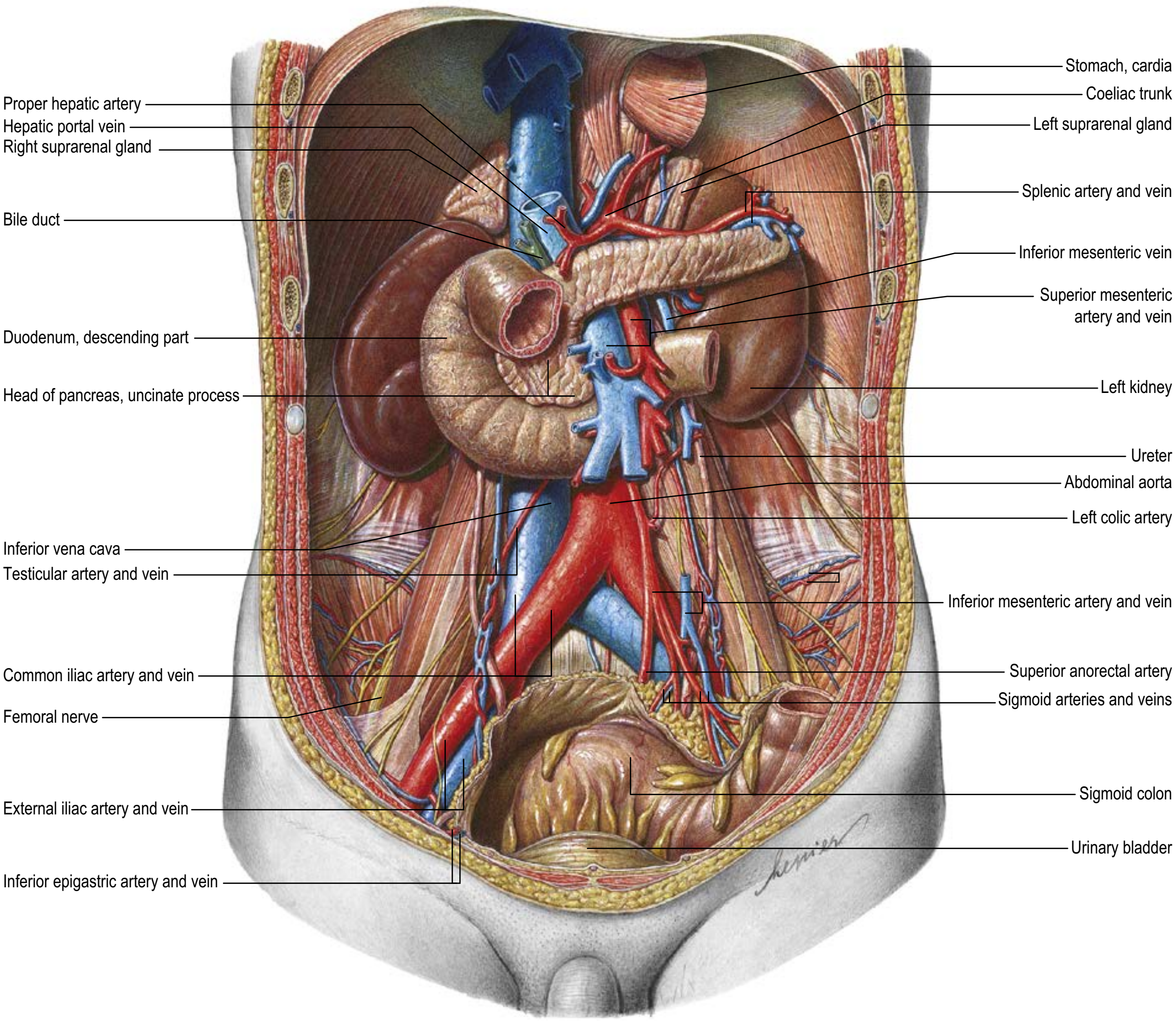
Proper hepatic artery
Hepatic portal vein
Right suprarenal gland
Bile duct
Duodenum, descending part
Head of pancreas, uncinate process
Inferior vena cava
Testicular artery and vein
Common iliac artery and vein
Femoral nerve
External iliac artery and vein
Inferior epigastric artery and vein
Stomach, cardia
Coeliac trunk
Left suprarenal gland
Splenic artery and vein
Inferior mesenteric vein
Superior mesenteric artery and vein
Left kidney
Ureter
Abdominal aorta
Left colic artery
Inferior mesenteric artery and vein
Superior anorectal artery
Sigmoid arteries and veins
Sigmoid colon
Urinary bladder

Fig. 72.1 Relations of the kidneys and ureters in the male retroperitoneum. (Sobotta Atlas of Human Anatomy © Elsevier GmbH, Urban & Fischer, Munich.)

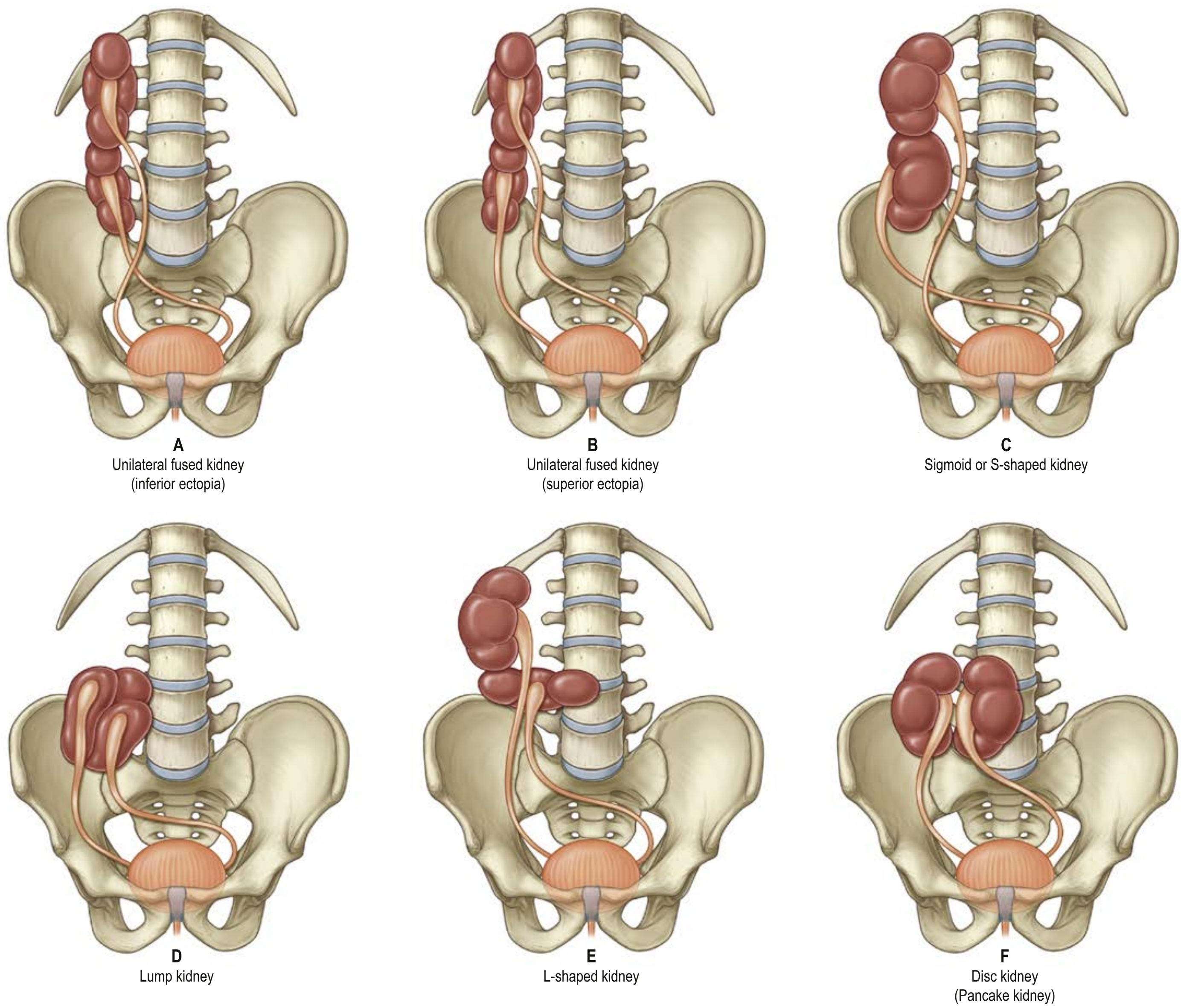

Fig. 72.2 The possible arrangements of crossed fused ectopic kidneys.

compensatory hypertrophy but, provided the single kidney is anatomically and functionally normal, the life expectancy of individuals with a single kidney is no different from that of those with two kidneys.

An ectopic kidney is found in the pelvis in 1 in 2500 live births. Kidneys so placed often have associated malrotation anomalies and can have marked fetal lobulation. Pelvic kidneys frequently become hydronephrotic as a result of an anteriorly placed ureter and an anomalous arterial supply; there is often an associated ureteropelvic (pelviureteric) junction obstruction.

Very rarely, and despite the normal location of the ureteric orifices within the urinary bladder, the two kidneys are on the same side and are usually fused (crossed fused renal ectopia). A solitary crossed fused renal ectopia may be associated with skeletal and other genitourinary anomalies. A number of different anatomical patterns can result, all of which are extremely rare (Fig. 72.2).

Horseshoe kidney Horseshoe kidneys are found in 1 in 400 individuals. A transverse bridge of renal tissue, the isthmus, often containing functioning renal substance, connects the two renal masses. The isthmus lies between the inferior poles, most commonly anterior to the great vessels; it is often inferior to the inferior mesenteric artery because this vessel can obstruct the normal ascent of the kidney during embryological development. The ureters curve anterior to the isthmus and often have a high origin from the renal pelvis (Fig. 72.3).

Renal fascia

The renal fascia (Gerota's fascia), is a dense, elastic connective tissue sheath that envelops each kidney and suprarenal gland, together with a layer of surrounding perirenal fat that is thickest at the renal borders and extends into the renal sinus at the hilum of the kidney (Fig. 72.4; see Fig. 61.2).

The renal fascia was originally described as two separate entities, the posterior fascia of Zuckerkandl and the anterior fascia of Gerota, which fused laterally to form the lateroconal fascia (Chesbrough et al 1989, Burkhill and Healy 2000). According to this view, the lateroconal fascia continued anterolaterally behind the colon to blend with the parietal peritoneum. However, Mitchell (1950) showed that the renal fascia is a single multi-laminated structure that is fused posteromedially with the muscular fasciae of psoas major and quadratus lumborum. It then extends anterolaterally behind the kidney as a bilaminated sheet, which, at a variable point, divides into a thin anterior layer, passing anterior to the kidney, and a thicker posterior layer that continues anterolaterally as the lateroconal fascia and fuses with the parietal peritoneum.

Classically, the anterior layer of renal fascia was thought to blend into the dense mass of connective tissue surrounding the great vessels in the root of the mesentery behind the duodenum and pancreas, thereby preventing communication between perirenal spaces across the midline. However, inspection of computed tomography (CT) images or of anatomical sections of cadavers, following injection of contrast or coloured latex, respectively, into the perirenal space, revealed that fluid could extend across the midline at the third to fifth lumbar levels through a narrow channel measuring 2–10 mm in the anteroposterior dimension. In the midline superiorly, the anterior and posterior layers of renal fascia fuse and are attached to the crura of the respiratory diaphragm. Inferiorly, the fasciae are separate for a variable craniocaudal distance. The posterior layer of renal fascia fuses with the psoas fascia, while the anterior layer of renal fascia extends across the midline anterior to the aorta and inferior vena cava; communication between the

The blood supply to horseshoe kidneys is variable. One vessel to each moiety is seen in 30% of horseshoe kidneys but multiple vessels are common; the isthmus can be supplied by a vessel directly from the aorta or from branches of the inferior mesenteric, common iliac or external iliac arteries. In many cases, aberrant vessels arising below the inferior border of the isthmus supply the isthmus. In view of this variable arterial anatomy, angiography or computed tomography (CT) scanning with vascular reconstruction is very helpful when planning surgery on horseshoe kidneys.

Horseshoe kidneys exhibit an associated congenital ureteropelvic junction obstruction in up to 30% of cases and have a chromosomal anomaly in 56% of cases (Scott 2002). Anomalous vessels crossing the ureter, and the abnormal course of the ureter as it passes over the kidney, can also cause obstruction and result in hydronephrosis or haematuria. The right and left major calyces can exist independently and not cross the midline (Iwanaga et al 2015).

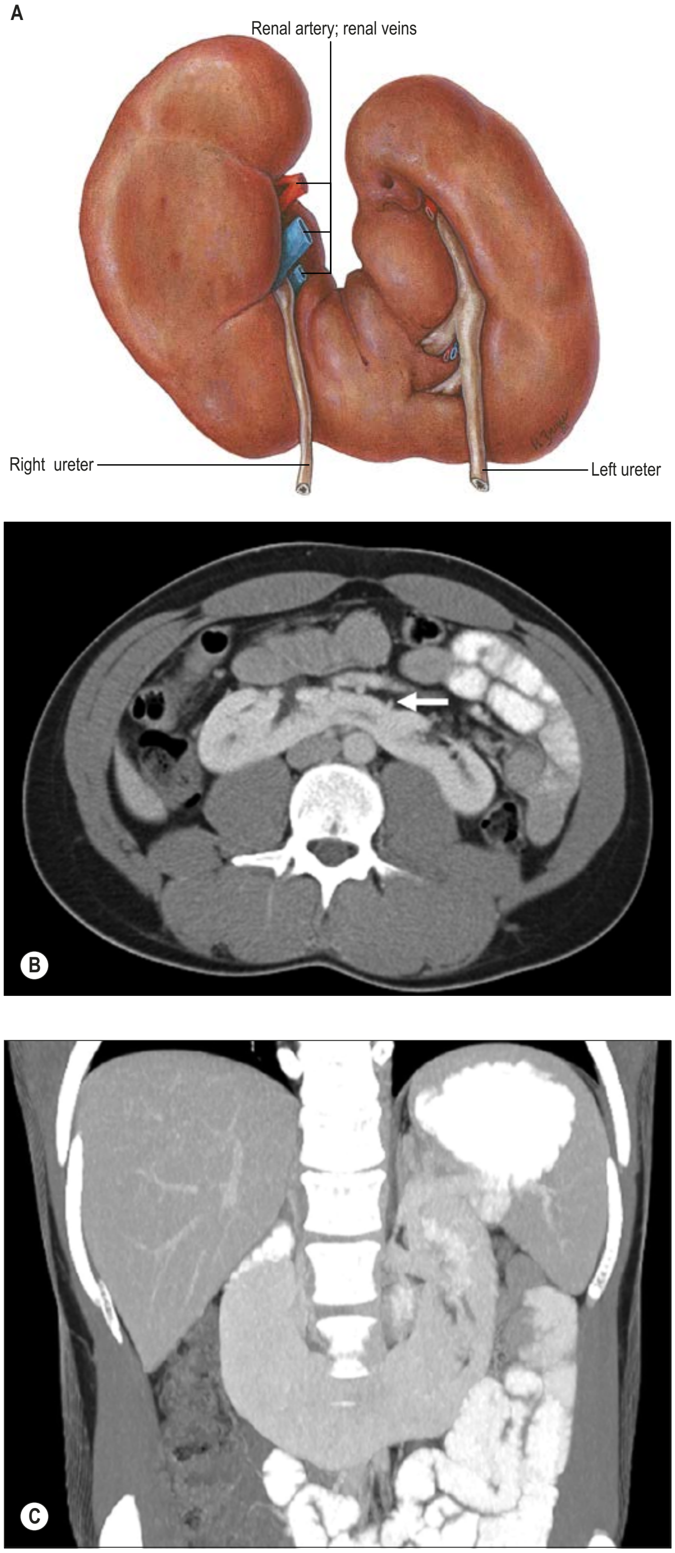

Fig. 72.3 **A**, A horseshoe kidney. Note the ureters pass anterior to the isthmus, and the relatively high insertion of the ureters into the renal pelvis on the left side. **B**, Axial contrast-enhanced computed tomography (CT) image. **C**, Coronal maximal intensity projection (MIP) image of the abdomen. **B** and **C** demonstrate midline connection of the two kidneys below the inferior mesenteric artery (**B**, arrow), in a horseshoe configuration. (A, Sobotta Atlas of Human Anatomy © Elsevier GmbH, Urban & Fischer, Munich.)

two sides is permitted, although it is very rarely of clinical significance. Below this level, the two fasciae once again merge and are attached to the aorta and inferior vena cava or iliac vessels. The containment of fluid to one side of the perirenal space that is observed in over two-thirds of clinical cases is attributed to the presence of fibrous septa.

Above the suprarenal glands, the anterior and posterior layers of renal fascia were previously said to fuse with each other and to the diaphragmatic fascia. This description of a closed superior cone is not universally accepted. Cadaveric dissections have shown that the superior aspect of the perirenal space is open and in continuity with the bare area of the liver on the right and the subphrenic space on the left. The posterior fascial layer blends bilaterally with the psoas fascia and fascia over quadratus lumborum, and with the diaphragmatic fascia. The anterior fascial layer on the right blends with the inferior aspect of the right coronary ligament at the level of the upper pole of the kidney and the bare area of the liver. On the left, the anterior layer fuses with the gastrosplenic ligament at the level of the suprarenal gland.

There is some debate concerning the inferior fusion of the renal fascia. Many investigators believe that, inferiorly, the anterior and posterior layers of the renal fascia fuse to produce an inverted cone that is open to the pelvis at its apex. Laterally, the anterior and posterior layers fuse with the iliac fascia; medially, they fuse with the periureteric connective tissue. The apex of the cone is open anatomically towards the iliac fossa but rapidly becomes sealed in inflammatory disease. An alternative view based on dissections of recently deceased cadavers after injections of coloured latex into the perirenal space, has shown that the anterior and posterior layers of renal fascia merge to form a single multilaminar fascia that contains the ureter in the iliac fossa. Anteriorly, this common fascia is loosely connected to the parietal peritoneum, and so denies free communication between the perirenal space and the pelvis, and between the perirenal and pararenal spaces.

Relations

The superior poles of both kidneys are thick and round and related to their respective suprarenal glands. The inferior poles are thinner and extend to within 2.5 cm of the iliac crests. The lateral borders are convex. The medial borders are convex adjacent to the poles and concave between them, and slope inferolaterally. In each, a deep vertical fissure opens anteromedially as the hilum of the kidney, which is bounded by anterior and posterior lips and contains the renal vessels and nerves, and the renal pelvis. The relative positions of the main hilar structures are the renal vein (anterior), the renal artery (intermediate) and the renal pelvis (posterior) (Fig. 72.5). Usually, an anterior branch from the renal artery runs over the superior margin of the renal pelvis to enter the hilum on the posterior aspect of the renal pelvis, and often leaves the hilum in the same plane. Above the hilum the medial border is related to the suprarenal gland and below to the origin of the ureter.

The convex anterior surface of the kidney faces anterolaterally and its posterior surface faces posteromedially. The relations of the left and right kidneys are shown in Fig. 72.6.

A small area of the superior pole of the right kidney is in contact with the right suprarenal gland, which can overlap the upper part of the medial border of the right kidney (Fig. 72.7). A large area below this is immediately related to the right lobe of the liver, separated by a layer of parietal peritoneum. A narrow medial area is directly related to the descending part of the duodenum. Inferiorly, the anterior surface is directly in contact laterally with the right colic flexure and medially with part of the small intestine.

A small medial area of the superior pole of the left kidney is related to the left suprarenal gland (see Fig. 72.7). The lateral half of the superior pole of the anterior surface is related to the spleen, from which it is separated by a layer of peritoneum. A central quadrilateral area lies in direct contact with the pancreas and the splenic vessels. Above this, a small, variable, triangular region, between the suprarenal and splenic areas, is in contact with the stomach, separated by a layer of peritoneum. Below the pancreatic and splenic areas a narrow lateral strip that extends to the lateral border of the kidney is directly related to the left colic flexure and the beginning of the descending colon. An extensive medial area is related to the jejunum. The gastric area is covered with the peritoneum of the omental bursa, and the splenic and jejunal areas are covered by the peritoneum of the greater sac. Behind the peritoneum covering the jejunal area, branches of the left colic vessels are related to the kidney.

The posteromedial surface of the kidneys is embedded in fat and devoid of peritoneum. The right and left kidneys are related to similar structures. Superiorly are the respiratory diaphragm and the medial and lateral arcuate ligaments. More inferiorly, moving in a medial to lateral direction, are psoas major, quadratus lumborum and the aponeurotic tendon of transversus abdominis, the subcostal vessels and the subcostal, iliohypogastric and ilioinguinal nerves. The upper pole of the right kidney is level with the twelfth rib, and that of the left with the eleventh and twelfth ribs. The respiratory diaphragm covered with parietal peritoneum separates the kidney from the parietal pleura, which descends to form the costodiaphragmatic recess; the diaphragm is sometimes defective or absent in the lumbocostal triangle immediately above the lateral arcuate ligament, and this allows perirenal adipose tissue to contact the diaphragmatic pleura.

A simple nephrectomy for benign disease removes the kidney from within the renal fascia; a radical nephrectomy (for cancer) classically removes the entire contents of the perirenal space, including the renal fascia and suprarenal gland, in order to give adequate clearance around the tumour.

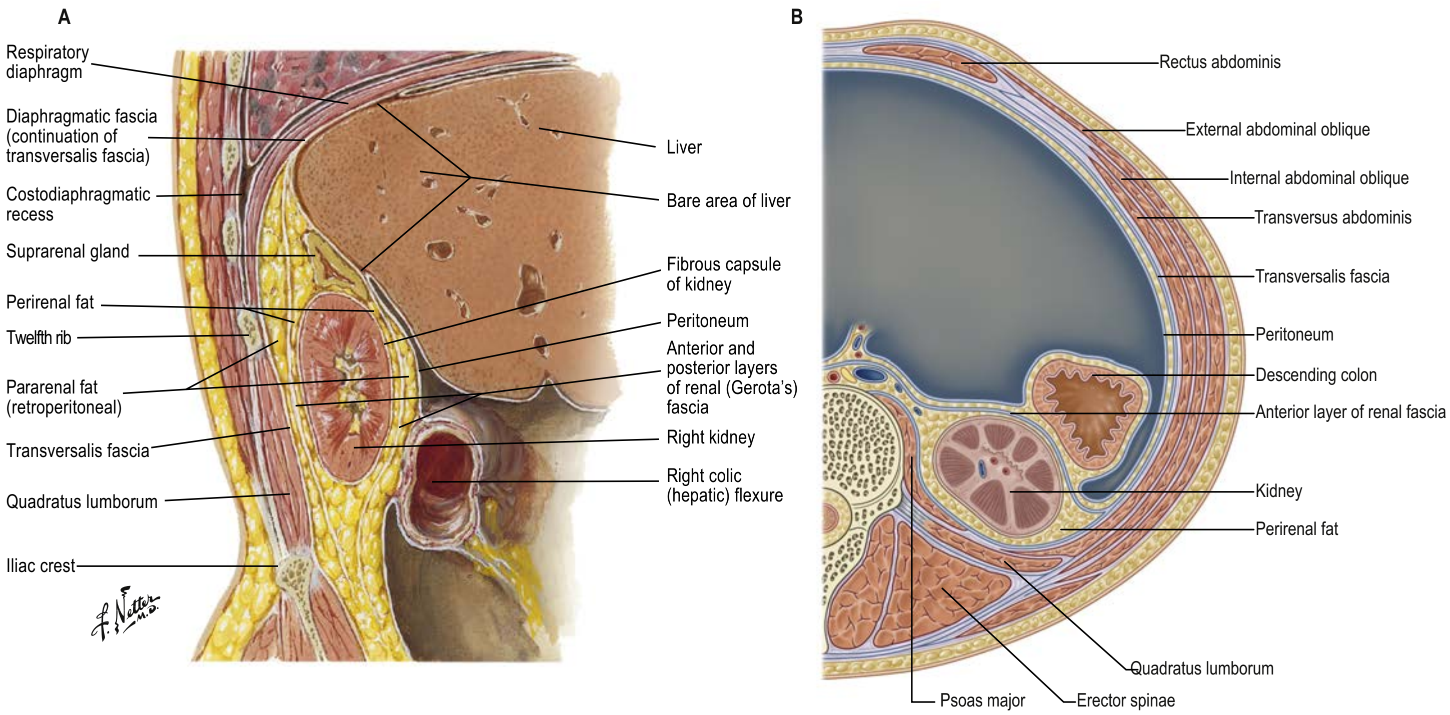
A
Respiratory diaphragm
Diaphragmatic fascia (continuation of transversalis fascia)
Costodiaphragmatic recess
Suprarenal gland
Perirenal fat
Twelfth rib
Pararenal fat (retroperitoneal)
Transversalis fascia
Quadratus lumborum
Iliac crest
Liver
Bare area of liver
Fibrous capsule of kidney
Peritoneum
Anterior and posterior layers of renal (Gerota's) fascia
Right kidney
Right colic (hepatic) flexure
F. Netter M.D.
B
Rectus abdominis
External abdominal oblique
Internal abdominal oblique
Transversus abdominis
Transversalis fascia
Peritoneum
Descending colon
Anterior layer of renal fascia
Kidney
Perirenal fat
Quadratus lumborum
Psoas major
Erector spinae

Fig. 72.4 **A**, A sagittal section through the posterior abdominal wall, showing the relations of the renal fascia of the right kidney. **B**, A transverse section, showing the relations of the renal fascia. (A, Reprinted from Netter Anatomy Illustration Collection, © Elsevier Inc. All Rights Reserved.)

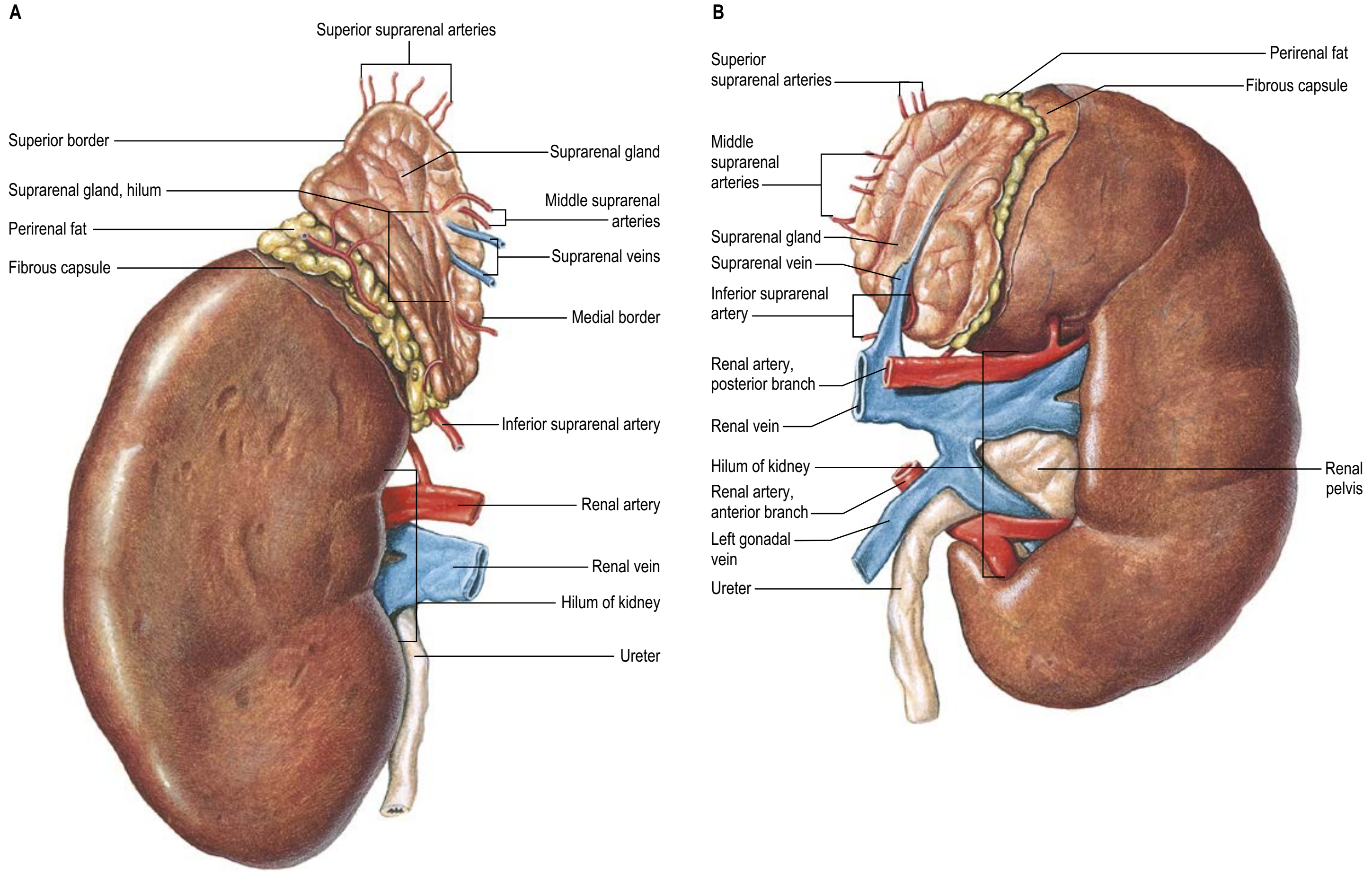
A
Superior suprarenal arteries
Superior border
Suprarenal gland, hilum
Perirenal fat
Fibrous capsule
Suprarenal gland
Middle suprarenal arteries
Suprarenal veins
Medial border
Inferior suprarenal artery
Renal artery
Renal vein
Hilum of kidney
Ureter
B
Superior suprarenal arteries
Middle suprarenal arteries
Suprarenal gland
Suprarenal vein
Inferior suprarenal artery
Renal artery, posterior branch
Renal vein
Hilum of kidney
Renal artery, anterior branch
Left gonadal vein
Ureter
Perirenal fat
Fibrous capsule
Renal pelvis

Fig. 72.5 **A**, The anterior aspect of the right kidney and suprarenal gland. **B**, The anterior aspect of the left kidney and suprarenal gland. Note that the left suprarenal vein enters the left renal vein. This is an important relationship to identify when performing a left nephrectomy. (A and B, Sobotta Atlas of Human Anatomy © Elsevier GmbH, Urban & Fischer, Munich.)

Internal macrostructure

The postnatal kidney has a thin fibrous capsule composed of collagen-rich connective tissue with some elastic and smooth muscle fibres. In renal disease, the capsule can become adherent.

The kidney itself can be divided into an internal renal medulla and external renal cortex (Fig. 72.8). The renal medulla consists of pale, striated, conical renal pyramids; their bases are peripheral, and their apices converge to the renal sinus. At the renal sinus, they project into calyces as papillae.

The renal cortex (see Fig. 72.13) is subcapsular, arching over the bases of the renal pyramids and extending between them towards the renal sinus as renal columns. Its peripheral regions are termed cortical arches and are traversed by radial, lighter-coloured

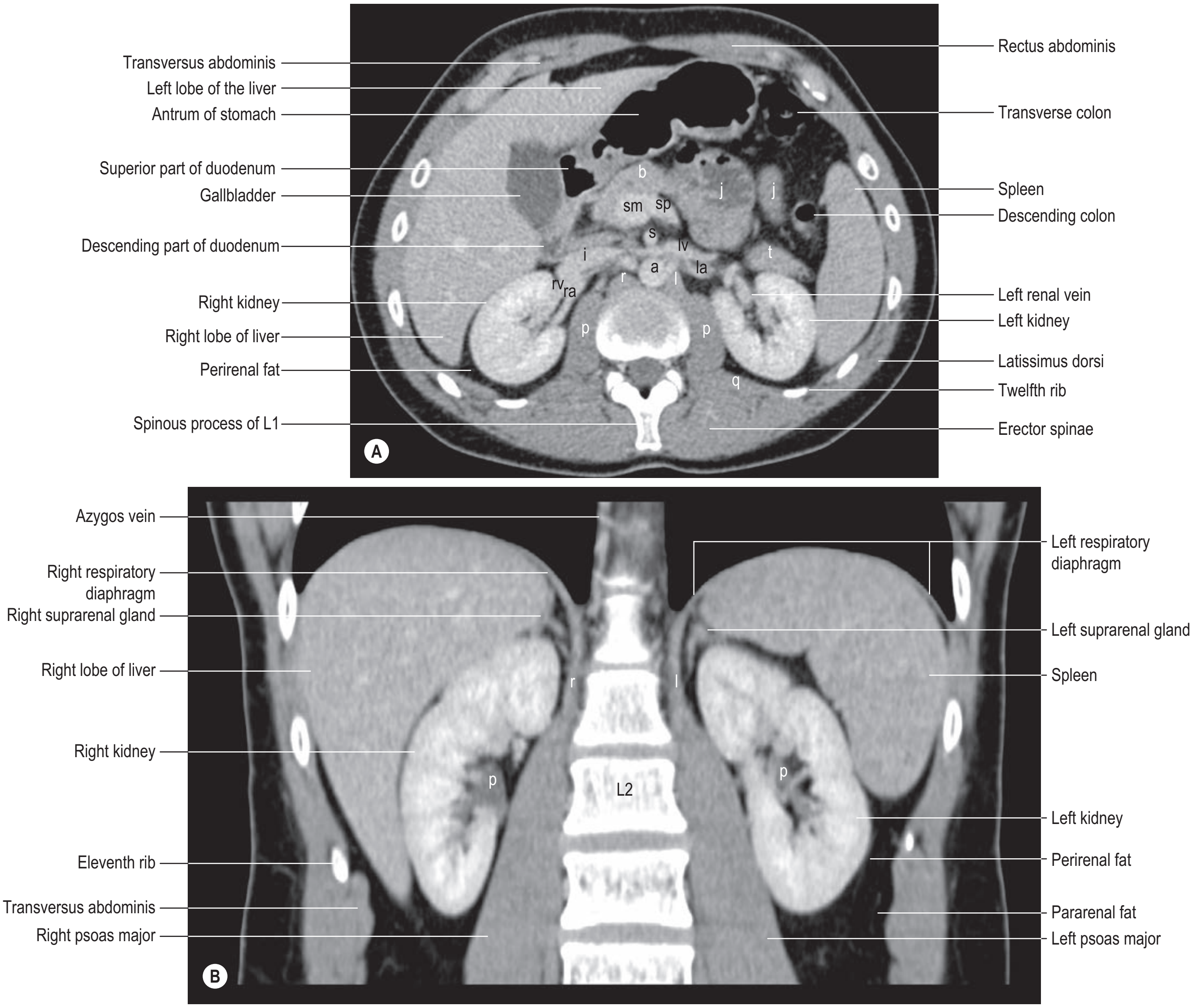
Transversus abdominis
Left lobe of the liver
Antrum of stomach
Superior part of duodenum
Gallbladder
Descending part of duodenum
Right kidney
Right lobe of liver
Perirenal fat
Spinous process of L1
Rectus abdominis
Transverse colon
Spleen
Descending colon
Left renal vein
Left kidney
Latissimus dorsi
Twelfth rib
Erector spinae
b
sm
sp
j
j
s
lv
i
t
a
la
r
l
rv
ra
p
p
q
A
Azygos vein
Right respiratory diaphragm
Right suprarenal gland
Right lobe of liver
Right kidney
Eleventh rib
Transversus abdominis
Right psoas major
Left respiratory diaphragm
Left suprarenal gland
Spleen
Left kidney
Perirenal fat
Pararenal fat
Left psoas major
r
l
p
L2
p
B

Fig. 72.6 Multislice CT scans of the kidneys. **A**, Axial plane CT with intravenous contrast medium at the level of the renal hila (L1-L2). Abbreviations: a, aorta; b, body of pancreas; i, inferior vena cava; j, jejunal loops; l, left crus of respiratory diaphragm; la, left renal artery; lv, left renal vein; p, psoas major; q, quadratus lumborum; r, right crus of respiratory diaphragm; ra, right renal artery; rv, right renal vein; s, superior mesenteric artery; sm, superior mesenteric vein; sp, splenic vein; t, tail of pancreas. **B**, Coronal multiplanar reformat from a CT with intravenous contrast medium through both kidneys and suprarenal glands. Abbreviations: l, left crus of respiratory diaphragm; r, right crus of respiratory diaphragm; p, renal pelvis. (A–B, Courtesy of Dr Tom Turmezei, Norfolk and Norwich University Hospital.) (C–D, *continued online*)

medullary rays, separated by darker tissue, the convoluted part. The rays taper towards the renal capsule and are peripheral prolongations from the bases of renal pyramids. The cortex is histologically divisible into outer and inner zones. The inner zone is demarcated from the renal medulla by tangential blood vessels (arcuate arteries and veins), which lie at the junction of the two; however, a thin layer of cortical tissue (subcortex) appears on the medullary side of this zone. The cortex close to the renal medulla is sometimes termed the juxtamedullary cortex.

Renal pelvis and calyces

The hilum of the kidney leads into a centrally located renal sinus, lined by the renal capsule and almost filled by the renal pelvis and renal vessels; the remaining space is filled by fat. Dissection into this plane can be challenging but is important in surgery on the renal pelvis, particularly open stone surgery. Within the renal sinus the collecting tubules of the nephrons of the kidney open on to the summits of the renal papillae to drain into minor calyces, which are funnel-shaped expansions of the upper urinary tract. The renal capsule covers the external surface of the kidney and continues through the hilum to line the renal sinus and fuse with the adventitial coverings of the minor calyces. Each minor calyx surrounds either a single renal papilla or, more rarely, groups of two or three renal papillae. The minor calyces unite with their neighbours to form two, or possibly three, larger chambers: the major calyces. There is wide variation in the arrangement of the calyces. As the posterior aspect of the kidney rotates laterally during its ascent *in utero*, the calyces that were lateral *in utero* become positioned anteriorly and the medial calyces move more posteriorly. The major calyces drain into the infundibula (MacLennan 2012). The renal pelvis is normally formed from the junction of two infundibula – one from the upper and one from the lower pole greater calyces – but there may be a third, which drains the calyces in the mid portion of the kidney. The major calyces are usually grouped so that three pairs drain into the upper pole infundibulum and four pairs into the lower one. If there is a middle infundibulum, the distribution is normally three pairs at the upper pole, two in the middle, and two at the lower pole. There is considerable variation in the arrangement of the infundibula and in the extent to which the renal pelvis is intrarenal or extrarenal. The funnel-shaped renal pelvis tapers as it passes inferomedially, traversing the hilum to become continuous with the ureter (see Figs 72.8–72.9). It is rarely possible to determine precisely where the renal pelvis ceases and the ureter begins; the region is usually extrahilar and normally lies adjacent to the lower part of the medial border of the kidney. Rarely, the entire renal pelvis has been found to lie inside the renal sinus so that the junction between it and the ureter occurs either in the vicinity of the hilum or completely within the renal sinus.

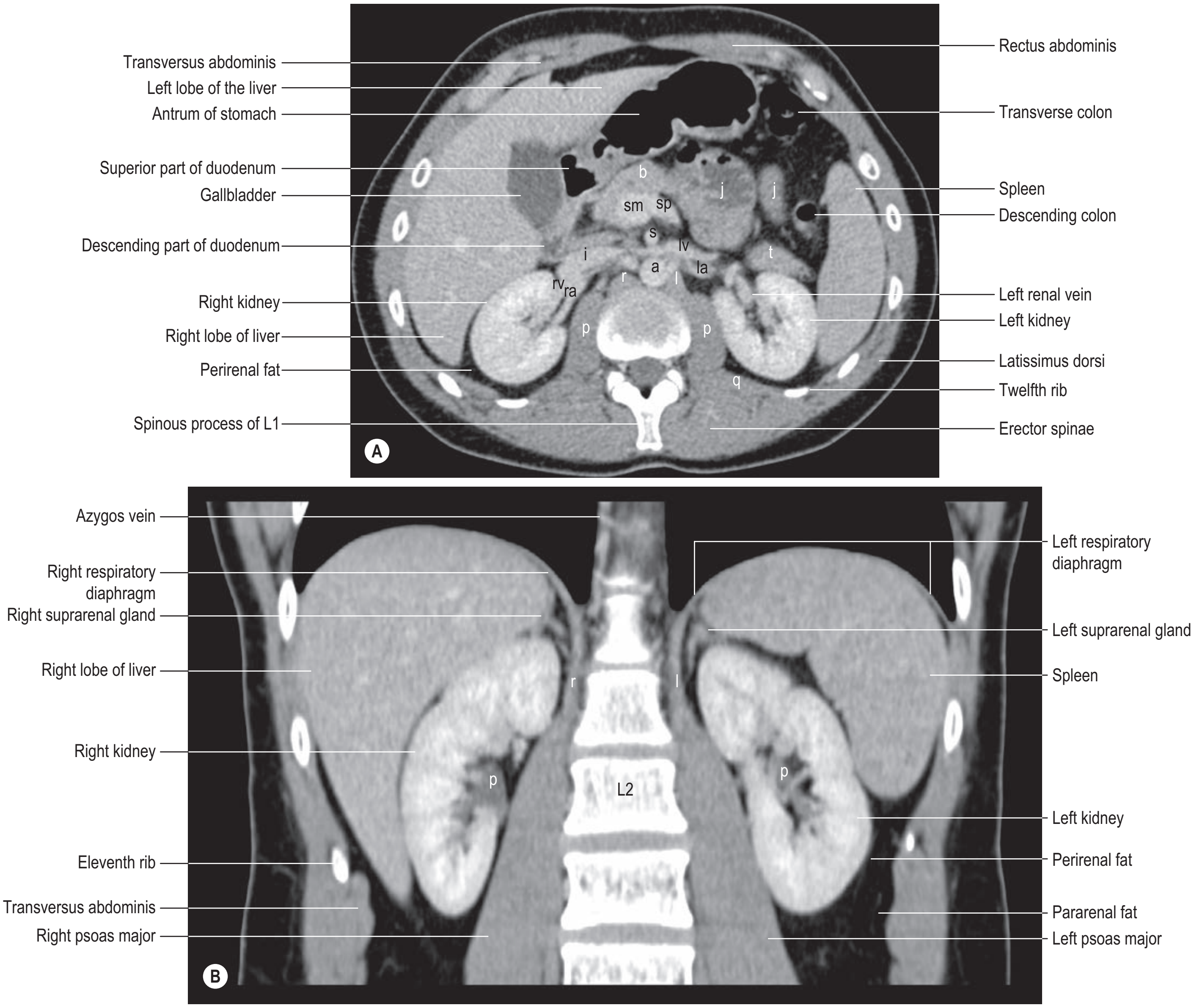
Transversus abdominis
Left lobe of the liver
Antrum of stomach
Superior part of duodenum
Gallbladder
Descending part of duodenum
Right kidney
Right lobe of liver
Perirenal fat
Spinous process of L1
Rectus abdominis
Transverse colon
Spleen
Descending colon
Left renal vein
Left kidney
Latissimus dorsi
Twelfth rib
Erector spinae
b
sm
sp
j
j
s
lv
i
t
a
la
r
l
rv
ra
p
p
q
A
Azygos vein
Right respiratory diaphragm
Right suprarenal gland
Right lobe of liver
Right kidney
Eleventh rib
Transversus abdominis
Right psoas major
Left respiratory diaphragm
Left suprarenal gland
Spleen
Left kidney
Perirenal fat
Pararenal fat
Left psoas major
r
l
p
p
L2
B

Fig. 72.6 Multislice CT scans of the kidneys. **A**, An axial plane CT with intravenous contrast medium at the level of the renal hila (L1-L2). Abbreviations: a, aorta; b, body of pancreas; i, inferior vena cava; j, jejunal loops; l, left crus of respiratory diaphragm; la, left renal artery; lv, left renal vein; p, psoas major; q, quadratus lumborum; r, right crus of respiratory diaphragm; ra, right renal artery; rv, right renal vein; s, superior mesenteric artery; sm, superior mesenteric vein; sp, splenic vein; t, tail of pancreas. **B**, A coronal multiplanar reformat from a CT with intravenous contrast medium through both kidneys and suprarenal glands. Abbreviations: l, left crus of respiratory diaphragm; r, right crus of respiratory diaphragm; p, renal pelvis.

The calyces, renal pelvis and ureter are well demonstrated radiologically following an intravenous injection of radio-opaque contrast that is excreted in the urine (computed tomographic urography, CTU) (Fig. 72.9), or after the introduction of radio-opaque contrast into the ureter by catheterization through a cystoscope (ascending or retrograde pyelography). Normal cupping of the minor calyces by projecting renal papillae can be obliterated by conditions that cause hydronephrosis, e.g. chronic distension of the ureter and renal pelvis due to upper or lower urinary tract obstruction, resulting in elevated pressure of the renal pelvis. An appreciation of the rotation of the kidneys, which results when the posterior calyces lie relatively medially and the anterior calyces lie laterally, is essential for interpreting contrast imaging of the collecting system of the kidneys.

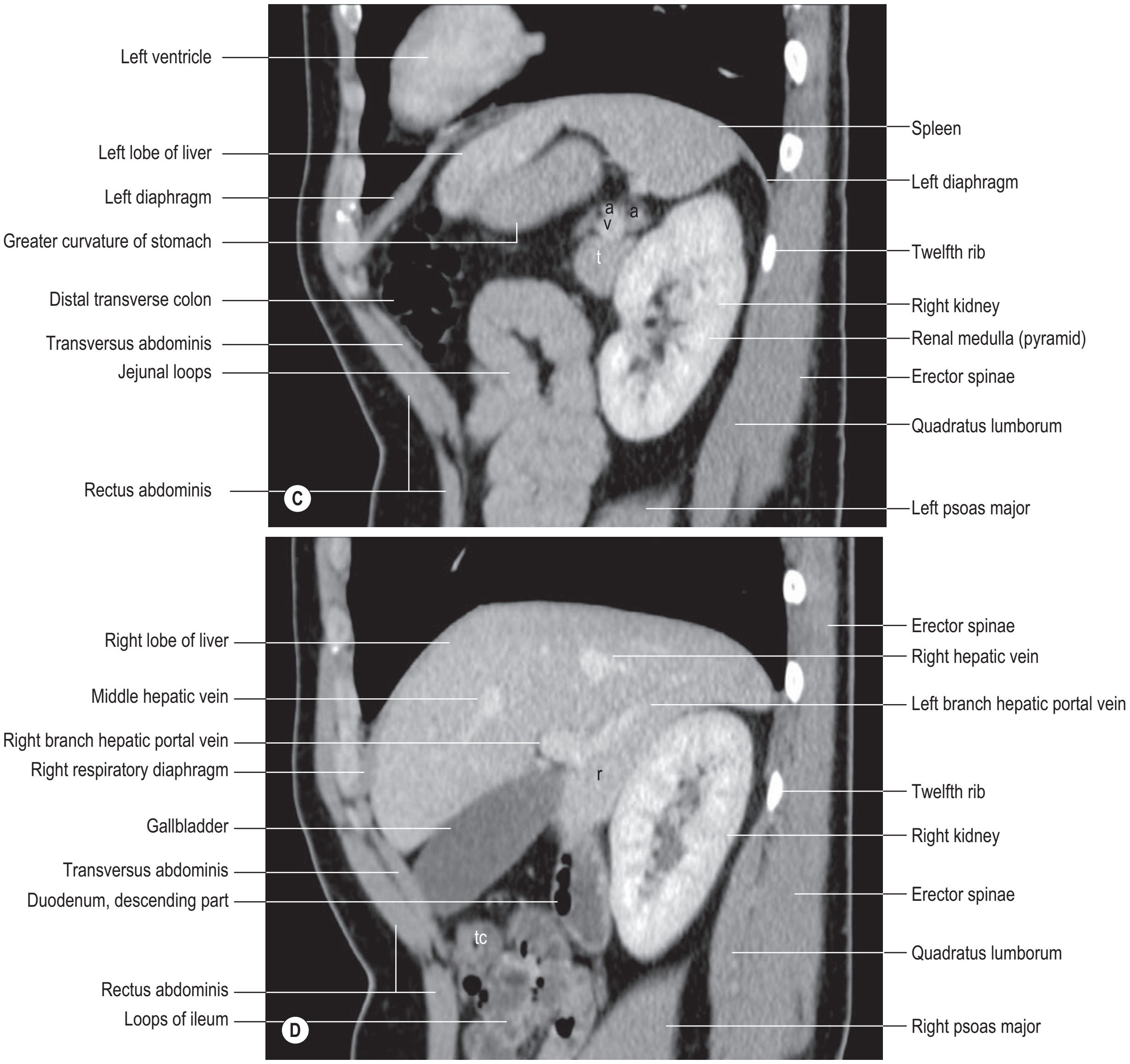
Left ventricle
Left lobe of liver
Left diaphragm
Greater curvature of stomach
Distal transverse colon
Transversus abdominis
Jejunal loops
Rectus abdominis
C
a
a
v
t
Spleen
Left diaphragm
Twelfth rib
Right kidney
Renal medulla (pyramid)
Erector spinae
Quadratus lumborum
Left psoas major
Right lobe of liver
Middle hepatic vein
Right branch hepatic portal vein
Right respiratory diaphragm
Gallbladder
Transversus abdominis
Duodenum, descending part
Rectus abdominis
Loops of ileum
D
r
tc
Erector spinae
Right hepatic vein
Left branch hepatic portal vein
Twelfth rib
Right kidney
Erector spinae
Quadratus lumborum
Right psoas major

Fig. 72.6, cont'd C, Sagittal multiplanar reformat from a CT with intravenous contrast medium throughout the left kidney. Abbreviations: a, splenic artery; t, tail of pancreas; v, splenic vein. **D**, Sagittal multiplanar reformat from a CT with intravenous contrast medium throughout the right kidney. Abbreviations: r, right lobe of liver; tc, transverse colon.

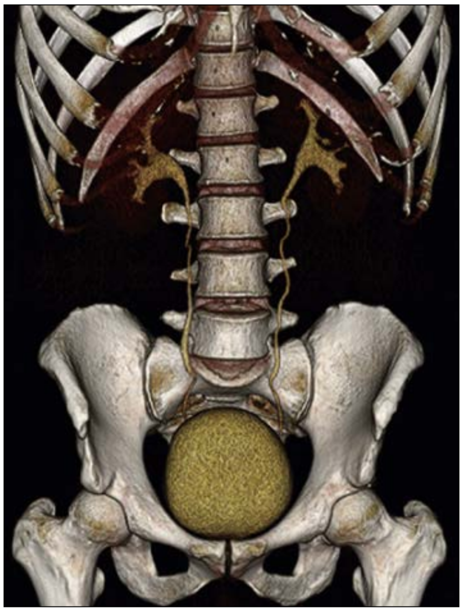

Fig. 72.9 A volume-rendered coronal CT urogram of a 39-year-old male; collecting systems, ureters and bladder are normal.

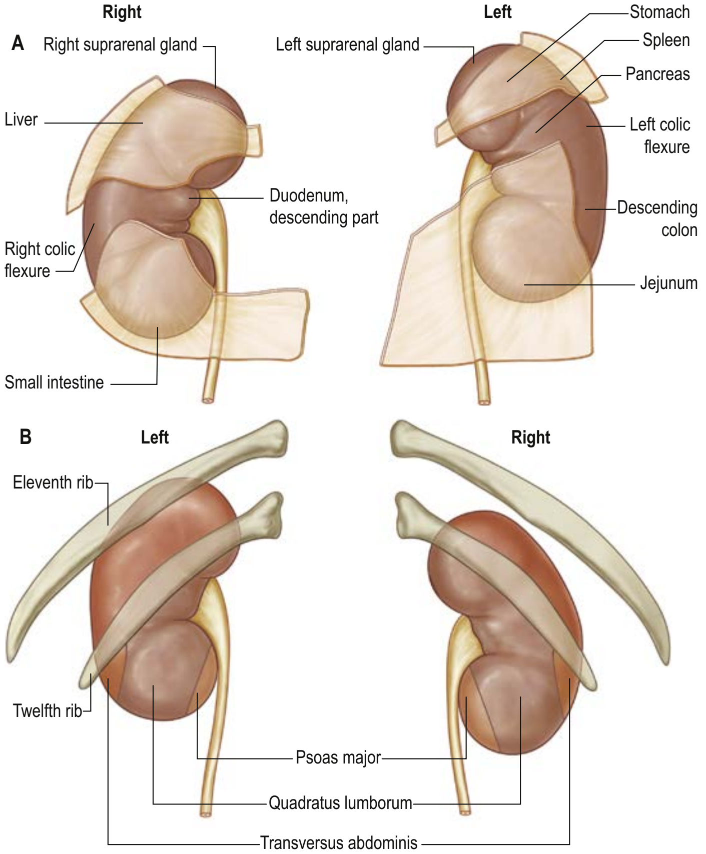

Fig. 72.7 The surfaces of the kidneys. **A**, Anterior, showing the areas related to neighbouring viscera. The areas where overlying viscera are separated from the kidney by peritoneum are shown. **B**, Posterior, showing the areas of relation to the posterior abdominal wall. (With permission from Drake RL, Vogl AW, Mitchell A et al (eds) Gray's Atlas of Anatomy. Elsevier, Churchill Livingstone. Copyright 2008.)

Vascular supply and lymphatic drainage

Renal arteries

The paired renal arteries take about 20% of the cardiac output to supply organs that represent less than 1% of total body weight. They branch laterally from the aorta at the right-angles just below the origin of the superior mesenteric artery (see Fig. 59.5A; **Fig. 72.10A, C**)). Both cross the corresponding crus of the respiratory diaphragm. The right renal artery is longer and often slightly higher, passing posterior to the inferior vena cava, right renal vein, head of the pancreas, and descending part of the duodenum. The left renal artery is often a little lower and passes behind the left renal vein, the body of the pancreas and the splenic vein. It may be crossed anteriorly by the inferior mesenteric vein.

A single renal artery to each kidney is present in approximately 70% of individuals (**Fig. 72.11**). The arteries vary in their level of origin and in their calibre, obliquity and precise relations (Merklin and Michels 1958). In its extrarenal course, each renal artery gives off one or more inferior suprarenal arteries, ureteric and capsular branches, and branches that supply perirenal tissue and the renal pelvis. Near the hilum of the kidney, each artery divides into an anterior and a posterior branch, and these divide into segmental arteries supplying the renal vascular segments. Accessory renal arteries are common (in approximately 30% of individuals) and usually arise from the abdominal aorta above or below (most commonly below) the renal artery and follow it to the hilum (**Figs 72.10B, D**). Accessory vessels to the inferior pole cross anterior to the ureter and can, by obstructing the ureter, cause hydronephrosis (**Fig. 72.12**). In children with ureteropelvic junction obstruction, a crossing vessel is found in 28% of cases (Veyrac et al 2003). Three anatomical variants of aberrant lower pole crossing vessels have been described: either anterior to the dilated renal pelvis or ureteropelvic junction, or inferior to the ureteropelvic junction, causing kinking of the ureter (Schneider et al 2013). Rarely, accessory renal arteries arise from the coeliac or superior mesenteric arteries near the aortic bifurcation, or from the common iliac arteries.

The subdivisions of the renal arteries are described sequentially as segmental, lobar, interlobar, arcuate and interlobular (cortical radiate) arteries, and afferent and efferent glomerular arterioles (**Fig. 72.13**).

Segmental arteries

Renal vascular segmentation was originally recognized by John Hunter in 1794, but the first detailed account of the primary pattern was produced in the 1950s from casts and radiographs of injected kidneys. Five arterial segments of the kidney have been identified (**Fig. 72.14A**). The superior segment occupies the anteromedial region of the superior pole. The anterior superior segment includes the rest of the superior pole and the central anterosuperior region. The inferior segment encompasses the whole inferior pole. The anterior inferior segment lies between the anterior and inferior segments. The posterior segment includes the whole posterior region between the superior and inferior segments. This is the pattern most commonly seen, and although there can be considerable variation, it is the pattern that clinicians most frequently encounter when performing partial nephrectomy. Anatomical and radiological analyses have suggested that there could be up to nine arterial segments for each kidney (Macchi et al 2019) (**Fig. 72.14B**). Whatever pattern is present, it is important to emphasize that vascular segments are supplied by virtual end arteries. In contrast, the larger intrarenal veins have no segmental organization and anastomose freely.

Brödel described a relatively avascular longitudinal zone (the 'bloodless' line of Brödel) along the convex renal border, which was proposed as the most suitable site for surgical incision (Brödel 1911). However, many vessels cross this zone and it is far from 'bloodless'; planned radial or intersegmental incisions are therefore preferable (Macchi et al 2018). Knowledge of the vascular anatomy of the kidney is important when partial nephrectomy is undertaken for renal cell carcinoma. In this surgery, the branches of the renal artery are defined so that the surgeon can safely excise the tumour while not compromising the vascular supply to the remaining renal tissue (Novick 1998).

Lobar, interlobar, arcuate and interlobular arteries

The initial branches of segmental arteries are lobar, usually one to each renal pyramid. Before reaching the renal pyramid they subdivide into two or three interlobar arteries, extending towards the cortex around each pyramid. At the junction of the renal cortex and medulla, interlobar arteries dichotomize into arcuate arteries, which diverge at right angles. As they arch between the renal cortex and medulla, each divides further, ultimately supplying interlobular arteries that diverge radially into the cortex. The terminations of adjacent arcuate arteries do not anastomose but end in the renal cortex as additional interlobular arteries. Though most interlobular arteries come from arcuate branches, some arise directly from arcuate, or even terminal, interlobar arteries (see Fig. 72.13). Interlobular arteries ascend towards the superficial cortex or can branch occasionally en route. Some are more tortuous and recurve towards the renal medulla at least once before proceeding towards the renal surface. Others traverse the surface as perforating arteries to anastomose with the capsular plexus (which is also supplied from the inferior suprarenal, renal and gonadal arteries).

Afferent and efferent glomerular arterioles

Afferent glomerular arterioles are mainly the lateral rami of interlobular arteries. A few arise from arcuate and interlobar arteries when they vary their direction and angle of origin: deeper ones incline obliquely back towards the renal medulla, the intermediate pass horizontally and the more superficial approach the surface of the kidney obliquely before ending in a glomerulus (see Fig. 72.13). Efferent glomerular arterioles from most glomeruli (except at juxtamedullary and, sometimes, intermediate cortical levels) soon divide to form a dense peritubular capillary plexus around the proximal and distal convoluted tubules; there are therefore two sets of capillaries – glomerular and peritubular – in series in the main renal cortical circulation, linked by efferent glomerular arterioles. The vascular supply of the renal medulla is largely from efferent arterioles of juxtamedullary glomeruli, supplemented by some from more superficial glomeruli, and 'aglomerular' arterioles (probably from degenerated glomeruli). Efferent glomerular arterioles passing into the renal medulla are relatively long, wide vessels, and contribute side branches to neighbouring capillary plexuses before entering the renal medulla, where each divides into 12–25 descending vasa recta. As their name suggests, these run straight to various depths in the renal medulla, contributing side branches to a radially elongated capillary plexus applied to the descending and ascending limbs of renal loops and to collecting ducts. The venous ends of capillaries converge to the ascending vasa recta, which drain into arcuate or interlobular veins. An essential feature of the vasa recta (particularly in the outer medulla) is

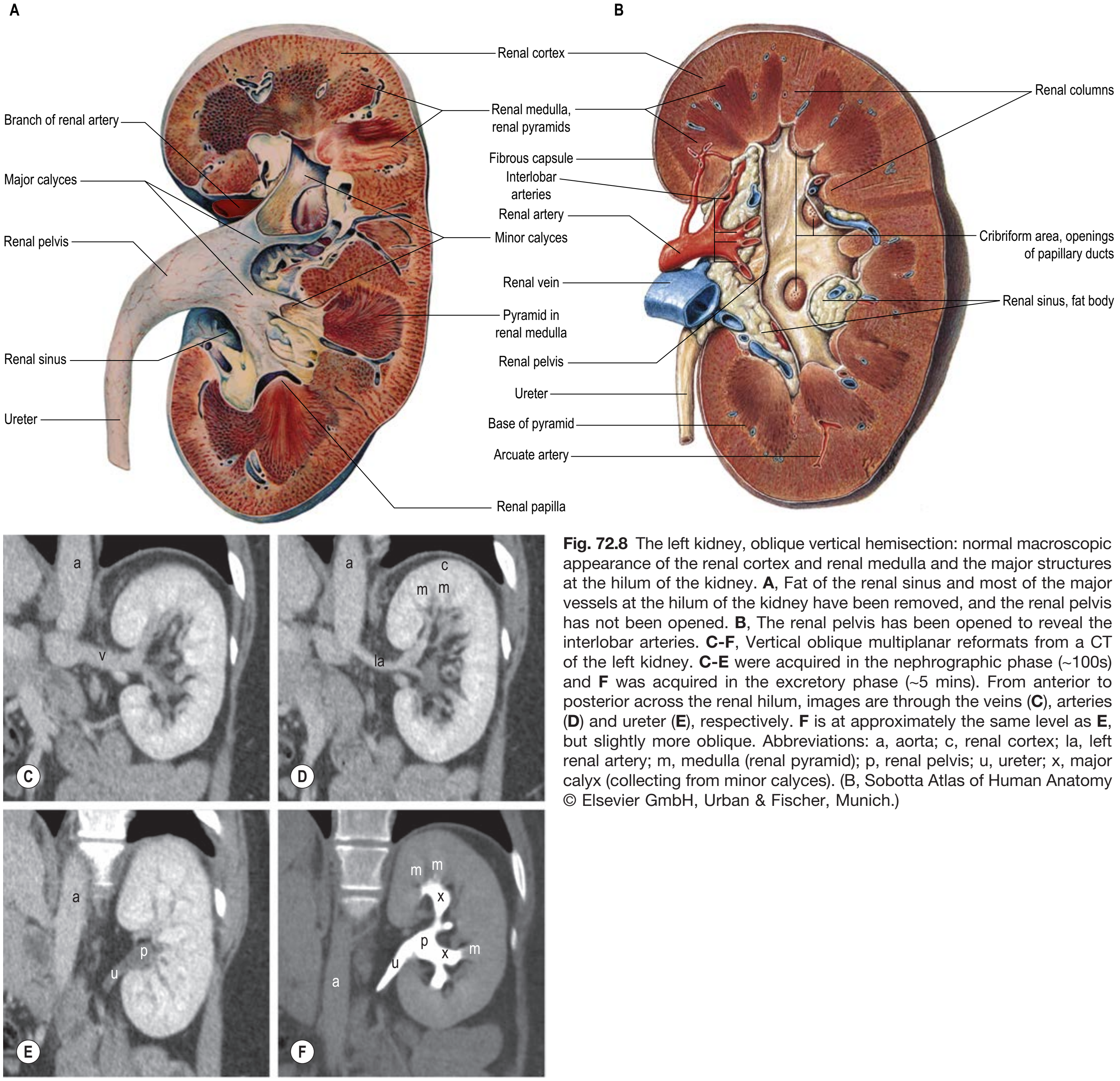
A
B
Branch of renal artery
Major calyces
Renal pelvis
Renal sinus
Ureter
Renal cortex
Renal medulla, renal pyramids
Fibrous capsule
Interlobar arteries
Renal artery
Minor calyces
Renal vein
Pyramid in renal medulla
Renal pelvis
Ureter
Base of pyramid
Arcuate artery
Renal papilla
Renal columns
Cribriform area, openings of papillary ducts
Renal sinus, fat body
a
v
C
a
c
m
m
la
D
a
p
u
E
m
m
x
p
x
m
u
a
F

Fig. 72.8 The left kidney, oblique vertical hemisection: normal macroscopic appearance of the renal cortex and renal medulla and the major structures at the hilum of the kidney. **A**, Fat of the renal sinus and most of the major vessels at the hilum of the kidney have been removed, and the renal pelvis has not been opened. **B**, The renal pelvis has been opened to reveal the interlobar arteries. **C-F**, Vertical oblique multiplanar reformats from a CT of the left kidney. **C-E** were acquired in the nephrographic phase (~100s) and **F** was acquired in the excretory phase (~5 mins). From anterior to posterior across the renal hilum, images are through the veins (**C**), arteries (**D**) and ureter (**E**), respectively. **F** is at approximately the same level as **E**, but slightly more oblique. Abbreviations: a, aorta; c, renal cortex; la, left renal artery; m, medulla (renal pyramid); p, renal pelvis; u, ureter; x, major calyx (collecting from minor calyces). (B, Sobotta Atlas of Human Anatomy © Elsevier GmbH, Urban & Fischer, Munich.)

that both descending and ascending vessels are grouped into vascular bundles, within which the external aspects of both types are closely apposed, bringing them close to the limbs of the nephron loops (of Henle) and collecting ducts. As these bundles converge centrally into the renal medulla, they contain fewer vessels; some terminate at successive levels in neighbouring capillary plexuses. This proximity of descending and ascending vessels to each other and to adjacent collecting ducts provides the structural basis for the countercurrent exchange and multiplier phenomena (Fig. 72.15). These complex renal vascular patterns show regional specializations that are closely adapted to the spatial organization and functions of renal corpuscles, tubules and ducts (see below).

Renal veins

Fine radicles from the venous ends of the peritubular plexuses converge to join interlobular veins, one with each interlobular artery. Many interlobular veins begin beneath the fibrous capsule of the kidney by the convergence of several stellate veins, which drain the most superficial zone of the renal cortex and so are named from their surface appearance. Interlobular veins pass to the corticomedullary junction and also receive some ascending vasa recta before ending in arcuate veins (which accompany arcuate arteries), and anastomose with neighbouring veins. Arcuate veins drain into interlobar veins, which anastomose and form the renal vein.

The large renal veins lie anterior to the renal arteries and open into the inferior vena cava almost at right-angles (see Fig. 59.6; Fig. 72.16). The left renal vein is three times longer than the right (7.5 cm and 2.5 cm, respectively): the left kidney is the preferred side for live donor nephrectomy for this reason. However, the left renal vein can also be double, one vein passing posterior and the other anterior to the aorta before draining into the inferior vena cava, an arrangement that is sometimes referred to as persistence of the 'renal collar'. The anterior vein can be absent, in which case

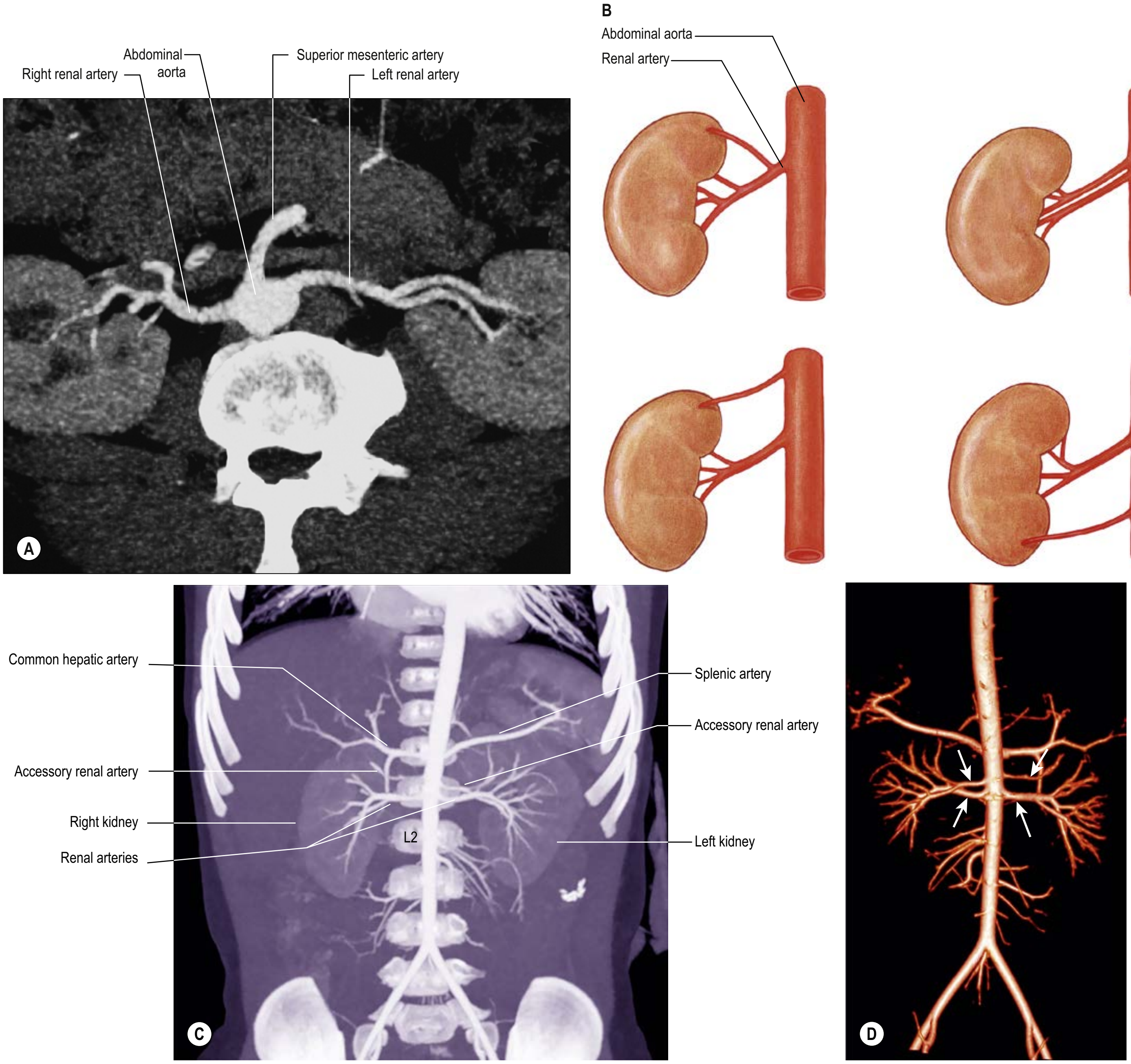
Abdominal aorta
Right renal artery
Superior mesenteric artery
Left renal artery
A
B
Abdominal aorta
Renal artery
Common hepatic artery
Accessory renal artery
Right kidney
Renal arteries
L2
Splenic artery
Accessory renal artery
Left kidney
C
D

Fig. 72.10 **A**, An axial multislice CT renal angiogram. **B**, Variations in the number and patterns of branching of the renal artery. **C**, Coronal maximal intensity projection (MIP) image of the abdomen. **D**, Volume-rendered abdominal angiogram from a paediatric patient showing a posterior view of the abdominal aorta and its branches, accessory renal arteries (upper arrows) and renal arteries (lower arrows). (B, Sobotta Atlas of Human Anatomy © Elsevier GmbH, Urban & Fischer, Munich. C–D, Courtesy of Jon C Betts Jr, Children's of Alabama, Birmingham, AL, USA.)

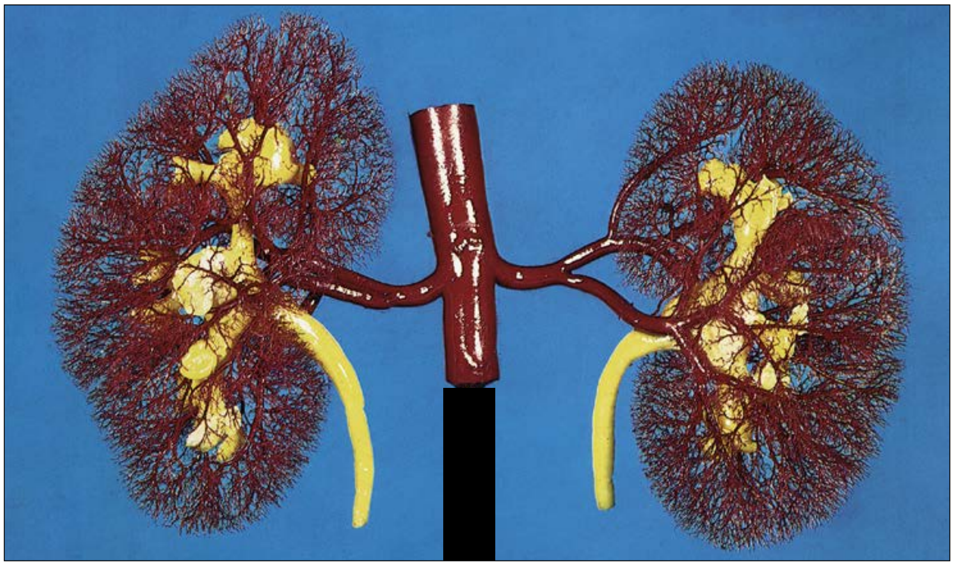

Fig. 72.11 A resin corrosion cast of the human kidneys. Ureters, renal pelves and calyces are yellow; aorta, renal arteries and their branches are red. (Prepared by the late DH Tompsett of the Royal College of Surgeons of England. With permission from the Museums of the Royal College of Surgeons.)

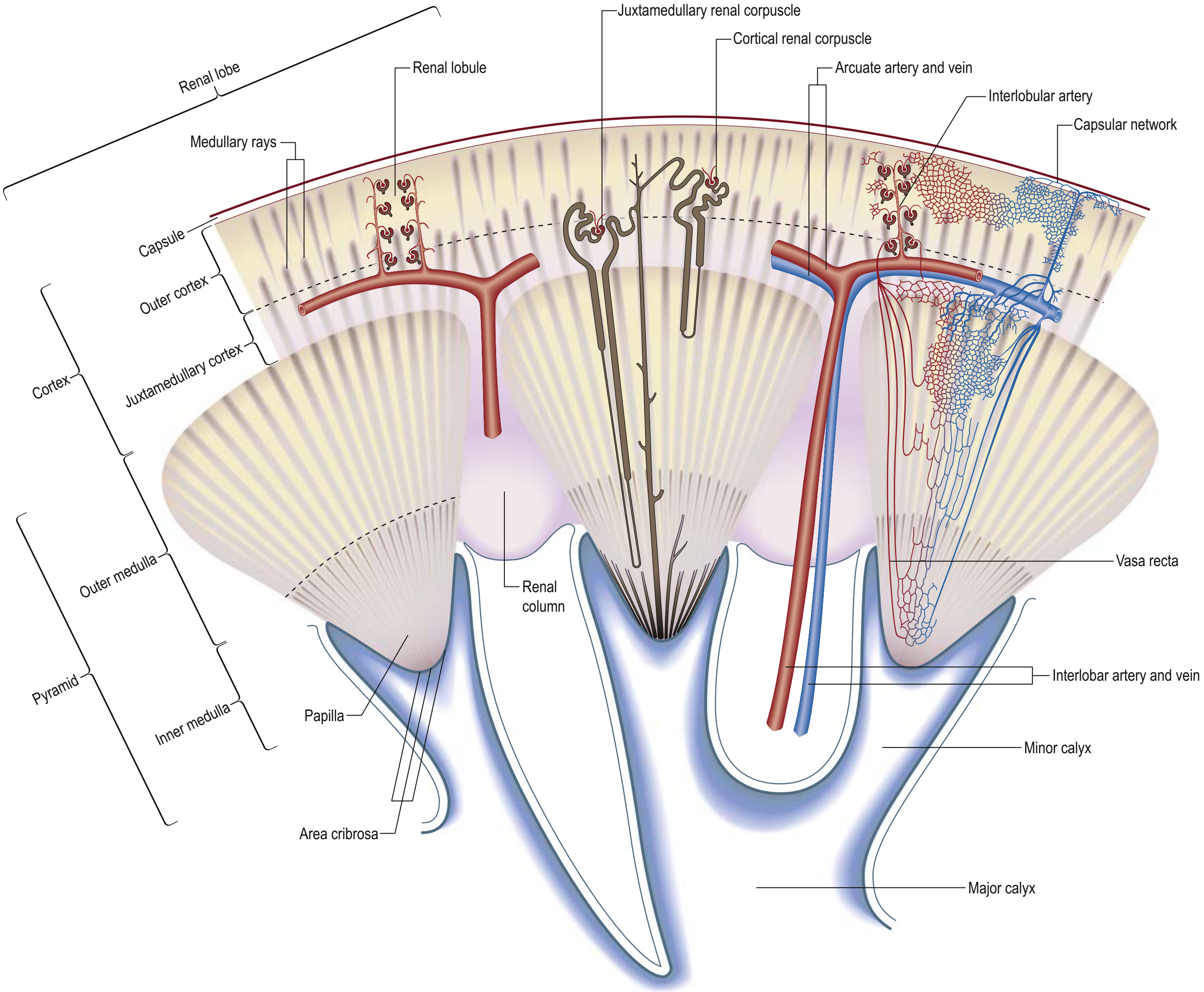
Renal lobe
Juxtamedullary renal corpuscle
Cortical renal corpuscle
Renal lobule
Arcuate artery and vein
Interlobular artery
Capsular network
Medullary rays
Capsule
Outer cortex
Cortex
Juxtamedullary cortex
Outer medulla
Pyramid
Inner medulla
Papilla
Area cribrosa
Renal column
Vasa recta
Interlobar artery and vein
Minor calyx
Major calyx

Fig. 72.13 The major structures in the renal cortex and medulla (left), the position of cortical and juxtamedullary nephrons (middle) and the major blood vessels (right).

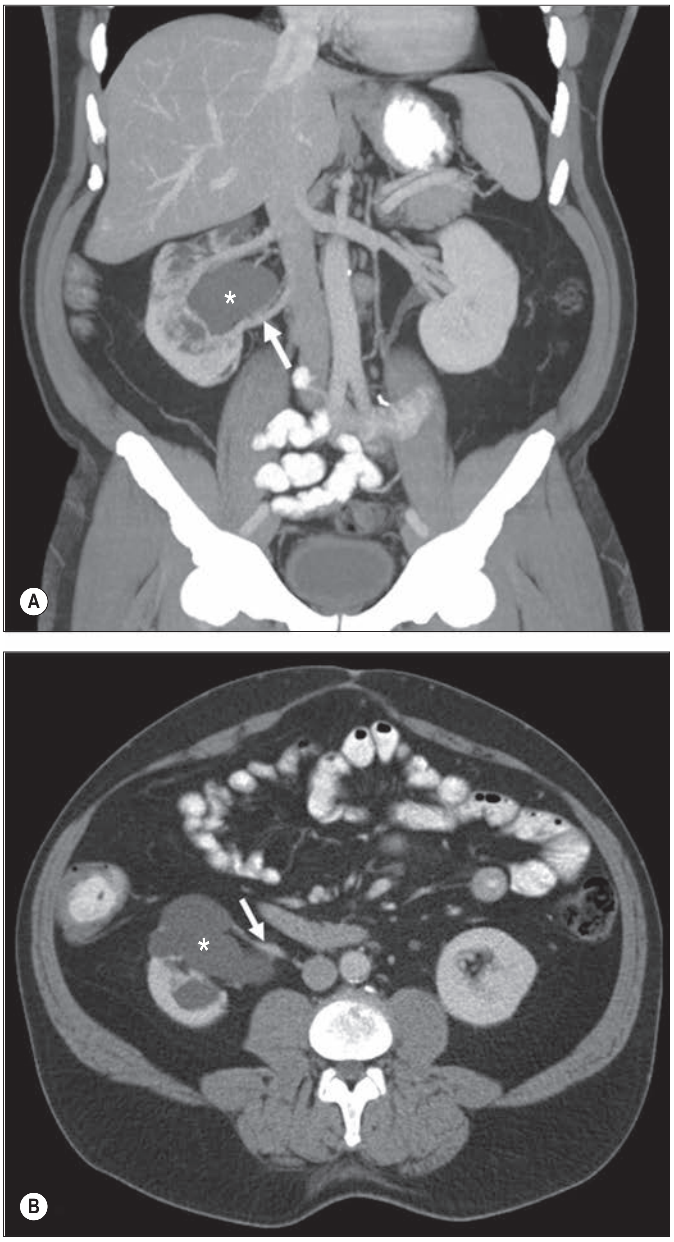

Fig. 72.12 Marked dilation of the right renal pelvis (*) and calyces, and non-dilation of the right ureter (with no associated lesion) due to ureteropelvic junction obstruction. Note a crossing inferior right renal vein (arrow) at the level of the obstruction. **A**, A coronal maximum-intensity projection of the abdomen. **B**, An axial contrast-enhanced CT image of the abdomen.

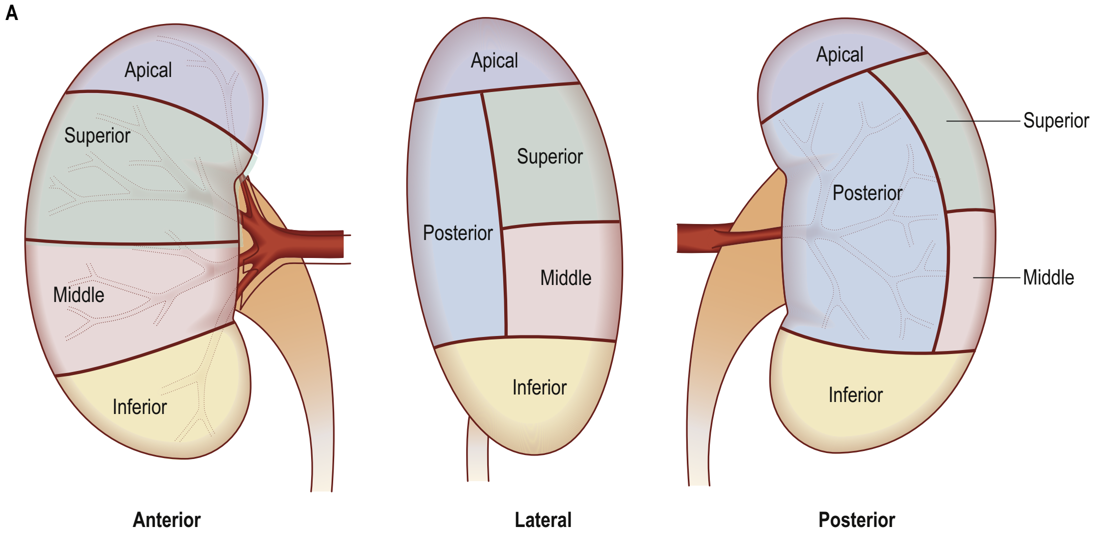

Fig. 72.14 A, The segmental arterial anatomy of the right kidney. The posterior division branches near the hilum of the kidney before the anterior division divides into the other segmental arteries. (Courtesy Dr Veronica Macchi, University of Padova, Padova, Italy.) (B, *continued online*)

there is a single retro-aortic left renal vein. These variations could negate any advantage of using the left kidney as a donor (Phelan et al 2009). The left renal vein runs from its origin in the hilum of the kidney, posterior to the splenic vein and the body of the pancreas, and then across the anterior aspect of the abdominal aorta, just below the origin of the superior mesenteric artery. Anterior nutcracker syndrome, characterized by left renal vein hypertension secondary to compression of the vein between the ventral surface of the abdominal aorta and the dorsal surface of the superior mesenteric artery, has been associated with haematuria and varicocele in children (Kurklinsky and Rooke 2010). The left gonadal vein enters the left renal vein from below, and the left suprarenal vein, usually receiving one of the left inferior phrenic veins, enters it above but nearer the midline (see Fig. 61.12). The left renal vein enters the inferior vena cava slightly superior to the right renal vein. The right renal vein lies posterior to the descending part of the duodenum and, sometimes, the head of the pancreas. It can be extremely short (less than 1 cm), such that safe nephrectomy can require excision of a cuff of the inferior vena cava.

Lymphatic drainage

Renal lymphatic vessels begin in three plexuses: around the renal tubules, under the renal capsule and in the perirenal fat (the latter two connect freely). Collecting vessels from the intrarenal plexus form four or five trunks that follow the renal vein to end in the lateral aortic nodes; the subcapsular collecting vessels join them as they leave the hilum of the kidney. The perirenal plexus drains directly into the same nodes.

Innervation

Rami from the coeliac ganglion and plexus, aorticorenal ganglion, least thoracic splanchnic nerve, first lumbar splanchnic nerve and aortic plexus form a dense plexus of autonomic nerves around the renal artery (see Fig. 59.4).

Small ganglia occur in the renal plexus, the largest usually behind the origin of the renal artery. The plexus continues into the kidney around the arterial branches and supplies the vessels, renal glomeruli and, especially, the cortical renal tubules. Axons from plexuses around the arcuate arteries innervate juxtamedullary efferent arterioles and vasa recta, which control the blood flow between the renal cortex and medulla without affecting the glomerular circulation. Axons from the renal plexus contribute to the ureteric and gonadal plexuses.

Microstructure

The kidney is composed of many tortuous, closely packed renal tubules, bounded by a delicate connective tissue in which run blood vessels, lymphatics and nerves. Each tubule consists of two embryologically distinct parts: the nephron, which produces urine, and the collecting duct, which completes the concentration of urine and through which urine passes out into the calyces of the kidney, the renal pelvis, the ureter and urinary bladder.

Nephron

The nephron consists of a renal corpuscle, concerned with filtration from the plasma, and a renal tubule, concerned with selective resorption from the filtrate to form the urine (see Fig. 72.13). Collecting ducts carry fluid from several renal tubules to a terminal papillary duct, opening into a minor calyx at the apex of a renal papilla. Papillary surfaces show numerous minute orifices of these ducts and pressure on a fresh kidney expresses urine from them.

Renal corpuscle

Renal corpuscles are small, rounded structures averaging 0.2 mm in diameter, visible in the renal cortex deep to a narrow peripheral cortical zone (**Fig. 72.17**; see Fig. 72.15). Each has a central glomerulus of vessels and a glomerular (Bowman's) capsule, from which the renal tubule originates.

There are about one million renal corpuscles in each kidney, their number (which can be determined, in part, by intrauterine factors) decreasing with age; this process is accelerated by raised blood pressure. After birth, new nephrons cannot be developed which means that a lost nephron can never be replaced. The decrease in corpuscular numbers with age is reflected in a corresponding reduction in the rate of glomerular filtration from the fourth decade onwards.

Glomerulus

A glomerulus is a collection of convoluted capillary blood vessels, united by a delicate mesangial matrix and supplied by an afferent arteriole that enters the capsule opposite the urinary pole, where the filtrate enters the tubule (the term glomerulus is often used to describe the entire renal corpuscle) (Davies et al 2001). An efferent arteriole emerges from the same point, the vascular pole of the corpuscle. Glomeruli are simple in form until late prenatal life; some remain so for about 6 months after birth, the majority maturing by 6 years and all by 12 years. Low birth weight, defined as a weight less than 2500 g, is associated with a reduction in the number and volume of glomeruli (Manalich et al 2000).

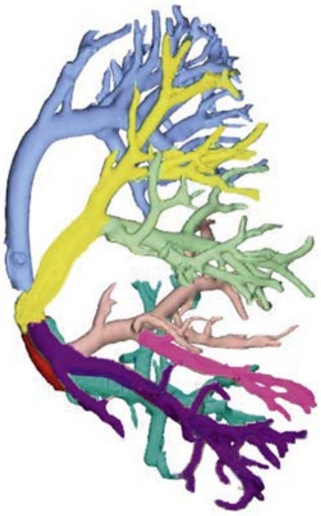

Fig. 72.14, cont'd B, A 3D elaboration of CT imaging of a vascular cast illustrating the segmental arterial anatomy of the right kidney. This specimen illustrates seven arterial segments each indicated with a separate colour. (Courtesy Dr Veronica Macchi, University of Padova, Padova, Italy.)

The left renal vein may have to be ligated during surgery for aortic aneurysm because it has such a close relationship with the aorta; this seldom results in any harm to the kidney, provided that the ligature is placed medial to the draining gonadal and suprarenal veins, since these usually provide adequate collateral venous drainage. The right renal vein has no significant collateral drainage and cannot be ligated with impunity.

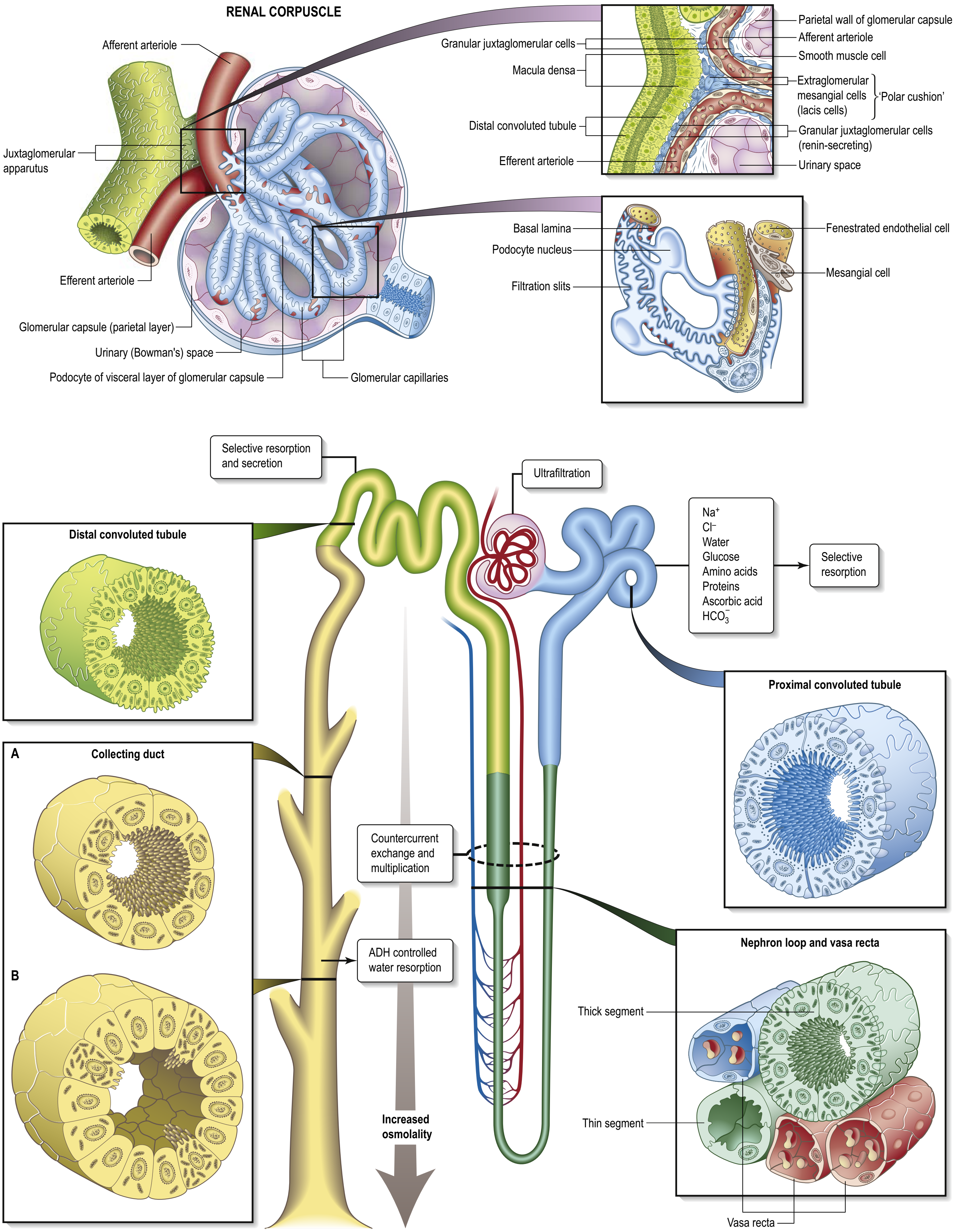
RENAL CORPUSCLE
Afferent arteriole
Juxtaglomerular apparatus
Efferent arteriole
Glomerular capsule (parietal layer)
Urinary (Bowman's) space
Podocyte of visceral layer of glomerular capsule
Glomerular capillaries
Granular juxtaglomerular cells
Macula densa
Distal convoluted tubule
Efferent arteriole
Parietal wall of glomerular capsule
Afferent arteriole
Smooth muscle cell
Extraglomerular mesangial cells (lacis cells)
'Polar cushion'
Granular juxtaglomerular cells (renin-secreting)
Urinary space
Basal lamina
Podocyte nucleus
Filtration slits
Fenestrated endothelial cell
Mesangial cell
Selective resorption and secretion
Ultrafiltration
Distal convoluted tubule
Na^+
Cl^-
Water
Glucose
Amino acids
Proteins
Ascorbic acid
HCO_3^-
Selective resorption
Proximal convoluted tubule
A
Collecting duct
B
Countercurrent exchange and multiplication
ADH controlled water resorption
Increased osmolality
Nephron loop and vasa recta
Thick segment
Thin segment
Vasa recta

Fig. 72.15 The regional microstructure and principal activities of a nephron and collecting duct. For clarity, a nephron of the long loop (juxtamedullary) type is shown. Abbreviations: ADH, antidiuretic hormone.

Glomerular capsule

The glomerular capsule is the blind expanded end of a renal tubule and is deeply invaginated by the glomerulus. It is lined by a simple squamous epithelium on its outer (parietal) wall; its glomerular, juxtacapillary (visceral) wall is composed of specialized epithelial podocytes. Between the two walls of the capsule is a flattened urinary (Bowman's) space continuous with the proximal convoluted tubule (**Fig. 72.17B**; see Figs 2.2A, 72.15).

Podocytes are stellate cells (Zhao and Burt 2007). Their major (primary) foot processes curve around the capillary loops and branch to form secondary processes that are applied closely to the basal lamina; secondary or tertiary processes give rise to terminal pedicels (**Fig. 72.18A**). Pedicels of one cell alternate with those of an adjacent cell and interdigitate tightly with each other, separated by narrow (25 nm) gaps: the filtration slits (**Fig. 72.18B**). The latter are covered by a dense, membranous, slit diaphragm, through which filtrate must pass to enter the urinary space. The differentiation of the adult podocyte phenotype is associated with the presence of several specific proteins, including nephrin, podocin, synaptopodin and GLEPP-1. Mutations in these proteins can cause important functional problems, e.g. the classic Finnish form of congenital nephritic syndrome is caused by a mutation of *NHPS1*, which codes for nephrin. The luminal membrane and the slit diaphragm are covered by a dense surface coat rich in sialoglycoprotein, which gives this surface a very high negative charge and is one of the key characteristics of the permselectivity barrier. Differentiated podocytes cannot replicate.

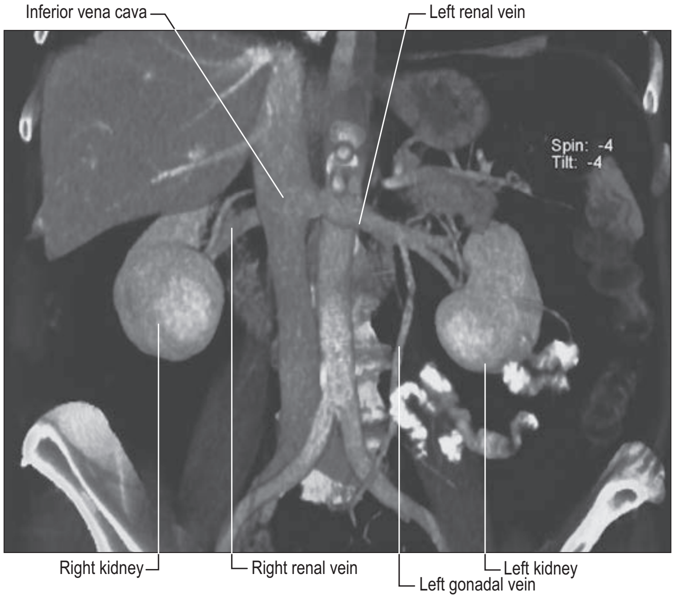

Fig. 72.16 A CT renal venogram, acquired from a multislice CT examination and reconstructed as a three-dimensional, surface-shaded reformat.

The glomerular endothelium is finely fenestrated. The principal barrier to the passage of fluid from capillary lumen to urinary space is the glomerular basal lamina, the fused endothelial and podocyte basal laminae (see Fig. 72.18B). This is usually 0.33 μm thick in humans and acts as a selective filter, allowing the passage from blood, under pressure, of water and various small molecules and ions in the circulation. Haemoglobin can cross the filter, but larger molecules and those of similar size with a negative charge are largely retained. Most protein that does enter the filtrate is selectively resorbed and degraded by cells of the proximal convoluted tubule.

The glomerular basal lamina serves as the skeleton of the glomerular tuft. Its outer aspect is completely covered by podocytes, and the interior is filled by capillaries and a delicate mesangial matrix (mesangium). The major components of the glomerular basal lamina are laminin and type IV collagen (both of which are expressed as unique isoforms), and heparan sulphate proteoglycans. The thickness of the glomerular basal lamina increases throughout childhood; the rate of increase slows after the age of 11 years (Ramage et al 2002).

Irregular mesangial cells, with phagocytic and contractile properties, lie within and secrete the glomerular mesangium, a specialized connective tissue that binds the loop of glomerular capillaries and fills the spaces between endothelial surfaces that are not invested by podocytes (see Figs 72.15, 72.17B). Mesangial cells are related to vascular pericytes and are concerned with the turnover of glomerular basal lamina. They clear the glomerular filter of immune complexes and cellular debris, and their contractile properties help to regulate blood flow. Similar cells, the extraglomerular mesangial (lacis) cells, lie outside the glomerulus at the vascular pole and form part of the juxtaglomerular apparatus.

Renal tubule

A renal tubule consists of a glomerular capsule that leads into a proximal convoluted tubule, connected to the capsule by a short neck and continuing into a sinuous or coiled convoluted part (see Fig. 72.15). This straightens as it approaches the medulla to become the descending limb of the nephron loop (loop of Henle), and then the ascending limb after an abrupt U-turn. The limbs of the nephron loop are narrower and thinner-walled within the deeper medullary tissue, where they become the descending and ascending thin segments. The thick ascending limb continues into the distal convoluted tubule. The nephron finally straightens once more as the connecting tubule, which ends by joining a collecting duct.

Collecting ducts originate in the cortical medullary rays and join others at intervals. They finally open into wider papillary ducts, which open on to a papilla, their numerous orifices forming a perforated cribriform area on the surface at its tip (see Fig. 72.13).

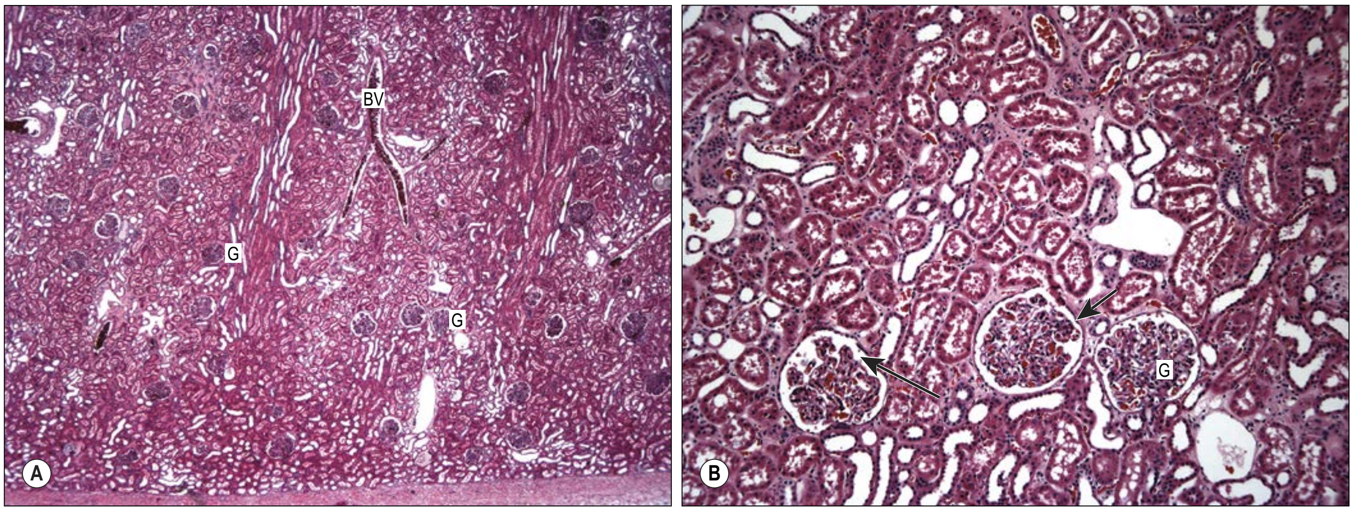

Fig. 72.17 **A**, A low-power histological section of the renal cortex, containing glomeruli (G), proximal and distal convoluted tubules and blood vessels (BV). **B**, A higher-power view of the section demonstrating several glomeruli (G) within a network of mesangium. The glomerular basement membrane of the capillaries is continuous with the glomerular capsule (short arrow) of the glomerulus, and is separated from it by Bowman's space (long arrow).

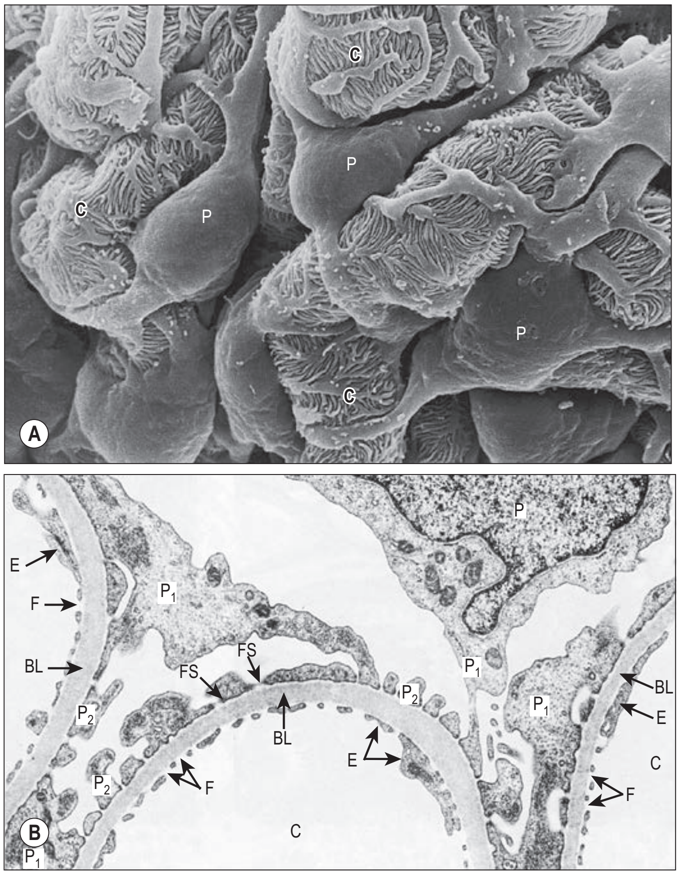

Fig. 72.18 **A**, A scanning electron micrograph showing podocytes forming the visceral layer of the glomerular capsule in the renal corpuscle. Their cell bodies (P) send out primary processes that branch several times and end in fine pedicels, which wrap tightly around the glomerular capillaries (C) and interdigitate with similar pedicels from a neighbouring podocyte. **B**, A transmission electron micrograph demonstrating the glomerular filtration apparatus. Note the endothelial cells of fenestrated capillaries, the filtration slits between podocyte pedicels and their thick shared basal lamina. Abbreviations: BL, basal lamina; C, lumina of capillary loops; E, endothelial cell cytoplasm; F, fenestrations; FS, filtration slits; P, podocyte; P_1 and P_2, primary and secondary foot processes that rest on the glomerular basal laminae. (A, With permission from Igaku-Shoin, Tokyo, from Fujita T, Tanaka K, Tokunaga J 1981 SEM Atlas of Cells and Tissues. B, With permission from Young B, Heath JW 2000 Wheater's Functional Histology. Edinburgh: Churchill Livingstone.)

Renal tubules are lined throughout by a single-layered epithelium (see Fig. 72.15; **Fig. 72.19**). The type of epithelial cell varies according to the functional roles of the different regions, e.g. active transport and passive diffusion of various ions and water into and out of the tubules; reabsorption of organic components such as glucose and amino acids; uptake of any proteins that leak through the glomerular filter.

The proximal convoluted tubule is lined by cuboidal or low columnar epithelium and has a brush border of tall microvilli on its luminal surface. The shape of the cells depends on tubular fluid pressure, which, in life, distends the lumen and flattens the cells (they become taller when glomerular blood pressure ceases post mortem or at biopsy). The cytoplasm of proximal tubular cells is strongly eosinophilic and the nuclei are euchromatic and central. The basal cytoplasm is rich in mitochondria, orientated perpendicularly and the basal plasma membrane is highly infolded. The lateral surfaces of adjacent epithelial cells interdigitate, increasing the complexity of the basolateral plasma membrane. The microvilli on the luminal surfaces significantly increase the area of plasma membrane in contact with tubular fluid, facilitating the transport of ions and small molecules against steep concentration gradients. The abundant mitochondria supply the energy, as adenosine triphosphate (ATP), needed for this process. Sodium/potassium adenosine triphosphatase (Na$^+$/K$^+$ ATPase) is located in apical and basal membranes, and the cytoplasm contains numerous other enzymes concerned with ion transport. Water and other solutes pass between cells (paracellular transport) passively, along osmotic and electrochemical gradients, probably through leaky apical tight junctions. Pinocytotic vesicles are found near the apical surface and represent the means by which small proteins and peptides from the filtrate are internalized and degraded by associated lysosomes. Peroxisomes and lipid droplets abound in the cytoplasm.

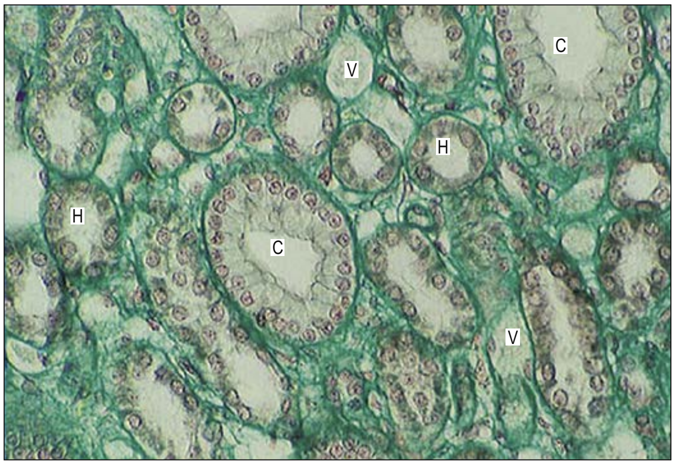

Fig. 72.19 A histological cross-section of a part of the renal medulla. Note the large collecting ducts (C) and smaller segments of the nephron loop (loop of Henle (H)), interspersed with vasa recta (V) (trichrome-stained).

The nephron loop consists of a thin segment (30 µm in diameter), lined by low cuboidal to squamous cells, and a thick segment (60 µm in diameter) composed of cuboidal cells like those in the distal convoluted tubule. The thin segment forms most of the nephron loop in juxtamedullary nephrons, which reach deep into the medulla. Few organelles appear in cells lining the thin segment, indicating that these cells play a passive rather than an active role in ion transport. The thick segment is composed of cuboidal epithelium with many mitochondria, deep basolateral folds and short apical microvilli, indicating a more active metabolic role. The thick ascending limb of the nephron loop is the source of Tamm–Horsfall glycoprotein, which is a crucial defence molecule (Wu et al 2018).

Cells of the distal tubule are cuboidal and resemble those in the proximal tubule. They have few microvilli, so the tubular lumen has a more distinct outline. The basolateral folds containing mitochondria are deep, almost reaching the luminal aspect. Enzymes concerned with active transport of sodium, potassium and other ions are abundant. At the junction of the straight and convoluted regions, the distal tubule comes close to the vascular pole of its parent renal corpuscle. Here, tubular cells form the macula densa, a sensory structure that is concerned with the regulation of blood flow and therefore the filtration rate. Cells in the terminal part of the distal tubule have fewer basal folds and mitochondria and constitute a connecting duct formed from metanephric mesenchyme during embryogenesis. Collecting ducts are lined by simple cuboidal or columnar epithelium. This increases in height from the renal cortex, where the ducts receive the contents of distal tubules, to the wide papillary ducts that discharge at the cribriform area (area cribrosa). The pale-staining principal cells have relatively few organelles or lateral interdigitations, and only occasional microvilli. A second cell type, intercalated or dark cells (also present in smaller numbers in the distal convoluted tubule), has longer microvilli and more mitochondria and secretes H$^+$ into the filtrate; these cells function in the maintenance of acid–base homeostasis.

Renal vessels

The renal, interlobar and arcuate arteries are typical large muscular arteries and the interlobular vessels resemble small muscular arteries. Afferent glomerular vessels have a typical arteriolar structure with a muscular coat 2–3 cells thick; this coat and the connective tissue components of the wall diminish near a glomerulus until a point 30–50 µm proximal to it, where arteriolar cells begin to show modifications typical of the juxtaglomerular apparatus. The efferent arterioles from most cortical glomeruli have thicker walls and a narrower calibre than corresponding afferents. Although the afferent arteriole is generally considered to be solely responsible for tubuloglomerular feedback, the peritubular and medullary capillaries possess a well-defined basal lamina. Additionally, their endothelial cells have typically fenestrated cytoplasm, as do the ascending vasa recta, whereas the descending vasa recta have a thicker, continuous endothelium (Davies 1991).

Other renal cells

Other cells essential for renal structure and function lie between the renal tubules and blood vessels. Connective tissue is inconspicuous in the cortex but prominent in the medulla, particularly in the papillae. Medullary interstitial cells, which may be modified fibroblasts, form vertical stacks of tangentially orientated cells between the more distal collecting ducts, like the rungs of a ladder. These cells secrete prostaglandins and may contribute, with cortical tubular cells, to the renal source of erythropoietin.

Calyces and renal pelvis

The wall of the proximal part of the urinary tract is composed of three layers: an outer connective tissue adventitia, an intermediate layer of smooth muscle and an inner mucosa. The mucosal lining of the renal calyces and pelvis is identical in structure to that of the ureter (see below). The adventitia consists of loose fibroelastic connective tissue that merges with retroperitoneal areolar tissue. Proximally, the coat fuses with the fibrous capsule of the kidney lining the renal sinus.

The smooth muscle of the renal calyces and pelvis is composed of two distinct types of smooth muscle cell. One type of muscle cell is identical to that described for the ureter and can be traced proximally through the ureteropelvic (pelviureteric) region and renal pelvis, as far as the minor calyces. The other type of cell forms the muscle coat of each minor calyx and continues into the major calyces and renal pelvis, where it forms a distinct inner layer. The cells also form a thin sheet of muscle that covers each minor calyx and extends across the renal parenchyma between the attachments of neighbouring minor calyces, thereby linking each minor calyx to its neighbours. This discrete inner layer of atypical smooth muscle ceases in the ureteropelvic region, so that the proximal ureter lacks such an inner layer. Pacemaker cells that initiate renal pelvic and ureteric peristalsis are sited within the calyces (Gosling and Dixon 1974, Lang et al 2006) and allow coordinated peristalsis of the ureter to take place six times a minute.

Production of urine

Glomerular filtration

Glomerular filtration (see Figs 72.13, 72.15) is the passage of water containing dissolved small molecules from the blood plasma to the urinary space in the glomerular capsule. Larger molecules, e.g. plasma proteins above 70 kDa and those with a net negative charge, polysaccharides, lipids and cells, are largely retained in the blood by the selective permeability of the glomerular basal lamina.

Filtration occurs along a steep pressure gradient between the large glomerular capillaries and the urinary space. Three structures separate the two: the capillary endothelium, the glomerular basal lamina and the foot process of the podocyte. Of these, the principal structure is the glomerular basal lamina (Fig. 72.18B). This gradient far exceeds the colloid osmotic pressure of blood, which opposes the outward flow of filtrate. In the peripheral renal cortex, the arteriolar pressure gradient is enhanced because afferent glomerular arterioles are wider than efferent ones. In all glomeruli, the rate of filtration can be altered by changes in the tone of the glomerular arterioles. When first formed, the glomerular filtrate is isotonic with glomerular blood and has an identical concentration of ions and small molecules.

The assessment of glomerular filtration is fundamental to the diagnosis of renal glomerular pathology and the management of drug therapy, where clearance depends on the glomerular filtration, and in chronic kidney disease to facilitate timely management decisions. Measurements of glomerular filtration rate (GFR) are based on the renal clearance of a marker in plasma, expressed as the volume of plasma completely cleared of the marker per unit time. Markers used to measure GFR can be endogenous (creatinine, urea) or exogenous (inulin, iothalamate). The ideal marker is endogenous, freely filtered by the glomerulus, neither reabsorbed nor secreted by the renal tubule, and eliminated only by the kidney.

Selective resorption

Selective resorption from the filtrate is an active process and occurs mainly in the proximal convoluted tubules, which resorb glucose, amino acids, phosphate, chloride, sodium, calcium and bicarbonate, and take up small proteins (e.g. albumin) by endocytosis. Cells of the proximal tubules are permeable to water, which passes out of the tubules passively, so that the filtrate remains locally isotonic with blood. The rest of the tubule reabsorbs most of the water (to a variable extent up to 95%), so that urine is generally much reduced in volume and hypertonic to blood when it reaches the calyces. The process depends on establishing high osmolality in the medullary interstitium in order to exert sufficient osmotic pressure on water-permeable regions of the tubule, and is achieved by a countercurrent multiplier mechanism.

Countercurrent multiplier mechanism

The countercurrent multiplier mechanism is responsible for producing a high osmolality in the extratubular interstitial tissue of the renal medulla. Water passes freely from the tubular lumen into the adjacent medullary interstitium along the descending limb of the nephron loop. This part of the tubule is less permeable to solutes. In the thick ascending limb, sodium and chloride ions are actively transported from the tubule lumen into interstitial spaces, while the tubular epithelium remains impermeable to water. The increased interstitial osmolality causes water to be withdrawn from the descending part of the nephron loop, thus concentrating the filtrate. Tubular fluid flows in a countercurrent on its descent into and ascent out of the renal medulla; it is augmented by new isotonic fluid entering the nephron loop, and depleted by hypotonic fluid leaving the loop as solutes are actively resorbed. The osmotic gradient within the interstitium is therefore multiplied from the corticomedullary boundary to the renal pyramids, where it reaches equilibrium at four to five times the osmolality of plasma. Although the tonicity of the tubular fluid changes during its passage through the steep osmotic gradient within the renal medulla, the osmotic gradient between ascending and descending limbs at each level never exceeds 200 mOsm/kg, a force that can be sustained by the cells of the tubular wall.

Countercurrent exchange mechanism

Rapid removal of ions from the renal medulla by the circulation of blood is minimized by another looped countercurrent system. This is the countercurrent exchange mechanism, in which arterioles entering the renal medulla pass for long distances parallel to the venules leaving it, before ending in capillary beds around tubules. This close apposition of oppositely flowing blood allows ions to diffuse directly from outflowing to inflowing blood, so that the vasa recta (see Fig. 72.13) conserve the high osmotic pressure in the renal medulla.

Concentration of urine

Because sodium and chloride ions are selectively resorbed by the cells of the ascending limbs and distal tubules under aldosterone control, the filtrate at the distal end of the convoluted tubules is hypotonic. As it reaches the collecting ducts, fluid descends again through the renal medulla and thus re-enters a region of high osmotic pressure. The cells lining the collecting ducts are variably permeable to water, under the influence of antidiuretic hormone (ADH). Water follows an osmotic gradient into the adjacent extratubular spaces, so that the tonicity of the filtrate gradually rises along collecting ducts, until, at the tip of the renal pyramids, it is above that of blood. This complex system is highly flexible and the balance between the rates of filtration and absorption can be varied to meet current physiological demands.

Control of hydrogen and ammonium ion concentrations is essential for the regulation of acids and bases in the blood. Secretion of various ions occurs at several sites. Over 91% of ingested potassium is excreted in urine, largely through secretion by cells of the distal tubule and collecting duct. (For further details of renal physiology, see Madias and Adrogué (2005), Tannen and Hallows (2005), Singh and Thomson (2011).)

Juxtaglomerular apparatus

The juxtaglomerular apparatus provides a tubuloglomerular feedback system that maintains systemic arterial blood pressure during a reduction in vascular volume and decrease in filtration rate. The elements of a juxtaglomerular apparatus are juxtaglomerular and extraglomerular mesangial cells, and the macula densa. The afferent and efferent arterioles at the vascular pole of a glomerulus and the macula densa of the distal tubule of the same nephron lie in close proximity, enclosing a small cone of tissue populated by extraglomerular mesangial cells (see Fig. 72.15). The cells of the tunica media of afferent, and to a lesser extent efferent, arterioles differ from typical smooth muscle cells. These juxtaglomerular cells are large, rounded, myoepithelioid cells and their cytoplasm contains many mitochondria and dense renin-containing vesicles, 10–40 nm in diameter. Each macula densa of the distal tubule is a cluster of up to 40 tightly packed cells in the tubule wall; the cells have large, oval nuclei and apically concentrated mitochondria. They

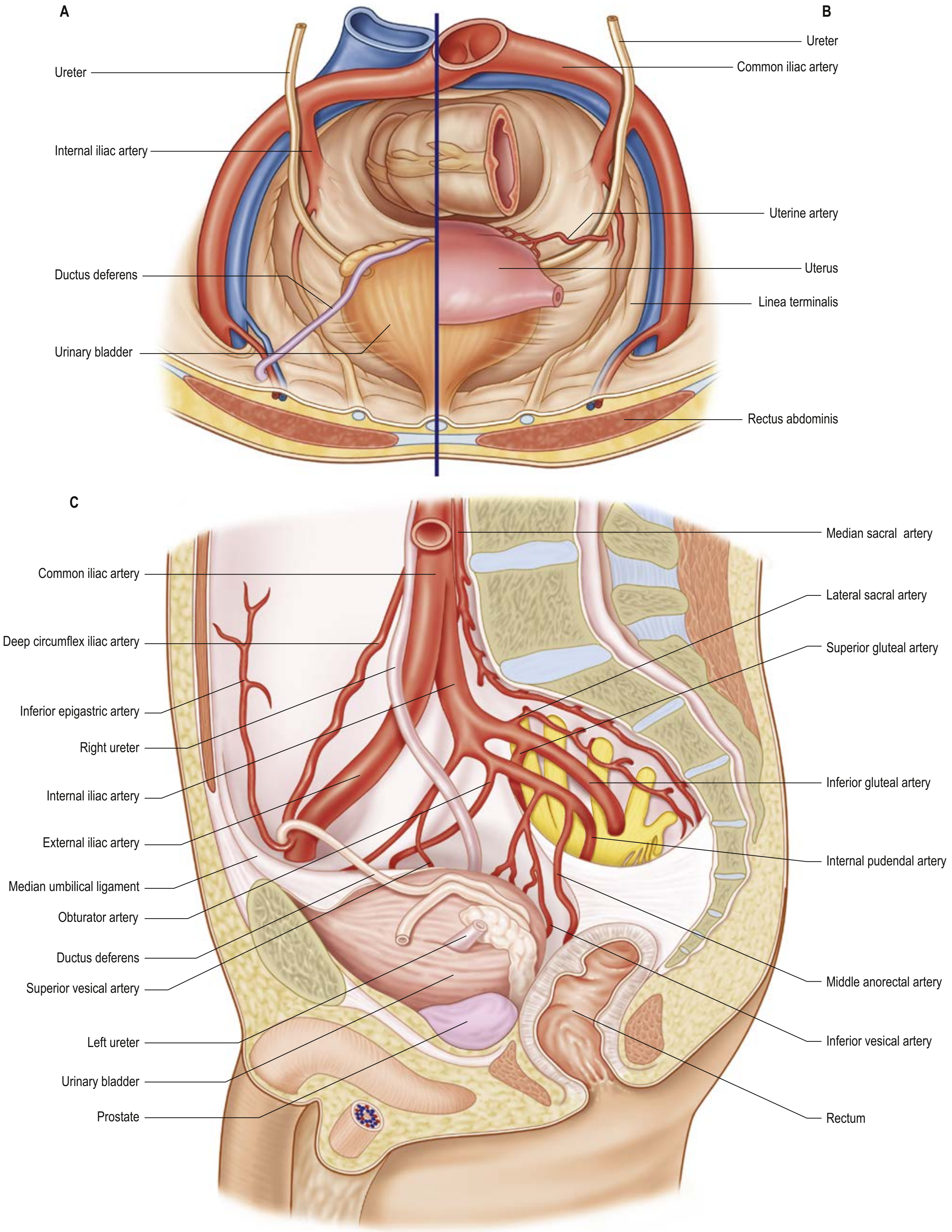
A
B
Ureter
Internal iliac artery
Ductus deferens
Urinary bladder
Ureter
Common iliac artery
Uterine artery
Uterus
Linea terminalis
Rectus abdominis
C
Common iliac artery
Deep circumflex iliac artery
Inferior epigastric artery
Right ureter
Internal iliac artery
External iliac artery
Median umbilical ligament
Obturator artery
Ductus deferens
Superior vesical artery
Left ureter
Urinary bladder
Prostate
Median sacral artery
Lateral sacral artery
Superior gluteal artery
Inferior gluteal artery
Internal pudendal artery
Middle anorectal artery
Inferior vesical artery
Rectum

Fig. 72.20 Relations of the abdominal and pelvic parts of the ureter. **A**, **B**, Relations of the distal part of the ureter, superior view. **A**, The male pelvis. **B**, The female pelvis. C, The male pelvis, sagittal section. (A, Sobotta Atlas of Human Anatomy © Elsevier GmbH, Urban & Fischer, Munich. B–C, With permission from Drake RL, Vogl AW, Mitchell A (eds) Gray's Anatomy for Students, 2nd ed. Elsevier, Churchill Livingstone. Copyright 2010.)

are osmoreceptors, sensing the sodium chloride content of the filtrate after its passage through the nephron loop.

When sodium chloride concentrations in the filtrate change, tubuloglomerular feedback mechanisms operate to maintain the inverse relationship between salt concentration and glomerular filtration rate. Juxtaglomerular cells release renin, an enzyme that acts on circulating angiotensinogen to activate the cascade whereby angiotensin II increases blood pressure (and therefore filtration rate), stimulates aldosterone and antidiuretic hormone release and increases sodium ion and water resorption, primarily from the distal tubule, to increase plasma volume. Macula densa cells are thought to respond to high salt concentration in the distal tubule by releasing nitric oxide, which inhibits the tubuloglomerular feedback response and reduces filtration rate. The role of macula densa cells in the stimulation of renin release to increase the filtration rate is less well understood.

The third element of the juxtaglomerular apparatus is a population of extraglomerular mesangial cells that form a network of stellate cells connecting the macula densa sensory cells with the juxtaglomerular effector cells. It is likely that extraglomerular mesangial cells transmit the sensory signal, possibly through gap junctions. They may also signal to contractile glomerular mesangial cells and effect vasoconstriction directly within the glomerulus. Adrenergic nerve fibres occur in small numbers among these cells.

URETER

The ureters are two muscular tubes that convey urine from the kidneys to the urinary bladder by peristaltic contractions (see Figs 72.1, 72.9, Fig. 72.20). Each measures 25–30 cm in length (in neonates 6–7 cm), is thick-walled and narrow, and is continuous superiorly with the funnel-shaped renal pelvis. Each descends slightly medially, anterior to psoas major and enters the pelvic cavity where it curves initially laterally, then medially, to open into the fundus of the urinary bladder. The diameter of the ureter is normally 3 mm, but is slightly less at its junction with the renal pelvis, at the linea terminalis near the medial border of psoas major, and where it runs within the wall of the urinary bladder, which is its narrowest part. These are the most common sites for renal stone impaction.

Relations

The ureter has abdominal, pelvic and intramural parts. The abdominal part travels from the renal pelvis to the linea terminalis and descends posterior to the peritoneum on the medial part of psoas major, which separates it from the tips of the transverse processes of the lumbar vertebrae. During surgery on intraperitoneal structures, the ureter can be tented up as the peritoneum is drawn anteriorly, resulting in iatrogenic injury. Anterior to psoas major, it crosses anterior to the genitofemoral nerve and is obliquely crossed by the gonadal vessels. It enters the lesser pelvis either anterior to the end of the common iliac vessels or at the origin of the external iliac vessels.

The right ureter is usually overlapped by the descending part of the duodenum at its origin. It descends lateral to the inferior vena cava and is crossed anteriorly by the right colic and ileocolic vessels. Near the superior aperture of the lesser pelvis it passes behind the lower part of the mesentery and the terminal ileum. The left ureter is lateral to the abdominal aorta and is crossed by the gonadal and left colic vessels. It passes posterior to the jejunum and sigmoid colon and its mesentery in the posterior wall of the intersigmoid recess. The inferior mesenteric vein has a long retroperitoneal course lying close to the medial aspect of the left ureter.

The pelvic part of the ureter extends from the linea terminalis to the point where it pierces the wall of the urinary bladder. At first, the ureter descends posterolaterally on the lateral wall of the lesser pelvis along the anterior border of the greater sciatic foramen, lying in extraperitoneal areolar tissue. Opposite the ischial spine, it turns anteromedially into fibrous adipose tissue above levator ani to reach the fundus of the bladder. On the pelvic side wall the ureter is anterior to the internal iliac artery and the origin of its anterior division; the internal iliac vein, lumbosacral trunk and sacroiliac joint are posterior relations. Laterally, it lies on the obturator fascia and progressively crosses to become medial to the umbilical, inferior vesical and middle anorectal arteries.

In males, the pelvic part of the ureter hooks under the ductus deferens (Fig. 72.21); it then passes anterior and slightly superior to the upper pole of the seminal gland to the wall of the urinary bladder. In females, the pelvic part of the ureter initially has the same relations as in males, but anterior to the internal iliac artery it is immediately behind the ovary, forming the posterior boundary of the ovarian fossa (see Fig. 75.8). In the anteromedial part of its course to the urinary bladder it is related to the uterine artery, uterine cervix and vaginal fornix. It lies in extraperitoneal connective tissue in the inferomedial part of the broad ligament of the uterus and can be injured during hysterectomy (see Fig. 75.7). In the broad ligament of the uterus, the uterine artery is anterosuperior to the ureter for approximately 2.5 cm and then crosses to its medial side to ascend alongside the uterus. The ureter turns forwards slightly above the lateral part of the vaginal fornix and is generally 2 cm lateral to the supravaginal part of the uterine cervix in this location. It then inclines medially to reach the urinary bladder, with a variable relation to the anterior aspect of the vagina. As the uterus is commonly deviated to one side, one ureter, usually the left, can be more extensively apposed to the vagina, and may cross the midline.

The distal 1–2 cm of the ureter, the intramural part, is surrounded by an incomplete collar of non-striated muscle (sheath of Waldeyer).

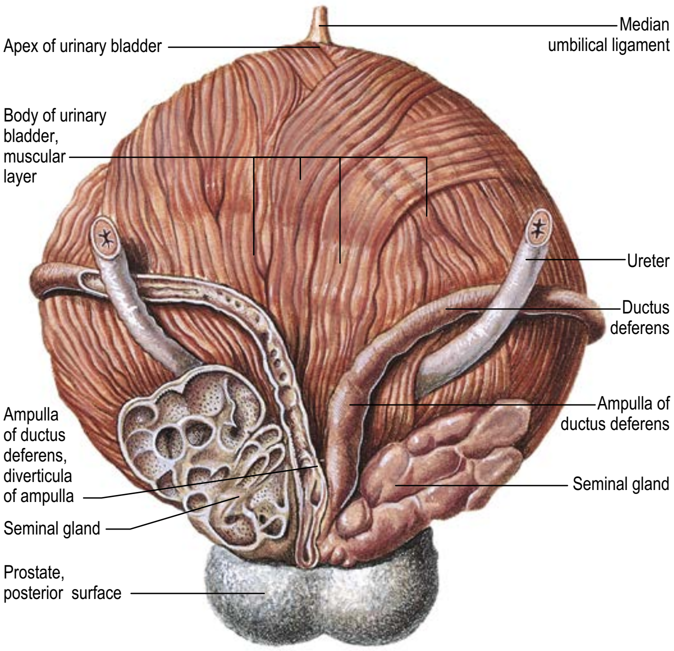
Apex of urinary bladder
Median umbilical ligament
Body of urinary bladder, muscular layer
Ureter
Ductus deferens
Ampulla of ductus deferens
Ampulla of ductus deferens, diverticula of ampulla
Seminal gland
Seminal gland
Prostate, posterior surface

Fig. 72.21 The posterior aspect of the male urogenital organs, showing the relationship of the distal ureter to the ductus deferens and seminal glands. (Sobotta Atlas of Human Anatomy © Elsevier GmbH, Urban & Fischer, Munich.)

The two ureters pierce the posterior aspect of the urinary bladder and run obliquely through its wall for a distance of 1.5–2.0 cm before terminating at the ureteric orifices (see Fig. 73.7B). This arrangement is believed to assist in preventing reflux of urine into the ureter, since the intramural parts of the ureters are thought to be occluded during increases in urinary bladder pressure at the time of micturition. There is no evidence of a classic ureteral sphincter mechanism in humans. The longitudinally orientated muscle bundles of the terminal ureters continue into the urinary bladder wall and become continuous with the superficial trigone muscle at the ureteric orifices. In both sexes, the ureteric orifices are usually 5 cm apart in the distended urinary bladder and 2.5 cm apart when the bladder is empty.

Vascular supply and lymphatic drainage

Arteries

The ureter is supplied by branches from the renal, gonadal and common iliac arteries, the internal iliac artery and its branches, and the abdominal aorta. The pattern of distribution is subject to much variation. The abdominal part of the ureter is supplied from vessels originating medial to the ureter; the pelvic part of the ureter is supplied by vessels lateral to the ureter (Fig. 72.22). There is a good longitudinal anastomosis between these branches on the wall of the ureter, which means that the ureter can be safely transected at any level intraoperatively, and a uretero-ureterostomy performed, without compromising its viability. The branches from the inferior vesical artery are constant in their occurrence and supply the distal part of the ureter, as well as a large part of the trigone of the bladder. The branch from the renal artery is also constant and is preserved whenever possible in renal transplantation to ensure good vascularity of the ureter.

Veins

The venous drainage of the ureters generally follows the arterial supply.

Lymphatic drainage

Lymph vessels draining the ureter begin in the submucosal, intramuscular and adventitial plexuses, which all communicate. Collecting vessels from the upper abdominal part of the ureter can join the renal collecting vessels or pass directly to the lateral aortic nodes near the origin of the gonadal artery; those from the lower abdominal part of the ureter drain to the common iliac nodes; and those from the pelvic part of the ureter drain to common, external or internal iliac nodes.

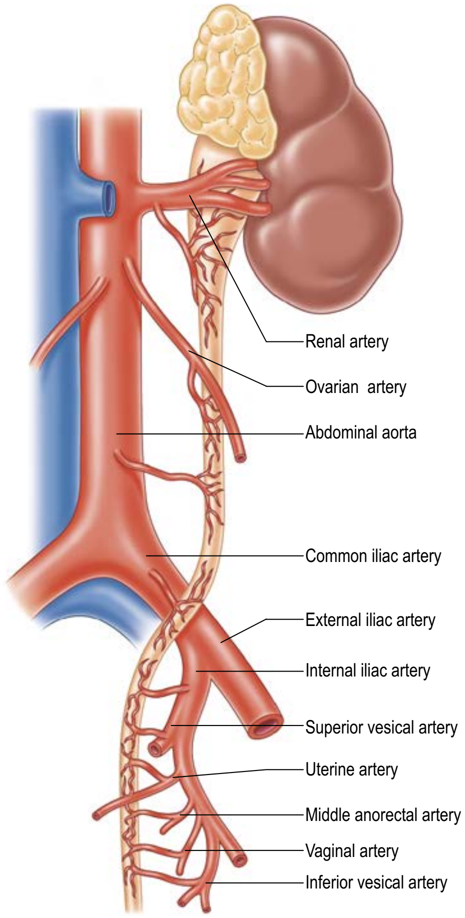

Fig. 72.22 The arterial supply of the female left ureter. The proximal part takes its blood supply medially and the distal part is supplied laterally. (With permission from Walsh PC, Retik AB, Vaughan ED et al (eds) 2002 Campbell's Urology, 8th ed. Philadelphia: Saunders.)

Innervation

The ureter is supplied from the lower three thoracic, first lumbar and the second to fourth sacral segments of the spinal cord by branches from the renal and abdominal aortic plexuses, and the superior and inferior hypogastric plexuses (see Figs 59.3, 73.8). The ureteric nerves consist of relatively large bundles of axons that form an irregular plexus in the adventitia of the ureter. The ureteric plexus receives branches from the renal and aortic plexuses (in its upper part); from the superior hypogastric plexus and hypogastric nerve (in its intermediate part); and from the hypogastric nerve and inferior hypogastric plexus (in its lower part). Numerous small branches penetrate the ureteric muscle coat; some of the adventitial nerves accompany the blood vessels and branch with them as they extend into the muscle layer; others are unrelated to the vascular supply and lie free in the adventitial connective tissue around the circumference of the ureter.

The density of innervation increases gradually from the renal pelvis and proximal (upper) ureter (where autonomic nerves are sparse) to a maximum density in the juxtavesical segment. At least three different neurotransmitter phenotypes – cholinergic, noradrenergic and peptidergic (substance P) – are well known and others have been reported. The functional significance of these different types of autonomic nerve fibres in relation to ureteric smooth muscle activity is not fully understood; although they are thought to influence the inherent motility of the ureter, they are not essential for the initiation and propagation of ureteric contraction waves. A branching plexus of fine cholinergic, noradrenergic and peptidergic axons occurs throughout the lamina propria and extends from the inner aspect of the muscle coat towards the base of the urothelium. Some of these axons form perivascular plexuses, while others lie in isolation from the vascular supply and could be sensory in function.

Ureteric peristalsis

Under normal conditions, contraction waves originate in the proximal part of the upper urinary tract and are propagated anterogradely towards the urinary bladder. Atypical smooth muscle cells in the wall of the minor calyces act individually or collectively as pacemaker sites. A peristaltic wave begins at one (or possibly more) of these sites. Once initiated, the contraction is propagated through the wall of the adjacent major calyx and activates the smooth muscle of the renal pelvis. Contraction waves are propagated away from the kidney, and so undesirable pressure rises are not directed against the renal parenchyma. Since there are several potential pacemaker sites, the initiation of contraction waves is unimpaired by partial nephrectomy; the minor calyces spared by the resection remain *in situ* to continue their pacemaking function. Pressures within the ureter at the time of peristalsis reach 20–80 cm H_2O.

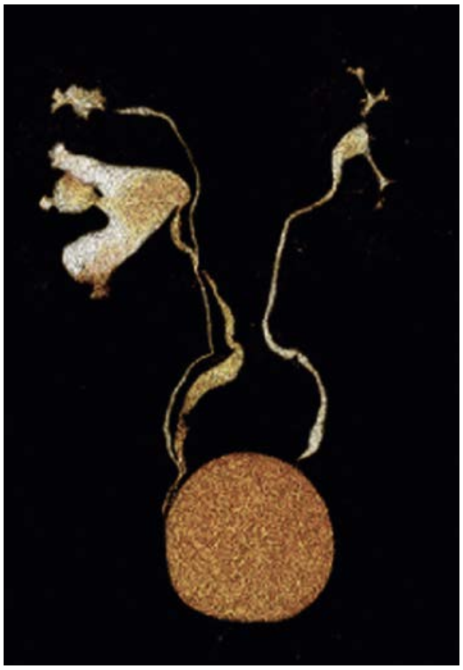

Fig. 72.23 A coronal CT urogram volume-rendered image demonstrates a duplicated right collecting system and ureter, along with dilation of the collecting system of the lower pole moiety. No urothelial lesion is seen.

Referred pain Excessive distension of the ureter or spasm of its muscle can be caused by a stone (calculus) and provokes severe pain (ureteric colic, which is commonly, but mistakenly, called renal colic). The pain is spasmodic and agonizing, particularly if the obstruction is gradually forced down the ureter by the muscle spasm. It is referred to cutaneous areas innervated from spinal segments that supply the ureter, mainly T11–L2, and shoots superomedially down to the scrotum or labium majus; it can extend into the proximal anterior aspect of the thigh by projection to the genitofemoral nerve (L1, L2). The cremaster, which has the same innervation, may retract the testis reflexly.

Renal and ureteric calculi An understanding of intrarenal and ureteric anatomy is essential for managing patients with calculi, particularly now that minimally invasive techniques are widely used to treat this common pathology.

Microstructure

Like the calyces and the renal pelvis, the wall of the ureter is composed of an external adventitia, a smooth muscle layer and an inner mucosal layer. The mucosal layer consists of a urothelium (transitional epithelium) (see Fig. 2.5D) and an underlying connective tissue lamina propria.

The ureteric adventitial blood vessels and connective tissue fibres are orientated parallel to the long axis of the ureter. Throughout its length, the muscle coat of the ureter is fairly uniform in thickness and, in cross-section, measures 750–800 μm in width. The muscle bundles that constitute this coat are frequently separated from one another by relatively large amounts of connective tissue. However, branches that interconnect muscle bundles are common and there is frequent interchange of muscle fibres between adjacent bundles. As a consequence of this extensive branching, individual muscle bundles do not spiral around the ureter, but form a complex meshwork of interweaving bundles. Moreover, unlike the gut, the muscle bundles

Experimental evidence indicates that autonomic nerves do not play a major part in the propagation of peristalsis. It seems more likely that they modulate the contractile events occurring in the musculature of the upper urinary tract. The most likely mechanism to account for impulse propagation is myogenic conduction mediated by the electrotonic coupling of one muscle cell to its immediate neighbours via intercellular gap junctions; there are numerous regions of close approach between ureteric smooth muscle cells and also between both types of muscle cell in the renal pelvis and calyces.

Smaller renal calculi are treated with extracorporeal shock wave lithotripsy. Stones in the lower pole of the kidney clear less well if the angle between the infundibulum of the major calyx containing the stone and the ureter is acute, or if there is a particularly long and narrow infundibulum. Percutaneous stone extraction is most frequently achieved by puncturing a posterior calyx with a needle. Ureteric calculi tend to be arrested in their descent in either the ureteropelvic region, or at the point where the ureter passes over the linea terminalis as it crosses the common iliac artery, or at the ureterovesical junction, because these are the three areas where the ureter is narrowest. The ureterovesical junction is the narrowest of these areas and can be responsible for arresting the passage of stones of as little as 2–3 mm. The kidney and proximal ureter move with respiration within the renal fascia, and this can affect the visualization and tracking of a stone, both at the time of extracorporeal shock wave lithotripsy and at retrograde endoscopy.

are so arranged that morphologically distinct longitudinal and circular layers cannot be clearly distinguished. In the upper part of the ureter, the inner muscle bundles tend to lie longitudinally while those on the outer aspect have a circular or oblique orientation. In the middle and lower parts, there are additional outer longitudinally orientated fibres, and as the ureterovesical junction is approached, the muscle coat consists predominantly of longitudinally orientated muscle bundles.

The mucosa of the ureter consists of an epithelium, the urothelium, lying on a layer of subepithelial fibroelastic connective tissue lamina propria. The latter varies in thickness from 350 to 700 µm and is a conduit for small blood vessels and bundles of unmyelinated nerve fibres. Occasional lymphocytes can be present in the lamina propria but their aggregation into definitive lymph nodules is rare. The urothelium is usually extensively folded, giving the ureteric lumen a stellate outline.

Developmental anomalies of the ureter

Double (duplex) ureters In 1 in 125 individuals, two ureters drain the renal pelvis on one side; this is termed a double (duplex) ureter (Fig. 72.23). Bilateral double ureters occur in approximately 1 in 800 cases. Double ureters are the product of two ureteric buds arising from the mesonephric duct; they share a single fascial sheath and can either fuse at any point along their course or remain separate until they insert through separate ureteric orifices into the urinary bladder.

Care must be taken not to compromise the blood supply of the second ureter when a single ureter of a double ureter system is excised or reimplanted. The ureter from the upper pole of the kidney (the longer ureter) inserts more medially and caudally in the urinary bladder than the ureter from the lower pole (Weigert–Meyer rule). This reflects the embryological development of the ureter: the ureteric bud that is initially more proximal on the mesonephric duct has a shorter time to be pulled cranially in the urinary bladder and so it inserts more distally in the mature bladder. The ureter from the lower pole has a shorter intramural course than the longer ureter and is prone to reflux.

Ectopic ureters An ectopic ureter is a ureter that has an abnormal anatomical location, e.g. not opening into the trigone of the urinary bladder. In the male, the ureter can insert at the neck of the bladder or posterior urethra, or, rarely, into the seminal gland, but it always inserts cranial to the external urethral sphincter. In the female, ectopic insertion can be distal to the external urethral sphincter in the urethra, or into the vagina, resulting in persistent childhood incontinence. Single ureters, and more commonly the longer ureter of a double ureter system, can insert more caudally and medially than is normal in some individuals.

Ureteroceles Ureteroceles are cystic dilations of the lower end of the ureter; the ureteric orifice is covered by a membrane that expands as it is filled with urine and then deflates as it empties. Ureteroceles can vary in size and usually have no influence on ureteric drainage; however, they can be a cause of obstruction in the ureter and pelvicalyceal system more proximally. Prolapsing ureteroceles, though small, prolapse from their position around the ureterovesical junction region into the urethra, causing intermittent urinary bladder outflow obstruction.

They are identified antenatally with ultrasound (Fig. 72.24). In adults, ureteroceles tend to be bilateral and small and are often found incidentally when the urinary tract is being imaged in the investigation of a coincidental pathology. Radiologically, they classically result in a 'cobra-head' halo around the ureteric orifice following administration of contrast on intravenous urography.

Retrocaval ureter Persistence of the posterior cardinal vein, associated with high confluence of the right and left common iliac veins or a double inferior vena cava, can result in a retrocaval (or circumcaval) ureter that passes behind the inferior vena cava, usually at the level of the inferior edge of the third (horizontal) part of the duodenum, before it emerges anterior to it to pass from medial to lateral. A retrocaval ureter occurs in one in 1500 individuals. Most commonly it has no clinical sequelae, although it can result in upper ureteric obstruction (Fig. 72.25).

For further reading on congenital anomalies of the kidney and urinary tract (CAKUT), see Schultza and Todab (2016).

Bonus e-book content

Fig. 72.6 **C–D**, Sagittal multiplanar reformats from CTs with intravenous contrast medium through the left and right kidneys.

Fig. 72.8 **C–F**, Vertical oblique multiplanar reformats of a CT of the left kidney.

Fig. 72.9 A volume-rendered coronal CT urogram, 39-year-old male.

Fig. 72.12 Ureteropelvic junction obstruction: dilation of right renal pelvis and calyces.

Fig. 72.14 **B**, A 3D elaboration of CT imaging of a vascular cast illustrating the segmental arterial anatomy of the right kidney. This specimen illustrates seven arterial segments each indicated with a separate colour.

Fig. 72.24 **A–B**, Sagittal grey scale ultrasound images: ureterocele in a 2-day-old girl.

Fig. 72.25 An intravenous urogram illustrating a retrocaval (or circumcaval) ureter.

Key references

Brödel M 1911 The intrinsic blood-vessels of the kidney and their significance in nephrotomy. Bull Johns Hopkins Hosp 12:10–13.
The original description of a relatively avascular longitudinal zone within the kidney, proposed as a site for surgical incision.

Burkhill GJ, Healy JC 2000 Anatomy of the retroperitoneum. Imaging 12:10–20.
A review of the imaging literature describing the contentious anatomy of the renal fascia.

Chesbrough RM, Burkhard TK, Martinez AJ et al 1989 Gerota versus Zuckerkandl: the renal fascia revisited. Radiology 173:845–6.
A paper that clarifies the original descriptions of the anterior and posterior layers of the renal fascia.

Gosling JA, Dixon JS 1974 Species variation in the location of upper urinary tract pacemaker cells. Invest Urol 11:418.
An early paper describing the identification of pacemaker cells in various species.

MacLennan GT 2012 Hinman's Atlas of Urosurgical Anatomy, 2nd ed. Philadelphia: Elsevier.
An atlas containing detailed illustrations of the genitourinary tract and its surrounding anatomy, supplemented by radiological, pathological and intraoperative images.

Merklin RJ, Michels NA 1958 The variant renal and suprarenal blood supply with data on the inferior phrenic, ureteral, and gonadal arteries: a statistical analysis based on 185 dissections and a review of the literature. J Int Coll Surg 29:41–76.
A review of renal vascular anatomy in almost 11,000 kidneys.

Mitchell GA 1950 The renal fascia. Br J Surg 37:257–66.
An account that demonstrates that the renal fascia is a multilaminar structure rather than a single fused fascia.

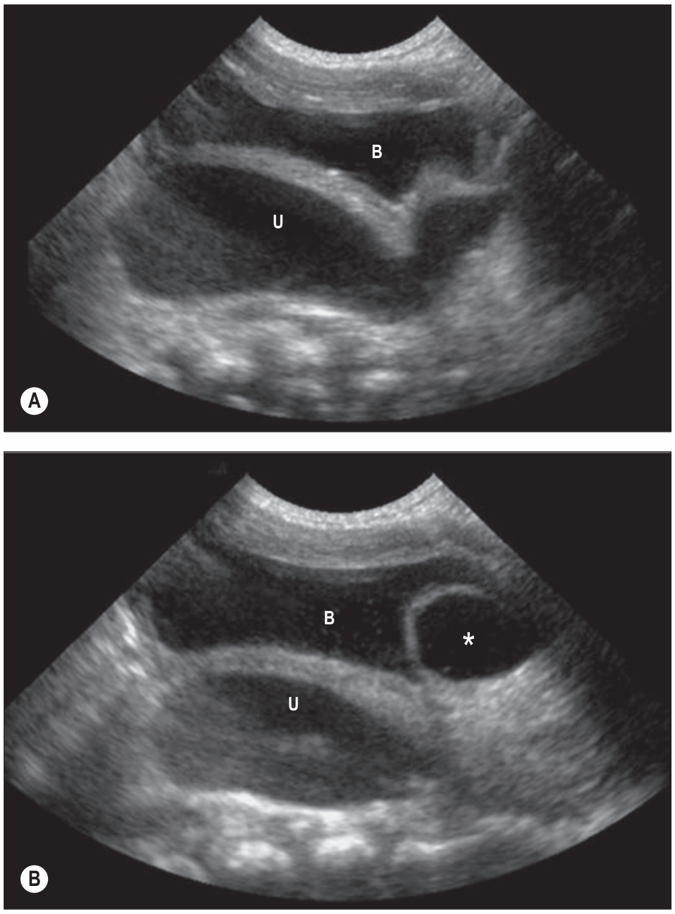

Fig. 72.24 A–B, Sagittal grey scale ultrasound images through the pelvis of a 2-day-old girl demonstrate a dilated left ureter (U), which contains layering echogenic debris, and an anechoic round filling defect (*) in the inferior bladder (B) with increased through-transmission and an echogenic rim, in keeping with a ureterocele.

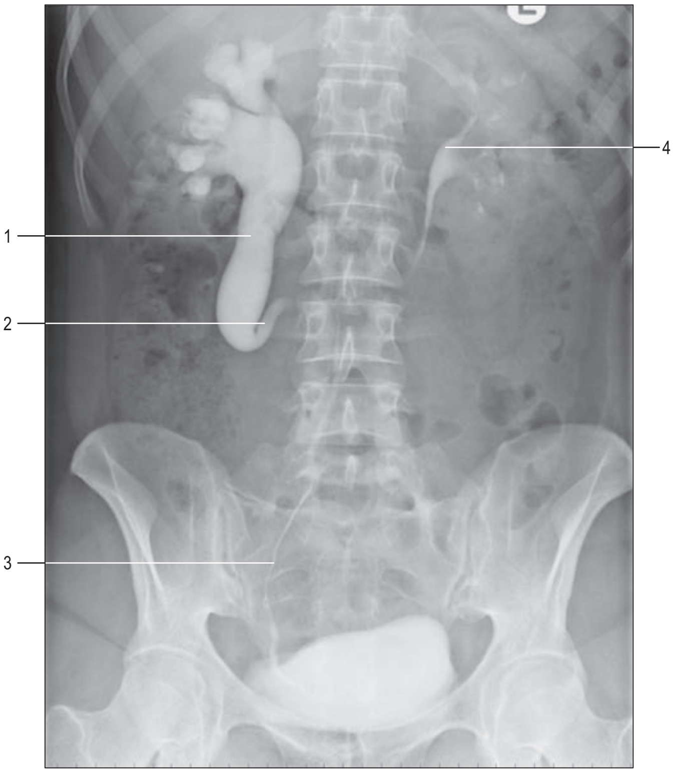

Fig. 72.25 An intravenous urogram showing a classic retrocaval (or circumcaval) ureter. A degree of obstruction has resulted in a markedly dilated upper ureter. The ureter passes cranially, medially and then caudally and can be followed into the renal pelvis. Key: 1, contrast within dilated collecting system of right kidney and upper ureter; 2, contrast within ureter turning behind inferior vena cava; 3, contrast within normal calibre ureter seen below the obstruction; 4, contrast within normal collecting system of left kidney and proximal ureter.

References

Brödel M 1911 The intrinsic blood-vessels of the kidney and their significance in nephrotomy. Bull Johns Hopkins Hosp 12:10–13.

The original description of a relatively avascular longitudinal zone within the kidney, proposed as a site for surgical incision.

Burkhill GJ, Healy JC 2000 Anatomy of the retroperitoneum. Imaging 12:10–20.

A review of the imaging literature describing the contentious anatomy of the renal fascia.

Chesbrough RM, Burkhard TK, Martinez AJ et al 1989 Gerota versus Zuckerkandl: the renal fascia revisited. Radiology 173:845–6.

A paper that clarifies the original descriptions of the anterior and posterior layers of the renal fascia.

Davies A, Blakeley AG, Kidd C 2001 The renal system. In: Human Physiology. Edinburgh: Elsevier, Churchill Livingstone; Ch. 8, pp. 713–97.

Davies JM 1991 The role of the efferent arteriole in tubuloglomerular feedback. Kidney Int Suppl 32:S71–3.

Gosling JA, Dixon JS 1974 Species variation in the location of upper urinary tract pacemaker cells. Invest Urol 11:418.

An early paper describing the identification of pacemaker cells in various species.

Iwanaga J, Saga T, Tabira Y et al 2015 Contrast imaging study of the horseshoe kidney for transplantation. Surg Radiol Anat 37:1267–71.

Kurklinsky AK, Rooke TW 2010 Nutcracker phenomenon and nutcracker syndrome. Mayo Clin Proc 85:552–9.

Lang RJ, Tonta MA, Zoltkowski BZ et al 2006 Pyeloureteric peristalsis: role of atypical smooth muscle cells and interstitial cells of Cajal-like cells as pacemakers. J Physiol 695–705.

Macchi V, Picardi E, Inferrera A et al 2018 Anatomic and radiologic study of renal avascular plane (Brödel's line) and its potential relevance on percutaneous and surgical approaches to the kidney. J Endourol 32:154–9.

Macchi V, Picardi EEE, Porzionato A et al 2019 Integration of anatomical and radiological analysis suggests more segments in the human kidney. Clin Anat 32:46–52.

MacLennan GT 2012 Hinman's Atlas of Urosurgical Anatomy, 2nd ed. Philadelphia: Elsevier.

An atlas containing detailed illustrations of the genitourinary tract and its surrounding anatomy, supplemented by radiological, pathological and intraoperative images.

Madias NE, Adrogué HJ 2005 Hypo-hypernatraemia: disorders of water balance. In: Davison AM, Cameron JS, Grunfeld J-P et al (eds) Oxford Textbook of Clinical Nephrology. Oxford: Oxford University Press; Ch. 2.1, vol. 1.

Manalich R, Reyes L, Herrera M et al 2000 Relationship between weight at birth and the number and size of renal glomeruli in humans: a histomorphometric study. Kidney Int 58:770–3.

Merklin RJ, Michels NA 1958 The variant renal and suprarenal blood supply with data on the inferior phrenic, ureteral, and gonadal arteries: a statistical analysis based on 185 dissections and a review of the literature. J Int Coll Surg 29:41–76.

A review of renal vascular anatomy in almost 11,000 kidneys.

Mirjalili SA, McFadden SL, Buckenham T et al 2012 A reappraisal of adult abdominal surface anatomy. Clin Anat 25:844–50.

Mitchell GA 1950 The renal fascia. Br J Surg 37:257–66.

An account that demonstrates that the renal fascia is a multilaminar structure rather than a single fused fascia.

Novick AC 1998 Anatomic approaches in nephron-sparing surgery for renal cell carcinoma. Atlas Urol Clin North Am 6:39.

Phelan PJ, Shields W, O'Kelly P et al 2009 Left versus right deceased donor renal allograft outcome. Transpl Int 22:1159–63.

Ramage IJ, Howatson AG, McColl JH et al 2002 Glomerular basement membrane thickness in children: a stereologic assessment. Kidney Int 62:895–900.

Schneider A, Ferreira CG, Delay C et al 2013 Lower pole vessels in children with pelviureteric junction obstruction: laparoscopic vascular hitch or dismembered pyeloplasty? J Pediatr Urol 9:419–23.

Schultza K, Todab LY 2016 Genetic basis of ureterocele. Curr Genomics 17:62–9.

Scott JE 2002 Fetal, perinatal, and infant death with congenital renal anomaly. Arch Dis Child 87:114–7.

Singh P, Thomson SC 2011 Renal homeostasis and tubuloglomerular feedback. Curr Opin Nephrol Hypertens 19:59–64.

Tannen RL, Hallows KR 2005 Hypo-hyperkalaemia. In: Davison AM, Cameron JS, Grunfeld J-P et al (eds) Oxford Textbook of Clinical Nephrology, vol 1. Oxford: Oxford University Press; Ch. 2.2.

Veyrac C, Baud C, Lopez C et al 2003 The value of colour Doppler ultrasonography for identification of crossing vessels in children with pelviureteric junction obstruction. Pediatr Radiol 33:745–51.

Wu TS, Li KJ, Yu CL et al 2018 Tamm–Horsfall protein is a potent immunomodulatory molecule and a disease biomarker in the urinary system. Molecules 23:1–14.

Zhao L, Burt AD 2007 The diffuse stellate cell system J Mol Histol 38:53–64.

CHAPTER 73

Bladder, prostate and urethra

URINARY BLADDER

The urinary bladder is a reservoir. Its size, shape, position and relations all vary according to its content and the state of the neighbouring viscera. When the bladder is empty, it lies entirely in the lesser pelvis, but as it distends it expands superiorly into the abdominal cavity (**Video 73.1**). An empty bladder is somewhat tetrahedral and has a fundus, body, neck, apex and superior and inferolateral surfaces.

Relations

The fundus of the bladder is triangular and located posteroinferiorly. In females it is closely related to the anterior vaginal wall (**Fig. 73.1**); in males it is related to the rectum, although it is separated from it superiorly by the rectovesical pouch and inferiorly by the seminal gland (vesicle) and ductus (vas) deferens on each side, and by the prostatoseminal fascia (Denonvilliers' fascia) (**Fig. 73.2**). The neck of the bladder, which is most fixed, lies most inferiorly, 3–4 cm behind the lower part of the pubic symphysis and just above the plane of the inferior aperture of the lesser pelvis. Essentially, the neck of the bladder is the internal urethral orifice, which lies in a constant position irrespective of the varying positions of the bladder and rectum. In males the neck rests on and is directly continuous with the base of the prostate; in females it is related to the pelvic fascia that surrounds the upper urethra. In both sexes the apex of the bladder, when not full, faces towards the upper part of the pubic symphysis. The median umbilical ligament (urachus) ascends behind the anterior abdominal wall from the apex of the bladder to the umbilicus, covered by peritoneum to form the median umbilical fold (see below).

The anterior aspect of the urinary bladder is separated from the transversalis fascia by adipose tissue in the potential retropubic space (of Retzius) (see Fig. 73.2D). This adheres more to the bladder than to the anterior surface of the prostate, which aids reliable identification of the region of the neck of the bladder surgically. In males each inferolateral surface is related anteriorly to the pubis and puboprostatic ligaments. In females the relations are similar, except that the pubovesical ligaments replace the puboprostatic ligaments (see later for a fuller description). The inferolateral surfaces are not covered by peritoneum. The triangular superior surface is bounded by lateral borders from the apex to the ureteric entrances, and by a posterior border that joins them. In males the superior surface is completely covered by peritoneum, which extends slightly on to the fundus and continues posteriorly into the rectovesical pouch and anteriorly into the median umbilical fold; it is in contact with the sigmoid colon and the terminal part of the ileum. In females the superior surface is largely covered by peritoneum, which is reflected posteriorly on to the uterus at the level of the anatomical internal os of the uterus (the junction of the body and isthmus of the uterus) to form the vesico-uterine pouch. The posterior part of the superior surface, devoid of peritoneum, is separated from the supravaginal part of the cervix by fibroareolar tissue.

These relations are important in managing bladder trauma. Extraperitoneal injuries can often be managed conservatively because urine is contained, whereas intraperitoneal injuries usually require surgical repair since urine within the abdominal cavity can cause peritonitis, ileus and infection.

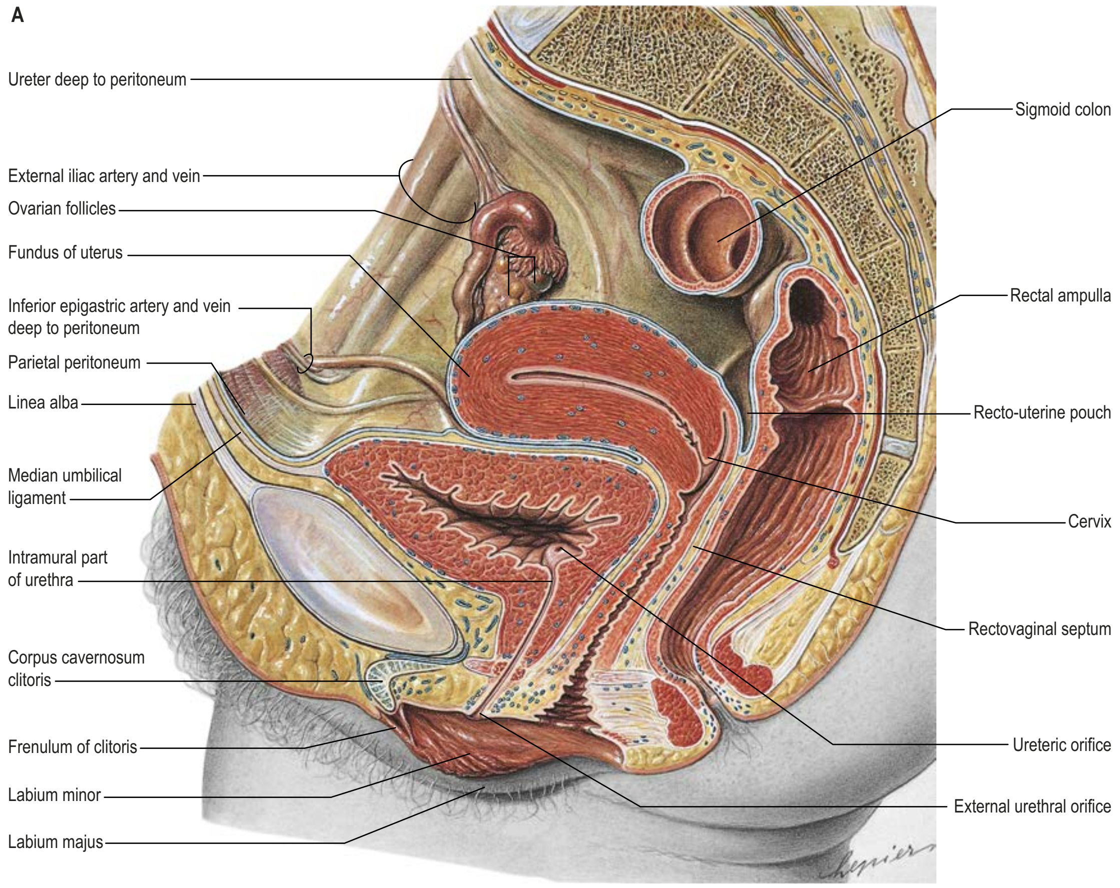
A
Ureter deep to peritoneum
External iliac artery and vein
Ovarian follicles
Fundus of uterus
Inferior epigastric artery and vein deep to peritoneum
Parietal peritoneum
Linea alba
Median umbilical ligament
Intramural part of urethra
Corpus cavernosum clitoris
Frenulum of clitoris
Labium minor
Labium majus
Sigmoid colon
Rectal ampulla
Recto-uterine pouch
Cervix
Rectovaginal septum
Ureteric orifice
External urethral orifice

Fig. 73.1 **A**, The relations of the female bladder, sagittal section of the pelvis. (Sobotta Atlas of Human Anatomy © Elsevier GmbH, Urban & Fischer, Munich.) (B, *continued online*)

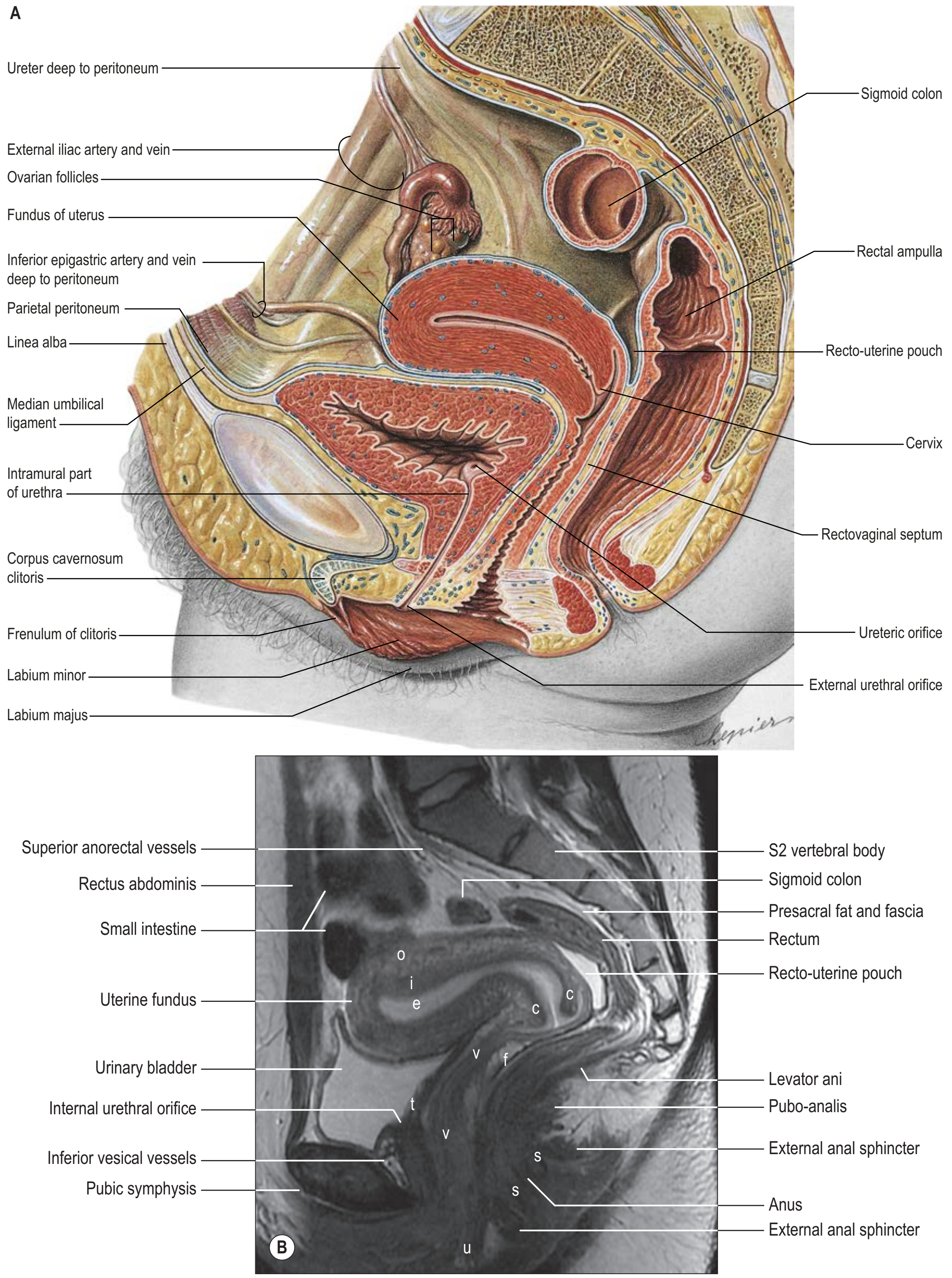
A
Ureter deep to peritoneum
External iliac artery and vein
Ovarian follicles
Fundus of uterus
Inferior epigastric artery and vein deep to peritoneum
Parietal peritoneum
Linea alba
Median umbilical ligament
Intramural part of urethra
Corpus cavernosum clitoris
Frenulum of clitoris
Labium minor
Labium majus
Sigmoid colon
Rectal ampulla
Recto-uterine pouch
Cervix
Rectovaginal septum
Ureteric orifice
External urethral orifice
B
Superior anorectal vessels
Rectus abdominis
Small intestine
Uterine fundus
Urinary bladder
Internal urethral orifice
Inferior vesical vessels
Pubic symphysis
S2 vertebral body
Sigmoid colon
Presacral fat and fascia
Rectum
Recto-uterine pouch
Levator ani
Pubo-analis
External anal sphincter
Anus
External anal sphincter
o
i
e
c
c
v
f
t
v
s
s
u

Fig. 73.1 **A**, The relations of the female bladder, sagittal section of the pelvis. **B**, Midline sagittal T2-weighted MRI through the female pelvis. Abbreviations: c, cervix; e, endometrium; f, rectovaginal fascia; i, inner myometrium; o, outer myometrium; s, internal anal sphincter; t, trigone; u, urethra; v, vagina. (A, Sobotta Atlas of Human Anatomy © Elsevier GmbH, Urban & Fischer, Munich.)

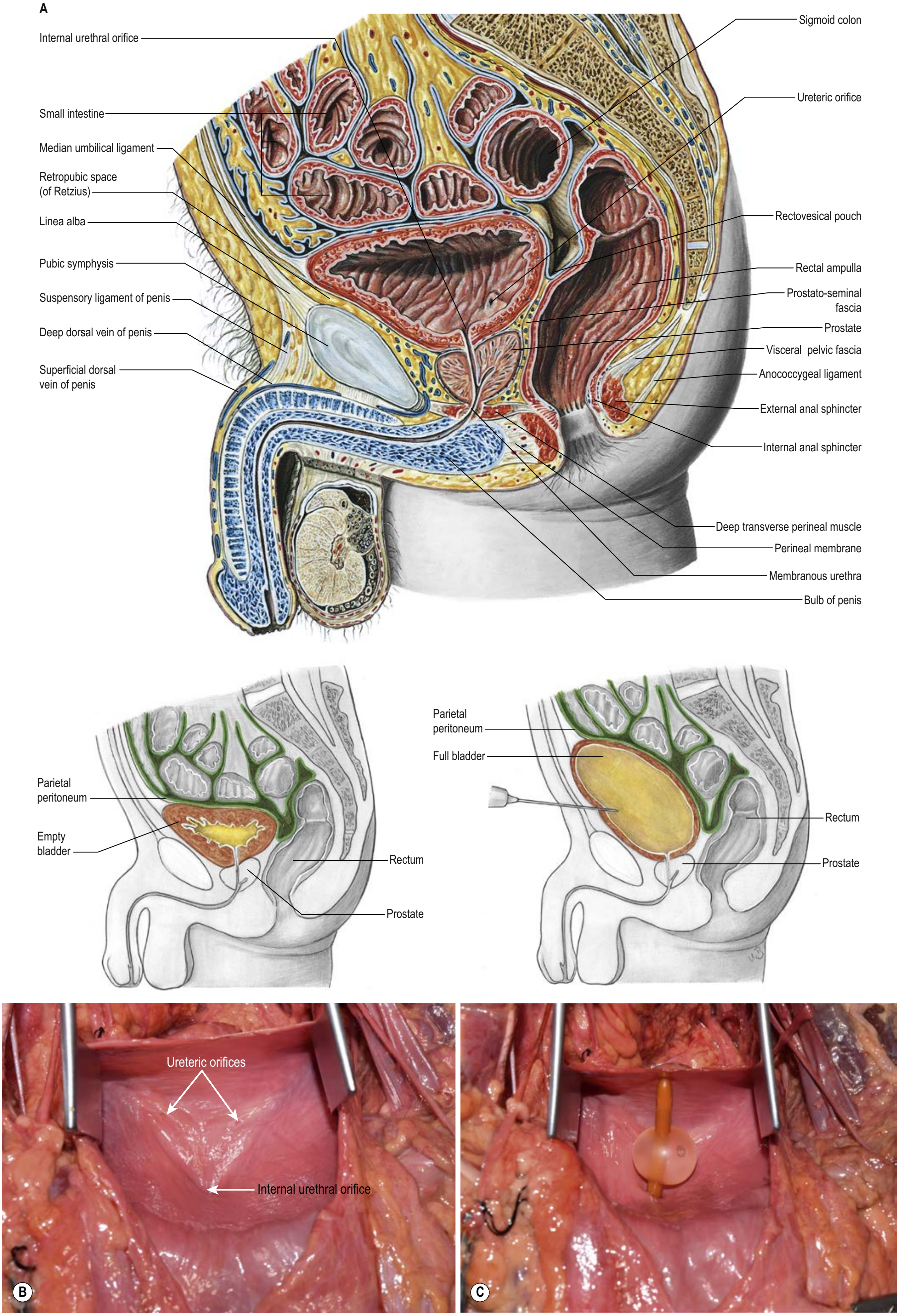
A
Internal urethral orifice
Small intestine
Median umbilical ligament
Retropubic space (of Retzius)
Linea alba
Pubic symphysis
Suspensory ligament of penis
Deep dorsal vein of penis
Superficial dorsal vein of penis
Sigmoid colon
Ureteric orifice
Rectovesical pouch
Rectal ampulla
Prostato-seminal fascia
Prostate
Visceral pelvic fascia
Anococcygeal ligament
External anal sphincter
Internal anal sphincter
Deep transverse perineal muscle
Perineal membrane
Membranous urethra
Bulb of penis
Parietal peritoneum
Empty bladder
Rectum
Prostate
Parietal peritoneum
Full bladder
Rectum
Prostate
Ureteric orifices
Internal urethral orifice
B
C

Fig. 73.2 **A**, The relationship of the bladder and prostate: sagittal section, male pelvis. The relationship of the bladder to the peritoneum and anterior abdominal wall on filling allows suprapubic cystostomy to be performed without intraperitoneal urine leakage. **B**, Anterior view of the opened urinary bladder in a male cadaver. Note the trigone of the bladder. **C**, A urinary bladder catheter has been placed through the internal urethral orifice and its balloon inflated to prevent dislodgment. (A, Sobotta Atlas of Human Anatomy © Elsevier GmbH, Urban & Fischer, Munich. B–C, Courtesy Dr R Shane Tubbs.) (D, *continued online*)

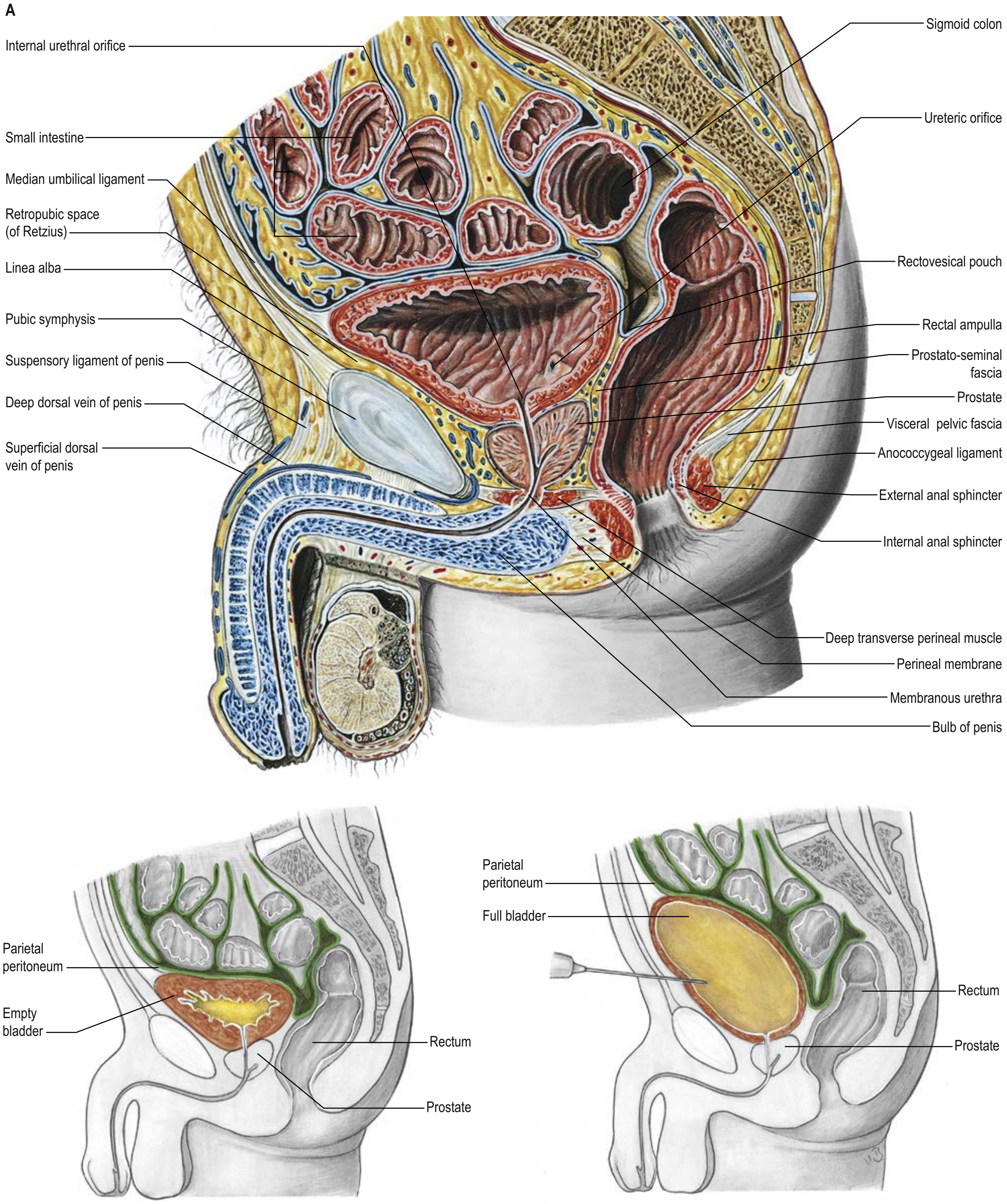
A
Internal urethral orifice
Small intestine
Median umbilical ligament
Retropubic space (of Retzius)
Linea alba
Pubic symphysis
Suspensory ligament of penis
Deep dorsal vein of penis
Superficial dorsal vein of penis
Sigmoid colon
Ureteric orifice
Rectovesical pouch
Rectal ampulla
Prostato-seminal fascia
Prostate
Visceral pelvic fascia
Anococcygeal ligament
External anal sphincter
Internal anal sphincter
Deep transverse perineal muscle
Perineal membrane
Membranous urethra
Bulb of penis
Parietal peritoneum
Empty bladder
Rectum
Prostate
Parietal peritoneum
Full bladder
Rectum
Prostate

Fig. 73.2 **A**, The relationship of the bladder and prostate: sagittal section, male pelvis. The relationship of the bladder to the peritoneum and anterior abdominal wall on filling of the bladder allows suprapubic cystostomy to be performed without intraperitoneal urine leakage.

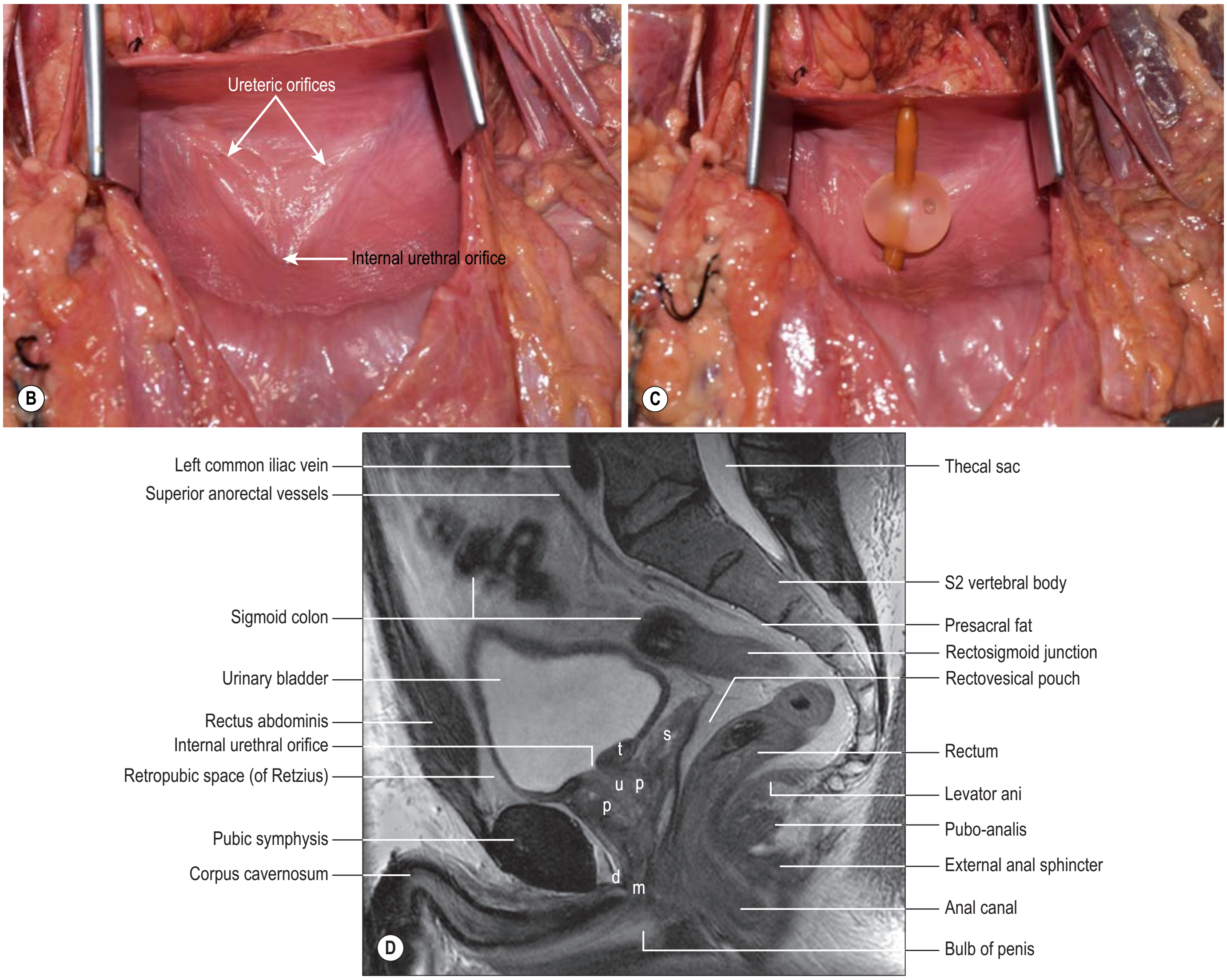
Ureteric orifices
Internal urethral orifice
B
C
Left common iliac vein
Superior anorectal vessels
Sigmoid colon
Urinary bladder
Rectus abdominis
Internal urethral orifice
Retropubic space (of Retzius)
Pubic symphysis
Corpus cavernosum
Thecal sac
S2 vertebral body
Presacral fat
Rectosigmoid junction
Rectovesical pouch
Rectum
Levator ani
Pubo-analis
External anal sphincter
Anal canal
Bulb of penis
t
s
u
p
p
d
m
D

Fig. 73.2, cont'd **B**, Anterior view of the opened urinary bladder in a male cadaver. Note the trigone of the bladder. **C**, A urinary bladder catheter has been placed through the internal urethral orifice and its balloon inflated to prevent dislodgment. **D**, Midline sagittal T2-weighted MRI of the male pelvis. Abbreviations: d, deep transverse perineal muscles; m, membranous urethra; p, prostate; s, seminal gland; t, trigone; u, prostatic urethra. (A, Sobotta Atlas of Human Anatomy © Elsevier GmbH, Urban & Fischer, Munich. B–C, Courtesy Dr R Shane Tubbs.)

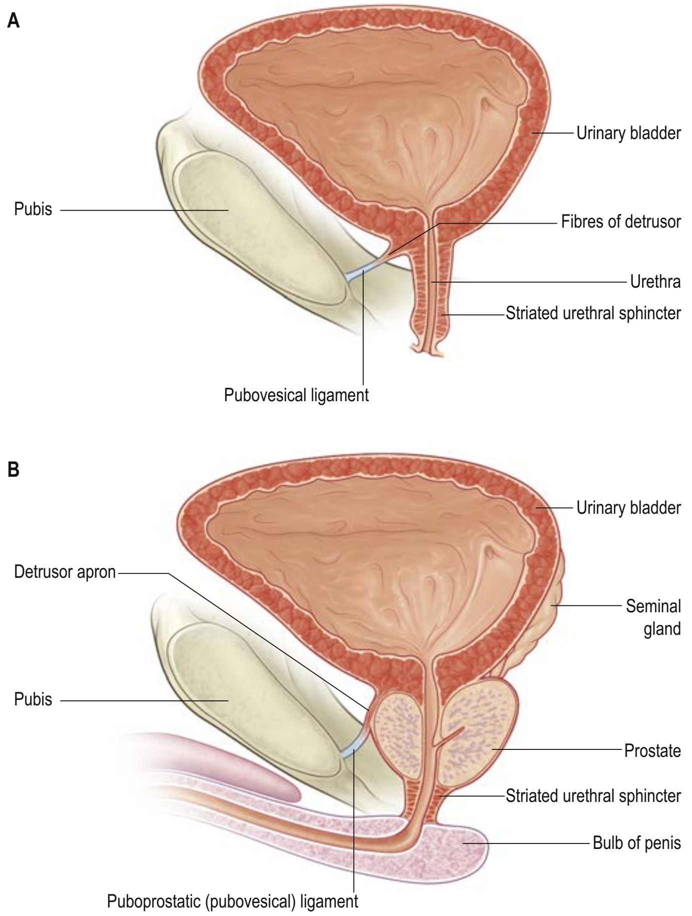

Fig. 73.4 Ligaments that anchor the neck of the bladder and pelvic part of the urethra to the pubis. **A**, In the female. **B**, In the male. In males, detrusor extends over the anterosuperior aspect of the prostate and inserts into the pubis. It condenses to form pubovesical/puboprostatic ligaments. (A, B, With permission from Drake RL, Vogl AW, Mitchell A et al Gray's Atlas of Anatomy. Elsevier, Churchill Livingstone. Copyright 2008.)

As the bladder fills it becomes ovoid (see Video 73.1). Anteriorly, it displaces the parietal peritoneum from the suprapubic region of the anterior abdominal wall. Its inferolateral surfaces become anterior and rest against the abdominal wall without intervening peritoneum for a distance above the pubic symphysis that varies with the degree of distension, but is commonly 5–7 cm. If normal catheterization of the urinary bladder via the urethra is unsuccessful, the distended bladder can be punctured just above the pubic symphysis without traversing the peritoneum (suprapubic cystostomy) (see Fig. 73.2A); surgical access to the bladder through the anterior abdominal wall is usually by this route. The summit of the full bladder points superiorly and anteriorly above the attachment of the median umbilical ligament, so that the peritoneum forms a supravesical fossa of varying depth between the summit and the anterior abdominal wall; this recess often contains coils of small intestine. The bladder is more cranially located at birth than in the adult because the lesser pelvis is shallow, and the internal urethral orifice is level with the upper border of the pubic symphysis. The bladder is then abdominal rather than pelvic and extends about two-thirds of the distance towards the umbilicus.

Ligaments of the urinary bladder

The urinary bladder is anchored anteroinferiorly to the pubis, lateral pelvic side walls and rectum by condensations of pelvic fascia (**Fig. 73.4**); although these condensations are not true anatomical ligaments, the term is applied in routine clinical use (see Ch. 71 for a further description of the visceral pelvic fascia).

In both sexes, stout bands of multilayered fibromuscular tissue, the puboprostatic (males only) and pubovesical ligaments, extend from the neck of the bladder to the inferior aspect of the pubis; they lie on each side of the median plane, leaving a midline urogenital hiatus through which numerous small veins pass. The puboprostatic and pubovesical ligaments have been variously and somewhat confusingly described in the literature. In the *Terminologia Anatomica*, both ligaments are listed as having medial and lateral components; the pubovesical ligament (presumably both medial and lateral parts) is also listed as synonymous with the medial puboprostatic ligament. Cadaveric dissection, histological and plastinated section studies (e.g. DeLancey 1989, Xu et al 2017) have identified the puboprostatic ligament as the anterior layer of the detrusor apron joined by decussated and un-decussated fibres of pubococcygeus; or part of the detrusor apron connecting the bladder to the pubic bone; or the merged fibres of the visceral endopelvic fascia. The pubovesical ligaments have been described as either an extension of the detrusor and its adventitia that is attached to the pubic bone and arcus tendineus fasciae pelvis, or the female equivalent of the medial puboprostatic ligaments, and either separate from the pubo-urethral ligaments or the superior extensions of the pubo-urethral ligaments.

The apex of the bladder is connected to the umbilicus by the remains of the urachus, which forms the median umbilical ligament (**Video 73.2**). The urachus is composed of longitudinal muscle fibres derived from detrusor and becomes more fibrous towards the umbilicus. It usually maintains a lumen lined with epithelium that persists into adult life but is only rarely complicated by a urachal cyst, sinus, fistula or adenocarcinoma.

Other ligaments that have been described in relation to the fundus of the urinary bladder are the lateral, uterosacral and cardinal ligaments. The lateral ligament was described by Miles in 1908: although never described in anatomical cadaveric dissection studies, it is recognized clinically as an important structure in the pararectal fossa at operation. It is a broad band of dense connective tissue, ranging in depth from 5 to 7 cm, and passing between the lateral wall of the pelvis and the fundus of the bladder at the point where the ureter terminates. It contains the middle anorectal artery and lymphatic vessels that pass from the distal rectum to the iliac nodes (Takahashi et al 2000). From the superior surface of the bladder, the peritoneum is carried off in a series of folds: the 'false' ligaments of the bladder. Anteriorly, there are three folds (**Fig. 73.5**): the median umbilical fold over the median umbilical ligament (urachus), and two medial umbilical folds over the occluded parts of the umbilical arteries. The inferior epigastric vessels (**Fig. 73.6**) are lateral to these folds on the anterior abdominal wall and when covered with peritoneum are termed lateral umbilical ligaments.

Urinary bladder interior

Mucosa of the bladder

Almost all of the bladder mucosa is attached only loosely to subjacent muscle (**Fig. 73.7**); it folds when the bladder empties, and the folds are stretched flat as it fills. Over the trigone of the bladder, immediately above and behind the internal urethral orifice, it is adherent to the subjacent muscle layer and is always smooth. The anteroinferior angle of the trigone is formed by the internal urethral orifice, its posterolateral angles by the ureteric orifices. The superior boundary of the trigone is a slightly curved interureteric crest, which connects the two ureteric orifices and is produced by the continuation into the bladder wall of the ureteric internal longitudinal muscle. During cystoscopy, the interureteric crest appears as a pale band and is a guide to the ureteric orifices (see Fig. 73.7A, B).

Trigone of the bladder

The smooth muscle of the trigone consists of two distinct layers, sometimes termed superficial trigone and deep trigone muscles. The latter is composed of muscle cells indistinguishable from those of detrusor, and is simply the posteroinferior portion of detrusor proper. The superficial trigone muscle represents a morphologically distinct component of the trigone, which, unlike detrusor, is composed of relatively small-diameter muscle bundles that are continuous proximally with those of the intramural ureters. It is relatively thin but is generally described as becoming thickened along its superior border to form the interureteric crest. Similar thickenings occur along the lateral edges of the superficial trigone. In both sexes, the superficial trigone muscle becomes continuous with the smooth muscle of the proximal urethra, and extends in the male along the urethral crest as far as the openings of the ejaculatory ducts.

Ureteric orifices and distal ureter

The slit-like ureteric orifices are placed at the posterolateral corners of the trigone of the bladder (see Figs 73.2B, 73.7A). In empty bladders they are approximately 2.5 cm apart and 2.5 cm from the internal urethral orifice; these measurements can be doubled when the bladder is distended. The distal 1.5–2.0 cm of the ureter (intramural part) passes obliquely through the bladder wall before ending as the ureteric orifices. As the bladder fills and intravesical hydrostatic pressure increases, the distal ureter is compressed and acts like a flap valve preventing reflux of urine toward the kidney.

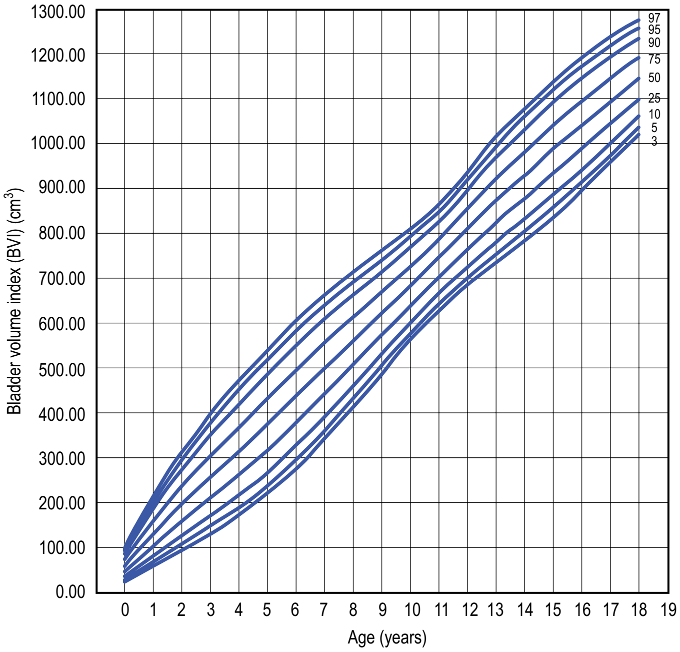

Fig. 73.3 Centiles of bladder volume index in children. (Redrawn with permission from Leung VY, Chu WC, Yeung CK et al 2007 Nomograms of total renal volume, urinary bladder volume and bladder wall thickness index in 3,376 children with a normal urinary tract. Pediatr Radiol 37:181–8.)

Urine samples can, therefore, be obtained in children by performing suprapubic needle puncture. A normogram of bladder volume index (BVI = length × width × depth of bladder), based on sonographic measurements in children, is shown in Fig. 73.3. The bladder progressively descends with growth and reaches the adult position shortly after puberty.

The urachus could be critical for maintaining fetal life when atresia of the urethra results in complete obstruction to the flow of amniotic fluid. Anhydramnios noted at 17 weeks' gestation has been reported to resolve by 21 weeks when the patent urachus acts as a fistula between the bladder and the amniotic cavity, preserving pulmonary and renal function (Stalberg and Gonzalez 2012).

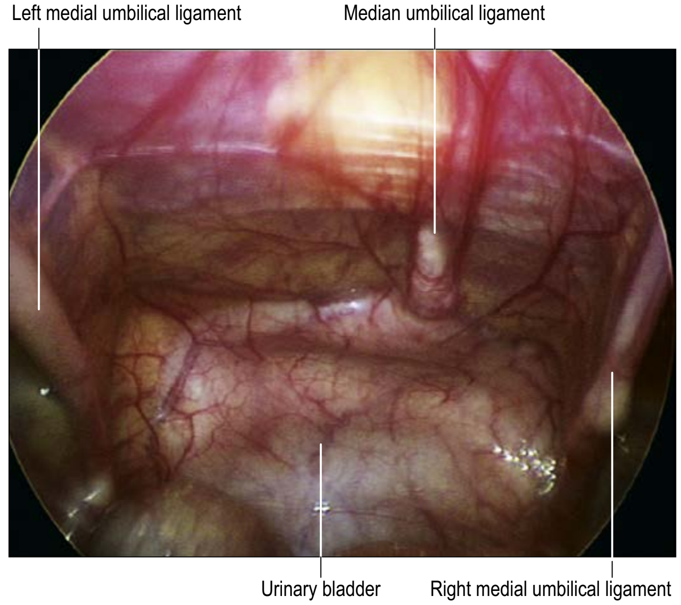
Left medial umbilical ligament
Median umbilical ligament
Urinary bladder
Right medial umbilical ligament

Fig. 73.5 A laparoscopic view of the empty bladder and median and medial umbilical folds in a 12-month-old boy. (Courtesy of Mr Girish Jawaheer.)

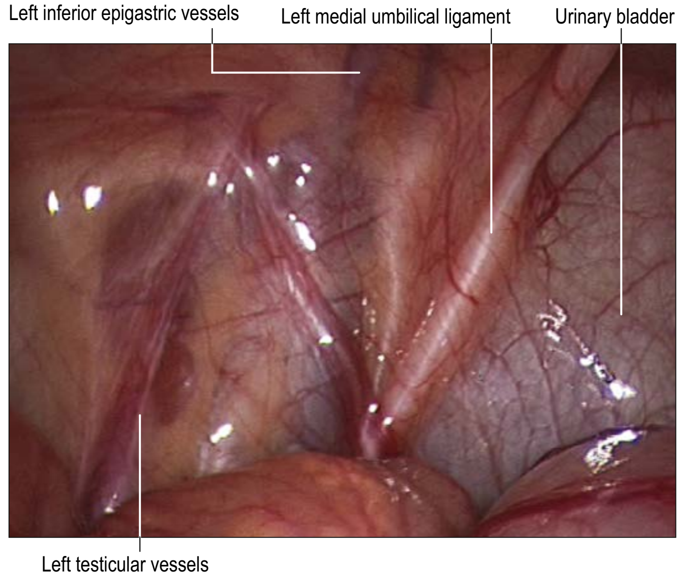
Left inferior epigastric vessels
Left medial umbilical ligament
Urinary bladder
Left testicular vessels

Fig. 73.6 A laparoscopic view of the left inferior epigastric vein (lateral umbilical ligament) in a 12-month-old boy. (Courtesy of Mr Girish Jawaheer.)

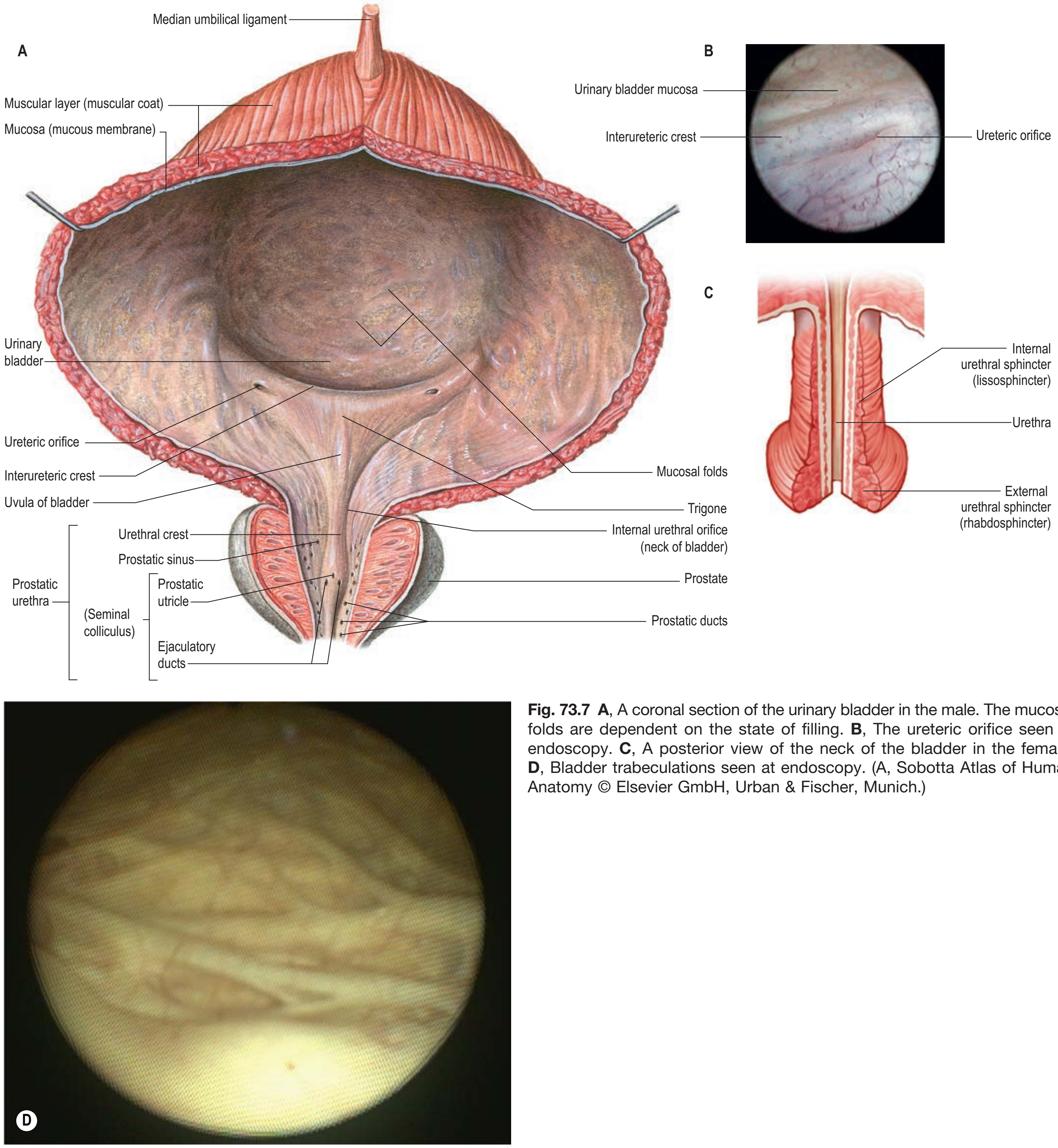
A
Median umbilical ligament
Muscular layer (muscular coat)
Mucosa (mucous membrane)
Urinary bladder
Ureteric orifice
Interureteric crest
Uvula of bladder
Urethral crest
Prostatic sinus
Prostatic urethra
(Seminal colliculus)
Prostatic utricle
Ejaculatory ducts
Mucosal folds
Trigone
Internal urethral orifice (neck of bladder)
Prostate
Prostatic ducts
B
Urinary bladder mucosa
Interureteric crest
Ureteric orifice
C
Internal urethral sphincter (lissosphincter)
Urethra
External urethral sphincter (rhabdosphincter)
D

Fig. 73.7 **A**, A coronal section of the urinary bladder in the male. The mucosal folds are dependent on the state of filling. **B**, The ureteric orifice seen at endoscopy. **C**, A posterior view of the neck of the bladder in the female. **D**, Bladder trabeculations seen at endoscopy. (A, Sobotta Atlas of Human Anatomy © Elsevier GmbH, Urban & Fischer, Munich.)

Internal urethral orifice

The internal urethral orifice is sited at the apex of the trigone of the bladder, the lowest part of this organ, and is usually somewhat crescentic in section. There is often an elevation immediately behind it in adult males (particularly past middle age), which is caused by the prostate.

Neck of the bladder

The smooth muscle of the neck of the bladder is histologically, histochemically and pharmacologically distinct from detrusor proper, so the neck of the bladder should be considered as a separate functional unit. Males and females have quite different arrangements of smooth muscle in this region, and will be described separately.

Females

In females the neck of the bladder consists of morphologically distinct smooth muscle (see Fig. 73.7C). The large-diameter fasciculi characteristic of detrusor are replaced by small-diameter fasciculi that extend obliquely or longitudinally into the urethral wall. In the normal female the neck of the bladder sits above the pelvic diaphragm, supported predominantly by the pubovesical ligaments (see Fig. 73.4A), the endopelvic fascia of the pelvic diaphragm and levator ani. These structures support the urethra at rest; with elevated intra-abdominal pressure, the pelvic diaphragm contracts, increasing urethral closure pressure to maintain continence. This anatomical arrangement commonly alters after parturition and with increasing age, such that the neck of the bladder lies beneath the pelvic diaphragm, particularly when intra-abdominal pressure rises. This means that the mechanism described above fails to maintain continence and females can experience stress incontinence (Klutke and Siegel 1995).

Males

In males the neck of the bladder is completely surrounded by a circular collar of smooth muscle with its own distinct adrenergic innervation, which extends distally to surround the intramural part of the urethra. These smooth muscle bundles are distinct from those that run in continuity from the neck of the bladder down to the prostatic urethra, and from the smooth muscle within the prostate. The bundles that form the internal urethral (preprostatic) sphincter are small compared with the muscle bundles of detrusor, and are separated by a relatively large connective tissue component rich in elastic fibres.

The neck of the bladder is sometimes called the proximal or internal urethral sphincter mechanism, to distinguish it from the distal or external urethral sphincter. The internal urethral sphincter contributes to urinary continence and, in the face of distal sphincteric incompetence, can at times maintain continence independently. Unlike detrusor and the rest of the urethral smooth muscle (in males and females), the internal urethral sphincter is richly supplied with sympathetic noradrenergic nerves and is almost totally devoid of parasympathetic cholinergic nerves (see below).

Urinary bladder outflow obstruction

The muscle of the bladder hypertrophies in progressive chronic obstruction to micturition, e.g. as a result of prostatic enlargement or urethral stricture, or in children with congenital bladder outflow obstruction, e.g. posterior urethral valves. The muscle fasciculi increase in size and, because they interlace in all directions, a thick-walled 'trabeculated bladder' is produced (see Fig. 73.7D). Mucosa between the fascicles forms 'diverticula' owing to the increased intravesical pressure required to pass urine through the obstruction. When outflow is obstructed, emptying may not be complete; some urine can remain and lead to infection and stone formation within the bladder. Back-pressure from a chronically distended bladder can gradually dilate the ureters, renal pelves and even the renal collecting ducts bilaterally and can result in progressive renal impairment.

Vascular supply and lymphatic drainage

Arteries

The bladder is supplied principally by the superior and inferior vesical arteries (see Figs 75.3, 72.20C), derived from the anterior division of the internal iliac artery and supplemented by the obturator and inferior gluteal arteries. In females, additional branches are derived from the uterine and vaginal arteries.

Superior vesical artery

The superior vesical artery arises from the patent part of the umbilical artery. It supplies many branches to the fundus of the bladder. The artery to the ductus deferens often originates from one of these branches and accompanies the ductus deferens to the testis, where it anastomoses with the testicular artery. Other branches of the superior vesical artery supply the ureter.

Inferior vesical artery

The inferior vesical artery often arises with the middle anorectal artery from the internal iliac artery. It supplies the fundus of the bladder, prostate, seminal glands and distal ureter, and sometimes provides the artery to the ductus deferens. Branches to the prostate communicate across the midline.

Veins

The veins that drain the bladder form a complicated plexus on its inferolateral surfaces and pass backwards in the lateral ligaments of the bladder to end in the internal iliac veins (see Fig. 75.3).

Lymphatic drainage

Lymphatics that drain the bladder begin in mucosal, intermuscular and adventitial plexuses (see Fig. 75.3). There are three sets of collecting vessels; most end in the external iliac nodes. Vessels from the trigone emerge on the exterior of the bladder to run superolaterally. Vessels from the superior surface of the bladder converge to the posterolateral angle and pass superolaterally to the external iliac nodes (some might drain to the internal or common iliac nodes). Vessels from the inferolateral surface of the bladder ascend to join those from the superior surface or run to the lymph nodes in the obturator fossa. Minute nodules of lymphoid tissue can occur along the lymph vessels of the bladder.

Innervation

The nerves supplying the bladder arise from the inferior hypogastric plexus, a mesh of autonomic nerves and ganglia lying on the lateral aspects of the rectum, internal genitalia and fundus of the bladder (Fig. 73.8). They consist of both sympathetic and parasympathetic components. For further reading, see Mundy et al (1999a).

Efferent fibres

Parasympathetic fibres arise from the second to the fourth sacral segments of the spinal cord and enter the inferior hypogastric plexus on the posterolateral aspects of the rectum as the pelvic splanchnic nerves. The sympathetic fibres are derived from neuronal cell bodies in the lower three thoracic and upper two lumbar segments of the spinal cord and form the coeliac and mesenteric plexuses in the abdomen; from here, the superior hypogastric plexus descends into the pelvis as fairly discrete nerve bundles within the extraperitoneal connective tissue posterior to the ureter on each side. The anterior part of the inferior hypogastric plexus is known as the vesical plexus. Small groups of autonomic neurones occur within the plexus and throughout all regions of the bladder wall. These multipolar intramural neurones are rich in acetylcholinesterase (AChE) and occur in ganglia containing up to 20 neuronal cell bodies. Most of the preganglionic nerve terminals correspond morphologically to presumptive cholinergic fibres. Noradrenergic terminals also relay on cell bodies in the inferior hypogastric plexus; it is not known whether similar nerves synapse on intramural bladder ganglia.

The urinary bladder is profusely supplied with nerves, which form a dense plexus among detrusor muscle cells. Most of these nerves contain AChE and are abundant throughout the muscle layer of the bladder. Axonal varicosities adjacent to detrusor muscle cells possess features that are considered to typify cholinergic nerve terminals, and contain clusters of small (50 nm diameter) agranular vesicles, occasional large (80–160 nm diameter) granulated vesicles and small mitochondria. Terminal regions approach to within 20 nm of the surface of the muscle cells and can be partially surrounded by Schwann cell cytoplasm; more often they are naked nerve endings.

Detrusor possesses a sparse but definite supply of sympathetic noradrenergic nerves that generally accompany the vascular supply and only rarely extend among the myocytes. Non-adrenergic, non-cholinergic nerves have been identified, and a number of other neurotransmitters or neuromodulators have been detected in intramural ganglia, including the peptide somatostatin. The superficial trigone muscle is associated with more noradrenergic (sympathetic) fibres than cholinergic (parasympathetic) nerves, a difference that supports the view that the superficial trigone muscle should be regarded as 'ureteric' rather than 'vesical' in origin. However, it should be emphasized that this muscle forms a very minor part of the total muscle mass of the neck of the bladder and proximal urethra in either sex and is probably of little significance in the physiological mechanisms that control these regions.

The smooth muscle of the neck of the bladder in males is predominantly orientated obliquely or circularly. It is sparsely supplied with cholinergic (parasympathetic) nerves but possesses a rich noradrenergic (sympathetic) innervation. There is a similar distribution of autonomic nerves in the smooth muscle of the prostate, seminal glands and ducti deferentia. Stimulation of sympathetic nerves causes contraction of smooth muscle in the wall of the genital tract, resulting in seminal emission. Concomitant sympathetic stimulation of the proximal urethral smooth muscle causes sphincteric closure of the internal urethral sphincter, preventing reflux of ejaculate into the bladder.

The lamina propria of the fundus and inferolateral walls of the bladder is virtually devoid of autonomic nerve fibres, apart from some noradrenergic and occasional cholinergic perivascular nerves. However, the density of nerves unrelated to blood vessels increases closer to the internal urethral orifice. At the neck of the bladder and trigone a nerve plexus of cholinesterase-positive axons extends throughout the lamina propria, independent of blood vessels. Some of the larger diameter axons are myelinated and others lie adjacent to the basal urothelial cells. In the absence of any obvious effector target sites, the subepithelial nerve plexuses of the bladder and the ureter are assumed to subserve a sensory function.

Afferent fibres

Visceral afferent nerves supplying the bladder are concerned with awareness of distension and pain and are stimulated by distension or spasm due to a stone, inflammation or malignant disease; they travel in sympathetic and parasympathetic nerves, predominantly the latter (Shoja et al 2013). Therefore, division of the sympathetic paths or of the

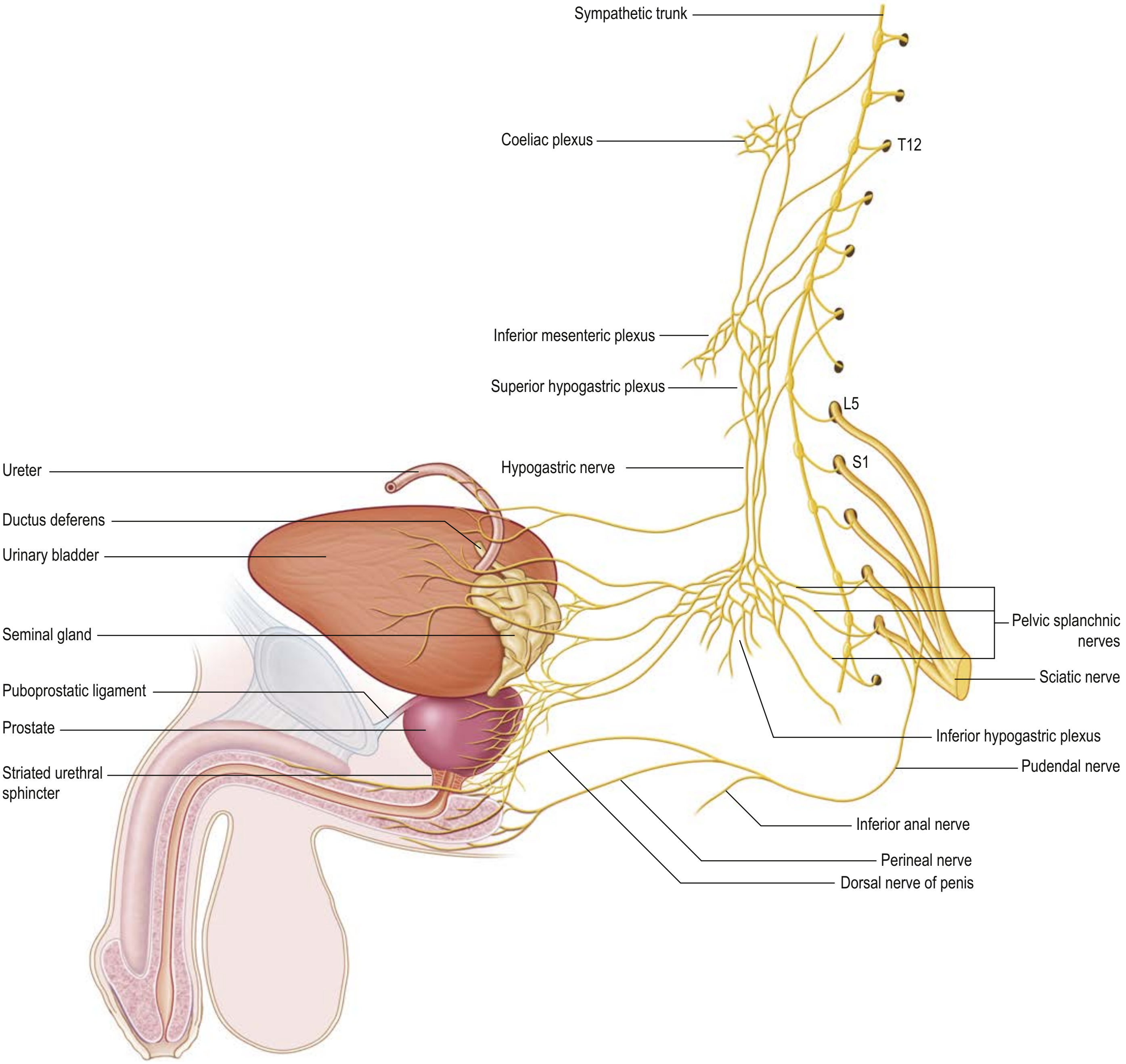
Sympathetic trunk
Coeliac plexus
T12
Inferior mesenteric plexus
Superior hypogastric plexus
L5
S1
Ureter
Hypogastric nerve
Ductus deferens
Urinary bladder
Seminal gland
Pelvic splanchnic nerves
Sciatic nerve
Puboprostatic ligament
Prostate
Inferior hypogastric plexus
Pudendal nerve
Striated urethral sphincter
Inferior anal nerve
Perineal nerve
Dorsal nerve of penis

Fig. 73.8 Innervation of the lower urinary tract and male genitalia. (Redrawn with permission from Dyck P, Thomas PK 2005 Peripheral Neuropathy. Saunders, Elsevier.)

superior hypogastric plexus does not materially relieve bladder pain, whereas considerable relief follows bilateral anterolateral cordotomy. Since nerve fibres mediating awareness of distension of the urinary bladder travel in the dorsal (posterior) columns, patients retain awareness of the need to micturate after anterolateral cordotomy. The nerve endings detecting noxious stimuli are probably of more than one type; a subepithelial plexus of fibres containing dense vesicles, which are probably afferent endings, has been described.

MICROSTRUCTURE

The bladder consists of four layers: urothelium (transitional epithelium), lamina propria, muscularis and adventitia (Fig. 73.9).

Urothelium

The urothelium is 4–7 cells thick; it can appear to be attenuated to 2–3 cells thick when the bladder is fully distended. It contains three distinctive cell layers: a basal layer, an intermediate layer and a superficial ('umbrella' cell) layer (see Fig. 73.9). The basal layer consists of small cuboidal cells from which the upper layers arise. The intermediate layers are polygonal and possess the capacity to stretch and flatten. The superficial layer forms a protective, almost impermeable, surface for the

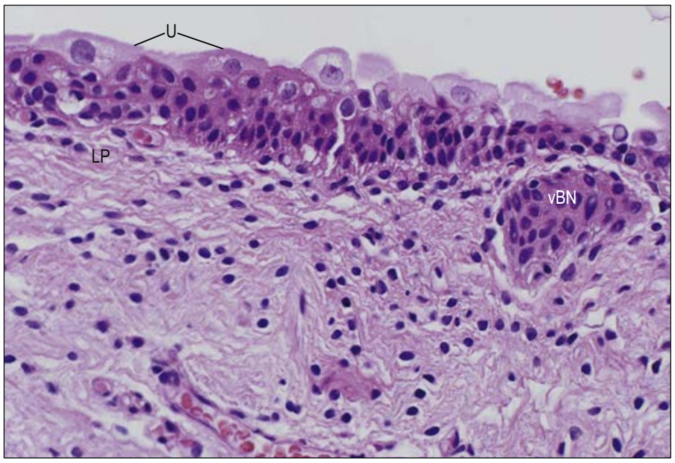

Fig. 73.9 The bladder is lined by urothelium with a surface 'umbrella cell' layer (U) and an intermediate region (3–5 cells thick). The lamina propria (LP) consists of stroma with blood vessels and von Brunn's nests (vBN).

The neck of the bladder is disrupted in the vast majority of men undergoing transurethral resection of the prostate and this can result in retrograde ejaculation. Similarly, an ejaculation can result when the sympathetic fibres are disrupted during retroperitoneal lymph node dissection surgery. Although this genital function of the neck of the bladder of the male is well established, it is not known whether the smooth muscle of this region contributes actively to the maintenance of urinary continence. In contrast, in females the smooth muscle of the neck of the bladder contains relatively few noradrenergic nerves but is richly supplied with cholinergic fibres. The sparse supply of sympathetic nerves presumably relates to the absence of a functioning 'genital' portion of the wall of the female urethra.

bladder mucosa and consists of large, sometimes multinucleated, cells displaying degenerative changes in their cytoplasm; these cells are ultimately exfoliated into the urine. The apical surface of the umbrella cell layer is covered by 16 nm protein particles packed hexagonally to form two-dimensional crystals of asymmetric unit membranes (AUMs), which contribute to the permeability barrier function of the urinary bladder, preventing reabsorption of urine across the urothelium into the blood stream. Islands or nests of urothelium (von Brunn's nests; see Fig. 73.9) can become separated from the surface during development and embedded in the underlying lamina propria; they can undergo central degeneration to form cysts (cystitis cystica).

Lamina propria

The lamina propria forms a connective tissue bed supporting the overlying urothelium, from which it is separated by a basal lamina. It is rich in capillaries, lymphatics and nerve endings, and contains elastic fibres and a thin, poorly defined, layer of smooth muscle fibres, muscularis mucosae, which is variably distributed within the bladder. This layer is often very superficial, lying close beneath the urothelium, but is sometimes deeper in the lamina propria, where it can be well developed; it must be distinguished from muscularis propria. Several functions have been proposed for the lamina propria, including acting as the capacitance layer of the bladder (determining bladder compliance and enabling adaptive changes to increasing volumes); providing factors that influence the growth of the urothelium and/or detrusor; and playing a role in signal transduction (Andersson and McCloskey 2014).

Interstitial cells of Cajal-like cells

Interstitial cells of Cajal (ICC) are a specialized population of cells involved in smooth muscle excitability that were initially described in the gastrointestinal tract (Chs 59, 64). Cells with a similar morphology but expressing platelet-derived growth receptor alpha (PDGFRα) rather than the tyrosine kinase receptor Kit that typifies ICC, and therefore designated interstitial cells of Cajal-like cells (ICC-LC), have been reported in the urethra, ductus deferens, prostate, bladder, corpus cavernosum penis, ureter, uterine tube and uterus, where they form a functional syncytium with nerves and smooth muscle cells. They may function as electrical pacemakers in the urethra and prostate. In the bladder they are closely apposed to detrusor smooth muscle cells, in the lamina propria and within the subepithelium; it has been tentatively suggested that one of their functions in the bladder is to act as intermediary cells transducing nerve signals to detrusor (Drumm et al 2014).

Muscularis propria

Detrusor is the muscularis propria of the bladder wall. It consists of three indistinct layers: an inner and outer longitudinal, and an intermediate circular layer. In contrast to muscularis mucosae, which consists of small wispy fibres, muscularis propria is made up of larger, poorly defined, bundles of smooth muscle cells that form well-defined inner circular and outer longitudinal layers at the neck of the bladder.

Adventitia

The adventitia partially covers the bladder. It is covered externally by mesothelium, beneath which there is a variable amount of vascularized adipose tissue that frequently extends into muscularis propria and, occasionally, into the lamina propria.

MALE URETHRA

The male urethra is 18–20 cm long and extends from the internal urethral orifice in the urinary bladder (**Fig. 73.10**) to the external urethral orifice at the end of the penis. It can be considered in two parts. The anterior urethra is subdivided into a proximal component, the bulbar part of the spongy urethra, which is surrounded by bulbospongiosus and entirely within the perineum, and a pendulous or penile component, which continues to the distal end of the penis. The posterior urethra is divided into intramural (preprostatic), prostatic and membranous parts. The urethra is a mere slit, except during the passage of fluid; in transverse section, it is transversely arched in the prostatic part, stellate in the intramural and membranous parts, transverse in the spongy parts, and sagittal at the external urethral orifice. The anterior urethra is approximately 16 cm long and lies within the perineum (proximally) and the penis (distally), surrounded by the corpus spongiosum penis. The posterior urethra is 4 cm long and lies in the pelvis proximal to the corpus spongiosum penis, where it is acted on by the urogenital sphincter mechanisms. Functionally, both parts act as a conduit.

Posterior part

Intramural part of the urethra

The intramural part of the urethra is approximately 1 cm long and extends from the fundus of the bladder to the prostate (see Fig. 73.7A). Small urethral glands (of Littré) at this site can contribute to benign prostatic hyperplasia (BPH) and symptoms of outflow obstruction in older men.

Prostatic urethra

The prostatic urethra is 3–4 cm long and tunnels through the substance of the prostate, closer to the anterior than the posterior surface of the gland (**Fig. 73.11**; see Fig. 73.7A). It is continuous above with the intramural part and emerges from the prostate slightly anterior to its apex (the most inferior point of the prostate). Throughout most of its length, the posterior wall has a midline ridge, the urethral crest, which projects into the lumen, causing it to appear crescentic in transverse section. On each side of the crest, the floor of a shallow depression, the prostatic sinus, is perforated by the orifices of 15–20 prostatic ducts. An elevation, the seminal colliculus (verumontanum) occurs at about the middle of the length of the urethral crest; at this point, the urethra turns anteriorly and contains the slit-like orifice of the prostatic utricle, a cul-de-sac approximately 6 mm long that runs upwards and backwards in the substance of the prostate behind its middle lobe, when present. The extent of angulation most often approximates 30–35° but can change with age and differs among individuals. The seminal colliculus is used as a surgical landmark for the external urethral sphincter or the membranous urethra during transurethral resection of the prostate (TURP) for benign enlargement of the gland. The two small openings of the ejaculatory ducts open on both sides of the seminal colliculus at 7 o'clock and 5 o'clock positions and are covered with a one-way valve (Li et al 2019).

The prostatic utricle is a cul-de-sac approximately 6 mm long, that runs upwards and backwards in the substance of the prostate behind its middle lobe. Its walls are composed of fibrous tissue, muscular fibres and mucous membrane, the latter pitted by the openings of numerous small glands. It develops from the paramesonephric ducts or urogenital sinus and has been considered homologous with the vagina of the female: it is sometimes called the 'vagina masculina', although the more usual view is that it is a uterine homologue, hence the name 'utricle'. Cystic dilation of the prostatic utricle (**Fig. 73.12**) can present in childhood with urinary tract infections, recurrent epididymitis or haematuria.

The lowest part of the prostatic urethra is fixed by the puboprostatic ligaments and is therefore immobile.

Membranous urethra

The membranous urethra is the shortest (2–2.5 cm), least dilatable and (except for the external urethral orifice), the narrowest section of the urethra. It descends with a slight ventral concavity from the prostate to the bulb of the penis, passing through the perineal membrane 2.5 cm posteroinferior to the pubic symphysis. The wall of the membranous urethra consists of a muscle coat that is separated from the epithelial lining by a narrow layer of fibroelastic connective tissue. The muscle coat contains a relatively thin layer of bundles of smooth muscle, which are continuous proximally with those of the prostatic urethra, and a prominent outer layer of circularly orientated striated muscle fibres, which together form the external urethral sphincter.

Urinary continence at the level of the membranous urethra is mediated by the radial folds of urethral mucosa, the submucosal connective tissue, the intrinsic urethral smooth muscle, the striated muscle fibres and puboperinealis. The muscle coat of the urethra and puboanalis (puborectalis) surround the membranous urethra and are attached to the inner surface of the ischiopubic ramus; fibres also reach up to the lowest part of the neck of the bladder and lie on the surface of the prostate. The striated external urethral sphincter has a posterior fibrous defect and is inserted throughout its length into the perineal body. It is related to the dorsal vascular complex anteriorly, levator ani laterally and the perineal body and rectourethralis posteriorly; it is suspended from the pubis by fibrous tissue that extends from its anterior and lateral parts to the puboprostatic ligaments posteriorly and to the suspensory ligament of the penis anteriorly. The bulbo-urethral glands (Cowper's glands) are embedded in the deep transverse perineal muscle and drain into the spongy urethra during sexual excitement.

Anterior part

The anterior, or spongy urethra lies within the corpus spongiosum penis (see Fig. 74.3). In the flaccid penis it is about 15 cm long and extends from the end of the membranous urethra to the external urethral orifice on the glans penis. It starts below the perineal membrane at a point anterior to the lowest level of the pubic symphysis as the bulbar part of the spongy urethra, the widest part of the urethra, surrounded by bulbospongiosus.

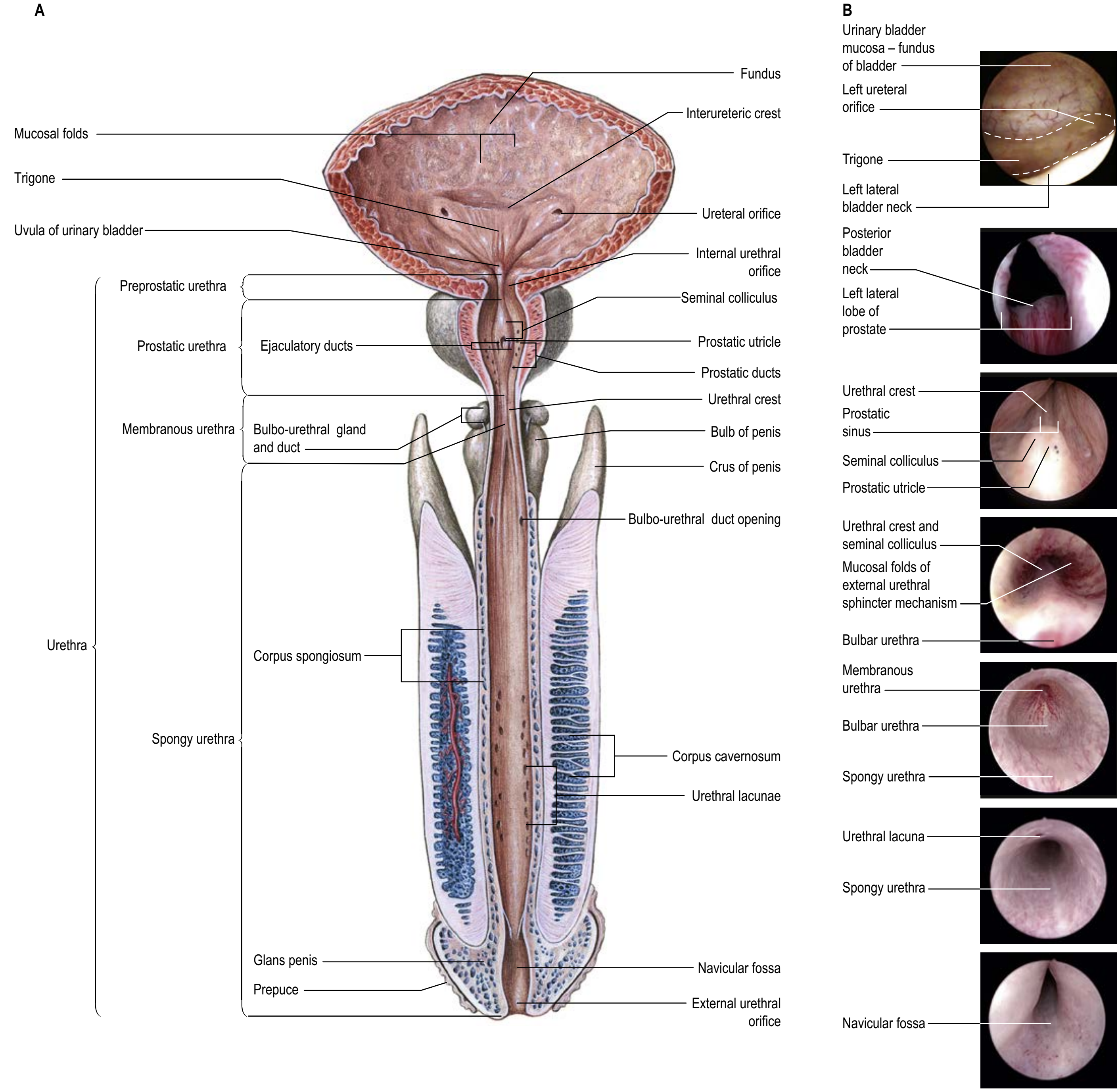
A
Fundus
Interureteric crest
Mucosal folds
Trigone
Ureteral orifice
Uvula of urinary bladder
Internal urethral orifice
Preprostatic urethra
Seminal colliculus
Prostatic urethra
Ejaculatory ducts
Prostatic utricle
Prostatic ducts
Urethral crest
Membranous urethra
Bulbo-urethral gland and duct
Bulb of penis
Crus of penis
Bulbo-urethral duct opening
Urethra
Corpus spongiosum
Spongy urethra
Corpus cavernosum
Urethral lacunae
Glans penis
Navicular fossa
Prepuce
External urethral orifice
B
Urinary bladder mucosa – fundus of bladder
Left ureteral orifice
Trigone
Left lateral bladder neck
Posterior bladder neck
Left lateral lobe of prostate
Urethral crest
Prostatic sinus
Seminal colliculus
Prostatic utricle
Urethral crest and seminal colliculus
Mucosal folds of external urethral sphincter mechanism
Bulbar urethra
Membranous urethra
Bulbar urethra
Spongy urethra
Urethral lacuna
Spongy urethra
Navicular fossa

Fig. 73.10 **A**, The male urethra. **B**, Endoscopic views (top to bottom): posterior bladder wall and trigone, neck of the bladder, urethral crest, membranous urethra, bulbar part of spongy urethra, spongy urethra, navicular fossa. (A, Sobotta Atlas of Human Anatomy © Elsevier GmbH, Urban & Fischer, Munich.)

The bulbo-urethral glands open into the bulbar part of the spongy urethra approximately 2.5 cm below the perineal membrane. The spongy urethra is a narrow, transverse slit when empty and has a diameter of approximately 6 mm when passing urine. It is dilated at its termination within the glans penis, where it is known as the navicular fossa. The external urethral orifice is the narrowest part of the urethra and is a sagittal slit about 6 mm long in the adult, bounded on each side by a small labium.

Traumatic injury to the male urethra

Available with the *Gray's Anatomy* e-book

Congenital anomalies of the male urethra

Available with the *Gray's Anatomy* e-book

Vascular supply and lymphatic drainage

Urethral artery

The urethral artery usually arises from the internal pudendal artery just below the perineal membrane, and travels through the corpus spongiosum penis to reach the glans penis. It supplies the urethra and the erectile tissue around it. The urethra is also supplied by the dorsal artery of the penis via its circumflex branches on each side, and in a retrograde fashion from the glans penis by its terminal branches. The blood supply through the corpus spongiosum penis is so plentiful that the urethra can be divided without compromising its vascular supply.

Veins

The venous drainage of the anterior urethra is to the dorsal veins of the penis and internal pudendal veins, which drain to the prostatic venous plexus. The posterior urethra drains into the prostatic and vesical venous plexuses, which drain into the internal iliac veins.

Lymphatic drainage

Vessels from the posterior urethra pass mainly to the internal iliac nodes; a few end in the external iliac nodes. Vessels from the membranous urethra accompany the internal pudendal artery. Vessels from the anterior urethra accompany those of the glans penis, most ending in the deep inguinal nodes; some can end in superficial inguinal nodes, while others traverse the inguinal canal to end in the external iliac nodes.

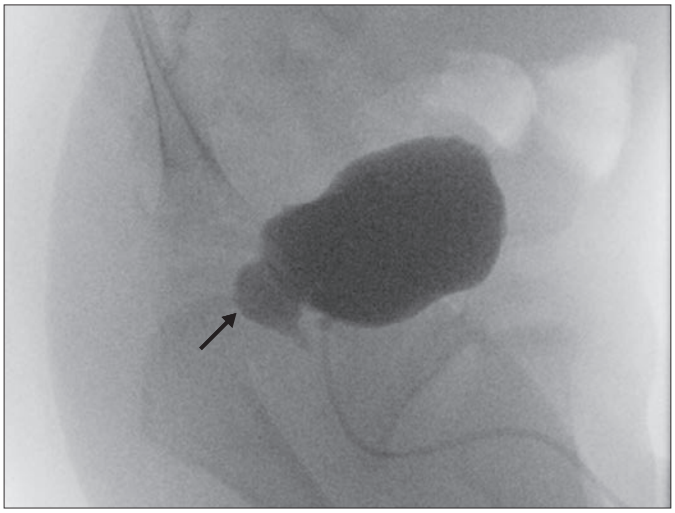

Fig. 73.12 Cystic dilation of the prostatic utricle (arrow) demonstrated in an 8-month-old child during a micturating cystourethrogram. (Courtesy of Mr Alok Godse.)

The mean length of the slit was found to be 5.4 mm in boys with a mean age of approximately seven years (Hutton and Babu 2007). The width of the external urethral orifice in uncircumcised boys between the ages of 5 months and 16 years varied from 3.5 to 7.5 mm (Orkiszewski and Madej 2010).

The urethral epithelium (e.g. distal spongy parts), presents the orifices of numerous small urethral glands that lie in the submucosa. It also contains a number of small pit-like recesses, or lacunae, of various sizes with orifices directed forwards. One, the lacuna magna, is larger than the rest and is situated in the roof of the navicular fossa.

The urethra can be ruptured by a fall-astride (straddle) injury to the bulbar part of the spongy urethra in the perineum, or by an injury related to a pelvic fracture. These injuries usually affect the junction of the membranous with the bulbar part of the spongy urethra across the perineal membrane. One complication associated with such injuries is extravasation of urine. After an injury to the bulbar part of the spongy urethra, urine usually extravasates between the perineal membrane and the membranous layer of the superficial fascia (Colles' fascia). As both of these are attached firmly to the ischiopubic rami, extravasated fluid cannot pass posteriorly because the two layers are continuous around superficial transverse perineal muscles. Laterally, the spread of urine is blocked by the pubic and ischial rami. Urine cannot enter the lesser pelvis through the perineal membrane if this remains intact, and so it tracks anteriorly into the loose connective tissue of the scrotum and penis, and, from there, to the anterior abdominal wall. If the posterior urethra is injured, urine is extravasated into the pelvic extraperitoneal tissue; if the perineal membrane is also torn, then urine may be extravasated into the perineum.

Hypospadias, found in 1 in 300 boys, most often results in the urethra opening on the distal, urethral surface of the penis. There is also an associated abnormality of the prepuce, which is longer dorsally and lacking ventrally, and often an associated chordee, which causes a ventral curvature of the penis. The microvessel density of the prepuce is reduced in children with hypospadias and this has surgical implications when preputial flaps are used for the repair of hypospadias (Yucel et al 2004, Çağrı Savaş et al 2011). Anomalies of arterial vascular anatomy of the prepuce have been described in boys with hypospadias, so it is important for hypospadias to be identified prior to circumcision because the abnormal prepuce is sometimes used for surgical correction of the deformity.

Epispadias occurs in approximately 1 in 100,000 boys; it is typically part of the exstrophy–epispadias complex but can occur in isolation. The urethra is either completely open dorsally or uncovered to the level of the pubic symphysis. Other features of epispadias include a shortened penis and dorsal chordee; the incidence of cryptorchidism is increased ten-fold.

Epispadias is a rare congenital anomaly that can affect the female urethra, either in isolation or as part of the exstrophy–epispadias complex. Isolated epispadias in girls is characterized by the urethra opening at the clitoris, which is typically bifid.

Posterior urethral valves occur in 1 in 5000–8000 males and are the most common cause of urinary outflow obstruction in infants. The most common type (type I) is believed to occur if the mesonephric (Wolffian) ducts open too anteriorly on to the primitive prostatic urethra; this abnormal migration of the ducts leaves behind thick vestigial tissue that forms rigid valve cusps extending caudally from the seminal colliculus. Megalourethra can be associated with posterior urethral valves. Congenital anterior urethral valves are a rare cause of urethral obstruction in boys and may be associated with posterior urethral valves and hypospadias.

Very rarely, urethral duplication occurs; the two urethrae almost invariably lie on top of each other rather than side by side. One of the urethrae, usually the more dorsal, may be blind-ending. A congenital prepubic sinus consists of a midline tract in the skin passing from the suprapubic region towards the anterior aspect of the urinary bladder without communication and is believed to be a variant of dorsal urethral duplication. Congenital urethrocutaneous fistulae are very rare anomalies in which the urethra opens on the ventral surface of the penis in the absence of chordee or hypospadias.

Congenital rectourethral fistulae can be present in children born with anorectal malformation. The prostatic or bulbar part of the spongy urethra is usually affected, and the rectum and urethra share a common wall immediately above the fistula site.

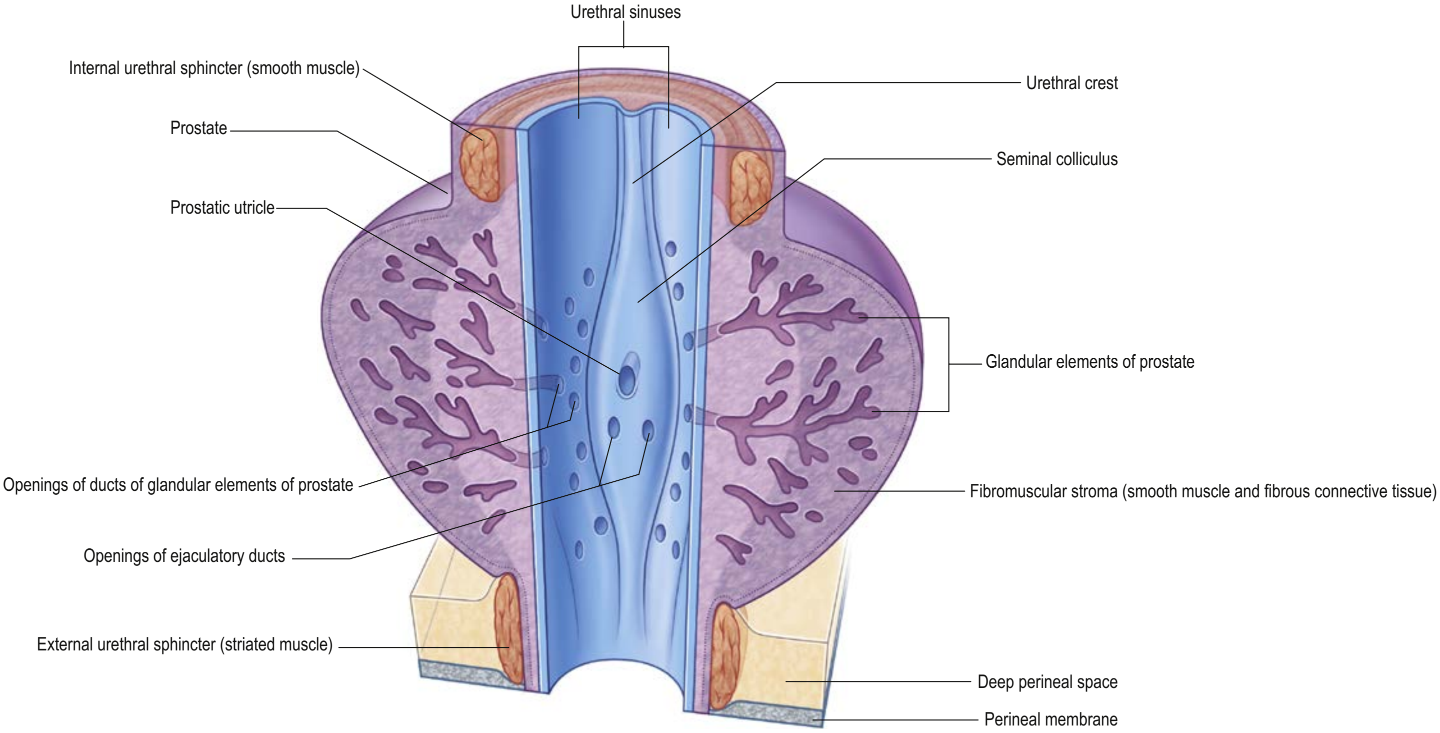
Urethral sinuses
Internal urethral sphincter (smooth muscle)
Urethral crest
Prostate
Seminal colliculus
Prostatic utricle
Glandular elements of prostate
Openings of ducts of glandular elements of prostate
Fibromuscular stroma (smooth muscle and fibrous connective tissue)
Openings of ejaculatory ducts
External urethral sphincter (striated muscle)
Deep perineal space
Perineal membrane

Fig. 73.11 The prostatic urethra. The raised part of the urethral crest is the seminal colliculus. (With permission from Drake RL, Vogl AW, Mitchell A (eds) Gray's Anatomy for Students, 2nd ed. Philadelphia: Elsevier, Churchill Livingstone. Copyright 2010.)

Innervation

The prostatic plexus supplies the smooth muscle of the prostate and prostatic urethra (see Fig. 73.8). On each side, it is derived from the inferior hypogastric plexus and lies on the posterolateral aspect of the seminal gland and prostate. The cavernous nerves of the penis pierce the bulb of the penis to innervate the corpora cavernosa. Sympathetic nerves that supply the internal urethral sphincter are derived from the inferior hypogastric plexus as it descends in the pelvis adjacent to the prostate; they function to prevent retrograde ejaculation. Parasympathetic preganglionic axons arise from neuronal cell bodies in the second to fourth sacral spinal cord segments. The nerve supply of the external urethral sphincter is controversial. It is generally believed to be supplied by neurones in the nucleus of the pudendal nerve (Onuf's nucleus) travelling in branches of the inferior hypogastric plexus and by perineal branches of the pudendal nerve lying on the perineal aspect of the pelvic diaphragm; in both instances, the axons arise from neurones in the second to fourth sacral spinal segments. In addition to somatic nerve fibres, immunohistochemical labelling has characterized sympathetic and parasympathetic fibres to the external urethral sphincter (Bessede et al 2016). Fibres from the nucleus of the pudendal nerve (somatic) travel with the inferior hypogastric plexus on each side; they subsequently branch off to run on the pelvic aspect of the pelvic diaphragm to enter the membranous urethra.

Microstructure

The epithelium lining the intramural part of the urethra and the proximal prostatic urethra is a typical urothelium (see Fig. 73.9). It is continuous with the urothelium lining the bladder and with the epithelium lining the prostatic ducts and ducts of the bulbo-urethral glands, the seminal glands and the ducti deferentia and ejaculatory ducts. These relations are important in the spread of urinary tract infections.

The epithelium below the openings of the ejaculatory ducts changes to a pseudostratified or stratified columnar type that also lines the membranous urethra and most of the spongy urethra. Mucus-secreting cells are common throughout this epithelium and frequently occur in small clusters in the spongy urethra. Branching tubular urethral glands secrete protective mucus on to the urethral epithelial lining and are especially numerous on its dorsal aspect. In the older male, many of the deep recesses of the urethral mucosa contain concretions similar to those found within prostatic glands (see Fig. 73.19A). Towards the distal end of the spongy urethra the epithelium changes once again, and becomes stratified squamous with well-defined connective tissue papillae. This type of epithelium also lines the navicular fossa and becomes keratinized at the external urethral orifice. The epithelial cells lining the navicular fossa are glycogen-rich, potentially providing a substrate for commensal lactobacilli that provide a defence against pathogenic organisms.

FEMALE URETHRA

The length of the female urethra increases from 23 mm at birth to 32 mm at 15 years (Hirdes et al 2010): it is approximately 4 cm long and 6 mm in diameter in the adult female. It begins at the internal urethral orifice of the bladder, approximately opposite the middle of the pubic symphysis, and runs anteroinferiorly behind the pubic symphysis, embedded in the anterior wall of the vagina (see Fig. 73.1). It crosses the perineal membrane and normally ends at the external urethral orifice in the vestibule of the vagina as an anteroposterior slit with rather prominent margins, directly anterior to the opening of the vagina and 2.5 cm behind the glans clitoris. It sometimes opens into the anterior vaginal wall. Except during the passage of urine, the anterior and posterior walls of the urethra are in apposition and the epithelium is thrown into longitudinal folds, one of which, on the posterior wall of the canal, is termed the urethral crest. Many small mucous periurethral glands and minute pit-like recesses or lacunae open along the urethra and can give rise to urethral diverticula. On each side, near the distal end of the urethra, the para-urethral glands (Skene's glands) are grouped together and open into the para-urethral ducts; each duct runs down in the submucous tissue and ends in a small aperture on the lateral margin of the external urethral orifice.

Vascular supply and lymphatic drainage

Urethral artery

The urethra is supplied principally by the vaginal artery, but also receives a supply from the inferior vesical artery.

Veins

The venous plexus around the urethra drains into the vesical venous plexus around the neck of the bladder and into the internal pudendal veins (see Fig. 75.3). An erectile plexus of veins along the length of the urethra is continuous with the erectile tissue of the vestibular bulb.

Lymphatic drainage

The lymphatics of the distal urethra drain into the internal and external iliac nodes, while those of the proximal urethra drain into the iliac, obturator and sacral nodes.

Innervation

Parasympathetic preganglionic axons arise from neuronal cell bodies in the intermediolateral nuclei of the intermediate column of grey matter of the second to fourth segments of the sacral part of the spinal cord, run in the pelvic splanchnic nerves, and synapse in the vesical plexus in or near the bladder wall (see Fig. 75.5B). Postganglionic fibres are distributed to the smooth muscle of the urethral wall. Somatic fibres to the skeletal muscle are also derived from the second to fourth segments of the sacral part of the spinal cord, and run in the pelvic splanchnic nerves but do not synapse in the vesical plexus. Sensory (visceral afferent) fibres run in the pelvic splanchnic nerves to the second to fourth segments of the sacral part of the spinal cord. Postganglionic sympathetic fibres arise from the plexus around the vaginal arteries.

Microstructure

The mucosa lining the female urethra consists of a stratified epithelium and a supporting lamina propria of loose fibroelastic connective tissue. The latter is bulky and well vascularized, and contains numerous thin-walled veins. Its abundant elastic fibres are orientated both longitudinally and circularly around the urethra. The lamina propria contains a fine nerve plexus, believed to be derived from sensory branches of the pudendal nerves. The proximal part of the urethra is lined by urothelium, identical in appearance to that of the neck of the bladder. Distally, the epithelium changes into a non-keratinized stratified squamous type that lines the major portion of the female urethra. This epithelium is keratinized at the external urethral orifice, where it becomes continuous with the skin of the vestibule of the vagina.

The wall of the female urethra consists of an outer muscular layer and an inner mucosa, which lines the lumen and is continuous with that of the bladder. The muscular layer consists of an outer sheath of skeletal muscle together with an inner coat of smooth muscle fibres. The female external urethral sphincter is anatomically separate from the adjacent periurethral skeletal muscle of the anterior part of the pelvic diaphragm. The muscle cells forming the external urethral sphincter are all small diameter, slow-twitch fibres.

The smooth muscle coat extends throughout the length of the urethra and consists of slender muscle bundles, most of which are orientated obliquely or longitudinally. A few circularly arranged muscle fibres occur in the outer aspect of the non-striated muscle layer and intermingle with the skeletal muscle fibres forming the inner part of the external urethral sphincter. Proximally, the smooth muscle of the urethra extends as far as the neck of the bladder, where it is replaced by fascicles of detrusor. This region of the female urethra lacks a well-defined circular smooth muscle component comparable with that of the male internal urethral sphincter. Distally, urethral smooth muscle bundles terminate in the subcutaneous adipose tissue surrounding the external urethral orifice.

The smooth muscle of the female urethra receives an extensive, presumptively cholinergic parasympathetic nerve supply but contains relatively few noradrenergic nerves. In the absence of an anatomical neck of the bladder sphincter, competence of the female neck of the bladder and proximal urethra is unlikely to depend totally on smooth muscle activity and is more probably related to the support provided by the ligamentous structures that surround them. The innervation and longitudinal orientation of most of the muscle fibres suggest that urethral smooth muscle in the female is active during micturition, serving to shorten and widen the lumen of the urethra.

MICTURITION AND URINARY CONTINENCE

The central integration of nervous control of the bladder and urethra is essential for normal micturition (**Fig. 73.13**). (For further reading see de Groat et al (2015), Bertrand et al (2016).)

Micturition consists of storage and voiding phases and is controlled primarily at cortical, pontine and spinal centres (Weledji et al 2019). Recent imaging studies have also shown that the cerebellum and thalamus are involved (Harvie et al 2019). During the storage phase the bladder accommodates an increasing volume of urine with no change in intravesical pressure, partly because of the viscoelastic properties of its walls and partly because a gating mechanism operates in the spinal cord that reflexively inhibits preganglionic parasympathetic activity. A gating mechanism in the pelvic ganglia prevents the activation of postganglionic parasympathetic neurones until preganglionic activity has reached a threshold level (Chancellor and Yoshimura 2002).

Normal functional bladder capacity in adults ranges from approximately 300 to 400 ml, but micturition commonly occurs at smaller volumes. Voluntary control is imposed from the inferior frontal and anterior cingulate gyri of the cerebral cortex. Filling to 500 ml may be tolerated; beyond this level, pain caused by tension in the bladder wall leads to the urgent desire to micturate. The pain is referred to the cutaneous areas supplied by the tenth thoracic to the second lumbar and the second to the fourth sacral spinal nerves, including the lower anterior abdominal wall, perineum and penis or clitoris. Threshold afferent stimulation activates the micturition centre in the rostral pons (the 'M' centre) (see Fig. 73.13), which drives preganglionic parasympathetic neurones in the intermediolateral nuclei of the intermediate column of grey matter of the second, third and fourth sacral spinal cord segments via descending spinal pathways. The axons of these neurones run to the inferior hypogastric plexus in the pelvic splanchnic nerves; they synapse on postganglionic neurones in ganglia lying within the plexus and in the wall of the bladder. Postganglionic axons ramify throughout the thickness of the detrusor muscle: when stimulated these axons release acetylcholine, which activates muscarinic receptors in detrusor and produces the sustained bladder contraction required for micturition. The external urethral sphincter maintains urethral closure.

Clinical urodynamic studies have demonstrated a number of age-related changes in the lower urinary tract, including reduced bladder capacity; increased uninhibited detrusor contractions; decreased urinary flow rate; and diminished urethral pressure profile (particularly in females) (Siroky 2004).

Urinary continence in the male

Urinary continence at the level of the membranous urethra is mediated by the radial folds of urethral mucosa, the submucosal connective tissue, the urethral smooth muscle, the striated external urethral sphincter and puboperinealis (**Fig. 73.14**). The external urethral sphincter represents the point of highest intraurethral pressure in the normal, contracted, state. The striated muscle component of the external urethral sphincter is devoid of muscle spindles. The skeletal muscle fibres themselves are unusually small in cross-section (15–20 μm in diameter) and are physiologically of the slow twitch type, unlike the pelvic diaphragm, which is a heterogeneous mixture of slow and fast twitch fibres of larger diameter. The slow twitch fibres of the external urethral sphincter are capable of sustained contraction over relatively long periods of time and actively contribute to the tone that closes the urethra and maintains urinary continence. They are innervated by neurones that lie in the nucleus of the pudendal nerve in the anterolateral nuclei of the anterior column of grey matter of the second to fourth sacral spinal cord segments. Their firing is controlled centrally by a storage centre within the rostral pons (the 'L' centre) (see Fig. 73.13). Just before the onset of voiding, the external urethral sphincter is relaxed by central inhibition of the nucleus of the pudendal nerve.

Urinary continence in the female

The urethral sphincter mechanism consists of the intrinsic striated and smooth muscle of the urethra, the mucosa and submucosal connective tissue, and puboanalis (which surrounds the urethra at the point of maximum concentration of those muscles). The striated muscle component of the urethral sphincter mechanism surrounds the middle and lower thirds of the urethra in the female. Proximally, it forms a complete ring around the urethra; more distally, it covers the anterior and lateral aspects of the urethra. It blends above with the smooth muscle of the neck of the bladder and below with the smooth muscle of the distal urethra and vagina. Contraction of this part of the sphincter compresses the urethra against the relatively fixed anterior vaginal wall. The external urethral sphincter has two subdivisions; inferolateral extensions to the ischial rami (compressor urethrae) and a circumferential band encompassing the urethra and vagina (urethrovaginal sphincter). The mucosa and submucosa of the urethra are oestrogen-dependent and atrophy postmenopausally, possibly resulting in stress incontinence.

PROSTATE

The prostate is a globular fibromuscular gland that surrounds the prostatic urethra from the fundus of the bladder to the membranous urethra (Myers 2001). It is enclosed by firmly adherent tissue (endopelvic fascia covering the adjacent part of levator ani) that has been variously termed the capsule of the prostate or the fascia of the prostate (Myers et al 2010) (**Fig. 73.15**). Histologically, it is a multilayered connective tissue (Hinata et al 2013). There is no true fibrous capsule at the base or apex of the prostate.

The muscular tissue within the prostate is mainly smooth muscle. Anterior to the urethra, a layer of smooth muscle merges with the main mass of muscle in the fibromuscular septa; it blends superiorly with vesical smooth muscle. Anterior to this layer, a transversely crescent-shaped mass of skeletal muscle is continuous inferiorly with the external urethral sphincter in the deep perineal space. Its fibres pass

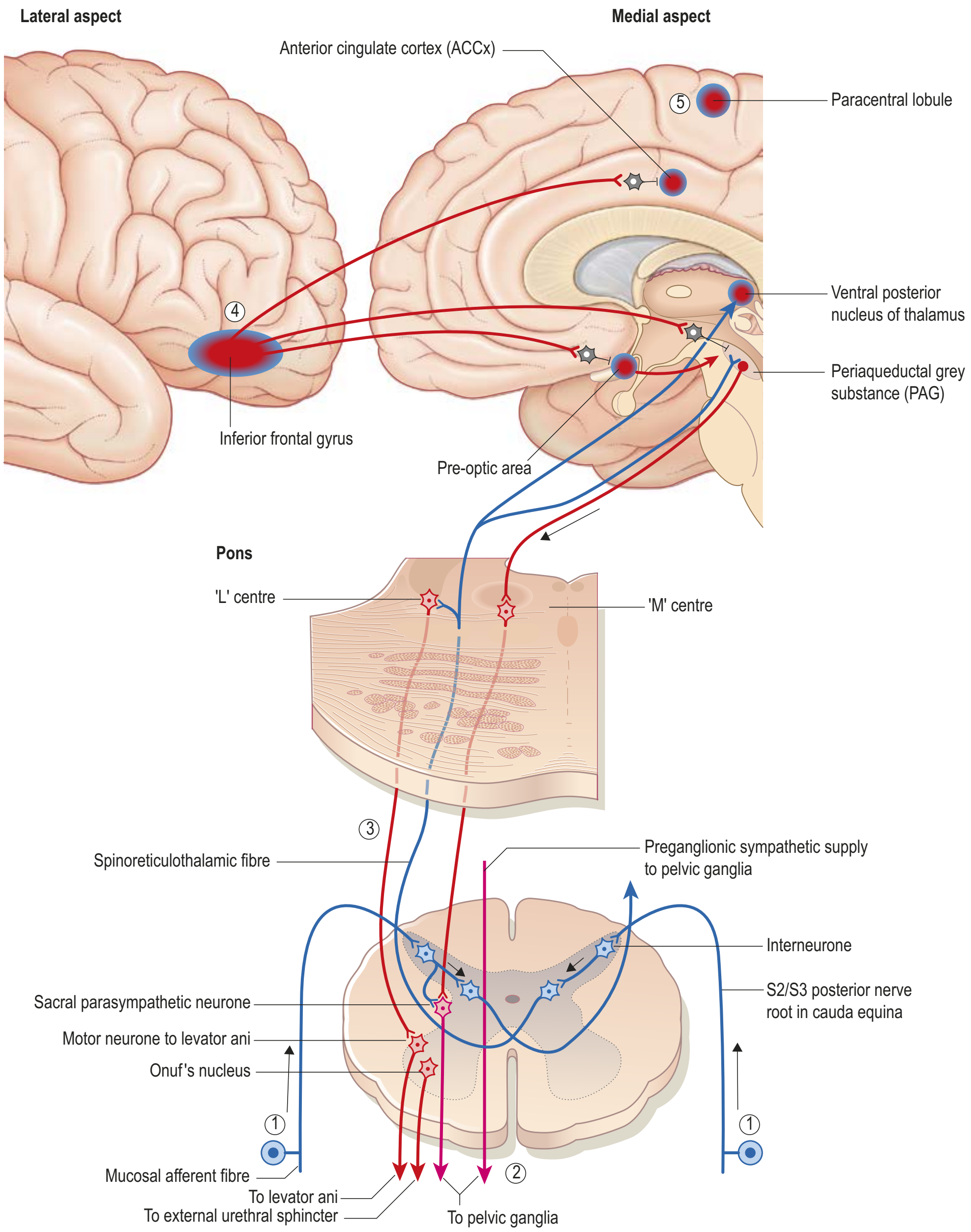
Lateral aspect
Medial aspect
Anterior cingulate cortex (ACCx)
⑤
Paracentral lobule
④
Ventral posterior nucleus of thalamus
Periaqueductal grey substance (PAG)
Inferior frontal gyrus
Pre-optic area
Pons
'L' centre
'M' centre
③
Spinoreticulothalamic fibre
Preganglionic sympathetic supply to pelvic ganglia
Interneurone
Sacral parasympathetic neurone
S2/S3 posterior nerve root in cauda equina
Motor neurone to levator ani
Onuf's nucleus
①
①
Mucosal afferent fibre
②
To levator ani
To external urethral sphincter
To pelvic ganglia

Fig. 73.13 The micturition control centre in the paramedian pontine reticular formation on each side consists of a medially placed micturition centre, 'M', and a laterally placed storage centre, 'L'. Neurones project from the 'M' centre and the storage centre 'L' to parasympathetic neurones in segments 2–4 of the sacral spinal cord, and to the motor neurone pool of the pudendal nerve, which is in the same segments and contains neurones that innervate the external urethral sphincter. At higher levels, neurones in the right prefrontal and anterior cingulate cortex, right preoptic nucleus and periaqueductal grey substance are involved in the control of micturition. Vesical afferents from stretch receptors in detrusor and trigonal mucosa relay the extent of bladder filling to the brain stem and thalamus via spinoreticulothalamic fibres (1). Parasympathetic activity and activity in the sympathetic system that maintains increases in bladder compliance (via β_2 receptors on detrusor fibres) is inhibited (2). Spinoreticular tract fibres synapsing in the 'L' nucleus in the pons activate the nucleus of the pudendal nerve to increase the tone of external urethral sphincter (3). If micturition is deferred, fibres projecting from the inferior frontal gyrus inhibit the right anterior cingulate gyrus, preoptic area and periaqueductal grey substance (4). Voluntary contraction of the pelvic diaphragm, controlled by the prefrontal cortex driving the perineal 'area' of the motor cortex (5), cannot be long sustained once filling is complete. (With permission from FitzGerald MJT, Folan-Curren J 2001 Clinical Neuroanatomy, 4th ed. London: Saunders.)

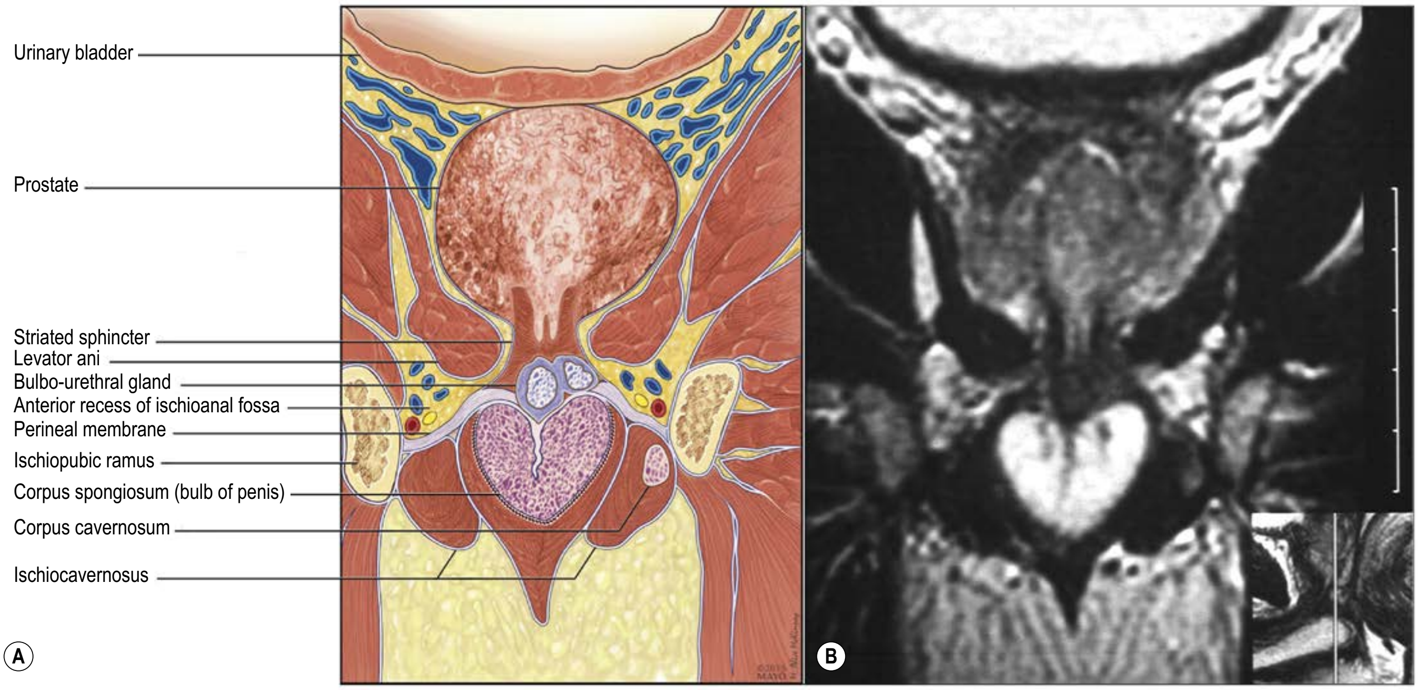
Urinary bladder
Prostate
Striated sphincter
Levator ani
Bulbo-urethral gland
Anterior recess of ischioanal fossa
Perineal membrane
Ischiopubic ramus
Corpus spongiosum (bulb of penis)
Corpus cavernosum
Ischiocavernosus
A
B

Fig. 73.14 A, Illustration of a coronal section through the male pelvis: prostate above, intervening striated urethral sphincter and perineal membrane with corporal bodies below. **B**, This coronal T2-weighted MRI includes the cephalad extension of the smooth muscle internal urethral sphincter, which cannot be discriminated from striated external urethral sphincter; bulbo-urethral glands are offset from expected symmetry. (A, B Courtesy of Robert P Myers MD, Akira Kawashima MD and Bernard F King MD, used with permission of Mayo Foundation for Medical Education and Research.)

transversely internal to the capsule and are attached to it laterally by diffuse collagen bundles; other collagen bundles pass posteromedially, merging with the prostatic fibromuscular septa and the urethral crest. This muscle, supplied by the pudendal nerve, probably compresses the urethra but it can also pull the urethral crest back and the prostatic sinuses forwards, dilating the urethra. Glandular contents may be expelled simultaneously into the urethra when it has expanded in this way, so that it contains 3–5 ml of seminal fluid prior to ejaculation.

The prostate lies at a low level in the lesser pelvis, behind the inferior border of the pubic symphysis and pubic arch (see Fig. 73.2A; **Figs 73.16–73.17**) and anterior to rectourethralis and the rectal ampulla, through which it can be palpated. It presents a base superiorly, an apex inferiorly, and posterior, anterior, lateral and posterolateral surfaces. The base of the prostate measures about 4 cm transversely. The gland is approximately 2 cm in its anteroposterior diameter and 3 cm in its vertical diameter. It weighs about 8 g in youth but almost invariably enlarges with the development of BPH; it usually weighs 40 g, but sometimes as much as 150 g or even more after the first five decades of life. The small prostate without BPH is described as a croissant shape and the enlarged gland is more doughnut-shaped. The shape of the prostate affects the relation of its apex to external urethral sphincter. This relationship is important when the prostate is removed at radical prostatectomy for cancer, and anastomosing the bladder to the urethra to maintain sphincter integrity. External urethral sphincter is flush to a large doughnut-type gland, so a perpendicular incision will separate the prostate and external urethral sphincter accurately. With a small prostate, external urethral sphincter fills the defect in the anterior aspect of the gland, so a perpendicular incision at the level of the posterior lip of the croissant-shaped gland will excise much of external urethral sphincter and leave the patient incontinent.

Superiorly, the base of the prostate is largely contiguous with the neck of the bladder. The apex is inferior, surrounding the junction of the prostatic and membranous parts of the urethra. The posterior relation of the apex of the prostate and external urethral sphincter is rectourethralis, a Y-shaped smooth muscle that originates from the outer longitudinal layer of the rectum posteriorly and travels to the membranous urethra anteriorly. Some fibres of this muscle insert laterally into levator ani (Muro et al 2018).

The anterior surface lies in the pubic arch, separated from it by the dorsal vascular complex (Santorini's plexus) and loosely attached adipose tissue. It is transversely narrow and convex, extending from the apex to the base of the gland. Near its superior limit it is connected to the pubis by the puboprostatic ligaments. The urethra emerges from this surface anterosuperior to the apex of the gland. The anterior part of the prostate is relatively deficient in glandular tissue and is largely composed of fibromuscular tissue. The anterior and lateral aspects of the prostate are covered by a layer of fascia derived from the endopelvic fascia on each side, called the fascia of the prostate. This adheres medially to the prostate, continues posteriorly over the lateral aspect of the prostate, neurovascular bundles and rectum (lateral rectal fascia), and passes distally over the urethra (see Fig. 73.15A). The prostatic venous plexus (see Fig. 73.16) lies between this extension of the endopelvic fascia and the prostate. Anteroinferiorly, the endopelvic and visceral fasciae of the prostate merge and blend with the puboprostatic ligaments. The anterior surface of the prostate and associated vascular plexus is covered by the detrusor apron (Myers 2002).

The inferolateral surfaces are related to the muscles of the pelvic side wall; the anterior fibres of levator ani embrace the prostate as the puboperinealis (Myers et al 2000). This muscle is separated from the prostate by a thin layer of connective tissue.

The posterior surface of the prostate is transversely flat and vertically convex. Near its base is a depression where it is penetrated by the two ejaculatory ducts. Below this, a shallow median sulcus is usually considered to mark a partial separation of the prostate into right and left lobes. The prostate is separated from the rectum by fatty areolar tissue and by the prostato-seminal fascia, a condensation of pelvic fascia that develops by obliteration of the rectovesical pouch from below upwards as fetal life progresses. At birth, the prostato-seminal fascia separates the prostate, the seminal glands and the ampullae of the ducti deferentia from the rectum. The superior limit of the prostato-seminal fascia is formed by the peritoneum of the rectovesical pouch; laterally, the fascia fuses with the lateral pelvic fascia. The lateral pelvic fascia is called the lateral fascia of the prostate anterior to the prostato-seminal fascia, and the lateral rectal fascia posterior to the prostato-seminal fascia.

The prostate is traversed by the urethra and ejaculatory ducts and contains the prostatic utricle. The urethra enters the prostate near its

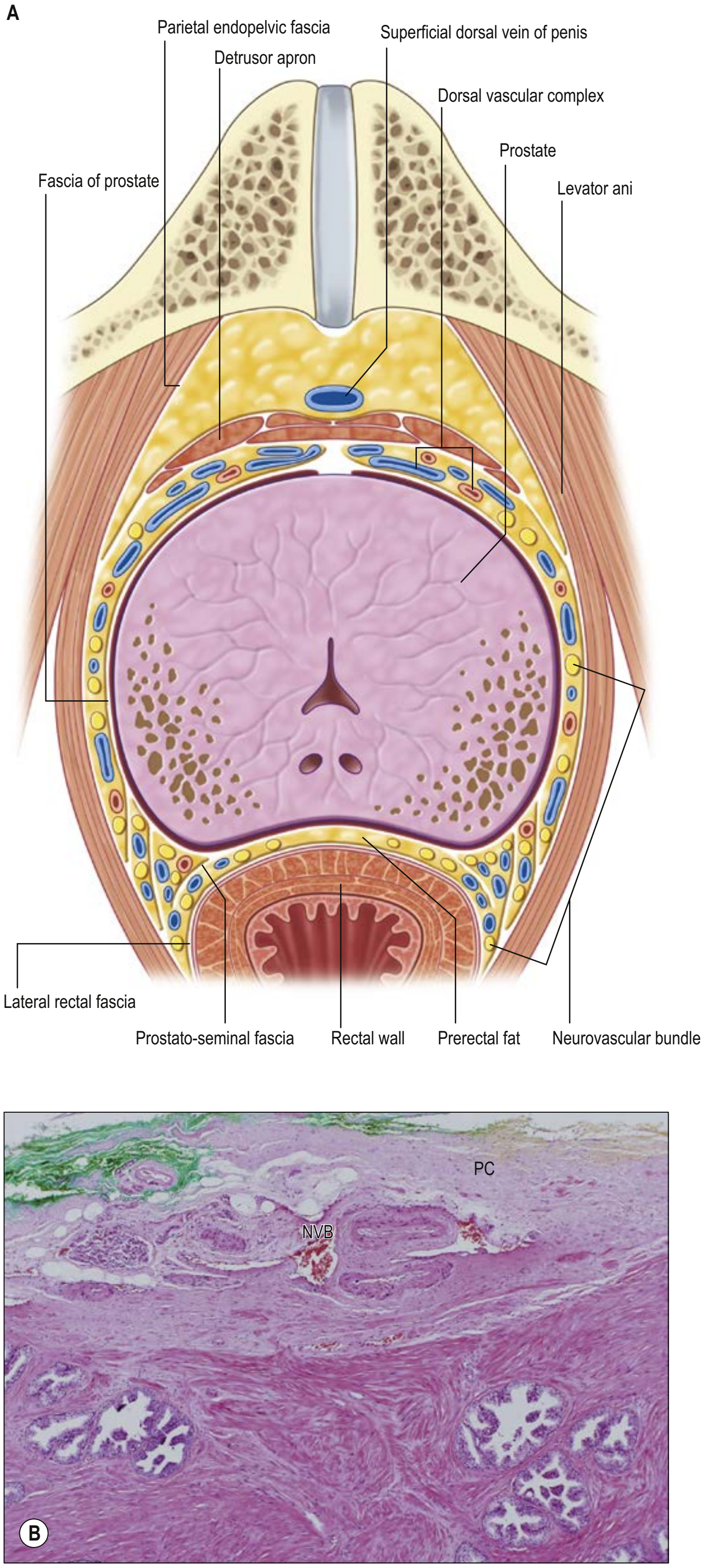

Fig. 73.15 A, The endopelvic fascia. The fascia covers the pelvic viscera and continues posteriorly over the lateral aspect of the prostate as the lateral fascia of the prostate and, on the lateral aspect of the rectum, as the lateral rectal fascia. Its relationship with the prostato-seminal fascia can be visualized as an 'H'. The deep dorsal vein and lateral branches run deep to the endopelvic fascia and the lateral fascia of the prostate, although they communicate with venous perforators to the pelvic side wall. The prostato-seminal fascia adheres to the prostate in the posterior midline but, like the lateral fascia of the prostate, is separated from the prostatic tissue by the neurovascular structures and fatty tissues elsewhere. Between the prostato-seminal fascia and the rectum is a fatty potential plane, clinically referred to as the prerectal space. **B**, The capsule of the prostate (PC) is a condensation of connective tissue (green) on the surface of the gland and encloses the neurovascular bundle (NVB). The prostatic fibromuscular stroma and glands lie beneath the capsule. (C, *continued online*)

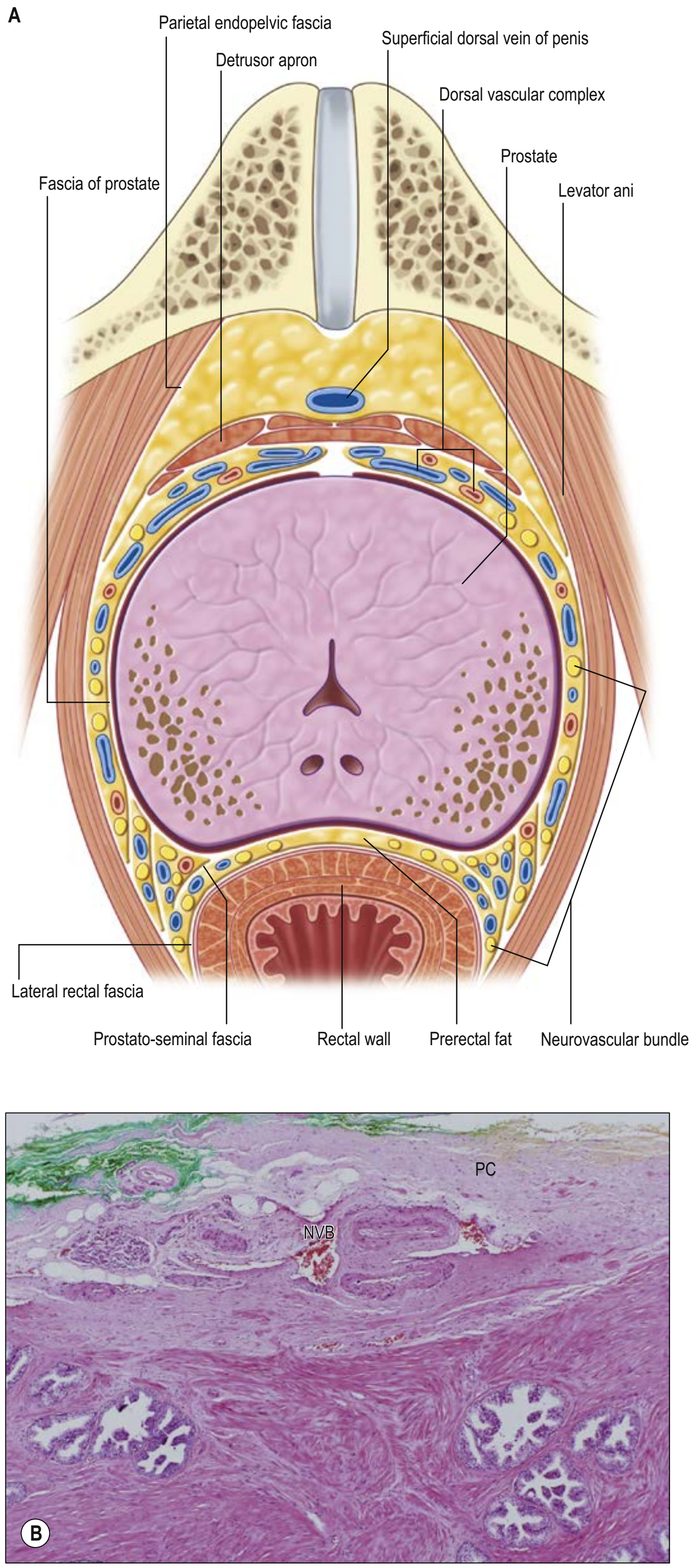
A
Parietal endopelvic fascia
Superficial dorsal vein of penis
Detrusor apron
Dorsal vascular complex
Prostate
Fascia of prostate
Levator ani
Lateral rectal fascia
Prostato-seminal fascia
Rectal wall
Prerectal fat
Neurovascular bundle
PC
NVB
B

Fig. 73.15 **A**, The endopelvic fascia. The fascia covers the pelvic viscera and continues posteriorly over the lateral aspect of the prostate as the lateral fascia of the prostate and, on the lateral aspect of the rectum, as the lateral rectal fascia . Its relationship with the prostato-seminal fascia can be visualized as an ‘H’. The deep dorsal vein and lateral branches run deep to the endopelvic fascia and the lateral fascia of the prostate, although they communicate with venous perforators to the pelvic side wall. The prostato-seminal fascia adheres to the prostate in the posterior midline but, like the lateral fascia of the prostate, is separated from the prostatic tissue by the neurovascular structures and fatty tissues elsewhere. Between the prostato-seminal fascia and the rectum is a fatty potential plane, clinically referred to as the prerectal space. **B**, The capsule of the prostate (PC) is a condensation of connective tissue (green) on the surface of the gland and encloses the neurovascular bundle (NVB). The prostatic fibromuscular stroma and glands lie beneath the capsule. (C, continued online)

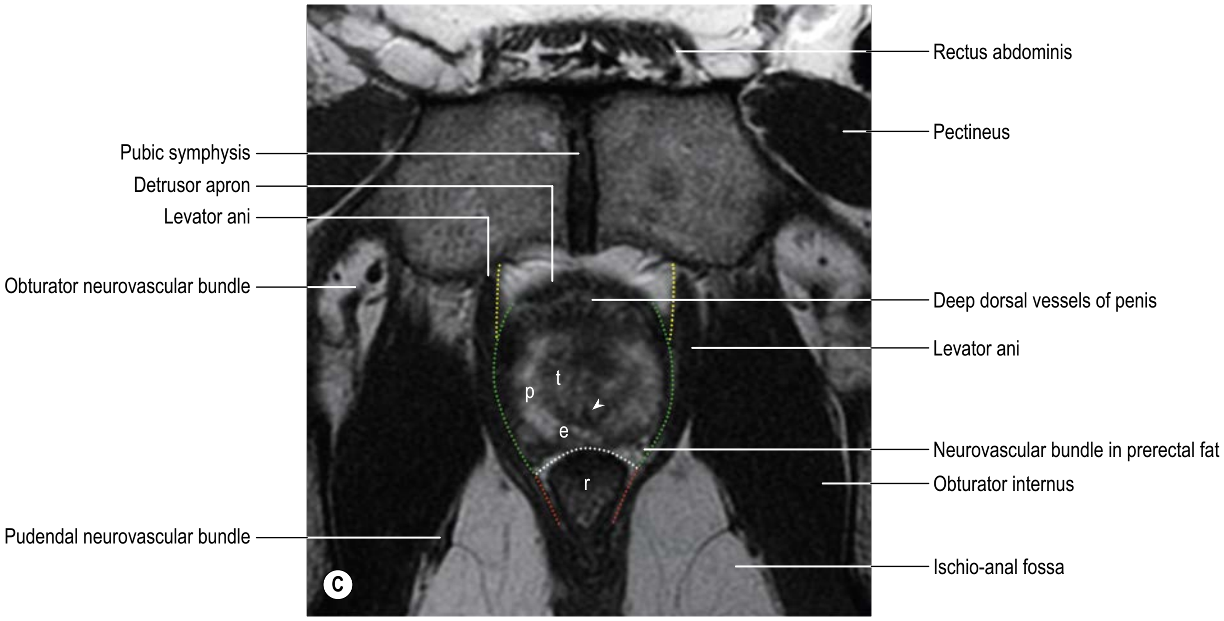
Rectus abdominis
Pectineus
Pubic symphysis
Detrusor apron
Levator ani
Obturator neurovascular bundle
Deep dorsal vessels of penis
Levator ani
p
t
e
r
Neurovascular bundle in prerectal fat
Obturator internus
Pudendal neurovascular bundle
Ischio-anal fossa
C

Fig. 73.15, cont'd C, A T2-weighted high resolution axial MRI of the prostate showing the courses of the endopelvic fascia as colour coded dotted lines: parietal endopelvic fascia (yellow); lateral prostatic fascia (green); lateral rectal fascia (red); Denonvilliers' fascia (white). The prostatic urethra is marked with an arrowhead. Abbreviations: e, ejaculatory duct; p, peripheral zone of prostate; r, rectum; t, transitional zone of prostate.

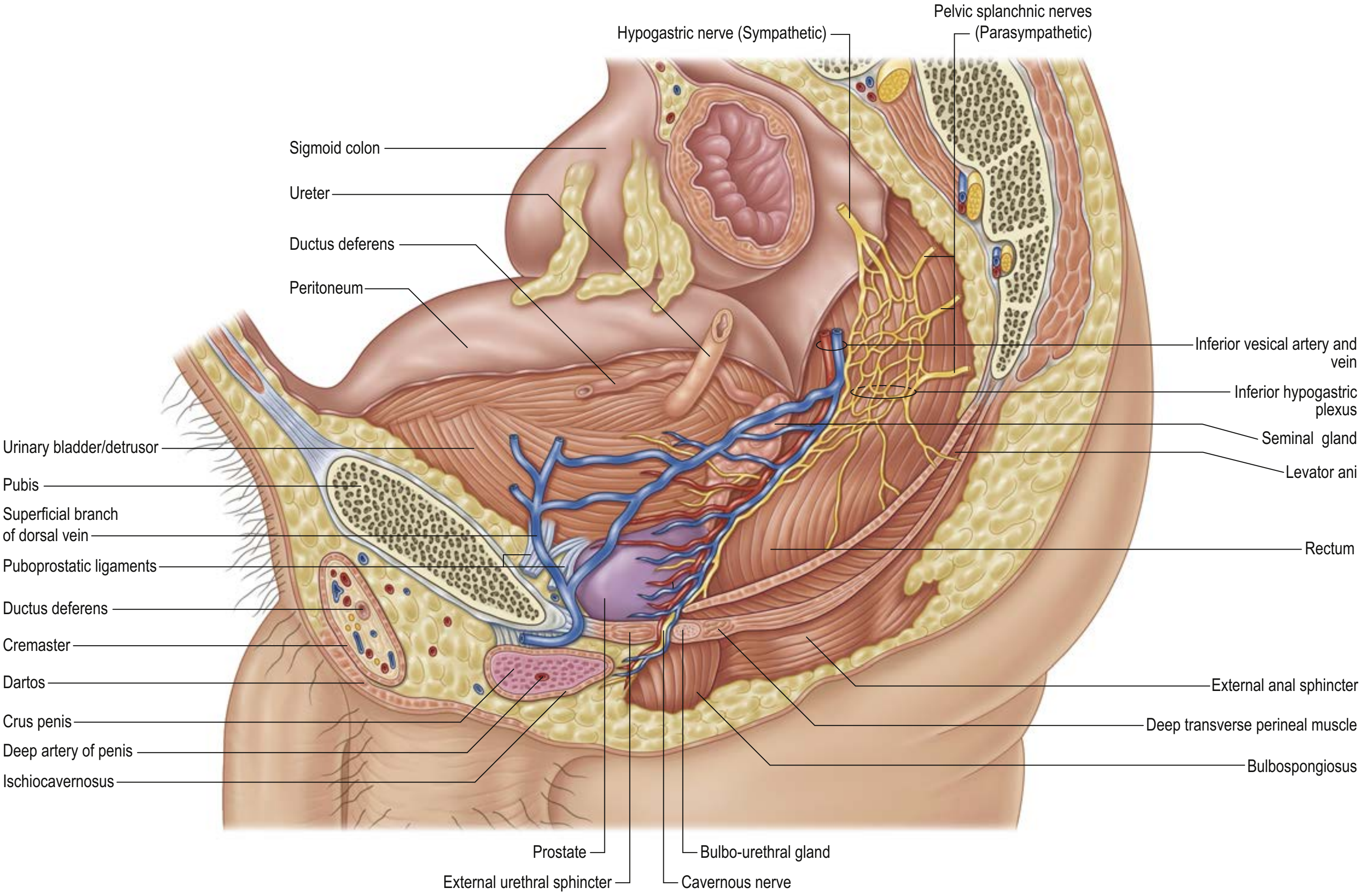
Hypogastric nerve (Sympathetic)
Pelvic splanchnic nerves (Parasympathetic)
Sigmoid colon
Ureter
Ductus deferens
Peritoneum
Inferior vesical artery and vein
Inferior hypogastric plexus
Seminal gland
Levator ani
Urinary bladder/detrusor
Pubis
Superficial branch of dorsal vein
Puboprostatic ligaments
Ductus deferens
Cremaster
Dartos
Crus penis
Deep artery of penis
Ischiocavernosus
Rectum
External anal sphincter
Deep transverse perineal muscle
Bulbospongiosus
Prostate
External urethral sphincter
Bulbo-urethral gland
Cavernous nerve

Fig. 73.16 A sagittal section of the male pelvis. The inferior hypogastric plexus lies with its midpoint level with the tip of the seminal glands. It gives branches to the prostate, bladder urethra, seminal glands, rectum and corpora cavernosa via the cavernous nerves. The cavernous nerves are the continuation of the neurovascular bundles, lying posterolateral to the prostate. These bundles can be injured at radical prostatectomy, resulting in impotence.

anterior border and usually passes between its anterior and middle thirds. The ejaculatory ducts pass anteroinferiorly through its posterior region to open into the prostatic urethra.

Zonal anatomy of the prostate

Based largely on histological studies, the prostate was once thought to be divided into five anatomical 'lobes' during early fetal life. Lowsley (1912) described five bilateral groups of prostatic buds that he designated as lobes: it is now recognized that prostatic bud initiation during development is stochastic, and that prostatic buds emerge and recede during the budding process (Cunha et al 2018, Shen et al 2018). In humans, until the onset of BPH, only three lobes are recognizable: left, right and middle lobes. Clinicians refer to left and right 'lobes' when they describe either what can be felt during transrectal palpation, or the endoscopically visible abnormalities in the diseased state when prostatic anatomy is distorted by, for example, BPH.

From an anatomical, and particularly from a morbid anatomical, perspective, the glandular tissue can be subdivided into three distinct zones (**Fig. 73.18**): peripheral (70% by volume), central (25% by volume) and transition (5% by volume) (Mundy et al 1999b). The zonal anatomy of the prostate is clinically important because most carcinomas arise in the peripheral zone, whereas BPH affects the transition zone, which may grow to form the bulk of the prostate (Yacoub and Oto 2018).

Non-glandular tissue (fibromuscular stroma) fills the space between the peripheral zones anterior to the intramural part of the urethra. The central zone surrounds the ejaculatory ducts posterior to the intramural part of the urethra and is more or less conical in shape, with its apex at the seminal colliculus. The fibromuscular stroma includes the smooth muscle detrusor apron superoanteriorly and striated urethral sphincter fibres that extend anteriorly over the anterior prostate on to the neck of the bladder. The transition zone lies around the distal part of the intramural part of the urethra just proximal to the apex of the central zone and the ejaculatory ducts; it includes the smooth muscle of the intramural part of the urethra. Its ducts enter the prostatic urethra just below the internal urethral sphincter and just above the ducts of the peripheral zone. The peripheral zone is cup-shaped and encloses the central transition zone and the intramural part of the urethra, except anteriorly, where the space is filled by the anterior fibromuscular stroma. Simple mucus-secreting glands lie in the tissue around the intramural part of the urethra, above the transition zone and surrounded by the internal urethral sphincter. These simple glands are similar to those in the female urethra and unlike the glands of the prostate.

On magnetic resonance imaging (MRI), the prostate has a zonal anatomy on T2-weighted images (see Fig. 73.17AB). The normal peripheral zone has high-signal intensity, as does fluid within the seminal glands. The central and transition zones have relatively low signal intensity and are often referred to as the 'central gland'. The seminal colliculus can be seen as high-signal within the central gland. The relations of the zones of the gland normally change with age. The central zone atrophies and the transition zone enlarges secondary to BPH. This often produces a low-signal band at the margin of the hypertrophied transition and compressed peripheral zones: the surgical pseudocapsule, which is well seen on T2-weighted MRI (Yacoub and Oto 2018).

As the transition zone grows, it produces the appearance of 'lobes' on either side of the urethra. In due course, these lobes can compress or distort the intramural and prostatic parts of the urethra and produce symptoms. The central zone surrounding the ejaculatory ducts is rarely involved in any disease. It shows certain histochemical characteristics that differentiate it from the rest of the prostate; it is thought to be derived from the mesonephric ducts (much like the epididymi, ducti deferentia and seminal glands), whereas the rest of the prostate is derived from the urogenital sinus (Ch. 22).

Vascular supply and lymphatic drainage

Arteries

The prostate is supplied by branches arising variably from the anterior division of the internal iliac, obturator, inferior vesical, internal pudendal and middle anorectal arteries or from a common trunk between the internal pudendal and inferior gluteal arteries (see Fig. 73.16). Less

SECTION 8

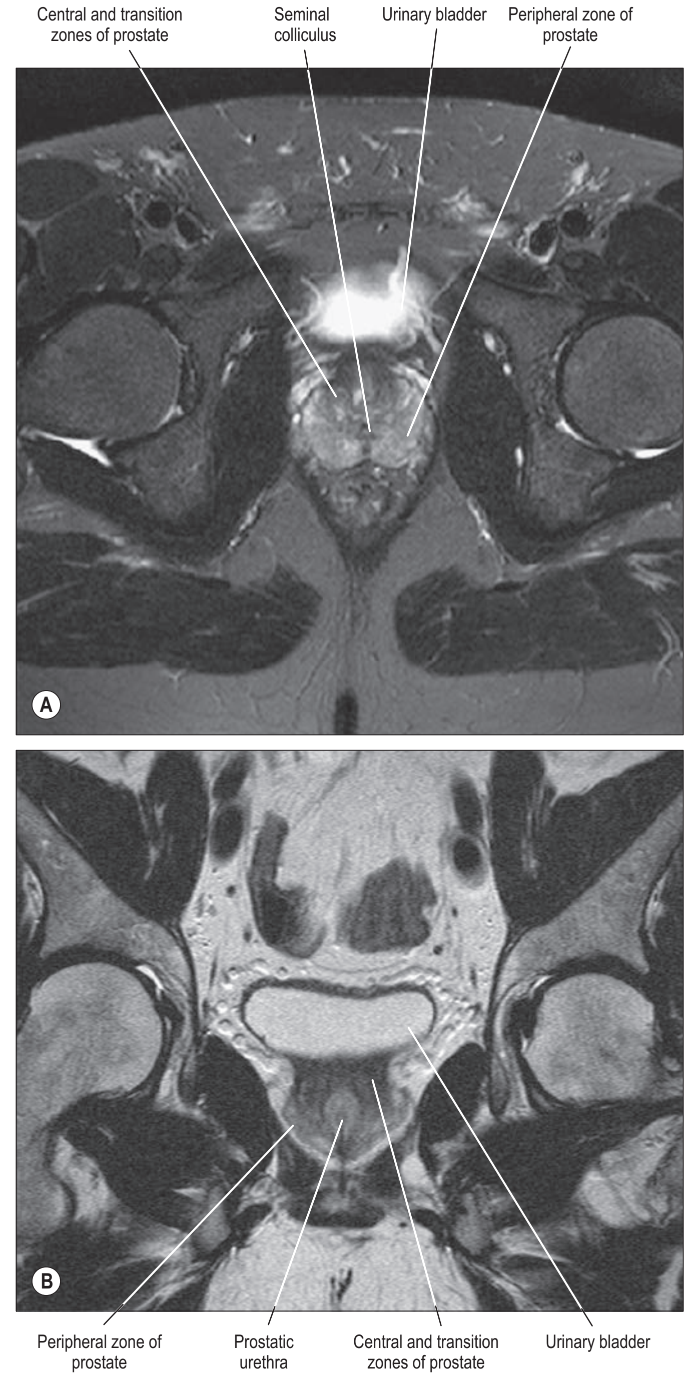
Central and transition zones of prostate
Seminal colliculus
Urinary bladder
Peripheral zone of prostate
A
B
Peripheral zone of prostate
Prostatic urethra
Central and transition zones of prostate
Urinary bladder

Fig. 73.17 Magnetic resonance imaging (MRI) of the prostate. **A**, A T2-weighted MRI showing the normal high signal of the peripheral zone and the intermediate signal of the central and transition zones and the seminal colliculus in the central gland. **B**, A T2-weighted coronal MRI of the prostate showing the zonal anatomy.

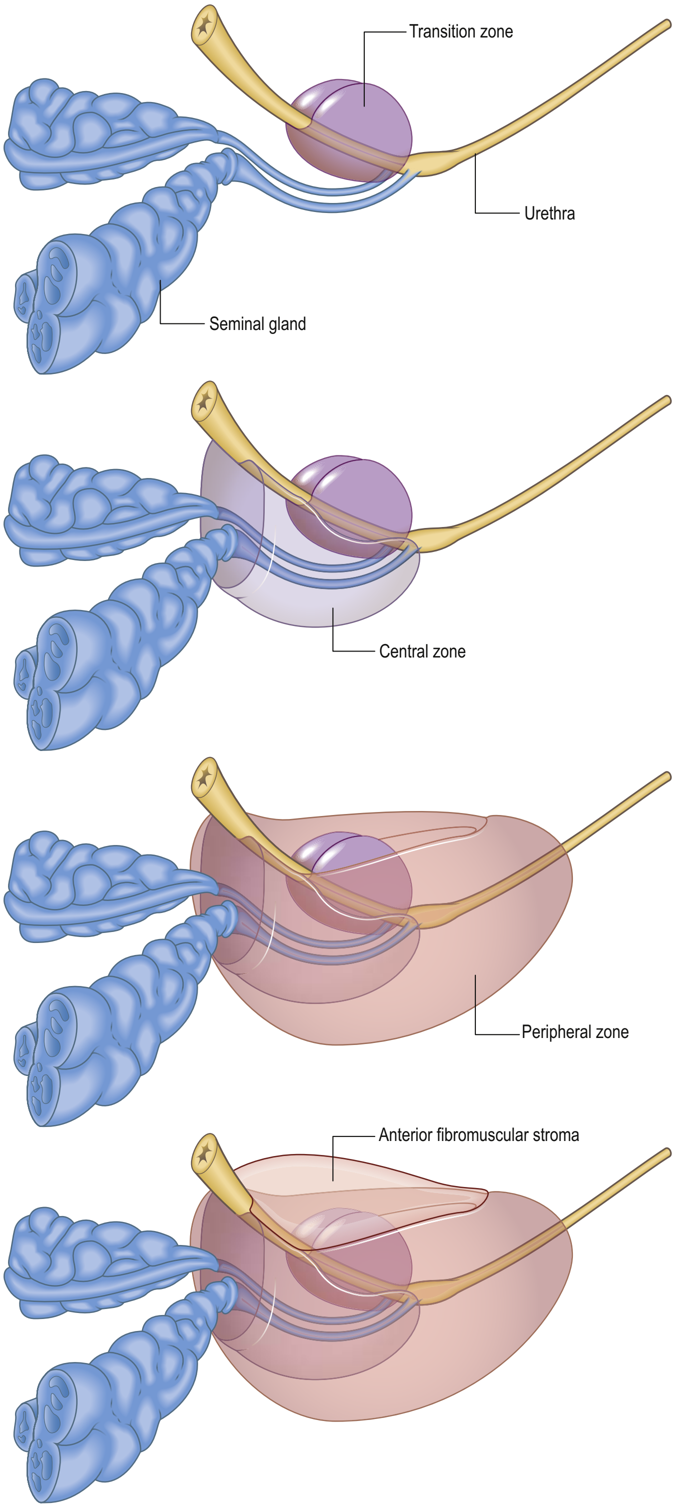
Transition zone
Urethra
Seminal gland
Central zone
Peripheral zone
Anterior fibromuscular stroma

Fig. 73.18 The zonal anatomy of the prostate. (With permission from Walsh PC, Retik AB, Vaughan ED et al (eds) 2002 Campbell's Urology, 8th ed. Philadelphia: Saunders.)

common origins of this vessel include the gluteal arteries, posterior division of the internal iliac artery, and accessory internal pudendal artery (Moya et al 2017). These perforate the gland along a posterolateral line from the junction of the prostate with the bladder down to the apex of the gland.

The inferior vesical artery often arises from the internal iliac artery with the middle anorectal artery. It gives rise to two groups of branches: the urethral and capsular. The urethral vessels enter at the junction between the bladder and prostate, principally posteriorly at the 5 and 7 o'clock positions, but also anteriorly at 1 and 11 o'clock positions. This arterial anatomy around the neck of the bladder is always apparent at transurethral resection of the prostate and open removal of BPH adenomas. The arteries to the capsule of the prostate run posterolaterally and inferiorly in the neurovascular bundles, providing perpendicular perforating vessels to the gland. The most constant in position and prominence is the apical perforator at the prostatourethral junction, an important landmark for this point and for the neurovascular bundle during radical prostatectomy.

Veins

The veins of the prostate run into a venous plexus around its anterolateral aspects, posterior to the inferior pubic ligament and the inferior part of the pubic symphysis. The chief tributary is the deep dorsal vein of the penis. The plexus also receives vesical and prostatic veins (which connect with the vesical venous plexus and internal pudendal vein) and drains into the internal iliac veins.

Lymphatic drainage

Lymphatic vessels from the ductus deferens drain into the external iliac nodes, while those from the seminal glands drain to the internal and external iliac nodes. Lymphatic vessels from the prostate end mainly in the internal iliac, sacral and obturator nodes. A vessel from the posterior surface

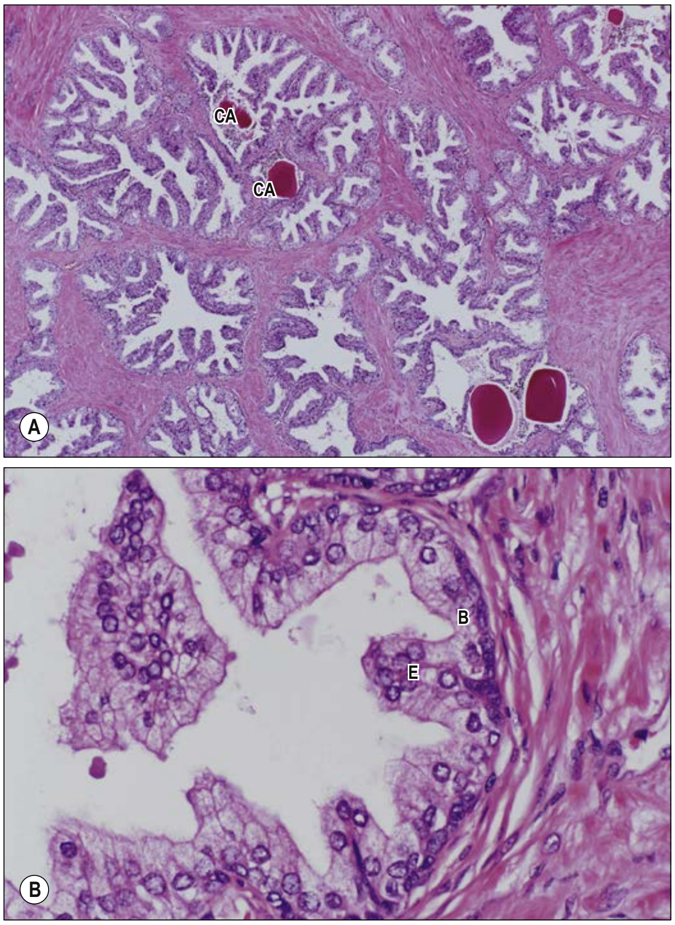

Fig. 73.19 **A**, Prostatic acini show papillary infoldings at the base of the gland (central zone). They are irregularly divided by fibromuscular stroma. Some acini contain eosinophilic (pink) secretions called corpora amylacea (CA) or prostatic concretions (×10, haematoxylin and eosin stain). **B**, Prostatic acini consist of a pseudostratified layer of epithelial cells (E), which line the lumen, including basal cells (B), which give rise to the mature epithelial cells.

of the prostate accompanies the urinary bladder vessels to the external iliac nodes, and another from the anterior surface of the prostate reaches the internal iliac nodes by joining vessels that drain the membranous urethra.

Innervation

The prostate is innervated by the inferior hypogastric plexus (see Figs 59.4, 73.8). The capsule of the prostate is covered by numerous nerve fibres and ganglia posterolaterally, forming the prostatic plexus. The greatest density of nerves is found in the internal urethral sphincter; there are fewer fibres in the anterior fibromuscular stroma, and the peripheral zone is the least densely innervated. Nerves containing neuropeptide Y and vasointestinal polypeptide are located in the subepithelial connective tissue, in the smooth muscle layers of the gland and in the walls of its blood vessels. Neurovascular bundles (Walsh and Donker 1982) containing autonomic nerves that supply the prostate, seminal glands, prostatic urethra, ejaculatory ducts, corpora cavernosa penis, corpus spongiosum penis, membranous and spongy parts of the urethra, and the bulbo-urethral glands are closely applied to, but separable from, the posterolateral surfaces of the prostate. They are intimately related to the fascia of the prostate. These nerves can be injured during radical prostate surgery for organ-confined prostate cancer, causing impotence, or sacrificed as part of wide local excision of the prostate (Tewari et al 2006, Pisipati et al 2014).

The pudendal nerve innervates the external urethral sphincter. The branches enter the muscle at the 5 and 7 o'clock positions. Sensory branches pass to the dorsal penis in association with the dorsal vascular complex and dorsal vein of the penis.

Microstructure

The glandular tissue consists of numerous follicles with frequent internal papillae. Follicles open into elongated canals that join to form 12–20 main ducts. The follicles are separated by loose connective tissue supported by extensions of the fibrous capsule and muscular stroma and enclosed in a delicate capillary plexus. Follicular epithelium is variable but predominantly columnar, and either single-layered or pseudostratified. Small colloid amyloid bodies (corpora amylacea) are frequent in the follicles (Fig. 73.19).

Prostatic ducts open mainly into the prostatic sinuses in the floor of the prostatic urethra. They have a pseudostratified epithelium in which the luminal layer is columnar and the basal layer is populated by small cuboidal cells. Secretions from the prostate and seminal gland form the bulk of seminal fluid: prostatic secretions are slightly acidic and contain acid phosphatase, amylase, prostate-specific antigen, fibrinolysin and zinc. Numerous neuroendocrine cells, containing neurone-specific enolase, chromogranin and serotonin (5-hydroxtryptamine, 5-HT), are present in the glandular epithelium; their numbers decline after middle age and their function is unknown.

Histological sections just above the level of the seminal colliculus reveal two concentric, partially circumurethral, zones of glandular tissue. The larger, outer peripheral zone contains long, branched glands with ducts that open mainly into the prostatic sinuses. The inner transition zone contains glands with ducts that open on the floor of the prostatic sinuses and seminal colliculus, and a group of simple mucosal glands that surround the intramural part of the urethra. Anteriorly, the peripheral zone and submucosal glands are absent in the anterior commissure of the prostate.

Age changes in the prostate

At birth, the prostate has a system of ducts embedded in a stroma that forms a large part of the gland. Follicles are represented by small end-buds on the ducts. Before birth, the epithelium of the ducts, seminal colliculus and prostatic utricle display hyperplasia and squamous metaplasia, possibly due to maternal oestrogens in the fetal blood. This subsides after birth and is followed by a period of quiescence lasting for 12–14 years.

At puberty, between the ages of approximately 14 and 18 years, the prostate enters a maturation phase and more than doubles in size. Growth is almost entirely due to follicular development, partly from end-buds on ducts and partly from modification of the ductal branches. Morphogenesis and differentiation of the epithelial cords starts in an intermediate part of the epithelial anlage and proceeds to the urethral and subcapsular parts of the gland; the latter is reached by the age of 17–18 years. The glandular epithelium is initially multilayered squamous or cuboidal and is transformed into a pseudostratified epithelium consisting of basal, exocrine secretory (including mucous) and neuroendocrine cells. The mucous cells are temporary and are lost as the gland matures. The remaining exocrine secretory cells produce a number of products, including acid phosphatase, prostate-specific antigen and β-microseminoprotein. Growth of the secretory component is associated with condensation of the stroma, which diminishes relative to the glandular tissue. These changes are probably a response to the secretion of testosterone by the testis.

During the third decade, the glandular epithelium grows by irregular multiplication of the epithelial infoldings into the lumen of the follicles. After the third decade, the size of the prostate remains virtually unaltered until 45–50 years, when the epithelial foldings tend to disappear, follicular outlines become more regular and amyloid bodies increase in number: all signs of prostatic involution. After 45–50 years, the prostate tends to develop BPH: an age-related condition (Roehrborn 2008). If a man lives long enough then BPH is inevitable, although not always symptomatic. Common symptoms include urinary frequency, hesitancy, urgency, nocturia, weak urinary stream and straining to urinate.

BPH begins as micronodules in the transition zone, which grow and coalesce to form macronodules around the inferior margin of the intramural part of the urethra just above the seminal colliculus. Macronodules, in turn, compress the surrounding normal tissue of the peripheral zone posteroinferiorly, creating a 'false capsule' around the hyperplastic tissue, which, coincidentally, provides a plane of cleavage for its surgical enucleation.

Bonus e-book content

Fig. 73.1 **B**, Midline sagittal T2-weighted MRI through the female pelvis.

Fig. 73.2 **D**, Midline sagittal T2-weighted MRI through the male pelvis.

Fig. 73.3 Centiles of urinary bladder volume index in children.

Fig. 73.5 Laparoscopic view of the empty bladder and median and medial umbilical folds in a 12-month-old boy.

Fig. 73.6 Laparoscopic view of the left inferior epigastric vein (lateral umbilical ligament) in a 12-month-old boy.

Fig. 73.12 Cystic dilation of the prostatic utricle demonstrated in an 8-month-old infant during a micturating cystourethrogram.

Fig. 73.15 **C**, A T2-weighted high resolution axial MRI of the prostate showing the courses of the endopelvic fascia.

Video 73.1 Laparoscopic view of bladder filling and emptying in relation to the rectovesical pouch.

Video 73.2 Laparoscopic view of the anterior abdominal wall and ligaments.

Key references

Harvie C, Weissbart SJ, Kadam-Halani P et al 2019 Brain activation during the voiding phase of micturition in healthy adults: a meta-analysis of neuroimaging studies. Clin Anat 32:13-19.

This study provides an insight into the supraspinal control of voiding in healthy adults and a framework with which to understand dysfunctional voiding.

Mundy AR, Fitzpatrick J, Neal D et al 1999a Structure and function of the lower urinary tract. In: The Scientific Basis of Urology. Oxford: Isis Medical Media; Ch. 11, pp. 217–42.

A detailed assessment of the structure and function of the lower urinary tract.

Mundy AR, Fitzpatrick J, Neal D et al (eds) 1999b The prostate and benign prostatic hyperplasia. In: The Scientific Basis of Urology. Oxford: Isis Medical Media; Ch. 13, pp. 257–76.

An account that includes a review of prostatic zonal anatomy.

Myers RP 2001 Practical surgical anatomy for radical prostatectomy. Urol Clin North Am 28:473–90.

An article that details the clinically relevant anatomy of the prostate and surrounding structures.

Walsh PC, Donker PJ 1982 Impotence following radical prostatectomy: insight into etiology and prevention. J Urol 128:492–7.

A landmark assessment of the importance of neurovascular anatomy in prostate surgery.

Yacoub JH, Oto A 2018 MR imaging of prostate zonal anatomy. Radiol Clin North Am 56:197–209.

The authors describe the zonal and periprostatic anatomy of the prostate as revealed on MR imaging.

Further reading

MacLennan GT 2012 Hinman's Atlas of UroSurgical Anatomy, 2nd ed. Philadelphia: Elsevier.

An atlas containing detailed illustrations of the genitourinary tract and its surrounding anatomy, supplemented by radiological, pathological and intraoperative images.

McNeal JE 1984 Anatomy of the prostate and morphogenesis of BPH. Prog Clin Biol Res 145:27–53.

A seminal paper describing the zonal anatomy of the prostate.

References

Andersson KE, McCloskey KD 2014 Lamina propria: the functional center of the bladder? Neurourol Urodyn 33:9–16.

Bertrand MM, Alsaid B, Droupy S et al 2016 Anatomical basis of the coordination between smooth and striated urethral and anal sphincters: loops of regulation between inferior hypogastric plexus and pudendal nerve. Immuno-histological study with 3D reconstruction. Surg Radiol Anat 38:963–72.

Bessede T, Sooriakumaran P, Takenaka A et al 2016 Neural supply of the male urethral sphincter: comprehensive anatomical review and implications for continence recovery after radical prostatectomy. World J Urol 35:549–65.

Cağrı Savaş M, Kapucuoğlu N, Gürsoy K et al 2011 The microvessel density of the hypospadiac prepuce in children. J Pediatr Urol 7:162–5.

Chancellor MB, Yoshimura N 2002 Physiology and pharmacology of the bladder and urethra. In: Walsh PC et al (eds) Campbell's Urology Study Guide, 10th ed. Philadelphia: Elsevier, Saunders; Ch. 23.

Cunha GR, Vezina CM, Ricke W et al 2018 Development of the human prostate. Differentiation 103:24–45.

de Groat WC, Griffiths D, Yoshimura N 2015 Neural control of the lower urinary tract. Comprehensive Physiol 5:327–96.

DeLancey JOL 1989 Pubovesical ligament: a separate structure from the urethral supports ('pubo-urethral ligaments'). Neurourol Urodyns 8:53–61.

Drumm BT, Koh SD, Andersson KE et al 2014 Calcium signalling in Cajal-like interstitial cells of the lower urinary tract. Nat Rev Urol 11:555–64.

Harvie C, Weissbart SJ, Kadam-Halani P et al 2019 Brain activation during the voiding phase of micturition in healthy adults: a meta-analysis of neuroimaging studies. Clin Anat 32:13–19.

This study provides an insight into the supraspinal control of voiding in healthy adults and a framework with which to understand dysfunctional voiding.

Hinata N, Sejima T, Takenaka A 2013 Progress in pelvic anatomy from the viewpoint of radical prostatectomy. Int J Urol 20:260–70.

Hirdes MM, de Jong TP, Dik P et al 2010 Urethral length in girls with lower urinary tract symptoms and forme fruste of female epispadias. J Pediatr Urol 6:372–5.

Hutton KA, Babu R 2007 Normal anatomy of the external urethral meatus in boys: implications for hypospadias repair. BJU Int 100:161–3.

Klutke CG, Siegel CL 1995 Functional female pelvic anatomy. Urol Clin North Am 22:487–98.

Li ZY, Xu Y, Liu C et al 2019 Anatomical study of the seminal vesicle system for transurethral seminal vesiculoscopy. Clin Anat 32:244–52.

Lowsley OS 1912 The development of the human prostate gland with reference to the development of other structures at the neck of the urinary bladder Am J Anat 13:299–349.

Miles WE 1908 A method of performing abdominoperineal excision for carcinoma of the rectum and of the terminal portion of the pelvic colon. Lancet 2:1812–14.

Moya C, Cuesta J, Friera A et al 2017 Cadaveric and radiologic study of the anatomical variations of the prostatic arteries. A review of the literature and a new classification proposal. Clin Anat 30:71–80.

Mundy AR, Fitzpatrick J, Neal D et al 1999a Structure and function of the lower urinary tract. In: The Scientific Basis of Urology. Oxford: Isis Medical Media; Ch. 11, pp. 217–42.

A detailed assessment of the structure and function of the lower urinary tract.

Mundy AR, Fitzpatrick J, Neal D et al (eds) 1999b The prostate and benign prostatic hyperplasia. In: The Scientific Basis of Urology. Oxford: Isis Medical Media; Ch. 13, pp. 257–76.

An account that includes a review of prostatic zonal anatomy.

Muro S, Tsukada Y, Harada M et al 2018 Spatial distribution of smooth muscle tissue in the male pelvic floor with special reference to the lateral extent of the rectourethralis muscle: application to prostatectomy and proctectomy. Clin Anat 31:1167–76.

Myers RP 2001 Practical surgical anatomy for radical prostatectomy. Urol Clin North Am 28:473–90.

An article that details the clinically relevant anatomy of the prostate and surrounding structures.

Myers RP 2002 Detrusor apron, associated vascular plexus, and avascular plane: relevance to radical retropubic prostatectomy – anatomic and surgical commentary. Urology 59:472–9.

An explanation of the neurological components of bladder function from the higher cortical centres to molecular events within the cells of detrusor.

Myers RP, Cahill DR, Kay PA et al 2000 Puboperineales: muscular boundaries of the male urogenital hiatus in 3D from magnetic resonance imaging. J Urol 164:1412–15.

Myers RP, Cheville JC, Pawlina W 2010 Making anatomic terminology of the prostate and contiguous structures clinically useful: historical review and suggestions for revision in the 21st century. Clin Anat 23:18–29.

Orkiszewski M, Madej J 2010 The meatal/urethral width in healthy uncircumcised boys. J Pediatr Urol 6:130–3.

Pisipati S, Ali A, Mandalapu RS et al 2014 Newer concepts in neural anatomy and neurovascular preservation in robotic radical prostatectomy. Indian J Urol 30:399–409.

Roehrborn CG 2008 Pathology of benign prostatic hyperplasia. Int J Impot Res 20:S11–S18.

Shen J, Cunha GR, Sinclair A et al 2018 Macroscopic whole-mounts of the human fetal uro-genital tract: indifferent stage to male and female differentiation. Differentiation 103:5–13.

Shoja MM, Sharma A, Mirzayan N 2013 Neuroanatomy of the female abdominopelvic region: a review with application to pelvic pain syndromes. Clin Anat 26:66–76.

Siroky MB 2004 The aging bladder. Rev Urol 6 Suppl 1(Suppl 1):S3–S7.

Stalberg K, Gonzalez R 2012 Urethral atresia and anhydramnios at 18 weeks of gestation can result in normal development. J Pediatr Urol 8:e33–5.

Takahashi T, Ueno M, Azekura K et al 2000 Lateral ligament: its anatomy and clinical importance. Semin Surg Oncol 19:386–95.

Tewari A, Takenaka A, Mtui E et al 2006 The proximal neurovascular plate and the trizonal neural architecture around the prostate gland: importance in the athermal robotic technique of nerve sparing prostatectomy. BJU Int 98:314–23.

Walsh PC, Donker PJ 1982 Impotence following radical prostatectomy: insight into etiology and prevention. J Urol 128:492–7.

A landmark assessment of the importance of neurovascular anatomy in prostate surgery.

Weledji EP, Eyongeta D, Ngounou E 2019 The anatomy of urination: what every physician should know. Clin Anat 32:60–7.

Xu Z, Cahpuis PH, Bokey L et al 2017 Nature and architecture of the puboprostatic ligament: a macro- and microscopic cadaveric study using epoxy sheet plastination. Urology 110:e1-263.e8.

Yacoub JH, Oto A 2018 MR imaging of prostate zonal anatomy. Radiol Clin North Am 56:197–209.

The authors describe the zonal and periprostatic anatomy of the prostate as revealed on MR imaging.

Yucel S, Guntekin E, Kukul E et al 2004 Comparison of hypospadiac and normal preputial vascular anatomy. J Urol 172:1973–6.

Further reading

Brewster SF 1985 The development and differentiation of human seminal vesicles. J Anat 143:45–55.

Brooks JD, Eggener SE, Chao WM 2002 Anatomy of the rectourethralis muscle. Eur Urol 41:94–100.

Hsieh MH, Eisenberg ML, Hittelman AB et al 2012 Caucasian male infants and boys with hypospadias exhibit reduced anogenital distance. Hum Reprod 27:1577–80.

Hurwitz RS, Woodhouse CR, Ransley P 1986 The anatomical course of the neurovascular bundles in epispadias. J Urol 136:68–70.

Kutikov A, Guzzo TJ, Malkowicz SB 2006 Clinical approach to the prostate: an update. Radiol Clin North Am 44:649–63.

This article details the practical approach to diseases of the prostate.

MacLennan GT 2012 Hinman's Atlas of UroSurgical Anatomy, 2nd ed. Philadelphia: Elsevier.

An atlas containing detailed illustrations of the genitourinary tract and its surrounding anatomy, supplemented by radiological, pathological and intraoperative images.

McNeal JE 1984 Anatomy of the prostate and morphogenesis of BPH. Prog Clin Biol Res 145:27–53.

A seminal paper describing the zonal anatomy of the prostate.

CHAPTER

74

Male reproductive system

The male reproductive system includes the gonads, spermatic cord, accessory sex glands and external genitalia. The male gonads, the testes, are responsible for spermatogenesis and steroidogenesis, thereby regulating reproductive function as well as normal physical and sexual development and behaviour. The accessory sex glands include the prostate, seminal glands (vesicles) and bulbo-urethral glands. Prostatic and seminal gland secretions constitute most of the seminal fluid volume, containing nutrients, growth factors and enzymes that are essential for normal spermatogenic function. Additionally, the anatomy of the male external genitalia, the scrotum and penis, is uniquely suited both to optimize the testicular environment for spermatogenesis and to facilitate seminal fluid delivery to the female reproductive tract. These functions are dependent on sensory and erectile capabilities.

TESTIS AND EPIDIDYMIS

Testis

In adults, the testes typically measure 4–5 cm in length, 2–3 cm in breadth and 3–4 cm in anteroposterior diameter (Tishler 1971); their weight ranges between 12 and 20 g. Average testicular volume ranges from 15 to 25 ml (Prader 1966, Goede et al 2011).

The testes are suspended in the scrotum by the spermatic cord (**Figs 74.2–74.3**). The left testis usually lies more inferiorly than the right; both are positioned obliquely, such that the superior pole is tilted anterolaterally while the inferior pole is tilted anteromedially. Their location in the scrotum, combined with the characteristics of the scrotal skin and the counter-current heat exchange mechanism of the pampiniform plexus, maintains the testes at a temperature 3–4 °C below body temperature.

The testes are enclosed in a tough capsule made up of three layers: an innermost vascular layer, an intermediate tunica albuginea and an outer tunica vaginalis (**Fig. 74.4**). The posterior aspect of the testis is the site of attachment of the epididymis and is therefore only partly covered by serosa. Here, the tunica albuginea projects inwards to form the mediastinum of the testis, and the tunica vaginalis projects outwards to cover the epididymis. Within the scrotum, the testes are separated by a septum.

Vascular layer The vascular layer (tunica vasculosa) contains a plexus of blood vessels and loose connective tissue. It lines the inner surface of the tunica albuginea and all of the surfaces and septations within the testis.

Tunica albuginea The tunica albuginea is a dense, blue–white layer composed primarily of collagen fibres. It covers the vascular layer and is surrounded by the visceral layer of the tunica vaginalis. At the posterior aspect of the testis it projects inwards as a thick but incomplete fibrous septum, the mediastinum of the testis, which extends from the superior to the inferior pole of the testis. It is here that vessels, nerves and efferent ductules traverse the testicular capsule (**Fig. 74.5**).

Tunica vaginalis The tunica vaginalis is a continuation of the processus vaginalis, the formation of which precedes the descent of the fetal testis from the abdomen to the scrotum. Following testicular migration into the scrotum, the portion of the processus vaginalis between the deep inguinal ring and the testis is obliterated, leaving a distal sac containing the testis. Failure to obliterate the processus vaginalis results in

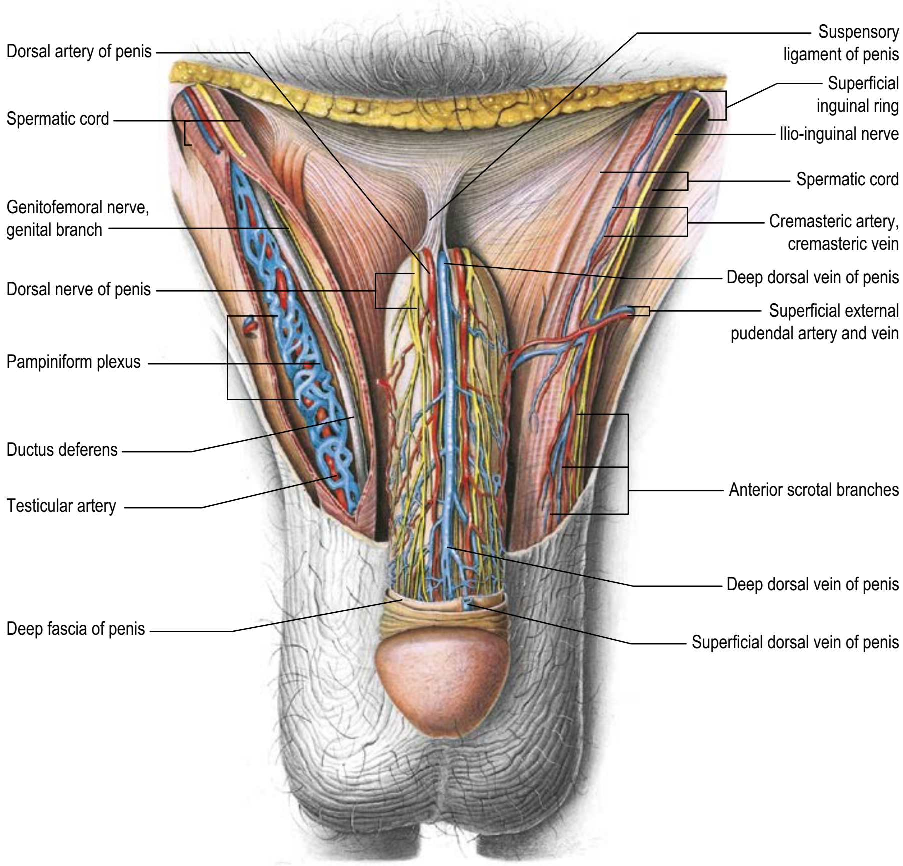
Dorsal artery of penis
Spermatic cord
Genitofemoral nerve, genital branch
Dorsal nerve of penis
Pampiniform plexus
Ductus deferens
Testicular artery
Deep fascia of penis
Suspensory ligament of penis
Superficial inguinal ring
Ilio-inguinal nerve
Spermatic cord
Cremasteric artery, cremasteric vein
Deep dorsal vein of penis
Superficial external pudendal artery and vein
Anterior scrotal branches
Deep dorsal vein of penis
Superficial dorsal vein of penis

Fig. 74.2 The male external genitalia illustrating the dorsal aspect of the penis. Nerves and vessels exposed by extensive removal of the skin and the superficial fascia of the penis. The layers of the spermatic cord have been incised on the right; note the pampiniform plexus surrounding the testicular artery. (Sobotta Atlas of Human Anatomy © Elsevier GmbH, Urban & Fischer, Munich.)

TABLE 74.1 **Volumes of the left and right testis as measured by ultrasonography.**

Age (years)	Boys (n)	Left volume	SD	Right volume	SD	Mean volume	SD
1	40	0.48	0.14	0.48	0.13	0.48	0.13
2	38	0.47	0.09	0.45	0.1	0.46	0.09
3	36	0.52	0.18	0.5	0.13	0.51	0.15
4	38	0.52	0.18	0.5	0.15	0.51	0.16
5	48	0.59	0.15	0.58	0.15	0.58	0.15
6	42	0.63	0.25	0.64	0.28	0.63	0.26
7	62	0.64	0.18	0.66	0.18	0.65	0.17
8	59	0.64	0.2	0.67	0.24	0.66	0.22
9	53	0.78	0.46	0.8	0.48	0.79	0.46
10	49	0.95	0.51	0.99	0.52	0.97	0.51
11	60	1.31	0.95	1.35	1.14	1.33	1.03
12	55	2.31	1.8	2.35	1.79	2.33	1.77
13	47	4.21	2.44	4.62	2.95	4.42	2.66
14	35	7.2	4.13	7.42	4.16	7.31	4.11
15	26	8.69	3.06	8.69	2.86	8.69	2.91
16	31	11.48	2.99	11.55	3.24	11.51	3.03
17	27	12.14	2.87	12.09	2.95	12.12	2.8
18	23	13.67	3.49	13.8	3.77	13.73	3.51

SD, standard deviation. All volumes in millilitres.

With permission from Goede J, Hack WW, Sijstermans K et al 2011 Normative values for testicular volume measured by ultrasonography in a normal population from infancy to adolescence. Horm Res Paediatr 76(1):56–64.

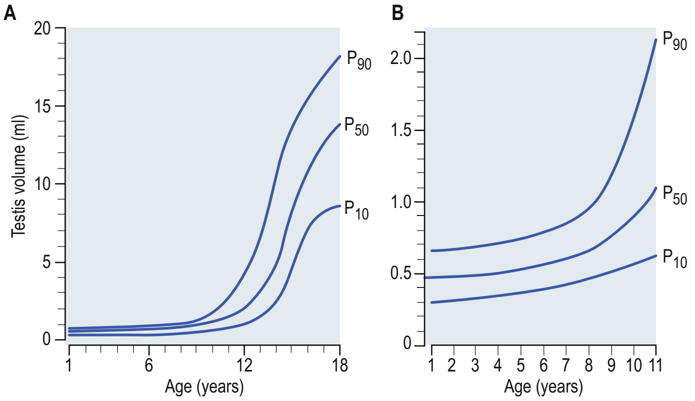

Fig. 74.1 **A**, Reference curves for mean testicular volume measured by ultrasonography. P_{10}, P_{50} and P_{90} indicate tenth, fiftieth and ninetieth centiles, respectively. **B**, Enlargement of the reference curves for mean testicular volume measured by ultrasonography. (With permission from Goede J, Hack WW, Sijstermans K et al 2011 Normative values for testicular volume measured by ultrasonography in a normal population from infancy to adolescence. Horm Res Paediatr 76:56–64.)

The volume of the left and right testis in males between infancy and adolescence as measured by ultrasonography is shown in Table 74.1; reference curves for mean testicular volume are shown in Fig. 74.1.

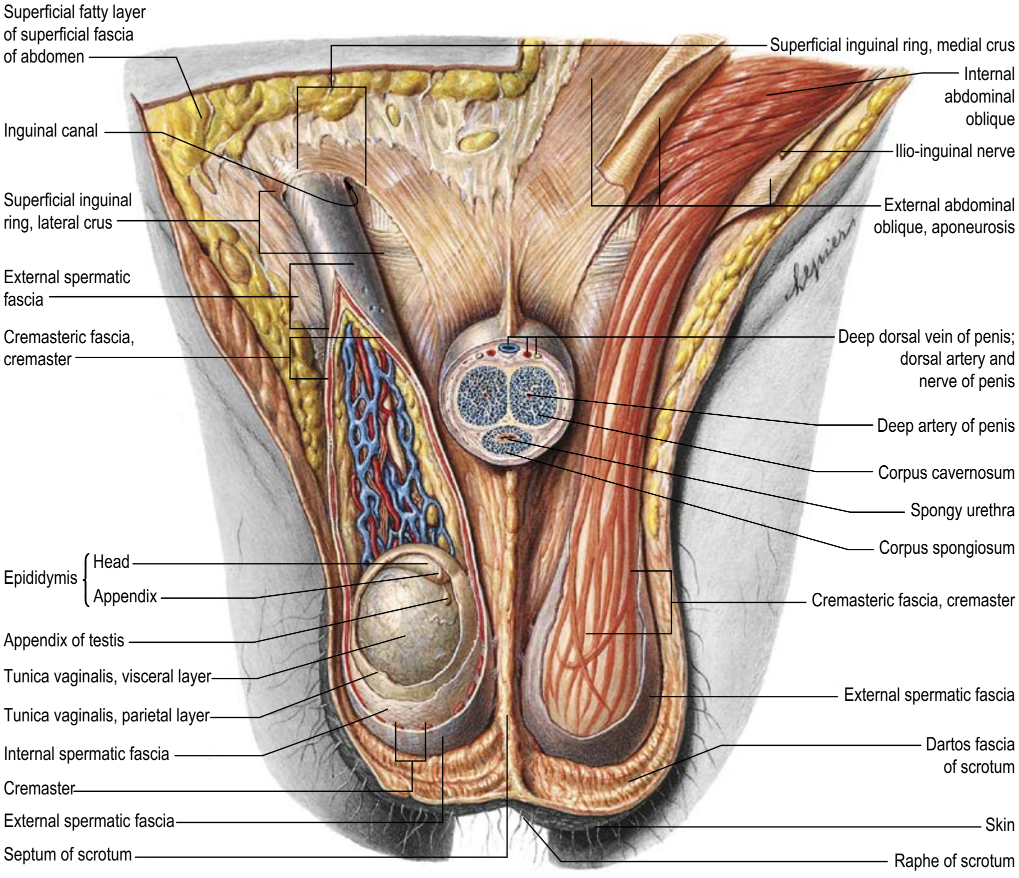
Superficial fatty layer of superficial fascia of abdomen
Inguinal canal
Superficial inguinal ring, lateral crus
External spermatic fascia
Cremasteric fascia, cremaster
Epididymis
Head
Appendix
Appendix of testis
Tunica vaginalis, visceral layer
Tunica vaginalis, parietal layer
Internal spermatic fascia
Cremaster
External spermatic fascia
Septum of scrotum
Superficial inguinal ring, medial crus
Internal abdominal oblique
Ilio-inguinal nerve
External abdominal oblique, aponeurosis
Deep dorsal vein of penis; dorsal artery and nerve of penis
Deep artery of penis
Corpus cavernosum
Spongy urethra
Corpus spongiosum
Cremasteric fascia, cremaster
External spermatic fascia
Dartos fascia of scrotum
Skin
Raphe of scrotum

Fig. 74.3 The male external genitalia. The skin of the abdomen and parts of the skin of the scrotum have been removed, and the body of the penis has been transected revealing the internal structure of the penis. The layers of the spermatic cord and the coverings of the testis have been dissected on the right. (Sobotta Atlas of Human Anatomy © Elsevier GmbH, Urban & Fischer, Munich.)

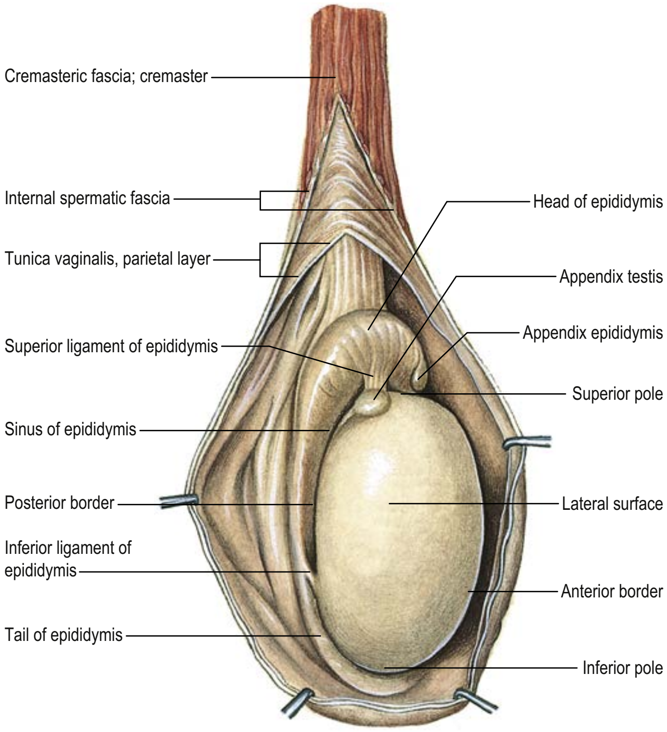
Cremasteric fascia; cremaster
Internal spermatic fascia
Tunica vaginalis, parietal layer
Superior ligament of epididymis
Sinus of epididymis
Posterior border
Inferior ligament of epididymis
Tail of epididymis
Head of epididymis
Appendix testis
Appendix epididymis
Superior pole
Lateral surface
Anterior border
Inferior pole

Fig. 74.4 The right testis, exposed by incising and laying open the cremasteric fascia and parietal layer of the tunica vaginalis on the lateral aspect of the testis. (Sobotta Atlas of Human Anatomy © Elsevier GmbH, Urban & Fischer, Munich.)

a persistent communication between the scrotum and peritoneal cavity (Fig. 74.6), which can lead to hydroceles and indirect inguinal hernias.

The tunica vaginalis is reflected from the surface of the testis on to the inner surface of the scrotum, forming visceral and parietal layers that are continuous at both poles of the testis. The visceral layer covers all aspects of the testis except the posterior aspect, where it is reflected towards the epididymis before becoming continuous with the parietal layer. The inner surface of the parietal layer has a smooth, moist mesothelium. The potential space between the visceral and parietal layers, the cavity (cavum) of the tunica vaginalis, is normally occupied by a thin film of clear, straw-coloured fluid. The volume of this fluid can increase with obstruction of lymphatic drainage due to inflammatory, traumatic or neoplastic conditions of the testis, resulting in a hydrocele.

Vascular supply and lymphatic drainage

Arteries

The arterial supply to the testis and epididymis is derived from three sources. In descending order of contribution, these are the testicular artery (supplying approximately two-thirds of the testicular blood supply), the artery to ductus deferens and the cremasteric artery (together contributing approximately one-third of the testicular blood supply) (Fig. 74.7) (Harrison and Barclay 1948, Raman and Goldstein 2004).

Testicular artery

The testicular artery usually arises from the abdominal aorta, inferior to the origin of the renal artery, and courses inferolaterally under the parietal peritoneum, along psoas major towards the pelvis. On the right, it courses anterior to the inferior vena cava and posterior to the middle colic and ileocolic arteries and the terminal ileum. On the left, it courses posterior to the inferior mesenteric vein, left colic artery and the descending colon. As the right and left testicular arteries enter the pelvis they lie anterior to the genitofemoral nerves, ureters and external iliac arteries. Both arteries then enter the deep inguinal ring and travel within the ipsilateral spermatic cord in the inguinal canal to the scrotum (see Figs 74.2, 74.5). The origin, number and course of the testicular arteries can vary (Asala et al 2001, Pai et al 2008, Kotian et al 2016, Kayalvizhi et al 2017).

Proximally, it supplies the upper and middle parts of the ureter (Daniel and Shackman 1952). Distally, in its course to the testis the testicular artery gives off one or more internal testicular arteries (MacLennan 2012) an inferior testicular artery, and branches supplying the head, body and tail of the epididymis (Macmillan 1954). The level at which this branching occurs is variable; in 31–88% of cases it occurs within the inguinal canal (Beck et al 1992, Jarow et al 1992). At the level of the testis, branches of the testicular artery enter the tunica albuginea in the mediastinum of the testis and ramify in the vascular layer before reaching their distribution. The testicular arteries ramify primarily in the anterior, medial and lateral portions of the inferior pole of the testis and in the anterior segment of the superior pole (Jarow 1991,

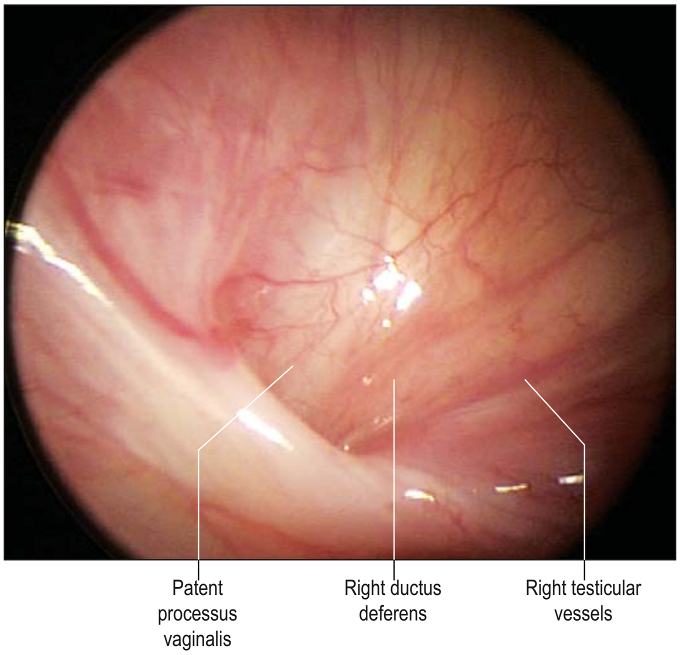
Patent processus vaginalis
Right ductus deferens
Right testicular vessels

Fig. 74.6 A laparoscopic view of a persistent communication between the scrotum and peritoneal cavity in a 4-month-old boy (patent processus vaginalis).

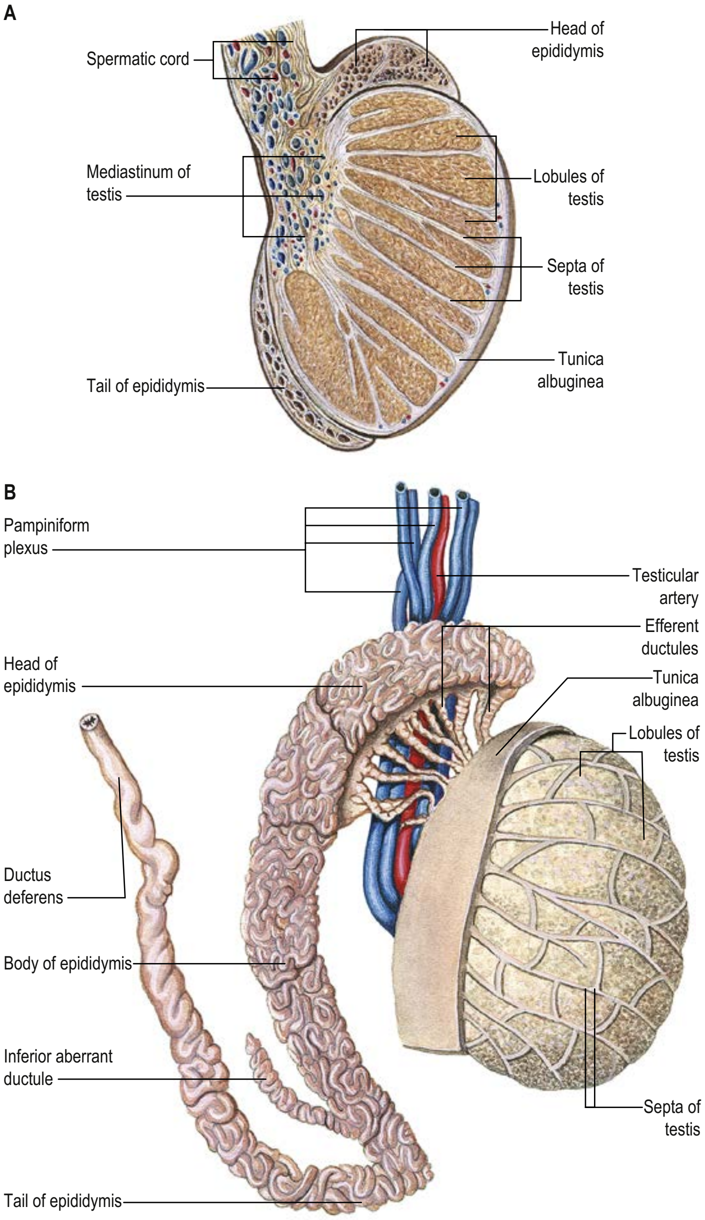
A
Spermatic cord
Head of epididymis
Mediastinum of testis
Lobules of testis
Septa of testis
Tunica albuginea
Tail of epididymis
B
Pampiniform plexus
Testicular artery
Efferent ductules
Tunica albuginea
Head of epididymis
Lobules of testis
Ductus deferens
Body of epididymis
Inferior aberrant ductule
Septa of testis
Tail of epididymis

Fig. 74.5 **A**, A sagittal section through the testis and epididymis. **B**, The arrangement of the efferent ductules of the testis and the mode of formation of the epididymis and ductus deferens. (Sobotta Atlas of Human Anatomy © Elsevier GmbH, Urban & Fischer, Munich.)

Mostafa et al 2008), which has important implications for planning testicular biopsies.

Artery to the ductus deferens

The artery to the ductus deferens is a branch of the superior or inferior vesical artery, which arises from the internal iliac artery (Mostafa et al 2008).

Cremasteric artery

The cremasteric artery is a branch of the inferior epigastric artery. It accompanies the spermatic cord and supplies cremaster and other coverings of the cord. Both the artery to the ductus deferens and the cremasteric artery enter the inguinal canal at the deep inguinal ring and travel the length of the spermatic cord alongside the testicular artery. The testicular artery and pampiniform plexus lie within the internal spermatic fascia, whereas the ductus deferens and its vessels, as well as cremaster and its vessels, lie outside the internal spermatic fascia but within the external spermatic fascia. In the scrotum there is a rich vascular anastomosis at the head of the epididymis, between the testicular artery and the epididymal artery, and at the tail of the epididymis between the testicular, epididymal, and cremasteric arteries and the artery to the ductus deferens.

Veins

Pampiniform plexus

Testicular veins emerge posteriorly from the testis, drain the epididymis and unite to form several highly anastomotic channels surrounding the testis known as the pampiniform plexus, a major component of the spermatic cord (see Fig. 74.2). This vascular arrangement means that counterflowing arteries and veins are separated only by the thickness of their vascular walls, permitting the exchange of heat and small molecules (Harrison 1949) and facilitating the maintenance of lower testicular temperatures. The pampiniform plexus ascends anterior to the ductus deferens and is drained by 3–4 veins in the inguinal canal. The veins enter the abdomen through the deep inguinal ring and coalesce into a single testicular vein that drains into the inferior vena cava on the right and the renal vein on the left. The right testicular vein joins the inferior vena cava at an acute angle, just inferior to the level of the renal veins, while the left testicular vein joins the left renal vein at a right angle (**Fig. 74.8**). The testicular veins contain valves.

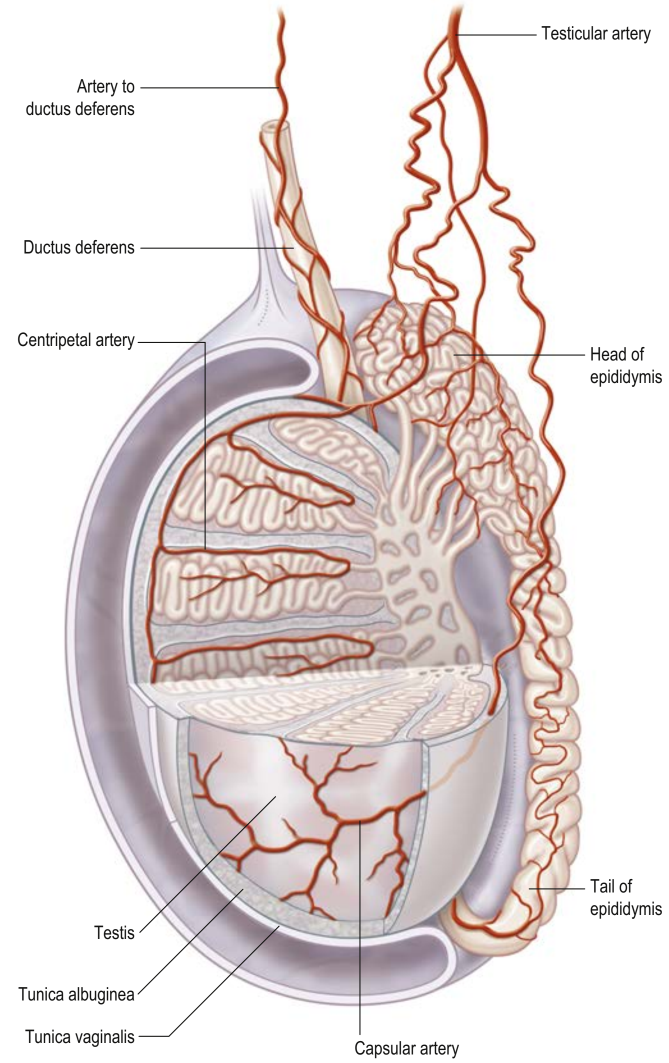
Testicular artery
Artery to ductus deferens
Ductus deferens
Centripetal artery
Head of epididymis
Tail of epididymis
Testis
Tunica albuginea
Tunica vaginalis
Capsular artery

Fig. 74.7 Sagittal and axial sections through the testis, to demonstrate its blood supply. Note the blood supply to the epididymis and ductus deferens.

Lymphatic drainage

Testicular lymphatic flow is abundant and consistent and follows the general retroperitoneal scheme of vertical drainage, with lateral flow from right to left. Lymphatic vessels from the right testis drain primarily into the right lateral aortic and lateral caval nodes, with some drainage into the left lateral aortic nodes. Lymphatic vessels from the left testis drain into the left and right lateral aortic and lateral caval nodes.

Innervation

The testis is innervated either by nerve fibres that arise from the tenth and eleventh thoracic spinal segments via the renal and aortic plexuses and accompany the testicular vessels, or by fibres that arise from the inferior hypogastric plexus and accompany the ductus deferens (Rauchenwald et al 1995). Interestingly, some afferent and efferent nerves have been shown to cross over to the contralateral inferior hypogastric plexus (Taguchi et al 1999), which could be one reason why pathological processes in one testis can affect the other.

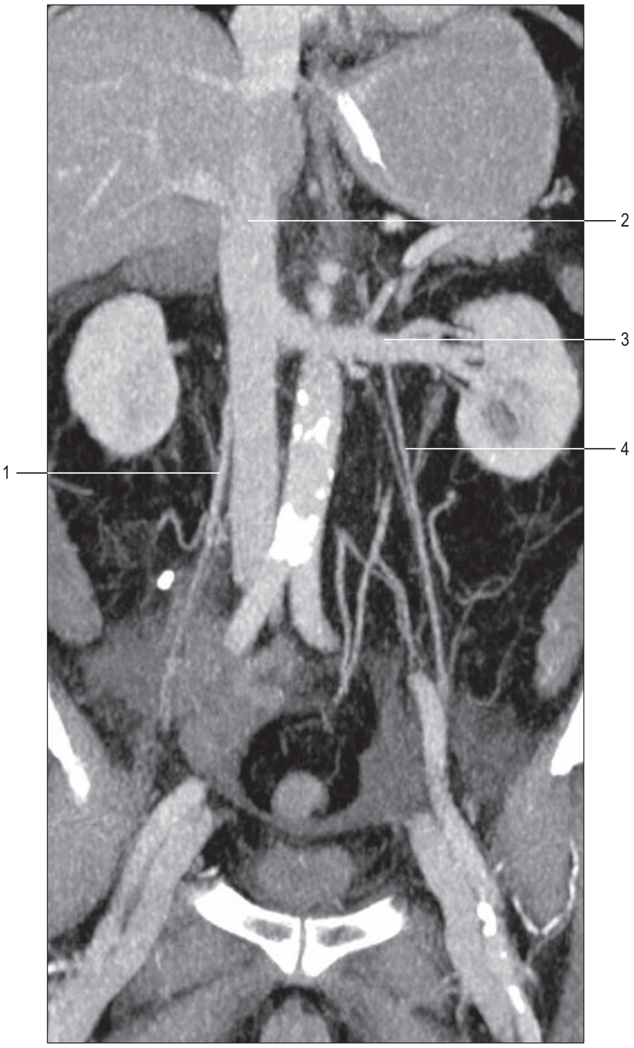

Fig. 74.8 Computed tomography showing the left testicular vein draining to the left renal vein and the right testicular vein draining to the inferior vena cava. Key: 1, right testicular vein; 2, inferior vena cava; 3, left renal vein; 4, left testicular vein.

The greater length of the left testicular vein and its angle of attachment into the left renal vein have been suggested as possible aetiologies for the occurrence of varicoceles. Additionally, the testicular veins can anastomose with the external pudendal and cremasteric veins and veins of the ductus deferens, allowing varicoceles to persist or recur after ablative procedures that do not address these potential collaterals.

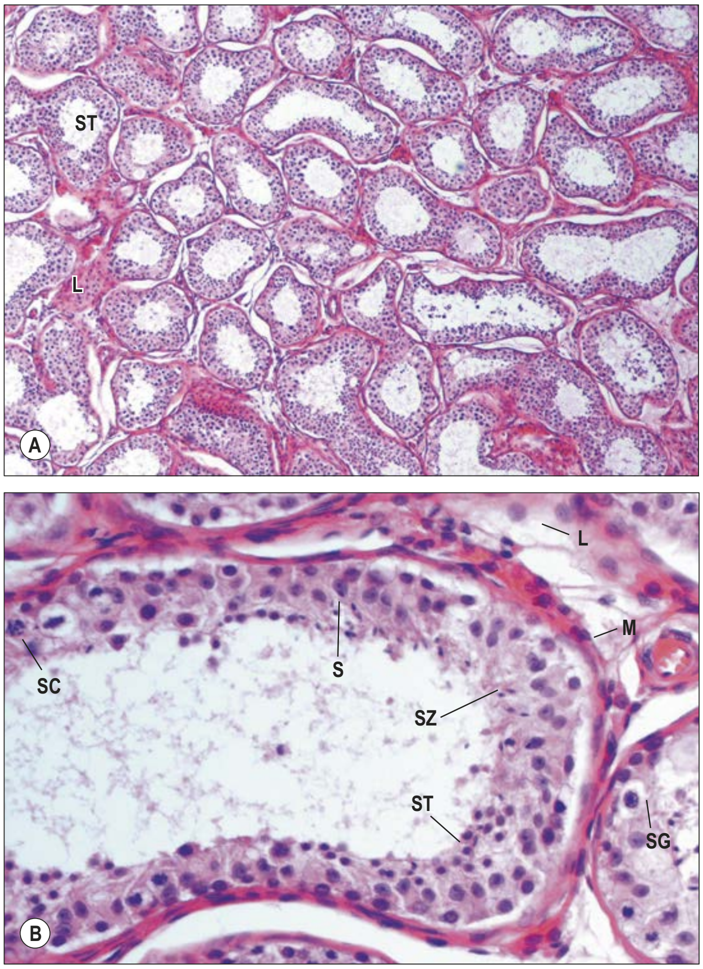

Fig. 74.10 **A**, Seminiferous tubules (ST; cut in various planes of section) and the interstitial endocrine cells (Leydig cells, L) of the testis. The seminiferous tubules are highly convoluted and lined by a stratified epithelium, which consists of cells in various stages of spermatogenesis and spermiogenesis (collectively referred to as the spermatogenic series). Non-spermatogenic cells are the Sertoli cells. **B**, A human seminiferous tubule showing the differentiation sequence of spermatozoa from basally situated spermatogonia (SG). Large primary spermatocytes (SC) have characteristic thread-like chromatin in various stages of prophase of the first meiotic division. Smaller haploid spermatids (ST) have round nuclei initially but mature to possess the dense, elongated nuclei and flagella of spermatozoa (SZ). Sertoli cells (S) are identified from their oval or pear-shaped nuclei, orientated perpendicular to the basal lamina, and from their prominent nucleoli. The tubule is surrounded by peritubular myoid cells (M). Clusters of interstitial endocrine cells (L) are seen in the interstitial connective tissue.

Microstructure

The testis is enclosed within a tough, collagenous tunica albuginea, which thickens posteriorly as the mediastinum of the testis. Blood and lymphatic vessels, and genital ducts all enter and leave the testis at the mediastinum (**Fig. 74.9**). Septations originating at the mediastinum of the testis extend internally to partition the testis into approximately 250 lobules that differ in size, the largest and longest lobules being near the centre (see Fig. 74.5). Each lobule contains 1–4 convoluted seminiferous tubules and interstitial tissue composed of interstitial endocrine cells (Leydig cells), mast cells, macrophages, nerves and blood vessels.

Seminiferous tubules are typically long, highly coiled and looped; both ends terminate in the mediastinum of the testis. Spermatogenesis occurs in the highly coiled portions (**Fig. 74.10**). As the tubules reach the apical portion of the lobule near the mediastinum of the testis they become much less convoluted and form short straight tubules (tubuli recti), which lack spermatogenic cells and are instead lined by cuboidal epithelium. Within the mediastinum of the testis, straight tubules anastomose to form the rete testis, which is lined by a flat epithelium. Here, tubular fluid is reabsorbed and spermatozoa become concentrated. The rete testis coalesces to form 7–15 efferent ductules, which act as conduits to carry spermatozoa into the head of the epididymis. The efferent ductules are lined by a ciliated columnar epithelium that also contains non-ciliated, actively endocytic cells. Outside the epithelial lining, the ductules are surrounded by a thin circular coat of smooth muscle.

The diameters of the seminiferous tubules decrease during the third trimester of pregnancy and immediately before birth, then gradually increase throughout childhood (Mendez and Emery 1979). Seminiferous tubules are responsible for up to 80% of the total testicular volume. It is estimated that the combined length of the 600–1200 tubules in the human testis is approximately 250 metres. Each tubule is surrounded by a basal lamina resting on a complex, stratified epithelium. In cross-section, the lumen of the seminiferous tubule is lined by Sertoli cells (sustentocytes) and contains spermatozoa in various stages of development, from spermatogonial stem cells near the base to progressively maturing forms (spermatogonia, spermatocytes, spermatids and spermatozoa) arranged systematically towards the centre of the tubule. Residual bodies, spherical structures derived from surplus spermatid cytoplasm shed during spermatozoal maturation, can be found among the spermatids.

Specialized tight junctional complexes between adjacent Sertoli cells form a functional 'blood–testis barrier' that subdivides the seminiferous tubule epithelium into basal and adluminal compartments. Spermatogonia and developing spermatocytes lie outside the blood–testis barrier in the basal compartment, whereas mature spermatocytes and spermatids are sequestered above the blood–testis barrier in the adluminal compartment.

Spermatogonia Spermatogonia, the germ cells for all spermatozoa, are descended from primordial germ cells that migrate into the genital cords of the developing testis. In the fully differentiated testis they are located along the basal laminae of the seminiferous tubules (see Fig. 74.10B). On the basis of their cellular and nuclear dimensions, distribution of nuclear chromatin, and histochemical and ultrastructural properties, spermatogonia are characterized as either dark-type A (Ad), pale-type A (Ap) or type B cells. Ad spermatogonia divide mitotically to maintain their own population and can differentiate to give rise to Ap cells, the precursors of type B cells, which are committed to the spermatogenesis cycle. Type B cells give rise to type I spermatocytes; they leave the basal compartment of the seminiferous tubule and cross the blood–testis barrier to enter the adluminal compartment in a step coordinated by Sertoli cells.

The generation of mature spermatozoa from spermatogonia takes approximately 64 days. In cross-section, a seminiferous tubule shows more than one phase of the cycle around its circumference because waves of progression through a spermatogenic cycle occur in spirals along the length of a tubule (see Fig. 74.10B).

Primary and secondary spermatocytes Primary spermatocytes have a diploid chromosome number with duplicated sister chromatids (4N DNA content). They are large cells with round nuclei in which the chromatin is condensed into dark, thread-like, coiled chromatids. They undergo meiosis I to give rise to secondary spermatids (2N), which rapidly undergo meiosis II to form haploid spermatids (N). Theoretically, each primary spermatocyte produces four spermatids; however, a proportion of spermatids degenerate during maturation, reducing the expected yield.

Spermatids Spermatids undergo a series of nuclear and cytoplasmic changes, termed spermiogenesis, in order to develop into mature spermatozoa. These changes take place while the spermatids are closely associated with Sertoli cells and linked to one another by cytoplasmic bridges. Spermiogenesis includes the development of the acrosome from Golgi vesicles, generation of the axoneme from the centrioles and formation of the acrosomal cap at the anterior pole of the spermatozoon. Concurrently, the nuclear chromatin condenses and the nucleus assumes a spearhead shape. The cytoplasmic volume shrinks, bringing the wall of the acrosomal vesicle into contact with the plasma membrane. A perinuclear sheath of microtubules develops from the posterior edge of the acrosome and extends towards the posterior pole of the spermatozoon. Here, the microtubules are arranged in the typical flagellar pattern of nine outer microtubules surrounding two central microtubules, the axonemal complex that extends longitudinally to form the tail of the spermatozoon. Mitochondria migrate along the axonemal complex and concentrate in the mid-piece of the tail. During the final phase of spermiogenesis, excess cytoplasm is detached from the spermatozoon as a residual body that is phagocytosed and degraded by Sertoli cells. During the formation of residual bodies, spermatids lose their cytoplasmic bridges and separate from one another before being released into the lumen of the seminiferous tubule.

Spermatozoa Spermatozoa released into the seminiferous tubule are structurally mature but usually non-motile. In the presence of excurrent ductal obstruction, testicular sperm can acquire motility (Jow et al 1993). The shape of the spermatozoon is ideally suited to rapid progressive motility (**Fig. 74.11**). Its head has minimal cytoplasm and measures approximately 4 μm × 3 μm. It contains an elongated, flattened nucleus

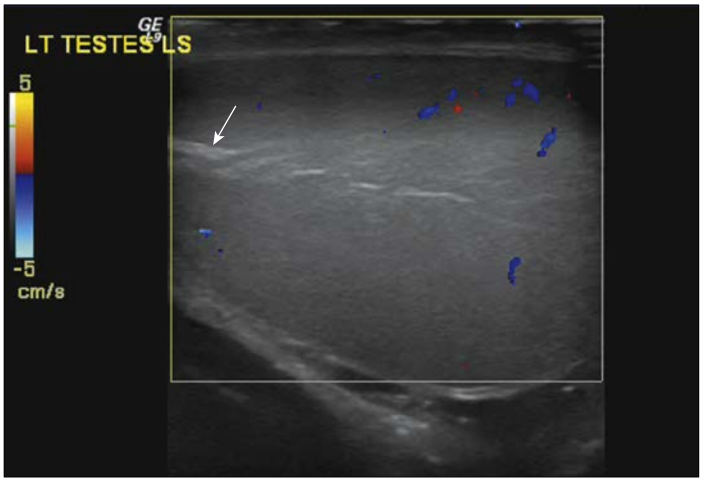
GE
LT TESTES LS
5
-5
cm/s

Fig. 74.9 A colour Doppler scan of the scrotal contents showing normal flow. The linear echogenic band (arrow) seen centrally represents the mediastinum of the testis, which is composed of fibroadipose tissues.

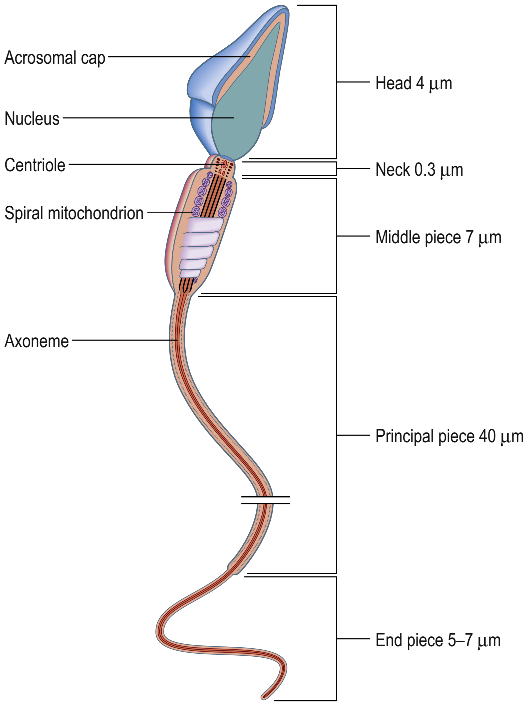
Acrosomal cap
Nucleus
Centriole
Spiral mitochondrion
Axoneme
Head 4 µm
Neck 0.3 µm
Middle piece 7 µm
Principal piece 40 µm
End piece 5–7 µm

Fig. 74.11 The main ultrastructural features of a mature spermatozoon.

with condensed, dark-staining chromatin, covered anteriorly by an acrosomal cap. The latter contains acid phosphatase, hyaluronidase and proteases necessary for oocyte fertilization. The head is connected by a short neck approximately 0.3 µm in length to a long tail, which is divided into middle, principal and end pieces. The mid-piece of the tail is a cylinder approximately 7 µm long. It consists of an axial bundle of microtubules, the axoneme, surrounded by a cylinder of nine outer dense fibres (ODFs), surrounded in turn by a helical mitochondrial sheath. The mid-piece is the powerhouse of the spermatozoon. The principal piece of the tail is responsible for motility. With a length of 40 µm and a diameter of 0.5 µm, the tail forms most of the volume of a spermatozoon. The axonemal complex is continuous from the neck region to the terminus of the tail, only the axoneme persisting in the final 5–7 µm.

Sertoli cells Sertoli cells (sustentocytes, nurse cells, supporting cells) have euchromatic and irregular nuclei that are aligned perpendicular to the basal lamina and contain one or two prominent nucleoli. They are variable in shape. Their basal end rests on the basal lamina while their apical end extends into the tubule lumen. Consistent with their phagocytic function, their cytoplasm is rich in lysosomes. Sertoli cells provide key support for spermatogenesis within the seminiferous tubules. Complex recesses in their plasma membranes serve to envelop spermatogonia, spermatids and spermatozoa until the latter are mature enough for release. Long cytoplasmic processes extend between spermatogonia in the basal compartment and spermatocytes in the adluminal compartment of the seminiferous tubule. Adjacent Sertoli cells are joined at this level by tight junctions that create a diffusion barrier between the extratubular and intratubular compartments. This so-called blood–testis barrier can be disrupted by trauma or inflammation, allowing self-directed immune responses to develop against sperm antigens, potentially leading to subfertility.

In addition to their role in spermatogenesis, Sertoli cells secrete proteinaceous fluid to facilitate spermatozoal transport through the seminiferous tubules and into the excurrent ducts. They also regulate the intratesticular hormonal milieu by secreting inhibin B and androgen-binding protein in response to stimulation by pituitary gland gonadotropins.

Interstitial endocrine cells and interstitial tissue The interstitial tissue between seminiferous tubules includes peritubular myoid cells, vessels, nerves and clusters of interstitial endocrine cells (Leydig cells). Myoid cells are contractile; their rhythmic activity helps propel non-motile spermatozoa through the seminiferous tubules towards the rete testis and excurrent ductal system. Interstitial endocrine cells are large polyhedral cells with eccentric nuclei containing 1–3 nucleoli, and pale-staining cytoplasm containing smooth endoplasmic reticulum, lipid droplets and characteristic needle-shaped, crystalloid inclusions (crystals of Reinke). In response to stimulation by pituitary gonadotropins they synthesize and secrete testosterone.

Age-related changes

Available with the *Gray's Anatomy* e-book

Puberty is associated with the development of an adult population of androgen-producing interstitial endocrine cells, which persist throughout adult life. The testes grow slowly until the age of 10 or 11 years, at which time there is a marked acceleration of growth. This increase in testicular size is largely due to the onset of spermatogenesis, characterized by proliferation and differentiation of previously dormant spermatogonial stem cells. Testicular size, sperm quality and quantity, and the numbers of Sertoli cells and interstitial endocrine cells have all been reported to decline with age, although no consistent or definitive age for the onset of this decline has been identified. Testicular volume occupied by seminiferous tubules decreases, whereas that occupied by interstitial tissue remains approximately constant.

The most frequently observed histological change in the ageing testis is the apparent variability in spermatogenesis; spermatogenesis is complete in some areas and reduced in others, or absent altogether as a result of tubular sclerosis. In tubules where spermatogenesis is complete, morphological abnormalities such as multinucleation can be observed in the germ cells. Germ cell loss, beginning with spermatids and progressively affecting the earlier stages of spermatogenesis, can also be seen. As a result, both sperm quality and quantity can be affected. In some males, this change is notable as early as the third or fourth decade of life.

Sperm motility and maturation Human spermatozoa acquire an increased capacity for motility as they migrate through the epididymis, which is manifested not only as an increase in the percentage of spermatozoa with motile tails but also as a qualitative change from an immature to a more mature pattern of motility. Spermatozoa in the proximal epididymis demonstrate high-amplitude, low-frequency tail movements, producing little motion. This is in contrast to spermatozoa in the tail of the epididymis, which demonstrate low-amplitude and high-frequency tail movements, resulting in considerably greater forward progression (Bedford et al 1973).

Whether and to what extent sperm motility depends on the interaction of human spermatozoa with a particular section of the epididymis is unknown. In patients with congenital absence or obstruction of the ductus deferens, spermatozoa in the distal epididymis demonstrate less effective motility than those in the proximal epididymis (Silber 1989, Schoysman and Bedford 1986). Therefore, intrinsic sperm processes as well as intrinsic epididymal function appear to be important in sperm maturation.

Following ejaculation, spermatozoa display their full pattern of motility. Although sperm motility is highest in the hours following ejaculation, motile human spermatozoa have been recovered from cervical mucus several days after insemination. However, this survival period may be of little relevance given that human spermatozoa are capable of migrating to their tubal destination within an hour of insemination.

After entering the female reproductive tract, spermatozoa undergo a process known as capacitation to render them capable of fertilizing the oocyte. Capacitation involves a number of structural and biochemical changes, including the development of hyperactivated motility and completion of the acrosome reaction. Independent of other sperm characteristics such as motility and morphology, capacitation is necessary for the development of functional spermatozoa.

Developmental anomalies of the testis

Cryptorchidism

Available with the *Gray's Anatomy* e-book

Retractile testis

Available with the *Gray's Anatomy* e-book

Torsion

Available with the *Gray's Anatomy* e-book

Hydrocele

Available with the *Gray's Anatomy* e-book

Splenogonadal fusion

Available with the *Gray's Anatomy* e-book

Transverse/crossed testicular ectopia

Available with the *Gray's Anatomy* e-book

Polyorchidism

Available with the *Gray's Anatomy* e-book

Epididymis

The epididymis lies posterior and slightly lateral to the testis. Anatomically, it is divided into three sections: head, body and tail. Between 8 and 12 efferent ductules from the superior pole of the testis drain into and form the head of the epididymis. Distally, the tail of the epididymis becomes continuous with the convoluted portion of the ductus deferens (see Fig. 74.5B). The epididymis is invested by the tunica vaginalis, continuous with that covering the testis. Laterally, a deep groove, the sinus of the epididymis, marks the boundary between the testis and epididymis. Testis–epididymis non-fusion has been described in children with cryptorchidism; non-fusion may involve the epididymal head or tail or the whole epididymis (Kraft et al 2011).

Epididymal cyst and spermatoceles

Available with the *Gray's Anatomy* e-book

Microstructure

The epididymal tubule is 3–4 metres long (Turner et al 1978) and is entirely encapsulated by the tunica vaginalis. Extensions from this connective tissue sheath enter the interductal spaces, forming septa that divide the tubule into histologically similar regions (Kormano and Reijonen 1976).

Functionally, the fetal testis is primarily an endocrine organ that produces testosterone and anti-Müllerian hormone. Seminiferous tubules do not become canalized until approximately the seventh month of gestation. Fetal interstitial endocrine cells responsible for androgen-induced differentiation of the male genitalia, degenerate after birth. A second wave of interstitial endocrine cell differentiation occurs 2–3 months after birth, briefly elevating testosterone levels in male infants. The interstitial endocrine cells of early infancy subsequently regress and the testis remains dormant during childhood. In a study of Japanese boys, gonocytes were reported to appear at about the age of 2 years, spermatocytes by 4 years and spermatids by 11 years (Yuasa et al 2001).

Sertoli cells are also affected by ageing and show a range of morphological changes including loss of differentiated characteristics, mitochondrial metaplasia and multinucleation. In interstitial endocrine cells there is a decline in the number of mitochondria and the quantity of smooth endoplasmic reticulum, paralleled by an increase in lipid droplets, crystalline inclusions and residual bodies. Some cells also become multinucleated. Functionally, these changes are manifested as a gradual age-related decline in circulating testosterone levels.

The descent of the testes from the abdominal cavity to the scrotum can be arrested at any point along the pathway of the testis, e.g. the deep inguinal ring, in the inguinal canal, or between the superficial inguinal ring and the scrotum. Retention in the inguinal canal is associated with a patent processus vaginalis and can be further complicated by a congenital hernia. Occasionally, the testis migrates outside its normal path of descent and lies in an ectopic location.

At birth, 3% of full-term male infants have a unilaterally undescended testis. By six months of age, this number decreases to less than 1%. Undescended testes are associated with a higher risk of infertility and testicular cancer later in life.

Orchidopexy is therefore recommended for patients with persistent cryptorchidism after 6 months of age and within 18 months of age. Available evidence suggests that orchidopexy at any age can improve spermatogenesis (Shin et al 1997) but does not decrease the risk of testicular cancer in a cryptorchid (undescended) testis. An inverse relationship has been reported between age at orchidopexy and total sperm count and sperm motility. The data support orchidopexy in the first year of life (Canavese et al 2009). Nevertheless, surgical correction maximizes the chance of early detection of a testicular mass and is the only means of restoring a normal milieu for spermatogenesis. Interestingly, interstitial endocrine cell function is usually unchanged by maldescent, so serum testosterone levels remain within the normal range in affected patients. In contrast, maldescent in children in the age range of 1–15 years is associated with Sertoli cell degeneration (Rune et al 1992).

Retractile testes are more common than undescended testes in boys. A retractile testis is one that moves to and fro between the inguinal region and the scrotum. Unlike undescended testes, retractile testes can be manipulated to the distal part of the scrotum on clinical examination. They are smaller than normal testes, having a mean volume of approximately 0.50 ml in children.

Testicular torsion refers to rotation of the testis around its blood supply leading to testicular ischaemia. Torsion can be extravaginal or intravaginal depending on whether it involves a rotation of both the testis and the tunica vaginalis, or of the testis alone, within an intact tunica vaginalis. In either case, torsion results in severe testicular pain secondary to tissue ischaemia. Fertility can be affected by a single episode of torsion. If unrelieved within 4–6 hours, permanent tissue loss can occur. Testicular torsion is therefore considered a surgical emergency.

Other structures in the scrotum such as the appendix of the testis (hydatid of Morgagni) (**Fig. 74.12**) and appendix of the epididymis (see Fig. 74.4) can also undergo torsion, resulting in scrotal pain that can be difficult to differentiate from testicular torsion. In some instances a 'blue dot' sign is noted at the superior pole of the testis, which is diagnostic. These structures are developmental remnants of the paramesonephric (Müllerian) and the mesonephric (Wolffian) ducts, respectively. There are no associated long-term sequelae.

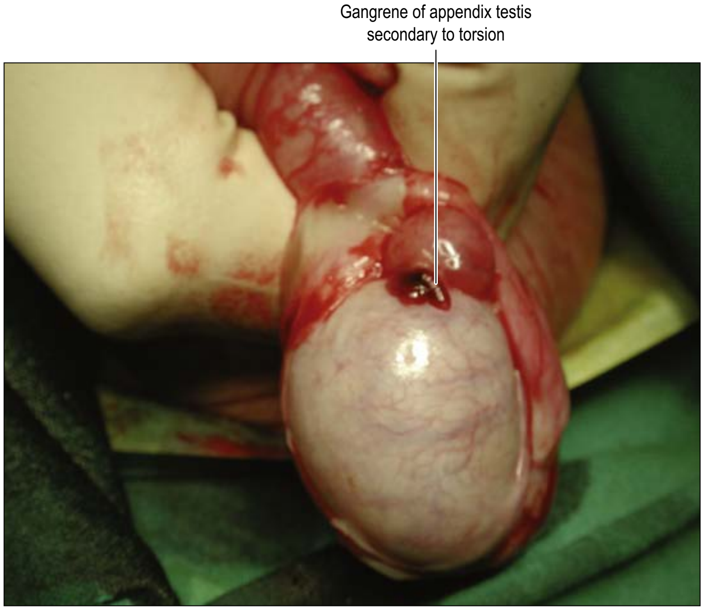

Fig. 74.12 Gangrene of the appendix of the testis secondary to torsion of the testis in an 8-year-old boy.

A patent processus vaginalis allows communication to occur between the peritoneal cavity and the spermatic cord or scrotum. Passage of peritoneal fluid into the scrotum presents as a communicating hydrocele and usually resolves spontaneously once the processus is obliterated by 18–24 months of age. Alternatively, if the processus vaginalis is patent proximally but obliterated distally, there could be a hydrocele or cyst of the spermatic cord. Surgical treatment can be indicated for persistent, non-communicating hydroceles. Hydroceles can also result from lymphatic vessel obstruction from a testicular tumour, epididymitis, orchitis or trauma. A 20% incidence of hydrocele has been reported in children having laparoscopic *en bloc* ligation of the spermatic vessels on the posterior abdominal wall (Palomo procedure). This complication is avoided by lymphatic-sparing surgery (Schwentner et al 2006).

Splenogonadal fusion is a rare congenital anomaly characterized by splenic tissue being connected to the gonad, resulting from an abnormal connection between the spleen and the gonad during gestation. It is more predominant in males and is almost invariably on the left side. It can be of the continuous type, where the testis is connected to the main spleen, or of the discontinuous type, where the testis is connected to ectopic splenic tissue.

Transverse/crossed testicular ectopia is an extremely rare condition in which both testes descend into a single inguinal canal or one side of the scrotum. The origin of the spermatic cord is normally located on each side. It can occur in association with persistent Müllerian duct syndrome (Tiryaki et al 2005).

Polyorchidism is a rare congenital anomaly in which there are more than two testes. The most common type consists of three testes; cases with four testes have also been reported. The supernumerary testes may or may not be connected to a ductus deferens.

Epididymal cysts arise from the epididymal tubules and can occur anywhere in the head, body or tail of the epididymis. Removal is unnecessary if they are asymptomatic, particularly given the risk of iatrogenic epididymal obstruction. Spermatoceles are cysts that are basically aneurysms of the efferent ducts that form the head of the epididymis and contain sperm. Removal is unnecessary unless they grow large and cause pain (Kaufman et al 2011). However, spermatoceles can be aspirated as a source of spermatozoa.

The head of the epididymis consists of 8–12 efferent ducts and the proximal segment of the duct of the epididymis. The efferent ducts become larger and more convoluted than they are in the testis. Each duct is 15–20 cm long and opens into an individual epididymal tubule. These tubules anastomose with one another along the length of the epididymis, eventually becoming a single, coiled tubule in the body of the epididymis. They are surrounded by contractile smooth muscle cells (**Fig. 74.13**), which are larger and more numerous in the distal epididymis. Peristaltic contractions generated by the smooth muscle propel the spermatozoa in an antegrade direction towards the tail of the epididymis.

Epithelium The pseudostratified epithelial lining of the epididymal tubule contains principal, basal, apical and clear cells. Principal cells are tall columnar cells with basally located, oval nuclei. They bear long stereocilia (15 µm) and function to resorb testicular fluid; approximately 90% of the total secretory fluid volume is absorbed in the epididymis. They also endocytose other components of seminal fluid and produce glycoproteins that are essential for sperm maturation. Basal cells lie between the bases of the principal cells and are thought to be precursors of them. Apical and clear cells are far less common than principal and basal cells. Apical cells are rich in mitochondria and are most abundant in the head of the epididymis. In contrast, clear cells are columnar and most abundant in the tail of the epididymis. They have few microvilli but numerous endocytic vesicles and lipid droplets. One of their functions is to acidify luminal fluid.

DUCTUS DEFERENS, SPERMATIC CORD AND EJACULATORY DUCT

Ductus deferens

The ductus deferens (vas deferens) is a tubular structure derived from the mesonephric duct. Its primary function is to transport sperm from the epididymis to the urethra, though absorptive and secretory functions have also been described (Hoffer 1976). As it arises from the tail of the epididymis, the ductus deferens is tortuous for 2–3 cm (see Fig. 74.5B). Beyond this convoluted segment it lies posterior and parallel to the vessels of the spermatic cord, passes through the inguinal canal (see Fig. 74.16), and emerges in the pelvis lateral to the inferior epigastric vessels (see Fig. 60.3). At the deep inguinal ring, the ductus deferens diverges from the testicular vessels, coursing medial to the structures of the pelvic side wall in order to reach the base of the prostate posteriorly. Here, the ductus deferens once again becomes tortuous and dilated (the ampulla of the ductus deferens) before culminating at the ejaculatory duct (see Fig. 72.21).

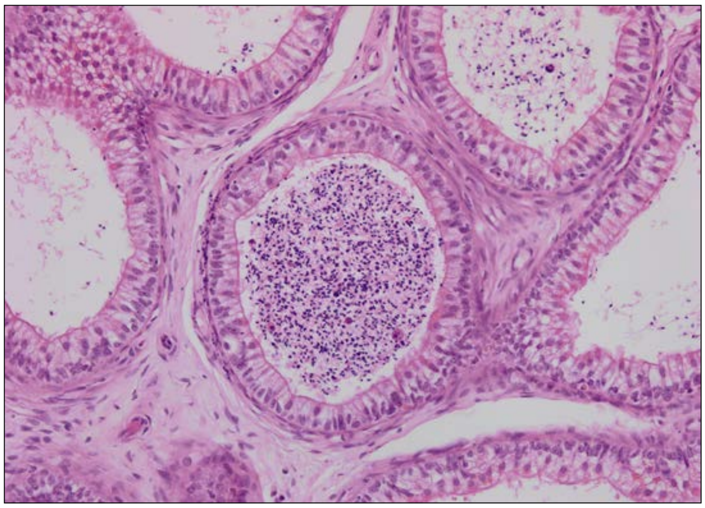

Fig. 74.13 The microstructure of the epididymis. The epididymal duct is lined by tall columnar pseudostratified epithelium bearing apical stereocilia. Accumulations of spermatozoa are seen in the lumen, e.g. centre field. (Courtesy of Mr Peter Helliwell, Department of Histopathology, Royal Cornwall Hospitals Trust, UK.)

Vascular supply and lymphatic drainage

The ductus deferens is supplied by the artery to the ductus deferens, which is derived from the superior or inferior vesical arteries, both of which are branches of the internal iliac artery (Zhang et al 2015). Rarely, it is derived directly from the internal iliac artery. Veins from the ductus deferens and seminal glands drain to the prostatic venous plexus, whereas the associated lymphatic vessels drain into the external and internal iliac nodes (MacLennan 2012, Mirilas and Mentessidou 2012).

Innervation

The ductus deferens is innervated by a rich autonomic plexus of primarily postganglionic sympathetic fibres derived from the inferior hypogastric plexus.

Microstructure

In humans, the ductus deferens is 30–35 cm in length and 2–3 mm in diameter, with a luminal diameter of 300–500 µm. In cross-section it consists of an outer adventitial sheath containing blood vessels and nerves; a thick, three-layered muscular wall of inner and outer longitudinal and middle circular smooth muscle; and an inner mucosal lining of pseudostratified columnar epithelium with non-motile cilia (**Fig. 74.14**). It has the greatest muscle to lumen ratio (approximately 10:1) of any hollow organ in the body. During ejaculation, the smooth muscle layers contract reflexively, propelling the sperm in an antegrade direction (see above).

Developmental anomalies of the ductus deferens

Available with the *Gray's Anatomy* e-book

Spermatic cord

The spermatic cord begins at the deep inguinal ring, extends the length of the inguinal canal, exits the canal at the superficial inguinal ring and suspends the testis in the scrotum (**Fig. 74.15**; see Fig. 74.3). Between the superficial inguinal ring and the testis the spermatic cord lies anterior to the proximal tendon of adductor longus. It is flanked anteriorly by the superficial external pudendal artery and posteriorly by the deep external pudendal artery. The ilio-inguinal nerve most commonly lies anterior to the spermatic cord as it traverses the inguinal canal (Oelrich and Moosman 1977, Ndiaye et al 2007).

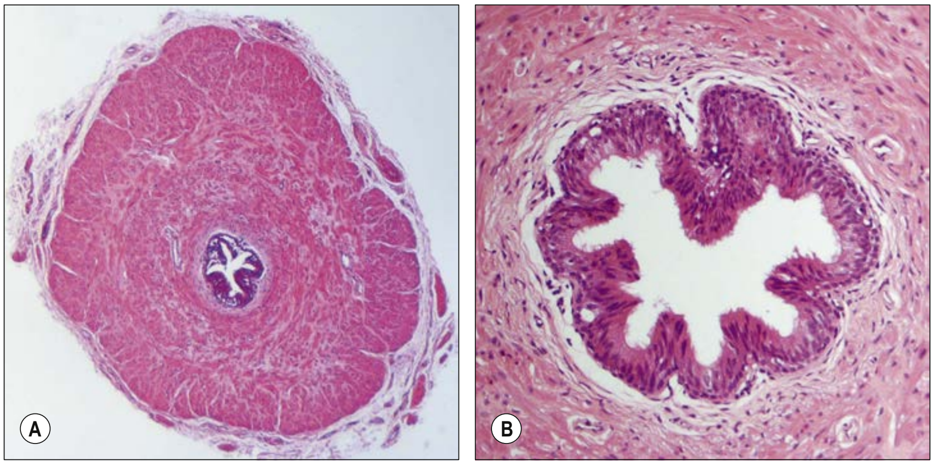

Fig. 74.14 The ductus deferens. **A**, A low-power view, transverse section. **B**, A higher-power view. The convoluted lumen is lined by pseudostratified columnar epithelial cells.

The ductus deferens can be congenitally absent, either unilaterally or bilaterally. When bilateral, the condition is associated with a mutation of the cystic fibrosis transmembrane conductance gene in 80% of affected males. This condition is characterized by low semen volume due to absent or hypoplastic seminal glands and azoospermia, though spermatogenesis is usually normal. An absent ductus deferens is usually the only genital manifestation of cystic fibrosis.

The anatomy of the ductus deferens is worthy of note in children with cryptorchidism (see above). At laparoscopic orchidopexy for intra-abdominal testis, it is important to exclude a ‘looping ductus deferens’ that enters the inguinal canal and loops back to the abdominal cavity (Shalaby et al 2011); failure to recognize this anatomical anomaly can result in iatrogenic injury to the ductus deferens.

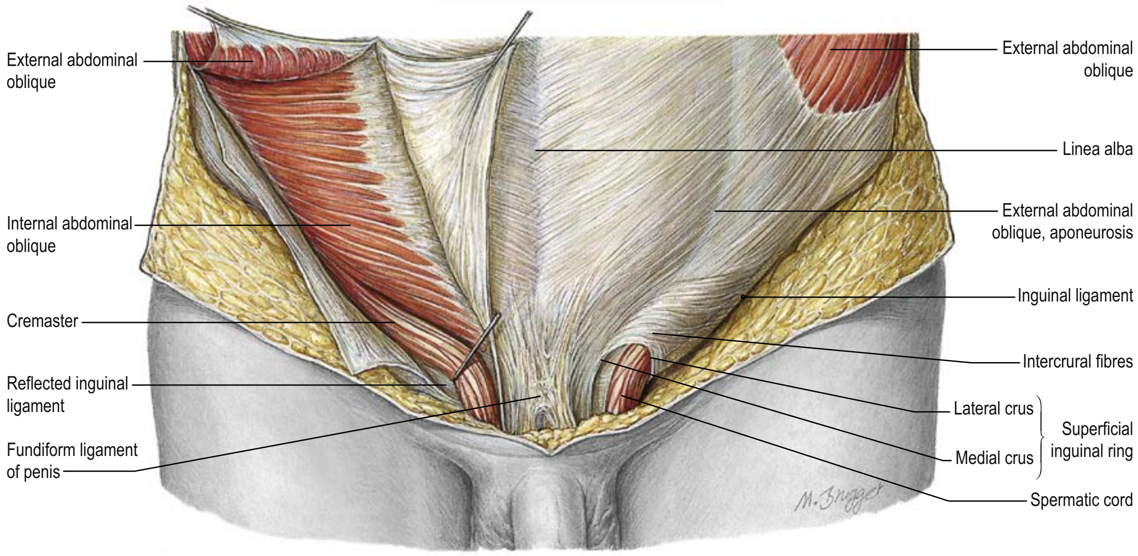
External abdominal oblique
Internal abdominal oblique
Cremaster
Reflected inguinal ligament
Fundiform ligament of penis
External abdominal oblique
Linea alba
External abdominal oblique, aponeurosis
Inguinal ligament
Intercrural fibres
Lateral crus
Medial crus
Superficial inguinal ring
Spermatic cord
M. Brugger

Fig. 74.15 The relation of the spermatic cord to the anterior abdominal wall. (Sobotta Atlas of Human Anatomy © Elsevier GmbH, Urban & Fischer, Munich.)

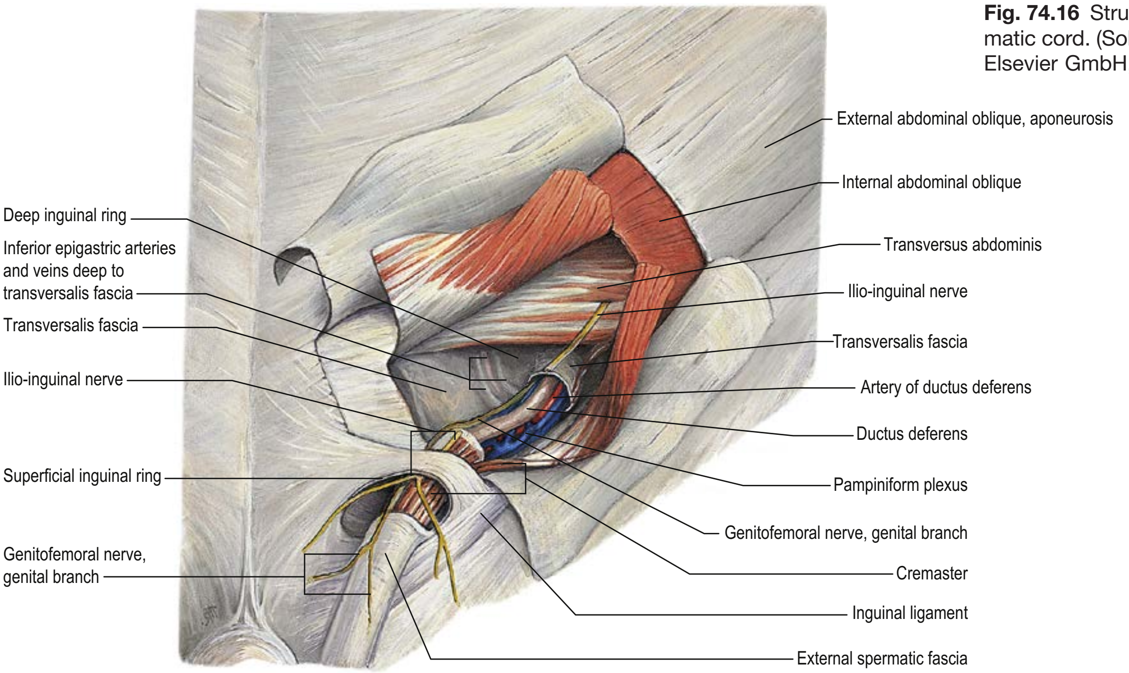
Deep inguinal ring
Inferior epigastric arteries and veins deep to transversalis fascia
Transversalis fascia
Ilio-inguinal nerve
Superficial inguinal ring
Genitofemoral nerve, genital branch
External abdominal oblique, aponeurosis
Internal abdominal oblique
Transversus abdominis
Ilio-inguinal nerve
Transversalis fascia
Artery of ductus deferens
Ductus deferens
Pampiniform plexus
Genitofemoral nerve, genital branch
Cremaster
Inguinal ligament
External spermatic fascia

Fig. 74.16 Structures contained within the spermatic cord. (Sobotta Atlas of Human Anatomy © Elsevier GmbH, Urban & Fischer, Munich.)

In addition to the artery, veins, lymphatic vessels and nerves serving the testis, which are contained within the internal spermatic fascia, the spermatic cord also includes the genital branch of the genitofemoral nerve, the cremasteric artery, the pampiniform plexus, and the artery to the ductus deferens all of which are contained within the external spermatic fascia (**Fig. 74.16**; see Fig. 74.2). The ilio-inguinal nerve usually lies on the anterior surface of the spermatic cord. Also, with immunohistochemistry, Oka et al (2016) identified parasympathetic fibres in the spermatic cord. The fascial layers are continuous with the layers of the abdominal wall. The internal spermatic fascia is derived from the transversalis fascia and forms a thin, loose layer around the spermatic cord. The cremasteric fascia contains skeletal muscle fibres derived from internal abdominal oblique and smooth muscle fibres (Schwarz and Hirtler 2017). The external spermatic fascia is continuous with the aponeurosis of external abdominal oblique.

Ejaculatory duct

The paired ejaculatory ducts are formed from the union of the duct of the seminal gland with the ampulla of the ductus deferens. Each is approximately 2 cm long and extends from the base of the prostate, between the median and lateral lobes, towards its opening on the seminal colliculus (see Fig. 73.11). The ducts become smaller and converge towards their ends. Ejaculatory duct obstruction, though rare, can lead to oligospermia or azoospermia. Causes include congenital cysts such as Müllerian duct cysts, or iatrogenic injury arising during urethral manipulation. In contrast to the walls of the ductus deferens, the walls of the ejaculatory ducts are thin. They consist of an outer fibrous layer, which decreases in thickness on their entry into the prostate; a thin layer of smooth muscle fibres; and a mucosa lined by columnar epithelium. The ducts dilate during ejaculation. Normal luminal wall dimensions of the ejaculatory duct are remarkably uniform among males; a luminal diameter greater than 2.3 mm defines a dilated or obstructed efferent duct (Nguyen et al 1996).

ACCESSORY GLANDULAR STRUCTURES

Seminal glands

The seminal glands (vesicles) are paired outpouchings of the terminal ductus deferens, located at the base of the prostate between the urinary bladder and the rectum (**Fig. 74.17**, see Fig. 72.21). In adults, the seminal gland measures 5–10 cm in length and 3–5 cm in diameter, with an average volume of 13 ml (Goldstein 2012). In most males the right seminal gland is slightly larger than the left; both glands become smaller with age.

In essence, each seminal gland is a coiled tube with irregular diverticula, contained within a dense, fibromuscular sheath and partly covered by peritoneum. The superior pole is a cul-de-sac while the

Ectopic suprarenal tissue (adrenal rest) is encountered within the distal end of the spermatic cord in 2% of children undergoing inguinal procedures. These tissues are typically bright yellow to orange in colour, round or oval in shape, and up to 5 mm in diameter; they contain the three layers of the suprarenal cortex but no medulla (Savas et al 2001).

The paradidymis (organ of Giraldes) is a small and variant collection of convoluted tubules arising from the ductus deferens just above the head of the epididymis. The tubules are lined with columnar ciliated epithelium and are likely to represent a vestigial remnant of the mesonephric duct (Sahni et al 1996, Favorito et al 2004).

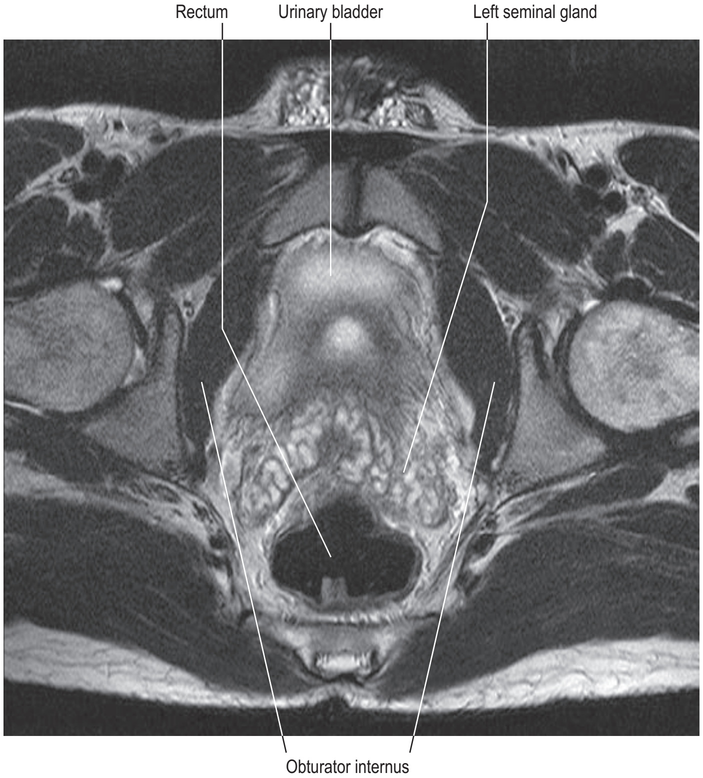

Fig. 74.17 T2-weighted axial magnetic resonance imaging (MRI) demonstrating the normal high signal in the seminal glands.

inferior pole narrows to a straight duct, which, together with the ductus deferens, culminates as the ejaculatory duct. The seminal glands are intimately associated with the prostate and urinary bladder anteriorly, the distal ureter superiorly, and the rectum and prostato-seminal fascia (Denonvilliers' fascia) posteriorly. The ampullae of the ductus deferens lie along the medial margins of the seminal glands, while the prostatic venous plexus lies laterally.

Agenesis of the seminal glands is a congenital anomaly associated with absence of the ductus deferentes (Tubbs et al 2016).

Vascular supply and lymphatic drainage

The primary blood supply to the seminal glands is from the vesiculodeferential artery, a branch of the umbilical artery (Braithwaite 1952). An additional source of blood supply is the inferior vesical artery, which arises from the internal iliac or the inferior gluteal artery. Venous drainage is provided by the vesiculodeferential veins and the vesical venous plexus. Lymphatic drainage, accordingly, occurs via the internal iliac nodes.

Innervation

The seminal glands receive preganglionic parasympathetic input from the pelvic splanchnic nerves and sympathetic (postganglionic) and parasympathetic (preganglionic) input from the inferior hypogastric plexus.

Microstructure

After puberty, the seminal glands mature into elongated, sac-like structures, produce a viscous white–yellow fluid that contributes at least two-thirds of the total ejaculate volume, and play an important role in sperm motility and metabolism. The secreted fluid is rich in fructose, coagulation proteins and prostaglandins and has a pH in the neutral to alkaline range. The wall of the seminal gland is composed of an external connective tissue layer, a middle smooth muscle layer (significantly thinner than the corresponding layer in the ductus deferens) and an internal mucosal layer with a highly folded, labyrinthine structure (**Fig. 74.18**). The mucosal layer is lined by cuboidal to pseudostratified columnar epithelium featuring typical protein-secreting cells. The seminal glands are not reservoirs for spermatozoa, except in cases of ejaculatory duct obstruction; they contract during ejaculation to release secretions into the ejaculatory duct.

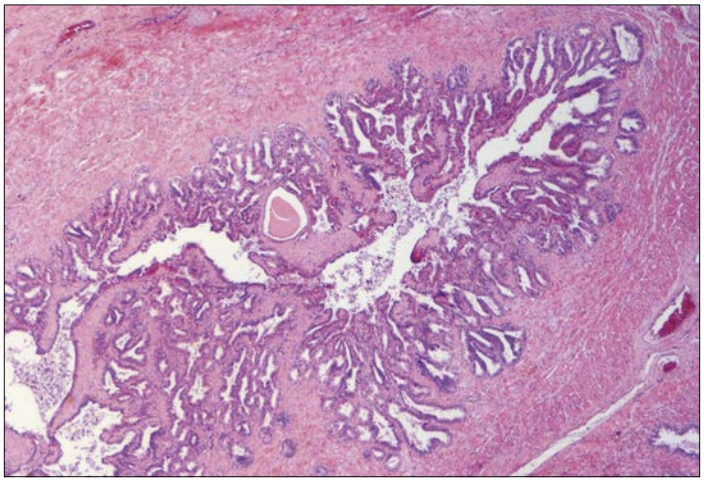

Fig. 74.18 The microstructure of the seminal glands, showing the tubulo-acinar structure.

Bulbo-urethral glands

The bulbo-urethral glands (Cowper's glands) are small, round, yellow, lobulated structures measuring approximately 1 cm in diameter and located lateral to the membranous urethra and superior to the perineal membrane. They are drained by long excretory ducts, each duct being almost 3 cm long, which pass obliquely and anteriorly from the region of the membranous urethra to penetrate the perineal membrane and open on the floor of the spongy urethra, approximately 2.5 cm below the perineal membrane. The glands are surrounded by muscle fibres that have long been considered to be part of the urinary sphincter. However, small bundles of muscle lying immediately lateral to the glands have been identified histologically as elements of the deep transverse perineal muscles that are apparently continuous with a 'tail' of the external urethral sphincter (Nakajima et al 2007). During sexual excitement, contraction of the muscle fibres leads to expulsion of clear mucus from the glands into the spongy urethra. Secretions of the bulbo-urethral glands constitute 5–10% of the total ejaculate volume.

Microstructure

Each bulbo-urethral gland consists of several lobules enclosed by a fibrous capsule. The secretory units are tubulo-alveolar in form. The glandular epithelium is columnar and secretes acidic and neutral mucins into the spongy urethra prior to ejaculation; the primary function of the secretions is lubrication. Diffuse mucosa-associated lymphoid tissue (MALT) is associated with the glands.

Peri-urethral glands

The peri-urethral glands (glands of Littré) are most numerous in the spongy urethra. Like the bulbo-urethral glands they secrete mucus into the urethra prior to ejaculation; the secretions also have a lubricating function.

EXTERNAL GENITALIA

Penis

The penis consists of an attached root in the perineum and a free, pendulous body, which is completely enveloped in skin (**Fig. 74.19**). At the junction of its fixed and pendulous parts, the penis is supported by the fundiform and suspensory ligaments, which anchor it to the pubic symphysis; they are composed primarily of elastic fibres continuous with the deep fascia of the penis (**Fig. 74.20B**). The body of the penis contains three erectile columns, the paired corpora cavernosa and the corpus spongiosum; the urethra; and the investing fasciae, blood vessels and nerves associated with these structures (**Fig. 74.20A**).

The corpora cavernosa lie in intimate apposition with one another along the length of the body of the penis (**Fig. 74.21**); the corpus spongiosum lies in the ventral groove between the corpora cavernosa. Proximally, posterior to the suspensory ligament of the penis, the corpora cavernosa diverge to form two tapering processes, the crura of the penis, which are firmly anchored to the ischiopubic rami (see Fig. 74.20B). The

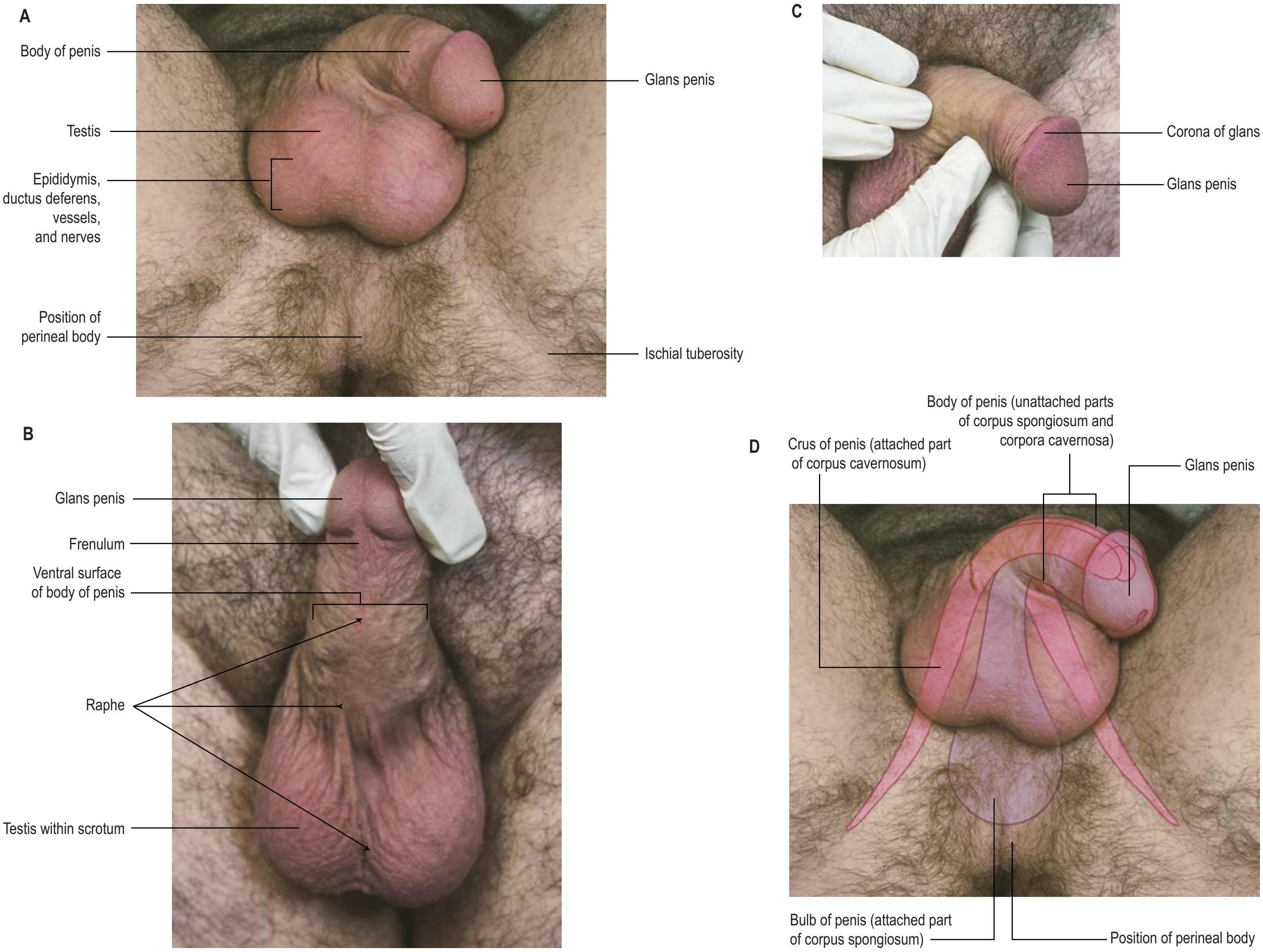
A
Body of penis
Glans penis
Testis
Epididymis, ductus deferens, vessels, and nerves
Position of perineal body
Ischial tuberosity
C
Corona of glans
Glans penis
B
Glans penis
Frenulum
Ventral surface of body of penis
Raphe
Testis within scrotum
D
Body of penis (unattached parts of corpus spongiosum and corpora cavernosa)
Crus of penis (attached part of corpus cavernosum)
Glans penis
Bulb of penis (attached part of corpus spongiosum)
Position of perineal body

Fig. 74.19 Male external genitalia. **A**, An inferior view. **B**, The ventral surface of the body of the penis. **C**, A lateral view of the body of the penis and glans. **D**, An inferior view of the male perineum; the erectile tissues of the penis are indicated with overlays. (With permission from Drake RL, Vogl AW, Mitchell A (eds) Gray's Anatomy for Students, 2nd ed. Elsevier, Churchill Livingstone. Copyright 2010.)

corpus spongiosum broadens between the two crura to form the bulb of the penis (Fig. 74.20C). At the distal end of the penis, the corpus spongiosum again enlarges and assumes a bulbous shape to form the glans penis. The rounded base of the glans, the corona, separates the glans from the body of the penis. The glans is covered by the prepuce, a loose fold of retractable skin attached to the ventral surface of the glans penis, under the corona, at the frenulum. The prepuce is a double membrane that variably encases the glans penis from which it is separated by a potential space (Favorito et al 2012).

Skin The skin of the body of the penis is thin, highly elastic and devoid of appendages (hair or glandular elements), except for preputial glands located at the base of the corona. It is also devoid of fat and quite mobile because of loose attachments between the superficial fascia of the penis and the underlying deep fascia of the penis (Buck's fascia) (Angermeier 2006). In contrast, the skin of the glans penis is immobile because it is directly attached to the underlying tunica albuginea. Blood supply to the penile skin is independent of the erectile bodies and is derived from the external pudendal arteries that enter the root of the penis and run longitudinally within the superficial fascia of the penis, forming a rich anastomotic network distally to the glans penis (Tuffaha et al 2014). Thus, it is possible to mobilize skin of the body of the penis on a vascular pedicle for surgical procedures such as urethral reconstruction.

The superficial penile fascia is devoid of fat and consists of loose connective tissue interspersed by fibres of dartos from the scrotum. In contrast, the deep fascia of the penis is a denser fascial sheath, which envelops both corpora cavernosa and splits to envelop the corpus spongiosum (Fig. 74.22B). Distally, it blends with the tunica albuginea covering all three corporal bodies. Proximally, it is continuous with dartos and the deep perineal fascia. Bleeding from a tear in the corporal bodies is usually contained within the deep fascia of the penis, and ecchymosis is limited to the body of the penis.

Root The root of the penis consists of three masses of erectile tissue in the urogenital triangle, namely the two crura and the bulb, firmly attached to the pubic arch and the perineal membrane respectively. The crura are the posterior extensions of the corpora cavernosa while the bulb is the dilated posterior end of the corpus spongiosum. The urethra enters the bulb via its posterior surface and travels the length of the body of the penis within the corpus spongiosum.

Body The major portion of the body of the penis consists of the paired corpora cavernosa. These contain erectile tissue enclosed within a dense fibroelastic sheath of connective tissue, the tunica albuginea (see Fig. 74.21E; Fig. 74.22). The outer longitudinal and inner circular fibres of the tunica form an undulating meshwork when the penis is flaccid but become tightly stretched on erection. The circular fibres surround each corpus separately, and the corpora are then surrounded as a unit by the outer longitudinal fibres. Smooth muscle bundles traverse the erectile bodies to form endothelium-lined cavernous sinuses, which give the erectile tissue a spongy appearance on gross examination. Blood flow into the sinuses leads to penile engorgement and compression of venous outflow channels, resulting in penile erection.

The corpora cavernosa are not distinct, separate structures but are divided in the midline by a fibrous septum that is continuous with the deep circular fibres of the tunica albuginea. The septum of the penis is complete and thick proximally but incomplete distally, permitting communication and exchange of blood flow between the corporal bodies. The wide median groove along the ventral aspect of the corpora cavernosa is occupied by the corpus spongiosum, containing the urethra. Dorsally, a similar but narrower groove contains the dorsal

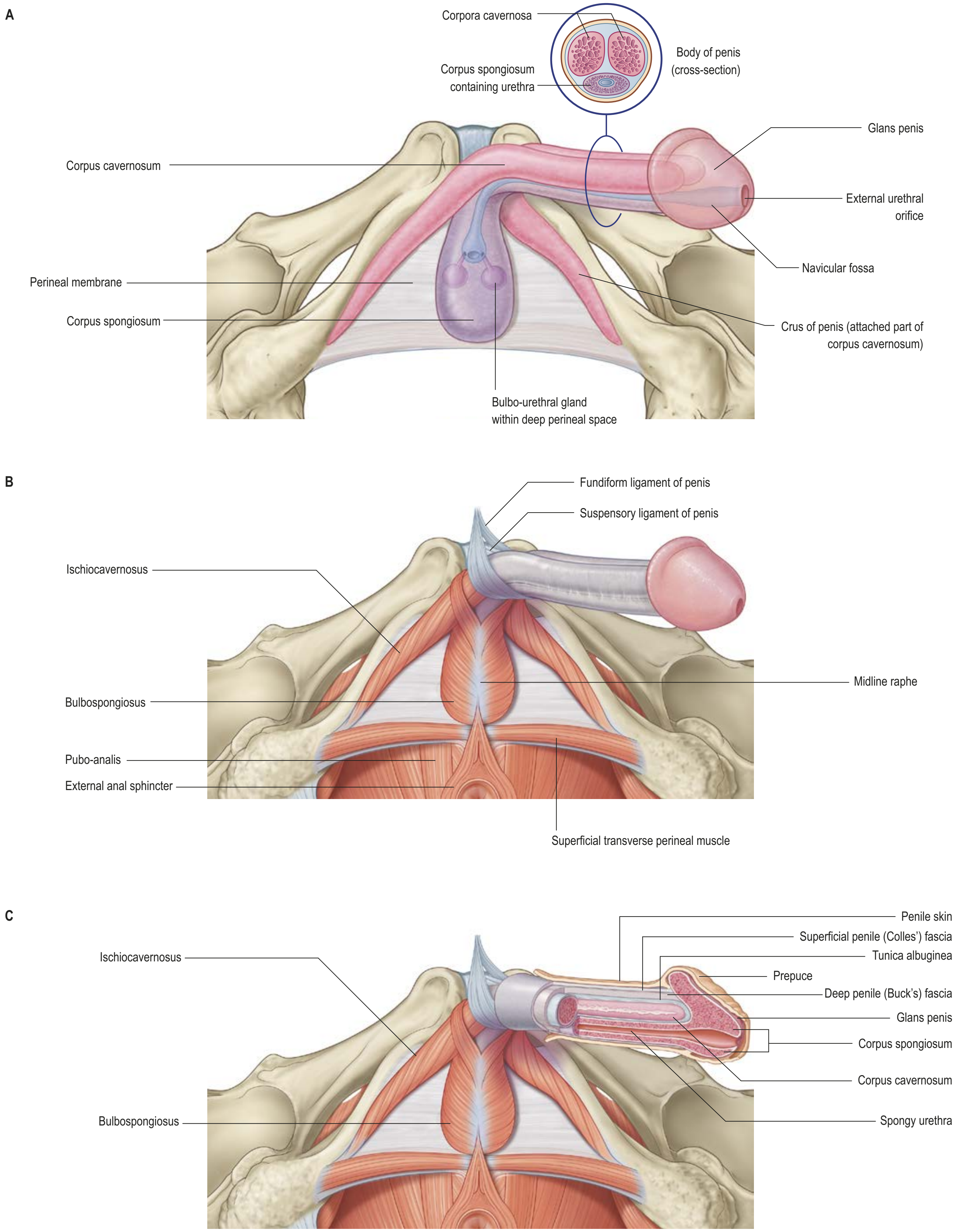
A
Corpora cavernosa
Corpus spongiosum containing urethra
Body of penis (cross-section)
Glans penis
Corpus cavernosum
External urethral orifice
Navicular fossa
Perineal membrane
Corpus spongiosum
Crus of penis (attached part of corpus cavernosum)
Bulbo-urethral gland within deep perineal space
B
Fundiform ligament of penis
Suspensory ligament of penis
Ischiocavernosus
Midline raphe
Bulbospongiosus
Pubo-analis
External anal sphincter
Superficial transverse perineal muscle
C
Penile skin
Superficial penile (Colles') fascia
Ischiocavernosus
Tunica albuginea
Prepuce
Deep penile (Buck's) fascia
Glans penis
Corpus spongiosum
Corpus cavernosum
Bulbospongiosus
Spongy urethra

Fig. 74.20 **A**, The erectile tissues of the penis. **B**, The muscles in the superficial perineal space. **C**, The muscles and erectile tissues of the penis in section. (A–B, With permission from Drake RL, Vogl AW, Mitchell A (eds) Gray's Anatomy for Students, 2nd ed. Elsevier, Churchill Livingstone. Copyright 2010. C, Adapted from Drake RL, Vogl AW, Mitchell A et al (eds) Gray's Atlas of Anatomy. Elsevier, Churchill Livingstone. Copyright 2008.)

neurovascular bundle. The corpora cavernosa end distally within the glans penis as individual, rounded cones (see Fig. 74.19D). The corpus spongiosum contains less erectile tissue than the corpora cavernosa and is enclosed by a thinner layer of tunica albuginea. The urethra traverses the length of the corpus spongiosum, terminating in a slit-like external urethral orifice at the distal end of the glans penis, which is itself an expansion of the corpus spongiosum. Numerous small sebaceous glands (preputial glands) lie along the proximal glans penis and their secretions combined with desquamated epithelial cells comprise smegma.

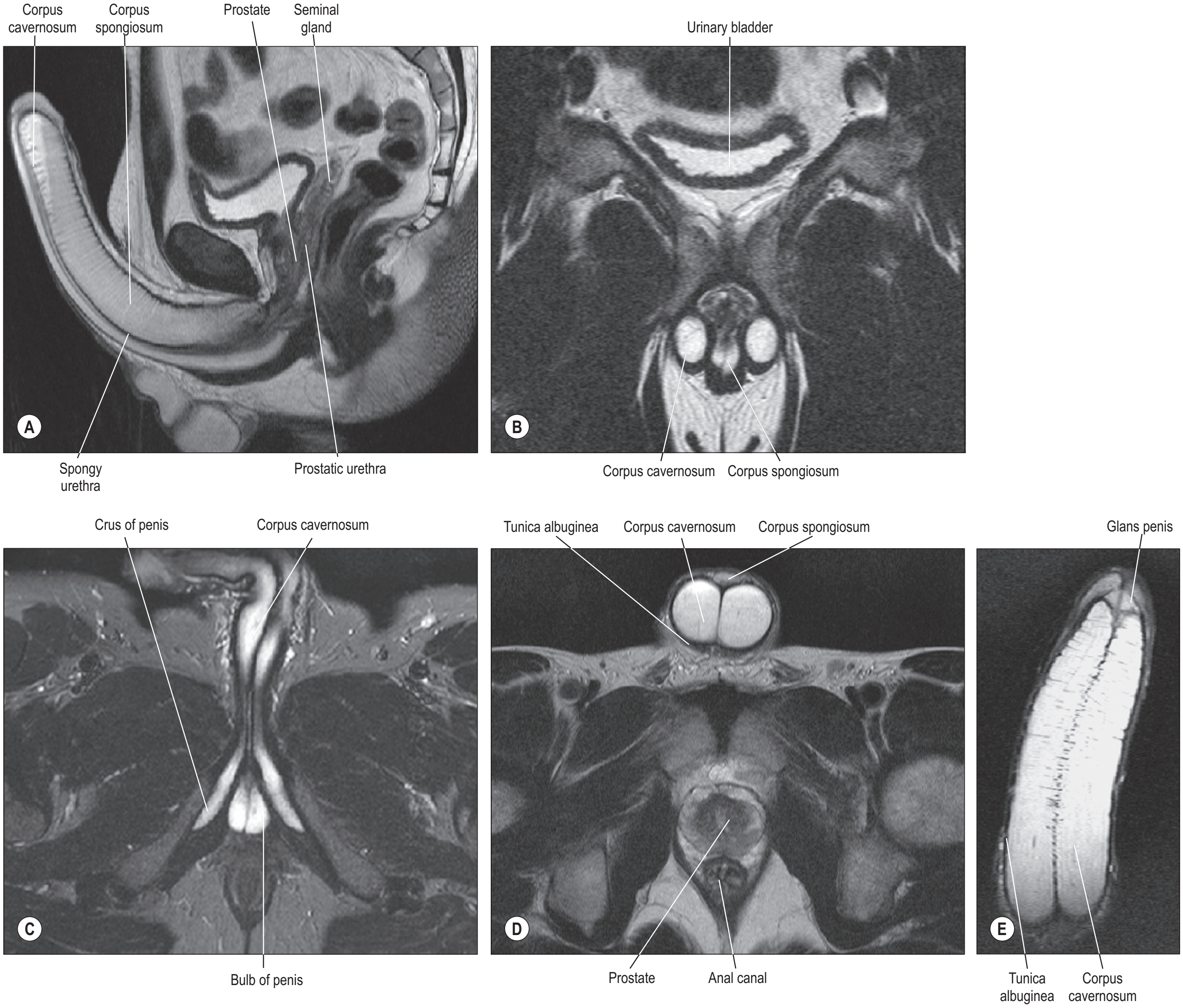

Fig. 74.21 A–B, MRI of the penis showing the corpora cavernosum and spongiosum. Note the corpus spongiosum flaring posteriorly into the bulb of the penis. **C**, MRI showing the bulb of the penis and the attachment of the posterior portion of the corpora cavernosa, the crura. **D–E**, MRI of the penis showing the tunica albuginea.

Vascular supply and lymphatic drainage

Arteries

Blood supply to the corporal bodies is derived from the internal pudendal artery, a branch of the internal iliac artery, which travels within the pudendal canal (Alcock's canal) before reaching the penis and perineum (Fig. 74.23). As it emerges from the pudendal canal, the internal pudendal artery gives rise to the perineal artery to supply ischiocavernosus and bulbospongiosus and the posterior surface of the scrotum, as well as the deep artery of the penis that supplies the deep structures of the penis (Fig. 74.24).

Arising from the perineal artery, the penile artery has three main branches: the artery to the bulb of the penis, the dorsal artery of the penis and the deep artery of the penis (Fig. 74.25) (Quartey 2006, MacLennan 2012).

Artery to the bulb of the penis The artery to the bulb of the penis penetrates the perineal membrane to enter the corpus spongiosum from above its posterolateral border and supplies the bulb of the penis and the urethra, in addition to the corpus spongiosum and glans penis.

Dorsal artery of the penis The dorsal artery of the penis passes between the crus of the penis and the pubis to reach the dorsal surface of the corpus cavernosum. It runs alongside the deep dorsal vein of the penis and the dorsal nerve of the penis and is attached, together with these structures, to the underside of the deep fascia of the penis. As it courses to the glans penis it gives off circumferential branches to the corpus spongiosum and spongy urethra. The rich blood supply to the corpus spongiosum allows the urethra to be divided safely during stricture repair.

Deep artery of the penis The deep artery of the penis is often a paired vessel that pierces the tunica albuginea of the corpora cavernosa proximally and then travels near the centre of the corporal bodies in the direction of the glans penis. Along its course it gives off several straight and helicine branches at regular intervals; they open directly into the cavernous spaces of the corporal bodies.

Variations in penile vascular anatomy are common and can include a single or absent cavernous artery or the presence of accessory pudendal arteries (Bare et al 1994, Matin 2006). While the penile arterial supply is commonly derived from both accessory and internal pudendal arteries, it can be derived exclusively from either the internal pudendal arteries or the accessory pudendal arteries (Droupy et al 1997). Recognizing such variation is extremely important for any surgeon contemplating penile revascularization surgery.

Veins

Blood leaving the penis is drained by one of three venous systems: superficial, intermediate or deep (see Figs 74.22B, 74.23). The superficial veins are contained within the superficial fascia of the penis and on its dorsolateral surface. They receive blood from the skin of the body of the penis and prepuce and coalesce to form a single superficial dorsal vein that drains into the long saphenous vein via the superficial external pudendal veins.

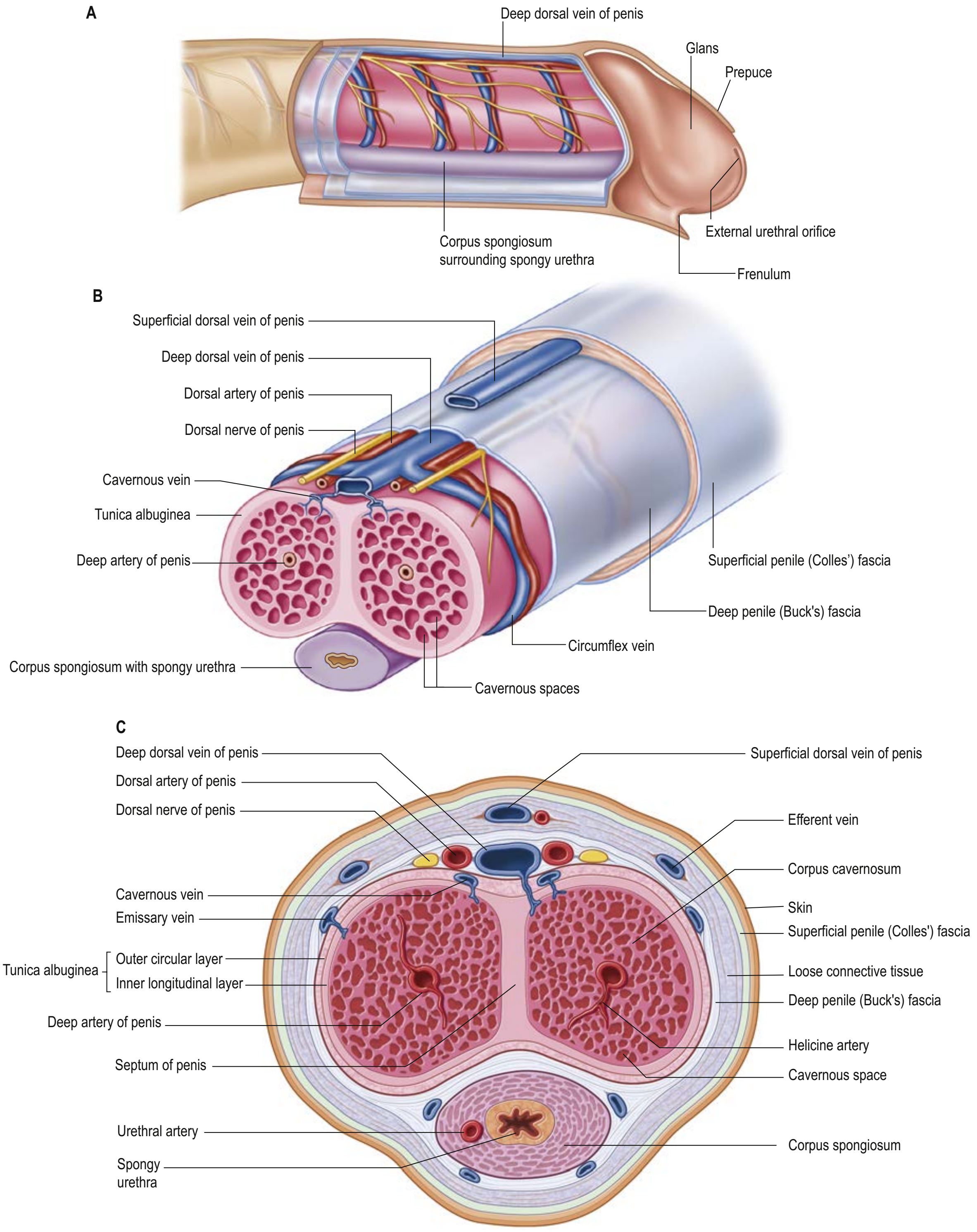
A
Deep dorsal vein of penis
Glans
Prepuce
External urethral orifice
Corpus spongiosum surrounding spongy urethra
Frenulum
B
Superficial dorsal vein of penis
Deep dorsal vein of penis
Dorsal artery of penis
Dorsal nerve of penis
Cavernous vein
Tunica albuginea
Deep artery of penis
Superficial penile (Colles') fascia
Deep penile (Buck's) fascia
Circumflex vein
Corpus spongiosum with spongy urethra
Cavernous spaces
C
Deep dorsal vein of penis
Dorsal artery of penis
Dorsal nerve of penis
Superficial dorsal vein of penis
Efferent vein
Corpus cavernosum
Cavernous vein
Emissary vein
Skin
Superficial penile (Colles') fascia
Tunica albuginea
Outer circular layer
Inner longitudinal layer
Loose connective tissue
Deep penile (Buck's) fascia
Deep artery of penis
Helicine artery
Septum of penis
Cavernous space
Urethral artery
Corpus spongiosum
Spongy urethra

Fig. 74.22 **A**, Layers of the penis and main structures. **B–C**, Cross-sectional anatomy of the body of the penis.

The intermediate drainage system contains the circumflex and deep dorsal veins, which lie within and beneath the deep fascia of the penis. This system receives blood from the glans penis, corpus spongiosum and distal two-thirds of the penis. Circumflex veins originate in the corpus spongiosum and course around the corpora cavernosa to meet the deep dorsal vein of the penis perpendicularly. They are only present in the distal two-thirds of the body of the penis and there are 3–10 of them. Intermediate venules in the erectile tissue of the corpora cavernosa arise from the cavernous spaces and drain into a subtunical capillary plexus. This plexus gives rise to emissary veins that course obliquely through the tunica albuginea and drain either into the circumflex veins or directly into the deep dorsal vein. The deep dorsal vein lies in the midline groove between the two corpora cavernosa. It passes inferior to the pubic symphysis at the level of the suspensory ligament of the penis, leaving the body of the penis at the crus, and drains into the prostatic venous plexus.

Deep venous drainage occurs via the crural and cavernous veins of the penis, the latter which travel almost the entire length of the corpus cavernosum and ultimately drain independent of the deep dorsal vein of the penis into the prostatic venous plexus (Hsu et al 2003). The emissary veins consolidate into 2–5 veins on the dorsomedial surface of the corpora cavernosa.

Lymphatic drainage

The penile and perineal skin is drained by lymphatic vessels that accompany the external pudendal veins to the superficial inguinal nodes. Lymphatic vessels from the glans penis pass to the deep inguinal and external iliac nodes, and those from the erectile tissue and spongy urethra pass to the internal iliac nodes.

Innervation

A rich sensory innervation to the glans penis is provided by the dorsal nerve of the penis, a branch of the pudendal nerve; it follows the course of the dorsal penile arteries (**Fig. 74.26**, see also Fig. 74.2). Small branches from the perineal nerve innervate the skin on the ventral surface of the penis as far distally as the glans (Uchio et al 1999).

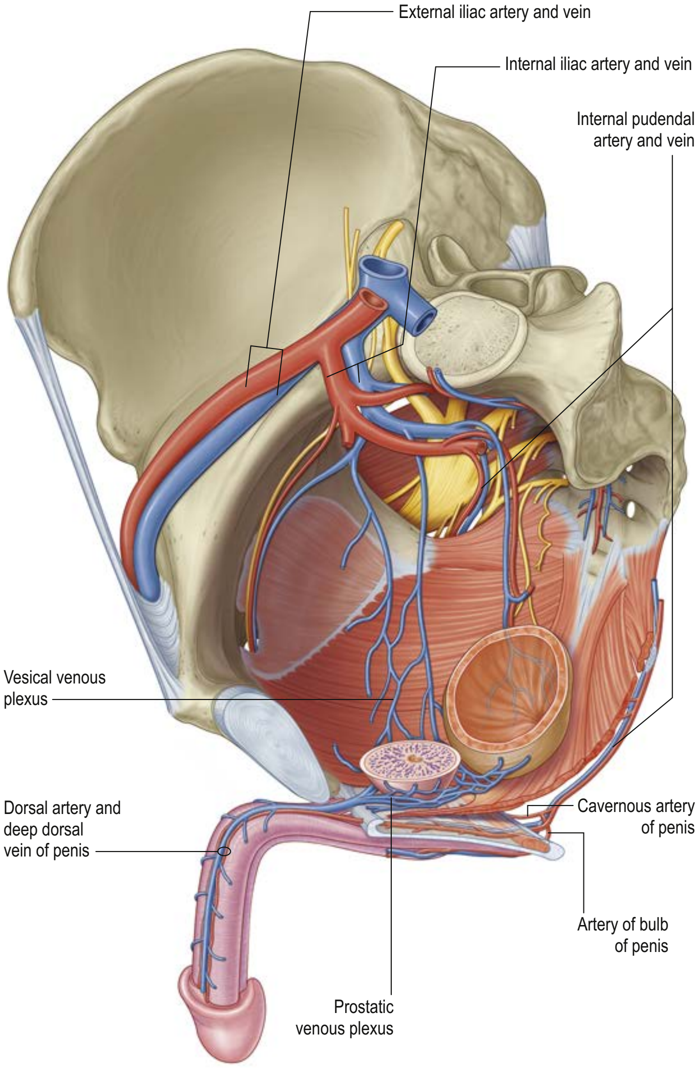
External iliac artery and vein
Internal iliac artery and vein
Internal pudendal artery and vein
Vesical venous plexus
Dorsal artery and deep dorsal vein of penis
Cavernous artery of penis
Artery of bulb of penis
Prostatic venous plexus

Fig. 74.23 Vessels related to the penis. (Adapted from Drake RL, Vogl AW, Mitchell A (eds) Gray's Anatomy for Students, 2nd ed. Elsevier, Churchill Livingstone. Copyright 2010.)

Sympathetic and parasympathetic input to the corpora cavernosa is provided by the cavernous nerves of the penis, which originate from the inferior hypogastric plexus. They course along the posterolateral aspect of the prostate before exiting the pelvis, together with the urethra, and entering the corpora cavernosa at the crura of the penis. Before entering the cavernous bodies, the cavernous nerve sends branches to the corpus spongiosum. Parasympathetic input to the penis (excitatory) originates in the neurones of the first four sacral spinal cord segments and travels via the pelvic splanchnic nerves to the inferior hypogastric plexus (see Fig. 74.26), where preganglionic fibres synapse on postganglionic neurones that give rise to the cavernous nerve. Sympathetic input to the penis (inhibitory) originates in the intermediolateral grey matter of the eleventh and twelfth thoracic and first lumbar spinal cord segments and travels through the sympathetic trunk before descending to the inferior hypogastric plexus. Parasympathetic stimulation produces vasodilatation while sympathetic innervation causes vasoconstriction, contraction of the seminal glands and prostate, and seminal fluid emission.

Microstructure

The corpora cavernosa are cylinders of spongy erectile tissue composed of interconnected endothelium-lined cavernous spaces, separated by smooth muscle trabeculae and surrounded by elastic and collagen fibres and loose areolar tissue. The cavernous spaces are larger in the centre. Terminal cavernous nerves and helicine arteries are intimately associated with smooth muscle. The helicine arteries are contracted and tortuous in the flaccid state and straight and dilated in the erect state.

The tunica albuginea surrounding the corpora consists of an inner circular and outer longitudinal layer of elastic fibres arranged in a latticed network. Venous drainage from the corpora cavernosa originates in the trabeculae between the peripheral cavernous spaces and the tunica albuginea (the subtunical capillary plexus) before exiting the corpora via the emissary veins (Banya et al 1989).

Emissary veins travel between the two layers of the tunica albuginea and exit the outer layer obliquely. The outer layer compresses the emissary veins when the penis becomes engorged with blood, preventing venous outflow, and thereby maintains the erection.

The structure of the corpus spongiosum is similar to that of the corpora cavernosa, with the exception of larger cavernous spaces and a thinner tunica albuginea. The glans penis has no tunical covering.

Erection and ejaculation

Penile erection is a neurovascular process, initiated by sexual stimulation and relaxation of the smooth muscle of the corpora cavernosa and mediated by various neurotransmitters produced by the parasympathetic nerves and the endothelium. The most important neurotransmitter is nitric oxide, which acts via the cyclic guanosine monophosphate (cGMP) second messenger system. Following smooth muscle relaxation there is rapid influx of blood from the helicine arteries, filling the cavernous spaces and leading to penile tumescence. The resulting distension compresses the emissary veins, preventing venous outflow. This so-called 'veno-occlusive mechanism' converts tumescence into an erection. Continuing cutaneous stimulation of the glans penis and frenulum contributes significantly towards maintaining an erection and initiating orgasm and ejaculation. Erection, therefore, depends on a variety of factors, including a normal psychogenic response to stimulation, intact parasympathetic nerves, healthy corporal smooth muscle capable of relaxation, patent arteries capable of delivering blood at the required rate, and a normal venous system. Following ejaculation, the sequence just described is reversed; smooth muscle contraction in response to sympathetic stimulation leads to penile detumescence.

Emission and ejaculation are separate but related processes. Emission is the transmission of seminal fluid from the ductus deferens, prostate and seminal glands into the prostatic urethra and is under sympathetic control. Ejaculation is the expulsion of seminal fluid from the prostatic urethra to the exterior and has both autonomic and somatic components. The first discernible event during ejaculation is contraction of bulbospongiosus, which occurs approximately six times and is under somatic control. Antegrade ejaculation also requires concomitant closure of the neck of the urinary bladder (Ch. 73). Relaxation of the external urethral sphincter, under autonomic control, permits seminal fluid to be expelled from the prostatic urethra to the spongy urethra and from there out the external urethral meatus to the exterior. The timing of this process is such that the ejaculate is expelled from the external urethral orifice between the second and final contraction of bulbospongiosus; in some males, ejaculation is pulsatile.

Erectile dysfunction and priapism

Available with the *Gray's Anatomy* e-book

Scrotum

The scrotum is composed of multiple layers of tissues including skin, dartos and external spermatic, cremasteric and internal spermatic fasciae (see Fig. 74.3). The internal spermatic fascia is loosely attached to the parietal layer of the tunica vaginalis.

The scrotal skin is thin, pigmented, devoid of fat, hair-bearing and rich in sebaceous and sweat glands. It is also richly innervated by cutaneous nerves that respond to stimulation of the skin and hairs and to changes in temperature. The appearance of the scrotal skin can vary from smooth to rugated depending on the degree of contraction of the underlying dartos. The midline raphe of the scrotum extends from the external urethral orifice down the ventral body of the penis and to the anus, signifying the line of fusion of the genital tubercles (see Fig. 22.20). It is a relatively avascular plane so it is a common location for single incisions used to access both scrotal compartments. Deep to the raphe of the scrotum, the scrotum is separated into two compartments by the septum of the scrotum composed of all the layers of the scrotal wall except the skin. The testes are suspended by the spermatic cords within these compartments.

Dartos is continuous with the superficial fascia of the penis (Colles' fascia) and the membranous layer of the superficial fascia of the abdomen (Scarpa's fascia). The external spermatic, cremasteric and internal spermatic layers of the scrotum are continuous with the corresponding layers in the spermatic cord and arise from the aponeuroses of external abdominal oblique and internal abdominal oblique and the transversalis fascia of the abdominal wall, Erectile dysfunction is the inability to achieve tumescence despite adequate sexual stimulation. The pathophysiology of erectile dysfunction is complex and involves vascular, neurogenic and psychogenic components. Common aetiologies underlying a diagnosis of erectile dysfunction include: inability to relax the cavernous smooth muscle; arterial insufficiency due to atheromatous disease; neurogenic dysfunction due to diabetes or surgery; and radiation therapy.

A prolonged erection that fails to subside after ejaculation is called priapism. Priapism can broadly be classified as high-flow (non-ischaemic) or low-flow (ischaemic). Low-flow priapism, which is due to impaired efflux of venous blood from the penis, is characterized by significant pain and is a medical emergency. If untreated, priapism leads to ischaemia of the corporal smooth muscle and irreversible erectile dysfunction. The aetiology of low-flow priapism includes conditions such as sickle-cell disease and leukaemia, and the use of intracavernosal injection therapy with prostaglandins. In contrast, high-flow priapism is the consequence of excessive blood flow into the penis, usually secondary to a fistula between the deep artery of the penis and cavernous spaces.

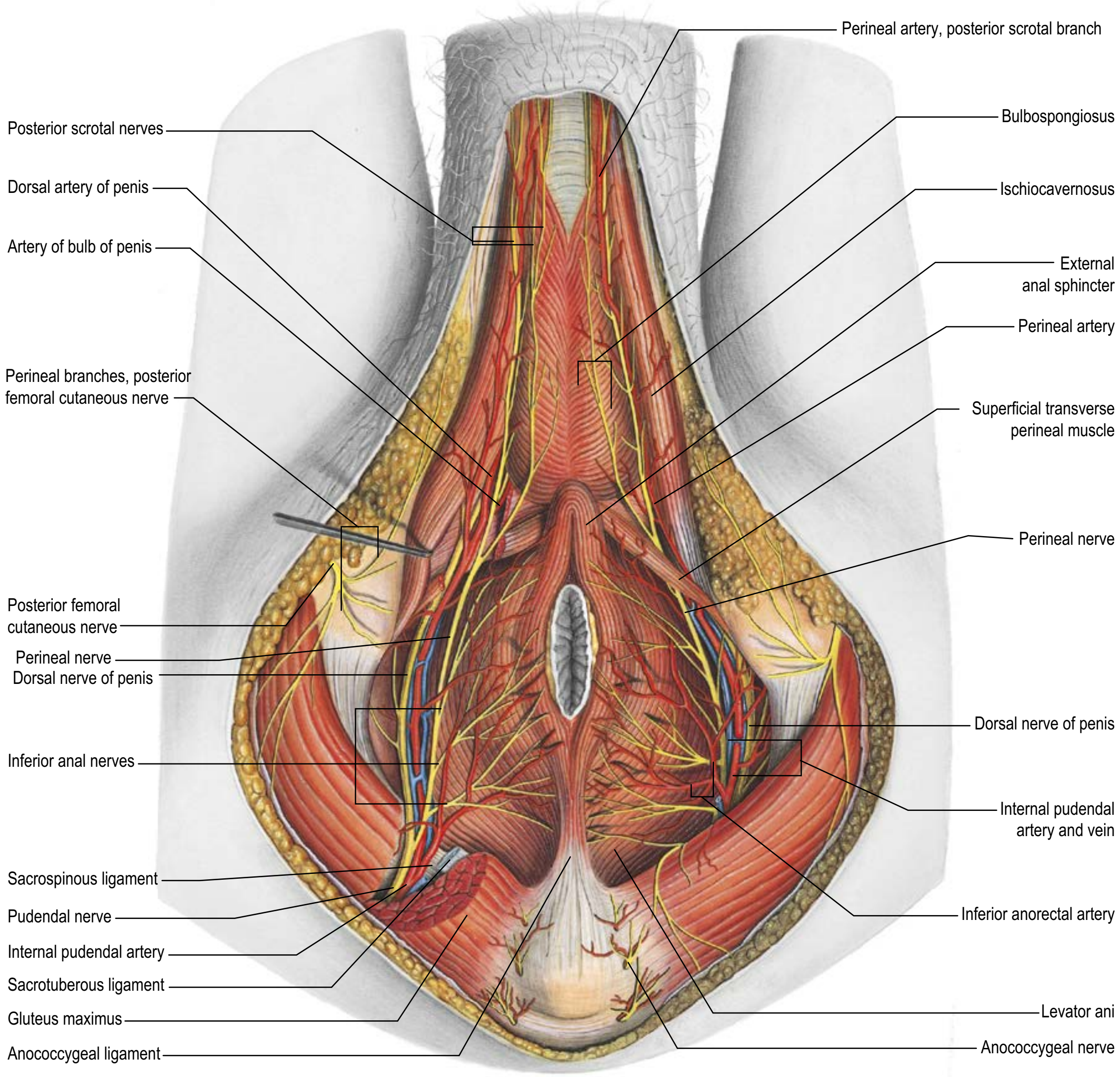
Posterior scrotal nerves
Dorsal artery of penis
Artery of bulb of penis
Perineal branches, posterior femoral cutaneous nerve
Posterior femoral cutaneous nerve
Perineal nerve
Dorsal nerve of penis
Inferior anal nerves
Sacrospinous ligament
Pudendal nerve
Internal pudendal artery
Sacrotuberous ligament
Gluteus maximus
Anococcygeal ligament
Perineal artery, posterior scrotal branch
Bulbospongiosus
Ischiocavernosus
External anal sphincter
Perineal artery
Superficial transverse perineal muscle
Perineal nerve
Dorsal nerve of penis
Internal pudendal artery and vein
Inferior anorectal artery
Levator ani
Anococcygeal nerve

Fig. 74.24 The blood vessels and nerves of the perineal region and external genitalia in the adult male. The fat body of the ischio-anal fossa has been removed and gluteus maximus has been incised in order to expose the course of the pudendal nerve and internal pudendal artery. (Sobotta Atlas of Human Anatomy © Elsevier GmbH, Urban & Fischer, Munich.)

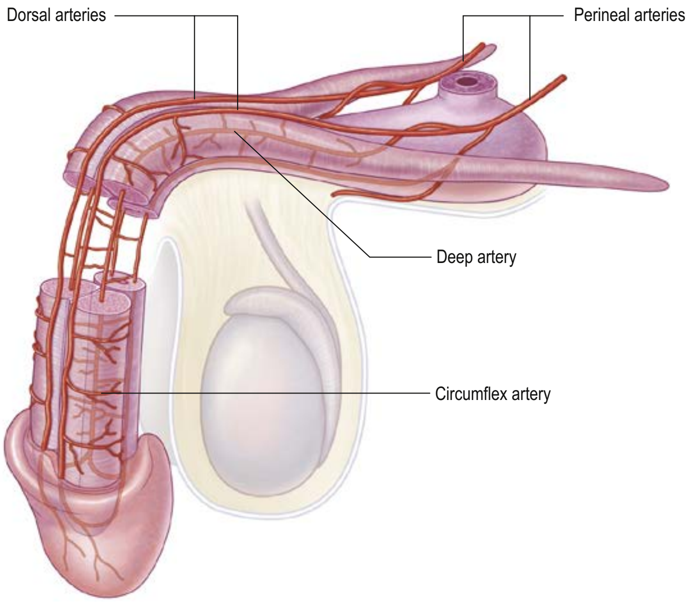
Dorsal arteries
Perineal arteries
Deep artery
Circumflex artery

Fig. 74.25 The arterial blood supply to the body of the penis.

respectively. The testis is also sometimes fixed to the scrotal wall at its inferior pole by a fibrous band known as the scrotal ligament (Cavalie et al 2018).

Developmental anomalies of the scrotum Congenital agenesis of the scrotum is a very rare anomaly characterized by absence of the scrotum; no rugae are noted in the perineum (Yilmaz et al 2013). Penoscrotal transposition, in which the scrotum is located superior and anterior to the penis, is a consequence of abnormal genital tubercle development and is associated with hypospadias, renal agenesis and dysplasia, and imperforate anus.

Vascular supply and lymphatic drainage

The arterial supply to the scrotum includes external pudendal branches of the femoral artery, posterior scrotal branches of the internal pudendal artery and the cremasteric artery, a branch from the inferior epigastric artery. Of note, the anterior scrotal wall is supplied primarily by branches of the external pudendal artery, which run parallel to the rugae and do not cross the raphe of the scrotum; this anatomical detail is important for planning appropriate incisions during scrotal surgery.

The scrotal vessels are arranged in a dense subcutaneous network, which facilitates heat loss and regulation of scrotal temperature. Venous drainage follows the arterial network and simple arteriovenous anastomoses are common.

Scrotal lymphatic vessels do not cross the raphe of the scrotum and therefore lymphatic drainage from the scrotum is always routed to the ipsilateral superficial inguinal nodes.

Innervation

Innervation of the skin of the anterior third of the scrotum is primarily derived from the first lumbar spinal cord segment by way of the ilio-inguinal nerve (anterior scrotal nerves) and genital branch of the

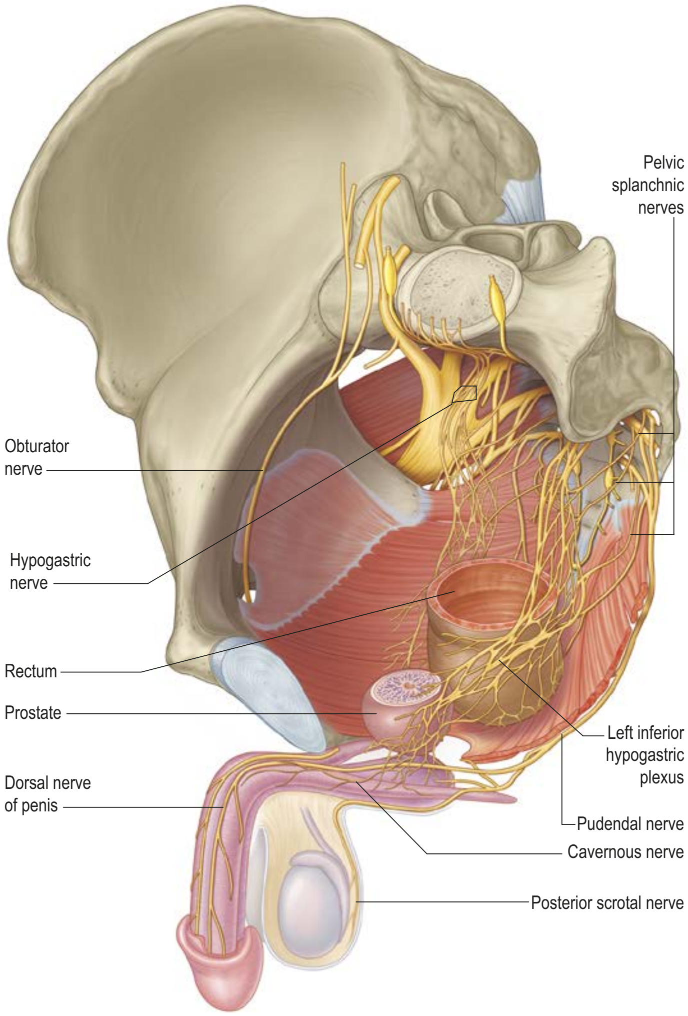

Fig. 74.26 The nerve supply to the penis. The corpus cavernosum of the penis receives both a parasympathetic and a sympathetic innervation from the cavernous nerves. Multiple cavernous nerves emanate from the prostatic plexus and intertwine with both dorsal nerves of the penis. The afferent fibres from the glans travel via the dorsal nerves of the penis and via the pudendal nerve. (Adapted from Drake RL, Vogl AW, Mitchell A (eds) Gray's Anatomy for Students, 2nd ed. Elsevier, Churchill Livingstone. Copyright 2010.)

genitofemoral nerve (see Fig. 74.2). Innervation of the skin of the posterior two-thirds of the scrotum is primarily derived from the third sacral spinal cord segment via the perineal nerve and perineal branches of the posterior femoral cutaneous nerve. In order to anaesthetize the scrotum, spinal anaesthesia must therefore be injected proximal to the L1 spinal cord level.

Key references

Angermeier KW 2006 Surgical anatomy of the penis. In: Novick AC, Jones JS, Gill IS et al (eds) Operative Urology at the Cleveland Clinic. Totowa: Humana Press, pp. 377–83.

A comprehensive atlas of urological surgery that includes details of robotic and laparoscopic prostatectomy, open and laparoscopic partial nephrectomy, renal transplantation and minimally invasive treatments for urological conditions.

Goldstein M 2012 Surgical management of male infertility. In: Wein A, Kavoussi LR, Novick AC et al (eds) Campbell-Walsh Urology, 10th ed. Philadelphia: Elsevier, Saunders, pp. 648–87.

A definitive and unparalleled summary of the indications and operative techniques for operations involving the male reproductive tract.

Macmillan EW 1954 The blood supply of the epididymis in man. Br J Urol 26:60–71.

An impressive and definitive arteriographical evaluation of the arterial supply and venous drainage of the human epididymis, including anastomoses with the testicular blood supply, and clinical implications in disease settings.

Nguyen HT, Etzell J, Turek PJ 1996 Normal human ejaculatory duct anatomy: a study of cadaveric and surgical specimens. J Urol 155:1639–42.

Gross and microscopic evaluation of the human ejaculatory duct, correlating microarchitecture to function, and defining anatomical measurements for the diagnosis of ejaculatory duct obstruction.

Oka S, Shiraishi K, Matsuyama H 2016 Microsurgical anatomy of the spermatic cord and spermatic fascia: distribution of lymphatics, and sensory and autonomic nerves. J Urol 195:1841–47.

An immunohistochenical examination of the distribution of the lymphatics and the sensory and autonomic innervation of the spermatic cord, using fresh spermatic cords and biopsied spermatic fascia.

Taguchi K, Tsukamoto T, Murakami G 1999 Anatomical studies of the autonomic nervous system in the human pelvis by the whole-mount staining method: left–right communicating nerves between bilateral pelvic plexuses. J Urol 161:320–5.

A histological evaluation of the various components of the inferior hypogastric plexus, correlating nerve morphology with function and demonstrating the presence of communication between nerves from the right and left plexuses, respectively.

Tubbs RS, Shoja M, Loukas M 2016 Bergman's Comprehensive Encyclopedia of Human Anatomic Variation. Hoboken: Wiley Blackwell.

A textbook dedicated to detailing the anatomical variations found in man.

Bonus e-book content

Fig. 74.1 A–B, Reference curves for mean testicular volume measured by ultrasonography.

Fig. 74.6 A laparoscopic view of a patent processus vaginalis in a 4-month-old boy.

Fig. 74.8 CT showing the left testicular vein draining to the left renal vein and the right testicular vein draining to the inferior vena cava.

Fig. 74.9 A colour Doppler scan of the scrotal contents showing normal flow.

Fig. 74.11 The main ultrastructural features of a mature spermatozoon.

Fig. 74.12 Gangrene of the appendix testis secondary to torsion of the testis in an 8-year-old boy.

Table 74.1 Testicular volumes measured by ultrasonography (infancy to adolescence).

Video 74.1 Dissection of the male pelvis and perineum.

References

Angermeier KW 2006 Surgical anatomy of the penis. In: Novick AC, Jones JS, Gill IS et al (eds) Operative Urology at the Cleveland Clinic. Totowa: Humana Press, pp. 377–383.

A comprehensive atlas of urological surgery that includes details of robotic and laparoscopic prostatectomy, open and laparoscopic partial nephrectomy, renal transplantation and minimally invasive treatments for urological conditions.

Asala S, Chaudhary SC, Masumbuko-Kahamba N et al 2001 Anatomical variations in the human testicular blood vessels. Ann Anat 183:545–9.

Banya Y, Ushiki T, Takagane H et al 1989 Two circulatory routes within the human corpus cavernosum penis: a scanning electron microscopic study of corrosion casts. J Urol 142: 879–883.

Bare RL, DeFranzo A, Jarow JP 1994 Intraoperative arteriography facilitates penile revascularization. J Urol 151:1019–21.

Beck EM, Schlegel PN, Goldstein M 1992 Intraoperative varicocele anatomy: a macroscopic and microscopic study. J Urol 148:1190–4.

The first large, detailed intraoperative study of spermatic cord anatomy in men with varicoceles.

Bedford JM, Calvin H, Cooper GW 1973 The maturation of spermatozoa in the human epididymis. J Reprod Fertil Suppl 18:199–213.

Braithwaite JL 1952 The arterial supply of the male urinary bladder. Br J Urol 24:64–71.

A comprehensive description of the arterial supply of the human bladder, including variations and anomalies.

Canavese F, Mussa A, Manenti M et al 2009 Sperm count of young men surgically treated for cryptorchidism in the first and second year of life: fertility is better in children treated at a younger age. Eur J Pediatr Surg 19:388–91.

Cavalie G, Bellier A, Marnas G et al 2018 Anatomy and histology of the scrotal ligament in adults: inconsistency and variability of the gubernaculum testis. Surg Radiol Anat 40:365–70.

Daniel O, Shackman R 1952 The blood supply of the human ureter in relation to ureterocolic anastomosis. Br J Urol 24:549–50.

Droupy S, Benoît G, Giuliano F et al 1997 Penile arteries in humans. Origin–distribution–variations. Surg Radiol Anat 19:161–7.

Favorito LA, Cavalcante AG, Babinski MA 2004 Study on the incidence of testicular and epididymal appendages in patients with cryptorchidism. Int Braz J Urol 30:49–52.

Favorito LA, Balassiano CM, Costa WS et al 2012 Development of the human foreskin during the fetal period. Histol Histopathol 27:1041–5.

Goede J, van der Voort-Doedens LM, Sijstermans K et al 2011 The volume of retractile testes. J Urol 186:2050–4.

Goldstein M 2012 Surgical management of male infertility. In: Wein A, Kavoussi LR, Novick AC et al (eds) Campbell-Walsh Urology, 10th ed. Philadelphia: Elsevier, Saunders, pp. 648–87.

A definitive and unparalleled summary of the indications and operative techniques for operations involving the male reproductive tract.

Harrison RJ 1949 The vascular supply to the human testis. J Anat 83:61.

Harrison RG, Barclay AE 1948 The distribution of the testicular artery (internal spermatic artery) to the human testis. Br J Urol 20:57–66.

A detailed anatomical study that significantly improved knowledge of the vascular supply of the human testis, with important implications for surgical techniques of orchidopexy.

Hoffer AP 1976 The ultrastructure of the ductus deferens in man. Biol Reprod 14:425–43.

An ultrastructural evaluation of the human ductus deferens, including an assessment of its contribution to sperm function and transport.

Hsu GL, Hsieh CH, Wen HS et al 2013 Penile venous anatomy: an additional description and its clinical implication. J Androl 24:921–27.

Jarow JP 1991 Clinical significance of intratesticular arterial anatomy. J Urol 145:777–9.

Jarow JP, Ogle A, Kaspar J et al 1992 Testicular artery ramification within the inguinal canal. J Urol 147:1290–2.

Jow WW, Steckel J, Schlegel PN et al 1993 Motile sperm in human testis biopsy specimens. J Androl 14:194–98.

Kayalvizhi I, Narayan RK, Kumar P 2017 Anatomical variations of testicular artery: a review. Folia Morphol 76:541–50.

Kaufman EC, Kim HH, Tanrikut C et al 2011 Microsurgical spermatocelectomy: technique and outcomes of a novel surgical approach. J Urol 185:238–42.

Kormano M, Reijonen K 1976 Microvascular structure of the human epididymis. Am J Anat 145:23–7.

Kotian SR, Pandey AK, Padmashali S et al 2016 A cadaveric study of the testicular artery and its clinical significance. J Vasc Bras 15:280–6.

Kraft KH, Mucksavage P, Canning DA et al 2011 Histological findings in patients with cryptorchidism and testis–epididymis nonfusion. J Urol 186:2045–9.

MacLennan GT 2012 Hinman's Atlas of UroSurgical Anatomy, 2nd ed. Philadelphia: Elsevier.

Macmillan EW 1954 The blood supply of the epididymis in man. Br J Urol 26:60–71.

An impressive and definitive arteriographical evaluation of the arterial supply and venous drainage of the human epididymis, including anastomoses with the testicular blood supply, and clinical implications in disease settings.

Matin SF 2006 Recognition and preservation of accessory pudendal arteries during laparoscopic radical prostatectomy. Urology 67:1012–5.

Mendez JA, Emery JL 1979 The seminiferous tubules of the testis before, around and after birth. J Anat 128:601–7.

Mirilas P, Mentessidou A 2012 Microsurgical subinguinal varicocelectomy in children, adolescents, and adults: surgical anatomy and anatomically justified technique. J Androl 33:338–49.

Mostafa T, Labib I, el-Khayat Y et al 2008 Human testicular artery supply: gross anatomy, corrosion case, and radiologic study. J Androl 90:2226–30.

Nakajima F, Takenaka A, Uchiyama E et al 2007 Macroscopic and histotopographic study of the deep transverse perineal muscle (musculus transversus perinei profundus) in elderly Japanese. Ann Anat 189:65–74.

Ndiaye A, Diop M, Ndoye JM et al 2007 Anatomical basis of neuropathies and damage to the ilioinguinal nerve during repairs of groin hernias (about 100 dissections). Surg Radiol Anat 29:675–81.

Nguyen HT, Etzell J, Turek PJ 1996 Normal human ejaculatory duct anatomy: a study of cadaveric and surgical specimens. J Urol 155:1639–42.

Gross and microscopic evaluation of the human ejaculatory duct, correlating microarchitecture to function, and defining anatomical measurements for the diagnosis of ejaculatory duct obstruction.

Oelrich TM, Moosman DA 1977 The aberrant course of the cutaneous component of the ilioinguinal nerve. Anat Rec 189:233–6.

Oka S, Shiraishi K, Matsuyama H 2016 Microsurgical anatomy of the spermatic cord and spermatic fascia: distribution of lymphatics, and sensory and autonomic nerves. J Urol 195:1841–7.

An immunohistochenical examination of the distribution of the lymphatics and the sensory and autonomic innervation of the spermatic cord, using fresh spermatic cords and biopsied spermatic fascia.

Pai MM, Vadgaonkar R, Rai R et al 2008 A cadaveric study of the testicular artery in the South Indian population. Singapore Med J 49:551–5.

Prader A 1966 Testicular size: assessment and clinical importance. Triangle 7:240–3.

A landmark paper introducing the use of a standardized orchidometer for measuring testicular volume and discussing the relationship between abnormal testicular size and various underlying medical disorders.

Quartey JKM 2006 Anatomy and blood supply of the urethra and penis. In: Schreiter F, Jordan G (eds) Urethral Reconstructive Surgery. Berlin, Springer; Ch. 3. pp. 12–17.

Raman J, Goldstein M 2004 Intraoperative characterization of arterial vasculature in spermatic cord. Urology 64:561–4.

Rauchenwald M, Steers WD, Desjardins C et al 1995 Efferent innervation of the rat testis. Biol Reprod 52:1136–43.

Rune GM, Mayr J, Neugebauer H et al 1992 Pattern of Sertoli cell degeneration in cryptorchid prepubertal testes. Int J Androl 15:19–31.

Sahni D, Jit K, Joshi K et al 1996 Incidence and structure of the appendices of the testis and epididymis. J Anat 189:341–8.

Savas C, Candir O, Bezir M et al 2001 Ectopic adrenocortical nodules along the spermatic cord of children. Int Urol Nephrol 32:681–5.

Schoysman RJ, Bedford JM 1986 The role of the human epididymis in sperm maturation and sperm storage as reflected in the consequences of epididymovasostomy. Fertil Steril 46:293–9.

Schwarz GM, Hirtler L 2017 The cremasteric reflex and its muscle – a paragon of ongoing scientific discussion: a systematic review. Clin Anat 30:498–507.

Schwentner C, Radmayr C, Lunacek A et al 2006 Laparoscopic varicocele ligation in children and adolescents using isosulphan blue: a prospective randomized trial. BJU Int 98:861–5.

Shalaby MM, Shoma AM, Elanany FG et al 2011 Management of the looping vas deferens during laparoscopic orchiopexy. J Urol 185:2455–7.

Shin D, Lemack GE, Goldstein M et al 1997 Induction of spermatogenesis and pregnancy after adult orchiopexy. J Urol 158:2242.

Silber SJ 1989 Role of epididymis in sperm maturation. Urology 33:47–51.

Taguchi K, Tsukamoto T, Murakami G 1999 Anatomical studies of the autonomic nervous system in the human pelvis by the whole-mount staining method: left-right communicating nerves between bilateral pelvic plexuses. J Urol 161:320–5.

A histological evaluation of the various components of the inferior hypogastric plexus, correlating nerve morphology with function and demonstrating the presence of communication between nerves from the right and left plexuses, respectively.

Tiryaki T, Hucumenoglu S, Atayurt H 2005 Transverse testicular ectopia associated with persistent Müllerian duct syndrome. A case report. Urol Int 74:190–2.

Tishler PV 1971 Diameter of testicles. N Engl J Med 285:1489.

Tubbs RS, Shoja M, Loukas M 2016 Bergman's Comprehensive Encyclopedia of Human Anatomic Variation. Hoboken: Wiley Blackwell.

A textbook dedicated to detailing the anatomical variations found in man.

Tuffaha SH, Sacks JM, Shores JT et al 2014 Using the dorsal, cavernosal, and external pudendal arteries for penile transplantation: technical considerations and perfusion territories. Plast Reconstr Surg 134:111e–119e.

Turner TT, D'Addario D, Howards SS 1978 Further observations on the initiation of sperm motility. Biol Reprod 19:1095–101.

Uchio EM, Yang CC, Kromm BG et al 1999 Cortical evoked responses from the perineal nerve. J Urol 162:1983–6.

Yilmaz E, Afsarlar CE, Karaman I et al 2013 Congenital hemiscrotal agenesis: report of a rare entity. J Pediatr Urol 991:e76–7.

Yuasa J, Ito H, Toyama Y et al 2001 Postnatal development of the testis in Japanese children based on observations of undescended testes. Int J Urol 8:490–494.

Zhang XP, Lin ZY, Zeng SX et al 2015 Blood vessels and nerves surrounding the seminal vesicles: a clinical anatomic study. Zhonghua Nan Ke Xue 21:877–80.

CHAPTER
75

Female reproductive system

The female reproductive system consists of the lower genital tract (vulva and vagina) and the upper tract (uterus and cervix with associated uterine (Fallopian) tubes and ovaries).

LOWER GENITAL TRACT

Vulva

The female external genitalia or vulva (pudendum) include the mons pubis, labia majora, labia minora, clitoris, vestibule of the vagina, vestibular bulbs and the greater vestibular glands (Bartholin's glands) (**Fig.** 75.1).

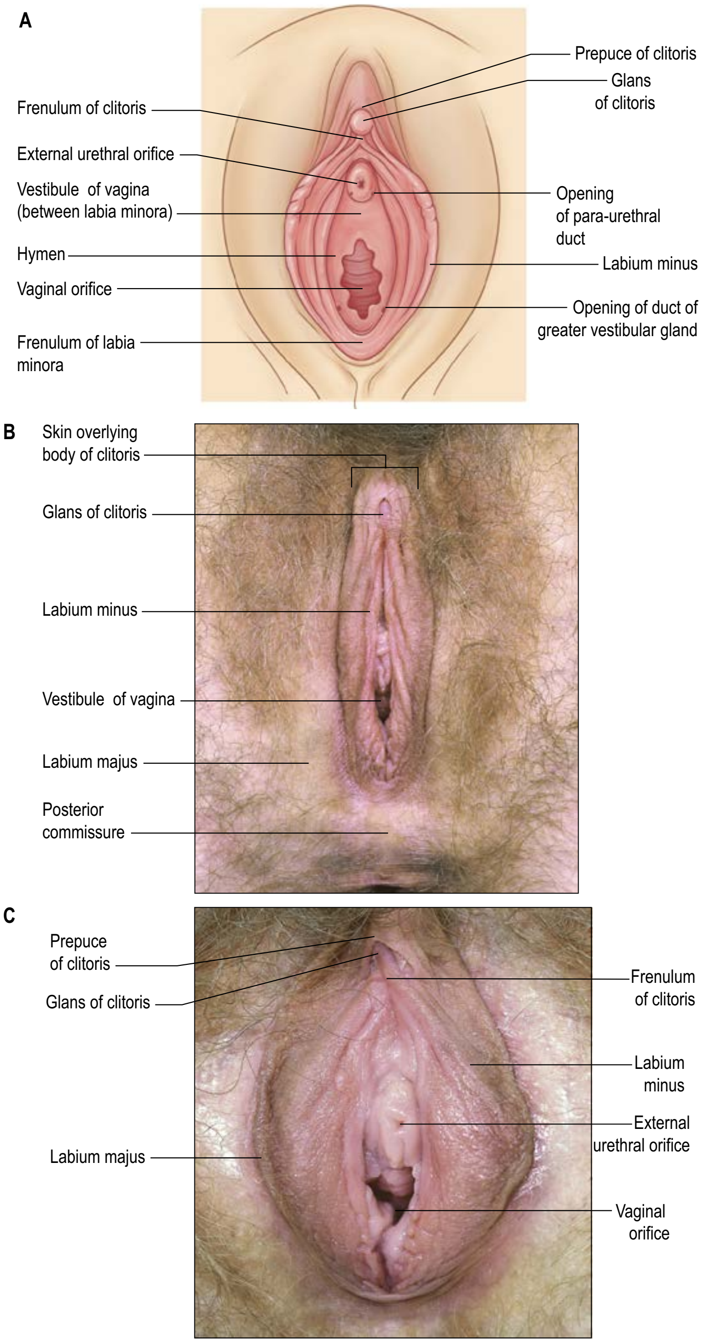
A
Prepuce of clitoris
Glans of clitoris
Frenulum of clitoris
External urethral orifice
Vestibule of vagina (between labia minora)
Opening of para-urethral duct
Hymen
Labium minus
Vaginal orifice
Opening of duct of greater vestibular gland
Frenulum of labia minora
B
Skin overlying body of clitoris
Glans of clitoris
Labium minus
Vestibule of vagina
Labium majus
Posterior commissure
C
Prepuce of clitoris
Glans of clitoris
Frenulum of clitoris
Labium minus
External urethral orifice
Labium majus
Vaginal orifice

Fig. 75.1 **A**, The superficial features of the vulva. **B**, The labia majora and other surrounding external genitalia. **C**, The labia minora. (A, With permission from Drake RL, Vogl AW, Mitchell A et al (eds) Gray's Atlas of Anatomy. Elsevier, Churchill Livingstone. Copyright 2008. B–C, With permission from Drake RL, Vogl AW, Mitchell A (eds) Gray's Anatomy for Students, 2nd ed. Elsevier, Churchill Livingstone. Copyright 2010.)

Mons pubis

The mons pubis is the rounded, hair-bearing area of skin and adipose tissue over the pubic symphysis and adjacent pubic bone. Before puberty, it is relatively flat and hairless, and the labia minora are poorly formed. Through adolescence and into adult life the mons pubis becomes prominent and develops coarse hair. It atrophies slightly after menopause.

Labia majora

The labia majora are two prominent, longitudinal folds of skin that extend back from the mons pubis to the perineum (see Fig. 75.1B). They form the lateral boundaries of the vulva. Each labium has an external pigmented surface covered with hairs and a smooth pink internal surface with large sebaceous follicles. Between these surfaces there is loose connective and adipose tissue intermixed with smooth muscle (resembling the dartos muscle of the scrotum), vessels, nerves and glands. The subcutaneous layer consists of a superficial fatty layer similar to the superficial fatty layer (Camper's fascia) of the anterior abdominal wall, and a deep membranous layer (Colles' fascia) continuous with the deep membranous layer (Scarpa's fascia) of the anterior abdominal wall. The round ligament of the uterus may end in the adipose tissue and skin in the anterior part of the labium majus. A patent processus vaginalis may also reach a labium majus. The labia majora join anteriorly to form the anterior commissure below the mons pubis. Posteriorly they do not join but instead merge into neighbouring skin, ending near and almost parallel to each other. The connecting skin between them posteriorly forms a ridge, the posterior commissure, which overlies the perineal body and is the posterior limit of the vulva.

Labia minora

The labia minora are two small cutaneous folds, devoid of fat and hair, that lie between the labia majora. They extend from the clitoris obliquely down, laterally and back, flanking the vaginal orifice. Anteriorly, each labium minus bifurcates. The upper layer of each side passes above the clitoris to form the prepuce, while the lower layer passes below the clitoris to form the frenulum of the clitoris (Fig. 75.1A–C). There are numerous sebaceous follicles on the medial surfaces. Sometimes, an extra labial fold (labium tertium) is found on one or both sides between the labia minora and majora. Adhesions between the labia minora are common in prepubertal girls; in postmenopausal females with severe atrophy they can predispose to urinary infections (Leung and Robson 1992, Gandhi et al 2016).

Vestibule of the vagina

The vestibule of the vagina is the cavity between the labia minora. It contains the vaginal and external urethral orifices and the openings of the two greater vestibular glands and of numerous mucous secreting, lesser vestibular glands. There is a shallow vestibular fossa between the vaginal orifice and the frenulum of the labia minora (Lee et al 2015). The posterior part of the vestibule of the vagina is a classic site where a fistulous opening of the rectum may be located in girls born with an imperforate anus (Bill et al 1975).

Urethra

The urethra opens into the vestibule of the vagina about 2.5 cm below the clitoris and above the vaginal orifice via the external urethral orifice, a short, sagittal cleft with slightly raised margins. The external urethral orifice is very distensible and varies in shape: the aperture can be rounded, slit-like, crescentic or stellate. The ducts of the para-urethral glands (Skene's glands) open on each side of the lateral margins of the urethra.

Bulbs of the vestibule

The bulbs of the vestibule lie on each side of the vestibule of the vagina (**Fig. 75.2B**). They are two elongated masses of erectile tissue, 3 cm long, which flank the vaginal orifice and unite anterior to it by a narrow commissure of the bulbs. Their posterior ends are expanded and are in contact with the greater vestibular glands. Their deep surfaces contact the inferior aspect of the perineal membrane; superficially, each is covered by bulbospongiosus (**Fig. 75.2A**) (Delancey 2011).

Greater vestibular glands (Bartholin's glands)

The greater vestibular glands are homologues of the male bulbo-urethral glands. They consist of two small, round or oval, reddish-yellow bodies that flank the vaginal orifice, in contact with and often overlapped by the posterior end of the vestibular bulb. Each opens into the vestibule of the vagina by a 2 cm long duct, situated in the groove between the hymen and the labium minus at approximately the 5 and 7 o'clock positions (Corton 2012). The glands are composed of tubulo-acinar tissue; the secretory cells are columnar and secrete a clear or whitish mucus for lubrication during sexual arousal.

Clitoris

The clitoris is an erectile structure, partially enclosed by the anterior bifurcated ends of the labia minora. It has a crus, root, body and glans (see Fig. 75.2). The body can be palpated through the skin. It contains two corpora cavernosa, composed of erectile tissue and enclosed in dense fibrous tissue, and separated medially by an incomplete fibrous pectiniform septum (septum of the corpora cavernosa). The fibrous tissue forms a suspensory ligament that is attached superiorly to the pubic symphysis. Each corpus cavernosum is attached to its ischiopubic ramus by a crus that extends from the root of the clitoris. The glans clitoris is a small, round tubercle of spongy erectile tissue at the end of the body, connected to the bulbs of the vestibule by thin bands of erectile tissue (pars intermedia). It is exposed between the anterior ends of the labia minora. Its epithelium has high cutaneous sensitivity, important in sexual responses. Congenital absence of the clitoris is very rare.

Vascular supply and lymphatic drainage of the vulva

Arteries

The arterial blood supply of the female external genitalia is derived from the superficial and deep external pudendal arteries which arise from the femoral artery superiorly and the internal pudendal artery inferiorly (**Figs 75.3A, 75.4**).

The blood supply to the adipose tissue of the labia majora must be carefully preserved during vaginal surgery, e.g. in creating a Martius fat pad flap to repair a vesicovaginal fistula where the blood supply has already been compromised by radiation or fibrosis (Delancey 2011).

Veins

Venous drainage of the skin of the external genitalia is via external pudendal veins to the long saphenous vein. Venous drainage of the clitoris is via deep dorsal veins to the internal pudendal vein, and via superficial dorsal veins to the external pudendal and long saphenous veins.

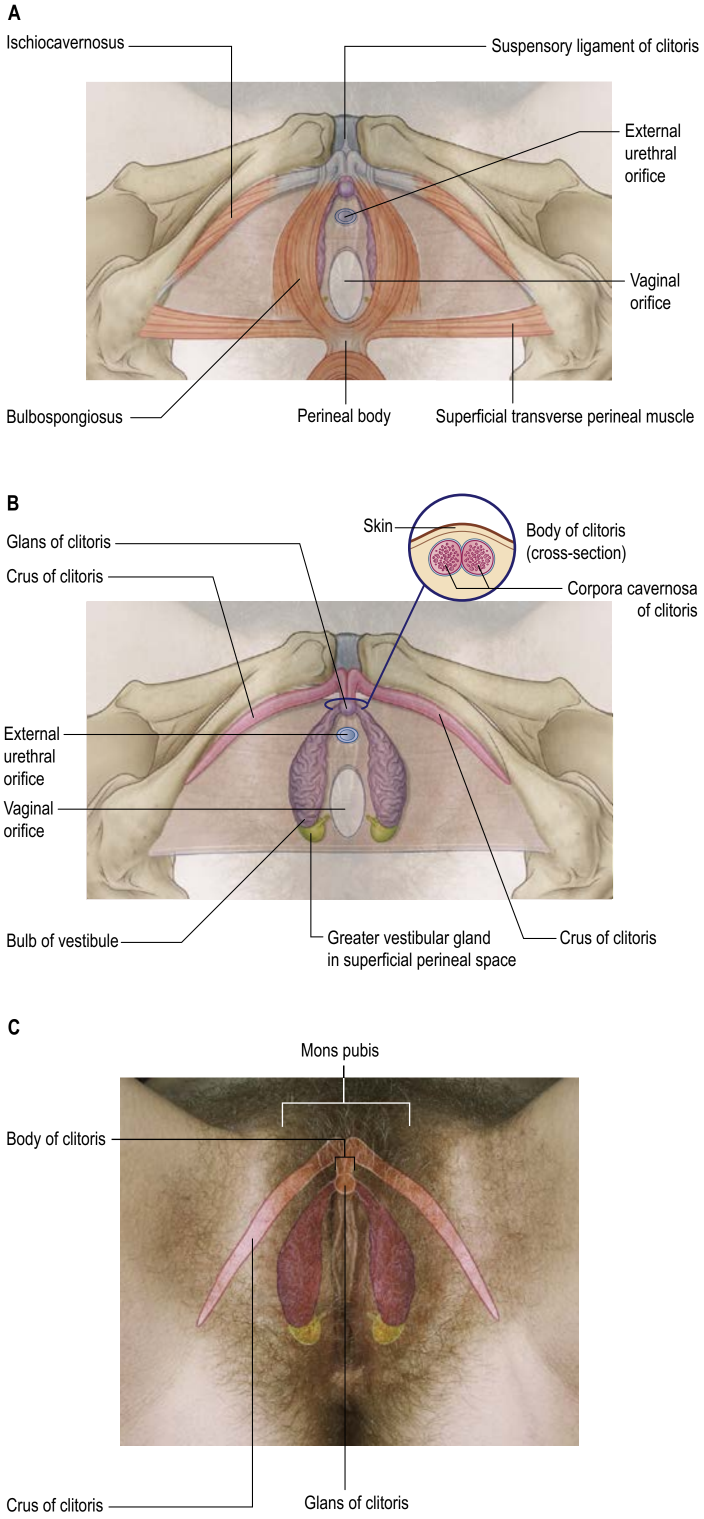
A
Ischiocavernosus
Suspensory ligament of clitoris
External urethral orifice
Vaginal orifice
Bulbospongiosus
Perineal body
Superficial transverse perineal muscle
B
Skin
Body of clitoris (cross-section)
Glans of clitoris
Crus of clitoris
Corpora cavernosa of clitoris
External urethral orifice
Vaginal orifice
Bulb of vestibule
Greater vestibular gland in superficial perineal space
Crus of clitoris
C
Mons pubis
Body of clitoris
Crus of clitoris
Glans of clitoris

Fig. 75.2 **A**, The muscles of the vestibule of the vagina and clitoris. **B**, The erectile tissues of the clitoris. **C**, The erectile tissues of the clitoris, vestibule of the vagina and greater vestibular gland with a surface anatomy overlay. (A–B, Adapted with permission from Drake RL, Vogl AW, Mitchell A (eds) Gray's Anatomy for Students, 2nd ed. Elsevier, Churchill Livingstone. Copyright 2010. C, With permission from Drake RL, Vogl AW, Mitchell A (eds) Gray's Anatomy for Students, 2nd ed. Elsevier, Churchill Livingstone. Copyright 2010.)

Lymphatic drainage

A meshwork of connecting vessels from the skin of the labia, clitoris and perineum join to form three or four collecting trunks that drain to superficial inguinal nodes lying on the cribriform fascia covering the femoral artery and vein; these nodes drain through the cribriform fascia to the deep inguinal nodes lying medial to the femoral vein (Corton 2012). The deep inguinal nodes drain via the femoral canal to the pelvic nodes (**Table 75.1**) . The last of the deep inguinal nodes lies under the inguinal ligament within the femoral canal and is often called Cloquet's node. Lymph vessels from the clitoris drain directly to the deep inguinal nodes, and direct clitoral lymphatics may pass to the internal iliac nodes (**Fig. 75.3B**). Lymph vessels in the perineum and lower part of the labia majora drain primarily to inguinal nodes.

Innervation

The main nerve supply of the vulva is the pudendal nerve (S2, S3 and S4) and its branches, the inferior anal and perineal nerves and the

TABLE 75.1 **Lymphatic drainage of the female genitalia**

Structure	Nodes
Vulva	
Upper labia, clitoris, and perineum	Superficial inguinal nodes
Perineum and lower labia majora	Superficial inguinal nodes Iliac nodes
Clitoris	Superficial inguinal nodes
	Direct to deep inguinal nodes
	Direct to internal iliac nodes
Vagina	
Proximal vagina	Internal and external iliac nodes
Middle vagina	Internal iliac nodes
Distal vagina	Superficial inguinal nodes
Uterus	
Fundus	Lateral aortic nodes
Body and cervix	External iliac nodes
	Internal iliac nodes
	Obturator nodes
Uterine tubes and round ligament of uterus	Lateral aortic nodes
	Internal iliac nodes
	Superficial inguinal nodes
Ovaries	Lateral aortic nodes

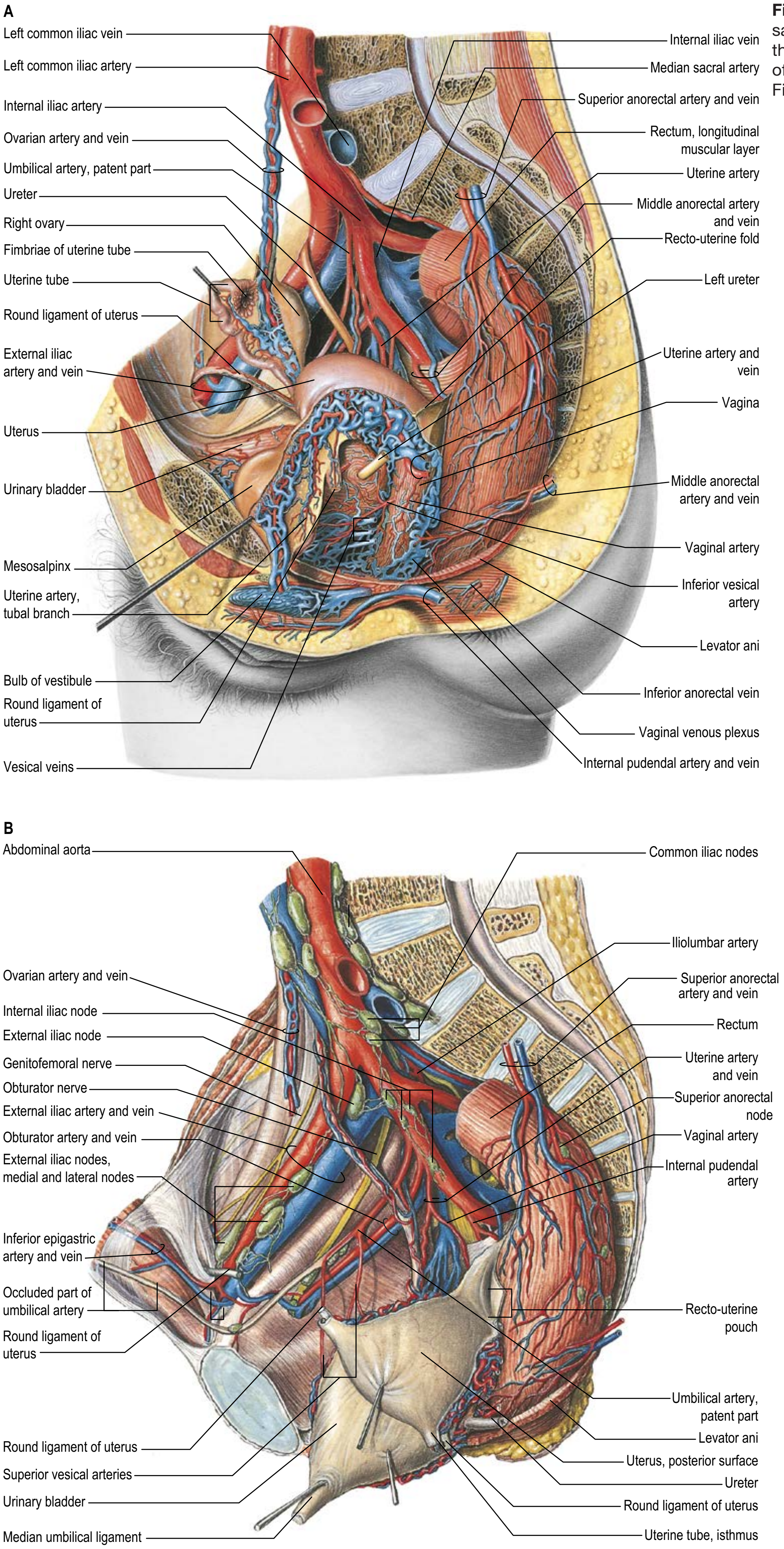
A
Left common iliac vein
Left common iliac artery
Internal iliac artery
Ovarian artery and vein
Umbilical artery, patent part
Ureter
Right ovary
Fimbriae of uterine tube
Uterine tube
Round ligament of uterus
External iliac artery and vein
Uterus
Urinary bladder
Mesosalpinx
Uterine artery, tubal branch
Bulb of vestibule
Round ligament of uterus
Vesical veins
Internal iliac vein
Median sacral artery
Superior anorectal artery and vein
Rectum, longitudinal muscular layer
Uterine artery
Middle anorectal artery and vein
Recto-uterine fold
Left ureter
Uterine artery and vein
Vagina
Middle anorectal artery and vein
Vaginal artery
Inferior vesical artery
Levator ani
Inferior anorectal vein
Vaginal venous plexus
Internal pudendal artery and vein
B
Abdominal aorta
Ovarian artery and vein
Internal iliac node
External iliac node
Genitofemoral nerve
Obturator nerve
External iliac artery and vein
Obturator artery and vein
External iliac nodes, medial and lateral nodes
Inferior epigastric artery and vein
Occluded part of umbilical artery
Round ligament of uterus
Round ligament of uterus
Superior vesical arteries
Urinary bladder
Median umbilical ligament
Common iliac nodes
Iliolumbar artery
Superior anorectal artery and vein
Rectum
Uterine artery and vein
Superior anorectal node
Vaginal artery
Internal pudendal artery
Recto-uterine pouch
Umbilical artery, patent part
Levator ani
Uterus, posterior surface
Ureter
Round ligament of uterus
Uterine tube, isthmus

Fig. 75.3 A, The vessels of the female pelvis: sagittal view. **B**, The nerves and lymphatics of the female pelvis: sagittal view. (Sobotta Atlas of Human Anatomy © Elsevier GmbH, Urban & Fischer, Munich.)

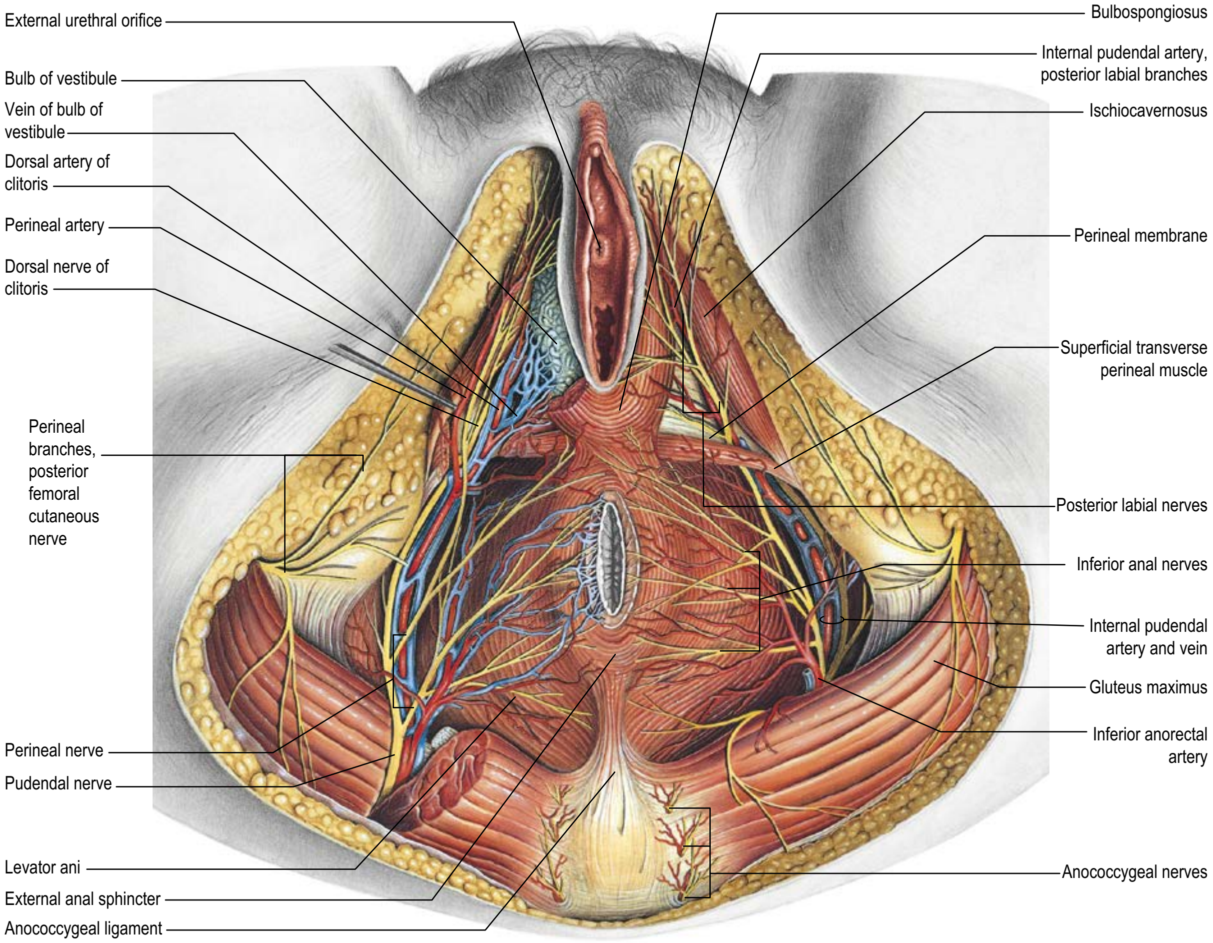
External urethral orifice
Bulb of vestibule
Vein of bulb of vestibule
Dorsal artery of clitoris
Perineal artery
Dorsal nerve of clitoris
Perineal branches, posterior femoral cutaneous nerve
Perineal nerve
Pudendal nerve
Levator ani
External anal sphincter
Anococcygeal ligament
Bulbospongiosus
Internal pudendal artery, posterior labial branches
Ischiocavernosus
Perineal membrane
Superficial transverse perineal muscle
Posterior labial nerves
Inferior anal nerves
Internal pudendal artery and vein
Gluteus maximus
Inferior anorectal artery
Anococcygeal nerves

Fig. 75.4 The muscles, vessels and nerves of the female perineum: inferior view. (Sobotta Atlas of Human Anatomy © Elsevier GmbH, Urban & Fischer, Munich.)

dorsal nerve of the clitoris (**Table 75.2**, **Fig. 75.5**; see Fig. 75.4; Shoja et al 2013, Jackson et al 2019). The sensory innervation differs between the anterior and posterior parts of the labium majus. The anterior third of the labium majus is supplied by the ilioinguinal nerve (anterior labial nerve) (L1), the posterior two-thirds are supplied by the pudendal nerve through the posterior labial branches of the perineal nerve (S3), and the lateral aspect is also innervated by the perineal branch of the posterior femoral cutaneous nerve (S2). Nerves of the external genitalia are susceptible to trauma and inflammation, leading to external genitalia pain syndromes or vulvodynia (Shoja et al 2013). The intimate relationship of the vagina to the urinary bladder, rectum and nerves of the external genitalia predispose to pelvic pain and dyspareunia.

Vagina

The vagina is a fibromuscular tube lined by non-keratinized stratified epithelium. It extends from the vestibule of the vagina (the opening between the labia minora) to the uterus. The upper end of the vagina surrounds the vaginal projection of the cervix of the uterus. The recess formed between the vaginal part of the cervix and vagina is the fornix; the different parts of the fornix are given separate names, i.e. anterior, posterior and lateral, but they are continuous (**Fig. 75.6**).

In the standing position, the vagina ascends posteriorly and superiorly, forming an angle of 60–70° with the horizontal plane (Corton 2012). It forms an angle of over 90° to the uterine axis (see Fig. 75.12); this angle varies with the contents of the urinary bladder and rectum. The proximal vagina is directed posteriorly towards the ischial spines. The width of the vagina increases as it ascends. The inner surfaces of the anterior and posterior vaginal walls are in contact with each other, forming a transverse slit. The vaginal mucosa is attached to the cervix of the uterus higher on the posterior cervical wall than on the anterior; the anterior wall is approximately 7.5 cm long and the posterior wall is approximately 9 cm long. The fibromuscular anterior wall of the vagina supports the fundus of the urinary bladder in its middle and upper portions, and the urethra (which is embedded in it) inferiorly. The fibromuscular posterior wall of the vagina supports the rectum. The upper quarter of the posterior vagina is separated from the rectum by the peritoneum of the recto-uterine pouch (pouch of Douglas), and by moderately dense fibromuscular tissue in its middle half (Delancey 2011). In its lower quarter, it is separated from the anal canal by the fibromuscular perineal body. The proximal vagina is supported laterally by levator ani, together with such ligaments as the cardinal and uterosacral. Pubovaginalis provides a U-shaped muscular sling around the mid-vagina. The distal vagina is surrounded by bulbospongiosus (see Fig. 75.4). As the ureters pass anteromedially to reach the fundus of the urinary bladder they pass close to the lateral parts of the fornix, where care must be taken to avoid injury during hysterectomy (**Fig. 75.7**). As they enter the urinary bladder, the ureters are usually anterior to the vagina; at this point, each ureter is crossed transversely by a uterine artery (**Fig. 75.8**).

The vagina opens externally via a sagittal orifice positioned below the external urethral orifice (see Fig. 75.1C). The size of the vaginal orifice varies; it is capable of great distension during childbirth and, to a lesser degree, during sexual intercourse. The hymen is a thin fold of mucous membrane situated just within the vaginal orifice. The internal surfaces of the folds are normally in contact with each other and the vaginal orifice appears as a cleft between them. The hymen varies greatly in shape and dimensions. When stretched, it is anular and widest posteriorly; it can also be semilunar and concave towards the mons pubis, cribriform, fringed, absent or complete and imperforate. The hymenal ring normally ruptures after first sexual intercourse, but can rupture earlier during non-sexual physical activity. Small round carunculae hymenales are its remnants after it has been ruptured. It has no established function.

Remnants of the caudal end of the mesonephric duct (Gartner's duct) (see Figs 22.13, 22.19) are occasionally seen protruding through the lateral parts of the fornix or lateral parts of the vagina and can cause cysts (Gartner's cysts). Prepubertal distal longitudinal folds are common within the vagina and they disappear during puberty (Altchek et al 2008).

TABLE 75.2 Innervation of the female genitalia

	Origin	Proximal course	Distal course	Organ	Function
Parasympathetic	S2–S4	Pelvic splanchnic nerves	Pelvic ganglia	Uterine tube Uterus	Vasodilation
		Cavernous nerves of clitoris		Vagina Clitoris	Transudation Erection
Sympathetic	T12, L1–L2	Superior mesenteric and renal plexuses	Ovarian plexus	Ovary	Vasoconstriction
		Superior hypogastric plexus	Hypogastric nerve		
			↓		
			Inferior hypogastric plexus		
			↓		
			Uterovaginal plexus	Uterine tube, uterus, proximal vagina	Contraction
Somatic	S2, S3, S4	Pudendal nerve	Dorsal nerve of clitoris	Clitoris	
		Pudendal nerve	Posterior labial nerves	Distal vagina Labia majora	Contraction
				Ischiocavernosus	
				Bulbospongiosus	

With permission from Shoja MM, Sharma A, Mirzaya N et al 2013 Neuroanatomy of the female abdominoplevic region: a review with application to pelvic pain syndromes. Clin Anat 26:66–76.

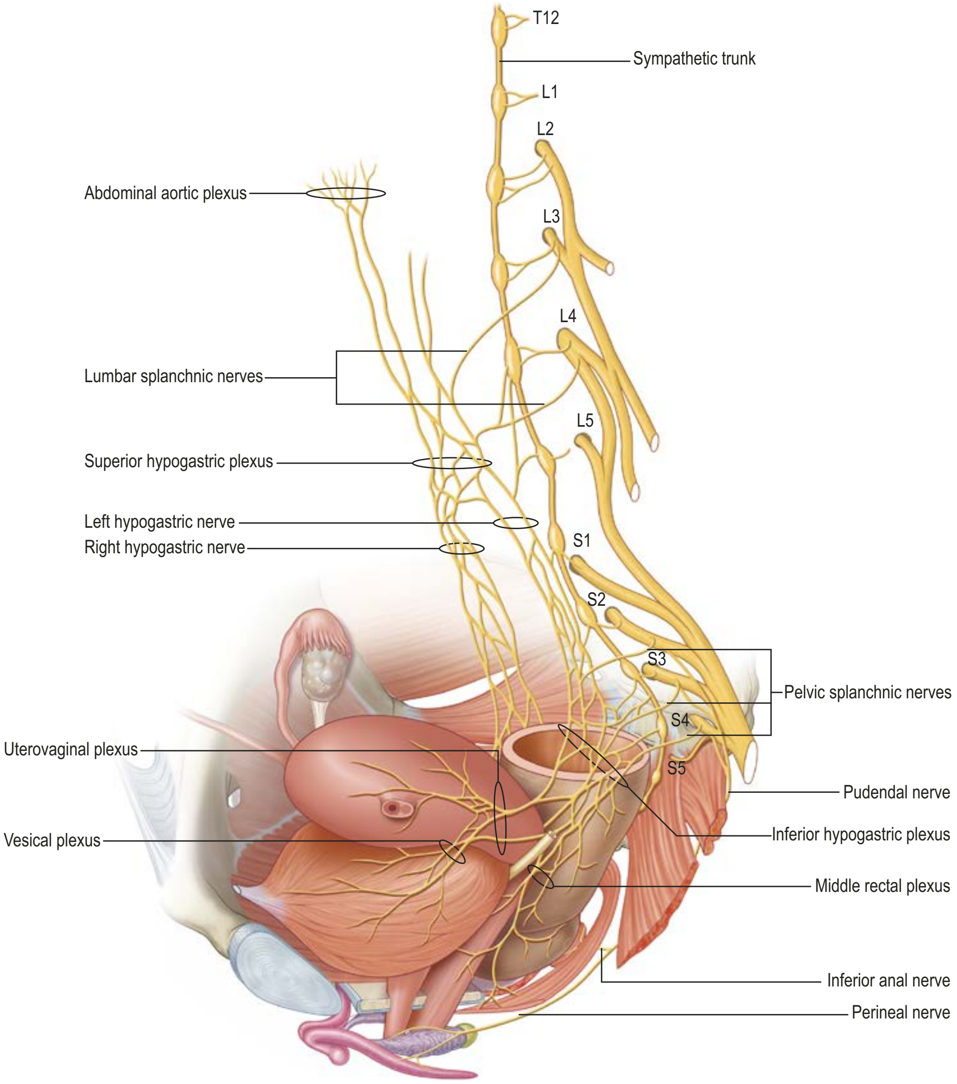
T12
Sympathetic trunk
L1
L2
Abdominal aortic plexus
L3
L4
Lumbar splanchnic nerves
L5
Superior hypogastric plexus
Left hypogastric nerve
Right hypogastric nerve
S1
S2
S3
Pelvic splanchnic nerves
S4
Uterovaginal plexus
S5
Pudendal nerve
Vesical plexus
Inferior hypogastric plexus
Middle rectal plexus
Inferior anal nerve
Perineal nerve

Fig. 75.5 The autonomic innervation of the female reproductive system. (Based on Barucha AE 2006 Pelvic floor: anatomy and function. Neurogastroenterol Motil 18:507–19.)

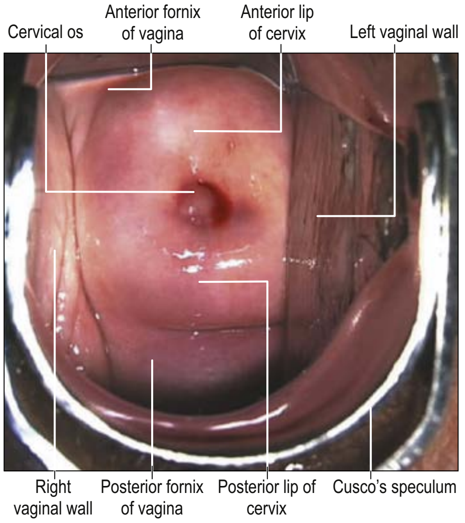
Cervical os
Anterior fornix of vagina
Anterior lip of cervix
Left vaginal wall
Right vaginal wall
Posterior fornix of vagina
Posterior lip of cervix
Cusco's speculum

Fig. 75.6 The cervix and vaginal fornix, as seen via a Cusco's bivalve speculum.

Vascular supply and lymphatic drainage

Arteries

The arterial supply of the vagina is derived from branches of the internal iliac arteries. Vaginal arteries anastomose with cervical branches of the uterine artery to form the midline azygos arteries of the vagina, which descend anterior and posterior to the vagina; these vessels also supply the bulb of the vestibule, fundus of the urinary bladder, and adjacent part of the rectum (see Fig. 75.3A). The uterine, internal pudendal and middle anorectal arteries may contribute to the blood supply of the vagina.

Veins

The vaginal veins, one on each side, arise from lateral venous plexuses that communicate with uterine, vesical and anorectal venous plexuses and drain to the internal iliac veins. The uterine and vaginal venous plexuses can provide collateral venous drainage for the lower limb.

Lymphatic drainage

Vaginal lymphatic vessels link with those of the cervix, rectum and vulva. They form three groups but the regions drained are not sharply demarcated. Upper vessels accompany the uterine artery to the internal and external iliac nodes; intermediate vessels accompany the vaginal artery to the internal iliac nodes; and vessels draining the vagina below the hymen, and from the vulva and perineal skin, pass to the superficial inguinal nodes (see Table 75.1).

Innervation

The distal vagina is supplied by the pudendal nerve (S2, S3 and S4). The proximal vagina is supplied by the pelvic splanchnic nerves (S2, S3 and, sometimes, S4) (see Fig. 75.5 and Table 75.2).

Developmental anomalies of the vagina

Available with the *Gray's Anatomy* e-book

Microstructure

The vagina has an external epithelial and an internal muscular layer: the epithelium adheres firmly to the muscular layer. There are two median longitudinal ridges on its epithelial surface, one anterior and the other posterior. Numerous transverse bilateral vaginal rugae extend from these vaginal columns, divided by sulci of variable depth, giving an appearance of conical papillae. These transverse rugosities are most

Developmental anomalies of the vagina include vaginal agenesis, absent hymen, transverse vaginal septum and persistent cloaca. Vaginal and renal agenesis, in the presence of other paramesonephric duct (Müllerian duct) anomalies, is termed Mayer–Rokitansky-Küster Hauser syndrome. An absent hymen in patients with vaginal agenesis is associated with renal agenesis (Kimberley et al 2012). A congenital transverse septum within the vagina manifests clinically during adolescence with primary amenorrhoea and haematocolpos. Children with a persistent cloaca have a congenital defect characterized by fusion of the rectum, vagina and urethra into a single common channel that varies in length from 1 to 7 cm.

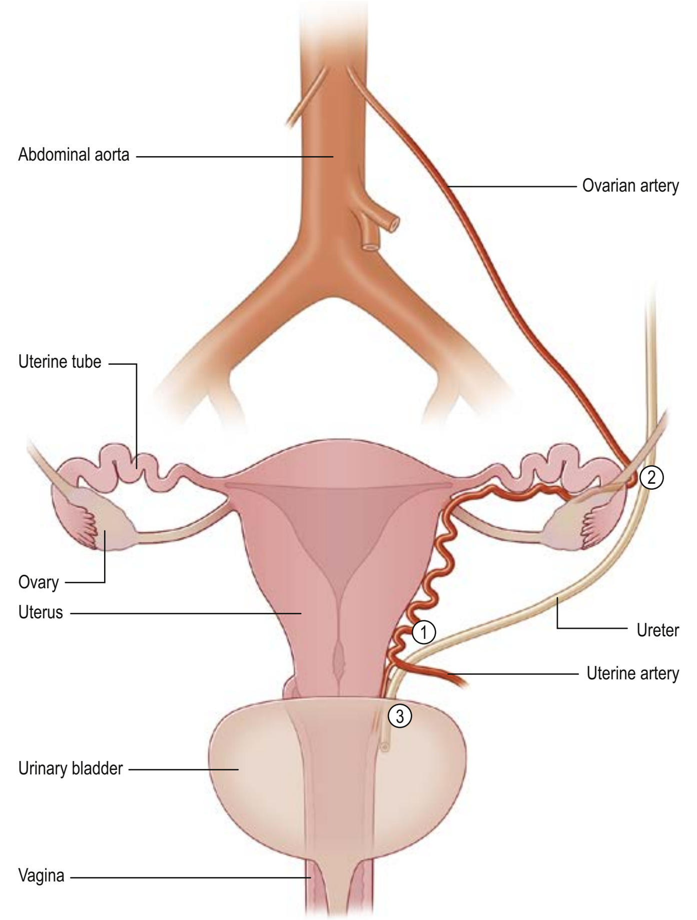

Fig. 75.7 The most common sites of ureteric injury during hysterectomy. Key: 1, distal ureter at the level of the uterine artery; 2, dorsal to the suspensory ligament of the ovary, near the pelvic brim; 3, intramural part of the ureter at the angle of the proximal vagina.

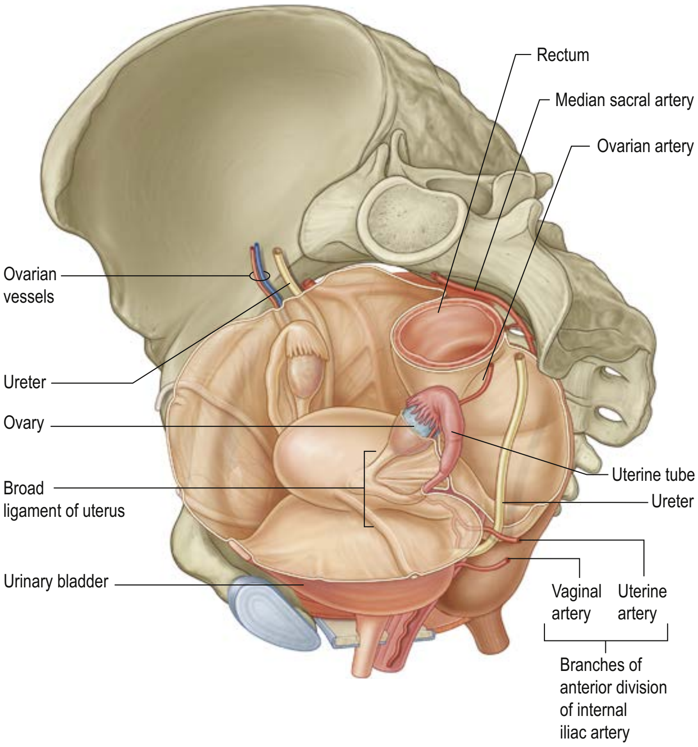

Fig. 75.8 The relationship of the ureter to the uterine and vaginal arteries. (With permission from Drake RL, Vogl AW, Mitchell A (eds) Gray's Anatomy for Students, 2nd ed. Elsevier, Churchill Livingstone. Copyright 2010.)

numerous on the posterior wall and near the orifice; they increase under the influence of oestrogen during puberty and pregnancy, are especially well developed before parturition, and decrease after the menopause

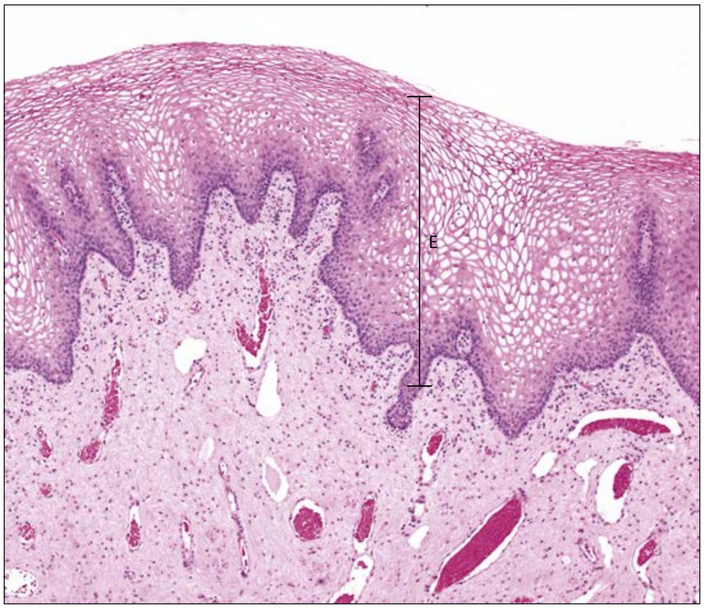

Fig. 75.9 Non-keratinized stratified squamous epithelium (E) covering the exocervical mucosa and vagina. The cells of the middle and upper layers appear clear owing to their glycogen content. (Courtesy of Mr Peter Helliwell and the late Dr Joseph Mathew, Department of Histopathology, Royal Cornwall Hospitals Trust, UK.)

(Corton 2012). The surface cells are stratified squamous non-keratinized epithelium, similar to and continuous with that of the ectocervical mucosa. After puberty the epithelium thickens and its superficial cells accumulate glycogen, which gives them a clear appearance in histological preparations.

The vaginal epithelium does not change markedly during the menstrual cycle, but its glycogen content increases after ovulation and then diminishes towards the end of the cycle. Natural vaginal bacteria, particularly *Lactobacillus acidophilus*, break down glycogen in the desquamated cellular debris to lactic acid. This produces a highly acidic (pH 3) environment that inhibits the growth of most other micro-organisms. There is less glycogen before puberty and after the menopause, when vaginal infections are more common. There are no mucous glands, but a fluid transudate from the lamina propria, supplemented by mucus production from the cervical glands (Fig. 75.9). The muscular layers are composed of smooth muscle and consist of a thick outer longitudinal and an inner circular layer; the two layers are not distinct but are connected by oblique interlacing fibres. The longitudinal fibres are continuous with the superficial muscle fibres of the uterus. A layer of loose connective tissue containing extensive vascular plexuses surrounds the muscle layers.

UPPER GENITAL TRACT

Uterus

The uterus is a thick-walled, muscular organ situated in the pelvis between the urinary bladder and the rectum (Figs 75.10–75.12). It lies posterior to the urinary bladder and vesico-uterine pouch and anterior to the rectum and recto-uterine pouch; it is mobile, which means that its position varies with distension of the urinary bladder and rectum. The broad ligaments are lateral.

The uterus is divided structurally and functionally into two main regions: the muscular body forms the upper two-thirds, and the fibrous cervix forms the lower third. In the adult nulliparous state, the cervix usually tilts forwards relative to the axis of the vagina (anteversion), and the body of the uterus tilts forwards relative to the cervix (anteflexion) (see Fig. 75.12). In 10–15% of females the whole uterus leans posteriorly at an angle to the vagina and is said to be retroverted. A uterus that angles posteriorly on its cervix is described as retroflexed.

Body

The body of the uterus is pear-shaped and extends from the fundus superiorly to the isthmus inferiorly. The uterine tubes enter the uterus on both sides at the utero-tubal junction: the round ligament of the uterus and proper ovarian ligament are inferoanterior and inferoposterior, respectively, to each junction. The dome-like fundus is superior

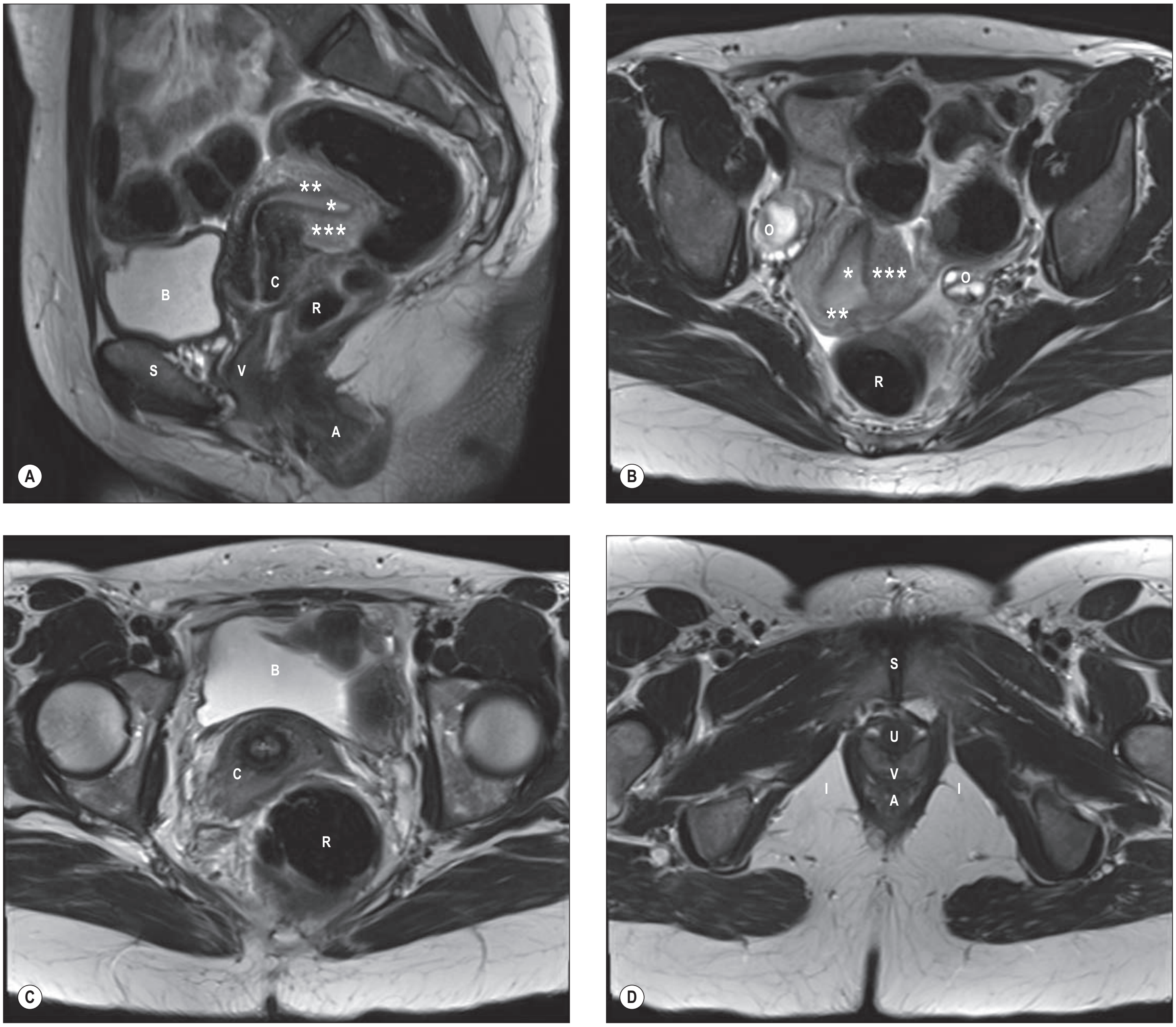

Fig. 75.10 T2-weighted magnetic resonance images through the pelvis, demonstrating normal female anatomy. **A**, Sagittal view. Abbreviations: A, anus; B, urinary bladder; C, cervix; R, rectum; S, pubic symphysis; V, vagina; *, endometrium; **, inner myometrium of uterus (also known as the junctional zone); ***, outer myometrium of uterus. **B–D**, Axial views. **B**, Abbreviations: O, ovary; R, rectum; *, endometrium, **, inner myometrium of uterus (junctional zone); ***, outer myometrium of uterus. **C**, Abbreviations: B, bladder; C, cervix (which, from external to internal, has several layers, as seen on T2-weighted MRI): a high-signal-intensity outer cervical stroma (contiguous with the outer myometrium); a low-signal-intensity inner cervical stroma (contiguous with the inner myometrium); high-signal-intensity cervical glands (contiguous with the endometrium); and a very high-signal-intensity cervical canal (contiguous with the uterine cavity); R, rectum. **D**, Abbreviations: A, anus; I, ischio-anal fossa; S, pubic symphysis; U, urethra; V, vagina.

to the entry points of the uterine tubes and is covered by peritoneum continuous with that of neighbouring surfaces. The fundus of the uterus is in contact with the small intestine and, occasionally, with a distended sigmoid colon. The lateral margins of the body of the uterus are convex; on each side, their peritoneum is reflected laterally to form the broad ligament, which extends as a flat sheet to the pelvic wall (see Figs 75.11B, 75.16). The anterior surface of the body of the uterus is covered by peritoneum reflected on to the urinary bladder at the vesico-uterine fold (see Fig. 75.14). This normally occurs at the level of the anatomical internal os, the most inferior margin of the body of the uterus. The vesico-uterine pouch, between the urinary bladder and uterus, is obliterated when the bladder is distended, but may be occupied by small intestine when the bladder is empty. The posterior surface of the uterus is convex transversely. Its peritoneal covering continues down to the cervix and proximal vagina and is then reflected back to the rectum along the surface of the recto-uterine pouch, which lies posterior to the uterus (see Fig. 75.15). The sigmoid colon and occasionally the terminal ileum lie posterior to the uterus.

The uterine cavity usually measures 6 cm from the external os of the uterus to the wall of the fundus and is flat in its anteroposterior plane (Salardi et al 1985). In coronal section, it is triangular, broad above where the two uterine tubes join the uterus, and narrow below at the anatomical internal os of the uterus. There is no change in the size of the uterus until approximately 7 years of age, when the body of the uterus enlarges more than the cervix.

Developmental anomalies of the uterus

Available with the *Gray's Anatomy* e-book

Cervix of the uterus

The adult, non-pregnant cervix is narrower and more cylindrical than the body of the uterus and is typically 2.5 cm long. The proximal end communicates with the isthmus of the uterus, and the distal end opens into the vagina at the external os (see Fig. 75.6). In

The paramesonephric (Müllerian) ducts can fail to fuse, resulting in a uterus that is not pear-shaped. There may only be a septum (septate uterus) or partial clefting of the uterus (bicornuate uterus); the most extreme example is a septate vagina, two cervices and two discrete uteri, each with one uterine tube (uterus didelphys) (Minto et al 2001) (see Fig. 22.15).

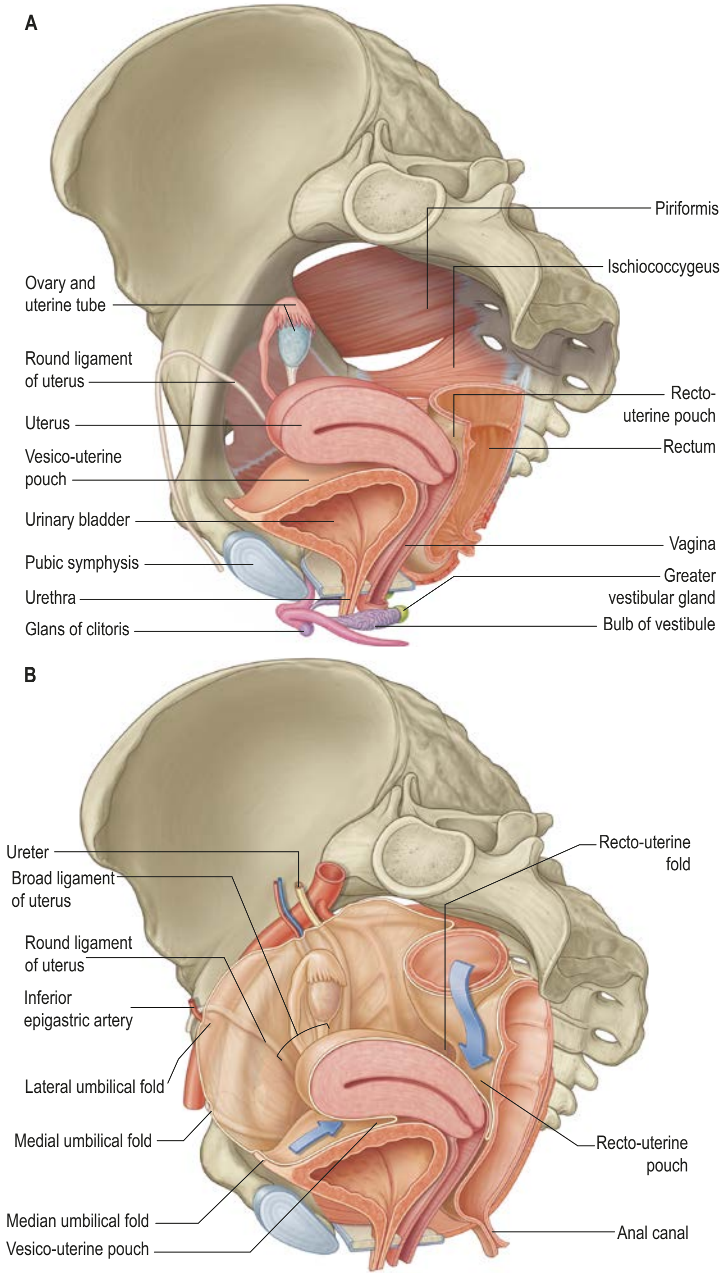
A
Piriformis
Ischiococcygeus
Ovary and uterine tube
Round ligament of uterus
Uterus
Recto-uterine pouch
Rectum
Vesico-uterine pouch
Urinary bladder
Pubic symphysis
Vagina
Greater vestibular gland
Urethra
Bulb of vestibule
Glans of clitoris
B
Ureter
Broad ligament of uterus
Recto-uterine fold
Round ligament of uterus
Inferior epigastric artery
Lateral umbilical fold
Medial umbilical fold
Recto-uterine pouch
Median umbilical fold
Vesico-uterine pouch
Anal canal

Fig. 75.11 **A**, Anatomical relations of the female genital tract, urinary bladder and rectum. **B**, Pelvic peritoneal reflections, showing the broad ligament and its contents. (A, With permission from Drake RL, Vogl AW, Mitchell A et al (eds) Gray's Atlas of Anatomy. Elsevier, Churchill Livingstone. Copyright 2008. B, With permission from Drake RL, Vogl AW, Mitchell A (eds) Gray's Anatomy for Students, 2nd ed. Elsevier, Churchill Livingstone. Copyright 2010.)

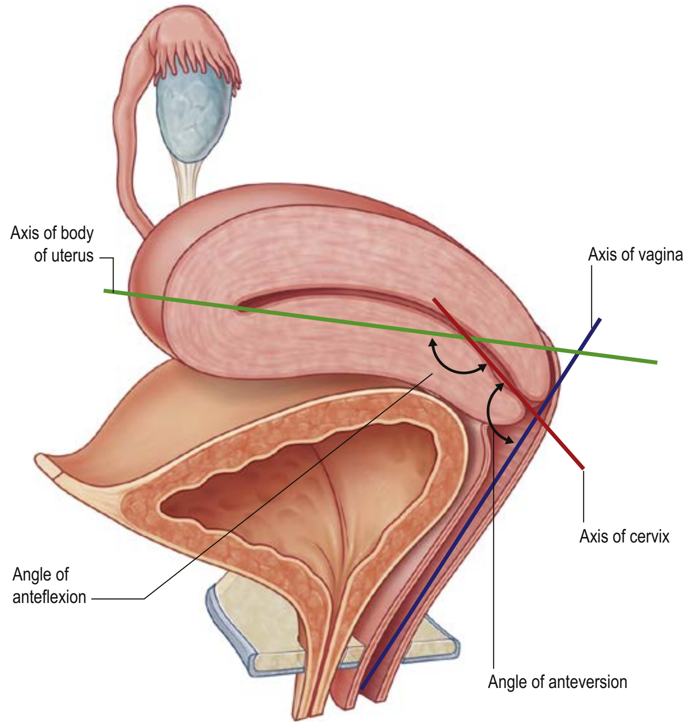
Axis of body of uterus
Axis of vagina
Axis of cervix
Angle of anteflexion
Angle of anteversion

Fig. 75.12 Angles of anteflexion and anteversion. (With permission from Drake RL, Vogl AW, Mitchell A (eds) Gray's Anatomy for Students, 2nd ed. Elsevier, Churchill Livingstone. Copyright 2010.)

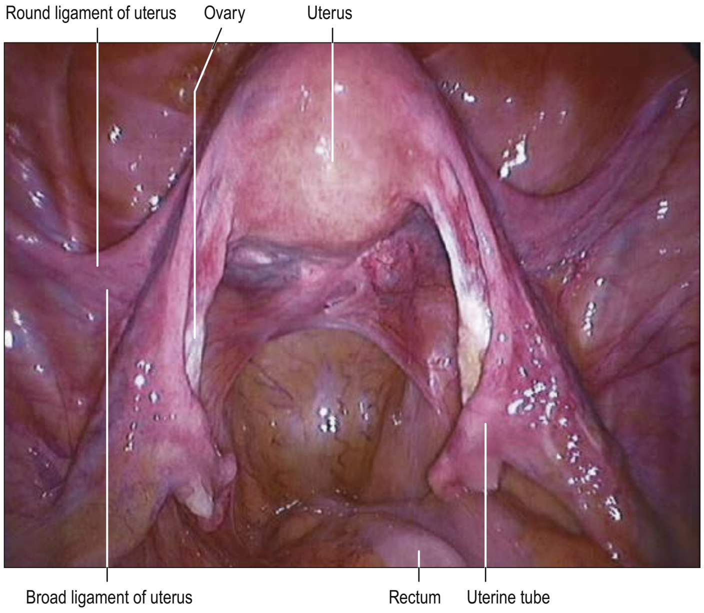
Round ligament of uterus
Ovary
Uterus
Broad ligament of uterus
Rectum
Uterine tube

Fig. 75.13 A laparoscopic view of the uterus. The patient is tilted head down so that the small intestine is moved away from the uterus to give this view.

nulliparous females the external os is usually a circular aperture, whereas it is a transverse slit after childbirth. Two longitudinal ridges, one each on its anterior and posterior walls, give off small, oblique, palmate folds that ascend laterally like the branches of a tree (arbor vitae uteri); the folds on opposing walls interdigitate to close the cervical canal. Once considered part of the cervix, the isthmus of the uterus (approximately 1 cm long) demarcates the body of the uterus from the cervix. Although unaffected in the first month of pregnancy, it is gradually taken up into the body of the uterus during the second month to form the 'lower uterine segment' (see below). In non-pregnant females the isthmus undergoes menstrual changes, although these are less pronounced than those occurring in the body of the uterus. The distal end of the cervix enters the proximal end of the vagina, thereby dividing the cervix into supravaginal and vaginal parts. The supravaginal part is separated anteriorly from the urinary bladder by connective tissue, the parametrium, which also passes to the sides of the cervix and laterally between the two layers of the broad ligaments.

Peritoneal folds and ligaments of the pelvis

The uterus is connected to a number of 'ligaments'. Some are true ligaments, in that they have a fibrous composition and provide support to the uterus; some provide no support to the uterus; and others are simply folds of peritoneum.

Peritoneal folds

The parietal peritoneum is reflected over the upper genital tract to produce anterior (vesico-uterine), posterior (recto-uterine) and lateral peritoneal folds. The lateral folds are commonly called the broad ligaments (Fig. 75.13).

Vesico-uterine and rectovaginal folds

The anterior or vesico-uterine fold consists of peritoneum reflected onto the urinary bladder from the uterus at the junction of its cervix and body (Fig. 75.14). The recto-uterine fold extends lower than the anterior fold and consists of peritoneum reflected from the posterior part

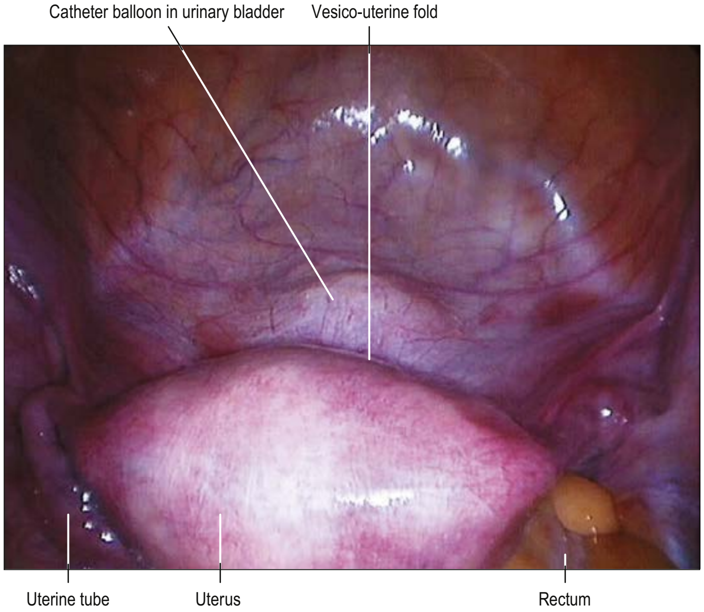

Fig. 75.14 A laparoscopic view of the anterior part of the pelvis, showing the vesico-uterine pouch anterior to the uterus.

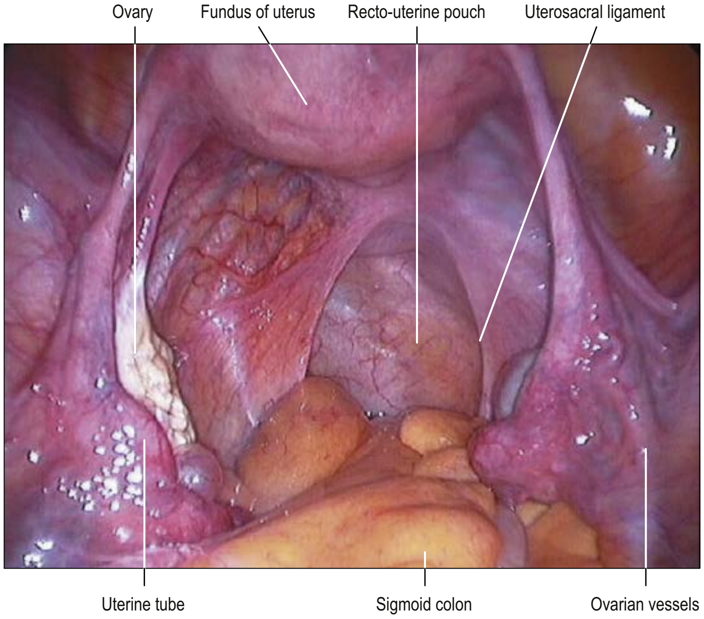

Fig. 75.15 A laparoscopic view of the posterior pelvis, showing the recto-uterine pouch (pouch of Douglas) with the sigmoid colon descending towards the rectum.

of the vaginal fornix on to the anterior surface of the rectum, thereby creating the recto-uterine pouch. The recto-uterine pouch is bounded anteriorly by the uterus, supravaginal part of the cervix and posterior part of the vaginal fornix; posteriorly by the rectum; and laterally by the uterosacral ligaments (Fig. 75.15).

Broad ligament

The lateral folds, or broad ligaments, extend on each side from the uterus to the lateral pelvic walls, where they become continuous with the peritoneum covering those walls (Figs 75.16–75.18). The upper border is free and the lower border is continuous with the peritoneum over the urinary bladder, rectum and side wall of the pelvis. The borders are continuous with each other at the free edge via the fundus of the uterus and diverge below near the superior surface of levator ani. A uterine tube lies in the upper free border on either side. The broad ligament is divided into an upper mesosalpinx, a posterior mesovarium and an inferior mesometrium.

Mesosalpinx and mesovarium

The mesosalpinx is attached above to the uterine tube and posteroinferiorly to the mesovarium (see Fig. 75.17). Superior and laterally it is attached to the suspensory ligament of the ovary; medially it is attached

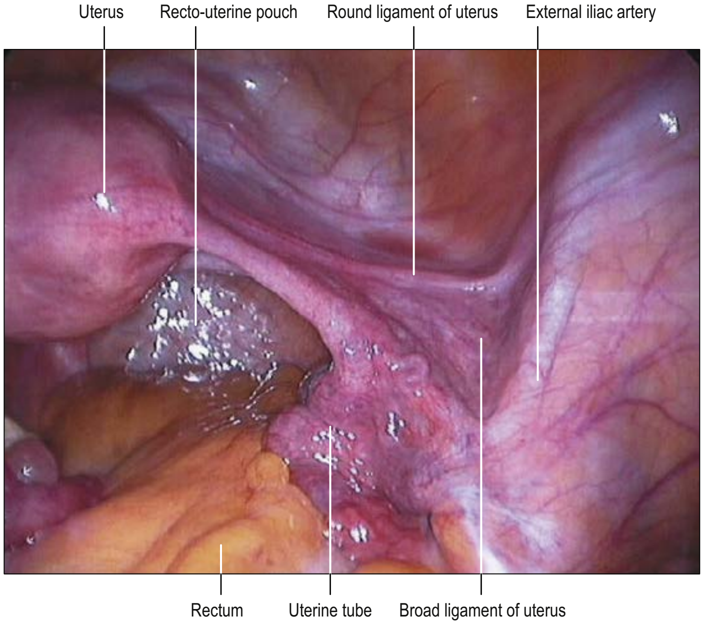

Fig. 75.16 A laparoscopic view of the broad ligament.

to the proper ovarian ligament. The fimbria of the uterine tube projects from its free lateral end. Between the ovary and uterine tube, the mesosalpinx contains vascular anastomoses between the uterine and ovarian vessels, the epoophoron and the paroophoron. The mesovarium projects from the posterior aspect of the broad ligament, of which it is the smaller part. It is attached to the hilum of the ovary and carries vessels and nerves to the ovary (see Fig. 75.17 and page 1321).

Mesometrium

The mesometrium is the largest part of the broad ligament and extends from the pelvic floor to the proper ovarian ligament and body of the uterus. The uterine artery passes between its two peritoneal layers typically 1.5 cm lateral to the cervix; it crosses the ureter shortly after its origin from the internal iliac artery and gives off a branch that passes superiorly to the uterine tube, where it anastomoses with the ovarian artery (Fig. 75.19). Between the pyramid formed by the infundibulum of the uterine tube, the upper pole of the ovary and the lateral pelvic wall, the mesometrium contains the ovarian vessels and nerves lying within the suspensory ligament of the ovary. This ligament continues laterally over the external iliac vessels as a distinct fold. The mesometrium also encloses the proximal part of the round ligament of the uterus, as well as smooth muscle and loose connective tissue.

Visceral ligaments of the pelvis

The visceral ligaments of the female pelvis include the round ligament of the uterus and the uterosacral, cardinal and pubocervical ligaments.

Round ligament of the uterus

Each round ligament of the uterus is a narrow band of smooth muscle 10–12 cm long, that extends from the utero-tubal junction through the broad ligament to enter the deep inguinal ring lateral to the inferior epigastric artery (see Figs 75.13, 75.16, 75.18). Although conventionally described as ending in the labium majus, a cadaveric dissection study showed that the round ligament of the uterus ended just outside the superficial inguinal ring in approximately 50% of specimens, with neither attachment nor extension to the caudal labium in any specimen (Bellier et al 2018). Near the uterus, the round ligament contains a considerable amount of smooth muscle, but this gradually diminishes and the terminal portion is purely fibrous. It also contains skeletal muscle, blood vessels, nerves and lymphatics that drain the uterine region around the utero-tubal junction to the superficial inguinal lymph nodes.

In the fetus, a projection of peritoneum (processus vaginalis) is carried with the round ligament of the uterus for a short distance into the inguinal canal. Although generally obliterated in adults, it is sometimes patent even in old age. A patent processus vaginalis in the inguinal canal is often referred to as the canal of Nuck; it can be asymptomatic or give rise to an indirect inguinal hernia or hydrocele of the canal of Nuck. In the canal, the ligament receives the same coverings as the spermatic cord, although they are thinner and blend with the ligament itself, which might not reach the mons pubis.

Uterosacral, cardinal and pubocervical ligaments

The uterosacral, cardinal and pubocervical ligaments are condensations of the visceral or endopelvic connective tissue that connect the pelvic viscera to the side wall of the pelvis; they radiate like the spokes of a wheel around the hub of the cervix of the uterus, providing it with considerable support (**Fig. 75.20**) (Delancey 2011). The connective tissue lateral to the uterus and the cervix, the parametrium, continues alongside the vagina as the paracolpium: it contains the vascular and connective tissues associated with the vagina. The uterosacral ligaments contain fibrous tissue and smooth muscle. They pass back from the cervix and body of the uterus on both sides of the rectum and are attached to the anterior aspect of the sacrum. They can be palpated laterally on rectal examination and can be felt as thick bands of tissue passing downwards on both sides of the posterior part of the vaginal fornix on vaginal examination. The cardinal ligaments (ligaments of Mackenrodt) extend from the sides of the cervix and lateral parts of the vaginal fornix, and are attached extensively on the pelvic wall (Eid et al 2018). The lower parts of the ureters and pelvic blood vessels traverse the cardinal ligaments. Fibres of the pubocervical ligament pass forwards from the anterior aspect of the cervix and upper vagina to diverge around the urethra, and are attached to the posterior aspect of the pubic bones.

The cardinal and uterosacral ligaments are almost vertically orientated in the standing position and maintain the near-horizontal axis of the upper vagina. The uterus and vagina are supported by the close interaction of the uterosacral and cardinal ligaments with the muscles of the pelvic floor, including the pelvic diaphragm, the perineal membrane and the perineal body. The support of the pelvic floor has been reviewed in detail by Delancey (2011) (see also Ch. 71).

Vascular supply and lymphatic drainage

Arteries

The arterial supply to the uterus comes primarily from the uterine artery (see Fig. 75.19; **Fig. 75.21**), which arises as a branch of the anterior division of the internal iliac artery. From its origin, the uterine artery crosses the ureter anteriorly in the broad ligament before branching as

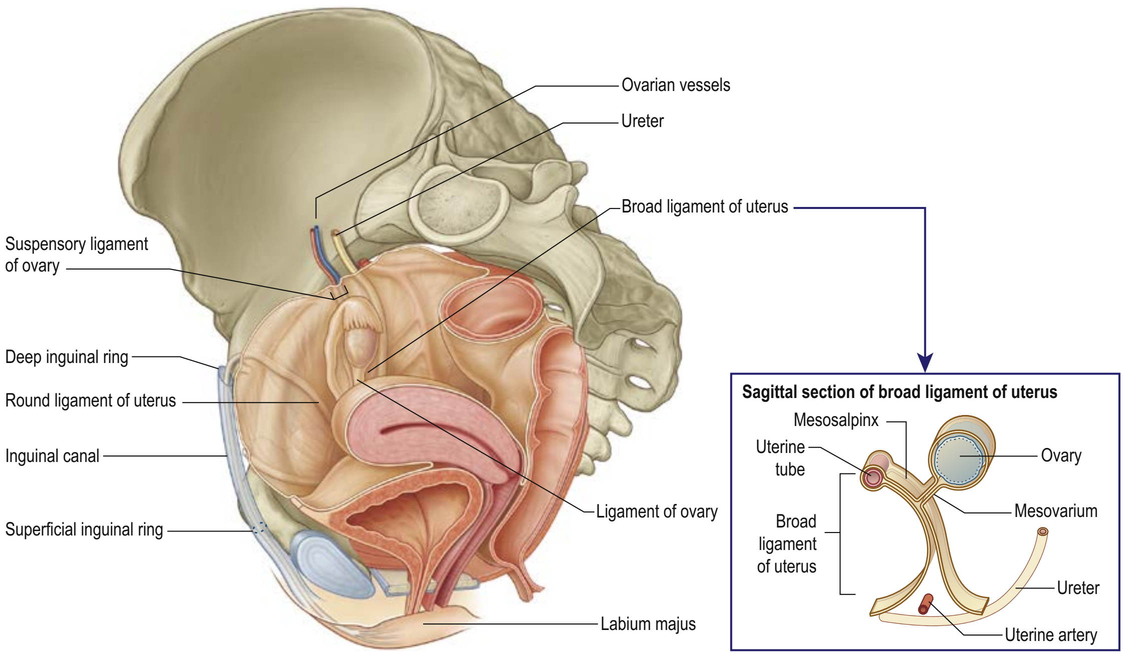
Ovarian vessels
Ureter
Broad ligament of uterus
Suspensory ligament of ovary
Deep inguinal ring
Round ligament of uterus
Inguinal canal
Superficial inguinal ring
Ligament of ovary
Labium majus
Sagittal section of broad ligament of uterus
Mesosalpinx
Uterine tube
Ovary
Broad ligament of uterus
Mesovarium
Ureter
Uterine artery

Fig. 75.17 Pelvic peritoneal reflections, demonstrating the broad ligament and its contents. (With permission from Drake RL, Vogl AW, Mitchell A (eds) Gray's Anatomy for Students, 2nd ed. Elsevier, Churchill Livingstone. Copyright 2010.)

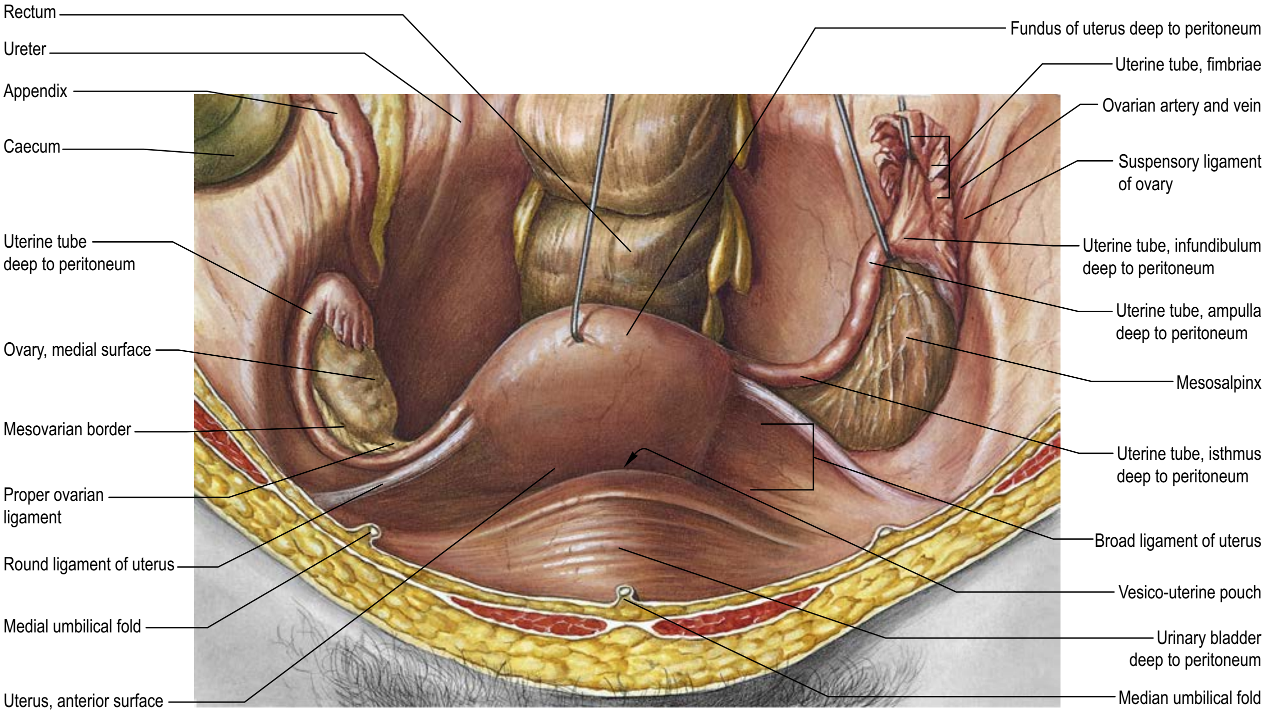
Rectum
Ureter
Appendix
Caecum
Uterine tube deep to peritoneum
Ovary, medial surface
Mesovarian border
Proper ovarian ligament
Round ligament of uterus
Medial umbilical fold
Uterus, anterior surface
Fundus of uterus deep to peritoneum
Uterine tube, fimbriae
Ovarian artery and vein
Suspensory ligament of ovary
Uterine tube, infundibulum deep to peritoneum
Uterine tube, ampulla deep to peritoneum
Mesosalpinx
Uterine tube, isthmus deep to peritoneum
Broad ligament of uterus
Vesico-uterine pouch
Urinary bladder deep to peritoneum
Median umbilical fold

Fig. 75.18 The ovaries and broad ligament of the uterus: superior view with the uterus lifted away from the urinary bladder. (Sobotta Atlas of Human Anatomy © Elsevier GmbH, Urban & Fischer, Munich.)

it reaches the uterus at the level of the cervico-isthmic junction (see Fig. 72.20B). One major branch ascends the uterus tortuously within the broad ligament until it reaches the region of the hilum of the ovary, where it anastomoses with branches of the ovarian artery. Another branch descends to supply the cervix and anastomoses with branches of the vaginal artery to form two median longitudinal vessels, the azygos arteries of the vagina, which descend anterior and posterior to the vagina. Although there are anastomoses with the ovarian and vaginal arteries, the dominance of the uterine artery is indicated by its marked hypertrophy during pregnancy.

The tortuosity of the vessels as they ascend in the broad ligaments is repeated in their branches within the uterine wall. Each uterine artery gives off numerous branches. These enter the uterine wall, divide and run circumferentially as groups of anterior and posterior arcuate arteries. They ramify and narrow as they approach the anterior and posterior midline so that no large vessels are present in these regions. However, the left and right arterial trees anastomose across the midline and unilateral ligation can be performed without serious effects. Terminal branches in the uterine muscle are tortuous and are called helicine arterioles. They provide a series of dense capillary plexuses in the myometrium and endometrium. From the arcuate arteries, many helical arteriolar rami pass into the endometrium. Their detailed appearance changes during the menstrual cycle. Helical arterioles are less prominent during the proliferative phase, whereas they grow in length and calibre, becoming even more tortuous, during the secretory phase.

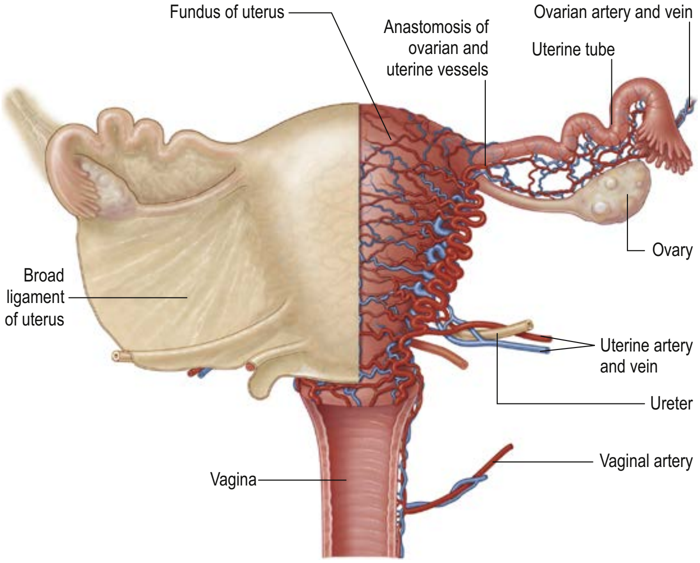

Fig. 75.19 The broad ligament (left) and blood supply to the uterus and ovaries (right). (With permission from Drake RL, Vogl AW, Mitchell A et al (eds) Gray's Atlas of Anatomy. Elsevier, Churchill Livingstone. Copyright 2008.)

Veins

The uterine veins extend laterally within the broad ligaments, running adjacent to the arteries and passing over the ureters. They drain into the internal iliac veins (see Fig. 75.3). The uterine venous plexus anastomoses with the vaginal and ovarian venous plexuses.

Lymphatic drainage

There are uterine lymphatics in the superficial (subperitoneal) and deep parts of the uterine wall. Collecting vessels from the body of the uterus and cervix pass laterally in the parametrium to three main groups of lymph nodes: the external and internal iliac and the obturator nodes (see Table 75.1). The external and internal iliac nodes surround their corresponding arteries. The obturator nodes lie in the so-called obturator fossa between the external and internal iliac vessels; the obturator nerve passes through the lower part of this group of lymph nodes.

Lymph vessels from the fundus of the uterus and the uterine tubes can accompany the lymph drainage of the ovaries to lateral aortic nodes (see Fig. 75.3B). The region surrounding the isthmus of the uterine tube can drain along the round ligament of the uterus to the superficial inguinal nodes.

Innervation

The nerve supply to the uterus is predominantly from the inferior hypogastric plexus (see Fig. 75.5) (Shoja et al 2013). Some branches ascend with, or near, the uterine arteries in the broad ligament. They supply the body of the uterus and uterine tubes and connect with tubal branches from the inferior hypogastric plexus and with the ovarian plexus. The branches to the uterus terminate in the myometrium and endometrium and usually accompany the vessels (see Table 75.2). Nerves to the cervix form a plexus that contains small paracervical ganglia. Branches can pass directly to the cervix of the uterus or be distributed along the vaginal arteries.

Efferent preganglionic sympathetic fibres are derived from neurones in the last thoracic and first lumbar spinal cord segments; the sites where they synapse on their postganglionic neurones are unknown but are presumably in the superior and/or inferior hypogastric plexus (Lee et al 1973). Preganglionic parasympathetic fibres arise from neurones in the second to fourth sacral spinal cord segments and relay in the paracervical ganglia. Sympathetic activity can produce uterine contraction and vasoconstriction, and parasympathetic activity can produce uterine inhibition and vasodilation, but these activities are complicated by hormonal control of uterine functions.

Microstructure

Body of the uterus

The uterus is composed of three main layers. From its lumen outwards, these are the endometrium (mucosa), myometrium (smooth muscle layer) and serosa (or adventitia) (**Fig. 75.22**).

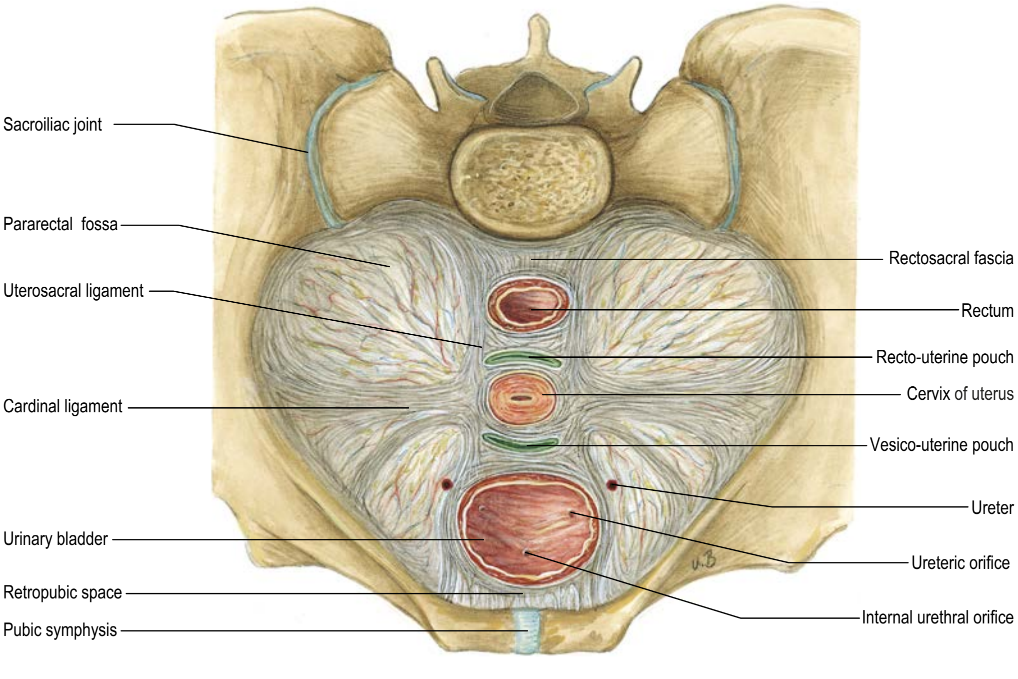

Fig. 75.20 The supporting ligaments of the pelvis, showing the cardinal ligaments. (Sobotta Atlas of Human Anatomy © Elsevier GmbH, Urban & Fischer, Munich.)

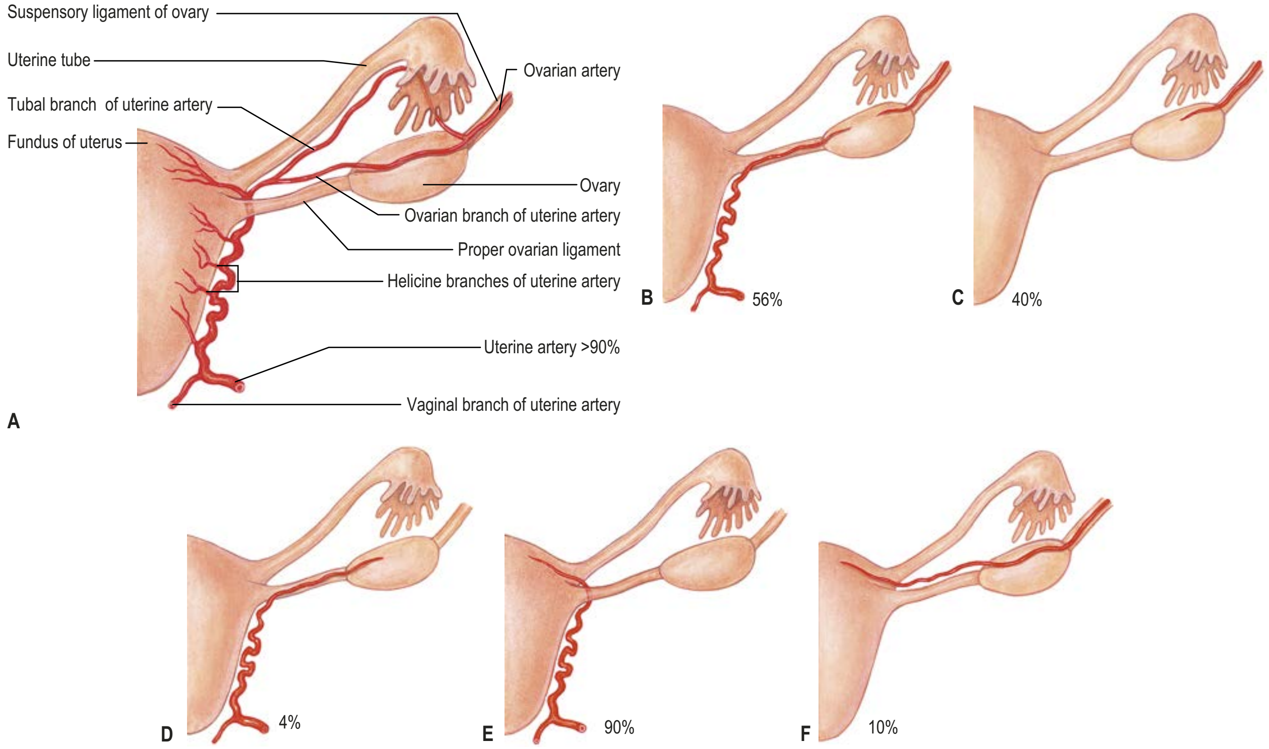
Suspensory ligament of ovary
Uterine tube
Tubal branch of uterine artery
Fundus of uterus
Ovarian artery
Ovary
Ovarian branch of uterine artery
Proper ovarian ligament
Helicine branches of uterine artery
Uterine artery >90%
Vaginal branch of uterine artery
A
B
56%
C
40%
D
4%
E
90%
F
10%

Fig. 75.21 **A**, The normal arterial supply to the uterus and ovary. **B–D**, Variations in arterial blood supply to the ovary. **E–F,** Variations in arterial blood supply to the fundus of the uterus. (A, Sobotta Atlas of Human Anatomy © Elsevier GmbH, Urban & Fischer, Munich.)

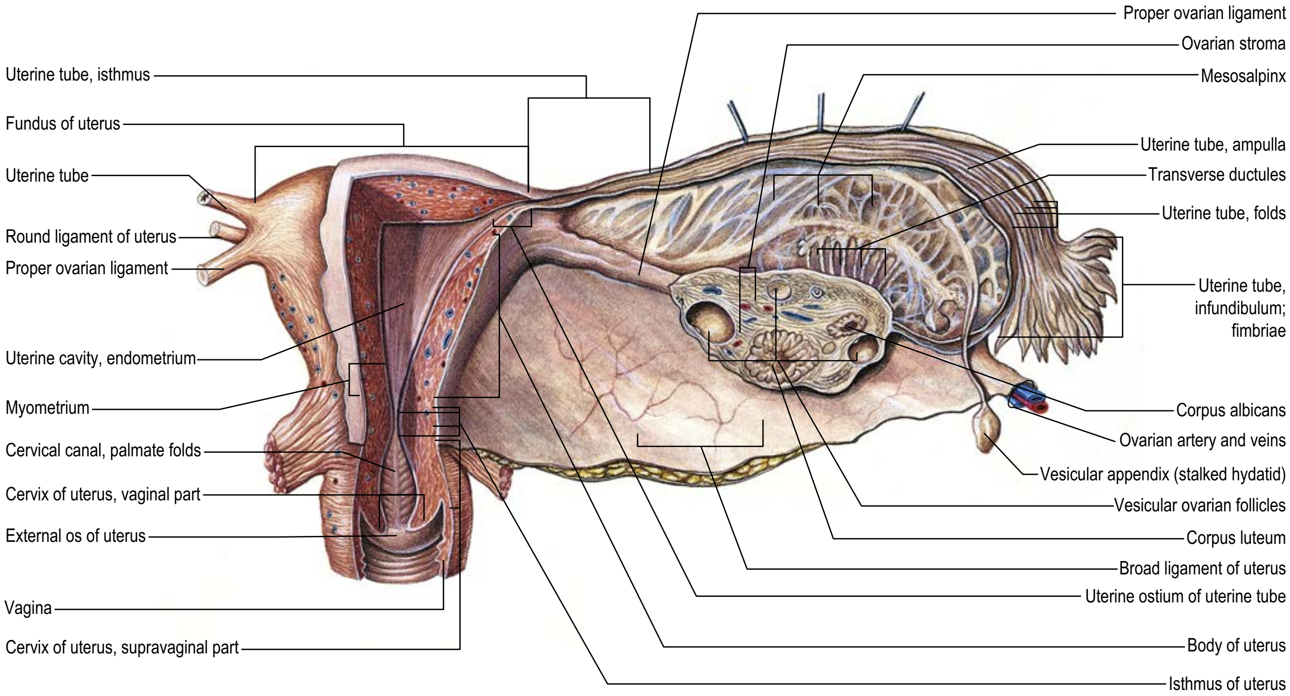
Uterine tube, isthmus
Fundus of uterus
Uterine tube
Round ligament of uterus
Proper ovarian ligament
Uterine cavity, endometrium
Myometrium
Cervical canal, palmate folds
Cervix of uterus, vaginal part
External os of uterus
Vagina
Cervix of uterus, supravaginal part
Proper ovarian ligament
Ovarian stroma
Mesosalpinx
Uterine tube, ampulla
Transverse ductules
Uterine tube, folds
Uterine tube, infundibulum; fimbriae
Corpus albicans
Ovarian artery and veins
Vesicular appendix (stalked hydatid)
Vesicular ovarian follicles
Corpus luteum
Broad ligament of uterus
Uterine ostium of uterine tube
Body of uterus
Isthmus of uterus

Fig. 75.22 The uterus, uterine tubes and ovaries. (Sobotta Atlas of Human Anatomy © Elsevier GmbH, Urban & Fischer, Munich.)

Endometrium

The endometrium is formed by a layer of connective tissue, the endometrial stroma, which supports a single-layered columnar epithelium. Before puberty, the epithelium is ciliated and cuboidal. It contains glands that are composed largely of columnar cells secreting glycoproteins and glycogen. After puberty, the structure of the endometrium varies with the stage of the menstrual cycle (see below). The glands are tubular, run perpendicular to the luminal surface and penetrate up to the myometrial layer. The stroma consists of a highly cellular connective tissue between the endometrial glands and contains blood and lymphatic vessels.

Myometrium

The myometrium is composed of smooth muscle and loose connective tissue and contains blood vessels, lymphatic vessels and nerves. It is dense and thick at the uterine midlevel and fundus but thin at the uterine ostium of the uterine tube. The body of the uterus has four muscular layers, submucosal, vascular, supravascular and subserosal. The submucosal (innermost) layer is composed of longitudinal and some oblique smooth muscle fibres. The vascular layer is external to the submucosal layer and is rich in blood vessels and longitudinal muscle. It is succeeded by the supravascular muscle layer where the muscle fibres are predominantly circular. The outer,

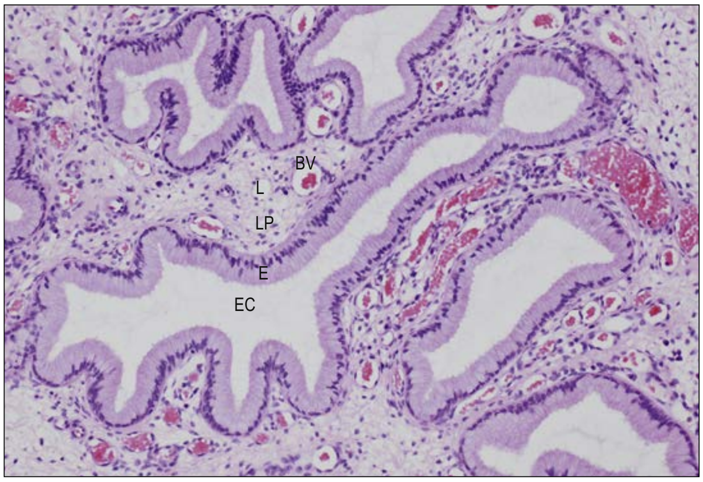

Fig. 75.23 The cervical glands. These are deep infoldings of the lining of the cervical canal (EC). The epithelium (E) is simple columnar and mucus-secreting. The underlying lamina propria (LP) is richly supplied with blood vessels (BV) and lymphatics (L). (Courtesy of Mr Peter Helliwell and the late Dr Joseph Mathew, Department of Histopathology, Royal Cornwall Hospitals Trust, UK.)

thin longitudinal muscle layer, the subserosal muscle layer, lies adjacent to the serosa.

The muscular fibres of the supravascular and subserosal layers converge at the lateral angles of the uterus and continue into the uterine tubes. Some fibres enter the broad ligaments as the round ligament of the uterus and the proper ovarian ligament, while others turn back into the uterosacral ligament. At the junction between the body and the cervix, the smooth muscle merges with dense, irregular connective tissue containing both collagen and elastin and forms most of the wall of the cervix. Bilateral longitudinal fibres extend in the lateral submucosal layer to the cervix. Their muscle fibres differ structurally from those of typical myometrium, and they may provide fast conducting pathways that coordinate the contractile activities of the uterine wall.

Serosa

The body of the uterus is covered by serosa, which continues downwards posteriorly to cover the supravaginal part of the cervix. The anterior cervix and the lateral surfaces of the body and cervix are not covered by peritoneum.

Cervix of the uterus

The cervix consists of fibroelastic connective tissue and contains relatively little (10%) smooth muscle. The elastin component of the cervical stroma is essential for the stretching capacity of the cervix during childbirth. The cervical canal is lined by a deeply folded mucosa with a surface epithelium of columnar mucous cells (Fig. 75.23). Branched tubular glands present within the mucosa are lined by a similar secretory epithelium. These glands extend obliquely upwards and outwards from the canal. They secrete clear, alkaline mucus, which is relatively viscous except at the midpoint of the menstrual cycle, when it becomes more copious and less viscous to encourage the passage of sperm. At the vaginal end of the cervix, the aperture of a gland may be blocked and it then fills with mucus to form a Nabothian follicle (or cyst). None of the mucosa is shed during menstruation, so unlike the body of the uterus it is not divided into functional and basal layers and lacks spiral arteries. The surface of the vaginal part of the cervix (ectocervical mucosa) is covered by stratified squamous non-keratinized epithelium, which contains glycogen.

The squamocolumnar junction, where the columnar secretory epithelium of the endocervical canal meets the stratified squamous covering of the ectocervical mucosa, is located at the external os of the uterus before puberty. As oestrogen levels rise during puberty the cervical os opens, exposing the endocervical columnar epithelium on to the ectocervical mucosa. This area of columnar cells on the ectocervical mucosa forms an area that is red and raw in appearance, called an ectropion (cervical erosion). It is then exposed to the acidic environment of the vagina and, through a process of squamous metaplasia (Ch. 2), transforms into stratified squamous epithelium. This area is thus known as the 'transformation zone' (Fig. 75.24). Other hyperoestrogenic states, such as pregnancy and the use of oral contraceptive pills, can also result in an ectropion. This area is the most usual site of cervical intraepithelial neoplasia (CIN), which can progress to malignancy. In postmenopausal females, the squamocolumnar junction recedes into the cervical canal.

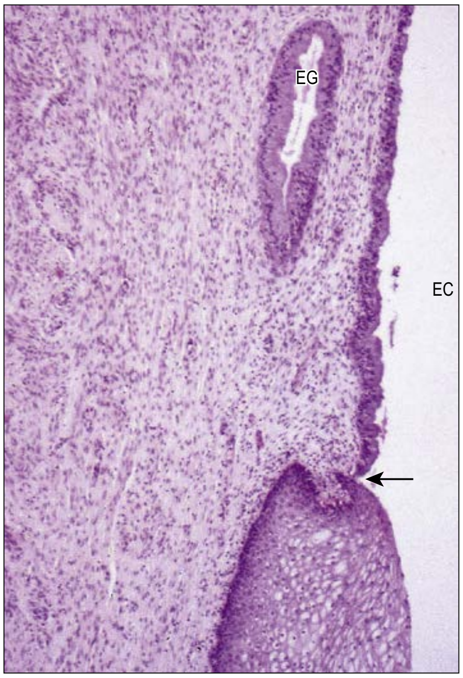

Fig. 75.24 The transformation zone of the cervix of the uterus. The single-layered columnar epithelium lining the cervical canal (EC) and its cervical glands (EG) changes abruptly (arrow) to the non-keratinized stratified squamous epithelium of the external os and exocervical mucosa (below arrow).

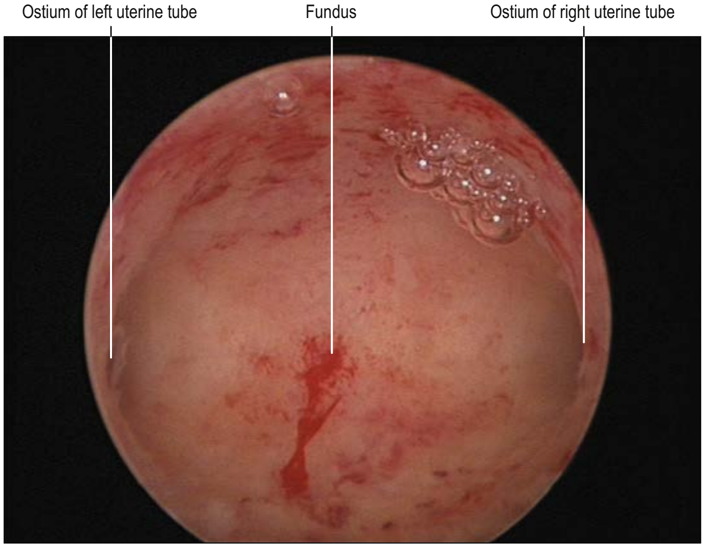

Fig. 75.26 A hysteroscopic view of the uterine cavity.

Magnetic resonance imaging of the uterus and vagina

Available with the *Gray's Anatomy* e-book

Uterine (Fallopian) tubes

The uterine tubes are attached to the upper part of the body of the uterus and their ostia open into the uterine cavity (Figs 75.26–75.28). The medial opening of the tube (uterine ostium of the uterine tube) is located at the superior angle of the uterine cavity. The tube passes laterally and superiorly and consists of four parts: uterine part, isthmus, ampulla and fimbria (see Fig. 75.22). The uterine part is 0.7 mm wide and 1 cm long and lies within the myometrium. It is continuous laterally with the isthmus, which is 1–5 mm wide and 3 cm long; it is rounded, muscular and firm. The isthmus is continuous laterally with the ampulla, the widest portion of the uterine tube with a maximum luminal diameter of 1 cm. The ampulla is 5 cm long and has a thin wall and a tortuously folded luminal surface. Typically, fertilization takes place in its lumen. The ampulla opens into the trumpet-shaped infundibulum at the abdominal ostium of the uterine tube. Fimbriae, numerous mucosal finger-like folds 1 mm wide, are

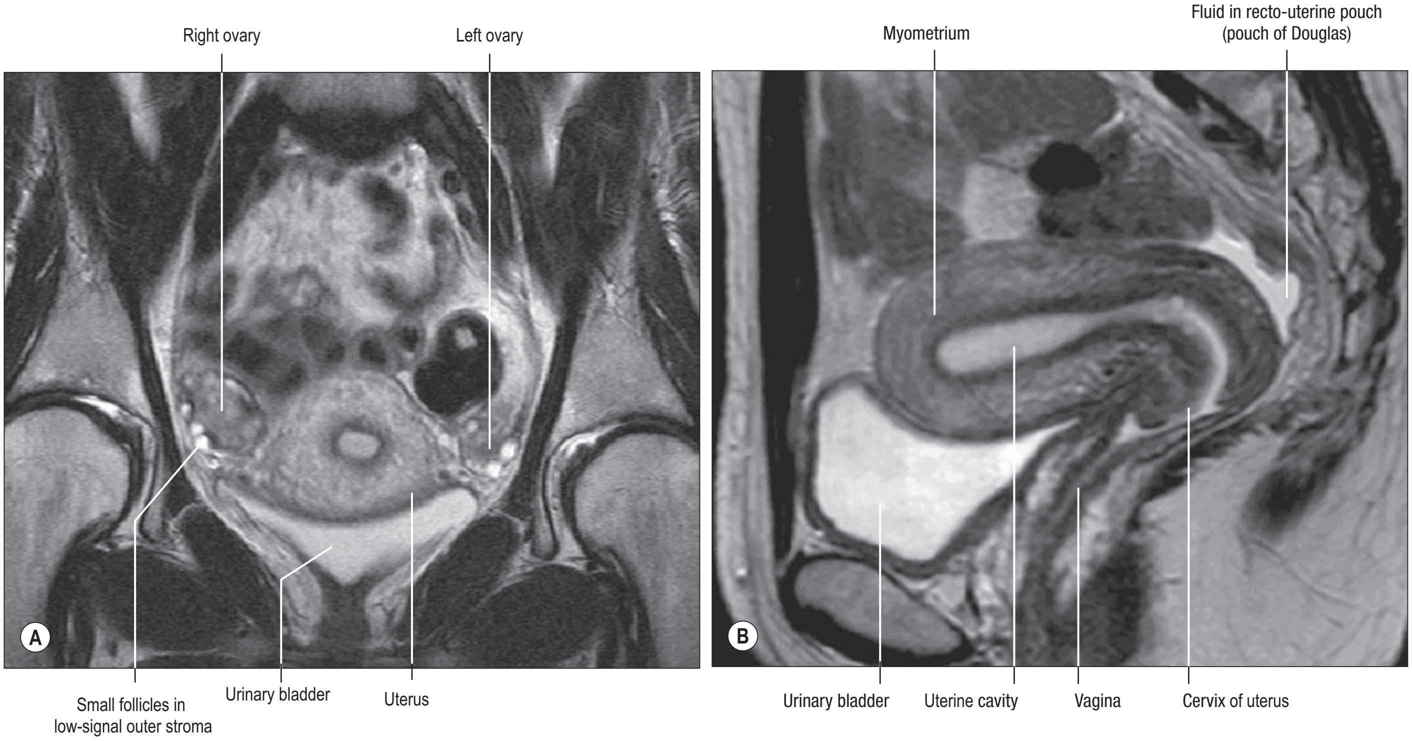

Fig. 75.25 T2-weighted MRI of the uterus and ovaries. **A**, A coronal T2-weighted MRI showing the uterus and both ovaries with the high-signal central stroma and lower-signal outer stroma. **B**, A sagittal T2-weighted MRI showing the zonal anatomy of the uterus.

Although MRI has limited clinical value for viewing the uterus and vagina, on T2-weighted magnetic resonance imaging (MRI) the uterus displays a zonal anatomy with three distinct zones: the endometrium, junctional zone and myometrium (**Fig. 75.25**) (Minto et al 2001). The endometrium and uterine cavity appear as a high-signal stripe; its thickness varies with the stage of the menstrual cycle. In the early proliferative phase it measures up to 5 mm, and widens to up to 1 cm in the mid-secretory phase. A low signal band, the junctional zone, borders the endometrium and represents the inner myometrium. It is of constant thickness and signal throughout the menstrual cycle and usually measures 5 mm. The outer myometrium is of medium-signal intensity during the proliferative phase and of high-signal intensity during the mid-secretory phase because of the increased vascularity and prominence of the arcuate vessels.

The uterus is smaller (only 4 cm in length) in prepubertal females, and on T2-weighted MRI the endometrium is minimal or absent and the junctional zone indistinct. In postmenopausal females the body of the uterus shrinks and the zonal anatomy is indistinct.

On T2-weighted MRI, the cervix has an inner, low-signal stroma continuous with the junctional zone of the uterus. This is often surrounded by an outer zone of intermediate signal intensity continuous with the outer myometrium. The appearances do not change with the menstrual cycle or oral contraceptive pill use. The central stripe is very high-signal and is a consequence of the secretions produced by the cervical glands.

The vagina is best seen on T2-weighted MRI as a thin layer of high-signal intensity of the mucosa and an outer low-signal layer of the submucosa and muscular layer (see Fig. 75.25). MRI accurately demonstrates congenital and acquired Müllerian duct anomalies including uterine and vaginal aplasia, duplication and septa (Grant et al 2010). Vaginal and perivaginal cysts are also well visualized with T2-weighted MRI.

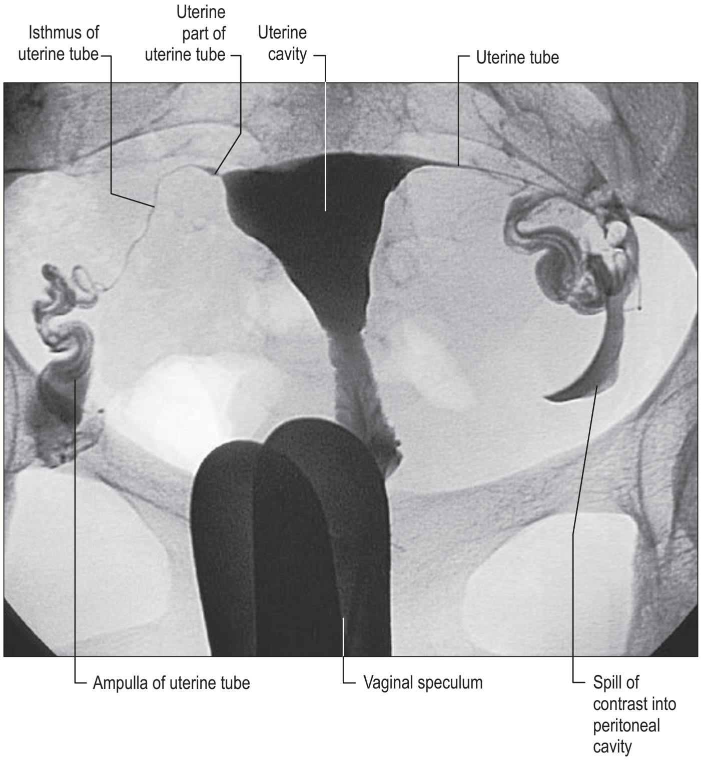

Fig. 75.27 A digitally subtracted hysterosalpingogram. Radiopaque contrast is introduced via a catheter inserted through the cervical os; the catheter is introduced using a vaginal speculum. The contrast fills the triangular-shaped uterine cavity. The lumina of the narrow uterine and isthmic parts of the uterine tubes may be traced inferolaterally from the superior angles as they expand into the wider ampullae. Some contrast media has escaped into the pelvic cavity from the abdominal ostia of the uterine tubes. (Courtesy of Dr Julia Hillier, Chelsea and Westminster Hospital, London.)

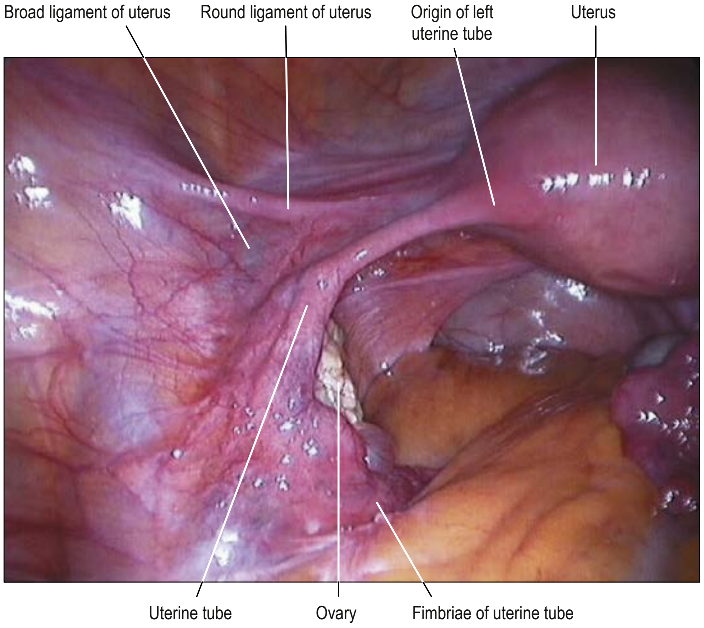

Fig. 75.28 A laparoscopic view of the origin of the uterine tube from the uterus.

attached to the ends of the infundibulum and extend from its inner circumference beyond the muscular wall of the uterine tube. One of these, the ovarian fimbria, is longer and more deeply grooved than the others and is typically applied to the tubal extremity of the ovary. At the time of ovulation, the fimbriae swell and extend as a result of engorgement of the vessels in the lamina propria, which aids capture of the released oocyte. All fimbriae are covered, like the mucosal lining throughout the tube, by a ciliated epithelium whose cilia beat towards the ampulla of the uterine tube.

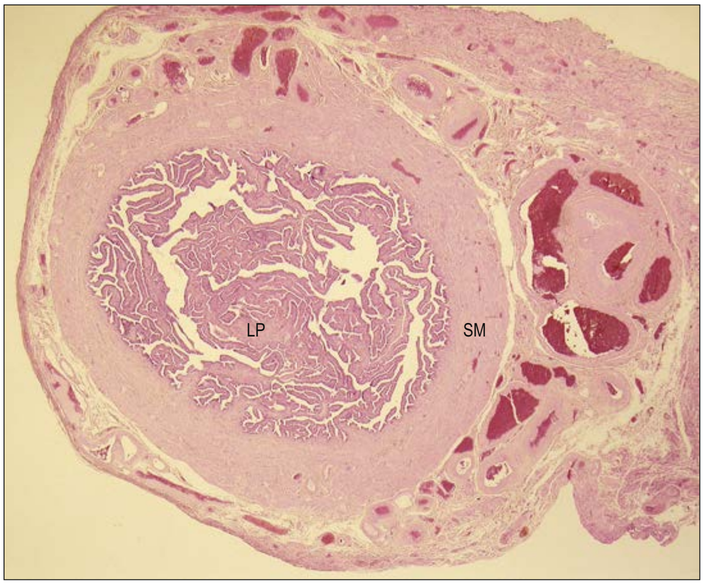

Fig. 75.29 The uterine tube (ampulla) with the mucosal lining thrown into extensive folds that fill the lumen. The superficial epithelium includes both secretory and ciliated cells, covering a lamina propria (LP). Smooth muscle (SM) occupies the wall of the tube. (Courtesy of Mr Peter Helliwell and the late Dr Joseph Mathew, Department of Histopathology, Royal Cornwall Hospitals Trust, UK.)

Vascular supply and lymphatic drainage

Arteries

The blood supply to the uterine tubes is derived from ovarian and uterine arteries (see Fig. 75.21A). The lateral third of the tube is supplied by the ovarian artery, which continues in the mesosalpinx to anastomose with branches from the uterine artery. The medial two-thirds of the uterine tube are supplied by the uterine artery.

Veins

Venous drainage is similar to the arterial supply. The venous drainage of the lateral two-thirds of the uterine tube is via the pampiniform plexus to the ovarian veins, which open into the inferior vena cava on the right side and the renal vein on the left. The medial two-thirds of the uterine tube drain via the uterine plexus to the internal iliac vein.

Lymphatic drainage

Lymph drainage is via ovarian vessels to the lateral aortic nodes and uterine vessels to the internal iliac nodes. It is possible for lymph to reach the inguinal nodes via the round ligament of the uterus (see Table 75.1).

Innervation

The uterine tubes are innervated by autonomic fibres that are distributed mainly with the ovarian and uterine arteries. Most of the tube has a dual sympathetic and parasympathetic supply (see Table 75.2). Preganglionic parasympathetic fibres are derived from the pelvic splanchnic nerves. The preganglionic sympathetic supply is derived from neurones in the intermediolateral nuclei of the tenth thoracic to the second lumbar spinal cord segments; postganglionic sympathetic fibres are most likely derived from the superior hypogastric plexus via the hypogastric nerves (see Fig. 75.5) (Chen et al 2014). Visceral afferent fibres travel with the sympathetic nerves and enter the spinal cord through corresponding dorsal roots; they can also travel with parasympathetic fibres. The ampullary submucosa contains modified Pacinian corpuscles.

Microstructure

The walls of the uterine tubes show typical visceral mucosal, muscular and serosal layers (**Fig. 75.29**). The mucosa is thrown into longitudinal folds, which are most pronounced distally at the infundibulum and decrease to shallow bulges in the uterine part. The mucosa is lined by a single-layered, tall, columnar epithelium, which contains mainly ciliated cells and secretory (peg) cells (so called because they project into the lumen further than their ciliated neighbours), and occasional intraepithelial lymphocytes. In the uterine tube, ciliated cells predominate distally and secretory cells proximally. Their activities vary with the

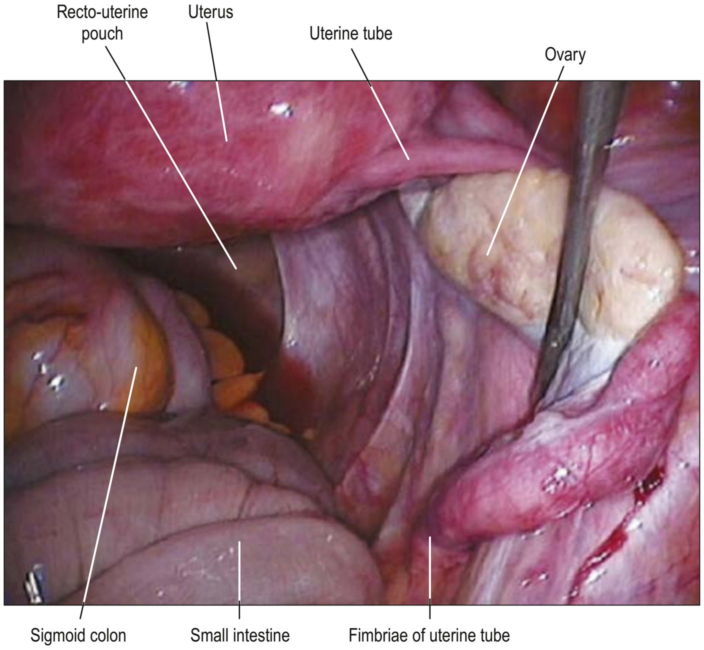

Fig. 75.30 A laparoscopic view of the right ovary, showing its distorted surface.

stage in the menstrual cycle and with age. Secretory cells are most active around the time of ovulation. Their secretions include nutrients for the gametes and aid capacitation of the spermatozoa. Ciliated cells increase in height and develop more cilia during the oestrogenic first half of the menstrual cycle. Their cilia waft the oocyte from the open-ended infundibulum towards the uterus in fluids secreted by the peg cells. The epithelium regresses in height towards the end of the cycle and postmenopausally, when ciliated cells are reduced in number.

The lamina propria provides vascular connective tissue support and abundant lymphatic drainage vessels. The smooth muscle of the muscular layer is arranged as an inner circular or spiral layer and an outer, thinner longitudinal layer. Together, their contractile activity produces peristaltic movements of the uterine tube, which assist propulsion of the gametes and the fertilised ovum. The uterine tubes are covered externally by a highly vascular serosa.

Ovaries

In the non-pregnant adult, the ovaries lie on each side of the uterus close to the lateral pelvic wall. They are suspended in the pelvic cavity by a double fold of peritoneum, the mesovarium, which is attached to the upper limit of the posterior aspect of the broad ligament. They are dull white in colour and consist of dense fibrous tissue, in which ova are embedded. Before regular ovulation begins they have a smooth surface, but their surfaces are distorted by scarring that follows the degeneration of successive corpora lutea, thereafter (Fritz and Speroff 2011) (**Fig. 75.30**). In the neonate, their dimensions are 1.3 × 0.6 × 0.4 cm. Before the first menstrual period (menarche) the ovaries are about one-third of the normal reproductive adult size. They gradually increase in size with body growth (Sforza et al 1993, Badouraki et al 2008): their average dimensions are 4 × 2 × 3 cm in reproductively mature females. The ovaries more than double in size during pregnancy and shrink significantly after menopause.

The lateral surface of the ovary contacts parietal peritoneum in the ovarian fossa. Behind the ovarian fossa are retroperitoneal structures including the ureter, internal iliac vessels, obturator vessels and nerve, and the origin of the uterine artery. The medial surface faces the uterus and uterine vessels in the broad ligament. Above the superior extremity are the fimbria and distal section of the uterine tube. The inferior extremity points downwards towards the pelvic floor. The mesovarian border faces the posterior leaf of the broad ligament. The free border faces the peritoneum, which overlies the upper part of the internal iliac artery and vein, and the ureter. On the right side, superior and lateral to the ovary, are the ileocaecal junction, caecum and appendix. On the left side, the sigmoid colon passes over the superior aspect of the ovary and joins the rectum, which lies between the medial surfaces of the two ovaries. The mesosalpinx lies below the uterine tube. The proper ovarian ligament is inferior and medial. The mesovarium and ovary lie inferiorly at its fimbrial end. The round ligament of the uterus is anterior to the uterine tube. The superior and posterior surfaces of the uterine tube lie free in the peritoneal cavity.

During embryonic and early fetal life the ovaries are situated in the lumbar region near the kidneys. They gradually descend along the gubernaculum, stopping at the lesser pelvis. The relationship between the location of the ovaries and surface landmarks is important for enabling the ovaries to be shielded from exposure to radiation during radiological procedures. In girls the ovaries lie at or below the iliac crest, just medial to the anterior superior iliac spine, and they lie above the pubic symphysis at all ages (Bardo et al 2009). There may be accessory ovarian tissue in the mesovarium or along the course of the gubernacula; rarely, the ovaries descend along the whole course of the gubernacula and are found in the labia majora. During pregnancy the ovaries are lifted high in the pelvis; by 14 weeks of gestation they become partly abdominal structures, and by the third trimester they are totally abdominal structures and lie vertically behind and lateral to the parous uterus.

Peritoneal and ligamentous supports of the ovary

The peritoneal and ligamentous supports of the ovary consist of the suspensory ligament of the ovary, proper ovarian ligament and the mesovarium.

Suspensory ligament of the ovary

The suspensory ligament of the ovary is a peritoneal fold attached to the upper part of the lateral surface of the ovary, which contains the ovarian vessels and nerves (see Fig. 75.18). On the right side, the suspensory ligament of the ovary is attached to a fold of peritoneum that is posterior and inferior to the caecum and appendix. The peritoneal attachment is higher on the left side than the right and is lateral to the junction of the descending and sigmoid colons. As it joins the peritoneum covering psoas major, the suspensory ligament of the ovary passes superiorly over the external iliac vessels, genitofemoral nerve and ureter.

Proper ovarian ligament

The proper ovarian ligament attaches the uterine (inferomedial) extremity of the ovary to the lateral angle of the uterus, posteroinferior to the uterine tube (see Fig. 75.22). It lies in the posterior leaf of the broad ligament and contains some smooth muscle cells. It is continuous with the medial border of the round ligament.

Mesovarium

The mesovarium is a short peritoneal fold that attaches the ovary to the back of the broad ligament. It carries blood vessels and nerves to the hilum of the ovary. The uterine tube arches over the ovary and ascends in relation to its mesovarian border, then curves over its tubal end and passes down on its posterior, free, border and medial surface.

Vascular supply and lymphatic drainage

Arteries

The ovarian arteries are branches of the abdominal aorta and originate below the renal arteries. Each descends behind the peritoneum and, at the linea terminalis, crosses the external iliac artery and vein to enter the lesser pelvis. Here, the artery turns medially in the suspensory ligament of the ovary and splits into a branch to the mesovarium that supplies the ovary and a branch that continues into the broad ligament, below the uterine tube, and supplies the tube. There are variations in the site of the division to the ovary and tube (see Fig. 75.21). On each side a branch passes lateral to the uterus to unite with the uterine artery. Other branches accompany the round ligaments through the inguinal canal to the skin of the labium majus and the inguinal region. Early in intrauterine life, the ovaries flank the vertebral column inferior to the kidneys, so the ovarian arteries are relatively short; they gradually lengthen as the ovaries descend into the pelvis.

Veins

The ovarian veins emerge from the ovary as a plexus (pampiniform plexus) in the mesovarium and suspensory ligament of the ovary (see Fig. 75.3A). Two veins emerge from the plexus and ascend with the ovarian artery; they usually merge into a single vessel before entering either the inferior vena cava on the right side or the renal vein on the left.

Lymphatic drainage

The main lymphatic drainage of the ovaries is along vessels that follow the ovarian veins to lateral aortic nodes situated near the origin of the renal arteries (see Table 75.1). There can also be drainage via pelvic nodes into lower lateral aortic nodes and, less commonly, via the round ligament of the uterus to the inguinal nodes (Kleppe et al 2015).

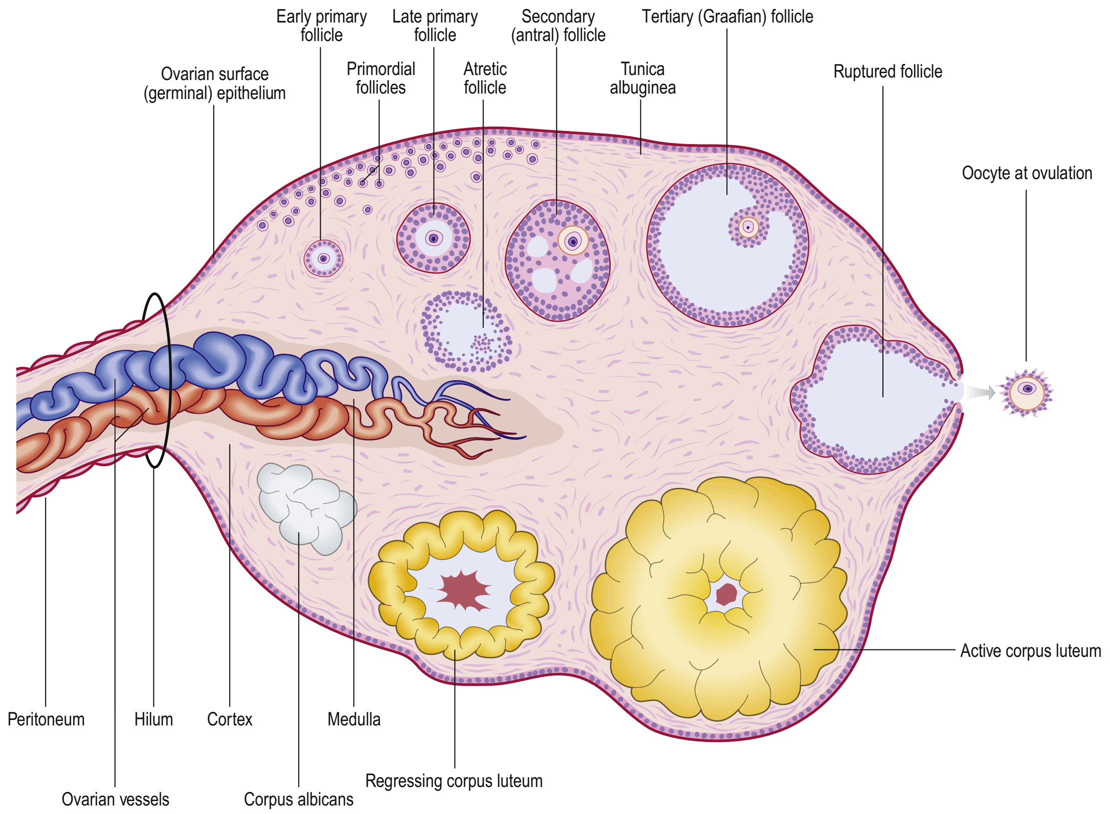

Fig. 75.31 The microstructure of the ovary and follicles at various stages in their cyclical development and the formation of corpora lutea and albicantia. Note that developing follicles are rarely seen in the human ovary.

Innervation

The ovarian innervation is derived from autonomic plexuses (see Table 75.2). The upper part of the ovarian plexus is formed from branches of the renal and aortic plexuses and the lower part is reinforced from the superior and inferior hypogastric plexuses. These plexuses consist of postganglionic sympathetic fibres, preganglionic parasympathetic fibres from the pelvic splanchnic nerves, and visceral afferent fibres (Lee et al 1973). The efferent preganglionic sympathetic fibres are derived from the tenth and eleventh thoracic spinal segments.

Microstructure

In young females the surface of the ovary is covered by a single layer of cuboidal epithelium, which contains some flatter cells. It appears dull white, in contrast to the shiny, smooth peritoneal mesothelial covering of the mesovarium, with which it is continuous. A white line around the anterior mesovarian border usually marks the transition between peritoneum and ovarian epithelium. The surface epithelium is also termed the germinal epithelium, but this is a misnomer because it is not the source of germ cells. Immediately beneath the epithelium there is a tough collagenous coat, the tunica albuginea. The ovarian tissue it surrounds is divisible into a cortex, containing the ovarian follicles, and a medulla, which receives the ovarian vessels and nerves at the hilum.

Ovarian cortex

Before puberty the cortex forms 35%, the medulla 20% and interstitial cells up to 45% of the volume of the ovary. After puberty, the cortex forms the major part of the ovary, enclosing the medulla except at the hilum. The cortex contains the ovarian follicles at various stages of development, and corpora lutea and their degenerative remnants, depending on age or stage of the menstrual cycle. The follicles and the structures derived from them are embedded in a dense stroma comprising a meshwork of thin collagen fibres and fusiform fibroblast-like cells, arranged in characteristic whorls. Stromal cells differ from fibroblasts in general connective tissue in that they contain lipid droplets, which accumulate during pregnancy. Stromal cells give rise to the thecal layers of maturing ovarian follicles.

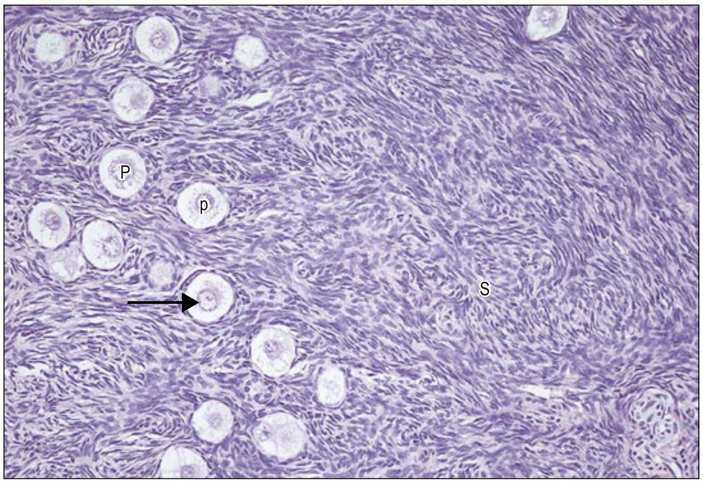

Fig. 75.32 Ovarian cortex with primordial (p) and early primary (P) follicles within the stroma (S); stimulated primary follicles have cuboidal cells forming their wall. A large oocyte nucleus is visible in the plane of section of most of the follicles (arrow). (Courtesy of Mr Peter Helliwell and the late Dr Joseph Mathew, Department of Histopathology, Royal Cornwall Hospitals Trust, UK.)

Ovarian follicles

Primordial follicles

The development of ovarian follicles can be divided into different stages (Fig. 75.31). At birth, the ovarian cortex contains a superficial zone of primordial follicles. These consist of primary oocytes 25 μm in diameter, each surrounded by a single layer of flat follicular cells. The oocyte nuclei are slightly eccentric and have a characteristically prominent nucleolus. They contain the diploid number of chromosomes (duplicated as sister chromatids), arrested at the diplotene stage of meiotic prophase after 16–20 weeks of fetal life (Fritz and Speroff 2011) (**Fig. 75.32**). Many follicles degenerate either during prepubertal (including prenatal) life, or through atresia at some stage after beginning the process of cyclical maturation during the child-bearing period. Their remnants are visible as atretic follicles, the remains of which accumulate throughout the period of reproductive life. After puberty, cohorts of up to 20 primordial follicles become activated in each menstrual cycle (fewer are activated with advancing age). Their development takes a number of cycles. Among the follicles activated in each cohort, usually only one from one or the other ovary becomes dominant, reaches maturity and releases its oocyte at ovulation.

Abnormal, non-growing follicles with indistinct germinal vesicle membranes and absent nucleoli are sometimes found in prepubertal

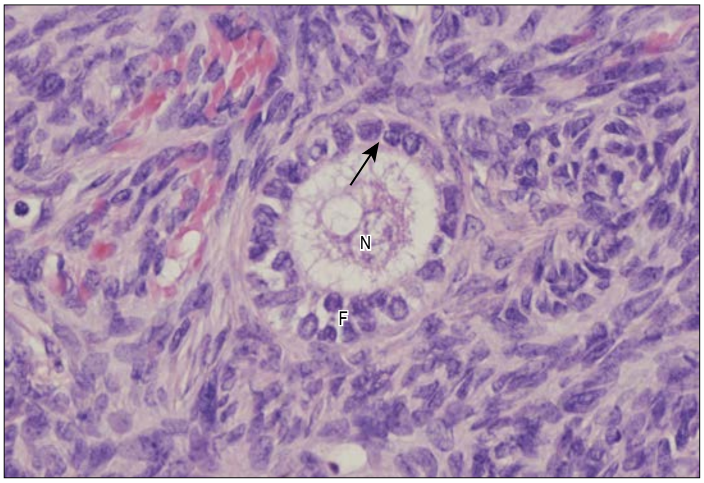

Fig. 75.33 A high-magnification micrograph of a primary follicle in a human ovarian cortex. The pale oocyte, with its eccentric nucleus (N), is separated from the follicle (F) by the zona pellucida (arrow). Cells of the follicle wall are in the early stages of proliferation to form a multilayered, late primary follicle. (Courtesy of Mr Peter Helliwell and the late Dr Joseph Mathew, Department of Histopathology, Royal Cornwall Hospitals Trust, UK.)

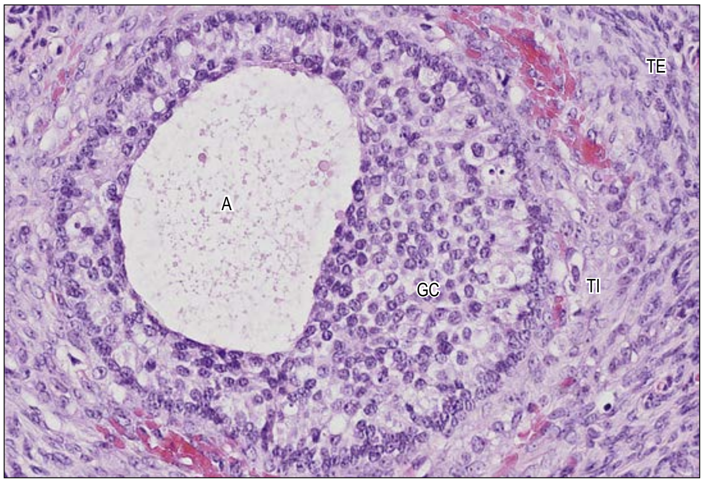

Fig. 75.34 An antral follicle, showing the layers of the developing follicle wall. Granulosa cells (GC) enclose the antrum (A), filled with follicular fluid, and surround the oocyte (not seen in the plane of section) within an eccentric cellular mass (right). The outer theca interna (TI) is a highly vascular layer that develops steroid secretory activity and is enclosed by the outermost theca externa (TE). (Courtesy of Mr Peter Helliwell and the late Dr Joseph Mathew, Department of Histopathology, Royal Cornwall Hospitals Trust, UK.)

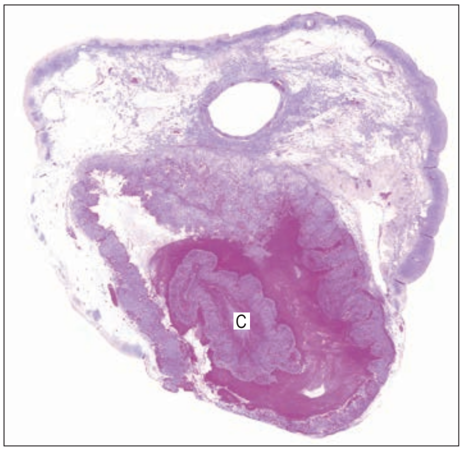

Fig. 75.35 A low-power view of a section of a human ovary, containing a corpus luteum (C). (Courtesy of Mr Peter Helliwell and the late Dr Joseph Mathew, Department of Histopathology, Royal Cornwall Hospitals Trust, UK.)

ovaries and occasionally in pubertal ovaries, but not in adult ovaries (Anderson et al 2014).

Primary follicles

Primary follicles develop from primordial follicles. The first sign is a change in the follicle cells from flattened to cuboidal, followed by their proliferation to give rise to a follicle consisting of a wall of granulosa cells surrounded by a thick basal lamina (Fig. 75.33).

Secondary follicles

Granulosa cell proliferation continues to form a multilayered follicular wall. Stromal cells immediately surrounding the follicle begin to differentiate into spindle-shaped cells that constitute the theca folliculi and which will become the theca interna. They are later surrounded by a more fibrous layer, the theca externa. At the same time, the oocyte increases in size and secretes a thick layer of extracellular proteoglycan-rich material – the zona pellucida – between its plasma membrane and the surrounding granulosa cells of the early follicle; this is important for the process of fertilization. The granulosa cells in contact with the zona pellucida send cytoplasmic processes radially inwards; these contact and communicate with oocyte microvilli at gap junctions (Motta et al 2003).

Antral follicles

Antral follicles develop from secondary follicles; the transition is not well defined and is a continuous process. The number of granulosa cells continues to increase. Cavities begin to form between them during a pre-antral phase and are filled with a clear fluid (follicular fluid), derived largely as an exudate from the thecal vasculature, containing hyaluronate, growth factors and steroid hormones secreted by the granulosa cells. The follicle is now about 200 μm in diameter and usually lies deep in the cortex. The cavities coalesce to form one large fluid-filled space, the antrum, which is surrounded by a thin uniform layer of granulosa cells, except at one pole of the follicle where a thickened granulosa layer envelops the eccentrically placed oocyte to form the cumulus oophorus. The oocyte has now reached its maximum size of about 160 μm (including the zona pellucida) and the inner and outer thecae are clearly differentiated (Fig. 75.34). As follicles mature, the theca interna becomes more prominent and its cells more rounded and typical of steroid-secreting endocrine cells. They produce androstenedione, from which the granulosa cells synthesize oestrogens (primarily oestradiol). Follicular development is stimulated by follicle-stimulating hormone (FSH).

Preovulatory (tertiary, Graafian) follicle

Although a number of follicles can progress to the secondary stage by about the first week of a menstrual cycle, usually only one follicle develops to maturity; the remainder become atretic. The surviving follicle increases considerably in size as the antrum takes up fluid from the surrounding tissues and expands to a diameter of 2 cm. The term 'Graafian follicle' is often used to describe this mature follicular stage (vesicular ovarian follicle). The oocyte with a surrounding ring of tightly adherent cells, the corona radiata, breaks away from the follicle wall and floats freely in the follicular fluid. The primary oocyte, which has remained in the first meiotic prophase since fetal life (see Fig. 1.24), completes its first meiotic division to produce the almost equally large secondary oocyte and a small first polar body with very little cytoplasm. The secondary haploid oocyte immediately begins its second meiotic division, but when it reaches metaphase the process is arrested until fertilization has occurred. The follicle moves to the superficial cortex, causing the surface of the ovary to bulge. The tissues at the point of contact (the stigma) with the tough tunica albuginea and ovarian surface epithelium are eroded until the follicle ruptures and its contents are released into the peritoneal cavity for capture by the fimbriae of the uterine tube. The oocyte at ovulation is still surrounded by its zona pellucida and corona radiata of granulosa cells. If fertilization does not occur, it begins to degenerate after 24–48 hours.

Corpus luteum

After ovulation, the remainder of the follicle becomes the corpus luteum (Fig. 75.35). The walls of the empty follicle collapse and fold. The granulosa cells increase in size and synthesize a cytoplasmic carotenoid pigment (lutein), giving them a yellowish colour (hence, corpus luteum). These large (30–50 μm) granulosa lutein cells form most of the corpus luteum. The basal lamina surrounding the follicle breaks down and numerous smaller theca lutein cells infiltrate the folds of the cellular mass, accompanied by capillaries and connective tissue. Extravasated blood from thecal capillaries accumulates in the centre as a small clot, but this rapidly resolves and is replaced by connective tissue. All lutein cells have a cytoplasm filled with abundant smooth endoplasmic reticulum, characteristic of steroid-synthesizing endocrine cells. Granulosa lutein cells secrete

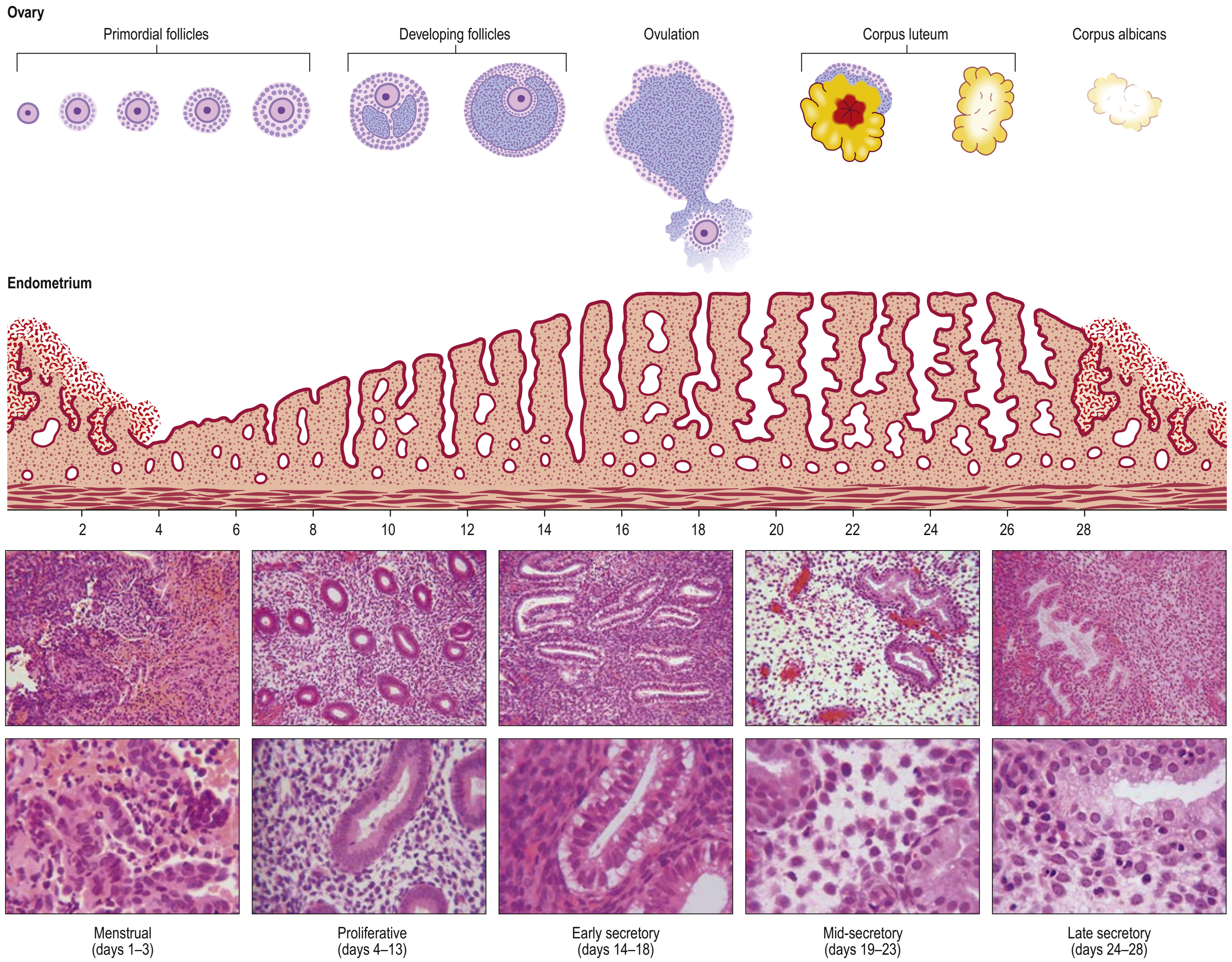

Fig. 75.36 Stages in the menstrual cycle with concomitant changes in the endometrium. Note that developing antral follicles are selected from cohorts of follicles recruited in earlier cycles. The ten lower panels are histological sections of endometrium at the cycle times indicated (low magnification on top and high magnification below in each case).

progesterone and oestradiol (from aromatization of the androstenedione synthesized by theca lutein cells). The two cell types also respond differently to circulating gonadotropins: theca lutein cells respond to luteinizing hormone (LH) and granulose lutein cells to FSH. Theca lutein cells express receptors for human chorionic gonadotrophin (hCG). If the oocyte is not fertilized, the corpus luteum (of menstruation) functions for 12–14 days after ovulation, then atrophies. The lutein cells undergo fatty degeneration, autolysis, removal by macrophages and gradual replacement with fibrous tissue. Eventually, after 2 months, a small, whitish, scar-like corpus albicans is all that remains.

If fertilization does occur, implantation of the blastocyst into the uterine endometrium usually begins 7 days later and the embryonic trophoblast then starts to produce hCG. The chorionic gonadotrophin stimulates the corpus luteum of menstruation to grow and it becomes a corpus luteum of pregnancy. It normally increases in diameter from 10 mm to 25 mm at 8 weeks of gestation and can be seen clearly on ultrasound. It secretes progesterone, oestrogen and relaxin and functions throughout pregnancy, although it gradually regresses as its endocrine functions are largely replaced by the placenta after 8 weeks' gestation. Its diameter is reduced by the end of pregnancy to 1 cm. Over the next few months it degenerates, like the corpus luteum of menstruation, to form a corpus albicans.

Ovarian medulla

The ovarian medulla is highly vascular. It contains numerous veins and spiral arteries that enter the hilum from the mesovarium and lie within a loose connective tissue stroma (Delson et al 1948). Small numbers of cells (hilus cells) with characteristics similar to interstitial (Leydig) cells in the testis are found in the medulla at the hilum; they may be a source of androgens.

Menopause

At the menopause, ovulation ceases and various microscopic changes ensue within the ovarian tissues. The stroma becomes denser, the tunica albuginea thickens and the ovarian surface epithelium thins. However, many follicles persist within the cortex.

MENSTRUAL CYCLE

The onset of menstruation (menarche) occurs between the tenth and seventeenth years of life, with a peak between 12 and 14 years. The uterus, ovaries and vagina undergo changes during the menstrual cycle, which normally lasts approximately 28 days. Usually, a single mature follicle ruptures mid-cycle (approximately day 14 of a 28-day cycle) to release a secondary oocyte. The wall of the follicle is then transformed into the corpus luteum, which secretes progesterone (luteal phase). About 10 days after ovulation the corpus luteum begins to regress, then it ceases to function and is replaced by fibrous tissue. The breakdown of the endometrium that follows this cessation of function is due to the falling levels of progesterone and oestrogen as the corpus luteum degenerates.

The changes that occur in the endometrium during the menstrual cycle can be divided into three phases: proliferative, secretory and menstrual (Fig. 75.36).

Proliferative phase

During the early proliferative phase, even before the menstrual flow ceases, the epithelium from the persisting basal parts of the uterine glands grows over the surface of the endometrium, which has been denuded by menstruation. Re-epithelialization is complete 5–6 days after the start of menstruation. Initially, the tissue is only 1–2 mm thick and is lined by low cuboidal epithelium. The glands are straight and narrow and their lining cells are low columnar. The apical cell surface contains microvilli; some cells are ciliated. The stroma is dense and contains small numbers of lymphocytes. During days 10–12 of the proliferative phase, the endometrium thickens. Cells divide in response to rising levels of oestrogen, which is produced by the ovary and acts through receptors present on both the stromal and the epithelial cells. The glands become tortuous and their lining epithelial cells become tall columnar in nature (Fritz and Speroff 2011).

Secretory phase

The secretory phase coincides with the luteal phase of the ovarian cycle. The endometrial changes are driven by progesterone and oestrogen, secreted by the corpus luteum. Steroid receptors in the endometrium activate a programme of new gene expression that over the following 7 days produces a highly regulated sequence of differentiative events, presumably required to prepare the tissue for blastocyst implantation. Part of the response is direct, but there is evidence that some of the effects are mediated through growth factors (Fritz and Speroff 2011). The first morphological effects of progesterone are evident 24–36 hours after ovulation (which occurs approximately 14 days before the next menstrual flow). During the early secretory phase, glycogen masses accumulate in the basal cytoplasm of the epithelial cells lining the glands, where they are often associated with lipids; giant mitochondria appear. There is an obviously increased polarization of the gland cells: nuclei are displaced towards the centre of the cells, and Golgi apparatus and secretory vesicles accumulate in the supranuclear cytoplasm. The nuclear channel system is prominent and the nuclei enlarge. Nascent secretory products can be detected immunohistochemically within the cells. Progestational effects on the stroma (known as the decidual reaction) are also evident in the early secretory phase. The nuclei are enlarged and the packing density of the resident stromal cells increases, due in part to the increase in volume of gland lumina and the onset of secretory activity in the epithelial compartment.

By the mid-secretory phase, the endometrium can be up to 6 mm deep. The basal epithelial glycogen mass is progressively transferred to the apical cytoplasm and nuclei return to the cell bases. The Golgi apparatus dilates and produces glycogen, mucin and other glycoproteins, secreted from the glandular epithelium into the lumen by a combination of apocrine and merocrine mechanisms; this activity reaches a maximum 6 days after ovulation. These secretory changes are considerably less pronounced in the basal gland cells and the luminal epithelium than in the glandular cell population of the functional layer. There is a notable stromal oedema and a corresponding decrease in the density of collagen fibrils. At the same time, the endoplasmic reticulum and Golgi apparatus become more prominent, and collagen is synthesized and degraded, presumably reflecting ongoing matrix remodelling.

During the late secretory phase, glandular secretory activity declines. Decidual differentiation occurs in the superficial stromal cells that surround blood vessels; this transformation includes nuclear rounding and an increased cytoplasmic volume, reflecting an increase in and dilation of the rough endoplasmic reticulum and Golgi systems, and cytoplasmic accumulation of lipid droplets and glycogen. The cells begin to produce basal lamina components including laminin and type IV collagen.

Ultrasound imaging of the uterus and its contents

Ultrasound is frequently used in the clinical evaluation of the endometrium. During the early secretory phase the endometrium is identified as a thin echogenic line, a consequence of specular reflection from the interface between its opposing surfaces. During the late proliferative phase the endometrium appears as a triple layer: a central echogenic line (produced by the apposed endometrial surfaces), surrounded by a thicker hypoechoic functional layer and bounded by an outer echogenic basal layer. During the secretory phase, the functional layer surrounding the echogenic line becomes more hyperechoic because of the increased mucus and glycogen within the glands and the increased number of interfaces caused by the development of tortuous spiral arteries (Fig. 75.37).

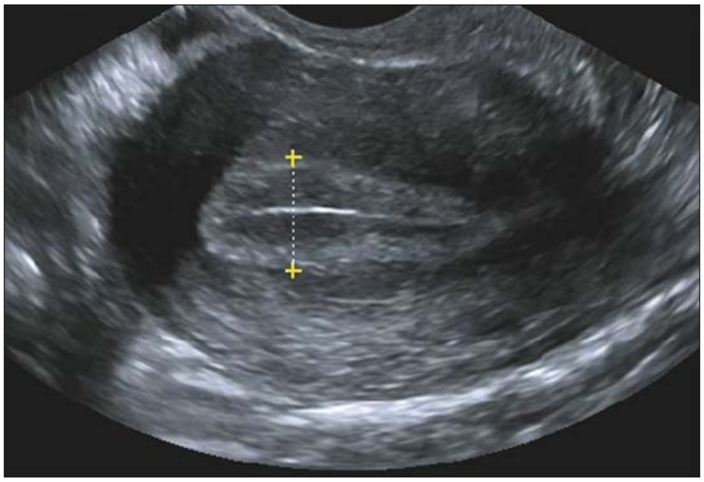

Fig. 75.37 Transvaginal ultrasound of the uterus, showing the triple-layered endometrium. The central echogenic line is produced by the interface of the opposing surfaces of the endometrium. The functional layer of the endometrium surrounding the echogenic line is hypoechoic on the left, in keeping with late proliferative phase, but is becoming more hyperechoic on the right, indicating the early secretory phase.

Menstrual phase

The premenstrual endometrium consists of two layers, an upper two-thirds, the functional layer (which will be shed), overlying the basal layer (which is retained). In the upper part of the functional layer (the compact layer), the necks of the glands are only slightly expanded and the stromal cells show a distinct decidual reaction. In the deeper part of the functional layer (the spongy layer) the uterine glands are tortuous, dilated and, ultimately, separated from one another by a small amount of connective tissue. The basal layer, next to the myometrium, is thin and contains the tips of the uterine glands embedded in an unaltered stroma.

As the corpus luteum regresses, those parts of the stroma showing a decidual reaction, together with the glandular epithelium, undergo degenerative changes and the endometrium often thins. Blood escapes from the superficial vessels of the endometrium, forming small haematomata beneath the surface epithelium (see below). The functional layer, next to the free surface, is shed piecemeal, leaving mainly the basal layer adjacent to the myometrium; 65–75% of the thickness of the endometrium can be shed. Blood and necrotic endometrium then begin to appear in the uterine lumen, to be discharged from the uterus through the vagina as the menstrual flow, which usually lasts 3–6 days.

Vascular changes within the uterus during the menstrual cycle

The vascular bed of the endometrium undergoes significant changes during the menstrual cycle. The arteries to the endometrium arise from a myometrial plexus and consist of short, straight vessels to the basal portion of the endometrium and more muscular spiral arteries to its superficial two-thirds. The venous drainage, consisting of narrow perpendicular vessels that anastomose by cross-branches, is common to both the superficial and the basal layers of the endometrium. The capillary bed consists of an endothelium with a basal lamina that is discontinuous during the proliferative phase but becomes more distinct by the mid-secretory phase. Pericytes make contact with the endothelial cells via cytoplasmic extensions that project through the basal lamina. Enlargement of the pericytes starts early in the secretory phase and leads to a conspicuous cuff of cells in the mid- and late secretory phases. The arterial supply to the basal part of the endometrium remains unchanged throughout the menstrual cycle. However, the spiral arteries supplying the compact (superficial) layer lengthen disproportionately, becoming increasingly coiled as their tips approach the uterine epithelium. This leads to a slowing of the circulation in the compact layer with some vasodilation. Immediately before the menstrual flow, these vessels begin to constrict intermittently, causing stasis of the blood and anaemia of the compact layer. During the periods of relaxation of the vessels, blood escapes from the devitalized capillaries and veins, causing the menstrual blood loss. The breakdown of the endometrium is a consequence of the falling levels of progesterone and oestrogen as the corpus luteum degenerates.

PREGNANCY AND PARTURITION

During pregnancy many morphological changes occur in the female reproductive system and associated abdominal structures. The uterus enlarges to accommodate the developing fetus and placenta, and

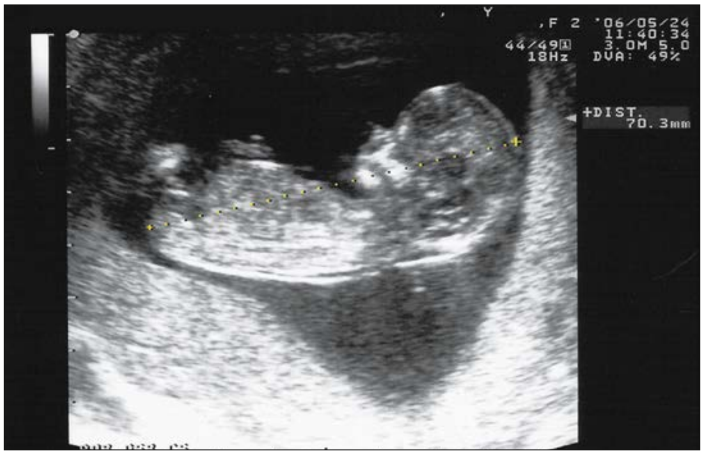

Fig. 75.38 Transabdominal ultrasound at 12 weeks, showing measurement of the crown–rump length to calculate the gestational age.

various alterations take place in the pelvic walls, floor and contents that allow for this expansion, and which anticipate parturition. At the end of gestation dramatic changes occur that facilitate the passage of the baby through the birth canal and, subsequently, allow the pelvic organs to return to the non-pregnant state (involution).

On average, human gestation is approximately 280 days (or 40 weeks) from the date of the last menstrual period (LMP): the duration of pregnancy can be expressed in postmenstrual weeks (Ch. 23). However, cycle irregularity or inaccurate recollection can lead to an inaccurate menstrual history: an accurate gestational age can be calculated by ultrasound measurement of the fetal crown–rump length during the first trimester (**Fig. 75.38**). A discrepancy of more than 5–7 days from the LMP-estimated age is usually reason to revise the estimated date of confinement. For females presenting after the first trimester, gestational dating can be based on other sonographically obtained fetal biometric measurements, such as the fetal biparietal diameter, head circumference and femur length, although precision gradually decreases in later pregnancy (see Fig. 23.5). The increased accuracy of gestational dating using sonographic fetal biometry rather than menstrual history alone has significantly reduced the number of pregnancies requiring induction of labour for post-term females.

Uterus in pregnancy

The function of the uterus in pregnancy is to retain the developing fetus and to provide a protected environment until a stage at which the fetus is capable of surviving *ex utero*. The uterus must grow, facilitate delivery of the fetus and then involute.

The uterus grows dramatically during pregnancy, increasing in weight from about 50 g at the beginning of pregnancy to up to 1 kg at term. Most of the weight gain is the result of increased vascularity and fluid retention by the myometrium. The increased growth of the uterine wall is driven by a combination of mechanical stretching and endocrine input. The mechanical load imposed on the uterine wall as gestation advances induces hypertrophy of uterine smooth muscle cells and is the major stimulus for increasing smooth muscle mass. There is some hyperplasia early in pregnancy, mainly from the growth of the media of the myometrial arteries and veins. The myometrium is relatively unresponsive to additional endocrine stimulation during most of pregnancy, a relative quiescence that is in part attributed to progesterone. However, a number of growth factors, e.g. insulin-like growth factor-1 (IGF-1), have been identified, which interact with oestrogen in promoting uterine growth. The myometrium thins with advancing gestation from 2–3 cm thick in early pregnancy to 1–2 cm at term.

The upper third of the cervix is gradually taken up into the body of the uterus during the second month to form the 'lower segment' (**Fig. 75.39**). The isthmus of the uterus hypertrophies like the body of the uterus during the first trimester and triples in length to about 3 cm. From the second trimester, the wall of the isthmus and that of the body are the same thickness and their junction is no longer visible externally. This condition persists until the middle of the third trimester, when the lower uterine segment thins to less than 1 cm in thickness. The thicker myometrium above this transition is the main contractile portion of the uterus that will generate the expulsive forces during labour. The thin lower uterine segment, which is thought to correspond to the level of the anatomical internal os, is just superior to the bladder and the reflections of the vesico-uterine pouch. It is more compliant and allows for the descent of the fetus in late pregnancy and during labour: it is the preferred site of incision during a caesarean section because it is thinner and less vascular than the upper uterus. In addition, because it is less contractile, there is a lower risk of uterine rupture in subsequent pregnancies than with an incision made in the body of the uterus during a 'classic' caesarean section.

The growing uterus generally emerges from the pelvis by postmenstrual week 12 and can be palpated on the maternal abdomen just above the pubic symphysis. By the 20th week of pregnancy the uterine fundus is at the level of the umbilicus and it reaches the xiphoid process of the sternum by 36 weeks. After 24 weeks, the distance between the pubic symphysis and the fundus of the uterus generally corresponds to the number of postmenstrual weeks and is often used in clinical care as a screening method to detect a pregnancy that is measuring suspiciously larger or smaller than expected. If there is more than a 2 cm discrepancy between uterine size and gestational week, a more accurate, sonographic assessment of fetal size and amniotic fluid volume is indicated.

Cervix of the uterus during pregnancy

During pregnancy the cervix of the uterus is a relatively rigid, fibromuscular structure that retains the developing fetus within the uterus. The rigidity of the cervix appears to be related to the orientation of its collagen fibres within a regular connective tissue matrix. The cervix gradually softens and shortens in the weeks preceding labour. During active labour, the cervix dilates to allow the fetus to descend through the birth canal. The exact processes that allow softening, effacement and dilation of the cervix are unclear, but are believed to include remodelling of the connective tissue matrix, probably mediated by increased activities of enzymes such as matrix metalloproteinase-1, reduced collagen concentration, a significant increase in the water content in the cervix, macrophage and neutrophil infiltration, and an increased level of apoptosis.

Transvaginal ultrasound examination allows for a robust evaluation of the cervix during pregnancy. Cervical length, dilation of the anatomical internal os and bulging of the membranes into the cervical canal can all be assessed. A shortened cervical length in mid-gestation detected by transvaginal ultrasound is a strong risk factor for premature delivery and has been used clinically to identify females at high risk of preterm delivery in order to plan appropriate management (Fonseca et al 2007, Owen et al 2009, Hassan et al 2011). Emerging sonographic and MRI technologies are being used to investigate both the biomechanical properties and the microstructure of the cervix in pregnancy and are beginning to shed light on the poorly understood mechanisms involved in both normal and pathological cervical shortening in human pregnancy (Feltovich et al 2012, House et al 2013). The advent of commercially available histochemical studies such as those testing for fetal fibronectin also look for substances known to increase with dilation of the cervix (Daskalakis et al 2000).

Relations of the uterus in pregnancy

With uterine expansion, the ovaries and uterine tubes are displaced upwards and laterally. The round ligaments of the uterus become hypertrophied and their course from the uterus down to the deep inguinal ring becomes more vertical. The broad ligaments tend to open out to accommodate the massive increase in sizes of the uterine and ovarian vessels. The uterine veins in particular can reach about 1 cm in diameter and appear to act as a significant reservoir for blood during uterine contractions. Lymphatics and nerves expand their territories (the significance of this increased innervation is not clear because paraplegic females are able to labour normally, albeit painlessly). Later in pregnancy, the increase in intra-abdominal pressure produced by the gravid uterus can cause eversion of the umbilicus. On the skin over the abdomen, a combination of stretching and hormonal changes can produce stretch marks (striae gravidarum). In multiparous patients, diastasis (divarification) of right and left rectus abdominis can occur to accommodate the enlarging fundus of the uterus further. In the supine position, the gravid uterus can cause aortocaval compression, leading to reduced venous return to the heart and decreased cardiac output. In some females this can result in symptomatic hypotension and symptoms of nausea and syncope. These symptoms are minimized if the patient lies on her left side, thereby deviating the gravid uterus and reducing compression of the inferior vena cava.

The jejunum, ileum and transverse colon tend to be displaced upwards by the enlarging uterus, whereas the caecum and appendix are displaced to the right and the sigmoid colon posteriorly and to the left. Upward and lateral displacement of the appendix in later pregnancy can cause difficulties in the diagnosis of appendicitis. The ureters are pushed laterally by the enlarging uterus and, in late pregnancy, can be

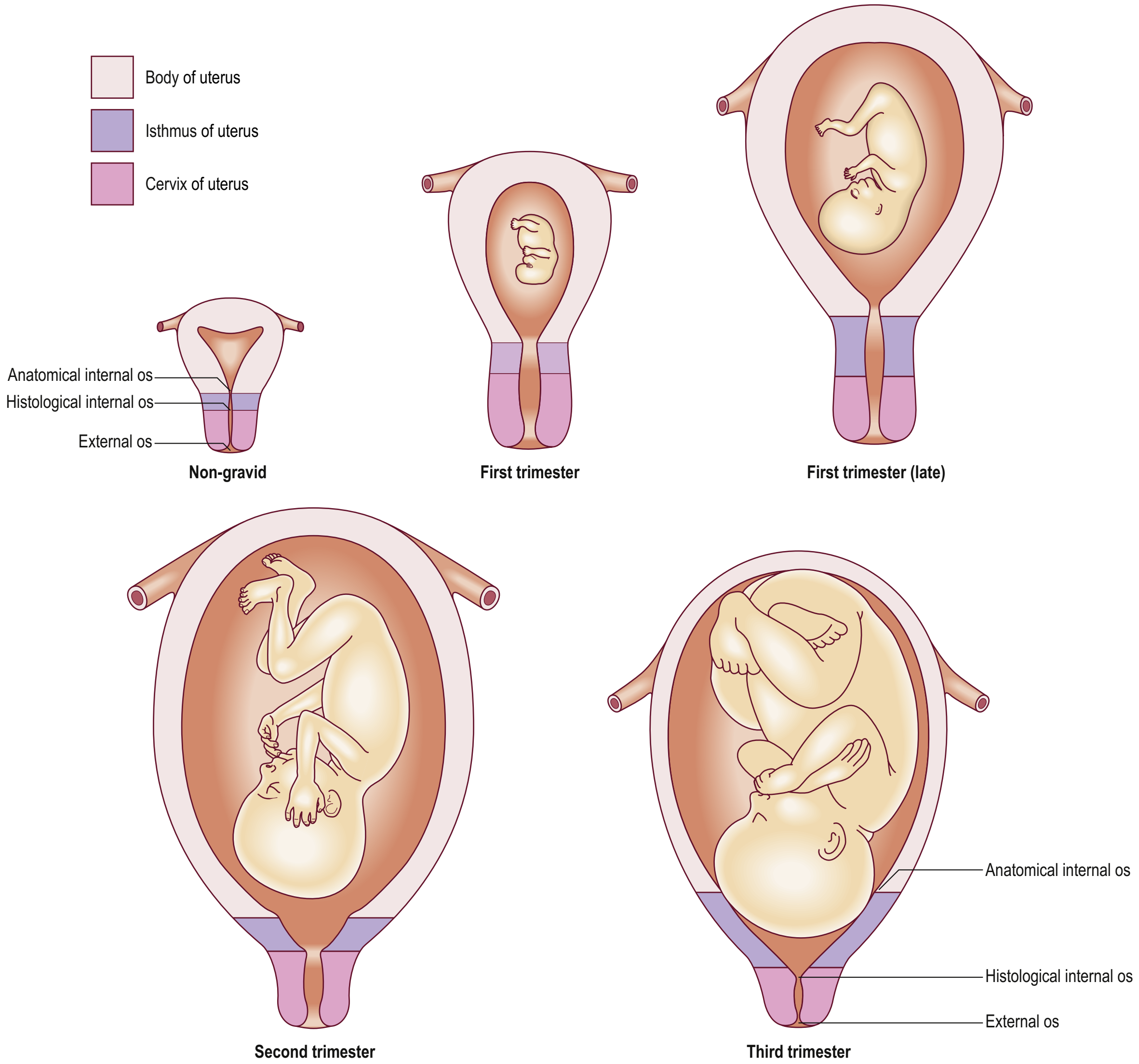

Fig. 75.39 A frontal view of the uterus, showing the location and extent of the body, isthmus and cervix in the non-gravid and gravid uterus at different stages in gestation. The isthmus forms the lower uterine segment with advancing gestation.

compressed at the level of the linea terminalis, resulting in hydronephrosis and pain in the lower back. However, mild ureteric dilation is normal in pregnancy and is caused by progesterone-induced relaxation of smooth muscle in the ureteric walls. The axis of the uterus is often dextrorotated by the presence of the sigmoid colon; this rotation must be considered when a hysterotomy is performed at the time of caesarean section to avoid injuring the large uterine vessels located bilaterally.

Pelvic changes in pregnancy

A pregnant uterus changes the centre of gravity of the body, especially in late pregnancy. In order to compensate for this, the mother tends to straighten her cervical and thoracic spine and throw her shoulders back, resulting in a compensatory increase in lumbar lordosis. There is also a softening of the pubic symphysis and sacroiliac joints, caused by production of relaxin and other pregnancy hormones, leading to mild pelvic instability that can result in a waddling gait. Softening also produces an increase in pelvic diameter, which is beneficial during labour. Significant joint relaxation can lead to pubic symphysis diastasis, which in severe cases can produce debilitating pain during walking.

Advances in three-dimensional ultrasound imaging permit real-time visualization of the anatomical relations and adaptations of the pelvic floor during pregnancy. They also make it possible to identify a pelvic diaphragm injury that can lead to symptomatic postpartum pelvic organ prolapse (Dietz and Lanzarone 2005, Shek et al 2012).

Placental development

The placenta is attached to the uterus at the point where the blastocyst becomes embedded, which is determined by a multitude of molecular signalling pathways (Ch. 9). In early pregnancy, the placental disc occupies a large proportion of the uterine cavity and will often appear to be situated near the anatomical internal os of the uterus. In most cases, growth and stretching of the uterus will usually draw the placenta upwards, away from the cervix of the uterus, by the end of pregnancy.

In about 1% of pregnancies, the position of the placenta will remain over or in close proximity to the anatomical internal os of the uterus at the end of pregnancy (**Fig. 75.40A–B**). This condition is called placenta praevia and can be associated with vaginal bleeding during pregnancy and labour. If the placenta covers the anatomical internal os of the uterus, or the lower edge is less than 1–2 cm from the anatomical internal os (marginal placental praevia), delivery by caesarean section is generally indicated.

Normal trophoblastic development includes the remodelling of maternal spiral arterioles to allow for low-resistance flow into the intervillous space. The uteroplacental vasculature is thus a low-resistance, high-capacitance system. Antenatal ultrasound Doppler velocimetry can be used during pregnancy to assess the resistance to flow in both the uterine and the umbilical arteries and can help in the management of high-risk pregnancies (**Fig. 75.41**).

Abnormally invasive placentation can occur when trophoblastic tissue invades through the decidua basalis and reaches the myometrium; this can lead to a morbidly adherent placenta and significant maternal morbidity. This condition, placenta accreta, occurs in approximately 3 per 1000 births. When the trophoblastic tissue invades the myometrium it is referred to as placenta increta; if the placental tissue reaches the uterine serosa it is called a placenta percreta. In extreme cases, a placenta percreta can also invade as far as the maternal bladder mucosa. These conditions often require a hysterectomy. Although several characteristics are known to increase the risk for placental invasion (such as placenta praevia, smoking, and multiple gestation), prior

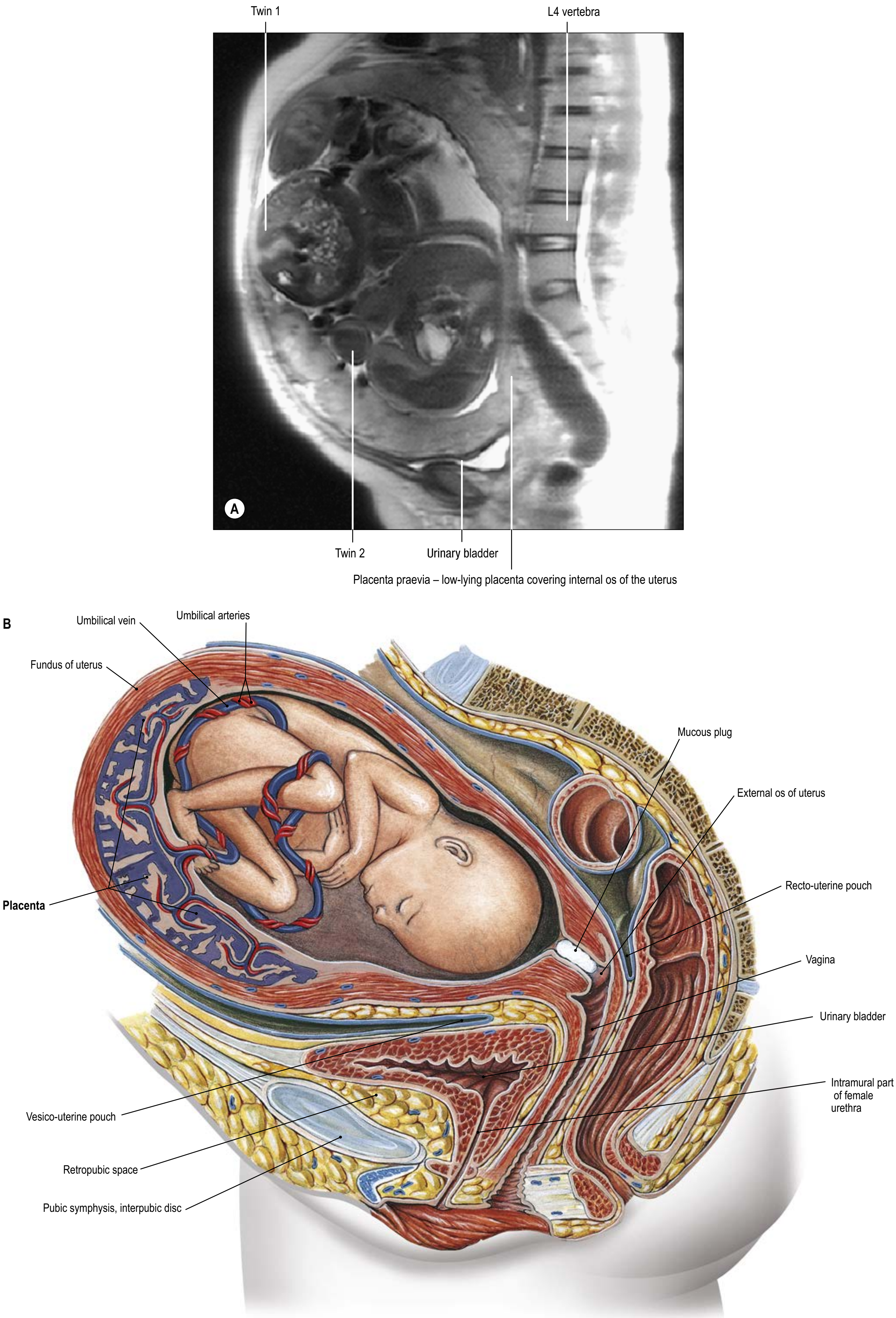
Twin 1
L4 vertebra
A
Twin 2
Urinary bladder
Placenta praevia – low-lying placenta covering internal os of the uterus
B
Umbilical vein
Umbilical arteries
Fundus of uterus
Mucous plug
External os of uterus
Recto-uterine pouch
Placenta
Vagina
Urinary bladder
Intramural part of female urethra
Vesico-uterine pouch
Retropubic space
Pubic symphysis, interpubic disc

Fig. 75.40 **A**, Sagittal T2-weighted MRI of a twin pregnancy with a placenta praevia overlying the internal os of the uterus. **B**, Uterus with fetus. The pelvis has been sectioned in the sagittal plane. (B, Sobotta Atlas of Human Anatomy © Elsevier GmbH, Urban & Fischer, Munich.)

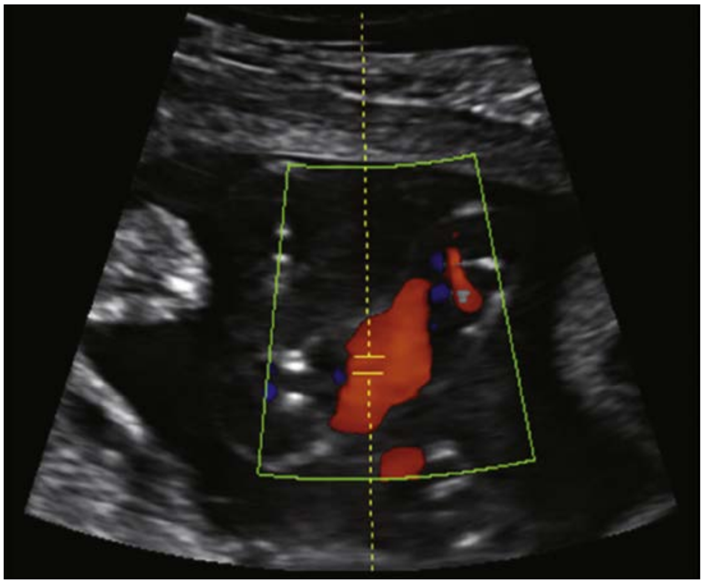

Fig. 75.41 Doppler examination of the maternal and fetal circulation in pregnancy. A pulsed Doppler showing normal waveforms in the umbilical arteries at 28 weeks.

uterine surgery, especially multiple prior caesarean sections, is the most significant risk factor (Fig. 75.42).

Labour

The onset of labour is defined as the combination of regular uterine contractions that are of sufficient intensity to produce progressive effacement and dilation of the cervix of the uterus. The process of labour is described in three main stages.

First stage

The first stage of labour is the period during which the cervix progressively dilates until the fetus is able to descend into the birth canal and the cervix of the uterus is no longer palpable on vaginal examination. There is little change in the uterine volume because myometrial contractions are isometric, so there is minimal shortening of the muscle fibres. Progress is determined by the equilibrium between forces generated by myometrial contractions, especially from the fundus, and the resistance of the cervix.

Second stage

The second stage of labour begins once the cervix is fully dilated, and ends with the delivery of the fetus. Cervical resistance is lost and myometrial activity results in isometric contractions that aid descent of the fetus through the birth canal. The head of the fetus usually enters the pelvis with the occiput facing laterally. As the head descends further, the occiput contacts the gutter-shaped levator ani and this promotes flexion and rotation of the occiput to the anterior position. With further descent, the occiput escapes under the pubic symphysis and the head is born by extension. At this point, the head of the fetus regains its normal relationship with its shoulders, and there is slight rotation (or restitution) of the head. Further external rotation occurs as the leading shoulder is directed medially by the maternal pelvic diaphragm. The body of the fetus is now born by lateral flexion as one shoulder slips underneath the pubic symphysis and the posterior shoulder is drawn over the frenulum of the labia minora.

Third stage

The third stage of labour is the time from delivery of the fetus until delivery of the placenta. Prior to separation of the placenta, a large proportion of the mother's cardiac output passes through the uterine circulation. After separation in the third stage of labour, maternal exsanguination is only prevented by marked uterine contraction; the criss-crossing myometrial fibres act as a tourniquet, restricting blood flow to the area that was the placental site. This process is usually expedited clinically by the administration of oxytocic drugs in an attempt to limit maternal blood loss. Any condition that predisposes to poor uterine contraction, such as retained placental tissue, polyhydramnios or multiple gestations, will increase the likelihood of postpartum haemorrhage (Salafia et al 2005).

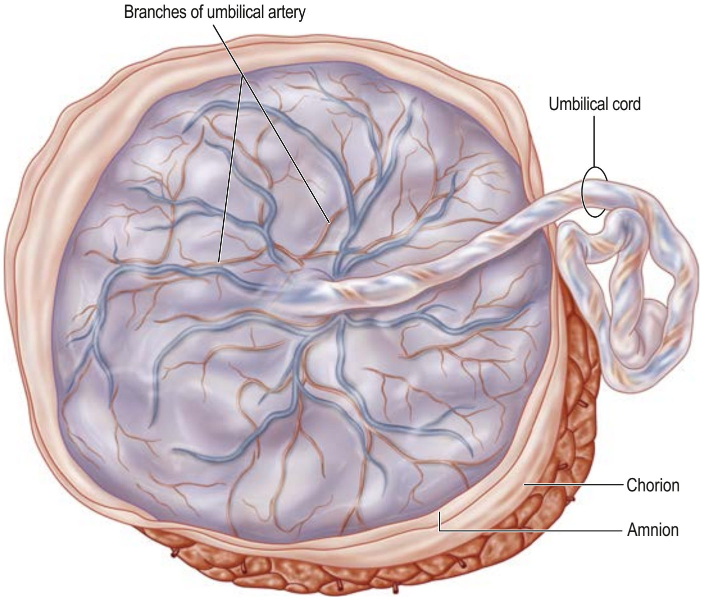

Fig. 75.43 Drawing of the fetal surface of a recently delivered placenta. The spiral umbilical vessels in the umbilical cord and their radiating branches are seen through the transparent amnion. The maternal surface is exposed in the lower and right corner of the figure. Note the fringes of amnion and chorion, the majority of which have been cut away near the placental margin.

Placenta after delivery

The placenta separates from the uterine wall along the plane of the functional layer and extends beyond the placental area, detaching the villous placenta with associated fibrinoid matrix and small amounts of basal decidua, the chorioamnion, together with a superficial layer of the fused capsular decidua, and the parietal decidua. When the placenta and membranes have been expelled, a thin functional layer remains above the uterine basal layer; it soon degenerates and is cast off in the early part of the puerperium. A new epithelial lining is regenerated from the remaining basal layer.

The expelled placenta is a flattened discoid mass with an approximately circular or oval outline (Fig. 75.43). It has an average volume of 500 ml (range 200–950 ml), a mean weight of 470 g (range 200–800 g), a diameter of 185 mm (range 150–200 mm), a thickness of 23 mm (range 10–40 mm), and a total villous surface area of 12–14 m^2. It is thickest at its centre (the original embryonic pole), and rapidly thins towards its periphery, where it continues as the chorion laeve (smooth chorion). The size of the placenta correlates well with the birth weight of the neonate.

Macroscopically, the fetal or inner surface, covered by amnion, is smooth, shiny and transparent, so that the mottled appearance of the subjacent chorion, to which it is closely applied, can be seen. The umbilical cord is usually attached near the centre of the fetal surface, and branches of the umbilical vessels radiate out under the amnion from this point; the veins are deeper and larger than the arteries. The maternal surface of the placenta is finely granular and mapped into some 15–30 lobes by a series of fissures or grooves. The placental lobes, which are often somewhat loosely termed cotyledons, correspond in large measure to the major branches of the umbilical vessels. The grooves correspond to the bases of incomplete placental septa, which become increasingly prominent from the end of the first trimester. They extend from the maternal aspect of the intervillous space towards the chorionic plate (see Fig. 9.5) but do not quite reach it. The septa are complex structures composed of components of the cytotrophoblastic shell and residual syncytium, together with maternally-derived material including decidual cells, occasional blood vessels and gland remnants, collagenous and fibrinoid extracellular matrix, and, in the later months of pregnancy, foci of degeneration.

In multiple pregnancies, the number of placentas is determined by the zygosity; for example, in twin gestations, dizygotic pregnancies will always have two placentas (dichorionic). Monozygotic pregnancies usually have a single placenta (monochorionic), but about one-third will have two; the number is determined by the timing of splitting of the embryonic mass (see Ch. 8 and Fig. 8.9). If the split occurs within 3 days of fertilization, each fetus will have its own placenta and amniotic sac (dichorionic diamniotic); splitting after the third day following fertilization results in a monochorionic diamniotic pregnancy (two amniotic sacs) and vascular communication within the two placental

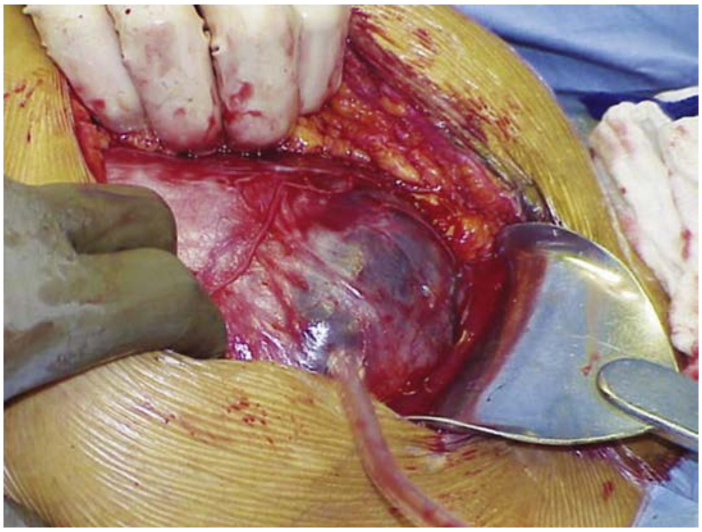

Fig. 75.42 Intraoperative photograph taken during a caesarean section in a patient with a placenta accreta. Note the hypervascularity caused by the placental tissue invading into, and almost through, the myometrial layer of the lower uterine segment, which is still covered with its serosal layer.

circulations (Fig. 75.44); splitting after the ninth day results in a single placenta and single amniotic sac (monochorionic monoamniotic); and splitting after the twelfth day results in conjoined twins.

Placental variations

The umbilical cord is usually attached near the centre of the placenta, although it can occasionally insert more laterally and closer to the placental margin; this condition is known as a battledore placenta (Fig. 75.45). Occasionally, the cord fails to reach the placenta itself and ends in the membranes as a velamentous insertion. When insertion of the cord is velamentous, the larger branches of the umbilical vessels traverse the membranes before they reach and ramify on the placenta (Fig. 75.46). They travel unprotected through the membranes to the placenta, and this puts the fetus at risk because compression or tearing of the vessels can disrupt blood flow to and from it. This can be particularly problematic when the vessels present themselves across the external os of the uterus, a condition called vasa praevia. An accessory (succenturiate) placental lobe is occasionally present, connected to the main organ by membranes and blood vessels. If it is inadvertently retained *in utero* after delivery of the main placental mass it can cause postpartum haemorrhage or infection. Other variations include membranous placenta, in which villous stems and their branches persist over the whole chorion; and vallate (circumvallate) placenta, where the placental margin is undercut by a deep groove caused by an abnormally central insertion of the membranes (Fig. 75.47).

Bonus e-book content

Fig. 75.25 T2-weighted MRI of the uterus and ovaries.

Fig. 75.42 Intraoperative photograph during a caesarean section, showing a placenta accreta.

Fig. 75.44 A vascular cast from a monochorionic diamniotic twin pregnancy.

Fig. 75.45 A battledore placenta.

Fig. 75.46 Velamentous insertion of the umbilical cord, showing the cord inserting into the chorioamniotic membranes rather than the placental disc.

Fig. 75.47 Circumvallate placenta.

Table 75.1 Lymphatic drainage of the female genitalia.

Table 75.2 Innervation of the female genitalia.

Video 75.1 Dissection of the female pelvis and perineum.

Key references

Corton MM 2012 Anatomy. In: Hoffman B, Schorge JO, Schaffer JI et al (eds) Williams Gynecology, 2nd ed. New York: McGraw Hill.
A chapter that provides a comprehensive review of pelvic organs, blood vessels, lymphatics and nerve supply and supports of the pelvic organs.

Delancey JO 2011 Surgical anatomy of the female pelvis. In: Rock JA, Jones HW (eds) Te Linde's Operative Gynecology, 10th ed. Philadelphia: Lippincott, Williams & Wilkins.
A chapter that provides a detailed review of the supports of the vagina and the pelvic organs.

Dietz HP, Lanzarone V 2005 Levator trauma after vaginal delivery. Obstet Gynecol 106:707–12.
A landmark study that prospectively identified levator trauma after vaginal delivery using non-invasive three-dimensional ultrasound.

Feltovich H, Hall TJ, Berghella V 2012 Beyond cervical length: emerging technologies for assessing the pregnant cervix. Am J Obstet Gynecol 207:345–54.
A review article that describes emerging imaging technologies for visualizing structural and architectural changes in the cervix in normal and abnormal pregnancies.

Grant LA, Sala E, Griffin N 2010 Congenital and acquired conditions of the vulva and vagina on magnetic resonance imaging: a pictorial review. Semin Ultrasound CT MR 31:347–62.
An article that reviews the typical imaging characteristics on MRI of the normal vagina, as well as congenital and acquired conditions of the vulva and vagina.

Hassan SS, Romero R, Vidyadhari D et al 2011 Vaginal progesterone reduces the rate of preterm birth in females with a sonographic short cervix: a multicenter, randomized, double-blind, placebo-controlled trial. Ultrasound Obstet Gynecol 38:18–31.
A landmark randomized, controlled clinical trial that demonstrates the utility of progesterone supplementation for reducing the risk of preterm birth in singleton pregnancies with a shortened cervix.

Kleppe M, Kraima AC, Kruitwagen RF et al 2015 Understanding lymphatic drainage pathways of the ovaries to predict sites for sentinel nodes in ovarian cancer. Int J Gynecol Cancer 25:1405–14.
A combined fetal and cadaveric study using immunohistochemistry to better elucidate lymphatic drainage from the human ovary.

Shek KL, Kruger J, Dietz HP 2012 The effect of pregnancy on hiatal dimensions and urethral mobility: an observational study. Int Urogynecol J 23:1561–7.
A study that demonstrates the anatomical changes that occur in the pelvic floor at the urethral hiatus during pregnancy.

Shoja MM, Sharma A, Mirzaya N et al 2013 Neuroanatomy of the female abdominopelvic region: a review with application to pelvic pain syndromes. Clin Anat 26:66–76.
A detailed review of the somatic and autonomic nerve supply of the female genital system and female pelvis.

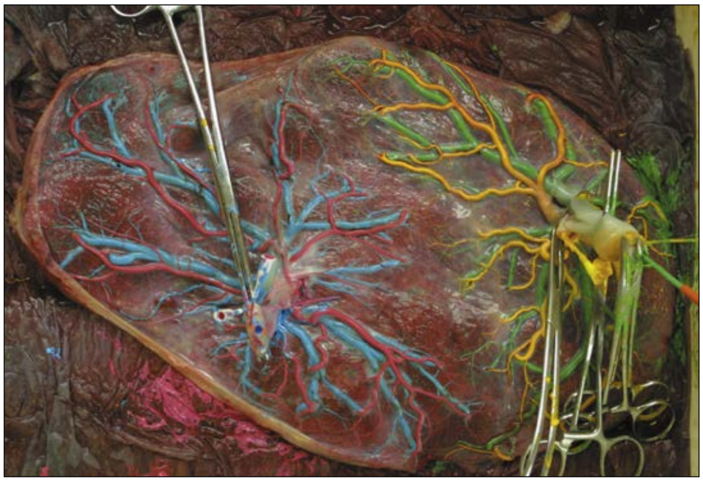

Fig. 75.44 A vascular cast from a monochorionic diamniotic twin pregnancy, showing vascular communications between the two placentas. (Courtesy of Dr Ling Wee, University College London Hospital.)

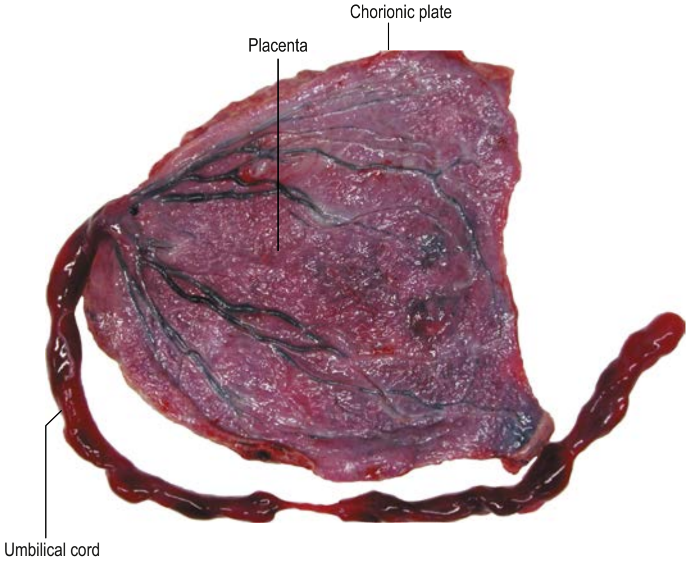
Chorionic plate
Placenta
Umbilical cord

Fig. 75.45 A battledore placenta showing the marginal insertion of the umbilical cord into the placenta. (Courtesy of Dr Michael Ashworth, Consultant Histopathologist, Great Ormond Street Hospital for Children, London.)

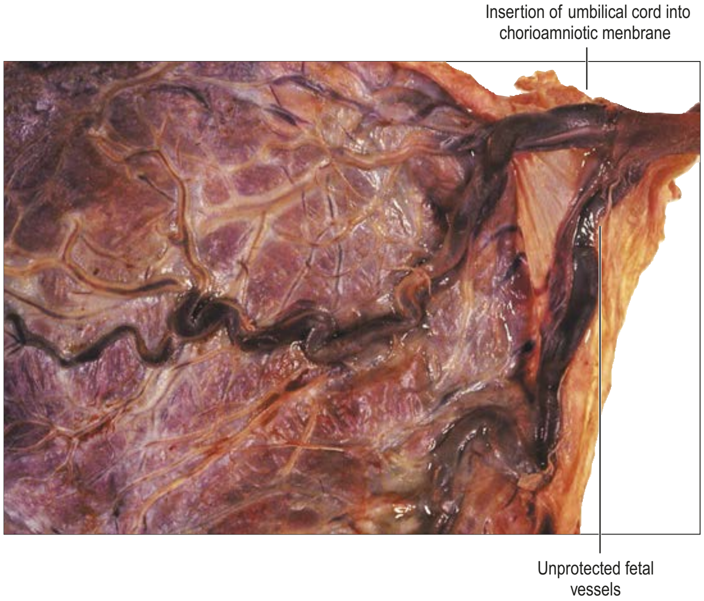
Insertion of umbilical cord into chorioamniotic menbrane
Unprotected fetal vessels

Fig. 75.46 Velamentous insertion of the umbilical cord, showing the cord inserting into the chorioamniotic membranes rather than the placental disc. (Courtesy of Dr Michael Ashworth, Consultant Histopathologist, Great Ormond Street Hospital for Children, London.)

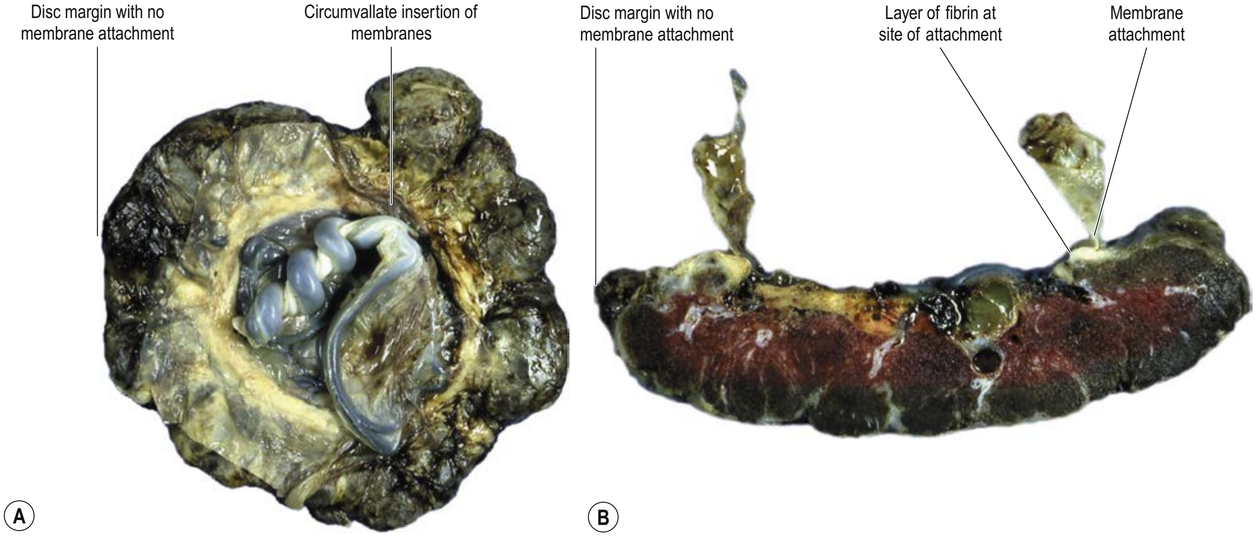
Disc margin with no membrane attachment
Circumvallate insertion of membranes
Disc margin with no membrane attachment
Layer of fibrin at site of attachment
Membrane attachment
A
B

Fig. 75.47 Circumvallate placenta. **A**, The fetal surface and a thick ring of membranes on the fetal surface of the placenta. **B**, A section through the placenta, showing that the membranes insert central to the edge of the placental disc. (Courtesy of Dr Michael Ashworth, Consultant Histopathologist, Great Ormond Street Hospital for Children, London.)

References

Altchek A, Wasserman B, Deligdisch L et al 2008 Prepubertal distal longitudinal vaginal folds. J Pediatr Adolesc Gynecol 21:351–4.

Anderson RA, McLaughlin M, Wallace WH et al 2014 The immature human ovary shows loss of abnormal follicles and increasing follicle developmental competence through childhood and adolescence. Hum Reprod 29:97–106.

Badouraki M, Christoforidis A, Economou I et al 2008 Sonographic assessment of uterine and ovarian development in normal girls aged 1 to 12 years. J Clin Ultrasound 36:539–44.

Bardo DM, Black M, Schenk K et al 2009 Location of the ovaries in girls from newborn to 18 years of age: reconsidering ovarian shielding. Pediatr Radiol 39:253–9.

Bellier A, Cavalié G, Marnas G 2018 et al The round ligament of the uterus: questioning its distal insertion. Morphologie 102:55–60.

Bill AH, Hall DG, Johnson RJ 1975 Position of rectal fistula in relation to the hymen in 46 girls with imperforate anus. J Pediatr Surg 10:361–5.

Chen C, Huang L, Liu P et al 2014 Neurovascular quantitative study of the uterosacral ligament related to nerve-sparing radical hysterectomy. Eur J Obstet Gynecol Reprod Biol 172:74–9.

Corton MM 2012 Anatomy. In: Hoffman B, Schorge JO, Schaffer JI et al (eds) Williams Gynecology, 2nd ed. New York: McGraw Hill.

A chapter that provides a comprehensive review of pelvic organs, blood vessels, lymphatics and nerve supply and supports of the pelvic organs.

Daskalakis GJ, Papantoniou NE, Koutsodimas NB et al 2000 Fetal fibronectin as a predictor of preterm birth. J Obstet Gynaecol 20:347–53.

Delancey JO 2011 Surgical anatomy of the female pelvis. In: Rock JA, Jones HW (eds) Te Linde's Operative Gynecology, 10th ed. Philadelphia: Lippincott, Williams & Wilkins.

A chapter that provides a detailed review of the supports of the vagina and the pelvic organs.

Delson B, Lubin S, Reynolds SRM 1948 Spiral arteries in the human ovary. Endocrinology 42:124–8.

Dietz HP, Lanzarone V 2005 Levator trauma after vaginal delivery. Obstet Gynecol 106:707–12.

A landmark study that prospectively identified levator trauma after vaginal delivery using non-invasive three-dimensional ultrasound.

Eid S, Iwanaga J, Oskouian RJ et al 2018 Comprehensive review of the cardinal ligament. Cureus 10:e2846.

Feltovich H, Hall TJ, Berghella V 2012 Beyond cervical length: emerging technologies for assessing the pregnant cervix. Am J Obstet Gynecol 207:345–54.

A review article that describes emerging imaging technologies for visualizing structural and architectural changes in the cervix in normal and abnormal pregnancies.

Fonseca EB, Celik E, Parra M et al 2007 Progesterone and the risk of preterm birth among females with a short cervix. N Engl J Med 357:462–9.

Fritz MA, Speroff L 2011 Clinical Gynecologic Endocrinology, 9th ed. Philadelphia: Lippincott, Williams & Wilkins.

Gandhi J, Chen A, Dagur G et al 2016 Genitourinary syndrome of menopause: an overview of manifestations, pathophysiology, etiology, evaluation, and management. Am J Obstet Gynecol 215:704–11.

Grant LA, Sala E, Griffin N 2010 Congenital and acquired conditions of the vulva and vagina on magnetic resonance imaging: a pictorial review. Semin Ultrasound CT MR 31:347–62.

An article that reviews the typical imaging characteristics on MRI of the normal vagina, as well as congenital and acquired conditions of the vulva and vagina.

Hassan SS, Romero R, Vidyadhari D et al 2011 Vaginal progesterone reduces the rate of preterm birth in females with a sonographic short cervix: a multicenter, randomized, double-blind, placebo-controlled trial. Ultrasound Obstet Gynecol 38:18–31.

A landmark randomized, controlled clinical trial that demonstrates the utility of progesterone supplementation for reducing the risk of preterm birth in singleton pregnancies with a shortened cervix.

House M, McCabe R, Socrate S 2013 Using imaging-based, three-dimensional models of the cervix and uterus for studies of cervical changes during pregnancy. Clin Anat 26:97–104.

Jackson LA, Hare AM, Carrick KS, et al 2019 Anatomy, histology, and nerve density of clitoris and associated structures: clinical application to vulvar surgery. Am J Obstet Gynecol 221:519.e1–10.

Kimberley N, Hutson JM, Southwell BR et al 2012 Vaginal agenesis, the hymen, and associated anomalies. J Pediatr Adolesc Gynecol 25:54–8.

Kleppe M, Kraima AC, Kruitwagen RF et al 2015 Understanding lymphatic drainage pathways of the ovaries to predict sites for sentinel nodes in ovarian cancer. Int J Gynecol Cancer 25:1405–14.

A combined fetal and cadaveric study using immunohistochemistry to better elucidate lymphatic drainage from the human ovary.

Lee JF, Maurer VM, Block GE 1973 Anatomic relations of pelvic autonomic nerves to pelvic operations. Arch Surg 107:324–8.

Lee MY, Dalpiaz A, Schwamb R et al 2015 Clinical pathology of Bartholin's glands: a review of the literature. Curr Urol 8:22–5.

Leung AK, Robson WL 1992 Labial fusion and urinary tract infection. Child Nephrol Urol 12:62–4.

Minto C, Hollings N, Hall-Craggs M et al 2001 Magnetic resonance imaging in the assessment of complex Müllerian anomalies. Br J Obstet Gynaecol 108:791–7.

An article that provides a detailed discussion of the formation and MRI appearance of congenital anomalies of the uterus and Fallopian tubes.

Motta PM, Nottola SA, Familiari G et al 2003 Morphodynamics of the follicular-luteal complex during early ovarian development and reproductive life. Int Rev Cytol 223:177–288.

An account that reviews the morphological and functional aspects of the ovarian follicle, corpus luteum and germ cells using light microscopy, electron microscopy and numerous drawings.

Owen J, Hankins G, Iams JD et al 2009 Multicenter randomized trial of cerclage for preterm birth prevention in high-risk females with shortened midtrimester cervical length. Am J Obstet Gynecol 201:375.e1-375.e8.

Salafia CM, Maas E, Thorp JM et al 2005 Measures of placental growth in relation to birth weight and gestational age. Am J Epidemiol 162:991–8.

Salardi S, Orsini LF, Cacciari E et al 1985 Pelvic ultrasonography in premenarcheal girls: relation to puberty and sex hormone concentrations. Arch Dis Child 60:120–5.

Sforza C, Ferrario VF, De Pol A et al 1993 Morphometric study of the human ovary during compartmentalization. Anat Rec 236:626–34.

Shek KL, Kruger J, Dietz HP 2012 The effect of pregnancy on hiatal dimensions and urethral mobility: an observational study. Int Urogynecol J 23:1561–7.

A study that demonstrates the anatomical changes that occur in the pelvic floor at the urethral hiatus during pregnancy.

Shoja MM, Sharma A, Mirzaya N et al 2013 Neuroanatomy of the female abdominopelvic region: a review with application to pelvic pain syndromes. Clin Anat 26:66–76.

A detailed review of the somatic and autonomic nerve supply of the female genital system and female pelvis.

COMMENTARY

8.1

The mesentery and the mesenteric model of abdominal compartmentalization

John Calvin Coffey, Kevin Gerard Byrnes, Peter Dockery, Dara Walsh

Abdominal compartmentalization

The peritoneal model of abdominal compartmentalization has long been the starting point for descriptions of abdominal anatomy. According to this model, abdominal digestive organs are organized along peritoneal lines and the position of each is described using the terms ‘intra’-, ‘extra’-, or ‘retro’-peritoneal (Snell 1992). However, some organs have both intra- and retro-peritoneal regions, a feature that is not explained by conventional embryological models of abdominal development. For example, the duodenum in the adult is ‘retro’-peritoneal in position while the rest of the small intestine is ‘intra’-peritoneal. The peritoneal landscape appears complex and regionalized into sacs, fossae and pouches that are described using an array of terms including fold, ligament, membrane and reflection. This heterogeneous terminology makes understanding abdominal anatomy challenging.

Abdominal organs are usually described as being individually connected to the rest of the body, typically mediated by a network of vascular and peritoneal links. The small intestine and the transverse and sigmoid colons are exceptions to this pattern and are conventionally described as linked to the rest of the body via their respective ‘mesenteries’ (Snell 1992). The peritoneal and fascial models that have been generated by the concept of multiple mesenteries are dauntingly complex. Fasciae within the abdomen are described as individual entities, a practice that arose in part because they were described separately, e.g. Toldt’s, Denonvilliers’ and Waldeyer’s fasciae (Congdon et al 1942, Coffey and Kiran 2017).

Mesenteric anatomy distal to the duodenojejunal flexure was clarified by the demonstration that the mesentery is continuous and connects the small and large intestines to the rest of the body (Coffey et al 2017). This perspective also explains peritoneal and fascial anatomy distal to the duodenojejunal flexure (Coffey et al 2017). Further research has now clarified the organization of the entire abdominal mesentery and all abdominal digestive organs, peritoneum and fasciae, on the basis of a mesenteric- rather than a peritoneal-based model of abdominal anatomy and compartmentalization.

Mesenteric model of abdominal compartmentalization

The abdominal mesentery is a collection of tissues that supports the growth of all abdominal digestive organs during embryological development and connects those organs to systems of the body throughout life. It is a continuous organ, beginning and ending at the oesophagogastric and anorectal junctions, respectively; all abdominal digestive organs are connected to it (Coffey and O’Leary 2016). The mesentery can be subdivided into three regions (upper, mid and lower) using two axes: the coeliac trunk represents the inferior boundary of the upper region and the upper limit of the mid-region (**Fig. 8.1.1**), and the superior mesenteric axis is the distal limit of the mid-region and the proximal limit of the lower region (see Fig. 8.1.1).

Emerging data indicate that the abdomen and its contents are compartmentalized along mesenteric lines. According to the mesenteric-based model of abdominal anatomy and compartmentalization, the abdomen is divided into two principal domains, mesenteric and non-mesenteric. The mesenteric domain contains all abdominal digestive organs positioned on the mesentery. The non-mesenteric domain comprises all non-digestive organs (i.e. the genitourinary organs) positioned on the musculoskeletal mainframe of the abdomen. The domains are connected, attached and linked anatomically. They are *connected* at the arterial inflow and venous drainage of the mesentery. The arterial inflow occurs at the coeliac trunk, and superior and inferior mesenteric arteries. Venous drainage occurs at the junction between the hepatic veins and the inferior vena cava. Both domains are *attached*, which means the posterior surface of the mesenteric domain is apposed to the anterior surface of the non-mesenteric domain: there is a fascia between apposed surfaces (Coffey et al 2017). The junction between fascia and the overlying mesentery is a conceptual zone that surgeons access when they detach the mesentery from its attachment to the posterior abdominal wall. At the periphery of the mesenteric domain, the two domains are *linked* by the peritoneal reflection, a serous mesothelial membrane that bridges the parietal peritoneum lining the non-mesenteric domain and the visceral peritoneum of the mesenteric domain.

The mesenteric-based model of abdominal compartmentalization explains several aspects of abdominal anatomy. Whilst the peritoneal landscape is generally regarded as extremely complex, it can be understood readily if approached with reference to the mesentery. From this perspective, the lining of organs of the mesenteric domain corresponds to ‘visceral’ peritoneum. The lining of the non-mesenteric domain corresponds to ‘parietal’ peritoneum. At the periphery of the mesenteric domain, parietal peritoneum detaches from the non-mesenteric domain and is reflected onto the mesenteric domain, where it continues as the lining of the latter (**Fig. 8.1.2**). The regions, sacs, pouches and cavities of the peritoneal landscape are regions of this model. Folds, ligaments and membranes are terms applied to different regions of peritoneal reflection.

Since all abdominal digestive organs are directly connected to the mesentery, it provides a reference frame for describing the positional anatomy of each. For example, the head of the pancreas is located in the mid-region of the mesentery whilst its neck and body are located in the upper region (**Fig. 8.1.3**). The location of each of the arteries supplying individual organs can also be explained in mesenteric terms. The same principle applies to the extrahepatic portal venous system. For example, the inferior mesenteric vein travels in the left mesocolon to reach the central zone of the mesentery, where it merges with the splenic and/or superior mesenteric vein to generate the hepatic portal vein (**Fig. 8.1.4**). The latter utilizes the mesoduodenum posterior to the pancreas to reach the liver. The shape of the periphery of the mesentery also explains the double spiral trajectory of the abdominal digestive tract (**Fig. 8.1.5**).

Mesenteric-based compartmentalization helps to clarify the organization of the fasciae of the abdomen. Where surfaces of the mesenteric and non-mesenteric domains are apposed, there is a fascia between them: the fasciae originally described by separate investigators are now perceived as different regions of the same tissue layer.

Mesenteric-based compartmentalization explains how abdominal digestive organs are linked to systems of the body. They are directly connected to the mesentery and, in turn, the mesentery collectively connects all of them to each system (and hence to the body). This perspective represents a radical departure from conventional descriptions, which hold that all abdominal digestive organs are centrally connected via a network of peritoneal derivatives.

Embryological development of mesenteric and non-mesenteric compartments

The earliest mesenteric correlate is a double fold of mesothelium directly connected to the developing abdominal wall along the posterior midline. Its shape changes rapidly as it stretches in different directions to generate an upper diverticulum, mid-region fold and lower region (de Bakker et al 2016). Early in development the posterior connection regresses until it is reduced to vascular and surface mesothelial (i.e. peritoneal) continuity. All abdominal digestive organs develop within, and remain connected to, the mesentery. Later in development, regions of the mesentery flatten back against the posterior abdominal wall (i.e. they become attached) as they are packaged into a final

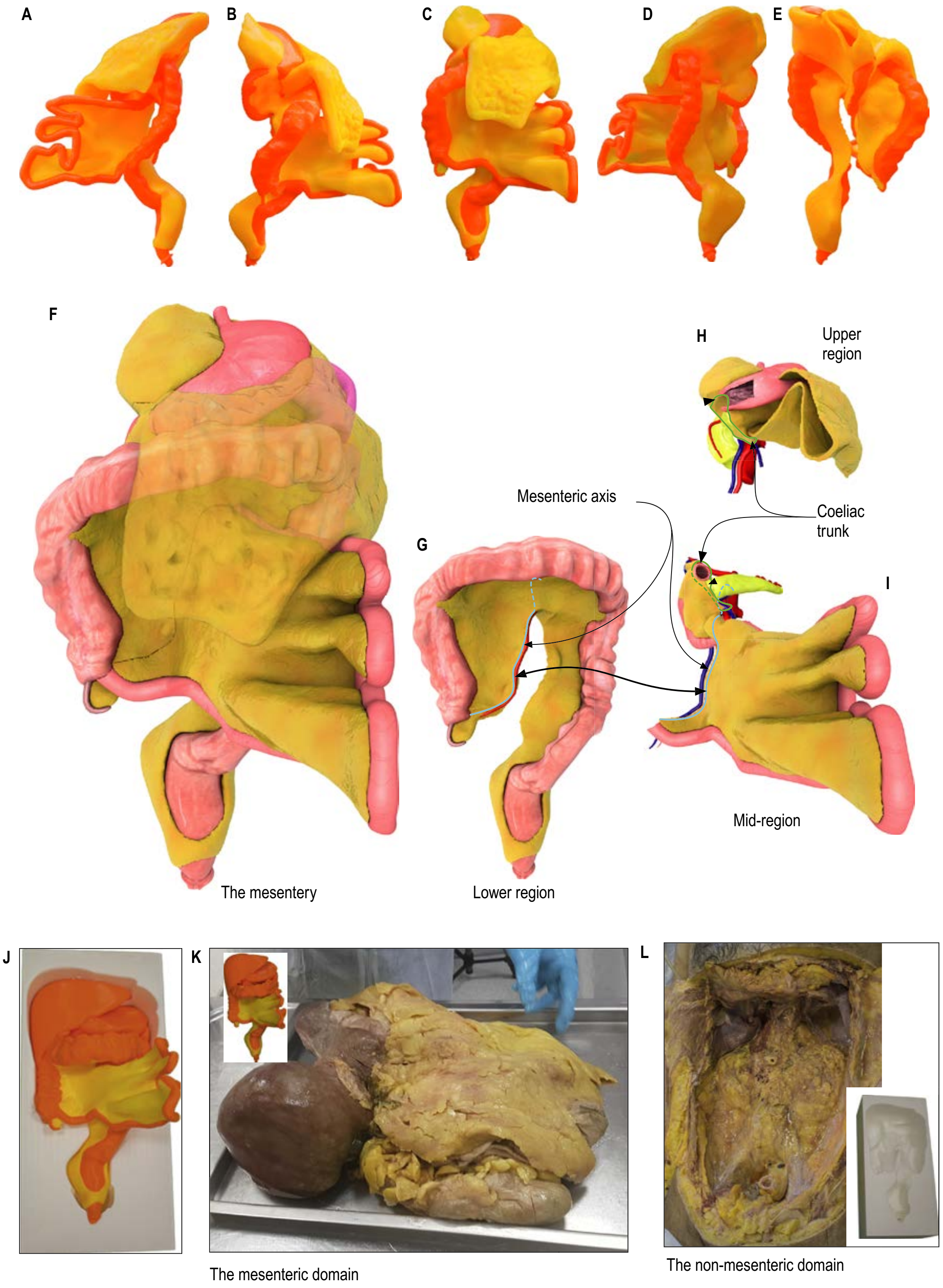
A
B
C
D
E
F
H
Upper region
Mesenteric axis
Coeliac trunk
G
I
Mid-region
The mesentery
Lower region
J
K
L
The mesenteric domain
The non-mesenteric domain

Fig. 8.1.1 The mesentery and mesenteric model of abdominal anatomy and compartmentalization. (**A–E**) Photographs of full-scale 3D printed mesentery demonstrating left lateral, right lateral, anterior, left posterolateral and right posterolateral views. (**F**) Photograph of 3D digital example of the mesentery. Photographs demonstrating the lower (**G**), mid (**H**) and upper (**I**) regions of the mesentery, delineated by the coeliac trunk and superior mesenteric artery. (**J**) Photograph of the 3D printed version of the mesenteric domain embedded in the 3D printed non-mesenteric domain of the abdomen. (**K**) *Ex vivo* mesenteric domain of the abdomen following excision (inset is the 3D printed mesenteric domain from **J**). (**L**) Photograph of cadaveric non-mesenteric domain after excision of the mesenteric domain (see **K**) (inset is the 3D printed non-mesenteric domain in **K**).

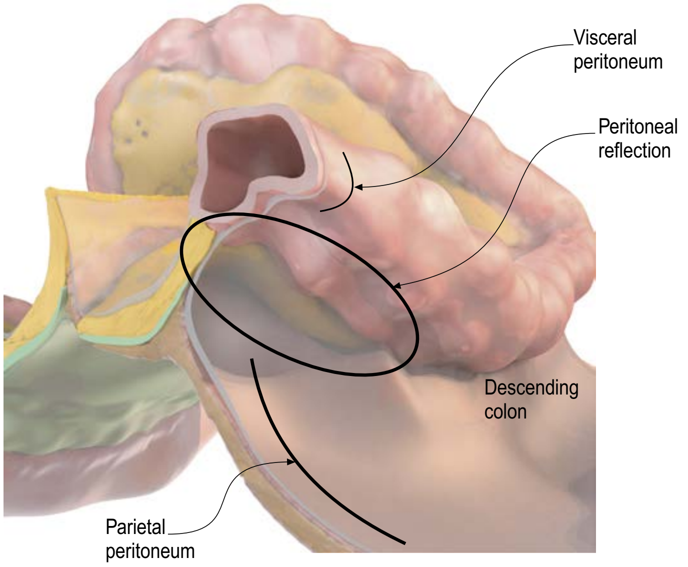

Fig. 8.1.2 The peritoneum. Photograph of a 3D digital sculpture demonstrating the anatomical relationship between the peritoneal reflection and parietal and visceral peritoneum.

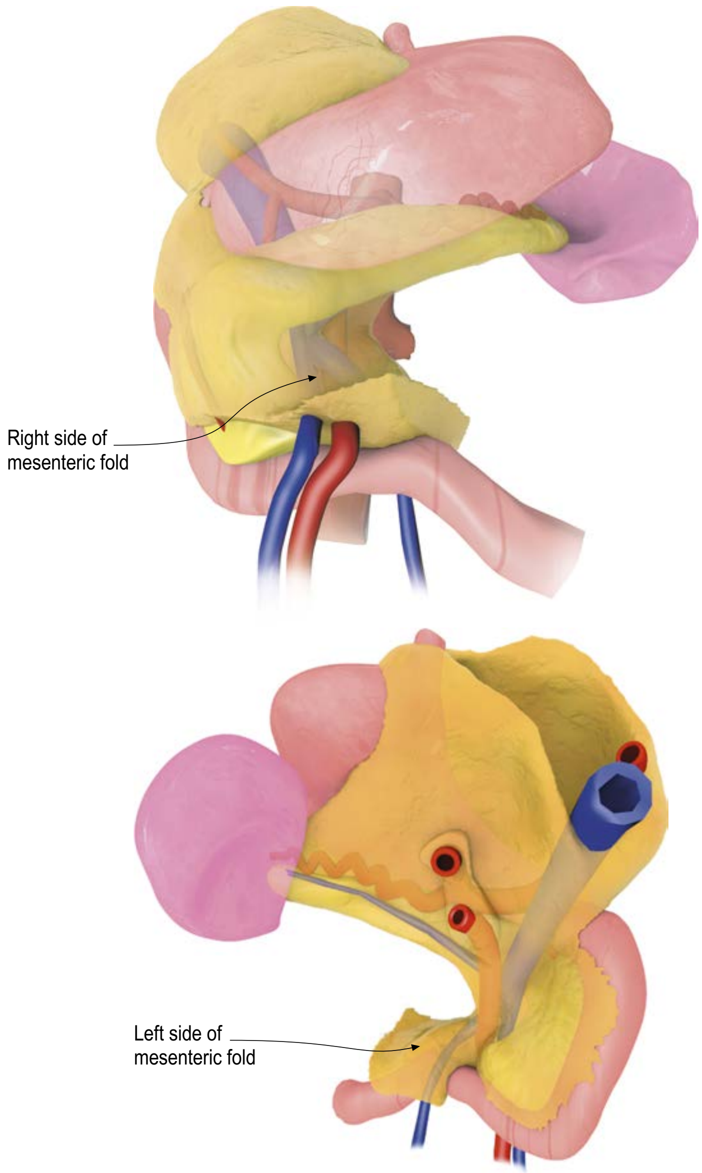

Fig. 8.1.3 The relationship of the pancreas to the mesentery. (**A**) A right lateral view of the central zone of the mesentery. The head of the pancreas is in the mesoduodenum forming the right side of the mesenteric fold at the central zone. The neck and body of the pancreas are in the mesentery of the upper region arching over the superior mesenteric artery and hepatic portal vein. (**B**) A left lateral view of the central zone of the mesentery. The position of the neck and body of the pancreas (within upper region mesentery) is apparent. The superior mesenteric artery and vein are in the apex of the central zone, where right and left sides converge, and are located posterior to the neck of the pancreas.

conformation. The mesenteric primordium is disconnected well in advance of differentiation of the abdominal digestive organs (i.e. the mesentery emerges first) (Byrnes et al 2019b). In the adult setting, all abdominal digestive organs remain connected to it, and it collectively connects them all to the posterior abdominal wall. This means the mesenteric organ occupies a structural and developmental primacy in the human digestive system.

History

Interestingly, the mesenteric model of abdominal anatomy and compartmentalization is not new. There are suggestions in classical texts that it was apparent to some Italian anatomists during the Renaissance. Several drawings from this era depict a complex of structures that includes all abdominal digestive organs centred on the mesentery (Byrnes et al 2019a). A vogue developed in the 19th century for describing multiple separate mesenteries (e.g. Gray 1858), and this approach was subsequently reflected in all mainstream reference texts. The concept of multiple separate mesenteries generated a complex peritoneal and fascial landscape that hampered investigation of the mesentery, which was largely ignored until recently. Interest in the mesentery was rekindled when surgeons recognized that its resection was required for good outcomes in patients undergoing surgery for cancer of abdominal digestive organs. Re-appraisal of mesenteric anatomy and embryological development led to the recognition of mesenteric continuity and connection with all abdominal digestive organs. These anatomical properties, which were recognized after adaptation of surgical techniques to dissection of the cadaveric human abdomen, could then be combined to generate the mesenteric model of abdominal compartmentalization. They were corroborated by observations related to embryological development of the mesentery. Given this, the mesenteric model is the first to comprehensively reconcile embryological, anatomical and surgical approaches to the abdomen, fields that had diverged considerably during the past century.

Implications

The model has wide scientific and clinical implications. Because it clarifies the organization of the abdomen and its contents, it enables the abdomen to be characterized systematically (i.e. scientifically). The characterization of mesenteric organ pharmacokinetics, lymphatic angiology, radiology and immunology has recently gained considerable momentum (Dalla Pria et al 2019). The model also enables the radiologist to build a composite picture of abdominal anatomy in paediatric and adult populations, which will facilitate a non-invasive interpretation of the nature and stage of abdominal diseases (Dalla Pria et al 2019). It will guide the surgeon in applying mesenteric-based strategies for managing intestinal cancer and inflammatory bowel disease (Heald et al 1982, Hohenberger et al 2009). For example, emerging data demonstrate that surgical techniques that reduce mesenteric inputs lead to improved outcomes in patients undergoing surgery for Crohn's disease (Coffey et al 2018, Fichera et al 2012). Mesenteric-based strategies are also showing promise in the surgical management of congenital abnormalities such as malrotation.

Future directions

It is important to determine the histological nature of the junction between each abdominal digestive organ and the mesentery. All signals that pass between the gastrointestinal tract and nervous system must traverse the mesentery. Accordingly, the gut–brain axis becomes the gut–mesentery–brain axis (Coffey and O'Leary 2016). The junction between the mesentery and abdominal digestive organ is highly relevant to the normal functioning of the body. It is noteworthy that despite the anatomical magnitude of this zone, it remains largely unstudied.

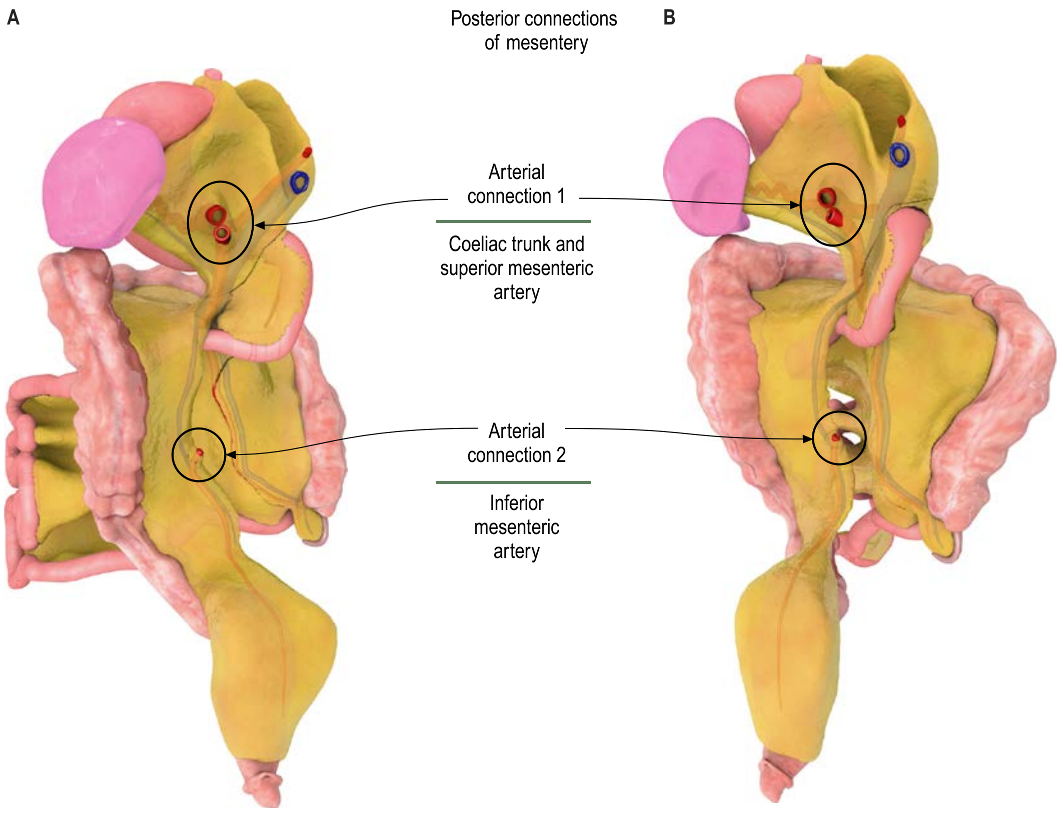
A
Posterior connections of mesentery
B
Arterial connection 1
Coeliac trunk and superior mesenteric artery
Arterial connection 2
Inferior mesenteric artery

Fig. 8.1.4 Left and right (**A** and **B**, respectively) posterolateral views of the mesenteric domain demonstrating the arterial connections and the course of the inferior mesenteric vein. The latter is located in the left mesocolon and travels from here to the splenic region of the transverse mesocolon. From there it accesses the left side of the central zone of the mesenteric fold where it joins either the splenic or superior mesenteric vein to form the hepatic portal vein.

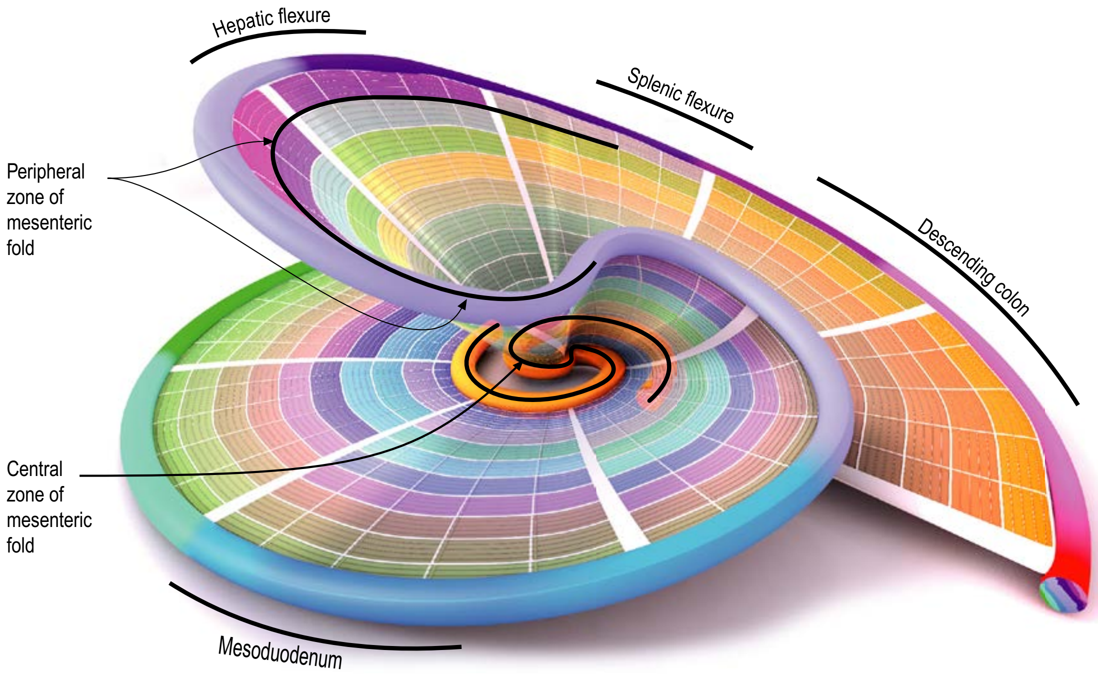
Hepatic flexure
Splenic flexure
Descending colon
Peripheral zone of mesenteric fold
Central zone of mesenteric fold
Mesoduodenum

Fig. 8.1.5 Double spiral. The central zone corresponds to the central zone of the mesenteric fold and the peripheral zone corresponds to the peripheral zone of the mesenteric fold. The edge of the shape broadly corresponds to the trajectory from the duodenum to the anorectal junction. The shape explains how an object (i.e. the mesentery) can have a folded shape centrally and a double spiral shape peripherally.

The contributions of the mesentery to visceral adiposity require investigation: the scale of the mesentery means it is the single largest contributor to visceral adiposity. Given the links between visceral adiposity and atherosclerosis, diabetes and hypertension, it is feasible that mesenteric inputs are major influences on the development of these conditions (Coffey and O'Leary 2016).

The mesenteric-based model of abdominal anatomy and compartmentalization is likely to provide surgeons with an anatomical roadmap that they can follow during multivisceral transplantation and is also likely to facilitate *ex vivo* surgical approaches in which a complex of organs is removed, surgically altered and then replaced *in situ*. This approach is adopted in the surgical management of tumours that are extensively invasive. Attempts to harness or re-activate the embryological potential of the mesentery are increasing in number and it is hoped such a mesentery-based approach could address the deficit in knowledge of the digestive organs available for transplantation (García-Arrarás et al 2019).

Conclusion

The mesenteric model of abdominal anatomy and compartmentalization provides an overarching model of abdominal anatomy. This is likely to help students better understand abdominal anatomy, assist the scientific investigation of human biology and the diagnosis and treatment of abdominal and systemic diseases.

References

Byrnes KG, McDermott KW, Coffey JC 2019a Mesenteric organogenesis. Semin Cell Dev Biol 92:1–3.

Byrnes KG, Walsh D, Lewton-Brain P et al 2019b Anatomy of the mesentery: historical development and recent advances. Semin Cell Dev Biol 92:4–11.

Coffey JC, Dockery P, Moran BJ et al 2017 Mesenteric and peritoneal anatomy. In: Coffey JC, Lavery I, Sehgal R (eds) Mesenteric Principles of Gastrointestinal Surgery: Basic and Applied Science. Boca Raton: CRC Press, pp. 11–40.

Coffey JC, Kiran R 2017 Toldt's fascia. In: Coffey JC, Lavery I, Sehgal R (eds) Mesenteric Principles of Gastrointestinal Surgery: Basic and Applied Science. Boca Raton: CRC Press, pp. 57–68.

Coffey CJ, Kiernan MG, Sahebally SM et al 2018 Inclusion of the mesentery in ileocolic resection for Crohn's disease is associated with reduced surgical recurrence. J Crohns Colitis 12:1139–50.

Coffey JC, O'Leary DP 2016 The mesentery: structure, function, and role in disease. Lancet Gastroenterol Hepatol 1:238–47.

Congdon ED, Blumberg R, Henry W 1942 Fascia of fusion and elements of the fused enteric mesenteries in the human adult. Am J Anat 70:251–79.

Dalla Pria HRF, Torres US, Velloni F et al 2019 The mesenteric organ: new anatomical concepts and an imaging-based review on its diseases. Semin Ultrasound CT MRI 40:515–32.

de Bakker BS, de Jong KH, Hagoort J et al 2016 An interactive three-dimensional digital atlas and quantitative database of human development. Science 354(6315).

Fichera A, Zoccali M, Kono T 2012 Anti-mesenteric functional end-to-end handsewn (Kono-S) anastomosis. J Gastrointest Surg 16:1412–16.

García-Arrarás JE, Bello SA, Malavez S 2019 The mesentery as the epicenter for intestinal regeneration. Semin Cell Dev Biol 92:45–54.

Gray H 1858 Anatomy Descriptive and Surgical. London: John W. Parker and Son.

Heald RJ, Husband EM, Ryall RD 1982 The mesorectum in rectal cancer surgery – the clue to pelvic recurrence? Br J Surg 69:613–16.

Hohenberger W, Weber K, Matzel K et al 2009 Standardized surgery for colonic cancer: complete mesocolic excision and central ligation – technical notes and outcome. Colorectal Dis 11:354–64; discussion 364–5.

Snell RS 1992 Clinical Anatomy for Medical Students, 4th ed. Boston: Little, Brown and Company.

CHAPTER

76

Pelvic girdle and lower limb: overview and surface anatomy

The structure of the lower limb is specialized for support of the body's weight, locomotion and maintenance of body stability (balance). Indeed, adaptations for weight-bearing and stability account for the major structural and functional differences between the upper and lower limbs. The inguinal (pelvicrural) and gluteal (buttock) regions are important anatomical junctional zones between the trunk and the lower limb through which longitudinally running nerves and vessels travel (Fig. 76.1). The inguinal region includes the transitional zones between the lower limb and abdominal cavity via the myopectineal orifice (the gap between the inguinal ligament and hip joint) and inguinal canal, and provides a gateway for the passage of various structures. Similarly, the obturator canal allows for the obturator nerve and vessels to traverse between the pelvis and thigh. The gluteal region communicates with the lower limb and the abdominopelvic cavity via the greater sciatic foramen, and with the lower limb and pelvic cavity and perineum via the lesser sciatic foramen.

BONES AND JOINTS

The bones of the lower limb are the three fused components of the pelvic girdle; the femur and patella (thigh); the tibia and fibula (leg; in anatomical nomenclature, leg refers to the part of the lower limb between the knee and ankle); and the tarsus, metatarsus, phalanges and sesamoid bones (foot) (Fig. 76.2). The pelvic bones (especially the ilium and ischium), femur, tibia and bones of the hindfoot are strong and their external (cortical) and internal (trabecular) structure is adapted for weight-bearing.

The joints of the pelvic girdle are the sacroiliac joints and the pubic symphysis. The lower limb is connected to the axial skeleton via the sacroiliac joint, a joint that consists of syndesmotic and synovial parts, and in which mobility has been sacrificed for stability and strength to allow for effective weight transmission from the trunk to the lower limb. Anteriorly, the two pubic bones are united at the pubic symphysis, a secondary cartilaginous joint that may display a slight degree of mobility during hip and sacroiliac movement, and during late pregnancy and childbirth. The hip joint is a synovial ball-and-socket articulation, and exhibits an effective compromise between mobility and stability that allows movement in all three orthogonal planes. The more distal joints have gained mobility at the expense of stability. The knee joint includes a complex synovial joint between the femur and the tibia, and a plane joint between the femur and the patella. This permits a range of up to about 140° of active flexion, extension to neutral or beyond, and voluntary medial and lateral rotation (approximately 60–70°) of the leg. The tibia and fibula articulate with each other at the superior and inferior tibiofibular joints. The superior joint, a plane synovial joint, allows slight gliding movement only. The inferior fibrous joint lies just above the ankle and allows a degree of fibular rotation linked to ankle motion. The ankle (talocrural) joint is formed by the distal ends of the tibia and fibula 'gripping' the talus, and enables about 70° of dorsiflexion and plantar flexion. There are multiple joints in the foot that may be classified topographically on the basis of whether they are in the hindfoot, midfoot or forefoot. Collectively, these joints allow the complex movements required as the foot fulfils its functional roles as a platform for standing and for shock absorption and propulsion in gait. The terminology used to describe motion of the ankle and foot, especially with respect to defining supination/pronation and inversion/eversion, is inconsistent (Greiner 2007, Doya et al 2010).

Both the knee and ankle are commonly subject to closed injuries, and the relatively superficial location of the knee renders it susceptible to open injury and infection. Although the ankle is frequently injured and is a major load-bearing joint, the incidence of clinically significant degenerative arthritis is surprisingly low when compared with that found in the hip and knee joints.

SKIN AND FASCIA

In the young adult and as an adaptation to weight-bearing, the skin of the lower limb is generally thicker than that of the upper limb. The soft tissues of the sole of the foot are particularly thickened in order to support weight during standing. The skin of the buttocks and posterior

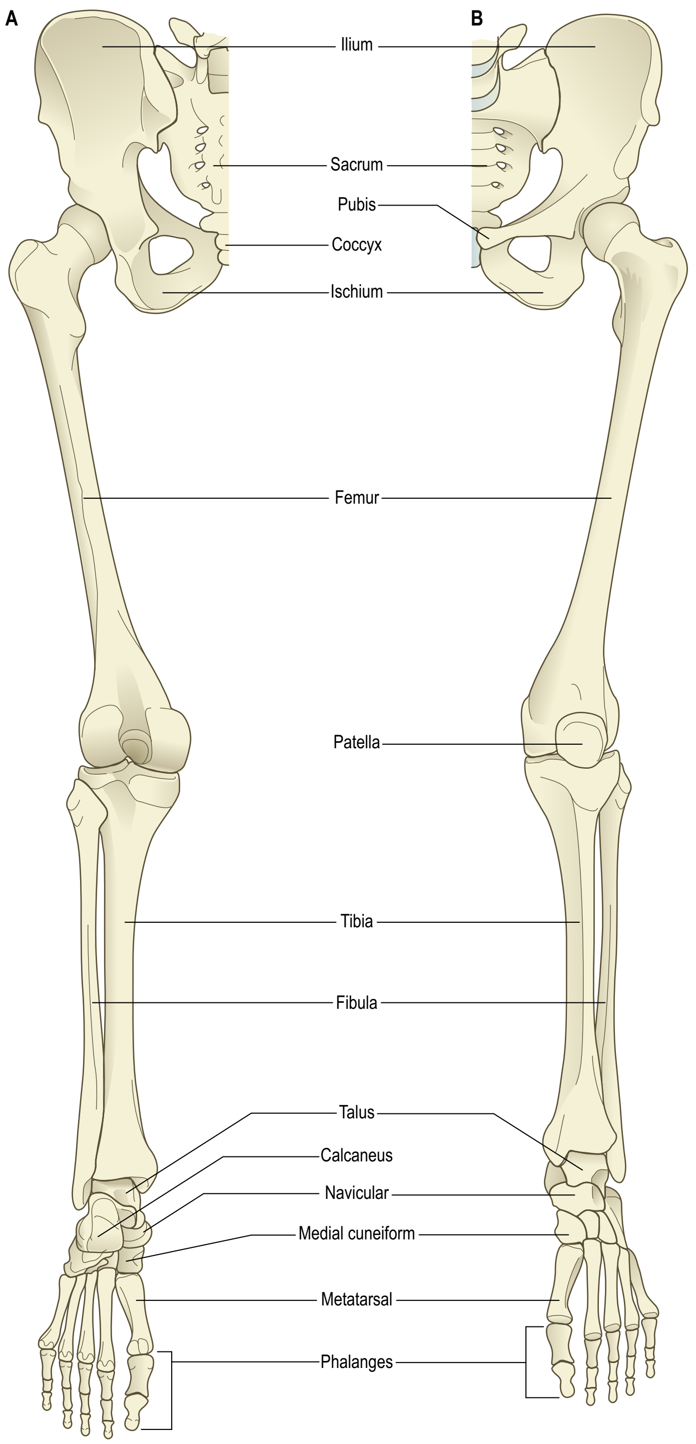

Fig. 76.2 An overview of the bones of the lower limb. **A**, Posterior aspect. **B**, Anterior aspect. (C, *continued online*)

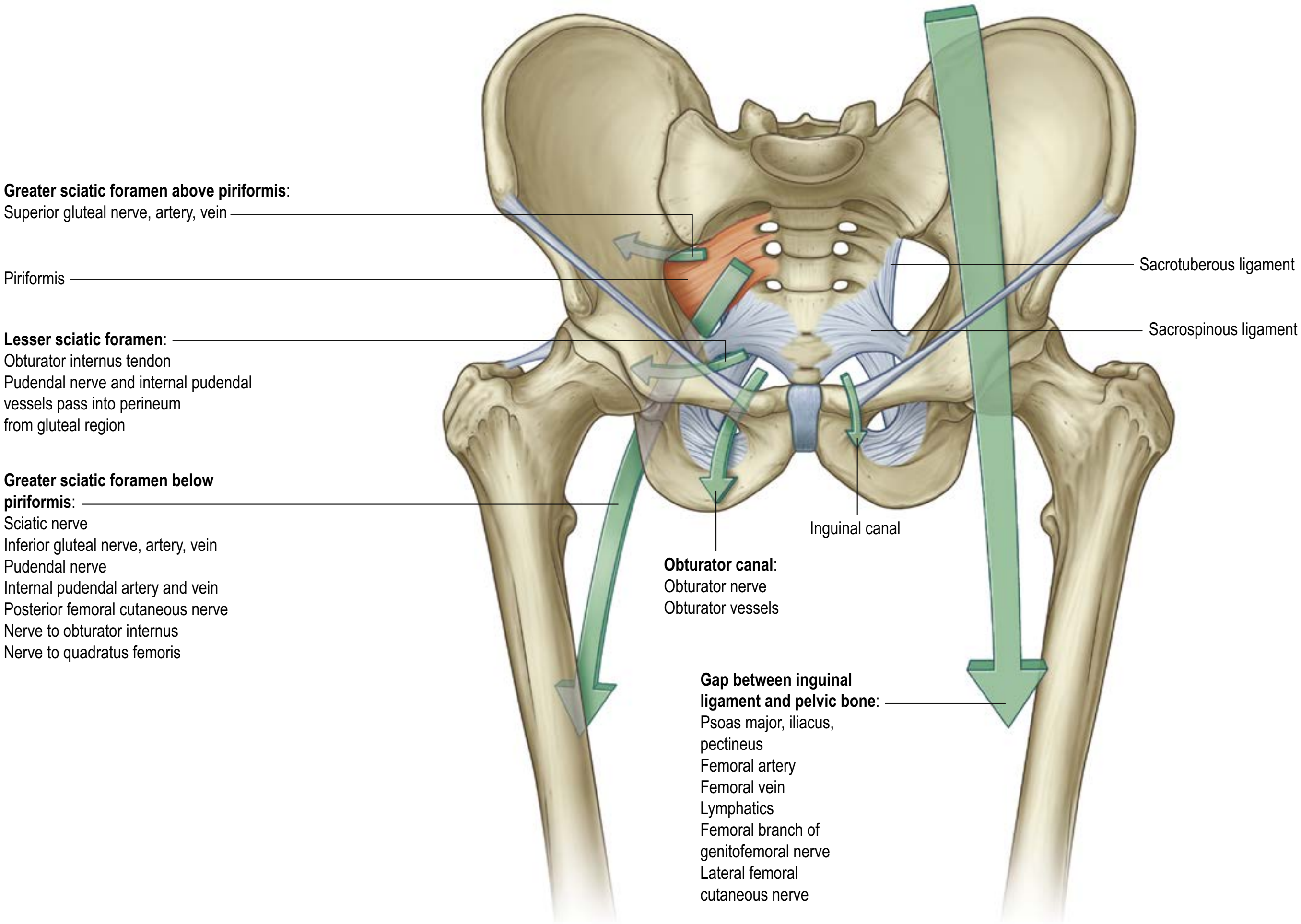
Greater sciatic foramen above piriformis:
Superior gluteal nerve, artery, vein
Piriformis
Lesser sciatic foramen:
Obturator internus tendon
Pudendal nerve and internal pudendal vessels pass into perineum from gluteal region
Greater sciatic foramen below piriformis:
Sciatic nerve
Inferior gluteal nerve, artery, vein
Pudendal nerve
Internal pudendal artery and vein
Posterior femoral cutaneous nerve
Nerve to obturator internus
Nerve to quadratus femoris
Sacrotuberous ligament
Sacrospinous ligament
Inguinal canal
Obturator canal:
Obturator nerve
Obturator vessels
Gap between inguinal ligament and pelvic bone:
Psoas major, iliacus, pectineus
Femoral artery
Femoral vein
Lymphatics
Femoral branch of genitofemoral nerve
Lateral femoral cutaneous nerve

Fig. 76.1 Gateways from the abdomen, pelvis and perineum to the lower limb. (With permission from Drake RL, Vogl AW, Mitchell A (eds) Gray's Anatomy for Students, 2nd ed. Elsevier, Churchill Livingstone. Copyright 2010.)

According to Cruveilhier (1841), all aponeurotic fasciae, including the deep fascia of the lower limb, are put under tension by specific myofascial expansions (more evident around joints) or dedicated muscles (e.g. tensor fasciae latae). These thickenings may act functionally as additional tendons. The pattern of soft tissue organization has a bearing on the physiological effects of the muscles and is crucial for efficient venous return from the limb. The fascial planes also control and direct the spread of pathological fluids (blood, pus) within the limb and play an important part in determining the degree and direction of displacement seen in long bone fractures.

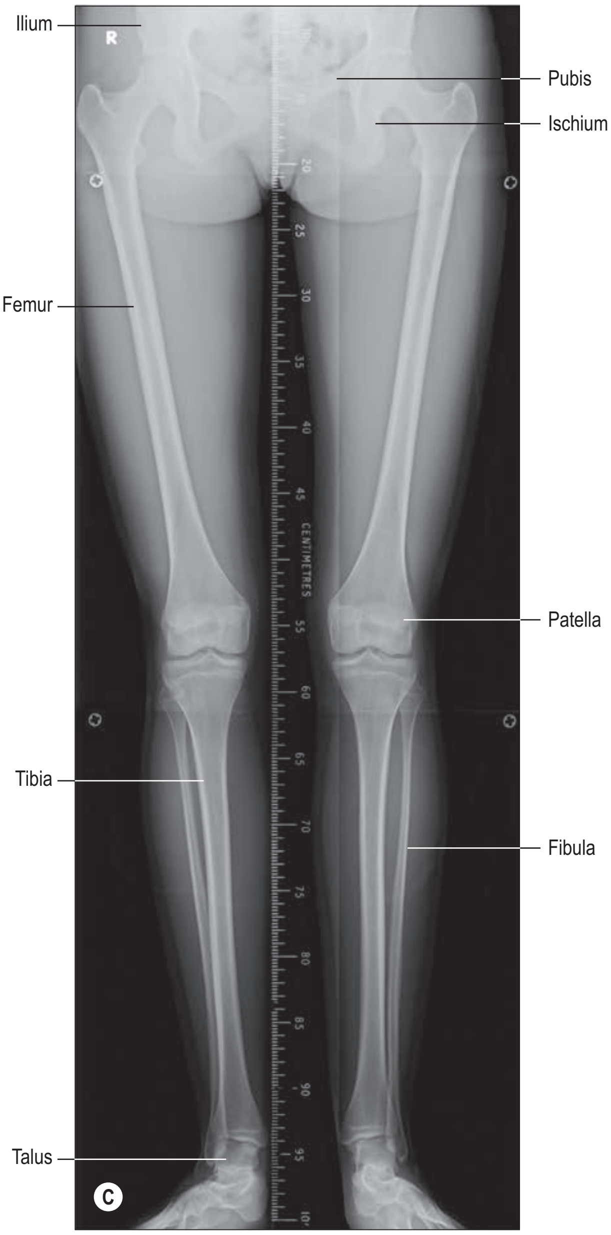
Ilium
R
Pubis
Ischium
Femur
Patella
Tibia
Fibula
Talus
C
CENTIMETRES

Fig. 76.2 C, Standing anteroposterior radiographs of the lower limbs of a 16-year-old female; two separate acquisitions stitched together. Note that the more distal long bone growth plates are still visible.

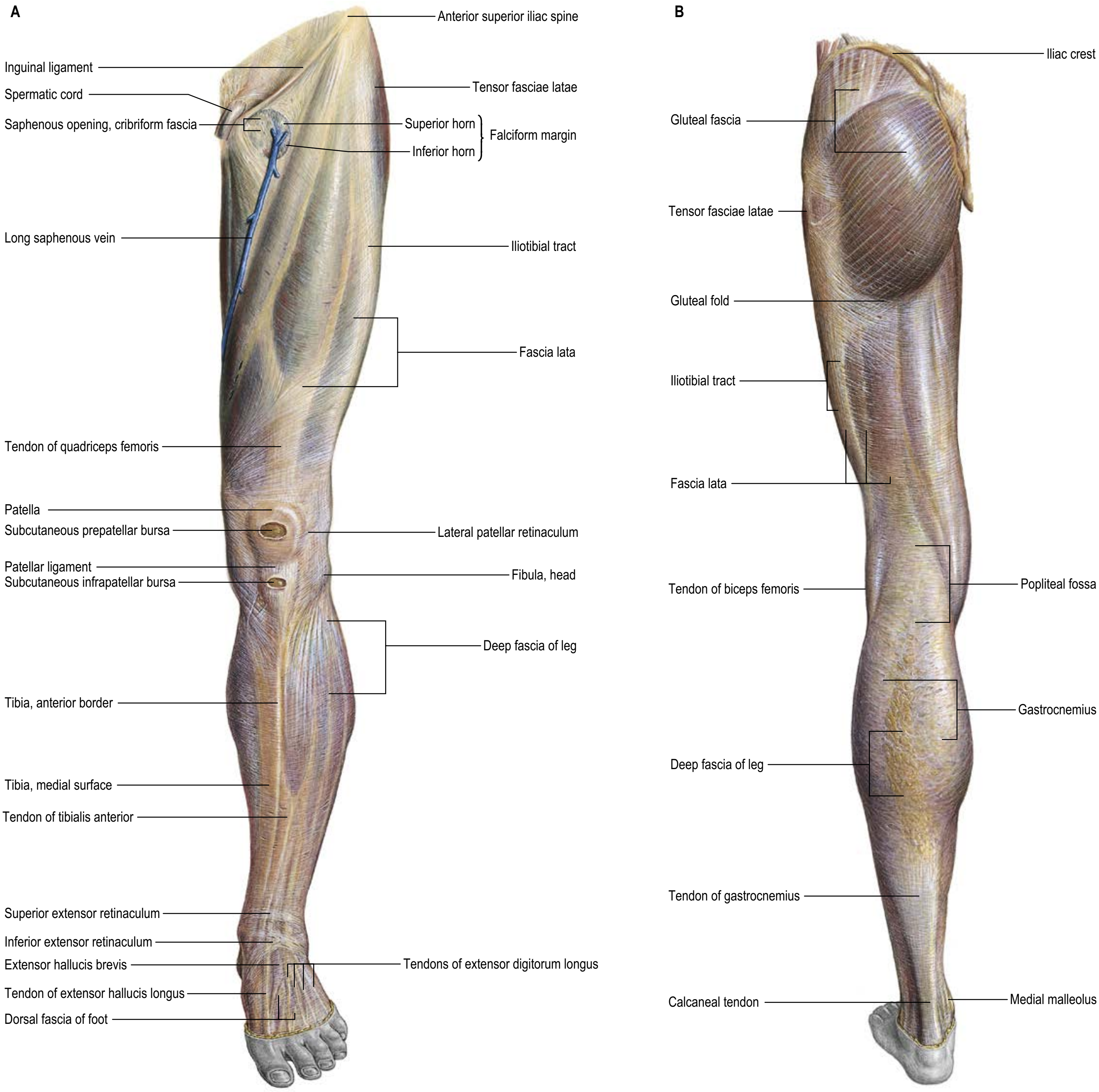
A
Anterior superior iliac spine
Inguinal ligament
Spermatic cord
Saphenous opening, cribriform fascia
Tensor fasciae latae
Superior horn
Inferior horn
Falciform margin
Long saphenous vein
Iliotibial tract
Fascia lata
Tendon of quadriceps femoris
Patella
Subcutaneous prepatellar bursa
Lateral patellar retinaculum
Patellar ligament
Subcutaneous infrapatellar bursa
Fibula, head
Deep fascia of leg
Tibia, anterior border
Tibia, medial surface
Tendon of tibialis anterior
Superior extensor retinaculum
Inferior extensor retinaculum
Extensor hallucis brevis
Tendons of extensor digitorum longus
Tendon of extensor hallucis longus
Dorsal fascia of foot
B
Iliac crest
Gluteal fascia
Tensor fasciae latae
Gluteal fold
Iliotibial tract
Fascia lata
Tendon of biceps femoris
Popliteal fossa
Gastrocnemius
Deep fascia of leg
Tendon of gastrocnemius
Calcaneal tendon
Medial malleolus

Fig. 76.3 The deep fascia of the lower limb. **A**, Anterior view. **B**, Posterior view. (A, B, Sobotta Atlas of Human Anatomy © Elsevier GmbH, Urban & Fischer, Munich.)

thigh bears weight in the sitting position and is relatively thick. The skin over the anteromedial aspect of the leg is particularly fragile and vulnerable in the elderly.

The superficial fascia (subcutaneous tissue; tela subcutanea; hypodermis) of the lower limb becomes thinner distally. It provides support for subcutaneous structures such as superficial veins and cutaneous nerves, and is connected to the adventitia of the superficial veins by thin bands that prevent the displacement of the veins during movement. The hypodermal plexus of arteries and veins controls blood flow through the skin, helping to regulate body temperature (Sterzi 1910).

The deep fascia of the gluteal region varies in thickness. The deep fascia of the thigh and leg is a well-defined layer that forms a tough circumferential ‘stocking-like’ structure that constrains the musculature (Fig. 76.3). It is attached to the medial and lateral intermuscular septa in the thigh, the patellar ligament, patella, tibial tuberosity and condyles, the head of the fibula at the knee, and the periosteum of the tibia, fibular head and lateral malleolus. The iliotibial tract, medial and lateral patellar retinacula, and the extensor, flexor and fibular retinacula at the ankle are important condensations. Septa pass from the deep surface of this fascial sheath to the bones within, defining discrete (osteofascial) compartments that contain functional muscle groups. The intermuscular septa and the interosseous membrane between the tibia and fibula also provide additional areas for the attachment of muscles.

The muscles of the thigh may be grouped into three compartments according to their function: anterior (extensor), medial (adductor) and posterior (flexor). Only the anterior and posterior compartments possess distinct fascial boundaries. A definite fascial separation into anterior (extensor), posterior (flexor) and lateral (evertor) compartments exists in the leg, and compartment syndrome is most common in this region (see below). The deep and superficial muscles in the flexor compartment of the leg are separated by the transverse intermuscular septum. The compartments of the foot, one on the dorsal aspect and four on the plantar surface, are described in Chapter 79.

Vessels and nerves run through all of the compartments and supply the muscles contained within them. The muscles acting within these closed compartments assist in maintaining the anti-gravity flow of venous blood.

The fascial boundaries that limit the compartments are largely inelastic, which means that any acute condition that leads to an increase in the volume of the compartmental contents, e.g. muscle swelling caused by trauma, haemorrhage or local infection, is likely to cause an increase in intracompartmental pressure. If unrelieved, this increased pressure will lead to compressive occlusion of the vessels in the compartment and consequent ischaemic damage to the nerves and muscles of the compartment, a phenomenon known as acute compartment syndrome. Chronic exertional compartment syndrome is characterized by exercise-induced leg pain that usually subsides with rest, thought to be caused by elevated intramuscular pressure that may result in decreased tissue perfusion, ischaemia and transient neurological impairments (Burrus et al 2015). The normal compartmental pressure of the leg is significantly higher in children than in adults: the average pressure in the compartments, measured when supine, varies between 13.3 and 16.6 mmHg in children, compared with 5.2 and 9.7 mmHg in adults (Staudt et al 2008). Pressures are higher when standing (Antle et al 2018).

The treatment of compartment syndrome relies on reducing abnormally elevated tissue pressure. Surgical decompression of the fasciae of the restricting compartment may be necessary; in order to prevent neurovascular injury during a fasciotomy, the exact course of the nerves and vessels within the affected compartment must be known (Apaydin et al 2008).

MUSCLES

The effects of extension and medial rotation of the limb that occur during fetal development are manifest in the relative positions of the muscle groups in the thigh and the leg, and in the adult pattern of segmental cutaneous innervation (dermatomes). The role of the muscles of the lower limb in the maintenance of equilibrium during gait and in stance is rarely emphasized sufficiently. Many of the muscles act frequently or predominantly from their distal attachments. During both stance and gait, the distal attachment is often fixed and the proximal attachment is mobile, e.g. the predominant action of gluteus medius is as a pelvic stabilizer rather than as a hip abductor. In contrast, in the upper limb, the proximal muscle attachments are usually fixed and the distal attachments are mobile, an arrangement that is consistent with the prehensile function of the hand. The lower limb contains many muscles that act on more than one joint, and it is unusual for any joint of the lower limb to move in isolation. Certain muscles are morphologically and functionally segregated, e.g. the anterior part of gluteus medius is active with medial (internal) rotation of the hip, while the posterior part contributes to lateral (external) rotation of the hip.

Muscles of the lower limb may be subdivided according to their location. (1) Muscles of the iliac region, psoas major and iliacus (together called iliopsoas) are the main flexors of the hip. They arise from the lumbar spine and inner surface of the ilium and are attached distally on the lesser trochanter of the femur. When present, psoas minor runs from the lumbar spine to the pubis. (2) The gluteal region includes the three named gluteal muscles and the deeper, short lateral rotators of the hip joint. Gluteus maximus lies most superficially and is a powerful extensor of the hip joint. Gluteus medius and minimus, passing between the ilium and the greater trochanter of the femur, are abductors of the hip. Their most important action is to stabilize the pelvis on the femur during gait, helped by tensor fasciae latae. Two of the short lateral rotators of the hip, piriformis and obturator internus, arise from within the pelvis, while the others, obturator externus, the gemelli and quadratus femoris, originate externally; all of these muscles are attached distally to the proximal femur. (3) The muscles of the thigh lie in three functional compartments. The anterior (extensor) compartment includes sartorius and quadriceps femoris (rectus femoris and vasti medialis, lateralis and intermedius). Sartorius and rectus femoris are attached proximally to the pelvis and can thus act on the hip joint as well as on the knee, whereas the vasti arise from the femoral shaft and are powerful knee extensors. The medial (adductor) compartment contains adductors brevis, longus and magnus and gracilis; pectineus may also be included. All five muscles cross the hip joint but only gracilis reaches beyond the knee. The muscles of the posterior (flexor) compartment, semitendinosus, semimembranosus and biceps femoris, are attached proximally to the ischial tuberosity and act to extend the hip and to flex and rotate the knee. Part of adductor magnus, as may be inferred from the extent of its proximal attachment and its dual innervation, shares the first of these functions with the hamstrings. Biceps femoris is the only muscle of the thigh that is attached distally to the fibula. (4) In the leg, the anterior (extensor) compartment includes the extensors (dorsiflexors) of the foot and the extrinsic toe extensors. Tibialis anterior, the main foot dorsiflexor, also inverts the foot at the subtalar joint, while the smallest muscle of the compartment, fibularis (peroneus) tertius, is a dorsiflexor that everts the foot. The lateral compartment contains the main evertors of the foot, fibularis (peroneus) longus and brevis; both muscles are also plantar flexors. The posterior (flexor/plantar flexor) compartment has superficial and deep components. The superficial component contains gastrocnemius, soleus and plantaris. Gastrocnemius and soleus are powerful plantar flexors of the foot: gastrocnemius and plantaris are attached proximally to the femur and distally to the calcaneus and can therefore act on the knee as well as at the ankle. The deep component of the flexor compartment contains popliteus, a rotator of the knee, tibialis posterior, the main invertor of the foot, and the extrinsic flexors of the toes. (5) The intrinsic muscles of the foot include one muscle on the dorsal surface (extensor digitorum brevis), and the muscles of the sole, arranged in four layers. The intrinsic muscles facilitate the actions of the extrinsic flexors of the toes, and provide subtle changes in the shape of the foot, thereby contributing to the control of foot posture during stance and gait.

VASCULAR SUPPLY AND LYMPHATIC DRAINAGE

The detailed regional descriptions of these systems are found in Chapters 77, 78 and 79.

Arteries

The femoral artery (the continuation of the external iliac artery) provides the principal arterial supply to the lower limb distal to the inguinal ligament and the gluteal fold (**Figs 76.4–76.5**). The femoral artery courses within the subsartorial (adductor) canal, which is located on the anteromedial aspect of the thigh. It passes through the adductor hiatus to become the popliteal artery on entering the posterior compartment of the thigh and soon thereafter divides into the anterior and posterior tibial arteries. The obturator and inferior gluteal vessels also contribute to the supply of the proximal part of the limb. In the embryo, the inferior gluteal artery supplies the main axial artery of the limb, which is represented in the adult by the artery to the sciatic nerve.

The bones of the lower limb receive their arterial supply from nutrient vessels, metaphysial arterial branches of the peri-articular anastomoses, and the arteries supplying the muscles that attach to their periosteum. The pattern of arterial supply is particularly relevant to fracture healing, the spread of infection and malignancy, and the planning of reconstructive surgical procedures. For further details, consult Cormack and Lamberty (1984), Taylor and Razaboni (1994) and Crock (1996).

Ischaemia of the lower limb due to peripheral arterial disease is a tremendous burden on healthcare resources. Obesity and smoking and diseases including diabetes, hypertension and atherosclerosis contribute to this pathology. Symptoms include intermittent claudication and wounds that do not heal well (see Sampson et al 2017). Physical examination of such patients may reveal decreased distal pulses (e.g. of the posterior tibial artery), pallor or a cool extremity.

Arterial perforators of the lower limb and surgical flaps

Achieving adequate and aesthetically satisfactory skin and soft tissue cover for large, superficial tissue defects is a perennial challenge in the field of plastic and reconstructive surgery, and accounts for a substantial part of a plastic surgeon's workload. Generally, split-thickness and full-thickness skin grafts are suitable only for very superficial defects. To achieve tissue coverage for deeper and larger tissue defects, one of a variety of autologous tissue flaps may be used. A fasciocutaneous flap is composed of skin, fat and deep fascia (fascia musculorum); a lower-extremity fasciocutaneous flap (Pontén 1981) is very useful in the repair of soft tissue defects of the leg.

The viability of a flap transplanted from one part of the body to another is crucially dependent on the blood supply of the flap. An appreciation of the angiosome concept (Chs 6, 7), coupled with technological advances in reconstructive microsurgery, has stimulated the development and use of perforator (or perforator-based) flaps. These

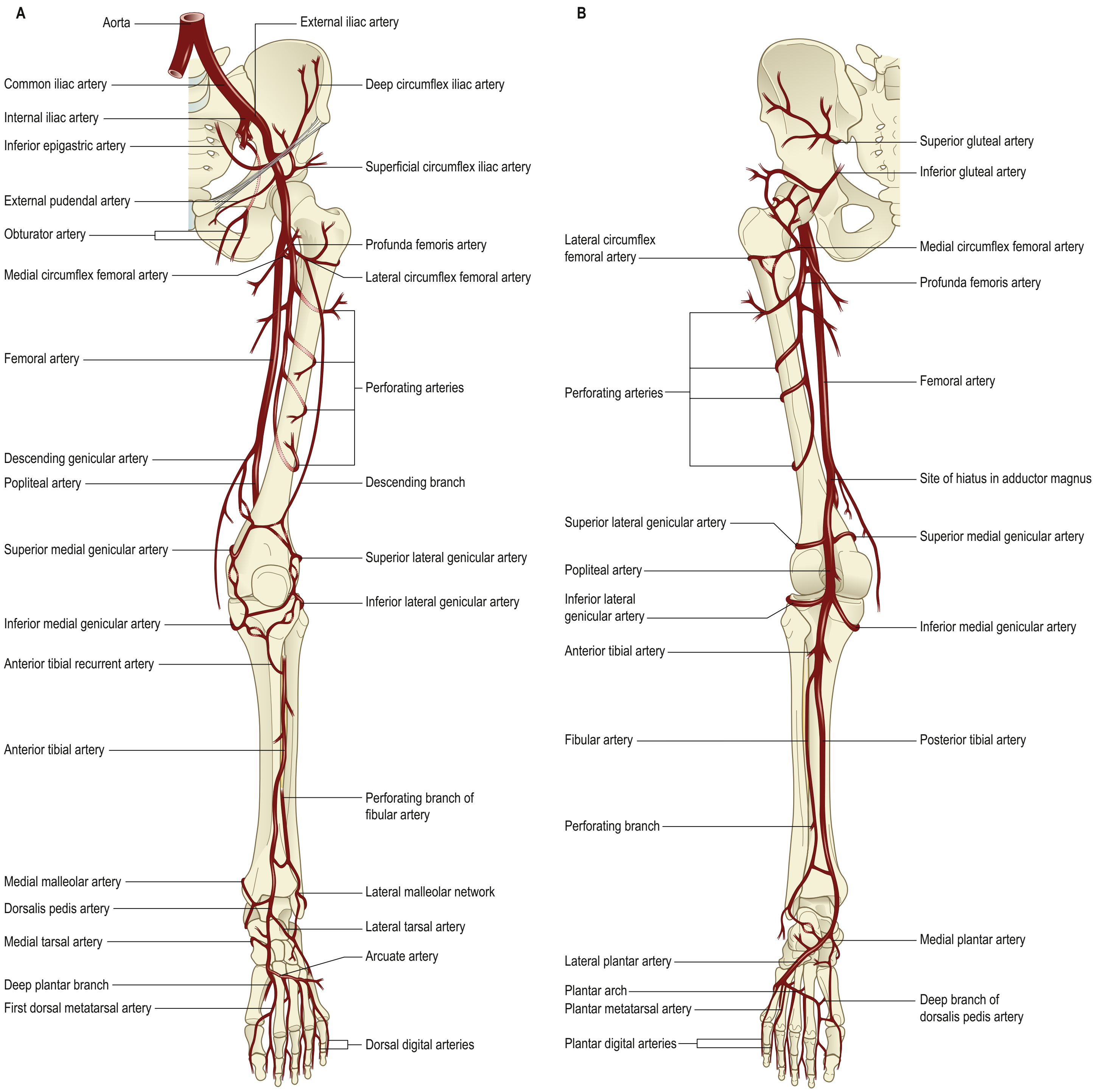
A
Aorta
External iliac artery
Common iliac artery
Deep circumflex iliac artery
Internal iliac artery
Inferior epigastric artery
Superficial circumflex iliac artery
External pudendal artery
Obturator artery
Profunda femoris artery
Medial circumflex femoral artery
Lateral circumflex femoral artery
Femoral artery
Perforating arteries
Descending genicular artery
Popliteal artery
Descending branch
Superior medial genicular artery
Superior lateral genicular artery
Inferior lateral genicular artery
Inferior medial genicular artery
Anterior tibial recurrent artery
Anterior tibial artery
Perforating branch of fibular artery
Medial malleolar artery
Lateral malleolar network
Dorsalis pedis artery
Lateral tarsal artery
Medial tarsal artery
Arcuate artery
Deep plantar branch
First dorsal metatarsal artery
Dorsal digital arteries
B
Superior gluteal artery
Inferior gluteal artery
Lateral circumflex femoral artery
Medial circumflex femoral artery
Profunda femoris artery
Femoral artery
Perforating arteries
Site of hiatus in adductor magnus
Superior lateral genicular artery
Superior medial genicular artery
Popliteal artery
Inferior lateral genicular artery
Inferior medial genicular artery
Anterior tibial artery
Fibular artery
Posterior tibial artery
Perforating branch
Medial plantar artery
Lateral plantar artery
Plantar arch
Deep branch of dorsalis pedis artery
Plantar metatarsal artery
Plantar digital arteries

Fig. 76.4 An overview of the arteries of the lower limb. **A**, Anterior aspect. **B**, Posterior aspect.

are flaps of skin or subcutaneous tissue supplied by one or more fascial 'perforators', i.e. arteries that reach the suprafascial plexus either directly from a source vessel, or indirectly from some other neighbouring tissue (Harry et al 2009) (**Fig. 76.6**). Perforator-based flaps are typically harvested with sparing of underlying muscle tissue and minimal trauma; their use is said to reduce postoperative pain, donor site morbidity and functional loss.

The lower limb is the largest donor site in the body for perforator-based flaps. Commonly used flaps include anterolateral thigh flaps, which provide a large amount of skin; superior and inferior gluteal artery perforator flaps used in breast reconstruction; vascularized fibular flaps for reconstruction of deficient bone; vascularized tensor fasciae latae flaps for tendon reconstruction; vascularized sural nerve flaps for nerve reconstruction; and the gracilis muscle flap, used in, for example, reanimation of paralysed muscle.

In the context of perforator flap surgery, the lower limb may be considered in terms of four anatomic regions: gluteal; anterior hip and thigh; knee and leg; ankle and foot. Each lower limb accounts for approximately 23% of the total body surface area (thigh 10.5%, leg 6.5%, buttock 2.5% and foot 3.5%) and contains an average of 90 arterial perforators (Fig. 76.7).

Pulses

The pulsation of the femoral artery is palpable as it enters the femoral triangle. Posterior to the knee joint, the popliteal pulse is difficult to identify due to the depth of the popliteal artery, and is best assessed with the knee in slight flexion. Distally, the posterior tibial artery is palpable just posterior to the medial malleolus and the dorsalis pedis pulse is located over the tarsal bones, immediately lateral to the tendon of extensor hallucis longus. Clinical signs of decreased or absent peripheral pulses, particularly the pedal pulses (posterior tibial artery and dorsalis pedis) bilaterally may be indicative of peripheral artery disease (Londero et al 2016).

Veins

The veins of the lower limb can be subdivided into a superficial group lying in the subcutaneous tissue and vessels that lie deep to the deep fascia and accompany the major arteries and their branches (**Figs 76.8–76.9**). Valves are present in both groups, but are more numerous in the deep veins. (They are also more numerous than in the veins of the upper limb.) Venous plexuses occur within and between some of the lower limb

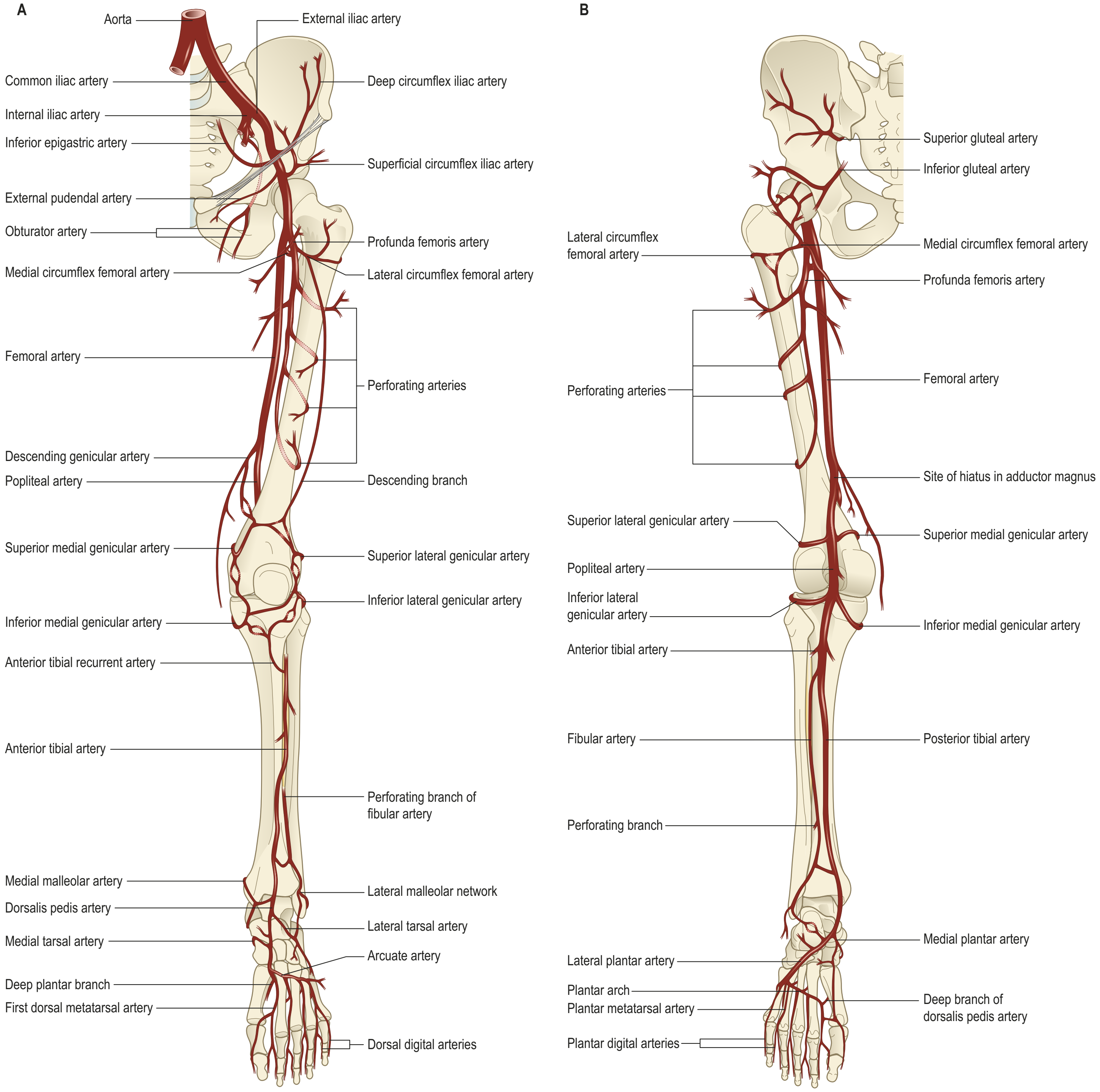
A
Aorta
External iliac artery
Common iliac artery
Deep circumflex iliac artery
Internal iliac artery
Inferior epigastric artery
Superficial circumflex iliac artery
External pudendal artery
Obturator artery
Profunda femoris artery
Medial circumflex femoral artery
Lateral circumflex femoral artery
Femoral artery
Perforating arteries
Descending genicular artery
Popliteal artery
Descending branch
Superior medial genicular artery
Superior lateral genicular artery
Inferior lateral genicular artery
Inferior medial genicular artery
Anterior tibial recurrent artery
Anterior tibial artery
Perforating branch of fibular artery
Medial malleolar artery
Lateral malleolar network
Dorsalis pedis artery
Lateral tarsal artery
Medial tarsal artery
Arcuate artery
Deep plantar branch
First dorsal metatarsal artery
Dorsal digital arteries
B
Superior gluteal artery
Inferior gluteal artery
Lateral circumflex femoral artery
Medial circumflex femoral artery
Profunda femoris artery
Perforating arteries
Femoral artery
Site of hiatus in adductor magnus
Superior lateral genicular artery
Superior medial genicular artery
Popliteal artery
Inferior lateral genicular artery
Inferior medial genicular artery
Anterior tibial artery
Fibular artery
Posterior tibial artery
Perforating branch
Medial plantar artery
Lateral plantar artery
Plantar arch
Plantar metatarsal artery
Deep branch of dorsalis pedis artery
Plantar digital arteries

Fig. 76.7 The source and location of the arterial perforators of the lower limb. **A**, Anterior aspect. **B**, Posterior aspect.

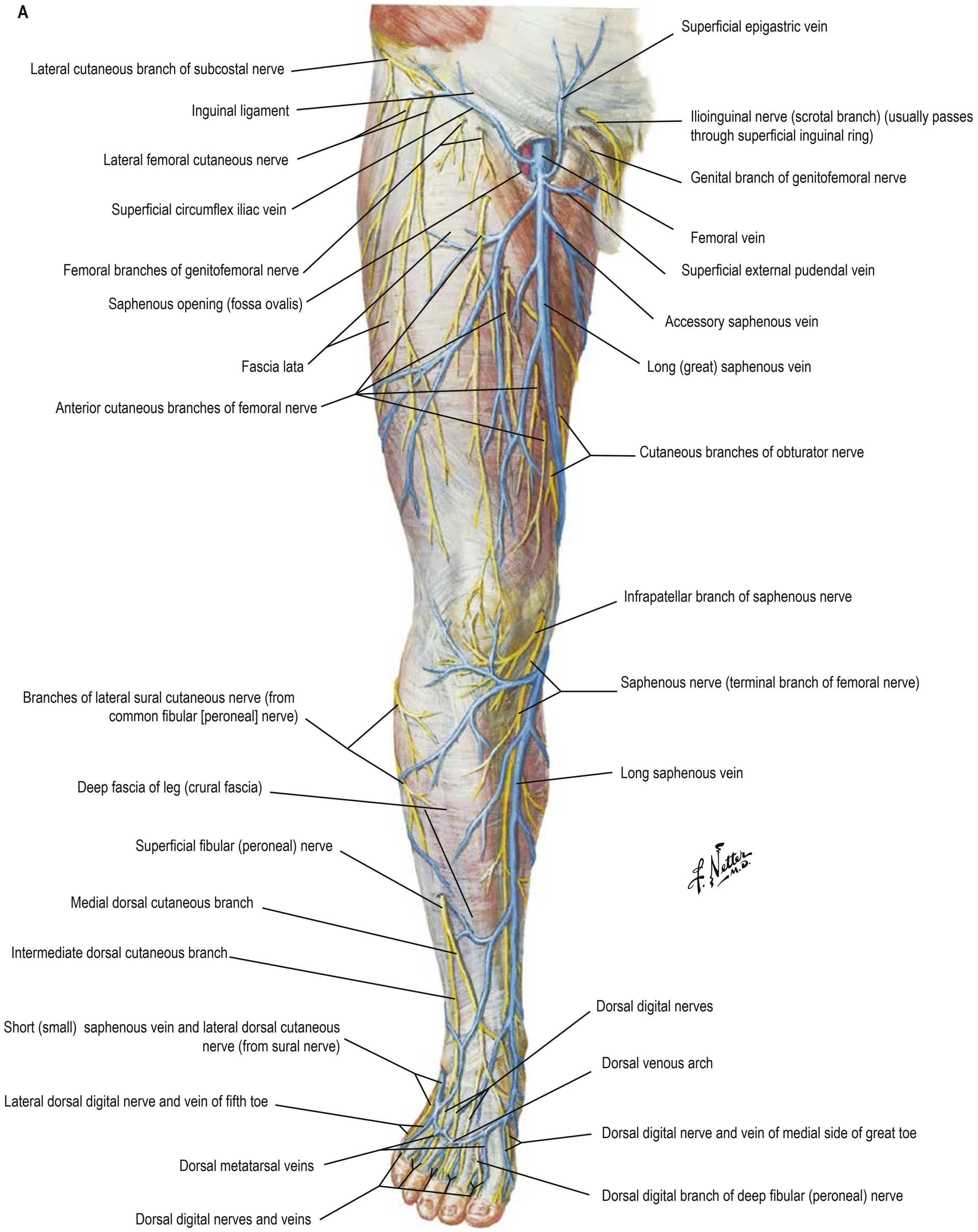
A
Lateral cutaneous branch of subcostal nerve
Inguinal ligament
Lateral femoral cutaneous nerve
Superficial circumflex iliac vein
Femoral branches of genitofemoral nerve
Saphenous opening (fossa ovalis)
Fascia lata
Anterior cutaneous branches of femoral nerve
Superficial epigastric vein
Ilioinguinal nerve (scrotal branch) (usually passes through superficial inguinal ring)
Genital branch of genitofemoral nerve
Femoral vein
Superficial external pudendal vein
Accessory saphenous vein
Long (great) saphenous vein
Cutaneous branches of obturator nerve
Infrapatellar branch of saphenous nerve
Saphenous nerve (terminal branch of femoral nerve)
Branches of lateral sural cutaneous nerve (from common fibular [peroneal] nerve)
Long saphenous vein
Deep fascia of leg (crural fascia)
Superficial fibular (peroneal) nerve
Medial dorsal cutaneous branch
Intermediate dorsal cutaneous branch
Dorsal digital nerves
Short (small) saphenous vein and lateral dorsal cutaneous nerve (from sural nerve)
Dorsal venous arch
Lateral dorsal digital nerve and vein of fifth toe
Dorsal digital nerve and vein of medial side of great toe
Dorsal metatarsal veins
Dorsal digital branch of deep fibular (peroneal) nerve
Dorsal digital nerves and veins
F. Netter M.D.

Fig. 76.9 **A**, The long (great) saphenous vein and its tributaries. (With permission from Netter FH, Atlas of Human Anatomy, 7th ed. Elsevier. Copyright 2019.)

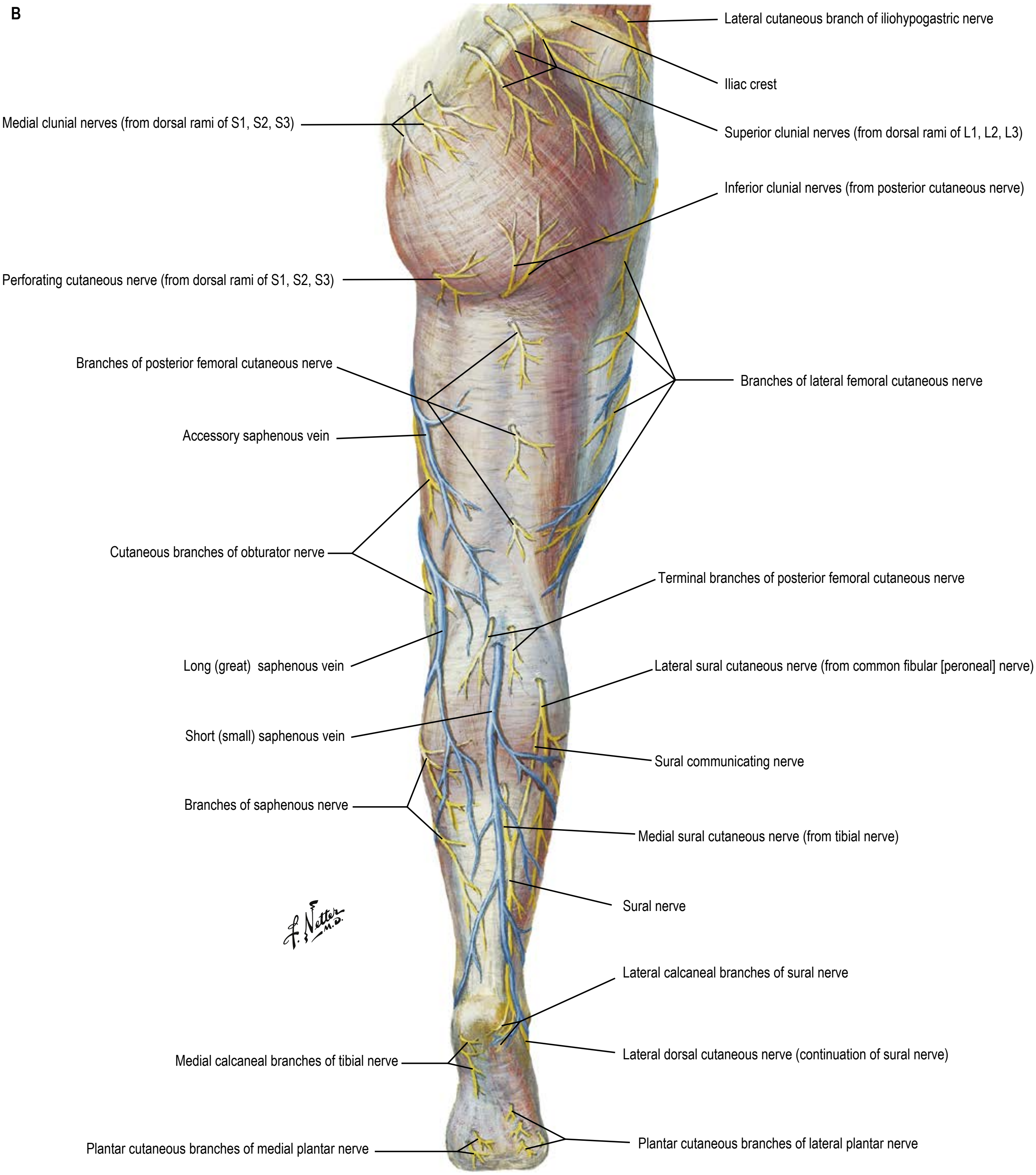
B
Lateral cutaneous branch of iliohypogastric nerve
Iliac crest
Medial clunial nerves (from dorsal rami of S1, S2, S3)
Superior clunial nerves (from dorsal rami of L1, L2, L3)
Inferior clunial nerves (from posterior cutaneous nerve)
Perforating cutaneous nerve (from dorsal rami of S1, S2, S3)
Branches of posterior femoral cutaneous nerve
Branches of lateral femoral cutaneous nerve
Accessory saphenous vein
Cutaneous branches of obturator nerve
Terminal branches of posterior femoral cutaneous nerve
Long (great) saphenous vein
Lateral sural cutaneous nerve (from common fibular [peroneal] nerve)
Short (small) saphenous vein
Sural communicating nerve
Branches of saphenous nerve
Medial sural cutaneous nerve (from tibial nerve)
Sural nerve
Lateral calcaneal branches of sural nerve
Medial calcaneal branches of tibial nerve
Lateral dorsal cutaneous nerve (continuation of sural nerve)
Plantar cutaneous branches of medial plantar nerve
Plantar cutaneous branches of lateral plantar nerve

Fig. 76.9, cont'd B, The short saphenous vein and its tributaries. (With permission from Netter FH, Atlas of Human Anatomy, 7th ed. Elsevier. Copyright 2019.)

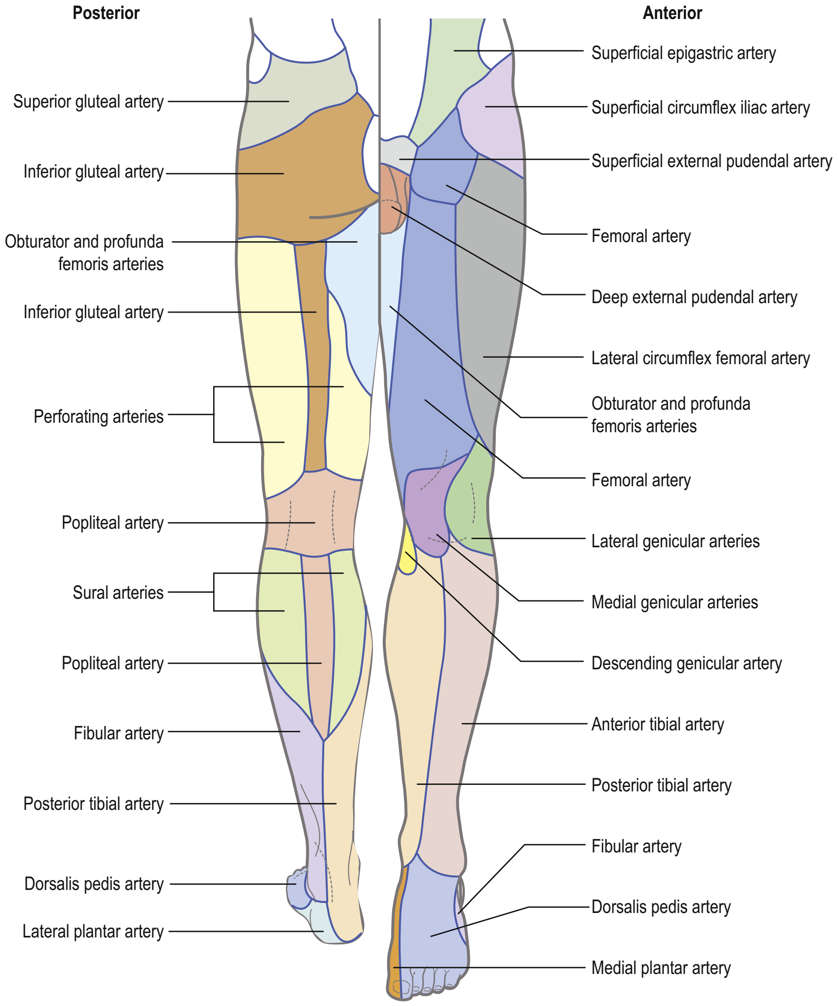
Posterior
Anterior
Superior gluteal artery
Inferior gluteal artery
Obturator and profunda femoris arteries
Inferior gluteal artery
Perforating arteries
Popliteal artery
Sural arteries
Popliteal artery
Fibular artery
Posterior tibial artery
Dorsalis pedis artery
Lateral plantar artery
Superficial epigastric artery
Superficial circumflex iliac artery
Superficial external pudendal artery
Femoral artery
Deep external pudendal artery
Lateral circumflex femoral artery
Obturator and profunda femoris arteries
Femoral artery
Lateral genicular arteries
Medial genicular arteries
Descending genicular artery
Anterior tibial artery
Posterior tibial artery
Fibular artery
Dorsalis pedis artery
Medial plantar artery

Fig. 76.5 The anatomical territories served by the cutaneous blood supply to the lower limb.

muscles. The two principal superficial veins are the long (great) and short (small) saphenous veins; their numerous tributaries are mostly unnamed, however, changes in clinical practice are driving a revision of the terminology (Caggiati et al 2002, 2005). The long saphenous vein can be harvested and used as a graft for peripheral vascular surgery, including coronary artery bypass (Kosinski 1926).

Plantar digital veins arise from plexuses in the plantar regions of the toes, connect with dorsal digital veins and unite to form four plantar metatarsal veins. These run in the intermetatarsal spaces and connect first with dorsal veins by means of perforating veins and then connect with each other to constitute a deep plantar venous arch adjacent to the deep plantar arterial arch. Medial and lateral plantar veins from the venous arch run near the corresponding arteries and communicate with the long and short saphenous veins before forming the posterior tibial veins posterior to the medial malleolus.

The posterior tibial veins accompany the posterior tibial artery. They receive veins from the calf muscles, especially the venous plexus in soleus, and connect with superficial veins and with the fibular veins. The latter accompany the fibular artery and receive tributaries from both soleus and superficial veins. The anterior tibial veins are continuations of the venae comitantes of the dorsalis pedis artery. They leave the extensor region between the tibia and fibula, pass through the proximal end of the interosseous membrane and unite with the posterior tibial veins at the distal border of popliteus to form the popliteal vein.

Venous (muscle) pumps

While standing, venous return from the lower limb depends largely on muscular activity, especially contraction of the calf and foot muscles, known as the 'muscle pump', aided by the tight sleeve of deep fascia (Ricci 2017). 'Perforating' veins connect the long saphenous vein with the deep veins, particularly near the ankle, distal calf and knee. Their valves are arranged so as to prevent flow of blood from the deep to the superficial veins. At rest, pressure in a superficial vein is equal to the height of the column of blood extending from that vein to the heart. When the posterior leg muscles contract, blood is pumped proximally into the deep veins and is normally prevented from flowing into the superficial veins by the valves in the perforating veins. During muscular relaxation, blood is drawn into the deep veins from the superficial veins. If the valves in the perforating veins become incompetent, these veins become sites of 'high-pressure leaks' during muscular contraction, and the superficial veins become dilated and varicose. There are similar perforating connections in the anterolateral region, where varicosities may also occur. Incompetence of the valves in the connecting veins between the long saphenous vein and femoral vein in the adductor canal may predispose to superficial varicosities along the medial aspect of the thigh (Dodd and Cockett 1976). Venous plexuses, which may be intramuscular (soleus) or intermuscular (in the foot and gluteal region), communicate with the axially running deep veins and are components of the 'muscle pump' mechanism.

Lymphatic drainage

Most lymph from the lower limb traverses a large intermediary inguinal group of nodes (Fig. 76.10). Peripheral nodes are few and are all deeply sited in the popliteal fossa except for an inconsistent node lying proximally on the interosseous membrane near the anterior tibial vessels. Enlarged popliteal nodes, often as a result of inflammation, malignancy or injury to the lateral side of the foot, may be palpated along the line of the popliteal vessels while the passively supported knee is gradually moved from extension to semi-flexion. Inguinal lymph nodes are found superficial and deep to the deep fascia. The superficial nodes may be divided into a lower vertical group that clothe the proximal part of the long saphenous vein, and an upper group that lie parallel to, but below, the inguinal ligament and which are related laterally to the superficial circumflex iliac and medially to the superficial external pudendal vessels. The deep nodes are few and lie alongside the medial aspect of

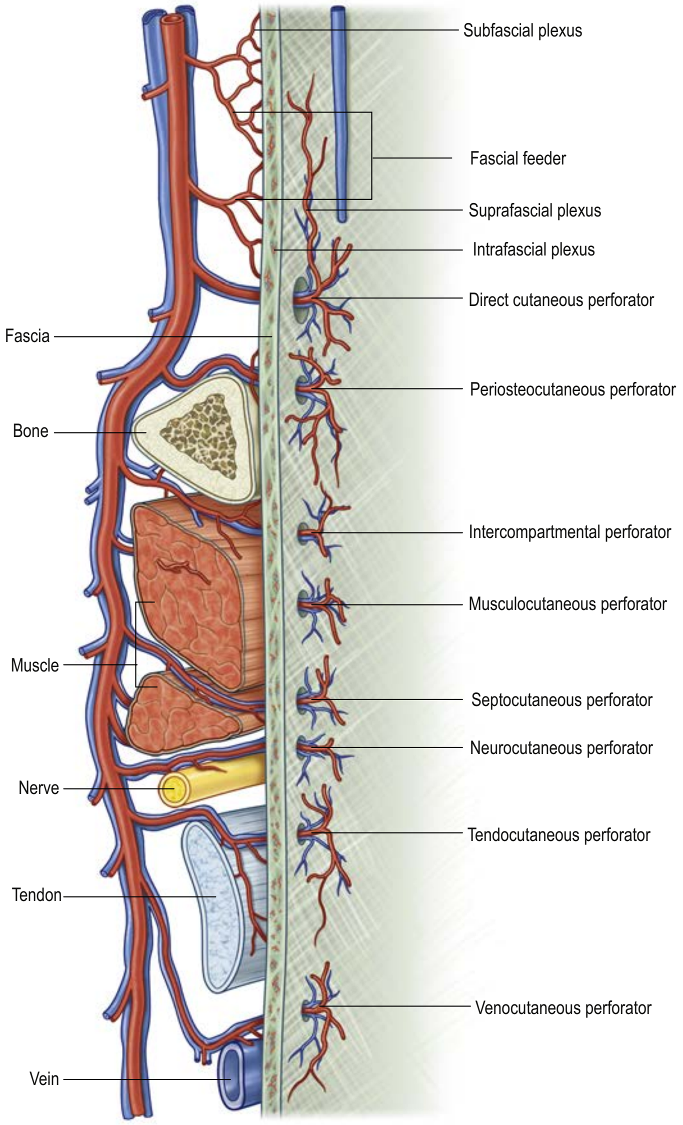
Subfascial plexus
Fascial feeder
Suprafascial plexus
Intrafascial plexus
Direct cutaneous perforator
Fascia
Periosteocutaneous perforator
Bone
Intercompartmental perforator
Musculocutaneous perforator
Muscle
Septocutaneous perforator
Neurocutaneous perforator
Nerve
Tendocutaneous perforator
Tendon
Venocutaneous perforator
Vein

Fig. 76.6 Types of arterial perforators.

the femoral vein. Lymph from the lower limb passes from the inguinal lymph nodes to the external and common iliac nodes, and ultimately drains to the lateral aortic nodes. Deep gluteal lymph reaches the same group through the internal and common iliac lymphatic vessels.

Superficial tissues

The superficial lymph vessels begin in subcutaneous plexuses. Collecting vessels leave the foot either medially with the long saphenous vein, or laterally with the short saphenous vein. Medial vessels are larger and more numerous. They start on the medial side of the dorsum of the foot, ascend anterior or posterior to the medial malleolus, accompany the long saphenous vein and drain to the distal superficial inguinal nodes. Lateral vessels begin on the fibular side of the dorsum of the foot. Some cross anteromedially in the leg to join the medial vessels and so pass to the distal superficial inguinal lymph nodes, while others accompany the short saphenous vein and drain to the popliteal nodes. Superficial lymph vessels from the gluteal region run anteriorly to the proximal superficial inguinal nodes.

Deeper tissues

The deep lymph vessels accompany the anterior and posterior tibial, fibular, popliteal and femoral vessels. Popliteal nodes interrupt the deep vessels from the foot and leg; deep vessels from the thigh pass to the deep inguinal nodes. The deep lymphatic vessels of the gluteal region follow their corresponding blood vessels. Those accompanying the superior gluteal vessels end in a node near the intrapelvic part of the superior gluteal artery, adjacent to the superior border of the greater sciatic foramen, while those that follow the inferior gluteal vessels traverse one or two of the small nodes inferior to piriformis and then pass to the internal iliac nodes.

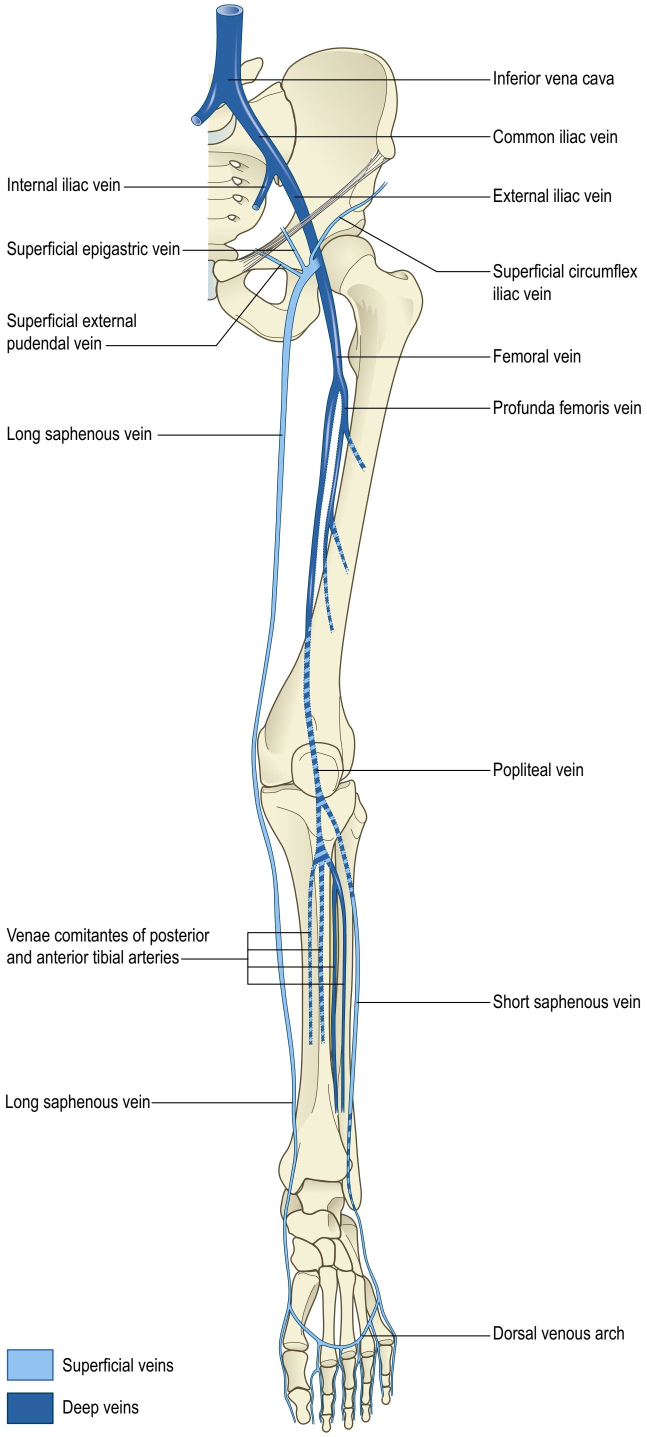
Inferior vena cava
Common iliac vein
Internal iliac vein
External iliac vein
Superficial epigastric vein
Superficial circumflex iliac vein
Superficial external pudendal vein
Femoral vein
Profunda femoris vein
Long saphenous vein
Popliteal vein
Venae comitantes of posterior and anterior tibial arteries
Short saphenous vein
Long saphenous vein
Dorsal venous arch
Superficial veins
Deep veins

Fig. 76.8 An overview of the veins of the lower limb.

INNERVATION

Overview of the lumbar and sacral plexuses

Nerves derived from the lumbar and sacral plexuses innervate the lower limb (Fig. 76.11). The lumbar plexus lies deep within psoas major, anterior to the transverse processes of the first three lumbar vertebrae. The sacral plexus lies in the pelvis on the anterior surface of piriformis, external to the pelvic fascia, which separates it from the inferior gluteal and internal pudendal vessels. The lumbosacral trunk (fourth and fifth lumbar ventral rami) emerges medial to psoas major on the posterior abdominal wall and lies on the ala of the sacrum before crossing the pelvic brim to join the first sacral ventral ramus. Contributions to the lumbosacral trunk may also be derived from the third lumbar nerve (Apaydin 2016).

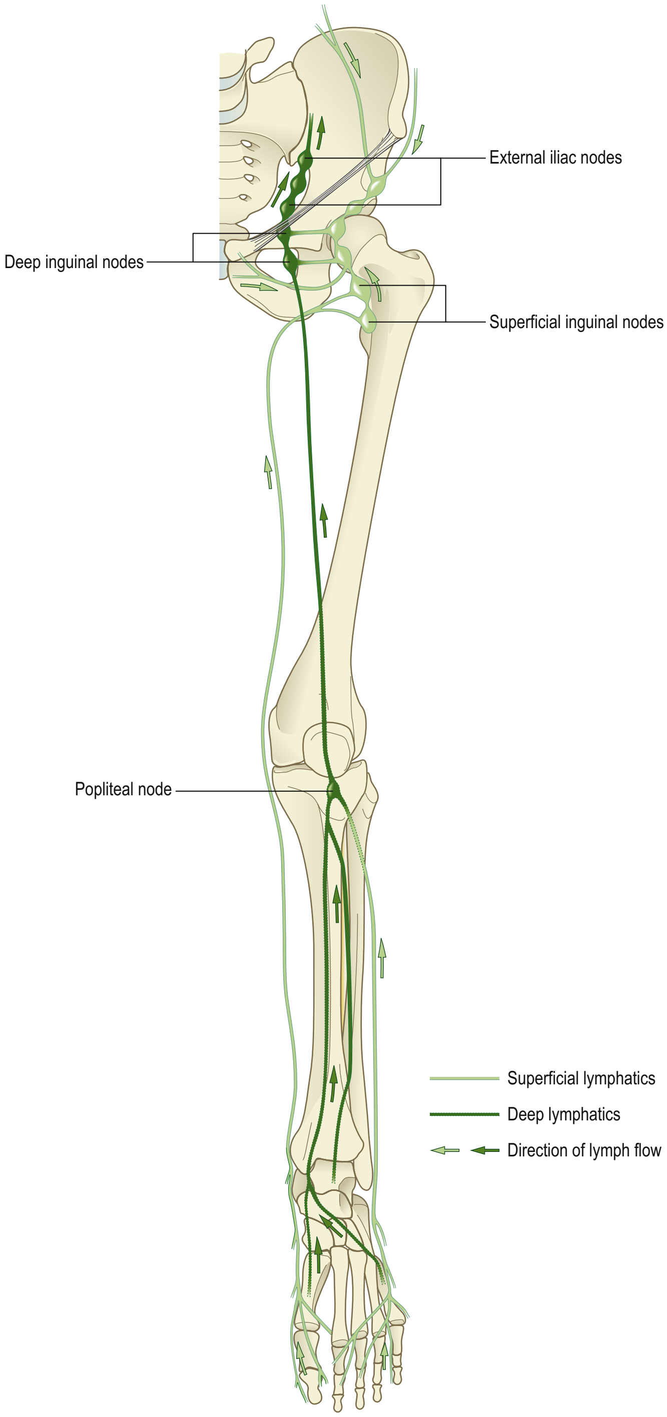

Fig. 76.10 An overview of the lymphatics of the lower limb.

Lesions of the lumbar and sacral plexuses

The deep and protected situation of the plexuses means that lesions are not common. The lumbar plexus may be involved in retroperitoneal pathology and the sacral plexus may be invaded by pelvic malignancies and both may be involved in the reticuloses, affected by plexiformneuromas, or damaged in fractures of the lumbar spine and pelvis or in other conditions that cause severe retroperitoneal and pelvic haemorrhage. Temporary lesions may occur after pregnancy and childbirth, e.g. after difficult forceps delivery of a large baby. Pain, which may be diffuse, is the most common feature. Iatrogenic injury can occur during surgical approaches to the abdomen and pelvis, particularly when operating within the retroperitoneal space and also during the lateral approach to spine.

Sciatica is pain in the lower back and hip region, radiating inferiorly along the posterior thigh to the leg. It is often caused by a herniated intervertebral disc, compressing the L5 or S1 ventral rami. The so-called piriformis syndrome, which may result from a variant or anomalous relationship between piriformis and the sciatic nerve, may also produce hip pain that radiates inferiorly along the course of the sciatic nerve. Diagnosis of specific nerve injuries relies on the distribution and characteristics of clinical findings in combination with supportive electrophysiological studies and/or MRI and CT scans. The clinical presentation of lesions can vary as a result of anatomical variation and overlapping innervation patterns. Generally, loss of hip flexion and knee extension indicates a lumbar lesion; loss of hip abduction, knee flexion, and plantarflexion and dorsiflexion are symptoms of sacral lesions (Ahmadian et al 2015).

Overview of the principal nerves of the lower limb

Femoral nerve (L2–L4)

The femoral nerve is the nerve of the anterior compartment of the thigh. It arises from the posterior divisions of the second to fourth lumbar ventral rami, descends through psoas major and emerges on its lateral border to pass between it and iliacus. It enters the thigh behind the inguinal ligament and lateral to the femoral sheath. Its terminal branches form in the femoral triangle about 2 cm distal to the inguinal ligament. In the abdomen, the nerve supplies small branches to iliacus and a branch to the proximal part of the femoral artery. It subsequently supplies a large cutaneous area on the anterior and medial thigh, medial leg and foot, and gives articular branches to the hip, knee and ankle. The femoral nerve is described in detail on pages 1391–1392.

The femoral nerve is susceptible to compression, resulting in isolated motor or sensory deficits, either within psoas major or as it passes under the inguinal ligament. Partial or complete nerve injury can occur during surgery directed to the hip, pelvis or spine; with femoral artery catheterization; from trauma; or as a result of a retroperitoneal haematoma or mass. Consequences include paralysis of the hip flexors and quadriceps (with loss of the patellar reflex) and sensory deficits in the medial and anterior thigh and medial side of the leg (saphenous branch).

Obturator nerve (L2–L4)

The obturator nerve is the nerve of the medial compartment of the thigh. It arises from the anterior divisions of the second to fourth lumbar ventral rami, descends through psoas major and emerges from its medial border at the pelvic brim. It crosses the sacroiliac joint behind the common iliac artery and lateral to the internal iliac vessels, runs along the lateral pelvic wall medial to obturator internus, and enters the thigh through the upper part of the obturator foramen. Near the foramen, it divides into anterior and posterior branches that are initially separated by part of obturator externus and more distally by adductor brevis. It provides articular branches to the hip and knee, and can supply the skin of the medial thigh and leg. An accessory obturator nerve may also be present and leaves the pelvis anterior to the pubis. The obturator nerve is described in detail on page 1392.

Isolated lesions of the obturator nerve are rare, and usually occur in combination with injury to other nerves of the lumbosacral plexus. They can result from an acetabular fracture, pelvic tumour, obturator hernia, prolonged labour or direct trauma, and can be produced iatrogenically following manipulation, transection or retraction during pelvic surgery. The obturator nerve can become entrapped within the fascia overlying adductor brevis. Resulting symptoms include radiating pain and numbness on the medial side of the thigh and adductor muscle paralysis. Pain or loss of sensation in the groin with weakness of adduction and medial rotation of the thigh may be noted.

Sciatic nerve (L4, L5, S1–S3)

The sciatic nerve is typically 2 cm wide at its origin and is the thickest nerve in the body. It travels in the posterior compartment of the thigh and supplies the leg and foot. It is formed in the pelvis from the ventral rami of the fourth lumbar to third sacral spinal nerves, enters the lower limb via the greater sciatic foramen inferior to piriformis and descends between the greater trochanter and ischial tuberosity. In its descent along the posterior thigh it is crossed by the long head of biceps femoris. The sciatic nerve 'divides' into the tibial and common fibular (peroneal) nerves proximal to the knee. The tibial nerve is derived from the anterior divisions of the sacral plexus and the common fibular nerve is derived from the posterior divisions of the plexus: the two large nerves are only loosely held together as the sciatic nerve and the level of their separation in the thigh is variable.

The sciatic nerve sends articular branches to the hip joint through its posterior capsule (these can be derived directly from the sacral plexus) and to the knee joint. The medial (tibial) component innervates the posterior thigh muscles, including the ischial part of adductor

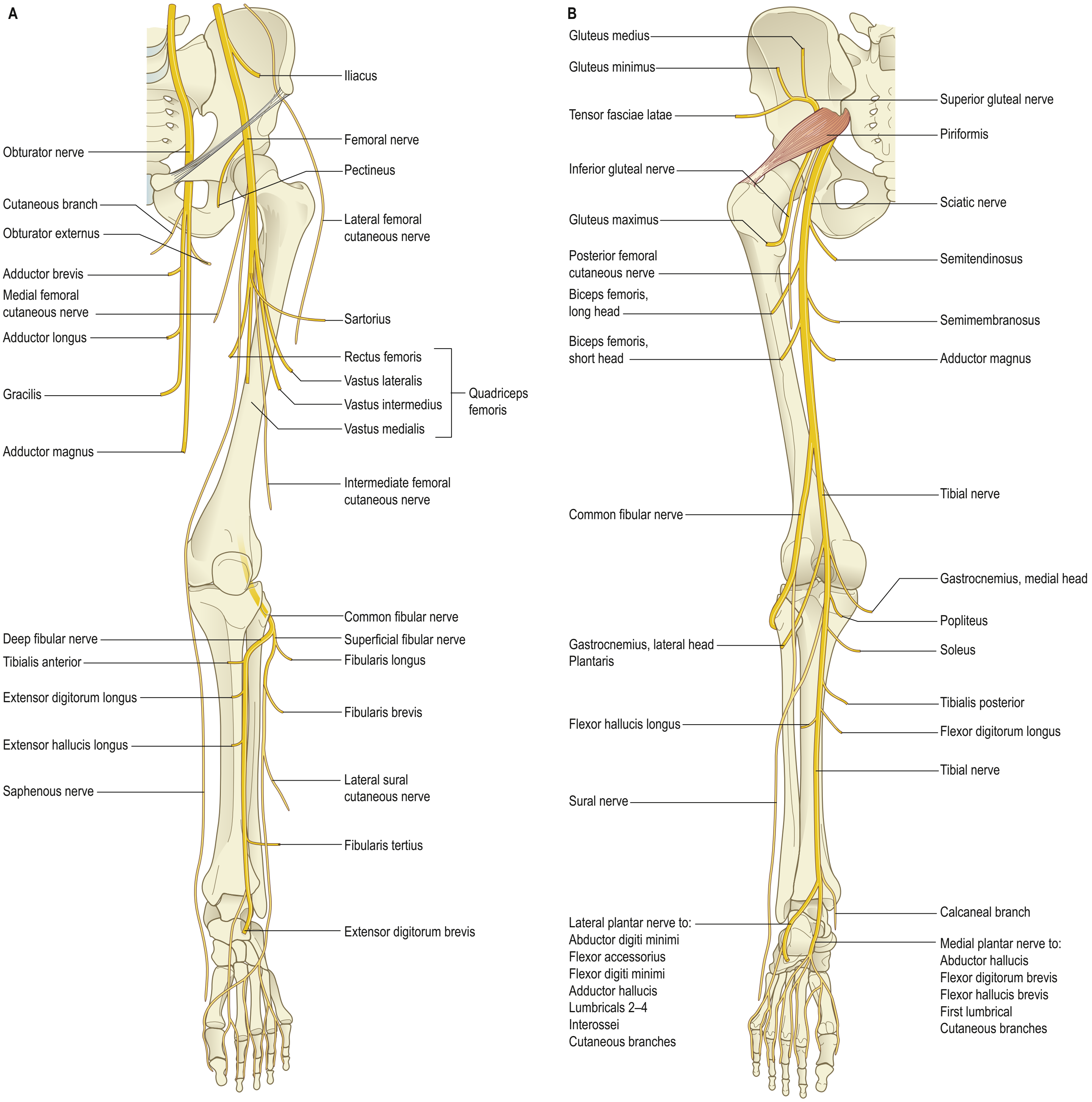
A
Iliacus
Obturator nerve
Femoral nerve
Pectineus
Cutaneous branch
Obturator externus
Lateral femoral cutaneous nerve
Adductor brevis
Medial femoral cutaneous nerve
Sartorius
Adductor longus
Rectus femoris
Vastus lateralis
Gracilis
Vastus intermedius
Quadriceps femoris
Vastus medialis
Adductor magnus
Intermediate femoral cutaneous nerve
Common fibular nerve
Deep fibular nerve
Superficial fibular nerve
Tibialis anterior
Fibularis longus
Extensor digitorum longus
Fibularis brevis
Extensor hallucis longus
Lateral sural cutaneous nerve
Saphenous nerve
Fibularis tertius
Extensor digitorum brevis
B
Gluteus medius
Gluteus minimus
Superior gluteal nerve
Tensor fasciae latae
Piriformis
Inferior gluteal nerve
Sciatic nerve
Gluteus maximus
Semitendinosus
Posterior femoral cutaneous nerve
Biceps femoris, long head
Semimembranosus
Biceps femoris, short head
Adductor magnus
Tibial nerve
Common fibular nerve
Gastrocnemius, medial head
Popliteus
Gastrocnemius, lateral head
Plantaris
Soleus
Tibialis posterior
Flexor hallucis longus
Flexor digitorum longus
Tibial nerve
Sural nerve
Calcaneal branch
Lateral plantar nerve to:
Abductor digiti minimi
Flexor accessorius
Flexor digiti minimi
Adductor hallucis
Lumbricals 2–4
Interossei
Cutaneous branches
Medial plantar nerve to:
Abductor hallucis
Flexor digitorum brevis
Flexor hallucis brevis
First lumbrical
Cutaneous branches

Fig. 76.11 The nerves of the lower limb, with their cutaneous and muscular branches. **A**, Anterior aspect. **B**, Posterior aspect. Adductor magnus has dual innervation.

magnus, but not the short head of biceps femoris, which is supplied by the lateral (common fibular) component. The common variations of the sciatic nerve have been classified into six types (Beason and Anson 1937). The sciatic nerve is described in detail on pages 1392–1393.

Sciatic nerve injury may result from gluteal trauma, hip fracture, vasculitis, myositis piriformis syndrome or iatrogenically damaged by misplaced gluteal injections or during total hip replacement surgery. Complete sciatic nerve palsy is rare, with injury to its common fibular component more frequent, possibly because it lies posterior, lateral and superficial to the tibial nerve.

Tibial nerve (L4, L5, S1–S3)

The tibial nerve is derived from the anterior divisions of the sacral plexus. It descends through the posterior thigh and popliteal fossa to the distal border of popliteus, passes anterior to soleus with the popliteal artery and continues into the leg. In the popliteal fossa, it initially lies lateral to the popliteal vessels, then becomes superficial to them and crosses to the medial side of the artery. In the leg, it is the nerve of the posterior compartment, descending with the posterior tibial vessels to lie between the heel and the medial malleolus and ending deep to the flexor retinaculum by dividing into the medial and lateral plantar nerves. The tibial nerve supplies articular branches to the knee and ankle joints, cutaneous branches to the back of the calf, the sole, the lateral border of the foot and the medial and lateral sides of the heel, and motor branches to gastrocnemius, plantaris, soleus, popliteus, tibialis posterior, flexor digitorum longus and flexor hallucis longus. The tibial nerve is described in detail on pages 1427–1428.

The tibial nerve is at risk of direct injury in the popliteal fossa, and can be compressed at the level of the tarsal tunnel as the nerve passes under the flexor retinaculum (tarsal tunnel syndrome). The medial plantar nerve may be compressed between abductor hallucis and the navicular bone ('jogger's foot'). Depending on the level of the injury, weakness of knee flexion, plantarflexion, inversion and toe flexion may result, accompanied by sensory loss in the lower lateral leg, heel and sole of the foot.

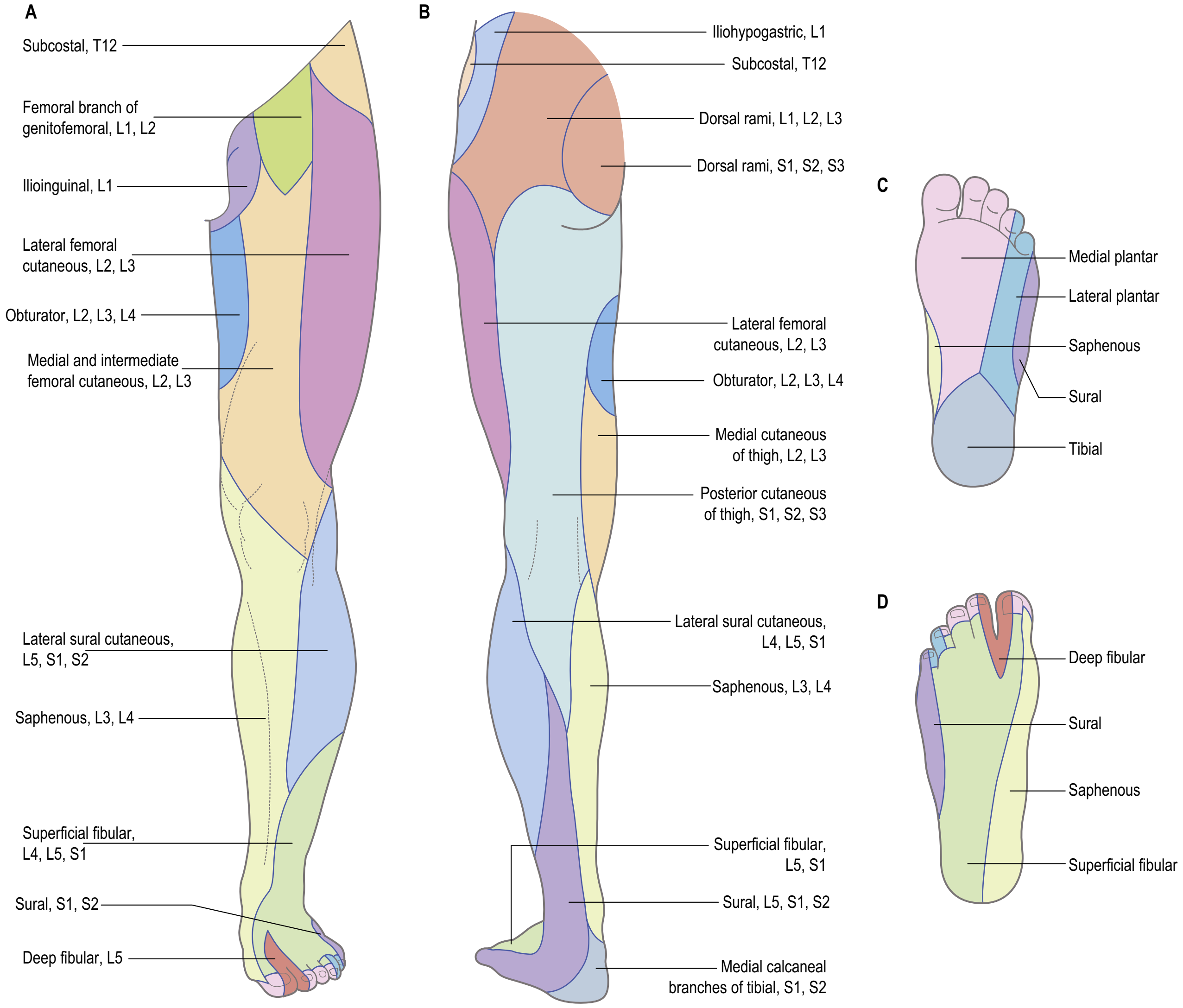
A
Subcostal, T12
Femoral branch of genitofemoral, L1, L2
Ilioinguinal, L1
Lateral femoral cutaneous, L2, L3
Obturator, L2, L3, L4
Medial and intermediate femoral cutaneous, L2, L3
Lateral sural cutaneous, L5, S1, S2
Saphenous, L3, L4
Superficial fibular, L4, L5, S1
Sural, S1, S2
Deep fibular, L5
B
Iliohypogastric, L1
Subcostal, T12
Dorsal rami, L1, L2, L3
Dorsal rami, S1, S2, S3
Lateral femoral cutaneous, L2, L3
Obturator, L2, L3, L4
Medial cutaneous of thigh, L2, L3
Posterior cutaneous of thigh, S1, S2, S3
Lateral sural cutaneous, L4, L5, S1
Saphenous, L3, L4
Superficial fibular, L5, S1
Sural, L5, S1, S2
Medial calcaneal branches of tibial, S1, S2
C
Medial plantar
Lateral plantar
Saphenous
Sural
Tibial
D
Deep fibular
Sural
Saphenous
Superficial fibular

Fig. 76.12 The cutaneous nerves of the lower limb: areas of distribution and spinal segments of origin. **A**, Anterior aspect. **B**, Posterior aspect. **C**, The sole of the foot. **D**, The dorsum of the foot.

Common fibular nerve (L4, L5, S1, S2)

The common fibular nerve (common peroneal nerve) is derived from the posterior divisions of the sacral plexus and is the nerve of the anterior and lateral compartments in the leg. It descends obliquely along the lateral side of the popliteal fossa to the fibular head, lying between the tendon of biceps femoris and the lateral head of gastrocnemius, then curves lateral to the neck of the fibula, lying on the bone deep to fibularis longus, and divides into superficial and deep fibular (peroneal) nerves. The common fibular nerve supplies the anterolateral part of the knee joint capsule and the proximal tibiofibular joint and the skin on the anterior, posterior and lateral surfaces of the proximal leg. The superficial fibular (peroneal) nerve supplies fibulares longus and brevis and the skin of the lower leg before dividing into medial and intermediate dorsal cutaneous nerves. The deep fibular (peroneal) nerve supplies muscular branches to tibialis anterior, extensors hallucis longus and digitorum longus and fibularis tertius, and an articular branch to the ankle joint, before dividing into lateral and medial terminal branches. The common fibular nerve is described in detail on page 1428.

The common fibular nerve is prone to iatrogenic or traumatic injury: patients with common fibular neuropathy present with foot drop. Injury specifically to the superficial fibular nerve will result in paralysis of eversion and sensory loss in the lower lateral aspect of the leg extending onto the dorsum of the foot. Damage to the deep fibular nerve results in paralysis of dorsiflexion and toe extension with sensory loss in the first interdigital web space.

Gluteal nerves (L4, L5, S1, S2)

The gluteal nerves arise from the posterior divisions of the sacral plexus. The superior gluteal nerve (L4, L5, S1) leaves the pelvis through the greater sciatic foramen superior to piriformis and supplies gluteus medius, gluteus minimus, tensor fasciae latae and the hip joint. The inferior gluteal nerve (L5, S1, S2) passes through the greater sciatic foramen inferior to piriformis and supplies gluteus maximus. The gluteal nerves are described in detail on page 1393.

Focal lesions of the superior and inferior gluteal nerves usually occur concurrently with those of the sciatic nerve, posterior femoral cutaneous nerve and/or pudendal nerve. However, both gluteal nerves are vulnerable to injury during total hip replacement, and less commonly due to blunt trauma or misplaced gluteal injections. Injury to the superior gluteal nerve causing paralysis of gluteus medius and minimus can result in Trendelenburg's sign, where the pelvis drops on the unsupported side (in the coronal plane) when standing on the affected limb. Injury to the inferior gluteal nerve results in weakness of gluteus maximus causing impaired hip extension (Kretschmer and Heinen 2015).

Cutaneous innervation

The cutaneous nerves supplying the skin of the lower limb are all branches of the lumbar and sacral plexuses, with the exception of some proximal nerves. The areas of distribution and spinal segments of origin of the cutaneous nerves of the lower limb are illustrated in Fig. 76.12. Variations in the composition and course of the cutaneous nerves of the lower limb are common.

For example, the ilioinguinal and iliohypogastric nerves may arise from a common trunk or the ilioinguinal nerve may be absent. The ilioinguinal nerve may also join the iliohypogastric nerve at the iliac crest. When the obturator nerve makes a more significant contribution to the cutaneous innervation, the medial cutaneous branch of the femoral nerve is relatively small. The cutaneous branch of the obturator nerve may be absent. The lateral femoral cutaneous nerve normally arises from L2 and L3, but L1 may also contribute. Although this nerve usually bifurcates after it exits the pelvis, it may bifurcate within the

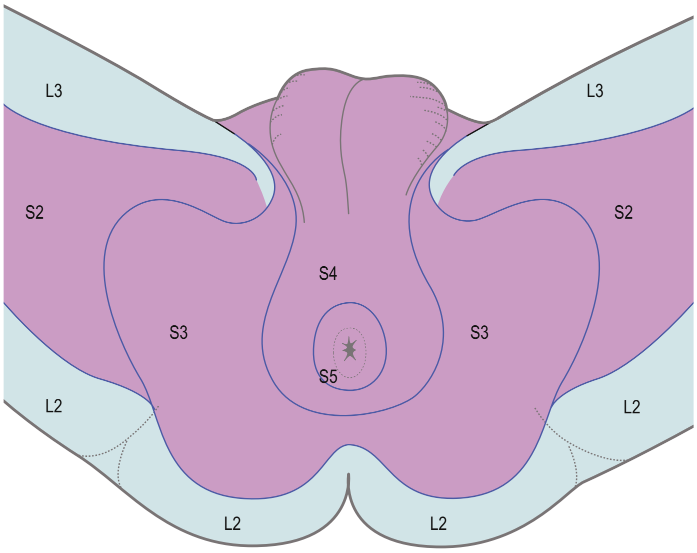

Fig. 76.13 Dermatomes of the perineum. (With permission from O'Brien M Aids to the Examination of the Peripheral Nervous System, 5th ed. Elsevier, Saunders. Copyright 2010.)

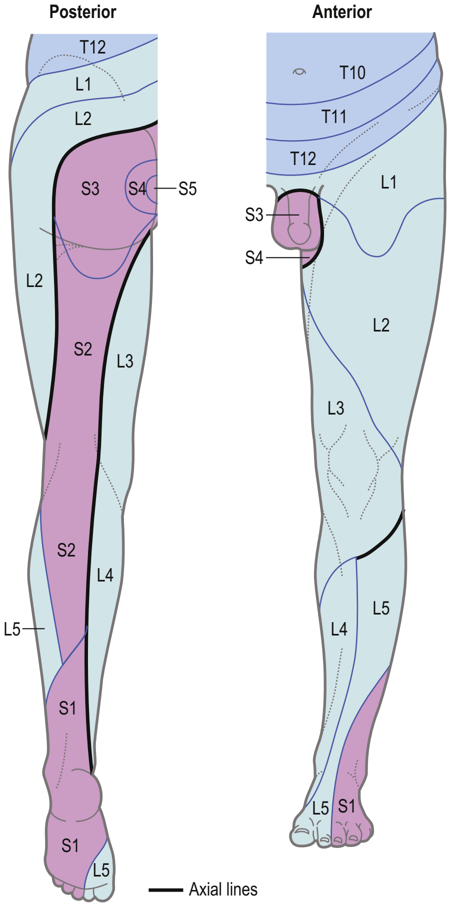

Fig. 76.14 Dermatomes of the lower limb. There is considerable variation and overlap between dermatomes, but the overlap across axial lines (heavy black) is minimal. (With permission from O'Brien M Aids to the Examination of the Peripheral Nervous System, 5th ed. Elsevier, Saunders. Copyright 2010.)

pelvic cavity: it may be absent on one side and/or may be replaced by the ilioinguinal nerve or a branch of the anterior femoral cutaneous nerve. The genital and femoral branches of the genitofemoral nerve may arise as separate offshoots of the lumbar plexus. The genital branch may receive fibres from the twelfth thoracic nerve or may be completely absent, and the femoral branch may have an extensive distribution to the skin of the upper two-thirds of the thigh. The sural nerve is subject to wide variation and may supply the dorsal cutaneous aspect of the lateral two-and-a-half toes, or may terminate in the foot without any digital branches.

Injury to the iliohypogastric, ilioinguinal and genitofemoral nerves most commonly occurs during surgical procedures involving the lower abdomen or spine, particularly inguinal surgery. Injury can result in anaesthesia, hyperaesthesia, neuralgia, or causalgia in the associated sensory distributions. The lateral femoral cutaneous nerve is most vulnerable to entrapment as it passes beneath the inguinal ligament just medial to the anterior superior iliac spine: injury results in paraesthesia or dysaesthesia on the anterolateral aspect of the thigh (meralgia paraesthetica) (Grossman et al 2001), which is usually intensified by walking or hip extension. Symptoms may be exacerbated when wearing tight belts or waist bands or as a result of pregnancy, obesity, rapid weight gain, diabetes or during hip surgery, hernia repair or iliac bone harvesting. The sural nerve may be injured at the level of the ankle joint following a fracture or sprain, compressed by wearing tight-fitting shoes or damaged during surgical procedures such as ankle arthroscopy or repair of the Achilles tendon: symptoms include pain or diminished sensation along the posterolateral aspect of the lower leg extending onto the lateral surface of the ankle and foot (Craig 2015).

Dermatomes

Our knowledge of the extent of individual dermatomes, especially in the limbs, is largely based on clinical evidence (Ladak et al 2014). While dermatomes have an orderly sequence and areas of consistency, they also demonstrate overlap and variability (Lee et al 2008). The dermatomes of the lower limb are innervated by spinal nerves T12 to S3 (see Fig. 76.12; **Figs 76.13–76.14**).

The preaxial border starts near the midpoint of the thigh and descends to the knee, then curves medially, descending to the medial malleolus and the medial side of the foot and hallux. The postaxial border starts in the gluteal region and descends to the centre of the popliteal fossa, then deviates laterally to the lateral malleolus and the lateral side of the foot. The ventral and dorsal axial lines exhibit corresponding obliquity. The ventral axial line starts proximally at the medial end of the inguinal ligament and descends along the posteromedial aspect of the thigh and leg to end proximal to the heel. The dorsal axial line begins in the lateral gluteal region and descends posterolaterally in the thigh to the knee; it inclines medially and ends proximal to the ankle. Considerable overlap exists between adjacent dermatomes innervated by nerves derived from consecutive spinal cord segments.

Autonomic innervation

The autonomic nerve supply to the limbs is exclusively sympathetic. Preganglionic sympathetic fibres to the lower limb are derived from neurones in the lateral horn of the lower thoracic (T10–T12) and upper lumbar (L1, L2) spinal cord segments. Fibres pass in white rami communicantes to the sympathetic trunk and synapse in the lumbar and sacral ganglia. Postganglionic fibres pass in grey rami communicantes to enter the lumbar and sacral plexuses; many are distributed to the skin via the cutaneous branches of the nerves derived from these plexuses. The blood vessels to the lower limb receive their sympathetic nerve supply via adjacent peripheral nerves. Postganglionic fibres accompanying the iliac arteries are destined mainly for the pelvis but may supply vessels in the proximal thigh.

Surgical or chemical lumbar sympathectomy may be indicated in arterial disease and in the management of plantar hyperhidrosis, and may be used to treat rest pain or other troublesome sensory symptoms of arterial disease, or in causalgia. A segment of the sympathetic trunk including the second and third lumbar ganglia is removed; preservation of the first lumbar ganglion is said to lessen the risk of ejaculatory problems.

Movements, muscles and segmental innervation

Most limb muscles are innervated by neurones derived from more than one segment of the spinal cord. The predominant segmental origin of the nerve supply for each of the muscles of the lower limb and for the movements that take place at the joints of the lower limb is summarized in **Tables 76.1–76.4** (Sharrard 1955). There is no consensus about the contribution that individual spinal nerves make to the innervation of individual muscles, and these listings are not exhaustive. The most positive identifications, which are limited, have been obtained by electrically stimulating spinal nerves and recording the evoked electromyographic activity in the muscles. Much of the information in Tables 76.1–76.4 is based on the clinical appreciation of deficits following lesions to various nerves. At the central nervous level of control, muscles

TABLE 76.1 **Segmental innervation of the muscles of the lower limb**

Segment	Muscles supplied
L1	Psoas major, psoas minor
L2	Psoas major, iliacus, sartorius, gracilis, pectineus, adductor longus, adductor brevis
L3	Psoas major, quadriceps femoris, adductors (magnus, longus, brevis)
L4	Psoas major, quadriceps femoris, tensor fasciae latae, adductor magnus, obturator externus, tibialis anterior, tibialis posterior
L5	Gluteus medius, gluteus minimus, obturator internus, semimembranosus, semitendinosus, extensor hallucis longus, extensor digitorum longus, fibularis tertius, popliteus
S1	Gluteus maximus, obturator internus, piriformis, biceps femoris, semitendinosus, popliteus, gastrocnemius, soleus, fibularis longus, fibularis brevis, extensor digitorum brevis
S2	Piriformis, biceps femoris, gastrocnemius, soleus, flexor digitorum longus, flexor hallucis longus, some intrinsic foot muscles
S3	Some intrinsic foot muscles (except abductor hallucis, flexor hallucis brevis, flexor digitorum brevis, extensor digitorum brevis)

TABLE 76.2 **Segmental innervation of joint movements of the lower limb**

Region	Muscles supplied	Segment
Hip	Flexors, adductors, medial rotators	L1–L3
	Extensors, abductors, lateral rotators	L5, S1
Knee	Extensors	L3, L4
	Flexors	L5, S1
Ankle	Dorsiflexors	L4, L5
	Plantar flexors	S1, S2
Foot	Invertors	L4, L5
	Evertors	L5, S1
	Intrinsic muscles	S2, S3

TABLE 76.3 **Movements, muscles and segmental innervation in the lower limb***

Joint	Movement	Muscle	Innervation	L1	L2	L3	L4	L5	S1	S2	S3
HIP	FLEXION	Psoas major	Spinal nn. L1–3	■	■	▨					
		Iliacus	Femoral n.		■	▨					
		Pectineus	Femoral n. or accessory obturator n.		■	▨					
		Rectus femoris	Femoral n.		▨	■	■				
		Adductor longus	Obturator n.		■	■	▨				
		Sartorius	Femoral n.		▨	▨					
	EXTENSION	Gluteus maximus	Inferior gluteal n.					■	■	▨	
		Adductor magnus	Obturator and tibial nn.		■	■	▨				
		Semitendinosus, semimembranosus, biceps femoris	Tibial and common fibular nn.					▨	■	▨	
	MEDIAL ROTATION	Iliacus	Femoral n.		■	▨					
		Gluteus medius and minimus	Superior gluteal n.				■	■	▨		
		Tensor fasciae latae	Superior gluteal n.				■	■	▨		
	LATERAL ROTATION	Superior and inferior gemelli	Nerve to obturator internus and nerve to quadratus femoris, respectively					▨	▨		
		Quadratus femoris	Nerve to quadratus femoris					▨	▨		
		Piriformis	Nerve to piriformis					▨	■	▨	
		Obturator internus	Nerve to obturator internus					▨	■		
		Obturator externus	Obturator n.			▨	■				
		Sartorius	Femoral n.		▨	▨					
	ADDUCTION	Gracilis	Obturator n.		■	▨					
		Adductor longus	Obturator n.		■	■	▨				
		Adductor magnus	Obturator and tibial nn.		■	■	▨				
		Adductor brevis	Obturator n.		▨	▨					
		Pectineus	Femoral n. or accessory obturator n.		■	▨					
	ABDUCTION	Tensor fasciae latae	Superior gluteal n.				■	■	▨		
		Gluteus medius and minimus	Superior gluteal n.				■	■	▨		
		Piriformis	Nerve to piriformis					▨	■	▨	
KNEE	FLEXION	Semimembranosus	Tibial n.					▨	■	▨	
		Semitendinosus	Tibial n.					▨	■	▨	
		Biceps femoris	Tibial and common fibular nn.					▨	■	▨	
		Gastrocnemius	Tibial n.						▨	▨	
	EXTENSION	Quadriceps femoris:									
		Rectus femoris	Femoral n.		▨	▨	▨				
		Vastus lateralis	Femoral n.		▨	▨	▨				
		Vastus intermedius	Femoral n.		▨	▨	▨				
		Vastus medialis	Femoral n.		▨	▨	▨				
ANKLE	DORSIFLEXION	Tibialis anterior	Deep fibular n.				▨	▨			
		Extensor digitorum longus	Deep fibular n.					▨	▨		
		Extensor hallucis longus	Deep fibular n.					■	▨		
		Fibularis tertius	Deep fibular n.					▨	▨		
	PLANTAR FLEXION	Gastrocnemius	Tibial n.						▨	▨	
		Soleus	Tibial n.						▨	▨	
		Flexor digitorum longus	Tibial n.					▨	■	■	
		Flexor hallucis longus	Tibial n.					▨	■	■	
		Fibularis longus	Superficial fibular n.					▨	▨		
		Tibialis posterior	Tibial n.				▨	▨			
	INVERSION	Tibialis anterior	Deep fibular n.				■	▨			
		Tibialis posterior	Tibial n.				▨	▨			
	EVERSION	Fibularis longus	Superficial fibular n.					▨	▨		
		Fibularis tertius	Deep fibular n.					▨	▨		
		Fibularis brevis	Superficial fibular n.					▨	▨		
TOES	FLEXION	Flexor digitorum longus	Tibial n.					▨	■	■	
		Flexor hallucis longus	Tibial n.					▨	■	■	
		Flexor hallucis brevis	Medial plantar n.						▨	▨	
		Flexor digitorum brevis	Medial plantar n.						▨	▨	
		Flexor accessorius (quadratus plantae)	Lateral plantar n.							▨	▨
		Flexor digiti minimi brevis	Lateral plantar n.							▨	▨
		Abductor hallucis	Medial plantar n.						▨	▨	
		Abductor digiti minimi	Lateral plantar n.							▨	▨
		Lumbricals	Medial and lateral plantar nn.							▨	▨
	EXTENSION	Extensor digitorum longus	Deep fibular n.					■	▨		
		Extensor hallucis longus	Deep fibular n.					■	▨		
		Extensor digitorum brevis	Deep fibular n.					▨	▨		
	ABDUCTION	Abductor hallucis	Medial plantar n.						▨		
		Abductor digiti minimi	Lateral plantar n.						▨	▨	▨
		Dorsal interossei	Lateral plantar n.							▨	▨
	ADDUCTION	Plantar interossei	Lateral plantar n.							▨	▨
		Adductor hallucis	Lateral plantar n.							▨	▨

*Royal blue shading denotes nerve roots from which there is a known dominant contribution. Turquoise shading denotes nerve roots from which the contribution is of similar degree.

TABLE 76.4 **The movements and muscles tested to determine the location of a lesion in the lower limb**

Movement	Muscle	Upper motor neurone*	Spinal nerve level	Reflex	Nerve
Hip flexion	Iliopsoas	++	L1, L2		Femoral
Hip adduction	Adductors	+	L2, L3	(+)	Obturator
Hip extension	Gluteus maximus		L5, S1		Inferior gluteal
Knee flexion	Hamstrings	+	S1		Sciatic
Knee extension	Quadriceps femoris		L3, L4	++	Femoral
Ankle dorsiflexion	Tibialis anterior	++	L4		Deep fibular
Ankle eversion	Fibularis longus and fibularis brevis		L5, S1		Superficial fibular
Ankle inversion	Tibialis posterior		L4, L5		Tibial
Ankle plantar flexion	Gastrocnemius/ soleus	+	S1, S2	++	Tibial
Great toe extension	Extensor hallucis longus		L5		Deep fibular

*The muscles listed in the 'Upper motor neurone' column are those that are preferentially affected in upper motor neurone lesions. The root level is the principal supply to a muscle.

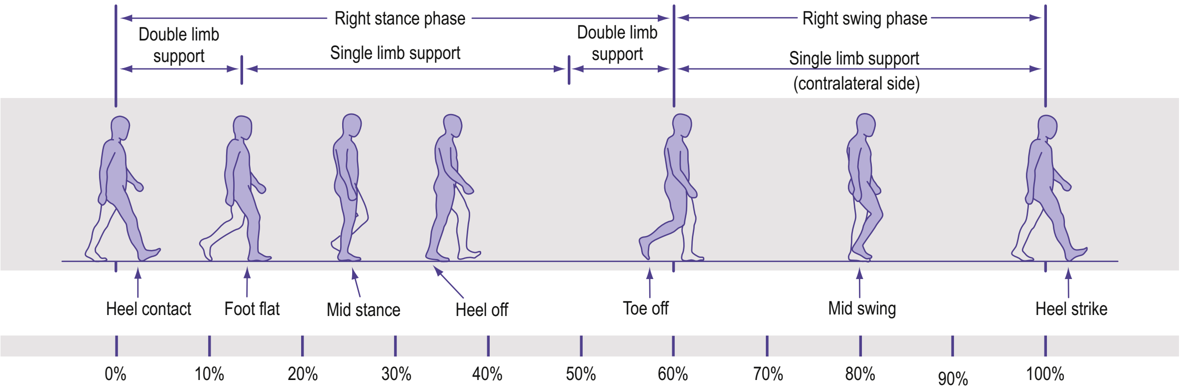

Fig. 76.15 An overview of the different phases of a normal gait cycle.

are not recognized as individual actuators but as components of movement, which means that they can contribute to several types of motion, acting variously as prime movers, antagonists, fixators or synergists. Some muscles have been included in more than one place in Table 76.3 on the basis that a muscle that acts across one joint can produce a combination of movements (e.g. flexion with medial rotation, or extension with adduction) and a muscle that crosses two joints can produce more than one movement.

Reflexes

Knee reflex (L2–L4). With the patient sitting and the knee supported and partially flexed, the patellar ligament is struck with a finger or percussion hammer. This results in extension of the knee joint.

Ankle reflex (S1, S2). With the patient sitting and the lower limb laterally rotated and partially flexed at the hip and knee, the foot is dorsiflexed by the examiner and the calcaneal tendon struck with a percussion hammer. This results in plantar flexion of the foot.

Plantar reflex. The plantar reflex is an important part of the clinical examination of the central nervous system. With the foot relaxed, the outer edge of the sole is stroked longitudinally with a blunt object such as the tip of the handle of a percussion hammer. Normally, this action elicits flexion of the toes. However, in patients with upper motor neurone lesions, the response includes extension of the great toe (Babinski's sign).

Neurological localization of a lesion

Available with the *Gray's Anatomy* e-book

GAIT

Overview of the gait cycle

Walking involves a cyclic repetition of movements that propel the body forwards (see Video 76.1). The gait cycle is usually defined as the interval between initial heel contact of one foot to the successive heel contact of the same foot. The terms used to describe the point at which the foot makes first contact with the ground varies. Heel contact or heel strike are used in some instances, but individuals with altered or pathological gait patterns may not be able to initiate contact with their heel (Wall et al 1987) and therefore the terms initial contact or foot strike are also common. Each gait cycle consists of two steps which together constitute a stride, and can be divided into two main phases: stance phase (when the foot is in contact with the ground) and swing phase (when the foot is off the ground).

At normal walking speed, the stance phase accounts for approximately 60% of the gait cycle, and swing phase occupies 40%. There are two single-limb support phases (where one foot is on the ground) which alternate with two periods of double-limb support (where both feet are on the ground simultaneously; at 0–10% and 50–60% of the gait cycle) (**Fig. 76.15**). Both stance and swing can be further divided into a number of different events or phases, although the terms ascribed to these vary.

The stance phase is usually described to consist of five events: heel contact, foot flat, mid stance, heel off and toe off. The gait cycle starts with heel contact, the point at which the heel meets the ground. With the foot still positioned in front of the body, foot flat (where the entire plantar surface of the foot is in contact with the ground) is reached, at approximately 10% of the gait cycle. This is sometimes also referred to as the 'loading response'. Transition is made to mid stance, the point at which the body's weight is aligned directly above the planted foot (at approximately 30% of the gait cycle). The point at which the heel rises off the ground is termed heel off (between approximately 30% and 40% of the gait cycle), and this occurs just before the contralateral foot makes contact with the ground (the double stance phase). The last event of stance is toe off defined as the instant the toes come off the ground (60% of the gait cycle). Push off is a term used to describe the period of ankle plantar flexion (approximately 40–60% of the gait cycle), but there is a lack of consensus on the primary functional role of this phase of gait (Zelik and Adamczyk 2016). The swing phase typically comprises three events: early (or initial), mid and late (or terminal) swing. Early swing encompasses the period between toe off to mid swing (60–75% of the gait cycle). Mid swing occurs slightly before to just after the mid stance phase of the opposite limb (approximately 75–85% of the gait cycle) and late swing encompasses the period from the end of mid swing through to heel contact (85–100% of the gait cycle) (Simoneau and Heiderscheit 2017) (see Fig. 76.15).

Joint kinematics and muscle activity

Available with the *Gray's Anatomy* e-book

SURFACE ANATOMY

Skeletal landmarks

Pelvis

The anterior superior iliac spine lies superior to the lateral end of the inguinal skin crease: the iliac crest is palpable from this point along its entire length (**Fig. 76.18**). A line (Tuffier's) or plane (supracristal) joining the most superior aspects, or highest points, of the iliac crests commonly crosses the vertebral body of L4 or L4–L5 intervertebral disc, corresponding to the region from the L3–L4 to the L4–L5 interspinous space (Render 1996, Walsh et al 2006) (**Fig. 76.19**). The supracristal plane is used as a landmark when performing a lumbar puncture. Its localization via palpation, especially in females and patients with a high body mass index (BMI), often places it at a more superior vertebral level, up to the L2–L3 interspinous space (Chakraverty et al 2007, Kim et al 2007). Inferiorly, the line may intersect the vertebral column at the spinous process of L5. Vertebral column flexion in the adult has little effect on the level of the supracristal plane (Kim et al 2003). In neonates, the plane sits at the L4–L5 interlaminar space level whilst prone, moving to the superior one third of the vertebral body of L5 during vertebral column flexion (van Schoor et al 2014): palpation commonly locates the plane at the L4–L5 or L5–S1 interspinous space (Baxter et al 2016).

The iliac crest terminates posteriorly as the posterior superior iliac spine, which is marked by an indentation in the overlying skin. Palpation places the posterior superior iliac spines most commonly at the level of the spinous process of S1 or S2 (range spinous process of S1 or S2). Radiographic assessment shows that the inferior margin of the posterior superior iliac spine consistently marks the S2 spinous process in most individuals (McGaugh et al 2007). The inferior limit

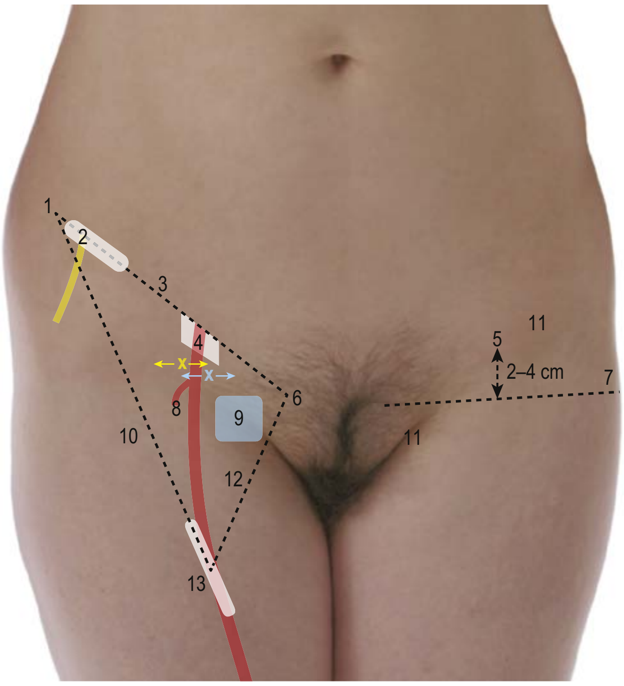

Fig. 76.18 The inguinal region and femoral triangle. Key: 1, anterior superior iliac spine; 2, lateral femoral cutaneous nerve and its zone of emergence into femoral triangle (white): range 0.3–7.3 cm (mean 2.1–3.5 cm) from the anterior superior iliac spine; 3, inguinal ligament; 4, femoral artery and zone of emergence (mid-inguinal point ±1.5 cm either side) into femoral triangle (white): the femoral nerve (yellow cross) and vein (blue cross) sit adjacent to the artery, and follow any variation in its position (arrows); 5, femoral head: located 2–4 cm above the midpoint of a line joining the greater trochanter to pubic tubercle; 6, pubic tubercle; 7, line joining the greater trochanter to the pubic tubercle; 8, profunda femoris artery: commonly arises 6.5±1.5 cm distal to the mid-inguinal point, on or just superior to the inguinal/groin crease; 9, zone of saphenofemoral junction location: almost always sits within a 3 cm × 3 cm zone situated 1–4 cm lateral and 0–3 cm inferior to the pubic tubercle; 10, sartorius; 11, inguinal/groin crease; 12, adductor longus; 13, zone of femoral artery entry into the adductor canal (white), approximately 28 cm (range 24–31 cm) from the anterior superior iliac spine. (Adapted from Drake R, Vogl AW, Mitchell AW et al (eds) Gray's Atlas of Anatomy. Elsevier, Churchill Livingstone. Copyright 2008.)

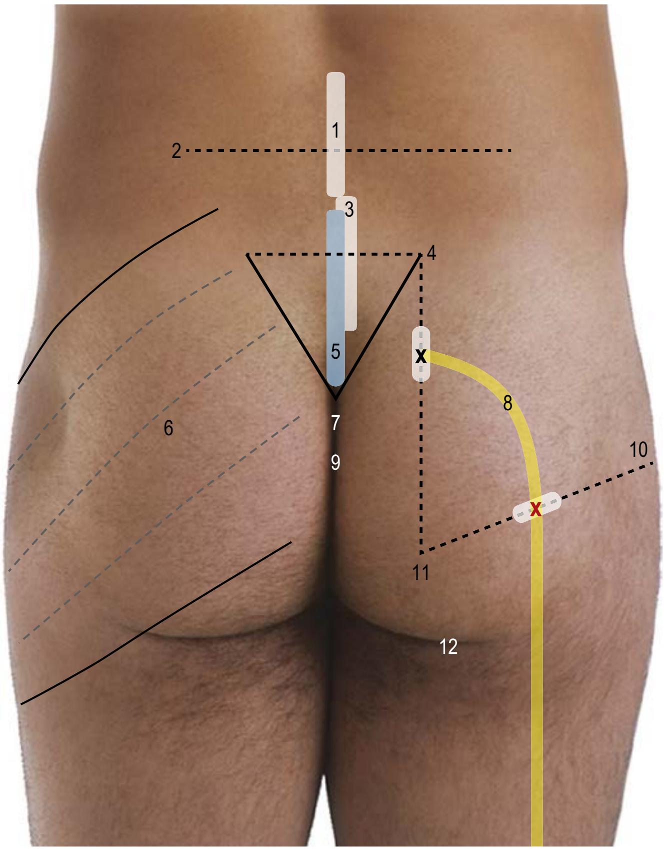

Fig. 76.19 The gluteal region and sciatic nerve. Key: 1, zone of supracristal plane intersection with vertebrae (white): ranges from the L2–L3 interspinous space to the spinous process of L5; 2, highest point of iliac crests (supracristal plane or Tuffier's line): most commonly intersects the vertebrae from the spinous process of L4 to the L4–L5 interspinous space; 3, zone of intersection between the vertebrae and a horizontal plane between the posterior superior iliac spines (white): ranges from the spinous process of L5 to S3 when determined via palpation (note the overlap with 5); 4, posterior superior iliac spine and interspinous plane: marked by a skin indentation, and commonly intersects the vertebral body or spinous process of S1 or S2; 5, zone of termination of dural sac (blue): ranges from L5–S1 intervertebral disc to vertebral body of S4, most commonly sits level with the inferior part of S1 to the inferior part of S2 vertebral body (note the overlap with 3); 6, gluteus maximus; 7, sacral hiatus bordered by sacral cornua, located at the apex of an approximately equilateral triangle with baseline measurement taken between the posterior superior iliac spines; 8, course of sciatic nerve: from a point 30 ± 5% of the distance down a line joining the posterior superior iliac spine to the ischial tuberosity (black X and white zone) to a point 50 ± 5% of the way along a line joining the ischial tuberosity to the upper greater trochanter (red X and white zone); 9, tip of coccyx within intergluteal cleft; 10, greater trochanter; 11, ischial tuberosity; 12, gluteal fold. (Adapted from Drake R, Vogl AW, Mitchell AW et al (eds) Gray's Atlas of Anatomy. Elsevier, Churchill Livingstone. Copyright 2008.)

of the dura mater, and therefore of the subarachnoid space, typically ranges from the inferior part of the vertebral body of S1 to the inferior part of the vertebral body of S2 (equating to the spinous processes of S1and S2, respectively) (Hansasuta et al 1999, Binokay et al 2006, Senoglu et al 2013): the inferior limit of the dura mater may vary from the L5–S1 intervertebral disc to the vertebral body of S4. The ischial tuberosity is covered by gluteus maximus and is palpable during hip flexion. The coccyx is palpable in the superior part of the intergluteal (natal, anal) cleft, which is the deep vertical midline groove between the left and right gluteal muscle masses. The sacral hiatus sits superior to the tip of the coccyx at a mean of 5.8 ± 0.9 cm and is flanked by the raised and palpable sacral cornua, which serve as reliable landmarks (Aggarwal et al 2009). In adults, the hiatus can be located at the inferior apex of an inverted equilateral triangle with its base measured between the posterior superior iliac spines; this arrangement may not always be observed (Senoglu et al 2005). The triangle is an unreliable marker of the sacral hiatus in neonates and young infants, since surface identification of the sacral hiatus by palpation is only possible when the sacral cornua are developed (Mirjalili et al 2015). The linear distance from the apex of the sacral hiatus to the termination of the dural sac is variable, from a mean of 3.2 ± 1.2 cm to 4.5 ± 1.2 cm, which is of relevance to caudal anaesthetic administration.

Femur

The greater trochanter of the femur is palpable on the superior part of the lateral thigh, inferior to the midpoint of the iliac crest and approximately level with a horizontal plane passing through the pubic tubercle (see Fig. 76.18). It can be used to guide surgeons during anterolateral approaches to the hip joint. A line (Nelaton's/Roser–Nelaton's) drawn from the anterior superior iliac spine to the ischial tuberosity passes superior to or over the greater trochanter. In a patient with hip dislocation or femoral neck fracture, the greater trochanter can be palpated superior to this line. The femoral shaft is not directly palpable but runs inferomedially from a point 2–3 cm medial to the lateral aspect of the greater trochanter to the midpoint of the patella. The femoral head sits 2–4 cm superior to the midpoint of a line joining the superior margin of the greater trochanter and the pubic tubercle.

When the knee is flexed, the medial surface of the medial condyle and the lateral surface of the lateral condyle of the femur may both be palpated, and portions of the articular surfaces of the femoral condyles can be examined on each side of the patellar ligament. The adductor tubercle is palpable superior to the medial femoral condyle, and is found by tracing the vertical tendon of adductor magnus inferiorly to its insertion.

Patella

The entire patella is palpable except for its articular surface. When the quadriceps femoris is relaxed in the fully extended knee, the patella can

In clinical practice, it is only necessary to test a relatively small number of muscles in order to determine the location of a lesion. Any muscle to be tested must satisfy a number of criteria. It should be visible, so that wasting or fasciculation can be observed, and the muscle consistency with contraction can be felt. It should have an isolated action, so that its function can be tested separately. It should help to differentiate between lesions at different levels in the neural axis and in the peripheral nerve, or between peripheral nerves. It should be tested in such a way that normal can be differentiated from abnormal, so that slight weakness can be detected early with reliability. Some preference should be given to muscles with an easily elicited reflex. Table 76.4 gives a list of movements and muscles chosen according to these criteria; in practice, these tests would be combined with tests of sensory function. Knowledge of the sequence in which motor branches leave a peripheral nerve to innervate specific muscles is helpful in localizing the level of a lesion.

The following provides an overview of lower limb joint kinematics of the pelvis, hip, knee, and ankle and foot during gait, along with associated muscle activity in each of the three planes. While most of the joint motion during gait takes place in the sagittal plane, important but smaller movements are also observed in the coronal (frontal) and horizontal (transverse) planes. Most of the data relating to muscle activity are derived from electromyographic studies, and relate to walking at a normal speed of about 1.3–1.4 m/sec (Murray et al 1964, Bohannon 1997). While general patterns of muscle activity are outlined (**Fig. 76.16**), it is important to note that significant variation may occur between individuals. In addition, other factors such as age, sex and gait speed can influence some aspects of joint kinematics and muscle activity. The trunk and upper limbs assist in maintaining balance and minimizing energy expenditure during gait, but their contributions are not considered in this section. For further details on gait, including kinetics (study of forces), please refer to Simoneau and Heiderscheit (2017).

Pelvis

In the sagittal plane, pelvic movement occurs through small arcs of anterior and posterior pelvic tilt (approximately 2–4° in total) and results from the forces produced by the hip joint capsule and the hip flexor and extensor muscles. At heel contact the pelvis is neutral, moving into a small amount of posterior pelvic tilt during the first period of double limb support. The pelvis then tilts anteriorly, reaching a position of anterior pelvic tilt just after mid stance. During the second half of the stance phase, the pelvis tilts posteriorly until around toe off. This changes to anterior pelvic tilt during early to mid swing, and then to posterior pelvic tilt in late swing (Thurston and Harris 1983).

A total excursion of about 10–15° of pelvic movement occurs in the coronal plane, termed 'pelvic-on-femoral (hip) abduction and adduction', in relation to the stance limb (Ch. 77, 'Movements'). During weight acceptance the contralateral side of the pelvis drops (pelvic on femoral adduction), due to the effect of body weight, controlled by eccentric activity of the hip abductors on the stance limb. During the remainder of the stance phase (20–60% of the gait cycle), the contralateral side of the pelvis (swing limb) is elevated (pelvic on femoral abduction) by concentric contraction of the hip abductors.

In the horizontal plane, pelvic rotation occurs around a vertical axis of rotation (Baker 2001). The total amount of pelvic rotation varies (range approximately 4–14°), and it is uncertain if differences exist between sexes. At heel contact of the right foot, the ipsilateral anterior superior iliac spine is further forward compared with its contralateral counterpart. Pelvic rotation occurs in a medial (internal, counterclockwise) direction for the first 15–20% of the gait cycle, and then changes to lateral (external, clockwise) rotation, whereby the contralateral anterior superior iliac spine moves forward along with the swing limb (Simoneau and Heiderscheit 2017). The anterior portions of gluteus medius and gluteus minimus contribute to the forward contralateral rotation of the pelvis (Semciw et al 2013, 2014).

Hip

In the sagittal plane, the hip moves through two arcs of motion during a normal stride, being extended during stance and flexed through the swing phase. The total range of motion is approximately 40–50°, with an average of 30–40° flexion and 5–10° extension. Maximum hip flexion is reached just before heel contact, at which stage the hip starts to extend in preparation for weight acceptance. Hip extension is produced by gluteus maximus (active in the first 30% of the gait cycle, from heel contact through to mid stance), and the hamstring muscles (active during the first 10% of gait cycle), with some assistance from adductor magnus during weight acceptance (Lyons et al 1983) (see Fig. 76.16). At heel contact, gluteus maximus also acts to control trunk flexion. The hip progressively extends as the body moves forward over the fixed foot, with maximum hip extension occurring just before toe off. Hip flexion is initiated at push off, and during the swing phase the hip flexors (including iliopsoas, rectus femoris and sartorius), assisted initially by the hip adductors, function to move the lower limb forwards and to elevate it to enable toe clearance. Iliopsoas activates before toe off, and together with the other hip flexors is active throughout approximately the first 50% of the swing phase (Keagy et al 1966, Andersson et al 1997); hip flexion during the second half of the swing phase occurs as a result of forward momentum obtained in early swing. The hip extensors contract eccentrically late in swing to decelerate the flexing hip.

As described in relation to pelvic kinematics, hip motion in the coronal plane during stance primarily occurs through 'pelvic-on-femoral' abduction and adduction. Gluteus medius and gluteus minimus, the two primary hip abductor muscles, demonstrate two bursts of activity during stance, and are most active during the first 40% of the gait cycle (see Fig. 76.16). These muscles initially function eccentrically to control the lowering of the contralateral pelvis on the side of the swing limb. They then contract concentrically, and are critical to ensuring frontal pelvic stability across the stance phase, particularly during single limb support (Ch. 77). During the swing phase the hip returns to its neutral frontal plane position, achieved through a combination of the motion of the pelvis (about the stance limb) and that of the advancing femur.

Hip medial and lateral rotation in the horizontal plane equates to approximately 6–7° in each direction. At heel contact, the femur is slightly laterally rotated. For most of the stance phase (the first 50% of the gait cycle) a net medial rotation movement occurs at the hip, as the contralateral pelvis is moved forward in the horizontal plane by the medial rotator muscles (tensor fasciae latae, anterior gluteus medius and gluteus minimus). This muscle group, together with the lateral rotators (six short lateral rotators, posterior gluteus medius, gluteus maximus), control the alignment of the hip in the horizontal plane. In particular, eccentric contraction of the lateral rotators may be important in controlling medial rotation of the lower limb during early stance. From early to mid-swing, the hip rotates laterally as the lower limb advances forward, and from mid swing to heel contact slight medial rotation is apparent.

Knee

The knee moves through a total sagittal range of motion from nearly full extension to approximately 65° flexion during the gait cycle (Bruening et al 2015). At heel contact, the knee is flexed slightly (approximately 5°), and continues to flex during the initial 15% of the gait cycle, to reach about 15–20°. This slight knee flexion contributes to shock absorption during weight acceptance onto the stance limb, and is controlled by eccentric activity of the quadriceps muscles (see Fig. 76.16). As body weight is transferred onto the stance limb, the knee gradually extends via contraction of the quadriceps muscles, attaining near full extension at the end of stance. The knee then begins to flex, serving to shorten the lower limb so to facilitate toe clearance, reaching 35° flexion at toe off and maximum flexion of approximately 60° at mid swing. Most of the knee flexion during swing occurs passively as a result of the hip flexing, with a potential small contribution from the plantar flexor muscles (Winter 1983, Sutherland 2001). Between mid to late swing the knee extends, nearly reaching full extension, and then begins to flex slightly just before heel contact. In the period just before to just after heel contact, the hamstrings contract eccentrically to decelerate knee extension. Co-contraction of the quadriceps and hamstring muscles in early stance, push off and late swing (highest levels of muscle excitation) (see Fig. 76.16) preserve knee joint stability during normal gait (Strazza et al 2017).

The knee is relatively stable in the coronal plane, but variation is evident in the direction of the reported motions. The knee is abducted slightly at heel contact (Lafortune et al 1992) and moves through a small range (approximately 3°) of inconsistent abduction–adduction during the first 80% of stance, with up to 5° of adduction apparent throughout the final 20% of stance (Ishii et al 1997, Benoit et al 2007). Throughout swing, the knee is abducted, with maximum abduction occurring near the point of maximum knee flexion.

Similar to coronal plane motion, knee movements in the horizontal plane are small (approximately 5–10° in total) and highly variable between individuals. The tibia is rotated laterally just before heel contact, with medial rotation initiated at heel contact and sustained during the first 25% of stance. At mid stance the tibiofemoral joint is

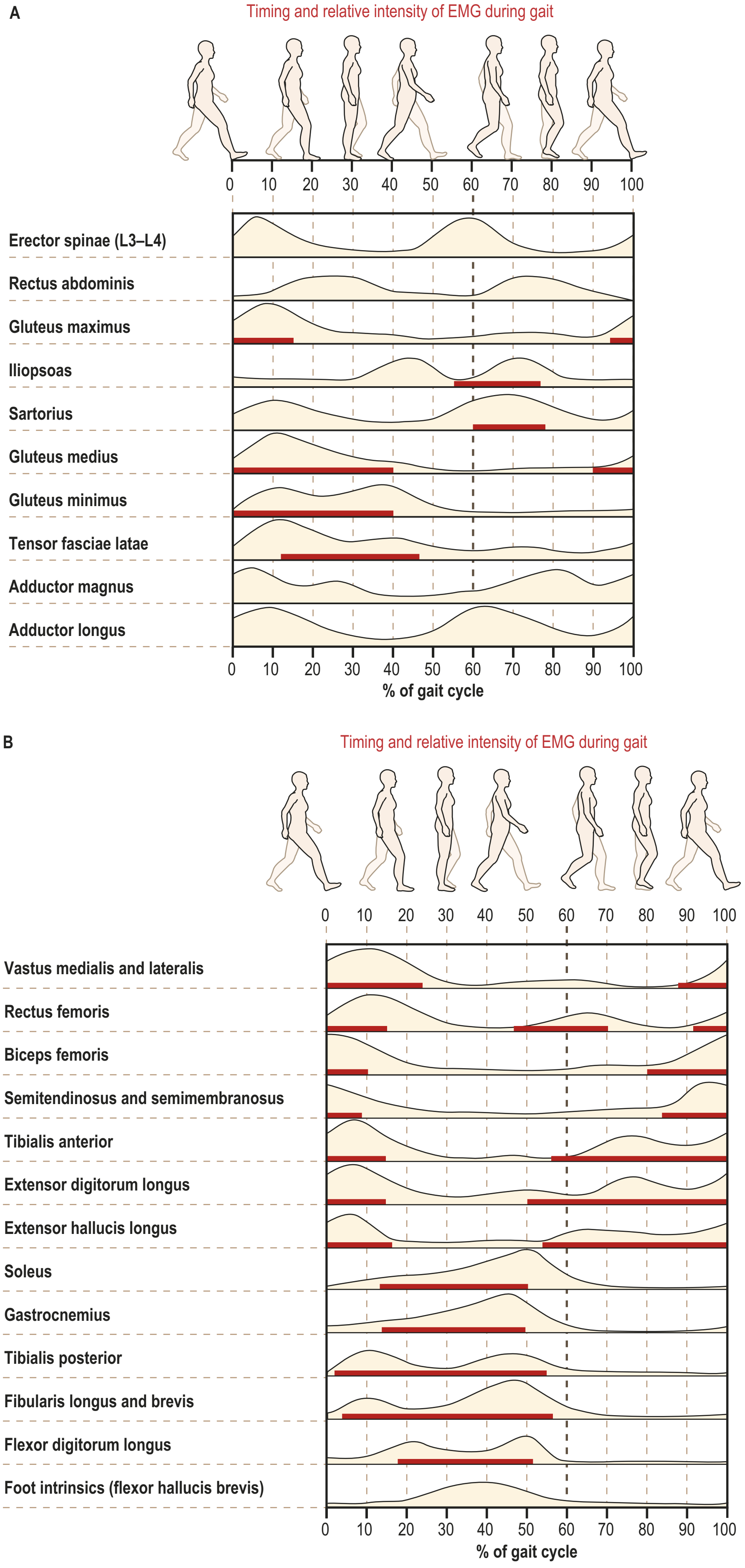

Fig. 76.16 A–B, An electromyographic (EMG) illustration showing the timing (red bars) and relative intensity (light brown shading) of muscle activation during walking. The Y axes depict the relative intensity of muscle activation for each muscle as a proportion of their maximum value obtained during the gait cycle. Based on this scaling, all muscles nearly fill the full vertical dimension of their respective graph, therefore precluding direct comparison of magnitude of muscle activation across muscles. (Adapted with permission from Simoneau GG, Heiderscheit BC Kinesiology of walking. In: Neumann DA (ed) Kinesiology of the Musculoskeletal System: Foundations for Rehabilitation, 3rd ed. Elsevier, Mosby. Copyright 2017.)

close to neutral, with lateral tibial rotation occurring in conjunction with the final 30° of extension, an event referred to as the 'screw home' movement or rotation (Levens et al 1948). Initiation of knee flexion, through to mid swing, is accompanied by medial rotation of the tibia (Perry and Burnfield 2010).

Ankle and foot

The total excursion of ankle (talocrural) joint plantar flexion and dorsiflexion in the sagittal plane is approximately 33°. At heel contact the foot is positioned in neutral or slight plantar flexion (0–5°). A short phase of rapid plantar flexion follows during the first 8% of the gait cycle, controlled by the eccentric activity of the ankle dorsiflexors (tibialis anterior, extensors digitorum longus and hallucis longus), enabling the foot to be positioned flat on the ground (Gray and Basmajian 1968, Hunt et al 2001). During stance (8–45% of the gait cycle), dorsiflexion occurs as the tibia moves forward over the foot. Dorsiflexion in this phase of gait reaches a maximum of approximately 10°, and is controlled by the plantar flexor muscles (gastrocnemius and soleus) which work eccentrically from just after foot flat to heel off to control the forward progression of the leg (see Fig. 76.16).

Just after heel off, the ankle begins to plantar flex due to concentric plantar flexion muscle contraction (including fibularis longus), with a major burst of activity occurring around push off (see Fig. 76.16): there are contrasting opinions as to whether push off contributes to the production of forward motion of the body during normal gait (centre of mass acceleration) and/or acceleration of leg swing (Hof et al 1992, Zelik and Adamczyk 2016). As the heel leaves the ground, gradual extension (up to 45°) occurs at the metatarsophalangeal joints. Due to the indirect connections between the deep plantar fascia and the toes, extension, of the great toe particularly, increases tension throughout the medial longitudinal arch (referred to as the 'windlass effect'). Maximum plantar flexion (approximately 15–20°) occurs just after toe off. During swing phase the ankle dorsiflexors (particularly tibialis anterior) contract concentrically to return the ankle to a neutral position, allowing the toes to clear the ground (Winter and Yack 1987). The intrinsic muscles of the foot are active from mid stance to toe off, stabilizing the forefoot and raising the medial longitudinal arch (see Fig. 76.16).

In the coronal plane interaction between the subtalar and transverse tarsal joints results in the tri-planar movements of supination and pronation. At heel contact, the subtalar joint is inverted (approximately 2–3°), and then rapidly everts until mid stance (Hunt et al 2001). Tibialis posterior is active throughout most of the stance phase, with muscle activity peaking from just after heel contact and then again at about 35% of the gait cycle (see Fig. 76.16). This muscle acts to resist pronation of the hindfoot (calcaneus and talus), and works synergistically with fibularis longus, to assist with mediolateral foot stability (Murley et al 2009, 2014). Following mid stance, the subtalar joint reverses its direction of movement, inverting (through concentric invertor muscle activity) to reach a neutral position about the time of heel off (Arndt et al 2004). Calcaneal inversion continues between heel off and toe off to reach approximately 6° of inversion, and during swing the hind foot returns to a slightly inverted position prior to heel contact.

Little ankle and foot movement occurs in the horizontal plane, and so this is not considered in this section.

Development of walking

The average child sits at 6 months, crawls at 9 months, walks with support at 10 months and walks without support around 12–14 months. The characteristic early gait matures rapidly and is similar to that of the adult by about 4–5 years (Sutherland et al 1980, Chester et al 2006). Some minor changes occur up to 7 years, which are largely a reflection of neurological development but are also related to stature (Volpe 2001). Early gait is jerky, unsteady and wide-based. Initial ground contact varies, and heel–toe, whole foot and toe–heel are all possible. Generally, a plantar flexed posture is adopted, which contrasts with the adult pattern. In adults, heel contact is accompanied by a straight knee which then flexes. A child strikes the ground with a flexed knee which is then extended in response to weight-bearing, and a short time is spent in single-leg stance (**Fig. 76.17**). The earliest changes are development of heel contact, knee flexion during stance, adult pattern of joint angles and reciprocal upper limb swing. Maturation is associated with diminution of base width and an increase in step length and velocity (Sutherland et al 1980).

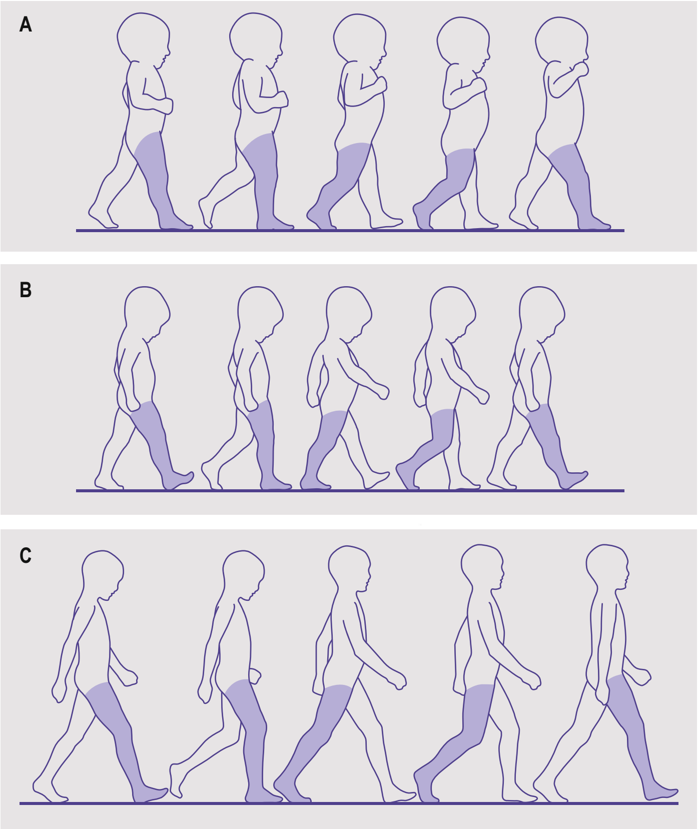

Fig. 76.17 Development of a mature gait. **A**, A 1-year-old infant. Note the flexed elbows and lack of arm swing. The foot is plantar flexed at contact. **B**, A 3-year-old child. Arm swing is now present, as is heel strike. **C**, A 6-year-old child. There is now an adult-type gait. (With permission from Benson MKD, Fixsen JA, MacNicol MF (eds) 2001 Development of mature gait. In: Children's Orthopaedics and Fractures, 2nd ed. Edinburgh: Churchill Livingstone.)

Ageing

With ageing, walking becomes more challenging as a consequence of reduced lower limb muscle strength and range of motion and impaired balance (Pirker and Katzenschlager 2016). Mean gait speed is relatively consistent up to about 70 years of age, and then declines by up to 1.2% per year (Alcock et al 2013), reaching less than 1.0 m/sec in those aged 80 years and over (Bohannon and Williams Andrews 2011). This decrease in speed is a function of both a shorter step length and an increase in time spent in the double-limb support phase; step width also increases thereby increasing the base of support, and gait becomes more variable and asymmetrical due to stride-to-stride fluctuations (Lord et al 2013). Alterations in kinematic attributes, that are independent of a reduced gait speed, include reduced hip extension with an associated increase in anterior pelvic tilt (Kerrigan et al 1998). Reductions in plantar flexion range with decreased ankle plantar flexion power during push off are also evident. Some of these age-related changes may indicate the adoption of a more stable walking pattern, to compensate for reduced physical ability (Menz et al 2003), or represent adaptations to alterations in sensory or motor systems (Aboutorabi et al 2016). Altered gait performance influences falls risk, and progressive deterioration in gait parameters occurs with cognitive impairment, with greater declines evident in the advanced stages of dementia (Allali et al 2016).

Running

The spatiotemporal descriptors of running are defined in a similar way to those of walking (see Video 76.2). However, while walking involves two periods of double-limb support phases (where both feet are on the ground simultaneously), in running each foot is on the ground (stance phase) for 40% (jogging, approximately 2.0–3.5 m/sec) to approximately 25% (sprinting, greater than 8.0 m/sec) of the stride (Högberg 1952, Mann and Hagy 1980). This results in an aerial phase – the 'double-float' phase – when neither foot is on the ground, a feature that demarcates running from walking. An increase in running speed is generally the result of taking longer strides and increasing stride frequency (Dorn et al 2012). The faster an individual runs, the shorter the stance phase, with the main difference between running and sprinting being the acceleration at the start of a sprint (Haugen et al 2019).

The stance and swing phases of the running gait cycle can be divided into a number of key events that include heel contact, mid stance, heel off, toe off and mid swing (Heiderscheit and Simoneau 2017). The start of the running cycle is defined as the instant the foot comes into contact with the ground, often referred to as foot strike. This can occur in three ways, with either the rearfoot (hindfoot or heel), midfoot or forefoot contacting the ground first; the rearfoot strike pattern is most common, accounting for up to approximately 85% of all runners (Lieberman et al 2010, Almeida et al 2015). Mid stance occurs when the body's weight is aligned directly above the planted foot or when the knees are side by side (at approximately 20% of the gait cycle), with the 'loading response' occupying the first 15% of the cycle. The timing of heel off (approximately 25% of the cycle) and toe off (30–40% of the cycle) varies with running speed. Like walking, mid swing occurs around the middle of the swing phase (approximately 70% of the running gait cycle).

The other periods of the running gait cycle include pre swing, early swing and late swing. During pre swing, which occurs between heel off and toe off, the lower limb muscles generate mechanical energy for propulsion. Early swing encompasses the period between toe off to mid swing, while late swing occurs from the end of mid swing through to foot strike (Heiderscheit and Simoneau 2017).

There are many factors that influence running mechanics including age, sex, speed and type of surface, and injuries are common. While the overall kinematics of running are similar to those of walking, the magnitude and timing of joint motion is different. For further details on the biomechanics of running, refer to Novacheck (1998) and Heiderscheit and Simoneau (2017).

TABLE 76.5 Common sites for iatrogenic upper limb nerve injury in primary care (adapted from Wallis et al 2018)

Nerve	Site	Procedure
Sciatic nerve	Gluteal region	Intramuscular injection
Lateral cutaneous of thigh	Anterior thigh	
Common fibular nerve	At the level of the fibular neck	Minor surgical procedure (skin lesion removal)
Sural nerve	Posterior leg	

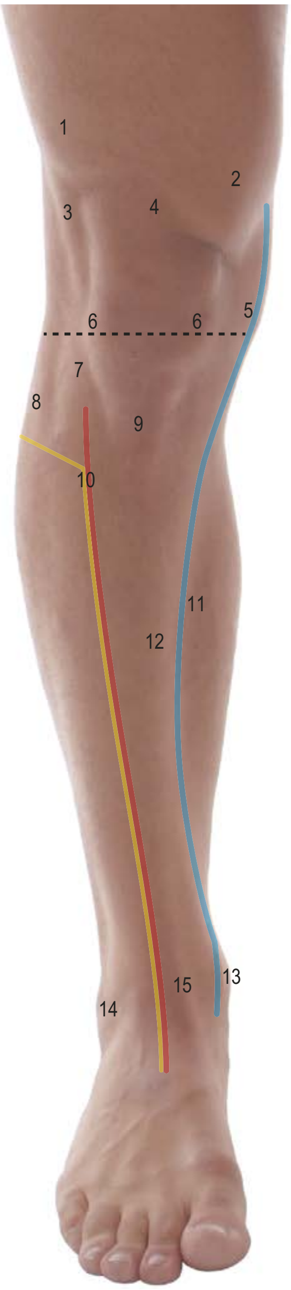

Fig. 76.20 The anterior aspect of the knee and leg. Key: 1, vastus lateralis; 2, vastus medialis; 3, iliotibial tract; 4, quadriceps tendon overlying suprapatellar bursa; 5, sartorius; 6, anterior horns of menisci: located above knee joint line (dotted line) and either side of patellar ligament; 7, tubercle of the iliotibial tract (Gerdy's); 8, fibular head; 9, patellar ligament insertion into tibial tuberosity; 10, anterior tibial artery and deep fibular nerve: the artery passes from halfway between fibular head and tibial tuberosity to a point halfway between the medial and lateral malleoli; 11, soleus and long saphenous vein (blue); 12, medial tibial border (subcutaneous); 13, medial malleolus: long saphenous vein and saphenous nerve pass anterior; 14, lateral malleolus; 15, tendon of tibialis anterior. (Adapted from Drake R, Vogl AW, Mitchell AW et al (eds) Gray's Atlas of Anatomy. Elsevier, Churchill Livingstone. Copyright 2008.)

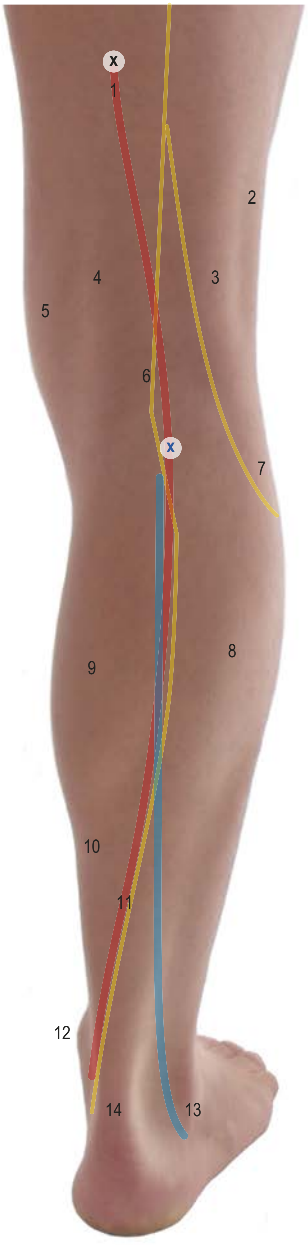

Fig. 76.21 The posterior aspect of the knee and leg. Key: 1, popliteal artery: passing from a point (black X) 2.5 cm medial to the posterior midline of the thigh at the junction of its middle and inferior one thirds to a point halfway between the femoral condyles/the midaxial line of the calf (blue X); 2, iliotibial tract; 3, tendon of biceps femoris and common fibular nerve (yellow) located medially; 4, semimembranosus and semitendinosus; 5, gracilis; 6, popliteal fossa; 7, head of fibula; 8, lateral head of gastrocnemius; 9, medial head of gastrocnemius; 10, soleus; 11, posterior tibial artery and tibial nerve: pass along a line from the midaxial line of the posterior leg, at the level of the fibular neck, to a point one-third of the way from the posterior border of the medial malleolus to the distal insertion of the calcaneal tendon; 12, medial malleolus; 13, lateral malleolus and short saphenous vein passing posteriorly; 14, calcaneal tendon insertion into calcaneus. (Adapted from Drake R, Vogl AW, Mitchell AW et al (eds) Gray's Atlas of Anatomy. Elsevier, Churchill Livingstone. Copyright 2008.)

be tilted and moved on the distal aspect of the femur. The inferior limit of the apex of the patella is located superior to the knee joint line by 1–2 cm (Fig. 76.20).

Knee

The patella and the femoral condyles have been described above. The tibial condyles form visible and palpable landmarks on the medial and lateral sides of the patellar ligament (see Fig. 76.20). The latter may be traced inferiorly from the apex of the patella to the tibial tuberosity, which is both visible and palpable. When the knee is flexed, the anterior margins of the tibial condyles can be felt: each forms the lower boundary of a depression at the side of the patellar ligament. The lateral condyle is the more prominent of the two. The joint line of the knee (tibiofemoral joint) corresponds to the upper margins of the tibial condyles and can be approximated by a line drawn around the limb at this level. The anterior horns of the menisci lie in the angles between this line and the edges of the patellar ligament. The iliotibial tract is attached to a bony prominence, the tubercle of the iliotibial tract (Gerdy's tubercle), on the anterior surface of the lateral tibial condyle which is normally approximately 1 cm inferior to the joint line and about 2 cm superolateral to the tibial tuberosity.

The head of the fibula forms a slight surface elevation on the posterior part of the proximal lateral leg. It lies vertically below the posterior part of the lateral condyle of the femur, 1–2 cm inferior to the knee joint line.

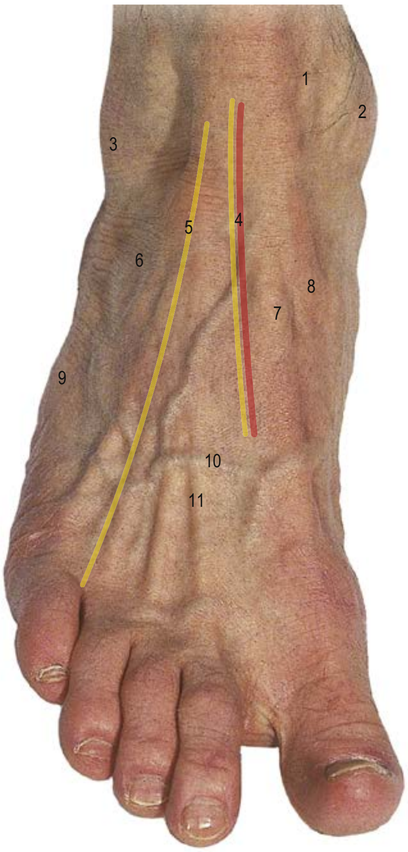

Fig. 76.22 The dorsal aspect of the foot and ankle. Key: 1, long saphenous vein and saphenous nerve; 2, medial malleolus; 3, lateral malleolus; 4, dorsalis pedis artery and deep fibular nerve: located immediately lateral to the tendon of extensor hallucis longus; 5, intermediate dorsal cutaneous nerve: visible passing towards the fourth toe during toe and ankle plantarflexion; 6, extensor digitorum brevis; 7, tendon of extensor hallucis longus; 8, tendon of tibialis anterior: insertion into medial cuneiform; 9, tuberosity of fifth metatarsal; 10, dorsal venous arch of foot; 11, tendon of extensor digitorum longus (to the second toe). (Adapted from Drake R, Vogl AW, Mitchell AW (eds) Gray's Anatomy for Students, 2nd ed. Elsevier, Churchill Livingstone. Copyright 2010.)

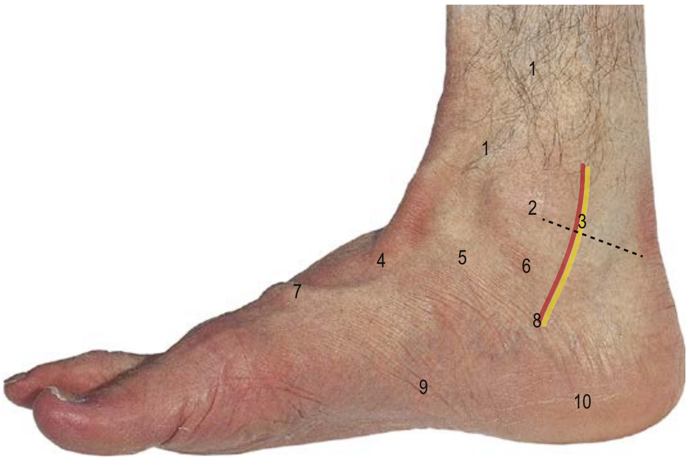

Fig. 76.23 The medial aspect of the foot and ankle. Key: 1, long saphenous vein and saphenous nerve; 2, medial malleolus; 3, posterior tibial artery and tibial nerve: located approximately one-third of the distance along a line passing from the posterior border of the medial malleolus to the distal part (insertion) of the calcaneal tendon; 4, tendon of tibialis anterior: insertion into medial cuneiform; 5, navicular tuberosity and tibialis posterior insertion; 6, sustentaculum tali; 7, dorsal venous arch; 8, region of the posterior tibial artery bifurcation into medial and lateral plantar arteries; 9, medial border of plantar aponeurosis; 10, medial calcaneal tubercle covered by fibro-fatty heel pad. (Adapted from Drake R, Vogl AW, Mitchell AW (eds) Gray's Anatomy for Students, 2nd ed. Elsevier, Churchill Livingstone. Copyright 2010.)

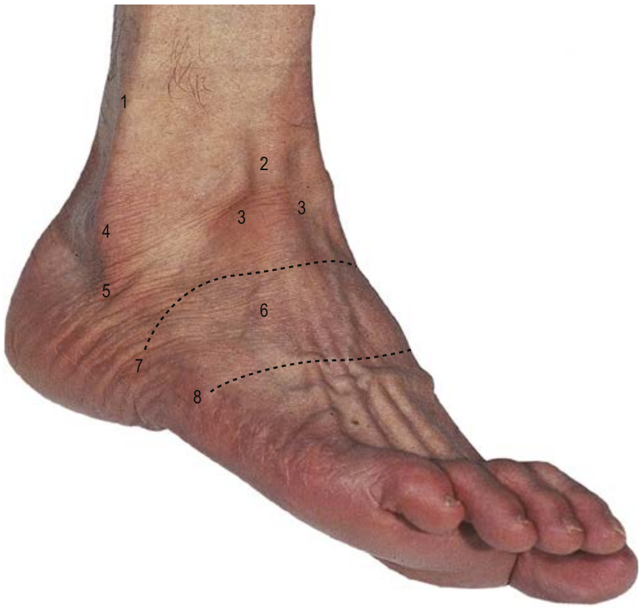

Fig. 76.24 The anterolateral aspect of the foot and ankle. Key: 1, tendons of fibularis longus and brevis; 2, tendons of extensor digitorum longus and fibularis tertius; 3, inferior extensor retinaculum; 4, lateral malleolus; 5, fibular trochlea; 6, tendon of fibularis tertius; 7, transverse tarsal (Chopart) joint line (dotted); 8, tuberosity of fifth metatarsal and tarsometatarsal (Lisfranc) joint line (dotted). (Adapted from Drake R, Vogl AW, Mitchell AW (eds) Gray's Anatomy for Students, 2nd ed. Elsevier, Churchill Livingstone. Copyright 2010.)

Leg and ankle

The subcutaneous medial surface of the tibia corresponds to the flat anteromedial aspect of the leg. Superiorly, this surface merges with the medial condyle of the tibia, and inferiorly, it is continuous with the visible prominence of the medial malleolus of the tibia (see Fig. 76.20; Figs 76.21–76.22). The anterior border of the tibia can be palpated distinctly throughout most of its extent, but inferiorly, it is partially covered by the tendon of tibialis anterior, which lies to its lateral side. The lateral malleolus of the fibula forms a large prominence on the lateral side of the ankle; it descends to a more inferior level than the medial malleolus and is located on a more posterior plane. The lateral aspect of the lateral malleolus is continuous superiorly with an elongated, subcutaneous, triangular area of the inferior shaft of the fibula. The lateral part of the anterior margin of the inferior end of the tibia can be palpated immediately anterior to the base of the lateral malleolus; the line of the ankle joint can be determined from it.

Foot

The anterior part of the upper surface of the calcaneus can be identified on the dorsum of the foot slightly anterior to the lateral malleolus. When the foot is passively inverted, the upper and lateral parts of the head of the talus can be both seen and palpated on the dorsal surface approximately 3 cm anterior to the distal end of the tibia; the extensor tendons cover the talus when the toes are extended. Regional tenderness can indicate a talar neck fracture.

The dorsal aspects of the bodies of the metatarsals can be palpated but they are partly covered by the extensor tendons of the toes. The tuberosity on the base of the fifth metatarsal forms a distinct palpable and visible projection on the lateral border of the foot.

The flat lateral surface of the calcaneus can be palpated on the lateral aspect of the heel and can be traced anteriorly, inferior to the lateral malleolus, where the tendons of fibularis longus and brevis cover it. The fibular (peroneal) trochlea, when sufficiently large, can be palpated as a raised tubercle of bone approximately 2 cm inferior to the tip of the lateral malleolus. A palpable depression just anterior to the lateral malleolus leads to the lateral end of the tarsal sinus.

On the medial side of the foot, the sustentaculum tali can be felt approximately 2 cm inferior to the medial malleolus; the tendon of flexor hallucis longus can be located inferiorly (Fig. 76.23). The tuberosity of the navicular is palpable and usually visible approximately 2.5 cm anterior to the sustentaculum tali. Anterior to this, the medial cuneiform can be identified, with the tendon of tibialis anterior inserting onto it. The superior and medial parts of the joint line between the medial cuneiform and the first metatarsal can be felt as a narrow groove.

When the foot is placed on the ground, it rests on the posterior part of the inferior surface of the calcaneus, the heads of the metatarsals and, to a lesser extent, on its lateral border, and the medial longitudinal arch of the foot is elevated from the ground. The medial and lateral tubercles of the calcaneus can be palpated on its inferior surface through the anterior part of the fibro-fatty heel pad, which covers them and may make their palpation difficult. The heads of the metatarsals are similarly covered by a fibro-fatty pad on the plantar surface of the foot, they are most easily palpated on the dorsum of the foot, with the digits in flexion.

The calcaneocuboid joint is about 2 cm posterior to the tuberosity on the base of the fifth metatarsal and is almost in line with the talonavicular joint: the position of the latter may be gauged from the talar head (**Fig. 76.24**). The calcaneocuboid and talonavicular joints collectively form the transverse tarsal (Chopart) joint. The tarsometatarsal (Lisfranc) joints approximate to a line joining the tip of the tuberosity of the fifth metatarsal to the tarsometatarsal joint of the great toe; the latter is located 2–3 cm anterior/distal to the tuberosity of the navicular and is palpable. The joint between the second metatarsal and the intermediate cuneiform is located 2–3 mm posterior to the line of the other tarsometatarsal joints. The metatarsophalangeal joints are located about 2.5 cm posterior to the web spaces of the toes and are palpable on the dorsal foot, from where they are accessible via a needle.

Musculotendinous and ligamentous landmarks

See **Video 76.3**.

Gluteal region and hip

The bulky prominence of the gluteal region is formed by gluteus maximus, a variable amount of subcutaneous fat and the normal alignment of the pelvis, which angles the ischial tuberosities posteriorly (see Fig. 76.19).

The gluteal fold, an almost horizontal fold of skin located inferior to the main bulk of the gluteal muscles, marks the upper limit of the posterior aspect of the thigh. It does not correspond to the inferior border of gluteus maximus but is formed by fibrous connections between the skin and the deep fascia. The vertical intergluteal (natal, anal) cleft, which separates the left and right gluteal regions inferiorly, begins superiorly level with the vertebral body of S3 or S4. The superior border of gluteus maximus begins on the iliac crest approximately 5–7 cm superolateral to the posterior superior iliac spine and runs inferiorly and laterally towards the apex of the greater trochanter. Its inferior border corresponds to a line drawn from the ischial tuberosity, through the midpoint of the gluteal fold, to a point approximately 9 cm below the greater trochanter. Although gluteus maximus overlaps the ischial tuberosity in the standing position, on sitting, it slides superior to the tuberosity, leaving it free to bear weight. Gluteus maximus can be felt to contract when the hip is extended against resistance. In neonates, gluteus maximus is relatively small and poorly developed.

Gluteus medius completely covers the underlying gluteus minimus. Both muscles lie in a slight depression superolateral to gluteus maximus and inferior to the anterior part of the iliac crest and both pass inferiorly to insert into the greater trochanter. They constitute the major abductors of the hip and can be felt to contract by asking the subject to stand on one limb. The ipsilateral muscles contract to stabilize the centre of gravity and maintain a relatively horizontal pelvic position. Paresis or paralysis causes the pelvis to drop towards the unsupported, contralateral side (Trendelenburg's sign).

Thigh

The inguinal ligament can be felt running between the anterior superior iliac spine and the pubic tubercle, especially when the thigh is abducted and laterally rotated (see Fig. 76.18). The inguinal/groin crease (line of Holden), where the membranous layer of the superficial fascia of the abdomen (Scarpa's fascia) joins the fascia lata of the thigh, lies inferior to the inguinal ligament by a mean of 6.7 ± 1.9 cm and is more inferior to the inguinal ligament in females than in males (7.5 ± 1.9 cm versus 6.3 ± 1.9 cm) (see Fig. 76.18) (Lechner et al 1988).

The femoral triangle is located on the proximal anterior thigh. It is bounded superiorly by the inguinal ligament and laterally by the medial border of the strap-like sartorius, which can be both seen and felt in a reasonably thin and muscular subject when the hip is flexed in the sitting position, while the knee is kept extended and the thigh is slightly abducted and rotated laterally. Sartorius can be traced inferomedially from the anterior superior iliac spine to approximately halfway down the medial side of the thigh; distally, it may be identified as a soft longitudinal ridge passing towards the posterior part (region) of the medial surface of the medial femoral condyle. The adductor group of muscles forms the bulky mass at the upper part of the medial thigh. The medial border of adductor longus forms the medial boundary of the femoral triangle and can be felt as a distinct ridge when the thigh is adducted against resistance. At its superior end, its prominent tendon of origin can be seen and palpated immediately inferior to the pubic tubercle, which is a useful guide to this bony landmark.

The anterior convexity of the anterior thigh is caused by the curvature of the femur covered by the muscle mass of quadriceps femoris. Rectus femoris appears as a raised ridge passing down the anterior aspect of the thigh to the base of the patella, when the sitting subject flexes the hip with the knee extended. Vastus medialis forms a rounded elevation both medial and superior to the patella, and vastus lateralis forms an elevation superolateral to the patella that is more proximal and less pronounced than that of vastus medialis (see Fig. 76.20). Vastus intermedius follows the course of the femoral shaft, and is covered by the three other muscles in the quadriceps group. The thick tendon of adductor magnus can be palpated on the distal medial thigh, deep within the indentation located between vastus medialis anteriorly and gracilis and sartorius posteriorly.

The iliotibial tract, a thickened portion of the deep fascia of the thigh (fascia lata), runs from the lateral aspect of the iliac crest to the tubercle of the iliotibial tract and produces the flattened appearance of the lateral thigh. It forms a defined ridge that is visible on the lateral aspect of the knee either when the knee is extended against gravity or when the contralateral limb is lifted from the floor while standing.

The muscles of the posterior thigh may be palpated from the ischial tuberosity inferiorly along the lateral (biceps femoris) and medial (semitendinosus and semimembranosus) aspects of the posterior thigh.

Knee

The large depression posterior to the knee that is visible when the joint is actively flexed against resistance corresponds to the popliteal fossa. The transverse skin crease of the popliteal fossa lies about 2–3 cm superior to the knee joint line. The fossa is bounded on its superolateral side by the prominent tendon of biceps femoris, which can be palpated between the finger and thumb and traced inferolaterally to the head of the fibula. Three tendons (of semitendinosus, gracilis and semimembranosus) can be felt on the superomedial side of the fossa. Semitendinosus is the most lateral and posterior, while gracilis is the most medial and anterior; both tendons stand out sharply and can be seen when the knee is flexed against resistance and the hip adducted against resistance. The tendon of semimembranosus may be palpated deeply in the interval between the tendons of semitendinosus and gracilis: it is much thicker than the other two tendons and broadens rapidly as it is traced proximally. The superior borders of the medial and lateral heads of gastrocnemius form the inferomedial and inferolateral boundaries, respectively, of the popliteal fossa.

The cord-like fibular collateral ligament may be felt passing from the apex of the fibular head to the lateral epicondyle of the femur when the knee is flexed and laterally directed pressure (varus force) is applied to the medial side of the knee. The medial and lateral patellar retinacula pass from the patella to the medial and lateral femoral condyles, respectively. They are best observed and palpated on either side of the patella when pushing the patella laterally or medially, whilst the knee is fully extended and quadriceps femoris is relaxed.

Leg

The muscles in the anterior osteofascial compartment of the leg form a raised prominence over the superior two-thirds of its anterolateral aspect; this prominence is accentuated when the foot is actively dorsiflexed against resistance. The muscles continue as tendons in the inferior one third of the leg. The tendon of tibialis anterior can be seen just lateral to the anterior border of the distal tibia and traced inferiorly and medially across the anterior aspect of the ankle to the medial cuneiform (see Figs 76.20, 76.22). The other tendons cannot be examined satisfactorily superior to the ankle. The tendons of tibialis posterior and flexor digitorum longus can be felt (rather indistinctly) immediately superior to the posterior border of the medial malleolus and close to the medial border of the tibia, when the foot is actively inverted and plantar flexed.

On the lateral aspect of the leg, fibularis longus can be seen as a narrow almost vertical ridge following the line of the fibula during active eversion and plantar flexion of the foot. It covers and hides fibularis brevis. The shaft of the fibula can only be palpated indistinctly between its neck and the area above the lateral malleolus.

The bulky muscular prominence of the posterior leg is formed by gastrocnemius and soleus, both of which can be identified either when the foot is plantar flexed against resistance, or when the heel is raised from the ground by standing on tiptoes (see Fig. 76.21). The two heads of gastrocnemius unite to form the inferior borders of the popliteal fossa. The medial head of gastrocnemius descends to a more inferior level than the lateral head. Soleus lies deep to gastrocnemius; when tensed, it bulges from under the medial and lateral margins of gastrocnemius, particularly on the lateral side, and its fleshy belly extends to a more distal level. Both muscles end inferiorly in the prominent calcaneal tendon, which can be palpated between the finger and thumb and followed inferiorly to its insertion into the posterior aspect of the calcaneus.

Foot

When the toes are actively extended, the bellies of extensor digitorum brevis and extensor hallucis brevis form a small elevation on the dorsal foot, just anterior to the lateral malleolus (see Fig. 76.22). During inversion of the ankle and extension of the toes, the prominent tendon of tibialis anterior is visible on the medial side of the dorsal foot, passing inferiorly and medially to the medial cuneiform. The tendon of extensor hallucis longus can be identified laterally as it passes toward the great toe; the tendons of extensor digitorum longus and fibularis tertius are further lateral as they pass deep to the inferior extensor retinaculum and immediately anterior to the lateral part of the distal tibia. More distally, the tendons of extensor digitorum longus and fibularis tertius diverge and can be traced to their insertions.

The tendon of tibialis posterior winds posterior to the medial malleolus and then curves anteriorly in the interval between the medial malleolus and the sustentaculum tali to reach the tuberosity of the navicular (see Fig. 76.23). The tendon is visible and palpable posterior to the malleolus when the foot is forcibly plantar flexed and inverted. The tendon of flexor digitorum longus lies immediately posterolateral to that of tibialis posterior. It curves forwards inferior to tibialis posterior and lies on the medial aspect of the sustentaculum tali. From there, it passes anteriorly and laterally to the centre of the plantar foot, where it divides into four tendons that pass to the base of the distal phalanx of each of the lateral four toes. The tendon of flexor hallucis longus lies inferior to, and grooves, the sustentaculum tali. As it passes towards the base of the distal phalanx of the great toe, it crosses the line of the flexor digitorum longus opposite the interval between the sustentaculum tali and the tuberosity of the navicular. Abductor hallucis may be seen or palpated in some subjects as a bulky mass along the medial border of the foot, passing from the medial calcaneal tubercle to the medial side of the base of the proximal phalanx of the great toe, just distal to the first metatarsophalangeal joint.

When the toes are maximally dorsiflexed, the plantar aponeurosis is easily palpated along the medial border of the foot, from just distal to the heel pad to the first metatarsophalangeal joint. It originates from the calcaneal tubercles, which may be palpable through the anterior part of the heel pad. Pain in the region of the medial calcaneal tubercle is commonly associated with plantar fasciitis.

Vessels, pulses and nerves

Arteries

The femoral artery enters the anterior thigh either halfway between the anterior superior iliac spine and the pubic symphysis (mid-inguinal point), or up to 1.5 cm on either side (medial to lateral) of this point (Hale et al 2010) (see Fig. 76.18). The artery normally passes directly anterior to the hip joint; its course may be represented by the upper two-thirds of a line joining its entry point into the thigh with the adductor tubercle, when the thigh is flexed, slightly abducted and rotated laterally. The profunda femoris artery (deep artery of the thigh) normally arises from the lateral side of the femoral artery, 6.5 ± 1.5 cm distal to the mid-inguinal point (Choy et al 2013), which is most commonly at or just superior to the level of the inguinal/groin crease (Lechner et al 1988). The femoral artery enters the adductor canal at the apex of the femoral triangle, about 27 cm (range 24–31 cm) from the anterior superior iliac spine along the line of sartorius, a point that is almost always distal to the midpoint of the thigh. It then travels deep to sartorius and the vastoadductor membrane towards the adductor hiatus. The length of the adductor canal is variable: 11.5 cm (range 8.9–14.5 cm) measured with ultrasound imaging (Wong et al 2017) and 7.6 cm (range 5.5–15 cm) in cadaveric dissections (Tubbs et al 2007). The adductor hiatus is commonly located approximately one third of the way up a line joining the midpoint of the femoral interepicondylar line to the superior part of the greater trochanter (Kale et al 2012).

Alternatively the adductor hiatus is located 65–75% of the way down a line drawn to join the midinguinal point (the midpoint of a line drawn between the anterior superior iliac spine and the pubic symphysis) to the adductor tubercle.

The course of the popliteal artery can be represented by a line extending from the junction of the middle and inferior one-third of the thigh, 2.5 cm medial to its posterior midline, to a point halfway between the femoral condyles, and continuing inferolaterally to the level of the tibial tuberosity, medial to the fibular neck, where it bifurcates into the anterior and posterior tibial arteries (see Fig. 76.21).

The anterior tibial artery may be represented by a line extending from a point halfway between the tibial tuberosity and the fibular head to a point midway between the anterior borders of the two malleoli (see Fig. 76.20). It passes onto the dorsal foot and becomes the dorsalis pedis artery, lateral to the tendon of extensor hallucis longus. The dorsalis pedis artery travels to the space between the bases of the first and second metatarsal bones. Near the second tarsometatarsal joint it gives off the arcuate artery which curves laterally over the bases of the second to fifth metatarsals.

The posterior tibial artery may be represented by a line drawn from a midaxial point on the posterior leg (approximately midway between the tibial condyles) at the level of the neck of the fibula, to a point one-third of the way between the posterior border of the medial malleolus and the distal part (insertion) of the calcaneal tendon (see Figs 76.21, 76.23). The same line represents the course of the tibial nerve. The nerve initially lies lateral to the popliteal artery, but then crosses the vessel to sit on its medial side. The posterior tibial artery bifurcates into the plantar arteries halfway between the medial malleolus and the medial calcaneal tubercle, approximately 1–2cm inferior to the inferior border of the medial malleolus.

The medial plantar artery passes anteriorly towards the base of the first metatarsal, where it branches. The lateral plantar artery passes obliquely laterally, towards the midpoint of the fifth metatarsal, reaching a point approximately 2–3 cm medial to the tuberosity of the fifth metatarsal. The deep plantar arch passes medially from the proximal end of the fourth to the proximal end of the first intermetatarsal space. Plantar and dorsal metatarsal arteries branch from the plantar arch and arcuate arteries, respectively, and pass along the intermetatarsal spaces toward the web spaces where they divide into plantar or dorsal digital arteries. These, together with the respective digital nerves, pass along the medial and lateral sides of the toes.

Pulses

Femoral artery. The pulsations of the femoral artery can be felt at its entry point into the proximal femoral triangle, where it can be compressed against either the superior pubic ramus or the hip joint. The pulse of the femoral artery is of value in assessing whether there is any significant cardiac output in cases of circulatory collapse. It is a common site for catheter insertion for radiological examinations such as cardiac angiography and for arterial puncture for blood gas analysis.

Popliteal artery. The pulse of the popliteal artery is the most difficult of the peripheral pulses to feel because the artery lies deep in the popliteal fossa. It is best examined with the subject lying supine or prone, with the knee flexed in order to relax the otherwise tense popliteal fascia that roofs the popliteal fossa. The popliteal pulse is then felt over the midline of the fossa by deep pressure against the popliteal surface of the femur.

Posterior tibial artery. The pulse of the posterior tibial artery can be felt by gentle palpation posterolateral to the medial malleolus as the artery lies between the tendons of flexor hallucis longus and flexor digitorum longus, approximately one-third of the way along a line connecting the posterior border of the medial malleolus to the distal part (insertion) of the calcaneal tendon.

Dorsalis pedis artery. The dorsalis pedis arterial pulse is found by palpation against the underlying tarsal bones, immediately lateral to the tendon of extensor hallucis longus, in the region extending from the midpoint between the malleoli to the proximal end of the first intermetatarsal space.

Veins

The femoral vein is located immediately medial to the femoral artery pulse, where it can be accessed (see Fig. 76.18). While femoral vein puncture is relatively easy and enables access to the right atrium, the use of this approach is relatively unpopular for long-term cannulation because of a greater incidence of thrombosis and sepsis. However, it is a useful site for venous sampling in a patient with collapsed veins. For femoral vein cannulation, the skin puncture site is approximately 1 cm medial to the femoral artery and just inferior to the inguinal ligament.

The dorsal venous arch of the foot is visible and curves across the metatarsals (see Fig. 76.22). The long saphenous vein arises from the medial end of the arch, and the short saphenous vein arises from the lateral end. The long saphenous vein can be seen and palpated anterior to the medial malleolus, after which it runs superiorly and posteriorly across the distal medial surface of the tibia: this is a useful site for surgical venous access (cut-down) or venous harvesting for cardiac bypass surgery (see Figs 76.20, 76.23). The vein then runs proximally along the posterior part of the medial border of the tibia, where it is accompanied by the saphenous nerve, to reach a point about 7–10 cm posterior to the medial patellar border. From here, the vein ascends the thigh to the saphenous opening, where it passes deep to enter the femoral vein. The saphenofemoral junction is almost always located in a 3 cm×3 cm zone located 1–4 cm lateral and 0–3 cm inferior to the pubic tubercle (Mirjalili et al 2014) (see Fig. 76.18). The junction may be nearer to the pubic tubercle in younger and thinner subjects. A saphena varix may form at the junction, producing a swelling.

The course of the short saphenous vein may be represented by a line passing superiorly along the midline of the posterior leg, from the posterior surface of the lateral malleolus to the popliteal fossa; together with the sural nerve, this vein is the key anatomical guide to surgical dissection of the popliteal fossa (see Fig. 76.21).

Nerves

The femoral nerve, or its terminal branches, is located immediately lateral to the femoral artery pulse in the proximal femoral triangle.

The surface marking for the course of the saphenous nerve in the leg matches that of the long saphenous vein (see above). The lateral femoral cutaneous nerve enters the femoral triangle 2.1–3.5 cm (range 0.3–7.3 cm) inferomedial to the anterior superior iliac spine, deep to the inguinal ligament (see Fig. 76.18) (Grothaus et al 2005, Bjurlin et al 2007, Ropars et al 2009). It then passes over the lateral border of sartorius up to 11.3 cm distal to the anterior superior iliac spine and over the anterior border of tensor fasciae latae 2.4–9.2 cm distal to the anterior superior iliac spine. The nerve is at risk of damage during anterolateral surgical approaches to the hip.

The course of the sciatic nerve can be represented by a curved line that starts at a point 30 ± 5% of the distance down a line joining the posterior superior iliac spine to the ischial tuberosity, and passes to a point 50 ± 5% along a line joining the ischial tuberosity to the greater trochanter (see Fig. 76.19) (Currin et al 2015). It then continues vertically and inferiorly in the midline of the posterior aspect of the thigh, deep to biceps femoris, to the superior apex of the popliteal fossa, where it divides into the tibial and common fibular nerves (if it has not already done so at a more superior level). In children up to 10 years of age, the sciatic nerve in the gluteal region is most commonly located within the middle one third of two reference lines: a line joining the posterior superior iliac spine to the ischial tuberosity and a line joining the greater trochanter to the ischial tuberosity (Selkirk et al 2016).

The surface marking for the course of the tibial nerve in the leg matches that of the posterior tibial artery (see above). The course of the sural nerve at the ankle can be approximated by a line running parallel to the calcaneal tendon that is situated halfway between the tendon and the lateral malleolus: this position is variable and the sural nerve is at risk from surgery in this region.

The course of the common fibular nerve can be indicated by a line that passes from the superior apex of the popliteal fossa, along the inferomedial side of the tendon of biceps femoris towards the neck of the fibula (see Fig. 76.21). The nerve then curves inferiorly and anteriorly around the neck of the fibula approximately 3 cm distal to the apex of the fibular head. The common fibular nerve is palpable medial and distal to the tendon of biceps femoris and over the neck of the fibula, although here it becomes less distinct as it passes deep to the origin of fibularis longus. The nerve is at particular risk of damage at the neck of the fibula, from either a tightly applied plaster cast or a fracture.

The deep fibular nerve starts on the lateral aspect of the neck of the fibula, passes downwards and medially, and becomes associated with the anterior tibial artery, with which it is landmarked (see Fig. 76.21). The superficial fibular nerve also begins on the lateral aspect of the neck of the fibula. It passes inferiorly along the line of the fibula to a point on the anterior border of fibularis longus, at the junction of the middle and inferior one-thirds of the leg, where it pierces the deep fascia to become subcutaneous and divides into intermediate and medial dorsal cutaneous branches. The intermediate dorsal cutaneous branch is normally both visible and palpable as a fine ridge passing over the dorsolateral aspect of the ankle and foot toward the fourth toe, especially with the ankle and toes in plantarflexion (see Fig. 76.22). The medial dorsal cutaneous branch is rarely visible and passes towards the second toe. These superficial nerves are at risk from surgery in the anterior ankle region (especially during arthroscopy).

Several of the nerves within the lower limb can be iatrogenically damaged along their course by relatively minor procedures (**Table 76.5**).

Clinical procedures

Regional nerve blocks

Nerves can be effectively anaesthetized with local anaesthetic injection for surgical or post-injury pain relief. Common injection sites for the lower limb are around the hip for thigh and knee pain, and around the ankle for foot surgery. For the deeper nerves around the hip, ultrasound guidance enables the anaesthetist to secure an accurate needle position and to monitor the distribution of the local anaesthetic in real time (Munirama and McLeod 2013). For example, blockade of the sciatic nerve in the gluteal region, femoral nerve in the anterior thigh and obturator nerve in the medial thigh may be undertaken to provide pain relief following total knee replacement; the tibial nerve at the posteromedial ankle, the sural nerve at the posterolateral ankle and the superficial fibular nerves at the anterior ankle may all be anaesthetized at the ankle to allow ‘awake foot surgery’.

Intramuscular injection

Intramuscular injections into the gluteal region using the classic dorsogluteal approach, with injections sited in the superior lateral quadrant, should be avoided to prevent iatrogenic damage to the sciatic nerve. Ventrogluteal approaches reduce the risk of iatrogenic neurovascular injury and are now recommended (Wallis et al 2018). For this approach, the palm of the examiner’s hand, contralateral to the side being injected, is placed over the greater trochanter with the index finger pointing toward the anterior superior iliac spine and the remaining fingers abducted. The injection is made at the centre of the region bordered by the index finger, the iliac crest and the middle finger. Many so-called ‘intramuscular’ injections given into the gluteal region are actually given into the fat due to an insufficient needle length. Another safe alternative is to inject into the lateral aspect of the thigh (vastus lateralis).

Joint injection and aspiration

Careful aseptic technique is essential for all joint aspirations and injections.

Hip. Intra-articular hip injections are typically performed under fluoroscopic or ultrasonographic guidance. With the patient lying supine, and after the positions of the femoral artery and the anterior superior iliac spine have been marked out, the needle is introduced anteriorly, approximately 5 cm distal to the anterior superior iliac spine and 4 cm lateral to the femoral arterial pulse, and passed posteriorly, a little proximally and medially. An alternative technique that is dependent on relative distances from surface landmarks, rather than imaging guidance, utilizes the site of the proximal anterolateral portal for hip arthroscopy as the point of needle insertion (Masoud and Said 2013).

Knee. The lateral retropatellar approach is used. With the patient supine and the knee extended, the needle is introduced at the level of the superior border of the patella and guided towards the suprapatellar bursa.

Popliteal fossa. Sciatic nerve blocks at the popliteal fossa in infants and children can be effectively performed above the popliteal skin crease by correcting the adult landmark of 10 cm by the calculated ratio of the femoral shaft length of a child to the femoral shaft length of an adult (Bernière et al 2008).

Ankle. The anterior approach entails introducing the needle between the tendons of tibialis anterior and extensor hallucis longus with the foot partially plantar flexed.

Arthroscopy portals

The placement of portals for arthroscopy is important for maximizing surgical access for visualization and for surgical instruments, and also for avoiding damage to structures such as nerves and blood vessels.

Hip. Arthroscopy of the hip is used for conditions such as femoro-acetabular impingement, acetabular labral tears, chondral defects and extra-articular causes of hip pain. A variety of entry portals have been described. The anterolateral portal is sited on the skin approximately 4 cm lateral to the femoral artery pulse and 4 cm inferior to the inguinal ligament. Under fluoroscopy, a needle traversing the skin 30–45° proximally is advanced into the joint. Other more lateral portals can be used; the lateral femoral cutaneous nerve and the sciatic nerve are potentially at risk.

Knee. The knee is the joint most frequently examined arthroscopically. The standard portals are placed anteriorly. When the knee is flexed at a right-angle, 'soft triangles' bordered by the patellar ligament, the femoral condyles and the tibia and anterior horns of the menisci are palpable on either side of the superior third of the patellar ligament. Small incisions can be made in the apices of these triangular areas at about the level of the inferior pole of the patella for the anterolateral portal, and slightly lower for the anteromedial portal. These portals will allow passage of an arthroscope and instruments, with good access to most of the joint. The patellar ligament and the infrapatellar branch of the saphenous nerve are at risk from the skin incisions. The nerve is less vulnerable than the ligament; its position is variable but it usually lies below the appropriate portal sites. In the days of open meniscal surgery, the nerve was usually divided and painful neuroma formation was not uncommon.

Posteromedial and posterolateral portals are useful when better access to the posterior knee is required. The saphenous and common fibular nerves, respectively, are at risk with these approaches, and anatomical knowledge is vital to ensure safe portal placement. Laterally, the incision should be anterior to the tendon of biceps femoris, which can easily be palpated. Medially, the situation is more difficult because the saphenous nerve and long saphenous vein travel superficial to the medial epicondylar region of the knee, approximately a hand's breadth posterior to the medial border of the patella. It is essential that sharp incision includes the skin only, and that dissection down to the joint capsule is undertaken bluntly. If the medial meniscus is sutured, the capsule must be exposed before tying off sutures to avoid ensnaring the nerve.

Ankle. The use of ankle arthroscopy is well established, especially in treating sports-related injuries. Anterior portals are standard. The anteromedial portal can be placed just medial to the tendon of tibialis anterior, in the palpable soft spot. However, this comes close to the long saphenous vein and saphenous nerve; limiting the sharp incision to the skin, followed by blunt deeper dissection, reduces the risk. Alternatively, the anteromedial portal can be chosen to pass between the lateral edge of tibialis anterior and extensor hallucis longus. The anterolateral portal is placed with the help of the arthroscope in the joint to check the position of a preliminary needle passed into it. The portal should pass lateral to fibularis tertius and extensor digitorum longus. The intermediate dorsal cutaneous branch of the superficial fibular nerve is at risk as it crosses the ankle anterior to the lateral malleolus, and therefore it is wise to mark the positions of the nerves and blood vessels with a pen before making any incision. The nerves can usually be felt at the front of the ankle, even in obese patients, and they are often seen if the ankle is pulled into maximal plantar flexion. Posterior ankle arthroscopy is controversial: there is a view that the proximity of the neurovascular bundle (medially) and the sural nerve (laterally) renders the procedure too hazardous. Keeping lateral to the tendon of flexor hallucis longus will safeguard the medial neurovascular bundle.

Placement of surgical incisions

Hip. Surgery of the hip joint is usually undertaken for congenital issues, slipped capital femoral epiphysis in children, trauma or arthroplasty. Anterior and anterolateral approaches, often used in children, put the lateral femoral cutaneous nerve at considerable risk. Even in more lateral approaches, the lateral femoral cutaneous nerve and the femoral and sciatic nerves are all at risk through traction. A popular anterolateral approach to the hip joint involves splitting and separating forwards the anterior part of gluteus medius and vastus lateralis as a single sheet of tissue for subsequent reattachment to the greater trochanter. This technique relies on the anatomical continuity of the tissue. If the splitting of gluteus medius is more than a few centimetres superior to the tip of the greater trochanter, then the superior gluteal nerve and vessels are at risk, and weakness of hip abduction and a limp may result. In the posterior approach to the hip joint, gluteus maximus is incised in the line of its fibres. This is followed by division of the tendons of the short lateral rotators (piriformis, obturator internus and externus and the gemelli) near their trochanteric attachments to reveal the joint capsule. Reflecting these cut tendons medially protects the sciatic nerve. The inferior and superior gluteal nerves are at risk during posterior approaches to the hip.

Knee. Most open knee surgery can be undertaken through an anterior midline longitudinal incision, which gives good access and means that any future surgery can usually be undertaken via the same wound. New incisions run the risk of skin necrosis and poor wound healing as a consequence of interfering with the cutaneous blood supply. Inevitable interruption of cutaneous nerves, including the infrapatellar branch of the saphenous nerve, means that there is always numbness lateral to a longitudinal incision.

The extensile approach to the posterior knee is extensive. The key is to expose the sural nerve and short saphenous vein and to trace them proximally. This will lead the surgeon into the popliteal fossa and, after opening the deep fascia, safely to the neurovascular bundle. The wound crosses a flexure crease. A scar perpendicular to the crease might induce a fixed flexion contracture of the joint and therefore an S-shaped incision is employed where the transverse segment runs in the line of the flexure crease.

Ankle and foot. Incisions around the foot and ankle frequently put cutaneous nerves at risk and such an injury can result in a neuroma. The sural nerve at the ankle has a notorious tendency to form neuromas if transected, often after repair of a ruptured calcaneal tendon.

Bonus e-book content

Fig. 76.1 Gateways from the abdomen, pelvis and perineum to the lower limb.

Fig. 76.2 **C**, Standing anteroposterior radiographs of the lower limbs of a 16-year-old female, in whom the more distal long bone growth plates are still visible.

Fig. 76.7 The source and location of the arterial perforators of the lower limb.

Fig. 76.9 **A**, The long (great) saphenous vein and its tributaries. **B**, The short saphenous vein and its tributaries.

Fig. 76.16 An electromyographic illustration showing the timing and relative intensity of muscle activation during walking.

Fig. 76.17 The development of a mature gait.

Table 76.1 Segmental innervation of the muscles of the lower limb.

Table 76.2 Segmental innervation of joint movements of the lower limb.

Table 76.3 Movements, muscles and segmental innervation in the lower limb.

Table 76.4 The movements and muscles tested to determine the location of a lesion in the lower limb.

Table 76.5 Common sites for iatrogenic upper limb nerve injury in primary care.

Video 76.1 Walking gait cycle.

Video 76.2 Running gait cycle.

Video 76.3 Lower limb surface anatomy.

Key references

Beason LE, Anson BJ 1937 The relation of the sciatic nerve and its subdivisions to the piriformis muscle. Anat Rec 70:1–5.

A classic description of the course of the sciatic nerve, including a classification system of the relation of the sciatic nerve with the piriformis muscle.

Crock HV 1996 Atlas of Vascular Anatomy of the Skeleton and Spinal Cord. London: Martin Dunitz.

A review of the arterial supply of the bones from nutrient vessels, metaphysial arterial branches of the peri-articular anastomoses, and the arteries supplying the muscles that attach to their periosteum.

Dodd H, Cockett FB 1976 The Pathology and Surgery of the Veins of the Lower Limb, 2nd ed. Edinburgh: Churchill Livingstone.

A review of the structure of the superficial and deep veins of the lower extremity. The pathological processes observed when the valves in the perforating veins become incompetent are considered. The aetiological factors and the pathogenesis of varicose veins are discussed.

Harry LE, Sandison A, Pearse MF et al 2009 Comparison of the vascularity of fasciocutaneous tissue and muscle for coverage of open tibia fracture. Plast Reconstr Surg 124:1211–9.

A consideration of the major advantage of using a fasciocutaneous reconstruction in terms of the decreased incidence of bone infection. The aesthetic results and the application to pathologies such as Volkmann's contracture are discussed.

Kosinski C 1926 Observations on the superficial venous system of the lower extremity. J Anat 60:131–42.

A discussion of the venous plexuses within and between some of the lower limb muscles. The two principal superficial veins and their numerous tributaries are discussed and their use as grafts during peripheral vascular surgery, including coronary artery bypass, is considered.

Pontén B 1981 The fasciocutaneous flap: its use in soft tissue defects of the lower leg. Br J Plast Surg 34:215–20.

The first description of lower extremity fasciocutaneous flaps. Their use in the repair of soft tissue defects is discussed.

Ricci S 2017 Anatomy. In: Goldman MP, Guex J-J, Weiss RA (eds) Sclerotherapy: Treatment of Varicose and Telangiectatic Leg Veins, 6th ed. Edinburgh: Elsevier; Ch. 1, pp. 1–26.

An up-to-date guide for the effective management of varicose veins and other vascular anomalies. Details regarding the latest techniques such as foam sclerotherapy, endovenous radiofrequency and laser closure, ambulatory phlebectomy and laser treatment of spider telangiectasia and possible complications are discussed.

Sharrard WJW 1955 The distribution of the permanent paralysis in the lower limb in poliomyelitis: a clinical and pathological study. J Bone Joint Surg Br 37:540–58.

A definition of the innervation patterns of the lower limb. The segmental origin of the nerve supply for each of the muscles of the lower limb and for the movements is discussed. The clinical consequences of damage to these segments are considered.

Simoneau GG, Heiderscheit BC 2017 Kinesiology of walking. In: Neumann DA (ed) Kinesiology of the Musculoskeletal System: Foundations for Rehabilitation, 3rd ed. St Louis: Elsevier; Ch. 15, pp. 653–705.

A recent publication that outlines the kinesiology of walking and includes detailed information on lower limb anatomy, joint kinematics, muscle activity, kinetics and gait dysfunction.

Sterzi G 1910 Il tessuto sottocutaneo [Subcutaneous Tissue]. Florence: Luigi Niccolai.

A discussion of the specific structure of the subcutaneous tissue of the lower limb and its participation in the integrity of the skin.

Taylor GI, Razaboni RM (eds) 1994 Michel Salmon: Anatomic Studies, Book 1. Arteries of the Muscles of the Extremities and Trunk. St Louis: Quality Medical Publishing.

A discussion of the arteries to the muscles of the lower extremity. The pattern of arterial supply is particularly relevant to fracture healing, the spread of infection and malignancy, and the planning of reconstructive surgical procedures.

References

Aboutorabi A, Arazpour M, Bahramizadeh M et al 2016 The effect of aging on gait parameters in able-bodied older subjects: a literature review. Aging Clin Exp Res 28:393–405.

Aggarwal A, Kaur H, Batra YK et al 2009 Anatomic consideration of caudal epidural space: a cadaver study. Clin Anat 22:730–7.

Ahmadian A, Abel N, Dakwar E 2015 Injuries to the nerves of the abdominopelvic region. In: Tubbs RS, Rizk E, Shoja MM et al (eds) Nerves and Nerve Injuries: Volume 2: Pain, Treatment, Injury, Disease and Future Directions. Elsevier Science; Ch. 35, pp. 545–55.

Alcock L, Vanicek N, O'Brien TD 2013 Alterations in gait speed and age do not fully explain the changes in gait mechanics associated with healthy older women. Gait Posture 37:586–92.

Allali G, Annweiler C, Blumen HM et al 2016 Gait phenotype from mild cognitive impairment to moderate dementia: results from the GOOD initiative. Eur J Neurol 23:527–41.

Almeida MO, Davis IS, Lopes AD 2015 Biomechanical differences of foot-strike patterns during running: a systematic review with meta-analysis. J Orthop Sports Phys Ther 45:738–55.

Andersson EA, Nilsson J, Thorstensson A 1997 Intramuscular EMG from the hip flexor muscles during human locomotion. Acta Physiol Scand 161:361–70.

Antle DM, Cormier L, Findlay M et al 2018 Lower limb blood flow and mean arterial pressure during standing and seated work: Implications for workplace posture recommendations. Prev Med Rep 10:117–22.

Apaydin N 2016 Lumbosacral plexus. In: Tubbs RS, Shoja MM, Loukas M (eds) Bergman's Comprehensive Encyclopedia of Human Anatomical Variation. Hoboken: John Wiley & Sons; Ch. 92, pp. 1114–9.

Apaydin N, Basarir K, Loukas M et al 2008 Compartmental anatomy of the superficial fibular nerve with an emphasis on fascial release operations of the leg. Surg Radiol Anat 30:47–52.

Arndt A, Westblad P, Winson I et al 2004 Ankle and subtalar kinematics measured with intracortical pins during the stance phase of walking. Foot Ankle Int 25:357–64.

Baker R 2001 Pelvic angles: a mathematically rigorous definition which is consistent with a conventional clincal understanding of the terms. Gait Posture 13:1–6.

Baxter B, Evans J, Morris R et al 2016 Neonatal lumbar puncture: are clinical landmarks accurate. Arch Dis Child Fetal Neonatal Ed 101:F448–F450.

Beason LE, Anson BJ 1937 The relation of the sciatic nerve and its subdivisions to the piriformis muscle. Anat Rec 70:1–5.

A classic description of the course of the sciatic nerve, including a classification system of the relation of the sciatic nerve with the piriformis muscle.

Benoit DL, Ramsey DK, Lamontagne M et al 2007 In vivo knee kinematics during gait reveals new rotation profiles and smaller translations. Clin Orthop Relat Res 454:81–8.

Bernière J, Schrayer S, Piana F et al 2008 A new formula of age-related anatomical landmarks for blockade of the sciatic nerve in the popliteal fossa in children using the posterior approach. Paediatr Anaesth 18:602–5.

Binokay F, Akgul E, Bicakci K et al 2006 Determining the level of the dural sac tip: magnetic resonance imaging in an adult population. Acta Radiol 47:397–400.

Bjurlin MA, Davis KE, Allin EF et al 2007 Anatomic variations in the lateral femoral cutaneous nerve with respect to pediatric hip surgery. Am J Orthop (Belle Mead NJ) 36:143–6.

Bohannon RW 1997 Comfortable and maximum walking speed of adults aged 20–79 years: reference values and determinants. Age Ageing 26:15–19.

Bohannon RW, Williams Andrews A 2011 Normal walking speed: a descriptive meta-analysis. Physiotherapy 97:182–9.

Bruening DA, Frimenko RE, Goodyear CD et al 2015 Sex differences in whole body gait kinematics at preferred speeds. Gait Posture 41:540–5.

Burrus MT, Werner BC, Starman JS et al 2015 Chronic leg pain in athletes. Am J Sports Med 43:1538–47.

Caggiati A, Bergan JJ, Gloviczki P et al 2002 Nomenclature of the veins of the lower limbs: an international interdisciplinary consensus statement. J Vasc Surg 36:416–22.

Caggiati A, Bergan JJ, Gloviczki P et al 2005 Nomenclature of the veins of the lower limb: extensions, refinements, and clinical application. J Vasc Surg 41:719–24.

Chakraverty R, Pynsent P, Isaacs K 2007 Which spinal levels are identified by palpation of the iliac crests and the posterior superior iliac spines? J Anat 210:232–6.

Chester VL, Tingley M, Biden EN 2006 A comparison of kinetic gait parameters for 3-13 year olds. Clin Biomech (Bristol, Avon) 21:726–32.

Choy KW, Kogilavani S, Norshalizah M et al 2013 Topographical anatomy of the profunda femoris artery and the femoral nerve: normal and abnormal relationships. Clin Ter 164:17–19.

Cormack GC, Lamberty BG 1984 Fasciocutaneous vessels: their distribution on the trunk and limbs, and their clinical application in tissue transfer. Anat Clin 6:121–31.

Craig A 2015 Nerve compression/entrapment sites of the lower limb. In: Tubbs RS, Rizk E, Shoja MM et al (eds) Nerves and Nerve Injuries: Volume 2: Pain, Treatment, Injury, Disease and Future Directions. Elsevier Science; Ch. 48, pp. 755–70.

Crock HV 1996 Atlas of Vascular Anatomy of the Skeleton and Spinal Cord. London: Martin Dunitz.

A review of the arterial supply of the bones from nutrient vessels, metaphysial arterial branches of the peri-articular anastomoses, and the arteries supplying the muscles that attach to their periosteum.

Cruveilhier J 1841 Descriptive Anatomy. London: Whittaker.

Currin SS, Mirjalili SA, Meikle G et al 2015 Revisiting the surface anatomy of the sciatic nerve in the gluteal region. Clin Anat 28:144–9.

Dodd H, Cockett FB 1976 The Pathology and Surgery of the Veins of the Lower Limb, 2nd ed. Edinburgh: Churchill Livingstone.

A review of the structure of the superficial and deep veins of the lower extremity. The pathological processes observed when the valves in the perforating veins become incompetent are considered. The aetiological factors and the pathogenesis of varicose veins are discussed.

Dorn TW, Schache AG, Pandy MG 2012 Muscular strategy in human running: dependence of running speed on hip and ankle muscle performance. J Exp Biol 215:1944–56.

Doya H, Haraguchi N, Niki H et al 2010 Proposed novel unified nomenclature for range of joint motion: method for measuring and recording for the ankles, feet, and toes. J Orthop Sci 15:531–9.

Gray EG, Basmajian JV 1968 Electromyography and cinematography of leg and foot ('normal' and flat) during walking. Anat Rec 161:1–15.

Greiner TM 2007 The jargon of pedal movements. Foot Ankle Int 28:109–25.

Grossman MG, Ducey SA, Nadler SS et al 2001 Meralgia paresthetica: diagnosis and treatment. J Am Acad Orthop Surg 9:336–44.

Grothaus MC, Holt M, Mekhail AO et al 2005 Lateral femoral cutaneous nerve: an anatomic study. Clin Orthop Relat Res 437:164–8.

Hale SJ, Mirjalili SA, Stringer MD 2010 Inconsistencies in surface anatomy: the need for an evidence-based reappraisal. Clin Anat 23:922–30.

Hansasuta A, Tubbs RS, Oakes WJ 1999 Filum terminale fusion and dural sac termination: study in 27 cadavers. Pediatr Neurosurg 30:176–179.

Harry LE, Sandison A, Pearse MF et al 2009 Comparison of the vascularity of fasciocutaneous tissue and muscle for coverage of open tibia fracture. Plast Reconstr Surg 124:1211–9.

A consideration of the major advantage of using a fasciocutaneous reconstruction in terms of the decreased incidence of bone infection. The aesthetic results and the application to pathologies such as Volkmann's contracture are discussed.

Haugen T, McGhie D, Ettema G 2019 Sprint running: from fundamental mechanics to practice – a review. Eur J Appl Physiol 119:1273–87.

Heiderscheit BC, Simoneau GG 2017 Kinesiology of running. In: Neumann DA (ed) Kinesiology of the Musculoskeletal System: Foundations for Rehabilitation, 3rd ed. St Louis: Elsevier; Ch. 16, pp. 706–27.

Hof AL, Nauta J, van der Knaap ER et al 1992 Calf muscle work and segment energy changes in human treadmill walking. J Electromyogr Kinesiol 2:203–16.

Högberg P 1952 Length of stride, stride frequency, 'flight' period and maximum distance between the feet during running with different speeds. Arbeitsphysiologie 14:4313–6.

Hunt AE, Smith RM, Torode M 2001 Extrinsic muscle activity, foot motion and ankle joint moments during the stance phase of walking. Foot Ankle Int 22:31–41.

Ishii Y, Terajima K, Terashima S et al 1997 Three-dimensional kinematics of the human knee with intracortical pin fixation. Clin Orthop Relat Res 434:144–50.

Kale A, Gayretli O, Ozturk A et al 2012 Classification and localization of the adductor hiatus: a cadaver study. Balkan Med J 29:395–400.

Keagy DR, Brumlik J, Bergan JJ 1966 Direct electromyography of the psoas major muscle in man. J Bone Joint Surg Am 48:1377–82.

Kerrigan DC, Todd MK, Della Croce U et al 1998 Biomechanical gait alterations independent of speed in the healthy elderly: evidence for specific limiting impairments. Arch Phys Med Rehabil 79:317–22.

Kim JT, Jung CW, Lee JR et al 2003 Influence of lumbar flexion on the position of the intercrestal line. Reg Anesth Pain Med 28:509–11.

Kim HW, Ko YJ, Rhee WI et al 2007 Interexaminer reliability and accuracy of posterior superior iliac spine and iliac crest palpation for spinal level estimations. J Manipulative Physiol Ther 30:386–9.

Kosinski C 1926 Observations on the superficial venous system of the lower extremity. J Anat 60:131–42.

A discussion of the venous plexuses within and between some of the lower limb muscles. The two principal superficial veins and their numerous tributaries are discussed and their use as grafts during peripheral vascular surgery, including coronary artery bypass, is considered.

Kretschmer T, Heinen C 2015 Iatrogenic injuries of the nerves. In: Tubbs RS, Rizk E, Shoja MM et al (eds) Nerves and Nerve Injuries: Volume 2: Pain, Treatment, Injury, Disease and Future Directions. Elsevier Science; Ch. 36, pp. 557–85.

Ladak A, Tubbs RS, Spinner RJ 2014 Mapping sensory nerve communications between peripheral nerve territories. Clin Anat 27:681–9.

Lafortune MA, Cavanagh PR, Sommer HJ 3rd et al 1992 Three-dimensional kinematics of the human knee during walking. J Biomech 25:347–57.

Lechner G, Jantsch H, Waneck R et al 1988 The relationship between the common femoral artery, the inguinal crease, and the inguinal ligament: a guide to accurate angiographic puncture. Cardiovasc Intervent Radiol 11:165–9.

Lee MWL, McPhee RW, Stringer MD 2008 An evidence-based approach to human dermatomes. Clin Anat 21:363–73.

Levens AS, Inman VT, Blosser JA 1948 Transverse rotation of the segments of the lower extremity in locomotion. J Bone Joint Surg Am 38:859–72.

Lieberman DE, Venkadesan M, Werbel WA et al 2010 Foot strike patterns and collision forces in habitually barefoot versus shod runners. Nature 463:531–5.

Londero LS, Lindholt JS, Thomsen MD et al 2016 Pulse palpation is an effective method for population-based screening to exclude peripheral arterial disease. J Vasc Surg 63:1305–10.

Lord S, Galna B, Verghese J et al 2013 Independent domains of gait in older adults and associated motor and nonmotor attributes: validation of a factor analysis approach. J Gerontol A Biol Sci Med Sci 68:820–7.

Lyons K, Perry J, Gronley JK et al 1983 Timing and relative intensity of hip extensor and abductor muscle action during level and stair ambulation: an EMG study. Phys Ther 63:1597–605.

Mann RA, Hagy J 1980 Biomechanics of walking, running, and sprinting. Am J Sports Med 8:345–50.

Masoud MA, Said HG 2013 Intra-articular hip injection using anatomic surface landmarks. Arthrosc Tech 2:e147–9.

McGaugh JM, Brisme JM, Dedrick GS et al 2007 Comparing the anatomical consistency of the posterior superior iliac spine to the iliac crest as reference landmarks for the lumbopelvic spine: a retrospective radiological study. Clin Anat 20:819–25.

Menz HB, Lord SR, Fitzpatrick RC 2003 Age-related differences in walking stability. Age Ageing 32:137–42.

Mirjalili SA, Muirhead JC, Stringer MD 2014 Redefining the surface anatomy of the saphenofemoral junction in vivo. Clin Anat 27:915–9.

Mirjalili SA, Taghavi K, Frawley G et al 2015 Should we abandon landmark–based technique for caudal anesthesia in neonates and infants? Pediatr Anesthes 25:511–6.

Munirama S, McLeod G 2013 Ultrasound-guided femoral and sciatic nerve blocks. Cont Ed Anaesth Crit Care Pain 13:136–40.

Murley GS, Buldt AK, Trump PJ et al 2009 Tibialis posterior EMG activity during barefoot walking in people with neutral foot posture. J Electromyogr Kinesiol 19:e69–77.

Murley GS, Menz HB, Landorf KB 2014 Electromyographic patterns of tibialis posterior and related muscles when walking at different speeds. Gait Posture 39:1080–5.

Murray MP, Drought AB, Ross CK 1964 Walking patterns of normal men. J Bone Joint Surg Am 46:335–60.

Novacheck TF 1998 The biomechanics of running. Gait Posture 7:77–95.

Perry J, Burnfield JM 2010 Gait analysis: normal and pathological function. Thorofare, NJ: Slack.

Pirker W, Katzenschlager R 2016 Gait disorders in adults and the elderly: a clinical guide. Wien Klin Wochenschr 129:81–95.

Pontén B 1981 The fasciocutaneous flap: its use in soft tissue defects of the lower leg. Br J Plast Surg 34:215–20.

The first description of lower extremity fasciocutaneous flaps. Their use in the repair of soft tissue defects is discussed.

Render CA 1996 The reproducibility of the iliac crest as a marker of lumbar spine level. Anaesthesia 51:1070–1.

Ricci S 2017 Anatomy. In: Goldman MP, Guex J-J, Weiss RA (eds) Sclerotherapy: Treatment of Varicose and Telangiectatic Leg Veins, 6th ed. Elsevier; Ch. 1, pp. 1–26.

An up-to-date guide for the effective management of varicose veins and other vascular anomalies. Details regarding the latest techniques such as foam sclerotherapy, endovenous radiofrequency and laser closure, ambulatory phlebectomy and laser treatment of spider telangiectasia and possible complications are discussed.

Ropars M, Morandi X, Huden D et al 2009 Anatomical study of the lateral femoral cutaneous nerve with special reference to minimally invasive anterior approach for total hip replacement. Surg Radiol Anat 31:199–204.

Sampson UKA, Fowkes FGR, Naidoo NG et al 2017 Peripheral artery disease. In: Prabhakaran D, Anand S, Gaziano TA et al (eds) Cardiovascular, Respiratory, and Related Disorders, 3rd ed (Disease Control Priorities Vol 5). Washington, DC: The International Bank for Reconstruction and Development/The World Bank; Ch. 14, pp. 253–62.

Semciw AI, Pizzari T, Murley GS et al 2013 Gluteus medius: an intramuscular EMG investigation of anterior, middle and posterior segments during gait. J Electromyogr Kinesiol 23:858–64.

Semciw AI, Green RA, Murley GS et al 2014 Gluteus minimus: an intramuscular EMG investigation of anterior and posterior segments during gait. Gait Posture 39:822–6.

Selkirk GD, Mclaughlin AC, Mirjalili SA 2016 Revisiting the surface anatomy of the sciatic nerve in the gluteal region in children using computed tomography. Clin Anat 29:211–6.

Senoglu N, Senoglu M, Oksuz H et al 2005 Landmarks of the sacral hiatus for caudal epidural block: an anatomical study. Br J Anaesth 95:692–5.

Senoglu N, Senoglu M, Ozkan F et al 2013 The level of termination of the dural sac by MRI and its clinical relevance in caudal epidural block in adults. Surg Radiol Anat 35:579–84.

Sharrard WJW 1955 The distribution of the permanent paralysis in the lower limb in poliomyelitis: a clinical and pathological study. J Bone Joint Surg Br 37:540–58.

A definition of the innervation patterns of the lower limb. The segmental origin of the nerve supply for each of the muscles of the lower limb and for the movements is discussed. The clinical consequences of damage to these segments are considered.

Simoneau GG, Heiderscheit BC 2017 Kinesiology of walking. In: Neumann DA (ed) Kinesiology of the Musculoskeletal System: Foundations for Rehabilitation, 3rd ed. Elsevier; Ch. 15, pp. 653–705.

A recent publication that outlines the kinesiology of walking and includes detailed information on lower limb anatomy, joint kinematics, muscle activity, kinetics and gait dysfunction.

Staudt JM, Smeulders MJ, van der Horst CM 2008 Normal compartment pressures of the lower leg in children. J Bone Joint Surg Br 90:215–9.

Sterzi G 1910 Il tessuto sottocutaneo [Subcutaneous Tissue]. Florence: Luigi Niccolai.

A discussion of the specific structure of the subcutaneous tissue of the lower limb and its participation in the integrity of the skin.

Strazza A, Mengarelli A, Fioretti S et al 2017 Surface-EMG analysis for the quantification of thigh muscle dynamic co-contractions during normal gait. Gait Posture 51:228–33.

Sutherland DH 2001 The evolution of clinical gait analysis part 1: kinesiological EMG. Gait Posture 14:61–70.

Sutherland DH, Olshen R, Cooper L et al 1980 The development of mature gait. J Bone Joint Surg Am 62:336–53.

Taylor GI, Razaboni RM (eds) 1994 Michel Salmon: Anatomic Studies, Book 1. Arteries of the Muscles of the Extremities and Trunk. St Louis: Quality Medical Publishing.

A discussion of the arteries to the muscles of the lower extremity. The pattern of arterial supply is particularly relevant to fracture healing, the spread of infection and malignancy, and the planning of reconstructive surgical procedures.

Thurston AJ, Harris JD 1983 Normal kinematics of the lumbar spine and pelvis. Spine 8:199–205.

Tubbs RS, Loukas M, Shoja MM et al 2007 Anatomy and potential clinical significance of the vastoadductor membrane. Surg Radiol Anat 29:569–73.

van Schoor A, Bosman MC, Bosenberg AT 2014 The value of Tuffier's line for neonatal neuraxial procedures. Clin Anat 27:370–5.

Volpe RG 2001 Pediatric gait. In: Thomson P, Volpe RG (eds) Introduction to Podopediatrics, 2nd ed. Edinburgh: Elsevier, Churchill Livingstone; Ch. 4, pp. 49–71.

Wall JC, Charteris J, Turnbull GI 1987 Two steps equals one stride equals what? The applicability of normal gait nomenclature to abnormal walking patters. Clin Biomech (Bristol, Avon) 2:119–25.

Wallis KA, Hills T, Mirjalili SA 2018 Minimising iatrogenic nerve injury in primary care. Br J Gen Pract 68:392–3.

Walsh JC, Quinlan JF, Butt K et al 2006 Variation in position of the L4/5 disc inter-space from the anatomical landmark: review of 450 radiographs and clinical applications. Eur J Orthop Surg Traumatol 16:203–6.

Winter DA 1983 Energy generation and absorption at the ankle and knee during fast, natural, and slow cadences. Clin Orthop Relat Res 175:147–54.

Winter DA, Yack HJ 1987 EMG profiles during normal human walking: stride-to-stride and inter-subject variability. Electroencephalogr Clin Neurophysiol 67:402–11.

Wong WY, Bjørn S, Strid JMC et al 2017 Defining the location of the adductor canal using ultrasound. Reg Anesth Pain Med 42:241–5.

Zelik KE, Adamczyk PG 2016 A unified perspective on ankle push-off in human walking. J Exp Biol 219:3676–83.

CHAPTER 77

Pelvic girdle, hip, gluteal region and thigh

The pelvic girdle consists of the paired hip bones (each composed of the ilium, ischium and pubis) and the sacrum. The two pubic bones articulate anteriorly at the pubic symphysis and the sacrum articulates posteriorly with the two iliac bones at the sacroiliac joint; the bones are virtually incapable of independent movement, except in the female during parturition or because of pathological change. The pelvic girdle serves as a weight-bearing and protective structure, as an attachment for trunk and lower limb muscles, and as the skeletal framework of a birth canal capable of accommodating the passage of a fetus.

The hip joint is a large synovial ball-and-socket type articulation between the head of the femur and the cup-shaped acetabulum. It permits extensive movements between the thigh and the pelvis, and between the trunk-and-pelvis (as a functional unit) and the thigh. The pivotal location of the hips serves as an essential mechanical link for many movements and postures of the body, including upright standing, locomotion, and bending toward and away from the ground.

The gluteal region or buttock is an area demarcated by the gluteal fold inferiorly, a line joining the greater trochanter and the anterior superior iliac spine laterally, the iliac crest superiorly and the midline medially. It contains a large bulk of skeletal muscle that covers several vulnerable neurovascular structures, and incorporates junctional zones between the lower limb, pelvis and perineum at the sciatic foramina. Direct and indirect musculoskeletal injuries in this region may damage the sciatic nerve and gluteal vessels.

The thigh consists of a cylinder of compact bone, the femoral shaft, surrounded by muscle groups traversed by important neurovascular structures. The muscles are grouped according to function and lie within three osteofascial compartments (anterior, posterior and medial) that are defined by fascial septa running between the femur and an enveloping tube of thick fascia, the fascia lata. The femoral artery gives off its major branch, the profunda femoris artery (deep artery of the thigh), in the anterior compartment. The sciatic nerve usually divides into its main branches, the tibial and common fibular nerves, as it passes through the posterior compartment of the thigh. The femoral nerve divides soon after entering the anterior compartment of the thigh beneath the inguinal ligament; the obturator nerve enters the medial thigh proximally and medially from the pelvis and divides into its main branches, which run anterior and posterior to adductor brevis.

SKIN AND SOFT TISSUES

Skin

See also Chapter 78.

Cutaneous vascular supply and lymphatic drainage

Buttock

Most of the skin of the buttock is supplied by musculocutaneous perforating vessels from the superior and inferior gluteal arteries. There are also small peripheral contributions from similar branches of the internal pudendal, iliolumbar and lateral sacral arteries.

Cutaneous veins are tributaries of vessels that correspond to the named arteries. Cutaneous lymphatic drainage is to the superficial inguinal nodes.

Thigh

The skin of the thigh distal to the inguinal ligament and gluteal fold is supplied mainly by branches of the femoral and profunda femoris arteries. There is some contribution from the obturator, inferior gluteal and popliteal arteries, and from direct cutaneous, musculocutaneous and fasciocutaneous vessels. For further details, consult Cormack and Lamberty (1994).

Cutaneous veins are tributaries of vessels that correspond to the named arteries. Cutaneous lymphatic drainage is to the superficial inguinal nodes, mainly via collecting trunks accompanying the long saphenous vein.

Innervation

For the dermatomes and cutaneous nerves, see Figs 76.12B, 76.13–76.14.

Soft tissues

Superficial fascia

The superficial fascia (subcutaneous tissue; tela subcutanea) of the thigh and buttock consists, as elsewhere in the limbs, of loose areolar tissue containing a variable quantity of fat. In some regions, particularly near the inguinal ligament, it splits into recognizable layers, between which may be found the branches of superficial vessels and nerves. It is thick in the inguinal region, where its two layers enclose the superficial inguinal lymph nodes, long saphenous vein and other smaller vessels. Here, the superficial layer is continuous with that of the abdominal fascia. The deep layer, a thin fibroelastic stratum, is most marked medial to the long saphenous vein and inferior to the inguinal ligament, and is interposed between the subcutaneous vessels and nerves and the deep fascia, fusing with the latter a little below the ligament. This membranous layer of subcutaneous tissue overlies the saphenous opening, blending with its circumference and with the femoral sheath. Over the opening, it is perforated by the long saphenous vein, by the superficial branches of the femoral artery other than the superficial circumflex iliac branch (which perforates the fascia lata separately), and lymphatic vessels; hence the term cribriform fascia. The subcutaneous tissue of the buttock is continuous superiorly with that over the low back and contains a variable quantity of fat.

Deep fascia

The deep fascia (fascia musculorum) covering the gluteal muscles varies in thickness. Over gluteus maximus it is thin, but over the anterior two-thirds of gluteus medius it forms the thick, strong gluteal aponeurosis. This is attached to the lateral border of the iliac crest superiorly, and splits anteriorly to enclose tensor fasciae latae and posteriorly to enclose gluteus maximus.

Fascia lata

The fascia lata, the expansive deep fascia that surrounds the thigh, is thicker in the proximal and lateral parts of the thigh where tensor fasciae latae and an expansion from gluteus maximus are attached to it. It is thin posteriorly and over the adductor muscles, but thicker around the knee, where it is strengthened by expansions from the tendon of biceps femoris laterally, sartorius medially and quadriceps femoris anteriorly. The fascia lata is attached superiorly and posteriorly to the back of the sacrum and coccyx, laterally to the outer margin of the iliac crest, anteriorly to the inguinal ligament, the iliac fascia and superior ramus of the pubis, and medially to the inferior ramus of the pubis, the ramus and tuberosity of the ischium, and the lower border of the sacrotuberous ligament. From the iliac crest, it descends as a dense layer over gluteus medius to the upper border of gluteus maximus, where it splits into two layers, one passing superficial and the other deep to the muscle, the layers reuniting at the lower border of the muscle.

Iliotibial tract

Over the flattened lateral surface of the thigh the fascia lata thickens to form a strong band, the iliotibial tract. The upper end of the tract splits into two layers, where it encloses and anchors tensor fasciae latae and receives, posteriorly, most of the tendon of gluteus maximus. The superficial layer ascends lateral to tensor fasciae latae to the iliac crest; the deeper layer passes up and medially, deep to the muscle, and blends

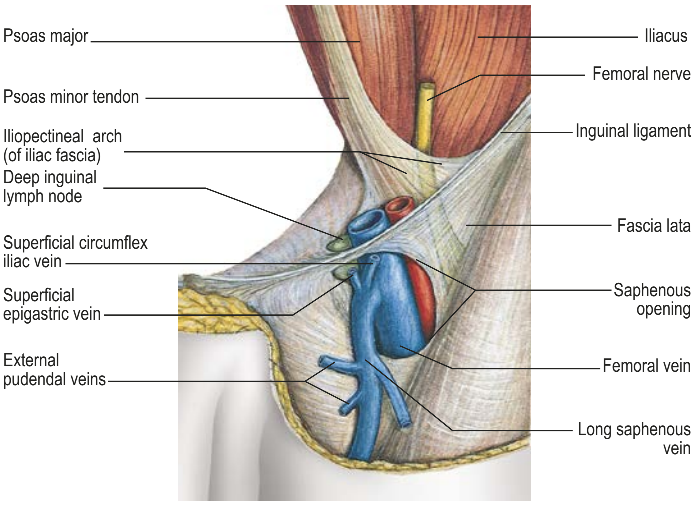

Fig. 77.1 The saphenous opening following removal of the cribriform fascia. (Sobotta Atlas of Human Anatomy © Elsevier GmbH, Urban & Fischer, Munich.)

with the lateral part of the capsule of the hip joint. Distally the iliotibial tract is attached to a smooth, triangular facet (Gerdy's tubercle) on the anterolateral aspect of the lateral condyle of the tibia, where it is superficial to, and blends with, an aponeurotic expansion from vastus lateralis. When the knee is extended against resistance, it stands out as a strong, visible ridge on the anterolateral aspect of the thigh and knee.

Distally the fascia lata is attached to all exposed bony points around the knee joint, such as the condyles of the femur and tibia, and the head of the fibula. On each side of the patella the deep fascia is reinforced by transverse fibres, which receive contributions from the lateral and medial vasti. The stronger lateral fibres are continuous with the iliotibial tract.

Intermuscular septa

The deep surface of the fascia lata yields two intermuscular septa, which are attached to the whole of the linea aspera of the posterior femur and to its proximal and distal prolongations. The lateral septum, thicker and stronger than the medial one, extends from the attachment of gluteus maximus to the lateral femoral condyle; it lies between vastus lateralis in front and the short head of biceps femoris behind, and provides partial attachment for them. The medial, thinner and weaker septum lies between vastus medialis and the adductors and pectineus. Numerous smaller septa, such as that separating the thigh adductors and flexors, pass between the individual muscles, ensheathing them and sometimes providing partial attachment for their fibres.

Saphenous opening

The saphenous opening is an aperture in the deep fascia, inferolateral to the medial end of the inguinal ligament, which allows passage for the long saphenous vein and other smaller vessels (**Fig. 77.1**). The cribriform fascia, which is pierced by these structures, fills in the aperture and must be removed to reveal it. Adjacent subsidiary openings may exist to transmit venous tributaries. In the adult, the approximate centre of the saphenous opening is 3 cm lateral to a point just distal to the pubic tubercle. The length and width of the opening vary considerably. The fascia lata in this part of the thigh displays superficial and deep strata (not to be confused with the superficial and deep layers of the subcutaneous tissue described above). They lie, respectively, anterior and posterior to the femoral sheath, with the saphenous opening situated where the two layers are in continuity. This serves to explain the somewhat oblique and spiral configuration of the saphenous opening.

The superficial layer, lateral and superior to the saphenous opening, is attached, in continuity, to the crest and anterior superior spine of the ilium, to the whole length of the inguinal ligament, and to the pecten pubis and lacunar ligament. It is reflected inferolaterally from the pubic tubercle as the arched falciform margin, which forms the superior, lateral and inferior boundaries of the saphenous opening; this margin adheres to the anterior layer of the femoral sheath, and the cribriform fascia is attached to it. The falciform margin is considered to have superior and inferior horns. The inferior horn is well defined, and is continuous behind the long saphenous vein with the deep stratum of the fascia lata.

The deep layer is medial to the saphenous opening and is continuous with the superficial stratum at its lower margin. Traced upwards, it covers pectineus, adductor longus and gracilis, passes behind the femoral sheath, with which it blends, and continues to the pecten pubis.

Femoral sheath

The femoral sheath is a funnel-shaped distal prolongation of extraperitoneal fascia, formed of transversalis fascia anterior to the femoral vessels, and of the iliac fascia posteriorly. It is wider proximally and its tapered distal end fuses with the vascular adventitia 3 or 4 cm distal to the inguinal ligament. At birth the sheath is shorter; it elongates when extension at the hips becomes habitual. The femoral branch of the genitofemoral nerve perforates its lateral wall. The medial wall slopes laterally and is pierced by the long saphenous vein and lymphatic vessels. Like the carotid sheath, the femoral sheath encloses a mass of connective tissue in which the vessels are embedded. Three compartments are described: a lateral compartment containing the femoral artery; an intermediate one for the femoral vein; and a medial compartment, the femoral canal, which contains lymph vessels and an occasional lymph node embedded in areolar tissue. The presence of this canal allows the femoral vein to distend. The canal is conical and approximately 1.25 cm in length. Its proximal (wider) end, termed the femoral ring, is bounded in front by the inguinal ligament, behind by pectineus and its fascia and the pectineal ligament, medially by the crescentic, lateral edge of the lacunar ligament and laterally by the femoral vein. The spermatic cord, or the round ligament of the uterus, is just above its anterior margin, while the inferior epigastric vessels are near its anterolateral rim. It is larger in women than in men: this is due partly to the relatively greater width of the female pelvis and partly to the smaller size of the femoral vessels in women. The ring is filled by condensed extraperitoneal tissue, the femoral septum, which is covered on its proximal aspect by the parietal peritoneum. Numerous lymph vessels that connect the deep inguinal to the external iliac lymph nodes traverse the femoral septum (**Fig. 77.2**).

Femoral hernia

Femoral hernia is described with other groin hernias in Chapter 60.

Iliac fascia

The iliac fascia covers psoas and iliacus. It is thin above but thickens progressively towards the inguinal ligament. The part covering psoas is thickened above as the medial arcuate ligament. Medially the fascia over psoas is attached by a series of fibrous arches to the intervertebral discs, the margins of vertebral bodies and the upper part of the sacrum. Laterally, it blends with the fascia anterior to quadratus lumborum above the iliac crest, and with the fascia covering iliacus below the crest. The iliac part is connected laterally to the whole of the inner lip of the iliac crest and medially to the pelvic brim, where it blends with the periosteum. At approximately the height of the anterior superior iliac spine, the iliac fascia forms an open, curved superior edge, known as the iliopectineal arch (see Fig. 77.1). This arch passes directly over the femoral nerve, and iliacus and psoas major. The medial extent of the arch is attached to the iliopubic ramus, where it receives a slip from the tendon of psoas minor, when this muscle is present (Neumann and Garceau 2015). The external iliac vessels are anterior to the fascia but the branches of the lumbar plexus are posterior to it. The fascia is separated from the peritoneum by loose extraperitoneal tissue. Lateral to the femoral vessels the iliac fascia is continuous with the posterior margin of the inguinal ligament and the transversalis fascia. Medially, it passes behind the femoral vessels to become the pectineal ligament, attached to the pecten pubis. At the junction of its lateral and medial parts, it is attached to the iliopubic ramus and the capsule of the hip joint. It thus forms a septum between the inguinal ligament and the hip bone, dividing the space here into a lateral part, the muscular space, containing psoas major, iliacus and the femoral nerve, and a medial part, the vascular space, transmitting the femoral vessels (see Fig. 77.2). The iliac fascia continues downwards to form the posterior wall of the femoral sheath.

Obturator membrane

The obturator membrane (**Fig. 77.3**; see Fig. 77.2A) is a thin aponeurosis that closes (obturates) most of the obturator foramen, leaving a superolateral aperture, the obturator canal, through which the obturator vessels and nerve leave the pelvis and enter the thigh. The membrane is attached to the sharp margin of the obturator foramen except at its inferolateral angle, where it is fixed to the pelvic surface of the ischial ramus, i.e. internal to the foramen. Its fibres are arranged mainly transversely in interlacing bundles; the uppermost bundle, which is attached to the obturator tubercles, completes the obturator canal. The outer and inner surfaces of the obturator membrane provide attachment for the obturator externus and internus, respectively. Some fibres of the pubofemoral ligament of the hip joint are attached to the outer surface.

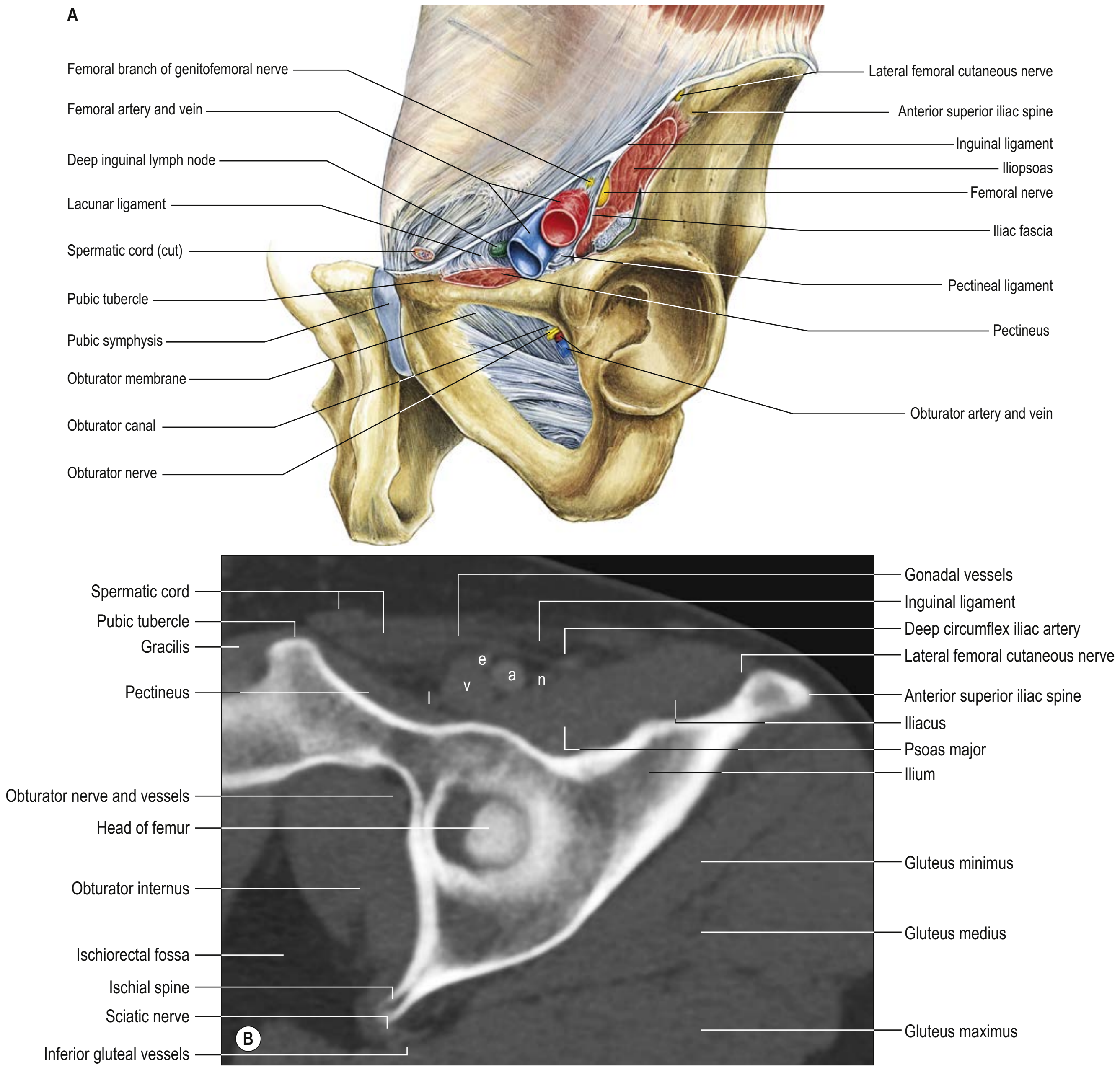
A
Femoral branch of genitofemoral nerve
Femoral artery and vein
Deep inguinal lymph node
Lacunar ligament
Spermatic cord (cut)
Pubic tubercle
Pubic symphysis
Obturator membrane
Obturator canal
Obturator nerve
Lateral femoral cutaneous nerve
Anterior superior iliac spine
Inguinal ligament
Iliopsoas
Femoral nerve
Iliac fascia
Pectineal ligament
Pectineus
Obturator artery and vein
Spermatic cord
Pubic tubercle
Gracilis
Pectineus
Obturator nerve and vessels
Head of femur
Obturator internus
Ischiorectal fossa
Ischial spine
Sciatic nerve
Inferior gluteal vessels
B
e
v
a
n
l
Gonadal vessels
Inguinal ligament
Deep circumflex iliac artery
Lateral femoral cutaneous nerve
Anterior superior iliac spine
Iliacus
Psoas major
Ilium
Gluteus minimus
Gluteus medius
Gluteus maximus

Fig. 77.2 **A**, Structures passing beneath the inguinal ligament. **B**, An oblique multiplanar reformat of a CT with intravenous contrast medium along the inguinal ligament. Key: a, femoral artery; e, inferior epigastric artery; l, deep inguinal lymph node; n, femoral nerve; v, femoral vein. (A, Sobotta Atlas of Human Anatomy © Elsevier GmbH, Urban & Fischer, Munich.)

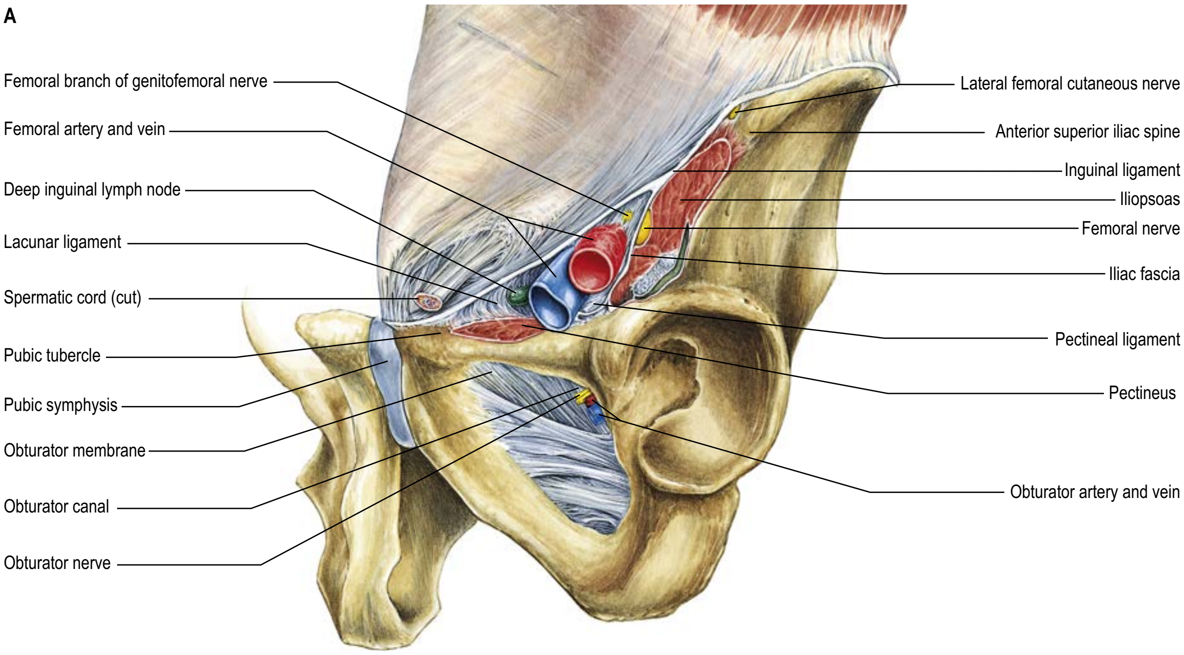
A
Femoral branch of genitofemoral nerve
Femoral artery and vein
Deep inguinal lymph node
Lacunar ligament
Spermatic cord (cut)
Pubic tubercle
Pubic symphysis
Obturator membrane
Obturator canal
Obturator nerve
Lateral femoral cutaneous nerve
Anterior superior iliac spine
Inguinal ligament
Iliopsoas
Femoral nerve
Iliac fascia
Pectineal ligament
Pectineus
Obturator artery and vein

Fig. 77.2 A, Structures passing beneath the inguinal ligament. (Sobotta Atlas of Human Anatomy © Elsevier GmbH, Urban & Fischer, Munich.) (B, *continued online*)

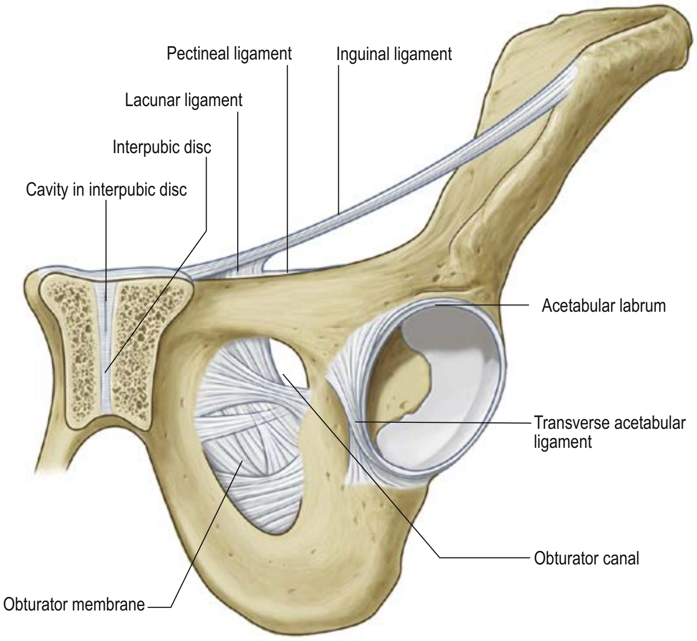
Pectineal ligament
Inguinal ligament
Lacunar ligament
Interpubic disc
Cavity in interpubic disc
Acetabular labrum
Transverse acetabular ligament
Obturator canal
Obturator membrane

Fig. 77.3 An anterolateral view of left bony pelvis, showing associated ligaments and the obturator membrane.

BONES

The relevant bones in this region include the pelvic girdle (which consists of two hip bones, sacrum and coccyx) and the two femurs.

Hip bone

The hip bone is large, irregular, constricted centrally and expanded above and below (Figs 77.4–77.5). Its lateral surface has a deep, cup-shaped acetabulum, articulating with the femoral head, anteroinferior to which is the large, oval or triangular obturator foramen. Above the acetabulum, the bone widens into an undulant plate surmounted by a sinuously curved iliac crest. The bone articulates in front with its fellow and posteriorly with the sacrum to form the pelvic girdle. Each hip bone has three parts, ilium, ischium and pubis, connected to each other by cartilage in youth but united as one bone in adults. The principal union is in the acetabulum. The ilium includes the upper acetabulum and expanded area above it; the ischium includes the posteroinferior acetabulum and bone posteroinferior to it; the pubis forms the anteroinferior acetabulum.

Acetabulum

The acetabulum (see Fig. 77.4A) is an approximately hemispherical cavity situated about the centre of the lateral aspect of the hip bone. It faces anteroinferiorly and is circumscribed by an irregular margin deficient inferiorly at the acetabular notch. The acetabular fossa forms the central floor and is rough and non-articular. The articular lunate surface is widest above (the 'dome'), where weight is transmitted to the femur. Consequently, fractures through this region tend to be associated with unsatisfactory outcomes. All three components of the hip bone contribute to the acetabulum, although unequally. The pubis forms the anterosuperior fifth of the articular surface, the ischium forms the floor of the fossa and rather more than the posteroinferior two-fifths of the articular surface, and the ilium forms the remainder.

Obturator foramen

The obturator foramen lies below and slightly anterior to the acetabulum, between the pubis and ischium. It is bordered above by the grooved obturator surface of the superior pubic ramus, medially by the pubic body and its inferior ramus, below by the ischial ramus, and laterally by the anterior border of the ischial body, including the margin of the acetabulum. It is almost closed by the obturator membrane, which is attached to its margins, except superolaterally, where a communication remains between the pelvis and thigh. This free edge of the membrane is attached to an anterior obturator tubercle at the anterior end of the inferior border of the superior pubic ramus, and a posterior obturator tubercle on the anterior border of the acetabular notch; these tubercles are sometimes indistinct. The foramen is large and oval in males, but smaller and nearly triangular in females.

Structure

The thicker parts of the hip bone are trabecular, encased by two layers of compact bone, while the thinner parts, as in the acetabulum and central iliac fossa, are often translucent and consist of a single lamina of compact bone. In the upper acetabulum and along the arcuate line, i.e. the route of weight transmission from the sacrum to the femur, the amount of compact bone is increased and the subjacent trabecular bone displays two sets of pressure lamellae. These start together near the upper auricular surface and diverge to meet two strong buttresses of compact bone, from which two similar sets of lamellar arches start and converge on the acetabulum. The anterior part of the iliac crest has been much studied with regard to distribution of cortical and trabecular bone. Whitehouse (1977) described the cortical bone as very porous, being only 75% bone, decreasing to 35% near the anterior superior iliac spine.

Studies of the internal stresses within the hip bone have revealed a pattern of trabeculae that corresponds well with the theoretically expected patterns of stress trajectories (Holm 1980). These patterns are considerably more complex than in any other major bone. Stresses are higher in the acetabular than in the iliac region. In the ilium, the pelvic surface is subjected to considerably less stress than is the gluteal surface.

Muscle attachments

See individual bones.

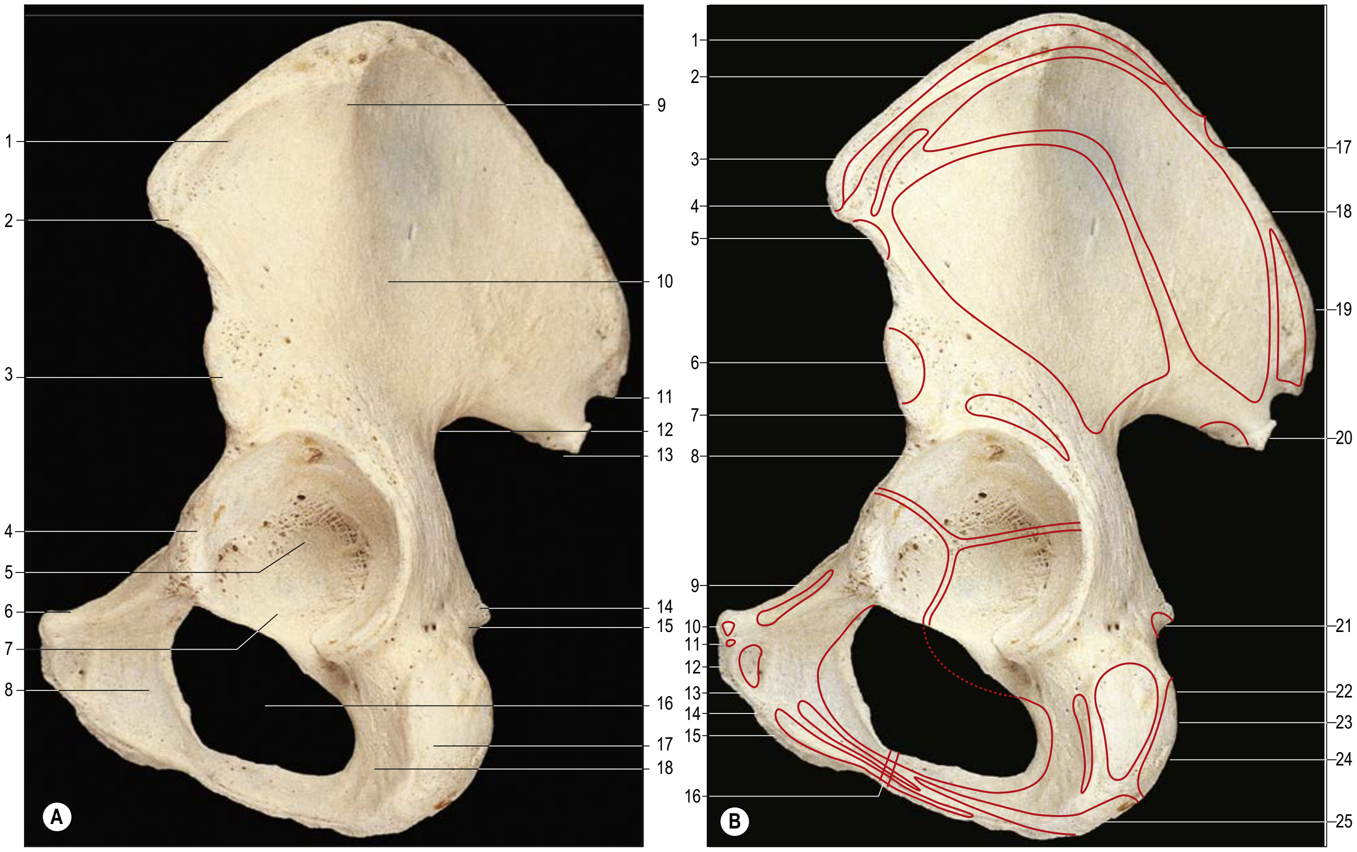

Fig. 77.4 Left hip bone. **A**, External aspect. **B**, Muscle attachments. **A**, Key: 1, iliac crest; 2, anterior superior iliac spine; 3, anterior inferior iliac spine; 4, iliopubic (iliopectineal) eminence; 5, acetabulum; 6, pubic tubercle; 7, acetabular notch; 8, pubis; 9, tubercle of iliac crest; 10, ilium; 11, posterior superior iliac spine; 12, greater sciatic notch; 13, posterior inferior iliac spine; 14, ischial spine; 15, lesser sciatic notch; 16, obturator foramen; 17, ischial tuberosity; 18, ischium. **B**, Key: 1, internal abdominal oblique; 2, external abdominal oblique; 3, tensor fasciae latae; 4, gluteus minimus; 5, sartorius; 6, rectus femoris, straight head; 7, rectus femoris, reflected head; 8, junction between ilium, ischium and pubis; 9, pectineus; 10, rectus abdominis, lateral head; 11, pyramidalis; 12, adductor longus; 13, obturator externus; 14, adductor brevis; 15, gracilis; 16, junction between ischium and pubis; 17, latissimus dorsi; 18, gluteus medius; 19, gluteus maximus; 20, piriformis; 21, gemellus superior; 22, semimembranosus; 23, quadratus femoris; 24, biceps femoris and semitendinosus; 25, adductor magnus.

Vascular supply

In the infant, nutrient arteries are clearly demonstrable for each component of the hip bone. Each nutrient artery branches in a fan-like fashion within its bone of supply (Crock 1996). Later, a periosteal arterial network develops, with contributions from numerous local arteries (see under individual bones).

Innervation

Periosteal innervation is by a network of nerves derived from branches of local nerves. These nerves also supply muscles attaching to the periosteum and the joints involving the hip bone. Autonomic nerves accompany nutrient arteries and branch within the bone.

Ossification

Ossification (Figs 77.6–77.7) is by three primary centres: one each for the ilium, ischium and pubis. The iliac centre appears above the greater sciatic notch prenatally at about postmenstrual weeks 9–10; the ischial centre in its body during postmenstrual weeks 13–16; and the pubic centre in its superior ramus during postmenstrual weeks 13–20. The pubis is often not recovered from prenatal remains due to its size and fragility and because it is the last of the hip bones to begin ossification (Scheuer and Black 2004). At birth the whole iliac crest, the acetabular floor and the inferior margin are cartilaginous. Gradual ossification of the three components of the acetabulum results in a triradiate cartilaginous stem extending medially to the pelvic surface as a Y-shaped epiphysial plate between the ilium, ischium and pubis, and including the anterior inferior iliac spine. Cartilage along the inferior margin also covers the ischial tuberosity, forms conjoined ischial and pubic rami, and continues to the pubic symphysial surface and along the pubic crest to the pubic tubercle.

The ossifying ischium and pubis fuse to form a continuous ischiopubic ramus at the seventh or eighth year. Secondary centres, other than for the acetabulum, appear at about puberty and fuse between the fifteenth and twenty-fifth years. There are usually two for the iliac crest (which fuse early), and single centres for the ischial tuberosity (in cartilage close to the inferior acetabular margin and spreading forwards), anterior inferior iliac spine (although it may ossify from the triradiate cartilage) and symphysial surface of the pubis (the pubic tubercle and crest may have separate centres). Progression of ossification of the iliac crest in girls is an index of skeletal maturity and is useful in determining the optimal timing of surgery for spinal deformity.

Between the ages of 8 and 9 years, three major centres of secondary ossification appear in the acetabular cartilage. The largest appears in the anterior wall of the acetabulum and fuses with the pubis, the second in the iliac acetabular cartilage superiorly, fusing with the ilium, and the third in the ischial acetabular cartilage posteriorly, fusing with the ischium. At puberty, these epiphyses expand towards the periphery of the acetabulum and contribute to its depth (Ponseti 1978). Fusion between the three bones within the acetabulum occurs between the sixteenth and eighteenth years. Delaere et al (1992) have suggested that ossification of the ilium is similar to that of a long bone, possessing three cartilaginous epiphyses and one cartilaginous process, although it tends to undergo osteoclastic resorption comparable with that of cranial bones. During development the acetabulum increases in breadth at a faster rate than it does in depth.

Avulsion fractures of pelvic apophyses may occur from excessive pull on tendons, usually in athletic adolescents. The most frequent examples of such injuries are those to the ischial tuberosity (hamstrings) and anterior inferior iliac spine (rectus femoris).

Pubis

The pubis (see Figs 77.4–77.5) is the ventral part of the hip bone and forms a median cartilaginous pubic symphysis with its fellow. The body of the pubis occupies the anteromedial part of the bone, and from the body a superior ramus passes up and back to the acetabulum and an inferior ramus passes back, down and laterally to join the ischial ramus inferomedial to the obturator foramen.

Body

The body, anteroposteriorly compressed, has anterior, posterior and symphysial (medial) surfaces and an upper border, the pubic crest. The

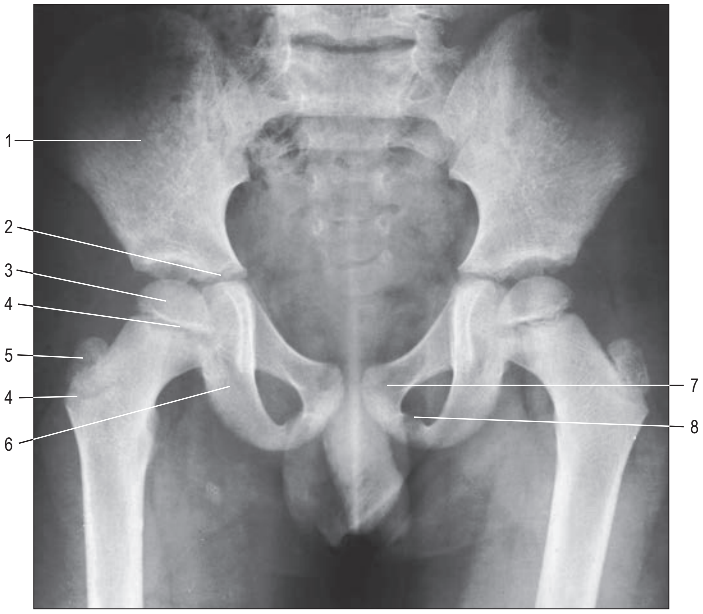

Fig. 77.7 An anteroposterior radiograph of the pelvis of a 7-year-old boy. Key: 1, ilium; 2, part of triradiate growth cartilage; 3, superior femoral epiphysis; 4, cartilaginous growth plates; 5, ossifying greater trochanter; 6, ischium; 7, pubis; 8, cartilage between inferior pubic and ischial rami.

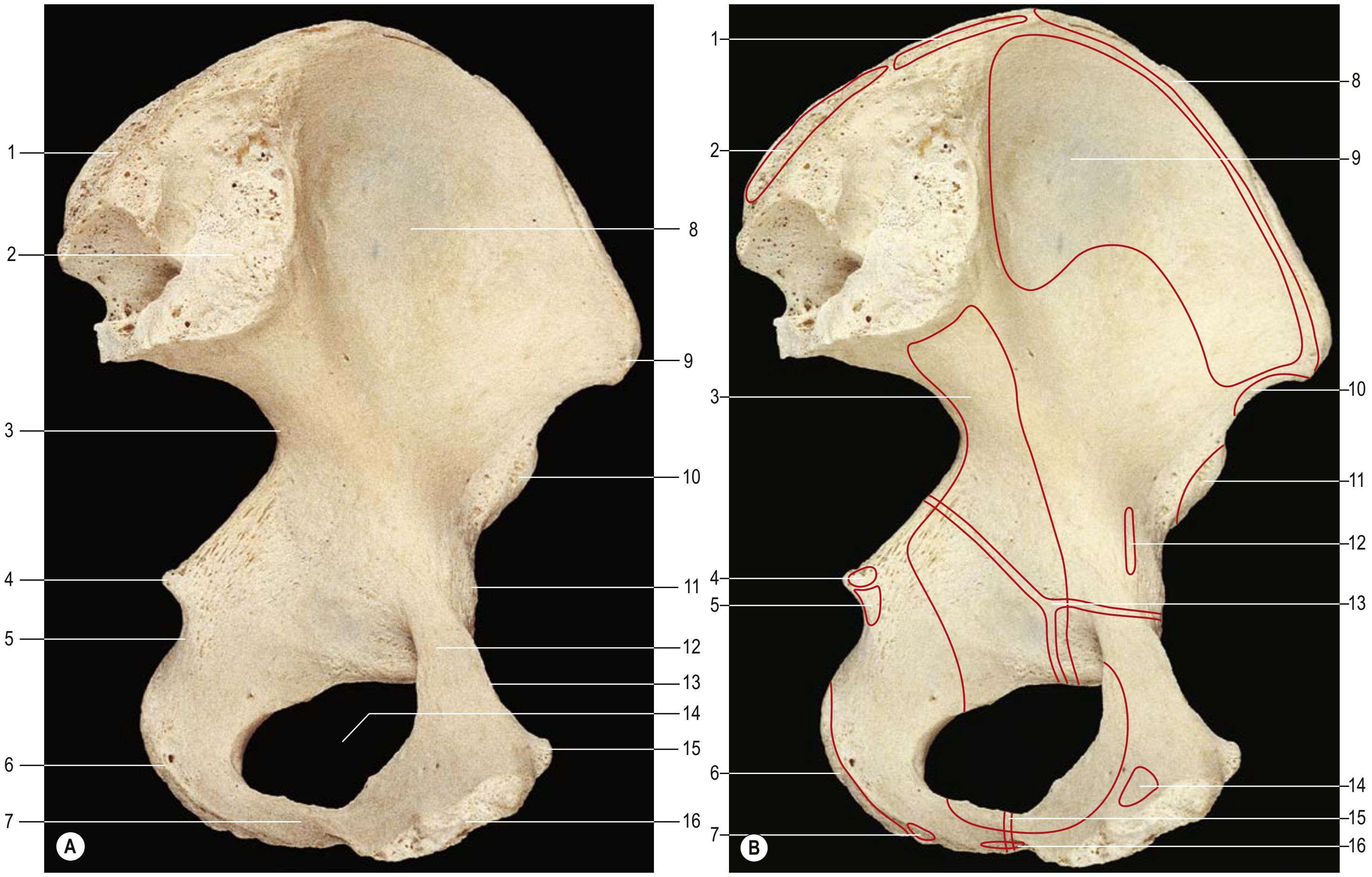

Fig. 77.5 Left hip bone. **A**, Internal (pelvic) aspect. **B**, Muscle attachments. **A**, Key: 1, iliac tuberosity; 2, auricular surface; 3, greater sciatic notch; 4, ischial spine; 5, lesser sciatic notch; 6, ischial tuberosity; 7, ischiopubic (inferior pubic) ramus; 8, iliac fossa; 9, anterior superior iliac spine; 10, anterior inferior iliac spine; 11, iliopubic (iliopectineal) eminence; 12, superior pubic ramus; 13, pecten pubis; 14, obturator foramen; 15, pubic tubercle; 16, symphysial surface. **B**, Key: 1, quadratus lumborum; 2, erector spinae; 3, obturator internus; 4, coccygeus; 5, levator ani; 6, sacrotuberous ligament; 7, transversus perinei superificalis; 8, transversus abdominis; 9, iliacus; 10, sartorius; 11, rectus femoris; 12, psoas minor; 13, junction between ilium, ischium and pubis; 14, levator ani; 15, junction between ischium and pubis; 16, sphincter urethrae.

anterior surface also faces inferolaterally; it is rough superomedially and smooth elsewhere, giving attachment to medial thigh muscles. The smooth posterior surface faces upwards and backwards as the oblique anterior wall of the lesser pelvis and is related to the urinary bladder. The symphysial surface is elongated and oval, united by cartilage to its fellow at the pubic symphysis. Denuded of cartilage, it has an irregular surface of small ridges and furrows or nodular elevations, varying considerably with age, features that are of forensic interest. The pubic crest is the rounded upper border of the body and overhangs the anterior surface; the pubic tubercle is a small rounded eminence on its lateral end. Both crest and tubercle are palpable; the latter partly is obscured in males by the spermatic cord that crosses above it from the scrotum to the anterior abdominal wall. The pubic rami diverge posterolaterally from the superolateral corners of the body.

The anterior surface of the pubic body faces the adductor region. The anterior pubic ligament attaches to its medial part along a rough strip, which is wider in females. The posterior surface is separated from the urinary bladder by retropubic fat. The puboprostatic ligaments are attached to this surface medial to levator ani.

Superior pubic ramus

The superior pubic ramus passes upwards, backwards and laterally from the body, superolateral to the obturator foramen, to reach the acetabulum. It is triangular in section and has three surfaces and borders. Its anterior, pectineal surface, tilted slightly up, is triangular in outline and extends from the pubic tubercle to the iliopubic ramus. It is bounded in front by the rounded obturator crest and behind by the sharp pecten pubis (pectineal line), which, with the crest, is the pubic part of the linea terminalis (i.e. anterior part of the pelvic brim). The posterosuperior, pelvic surface, medially inclined, is smooth and narrows into the posterior surface of the body, which is bounded above by the pecten pubis and below by a sharp inferior border. The obturator surface, directed down and back, is crossed by the obturator groove sloping down and forwards. Its anterior limit is the obturator crest and its posterior limit is the inferior border.

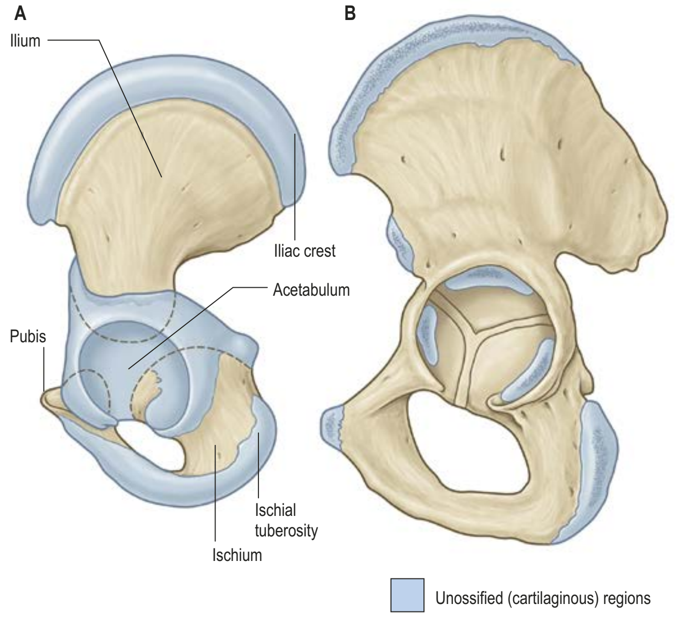

Fig. 77.6 The hip bone. **A**, At birth. **B,** In adolescence; more heavily stippled areas indicate the secondary centres of ossification.

Inferior pubic ramus

The inferior pubic ramus, an inferolateral process of the body, descends inferolaterally to join the ischial ramus medial to, and below, the obturator foramen. The union may be locally thickened, but not obviously so in adults. The ramus has two surfaces and borders. The anterolateral surface, continuous above with that of the pubic body, faces the thigh and is marked by muscles. It is limited laterally by the margin of the obturator foramen, and medially by the rough anterior border. The posteromedial surface is continuous above with that of the body and is transversely convex; its medial part is often everted in males and gives attachment to the crus of the penis. This surface faces the perineum medially, its smooth lateral part tilted up towards the pelvic cavity.

The internal surface is indistinctly divided into medial, intermediate and lateral areas. The medial area faces inferomedially in direct contact with the crus of the penis or clitoris and is limited above and behind by an indistinct ridge for attachment of the fascia overlying the superficial perineal muscles. The medial margin of the ramus, strongly everted in males, provides attachment for the fascia lata and the stratum membranosum perinei.

Pubic tubercle

The pubic tubercle provides attachment to the medial end of the inguinal ligament. It forms part of the floor of the superficial inguinal ring and is crossed by the spermatic cord.

Pecten pubis

The pecten pubis is the sharp, superior edge of the pectineal surface. The conjoint tendon (inguinal falx) and lacunar ligament are attached at its medial end and a strong, fibrous pectineal ligament is attached along the rest of its surface. The smooth pelvic surface is separated from parietal peritoneum only by areolar tissue, in which the lateral umbilical ligament descends forwards across the ramus and, laterally, the vas ductus deferens (vas deferens) passes backwards. The obturator groove, which is converted to a canal by the upper borders of the obturator membrane and obturator muscles, transmits the obturator vessels and nerve from the pelvis to the thigh. Some fibres of the pubofemoral ligament are attached to the lateral end of the obturator crest.

Muscle attachments

The tendon of adductor longus is attached on the anterior (external) surface of the body, below the pubic crest. Below adductor longus, gracilis is attached to a line near the lower margin extending down on to the inferior ramus. Above gracilis, adductor brevis is attached to the body and inferior ramus. Above again, obturator externus is attached to the anterior surface, spreading on to the inferior pubic and ischial rami. Adductor magnus usually extends from the ischial ramus on to the lower part of the inferior pubic ramus between adductor brevis and obturator externus. Pectineus is attached to the pectineal surface of the superior ramus along its upper part. Ascending loops of cremaster are attached to the pubic tubercle. The lateral part of rectus abdominis and, inferiorly, pyramidalis, are attached lateral to the tubercle, on the pubic crest. Medially, the crest is crossed by the medial part of rectus abdominis, ascending from ligamentous fibres that interlace in front of the pubic symphysis. Anterior fibres of levator ani are attached on the posterior (internal) surface of the body near its centre. More laterally, obturator internus is attached on this surface, extending on to both rami. Psoas minor, when present, is attached near the centre of the pecten pubis (Neumann and Garceau 2015).

Vascular supply

The pubis is supplied by a periosteal anastomosis of branches from the obturator, inferior epigastric and medial circumflex femoral arteries. The superficial and deep external pudendal arteries may also contribute. Multiple vascular foramina are present, mainly at the lateral (acetabular) end of the bone, but there is no consistently placed nutrient foramen.

Innervation

The pubic periosteum is innervated by branches of the nerves that supply muscles attached to the bone, the hip joint and the symphysis pubis.

Ossification

Ossification of the pubis is described on page 1355.

Ilium

The ilium has upper and lower parts and three surfaces (see Figs 77.4–77.5). The smaller, lower part forms a little less than the upper two-fifths of the acetabulum. The upper part is much expanded, and has gluteal, sacropelvic and iliac (internal) surfaces. The posterolateral gluteal surface is an extensive rough area; the anteromedial iliac fossa is smooth and concave; and the sacropelvic surface is medial and posteroinferior to the fossa, from which it is separated by the medial border.

Iliac crest

The iliac crest is the superior border of the ilium. It is convex upwards but sinuous from side to side, being internally concave in front and convex behind. Its ends project as anterior and posterior superior iliac spines. The anterior superior iliac spine is palpable at the lateral end of the inguinal fold; the lateral end of the inguinal ligament is attached to the anterior superior iliac spine. The posterior superior iliac spine is not easily palpable but is often indicated by a dimple, approximately 4 cm lateral to the second sacral spinous process, above the medial gluteal region.

The iliac crest has ventral and dorsal segments. The ventral segment occupies slightly more than the anterior two-thirds of the iliac crest and its prominence is associated with changes in iliac form as a result of the emergence of the upright posture. It has internal and external lips and a rough intermediate zone that is narrowest centrally. The dorsal segment, which occupies approximately the posterior one-third in humans, is a feature of all land vertebrates. It has two sloping surfaces separated by a longitudinal ridge ending at the posterior superior spine. The interosseous and posterior sacroiliac ligaments arise from the medial margin of the dorsal segment. The tubercle of the iliac crest projects outwards from the outer lip approximately 5 cm posterosuperior to the anterior superior spine. The summit of the iliac crest, a little behind its midpoint, is level with the fourth lumbar vertebral body in adults and with the fifth lumbar vertebral body in children aged 10 years or less (Tame and Burstal 2003).

Anterior border

The anterior border descends to the acetabulum from the anterior superior spine. Superiorly, it is concave forwards. Inferiorly, immediately above the acetabulum, is a rough anterior inferior iliac spine, which is divided indistinctly into an upper area for the straight head of rectus femoris and a lower area extending laterally along the upper acetabular margin to form a triangular impression for the proximal end of the iliofemoral ligament.

Posterior border

The posterior border is irregularly curved and descends from the posterior superior spine, at first forwards, with a posterior concavity forming a small notch. At the lower end of the notch is a wide, low projection: the posterior inferior iliac spine. Here the border turns almost horizontally forwards for approximately 3 cm, then down and back to join the posterior ischial border. Together these borders form a deep notch, the greater sciatic notch, which is bounded above by the ilium and below by the ilium and ischium. The upper fibres of the sacrotuberous ligament are attached to the upper part of the posterior border. The superior rim of the notch is related to the superior gluteal vessels and nerve. The lower margin of the greater sciatic notch is covered by piriformis and is related to the exiting sciatic nerve.

Medial border

The medial border separates the iliac fossa and the sacropelvic surface. It is indistinct near the crest, rough in its upper part, then sharp where it bounds an articular surface for the sacrum, and finally rounded. The latter part is the arcuate line, which inferiorly reaches the posterior part of the iliopubic ramus, marking the union of the ilium and pubis.

Gluteal surface

The gluteal surface, facing inferiorly in its posterior part and laterally and slightly downwards in front, is bounded above by the iliac crest, and below by the upper acetabular border and by the anterior and posterior borders. It is rough and curved, convex in front, concave behind and marked by three gluteal lines. The posterior gluteal line is shortest, descending from the external lip of the crest approximately 5 cm in front of its posterior limit and ending in front of the posterior inferior iliac spine. Above, it is usually distinct, but inferiorly it is poorly defined and frequently absent. The anterior gluteal line, the longest, begins near the midpoint of the superior margin of the greater sciatic notch and ascends forwards into the outer lip of the crest, a little anterior to its tubercle. The inferior gluteal line, seldom well marked, begins posterosuperior to the anterior inferior iliac spine, curving posteroinferiorly to end near the apex of the greater sciatic notch. Between the inferior gluteal line and the acetabular margin is a rough, shallow groove. Behind the acetabulum, the lower gluteal surface is continuous with the posterior ischial surface, the conjunction marked by a low elevation.

The articular capsule is attached to an area adjoining the acetabular margin, most of which is covered by gluteus minimus. Posteroinferiorly, near the union of the ilium and ischium, the bone is related to piriformis.

Iliac fossa

The iliac fossa, the internal concavity of the ilium, faces anterosuperiorly. It is limited above by the iliac crest, in front by the anterior border and behind by the medial border, separating it from the sacropelvic surface. It forms the smooth and gently concave posterolateral wall of the greater pelvis. Below it is continuous with a wide shallow groove, bounded laterally by the anterior inferior iliac spine and medially by the iliopubic ramus.

The converging fibres of iliacus occupy the wide groove between the anterior inferior iliac spine and the iliopubic ramus laterally and the tendon of psoas major medially; the tendon is separated from the underlying bone by a bursa. The right iliac fossa contains the caecum, and often the vermiform appendix and terminal ileum. The left iliac fossa houses the terminal part of the descending colon and the proximal sigmoid colon.

Sacropelvic surface

The sacropelvic surface, the posteroinferior part of the medial iliac surface, is bounded posteroinferiorly by the posterior border, anterosuperiorly by the medial border, posterosuperiorly by the iliac crest and anteroinferiorly by the line of fusion of the ilium and ischium. It is divided into iliac tuberosity and auricular and pelvic surfaces. The iliac tuberosity, a large, rough area below the dorsal segment of the iliac crest, shows cranial and caudal areas separated by an oblique ridge and connected to the sacrum by the interosseous sacroiliac ligament. The sacropelvic surface gives attachment to the posterior sacroiliac ligaments and, behind the auricular surface, to the interosseous sacroiliac ligament. The iliolumbar ligament is attached to its anterior part. The auricular surface, immediately anteroinferior to the tuberosity, articulates with the lateral sacral mass. Shaped like an ear, its widest part is anterosuperior, and its 'lobule' posteroinferior and on the medial aspect of the posterior inferior spine. Its edges are well defined but the surface, though articular, is rough and irregular. It articulates with the sacrum and is reciprocally shaped. The anterior sacroiliac ligament is attached to its sharp anterior and inferior borders. The narrow part of the pelvic surface, between the auricular surface and the upper rim of the greater sciatic notch, often shows a rough pre-auricular sulcus (that is usually better defined in females) for the lower fibres of the anterior sacroiliac ligament. For the reliability of this feature as a sex discriminant, refer to Finnegan (1978) and Brothwell and Pollard (2001). The pelvic surface is anteroinferior to the acutely curved part of the auricular surface, and contributes to the lateral wall of the lesser pelvis. Its upper part, facing down, is between the auricular surface and the upper limb of the greater sciatic notch; the lower part faces medially and is separated from the iliac fossa by the arcuate line. Anteroinferiorly, the pelvic surface extends to the line of union between the ilium and ischium.

Muscle attachments

The attachment of sartorius extends down the anterior border below the anterior superior iliac spine. The iliac crest gives attachment to the anterolateral and dorsal abdominal muscles, and to the fasciae and muscles of the lower limb. The fascia lata and iliotibial tract are attached to the outer lip and tubercle of its ventral segment. Tensor fasciae latae is attached anterior to the tubercle. The lower fibres of external oblique and, just behind the summit of the crest, the lowest fibres of latissimus dorsi are attached to its anterior two-thirds. A variable interval exists between the most posterior attachment of external oblique and the most anterior attachment of latissimus dorsi, and here the crest forms the base of the lumbar triangle through which herniation of abdominal contents may rarely occur. Internal oblique is attached to the intermediate area of the crest. Transversus abdominis is attached to the anterior two-thirds of the inner lip of the crest, and behind this to the thoracolumbar fascia and quadratus lumborum. The most superior fibres of gluteus maximus are attached to the dorsal segment of the crest on its lateral slope. Erector spinae arises from the medial slope of the dorsal segment. The straight head of rectus femoris is attached to the upper area of the anterior inferior spine. Some fibres of piriformis are attached in front of the posterior inferior spine on the upper border of the greater sciatic foramen.

The gluteal surface is divided by three gluteal lines into four areas. Behind the posterior line, the upper rough part gives attachment to the upper fibres of gluteus maximus and the lower, smooth region to part of the sacrotuberous ligament and iliac head of piriformis. Gluteus medius is attached between the posterior and anterior lines, below the iliac crest, and gluteus minimus is attached between the anterior and inferior lines. The fourth area, below the inferior line, contains vascular foramina.

The reflected head of rectus femoris attaches to a curved groove above the acetabulum. Iliacus is attached to the upper two-thirds of the iliac fossa and is related to its lower one-third. The medial part of quadratus lumborum is attached to the anterior part of the sacropelvic surface, above the iliolumbar ligament. Piriformis is sometimes partly attached lateral to the pre-auricular sulcus, and part of obturator internus is attached to the more extensive remainder of the pelvic surface.

Vascular supply

Branches of the iliolumbar artery run between iliacus and the ilium; one or more enter large nutrient foramina lying posteroinferiorly in the iliac fossa. The superior gluteal, obturator and superficial circumflex iliac arteries contribute to the periosteal supply. The obturator artery may supply a nutrient branch. Vascular foramina on the ilium underlying the gluteal muscles may lead into large vascular canals in the bone.

Innervation

The periosteum is innervated by branches of nerves that supply muscles attached to the bone, the hip joint and the sacroiliac joint.

Ossification

Ossification of the ilium is described on page 1355.

Ischium

The ischium, the inferoposterior part of the hip bone, has a body and ramus. The body has upper and lower ends and femoral, posterior and pelvic surfaces (see Figs 77.4–77.5). Above, it forms the posteroinferior part of the acetabulum; below, its ramus ascends anteromedially at an acute angle to meet the inferior pubic ramus, thereby completing the boundary of the obturator foramen. The ischiofemoral ligament is attached to the lateral border below the acetabulum (Fuss and Bacher 1991).

The femoral surface faces downwards, forwards and laterally towards the thigh. It is bounded in front by the margin of the obturator foramen. The lateral border, indistinct above but well defined below, forms the lateral limit of the ischial tuberosity. At a higher level the femoral surface is covered by piriformis, from which it is partially separated by the sciatic nerve and the nerve to quadratus femoris. The posterior surface, facing superolaterally, is continuous above with the iliac gluteal surface, and here a low convexity follows the acetabular curvature. Inferiorly, this surface forms the upper part of the ischial tuberosity, above which is a wide, shallow groove on its lateral and medial aspects. Above the ischial tuberosity the posterior surface is crossed by the tendon of obturator internus and the gemelli. The nerve to quadratus femoris lies between these structures and the ischium. The ischial tuberosity is a large, rough area on the lower posterior surface and inferior extremity of the ischium. Though obscured by gluteus maximus in hip extension, it is more readily palpable in hip flexion. It is 5 cm from the midline and about the same distance above the gluteal fold. It is elongated and widest above, and tapers inferiorly. The posterior aspect of the ischium lies between its lateral and posterior borders. The posterior border blends above with that of the ilium, helping to complete the inferior rim of the greater sciatic foramen, the posterior end of which has a conspicuous ischial spine. Below this the rounded border forms the floor of the lesser sciatic foramen, between the ischial spine and tuberosity. The pelvic surface is smooth and faces the pelvic cavity; inferiorly, it forms part of the lateral wall of the ischio-anal fossa.

Ischial ramus

The ischial ramus has anteroinferior and posterior surfaces continuous with the corresponding surfaces of the inferior pubic ramus. The anteroinferior surface is roughened by the attachment of the medial thigh muscles. The smooth posterior surface is partly divided into perineal and pelvic areas, like the inferior pubic ramus. The upper border completes the obturator foramen; the rough lower border, together with the medial border of the inferior pubic ramus, contributes to the pubic arch. The fascia overlying the superficial muscles of the perineum is attached below the ridge between the perineal and pelvic areas of the posterior surface of the ischial ramus. Above the ridge, areas give attachment to the crus of the penis or clitoris and the external urethral sphincter. The lower border of the ramus provides an attachment for the fascia lata and the stratum membranosum perinei.

Ischial tuberosity

The ischial tuberosity is divided nearly transversely into upper and lower areas. The upper area is subdivided by an oblique line into superolateral and inferomedial parts. The lower area, narrowing as it curves on to the inferior ischial aspect, is subdivided by an irregular vertical ridge into lateral and medial areas. The medial area is covered by fibroadipose tissue that usually contains the sciatic bursa of gluteus maximus, which supports the body in sitting. Medially the tuberosity is limited by a curved ridge that passes on to the ramus and which gives attachment to the sacrotuberous ligament and its falciform process.

Ischial spine

The ischial spine projects downwards and a little medially (see Fig. 77.4B). The sacrospinous ligament is attached to its margins, separating the greater from the lesser sciatic foramen. The ligament is crossed posteriorly by the internal pudendal vessels, pudendal nerve and the nerve to obturator internus.

Muscle attachments

Part of obturator externus is attached to the lower femoral surface of the ischial body. Part of obturator externus, the anterior fibres of adductor magnus and, near the lower border, gracilis are all attached to the anterior surface of the ischial ramus. Between adductor magnus and gracilis, the attachment of adductor brevis may descend from the inferior pubic ramus. The posterior surface is divided into pelvic and perineal areas. The pelvic area, facing back, has part of obturator internus attached to it. The perineal area faces medially; its upper part is related to the crus of the penis or clitoris, and its lower part gives attachment to sphincter urethrae, ischiocavernosus and the superficial transverse perineal muscle.

The ischial tuberosity gives attachment to the posterior thigh muscles. Quadratus femoris is attached along the upper part of its lateral border. The upper area of the tuberosity is subdivided by an oblique line into a superolateral part for semimembranosus and an inferomedial part for the long head of biceps femoris and semitendinosus. The lower area is subdivided by an irregular vertical ridge into lateral and medial areas. The larger lateral area is for part of adductor magnus. Superomedial to the tuberosity, the posterior surface has a wide, shallow groove, usually covered by hyaline cartilage, with a bursa between it and the tendon of obturator internus. Gemellus inferior is attached to the lower margin of the groove, near the tuberosity. Gemellus superior is attached to the upper margin, near the ischial spine. Forceful activation and/or severe stretch of the hamstrings can result in an avulsion fracture of the ischial tuberosity.

The pelvic surface of the ischial spine gives attachment to coccygeus and to the most posterior fibres of levator ani. Obturator internus is attached to the upper part of the smooth pelvic ischial surface and converges on the bony part of the lesser sciatic foramen, covering the rest of this surface other than the pelvic aspect of the ischial spine; the muscle and its fascia separate the bone from the ischio-anal fossa.

Vascular supply

There are multiple vascular foramina at the acetabular margins and a few are usually present on the pelvic surface. Branches of the obturator, medial circumflex femoral and inferior gluteal arteries supply the ischium.

Innervation

The periosteum is innervated by branches of nerves that supply the hip joint and muscles attached to the bone.

Ossification

Ossification of the ischium is described on page 1355.

Sacrum

See Chapter 46.

Coccyx

See Chapter 46.

Bony pelvis as a whole

The term pelvis ('basin') is applied variously to the skeletal ring formed by the hip bones and the sacrum, the cavity therein and even the entire region where the trunk and lower limbs meet (Fig. 77.8). It is used here in the skeletal sense, to describe the irregular osseous girdle between the femoral heads and fifth lumbar vertebra. It is large because its primary function is to withstand the forces of body weight and musculature. In this section, its obstetric, forensic and anthropological significance will be considered.

The pelvis can be regarded as having greater and lesser segments, the false and true pelves, respectively. The segments are arbitrarily

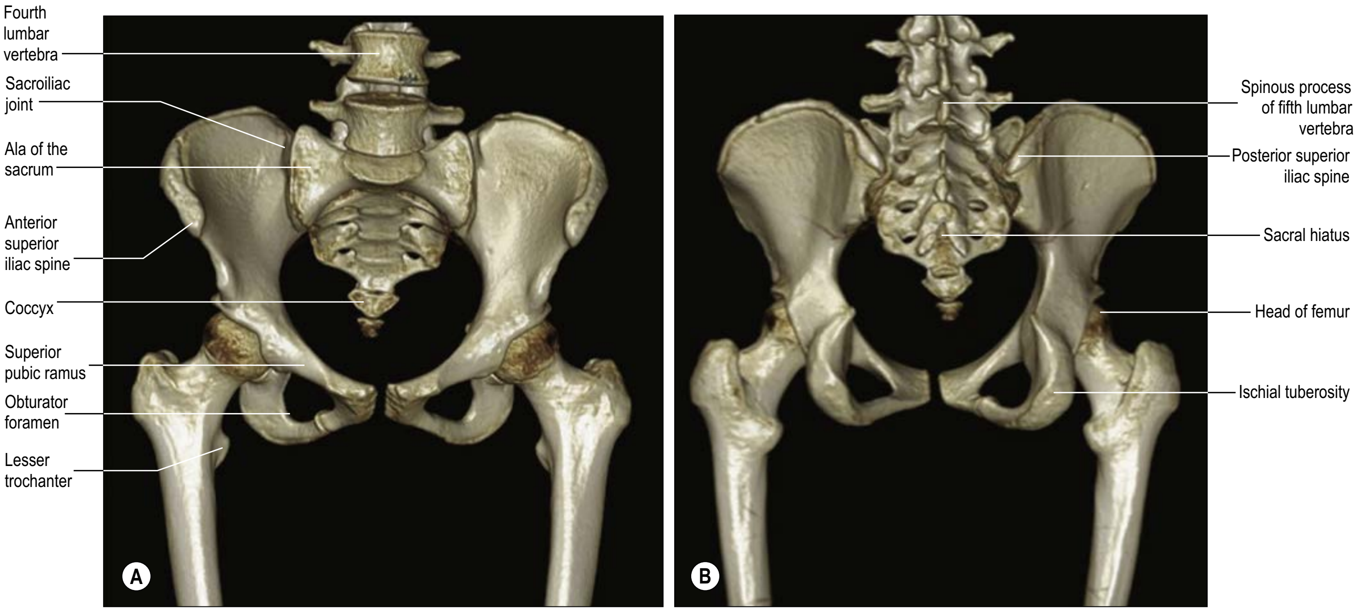

Fig. 77.8 Anterior (**A**) and posterior (**B**) views of the female pelvis, upper femur and lower lumbar spine, using three-dimensional computed tomography. (Courtesy of Dr Yoginder Vaid and Mr Jon C Betts, Jr.)

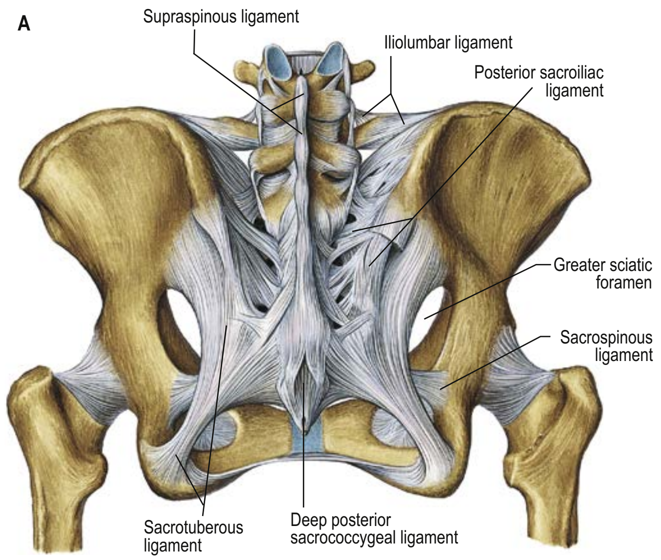

Fig. 77.9 The greater and lesser sciatic foramina, **A**, Posterior aspect of the pelvis. (Sobotta Atlas of Human Anatomy © Elsevier GmbH, Urban & Fischer, Munich.) (B, *continued online*.)

divided by an oblique plane passing through the sacral promontory posteriorly and the lineae terminales elsewhere. Each linea terminalis includes the iliac arcuate line, pectineal line (pecten pubis) and pubic crest.

Greater pelvis

The greater pelvis consists of the ilium and pubis above the lineae terminales and the base of the sacrum. This junctional zone is structurally massive and forms powerful arches from the acetabular fossae to the vertebral column around the visceral cavity, which is part of the abdomen. It has little anterior wall because of the pelvic inclination.

Pelvic inlet (superior pelvic aperture)

The pelvic inlet or brim may be round or oval in shape, and is indented posteriorly by the sacral promontory. The pelvic brim is obstetrically important and has also long been measured for anthropological reasons, as has the pelvic cavity.

By convention, the pelvic inlet is described in three dimensions. The anteroposterior diameter (true conjugate) is measured between the midpoints of the sacral promontory and upper border of the pubic symphysis, and on average is 10 cm in the adult male and 11.2 cm in the adult female. The transverse diameter is the maximum distance between similar points (assessed by eye) on opposite sides of the pelvic brim, and is on average 12.5 cm in the adult male and 13.1 cm in the adult female. The oblique diameter is measured from the iliopubic ramus to the opposite sacroiliac joint, and is on average 12 cm in the adult male and 12.5 cm in the adult female. These measurements vary with the individual and with racial group. In children, dimensions of the thorax and spine are significantly correlated with the width of the pelvic inlet, which are age-independent predictors of paediatric chest width and may be useful in assessing growth of the thorax and spine in children with early-onset spinal deformity (Emans et al 2005).

Articulated bony pelvis

The lesser pelvis encloses a true basin when soft tissues of the pelvic floor are in place. Skeletally, it is a narrower continuation of the greater pelvis, with irregular but more complete walls around its cavity. Of obstetric importance, it has a curved median axis, and superior and inferior openings. The superior opening is occupied by viscera. The pelvic floor, viscera and subjacent perineal sphincters close the inferior opening.

Cavity of the lesser pelvis

The cavity of the lesser pelvis is short, curved and markedly longer in its posterior wall. Anteroinferiorly, it is bounded by pubic bones, their rami and symphysis. Posteriorly, it is bounded by the concave anterior sacral surface and coccyx. Laterally, on each side its margins are the smooth quadrangular pelvic aspect of the fused ilium and ischium. The region so enclosed is the pelvic cavity proper, through which pass the rectum, urinary bladder and parts of the reproductive organs. The cavity in females must also permit passage of the fetus.

The pelvic cavity diameters are measured at approximately the midlevel. The anteroposterior diameter is measured between the midpoints of the third sacral segment and posterior surface of the pubic symphysis, and is about 10.5 cm in the adult male and 13 cm in the adult female. The transverse diameter is the widest transverse distance between the side walls of the cavity, and often the greatest transverse dimension in the whole cavity. It measures about 12 cm in the adult male and 12.5 cm in the adult female. The oblique diameter is the distance from the lowest point of one sacroiliac joint to the midpoint of the contralateral obturator membrane, and measures about 11 cm in the adult male and 13.1 cm in the adult female. All measurements vary with the individual and with racial group.

Pelvic outlet (inferior pelvic aperture)

Less regular in outline than the pelvic inlet, the pelvic outlet is indented behind by the coccyx and sacrum, and bilaterally by the ischial tuberosities. Its perimeter thus consists of three wide arcs. Anteriorly is the pubic arch, between the converging ischiopubic rami. Posteriorly and laterally on both sides are the sciatic notches between the sacrum and ischial tuberosities. The sciatic notches are divided by the sacrotuberous and sacrospinous ligaments into greater and lesser sciatic foramina (Fig. 77.9).

With ligaments included, the pelvic outlet is rhomboidal. Its anterior limbs are the ischiopubic rami (joined by the inferior pubic (arcuate) ligament) and its posterior margins are the sacrotuberous ligaments, with the coccyx in the midline. The outlet is thus not rigid in its posterior half, being limited by ligaments and the coccyx, all slightly yielding. Even with the sacrum taken as the posterior midline limit (more reliable for measurement), there is typically slight mobility at the sacroiliac joints. Note also that a plane of the pelvic outlet is merely conceptual. The anterior, ischiopubic part has a plane that is inclined down and back to a transverse line between the lower limits of the ischial tuberosities, and the posterior half has a plane approximating to the sacrotuberous ligaments, sloping down and forwards to the same line.

Three measurements are made for the pelvic outlet. The anteroposterior diameter is usually measured from the apex of the coccyx to the midpoint of the lower rim of the pubic symphysis. The lowest sacral point may also be used (on average: male 8 cm, female 12.5 cm). The transverse (bituberous) diameter is measured between the ischial tuberosities at the lower borders of their medial surfaces (on average: male 8.5 cm, female 11.8 cm). The oblique diameter extends from the midpoint of the sacrotuberous ligament on one side to the contralateral ischiopubic junction (on average: male 10 cm, female 11.8 cm). All measurements vary among individuals and racial groups.

Other measurements

Apart from these main measurements, by consensus the basis of pelvic osteometry, other planes and measurements are used in obstetric practice. The plane of greatest pelvic dimensions is an obstetric concept. It represents the most capacious pelvic level, between the pelvic brim and midlevel plane, and corresponds with the latter anteriorly at the middle part of the pubic symphysis and posteriorly at the level of the second and third sacral segments.

The plane of least dimensions is said to be at about mid-pelvic level. Its transverse diameter is between the apices of the ischial spines. This measurement is about 9.5 cm in an adult female and is just wide enough to allow passage of the biparietal diameter of a fetal head (about 9 cm). Not surprisingly, most difficult parturition occurs here.

The above measurements are sometimes made in clinical practice using radiographs or magnetic resonance imaging (MRI) pelvimetry. Precise measurement is not possible without radiological techniques, and even these do not consider the adjacent soft tissues.

Pelvic axes and inclination

The axis of the superior pelvic aperture traverses its centre at right-angles to its plane, directed down and backwards (Fig. 77.10). When prolonged (projected), it passes through the umbilicus and mid-coccyx. An axis is similarly established for the inferior aperture: projected upwards, it impinges on the sacral promontory. Axes can likewise be constructed for any plane, and one for the whole cavity is a concatenation of an infinite series of such lines (see Fig. 77.10).

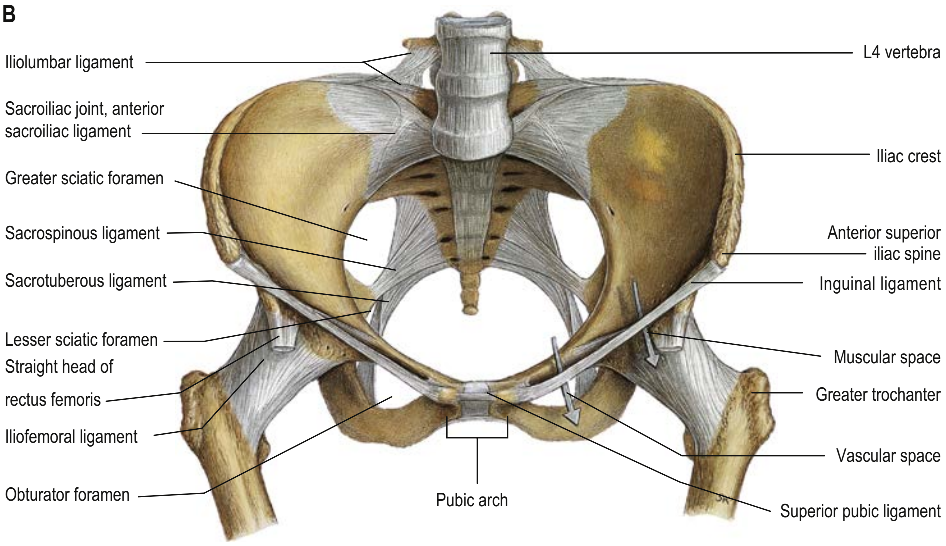

Fig. 77.9 B, Anterior aspect of the pelvis. Note the arrows indicating vascular and muscular spaces. (Sobotta Atlas of Human Anatomy © Elsevier GmbH, Urban & Fischer, Munich.)

The skeletal pelvis supports and protects the contained viscera but is primarily part of the lower limbs, affording wide attachment for muscles of the thigh, leg and trunk. It constitutes the major mechanism for transmitting the weight of the head, trunk and upper limbs to the lower limbs. It may be considered as two arches divided by a coronal trans-acetabular plane. The posterior arch, chiefly concerned in transmitting weight, consists of the upper three sacral vertebrae and strong pillars of bone from the sacroiliac joints to the acetabular fossae. The anterior arch, formed by the pubic bones and their superior rami, connects these lateral pillars as a tie beam to prevent separation; it also acts as a compression strut against medial femoral thrust. The sacrum, as the summit of the posterior arch, is loaded at the lumbosacral joint. Theoretically, this force has two components: one thrusting the sacrum downwards and backwards between the iliac bones, the other thrusting its upper end downwards and forwards. Sacroiliac joint movements are regulated by osseous shape and massive ligaments. The first component therefore acts against the wedge, its tendency to separate iliac bones resisted by the sacroiliac and iliolumbar ligaments and pubic symphysis.

Vertical coronal sections through the sacroiliac joints suggest division of the (synovial) articular region of the sacrum into three segments. In the anterosuperior segment, involving the first sacral vertebra, the articular surfaces are slightly sinuous and almost parallel. In the middle segment, the posterior width between the articular markings is greater than the anterior, and centrally a sacral concavity fits a corresponding iliac convexity, an interlocking mechanism relieving the strain on the ligaments produced by body weight. In the posteroinferior segment, the anterior sacral width is greater than the posterior and here its sacral surfaces are slightly concave. Anteroinferior sacral dislocation by the second component (of force) is prevented, therefore, mainly by the middle segment, owing to its cuneiform shape and interlocking mechanism. However, some rotation occurs, in which the anterosuperior segment tilts down and the posteroinferior segment up. 'Superior' segmental movement is limited to a small degree by wedging but primarily by tension in the sacrotuberous and sacrospinous ligaments. In all movements, the sacroiliac and iliolumbar ligaments and pubic symphysis resist separation of the iliac bones.

The pelvis provides the most marked skeletal differences between male and female. Although there is some skeletal sexual dimorphism in infancy and childhood, most researchers agree that this is minimal. There are methods that focus on the shape of the greater sciatic notch, but they are quite unreliable. Sexual differences in adults are divisible into metrical and non-metrical features; the range of most features overlaps between the sexes.

Differences are inevitably linked to function. Although the primary pelvic function in both sexes is locomotor, the pelvis, particularly the lesser pelvis, is adapted to parturition in females, and these changes variably affect the proportions and dimensions of the greater pelvis (Betti and Manica 2018). Since males are stereotypically more muscular and therefore more heavily built, overall pelvic dimensions, such as the intercristal distance (distance between the iliac crests), are greater, markings for muscles and ligaments more pronounced, and general architecture more robust. The male iliac crest is more rugged and more medially inclined at its anterior end; in females the iliac crests are less curved in all parts. The iliac alae are more vertical in females but do not ascend so far; the iliac fossae are therefore shallower. These iliac peculiarities probably account for the greater prominence of female hips.

The male is more robust above the pelvis, with consequent differences at the lumbosacral and hip joints. The sacral basal articular facet for the fifth lumbar vertebra and intervening intervertebral disc is more than one-third of the total sacral basal width in males but less than one-third in females, in whom the sacrum is also relatively broader, accentuating this difference. The female has relatively broader sacral alae. The male acetabulum is larger, and its diameter is approximately equal to the distance between its anterior rim and pubic symphysis. In females, acetabular diameter is usually less than this distance, not only because it is smaller but also because the anterolateral wall of the cavity is comparatively and often absolutely wider. The height of the female pubic symphysis and adjoining parts of the pubis and ischium, which form the anterior pelvic wall, are also less, producing a somewhat triangular obturator foramen, which is more ovoid in males. Differing pubic growth is also expressed in the pubic arch below the pubic symphysis and between the inferior pubic rami. It is more angular in males, being 50–60°; in females it is rounded, less easy to measure and usually 80–85°. A greater separation of the pubic tubercles in females contributes to the pubic width. The ischiopubic rami are also much more lightly built and narrowed near the symphysis; in males they bear a distinctly rough, everted area for attachment of the penile crura and in females the corresponding attachment for the clitoris is the ventral arc. The ischial spines are closer in males and are more inturned. The greater sciatic notch is usually wider in females: mean values for males and females are 50.4° and 74.4°, respectively. The greater female values for angle and width are associated with increased backward sacral tilt and greater anteroposterior pelvic diameter, especially at lower levels.

The sacrum also displays metrical sexual differences. Female sacra are less curved, the curvature being most marked between the first and second segments and the third and fifth, with an intervening flatter region. Male sacra are more evenly curved, and relatively long and narrow, and more often exceed five segments (by addition of a lumbar or coccygeal vertebra). The sacral index compares sacral breadth (between the most anterior points on the auricular surfaces) with length (between midpoints on the anterior margins of the promontory and apex): average values for males and females are 105% and 115%, respectively. Auricular surfaces are relatively smaller and more oblique in females, but extend on to the upper three sacral vertebrae in both sexes. The dorsal auricular border is more concave in females. Many differences may be summarized in the generalization that the pelvic cavity is longer and more conical in males, and shorter and more cylindrical in females; the axis is curved in both. Differences are greater at the inferior aperture than at the brim, where in absolute measurements males are not as different from females as sometimes stated.

In forensic practice, identification of human skeletal remains (which are sometimes fragmentary) usually involves estimation of sex, and this is most reliably established from an examination of the pelvis. Even fragments of the pelvis can be useful in this respect, and may be considered alongside skull robusticity or gracility and long bone metrics. Pelvic features taken into account include the subpubic angle, pubic width, sacral curvature, width of the greater sciatic notch, and the proportion of the body of the first sacral vertebra compared to the alae. It is important to consider all data available for measuring skeletal sexual dimorphism of the pelvis and skull, as assessment of sex from isolated and often incomplete human remains is less reliable. For further details, consult White and Folkens (2005).

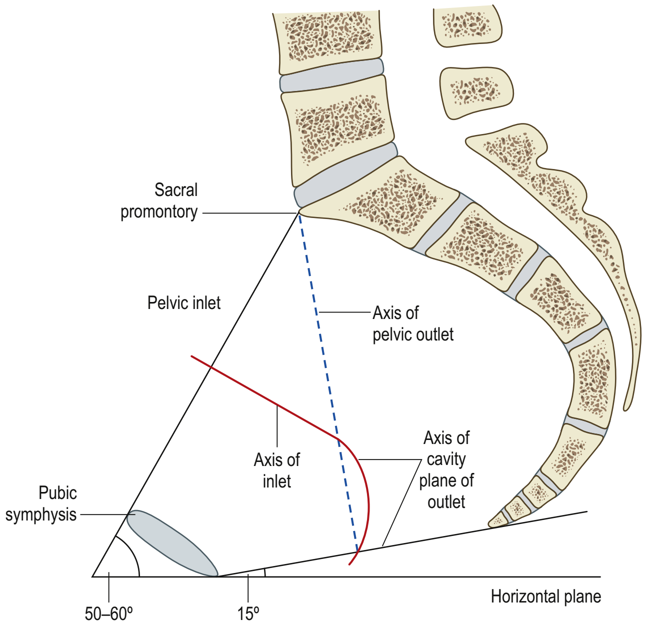

Fig. 77.10 A median sagittal section through the female pelvis, showing the planes of the inlet and outlet and the axis of the pelvic cavity.

The fetal head, however, descends in the axis of the inlet as far as the level of the ischial spines; it is then directed forwards into the axis of the vagina at right-angles to that axis. The form of this pelvic axis and the disparity in depth between the anterior and posterior contours of the cavity are prime factors in the mechanism of fetal transit in the pelvic canal.

In the standing position, the pelvic canal curves obliquely backwards relative to the trunk and abdominal cavity. The whole pelvis is tilted forwards, the plane of the pelvic brim making an angle of 50–60° with the horizontal. The plane of the pelvic outlet is tilted to about 15°. Strictly, the pelvic outlet has two planes: an anterior passing backwards from the pubic symphysis and a posterior passing forwards from the coccyx, both descending to meet at the intertuberous line. In standing, the pelvic aspect of the pubic symphysis faces nearly as much upwards as backwards and the sacral concavity is directed anteroinferiorly. The front of the pubic symphysis and anterior superior iliac spines are in the same vertical plane. While sitting, body weight is transmitted through the inferomedial parts of the ischial tuberosities, with variable soft tissues intervening. The anterior superior iliac spines are in a vertical plane through the acetabular centres, and the whole pelvis is tilted back with the lumbosacral angle somewhat diminished at the sacral promontory.

Pelvic mechanism

Available with the *Gray's Anatomy* e-book

Sexual differences in the pelvis

Available with the *Gray's Anatomy* e-book

Femur

The femur is the longest and strongest bone in the human body (Figs 77.11–77.12). Its length is associated with a striding gait, and its strength with the weight and muscular forces it is required to withstand. Its shaft, almost cylindrical along most of its length, is bowed forwards. It has a proximal rounded, articular head projecting medially from its short neck, which, in turn, is a medial extension of the proximal shaft. The distal extremity is wider and more substantial, and presents two condyles that articulate with the tibia. In standing, the femoral shafts show an inclination upwards and outwards from their tibial articulations, with the femoral heads being separated by the pelvic width. Since the tibia and fibula descend vertically from the knees, the ankles are also in the line of body weight in standing or walking. The degree of femoral obliquity varies between individuals but is generally greater in women, reflecting the relatively greater pelvic breadth and shorter femora. Proximally, the femur consists of a head, neck and greater and lesser trochanters.

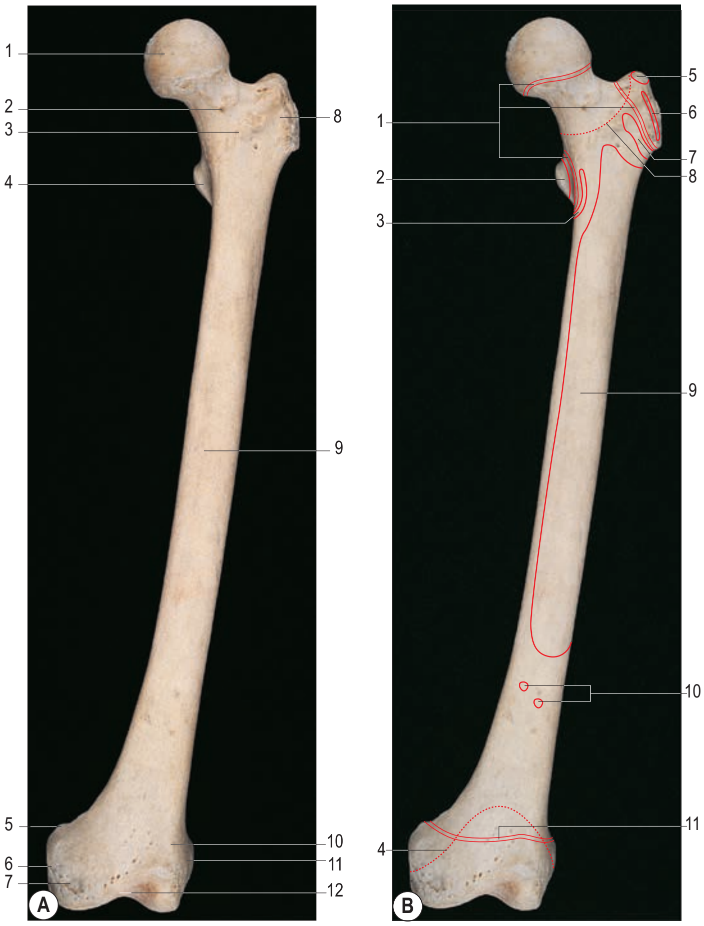

Fig. 77.11 Left femur. **A**, Anterior aspect. **B**, Muscle attachments. **A**, Key: 1, head; 2, neck; 3, intertrochanteric line; 4, lesser trochanter; 5, adductor tubercle; 6, medial epicondyle; 7, medial condyle; 8, greater trochanter; 9, shaft; 10, lateral condyle; 11, lateral epicondyle; 12, patellar surface. **B**, Key: 1, epiphysial lines (growth plates); 2, psoas major; 3, vastus medialis; 4, attachment site of hip joint capsule; 5, piriformis; 6, gluteus minimus; 7, vastus lateralis; 8, attachment site of knee joint capsule; 9, vastus intermedius; 10, articularis genus; 11, epiphysial line (growth plate).

Femoral head

The femoral head faces anterosuperomedially to articulate with the acetabulum (Fig. 77.13). The head, often described as rather more than half a 'sphere', is not part of a true sphere but is spheroidal. Its smoothness is interrupted posteroinferior to its centre by a small, rough fovea, to which the ligament of the head of the femur (ligamentum teres) is attached. The head is intracapsular and is encircled, distal to its equator, by the acetabular labrum. Its articular margin is distinct, except anteriorly, where the articular surface extends on to the neck. The anterior surface of the head is separated inferomedially from the femoral artery by the tendon of psoas major, the iliopectineal bursa and the articular capsule.

Femoral neck

The femoral neck (see Fig. 77.13) is approximately 5 cm long, narrowest in its mid part and widest laterally, and connects the head to the shaft at an average angle of approximately 127° (Gilligan et al 2013) (angle of inclination; neck–shaft angle). The neck is also anteriorly rotated with respect to the shaft (angle of anteversion) some 10–15°, although values of this angle vary between individuals and between populations (Eckhoff et al 1994). The contours of the neck are rounded; the upper surface is almost horizontal and slightly concave, while the lower is straighter but oblique, directed inferolaterally and backwards to the shaft near the lesser trochanter. On all aspects the neck expands as it approaches the articular surface of the head. Morphological variation of this bony expansion may cause painful impingement between the femoral neck and acetabular labrum at the

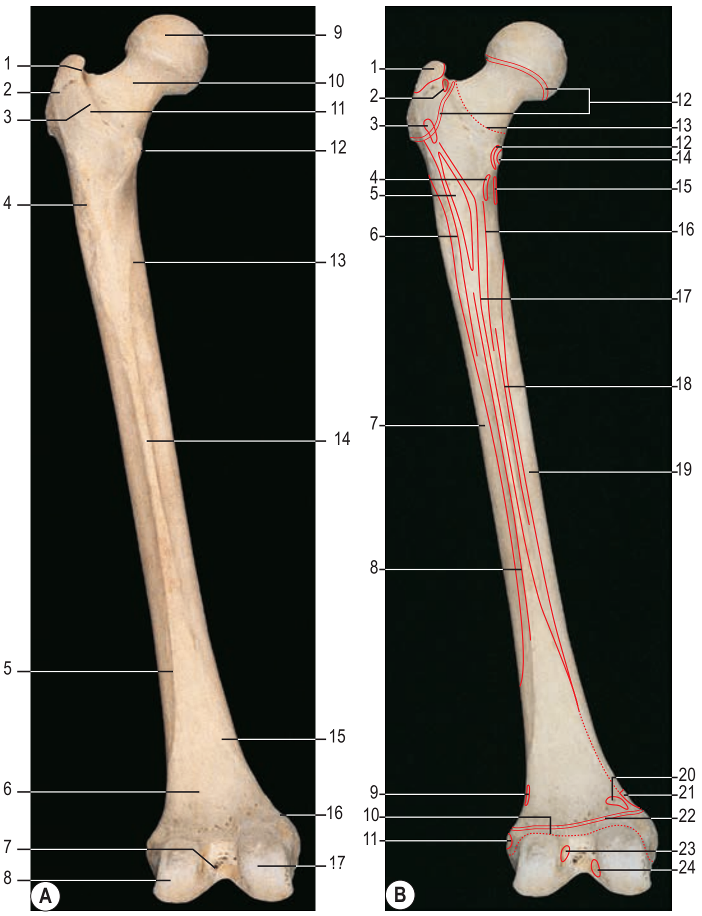

Fig. 77.12 Left femur. **A**, Posterior aspect. **B**, Muscle attachments. **A**, Key: 1, trochanteric fossa; 2, greater trochanter; 3, quadrate tubercle; 4, gluteal tuberosity; 5, lateral supracondylar line; 6, popliteal surface; 7, intercondylar fossa; 8, lateral condyle; 9, head; 10, neck; 11, intertrochanteric crest; 12, lesser trochanter; 13, spiral (pectineal) line; 14, linea aspera; 15, medial supracondylar line; 16, adductor tubercle; 17, medial condyle. **B**, Key: 1, gluteus medius; 2, obturator externus; 3, quadratus femoris; 4, pectineus; 5, gluteus maximus; 6, vastus lateralis; 7, vastus intermedius; 8, biceps femoris, short head; 9, plantaris; 10, attachment site of knee joint capsule; 11, gastrocnemius, lateral head; 12, epiphysial lines (growth plates); 13, attachment site of hip joint capsule; 14, psoas major; 15, iliacus; 16, adductor brevis; 17, adductor magnus; 18, adductor longus; 19, vastus medialis; 20, gastrocnemius, medial head; 21, adductor magnus; 22, epiphysial line (growth plate); 23, anterior cruciate ligament; 24, posterior cruciate ligament.

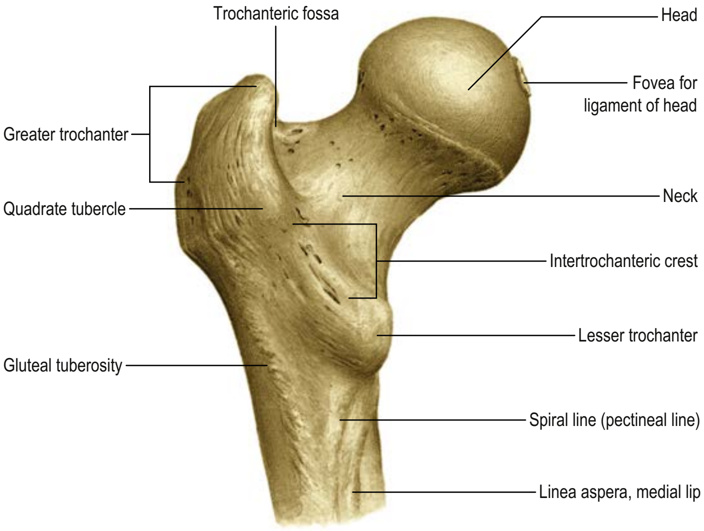

Fig. 77.13 The proximal end of the femur, posterior aspect. (Sobotta Atlas of Human Anatomy © Elsevier GmbH, Urban & Fischer, Munich.)

extremes of flexion and medial (internal) rotation positions. The anterior surface of the neck is flat and marked at the junction with the shaft by a rough intertrochanteric line. The posterior surface, facing posteriorly and superiorly, is transversely convex, and concave in its long axis; its junction with the shaft is marked by a rounded intertrochanteric crest. There are numerous vascular foramina, especially anteriorly and posterosuperiorly.

The anterior surface is intracapsular, the capsule attaching laterally to the intertrochanteric line. Facets, often covered by extensions of articular cartilage, and various imprints frequently occur here. On the posterior surface the capsule does not reach the intertrochanteric crest; little more than the medial half of the neck is intracapsular. The anterior surface adjoining the head and covered by cartilage is related to the iliofemoral ligament. A groove, produced by the tendon of obturator externus as it approaches the trochanteric fossa, spirals across the posterior surface of the neck of the femur in a proximolateral direction.

Greater trochanter

The greater trochanter is large and quadrangular, projecting up from the junction of the neck and shaft (see Fig. 77.13). The leverage of many hip muscles is enhanced by their attachment to this prominent bony feature. Its posterosuperior region projects superomedially to overhang the adjacent posterior surface of the neck and here its medial surface presents the rough trochanteric fossa. The proximal border of the trochanter lies approximately a hand's breadth below the iliac tuberculum, level with the centre of the femoral head. It has an anterior rough impression. Its lateral surface, continuous distally with the lateral surface of the femoral shaft, is crossed anteroinferiorly by an oblique, flat strip, which is wider above. This surface is readily palpable, especially when the muscles are relaxed.

Lesser trochanter

The lesser trochanter is a conical posteromedial projection of the shaft at the posteroinferior aspect of its junction with the neck. Its summit and anterior surface are rough, but its posterior surface, at the distal end of the intertrochanteric crest, is smooth. It is not palpable. The lesser trochanter serves as the primary attachment for the large iliopsoas muscle.

Intertrochanteric line

The intertrochanteric line, a prominent ridge at the junction of the anterior surfaces of the neck and shaft, descends medially from a tubercle on the upper part of the anterior aspect of the greater trochanter to a point on the lower border of the neck, anterior to the lesser trochanter, where there may also be a tubercle. This line is the lateral limit of the hip joint capsule anteriorly. The upper and lower bands of the iliofemoral ligament are attached to its proximal and distal ends and the associated tubercles. Distally, it is continuous with the spiral (pectineal) line.

Intertrochanteric crest

The intertrochanteric crest, a smooth and prominent ridge at the junction of the posterior surface of the neck with the shaft, descends medially from the posterosuperior angle of the greater trochanter to the lesser trochanter. A little above its centre is the low, rounded quadrate tubercle. It is covered by gluteus maximus, from which it is separated, medial to the tubercle, by quadratus femoris and the upper border of adductor magnus.

Gluteal tuberosity

The gluteal tuberosity, accepting the tendon of the gluteus maximus, may be an elongated depression or a ridge. It may at times be prominent enough to merit the title of a third trochanter.

Shaft

The shaft is surrounded by muscles and is impalpable (see Figs 77.11B, 77.12B). The distal anterior surface, for 5–6 cm above the patellar articular surface, is covered by a suprapatellar bursa, between bone and muscle. The proximal two-thirds of the anterior and lateral surfaces are covered by vastus intermedius. The medial surface, devoid of attachments, is covered by vastus medialis.

The shaft is narrowest centrally, expanding a little at its proximal end, and substantially more at its distal end. Its long axis makes an angle of approximately 10° with the vertical, and diverges 5–7° from the long axis of the tibia. Its middle one-third has three surfaces and borders. The extensive anterior surface, smooth and gently convex, is between the lateral and medial borders, which are both round and indistinct. The posterolateral surface is bounded posteriorly by the broad, rough and often raised, linea aspera, usually a crest with lateral and medial edges. Its subjacent compact bone is augmented to withstand compressive forces, which are concentrated here by the anterior curvature of the shaft. The linea aspera gives at least partial attachment to adductors longus and brevis, adductor magnus, vastus medialis and lateralis, intermuscular septa (partially continuous with the fascia lata of the thigh), and the short head of biceps femoris, all inseparably blended at their attachments. Perforating arteries cross the linea aspera laterally under tendinous arches in adductor magnus and biceps femoris. Nutrient foramina, directed proximally, appear in the linea aspera, varying in number and site, one usually near its proximal end, a second usually near its distal end. The posteromedial surface, smooth like the others, is bounded in front by the indistinct medial border and behind by the linea aspera. In its proximal third the shaft has a fourth, posterior surface, bounded medially by the narrow, rough spiral line. Laterally, this surface is limited by the broad, rough gluteal tuberosity, ascending a little laterally to the greater trochanter and descending to the lateral edge of the linea aspera. In its distal one-third, the posterior surface of the shaft presents a further surface, the popliteal surface (see below) between the medial and lateral supracondylar lines. These lines are continuous above with the corresponding edges of the linea aspera. The lateral line is most distinct in its proximal two-thirds, where the short head of biceps femoris and lateral intermuscular septum are attached. Its distal third has a small, rough area for the attachment of plantaris, often encroaching on the popliteal surface. The medial line is indistinct in its proximal two-thirds, where vastus medialis is attached. Distally, the femoral vessels entering the popliteal fossa from the adductor canal cross the medial line obliquely. Further distally, the line is often sharp for 3 or 4 cm proximal to the adductor tubercle.

The popliteal surface, triangular in outline, lies between the medial and lateral supracondylar lines. In its distal medial part, it is rough and slightly elevated. Forming the proximal part of the floor of the popliteal fossa, the popliteal surface is covered by a variable amount of fat that separates the popliteal artery from bone. The superior medial genicular artery, a branch of the popliteal artery, arches medially above the medial condyle. It is separated from bone by the medial head of gastrocnemius. The latter is attached a little above the condyle; further distally, there may be a smooth facet underlying a bursa for the medial head of gastrocnemius. More medially, there is often an imprint proximal to the articular surface; in deep flexion, this is close to a rough tubercle on the medial tibial condyle for the attachment of semimembranosus. The superior lateral genicular artery arches up laterally proximal to the lateral condyle but is separated from bone by the attachment of plantaris to the distal part of the lateral supracondylar line.

Distal end

The distal end of the femur is widely expanded as a bearing surface for transmission of weight to the tibia (**Fig. 77.14**). It bears two massive condyles, which are partly articular. Anteriorly, the condyles are confluent and continue into the shaft; posteriorly, they are separated by a deep intercondylar fossa and project beyond the plane of the popliteal surface. The articular surface is a broad area, like an inverted U, for the patella and the tibia. The patellar surface extends anteriorly on both condyles, especially the lateral. It is transversely concave, vertically convex and grooved for the posterior patellar surface. The tibial surface is divided by the intercondylar fossa but is anteriorly continuous with the patellar surface. Its medial part is a broad strip on the convex inferoposterior surface of the medial condyle, and is gently curved with a medial convexity. Its lateral part covers similar aspects of the lateral condyle but is broader and passes straight back. The tibial surfaces are convex in all directions. The medial and lateral tibial surfaces have dissimilar anteroposterior curvatures; as evident in Fig. 77.14, the medial condyle curves more obliquely than the lateral. As described in Chapter 78 on the knee, these differences are believed to be important determinants in the mechanics of locking the knee in full extension.

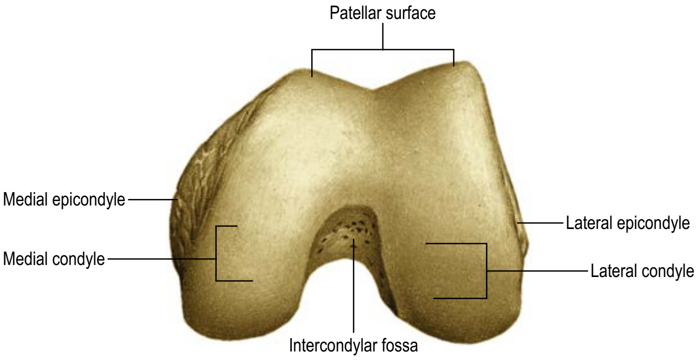

Fig. 77.14 The distal end of the femur, articular surface. (Sobotta Atlas of Human Anatomy © Elsevier GmbH, Urban & Fischer, Munich.)

Patellar surface

The patellar surface extends more proximally on the lateral side. Its proximal border is therefore oblique and runs distally and medially, separated from the tibial surfaces by two faint grooves that cross the condyles obliquely. The lateral groove is the more distinct. It runs laterally and slightly forwards from the front of the intercondylar fossa and expands to form a faint triangular depression, resting on the anterior edge of the lateral meniscus when the knee is fully extended. The medial groove is restricted to the medial part of the medial condyle and rests on the anterior edge of the medial meniscus in full extension. Where it ceases, the patellar surface continues back to the lateral part of the medial condyle as a semilunar area adjoining the anterior region of the intercondylar fossa. This area articulates with the medial vertical facet of the patella in full flexion; its outline is indistinct in most femora.

Intercondylar fossa

The intercondylar fossa separates the two condyles distally and behind. In front, the distal border of the patellar surface limits it, and behind an intercondylar line limits it, separating it from the popliteal surface. It is intracapsular but largely extrasynovial. Its lateral wall, the medial surface of the lateral condyle, bears a flat posterosuperior impression that spreads to the floor of the fossa near the intercondylar line for the proximal attachment of the anterior cruciate ligament. The medial wall of the fossa, i.e. the lateral surface of the medial condyle, bears a similar larger area, but far more anteriorly, for the proximal attachment of the posterior cruciate ligament. Both impressions are smooth and largely devoid of vascular foramina, whereas the rest of the fossa is rough and pitted by vascular foramina. A bursal recess between the ligaments may ascend to the fossa. The capsular ligament and, laterally, the oblique popliteal ligament are attached to the intercondylar line. The infrapatellar synovial fold is attached to the anterior border of the fossa.

Lateral condyle

The lateral condyle (see Fig. 77.14) is larger anteroposteriorly than the medial condyle. Its most prominent point is the lateral epicondyle to which the fibular collateral ligament is attached (**Fig. 77.15**). A short groove, deeper in front, separates the lateral epicondyle inferiorly from the articular margin. This groove allows the tendon of popliteus to run deep to the fibular collateral ligament and insert

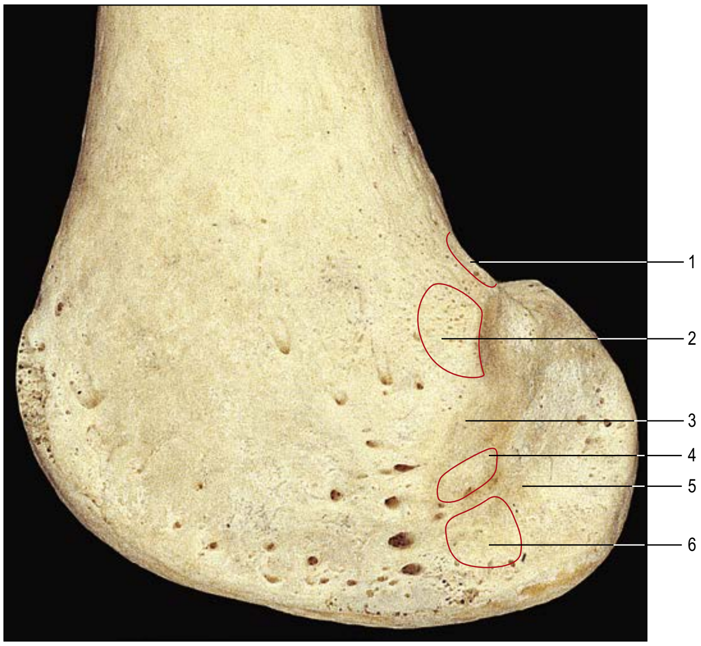

Fig. 77.15 The distal end of the femur, lateral aspect. Key: 1, attachment of plantaris; 2, attachment of lateral head of gastrocnemius; 3, lateral epicondyle; 4, attachment of fibular collateral ligament; 5, groove for popliteus in full flexion; 6, attachment of popliteus. Note multiple nutrient foramina.

inferior and anterior to the ligament insertion. Adjoining the joint margin is a strip of condyle, 1 cm broad. It is intracapsular and covered by synovial membrane except for the attachment of popliteus.

The medial surface is the lateral wall of the intercondylar fossa. Its lateral surface projects beyond the shaft. Part of the lateral head of gastrocnemius is attached to an impression posterosuperior to the lateral epicondyle.

Medial condyle

The medial condyle has a bulging, convex medial aspect, which is easily palpable. Proximally, its adductor tubercle, which may only be a facet rather than a projection, receives the tendon of adductor magnus. The medial prominence of the condyle, the medial epicondyle, is anteroinferior to the tubercle. The lateral surface of the condyle is the medial wall of the intercondylar fossa. The condyle projects distally so that, despite the obliquity of the shaft, the profile of the distal end is almost horizontal. A curved strip, 1 cm wide and adjoining the medial articular margin, is covered by synovial membrane and is inside the joint capsule. Proximal to this, the medial epicondyle receives the tibial collateral ligament.

Structure

The femoral shaft is a cylinder of compact bone with a large medullary cavity. The wall is thick in its middle third, where the femur is narrowest and the medullary cavity most capacious. Proximally and distally the compact wall becomes progressively thinner, and the cavity gradually fills with trabecular bone. The extremities, especially the articular areas, consist of trabecular bone within a thin shell of compact bone, their trabeculae being disposed along lines of greatest stress. At the proximal end the main trabeculae form a series of plates orthogonal to the articular surface, converging to a central dense wedge, which is supported by strong trabeculae passing to the sides of the neck, especially along its upper and lower profiles (**Fig. 77.16**). Force applied to the femoral head is therefore transmitted to the wedge and from there to the junction of the neck and shaft. This junction is strengthened by dense trabeculae extending laterally from the lesser trochanter to the end of the superior aspect of the neck, thus resisting tensile or shearing forces applied to the neck through the head (**Fig. 77.17**). Tensile and compressive tests indicate that axial trabeculae of the femoral head withstand much greater stresses than peripheral trabeculae. A smaller bar across the junction of the greater trochanter with the neck and shaft resists shearing caused by forces produced by local muscles such as the gluteus medius. A thin vertical plate, the so-called calcar femorale, ascends from the compact wall near the linea aspera into the trabeculae of the neck (see Fig. 77.17). Medially, it joins the posterior wall of the neck; laterally, it continues into the greater trochanter, where it disperses into general trabecular bone. It is thus in a plane anterior to the trochanteric crest and base of the lesser trochanter. Dixon (1910) demonstrated that the trabecular framework of the proximal femur was spiral, and that the 'arches' were simplified sectional profiles of this spiral. At the distal end of the femur, trabeculae spring from the entire internal surface of compact bone, descending perpendicular to the articular surface. Proximal to the condyles these are strongest and most accurately perpendicular. Horizontal planes of trabecular bone, arranged like crossed girders, form a series of cubical compartments.

Muscle attachments

The greater trochanter provides attachment for glutei medius and minimus. Gluteus minimus is attached to its rough anterior impression and gluteus medius to its posterosuperior aspect and an oblique line on its lateral surface. The bone is separated from the tendons of gluteus minimus and medius by several bursae (Woodley et al 2008). The area behind it is covered by deep fibres of gluteus maximus, with part of its trochanteric bursa interposed. The tendon of piriformis is attached to the upper border of the trochanter and the common (tricipital) tendon of obturator internus and the gemelli is attached to its medial surface. The trochanteric fossa receives the tendon of obturator externus. Psoas major is attached to the summit and anteromedial surface of the lesser trochanter, and iliacus to the medial or anterior surface of its base, descending a little behind the spiral line as its tendon fuses with that

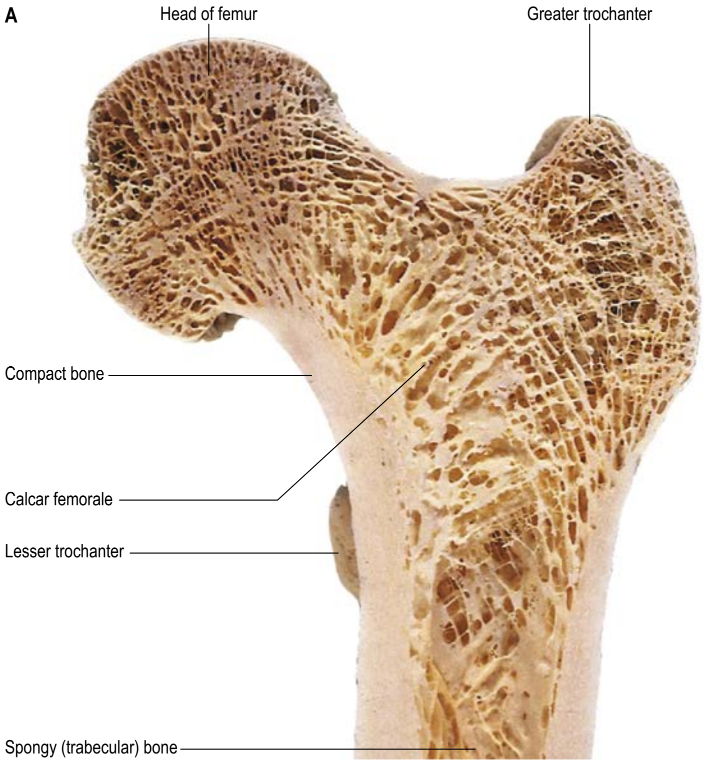
A
Head of femur
Greater trochanter
Compact bone
Calcar femorale
Lesser trochanter
Spongy (trabecular) bone

Fig. 77.17 A, A coronal section through the proximal end of the femur showing the trabecular architecture, calcar femorale and variations in cortical thickness. (Sobotta Atlas of Human Anatomy © Elsevier GmbH, Urban & Fischer, Munich.) (B, *continued online*)

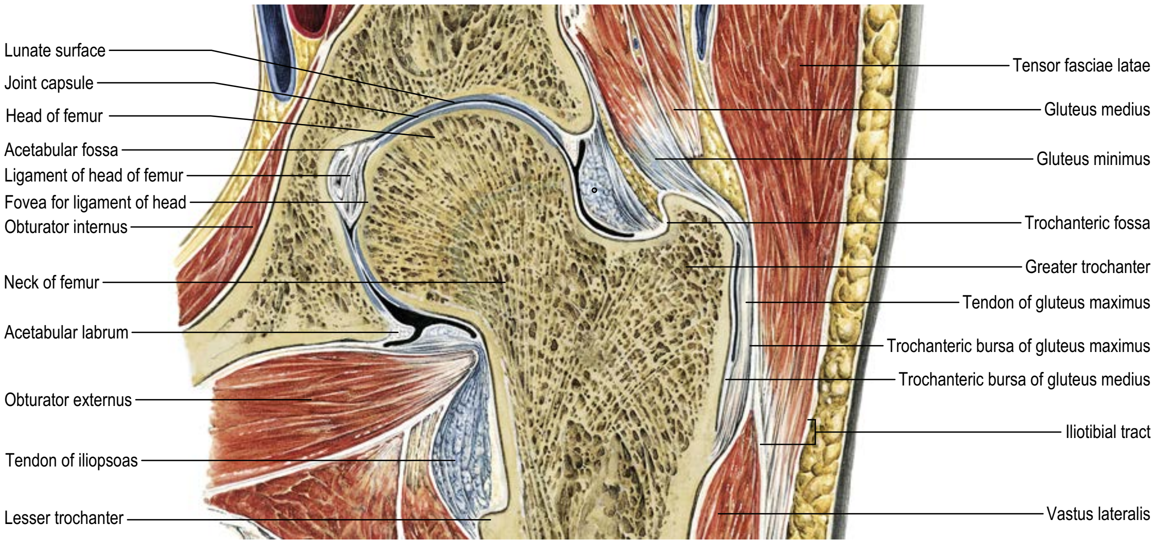
Lunate surface
Joint capsule
Head of femur
Acetabular fossa
Ligament of head of femur
Fovea for ligament of head
Obturator internus
Neck of femur
Acetabular labrum
Obturator externus
Tendon of iliopsoas
Lesser trochanter
Tensor fasciae latae
Gluteus medius
Gluteus minimus
Trochanteric fossa
Greater trochanter
Tendon of gluteus maximus
Trochanteric bursa of gluteus maximus
Trochanteric bursa of gluteus medius
Iliotibial tract
Vastus lateralis

Fig. 77.16 A coronal section through the left hip joint. (Sobotta Atlas of Human Anatomy © Elsevier GmbH, Urban & Fischer, Munich.)

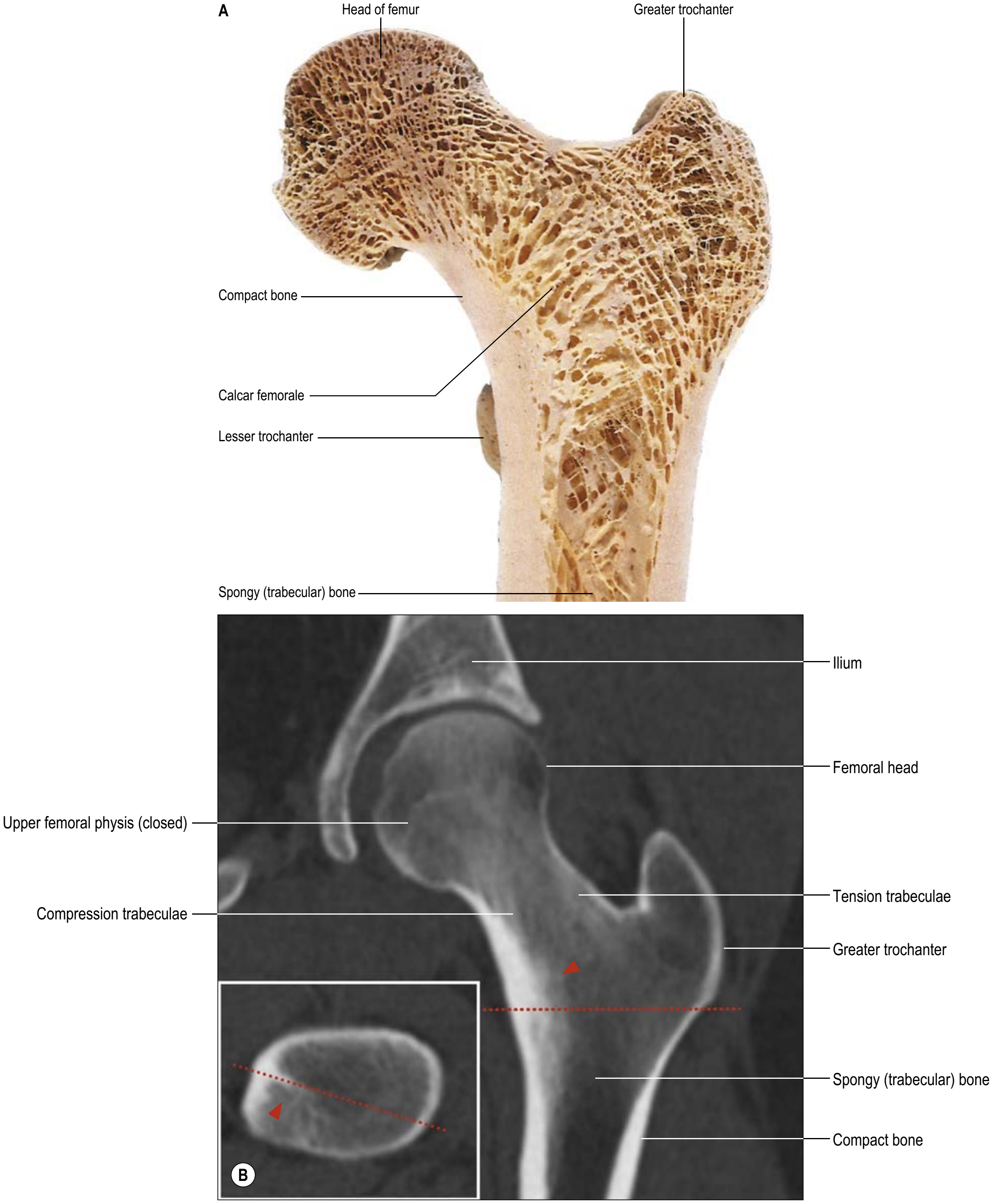
A
Head of femur
Greater trochanter
Compact bone
Calcar femorale
Lesser trochanter
Spongy (trabecular) bone
Ilium
Femoral head
Upper femoral physis (closed)
Compression trabeculae
Tension trabeculae
Greater trochanter
Spongy (trabecular) bone
Compact bone
B

Fig. 77.17 **A**, A coronal section through the proximal end of the femur showing the trabecular architecture, calcar femorale and variations in cortical thickness. **B**, A coronal oblique CT of the proximal femur showing the calcar femorale (arrowheads) with the axial plane inset; the dotted red lines show the respective cross-sections. (A, Sobotta Atlas of Human Anatomy © Elsevier GmbH, Urban & Fischer, Munich.)

of psoas major. Adductor magnus (upper part) passes over the posterior surface of the lesser trochanter, sometimes separated by an interposed bursa.

The most proximal fibres of vastus lateralis are attached to the proximal end of the intertrochanteric line, and those of vastus medialis to the distal end. Quadratus femoris is attached to the quadrate tubercle and the immediately distal bone. Vastus intermedius is attached to the anterior and lateral surfaces of the proximal three-quarters of the femoral shaft. Slips of articularis genus are attached distal to this.

The gluteal tuberosity receives the deeper fibres of the distal half of gluteus maximus and, at its medial edge, the uppermost fibres of adductor magnus. Distal to this, adductor magnus is attached to the linea aspera and, by an aponeurosis, to the proximal part of the medial supracondylar ridge. Its remaining fibres form a large tendon attached to the adductor tubercle, with an aponeurotic expansion to the distal part of the medial supracondylar ridge.

Pectineus and adductor brevis are attached to the posterior femoral surface between the gluteal tuberosity and spiral line. The pectineal attachment is a line, sometimes slightly rough, from the base of the lesser trochanter to the linea aspera. Adductor brevis is attached lateral to pectineus and beyond this to the proximal part of the linea aspera, medial to adductor magnus. Adductor longus, intermuscular septa and the short head of biceps femoris are also attached to the linea aspera. Vastus lateralis has a linear attachment from the anterior surface of the base of the greater trochanter to the proximal end of the gluteal tuberosity, and along the lateral margin of the latter to the proximal half of the lateral edge of the linea aspera. Vastus medialis is attached from the distal end of the intertrochanteric line along the spiral line to the medial edge of the linea aspera and thence to the medial supracondylar line, which also receives many fibres from the aponeurotic attachments of adductor magnus.

The medial head of gastrocnemius is attached to the posterior surface a little above the medial condyle. The short head of biceps femoris is attached to the proximal two-thirds of the lateral supracondylar line. Plantaris attaches to the line distally. Vastus medialis is attached to the proximal two-thirds of the medial supracondylar line.

Part of the lateral head of gastrocnemius is attached posterosuperiorly to the lateral epicondyle. Popliteus is attached anteriorly in the groove on the outer aspect of the lateral epicondyle. Its tendon passes deep to the fibular collateral ligament (see Fig. 77.15). The tendon lies in the groove in full knee flexion; in extension it crosses the articular margin and may form an impression on it.

Vascular supply

The blood supply of the femoral head is derived from an arterial ring around the neck, just outside the attachment of the fibrous capsule, constituted by the medial and lateral circumflex femoral arteries with minor contributions from the superior and inferior gluteal vessels. Branches from the arterial ring pierce the capsule (under its zona orbicularis) to ascend the neck beneath the reflected synovial membrane. These vessels become the retinacular arteries and form a subsynovial intracapsular anastomosis. Here the vessels are at risk with a displaced fracture of the femoral neck. Interruption of blood supply in this way can lead to avascular necrosis of the femoral head. If the fracture is intracapsular, not only is the intraosseous blood supply damaged but the retinacular vessels are also vulnerable. If the fracture is extracapsular, the retinacular vessels will remain intact and avascular necrosis of the femoral head is much less likely. The ascending cervical vessels give off metaphysial branches that enter the neck, while the intracapsular ring gives off lateral and inferior epiphysial branches. A small medial epiphysial supply reaches the head along the ligament of the head of femur by the acetabular branches of the obturator and medial circumflex femoral arteries, which anastomose with the other epiphysial vessels (Seeley et al 2016). During growth, the epiphysial plate separates the territories of the metaphysial and epiphysial vessels; these vessels anastomose freely after osseous union of the head and neck. Observations of developmental patterns of this supply in late fetal and early postnatal periods have revealed that although the medial and lateral circumflex femoral arteries at first contribute equally, two major branches of the medial provide the final supply, both posterior to the neck. The supply from the lateral circumflex femoral artery diminishes and the arterial ring is interrupted. As the femoral neck elongates, the extracapsular circle becomes more distant from the epiphysial part of the head.

The trochanteric regions and subtrochanteric shaft are supplied by the trochanteric and cruciate arterial anastomoses. More distally in the shaft, nutrient foramina, directed proximally, are found in the linea aspera, varying in number and site: one is usually near its proximal end and a second usually near its distal end. The main nutrient artery is usually derived from the second perforating artery (see p. 1389). If two nutrient arteries occur, they may branch from the first and third perforators. Periosteal vessels arise from the perforators and from the profunda femoris artery, and run circumferentially rather than longitudinally. The distal metaphysis has many vascular foramina. Arterial supply here is from the genicular anastomosis. For further details, consult Crock (1980, 1996).

In general, the pattern of venous drainage of the head and neck corresponds to that of the arteries, though there may be a single large cervical vein posteroinferiorly.

Innervation

The periosteal innervation is derived proximally from nerves that supply the hip joint, distally from those supplying the knee, and in all areas from nerves that innervate muscles attached to the bone.

Ossification

The femur ossifies from five centres: in the shaft, head, greater and lesser trochanters and the distal end (**Figs 77.18–77.19**). Other than the clavicle, it is the first long bone to ossify.The process starts in the mid-shaft during embryonic stages 22 and 23 (postfertilization days 52–58) and extends to produce a miniature shaft that is largely ossified at birth. Secondary centres appear in the distal end (from which the condyles and epicondyles are formed) during postmenstrual weeks 33–36; in the greater trochanter during the fourth year; and in the lesser trochanter between the twelfth and fourteenth years. In the infant, the femoral head is entirely cartilaginous: it cannot be seen on plain radiographs and is best visualized using ultrasound (**Fig. 77.20**). The centre in the cartilaginous head is restricted to it until the tenth year, so that the epiphysial line (see Fig. 77.7) is horizontal and the inferomedial part of the articular surface is on the neck. The medial epiphysial margin later grows over this part of the articular surface. Thus, the mature epiphysis is a hollow cup on the summit of the neck. The epiphysial line follows the articular margin except where it is separated superiorly from the articular surface by a non-articular area where blood vessels enter the head (Trueta 1957). The epiphyses fuse independently: the lesser trochanter soon after puberty, followed by the greater trochanter. The capital epiphysis fuses in the fourteenth year in females and seventeenth year in males. The epiphysis at the distal end fuses in the sixteenth year in females, and eighteenth year in males. The distal epiphysial plate traverses the adductor tubercle.

Growth plate considerations

Trauma to any epiphysial plate can lead to bony union between epiphysis and metaphysis, and so cause premature cessation of growth. Any surgery in the hip region in children can injure the growth plate, resulting in abnormal proximal femoral development. In the case of fractures involving the epiphysis, expeditious restoration of normal bony alignment is essential in order to minimize the risk of subsequent abnormal growth.

The growth plate represents a line of weakness and predisposes to fracture from injury. Such acute injuries affecting the capital epiphysis are uncommon. However, a more chronic fracture through the capital epiphysis occurs in slipped capital femoral epiphysis (see Fig. 77.29). The condition affects pubescent adolescents, especially males. The femoral head epiphysis displaces posteriorly off the femoral neck. If it heals in this position, lower limb deformity and restricted hip

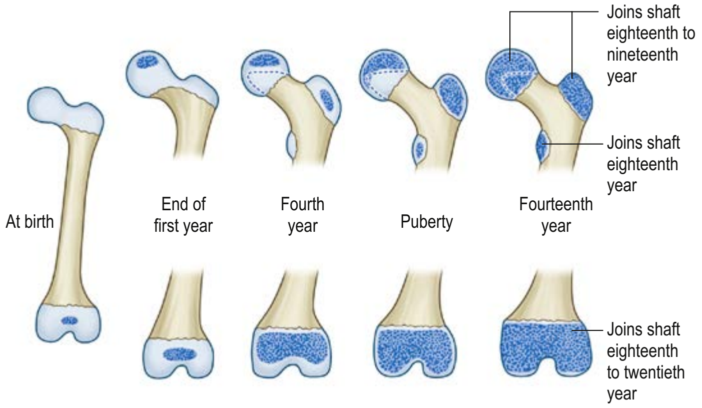
Joins shaft eighteenth to nineteenth year
Joins shaft eighteenth year
At birth
End of first year
Fourth year
Puberty
Fourteenth year
Joins shaft eighteenth to twentieth year

Fig. 77.18 Stages in ossification of the femur (not to scale).

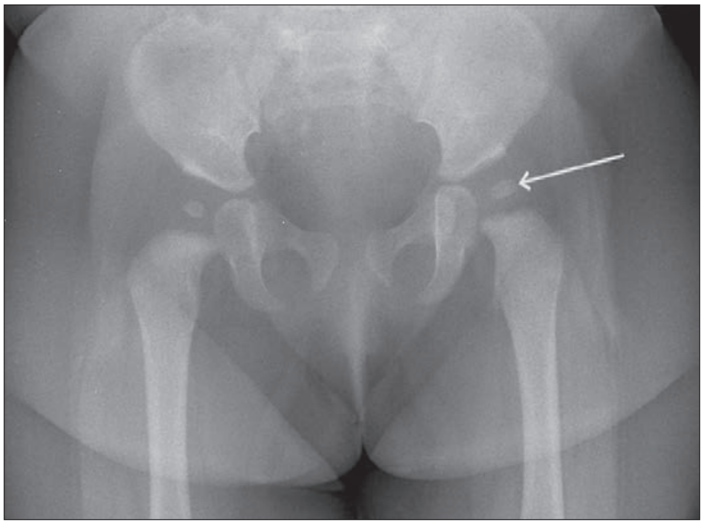

Fig. 77.19 A radiograph of the pelvis of a 9-month-old infant showing the centre of ossification of the femoral epiphysis (arrow). (Courtesy of Mr Christopher Edward Bache.)

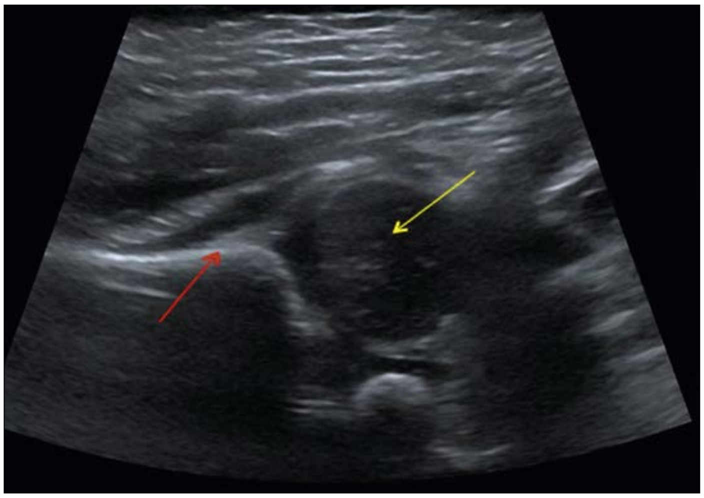

Fig. 77.20 An ultrasound image of a 4-week-old baby taken in the lateral position and demonstrating the cartilaginous femoral head (yellow arrow) and edge of the acetabulum (red arrow). (Courtesy of Mr Christopher Edward Bache.)

movement occur. A classic hallmark is obligatory lateral (external) rotation of the femur as the hip is flexed. Treatment varies according to the time taken for the 'slip' to occur. Normal anatomical restoration is not attempted because of an increased incidence of avascular necrosis. The position of the femoral head may be accepted as it is and fixed with screws in this position to stop further displacement. This treatment will deliberately cause premature growth plate fusion and so prevent future 'slippage'. Since the distal femoral growth plate accounts for most of the normal increase in longitudinal growth of the femoral shaft, an acceptable limb length difference usually results.

Infection of bone in neonates and young children tends to arise via bacteria in the blood stream that usually 'seed' in the metaphysial region, probably as a consequence of the vascular 'arcade' arrangement of arteries in this part of the bone. The proximal femoral growth plate is intra-articular. As a result, infection in the proximal femoral metaphysis can spread into the joint and result in a septic arthritis that can destroy the hip joint permanently.

The distal end of the femur is the only epiphysis in which ossification consistently starts just before birth; the phenomenon therefore serves as a reliable indicator of the gestational maturity of a stillborn baby. Since the epiphysial plate is level with the adductor tubercle, the epiphysis is partly extra-articular. Operations here may damage the distal epiphysial cartilage in children and result in subsequent shortening of the leg.

JOINTS

Pubic symphysis

The pubic bones meet in the midline at the pubic symphysis, a secondary cartilaginous joint (see Figs 77.2–77.3).

Articulating surfaces The articulating surfaces are the medial (symphysial) surfaces of the pubic bones, each covered by a thin layer of tightly adherent hyaline cartilage (surface growth cartilage in the young). The junction is not flat but is marked by reciprocal crests and papillae. Theoretically, this would resist shearing. The surfaces of hyaline cartilage are connected by fibrocartilage, varying in thickness and constituting the interpubic disc. The interpubic disc often contains a cleft, which rarely appears before the tenth year and may have a synovial lining (Becker et al 2010). The cleft, which is larger and more prevalent in females, is usually posterosuperior but may extend the length and/or depth of the disc.

Ligaments The interpubic disc is strengthened anteriorly by several interlacing collagenous fibrous layers, passing obliquely from bone to bone, decussating with fibres of the external oblique aponeuroses and the medial tendons of the recti abdominis. These layers constitute the anterior pubic ligament. There are less well developed posterior fibres, sometimes named the posterior pubic ligament. The main ligaments of the joint are the superior and inferior pubic ligaments. The superior pubic ligament connects the bones above, extending to the pubic tubercles. The inferior pubic ligament, a thick arch of fibres, connects the lower borders of the symphysial pubic surfaces bounding the pubic arch. It blends superiorly with the interpubic disc and extends laterally to the inferior pubic rami. Its inferior edge is separated from the anterior border of the perineal membrane by an opening, which is traversed by the deep dorsal vein of the penis or clitoris.

Vascular supply The pubic symphysis is supplied by pubic branches of the obturator, superficial external pudendal and inferior epigastric arteries.

Innervation The pubic symphysis is innervated by branches from the iliohypogastric, ilioinguinal and pudendal nerves.

Factors maintaining stability The interpubic disc and the superior and inferior ligaments are the main stabilizing factors of the pubic symphysis.

Movements Angulation, rotation and displacement are possible but slight, and are likely during movement at the sacroiliac and hip joints. The movements at the pubic symphysis range between 0.1 and 2 mm and are greater in the vertical axis than along the sagittal and transverse axes (Walheim et al 1984). Excessive movement may occur following an injury. Some separation occurs late in gestation and during childbirth; on occasion, this is considerable.

Relations Anteriorly the pubic symphysis is related to subcutaneous tissue and skin. Because of the obliquity of the joint, the proximal ends of the penile or clitoral shafts lie anterior to the lower half of the joint. Inferiorly the urethra lies about 2.5 cm away in the male, and somewhat closer in the female, as it passes through the perineal membrane. Closer to the joint, the deep dorsal vein of the penis or clitoris passes between the inferior pubic ligament and the anterior border of the perineal membrane. Posteriorly the upper part of the joint is separated from the inferolateral surfaces of the urinary bladder by the retropubic fat pad. Inferiorly in the male the prostatic venous plexus separates the prostate from the lower part of the joint. The region is sometimes termed the retropubic space (of Retzius). These relationships explain why traumatic disruption of the anterior bony pelvis may be associated with serious urogenital injury.

Sacroiliac joint

The sacroiliac joint occurs between the sacral and iliac auricular surfaces and, in essence, is a stress-relieving joint (Bogduk 2012, Vleeming et al 2012) (see Fig. 77.8A). The joint consists of syndesmotic and synovial parts. Fibrous adhesions and gradual obliteration occur in both sexes, earlier in males and after menopause in females. Radiological evidence of obliteration in normal subjects is occasionally seen before 50 years but is not uncommon thereafter; in old age, the joint may be completely fibrosed and occasionally even ossified.

Articulating surfaces The surfaces are nearly flat in infants, whereas in adults they are irregular, often markedly so, and sometimes undulant. The curvatures and irregularities, greater in males, are reciprocal; they restrict movements and contribute to the considerable strength of the joint in transmitting weight from the vertebral column to the lower limbs. The sacral surface is covered by hyaline cartilage, which is thicker anteriorly than posteriorly in adults. The thinner cartilage on the iliac surface is also hyaline in type, as confirmed by the presence of type II collagen.

Fibrous capsule The capsule is attached close to both articular margins.

Ligaments The ligaments of the sacroiliac joint are the anterior, interosseous and posterior sacroiliac, iliolumbar, sacrotuberous and sacrospinous ligaments.

Anterior sacroiliac ligament The anterior sacroiliac ligament (see Fig. 77.9A), an anteroinferior capsular thickening, is particularly well developed near the arcuate line and the posterior inferior iliac spine, where it connects the third sacral segment to the lateral side of the pre-auricular sulcus. It is thin elsewhere.

Interosseous sacroiliac ligament The interosseous sacroiliac ligament is the major bond between the bones, filling the irregular space posterosuperior to the joint. The posterior sacroiliac ligament covers it superficially. Its deeper part has superior and inferior bands passing from depressions posterior to the sacral auricular surface to those on the iliac tuberosity. These bands are covered by, and blend with, a more superficial fibrous sheet connecting the posterosuperior margin of a rough area posterior to the sacral auricular surface to the corresponding margins of the iliac tuberosity. This sheet is often partially divided into superior and inferior parts, the former uniting the superior articular process and lateral crest on the first two sacral segments to the neighbouring ilium as a short posterior iliac ligament (see Fig. 46.70).

Posterior sacroiliac ligament The posterior sacroiliac ligament (see Fig. 77.9B) overlies the interosseous ligament: the dorsal rami of the sacral spinal nerves and vessels intervene. It consists of several weak fasciculi connecting the intermediate and lateral sacral crests to the posterior superior iliac spine and posterior end of the internal lip of the iliac crest. Inferior fibres, from the third and fourth sacral segments, ascend to the posterior superior iliac spine and posterior end of the internal lip of the iliac crest; they may form a separate long posterior sacroiliac ligament. This ligament is continuous laterally with part of the sacrotuberous ligament and medially with the posterior lamina of the thoracolumbar fascia.

Iliolumbar ligament See Chapter 46.

Sacrotuberous ligament The sacrotuberous ligament (see Figs 77.9, 46.70) is attached by its broad base to the posterior superior iliac spine, the posterior sacroiliac ligaments (with which it is partly blended), lateral sacral crest and the lateral margins of the lower sacrum and upper coccyx. Its oblique fibres descend laterally, converging to form a thick, narrow band that widens again below and is attached to the medial margin of the ischial tuberosity. It then spreads along the ischial ramus as the falciform process, whose concave edge blends with the fascial sheath of the internal pudendal vessels and pudendal nerve. The lowest fibres of gluteus maximus are attached to the posterior surface of the ligament; superficial fibres of the lower part of the ligament continue into the superficial fibres of the tendon of the long head of biceps femoris. The coccygeal branches of the inferior gluteal artery, the perforating cutaneous nerve and filaments of the coccygeal plexus pierce the ligament.

Sacrospinous ligament The thin, triangular sacrospinous ligament (see Fig. 77.9) extends from the ischial spine to the lateral margins of the sacrum and coccyx anterior to the sacrotuberous ligament, with which it blends in part. Its anterior surface is the coccygeus muscle, i.e. muscle and ligament are coextensive. The sacrospinous ligament is often regarded as a degenerate part of coccygeus.

Sciatic foramina The sacrotuberous and sacrospinous ligaments convert the sciatic notches into foramina (see Fig. 77.9).

Greater sciatic foramen The greater sciatic foramen is bounded anterosuperiorly by the greater sciatic notch, posteriorly by the sacrotuberous ligament and inferiorly by the sacrospinous ligament and ischial spine (see Fig. 77.9). It is partly filled by the emerging piriformis, above which the superior gluteal vessels and nerve leave the pelvis. Below it, the inferior gluteal vessels and nerve, internal pudendal vessels and pudendal nerve, sciatic and posterior femoral cutaneous nerves and the nerves to obturator internus and quadratus femoris all leave the pelvis.

Lesser sciatic foramen The lesser sciatic foramen is bounded anteriorly by the ischial body, superiorly by its spine and sacrospinous ligament, and posteriorly by the sacrotuberous ligament (see Fig. 77.9A). It transmits the tendon of obturator internus, the nerve to obturator internus, and the internal pudendal vessels and pudendal nerve.

Vascular supply and lymphatic drainage The arterial supply of the sacroiliac joint is derived from the iliolumbar, superior gluteal and superior lateral sacral arteries, with corresponding venous drainage. Lymphatic drainage follows the arteries, reaching the iliac and lumbar nodes.

Innervation Nerve fibres ramify within the joint capsule and adjoining ligaments, but their source is uncertain. It is thought that the joint probably receives branches from the anterior and posterior rami of the first two sacral spinal nerves, and from the superior gluteal nerve, and that there may also be contributions from the obturator nerve and the lumbosacral trunk.

The sacroiliac joint has sometimes been implicated as the source of pain in the lower back and buttocks. Diagnosing sacroiliac joint-mediated pain is difficult because the presenting complaints are similar to those seen with other causes of back pain. Patients with sacroiliac joint-mediated pain rarely report pain above the level of L5; most localize their pain to the area around the posterior superior iliac spine.

Factors maintaining stability The sacroiliac joint is one of the most stable joints in the body and supports the weight of the trunk. The reciprocal irregularity of the joint surfaces allows very little movement. The tendency of the sacrum to be forced downwards by the trunk is resisted by the extremely strong posterior ligaments, while the iliolumbar ligaments help to resist displacement of the fifth lumbar vertebra over the sacrum. The sacrotuberous and sacrospinous ligaments oppose upward tilting of the lower part of the sacrum when downward thrust is applied at its upper end.

Movements Primary movement of the sacroiliac joint is minimal (Vleeming et al 2012). All muscles that cross the joint act on the lumbar spine or on the hip. Such movements as do occur are secondarily imposed on the joint as the pelvis moves. Data from living subjects are technically difficult to obtain, and those based on plain radiographs are unreliable. Studies using implanted tantalum spheres and biplanar radiography have shown mean rotational ranges of less than 2°. Even when there is recordable movement, the direction of movement is irregular. Biplanar radiography has also shown that the axes of movement of the sacroiliac joint during hip movement are oblique, and that the axes differ in flexion and extension.

During pregnancy, the pelvic joints and ligaments loosen under the influence of the hormone relaxin. Movements in the joints increase. Relaxation renders the sacroiliac locking mechanism less effective, permitting greater rotation and perhaps allowing alterations in pelvic diameters at childbirth, although the effect is probably small. The impaired locking mechanism diverts the strain of weight-bearing to the ligaments, with frequent sacroiliac strain after pregnancy.

Relations The sacroiliac joints have many important anterior relations. The internal and external iliac veins join to form the common iliac veins immediately anteriorly, separating the joints from the bifurcations of the common iliac arteries and, more anteriorly, the ureters. The lumbosacral trunk and the obturator nerve cross the anterior aspect of the joint behind the vessels. Piriformis partly attaches to the anterior capsule, separating the joint from the upper part of the sacral plexus.

Variants Accessory sacroiliac articulations are not uncommon. They develop behind the articular surface between the lateral sacral crest and posterior superior iliac spine and iliac tuberosity, and are acquired fibrocartilaginous joints resulting from the stresses of weight-bearing. They have a joint capsule, are saddle-shaped, and may be single, double, unilateral or bilateral (Weisl 1954).

Hip

The hip joint is a synovial joint of ball-and-socket (multiaxial spheroidal) type between the head of the femur and the cup-shaped (cotyloid) acetabulum; its centre lies a little inferior to the middle one-third of the inguinal ligament (**Fig. 77.21**).

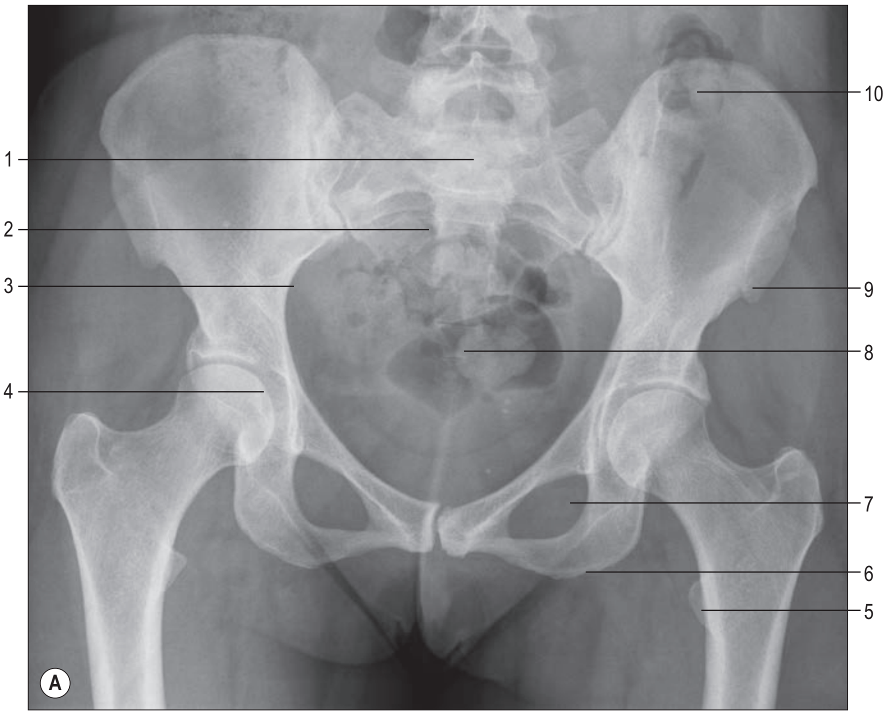

Fig. 77.21 Anteroposterior radiograph of an adult female pelvis. Key: 1, sacral promontory; 2, margin of anterior sacral foramen; 3, linea terminalis; 4, fovea for ligament of head; 5, lesser trochanter of left femur; 6, left ischial tuberosity; 7, left obturator foramen; 8, coccyx; 9, left anterior inferior iliac spine; 10, gas in sigmoid colon. (B, *continued online*)

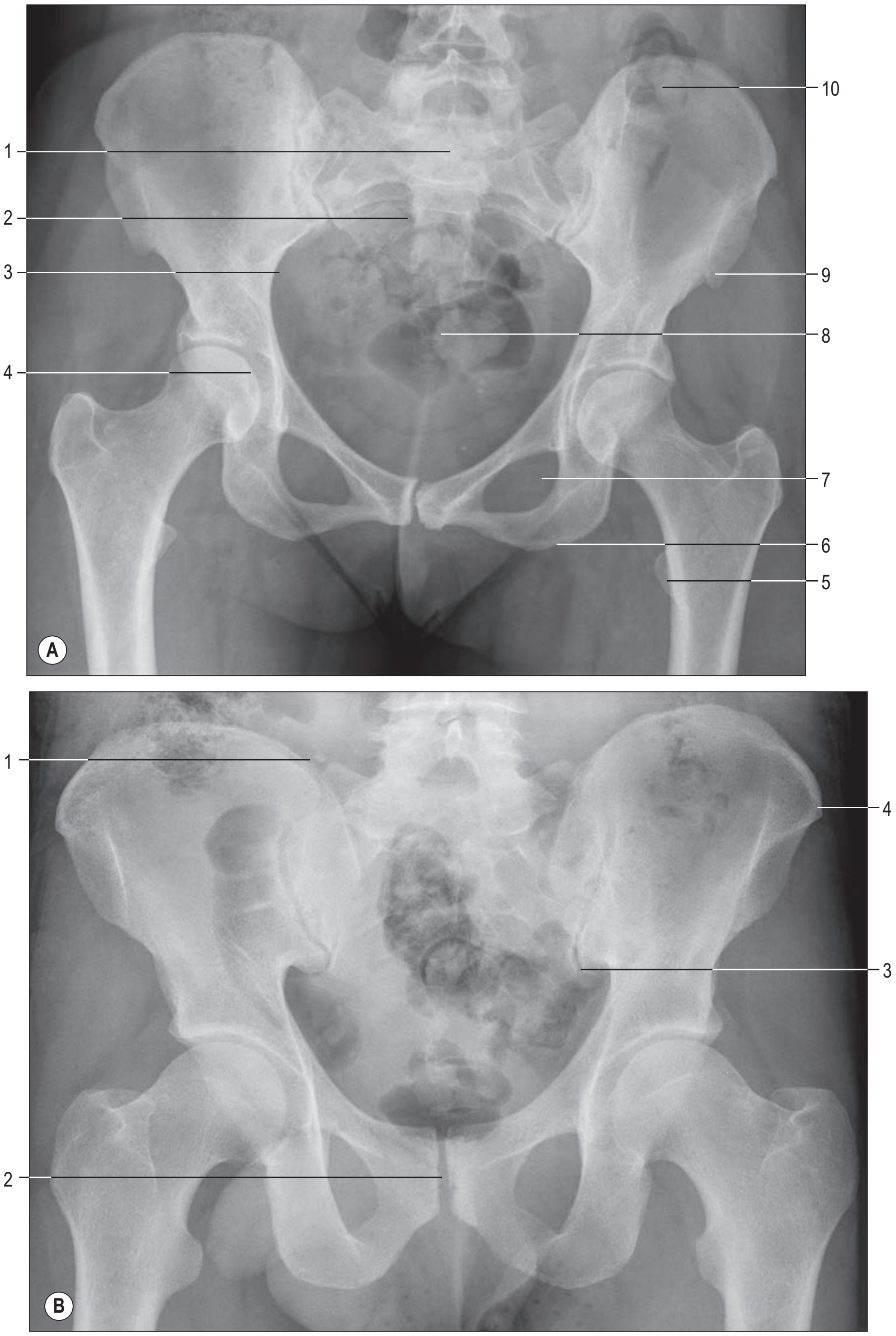

Fig. 77.21 Anteroposterior radiograph of an adult female pelvis. Key: 1, sacral promontory; 2, margin of anterior sacral foramen; 3, linea terminalis; 4, fovea for ligament of head; 5, lesser trochanter of left femur; 6, left ischial tuberosity; 7, left obturator foramen; 8, coccyx; 9, left anterior inferior iliac spine; 10, gas in sigmoid colon. **B**, Anteroposterior radiograph of an adult male pelvis (the hip joint is normal). Key: 1, ossification in right iliolumbar ligament; 2, pubic symphysis; 3, inferior margin of left sacroiliac joint; 4, left anterior superior iliac spine.

Articulating surfaces The femoral head can be landmarked from the surface roughly 2–4 cm superior to an approximate midpoint of a line joining the superior margin of the greater trochanter to the pubic tubercle. The articular surfaces of the femoral head and the acetabulum are reciprocally curved but neither coextensive nor completely congruent (see Fig. 77.21; see Fig. 77.16). The close-packed position of the hip joint is one of full extension, with slight abduction and medial rotation (see also Table 5.4). This position winds up most of the joint's capsular ligaments, which can provide an important element of articular stability. The femoral head is covered by articular cartilage, except over the fovea where the ligament of the head of the femur (ligamentum teres) is attached. Anteriorly, the cartilage extends laterally over a small area on the adjoining neck. Articular cartilage is, generally, thicker centrally than peripherally. Cartilage thickness is maximal anterosuperiorly in the acetabulum and anterolaterally on the femoral head, the two areas that correspond to the principal load-bearing areas within the joint. The acetabular articular surface, the lunate surface, is an incomplete ring, broadest anterosuperiorly where the pressure of body weight falls in the erect posture, and narrowest in its pubic region. It is deficient inferiorly opposite the acetabular notch. The lunate surface is covered by articular cartilage, which is thickest where the surface is broadest. The acetabular fossa, the central non-articular area in the floor of the acetabulum, is devoid of cartilage but contains fibroelastic fat largely covered by synovial membrane. The acetabular labrum, a fibrocartilaginous rim attached to the acetabular margin, serves to deepen the acetabulum and bridges the acetabular notch by attaching to the peripheral edge of the transverse acetabular ligament. The acetabular labrum is triangular in section, attached by its base to the acetabular margin and blending with adjacent articular cartilage; its acute free edge projects beyond the acetabular margin. The diameter of the acetabular cavity is constricted by the labral rim, which embraces the femoral head, thereby contributing to the stability of the articulation. The acetabular labrum increases the surface area for joint contact as well as sealing the joint, allowing optimal intra-articular distribution of synovial fluid (Ferguson et al 2003, Cadet et al 2012). It thus facilitates nutrition of the articular cartilage and helps to reduce intra-articular friction (Safran et al 2011, Song et al 2012). Nerve endings found within the labrum suggest this structure may be a source of proprioception or, when injured, of pain (Kim and Azuma 1995, Alzaharani et al 2014). A torn acetabular labrum can be detected using MRI, to identify the site and severity of the lesion (**Fig. 77.22**).

Acetabular labrum and impingement injury

Available with the *Gray's Anatomy* e-book

Fibrous capsule The fibrous capsule of the hip joint is strong and dense. It is attached superiorly to the acetabular margin 5–6 mm medial to the labral attachment, anteriorly to the outer labral aspect and, near the acetabular notch, to the transverse acetabular ligament and the adjacent rim of the obturator foramen. From its acetabular attachment, it extends laterally to surround the femoral head and neck, and is attached anteriorly to the intertrochanteric line, superiorly to the base of the femoral neck, posteriorly 1 cm superomedial to the intertrochanteric crest, and inferiorly to the femoral neck near the lesser trochanter (see Fig. 77.12B). Anteriorly, many fibres ascend along the neck as longitudinal retinacula, containing blood vessels for both the femoral head and the neck. The capsule is thicker anterosuperiorly, where maximal stress occurs, particularly while standing with the hip extended. Posteroinferiorly, it is relatively thin and loosely attached. The capsule as a whole has two sets of fibres, circular and longitudinal. The circular fibres (zona orbicularis) are internal and form a collar round the femoral neck; although partly blended with the pubofemoral and ischiofemoral ligaments, these fibres are not directly attached to bone. Externally, longitudinal fibres are most numerous in the anterosuperior region, where they are reinforced by the iliofemoral ligament. The capsule is also strengthened inferiorly by the pubofemoral ligament, and posteriorly by the ischiofemoral ligament. Externally the capsule is rough, covered by muscles and tendons, and separated anteriorly from psoas major and iliacus by a bursa. The capsular attachment to the femur lies well distal to the growth plate of the femoral head both anteriorly and posteriorly, and so the upper femoral epiphysis is entirely intracapsular. The capsular attachment intersects the growth plate of the greater trochanter on the superior surface of the base of the neck.

Iliocapsularis

Available with the *Gray's Anatomy* e-book

Relations The joint capsule is surrounded by muscles (**Fig. 77.24**). Anteriorly, lateral fibres of pectineus separate the capsule from the femoral vein. Lateral to this, the tendon of psoas major, with iliacus lateral to it, descends en route to the lesser trochanter, partly separated from the capsule by a bursa. The femoral artery is anterior to the tendon of psoas major, and the femoral nerve lies deep in a groove between the tendon and iliacus. More laterally the straight head of rectus femoris crosses the joint with a deep layer of the iliotibial tract, which blends with the capsule under the lateral border of the muscle. Superiorly the reflected head of rectus femoris contacts the capsule medially, while gluteus minimus covers it laterally, being either closely adherent or comingled (Walters et al 2014). Inferiorly, medial fibres of pectineus adjoin the capsule and, more posteriorly, obturator externus spirals obliquely to its posterior aspect. Posteroinferiorly the capsule is covered by the tendon of obturator externus, separating it from quadratus femoris and accompanied by an ascending branch of the medial circumflex femoral artery. Superior to this the tendon of obturator internus and the gemelli contact the joint capsule, separating it from the sciatic nerve. The nerve to quadratus femoris is deep to the obturator internus tendon and descends medially on the capsule. Superior to this the posterior surface of the joint is crossed by piriformis.

Ligaments The ligaments of the hip joint are the iliofemoral, pubofemoral, ischiofemoral and transverse acetabular ligaments, and the ligament of the head of the femur (**Fig. 77.25**). As the hip moves, the capsular ligaments wind and unwind, tightening around the hip, and affecting stability, excursion and joint capacity (Fuss and Bacher 1991). Joint capacity is maximal when the hip joint is held in a partially flexed and abducted position; a patient with an effusion in the hip joint is therefore most comfortable when the joint is held in this position.

Iliofemoral ligament The iliofemoral ligament is very strong and is shaped like an inverted Y, lying anteriorly and intimately blended with the capsule. Its apex is attached between the anterior inferior iliac spine and acetabular margin, its base to the intertrochanteric line. It is composed of a medially placed, thicker descending part and a laterally placed, transverse part, which is typically distinguishable anteriorly. The obliquely disposed transverse part is attached to a tubercle at the superolateral end of the intertrochanteric line, while the vertically oriented descending part reaches the inferomedial end of the line.

Pubofemoral ligament The pubofemoral ligament is triangular, with a base that is attached to the iliopubic ramus, superior pubic ramus, obturator crest and membrane. It blends distally with the capsule and deep surface of the descending part of the iliofemoral ligament and has been described as consisting of multiple crura (Fuss and Bacher 1991).

Ischiofemoral ligament The ischiofemoral ligament thickens the posterior aspect of the capsule. The central part spirals superolaterally from the ischium, where it is attached posteroinferior to the acetabulum, then courses posterior to the femoral neck to attach distally to the greater trochanter deep to the iliofemoral ligament. Some fibres blend with the zona orbicularis. Some of the more inferior fibres of the ischiofemoral ligament embrace the posterior circumference of the femoral neck.

Transverse acetabular ligament The transverse acetabular ligament (see Fig. 77.3) is continuous peripherally with the labrum but does not possess any cartilage cells. Its strong, flat fibres cross the acetabular notch, forming a foramen through which vessels and nerves pass to enter the joint.

Ligament of the head of the femur The ligament of the head of the femur (ligamentum teres) is a triangular and somewhat flattened band of connective tissue (see Fig. 77.24; **Fig. 77.26**). Its apex is attached anterosuperiorly in the fovea for the ligament of the head of the femur while its base is attached principally to both edges of the acetabular notch, between which it blends with the transverse acetabular ligament. It also receives variable contributions from the margins of the acetabular fossa and hip

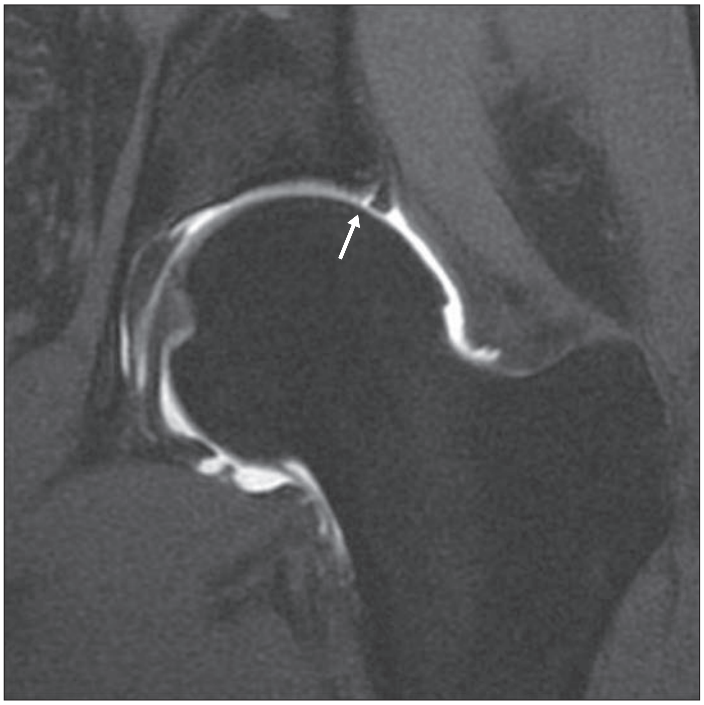

Fig. 77.22 T1-weighted fat-saturated MR arthrogram of the left hip joint (coronal section). The arrow points to a torn acetabular labrum at the anterosuperior margin of the acetabulum.

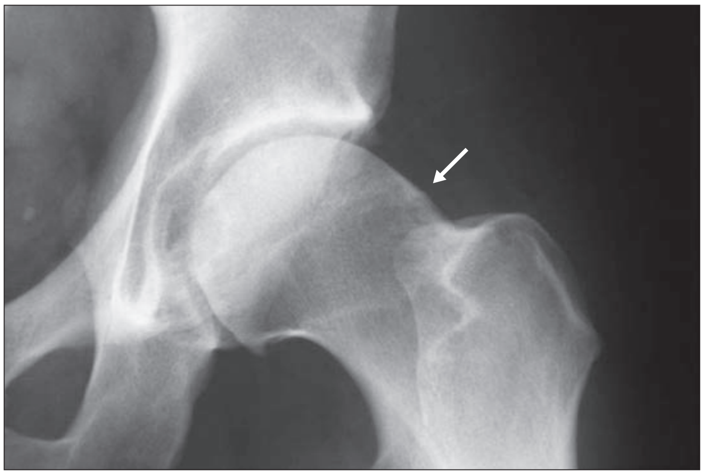

Fig. 77.23 Pre-surgical radiograph of a hip with a cam deformity of the femoral head–neck junction (arrow). Note the loss of sphericity in the femoral head and the loss of the tapering of the neck. (Image courtesy of John T Heinrich, MD, Milwaukee Orthopaedic Group Limited, Milwaukee, WI, USA.)

The shape of the bones of the hip normally limits large and potentially damaging contact stress on adjacent connective tissues, especially during the extremes of movement. Consider, for example, the normal shape of the femoral head and neck region. Similar to the shape of a light bulb, the spherical femoral head narrows gradually at its junction with the neck of the femur. This tapering limits large contact stress between the femoral neck and the margin of the acetabulum. However, tapering may be lost because of natural variation or underlying pathology, resulting in a specific deformity that has been referred to as a cam deformity because the head and neck of the femur, together, resemble a camshaft. Although often subtle, this deformity may be detected radiographically (see arrow in Fig. 77.23). In some patients with a cam deformity, extreme and repeated motions of the hip, typically involving combinations of flexion, medial rotation and adduction, can create damaging impingement between the hard and bulbous femoral neck and the softer acetabular labrum. The anterosuperior section of the labrum is particularly vulnerable to this type of injury, which is a painful and often motion-limiting condition referred to as femoroacetabular impingement syndrome. The repeatedly traumatized section of the labrum can become enlarged, fragmented or torn. When the acetabular labrum is torn, a hip joint may become unstable as a consequence of the loss of the natural suction seal around the joint. In some advanced cases, the impingement trauma may create lesions at the chondrolabral junction, resulting in damage to the adjacent articular cartilage, potentially predisposing the hip joint to degenerative arthritis (osteoarthrosis) (Beck et al 2005). Treatment may involve arthroscopic repair of the acetabular labrum and cartilage, as well as reshaping the area of the femoral head and neck responsible for the impingement.

Iliocapsularis (also called iliacus minor or iliotrochantericus) is a little-known but constant muscle that lies immediately deep to the tendon of iliopsoas and overlies the anterior hip capsule (Babst et al 2011, Ward et al 2000). Typically present as just a few strands of fibres, it originates from the anteromedial hip capsule and anteroinferior iliac spine, and is attached just distal to the lesser trochanter. Although the function of the muscle is uncertain, it may draw the capsule taut as a way of reducing its impingement during hip flexion. For reasons not understood, the size of the iliocapsularis has been shown to be larger in hips with radiological evidence of developmental hip dysplasia (Haefeli et al 2015)

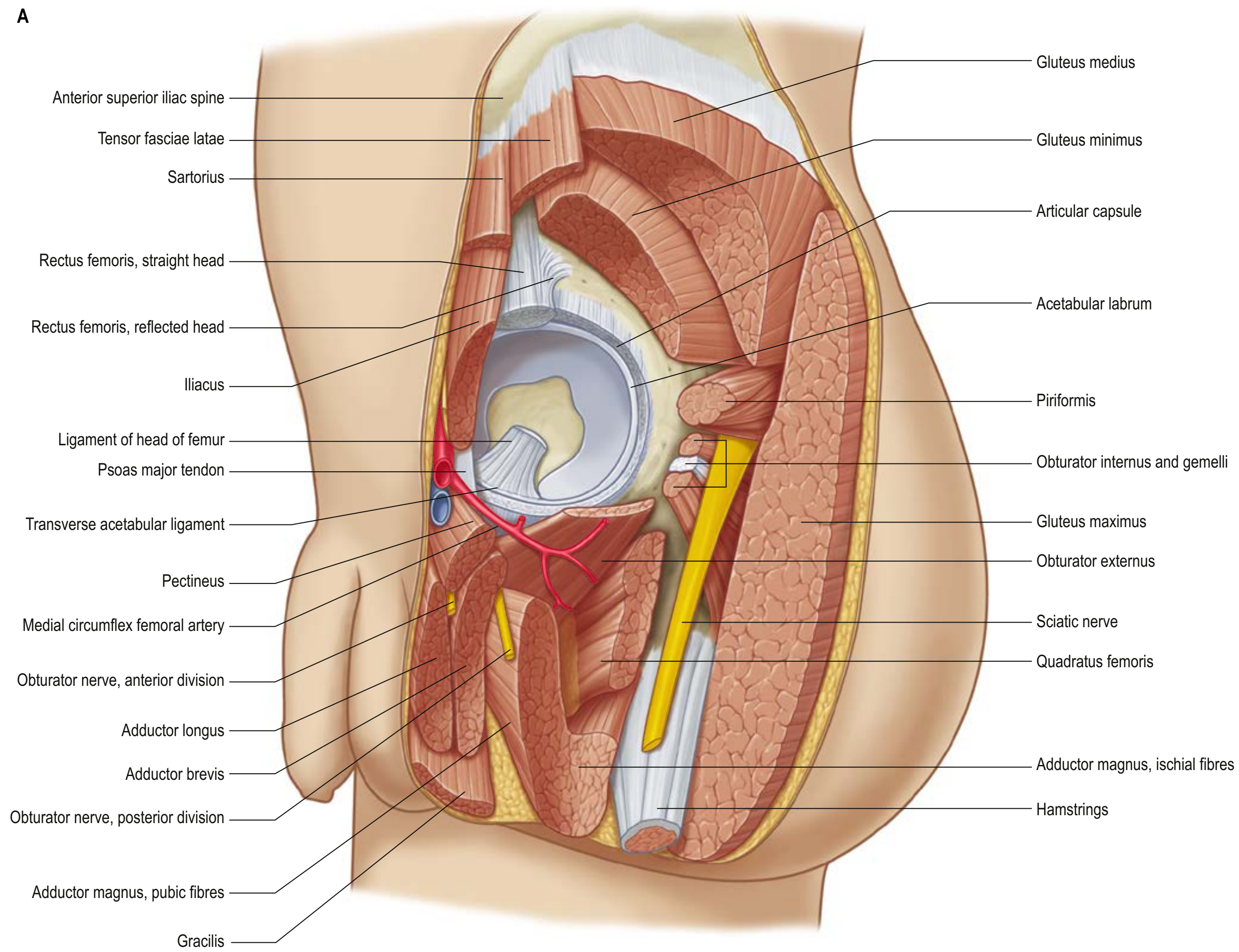
A
Anterior superior iliac spine
Tensor fasciae latae
Sartorius
Rectus femoris, straight head
Rectus femoris, reflected head
Iliacus
Ligament of head of femur
Psoas major tendon
Transverse acetabular ligament
Pectineus
Medial circumflex femoral artery
Obturator nerve, anterior division
Adductor longus
Adductor brevis
Obturator nerve, posterior division
Adductor magnus, pubic fibres
Gracilis
Gluteus medius
Gluteus minimus
Articular capsule
Acetabular labrum
Piriformis
Obturator internus and gemelli
Gluteus maximus
Obturator externus
Sciatic nerve
Quadratus femoris
Adductor magnus, ischial fibres
Hamstrings

Fig. 77.24 **A**, A schematic dissection to display the structures surrounding the hip joint. The femoral head has been disarticulated and removed. (B, *continued online*)

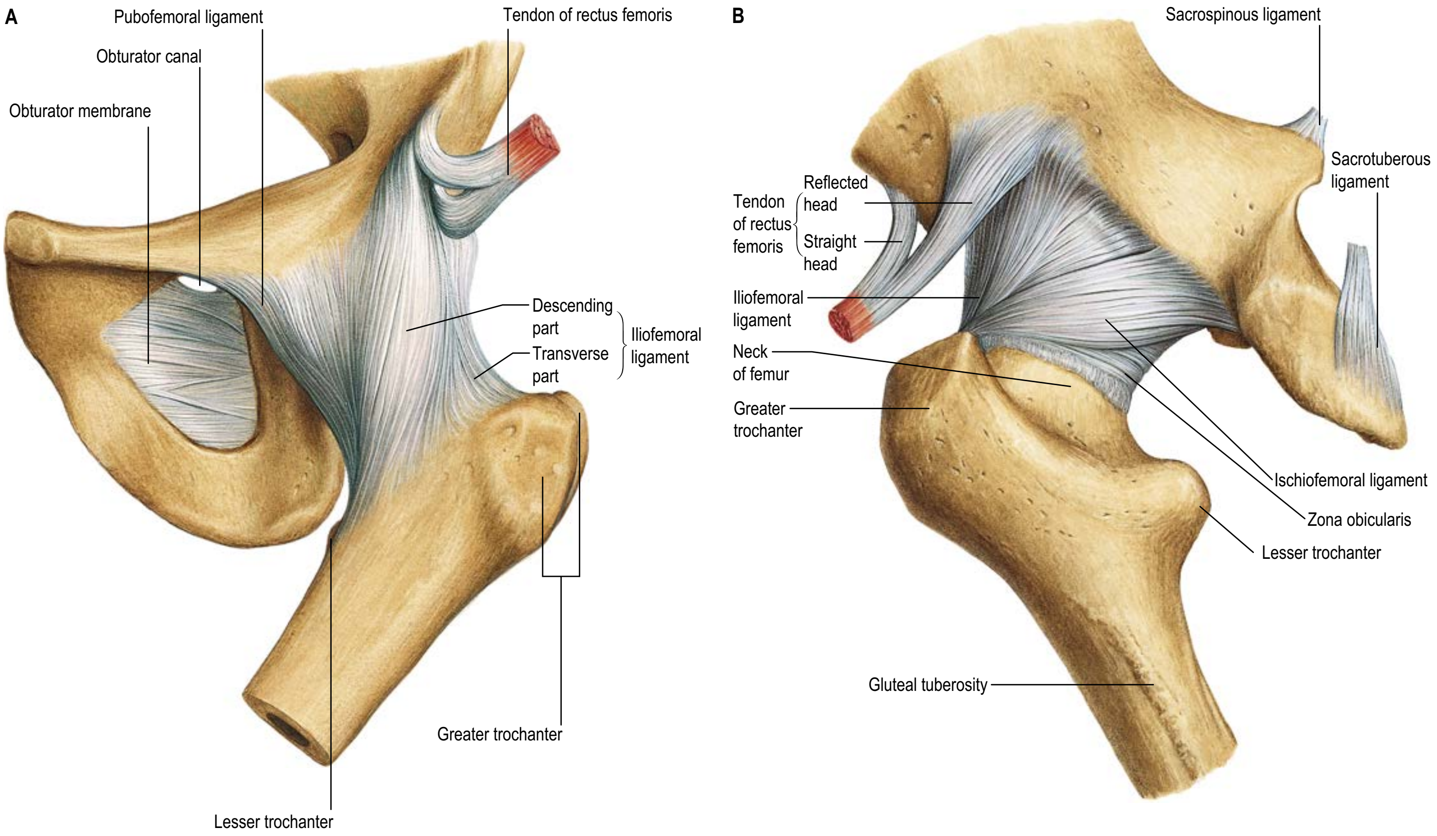
A
Pubofemoral ligament
Obturator canal
Obturator membrane
Tendon of rectus femoris
Descending part
Transverse part
Iliofemoral ligament
Greater trochanter
Lesser trochanter
B
Sacrospinous ligament
Sacrotuberous ligament
Tendon of rectus femoris
Reflected head
Straight head
Iliofemoral ligament
Neck of femur
Greater trochanter
Ischiofemoral ligament
Zona obicularis
Lesser trochanter
Gluteal tuberosity

Fig. 77.25 Ligaments of the hip joint. **A**, Anterior aspect. **B**, Posterior aspect. (Sobotta Atlas of Human Anatomy © Elsevier GmbH, Urban & Fischer, Munich.)

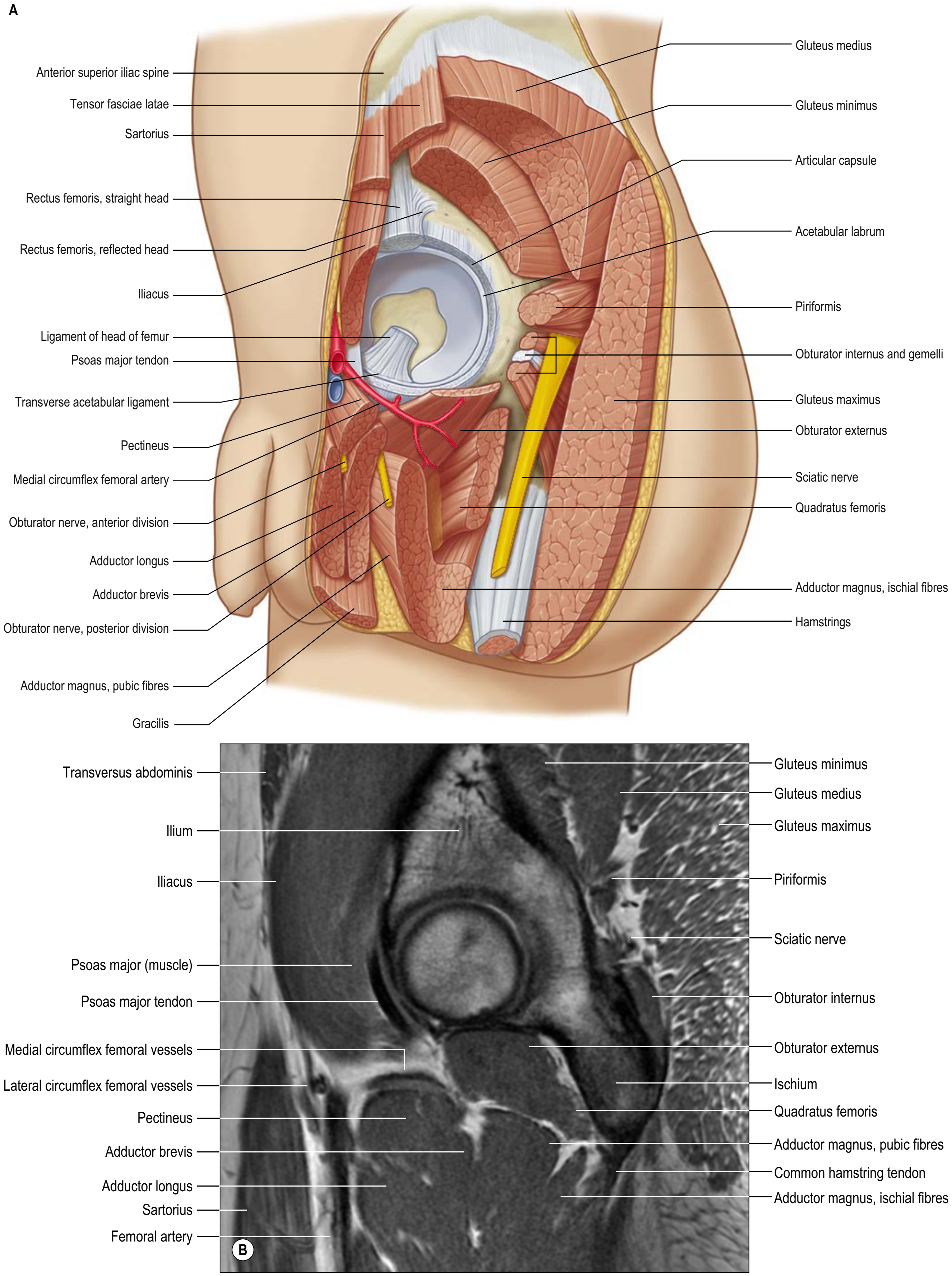
A
Anterior superior iliac spine
Tensor fasciae latae
Sartorius
Rectus femoris, straight head
Rectus femoris, reflected head
Iliacus
Ligament of head of femur
Psoas major tendon
Transverse acetabular ligament
Pectineus
Medial circumflex femoral artery
Obturator nerve, anterior division
Adductor longus
Adductor brevis
Obturator nerve, posterior division
Adductor magnus, pubic fibres
Gracilis
Gluteus medius
Gluteus minimus
Articular capsule
Acetabular labrum
Piriformis
Obturator internus and gemelli
Gluteus maximus
Obturator externus
Sciatic nerve
Quadratus femoris
Adductor magnus, ischial fibres
Hamstrings
B
Transversus abdominis
Ilium
Iliacus
Psoas major (muscle)
Psoas major tendon
Medial circumflex femoral vessels
Lateral circumflex femoral vessels
Pectineus
Adductor brevis
Adductor longus
Sartorius
Femoral artery
Gluteus minimus
Gluteus medius
Gluteus maximus
Piriformis
Sciatic nerve
Obturator internus
Obturator externus
Ischium
Quadratus femoris
Adductor magnus, pubic fibres
Common hamstring tendon
Adductor magnus, ischial fibres

Fig. 77.24 **A**, A schematic dissection to display the structures surrounding the hip joint. The femoral head has been disarticulated and removed. **B**, A sagittal proton density MRI through the left hip showing the muscles around the joint.

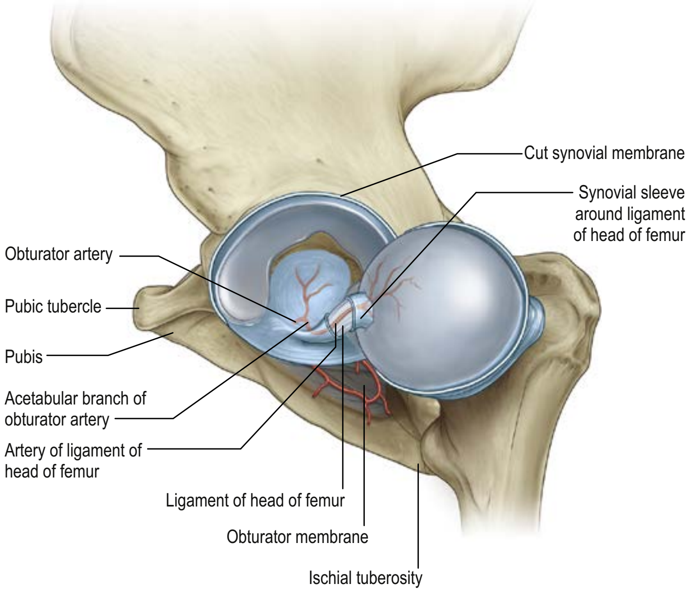
Cut synovial membrane
Synovial sleeve around ligament of head of femur
Obturator artery
Pubic tubercle
Pubis
Acetabular branch of obturator artery
Artery of ligament of head of femur
Ligament of head of femur
Obturator membrane
Ischial tuberosity

Fig. 77.26 Interior aspect of the hip joint to show the ligament of the head of the femur. (With permission from Drake RL, Vogl AW, Mitchell A et al (eds) Gray's Atlas of Anatom. Elsevier, Churchill Livingstone. Copyright 2008.)

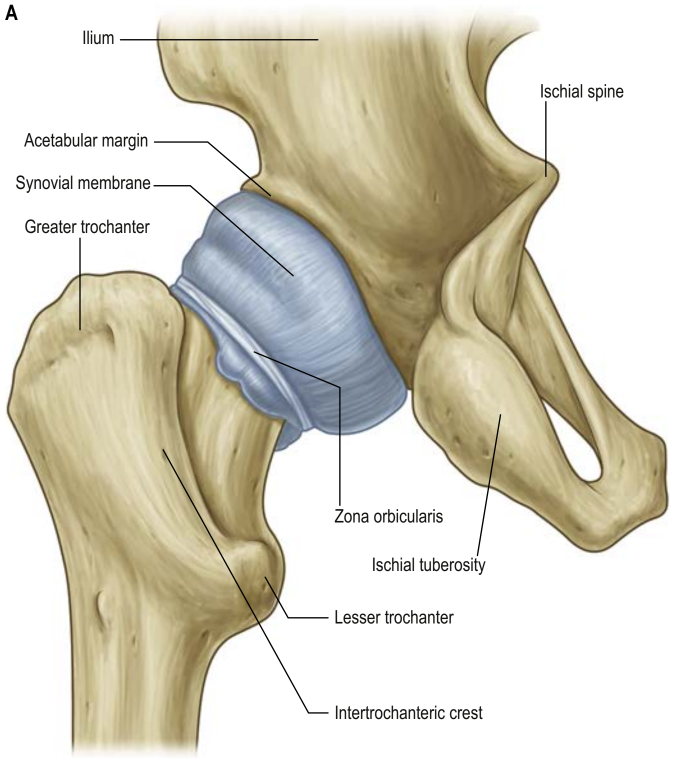

Fig. 77.28 **A**, Synovial cavity of the left hip joint (distended): posterior aspect. (B, *continued online*)

joint capsule (Perumal et al 2019), is ensheathed by synovial membrane and varies in strength. The ligamentum teres is typically not physically compressed between the socket and the femoral head because of the depth and shape of the acetabular fossa. Occasionally the synovial sheath exists by itself in the absence of the ligament; rarely, both the ligament and sheath are absent.

Although the ligament of the head of the femur is known primarily for lending structural support to the blood vessels that travel to and from the femoral head, speculation exists that it may also have a role in stabilizing the hip joint *in utero*. In the adult, it is mostly elongated and assumed to be taut when the hip joint is semi-flexed, laterally rotated and adducted, the position where the capsular ligaments, as a whole, offer least stability to the joint (Martin et al 2012). The degree to which the ligament of the head of the femur offers functional stability to the adult hip is uncertain, although it is likely to be secondary to that provided by the capsular ligaments and muscle activation.

Medical interest in the ligament of the head of the femur has increased with the advancing technology associated with medical imaging and arthroscopic hip surgery (Gray and Villar 1997, Botser et al 2011; **Fig. 77.27**).Free nerve endings have been identified within this ligament, suggesting that this structure may be a source of pain when it is injured or degenerating (Leunig et al 2000). The afferent innervation in the healthy state may serve as a source of proprioception or protection of the joint (Bardakos and Villar 2009).

Synovial membrane Starting from the femoral articular margin, the synovial membrane covers the intracapsular part of the femoral neck, and then passes to the internal surface of the capsule to cover the acetabular labrum, the ligament of the head of the femur and fat in the acetabular fossa (**Fig. 77.28**). It is thin on the deep surface of the iliofemoral ligament where it is compressed against the femoral head, and sometimes is even absent here.

Bursae The hip joint may communicate with the subtendinous iliopectineal bursa through a circular aperture between the pubofemoral ligament and the descending part of the iliofemoral ligament. More distant bursae are associated with the tendons of the distal attachments of the gluteus medius (subgluteus maximus or 'trochanteric' bursa) and minimus at the greater trochanter, and between gluteus maximus and the proximal tendon of vastus lateralis (Woodley et al 2008).

Vascular supply and lymphatic drainage Articular arteries are branches from the obturator, medial circumflex femoral, and superior and inferior gluteal arteries; they form the cruciate and trochanteric anastomoses. There is a corresponding venous drainage.

The blood supply to the hip in the child is different from that in the adult and this has very important implications clinically. Since the growth plate is avascular, the only blood supply to the femoral head is conveyed through the retinacular vessels, which are mainly tributaries of the medial circumflex femoral artery. These retinacular arteries enter the joint capsule in the trochanteric fossa and ascend the femoral neck on its outer aspect superiorly and posteriorly. They pass around the edge of the growth plate (physis) and enter the femoral head. A minor contribution to the vascular supply comes from the ligament of the head of the femur. Any damage to these vessels (e.g. trauma, infection) can result in the devastating complication of avascular necrosis of the femoral head. The growth plate represents a line of weakness and predisposes to fracture from injury. Acute injuries affecting the capital epiphysis are uncommon. A more chronic fracture through the capital epiphysis resulting in slipped capital femoral epiphysis, where the femoral head epiphysis displaces posteriorly off the femoral neck, occurs in pubescent adolescents, especially males (**Fig. 77.29**).

Lymphatics from the anterior aspect of the hip joint drain to the deep inguinal nodes, while those from the medial and posterior aspects of the joint travel with the obturator and gluteal arteries, respectively, to reach the internal iliac nodes.

Innervation The anterior capsule of the hip joint is innervated by the femoral, obturator and accessory obturator (when present) nerves. The posterior capsule is innervated by the sciatic and superior gluteal nerves, and by the nerve to quadratus femoris (Gardner 1948, Birnbaum et al 1997).

Hip and groin pain

Pain emanating from the hip and groin has many possible causes. True pain from the hip joint is typically felt deep in the crease of the groin, secondary to intra-articular pathology such as osteoarthritis, a torn acetabular labrum, or femoro-acetabular impingement. Pain over the lateral aspect of the hip usually suggests a local problem such as gluteus medius or minimus tendinopathy and associated trochanteric bursitis (Bird et al 2001, Grimaldi and Fearon 2015). Pain in the buttock is only occasionally derived from the hip joint; most frequently, it is referred from the lumbosacral spine or may be caused by vascular claudication. Pain in the groin may be associated with inguinal or femoral hernias. In the younger age group, it afflicts those engaged in sports, especially running ball sports; the pain is sometimes due to hernia but most often is related to adductor longus tendinosis ('groin strain'). Attritional chronic overload of the anterior abdominal wall at its attachments to the pubis and inguinal ligament, or of external abdominal oblique at

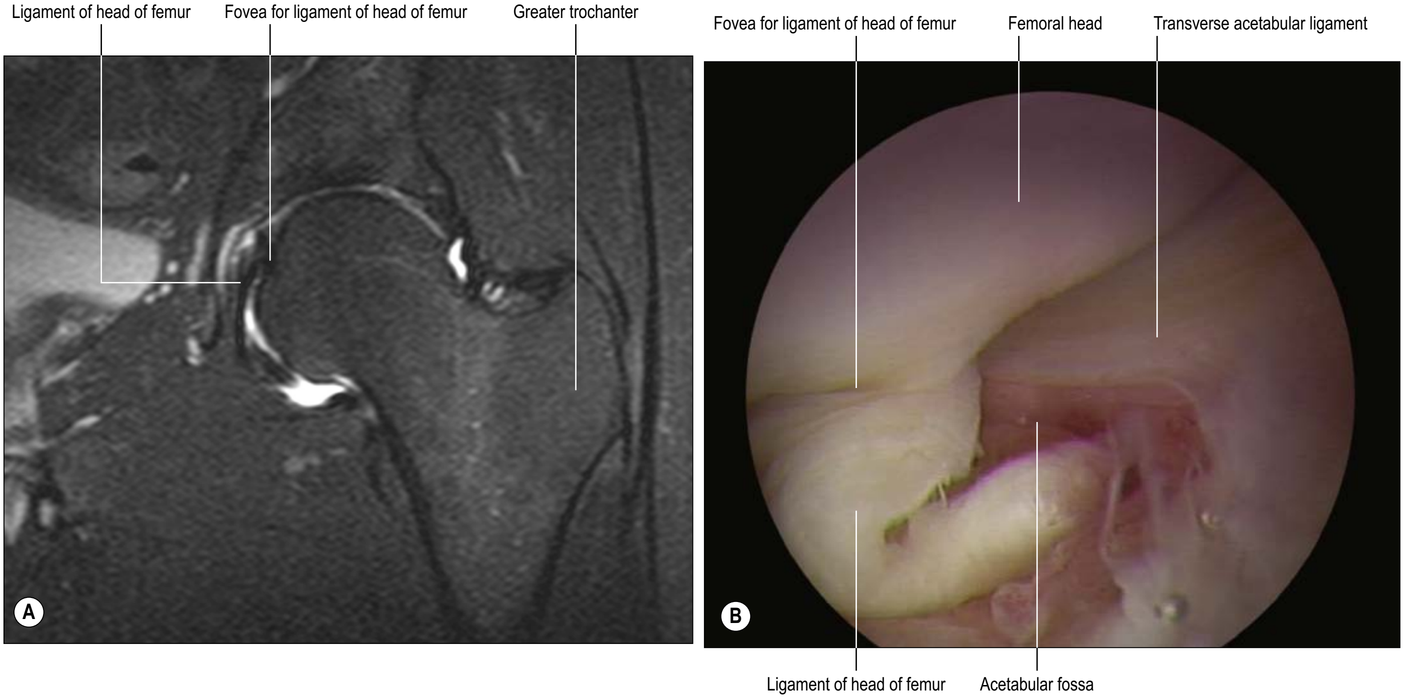
Ligament of head of femur
Fovea for ligament of head of femur
Greater trochanter
A
Fovea for ligament of head of femur
Femoral head
Transverse acetabular ligament
B
Ligament of head of femur
Acetabular fossa

Fig. 77.27 An intact ligament of the head of the femur in a left adult hip. **A**, T2-weighted fat-saturated MR arthrogram of the hip joint (coronal section). **B**, Photograph taken through an arthroscope of a slightly distracted hip joint. (A, Courtesy of Michael O'Brien MD, Wisconsin Radiology Specialists, Milwaukee, WI, USA. B, Courtesy of John T Heinrich MD, Milwaukee Orthopaedic Group Limited, Milwaukee, WI, USA.)

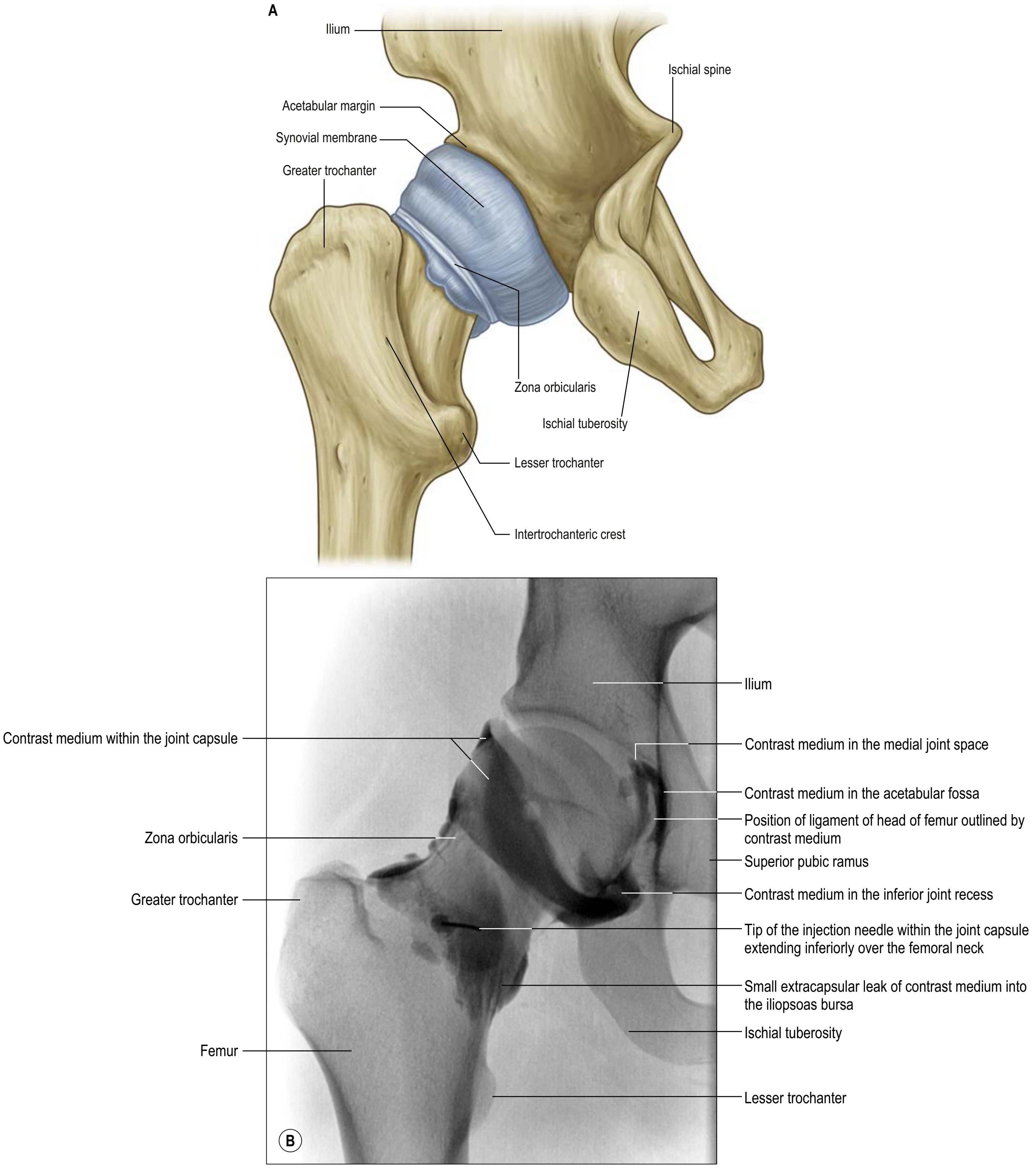
A
Ilium
Acetabular margin
Synovial membrane
Greater trochanter
Ischial spine
Zona orbicularis
Ischial tuberosity
Lesser trochanter
Intertrochanteric crest
B
Ilium
Contrast medium within the joint capsule
Contrast medium in the medial joint space
Contrast medium in the acetabular fossa
Position of ligament of head of femur outlined by contrast medium
Zona orbicularis
Superior pubic ramus
Greater trochanter
Contrast medium in the inferior joint recess
Tip of the injection needle within the joint capsule extending inferiorly over the femoral neck
Small extracapsular leak of contrast medium into the iliopsoas bursa
Ischial tuberosity
Femur
Lesser trochanter

Fig. 77.28 **A**, Synovial cavity of the left hip joint (distended): posterior aspect. **B**, A fluoroscopic arthrogram of the right hip. Contrast medium tends not to appear in the superior joint space unless a large volume is injected that then separates the opposed articular cartilage surfaces.

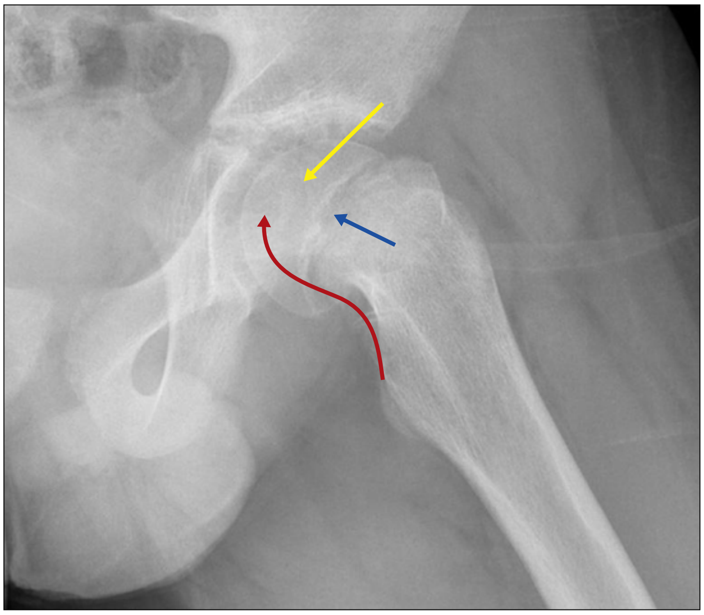

Fig. 77.29 Radiograph of the left hip of a 14-year-old boy. The yellow arrow shows posterior displacement of the femoral head in the slipped capital femoral epiphysis. The red arrow indicates the course of the retinacular vessels along the posterior aspect of the femoral neck. The blue arrow indicates the growth plate (physis). (Courtesy of Mr Christopher Edward Bache.)

the superficial inguinal ring, is a common occurrence. Rarely, problems may occur at the pubic symphysis.

Biomechanics of the hip joint

The transition from quadrupedal to bipedal gait was a considerable biomechanical milestone in the evolution of *Homo sapiens*. The biomechanical features of the human lower limb, which functions primarily to allow stance and bipedal propulsion, are very different from those of the quadruped lower limb, and these differences are reflected in the anatomy and biomechanics of the human hip, knee, ankle and foot joints.

Stability and movement

The hip joint is normally very stable. The femoral head is closely fitted to the acetabulum in an area exceeding half a sphere, forming a multiaxial spheroidal ('ball and socket') joint that allows relatively unhindered motion in three degrees of freedom, i.e. flexion/extension, abduction/adduction and medial/lateral rotation. However, the femoral head is also embraced closely by the acetabular labrum, which restrains it in the socket and innately limits its capacity for translational motion in anteroposterior, transverse and vertical directions. The thick capsule is reinforced by the three major ligaments: iliofemoral, pubofemoral and ischiofemoral. The iliofemoral ligament is the strongest, and is progressively tightened when the femur extends to and beyond the line of the trunk. The pubofemoral and ischiofemoral ligaments also tighten when this happens and, as the joint approaches the close-packed position, resistance to an extending torque increases rapidly. The transverse acetabular ligament and ligament of the head of the femur may also contribute to stability.

A 'vacuum effect' within the hip joint is present, which means that only slight separation of the articular surfaces can be achieved by strong traction on the joint. To aid insertion of an arthroscope, a needle is first inserted into the joint to eliminate the suction effect; the joint will subsequently open sufficiently with traction. Traumatic dislocation usually occurs only when the joint is subjected to extreme force.

Femur

The femur is essentially a tubular structure with distortions that consist of bows and twists. The most notable is the anterior bow in its mid portion, where the radius of curvature is relatively constant along the length of the femoral shaft. In the coronal plane, the femoral neck is inclined obliquely to the shaft at an angle of about 125°, although this angle can vary considerably (Fig. 77.30). Although both the neck–shaft angle (collodiaphysial angle; Mikulicz angle) and neck length are variable, the centre of the neck in the coronal plane is at the level of the apex of the greater trochanter. The neck–shaft angle facilitates freedom of movement of the femur, enabling it to swing clear of the pelvis. The neck also provides an adequate lever for the action of the muscles acting about the hip joint, most notably the hip abductors, which are attached to the proximal femur. The neck–shaft angle is widest at birth and diminishes gradually until the age of 10 years (Birkenmaier et al 2010); it is smaller in females. In the axial plane, the femoral neck is anteverted, i.e. rotated anteriorly relative to the posterior surfaces of the femoral condyles; in the adult, this angle is typically about 10–15° (Fig. 77.31A). Excessive anteversion may exist when this angle is significantly greater than 10–15° (Fig. 77.31B). At birth, the angle of anteversion is typically about 35–40°. As the child develops, forces from muscles and gravity cause the angle of anteversion to decrease gradually, approaching 15° by young adulthood. Excessive anteversion usually persists beyond childhood in cases of abnormal motor development, such as can be seen with cerebral palsy.

The degree of anteversion affects many aspects of lower limb biomechanics, including the moment (lever) arms of the hip abductor and medial rotator muscles (the perpendicular distance from the centre of rotation of the femur to the line of action of the resultant muscle force); patellar tracking (the motion of the patella relative to the femur); and foot orientation.

Acetabulum

The acetabulum consists of the confluence of the ilium, ischium and pubis at the triradiate cartilage. By itself, the acetabulum covers an area slightly less than a hemisphere; it is deepened by the acetabular labrum. The degree of acetabular anteversion is about 17° (16° males and 18° females) (Reikeras et al 1983). In the coronal plane, the acetabular axis is inclined inferiorly approximately 45° from the horizontal.

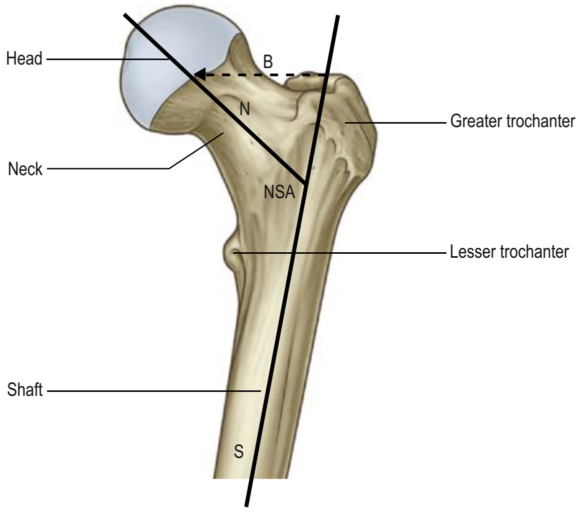

Fig. 77.30 The neck–shaft angle (NSA) is shown between the long axis of the femoral shaft (S) and the axis of the femoral neck (N). In addition, in most hips, a line nearly perpendicular to S from the tip of the greater trochanter (B) passes through the centre of the femoral head. This approximation can be utilized in judging the position of the femoral osteotomy in hip arthroplasty.

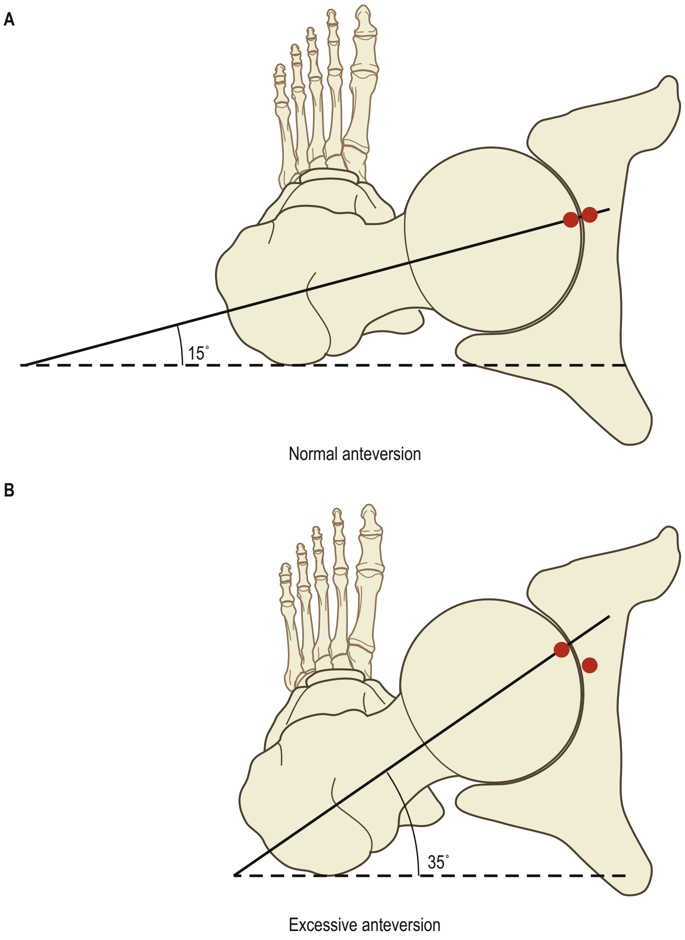

Fig. 77.31 **A**, Superior view of a proximal femur showing normal anteversion. **B**, Superior view of a proximal femur with excessive anteversion. (With permission from Neumann D, Kinesiology of the Musculoskeletal System, 3rd ed. Elsevier, Mosby. Copyright 2017.)

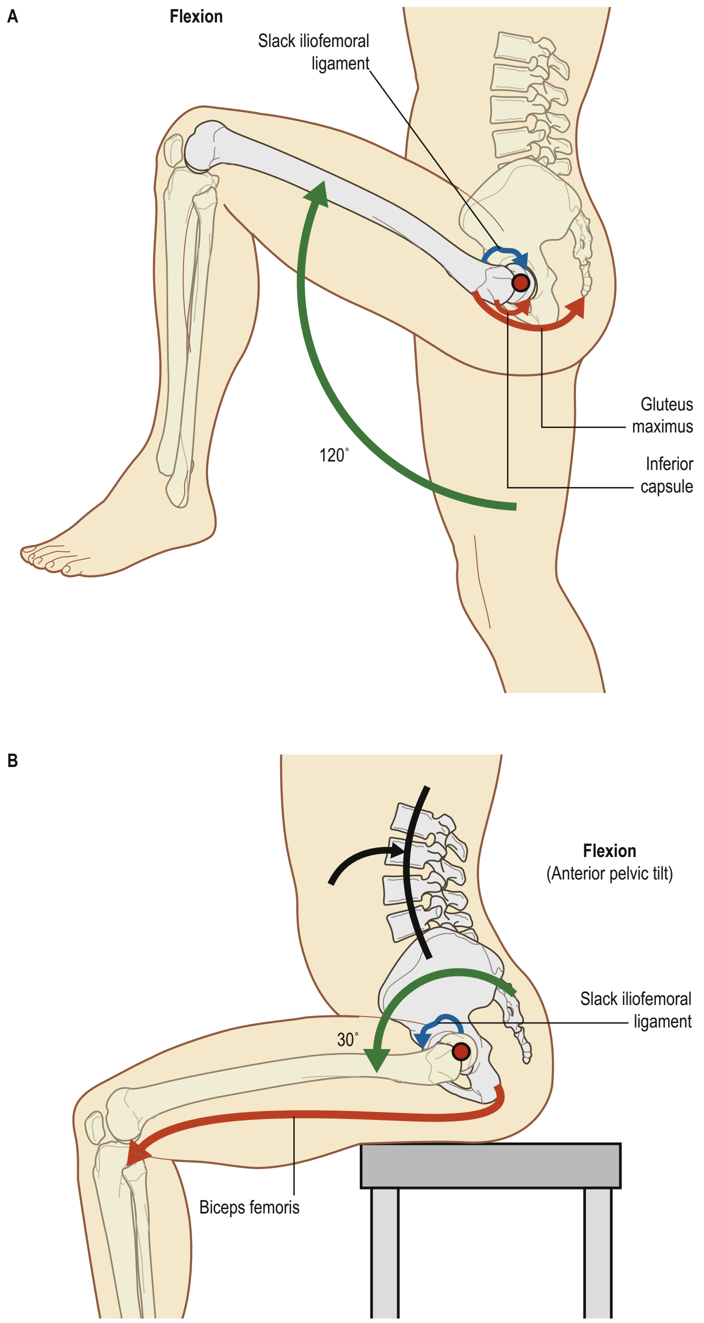

Fig. 77.32 Hip flexion shown from two kinematic perspectives, as indicated by the green curved arrows. **A**, Femoral-on-pelvic flexion. **B**, Pelvic-on-femoral flexion. Note the directional-specific motion of the lumbar spine in **B**; this is a necessity, assuming the trunk remains upright. Tissues that are elongated or pulled taut are indicated by orange arrows; tissues slackened are indicated by blue wavy arrows. In all cases, muscles are assumed to be inactive but stretched. The red circle indicates the axis of rotation at the hip. (With permission from Neumann D, Kinesiology of the Musculoskeletal System, 3rd ed. Elsevier, Mosby. Copyright 2017.)

Movements

Two terms can conveniently describe the kinematics (movements) at the hip. Femoral-on-pelvic hip kinematics describes the rotation of the femur about a relatively fixed pelvis. Conversely, pelvic-on-femoral (hip) kinematics describes the rotation of the pelvis, and often the superimposed trunk, over a relatively fixed femur or set of femurs. Regardless of whether the femur or the pelvis is the moving segment, kinematics are described for all three cardinal planes on the assumption that movements are initiated from the anatomical position.

Flexion and extension are motions that occur in the sagittal plane. To appreciate the hip joint arthrokinematics that accompany the associated femoral-on-pelvic motions, the length and angulation of the femoral neck in relation to the shaft must be considered. As the hip (femur) is flexed about 120° towards the anterior thoracic wall, or extended 10–20° beyond the plane of the trunk, the femoral head 'spins' in the acetabulum about a side-to-side (medial–lateral) axis of rotation. Conversely, from a pelvic-on-femoral perspective, the acetabula rotate around a similar axis in flexion and extension relative to stationary femoral heads (compare Figs 77.32A and B). Depending on the accompanying trunk movement, the lumbar vertebrae will either flex or extend in rhythm with the rotating pelvis. Consider, for example, a short-arc anterior rotation (or tilt) of the pelvis over both femurs while the upper trunk remains stationary. During this motion, the lumbar vertebrae extend slightly towards greater lordosis. By comparison, rotating both the pelvis and the trunk over both femurs (as in reaching towards the ground with knees held extended), the pelvis and the thoracolumbar vertebrae both flex, thereby augmenting the overall forward motion of the body as a whole.

Abduction and adduction of the hip joint occur in the coronal plane about an anterior-to-posterior axis of rotation through the femoral head. With the pelvis fixed, the femur abducts about 40° (Fig. 77.33A). Conversely, pelvic-on-femoral (hip) motions that occur in the coronal

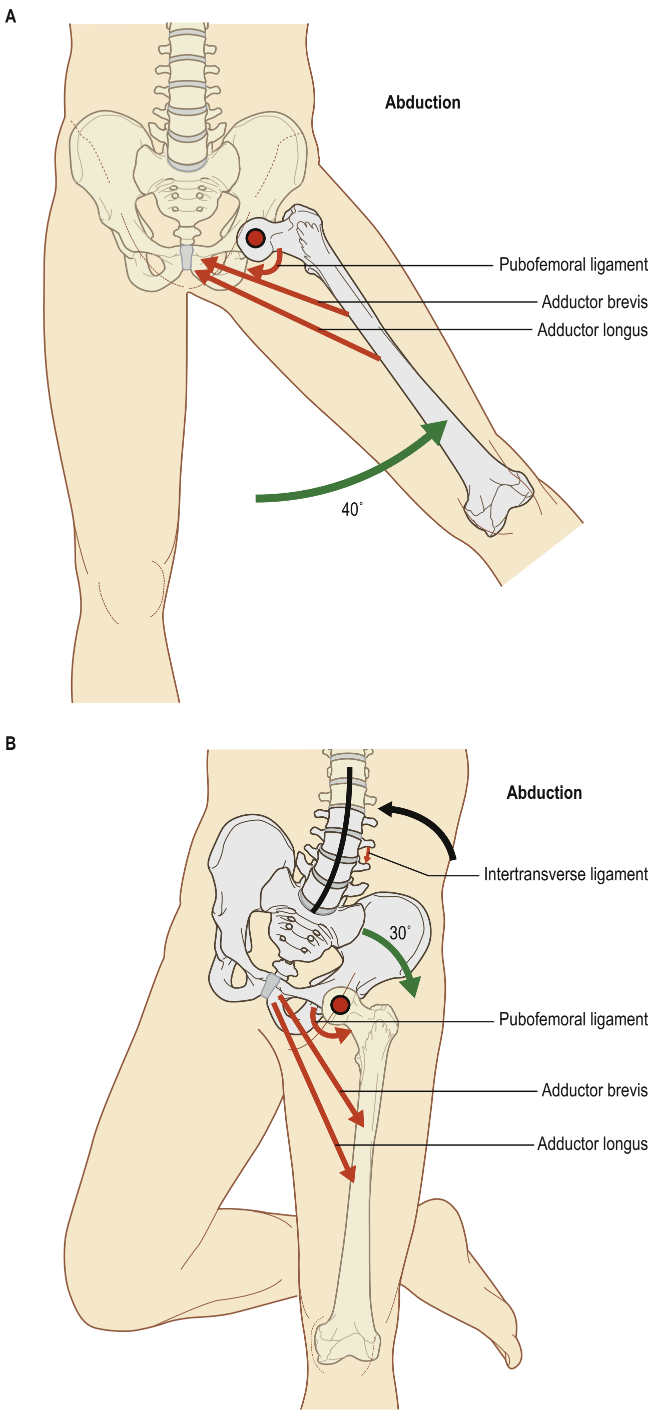

Fig. 77.33 Hip abduction shown from two kinematic perspectives, as indicated by the green curved arrows. **A**, Femoral-on-pelvic abduction. **B**, Pelvic-on-femoral abduction. Note the directional-specific motion of the lumbar spine in **B**; this is a necessity, assuming the trunk remains upright. Tissues that are elongated or pulled taut are indicated by orange arrows. In all cases, muscles are assumed to be inactive but stretched. The red circle indicates the axis of rotation at the hip. (With permission from Neumann D, Kinesiology of the Musculoskeletal System, 3rd ed. Elsevier, Mosby. Copyright 2017.)

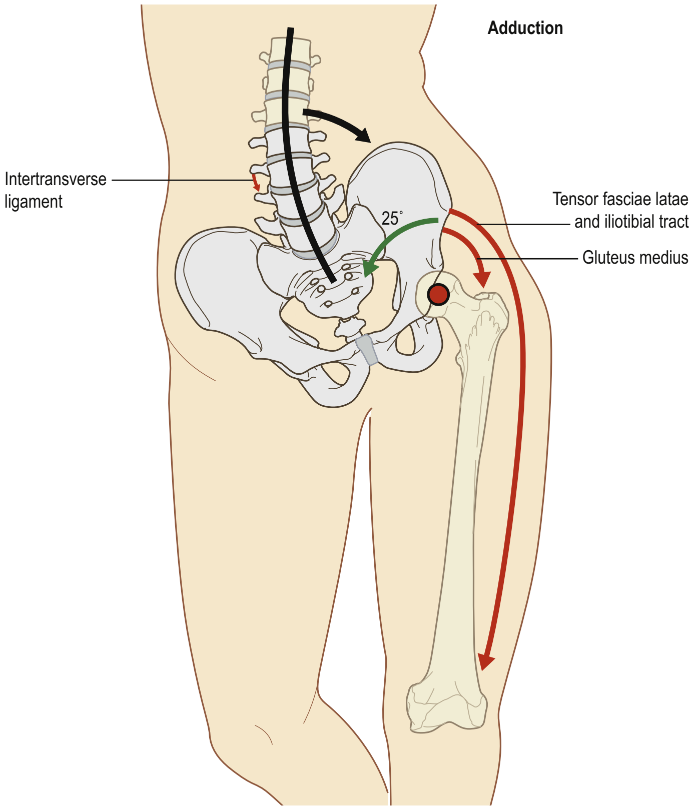

Fig. 77.34 Hip adduction shown from a pelvic-on-femoral perspective, as indicated by the green curved arrow. Note the directional-specific motion of the lumbar spine; this is a necessity, assuming the trunk remains upright. Tissues that are elongated or pulled taut are indicated by orange arrows. In all cases, muscles are assumed to be inactive but stretched. The red circle indicates the axis of rotation at the hip. (With permission from Neumann D, Kinesiology of the Musculoskeletal System, 3rd ed. Elsevier, Mosby. Copyright 2017.)

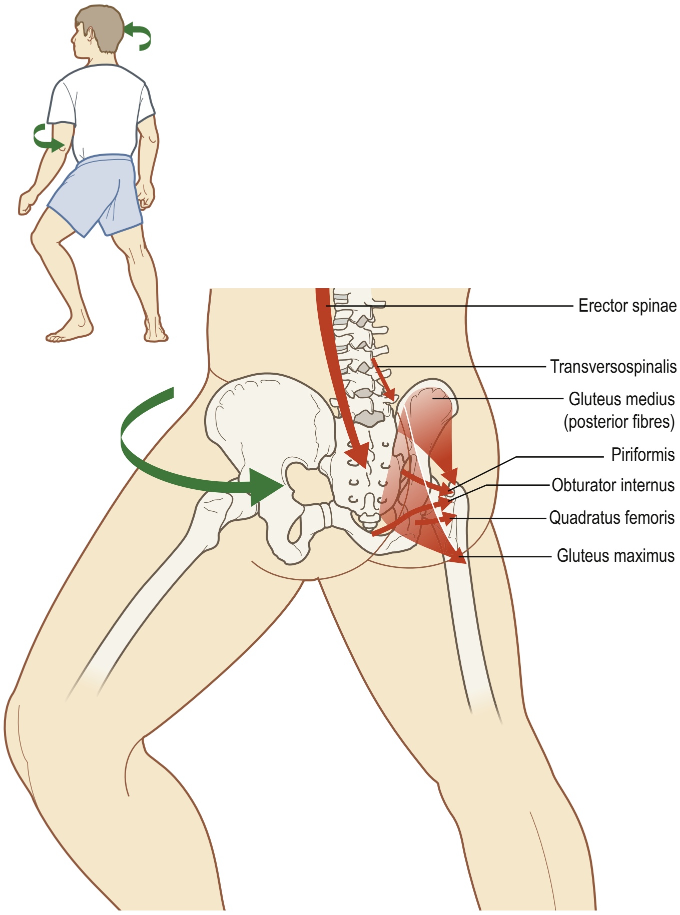

Fig. 77.35 The right lateral rotator muscles of the hip contract to produce lateral rotation of the right hip, from a pelvic-on-femoral perspective. Back extensor muscles are also shown active, rotating the lower trunk to the left. (With permission from Neumann D, Kinesiology of the Musculoskeletal System, 3rd ed. Elsevier, Mosby. Copyright 2017.)

plane are best described assuming a person is bearing weight firmly on one lower limb, referred to hereafter as the 'support' hip. Abduction at the support hip occurs by raising the contralateral side of the pelvis a few degrees (Fig. 77.33B). Marked tightness in the hip adductor muscles or medial capsule of the hip on the support hip can limit this pelvic motion. Adduction at the support hip occurs by lowering the contralateral side of the pelvis (Fig. 77.34). Assuming that the trunk remains nearly stationary during these short-arc pelvic-on-femoral motions, the lumbar spine laterally bends slightly as a way to offset undesired thoracic motion. The lumbar vertebrae, therefore, act to decouple motion of the pelvis (moving on the femur) from undesired motions between the thorax and pelvis (Neumann 2017). This decoupling function of the lumbar vertebrae is especially useful during walking as a way of partially fixing the spatial orientation of the upper thorax, as well as the associated craniocervical region and the embedded senses of vision and equilibrium. This kinematic linkage between the spine, pelvis and femur exists in essentially all hip motions to varying degrees, and is an important characteristic of normal walking.

Medial and lateral rotation of the hip joint occurs in the horizontal (transverse) plane about a vertical axis of rotation. With the pelvis fixed, the femur rotates medially about 35°. The extended hip rotates laterally about 45°. Horizontal plane movements of the hip joint from a pelvic-on-femoral perspective, as explained above, are best described assuming a person is bearing weight over a given 'support' hip. Consider, for example, running and rapidly changing directions while one lower limb is securely planted on the ground. During lateral rotation of the support hip, the iliac crest located contralateral to the support limb rotates posteriorly in the transverse plane, an action driven strongly by gluteus maximus (Fig. 77.35). Conversely, pelvic-on-femoral (hip) medial rotation occurs as the contralateral iliac crest region rotates anteriorly.

As stated above, the axis of rotation for horizontal plane motions at the hip joint occurs about a vertical axis of rotation. The slight anterior bowing for the femoral shaft, coupled with the natural angle between the femoral shaft and neck, means that this axis is not intramedullary; rather it passes just posterior and slightly medial to the shaft. The position of this 'mechanical' (versus medullary) axis becomes biomechanically relevant when considering the actions and moment arms of certain hip muscles, most notably for adductor muscles that also function as medial rotators (Neumann 2010).

Forces acting on the hip

In quiet upright standing, the femoral heads support the weight of the trunk, upper limbs and head. About two-thirds of body weight is located above the hips, and so each femoral head normally accepts about one-third of body weight. This force is compressive in nature, as gravity pulls the acetabula against the femoral heads. When viewed in the sagittal plane, minimal muscle forces suffice to maintain equilibrium as long as the weight of the upper body is directed over or behind the femoral heads. If the upper body leans anteriorly, shifting the upper body weight vector anteriorly beyond the femoral heads and thereby producing a hip flexion moment, posterior thigh muscles can counter such rotation. As the capsular ligaments of the hip slacken in flexion, none of them is able to resist the forward lean.

Hip joint compression forces vary from one-third of body weight, when both feet are on the ground during standing at ease, to some four times body weight when the other foot is lifted, as during walking. This represents at least a ten-fold increase in compression forces, explaining, in part, why persons with a painful hip often limit the time spent in single-limb stance. The large compression forces generated while walking originate primarily from two sources: gravity and muscle activation. During the stance phase, gravity pulls the upper body and acetabulum inferiorly on the femoral heads (as described above for quiet standing). More significantly, each femoral head is pushed superiorly against its socket as the foot strikes and then pushes against the ground. Although activation of muscles is responsible for a greater portion of joint compression at the hip, the influences of gravity and of capsular tension (when the hip joint is extended) should not be ignored.

As the lower limb is swinging anteriorly and free of contact with the ground, hip joint compression force is estimated to be at about 50%

of body weight (Correa et al 2010). Such joint force is essentially myogenic. Consider, for example, a contracting iliopsoas pulling the femoral head against the acetabulum as it simultaneously advances the lower limb in walking.

In contrast, during the stance phase of walking, hip joint forces may reach four times body weight. These forces are mainly caused by the pull of the hip abductor muscles (primarily gluteus medius, gluteus minimus and tensor fasciae latae). This muscular action, essential to normal bipedal gait, provides the necessary coronal plane stabilization of the pelvis relative to the femoral head of the stance limb.

The importance of hip abductor muscle activation during the stance phase of walking can be well appreciated by understanding the simple mechanics of standing on one limb (**Fig. 77.36**). The lever arm (a) of left hip abductor force (Ab) is about half the length of the lever arm (b) associated with body weight (BW). To balance the competing (coronal plane) gravitational moments about the stance hip, the hip abductors must produce a force about twice superincumbent body weight. Thus, the acetabulum is pulled inferiorly against the femoral head not only by the body weight but also by the force created by the activated hip abductor muscles. The sum of the muscular and gravitational forces therefore approaches 2.5 times the total weight of the person. These downward forces on the head of the femur are counteracted by an upward joint reaction force of equal magnitude (JRF in Fig. 77.36). Both magnitude and direction of the joint reaction force are strongly influenced by the pull of the hip abductor muscles.

The above analysis is for standing quietly on one limb. During walking, however, the joint reaction force routinely reaches at least four times body weight, reflecting both the high ground reaction forces and the need for the hip abductor muscles to decelerate rotations of the pelvis (Bergmann et al 1993). Hip joint forces reach still greater values during running or stair-climbing (see review in Stansfield and Nicol 2002).

Compression forces produced by the gluteus medius during stance phase are directed superiorly and slightly anteromedially within the acetabulum (Correa et al 2010), a region naturally protected by thick articular cartilage. In the healthy hip joint, the muscular-based compressive forces serve important functions, such as helping to stabilize the articulation and stimulate the morphological development of the growing hip. Forces that cross the hip typically do not harm the joint because they are absorbed by healthy articular cartilage and congruent joint surfaces. Failure of these conditions to absorb forces in the joint may predispose to osteoarthritis of the hip.

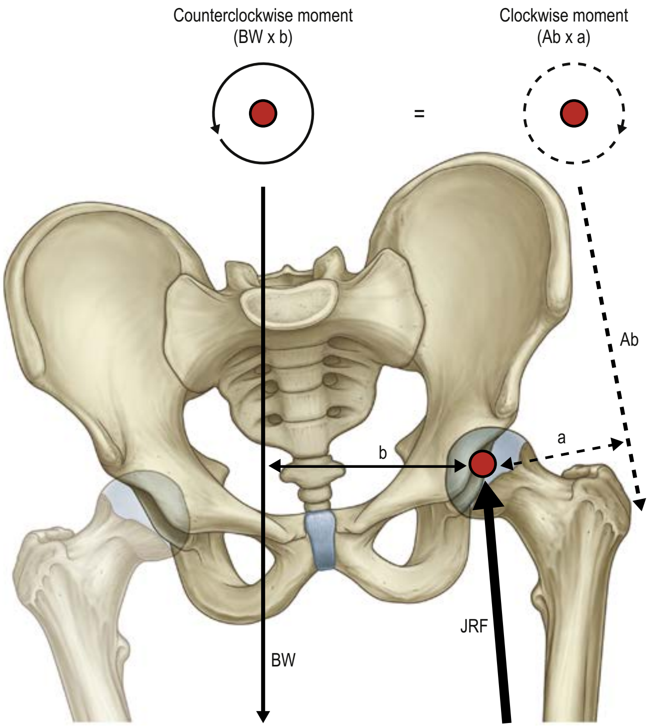

Fig. 77.36 While standing on one (left) lower limb, body weight (BW) line of force, i.e. total body weight minus the weight of the left lower limb, passes just lateral to the midline, exerting a counterclockwise moment about the stance hip (BW × b). An equal but clockwise moment is required about the stance hip for mechanical equilibrium: a moment produced by the force of the abductors (Ab), whose lever arm (a) is approximately half that of the lever arm (b). The two moments are in balance when (Ab × a = BW × b). The abductor force required to maintain equilibrium is approximately twice that of BW, resulting in a joint reaction force (JRF) nearly 2.5 times that of total weight of the subject's body.

The three factors that influence both the magnitude and the direction of compressive forces acting on the hip are the position of the centre of gravity; the abductor moment arm, which is a function of neck length (offset) and neck–shaft angle; and the amount of body weight. Shortening of the lever arm of the abductors, such as occurs in coxa valga or excessive femoral anteversion, or in a remodelled proximal femur in advanced hip osteoarthritis, would increase abductor muscle demand and thus increase joint reaction force as well. If the muscles cannot meet this demand, the pelvis cannot be held level in standing on one limb, a problem known as either a compensated or an uncompensated Trendelenburg sign. The Trendelenburg sign is said to be compensated if the pelvis is brought towards the affected stance limb as a way of shortening the body weight's lever arm. Conversely, the Trendelenburg sign is said to be uncompensated if the pelvis drops away from the affected stance limb uncontrollably.

Muscles producing hip joint movements

Flexion is primarily produced by psoas major, iliacus and rectus femoris, assisted by pectineus, tensor fasciae latae and sartorius. The adductors, particularly adductor longus and brevis, also assist, especially when the hip is near full extension. Effective action of the hip flexor muscles requires strong synergistic activation of the abdominal muscles to stabilize the pelvis.

Extension is produced by gluteus maximus, the long head of biceps femoris, semitendinosus, semimembranosus and adductor magnus. The posterior fibres of gluteus medius assist with this action (Neumann 2010). In the fully erect posture, a vertical line through the centre of gravity of the body normally passes just posterior to a line joining the centres of the femoral heads. The body therefore tends to incline posteriorly but this is counterbalanced by ligamentous tension and congruence and compression of the articular surfaces within the hip joints in the close-packed position. Under increased loading of the trunk or leaning posteriorly, these resistive but passive factors are assisted by active force produced by the hip joint flexors. In swaying anteriorly at the ankles, or when the arms are stretched forwards, and also in forward-bending at the hip, the line of body weight moves anterior to the medial–lateral axis of rotation through the hip joints. The posture adopted, or the rate of change of posture, is largely controlled by the hamstrings, which, besides being powerful flexors of the knee, are strong extensors of the hip. Gluteus maximus becomes particularly active when the thigh is extended against resistance, as in rising from a bending position or during climbing.

Abduction is produced by gluteus medius, gluteus minimus and tensor fasciae latae, assisted by the piriformis and sartorius. The motion is limited by adductor muscle tension, the pubofemoral ligament and the extreme medial bands of the descending part of the iliofemoral ligament. The abductor muscles, most notably glutei medius and minimus, are active periodically at precise phases of the walking or running cycle to ensure coronal plane stability of the pelvis.

Adduction is produced by adductor longus, brevis and magnus, and gracilis, assisted by pectineus, quadratus femoris and the inferior fibres of gluteus maximus. The range of adduction is limited by the increasing tension in the abductor muscles, the transverse part of the iliofemoral ligament and the fascia lata of the thigh.

Medial rotation is produced by the anterior fibres of glutei minimus and medius, and assisted by most adductor muscles and, to a lesser extent, the tensor fasciae latae. The strength of medial rotation naturally increases as the hip is flexed because this position increases the moment arm of most medial rotator muscles (Delp et al 1999). Medial rotation is limited by tension in lateral rotator muscles such as piriformis, the ischiofemoral ligament and the adjacent posterior joint capsule (Wagner et al 2012).

Lateral rotation is produced by gluteus maximus, obturator internus, superior and inferior gemelli, quadratus femoris and piriformis, assisted by obturator externus and sartorius. Lateral rotation, a stronger motion than medial rotation, is limited by tension in the medial rotator muscles and the transverse part of the iliofemoral ligament (Myers et al 2011).

MUSCLES

Muscles of the iliac region

Although there is no 'iliac region' as such, this heading conveniently describes a group of three muscles that originate from the lumbar vertebral column (psoas major and minor) and the ilium (iliacus). Psoas major and iliacus are attached together on the femur as flexors of the hip joint and are often considered as a functional unit, iliopsoas. Psoas minor, when present, only reaches the anterior pelvis, near the iliopubic junction, and therefore does not act directly on the femur.

Psoas major

Attachments Psoas major is a long muscle that lies on either side of the lumbar vertebral column and the pelvic brim (Fig. 77.37; see Fig. 61.7). Its proximal attachments are complex. They include the anterior surfaces and lower borders of the transverse processes of all the lumbar vertebrae. There are five digitations, each from the bodies of two adjoining vertebrae and their intervertebral disc. The highest of these arises from the lower margin of the body of the twelfth thoracic vertebra, the upper margin of the body of the first lumbar vertebra and the interposed intervertebral disc. The lowest arises from the adjacent margins of the bodies of the fourth and fifth lumbar vertebrae and the interposed disc. A series of tendinous arches extend across the narrow parts of the bodies of the lumbar vertebrae between the digitations already described. The lumbar arteries and veins, and filaments from the sympathetic trunk, pass medial to these arches. The upper four lumbar intervertebral foramina bear important relations to these attachments of the muscle. The foramina lie anterior to the transverse processes and posterior to the attachments to vertebral bodies, intervertebral discs and tendinous arches. Thus, the roots of the lumbar plexus enter the muscle directly, the plexus is lodged within it, and its branches emerge from its borders and surfaces.

The muscle descends along the pelvic brim, continues posterior to the inguinal ligament and anterior to the capsule of the hip joint, and converges to a tendon that, having received on its lateral side nearly all the fibres of iliacus, becomes attached to the lesser trochanter of the femur. The large subtendinous iliac bursa, which occasionally communicates with the cavity of the hip joint, separates the tendon from the pubis and the capsule of the joint.

The complex vertebral attachments of psoas major sometimes display minor numerical variations.

Relations The upper limit of psoas major is posterior to the diaphragm in the lowest part of the posterior mediastinum. It may be in contact with the posterior extremity of the pleural sac. In the abdomen its anterolateral surface is related to the medial arcuate ligament (a linear, arched thickening in the psoas fascia), extraperitoneal tissue and peritoneum, the kidney, psoas minor, renal vessels, ureter, testicular or ovarian vessels and the genitofemoral nerve. Anteriorly the right psoas is overlapped by the inferior vena cava and crossed by the terminal part of the ileum; the colon crosses the left psoas. Its posterior surface is related to the transverse processes of the lumbar vertebrae and the medial edge of quadratus lumborum. The lumbar plexus is embedded posteriorly in the substance of psoas major. Medially the muscle is related to the bodies of the lumbar vertebrae and lumbar vessels. Along its anteromedial margin it is in contact with the sympathetic trunk, aortic lymph nodes and, along the pelvic brim, with the external iliac artery. This margin is covered by the inferior vena cava on the right side, and lies posterior and lateral to the abdominal aorta on the left side. In the thigh, iliopsoas is related anteriorly to the fascia lata and the femoral artery, and posteriorly to the capsule of the hip joint, from which it is separated by a bursa. At its medial border it is related to pectineus and the medial circumflex femoral artery, and to the femoral vein, which may overlap it slightly. At its lateral border it is related to the femoral nerve and iliacus. The femoral nerve descends at first through the fibres of psoas major, and then in the furrow between it and iliacus.

Branches of the lumbar plexus diverge from the abdominal part of psoas major. Emerging from the lateral border, from above downwards, are the iliohypogastric, ilioinguinal and lateral femoral cutaneous and femoral nerves. Emerging from the anterolateral surface is the genitofemoral nerve. The obturator and accessory obturator nerves (when present) and the upper root of the lumbosacral trunk all emerge from the medial border.

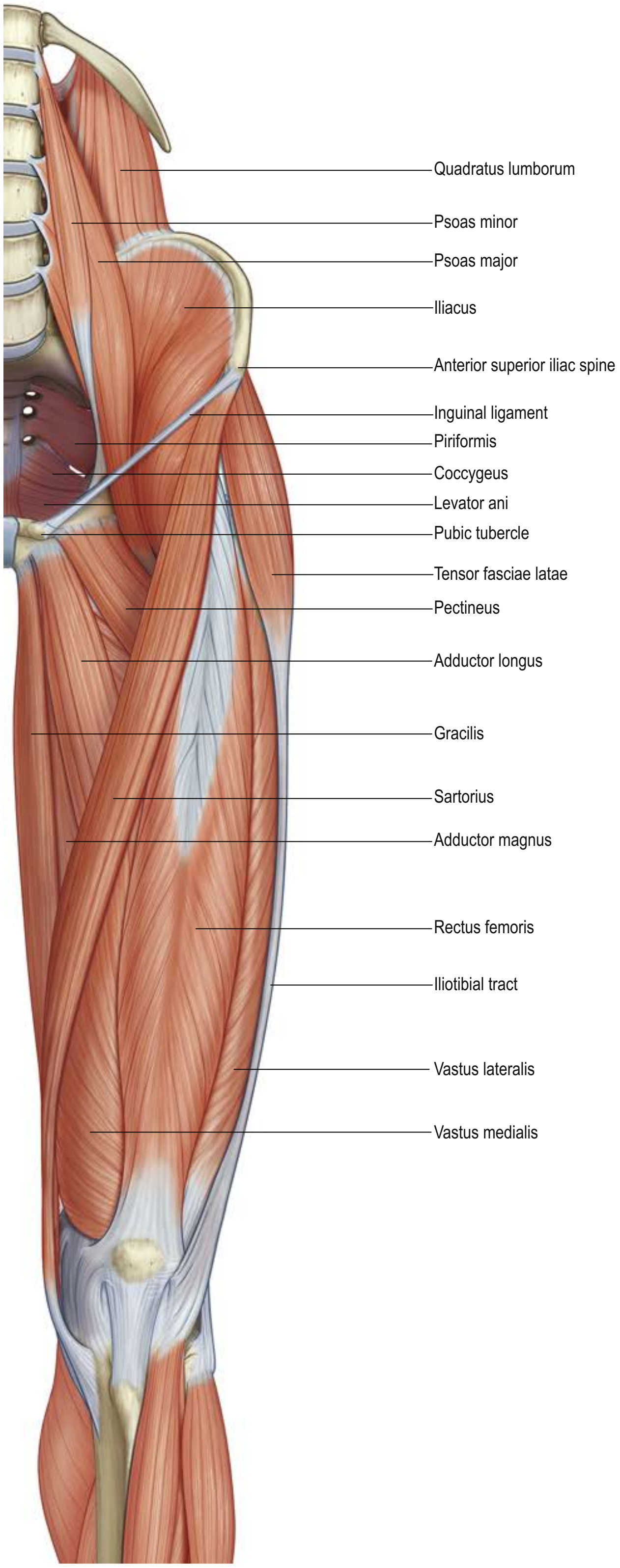

Fig. 77.37 The hip flexors and superficial muscles of the thigh, anterior view.

Vascular supply Psoas major is supplied by a rich network of arteries derived from the lumbar, iliolumbar, obturator, external iliac and femoral arteries. In general terms, the upper part of the muscle is supplied by the lumbar arteries, the mid part by the anterior branch of the iliolumbar artery (the main artery to the muscle) with contributions from the deep circumflex and external iliac arteries, and the distal part by the femoral artery and its branches. The psoas sheath has an arterial supply independent from that of the muscle, though the same vessels contribute.

Innervation Psoas major is innervated by the ventral rami of the lumbar spinal nerves, mainly L2, L3 and L4 (Mahan et al 2017).

Actions Psoas major acts together with iliacus; the combination is referred to as iliopsoas. See below.

Testing This is considered below with iliacus.

Psoas minor

Attachments The presence of a psoas minor (see Fig. 77.37) has been reported in about 40–60% of individuals (Neumann and Garceau 2015). When present, it lies anterior to psoas major, entirely within the abdomen. It arises from the sides of the bodies of the twelfth thoracic and first lumbar vertebrae, and from the intervertebral disc between them. It ends in a long, flat tendon that is attached to the pecten pubis, iliopubic ramus and, laterally, to the iliac fascia.

Relations Psoas minor lies on psoas major, and its proximal anterior relations are those of the anterior or anteromedial surface of that muscle.

Vascular supply The main arterial supply to psoas minor is from the lumbar arteries, though there may be minor contributions from other vessels of the network that supplies psoas major.

Innervation Psoas minor is innervated by a branch from L1.

Actions Psoas minor may flex the trunk; although due to the muscle's small size, its relative contribution to this action would be slight. Although speculation, the muscle's firm attachment into the iliac fascia may help stabilize the position of the underlying psoas major (see Commentary 9.2) (Neumann and Garceau 2015).

Testing Psoas minor cannot be tested clinically.

Iliacus

Attachments Iliacus (see Figs 77.37, 61.13) is a triangular sheet of muscle that arises from the superior two-thirds of the concavity of the iliac fossa, the inner lip of the iliac crest, the ventral sacroiliac and iliolumbar ligaments, and the upper surface of the lateral part of the sacrum (see Fig. 46.49). In front, it reaches as far as the anterior superior and anterior inferior iliac spines, and receives a few fibres from the upper part of the capsule of the hip joint (iliocapsularis, p. 1369.e1). Most of its fibres converge into the lateral side of the strong tendon of psoas major, and the muscles then insert together into the lesser trochanter, but some fibres attach directly to the femur 2.5 cm below and in front of the lesser trochanter.

Relations In the abdomen the anterior surface of iliacus is related to its fascia (which separates the muscle from extraperitoneal tissue and peritoneum), the lateral femoral cutaneous nerve, the caecum (on the right) and the iliac part of the descending colon (on the left). On its posterior surface is the iliac fossa, and at its medial border, psoas major and the femoral nerve. In the thigh its anterior surface is in contact with the fascia lata, rectus femoris, sartorius and the profunda femoris artery, and its posterior surface is in contact with the capsule of the hip joint, from which it is partially separated by a bursa it shares with psoas major.

Vascular supply Iliacus is supplied by the same arterial network as psoas major, and there is mutual overlap of the arterial territories of each muscle. The main supply is from the iliac branches of the iliolumbar artery, with contributions from the deep circumflex iliac and obturator arteries, and branches of the femoral artery.

Innervation Iliacus is innervated by branches of the femoral nerve, L2 and L3.

Actions The combined actions of the psoas major and iliacus (iliopsoas) have a large kinetic influence across the midsection of the body, extending between the thoracolumbar junction to the hip joints. The iliopsoas flexes the thigh on the pelvis. When the iliopsoas of both sides acts from fixed femurs, they contract to effectively bend the trunk and pelvis forwards against resistance, as in raising the trunk to sit upright from a recumbent, supine position. In symmetrical upright stance, iliopsoas has some action from below to maintain the vertebral column upright. Psoas major is active in balancing the trunk while sitting. When active bilaterally, the psoas major likely contributes frontal plane stability to the lumbar spine (Hu et al 2011).

Testing Iliopsoas may be tested clinically by actively flexing the hip against resistance, in the supine position with the hip and knee flexed.

Muscles of the gluteal region

Tensor fasciae latae

Attachments Tensor fasciae latae (see Fig. 77.37) arises from the anterior 5 cm of the outer lip of the iliac crest, from the lateral surface of the anterior superior iliac spine and part of the border of the notch below it, between gluteus medius and sartorius, and from the deep surface of the fascia lata. Proximal attachments may extend to the aponeurotic fascia superficial to gluteus medius. The short muscle belly descends between, and is attached to, the two layers of the iliotibial tract of the fascia lata, ultimately attaching to the lateral condyle region of the tibia.

Vascular supply The muscle itself is supplied mainly by a large ascending branch of the lateral circumflex femoral artery. The tensor fasciae latae musculocutaneous flap is raised on this pedicle. The superior part of the muscle receives branches from the superior gluteal artery. The fascia surrounding the muscle is supplied on its superficial aspect by the superficial circumflex iliac artery and on its deep surface by the lateral circumflex femoral artery.

Innervation Tensor fasciae latae is innervated by the superior gluteal nerve, L4, L5 and S1.

Actions Tensor fasciae latae is a hip flexor and abductor; its role in medial rotation (from the anatomical position) is minimal (Neumann 2010). The muscle helps to maintain upright posture while minimizing energy expenditure on muscle activity. When the subject is standing it acts from below to steady the pelvis on the head of the femur and, through the iliotibial tract, helps maintain the extended knee in a locked position. The muscle aids gluteus medius in stabilizing the pelvis over the femur in the frontal plane, when standing on one limb (see Fig. 77.36).

Testing When the thigh is flexed against gravity and the knee is extended, an angular depression appears immediately below the anterior superior iliac spine; its lateral boundary is tensor fasciae latae. If the thigh is then abducted against resistance, the muscle can be felt and sometimes seen.

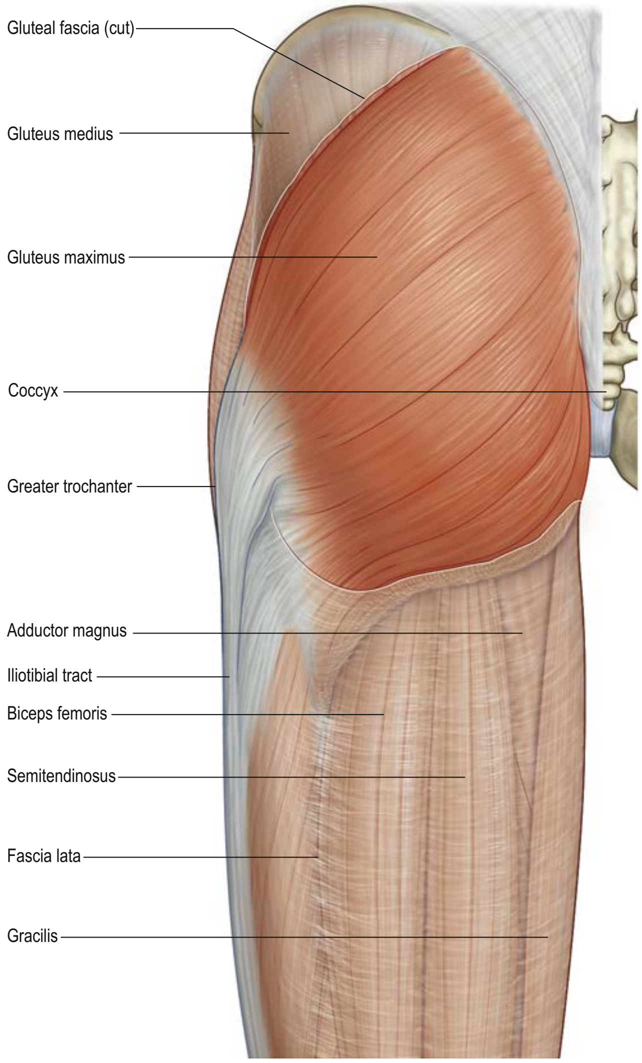

Fig. 77.38 Gluteus maximus, posterior view with the posterior thigh muscles seen through the overlying fascia lata.

Gluteus maximus

Attachments Gluteus maximus (Fig. 77.38) is the largest and most superficial muscle in the gluteal region. It is a broad, thick, quadrilateral mass, which, with its overlying adipose fascia, forms the familiar prominence of the buttock. Gluteus maximus is thicker and more extensive in humans than in any non-human primate, features that presumably correlate with the evolutionary transition to bipedality and a permanently upright posture. The muscle has a coarse fascicular architecture, with large bundles of fibres separated by fibrous septa. It arises from the posterior gluteal line of the ilium and the rough area of bone, including the crest, immediately above and behind it; from the aponeurosis of erector spinae; the dorsal surface of the lower part of the sacrum and the side of the coccyx; the sacrotuberous ligament; and the fascia (gluteal aponeurosis) that covers gluteus medius. There may be additional slips from the lumbar aponeurosis or ischial tuberosity. The muscle may also be bilaminar. The fibres descend laterally; the upper part of the muscle, together with the superficial fibres of the lower part, ends in a thick tendinous lamina that passes lateral to the greater trochanter and is attached to the iliotibial tract of the fascia lata. The deeper fibres of the lower part of the muscle attach to the gluteal tuberosity between vastus lateralis and adductor magnus.

Relations A thin fascia separates the superficial surface of gluteus maximus from the overlying thick, adipose subcutaneous tissue. The deep surface of the muscle is related to the ilium, sacrum, coccyx, sacrotuberous ligament, part of gluteus medius, piriformis, the gemelli, obturator internus, quadratus femoris, the ischial tuberosity, greater trochanter, and the attachments of biceps femoris, semitendinosus, semimembranosus and adductor magnus to the ischial tuberosity. Three main bursae lie deep to gluteus maximus, the: trochanteric, over the greater trochanter; gluteofemoral, between the tendon of gluteus maximus and the proximal tendon of vastus lateralis; and ischiofemoral, over the gluteal tuberosity, which is less commonly present.

The superficial division of the superior gluteal artery reaches the deep surface of the muscle between piriformis and gluteus medius. The inferior gluteal and internal pudendal vessels, the sciatic, pudendal and posterior femoral cutaneous nerves, muscular branches from the sacral femoral cutaneous nerves, and muscular branches from the sacral plexus all typically leave the pelvis below piriformis. The first perforating artery and the terminal branches of the medial circumflex femoral artery are also deep to the lower part of gluteus maximus. The upper border of gluteus maximus is thin and overlies gluteus medius. Its prominent lower border is free and slopes downwards and laterally. The muscle is crossed by the horizontal gluteal fold (the posterior flexure line of the hip joint), which marks the upper limit of the back of the thigh on the surface.

Vascular supply The dominant vascular pedicle is usually that of the inferior gluteal artery, which supplies approximately two-thirds of the muscle. The remainder is supplied mainly by the superior gluteal artery, though this may sometimes be the dominant vessel. The lateral and distal borders of the muscle receive a supply from the first perforator given off from the profunda femoris artery and from the medial circumflex femoral artery. Minor branches may be derived from the lateral circumflex femoral, lateral sacral and internal pudendal arteries.

Gluteus maximus musculocutaneous flaps may be based on either of the gluteal vessels or on the first perforator given off from the profunda femoris artery, depending on the site and size of the defect requiring coverage.

Innervation Gluteus maximus is innervated by the inferior gluteal nerve, L5, S1 and S2.

Actions Acting from the pelvis, gluteus maximus can extend the flexed thigh and bring it to and beyond a line extending from the trunk. Acting from its distal attachment, it may prevent the forward momentum of the trunk from producing flexion at the supporting hip during bipedal gait. The muscle is generally inactive during quiet standing, when swaying forwards at the ankle joints, or when bending forwards at the hip joints to touch the toes. However, it acts with the hamstrings in raising the trunk after stooping, by rotating the pelvis backwards on the head of the femur. It is intermittently active in the walking cycle and in climbing stairs, and continuously active in strong lateral rotation of the thigh. Its upper fibres are active in powerful abduction of the thigh. It is a tensor of the fascia lata, and through the iliotibial tract it stabilizes the femur on the tibia when the extensor muscles of the knee are relaxed.

Testing Gluteus maximus may be tested by extension of the hip against resistance, in the prone position with the knees held flexed.

Gluteus medius

Attachments Gluteus medius is a broad, thick muscle (see Fig. 77.38; Fig. 77.39A). It arises from the outer surface of the ilium between the iliac crest and posterior gluteal line above, and the anterior gluteal line below, and also from the gluteal aponeurosis superficial to its upper part. The fibres converge to a flat tendon that has two attachments: a cord-like tendon that attaches to the posterosuperior aspect of the trochanter, and a ridge that slants downwards and forwards on the lateral surface of the greater trochanter. The distal tendon of gluteus medius commonly fuses with the distal tendon of gluteus minimus as it approaches the greater trochanter, and its posterior edge sometimes blends with piriformis. The muscle may be composed of three parts (anterior, middle and posterior).

Relations The posterior third of gluteus medius is covered by gluteus maximus but it is superficial in its anterior two-thirds, where a strong layer of deep fascia (gluteal aponeurosis) covers it. Its deep surface is related to gluteus minimus. Branches of the deep divisions of the superior gluteal nerve and artery run between the gluteus medius and minimus muscles, and are vulnerable during anterolateral and lateral approaches to the hip that involve splitting gluteus medius. The tendon

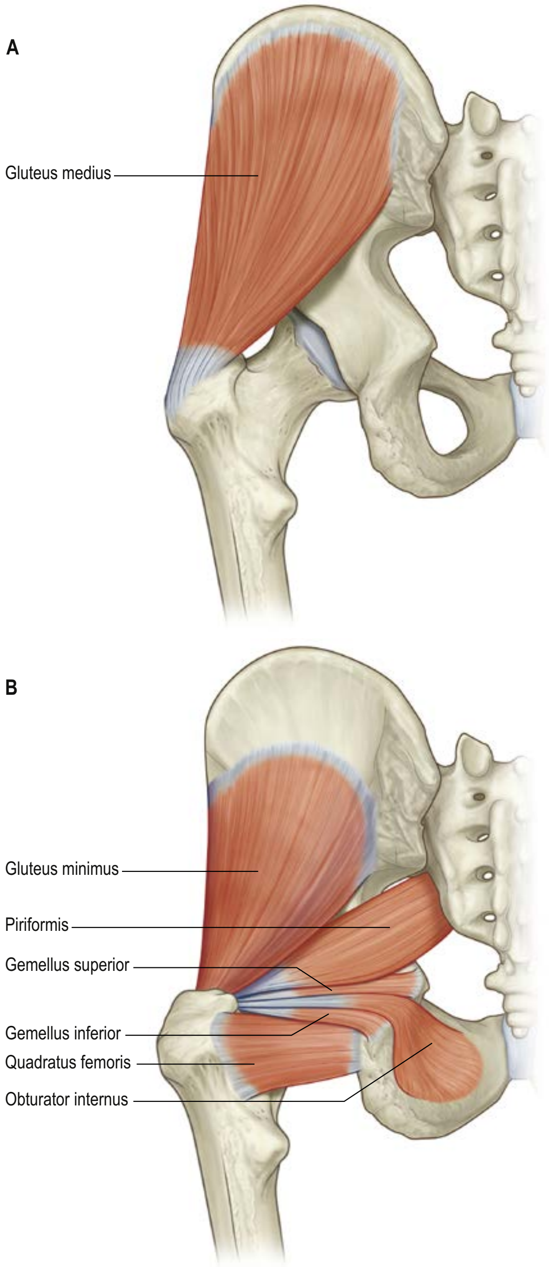

Fig. 77.39 **A**, Gluteus medius, posterior view. **B**, Gluteus minimus and short lateral rotators of the hip, posterior view.

glides on the anterosuperior part of the lateral surface of the trochanter, where at least one bursa separates it from the bone.

Vascular supply The main supply to gluteus medius is from the deep branch of the superior gluteal artery (**Fig. 77.40A**). The distal part of the muscle is supplied by the trochanteric anastomosis.

Innervation Gluteus medius is innervated by the superior gluteal nerve, L4, L5 and S1.

Actions These are considered below with gluteus minimus.

Testing This is considered below with gluteus minimus.

Gluteus minimus

Attachments Gluteus minimus lies deep to gluteus medius (**Fig. 77.39B**). The fan-shaped muscle arises from the outer surface of the ilium between the anterior and inferior gluteal lines and, behind, from the margin of the greater sciatic notch. The fibres converge below to the deep surface of an aponeurosis that ends in a tendon attached to an anterolateral ridge on the greater trochanter and contributes an expansion to the capsule of the hip joint.

The muscle may be comprised of anterior and posterior parts. Separate slips may pass to piriformis, gemellus superior or vastus lateralis, and its distal tendon often blends with that of gluteus medius.

Relations Branches of the deep division of the superior gluteal artery and nerve run on the superficial surface of the muscle. The reflected tendon of rectus femoris and the capsule of the hip joint are deep to gluteus minimus. At least one bursa separates the tendon from the medial part of the anterior surface of the greater trochanter.

Vascular supply Gluteus minimus is supplied from both its surfaces, from the main trunk and the deep branch of the superior gluteal artery, with a contribution at its femoral attachment from the trochanteric anastomosis (see Fig. 77.40).

Innervation Gluteus minimus is innervated by the superior gluteal nerve, L4, L5 and S1.

Actions of gluteus medius and gluteus minimus Both gluteus medius and minimus, acting from the pelvis, abduct the thigh, and their anterior and posterior fibres rotate it medially and laterally, respectively. Acting from the femur, they play an essential part in maintaining the trunk upright when the foot of the opposite side is raised from the ground in walking and running (see Fig. 77.36). In this phase, the body weight tends to make the pelvis sag downwards on the unsupported side. This is counteracted by the gluteus medius and minimus of the supporting side, which, acting from below, exert such powerful traction on the hip bone that the pelvis is actually raised a little on the unsupported side. In symmetrical standing with the feet somewhat separated, the abductor muscles are usually 'silent' on electromyography.

Testing The supportive effect of the gluteus medius and minimus on the pelvis when the contralateral foot is raised depends on the following conditions. The two muscles, and their innervation, must be functioning normally. The components of the hip joint, which forms the fulcrum, must be in their usual relation. The neck of the femur must be intact, with its normal angulation to the shaft.

When any one of these conditions is not fulfilled, e.g. in paralysis of the glutei, developmental dysplasia of the hip or coxa vara, the supporting mechanism is upset and the pelvis drops on the unsupported side when the patient tries to stand on the affected limb. This is known clinically as an uncompensated Trendelenburg's sign. Individuals with paralysis of gluteus medius and minimus have a characteristic lurching gait:

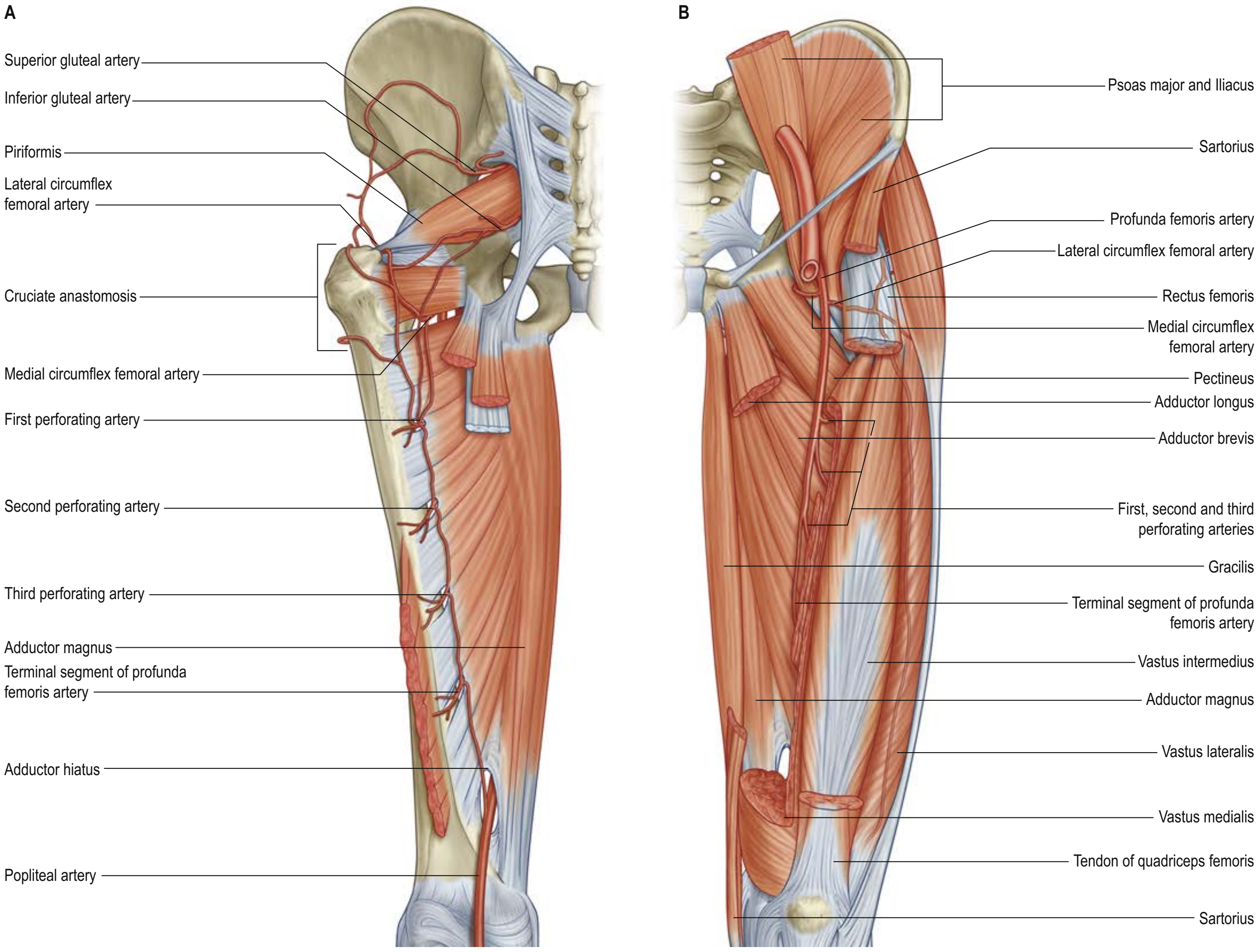
A
Superior gluteal artery
Inferior gluteal artery
Piriformis
Lateral circumflex femoral artery
Cruciate anastomosis
Medial circumflex femoral artery
First perforating artery
Second perforating artery
Third perforating artery
Adductor magnus
Terminal segment of profunda femoris artery
Adductor hiatus
Popliteal artery
B
Psoas major and Iliacus
Sartorius
Profunda femoris artery
Lateral circumflex femoral artery
Rectus femoris
Medial circumflex femoral artery
Pectineus
Adductor longus
Adductor brevis
First, second and third perforating arteries
Gracilis
Terminal segment of profunda femoris artery
Vastus intermedius
Adductor magnus
Vastus lateralis
Vastus medialis
Tendon of quadriceps femoris
Sartorius

Fig. 77.40 The arteries and muscles of the left gluteal and femoral regions. **A**, Posterior aspect. **B**, Anterior aspect. (With permission from Drake RL, Vogl AW, Mitchell A (eds) Gray's Anatomy for Students, 2nd ed. Elsevier, Churchill Livingstone. Copyright 2010.)

during the single-limb support phase of walking, the trunk leans to the side of the weakened muscles (compensated Trendelenburg sign) (Neumann 2017). Provided that these two muscles are intact, paralysis of other muscles acting on the hip joint produces remarkably little deficit in gait, at least when walking on level surfaces at a relatively slow speed.

Gluteus medius and minimus may be tested together by medial rotation of the thigh against resistance, in the supine position with hip and knee flexed. Both muscles may be tested together with tensor fasciae latae by abduction of the lower limb against resistance, in the supine position with the knee extended.

Piriformis

Attachments Piriformis (see Figs 77.39B, 77.40A) occupies a central position in the buttock, where it lies in the same plane as gluteus medius. It arises from the anterior surface of the sacrum by three digitations, which are attached to the portions of bone between the pelvic sacral foramina, and to the grooves leading from the foramina (see Fig. 46.49). It also arises from the gluteal surface of the ilium near the posterior inferior iliac spine, from the capsule of the adjacent sacroiliac joint, and sometimes from the upper part of the pelvic surface of the sacrotuberous ligament. The muscle passes out of the pelvis through the greater sciatic foramen, which it substantially fills. Here it constitutes an important surgical landmark in the identification of structures that emerge above and below it. It inserts into the medial side of the upper border of the greater trochanter of the femur via a rounded tendon that lies behind and above, but is often partially blended with, the common tendon of obturator internus and the gemelli. The muscle itself may be fused with gluteus medius.

Relations Within the pelvis, the anterior surface of piriformis is related to the rectum (especially on the left), the sacral plexus of nerves and branches of the internal iliac vessels. The posterior surface lies against the sacrum. Outside the pelvis, its anterior surface is in contact with the posterior surface of the ischium and capsule of the hip joint, and its posterior surface with gluteus maximus. Its upper border is in contact with gluteus medius and the superior gluteal vessels and nerve, its lower border with coccygeus and gemellus superior. The inferior gluteal and internal pudendal vessels, the sciatic, posterior femoral cutaneous and pudendal nerves, and muscular branches from the sacral plexus appear in the buttock in the interval between piriformis and gemellus superior. The relationship between piriformis and the sciatic nerve, however, is variable. The undivided nerve may emerge above the muscle or through the muscle. The major divisions of the nerve may lie either side of the muscle, or (the most common variant) one division passes between the heads of a divided muscle and one division either above or below (Beaton and Anson 1937).

Vascular supply In the buttock, piriformis is supplied mainly from the superior gluteal artery, with contributions from the gemellar branches of the internal pudendal. There may be a separate branch from the inferior gluteal artery (see Fig. 77.40A). In the pelvis, the main supply is from the lateral sacral artery, with contributions from both gluteal vessels.

Innervation Piriformis is innervated by the superior gluteal nerve and branches from ventral rami of S1 and S2 (Iwanaga et al 2018).

Actions Piriformis rotates the extended thigh laterally, but abducts the flexed thigh.

Testing Clinically, it is not possible to test piriformis alone; however, for suspected dysfunction of piriformis the best provocative test is to ask the seated subject to abduct the thighs. Buttock pain suggests piriformis involvement.

Obturator internus

Attachments Obturator internus (see Figs 77.39B, 77.42) is situated partly within the true pelvis and partly posterior to the hip joint. It arises from the internal surface of the anterolateral wall of the lesser pelvic cavity. Its attachments, which almost surround the obturator foramen, are to the inferior ramus of the pubis, the ischial ramus and the pelvic surface of the hip bone below and behind the pelvic brim, to the upper part of the greater sciatic foramen above and behind, to the obturator foramen below and in front. It also arises from the medial part of the pelvic surface of the obturator membrane, from the tendinous arch that completes the obturator canal, and, to a small extent, from the obturator fascia that covers the muscle. The fibres converge towards the lesser sciatic foramen and end in four or five tendinous bands on the deep surface of the muscle. These bands make a lateral right-angled turn around the grooved surface of the ischium between its spine and tuberosity. The grooved surface is covered with a smooth layer of hyaline cartilage and is separated from the tendon by a bursa; ridges on the surface correspond to furrows between the tendinous bands. These bands leave the pelvis through the lesser sciatic foramen and unite to form a single flattened tendon that passes horizontally across the capsule of the hip joint. The gemelli fuse with this tendon before it inserts on to an anterior impression on the medial surface of the greater trochanter anterosuperior to the trochanteric fossa. A long, narrow bursa is usually interposed between the tendon and the capsule of the hip joint, and occasionally communicates with the bursa between the tendon and the ischium.

Relations Within the pelvis, the anterolateral surface of the muscle is in contact with the obturator membrane and inner surface of the lateral wall of the pelvis. Its posteromedial surface is related to the obturator fascia, the origin of levator ani and the sheath that surrounds the internal pudendal vessels and pudendal nerve, and forms the lateral wall of the ischio-anal fossa. Outside the pelvis, the muscle is covered by gluteus maximus, is crossed posteriorly by the sciatic nerve and passes behind the hip joint. As the tendon of obturator internus emerges from the lesser sciatic foramen, it may be covered above and below by the two gemelli, which form a muscular canal for it. Near its termination, the gemelli may pass anterior to the tendon and form a groove in which it lies.

Vascular supply The main arterial supply of the extrapelvic part of obturator internus is from the gemellar branches of the internal pudendal artery. Intrapelvic and extrapelvic parts are supplied by the branches of the obturator artery.

Innervation Obturator internus is innervated by the nerve to obturator internus, L5 and S1.

Actions These are considered below with the actions of obturator externus.

Testing This is considered below with the testing of obturator externus.

Obturator externus

Attachments Obturator externus (**Fig. 77.41**) is a flat, triangular muscle covering the external surface of the anterior pelvic wall. It arises from the anteromedial two-thirds of the external surface of the obturator membrane, and from the adjacent bone of the pubic and ischial rami, extending for a short distance on to their pelvic surfaces between the margin of the obturator foramen and the obturator membrane. The whole muscle, and the tendon into which its fibres converge, spiral backwards, laterally and upwards, and thus cross the inferior aspect and

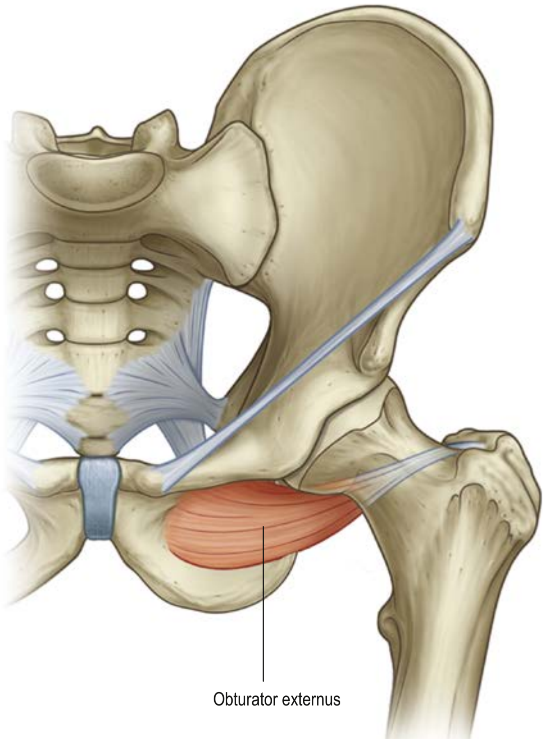

Fig. 77.41 Obturator externus, anterior aspect. (Adapted from Drake RL, Vogl AW, Mitchell A (eds) Gray's Anatomy for Students, 2nd ed. Elsevier, Churchill Livingstone. Copyright 2010.)

then the back of the neck of the femur and lower part of the capsule of the hip joint to end in the trochanteric fossa of the femur.

Relations A bursa, which communicates with the hip joint, may be interposed between the tendon and the hip joint capsule and femoral neck. The obturator vessels lie between the muscle and the obturator membrane. The anterior branch of the obturator nerve reaches the thigh by passing in front of the muscle, and the posterior branch by piercing it.

Vascular supply Obturator externus receives a variable pattern of supply from the obturator and medial circumflex femoral arteries.

Innervation Obturator externus is innervated by the posterior branch of the obturator nerve, L3 and L4.

Actions It has been suggested that the short rotator muscles around the hip joint (piriformis, obturator externus and internus, the gemelli and quadratus femoris) are more important as postural muscles than as prime movers, acting as adjustable ligaments to maintain the stability and integrity of the hip. However, these muscles are largely inaccessible to direct observation, and, because of the hazards presented by their close relationship to important neurovascular structures, little electromyographic data are available in humans (Hodges et al 2014). In both bipedal walking and vertical climbing, obturator externus is recruited during the early part of the swing phase; in climbing it effects lateral rotation of the thigh, and in walking it probably counteracts the tendency to medial rotation produced by the anterior adductor muscles at this stage of the cycle. Obturator internus differs from obturator externus in its pattern of use but its role in bipedal walking remains unclear. Its attachments suggest that it, like the gemelli, is a lateral rotator of the extended thigh and perhaps an abductor of the flexed thigh. These actions may be used to antagonize unwanted components of movement produced by the primary locomotor muscles.

Testing The short rotators cannot be tested individually, but lateral rotation of the extended hip and abduction of the flexed hip against resistance tests them as a group.

Gemellus inferior and gemellus superior

Attachments Gemellus inferior arises from the upper part of the lateral surface of the ischial tuberosity, immediately below the groove for the tendon of obturator internus (Fig. 77.42). It blends with the lower border of this tendon, and inserts with it into the medial surface of the greater trochanter.

Gemellus superior, the smaller of the two gemelli, arises from the dorsal surface of the ischial spine, blends with the upper border of the tendon of obturator internus, and inserts with it into the medial surface of the greater trochanter. It is sometimes absent.

The two gemelli can be regarded as accessory to obturator internus (see Fig. 77.39B).

Relations The relations of the gemelli are as described for the extrapelvic part of obturator internus.

Vascular supply Gemellus superior is supplied by the internal pudendal artery and its gemellar branches; by the inferior gluteal artery; and sometimes also by the superior gluteal artery. Gemellus inferior is supplied mainly by the medial circumflex femoral artery.

Innervation Gemellus superior is innervated by the nerve to obturator internus, L5, S1 and S2. Gemellus inferior is innervated by the nerve to quadratus femoris, L4, L5 and S1.

Actions The gemelli rotate the extended thigh laterally and may contribute to abduction of the flexed thigh.

Testing This is considered above with the testing of obturator externus.

Quadratus femoris

Attachments Quadratus femoris (see Fig. 77.39B) is a flat, quadrilateral muscle lying between gemellus inferior and the upper margin of adductor magnus, from which it is separated by the transverse branch of the medial circumflex femoral artery. It arises from the upper part of the external aspect of the ischial tuberosity and inserts on to a small tubercle a little above the middle of the trochanteric crest of the femur and into the bone for a short distance below. It may be absent.

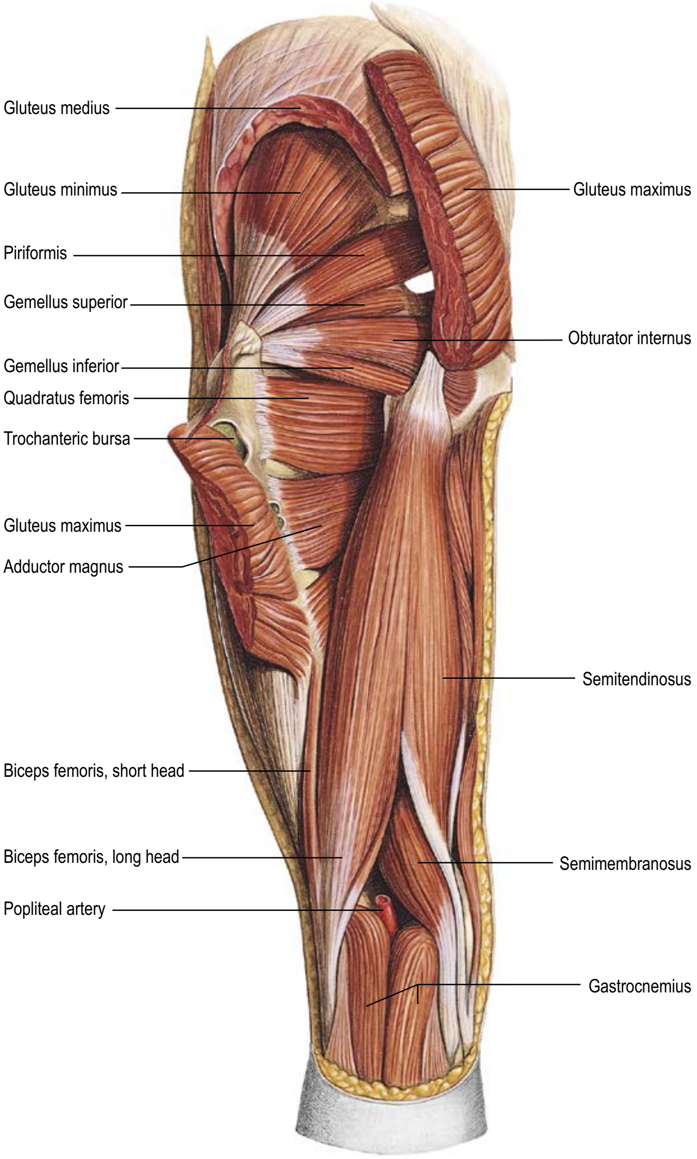

Fig. 77.42 The posterior thigh and gluteal muscles with gluteus maximus and medius partially removed. (Sobotta Atlas of Human Anatomy © Elsevier GmbH, Urban & Fischer, Munich.)

Relations The muscle passes behind the hip joint and the neck of the femur, separated from them by the tendon of obturator externus and the ascending branch of the medial circumflex femoral artery (which may cause troublesome bleeding if injured during the posterior surgical approach to the hip). The sciatic nerve crosses the muscle posteriorly. A bursa is often present between the muscle and the lesser trochanter.

Vascular supply Branches pass to the superficial surface of the muscle from the inferior gluteal artery and from the medial circumflex femoral artery, which also supplies the deep surface.

Innervation Quadratus femoris is innervated by the nerve to quadratus femoris, L5 and S1.

Actions Quadratus femoris produces lateral rotation of the thigh.

Testing This is considered above with the testing of obturator externus..

Muscles of the thigh

There are three functional groups of muscle in the thigh, namely: anterior (extensor), posterior (flexor) and medial (adductor). The anterior and posterior groups occupy separate osteofascial compartments that are limited peripherally by the fascia lata and separated from each other by the femur and the medial and lateral intermuscular septa (see Fig. 77.43). The presence and position of the femoral neck cause the femoral shaft to lie obliquely; consequently, the anterior muscle group, quadriceps femoris, runs obliquely distally and medially and so applies a pull to the patella that is both laterally and proximally directed. The adductor muscles do not possess a separate compartment limited by fascial planes, but occupy the region between quadriceps femoris and the medial margin of the thigh. They are attached distally to the posterior surface of the femur and lie more posteriorly than quadriceps femoris. The posterior muscle group, the hamstrings, lie behind the adductors. The attachments of these muscles often determine the nature and direction of displacement of femoral shaft fractures.

The muscles of the three compartments of the thigh are described below. Of note, adductor magnus, adductor longus and pectineus could each be considered to be constituents of two compartments, i.e. adductor magnus in the posterior and the medial compartments, and adductor longus and pectineus in the anterior and the medial compartments.

The nerve supply to the compartments of the thigh mainly follows the 'one compartment – one nerve' principle. Thus, the femoral nerve supplies the muscles of the anterior compartment, the obturator nerve supplies the medial compartment muscles and the sciatic nerve supplies those in the posterior compartment. The dual functional and compartmental attribution of adductor magnus and pectineus are reflected in their dual nerve supplies.

In contrast to the motor innervation, the arterial supply to the compartmental muscle groups does not exhibit such a direct relationship. All groups receive a supply from the femoral system, particularly from the profunda femoris artery and its branches. The adductors receive a contribution from the obturator artery, and the hamstrings receive a proximal supply from the inferior gluteal artery. Further details are given in the descriptions of the individual muscles.

Anterior compartment

The muscles of the anterior compartment (**Figs 77.43–77.45**; see Fig. 77.37) include sartorius and rectus femoris, which can act at both the hip and knee joints, and vasti medialis, lateralis and intermedius, which act only at the knee. Articularis genus completes the group: it is thought to retract the synovial capsule of the knee joint. Rectus femoris and the vasti extend the knee joint through a common tendon and hence are collectively termed quadriceps femoris. Adductor longus and pectineus are sometimes considered to be part of both the anterior and the adductor compartments.

Sartorius

Attachments Sartorius is a narrow strap muscle and is the longest muscle in the body (Figs 77.44; see Fig. 77.37). It arises by tendinous fibres from the anterior superior iliac spine and the upper half of the notch below it. It crosses the thigh obliquely over to the medial side and then descends more vertically to the medial side of the knee. The muscle fibres terminate at this point and a thin, flattened tendon curves obliquely forwards and expands into a broad aponeurosis. The aponeurosis is attached to the proximal part of the medial surface of the tibia in front of gracilis and semitendinosus, together forming the so-called pes anserinus (**Fig. 77.46**). A slip from its upper margin blends with the capsule of the knee joint, and another from its lower margin merges with the superficial layer of the deep fascia on the medial side of the leg. This sheet of tissue passes inferiorly to lie superficial to and over the distal insertions of gracilis and semitendinosus. It must be split by sharp dissection to reveal these two tendons if they need to be harvested, e.g. in cruciate ligament surgery.

In some cases, sartorius is absent, while in others, the muscle may possess an extra head; when the latter occurs, the extra head is attached to the pectineal line or to the femoral sheath. Variations in the distal attachment of sartorius, in the vicinity of the knee, have been described.

Relations The relations of sartorius are described in the femoral triangle (see below).

Vascular supply The main arterial supply to sartorius is derived from multiple branches of the femoral system and enters the medial half of the muscle from its deep surface. Vessels supplying the proximal third of sartorius may arise from the femoral artery, the profunda femoris artery, the 'artery of the quadriceps' or the lateral circumflex femoral artery. There may be an additional proximal supply from the superficial circumflex iliac artery. Those vessels supplying the middle third of the muscle arise from the femoral artery. The distal vessels arise from the femoral artery within the adductor canal and from the descending genicular artery.

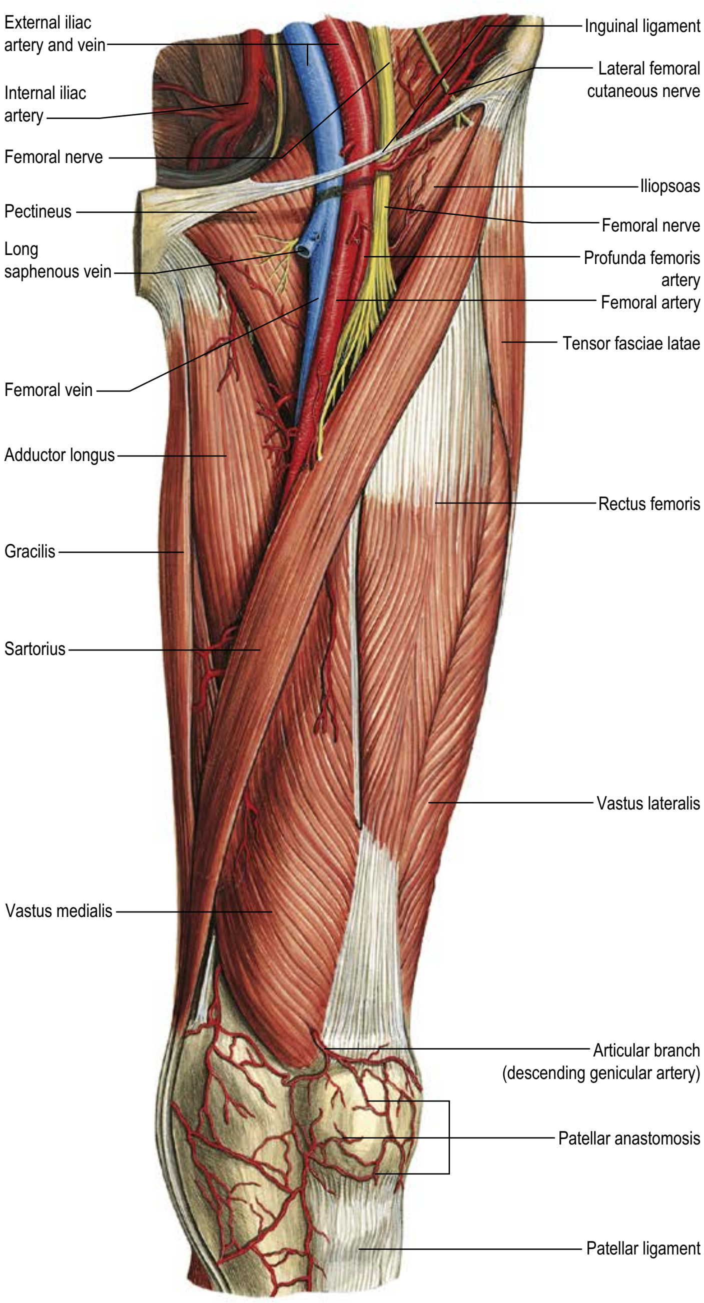

Fig. 77.44 The left femoral triangle; anterior aspect of the thigh. (Sobotta Atlas of Human Anatomy © Elsevier GmbH, Urban & Fischer, Munich.)

Innervation Sartorius is innervated by the femoral nerve, L2 and L3.

Actions Sartorius assists in flexing and medially rotating the leg (at the knee). The muscle also flexes the thigh on the pelvis, particularly when combined with knee flexion and helps to abduct the thigh and to rotate it laterally.

Testing When combining flexion and lateral rotation of the hip against gravity, sartorius can typically be seen and felt in the living, lean subject.

Femoral triangle

The femoral triangle is a depressed, intermuscular space in the anteromedial aspect of the proximal thigh, lying immediately distal to the inguinal ligament. The latter constitutes the base of the femoral triangle's inverted triangular outline. Its lateral boundary is the medial margin of sartorius. Its medial boundary is the medial margin of adductor longus. Its distal extremity, the apex, is where sartorius overlaps adductor longus (see Fig. 77.44). Its floor is provided laterally by iliacus and psoas major, and medially by pectineus and adductor longus, and the overlying fascia lata forms the roof. The femoral vessels, passing from mid-base to apex, are in the deepest part of the triangle. Lying

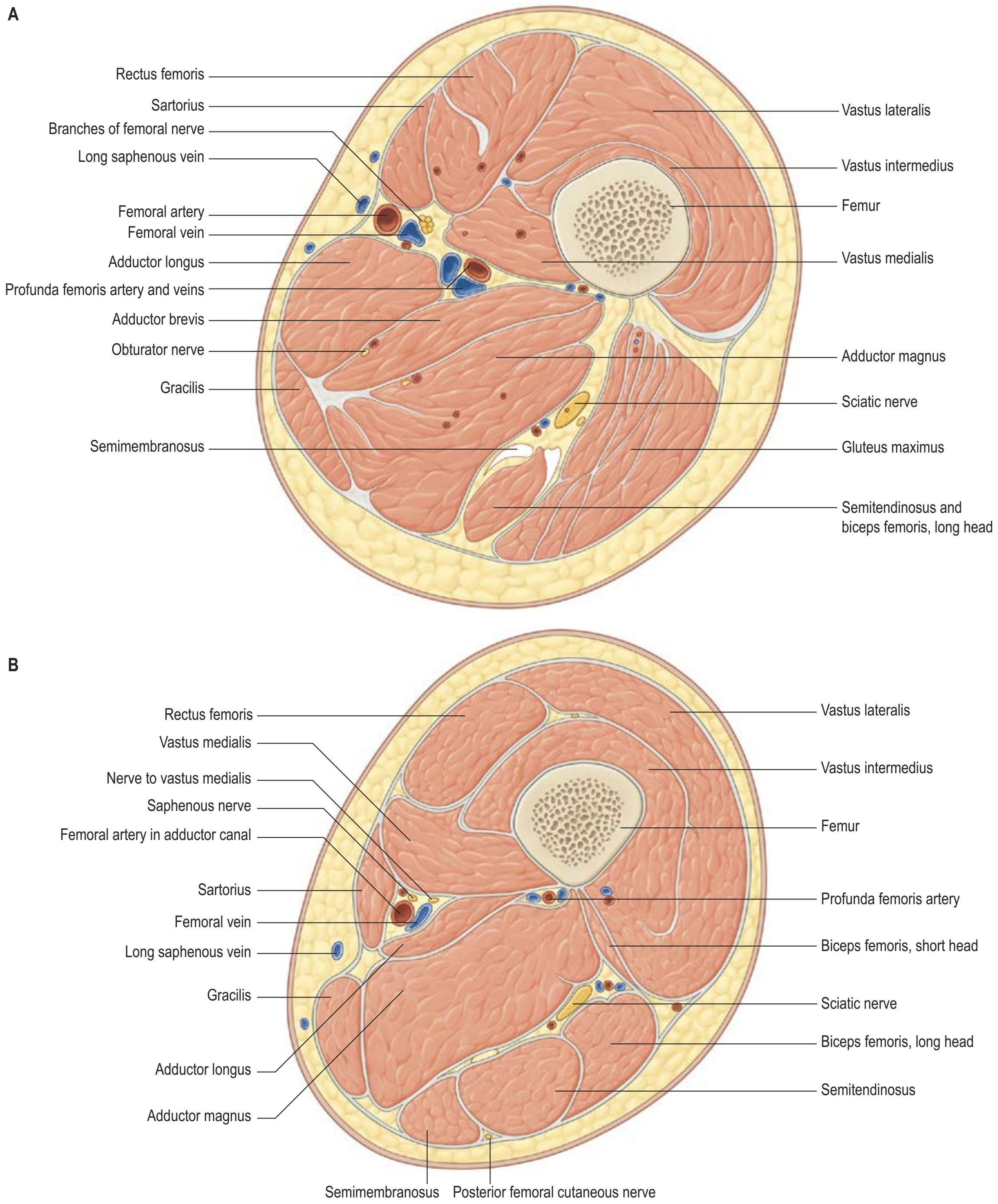
A
Rectus femoris
Sartorius
Branches of femoral nerve
Long saphenous vein
Femoral artery
Femoral vein
Adductor longus
Profunda femoris artery and veins
Adductor brevis
Obturator nerve
Gracilis
Semimembranosus
Vastus lateralis
Vastus intermedius
Femur
Vastus medialis
Adductor magnus
Sciatic nerve
Gluteus maximus
Semitendinosus and biceps femoris, long head
B
Rectus femoris
Vastus medialis
Nerve to vastus medialis
Saphenous nerve
Femoral artery in adductor canal
Sartorius
Femoral vein
Long saphenous vein
Gracilis
Adductor longus
Adductor magnus
Semimembranosus
Posterior femoral cutaneous nerve
Vastus lateralis
Vastus intermedius
Femur
Profunda femoris artery
Biceps femoris, short head
Sciatic nerve
Biceps femoris, long head
Semitendinosus

Fig. 77.43 Transverse sections through the thigh. **A**, At the level of the apex of the femoral triangle. **B**, At the level of the mid-thigh.

continued

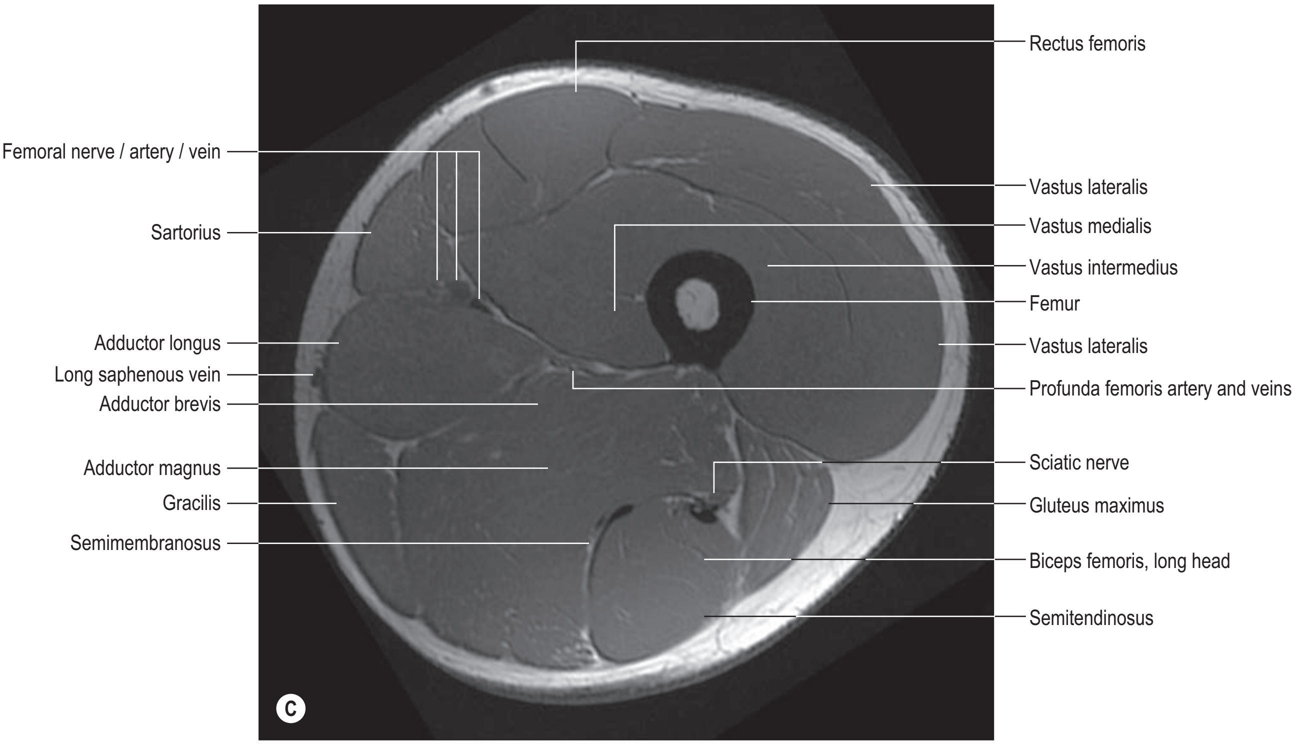
Rectus femoris
Femoral nerve / artery / vein
Vastus lateralis
Sartorius
Vastus medialis
Vastus intermedius
Femur
Adductor longus
Vastus lateralis
Long saphenous vein
Adductor brevis
Profunda femoris artery and veins
Adductor magnus
Sciatic nerve
Gracilis
Gluteus maximus
Semimembranosus
Biceps femoris, long head
Semitendinosus
C

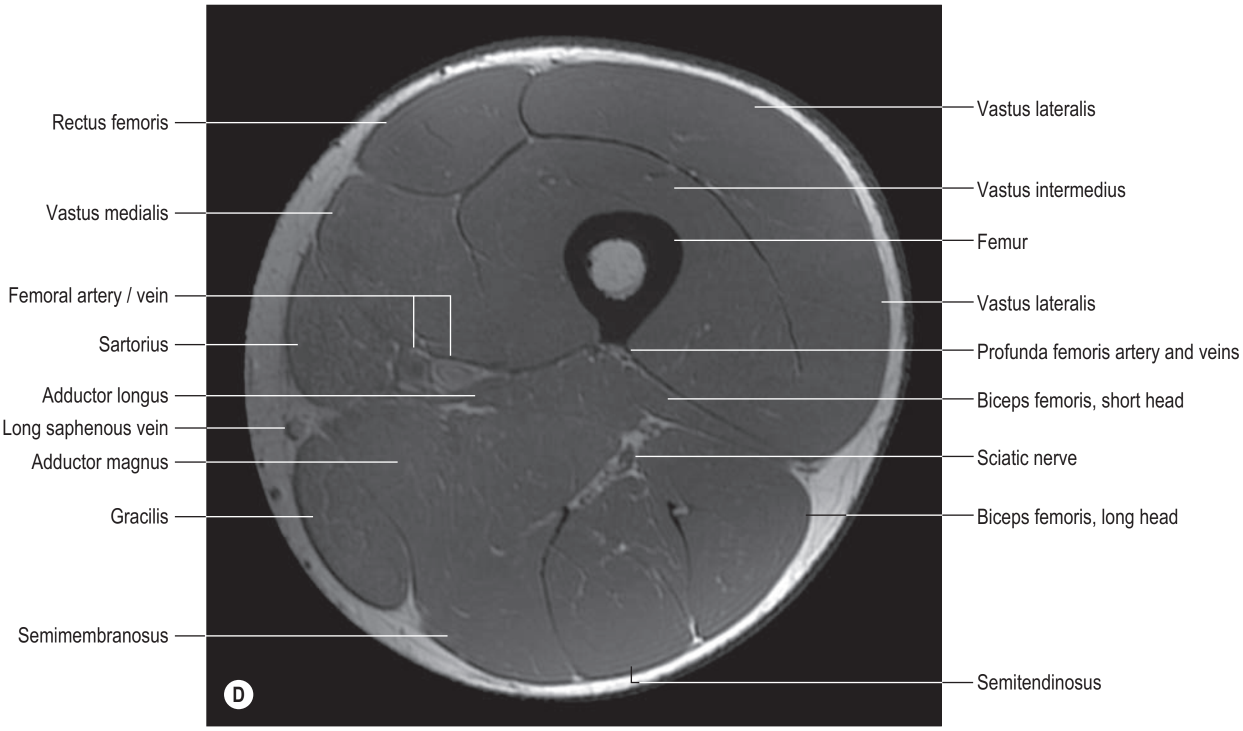
Vastus lateralis
Rectus femoris
Vastus intermedius
Vastus medialis
Femur
Femoral artery / vein
Vastus lateralis
Sartorius
Profunda femoris artery and veins
Adductor longus
Biceps femoris, short head
Long saphenous vein
Adductor magnus
Sciatic nerve
Gracilis
Biceps femoris, long head
Semimembranosus
Semitendinosus
D

Fig. 77.43, cont'd **C** and **D** are axial T1-weighted images of the thigh, **C** at the level of the apex of the femoral triangle and **D** at the level of the mid-thigh.

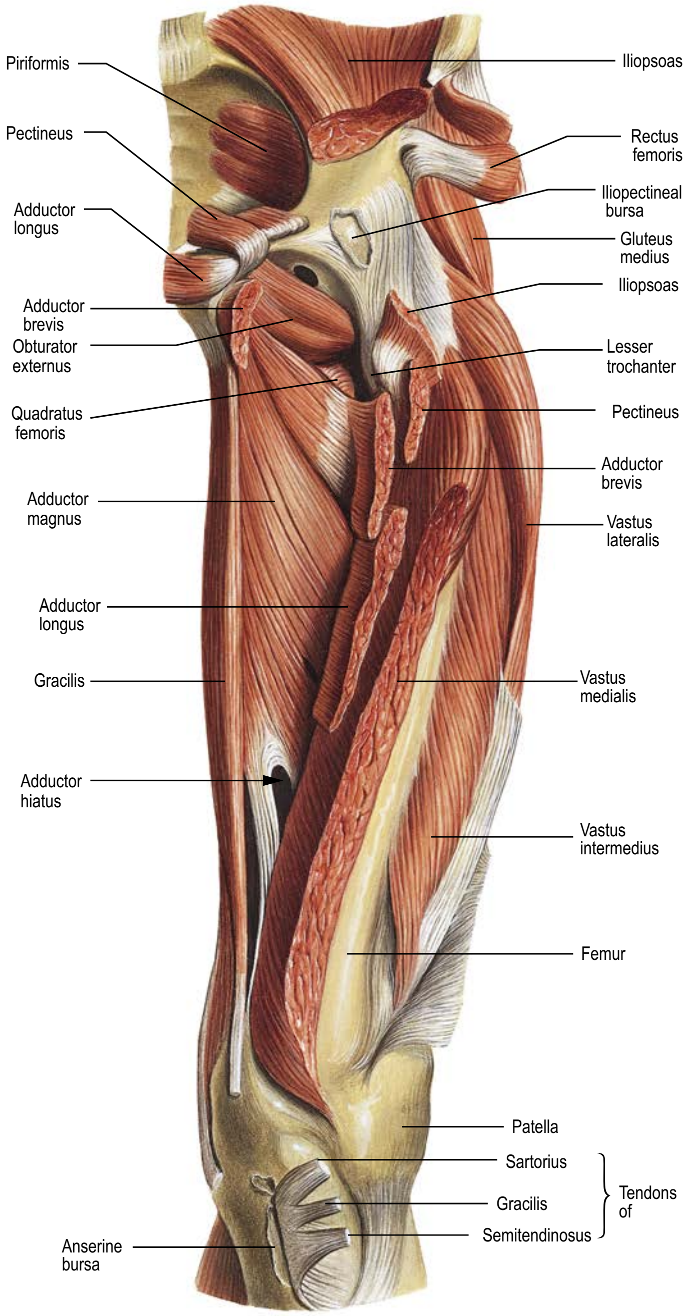
Piriformis
Pectineus
Adductor longus
Adductor brevis
Obturator externus
Quadratus femoris
Adductor magnus
Adductor longus
Gracilis
Adductor hiatus
Anserine bursa
Iliopsoas
Rectus femoris
Iliopectineal bursa
Gluteus medius
Iliopsoas
Lesser trochanter
Pectineus
Adductor brevis
Vastus lateralis
Vastus medialis
Vastus intermedius
Femur
Patella
Sartorius
Gracilis
Semitendinosus
Tendons of

Fig. 77.45 The adductor muscles of the thigh, anterior aspect. (Sobotta Atlas of Human Anatomy © Elsevier GmbH, Urban & Fischer, Munich.)

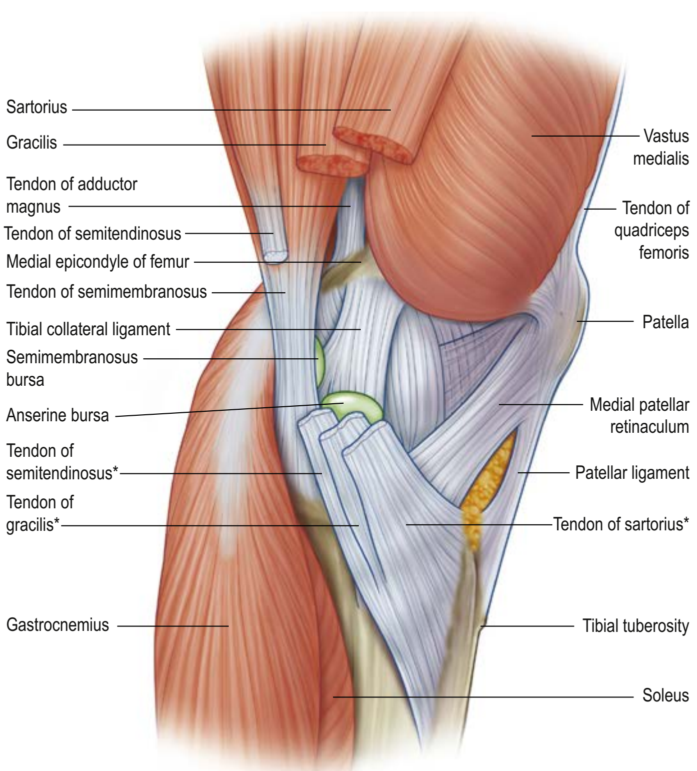
Sartorius
Gracilis
Tendon of adductor magnus
Tendon of semitendinosus
Medial epicondyle of femur
Tendon of semimembranosus
Tibial collateral ligament
Semimembranosus bursa
Anserine bursa
Tendon of semitendinosus*
Tendon of gracilis*
Gastrocnemius
Vastus medialis
Tendon of quadriceps femoris
Patella
Medial patellar retinaculum
Patellar ligament
Tendon of sartorius*
Tibial tuberosity
Soleus

Fig. 77.46 The distal attachment of muscles of the thigh, medial aspect. Note the three tendons of the pes anserinus attaching to the medial, proximal tibia (asterisks).

lateral to the artery and outside the femoral sheath is the femoral nerve, which, on entering the femoral triangle, divides into multiple branches. The triangle also contains fat and lymph nodes.

Quadriceps femoris

Quadriceps femoris (see Figs 77.37, 77.43, 77.44), the great extensor muscle of the leg, covers almost all of the front and sides of the femur. It can be divided into four parts, each named individually. One, rectus femoris, arises from the ilium and travels straight down the middle of the thigh, its shape and path determining its name. The other three arise from the shaft of the femur and surround it (apart from the linea aspera) from the trochanters to the condyles: vastus lateralis is lateral to the femur, vastus medialis is medial to it, and vastus intermedius lies immediately anterior to the femur. Rectus femoris crosses both hip and knee joints, while the three vasti only cross the knee joint.

The tendons of the four components of quadriceps femoris unite in the lower part of the thigh to form a single strong tendon attached to the base of the patella, and some fibres continue over it to blend with the patellar ligament. The patella is a sesamoid bone in the quadriceps femoris tendon, and the patellar ligament, which extends from the patellar apex to the tibial tuberosity, is the continuation of the main tendon. The medial and lateral patellar retinacula are expansions from its borders. The suprapatellar bursa (a synovial extension of the knee joint) lies between the femur and the suprapatellar part of the quadriceps femoris tendon. The deep infrapatellar bursa lies between the patellar ligament and the proximal end of the tibia.

The arterial supply to the quadriceps femoris has been traditionally ascribed to a single branch of either the profunda femoris artery or the lateral circumflex femoral artery, the 'artery of the quadriceps'. This vessel, which may be large, occasionally arises directly from the femoral artery. However, according to Taylor and Razaboni (1994), this artery does not supply all four components of quadriceps femoris; vastus medialis is supplied directly from the femoral artery. The supply of the individual muscle components is described below; their sheaths may have an additional and variable supply.

Quadriceps femoris as a group shows little anatomical variation.

Rectus femoris

Attachments Rectus femoris is fusiform. Its superficial fibres are bipennate, the deep fibres parallel. It has a double origin on the ilium: a straight tendon arises from the anterior inferior iliac spine, and a thinner, flatter reflected tendon from a groove above the acetabulum and from the fibrous capsule of the hip joint. The two unite at an acute angle and spread into an aponeurosis that is prolonged downwards on the anterior surface of the muscle; the muscular fibres arise from this aponeurosis. The fibres end in a broad, thick aponeurosis that forms over the lower two-thirds of its posterior surface and gradually narrows into the thick, flat tendon by which it is attached to the base of the patella. This constitutes the superficial central part of the quadriceps femoris tendon. A third head of rectus femoris may exist; it attaches deeply to the iliofemoral ligament and superficially to the tendon of gluteus minimus as it attaches on to the femur (Tubbs et al 2006). Rectus femoris may also arise from the anterior superior iliac spine, and its reflected head may be absent.

Relations Proximally, the muscle is covered by tensor fasciae latae, iliacus and sartorius. The reflected head lies beneath gluteus minimus. The capsule of the hip joint, vastus intermedius, the anterior borders of vasti lateralis and medius, the lateral circumflex femoral artery and some branches of the femoral nerve all lie deep to rectus femoris.

Vascular supply There are two main vascular pedicles: a superior and an inferior. The superior enters rectus femoris at the junction of its upper and middle thirds, and arises from the 'artery of the quadriceps'. The inferior and larger branch arises from the 'artery of the quadriceps' at about mid-thigh level and enters the muscle a few centimetres more distally. There are additional contributions from the lateral circumflex femoral artery and, less often, from the superficial circumflex iliac artery.

Vastus medialis

Attachments Vastus medialis arises from the lower part of the intertrochanteric line, spiral line, medial lip of the linea aspera, proximal part of the medial supracondylar line, the tendons of adductor longus and magnus, and the medial intermuscular septum. Its fibres pass downwards and forwards at an average angle of 15° to the long axis of the femur, most of them into an aponeurosis on the deep surface of the muscle that is attached to the medial border of the patella and to the quadriceps femoris tendon. An expansion from this aponeurosis reinforces the capsule of the knee joint and is attached below to the medial condyle of the tibia.

The lowest fibres are nearly horizontal and form a bulge in the living subject, medial to the upper half of the patella. Some authors distinguish this part of the muscle as the vastus medialis obliquus, with fibres that originate largely from the tendon of adductor magnus and insert into the medial border of the patella. This muscle likely has a unique role in dynamically aligning the patellofemoral joint.

Relations Vastus medialis is partly covered by rectus femoris and sartorius. In the central part of the thigh it forms the lateral wall of the adductor canal (Hunter's canal; subsartorial canal).

Vascular supply Vastus medialis is supplied by three branches of the femoral artery. The superior and middle branches arise, sometimes from a common trunk, proximal to the adductor canal, while the inferior arises within the canal. There may also be minor branches from the profunda femoris artery and descending genicular arteries.

Vastus lateralis

Attachments Vastus lateralis is the largest component of quadriceps femoris. It arises by a broad aponeurosis from the upper part of the intertrochanteric line, the anterior and inferior borders of the greater trochanter, the lateral lip of the gluteal tuberosity and the proximal half of the lateral lip of the linea aspera. This aponeurosis covers the proximal three-quarters of the muscle; many additional fibres arise from its deep surface. A few fibres also arise from the tendon of gluteus maximus and the lateral intermuscular septum between vastus lateralis and the short head of biceps femoris. The muscular mass thus formed is attached to a strong aponeurosis on the deep surface of the lower part of the muscle. This narrows to a flat tendon, which attaches to the base and lateral border of the patella and blends into the compound quadriceps femoris tendon. It contributes an expansion to the capsule of the knee joint that descends to the lateral condyle of the tibia and blends with the iliotibial tract.

Relations Vastus lateralis is covered laterally by the fascia lata and the aponeurotic insertions of tensor fasciae latae and gluteus maximus. It is separated from vastus intermedius by branches of the femoral nerve and the lateral circumflex femoral artery. Posteriorly, it is separated from biceps femoris by the lateral intermuscular septum.

Vascular supply There are three main arteries of supply: the superior medial artery arises directly from the lateral circumflex femoral artery; the inferior medial (the largest of the three) from the 'artery of the quadriceps'; and the lateral from the first perforating branch given off from the profunda femoris artery.

Vastus intermedius

Attachments Vastus intermedius arises from the anterior and lateral surfaces of the upper two-thirds of the femoral shaft, and from the lower part of the lateral intermuscular septum. Its fibres end on the anterior surface of the muscle in an aponeurosis that forms the deep part of the quadriceps femoris tendon and is attached to the lateral border of the patella and the lateral condyle of the tibia.

Vastus intermedius appears to be inseparable from vastus medialis. However, when rectus femoris is reflected, a narrow cleft can be seen extending upwards from the medial border of the patella between the two muscles, sometimes as far as the lower part of the intertrochanteric line; proximal to this, the two muscles are frequently fused.

Relations Vastus intermedius is almost completely covered by the other components of quadriceps femoris, except laterally, where a small part becomes superficial behind vastus lateralis.

Vascular supply Vastus intermedius receives a lateral artery of supply, which arises from the 'artery of the quadriceps', and a medial artery that arises directly from the profunda femoris artery. Arteries to the other components of quadriceps femoris may also contribute. There is an anastomotic network deep to the muscle that supplies the suprapatellar bursa and articularis genus, and may form a collateral pathway when the femoral artery is blocked.

Articularis genus

Articularis genus is a small muscle, usually distinct from vastus intermedius but occasionally blending with it. It consists of several relatively thin muscular bundles that arise from the anterior surface of the lower part of the femoral shaft and are attached to a proximal reflection of the synovial membrane of the knee joint (Woodley et al 2012). It is visible during knee arthroscopy when viewed looking superiorly from within the suprapatellar bursa (Ch. 78).

Innervation of quadriceps femoris

Quadriceps femoris and articularis genus are supplied by the femoral nerve, L2, L3 and L4.

Actions of quadriceps femoris

Quadriceps femoris extends the knee. Rectus femoris helps to flex the thigh on the pelvis; if the thigh is fixed, it helps to flex the pelvis on the thigh. Rectus femoris can flex the hip and extend the knee simultaneously. There is little or no activity in quadriceps femoris during quiet standing, as long as the knee is mechanically locked by action of gravity falling through or in front of the centre of rotation at the knee. Rectus femoris pulls the patella along the line of the mechanical axis of the lower limb (i.e. the line connecting the centres of the hip, knee and ankle). The remaining muscles in the group are attached to the shaft of the femur and their pull (notably the vastus lateralis) is lateral as well as proximal. An important dynamic function of vastus medialis obliquus is to counter this lateral vector on the patella during knee extension. Other static factors that help are the depth of the femoral patellar surface, the buttressing effect of the lateral femoral condyle in the groove and the restraining action of the medial patellofemoral ligament. Although difficult to establish a direct cause-and-effect relationship, in theory, inadequacy of vastus medialis obliquus may have a mechanical role in abnormal patellar 'tracking' and associated pain (Sheehan et al 2012). Improving patellar 'tracking' on the femur is an important part of surgical and physiotherapy regimens for patellofemoral problems.

Articularis genus retracts the synovial suprapatellar bursa proximally during extension of the leg, presumably to prevent interposition of redundant synovial folds between patella and femur (Grob et al 2017).

Testing The quadriceps femoris is tested by extending the knee against resistance, in the supine position with the hip flexed.

Adductor compartment

The muscles of the adductor compartment, namely gracilis, pectineus, adductor longus, adductor brevis and adductor magnus (see Figs 77.37, 77.40, 77.43–77.44), have evolved, as their nerve supply suggests, from both flexor and extensor columns. All five muscles cross the hip joint but only gracilis reaches beyond the knee. They are known collectively as the adductors of the thigh, although their actions are more complex than this, e.g. acting from below they have important roles in balancing the trunk on the lower limb during walking.

Their blood supply is derived from the profunda femoris artery, medial circumflex femoral, femoral and obturator arteries. The profunda femoris artery (or sometimes the first perforator) supplies a large branch, the 'artery of the adductor muscles'.

Gracilis

Attachments Gracilis (see Figs 77.43–77.46) is the most superficial of the adductor group. It is thin and flat, broad above, and narrow and tapering below. It arises by a thin aponeurosis from the medial margins of the lower half of the body of the pubis, the whole of the inferior pubic ramus, and the adjoining part of the ischial ramus. The fibres descend vertically into a rounded tendon, often harvested as a knee ligament graft, which passes across the medial condyle of the femur posterior to the tendon of sartorius. It then curves around the medial condyle of the tibia, where it fans out and is attached to the upper part of the medial surface of the tibia, just below the condyle, forming part of the pes anserinus (see Fig. 77.46). A few fibres from the lower part of the tendon continue into the deep fascia of the lower leg. Often there is a slip that blends with the tendon of the medial head of gastrocnemius. Unless divided, this can lead to problems during surgical harvesting of the gracilis tendon.

Relations The muscle is covered medially by the fascia lata throughout most of its length. Deep to gracilis lie adductor brevis and adductor magnus. The tibial attachment is immediately proximal to that of semitendinosus, and is just behind and blended with the upper edge of the elongated tendon of sartorius. It is separated from the tibial collateral ligament of the knee joint by the anserine bursa.

Vascular supply The arterial supply to gracilis enters via its lateral surface. The main pedicle arises from the 'artery to the adductors', a branch of the profunda femoris artery, and enters at the junction of the upper and middle thirds of the muscle. The gracilis musculocutaneous flap is based on this pedicle. A less important artery enters the distal third of the muscle from the femoral artery. There is a minor proximal supply from the medial circumflex femoral artery.

Innervation Gracilis is innervated by the obturator nerve, L2 and L3.

Actions Gracilis flexes the leg and rotates it medially. It also adducts and assists with flexion of the thigh. When the foot is fixed, gracilis (along with sartorius and semitendinosus) can stabilize the medial side of the knee, and thus may be considered a 'dynamic tibial collateral ligament'.

Testing The tendon can be palpated posteromedially at the knee, as the knee is actively flexed and rotated medially. Gracilis can also be tested with the other adductors of the hip.

Adductor longus

Attachments Adductor longus (see Figs 77.37, 77.43–77.44), the most anterior of the three adductors, is a large, fan-shaped muscle that lies in the same plane as pectineus. It arises by a narrow tendon with a flattened (sometimes C-shaped) cross-section, which is attached to the front of the pubis in the angle between the crest and the symphysis. It expands into a broad fleshy belly that descends posterolaterally and inserts by an aponeurosis into the linea aspera in the middle third of the femur, between vastus medialis and adductors magnus and brevis, usually blending with all of these muscles. Its proximal attachment is vulnerable to overload from sporting activity: this is one cause of sports-related groin pain.

Adductor longus is occasionally double.

Relations Anterior to adductor longus are the spermatic cord, fascia lata (which separates it from the long saphenous vein) and, near its attachment, the femoral artery and vein and sartorius. Posteriorly are adductor brevis and adductor magnus, the anterior branch of the obturator nerve and, near its attachment, the deep artery and vein of the thigh. Lateral and medial to adductor longus are, respectively, pectineus and gracilis.

Vascular supply The main supply to adductor longus is to the central part of the muscle from the 'artery to the adductors', a branch of the profunda femoris artery. There is an additional proximal supply from the medial circumflex femoral artery, and a more distal supply from the femoral artery and sometimes the descending genicular artery.

Innervation Adductor longus is innervated by the anterior division of the obturator nerve, L2, L3 and L4.

Adductor brevis

Attachments Adductor brevis (see Figs 77.40B, 77.43) lies posterior to pectineus and adductor longus. It arises by a narrow attachment from the external aspect of the body and inferior ramus of the pubis, between gracilis and obturator externus. Like adductor longus, it is somewhat triangular, and expands as it descends posterolaterally to insert via an aponeurosis into the femur, along a line from the lesser trochanter to the linea aspera, and on the upper part of the linea immediately behind pectineus and the upper part of adductor longus.

Adductor brevis often has two or three separate parts, or may be integrated into adductor magnus.

Relations Anteriorly lie pectineus, adductor longus, the profunda femoris artery and the anterior branch of the obturator nerve; posteriorly are adductor magnus and the posterior branch of the obturator nerve. The upper border of adductor brevis is related to the medial circumflex femoral artery, obturator externus, and the conjoined tendon of psoas major and iliacus. Its lower border is related to gracilis and adductor magnus. The second perforating artery, or first and second perforating arteries, pierces it near its femoral attachment.

Vascular supply The vascular supply to adductor brevis is variable. Usually the main arterial supply is directly from the profunda femoris artery distally and from the 'artery to the adductors' more proximally. There is an additional proximal supply from the medial circumflex femoral artery. The deep surface receives branches from the obturator artery.

Innervation Adductor brevis is innervated by the obturator nerve, L2 and L3.

Adductor magnus

Attachments Adductor magnus (**Fig. 77.47**; see Figs 77.40, 77.43, 77.45), a massive triangular muscle, arises from a small part of the inferior ramus of the pubis, from the conjoined ischial ramus, and from the inferolateral aspect of the ischial tuberosity. The short, horizontal fibres from the pubic ramus are inserted into the medial margin of the gluteal tuberosity of the femur, medial to gluteus maximus; this part of the muscle, in a plane anterior to the rest, is sometimes called adductor minimus. The fibres from the ischial ramus fan out downwards and laterally, to insert via a broad aponeurosis into the linea aspera and the proximal part of the medial supracondylar line. The medial (ischiocondylar) part of the muscle, composed mainly of fibres from the ischial tuberosity, is a thick mass that descends almost vertically, and ends in the lower third of the thigh in a rounded tendon as it approaches its distal attachment to the adductor tubercle on the medial condyle of the femur. The tendon is connected by a fibrous expansion to the medial supracondylar line.

The long, linear attachment of the muscle is interrupted by a series of osseo-aponeurotic openings, bridged by tendinous arches attached to the bone. The upper four are small and transmit the perforating branches and the termination of the profunda femoris artery. The lowest is large and allows the femoral vessels to cross to the popliteal fossa.

The vertical, ischiocondylar part of the muscle varies in its degree of separation from the rest. The upper border of adductor magnus may fuse with quadratus femoris.

Relations Anteriorly lie pectineus, adductor brevis and adductor longus, the femoral and deep femoral vessels, and the posterior branch of the obturator nerve. A bursa separates the proximal part of the muscle from the lesser trochanter of the femur. Posteriorly are the sciatic nerve, gluteus maximus, biceps femoris, semitendinosus and semimembranosus. The superior border of adductor magnus is parallel with quadratus femoris, and the transverse branch of the medial circumflex femoral artery passes between these two muscles. Its medial border is related to gracilis, sartorius and the fascia lata.

Vascular supply As expected from its position, adductor magnus is supplied from both its anterior and its posterior aspects. The contribution from the anterior compartment is the more important. The profunda femoris artery, obturator artery and femoral artery all contribute; the main supply comes directly from the distal part of the profunda femoris artery. Distally, there may be contributions from the femoral and descending genicular arteries. Posteriorly, there are branches from the medial circumflex femoral, the first and second perforating and the popliteal vessels.

Innervation Adductor magnus is composite and is doubly innervated by the obturator nerve and by the tibial division of the sciatic nerve (L2, L3 and L4), which supplies the ischiocondylar part. Both nerves are derived from anterior divisions in the lumbosacral plexus, indicating a primitive flexor origin for both parts of the muscle.

Actions the adductors

Although the adductors all adduct the femur, they commonly act as synergists in the complex patterns such as that used in walking, running and climbing, and to some degree as controllers of posture. Adductors magnus and longus are probably medial rotators of the thigh. The adductors are relatively inactive during adduction of the abducted thigh in the erect posture (when gravity assists), but active in other postures,

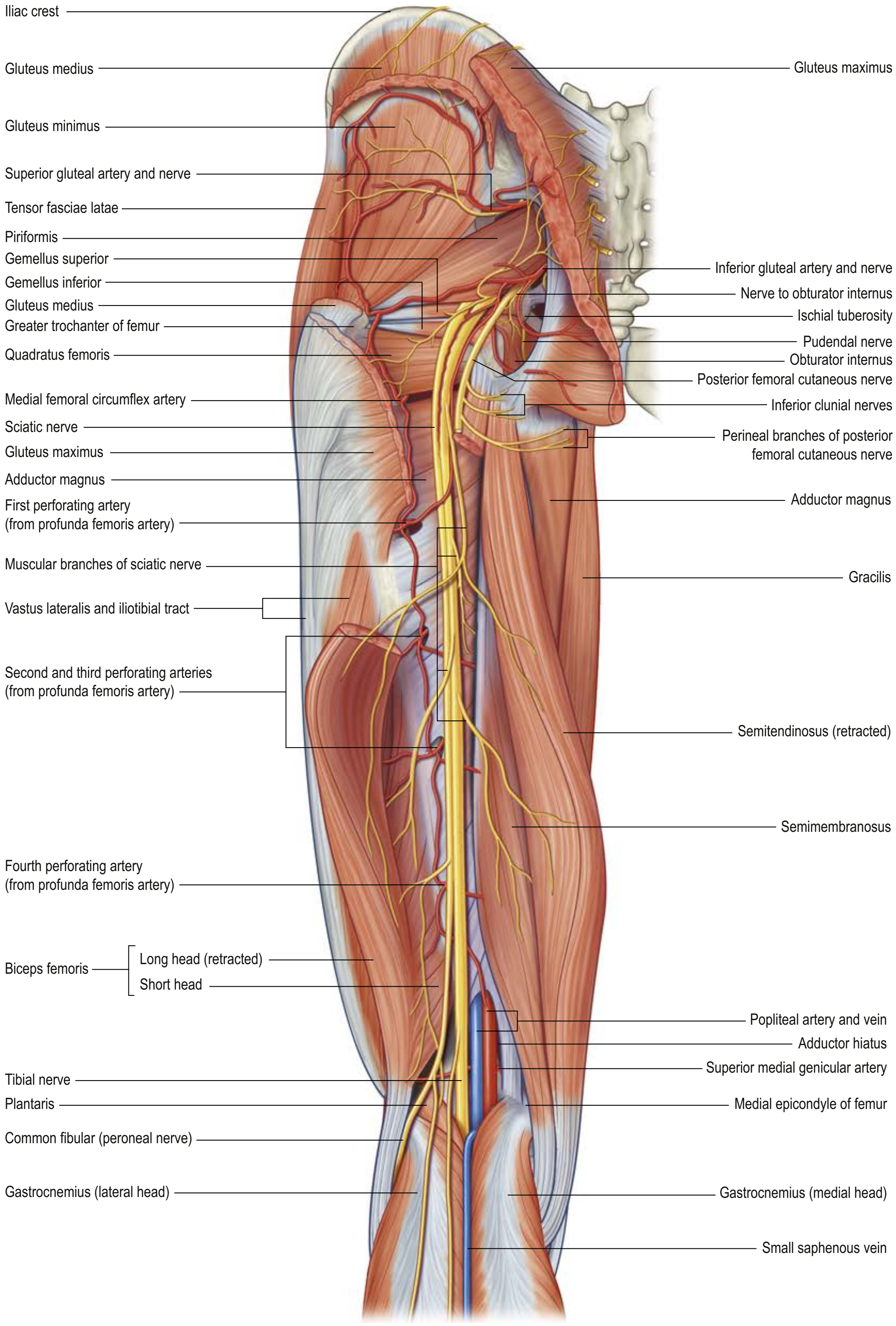
Iliac crest
Gluteus medius
Gluteus minimus
Superior gluteal artery and nerve
Tensor fasciae latae
Piriformis
Gemellus superior
Gemellus inferior
Gluteus medius
Greater trochanter of femur
Quadratus femoris
Medial femoral circumflex artery
Sciatic nerve
Gluteus maximus
Adductor magnus
First perforating artery
(from profunda femoris artery)
Muscular branches of sciatic nerve
Vastus lateralis and iliotibial tract
Second and third perforating arteries
(from profunda femoris artery)
Fourth perforating artery
(from profunda femoris artery)
Biceps femoris
Long head (retracted)
Short head
Tibial nerve
Plantaris
Common fibular (peroneal nerve)
Gastrocnemius (lateral head)
Gluteus maximus
Inferior gluteal artery and nerve
Nerve to obturator internus
Ischial tuberosity
Pudendal nerve
Obturator internus
Posterior femoral cutaneous nerve
Inferior clunial nerves
Perineal branches of posterior
femoral cutaneous nerve
Adductor magnus
Gracilis
Semitendinosus (retracted)
Semimembranosus
Popliteal artery and vein
Adductor hiatus
Superior medial genicular artery
Medial epicondyle of femur
Gastrocnemius (medial head)
Small saphenous vein

Fig. 77.47 The neurovascular structures of the gluteal region and posterior thigh. (With permission from Netter FH Atlas of Human Anatomy, 5th ed. Elsevier, Saunders. Copyright 2011.)

such as the supine position, or during adduction of the flexed thigh when standing. They are also active during flexion (adductor longus and brevis) and extension (adductor magnus) of the thigh at the hip joint. In symmetrical easy standing their activity is minimal.

Testing the adductors The adductors are usually tested as a group by adduction of the thigh against resistance, in the supine position with the knee extended. The tendon of adductor magnus can be felt just proximal to the adductor tubercle on the medial condyle of the femur. Clinical testing of the other actions mentioned above is not feasible for each of the individual muscles.

Pectineus

Attachments Pectineus (see Figs 77.37, 77.40) is a flat, quadrangular muscle that contributes to the medial aspect of the floor in the femoral triangle. The muscle may also be considered as part of the anterior compartment of the thigh, which is consistent with the muscle's partial femoral nerve innervation. It arises from the pecten pubis, from the bone anterior to it between the iliopubic ramus and the pubic tubercle, and from the fascia on its own anterior surface. The fibres descend posterolaterally to be attached along a line from the lesser trochanter to the linea aspera. Proximally, it may be partially or wholly attached to the capsule of the hip joint.

Relations Pectineus is related anteriorly to the deep lamina of the fascia lata, which separates it from the femoral vessels and long saphenous vein; posteriorly, to the capsule of the hip joint, adductor brevis, obturator externus and the anterior branch of the obturator nerve; laterally, to psoas major and the medial circumflex femoral vessels; and medially, to the lateral margin of adductor longus.

Vascular supply The main arterial supply to pectineus is derived from the medial circumflex femoral artery, which enters the superficial surface of the muscle. There may be a branch from the femoral artery more proximally, and a deep supply from the obturator artery.

Innervation Pectineus is innervated by the femoral nerve, L2 and L3, and the accessory obturator nerve, L3 (when present). Occasionally, it receives a branch from the obturator nerve. The muscle may be incompletely divided into dorsal and ventral layers, which are supplied by the obturator and femoral (or rarely, accessory obturator) nerves, respectively.

Actions Pectineus adducts the thigh and flexes it on the pelvis.

Testing The action of pectineus cannot be tested clinically in isolation.

Adductor canal

The adductor canal is a trough-shaped intermuscular tunnel occupying the distal two-thirds of the medial aspect of the thigh (see Fig. 77.43B). It starts at the apex of the femoral triangle and extends distally as far as the distal attachment of the tendon of adductor magnus. It is triangular in section and is bounded anterolaterally by vastus medialis; posteromedially by adductor longus; and distal to adductor longus, by adductor magnus. Its anteromedial boundary (often referred to as the roof) is a strong and dense fascia that extends from the medial surface of vastus medialis to the medial edge of the adductors longus and magnus, overlapping in its stride the femoral vessels in the adductor canal. This fascia, on account of being overlain by sartorius, is termed the subsartorial fascia.

The adductor canal contains the femoral artery and vein, the descending genicular and muscular branches of the femoral artery and their corresponding venous tributaries, the saphenous nerve, and the nerve to vastus medialis (until it enters its muscle). The femoral vessels pass from the adductor canal into the popliteal fossa via the adductor hiatus, an opening in the tendon of adductor magnus adjacent to the femoral shaft, two-thirds of the way down the adductor canal.

Posterior compartment

The posterior thigh muscles, biceps femoris, semitendinosus and semimembranosus, are colloquially termed the 'hamstrings'. They cross both hip and knee joints, and integrate extension at the hip with flexion at the knee. As the muscles span the back of the knee, they form the proximal lateral and medial margins of the popliteal fossa.

The muscles of the posterior compartment (see Figs 77.38, 77.42–77.43) receive their blood supply from the perforating branches of the profunda femoris artery, most importantly through the first perforator given off from this artery. This vessel has important anastomoses with the inferior gluteal artery (on or within semitendinosus) and with the medial circumflex femoral artery, while the third perforator anastomoses with the superior medial genicular artery within the short head of biceps femoris. This anastomotic chain forms an important collateral arterial pathway when the femoral artery is blocked.

Semitendinosus

Attachments Semitendinosus (see Figs 77.42, 77.43B, 77.47), notable for the length of its distal tendon, lies posteromedially in the thigh. It arises from an inferomedial impression on the upper area of the ischial tuberosity (see Fig. 77.4B), by a tendon it shares with the long head of biceps femoris, and from an aponeurosis connecting the adjacent anterior surfaces of the two muscles for 7.5 cm from their common origin. The belly is fusiform and ends a little below mid-thigh in a long, rounded tendon that runs on the posterior surface of semimembranosus. The tendon curves around the medial condyle of the tibia, passes over the tibial collateral ligament (from which it is separated by the anserine bursa), and inserts into the upper part of the medial surface of the tibia behind the attachment of sartorius and distal to that of gracilis (see Fig. 77.46). At its termination, it is united with the tendon of gracilis and gives off a prolongation to the deep fascia of the leg and to the medial head of gastrocnemius. A tendinous intersection is usually present near the midpoint of the muscle, which may also receive a muscular slip from the long head of biceps femoris. These connections with the medial head of gastrocnemius and biceps femoris can cause difficulty when harvesting the tendon surgically for a graft.

Relations Semitendinosus lies on the posterior surface of semimembranosus throughout its length. The relations of the distal part of the muscle are described above and with the pes anserinus.

Vascular supply The two main arteries of supply to semitendinosus are superior and inferior. The superior is derived from either the medial circumflex femoral artery or the first perforating artery. The inferior and larger branch arises from the first perforator distal to the origin of the superior branch. An accessory supply at the ischial attachment is derived from the inferior gluteal artery, and at the tibial attachment from the inferior medial genicular artery.

Innervation Semitendinosus is innervated by the sciatic nerve, L5, S1 and S2, through its tibial division (see Fig. 77.47).

Semimembranosus

Attachments Semimembranosus (see Figs 77.43, 77.47), so named because of the flattened form of its upper attachment, is posteromedial in the thigh. It arises by a long, flat tendon from a superolateral impression on the ischial tuberosity (see Fig. 77.4B). Inferomedially, the tendinous fibres intermingle to some extent with those of biceps femoris and semitendinosus. The tendon receives, from the ischial tuberosity and ramus, two fibrous expansions that flank adductor magnus. It then broadens and descends deep to semitendinosus and the long head of biceps femoris. Muscle fibres arise from the tendon at about mid-thigh and converge to a second aponeurosis on the posterior aspect of the lower part of the muscle, which tapers to the heavy, rounded tendon of the distal attachment. The tendon divides at the level of the knee into five components. The main one is attached to a tubercle (sometimes called the tuberculum tendinis) on the posterior aspect of the medial tibial condyle. The others are: a series of slips to the medial margin of the tibia, immediately behind the tibial collateral ligament; a thin fibrous expansion to the fascia over popliteus; a cord-like tendon to the inferior lip and adjacent part of the groove on the back of the medial tibial condyle, deep to the tibial collateral ligament; and a strong expansion that passes obliquely upwards to the femoral intercondylar line and lateral femoral condyle, and forms much of the oblique popliteal ligament of the knee joint.

Semimembranosus varies considerably in size and may be absent. It may be double, and arise mainly from the sacrotuberous ligament. Slips to the femur or to adductor magnus may occur.

Relations Semimembranosus overlaps the popliteal vessels and is itself partly overlapped by semitendinosus throughout its extent (see Fig. 77.42). Its deep surface lies on adductor magnus. The sciatic nerve lies laterally and surprisingly close to the surface. The distal end of the muscle partially overlies the medial head of gastrocnemius before passing anteromedially to it. An important bursa lies between the semimembranosus tendon and gastrocnemius, and often communicates with the knee joint and with a smaller bursa between the tendon and the posterior tibial margin.

Vascular supply Semimembranosus is supplied from the perforating arteries, usually from all, though predominantly from the first. Sometimes the predominant artery arises from the fourth perforator. A branch of the femoral or popliteal artery supplies the distal part of the muscle, and there may be a contribution from the inferior gluteal artery at the proximal attachment.

Innervation Semimembranosus is innervated by the sciatic nerve, L5, S1 and S2, through its tibial division.

Biceps femoris

Attachments Biceps femoris (see Figs 77.43, 77.47) occupies a posterolateral position in the thigh. It has two proximal attachments. One, the long head, arises from an inferomedial impression on the upper area of the ischial tuberosity (see Fig. 77.4B), via a tendon that it shares with semitendinosus, and some superficial fibres blend with the lower part of the sacrotuberous ligament. The other, the short head, arises from the lateral lip of the linea aspera, between adductor magnus and vastus lateralis. This attachment extends proximally almost to gluteus maximus and distally along the lateral supracondylar line to within 5 cm of the lateral femoral condyle, and from the lateral intermuscular septum. The long head forms a fusiform belly that descends laterally across the sciatic nerve. The fibres end in an aponeurosis that covers the posterior surface of the muscle. This aponeurosis receives on its deep surface the fibres of the short head, and gradually narrows to a tendon (the lateral hamstring). The main part of the tendon splits round the fibular collateral ligament and is attached to the head of the fibula. The remainder splits into three laminae. The intermediate lamina fuses with the fibular collateral ligament, while the others pass superficial and deep to the ligament to attach to the lateral condyle of the tibia.

The short head may be absent. Additional slips may arise from the ischial tuberosity, linea aspera or medial supracondylar line.

Relations Proximally, biceps femoris is covered by gluteus maximus, but elsewhere it lies relatively superficially. Deep to it lie semimembranosus proximally, and the sciatic nerve, adductor magnus and the lateral head of gastrocnemius more distally. Semitendinosus and semimembranosus lie medially. A bursa may lie between the tendon and the fibular collateral ligament. The common fibular nerve descends along the medial border of the tendon of biceps femoris, separating it distally from the lateral head of gastrocnemius.

As a guide during surgery, it is safest to find a nerve proximally and dissect it free distally. The common fibular nerve is found emerging posterior to the biceps femoris tendon, which is a useful guide to locating the nerve and avoiding iatrogenic injury. The nerve is adherent to the tendon; if part of the fibular head or the attachment of the tendon of biceps femoris, usually with the insertion of the fibular collateral ligament, is avulsed, then the tendon will exert proximal traction on the nerve, which may contribute to common fibular nerve traction injury. When the lateral meniscus is sutured arthroscopically, care must be taken that all needle passages are anterior to biceps femoris. A proximal fibular fracture may result in the nerve being trapped in the fracture line.

Vascular supply The long head of biceps femoris is supplied by the first and second perforating arteries. There are accessory supplies at the ischial attachment from the inferior gluteal and medial circumflex femoral arteries, and in the distal quarter from the superior lateral genicular artery. The short head is supplied superiorly by the second or third perforating artery and inferiorly by the superior lateral genicular artery.

Innervation Biceps femoris is innervated by the sciatic nerve, L5, S1 and S2: the long head through the tibial division and the short head through the common fibular division, a distribution that reflects the composite derivation from flexor and extensor musculature.

Actions of the hamstrings

Acting from above, the posterior thigh muscles flex the knee. Acting from below, they extend the hip joint, pulling the trunk upright from a stooping posture against the influence of gravity. When the knee is semi-flexed, biceps femoris can act as a lateral rotator and semimembranosus and semitendinosus as medial rotators of the lower leg on the thigh at the knee. As is the case with quadriceps femoris, the adductors and gluteus maximus, the hamstrings are typically quiescent in easy symmetrical standing. However, any action that takes the centre of gravity in front of a transverse axis through the hip joints, e.g. forward reaching, forward sway at the ankle joints or forward bending at the hips, is immediately accompanied by strong contraction of the hamstrings. This is in marked contrast to gluteus maximus, which contracts only when there is a call for powerful extension at the hip joint.

Often, activation of the hamstring muscles occurs in conjunction with simultaneous movements of the hip and the knee. For example, consider rising from a deep squat position by combining simultaneous extension of the hips and knees. In this example, the activated hamstrings are pulling the hips into extension, while they are simultaneously being elongated as they cross the posterior side of the extending knee. Such a biomechanical scenario (which is typical in most biarticular muscles throughout the body) helps maintain an overall muscle length that is conducive to effective force production (Neumann 2017).

When relaxed, these muscles show considerable variation in length; in some individuals, the muscles are so short as to impose a serious limitation on flexion of the trunk at the hip joints when the knees are kept extended. Movements such as stooping must then be accomplished by flexing the vertebral column or squatting. Perhaps the need for more stress on the lumbar spine accounts for the occurrence of hamstring tightness in adolescents who develop spondylolysis. These muscles are prone to tearing, which may be related to the relative complexity of muscles that cross two joints, or to the fact that they are subject to large forces being produced as the muscles are active in an eccentric fashion.

Testing The posterior thigh muscles are tested clinically by active knee flexion against resistance in the supine or prone position. In the prone position, the individual hamstring tendons can be identified more easily. When the knee is flexed against resistance, the tendon of biceps femoris can be felt lateral to the popliteal fossa. Medial to the fossa, the tendons of gracilis (which is the more medial) and semitendinosus stand out sharply. The semimembranosus tendon is just palpable in the interval between them (and also by deep pressure from a 'pincer' grip beyond their margins).

VASCULAR SUPPLY AND LYMPHATIC DRAINAGE

Arteries

Common iliac and external iliac arteries and veins

The common iliac and external iliac arteries and veins are described in Chapter 71.

Gluteal vessels

The superior and inferior gluteal arteries (see Fig. 77.47) are described in Chapter 71.

Arteria comitans nervi ischiadici (artery to sciatic nerve)

The arteria comitans nervi ischiadici is a direct or indirect branch of the internal iliac artery, and runs on the surface of, or within, the sciatic nerve. It represents the primitive axial artery of the lower limb. The artery is usually a very small vessel; occasionally, it persists as a large vessel, in which case the femoral artery is correspondingly reduced in size. The artery may participate in collateral circulatory pathways.

Femoral artery

The femoral artery (see Figs 77.2, 77.43–77.44; **Fig. 77.48**) is a continuation of the external iliac artery (Benninger 2014). It begins behind the inguinal ligament, midway between the anterior superior iliac spine and the pubic symphysis, descends along the anteromedial part of the thigh in the femoral triangle, enters and passes through the adductor (subsartorial) canal, and becomes the popliteal artery as it passes through an opening in adductor magnus near the junction of the middle and distal thirds of the thigh. Its first 3 or 4 cm are enclosed, with the femoral vein, in the femoral sheath. The femoral artery gives off several branches in the proximal thigh, including the superficial epigastric, superficial circumflex iliac, superficial external pudendal, deep external pudendal and the profunda femoris artery. It gives off the descending genicular artery within the adductor canal.

Rarely, the femoral artery divides, distal to the origin of the profunda femoris artery, into two trunks that reunite near the adductor opening. The inferior gluteal artery, accompanying the sciatic nerve to the popliteal fossa and representing a persistence of the original axial artery, may replace it. The external iliac artery is then small, ending as the deep artery of the thigh.

Relations Anterior to the artery in the femoral triangle are the skin, subcutaneous tissue, superficial inguinal lymph nodes, fascia lata, femoral sheath, superficial circumflex iliac vein (crossing in the subcutaneous tissue) and the femoral branch of the genitofemoral nerve (which is at first lateral and then anterior). Near the apex of the triangle, the medial femoral cutaneous nerve crosses in front of the artery from the lateral to the medial side. Posteriorly, the posterior wall of the femoral sheath separates the artery from the tendons of psoas, pectineus and adductor longus. The artery is separated from the hip joint by the tendon of psoas major, from pectineus by the femoral vein and deep femoral vessels, and from adductor longus by the femoral vein. Proximally, the nerve to pectineus passes medially behind the artery. The femoral nerve lies lateral to the artery, outside the femoral sheath. The femoral vein is medial to the artery in the proximal part of the triangle and becomes posterior distally at the apex.

Within the adductor canal, the artery is covered by skin, subcutaneous tissue, deep fascia, sartorius and the fibrous roof (subsartorial fascia) of the canal. The saphenous nerve lies at first lateral, then anterior and finally medial to the artery. Adductor longus and adductor magnus are posterior, vastus medialis and its nerve are anterolateral, and the femoral vein is also posterior proximally but it becomes lateral distally (see Fig. 77.48; **Fig. 77.49**).

Compression of the femoral artery is most effective just distal to the inguinal ligament, where it is superficial and separated from the bone (iliopubic ramus) only by the psoas major tendon. For this reason, arterial injury proximal to the inguinal ligament, such as laceration by

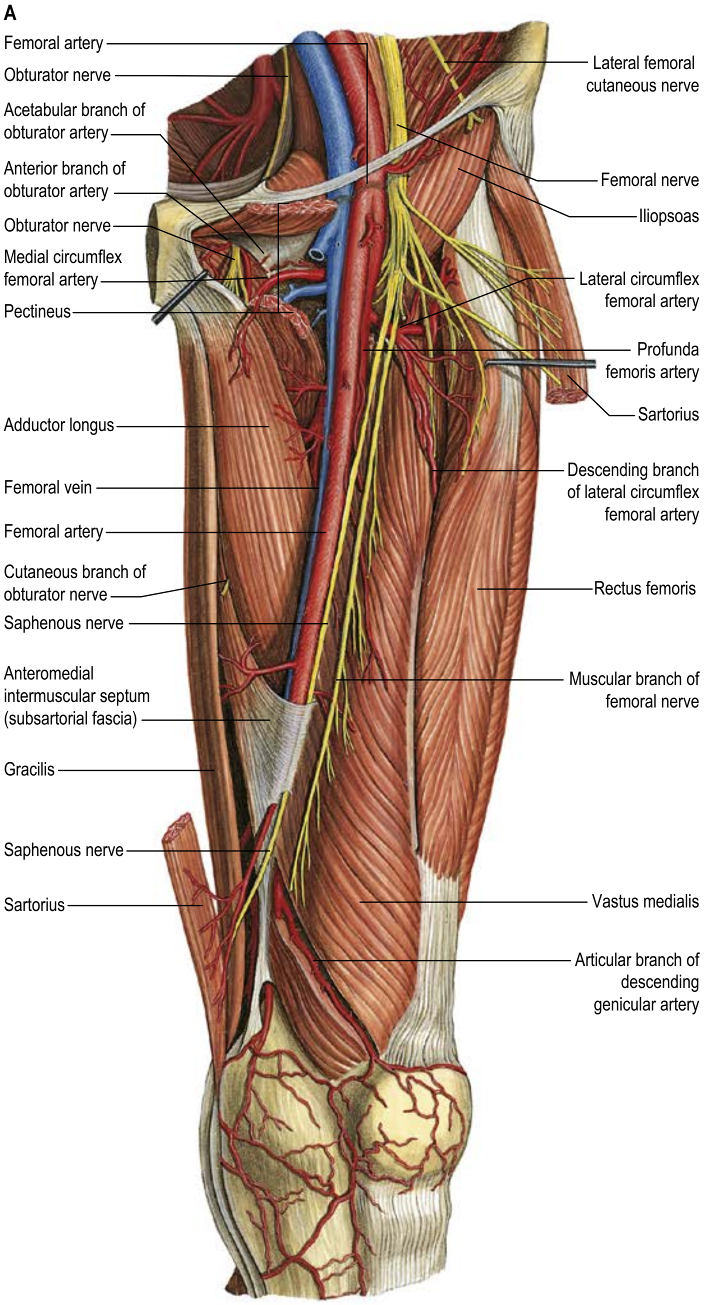
A
Femoral artery
Obturator nerve
Acetabular branch of obturator artery
Anterior branch of obturator artery
Obturator nerve
Medial circumflex femoral artery
Pectineus
Adductor longus
Femoral vein
Femoral artery
Cutaneous branch of obturator nerve
Saphenous nerve
Anteromedial intermuscular septum (subsartorial fascia)
Gracilis
Saphenous nerve
Sartorius
Lateral femoral cutaneous nerve
Femoral nerve
Iliopsoas
Lateral circumflex femoral artery
Profunda femoris artery
Sartorius
Descending branch of lateral circumflex femoral artery
Rectus femoris
Muscular branch of femoral nerve
Vastus medialis
Articular branch of descending genicular artery

Fig. 77.48 A, The neurovascular structures of the anteromedial thigh. (Sobotta Atlas of Human Anatomy © Elsevier GmbH, Urban & Fischer, Munich.) (B–C, *continued online*)

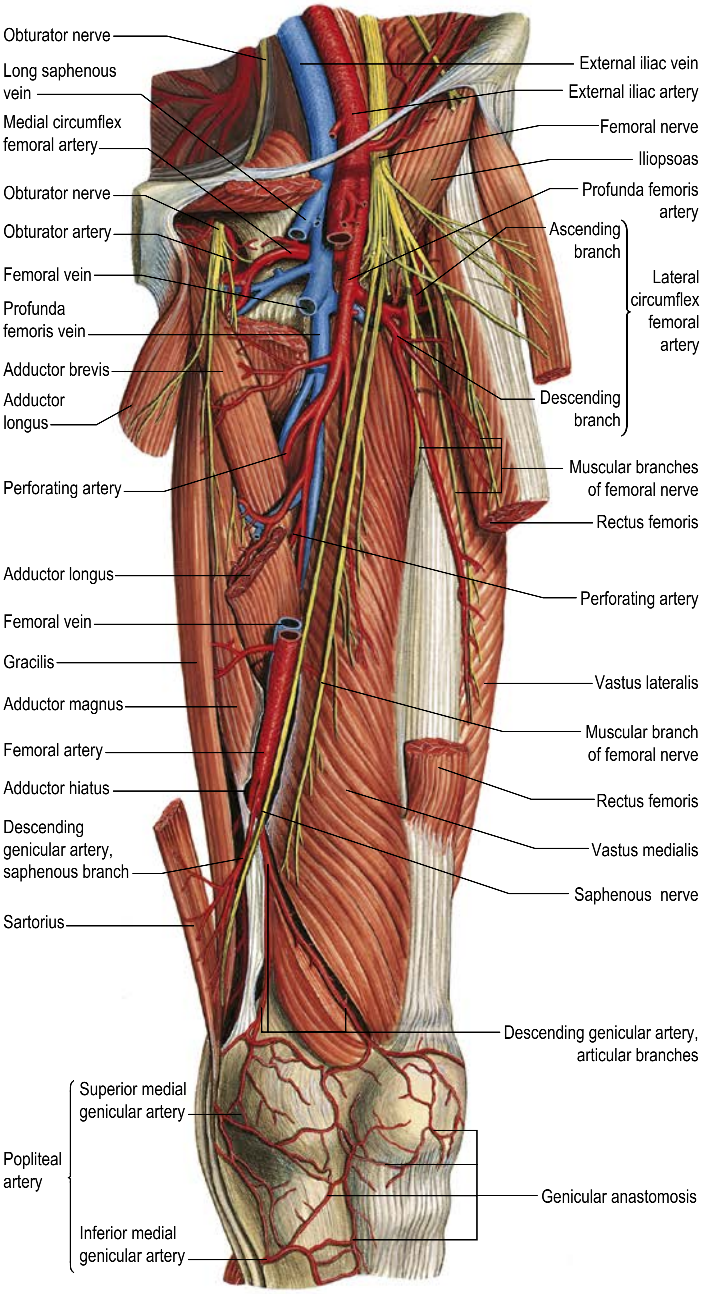
Obturator nerve
Long saphenous vein
Medial circumflex femoral artery
Obturator nerve
Obturator artery
Femoral vein
Profunda femoris vein
Adductor brevis
Adductor longus
Perforating artery
Adductor longus
Femoral vein
Gracilis
Adductor magnus
Femoral artery
Adductor hiatus
Descending genicular artery, saphenous branch
Sartorius
Popliteal artery
Superior medial genicular artery
Inferior medial genicular artery
External iliac vein
External iliac artery
Femoral nerve
Iliopsoas
Profunda femoris artery
Ascending branch
Lateral circumflex femoral artery
Descending branch
Muscular branches of femoral nerve
Rectus femoris
Perforating artery
Vastus lateralis
Muscular branch of femoral nerve
Rectus femoris
Vastus medialis
Saphenous nerve
Descending genicular artery, articular branches
Genicular anastomosis

Fig. 77.49 The neurovascular structures of the anterior thigh. This is a deeper dissection than is shown in Fig. 77.48. (Sobotta Atlas of Human Anatomy © Elsevier GmbH, Urban & Fischer, Munich.)

a knife, cannot be controlled simply by compression. Gaining proximal control of bleeding involves major exposure of the more proximal arteries as a life-saving manoeuvre.

Branches

The branches of the femoral artery include the superficial epigastric, superficial circumflex iliac, superficial external pudendal, deep external pudendal arteries, muscular branches, the profunda femoris artery and the descending genicular artery (see Fig. 76.4).

Superficial epigastric artery

The superficial epigastric artery arises anteriorly from the femoral artery approximately 1 cm distal to the inguinal ligament, and traverses the cribriform fascia to ascend anterior to the ligament and run in the abdominal subcutaneous tissue almost to the umbilicus. It supplies the superficial inguinal lymph nodes, subcutaneous tissue and skin, and anastomoses with branches of the inferior epigastric artery and its contralateral fellow.

Superficial circumflex iliac artery

The superficial circumflex iliac artery is the smallest superficial branch of the femoral artery and arises near or with the superficial epigastric artery. It usually emerges through the fascia lata, lateral to the saphenous opening, and turns laterally distal to the inguinal ligament towards the anterior superior iliac spine. It supplies the skin, subcutaneous tissue and superficial inguinal lymph nodes, anastomosing with the deep circumflex iliac, superior gluteal and lateral circumflex femoral arteries.

The superficial circumflex iliac artery is the basis for the important axial-pattern pedicled groin skin flap. Free flaps based on the vessel may also be raised.

Superficial external pudendal artery

The superficial external pudendal artery arises medially from the femoral artery, close to the preceding branches. Emerging from the cribriform fascia, it passes medially, usually deep to the long saphenous vein, across the spermatic cord (or round ligament) to supply the lower abdominal, penile, scrotal or labial skin, and anastomoses with branches of the internal pudendal artery.

Deep external pudendal artery

The deep external pudendal artery passes medially across pectineus and anterior or posterior to adductor longus, covered by fascia lata, which it pierces to supply the skin of the perineum and scrotum or labium majus. Its branches anastomose with the posterior scrotal or labial branches of the internal pudendal artery.

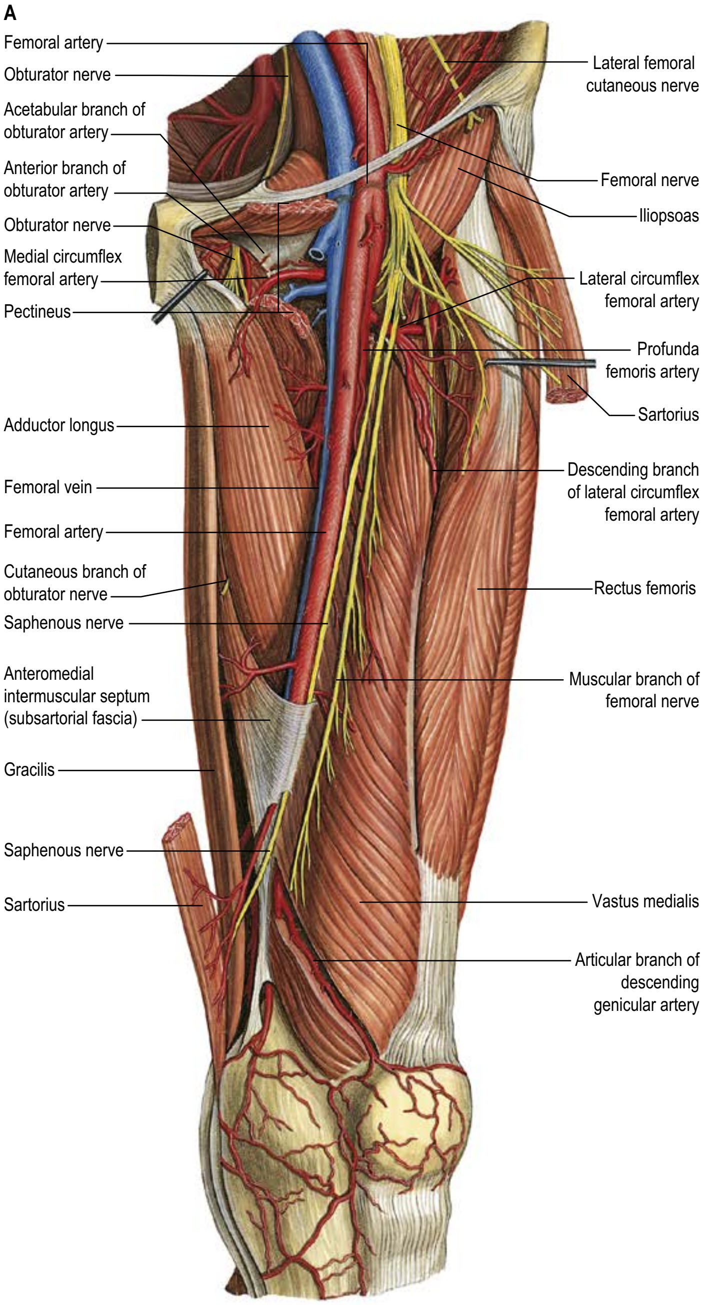
A
Femoral artery
Obturator nerve
Acetabular branch of obturator artery
Anterior branch of obturator artery
Obturator nerve
Medial circumflex femoral artery
Pectineus
Adductor longus
Femoral vein
Femoral artery
Cutaneous branch of obturator nerve
Saphenous nerve
Anteromedial intermuscular septum (subsartorial fascia)
Gracilis
Saphenous nerve
Sartorius
Lateral femoral cutaneous nerve
Femoral nerve
Iliopsoas
Lateral circumflex femoral artery
Profunda femoris artery
Sartorius
Descending branch of lateral circumflex femoral artery
Rectus femoris
Muscular branch of femoral nerve
Vastus medialis
Articular branch of descending genicular artery

Fig. 77.48 **A**, The neurovascular structures of the anteromedial thigh.

continued

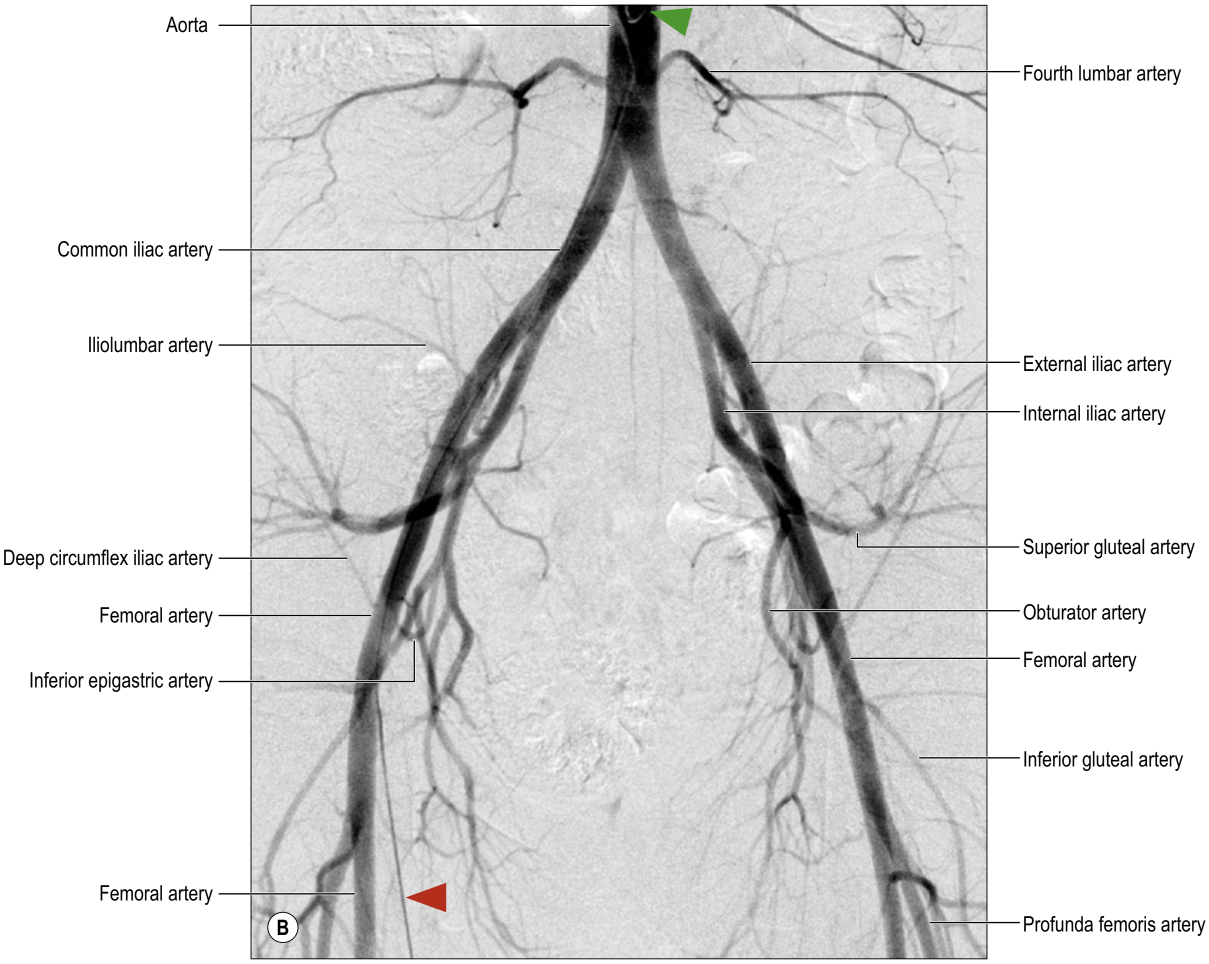
Aorta
Fourth lumbar artery
Common iliac artery
Iliolumbar artery
External iliac artery
Internal iliac artery
Superior gluteal artery
Deep circumflex iliac artery
Obturator artery
Femoral artery
Femoral artery
Inferior epigastric artery
Inferior gluteal artery
Femoral artery
Profunda femoris artery
B

Fig. 77.48, cont'd B, A frontal digital subtraction angiogram of the aortic bifurcation to the common femoral bifurcation; contrast medium is injected via a catheter (red arrowhead) entering via the right common femoral artery and passing to its coiled tip just at the superior margin of the image (green arrowhead).

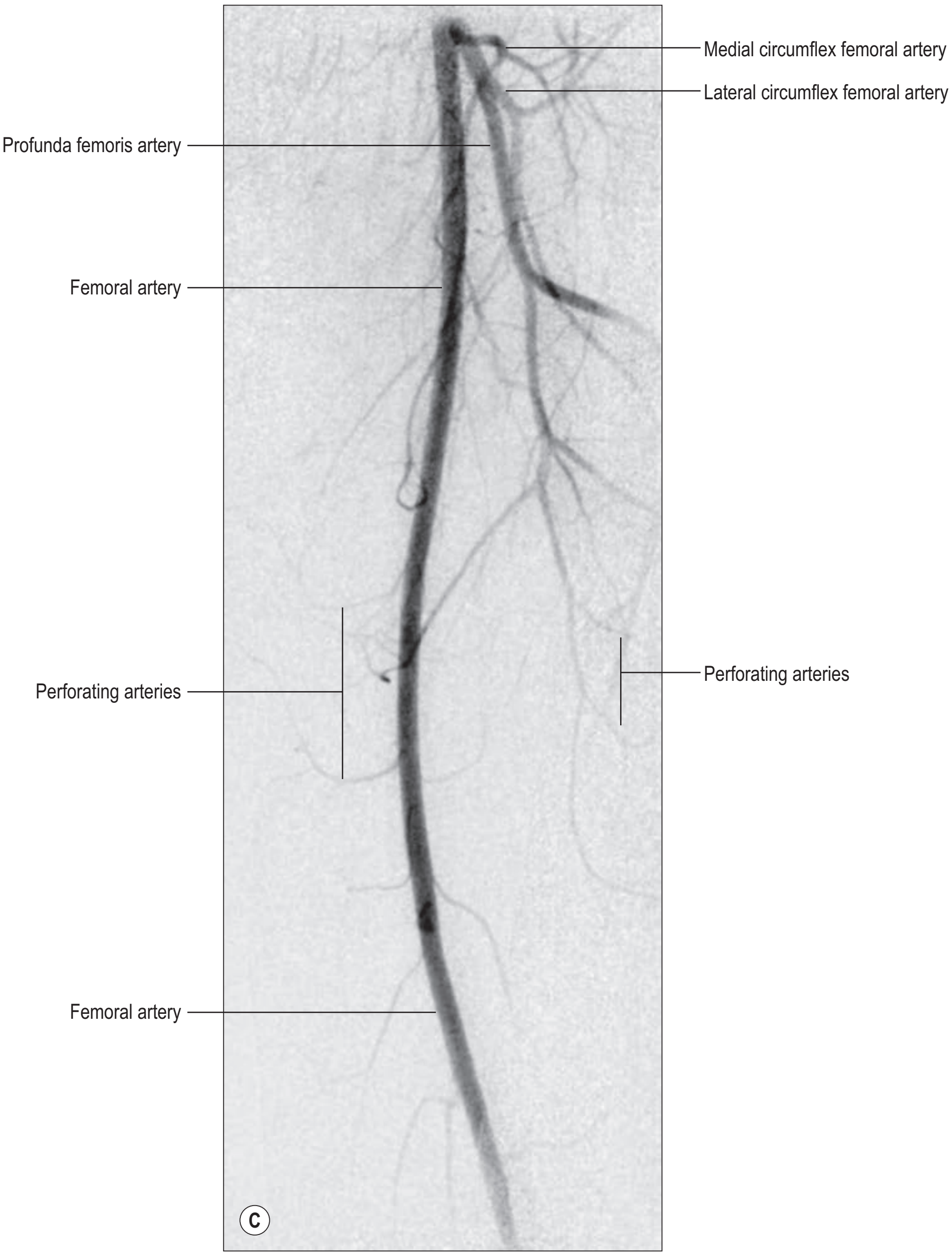
Medial circumflex femoral artery
Lateral circumflex femoral artery
Profunda femoris artery
Femoral artery
Perforating arteries
Perforating arteries
Femoral artery
C

Fig. 77.48, cont'd C, A frontal digital subtraction angiogram of the left common femoral bifurcation to the distal superficial artery. (A, Sobotta Atlas of Human Anatomy © Elsevier GmbH, Urban & Fischer, Munich.)

Muscular branches

These branches supply sartorius, vastus medialis and the adductors.

Profunda femoris artery (deep artery of the thigh)

The profunda femoris artery (see Figs 77.40, 77.43B, 77.48–77.49) is a large branch that arises posterolaterally from the femoral artery about 3.5 cm distal to the inguinal ligament. At first lateral to the femoral artery, it spirals posterior to this and the femoral vein to reach the medial side of the femur. It passes between pectineus and adductor longus, then between the latter and adductor brevis, before it descends between adductor longus and adductor magnus. It pierces adductor magnus and anastomoses with the upper muscular branches of the popliteal artery. This terminal part is sometimes named the fourth perforating artery.

The profunda femoris artery is the main supply to the adductor, extensor and flexor muscles, and also anastomoses with the internal and external iliac arteries above and with the popliteal artery below. It is a major collateral artery of the lower limb in patients with femoropopliteal arterial occlusive disease (see Fig. 77.49) (Shakeri et al 2010).

The profunda femoris artery sometimes arises from the posterior aspect of the femoral artery, and more rarely from the medial aspect. If it arises posteriorly, it may cross anterior to the femoral vein and then pass backwards around its medial side.

Relations Posteriorly, in proximodistal order, lie iliacus, pectineus, adductor brevis and adductor magnus. Anteriorly, the femoral and deep femoral veins, and distally, adductor longus, separate the profunda femoris artery from the femoral artery. Laterally, vastus medialis separates the proximal part of the artery from the femur.

Branches The profunda femoris artery gives off the lateral and medial circumflex arteries in the proximal thigh, and perforating and muscular branches more distally.

Lateral circumflex femoral artery The lateral circumflex femoral artery (see Figs 77.48–77.49) is a laterally running branch given off near the root of the profunda femoris artery. It passes between the divisions of the femoral nerve, posterior to sartorius and rectus femoris, and divides into ascending, transverse and descending branches. The ascending branch ascends along the intertrochanteric line, under tensor fasciae latae, lateral to the hip joint. It anastomoses with the superior gluteal and deep circumflex iliac arteries, supplying the greater trochanter, and, with branches of the medial circumflex femoral, forms an anastomotic ring round the femoral neck, from which the femoral neck and head are supplied. The ascending branch forms the pedicle of the tensor fasciae latae musculocutaneous flap. The descending branch descends posterior to rectus femoris, along the anterior border of vastus lateralis, which it supplies; a long branch descends in vastus lateralis to the knee (Tayfur et al 2010), anastomosing with the superior lateral genicular branch of the popliteal artery, accompanied by the nerve to vastus lateralis. The fasciocutaneous perforators that arise from the descending branch supply the anterolateral thigh fasciocutaneous flap. The transverse branch, the smallest, passes laterally anterior to vastus intermedius and pierces vastus lateralis to wind round the femur, just distal to the greater trochanter. It anastomoses with the medial circumflex, inferior gluteal and first perforating arteries, forming a cruciate anastomosis.

The lateral circumflex femoral artery may arise from the femoral artery or as a common trunk with the profunda femoris artery and the medial circumflex femoral artery. The ascending and descending branches may occasionally arise separately (Siddharth et al 1985).

Medial circumflex femoral artery The medial circumflex femoral artery (see Figs 77.48–77.49) usually originates from the posteromedial aspect of the profunda femoris artery, but sometimes originates from the femoral artery itself or as a common trunk with either the profunda femoris artery or the lateral circumflex femoral artery or both (Siddharth et al 1985). It supplies the adductor muscles and curves medially round the femur between pectineus and psoas major and then obturator externus and adductor brevis, finally appearing between quadratus femoris and the upper border of adductor magnus, dividing into transverse and ascending branches. The transverse branch takes part in the cruciate anastomosis. The ascending branch ascends on the tendon of obturator externus, anterior to quadratus femoris, to the trochanteric fossa, where it anastomoses with branches of the gluteal and lateral circumflex femoral arteries. An acetabular branch at the proximal edge of adductor brevis enters the hip joint under the transverse acetabular ligament with one from the obturator artery. It supplies the fat in the fossa and reaches the femoral head along its ligament. For details of the blood supply of the proximal end of the femur, consult Crock (1996).

Perforating arteries The perforating arteries (see Fig. 77.40) perforate the femoral attachment of adductor magnus to reach the flexor aspect of the thigh. There are three perforating branches, and the terminal part of the profunda femoris artery itself becomes the fourth perforator. They pass close to the linea aspera under small tendinous arches and give off muscular, cutaneous and anastomotic branches. Diminished, they pass deep to the short head of biceps femoris (the first usually through the attachment of gluteus maximus), traverse the lateral intermuscular septum and enter vastus lateralis. The first arises proximal, the second anterior and the third distal to adductor brevis. The first perforating artery passes back between pectineus and adductor brevis (sometimes through the latter), pierces adductor magnus near the linea aspera to supply adductor brevis, adductor magnus, biceps femoris and gluteus maximus, and anastomoses with the inferior gluteal, medial and lateral circumflex femoral and second perforating arteries. The larger second perforating artery, often arising with the first, pierces the attachments of adductor brevis and magnus, divides into the ascending and descending branches supplying the posterior thigh muscles and anastomoses with the first and third perforating arteries. The femoral nutrient artery usually arises from it. When two nutrient arteries exist, they usually arise from the first and third perforators. The third perforating artery starts distal to adductor brevis, pierces the attachment of adductor magnus and divides into branches to the posterior thigh muscles. It anastomoses proximally with the perforating arteries, and distally with the end of the profunda femoris artery and muscular branches of the popliteal. The femoral nutrient artery may arise from it. Side branches of the diaphysial nutrient and other branches of the profunda femoris artery provide subsidiary cortical arteries.

The perforating arteries form a double chain of anastomoses, initially in the adductor muscles and subsequently near the linea aspera.

Muscular branches Numerous muscular branches arise from the profunda femoris artery. Some end in the adductors, and others pierce adductor magnus, supply the flexors and anastomose with the medial circumflex femoral artery and superior muscular branches of the popliteal artery. The profunda femoris artery is thus the main supply to the thigh muscles.

Descending genicular artery

The descending genicular artery (see Figs 77.48–77.49, 78.1), the distal branch of the femoral artery, arises just proximal to the adductor opening and immediately supplies a saphenous branch. It then descends in vastus medialis, anterior to the tendon of adductor magnus, to the medial side of the knee, where it anastomoses with the superior medial genicular artery. Muscular branches supply vastus medialis and adductor magnus, and give off articular branches that anastomose around the knee joint. One articular branch crosses above the femoral patellar surface, forming an arch with the superior lateral genicular artery and supplying the knee joint. The saphenous branch (saphenous artery) emerges distally through the roof of the adductor canal to accompany the saphenous nerve to the medial side of the knee. It passes between sartorius and gracilis, and supplies the skin of the proximomedial area of the leg; it anastomoses with the inferior medial genicular artery.

Arterial anastomoses around the hip

In the fetus, a peri-acetabular vascular circle formed by the superior and inferior gluteal, internal pudendal and obturator arteries reduces the risk of bony necrosis of this region in children. However, there is a zone at the anterior portion of the acetabulum where the blood supply is less abundant (Damsin et al 1992).

Anastomoses on the posterior aspect of the thigh

An important chain of anastomoses extends on the posterior aspect of the thigh from the gluteal region to the popliteal fossa. It is formed in proximodistal order by anastomoses between the gluteal arteries and terminal branches of the medial circumflex femoral artery; the circumflex femoral arteries and the first perforating artery; the perforating arteries themselves; and between the fourth perforating artery and the superior muscular branches of the popliteal artery (see Fig. 76.4). The trochanteric and cruciate anastomoses are the proximal elements of this chain.

Trochanteric anastomosis

The trochanteric anastomosis lies near the trochanteric fossa of the femur and is an anastomosis between the ascending branch of the medial circumflex femoral artery and descending branches of the superior and inferior gluteal arteries. The lateral circumflex femoral artery and the first perforating artery from the profunda femoris artery may also contribute, creating an extracapsular 'arterial ring of the femoral neck' (Crock 1996). Branches from this ring, the retinacular vessels, pierce the capsule and ascend along the femoral neck to give the main blood supply to the head of the femur.

Cruciate anastomosis

The cruciate anastomosis lies at the level of the lesser trochanter, near the lower edge of the femoral attachment of quadratus femoris, and is an anastomosis between the transverse branches of the medial and lateral circumflex femoral arteries, a descending branch of the inferior gluteal artery and an ascending branch from the first perforating artery.

Collateral circulation in proximal femoral artery occlusion

After occlusion of the femoral artery proximal to the origin of the profunda femoris artery, five main anastomotic channels are available. These are between branches of the superior and inferior gluteal arteries, the medial and lateral circumflex femoral arteries and the first perforating branch of the profunda femoris artery; the obturator branch of the internal iliac artery and the medial circumflex femoral artery; the internal pudendal branch of the internal iliac artery and the superficial and deep external pudendal branches of the femoral artery; a deep circumflex iliac branch of the external iliac artery, the lateral circumflex femoral branch of the deep artery of the thigh and the superficial circumflex iliac branch of the femoral artery; and the inferior gluteal branch of the internal iliac artery and perforating branches of the profunda femoris artery.

Perforator flaps in the hip and thigh

Gluteal region

The gluteal region of the lower limb has an average of 21 perforators, which arise from three main source arteries: namely, the superior and inferior gluteal and the internal pudendal arteries (see Fig. 76.7). The flaps based on these perforators are used as free flaps for breast reconstruction and as local flaps for covering defects in the sacral and perineal region.

Hip and thigh region

The hip and thigh region has six source arteries and an average of 50 arterial perforators. The thigh can be divided into four areas: anteromedial; anterolateral and trochanteric; posteromedial; and posterolateral. The perforators that supply the anteromedial thigh are derived from the femoral artery, and those for the anterolateral thigh are derived from branches of the lateral circumflex femoral artery. Perforators that supply the skin over the posteromedial and posterolateral thigh regions are derived from the profunda femoris artery and the popliteal arteries. Skin flaps based on the superficial circumflex iliac, superficial external pudendal and superficial inferior epigastric arteries have been used as local flaps, tube pedicles and free tissue transfers. Other popular skin flaps are tensor fasciae latae (TFL) perforator flaps, anterolateral thigh (ALT) and anteromedial thigh (AMT) flaps, the gracilis perforator flap and posterior thigh flaps.

Veins

Femoral vein

The femoral vein accompanies its artery, beginning at the adductor opening as the continuation of the popliteal vein, and ending posterior to the inguinal ligament as the external iliac vein (see Figs 77.1–77.2, 77.44, 76.8). The vein is posterolateral to the femoral artery in the distal adductor canal. More proximally in the canal, and in the distal femoral triangle (i.e. at its apex), the vein lies posterior to the artery and proximally, at the base of the triangle, the vein lies medial to the artery. The vein occupies the middle compartment of the femoral sheath, between the femoral artery and femoral canal; fat in the canal permits expansion of the vein.

The femoral vein has numerous muscular tributaries. The profunda femoris vein (deep vein of the thigh, deep femoral vein) joins the femoral vein posteriorly 4–12 cm distal to the inguinal ligament, and the long saphenous vein then enters anteriorly. Veins accompanying the superficial epigastric, superficial circumflex iliac and external pudendal arteries join the long saphenous vein before it enters the saphenous opening. Lateral and medial circumflex femoral veins are usually tributaries of the femoral vein. There are usually four or five valves in the femoral vein; the two most constant are just distal to the entry of profunda femoris and near the inguinal ligament.

Profunda femoris vein (deep vein of the thigh)

The profunda femoris vein lies anterior to its artery and receives tributaries corresponding to the branches of the artery. Through these tributaries it connects distally with the popliteal vein and proximally with the inferior gluteal veins. It sometimes drains the medial and lateral circumflex femoral veins and has a valve just before it empties into the femoral vein.

Long saphenous vein

The long (great) saphenous vein (see Fig. 76.9A), the longest vein in the body, starts distally as a continuation of the medial marginal vein of the foot, and ends in the femoral vein a short distance distal to the inguinal ligament. It ascends immediately anterior to the medial malleolus, crosses the distal third of the medial surface of the tibia obliquely in an anteroposterior direction to reach its medial border, and then ascends a little behind the border to the knee. Proximally, it is posteromedial to the medial tibial and femoral condyles and then ascends the medial aspect of the thigh. It passes through the saphenous opening and finally opens into the femoral vein. The ‘centre’ of the opening is often said to be 2.5–3.5 cm inferolateral to the pubic tubercle, and the vein is then represented by a line drawn from this point to the adductor tubercle. However, the saphenous opening varies greatly in size and disposition so that this ‘centre’ is not a reliable surface marking for the saphenofemoral junction.

In its course through the thigh, the long saphenous vein is accompanied by the medial branches of the anterior cutaneous branches of the femoral nerve. At the knee, the saphenous branch of the descending genicular artery (the saphenous artery) and, in the leg and foot, the saphenous nerve all lie anterior to the vein. The vein is often duplicated, especially distal to the knee. It has 10–20 valves, which are more numerous in the leg than in the thigh. One is present just before the vein pierces the cribriform fascia, another at its junction with the femoral vein. In almost its entire extent the vein lies in subcutaneous tissue, but it has many connections with the deep veins, especially in the leg.

Tributaries

At the ankle, the long saphenous vein drains the sole of the foot by medial marginal veins. In the leg, it often connects with the short saphenous vein and with deep veins via perforating veins. Just distal to the knee, it usually receives three large tributaries from the front of the leg, the medial malleolar region (connecting with some of the ‘perforating’ veins) and the calf (communicating with the short saphenous vein). The tributary draining the medial malleolar region is formed distally from a fine network or ‘corona’ of delicate veins just over the medial malleolus, and then ascends the medial aspect of the calf as the posterior arch vein. This vein was first illustrated by Leonardo da Vinci, whose name is sometimes given to it. It connects with posterior tibial venae comitantes by a series of perforating (communicating) veins. There are usually three, equally spaced between the medial malleolus and the mid-calf. More than three such perforators are uncommon, and an arch vein perforator above mid-calf is only very rarely found.

Above the posterior crural arch vein, perforating veins join the long saphenous vein or one of its main tributaries at two main sites. The first is at a level in the upper calf indicated by its name, the tibial tubercle perforator; the second is in the lower/intermediate third of the thigh, where it perforates the deep fascia roof of the subsartorial canal to join the femoral vein.

In the thigh, the long saphenous vein receives many tributaries. Some open independently, while others converge to form large named channels that frequently pass towards the basal half of the femoral triangle before joining the long saphenous near its termination. These may be grouped as follows: one or more large posteromedial tributaries, one or more large anterolateral tributaries, and four or more peri-inguinal veins. The posteromedial vein of the thigh, large and sometimes double, drains a large superficial region indicated by its name; it has (as have the other tributaries) radiological and surgical significance. One of its lower radicles is often continuous with the short saphenous vein. The posteromedial vein is sometimes named the accessory saphenous vein, though some restrict the term accessory to a lower (more distal) posteromedial tributary when two (or more) are present. Another large vessel, the anterolateral vein of the thigh (anterior femoral cutaneous vein), usually commences from an anterior network of veins in the distal thigh and crosses the apex and distal half of the femoral triangle to reach the long saphenous vein. As the latter traverses the saphenous opening, it is joined by the superficial epigastric, superficial circumflex iliac and superficial external pudendal veins. Their mode of union varies. Superficial epigastric and circumflex iliac veins drain the inferior abdominal wall, the latter also receiving tributaries from the proximolateral region of the thigh. The superficial epigastric or the femoral vein may connect with the lateral thoracic veins by means of a thoracoepigastric vein that runs superficially on the anterolateral aspect of the trunk. This vein connects the inferior and superior caval areas of drainage and may be dilated and visible in cases of inferior caval obstruction. Superficial external pudendal veins drain part of the scrotum/labia; one is joined by the superficial dorsal vein of the penis/clitoris. The deep external pudendal veins join the long saphenous vein at the saphenous opening.

The long saphenous vein is often harvested for grafts used in both peripheral and coronary arterial surgery.

Lymphatic drainage

Superficial inguinal nodes

The superficial inguinal nodes form proximal and distal groups. The proximal group usually consists of five or six nodes just distal to the inguinal ligament. Its lateral members receive afferent vessels from the gluteal region and the adjoining infra-umbilical anterior abdominal wall. Medial members receive superficial vessels from the external genitalia (including the inferior vagina), inferior anal canal and perianal region, adjoining abdominal wall, umbilicus and vessels accompanying the round ligament. The distal group usually consists of four or five nodes along the termination of the long saphenous vein. They receive all the superficial vessels of the lower limb, except those from the posterolateral calf. All superficial inguinal nodes drain to the external iliac nodes, some via the femoral canal and others anterior or lateral to the femoral vessels. Numerous vessels interconnect individual nodes.

Superficial inguinal nodes are frequently enlarged in disease or injury in their region of drainage. Thus the proximal inguinal nodes are almost invariably affected in malignant or infective disease of the prepuce, penis, labia majora, scrotum, perineum, anus and lower vagina, or in diseases affecting the skin and superficial structures in these regions, in the infra-umbilical part of the abdominal wall or in the gluteal region. The distal group is implicated only in disease or injury of the limb.

Deep inguinal nodes

The deep inguinal nodes vary from one to three, and are situated medial to the femoral vein. One lies just distal to the saphenofemoral junction, another in the femoral canal, and the most proximal node lies laterally in the femoral ring. The middle node is the most inconstant and the proximal node is often absent. All receive deep lymphatics that accompany the femoral vessels, lymph vessels from the glans penis or clitoris and a few efferents from the superficial inguinal nodes. Their own efferents traverse the femoral canal to the external iliac nodes.

INNERVATION

Lumbar plexus and branches

The lumbar plexus is formed by the first three and most of the fourth lumbar ventral rami (see Fig. 61.16). The iliohypogastric, ilioinguinal and genitofemoral nerves are described in Chapter 61.

Lateral femoral cutaneous nerve

The lateral femoral cutaneous nerve (lateral cutaneous nerve of the thigh) arises from the dorsal branches of the second and third lumbar ventral rami and emerges from the lateral border of psoas major, crossing iliacus obliquely towards the anterior superior iliac spine. It supplies the parietal peritoneum in the iliac fossa. The right nerve passes posterolateral to the caecum, separated from it by the iliac fascia and peritoneum; the left passes behind the lower part of the descending colon. Both pass behind or through the inguinal ligament, variably medial to the anterior superior iliac spine (commonly 1 cm) and anterior to or through sartorius into the thigh, where they divide into anterior and posterior branches. The anterior branch becomes superficial approximately 10 cm distal to the anterior superior iliac spine and supplies the skin of the anterior and lateral thigh as far distally as the knee. It connects terminally with the cutaneous branches of the anterior division of the femoral nerve and the infrapatellar branch of the saphenous nerve, forming the peripatellar plexus. The posterior branch pierces the fascia lata higher than the anterior, and divides to supply the skin on the lateral surface from the greater trochanter to about mid-thigh. It may also supply skin of the gluteal region.

Lesions of the lateral femoral cutaneous nerve

The lateral femoral cutaneous nerve may become entrapped at three sites along its course: close to the vertebral column; within the abdominal cavity as the nerve travels across the pelvis; and as it leaves the pelvis. This last site is where the nerve is most commonly damaged, and entrapment is thought to occur as the nerve passes through or deep to the inguinal ligament just medial to the anterior superior iliac spine. The angulation of the nerve as it crosses the iliac crest means that it is vulnerable to compression during movement, e.g. hip extension may increase angulation and tension on the nerve.

Injury produces an area of impaired sensation, often with pain and paraesthesia on the anterolateral aspect of the thigh (meralgia paraesthetica) in the distal cutaneous distribution of the nerve. This area does not extend across the midline anteriorly, it does not extend below the knee and it does not extend behind the hamstring tendons laterally. Symptoms may be exacerbated when wearing tight belts or tight-waisted clothes or as a result of a recent weight gain or pregnancy. Exceptionally, the posterior branch of the lateral femoral cutaneous nerve, which supplies a thin strip from the greater trochanter of the femur down about two-thirds of the way to the knee, may be affected separately. This branch leaves the main trunk of the nerve, usually distal to the inguinal ligament, and it then turns laterally to pierce tensor fasciae latae, where it may become entrapped.

Femoral nerve

The femoral nerve is the largest branch of the lumbar plexus and arises from the dorsal branches (posterior divisions) of the second to fourth lumbar ventral rami (see Figs 77.44, 77.48–77.49, 76.11A). It descends through psoas major, emerging low on its lateral border, and then passes between psoas and iliacus, deep to the iliac fascia. Passing behind the inguinal ligament into the thigh, it is split into anterior and posterior divisions by the lateral circumflex femoral artery. Behind the inguinal ligament, it is separated from the femoral artery by part of psoas major. In the abdomen, the nerve supplies small branches to iliacus and pectineus and a branch to the proximal part of the femoral artery; the latter branch sometimes arises in the thigh.

Nerve to pectineus

The nerve to pectineus branches from the medial side of the femoral nerve near the inguinal ligament. It passes behind the femoral sheath and enters the anterior aspect of the muscle.

Anterior division of the femoral nerve

The anterior division of the femoral nerve supplies intermediate and medial femoral cutaneous nerves and branches to sartorius.

Medial femoral cutaneous nerve of the thigh The medial femoral cutaneous nerve (medial cutaneous nerve of the thigh) is at first lateral to the femoral artery. It crosses anterior to the artery at the apex of the femoral triangle and divides into anterior and posterior branches. Before doing so, it sends a few fibres through the fascia lata to supply the skin of the medial side of the thigh, near the long saphenous vein; one branch emerges via the saphenous opening, while another becomes subcutaneous about mid-thigh. The anterior branch descends on sartorius, perforates the fascia lata beyond mid-thigh, and divides into a branch that supplies the skin as low as the medial side of the knee, and another that runs lateral to the former and connects with the infrapatellar branch of the saphenous nerve. The posterior branch descends along the posterior border of sartorius to the knee, pierces the fascia lata, connects with the saphenous nerve and gives off several cutaneous rami, some as far as the medial side of the leg. The nerve contributes to the subsartorial plexus (see below).

Intermediate cutaneous nerve of the thigh The intermediate femoral cutaneous nerve (intermediate cutaneous nerve of the thigh) usually pierces the fascia lata some 8 cm below the inguinal ligament, either as two branches or as one trunk that quickly divides into two. These descend on the front of the thigh, supplying the skin as far as the knee and ending in the peripatellar plexus. The lateral branch of the intermediate cutaneous nerve communicates with the femoral branch of the genitofemoral nerve, frequently piercing sartorius and sometimes supplying it.

Nerve to sartorius The main nerve to sartorius arises from the femoral nerve in common with the intermediate cutaneous nerve of the thigh.

Posterior division of the femoral nerve

The branches of the posterior division of the femoral nerve are the saphenous nerve and branches to quadriceps femoris and the knee joint.

Saphenous nerve See Chapter 78.

Muscular branches The muscular branches of the posterior division of the femoral nerve supply quadriceps femoris. A branch to rectus femoris enters its proximal posterior surface and also supplies the hip joint. A larger branch to vastus lateralis forms a neurovascular bundle with the descending branch of the lateral circumflex femoral artery in its distal part and also supplies the knee joint. A branch to vastus medialis descends through the proximal part of the adductor canal, lateral to the saphenous nerve and femoral vessels, and enters the muscle at about its midpoint, sending a long articular filament distally along the muscle to the knee. Two or three branches to vastus intermedius enter its anterior surface about mid-thigh; a small branch from one of these descends through the muscle to supply articularis genus and the knee joint.

Vascular branches

Vascular branches of the femoral nerve supply the femoral artery and its branches.

Lesions of the femoral nerve

The main trunk of the femoral nerve is not subject to an entrapment neuropathy, but it may be compressed by retroperitoneal tumours or retroperitoneal haemorrhage in patients on anticoagulants or with a bleeding diathesis. A localized lesion of the femoral nerve may occur in diabetes mellitus (one of the forms of diabetic amyotrophy). The most striking feature of femoral neuropathy is wasting and weakness of quadriceps femoris, which results in difficulty in walking and a tendency for the leg to collapse. Pain and paraesthesia may occur on the anterior and medial aspect of the thigh, extending down the medial aspect of the leg in the distribution of the saphenous branch of the femoral nerve.

Obturator nerve

The obturator nerve arises from the ventral branches of the second to fourth lumbar ventral rami. The branch from the third is the largest while that from the second is often very small. The nerve descends in psoas major, emerging from its medial border at the pelvic brim to pass behind the common iliac vessels and lateral to the internal iliac vessels. It then descends forwards along the lateral wall of the lesser pelvis on obturator internus, anterosuperior to the obturator vessels, to the obturator foramen, entering the thigh by its upper part. Near the foramen, it divides into anterior and posterior branches, separated at first by part of obturator externus and lower down by adductor brevis.

Anterior branch

The anterior branch (see Fig. 77.49) leaves the pelvis anterior to obturator externus, descending in front of adductor brevis, behind pectineus and adductor longus. At the lower border of adductor longus it communicates with the medial cutaneous and saphenous branches of the femoral nerve, to form a subsartorial plexus that supplies the skin on the medial side of the thigh (see below). It descends on, and supplies, the femoral artery. Near the obturator foramen, the anterior branch supplies the hip joint. Behind pectineus it supplies adductor longus, gracilis, usually adductor brevis and often pectineus, and connects with the accessory obturator nerve (when present). Occasionally, the communicating branch to the femoral medial cutaneous and saphenous branches continues as a cutaneous branch to the thigh and leg. When this occurs, the nerve emerges from behind the distal border of adductor longus to descend along the posterior margin of sartorius to the knee, where it pierces the deep fascia and connects with the saphenous nerve to supply the skin halfway down the medial side of the leg.

Subsartorial nerve plexus The medial cutaneous nerve of the thigh forms a subsartorial plexus with branches of the saphenous and obturator nerves, deep to the fascia lata, at the lower border of adductor longus. When the communicating branch of the obturator nerve is large and reaches the leg, the posterior branch of the medial cutaneous nerve is small, and ends in the plexus from which it gives rise to a few cutaneous filaments.

Posterior branch

The posterior branch pierces obturator externus anteriorly, supplies it and passes behind adductor brevis to the front of adductor magnus, dividing into branches to this and adductor brevis when the latter is not supplied by the anterior division. It usually sends an articular filament to the knee joint, which either perforates adductor magnus distally or traverses its opening with the femoral artery to enter the popliteal fossa. Within the fossa, the nerve descends on the popliteal artery to the back of the knee, pierces its oblique posterior ligament and supplies the articular capsule. It gives filaments to the popliteal artery.

Lesions of the obturator nerve

Isolated lesions of the obturator nerve are rare, but may occasionally occur as a result of direct trauma (sometimes during parturition) or in anterior dislocations of the hip. The nerve may also be damaged by an obturator hernia, or be involved together with the femoral nerve in retroperitoneal lesions that occur close to the origins of the lumbar plexus. Compression of the nerve by herniated bowel loops at the obturator foramen can result in pain referred to the hip, medial thigh and knee, the so-called Howship–Romberg sign. A more distal nerve entrapment syndrome causing chronic medial thigh pain has been described in athletes with large adductor muscles.

Accessory obturator nerve

Occasionally present, the accessory obturator nerve is small and arises from the ventral branches of the third and fourth lumbar ventral rami. It descends along the medial border of psoas major, crosses the superior pubic ramus behind pectineus and divides into branches; one branch enters the deep surface of pectineus, another supplies the hip joint, and a third connects with the anterior branch of the obturator nerve. Sometimes the accessory obturator nerve is very small and only supplies pectineus. Any branch may be absent and others may occur; an additional branch sometimes supplies adductor longus.

Sacral plexus and branches

The branches of the sacral plexus (see Fig. 76.11B) are shown in Table 77.1.

Sciatic nerve

The sciatic nerve is 2 cm wide at its origin and is the thickest nerve in the body. It leaves the pelvis via the greater sciatic foramen, usually below piriformis, and descends between the greater trochanter and ischial tuberosity, along the back of the thigh, dividing into the tibial and common fibular nerves at a varying level proximal to the knee (**Fig. 77.50**; see Fig. 76.11B). Superiorly, it lies deep to gluteus maximus, resting first on the posterior ischial surface with the nerve to quadratus femoris between them. It then crosses posterior to obturator internus, the gemelli and quadratus femoris, separated by the latter from obturator externus and the hip joint. It is accompanied medially by the posterior femoral cutaneous nerve and the inferior gluteal artery. More distally, it lies behind adductor magnus and is crossed posteriorly by the long head of biceps femoris. Its course corresponds to a line drawn from just medial to the midpoint between the ischial tuberosity and greater trochanter to the apex of the popliteal fossa.

Articular branches arise proximally to supply the hip joint through its posterior capsule; these are sometimes derived directly from the sacral plexus. Muscular branches are distributed to biceps femoris, semitendinosus, semimembranosus and the ischial part of adductor magnus.

The point of division of the sciatic nerve into its tibial and common fibular components is very variable. The common site is at the junction of the middle and lower thirds of the thigh, near the apex of the popliteal fossa, but the division may occur at any level above this point and, rarely, may occur below it (Beaton and Anson 1937).

Blood supply to the sciatic nerve

In the gluteal region, the sciatic nerve is supplied by the inferior gluteal artery and cruciate anastomosis (the medial and lateral circumflex femoral arteries, inferior gluteal artery and the first perforating branch of the profunda femoris artery) (see Figs 77.40A, 77.47). On rare

TABLE 77.1 The branches of the sacral plexus

	Ventral divisions	Dorsal divisions
Nerve to quadratus femoris and gemellus inferior	L4–S1	
Nerve to obturator internus and gemellus superior	L5–S2	
Nerve to piriformis		L4–S2
Superior gluteal		L4–S1
Inferior gluteal		L5–S2
Posterior femoral cutaneous	S2, S3	S1, S2
Tibial (sciatic)	L4–S3	
Common fibular (sciatic)		L4–S2
Perforating cutaneous		S2, S3
Pudendal	S2–S4	
Branches to levator ani, coccygeus and external anal sphincter	S4	

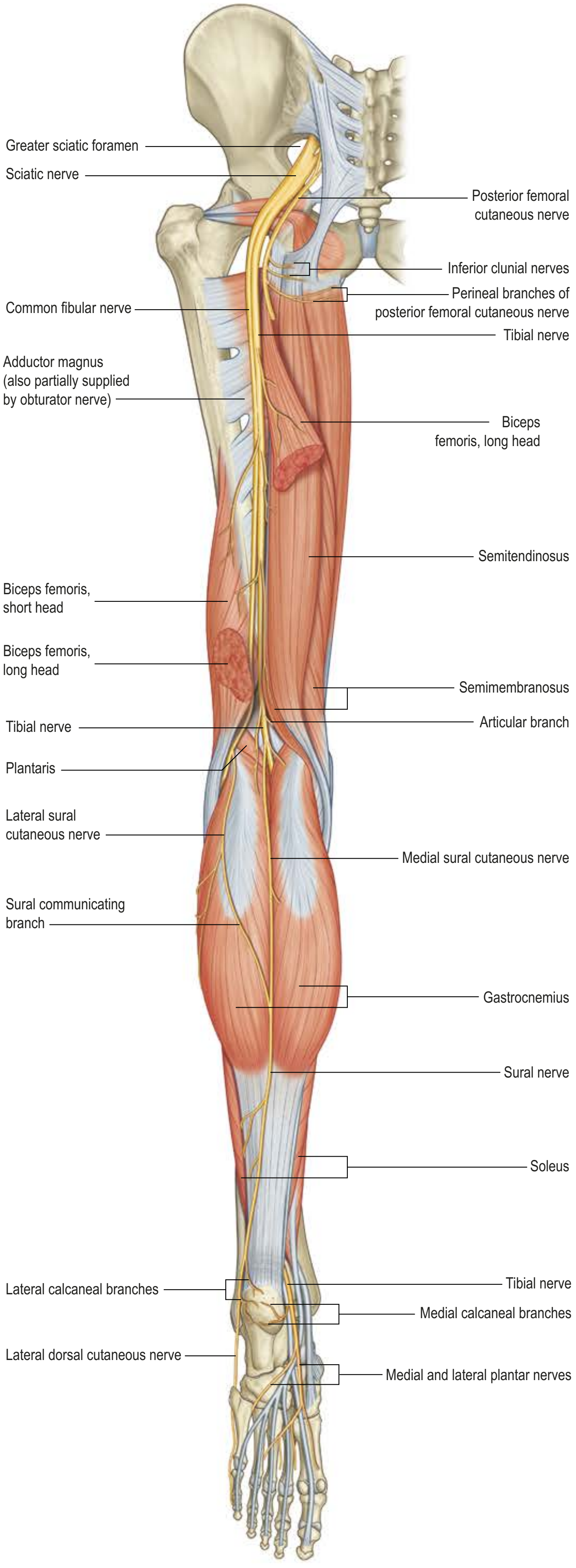
Greater sciatic foramen
Sciatic nerve
Posterior femoral cutaneous nerve
Inferior clunial nerves
Perineal branches of posterior femoral cutaneous nerve
Common fibular nerve
Tibial nerve
Adductor magnus (also partially supplied by obturator nerve)
Biceps femoris, long head
Semitendinosus
Biceps femoris, short head
Biceps femoris, long head
Semimembranosus
Articular branch
Tibial nerve
Plantaris
Lateral sural cutaneous nerve
Medial sural cutaneous nerve
Sural communicating branch
Gastrocnemius
Sural nerve
Soleus
Tibial nerve
Lateral calcaneal branches
Medial calcaneal branches
Lateral dorsal cutaneous nerve
Medial and lateral plantar nerves

Fig. 77.50 The sciatic nerve and its branches, posterior view.

occasions, it is supplied by branches from the superior gluteal or internal pudendal arteries, which reach the nerve on its medial side. Lower in the thigh, arterial branches derived from the perforating branches of the profunda femoris artery or the anastomotic chain between them or, occasionally, from the popliteal artery, enter the nerve on its lateral or anterolateral side (Sunderland 1945). The numerous arterial branches to the sciatic nerve anastomose with each other to form extraneural and intraneural arterial chains (Sunderland 1945, Ugrenovic et al 2013).

Lesions of the sciatic nerve

The sciatic nerve supplies the posterior thigh muscles and all the muscles below the knee, which means that a complete palsy of the sciatic nerve results in a flail foot and severe difficulty in walking. Fortunately, complete sciatic nerve palsy is very rare. The nerve is vulnerable in posterior dislocation of the hip. As it leaves the pelvis, it passes either below piriformis or sometimes through the muscle, and at that point it may very rarely become entrapped or tethered; the piriformis syndrome is a controversial condition in which an anomalous relationship between piriformis and the sciatic nerve is thought to cause pain in the buttocks and along the course of the sciatic nerve. External compression over the buttock, e.g. in patients who lie immobile on a hard surface for a considerable length of time, can injure the nerve. However, the most common cause of serious sciatic nerve injury (and of the resulting major medicolegal claims) is iatrogenic (Dillow et al 2013). The nerve may be damaged in misplaced therapeutic injections into gluteus maximus. Sciatic nerve palsy occurs after total hip replacement or similar surgery in 1% of cases, and may be caused by sharp injury, burning from bone cement, traction from instruments, manipulation of the hip, inadvertent lengthening of the femur, or haematoma surrounding the nerve. For some reason, possibly anatomical, the common fibular component of the sciatic nerve is more usually affected, resulting in a foot drop and a high-stepping gait.

Inferior gluteal nerve

The inferior gluteal nerve arises from the dorsal branches of the fifth lumbar and first and second sacral ventral rami. It leaves the pelvis via the greater sciatic foramen below piriformis, and divides into branches that enter the deep surface of gluteus maximus (see Fig. 77.47).

Superior gluteal nerve

The superior gluteal nerve arises from the dorsal branches of the fourth and fifth lumbar and first sacral ventral rami. Accompanied by the superior gluteal vessels, the nerve leaves the pelvis via the greater sciatic foramen above piriformis, and divides into superior and inferior branches (see Fig. 77.47). The superior branch accompanies the upper branch of the deep division of the superior gluteal artery to supply gluteus medius and occasionally gluteus minimus. The inferior branch runs with the lower ramus of the deep division of the superior gluteal artery across gluteus minimus, supplies the glutei medius and minimus, and ends in tensor fasciae latae.

Pudendal nerve

See Fig. 61.16 and Chapter 61.

Perforating cutaneous nerve

The perforating cutaneous nerve usually arises from the posterior aspects of the second and third sacral ventral spinal rami. It pierces the sacrotuberous ligament, curves round the inferior border of gluteus maximus and supplies the skin over the inferomedial aspect of this muscle. The nerve may arise from the pudendal nerve or it may be absent, in which case it may be replaced either by a branch from the posterior femoral cutaneous nerve or from the third and fourth, or fourth and fifth, sacral ventral rami.

Nerve to quadratus femoris

The nerve to quadratus femoris arises from the ventral branches of the fourth lumbar to the first sacral ventral rami. It leaves the pelvis via the greater sciatic foramen below piriformis, descends on the ischium deep to the sciatic nerve, the gemelli and the tendon of obturator internus, and supplies gemellus inferior, quadratus femoris and the hip joint.

Nerve to obturator internus

The nerve to obturator internus arises from the ventral branches of the fifth lumbar and first and second sacral ventral rami. It leaves the pelvis via the greater sciatic foramen below piriformis, supplies a branch to the upper posterior surface of gemellus superior, crosses the ischial spine lateral to the internal pudendal vessels, re-enters the pelvis via the lesser sciatic foramen, and enters the pelvic surface of obturator internus.

Posterior femoral cutaneous nerve (posterior cutaneous nerve of the thigh)

The posterior femoral cutaneous nerve (posterior cutaneous nerve of the thigh) arises from the dorsal branches of the first and second, and the ventral branches of the second and third sacral rami. It leaves the pelvis via the greater sciatic foramen below piriformis and descends under gluteus maximus with the inferior gluteal vessels, lying posterior or medial to the sciatic nerve (see Fig. 77.47). It descends in the back of the thigh superficial to the long head of biceps femoris, deep to the fascia lata. It pierces the deep fascia behind the knee and accompanies the short saphenous vein to mid-calf, its terminal twigs connecting with the sural nerve. Its branches are cutaneous and are distributed to the gluteal region, perineum, posterior thigh and proximal posterior leg.

Three or four gluteal branches (inferior clunial nerves) curl round the lower border of gluteus maximus to supply the skin over the inferolateral portion of the muscle. The perineal branch supplies the superomedial skin in the thigh, curves forwards across the hamstrings below the ischial tuberosity, pierces the fascia lata and then runs in the superficial perineal fascia to the scrotal or labial skin. It communicates with the inferior rectal and posterior scrotal or labial branches of the perineal nerve, and gives numerous branches to the skin of the back and medial side of the thigh, the popliteal fossa and the proximal part of the back of the leg. One study found the perineal branch of the posterior cutaneous nerve of the thigh in about one-half of specimens (Tubbs et al 2009).

Nerve to piriformis

The nerve to piriformis usually arises from the dorsal branches of the first and second sacral ventral rami (sometimes only the second) and enters the anterior surface of piriformis.

Visceral and pelvic muscular branches of sacral plexus

Visceral and muscular branches of the sacral plexus are described in Chapter 71.

Bonus e-book content

Fig. 77.2 **B,** An oblique multiplanar reformat of a CT with intravenous contrast medium along the inguinal ligament.

Fig. 77.7 An anteroposterior radiograph of the pelvis of a boy aged 7 years.

Fig. 77.9 The greater and lesser sciatic foramina. **B,** Anterior aspect. Note the arrows indicating vascular and muscular spaces.

Fig. 77.17 **B,** A coronal oblique CT of the proximal femur showing the calcar femorale.

Fig. 77.19 A radiograph of the pelvis of a 9-month-old infant showing the centre of ossification of the femoral epiphysis.

Fig. 77.20 An ultrasound image of a 4-week-old baby taken in the lateral position and demonstrating the cartilaginous femoral head and edge of the acetabulum.

Fig. 77.21 **B**, Anteroposterior radiograph of an adult male pelvis; the hip joint is normal.

Fig. 77.22 T1-weighted fat-saturated MR arthrogram of the left hip joint (coronal section).

Fig. 77.23 Pre-surgical radiograph of a hip with a cam deformity of the femoral head–neck junction.

Fig. 77.24 **B**, A sagittal proton density MRI through the left hip showing the muscles around the joint.

Fig. 77.27 **A**, T2-weighted fat-saturated MR arthrogram of the hip joint (coronal section). **B**, Photograph taken through an arthroscope of a slightly distracted hip joint.

Fig. 77.28 **B**, A fluoroscopic arthrogram of the right hip.

Fig. 77.29 Radiograph of the left hip of a 14-year-old boy.

Fig. 77.43 **A–B** Transverse sections through the thigh. **C–D**, T1-weighted images of the thigh.

Fig. 77.48 **B–C,** Frontal digital subtraction angiograms of the aortic bifurcation to the common femoral bifurcation and the left common femoral bifurcation to the distal superficial artery.

Key references

Dixon AF 1910 The architecture of the cancellous tissue forming the upper end of the femur. J Anat Physiol 44:223–30.

A neglected and original work with far-reaching implications for the understanding of femoral structure.

Fuss FK, Bacher A 1991 New aspects of the morphology and function of the human hip joint ligaments. Am J Anat 192:1–13.

An examination of how the motion of the hip affects the length and subsequent stretch on the hip capsular ligaments in dissected, cadaveric hips.

Gilligan I, Chandraphak S, Mahakkanukrauh P 2013 Femoral neck-shaft angle in humans: variation relating to climate, clothing, lifestyle, sex, age and side. J Anat 223:133–51.

An analysis of over 8000 femora representing 100 human groups, which found an average femoral neck-shaft angle of approximately 127°.

Leunig M, Beck M, Stauffer E et al 2000 Free nerve endings in the ligamentum capitis femoris. Acta Orthop Scand 71:452–4.

An immunohistochemical study of free nerve endings in the ligament of the head of the femur (ligamentum teres; ligamentum capitis femoris).

Neumann DA 2010 Kinesiology of the hip: a focus on muscular actions. J Orthop Sports Phys Ther 40:82–94.

A review of the interactions among the muscles that cross the hip joint, with particular reference to how these interactions influence normal movement and physical rehabilitation of the lower limb.

Scheuer L, Black S 2004 The Juvenile Skeleton. London: Elsevier, Academic Press.

An invaluable reference to the skeleton of the juvenile. Relevant to the fields of anthropology, archaeology, anatomy, skeletal biology and forensic science.

Taylor GI, Razaboni RM (eds) 1994 Michael Salmon: Anatomic Studies. Book 1, Arteries of the Muscles of the Extremities and the Trunk. St Louis: Quality Medical Publishing.

A translated, updated and edited version of a classic French text, first published in 1933. Now a major source book in plastic surgery.

Tubbs RS, Miller J, Loukas M et al 2009 Surgical and anatomical landmarks for the perineal branch of the posterior femoral cutaneous nerve: implications in perineal pain syndromes. Laboratory investigation. J Neurosurg 111:332–5.

An original study on the perineal branch of the posterior femoral cutaneous nerve.

Vleeming A, Schuenke MD, Masi AT et al 2012 The sacroiliac joint: an overview of its anatomy, function and potential clinical implications. J Anat 221:537–67.

A thorough, critical review of the anatomy and biomechanics of the sacroiliac joints.

Wagner FV, Negrao JR, Campos J et al 2012 Capsular ligaments of the hip: anatomic, histologic, and positional study in cadaveric specimens with MR arthrography. Radiology 263:189–98.

An evaluation using MRI and dissection of the length and subsequent tension in the capsular ligaments of the hip in ten cadaveric specimens at the extremes of extension, flexion, abduction, adduction, and medial and lateral rotation.

References

Alzaharani A, Bali K, Gudena R et al 2014 The innervation of the human acetabular labrum and hip joint: an anatomic study. BMC Musculoskelet Disord 15:41.

Babst D, Steppacher SD, Ganz R et al 2011 The iliocapsularis muscle: an important stabilizer in the dysplastic hip. Clin Orthop Relat Res 469:1728–34.

Bardakos NV, Villar RN 2009 The ligamentum teres of the adult hip. J Bone Joint Surg Br 91:8–15.

Beaton LE, Anson BJ 1937 The relationship of the sciatic nerve and of its subdivisions to the piriformis muscle. Anat Rec 70:1–5.

Beck M, Kalhor M, Leunig M et al 2005 Hip morphology influences the pattern of damage to the acetabular cartilage: femoroacetabular impingement as a cause of early osteoarthritis of the hip. J Bone Joint Surg Br 87:1012–18.

Becker I, Woodley SJ, Stringer MD 2010 The adult human pubic symphysis: a systematic review. J Anat 217:475–87.

Benninger B 2014 Novel femoral artery terminology: integrating anatomy and clinical procedures leading to standardized intuitive nomenclature. Clin Anat 27:1085–8.

Bergmann G, Graichen F, Rohlmann A 1993 Hip joint loading during walking and running, measured in two patients. J Biomech 26:969–90.

Betti L, Manica A 2018 Human variation in the shape of the birth canal is significant and geographically structured. Proc R Soc B 285:20181807.

Bird PA, Oakley SP, Shnier R et al 2001 Prospective evaluation of magnetic resonance imaging and physical examination findings in patients with greater trochanteric pain syndrome. Arthritis Rheum 44:2138–45.

Birkenmaier C, Jorysz G, Jansson V et al 2010 Normal development of the hip: a geometrical analysis based on planimetric radiography. J Pediatr Orthop B 19:1–8.

Birnbaum K, Prescher A, Hessler S et al 1997 The sensory innervation of the hip joint – an anatomical study. Surg Radiol Anat 19:371–5.

Bogduk N 2012 Clinical Radiologic Anatomy of the Lumbar Spine, 5th ed. New York: Churchill Livingstone.

Botser IB, Martin DE, Stout CE et al 2011 Tears of the ligamentum teres: prevalence in hip arthroscopy using 2 classification systems. Am J Sports Med 39(Suppl):117S–25S.

Brothwell DR, Pollard AM 2001 Handbook of Archaeological Sciences. Chichester: Wiley.

Cadet ER, Chan AK, Vorys GC et al 2012 Investigation of the preservation of the fluid seal effect in the repaired, partially resected, and reconstructed acetabular labrum in a cadaveric hip model. Am J Sports Med 40:2218–23.

Cormack GC, Lamberty BGH 1994 The Arterial Anatomy of Skin Flaps. Edinburgh: Elsevier, Churchill Livingstone.

Correa TA, Crossley KM, Kim HJ et al 2010 Contributions of individual muscles to hip joint contact force in normal walking. J Biomech 43:1618–22.

Crock HV 1980 An atlas of the arterial supply of the head and neck of the femur in man. Clin Orthop Relat Res 152:17–27.

Crock HV 1996 Atlas of Vascular Anatomy of the Skeleton and Spinal Cord. London: Martin Dunitz.

Damsin JP, Lazennec JY, Gonzales M et al 1992 Arterial supply of the acetabulum in the fetus: application to periacetabular surgery in childhood. Surg Radiol Anat 4:215–21.

Delaere O, Kok V, Nyssen-Behets C et al 1992 Ossification of the human fetal ilium. Acta Anat 143:330–4.

Delp SL, Hess WE, Hungerford DS et al 1999 Variation of rotation moment arms with hip flexion. J Biomech 32:493–501.

Dillow JM, Rosett RL, Petersen TR et al 2013 Ultrasound-guided parasacral approach to the sciatic nerve block in children. Paediatr Anaesth 23:1042–7.

Dixon AF 1910 The architecture of the cancellous tissue forming the upper end of the femur. J Anat Physiol 44:223–30.

A neglected and original work with far-reaching implications for the understanding of femoral structure.

Eckhoff DG, Kramer RC, Watkins JJ et al 1994 Variation in femoral anteversion. Clin Anat 7:72–5.

Emans JB, Ciarlo M, Callahan M et al 2005 Prediction of thoracic dimensions and spine length based on individual pelvic dimensions in children and adolescents: an age-independent, individualized standard for evaluation of outcome in early onset spinal deformity. Spine 30:2824–9.

Ferguson SJ, Bryant JT, Ganz R et al 2003 An in vitro investigation of the acetabular labral seal in hip joint mechanics. J Biomech 36:171–8.

Finnegan M 1978 Non-metric variation of the infracranial skeleton. J Anat 125:33–7.

Fuss FK, Bacher A 1991 New aspects of the morphology and function of the human hip joint ligaments. Am J Anat 192:1–13.

An examination of how the motion of the hip affects the length and subsequent stretch on the hip capsular ligaments in dissected, cadaveric hips.

Gardner E 1948 The innervation of the hip joint. Anat Rec 101:353–71.

Gilligan I, Chandraphak S, Mahakkanukrauh P 2013 Femoral neck-shaft angle in humans: variation relating to climate, clothing, lifestyle, sex, age and side. J Anat 223:133–51.

An analysis of over 8000 femora representing 100 human groups, which found an average femoral neck-shaft angle of approximately 127°.

Gray AJ, Villar RN 1997 The ligamentum teres of the hip: an arthroscopic classification of its pathology. Arthroscopy 13:575–8.

Grimaldi A, Fearon A 2015 Gluteal tendinopathy: integrating pathomechanics and clinical features in its management. J Orthop Sports Phys Ther 45:910–22.

Grob K, Gilbey H, Manestar M et al 2017 The anatomy of the articularis genus muscle and its relation to the extensor apparatus of the knee. JB JS Open Access. 2: e0034.

Haefeli PC, Steppacher SD, Babst D et al 2015 An increased iliocapsularis-to-rectus-femoris ratio is suggestive for instability in borderline hips. Clin Orthop Relat Res 473:3725–34.

Hodges PW, McLean L, Hodder J 2014: Insight into the function of the obturator internus muscle in humans: observations with development and validation of an electromyography recording technique. J Electromyogr Kines 24:489–96.

Holm NJ 1980 The internal stress pattern of the os coxae. Acta Orthop Scand 51:421–8.

Hu H, Meijer OG, van Dieen JH et al 2011 Is the psoas a hip flexor in the active straight leg raise? Eur Spine J 20:759–65.

Iwanaga J, Eid S, Simonds E et al 2018 The majority of piriformis muscles are innervated by the superior gluteal nerve. Clin Anat 32:282–6.

Kim YT, Azuma H 1995 The nerve endings of the acetabular labrum. Clin Orthop 320:176–81.

Leunig M, Beck M, Stauffer E et al 2000 Free nerve endings in the ligamentum capitis femoris. Acta Orthop Scand 71:452–4.

An immunohistochemical study of free nerve endings in the ligament of the head of the femur (ligamentum teres; ligamentum capitis femoris).

Mahan MA, Sanders LE, Guan J et al 2017. Anatomy of psoas muscle innervation: cadaveric study. Clin Anat 30:479–86.

Martin RL, Palmer I, Martin HD 2012 Ligamentum teres: a functional description and potential clinical relevance. Knee Surg Sports Traumatol Arthrosc 20:1209–14.

Myers CA, Register BC, Lertwanich P et al 2011 Role of the acetabular labrum and the iliofemoral ligament in hip stability: an in vitro biplane fluoroscopy study. Am J Sports Med 39(Suppl):85S–91S.

Neumann DA, Garceau L 2015 A proposed novel function of the psoas minor revealed through cadaver dissection. Clin Anat 28:243–52.

Neumann DA 2010 The actions of hip muscles. J Orthop Sports Phys Ther 40:82–94.

A review of the interactions among the muscles that cross the hip joint, with particular reference to how these interactions influence normal movement and physical rehabilitation of the lower limb.

Neumann DA 2017 Kinesiology of the Musculoskeletal System: Foundations for Physical Rehabilitation, 3rd ed. Elsevier.

Perumal V, Techataweewan N, Woodley SJ et al 2019 Clinical anatomy of the head of the femur. Clin Anat 32:90–8.

Ponseti IV 1978 Growth and development of the acetabulum in the normal child. J Bone Joint Surg Am 60:575–85.

Reikeras O, Bjerkreim I, Kolbenstvedt A 1983 Anteversion of the acetabulum and femoral neck in normals and in patients with osteoarthritis of the hip. Acta Orthop Scand 54:18–23.

Safran MR, Giordano G, Lindsey DP et al 2011 Strains across the acetabular labrum during hip motion: a cadaveric model. Am J Sports Med 39(Suppl):92S–102S.

Scheuer L, Black S 2004 The Juvenile Skeleton. London: Elsevier, Academic Press.

An invaluable reference to the skeleton of the juvenile. Relevant to the fields of anthropology, archaeology, anatomy, skeletal biology and forensic science.

Seeley MA, Georgiadis AG, Sankar WN 2016 Hip vascularity: a review of the anatomy and clinical implications. J Am Acad Orthop Surg 24:515–26.

Shakeri A, Tubbs RS, Shoja MM et al 2010 Analysis of the profunda femoris artery with superficial femoral artery occlusive disease. Biomed Int 1:62–5.

Sheehan FT, Borotikar BS, Behnam AJ et al 2012 Alterations in in vivo knee joint kinematics following a femoral nerve branch block of the vastus medialis: implications for patellofemoral pain syndrome. Clin Biomech 27:525–31

Siddharth P, Smith NL, Mason RA et al 1985 Variational anatomy of the deep femoral artery. Anat Rec 212:206–9.

Song Y, Ito H, Kourtis L et al 2012 Articular cartilage friction increases in hip joints after the removal of acetabular labrum. J Biomech 45:524–30.

Stansfield BW, Nicol AC 2002 Hip joint contact forces in normal subjects and subjects with total hip prostheses: walking and stair and ramp negotiation. Clin Biomech 17:130–9

Sunderland S 1945 Blood supply of the sciatic nerve and its popliteal divisions in man. Arch Neurol Psychiatry 54:283–9.

Tame SJ, Burstal R 2003 Investigation of the radiological relationship between iliac crests, conus medullaris and vertebral level in children. Paediatr Anaesth 13:676–80.

Tayfur V, Magden O, Edizer M, Atabey A. 2010 Anatomy of vastus lateralis muscle flap. J Craniofac Surg 21:1951–3.

Taylor GI, Razaboni RM (eds) 1994 Michael Salmon: Anatomic Studies. Book 1, Arteries of the Muscles of the Extremities and the Trunk. St Louis: Quality Medical Publishing.

A translated, updated and edited version of a classic French text, first published in 1933. Now a major source book in plastic surgery.

Trueta J 1957 The normal vascular anatomy of the femoral head during growth. J Bone Joint Surg Br 39:358–94.

Tubbs RS, Miller J, Loukas M et al 2009 Surgical and anatomical landmarks for the perineal branch of the posterior femoral cutaneous nerve: implications in perineal pain syndromes. Laboratory investigation. J Neurosurg 111:332–5.

An original study on the perineal branch of the posterior femoral cutaneous nerve.

Tubbs RS, Stetler W Jr, Savage AJ et al 2006 Does a third head of the rectus femoris muscle exist? Folia Morphol (Warsz) 65:377–80.

Ugrenovic SZ, Jovanovic ID, Kovacevic P et al 2013 Similarities and dissimilarities of the blood supplies of the human sciatic, tibial, and common peroneal nerves. Clin Anat 26:875–82.

Vleeming A, Schuenke MD, Masi AT et al 2012 The sacroiliac joint: an overview of its anatomy, function and potential clinical implications. J Anat 221:537–67.

A thorough, critical review of the anatomy and biomechanics of the sacroiliac joints.

Wagner FV, Negrao JR, Campos J et al 2012 Capsular ligaments of the hip: anatomic, histologic, and positional study in cadaveric specimens with MR arthrography. Radiology 263:189–98.

An evaluation using MRI and dissection of the length and subsequent tension in the capsular ligaments of the hip in ten cadaveric specimens at the extremes of extension, flexion, abduction, adduction, and medial and lateral rotation.

Walheim G, Olerud S, Ribbe T 1984 Mobility of the pubic symphysis: measurements by an electromechanical method. Acta Orthop Scand 55:203–8.

Walters BL, Cooper JH, Rodriguez JA 2014 New findings in hip capsular anatomy: dimensions of capsular thickness and pericapsular contributions. Arthroscopy 30:1235–45.

Ward WT, Fleisch ID, Ganz R 2000 Anatomy of the iliocapsularis muscle. Relevance to surgery of the hip. Clin Orthop Relat Res 374:278–85.

Weisl H 1954 The articular surfaces of the sacroiliac joint and their relation to the movements of the sacrum. Acta Anat 22:1–14.

White TD, Folkens PA 2005 The Human Bone Manual. Boston: Elsevier Academic.

Whitehouse WJ 1977 Cancellous bone in the anterior part of the iliac crest. Calcif Tissue Res 23:67–76.

Woodley SJ, Mercer SR, Nicholson HD 2008 Morphology of the bursae associated with the greater trochanter of the femur. J Bone Joint Surg Am 90:284–94.

Woodley SJ, Latimer CP, Meikle GR et al 2012 Articularis genus: an anatomic and MRI study in cadavers. J Bone Joint Surg Am 94:59–67.

CHAPTER

78

Knee and leg

The knee is the largest synovial joint in the body. It consists of three functional compartments that collectively form a dynamic, specialized hinge joint. During gait, the knee is able to withstand impressive weight-bearing loads while conducting precision movements, providing a stable yet fluid mechanism for relatively efficient bipedal locomotion. The complex arrangement of intra- and extracapsular ligaments that helps to counter the considerable biomechanical demands that are imposed on the joint can also be involved in disease (i.e. tri-compartment disease). The leg consists of two bones, with an interosseous membrane between them: the larger tibia, which transmits most of the stress of walking, and the smaller fibula, which provides secondary support and ankle stability. Muscles of the three compartments of the leg primarily permit movement of the ankle, foot and toes.

SKIN AND SOFT TISSUES

Skin

Vascular supply and lymphatic drainage

Knee

The arterial supply of the skin covering the knee is derived from genicular branches of the popliteal artery, the descending genicular branch of the femoral artery and the anterior recurrent branch of the anterior tibial artery, with small contributions from muscular branches to vastus medialis and the posterior thigh muscles (**Fig. 78.1**). For further details, consult Cormack and Lamberty (1994).

Cutaneous veins are tributaries of vessels that correspond to the named arteries. Cutaneous lymphatic drainage is initially to the superficial inguinal nodes, possibly also to the popliteal nodes, and then to the deep inguinal nodes.

Leg

The cutaneous arterial supply of the leg is derived from branches of the popliteal, anterior and posterior tibial and fibular vessels (see Fig. 76.5). Multiple fasciocutaneous perforating branches from each vessel pass along intermuscular septa to reach the skin; musculocutaneous perforators traverse muscles before reaching the skin. In some areas there is an additional, direct cutaneous supply from vessels that accompany cutaneous nerves, e.g. the descending genicular artery (saphenous artery) and superficial sural arteries. Fasciocutaneous and direct cutaneous arterial branches are oriented longitudinally in the skin, whereas the musculocutaneous branches are more radially oriented. For further details, consult Cormack and Lamberty (1994).

Cutaneous veins are tributaries of vessels that correspond to the named arteries. Cutaneous lymphatic vessels running on the medial side of the leg accompany the long saphenous vein and drain to the superficial inguinal nodes, and those from the lateral and posterior

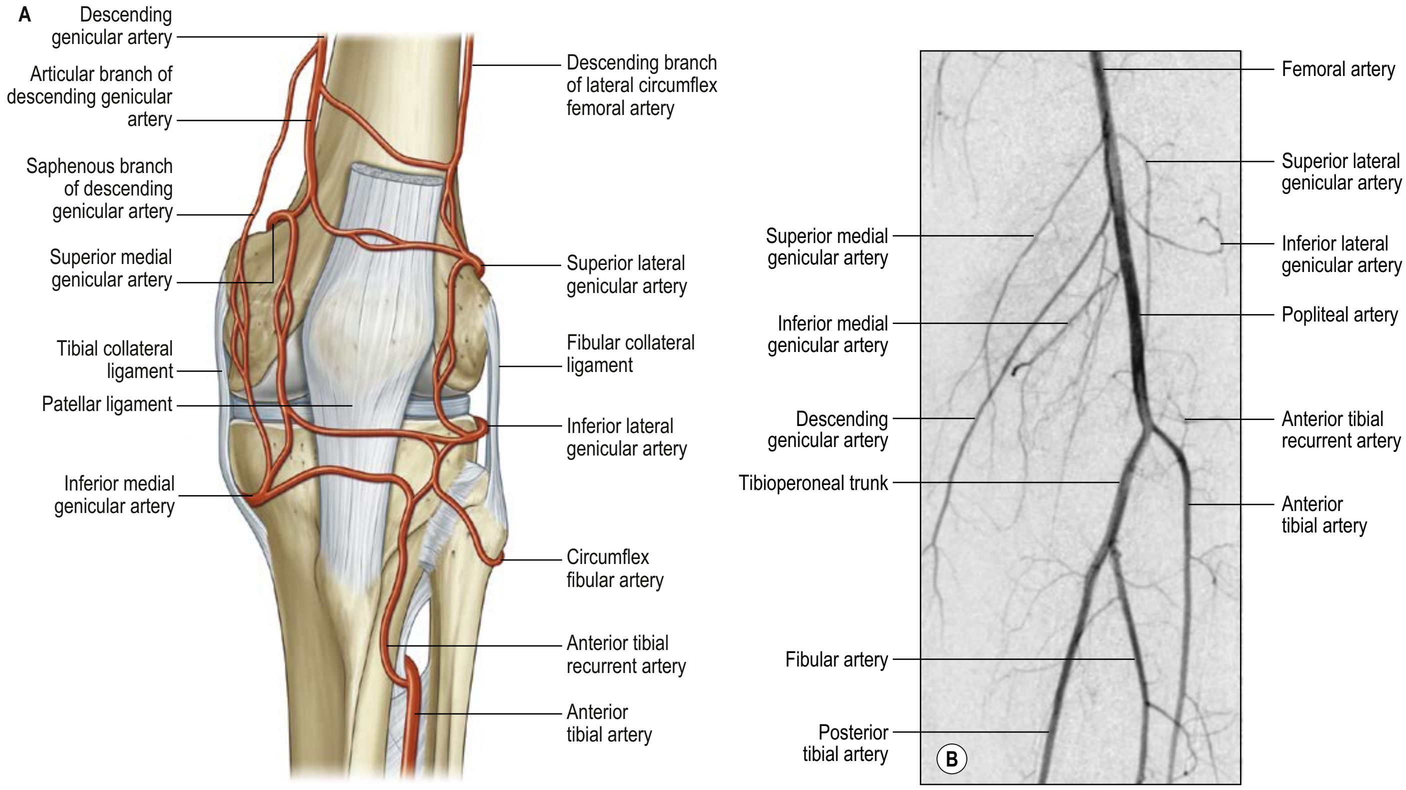
A
Descending genicular artery
Articular branch of descending genicular artery
Saphenous branch of descending genicular artery
Superior medial genicular artery
Tibial collateral ligament
Patellar ligament
Inferior medial genicular artery
Descending branch of lateral circumflex femoral artery
Superior lateral genicular artery
Fibular collateral ligament
Inferior lateral genicular artery
Circumflex fibular artery
Anterior tibial recurrent artery
Anterior tibial artery
Superior medial genicular artery
Inferior medial genicular artery
Descending genicular artery
Tibioperoneal trunk
Fibular artery
Posterior tibial artery
B
Femoral artery
Superior lateral genicular artery
Inferior lateral genicular artery
Popliteal artery
Anterior tibial recurrent artery
Anterior tibial artery

Fig. 78.1 **A**, The arterial anastomoses around the left knee joint, anterior aspect. **B**, Frontal digital subtraction angiogram of the left distal femoral artery to the trifurcation.

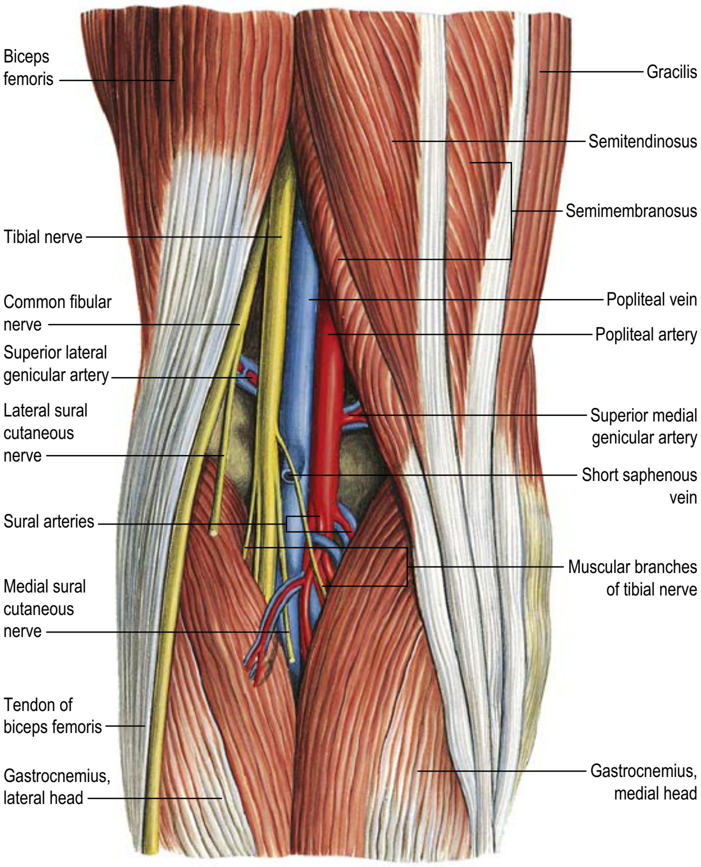
Biceps femoris
Tibial nerve
Common fibular nerve
Superior lateral genicular artery
Lateral sural cutaneous nerve
Sural arteries
Medial sural cutaneous nerve
Tendon of biceps femoris
Gastrocnemius, lateral head
Gracilis
Semitendinosus
Semimembranosus
Popliteal vein
Popliteal artery
Superior medial genicular artery
Short saphenous vein
Muscular branches of tibial nerve
Gastrocnemius, medial head

Fig. 78.2 The left popliteal fossa. (With permission from Waschke J, Paulsen F (eds) Sobotta Atlas of Human Anatomy, 15th ed. Elsevier, Urban & Fischer. Copyright 2013.)

sides of the leg accompany the short saphenous vein and pierce the deep fascia to drain into the popliteal nodes.

Innervation

Leg

The skin of the leg is supplied by branches of the saphenous, posterior femoral cutaneous, common fibular and tibial nerves (see p. 1391 and Figs 76.11–76.12, 76.20–76.21).

Infrapatellar branch of the saphenous nerve

The infrapatellar branch of the saphenous nerve reaches the anterior aspect of the knee from the medial side. It is invariably divided in medial surgical approaches to the knee, which accounts for the numbness that inevitably occurs following such procedures. A painful neuroma may form if the nerve is partially sectioned, e.g. by the incision for an arthroscopy portal or a small medial arthrotomy. The position of the nerve relative to the line of the joint is variable. In most cases, it crosses just below the joint line, passing over the patellar ligament at its insertion on to the tibia. For further details, see Tennant et al (1998).

Peripatellar plexus

Proximal to the knee, the infrapatellar branch of the saphenous nerve connects with branches of the medial and intermediate femoral cutaneous nerves, and lateral femoral cutaneous nerve. Distal to the knee, it connects with other branches of the saphenous nerve. This fine, subcutaneous network of communicating nerve fibres over and around the patella is termed the peripatellar plexus.

Soft tissues

Popliteal fossa

The popliteal fossa (Figs 78.2–78.3) is a diamond-shaped region posterior to the knee, bordered by muscles in the posterior compartment of the thigh and leg. The boundaries are biceps femoris proximolaterally; semimembranosus and the overlying semitendinosus proximomedially; the lateral head of gastrocnemius with the underlying plantaris distolaterally; and the medial head of gastrocnemius distomedially. The anterior boundary (or floor) of the fossa is formed, in proximodistal sequence, by the popliteal surface of the femur, the oblique popliteal ligament (overlying the posterior surface of the capsule of the knee joint), and the posterior aspect of the proximal tibia covered by popliteus and its fascia. The deep fascia (fascia musculorum) acts as the roof of the fossa and is continuous with the fascia lata proximally and with the deep fascia of the leg distally. It is a dense layer that is strongly reinforced by transverse fibres and is often perforated by the short saphenous vein and medial and lateral sural cutaneous nerves; these structures are useful landmarks in the direct posterior approach to the knee joint.

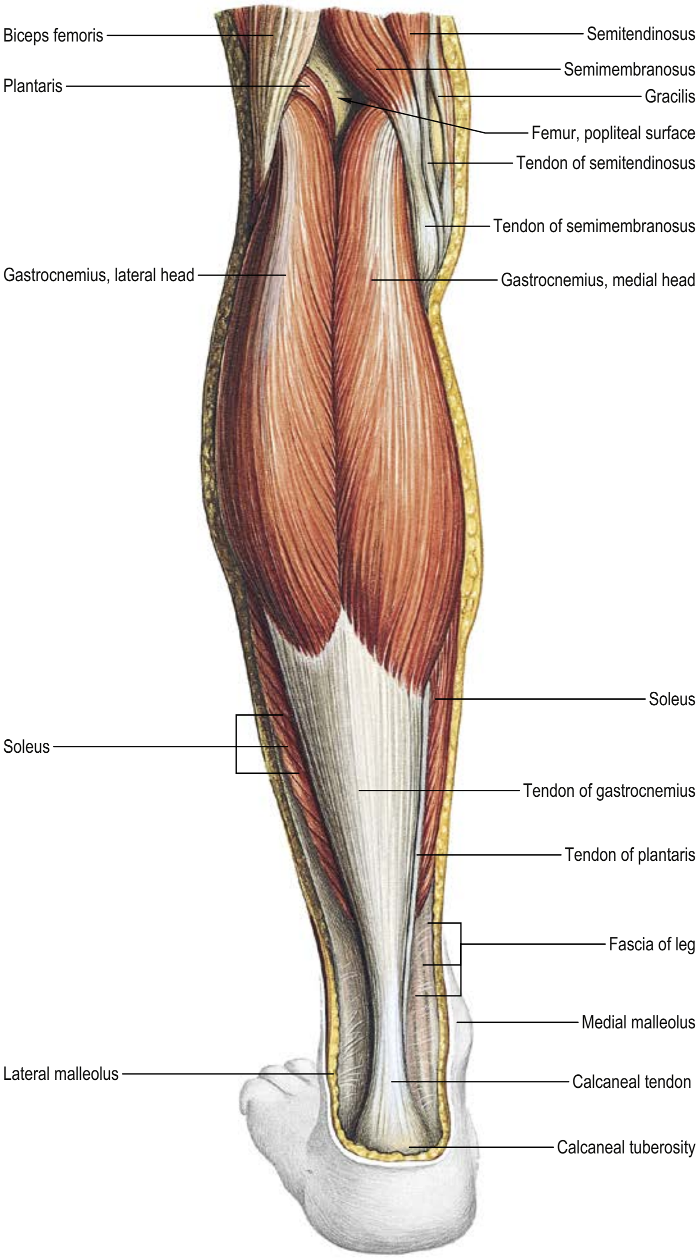
Biceps femoris
Plantaris
Gastrocnemius, lateral head
Soleus
Lateral malleolus
Semitendinosus
Semimembranosus
Gracilis
Femur, popliteal surface
Tendon of semitendinosus
Tendon of semimembranosus
Gastrocnemius, medial head
Soleus
Tendon of gastrocnemius
Tendon of plantaris
Fascia of leg
Medial malleolus
Calcaneal tendon
Calcaneal tuberosity

Fig. 78.3 Muscles of the calf, superficial view including the boundaries of the popliteal fossa. (With permission from Waschke J, Paulsen F (eds) Sobotta Atlas of Human Anatomy, 15th ed. Elsevier, Urban & Fischer. Copyright 2013.)

The popliteal fossa is approximately 2.5 cm wide. Distally, its contents are protected and hidden by the heads of gastrocnemius, which contact each other. The fossa contains the popliteal vessels (see Fig. 78.2; Fig. 78.4), tibial and common fibular nerves, short saphenous vein, medial and lateral sural cutaneous nerves, posterior femoral cutaneous nerve, articular branch of the obturator nerve, lymph nodes, fat and a variable number of bursae. The tibial nerve descends centrally immediately anterior to the deep fascia, crossing the vessels posteriorly from lateral to medial. The common fibular nerve descends laterally immediately medial to the tendon of biceps femoris. When the popliteal vessels enter the proximal region of the popliteal fossa, they maintain a side-by-side relationship, which shifts to an over–under relationship as they descend through the fossa and are held together by

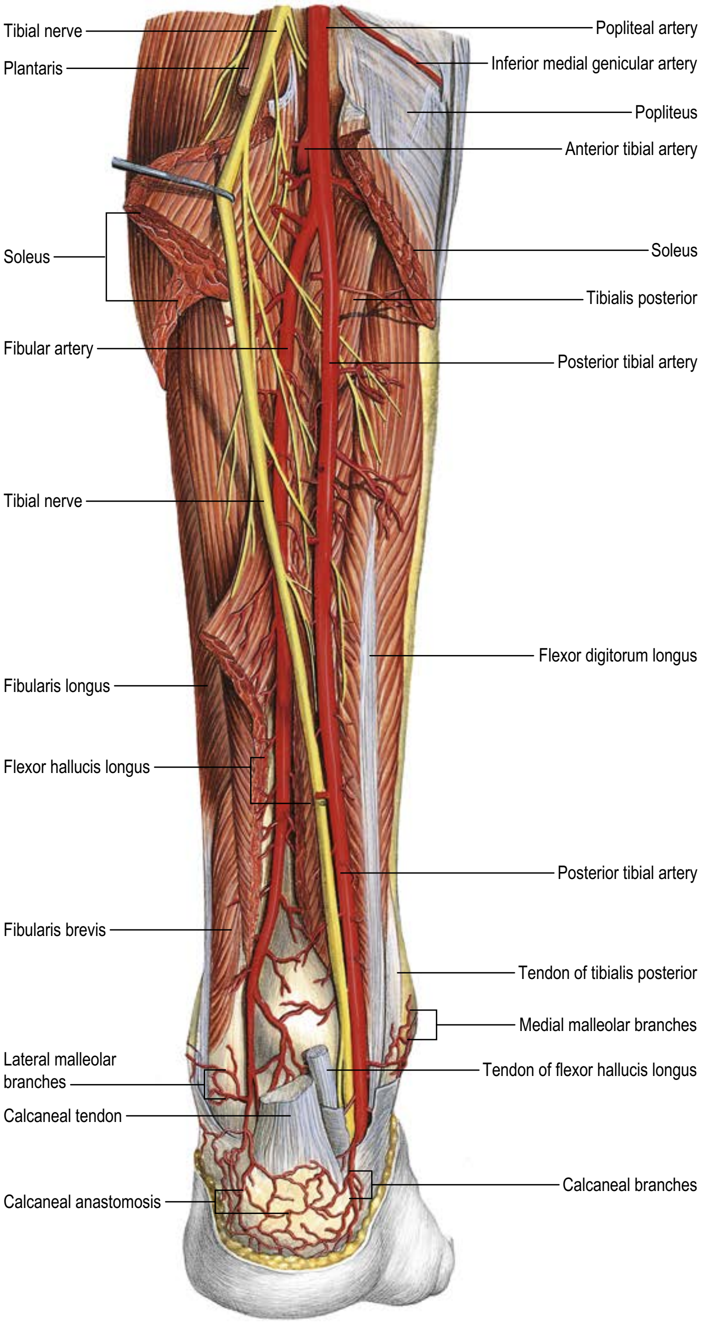
Tibial nerve
Plantaris
Soleus
Fibular artery
Tibial nerve
Fibularis longus
Flexor hallucis longus
Fibularis brevis
Lateral malleolar branches
Calcaneal tendon
Calcaneal anastomosis
Popliteal artery
Inferior medial genicular artery
Popliteus
Anterior tibial artery
Soleus
Tibialis posterior
Posterior tibial artery
Flexor digitorum longus
Posterior tibial artery
Tendon of tibialis posterior
Medial malleolar branches
Tendon of flexor hallucis longus
Calcaneal branches

Fig. 78.4 The left popliteal, posterior tibial and fibular arteries, posterior aspect. (With permission from Waschke J, Paulsen F (eds) Sobotta Atlas of Human Anatomy, 15th ed. Elsevier, Urban & Fischer. Copyright 2013.)

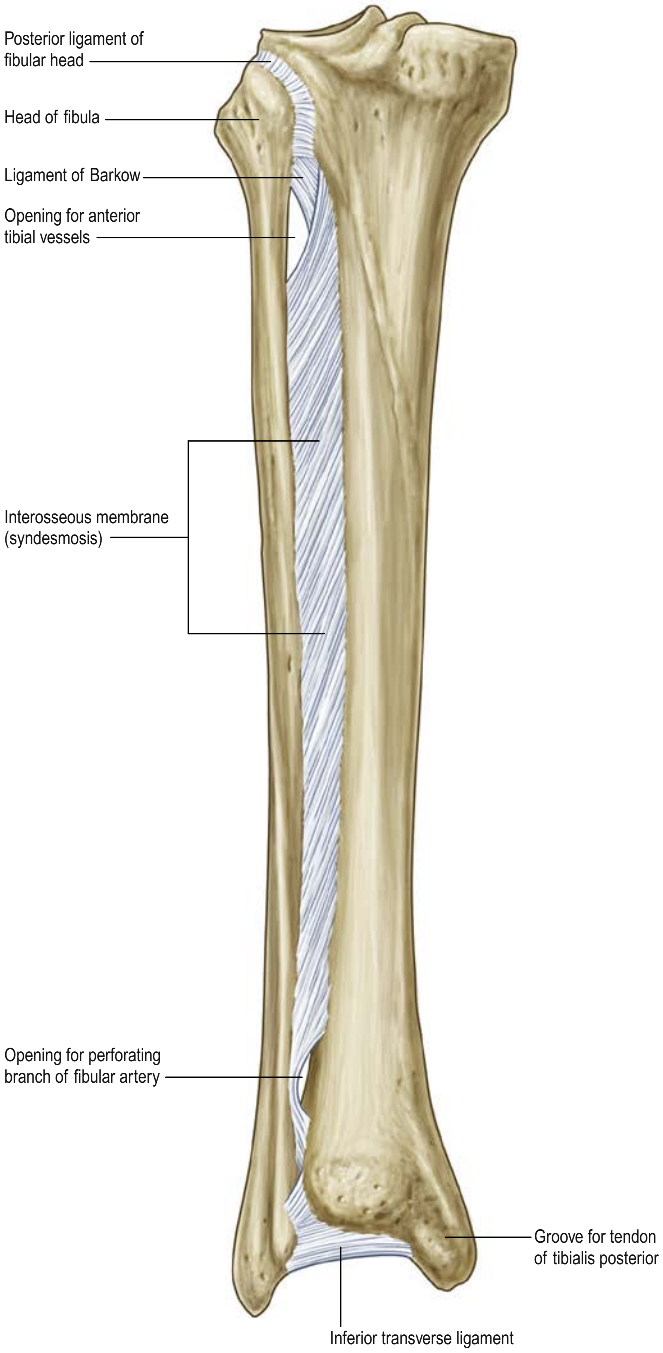
Posterior ligament of fibular head
Head of fibula
Ligament of Barkow
Opening for anterior tibial vessels
Interosseous membrane (syndesmosis)
Opening for perforating branch of fibular artery
Groove for tendon of tibialis posterior
Inferior transverse ligament

Fig. 78.5 The posterior aspect of the interosseous membrane. Note the contrasting direction of the fibre bundles around the vascular openings.

dense areolar tissue within the fossa. This may potentially compromise the popliteal artery in distal femoral fractures. The popliteal vein is generally located posterior to the artery. Proximally, the vein lies lateral to the artery, crossing to its medial side distally. At times, the popliteal vein may be duplicated, so that the artery lies between the veins, which are usually bridged by connecting channels. An articular branch from the obturator nerve descends along the artery to the knee. Six or seven popliteal nodes are embedded in the fat, one under the deep fascia near the termination of the short saphenous vein, one between the popliteal artery and knee joint, and the others intimate with the popliteal vessels.

Deep fascia

The deep fascia of the leg is continuous with the fascia lata and is attached around the knee to the patellar margin, the patellar ligament, the tuberosity and condyles of the tibia, and the head of the fibula. Posteriorly, it covers the popliteal fossa as the popliteal fascia. It receives lateral expansions from the tendon of biceps femoris and multiple medial expansions from the tendons of sartorius, gracilis, semitendinosus and semimembranosus. The deep fascia blends with the periosteum on the subcutaneous surface of the tibia and the subcutaneous surfaces of the fibular head and lateral malleolus, and is continuous below with the extensor and flexor retinacula. It is thick and dense in the proximal and anterior part of the leg, where fibres of tibialis anterior and extensor digitorum longus are attached to its deep surface, and is thinner posteriorly, where it covers gastrocnemius and soleus. On the lateral side, it is continuous with the anterior and posterior intermuscular septa of the leg, which are attached to the anterior and posterior borders of the fibula, respectively.

Transverse intermuscular septum

The transverse intermuscular septum of the leg is a fibrous stratum between the superficial and deep muscles of the calf. It extends transversely from the medial margin of the tibia to the posterior border of the fibula. Proximally, where it is thick and dense, it is attached to the soleal ridge of the tibia and to the fibula, inferomedial to the fibular attachment of soleus. Between these bony attachments, it is continuous with the fascia covering popliteus, which is, in effect, an expansion from the tendon of semimembranosus. At intermediate levels it is thin but distally, where it covers the tendons behind the malleoli, it is thick and continuous with the flexor and superior fibular retinacula.

Interosseous membrane

The interosseous membrane connects the interosseous borders of the tibia and fibula (Fig. 78.5). It is interposed between the anterior and posterior groups of crural muscles; some members of each group are

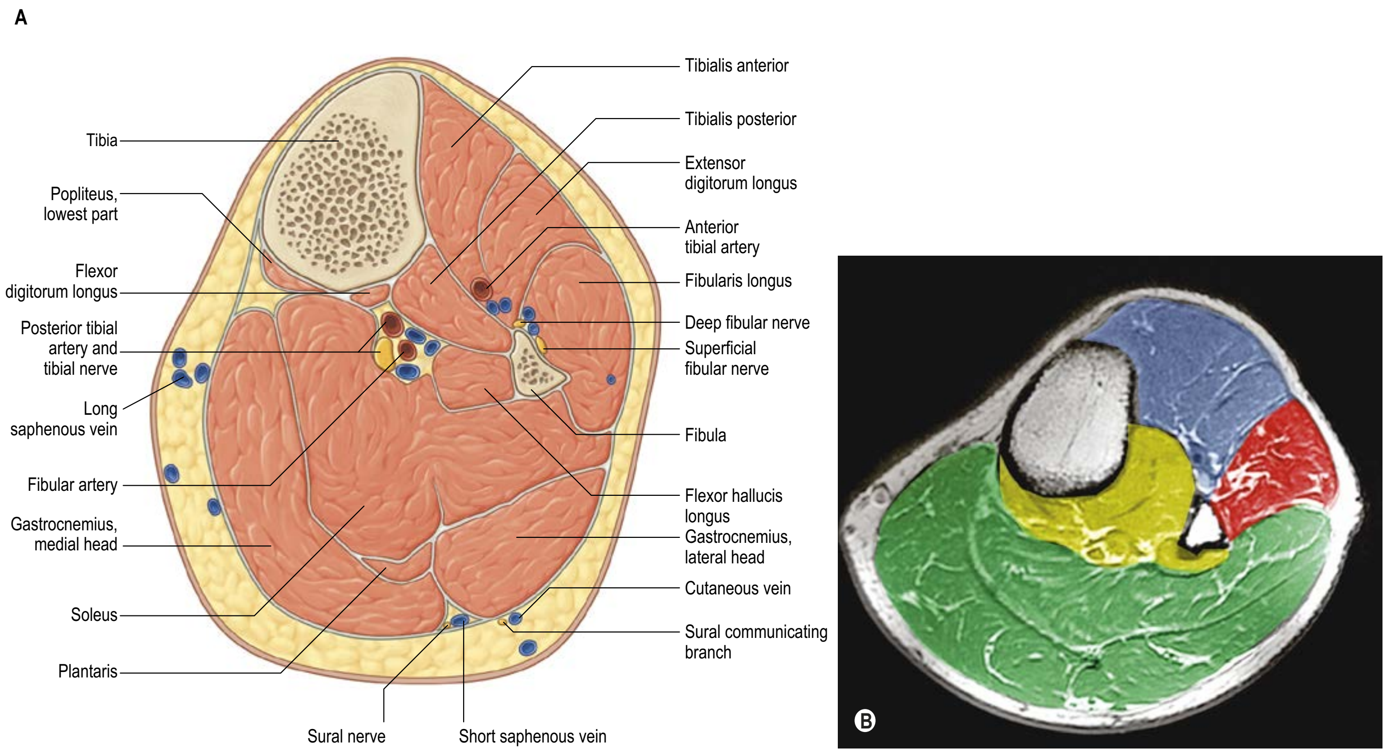

Fig. 78.6 **A**, A transverse (axial) section through the left leg, approximately 10 cm distal to the knee joint. **B,** A colour-coded axial magnetic resonance image (MRI) of the leg. Key: anterior (blue), lateral (red) and posterior (deep part yellow and superficial part green) compartments of the leg. (C, *continued online*)

attached to the corresponding surface of the interosseous membrane. The anterior tibial artery passes forwards through a large oval opening near the proximal end of the membrane, and the perforating branch of the fibular artery pierces it distally. An associated ligament (ligament of Barkow), in the same plane as the interosseous membrane, may be found uniting the proximal tibiofibular joint; when present, it forms the upper half of this oval opening (see Fig. 78.5) (Tubbs et al 2009). Its fibres are predominantly oblique and most descend laterally; those that descend medially include a bundle at the proximal border of the proximal opening. The thickness of the interosseous membrane differs between its thin centre and thick tibial and fibular borders. The membrane is continuous distally with the interosseous ligament of the distal tibiofibular joint.

Retinacula

The retinacula at the ankle joint are described in Chapter 79.

Compartments of the leg

The compartments of the leg are particularly well defined and are the most common sites at which osteofascial compartment syndromes occur. The three main compartments are anterior (extensor), lateral (fibular) and posterior (flexor) (**Fig. 78.6**). The posterior compartment is divided into deep and superficial parts by the transverse intermuscular septum. These compartments are enclosed by the unyielding deep fascia and separated from each other by the bones of the leg and interosseous membrane, and by the anterior and posterior intermuscular septa that pass from the deep fascia to the fibula. The anterior compartment, the least expansile of the three, is bounded by the deep fascia, the interosseous surfaces of the tibia and fibula, the interosseous membrane and the anterior intermuscular septum. The lateral compartment lies between the anterior and posterior intermuscular septa, and is bordered laterally by the deep fascia and medially by the lateral surface of the fibula. The posterior compartment is bounded by the deep fascia, the posterior intermuscular septum, the fibula and tibia, and the interosseous membrane. Its relatively expansile superficial component is separated from the compacted deep component by the transverse intermuscular septum, reinforced by the deep aponeurosis of soleus. Knowledge of the compartmental anatomy of the leg is important in planning the treatment of compartment syndromes and for soft tissue tumour resections of the leg.

The nerve supply of the muscles in the compartments follows the 'one compartment – one nerve' principle: the deep fibular nerve supplies the anterior compartment, the superficial fibular nerve supplies the lateral compartment and the tibial nerve supplies the posterior compartment. Magnetic resonance imaging (MRI) is the best imaging modality for evaluating the soft tissues of the leg. Most of the muscle in the anterior compartment is supplied by the anterior tibial artery, with an additional contribution from the fibular artery to extensor hallucis longus. The muscles of the posterior compartment are supplied by the popliteal, posterior tibial and fibular arteries. The muscles of the lateral compartment are supplied by the anterior tibial and fibular arteries, and to a lesser extent proximally, by a branch from the popliteal artery.

Trauma and soft tissues of the leg

Available with the *Gray's Anatomy* e-book

BONES

The relevant bones are the femur (described in Chapter 77), tibia, fibula and patella.

Tibia

The tibia lies medial to the fibula and is exceeded in length only by the femur (**Figs 78.7–78.8**). The tibial shaft is triangular in section and has expanded ends; a strong medial malleolus projects distally from the smaller distal end. The anterior border of the shaft is sharp and curves medially towards the medial malleolus. Together with the medial and lateral borders, it defines the three surfaces of the bone. The exact shape and orientation of these surfaces show individual and racial variations. In children, the mean tibial length is greater in males than in females (Oeffinger et al 2010).

Proximal end

The expanded proximal end bears the weight transmitted through the femur. It consists of medial and lateral condyles, an intercondylar area and the tibial tuberosity.

Condyles The tibial condyles overhang the proximal part of the posterior surface of the shaft. Both condyles have articular facets on their superior surfaces, separated by an irregular, non-articular intercondylar area. The condyles are visible and palpable at the sides of the patellar ligament, the lateral being more prominent. In the passively flexed knee, the anterior margins of the condyles are palpable in depressions that flank the patellar ligament.

The relative paucity of soft tissue in the shin region and the subcutaneous position of the medial surface of the tibia means that even trivial soft tissue injury may lead to serious problems such as ulceration and osteomyelitis. In the elderly these soft tissues are often especially thin and unhealthy, reflecting the effects of ageing and venous stasis (see p. 1427). Tibial fractures are common in the young and, partly as a result of poor soft tissue coverage, they are often open injuries. Diminished blood supply to the bone, caused by traumatic stripping of attached soft tissues, and the risk of contamination add greatly to the risk of non-union and infection of the fracture. Healing of fractures at the junction of the middle and lower thirds of the tibia is compromised by the relatively poor blood supply to this region. Injury to the leg may result in elevated pressures of one or more compartments (so-called compartment syndrome); this clinical scenario is manifested by the 'six Ps': pain, paraesthesiae, pallor, paralysis, pulselessness and poikilothermia (differing temperatures in the affected and unaffected limbs).

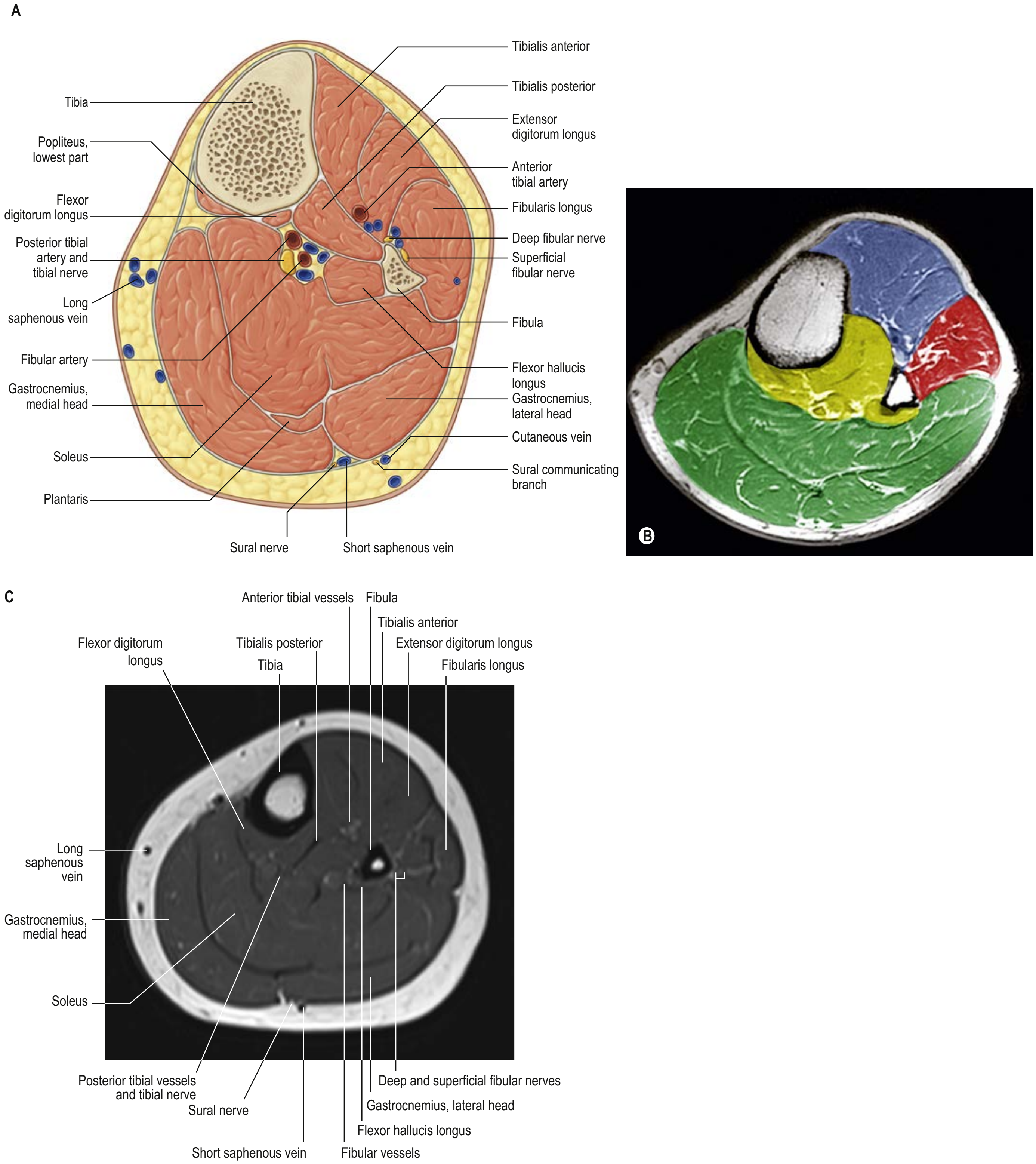
A
Tibialis anterior
Tibialis posterior
Tibia
Extensor digitorum longus
Popliteus, lowest part
Anterior tibial artery
Flexor digitorum longus
Fibularis longus
Deep fibular nerve
Posterior tibial artery and tibial nerve
Superficial fibular nerve
Long saphenous vein
Fibula
Fibular artery
Flexor hallucis longus
Gastrocnemius, medial head
Gastrocnemius, lateral head
Cutaneous vein
Soleus
Sural communicating branch
Plantaris
Sural nerve
Short saphenous vein
B
C
Anterior tibial vessels
Fibula
Tibialis anterior
Flexor digitorum longus
Tibialis posterior
Extensor digitorum longus
Tibia
Fibularis longus
Long saphenous vein
Gastrocnemius, medial head
Soleus
Posterior tibial vessels and tibial nerve
Deep and superficial fibular nerves
Sural nerve
Gastrocnemius, lateral head
Flexor hallucis longus
Short saphenous vein
Fibular vessels

Fig. 78.6 **A**, A transverse (axial) section through the left leg, approximately 10 cm distal to the knee joint. **B,** A colour-coded axial magnetic resonance image (MRI) of the leg. Key: anterior (blue), lateral (red) and posterior (deep part yellow and superficial part green) compartments of the leg. **C**, An axial T2-weighted MRI of the upper leg.

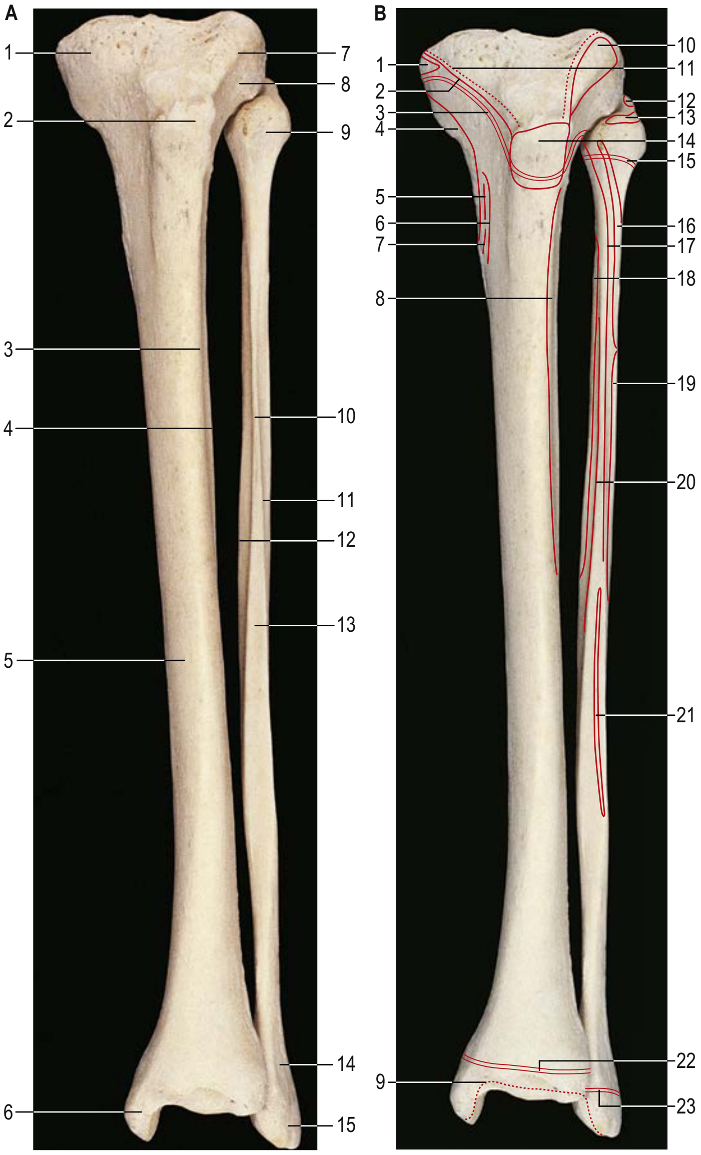

Fig. 78.7 **A**, The left tibia and fibula showing sites of muscular and capsular attachment and epiphysial lines, anterior aspect. Key: 1, medial condyle; 2, tibial tuberosity; 3, anterior border of tibia; 4, interosseous border of tibia; 5, medial surface; 6, medial malleolus; 7, Gerdy's tubercle; 8, lateral condyle; 9, head of fibula; 10, interosseous border of fibula; 11, anterior border of fibula; 12, medial crest; 13, anterior surface; 14, subcutaneous area; 15, lateral malleolus. **B**, Muscle attachments. Key: 1, semimembranosus; 2, medial patellar retinaculum; 3, epiphysial line (growth plate); 4, tibial collateral ligament; 5, gracilis; 6, sartorius; 7, semitendinosus; 8, tibialis anterior; 9, attachment site of ankle joint capsule; 10, iliotibial tract; 11, attachment site of knee joint capsule; 12, fibular collateral ligament; 13, biceps femoris; 14, patellar ligament; 15, epiphysial line (growth plate); 16, fibularis longus; 17, extensor digitorum longus; 18, tibialis posterior; 19, fibularis brevis; 20, extensor hallucis longus; 21, fibularis tertius; 22, epiphysial line (growth plate); 23, epiphysial line (growth plate).

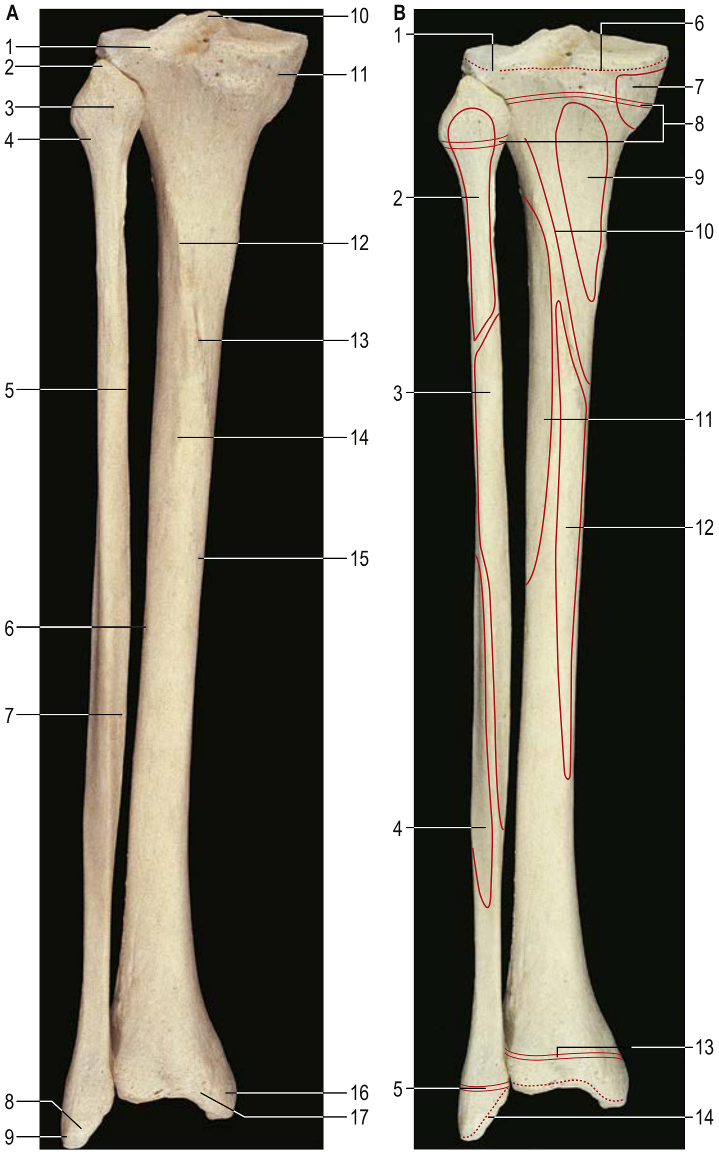

Fig. 78.8 **A**, The left tibia and fibula showing sites of muscular and capsular attachment and epiphysial lines, posterior aspect. Key: 1, groove for tendon of popliteus; 2, apex of head of fibula; 3, head of fibula; 4, neck of fibula; 5, medial crest; 6, interosseous border of tibia; 7, posterior border; 8, groove for fibular tendons; 9, lateral malleolus; 10, intercondylar eminence; 11, groove for semimembranosus attachment; 12, soleal line; 13, nutrient foramen; 14, vertical line; 15, medial border of tibia; 16, medial malleolus; 17, groove for tibialis posterior tendon. **B**, Muscle attachments. Key: 1, gap in capsule for popliteus tendon; 2, soleus; 3, flexor hallucis longus; 4, fibularis brevis; 5, epiphysial line (growth plate); 6, attachment site of knee joint capsule; 7, semimembranosus; 8, epiphysial lines (growth plates); 9, popliteus; 10, soleus; 11, tibialis posterior; 12, flexor digitorum longus; 13, epiphysial line (growth plate); 14, attachment site of ankle joint capsule.

The fibular articular facet on the posteroinferior aspect of the lateral condyle faces distally and posterolaterally. The angle of inclination of the superior tibiofibular joint varies between individuals, and may be horizontal or oblique. Superomedial to it, the condyle is grooved on its posterolateral aspect by the tendon of popliteus; a synovial recess intervenes between the tendon and bone. The anterolateral aspect of the condyle is separated from the lateral surface of the shaft by a sharp margin for the attachment of deep fascia. The distal attachment of the iliotibial tract makes a flat and usually definite marking (Gerdy's tubercle) on its anterior aspect. This tubercle, which is triangular and facet-like, is usually palpable through the skin.

The anterior condylar surfaces are continuous with a large triangular area whose apex is distal and formed by the tibial tuberosity. The lateral edge is a sharp ridge between the lateral condyle and lateral surface of the shaft.

Tibial tuberosity The tibial tuberosity is the truncated apex of a triangular area where the anterior condylar surfaces merge. It projects only a little, and is divided into distal rough and proximal smooth regions. The distal region is palpable and is separated from skin by the subcutaneous infrapatellar bursa. A line across the tibial tuberosity marks the distal limit of the proximal tibial growth plate (see Fig. 78.7). The patellar ligament is attached to the smooth bone proximal to this, its superficial fibres reaching a rough area distal to the line. The deep infrapatellar bursa and fibroadipose tissue intervene between the bone and tendon proximal to its site of attachment. The latter may be marked distally by a somewhat oblique ridge, on to which the lateral fibres of the patellar ligament are inserted more distally than the medial fibres. This knowledge is necessary for avoiding damage to this structure when performing an osteotomy just above the tibial tuberosity in a lateral to medial direction. In habitual squatters, a vertical groove on the anterior surface of the lateral condyle is occupied by the lateral edge of the patellar ligament in full flexion of the knee.

Shaft

The shaft is triangular in section and has (antero)medial, lateral and posterior surfaces separated by anterior, lateral (interosseous) and medial borders. It is narrowest at the junction of the middle and distal thirds, and expands gradually towards both ends. The anterior border descends from the tuberosity to the anterior margin of the medial malleolus and is subcutaneous throughout. Except in its distal quarter, where it is indistinct, it is a sharp crest. It is slightly sinuous, and turns medially in the distal quarter. The interosseous border begins distal and anterior to the fibular articular facet and descends to the anterior border of the fibular notch; it is indistinct proximally. The interosseous membrane is attached to most of its length, connecting the tibia to the fibula. The medial border descends from the anterior end of the groove on the medial condyle to the posterior margin of the medial malleolus. Its proximal and distal quarters are ill defined but its central region is sharp and distinct.

The anteromedial surface, between the anterior and medial borders, is broad, smooth and almost entirely subcutaneous. The lateral surface, between the anterior and interosseous borders, is also broad and smooth. It faces laterally in its proximal three-quarters and is transversely concave. Its distal quarter bends to face anterolaterally, on account of the medial deviation of the anterior and distal interosseous borders. This part of the surface is somewhat convex. The posterior surface, between the interosseous and medial borders, is widest above, where it is crossed distally and medially by an oblique, rough soleal line. A faint vertical line descends from the centre of the soleal line for a short distance before becoming indistinct. A large vascular groove adjoins the end of the line and descends distally into a nutrient foramen. Deep fascia and, proximal to the medial malleolus, the medial end of the superior extensor retinaculum are attached to the anterior border. Posterior fibres of the tibial collateral ligament and slips of semimembranosus and the popliteal fascia are attached to the medial border proximal to the soleal line, and some fibres of soleus and the fascia covering the deep calf muscles are attached distal to the line. The distal medial border runs into the medial lip of a groove for the tendon of tibialis posterior. The interosseous membrane is attached to the lateral border, except at either end of this border. It is indistinct proximally where a large gap in the membrane transmits the anterior tibial vessels. Distally, the border is continuous with the anterior margin of the fibular notch, to which the anterior tibiofibular ligament is attached.

The anterior part of the tibial collateral ligament is attached to an area approximately 5 cm long and 1 cm wide near the medial border of the proximal medial surface. The remaining medial surface is subcutaneous and crossed obliquely by the long saphenous vein. Tibialis anterior is attached to the proximal two-thirds of the lateral surface. The distal third, devoid of attachments, is crossed in mediolateral order by the tendons of tibialis anterior (lying just lateral to the anterior border), extensor hallucis longus, the anterior tibial vessels and deep fibular nerve, extensor digitorum longus and fibularis tertius.

On the posterior surface, popliteus is attached to a triangular area proximal to the soleal line, except near the fibular articular facet. The popliteal aponeurosis, soleus and its fascia, and the transverse intermuscular septum are all attached to the soleal line; the proximal end of the line does not reach the interosseous border, and is marked by a tubercle for the medial end of the tendinous arch of soleus. Lateral to the tubercle, the posterior tibial vessels and tibial nerve descend on tibialis posterior. Distal to the soleal line, a vertical line separates the attachments of flexor digitorum longus and tibialis posterior. Nothing is attached to the distal quarter of this surface, but the area is crossed medially by the tendon of tibialis posterior travelling to a groove on the posterior aspect of the medial malleolus. Flexor digitorum longus crosses obliquely behind tibialis posterior; the posterior tibial vessels and nerve and flexor hallucis longus contact only the lateral part of the distal posterior surface.

Distal end

The slightly expanded distal end of the tibia has anterior, medial, posterior, lateral and distal surfaces. It projects inferomedially as the medial malleolus. The distal end of the tibia, when compared to the proximal end, is laterally rotated (tibial torsion). The torsion begins to develop *in utero* and progresses throughout childhood, mainly during the first four years of life (Kristiansen et al 2001), until skeletal maturity is attained. Some of the femoral neck anteversion seen in the newborn may persist in adult females: this causes the femoral shaft and knee to be medially rotated, which may lead the tibia to develop a compensatory external torsion to counteract the tendency of the feet to turn inwards. Tibial torsion is approximately 30° in Caucasian and Asian populations, but is significantly greater in Africans (Eckhoff et al 1994).

The smooth anterior surface projects beyond the distal surface, from which it is separated by a narrow groove. The capsule of the ankle joint is attached to an anterior groove near the articular surface. The medial surface is smooth and continuous above and below with the medial surfaces of the shaft and medial malleolus, respectively; it is subcutaneous and visible. The posterior surface is smooth except where it is crossed near its medial end by a nearly vertical but slightly oblique groove, which is usually conspicuous and extends to the posterior surface of the malleolus. The groove is adapted to the tendon of tibialis posterior, which usually separates the tendon of flexor digitorum longus from the bone. More laterally, the posterior tibial vessels, tibial nerve and flexor hallucis longus contact this surface. The lateral surface is the triangular fibular notch; its anterior and posterior edges project and converge proximally to the interosseous border. The floor of the notch is roughened proximally by a substantial interosseous ligament but is smooth distally and is sometimes covered by articular cartilage. The anterior and posterior tibiofibular ligaments are attached to the corresponding edges of the notch. The distal surface articulates with the talus and is wider in front, concave sagittally and slightly convex transversely, i.e. saddle-shaped. Medially, it continues into the malleolar articular surface, which may extend into the groove that separates it from the anterior surface of the shaft. Such extensions, medial or lateral or both, are squatting facets, and they articulate with reciprocal talar facets in extreme dorsiflexion. These features have been used in the field of forensic medicine to identify the race of skeletal material.

Medial malleolus The short, thick medial malleolus has a smooth lateral surface with a crescentic facet that articulates with the medial surface of the talus. Its anterior aspect is rough and its posterior aspect features the continuation of the groove from the posterior surface of the tibial shaft for the tendon of tibialis posterior. The distal border is pointed anteriorly, posteriorly depressed and gives attachment to the deltoid ligament. The tip of the medial malleolus does not project as far distally as the tip of the lateral malleolus, the latter also being the more posteriorly located of the two malleoli. The capsule of the ankle joint is attached to the anterior surface of the medial malleolus, and the flexor retinaculum is attached to its prominent posterior border.

Muscle attachments

The patellar ligament is attached to the proximal half of the tibial tuberosity. Semimembranosus is attached to the distal edge of the groove on the posterior surface of the medial condyle; a tubercle at the lateral end of the groove is the main attachment of the tendon of this muscle. Slips from the tendon of biceps femoris are attached to the lateral tibial condyle anteroproximal to the fibular articular facet (see Fig. 78.7B). Proximal fibres of extensor digitorum longus and (occasionally) fibularis longus are attached distal to this area. Slips of semimembranosus are attached to the medial border of the shaft posteriorly, proximal to the soleal line. Some fibres of soleus attach to the posteromedial surface distal to the line. Semimembranosus is attached to the medial surface proximally, near the medial border, behind the attachment of the anterior part of the tibial collateral ligament. Anterior to this area (in anteroposterior sequence) are the linear attachments of the tendons of sartorius, gracilis and semitendinosus; these rarely mark the bone. Tibialis anterior is attached to the proximal two-thirds of the lateral (extensor) surface. Popliteus is attached to the posterior surface in a triangular area proximal to the soleal line, except near the fibular articular facet (see Fig. 78.8B). Soleus and its associated fascia are attached to the soleal line itself. Flexor digitorum longus and tibialis posterior are attached to the posterior surface distal to the soleal line, medial and lateral, respectively, to the vertical line (see above).

Vascular supply

The proximal end of the tibia is supplied by metaphysial arteries from the genicular anastomosis. The nutrient foramen usually lies near the soleal line and transmits a branch of the posterior tibial artery; the nutrient vessel may also arise at the level of the popliteal bifurcation or as a branch from the anterior tibial artery. On entering the bone, the nutrient artery divides into ascending and descending branches. The periosteal supply to the shaft arises from the anterior tibial artery and from muscular branches. The distal metaphysis is supplied by branches from the arterial anastomosis around the ankle.

Innervation

The proximal and distal ends of the tibia are innervated by branches from the nerves that supply the knee joint and ankle joint, respectively. The periosteum of the shaft is supplied by branches from the nerves that innervate the muscles attached to the tibia.

Ossification

The tibia ossifies from three centres: one in the shaft and one in each epiphysis. Ossification (**Fig. 78.9**) begins in mid-shaft during stages 21–23 (50–58 days post fertilization). The proximal epiphysial centre is usually present at birth: at approximately 10 years, a thin anterior process from the centre descends to form the smooth part of the tibial tuberosity. A separate centre for the tuberosity may appear at about the

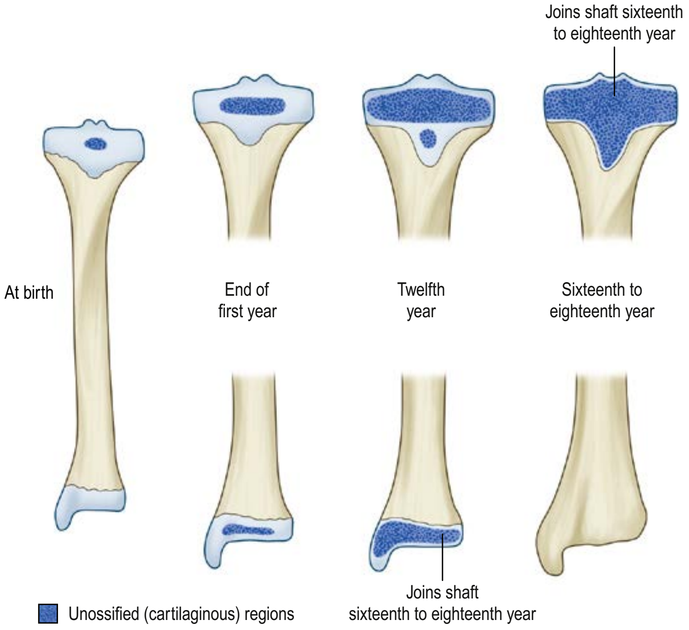
Joins shaft sixteenth to eighteenth year
At birth
End of first year
Twelfth year
Sixteenth to eighteenth year
Joins shaft sixteenth to eighteenth year
▨ Unossified (cartilaginous) regions

Fig. 78.9 Stages in the ossification of the tibia (not to scale).

twelfth year and soon fuses with the epiphysis. Distal strata of the epiphysial plate are composed of dense collagenous tissue in which the fibres are aligned with the patellar ligament. Exaggerated traction stresses may account for Osgood–Schlatter disease, in which fragmentation of the epiphysis of the tibial tuberosity occurs during adolescence and produces a painful swelling around it. Healing occurs once the growth plate fuses, leaving a bony protrusion. Prolonged periods of traction with the knee extended, both in children and adolescents, can lead to growth arrest of the anterior part of the proximal epiphysis, which results in bowing of the proximal tibia as the posterior tibia continues to grow. The proximal epiphysis fuses in the sixteenth year in females and the eighteenth in males. The distal epiphysial centre appears early in the first year and joins the shaft at about the fifteenth year in females and the seventeenth in males. The medial malleolus is an extension from the distal epiphysis and starts to ossify in the seventh year; it may have its own separate ossification centre. An accessory ossification centre sometimes appears at the tip of the medial malleolus, more often in females than in males. It fuses during the eighth year in females and the ninth year in males; it should not be confused with an os subtibiale, which is a rare accessory bone found on the posterior aspect of the medial malleolus. The average growth rate of the distal tibia decreases from a plateau of about 11 years of age in boys and 10 years of age in girls (Kärrholm et al 1984).

Fibula

The fibula (see Figs 78.7–78.8) is much more slender than the tibia and is not directly involved in transmission of weight. It has a proximal head, a narrow neck, a long shaft and a distal lateral malleolus. The shaft varies in form, being variably moulded by attached muscles; these variations may be confusing.

Head

The head of the fibula is irregular in shape and projects anteriorly, posteriorly and laterally. A round facet on its proximomedial aspect articulates with a corresponding facet on the inferolateral surface of the lateral tibial condyle. It faces proximally and anteromedially, and has an inclination that may vary among individuals from almost horizontal to an angle of up to 45°. A blunt apex projects proximally from the posterolateral aspect of the head and is often palpable approximately 2 cm distal to the knee joint. The fibular collateral ligament is attached in front of the apex, embraced by the main attachment of biceps femoris. The tibiofibular joint capsule is attached to the margins of the articular facet. The common fibular nerve crosses posterolateral to the neck and can be rolled against the underlying bone at this location.

Shaft

The shaft has three borders and surfaces, each associated with a particular group of muscles. The anterior border ascends proximally from the apex of an elongated triangular area that is continuous with the lateral malleolar surface, to the anterior aspect of the fibular head. The posterior border, continuous with the medial margin of the posterior groove on the lateral malleolus, is usually distinct distally but often rounded in its proximal half. The interosseous border is medial to the anterior border and somewhat posterior. Over the proximal two-thirds of the fibular shaft the two borders approach each other, with the surface between the two being narrowed to 1 mm or less.

The lateral surface, between the anterior and posterior borders and associated with the fibular muscles, faces laterally in its proximal three-quarters. The distal quarter spirals posterolaterally to become continuous with the posterior groove of the lateral malleolus. The anteromedial (sometimes simply termed anterior, or medial) surface, between the anterior and interosseous borders, usually faces anteromedially but often directly anteriorly. It is associated with the extensor muscles. Though wide distally, it narrows in its proximal half and may become a mere ridge. The posterior surface, between the interosseous and posterior borders, is the largest and is associated with the flexor muscles. Its proximal two-thirds are divided by a longitudinal medial crest, separated from the interosseous border by a grooved surface that is directed medially. The remaining surface faces posteriorly in its proximal half; its distal half curves on to the medial aspect. Distally, this area occupies the fibular notch of the tibia, which is roughened by the attachment of the principal interosseous tibiofibular ligament. The triangular area proximal to the lateral surface of the lateral malleolus is subcutaneous; muscles cover the rest of the shaft.

The anterior border is divided distally into two ridges that enclose a triangular subcutaneous surface. The anterior intermuscular septum is attached to its proximal three-quarters. The lateral end of the superior extensor retinaculum is attached distally on the anterior border of the triangular area and the lateral end of the superior fibular retinaculum is attached distally on the posterior margin of the triangular area. The interosseous border ends at the proximal limit of the rough area for the interosseous ligament. The interosseous membrane attached to this border does not reach the fibular head, which leaves a gap through which the anterior tibial vessels pass. The posterior border is proximally indistinct, and the posterior intermuscular septum is attached to all but its distal end. The medial crest is related to the fibular artery. A layer of deep fascia separating the tendon of tibialis posterior from flexor hallucis longus and flexor digitorum longus is attached to the medial crest.

Lateral malleolus

The distal end of the fibula forms the lateral malleolus, which projects distally and posteriorly (see Figs 78.7–78.8). Its lateral aspect is subcutaneous while its posterior aspect has a broad groove with a prominent lateral border. Its anterior aspect is rough, round and continuous with the tibial inferior border. The medial surface has a triangular articular facet, vertically convex, its apex distal, which articulates with the lateral talar surface. Behind this facet is a rough malleolar fossa pitted by vascular foramina. The posterior tibiofibular ligament and, more distally, the posterior talofibular ligament, are attached in the fossa. The anterior talofibular ligament is attached to the anterior surface of the lateral malleolus; the calcaneofibular ligament is attached to the notch anterior to its apex. The tendons of fibularis brevis and longus groove its posterior aspect; the latter is superficial and covered by the superior fibular retinaculum.

Muscle attachments

The main attachments of biceps femoris embrace the fibular collateral ligament in front of the apex of the fibular head. Extensor digitorum longus is attached to the head anteriorly, fibularis longus anterolaterally, and soleus posteriorly. Extensor digitorum longus, extensor hallucis longus and fibularis tertius are attached to the anteromedial (extensor) surface. Fibularis longus is attached to the whole width of the lateral (fibular) surface in its proximal third, but in its middle third only to its posterior part, behind fibularis brevis. The latter continues its attachment almost to the distal end of the shaft.

Muscle attachments to the posterior surface, which is divided longitudinally by the medial crest, are complex. Between the crest and interosseous border, the posterior surface is concave. Tibialis posterior is attached throughout the proximal three-quarters of this area, and an intramuscular tendon may ridge the bone obliquely. Soleus is attached between the crest and the posterior border on the proximal quarter of the posterior surface and its tendinous arch is attached to the surface proximally (see Fig. 78.8B). Flexor hallucis longus is attached distal to soleus on the posterior surface and almost reaches the distal end of the shaft.

Vascular supply

A little proximal to the midpoint of the posterior surface (14–19 cm from the apex), a distally directed nutrient foramen on the fibular shaft receives a branch of the fibular artery. An appreciation of the detailed anatomy of the fibular artery in relation to the fibula is fundamental to the raising of osteofasciocutaneous free flaps. Free vascularized diaphysial grafts may also be taken on a fibular arterial pedicle. The proximal and distal ends receive metaphysial vessels from the arterial anastomoses at the knee and ankle, respectively (Taylor and Razaboni 1994).

Innervation

The proximal and distal ends of the bone are supplied by branches of nerves that innervate the knee and superior tibiofibular joint, and the ankle and inferior tibiofibular joints, respectively. The periosteum of the shaft is supplied by branches from the nerves that innervate the muscles attached to the fibula.

Ossification

The fibula ossifies from three centres: one each for the shaft and the extremities. The process begins in the shaft during stage 23 (approximately 53–58 days post fertilization); in the distal end in the first year; and in the proximal end at about the third year in females and the fourth year in males. The distal epiphysis unites with the shaft at about the fifteenth year in females and the seventeenth year in males, whereas the proximal epiphysis does not unite until about the seventeenth year in females and the nineteenth year in males. A longitudinal radiographic study of children has shown that the proximal growth plate of the fibula contributes more to growth than the proximal growth plate of the tibia, their growth contributions being 61% and 57%, respectively (Pritchett and Bortel 1997).

Patella

The patella is the largest sesamoid bone in the body (Figs 78.10–78.11) and is embedded in the tendon of quadriceps femoris, lying anterior to the distal femur (femoral condyles). It is flat, distally tapered and proximally curved, and has anterior and articular surfaces, three borders and an apex, which is the distal end of the bone. Most surfaces and borders are palpable. With the knee in extension, the apex is positioned proximal to the line of the knee joint by 1–2 cm.

The subcutaneous, convex anterior surface is perforated by numerous nutrient vessels. It is longitudinally ridged, separated from the skin by the subcutaneous prepatellar bursa, and covered by an expansion from the tendon of quadriceps femoris, which blends distally with superficial fibres of the patellar ligament (inaccurately named because this structure is the continuation of the tendon of quadriceps femoris). The posterior surface has a proximal smooth, oval articular area, crossed by a smooth vertical ridge, which fits the intercondylar groove on the femoral patellar surface and divides the patellar articular area into medial and lateral facets; the lateral is usually larger. Each facet is divided by faint horizontal lines into approximately equal thirds. A seventh 'odd' facet is present as a narrow strip along the medial border of the patella; it contacts the medial femoral condyle in extreme knee flexion. Distal to the articular surface, the apex is roughened by the attachment of the patellar ligament. Proximal to this, the area between the roughened apex and the articular margin is covered by an infrapatellar fat pad. The patellar articular cartilage is the thickest in the body, reflecting the magnitude of the stresses to which it is subjected.

The thick superior border (surface) of the patella slopes anteroinferiorly. Its medial and lateral borders are thinner and converge distally; the expansions of the tendons of vasti medialis and lateralis (medial and lateral patellar retinacula, respectively) are attached to them. The lateral retinaculum receives contributions from the iliotibial tract. Ossification occasionally extends from the lateral margin of the patella into the tendon of vastus lateralis.

The shape of the patella can vary and certain configurations are associated with patellar instability. Not infrequently, a bipartite and, less commonly, a tripartite patella are seen on imaging (Oohashi et al 2010). The bone seems to be in separate parts, usually with a smaller superolateral fragment: this has long been attributed to the presence of a separate ossification centre but, in some cases, could represent failed union following either a stress fracture or a violent contraction of quadriceps femoris (e.g. landing on the feet after jumping from a substantial height) resulting in a traumatic fracture.

Structure The patella consists of more or less uniformly dense trabecular bone, covered by a thin compact lamina. Trabeculae beneath the anterior surface are parallel to the surface; elsewhere, they radiate from the articular surface into the substance of the bone.

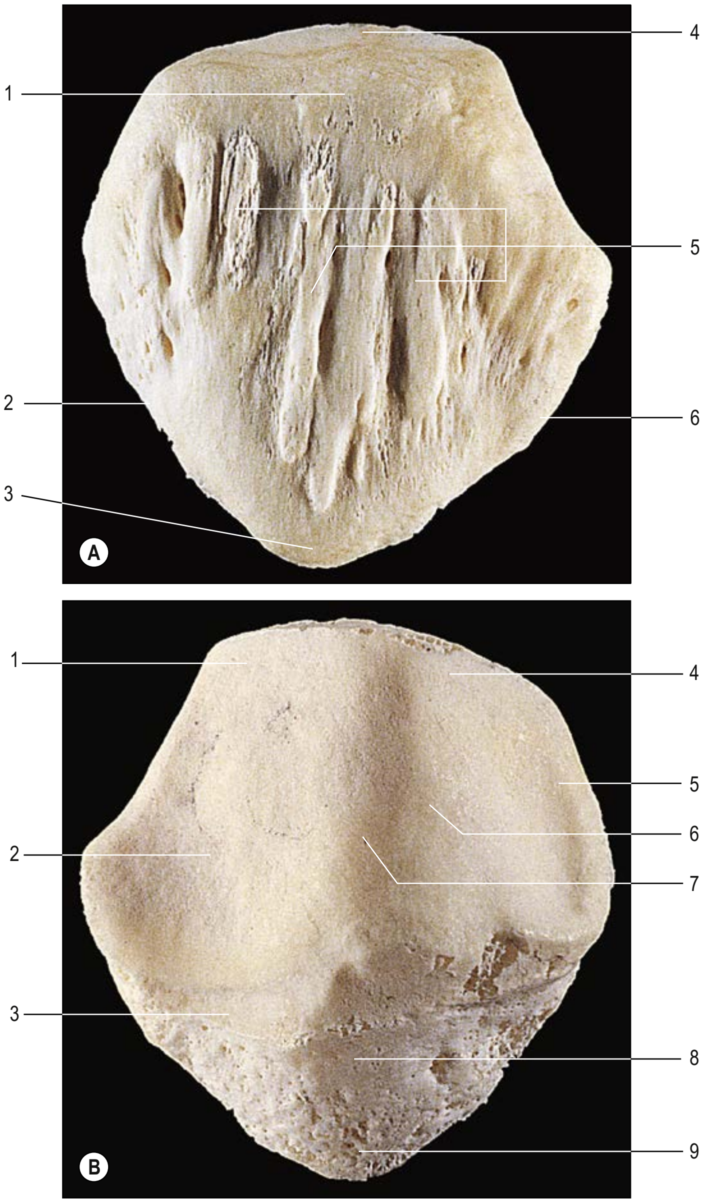

Fig. 78.10 The left patella, showing sites of muscular and soft tissue attachment and articular surfaces. **A**, Anterior aspect. Key: 1, area of attachment of rectus femoris; 2, medial border: attachment of medial retinaculum (expansion); 3, apex; 4, area of attachment of vastus intermedius; 5, markings of attachment of tendon of quadriceps femoris; 6, lateral border, for attachment of lateral retinaculum (expansion). **B**, Articular (posterior) surface. Key: 1, upper lateral facet: in contact with femur in flexion of the knee; 2, lower lateral facet: in contact with femur in extension of the knee; 3, area overlain by edge of circumferential fat pad; 4, upper medial facet: in contact with femur in flexion of the knee; 5, medial vertical ('odd') facet: in contact with femur in extreme flexion of the knee; 6, lower medial facet: in contact with femur in extension of the knee; 7, ridge; 8, area covered by infrapatellar fat pad; 9, area for attachment of patellar ligament.

Muscle attachments Quadriceps femoris is attached to the superior surface, except near its posterior margin; the attachment extends distally on to the anterior surface. The attachment for rectus femoris is anteroinferior to that for vastus intermedius. Rough markings can be traced in continuity around the periphery of the bone from the anterosuperior surface to the deep surface of the apex. Those at the lateral and medial borders represent the attachments of vasti lateralis and medialis, and those at the apex represent the attachment of the patellar ligament.

Vascular supply The arterial supply of the patella is derived from the genicular anastomosis, particularly from the genicular branches of the popliteal artery and from the anterior tibial recurrent artery. An anatomical study in children and fetuses confirmed that this network is already well developed in these age groups (Hamel et al 2012).

Ossification Several centres appear during the third to sixth years and these coalesce rapidly. Accessory marginal centres appear later and fuse with the central mass.

An os subfibulare is an occasional and separate entity and lies posterior to the tip of the fibula, whereas the distal fibular apophysis lies anteriorly. An os retinaculi is rarely encountered; if present, it overlies the bursa of the distal fibula within the fibular retinaculum.

Fibular dimelia is characterized by duplication of the fibula, tibial aplasia and partial duplication of the foot with pre-axial mirror polydactyly, and may be associated with ulnar dimelia and calcaneal duplication. It resembles duplication of the zone of polarizing activity that defines the postaxial border, but along the preaxial limb border of the limb (Ch. 19) (Bayram et al 1996, Ganey et al 2000, Verghese et al 2007).

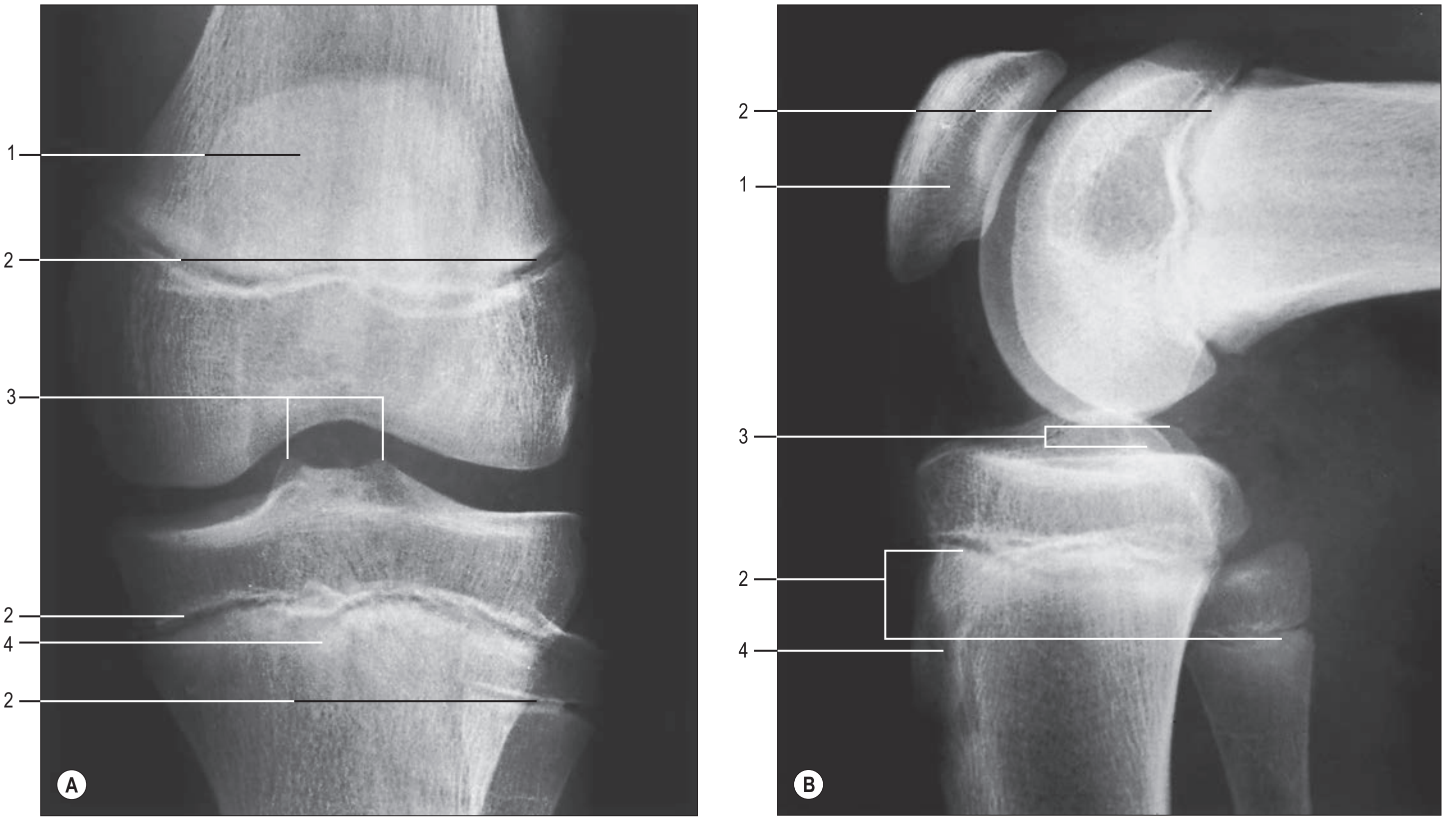

Fig. 78.11 Anteroposterior (**A**) and lateral (**B**) radiographs of the knee of a boy aged 14 years. Key: 1, patella; 2, cartilaginous growth plates; 3, intercondylar eminence; 4, prolongation of proximal tibial epiphysis and growth plate forming the tibial tuberosity.

JOINTS

Superior tibiofibular joint

The superior (proximal) tibiofibular joint is a synovial joint (plane variety) between the lateral tibial condyle and head of the fibula.

Articulating surfaces The articulating surfaces vary in size, form and inclination. The joint line may be transverse or oblique (in the latter case, the joint surfaces are inclined at an angle of greater than 20°). The fibular facet is usually elliptical or circular, and almost flat or slightly grooved. The surfaces are covered with hyaline cartilage. The volume of articular cartilage peaks at Tanner stage 2; boys gain articular cartilage faster than girls. The rate of cartilaginous volume development is +233 μl/year for the patella, +350 μl/year for the medial tibial compartment and +256 μl/year for the lateral tibial compartment (Jones et al 2003).

Fibrous capsule The capsule is attached to the margins of the articular surfaces of the tibia and fibula, and is thickened anteriorly and posteriorly.

Ligaments The ligaments of the superior tibiofibular joint are not entirely separate from the capsule. The anterior ligament is made up of two or three flat bands, which pass obliquely up from the fibular head to the front of the lateral tibial condyle in close relation to the tendon of biceps femoris. The posterior ligament is a thick band that ascends obliquely between the posterior aspect of the fibular head and the lateral tibial condyle, covered by the popliteal tendon.

Synovial membrane The synovial membrane of the superior tibiofibular joint is occasionally continuous with that of the knee joint via the subpopliteal recess.

Vascular supply and lymphatic drainage The superior tibiofibular joint receives an arterial supply from the anterior and posterior tibial recurrent branches of the anterior tibial artery. Lymphatics follow the arteries and drain to the popliteal nodes.

Innervation The superior tibiofibular joint is innervated by branches from the deep fibular nerve and from the nerve to popliteus.

Factors maintaining stability Stability of the superior tibiofibular joint is maintained by the fibrous capsule and the anterior and posterior ligaments, assisted by the biceps femoris tendon and the interosseous membrane of the leg.

Movements Very little movement other than limited gliding takes place at the superior tibiofibular joint. Some movement must occur in conjunction with movement at the inferior tibiofibular joint; however, surgical fusion (arthrodesis) of the superior tibiofibular joint seems to have no effect on movements of the ankle joint.

Relations The common fibular nerve runs posterior to the head of the fibula, medial to the tendon of biceps femoris, which is closely associated with the anterior capsule. The anterior and posterior tibial branches of the popliteal artery, and the fibular artery are all vulnerable inferomedial to the joint.

Patellofemoral joint

The patellofemoral joint is a synovial joint and is part of the knee joint.

Articulating surfaces The articular surface of the patella is adapted to that of the femur. The latter extends on to the anterior surfaces of both femoral condyles like an inverted U. Since the whole area is concave transversely and convex in the sagittal plane, it is an asymmetric sellar surface. The 'odd' facet on the articular surface of the patella contacts the anterolateral aspect of the medial femoral condyle in full flexion, when the highest lateral patellar facet contacts the anterior part of the lateral femoral condyle. As the knee extends, the middle patellar facets contact the lower half of the femoral surface; in full extension, only the lowest patellar facets are in contact with the femur. In summary, on flexion, the patellofemoral contact point moves proximally and the contact area broadens to cope with the increasing stress that accompanies progressive knee flexion.

Fibrous capsule See page 1407.

Ligaments The patellar ligament is an essential component of the extensor mechanism of the knee. The key medial structures involved in

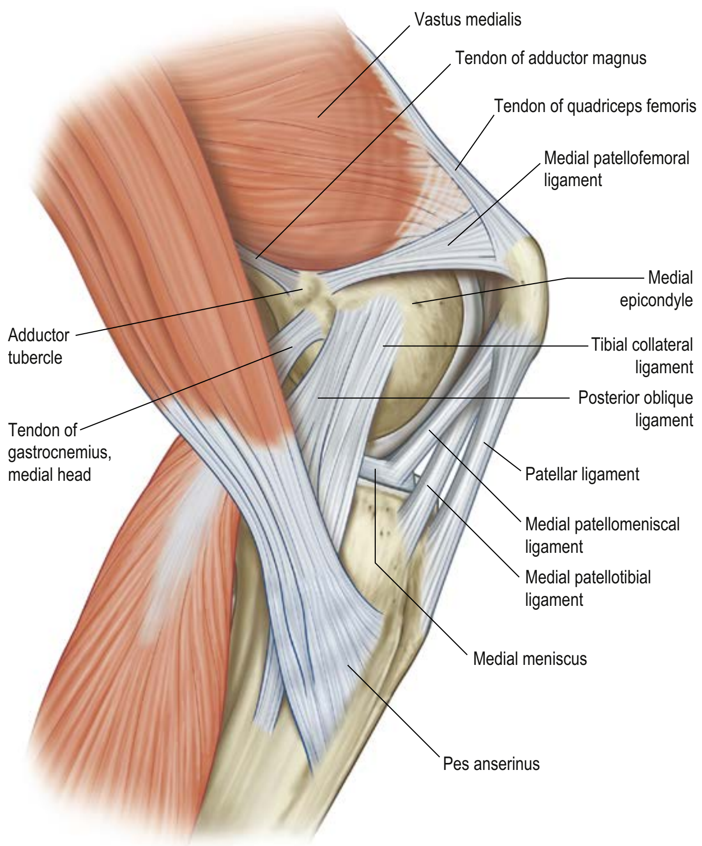
Vastus medialis
Tendon of adductor magnus
Tendon of quadriceps femoris
Medial patellofemoral ligament
Medial epicondyle
Adductor tubercle
Tibial collateral ligament
Posterior oblique ligament
Tendon of gastrocnemius, medial head
Patellar ligament
Medial patellomeniscal ligament
Medial patellotibial ligament
Medial meniscus
Pes anserinus

Fig. 78.12 Insertions of the medial patellar ligaments on the femur, patella tibia, and medial meniscus in a left knee (compare with Fig. 78.19).

patellofemoral joint stabilization are the medial patellofemoral, patellotibial and medial patellomeniscal ligaments (Fig. 78.12).

Patellar ligament sheath and patellar ligament The patellar ligament is a continuation of the tendon of quadriceps femoris and therefore is a misnomer. It continues from the patella to the tibial tuberosity (see Figs 77.44 and 77.46). It is strong, flat and 6–8 cm in length. Proximally, it is attached to the apex of the patella and adjoining margins, to roughened areas on the anterior surface and to a depression on the distal posterior patellar surface. Distally, it is attached to the superior smooth area of the tibial tuberosity. This attachment is oblique, and is more distal laterally. Its superficial fibres are continuous over the patella with the tendon of quadriceps femoris, the medial and lateral parts of which descend, flanking the patella, to the sides of the tibial tuberosity, where they merge with the fibrous capsule as the medial and lateral patellar retinacula. The patellar ligament is separated from the synovial membrane by a large infrapatellar fat pad and from the tibia by a bursa, and lies within its own well-defined sheath.

In the procedure of tibial osteotomy, the tibia is cut transversely just above the insertion of the patellar ligament. Failure to appreciate the obliquity of the tibial attachment of the tendon may lead to inadvertent division of the tendon during this procedure. The middle third of the patellar ligament may be harvested for surgical repair of a cruciate ligament.

Medial patellofemoral ligament The femoral attachment of the medial patellofemoral ligament is consistently anterior and distal to the adductor tubercle with soft tissue attachments to the tendon of adductor magnus. Its fibres course deep to vastus medialis obliquus to attach broadly to the proximal third of the superomedial aspect of the patella, with a long, thin attachment adjacent to the quadriceps tendon and superficial to the patellar articular cartilage and joint capsule.

Medial patellotibial and patellomeniscal ligaments The medial patellotibial ligament is a thin, single-layered structure (compared to the rounded, cord-like medial patellomeniscal ligament) located superficial and intimately adherent to the medial capsule. Both ligaments insert on the inferomedial patella; a portion of the patellar attachment lies deep to the patellar ligament but superficial to the patellar articular cartilage and deeper joint capsule. From its patellar attachment site, the medial patellotibial ligament passes inferomedially to the medial tibial tubercle of the anteromedial proximal tibia. The medial patellomeniscal ligament courses more horizontally than the medial patellotibial ligament and has a distinct attachment medial to the anterior horn of the medial meniscus (Kruckeberg et al 2018).

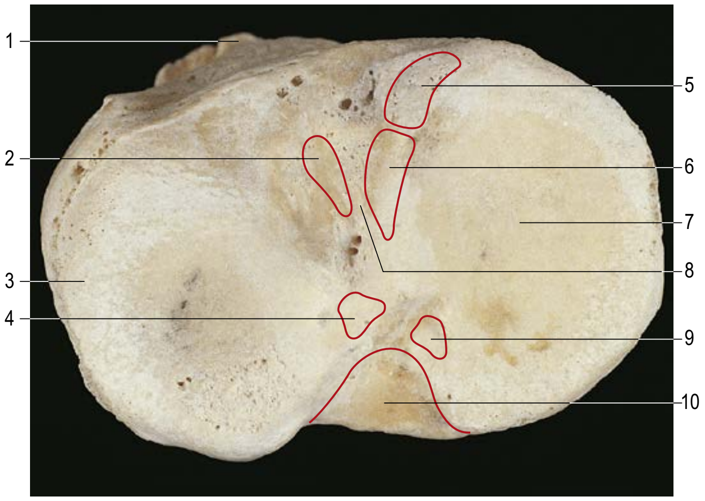

Fig. 78.13 The left tibial plateau, showing sites of ligamentous and meniscal attachments and articular surfaces. Key: 1, tibial tuberosity; 2, attachment of anterior horn, lateral meniscus; 3, lateral condyle; 4, attachment of posterior horn, lateral meniscus; 5, attachment of anterior horn, medial meniscus; 6, attachment of anterior cruciate ligament; 7, medial condyle; 8, intercondylar eminence; 9, attachment of posterior horn, medial meniscus; 10, attachment of posterior cruciate ligament.

Lateral patellar dislocation is a relatively frequent injury, with an overall annual incidence of approximately 23.2 per 100,000 person years; the highest incidence, of approximately 147.7 per 100,000 person years, is in adolescents aged 14–18 years (Sanders et al 2018). The medial patellofemoral ligament is the primary medial stabilizer of the patella throughout the first 30° of flexion and is the most commonly injured ligament with a lateral patellar dislocation. The medial patellotibial and patellomeniscal ligaments have a role in restricting lateral translation, patellar tilt and patellar rotation at increased degrees of knee flexion. They also maintain normal kinematics of the patellofemoral joint, particularly at higher flexion angles. Patellar re-dislocation occurs in 15–72% of patients treated non-operatively. However, significant reductions in patellar re-dislocation rates have been reported following surgical intervention, with medial patellofemoral ligament reconstruction (Zimmerer et al 2018).

All other aspects of the patellofemoral joint are described with the tibiofemoral joint.

Tibiofemoral joint

The tibiofemoral joint is a complex synovial joint and is part of the knee joint.

Articulating surfaces The articulating surfaces of the tibiofemoral joint are the proximal tibial surface, the intercondylar area and the femoral surface.

Proximal tibial surface The proximal tibial surface (unofficially referred to as the tibial plateau) slopes posteriorly and downwards relative to the long axis of the shaft (Fig. 78.13). The tilt, which is maximal at birth, decreases with age, and is more marked in habitual squatters. The tibial plateau presents medial and lateral articular surfaces (facets) for articulation with the corresponding femoral condyles. The posterior surface, distal to the articular margin, displays a horizontal, rough groove to which the capsule and posterior part of the tibial collateral ligament are attached. The anteromedial surface of the medial tibial condyle is a rough strip, separated from the medial surface of the tibial shaft by an inconspicuous ridge. The medial patellar retinaculum is attached to the medial tibial condyle along its anterior and medial surfaces, which are marked by vascular foramina.

The medial articular surface is oval (long axis anteroposterior) and longer than the lateral articular surface. Around its anterior, medial and posterior margins, it is related to the medial meniscus; the meniscal imprint, wider posteriorly and narrower anteromedially, is often discernible. The surface is flat in its posterior half and the anterior half slopes superiorly about 10°. The meniscus covers much of the posterior surface so that, overall, a concave surface is presented to the medial femoral condyle. Its lateral margin is raised as it reaches the intercondylar region.

The lateral tibial condyle overhangs the shaft of the tibia posterolaterally above a small circular facet for articulation with the fibula. The lateral articular surface is more circular and coapted to its meniscus. In the sagittal plane, the articular surface is fairly flat centrally, and anteriorly and

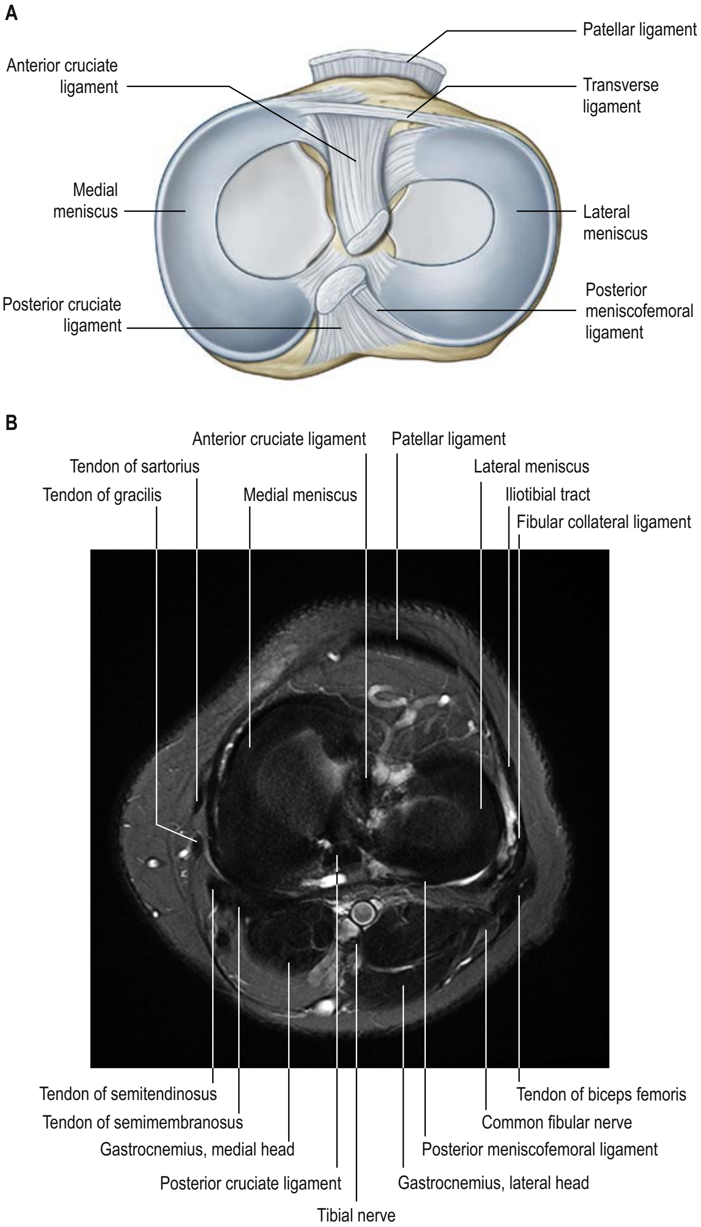
A
Patellar ligament
Anterior cruciate ligament
Transverse ligament
Medial meniscus
Lateral meniscus
Posterior cruciate ligament
Posterior meniscofemoral ligament
B
Anterior cruciate ligament
Patellar ligament
Tendon of sartorius
Lateral meniscus
Tendon of gracilis
Medial meniscus
Iliotibial tract
Fibular collateral ligament
Tendon of semitendinosus
Tendon of biceps femoris
Tendon of semimembranosus
Common fibular nerve
Gastrocnemius, medial head
Posterior meniscofemoral ligament
Posterior cruciate ligament
Gastrocnemius, lateral head
Tibial nerve

Fig. 78.14 **A**, The superior aspect of the left tibia, showing the menisci and the attachments of the cruciate ligaments. **B**, Compounded image of two sequential axial MRI slices (T2-weighted with fat suppression) at the left knee joint showing the menisci and related ligaments. (A, With permission from Drake RL, Vogl AW, Mitchell A et al (eds) Gray's Atlas of Anatomy. Elsevier, Churchill Livingstone. Copyright 2008.)

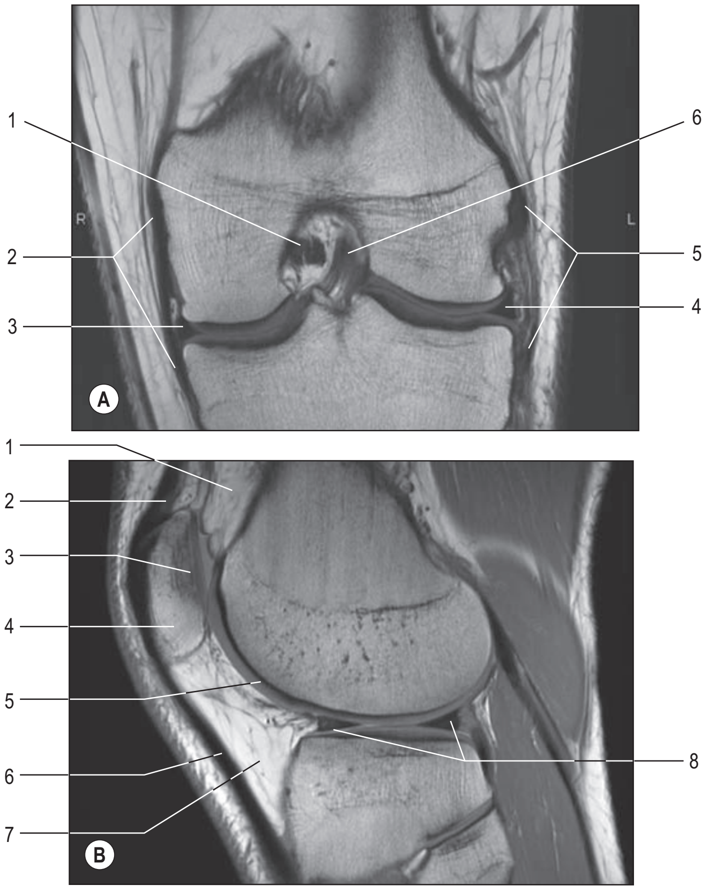
1
2
3
R
L
6
5
4
A
1
2
3
4
5
6
7
8
B

Fig. 78.15 Left knee joint. **A,** T1-weighted coronal magnetic resonance image (MRI). Key: 1, posterior cruciate ligament; 2, tibial collateral ligament; 3, medial meniscus; 4, lateral meniscus; 5, fibular collateral ligament; 6, anterior cruciate ligament. **B,** Medial meniscus, proton density (PD) weighted sagittal MRI. Key: 1, suprapatellar fat pad; 2, tendon of quadriceps femoris; 3, patellar articular cartilage; 4, patella; 5, femoral articular cartilage; 6, patellar ligament; 7, infrapatellar fat pad; 8, medial meniscus.

posteriorly the surface slopes inferiorly. Overall, this creates a rather convex surface so that, with the lateral femoral condyle in contact, there are anterior and posterior recesses (triangular in section), which are occupied by the anterior and posterior meniscal 'horns'. Elsewhere, the surface has a raised medial margin that spreads to the lateral intercondylar tubercle. Its articular margins are sharp, except posterolaterally, where the edge is rounded and smooth: here the tendon of popliteus is in contact with bone.

Intercondylar area The rough-surfaced area between the condylar articular surfaces is narrowest centrally where there is an intercondylar eminence, the edges of which project slightly proximally as the lateral and medial intercondylar tubercles. The intercondylar area widens behind and in front of the eminence as the articular surfaces diverge (see Fig. 78.13; **Fig. 78.14**).

The anterior intercondylar area is widest anteriorly. Anteromedially, anterior to the medial articular surface, a depression marks the site of attachment of the anterior horn of the medial meniscus. Behind this, a smooth area receives the anterior cruciate ligament. The anterior horn of the lateral meniscus is attached anterior to the intercondylar eminence, lateral to the anterior cruciate ligament. The eminence, with medial and lateral tubercles, is the narrow central part of the area. The raised tubercles are thought to provide a slight stabilizing influence on the femur. It is believed that the eminence becomes prominent once walking commences and that the tibial condyles transmit the weight of the body through the tibia.

The posterior horn of the lateral meniscus is attached to the posterior slope of the intercondylar area. The posterior intercondylar area inclines down and backwards behind the posterior horn of the lateral meniscus. A depression behind the base of the medial intercondylar tubercle is for the attachment of the posterior horn of the medial meniscus. The rest of the area is smooth and provides attachment for the posterior cruciate ligament, spreading back to a ridge to which the capsule is attached.

Femoral surface. The femoral condyles, bearing articular cartilage, are almost wholly convex. There are various opinions as to the contours of their sagittal profiles. One view is that they are spiral with a curvature increasing posteriorly ('a closing helix'), that of the lateral condyle being greater. An alternative view is that the articular surface for contact with the tibia on the medial femoral condyle describes the arcs of two circles. According to this view, the anterior arc makes contact with the tibia near extension and is part of a virtual circle of larger radius than the more posterior arc, which makes contact during flexion. The lateral femoral condyle is believed to describe a single arc and thus to possess a single radius of curvature.

Tibiofemoral congruence is improved by the menisci, which are shaped to produce concavity of the surfaces presented to the femur; the combined lateral tibiomeniscal surface is deeper. The lateral femoral condyle has a faint groove anteriorly, which rests on the peripheral edge of the lateral meniscus in full extension. A similar groove appears on the medial condyle but does not reach its lateral border, where a narrow strip contacts the medial patellar articular surface in full flexion. These grooves demarcate the femoral patellar and condylar surfaces. The differences between the shapes of the articulating surfaces correlate with the movements of the knee joint.

Menisci The menisci (semilunar cartilages) are crescentic, intracapsular, fibrocartilaginous laminae (see Fig. 78.14; **Fig. 78.15**). They serve to widen, deepen and prepare the tibial articular surfaces that receive the femoral condyles. Their peripheral attached borders are thick and convex, and their free, inner borders are thin and concave. Their peripheries are vascularized by capillary loops from the fibrous capsule and synovial membrane, while their inner regions are less vascular. Tears of the menisci are common. Peripheral tears (e.g. in the vascularized zone) have the potential to heal satisfactorily, especially with surgical intervention. Tears in the less vascular or inner zones seldom heal spontaneously; if surgery is indicated, these menisci are often resected. The meniscal horns are richly innervated compared with the remainder of the meniscus. The central one-third is devoid of innervation (Gronblad et al 1985). The proximal surfaces are smooth and concave, and in contact with the articular cartilage on the femoral condyles. The distal surfaces are smooth and flat, resting on the tibial articular cartilage. Each covers approximately two-thirds of its tibial articular surface. Canal-like structures open on to the surface of the menisci in infants and young children, and may transport nutrients to deeper, less vascular areas.

Two structurally different regions of the menisci have been identified. The inner two-thirds of each meniscus consist of radially organized collagen bundles, and the peripheral one-third consists of larger circumferentially arranged bundles (Ghadially et al 1983). Thinner collagen bundles parallel to the surface line the articular surfaces of the inner part, while the outer portion is covered by synovium. This structural arrangement suggests specific biomechanical functions for the two regions: the inner portion of the meniscus is suited to resisting compressive forces while the periphery is capable of resisting tensional forces. With ageing and degeneration, compositional changes occur within the menisci, which reduce their ability to resist tensional forces. Outward displacement of the menisci by the femoral condyles is resisted by firm anchorage of the peripheral circumferential fibres to the intercondylar bone at the meniscal horns.

Alternatively, each meniscus can be considered as consisting of three contiguous segments, namely an anterior horn/root, a body, and a posterior horn/root. The anterior roots of both menisci have relatively simple, planar insertions into the tibial plateau, while the posterior roots reveal complex, three-dimensional insertions into the tibial plateau.

The menisci spread load by increasing the congruity of the articulation, provide stability by their physical presence and proprioceptive feedback, and may cushion the underlying bone from the considerable forces generated during extremes of flexion and extension of the knee. They play a vital role in protecting against osteochondral damage of the tibiofemoral joint with specific importance afforded to the meniscal root. The loss of attachment at the root of the meniscus impairs the ability to maintain hoop strain when loading the tibiofemoral joint. (Hoop strain refers to the circumferential nature of the stress on meniscal fibres during axial loading.) This decrease in hoop strain resistance is responsible for increased articular cartilage contact pressure, which can lead to rapid degenerative changes (Krych et al 2017). An avulsion of the posterior root of the medial meniscus is biomechanically equivalent to a complete meniscectomy due to abnormally high peak tibiofemoral contact pressures (Allaire et al 2008).

Medial meniscus The medial meniscus is broader posteriorly and is almost a semicircle in shape (see Fig. 78.14). The anatomical location of the anterior root attachment of the medial meniscus has been described using surgical and arthroscopic vantage points. With reference to relevant open surgical landmarks, the centre of the anterior root is proximal to the superior aspect of the medial edge of the tibial tuberosity, and proximomedial to the centre of the superior edge of the tibial tuberosity. With regard to arthroscopic landmarks, the centre of the anterior root is anterior to the apex of the medial tibial eminence, anteromedial to the centre of the anterior cruciate ligament, and anteromedial to the centre of the lateral root of the lateral meniscus. The central, prominent root fibres that attach to the tibia encompass an area of approximately 56.3 mm^2 (LaPrade et al 2014). When the transverse (anterior intermensical) ligament is present it spans between the posteromedial aspect of the anterior horn of the medial meniscus and the anterolateral aspect of the anterior root of the lateral meniscus.

The posterior root is attached posterior to the apex of the medial tibial plateau, lateral to the inflection point of the articular cartilage of the medial tibial plateau, and anteromedial to the tibial attachment of the posterior cruciate ligament. The footprint area formed by the central fibres of the posterior root at its attachment is approximately 30.4 mm^2 (Johannsen et al 2012).

The peripheral border of the meniscus is attached to the fibrous capsule and the deep surface of the tibial collateral ligament. The tibial attachment of the meniscus is known as the ‘coronary or meniscotibial ligament’. Collectively, these attachments ensure that the medial meniscus is relatively fixed and moves much less than the lateral meniscus.

Lateral meniscus The lateral meniscus forms approximately four-fifths of a circle and covers a larger area than the medial meniscus (see Fig. 78.14). Its breadth, except at its short tapered horns, is more or less uniform. It is grooved posterolaterally by the tendon of popliteus, separating it from the fibular collateral ligament. The central fibres of its anterior root are attached anteromedial to the apex of the lateral tibial eminence, and anterolateral to the centre of the tibial attachment of the anterior cruciate ligament. The tibial attachment area of the anterior root is approximately 140.7 mm^2, and there is significant overlap with the tibial footprint of the anterior cruciate ligament (LaPrade et al 2014).

The posterior root is attached posteromedial to the lateral tibial eminence apex, medial to the edge of the lateral articular cartilage, anterior to the tibial attachment of the posterior cruciate ligament, and anterolateral to the posterior root of the medial meniscus. Its footprint area is approximately 39.2 mm^2. In addition to the main attachment a continuation of the posterior fibres pass to the posterior aspect of the lateral margin of the medial tibial eminence (Johannsen et al 2012). Near its posterior attachment, it commonly sends a posterior meniscofemoral ligament superomedially behind the posterior cruciate ligament to the medial femoral condyle. An anterior meniscofemoral ligament may also connect the posterior horn to the medial femoral condyle anterior to the posterior cruciate ligament. The meniscofemoral ligaments are often the sole attachments of the posterior horn of the lateral meniscus. More laterally, part of the tendon of popliteus is attached to the lateral meniscus, and so mobility of its posterior horn may be controlled by the meniscofemoral ligaments and by popliteus. A meniscofibular ligament occurs in most knee joints. As with the medial meniscus, there is a tibial attachment via the so-called coronary ligament, but the meniscus has no peripheral bony attachment in the region of popliteus; in the surgical literature, this gap is referred to as the popliteus hiatus.

Discoid lateral meniscus A discoid lateral meniscus occasionally occurs, often bilaterally. The distinguishing features of a discoid lateral meniscus are its shape and posterior ligamentous attachments. The following classification of the abnormality is based on the work of Watanabe et al (1979). In its mildest form, the partial discoid meniscus is simply a wider form of the normal lateral meniscus. The acute, medial free edge is interposed between the femoral and tibial condyles but it does not completely cover the tibial plateau. A complete discoid meniscus appears as a biconcave disc with a rolled medial edge and covers the lateral tibial plateau. The Wrisberg type of meniscus has the same shape as a complete discoid meniscus but its only peripheral posterior attachment is by the meniscofemoral ligaments. In this case, the normal tibial attachment of the posterior horn of the lateral meniscus is lacking but the posterior meniscofemoral ligament persists. As a result, this type of meniscus is attached anteriorly to the tibia and posteriorly to the femur, which renders the posterior horn unstable. Under these circumstances, the meniscus is liable to become caught between the femur and tibia: this accounts for the classic presenting symptom of the ‘clunking knee’ in some patients. The aetiology of discoid meniscus is not clear. Most are asymptomatic and are often found by chance at arthroscopy. However, they may cause difficulty in gaining access to the lateral compartment at arthroscopy. A discoid medial meniscus is extremely rare.

Transverse ligament of the knee The transverse ligament of the knee connects the anterior convex margin of the lateral meniscus to the anterior horn of the medial meniscus (see Figs 78.14, 78.22). It varies in thickness and is often absent. Its exact role is conjectural, although one study found that the ligament was slightly taut in knee extension (Tubbs et al 2008); presumably, it helps to decrease tension generated in the longitudinal circumferential fibres of the menisci when the knee is subjected to load. A posterior meniscomeniscal ligament is sometimes present.

Meniscofemoral ligaments Two meniscofemoral ligaments connect the posterior horn of the lateral meniscus to the inner (lateral) aspect of the medial femoral condyle (**Fig. 78.16B**). The anterior meniscofemoral ligament (ligament of Humphrey) passes anterior to the posterior cruciate ligament. The posterior meniscofemoral ligament (ligament of Wrisberg) passes behind the posterior cruciate ligament and attaches proximal to the margin of attachment of the posterior cruciate.

Anatomical cadaveric studies found that at least one meniscofemoral ligament was typically present in the knees examined; both sometimes coexisted (Gupte et al 2003). Biomechanical studies have revealed the cross-sectional area and strength of the meniscofemoral ligaments to be comparable to those of the posterior fibre bundle of the posterior cruciate ligament.

The meniscofemoral ligaments are believed to act as secondary restraints, supporting the posterior cruciate ligament in minimizing displacement caused by posteriorly directed forces on the tibia. They are also involved in controlling the motion of the lateral meniscus in conjunction with the tendon of popliteus during knee flexion.

Soft tissues

Recent advances in imaging and surgery on knee ligaments have contributed to an improved understanding of anatomy, particularly of the medial and lateral soft tissues of the knee.

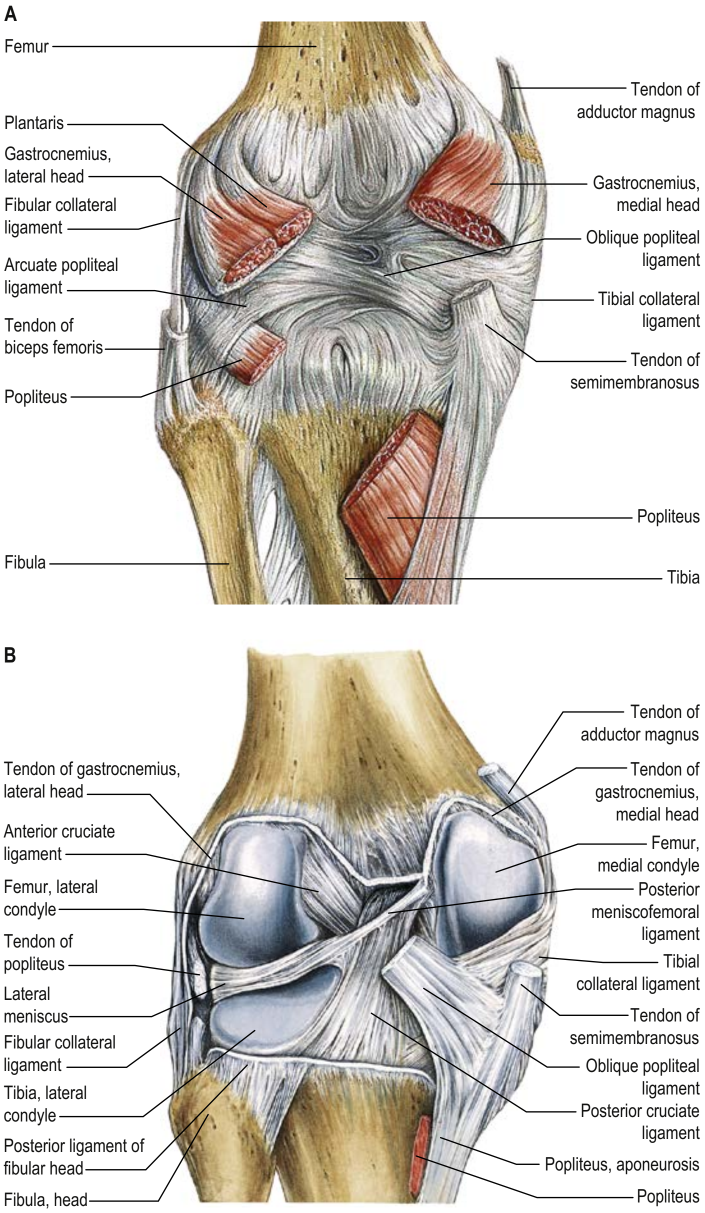
A
Femur
Plantaris
Gastrocnemius, lateral head
Fibular collateral ligament
Arcuate popliteal ligament
Tendon of biceps femoris
Popliteus
Fibula
Tendon of adductor magnus
Gastrocnemius, medial head
Oblique popliteal ligament
Tibial collateral ligament
Tendon of semimembranosus
Popliteus
Tibia
B
Tendon of gastrocnemius, lateral head
Anterior cruciate ligament
Femur, lateral condyle
Tendon of popliteus
Lateral meniscus
Fibular collateral ligament
Tibia, lateral condyle
Posterior ligament of fibular head
Fibula, head
Tendon of adductor magnus
Tendon of gastrocnemius, medial head
Femur, medial condyle
Posterior meniscofemoral ligament
Tibial collateral ligament
Tendon of semimembranosus
Oblique popliteal ligament
Posterior cruciate ligament
Popliteus, aponeurosis
Popliteus

Fig. 78.16 A posterior dissection of the knee. **A**, Capsule intact. **B**, Capsule removed. (With permission from Waschke J, Paulsen F (eds) Sobotta Atlas of Human Anatomy, 15th ed. Elsevier, Urban & Fischer. Copyright 2013.)

Fibrous capsule and retinacula

The joint capsule is a fibrous membrane of variable thickness. Anteriorly it is replaced by the patellar ligament and does not pass proximal to the patella or over the patellar area. Elsewhere it lies deep to expansions from vasti medialis and lateralis, separated from them by a plane of vascularized loose connective tissue. The expansions are attached to the patellar margins and patellar ligament, extending back to the corresponding collateral (tibial and fibular) ligaments and distally to the tibial condyles. They form medial and lateral patellar retinacula, the lateral being reinforced by the iliotibial tract.

Posteriorly the capsule contains vertical fibres that arise from the articular margins of the femoral condyles and intercondylar fossa, and from the proximal tibia. The fibres mainly pass downwards and somewhat medially. The oblique popliteal ligament is a well-defined thickening across the posteromedial aspect of the capsule, and is one of the major extensions from the tendon of semimembranosus.

Medial ligaments and soft tissues

The medial soft tissues are arranged in three layers from superficial to deep (Warren and Marshall 1979).

Layer 1 Layer 1 is the deep fascia that invests sartorius. The saphenous nerve and its infrapatellar branch are superficial to the deep fascia of the leg. Sartorius inserts into the fascia as an expansion rather than as a distinct tendon. The fascia spreads inferiorly and anteriorly to lie superficial to the distinct and readily identifiable tendons of gracilis and semitendinosus and their insertions. These tendons are commonly harvested for surgical reconstruction of damaged cruciate ligaments. To gain access to them, the upper edge of sartorius can be identified and the sartorius (layer 1) fascia is incised to reveal the tendons. Deep to the tendons is the anserine bursa, which overlies the superficial part of the tibial collateral ligament; this bursa sometimes becomes inflamed, especially in track and field athletes. Posteriorly, layer 1 overlies the tendons of gastrocnemius and the structures of the popliteal fossa. Anteriorly, layer 1 blends with the anterior limit of layer 2 and the medial patellar retinaculum. More inferiorly, layer 1 blends with the periosteum.

A condensation of tissue passes from the medial border of the patella to the medial epicondyle of the femur (the medial patellofemoral ligament), the anterior horn of the medial meniscus (the meniscopatellar ligament) and the medial tibial condyle (the patellotibial ligament).

Layer 2 Layer 2 is the plane of the superficial part of the tibial collateral ligament (medial collateral ligament) (**Fig. 78.17**). The tendons of gracilis and semitendinosus lie between layers 1 and 2. The superficial part of the tibial collateral ligament is the largest structure of the medial aspect of the knee, measuring approximately 10–12 cm in length (Fig. 78.17; see Fig. 78.15). It has one femoral and two tibial (proximal and distal) attachments. The femoral attachment is to a small depression just proximal and posterior to the centre of the medial epicondyle of the femur. As the superficial part of the tibial collateral ligament passes distally, it is separated from the tibia by the inferior medial genicular artery and vein, and a corresponding branch from the tibial nerve. Its proximal tibial attachment is primarily to soft tissues (the anterior arm of the tendon of semimembranosus) rather than directly to bone. The distal tibial attachment is broad-based and located just anterior to the posteromedial crest of the tibia: the majority of the fibres are located within the anserine bursa (LaPrade et al 2007). There is a vertical split in layer 2 anterior to the superficial part of the tibial collateral ligament. The fibres anterior to the split pass superiorly to blend with the fascia over vastus medialis and layer 1 in the medial patellar retinaculum. The fibres posterior to the split pass superiorly to the medial epicondyle and continue anteriorly as the medial patellofemoral ligament (see Figs 78.12, 78.17).

Layer 3 Layer 3 is formed by the joint capsule, including the deep part of the tibial collateral ligament (mid-third capsular ligament) and can be separated from layer 2 everywhere except anteriorly close to the patella, where it blends with the more superficial layers. The deep part of the tibial collateral ligament is a distinct thickening of the anterior aspect of the medial joint capsule. It is deep to, and roughly parallels, the anterior aspect of the superficial part of the tibial collateral ligament. The deep part of the tibial collateral ligament consists of two components: the meniscotibial and meniscofemoral ligaments. The meniscotibial component is attached just distal to the tibial joint line. It is shorter and thicker than the meniscofemoral component, which is attached proximal to the femoral joint line (LaPrade et al 2015). Anteriorly the separation of the superficial and deep parts of the tibial collateral ligament is distinct, whereas posteriorly layers 2 and 3 blend to form a conjoined posteromedial capsule.

Factors maintaining medial stability The tibial collateral ligament is important for stabilization of the medial knee, and is the most commonly injured ligament of the knee. The superficial and deep parts of the tibial collateral ligament are the primary and secondary static stabilizers, respectively, to valgus motion. The primary stabilizer for lateral (external) rotation is the distal attachment of the superficial part of the tibial collateral ligament; the proximal attachment of the superficial part of the tibial collateral ligament and the deep part of the tibial collateral ligament have secondary roles. The posterior oblique ligament also plays a significant role in resisting posteromedial rotatory instability of the knee (Griffith et al 2009).

Lateral ligaments and soft tissues

The arrangement of the lateral soft tissues of the knee is controversial. Three distinct layers are recognized (Seebacher et al 1982), but views as to their contents vary. The first layer may be divided into superficial (oblique fibres of the iliotibial tract ending on the patella) and deep (lateral patellofemoral ligament, the transverse retinaculum and the patellotibial band) parts. These two parts are joined posteriorly by the iliotibial tract. The second layer contains the fibular collateral ligament, patellofemoral ligament, fabellofibular ligament and arcuate ligament,

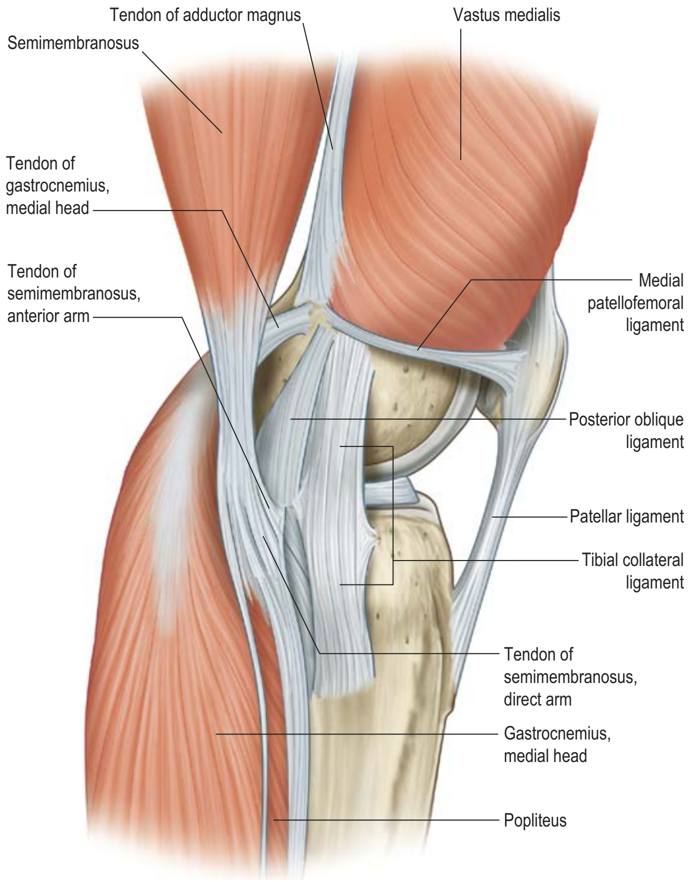
Tendon of adductor magnus
Vastus medialis
Semimembranosus
Tendon of gastrocnemius, medial head
Tendon of semimembranosus, anterior arm
Medial patellofemoral ligament
Posterior oblique ligament
Patellar ligament
Tibial collateral ligament
Tendon of semimembranosus, direct arm
Gastrocnemius, medial head
Popliteus

Fig. 78.17 The major components of the medial aspect of the knee.

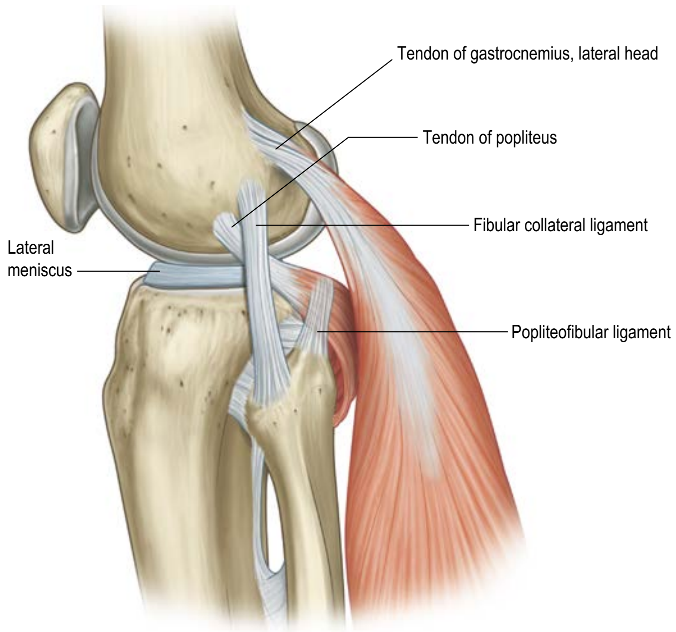
Tendon of gastrocnemius, lateral head
Tendon of popliteus
Fibular collateral ligament
Lateral meniscus
Popliteofibular ligament

Fig. 78.18 The three major components of the posterolateral corner: lateral collateral ligament, tendon of popliteus and popliteofibular ligament.

and the third layer is the joint capsule. An alternative view is that the first layer consists only of the oblique iliotibial tract fibres; the second layer contains the lateral patellofemoral ligament, the transverse retinaculum and the patellotibial band; and the third layer consists of superficial and deep portions, where the superficial part contains the fibular collateral ligament, patellofemoral ligament, fabellofibular ligament and the arcuate ligament and the deep part contains the joint capsule (Miller and Azar 2017). The recently described anterolateral ligament (Stijak et al 2016) of the knee may be a component of the superficial layer (Claes et al 2013).

The lateral patellar retinaculum consists of superficial oblique and deep transverse portions. The former runs from the iliotibial tract to the patella. The latter is thicker and subdivided into three parts: the lateral patellofemoral ligament, running from the lateral patellar border to the lateral epicondyle of the femur; the transverse retinaculum, running from the iliotibial tract to the mid-patella; and the patellotibial band, running from the patella to the lateral tibial condyle.

The fascia lata and the iliotibial tract lie posterior to the lateral retinaculum. They come together distally to insert on to the tibia at a tubercle (Gerdy's tubercle) on the anterolateral proximal tibia; some fibres continue to insert on the tibial tuberosity. Proximally, the fascia lata merges with the lateral intermuscular septum. Posteriorly, it blends with the fascia over biceps femoris. Here, as it emerges from behind the biceps femoris tendon, the common fibular nerve lies in a thin layer of fat bound by the fascia.

Posterolateral corner of the knee

The posterolateral corner of the knee contains several important structures that maintain varus and rotational stability throughout all ranges of motion; the three primary stabilizers are the fibular collateral ligament, popliteus tendon and popliteofibular ligament (Crespo et al 2015, Serra Cruz et al 2016) (**Fig. 78.17**).

The fibular collateral ligament has a mean length of 7 cm and arises from a depression located just proximal and posterior to the lateral epicondyle, posterior to the insertion of popliteus. It passes underneath the superficial layer of the iliotibial tract and is inserted approximately 2.8 cm distal to the tip of the fibular head, with the majority of fibres extending to encompass the distal one-third of the lateral aspect of the fibular head. The fibular collateral ligament is separated from the capsule by a thin layer of fat and the inferior lateral genicular vessels. It is the primary restraint to varus stress on the knee and assists in limiting lateral rotation when the knee is slightly flexed.

The femoral insertion of the popliteus tendon constitutes the most anterior femoral insertion site of the posterolateral corner (see p. 1416).

The single most important stabilizer of the posterolateral knee is the popliteofibular (short external lateral) ligament that spans between the musculotendinous junction of popliteus and the posteromedial aspect of the fibular head. This ligament has a smaller anterior and a larger posterior division that embrace the musculotendinous junction of popliteus. The distolateral attachment of the anterior division is positioned on the anterior downslope of the medial aspect of the fibular styloid process. In a similar fashion, the posterior division is attached to the tip and posteromedial aspect of the fibular styloid process. The popliteofibular ligament contributes to the external rotatory stability of the knee (Chahla et al 2016). Its connection to the tendon of popliteus also allows 'dynamic' tensioning.

The fabellofibular ligament is a condensation of fibres that runs either from the fabella (a sesamoid bone sometimes found within the tendon of the lateral head of gastrocnemius) or from the lateral head of gastrocnemius (if the fabella is absent), to the apex of the head of the fibula. The arcuate ligament is a condensation of fibres that runs from the apex of the head of the fibula, posteromedially over the emerging tendon of popliteus below the level of the tibial joint surface, to the tibial intercondylar area. The lateral joint capsule is thin and blends posteriorly with the arcuate ligament. Anteriorly, it forms the weak, lax coronary or meniscotibial ligament, which attaches the inferior border of the meniscus to the lateral tibia.

Intra-articular ligaments

Cruciate ligaments

The cruciate ligaments, so named because they cross each other, are very strong, richly innervated intracapsular structures. The point of crossing is located a little posterior to the articular centre. They are named anterior and posterior with reference to their tibial attachments (**Figs 78.19–78.22**; see Fig. 78.25). A synovial membrane almost surrounds the ligaments but is reflected posteriorly from the posterior cruciate ligament to adjoining parts of the capsule; the intercondylar part of the posterior region of the fibrous capsule therefore has no synovial covering.

Anterior cruciate ligament The anterior cruciate ligament is attached to the anterior intercondylar area of the tibia, just anterior and slightly lateral to the medial intercondylar tubercle, partly blending with the anterior horn of the lateral meniscus (see Fig. 78.14). It ascends posterolaterally, twisting on itself and fanning out to attach high on the posteromedial aspect of the lateral femoral condyle (Girgis et al 1975). The average length and width of an adult anterior cruciate ligament are 38 mm and 11 mm, respectively. It is formed of two, or possibly three, functional bundles that are not apparent to the

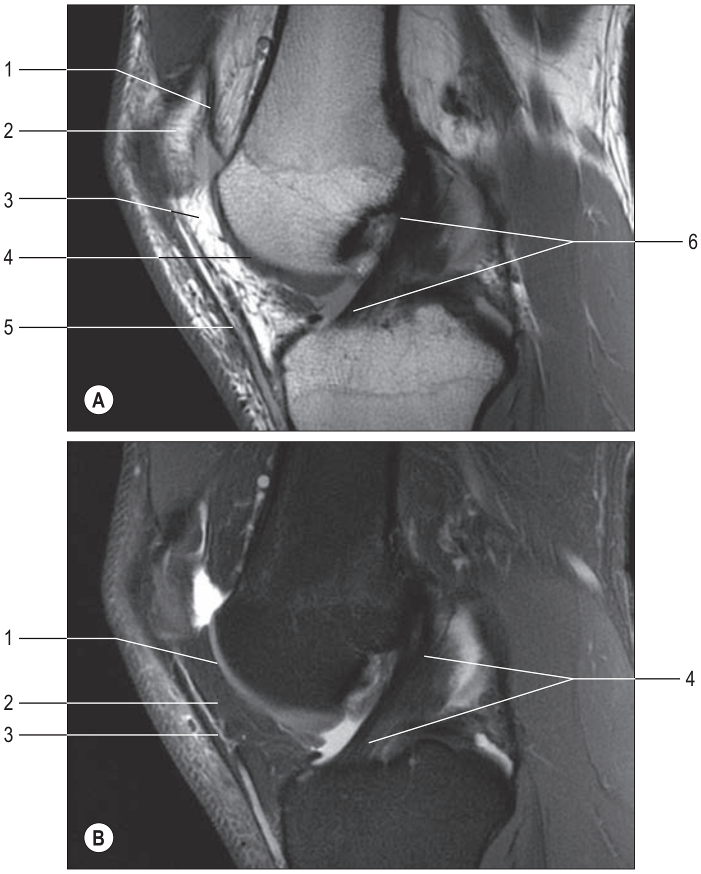

Fig. 78.19 **A**, MRI of the anterior cruciate ligament. **A**, Proton density (PD)-weighted sagittal view. Key: 1, suprapatellar bursa; 2, patella; 3, infrapatellar fat pad; 4, femoral articular cartilage; 5, patellar ligament; 6, anterior cruciate ligament. **B**, T2-weighted sagittal image. Key: 1, femoral articular cartilage; 2, infrapatellar fat pad; 3, patellar ligament; 4, anterior cruciate ligament.

naked eye but can be demonstrated by microdissection techniques. The bundles are named anteromedial, intermediate and posterolateral, according to their tibial attachments (Amis and Dawkins 1991; Clarke et al 2018).

Posterior cruciate ligament The posterior cruciate ligament is thicker and stronger than the anterior cruciate ligament (see Fig. 78.14), the average length and width of an adult posterior cruciate ligament being 38 mm and 13 mm, respectively. It is attached to the lateral surface of the medial femoral condyle and extends up on to the anterior part of the roof of the intercondylar fossa, where its attachment is extensive in the anteroposterior direction. Its fibres are adjacent to the articular surface. They pass distally and posteriorly to a fairly compact attachment posteriorly in the intercondylar region and in a depression on the adjacent posterior tibia. This gives a fan-like structure in which fibre orientation is variable. Anterolateral and posteromedial bundles have been defined; they are named (against convention) according to their femoral attachments. The anterolateral bundle tightens in flexion while the posteromedial bundle is tight in extension of the knee. Each bundle slackens as the other tightens. Unlike the anterior cruciate ligament, it is not isometric during knee motion, i.e. the distance between attachments varies with knee position. The posterior cruciate ligament ruptures less commonly than the anterior cruciate ligament and rupture is usually better tolerated by patients than rupture of the anterior cruciate ligament.

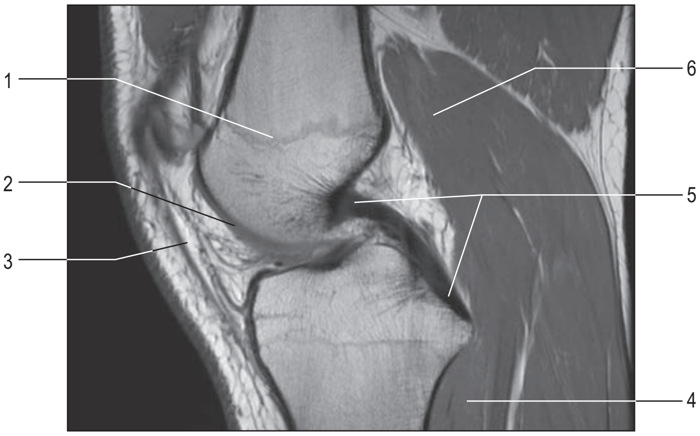

Fig. 78.20 Posterior cruciate ligament, PD-weighted sagittal MRI. Key: 1, epiphyseal line; 2, femoral articular cartilage; 3, patellar ligament; 4, popliteus; 5, posterior cruciate ligament; 6, gastrocnemius.

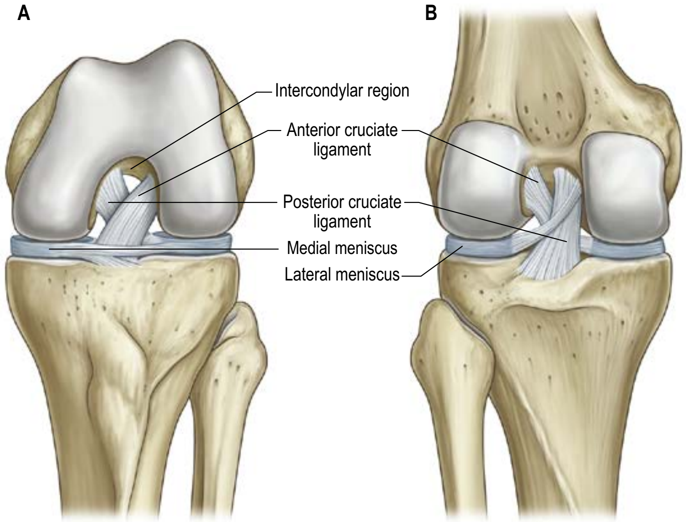

Fig. 78.21 The left knee joint. **A**, Anterior aspect in full flexion. **B**, Posterior aspect in extension. (With permission from Drake RL, Vogl AW, Mitchell A et al (eds) Gray's Atlas of Anatomy. Elsevier, Churchill Livingstone. Copyright 2008.)

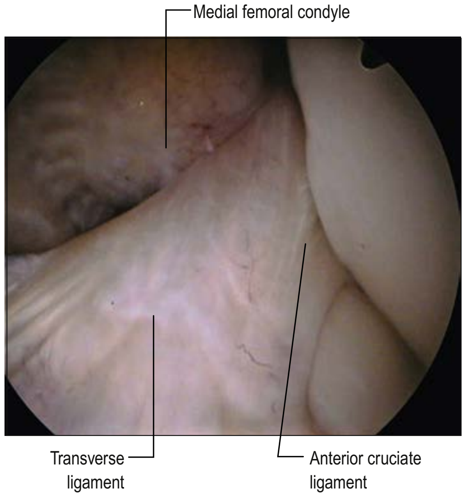

Fig. 78.22 Arthroscopic view of the anterior and posterior cruciate ligaments of the left knee. (With permission from Scott W 2006 Insall & Scott Surgery of the Knee, Fourth Edition. Churchill Livingstone Elsevier.)

Synovial membrane, plicae and fat pads

The synovial membrane of the knee is the most extensive and complex in the body. It forms a large suprapatellar bursa between quadriceps femoris and the lower femoral shaft proximal to the superior patellar border (Figs 78.23–78.24). The bursa is an extension of the joint cavity. The attachment of articularis genus to its proximal aspect prevents the bursa from collapsing into the joint. Alongside the patella, the membrane extends beneath the aponeuroses of the vasti, especially under vastus medialis. It extends proximally a hand's breadth above the superior pole of the patella. Distal to the patella, the synovial membrane is separated from the patellar ligament by an infrapatellar fat pad. Where it lies beneath the fat pad, the membrane projects into the joint as two fringes, alar folds, which bear villi. The folds converge posteriorly to form a single infrapatellar fold or plica (ligamentum mucosum), which curves posteriorly to its attachment in the femoral intercondylar fossa (Fig. 78.25). This fold may be a vestige of the inferior boundary of an

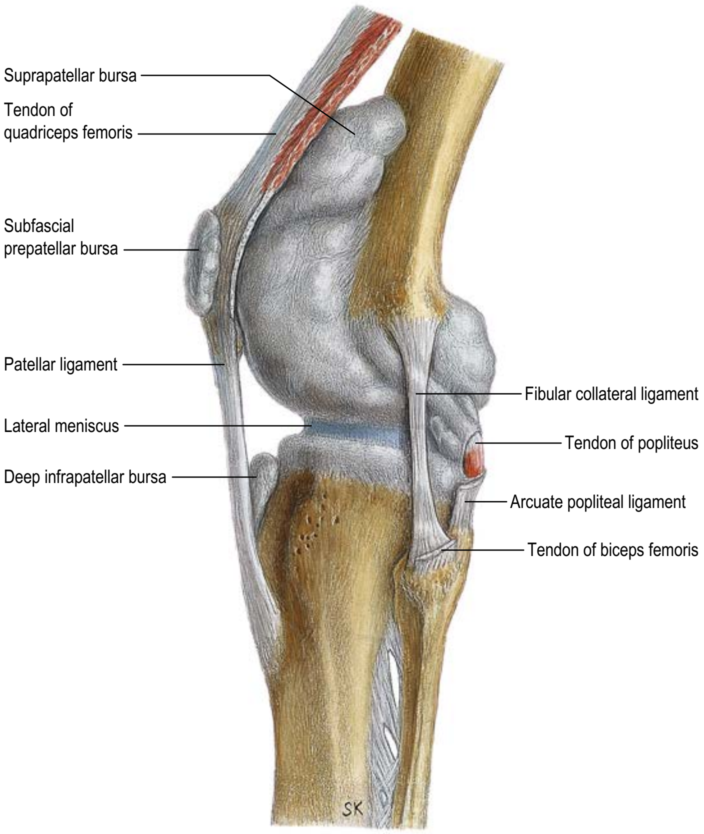
Suprapatellar bursa
Tendon of quadriceps femoris
Subfascial prepatellar bursa
Patellar ligament
Lateral meniscus
Deep infrapatellar bursa
Fibular collateral ligament
Tendon of popliteus
Arcuate popliteal ligament
Tendon of biceps femoris
SK

Fig. 78.23 The left knee joint, lateral aspect. The synovial cavity is distended and the synovial membrane appears grey. (With permission from Waschke J, Paulsen F (eds) Sobotta Atlas of Human Anatomy, 15th ed. Elsevier, Urban & Fischer. Copyright 2013.)

originally separate femoropatellar joint. The extent of the infrapatellar plica ranges from a thin cord to a complete sheet that can obstruct the passage of instruments during knee arthroscopy. When substantial, it has been mistaken for the anterior cruciate ligament, which is directly posterior to it. The medial plica extends in the midline anteriorly from the medial alar fold medially to the suprapatellar bursa. Occasionally, it can be thickened and inflamed, usually following acute or chronic trauma.

The suprapatellar plicae are remnants of an embryonic septum that completely separates the suprapatellar bursa from the knee joint. Occasionally, a septum persists, either in its entirety or perforated by a small peripheral opening.

The infrapatellar fat pad is the largest part of a circumferential extrasynovial fatty ring that extends around the patellar margins (Newell 1991).

At the sides of the joint, the synovial membrane descends from the femur and lines the capsule as far as the menisci, whose surfaces have no synovial covering. Posterior to the lateral meniscus, the membrane forms a subpopliteal recess between a groove on the meniscal surface and the tendon of popliteus, which may connect with the superior tibiofibular joint. The relationship of the synovial membrane to the cruciate ligaments is described above.

Bursae

Numerous bursae are associated with the knee. Anteriorly, there is a large subcutaneous prepatellar bursa between the lower half of the patella and skin; a small, deep infrapatellar bursa between the tibia and patellar ligament; a subcutaneous infrapatellar bursa between the distal part of the tibial tuberosity and skin; and a large suprapatellar bursa, which is the superior extension of the knee joint cavity (see Fig. 78.24). Posterolaterally, there are bursae between the lateral head of gastrocnemius (lateral subtendinous bursa of gastrocnemius) and the joint capsule (this bursa is sometimes continuous with the joint cavity); the fibular collateral ligament and the tendon of biceps femoris; the fibular collateral ligament and the tendon of popliteus; and the tendon of popliteus and the lateral femoral condyle, which is usually an extension of the synovial cavity of the joint. The last two bursae may communicate with each other.

Medially, the arrangement of the bursae is complex. The bursa between the medial head of gastrocnemius and the fibrous capsule is prolonged

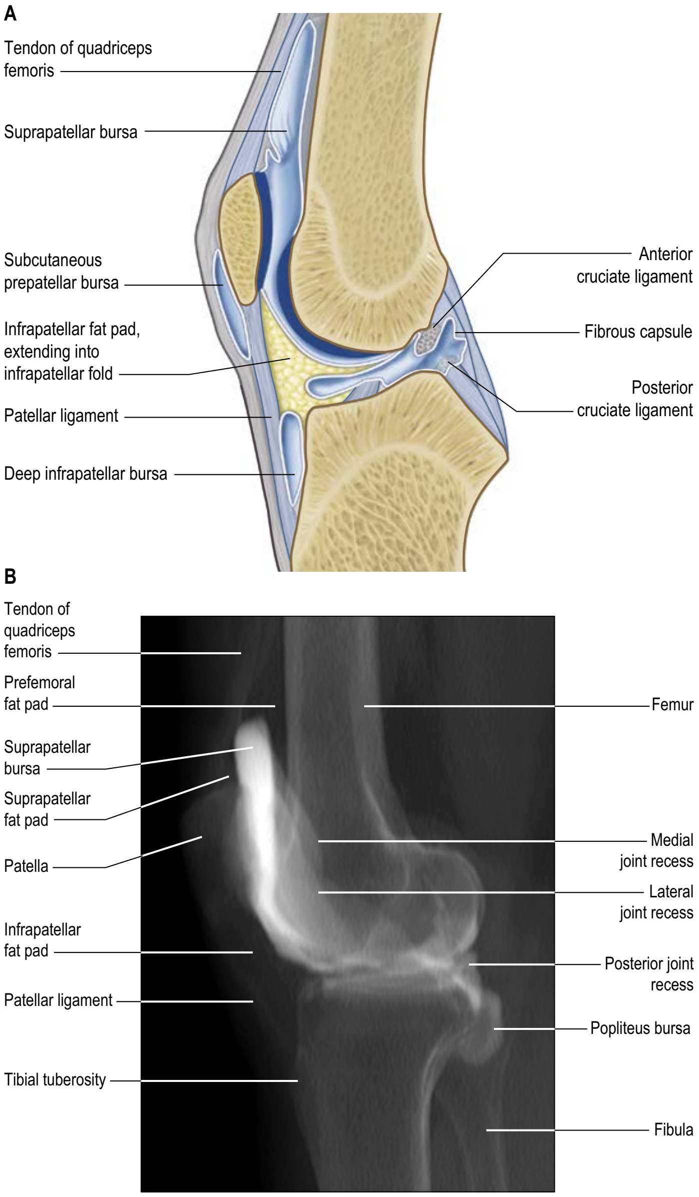
A
Tendon of quadriceps femoris
Suprapatellar bursa
Subcutaneous prepatellar bursa
Infrapatellar fat pad, extending into infrapatellar fold
Patellar ligament
Deep infrapatellar bursa
Anterior cruciate ligament
Fibrous capsule
Posterior cruciate ligament
B
Tendon of quadriceps femoris
Prefemoral fat pad
Suprapatellar bursa
Suprapatellar fat pad
Patella
Infrapatellar fat pad
Patellar ligament
Tibial tuberosity
Femur
Medial joint recess
Lateral joint recess
Posterior joint recess
Popliteus bursa
Fibula

Fig. 78.24 **A**, A sagittal section through the left knee joint, lateral aspect. **B**, Sagittal mean intensity projection of the knee from a CT arthrogram.

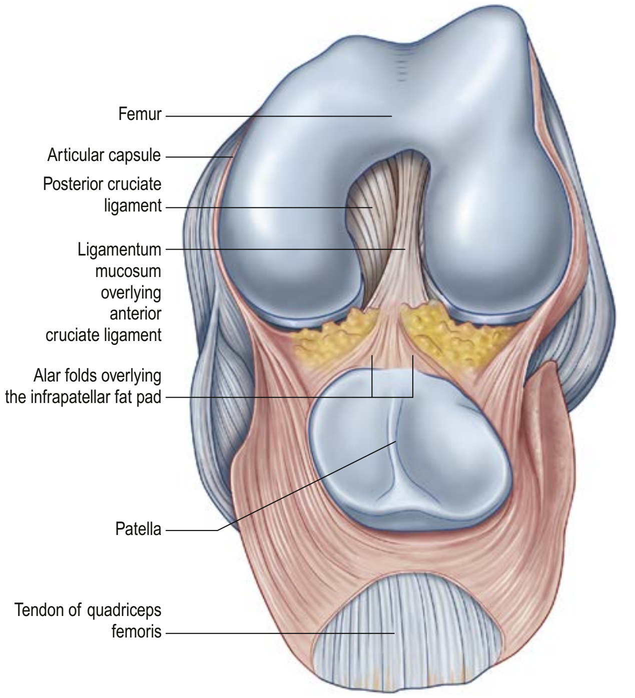
Femur
Articular capsule
Posterior cruciate ligament
Ligamentum mucosum overlying anterior cruciate ligament
Alar folds overlying the infrapatellar fat pad
Patella
Tendon of quadriceps femoris

Fig. 78.25 The left knee joint in full flexion. The tendon of quadriceps femoris has been sectioned and the patella retracted distally. Compare with Fig. 78.14A.

between the medial tendon of gastrocnemius and the tendon of semimembranosus (the semimembranosus bursa), and usually communicates with the joint. The bursa between the tendon of semimembranosus and the medial tibial condyle and the medial head of gastrocnemius may communicate with this bursa. The anserine bursa is located between the tibial collateral ligament and the tendons of sartorius, gracilis and semitendinosus. Bursae that vary in both number and position lie deep to the tibial collateral ligament between the joint capsule, femur, medial meniscus, tibia or tendon of semimembranosus. Occasionally, there may be a bursa between the tendons of semimembranosus and semitendinosus. Posteriorly, bursae associated with the knee are variable.

The clinically important bursae are the anterior group, the anserine bursa and the semimembranosus bursa. Inflammation of the subcutaneous prepatellar bursa and infrapatellar bursa are referred to colloquially as 'housemaid's knee' and 'clergyman's knee', respectively. The anserine bursa can become inflamed, especially in athletes. In adults, bursal inflammation producing a popliteal fossa swelling commonly occurs secondary to degeneration within the knee joint; regardless of its size and position, it almost always arises from the plane between semimembranosus and the tendon of the medial head of gastrocnemius.

Relations and 'at risk' structures

The tendon of quadriceps femoris (which encloses and is attached to the non-articular surfaces of the patella), the patellar ligament, tendinous expansions from vasti medialis and lateralis (which extend over the anteromedial and anterolateral aspects of the capsule, respectively), and the patellar retinacula all lie anterior to the knee joint. Posteromedially are sartorius and the tendon of gracilis (which lies along its posterior border); both descend across the joint. Posterolaterally the tendon of biceps femoris and the common fibular nerve (which lies medial to the tendon) are in contact with the capsule, and thereby separated from the tendon of popliteus. Posteriorly the popliteal artery and associated lymph nodes lie posterior to the oblique popliteal ligament; the popliteal vein is posteromedial or medial, and the tibial nerve is posterior to both. The nerve and vessels are overlapped by both heads of gastrocnemius and laterally by plantaris. Gastrocnemius contacts the capsules on either side of the vessels. Semimembranosus lies between the capsule and semitendinosus, medial to the medial head of gastrocnemius.

BIOMECHANICS OF THE KNEE

The knee joint is a complex synovial joint consisting of the tibiofemoral and patellofemoral articulations. It functions to control the centre of body mass and posture in the activities of daily living. This necessitates a large range of movement in three dimensions coupled with the ability to withstand high forces. These conflicting parameters of mobility and stability are only achieved by the interactions between the articular surfaces, the passive stabilizers and the muscles that cross the joint.

The relatively incongruent nature of the joint surfaces makes the knee joint inherently mobile. In addition, because it acts as a pivot between the longest bones in the body, and is subjected to considerable loads in locomotion, the joint is also potentially at risk of injury if any of the multiple factors providing joint stability are compromised. The long bones may act as levers, increasing the stresses on the stabilizing ligaments.

Movements

Movements at the knee are customarily described as flexion, extension, medial (internal) and lateral (external) rotation. Flexion and extension differ from true hingeing, in that the articular surface profiles of the femoral and tibial articular surfaces produce a variably placed axis of rotation during the flexion arc, and when the foot is fixed, flexion entails corresponding conjunct (coupled) lateral rotation. These conjunct rotations are a product of the complex geometry of the articular surfaces and, to an extent, the disposition of the associated ligaments. There is differential motion in the medial and lateral tibiofemoral compartments. Laterally, there is considerable displacement of the femur on the tibia, with rolling as well as sliding at the joint surface. In contrast, medially, for most of the flexion arc there is minimal relative motion of the femur and tibia, and the motion almost exclusively involves one joint surface sliding on the other. In full flexion, the lateral femoral condyle is close to posterior subluxation off the lateral tibial articular surface. Medially, significant posterior femoral displacement only occurs when flexion exceeds 120°. The menisci move with the femoral condyles, the anterior horns more than the posterior, and the lateral meniscus considerably more than the medial.

The axial rotations have a smaller range than the arc of flexion and extension. These rotations are conjunct, and integral with flexion and extension, i.e. they are obligatory. They can also be adjunct and independent, i.e. voluntary, and are best demonstrated with the knee semi-flexed. The degree of axial rotation therefore varies with flexion and extension.

The range of extension is 5–10° beyond the 'straight position'. Active flexion is approximately 120° with the hip extended, 140° when it is flexed, and 160° when aided by a passive element, e.g. sitting on the heels. Voluntary rotation is 60–70° but conjunct rotation only 20°.

Conjunct medial rotation of the femur on the tibia in the later stages of extension is part of a 'locking' mechanism, the so-called 'screw-home movement', which is an asset when the fully extended knees are subjected to strain. Full extension results in the close-packed position, with maximal spiralization and tightening of the ligaments. The roles of the articular surfaces, musculature and ligaments in generating conjunct rotations remain controversial (Girgis et al 1975, Rajendran 1985) but the following points can be made. The lateral combined meniscotibial 'receiving surface' is smaller, more circular and more deeply concave. Since the articular surface is virtually convex in sagittal section, the depth of the receiving surface is largely due to the presence of the lateral meniscus. The lateral femoral articular surface is also smaller. Consequently, the lateral femoral condyle approaches full congruence with the opposed surface some 30° before full extension (well before the medial condyle). Simple extension cannot continue, but medial rotation of the femur occurs on a vertical axis through its head and medial condyle; the medial femoral condyle moves very little in the sagittal plane and is stabilized by the 'upslope' of the anterior half of the medial tibia, while rotation of the lateral femoral condyle and meniscus brings the anterior horn of the latter on to the anterior 'downslope' of the lateral tibial condyle. Rotation and extension follow simultaneously and smoothly until final close packing of both condyles is accomplished. At the beginning of flexion from full extension (with the foot fixed), lateral femoral rotation occurs, which 'unlocks' the joint. While joint surfaces and many ligaments are involved, electromyographic evidence reveals that contraction of popliteus is important, and that it pulls down and backwards on the lateral femoral condyle, lateral to the axis of femoral rotation. It also retracts the posterior horn during lateral rotation and continuing flexion, via its attachment to the lateral meniscus, and so prevents traumatic compression.

Any position of extension adopted is a balance between forces (torque) extending the joint and passive mechanisms resisting them. The range near to close packing is functionally important. In symmetrical standing, the line of the body's weight is anterior to the transverse axes of the knee joints, but the passive mechanisms noted above preserve posture with minimal muscular effort (Joseph 1960). Active contraction of quadriceps femoris and a close-packed position only occurs in asymmetrical postures, e.g. in leaning forward, during heavy loading, or when powerful thrust is needed.

In knee extension, parts of the cruciate ligaments, the tibial and fibular collateral ligaments, the posterior capsular region, the oblique popliteal ligament, skin and fasciae are all taut. Passive and sometimes active tension exists in the posterior thigh muscles and gastrocnemius, and the anterior part of the medial meniscus is compressed between the femoral and tibial condyles. During extension, the patellar ligament is tightened by quadriceps femoris but is relaxed in the erect attitude. When the knee flexes, the fibular collateral ligament and the posterior part of the tibial collateral ligament relax but the cruciate ligaments and the anterior part of the tibial collateral ligament remain taut; the posterior parts of the menisci are compressed between the femoral and tibial condyles. Flexion is checked by quadriceps femoris, anterior parts of the knee joint capsule, posterior cruciate ligament and compression of soft tissues behind the knee. In extreme passive flexion, contact of the calf with the thigh may be the limiting factor and parts of both cruciate ligaments are also taut. In addition to conjunct rotation with terminal extension or initial flexion, relaxed collateral ligaments also allow independent medial and lateral rotation (adjunct rotation) when the joint is flexed.

Accessory movements

Wider rotation can be obtained by passive movements when the knee is semi-flexed. To a limited extent, the tibia can also be translated backwards and forwards on the femur. Abduction and adduction are prevented in full extension by the collateral ligaments and secondary restraints such as the cruciate ligaments. With the knee slightly flexed, limited adduction and abduction are possible, both passive and active. Slight separation of the femur and tibia can be achieved by strong traction on the leg with countertraction applied to the thigh.

Physiological knee joint laxity may occur during puberty. Increased knee joint flexibility is seen more frequently in adolescent girls than boys. There is an inverse relationship between Tanner stage and the degree of laxity with a progressive decrease of sagittal laxity at the onset of Tanner stage 2 (Falciglia et al 2009).

Muscles producing movements

Flexion Flexion is produced by biceps femoris, semitendinosus and semimembranosus, assisted by gracilis, sartorius and popliteus. With the foot stationary, gastrocnemius and plantaris also assist (see Fig. 78.3).

Extension Extension is produced by quadriceps femoris, assisted by tensor fasciae latae.

Medial rotation of the flexed leg Medial rotation of the flexed leg is produced by popliteus, semimembranosus and semitendinosus, assisted by sartorius and gracilis.

Lateral rotation of the flexed leg Lateral rotation of the flexed leg is produced by biceps femoris.

Patellofemoral joint The alignment of the femoral and tibial shafts is such that the pull of quadriceps femoris on the patella imparts a force on the patella that is directed both superiorly and laterally. The static bony factors that counter this tendency to move laterally are the congruity of the patellofemoral joint and the buttressing effect of the larger lateral part of the patellar surface of the femur, which, clinically, is often referred to as the trochlear groove. Instability of the patella may result if the patella is small or if the patellar surface of the femur is too shallow. The static ligamentous factors are the medial patellofemoral ligament and medial patellar retinaculum.

Dynamic neuromuscular control is important. The most distal part of vastus medialis (vastus medialis obliquus) consists of transverse fibres that are attached directly to the medial edge of the patella: these pull the patella medially, countering the tendency to move laterally. This is the muscle that is preferentially strengthened in a physical therapy programme aimed at treating patellofemoral conditions often associated with patella tracking problems such as those seen in growing adolescents.

Tibiofemoral joint The tibiofemoral joint surfaces are inherently mobile, especially laterally. Medially, some stability is afforded by the relatively concave tibial surface and the relatively fixed posterior horn of the medial meniscus. Both medially and laterally the menisci are helpful, particularly as they move with the femoral condyles. Ligaments play a major role in constraining mobility because they bind the bones in positions of extreme stress and also provide proprioceptive feedback, aiding coordination of stabilizing muscle activity. To take a somewhat ‘two-dimensional’ view, the tibial and fibular collateral ligaments may be considered as sensors (resistors) of valgus and varus forces on the knee, respectively, and the anterior and posterior cruciate ligaments as sensors (resistors) of anterior and posterior tibial translation, respectively. However, in reality the situation is more complex than this. The stresses are rarely applied in orthogonal planes and so a combination of forces, especially rotational, is involved. Moreover, many structures other than the collateral and cruciate ligaments are involved in stabilizing the joint. The ‘posterolateral corner’, which is the primary restraint to varus and rotational forces of the tibia, consists of the popliteofibular, fabellofibular, arcuate and fibular collateral ligaments and iliotibial tract, together with popliteus, the lateral head of gastrocnemius and biceps femoris (see Fig. 78.21). The ‘posteromedial corner’, which resists tibial rotation, consists of the posterior oblique portion of the superficial part of the tibial collateral ligament, and the capsule including the oblique popliteal ligament and semimembranosus (see Fig. 78.17). Since stresses are often a combination of force plus rotation, structures usually operate together rather than in isolation.

Loading at the knee

During level walking, the force across the tibiofemoral joint for most of the cycle is between two and four times body weight, and can be more. In contrast, the force across the patellofemoral joint is no more than 50% of body weight. Peak force transmission across the joint increases sequentially as the menisci, articular cartilage and subchondral bone are damaged or removed. Walking up or down stairs has little influence on tibiofemoral forces, but significantly increases patellofemoral forces to two (walking up) or three (walking down) times body weight, reflecting the changed angle of the tendon of quadriceps femoris and patellar ligament during flexion. There are two mechanisms for ameliorating forces transmitted across the patella: the extensor lever arm is lengthened as the axis of rotation moves posteriorly during flexion, and the contact area between the patella and femur almost triples between 30° and 90°. To cope with the potential large forces generated by activities such as running, the patella has the thickest articular cartilage in the body.

Knee joint kinematics

The surfaces of the tibia and femur are not as conforming as those of the relatively congruent hip joint. Although this variation in geometry permits motion to occur in six degrees of freedom (**Fig. 78.26**), the primary motion of the knee occurs in the sagittal plane, and a relatively minor degree of movement occurs in the transverse plane. The knee joint may therefore be described simplistically as a modified hinge joint allowing flexion–extension and a measure of rotatory motion. Knee motion is normally defined as starting from 0° (the neutral position), when the tibia and femur are in line in the sagittal plane. Biomechanically, it is important that the knee reaches the neutral position in extension because that allows the leg to support the body weight like a simple strut when the subject is standing still. When the subject is standing upright, if the knee is flexed, the vertical line of action of the body weight passes posterior to the centre of rotation of the knee, tending to cause the body to tilt posteriorly. To counterbalance this, continuous quadriceps femoris contraction is required, causing expenditure of energy.

Active knee flexion leads to approximately 130° flexion. The active motion is limited by apposition of the soft tissue masses (posterior thigh and calf). Passive flexion may reach 160°. This is required in people who habitually kneel as part of daily life, and is a challenge for designers of knee prostheses. It can be observed that such deep flexion is often accompanied by tibial medial rotation, so that, when the subject is kneeling, the buttocks can rest on the feet. This movement carries the lateral tibial plateau anteriorly, so that it does not engage with the femoral lateral condyle in deep knee flexion. The femoral

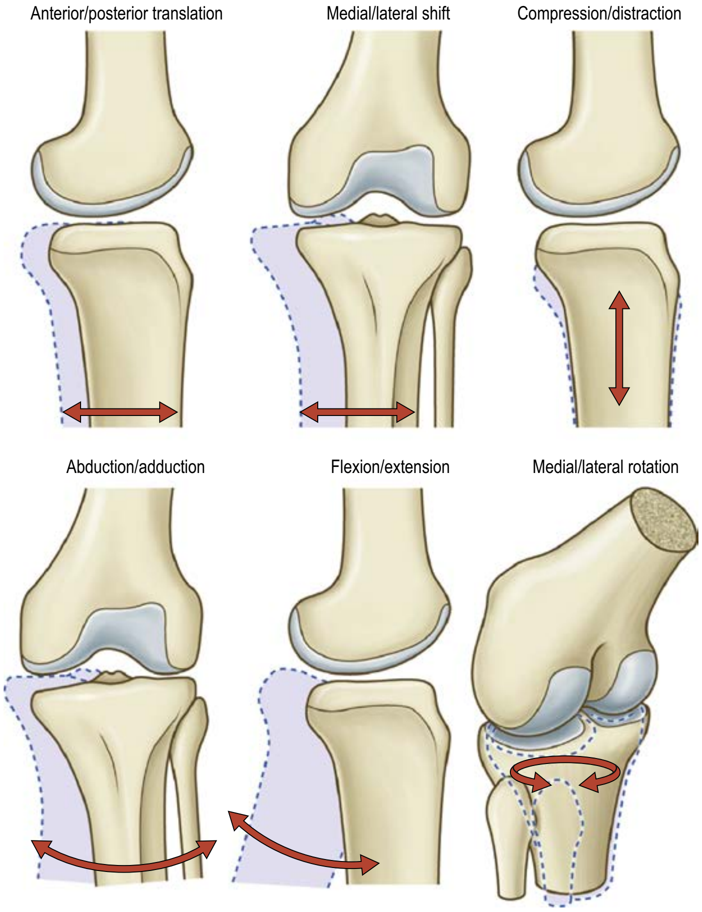

Fig. 78.26 The knee joint motion in three dimensions, described using six independent variables (degrees of freedom).

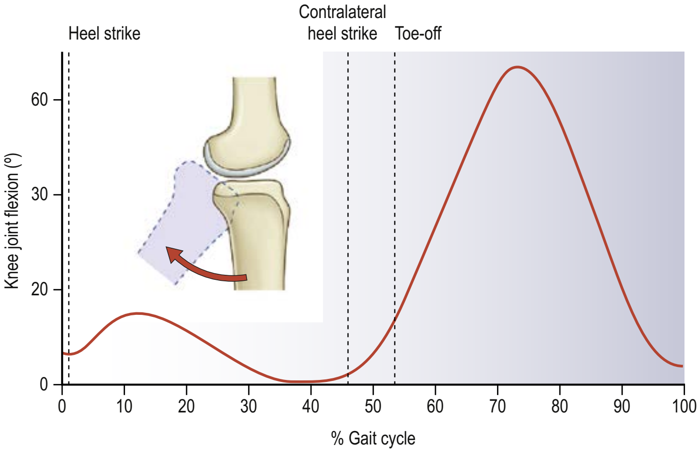

Fig. 78.27 Knee flexion–extension motion during gait.

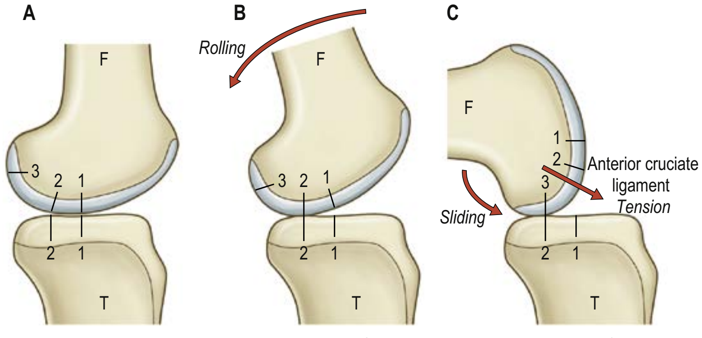

Extension: Central contact of femur on to tibia (F1 on to T1)

Early flexion: Posterior rolling. Contact now moves back to F2 on to T2

Deeper flexion: Anterior cruciate ligament prevents the femur from rolling back further, so now it slides on the tibia. F3 moves on to T2

Fig. 78.28 Knee joint kinematics during gait: rolling and sliding (flexion, anterior translation).

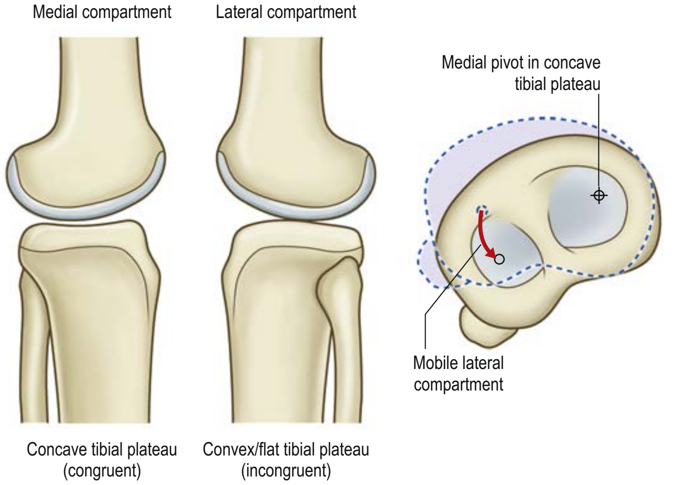
Medial compartment
Lateral compartment
Medial pivot in concave tibial plateau
Mobile lateral compartment
Concave tibial plateau (congruent)
Convex/flat tibial plateau (incongruent)

Fig. 78.29 The shape of the articular surfaces providing mobility of the lateral compartment.

condyle passes posteriorly and rides over the horn of the lateral meniscus.

The most frequently employed knee movement occurs when walking (Fig. 78.27). When the leg is swinging past the supporting leg, the knee must be flexed in order to avoid dragging the toes on the ground; this requires approximately 65° knee flexion. When the swinging leg approaches the first contact with the ground, the knee extends, to move the foot forwards for heel contact. If the knee remained extended, this would then cause the body to move in a circular arc, centred at the ankle, causing the centre of gravity to move upwards and then back down again, leading to more energy expenditure. It would also increase the forces on the knee because the leg would act more like a rigid strut, unable to dissipate the impact forces when the foot hit the ground. All these problems are overcome by flexing the knee 15° in the mid-stance phase (see Fig. 78.27); the centre of gravity of the body can move forwards at approximately constant height, and the impact energy is absorbed by stretching quadriceps femoris.

Tibial medial–lateral rotation also occurs during gait: the tibia rotates laterally during terminal extension, a phenomenon known as 'screw-home'. It is surmised that this rotation helps to lock the geometry and tighten the soft tissues, thereby maintaining the knee in a stable position prior to the impact load of weight-bearing. The knee acts as one link in a chain of limb segments, and this screw-home relates to rotation of both the foot and hip. When the foot is swung forwards for heel contact, the pelvis rotates so that the hip is moved forwards, a movement that entails lateral rotation of the hip. During stance, the femur is medially rotated against the locked knee. Tibial lateral rotation also causes inversion of the foot at the subtalar joint, raising the arch and locking the structure of the foot. The knee flexion that occurs after the impact on the ground allows the tibia to rotate medially so that the foot everts, softening its structure and allowing it to deform and absorb energy. Conversely, towards toe-off, the knee extends, rotating the tibia laterally, so the foot is again a rigid lever with which to push the body forwards.

Articular kinematics

Consideration of knee motion at a smaller scale, i.e. within the joint, is difficult to separate from the actions of the ligaments that act as passive restraints to tibiofemoral joint movements, and are discussed below.

Sagittal sections of the knee reveal that the arcs of the femoral condyles are much longer than the anterior–posterior length of the tibial plateau. This means that if the knee flexed with a purely rolling motion, then the femur would roll off the back of the tibia long before the knee reaches full flexion (Fig. 78.28). This does not happen because the femur slides anteriorly at the same time as it rolls posteriorly, and thus remains in correct articulation. If the knee were to possess a fully conforming roller-in-trough geometry, as in the humero-ulnar joint, then flexion would occur by pure sliding movement between the joint surfaces. This conformity is not possible at the knee because it would inhibit the tibial medial–lateral rotation that is needed during locomotion.

In the locked, fully extended knee, the anterodistal femoral articular surfaces press on to the anterior horns of the menisci. This tends to cause the femur to slide posteriorly, tensing the anterior cruciate ligament and slackening the posterior cruciate ligament. With knee flexion, the femur lifts off the anterior horns of the menisci, leading to contact between the smaller radii of the posterior parts of the femoral condyles and the tibial plateau plus the posterior horns of the menisci. This means that the centre of contact moves posteriorly in early knee flexion. After this, the femoral condyles have approximately circular sagittal sections. The femur is now prevented from rolling back any further by tension in the anterior cruciate ligament.

Articular mechanics

The combined effect of the external and internal loads on the knee is to impose considerable forces on the articular cartilage. This may be analysed as a vertical (compressive) component and a horizontal (shear or friction) component. The friction component is a combination of the compressive force and the friction characteristics of the joint surfaces.

Compression

The compressive force is distributed over an area to produce a contact pressure (contact stress). The contact pressure is, therefore, dependent on the area of contact as well as the load itself. Fully conforming articular surface geometry would allow the greatest area of contact, and thus would minimize contact pressure; however, this is not present in the knee. The medial compartment of the knee is semi-conforming with a convex femoral condyle articulating over a concave medial tibial plateau. The lateral compartment has less conformity; the lateral tibial plateau is flat or slightly convex in sagittal sections. These different shapes reflect the differential movement of the medial and lateral compartments. In normal movement, the screw-home rotation of the tibia occurs about a medial axis, which means that most of the rotation of the tibia is due to an anterior–posterior translation of the lateral compartment (Fig. 78.29).

In order to maintain some degree of conformity, and also to minimize contact pressure between the femur and tibia, the menisci are wedge-shaped in cross-section, thereby increasing the area over which the compressive force on the knee is distributed. In the absence of the menisci,

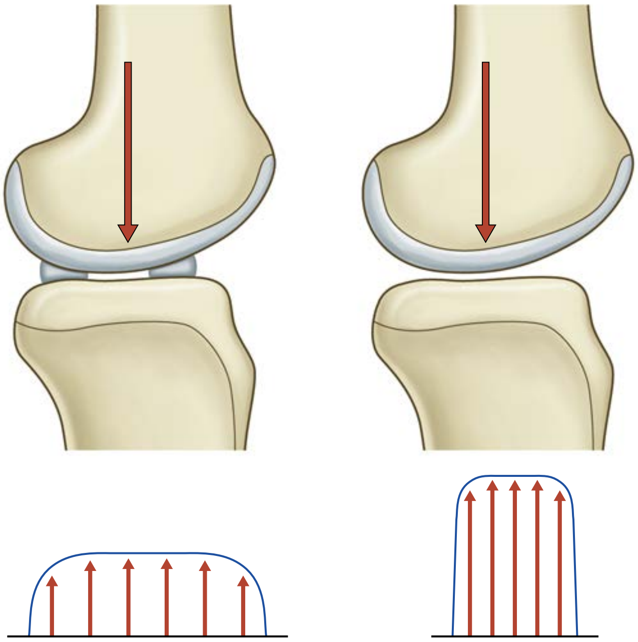

Fig. 78.30 The function of the menisci in increasing articular conformity, with increased peak pressure before and after meniscectomy.

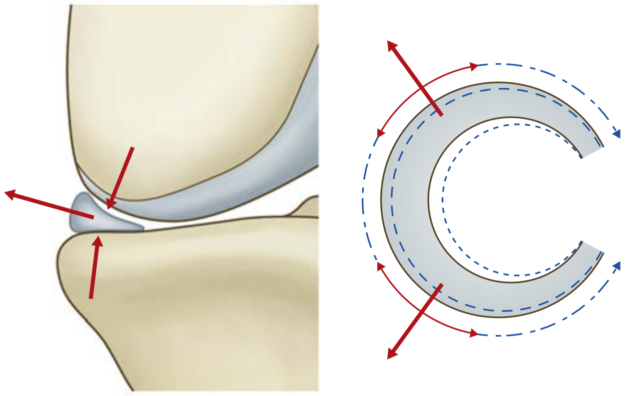

Fig. 78.31 The load-carrying mode of the menisci. Conversion of axial load into meniscal hoop stresses.

the load is carried by a much smaller area of cartilage, resulting in higher contact stresses on the articular cartilage (Fig. 78.30). This helps to explain the prevalence of osteoarthrosis following meniscectomy.

The menisci are most firmly attached at the intercondylar eminence of the tibia, which means that they can translate anteriorly and posteriorly to 'follow' the femoral rollback. The lateral meniscus is more mobile because it is attached to the capsule less tightly than the medial meniscus. The anterior–posterior movement of the menisci is approximately half the magnitude of the anterior–posterior movement of the femur, suggesting that the conformity of the joint changes during flexion of the knee joint.

The distal aspect of the femur, resting on the menisci in the extended knee, has a large radius of curvature and thus fits against the entire area of the menisci. However, as the knee flexes, the smaller radii of the posterior parts of the femoral condyles cause the femur to lift off the anterior horns of the menisci, and the femoral contact is now solely on the posterior horns in the flexed knee. This, combined with the large joint forces that are generated when arising from a seated position, explains why there are often spontaneous tears of the posterior horns in older patients, when standing up from a squatting position.

The load-carrying mode of the menisci is shown in Fig. 78.31. When the femoral condyle presses down on the meniscus, it tends to squeeze the meniscus out of the joint because of its tapered cross-section. This causes the diameter of the circular shape of the meniscus (and therefore the meniscal circumference) to increase. This is resisted by 'hoop tension' in strong fibres that pass around the periphery of the meniscus, and transmit the tension to the tibial plateau via strong insertional ligaments. As the tissue is adapted to resist hoop stresses, it has much greater hoop strength (approximately 100 MPa) than radial strength (approximately 3 MPa), which explains why bucket handle tears occur. It also explains why a circumferential tear does not have such a serious effect on meniscal function because the circumferential fibres can still transmit the loads, whereas a radial tear breaks the load-carrying fibres.

Friction

The knee acts as a bearing that transmits forces and movements between the limb segments. Load-bearing synovial joints move with remarkably little friction and their surfaces must withstand many millions of impact loads, which tend to cause fatigue failure and breakdown of the surfaces.

During walking, every step involves phases of action that vary the loading and velocity conditions at the knee joint. A variety of lubrication mechanisms normally prevent joint surface damage. Thus, in the swing phase, when the foot is off the ground, the joint surfaces are loaded lightly, and have high relative velocity while the knee flexes and extends. This allows the synovial fluid to separate the surfaces, giving fluid film lubrication, with very low friction and no wear (Fig. 78.32). At the time of heel contact, a large impact load acts to compress the surfaces together. At a microscopic level, the surfaces do not come into contact because of the squeeze-film effect: in essence, the impact occurs so rapidly (less than 0.1 sec) that the synovial fluid cannot all be squeezed out of the joint space because of its viscosity and the narrowness of the space. In the mid-stance phase, the flexion–extension motion again entrains the synovial fluid in between the joint surfaces, producing what is known as a hydrodynamic effect: the fluid is trapped between the surfaces by the motion and therefore it acts to separate them. Finally, when the foot is pushing off the body weight, there is little motion and the thin fluid film diminishes under the compressive load. If the squeeze-film effect were insufficient, then the joint surfaces would come into direct contact were it not for the fact that the synovial fluid contains large protein molecules that are trapped on the cartilage surfaces when the fluid is expelled. This molecular layer acts as a boundary lubricant, protecting the cartilage in the same way that grease protects a synthetic bearing.

Many aspects of the arthritic breakdown of the cartilage can be explained on the basis of lubrication biomechanics. Thus, in joints affected by osteoarthrosis, synovial fluid is known to have a lower viscosity than that in normal joints. The viscosity is lower still in joints afflicted with rheumatoid arthritis and is unable to prevent attritional damage to the cartilage surfaces.

Soft tissue mechanics

The knee joint relies on active (musculotendinous) and passive (ligamentous) restraints to maintain its stability. The muscles provide the loading to move the joint: quadriceps femoris, hamstrings and gastrocnemius control both flexion/extension and medial–lateral rotation. However, they also cause anterior–posterior shear forces that are resisted primarily by the cruciate ligaments. This tethering effect is critical in allowing the joint to move physiologically, maintaining congruency and stability.

The passive stabilizers of the joint act by resisting unwanted displacements between the bones. This may be to control the path of motion or to limit the range of motion. When the muscles or some other external force (due to body weight or impact) cause the bones to displace, the ligaments are stretched, and so develop tensile forces that resist the displacement and allow the joint to maintain its stability. Disruption of any of these passive restraints may cause a mechanical instability, which is an abnormally increased displacement due to an applied force (in biomechanical terms this is called excess laxity).

Primary and secondary restraints

On testing the laxity in any of the degrees of freedom of the joint (e.g. in the anterior drawer test, a bedside clinical test in which the subject is placed in the supine position with the knee to be tested flexed to 80–90° before passive forward traction is applied to the tibia), there are usually combinations of ligaments that are tensed. Some of these are better aligned to resist the applied load or displacement. These are termed primary restraints, and are exemplified by the cruciate ligaments and the tibial and fibular collateral ligaments. Secondary restraints are less well aligned but still have a significant restraining effect. These are exemplified by the menisci and by the meniscofemoral ligaments (see p. 1406). In the example in Fig. 78.33, the anterior cruciate ligament is well aligned to resist the applied anterior force. With an absent anterior cruciate ligament, the tibial collateral ligament can resist the applied force; however, it does so by being loaded to a much higher level than the original loading on the anterior cruciate ligament. The size of the lines in the

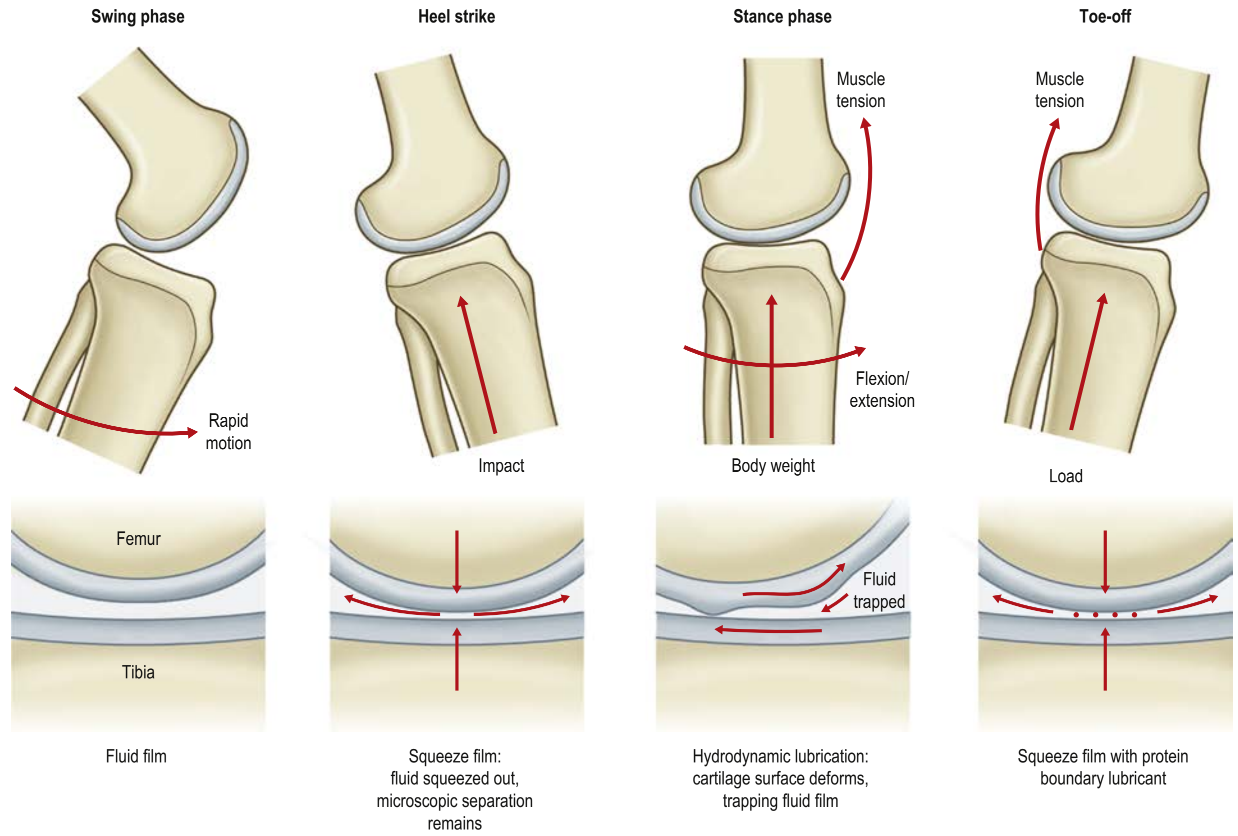
Swing phase
Heel strike
Stance phase
Toe-off
Muscle tension
Muscle tension
Rapid motion
Impact
Body weight
Flexion/ extension
Load
Femur
Tibia
Fluid trapped
Fluid film
Squeeze film: fluid squeezed out, microscopic separation remains
Hydrodynamic lubrication: cartilage surface deforms, trapping fluid film
Squeeze film with protein boundary lubricant

Fig. 78.32 The different modes of knee joint motion and lubrication when walking.

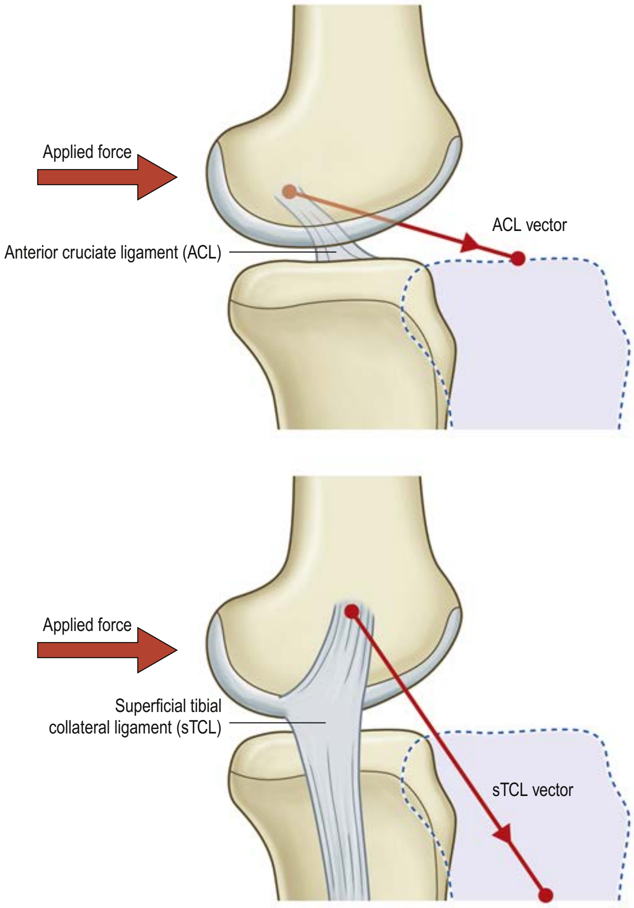
Applied force
Anterior cruciate ligament (ACL)
ACL vector
Applied force
Superficial tibial collateral ligament (sTCL)
sTCL vector

Fig. 78.33 Primary and secondary restraints to anteroposterior forces. The example shows the anterior cruciate ligament (ACL) and superficial part of the tibial collateral ligament (sTCL).

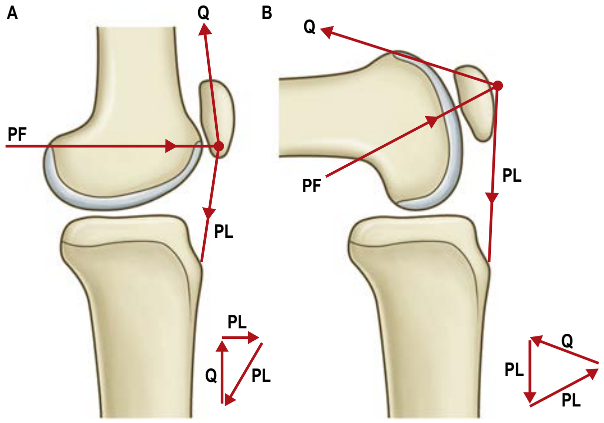
A
Q
B
Q
PF
PF
PL
PL
PL
Q
PL
Q
PL
PL

PL = Patellar ligament force **PF** = Patellofemoral joint reaction force **Q** = Quadriceps femoris traction force

Fig. 78.34 The patellofemoral joint force with knee extension (**A**) and with 90° of knee flexion (**B**).

vector diagram demonstrate this principle: although joint laxity may remain normal initially following rupture of a primary restraint, it may subsequently result in the overload of a secondary restraint and, ultimately, in further soft tissue failure.

The patellofemoral joint is most heavily loaded during weight-bearing activities when the knee is flexed. Analyses of rising from a chair have predicted that the patellar ligament tension at 90° of knee flexion may be greater than the tibiofemoral joint, which is loaded at the same time (Amis and Farahmand 1996).

In the frontal plane, quadriceps femoris and the patellar ligament tensions combine to cause a lateralizing force vector termed the Q-angle effect. The Q angle is defined as the difference between the resultant force vector of quadriceps femoris, which is normally parallel to the femoral shaft, and the patellar ligament (Fig. 78.34). Clinically, the Q angle is changed by the position of hip rotation, tibial rotation and quadriceps femoris tension. The clinical Q angle is 12–15° (males) and 15–18° (females), which means that there is a greater lateralizing force vector on the patellofemoral joint in females. Contraction of quadriceps femoris, therefore, tends to displace the patella laterally, which is resisted by the geometry of the joint and by the ligaments. Vastus medialis obliquus acts medially and posteriorly as much as it acts proximally, and so its tension helps to resist the Q-angle effect.

MUSCLES

Muscles of the knee

The majority of muscles that act on the knee joint (quadriceps femoris, semimembranosus, biceps femoris, semitendinosus, articularis genus) are described in Chapter 77. Gastrocnemius and popliteus are described below.

Popliteus

Attachments Popliteus is a flat muscle that forms the floor of the lower part of the popliteal fossa (see Figs 78.16A, 78.38A). It arises within the capsule of the knee joint by a strong tendon, 2.5 cm long, which is attached to a depression at the anterior end of the groove (groove for popliteus) on the lateral aspect of the lateral condyle of the femur (see Figs 78.8B, 78.17). Medially, this tendon is joined by collagenous fibres arising from the arcuate popliteal ligament; the fibrous capsule adjacent to the lateral meniscus; and the outer margin of the meniscus.

Popliteus is attached to the medial aspect of the head of the fibula by the popliteofibular ligament, which passes laterally and inferiorly from the popliteus tendon in a sheet of tissue that is normally about 2 cm^2 (see Fig. 78.17). This ligament is the single most important stabilizer of the posterolateral region of the knee and resists lateral rotation of the tibia on the femur. Failure to recognize and reconstruct damage to this ligament and to the related ligamentous structures is the most common reason for a poor result from an otherwise well-performed operation for repair of ruptured cruciate ligaments.

Fleshy fibres expand from the inferior limit of the tendon to form a somewhat triangular muscle that descends medially to be inserted into the medial two-thirds of the triangular area above the soleal line on the posterior surface of the tibia, and into the tendinous expansion that covers its surface (see Fig. 78.8).

An additional head may arise from the sesamoid bone in the lateral head of gastrocnemius. Very rarely, two other muscles may be found deeply situated behind the knee. Popliteus minor runs from the posterior surface of the lateral tibial condyle, medial to plantaris, to the oblique popliteal ligament. Peroneotibialis runs deep to popliteus from the medial side of the fibular head to the upper end of the soleal line.

Relations Popliteus is covered posteriorly by a dense aponeurotic expansion, which is largely derived from the tendon of semimembranosus. Gastrocnemius, plantaris, the popliteal vessels and the tibial nerve all lie posterior to the expansion. The popliteal tendon is intracapsular and is deep to the fibular collateral ligament and the tendon of biceps femoris (see Figs 78.16A, 78.23). It is invested on its deep surface by synovial membrane, and grooves the posterior border of the lateral meniscus and the adjoining part of the tibia before it emerges inferior to the posterior band of the arcuate ligament. This region is called the 'popliteus hiatus'; the lateral meniscus has no peripheral bony attachment here and is therefore rather mobile.

Vascular supply The arterial supply of popliteus is derived mainly from the inferior medial and lateral genicular arteries (see Fig. 78.1). The latter may cross either superficial or deep to the muscle. There are additional contributions from the nutrient artery of the tibia (from the posterior tibial artery), the proximal part of the posterior tibial artery and the posterior tibial recurrent artery.

Innervation Popliteus is innervated by a branch of the tibial nerve (L4, L5 and S1) (see Fig. 78.4) that winds around the distal border of popliteus and enters the anterior surface of the muscle; this nerve also innervates the superior tibiofibular joint and the interosseous membrane of the leg.

Actions Popliteus rotates the tibia medially on the femur or, when the tibia is fixed, rotates the femur laterally on the tibia. It is usually regarded as the muscle that 'unlocks' the joint at the beginning of flexion of the fully extended knee; electromyography supports this view. Its connection with the arcuate popliteal ligament, fibrous capsule and lateral meniscus has led to the suggestion that popliteus may retract the posterior horn of the lateral meniscus during lateral rotation of the femur and flexion of the knee joint, thus protecting the meniscus from being crushed between the femur and the tibia during these movements. The muscle is markedly active in crouching, perhaps to provide stability as the tibia rotates medially during flexion of the knee. However, the main function is likely to be provision of dynamic stability to the posterolateral part of the knee by preventing excessive lateral rotation of the tibia, partly by its direct action, but more significantly by tensing the popliteofibular ligament.

Muscles of the leg

The muscles of the leg consist of an anterior group of extensor muscles, which produce dorsiflexion (extension) of the ankle; a posterior group of flexor muscles, which produce plantar flexion (flexion); and a lateral group of muscles, which evert the ankle and are derived embryologically from the anterior muscle group. The greater bulk of the muscles in the calf is commensurate with the powerful propulsive role of the plantar flexors in walking and running.

Anterior (extensor) compartment

The anterior compartment contains muscles that dorsiflex the ankle when acting from above (**Fig. 78.35A**; see Fig. 78.6). When acting from below, they pull the body forwards on the fixed foot during walking. Two of the muscles, extensor digitorum longus and extensor hallucis longus, also extend the toes, and two muscles, tibialis anterior and fibularis tertius, have the additional actions of inversion and eversion, respectively.

Tibialis anterior

Attachments Tibialis anterior is a superficial muscle and is therefore readily palpable lateral to the tibia. It arises from the lateral condyle and proximal one-half to two-thirds of the lateral surface of the tibial shaft; the adjoining anterior surface of the interosseous membrane; the deep surface of the deep fascia; and the intermuscular septum between itself and extensor digitorum longus (see Figs 78.6A, 78.7B). The muscle descends vertically and ends in a tendon on its anterior surface in the lower third of the leg. The tendon passes through the medial compartments of the superior and inferior retinacula, inclines medially, and is inserted on to the medial and inferior surfaces of the medial cuneiform and the adjoining part of the base of the first metatarsal (see Fig. 79.5B).

Attachments to the talus, first metatarsal head, base of the proximal phalanx of the hallux and extensor retinaculum have been recorded.

Relations Tibialis anterior overlaps the anterior tibial vessels and deep fibular nerve in the upper part of the leg. It lies on the tibia and interosseous membrane. Extensor digitorum longus and extensor hallucis longus lie laterally.

Vascular supply The main body of tibialis anterior is supplied by a series of medial and anterior branches of the anterior tibial artery; the branches may occur in two columns (**Fig. 78.36**). There is a proximal accessory supply from the anterior tibial recurrent artery. The tendon is supplied by the anterior medial malleolar artery and network, dorsalis pedis artery, medial tarsal arteries, and by the medial malleolar and calcaneal branches of the posterior tibial artery (see Fig. 79.10).

Innervation Tibialis anterior is innervated by the deep fibular nerve, L4 and L5.

Actions Tibialis anterior dorsiflexes and inverts the foot. It is most active when both movements are combined, as in walking. Its tendon can be seen through the skin lateral to the anterior border of the tibia and can be traced downwards and medially across the front of the ankle to the medial side of the foot. Tibialis anterior elevates the first metatarsal base and medial cuneiform, and rotates their dorsal aspects laterally.

The muscle is usually quiescent while standing, since the weight of the body acts through vertical lines that pass anterior to the ankle joints. Acting from below, it helps to counteract any tendency to overbalance backwards by flexing the leg forwards at the ankle. It has a role in supporting the medial part of the longitudinal arch of the foot; although electromyographically detectable activity is minimal during standing, it

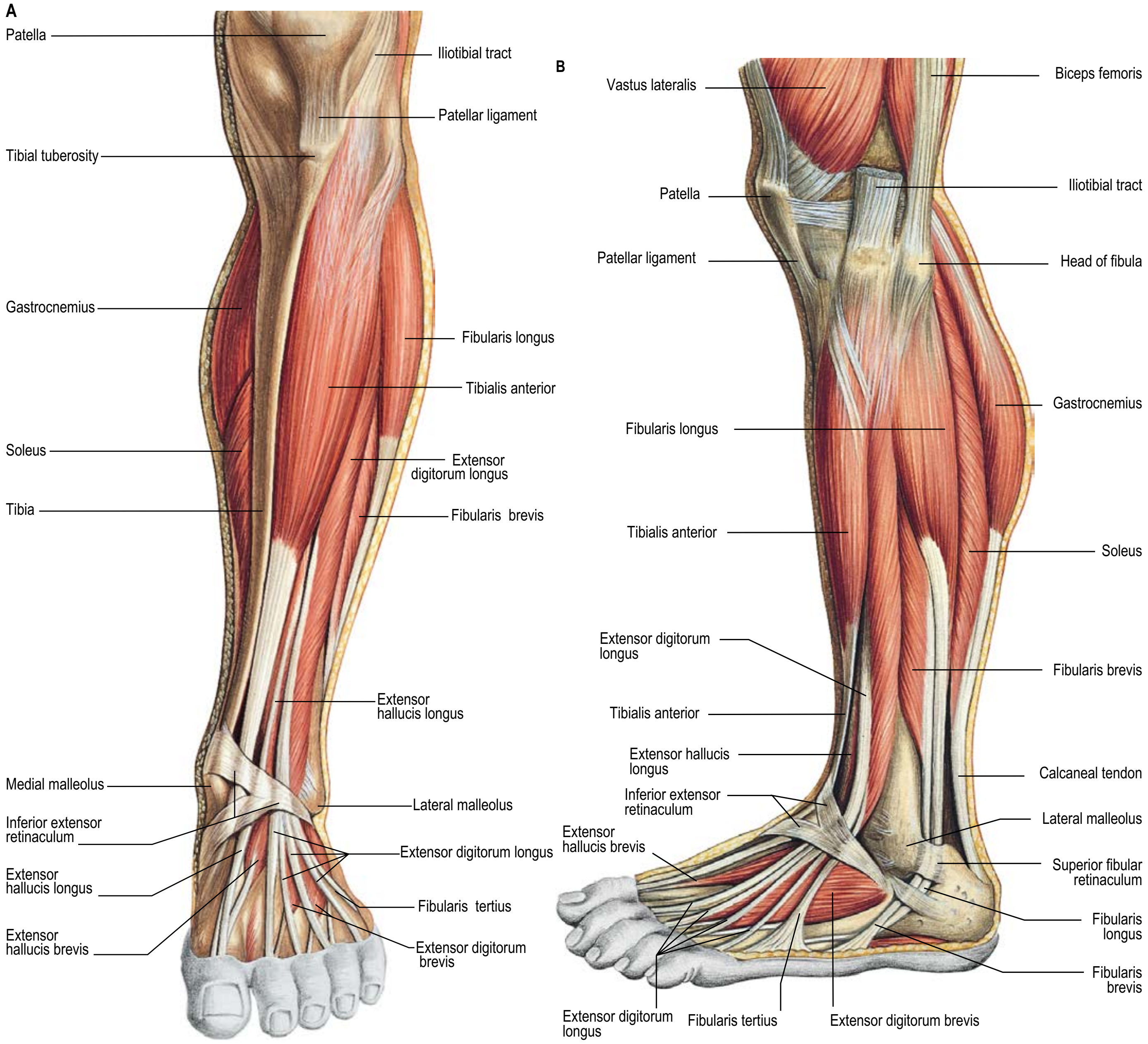
A
Patella
Iliotibial tract
Patellar ligament
Tibial tuberosity
Gastrocnemius
Fibularis longus
Tibialis anterior
Soleus
Extensor digitorum longus
Tibia
Fibularis brevis
Extensor hallucis longus
Medial malleolus
Lateral malleolus
Inferior extensor retinaculum
Extensor digitorum longus
Extensor hallucis longus
Fibularis tertius
Extensor hallucis brevis
Extensor digitorum brevis
B
Vastus lateralis
Biceps femoris
Patella
Iliotibial tract
Patellar ligament
Head of fibula
Gastrocnemius
Fibularis longus
Tibialis anterior
Soleus
Extensor digitorum longus
Fibularis brevis
Tibialis anterior
Extensor hallucis longus
Calcaneal tendon
Inferior extensor retinaculum
Lateral malleolus
Extensor hallucis brevis
Superior fibular retinaculum
Fibularis longus
Fibularis brevis
Extensor digitorum longus
Fibularis tertius
Extensor digitorum brevis

Fig. 78.35 Muscles of the left leg and foot. The fasciae have been removed. **A**, Anterior view. **B**, Lateral view. (With permission from Waschke J, Paulsen F (eds) Sobotta Atlas of Human Anatomy, 15th ed. Elsevier, Urban & Fischer. Copyright 2013.)

is manifest during any movement that increases the arch, such as toe-off in walking and running.

Testing Tibialis anterior can be seen to act when the foot is dorsiflexed against resistance. Dorsiflexion is best tested by asking the subject to walk on their heels.

Extensor hallucis longus

Attachments Extensor hallucis longus lies between, and is partly overlapped by, tibialis anterior and extensor digitorum longus (see Figs 78.6A, 78.35). It arises from the middle half of the medial surface of the fibula, medial to extensor digitorum longus (see Fig. 78.7B), and from the adjacent anterior surface of the interosseous membrane. Its fibres run distally and end in a tendon that forms on the anterior border of the muscle. The tendon passes deep to the superior extensor retinaculum and through the inferior extensor retinaculum, crosses anterior to the anterior tibial vessels to lie on their medial side near the ankle, and is inserted on to the dorsal aspect of the base of the distal phalanx of the hallux (see Fig. 79.5). At the metatarsophalangeal joint, a thin prolongation from each side of the tendon covers the dorsal surface of the joint. An expansion from the medial side of the tendon to the base of the proximal phalanx is usually present (see Fig. 79.1).

Extensor hallucis longus is sometimes united with extensor digitorum longus and may send a slip to the second toe.

Relations The anterior tibial vessels and deep fibular nerve lie between extensor hallucis longus and tibialis anterior. Extensor hallucis longus lies lateral to the artery proximally, crosses it in the lower third of the leg and is medial to it on the foot.

Vascular supply Extensor hallucis longus is supplied by the anterior tibial artery via obliquely running branches, with a variable contribution from the perforating branch of the fibular artery (see Fig. 78.36). More distally, the tendon is supplied via the anterior medial malleolar artery and network, the dorsalis pedis artery and the plantar metatarsal artery of the first digit via perforating branches.

Innervation Extensor hallucis longus is innervated by the deep fibular nerve, L5.

Actions Extensor hallucis longus extends the hallux and dorsiflexes the foot. When the hallux is actively extended, relatively little external force is required to overcome the extension of the distal phalanx, whereas considerable force is needed to overcome the extension of the proximal phalanx.

Testing When the hallux is extended against resistance the tendon of extensor hallucis longus can be seen and felt on the lateral side of the tendon of tibialis anterior.

Extensor digitorum longus

Attachments Extensor digitorum longus arises from the inferior surface of the lateral condyle of the tibia, the proximal three-quarters of the medial surface of the fibula, the adjacent anterior surface of the

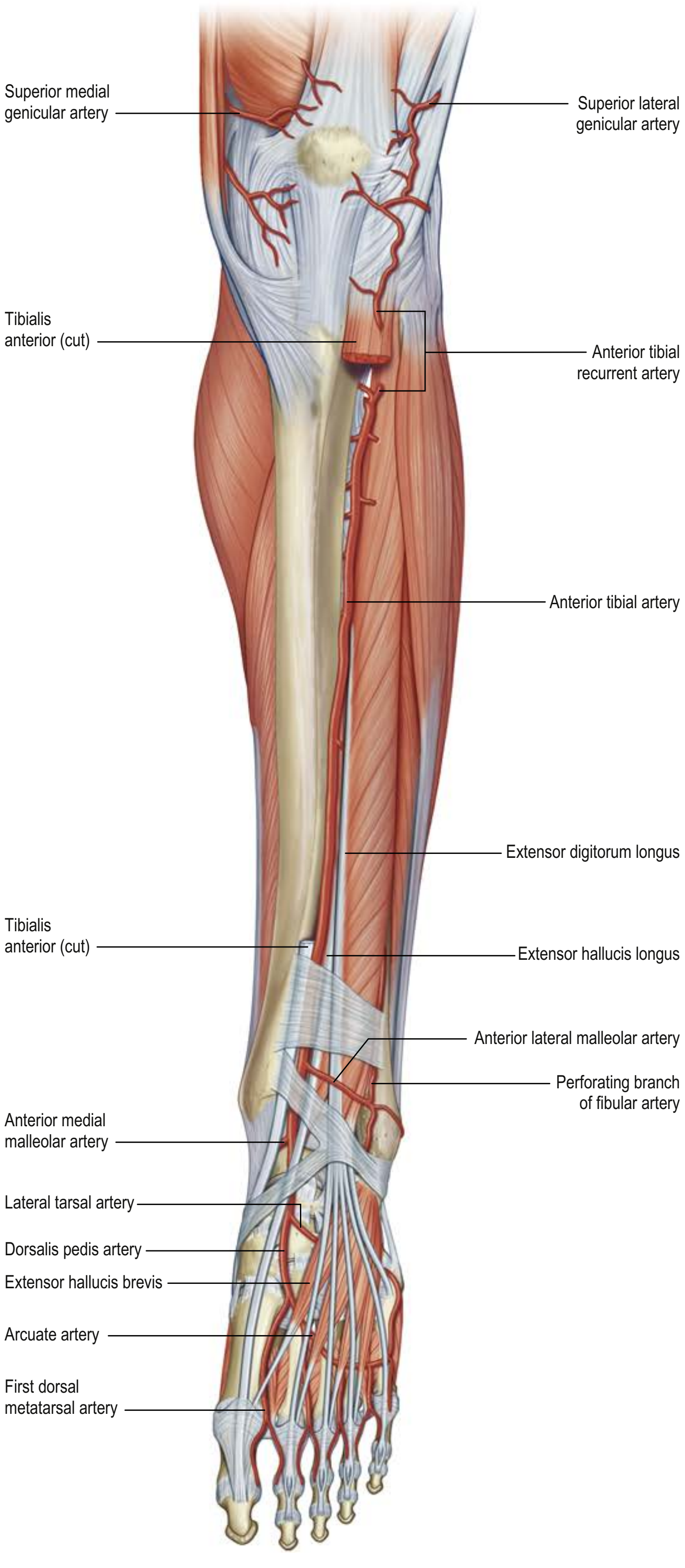
Superior medial genicular artery
Superior lateral genicular artery
Tibialis anterior (cut)
Anterior tibial recurrent artery
Anterior tibial artery
Extensor digitorum longus
Tibialis anterior (cut)
Extensor hallucis longus
Anterior lateral malleolar artery
Perforating branch of fibular artery
Anterior medial malleolar artery
Lateral tarsal artery
Dorsalis pedis artery
Extensor hallucis brevis
Arcuate artery
First dorsal metatarsal artery

Fig. 78.36 The left anterior tibial and dorsalis pedis arteries. To expose the anterior tibial artery, a large part of tibialis anterior has been excised.

interosseous membrane, the deep surface of the deep fascia, the anterior intermuscular septum and the fascial septum between itself and tibialis anterior (see Figs 78.6A, 78.7B). These origins form the walls of an osseo-aponeurotic tunnel. Extensor digitorum longus becomes tendinous at about the same level as tibialis anterior, and the tendon passes deep to the superior extensor retinaculum and within a loop of the inferior extensor retinaculum with fibularis tertius (see Fig. 78.35A). It divides into four slips, which run forwards on the dorsum of the foot and are attached in the same way as the tendons of extensor digitorum in the hand. At the metatarsophalangeal joints, the tendons to the second, third and fourth toes are each joined on the lateral side by a tendon of extensor digitorum brevis. The so-called dorsal digital expansions thus formed on the dorsal aspects of the proximal phalanges, as in the fingers, receive contributions from the appropriate lumbrical and interosseous muscles. The expansion narrows as it approaches a proximal interphalangeal joint, and divides into three slips. These are a central (axial) slip, attached to the base of the middle phalanx, and two collateral (coaxial) slips, which reunite on the dorsum of the middle phalanx and are attached to the base of the distal phalanx (see Figs 79.1, 79.5A).

The tendons to the second and fifth toes are sometimes duplicated, and accessory slips may be attached to metatarsals or to the hallux.

Relations Extensor digitorum longus lies on the lateral tibial condyle, fibula, lower end of the tibia, ankle joint and extensor digitorum brevis. Tibialis anterior and extensor hallucis longus lie medially in the leg, and the fibular muscles lie laterally. In the upper part of the leg, the anterior tibial vessels and deep fibular nerve lie between extensor digitorum longus and tibialis anterior; the nerve runs obliquely and medially beneath its upper part.

Vascular supply The main blood supply to extensor digitorum longus is derived from anteriorly and laterally placed branches of the anterior tibial artery, supplemented distally from the perforating branch of the fibular artery (see Fig. 78.36). Proximally, there may also be a supply from the inferior lateral genicular, popliteal or anterior tibial recurrent arteries. At the ankle and in the foot the tendons are supplied by the anterior lateral malleolar artery and malleolar network, and by lateral tarsal, metatarsal, plantar and digital arteries (see Fig. 79.10).

Innervation Extensor digitorum longus is innervated by the deep fibular nerve, L5, S1.

Actions Extensor digitorum longus extends the lateral four toes. Acting synergistically with tibialis anterior, extensor hallucis longus and fibularis tertius, it is a dorsiflexor of the ankle. Acting with extensor hallucis longus, it helps tighten the plantar aponeurosis.

Testing The tendons of extensor digitorum longus can be seen when the toes are extended against resistance.

Fibularis tertius

Attachments Fibularis tertius (peroneus tertius) often appears to be part of extensor digitorum longus and might be described as its 'fifth tendon'. The muscle fibres of fibularis tertius arise from the distal third or more of the medial surface of the fibula, the adjoining anterior surface of the interosseous membrane, and the anterior intermuscular septum. The tendon passes deep to the superior extensor retinaculum and within the loop of the inferior extensor retinaculum alongside the extensor digitorum longus (see Figs 78.35, 79.2A). It is inserted on to the medial part of the dorsal surface of the base of the fifth metatarsal; a thin expansion usually extends forwards along the medial border of the shaft of the bone (see Fig. 79.5A).

Relations Fibularis tertius lies lateral to extensor digitorum longus.

Vascular supply Fibularis tertius is supplied by the same vessels as extensor digitorum longus. In the foot it receives an additional supply from the termination of the arcuate artery and the fourth dorsal metatarsal artery.

Innervation Fibularis tertius is innervated by the deep fibular nerve, L5, S1.

Actions Electromyographic studies show that during the swing phase of gait, fibularis tertius acts with extensor digitorum longus and tibialis anterior to produce dorsiflexion of the foot, and with fibularis longus and fibularis brevis to effect eversion of the foot (Jungers et al 1993). This levels the foot and helps the toes to clear the ground, an action that improves the efficiency and enhances the economy of bipedal locomotion. Fibularis tertius is not active during the stance phase, a finding that is at variance with the suggestion that the muscle acts primarily to support the lateral longitudinal arch and to transfer the centre of pressure of the foot medially.

Testing Fibularis tertius cannot be tested in isolation, but its tendon can sometimes be seen and felt when the foot is dorsiflexed against resistance.

Lateral (fibular, peroneal) compartment

The lateral compartment contains fibularis (peroneus) longus and fibularis (peroneus) brevis (see Figs 78.6, 78.35B). Both muscles evert the foot and are plantar flexors of the ankle, and both probably play a part in balancing the leg on the foot in standing and walking.

Fibularis longus

Attachments Fibularis longus is the more superficial of the two muscles of the lateral compartment. It arises from the head and proximal two-thirds of the lateral surface of the fibula, the deep surface of the deep fascia, the anterior and posterior intermuscular septa, and occasionally by a few fibres from the lateral condyle of the tibia (see Fig. 78.6A, 78.7B). The muscle belly ends in a long tendon that runs distally behind the lateral malleolus in a groove it shares with the tendon of fibularis brevis. The groove is converted into a canal by the superior fibular retinaculum, so that the tendon of fibularis longus and that of fibularis brevis, which lies in front of the longus tendon, are contained in a common synovial sheath. If the fibular retinaculum is ruptured by injury and fails to heal, the tendons can dislocate from the groove. The fibularis longus tendon runs obliquely forwards on the lateral side of the calcaneus, below the fibular trochlea and the tendon of fibularis brevis, and deep to the inferior fibular retinaculum. It crosses the lateral side of the cuboid and then runs under the cuboid in a groove that is converted into a canal by the long plantar ligament (see Fig. 79.18). It crosses the sole of the foot obliquely and is attached by two slips, one to the lateral side of the base of the first metatarsal and one to the lateral aspect of the medial cuneiform (see Fig. 79.5A); occasionally, a third slip is attached to the base of the second metatarsal. The tendon changes direction below the lateral malleolus and on the cuboid bone. At both sites it is thickened, and at the second site a sesamoid fibrocartilage (sometimes a bone, the os peroneum) is usually present. A second synovial sheath invests the tendon as it crosses the sole of the foot (see Fig. 79.21B).

Relations Proximally, fibularis longus lies posterior to extensor digitorum longus and anterior to soleus and flexor hallucis longus. Distally, in the leg, it lies posterior to fibularis brevis. Between its attachments to the head and shaft of the fibula there is a gap through which the common fibular nerve passes.

Vascular supply of lateral compartment Usually, the predominant supply of the lateral compartment muscles is derived from branches of the anterior tibial artery; the superior is commonly the larger. There is also a lesser, variable, contribution from the fibular artery in the distal part of the leg (see Fig. 78.4). A fibular branch may replace the inferior branch of the anterior tibial artery; less commonly, the fibular artery provides the main supply to the whole compartment. The upper part of fibularis longus is also supplied by the circumflex fibular branch of the posterior tibial artery, which is usually a branch of the anterior tibial artery. The companion artery to the common fibular nerve, a branch of the popliteal artery, provides a minor contribution proximally. Distally, the tendons are supplied by the fibular perforating, anterior lateral malleolar, lateral calcaneal, lateral tarsal, arcuate, lateral and medial plantar arteries (see Fig. 79.10).

Innervation Fibularis longus is innervated by the superficial fibular nerve, L5, S1.

Actions There is little doubt that fibularis longus can evert the foot and plantar flex the ankle, and possibly act on the leg from its distal attachments. The oblique direction of its tendon across the sole also enables it to support the longitudinal and transverse arches of the foot (see p. 1454). With the foot off the ground, eversion is visually and palpably associated with increased prominence of both tendon and muscle. It is not clear to what extent this helps to maintain plantigrade contact of the foot in normal standing, but electromyographic recordings show little or no fibular activity under these conditions. Fibularis longus and brevis come strongly into action to maintain the concavity of the foot during toe-off and tip-toeing. If the subject deliberately sways to one side, fibularis longus and brevis contract on that side, but their involvement in influencing postural interactions between the foot and leg remains uncertain.

Testing Fibularis longus and brevis are tested together by eversion of the foot against resistance; the tendons can be identified laterally at the ankle and in the foot.

Fibularis brevis

Attachments Fibularis brevis arises from the distal two-thirds of the lateral surface of the fibula, anterior to fibularis longus (see Figs 78.7B, 78.8B), and from the anterior and posterior crural intermuscular septa. It passes vertically downwards and ends in a tendon that passes behind the lateral malleolus together with, and anterior to, that of fibularis longus. The two tendons run deep to the superior fibular retinaculum in a common synovial sheath. The tendon of fibularis brevis then runs forwards on the lateral side of the calcaneus above the fibular trochlea and the tendon of fibularis longus, and is inserted into a tuberosity on the lateral side of the base of the fifth metatarsal (see Fig. 79.5).

Relations Anteriorly lie extensor digitorum longus and fibularis tertius. Fibularis longus and flexor hallucis longus are posterior. On the lateral surface of the calcaneus the tendons of fibularis longus and fibularis brevis occupy separate osteofascial canals formed by the calcaneus and the inferior fibular retinaculum; each tendon is enveloped in a separate distal prolongation of the common synovial sheath (see Fig. 79.2A).

Vascular supply This is considered with the vascular supply of the lateral compartment (above).

Innervation Fibularis brevis is innervated by the superficial fibular nerve, L5, S1.

Actions Fibularis brevis may limit inversion of the foot and so relieve strain on the ligaments that are tightened by this movement (the lateral part of interosseous talocalcaneal, lateral talocalcaneal and calcaneofibular ligaments). It participates in eversion of the foot and may help to steady the leg on the foot. See also ‘Fibularis longus’.

Testing This is considered with testing of fibularis longus.

Variants of fibular muscles Tendinous slips from fibularis longus may extend to the base of the third, fourth or fifth metatarsals, or to adductor hallucis. Fusion of fibularis longus and brevis has been reported but is rare. Fibularis tertius is highly variable in its form and bulk but is seldom completely absent; its distal attachment may be to the fourth metatarsal rather than the fifth. Two other variant fibular muscles, arising from the fibula between fibularis longus and fibularis brevis, have been described. These are fibularis accessorius, whose tendon joins that of fibularis longus in the sole, and fibularis quartus, which arises posteriorly and inserts on to the calcaneus or on to the cuboid.

Posterior (flexor) compartment

The muscles in the posterior compartment of the lower leg form superficial and deep groups, separated by the transverse intermuscular septum.

Superficial flexor group

The superficial muscles, gastrocnemius, plantaris and soleus, form the bulk of the calf (**Fig. 78.37**; see Figs 78.3, 78.6). Gastrocnemius and soleus, collectively known as the triceps surae, constitute a powerful muscular mass whose main function is plantar flexion of the foot, although soleus in particular has an important postural role (see below). Their large size is a defining human characteristic, and is related to the upright stance and bipedal locomotion of the human. Gastrocnemius and plantaris act on both the knee and the ankle joints, soleus on the latter alone.

Gastrocnemius

Attachments Gastrocnemius is the most superficial muscle of the group and forms the ‘belly’ of the calf (see Figs 78.3, 78.37). It arises by two heads, connected to the condyles of the femur by strong, flat tendons. The medial, larger head is attached to a depression at the upper and posterior part of the medial condyle behind the adductor tubercle, and to a slightly raised area on the popliteal surface of the femur just above the medial condyle. The lateral head is attached to a recognizable area on the lateral surface of the lateral condyle and to the lower part of the corresponding supracondylar line (see Fig. 77.12B). Both heads also arise from subjacent areas of the capsule of

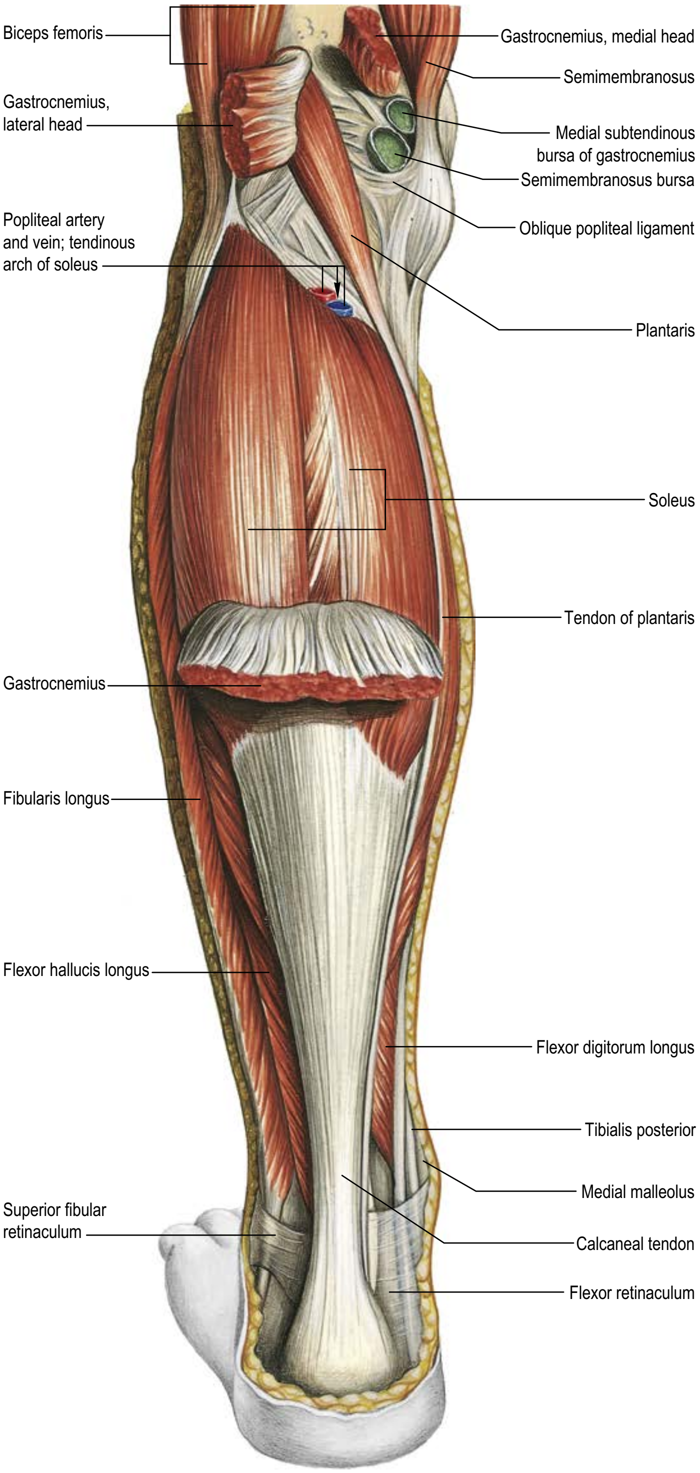

Fig. 78.37 Muscles of the left leg, posterior aspect. Gastrocnemius has been partially removed. (With permission from Waschke J, Paulsen F (eds) Sobotta Atlas of Human Anatomy, 15th ed. Elsevier, Urban & Fischer. Copyright 2013.)

the knee joint. The tendinous attachments expand to cover the posterior surface of each head with an aponeurosis, from the anterior surface of which the muscle fibres arise. The fleshy part of the muscle extends to about mid-calf. The muscle fibres of the larger medial head extend lower than those of the lateral head. As the muscle descends, the muscle fibres begin to insert into a broad aponeurosis that develops on its anterior surface; up to this point, the muscular masses of the two heads remain separate. The aponeurosis gradually narrows and receives the tendon of soleus on its deep surface to form the calcaneal tendon (for a detailed description of the calcaneal tendon, see Chapter 79).

On occasion, the lateral head, or the whole muscle, is absent. A third head arising from the popliteal surface of the femur is sometimes present.

Relations Proximally, the two heads of gastrocnemius form the lower boundaries of the popliteal fossa. The lateral head is partially overlaid by the tendon of biceps femoris, the medial head by semimembranosus (see Fig. 78.2). Over the rest of its length, the muscle is superficial and the two heads can easily be seen in the living subject. The superficial surface of the muscle is separated by the deep fascia from the short saphenous vein and the fibular communicating and sural nerves. The common fibular nerve crosses behind the lateral head of the muscle, partly under cover of biceps femoris. The deep surface lies posterior to the oblique popliteal ligament, popliteus, soleus, plantaris, popliteal vessels and the tibial nerve. A bursa, which communicates with the knee joint, is located anterior to the tendon of the medial head (see Fig. 78.37); if the bursa expands into the popliteal fossa, it does so in the plane between the medial head of gastrocnemius and semimembranosus. The tendon of the lateral head frequently contains a sesamoid bone, the fabella, where it moves over the lateral femoral condyle. A sesamoid bone may occasionally occur in the tendon of the medial head.

Vascular supply Each head of gastrocnemius is supplied by its own sural artery. These arteries are branches of the popliteal artery and arise at variable levels, usually at the level of the tibiofemoral joint line. The medial sural artery almost always arises more proximally than the lateral; the medial may arise proximal to the joint line, the lateral sometimes distal to the line. Each sural artery enters the corresponding muscle head with its nerve of supply, the pedicle entering the muscle near its axial border at the level of the middle of the popliteal fossa. Medial or lateral gastrocnemius musculocutaneous flaps may be raised, each based on its neurovascular pedicle. Minor accessory sural arteries arise from the popliteal or from the superior genicular arteries.

The blood supply to the calcaneal tendon is described in Chapter 79.

Innervation Gastrocnemius is innervated by the tibial nerve, S1 and S2.

Actions The action of gastrocnemius is considered with soleus.

Testing Gastrocnemius is tested by plantar flexion of the foot against resistance, in the supine position and with the knee extended. Plantar flexion (gastrocnemius and soleus) is best tested by asking the subject to perform repetitive unilateral toe rises.

Plantaris

Attachments Plantaris arises from the lower part of the lateral supracondylar line and the oblique popliteal ligament (see Figs 77.12B, 78.37). Its small fusiform belly is 7–10 cm long and ends in a long slender tendon, which crosses obliquely, in an inferomedial direction, between gastrocnemius and soleus, then runs distally along the medial border of the calcaneal tendon and inserts on to the calcaneus just medial to the calcaneal tendon (see Fig. 79.5A). Occasionally, it ends by fusing with the calcaneal tendon.

The muscle is sometimes double, and occasionally absent. Occasionally, its tendon merges with the flexor retinaculum or with the fascia of the leg.

Vascular supply Plantaris is supplied superficially by the lateral sural and popliteal arteries, and deeply by the superior lateral genicular artery. The distal tendon shares a blood supply with the calcaneal tendon.

Innervation Plantaris is innervated by the tibial nerve, often from the ramus that supplies the lateral head of gastrocnemius, S1 and S2.

Actions In many mammals, plantaris is well developed and inserts directly or indirectly into the plantar aponeurosis. In humans, the muscle is almost vestigial and is normally inserted well short of the plantar aponeurosis, usually into the calcaneus. It is therefore presumed to act with gastrocnemius.

Soleus

Attachments Soleus is a broad, flat muscle situated immediately deep (anterior) to gastrocnemius (see Figs 78.6, 78.37). It arises from the posterior surface of the head and proximal quarter of the shaft of the fibula; the soleal line and the middle third of the medial border of the tibia (see Fig. 78.8B); and from a fibrous band between the tibia and fibula (tendinous arch of the soleus) that arches over the popliteal vessels and tibial nerve. This origin is aponeurotic; most of the muscular fibres arise from its posterior surface and pass obliquely to the tendon of insertion on the posterior surface of the muscle. Other muscle fibres arise from the anterior surface of the aponeurosis. They are short, oblique and bipennate in arrangement, and converge on a narrow, central intramuscular tendon that merges distally with the principal tendon. The latter gradually becomes thicker and narrower, and joins the tendon of gastrocnemius to form the calcaneal tendon. The muscle is covered proximally by gastrocnemius, but below mid-calf it is broader than the tendon of gastrocnemius and is readily accessible on either side of the tendon.

An accessory part of the muscle is sometimes present distally and medially. It may be inserted into the calcaneal tendon, the calcaneus or the flexor retinaculum.

Relations The superficial surface of soleus is in contact with gastrocnemius and plantaris. Its deep surface is related to flexor digitorum longus, flexor hallucis longus, tibialis posterior and the posterior tibial vessels and tibial nerve, from all of which it is separated by the transverse intermuscular septum of the leg.

Vascular supply Soleus is supplied by two main arteries: the superior arises from the popliteal artery at about the level of the soleal arch, and the inferior from the proximal part of the fibular artery or sometimes from the posterior tibial artery. A secondary supply is derived from the lateral sural, fibular or posterior tibial vessels.

There is a venous plexus within the muscle belly that is important physiologically as part of the muscle pump complex (see below). Pathologically, it is a common site of deep vein thrombosis.

Innervation Soleus is innervated by two branches from the tibial nerve, S1 and S2.

Actions These are considered with the actions of triceps surae (below).

Testing Soleus is tested by plantar flexion of the foot against resistance in the supine position, with hip and knee flexed; the muscle belly can be palpated separately from those of gastrocnemius.

Actions of triceps surae

Gastrocnemius and soleus are the chief plantar flexors of the foot; gastrocnemius is also a flexor of the knee. The muscles are usually large and correspondingly powerful. Gastrocnemius provides force for propulsion in walking, running and leaping. Soleus, acting from below, is said to be more concerned with steadying the leg on the foot in standing. This postural role is also suggested by its high content of slow, fatigue-resistant (type 1) muscle fibres. In many adult mammals the proportion of this type of fibre in soleus approaches 100%. However, such a rigid separation of functional roles seems unlikely in humans; soleus probably participates in locomotion, and gastrocnemius in posture. Nevertheless, the ankle joint is loose-packed in the erect posture, and since the weight of the body acts through a vertical line that passes anterior to the joint, a strong brace is required behind the joint to maintain stability. Electromyography shows that these forces are supplied mainly by soleus; during symmetrical standing, soleus is continuously active, whereas gastrocnemius is recruited only intermittently. The relative contributions of soleus and gastrocnemius to phasic activity of the triceps surae in walking have yet to be satisfactorily analysed.

Deep flexor group

The deep flexor group (see Fig. 78.6; **Fig. 78.38**) lies beneath (anterior to) the transverse intermuscular septum and consists of popliteus, which acts on the knee joint, and flexor digitorum longus, flexor hallucis longus and tibialis posterior, which all produce plantar flexion at the ankle in addition to their specific actions on joints of the foot and digits.

Popliteus

Popliteus is described on page 1416.

Flexor digitorum longus

Attachments Flexor digitorum longus is thin and tapered proximally, but widens gradually as it descends (see Fig. 78.38). It arises from the posterior surface of the tibia medial to tibialis posterior from just below the soleal line to within 7 or 8 cm of the distal end of the bone (see Fig. 78.8B); it also arises from the fascia covering tibialis posterior. The muscle ends in a tendon that extends along almost the whole of its posterior surface. The tendon gradually crosses tibialis posterior on its superficial aspect and passes behind the medial malleolus where it shares a groove with tibialis posterior, from which it is separated by a fibrous septum, i.e. each tendon occupies its own compartment lined by a synovial sheath (see Fig. 79.2B). The tendon of flexor digitorum longus then curves obliquely forwards and laterally, in contact with the medial side of the sustentaculum tali, passes deep to the flexor retinaculum, and enters the sole of the foot on the medial side of the tendon of flexor hallucis longus. It crosses superficial to that tendon and receives a strong slip from it (and may also send a slip to it). The tendon of flexor digitorum longus then passes forwards as four separate tendons, one each for the second to fifth toes, deep to the tendons of flexor digitorum brevis. After giving rise to the lumbricals, it passes through the fibrous sheaths of the lateral four toes. The tendons of flexor accessorius insert into the long flexor tendons of the second, third and fourth digits (see Fig. 79.21); flexor hallucis longus makes a variable contribution through the connecting slip mentioned above. The long flexor tendons of the lateral four digits are attached to the plantar surfaces of the bases of their distal phalanges; each passes between the slips of the corresponding tendon of flexor digitorum brevis at the base of the proximal phalanx (see Figs 79.5B, 79.23).

A supplementary head of the muscle, flexor accessorius longus, with its own tendon, may arise from the fibula, tibia or deep fascia and insert into the main tendon or into flexor accessorius in the foot. It may send communicating slips to tibialis anterior or to flexor hallucis longus.

Relations Flexor digitorum longus lies medial to flexor hallucis longus. In the leg, its superficial surface is in contact with the transverse intermuscular septum, which separates it from soleus, and distally from the posterior tibial vessels and tibial nerve. Its deep surface is related to the tibia and to tibialis posterior. In the foot, it is covered by abductor hallucis and flexor digitorum brevis, and it crosses superficial to flexor hallucis longus.

Vascular supply A series of transversely running branches of the posterior tibial artery enters the lateral border of flexor digitorum longus. There may be a secondary supply from fibular branches to flexor hallucis longus. The tendons are supplied by the vessels of the ankle and sole of the foot.

Innervation Flexor digitorum longus is innervated by branches of the tibial nerve, L5, S1 and S2.

Actions These are considered with the actions of the deep digital flexors (below).

Testing Flexor digitorum longus is tested by flexing the toes against resistance. Aberrant function of flexor digitorum longus is implicated in toe deformities such as hammer toe, claw toe and mallet toe. Its tendon may be used in transfer procedures for the surgical treatment of tibialis posterior tendon dysfunction.

Flexor hallucis longus

Attachments Flexor hallucis longus arises from the distal two-thirds of the posterior surface of the fibula (except for the lowest 2.5 cm of this surface); the adjacent interosseous membrane and the posterior crural intermuscular septum; and from the fascia covering tibialis posterior, which it overlaps to a considerable extent (see Fig. 78.38). Its fibres pass obliquely down to a tendon that occupies nearly the whole length of the posterior aspect of the muscle. This tendon grooves the posterior surface of the lower end of the tibia, then, successively, the posterior surface of the talus and the inferior surface of the sustentaculum tali of the calcaneus (see Fig. 79.2B). Fibrous bands convert the grooves on the talus and calcaneus into a canal lined by a synovial sheath. In dancers, overuse causes thickening of the tendon in this region, and pain and even 'triggering' can occur (hallux saltans). In the sole of the foot, the tendon of flexor hallucis longus passes forwards in the second layer like a bowstring. It crosses the tendon of flexor digitorum longus from lateral to medial, curving obliquely superior to it (see Fig. 79.21B). At the crossing point (knot of Henry), it gives off two strong slips to the medial two divisions of the tendons of flexor digitorum longus and then crosses the lateral part of flexor hallucis brevis to reach the interval between the sesamoid bones under the head of the first metatarsal. It continues on the plantar aspect of the hallux, and runs in an osseo-aponeurotic tunnel to be attached to the plantar aspect of the base of the distal phalanx (see Figs 79.5B, 79.23). The tendon is retained in position over the lateral part of flexor

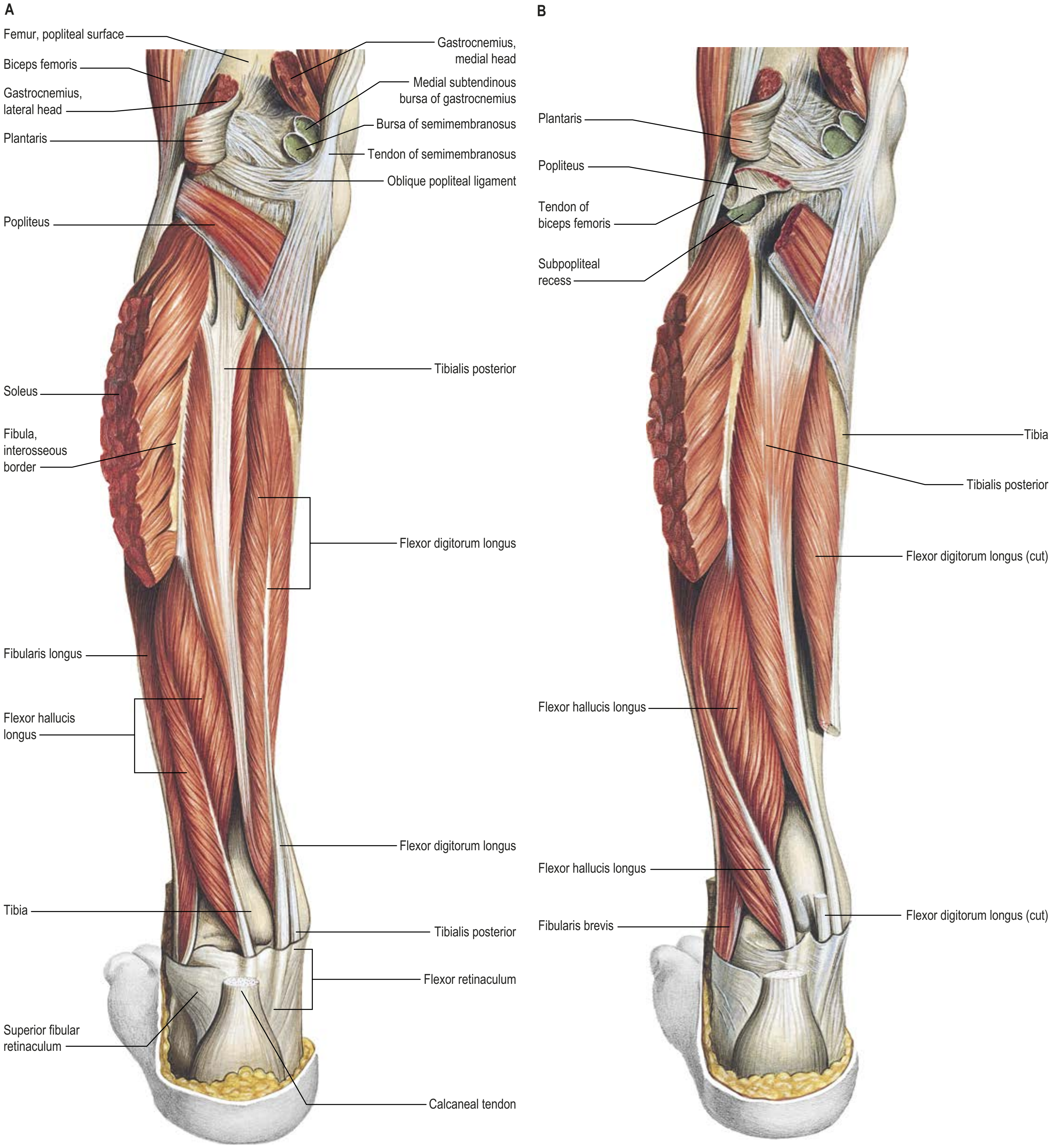
A
Femur, popliteal surface
Biceps femoris
Gastrocnemius, lateral head
Plantaris
Popliteus
Soleus
Fibula, interosseous border
Fibularis longus
Flexor hallucis longus
Tibia
Superior fibular retinaculum
Gastrocnemius, medial head
Medial subtendinous bursa of gastrocnemius
Bursa of semimembranosus
Tendon of semimembranosus
Oblique popliteal ligament
Tibialis posterior
Flexor digitorum longus
Flexor digitorum longus
Tibialis posterior
Flexor retinaculum
Calcaneal tendon
B
Plantaris
Popliteus
Tendon of biceps femoris
Subpopliteal recess
Flexor hallucis longus
Flexor hallucis longus
Fibularis brevis
Tibia
Tibialis posterior
Flexor digitorum longus (cut)
Flexor digitorum longus (cut)

Fig. 78.38 Muscles of the left leg, posterior aspect. **A**, The superficial muscles have been extensively removed. **B**, The superficial muscles have been extensively removed, popliteus has been sectioned and the tendon of flexor digitorum longus removed as it crosses the tendon of tibialis posterior. (With permission from Waschke J, Paulsen F (eds) Sobotta Atlas of Human Anatomy, 15th ed. Elsevier, Urban & Fischer. Copyright 2013.)

hallucis brevis by the diverging stems of the distal band of the medial intermuscular septum.

The distal extent of the muscle belly is a distinctive characteristic; in the posteromedial surgical approach to the ankle, flexor hallucis longus is readily identifiable by the fact that muscle fibres are evident almost to calcaneal level. In athletes, the muscle fibres may be present so far inferiorly into the tendon as to be susceptible to impingement when pulled into the tunnel at the talus.

The connecting slip to flexor digitorum longus varies in size; it usually continues into the tendons for the second and third toes but is sometimes restricted to the second toe and occasionally extends to the fourth toe.

Relations Soleus and the calcaneal tendon lie superficial (i.e. posterior) to flexor hallucis longus, separated by the transverse intermuscular septum. Deeply situated are the fibula, tibialis posterior, fibular vessels, distal part of the interosseous membrane and the talocrural joint. Laterally lie fibularis longus and fibularis brevis; medially are tibialis posterior, posterior tibial vessels and the tibial nerve. Flexor hallucis longus is an important surgical landmark at the ankle; staying lateral to it prevents injury to the neurovascular bundle.

Vascular supply Flexor hallucis longus is supplied by numerous branches of the fibular artery (see Fig. 78.4). The tendon is supplied by arteries of the ankle and foot.

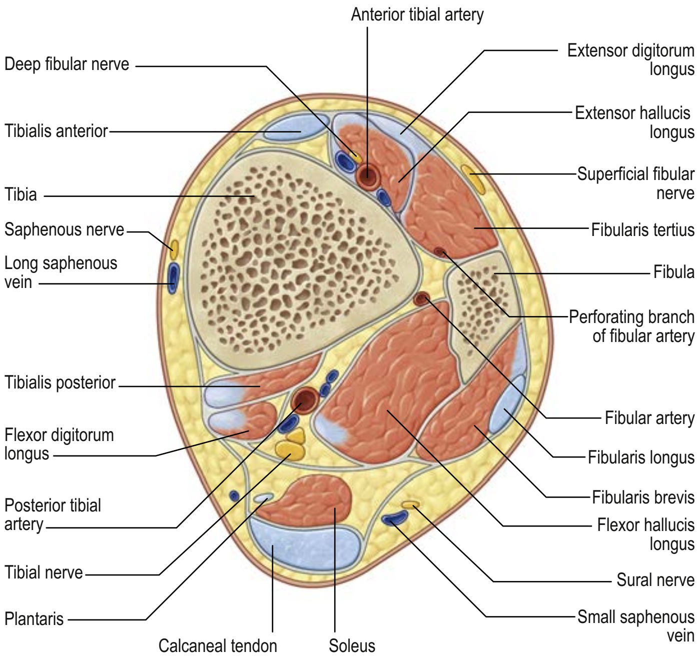

Fig. 78.39 A transverse section through the left leg, approximately 6 cm proximal to the medial malleolus.

Innervation Flexor hallucis longus is innervated by branches of the tibial nerve, L5, S1 and S2 (mainly S1).

Testing Flexor hallucis longus is tested by flexion of the hallux against resistance.

Actions of deep digital flexors

Both flexor hallucis longus and flexor digitorum longus can act as plantar flexors but this action is weak compared with that of gastrocnemius and soleus. When the foot is off the ground, both muscles flex the phalanges, acting primarily on the distal phalanges. When the foot is on the ground and under load, they act synergistically with the small muscles of the foot and, especially in the case of flexor digitorum longus, with the lumbricals and interossei to maintain the pads of the toes in firm contact with the ground, enlarging the weight-bearing area and helping to stabilize the heads of the metatarsals, which form the fulcrum on which the body is propelled forwards. Activity in the long digital flexors is minimal during quiet standing, so they apparently contribute little to the static maintenance of the longitudinal arch, but they become very active during toe-off and tip-toe movements.

Tibialis posterior

Attachments Tibialis posterior is the most deeply placed muscle of the flexor group (see Figs 78.6, 78.38). At its origin it lies between flexor hallucis longus and flexor digitorum longus, and is overlapped by both, but especially by the former. Its proximal attachment consists of two tapered processes, separated by an angular interval that is traversed by the anterior tibial vessels. The medial process arises from the posterior surface of the interosseous membrane, except at its most distal part, and from a lateral area on the posterior surface of the tibia between the soleal line above and the junction of the middle and lower thirds of the shaft below. The lateral part arises from a medial strip of the posterior fibular surface in its upper two-thirds (see Figs 78.7B, 78.8B). The muscle also arises from the transverse intermuscular septum, and from the intermuscular septa that separate it from adjacent muscles. In the distal quarter of the leg, its tendon passes deep to that of flexor digitorum longus, with which it shares a groove behind the medial malleolus, each enclosed in a separate synovial sheath (see Fig. 79.2B). It then passes deep to the flexor retinaculum and superficial to the deltoid ligament to enter the foot. In the foot, it is at first inferior to the plantar calcaneonavicular ligament, where it contains a sesamoid fibrocartilage. The tendon then divides into two. The more superficial and larger division, which is a direct continuation of the tendon, is attached to the tuberosity of the navicular, from which fibres continue to the inferior surface of the medial cuneiform. A tendinous band also passes laterally and a little proximally to the tip and distal margin of the sustentaculum tali. The deeper lateral division gives rise to the tendon of origin of the medial limb of flexor hallucis brevis, and then continues between this muscle and the navicular and medial cuneiform to end on the intermediate cuneiform and the bases of the second, third and fourth metatarsals; the slip to the fourth metatarsal is the strongest (see Fig. 79.5B).

The slips to the metatarsals vary in number. Slips to the cuboid and lateral cuneiform may also occur. An additional muscle, the tibialis secundus, has been described running from the back of the tibia to the capsule of the ankle joint.

Relations The superficial surface of tibialis posterior is separated from soleus by the transverse intermuscular septum, and is related to flexor digitorum longus, flexor hallucis longus, the posterior tibial vessels, the tibial nerve and the fibular vessels. The deep surface is in contact with the interosseous membrane, tibia, fibula and ankle joint.

Vascular supply Tibialis posterior is supplied by numerous branches of small calibre arising from the posterior tibial and fibular arteries. The tendon is supplied by arteries of the medial malleolar network and by the medial plantar artery.

Innervation Tibialis posterior is innervated by the tibial nerve, L4 and L5.

Actions Tibialis posterior is a powerful muscle that, on contraction, has an excursion of only 1–2 cm. It is the principal invertor of the foot and also initiates elevation of the heel; it is responsible for the hindfoot varus that occurs during a single heel raise. Due to its insertions on to the cuneiforms and the bases of the metatarsals, it has long been thought to assist in elevating the longitudinal arch of the foot, although electromyography shows that it is actually quiescent in standing. It is phasically active in walking, during which it probably acts with the intrinsic foot musculature and the lateral leg muscles to control the degree of pronation of the foot and the distribution of weight through the metatarsal heads. It is said that when the body is supported on one leg, the invertor action of tibialis posterior, exerted from below, helps to maintain balance by resisting any tendency to sway laterally.

Tibialis posterior is also important in the maintenance of the medial part of the longitudinal arch of the foot. In overweight individuals with pes planus (flat foot deformity), unaccustomed activity can result in inflammation and degeneration of the terminal portion of the tendon, which leads to elongation of the tendon, attenuation of the spring ligament and progressive collapse of the medial longitudinal arch. As the excursion is so short, the muscle cannot compensate for the lengthening of its tendon, a failure that results in tibialis posterior tendon dysfunction.

Testing Tibialis posterior is tested by asking the subject to move the foot into a position of maximal plantar flexion and inversion against the resistance of the examiner's hand; the tendon can be seen and felt just proximal to the medial malleolus. Testing tibialis posterior function is important in establishing a diagnosis of a common fibular nerve neuropathy and differentiating it from an L5 radiculopathy, which are two common clinical conditions. In a common fibular nerve neuropathy, tibialis posterior has normal function, whereas in an L5 radiculopathy, tibialis posterior is weak.

VASCULAR SUPPLY AND LYMPHATIC DRAINAGE

Arteries

Popliteal artery

The popliteal artery is the continuation of the femoral artery and crosses the popliteal fossa (see Figs 78.1B, 78.2, 78.4). It descends laterally from the opening in adductor magnus to the femoral intercondylar fossa, inclining obliquely to the distal border of popliteus, where it divides into the anterior and posterior tibial arteries. This division usually occurs at the proximal end of the interosseous space between the wide tibial metaphysis and the slender fibular metaphysis. The artery is relatively tethered at the adductor hiatus and again distally by the fascia related to soleus, and is therefore susceptible to damage following knee injuries, e.g. dislocation. Aneurysms of the popliteal artery are not uncommon.

Variations in the popliteal artery The popliteal artery may occasionally bifurcate more superiorly and divide into its terminal branches proximal to popliteus, or it may trifurcate into anterior and posterior tibial and fibular arteries. Either the anterior tibial or the posterior tibial artery may be reduced or increased in size. The size of the fibular artery is usually inversely related to the size of the anterior and posterior tibial arteries. Rarely, the anterior tibial artery is the source of the fibular artery, a variation that is almost always associated with a high bifurcation of the popliteal artery.

The popliteal and inferior gluteal arteries may be joined by a large anastomotic vessel; in such cases, the femoral artery is hypoplastic (Kawashima and Sasaki 2010). When this occurs, the popliteal artery usually has an abnormal relationship to popliteus, running deep to the muscle before dividing into its terminal branches. The popliteal artery may pass medially beneath the medial head of gastrocnemius, or may pass beneath an aberrant band of muscle in the popliteal fossa; in either case, contraction of the muscles may occlude the artery – a condition that may present with claudication on exertion. The popliteal vein is usually superficial and adjacent to the artery, but it may run deep to the artery, or be separated from it by a slip of muscle derived from the medial head of gastrocnemius.

Relations Anteriorly, from proximal to distal, are the fat covering the femoral popliteal surface, the capsule of the knee joint and the fascia of popliteus. Posteriorly are semimembranosus (proximally) and gastrocnemius and plantaris (distally). In between, the artery is separated from the skin and fasciae by fat and crossed from its lateral to its medial side by the tibial nerve and popliteal vein; the vein lies between the nerve and artery and is adherent to the latter. Laterally are biceps femoris, the tibial nerve, popliteal vein and lateral femoral condyle (all proximal), and plantaris and the lateral head of gastrocnemius (distal). Medially are semimembranosus and the medial femoral condyle (proximal), and the tibial nerve, popliteal vein and medial head of gastrocnemius (distally). The relations of the popliteal nodes are described below.

Branches

Genicular anastomosis

There is an intricate arterial anastomosis around the patella and femoral and tibial condyles (see Fig. 78.1). A superficial network spreads between the fascia and skin around the patella and in the fat deep to the patellar ligament. A deep network lies on the femur and tibia near their adjoining articular surfaces, and supplies the bone, articular capsule and synovial membrane. The vessels involved in this anastomosis are superior medial and lateral genicular; inferior medial and lateral genicular; descending genicular; descending branch of the lateral circumflex femoral; circumflex fibular; and anterior and posterior tibial recurrent arteries. For details, consult Scapinelli (1968).

Superior genicular arteries The superior genicular arteries branch from the popliteal artery, curving round proximal to both femoral condyles to reach the anterior aspect of the knee. The superior medial genicular artery lies under semimembranosus and semitendinosus, proximal to the medial head of gastrocnemius and deep to the tendon of adductor magnus. It divides into a branch to vastus medialis that anastomoses with the descending genicular and inferior medial genicular arteries, and a branch that ramifies on the femur and anastomoses with the superior lateral genicular artery. Its size varies inversely with that of the descending genicular artery. The superior lateral genicular artery passes under the tendon of biceps femoris, pierces the lateral intermuscular septum and divides into superficial and deep branches. The superficial branch supplies vastus lateralis and anastomoses with the descending branch of the lateral circumflex femoral and inferior lateral genicular arteries, while the deep branch anastomoses with the superior medial genicular artery, forming an anterior arch across the femur with the descending genicular artery. The superficial branch is vulnerable if the lateral patellar retinaculum is divided surgically.

Middle genicular artery The middle genicular artery is small. It arises from the popliteal artery near the midpoint of the posterior aspect of the knee joint. It pierces the oblique popliteal ligament to supply the cruciate ligaments and synovial membrane.

Inferior genicular arteries The inferior medial and lateral genicular arteries arise from the popliteal artery deep to gastrocnemius. The inferior medial genicular artery is deep to the medial head of gastrocnemius. It descends along the proximal margin of popliteus, which it supplies; passes inferior to the medial tibial condyle, under the tibial collateral ligament; and then ascends anteromedial to the knee joint at the anterior border of the tibial collateral ligament. It supplies the joint and the tibia, and anastomoses with the inferior lateral and superior medial genicular arteries and with the anterior tibial recurrent artery and saphenous branch of the descending genicular artery. The inferior lateral genicular artery runs laterally across popliteus and forwards over the head of the fibula to the front of the knee joint, passing under the lateral head of gastrocnemius, the fibular collateral ligament and the tendon of biceps femoris. Its branches anastomose with the inferior medial and superior lateral genicular arteries; anterior and posterior tibial recurrent arteries; and the circumflex fibular branch of the posterior tibial artery.

Cutaneous branches: the superficial sural arteries The superficial sural arteries are three vessels that leave the popliteal artery, or its side branches, descend between the heads of gastrocnemius and perforate the deep fascia to supply the skin on the back of the leg. The central or median vessel is usually larger than the medial or lateral vessels, and usually accompanies the sural nerve.

Fasciocutaneous free and pedicled flaps may be raised on the superficial sural arteries.

Superior muscular branches The superior muscular branches are two or three vessels that arise proximally and pass to adductor magnus and the posterior thigh muscles. They anastomose with the termination of the profunda femoris artery.

Sural arteries The two sural arteries are large and arise behind the knee joint to supply gastrocnemius, soleus and plantaris. They are used in gastrocnemius musculocutaneous flaps.

Anterior tibial artery

The anterior tibial artery arises at the distal border of popliteus (**Fig. 78.40**; see Figs 76.4, 78.1, 78.4, 78.36). At first in the flexor compartment, it passes between the heads of tibialis posterior and through the oval aperture in the proximal part of the interosseous membrane to reach the extensor (anterior) compartment, passing medial to the fibular neck; it is vulnerable here during tibial osteotomy. Descending on the anterior aspect of the membrane, it approaches the tibia and, distally, lies anterior to it. At the ankle, the anterior tibial artery is located approximately midway between the malleoli, and it continues on the dorsum of the foot, lateral to extensor hallucis longus, as the dorsalis pedis artery (see Fig. 79.1).

The anterior tibial artery may, on occasion, be small but it is rarely absent. Its function may be replaced by perforating branches from the posterior tibial artery or by the perforating branch of the fibular artery. It occasionally deviates laterally, regaining its usual position at the ankle. It may also be larger than normal, in which case its territory of supply in the foot may be increased to include the plantar surface.

Relations In its proximal two-thirds the anterior tibial artery lies on the interosseous membrane, and in its distal third it is anterior to the tibia and ankle joint. Proximally, it lies between tibialis anterior and extensor digitorum longus, then between tibialis anterior and extensor hallucis longus. At the ankle it is crossed superficially from the lateral side by the tendon of extensor hallucis longus and then lies between this tendon and the first tendon of extensor digitorum longus. Its proximal two-thirds are covered by adjoining muscles and deep fascia, its distal third by the skin, fasciae and extensor retinacula. It is accompanied by venae comitantes. The deep fibular nerve, curling laterally round the fibular neck, reaches the lateral side of the artery where it enters the extensor region, is then anterior to the artery in the middle third of the leg, and becomes lateral again distally.

Branches

The named branches of the anterior tibial artery are the posterior and anterior tibial recurrent, muscular, perforating, and anterior medial and lateral malleolar arteries (see Figs 76.7, 79.10A).

Posterior tibial recurrent artery The posterior tibial recurrent artery is an inconstant branch that arises before the anterior tibial artery reaches the extensor compartment of the leg. It ascends anterior to popliteus, anastomosing with the inferior genicular branches of the popliteal artery. It supplies the superior tibiofibular joint.

Anterior tibial recurrent artery The anterior tibial recurrent artery arises near the posterior tibial recurrent artery. It ascends in tibialis anterior, ramifies on the front and sides of the knee joint, and joins the patellar anastomosis, which interconnects with the genicular branches of the popliteal and circumflex fibular arteries.

Muscular branches Numerous branches supply the adjacent muscles. Some then pierce the deep fascia to supply the skin, while others

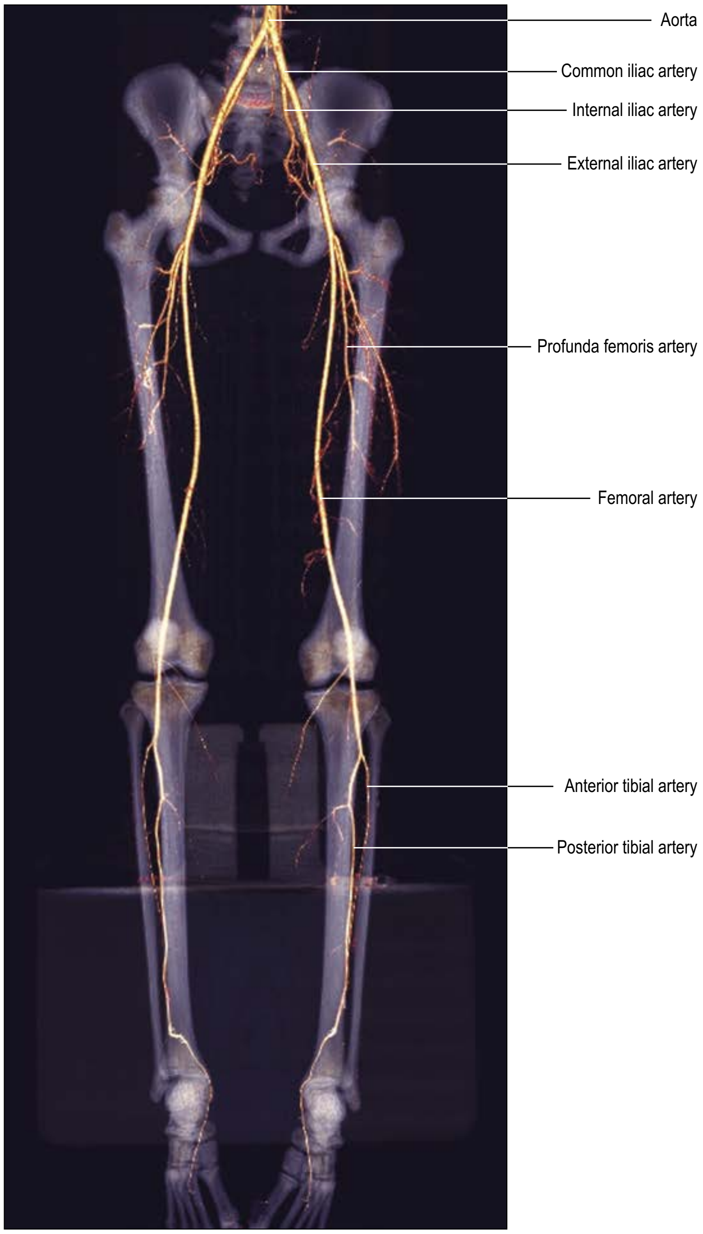

Fig. 78.40 Three-dimensional CT imaging illustrating the arterial supply of the lower limb. Note the relationships of the arteries to the surrounding bones. (Courtesy of Dr Yoginder Vaid and Mr Jon C Betts, Jr.)

traverse the interosseous membrane to anastomose with branches of the posterior tibial and fibular arteries.

Perforating branches Most of the fasciocutaneous perforators pass along the anterior fibular fascial septum behind extensor digitorum longus before penetrating the deep fascia to supply the skin.

Anterior medial malleolar artery The anterior medial malleolar artery arises approximately 5 cm proximal to the ankle. It passes posterior to the tendons of extensor hallucis longus and tibialis anterior medial to the joint, where it joins branches of the posterior tibial and medial plantar arteries.

Anterior lateral malleolar artery The anterior lateral malleolar artery runs posterior to the tendons of extensor digitorum longus and fibularis tertius to the lateral side of the ankle and anastomoses with the perforating branch of the fibular artery and ascending branches of the lateral tarsal artery.

Posterior tibial artery

The posterior tibial artery begins at the distal border of popliteus, between the tibia and fibula (see Figs 76.4B, 78.1B, 78.4, 78.40). It descends medially in the flexor compartment and divides under abductor hallucis, midway between the medial malleolus and the calcaneal tubercle, into the medial and lateral plantar arteries. The artery may be much reduced in length or in calibre; the fibular artery then takes over its distal territory of supply and may consequently be increased in size.

Relations The posterior tibial artery is successively posterior to tibialis posterior, flexor digitorum longus, the tibia and the ankle joint. Proximally, gastrocnemius, soleus and the transverse intermuscular septum of the leg are superficial to the artery, and distally, it is covered only by skin and fascia. It is parallel with and approximately 2.5 cm anterior to the medial border of the calcaneal tendon; terminally, it is deep to the flexor retinaculum. The artery is accompanied by two veins and the tibial nerve. The nerve is at first medial to the artery but soon crosses behind it and subsequently becomes largely posterolateral in position.

Branches

The named branches of the posterior tibial artery are the circumflex fibular, nutrient, muscular, perforating, communicating, medial malleolar, calcaneal, lateral and medial plantar, and fibular arteries (see Figs 76.7B, 79.10).

Circumflex fibular artery The circumflex fibular artery, which sometimes arises from the anterior tibial artery, passes laterally round the neck of the fibula through the soleus to anastomose with the inferior medial and lateral genicular and anterior tibial recurrent arteries. It supplies bone and related articular structures.

Nutrient artery of the tibia The nutrient artery of the tibia arises from the posterior tibia near its origin. After giving off a few muscular branches, it descends into the bone immediately distal to the soleal line. It is one of the largest of the nutrient arteries.

Muscular branches Muscular branches are distributed to the soleus and deep flexors of the leg.

Perforating branches Approximately five fasciocutaneous perforators emerge between flexor digitorum longus and soleus, and pass through the deep fascia, often accompanying the perforating veins that connect the deep and superficial venous systems. The arterial perforators then divide into anterior and posterior branches to supply the regional periosteum and skin. These vessels are utilized in raising medial fasciocutaneous perforator flaps in the leg.

Communicating branch The communicating branch runs posteriorly across the tibia approximately 5 cm above its distal end, deep to flexor hallucis longus, to join a communicating branch of the fibular artery.

Medial malleolar branches The medial malleolar branches pass round the medial malleolus to the medial malleolar network, which supplies the skin.

Calcaneal branches Calcaneal branches arise just proximal to the terminal division of the posterior tibial artery. They pierce the flexor retinaculum to supply fat and skin behind the calcaneal tendon and in the heel, and muscles on the tibial side of the sole; the branches anastomose with medial malleolar arteries and calcaneal branches of the fibular artery.

Medial plantar artery The medial plantar artery is the smaller terminal branch of the posterior tibial artery and passes distally along the medial side of the foot, medial to the medial plantar nerve (see Figs 76.4B, 79.26). At first deep to abductor hallucis, it runs distally between this muscle and flexor digitorum brevis, and supplies both. Near the first metatarsal base its size, already diminished by muscular branches, is further reduced to a superficial stem that divides to form three superficial digital branches. These accompany the digital branches of the medial plantar nerve and join the first to third plantar metatarsal arteries. The main trunk of the medial plantar artery then runs on to reach the medial border of the hallux, where it anastomoses with a branch of the first plantar metatarsal artery.

Lateral plantar artery The lateral plantar artery is the larger terminal branch of the posterior tibial artery (see Figs 76.4B, 79.26). It passes distally and laterally to the fifth metatarsal base, lateral to the lateral plantar nerve. (The medial and lateral plantar nerves lie between the corresponding plantar arteries.) Turning medially with the deep branch of the lateral plantar nerve, it reaches the interval between the first and second metatarsal bases, and unites with the deep plantar artery to complete the plantar arch. As it passes laterally, it is first between the calcaneus and abductor hallucis, then between flexor digitorum brevis and flexor accessorius. Running distally to the fifth metatarsal base, it passes between flexor digitorum brevis and abductor digiti minimi, and is covered by the plantar aponeurosis, superficial fascia and skin.

Branches Muscular branches supply the adjoining muscles. Superficial branches supply the skin and subcutaneous tissue along the lateral sole. Anastomotic branches run to the lateral border of the foot, joining branches of the lateral tarsal and arcuate arteries. A calcaneal branch sometimes pierces abductor hallucis to supply the skin of the heel.

Fibular artery

The fibular artery arises from the posterior tibial artery approximately 2.5 cm distal to popliteus and passes obliquely to the fibula, descending along its medial crest either in a fibrous canal between tibialis posterior and flexor hallucis longus or within flexor hallucis longus (see Figs 76.4B, 78.4, 78.39). Reaching the inferior tibiofibular syndesmosis, it divides into calcaneal branches that ramify on the lateral and posterior surfaces of the calcaneus. Proximally, it is covered by soleus and the transverse intermuscular septum between soleus and the deep muscles of the leg, and distally it is overlapped by flexor hallucis longus.

The fibular artery may branch high from the posterior tibial artery or may even branch from the popliteal artery separately, resulting in a true 'trifurcation'. It may also branch more distally from the posterior tibial artery, sometimes 7 or 8 cm distal to popliteus. Its size tends to be inversely related to the size of the other arteries of the leg. It may be reduced in size but is more often enlarged, when it may join, reinforce or even replace the posterior tibial artery in the distal leg and foot.

Branches

The fibular artery has muscular, nutrient, perforating, communicating and calcaneal branches (see Fig. 79.10).

Muscular branches Multiple short branches supply soleus, tibialis posterior, flexor hallucis longus and the fibular muscles.

Nutrient artery The nutrient artery branches from the main trunk approximately 7 cm from its origin and enters the fibula 14–19 cm from the apex of the head of the fibula.

Perforating branches The main perforating branch traverses the interosseous membrane approximately 5 cm proximal to the lateral malleolus to enter the extensor compartment, where it anastomoses with the anterior lateral malleolar artery. Descending anterior to the inferior tibiofibular syndesmosis, it supplies the tarsus and anastomoses with the lateral tarsal artery. This branch is sometimes enlarged and may replace the dorsalis pedis artery.

Fasciocutaneous perforators from the lateral muscular branches pass along the posterior fibular fascial septum to penetrate the deep fascia and reach the skin. These vessels are utilized in raising fasciocutaneous posterolateral leg flaps (see below).

Communicating branch The communicating branch connects to a communicating branch of the posterior tibial artery approximately 5 cm proximal to the ankle.

Calcaneal branches Calcaneal (terminal) branches anastomose with the anterior lateral malleolar and calcaneal branches of the posterior tibial artery.

Perforator flaps in the knee and leg

The perforators, which arise from the rich vascular anastomosis around the patella, generally traverse the tendon of quadriceps femoris to supply the skin over the patella and the peripatellar region (see Fig. 76.7). The skin flaps based on these perforators may be used as distally based or proximally based flaps to cover defects over the knee and popliteal region. The direct cutaneous branch of the popliteal artery and a superficial sural artery, which accompanies the sural nerve, provide additional perforators to the skin over the back of the knee. The posterior tibial artery gives off an average of ten perforators to the skin covering the anteromedial and posterior parts of the leg. In the upper third of the leg, the perforating vessels are predominantly muscular and periosteocutaneous, while in the lower third, the perforating vessels are mainly direct subcutaneous types. They anastomose with the perforating branches of the anterior tibial artery anteriorly and fibular artery posteriorly. Inferiorly, the posterior tibial artery forms a rich anastomotic ring around the ankle joint with the fibular and anterior tibial arteries. Perforators from these vessels supply the calcaneal tendon and the overlying skin. The posterior tibial artery gives off three direct cutaneous perforators in the lower part of the leg; a distally based skin or adipofascial flap based on one of these perforators may be used to reconstruct a defect over the anterior or the posterior aspect of the lower leg. The anterior tibial artery gives off an average of six perforators, which supply the anterolateral part of the leg. They emerge in two longitudinal rows; one perforator is fairly large and accompanies the superficial fibular nerve. A small skin flap based on any one of these perforators may be used to cover small defects over the tibia, and a neurocutaneous flap that includes the superficial fibular nerve may be used.

The fibular artery has an average of five perforators. A constant perforator pierces the deep fascia approximately 5 cm above the lateral malleolus and divides into an ascending and a descending branch. A vascularized fibula graft based on the fibular artery is now the standard graft used in reconstruction of the mandible, while small fasciocutaneous and adipofascial flaps based on the perforators of the fibular artery are useful in covering soft tissue defects over the heel and proximal part of the foot.

Veins

Deep veins

The veins draining the knee and leg correspond in name to the arteries and run with them; the named smaller veins drain into the popliteal and femoral veins.

Popliteal vein

The popliteal vein ascends through the popliteal fossa to the opening in adductor magnus, where it becomes the femoral vein (see Figs 76.8, 77.47). Its relationship to the popliteal artery changes as the vein ascends: distally, it is medial to the artery; between the heads of gastrocnemius, it is superficial (posterior) to the artery; and proximal to the knee joint, it is posterolateral to the artery. Its tributaries are the short saphenous vein; veins corresponding to branches of the popliteal artery; and muscular veins, including a large branch from each head of gastrocnemius. There are usually four or five valves in the popliteal vein.

Posterior tibial veins

The posterior tibial veins accompany the posterior tibial artery (see Fig. 76.8). They receive tributaries from the calf muscles (especially from the venous plexus in the soleus) and connections from superficial veins and the fibular veins.

Fibular veins

The fibular veins, running with their artery, receive tributaries from soleus and from superficial veins.

Anterior tibial veins

The anterior tibial veins, continuations of the venae comitantes of the dorsalis pedis artery, leave the anterior compartment between the tibia and fibula, and pass through the proximal end of the interosseous membrane. They unite with the posterior tibial veins to form the popliteal vein at the distal border of popliteus.

Superficial veins

Long saphenous vein

The course of the long saphenous vein is described in Chapter 77.

Short saphenous vein

The short saphenous vein (small saphenous vein) begins posterior to the lateral malleolus as a continuation of the lateral marginal vein (see Fig. 76.9B). In the lower third of the calf, it ascends lateral to the calcaneal tendon, lying on the deep fascia and covered only by subcutaneous tissue and skin. Inclining medially to reach the midline of the calf, it penetrates the deep fascia, within which it ascends on gastrocnemius, only emerging between the deep fascia and gastrocnemius gradually at about the junction of the middle and proximal thirds of the calf (usually well below the lower limit of the popliteal fossa). Continuing its ascent, it passes between the heads of gastrocnemius and proceeds to its termination in the popliteal vein, 3–7.5 cm above the knee joint.

Tributaries

The short saphenous vein connects with deep veins on the dorsum of the foot, receives many cutaneous tributaries in the leg, and sends several communicating branches proximally and medially to join the long saphenous vein. Sometimes a communicating branch ascends medially to the accessory saphenous vein: this may be the main continuation of the short saphenous vein. In the leg, the short saphenous vein lies near the sural nerve and contains 7–13 valves, with one near its termination. Its mode of termination is variable: it may join the long saphenous vein in the proximal thigh or it may bifurcate, one branch joining the long saphenous vein and the other joining the popliteal or deep posterior femoral veins. Sometimes it drains distal to the knee in the long saphenous or sural veins.

Venous disease

Chronic venous disease is common. Sustained overdistension of the superficial veins of the lower limb may result in the development of short, dilated venous segments or varicosities. Varicose veins can occur as a consequence of venous valve failure at the proximal end of the long saphenous vein at the saphenofemoral junction, or in the perforating veins that pass from the superficial system to the high-pressure deep veins. Varicose veins have thin walls and 'leak' red blood cells into adjacent soft tissues. As these cells are broken down, haemosiderin is deposited in the soft tissues, resulting in a brown pigmentation. This phenomenon, together with the fact that venous stasis produces oedema, renders the soft tissues of the leg unhealthy and prone to ulceration, particularly after minor trauma.

Acute venous disease occurs most commonly in the posterior compartment of the leg. This is attributed to the sluggish blood flow that occurs, at times, in the deep veins of the calf. This relative stasis predisposes to the formation of venous thrombi. Fragments of these thrombi may become dislodged and carried in the venous return to the heart to cause a life-threatening pulmonary embolism. Blockage of the normal venous system may contribute to increased local venous pressure and oedema.

Lymphatic drainage

Lymphatic drainage is to the popliteal nodes (see Fig. 76.10). Most of the lymph vessels accompany the genicular arteries; some vessels from the joint drain directly into a node between the popliteal artery and the posterior capsule of the knee joint.

Popliteal nodes

There are usually six small lymph nodes embedded in the fat of the popliteal fossa. One, near the termination of the short saphenous vein, drains the superficial region served by this vessel. Another lies between the popliteal artery and the posterior aspect of the knee, receiving direct vessels from the knee joint and those accompanying the genicular arteries. The remainder flank the popliteal vessels, receiving trunks that accompany the anterior and posterior tibial vessels. Popliteal lymphatic vessels ascend close to the femoral vessels to reach the deep inguinal nodes; some may accompany the long saphenous vein to the superficial inguinal nodes.

INNERVATION

Knee joint

The knee joint is innervated by branches from the obturator, femoral, tibial and common fibular nerves (see Fig. 76.11) (Freeman and Wyke 1967). The articular branch of the obturator nerve is the terminal branch of its posterior division. Muscular branches of the femoral nerve, especially to vastus medialis, supply articular branches to the knee joint. Genicular branches from the tibial and common fibular nerves accompany the genicular arteries, and those from the tibial nerve travel with the medial and middle genicular arteries, while those from the common fibular nerve travel with the lateral genicular and anterior tibial recurrent arteries.

Saphenous nerve

The saphenous nerve is the largest and longest cutaneous branch of the femoral nerve and the longest nerve in the body (see Figs 76.11A, 77.48). It descends lateral to the femoral artery in the femoral triangle and enters the adductor canal, where it crosses anterior to the artery to lie medial to it. At the distal end of the canal, it leaves the artery and emerges through the aponeurotic covering with the saphenous branch of the descending genicular artery. As it leaves the adductor canal, it gives off an infrapatellar branch that contributes to the peripatellar plexus and then pierces the fascia lata between the tendons of sartorius and gracilis, becoming subcutaneous to supply the skin anterior to the patella. It descends along the medial border of the tibia with the long saphenous vein and divides distally into a branch that continues along the tibia to the ankle and a branch that passes anterior to the ankle to supply the skin on the medial side of the foot, often as far as the first metatarsophalangeal joint (see Fig. 76.12A). The saphenous nerve connects with the medial branch of the superficial fibular nerve. Near the mid-thigh, it provides a branch to the subsartorial plexus. The nerve may become entrapped as it leaves the adductor canal.

Tibial nerve

The tibial nerve, the larger component of the sciatic nerve, is derived from the ventral branches (anterior divisions) of the fourth and fifth lumbar and first to third sacral ventral rami. It descends along the back of the thigh and popliteal fossa to the distal border of popliteus. It then passes anterior to the arch of soleus with the popliteal artery and continues into the leg. In the thigh, it is overlapped proximally by the hamstring muscles but it becomes more superficial in the popliteal fossa, where it is lateral to the popliteal vessels (see Fig. 77.47). At the level of the knee, the tibial nerve becomes superficial to the popliteal vessels and crosses to the medial side of the artery. In the distal popliteal fossa, it is overlapped by the junction of the two heads of gastrocnemius.

In the leg, the tibial nerve descends with the posterior tibial vessels to lie between the heel and the medial malleolus (see Fig. 78.4). Proximally it is deep to soleus and gastrocnemius, but in its distal third is covered only by skin and fasciae, and overlapped sometimes by flexor hallucis longus. At first medial to the posterior tibial vessels, it crosses behind them and descends lateral to them until it bifurcates. It lies on tibialis posterior for most of its course except distally, where it adjoins the posterior surface of the tibia. The tibial nerve ends under the flexor retinaculum by dividing into the medial and lateral plantar nerves.

Branches

The branches of the tibial nerve are articular, muscular, sural, medial calcaneal and medial and lateral plantar nerves. The medial and lateral plantar nerves and the medial calcaneal nerve are described in Chapter 79.

Articular branches Articular branches to the knee joint accompany the superior and inferior medial genicular arteries and the middle genicular artery; they form a plexus with a branch from the obturator nerve and also supply the oblique popliteal ligament. The branches accompanying the superior and inferior medial genicular arteries supply the medial part of the capsule. A branch of the nerve to popliteus (tibial nerve) supplies the posterior portion of the superior tibiofibular joint. Just before the tibial nerve bifurcates, it gives off branches that supply the ankle joint.

Muscular branches Proximal muscular branches arise between the heads of gastrocnemius and supply gastrocnemius, plantaris, soleus and popliteus. The nerve to soleus enters its superficial aspect. The branch to popliteus descends obliquely across the popliteal vessels, curling round the distal border of the muscle to its anterior surface. It also supplies tibialis posterior, the superior tibiofibular joint and the tibia, and gives off an interosseous branch that descends near the fibula to reach the distal tibiofibular joint.

Muscular branches in the leg, either independently or by a common trunk, supply soleus (on its deep surface), tibialis posterior, flexor digitorum longus and flexor hallucis longus (see Fig. 78.4). The branch to flexor hallucis longus accompanies the fibular vessels.

Sural nerve The sural nerve descends between the heads of gastrocnemius, pierces the deep fascia proximally in the leg, and is joined at a variable level by the sural communicating branch of the common fibular nerve. Some authors term this branch the lateral sural cutaneous nerve, and call the main trunk (from the tibial nerve) the medial sural cutaneous nerve (see Fig. 76.9B). The sural nerve descends lateral to the calcaneal tendon, near the short saphenous vein, to the region between the lateral malleolus and the calcaneus, and supplies the posterior and lateral skin of the distal third of the leg. It then passes distal to the lateral malleolus along the lateral side of the foot and fifth toe, supplying the overlying skin (see Fig. 76.12). It connects with the posterior femoral cutaneous nerve in the leg and with the superficial fibular nerve on the dorsum of the foot.

The sural nerve is often used as an autologous peripheral nerve graft on the grounds that it is easily harvested, readily identified and exclusively cutaneous.

Lesions of the tibial nerve

The tibial nerve is vulnerable to direct injury in the popliteal fossa, where it lies superficial to the popliteal vessels at the level of the knee, or to compression at the tendinous arch of the soleus. It may be damaged in compartment syndrome that affects the deep flexor compartment of the calf. The tibial nerve or the medial and lateral plantar nerves may become entrapped beneath the flexor retinaculum or the so-called plantar tunnels (beneath the fascia of the abductor hallucis) at the ankle, resulting in tarsal tunnel syndrome.

Common fibular nerve

The common fibular nerve (common peroneal nerve) is approximately half the size of the tibial nerve and is derived from the dorsal branches of the fourth and fifth lumbar and first and second sacral ventral rami. It descends obliquely along the lateral side of the popliteal fossa to the fibular head, medial to biceps femoris. It lies between the tendon of biceps femoris, to which it is bound by fascia, and the lateral head of gastrocnemius (**Fig. 78.41**; see Fig. 76.11). The nerve then passes into the anterolateral compartment of the leg through a tight opening in the thick fascia overlying tibialis anterior. It curves lateral to the fibular neck, deep to fibularis longus, and divides into superficial and deep fibular nerves; an articular trunk, derived from the deep fibular nerve, provides an articular branch that travels with the anterior tibial recurrent artery and a proximal branch to tibialis anterior.

Branches

The common fibular nerve has articular and cutaneous branches, and terminates as the superficial and deep fibular nerves.

Articular branches There are three articular branches. Two accompany the superior and inferior lateral genicular arteries; they may arise in common. The third, the recurrent articular branch, arises near the termination of the common fibular nerve. It ascends with the anterior recurrent tibial artery through tibialis anterior and supplies the anterolateral part of the knee joint capsule and the proximal tibiofibular joint.

Cutaneous branches The two cutaneous branches, often from a common trunk, are the lateral sural and sural communicating nerves (see Fig. 76.9). The lateral sural cutaneous nerve (lateral cutaneous nerve of the calf) supplies the skin on the anterior, posterior and lateral surfaces of the proximal leg (see Fig. 76.12A). The sural communicating nerve arises near the head of the fibula and crosses the lateral head of gastrocnemius to join the sural nerve. It may descend separately as far as the heel.

Lesions of the common fibular nerve

The common fibular nerve is relatively unprotected as it traverses the lateral aspect of the neck of the fibula and is easily compressed at this site, e.g. by plaster casts or ganglia. The nerve may also become entrapped by a fascial band beneath fibularis longus within the so-called fibular tunnel, between the attachments of fibularis longus to the head and shaft of the fibula (van den Bergh et al 2013). Traction lesions can accompany dislocations of the lateral compartment of the knee, and are most likely to occur if the distal attachments of biceps femoris and the ligaments that insert on to the fibular head are avulsed, possibly with a small part of the fibular head; the nerve is tethered to the tendon of biceps femoris by dense fascia and so is pulled proximally. Severe traction lesions may produce longitudinal injuries affecting a long segment of the common fibular nerve. Torsional injury following ankle injury (sprain or fracture) may result in common fibular neuropathy; the injury is transmitted from the ankle along the interosseous membrane to the proximal leg (Lalezari et al 2012). Patients with such injury present with a foot drop. Physical examination reveals weakness or paralysis of ankle dorsiflexion, toe extension and eversion of the foot, but inversion and plantar flexion are normal. Sensation on the dorsum of the foot, including the first dorsal web space, is diminished. The ankle reflex is preserved. Since the common fibular nerve divides at the fibular neck into the superficial and deep fibular nerves, injuries to the nerve at this level may damage either the main trunk or its branches. Electrodiagnostic studies can help localize a common fibular nerve injury to the fibular neck region. At this level, nerve conduction studies may show slowed velocities and electromyography would demonstrate denervation in the muscles innervated by the common fibular nerve (such as tibialis anterior or fibularis longus), whereas more proximally innervated muscles (particularly the short head of biceps femoris) would be normal.

Superficial fibular nerve

The superficial fibular nerve (superficial peroneal nerve) begins at the bifurcation of the common fibular nerve. It lies deep to fibularis longus at first (see Fig. 78.6A), then passes anteroinferiorly between fibularis longus and brevis and extensor digitorum longus, and pierces the deep fascia in the distal third of the leg (see Fig. 78.41). It divides into a large medial dorsal cutaneous nerve and a smaller, more laterally placed, intermediate dorsal cutaneous nerve, usually after piercing the deep fascia (see Fig. 76.9A), but sometimes while it is still deep to the fascia. As the nerve lies between the muscles it supplies fibularis longus, fibularis brevis and the skin of the lower leg. The deep course, i.e. the compartmental localization, and the peripheral digital distribution of the superficial fibular nerve are subject to considerable variation (Kosinski 1926, Solomon et al 2001).

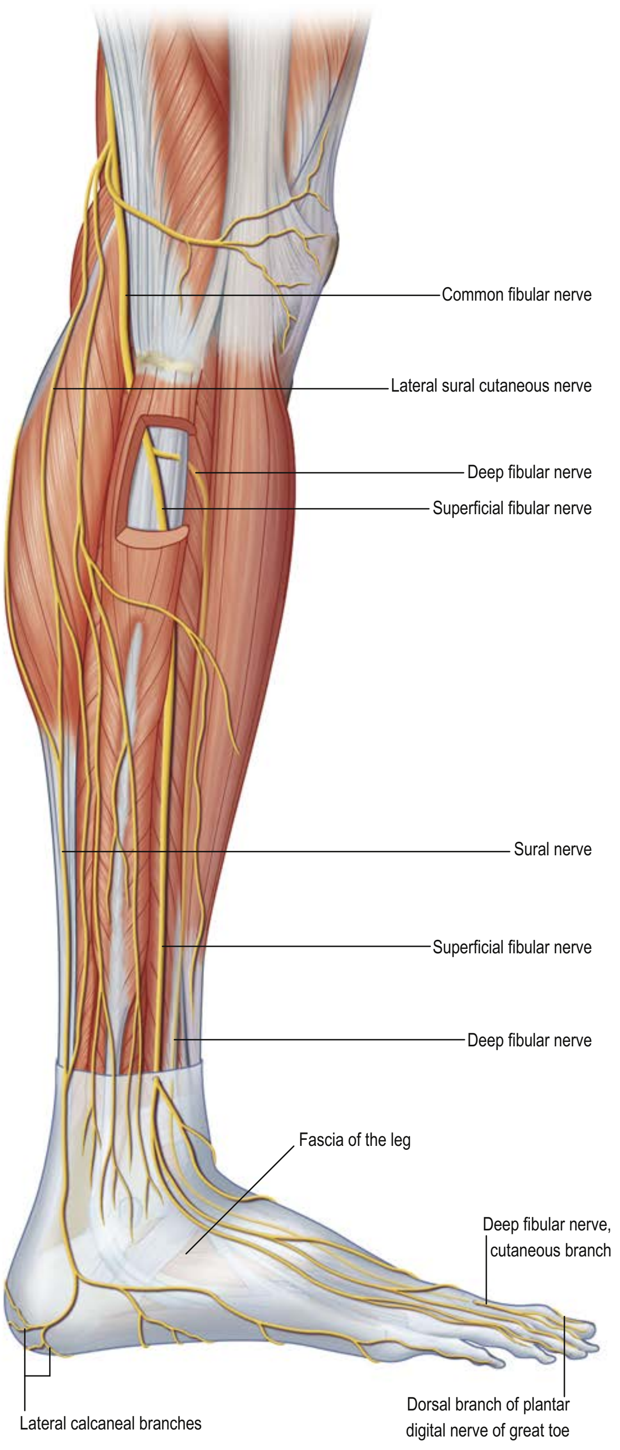

Fig. 78.41 The course, relations and branches of the right common fibular nerve. (Courtesy of Rolfe Birch, all rights reserved, published in Birch R, Surgical Disorders of the Peripheral Nerve, 2nd ed. 2011. Springer-Verlag, London.)

Branches

The medial dorsal cutaneous nerve passes in front of the ankle joint and divides into two dorsal digital branches; one of these supplies the medial side of the hallux and the other supplies the adjacent side of the second and third toes. It communicates with the saphenous and deep fibular nerves. The smaller intermediate branch crosses the dorsum of the foot laterally. It divides into dorsal digital branches that supply the contiguous sides of the third to fifth toes and the skin of the lateral aspect of the ankle (see Fig. 76.12A, C), where it connects with the sural nerve. Both branches, especially the intermediate, are at risk during the placement of portal skin incisions for arthroscopy and during surgical approaches to the lateral malleolus. Branches of the superficial fibular nerve supply the skin of the dorsum of all the toes except that of the lateral side of the fifth toe (supplied by the sural nerve) and the adjoining sides of the great and second toes (supplied by the medial terminal branch of the deep fibular nerve). Some of the lateral branches of the superficial fibular nerve are frequently absent and are replaced by sural nerve branches.

Accessory fibular nerves An accessory superficial fibular nerve and an accessory deep fibular nerve have been described as variant branches of the superficial fibular nerve; both are probably the product of atypical branching of the parent nerve deep to the deep fascia (see above).

Lesions of the superficial fibular nerve

A lesion of the superficial fibular nerve causes weakness of foot eversion and sensory loss on the lateral aspect of the leg that extends on to the dorsum of the foot. The nerve can be subject to entrapment as it penetrates the deep fascia of the leg and it may also be involved in compartment syndrome that affects the lateral compartment of the leg.

Deep fibular nerve

The deep fibular nerve (deep peroneal nerve) begins at the bifurcation of the common fibular nerve, between the fibula and the proximal part of fibularis longus (see Fig. 78.41). It passes obliquely forwards deep to extensor digitorum longus to the front of the interosseous membrane and reaches the anterior tibial artery in the proximal third of the leg. It descends with the artery to the ankle, where it divides into lateral and medial terminal branches. As it descends, the nerve is first lateral to the artery, then anterior and finally lateral again at the ankle.

Branches

The deep fibular nerve supplies muscular branches to tibialis anterior, extensor hallucis longus, extensor digitorum longus and fibularis tertius, and an articular branch to the ankle joint.

The lateral terminal branch crosses the ankle deep to extensor digitorum brevis, enlarges as a pseudoganglion and supplies extensor digitorum brevis. From the enlargement, three minute interosseous branches supply the tarsal and metatarsophalangeal joints of the middle three toes.

The medial terminal branch runs distally on the dorsum of the foot lateral to the dorsalis pedis artery, and connects with the medial branch of the superficial fibular nerve in the first interosseous space. It divides into two dorsal digital nerves, which supply adjacent sides of the great and second toes (see Figs 76.9A, 76.12C). Before dividing, it gives off an interosseous branch, which supplies the first metatarsophalangeal joint. The deep fibular nerve may end as three terminal branches.

Lesions of the deep fibular nerve

Isolated injury to the deep fibular nerve may result from compartment syndrome that affects the anterior compartment of the leg or from an intraneural ganglion cyst (mucinous cyst within the nerve derived from the superior tibiofibular joint via the articular branch that travels with the anterior tibial recurrent artery (Spinner et al 2003)). Individuals with lesions of the deep fibular nerve have weakness of ankle dorsiflexion and extension of all toes but normal foot eversion. Sensory impairment is confined to the first interdigital web space.

Bonus e-book content

Fig. 78.6 C, An axial T2-weighted MRI of the upper leg.

Key references

Amis AA, Dawkins GP 1991 Functional anatomy of the anterior cruciate ligament. Fibre bundle actions related to ligament replacements and injuries. J Bone Joint Surg Br 73:260–7.

A study of three functional components of the anterior cruciate ligament. Fibre length changes suggested that the 'isometric point' aimed at by some ligament replacements lay anterior and superior to the femoral origin of the intermediate fibre bundle and towards the roof of the intercondylar notch.

Freeman MAR, Wyke B 1967 The innervation of the knee joint: an anatomical and histological study in the cat. J Anat 101:505–32.

A classic paper that investigates the gross anatomy and histology of the articular innervation of the knee joint. Four articular nerve endings were classified.

Girgis FG, Marshall JL, Al Monajem ARS 1975 The cruciate ligaments of the knee joint. Clin Orthop 106:216–31.

A cadaveric study that described the anterior cruciate ligament as having an anteromedial and posterolateral band. It suggested that the anteromedial band was responsible for the anteroposterior drawer sign with flexion.

LaPrade CM, Ellman MB, Rasmussen MT et al 2014 Anatomy of the anterior root attachments of the medial and lateral menisci: a quantitative analysis. Am J Sports Med 42:2386–92.

A cadaveric study that described the quantitative and qualitative anatomy of the anterior root attachments of the medial and lateral menisci, with regard to pertinent open and arthroscopic landmarks.

LaPrade MD, Kennedy MI, Wijdicks CA et al 2015 Anatomy and biomechanics of the medial side of the knee and their surgical implications. Sports Med Arthrosc Rev 23:63–70.

A review of the anatomy and biomechanics of structures on the medial side of the knee.

LaPrade RF, Engebretsen AH, Ly TV et al 2007 The anatomy of the medial part of the knee. J Bone Joint Surg Am 89:2000–10.

A cadaveric study that described the qualitative anatomy of medial knee structures and a quantitative evaluation of their anatomic attachment sites in reference to pertinent osseous landmarks.

Seebacher JR, Inglis AE, Marshall JL et al 1982 The structure of the posterolateral aspect of the knee. J Bone Joint Surg Am 64:536–41.

A work that established the current interpretation of the anatomy of the soft tissues of the knee.

Taylor GI, Razaboni RM (eds) 1994 Michael Salmon: Anatomic Studies. Book 1, Arteries of the Muscles of the Extremities and the Trunk. St Louis: Quality Medical Publishing.

A translated, edited version of a classic French text, first published in 1933. Now a major source book in plastic surgery.

Tubbs RS, Michelson J, Loukas M et al 2008 The transverse genicular ligament: anatomical study and review of the literature. Surg Radiol Anat 30:5–9.

A cadaveric study that identified the transverse ligament of the knee in 55% of specimens, with two specimens exhibiting a duplicated ligament.

Warren LF, Marshall JL 1979 The supporting structures and layers on the medial side of the knee: an anatomical analysis. J Bone Joint Surg Am 61:56–62.

A cadaveric study of the medial knee that established a three-layer pattern for the regional ligaments.

References

Allaire R, Muriuki M, Gilbertson L et al 2008 Biomechanical consequences of a tear of the posterior root of the medial meniscus. Similar to total meniscectomy. J Bone Joint Surg Am 90:1922–31.

Amis AA, Dawkins GP 1991 Functional anatomy of the anterior cruciate ligament. Fibre bundle actions related to ligament replacements and injuries. J Bone Joint Surg Br 73:260–7.

A study of three functional components of the anterior cruciate ligament. Fibre length changes suggested that the 'isometric point' aimed at by some ligament replacements lay anterior and superior to the femoral origin of the intermediate fibre bundle and towards the roof of the intercondylar notch.

Amis AA, Farahmand F 1996 Biomechanics masterclass: extensor mechanism of the knee. Curr Orthop 10:102–9.

Bayram H, Herdem M, Temoçin AK 1996 Fibular dimelia and mirror foot without associated anomalies. Clin Genet 49:311–13.

Chahla J, Moatshe G, Dean CS et al 2016 Posterolateral corner of the knee: current concepts. Arch Bone Jt Surg 4:97–103.

Claes S, Vereecke E, Maes M et al 2013 Anatomy of the anterolateral ligament of the knee. J Anat 223:321–8.

Clarke HD, Kransdorf MJ, Conley CR et al 2018 Anatomy. In: Scott WN (ed), Insall & Scott Surgery of the Knee, 6 ed. Elsevier; Section 1 Basic Science. pp. 2–49.

Cormack GC, Lamberty BGH 1994 The Arterial Anatomy of Skin Flaps. Edinburgh: Elsevier, Churchill Livingstone.

Crespo B, James EW, Metsavaht L et al 2015 Injuries to posterolateral corner of the knee: a comprehensive review from anatomy to surgical treatment. Rev Bras Ortop 50:363–70.

Eckhoff DG, Kramer RC, Watkins JJ et al 1994 Variation in tibial torsion. Clin Anat 7:76–9.

Falciglia F, Guzzanti V, Di Ciommo V et al 2009 Physiological knee laxity during pubertal growth. Bull NYU Hosp Jt Dis 67:325–9.

Freeman MAR, Wyke B 1967 The innervation of the knee joint: an anatomical and histological study in the cat. J Anat 101:505–32.

A classic paper that investigates the gross anatomy and histology of the articular innervation of the knee joint. Four articular nerve endings were classified.

Ganey TM, Carey TP, O'Neal ML et al 2000 Morphologic and radiographic characterization of fibular dimelia. J Pediatr Orthop B 9:293–305.

Ghadially FN, Lalonde JM, Wedge JH 1983 Ultrastructure of normal and torn menisci of the human knee joint. J Anat 136:773–91.

Girgis FG, Marshall JL, Al Monajem ARS 1975 The cruciate ligaments of the knee joint. Clin Orthop 106:216–31.

A cadaveric study that described the anterior cruciate ligament as having an anteromedial and posterolateral band. It suggested that the anteromedial band was responsible for the anteroposterior drawer sign with flexion.

Griffith CJ, LaPrade RF, Johansen S et al 2009 Medial knee injury: part 1, static function of the individual components of the main medial knee structures. Am J Sports Med 37:1762–70.

Gronblad M, Korkala O, Leisi P et al 1985 Innervation of synovial membrane and meniscus. Acta Orthop Scand 56:484–6.

Gupte CM, Bull AMJ, Thomas RD et al 2003 A review of the function and biomechanics of the meniscofemoral ligaments. Arthroscopy 19:161–71.

Hamel A, Ploteau S, Lancien M et al 2012 Arterial supply to the tibial tuberosity: involvement in patellar ligament transfer in children. Surg Radiol Anat 34:311–16.

Johannsen AM, Civitarese DM, Padalecki JR et al 2012 Qualitative and quantitative anatomic analysis of the posterior root attachments of the medial and lateral menisci. Am J Sports Med 40:2342–7.

Jones G, Ding C, Glisson M et al 2003 Knee articular cartilage development in children: a longitudinal study of the effect of sex, growth, body composition, and physical activity. Pediatr Res 54:230–6.

Joseph J 1960 Man's Posture: Electromyographic Studies. Springfield, IL: Thomas.

Jungers WL, Meldrum DJ, Stern JT Jr 1993 The functional and evolutionary significance of the human peroneus tertius muscle. J Hum Evol 25:377–86.

Kärrholm J, Hansson LI, Selvik G 1984 Longitudinal growth rate of the distal tibia and fibula in children. Clin Orthop Relat Res 191:121–8.

Kawashima T, Sasaki H 2010 Reasonable classical concepts in human lower limb anatomy from the viewpoint of the primitive persistent sciatic artery and twisting human lower limb. Okajimas Folia Anat Jpn 87:141–9.

Kosinski C 1926 The course, mutual relations and distribution of the cutaneous nerves of the metazonal regions of the leg and foot. J Anat Physiol 60:274–97.

Kristiansen LP, Gunderson RB, Steen H et al 2001 The normal development of tibial torsion. Skeletal Radiol 30:519–22.

Kruckeberg BM, Chahla J, Moatshe G et al 2018 Quantitative and qualitative analysis of the medial patellar ligaments: an anatomic and radiographic study. Am J Sports Med 46:153–62.

Krych AJ, Reardon PJ, Johnson NR et al 2017 Non-operative management of medial meniscus posterior horn root tears is associated with worsening arthritis and poor clinical outcome at 5-year follow-up. Knee Surg Sports Traumatol Arthrosc 25:383–9.

Lalezari S, Amrami KK, Tubbs RS et al 2012 Interosseous membrane: the anatomic basis for combined ankle and common fibular (peroneal) nerve injuries. Clin Anat 25:401–6.

LaPrade CM, Ellman MB, Rasmussen MT et al 2014 Anatomy of the anterior root attachments of the medial and lateral menisci: a quantitative analysis. Am J Sports Med 42:2386–92.

A cadaveric study that described the quantitative and qualitative anatomy of the anterior root attachments of the medial and lateral menisci with regards to pertinent open and arthroscopic landmarks.

LaPrade MD, Kennedy MI, Wijdicks CA et al 2015 Anatomy and biomechanics of the medial side of the knee and their surgical implications. Sports Med Arthrosc Rev 23:63–70.

A review of the anatomy and biomechanics of structures on the medial side of the knee.

LaPrade RF, Engebretsen AH, Ly TV et al 2007 The anatomy of the medial part of the knee. J Bone Joint Surg Am 89:2000–10.

A cadaveric study that described the qualitative anatomy of medial knee structures and a quantitative evaluation of their anatomic attachment sites in reference to pertinent osseous landmarks.

Miller RH, Azar FM 2017 Knee injuries. In: Azar FM, Beaty JH, Canale ST (eds) Campbell's Operative Orthopaedics, 13 ed. Elsevier; Ch. 45, pp. 2121–97.

Newell RLM 1991 A complete intra-articular fat pad around the human patella. J Anat 179:232.

Oeffinger D, Conaway M, Stevenson R et al 2010 Tibial length growth curves for ambulatory children and adolescents with cerebral palsy. Dev Med Child Neurol 52:e195–201.

Oohashi Y, Koshino T, Oohashi Y 2010 Clinical features and classification of bipartite or tripartite patella. Knee Surg Sports Traumatol Arthrosc 18:1465–9.

Pritchett JW, Bortel DT 1997 Single bone straight line graphs for the lower extremity. Clin Orthop Relat Res 342:132–40.

Rajendran K 1985 Mechanism of locking at the knee joint. J Anat 143:189–94.

Sanders TL, Pareek A, Hewett TE et al 2018 Incidence of first-time lateral patellar dislocation: a 21-year population-based study. Sports Health 10:146–51.

Scapinelli R 1968 Studies on the vasculature of the human knee joint. Acta Anat 70:305–31.

Seebacher JR, Inglis AE, Marshall JL et al 1982 The structure of the posterolateral aspect of the knee. J Bone Joint Surg Am 64:536–41.

A work that established the current interpretation of the anatomy of the soft tissues of the knee.

Serra Cruz R, Mitchell JJ, Dean CS et al 2016 Anatomic posterolateral corner reconstruction. Arthrosc Tech 5:e563–72.

Solomon LB, Ferris L, Tedman R et al 2001 Surgical anatomy of the sural and superficial fibular nerves with an emphasis on the approach to the lateral malleolus. J Anat 199:717–23.

Spinner RJ, Atkinson JL, Tiel RL 2003 Peroneal intraneural ganglia: the importance of the articular branch. A unifying theory. J Neurosurg 99:330–43.

Stijak L, Bumbaširević M, Radonjić V et al 2016 Anatomic description of the anterolateral ligament of the knee. Knee Surg Sports Traumatol Arthrosc 24: 2083–8.

Taylor GI, Razaboni RM (eds) 1994 Michael Salmon: Anatomic Studies. Book 1, Arteries of the Muscles of the Extremities and the Trunk. St Louis: Quality Medical Publishing.

A translated, edited version of a classic French text, first published in 1933. Now a major source book in plastic surgery.

Tennant TD, Birch NC, Holmes MJ et al 1998 Knee pain and the infrapatellar branch of the saphenous nerve. J R Soc Med 91:573–5.

Tubbs RS, Apaydin N, Uz A et al 2009 The clinical anatomy of the ligament of Barkow at the proximal tibiofibular joint. Surg Radiol Anat 31:161–3.

Tubbs RS, Michelson J, Loukas M et al 2008 The transverse genicular ligament: anatomical study and review of the literature. Surg Radiol Anat 30:5–9.

A cadaveric study that identified the transverse ligament of the knee in 55% of specimens, with two specimens exhibiting a duplicated ligament.

van den Bergh FR, Vanhoenacker FM, De Smet E et al 2013 Peroneal nerve: Normal anatomy and pathologic findings on routine MRI of the knee. Insights Imaging 4:287–99.

Verghese R, Shah H, Rebello G et al 2007 Pre-axial mirror polydactyly associated with tibial deficiency: a study of the patterns of skeletal anomalies of the foot and leg. J Child Orthop 1:49–54.

Warren LF, Marshall JL 1979 The supporting structures and layers on the medial side of the knee: an anatomical analysis. J Bone Joint Surg Am 61:56–62.

A cadaveric study of the medial knee that established a three-layer pattern for the regional ligaments.

Watanabe M, Takeda S, Ikeuchi H 1979 Atlas of Arthroscopy. Berlin: Springer.

Zimmerer A, Sobau C, Balcarek P 2018 Recent developments in evaluation and treatment of lateral patellar instability. J Exp Orthop 5:3.

CHAPTER

79

Ankle and foot

The ankle joint (talocrural joint) is a diarthrodial articulation involving the distal tibia and fibula and the body of the talus; it is the only example in the human body of a true mortise joint. The human foot is a complex structure adapted to allow orthograde bipedal stance and locomotion and is the only part of the body that is in regular contact with the ground (Jones 1949). There are 28 separate bones in the human foot, including the sesamoid bones of the first metatarsophalangeal joint, and 31 joints, including the ankle joint. The hindfoot comprises the calcaneus and talus; the midfoot comprises the navicular, cuboid and three cuneiforms; the forefoot comprises five metatarsals, 14 phalanges and two sesamoid bones. With regard to the nomenclature of the surfaces of the foot, the terms 'plantar' and 'dorsal' are used to denote inferior and superior surfaces, respectively.

SKIN AND SOFT TISSUES

Skin

Vascular supply and lymphatic drainage

The skin around the ankle is supplied by anterior lateral and anterior medial malleolar arteries from the anterior tibial artery, posterior medial malleolar branches from the posterior tibial artery, posterior lateral malleolar branches from the fibular artery, and fasciocutaneous perforators from the anterior and posterior tibial and fibular arteries. The main blood supply to the medial side of the heel is from the medial calcaneal branches of the posterior tibial artery or, sometimes, the lateral plantar artery passing through the flexor retinaculum (Attinger et al 1997). The skin of the lateral side of the heel is supplied by lateral calcaneal branches of the fibular artery and the lateral tarsal artery. The arterial supply to the skin of the foot is rich and is derived from branches of the dorsalis pedis (the direct continuation of the anterior tibial artery), posterior tibial and fibular arteries. The skin covering the dorsum of the foot is supplied by the dorsalis pedis artery and by its continuation, the first dorsal metatarsal artery, with smaller contributions from the anterior perforating branch of the fibular artery and the marginal anastomotic arteries on the medial and lateral borders of the foot. The skin covering the plantar surface of the foot is supplied by perforating branches of the medial and lateral plantar arteries (the terminal branches of the posterior tibial artery). The skin of the forefoot is supplied by cutaneous branches of the common digital arteries.

Cutaneous venous drainage is via dorsal and plantar venous arches draining into medial and lateral marginal veins. The medial and lateral marginal veins form the long (great) and short (small) saphenous veins, respectively. On the plantar aspect of the foot, a superficial venous network forms an intradermal and subdermal mesh that drains to the medial and lateral marginal veins. Venous branches that accompany the medial and lateral plantar arteries arise from a deep venous network. Uniquely within the lower limb, venous flow in the foot is bidirectional. However, when valves are present, flow is from the plantar to the superficial dorsal system. From here, blood leaves the foot in the superficial and deep veins of the lower limb.

Superficial lymphatic drainage of all areas of the leg and foot (except the superficial posterolateral area) is via lymphatic vessels that accompany the long saphenous vein and its tributaries. The superficial posterolateral foot and leg drain into the popliteal lymph nodes via lymphatic vessels that accompany the short saphenous vein. Deep lymphatic vessels that accompany the dorsalis pedis, posterior tibial and fibular arteries drain into the popliteal lymph nodes.

Innervation

The skin covering the ankle and foot is innervated by nerves derived from the fourth and fifth lumbar and first sacral spinal nerves (see Figs 76.12, 76.14). Innervation of the dorsum of the foot is provided medially by the saphenous nerve, centrally by the superficial fibular nerve and laterally by the sural nerve; the deep fibular nerve supplies the dorsum of the first web space. Dorsal branches of the medial and lateral plantar nerves innervate the nail beds. The plantar aspect of the foot is innervated by the medial and lateral plantar nerves, which arise as terminal branches of the tibial nerve. The medial plantar nerve supplies sensation to the plantar aspect of the great toe and the second, the third and the medial half of the fourth toes. The lateral plantar nerve supplies the remaining lateral aspect of the fourth and the entire fifth toe. The heel is innervated by calcaneal branches of the tibial and sural nerves. Injury to any of these nerves can lead to painful neuromas and loss of protective sensation, the latter is a common complication in diabetic neuropathy, which is one of the major risk factors in developing diabetic foot ulcers.

Nail apparatus

A toenail consists of a nail plate with the underlying nail matrix and nail bed. The nail apparatus is described in Chapter 7. The toenail is commonly a site of several pathologies, including onychomycosis and onychocryptosis (Jules 1989, Eekhof et al 2012).

Soft tissues

Retinacula at the ankle

In the vicinity of the ankle joint, the tendons of the muscles of the leg are bound down by localized, band-shaped thickenings of the deep fascia termed retinacula, which collectively serve to prevent bowstringing of the underlying tendons during muscle contraction. The retinacula can be considered as specialized deep fascia that may have a role in spatial proprioception (Stecco et al 2010).

There are superior and inferior extensor retinacula, a flexor retinaculum and superior and inferior fibular retinacula.

Extensor retinacula

Superior extensor retinaculum

The superior extensor retinaculum binds down the tendons of tibialis anterior, extensor hallucis longus, extensor digitorum longus and fibularis tertius immediately proximal to the anterior aspect of the ankle joint (**Fig. 79.1**). The anterior tibial vessels and deep fibular nerve pass deep to the retinaculum, and the superficial fibular nerve passes superficially. The retinaculum is attached laterally to the distal end of the anterior border of the fibula and medially to the anterior border of the tibia. Its proximal border is continuous with the deep fascia of the leg, and dense connective tissue connects its distal border to the inferior extensor retinaculum. Laterally, it blends with the superior fibular retinaculum and medially it blends with the upper border of the extensor retinaculum. The tendon of tibialis anterior is the only extensor tendon that possesses a synovial sheath at the level of the superior extensor retinaculum, which means that tenosynovitis of tibialis anterior can cause pain at the level of the superior extensor retinaculum (Genç et al 2013).

Inferior extensor retinaculum

The inferior extensor retinaculum is a Y-shaped band lying anterior to the ankle joint (see Fig. 78.35; **Fig. 79.2**). The stem of the Y is at the lateral end, where it is attached to the upper surface of the calcaneus, anterior to the calcaneal sulcus. The band passes medially, forming a strong loop around the tendons of fibularis tertius and extensor digitorum longus (see Fig. 79.2A). From the deep surface of the loop, a band passes laterally behind the interosseous talocalcaneal and cervical ligaments and is attached to the calcaneal sulcus. At the medial end of the loop, two diverging limbs extend medially to complete the 'Y' shape of the retinaculum. The proximal limb consists of two layers. The deep layer passes deep to the tendons of extensor hallucis longus and tibialis anterior, but superficial to the anterior tibial vessels and deep fibular nerve, to reach the medial malleolus. The superficial layer crosses superficial to the tendon of extensor hallucis longus and then adheres firmly to the deep one; in some cases, it continues superficial to the tendon of tibialis anterior, before blending with the deep layer. The distal limb

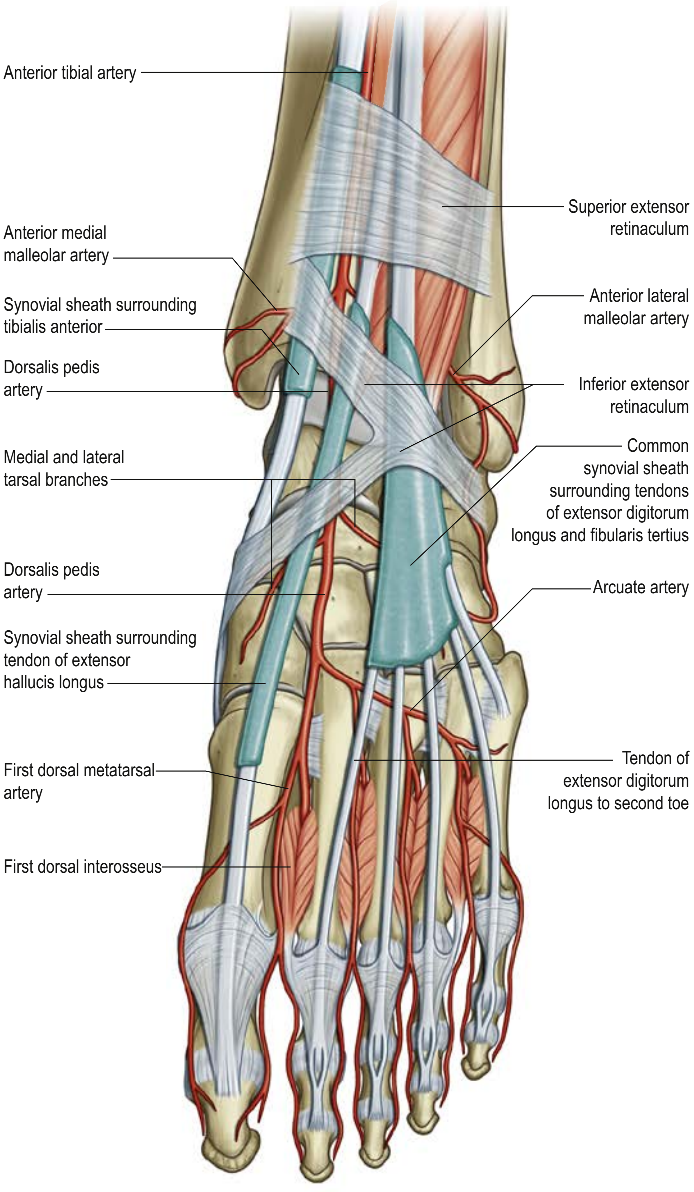
Anterior tibial artery
Anterior medial malleolar artery
Synovial sheath surrounding tibialis anterior
Dorsalis pedis artery
Medial and lateral tarsal branches
Dorsalis pedis artery
Synovial sheath surrounding tendon of extensor hallucis longus
First dorsal metatarsal artery
First dorsal interosseus
Superior extensor retinaculum
Anterior lateral malleolar artery
Inferior extensor retinaculum
Common synovial sheath surrounding tendons of extensor digitorum longus and fibularis tertius
Arcuate artery
Tendon of extensor digitorum longus to second toe

Fig. 79.1 The synovial sheaths of the tendons of the ankle, anterior aspect. (With permission from Drake RL, Vogl AW, Mitchell A (eds) Gray's Anatomy for Students, 2nd ed. Elsevier, Churchill Livingstone. Copyright 2010.)

extends downwards and medially and blends with the plantar aponeurosis. It is superficial to the tendons of extensor hallucis longus and tibialis anterior, the dorsalis pedis artery and the terminal branches of the deep fibular nerve.

Flexor retinaculum

The flexor retinaculum is attached anteriorly to the medial malleolus, distal to which it is continuous with the deep fascia on the dorsum of the foot (see Fig. 79.2B). From its malleolar attachment, it extends posteroinferiorly to the medial process of the calcaneus and the plantar aponeurosis. Proximally, there is no clear demarcation between its border and the deep fascia of the leg, especially the deep transverse layer of the deep fascia. Distally, its border is continuous with the plantar aponeurosis and many fibres of abductor hallucis are attached to it. The flexor retinaculum converts grooves on the tibia and calcaneus into canals for the tendons, and bridges over the posterior tibial vessels and tibial nerve. As these structures enter the sole, they are, from medial to lateral, the tendons of tibialis posterior and flexor digitorum longus, the posterior tibial vessels, the tibial nerve and the tendon of flexor hallucis longus (see Fig. 79.15).

Fibular retinacula

The fibular retinacula are fibrous bands that retain the tendons of fibularis longus and brevis in position as these tendons cross the lateral aspect of the ankle region (see Fig. 79.2A).

Superior fibular retinaculum

The superior fibular retinaculum is a short band that extends from the back of the lateral malleolus to the deep transverse fascia of the leg and the lateral surface of the calcaneus. Damage to the retinaculum can lead to instability of the tendons of fibularis longus and brevis.

Inferior fibular retinaculum

The inferior fibular retinaculum is continuous in front with the inferior extensor retinaculum, and is attached posteriorly to the lateral surface of the calcaneus. Some of its fibres are fused with the periosteum on the fibular trochlea (peroneal trochlea or tubercle) of the calcaneus, forming a septum between the tendons of fibularis longus and brevis.

Synovial sheaths at the ankle

Anterior to the ankle, the synovial sheath for tibialis anterior extends from the proximal margin of the superior extensor retinaculum to the interval between the diverging limbs of the inferior retinaculum (see Figs 79.1, 79.2B). A common sheath encloses the tendons of extensor digitorum longus and fibularis tertius, starting just above the level of the malleoli, and reaching to the level of the base of the fifth metatarsal (see Figs 79.1, 79.2A). Although variable, the sheath for extensor hallucis longus begins near that for extensor digitorum longus and extends as far as the base of the first metatarsal (see Figs 79.1–79.2).

Posteromedial to the ankle, the sheath for tibialis posterior starts approximately 4 cm above the medial malleolus and ends just proximal to the attachment of the tendon to the tuberosity of the navicular (see Fig. 79.2B). The sheath for flexor hallucis longus begins at the level of the medial malleolus and extends distally as far as the base of the first metatarsal (see Fig. 79.2B). Occasionally, as a result of overuse, particularly in ballet dancers where balance on the tips of the toes *en pointe* involves sustained extreme plantar flexion of the ankle and great toe in the weight-bearing position, a fibrous nodule may develop in the tendon, just proximal to the tendon sheath. This may result in the thickened tendon being caught intermittently in the sheath, causing pain and 'triggering' of the great toe, a condition referred to as hallux saltans. Surgical opening of the sheath may be required. In athletes, the muscle belly of flexor hallucis longus may be abnormally large and may extend further distally than usual; it can also catch at the opening of the sheath. The sheath for flexor digitorum longus begins slightly superior to the level of the medial malleolus and ends at the level of the navicular.

Posterolateral to the ankle, the tendons of fibularis longus and brevis are enclosed in a single sheath deep to the superior fibular retinaculum. This sheath splits into two separate sheaths enclosing the tendons of fibularis longus and brevis deep to the inferior fibular retinaculum (see Fig. 79.2A): it extends for about 4 cm both proximally and distally from the lateral malleolus.

Plantar aponeurosis

The plantar aponeurosis is composed of densely compacted collagen fibres orientated mainly longitudinally, but also transversely (**Fig. 79.3**). Its medial and lateral borders overlie the intrinsic muscles of the great and fifth toes, respectively, while its dense central part overlies the extrinsic and intrinsic flexors of the digits.

The central part is the strongest and thickest. The fascia is narrow posteriorly, where it is attached to the medial process of the calcaneal tuberosity proximal to flexor digitorum brevis, and traced distally it becomes broader and somewhat thinner. Just proximal to the level of the metatarsal heads, it divides into five bands, one for each toe. As these five digital bands diverge below the metatarsal shafts, they are united by transverse fibres. Proximal, plantar and a little distal to the metatarsal heads and the metatarsophalangeal joints, the superficial stratum of each of the five bands is connected to the dermis by skin ligaments (retinacula cutis) (see Fig. 7.19). These ligaments reach the skin of the first metatarsophalangeal joint proximal to, and in the floors of, the furrows that separate the toes from the sole: Ledderhose's disease (plantar fibromatosis) may involve these ligaments, producing contractures of the affected digits (Espert et al 2018). The deep stratum of each digital band of the aponeurosis yields two septa that flank the digital flexor tendons and separate them from the lumbricals and the digital vessels and nerves. These septa pass deeply to fuse with the interosseous fascia, the deep transverse metatarsal ligaments (which run between the heads of adjacent metatarsals), the plantar ligaments of the metatarsophalangeal joints, and the periosteum and fibrous flexor sheaths at the base of each proximal phalanx. Pads of fat develop in the web spaces between the metatarsal heads and the bases of the proximal phalanges, and they cushion the digital nerves and vessels from adjoining

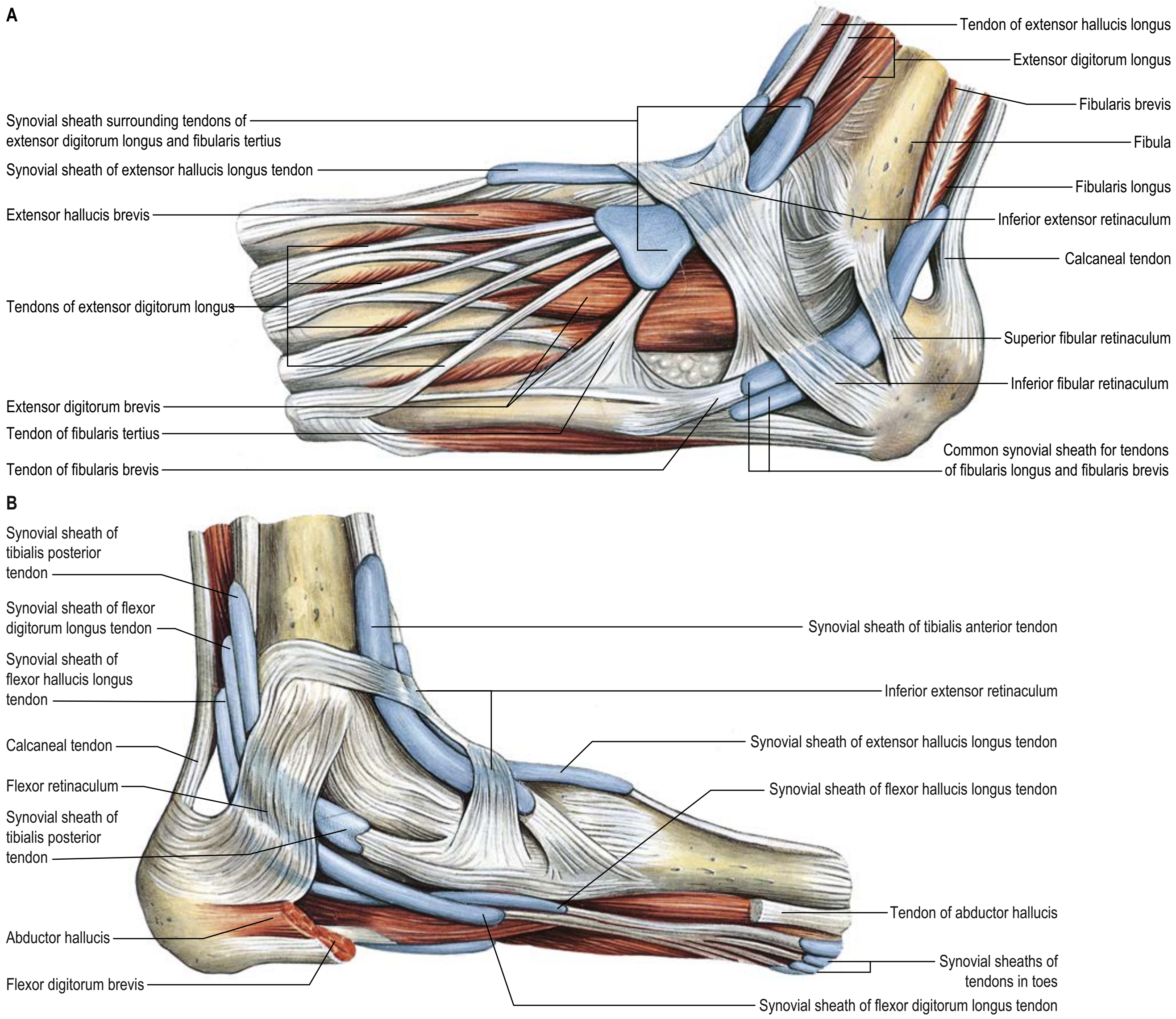
A
Tendon of extensor hallucis longus
Extensor digitorum longus
Fibularis brevis
Fibula
Fibularis longus
Inferior extensor retinaculum
Calcaneal tendon
Superior fibular retinaculum
Inferior fibular retinaculum
Common synovial sheath for tendons of fibularis longus and fibularis brevis
Synovial sheath surrounding tendons of extensor digitorum longus and fibularis tertius
Synovial sheath of extensor hallucis longus tendon
Extensor hallucis brevis
Tendons of extensor digitorum longus
Extensor digitorum brevis
Tendon of fibularis tertius
Tendon of fibularis brevis
B
Synovial sheath of tibialis posterior tendon
Synovial sheath of flexor digitorum longus tendon
Synovial sheath of flexor hallucis longus tendon
Calcaneal tendon
Flexor retinaculum
Synovial sheath of tibialis posterior tendon
Abductor hallucis
Flexor digitorum brevis
Synovial sheath of tibialis anterior tendon
Inferior extensor retinaculum
Synovial sheath of extensor hallucis longus tendon
Synovial sheath of flexor hallucis longus tendon
Tendon of abductor hallucis
Synovial sheaths of tendons in toes
Synovial sheath of flexor digitorum longus tendon

Fig. 79.2 The synovial sheaths of the tendons of the ankle. **A**, Lateral aspect. **B**, Medial aspect. (Sobotta Atlas of Human Anatomy © Elsevier GmbH, Urban & Fischer, Munich.)

tendinous structures and extraneous plantar pressures. Just distal to the metatarsal heads, a plantar interdigital ligament (superficial transverse metatarsal ligament) blends progressively with the deep aspect of the superficial stratum of the plantar aponeurosis where it enters the toes (see Fig. 79.3). The central part of the plantar aponeurosis thus provides an intermediary structure between the skin and the osteoligamentous framework of the foot via numerous cutaneous retinacula and deep septa that extend to the metatarsals and phalanges. The central part is also continuous with the medial and lateral parts: at the junctions, two intermuscular septa, medial and lateral, extend in oblique vertical planes between the medial, intermediate and lateral groups of plantar muscles to reach bone. Thinner, horizontal intermuscular septa, derived from the vertical intermuscular septa, pass between the muscle layers.

The lateral part of the plantar aponeurosis, which covers abductor digiti minimi, is thin distally and thick proximally, where it forms a strong band that sometimes contains muscle fibres, between the lateral process of the calcaneal tuberosity and the base of the fifth metatarsal. It is continuous medially with the central part of the aponeurosis, and with the fascia on the dorsum of the foot around its lateral border. The medial part of the plantar aponeurosis, which covers abductor hallucis, is thin. It is continuous proximally with the flexor retinaculum, medially with the dorsal fascia of the foot, and laterally with the central part of the plantar aponeurosis.

Plantar heel pain

Available with the *Gray's Anatomy* e-book

Fascial compartments of the foot

There are four main compartments of the plantar aspect of the foot: medial, central (or intermediate), lateral and interosseous (Fig. 79.4). The medial compartment contains abductor hallucis and flexor hallucis brevis, as well as the tendon of flexor hallucis longus. The medial compartment is bounded inferiorly and medially by the medial part of the plantar aponeurosis and its medial extension, laterally by an intermuscular septum, and dorsally by the first metatarsal. The central compartment contains flexor digitorum brevis, the lumbricals, flexor accessorius (quadratus plantae), adductor hallucis, and the tendons of flexor digitorum longus. The central compartment is bounded by the plantar aponeurosis inferiorly, the osseofascial tarsometatarsal structures dorsally and intermuscular septa medially and laterally. The lateral compartment contains abductor digiti minimi and flexor digiti minimi brevis, and its boundaries are the fifth metatarsal dorsally, the plantar aponeurosis inferiorly and laterally, and an intermuscular septum medially. The interosseous compartment contains the seven interossei and its boundaries are the interosseous fascia and the metatarsals.

The dorsal aspect of the foot effectively contains a single compartment occupied by the extrinsic extensor tendons and extensor digitorum brevis, and roofed by the deep dorsal fascia. The deep fascia on the dorsum of the foot (fascia dorsalis pedis) is a thin layer, continuous above with the inferior extensor retinaculum and covering the dorsal extensor tendons and extensor digitorum brevis.

Lateral intermuscular septum

The lateral intermuscular septum is incomplete, especially at its proximal end where the lateral plantar artery and nerve enter the lateral compartment. Distally, its deep attachments are to the fibrous sheath of fibularis longus and to the fifth metatarsal.

Medial intermuscular septum

The medial intermuscular septum is incomplete where the tendon of flexor digitorum longus enters the central compartment and where

Plantar fasciopathy (fasciosis) is a common cause of plantar heel pain (Riel et al 2017). Many contributing aetiological factors have been reported, such as age, body weight, systemic disease, genetics, biomechanical dysfunction or deformity, footwear, occupation, activity, or lifestyle. Histological findings show fragmentation and degeneration of the plantar fascia in the absence of inflammatory changes. On imaging, thickening of the plantar fascia together with other findings such as plantar calcaneal spurs, perifascial oedema and bone marrow oedema, may also be present.

Clinically, palpation of the plantar aponeurosis at the medial tubercle of the calcaneus may result in localized tenderness and exacerbated heel pain in patients. Multiple treatment options, from conservative therapy to surgical intervention, may be used to provide pain relief. Non-operative approaches include foot orthoses and night splints, injections with a combination of corticosteroids and local anaesthetics, injections of autologous platelet-rich plasma, extracorporeal shockwave therapy, dry needling, laser therapy and stretching or strengthening exercises (Salvioli et al 2017, Monteagudo et al 2018). Surgical treatments include partial or complete release of the plantar aponeurosis; gastrocnemius recession is considered a safe, current alternative for surgical correction (Molund et al 2018).

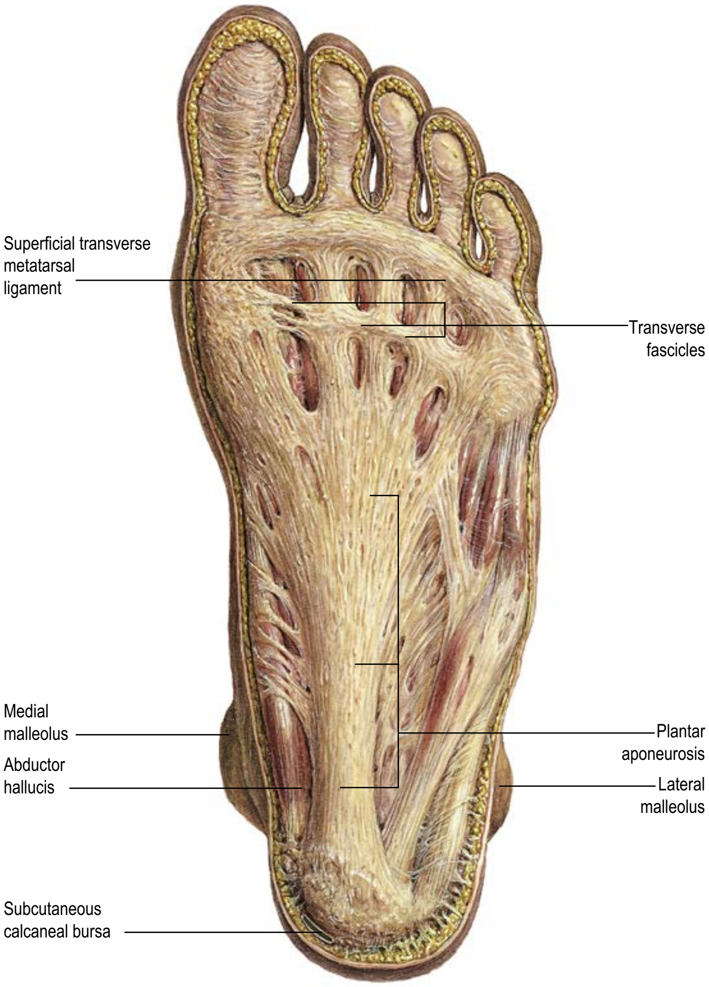

Fig. 79.3 The plantar aponeurosis. (Sobotta Atlas of Human Anatomy © Elsevier GmbH, Urban & Fischer, Munich.)

adductor hallucis and the lateral head of flexor hallucis brevis enter the medial compartment. The septum divides into three bands, proximal, intermediate and distal, each of which displays lateral and medial divisions as it approaches its deep attachments. The proximal band is attached laterally to the cuboid and blends medially with the tendon of tibialis posterior. The middle band is attached laterally to the cuboid and the long plantar ligament and medially to the medial cuneiform. The distal band divides to enclose the tendon of flexor hallucis longus and is attached to the fascia over flexor hallucis brevis.

Compartment syndrome in the foot

A compartment syndrome results from an increase in intracompartmental pressure sufficient to impair venous outflow from that compartment. Blood enters the compartment at arterial pressure, but with no outflow, this increases compartment pressures until they exceed the arterial pressure. At this point the inflow of arterial blood ceases, leading to muscle and nerve ischaemia. Failure to relieve the increased pressure in the compartment surgically results in necrosis of the soft tissues within the compartment. The most common cause of compartment syndrome in the foot is trauma, usually of high-energy (high-impact) type; crush injuries, calcaneal fractures and disruption of the tarsometatarsal joints are the usual antecedents (Dodd and Le 2013).

Specialized adipose tissue (heel and metatarsal pads)

The heel is subject to repeated high impacts and is anatomically adapted to withstand these pressures. The adult heel pad has a mean thickness of 18 mm and a mean epidermal thickness of 0.64 mm (dorsal epidermal thickness averages 0.069 mm). The heel pad contains elastic adipose tissue organized as spiral fibrous septa anchored to each other, to the calcaneus and to the skin. The septa are U-shaped, fat-filled columns designed to resist compressive loads and are reinforced internally with elastic diagonal and transverse fibres that separate the fat into compartments.

In the forefoot, the subcutaneous tissue consists of fibrous lamellae arranged in a complex whorl containing adipose tissue attached via vertical fibres to the dermis superficially and the plantar aponeurosis deeply. The fat is particularly thick in the region of the metatarsophalangeal joints, which cushions the foot during the toe-off phase of gait. Like the heel pad, the metatarsal fat pad is designed to withstand compressive and shearing forces. Atrophy of either may be a cause of persistent pain in the distal plantar region.

BONES

Functionally, the skeleton of the foot may be divided into the tarsus, metatarsus and phalanges. Anatomically, it may be divided into the hindfoot (calcaneus and talus), midfoot (navicular, cuboid and cuneiforms), and forefoot (metatarsals, phalanges and sesamoid bones of the great toe).

Distal tibia

The distal end of the tibia has anterior, medial, posterior, lateral and distal surfaces, and projects inferomedially as the medial malleolus (see Figs 78.7, 79.3). The distal surface, also called the tibial plafond, articulates with the talus and is wider anteriorly than posteriorly. It is concave sagittally and slightly convex transversely, and continues medially into the malleolar articular surface. The medial malleolus is short and thick, and has a smooth lateral surface with a crescentic or comma-shaped facet that articulates with the medial surface of the talar body. The distal end of the tibia, including its ossification, is described in detail in Chapter 78 (see Fig. 78.9).

Ligamentous attachments No muscles are attached to the distal tibia. The interosseous membrane, the deltoid ligament and the anterior and posterior tibiofibular ligaments are attached to the distal tibia.

Vascular supply The distal tibia is supplied by an arterial network formed by branches of the dorsalis pedis, posterior tibial and fibular arteries.

Innervation The distal tibia is innervated by branches from the deep fibular, tibial, saphenous and sural nerves.

Distal fibula

The distal end of the fibula or lateral malleolus projects distally and posteriorly relative to the medial malleolus (see Figs 79.3, 78.7, 78.8). Its lateral aspect is subcutaneous, the posterior surface has a broad groove with a prominent lateral border, and the anterior surface is rough and somewhat rounded and articulates with the anteroinferior aspect of the tibia. The medial surface has a triangular articular facet and is vertically convex with its apex directed distally. It articulates with the lateral talar surface. Behind the facet is a rough malleolar fossa for ligamentous attachment. The distal end of the fibula, including its ossification, is described in detail in Chapter 78.

Ligamentous attachments No muscles are attached to the distal fibula below the level of the interosseous ligament. The ligamentous attachments are those of the lateral ligament complex, i.e. the anterior talofibular, the calcaneofibular and the posterior talofibular ligaments. The interosseous membrane is attached on its medial aspect.

Vascular supply The distal fibula is supplied by an arterial network made up of branches of the dorsalis pedis, posterior tibial and fibular arteries.

Innervation The distal fibula is innervated by the deep fibular, tibial, saphenous and sural nerves.

Tarsus

The seven tarsal bones occupy the proximal half of the foot (**Figs 79.5–79.6, 79.8**). The tarsus and carpus are homologous, but the tarsal elements are larger, reflecting their role in supporting and distributing body weight. As in the carpus, tarsal bones are arranged in proximal and distal rows, but medially, there is an additional single intermediate tarsal element, the navicular. The proximal row is made up of the talus and calcaneus; the long axis of the talus is inclined anteromedially and inferiorly, and its distally directed head is medial to the calcaneus and at a

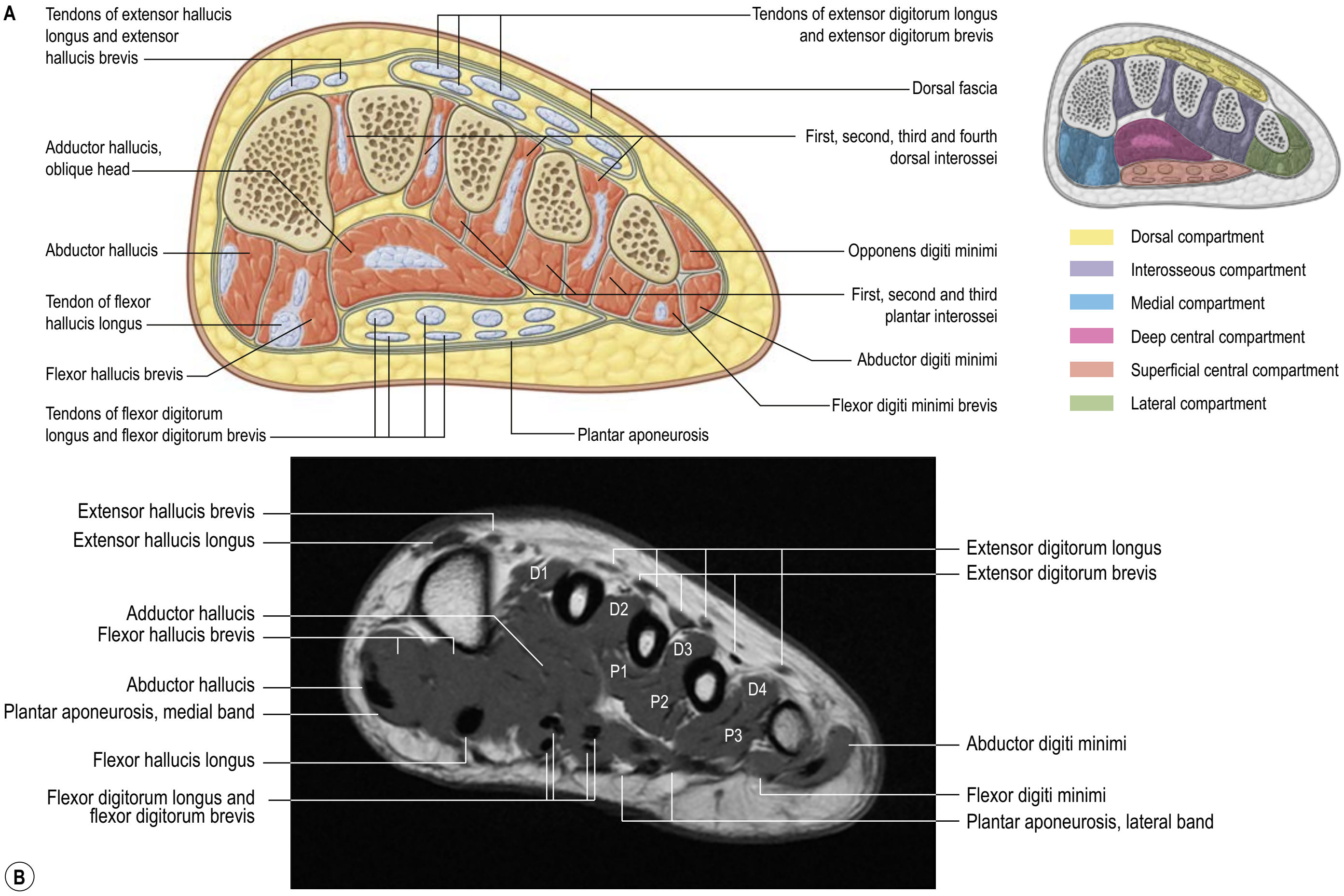
A
Tendons of extensor hallucis longus and extensor hallucis brevis
Adductor hallucis, oblique head
Abductor hallucis
Tendon of flexor hallucis longus
Flexor hallucis brevis
Tendons of flexor digitorum longus and flexor digitorum brevis
Plantar aponeurosis
Tendons of extensor digitorum longus and extensor digitorum brevis
Dorsal fascia
First, second, third and fourth dorsal interossei
Opponens digiti minimi
First, second and third plantar interossei
Abductor digiti minimi
Flexor digiti minimi brevis
Dorsal compartment
Interosseous compartment
Medial compartment
Deep central compartment
Superficial central compartment
Lateral compartment
Extensor hallucis brevis
Extensor hallucis longus
Adductor hallucis
Flexor hallucis brevis
Abductor hallucis
Plantar aponeurosis, medial band
Flexor hallucis longus
Flexor digitorum longus and flexor digitorum brevis
D1
D2
D3
D4
P1
P2
P3
Extensor digitorum longus
Extensor digitorum brevis
Abductor digiti minimi
Flexor digiti minimi
Plantar aponeurosis, lateral band
B

Fig. 79.4 A, A coronal section through the midfoot showing the main fascial compartments. **B**, Coronal T1-weighted MRI through the midfoot.

superior level. The distal row contains, from medial to lateral, the medial, intermediate and lateral cuneiforms and the cuboid. Collectively, these bones display an arched transverse alignment that is dorsally convex. Medially, the navicular is interposed between the head of the talus and the cuneiforms. Laterally, the calcaneus articulates with the cuboid.

The tarsus and metatarsus are arranged to form intersecting longitudinal and transverse arches. Hence, thrust and weight are not transmitted from the tibia to the ground (or *vice versa*) directly through the tarsus, but are distributed through the tarsals and metatarsals to the ends of the longitudinal arches. For the purposes of description, each tarsal bone is arbitrarily considered to be cuboidal in form, with six surfaces. The ossification sites and timing of ossification are summarized in Figs 79.7–79.8A.

Individual tarsal bones

Talus

The talus is an intercalated bone with no tendinous attachments. It is the osseous link between the foot and leg through the ankle joint (see Figs 79.8B, 79.17, 79.19).

Head

Directed distally and somewhat inferomedially, the head has a distal surface which is ovoid and convex; its long axis is also inclined inferomedially to articulate with the proximal navicular surface (see Fig. 79.5A). The plantar surface of the head has three articular areas, separated by smooth ridges (Fig. 79.9C). The most posterior and largest is oval and slightly convex, and rests on a shelf-like medial calcaneal projection, the sustentaculum tali. Anterolateral to this and usually continuous with it, a flat articular facet rests on the anteromedial part of the dorsal (proximal) calcaneal surface; distally, it continues into the navicular surface. Between the two calcaneal facets, a part of the talar head, covered with articular cartilage, is in contact with the plantar calcaneonavicular (spring) ligament, which is covered here, superiorly, by fibrocartilage. When the foot is inverted passively, the dorsolateral aspect of the head is visible and palpable approximately 3 cm distal to the tibia; it is hidden by extensor tendons when the toes are dorsiflexed.

Neck

The neck is the narrow, medially inclined region between the head and body (see Fig. 79.9C). Its rough surfaces are for ligaments. The medial plantar surface has a deep sulcus tali that, when the talus and calcaneus are articulated, forms the roof of the tarsal sinus, which is occupied by interosseous talocalcaneal and cervical ligaments.

The long axis of the neck, inclined downwards, distally and medially, makes an angle of approximately 150° with that of the body; it is smaller (130–140°) at birth, accounting in part for the inverted foot in young children. The dorsal talonavicular ligament and ankle articular capsule are attached distally to the dorsal surface of the talus, which means that the proximal part of this surface lies within the capsule of the ankle joint. The medial articular facet of the talar body and part of the trochlear surface may extend on to the neck. The anterior talofibular ligament is attached on the lateral aspect of the neck, spreading along the adjacent anterior border of the lateral surface. The interosseous talocalcaneal and cervical ligaments are attached to the inferior surface of the neck. A dorsolateral, so-called 'squatting facet' is commonly present on the talar neck in those individuals who habitually adopt the squatting position; it articulates with the anterior tibial margin in extreme dorsiflexion and may be doubled.

Body

The body is cuboidal, covered dorsally by a trochlear surface articulating with the distal end of the tibia. It is anteroposteriorly convex, gently concave transversely, widest anteriorly and, therefore, sellar in shape (see Fig. 79.9C). The triangular lateral surface is smooth and vertically concave for articulation with the lateral malleolus. Superiorly, it is continuous with the trochlear surface; inferiorly, its apex is a lateral process. Proximally, the medial surface is (posterosuperiorly) covered by a comma-shaped facet, which is deeper in front and articulates with the medial malleolus. Distally, this surface is rough and contains numerous vascular foramina. The small posterior surface features a rough projection termed the posterior process. The process is marked by an oblique groove between two tubercles. The lateral tubercle is usually larger; the medial is less prominent and lies immediately behind the sustentaculum tali. The plantar surface articulates with the middle third of the dorsal calcaneal surface by an oval concave facet, its long axis directed distolaterally at an angle of

In a hypermobile flat foot undergoing pronation, the talar head is unsupported medially by the sustentaculum tali. The resulting lack of support results in a visible medial protrusion of the talar head as the foot adducts and plantar flexes towards the ground (Michaud 2011).

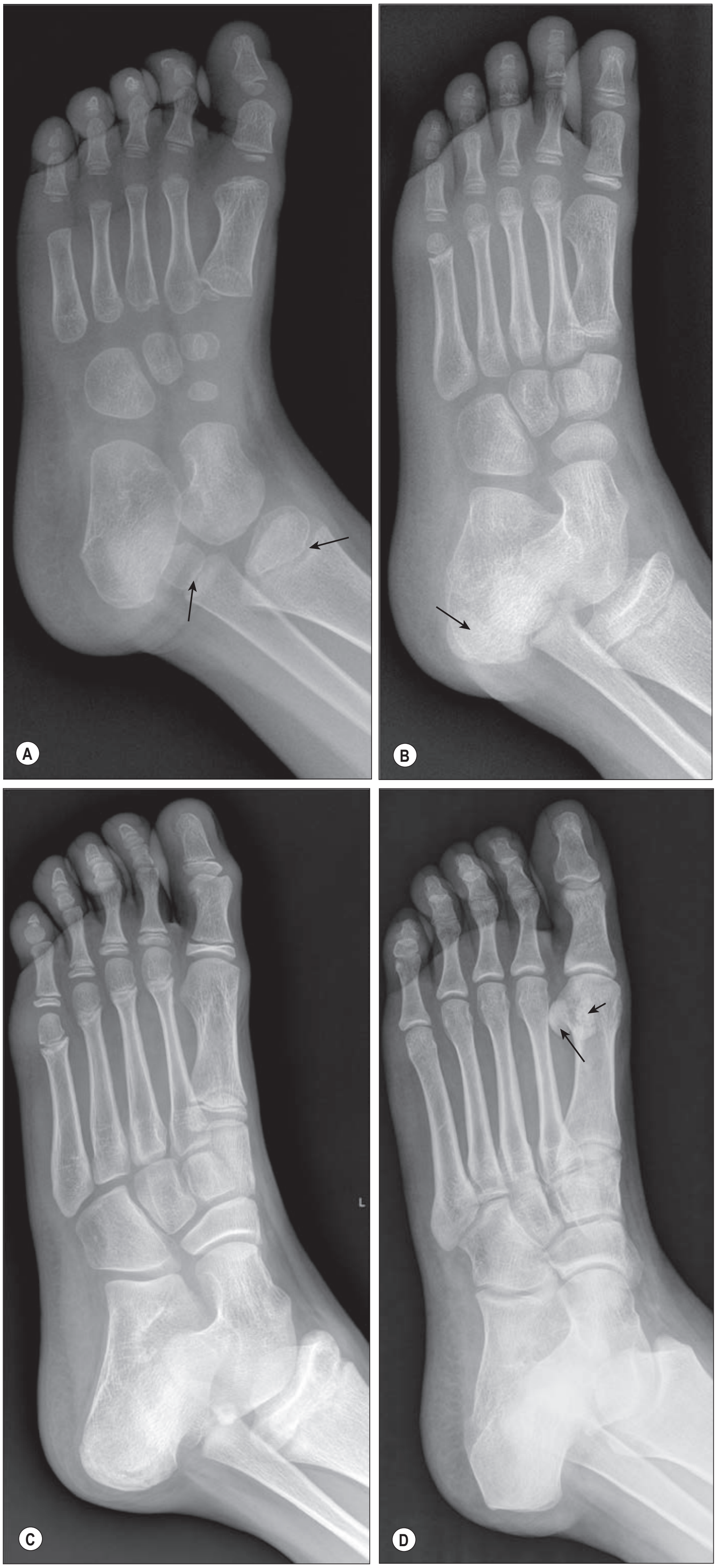

Fig. 79.7 A, Plain film oblique radiograph of a normal left ankle and foot in a 2-year-old infant. Note the epiphysial plates of the distal tibia and fibula (arrows). **B**, Plain film oblique radiograph of a normal left ankle and foot; 6-year-old child. Note the calcaneal apophysis (arrow). **C**, Plain film oblique radiograph of a normal left ankle and foot; 11-year-old juvenile. Note that the sesamoid bones of the first metatarsophalangeal joints are not visible because they have not yet ossified. **D**, Plain film oblique radiograph of a normal left ankle and foot of a skeletally mature adult. Note the presence of the sesamoid bones of the first metatarsophalangeal joints (arrows). The medial sesamoid is bipartite (short arrow), which is an anatomical variation. (Courtesy of Douglas N. Mintz, MD, Department of Radiology and Imaging, Hospital for Special Surgery, New York, NY.)

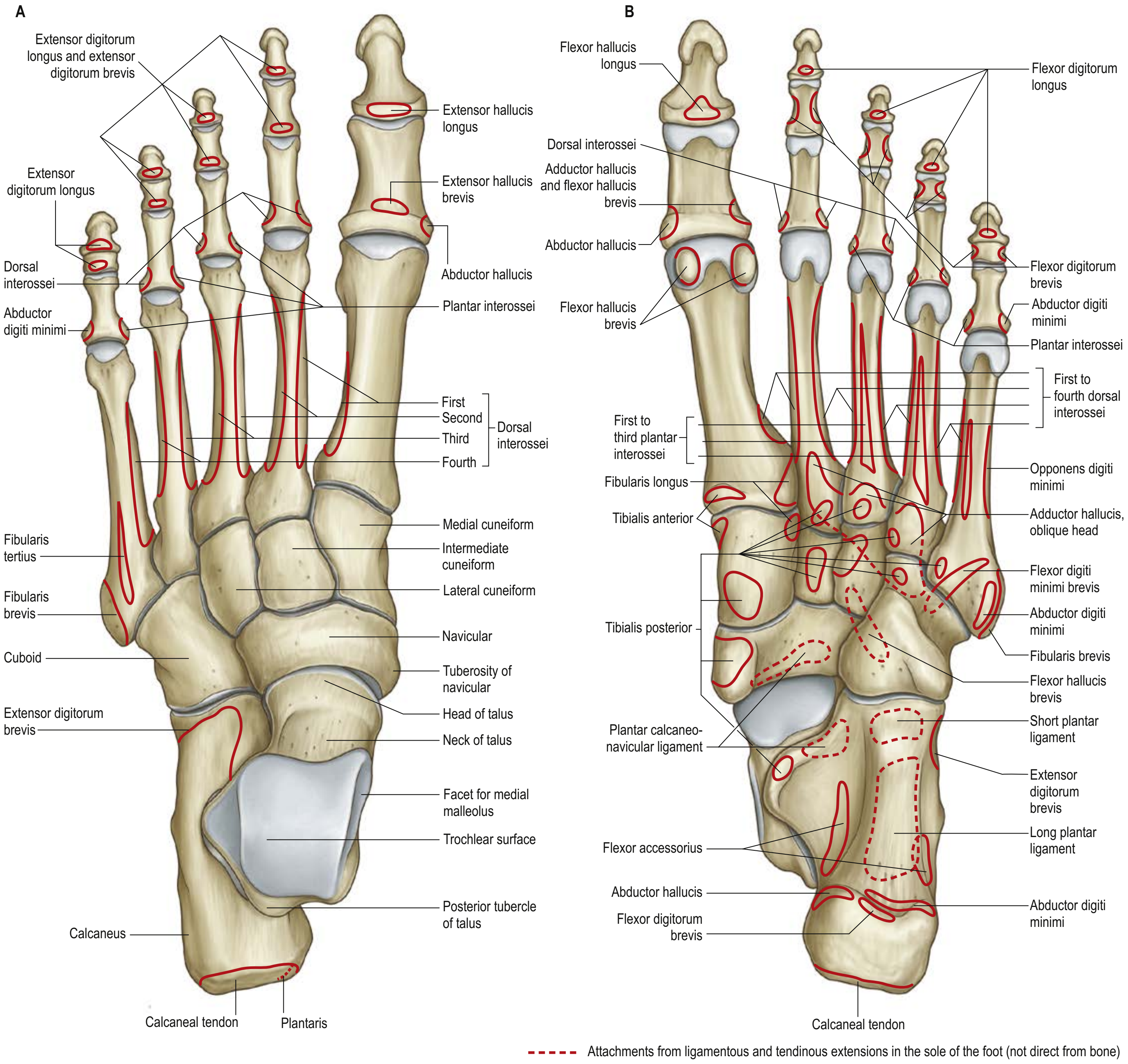
A
Extensor digitorum longus and extensor digitorum brevis
Extensor digitorum longus
Dorsal interossei
Abductor digiti minimi
Extensor hallucis longus
Extensor hallucis brevis
Abductor hallucis
Plantar interossei
First
Second
Third
Fourth
Dorsal interossei
Medial cuneiform
Intermediate cuneiform
Lateral cuneiform
Navicular
Fibularis tertius
Fibularis brevis
Cuboid
Tuberosity of navicular
Head of talus
Extensor digitorum brevis
Neck of talus
Facet for medial malleolus
Trochlear surface
Posterior tubercle of talus
Calcaneus
Calcaneal tendon
Plantaris
B
Flexor hallucis longus
Flexor digitorum longus
Dorsal interossei
Adductor hallucis and flexor hallucis brevis
Abductor hallucis
Flexor digitorum brevis
Abductor digiti minimi
Flexor hallucis brevis
Plantar interossei
First to fourth dorsal interossei
First to third plantar interossei
Opponens digiti minimi
Fibularis longus
Tibialis anterior
Adductor hallucis, oblique head
Flexor digiti minimi brevis
Abductor digiti minimi
Tibialis posterior
Fibularis brevis
Flexor hallucis brevis
Short plantar ligament
Plantar calcaneonavicular ligament
Extensor digitorum brevis
Long plantar ligament
Flexor accessorius
Abductor hallucis
Abductor digiti minimi
Flexor digitorum brevis
Calcaneal tendon
Attachments from ligamentous and tendinous extensions in the sole of the foot (not direct from bone)

Fig. 79.5 The skeleton of the left foot, with muscle attachments. **A**, Dorsal aspect. **B**, Plantar aspect. The attachments of tibialis posterior to the metatarsals vary; those to the third and fifth metatarsals are sometimes absent.

approximately 45° with the median plane. The medial edge of the trochlear surface is straight, but its lateral edge inclines medially in its posterior part and is often broadened into a small, elongated triangular area, which is in contact with the posterior tibiofibular ligament in dorsiflexion.

The posterior talofibular ligament is attached to the lateral tubercle of the posterior process (posterolateral tubercle). Its attachment extends up to the groove, or depression, between the process and posterior trochlear border. The posterior talocalcaneal ligament is attached to the plantar border of the posterior process. The groove between the tubercles of the process contains the tendon of flexor hallucis longus and continues distally into the groove on the plantar aspect of the sustentaculum tali. The medial talocalcaneal ligament is attached below to the medial tubercle, whereas the most posterior superficial fibres of the deltoid ligament are attached above the tubercle. The deep fibres of the deltoid ligament are attached more superiorly to the rough area immediately below the comma-shaped articular facet on the medial surface.

Ligamentous attachments No muscles are attached to the talus. However, many ligaments are attached to the bone, and these confer stability to the talocrural, subtalar and talocalcaneonavicular joints.

Vascular supply The talar blood supply is rather tenuous because of the lack of muscle attachments. The first comprehensive account of talar blood supply was provided by Wildenauer in 1950. The extraosseous blood supply is via the posterior tibial, dorsalis pedis and fibular arteries (Fig. 79.10). The artery of the tarsal canal arises from the posterior tibial artery approximately 1 cm proximal to the origin of the medial and lateral plantar arteries (Fig. 79.11) and passes anteriorly between the sheaths of flexor digitorum longus and flexor hallucis longus to enter the tarsal canal, in which it lies anteriorly, close to the talus. (The 'tarsal canal' is the term that is commonly used to describe the tunnel-shaped medial end of the tarsal sinus.) Branches from the arterial network in the tarsal canal enter the talus. The artery continues through the tarsal canal into the lateral part of the tarsal sinus, where it anastomoses with the artery of the tarsal sinus, forming a vascular sling under the talar neck. A branch of the artery of the tarsal canal known as the deltoid branch passes deep to the deltoid ligament and supplies part of the medial aspect of the talar body. Sometimes, it arises from the posterior tibial

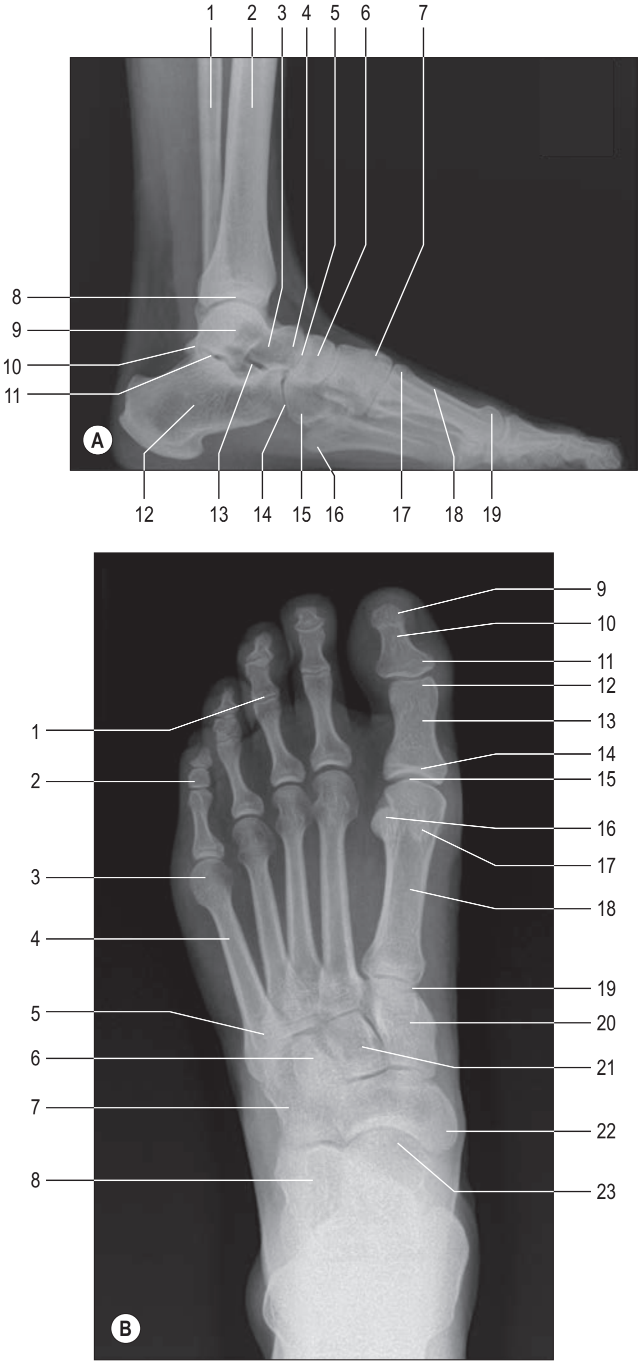
1
2
3
4
5
6
7
8
9
10
11
12
13
14
15
16
17
18
19
A
1
2
3
4
5
6
7
8
9
10
11
12
13
14
15
16
17
18
19
20
21
22
23
B

Fig. 79.6 **A**, A lateral radiograph of the adult ankle and foot in full plantigrade contact with the ground, during symmetrical standing, in a male aged 24 years. Key: 1, fibula; 2, tibia; 3, talar neck; 4, talar head; 5, talonavicular joint; 6, navicular; 7, medial cuneiform; 8, talocrural joint; 9, talar body; 10, posterior process of talus; 11, subtalar joint; 12, calcaneus (note the trabecular pattern); 13, tarsal sinus; 14, calcaneocuboid joint; 15, cuboid; 16, styloid process of the fifth metatarsal; 17, base of the first metatarsal; 18, shaft of the first metatarsal; 19, head of the first metatarsal. **B**, A dorsoplantar radiograph of the adult foot in full plantigrade contact with the ground, during symmetrical standing, in a male aged 24 years. Key: 1, interphalangeal joint; 2, middle phalanx; 3, head of fifth metatarsal; 4, shaft of fifth metatarsal; 5, base of fifth metatarsal; 6, lateral cuneiform; 7, cuboid; 8, calcaneus; 9, head of distal phalanx; 10, shaft of distal phalanx; 11, base of distal phalanx; 12, head of proximal phalanx; 13, shaft of proximal phalanx; 14, base of proximal phalanx; 15, first metatarsophalangeal joint; 16, lateral (fibular) sesamoid; 17, medial (tibial) sesamoid; 18, shaft of first metatarsal; 19, first metatarsocuneiform joint; 20, medial cuneiform; 21, intermediate cuneiform; 22, tuberosity of navicular; 23, talar head. (Courtesy of New York College of Podiatric Medicine, New York, NY.)

artery; rarely, it arises from the medial plantar artery; it may be the only remaining arterial supply to the talus when this bone is fractured. The dorsalis pedis artery supplies branches to the superior aspect of the talar neck and also gives off the artery of the tarsal sinus. This large vessel is always present and anastomoses with the artery of the tarsal canal. The artery of the tarsal sinus receives a contribution from the anterior perforating branch of the fibular artery and supplies direct branches to the talus. The fibular artery provides small branches, which form a plexus of vessels posteriorly with branches of the posterior tibial artery; however, the contribution that the fibular artery makes to the talar blood supply is thought to be insignificant.

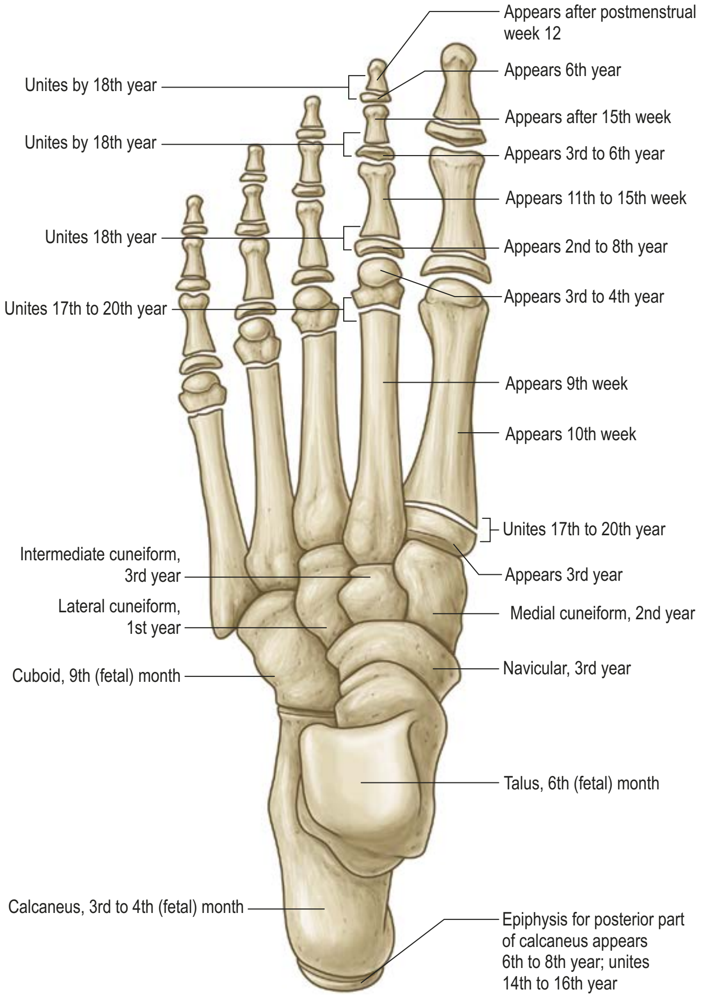
Appears after postmenstrual week 12
Unites by 18th year
Appears 6th year
Appears after 15th week
Unites by 18th year
Appears 3rd to 6th year
Appears 11th to 15th week
Unites 18th year
Appears 2nd to 8th year
Appears 3rd to 4th year
Unites 17th to 20th year
Appears 9th week
Appears 10th week
Unites 17th to 20th year
Intermediate cuneiform, 3rd year
Appears 3rd year
Lateral cuneiform, 1st year
Medial cuneiform, 2nd year
Cuboid, 9th (fetal) month
Navicular, 3rd year
Talus, 6th (fetal) month
Calcaneus, 3rd to 4th (fetal) month
Epiphysis for posterior part of calcaneus appears 6th to 8th year; unites 14th to 16th year

Fig. 79.8 The approximate dates of ossification of the individual bones of the foot and their epiphyses.

The intraosseous blood supply of the talar head arises medially from branches of the dorsalis pedis and laterally via vessels that arise from the anastomosis between the arteries of the tarsal canal and tarsal sinus. The middle third of the talar body, other than its most superior aspect, and the lateral third, other than its posterior aspect, are supplied mainly by the anastomotic arcade in the tarsal canal. The medial third of the body of the talus is supplied by the branch of the artery of the tarsal canal to the deltoid ligament.

Innervation The talus is innervated by branches from the deep fibular, tibial, saphenous and sural nerves.

Ossification A single ossification centre appears during postmenstrual weeks 21–24 (see Fig. 79.8). The posterolateral process sometimes fuses with an accessory bone called the os trigonum.

Talar fractures Since 70% of the surface of the talus is covered by articular cartilage, displaced talar neck fractures, where the blood supply to the talar body is interrupted, may result in avascular necrosis and non-union. A systematic review by Halvorson et al (2012) reported that approximately 33% of talar neck fractures progress to avascular necrosis, 20% progress to malunions and 5% progress to non-unions. In general, these complications do not occur in non-displaced fractures. If a subchondral lucency is seen in the talus on radiographs at 8 weeks after fracture of the talar neck (Hawkins sign), it may be assumed that vascularity to the talar body is intact and that the fracture is likely to heal satisfactorily.

This accessory bone is found occasionally; it arises from a separate ossification centre that appears between 8 and 11 years of age. When the os trigonum fuses to the posterolateral process of the talus it is called the trigonal process (Stieda's process). Another (rare) accessory bone of the foot is the os supratalare, which lies on the dorsal aspect of the talus and rarely measures more than 4 mm in length.

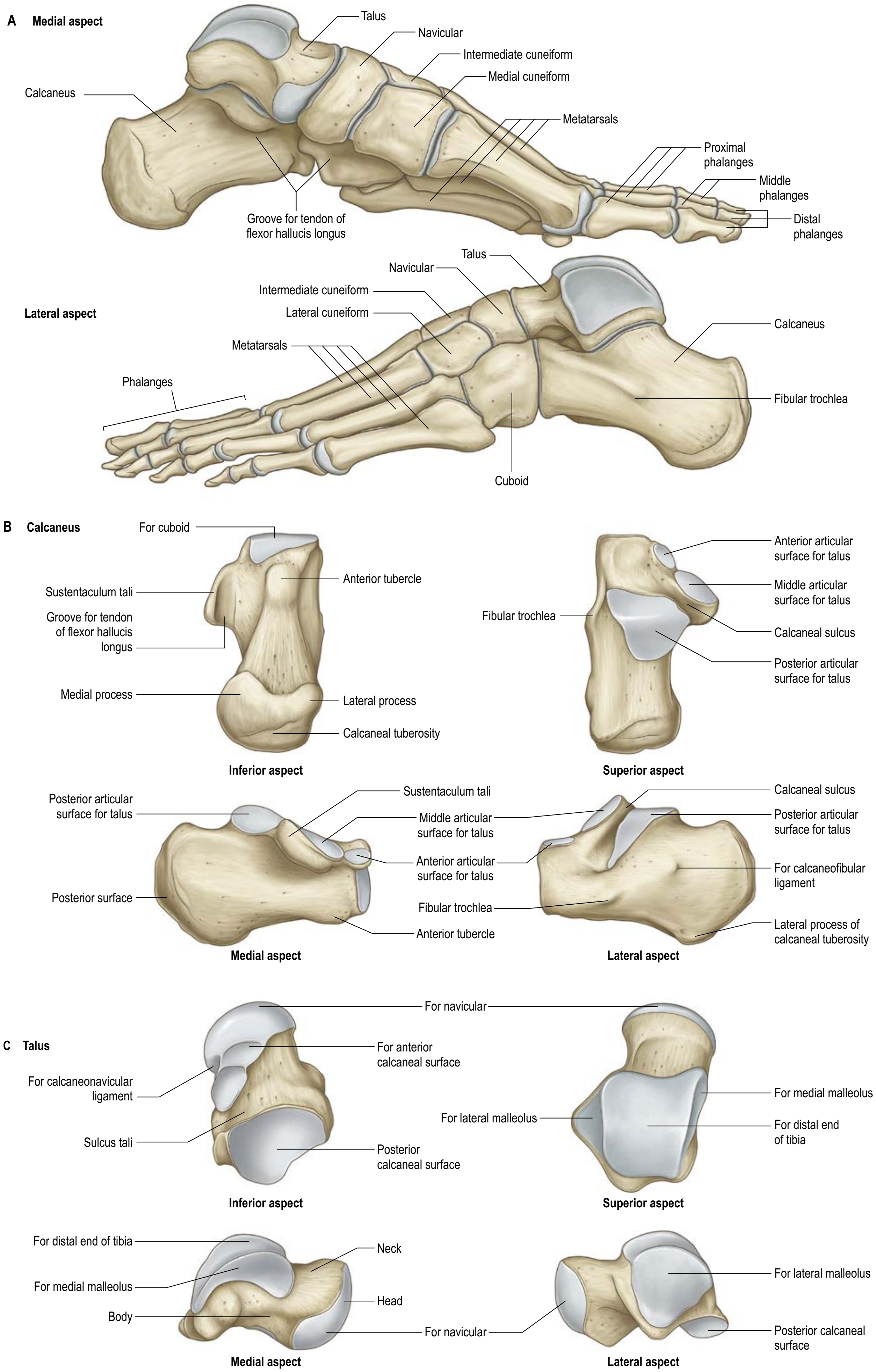
A Medial aspect
Talus
Navicular
Intermediate cuneiform
Medial cuneiform
Calcaneus
Metatarsals
Proximal phalanges
Middle phalanges
Distal phalanges
Groove for tendon of flexor hallucis longus
Lateral aspect
Talus
Navicular
Intermediate cuneiform
Lateral cuneiform
Metatarsals
Phalanges
Calcaneus
Fibular trochlea
Cuboid
B Calcaneus
For cuboid
Sustentaculum tali
Anterior tubercle
Groove for tendon of flexor hallucis longus
Medial process
Lateral process
Calcaneal tuberosity
Inferior aspect
Fibular trochlea
Anterior articular surface for talus
Middle articular surface for talus
Calcaneal sulcus
Posterior articular surface for talus
Superior aspect
Posterior articular surface for talus
Posterior surface
Sustentaculum tali
Middle articular surface for talus
Anterior articular surface for talus
Fibular trochlea
Anterior tubercle
Medial aspect
Calcaneal sulcus
Posterior articular surface for talus
For calcaneofibular ligament
Lateral process of calcaneal tuberosity
Lateral aspect
C Talus
For navicular
For anterior calcaneal surface
For calcaneonavicular ligament
Sulcus tali
Posterior calcaneal surface
Inferior aspect
For lateral malleolus
For medial malleolus
For distal end of tibia
Superior aspect
For distal end of tibia
For medial malleolus
Body
Neck
Head
For navicular
Medial aspect
For lateral malleolus
Posterior calcaneal surface
Lateral aspect

Fig. 79.9 The skeleton of the foot. **A**, Foot bones. **B**, Calcaneus. **C**, Talus.

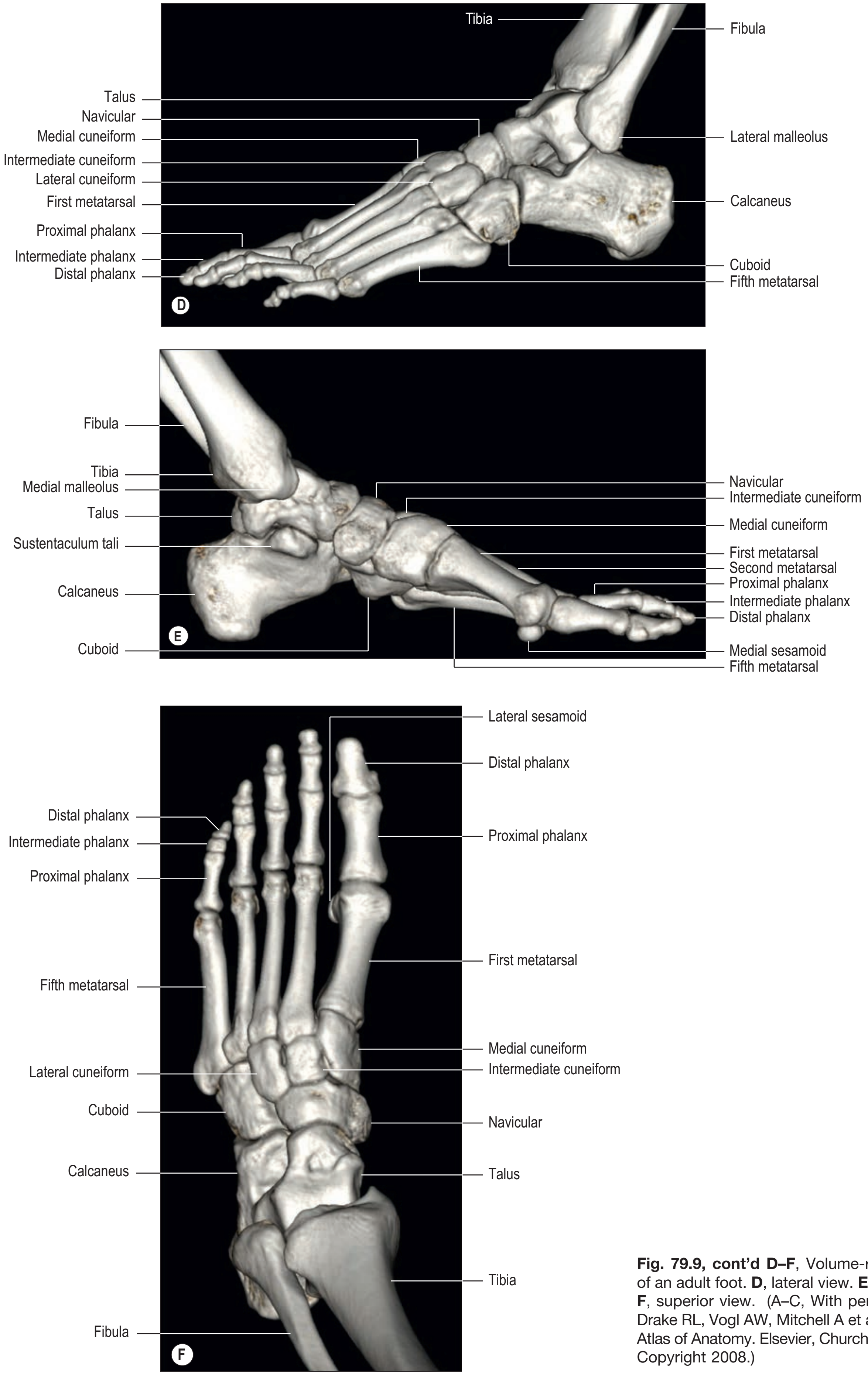
Tibia
Fibula
Talus
Navicular
Medial cuneiform
Intermediate cuneiform
Lateral cuneiform
First metatarsal
Proximal phalanx
Intermediate phalanx
Distal phalanx
Lateral malleolus
Calcaneus
Cuboid
Fifth metatarsal
D
Fibula
Tibia
Medial malleolus
Talus
Sustentaculum tali
Calcaneus
Cuboid
E
Navicular
Intermediate cuneiform
Medial cuneiform
First metatarsal
Second metatarsal
Proximal phalanx
Intermediate phalanx
Distal phalanx
Medial sesamoid
Fifth metatarsal
Lateral sesamoid
Distal phalanx
Proximal phalanx
Distal phalanx
Intermediate phalanx
Proximal phalanx
Fifth metatarsal
First metatarsal
Medial cuneiform
Intermediate cuneiform
Lateral cuneiform
Cuboid
Navicular
Calcaneus
Talus
Tibia
Fibula
F

Fig. 79.9, cont'd D–F, Volume-rendered CTs of an adult foot. **D**, lateral view. **E**, medial view. **F**, superior view. (A–C, With permission from Drake RL, Vogl AW, Mitchell A et al (eds) Gray's Atlas of Anatomy. Elsevier, Churchill Livingstone. Copyright 2008.)

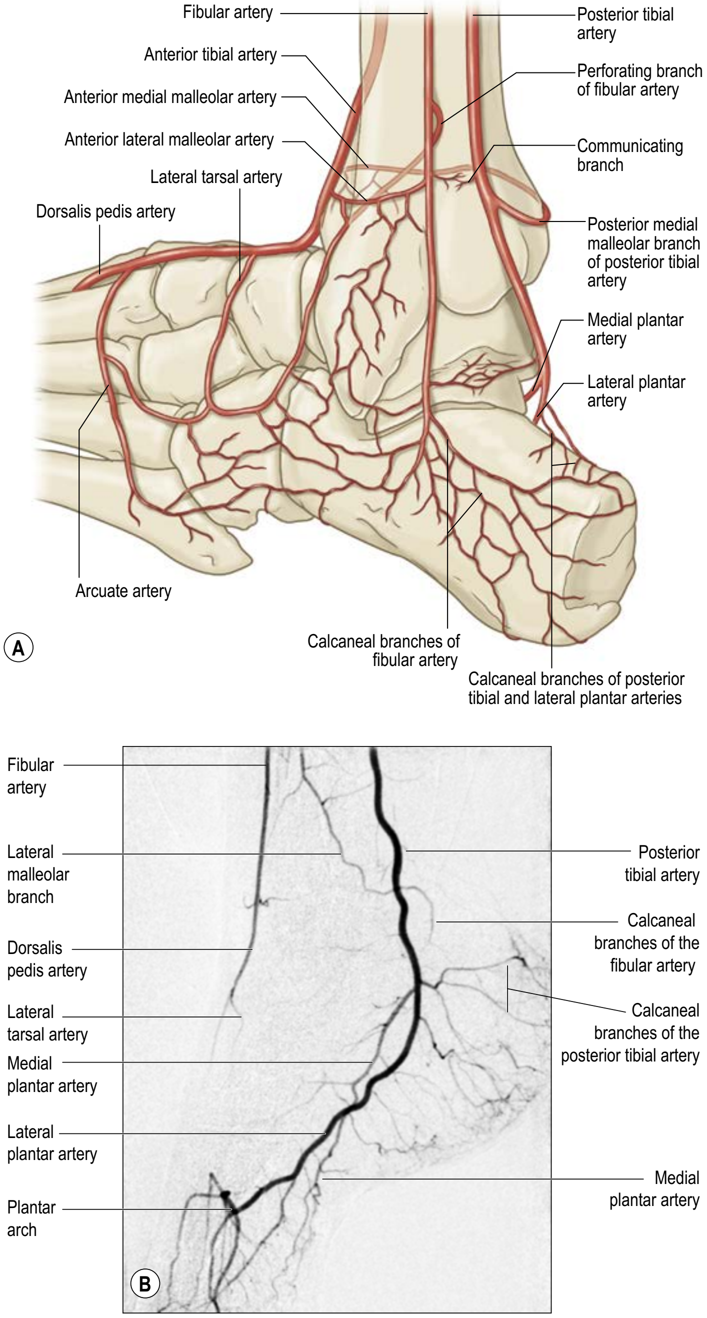
Fibular artery
Posterior tibial artery
Anterior tibial artery
Perforating branch of fibular artery
Anterior medial malleolar artery
Anterior lateral malleolar artery
Communicating branch
Lateral tarsal artery
Dorsalis pedis artery
Posterior medial malleolar branch of posterior tibial artery
Medial plantar artery
Lateral plantar artery
Arcuate artery
A
Calcaneal branches of fibular artery
Calcaneal branches of posterior tibial and lateral plantar arteries
Fibular artery
Lateral malleolar branch
Dorsalis pedis artery
Lateral tarsal artery
Medial plantar artery
Lateral plantar artery
Plantar arch
Posterior tibial artery
Calcaneal branches of the fibular artery
Calcaneal branches of the posterior tibial artery
Medial plantar artery
B

Fig. 79.10 **A**, The arterial anastomoses of the ankle, tarsus and metatarsus. **B**, Lateral digital subtraction angiogram of the ankle and foot.

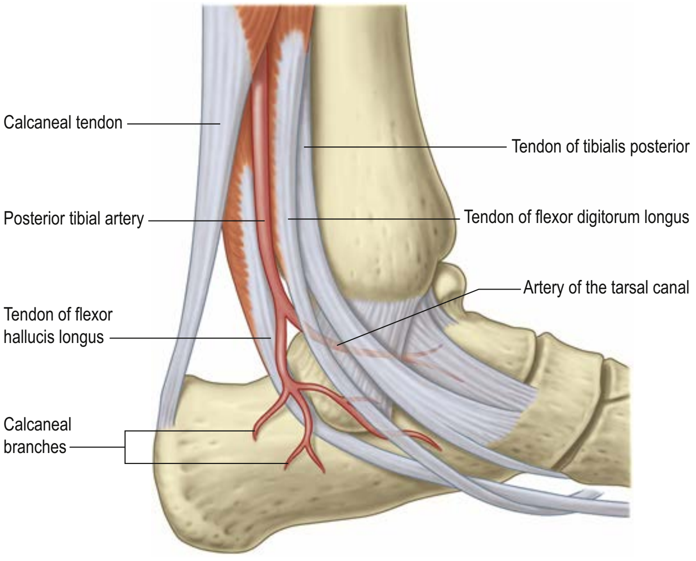
Calcaneal tendon
Tendon of tibialis posterior
Posterior tibial artery
Tendon of flexor digitorum longus
Artery of the tarsal canal
Tendon of flexor hallucis longus
Calcaneal branches

Fig. 79.11 Branches of the posterior tibial artery, posteromedial view of the ankle.

Calcaneus

The calcaneus is the largest of the tarsal bones and projects posterior to the tibia and fibula as a short lever for muscles of the calf attached to its posterior surface. It is irregularly cuboidal, with its long axis inclined distally upwards and laterally (Fig. **79.9A–B**). It has a relatively thin cortex (Daftary et al 2005). The superior or proximal surface is divisible into three areas. The posterior third is rough and concavo-convex; the convexity is transverse and supports fibroadipose tissue (Kager's fat pad) between the calcaneal tendon and ankle joint. The middle third carries the posterior talar facet, which is oval and convex anteroposteriorly. The anterior third is partly articular; distal (anterior) to the posterior articular facet, a rough depression, the calcaneal sulcus, narrows into a groove on the medial side and completes the tarsal sinus with the talus (see Fig. 79.9B). (The tarsal sinus is a conical hollow bounded by the talus medially, superiorly and laterally, with the superior surface of the calcaneus below. Its medial end is narrow and tunnel-shaped, and is often referred to as the tarsal canal.) Distal and medial to this groove, an elongated articular area covers the sustentaculum tali (talar shelf) and extends distolaterally on the body of the bone. This facet is often divided into middle and anterior talar facets by a non-articular interval at the anterior limit of the sustentaculum tali (the incidence of this subdivision varies with sex, race and occupation). Rarely, all three facets on the upper surface of the calcaneus are fused into one irregular area.

The anterior surface is the smallest, and is an obliquely set concavo-convex articular facet for the cuboid. The posterior surface is divided into three regions: a smooth proximal (superior) area separated from the calcaneal tendon by a bursa and adipose tissue (tip of the Kager's fat pad); a middle area, which is the largest, limited above by a groove and below by a rough ridge for the calcaneal tendon; and a distal (inferior) area, vertically striated and inclined downwards and forwards, which is the subcutaneous weight-bearing surface.

The plantar surface is rough, especially proximally as the calcaneal tuberosity, which has lateral and medial processes that extend distally, separated by a notch. The medial process is longer and broader (see Fig. 79.9B). Further distally, an anterior tubercle marks the distal limit of the attachment of the long plantar ligament.

The lateral surface is almost flat. Proximally, it is deeper and palpable on the lateral aspect of the heel distal to the lateral malleolus. Distally, it presents the fibular trochlea (see Figs 79.9A–B), which is exceedingly variable in size and palpable 2 cm distal to the lateral malleolus when well developed. It bears an oblique groove for the tendon of fibularis longus and a shallower proximal groove for the tendon of fibularis brevis. About 1 cm or more behind and above the fibular trochlea, a second elevation may exist for attachment of the calcaneofibular part of the lateral ligament.

The medial surface is vertically concave. The concavity is accentuated by the sustentaculum tali, which projects medially from the distal part of its upper border (see Fig. 79.9B). Superiorly the process bears the middle talar facets and inferiorly a groove is continuous with that on the talar posterior surface for the tendon of flexor hallucis longus (see Fig. 79.9A–B). The medial aspect of the sustentaculum tali can be felt immediately distal to the tip of the medial malleolus, and occasionally, it is also grooved by the tendon of flexor digitorum longus.

Muscle and ligamentous attachments The interosseous talocalcaneal and cervical ligaments and the medial root of the inferior extensor retinaculum are attached in the calcaneal sulcus. The non-articular area distal to the posterior talar facet is the site of attachment of extensor digitorum brevis (in part), the principal band of the inferior extensor retinaculum and the stem of the bifurcate ligament.

Abductor hallucis and the superficial part of the flexor retinaculum and, distally, the plantar aponeurosis and flexor digitorum brevis are all attached to the medial process (medial condyle) of the calcaneal tuberosity at its prominent medial margin. The medial process of the calcaneal tuberosity is the primary weight-bearing portion of the calcaneus. Clinically, pain over the medial tuberosity is often associated with plantar fasciopathy) (Yi et al 2011). Abductor digiti minimi is attached to the lateral process, extending medially to the medial process. The long plantar ligament is attached to the rough region between the processes proximally, and extends to the anterior tubercle distally. The plantar calcaneocuboid ligament (short plantar ligament) is attached to the tubercle and the area distal to it. The lateral tendinous head of flexor accessorius is attached distal to the lateral process near the lateral margin of the long plantar ligament. Plantaris is attached to the posterior surface near the medial side of the calcaneal tendon. The anterior part of the lateral surface is crossed by the fibular

A detailed analysis of patterns of anterior talar articular facets in a series of 401 Indian calcanei revealed four types. Type I (67%) showed one continuous facet on the sustentaculum extending to the distomedial calcaneal corner; type II (26%) presented two facets, one sustentacular and one distal calcaneal; type III (5%) possessed only a single sustentacular facet; and type IV (2%) showed confluent anterior and posterior facets (Gupta et al 1977).

tendons but is largely subcutaneous. The calcaneofibular ligament is attached 1–2 cm proximal to the fibular trochlea, usually to a low, rounded elevation.

The dorsal surface of the sustentaculum tali is part of the talocalcaneonavicular joint. The plantar surface is grooved by the tendon of flexor hallucis longus, and margins of the groove give attachment to the deep part of the flexor retinaculum. The plantar calcaneonavicular ligament is attached distally to the medial margin of the sustentaculum tali, which is narrow, rough and convex. A slip from the tendon of tibialis posterior, and superficial fibres of the deltoid ligament and medial talocalcaneal ligaments, are attached proximally. Distal to the attachment of the deltoid ligament, the tendon of flexor digitorum longus is related to the margin of the sustentaculum tali and may form a groove in it. The large medial head of flexor accessorius is attached distal to the groove for flexor hallucis longus.

Vascular supply The calcaneus receives its arterial supply from the medial and lateral calcaneal arteries (arising from the posterior tibial and fibular arteries, respectively), the fibular artery, posterior calcaneal anastomosis (formed from the posterior tibial and fibular arteries), medial and lateral plantar arteries, artery of the tarsal sinus and tarsal canal, branches of the lateral tarsal artery and perforating fibular arteries.

Innervation The calcaneus is innervated by branches of the tibial, sural and deep fibular nerves.

Ossification The calcaneus is the only tarsal bone that always has two ossification centres (see Fig. 79.8). In addition to the main ossification centre, there is a scale-like posterior apophysis that covers most of the posterior, and part of the plantar, surfaces. The main centre appears prenatally during postmenstrual weeks 9–12, whereas the posterior apophysis appears in the sixth year in females and the eighth year in males, fusing in the fourteenth and sixteenth years, respectively.

An os calcaneus secundarius, an accessory bone rather than a secondary ossification centre, occasionally occurs. When present, it is located on the 'anterior process' of the calcaneus, from which the bifurcate ligament arises, in an interval between the anteromedial aspect of the calcaneus, the proximal ends of the cuboid and navicular, and the head of the talus. Other rare accessory bones of the calcaneus include the calcaneus accessorius in the region of the fibular trochlea; the os sustentaculi on the posterior aspect of the sustentaculum tali; the os subcalcis on the plantar aspect of the calcaneus slightly posterior to the origin of the plantar aponeurosis; and the os aponeurosis plantaris, which lies within the plantar aponeurosis in close proximity to the medial process of the calcaneal tuberosity.

Navicular

The navicular articulates with the talar head proximally and with the cuneiform bones distally (see Fig. 79.9A; **Fig. 79.12**). In convex pes planovalgus (vertical talus), the navicular is subluxed dorsally and articulates instead with the talar neck. The downward displacement of the talar head creates a characteristic convex 'rocker-bottom foot'. The distal surface of the navicular is transversely convex and divided into three facets (the medial being the largest) for articulation with the cuneiforms. The proximal surface is oval and concave, and articulates with the talar head. Other than proximal and distal articular surfaces, the remaining surfaces are rough for ligamentous attachments and tendinous articulations. The dorsal surface is convex. The medial surface projects proximally as a prominent tuberosity, palpable approximately 2.5 cm distal and plantar to the medial malleolus. The plantar surface is concave, and separated from the tuberosity medially by a groove for the tendon of tibialis posterior. The lateral irregular surface often bears a facet for articulation with the cuboid.

The facet for articulation with the medial cuneiform is approximately triangular in shape: its rounded apex is medial and its 'base', facing laterally, is often markedly curved; the articular facets for the intermediate and lateral cuneiforms are also triangular, with plantar-facing apices. The facet for the lateral cuneiform may appear as a wide crescent or a semicircle rather than a triangle. Dorsal talonavicular, cuneonavicular and cubonavicular ligaments are attached to the dorsal navicular surface.

Muscle and ligamentous attachments The navicular tuberosity is the main attachment site of tibialis posterior; a groove lateral to the tuberosity transmits part of the tendon distally to the cuneiforms and middle three metatarsal bases. The plantar calcaneonavicular ligament

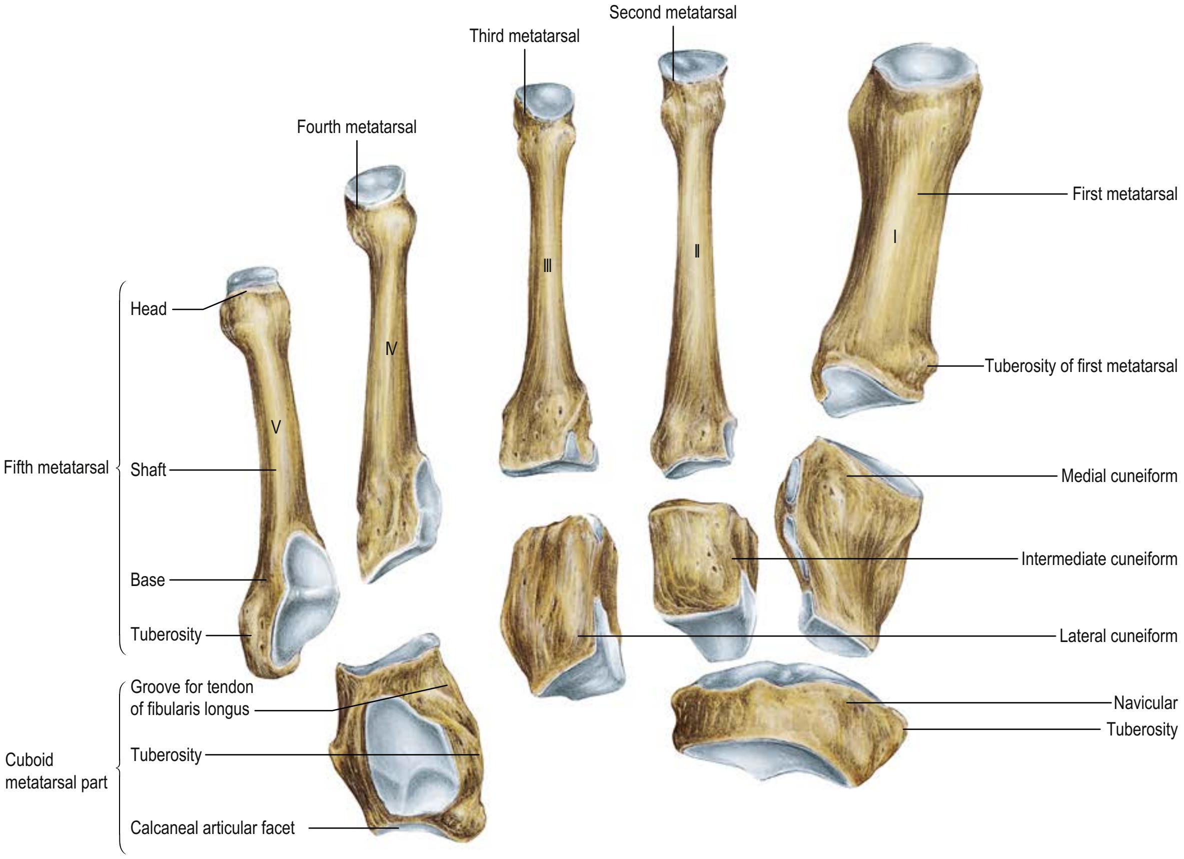

Fig. 79.12 The skeleton of the tarsals and metatarsals, dorsal aspect. (Sobotta Atlas of Human Anatomy © Elsevier GmbH, Urban & Fischer, Munich.)

Calcaneal apophysitis (Sever's disease) is a self-limiting inflammatory condition seen in some child athletes, boys more commonly than girls. It is not a true apophysitis and the use of imaging for its initial diagnosis is a subject of controversy (Kose 2010, Rachel et al 2011). Calcaneal apophysitis is often treated with physiotherapy and/or therapeutic heel lifts, but simply monitoring the condition can also be efficacious (Wiegerinck et al 2016).

is attached to a slight projection lateral to the groove and adjacent to the proximal surface (see Fig. 79.5B). The calcaneonavicular part of the bifurcate ligament is attached to the rough part of the lateral surface.

Vascular supply The dorsal aspect of the navicular is supplied by the dorsalis pedis artery, either directly or from a branch of the main artery. The medial plantar artery supplies its plantar aspect, and the tuberosity is supplied by an anastomosis between the dorsalis pedis and medial plantar arteries.

Innervation The navicular is innervated by the deep fibular and medial plantar nerves.

Ossification The navicular ossification centre appears during the third year (see Fig. 79.8). It is sometimes affected by avascular necrosis between the ages of 4 and 7 years (Köhler's disease).

An accessory navicular bone, considered to be an anatomical variant, occasionally occurs (Keles-Celik et al 2017), arising from a separate ossification centre in the region of the posteromedial aspect of the navicular tuberosity. There are three distinct types of accessory navicular. Type I is probably a sesamoid bone within the plantar aspect of the tendon of tibialis posterior at the level of the inferior calcaneonavicular ligament. In type II, the accessory bone is separated from the body of the navicular by a synchondrosis. These types are sometimes known as os tibiale externum or naviculare secundarium. In Type III, commonly called the cornuate navicular or gorilloid navicular (Haffner and Conklin 2016), the accessory bone is united to the navicular by a bony ridge, and may represent the possible end stage of type II. An accessory navicular may be the source of pain in athletes. Type II is the most commonly symptomatic variant: it has been suggested that the pull of the tendon of tibialis posterior, the degree of foot pronation and the location of the accessory bone in relation to the undersurface of the navicular, may produce tension, shear and/or compression forces on the synchondrosis. An accessory navicular is one aetiological factor in posterior tibial tendon dysfunction. The altered mechanics cause abnormal stresses, leading to tendon degeneration, decreased strength and possible tendon rupture.

Rarely, the navicular is bipartite and it arises from two distinct centres of ossification: this can lead to premature degeneration within the talocalcaneonavicular joint (Müller–Weiss disease). Occasionally, a small bone, os talonaviculare dorsale, is found within the talocalcaneonavicular joint on its dorsal aspect: it represents either a separate accessory bone or a fractured osteophyte of the proximal dorsal aspect of the navicular. A bipartite navicular is sometimes found with cuneonavicular coalitions.

Cuboid

The cuboid, the most lateral bone in the distal tarsal row, lies between the calcaneus proximally and the fourth and fifth metatarsals distally (see Figs 79.9A, 79.12). Its dorsolateral surface is rough for the attachment of ligaments. The plantar surface is crossed distally by an oblique groove for the tendon of fibularis longus and bounded proximally by a ridge that ends laterally in the tuberosity of the cuboid, the lateral aspect of which is faceted for a sesamoid bone or cartilage that is frequently found in the tendon of fibularis longus. Proximal to its ridge, the rough plantar surface extends proximally and medially because of the obliquity of the calcaneocuboid joint, making its medial border much longer than the lateral. The lateral surface contains the groove for fibularis longus, extending from a deep notch on its plantar edge. The medial surface, which is much more extensive and partly non-articular, bears an oval facet for articulation with the lateral cuneiform and proximal to this another facet (sometimes absent) for articulation with the navicular; the two form a continuous surface separated by a smooth vertical ridge. The distal surface is divided vertically into a medial quadrilateral articular area for the base of the fourth metatarsal and a lateral triangular area, its apex lateral, for the base of the fifth metatarsal. The proximal surface, triangular and concavo-convex, articulates with the distal calcaneal surface; its medial plantar angle projects proximally and inferiorly to the distal end of the calcaneus.

Muscle and ligamentous attachments The dorsal calcaneocuboid, cubonavicular, cuneocuboid and cubometatarsal ligaments are attached to the dorsal surface. Deep fibres of the long plantar ligament are attached to the proximal edge of the plantar ridge. Slips from the tendons of tibialis posterior and flexor hallucis brevis are attached to the projecting proximomedial part of the plantar surface. Interosseous, cuneocuboid and cubonavicular ligaments are attached to the rough part of the medial cuboidal surface. Proximally, the medial calcaneocuboid ligament, which is the lateral limb of the bifurcate ligament, is also attached to this surface. The placement and trapezoidal shape of the cuboid give it the ability to act as the 'keystone' of the lateral longitudinal arch of the foot. During normal gait, the tension of the calcaneocuboid joint helps 'lock' the mid-tarsal joint and acts as a major stabilizer of the foot.

Vascular supply The cuboid is supplied by deep branches of the medial and lateral plantar arteries and by branches from the dorsal arterial network.

Innervation The cuboid is innervated by branches from the lateral plantar, sural and deep fibular nerves.

Ossification The cuboid frequently begins to ossify before birth, the primary ossification centre appearing just before birth during postmenstrual weeks 37–41 (see Fig. 79.8). An os cuboides secundarium is a rare accessory bone situated on the plantar aspect of the cuboid and is sometimes involved in the infrequently reported cubonavicular coalitions.

Cuneiforms

The wedge-like cuneiform bones articulate with the navicular proximally and with the bases of the first to third metatarsals distally; the medial cuneiform is the largest, the intermediate is the smallest. The dorsal surfaces of the intermediate and lateral cuneiforms form the base of the wedge. The wedge is reversed in the medial cuneiform, which is a prime factor in shaping the transverse arch. The proximal surfaces of all three form a concavity for the distal surface of the navicular. The medial and lateral cuneiforms project distally beyond the intermediate cuneiform and so form a recess (mortise) for the second metatarsal base.

Medial cuneiform

The medial cuneiform (see Figs 79.5, 79.9A, 79.12) articulates with the navicular and base of the first metatarsal. It has a narrow dorsal surface. The distal surface is a kidney-shaped facet for the first metatarsal base, its 'hilum' being lateral. The proximal surface bears a piriform facet for the navicular, which is concave vertically and dorsally narrowed. The medial surface, subcutaneous, is vertically convex; its distal plantar angle carries a large impression that receives the principal attachment of the tendon of tibialis anterior (see Fig. 79.5B). The lateral surface is partly non-articular; there is a smooth right-angled strip along its proximal and dorsal margins for the intermediate cuneiform. Its distal dorsal area is separated by a vertical ridge from a small, almost square, facet for articulation with the dorsal part of the medial surface of the second metatarsal base. Plantar to this, the medial cuneiform is attached to the medial side of the second metatarsal base by a strong ligament (Lisfranc's ligament). Proximally, an intercuneiform interosseous ligament connects this surface to the intermediate cuneiform. The distal and plantar areas of the surface are roughened by attachment of part of the tendon of fibularis longus.

Muscle attachments The plantar surface receives a slip from the tendon of tibialis posterior, in addition to part of the insertion of the tendon of fibularis longus. The medial surface receives the attachment of most of the tendon of tibialis anterior.

Vascular supply The medial cuneiform is supplied via its dorsal, medial and lateral surfaces, mainly from the dorsal arterial network.

Innervation The medial cuneiform is supplied by the deep fibular and medial plantar nerves.

Ossification The medial cuneiform may have two separate ossification centres, which appear during the second year of life (see Fig. 79.8). Very rarely, the medial cuneiform is bipartite and there is a horizontal cleavage plane between the two parts. The os cuneo-1 metatarsale-I plantare is a rare accessory bone that occurs on the plantar aspect of the foot at the base of the first metatarsal and articulates with the plantar base of the first metatarsal and the medial cuneiform.

Intermediate cuneiform

The intermediate (middle) cuneiform articulates proximally with the navicular and distally with the second metatarsal base (see Figs 79.5A, 79.12). It has a narrow plantar surface that receives a slip from the tendon of tibialis posterior. The distal and proximal surfaces are both triangular articular facets. The medial surface is partly articular; it articulates via a smooth, angled region that is occasionally double with the medial cuneiform along its proximal and dorsal margins. The lateral surface is also partly articular; along its proximal margin a vertical segment, usually indented, abuts the lateral cuneiform. Strong interosseous ligaments connect the non-articular parts of both surfaces to the adjacent cuneiforms. An intricate arrangement of dorsal and plantar ligaments spans the tarsometatarsal joint, connecting the most distal row of tarsals to their respective metatarsals. However, the plantar ligament between the intermediate cuneiform and the base of the second metatarsal is uniquely absent (Castro et al 2010, Chaney 2010).

Muscle attachments Part of the tendon of tibialis posterior is attached to the intermediate cuneiform.

Vascular supply The intermediate cuneiform is supplied via its dorsal, medial and lateral surfaces, mainly from the dorsal arterial network.

Innervation The intermediate cuneiform is innervated by the deep fibular and medial plantar nerves.

Ossification The ossification centre appears during the third year of life (see Fig. 79.8). The os cuneo-2 metatarsale-II dorsale, a rare accessory bone, lies on the dorsal aspect of the joint between the intermediate cuneiform and the second metatarsal. It is wedge-shaped with its base orientated dorsally.

Lateral cuneiform

The lateral cuneiform lies between the intermediate cuneiform and cuboid, and also articulates with the navicular and, distally, with the third metatarsal base (see Figs 79.5A, 79.12). Like the intermediate cuneiform, its dorsal surface, which is rough and almost rectangular, is the base of a wedge. The plantar surface is narrow and receives a slip from tibialis posterior and sometimes part of flexor hallucis brevis. The distal surface is a triangular articular facet for the third metatarsal base. The proximal surface is rough on its plantar aspect, but its dorsal two-thirds articulate with the navicular by a triangular facet. The medial surface is partly non-articular and has a vertical segment, indented by the intermediate cuneiform, on its proximal margin; on its distal margin, a narrower strip (often two small facets) articulates with the lateral side of the second metatarsal base. The lateral surface, also partly non-articular, bears a triangular or oval proximal facet for the cuboid; a semilunar facet on its dorsal and distal margin articulates with the dorsal part of the medial side of the fourth metatarsal base. Non-articular areas of the medial and lateral surfaces receive intercuneiform and cuneocuboid ligaments, respectively, which are important in the maintenance of the transverse arch of the foot.

Muscle attachments The plantar surface of the lateral cuneiform receives a slip from the tendon of tibialis posterior and, occasionally, part of flexor hallucis brevis.

Vascular supply The lateral cuneiform is supplied via its dorsal, medial and lateral surfaces, mainly from the dorsal arterial network.

Innervation The lateral cuneiform is innervated by branches of the deep fibular and lateral plantar nerves.

Ossification The lateral cuneiform ossifies during the first year of life (see Fig. 79.8).

Tarsal coalition

Tarsal coalition is a hereditary condition in which there is a fibrous, cartilaginous or osseous union of two or more tarsal bones. The aetiology of tarsal coalition is unclear; suggestions include genetic predisposition, an autosomal dominant inherited pattern, trauma, arthritic changes, and/or osteochondroses of the tarsal bones (e.g. Köhler's disease) (Klammer et al 2018).

Metatarsus

The five metatarsals lie in the distal half of the foot and connect the tarsus with the phalanges. Like the metacarpals, they are miniature long bones and have a shaft, proximal base and distal head (see Fig. 79.9). Except for the first and fifth, the shafts are long and slender, longitudinally convex dorsally, and concave on their plantar aspects. Prismatic in section, they taper distally. Their bases articulate with the distal tarsal row and with adjacent metatarsal bases. The line of each tarsometatarsal joint, except the first, inclines proximally and laterally with the metatarsal bases being oblique relative to their shafts. The heads articulate with the proximal phalanges, each by a convex surface that passes farther on to its plantar aspect, where it ends on the summits of two eminences. The sides of the heads are flat, with a depression surmounted by a dorsal tubercle for a collateral ligament of the metatarsophalangeal joint.

On occasion, an os intermetatarseum is encountered between the medial cuneiform and the bases of the first and second metatarsals and represents a rare accessory bone in this region.

Individual metatarsals

First metatarsal

The first metatarsal (see Figs 79.5, 79.12) is the shortest and thickest, and has a strong shaft, of marked prismatic form. The base sometimes has a lateral facet or ill-defined smooth area as a result of contact with the second metatarsal. Its large proximal surface, usually indented on the medial and lateral margins, articulates with the medial cuneiform. Its circumference is grooved for tarsometatarsal ligaments and, medially, part of the tendon of tibialis anterior is attached; its plantar angle has a rough, oval, lateral prominence for the tendon of fibularis longus. The medial head of the first dorsal interosseous is attached to the flat lateral surface of the shaft. The large head has a plantar elevation, the crista, which separates two grooved facets (of which the medial is larger), on which sesamoid bones glide. The most common joint deformity related to the first metatarsal is hallux abducto valgus (bunion) (see Fig. 79.20).

Second metatarsal

The second metatarsal is the longest (see Figs 79.5, 79.12). Its cuneiform base bears four articular facets. The proximal one, concave and triangular, is for the intermediate cuneiform. The dorsomedial one, for the medial cuneiform, is variable in size and usually continuous with that for the intermediate cuneiform. Two lateral facets, dorsal and plantar, are separated by non-articular bone, each divided by a ridge into distal demifacets, which articulate with the third metatarsal base, and a proximal pair (sometimes continuous) for the lateral cuneiform. The areas of these facets vary, particularly the plantar facet, which may be absent. An oval pressure facet, caused by contact with the first metatarsal, may appear on the medial side of the base, plantar to that for the medial cuneiform. Because of its length, its steep inclination, and the position of its base recessed in the tarsometatarsal joint, it is at risk of stress overload; perhaps this is why it is a common site for stress fractures (particularly in athletes) and an avascular phenomenon in its head (Freiberg's infraction). The second metatarsal head is affected in 68% of cases, the third metatarsal head in 27% of cases, and the fourth metatarsal head in 3% of cases. Freiberg's disease is the only osteochondrosis more common in females and occurs at a ratio of 5 : 1 with peak age of onset between 11 and 17 years (Carmont et al 2009, Cerrato 2011).

Third metatarsal

The third metatarsal (see Figs 79.5, 79.12) has a flat triangular base, articulating proximally with the lateral cuneiform, medially with the second metatarsal, via dorsal and plantar facets, and laterally, via a single facet, with the dorsal angle of the fourth metatarsal. The medial plantar facet is frequently absent. The third tarsometatarsal joint is relatively immobile and predisposes the third metatarsal to stress fracture.

Fourth metatarsal

The fourth metatarsal is smaller than the third (see Figs 79.5, 79.12). Its base has, proximally, an oblique quadrilateral facet for articulation with the cuboid; laterally, a single facet for the fifth metatarsal; and medially, an oval facet for the third metatarsal. The latter is sometimes divided by a ridge, in which case the proximal part articulates with the lateral cuneiform.

Fifth metatarsal

The fifth metatarsal has a tuberosity on the lateral side of its base (see Figs 79.5, 79.12). The base articulates proximally with the cuboid by a triangular, oblique surface, and medially with the fourth metatarsal. The tuberosity can be seen and palpated midway along the lateral border of the foot; in acute inversion it may be fractured. The metaphysial–diaphysial junction of the fifth metatarsal base is prone to traumatic or stress fractures. It is believed that fractures at this level damage the nutrient artery and the extraosseous arterial plexus, resulting in compromised vascularity of the fracture site, consequent poor fracture healing and non-union that often requires surgical fixation.

Muscle attachments The first metatarsal receives attachments from the tendon of tibialis anterior medially, and the tendon of fibularis longus on its plantar aspect (see Fig. 79.5). It gives origin to the medial head of the first dorsal interosseus on the proximal aspect of the lateral surface. The lateral head of the first dorsal interosseous and the medial head of

Harris and Beath (1948) were the first to recognize an association between tarsal coalitions and 'peroneal (fibular) spastic flat foot'. The two most common examples are talocalcaneal and calcaneonavicular coalitions, which usually present with symptoms early in the second decade of life. They are often, but not invariably, associated with flat feet (pes planus). A talonavicular coalition is rare (Brennan et al 2012), but when present, it is often associated with a 'ball-and-socket' ankle joint. Surgical resection of tarsal coalitions may eradicate associated pain but seldom improves the range of movement.

the second are attached to the medial and lateral surfaces, respectively of the shaft of the second metatarsal. The lateral heads of the second dorsal interosseous and first plantar interosseous are attached to the medial surface of the shaft of the third metatarsal and the medial head of the third dorsal interosseous is attached to its lateral surface. The lateral head of the third dorsal and second plantar interossei are attached to the medial surface of the fourth metatarsal and the medial head of the fourth dorsal interosseous is attached to the lateral surface.

The tendon of fibularis tertius is attached to the medial part of the dorsal surface and medial border of the shaft of the fifth metatarsal, and that of fibularis brevis to the dorsal surface of the tuberosity. A strong band of the plantar aponeurosis, sometimes containing muscle, connects the apex of the tuberosity to the lateral process of the calcaneal tuberosity. It is this attachment, and not that of fibularis brevis, that is responsible for avulsion fractures of the tuberosity. The tendon of abductor digiti minimi grooves the plantar surface of the base of the fifth metatarsal and flexor digiti minimi brevis is attached here. The lateral heads of the fourth dorsal and the third plantar interossei are attached to the medial side of the shaft of the fifth metatarsal.

Vascular supply The first metatarsal is supplied by the first dorsal and first plantar metatarsal arteries and a superficial branch of the medial plantar artery (see Fig. 76.7), together forming a periosteal arterial network. A nutrient artery enters the lateral surface of the mid diaphysis. The head receives a medial, lateral and plantar supply from these arteries. The blood supply of the second, third and fourth metatarsals follows the same pattern as that described for the first metatarsal, i.e. each bone is supplied by branches of the dorsal and plantar metatarsal arteries, the nutrient artery enters the diaphysis on its lateral side near the metatarsal base and a constant plantar vessel supplies the head. The fifth metatarsal is supplied by dorsal and plantar metatarsal arteries and an inconstant fibular marginal artery, and the nutrient artery enters the diaphysis proximally and medially.

Innervation With the exception of the fifth metatarsal, all of the metatarsals are innervated by the deep fibular nerve. The medial and lateral plantar nerves also supply the first and second metatarsals, and the third and fourth metatarsals, respectively. The fifth metatarsal is innervated by branches from the sural, superficial fibular and lateral plantar nerves.

Ossification Each metatarsal ossifies from a primary centre for the shaft and a secondary centre in either the base (first metatarsal) or head (second–fourth metatarsals) (see Fig. 79.8). The two centres of ossification in the first metatarsal, in the shaft and base, appear after postmenstrual week 12 and the third year of life, respectively, and fuse between the seventeenth and twentieth years. There may be a third centre in the first metatarsal head. The second, third and fourth metatarsals have two centres of ossification, one in the shaft and one distally in the metatarsal head. Ossification of the shaft starts after postmenstrual week 12 and ossification of the metatarsal head starts between the third and fourth years; fusion occurs between the seventeenth and twentieth years. There are three centres of ossification in the fifth metatarsal: at the base in the region of the tuberosity (an apophysis), in the shaft, and distally in the metatarsal head. Ossification of the shaft starts after postmenstrual week 12 and ossification of the metatarsal head starts between the third and fourth years. Fusion of the distal and shaft centres occurs between the seventeenth and twentieth years and the proximal apophysis fuses earlier. An os vesalianum pedis is a rare variant that should not be confused with the basal apophysis (**Fig. 79.13**).

Phalanges of the foot

In general, the phalanges of the foot resemble those of the hand; there are two in the great toe and three in each of the other toes (see Figs 79.5, 79.9). On occasion, there are only two phalanges in the little toe and, rarely, this is the case with the other toes. The phalanges of the toes are much shorter than their counterparts in the hand, and their shafts, especially those of the proximal set, are compressed from side to side. In the proximal phalanges, the compressed shaft is convex dorsally, with a plantar concavity. The base is concave for articulation with a metatarsal head, and the head is a trochlea for the middle phalanx. Middle phalanges are small and short, but broader than their proximal counterparts. Distal phalanges resemble those in the fingers, but are smaller and flatter. Each has a broad base for articulation with a middle phalanx and an expanded distal end. A rough tuberosity on the plantar aspect of the latter supports the pulp of the toe and provides a weight-bearing area.

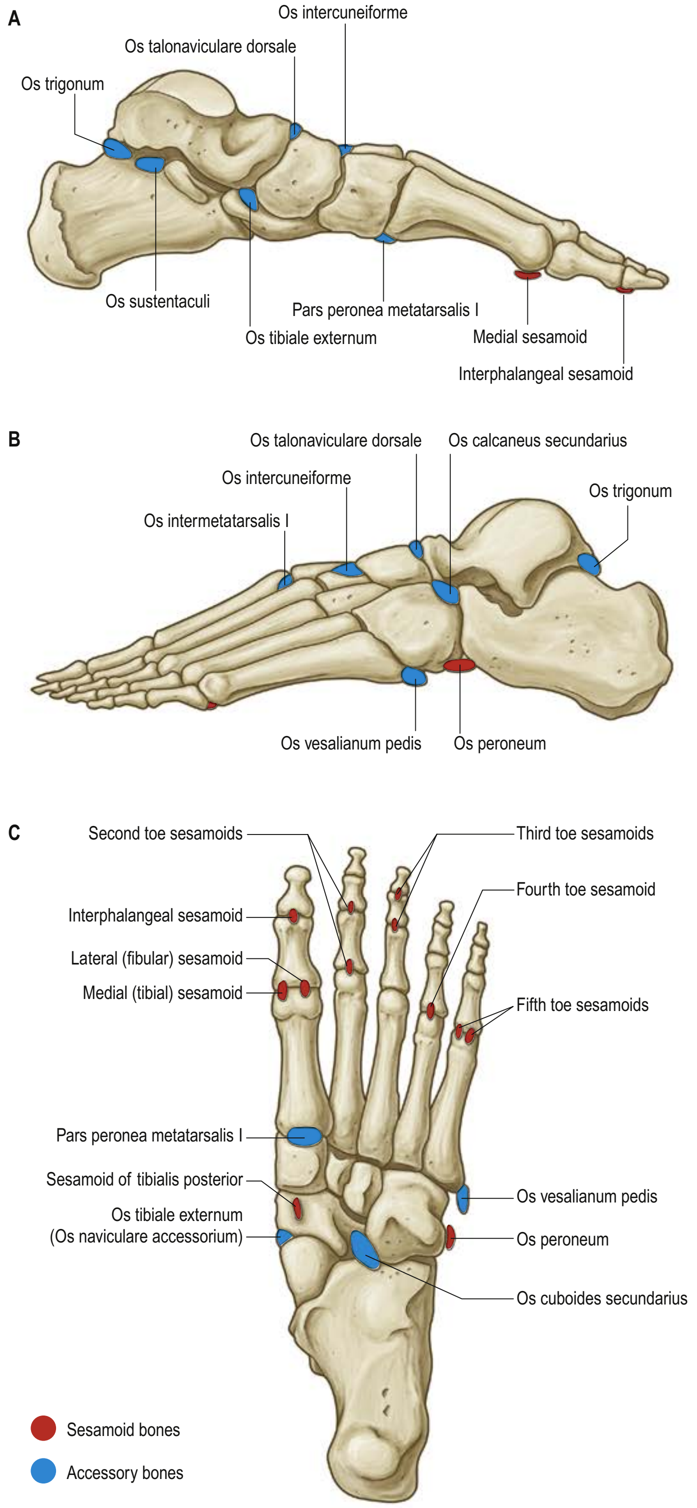
A
Os intercuneiforme
Os talonaviculare dorsale
Os trigonum
Os sustentaculi
Pars peronea metatarsalis I
Os tibiale externum
Medial sesamoid
Interphalangeal sesamoid
B
Os talonaviculare dorsale
Os calcaneus secundarius
Os intercuneiforme
Os trigonum
Os intermetatarsalis I
Os vesalianum pedis
Os peroneum
C
Second toe sesamoids
Third toe sesamoids
Fourth toe sesamoid
Interphalangeal sesamoid
Lateral (fibular) sesamoid
Medial (tibial) sesamoid
Fifth toe sesamoids
Pars peronea metatarsalis I
Sesamoid of tibialis posterior
Os vesalianum pedis
Os tibiale externum
(Os naviculare accessorium)
Os peroneum
Os cuboides secundarius
● Sesamoid bones
● Accessory bones

Fig. 79.13 Sites of sesamoid and accessory bones found in the left foot. **A**, Medial aspect. **B**, Lateral aspect. **C**, Plantar aspect.

Muscle attachments The tendons of the long digital flexors and extensors are attached to the plantar and dorsal aspects of the bases of the distal phalanges of the lateral four toes. Flexor hallucis longus and extensor hallucis longus are similarly attached to the great toe. The tendons of flexor digitorum brevis and extensor digitorum brevis are attached to the bases of the middle phalanges. The proximal phalanges of the second, third, fourth and fifth toes each receive a lumbrical on their medial side; those of the second, third and fourth toes also receive an interosseous muscle on both sides.

Vascular supply The proximal phalanges receive most of their blood supply from the dorsal digital arteries. The middle phalanges are supplied by plantar and dorsal digital arteries. The distal phalanges receive their supply mainly from plantar digital arteries.

Innervation The phalanges are innervated by the plantar and dorsal digital nerves.

Ossification Phalanges are ossified from a primary centre for the shaft and a basal epiphysis (see Fig. 79.8). Primary centres for the distal phalanges appear after postmenstrual week 12 and somewhat later in the fifth digit. Primary centres for the proximal phalanges appear after postmenstrual week 12, and later for the middle phalanges, but there is wide variation. Basal centres appear between the second and eighth years (usually second or third in the great toe), and union with the shaft occurs by the eighteenth year. There is considerable variation in ossification and fusion dates.

Sesamoid bones

Most sesamoid bones are only a few millimetres in diameter and their shape is variable. Some have a predictable location (see below), but many others vary in terms of location and frequency of occurrence (see Fig. 79.13). Some sesamoid bones ossify, whereas others remain cartilaginous. Most sesamoid bones are embedded in tendons in close proximity to joints (Yammine 2015). Their precise role is not understood; it is believed that they may alter the direction of muscle pull, decrease friction and modify pressure.

Medial and lateral sesamoid bones of the first metatarsophalangeal joint

The two constant sesamoid bones within the foot are those of the first metatarsophalangeal articulation (see Figs 79.7, 79.8B, 79.9E). The medial (tibial) sesamoid bone is generally larger than the lateral (fibular) sesamoid bone and lies slightly more distally. During dorsiflexion of the great toe, the sesamoid bones lie below the first metatarsal head, offering protection to the otherwise exposed plantar aspect of the first metatarsal head. The medial sesamoid is approximately 10 mm wide and 14 mm long, and the lateral sesamoid is usually smaller (approximately 8 mm wide and 10 mm long); the overall sizes of the sesamoid bones vary considerably.

The sesamoid bones are embedded within the double tendon of flexor hallucis brevis (see Fig. 79.5B) and articulate on their dorsal surfaces with the plantar facets of the first metatarsal head. They are separated by the crista or intersesamoidal ridge, which provides stability to the sesamoid bone complex. (This ridge can be eroded to the point of obliteration in severe cases of hallux abducto valgus.) The sesamoid bones are connected to the plantar base of the proximal phalanx through the plantar plate. A thin layer of the tendon of flexor hallucis brevis covers the plantar surface of each sesamoid, whereas the dorsal or superior surface is covered by hyaline cartilage. The sesamoid bones are suspended by a sling-like mechanism made up of the collateral ligaments of the first metatarsophalangeal joint and the sesamoid ligaments on either side of the joint. The plantar aponeurosis also has an attachment to the sesamoid bones.

Approximately 30% of these sesamoid bones are bipartite (see Fig. 79.7D). The medial is much more commonly affected and may have two, three or four parts, but the fibular sesamoid rarely has more than two. The condition may be bilateral. The sesamoid bones may be congenitally absent.

Muscle attachments The medial sesamoid bone receives an attachment from abductor hallucis that medially stabilizes the sesamoid complex. The lateral sesamoid receives some fibres from the tendon of adductor hallucis and this provides lateral stabilization. The medial and lateral sesamoid bones are connected by the intersesamoid ligament, which forms the floor of the tendinous canal for the tendon of flexor hallucis longus. The mean length and width of the intersesamoid ligament on its plantar aspect (outside the capsule) is approximately 8.5 mm and 6.3 mm compared to 6.5 mm and 2.2 mm on its dorsal aspect (within the capsule); it is about 3 mm thick. With the application of hallux abducto valgus deforming forces, the size of the sesamoid bones may change, resulting in lengthening of the intersesamoid ligament (Fiacco et al 2017).

Vascular supply There are three patterns of blood supply to the sesamoid bones. In 50% of cases, the arterial supply is derived from the medial plantar artery and the deep plantar arch; in 25% of cases, it is predominantly from the deep plantar arch; and in 25% of cases, from the medial plantar artery alone. The major arterial blood supply to the sesamoid bones enters from the proximal and plantar aspects, and only a minor contribution enters through their distal poles.

Innervation The medial and lateral sesamoid bones are innervated by the plantar digital nerves.

Ossification The ossification centres of the sesamoid bones can be multiple or single.

Other sesamoid and accessory bones

Accessory or inconstant sesamoid bones may occur under any weight-bearing surface of the foot but are most common under the second to fifth metatarsal heads. They are extremely variable in size and their incidence is difficult to determine (Yammine 2015).

A true sesamoid bone occasionally occurs in the tendon of tibialis posterior. It lies on the plantar aspect of the navicular tuberosity within the tendon at the level of the inferior border of the calcaneonavicular ligament (see p. 1441, accessory navicular). Very rarely, a sesamoid bone is found within the tendon of tibialis anterior near its insertion at the level of the anteroinferior corner of the medial cuneiform, where there is an articular facet. An os peroneum is a sesamoid bone within the tendon of fibularis longus that articulates with the lateral surface of the calcaneus, the calcaneocuboid joint or, more frequently, the plantar aspect of the cuboid where there is an articular facet. The bone is situated where the tendon of fibularis longus angles around the plantar aspect of the lateral border of the cuboid and is usually cartilaginous. The frequency of the os peroneum has been reported to be as low as 4.7% and as high as 90% (Oyedele et al 2006, Coskun et al 2009, Muehleman et al 2009).

JOINTS

Ankle (talocrural) joint

The ankle joint is a hinge joint, approximately uniaxial. The lower end of the tibia and its medial malleolus, together with the lateral malleolus of the fibula and inferior transverse tibiofibular ligament, form a deep recess (‘mortise’) for the body of the talus. Although it appears to be a simple hinge, its axis of rotation is dynamic, shifting during dorsiflexion and plantar flexion. Starting from the plantigrade position, the normal range of dorsiflexion is 10° when the knee is straight, and 30° with the knee flexed (when the calcaneal tendon will be relaxed). The range of normal plantar flexion is 30°. (The values of these ranges are all approximate.) Dorsiflexion results in the joint adopting the ‘close-packed’ position, with maximal congruence and ligamentous tension; from this position, all major thrusting movements are exerted, in walking, running and jumping. The malleoli grip the talus, and no appreciable lateral movement can occur without stretch of the inferior tibiofibular syndesmosis, even in relaxation. The superior talar surface is broader in front, and in dorsiflexion, the malleolar gap is increased by slight lateral rotation of the fibula, by ‘give’ at the inferior tibiofibular syndesmosis, and gliding at the superior tibiofibular joint. Normal ankles show valgus inclination at birth. The morphology changes in the first few years of life and the ankle reaches the adult position by the age of three years (Nakai et al 2000).

Articulating surfaces Articular surfaces are covered by hyaline cartilage. The talar trochlear surface is convex sagittally, gently concave transversely and wider anteriorly; the distal tibial articular surface is reciprocally curved. The talar articular surface for the medial malleolus is a proximal area on the medial talar surface, and is fairly flat, comma-shaped and deeper anteriorly. The larger lateral talar articular surface is triangular and vertically concave, while the articular surface on the lateral malleolus is reciprocally curved. Posteriorly, the edge between the trochlear and fibular articular surfaces of the talus is bevelled to a narrow, flat triangular area that articulates with the inferior transverse tibiofibular ligament (Fig. 79.14A); all surfaces are contiguous. The bones are held together by a fibrous capsule, and by medial collateral (deltoid), anterior and posterior talofibular and calcaneofibular ligaments.

Fibrous capsule Around the joint, the fibrous capsule is thin anteriorly and posteriorly. It is attached proximally to the borders of the tibial and malleolar articular surfaces, and distally to the talus near the margins of its trochlear surface, except anteriorly where it reaches the dorsum of the talar neck. The capsule is strengthened by strong collateral ligaments. Its posterior part consists mainly of transverse fibres. It blends with the inferior transverse ligament and is thickened laterally where it reaches the fibular malleolar fossa.

Ligaments The ligaments of the ankle joint are the medial and lateral collateral ligaments.

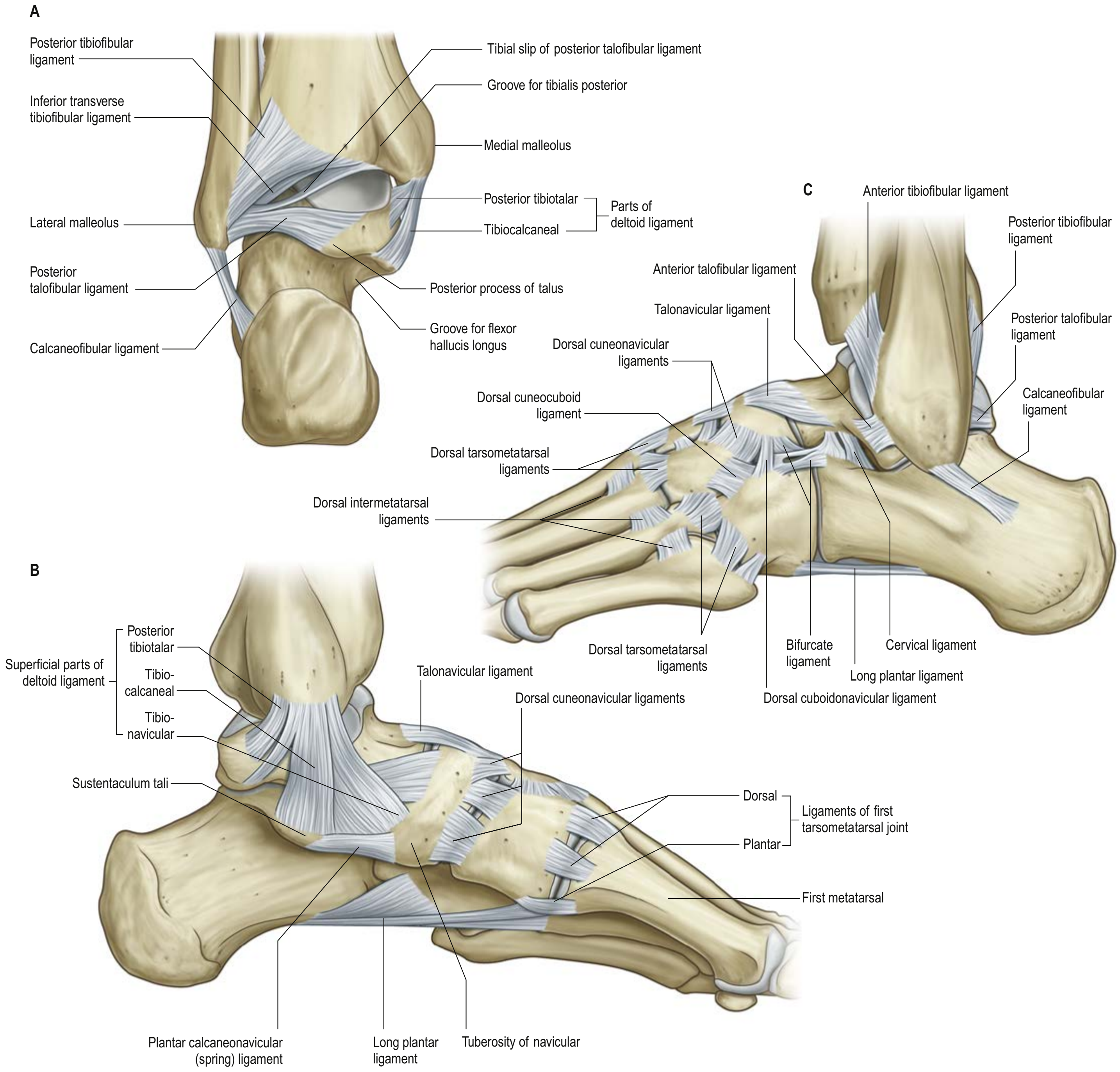
A
Posterior tibiofibular ligament
Inferior transverse tibiofibular ligament
Lateral malleolus
Posterior talofibular ligament
Calcaneofibular ligament
Tibial slip of posterior talofibular ligament
Groove for tibialis posterior
Medial malleolus
Posterior tibiotalar
Tibiocalcaneal
Parts of deltoid ligament
Posterior process of talus
Groove for flexor hallucis longus
B
Superficial parts of deltoid ligament
Posterior tibiotalar
Tibio-calcaneal
Tibio-navicular
Sustentaculum tali
Talonavicular ligament
Dorsal cuneonavicular ligaments
Dorsal
Plantar
Ligaments of first tarsometatarsal joint
First metatarsal
Plantar calcaneonavicular (spring) ligament
Long plantar ligament
Tuberosity of navicular
C
Anterior tibiofibular ligament
Posterior tibiofibular ligament
Anterior talofibular ligament
Talonavicular ligament
Posterior talofibular ligament
Dorsal cuneonavicular ligaments
Dorsal cuneocuboid ligament
Calcaneofibular ligament
Dorsal tarsometatarsal ligaments
Dorsal intermetatarsal ligaments
Dorsal tarsometatarsal ligaments
Bifurcate ligament
Cervical ligament
Long plantar ligament
Dorsal cuboidonavicular ligament

Fig. 79.14 The left ankle and tarsal joints. **A**, Posterior aspect. **B**, Medial aspect. **C**, Lateral aspect.

Medial collateral ligament (deltoid ligament) The medial collateral ligament (deltoid ligament) is a strong, triangular band, attached to the apex and the anterior and posterior borders of the medial malleolus. While up to eight different bands have been reported (Panchani et al 2014), they are variable in their presentation (**Fig. 79.14B**). Of its superficial fibres, anterior (tibionavicular) fibres pass anteriorly to the navicular tuberosity, behind which they blend with the medial margin of the plantar calcaneonavicular ligament (fibers to spring ligament); intermediate (tibiocalcaneal) fibres descend almost vertically to the entire length of the sustentaculum tali; posterior (superficial posterior tibiotalar) fibres pass posterolaterally to the medial side of the talus and its medial tubercle; and additional fibres posterior to the sustentaculum tali (rare variant) have been reported. Of its deep fibres, anterior (anterior tibiotalar) fibres pass from the medial malleolus to the non-articular part of the medial talar surface; intermediate fibres deep to the tibiocalcaneal ligament (rare variant) descend almost vertically to the entire length of the sustentaculum tali; posterior (deep posterior tibiotalar) fibres pass posterolaterally to the medial side of the talus and its medial tubercle; and additional fibres may pass to the spring ligament (Pankovich and Shivaram 1979, Milner and Soames 1998, Boss and Hintermann 2002, Yammine 2017). The tendons of tibialis posterior and flexor digitorum longus cross the ligament. The medial collateral ligament of the ankle is rarely injured alone: tears are commonly associated with a fracture of the distal fibula. Chronic instability is rare.

Lateral collateral ligament The lateral collateral ligament has three discrete parts. The anterior talofibular ligament extends anteromedially from the anterior margin of the lateral malleolus to the talus, attached anterior to its lateral articular facet and to the lateral aspect of its neck (**Fig. 79.14C**). The posterior talofibular ligament runs almost horizontally from the distal part of the lateral malleolar fossa to the lateral tubercle of the posterior talar process (Fig. 79.14A); a 'tibial slip' of fibres, also known as transverse fibres of the posterior talofibular ligament, connects it to the medial malleolus. The calcaneofibular ligament, a long cord, runs from a depression anterior to the apex of the lateral malleolus to a tubercle on the lateral calcaneal surface and is crossed by the tendons of fibularis longus and brevis (see Fig. 79.14A,C). The lateral ligament complex, more specifically, the anterior talofibular ligament, is injured most commonly with inversion sprains; the posterior talofibular ligament is almost always spared. Although the resulting increased laxity is tolerated in most cases, some require surgical reconstruction.

Synovial membrane The joint is lined by a synovial membrane that projects into the inferior tibiofibular joint.

Vascular supply and lymphatic drainage The ankle joint is supplied by malleolar branches of the anterior and posterior tibial and fibular arteries. Lymphatic drainage is via vessels accompanying the arteries and via the long and short saphenous veins, superficially. The blood supply of the medial collateral ligament is derived from three extraosseous arteries (medial tarsal, tibialis anterior and tibialis posterior arteries) and at least one intraosseous source (at the site of its attachments to the medial malleolus and the medial aspect of the talus) (Haynes et al 2017).

Innervation The ankle joint is innervated by branches from the deep fibular, saphenous, sural and tibial nerves (or medial and lateral plantar nerves, depending on the level of division of the tibial nerve). Occasionally, the superficial fibular nerve also supplies the ankle joint. For a comprehensive account of the innervation of the ankle joint (and other foot joints), see Gardner and Gray (1968) and Sarrafian (2011).

Relations Anteriorly, from medial to lateral, are tibialis anterior, extensor hallucis longus, the anterior tibial vessels, deep fibular nerve, extensor digitorum longus and fibularis tertius; posteromedially, from medial to lateral, are tibialis posterior, flexor digitorum longus, the posterior tibial vessels, tibial nerve and flexor hallucis longus; in the groove behind the lateral malleolus are the tendons of fibularis longus and brevis. The tendon of fibularis brevis lies anterior to the tendon of fibularis longus at this level (Fig. 79.15). The long saphenous vein and saphenous nerve cross the ankle joint medial to the tendon of tibialis anterior and anterior to the medial malleolus, the nerve lying posterior to the vein. All of these structures are at risk during surgery on the ankle, the main structures at risk being the neurovascular structures located anteriorly and posteromedially. Branches of the superficial fibular nerve are at risk of injury on the anterolateral aspect of the ankle, particularly during ankle arthroscopy.

Factors maintaining stability Passive stability is conferred upon the ankle mainly by the medial and lateral ligament complexes, the distal tibiofibular ligaments, the tendons crossing the joint, the bony contours and the capsular attachments. Gravity, muscle action and ground

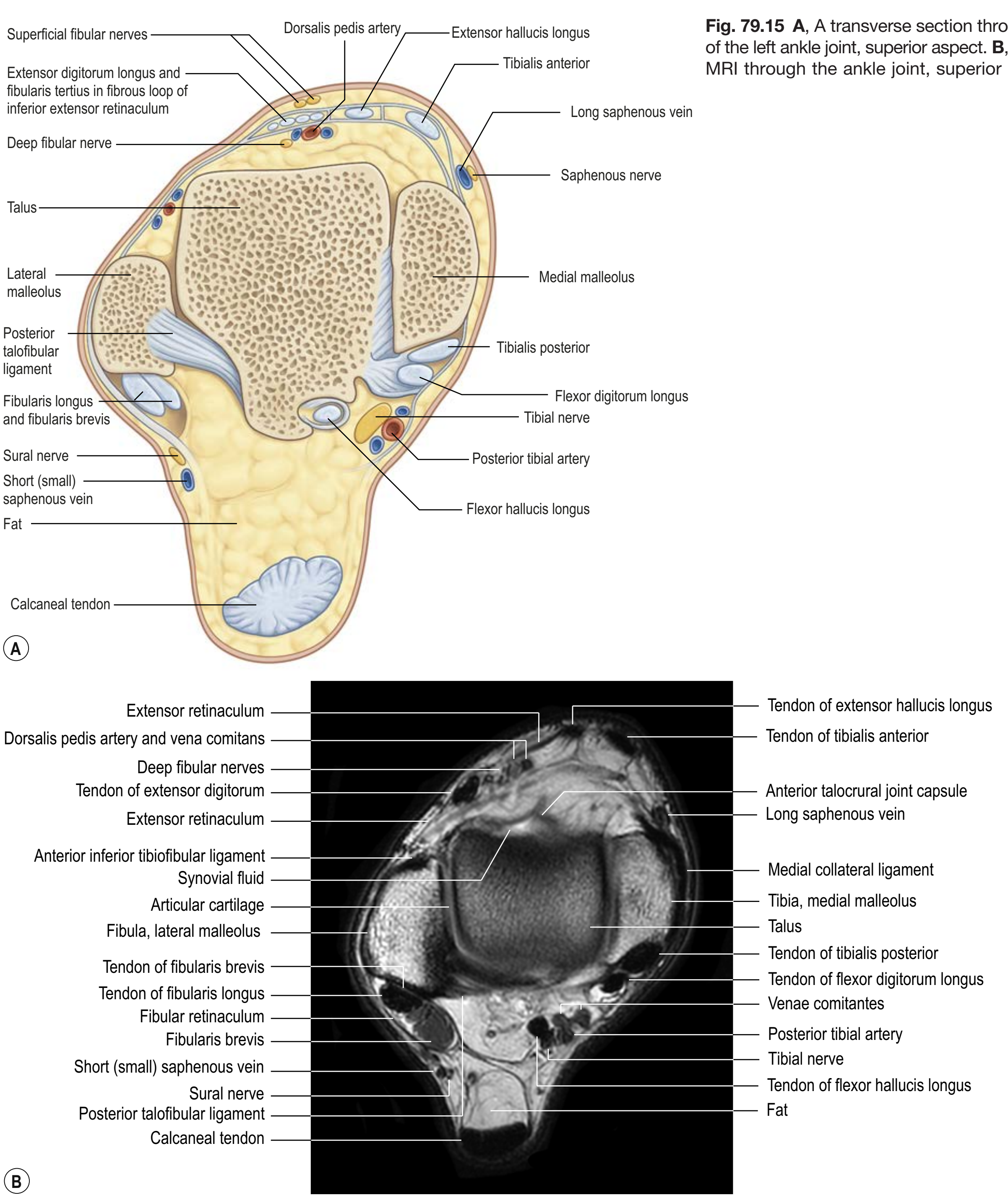

Fig. 79.15 **A**, A transverse section through the lower part of the left ankle joint, superior aspect. **B**, Axial T2-weighted MRI through the ankle joint, superior aspect.

Superficial fibular nerves
Dorsalis pedis artery
Extensor hallucis longus
Tibialis anterior
Extensor digitorum longus and fibularis tertius in fibrous loop of inferior extensor retinaculum
Long saphenous vein
Deep fibular nerve
Saphenous nerve
Talus
Lateral malleolus
Medial malleolus
Posterior talofibular ligament
Tibialis posterior
Fibularis longus and fibularis brevis
Flexor digitorum longus
Tibial nerve
Sural nerve
Posterior tibial artery
Short (small) saphenous vein
Flexor hallucis longus
Fat
Calcaneal tendon
A
Extensor retinaculum
Tendon of extensor hallucis longus
Dorsalis pedis artery and vena comitans
Tendon of tibialis anterior
Deep fibular nerves
Tendon of extensor digitorum
Anterior talocrural joint capsule
Extensor retinaculum
Long saphenous vein
Anterior inferior tibiofibular ligament
Medial collateral ligament
Synovial fluid
Articular cartilage
Tibia, medial malleolus
Fibula, lateral malleolus
Talus
Tendon of fibularis brevis
Tendon of tibialis posterior
Tendon of fibularis longus
Tendon of flexor digitorum longus
Fibular retinaculum
Venae comitantes
Fibularis brevis
Posterior tibial artery
Short (small) saphenous vein
Tibial nerve
Sural nerve
Tendon of flexor hallucis longus
Posterior talofibular ligament
Fat
Calcaneal tendon
B

reaction forces provide dynamic stability. Stability requires the continuous action of soleus assisted by gastrocnemius, increasing when leaning forwards, and decreasing when leaning backwards. If backward sway takes the projection of the centre of gravity ('weight line') posterior to the transverse axes of the ankle joints, the muscles that plantar flex and dorsiflex relax and contract, respectively.

Failure of the fibular muscles can lead progressively to varus instability of the ankle, whereas long-standing failure of the tendon of tibialis posterior, posterior tibial tendon dysfunction, can result in valgus instability of the ankle and particularly a planovalgus foot deformity commonly referred to as adult-acquired flat-foot deformity.

Posterior tibial tendon dysfunction

Available with the *Gray's Anatomy* e-book

Muscles producing movement Dorsiflexion is produced by tibialis anterior, assisted by extensor digitorum longus, extensor hallucis longus and fibularis tertius. Plantar flexion is produced by gastrocnemius and soleus, assisted by plantaris, tibialis posterior, flexor hallucis longus and flexor digitorum longus.

Ankle fractures Ankle fractures are common and of importance because failure to achieve accurate anatomical alignment in the treatment of these fractures often results in significant long-term morbidity. Except for very simple and non-displaced fractures, most ankle fractures are associated with a ligamentous injury. The direction and nature of forces applied to the ankle correlate with the fracture pattern and concomitant ligament injury.

Inferior tibiofibular joint

The inferior tibiofibular joint is usually considered a syndesmosis. It consists of the anterior and posterior tibiofibular and interosseous ligaments.

Articulating surfaces The distal tibiofibular joint is between the rough, medial convex surface on the distal end of the fibula and the concave surface of the fibular notch of the tibia. These surfaces are separated distally for approximately 4 mm by a synovial prolongation from the ankle joint, and may be covered by articular cartilage in their lowest parts.

Fibrous capsule The inferior tibiofibular joint does not have a capsule.

Ligaments The ligaments of the inferior tibiofibular joint are the anterior, interosseous and posterior ligaments.

Anterior tibiofibular ligament The anterior tibiofibular ligament is a flat band that descends laterally between the adjacent margins of the tibia and fibula, anterior to the syndesmosis (see Fig. 79.14C). Bassett's ligament is a variant that presents as a low-lying slip of the ligament inserted so far distally on the fibula that it may cause irritation of the lateral aspect of the talus; it is amenable to arthroscopic removal (Subhas et al 2008).

Interosseous tibiofibular ligament The interosseous tibiofibular ligament is continuous with the interosseous membrane. It contains many short bands between the rough adjacent tibial and fibular surfaces and is the strongest union between the bones.

Posterior tibiofibular ligament The posterior tibiofibular ligament is stronger than the anterior, and is placed similarly on the posterior aspect of the syndesmosis (see Fig. 79.14A). Its distal, deep part is the inferior transverse ligament, a thick band of yellow fibres that crosses from the proximal end of the lateral malleolar fossa to the posterior border of the tibial articular surface almost to the medial malleolus. The ligament projects distal to the bones, in contact with the talus. Its colour reflects its content of yellow elastic fibres.

Synovial membrane The synovial membrane of the ankle joint projects into the distal 4 mm or so of the inferior tibiofibular joint.

Vascular supply and lymphatic drainage The inferior tibiofibular joint is supplied by the perforating branch of the fibular artery and lateral malleolar branches of the anterior and posterior tibial arteries. Lymphatic drainage is via vessels corresponding to the arteries, and via vessels that accompany the long and short saphenous veins.

Innervation The inferior tibiofibular joint is innervated by branches from the deep fibular and sural nerves.

Relations No significant structures pass anterior to the anterior aspect of the inferior tibiofibular joint but the superficial fibular nerve is at risk during surgery to this area. Posteriorly the fibular artery passes over the posterior tibiofibular ligament and is at risk in the posterolateral approach to the fibula.

Factors maintaining stability Stability is maintained in part by the bone contours, but mainly by the dense anterior and posterior tibiofibular and the interosseous ligaments.

Muscles producing movement No muscles act on the inferior tibiofibular joint, which moves only slightly. Because of the varying slope of the lateral surface of the body of the talus, the fibula undergoes a small degree of lateral rotation during dorsiflexion at the ankle, and this results in slight widening of the interval between the bones. Testing for a significant disruption of this joint is usually carried out with the patient under anaesthesia and involves applying a lateral rotation and abduction force, looking for abnormal widening of the syndesmosis. Another helpful clinical test for evaluating a syndesmotic injury is the Hopkinson squeeze test. This test is carried out by compressing the fibula to the tibia at the midpoint of the leg. An injured syndesmosis will result in pain in the area of the inferior tibiofibular joint (Hopkinson et al 1990, Scheyerer et al 2011). Excessive anterior/posterior glide of the fibula relative to the tibia also indicates a disruption of the joint.

Tarsal joints

Talocalcaneal joint

Anterior and posterior articulations between the calcaneus and talus form a functional unit termed the talocalcaneal or subtalar joint (see Fig. 79.17, 79.19). The posterior articulation is referred to as the talocalcaneal joint and the anterior articulation is regarded as part of the talocalcaneonavicular joint. The talocalcaneal joint is a modified multiaxial joint and its permitted movements are considered together with those at other tarsal joints. The bones are connected by a fibrous capsule and by lateral, medial, interosseous talocalcaneal and cervical ligaments.

Articulating surfaces The subtalar joint proper involves the concave posterior calcaneal facet on the posterior part of the inferior surface of the talus and the convex posterior facet on the superior surface of the calcaneus (**Fig. 79.16**).

Fibrous capsule The fibrous capsule envelops the joint; its fibres are short and attached to its articular margins.

Ligaments The ligaments of the talocalcaneal joint are the lateral, medial and interosseous talocalcaneal ligaments and the cervical ligament.

Lateral talocalcaneal ligament The lateral talocalcaneal ligament is a short flat fasciculus that descends obliquely and runs inferoposteriorly from the lateral process of the talus to the lateral calcaneal surface and is attached anterosuperior to the calcaneofibular ligament.

Medial talocalcaneal ligament The medial talocalcaneal ligament connects the medial tubercle of the talus to the posterior aspect of the sustentaculum tali and adjacent medial surface of the calcaneus. Its fibres blend with the medial collateral (deltoid) ligament of the ankle joint; the most posterior fibres line the groove for flexor hallucis longus between the talus and calcaneus.

Interosseous talocalcaneal ligament The interosseous talocalcaneal ligament is a broad, flat bilaminar transverse band in the tarsal sinus (see Fig. 79.16A; **Fig. 79.17**). It descends obliquely and laterally from the sulcus tali to the calcaneal sulcus. The posterior lamina of the ligament is associated with the talocalcaneal joint, and the anterior lamina with the talocalcaneonavicular joint. Its medial fibres are taut in eversion of the foot.

The aetiology of posterior tibial tendon dysfunction is complex. The incidence is greater in obese, middle-aged women. There are multiple contributory factors such as diabetes mellitus and hypertension, which are further complicated by steroid exposure or previous trauma or surgery in the region of the tendon of tibialis posterior. There is often a progressive disruption not only of this tendon, but also of multiple ligamentous complexes such as the spring ligament and those supporting the naviculocuneiform and tarsometatarsal ligaments. This leads to a marked collapse of the medial longitudinal arch, which can be staged using the original Johnson and Strom (1989) classification system and that of Myerson (1997). Along with the varying methods used to diagnose posterior tibial tendon dysfunction, a clinically important test is the single heel-rise test used in the initial stages of adult-acquired flat-foot deformity (Abousayed et al 2017).

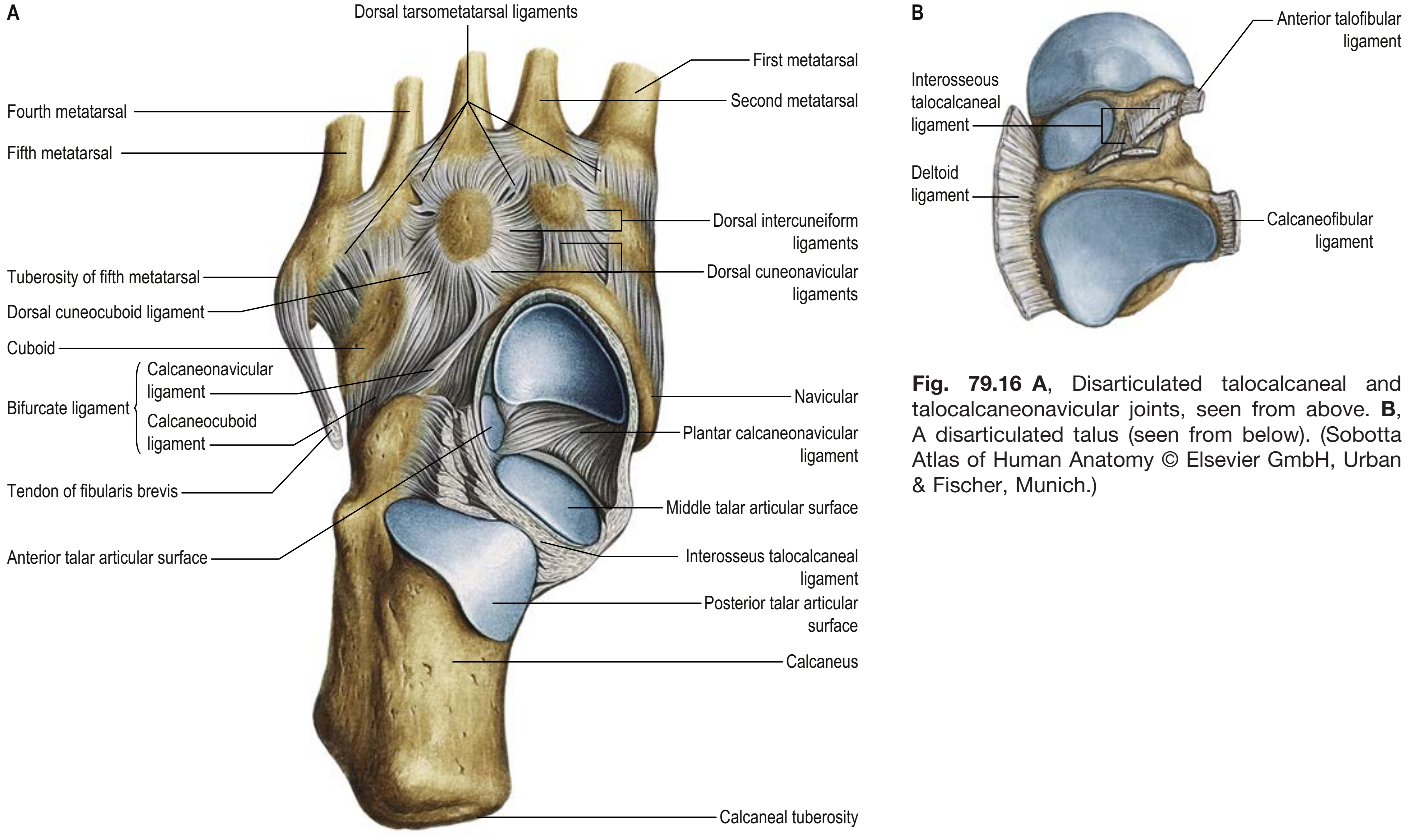
A
Dorsal tarsometatarsal ligaments
First metatarsal
Second metatarsal
Fourth metatarsal
Fifth metatarsal
Dorsal intercuneiform ligaments
Dorsal cuneonavicular ligaments
Tuberosity of fifth metatarsal
Dorsal cuneocuboid ligament
Cuboid
Bifurcate ligament
Calcaneonavicular ligament
Calcaneocuboid ligament
Navicular
Plantar calcaneonavicular ligament
Tendon of fibularis brevis
Middle talar articular surface
Anterior talar articular surface
Interosseus talocalcaneal ligament
Posterior talar articular surface
Calcaneus
Calcaneal tuberosity
B
Anterior talofibular ligament
Interosseous talocalcaneal ligament
Deltoid ligament
Calcaneofibular ligament

Fig. 79.16 A, Disarticulated talocalcaneal and talocalcaneonavicular joints, seen from above. **B**, A disarticulated talus (seen from below). (Sobotta Atlas of Human Anatomy © Elsevier GmbH, Urban & Fischer, Munich.)

Posterior talocalcaneal ligament The posterior talocalcaneal ligament is attached to the plantar border of the posterior process (posterolateral tubercle) of the body of the talus.

Cervical ligament The cervical ligament is just lateral to the tarsal sinus and attached to the superior calcaneal surface (see Fig. 79.14C). It is medial to the attachment of extensor digitorum brevis, from where it ascends medially to an inferolateral tubercle on the talar neck (Barclay-Smith 1896). It is considered to be taut in inversion of the foot. For morphometric data on the cervical ligament and its relationship to the interosseous talocalcaneal ligament see Poonja et al (2017).

Synovial membrane The synovial cavity of the talocalcaneal joint is usually quite separate and does not communicate with those of other tarsal joints. However, direct communication with the ankle joint has been observed in rare instances.

Innervation The talocalcaneal joint is innervated by branches of the tibial, medial plantar and sural nerves.

Relations Posteromedially, in the region of the posterior aspect of the talocalcaneal joint, and viewed from anterior to posterior, veins are seen on either side of the posterior tibial artery, the tibial nerve and the tendon of flexor hallucis longus. These neurovascular structures are at risk in posteromedial approaches to the ankle and talocalcaneal joints. On the lateral side, the tendon of fibularis brevis lies anterior to the tendon of fibularis longus and both pass behind the lateral malleolus close to the talocalcaneal joint. The sural nerve lies just posterior to the tendons of fibularis longus and brevis.

Factors maintaining stability Stability is conferred by the bony contours of the hindfoot plus the above-mentioned ligaments: it is not known which ligaments provide the most stability. An additional ligamentous restraint is provided by the calcaneofibular component of the lateral ligament complex, and the tendons crossing the articulation add stability.

Muscles producing movement Heel inversion is controlled by tibialis anterior, tibialis posterior and the gastrocnemius–soleus complex via the calcaneal tendon, and the extrinsic flexors of the toes also contribute. Eversion of the foot results from the pull of fibularis longus, brevis and tertius in addition to the extrinsic muscles that extend the toes.

Talocalcaneonavicular joint

The talocalcaneonavicular joint is a compound, multiaxial articulation (see Fig. 79.19A–B). In terms of function, and in clinical practice, it is helpful to regard this complex joint as consisting of two articulations, the anterior part of the 'subtalar' joint and the talonavicular joint. Barclay-Smith provided an eloquent account of the joint in 1896, and for a more recent study see Bonnel et al (2011).

Articulating surfaces The ovoid talar head is continuous with the triple-faceted anterior area of its inferior surface. This part fits the concavity formed collectively by the posterior surface of the navicular, the middle and anterior talar facets of the calcaneus, and the superior fibrocartilaginous surface of the plantar calcaneonavicular ligament (spring ligament). The bones are connected by a fibrous capsule, by the talonavicular and plantar calcaneonavicular ligaments, and by the calcaneonavicular part of the bifurcate ligament.

Fibrous capsule The fibrous capsule is poorly developed, except posteriorly, where it is thick and blends with the anterior part of the interosseous ligament filling the tarsal sinus.

Ligaments The ligaments of the talocalcaneonavicular joint are the talonavicular and plantar calcaneonavicular (spring) ligaments.

Talonavicular ligament The talonavicular ligament is a broad, thin band (see Fig. 79.14B–C). It connects the dorsal surfaces of the neck of the talus and the navicular and is covered by extensor tendons. The plantar calcaneonavicular ligament and the calcaneonavicular part of the bifurcate ligament (see Fig. 79.14B–C) are the plantar and lateral ligaments, respectively, of the joint. Although the calcaneus and navicular do not articulate directly, they are connected by the calcaneonavicular part of the bifurcate ligament and the plantar calcaneonavicular ligament.

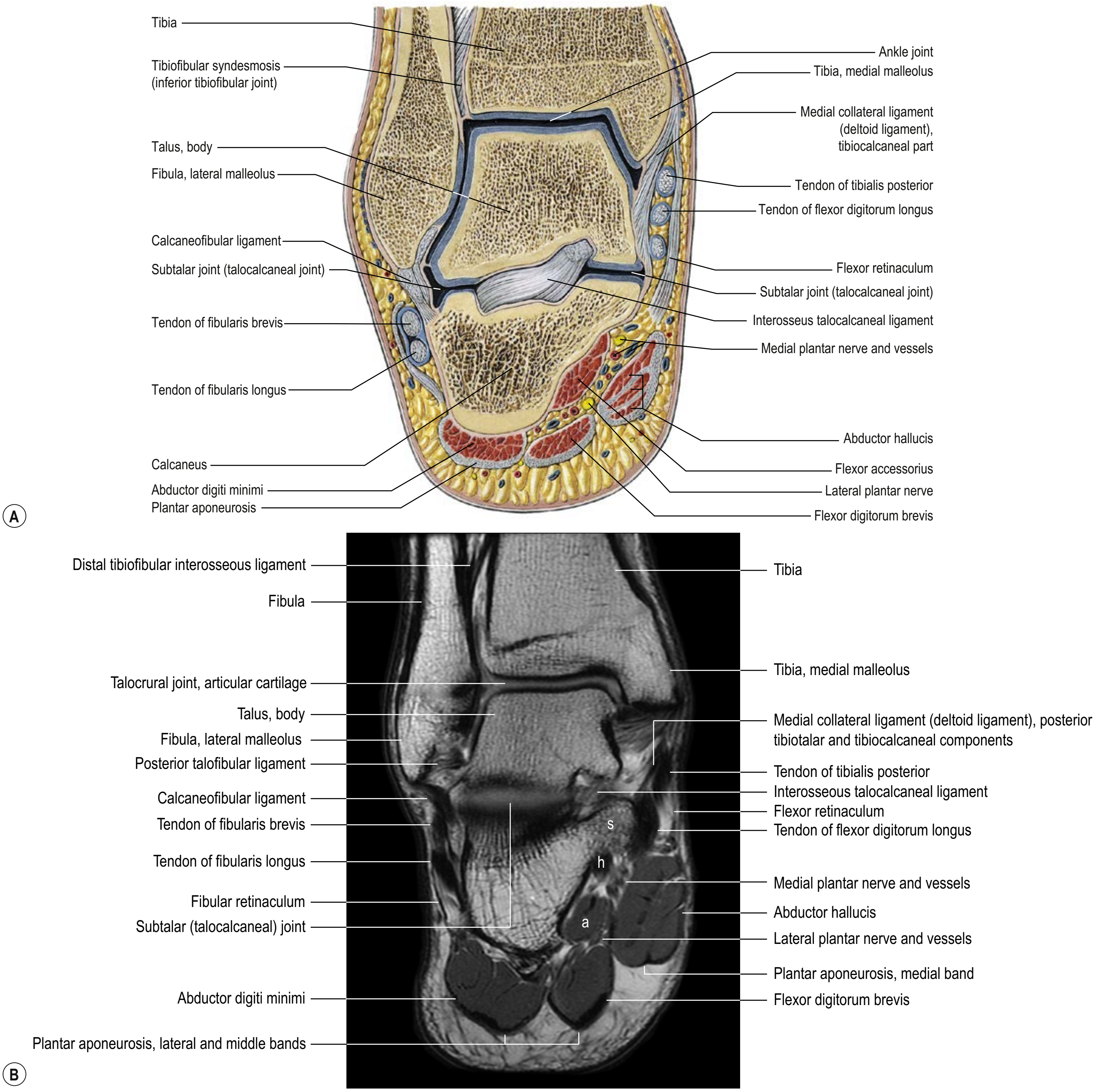
Tibia
Tibiofibular syndesmosis (inferior tibiofibular joint)
Talus, body
Fibula, lateral malleolus
Calcaneofibular ligament
Subtalar joint (talocalcaneal joint)
Tendon of fibularis brevis
Tendon of fibularis longus
Calcaneus
Abductor digiti minimi
Plantar aponeurosis
A
Ankle joint
Tibia, medial malleolus
Medial collateral ligament (deltoid ligament), tibiocalcaneal part
Tendon of tibialis posterior
Tendon of flexor digitorum longus
Flexor retinaculum
Subtalar joint (talocalcaneal joint)
Interosseus talocalcaneal ligament
Medial plantar nerve and vessels
Abductor hallucis
Flexor accessorius
Lateral plantar nerve
Flexor digitorum brevis
Distal tibiofibular interosseous ligament
Fibula
Talocrural joint, articular cartilage
Talus, body
Fibula, lateral malleolus
Posterior talofibular ligament
Calcaneofibular ligament
Tendon of fibularis brevis
Tendon of fibularis longus
Fibular retinaculum
Subtalar (talocalcaneal) joint
Abductor digiti minimi
Plantar aponeurosis, lateral and middle bands
B
Tibia
Tibia, medial malleolus
Medial collateral ligament (deltoid ligament), posterior tibiotalar and tibiocalcaneal components
Tendon of tibialis posterior
Interosseous talocalcaneal ligament
Flexor retinaculum
Tendon of flexor digitorum longus
Medial plantar nerve and vessels
Abductor hallucis
Lateral plantar nerve and vessels
Plantar aponeurosis, medial band
Flexor digitorum brevis
s
h
a

Fig. 79.17 A, A coronal section through the left ankle and talocalcaneal joint (seen from behind). **B**, Coronal proton density MRI of the talocrural joint. Key: a, flexor accessorius; s, sustentaculum tali; h, tendon of flexor hallucis longus. (A, Sobotta Atlas of Human Anatomy © Elsevier GmbH, Urban & Fischer, Munich.)

Plantar calcaneonavicular (spring) ligament The plantar calcaneonavicular (spring) ligament is a broad, thick band connecting the anterior margin of the sustentaculum tali to the plantar surface of the navicular (see Figs 79.14B, 79.16A; **Fig. 79.18**). It ties the calcaneus to the navicular below the head of the talus as part of its articular cavity and it maintains the medial longitudinal arch of the foot. According to Davis et al (1996), the spring ligament is made up of two distinct parts, a superomedial calcaneonavicular portion and an inferior calcaneonavicular portion.

The dorsal surface of the superomedial calcaneonavicular portion has a triangular fibrocartilaginous facet on which part of the talar head rests (see Fig. 79.16A). Its plantar surface is supported medially by the tendon of tibialis posterior and laterally by the tendons of flexors hallucis longus and digitorum longus. Its medial border is blended with the anterior superficial fibres of the medial (deltoid) ligament. Jennings and Christensen (2008) showed that transection of the spring ligament leads to instability of the hindfoot, including talar head plantar flexion and adduction, consistent with pes planovalgus (adult-acquired flatfoot) deformity. The inferior calcaneonavicular portion can become attenuated in adult-acquired flat-foot deformity, and may require surgical correction.

Synovial membrane The talocalcaneonavicular joint is a synovial joint: its cavity sometimes communicates with that of the talocalcaneal joint.

Innervation The talocalcaneonavicular joint is innervated by the deep fibular and medial plantar nerves.

Relations On the medial side, from dorsal to plantar, the tendons of tibialis posterior and flexor digitorum longus lie above the sustentaculum tali, and the tendon of flexor hallucis longus lies below.

The superomedial portion is the larger of the two and originates from the superomedial aspect of the sustentaculum tali and the anterior edge of the anterior facet of the calcaneus. The inferior calcaneonavicular portion originates from between the middle and anterior calcaneal facets on the anterior limit of the sustentaculum tali. Both portions are attached to the inferior surface of the midnavicular; the superomedial portion is attached medial to the inferior portion.

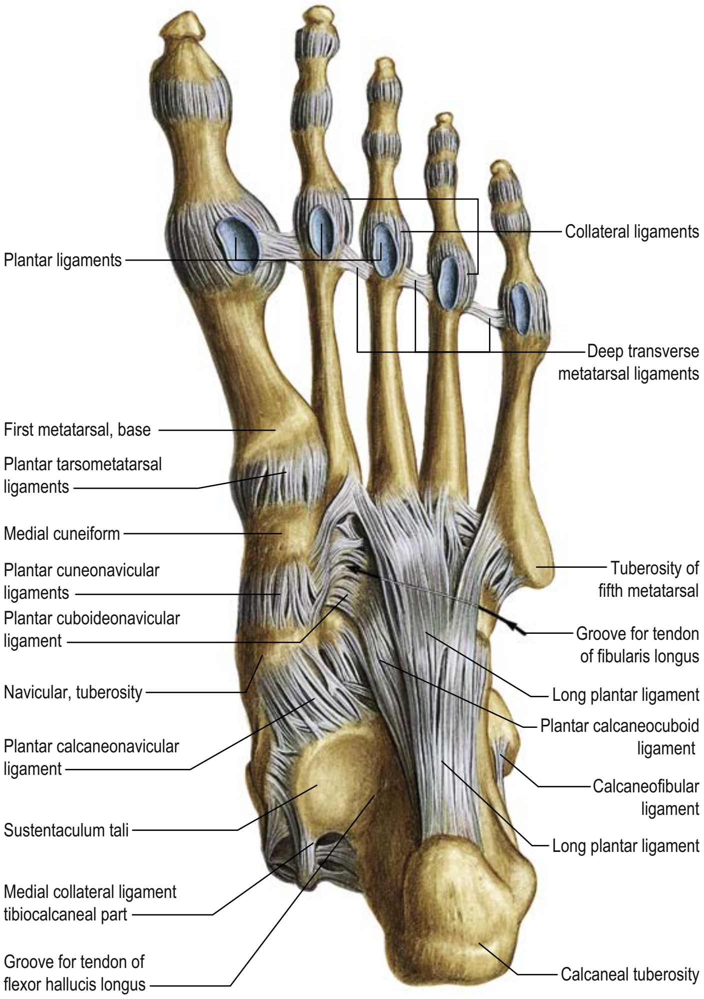
Plantar ligaments
Collateral ligaments
Deep transverse metatarsal ligaments
First metatarsal, base
Plantar tarsometatarsal ligaments
Medial cuneiform
Plantar cuneonavicular ligaments
Plantar cuboideonavicular ligament
Tuberosity of fifth metatarsal
Groove for tendon of fibularis longus
Navicular, tuberosity
Long plantar ligament
Plantar calcaneocuboid ligament
Plantar calcaneonavicular ligament
Calcaneofibular ligament
Sustentaculum tali
Long plantar ligament
Medial collateral ligament tibiocalcaneal part
Groove for tendon of flexor hallucis longus
Calcaneal tuberosity

Fig. 79.18 Ligaments on the plantar aspect of the left foot. (Sobotta Atlas of Human Anatomy © Elsevier GmbH, Urban & Fischer, Munich.)

At this point, flexor hallucis longus is deep to the medial and lateral plantar branches of the posterior tibial artery and the tibial nerve. These latter structures are at risk during medial approaches to the joint, e.g. resection of talocalcaneal coalition. Dorsally from medial to lateral, the tendons of tibialis anterior and extensor hallucis longus, the deep fibular nerve, dorsalis pedis artery and the muscle belly of extensor hallucis brevis all pass medially and deep to the tendons of extensor digitorum longus and fibularis tertius. Structures at risk during the dorsal approach to the talonavicular joint include the branches of the superficial fibular nerve superficially and the dorsalis pedis artery and deep fibular nerve deep to the inferior extensor retinaculum.

Factors maintaining stability Stability of the joint is due to a combination of factors, bony contours, the strong plantar calcaneonavicular (spring) ligament and the calcaneonavicular component of the bifurcate ligament.

Muscles producing movement The muscles producing movement are as described above for the talocalcaneal joint.

Calcaneocuboid joint

The calcaneocuboid joint is a saddle (sellar) or biaxial joint with concavo-convex surfaces (Bonnel et al 2013). It is at the same level as the talonavicular joint: together these joints represent the transverse tarsal joint.

Articulating surfaces The articular surfaces of the calcaneocuboid joint, which is 2 cm proximal to the tubercle on the fifth metatarsal base, are between the anterior (distal) surface of the calcaneus and the posterior (proximal) surface of the cuboid.

Fibrous capsule The fibrous capsule is thickened dorsally as the dorsal calcaneocuboid ligament. The synovial cavity of this joint is separate, and does not communicate with those of other tarsal articulations.

Ligaments The ligaments of the calcaneocuboid joint are the bifurcate, long plantar and plantar calcaneocuboid ligaments.

Bifurcate ligament The bifurcate ligament (Chopart's ligament) is a strong Y-shaped structure (see Figs 79.14C, 79.16A). It is attached by its stem proximally to the anterior part of the upper calcaneal surface, and distally it divides into flat-shaped calcaneocuboid and cord-shaped calcaneonavicular bands. The mean length and width of the calcaneocuboid band is approximately 11 mm and 7 mm compared to the calcaneonavicular band, which measures 23 mm and 7 mm, respectively (Kafka et al 2019).

Long plantar ligament The long plantar ligament is the longest ligament associated with the tarsus and is a most powerful factor limiting depression of the lateral longitudinal arch (see Figs 79.14B–C, 79.18; Fig. 79.19). It extends from the plantar surface of the calcaneus (anterior to the processes of its tuberosity) and from its anterior tubercle, to the ridge and tuberosity on the plantar surface of the cuboid. Deep fibres are attached to the cuboid and more superficial fibres continue to the bases of the second to the fourth, and sometimes the fifth, metatarsals. This ligament, together with the groove on the plantar surface of the cuboid, makes a tunnel for the tendon of fibularis longus.

Plantar calcaneocuboid ligament The plantar calcaneocuboid (short plantar) ligament also supports the lateral longitudinal arch. It is deeper than the long plantar ligament, from which it is separated by areolar tissue (see Fig. 79.18) and is a short, wide and strong band that stretches from the anterior calcaneal tubercle and the depression anterior to it, to the adjoining part of the plantar surface of the cuboid.

Synovial membrane A synovial membrane lines the calcaneocuboid joint.

Innervation The calcaneocuboid joint is innervated on its plantar aspect by the lateral plantar nerve and dorsally by the sural and deep fibular nerves.

Relations Fibularis longus and abductor digiti minimi pass close to the joint, the lateral plantar nerve passes medially, and extensor digitorum brevis overlies the lateral aspect of the joint. The sural nerve and the tendon of fibularis longus are at risk during approaches to an os peroneum.

Factors maintaining stability The calcaneocuboid joint only permits a small amount of movement; its stability reflects the bony contours and strong ligaments described above.

Muscles producing movement Gliding occurs between the calcaneus and cuboid, with conjunct rotation on each other during inversion and eversion of the entire foot. The same muscles that act on the talocalcaneal and talocalcaneonavicular joints bring about these movements.

Naviculocuneiform joint

The naviculocuneiform joint is a compound joint, often described as a plane joint.

Articulating surfaces The navicular articulates distally with the cuneiform bones where the distal navicular surface is transversely convex and divided into three facets by low ridges that are adapted to the proximal, slightly curved, surfaces of the cuneiforms.

Fibrous capsule The fibrous capsule is continuous with those of the intercuneiform and cuneocuboid joints, and it is also connected to the second and third cuneometatarsal joints and intermetatarsal joints between the second to fourth metatarsals.

Ligaments The ligaments of the naviculocuneiform joint are the dorsal and plantar ligaments.

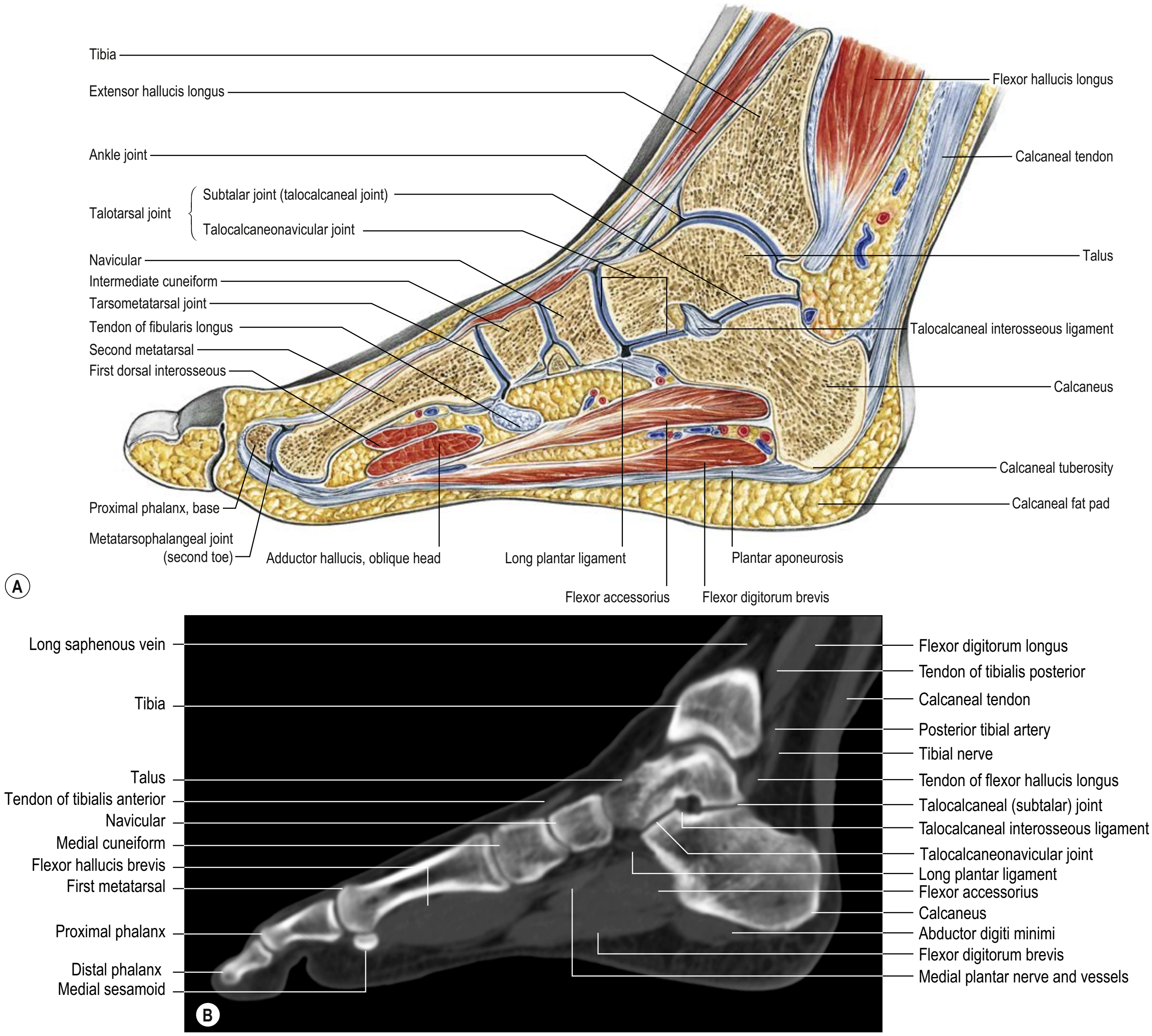
Tibia
Extensor hallucis longus
Ankle joint
Talotarsal joint
Subtalar joint (talocalcaneal joint)
Talocalcaneonavicular joint
Navicular
Intermediate cuneiform
Tarsometatarsal joint
Tendon of fibularis longus
Second metatarsal
First dorsal interosseous
Proximal phalanx, base
Metatarsophalangeal joint (second toe)
Adductor hallucis, oblique head
Long plantar ligament
Plantar aponeurosis
Flexor accessorius
Flexor digitorum brevis
Flexor hallucis longus
Calcaneal tendon
Talus
Talocalcaneal interosseous ligament
Calcaneus
Calcaneal tuberosity
Calcaneal fat pad
A
Long saphenous vein
Tibia
Talus
Tendon of tibialis anterior
Navicular
Medial cuneiform
Flexor hallucis brevis
First metatarsal
Proximal phalanx
Distal phalanx
Medial sesamoid
Flexor digitorum longus
Tendon of tibialis posterior
Calcaneal tendon
Posterior tibial artery
Tibial nerve
Tendon of flexor hallucis longus
Talocalcaneal (subtalar) joint
Talocalcaneal interosseous ligament
Talocalcaneonavicular joint
Long plantar ligament
Flexor accessorius
Calcaneus
Abductor digiti minimi
Flexor digitorum brevis
Medial plantar nerve and vessels
B

Fig. 79.19 **A**, A sagittal section of the foot showing ankle and tarsal joints. **B**, A sagittal CT multiplanar reconstruction through the medial aspect of the foot. (A, Sobotta Atlas of Human Anatomy © Elsevier GmbH, Urban & Fischer, Munich.) (C, *continued online*)

Dorsal and plantar ligaments The dorsal and plantar ligaments connect the navicular to each cuneiform; of the three dorsal ligaments, one is attached to each cuneiform. The fasciculus from the navicular to the medial cuneiform is continued as the capsule of the joint around its medial aspect, and then blends medially with the plantar ligament. Plantar ligaments have similar attachments and receive slips from the tendon of tibialis posterior.

Synovial membrane The synovial membrane lines the fibrous capsule in the manner outlined above.

Innervation The naviculocuneiform joint is innervated dorsally by branches from the deep fibular nerve. The medial plantar nerve innervates the medial and intermediate naviculocuneiform joints, and the lateral plantar nerve innervates the lateral naviculocuneiform joint.

Relations The tendon of tibialis posterior sends fibres to the medial cuneiform and crosses the joint on its medial side; it is vulnerable to injury when a medial surgical approach is used, as are the dorsal venous arch and the saphenous nerve. The tendon of tibialis anterior passes over the dorsomedial aspect of the joint and the tendon of extensor hallucis longus is lateral. From medial to lateral, the deep fibular nerve, dorsalis pedis artery and extensor hallucis brevis run over the intermediate cuneiform and all are vulnerable during dorsal exposure of the joint. On the lateral aspect of the joint, the superficial structures at risk are the superficial fibular nerve and the dorsal venous arch of the foot.

Muscles producing movement Movements at the naviculocuneiform, cuboideonavicular, intercuneiform and cuneocuboid joints are slight, subtle gliding and rotational movements that occur during pronation or supination of the foot. When alterations occur in a loaded foot in contact with the ground, they increase suppleness when the forefoot is stressed, e.g. in the initial thrust of running and jumping. The muscles responsible for these slight movements are tibialis anterior, tibialis posterior, fibularis longus and brevis, and the long flexors and extensors of the toes.

Cuboideonavicular joint

The cuboideonavicular joint is usually a fibrous joint in which the bones are connected by dorsal, plantar and interosseous ligaments. However, this syndesmosis is often a synovial joint that is almost plane, and its articular capsule and synovial lining are continuous with that of the naviculocuneiform joint. The dorsal ligament extends distolaterally, and

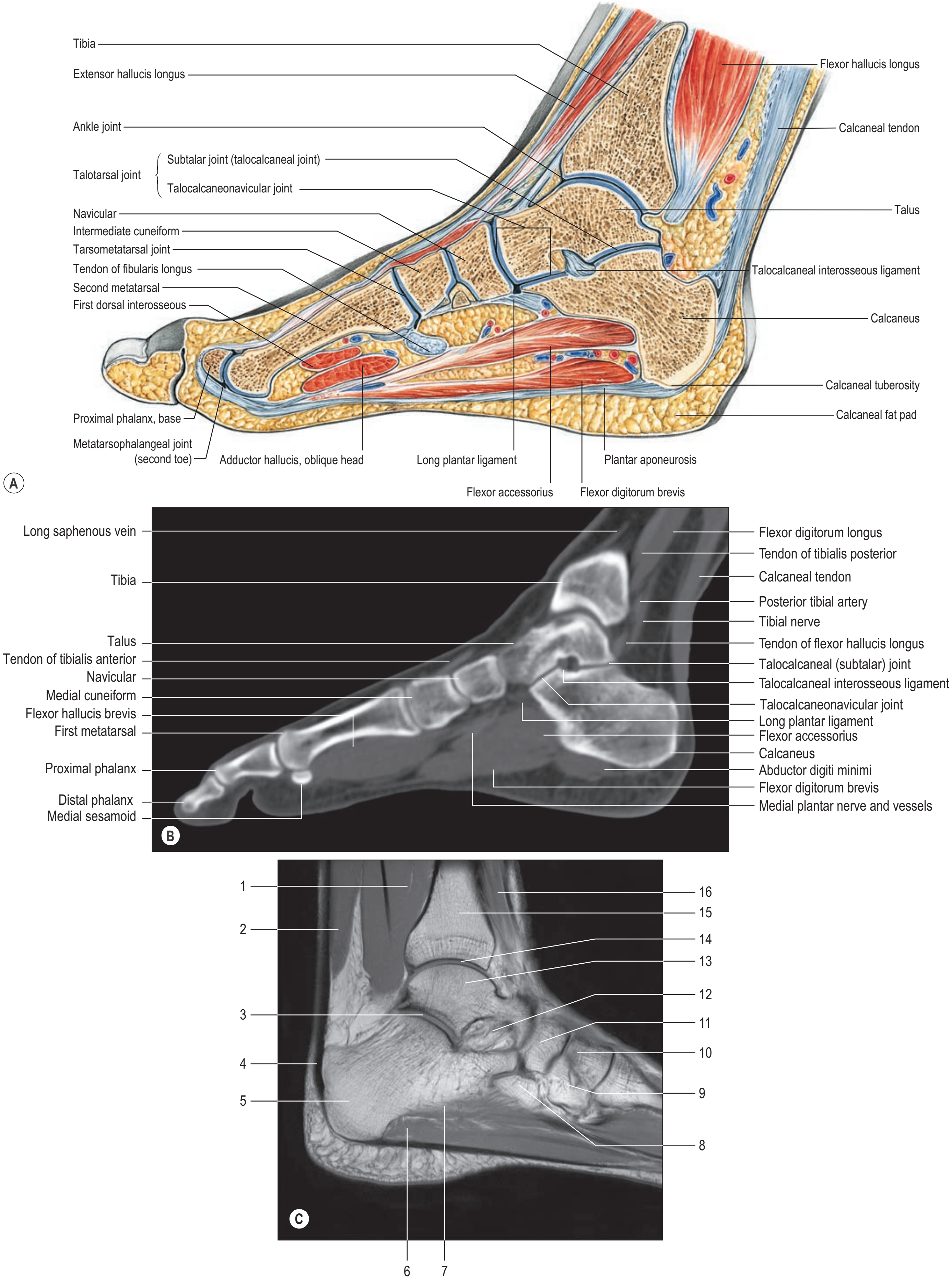
Tibia
Extensor hallucis longus
Ankle joint
Talotarsal joint
Subtalar joint (talocalcaneal joint)
Talocalcaneonavicular joint
Navicular
Intermediate cuneiform
Tarsometatarsal joint
Tendon of fibularis longus
Second metatarsal
First dorsal interosseous
Proximal phalanx, base
Metatarsophalangeal joint (second toe)
Adductor hallucis, oblique head
Long plantar ligament
Flexor accessorius
Flexor digitorum brevis
Plantar aponeurosis
Flexor hallucis longus
Calcaneal tendon
Talus
Talocalcaneal interosseous ligament
Calcaneus
Calcaneal tuberosity
Calcaneal fat pad
A
Long saphenous vein
Tibia
Talus
Tendon of tibialis anterior
Navicular
Medial cuneiform
Flexor hallucis brevis
First metatarsal
Proximal phalanx
Distal phalanx
Medial sesamoid
Flexor digitorum longus
Tendon of tibialis posterior
Calcaneal tendon
Posterior tibial artery
Tibial nerve
Tendon of flexor hallucis longus
Talocalcaneal (subtalar) joint
Talocalcaneal interosseous ligament
Talocalcaneonavicular joint
Long plantar ligament
Flexor accessorius
Calcaneus
Abductor digiti minimi
Flexor digitorum brevis
Medial plantar nerve and vessels
B
1
2
3
4
5
16
15
14
13
12
11
10
9
8
C
6
7

Fig. 79.19 A, A sagittal section of the foot showing ankle and tarsal joints. **B,** A sagittal CT multiplanar reconstruction through the medial aspect of the foot. **C,** A sagittal turbo spin-echo, T1-weighted MRI of the left ankle and hindfoot of a female aged 26 years. Key: 1, flexor digitorum longus; 2, soleus; 3, talocalcaneal (subtalar) joint; 4, calcaneal tendon; 5, calcaneus; 6, flexor digitorum brevis; 7, flexor accessorius; 8, cuboid; 9, lateral cuneiform; 10, intermediate cuneiform; 11, navicular; 12, talocalcaneal interosseous ligament; 13, talus; 14, talocrural joint; 15, tibia; 16, tibialis anterior. (A, Sobotta Atlas of Human Anatomy © Elsevier GmbH, Urban & Fischer, Munich. C, Courtesy of Robert J. Ward, MD, Tufts University School of Medicine, Boston, MA.).

the plantar nearly transversely from the cuboid to the navicular. The interosseous ligament is made of strong transverse fibres and connects non-articular parts of adjacent surfaces to the two bones.

Intercuneiform and cuneocuboid joints

The intercuneiform and cuneocuboid joints are all synovial and approximately plane or slightly curved. Their articular capsules and synovial linings are continuous with those of the naviculocuneiform joints. The bones are connected by dorsal, plantar and interosseous ligaments (see Figs 79.14B–C, 79.16A).

Ligaments The ligaments of the intercuneiform and cuneocuboid joints are the dorsal, plantar and interosseous ligaments.

Dorsal and plantar ligaments The dorsal and plantar ligaments each have three transverse bands that pass between the medial and intermediate cuneiforms, the intermediate and lateral cuneiforms, and the lateral cuneiform and cuboid. The plantar ligaments receive slips from the tendon of tibialis posterior.

Interosseous ligaments The interosseous ligaments connect non-articular areas of adjacent surfaces and are strong agents in maintaining the transverse arch.

Innervation The intercuneiform and cuneocuboid joints are innervated dorsally by branches of the deep fibular nerve. The plantar aspect of the medial two joints is innervated from the medial plantar nerve, and the plantar aspect of the lateral joints is innervated by branches of the lateral plantar nerve.

Muscles producing movement The muscles producing movement are as described above for the naviculocuneiform joint.

Tarsometatarsal joints

Tarsometatarsal articulations are approximately plane synovial joints.

Articulating surfaces The first metatarsal articulates with the medial cuneiform; the second is recessed between the medial and lateral cuneiforms and articulates with the intermediate cuneiform; the third articulates with the lateral cuneiform; the fourth articulates with the lateral cuneiform and the cuboid; and the fifth articulates with the cuboid. The joints are approximately on an imaginary line traced from the tubercle of the fifth metatarsal to the tarsometatarsal joint of the great toe, except for that between the second metatarsal and intermediate cuneiform, which is 2–3 mm proximal to this line (see Figs 79.5A, 79.12). Ryan et al (2012) reported that the average joint depths for the first, second and third metatarsal–cuneiform joints were 32.3, 26.9 and 23.6 mm, respectively.

Fibrous capsule The tarsometatarsal joint of the great toe has its own capsule. The articular capsules and cavities of the second and third toes are continuous with those of the intercuneiform and naviculocuneiform joints, but are separated from the fourth and fifth joints by an interosseous ligament between the lateral cuneiform and fourth metatarsal base.

Ligaments The bones are connected by dorsal and plantar tarsometatarsal and cuneometatarsal interosseous ligaments (see Figs 79.16A, 79.18).

Dorsal ligaments The dorsal ligaments are strong and flat. The first metatarsal is joined to the medial cuneiform by an articular capsule, and the other tarsometatarsal capsules blend with the dorsal and plantar ligaments. The second metatarsal receives a band from each cuneiform, the third from the lateral cuneiform, the fourth from the lateral cuneiform and the cuboid, and the fifth from the cuboid alone.

Plantar ligaments The plantar ligaments are longitudinal and oblique bands that are less regular than the dorsal ligaments. Those for the first and second metatarsals are strongest. The second and third metatarsals are joined by oblique bands to the medial cuneiform, and the fourth and fifth metatarsals are joined by a few fibres to the cuboid.

Cuneometatarsal interosseous ligaments There are three cuneometatarsal interosseous ligaments. The strongest, known as Lisfranc's ligament, passes from the lateral surface of the medial cuneiform to the adjacent angle of the second metatarsal and is crucial to the stability of the tarsometatarsal joint complex (Johnson et al 2008). Disruption of this ligament can lead to instability and deformity, and subsequent degenerative changes. A second ligament connects the lateral cuneiform to the adjacent angle of the second metatarsal, but it does not divide the joint between the second metatarsal and lateral cuneiform and is inconstant. A third ligament connects the lateral angle of the lateral cuneiform to the adjacent fourth metatarsal base.

Synovial membrane The first tarsometatarsal joint has its own capsule, with a synovial lining. The other joints are similarly arranged; there is a communication between the second and third and between the fourth and fifth tarsometatarsal joints.

Innervation The interosseous cuneometatarsal ligaments are innervated dorsally via the deep fibular nerve. The plantar aspects of the medial two joints are innervated by branches of the medial plantar nerve, and the plantar aspects of the lateral joints are innervated by branches of the lateral plantar nerve.

Relations From medial to lateral, the saphenous nerve, dorsal venous arch, tendon of extensor hallucis longus, dorsalis pedis artery, deep fibular nerve, extensor hallucis brevis and the tendons of extensor digitorum longus, extensor digitorum brevis, fibularis tertius and fibularis brevis all cross the dorsal aspect of the tarsometatarsal joints. Branches of the superficial fibular nerve are variable in location on the dorsum and the sural nerve lies just inferior to the tendon of fibularis brevis in the subcutaneous tissues. Surgery involving the tarsometatarsal joints is performed through a dorsal approach, and therefore all of these structures are potentially at risk of injury.

Factors maintaining stability The major stabilizers of the tarsometatarsal joints are the associated ligaments. However, despite the strength of the ligaments, this joint complex is vulnerable to injury because of the lack of ligamentous connection between the first and second metatarsal bases. The medial interosseous ligament or Lisfranc's ligament is responsible for the tell-tale avulsion fracture of the second metatarsal base, which may be the only radiographic indication of abnormality after injury to this part of the foot. It is a highly significant injury that is often missed; failure to recognize and treat it by surgical reduction and fixation can lead to long-term disability.

Muscles producing movement Movements between the tarsals and metatarsals are limited to flexion and extension, except in the first tarsometatarsal joint, where some abduction and rotation occur. The muscles that produce this motion are tibialis anterior and fibularis longus. Flexion and extension are brought about by the long and short flexors and extensors of the toes. Movement between the medial cuneiform and first metatarsal, and between the fourth and fifth metatarsal bases and the cuboid, is moderate and allows the foot to adapt to uneven surfaces, whereas movement between the second and third metatarsal bases and their corresponding cuneiforms is very limited.

Intermetatarsal joints

The intermetatarsal ligaments are very strong. They are present between all the lateral four metatarsals, but absent between the first and second metatarsals. The base of the second metatarsal is joined to the first tarsometatarsal joint by the cuneometatarsal interosseous ligament.

Ligaments The ligaments of the intermetatarsal joints include the dorsal and plantar intermetatarsal ligaments (see Fig. 79.14B).

Dorsal and plantar intermetatarsal ligaments As with their dorsal counterparts, the plantar intermetatarsal ligaments are longitudinal, oblique or transverse and they vary considerably in both number and organization. The plantar ligaments are significantly stronger than the corresponding dorsal ligaments. The strongest is the second oblique plantar ligament, which connects the medial cuneiform to the bases of the second and third metatarsals.

Other ligaments All the metatarsal heads are connected indirectly by deep transverse metatarsal ligaments. Dorsal and plantar ligaments pass transversely between adjacent bases. Interosseous ligaments are strong transverse bands that connect non-articular parts of the adjacent surfaces.

Metatarsophalangeal joints

Metatarsophalangeal articulations are ovoid or ellipsoid joints between the rounded metatarsal heads and shallow cavities on the proximal phalangeal bases. They are usually 2.5 cm proximal to the web spaces of the toes.

Articulating surfaces Articular surfaces cover the distal and plantar, but not the dorsal, aspects of the metatarsal heads. The plantar aspect of the first metatarsal head has two longitudinal grooves separated by a ridge (crista). Each articulates with a sesamoid bone embedded in the capsule of the joint, formed here by the two tendons of flexor hallucis brevis (see Figs 79.5B, 79.13). The sesamoid bones are connected to each other by the intersesamoid ligament, which forms the floor of the tendinous canal for the tendon of flexor hallucis longus. The medial sesamoid bone receives an attachment from abductor hallucis and the lateral sesamoid bone receives an attachment from adductor hallucis, forming the conjoint tendon. Both sesamoid bones act to create a longer lever arm for the tendon of flexor hallucis brevis. Articular areas on the proximal phalangeal bases are concave. The ligaments are capsular, plantar, deep transverse metatarsal and collateral.

Fibrous capsules Fibrous capsules are attached to their articular margins. They are thin dorsally, and may be separated from the extrinsic extensor tendons by small bursae, or they may be replaced by the tendons, but they are inseparable from the plantar and collateral ligaments. The plantar aponeurosis blends with the plantar capsule to form the 'plantar plate', which inserts distally into the base of the proximal phalanx via medial and lateral bundles. Proximally, the plate is attached to the metatarsal head via a thin synovial fold. It also receives an attachment from the accessory collateral ligament.

Ligaments The ligaments of the metatarsophalangeal joints are the plantar, deep transverse metatarsal and collateral ligaments (see Fig. 79.18).

Plantar ligaments The plantar ligaments are thick and dense. They lie between and blend with the collateral ligaments, being loosely attached to the metatarsals and firmly attached to the phalangeal bases. Their margins blend with the deep transverse metatarsal ligaments. Their deep surfaces extend the articular areas for the metatarsal heads. Their plantar surfaces are grooved for the flexor tendons; the fibrous sheaths of the tendons connect with the edges of the grooves (see Fig. 79.18).

Deep transverse metatarsal ligaments The deep transverse metatarsal ligaments are four short, wide, flat bands that unite the plantar ligaments of adjoining metatarsophalangeal joints. The interossei are dorsal to, and the lumbricals, digital vessels and nerves are plantar to, these ligaments. They resemble the deep transverse metacarpal ligaments except that, in the foot, there is a deep transverse metatarsal ligament between the plantar ligament of the second metatarsophalangeal joint and that of the first metatarsophalangeal joint (see Fig. 79.18). Transection of the deep transverse metatarsal ligament during neuroma removal may splay the metatarsals, increasing the intermetatarsal angle (Preston et al 2018).

Collateral ligaments The collateral ligaments are strong cords flanking each joint. They are attached to the dorsal tubercles on the metatarsal heads and the corresponding side of the phalangeal bases, and they slope inferodistally. The first metatarsophalangeal joint also contains metatarsosesamoid ligaments. On either side, the ligaments arise from the metatarsal head with a narrow origin and then fan out to insert on the border of the proximal phalanx and the plantar plate. Each collateral ligament consists of a phalangeal collateral ligament, which inserts into the base of the proximal phalanx, and an accessory collateral ligament, which inserts into the plantar plate.

Synovial membrane Each metatarsophalangeal joint is a separate synovial joint.

Innervation The main nerve supply of the metatarsophalangeal joints is from branches of the plantar digital nerves, which supply the first, second, third and medial half of the fourth metatarsophalangeal joint on their plantar aspects. Digital branches of the lateral plantar nerve supply the lateral half of the fourth joint, and both medial and lateral aspects of the fifth joint, on their plantar sides. The medial dorsal cutaneous branch of the superficial fibular nerve supplies the dorsomedial side of the hallucal metatarsophalangeal joint. The deep fibular nerve supplies the dorsolateral side of the hallucal metatarsophalangeal joint and the medial side of the metatarsophalangeal joint of the second toe.

Relations Dorsally the tendon of extensor hallucis longus lies medial to the tendon of extensor hallucis brevis. The same arrangement occurs in the lateral four toes with the tendons of extensor digitorum longus and brevis. The interossei are plantarmedial and plantarlateral, dorsal to the transverse intermetatarsal ligament, whereas the lumbrical tendons and the digital artery and nerve are plantar to the transverse intermetatarsal ligament. The extrinsic and intrinsic flexors lie on the plantar aspect of the joint in the midline. If approaching the metatarsophalangeal joint surgically from the plantar surface, it is important not to stray from the midline.

Factors maintaining stability The first metatarsophalangeal joint owes its stability to its capsuloligamentous structures and to flexor and extensor hallucis brevis, with a small contribution from flexor and extensor hallucis longus or the bony contours. The collateral ligaments and plantar plates stabilize the metatarsophalangeal joints of the lateral four toes. Rupture of the plantar plate can lead to dorsal dislocation of the digit on its articulating metatarsal. The resulting extension at the metatarsophalangeal joint creates a hammer toe deformity.

Muscles producing movement The types of movements at these joints are like those that occur at the corresponding joints in the hand, but the range of movement is quite different. In contrast to the metacarpophalangeal joints, the range of active extension at the metatarsophalangeal joints (50–60°) is greater than that of flexion (30–40°); this is an adaptation to the needs of walking, and is most marked in the joint of the great toe, where flexion is a few degrees while extension may reach 90°. When the foot is on the ground, the metatarsophalangeal joints are already extended to at least 25° because the metatarsals incline proximally in the longitudinal arches of the foot (see Fig. 79.9A). The range of passive movements in these joints is 90° (extension) and 45° (flexion), according to Kapandji (2011). The muscles producing movements at the metatarsophalangeal joints are as follows.

Flexion Flexor digitorum brevis, lumbricals and interossei, assisted by flexor digitorum longus and flexor accessorius. In the fifth toe, flexor digiti minimi brevis assists. For the great toe, flexors hallucis longus and brevis and the oblique head of the adductor hallucis are the only flexors.

Extension Extensor digitorum longus and extensor digitorum brevis, extensor hallucis longus.

Adduction Adductor hallucis; in the third to fifth toes, the first, second and third plantar interossei, respectively.

Abduction Abductor hallucis; in the second toe, the first and second dorsal interossei; in the third and fourth toes, the corresponding dorsal interossei; in the fifth toe, abductor digiti minimi. Note that the line of reference for adduction and abduction in the foot is along the second digit, which has the least mobile metatarsal. The second toe may therefore be 'abducted' medially and laterally by the first and second dorsal interossei, respectively.

Hallux abducto valgus Hallux abducto valgus is a common condition, occurring mainly in individuals who have a genetic predisposition. Footwear is implicated in this condition, which presumably accounts for the greater incidence in females. This is because high heel shoes can hold the foot in an artificially supinated position, and the pointed toe box of the shoes can compress the toes towards the midline. However, it is more of an accelerating factor than a sole causative one. Hallux abducto valgus is a tri-planar deformity, and is associated with transverse abduction (from the midline of the foot), sagittal elevation and frontal plane rotation of the first metatarsal, which abducts and rotates the hallux in valgus (**Fig. 79.20**). While frontal plane rotation is a prevalent part of hallux abducto valgus, it is rarely considered in surgical correction, which may account for the high recurrence rates of this deformity (Hatch et al 2018).

The more spheroidal the shape of the first metatarsal head, the more likely it is to be unstable. Conversely, a flat metatarsal head is less likely to be associated with hallux abducto valgus. No muscle inserts into the first metatarsal head, and therefore its position is determined by the

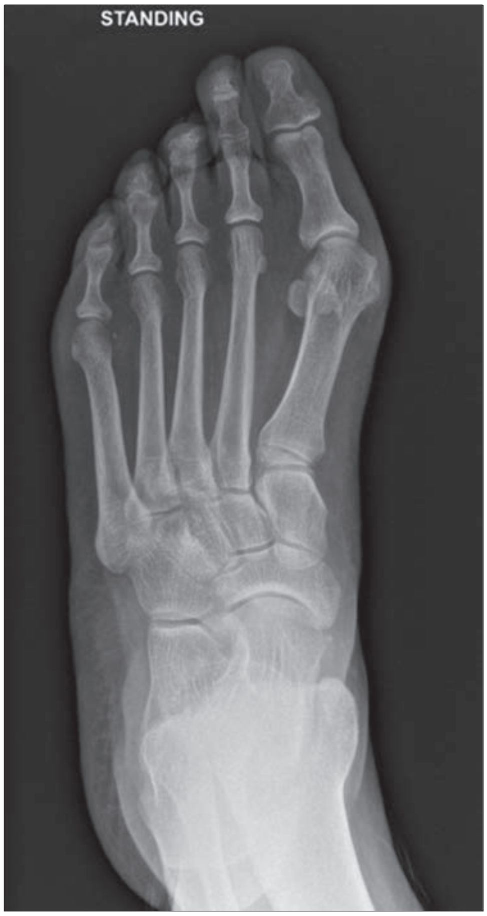

Fig. 79.20 Radiograph of the left foot of a skeletally mature adult with a hallux abducto valgus (bunion) deformity.

position of the proximal phalanx. Furthermore, the base of the first metatarsal (the first metatarsal cuneiform joint) has no ligamentous attachments to the lateral four metatarsals. This creates an intrinsic instability that can more easily allow the first metatarsal to drift (Burns and Mecham 2014).

As the proximal phalanx moves laterally on the metatarsal head, it pushes the head medially. This leads to attenuation of the medial soft tissue structures and contracture of the lateral ones. The extensor tendon axis, once midline, becomes a deforming force as the metatarsophalangeal joint is positioned medial to the tendon. The sesamoid sling (i.e. plantar plate and flexor hallucis brevis), which is anchored laterally by adductor hallucis, remains in place as the head moves medially and everts, giving the illusion on a radiograph of displacing the sesamoid bones from beneath the metatarsal head. In reality, the sesamoids stay locked in the sling, and it is the metatarsal head that is displaced and may play a role in the increased size of the medial eminence (the visible medial protuberance of a bunion deformity) as the deformity progresses into late stage changes (Burns and Mecham 2014). As this happens, the weakest point of the medial capsule fails, so that abductor hallucis slips under the metatarsal head. This leads to failure of the intrinsic muscles to stabilize the joint, and the pull of abductor hallucis leads to spinning of the proximal phalanx, which results in a varus deformity. Failure to intervene surgically inevitably results in a progressive deformity.

Interphalangeal joints

Interphalangeal articulations are almost pure hinge joints in which the trochlear surfaces on the phalangeal heads articulate with reciprocally curved surfaces on adjacent phalangeal bases. Each has an articular capsule and two collateral ligaments, as occurs in the metatarsophalangeal joints. The plantar surface of the capsule is a thickened fibrous plate, like the plantar metatarsophalangeal ligaments, and is often termed the plantar ligament.

Innervation The interphalangeal articulations are innervated by branches from the plantar digital nerves. The medial dorsal cutaneous branch of the superficial fibular nerve also supplies the interphalangeal joint of the great toe. Branches of the deep fibular, intermediate dorsal cutaneous and sural nerves sometimes supply the joints of the lateral four toes.

Muscles producing movement Movements are flexion and extension, which are greater in amplitude between the proximal and middle phalanges than between the middle and distal. Flexion is marked, but extension is limited by tension of the flexor muscles and plantar ligaments. Abduction, adduction and rotation occur to a minor extent. The muscles producing movements at the interphalangeal joints are as follows.

Flexion Flexor digitorum longus, flexor digitorum brevis and flexor hallucis longus. Flexor accessorius assists flexor digitorum longus to maintain a flexed toe and neutralize the medial pull of flexor digitorum longus.

Extension Extensor digitorum longus, extensor digitorum brevis, extensor hallucis longus and extensor hallucis brevis.

ARCHES OF THE FOOT

Three main arches are recognized in the foot: medial and lateral longitudinal and transverse. The roles of the arches in the biomechanics of the foot are discussed later in this chapter.

Medial longitudinal arch

The medial margin of the foot arches up between the heel proximally and the medial three metatarsophalangeal joints to form a visible arch (see Fig. 79.9A). It is made up of the calcaneus, talar head, navicular, the three cuneiforms and the medial three metatarsals. The posterior and anterior pillars are the posterior part of the inferior calcaneal surface and the three metatarsal heads, respectively. The bones themselves contribute little to the stability of the arch, whereas the ligaments contribute significantly. The most important ligamentous structure is the plantar aponeurosis, which acts as a tie beam between the supporting pillars (Hicks 1954). Dorsiflexion, especially of the great toe, draws the two pillars together, thus heightening the arch: the so-called ‘windlass’ mechanism. Next in importance is the spring ligament, which supports the head of the talus. If this ligament attenuates, the navicular and calcaneus separate, allowing the talar head, the highest point of the arch, to descend, leading to a flat-foot deformity. The talocalcaneal ligaments and the anterior fibres of the deltoid ligament, from the tibia to the navicular, also contribute to the stability of the arch. Muscles play a role in the maintenance of the medial longitudinal arch. Flexor hallucis longus acts as a bowstring. Flexor digitorum longus, abductor hallucis and the medial half of flexor digitorum brevis also contribute but to a lesser extent. Tibialis posterior and anterior invert and adduct the foot, and so help to raise its medial border. The importance of tibialis posterior is manifest by the collapse of the medial longitudinal arch that accompanies failure of its tendon (see below, pes planus).

Lateral longitudinal arch

The lateral longitudinal arch is a much less pronounced arch than the medial one. The bones making up the lateral longitudinal arch are the calcaneus, the cuboid and the fourth and fifth metatarsals; they contribute little to the arch in terms of stability (see Fig. 79.9A). The pillars are the calcaneus posteriorly and the lateral two metatarsal heads anteriorly. Ligaments play a more important role in stabilizing the arch, especially the lateral part of the plantar aponeurosis and the long and short plantar ligaments. However, the tendon of fibularis longus makes the most important contribution to the maintenance of the lateral arch. The lateral two tendons of flexor digitorum longus (and flexor accessorius), the muscles of the first layer (lateral half of flexor digitorum brevis and abductor digiti minimi), and fibularis brevis and tertius also contribute to the maintenance of the lateral longitudinal arch.

Transverse arch

The bones involved in the transverse arch are the bases of the five metatarsals, the cuboid and the cuneiforms (see Fig. 79.9A). The intermediate and lateral cuneiforms are wedge-shaped and thus adapted to maintenance of the transverse arch. The ligaments, which bind the cuneiforms and the metatarsal bases, mainly provide the stability of the arch, as does the tendon of fibularis longus, which tends to approximate the medial and lateral borders of the foot. A shallow arch is maintained at the metatarsal heads by the deep transverse ligaments, transverse fibres that tie together the digital slips of the plantar aponeurosis, and, to a lesser extent, by the transverse head of adductor hallucis.

Pes planus and pes cavus

The term pes planus denotes an excessively flat foot. There is no precise degree of flatness that defines pes planus but it may be either physiological or pathological. In physiological pes planus, the feet are flexible and rarely problematic. There is a high prevalence in children of preschool age. In the 2–6 years age group, normal arch volumes in the sitting and standing positions correlate with the height of the navicular (lowest palpable medial projection of the navicular to the floor) (Chang et al 2012). In marked contrast, pathological pes planus is often associated with stiffness and pain. The windlass (or ‘Jack’s great toe’) test involves passively dorsiflexing the great toe at the metatarsophalangeal joint. This tightens the plantar aponeurosis and, in flexible pes planus, results in accentuation of the medial longitudinal arch. In pathological pes planus, no accentuation of the arch is seen. Another test can also be carried out by asking the individual to stand with both feet plantar flexed while viewing the hindfoot from behind. In flexible flat feet, the calcaneus swings into a varus position; in pathological pes planus it does not. Abduction of the forefoot associated with pes planus causes most of the lesser digits to be visible from this view (‘too many toes sign’). Causes of pathological pes planus include tarsal coalition, disruption of the tendon of tibialis posterior, rupture of the spring ligament, tarsometatarsal arthritis (and subsequent collapse), and hindfoot (talocalcaneal or subtalar joint) degenerative or inflammatory arthritis.

Pes cavus denotes an excessively high-arched foot. The majority of cases arise as a result of a neurological disorder (e.g. Charcot–Marie–Tooth disease, tethered spinal cord, poliomyelitis). According to the anatomical location of the deformity, pes cavus may be classified into hindfoot, midfoot or forefoot cavus. When pes cavus involves all three parts of the foot, it is called ‘global’ cavus. In Charcot–Marie–Tooth disease, an overactive fibularis longus leads to plantar hyperflexion of the first metatarsal. To keep the forefoot in contact with the ground, the patient develops a progressive compensatory hindfoot varus. If ignored, the hindfoot varus, which is initially flexible, becomes fixed. Charcot foot deformity, a relatively rare arthropathy that presents in conjunction with peripheral neuropathy, but separate from Charcot–Marie–Tooth disease, often leads to a total collapse of the midfoot. This creates a pathological flatfoot that can progress to a 'rocker-bottom deformity' as the downward pressure from the leg acts in concert with the upward pull of the calcaneal (Achilles) tendon. As a corrective measure for this, the calcaneal tendon is often lengthened surgically (Ramanujam and Zgonis 2017).

MUSCLES

The muscles acting on the foot may be divided into extrinsic and intrinsic groups.

Extrinsic muscles

The extrinsic muscles are described in Chapter 78. Their tendons cross the ankle and move and stabilize this joint. Distally, the tendons also act on the joints of the foot and help to stabilize them. The muscles can be grouped according to their arrangement in the leg. The extensors arise in the anterior compartment of the leg and their tendons pass anterior to the ankle, where they are bound down by the extensor retinacula. The lateral group arises in the relatively narrow lateral compartment of the leg and their tendons pass posterior to the lateral malleolus, bound down by the fibular retinacula. The flexors arise in the posterior compartment of the leg and their tendons pass posterior to the ankle, where the tendons of the superficial group of flexors are inserted into the calcaneus (see below), and the tendons of the deep group of flexors are bound down by the flexor retinaculum (see Figs 78.36, 79.1–79.2).

Anterior group

Tibialis anterior, extensor hallucis longus, extensor digitorum longus and fibularis tertius are described in Chapter 78.

Lateral group

Fibularis longus and fibularis brevis are described in Chapter 78.

Posterior group

Superficial group

Gastrocnemius, soleus and plantaris are described in Chapter 78; the calcaneal tendon is described below.

Calcaneal tendon

The calcaneal (Achilles) tendon is the common tendon of gastrocnemius and is the thickest and strongest tendon in the human body (see Fig. 79.2). Approximately 15 cm long, it begins near the middle of the calf. Its anterior surface receives muscle fibres from soleus almost to its inferior end. It gradually becomes more rounded until approximately 4 cm above the calcaneus; below this level, it expands and becomes attached to the midpoint of the posterior surface of the calcaneus. Age-dependent variability in the terminal insertion site of the calcaneal tendon (Snow et al 1995, Kim et al 2010, Kim et al 2011) may explain why calcaneal tendinopathy is infrequently found in children and adolescents and also has implications for the appropriate siting of surgical entry portals about the calcaneal tendon insertion in order to reduce the risk of iatrogenic injury to the tendon (Lohrer et al 2008). The fibres of the calcaneal tendon are not aligned strictly vertically and display a variable degree of spiralization (Cummins and Anson 1946, Edama et al 2015). They spiral laterally through 90° as they descend, so that the fibres associated with gastrocnemius are inserted more laterally on the calcaneus, and those associated with soleus are inserted more medially. The fibres in the tendon of plantaris (described in Ch. 78) exhibit varying degrees of blending with the fibres of the calcaneal tendon, sometimes blending entirely at its insertion or inserting into the plantar aponeurosis.

Tensile properties The calcaneal tendon is subjected to large loads: it may reach tensile stresses of up to four times body weight (2600 N) during walking and up to eight times body weight (5330 N) during running (Finni et al 1998, Giddings et al 2000). Despite being the strongest tendon in the body, the calcaneal tendon is particularly susceptible to tendinopathy. In general, tendon disorders are thought to be related to increasing age, yet the association between ageing and the underlying biological and mechanical changes (e.g. stiffness) of the calcaneal tendon is inconclusive (Stenroth et al 2012, Waugh et al 2012).

Vascular supply The blood supply to the calcaneal tendon is poor; the predominant artery is a recurrent branch of the posterior tibial artery, which mainly supplies peritendinous tissues (Salmon et al 1994). There is an additional supply from the paratenon (Carr and Norris 1989, Chen et al 2009), as well as a supply proximally from intramuscular arterial branches and distally from the calcaneus. Microdissection and angiographic studies have identified three main vascular territories: a proximal section, a hypovascular midsection and a distal section (Ahmed et al 1998, Zantop et al 2003, Chen et al 2009). The posterior tibial artery primarily supplies the proximal and distal sections, and the midsection receives a relatively poor blood supply from the fibular artery (Chen et al 2009). These findings support previous work showing that the hypovascular midsection of the calcaneal tendon (the 'watershed area') is the area most prone to rupture and also underscore the importance of avoiding disruption of the vascular supply to the tendon during percutaneous surgery. The vascularity of the skin overlying the calcaneal tendon varies according to location: the skin on the medial side of the tendon is supplied by the posterior tibial artery and on the lateral side by the fibular artery (Yepes et al 2010). The skin covering the posterior aspect of the tendon is the most poorly vascularized: medial or lateral incisions of the skin surrounding the tendon should reduce post-surgical healing complications relative to a direct posterior approach.

The calcaneal tendon is not the only plantar flexor of the ankle, which is one of the reasons why ruptures of the calcaneal tendon may not always be clinically apparent. However, it is a frequent site of pathology because of its susceptibility to rupture, degenerative change (tendinosis) and inflammation (paratendinitis); the area of relative avascularity in the midsection of the tendon is where the majority of problems occur.

Ruptures of the calcaneal tendon are often diagnosed by a palpable dell in the area of the tendon rupture, or by the Simmonds–Thompson test in which the patient lies prone on the examination table with the injured lower leg off the table. As the gastrocnemius–soleus complex is squeezed, a lack of movement at the ankle indicates a complete rupture of the tendon (positive test result). However, this lack of motion is dependent upon the rupture of soleus compared to the aponeurosis of gastrocnemius, and can sometimes result in a false positive (Douglas et al 2009).

Relations The calcaneal tendon is subcutaneous. The sural nerve crosses its lateral border about 10 cm above its insertion. The nerve is especially vulnerable here during surgery: percutaneous Achilles tendon lengthening is usually undertaken with the most proximal incision being performed medially to avoid iatrogenic injury to the nerve. Distally, there are bursae superficial and deep to the tendon. The muscle belly of flexor hallucis longus lies deep to the deep fascia on the anterior surface of the tendon.

Actions The calcaneal tendon produces plantar flexion of the ankle joint.

Heel bursae Bursae are found in three locations about the heel. A retrocalcaneal bursa is almost always present between the calcaneal tendon and the posterior surface of the calcaneus. It has an anterior wall composed of fibrocartilage and a thin posterior wall that blends with the thin epitenon (epitendineum) of the calcaneal tendon. Dorsiflexion of the ankle results in compression of the bursa. A prominent superolateral calcaneal tuberosity, often associated with a retrocalcaneal bursa, may impinge on the deep aspect of the calcaneal tendon where it is inserted onto the calcaneus (Haglund's disease). Symptoms are exacerbated by dorsiflexion of the ankle because this movement increases the pressure within the bursa and causes impingement of the calcaneus against the insertion of the tendon. Less common are an adventitious bursa superficial to the calcaneal tendon, and a subcalcaneal bursa between the inferior surface of the calcaneus and the origin of the plantar aponeurosis.

Plantaris

Plantaris is described in Chapter 78.

Deep group

The deep muscles of the calf include popliteus, which acts on the knee joint, and flexor hallucis longus, flexor digitorum longus and tibialis posterior, which all act on the ankle joint and the joints of the foot.

Flexor hallucis longus

Flexor hallucis longus is described on page 1421. The tendon of flexor hallucis longus is described below.

Flexor digitorum longus

Flexor digitorum longus is described on page 1421.

Tibialis posterior

Tibialis posterior is described on page 1423.

Intrinsic muscles

The intrinsic muscles, i.e. those contained entirely within the foot, follow the primitive limb pattern of plantar flexors and dorsal extensors. Considerable anatomical variation is evident in the intrinsic muscles (Kafka et al 2016).

The plantar muscles may be divided into medial, central, lateral and interosseous compartments. The medial and lateral compartments consist of the intrinsic muscles of the great and fifth toes, abductor hallucis and abductor digiti minimi, respectively; the central compartment includes the lumbricals, intrinsic digital flexors, adductor hallucis and the tendons of flexor digitorum longus; and the interosseous compartment contains the seven interossei. It is customary to group the muscles in four layers because this is the order in which they are encountered during dissection. However, in clinical practice and in terms of function, the grouping into medial, central, lateral and interosseous compartments is often more useful. The vascular supply and innervation of the intrinsic muscles of the foot are given at the end of this section.

Plantar muscles of the foot: first layer

This superficial layer includes abductor hallucis, abductor digiti minimi and flexor digitorum brevis (**Figs 79.21–79.22**). All three extend from the calcaneal tuberosity to the toes, and all assist in maintaining the concavity of the foot.

Abductor hallucis

Attachments The abductor hallucis arises principally from the flexor retinaculum, but also from the medial process of the calcaneal tuberosity, the plantar aponeurosis, and the intermuscular septum between abductor hallucis and flexor digitorum brevis. The muscle fibres end in a tendon that is attached, together with the medial tendon of flexor hallucis brevis, to the medial side of the base of the proximal phalanx of the great toe: some fibres are frequently attached more proximally to the medial sesamoid bone of this toe. The muscle may also send fibres to the dermis along the medial border of the foot.

Relations Abductor hallucis lies along the medial border of the foot and covers the origins of the plantar vessels and nerves (see Fig. 79.22). The space thus created by abductor hallucis and its relationship to the calcaneus is called the porta pedis: it is often manually enlarged during decompression of the tarsal tunnel neurovascular bundle (McSweeney and Cichero 2015).

Actions Abductor hallucis produces abduction of the great toe relative to the longitudinal axis of the foot at the shaft of the second metatarsal.

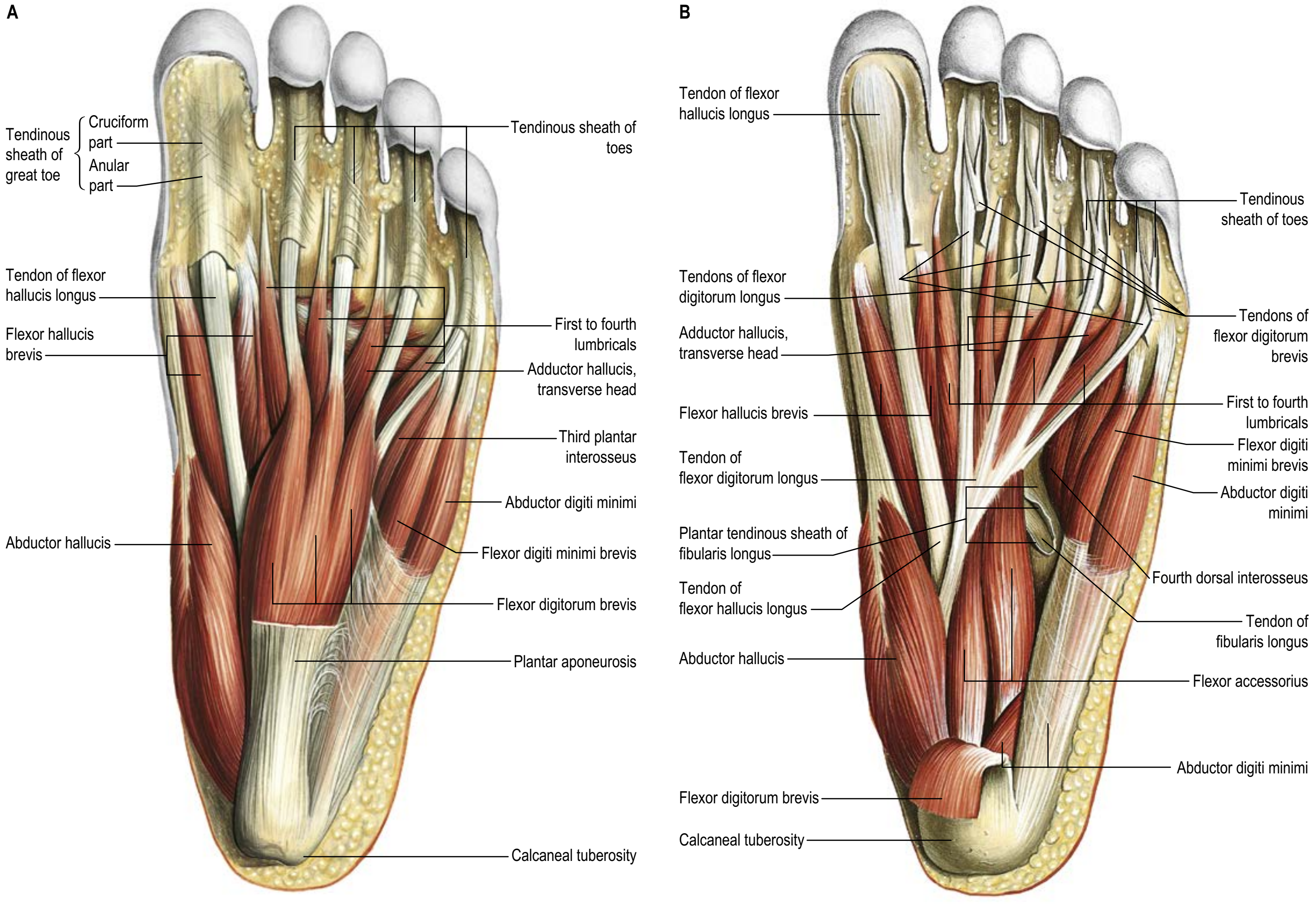
A
Tendinous sheath of great toe
Cruciform part
Anular part
Tendinous sheath of toes
Tendon of flexor hallucis longus
Flexor hallucis brevis
First to fourth lumbricals
Adductor hallucis, transverse head
Third plantar interosseus
Abductor digiti minimi
Abductor hallucis
Flexor digiti minimi brevis
Flexor digitorum brevis
Plantar aponeurosis
Calcaneal tuberosity
B
Tendon of flexor hallucis longus
Tendinous sheath of toes
Tendons of flexor digitorum longus
Tendons of flexor digitorum brevis
Adductor hallucis, transverse head
Flexor hallucis brevis
First to fourth lumbricals
Flexor digiti minimi brevis
Tendon of flexor digitorum longus
Abductor digiti minimi
Plantar tendinous sheath of fibularis longus
Fourth dorsal interosseus
Tendon of flexor hallucis longus
Tendon of fibularis longus
Abductor hallucis
Flexor accessorius
Abductor digiti minimi
Flexor digitorum brevis
Calcaneal tuberosity

Fig. 79.21 Muscles of the sole of the foot. **A**, First layer. **B**, Second layer. (Sobotta Atlas of Human Anatomy © Elsevier GmbH, Urban & Fischer, Munich.)

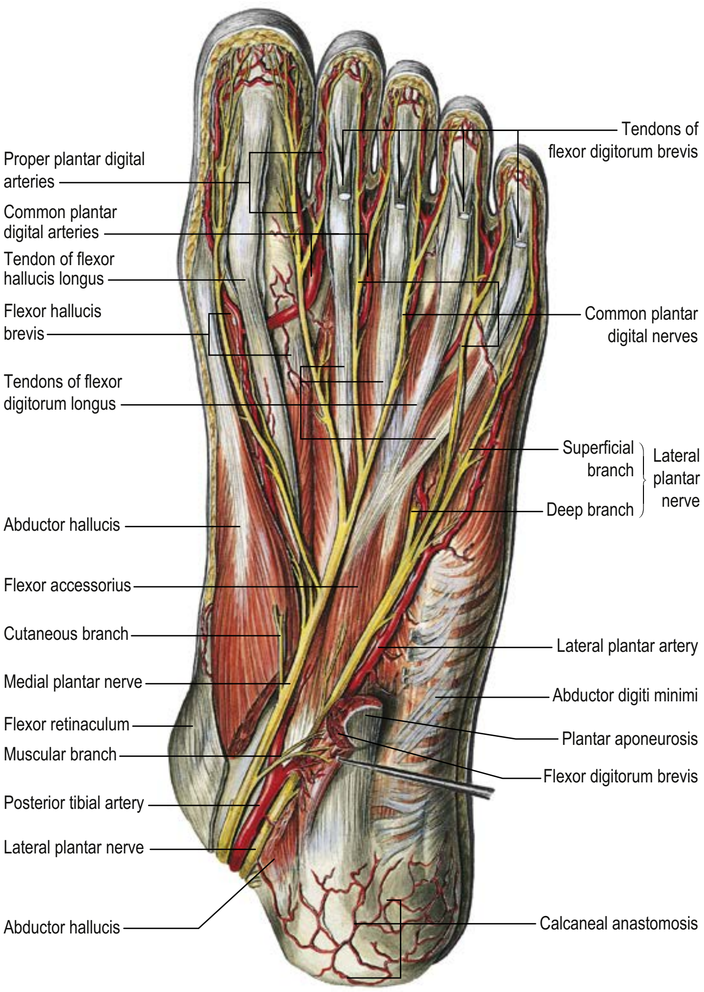

Fig. 79.22 Plantar nerves and vessels in relation to muscle layers. (Sobotta Atlas of Human Anatomy © Elsevier GmbH, Urban & Fischer, Munich.)

Testing Abductor hallucis is tested clinically by asking the subject to resist a forcibly applied lateral deviation of the proximal phalanx of the great toe.

Clinical anatomy The abductor hallucis fascia is strong and can be used in soft tissue augmentation following correction of hallux abducto valgus deformity. Rarely, persistent, exaggerated tonus in the muscle may be a cause of varus deformity of the foot, necessitating surgical intervention. An abductor hallucis flap is sometimes used for provision of soft tissue coverage.

Flexor digitorum brevis

Attachments Flexor digitorum brevis arises by a narrow tendon from the medial process of the calcaneal tuberosity, from the central part of the plantar aponeurosis, and from the intermuscular septa between it and adjacent muscles (see Fig. 79.21A). It divides into four tendons that pass to the lateral four toes and enter digital tendinous sheaths accompanied by the tendons of flexor digitorum longus, which lie deep to them. At the bases of the proximal phalanges, each tendon divides around the corresponding tendon of flexor digitorum longus. The two slips then reunite and partially decussate, forming a tunnel through which the tendon of flexor digitorum longus passes to the distal phalanx. The tendon of flexor digitorum brevis divides again and is attached to both sides of the shaft of the middle phalanx. The way in which this tendon divides and is attached to the phalanges is identical to the arrangement of the tendons of flexor digitorum superficialis in the hand. The slip to a given toe may be absent, or it may be replaced by a small muscular slip from the extrinsic flexor tendons or from flexor accessorius. Conversely, the slip may be joined by a second, supernumerary slip.

Relations Flexor digitorum brevis lies immediately deep to the central part of the plantar aponeurosis. Its deep surface is separated from the lateral plantar vessels and nerves by a thin layer of fascia.

Actions Flexor digitorum brevis flexes the lateral four toes at the proximal interphalangeal joint, with equal effect in any position of the ankle joint.

Testing To test the action of flexor digitorum brevis, the examiner passively extends the distal interphalangeal joint and asks the subject to flex the toes at the proximal interphalangeal joint. Contracture of the tendons of flexor digitorum brevis can lead to toe deformities, and release or lengthening procedures may be required. The muscle belly is sometimes excised as a flap to cover a soft tissue defect.

Abductor digiti minimi

Attachments Abductor digiti minimi arises from both processes of the calcaneal tuberosity, the plantar surface of the bone between them, the plantar aponeurosis and the intermuscular septum between the muscle and flexor digitorum brevis. An accessory slip from the base of the fifth metatarsal may be present. The tendon of abductor digiti minimi glides in a smooth groove on the plantar surface of the base of the fifth metatarsal and is attached, with flexor digiti minimi brevis, to the lateral side of the base of the proximal phalanx of the fifth toe, which means that it is more a flexor than an abductor. Some of the fibres arising from the lateral calcaneal process usually reach the tip of the tuberosity of the fifth metatarsal (see Fig. 79.5B) and may form a separate muscle, abductor ossis metatarsi digiti quinti.

Relations Abductor digiti minimi lies along the lateral border of the foot, and its medial margin is related to the lateral plantar vessels and nerve (see Fig. 79.22).

Actions Despite its name, abductor digiti minimi is more a flexor than an abductor of the metatarsophalangeal joint of the fifth toe.

Plantar muscles of the foot: second layer

The second layer consists of flexor accessorius and the four lumbrical muscles. The tendons of flexor hallucis longus and flexor digitorum longus run in the same plane as the muscles of the second layer (see Fig. 79.21B); flexor hallucis longus and flexor digitorum longus are described on pages 1421–1423.

Flexor tendinous sheaths

The terminations of the tendons of the extrinsic and intrinsic flexor muscles are contained in osseo-aponeurotic canals similar to those that occur in the fingers. These canals are bounded above by the phalanges and below by fibrous bands, the digital fibrous tendon sheaths (see Fig. 79.21A), which arch across the tendons and are attached on either side to the margins of the phalanges. Along the proximal and middle phalanges, the fibrous bands are strong and the fibres are transverse (anular part); opposite the joints they are much thinner and the fibres decussate (cruciform part). Each osseo-aponeurotic canal has a synovial lining that is reflected around its tendon. Vincula tendinum are arranged within this sheath, as they are in the fingers.

Flexor accessorius (quadratus plantae)

Attachments Flexor accessorius (quadratus plantae) usually arises by two heads (see Fig. 79.21B), with the long plantar ligament situated deeply in the interval between the two heads (see Fig. 79.23). The medial head is larger and is attached to the medial concave surface of the calcaneus, below the groove for the tendon of flexor hallucis longus. The lateral head is flat and tendinous, and is attached to the calcaneus distal to the lateral process of the tuberosity, and to the long plantar ligament. Flexor accessorius is inserted into the tendon of flexor digitorum longus via muscular, tendinous or aponeurotic insertions at the point where it is bound by a fibrous slip to the tendon of flexor hallucis longus and where it divides into its four tendons.

Either head may be absent (absence of the lateral head is more common than absence of the medial head); complete absence of the muscle or an additional third head are rare (Pretterkleiber 2018, Edama et al 2019). The distal attachment to the tendons of flexor digitorum longus may vary, which means that the fourth and fifth long flexor tendons may, at times, fail to receive slips from flexor accessorius.

Relations The medial plantar nerve passes medial to and the lateral plantar nerve passes superficial to flexor accessorius.

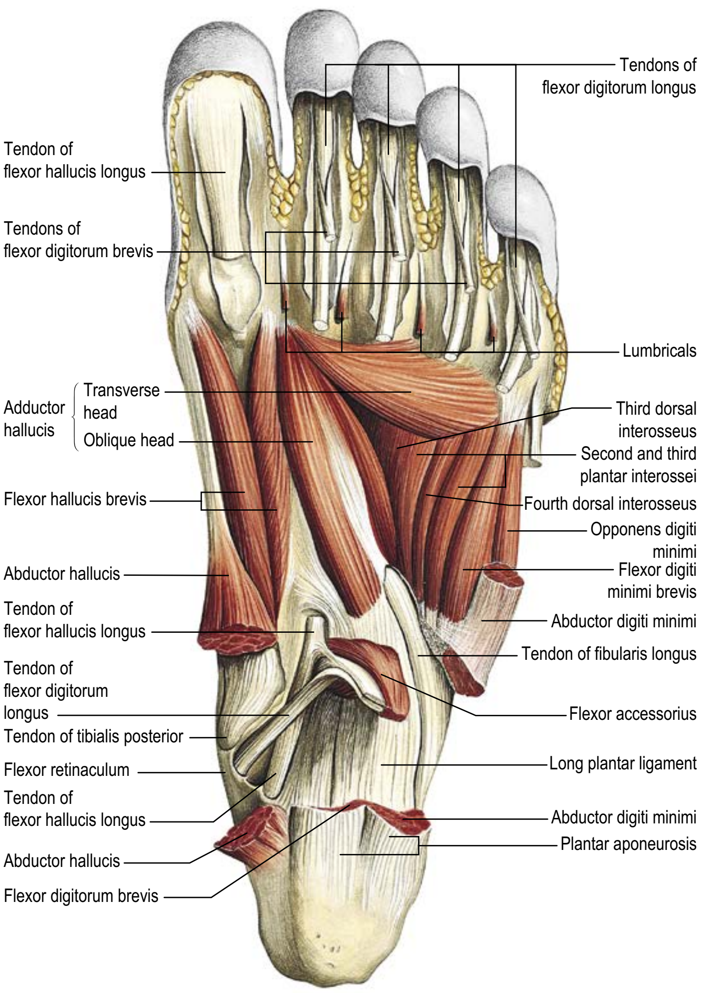
Tendons of flexor digitorum longus
Tendon of flexor hallucis longus
Tendons of flexor digitorum brevis
Lumbricals
Adductor hallucis
Transverse head
Oblique head
Third dorsal interosseus
Second and third plantar interossei
Flexor hallucis brevis
Fourth dorsal interosseus
Opponens digiti minimi
Abductor hallucis
Flexor digiti minimi brevis
Tendon of flexor hallucis longus
Abductor digiti minimi
Tendon of fibularis longus
Tendon of flexor digitorum longus
Flexor accessorius
Tendon of tibialis posterior
Long plantar ligament
Flexor retinaculum
Tendon of flexor hallucis longus
Abductor digiti minimi
Plantar aponeurosis
Abductor hallucis
Flexor digitorum brevis

Fig. 79.23 Muscles of the sole of the foot, third layer. (Sobotta Atlas of Human Anatomy © Elsevier GmbH, Urban & Fischer, Munich.)

Actions By pulling on the tendons of flexor digitorum longus, flexor accessorius provides a means of flexing the lateral four toes in any position of the ankle joint.

Lumbrical muscles

Attachments The lumbrical muscles are four small muscles (numbered from the medial side of the foot) that are accessory to the tendons of flexor digitorum longus (see Fig. 79.21). They arise from these tendons as far back as their angles of separation, each springing from the sides of two adjacent tendons, except for the first lumbrical, which arises only from the medial border of the first tendon. The muscles end in tendons that pass distally on the medial sides of the four lateral toes and are attached to the dorsal digital expansions on their proximal phalanges.

Relations The lumbricals are intimately related to the tendons of flexor digitorum longus before the latter enter their corresponding fibrous flexor sheaths. The lumbricals remain outside the fibrous flexor sheaths and cross the plantar aspects of the deep transverse metatarsal ligaments before reaching the dorsal digital expansions.

Actions The lumbricals help to maintain extension of the interphalangeal joints of the toes. In injuries of the tibial nerve, and in conditions such as the hereditary motor–sensory neuropathies (e.g. Charcot–Marie–Tooth disease), lumbrical dysfunction contributes to clawing of the toes.

Plantar muscles of the foot: third layer

The third layer of the foot contains the shorter intrinsic muscles of the toes, i.e. flexor hallucis brevis, adductor hallucis and flexor digiti minimi brevis (**Fig. 79.23**).

Flexor hallucis brevis

Attachments Flexor hallucis brevis has a bifurcated tendon of origin (see Figs 79.21A, B, 79.23). The lateral limb arises from the medial part of the plantar surface of the cuboid, posterior to the groove for the tendon of fibularis longus, and from the adjacent part of the lateral cuneiform. The medial limb has a deep attachment directly continuous with the lateral division of the tendon of tibialis posterior, and a more superficial attachment to the middle band of the medial intermuscular septum. The belly of the muscle divides into medial and lateral parts, with two tendons that are attached to the sides of the base of the proximal phalanx of the great toe: the medial part blends with the tendon of abductor hallucis and the lateral part blends with the tendon of adductor hallucis, as they reach their terminations.

A sesamoid bone usually occurs in each tendon near its attachment. Clinical problems with flexor hallucis brevis are usually related to the associated sesamoid bones. However, excision of both sesamoid bones leads to disruption of both tendons and a subsequent extension deformity at the first metatarsophalangeal joint; such surgery is, therefore, not recommended.

Accessory slips may arise proximally from the calcaneus or long plantar ligament. A tendinous slip may extend to the proximal phalanx of the second toe.

Relations Flexor hallucis brevis lies on the underside of the first metatarsal shaft; abductor hallucis lies medially. The medial digital nerve to the great toe and the tendon of flexor hallucis longus both pass to the great toe on its plantar surface. The medial plantar nerve lies more superficially on its lateral side.

Actions Flexor hallucis brevis flexes the proximal phalanx of the great toe.

Testing The individual is asked to flex the first metatarsophalangeal joint with the interphalangeal joint extended, thereby eliminating the action of flexor hallucis longus.

Adductor hallucis

Attachments Adductor hallucis arises by oblique and transverse heads (see Figs 79.21–79.23). The oblique head arises from the bases of the second, third and fourth metatarsals, and from the fibrous sheath of the tendon of fibularis longus. The transverse head is a narrow, flat fasciculus that arises from the plantar metatarsophalangeal ligaments of the third, fourth and fifth toes (sometimes only from the third and fourth), and from the deep transverse metatarsal ligaments between them. The oblique head has medial and lateral parts. The medial part blends with the lateral part of flexor hallucis brevis and is attached to the lateral sesamoid bone of the great toe. The lateral part joins the transverse head and is also attached to the lateral sesamoid bone and directly to the base of the first phalanx of the great toe. There is no phalangeal attachment for the transverse part of the muscle and fibres that fail to reach the lateral sesamoid bone are attached with the oblique part. The transverse part of adductor hallucis is sometimes absent; part of the muscle may be attached to the first metatarsal, constituting an opponens hallucis; and a slip may also extend to the proximal phalanx of the second toe.

Relations Adductor hallucis lies plantar to the metatarsal shafts and the interossei, and the long and short toe flexors. The medial and lateral plantar arteries and nerves are superficial, and flexor hallucis brevis is proximal and medial.

Actions Adductor hallucis partly flexes the proximal phalanx of the great toe, but also stabilizes the metatarsal heads.

Clinical anatomy Adductor hallucis has traditionally been thought of as a major deforming force in hallux abducto valgus. While this muscle may need to be released during a distal soft tissue release, this procedure is only generally necessary in reducing severe bunion deformities (Yammine and Assi 2018).

Flexor digiti minimi brevis

Attachments Flexor digiti minimi brevis arises from the medial part of the plantar surface of the base of the fifth metatarsal, and from the sheath of fibularis longus (see Figs 79.21, 79.23). It has a distal tendon that is inserted into the lateral side of the base of the proximal phalanx of the fifth toe and usually blends laterally with the tendon of abductor digiti minimi. Occasionally, some of its deeper fibres extend to the lateral part of the distal half of the fifth metatarsal, constituting what may be described as a distinct muscle, opponens digiti minimi.

Relations The fifth metatarsal shaft lies on the deep surface of flexor digiti minimi brevis, the interossei lie medially and abductor digiti minimi is lateral. The most lateral branch of the lateral plantar nerve lies superficially and just medial to flexor digiti minimi brevis.

Actions Flexor digiti minimi brevis flexes the metatarsophalangeal joint of the fifth toe.

Plantar muscles of the foot: fourth layer

The fourth layer of muscles of the foot consists of the plantar and dorsal interossei and the tendons of tibialis posterior and fibularis longus (tibialis posterior and fibularis longus are described in Chapter 78). The interossei resemble their counterparts in the hand except that, when describing adduction and abduction of the toes, the axis of reference is a longitudinal axis corresponding to the shaft of the second metatarsal (unlike in the hand, where reference is made to the longitudinal axis of the third metacarpal).

Dorsal interossei

Attachments The dorsal interossei (**Fig. 79.24A**; see Fig. 79.1) are situated between the metatarsals and are four bipennate muscles, each arising by two heads from the sides of the adjacent metatarsals. Their tendons are attached to the bases of the proximal phalanges and to the dorsal digital expansions. The first inserts into the medial side of the second toe and the other three pass to the lateral sides of the second, third and fourth toes.

Relations A perforating artery passes to the dorsum of the foot through an angular space between the heads of each of the three lateral muscles. The corresponding space between the heads of the first muscle transmits the terminal part of the dorsalis pedis artery to the sole (see Fig. 79.1).

Actions Dorsal interossei abduct the toes relative to the longitudinal axis of the second metatarsal. They also flex the metatarsophalangeal joints and extend the interphalangeal joints of the lateral four toes. The great and fifth toes have their own abductors.

Clinical anatomy Denervation of the interossei leads to claw-toe deformities: development of clawed toes should alert the clinician to the possibility of a neuropathic process (e.g. Charcot–Marie–Tooth disease, tethered spinal cord, longstanding diabetic neuropathy).

Plantar interossei

There are three plantar interossei (**Fig. 79.24B**). They lie below, rather than between, the metatarsals, and each is connected to only one metatarsal. They are unipennate, unlike the dorsal interossei. They arise from the bases and medial sides of the third, fourth and fifth metatarsals, and are inserted into the medial sides of the bases of the proximal phalanges of the numerically corresponding toes, and into their dorsal digital expansions.

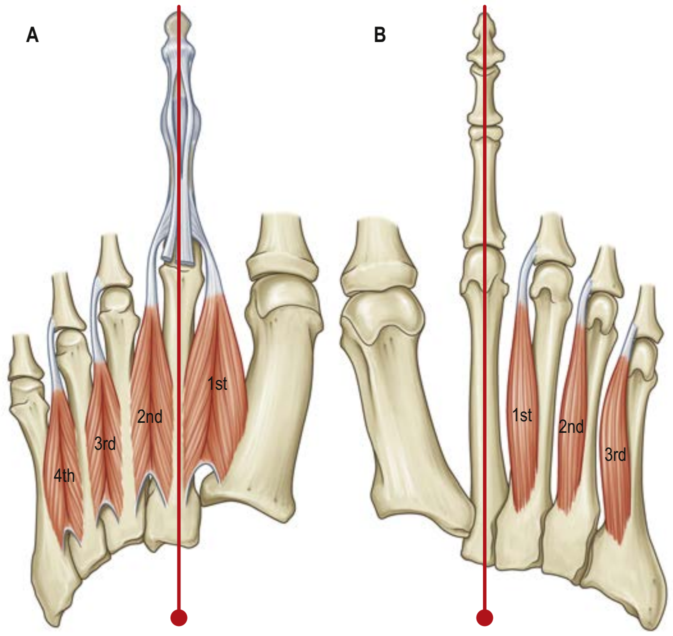

Fig. 79.24 The interossei of the left foot. **A**, The dorsal interossei viewed from the dorsal aspect. **B**, The plantar interossei viewed from the plantar aspect. The axis to which the movements of abduction and adduction are referred is indicated.

Relations The plantar interossei lie plantar to the dorsal interossei and deep to the muscles of the third layer.

Actions Plantar interossei adduct the third, fourth and fifth toes, flex the metatarsophalangeal joints and extend the interphalangeal joints.

Clinical anatomy The clinical anatomy of the plantar interossei is similar to that of the dorsal interossei.

Extensor muscles of the foot

Extensor digitorum brevis and extensor hallucis brevis

Attachments Extensor digitorum brevis (see Fig. 79.2A) is a thin muscle that arises from the distal part of the superolateral surface of the calcaneus in front of the shallow lateral groove for fibularis brevis, from the interosseous talocalcaneal ligament, and from the deep surface of the stem of the inferior extensor retinaculum. It slants distally and medially across the dorsum of the foot and ends in four tendons. The medial part of the muscle is usually a more or less distinct slip, ending in a tendon that crosses the dorsalis pedis artery superficially and is inserted into the dorsal aspect of the base of the proximal phalanx of the great toe; this slip is termed extensor hallucis brevis. The other three tendons are attached to the lateral sides of the tendons of extensor digitorum longus for the second, third and fourth toes. Extensor digitorum brevis is subject to variation, e.g. accessory slips from the talus and navicular; an extra tendon to the fifth digit; absence of one or more tendons; additional connections to the adjacent dorsal interossei.

Relations Extensor hallucis brevis, the most medial tendon, courses dorsomedially and passes superficial to the dorsalis pedis artery and the deep fibular nerve. The remaining three tendons pass obliquely deep to the corresponding tendons of extensor digitorum longus.

Actions The muscle assists in extending the phalanges of the middle three toes via the tendons of extensor digitorum longus and assists in extension of the metatarsophalangeal joint of the great toe.

Clinical anatomy Laceration of extensor digitorum brevis leads to little in the way of functional impairment because the long extensors can compensate for the loss of the muscle. The proximal part of the muscle can be used as interposition material to prevent bone fusion after resection of a calcaneonavicular bar (a common tarsal coalition). The muscle belly and tendon of extensor hallucis brevis serve as guides to the location of the dorsalis pedis artery and deep fibular nerve, and the tendon of extensor hallucis brevis can be used as a local graft.

Vascular supply to the intrinsic muscles of the foot

Abductor hallucis is supplied by the medial malleolar network, medial calcaneal branches of the lateral plantar artery (see Fig. 79.10), the medial plantar artery (directly and via superficial and deep branches), the first plantar metatarsal artery and perforators from the plantar arterial arch. Flexor digitorum brevis is supplied by the lateral and medial plantar arteries, the plantar metatarsal arteries and the plantar digital arteries to the lateral four toes. Abductor digiti minimi is supplied by the medial and lateral plantar arteries (see Figs 79.22, 79.26), the plantar digital artery to the lateral side of this muscle, branches from the deep plantar arch, the fourth plantar metatarsal artery and end twigs from the arcuate and lateral tarsal arteries (see Fig. 79.10). Flexor accessorius is supplied by the stem of the medial plantar artery (to the medial head), the lateral plantar artery and the deep plantar arch. The lumbricals are supplied by the lateral plantar artery and deep plantar arch and by four plantar metatarsal arteries (four distal perforating arteries joined by three proximal perforating arteries). Their tendons are supplied by twigs from the dorsal digital arteries and their parent dorsal metatarsal arteries to the lateral four toes. Flexor hallucis brevis is supplied by branches of the medial plantar artery, the first plantar metatarsal artery, the lateral plantar artery and the deep plantar arch. Adductor hallucis is supplied by branches of the medial and lateral plantar arteries, the deep plantar arch and the first to fourth plantar metatarsal arteries. Flexor digiti minimi brevis is supplied by end twigs of the arcuate and lateral tarsal arteries, and the lateral plantar artery and its digital (plantar) branch to the lateral side of the fifth toe. Dorsal interossei are supplied by the arcuate artery, lateral and medial tarsal arteries, the first to fourth plantar arteries and the first to fourth dorsal metatarsal arteries (receiving proximal and distal perforating arteries), and by the dorsal digital arteries of the lateral four toes. Plantar interossei are supplied by the lateral plantar artery, the deep plantar arch, the second to fourth plantar metatarsal arteries and the dorsal digital arteries of the lateral three toes. Extensor digitorum brevis is supplied by the anterior perforating branch of the fibular artery, the anterior lateral malleolar artery, lateral tarsal arteries, dorsalis pedis artery, arcuate artery, the first, second and third dorsal metatarsal arteries, proximal and distal perforating arteries, and the dorsal digital arteries to the medial four toes (including the great toe).

Innervation of the intrinsic muscles of the foot

Abductor hallucis is innervated by the medial plantar nerve, S1 and S2. Contraction of the muscle confirms an intact medial plantar nerve when the integrity of this nerve is in question. Flexor digitorum brevis is innervated by the medial plantar nerve, S1 and S2. Abductor digiti minimi and flexor accessorius are innervated by the lateral plantar nerve, S1, S2 and S3. The first lumbrical is supplied by the medial plantar nerve, and the other lumbricals are supplied by the deep branch of the lateral plantar nerve, S2 and S3. Flexor hallucis brevis is supplied by the medial plantar nerve, S1 and S2. Adductor hallucis is innervated by the deep branch of the lateral plantar nerve, S2 and S3. Flexor digiti minimi brevis is innervated by the superficial branch of the lateral plantar nerve, S2 and S3. Dorsal interossei are supplied by the deep branch of the lateral plantar nerve, S2 and S3, except that of the fourth intermetatarsal space, which is supplied by the superficial branch of the lateral plantar nerve. Plantar interossei are supplied by the deep branch of the lateral plantar nerve, S2 and S3, except that of the fourth intermetatarsal space, which is supplied by the superficial branch of the lateral plantar nerve. Extensor digitorum brevis is supplied by the lateral terminal branch of the deep fibular nerve, L5 and S1.

VASCULAR SUPPLY

Arteries

Dorsalis pedis artery

The dorsalis pedis artery (see Fig. 79.1; **Fig. 79.25**) is usually the continuation of the anterior tibial artery distal to the ankle. It passes to the proximal end of the first intermetatarsal space, where it turns into the sole between the heads of the first dorsal interosseous to complete the deep plantar arch, and provides the first plantar metatarsal artery. The artery may be larger than normal, to compensate for a small lateral plantar artery. It often diverges laterally from its usual route and, rarely, may be absent (Robertson et al 1990), in which case it is replaced by a large perforating branch of the fibular artery.

Relations The dorsalis pedis artery crosses, successively, the talocrural articular capsule, talus, navicular and intermediate cuneiform and their ligaments. The skin, fasciae, inferior extensor retinaculum and, near its termination, extensor hallucis brevis, are all superficial. The tendon of extensor hallucis longus is medial and the medial tendon of extensor digitorum longus and the medial terminal branch of the deep fibular nerve are both lateral. The tendons and navicular tuberosity are useful landmarks in palpation for the planning of safe anatomical approaches in surgery of the ankle and foot.

Branches

The dorsalis pedis artery gives rise to the tarsal, arcuate and first dorsal metatarsal arteries (see Figs 79.1, 79.10, 79.25).

Tarsal arteries Two tarsal arteries, lateral and medial, arise as the dorsalis pedis artery crosses the navicular (see Fig. 79.25). The lateral tarsal artery runs laterally under extensor digitorum brevis: it supplies this muscle and the tarsal articulations, and anastomoses with branches of the arcuate, anterior lateral malleolar and lateral plantar arteries, and the perforating branch of the fibular artery. Two or three medial tarsal arteries ramify on the medial border of the foot and join the medial malleolar arterial network.

Arcuate artery The arcuate artery (see Fig. 79.25) arises near the medial cuneiform, passes laterally over the metatarsal bases, deep to the tendons of the digital extensors, and anastomoses with the lateral tarsal and plantar arteries. It supplies the second to fourth dorsal metatarsal arteries, running distally superficial to the corresponding dorsal interossei, and divides into two dorsal digital branches for the adjoining toes in the interdigital clefts. Proximally, these branches receive proximal perforating branches from the deep plantar arch. Distally, they are joined by distal perforating branches from the plantar metatarsal arteries. The fourth dorsal metatarsal artery sends a branch to the lateral side of the fifth toe. The frequency of the arcuate artery has been reported to range from 10% to 67%, depending on the precise definition of the artery (DiLandro et al 2001).

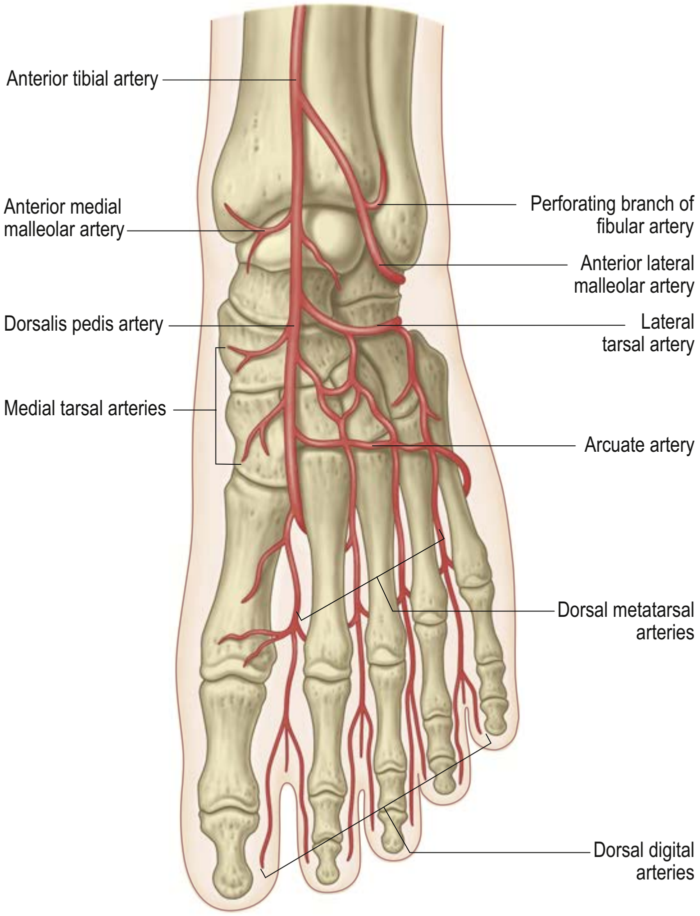
Anterior tibial artery
Anterior medial malleolar artery
Dorsalis pedis artery
Medial tarsal arteries
Perforating branch of fibular artery
Anterior lateral malleolar artery
Lateral tarsal artery
Arcuate artery
Dorsal metatarsal arteries
Dorsal digital arteries

Fig. 79.25 The dorsal arteries of the foot.

First dorsal metatarsal artery The first dorsal metatarsal artery (see Fig. 79.25) arises just before the dorsalis pedis artery enters the sole. It runs distally on the first dorsal interosseous and divides at the cleft between the first and second toes. One branch passes under the tendon of extensor hallucis longus and supplies the medial side of the great toe and the other bifurcates to supply the adjoining sides of the great and second toes.

Cutaneous vessels from the dorsalis pedis artery The dorsalis pedis artery and its first dorsal metatarsal branch give rise to small direct cutaneous branches that supply the skin of the dorsal foot between the extensor retinaculum and the first web space. This vessel provides the basis for a fasciocutaneous flap raised from this region that may be used to cover superficial defects elsewhere.

Deep plantar arch

The deep plantar arch (see Fig. 79.26) is deeply situated, extending from the fifth metatarsal base to the proximal end of the first intermetatarsal space. Convex distally, it is plantar to the bases of the second to fourth metatarsals and corresponding interossei, but dorsal to the oblique part of adductor hallucis.

Branches

The deep plantar arch gives rise to three perforating and four plantar metatarsal branches, and numerous branches that supply the skin, fasciae and muscles in the sole. Three perforating branches ascend through the proximal ends of the second to fourth intermetatarsal spaces, between the heads of dorsal interossei, and anastomose with the dorsal metatarsal arteries. Four plantar metatarsal arteries extend distally between the metatarsals in contact with the interossei (**Fig. 79.26**). Each divides into two

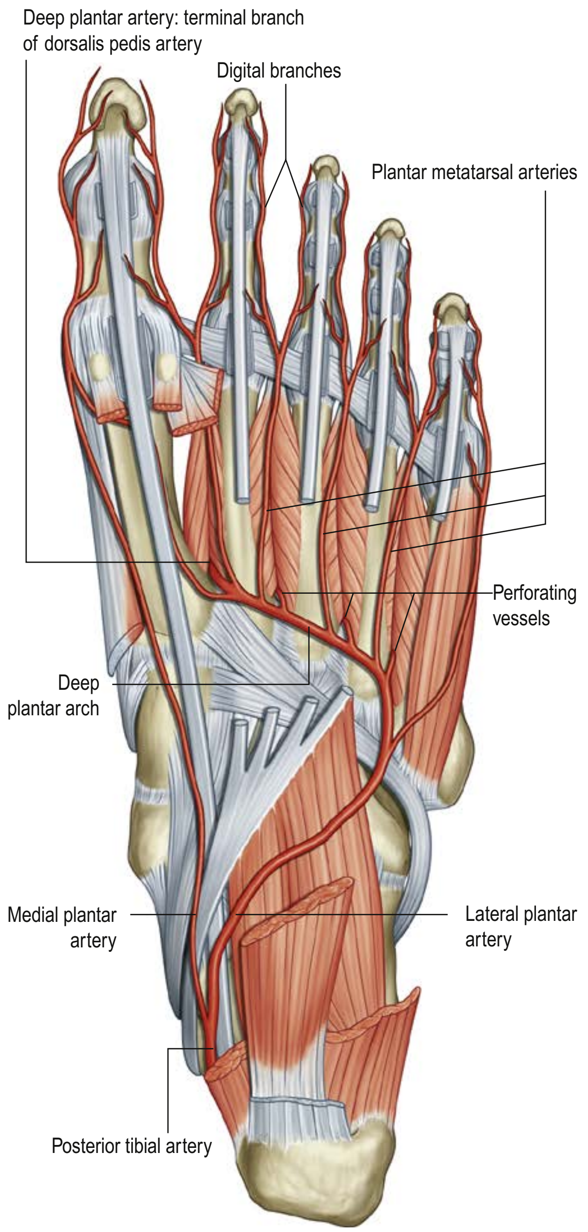

Fig. 79.26 The plantar arteries. (Adapted with permission from Drake RL, Vogl AW, Mitchell A (eds) Gray's Anatomy for Students, 4th ed. Elsevier, Churchill Livingstone. Copyright 2019.)

plantar digital arteries, supplying the adjacent digital aspects. Near its division, each plantar metatarsal artery sends a distal perforating branch dorsally to join a dorsal metatarsal artery. The first plantar metatarsal artery springs from the junction between the lateral plantar and dorsalis pedis arteries, and sends a digital branch to the medial side of the great toe. The lateral digital branch for the fifth toe arises directly from the lateral plantar artery near the fifth metatarsal base. Haemorrhage from the deep plantar arch is difficult to control because of the depth of the vessel and its important close relations.

Surface anatomy

The lateral plantar artery begins between the heel and medial malleolus, and crosses obliquely to a point 2.5 cm medial to the tuberosity of the fifth metatarsal. With a slight distal convexity, it reaches the proximal end of the first intermetatarsal space.

Posterior tibial artery

Before the posterior tibial artery divides into its two main terminal branches, it gives off a communicating branch that runs posteriorly across the tibia approximately 5 cm above its distal end, deep to flexor hallucis longus, and joins a communicating branch of the fibular artery; calcaneal branches that arise just proximal to the termination of the posterior tibial artery, pierce the flexor retinaculum and supply the skin and fat behind the calcaneal tendon; and the artery of the tarsal canal.

Branches The terminal branches of the posterior tibial artery are the medial and lateral plantar arteries.

Branches

Medial plantar artery The medial plantar artery is the smaller terminal branch of the posterior tibial artery (see Fig. 79.26). It arises midway between the medial malleolus and the medial calcaneal tubercle, and passes distally along the medial side of the foot, with the medial plantar nerve lateral to it. At first deep to abductor hallucis, it runs distally between abductor hallucis and flexor digitorum brevis, supplying both muscles. Near the first metatarsal base, when its calibre is already diminished as a result of supplying numerous muscular branches, it is further diminished by a superficial stem. It passes to the medial border of the great toe, where it anastomoses with a branch of the first plantar metatarsal artery. Its superficial stem then trifurcates and supplies three superficial digital branches that accompany the digital branches of the medial plantar nerve and join the first to third plantar metatarsal arteries.

Lateral plantar artery The lateral plantar artery is the larger terminal branch of the posterior tibial artery (see Fig. 79.26). It passes distally and laterally to the fifth metatarsal base; the lateral plantar nerve is medial. Turning medially, and accompanied by the deep branch of the nerve, the artery gains the interval between the first and second metatarsal bases where it unites with the dorsalis pedis artery to complete the deep plantar arch. As it passes laterally, it is first between the calcaneus and abductor hallucis, then between flexor digitorum brevis and flexor accessorius. Running distally to the fifth metatarsal base, it passes between flexor digitorum brevis and abductor digiti minimi and is covered by the plantar aponeurosis, superficial fascia and skin.

Muscular branches supply the adjoining muscles. Superficial branches emerge along the intermuscular septum to supply the skin and subcutaneous tissue over the lateral part of the sole. Anastomotic branches run to the lateral border and join branches of the lateral tarsal and arcuate arteries. A calcaneal branch sometimes pierces abductor hallucis to supply the skin of the heel. The medial and lateral plantar arteries sometimes anastomose superficial to flexor digitorum brevis to form the superficial plantar arch.

Perforator flaps in the ankle and foot region

The arteries around the ankle and in the foot are the medial and lateral calcaneal arteries, medial and lateral plantar arteries and the dorsalis pedis artery (see Figs 76.7, 78.10). In the foot, the two plantar arteries and communicating arteries from the dorsalis pedis artery give rise to multiple small perforators. In the sole of the foot, the perforators emerge on either side of the plantar aponeurosis and also pass through it, to supply the skin. 'Island flaps' from these perforators may be advanced to reconstruct small defects in the weight-bearing area. The skin of the sole of the foot is highly specialized: ideally, defects in this region should therefore be reconstructed using local skin.

Deep and superficial venous systems in the foot

Superficial veins of the foot

The named superficial veins are the long and short saphenous. Their numerous tributaries are mostly unnamed (named vessels will be noted; see Fig. 76.9A). As in the upper limb chapter, the vessels are here described centripetally from peripheral to major drainage channels.

Dorsal digital veins receive rami from the plantar digital veins in the clefts between the toes and then join to form dorsal metatarsal veins, which are united across the proximal parts of the metatarsals in a dorsal venous arch. Proximal to this arch, an irregular dorsal venous network receives tributaries from deep veins and is continuous proximally with a venous network in the leg. At each side of the foot, this network connects with medial and lateral marginal veins that are both formed mainly by veins from more superficial parts of the sole. In the sole, superficial veins form a plantar cutaneous arch across the roots of the toes and also drain into the medial and lateral marginal veins.

Deep veins of the foot

Plantar digital veins arise from plexuses in the plantar regions of the toes. They connect with dorsal digital veins to form four plantar metatarsal veins that run proximally in the intermetatarsal spaces. These connect via perforating veins with dorsal veins to form the deep plantar venous arch situated alongside the deep plantar arterial arch. From this venous arch, medial and lateral plantar veins run near the corresponding arteries, communicate with the long and short saphenous veins and form the posterior tibial veins behind the medial malleolus (see Fig. 76.8).

Proximal to the deep plantar arch there is a plantar cutaneous venous plexus, especially dense in the fat of the heel. It connects with the plantar cutaneous venous arch and other deep veins, but drains mainly into the marginal veins. The veins of the sole are an important part of the lower limb 'venous pump' system aiding propulsion of blood up the limb (Broderick et al 2008). Intermittent foot compression devices are available to enhance this flow and so reduce the risk of deep vein thrombosis during periods of increased risk, e.g. after surgery.

INNERVATION

Superficial fibular nerve

The superficial fibular nerve is described on page 1428.

Deep fibular nerve

The deep fibular nerve is described on page 1429.

Tibial nerve

The branches of the tibial nerve that innervate structures in the ankle and foot are articular, muscular, sural, medial calcaneal and medial and lateral plantar nerves. The course and distribution of the tibial nerve in the calf are described on page 1427.

Medial calcaneal nerve The medial calcaneal nerve arises from the tibial nerve and perforates the flexor retinaculum to supply the skin of the heel and medial side of the sole.

Medial plantar nerve The medial plantar nerve is the larger terminal division of the tibial nerve, and lies lateral to the medial plantar artery. From its origin under the flexor retinaculum, it passes deep to abductor hallucis, then appears between it and flexor digitorum brevis, gives off a medial proper digital nerve to the great toe, and divides near the metatarsal bases into three common plantar digital nerves (Fig. 79.27; see Fig. 79.22).

Cutaneous branches pierce the plantar aponeurosis between abductor hallucis and flexor digitorum brevis to supply the skin of the sole of the foot. Muscular branches supply abductor hallucis, flexor digitorum brevis, flexor hallucis brevis and the first lumbrical. The first two branches arise near the origin of the nerve and enter the deep surfaces of the muscles. The branch to flexor hallucis brevis is from the hallucal medial digital nerve, and the branch to the first lumbrical from the first common plantar digital nerve. Articular branches supply the joints of the tarsus and metatarsus.

Three common plantar digital nerves pass between the slips of the plantar aponeurosis, each dividing into two proper digital branches. The first supplies adjacent sides of the great and second toes; the second supplies adjacent sides of the second and third toes; and the third supplies adjacent sides of the third and fourth toes and also connects with the lateral plantar nerve. The first gives a branch to the first lumbrical. Each proper digital nerve has cutaneous and articular branches, and near the distal phalanges, a dorsal branch supplies structures around the nail. Abductor hallucis, flexor hallucis brevis and the first lumbrical are all supplied by the medial plantar nerve.

Lateral plantar nerve The lateral plantar nerve supplies the skin of the fifth toe, the lateral half of the fourth toe and most of the deep muscles of the foot (see Figs 79.22, 79.27). It is located medial to the lateral plantar artery and courses anteriorly towards the tubercle of the fifth metatarsal. It passes between flexor digitorum brevis and flexor accessorius and ends between flexor digiti minimi brevis and abductor digiti minimi by dividing into superficial and deep branches. Before dividing, it supplies flexor accessorius and abductor digiti minimi, and gives off small branches that pierce the plantar aponeurosis to supply the skin of the lateral part of the sole (see Fig. 79.27). The superficial branch splits into two common plantar digital nerves: the lateral supplies the lateral side of the fifth toe, flexor digiti minimi brevis and the two interossei in the fourth intermetatarsal space; the medial connects with the third common plantar digital branch of the medial plantar nerve and divides to supply the adjoining sides of the fourth and fifth toes. The deep branch accompanies the lateral plantar artery deep to the flexor tendons and adductor hallucis, and supplies the second to fourth lumbricals, adductor hallucis and all the interossei (except those of the fourth intermetatarsal space). Branches to the second and third lumbricals pass distally deep to the transverse head of adductor hallucis, travelling around its distal border to reach the lumbricals. See Video 79.1.

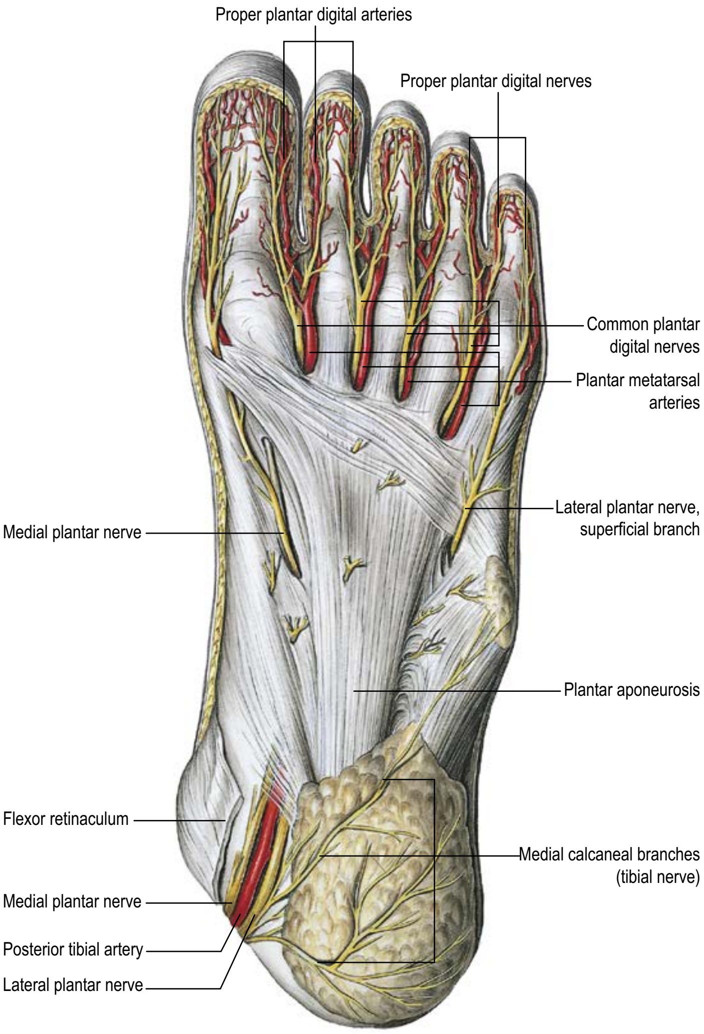
Proper plantar digital arteries
Proper plantar digital nerves
Common plantar digital nerves
Plantar metatarsal arteries
Lateral plantar nerve, superficial branch
Medial plantar nerve
Plantar aponeurosis
Flexor retinaculum
Medial calcaneal branches (tibial nerve)
Medial plantar nerve
Posterior tibial artery
Lateral plantar nerve

Fig. 79.27 The plantar digital nerves. (Sobotta Atlas of Human Anatomy © Elsevier GmbH, Urban & Fischer, Munich.)

Nerve entrapment syndromes in the foot

All nerves of the foot can be affected by entrapment, leading classically to a burning sensation in the distribution of that nerve. Tarsal tunnel syndrome is much less common than carpal tunnel syndrome. The flexor retinaculum may compress the tibial nerve or either of its branches (medial and lateral plantar nerves); entrapment at this level is most commonly due to a space-occupying lesion, e.g. a ganglion, or to compression by either a leash of vessels or the deep fascia associated with abductor hallucis. Compression of the first branch of the lateral plantar nerve (Baxter's nerve) by the deep fascia that covers abductor hallucis has been implicated as a possible cause of chronic heel pain and of plantar fasciopathy. (Plantar fasciopathy, often caused by repetitive high-impact injury to the foot, may be associated with pain, especially over the medial calcaneal process, which may be exacerbated by passive ankle or great toe flexion.) The medial plantar nerve can be compressed at the 'knot of Henry', which is the point where the tendon of flexor hallucis longus crosses deep to the tendon of flexor digitorum longus, to reach its medial side in the sole of the foot. The superficial fibular nerve can be damaged in severe inversion injuries of the ankle, and the deep fibular nerve is sometimes compressed by osteophytes in the region of the second tarsometatarsal joint. Sural nerve entrapment is usually not due to compression by fascial elements. Entrapment of the third common digital nerve as it passes deep to the intermetatarsal ligament of the third (or less commonly the second) web space can result in a Morton's neuroma, which is probably the most common form of nerve entrapment in the foot.

Patients with Morton's neuroma usually present with a main complaint of pain in the area of the third and fourth metatarsal heads, and tingling, shooting pain, or numbness over the lateral aspect of the third and medial aspect of the fourth digits. While there is no pathognomonic clinical test, diagnostic imaging coupled with clinical tests can provide convergent validity to help with diagnosis (Owens et al 2011). Two commonly used clinical tests are web-space tenderness and forefoot squeeze tests. The web-space tenderness test is performed by placing the side of the thumb into the third web space and pressing down. The forefoot squeeze test is performed by squeezing the forefoot from side to side while concurrently performing the web-space test.

BIOMECHANICS OF THE FOOT

Planes of motion

The terms describing movement along the planes of motion in the foot and ankle, particularly in relation to the use of supination and inversion, and pronation and eversion, respectively, are inconsistently applied (Greiner 2007, Doya et al 2010). Plantar flexion and dorsiflexion refer to movement in the sagittal plane and occur principally, but not exclusively, at the ankle, metatarsophalangeal and interphalangeal joints. Motion along the frontal or coronal plane involves inversion, which is a tilting of the plantar surface of the foot towards the midline, and eversion, a tilting away from the midline. These movements take place principally in the talocalcaneal and transverse tarsal joints. Adduction is movement of the foot towards the midline in the transverse plane; abduction is movement away from the midline in the transverse plane. These movements occur in the transverse tarsal joints and, to a limited degree, in the first tarsometatarsal and metatarsophalangeal joints.

Supination describes a tri-planar motion, and is a combination of adduction, inversion and plantar flexion. Pronation is the opposite tri-planar motion, i.e. a combination of abduction, eversion and dorsiflexion. Pronation and supination are usually better terms than eversion and inversion, because the latter rarely occur in isolation and the former describe the 'compound' motion that usually occurs.

Active movements occur at the ankle, talocalcaneonavicular and subtalar joints. Movements at the ankle joint are almost entirely restricted to dorsiflexion and plantar flexion, but slight rotation may occur in plantar flexion. The ranges of movement at the talocalcaneonavicular and subtalar joints are greater: supination and pronation mainly occur here.

Standing

Humans are bipedal and stand with an erect trunk and knees that are almost straight. Humans are also plantigrade, i.e. the whole length of the foot is set down on the ground, whereas most medium to large mammals are digitigrade, i.e. they stand and walk on their toes, and ungulates stand on hooves on the tips of their toes. In the sagittal plane, body weight acts along a line that passes a few centimetres anterior to the tibiotalar joint, exerting a moment that must be balanced by the plantar flexor muscles.

Movements of the foot

The foot has two major functions: to support the body in standing and progression, and to lever it forwards and absorb shock in walking, running and jumping (Alexander 1992). To fulfil the first function, the pedal platform must be able to spread the stresses of standing and moving, and be pliable enough to accommodate walking or running over uneven and sloping surfaces. To fulfil the second function, the foot must be transformable into a strong, adjustable lever in order to resist inertia and powerful thrust; a segmented lever can best meet such stresses if it is arched.

In infants and young children, fatty connective tissue on the plantar aspect may give the foot a flat appearance and soft tissues modify its appearance to varying degrees at all ages. The thickness of the medial midfoot plantar fat pad ranges from 3.1 to 4.9 mm (Riddiford-Harland et al 2007). However, the skeleton of the human foot is normally arched, and the sole of the foot is usually visibly concave. These arches vary individually in their height, especially the medial part of the longitudinal arch. Since they are dynamic, their heights also differ in different phases of activity.

The medial longitudinal arch contains the calcaneus, talus, navicular, cuneiform and medial three metatarsals. Its summit, at the superior talar articular surface, takes the full thrust from the tibia and passes it backwards to the calcaneus, and forwards through the navicular and cuneiforms to the metatarsals. When the foot is grounded, these forces are transmitted through the three metatarsal heads and calcaneus (especially its tuberosity). The medial arch is higher, and more mobile and resilient than the lateral arch, and its flattening progressively tightens the plantar calcaneonavicular ligament and plantar aponeurosis. The lateral arch is adapted to transmit weight and thrust rather than to absorb such forces; the long plantar and plantar calcaneocuboid ligaments tighten as it flattens.

The lateral arch makes contact with the ground more extensively than the medial arch. As the foot flattens, an increasing fraction of load traverses the soft tissues that are inferior to the entire arch. The whole lateral border usually touches the ground, whereas the medial border does not. The medial border is visibly concave, usually even in standing, which explains the familiar outline of human footprints (although this varies with the position of the feet, the development of associated soft tissues and the nature of the surface) (Fig. 79.28). In any activity, as soon as the heel rises, the toes are extended and muscular structures (including the plantar aponeurosis) tighten up in the sole, accentuating the longitudinal arches: it has been suggested that tension diminishes in the deeper plantar ligaments in this phase. The sole is transversely concave, both in skeletal form and usually in external appearance; serial transverse arches are most developed inferior to the metatarsus and adjoining tarsus.

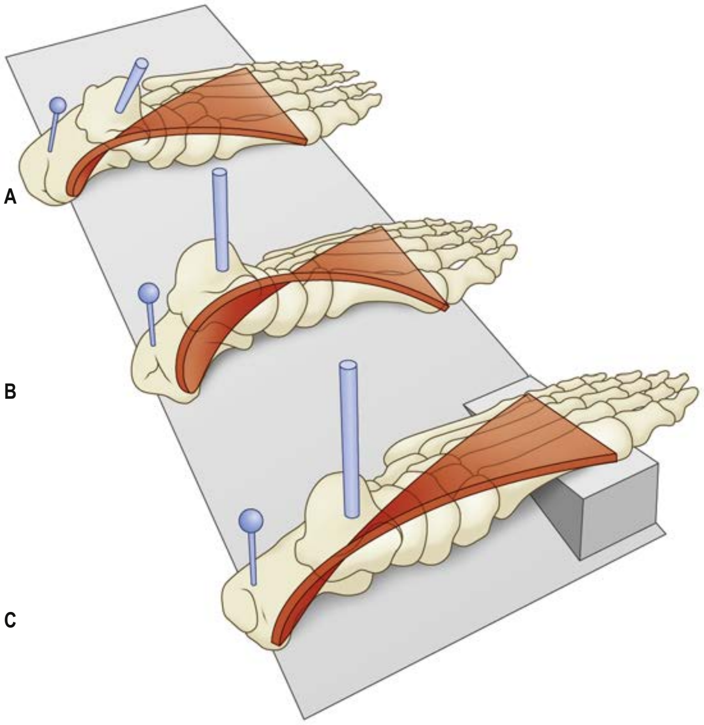

Fig. 79.28 The concept of the foot skeleton as a twisted plate that may be untwisted (supination) or further twisted (pronation) during the maintenance of a plantigrade stance in various positions of the foot. **A**, The foot skeleton in supination, as in standing with the feet widely separated. Note the marked medial tilting of the talus and, to a lesser degree, of the calcaneus and the depression of the medial longitudinal arch. **B**, Relative pronation of the foot, as in standing with the feet close together. **C**, Supination of the foot when standing on an inclined surface; if the position of the wedge had been reversed, the foot skeleton would, of course, approach maximal pronation. (Based on MacConaill MA 1945 The postural mechanism of the human foot. Proc Roy Irish Acad 50:265–78.)

Transmission of force occurs at the metatarsal heads, to some degree along the lateral border of the foot, and through subjacent soft tissues.

In standing, with only body weight to support, both the intrinsic and extrinsic muscles appear to relax (Perry 2010). If the longitudinal arches are allowed to sink as a result of muscular relaxation, the plantar ligaments support the bones in an arched form. The medial arch is more elevated when the feet are together than when they are apart, i.e. inversion with supination increases as the feet are separated. This medial sag can be countered by voluntary contraction of muscles such as tibialis anterior. Whatever the position of the feet, pronation and supination ensure that in standing, a maximal weight-bearing area is grounded from the metatarsal heads along the lateral border of the foot to the calcaneus. The twist of the ligamentous skeleton of the foot imparted by pronation (which is partly undone in supination) prompts the likening of the foot to a twisted but resilient plate (see Fig. 79.28), where adequate ground contact is ensured whatever the angle between the foot and leg, and adaptable resilience is imparted in standing and progression.

Bonus e-book content

Fig. 79.7 A–D, Radiographs showing ossification of the developing ankle and foot (at 2, 6 and 11 years) and in the adult.

Fig. 79.19 C, Turbo spin-echo, T1-weighted MRI of the left ankle of a female aged 26.

Fig. 79.20 Left foot radiograph of a skeletally mature adult with a hallux abducto valgus (bunion) deformity.

Video 79.1 Ankle block: surface anatomy.

Key references

Barclay-Smith E 1896 Astragalo-calcaneo-navicular joint. J Anat 30:390–412.

The first description of the astragalo-calcaneo-navicular joint. The paper explained the importance of the joint complex in terms of hindfoot motion.

Chen TM, Rozen WM, Pan WR et al 2009 The arterial anatomy of the Achilles tendon: anatomical study and clinical implications. Clin Anat 22:377–385.

A demonstration that the calcaneal tendon has three main territories of vascularity: a proximal section, mid-section and distal section. The mid-section had the poorest blood supply of all three territories.

DiLandro AC, Lilja EC, Lepore FL et al 2001 The prevalence of the arcuate artery: a cadaveric study of 72 feet. J Am Podiatr Med Assoc 91:300–5.

A large cadaveric study in which the authors found that the arcuate artery was present in only 16.7% of their sample of feet. They established that the lateral tarsal artery supplied the second to fourth dorsal metatarsal arteries in 47.2% of their sample, an arrangement that was more frequently found than the commonly described arcuate artery.

Eekhof JA, Van Wijk B, Knuistingh Neven A et al 2012 Interventions for ingrowing toenails. Cochrane Database Syst Rev 4:CD001541.

A meta-analysis of the efficacy of procedures used to treat ingrown toenails.

Jones FW 1949 Structure and Function as Seen in the Foot, 2nd ed. London: Baillière, Tindall & Cox.

This remains one of the classic texts on the foot.

Kim PJ, Richey JM, Wissman LR et al 2010 The variability of the Achilles tendon insertion: a cadaveric examination. J Foot Ankle Surg 49:417–20.

A description of the variability in the terminal insertion site of the calcaneal tendon that may be dependent on age.

Wildenauer E 1950 Die Blutversorgung des Talus. Zeitschrift für Anatomie und Entwicklungsgeschichte 115:32–6.

The first comprehensive account of talar blood supply and the identification of the important artery of the tarsal canal.

References

Abousayed MM, Alley MC, Shakked R et al 2017 Adult acquired flatfoot deformity: etiology, diagnosis, and management. JBJS Rev 5:e7.

Ahmed IM, Lagopoulos M, McConnell P et al 1998 Blood supply of the Achilles tendon. J Orthop Res 16:591–6.

Alexander RM 1992 The Human Machine. New York: Columbia University Press.

Attinger C, Cooper P, Blume P 1997 Vascular anatomy of the foot and ankle. Oper Tech Plast Reconstr Surg 4:183–98.

Barclay-Smith EB 1896 Astragalo-calcaneo-navicular joint. J Anat 30:390–412.

The first description of the astragalo-calcaneo-navicular joint. The paper explained the importance of the joint complex in terms of hindfoot motion.

Bonnel F, Teissier P, Maestro M et al 2011 Biometry of bone components in the talonavicular joint: a cadaver study. Orthop Traumatol Surg Res 97:S66–73.

Bonnel F, Teissier P, Colombier JA et al 2013 Biometry of the calcaneocuboid joint: biomechanical implications. Foot Ankle Surg 19:70–5.

Boss AP, Hintermann B 2002 Anatomical study of the medial ankle ligament complex. Foot Ankle Int 23:547–53.

Brennan SA, Kiernan C, Maleki F et al 2012 Talonavicular synostosis with lateral ankle instability – a case report and review of the literature. Foot Ankle Surg 18:e34–6.

Broderick BJ, Corley GJ, Quondamatteo F et al 2008 A haemodynamic study of the physiological mechanisms of the venous pump in the healthy human foot. Conf Proc IEEE Eng Med Biol Soc 2008:1411–14.

Burns PR, Mecham B 2014 Biodynamics of hallux abductovalgus etiology and preoperative evaluation. Clin Podiatr Med Surg 31:197–212.

Carmont MR, Rees RJ, Blundell CM 2009 Current concepts review: Freiberg's disease. Foot Ankle Int 30:167–76.

Carr AJ, Norris SH 1989 The blood supply of the calcaneal tendon. J Bone Joint Surg Br 71:100–1.

Castro M, Melao L, Canella C et al 2010 Lisfranc joint ligamentous complex: MRI with anatomic correlation in cadavers. AJR Am J Roentgenol 195:W447–55.

Cerrato RA 2011 Freiberg's disease. Foot Ankle Clin 16:647–58.

Chaney DM 2010 The Lisfranc joint. Clin Podiatr Med Surg 27:547–60.

Chang HW, Lin CJ, Kuo LC et al 2012 Three-dimensional measurement of foot arch in preschool children. Biomed Eng Online 11:76.

Chen TM, Rozen WM, Pan WR et al 2009 The arterial anatomy of the Achilles tendon: anatomical study and clinical implications. Clin Anat 22:377–85.

A demonstration that the calcaneal tendon has three main territories of vascularity: a proximal section, mid-section and distal section. The mid-section had the poorest blood supply of all three territories.

Coskun N, Yuksel M, Cevener M et al 2009 Incidence of accessory ossicles and sesamoid bones in the feet: a radiographic study of the Turkish subjects. Surg Radiol Anat 31:19–24.

Cummins EJ, Anson BJ 1946 The structure of the calcaneal tendon (of Achilles) in relation to orthopedic surgery, with additional observations on the plantaris muscle. Surg Gynecol Obstet 83:107–16.

Daftary A, Haims AH, Baumgaertner MR 2005 Fractures of the calcaneus: a review with emphasis on CT. Radiographics 25:1215–26.

Davis WH, Sobel M, DiCarlo EF et al 1996 Gross, histological, and microvascular anatomy and biomechanical testing of the spring ligament complex. Foot Ankle Int 17:95–102.

DiLandro AC, Lilja EC, Lepore FL et al 2001 The prevalence of the arcuate artery: a cadaveric study of 72 feet. J Am Podiatr Med Assoc 91:300–5.

A large cadaveric study in which the authors found that the arcuate artery was present in only 16.7% of their sample of feet. They established that the lateral tarsal artery supplied the second to fourth dorsal metatarsal arteries in 47.2% of their sample, an arrangement that was more frequently found than the commonly described arcuate artery.

Dodd A, Le I 2013 Foot compartment syndrome: diagnosis and management. J Am Acad Orthop Surg 21:657–64.

Douglas J, Kelly M, Blachut P 2009 Clarification of the Simmonds–Thompson test for rupture of an Achilles tendon. Can J Surg 52:40–1.

Doya H, Haraguchi N, Niki H et al 2010 Proposed novel unified nomenclature for range of joint motion: method for measuring and recording for the ankles, feet, and toes. J Orthop Sci 15:531-9.

Edama M, Kubo M, Onishi H et al 2015 The twisted structure of the human Achilles tendon. Scand J Med Sci Sports 25:e497–503.

Edama M, Takabayashi T, Inai T et al 2019 The relationships between the quadratus plantae and the flexor digitorum longus and the flexor hallucis longus. Surg Radiol Anat 41:689–92.

Eekhof JA, Van Wijk B, Knuistingh Neven A et al 2012 Interventions for ingrowing toenails. Cochrane Database Syst Rev 4:CD001541.

A meta-analysis of the efficacy of procedures used to treat ingrown toenails.

Espert M, Anderson MR, Baumhauer JF 2018 Current concepts review: plantar fibromatosis. Foot Ankle Int 39:751–7.

Fiacco RC, Ream GM, Wilson C et al 2017 Relationship between the intersesamoid ligament and sesamoid bones in cadaveric feet with hallux valgus. Cureus 9:e1819.

Finni T, Komi PV, Lukkariniemi J 1998 Achilles tendon loading during walking: application of a novel optic fiber technique. Eur J Appl Physiol 77:289–91.

Gardner E, Gray DJ 1968 The innervation of the joints of the foot. Anat Rec 161:141–8.

Genç B, Solak A, Mayda A et al 2013 Isolated tuberculous tenosynovitis of the anterior tibial and extensor digitorum longus tendons. J Clin Imaging Sci 3:37.

Giddings VL, Beaupré GS, Whalen RT et al 2000 Calcaneal loading during walking and running. Med Sci Sports Exerc 32: 627–34.

Greiner TM 2007 The jargon of pedal movements. Foot Ankle Int 28:109–25.

Gupta SC, Gupta CD, Arora AK 1977 Pattern of talar articular facets in Indian calcanei. J Anat 124:651–5.

Haffner M, Conklin M 2016 Bones of the lower limb. In: Tubbs RS, Shoja MM, Loukas M (eds) Bergman's Comprehensive Encyclopedia of Human Anatomical Variation. Hoboken: John Wiley; Ch. 13, pp. 89–115.

Halvorson JJ, Winter SB, Teasdall RD et al 2012 Talar neck fractures: a systematic review of the literature. J Foot Ankle Surg 52:56–61.

Harris RI, Beath T 1948 Etiology of peroneal spastic flat foot. J Bone Joint Surg Br 30:624–34.

Hatch DJ, Santrock RD, Smith B et al 2018 Triplane hallux abducto valgus classification. J Foot Ankle Surg 57:972–81.

Haynes JA, Gosselin M, Cusworth B et al 2017 The arterial anatomy of the deltoid ligament: a cadaveric study. Foot Ankle Int 38:785–90.

Hicks JH 1954 The mechanics of the foot. II. The plantar aponeurosis and the arch. J Anat 88:25–30.

Hopkinson WJ, St Pierre P, Ryan JB et al 1990 Syndesmosis sprains of the ankle. Foot Ankle 10:325–30.

Jennings MM, Christensen JC 2008 The effects of sectioning the spring ligament on rearfoot stability and posterior tibial tendon efficiency. J Foot Ankle Surg 47:219–24.

Johnson KA, Strom DE 1989 Tibialis posterior tendon dysfunction. Clin Orthop Relat Res 239:196–206.

Johnson A, Hill K, Ward J, Ficke J 2008 Anatomy of the Lisfranc ligament. Foot Ank Spec 1:19–23.

Jones FW 1949 Structure and Function as Seen in the Foot, 2nd ed. London: Baillière, Tindall & Cox.

A work that remains one of the classic texts on the foot.

Jules KT 1989 Nail infections. Clin Podiatr Med Surg 6:403–16.

Kafka RM, Aveytua IL, Fiacco RC et al 2016 Intrinsic muscles of the foot In: Tubbs, RS, Shoja MM, Loukas M (eds) Bergman's Comprehensive Encyclopedia of Human Anatomic Variation. Hoboken: John Wiley; Ch. 42, pp. 438–48.

This chapter provides an extensive description of the known variations of the intrinsic muscles of the foot and includes helpful illustrations.

Kafka RM, Aveytua IL, Choi PJ et al 2019 Anatomico-radiological study of the bifurcate ligament of the foot with clinical significance. Cureus 11:e3847

Kapandji IA 2011 The Physiology of the Joints. Volume 2, The Lower Limb, 6th ed. Edinburgh: Elsevier, Churchill Livingstone.

Keles-Celik N, Kose O, Sekerci R et al 2017 Accessory ossicles of the foot and ankle: disorders and a review of the literature. Cureus 9:e1881.

Kim PJ, Richey JM, Wissman LR et al 2010 The variability of the Achilles tendon insertion: a cadaveric examination. J Foot Ankle Surg 49:417–20.

A description of the variability in the terminal insertion site of the calcaneal tendon that may be dependent on age.

Kim PJ, Martin E, Ballehr L et al 2011 Variability of insertion of the Achilles tendon on the calcaneus: an MRI study of younger subjects. J Foot Ankle Surg 50:41–3.

Klammer G, Espinosa N, Iselin LD 2018 Coalitions of the tarsal bones. Foot Ankle Clin 23:435–49.

Kose O 2010 Do we really need radiographic assessment for the diagnosis of non-specific heel pain (calcaneal apophysitis) in children? Skeletal Radiol 39:359–61.

Lohrer H, Arentz S, Nauck T et al 2008 The Achilles tendon insertion is crescent-shaped: an in vitro anatomic investigation. Clin Orthop Relat Res 466:2230–7.

McSweeney SC, Cichero M 2015 Tarsal tunnel syndrome: a narrative literature review. Foot 25:244–50.

Michaud TC 2011 Human Locomotion: The Conservative Management of Gait-Related Disorders. Newton, MA: Newton Biomechanics.

Milner CE, Soames RW 1998 The medial collateral ligaments of the human ankle joint: anatomical variations. Foot Ankle Int 19:289–92.

Molund M, Husebye EE, Hellesnes J et al 2018 Proximal medial gastrocnemius recession and stretching versus stretching as treatment of chronic plantar heel pain. Foot Ankle Int 39:1423–31.

Monteagudo M, de Albornoz PM, Gutierrez B et al 2018 Plantar fasciopathy: a current concepts review. EFORT Open Rev 3:485–93.

Muehleman C, Williams J, Bareither ML 2009 A radiologic and histologic study of the os peroneum: prevalence, morphology, and relationship to degenerative joint disease of the foot and ankle in a cadaveric sample. Clin Anat 22:747–54.

Myerson MS 1997 Adult acquired flatfoot deformity: treatment of dysfunction of the posterior tibial tendon. Instr Course Lect 46:393–405.

Nakai T, Takakura Y, Tanaka Y 2000 Morphologic changes of the ankle in children as assessed by radiography and arthrography. J Orthop Sci 5:134–8.

Owens R, Gougoulias N, Guthrie H et al 2011 Morton's neuroma: clinical testing and imaging in 76 feet, compared to a control group. Foot Ankle Surg 17:197–200.

Oyedele O, Maseko C, Mkasi N et al 2006 High incidence of the os peroneum in a cadaver sample in Johannesburg, South Africa: possible clinical implications? Clin Anat 19:605–10.

Panchani PN, Chappell TM, Moore GD et al 2014 Anatomic study of the deltoid ligament of the ankle. Foot Ankle Int 35:916–21.

A large cadaveric study in which the authors studied the morphology and variations of the bands that comprise the deltoid ligament. They reported that the ligament can be composed of up to eight different bands.

Pankovich AM, Shivaram MS 1979 Anatomical basis of variability in injuries of the medial malleolus and the deltoid ligament. I. Anatomical studies. Acta Orthop Scand 50:217–23.

Perry J 2010 Gait Analysis: Normal and Pathological Function, 2nd ed. Thorofare, NJ: Slack.

Poonja AJ, Hirano M, Khakimov D et al 2017 Anatomical study of the cervical and interosseous talocalcaneal ligaments of the foot with surgical relevance. Cureus 9:e1382.

Preston N, Peterson D, Allen J et al 2018 Deep transverse metatarsal ligament transection in Morton's neuroma excision: a cadaveric study examining effects on metatarsal alignment. Foot Ankle Spec 11:342–6.

Pretterklieber B 2018 Morphological characteristics and variations of the human quadratus plantae muscle. Ann Anat 216: 9–22.

Rachel JN, Williams JB, Sawyer JR et al 2011 Is radiographic evaluation necessary in children with a clinical diagnosis of calcaneal apophysitis (Sever disease)? J Pediatr Orthop 31:548–50.

Ramanujam C, Zgonis T 2017 Surgical correction of the Achilles tendon for diabetic foot ulcerations and Charcot neuroarthropathy. Clin Podiatr Med Surg 34:275–80.

Riddiford-Harland DL, Steele JR, Baur LA 2007 The use of ultrasound imaging to measure midfoot plantar fat pad thickness in children. J Orthop Sports Phys Ther 37:644–7.

Riel H, Cotchett M, Delahunt E et al 2017 Is 'plantar heel pain' a more appropriate term than 'plantar fasciitis'? Time to move on. Br J Sports Med 17:1576–7.

Robertson GS, Ristic CD, Bullen BR 1990 The incidence of congenitally absent foot pulses. Ann R Coll Surg Engl 72:99–100.

Ryan JD, Timpano ED, Brosky TA 2nd 2012 Average depth of tarsometatarsal joint for trephine arthrodesis. J Foot Ankle Surg 51:168–71.

Salmon M, Taylor GI, Razaboni RM 1994 Anatomic Studies: Arteries of the Muscles of the Extremities and the Trunk: Arterial Anastomotic Pathways of the Extremities. St Louis: Quality Medical Publishers.

Salvioli S, Guidi M, Macrotulli G 2017 The effectiveness of conservative, non-pharmacological treatment, of plantar heel pain: a systematic review with meta-analysis. Foot 33:57–67.

Sarrafian SK 2011 Anatomy of the Foot and Ankle: Descriptive, Topographic, Functional, 3rd ed. Philadelphia: Lippincott Williams & Wilkins.

Scheyerer MJ, Helfet DL, Wirth S 2011 Diagnostics in suspicion of ankle syndesmotic injury. Am J Orthop (Belle Mead NJ) 40:192–7.

Snow SW, Bohne WH, DiCarlo E 1995 Anatomy of the Achilles tendon and plantar fascia in relation to the calcaneus in various age groups. Foot Ankle Int 16:418–21.

Stecco C, Macchi V, Porzionato A, Morra A et al 2010 The ankle retinacula: morphological evidence of the proprioceptive role of the fascial system. Cells Tissues Organs 192:200–10.

Stenroth L, Peltonen J, Cronin NJ et al 2012 Age-related differences in Achilles tendon properties and triceps surae muscle architecture in vivo. J Appl Physiol 113:1537–44.

Subhas N, Vinson EN, Cothran RL et al 2008 MRI appearance of surgically proven abnormal accessory anterior–inferior tibiofibular ligament (Bassett's ligament). Skeletal Radiol 37:27–33.

Waugh CM, Blazevich AJ, Fath F et al 2012 Age-related changes in mechanical properties of the Achilles tendon. J Anat 220:144–55.

Wiegerinck J, Zwiers R, Sierevelt IN, et al 2016 Treatment of calcaneal apophysitis: wait and see versus orthotic device versus physical therapy: a pragmatic therapeutic randomized clinical trial. J Pediatr Orthop 36:152–7.

Wildenauer E 1950 Die Blutversorgung des Talus. Zeitschrift für Anatomie und Entwicklungsgeschichte 115:32–6.

The first comprehensive account of talar blood supply and the identification of the important artery of the tarsal canal.

Yammine K 2015 The sesamoids of the feet in humans: a systematic review and meta-analysis. Anat Sci Int 90:144–60.

Yammine K 2017 The morphology and prevalence of the deltoid complex ligament of the ankle. A meta-analysis of cadaveric studies. Foot Ankle Spec 10:55–62.

Yammine K, Assi C 2018 A meta-analysis of comparative clinical studies of isolated osteotomy versus osteotomy with lateral soft tissue release in treating hallux valgus. Foot Ankle Surg 25:684–90.

Yepes H, Tang M, Geddes C et al 2010 Digital vascular mapping of the integument about the Achilles tendon. J Bone Joint Surg Am 92:1215–20.

Yi TI, Lee GE, Seo IS et al 2011 Clinical characteristics of the causes of plantar heel pain. Ann Rehabil Med 35:507–13.

Zantop T, Tillmann B, Petersen W 2003 Quantitative assessment of blood vessels of the human Achilles tendon: an immunohistochemical cadaver study. Arch Orthop Trauma Surg 123:501–4.

COMMENTARY

9.1

Functional anatomy and biomechanics of the pelvis

Andry Vleeming, Frank H. Willard

This commentary focuses on the anatomy and biomechanics of the pelvic girdle and, specifically, the sacroiliac joints. In bipeds, the pelvis serves as a basic platform with three large levers acting on it (the spine and two lower limbs). Movement of the pelvic platform upon the hip joints relative to the femur, such as flexion and extension (pelvic ante- and retroversion), and rotation and abduction/adduction, strongly influences lumbar spinal movement. As well as this substantial external pelvic motion, internal pelvic motion through the sacroiliac joint is essential for effectively transferring loads between the spine and lower limbs. It has been postulated that the sacroiliac joints act as important stress relievers in the 'force–motion' relationships between the trunk and lower limb (Vleeming et al 2007). These joints ensure that the pelvic girdle is a flexible ring of bone that will not easily fracture under the great forces to which it might be subject, either from trauma or from its many bipedal functions (Lovejoy 1988). Analysis of gait mechanics demonstrates that the sacroiliac joints provide sufficient flexibility for the intrapelvic forces to be transferred effectively to and from the lumbar spine and lower extremities (Vleeming et al 2007).

The sacroiliac joint is a highly specialized joint that lends stable (yet flexible) support to the upper body. Both the tightness of the well-developed dorsal fibrous apparatus and the specific architecture of the sacroiliac joint result in limited mobility. Numerous researchers have tried to model sacroiliac joint function by studying its principal displacement characteristics. A common assumption of these studies is that increased loading on the sacrum leads to tilting of the sacrum ventrally (nutation), a process by which most dorsal sacroiliac joint ligaments are stretched and the dorsal aspects of the iliac bones are drawn together (Solonen 1957, Vleeming et al 1990a, Vleeming et al 1990b). Counternutation normally takes place in unloaded situations, such as lying. Nutation implies a forward tilting of the sacrum relative to a posterior rotation of the ilia, and vice versa in counternutation.

Sacroiliac joint movement

Pelvic motion of males and females has been investigated by roentgen stereophotogrammetric motion analysis (RSA). RSA is a technique for measuring small movements and is regarded as the gold standard for determining mobility in orthopaedics (Kibsgård et al 2012). It has been used to measure the mean sacroiliac joint mobility, especially around the sagittal axis, in patients with pelvic girdle pain (PGP; Sturesson 2007). The average mobility for males was about 40% less than for females. However, there was no detectable decrease in total mobility in either gender with age (in patients up to 50 years old). In fact, there was a significant increase of mobility with age for both moving from a 'supine to sitting position' and from 'standing to lying prone with hyperextension' position, particularly in females. Likewise, gender differences of symphysial motion were analysed in a group of 45 asymptomatic individuals. In males, the average frontal plane movement was 1.4 mm, and in nulliparous females 1.6 mm. However, in multiparous females, motion increased to 3.1 mm (Garras et al 2008).

The increased sacroiliac joint mobility in females compared to males has possible anatomical correlates. The curvature of the sacroiliac joint surfaces is usually less pronounced in females to allow for greater mobility (Vleeming et al 1990a). Also, the pubic angle differs between males and females (Vleeming et al 2012). The increase in mobility of the pelvic ring seen in the post-pubescent female pelvis is functional in allowing passage for the child during labour. When the data are combined from published studies employing RSA and appropriate placing of markers, the maximum sagittal rotation of the sacroiliac joint never exceeds 3.6° and translation of the joint never exceeds 2 mm (Kibsgård et al 2012). If these data are amalgamated with the observation that osteophytosis is rare in females, regardless of age (1.83% of females), and is not very common in males (12.27%; Dar et al 2008), it appears that small sacroiliac joint movements are present, even at an advanced age (Vleeming et al 2012).

Sacroiliac joint stability

To illustrate the importance of both myofascial and ligamentous stability of the sacroiliac joint, the biomechanical principles of form and force closure were introduced (Vleeming et al 1990a, Vleeming et al 1990b). Form closure refers to a theoretical stable situation in a joint with closely fitting surfaces, where no extra forces are needed to maintain the state of the system. With force closure (leading to joint compression), both a lateral force and friction are needed to withstand vertical load. The structural features that contribute to sacroiliac joint form closure are complementary ridges and grooves of the articular surfaces; dorsocranial 'wedging' of the sacrum into the ilia; a particular high coefficient of friction in the sacroiliac joint (Vleeming et al 1990a, Vleeming et al 1990b); and the integrity of the dorsal binding ligaments in particular, which are among the strongest in the body (Vleeming et al 1990a). Both form and force closure are necessary for balancing friction/compression in the sacroiliac joint. Force closure is the result of altered joint reaction forces by tensing ligaments, fasciae, muscles and ground reaction forces (Vleeming et al 1990a, Vleeming et al 1990b). Force closure ideally generates a perpendicular compressional reaction force to the sacroiliac joint to overcome the forces of gravity (Vleeming et al 1990b).

Biomechanical considerations and the active straight leg raise test in pelvic girdle pain patients

PGP patients, who test positively on the functional active straight leg raise test, show an inability to raise the leg while lying supine. This test can temporarily be normalized by manual anterior compression of the pelvis or the use of a pelvic belt. This suggests that increased unilateral motion of the sacroiliac joint could lead to impairment and failure to lift the leg (Mens et al 1999).

Likewise, Sturesson (2007), using RSA, studied the effects of surgical application of an anterior external fixation frame for severe PGP patients. This resulted in a mean reduction of movement of the sacroiliac joint around the helical axis of 59% and around the X-axis of 74%. In addition, the active straight leg raise test and other evidence-based PGP tests were normalized (Vleeming et al 2008). When the frame was tightened, a nutation movement of the sacrum was noticed (Sturesson 2007).

This and other studies mentioned in this brief commentary imply that 'too much movement' of the sacroiliac joint could be a significant factor in the onset of PGP (Vleeming et al 2008).

References

Dar G, Khamis S, Peleg S et al 2008 Sacroiliac joint fusion and the implications for manual therapy diagnosis and treatment. Man Ther 13:155–8.

Garras DN, Carothers JT, Olson SA 2008 Single-leg-stance (flamingo) radiographs to assess pelvic instability: how much motion is normal? J Bone Joint Surg Am 90:2114–18.

Kibsgård TJ, Røise O, Stuge B et al 2012 Precision and accuracy measurement of radiostereometric analysis applied to movement of the sacroiliac joint. Clin Orthop Relat Res 470:3187–94.

Lovejoy CO 1988 Evolution of human walking. Sci Am 25:118–25A.

Mens JM, Vleeming A, Snijders CJ et al 1999 The active straight leg raising test and mobility of the pelvic joints. Eur Spine J 8:468–73.
Solonen KA 1957 The sacroiliac joint in the light of anatomical, roentgenological and clinical studies. Acta Orthop Scand 27:1–127.
Sturesson B 2007 Movement of the sacroiliac joint with special reference to the effect of load. In: Vleeming A, Mooney V, Stoeckart R (eds) Movement, Stability and Lumbopelvic Pain: Integration of Research and Therapy, 2nd ed. Edinburgh: Elsevier, Churchill Livingstone, pp. 343–52.
Vleeming A, Stoeckart R, Volkers AC et al 1990a Relation between form and function in the sacroiliac joint. Part I: Clinical anatomical aspects. Spine 15:130–2.
Vleeming A, Volkers AC, Snijders CJ et al 1990b Relation between form and function in the sacroiliac joint. Part II: Biomechanical aspects. Spine 15:133–6.
Vleeming A, Mooney V, Stoeckart R (eds) 2007 Movement, Stability and Lumbopelvic Pain: Integration of Research and Therapy, 2nd ed. Edinburgh: Elsevier, Churchill Livingstone, p. 658.
Vleeming A, Albert HB, Ostgaard HC et al 2008 European guidelines for the diagnosis and treatment of pelvic girdle pain. Eur Spine J 17:794–819.
Vleeming A, Schuenke MD, Masi AT et al 2012 The sacroiliac joint: an overview of its anatomy, function and potential clinical implications. J Anat 221:537–67.

COMMENTARY

9.2

A proposed novel action of psoas minor

Donald Anthony Neumann

Psoas minor is a curious muscle in humans, lacking a clear and universally agreed function and reported to be present in only 33–65% of individuals (Seib 1934, Gandhi et al 2013, Neumann and Garceau 2015, Tubbs et al 2016). This commentary proposes a novel functional role for psoas minor, with the aim of stimulating interest in this muscle, both anatomically and clinically.

Psoas minor is located retroperitoneally deep in the abdomen, running nearly parallel with and immediately anterior to the much larger psoas major (**Fig. 9.2.1**). Although structural variation is not uncommon, it typically originates proximally on the vertebral bodies of T12–L1 and the intervening intervertebral disc (Moore et al 2014; see Ch. 77). The relatively long tendon of psoas minor typically has a distal bony attachment to the iliopubic ramus (see Fig. 9.2.1): this attachment is usually medial to the anterior edge of the acetabulum and medial and slightly superior to the iliopubic eminence (Neumann and Garceau 2015). Therefore, unlike psoas major, psoas minor typically has a bony distal attachment to the pelvis, not to the femur, that likely accounts for its described functions as a weak flexor of the trunk or of the lumbar spine (Oatis 2008, Drake et al 2020). However, given its small muscle belly and the presence of other larger surrounding muscles that are capable of these actions, it seems unlikely that these are either the sole or dominant functions of psoas minor.

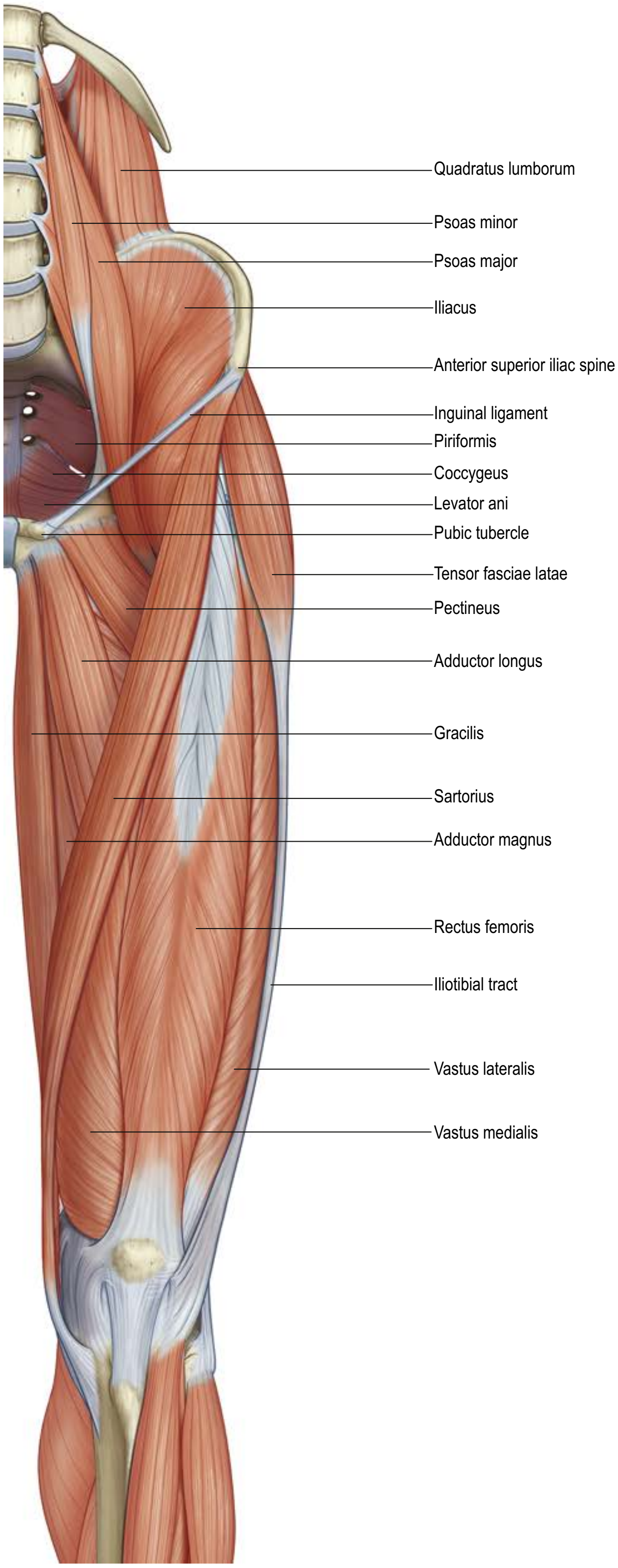

Fig. 9.2.1 Psoas minor running parallel to and in contact with the psoas major.

Anatomical connections between the tendon of psoas minor and the iliac fascia

In addition to the distal attachment of psoas minor to the pelvis, anatomy textbooks usually report a secondary attachment into adjacent fascia. In a cadaveric study, the tendon of psoas minor was found to be consistently fused with the structural 'backbone' of the iliac fascia, and the entire musculofascial entity was referred to as the psoas minor–iliac fascia complex (Neumann and Garceau 2015). Detailed measurements showed that the iliac fascia component of this complex draped directly over the distal, pre-tendinous portion of iliopsoas and the femoral nerve (**Fig. 9.2.2A**). The variably curved superior edge of the iliac fascia has been referred to as the iliopectineal arch (Agur and Dalley 2013), and this is the term that will be used throughout this commentary.

A composite tracing of the location of the iliac fascia obtained through study of cadaveric specimens is shown in **Fig. 9.2.2B** (Neumann and Garceau 2015). Of the 21 hips in which psoas minor was present, the muscle was attached distally to bone *and* to the iliac fascia in 19 (90.5%) (see vertical and horizontal red areas in Fig. 9.2.2B, respectively). In the remaining two hips (from the same cadaver) psoas minor was attached distally only to the iliac fascia (which was fully formed). Thus, in all cases, the tendon of psoas minor was firmly blended with the iliac fascia. The location of this tendon–fascial junction was on average 69.9 ± 9.0 mm medial and 29.8 ± 16.1 mm superior to the anterior–superior iliac spine (see Fig. 9.2.2B), placing the tendon–fascial junction immediately lateral and anterior to the sacroiliac joint.

As is apparent in the composite perspective in Fig. 9.2.2B, the arched superior edge of the iliac fascia (i.e. the iliopectineal arch) was generally concave, faced superiorly and could be pulled up and away from the underlying iliopsoas. The superior–medial aspect of the iliac fascia was attached to bone and crossed the sacroiliac joint in 11 hips (52.4%). Inferior to the sacroiliac joint, the fascia was attached to the inner pelvic brim and eventually became continuous with the pelvic attachment of the tendon of psoas minor (see Fig. 9.2.2B). The iliac fascia continued and was attached inferiorly to a point generally medial to the iliopubic junction, i.e. the junction between the anterior ilium and superior pubic ramus. En route, some fibres flowed posteromedially to interlace with the external fascia covering the superior part of obturator internus.

The lateral extent of the iliopectineal arch was attached to bone in a region immediately superior and inferior to the anterior superior iliac spine. However, the posterior side of the iliac fascia lacked

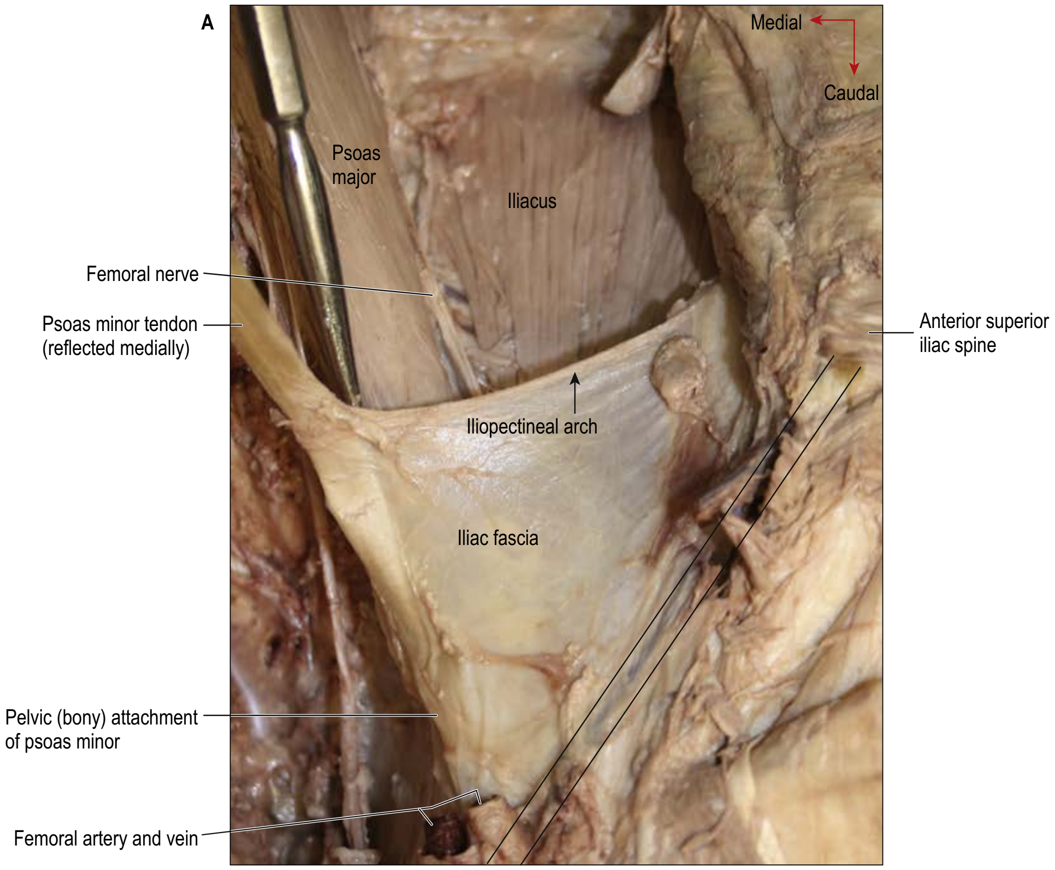
A
Medial
Caudal
Psoas major
Iliacus
Femoral nerve
Psoas minor tendon (reflected medially)
Anterior superior iliac spine
Iliopectineal arch
Iliac fascia
Pelvic (bony) attachment of psoas minor
Femoral artery and vein

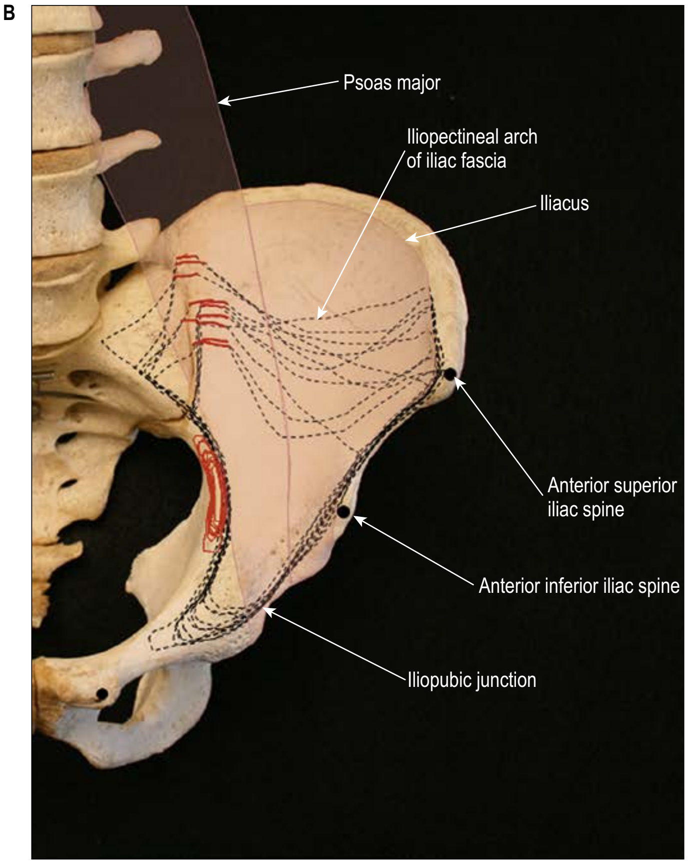
B
Psoas major
Iliopectineal arch of iliac fascia
Iliacus
Anterior superior iliac spine
Anterior inferior iliac spine
Iliopubic junction

Fig. 9.2.2 Anterior views of the iliac fascia component of the left psoas minor–iliac fascia complex. **A**, Psoas minor tendon blending with the iliac fascia (see tip of probe). Note that the tendon of psoas minor has been manually pulled medially. Normally, *in situ,* the tendon of psoas minor lies nearly parallel and in contact with the anterior belly of psoas major. Parallel black lines show the approximate location of the inguinal ligament. **B**, Pictorial summary of the distal attachments of the psoas minor–iliac fascia complex. The dashed black lines represent the location of the iliac fascia. The locations of the attachment of the tendon of psoas minor into the iliac fascia are indicated by variably spaced, red horizontal areas; and into the pelvic bone by overlapping red, vertical areas. For perspective, the estimated location of psoas major and iliacus, which for the most part lie deep to the iliac fascia, are depicted using a translucent outline. (Adapted with permission from Neumann DA, Garceau LR 2015 A proposed novel function of the psoas minor revealed through cadaver dissection. Clin Anat 28:243–52.)

a pelvic attachment. The anterior surface of the iliac fascia blended with the deep part of the inguinal ligament and the proximal fascia lata of the thigh. A near continuous sheet of iliac fascia therefore existed between the iliopectineal arch superiorly and fascia lata inferiorly, providing an open vertical aponeurotic sleeve that allowed unrestricted passage of the underlying iliopsoas and femoral nerve into the thigh (see Video 9.2.1 and Fig. 9.2.3). Although iliopsoas and the femoral nerve passed posterior to the iliac fascia, the femoral vein and artery (embedded within the femoral sheath) passed superficial to the fascia. The anterior surface of iliopsoas and the femoral nerve were in direct contact with the posterior surface of the iliac fascia, whereas the posterior surface of iliopsoas was in firm contact with a segment of the anterior pelvic brim.

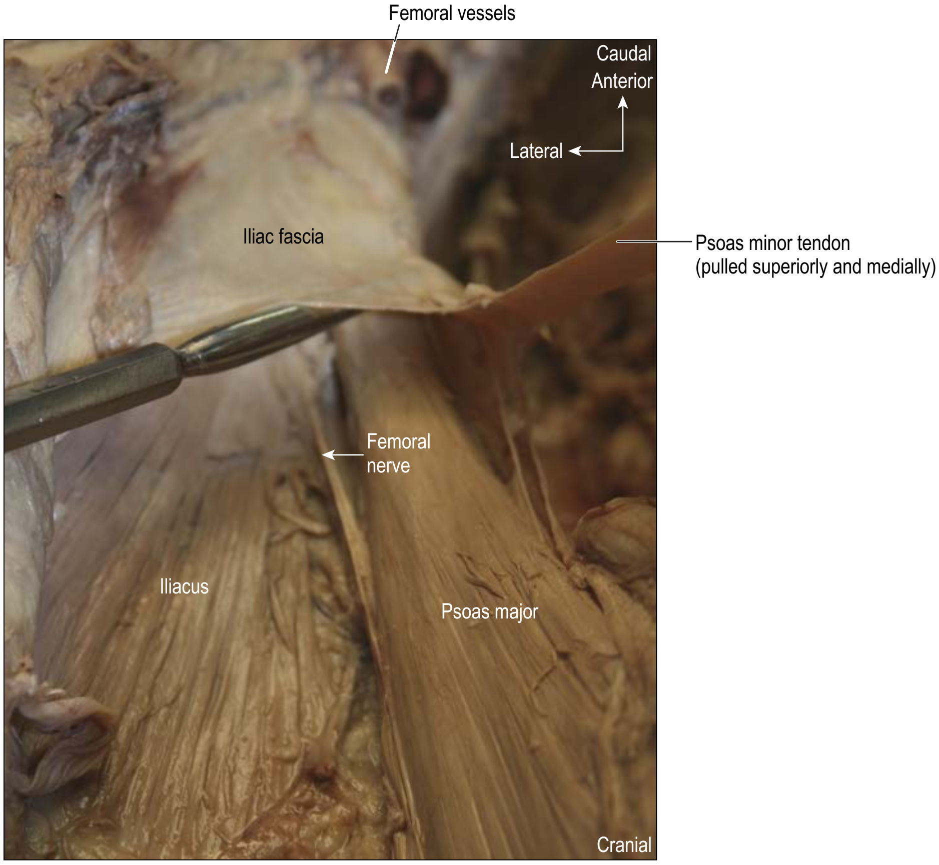

Fig. 9.2.3 Anterior view showing the left pelvic region of a cadaver, with intestines and inguinal ligament removed (orientation seen in Fig. 9.2.2A has been reversed). The probe is shown lifting the iliopectineal arch (and iliac fascia) away from the underlying left iliacus, psoas major and femoral nerve. The tendon of psoas minor has been manually pulled superiorly and medially, adding to the tension in the iliac fascia. Caudally, the iliac fascia blends with the fascia lata of the proximal thigh.

Possible biomechanical and clinical significance of the psoas minor–iliac fascia complex

When present, the tendon of psoas minor is consistently attached to and reinforces the medial and central part of the iliac fascia (Neumann and Garceau 2015). Based on this anatomical connection, an active force produced by psoas minor could, to some degree, adjust the tension within the iliac fascia, and potentially within the proximal part of the fascia lata (see arrows in **Fig. 9.2.4**). In this way, psoas minor may provide some degree of mechanical stability to the underlying iliopsoas as it crosses over the femoral head and across the anterior pelvic brim. Such an active tensioning may confer useful biomechanical functions to iliopsoas as a hip flexor. Although speculative, it may be that the myogenic tensioning within the iliac fascia prevents an activated iliopsoas from 'bowstringing' away from the anterior pelvic brim, especially when strongly contracting to move the thigh into a high flexion angle. Excessive bowstringing of iliopsoas and its tendon away from the femoral head would increase the hip flexion moment arm (leverage) of the muscle, resulting in *less* rotation of the joint (flexion of the hip, in this case) per linear unit of muscle contraction. Such a counterproductive biomechanical scenario would exist for *any* muscle that bowstrings across a joint (Neumann 2017). Excessive bowstringing of the tendon of iliopsoas could reduce the range of available active hip flexion, which may limit the ease of activities that require end range flexion, such as putting on shoes and socks. Whether psoas minor has the physiological strength for generating enough active counter-tension in the iliac fascia to prevent iliopsoas bowstringing during hip flexion is not known. To add insight into this notion, Neumann and Garceau (2015) estimated that, on average, psoas minor could theoretically produce a maximal force of 21 N (2.1 kg) based on an average cross-sectional area of 52.5 mm^2. Although this is an estimate, it does provide some context when considering whether psoas minor has the force potential to offer mechanical stability to the much stronger iliopsoas. Further study is needed to verify this biomechanical proposition.

The mechanism described in the previous paragraph could, in theory, also allow the psoas minor–iliac fascia complex to provide varying control of the *medial–lateral* position of the underlying iliopsoas as it runs across the femoral head, anterior capsule region, iliopectineal eminence and the pelvic brim. Could such control influence the contact stress between the distal region of iliopsoas and adjacent structures? This question is clinically relevant given the many poorly understood painful conditions or pathologies in the anterior hip region that may involve iliopsoas. Such conditions include iliopsoas 'snapping hip' syndrome (Byrd 2006, Lewis 2010, Philippon et al 2014); iliopsoas impingement (Dora et al 2007); iliopsoas bursitis or tendonitis (Blankenbaker et al 2006, Nunley et al 2010, Philippon et al 2011); and, possibly, acetabular labral pathology (Philippon et al 2014). An intriguing question arises as to the possible clinical consequences of not possessing a psoas minor, and therefore lacking the proposed active tensioning mechanism for the iliac fascia. Would absence of psoas minor predispose to developing painful iliopsoas-associated pathology?

A primary fascial-based stabilization role for a muscle: is this a novel concept?

Several examples exist within the body where a sheath of connective tissue *passively* stabilizes the position of underlying muscles or tendons. Consider for example the role of the fibrous lacertus for elbow flexion, the anular pulleys for digital flexion, or the extensor retinaculum for ankle dorsiflexion or wrist extension. This commentary proposes that a similar anatomical mechanism might exist for iliopsoas, with regard to its mechanical potential to bowstring away from the hip during high angle hip flexion (Yoshio et al 2002). It is arguable that this stability could be furnished not only by passive tension, as in the examples cited above, but also through force generated by psoas minor and transferred through the iliac fascia. In theory, sensory receptors within the psoas minor–iliac fascia complex may provide input to the central nervous system. As such, the nervous system may better determine the necessary motor activation of psoas minor to mechanically stabilize the iliopsoas tendon during active motion. Perhaps psoas minor and iliopsoas are activated 'in phase' with each other during vigorous movements

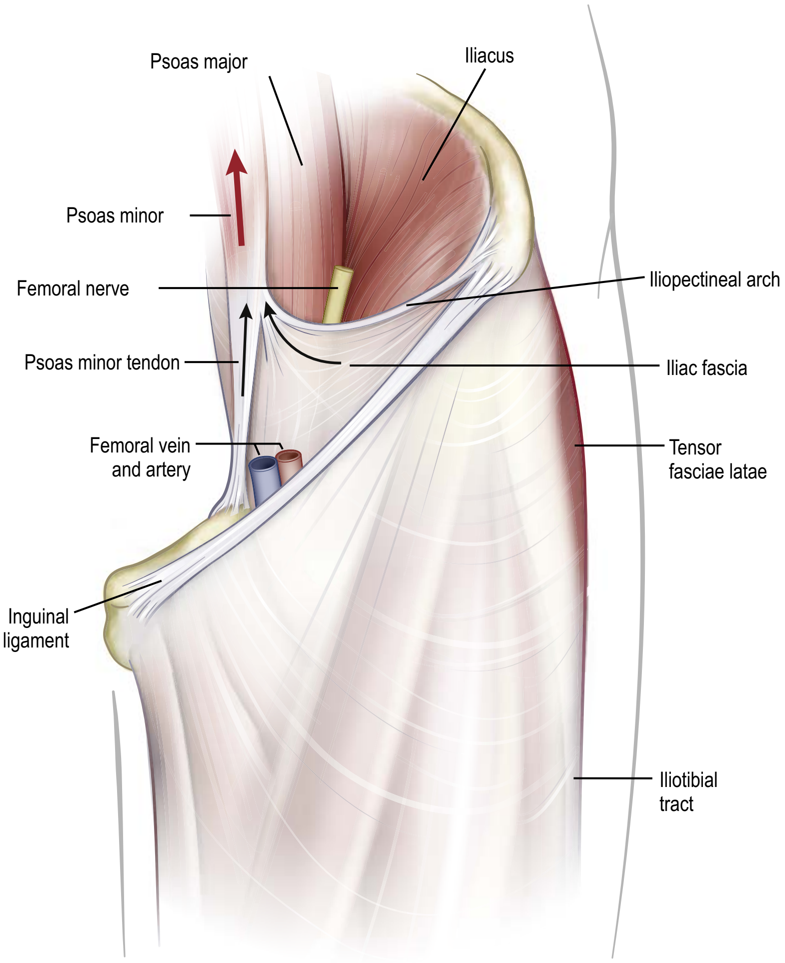

Fig. 9.2.4 The left proximal thigh and pelvic region, intestines removed. Red arrow, active force produced by contraction of psoas minor; black arrows, tension that could be transferred throughout the iliac fascia and into the proximal part of the fascia lata of the thigh.

involving high flexion angles, such as cycling or running up hill, which is an idea that remains unstudied.

The proposition that one muscle can serve as an *active* stabilizer for another, as postulated for psoas minor, is not unique. Examples include quadratus plantae, which may help guide the position of the common tendon of flexor digitorum longus in the foot, and palmaris longus as it stabilizes the palmar aponeurosis in the hand, a structural arrangement that prevents bowstringing of the extrinsic digital flexor tendons and median nerve within the carpal tunnel during extreme wrist flexion.

Closing remarks

Although not proven, it is proposed that psoas minor functions as a dedicated accessory muscle to iliopsoas. More specifically, the primary function of the psoas minor–iliac fascia complex is postulated to enhance the biomechanical stability and function of the underlying iliopsoas. Such a stabilizing role appears more likely than the traditional description of psoas minor as a trunk flexor.

Further study is warranted to test the hypotheses raised in this commentary. Such research could involve: (1) large-scale dissection studies to determine the cross-sectional area, morphological variation, pennation angle and innervation of the psoas minor–iliac fascia complex; (2) measurement of the strength and stiffness characteristics of the iliac fascia; (3) instrumenting the psoas minor–iliac fascia complex and cadaveric hips with force (strain) and kinematic measurement hardware; (4) computer and mathematical modelling; and (5) *in vivo* electromyographical or ultrasound analyses. One specific aim of this research would be to analyse whether psoas minor is physiologically capable of producing enough force to stabilize the position of iliopsoas across a range of hip positions. Ultimately, research may be justified to determine whether an association exists between the presence or absence of psoas minor and the likelihood of developing anterior hip pain and other associated pathologies involving iliopsoas.

Although this commentary has generated more questions than it has answered, it seeks to share a hypothesis with anatomists, kinesiologists, physiotherapists, surgeons and other clinicians who treat musculoskeletal problems involving the anterior aspect of the hip.

References

Agur AMR, Dalley AF 2013 Grant's Atlas of Anatomy, 13th ed. Philadelphia, PA: Lippincott Williams & Wilkins.

Blankenbaker DG, DeSmet AA, Keene JS 2006 Sonography of the iliopsoas tendon and injection of the iliopsoas bursa for diagnosis and management of the painful snapping hip. Skeletal Radiol 35:565–71.

Byrd JW 2006 Evaluation and management of the snapping iliopsoas tendon. Instr Course Lect 55:347–55.

Dora C, Houweling M, Koch P et al 2007 Iliopsoas impingement after total hip replacement: the results of non-operative management, tenotomy or acetabular revision. J Bone Joint Surg Br 89:1031–5.

Drake RL, Vogl AW, Mitchell AWM 2020 Gray's Anatomy for Students, 4th ed. Philadelphia, PA: Elsevier.

Gandhi S, Gupta N, Thakur A et al 2013 Anatomical and clinical insight of variant morphologies of psoas minor muscle: a case report. Int J Cur Rev 5:106–10.

Lewis CL 2010 Extra-articular snapping hip: a literature review. Sports Health 2:186–90.

Moore KL, Dalley AF, Agur AMR 2014 Clinically Oriented Anatomy, 7th ed. Philadelphia, PA: Lippincott Williams & Wilkins.

Neumann DA 2017 Kinesiology of the Musculoskeletal System: Foundations for Rehabilitation, 3rd ed. St Louis, MO: Elsevier.

Neumann DA, Garceau LR 2015 A proposed novel function of the psoas minor revealed through cadaver dissection. Clin Anat 28:243–52.

Nunley RM, Wilson JM, Gilula L et al 2010 Iliopsoas bursa injections can be beneficial for pain after total hip arthroplasty. Clin Orthop Relat Res 468:519–26.

Oatis CA 2008 Kinesiology: The Mechanics and Pathomechanics of Human Movement, 2nd ed. Philadelphia, PA: Lippincott Williams & Wilkins.

Philippon MJ, Decker MJ, Giphart JE et al 2011 Rehabilitation exercise progression for the gluteus medius muscle with consideration for iliopsoas tendinitis: an in vivo electromyography study. Am J Sports Med 39:1777–85.

Philippon MJ, Devitt BM, Campbell KJ et al 2014 Anatomic variance of the iliopsoas tendon. Am J Sports Med 42:807–11.

Seib GA 1934 Incidence of the m. psoas minor muscle in man. Am J Phys Anthropol 19:229–46.

Tubbs RS, Shoja MM, Loukas M 2016 Bergman's Comprehensive Encyclopedia of Human Anatomical Variation. Hoboken, NJ: John Wiley & Sons.

Yoshio M, Murakami G, Sato T et al 2002 The function of the psoas major muscle: passive kinetics and morphological studies using donated cadavers. J Orthop Sci 7:199–207.

COMMENTARY

9.3

Anterolateral ligament of the knee

Robert F. LaPrade

There has been significant interest over the past decade concerning the 'rediscovery' of the anterolateral ligament (ALL) of the knee. The structure was initially defined by Paul Segond in 1879 as a pearly, fibrous band that became tensioned during internal rotation of the knee (Segond 1879). Strictly speaking, the 'rediscovery' of the ALL by Claes et al (2013) was a clarification of the previous literature and reflected increasing recognition that anterior cruciate ligament (ACL) reconstruction alone did not always eliminate a patient's pivot shift test. This fibrous band along the anterolateral aspect of the knee has been variously identified as retrograde iliotibial tract fibres (Lobenhoffer et al 1987), the capsulo-osseous layer of the iliotibial tract (Terry et al 1993), the mid-third lateral capsular ligament (LaPrade et al 2000), and more recently, as the ALL (Vieira et al 2007).

It is important to realise that while the ALL has been recognized as a thickening within the mid-third of the lateral capsular ligament, there is still no clear definition of its anatomical attachment sites. The femoral attachment of the ALL has been identified proximal and posterior to the lateral epicondyle (Kennedy et al 2015) and the tibial attachment has been located consistently midway between the anterior aspect of the fibular head and Gerdy's tubercle (Claes et al 2013, Helito et al 2013, Dodds et al 2014, Caterine et al 2015, Kennedy et al 2015).

The femoral attachment of the ALL has been difficult to define. Some of the first descriptions indicated a femoral attachment on or near the insertion of the popliteus tendon (Vincent et al 2012), or a shared femoral origin with the fibular collateral ligament (FCL), adjacent to the lateral epicondyle (Claes et al 2013). Helito et al (2013) described a femoral attachment anterior and distal to the FCL femoral attachment site, while Dodds et al (2014) reported the femoral attachment as proximal and posterior to the femoral FCL attachment site. Caterine et al (2015) reported significant anatomical variability, identifying attachments at either the proximal and posterior or the anterior and distal attachment sites. Most recently, Kennedy et al (2015) consistently located a femoral attachment approximately 7.0 mm from the lateral epicondyle and 4.7 mm posterior and proximal to the FCL femoral attachment, with an overall attachment area of 67.7 mm^2 (Fig. 9.3.1). Lateral radiographs yielded a relative distance of 8.4 mm posterior and proximal to the lateral epicondyle, and an approximate distance of 22.3 mm proximal to the joint line.

The tibial attachment site of the ALL has been fairly consistently described across multiple studies over the years as a thickening of the lateral capsule, traversing anterodistal from its origin, and coming under tension when an internal rotation load is applied to the knee at 30° of flexion. This insertion has an area of approximately 64.9 mm^2, and is strongly correlated with the location of a bony avulsion on the anterolateral aspect of the knee (Segond fracture) that occasionally accompanies ACL injuries. The attachment is approximately midway between the anterior aspect of the fibular head and Gerdy's tubercle, with relative distances of 26.1 mm and 24.7 mm from these points, respectively (Kennedy et al 2015). It has been estimated radiographically as 13.1 mm distal to the lateral tibial plateau, with anterior–posterior radiographs yielding a planar distance of 19.0 mm posterior and superior to the centre of Gerdy's tubercle. Additional attachments of the ALL to the meniscotibial portion of the mid-third lateral capsular ligament, the anterior arm of the short head of biceps femoris, and the capsulo-osseous layer of the iliotibial tract, have all been identified.

The occurrence of Segond fractures together with ACL injuries and the high failure rate of ACL reconstructions prompted the idea that perhaps the structures responsible for the kinematics associated with these injuries were not being fully restored. Upon concomitant sectioning of the ACL and ALL in a robotic study, Rasmussen et al (2016) found a significant increase in axial plane tibial translation during a simulated pivot shift relative to isolated ACL-deficient states, in addition to increases in internal rotation. This study supported the proposal that the ALL was acting as a secondary stabilizer throughout knee flexion during applied internal rotation torque and pivot shift testing and that its absence altered the stability of the knee and ultimately overburdened grafts utilized for ACL reconstructions. Nitri et al (2016) showed that concurrent reconstruction of both ACL and ALL was successful in improving rotary stability relative to isolated ACL reconstruction in ALL–ACL deficient knees. This was supported by Schon et al (2016) who also showed that ALL reconstructions resulted in a significant overconstraint of internal rotation beyond 30° of knee flexion.

In conclusion, the ALL is a capsular thickening of the lateral knee, originating proximal and posterior to the lateral epicondyle and coursing anterodistal to the anterolateral tibia, which can be reproducibly identified by reference to surrounding anatomical and bony landmarks. Imaging correlates ALL failure with the identical location of Segond fractures on the tibia, reinforcing its importance as a stabilizer of internal rotation in the ACL-deficient knee. Although the ALL appears to be vital for secondary stabilization of internal rotation, especially in conditions of ACL deficiency, further studies are necessary when considering ALL-supplemented reconstructions in the treatment of ACL injuries.

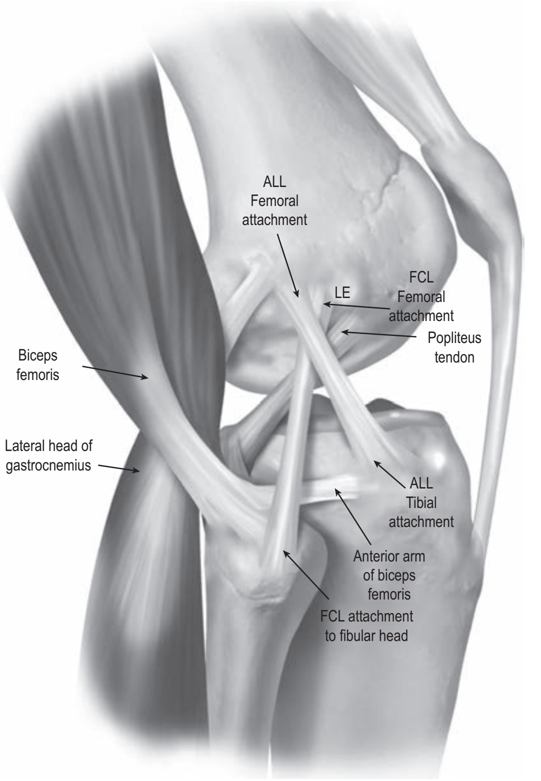

Fig. 9.3.1 Attachment sites for the main structures of the lateral knee (lateral view, right knee). The anterolateral ligament (ALL) is attached posterior and proximal to the femoral attachment of the fibular collateral ligament (FCL), and courses anterodistal to its insertion onto the tibia midway between Gerdy's tubercle and the anterior margin of the fibular head. Abbreviations: ALL, anterolateral ligament; FCL, fibular collateral ligament; LE, lateral epicondyle. (With permission from SAGE Publications Inc., from Kennedy MI, Claes S, Fuso FA et al 2015 The anterolateral ligament: an anatomic, radiographic, and biomechanical analysis. Am J Sports Med 43:1606–15. Copyright SAGE Publications Inc., Thousand Oaks, CA.)

References

Caterine S, Litchfield R, Johnson M et al 2015 A cadaveric study of the anterolateral ligament: re-introducing the lateral capsular ligament. Knee Surg Sports Traumatol Arthrosc 23:3186–95.

Claes S, Vereecke E, Maes M et al 2013 Anatomy of the anterolateral ligament of the knee. J Anat 223:321–8.

Dodds AL, Halewood C, Gupte CM et al 2014 The anterolateral ligament: anatomy, length changes and association with the Segond fracture. Bone Joint J 96-B:325–31.

Helito CP, Demange MK, Bonadio MB et al 2013 Anatomy and histology of the knee anterolateral ligament. Orthop J Sports Med 1:2325967113513546.

Kennedy MI, Claes S, Fuso FA et al 2015 The anterolateral ligament: an anatomic, radiographic, and biomechanical analysis. Am J Sports Med 43:1606–15.

LaPrade RF, Gilbert TJ, Bollom TS et al 2000 The magnetic resonance imaging appearance of individual structures of the posterolateral knee. A prospective study of normal knees and knees with surgically verified grade III injuries. Am J Sports Med 28:191–9.

Lobenhoffer P, Posel P, Witt S et al 1987 Distal femoral fixation of the iliotibial tract. Arch Orthop Trauma Surg 106:285–90.

Nitri M, Rasmussen MT, Williams BT et al 2016 An in vitro robotic assessment of the anterolateral ligament, part 2: anterolateral ligament reconstruction combined with anterior cruciate ligament reconstruction. Am J Sports Med 44:593–601.

Rasmussen MT, Nitri M, Williams BT et al 2016 An in vitro robotic assessment of the anterolateral ligament, part 1: secondary role of the anterolateral ligament in the setting of an anterior cruciate ligament injury. Am J Sports Med 44:585–92.

Schon JM, Moatshe G, Brady AW et al 2016 Anatomic anterolateral ligament reconstruction of the knee leads to overconstraint at any fixation angle. Am J Sports Med 44:2546–56.

Segond P 1879 Recherches cliniques et expérimentales sur les épanchements sanguins du genou par entorse. Progrès Médical (Paris) 1–85.

Terry GC, Norwood LA, Hughston JC et al 1993 How iliotibial tract injuries of the knee combine with acute anterior cruciate ligament tears to influence abnormal anterior tibial displacement. Am J Sports Med 21:55–60.

Vieira EL, Vieira EA, da Silva RT 2007 An anatomic study of the iliotibial tract. Arthroscopy 23:269–74.

Vincent JP, Magnussen RA, Gezmez F et al 2012 The anterolateral ligament of the human knee: an anatomic and histologic study. Knee Surg Sports Traumatol Arthrosc 20:147–52.

CHAPTER

80

The anatomy of the peripheral nervous system

The peripheral nervous system (PNS) is composed of spinal and cranial nerves, their associated ganglia (autonomic and sensory) and their ramifications that transmit afferent and efferent information between the central nervous system (CNS) and the rest of the body. It also includes the peripheral part of the autonomic nervous system (ANS), notably the sympathetic trunks and the sympathetic and parasympathetic ganglia and their ramifications, and the enteric nervous system (ENS), composed of plexuses of nerve fibres and cell bodies in the wall of the gastrointestinal tract, and the visceral afferent system.

CRANIAL NERVES

Cranial nerves are the means by which the brain receives information from, and controls the activities of, the head and neck and the thoracic and greater part of the abdominal viscera. There are 12 pairs of cranial nerves, individually named and numbered (Roman numerals) in a rostrocaudal sequence (see Table 24.1). Unlike spinal nerves, only some cranial nerves are mixed in function, i.e. they carry both sensory and motor fibres; others are purely sensory or motor. The first cranial nerve (I; olfactory) has an ancient lineage and is derived from the forerunner of the cerebral hemisphere. It retains this unique position through the connections of the olfactory bulb, and is the only sensory cranial nerve that projects directly to the cerebral cortex rather than indirectly via the thalamus. The areas of cerebral cortex receiving olfactory input have a primitive cellular organization and are an integral part of the limbic system, which is concerned with the emotional aspects of behaviour. The second cranial nerve (II; optic) consists of the axons of second-order visual neurones and these terminate in the thalamus. Most of the component fibres of the other 10 pairs of cranial nerves originate from, or terminate in, named cranial nerve nuclei in the brainstem.

OLFACTORY NERVE

The olfactory nerve is the first cranial nerve and, as its name suggests, is concerned with olfaction (the sense of smell). It is composed of bundles of very small unmyelinated axons derived from olfactory receptor neurones in the olfactory mucosa. The axons are in varying stages of maturity, reflecting the constant turnover of olfactory neurones that takes place in the olfactory epithelium. Bundles of axons are surrounded by olfactory ensheathing cells and form a plexiform network in the subepithelial lamina propria of the mucosa. The bundles unite into as many as 20 branches that cross the cribriform plate of the ethmoid bone in lateral and medial groups, and enter the overlying olfactory bulb, where they end in glomeruli. Each branch is ensheathed by dura mater and pia/arachnoid as it passes through the cribriform plate (see Fig. 39.13A). The dura subsequently becomes continuous with the nasal periosteum, and the pia/arachnoid merges with the connective tissue sheaths that surround the nerve bundles, an arrangement that may facilitate the spread of infection into the cranial cavity from the nasal cavity.

The olfactory bulb is continuous posteriorly with the olfactory tract, through which the output of the bulb projects directly to the ipsilateral retrobulbar area (anterior olfactory nucleus), olfactory tubercle, prepiriform area, amygdala and rostral entorhinal cortex. There is a clear laminar structure in the olfactory bulb (Fig. 32.32A). Different odour molecules are represented by different patterns of spatial activity in the olfactory bulb (Shepherd 2006).

In severe injuries involving the anterior cranial fossa, the olfactory bulb may be separated from the olfactory nerves or the nerves may be torn, producing anosmia, i.e. loss of olfaction. Fractures may involve the meninges, so that cerebrospinal fluid may leak into the nose, resulting in cerebrospinal rhinorrhoea. These injuries open up avenues for intracranial infection from the nasal cavity.

OPTIC NERVE

The optic nerve is the second cranial nerve and contains the axons of retinal ganglion cells. The two optic nerves join to form the optic chiasma which is usually positioned over the diaphragma sellae and pituitary gland (normofixed), although it may be prefixed (above the tuberculum sellae) or postfixed (above the dorsum sellae). On entering the optic nerve, retinal ganglion cell axons initially maintain their relative retinal positions, with axons from the fovea forming a lateral wedge. This retinotopic mapping is largely maintained within the optic nerve, although nearer the chiasma the foveal axons take a position in the centre of the optic nerve while temporal fibres occupy their previous lateral location. A substantial rearrangement of axons takes place at the chiasma. Most axons arising from the nasal half of a line bisecting the fovea within each retina cross in the chiasma to enter the contralateral optic tract. Fibres from the temporal hemi-retinas do not generally cross in the chiasma.

The axons within the optic tract were thought to maintain their topographic order and each tract was assumed to be a single representation of the contralateral hemifield. However, it is now clear that axons are mainly organized in functional groupings, larger superficial axons representing the magnocellular pathway and deeper axons originating from midget ganglion cells and forming the parvocellular pathway. This arrangement is chronotopic, the deeper axons developing earlier during axogenesis than the more superficial ones (Reese 1993).

Almost all (90%) of the retinal ganglion cell axons terminate on neurones in the lateral geniculate nucleus. Extrageniculate axons (10%) leave the optic tract before the lateral geniculate nucleus: they may leave the optic chiasma dorsally and project to the suprachiasmatic nucleus of the hypothalamus, or may branch off the optic tract at the superior brachium and project to the superior colliculus, pretectal areas and inferior pulvinar.

The optic nerve is usually described in four parts, intracranial (approximately 10 mm), intracanalicular (approximately 10 mm), intraorbital (25–30 mm), and intraocular (1 mm). The intracranial part arises from the optic chiasma in the suprasellar cistern. It is surrounded by the optic sheath and its dorsal surface is covered by the falciform ligament. The intracanalicular part passes through the optic canal together with the ophthalmic artery: this is the weakest point of the anterior visual pathway because the nerve is fixed to its bony surroundings by fibrous adhesions. The intraorbital part passes forwards, laterally and downwards, and pierces the sclera at the lamina cribrosa, slightly medial to the posterior pole: it has a somewhat tortuous course within the orbit that allows for movements of the eyeball (Demer 2016). The subarachnoid space surrounding the intracranial part is continuous with the subarachnoid space around the intracanalicular and intraorbital parts. The dural sheath surrounding the optic nerve originates at the level of the optic canal and accompanies the optic nerve to the sclera. The intraorbital part of optic nerve has important relationships with other orbital structures (see Fig. 44.4). As it leaves the optic canal, it lies superomedial to the ophthalmic artery, and is separated from lateral rectus by the oculomotor, nasociliary and abducens nerves, and sometimes by the ophthalmic veins. It is closely related to the origins of the four recti, whereas more anteriorly, where the muscles diverge, it is separated from them by a substantial amount of orbital fat. Just beyond the optic canal, the ophthalmic artery and the nasociliary nerve cross the optic nerve to reach the medial wall of the orbit. The central artery of the retina enters the substance of the optic nerve about halfway along its length. Near the back of the eyeball, the optic nerve is surrounded by the long and short ciliary nerves and vessels.

OCULOMOTOR NERVE

The oculomotor nerve is the third cranial nerve and innervates levator palpebrae superioris and four of the extraocular muscles (superior, inferior and medial rectus and inferior oblique) (see Fig. 44.15). It also conveys preganglionic parasympathetic fibres from cell bodies in the Edinger–Westphal nucleus that relay in the ciliary ganglion.

Oculomotor nuclear complex

The nuclear complex from which the oculomotor nerve arises consists of several groups of large motor neurones that are collectively designated the oculomotor nucleus, and the smaller preganglionic parasympathetic Edinger–Westphal nucleus (see Figs 28.3, 28.16). The nuclear complex lies at the ventromedial aspect of the periaqueductal grey matter, superior to the trochlear nuclei and is partially enclosed by the fibres of the median longitudinal fasciculi. It is approximately 5 mm long and is divisible into neuronal groups that correlate with the distribution of motor fibres within the oculomotor nerve. Afferent inputs to the oculomotor nuclear complex include fibres from the rostral interstitial nucleus of the medial longitudinal fasciculus and the interstitial nucleus of Cajal, both of which are involved in the control of vertical and torsional gaze. Other inputs come, directly or indirectly, from the nuclei of the posterior commissure and, via these nuclei, from the frontal eye fields, the superior colliculus, the dentate nucleus and cortical areas. The medial longitudinal fasciculus carries afferent connections from the trochlear, abducens and vestibular nuclei.

The fibres from the medial vestibular nucleus project to the medial rectus subnucleus. In order from dorsal to ventral, the oculomotor neurone groups innervate the ipsilateral inferior rectus, inferior oblique and medial rectus. A medially placed column of cells innervates the contralateral superior rectus through axons that decussate in the caudal part of this subnucleus. A median subnucleus of large neurones, designated the caudal central nucleus, lies at the caudal pole of the oculomotor nucleus adjacent to the superior rectus and medial rectus subnuclei. Fascicles of axons from these subnuclei course forwards in the midbrain, through the tegmentum, red nucleus and medial substantia nigra, to emerge as the oculomotor nerve in the interpeduncular fossa. The fascicles are most probably arranged from medial to lateral subserving the pupil, inferior rectus, medial rectus, levator palpebrae superioris and superior rectus, and inferior oblique.

Intra- and extracranial course

For descriptive purposes, the oculomotor nerve is usually divided into cisternal, cavernous and orbital portions: surgically oriented classifications derived from combined microsurgical and endoscopic cadaveric dissection studies have proposed five or seven parts (Iaconetta et al 2010, Park et al 2017).

The cisternal portion of the oculomotor nerve emerges from the midbrain, either through the medial sulcus of the crus cerebri in the caudal part of the interpeduncular fossa or through the medial or the middle part of the crus cerebri. It usually passes forwards and laterally through the interpeduncular cistern between the posterior communicating artery and the superior cerebellar artery: this portion of the nerve is supplied by the P1 and P2 segments of the posterior cerebral artery. The pupilloconstrictor fibres lie superficially on the dorsomedial surface of the cisternal portion of oculomotor nerve, a location that renders them vulnerable to aneurysmal compression (Kerr and Hollowell 1964, Shechtman et al 2007), whereas a pupil-sparing palsy of the oculomotor nerve is pathognomonic of an ischaemic lesion, which tends to involve the central region of the nerve. The oculomotor nerve next passes inferolateral to the posterior communicating artery and inferomedial to the uncus and enters the roof of the cavernous sinus through the oculomotor trigone. This cavernous portion of the nerve passes along the lateral dural wall of the cavernous sinus, dividing into superior and inferior divisions that run beneath the trochlear and ophthalmic nerves. The two divisions enter the orbit through the superior orbital fissure, within the common tendinous ring of the recti, and separated by the nasociliary branch of the ophthalmic nerve.

The superior division of the oculomotor nerve passes above the optic nerve to enter the inferior (ocular) surface of superior rectus. It supplies this muscle and gives off a branch that runs to innervate levator palpebrae superioris. The inferior division of the oculomotor nerve divides into medial, central and lateral branches. The medial branch passes beneath the optic nerve to enter the lateral (ocular) surface of medial rectus; the central branch runs downwards and forwards to enter the superior (ocular) surface of inferior rectus; the lateral branch travels forwards on the lateral side of inferior rectus to enter the orbital surface of inferior oblique and also communicates with the ciliary ganglion to distribute parasympathetic fibres to sphincter pupillae and the ciliary muscle.

Edinger–Westphal nucleus

The Edinger–Westphal nucleus lies dorsal to the main oculomotor nucleus. It is composed of small, multipolar, preganglionic parasympathetic (general visceral efferent, GVE) neurones. Afferent inputs to the nucleus come primarily from the pretectal nuclei bilaterally, mediating the pupillary light reflex, and from the visual cortex, mediating accommodation. Efferent fibres from the nucleus travel in the oculomotor nerve to synapse with postganglionic neurones in the ciliary ganglion (Kozicz et al 2011), and also descend through the medial longitudinal fasciculus to innervate the medial and descending vestibular nuclei (Nieuwenhuys et al 2008).

TROCHLEAR NERVE

The trochlear nerve is the fourth cranial nerve and innervates superior oblique. It has the longest intracranial course and the smallest diameter of all of the cranial nerves, and is also the only cranial nerve to emerge from the dorsal surface of the brainstem, lateral to the lower edge of the inferior colliculus.

Trochlear nucleus

The trochlear nucleus is a small ovoid mass of grey matter just to the side of the midline (see Fig. 28.15). It is bounded by the periaqueductal grey matter dorsally and is enveloped by the fibres of the longitudinal fasciculi ventrally and laterally (Naidich et al 2009). The nucleus is part of the somatic efferent column in line with the oculomotor, abducens and hypoglossal nuclei. Afferent inputs to the trochlear nucleus include fibres from the rostral intermediate nucleus of the medial longitudinal fasciculus and from the interstitial nucleus of Cajal, both of which are involved in the control of vertical and torsional gaze. Other inputs come from the vestibular, abducens and oculomotor nuclei and, directly or indirectly, from the nuclei of the posterior commissure (nuclei of Darkschewitsch and of Cajal) and, via these nuclei, from the superior colliculus, frontal eye fields and other cortical areas. Other afferents arrive from the nucleus prepositus hypoglossi. Efferent trochlear fibres first course dorsally and caudally, just deep to the outer perimeter of the periaqueductal grey matter and medial to the mesencephalic trigeminal nucleus. The trochlear nerves then decussate within the superior medullary velum of the fourth ventricle. A few fibres may remain ipsilateral.

Intra- and extracranial course

The nerves emerge from the dorsal surface of the brainstem just caudal to the inferior colliculus and to each side of the frenulum veli. At the point of emergence, a variable number of rootlets, usually two, unite to form the nerve trunks that curve ventrally through the perimesencephalic cisterns, between the superior cerebellar arteries below and the posterior cerebral arteries above. The cisternal portion of each nerve courses anterolaterally, winding round the cerebral peduncle toward the tentorium cerebelli through the quadrigeminal and ambient cisterns. The nerve passes anteriorly along the infratentorial groove of the tentorium cerebelli and penetrates the roof of the cavernous sinus at the junction of the anterior and posterior petroclinoid dural folds. The cavernous portion continues along the lateral wall of the cavernous sinus below the oculomotor nerve, crossing this nerve at the level of the optic strut to become the most superior structure in the cavernous sinus. The trochlear nerve enters the orbit through the superior orbital fissure outside the common tendinous ring, superior to levator palpebrae superioris and medial to the frontal and lacrimal nerves (see Fig. 44.16). The orbital portion runs medially across levator palpebrae superior and superior rectus to reach superior oblique: its branches typically end on the posterior one-third of the muscle, most often on the medial aspect (Joo and Rhoton 2015).

TRIGEMINAL NERVE

The trigeminal nerve is the fifth cranial nerve and has extensive sensory, motor and autonomic components.

Sensory nuclei and central connections

The trigeminal nerve has three sensory nuclei (spinal tract, principal and mesencephalic) and one motor nucleus. On entering the pons, the fibres of the sensory root of the trigeminal nerve run dorsomedially towards the principal sensory nucleus. About 50% of the fibres divide into ascending and descending branches and the others ascend or descend without division. The descending fibres form the spinal tract of the trigeminal nerve, which terminates in the medially adjacent spinal nucleus of the trigeminal nerve. Some ascending trigeminal fibres, many of them heavily myelinated, synapse around the small neurones in the principal sensory nucleus, which lies lateral to the motor nucleus and medial to the middle cerebellar peduncle, and is continuous inferiorly with the spinal nucleus of the trigeminal nerve. The principal nucleus is considered to be mainly concerned with tactile stimuli. Other ascending fibres enter the mesencephalic nucleus, a column of unipolar cells with peripheral branches that may convey proprioceptive impulses from the masticatory muscles, and possibly also from the teeth, the facial and oculogyric muscles. Its neurones are unique in being the only primary sensory unipolar neurones that have cell bodies in the CNS. It is the relay for the 'jaw jerk', the only significant supraspinal monosynaptic reflex. Nerve fibres that ascend to the mesencephalic nucleus may give collaterals to the motor nucleus of the trigeminal nerve and to the cerebellum. Most fibres that arise in the trigeminal sensory nuclei cross the midline, ascend in the trigeminal lemniscus and end in the contralateral ventral posteromedial thalamic nucleus, from which third-order neurones project to the postcentral gyrus (areas 3, 1, 2).

Motor nucleus

The motor nucleus of the trigeminal nerve is ovoid in outline and lies in the upper pontine tegmentum, under the lateral part of the floor of the fourth ventricle. It lies medial to the principal sensory nucleus from which it is separated by fibres of the trigeminal nerve. It forms the rostral part of the pharyngeal (special visceral) efferent column. The motor nucleus contains characteristic large multipolar neurones interspersed with smaller multipolar cells, organized into a number of relatively discrete subnuclei that drive individual muscles. It receives fibres from both corticonuclear tracts. These fibres leave the tracts at the nuclear level or higher in the pons (aberrant corticospinal fibres), descend in the medial lemniscus and may end on motor neurones or interneurones. The motor nucleus receives afferents from the sensory nuclei of the trigeminal nerve, possibly including some from the mesencephalic nucleus, that form monosynaptic reflex arcs for proprioceptive control of the masticatory muscles. It also receives afferents from the reticular formation, red nucleus and tectum, the medial longitudinal fasciculus and possibly from the locus coeruleus. Collectively these represent pathways by which salivary secretion and mastication may be coordinated.

Tensor tympani and stapedius reflex

Loud sound elicits reflex contraction of tensor tympani and stapedius, attenuating movement of the tympanic membrane and the ossicular chain. Afferent impulses travel in the cochlear nerve to the cochlear nuclei in the brainstem. Efferent fibres to tensor tympani arise in the motor nucleus of the trigeminal nerve and travel in the mandibular division of the nerve. Efferent fibres to stapedius originate in the facial nucleus and travel in the facial nerve.

Jaw jerk reflex

The jaw jerk reflex is a deep tendon reflex, elicited by tapping on the midline of the mandible. Rapid stretching of the muscles that close the jaw (masseter, temporalis, medial pterygoid) activates muscle spindle afferents that travel via the mandibular division of the trigeminal nerve to the mesencephalic trigeminal nucleus. Collaterals project monosynaptically to the motor nucleus of the trigeminal nerve in the pons, establishing a two-neurone reflex arc.

Intra- and extracranial course

Embryologically, each division of the trigeminal nerve is associated with a developing facial process that gives rise to a specific area of the adult face: the ophthalmic nerve is associated with the frontonasal process, the maxillary nerve with the maxillary process, and the mandibular nerve with the mandibular process.

Ophthalmic nerve

The ophthalmic division of the trigeminal nerve is a sensory nerve. It arises from the trigeminal ganglion in the middle cranial fossa and passes forwards along the lateral dural wall of the cavernous sinus, giving off three main branches, the lacrimal, frontal and nasociliary nerves, just before it reaches the superior orbital fissure. These branches subsequently travel through the orbit to supply targets that are primarily in the upper part of the face (conjunctiva, skin over the forehead, upper eyelid and much of the external surface of the nose via the supraorbital, lacrimal, infratrochlear and external nasal nerves).

Lacrimal nerve

The lacrimal nerve is the smallest of the main ophthalmic branches. It enters the orbit through the superior orbital fissure, outside the common tendinous ring and lateral to the frontal and trochlear nerves. It passes forwards along the lateral wall of the orbit on the superior border of lateral rectus, and travels through the lacrimal gland and the orbital septum to supply the conjunctiva and skin covering the lateral part of the upper eyelid. The nerve also communicates with the zygomatic branch of the maxillary nerve, which may carry some postganglionic parasympathetic fibres from the pterygopalatine ganglion to the lacrimal gland. Occasionally, the lacrimal nerve is absent, in which case it is replaced by the zygomaticotemporal nerve; the relationship is reciprocal, and when the zygomaticotemporal nerve is absent it is replaced by a branch of the lacrimal nerve. The lacrimal nerve anastomoses with filaments of the facial nerve.

Frontal nerve

The frontal nerve is the largest branch of the ophthalmic nerve. It enters the orbit through the superior orbital fissure outside the common tendinous ring, and lies between the lacrimal nerve laterally and the trochlear nerve medially. It passes forwards towards the rim of the orbit on levator palpebrae superioris, and about halfway along this course it divides into the supraorbital and supratrochlear nerves.

Supraorbital nerve

The supraorbital nerve is the larger of the two terminal branches of the frontal nerve. It continues forwards along levator palpebrae superioris until it leaves the orbit through the supraorbital notch or foramen to emerge onto the forehead. It supplies the mucous membrane that lines the frontal sinus, the conjunctiva and the skin covering the upper eyelid via palpebral branches. It ascends on the forehead with the supraorbital artery, and divides into medial and lateral branches that supply the skin of the scalp nearly as far back as the lambdoid suture. These branches are at first deep to the frontal belly of occipitofrontalis. The medial branch perforates the muscle to reach the skin, while the lateral branch pierces the epicranial aponeurosis. The postganglionic sympathetic fibres that innervate the sweat glands of the supraorbital area probably travel in the supraorbital nerve, having entered the ophthalmic nerve via its communication with the abducens nerve within the cavernous sinus.

Supratrochlear nerve

The supratrochlear nerve is the smaller terminal branch of the frontal nerve. It runs anteromedially in the roof of the orbit, passes above the trochlea for the tendon of superior oblique, and supplies a descending filament to the infratrochlear branch of the nasociliary nerve. The nerve emerges between the trochlea and the supraorbital foramen at the frontal notch, curves up on the forehead close to the bone with the supratrochlear artery, and supplies the conjunctiva and the skin of the upper eyelid. It then ascends beneath corrugator and the frontal belly of occipitofrontalis before dividing into branches that pierce these muscles to supply the skin of the lower forehead near the midline.

Nasociliary nerve

The nasociliary nerve is intermediate in size between the frontal and lacrimal nerves. It is more deeply placed in the orbit, which it enters through the common tendinous ring, lying between the two rami of the oculomotor nerve. It crosses the optic nerve with the ophthalmic artery and runs obliquely below superior rectus and superior oblique to reach the medial orbital wall, where it gives off the anterior and posterior ethmoidal nerves. The nasociliary nerve has long ciliary and infratrochlear branches and a connection with the ciliary ganglion.

Anterior ethmoidal nerve

The anterior ethmoidal nerve passes through the anterior ethmoidal foramen and canal and enters the cranial cavity. It runs forwards in a groove on the upper surface of the cribriform plate beneath the dura mater, descends through a slit lateral to the crista galli into the nasal cavity, where it occupies a groove on the internal surface of the nasal bone, and supplies the roof of the nasal cavity. It gives off medial and lateral internal nasal branches that supply the anterior and upper parts of the septum and the anterior part of the lateral wall, respectively, before emerging at the inferior margin of the nasal bone as the external nasal nerve, which descends through the lateral wall of the nose and supplies the skin of the nose below the nasal bones to the nasal tip but excluding the alar portion around the external nares: damage following nasal trauma may result in paraesthesia of the nasal tip.

Posterior ethmoidal nerve

The posterior ethmoidal nerve leaves the orbit by the posterior ethmoidal foramen and supplies the ethmoidal and sphenoidal sinuses.

Infratrochlear nerve

The infratrochlear nerve leaves the orbit below the trochlea and supplies the skin of the eyelids, the conjunctiva, lacrimal sac, lacrimal caruncle and the side of the nose above the medial canthus.

Long ciliary nerves

Two or three long ciliary nerves branch from the nasociliary nerve as it crosses the optic nerve. They accompany the short ciliary nerves, pierce the sclera near the attachment of the optic nerve, and run forwards between the sclera and choroid. They supply the ciliary body, iris and cornea, and contain postganglionic sympathetic fibres for dilator pupillae from neurones in the superior cervical ganglion. An alternative pathway for the supply of the dilator pupillae is via the sympathetic root associated with the ciliary ganglion.

Ramus communicans to the ciliary ganglion

The ramus communicans to the ciliary ganglion usually branches from the nasociliary nerve as the latter enters the orbit lateral to the optic nerve. It is sometimes joined by a filament from the internal carotid sympathetic plexus or from the superior ramus of the oculomotor nerve as it enters the posterosuperior angle of the ganglion.

Maxillary nerve

The maxillary division of the trigeminal nerve is a sensory nerve. It leaves the skull via the foramen rotundum and enters the upper part of the pterygopalatine fossa where many of its extracranial branches are given off. It crosses the pterygopalatine fossa, giving off two large ganglionic branches that contain fibres destined for the nose, palate and pharynx and that all pass through the pterygopalatine ganglion without synapsing. The maxillary nerve then inclines sharply laterally on the posterior surface of the orbital process of the palatine bone and on the upper part of the posterior surface of the maxilla in the inferior orbital fissure (which is continuous posteriorly with the pterygopalatine fossa): it lies outside the orbital periosteum, and gives off zygomatic, and then posterior superior alveolar branches. About halfway between the orbital apex and the orbital rim, the maxillary nerve turns medially to enter the infraorbital canal as the infraorbital nerve. Named branches from the main trunk are meningeal, ganglionic, zygomatic, posterior, middle and anterior superior alveolar and infraorbital nerves. Named branches from the pterygopalatine ganglion are orbital, nasopalatine, posterior superior nasal, greater (anterior) palatine, lesser (posterior) palatine and pharyngeal nerves.

Meningeal nerve

The meningeal branch of the maxillary nerve arises within the middle cranial fossa and runs with the middle meningeal vessels. It contributes to the innervation of the dura mater (see Fig. 25.3B).

Ganglionic branches

Two ganglionic branches usually connect the maxillary nerve to the pterygopalatine ganglion.

Zygomatic nerve

The zygomatic branch of the maxillary nerve leaves the pterygopalatine fossa through the inferior orbital fissure with the maxillary nerve and lies close to the base of the lateral wall of the orbit. Soon after entering the orbit the nerve divides into two branches, the zygomaticotemporal and the zygomaticofacial nerves, which run within the orbit for only a short distance before passing onto the face through the lateral wall of the orbit. They may enter separate canals within the zygomatic bone or the zygomatic nerve itself may enter the bone before dividing.

Zygomaticotemporal nerve

The zygomaticotemporal nerve traverses a canal in the zygomatic bone and emerges into the anterior part of the temporal fossa, where it ascends between the bone and temporalis before piercing the temporal fascia about 2 cm above the zygomatic arch to supply the skin of the temple. It communicates with the facial and auriculotemporal nerves. As it pierces the deep layer of the temporal fascia, it sends a slender twig between the two layers of the fascia towards the lateral angle of the eye. It was thought that the branch carried parasympathetic postganglionic fibres from the pterygopalatine ganglion to the lacrimal gland, but it is now believed that these fibres innervate the lacrimal gland directly.

Zygomaticofacial nerve

The zygomaticofacial nerve traverses the inferolateral angle of the orbit and emerges on the face through a foramen in the zygomatic bone. It perforates orbicularis oculi to supply the skin on the prominence of the cheek and forms a plexus with zygomatic branches of the facial nerve and palpebral branches of the maxillary nerve. The nerve is absent occasionally.

Infraorbital nerve

The infraorbital nerve can be regarded as the terminal branch of the maxillary nerve. It leaves the pterygopalatine fossa to enter the orbit at the inferior orbital fissure and at first it lies in the infraorbital groove on the floor of the orbit. As it approaches the rim of the orbit it runs into the infraorbital canal through which it passes to emerge onto the face at the infraorbital foramen, where it lies between levator labii superioris and levator anguli oris. It gives off palpebral, nasal and superior labial branches. The palpebral branches ascend deep to orbicularis oculi, pierce the muscle to supply the skin in the lower eyelid, and join the facial and zygomaticofacial nerves near the lateral canthus. Nasal branches supply the skin of the side of the nose, the vestibule and the movable part of the nasal septum, and join the external nasal branch of the anterior ethmoidal nerve. Superior labial branches, which are large and numerous, descend behind levator labii superioris to supply the skin of the anterior part of the cheek and upper lip. They are joined by branches from the facial nerve to form the infraorbital plexus.

Orbital branches

Fine orbital branches enter the orbit through the inferior orbital fissure and supply orbital periosteum. Some fibres also pass through the posterior ethmoidal foramen to supply the sphenoidal and ethmoidal sinuses. The orbital branches probably join branches of the internal carotid nerve to form a 'retro-orbital' plexus from which orbital structures such as the lacrimal gland and orbitalis receive an autonomic innervation.

Posterior superior nasal nerves (lateral and medial)

The posterior superior alveolar nerves enter the back of the nasal cavity through the sphenopalatine foramen. Lateral posterior superior nasal nerves innervate the mucosa covering the posterior part of the superior and middle nasal turbinates (conchae) and lining the posterior ethmoidal sinuses. Two or three medial posterior superior nasal nerves cross the nasal roof below the opening of the sphenoidal sinus to supply the mucosa of the posterior part of the roof and of the nasal septum.

Nasopalatine nerve

The nasopalatine nerve leaves the pterygopalatine fossa through the sphenopalatine foramen and enters the nasal cavity. It passes across the cavity to the back of the nasal septum, runs downwards and forwards on the septum in a groove in the vomer, and then turns down through the incisive fossa in the anterior part of the hard palate to enter the roof of the mouth. When an anterior and a posterior incisive foramen exist in this fossa, the left nasopalatine nerve typically passes through the anterior foramen, and the right nerve passes through the posterior foramen. The nasopalatine nerve supplies the inferior part of the nasal septum and the anterior part of the hard palate, where it communicates with the greater palatine nerve.

Surgical division of the nasopalatine nerve, for example during the removal of an ectopic canine tooth, causes no obvious sensory deficit in the anterior part of the palate, which suggests that either the territory of the greater palatine nerve reaches as far forwards as the gingivae lingual to the incisor teeth or that the nasopalatine nerve has significant regenerative potential.

Palatine nerves (greater and lesser)

The greater and lesser palatine nerves pass downwards from the pterygopalatine ganglion through the greater palatine canal. The greater palatine nerve descends through the greater palatine canal, emerges on the hard palate from the greater palatine foramen and runs forwards in a groove on the inferior surface of the bony palate almost to the incisor teeth. It supplies the gingivae, mucosa and glands of the hard palate and also communicates with the terminal filaments of the nasopalatine nerve. In the greater palatine canal it gives off posterior inferior nasal branches that emerge through the perpendicular plate of the palatine bone and ramify over the inferior nasal turbinate (concha) and walls of the middle and inferior meatuses. As it leaves the greater palatine canal, it gives off branches which are distributed to both surfaces of the adjacent part of the soft palate.

The lesser (middle and posterior) palatine nerves are much smaller than the greater palatine nerve. They descend through the greater palatine canal, from which they diverge low down to emerge through the lesser palatine foramina in the tubercle or pyramidal process of the palatine bone. They innervate the uvula, tonsil and soft palate.

Fibres conveying taste impulses from the palate probably pass via the palatine nerves to the pterygopalatine ganglion. They pass through the ganglion without synapsing, and leave via the greater petrosal nerve. Their cell bodies are located in the facial ganglion and their central processes pass via the sensory root of the facial nerve (nervus intermedius) to the gustatory nucleus in the nucleus of the tractus solitarius.

Pharyngeal nerve

The pharyngeal branch of the maxillary nerve leaves the pterygopalatine ganglion posteriorly. It passes through the palatovaginal canal with the pharyngeal branch of the maxillary artery and supplies the mucosa of the nasopharynx behind the pharyngotympanic tube.

Superior alveolar nerves

The teeth in the upper jaw are supplied by the three superior alveolar (dental) nerves that arise from the maxillary nerve either in the pterygopalatine fossa or in the infraorbital groove and canal.

The posterior superior alveolar (dental) nerve leaves the maxillary nerve in the pterygopalatine fossa and runs anteroinferiorly to pierce the infratemporal surface of the maxilla, at which point it is possible to perform a local anaesthetic block that will anaesthetize the pulps of the premolar and molar ipsilateral teeth; it then descends under the mucosa of the maxillary sinus. After supplying the lining of the sinus, the nerve divides into small branches that link up as the molar part of the superior alveolar plexus, supplying twigs to the molar teeth. It also supplies a branch to the upper molar gingivae and the adjoining part of the cheek.

The middle superior alveolar (dental) nerve arises from the infraorbital nerve as it runs in the infraorbital groove, and runs downwards and forwards in the lateral wall of the maxillary sinus. It ends in small branches that link up with the superior dental plexus, supplying small rami to the upper premolar teeth. This nerve is variable; it may be duplicated, triplicated, or absent.

The anterior superior alveolar (dental) nerve leaves the lateral side of the infraorbital nerve near the midpoint of its canal and traverses the canalis sinuosus in the anterior wall of the maxillary sinus. It curves first under the infraorbital foramen, then passes medially towards the nose, and finally turns downwards and divides into branches to supply the incisor and canine teeth. It assists in the formation of the superior dental plexus and gives off a nasal branch that passes through a minute canal in the lateral wall of the inferior meatus to supply the mucous membrane of the anterior area of the lateral wall as high as the opening of the maxillary sinus, and the floor of the nasal cavity near the anterior nasal spine. It communicates with the nasal branches of the pterygopalatine ganglion and finally emerges near the root of the anterior nasal spine to supply the adjoining part of the nasal septum.

Mandibular nerve

The mandibular division of the trigeminal nerve is the largest division of the trigeminal nerve and is a mixed nerve. Its sensory branches supply the mandibular teeth and gingivae, the skin in the temporal region, part of the auricle and the lower lip, the lower part of the face and the mucosa of the anterior two-thirds (presulcal part) of the tongue and the floor of the oral cavity. The motor branches innervate the muscles of mastication, tensor veli palatini, tensor tympani, anterior belly of digastric and mylohyoid. The large sensory root emerges from the lateral part of the trigeminal ganglion and exits the cranial cavity through the foramen ovale. The small motor root passes under the ganglion and through the foramen ovale to unite with the sensory root just outside the skull. As it descends from the foramen ovale, the mandibular nerve is usually around 4 cm from the surface and a little anterior to the neck of the mandible. It immediately passes between tensor veli palatini, which is medial, and lateral pterygoid, which is lateral, gives off a meningeal branch and the nerve to medial pterygoid from its medial side, and then divides into a small anterior and large posterior trunk. The anterior trunk gives off branches to the four main muscles of mastication and a buccal branch which is sensory to the cheek. The posterior trunk gives off three main sensory branches, the auriculotemporal, lingual and inferior alveolar nerves, and motor fibres to supply mylohyoid and the anterior belly of digastric.

Meningeal branch (nervus spinosus)

The meningeal branch re-enters the middle cranial fossa through the foramen spinosum with the middle meningeal artery. It divides into anterior and posterior branches that accompany the main divisions of the middle meningeal artery and supply the dura mater in the middle cranial fossa and, to a lesser extent, in the anterior fossa and calvaria (see Fig. 25.3B).

Nerve to medial pterygoid

The nerve to medial pterygoid is a slender ramus that enters the deep aspect of the muscle. It supplies one or two filaments that pass through the otic ganglion without interruption to supply tensor tympani and tensor veli palatini.

Anterior trunk of mandibular nerve

The anterior trunk of the mandibular nerve gives rise to the buccal nerve, which is sensory, and the masseteric, deep temporal and lateral pterygoid nerves, which are all motor.

Buccal nerve

The buccal nerve passes between the two heads of lateral pterygoid, giving off motor fibres to the muscle as it passes through it. The nerve then descends deep to the tendon of temporalis, passes laterally anterior to masseter, and anastomoses with the buccal branches of the facial nerve. It may give off the anterior deep temporal nerve. The buccal nerve supplies sensation to the skin over the anterior part of buccinator, the corresponding buccal mucous membrane and the posterior part of the buccal gingivae opposite the second and third molar teeth. It may also give off a branch that passes through a small retromolar foramen to supply the molar teeth.

Nerve to masseter

The nerve to masseter passes laterally above lateral pterygoid onto the skull base, anterior to the temporomandibular joint and posterior to the tendon of temporalis. It crosses the posterior part of the mandibular notch with the masseteric artery and ramifies on and enters the deep surface of masseter. It provides articular branches to the temporomandibular joint.

Deep temporal nerves

There are usually two deep temporal nerves, anterior and posterior, although there may be a middle branch. They pass above lateral pterygoid to enter the deep surface of temporalis. The anterior branch may arise as a branch of the buccal nerve or from the nerve to masseter; the small posterior nerve sometimes arises in common with the nerve to masseter. Branches from the buccal nerve and the nerve to masseter may supply the inferior aspect of temporalis independently from the deep temporal nerves.

Nerve to lateral pterygoid

The nerve to lateral pterygoid enters the deep surface of the muscle. It may arise separately from the anterior division of the mandibular nerve or from the buccal nerve.

Posterior trunk of mandibular nerve

The posterior trunk of the mandibular nerve is larger than the anterior and is mainly sensory, although it receives fibres from the motor root for the nerve to mylohyoid. It divides into auriculotemporal, lingual and inferior alveolar (dental) nerves.

Auriculotemporal nerve

The auriculotemporal nerve usually has two roots that encircle the middle meningeal artery. It runs back under lateral pterygoid on the surface of tensor veli palatini, passes between the sphenomandibular ligament and the neck of the mandible, and then runs laterally behind the temporomandibular joint related to the upper part of the parotid gland. Emerging from behind the joint, it ascends over the posterior root of the zygoma, posterior to the superficial temporal vessels, and divides into superficial temporal branches. It communicates with the facial nerve and otic ganglion. The rami to the facial nerve, usually two, pass anterolaterally behind the neck of the mandible to join the facial nerve at the posterior border of masseter. Filaments from the otic ganglion join the roots of the auriculotemporal nerve close to their origin. The auriculotemporal nerve emerges onto the face behind the temporomandibular joint within the superior surface of the parotid gland, ascends posterior to the superficial temporal vessels, passes over the posterior root of the zygoma, and divides into superficial temporal branches. The cutaneous branches of the auriculotemporal nerve supply the tragus and part of the adjoining auricle of the ear and the posterior part of the temple. The nerve may be damaged during parotid gland surgery, resulting in impaired sensation over the tragus and temple. The auriculotemporal nerve communicates with the temporofacial division of the facial nerve, usually by two rami that pass anterolaterally behind the neck of the mandible. These communications anchor the facial nerve close to the lateral surface of the condylar process of the mandible and limit its mobility during surgery. Communications with the temporal and zygomatic branches of the facial nerve loop around the transverse facial and superficial temporal vessels.

Lingual nerve

The lingual nerve is sensory to the mucosa of the floor of the mouth, mandibular lingual gingivae and mucosa of the presulcal part of the tongue (excluding the circumvallate papillae, which are supplied by the glossopharyngeal nerve). It also carries postganglionic parasympathetic fibres from the submandibular ganglion to the sublingual and anterior lingual glands. It arises from the posterior trunk of the mandibular nerve and at first runs beneath lateral pterygoid and superficial to tensor veli palatini, where it is joined by the chorda tympani branch of the facial nerve, and often by a branch of the inferior alveolar nerve. Emerging from under cover of lateral pterygoid, the lingual nerve then runs downwards and forwards on the surface of medial pterygoid, and is thus carried progressively closer to the medial surface of the mandibular ramus. It becomes intimately related to the bone a few millimetres below and behind the junction of the vertical ramus and horizontal body of the mandible. Here it lies anterior to, and slightly deeper than, the inferior alveolar (dental) nerve. It next passes below the mandibular attachment of the superior pharyngeal constrictor and pterygomandibular raphe, closely applied to the periosteum of the medial surface of the mandible, until it lies opposite the posterior root of the lower third molar tooth, where it is covered only by the gingival mucoperiosteum. At this point it usually lies approximately 3 mm below the alveolar crest with a mean distance from the bone of 2 mm: it may be in direct contact with the bone (25%) or lie above the alveolar crest (15%). The nerve next passes medial to the mandibular origin of mylohyoid, and this carries it progressively away from the mandible, separating it from the alveolar bone covering the mesial root of the lower third molar tooth. It then passes downwards and forwards on the deep surface of mylohyoid (i.e. the surface nearer the mucosa covering the floor of the mouth), crossing the lingual sulcus beneath the mucosa. In this position, the lingual nerve lies on the deep portion of the submandibular gland, which bulges over the top of the posterior border of mylohyoid. The nerve passes below the submandibular duct, which crosses it from medial to lateral, and curves upwards, forwards and medially to enter the tongue by medial and lateral branches. Within the tongue, the medial branch sends small branches to the medial part of the ventrolateral tongue, and the lateral branch runs along the lateral border of the tongue and sends larger branches to innervate the mucosa of the anterior tip of the tongue. The lingual nerve is connected to the submandibular ganglion by two or three branches. It forms connecting loops with twigs of the hypoglossal nerve at the anterior margin of hyoglossus (Fitzgerald and Law 1958) and within the tongue (Zur et al 2004).

The lingual nerve is at risk during surgical removal of (impacted) lower third molars: patients occasionally develop lingual sensory disturbance postoperatively but this is rarely persistent (Renton 2011). The nerve is also at risk during operations to remove the submandibular salivary gland because the submandibular duct must be dissected from the lingual nerve, and also because its connection to the submandibular ganglion pulls it into the operating field.

Inferior alveolar (dental) nerve

The inferior alveolar nerve descends behind lateral pterygoid. At the lower border of the muscle the nerve passes between the sphenomandibular ligament and the mandibular ramus and enters the mandibular canal via the mandibular foramen. Just before entering the mandibular canal, the inferior alveolar nerve gives off a small mylohyoid branch that also carries fibres that innervate the anterior belly of digastric. Below lateral pterygoid, the nerve is accompanied by the inferior alveolar artery, a branch of the first part of the maxillary artery, which enters the canal with its associated veins. In the mandibular canal, the inferior alveolar nerve runs downwards and forwards, generally below the apices of the teeth until it is below the first and second premolars, where it divides into terminal incisive and mental branches. The incisive branch continues forwards in a bony canal or in a plexiform arrangement, giving off branches to the first premolar, canine and incisor teeth, and to the associated labial gingivae. The lower central incisor teeth receive a bilateral innervation, fibres probably crossing the midline within the periosteum to re-enter the bone via numerous canals in the labial cortical plate. The mental nerve passes upwards, backwards and outwards to emerge from the mandible via the mental foramen between and just below the apices of the premolar teeth. It immediately divides into three branches, two of which pass upwards and forwards to form an incisor plexus labial to the teeth that supplies the labial gingivae (and probably the periosteum). From this plexus and from the dental branches, fibres turn downwards and then lingually to emerge on the lingual surface of the mandible on the posterior aspect of the mental symphysis or opposite the premolar teeth, probably communicating with the lingual or mylohyoid nerves. The third branch of the mental nerve passes through the intermingled fibres of depressor anguli oris and platysma to supply the skin of the lower lip and chin. Branches of the mental nerve communicate with terminal filaments of the mandibular branch of the facial nerve.

Nerve to mylohyoid

The nerve to mylohyoid is given off from the inferior alveolar nerve just before that nerve enters the mandibular canal. It pierces the sphenomandibular ligament and enters a shallow groove on the medial surface of the mandible, following a course roughly parallel to its parent nerve. It passes below the origin of mylohyoid to lie on the superficial surface of the muscle, between it and the anterior belly of digastric, both of which it supplies. Although primarily a motor nerve supplying mylohyoid and the anterior belly of digastric, the mylohyoid nerve carries some sensory fibres that may enter the mandible via one or more small retromental foramina in the vicinity of the genial tubercles to supply some sensation to the anterior teeth, and it may also give a few filaments to supply the skin over the point of the chin.

Dental extractions

Variations in the fascicular organization of the inferior alveolar nerve are clinically important when extracting impacted third molars. The nerve may appear as a single bundle lying a few millimetres below the roots of the teeth, or it may lie much lower and almost reach the lower border of the bone, so that it gives off a variable number of large rami that pass anterosuperiorly towards the roots before dividing to supply the teeth and interdental septa. Only rarely is it plexiform. The nerve may lie on the lingual or buccal side of the mandible (slightly more commonly on the buccal side). Even when the third molar tooth is in a normal position, the nerve may be so intimately related to it that it grooves its root. Exceptionally, the nerve may be similarly related to the second molar tooth.

Failure to achieve complete anaesthesia to the mandibular teeth following an inferior alveolar nerve block (which should anaesthetize the nerve before it enters the mandibular canal) suggests that there are alternative pathways for sensory nerves to innervate the teeth. Knowledge of these pathways is important in helping clinicians to obtain complete dental anaesthesia. There are anatomical variations in the distribution of the inferior alveolar nerve, the buccal branch of the mandibular nerve, the mylohyoid nerve, the lingual nerve, the deep temporal nerves and the cervical plexus. The inferior alveolar nerve may give multiple branches before entering the mandibular canal that may re-enter the mandible via small accessory foramina in the retromolar region to supply sensation to the molar teeth: one or more of these branches may escape anaesthesia following inferior alveolar nerve block. If a successful inferior alveolar nerve block does not completely anaesthetize teeth in a jaw quadrant, additional local injections of anaesthetic solution around the tooth in question may be necessary to block alternative pathways. There is also the possibility of overlap across the midline involving the incisive and mylohyoid nerves. In children, there is evidence to suggest that the lingula is variable in position and its position from the occlusion plane increases with age: it is therefore not considered an appropriate landmark for inferior alveolar nerve block.

Neural connections between branches of trigeminal and other nerves

Communications exist between the inferior alveolar and lingual nerves. If the lingual nerve is not anaesthetized during an inferior alveolar nerve block, this pathway could account for any remaining sensation in the teeth. Although the deep temporal nerves are primarily motor, it has been suggested that terminal branches may pass from the substance of temporalis to enter the mandible through foramina in the retromolar region to supply some sensation to molar teeth. In the cervical plexus, the great auricular nerve, formed by the anterior primary rami of the second and third cervical spinal nerves, supplies skin over the angle of the mandible: it is possible that this nerve may provide a branch that penetrates the mandible to supply one or more of the cheek teeth.

ABDUCENS NERVE

The abducens nerve is the sixth cranial nerve and innervates the ipsilateral lateral rectus.

Abducens nucleus and central connections

The abducens nucleus lies in the floor of the fourth ventricle, just lateral to the midline, immediately subjacent to the facial colliculus and slightly lateral to the medial longitudinal fasciculus (see Fig. 28.4). The abducens nucleus is composed of approximately 6500 neurones that align with the trochlear, oculomotor and hypoglossal nuclei to form the general somatic efferent column (GSE). Within the nucleus, large motor neurones are intermixed with small multipolar interneurones, the latter being most heavily concentrated in the lateral and ventral aspects of the nucleus. The abducens nucleus receives afferent connections from multiple sources, including corticonuclear fibres (principally contralateral, some of the fibres are aberrant corticospinal fibres that descend from the midbrain to this level in the medial lemniscus); the medial longitudinal fasciculus (connecting the abducens nucleus to oculomotor, trochlear and vestibular nuclei); the tectobulbar tract (from the deep layers of the superior colliculus); the paramedian pontine reticular formation (rostral and caudal to the nucleus); the nucleus prepositus hypoglossi; and the contralateral medullary reticular formation.

Neural Control of Gaze

Although the detailed anatomical substrates for the different types of eye movement differ, they share common neural circuitry that lies mainly in the pons and midbrain, for horizontal and vertical gaze movements, respectively (see Fig. 44.12). The common element for all types of horizontal gaze movements is the abducens nucleus. It contains motor neurones that innervate the ipsilateral lateral rectus and interneurones that project via the medial longitudinal fasciculus to the contralateral oculomotor nucleus, which controls medial rectus. A lesion of the abducens nucleus leads to a total loss of ipsilateral horizontal conjugate gaze. A lesion of the medial longitudinal fasciculus produces slowed or absent adduction of the ipsilateral eye, usually associated with jerky movements (nystagmus) of the contralateral abducting eye, a syndrome called internuclear ophthalmoplegia (Leigh and Zee 2015). The gaze motor command involves specialized areas of the reticular formation of the brainstem, which receive a variety of supranuclear inputs. The main region for the generation of horizontal saccades is the paramedian pontine reticular formation, located on each side of the midline in the central paramedian part of the tegmentum, and extending from the pontomedullary junction to the pontopeduncular junction. Each paramedian pontine reticular formation contains excitatory neurones (referred to as 'burst' neurones) that discharge at high frequencies just prior to and during ipsilateral saccades. Excitatory burst neurones make monosynaptic connections with the ipsilateral abducens nucleus. Omnipause neurones in the pontine nucleus raphe interpositus, located in the midline between the rootlets of the abducens nerves, discharge tonically during fixation but stop firing immediately prior to a saccade. They appear to exert an inhibitory influence on the burst neurones and act as a switch to change from fixation to saccadic mode (Ramat et al 2007).

The tonic activity of neurones in the nucleus prepositus hypoglossi and medial vestibular nucleus is thought to provide an eye position signal to maintain the eccentric position of the eye against the viscoelastic forces in the orbit. These forces tend to move the eyeball back to looking straight ahead, i.e. the primary position, after a saccade. Vestibular nuclei and the perihypoglossal complex project directly to the abducens nuclei: these projections probably also carry smooth pursuit signals, via the cerebellum.

The final common pathway for vertical gaze movements is formed by the oculomotor and trochlear nuclei. The rostral interstitial nucleus of the medial longitudinal fasciculus contains both excitatory burst neurones that discharge in relation to up-and-down vertical saccadic movements and project to motor neurones involved in vertical gaze, and omnipause neurones that act similarly to those for horizontal gaze. The rostral interstitial nucleus of the medial longitudinal fasciculus projects through the posterior commissure to its equivalent on the other side of the mesencephalon for upgaze, as well as directly to the ipsilateral oculomotor and trochlear nuclei for downgaze (see Fig. 44.12). Neurones in and around the interstitial nucleus of Cajal, which lies slightly caudal to the rostral interstitial nucleus of the medial longitudinal fasciculus, provide signals for vertical gaze holding. Vertical gaze palsies can affect upgaze, downgaze or both. Lesions within the posterior commissure predominantly give rise to disturbances in upgaze, associated with other signs of dorsal midbrain syndrome, e.g. pupillary abnormalities (light–near dissociation). Discrete lesions placed more ventrally in the region of the rostral interstitial nucleus of the medial longitudinal fasciculus may cause mixed up-and-down, or mainly downgaze disturbances (Leigh and Zee 2015).

Intra- and extracranial course

The axons of the motor neurones in the abducens nucleus spread diffusely from the ventromedial aspect of the nucleus. Fifteen to twenty fascicles pass ventrally, laterally and caudally, directly through the intervening reticular formation, trapezoid body, medial lemniscus, pontocerebellar fibres, pontine nuclei and descending corticospinal tracts to emerge from the brainstem at the pontomedullary sulcus about 1–2 cm lateral to the midline. In their course, the rootlets typically coalesce to emerge from the brainstem as a compact bundle of fibres. Occasionally all or some of the rootlets may emerge rostral to the pontomedullary sulcus. The nerve runs upward, anteriorly and slightly laterally across the prepontine cistern between the pons and clivus, pierces the inner layer of dura mater and runs through the inferior venous compartment of the petroclival venous confluence in a bow-shaped canal, Dorello's canal. It then bends sharply across the upper border of the petrous part of the temporal bone to enter the cavernous sinus, where it lies lateral to the cavernous segment of the internal carotid artery but medial to the oculomotor, trochlear, ophthalmic and maxillary nerves that also course through the sinus (but merely invaginate the lateral dural wall of the sinus). The abducens nerve enters the orbit through the inferomedial part of the superior orbital fissure, within the common tendinous ring, at first below, and then between, the two divisions of the oculomotor nerve and lateral to the nasociliary nerve (see Fig. 44.15). It passes forwards to enter the medial (ocular) surface of lateral rectus, most often in the posterior one-third of the muscle (Joo et al 2012).

FACIAL NERVE

The facial nerve is the seventh cranial nerve. It contains special visceral/branchial efferent (SVE) motor axons that supply muscles derived from the second branchial arch, namely the mimetic facial muscles, buccinator, stapedius, platysma, the posterior belly of digastric and stylohyoid. The craniofacial muscles innervated by the facial nerve typically lack muscle spindles: proprioceptive information may be mediated by modified cutaneous mechanoreceptors or capsular corpuscle-like structures within the muscles. The facial nerve contains two, possibly three, types of sensory axon. Special visceral afferent (SVA) axons carry taste from the anterior two-thirds of the tongue via the chorda tympani, and general sensory afferent (GSA) axons carry cutaneous sensation, including pain, from the posterior aspect of the external acoustic meatus, with the caveat that the innervation of this region is complex and largely contributed by Arnold's nerve: these axons are thought to be responsible for coughing during cerumen removal, idiopathic otalgia, Hitselberger's sign and to be the site of vesicular eruptions in Ramsay Hunt syndrome.

General visceral efferent (GVE) fibres in the facial nerve arise from preganglionic parasympathetic neurones in the superior salivatory nucleus and pass via either the chorda tympani to the submandibular ganglion or the greater petrosal nerve and the nerve of the pterygoid canal to the pterygopalatine ganglion. The GVE, SVA, GSA axons form the nervus intermedius (intermediate nerve, nerve of Wrisberg).

Facial nucleus and central connections

The facial (motor) nucleus is situated caudal, ventral and lateral to the abducens nucleus. It lies within the caudal pontine reticular formation, ventromedial to the spinal tract and nucleus of the trigeminal nerve (see Figs 28.11, 28.13) (Haines and Mihailoff 2017). Groups of neurones form columns that innervate individual muscles or that correspond to branches of the facial nerve. The facial nucleus receives corticonuclear fibres for volitional control of the facial musculature. Within the nucleus, neurones that innervate the muscles of the scalp and upper face are innervated by bilateral corticonuclear fibres. They lie dorsal to the neurones that innervate the muscles of the lower face, which receive a predominately contralateral innervation. Clinically, therefore, upper and lower motor neurone lesions affecting the facial nerve can be differentiated because upper motor neurone lesions cause paralysis that is confined to the contralateral lower face (supranuclear facial palsy), whilst lower motor neurone lesions cause complete ipsilateral facial paralysis (Bell's palsy). The facial nucleus also receives ipsilateral afferents from the nucleus solitarius and from the sensory nucleus of the trigeminal nerve, establishing important reflex connections.

Efferent fibres that arise from large motor neurones of the facial nucleus form the motor root of the facial nerve. At first, the facial fibres course dorsomedially towards the floor of the fourth ventricle as a diffuse spread of fibres that pass dorsal and medial to the abducens nucleus. They then coalesce into a defined fibre bundle that re-curves dorsally and laterally over the rostral pole of the abducens nucleus, creating a bulge in the floor of the fourth ventricle, the facial colliculus (see Fig. 28.11). The fibres descend ventrolaterally through the reticular formation and pass between their nucleus of origin medially and the nucleus of the spinal tract of the trigeminal nerve laterally. The facial nerve emerges from the brainstem at the supraolivary fossette, between the olive and restiform body, and passes laterally through the cerebellopontine angle cistern to the porus acusticus of the internal acoustic meatus (internal auditory canal).

Intracranial and intratemporal course

The facial nerve has intracranial (cisternal), intratemporal and extratemporal portions. The intratemporal portion is further divided into meatal, labyrinthine, tympanic (horizontal) and mastoid (vertical) segments (see

Fig. 42.12). The cisternal portion emerges from the ventrolateral aspect of the caudal border of the pons. The meatal portion enters the porus acusticus of the internal acoustic meatus accompanied by the nervus intermedius, the vestibulocochlear nerve and the labyrinthine vessels. In this part of its course, the facial nerve lacks a fibrous sheath or endoneurium and is surrounded by a thin layer of arachnoid. The motor root, which supplies the muscles of the face, and the nervus intermedius, which contains sensory fibres concerned with the perception of taste and parasympathetic (secretomotor) fibres to various glands, are still separate components; they usually merge within the meatus. The labyrinthine segment runs from the fundus of the internal acoustic meatus to the geniculate ganglion, where the nerve makes the first bend or genu (see Fig. 42.12). The labyrinthine segment is the shortest and narrowest part of the facial nerve; its lack of anastomosing arterial cascades renders it susceptible to vascular compression. The tympanic part initially curves around the oval window niche, then lies just anterior and inferior to the lateral semicircular canal and bends again at the second genu to become the vertical or mastoid part. The mastoid part is the longest of the petrous segments and runs from the pyramidal process to the stylomastoid foramen. The tympanic and mastoid segments of the facial nerve are supplied by the facial arch, formed by the petrosal branch of the middle meningeal artery and the stylomastoid branch of the posterior auricular artery.

The branches that arise from the facial nerve within the temporal bone can be divided into those that come from the geniculate ganglion (greater petrosal nerve) and those that arise within the facial canal (nerve to stapedius and chorda tympani).

Greater petrosal nerve

The greater (superficial) petrosal nerve, a branch of the nervus intermedius, is the main branch from the geniculate ganglion. It passes anteriorly, receives a branch from the tympanic plexus and traverses a hiatus on the anterior surface of the petrous part of the temporal bone. It enters the middle cranial fossa, runs forwards in a groove on the bone above the lesser petrosal nerve, and then passes beneath the trigeminal ganglion to reach the foramen lacerum. Here it is joined by the deep petrosal nerve from the internal carotid sympathetic plexus, to become the nerve of the pterygoid canal (Vidian nerve). The greater petrosal nerve contains parasympathetic fibres destined for the pterygopalatine ganglion, and taste fibres from the palate. The geniculate ganglion also communicates with the lesser petrosal nerve.

Nerve to stapedius

The nerve to stapedius arises from the facial nerve in the facial nerve canal behind the pyramidal eminence of the posterior wall of the tympanic cavity and passes forwards through a small canal to reach the muscle.

Chorda tympani

The chorda tympani (see Figs 42.11, 42.12) leaves the facial nerve some 6 mm above the stylomastoid foramen and runs anterosuperiorly in a canal to enter the tympanic cavity via the posterior canaliculus. It then curves anteriorly in the substance of the tympanic membrane between its mucous and fibrous layers, and crosses medial to the upper part of the handle of the malleus to the anterior wall of the tympanic cavity, where it enters the anterior canaliculus. It exits the skull and enters the infratemporal fossa by passing through the medial end of the petrotympanic fissure posterior to the capsule of the temporomandibular joint. It next descends medial to the spine of the sphenoid bone, which it sometimes grooves, lying posterolateral to tensor veli palatini. It is crossed medially by the middle meningeal artery, the roots of the auriculotemporal nerve and the inferior alveolar nerve (see Fig. 38.23) and joins the posterior aspect of the lingual nerve at an acute angle. The chorda tympani carries taste fibres from the anterior two-thirds of the tongue (but not the from the circumvallate papillae) and efferent preganglionic parasympathetic secretomotor fibres destined for the submandibular ganglion in the floor of the mouth.

Dehiscences of the facial nerve canal

The facial nerve may be somewhat variable in its anatomical course through the temporal bone (Proctor and Nager 1982, Proctor 1991). It may split into two or three strands, starting at the geniculate ganglion, and then make its way across the promontory to the stylomastoid foramen, or pass a few millimetres posteriorly to its second genu, before it turns inferiorly posterior to the fossa incudis, a position where it is particularly vulnerable during surgical exploration of the mastoid antrum. The more proximal the division into strands, the more bizarre is the subsequent course. More distal bifurcations pass either side of the fenestra vestibuli. It may be dehiscent, particularly in its second part, when it occasionally overhangs the stapes, or run inferior to the stapedial superstructure, a position that renders it vulnerable during surgery to the stapes (Barnes et al 2001). The motor fibres to the face may be carried through the chorda tympani, which is then enlarged. When this is the case, the distal facial nerve dwindles to a fibrous strand in a narrowed stylomastoid foramen. In chronic bone disease in the tympanic cavity, the facial nerve may be exposed in its canal. Inflammation may lead to facial paralysis of the infranuclear or lower motor neurone type.

Extratemporal course

The facial nerve emerges from the base of the skull at the stylomastoid foramen and almost immediately gives off the nerves to the posterior belly of digastric and stylohyoid and the posterior auricular nerve, which supplies the occipital belly of occipitofrontalis and some of the intrinsic auricular muscles (see Fig. 36.23). The nerve next enters the parotid gland high up on its posteromedial surface and passes forwards and downwards behind the mandibular ramus. Within the substance of the gland, it branches into superior (temporofacial) and inferior (cervicofacial) trunks, usually just behind and superficial to the retromandibular vein. The trunks branch further to form a parotid plexus (pes anserinus). Five main terminal branches arise from the plexus, diverge within the gland and leave by its anteromedial surface, medial to its anterior margin, to supply the muscles of facial expression (see Fig. 36.23). Six distinctive anastomotic patterns were originally classified by Davis et al (1956) and these are illustrated in Fig. 36.24. Numerous microdissection studies have demonstrated considerable individual variation in branching patterns and anastomoses between branches, both within the parotid and on the face (e.g. Lineaweaver et al 1997, Kwak et al 2004): the account that follows is therefore an overview. In surgical terms, these anastomoses are important and presumably explain why accidental or deliberate division of a small branch often fails to result in the expected facial nerve weakness.

The temporal branch usually divides into anterior and posterior rami soon after piercing the parotidomasseteric fascia below the zygomatic arch; there is often a middle (frontal) ramus. These rami cross the arch in subcutaneous tissue, lying in the subgaleal space: their course is extremely variable.

Twigs supply intrinsic muscles on the lateral surface of the auricle and the anterior and superior auricular muscles. They communicate with the zygomaticotemporal branch of the maxillary nerve and the auriculotemporal branch of the mandibular nerve. The more anterior branches supply the frontal belly of occipitofrontalis, orbicularis oculi and corrugator and join the supraorbital and lacrimal branches of the ophthalmic nerve.

Zygomatic branches

Zygomatic branches are generally multiple. They cross the zygomatic bone to the lateral canthus of the eye and supply orbicularis oculi and may also supply muscles innervated by the buccal branch. Twigs communicate with filaments of the lacrimal nerve and the zygomaticofacial branch of the maxillary nerve.

Buccal nerve

The buccal branch of the facial nerve is usually single. It has a close relationship to the parotid duct for about 2.5 cm after emerging from the parotid gland and typically lies below the duct. Superficial branches run beneath the subcutaneous fat and the superficial musculo-aponeurotic system (SMAS). Some branches pass deep to procerus and join the infratrochlear and external nasal nerves. Upper deep branches supply zygomaticus major and levator labii superioris and form an infraorbital plexus with the superior labial branches of the infraorbital nerve. They also supply levator anguli oris, zygomaticus minor, levator labii superioris alaeque nasi and the small nasal muscles (these branches are sometimes described as lower zygomatic branches). Lower deep branches supply buccinator and orbicularis oris and communicate with filaments of the buccal branch of the mandibular nerve.

Marginal mandibular nerve

There are usually two marginal mandibular nerves. They run forwards towards the angle of the mandible under platysma, and then turn upwards across the body of the mandible to pass under depressor anguli oris. The branches supply risorius and the muscles of the lower lip and chin. Filaments communicate with the mental nerve. The marginal mandibular branch has an important surgical relationship with the inferior border of the mandible.

Cutaneous branches

Cutaneous branches of the facial nerve accompany the auricular branch of the vagus and probably supply small areas on both aspects of the auricle, in the depression of the concha and over its eminence.

The facial nerve has intra- or extracranial connections with the cutaneous branches of all three divisions of the trigeminal nerve (including branches of the auriculotemporal, buccal, mental, lingual, infraorbital, zygomatic and ophthalmic nerves); with branches of the vestibulocochlear, glossopharyngeal and vagus nerves; and with branches of the cervical plexus (including the great auricular, greater and lesser occipital and transverse cervical nerves). These cutaneous connections are significant in facilitating the perineural spread of tumours that arise either within the parotid or on the face and explains why some patients with perineural spread from cutaneous or parotid malignancies may present with vocal cord palsy.

Cervical branch

The cervical branch of the facial nerve emerges from the lower part of the parotid gland and runs anteroinferiorly under platysma to the anterior neck. Typically single, it supplies platysma and communicates with the transverse cutaneous cervical nerve.

Lesions of the facial nerve

Facial paralysis may be due to an upper motor neurone lesion (when frontalis is partially spared because of the bilateral cortical representation of the muscles of the upper part of the face) or a lower motor neurone lesion (when all branches may be involved). Lower motor neurone facial paralysis is most commonly idiopathic (Bell's palsy). There are a large number of other recognized causes that include geniculate herpes zoster (Ramsay Hunt syndrome), and malignant tumours of the parotid gland and temporal bone. Iatrogenic damage also accounts for a significant number of palsies, most often acquired in vestibular schwannoma, parotid and middle ear or mastoid surgery.

Bell's palsy

Bell's palsy is an idiopathic lower motor neurone facial palsy. It may be complete or partial, and is characterized by a flaccid paralysis of the ipsilateral mimetic facial muscles (muscles of facial expression); decreased lacrimation in the ipsilateral eye (which is controlled by neurones in the greater petrosal nerve); and hyperacusis or decreased tolerance of loud noises in the ipsilateral ear as a result of paralysis of stapedius. Its cause remains the subject of speculation but is most probably a herpes virus infection (Zandian et al 2014). Magnetic resonance imaging studies suggest that there are inflammatory changes in the labyrinthine and perigeniculate segments of the facial nerve. In the vast majority of cases, spontaneous full recovery takes place after a few weeks.

VESTIBULOCOCHLEAR NERVE

The vestibulocochlear nerve is the eighth cranial nerve. As its name suggests, it consists of two components, the vestibular nerve, concerned with balance, and the cochlear nerve, concerned with hearing.

Vestibular nuclei and central connections

The vestibular nuclear complex is situated beneath the floor of the fourth ventricle. It has traditionally been divided into four cellular masses, the lateral nucleus (of Deiter), medial nucleus (of Schwalbe), superior nucleus (of Bechterew) and inferior (spinal, descending) vestibular nucleus (see Figs 28.8, 28.11) (Haines and Mihailoff 2017). The nucleus prepositus hypoglossi, located medial to the medial vestibular nucleus, may also be regarded as a vestibular nucleus. Cell groups X and Y have been identified as accessory nuclei of the vestibular complex.

The medial vestibular nucleus is the largest of the vestibular nuclei. It lies lateral and superior to the visceromotor nuclei of the glossopharyngeal and vagus nerves, is crossed dorsally by the striae medullares of the fourth ventricle and is continuous with the nucleus intercalatus below. The superior vestibular nucleus is small and lies above the medial and lateral nuclei. It extends higher into the pons than the other subdivisions and occupies the upper part of the vestibular area. The inferior vestibular nucleus is the smallest of the group. It lies between the medial vestibular nucleus and the restiform body, from the level of the upper end of the nucleus gracilis to the pontomedullary junction, and is traversed by descending fibres of the vestibular nerve, from the cerebellum and the vestibulospinal tract. The lateral vestibular nucleus lies ventrolateral to the upper portion of the medial nucleus, just above the inferior nucleus and ascends almost to the level of the abducens nucleus. Its rostral end is continuous with the caudal end of the superior nucleus. It projects to the spinal cord through the lateral vestibulospinal tract (Voogd 2016). The lateral vestibular nucleus can be subdivided into dorsal and ventral components. The dorsal portion contains giant cells and is located within the juxtarestiform body: it receives no direct vestibular afferents, but receives Purkinje cell axons from the anterior vermis, and extends efferent connections to the cerebellum. The ventral portion contains cells of various sizes and is located medial to the juxtarestiform body

Vestibulocerebellar fibres (primary and secondary) travel via the juxtarestiform body mainly to the flocculus and nodule. Cerebellovestibular fibres pass to the nuclei, also via the juxtarestiform body: they arise mainly in the flocculus and nodule (posterior lobe), but some fibres are derived from the anterior lobe and the fastigial nucleus. A few vestibular fibres enter the cerebellum directly through the juxtarestiform body and end in the fastigial nucleus, flocculonodular lobe and uvula.

The vestibular nuclei receive afferent fibres from multiple sources, including the vestibular portion of the vestibulocochlear nerve, cerebellum, brainstem reticular formation and spinal cord. Myelinated fibres in the vestibular nerve enter the medulla between the restiform body and the spinal tract of the trigeminal nerve and bifurcate into ascending and descending branches. Most ascending vestibular fibres end in the superior vestibular nucleus. Descending vestibular fibres traverse the juxtarestiform body and give off extensive transverse collaterals to the inferior and medial (but not the lateral) vestibular nuclei. Additional afferent fibres descend from the cerebral cortex to innervate the vestibular nuclei bilaterally.

Afferent fibres arising from the interstitial nucleus of Cajal descend through the medial longitudinal fasciculus to synapse in the ipsilateral superior and medial vestibular nuclei and the nucleus prepositius hypoglossi. Afferent fibres from the Edinger–Westphal nucleus project to the medial and inferior vestibular nuclei, which also receive root fibres from the upper cervical nerve roots (C2, C3). The lateral vestibular nucleus and inferior portions of the medial and inferior vestibular nuclei receive ipsilateral spinovestibular fibres that ascend from lower spinal levels through the dorsal spinocerebellar tract.

The vestibular nuclei project extensively to the cerebellum and also receive fibres from the cerebellar cortex and the fastigial nuclei. Vestibulocerebellar fibres pass through the juxtarestiform body to the cerebellum (Carpenter and Sutin 1983). A few vestibular nerve fibres bypass the vestibular nuclei and traverse the juxtarestiform body to terminate directly in the fastigial nucleus, the flocculonodular lobe and uvula.

Evidence suggests that the vestibular apparatus is spatially represented in these nuclei. Efferents from the lateral vestibular nucleus descend to the spinal cord through the ipsilateral lateral vestibulospinal tract and extend along the full length of the spinal cord to exert a facilitatory influence on spinal reflex activity and on extensor muscle tone. Vestibular nuclear efferents form a major part of the medial longitudinal fasciculus, through which interconnections between the vestibular and oculogyric nuclei and the pontine reticular formation enable conjugate eye movements that compensate for head movements perceived by the labyrinths. The reflex arcs stabilize visual fixation despite changing head position. Vestibular efferents project to the thalamus (probably via the posterior portions of the ventroposterior complex and the medial pulvinar), which in turn projects to the primary vestibular cortex in the parietal lobe at the junction of the intraparietal and postcentral sulci, adjacent to the head portion of the postcentral gyrus. There may be additional representation of the vestibular system in the superior temporal gyrus near to the auditory cortex.

Vestibular ganglion

The somata of the bipolar neurones that form the vestibular nerve are in the vestibular (Scarpa's) ganglion located in the trunk of the nerve within the lateral end of the internal acoustic meatus (see Fig. 43.12B). They vary considerably in size, with circumferences ranging from 45 to 160 μm (Felix et al 1987): no topographically ordered distribution relating to size has been found. The somata are notable for their abundant granular endoplasmic reticulum, which in places forms Nissl bodies, and prominent Golgi complexes. They are covered by a thin layer of satellite cells and are often arranged in pairs, closely abutting each other so that only a thin layer of endoneurium separates the adjacent coverings of satellite cells. This arrangement has led to speculation that ganglion cells may affect each other directly by electrotonic spread (ephaptic transmission: see Felix et al (1987)). Two distinct sympathetic components have been identified in the vestibular ganglion, a perivascular adrenergic system derived from the stellate ganglion, and a blood vessel-independent system derived from the superior cervical ganglion.

The central processes of the vestibular ganglion cells travel via the vestibular nerve, enter the brainstem at the cerebellopontine angle and terminate in the vestibular nuclear complex (see below). Neurones in this complex project to motor nuclei in the brainstem and upper spinal cord, and to the cerebellum and thalamus. Thalamic efferent projections pass to a cortical vestibular area that is probably located near the intraparietal sulcus in area 2 of the primary somatosensory cortex.

The peripheral processes of the vestibular ganglion cells are aggregated into definable nerves, each with a specific distribution. The main nerve divides at and within the ganglion into superior and inferior divisions connected by an isthmus. The superior division, the larger of the two, passes through the small holes in the superior vestibular area at the fundus of the internal acoustic meatus (see Fig. 43.3) and supplies the ampullary crests of the lateral and anterior semicircular canals via the lateral and anterior ampullary nerves, respectively. A secondary branch of the lateral ampullary nerve supplies the macula of the utricle; however, the greater part of the utricular macula is innervated by the utricular nerve, which is a separate branch of the superior division. Another branch of the superior division supplies part of the saccule. The inferior division passes through small holes in the inferior vestibular area (see Fig. 43.3) to supply the remainder of the saccule and the posterior ampullary crest via saccular and singular branches, respectively; the latter passes through the foramen singulare. Occasionally, a very small supplementary or accessory branch innervates the posterior crest; it is probably a vestigial remnant of the crista neglecta, an additional area of sensory epithelium found in some other mammals but seldom in humans.

Afferent and efferent cochlear fibres are also present in the inferior division of the vestibular nerve but leave at the anastomosis of Oort to join the main cochlear nerve (see review by Warr (1992)). Another anastomosis, the vestibulofacial anastomosis, is situated more centrally between the facial and vestibular nerves and is the point at which fibres originating in the intermediate nerve pass from the vestibular nerve to the main trunk of the facial nerve.

There are approximately 20,000 fibres in the vestibular nerve, of which 12,000 travel in the superior division and 8000 travel in the inferior division. The distribution of fibre diameters is bimodal, with peaks at 4 μm and 6.5 μm. The smaller fibres go mainly to the type II hair cells and the larger fibres tend to supply the type I hair cells. In addition to the afferents, efferent and autonomic fibres have been identified. Efferent fibres synapse exclusively with the afferent calyceal terminals around type I cells and usually with the afferent boutons on type II cells, although a few are in direct contact with the cell bodies of type II cells. The autonomic fibres do not contact vestibular sensory cells but terminate beneath the sensory epithelia.

Cochlear nuclei and central connections

The primary afferents of the auditory pathway are the central processes of type I and II sensory neurones in the spiral ganglion of Corti in the cochlea. They travel in the cochlear division of the vestibulocochlear nerve and enter the brainstem just caudal to the vestibular division of the vestibulocochlear nerve at the cerebellopontine angle. The axons bifurcate and terminate in the dorsal (posterior) and ventral (anterior) cochlear nuclei lying along the lateral surface of the restiform body. The dorsal cochlear nucleus forms a bulge, the auditory tubercle (auditory eminence) on the posterior surface of the restiform body and also forms the floor of the lateral recess of the fourth ventricle; it is continuous medially with the vestibular area in the floor of the fourth ventricle (see Fig. 28.9). The ventral cochlear nucleus lies between the cochlear and vestibular fibres of the vestibulocochlear nerve. The dorsal and ventral cochlear nuclei are separated only by a thin stratum of nerve cell bodies and fibres.

The axons of type 1 spiral ganglion cells enter the ventral cochlear nucleus and bifurcate within its centre, dividing it into anterior and posterior ventral subnuclei. The fibres are organized into dorsoventrally oriented sheets in which fibres conveying low frequency sounds from apical spiral ganglion cells terminate ventrally and fibres conveying high frequency sounds from the basal turn of the spiral ganglion terminate dorsally. Posterior processes of type I ganglion cells pass to the caudal pole of the ventral nucleus, from which they enter the dorsal cochlear nucleus. Thin unmyelinated axons of type 2 spiral ganglion cells contact clusters of small interneurones scattered through the cochlear nuclei.

The axons that emerge from the cochlear nuclei are aggregated into three, mostly transverse, fibre bundles, the dorsal and intermediate acoustic striae and the trapezoid body. The dorsal cochlear nucleus projects via the dorsal acoustic stria to the contralateral inferior colliculus. The dorsal acoustic stria curves dorsally and medially, dorsal to the restiform body, traverses the reticular formation ventral to the striae medullares, crosses the midline, passes to the contralateral superior olivary complex, and ascends in the contralateral lateral lemniscus. The ventral cochlear nucleus projects via the trapezoid body or the intermediate acoustic stria to relay centres in either the superior olivary complex, the nuclei of the lateral lemniscus, or the inferior colliculus. Initially, the intermediate acoustic stria accompanies the dorsal acoustic stria as they pass medially, immediately dorsal to the restiform body, but it then separates from the dorsal acoustic stria, angles sharply ventrally in the ipsilateral tegmentum, passes through the spinal trigeminal nucleus, joins the trapezoid body, and crosses the midline to join and ascend with the contralateral lateral lemniscus.

The cochlear nerve also conveys efferent fibres that pass outward from the brainstem to terminate on the hair cells and on the cells of the spiral ganglion.

Intratemporal and intracranial course

The vestibulocochlear nerve emerges from the cerebellopontine angle (see Figs 28.4–28.5). It courses through the posterior cranial fossa in close association with the facial nerve, nervus intermedius and labyrinthine vessels. Together with these structures, it enters the petrous temporal bone via the porus acusticus of the internal acoustic meatus (see Fig. 43.3), and divides into an anterior trunk, the cochlear nerve, and a posterior trunk, the vestibular nerve. Both contain the centrally directed axons of bipolar neurones, together with a smaller number of efferent fibres that arise from brainstem neurones and terminate on cochlear and vestibular sensory neurones. In humans, the intratemporal portion of the vestibulocochlear nerve consists of two histologically distinct portions: a central glial zone adjacent to the brainstem, and a peripheral or non-glial zone (Bridger and Farkashidy 1980). In the glial zone, the axons are supported by central neuroglia, whereas in the non-glial zone they are ensheathed by Schwann cells. The non-glial zone sometimes extends into the cerebellopontine angle medial to the internal acoustic meatus in human vestibulocochlear nerves. During development, a gap of several weeks has been reported between the onset of Schwann cell myelination distally and glial myelination proximally; it has been suggested that the gap may coincide with the time of the final maturation of the organ of Corti. For further details about the development of the human cochlear nerve, see Ray et al (2005)).

In audiological practice, it is important to distinguish between intratemporal and intracranial lesions. However, this surgical distinction does not correlate with the precise anatomical description of peripheral and central portions of the auditory and vestibular systems. Clinically, the term 'peripheral auditory lesion' is used to describe lesions peripheral to the spiral ganglion, and the term 'peripheral vestibular disturbance' includes lesions of the vestibular ganglion and the entire vestibular nerve.

GLOSSOPHARYNGEAL NERVE

The glossopharyngeal nerve is the ninth cranial nerve (see Figs 35.8, 35.11, 35.19). It contains motor fibres to stylopharyngeus; parasympathetic secretomotor fibres to the parotid gland (derived from the inferior salivatory nucleus); sensory fibres to the tympanic cavity, pharyngotympanic tube, fauces, tonsils, nasopharynx, uvula and posterior (postsulcal) third of the tongue; and gustatory fibres from the circumvallate papillae.

Nucleus ambiguus

The nucleus ambiguus is a complex group of large motor neurones situated deep in the medullary reticular formation (see Figs 28.3, 28.9). Rostrally, it extends as far as the rostral end of the vagal nucleus and caudally it is in line with, but not continuous with, the nucleus of the accessory nerve. A small retrofacial nucleus separates the upper end of the nucleus ambiguus from the facial nucleus. The nucleus ambiguus contains cellular subgroups that exhibit some topographical representation. Relatively discrete groups of cells in the caudal region innervate individual laryngeal muscles; neurones in the intermediate area innervate the pharynx; neurones in the rostral area innervate the oesophagus and soft palate.

The nucleus ambiguus contributes special visceral efferent fibres to the glossopharyngeal nerve and may give general visceral efferent fibres to the vagus nerve. Fibres emerging from the nucleus ambiguus pass dorsomedially, then curve laterally. Rostral fibres join the glossopharyngeal nerve and caudal fibres join the vagus nerve and are distributed to the pharyngeal constrictors, intrinsic laryngeal muscles and striated muscles of the palate and upper oesophagus. A specific caudal pool of laryngeal motor neurones gives rise to the recurrent laryngeal nerve.

Extracranial course

The glossopharyngeal nerve leaves the skull through the anteromedial part of the jugular foramen, anterior to the vagus and accessory nerves, and in a separate dural sheath. In the foramen, it is lodged in a deep groove leading from the cochlear aqueductal depression, separated by the inferior petrosal sinus from the vagus and accessory nerves. The groove is bridged by fibrous tissue, which is sometimes calcified. After leaving the foramen, the nerve passes forwards between the internal jugular vein and internal carotid artery, and then descends anterior to the latter, deep to the styloid process and its attached muscles, to reach the posterior border of stylopharyngeus. It curves forwards on stylopharyngeus and either pierces the lower fibres of the superior pharyngeal constrictor or passes between it and the middle constrictor to be distributed to the palatine tonsil, the mucosae of the pharynx and postsulcal part of the tongue, the vallate papillae and oral mucous glands.

Two ganglia, superior and inferior, are situated on the glossopharyngeal nerve as it traverses the jugular foramen. The superior ganglion is in the upper part of the groove occupied by the nerve in the jugular foramen. It is small, has no branches and is usually regarded as a detached part of the inferior ganglion. The inferior ganglion is larger and lies in a notch in the lower border of the petrous part of the temporal bone. Its cells are typical unipolar neurones, their peripheral branches convey gustatory and tactile signals from the mucosa of the tongue (posterior third, including the sulcus terminalis and vallate papillae) and general sensation from the oropharynx, where the glossopharyngeal nerve is responsible for initiating the gag reflex.

The glossopharyngeal nerve has tympanic, carotid, pharyngeal, muscular, tonsillar and lingual branches.

Communicating branches

The glossopharyngeal nerve communicates with the sympathetic trunk and vagus and facial nerves. Its inferior ganglion is connected with the superior cervical sympathetic ganglion. Two filaments from the inferior ganglion pass to the vagus, one to its auricular branch and the other to its superior ganglion. A branch to the facial nerve arises from the glossopharyngeal nerve below the inferior ganglion and perforates the posterior belly of digastric to join the facial nerve near the stylomastoid foramen.

Tympanic nerve

The tympanic nerve leaves the inferior ganglion, ascends to the tympanic cavity through the tympanic canaliculus and divides into branches that contribute to the tympanic plexus on the promontory. The lesser petrosal nerve is derived from the tympanic plexus.

Carotid branch

The carotid branch is often double. It arises just below the jugular foramen and descends on the internal carotid artery to the wall of the carotid sinus and to the carotid body. The nerve contains primary afferent fibres from chemoreceptors in the carotid body and from the baroreceptors lying in the carotid sinus wall. It may communicate with the inferior ganglion of the vagus, or with one of its branches, and with a sympathetic branch from the superior cervical ganglion (see Fig. 35.20).

Pharyngeal branches

The pharyngeal branches are three or four filaments that unite with the pharyngeal branch of the vagus and the laryngopharyngeal branches of the sympathetic trunk to form the pharyngeal plexus near the middle pharyngeal constrictor. They constitute the route by which the glossopharyngeal nerve supplies sensory fibres to the mucosa of the pharynx.

Muscular branch

The muscular branch supplies stylopharyngeus.

Tonsillar, lingual and lesser petrosal branches and the tympanic plexus

The tympanic plexus supplies branches to the mucosa of the tympanic cavity, pharyngotympanic tube and mastoid air cells. The nerves that constitute the tympanic plexus ramify on the surface of the promontory on the medial wall of the tympanic cavity. They are derived from the tympanic branch of the glossopharyngeal nerve and the caroticotympanic nerves. The former arises from the inferior ganglion of the glossopharyngeal nerve and reaches the tympanic cavity via the tympanic canaliculus for the tympanic nerve. The superior and inferior caroticotympanic nerves are postganglionic sympathetic fibres derived from the carotid sympathetic plexus that traverse the wall of the carotid canal to join the plexus.

The lesser petrosal nerve, which may be regarded as the continuation of the tympanic branch of the glossopharyngeal nerve, traverses the tympanic plexus. It occupies a small canal below that for tensor tympani. It runs past, and receives a connecting branch from, the geniculate ganglion of the facial nerve. The lesser petrosal nerve emerges from the anterior surface of the temporal bone via a small opening lateral to the hiatus for the greater petrosal nerve and then traverses either the foramen ovale or the sphenopetrosal fissure or the innominate canal (of Arnold) to join the otic ganglion. Postganglionic secretomotor fibres leave this ganglion in the auriculotemporal nerve to supply the parotid gland. The tympanic plexus sends a branch to the greater petrosal nerve via an opening anterior to the fenestra vestibuli.

The tonsillar region is innervated by tonsillar branches of the maxillary and glossopharyngeal nerves. The fibres from the maxillary nerve pass through, but do not synapse in, the pterygopalatine ganglion; they are distributed through the lesser palatine nerves and form a plexus (the circulus tonsillaris) around the tonsil together with the tonsillar branches of the glossopharyngeal nerve. Nerve fibres from this plexus are also distributed to the soft palate and the region of the oropharyngeal isthmus. The tympanic branch of the glossopharyngeal nerve supplies the mucous membrane lining the tympanic cavity. Infection, malignancy and postoperative inflammation of the tonsil and tonsillar fossa may therefore be accompanied by pain referred to the ear.

Lesions of the glossopharyngeal nerve

There are anastomoses between the glossopharyngeal, vagus, greater auricular and other branches of the cervical plexus that may be significant when treating patients with skull base pathology. Damage to the glossopharyngeal nerve is rarely seen without associated involvement of other lower cranial nerves. Transient or sustained hypertension may follow surgical section of the nerve and indicates involvement of the carotid branch. Isolated lesions of the glossopharyngeal nerve lead to loss of sensation over the ipsilateral soft palate, fauces, pharynx and posterior third of the tongue, although this is difficult to assess clinically, and confirmation requires galvanic stimulation. The palatal and pharyngeal (gag) reflexes are reduced or absent and salivary secretion from the parotid gland may also be reduced. Weakness of stylopharyngeus cannot be tested individually. Glossopharyngeal neuralgia consists of episodic brief but severe pain, often precipitated by swallowing and experienced in the throat, behind the angle of the jaw and within the ear. Superior jugular bulb thromboses (e.g. in otitis media) and jugular foramen syndrome (associated with nasopharyngeal carcinoma or a jugular paraganglioma) may cause lesions of the adjacent glossopharyngeal, vagus and accessory nerves, with associated weakness in the muscles supplied in the pharynx and larynx.

VAGUS NERVE

The vagus is the tenth cranial nerve. It is a large mixed nerve, containing branchiomotor nerve fibres, general visceral afferents and preganglionic parasympathetic fibres. The vagus has a more extensive course and distribution than any other cranial nerve, running through the neck, thorax and abdomen. The proportion of efferent parasympathetic nerve fibres it contains varies at different levels but is small relative to its sensory and sensorimotor content. The branchiomotor fibres arise from neurones in the nucleus ambiguus in the medulla oblongata and are distributed to the constrictor muscles of the pharynx and the intrinsic muscles of the larynx. The preganglionic parasympathetic nerves arise from cell bodies in the vagal dorsal nucleus in the medulla oblongata, travel in the nerve and in its pulmonary, cardiac, oesophageal, gastric and intestinal branches and relay/synapse in minute ganglia in the visceral walls (see Fig. 56.6) (Mussa and Verberne 2013).

The general visceral afferent fibres carry sensation from thoracic and abdominal viscera and from aortic arch baroreceptors and chemoreceptors and end in the nucleus solitarius of the medulla. Their cell bodies are in the superior and inferior vagal ganglia. Their peripheral processes are distributed to terminals in the pharyngeal and oesophageal walls where, acting synergistically with glossopharyngeal visceral afferents in the pharynx, they are concerned with swallowing reflexes. Vagal afferents are also believed to innervate the thyroid and parathyroid glands. In the heart, vagal afferents innervate the walls of the great vessels, the aortic bodies and pressor receptors, where they are stimulated by raised intravascular pressure. In the lungs they are distributed via the pulmonary plexuses: they supply bronchial mucosa, where they are probably involved in cough reflexes; bronchial muscle, where they encircle myocytes and end in tendrils, which are sometimes regarded as muscle spindles and which are believed to be stimulated by change in the length of myocytes; interalveolar connective tissue, where their knoblike endings, together with terminals on myocytes, may evoke Hering–Breuer reflexes; the adventitia of pulmonary arteries, where they may be pressor receptors; and the intima of pulmonary veins, where they may be chemoreceptors. Vagal visceral afferent fibres also end in the gastric and intestinal walls, digestive glands and the kidneys. Fibres ending in the gut and its ducts respond to stretch or contraction. Gastric impulses may evoke sensations of hunger and nausea.

About 5% of the vagal afferents project directly to, and terminate in, the upper cervical spinal cord (C1–C2), where they are believed to contribute to referred sensations, as well as to propriospinal mechanisms of nociceptive modulation. Almost all the central processes of vagal and glossopharyngeal afferent fibres end in the nucleus solitarius of the medulla.

Dorsal motor nucleus of the vagus

The dorsal motor nucleus of the vagus lies slightly dorsolateral to the hypoglossal nucleus, from which it is separated by the nucleus intercalatus (see Fig. 28.8). The vagal nucleus extends caudally to the first cervical spinal segment and rostrally to the open portion of the medulla subjacent to the vagal trigone of the fourth ventricle. It is a general visceral efferent nucleus and is the largest parasympathetic nucleus in the brainstem. Most (80%) of its neurones give rise to the preganglionic parasympathetic fibres that pass into the vagus nerve. The remainder are interneurones or neurones that project centrally. The nucleus innervates the cardiac and smooth muscle of the thoracic viscera (heart, bronchi, lungs, oesophagus) and abdomen (stomach, liver, pancreas, spleen, small intestine and proximal part of the colon), and glandular epithelium. Sparse sensory afferents from the nodose ganglion project directly to the dorsal and lateral edges of the dorsal vagal nucleus, and possibly beyond it into the nucleus of the solitary tract (Holstein 2012).

Neurones within the nucleus are heterogeneous and can be classified into nine subnuclei, grouped into rostral, intermediate and caudal divisions. Topographic maps of visceral representation in animals suggest that the heart and lungs are represented in the caudal and lateral parts of the nucleus; the stomach and pancreas in intermediate regions; and the remaining abdominal organs in the rostral and medial parts of the nucleus.

Extracranial course

The vagus nerve exits the skull through the jugular foramen, accompanied by the accessory nerve, with which it shares an arachnoid and a dural sheath. Both nerves lie anterior to a fibrous septum that separates them from the glossopharyngeal nerve. The vagus descends vertically in the neck in the carotid sheath, between the internal jugular vein and the internal carotid artery, to the upper border of the thyroid cartilage, and then passes between the vein and the common carotid artery to the root of the neck. Its relationships in this part of its course are therefore similar to those described for these structures (see Figs 35.7A, 35.8, 35.17). Its further course differs on the two sides. The right vagus descends posterior to the internal jugular vein to cross the first part of the subclavian artery and enter the thorax. The left vagus enters the thorax between the left common carotid and subclavian arteries, and behind the left brachiocephalic vein.

After emerging from the jugular foramen, the vagus bears two marked enlargements: a small, round, superior (jugular) ganglion and a larger inferior (nodose) ganglion.

Superior (jugular) ganglion

The superior ganglion is greyish, spherical and approximately 4 mm in diameter. It is connected to the inferior glossopharyngeal ganglion and the sympathetic trunk, the latter by a filament from the superior cervical ganglion.

Inferior (nodose) ganglion

The inferior or nodose ganglion is larger than the superior ganglion, and is elongated and cylindrical in shape with a length of 25 mm and a maximum breadth of 5 mm. It is connected with the hypoglossal nerve, the loop between the first and second cervical spinal nerves, and with the superior cervical sympathetic ganglion. Most visceral afferent axons travelling in the vagus nerve are the peripheral processes of cell bodies located in the nodose ganglion.

Both vagal ganglia are exclusively sensory and contain somatic, special visceral and general visceral afferent neurones. The superior ganglion is mainly somatic and most of its neurones enter the auricular nerve, whilst neurones in the inferior ganglion are concerned with visceral sensation from the heart, larynx, lungs and the alimentary tract from the pharynx to the transverse colon. Some fibres transmit impulses from taste endings in the vallecula and epiglottis. Large afferent fibres are derived from muscle spindles in the laryngeal muscles. Vagal sensory neurones in the nodose ganglion may show some somatotopic organization. Both ganglia are traversed by parasympathetic and perhaps some sympathetic fibres, but there is no evidence that vagal parasympathetic components relay in the inferior ganglion. Preganglionic motor fibres from the dorsal vagal nucleus and the special visceral efferents from the nucleus ambiguus, which descend to the inferior vagal ganglion, commonly form a visible band that skirts the ganglion in some mammals. These larger fibres probably provide motor innervation to the larynx in the recurrent laryngeal nerve, together with some contribution to the superior laryngeal nerve supplying cricothyroid.

Vagus nerve in the neck

The branches of the vagus in the neck are the meningeal, auricular, pharyngeal, carotid body, superior and recurrent laryngeal nerves and cardiac branches.

Meningeal branches

Meningeal branches appear to start from the superior vagal ganglion and pass through the jugular foramen to be distributed to the dura mater in the posterior cranial fossa (see Fig. 25.3B).

Auricular branch

The auricular branch (Arnold's nerve) arises from the superior vagal ganglion and is joined by a branch from the inferior ganglion of the glossopharyngeal nerve. It passes behind the internal jugular vein and enters the mastoid canaliculus on the lateral wall of the jugular fossa. Traversing the temporal bone, it crosses the facial canal approximately 4 mm above the stylomastoid foramen and here supplies an ascending branch to the facial nerve. Fibres of the nervus intermedius may pass to the auricular branch at this point, which may explain the cutaneous vesiculation in the auricle that sometimes accompanies geniculate herpes. The auricular branch then traverses the tympanomastoid fissure and divides into two rami. One ramus joins the posterior auricular nerve and the other is distributed to the skin of part of the ear and to the external acoustic meatus.

Pharyngeal branch

The pharyngeal branch of the vagus is the main motor nerve of the pharynx and consists of axons arising from neuronal cell bodies in the nucleus ambiguus. It supplies all the muscles of the soft palate (excluding tensor veli palatini, which is supplied by the mandibular division of the trigeminal nerve via the nerve to medial pterygoid) and all the muscles of the pharynx (excluding stylopharyngeus, which is supplied by the glossopharyngeal nerve). It emerges from the upper part of the inferior vagal ganglion, passes between the external and internal carotid arteries to reach the upper border of the middle pharyngeal constrictor, and divides into numerous filaments that join rami of the sympathetic trunk and glossopharyngeal nerve to form the pharyngeal plexus. It also gives off a minute filament, the ramus lingualis vagi, which joins the hypoglossal nerve as it curves round the occipital artery.

Branches to the carotid body

Branches to the carotid body are variable in number. They may arise from the inferior ganglion or travel in the pharyngeal branch, or in the superior laryngeal nerve. They form a plexus with the glossopharyngeal rami and branches of the cervical sympathetic trunk.

Superior laryngeal nerve

The superior laryngeal nerve is larger than the pharyngeal branch and issues from the middle of the inferior vagal ganglion. It receives one or more communicating branches from the superior cervical sympathetic ganglion; most frequently, the connection is with the external laryngeal nerve. The sympathetic communication contributes to the innervation of the carotid body (Monfared et al 2002) and the thyroid gland (Sun and Chang 1991). The superior laryngeal nerve descends alongside the pharynx, at first posterior, then medial, to the internal carotid artery: it may be found on the lateral side of the artery. It divides into a smaller, external, and a larger, internal, branch, approximately 1.5 cm below the ganglion: rarely, both branches may arise from the ganglion (see Figs 35.8, 41.12).

Internal laryngeal nerve

The internal laryngeal nerve passes forwards approximately 7 mm before piercing the thyrohyoid membrane, usually at a higher level than the superior thyroid artery (Durham and Harrison 1962). It splits into superior, middle and inferior branches on entering the larynx. The superior branch supplies the mucosa of the piriform fossa. The large middle branch is distributed to the mucosa of the ventricle, specifically the quadrangular membrane, and therefore probably conveys the afferent component of the cough reflex. The inferior ramus is mainly distributed to the mucosa of the ventricle and subglottic cavity. On the medial wall of the piriform fossa, descending branches give twigs to the interarytenoid muscle and share a number of communicating branches with the recurrent laryngeal nerve (Sanders and Mu 1998).

The internal laryngeal nerve is sensory to the laryngeal mucosa down to the level of the vocal folds. It also carries afferent fibres from the laryngeal neuromuscular spindles and other stretch receptors. It descends to the thyrohyoid membrane, pierces it above the superior laryngeal artery and divides into an upper and lower branch. The upper branch is horizontal and supplies the mucosa of the pharynx, the epiglottis, vallecula and laryngeal vestibule. The lower branch descends in the medial wall of the piriform recess, supplies the aryepiglottic fold, the mucosa on the back of the arytenoid cartilage and one or two branches to transverse arytenoid (the latter unite with twigs from the recurrent laryngeal to supply the same muscle). The internal laryngeal nerve ends by piercing the inferior pharyngeal constrictor to unite with an ascending branch from the recurrent laryngeal nerve. As it ascends in the neck, it supplies branches, more numerous on the left, to the mucosa and tunica muscularis of the oesophagus and trachea, and to the inferior constrictor.

External laryngeal nerve

The external laryngeal nerve, smaller than the internal, descends behind sternohyoid with the superior thyroid artery, but on a deeper plane. It lies first on (occasionally within) the inferior pharyngeal constrictor, to which it contributes some small branches, and then pierces it to curve round the inferior thyroid tubercle. It passes beneath the attachment of sternothyroid to the oblique line of the thyroid cartilage to reach cricothyroid, which it supplies. A communicating nerve continues from the posterior surface of cricothyroid, crosses the piriform fossa and enters thyroarytenoid, where it anastomoses with branches from the recurrent laryngeal nerve. It has been suggested that these communicating branches may provide both additional motor components to thyroarytenoid and sensory fibres to the mucosa in the region of the subglottis. An anastomosis between the external and internal laryngeal nerves has also been described (Kochilas et al 2008). The external laryngeal nerve also gives branches to the pharyngeal plexus and communicates with the superior cardiac nerve and superior cervical sympathetic ganglion.

The close relationship of the external laryngeal nerve to the superior thyroid artery puts the nerve at potential risk when the artery is clamped during thyroid lobectomy, particularly when it is close to the artery (in approximately 20% of cases), or where, instead of crossing the superior thyroid vessels approximately 1 cm or more above the superior pole of the gland, it actually passes below this point (in some 20% of cases) (Cernea et al 1992, Kierner et al 1998). The external laryngeal nerve is also at risk in parathyroidectomy, carotid endarterectomy and anterior cervical spine procedures.

Recurrent laryngeal nerve

The recurrent laryngeal nerve supplies all the laryngeal muscles except cricothyroid, communicates with the internal laryngeal nerve and carries sensory filaments from the laryngeal mucosa below the vocal folds and from laryngeal stretch receptors. The nerve differs in origin and course on the two sides. On the right, it almost always arises from the vagus anterior to the first part of the subclavian artery, and curves backwards below and then behind it to ascend obliquely to the side of the trachea behind the common carotid artery. Near the lower pole of the lateral lobe of the thyroid gland, it is closely related to the inferior thyroid artery and crosses either in front of, behind or between its branches. On the left, the recurrent laryngeal nerve arises from the vagus on the left of the aortic arch, curves below it immediately behind the attachment of the ligamentum arteriosum to the concavity of the aortic arch and ascends to the side of the trachea (see Fig. 57.61). As the recurrent laryngeal nerve curves round either the subclavian artery or the aortic arch, it gives cardiac filaments to the deep cardiac plexus.

On both sides, the recurrent laryngeal nerve ascends in or near the tracheo-oesophageal groove. It is closely related to the medial surface of the thyroid gland before it passes under the lower border of the inferior constrictor, and it enters the larynx behind the articulation of the inferior thyroid cornu with the cricoid cartilage, passing either deep to (usually) or between (sometimes) the fibres of cricopharyngeus at its attachment to the lateral aspect of the cricoid cartilage. The nerve supplies cricopharyngeus as it passes. At this point, the nerve is in intimate proximity to the posteromedial aspect of the thyroid gland. The main trunk divides into two or more branches, usually below the lower border of the inferior constrictor, although branching may take place higher up. The anterior branch is mainly motor and is sometimes called the inferior laryngeal nerve (a term that is best avoided to prevent any confusion with a former synonym for the recurrent laryngeal nerve). It ascends posterior to the cricothyroid joint and its ligament, usually covered by fibres of posterior cricoarytenoid, then bends over the joint and continues forwards over lateral cricoarytenoid before terminating within thyroarytenoid. It innervates posterior cricoarytenoid by one or more branches, and interarytenoid, lateral cricoarytenoid and thyroarytenoid (Maranillo et al 2005). The posterior branch of the recurrent laryngeal nerve is mainly sensory and ascends deep to posterior cricoarytenoid to join the descending branch of the internal laryngeal nerve.

The recurrent laryngeal nerve does not always lie in a protected position in the tracheo-oesophageal groove but may be slightly anterior to it (more often on the right), and it may be markedly lateral to the trachea at the level of the lower part of the thyroid gland. The upper part of the nerve has a close but variable relationship to the inferior thyroid artery. On the right, it is as often anterior to, or posterior to, or intermingled with, the terminal branches of the artery; on the left, the nerve is usually posterior to the artery, though occasionally lies anterior to it. The stated incidences of these relationships vary between different authors. The recurrent laryngeal nerve has a highly variable branching pattern (see Fig. 41.13) (Henry et al 2016).

A very rare anomaly of relevance to laryngeal pathology and surgery is the 'non-recurrent' laryngeal nerve, where the right recurrent laryngeal nerve arises directly from the vagus nerve trunk high up in the neck and enters the larynx close to the inferior pole of the thyroid gland. Only the right side is affected, and it is always associated with an abnormal origin of the right subclavian artery from the aortic arch on the left side. If unrecognized, a non-recurrent laryngeal nerve may be susceptible to injury during surgery. It may also potentially be compressed by small tumours of the thyroid gland (Friedman et al 1986).

Pharyngeal plexus

Almost all of the nerve supply to the pharynx, whether motor or sensory, is derived from the pharyngeal plexus, which is formed by the pharyngeal branches of the glossopharyngeal and vagus nerves with contributions from the superior cervical sympathetic ganglion. The plexus lies on the external surface of the pharynx, especially on the middle constrictor. Filaments from the plexus ascend or descend external to the superior and inferior constrictors before branching within the muscular layer and mucosa of the pharynx. Whether a 'cranial root' of the accessory nerve serves as the conduit for the major motor drive to the pharyngeal plexus, albeit via the vagus nerve, is a matter of debate. The plexiform connections that may be demonstrated between the accessory nerve and the vagus nerve within the posterior cranial fossa are too variable and insubstantial to support this function.

Laryngeal nerve anastomoses

Anastomotic communications between the internal, external and recurrent laryngeal nerves probably explain why normal or near normal voice function can be present following neck surgery when one or more branches of these nerves have been divided (Naidu et al 2014, Sanudo et al 1999, Henry et al 2017). Numerous communications have been described (Sanudo et al 1999, Furlan et al 2002). The ansa Galeni, lying on the interarytenoid muscles, forms a direct connection between the recurrent and internal laryngeal nerves: it may be a single or double trunk or a plexus. The cricoid communication connects branches that originate bilaterally from the recurrent laryngeal nerve with the superior branch of the deep portion of the arytenoid plexus. The thyroarytenoid communication links the ascending branch of the recurrent laryngeal nerve and the descending branch from the anterior branch of the internal laryngeal nerve. There are also communications between the external laryngeal and recurrent laryngeal nerves, the internal and external laryngeal nerves and the recurrent laryngeal and superior laryngeal nerves. The anastomosis between the recurrent laryngeal nerve and the sympathetic trunk probably explains why ptosis is a rare complication following thyroidectomy.

Lesions of the vagus nerve and recurrent laryngeal nerve paralysis

The consequences of vagal nerve lesions are complex, reflecting the long course of the nerve and the possible involvement of three of its branches, namely the pharyngeal, superior laryngeal and recurrent laryngeal nerves. Collectively these nerves innervate the muscles of the larynx, soft palate and pharynx, and injury may therefore have deleterious effects on phonation and/or soft palate movements and/or swallowing. A lesion of the vagus nerve above the level at which the pharyngeal branch is given off will affect both the superior and recurrent laryngeal nerves. This causes immobility of the vocal fold on the affected side and imparts a breathy voice with lack of pitch and limited loudness. The affected fold is paralysed and lies in the so-called 'cadaveric' position halfway between abduction and adduction. If the lesion is unilateral, the voice is weak and hoarse, but if it is bilateral, phonation is almost absent, the vocal pitch cannot be altered, and the cough is weak and ineffective. There will also be a degree of hypernasality because of the effects on movements of the soft palate caused by paralysis of levator veli palatini. Unilateral palsies impact very significantly on the quality of life of the patient because of impaired vocalization and a tendency to aspirate. Bilateral palsies are extremely serious and a tracheostomy may be required to protect the airway.

A lesion affecting the superior laryngeal nerve may be unilateral or bilateral. Complete section is most likely during the ligation of the vessels forming the vascular pedicle of the superior pole of the thyroid gland during thyroid lobectomy. Unilateral lesions may result in the vocal folds appearing relatively normal and the effect on voice is barely noticeable and is often overlooked. A more detailed examination may detect some shortening of the vocal folds on the affected side with asymmetric tilt of the epiglottis and the anterior larynx canted towards the unaffected side. The result is a mildly hoarse voice with loss of pitch control. Bilateral superior laryngeal nerve lesions result in shortening of both vocal folds, the overhanging of the epiglottis over the folds and reduced tilt between the thyroid and cricoid cartilage. Effects on the voice are correspondingly greater, with reduced loudness and pitch but variable breathiness.

Damage to the internal laryngeal nerve causes loss of mechanoreceptive and proprioceptive sensation from the larynx. Unilateral loss produces a feeling that something is stuck in the throat, whereas bilateral loss will result in aspiration and can cause dysphagia, with a risk of choking.

Unilateral complete palsy of the recurrent laryngeal nerve is more common on the left side, presumably because the nerve is longer on this side. There is isolated paralysis of all the laryngeal muscles on the affected side except cricothyroid, which is innervated by the external laryngeal nerve. The patient may be asymptomatic or have a hoarse, breathy voice and there will be diminished ability to manipulate pitch. The hoarseness may be permanent or may become less severe with time as the contralateral fold develops the ability to hyperadduct and oppose the paralysed fold, thereby closing the glottis during phonation and coughing, although this is seldom enough to restore full voice quality. There may be aspiration of food and drink. Bilateral lesions of the recurrent laryngeal nerve result in both vocal folds being paralysed and taking up a paramedian position. Phonation can be nearly normal because the vocal folds lie so close to the midline, but there will be audible stridor and a compromised airway.

Clinically the position of the vocal fold in the acute phase after section of the recurrent laryngeal nerve is very variable. Though stridor is more common after bilateral lesions and sometimes only audible to the educated ear, the folds may be sufficiently abducted so that there is little problem with airway obstruction at rest, although the voice is always weaker in this situation. The folds are slightly more widely separated in chronic lesions, which renders the voice weaker but with a less precarious airway. Atrophy and fibrosis of paraglottic muscles probably affect the position of paralysed vocal folds in chronic lesions to a greater degree than variations in the strength of the apposing adductor and abductor muscle groups.

For many years, conventional wisdom held that movements of abduction were affected to a greater degree than those of adduction when the recurrent laryngeal nerve was partially damaged (Semon's law). This effect was thought to reflect the internal segregation within the recurrent laryngeal nerve of axons supplying the laryngeal abductor muscles. The hypothesis was later undermined by the demonstration that axons destined for particular laryngeal muscles are randomly distributed within the nerve. The weak abductive action of cricothyroid that is said to produce lengthening of the vocal folds has been suggested as the explanation for the relative sparing of abduction in these lesions, but is difficult to reconcile with the alternative view that cricothyroid may be a slight adductor of the vocal folds (Mu and Sanders 2009, Wadie et al 2013). It is likely that predicting the effect of partial lesions of the recurrent laryngeal nerve is complicated by the variable patterns of anastomoses between the laryngeal nerves. For further reading, see Aronson and Bless (2009) and Blitzer et al (2009).

Vagus nerve in the thorax

Preganglionic parasympathetic axons arise from neuronal cell bodies in the dorsal motor nucleus of the vagus in the medulla oblongata. Those destined for the thoracic viscera travel in the pulmonary, cardiac and oesophageal branches of the vagus nerve and synapse in minute ganglia in the walls of the target viscera. Axons travelling in cardiac branches join the cardiac plexuses and synapse in ganglia distributed freely over both atria, the interatrial septum and peri-nodal subepicardial tissue. Postganglionic fibres are distributed to the atria and the atrioventricular bundle and are concentrated around the sinuatrial and, to a lesser extent, the atrioventricular nodes. Cardiac branches slow the heart rate and diminish the force of contraction and may indirectly influence ventricular muscle via their effect on the atrioventricular node. The direct postganglionic parasympathetic innervation of the ventricles is sparse. The smaller branches of the coronary arteries are innervated mainly by parasympathetic vagal neurones, whereas the larger arteries are innervated mainly by sympathetic neurones. All cardiac branches of the vagus nerves contain both afferent and efferent fibres. Pulmonary branches contain axons that synapse in ganglia of the pulmonary plexuses: they are motor (bronchoconstrictor) to the circular non-striated muscle fibres of the bronchi and bronchioles (and therefore bring about bronchoconstriction), and secretomotor to the mucous glands of the respiratory epithelium.

Right vagus nerve

The right vagus nerve descends posterior to the right internal jugular vein in the neck and crosses the first part of the right subclavian artery to enter the thorax; the ansa subclavia is lateral, and the phrenic nerve is further lateral. After giving off the right recurrent laryngeal nerve, it descends through the superior mediastinum, at first posterior to the right brachiocephalic vein, and then lateral to the trachea and posteromedial to the superior vena cava. Superiorly, the right mediastinal part of the parietal pleura and superior lobe of the lung are lateral; inferiorly, the azygos vein and its arching terminal portion separate the right vagus nerve from the parietal pleura (see Fig. 56.7A). The nerve next passes posterior to the right main bronchus and lies on the posterior aspect of the right lung hilum. Here, it gives off posterior bronchial branches that unite with rami from the second to fifth/sixth thoracic sympathetic ganglia to form the right posterior pulmonary plexus. Two or three branches descend from the inferior part of this plexus on the posterior aspect of the oesophagus to join a left vagal branch and form the posterior oesophageal plexus. The anterior vagal trunk, containing nerve fibres from both vagus nerves, leaves the plexus and passes inferiorly on the posterior surface of the oesophagus, entering the abdomen by passing through the oesophageal hiatus in the respiratory diaphragm.

Left vagus nerve

The left vagus nerve enters the thorax posterior to the left brachiocephalic vein, between the left common carotid artery (anterior) and left subclavian artery (posterior). It descends through the superior mediastinum, crosses the left side of the aortic arch, gives off the left recurrent laryngeal nerve and then passes posterior to the left lung hilum (see Fig. 56.7B). Superior to the aortic arch, it is crossed anterolaterally by the left phrenic nerve, and on the arch, it is crossed laterally by the left superior intercostal vein and sometimes by a continuation of the accessory hemiazygos vein. Posterior to the hilum of the left lung, the left vagus nerve gives off posterior bronchial branches that unite with rami of the second to fourth thoracic sympathetic ganglia to form the left posterior pulmonary plexus. Two or three branches descend anteriorly on the oesophagus and join with a ramus from the right posterior pulmonary plexus to form the anterior oesophageal plexus. The posterior vagal trunk, containing nerve fibres from both vagus nerves, passes inferiorly on the anterior surface of the oesophagus and enters the abdomen through the oesophageal hiatus. Numerous branches from the anterior vagal and left sympathetic trunks are distributed to the descending thoracic aorta. This pathway transmits the typical intense, excruciating pain of an intramural aortic haematoma from aortic dissection or laceration.

Vagus nerve in the abdomen

The vagus nerves supply parasympathetic innervation to the abdominal viscera as far as the distal transverse colon, i.e. they supply the derivatives of the foregut and midgut, whereas the derivatives of the hindgut are supplied by parasympathetic fibres travelling via the pelvic splanchnic nerves; the overlap between these two supplies is variable. The vagal trunks are derived from the oesophageal plexus and enter the abdomen via the oesophageal hiatus, closely related to the anterior and posterior walls of the abdominal part of the oesophagus (see Fig. 56.6). The anterior vagal trunk is mostly derived from the left vagus and the posterior vagal trunk from the right vagus. The nerves supply the abdominal part of the oesophagus and stomach directly. The anterior vagal trunk gives off a hepatic branch, which innervates the liver and its vasculature, including the gallbladder and bile ducts, and the other structures in the free edge of the lesser omentum (hepatoduodenal ligament). The posterior vagal trunk supplies branches to the coeliac plexus: these fibres frequently constitute the largest portion of the fibres contributing to the plexus and arise directly from the posterior vagal trunk and from its gastric branch, and run beneath the peritoneum, deep to the posterior wall of the superior part of the omental bursa, to reach the coeliac plexus. Their synaptic relays with postganglionic neurones are situated in the myenteric (Auerbach's) and submucosal (Meissner's) plexuses in the wall of the hollow viscera.

ACCESSORY NERVE

The accessory nerve is the eleventh cranial nerve: its integrity is fundamental to thoracoscapular function and essential for scapulohumeral rhythm (Camp and Birch 2011).

Traditionally, it has been described as having a cranial root composed of a variable number of small rootlets that emerge from the post-olivary groove of the dorsolateral medulla, caudal to the rootlets of the vagus, and a spinal root composed of fibres derived from the cervical segments of the spinal cord (see below). According to this description, the cranial rootlets carry axons of motor neurones located in the caudal part of the nucleus ambiguus, and the spinal rootlets carry axons of motor neurones located in a nucleus in the ventral horn of the cervical spinal cord in line with the nucleus ambiguus. The spinal root ascends within the vertebral canal and enters the skull via the foramen magnum. The cranial and spinal roots join, either before or within the jugular foramen, and the bundle so formed then divides into internal and external branches on leaving the jugular foramen. The internal branch joins the vagus nerve and its fibres innervate branchiomeric muscles via the pharyngeal and laryngeal branches of the vagus nerve and the external branch descends to the neck and innervates sternocleidomastoid and trapezius.

There is an alternative view that the cranial root of the accessory nerve is anatomically and functionally part of the vagus nerve, and that the spinal root is, *de facto*, the accessory nerve. The issue is not simply one of contentious anatomical terminology; rather, it reflects the need to clarify the relevant microsurgical anatomy in order to minimize potential complications during surgery in the region. Paradoxically, meticulous cadaveric dissection studies, often undertaken stereomicroscopically, have failed to reach a consensus, finding either no connections between rootlets arising from the dorsolateral medulla and the spinal root of the accessory nerve because the cranial root was absent, or significant variations in the arrangement and size of plexiform connections between the cranial rootlets and the spinal root. Plexiform interconnections between neighbouring cranial nerves are not uncommon and are certainly not confined to the accessory and vagus nerves (Shoja et al 2014); their functional significance is often uncertain. (For further reading, see Krammer et al (1987), Lachman et al (2002), Ryan et al (2007), Wiles et al (2007), Benninger and McNeil (2010), Skinner (2011), Liu et al (2014), Tubbs et al (2014).)

Spinal nucleus

The (spinal) accessory nerve arises from an elongated nucleus of motor neurones in the lateral aspect of the ventral horn. Some rootlets emerge directly, while others turn cranially before exiting; their line of exit is irregular rather than linear. They join to form a trunk, the accessory nerve, which ascends intradurally within the vertebral canal between the ligamentum denticulatum and the dorsal roots of the spinal nerves. The nerve enters the skull via the foramen magnum, behind the vertebral artery. It then turns upwards and passes laterally to reach the jugular foramen, which it traverses in a common dural sheath with the vagus, but separated from that nerve by a fold of arachnoid mater.

Extracranial course

As the accessory nerve exits the jugular foramen, it runs posterolaterally and passes either medial or lateral to the internal jugular vein; occasionally, it may pass through the vein. The extradural part of the nerve then crosses the transverse process of the atlas and is crossed by the occipital artery before descending obliquely, medial to the styloid process, stylohyoid and the posterior belly of digastric. Running with the superior sternocleidomastoid branch of the occipital artery, it reaches the upper part of sternocleidomastoid and enters its deep surface, to form an anastomosis with fibres from C2 alone, C3 alone, or C2 and C3 (the ansa of Maubrac). It may also communicate with the ventral root of the first cervical nerve (McKenzie branch).

The accessory nerve occasionally terminates in sternocleidomastoid. More commonly it emerges, usually as one trunk, 5–10 mm cephalad to the point where the great auricular nerve winds around sternocleidomastoid, and moves from a plane posterior to the muscle to one that is anterior. The relationship between the accessory nerve and the great auricular nerve in the posterior triangle is the key to exposure of the accessory nerve: the general relations of the posterior triangle vary with individual physique, but this relation between the two nerves is reliably consistent. The accessory nerve then runs across the fatty areolar tissue at the apex of the posterior triangle, in close relation to the superior superficial cervical lymph nodes in levels Va and Vb, deep to platysma. It is separated from the underlying levator scapulae by this areolar tissue, and, more deeply, by the prevertebral fascia (see Fig. 35.7A). One slender branch passes to the upper fibres of trapezius either deep to sternocleidomastoid or just beyond it. The nerve pierces the fascia covering the deep surface of trapezius close to the anterior border of the muscle and then runs caudally about 2 cm from that border. It passes down in a characteristic sinuous fashion, accompanied by slender vessels to the deep, inner face of trapezius. A branch from the cervical plexus (third and fourth cervical ventral rami) joins the nerve just above the clavicle. Intraoperative stimulation of this branch rarely evokes a muscular response; it probably conveys afferent fibres from the middle and lower parts of trapezius. The nerve now turns medially, continuing in parallel to the spine of the scapula about 4 cm above it. At the medial end of the spine, the nerve turns caudally again, passing down parallel to the medial border of the scapula. It divides into terminal muscular branches about 7 cm distal to the scapular spine. Although sternocleidomastoid, and the middle and the lower portions of trapezius, may be partially supplied by branches from the cervical plexus, the upper part of trapezius is innervated solely by the accessory nerve.

The cervical course of the accessory nerve follows a line from the lower anterior part of the tragus to the tip of the transverse process of the atlas, and then across sternocleidomastoid and the posterior triangle to a point on the anterior border of trapezius 3–5 cm above the clavicle.

The accessory nerve is thought to provide the sole motor supply to sternocleidomastoid; the second and third cervical nerves are believed to carry proprioceptive fibres from it. The supranuclear pathway of fibres destined for sternocleidomastoid is not simple; current evidence favours bilateral hemispheric innervation, although opinion varies as to the extent of the ipsilateral input. The motor supply to the descending (upper) and transverse (middle) portions of trapezius is primarily from the accessory nerve under predominantly contralateral supranuclear control. Usually, trapezius receives an innervation from the cervical plexus, in most cases from C3 and C4 (Tubbs et al 2011). A study using intraoperative electroneurography and histochemical analyses found that, when present, the cervical fibres did not consistently innervate all three parts of the muscle (descending, transverse and ascending), and that fibres from C2 usually travelled via the accessory nerve, while fibres from C3 and C4 innervated trapezius independently (Pu et al 2008). In addition, to their motor contribution, C3 and C4 also carry proprioceptive fibres from trapezius.

On the basis of the incomplete denervation of the muscle that sometimes happens following sacrifice of both the accessory nerve and the cervical plexus, it has been suggested that trapezius receives a partial motor supply from other sources, possibly via thoracic roots. (For a detailed review of the applied surgical anatomy of the accessory nerve plexus, see Brown (2002).)

Sensory ganglia have been described along the course of the intradural portion of the nerve.

Lesions of the accessory nerve

Lesions of the accessory nerve may be sustained centrally, at its exit from the skull or in the neck. The supranuclear fibres that influence motor neurones innervating sternocleidomastoid decussate twice; a lesion of the corticospinal system above the pons therefore produces weakness of the ipsilateral sternocleidomastoid and contralateral trapezius. Episodic contraction of sternocleidomastoid and trapezius, often accompanied by contraction of other muscle groups, e.g. splenius capitis, occurs in spasmodic torticollis, a focal dystonia. In jugular foramen syndrome, caused by pathologies including nasopharyngeal carcinoma or a jugular paraganglioma, lesions of the glossopharyngeal, vagus and accessory nerves coexist. The accessory nerve can be injured more distally in the neck by trauma or by surgical exploration in the posterior triangle, particularly at the apex of the triangle. Typically, there is immediate pain, then dropping of the shoulder and a remarkable loss of function. The average ISHA is about 50°. The pain is characteristic: often severe, deep-seated, dull, constant and boring in nature, and felt around the scapula and the posterior aspect of the neck and shoulder. The posture of the scapula is also characteristic: because of the loss of the great suspensory muscle, trapezius, the scapula drops down and away from the spinal column (see Fig. 49.37). There is often winging of the scapula, easily distinguished from that caused by paralysis of serratus anterior by the posture of the scapula (see Fig. 49.38). The nerve appears to be relatively immune to the harmful effects of delayed repair, even as late as 4 years after injury, with early relief of pain long before there is reinnervation of muscle (Camp and Birch 2011).

HYPOGLOSSAL NERVE

The hypoglossal nerve is the twelfth cranial nerve and is motor to all the muscles of the tongue except palatoglossus.

Hypoglossal nucleus and central connections

The hypoglossal nucleus lies near the midline in the dorsal medullary grey matter. It is approximately 2 cm long and extends from the hypoglossal trigone in the floor of the fourth ventricle into the closed part of the medulla (see Figs 28.3, 28.5, 28.8). It consists of large motor neurones interspersed with myelinated fibres and is organized into dorsal and ventral nuclear tiers, each divisible into medial and lateral subnuclei. A musculotopic organization of motor neurones within the nuclei corresponds to the structural and functional divisions of tongue musculature. Experimental evidence suggests that motor neurones of the medial division of the hypoglossal nucleus innervate tongue muscles that are orientated in planes transverse to the long axis of the tongue (transverse and vertical intrinsics and genioglossus), whereas motor neurones of the lateral division innervate tongue muscles that are orientated parallel to this axis (styloglossus, hyoglossus, superior and inferior longitudinal).

The hypoglossal nucleus receives corticonuclear fibres from the precentral gyrus and adjacent areas, predominately from the contralateral hemisphere. The corticonuclear fibres synapse either directly on motor neurones of the nucleus or on interneurones. Most medial hypoglossal subnuclei receive projections from both cerebral hemispheres. The hypoglossal nucleus may connect with the cerebellum via the adjacent perihypoglossal nucleus, and perhaps also with the medullary reticular formation, the trigeminal sensory nucleus and the nucleus solitarius (Holstein 2012).

Hypoglossal fibres emerge from the ventral aspect of the nucleus and traverse the reticular formation lateral to both the medial lemniscus and the medial accessory olivary nucleus. They continue ventrally, between the medial accessory and the principal inferior olivary nuclei, and then curve laterally to emerge from the brainstem as a series of 10–15 rootlets arranged linearly along the preolivary sulcus (see Fig. 28.8) (Yousry et al 2002). These rootlets coalesce into two bundles that exit separately through the hypoglossal canal and unite extradurally.

Extracranial course

The hypoglossal rootlets run laterally behind the vertebral artery, collected into two bundles that perforate the dura mater separately opposite the hypoglossal canal in the occipital bone, and unite after traversing it. The canal is sometimes divided by a spicule of bone. The nerve emerges from the canal in a plane medial to the internal jugular vein, internal carotid artery and glossopharyngeal, vagus and accessory nerves, and passes inferolaterally behind the internal carotid artery and glossopharyngeal and vagus nerves to the interval between the artery and the internal jugular vein (see Fig. 35.8). Here, it makes a half-spiral turn round the inferior vagal ganglion, united to it by connective tissue. It then descends almost vertically between the vessels and anterior to the vagus to a point level with the angle of the mandible, becoming superficial below the posterior belly of digastric and emerging between the internal jugular vein and internal carotid artery. Often associated with a plexus of veins around the junction of the common facial and internal jugular veins (vena comitans nervi hypoglossi), excessive bleeding here during neck dissection can lead to nerve damage. The nerve loops round the inferior sternocleidomastoid branch of the occipital artery, crosses lateral to both internal and external carotid arteries and the loop of the lingual artery a little above the tip of the greater cornu of the hyoid, and is itself crossed by the facial vein (see Figs 35.7A, 35.8, 35.17). The nerve next inclines upwards and forwards on hyoglossus, passing deep to stylohyoid, the tendon of digastric and the posterior border of mylohyoid. Between mylohyoid and hyoglossus, the hypoglossal nerve lies below the deep part of the submandibular gland, the submandibular duct and the lingual nerve, with which it communicates. It then passes on to the lateral aspect of genioglossus, continuing forwards in its substance as far as the tip of the tongue (see Fig. 37.11A). It distributes fibres to styloglossus, hyoglossus and genioglossus and to the intrinsic muscles of the tongue. Cadaveric tongues stained using Sihler's stain (a whole mount nerve staining technique that renders a large specimen transparent while counterstaining all nerves) or acetylcholinesterase or silver stains, show the basic mammalian intralingual pattern of hypoglossal nerve distribution but with notable differences, even from non-human primates. Thus, many muscle fibres, particularly in the transverse group of intrinsic muscles, contain multiple *en grappe* motor end-plates (suggesting that they are some variant of slow tonic muscle fibres). Presumably, these specializations facilitate the fine motor control of tongue shape that is required in speech and swallowing (Mu and Sanders 2010) (see Fig. 37.13).

The hypoglossal nerve has meningeal, descending, thyrohyoid, geniohyoid and communicating branches.

Meningeal branches

Meningeal branches leave the nerve in the hypoglossal canal and return through it to supply the diploë of the occipital bone, the dural walls of the occipital and inferior petrosal sinuses, and much of the floor of the anterior wall of the posterior cranial fossa, probably through pathways other than that of the hypoglossal nerve, e.g. upper cervical spinal nerves (see Fig. 25.3B).

Descending branch

The descending branch (descendens hypoglossi) contains fibres from the first cervical spinal nerve. It leaves the hypoglossal nerve when it curves around the occipital artery, and runs down on the carotid sheath. It provides a branch to the superior belly of omohyoid before joining the descendens cervicalis to form the ansa cervicalis (see Figs 35.7A, 35.8).

Nerves to thyrohyoid and geniohyoid

The nerves to thyrohyoid and geniohyoid arise near the posterior border of hyoglossus and are derived from the first cervical ventral ramus.

Communicating branches

The hypoglossal nerve communicates with the sympathetic trunk, the lingual, glossopharyngeal and vagus nerves and the pharyngeal plexus. Near the atlas it is joined by branches from the superior cervical sympathetic ganglion and a filament from the loop between the first cervical ventral ramus and the ascending branch of the second cervical ventral ramus that leaves the hypoglossal nerve as the upper root of the ansa cervicalis. The vagal connections are close to the skull; numerous filaments pass between the hypoglossal nerve and the inferior vagal ganglion in the connective tissue that unites them. As the hypoglossal nerve curves round the occipital artery it receives the ramus lingualis vagi from the pharyngeal plexus. Near the anterior border of hyoglossus it is connected with the lingual nerve by many filaments that ascend on the muscle.

Lesions of the hypoglossal nerve

The hypoglossal nerve may be damaged during neck dissection. Complete hypoglossal division causes unilateral lingual paralysis and eventual hemiatrophy; the protruded tongue deviates to the paralysed side, and, on retraction, the wasted and paralysed side rises higher than the unaffected side. The larynx may deviate towards the active side in swallowing, as a consequence of the unilateral paralysis of the hyoid depressors associated with loss of the first cervical ventral ramus, which runs with the hypoglossal nerve. If paralysis is bilateral, the tongue is motionless. Taste and tactile sensibility are unaffected but articulation is slow and swallowing very difficult.

The hypoglossal nerve is often used to reanimate the face in patients, particularly the elderly, when their facial nerves have been transected. Direct end-to-end, end-to-side or split-nerve grafts are reliable and offer a robust, effective and quick alternative to more complex reanimation procedures.

SPINAL NERVES

Spinal nerves are the means by which the central nervous system receives information from, and controls the activities of, the trunk and limbs. There are 31 pairs of spinal nerves (8 cervical, 12 thoracic, 5 lumbar, 5 sacral, 1 coccygeal): they contain a mixture of sensory and motor fibres. The abbreviations C, T, L, S and Co, with appropriate numerals, are commonly applied to individual nerves as their 'root value'.

Spinal nerves pass through intervertebral foramina. At thoracic, lumbar, sacral and coccygeal levels, the numbered nerve exits the vertebral canal by passing below the pedicle of the corresponding vertebra, e.g. the fourth lumbar nerve (L4) nerve exits the intervertebral foramen between the fourth and fifth lumbar vertebrae. However, in the cervical region, the upper seven cervical nerves (C1–C7) pass above their corresponding vertebrae. The first cervical nerve (C1) exits the vertebral canal between the occipital bone and atlas, and is often termed the suboccipital nerve. The last pair of cervical nerves does not have a correspondingly numbered vertebra and the eighth cervical nerve passes between the seventh cervical and first thoracic vertebrae.

Appearance and orientation of roots at each spinal level

The size and direction of spinal nerve roots vary. The upper four cervical roots are small, while the lower four are large. Cervical dorsal roots have a thickness ratio to the ventral roots of 3:1, which is greater than in other regions. The first dorsal root is an exception, because it is smaller than its ventral counterpart, and is occasionally absent. The first and second cervical spinal roots are short and run almost horizontally to their exits from the vertebral canal, whereas from the third to the eighth cervical levels the roots slope obliquely down. Obliquity and length increase successively, although the distance between spinal attachment and vertebral exit never exceeds the height of one vertebra. There is an alternative view that the upper cervical roots descend, the fifth is horizontal, the sixth to eighth ascend, the first two thoracic roots are horizontal, the next three ascend, the sixth is horizontal and the rest descend (Kubik and Müntener 1969): this view is based on the observation that the cervicothoracic part of the spinal cord grows more in length than other parts.

Thoracic roots, except the first, are small, and the dorsal root only slightly exceeds the ventral in thickness. They increase successively in length. In the lower thoracic region, the roots descend in contact with the spinal cord for at least two vertebrae before emerging from the vertebral canal.

Lower lumbar and upper sacral roots are the largest, and their rootlets are the most numerous. Coccygeal roots are the smallest. Lumbar, sacral and coccygeal roots descend with increasing obliquity to their exits (Kubik and Müntener 1969). The spinal cord ends near the lower border of the first lumbar vertebra, which means that the lengths of successive roots rapidly increase: the consequent collection of roots forms the cauda equina (see Fig. 47.1A). The largest roots, and hence the largest spinal nerves, are continuous with the spinal cervical and lumbar enlargements and innervate the upper and lower limbs.

Spinal ganglia (dorsal root ganglia)

Spinal ganglia (dorsal root ganglia, DRG) are large groups of sensory neurones on the dorsal spinal roots. Each is oval and reddish: its size is related to that of its root. A ganglion is bifid medially where the two fascicles of a dorsal root emerge to enter the spinal cord. Ganglia usually lie in the intervertebral foramina, immediately lateral to the perforation of the dura mater by the roots (see Fig. 47.6A). However, the first cervical ganglion (when present) lies on the vertebral arch of the atlas and the second lies posterior to the lateral atlanto-axial joint; the sacral ganglia lie inside the vertebral canal; and the coccygeal ganglion usually lies within the dura mater. Small aberrant ganglia sometimes occur on the upper cervical dorsal roots between the spinal ganglia and the cord.

Spinal nerves proper

Immediately distal to the spinal ganglia, ventral and dorsal roots unite to form spinal nerves. These very soon divide into dorsal and ventral rami, both of which receive fibres from both roots (see Fig. 47.6A). At all levels above the sacral, this division occurs within the intervertebral foramen. Division of the sacral spinal nerves occurs within the sacral vertebral canal, and the dorsal and ventral rami exit separately through posterior and anterior sacral foramina at each level. Spinal nerves trifurcate at some cervical and thoracic levels, in which case the third branch is called a ramus intermedius. At or distal to its origin, each ventral ramus gives off recurrent meningeal (sinuvertebral) branches and receives a grey ramus communicans from the corresponding sympathetic ganglion. All the thoracic and first and second lumbar ventral rami each contribute a white ramus communicans to the corresponding sympathetic ganglia. The second, third and fourth sacral nerves supply visceral branches that carry a preganglionic parasympathetic outflow direct to the pelvic plexuses.

Cervical spinal nerves enlarge from the first to the sixth nerve. The seventh and eighth cervical and the first thoracic nerves are similar in size to the sixth cervical nerve. The remaining thoracic nerves are relatively small. Lumbar nerves are large, increasing in size from the first to the fifth. The first sacral nerve is larger than the other sacral nerves, which progressively decrease in size. The coccygeal nerves are the smallest spinal nerves.

In the radicular ('root') canal and intervertebral foramen, a spinal nerve is related to the spinal artery of that level and its radicular branch, and to a small plexus of veins. At the outer end of the foramen, the nerve may lie above or below transforaminal ligaments. The size of a spinal nerve and associated structures within the intervertebral foramen is not in direct relation to the size of the foramen through which the nerve exits: the fifth lumbar nerve is the largest of the lumbar nerves but its foramen is smaller than those of the first four lumbar nerves, and so it is particularly liable to compression.

Meningeal nerves

Recurrent meningeal (or sinuvertebral) nerves (see Fig. 47.9) occur at all vertebral levels. They are mixed sensory and sympathetic nerves, represented by numerous fine filaments amongst which as many as four larger trunks may be evident. At cervical levels the autonomic roots arise from the grey rami that form the vertebral nerve. At thoracic and lumbar levels, each nerve is formed by a somatic root from the ventral ramus and by an autonomic root from the grey ramus communicans of that segment. Each nerve pursues a recurrent course through the intervertebral foramen, passing ventral to the spinal nerve, to enter the vertebral canal, where it divides into ascending, descending and transverse branches. These branches communicate with corresponding branches from the segments above and below, and from the contralateral side, forming arcades along the floor of the vertebral canal. Meningeal branches of the arcades form a plexus on the ventral surface of the dural sac and nerve root sleeves that attenuates laterally; the posterior paramedian dura is devoid of nerve endings. Skeletal branches are distributed to the posterior longitudinal ligament, the periosteum of the vertebral bodies, and to the posterior and posterolateral aspects of the intervertebral discs (Garcia-Cosamalon et al 2010). Vascular branches accompany the veins and arteries of the vertebral canal and those of the vertebral bodies. The upper three cervical meningeal nerves ascend through the foramen magnum into the posterior cranial fossa, where they innervate the dura mater that covers the clivus; en route, they innervate the median atlanto-axial joint and its ligaments.

Variations of spinal roots and nerves

The courses of spinal roots and nerves in relation to the thecal sac and vertebral and radicular canals may be aberrant. An individual intervertebral foramen may contain a duplicated sheath, nerve and roots, which will then be absent at an adjacent level. Abnormal communications between roots may occur within the vertebral canal. These anomalies have been described and classified for the lumbosacral spine by Neidre and Macnab (1983).

Functional components of spinal nerves

A typical spinal nerve contains somatic efferent fibres and somatic and visceral afferent fibres. Some, but not all, spinal nerves also contain preganglionic autonomic fibres.

Somatic components

Somatic efferent fibres innervate skeletal muscles and are axons of α, β and γ neurones in the spinal ventral grey column. Somatic afferent fibres are the peripheral processes of unipolar neurones in the spinal ganglia and convey impulses into the CNS from receptors in the skin, subcutaneous tissues, muscles, tendons, fasciae and joints.

Visceral components

Visceral efferent fibres

Preganglionic visceral efferent sympathetic fibres are axons of neurones in the spinal intermediolateral grey column throughout the thoracic and upper two or three lumbar segments; they join the sympathetic trunk via corresponding white rami communicantes and synapse with postganglionic neurones that are distributed to smooth muscle, myocardium or exocrine glands.

Preganglionic visceral efferent parasympathetic fibres are axons of neurones in the spinal lateral grey column of the second to fourth sacral segments; they leave the ventral rami of corresponding sacral nerves and synapse in pelvic ganglia. Postganglionic axons are distributed mainly to smooth muscle or glands in the walls of the pelvic viscera.

Visceral afferent fibres

General visceral afferent fibres from the viscera and blood vessels accompany their efferent counterparts. They respond to various stimuli including excessive muscular contraction or distension, ischaemia and inflammation; their neuronal somata are located in the glossopharyngeal and vagal ganglia and in thoracic and lumbosacral dorsal root ganglia (visceral afferent fibres that run mainly with sympathetic efferent fibres). Their central projections reach the brainstem and spinal cord, respectively. Sensory fibres in the vagus are more numerous in the derivatives of the foregut than those of the derivatives of the midgut and are concerned with physiological responses such as satiety, whereas pain and discomfort are mediated by spinal pathways.

The somata of glossopharyngeal general visceral afferents are in the glossopharyngeal ganglia. Their peripheral processes innervate the postsulcal lingual region, the palatine tonsils and pharynx, but they do not innervate taste buds. They also innervate the carotid sinus and the carotid body, which contain receptors sensitive to tension and changes in chemical composition of the blood. Impulses from these receptors are essential to circulatory and respiratory reflexes.

The somata of vagal general visceral afferent fibres are in the superior and inferior vagal ganglia. Their peripheral processes are distributed to terminals in the pharyngeal and oesophageal walls where, acting synergistically with glossopharyngeal visceral afferents in the pharynx, they are concerned with swallowing reflexes. Vagal afferents are also believed to innervate the thyroid and parathyroid glands. In the heart, vagal afferents innervate the walls of the great vessels, the aortic bodies and pressor receptors, where they are stimulated by raised intravascular pressure. In the lungs they are distributed via the pulmonary plexuses. They supply bronchial mucosa, where they are probably involved in cough reflexes; bronchial muscle, where they encircle myocytes and end in tendrils, which are sometimes regarded as muscle spindles and which are believed to be stimulated by change in the length of myocytes; interalveolar connective tissue, where their knob-like endings, together with terminals on myocytes, may evoke Hering–Breuer reflexes; the adventitia of pulmonary arteries, where they may be pressor receptors; and the intima of pulmonary veins, where they may be chemoreceptors. Vagal visceral afferent fibres also end in the gastric and intestinal walls, digestive glands and the kidneys. Fibres ending in the gut and its ducts respond to stretch or contraction. Gastric impulses may evoke sensations of hunger and nausea.

Visceral afferents that enter the spinal cord through spinal nerve roots branch extensively and synapse on viscerosomatic neurones in the dorsal horn and intermediate grey matter. Almost all the central processes of vagal and glossopharyngeal afferent fibres end in the nucleus solitarius of the medulla. About 5% of the vagal afferents project directly to, and terminate in, the upper cervical spinal cord (C1–C2), where they are believed to contribute to referred sensations, as well as to propriospinal mechanisms of nociceptive modulation. Visceral afferents establish connections within the CNS that mediate autonomic reflexes. In addition, afferent impulses probably mediate visceral sensations such as hunger, nausea, sexual excitement, vesical distension, etc. Visceral pain fibres may follow these routes. Although viscera are insensitive to cutting, crushing or burning, excessive tension in smooth muscle and some pathological conditions produce visceral pain. In visceral disease, vague pain may be felt near the viscus itself (visceral pain) or in a cutaneous area or other tissue whose somatic afferents enter spinal segments receiving afferents from the viscus, a phenomenon known as referred pain. If inflammation spreads from a diseased viscus to the adjacent parietal serosa (e.g. the peritoneum), somatic afferents will be stimulated, causing local somatic pain, which is commonly spasmodic. Referred pain is often associated with local cutaneous tenderness. For further reading on visceral pain, see Bielefeldt and Gebhart (2013).

Afferent fibres in pelvic splanchnic nerves innervate pelvic viscera and the distal part of the colon. Vesical receptors are widespread; those in muscle strata are associated with thickly myelinated fibres and are believed to be stretch receptors, possibly activated by contraction. Pain fibres from the bladder and proximal urethra traverse both the pelvic splanchnic nerves and the inferior hypogastric plexus, hypogastric nerves, superior hypogastric plexus and lumbar splanchnic nerves to reach their cell bodies in ganglia on the lower thoracic and upper lumbar dorsal spinal roots; the significance of this dual sensory pathway is uncertain. Lesions of the cauda equina abolish pain from vesical overdistension, but hypogastric section is ineffective. Pain fibres from the uterus traverse the hypogastric plexus and lumbar splanchnic nerves to reach somata in the lowest thoracic and upper lumbar spinal ganglia, and hypogastric division may relieve dysmenorrhoea. Afferents from the uterine cervix traverse the pelvic splanchnic nerves to reach their somata in the upper sacral spinal ganglia; stretching the cervix uteri causes pain but cauterization and biopsy excisions do not.

In general, afferent fibres that accompany pre- and postganglionic sympathetic fibres have a segmental arrangement and end in spinal cord segments from which preganglionic fibres innervate the region or viscus concerned. General visceral afferents entering thoracic and upper lumbar spinal segments are largely concerned with pain. Nociceptive impulses from the pharynx, oesophagus, stomach, intestines, kidneys, ureter, gallbladder and bile ducts seem to be carried in sympathetic pathways. Cardiac nociceptive impulses enter the spinal cord in the first to fifth thoracic spinal nerves, mainly via the middle and inferior cardiac nerves, but some fibres pass directly to the spinal nerves. It is said that there are no general visceral afferents in the superior cardiac nerves. Peripherally, the fibres pass through the cardiac plexuses and along the coronary arteries. Myocardial anoxia may evoke symptoms of angina pectoris in which pain is typically presternal, and is also referred to much of the left chest, and radiates to the left shoulder, the medial aspect of the left arm, along the left side of the neck to the jaw and occiput, and down to the epigastrium. Cardiac afferents carried in vagal cardiac branches are concerned with the reflex depression of cardiac activity. Ureteric pain fibres, also running with sympathetic fibres, are presumably involved in the agonizing renal colic that follows obstruction by calculi. Afferent fibres from the testis and ovary run through the corresponding plexuses to somata in the tenth and eleventh thoracic dorsal root ganglia.

Some primary afferent neurones, innervating the gut, lungs, heart and blood vessels, also appear to have an efferent function in that they release transmitters from their peripheral endings during the axon reflex. The primary substances released in this way are substance P, calcitonin gene-related peptide (CGRP) and ATP. These act on target cells to produce vasodilation, increased venular permeability, changes in smooth muscle contractility, degranulation of mast cells and a variety of effects on leukocytes and fibroblasts, a process collectively known as 'peripheral neurogenic inflammation'. The local release of such substances may play a trophic role in the maintenance of tissue integrity and repair in response to injury (for further reading, see Xanthos and Sandkühler (2014)).

RAMI OF THE SPINAL NERVES

Spinal nerves exit from the vertebral canal via their corresponding intervertebral foramina. They then divide to form a large ventral (anterior) ramus and a smaller dorsal (posterior) ramus. In general terms, the ventral rami innervate the limbs and the muscles and skin of the anterolateral trunk. The axons within the ventral rami serving the neck, upper and lower limbs are redistributed within cervical, brachial and lumbosacral plexuses, respectively. Thoracic ventral rami run independently and retain a largely segmental distribution. Dorsal (posterior) rami of spinal nerves are usually smaller than the ventral rami and are directed posteriorly. Retaining a segmental distribution, all, except for the first cervical, fourth and fifth sacral and the coccygeal, divide into medial and lateral branches that supply the muscles and skin of the posterior regions of the neck and trunk (see Fig. 47.8).

Dorsal rami

Cervical dorsal spinal rami

Each cervical spinal dorsal ramus, except the first, divides into medial and lateral branches that all innervate muscles. In general, only medial branches of the second to fourth, and usually the fifth, supply the skin. Except for the first and second, each dorsal ramus passes posteriorly medial to a posterior intertransverse muscle (which it supplies), curving round the articular process into the interval between semispinalis capitis and semispinalis cervicis.

First cervical dorsal ramus (suboccipital nerve)

The first cervical dorsal ramus, the suboccipital nerve, is larger than the ventral (see Fig. 46.78). It emerges superior to the posterior arch of the atlas and inferior to the vertebral artery, and enters the suboccipital triangle to supply rectus capitis posterior major and minor, obliquus capitis superior and inferior, and semispinalis capitis. A filament from the branch to inferior oblique joins the second dorsal ramus. The suboccipital nerve occasionally has a cutaneous branch that accompanies the occipital artery to the scalp, and connects with the greater and lesser occipital nerves. It may also communicate with the accessory nerve.

Second cervical dorsal ramus

The second cervical dorsal ramus is slightly larger than the ventral and all the other cervical dorsal rami (see Figs 36.22, 46.78). It runs between the lamina of the axis and inferior oblique, below which it divides into a large medial and smaller lateral branch. The dorsal ramus or its medial branch receives communicating branches from the first cervical dorsal ramus that pass both through and around inferior oblique. A descending communicating branch crosses the facet joint between the second and third cervical vertebrae to reach the third cervical dorsal ramus.

Greater occipital nerve

The medial branch, termed the greater occipital nerve, passes transversely across inferior oblique deep to semispinalis capitis, which it innervates. Near the origin of inferior oblique, it turns rostrally along rectus capitis posterior major, where it receives a communicating branch from the third occipital nerve before turning dorsally to pierce semispinalis capitis. It emerges on to the scalp by passing above an aponeurotic sling between trapezius and sternocleidomastoid near their occipital attachments. It ascends with the occipital artery and divides into branches that connect with the third occipital and lesser occipital nerves, and which supply the back of the auricle and the skin of the scalp as far forwards as the coronal suture. The lateral branch of the second cervical dorsal ramus supplies longissimus capitis, semispinalis capitis and splenius capitis, and sends a communicating branch to the lateral branch of the third cervical dorsal ramus.

Greater occipital neuralgia Greater occipital neuralgia is a syndrome of pain and paraesthesiae felt in the distribution of the greater occipital nerve. This is usually caused by damage or irritation to the greater occipital nerve but more rarely can result from a similar process in the lesser occipital nerve or both greater and lesser occipital nerves. A similar syndrome may be caused by upper facet joint arthritis involving the second cervical root (Vanelderen et al 2010).

Third cervical dorsal ramus

The third cervical dorsal ramus is intermediate in size between the second and fourth. It courses back round the articular pillar of the third cervical vertebra, medial to the posterior intertransverse muscle, and divides into medial and lateral branches. The lateral branch passes dorsally across the surface of semispinalis capitis to supply it and the overlying longissimus capitis and splenius capitis. It receives a communicating branch from the lateral branch of the second cervical dorsal ramus, and sends a similar branch to the lateral branch of the fourth cervical dorsal ramus. The deep medial branch curves dorsally and medially around the waist of the articular pillar before ending in multifidus. It sends an articular branch to the facet joint between the third and fourth cervical vertebrae, and may also send a branch into semispinalis capitis. The superficial medial branch, the third occipital nerve, curves around the lateral and dorsal surfaces of the facet joint between the second and third cervical vertebrae, which it supplies. It continues transversely, deep to semispinalis, which it supplies, and sends a communicating branch to the greater occipital nerve. Just above the second cervical spinal process, the third occipital nerve turns dorsally to pierce semispinalis capitis, splenius capitis and trapezius, and becomes cutaneous over a small area immediately below the superior nuchal line. Communicating branches join the cutaneous branches of the greater and lesser occipital nerves.

Dorsal rami of the lower five cervical nerves

The dorsal rami of the lower five cervical nerves curve back round the vertebral articular pillars and divide into lateral and medial branches. The lateral branches supply longissimus cervicis, splenius cervicis and iliocostalis cervicis. The medial branches curve around the lateral and dorsal surfaces of the articular pillar of their segment, deep to semispinalis capitis. They send articular branches to the facet joints above and below their course before entering and supplying multifidus. Terminal branches reach interspinalis at each segment. Cutaneous branches arise consistently from the fourth, and commonly from the fifth, sixth and eighth, but not usually from the seventh medial branches. These branches pass across multifidus or through semispinalis cervicis and turn dorsally around the medial border of semispinalis capitis, to pierce splenius cervicis and trapezius and reach the skin.

Thoracic dorsal spinal rami

The dorsal rami of the thoracic spinal nerves supply the intrinsic muscles of the back and the overlying postvertebral skin on a segmental basis (see Figs 46.3, 47.8). At each segmental level, they pass dorsally through an aperture bounded by the transverse processes superiorly and inferiorly, the facet joint medially and the superior costotransverse ligament laterally. Thereafter, each dorsal ramus follows a prolonged course laterally, between the anterior lamella of the superior costotransverse ligament anteriorly, and the costolamellar ligament and the posterior lamella of the superior costotransverse ligament posteriorly. In this narrow space, the dorsal ramus divides into lateral and medial branches. The lateral branches continue laterally as far as the costotransverse joint, above which they turn dorsally and inferiorly to supply levatores costarum, and enter longissimus thoracis and iliocostalis. Lateral branches from the upper six thoracic dorsal rami remain intramuscular. Those from the lower six levels emerge from iliocostalis lumborum to pierce serratus posterior inferior and latissimus dorsi in line with the costal angles. They descend across as many as four ribs before becoming superficial. The twelfth thoracic lateral branch sends a filament medially along the iliac crest and then passes down to the anterior gluteal skin. Some upper thoracic lateral branches may become cutaneous.

Each medial branch hooks dorsally around the lateral margin of the posterior lamella of the superior costotransverse ligament, lying a variable distance above the tip of the transverse process. At the first to fourth, and at the ninth and tenth thoracic levels, the medial branches cross the superior tip of the transverse process to turn inferiorly and medially across the posterior surface of the transverse process, lying between the attachment sites of multifidus medially and semispinalis laterally. Each nerve continues this oblique course to supply multifidus and semispinalis. At the fifth to eighth thoracic levels, the medial branches assume a course parallel to that of other levels, but do not reach the transverse process, instead passing superior and dorsal to the plane of the transverse processes. At the eleventh and twelfth levels, in keeping with the relatively short transverse processes at these levels, the medial branches run close to the superior articular processes. Each medial branch supplies articular branches to the facet joints above and below its course. Medial branches of the upper six thoracic dorsal rami furnish cutaneous branches that pierce trapezius and the rhomboids to reach the skin near the spinous processes. Cutaneous branches may occasionally arise from the medial branches of the lower six thoracic dorsal rami.

Lumbar dorsal spinal rami

After leaving its spinal nerve, each of the first to fourth lumbar dorsal rami passes through an aperture in the dorsal leaf of the intertransverse ligament just above a transverse process (see Fig. 47.10). Each dorsal ramus supplies the overlying medial intertransverse muscle before dividing into lateral and medial branches. The lateral branches supply the longissimus and iliocostalis components of the lumbar erector spinae. The upper three lumbar lateral branches emerge from the lateral border of iliocostalis lumborum and pierce the aponeurosis of latissimus dorsi to become cutaneous. They cross the iliac crest to reach the gluteal skin; some reach as far as the level of the greater trochanter. Medial branches cross the junction of the superior articular process and transverse process, and hook medially between the mammillary and accessory processes, deep to the mammillo-accessory ligament. Medial to the ligament, each medial branch sends articular branches to the facet joints above and below its course, before entering multifidus, which it supplies. Medial branch blocks are quite useful in the treatment of facet-mediated low back pain. Terminal branches reach interspinalis at each segment.

The fifth dorsal ramus has a longer course than other dorsal rami. It arches over the ala of the sacrum, lying against the root of the first sacral superior articular process. Opposite the base of the lumbosacral joint, it sends a branch into the lowest fibres of longissimus thoracis, and a communicating branch to the first sacral dorsal ramus, before terminating as a branch that hooks around the lumbosacral joint to end in multifidus.

Sacral dorsal spinal rami

Sacral dorsal rami are small, diminishing in size inferiorly; other than the fifth, all emerge through the dorsal sacral foramina. The upper three are covered at their exit by multifidus, and divide into medial and lateral branches. Medial branches are small and end in multifidus. Lateral branches join together and with branches of the last lumbar and fourth sacral dorsal rami to form loops dorsal to the sacrum. Branches from these loops run dorsal to the sacrotuberous ligament and form a second series of loops under gluteus maximus. From these, two or three gluteal branches pierce gluteus maximus (along a line from the posterior superior iliac spine to the coccygeal apex) to supply the posterior gluteal skin.

The dorsal rami of the fourth and fifth sacral nerves are small and lie caudal to multifidus. They unite with each other and with the coccygeal dorsal ramus to form loops dorsal to the sacrum; filaments from these supply the skin over the coccyx.

Coccygeal dorsal spinal ramus

The coccygeal dorsal spinal ramus does not divide into medial and lateral branches. It communicates with the fourth and fifth sacral dorsal rami.

Ventral rami

Ventral rami innervate the skin of the anterolateral neck and trunk and the skin covering the upper and lower limbs. The second to the fourth cervical ventral rami (C2– C4) innervate the skin of the neck (branches from the cervical plexus); the fifth to the eighth cervical ventral rami (C5–C8) and the first thoracic ventral ramus (T1) innervate the skin of the upper limb (branches from the brachial plexus); the second thoracic to the first lumbar ventral rami (T2–L1) innervate the skin of the anterolateral trunk; the first or second thoracic ventral rami to the third sacral ventral ramus (L1/2–S3) innervate the skin of the lower limb and perineum (branches of the lumbar and sacral plexuses). Ventral rami supply the flexor musculature of the neck and body wall segmentally and the infrahyoid muscles and the muscles of the limbs via cervical (C1–C4), brachial (C5–T1/2), lumbar (L1–L4/5) and sacral (L4/5–S3) plexuses.

Cervical ventral rami

Broadly speaking, cervical ventral rami innervate the anterior and lateral groups of prevertebral muscles; the respiratory diaphragm (via the phrenic nerve); the muscles and joints of the upper limb and most of the infrahyoid muscles; and the skin of the anterolateral neck, the radial side of the upper limb and the palmar and dorsal surfaces of the hand (via the cervical and brachial plexuses).

Cervical ventral rami, except the first, appear between the anterior and posterior intertransverse muscles. The upper four form the cervical plexus, and the lower four, together with most of the first thoracic ventral ramus, form the brachial plexus. Each receives at least one grey ramus communicans, the upper four from the superior cervical sympathetic ganglion, the fifth and sixth from the middle ganglion, and the seventh and eighth from the cervicothoracic ganglion.

The first cervical ventral ramus, the suboccipital nerve, emerges above the posterior arch of the atlas, and passes forwards lateral to its lateral mass and medial to the vertebral artery. It supplies rectus capitis lateralis, emerges medial to it, descends anterior to the transverse process of the atlas and posterior to the internal jugular vein, and joins the ascending branch of the second cervical ventral ramus.

The second cervical ventral ramus issues between the vertebral arches of the atlas and axis. It ascends between their transverse processes, passes anterior to the first posterior intertransverse muscle and emerges lateral to the vertebral artery, generally between longus capitis and levator scapulae. The ramus divides into an ascending branch, which joins the first cervical nerve, and a descending branch, which joins the ascending branch of the third cervical ventral ramus.

The third cervical ventral ramus appears between longus capitis and scalenus medius. The remaining ventral rami emerge between scalenus anterior and the scalenus medius.

Phrenic nerve

The phrenic nerve is a mixed somatic sensory and motor nerve that provides the sole motor supply to the respective hemirespiratory diaphragm. It is derived mostly from the ipsilateral fourth cervical ventral ramus, with contributions from the ipsilateral third and fifth cervical ventral rami (see Figs 35.17–35.18). The nerve is formed at the upper part of the lateral border of scalenus anterior and descends almost vertically across its anterior surface behind the prevertebral fascia. It descends posterior to sternocleidomastoid, the inferior belly of omohyoid (near its intermediate tendon), the internal jugular vein, transverse cervical and suprascapular arteries and, on the left, the thoracic duct. At the root of the neck, the phrenic nerve runs anterior to the second part of the subclavian artery, from which it is separated by scalenus anterior (some accounts state that on the left side the nerve passes anterior to the first part of the subclavian artery) and posterior to the subclavian vein. The phrenic nerve crosses serratus anterior from lateral to medial (lying under the prevertebral fascia) and enters the thorax by crossing medially anterior to the internal thoracic artery.

In the neck, each nerve receives variable filaments from the cervical sympathetic ganglia or their branches and may also connect with internal thoracic sympathetic plexuses.

Within the thoracic cavity, the right and left phrenic nerves descend anterior to the pulmonary hila, between the fibrous pericardium and mediastinal parietal pleura, accompanied by the pericardiacophrenic vessels. Each phrenic nerve supplies sensory branches to the mediastinal pleura, fibrous pericardium and parietal layer of serous pericardium: the right phrenic nerve supplies the part of the right crus that lies to the right of the oesophagus, and the left phrenic nerve supplies the left crus and the part of the right crus that lies on the left of the oesophagus.

The right and left phrenic nerves differ in their intrathoracic relationships (Rajanna 1947).

Right phrenic nerve

The right phrenic nerve is shorter and more vertical than the left. At the root of the neck it is separated from the second part of the right subclavian artery by scalenus anterior (see Fig. 55.10A). It then passes inferomedially through the superior thoracic aperture between the first part of the right subclavian artery and the right subclavian vein. Occasionally, the right or left phrenic nerves may pass anterior to, or through the anterior wall of, the respective subclavian vein (Paraskevas et al 2011). Around the level of the first rib or the first costal cartilage, the right phrenic nerve crosses the right internal thoracic artery either superiorly between the artery and the first rib, or inferiorly, pressed against the artery by the apex of the right lung and its covering pleura (Owens et al 1994). The nerve continues to descend, passing immediately lateral to the right brachiocephalic vein, the superior vena cava, the fibrous pericardium covering the right side of the right atrium and the inferior vena cava. It branches just superior to, or at the level of, the respiratory diaphragm.

Left phrenic nerve

At the root of the neck, the left phrenic nerve commonly leaves the medial border of scalenus anterior and passes anterior to the first part of the left subclavian artery and posterior to the left subclavian vein and the thoracic duct (see Fig. 55.10B). Sometimes the right and left phrenic nerves are symmetrical in their cervical course, in which case the left phrenic nerve is initially separated from the second part of the left subclavian artery by scalenus anterior. After passing through the superior thoracic aperture the left phrenic nerve crosses the left internal thoracic artery, most commonly superiorly, around the level of the first rib or the first costal cartilage (Owens et al 1994). It descends across the medial aspect of the apex of the left lung and its pleural covering to pass between the left common carotid and left subclavian arteries. The nerve then descends anteromedially and passes anterior and close to the left vagus nerve while in the region superior to the aortic arch and posterior to the left brachiocephalic vein. It continues inferiorly, passing anterior to the left superior intercostal vein, the aortic arch and the left pulmonary hilum, after which it passes inferolaterally and to the left, over the fibrous pericardium covering the left atrium and left ventricle (see Fig. 55.9). As it passes over the fibrous pericardium, the left phrenic nerve is located more anterior than the right phrenic nerve and is therefore at greater risk of damage during the placement of surgical incisions to access the pericardial cavity.

Diaphragmatic relationships The right phrenic nerve passes through the central tendon of the respiratory diaphragm, either via the caval foramen or just lateral to it. The left phrenic nerve passes through the muscular part of the respiratory diaphragm anterior to the central tendon, just lateral to the fibrous pericardium covering the left pulmonary border of the heart, and posterior to the cardiac apex (see Fig. 55.9). At or slightly superior to the respiratory diaphragm each phrenic nerve supplies fine branches to the parietal pleura that lies above the central part of the diaphragm. Typically, the trunk of each nerve then divides into three branches (anterior or sternal, anterolateral and posterior) as it passes through the respiratory diaphragm (see Fig. 55.1A). The main branches may be submerged in diaphragmatic muscle or lie inferior to it. They supply motor fibres to the muscle and sensory fibres to the peritoneum and pleura related to the central part of the respiratory diaphragm. They also relay proprioceptive fibres from the musculature. The anterior (sternal) branch runs anteromedially towards the sternum and connects with its contralateral counterpart. The anterolateral branch runs to the lateral folia of the central tendon. The short posterior branch divides into a posterolateral ramus that passes posterior to the left or right folia of the central tendon and a posterior ramus that supplies the crura of the respiratory diaphragm. The posterolateral and posterior crural branches may arise separately from the phrenic nerve.

Phrenic ganglia The right phrenic nerve continues its course inferior to the respiratory diaphragm and frequently connects to the right phrenic ganglion. An additional, smaller, right accessory phrenic ganglion is sometimes located proximally along the phrenic nerve, close to its exit from the caval foramen. The right phrenic ganglion has plexiform communications with the coeliac and aorticorenal ganglia and with the right suprarenal gland (see Fig. 55.11). A left phrenic ganglion is less commonly seen; when present, it exhibits plexiform communications to several autonomic ganglia. Both phrenic nerves and ganglia are closely related to the diaphragmatic crura, therefore sutures for crural approximation in the repair of hiatal hernia must be placed superior to the ganglia in order to avoid iatrogenic injuries to the autonomic supply of the respiratory diaphragm and abdomen (Loukas et al 2016).

Referred pain Diaphragmatic irritation or pain is frequently felt at the tip of the shoulder, reflecting the common spinal nerve root origins of the phrenic and supraclavicular nerves (the ventral rami of the third and fourth cervical spinal nerves). It usually occurs when there is inflammation of the diaphragmatic parietal pleura, e.g. in basal pneumonia, pleural effusions, malignant disease, or irritation of the diaphragmatic parietal peritoneum, e.g. in pneumoperitoneum or subphrenic abscess, where involuntary diaphragmatic contraction (hiccups) may also occur.

Accessory phrenic nerve

The accessory phrenic nerve is composed of fibres from the fifth cervical ventral ramus that run in a branch of the nerve to subclavius. This lies lateral to the phrenic nerve and descends posterior (occasionally anterior) to the subclavian vein. The accessory phrenic nerve usually joins the phrenic nerve near the first rib but may not do so until near the pulmonary hilum or beyond. The accessory phrenic nerve may be derived from the fourth or sixth cervical ventral rami or from the ansa cervicalis.

Thoracic ventral rami

Thoracic ventral rami, unlike their cervical and lumbar counterparts, have retained a largely segmental distribution to the body wall (see Figs 24.10, 47.7, 53.3). The first to the eleventh intercostal nerves pass in the intercostal spaces between adjacent ribs, and the twelfth (subcostal nerve) passes below the twelfth rib. Each is connected with an adjacent ganglion of the sympathetic trunk by pre- and postganglionic branches (white and grey rami communicantes, respectively) (see Figs 24.13, 53.21). The majority of the intercostal nerves are distributed to the thoracic and, in the case of the more inferiorly located nerves, abdominal walls. The greater part of the first thoracic ventral ramus passes into the brachial plexus (see Fig. 48.6), together with variable proportions of the second and sometimes third thoracic ventral rami via the intercostobrachial nerves. The fourth to sixth intercostal nerves supply only the thoracic wall, whereas the seventh to eleventh nerves supply the thoracic and abdominal walls. The subcostal nerve is distributed to the abdominal wall and skin covering the superior part of the lateral aspect of the gluteal region and thigh. Communicating branches may link the intercostal nerves across the intercostal spaces posteriorly (see Fig. 56.6). The breast is mainly innervated by the anterior and lateral cutaneous branches of the fourth to sixth intercostal nerves. The nipple is innervated by a plexus formed primarily from cutaneous branches of the fourth intercostal nerve.

The ventral rami of the sixth to eleventh intercostal nerves, the subcostal nerve (twelfth thoracic) and first lumbar nerve (iliohypogastric and ilioinguinal nerves) innervate the muscles and skin of the anterior abdominal wall (Rozen et al 2008). The seventh to the twelfth thoracic ventral rami continue anteriorly into the abdominal wall (see Fig. 60.5). Approaching the costal arch, the seventh to tenth intercostal nerves curve medially across the deep surface of the costal cartilages between the digitations of the respiratory diaphragm and transversus abdominis. The subcostal nerve often gives a branch to the first lumbar ventral ramus (dorsolumbar nerve), and in these cases, therefore, contributes to the lumbar plexus. It accompanies the subcostal vessels along the inferior border of the twelfth rib, passing posterior to the lateral arcuate ligament and kidney, and anterior to the proximal part of quadratus lumborum.

All these segmental nerves run anteriorly within a thin layer of fascia in the neurovascular plane between transversus abdominis and internal abdominal oblique, where they branch and interconnect with adjacent nerves and give off branches to the lateral musculature (Rozen et al 2008). Cutaneous branches supply the skin of the lateral and anterior abdominal walls. The nerves enter the rectus sheath at its lateral margin by penetrating the posterior lamina of internal abdominal oblique and penetrating rectus abdominis on its posterior aspect. Here they give off muscular branches to rectus abdominis, transversus abdominis and pyramidalis and cutaneous branches that pierce the anterior layer of the rectus sheath to supply overlying skin.

The ninth intercostal nerve supplies skin proximal to the umbilicus, the tenth intercostal nerve supplies skin that consistently includes the umbilicus, and the eleventh intercostal nerve supplies skin distal to the umbilicus (see Figs 24.10, 60.5). The subcostal nerve supplies the skin over the anterior gluteal region just distal to the iliac crest and the skin of the distal abdomen and inguinal region (overlapping with the L1 dermatome in this region) (Lee et al 2008). A typical dermatome map of the anterior abdominal wall is shown in Fig. 24.10. The inferior intercostal nerves and subcostal nerve also provide sensory fibres to the costal parts of the respiratory diaphragm and parietal peritoneum.

The anterolateral abdominal wall muscles are innervated by several segmental nerves and injury to a single nerve rarely causes a clinically detectable loss of muscle tone. The overlap between sequential dermatomes means that significant cutaneous anaesthesia and muscle denervation are appreciated only after at least two sequential nerves have been surgically sectioned.

PERIPHERAL NERVE PLEXUSES

Cervical plexus

The cervical plexus is formed by the ventral rami of the upper four cervical nerves, and supplies some neck muscles, including most of the infrahyoid group, and areas of skin on the head, neck and chest (see Figs 33.6, 35.5B). It lies in the neck opposite a line drawn down the side of the neck from the root of the auricle to the level of the upper border of the thyroid cartilage. It lies deep to the internal jugular vein, the deep fascia and sternocleidomastoid, and anterior to scalenus medius and levator scapulae. Each ramus, except the first, divides into ascending and descending parts, which unite in communicating loops. Cutaneous branches from the first loop (second and third cervical ventral rami) supply the head and neck, and those from the second loop (third and fourth cervical ventral rami) supply the shoulder and chest. Muscular and communicating branches arise from the same nerves. The branches are superficial or deep: superficial branches perforate the cervical fascia to supply the skin and either ascend (the lesser occipital, great auricular and transverse cervical nerves) or descend (supraclavicular nerves) (see Fig. 35.1B). Deep branches form medial and lateral series and generally supply muscles.

Lesser occipital nerve

The lesser occipital nerve is derived mainly from the second cervical ventral ramus (although fibres from the third cervical nerve may sometimes contribute). It first passes anterior to the plane of the accessory nerve before winding around it and becoming anterior to it. It next ascends along the posterior margin of sternocleidomastoid. Near the cranium it perforates the deep fascia and passes up on to the scalp behind the auricle to supply the skin and connect with the great auricular and greater occipital nerves and the auricular branch of the facial nerve. Its auricular branch supplies the skin on the upper third of the medial aspect of the auricle and connects with the posterior branch of the great auricular nerve. The auricular branch is occasionally derived from the greater occipital nerve. It has been suggested that compression or stretching of the lesser occipital nerve contributes to cervicogenic headache (Lucas et al 1994).

Great auricular nerve

The great auricular nerve is the largest ascending branch of the cervical plexus. It arises from the second and third cervical ventral rami, encircles the posterior border of sternocleidomastoid, perforates the deep fascia and ascends on the muscle beneath platysma with the external jugular vein. On reaching the parotid gland, it divides into anterior and posterior branches. The anterior branch is distributed to the facial skin over the parotid gland and connects in the gland with the facial nerve. This cross-innervation between somatic sensory fibres and parasympathetic secretomotor fibres is considered to be part of the anatomical basis for the phenomenon of gustatory sweating (Frey's syndrome), seen after parotidectomy with its inherent disruption of the secretomotor nerve supply. The posterior branch supplies the skin over the mastoid process and on the back of the auricle (except its upper part); a filament pierces the auricle to reach the lateral surface, where it is distributed to the lobule and concha. Efforts are made to preserve the posterior branch at parotid surgery in order to avoid a sensory deficit of the auricle. The posterior branch communicates with the lesser occipital nerve, the auricular branch of the vagus and the posterior auricular branch of the facial nerve. Division of the greater auricular nerve during neck surgery results in loss of sensation of a variable amount of the lower half of the auricle, which some patients initially find unpleasant.

Transverse cervical nerve

The transverse cervical nerve arises from the second and third cervical ventral rami. It curves round the posterior border of sternocleidomastoid near its midpoint and runs obliquely forwards, deep to the external jugular vein, to the anterior border of the muscle. It perforates the deep cervical fascia, and divides under platysma into ascending and descending branches that are distributed to the anterolateral areas of the neck. The ascending branches ascend to the submandibular region, forming a plexus with the cervical branch of the facial nerve beneath platysma. Some branches pierce platysma and are distributed to the skin of the upper anterior areas of the neck. The descending branches pierce platysma and are distributed anterolaterally to the skin of the neck.

Supraclavicular nerves

The supraclavicular nerves arise from a common trunk formed from branches from the third and fourth cervical ventral rami and emerge at the posterior border of sternocleidomastoid. Descending under platysma and the deep cervical fascia, the trunk divides into medial, intermediate and lateral (posterior) branches, which diverge to pierce the deep fascia a little above the clavicle. The medial supraclavicular nerves run inferomedially across the external jugular vein and the clavicular and sternal heads of sternocleidomastoid to supply the skin as far as the midline and as low as the second rib. They also supply the sternoclavicular joint. The intermediate supraclavicular nerves cross the clavicle to supply the skin over pectoralis major and deltoid down to the level of the second rib, next to the area of supply of the second thoracic nerve. Overlap between these nerves is minimal. The lateral supraclavicular nerves descend superficially across trapezius and the acromion, supplying the skin of the upper and posterior parts of the shoulder.

Deep branches – medial series

Communicating branches

Communicating branches pass from the loop between the first and second cervical ventral rami to the vagus and hypoglossal nerves and to the sympathetic trunk. The hypoglossal branch later leaves the hypoglossal nerve as a series of branches, namely: the meningeal, superior root of ansa cervicalis, nerves to thyrohyoid and geniohyoid. A branch also connects the fourth and fifth cervical ventral rami. The first four cervical ventral rami each receive a grey ramus communicans from the superior cervical sympathetic ganglion.

The superior root of the ansa cervicalis (descendens hypoglossi) (see Figs 35.7A, 35.8) leaves the hypoglossal nerve where it curves round the occipital artery and then descends anterior to or in the carotid sheath. It contains fibres from the first cervical ventral ramus. After giving a branch to the superior belly of omohyoid, it is joined by the inferior root of the ansa from the second and third cervical ventral rami. The two roots form the ansa cervicalis (ansa hypoglossi), from which branches supply sternohyoid, sternothyroid and the inferior belly of omohyoid. Another branch is said to descend anterior to the vessels into the thorax to join the cardiac and phrenic nerves.

Muscular branches

Muscular branches supply rectus capitis lateralis (C1), rectus capitis anterior (C1, C2), longus capitis (C1–C3) and longus colli (C2–C4). The inferior root of the ansa cervicalis and the phrenic nerve are additional muscular branches.

The inferior root of the ansa cervicalis (nervus descendens cervicalis) (see Figs 35.7A, 35.8) is formed by the union of branches from the second and third cervical ventral rami. It descends on the lateral side of the internal jugular vein, crosses it a little below the middle of the neck, and continues forwards to join the superior root anterior to the common carotid artery, forming the ansa cervicalis (ansa hypoglossi), from which all infrahyoid muscles except thyrohyoid are supplied. The inferior root almost always comes from the second and third cervical ventral rami, but sometimes from the second to fourth, and occasionally from the third alone. Occasionally, it may be derived either from the second alone or from the first to third cervical ventral rami.

Deep branches – lateral series

Communicating branches

Lateral deep branches of the cervical plexus (C2–C4) may connect with the accessory nerve within sternocleidomastoid, the posterior triangle or beneath trapezius.

Muscular branches

Muscular branches are distributed to sternocleidomastoid (C2–C4), trapezius (C2 and possibly C3), levator scapulae (C3, C4) and scalenus medius (C3, C4). Branches to trapezius cross the posterior triangle obliquely below the accessory nerve.

Brachial plexus

The brachial plexus is formed by the union of the ventral rami of the lower four cervical nerves and the greater part of the ventral ramus of the first thoracic spinal nerve. It may also receive contributions from the fourth cervical and second thoracic ventral rami. As its name suggests, its branches supply the muscles, joints and skin of the upper limb.

At its origin, the brachial plexus lies in the posterior triangle of the neck, in the angle between the clavicle and the lower posterior border of sternocleidomastoid. It emerges between the scaleni anterior and medius, superior to the third part of the subclavian artery, and is covered by platysma, deep fascia and skin, through which it is palpable (see Fig. 35.17). It is crossed by the supraclavicular nerves, the nerve to subclavius, the inferior belly of omohyoid, the external jugular vein and the superficial ramus of the transverse cervical artery. The plexus passes posterior to the medial two-thirds of the clavicle, subclavius and the suprascapular vessels, and lies on the first digitation of serratus anterior and subscapularis. In the axilla, the lateral and posterior cords of the brachial plexus are anterior and lateral to the first part of the axillary artery, respectively, and the medial cord is behind the artery. The cords assume their appropriate relations around the second part of the artery, deep to pectoralis major. In the lower axilla, the cords divide into nerves that supply the upper limb (see Fig. 49.35). Other than the medial root of the median nerve, these nerves are related to the third part of the artery in the same way as their cords are related to the second part, i.e. branches of the lateral cord are lateral to the artery, branches of the medial cord are medial, and branches of the posterior cord are posterior.

Blood supply The blood supply to the brachial plexus is derived from vessels that arise from the subclavian and vertebral arteries. Important branches pass from the vertebral artery to the fifth and sixth cervical ventral rami and the more proximal cervical nerves. Branches from the costocervical trunk provide a rich supply to the eighth cervical and first thoracic ventral rami. Extensive contributions come from the suprascapular and superficial cervical arteries that arise from the thyrocervical trunk. In at least one-third of cases the superficial cervical and dorsal scapular arteries arise from the thyrocervical trunk as the transverse cervical artery. In clinical terms, the arteries arising from the thyrocervical trunk have become the lifeline to the upper limb and must be preserved during operations in cases when the ruptured subclavian artery has not been repaired. The dorsal scapular artery may arise from the third part of the subclavian artery to pass between the upper and middle trunks of the brachial plexus.

Trunks of the brachial plexus

The upper trunk is formed by the fifth and sixth cervical ventral rami, where these nerves emerge from deep to scalenus anterior. The middle trunk is the continuation of the seventh cervical ventral ramus. The lower trunk is formed by the eighth cervical and first thoracic ventral rami, and passes over the anterosuperior surface of the first rib. The first thoracic ventral ramus takes an upward course across the deep face of the neck of the first rib behind the pleura and the vertebral and subclavian arteries towards the lower trunk. The formation of the trunks is fairly consistent; they lie in front of one another rather than side by side, with the subclavian artery passing anteromedially. The phrenic nerve crosses the fifth cervical ventral ramus to pass anteromedially on the surface of scalenus anterior. The upper trunk, its divisions and the suprascapular nerve can all be palpated in the supraclavicular fossa in a subject of normal physique. The examining finger identifies first the subclavian pulse and then the nerves, whilst rolling the fingertip laterally (see Video 48.1).

Divisions of the brachial plexus

The trunks divide into anterior and posterior divisions. The upper trunk divides 2–3 cm above the clavicle, and the divisions of the middle and lower trunks are formed deep to the clavicle. The posterior divisions of the upper and middle trunks are consistently larger than their anterior divisions. The posterior division of the lower trunk is consistently smaller than the anterior division and is absent in about 10% of cases.

Cords of the brachial plexus

The cords are formed by the confluence of divisions: the lateral cord from the anterior divisions of the upper and middle trunks; the posterior cord by all three posterior divisions; and the medial cord by the anterior division of the lower trunk and, sometimes, by a branch from the anterior division of the middle trunks. The divisions of the trunks and the formation of the cords represent an important anatomical and functional differentiation. The posterior divisions and posterior cord innervate postaxial (extensor) musculature; the anterior divisions and the lateral and medial cords innervate preaxial (flexor) musculature.

The formation and relations of the three cords are variable and, indeed, their designations somewhat misleading. Immediately inferior to the clavicle, the posterior cord is lateral, the medial cord is posterior, and the lateral cord is anterior, in relation to the axillary artery; the cords assume their appropriate relations about the axillary artery deep to pectoralis minor. There is considerable variation in this arrangement; most commonly, the axillary artery lies anterior to the three cords and the median nerve.

The branches of the posterior cord, the largest of the three trunks, are consistent. In sequence, they are the upper subscapular, thoracodorsal, lower subscapular, axillary and radial nerves. The branches of the medial cord are usually predictable; the medial pectoral nerve and medial cutaneous nerve of the forearm are succeeded by the division into the medial root of the median nerve and the ulnar nerve. The ulnar nerve may arise as two or three branches. The greatest variation in the formation of trunk nerves is found within the lateral cord. Occasionally, the musculocutaneous nerve arises more distally than usual, either directly from the lateral cord as two or three branches or even from the median nerve itself. Sometimes, the highest of these branches enters coracobrachialis no more than 2 or 3 cm below the coracoid process. The lateral root of the median nerve may arise as two or three branches, and in some cases, it appears as a branch of the musculocutaneous nerve.

Terminal branches of the brachial plexus

Suprascapular nerve

The suprascapular nerve (fifth and sixth cervical ventral rami) is a large branch of the upper trunk: it is usually the first branch of the upper trunk but frequently arises directly from the fifth cervical ventral ramus (see Figs 35.17, 49.35).

It runs laterally, deep to trapezius and omohyoid, and enters the supraspinous fossa through the suprascapular notch inferior to the superior transverse scapular ligament. It runs deep to supraspinatus and supplies it. It curves round the lateral border of the spine of the scapula with the suprascapular artery to reach the infraspinous fossa, where it gives two branches to infraspinatus and articular rami to the glenohumeral and acromioclavicular joints. The suprascapular nerve rarely has a cutaneous branch: when present, it pierces deltoid close to the tip of the acromion and supplies the skin of the proximal third of the arm within the territory of the axillary nerve.

The suprascapular nerve is essential for abduction and lateral rotation at the glenohumeral joint. When the nerve or the rotator cuff is torn, or both are injured, the ISHA is so reduced that the patient is unable to move the arm away from the body. At rest, the head of the humerus drops inferiorly and migrates proximally in attempted abduction (see Fig. 49.41). In isolated cuff tears, the ISHA opens to about 30° or even more. In isolated axillary palsy, the ISHA is sometimes normal, or, more often, reduced by about 20° (see Figs 49.42–49.43).

Nerve to subclavius

The slender nerve to subclavius (fifth and sixth cervical ventral rami) springs from the upper trunk and passes anteriorly. It descends anterior to the plexus and the subclavian artery and passes above the subclavian vein to supply subclavius.

Lateral pectoral nerve

The lateral pectoral nerve (fifth and sixth cervical ventral rami) is larger than the medial, and may arise either from the anterior divisions of the upper and middle trunks, or by a single branch from the lateral cord, just above or deep to the clavicle. It crosses anterior to the axillary artery and vein, pierces the clavipectoral fascia and supplies the deep surface of pectoralis major. It sends a branch to the medial pectoral nerve, forming a loop in front of the first part of the axillary artery to supply some fibres to pectoralis minor.

Medial pectoral nerve

The medial pectoral nerve (eighth cervical and first thoracic ventral rami) branches from the medial cord while the latter lies posterior to the axillary artery and curves forwards between the axillary artery and vein. Anterior to the artery, it joins a ramus of the lateral pectoral nerve and enters the deep surface of pectoralis minor, which it supplies. Two or three branches pierce pectoralis minor and others may pass round its inferior border to end in pectoralis major.

Upper (superior) subscapular nerve

The superior subscapular nerve is smaller than the inferior. It arises from the posterior cord (fifth and sixth cervical ventral rami), enters subscapularis at a high level, and is frequently double.

Lower (inferior) subscapular nerve

The inferior subscapular nerve arises from the posterior cord (fifth and sixth cervical ventral rami). It supplies the lower part of subscapularis and ends in teres major, which is sometimes supplied by a separate branch.

Thoracodorsal nerve

The thoracodorsal nerve arises from the posterior cord (sixth, seventh and eighth cervical ventral rami) between the subscapular nerves. It accompanies the subscapular artery along the posterior axillary wall and supplies latissimus dorsi, reaching its distal border (see Fig. 49.29). The muscles, joints and skin of the upper limb are innervated by the fifth, sixth, seventh and eighth cervical ventral rami and nearly all of the first thoracic ventral ramus, collectively forming the brachial plexus (see Figs 48.6–48.7). A branch from the fourth and fifth cervical rami, which contributes to the innervation of the glenohumeral and elbow flexor muscles, is seen occasionally at operation: a muscular contribution from the second thoracic ventral ramus is rare. The rami enter the posterior triangle of the neck between scalenus anterior and medius. Rami from the seventh and eighth cervical ventral rami are the largest (C8 contains about 30,000 myelinated axons) and those from the fifth cervical ventral ramus and the first thoracic ventral ramus are the smallest (between 15,000 and 20,000 myelinated axons). An adult brachial plexus contains between 120,000 and 150,000 myelinated axons, of which 25% innervate the shoulder girdle and glenohumeral joint. The proportion of motor fibres is greatest in the fifth and eighth cervical ventral rami; the sensory contribution is greatest in the seventh cervical ventral ramus. A complex interchange of branches, before the main nerves of the upper limb are formed, produces the trunks, divisions and cords of the brachial plexus.

Dorsal scapular nerve

The dorsal scapular nerve arises above the clavicle from the proximal segment of the fifth cervical ventral ramus. It passes posteriorly, piercing scalenus medius, to run down in the plane between levator scapulae and serratus posterior superior and the posterior scalene muscles. It continues along the anterior border of the rhomboid muscles about 1.5 cm medial to the vertebral border of the scapula and is closely related to the dorsal scapular artery. The dorsal scapular nerve innervates the rhomboid muscles and, together with branches from the third and fourth cervical ventral rami, it supplies levator scapulae.

Long thoracic nerve (nerve to serratus anterior)

The long thoracic nerve is formed by branches that arise above the clavicle from the proximal segments of the ventral rami of the fifth, sixth and seventh cervical ventral rami. It innervates serratus anterior, a muscle that is essential for the function of the thoracoscapular joint. The muscular branches from the rami join deep to scalenus medius, and the trunk passes down posterolateral to the muscle, on the floor of the posterior triangle deep to the suprascapular nerve. The branches from the fifth and sixth cervical ventral rami are the largest. The nerve follows a sinuous course deep to the investing fascia covering the anterior faces of the digitations of serratus anterior. It is accompanied here by a branch of the thoracodorsal artery, and inclines posterolaterally towards the mid-axillary line.

The long thoracic nerve is frequently injured during operations around the first rib, in the posterior triangle and in the axilla, and by misplaced intercostal drains. It is particularly susceptible to involvement in neuralgic amyotrophy. Serratus palsy is usual in preganglionic injury to the ventral rami of the fifth, sixth and seventh cervical ventral rami. Pain and loss of function are usual and are only slightly less than those seen after accessory nerve palsy. The signs are characteristic. The active ISHA is, on average, 130°; this is the only nerve lesion in which the active ISHA actually exceeds the total range of active abduction. The scapula is pulled upwards and towards the spine by the unopposed action of trapezius (see Fig. 49.39), an action that is increased by the weight of the limb, which contributes to the winging and is most notable in protraction.

Axillary (circumflex) nerve

The axillary nerve arises from the posterior cord (fifth and sixth cervical ventral rami) (see Figs 48.8, 49.33, 49.35) and innervates teres minor and deltoid, and the skin overlying deltoid on the lateral aspect of the shoulder. Initially it is lateral to the radial nerve, posterior to the axillary artery and anterior to subscapularis. At the lower border of subscapularis, it curves back inferior to the humeroscapular articular capsule and, together with the posterior circumflex humeral vessels, traverses a quadrangular space bounded above by subscapularis (anteriorly) and teres minor (posteriorly), below by teres major, medially by the long head of triceps, and laterally by the surgical neck of the humerus. It divides in the space into anterior and posterior branches. The anterior branch curves round the neck of the humerus with the posterior circumflex humeral vessels, deep to deltoid, to reach the anterior part of the muscle. At the level of the anterior border of the acromion, the nerve often consists of two or more thin filaments that supply the anterior deltoid; it gives off a few small cutaneous branches that pierce deltoid and ramify in the skin over its lower part. The posterior branch courses medially and posteriorly along the attachment of the lateral head of triceps, inferior to the glenoid rim. It usually lies medial to the anterior branch in the quadrangular space. It gives off the nerve to teres minor and the upper lateral cutaneous nerve of the arm at the lateral edge of the attachment of the long head of triceps. The nerve to teres minor enters the muscle on its inferior surface. The posterior branch frequently supplies the posterior aspect of deltoid, usually via a separate branch from the main stem, but occasionally from the superior lateral cutaneous nerve of the arm. However, the posterior part of deltoid has a more consistent supply from the anterior branch of the axillary nerve, which should be remembered when performing a posterior deltoid-splitting approach to the shoulder. The upper lateral cutaneous nerve of the arm pierces the deep fascia at the medial border of the posterior aspect of deltoid, and supplies the skin over the lower part of deltoid and the upper part of the long head of triceps. The posterior branch is intimately related to the inferior aspects of the glenoid and shoulder joint capsule. There is often an enlargement or pseudoganglion on the branch to teres minor. The axillary trunk supplies a branch to the shoulder joint below subscapularis.

Lesions of the axillary nerve

The axillary nerve innervates deltoid. Although a good range of elevation is usually maintained by an intact abductor mechanism, strength and stamina are greatly reduced. Early diagnosis of rupture of the axillary nerve can prove difficult; the nerve is deeply seated, which means that Tinel's sign is rarely detectable. Active movement is restricted by pain and by the restraint of any sling. The loss of sensation varies and there may not be complete anaesthesia. Patients with an intact suprascapular nerve and an intact rotator cuff are able to initiate abduction and many can fully elevate the arm, or nearly so. The power of forward flexion and of abduction is reduced to, at most, 30–40% of normal, whereas extension, with the shoulder at 90° of abduction, is 10% or less. One useful test is to palpate the posterior third of deltoid with the fingers and ask the patient to move the elbow gently backwards. It should be possible to detect activity in the muscle when the arm is supported in a sling or by the examiner's arm.

Musculocutaneous nerve

The musculocutaneous nerve (fifth, sixth and seventh cervical ventral rami) is one of the two terminal branches of the lateral cord, the other being the lateral root of the median nerve (see Fig. 48.13). This division usually occurs at the level of the third part of axillary artery, where the lateral cord lies lateral to the vessel, but it may occur more proximally, where the cord is anterior to the second part of the artery. The nerve may also arise as two or three branches from the cord, or even from the median nerve. It pierces coracobrachialis a variable distance below the tip of the coracoid process and then descends laterally between biceps brachii and brachialis to the lateral side of the arm. The first branch, to coracobrachialis, may pass into the muscle no more than 2 cm distal to the tip of the coracoid; fibres from C7 may branch directly from the lateral cord. Branches to biceps brachii and brachialis leave after the musculocutaneous nerve has pierced coracobrachialis. There are usually two branches to brachialis, and the lower branch also supplies the anterior aspect of the elbow joint. The nerve to biceps brachii is consistently accompanied by a vascular pedicle. The nerve now inclines lateral and deep, into the plane between brachialis posteriorly and biceps anteriorly, where it supplies a small branch to the humerus that enters the shaft with the nutrient artery. Below the branches to brachialis, the musculocutaneous nerve continues as the lateral cutaneous nerve of the forearm, deep to biceps, before emerging lateral to it about 11 cm above the lateral epicondyle, and then running down the lateral aspect of the forearm.

The musculocutaneous nerve has frequent variations. It may run behind coracobrachialis or adhere for some distance to the median nerve and pass behind biceps brachii. Some fibres of the median nerve may run in the musculocutaneous nerve, leaving it to join their proper trunk; less frequently, the reverse occurs, and the median nerve sends a branch to the musculocutaneous nerve. Occasionally, the musculocutaneous nerve also supplies pronator teres and may innervate the skin over the first metacarpal and the lateral part of the thenar eminence.

Lateral cutaneous nerve of the forearm

The lateral cutaneous nerve of the forearm is the cutaneous division of the musculocutaneous nerve. It lies between biceps brachii and brachialis, inclining from the medial to the lateral side, then passes through the cubital fossa lateral to the tendon of biceps brachii and deep to the cephalic vein and descends along the radial border of the forearm to the wrist (see Figs 49.33–49.34, 50.31–50.32). It supplies the skin of the anterolateral surface of the forearm (see Fig. 49.1) and connects with the posterior cutaneous nerve of the forearm and the terminal branch of the radial nerve by branches that pass around the radial border of the forearm. Its trunk gives rise to a slender recurrent branch that extends along the cephalic vein as far as the middle third of the upper arm, distributing filaments to the skin over the distal third of the anterolateral surface of the upper arm close to the vein. At the wrist joint, the lateral cutaneous nerve of the forearm is anterior to the radial artery. It gives off filaments that pierce the deep fascia and accompany the artery to the dorsum of the carpus. The nerve then passes to the base of the thenar eminence, where it ends in cutaneous rami, some of which connect with the terminal branch of the radial nerve and the palmar cutaneous branch of the median nerve.

Medial cutaneous nerve of the arm

The medial cutaneous nerve of the arm (eighth cervical ventral ramus and first thoracic ventral ramus) is the smallest and most medial branch of the brachial plexus, arising from the medial cord (see Fig. 49.35). It crosses the axilla, either anterior or posterior to the axillary vein, then passes medial to the axillary vein, communicates with the intercostobrachial nerve, and descends medial to the brachial artery and basilic vein. It pierces the deep fascia at the midpoint of the upper arm to supply the skin over the medial aspect of the distal third of the upper arm (see Fig. 49.34). It connects with the posterior branch of the medial cutaneous nerve of the forearm. Sometimes, the medial cutaneous nerve of the arm and the intercostobrachial nerve are connected in a plexiform manner in the axilla. The intercostobrachial nerve may be large and reinforced by part of the lateral cutaneous branch of the third intercostal nerve. In these cases, it replaces the medial cutaneous nerve of the arm and receives a connection representing the latter from the brachial plexus (occasionally, this connection is absent).

Medial cutaneous nerve of the forearm

The medial cutaneous nerve of the forearm comes from the medial cord (first thoracic ventral ramus) (see Fig. 49.34). It lies initially between the axillary artery and vein, and gives off a ramus that pierces the deep fascia to supply the skin over the biceps, almost to the elbow. The nerve descends medial to the brachial artery, pierces the deep fascia with the basilic vein midway in the arm, and divides into anterior and posterior branches before it enters the forearm (see Figs 49.34, 50.31–50.32). The larger anterior branch usually passes anterior to, or occasionally behind, the median cubital vein, and descends anteromedially in the forearm to supply the skin as far as the wrist. It curves round to the dorsum of the forearm, descending on its medial border to the wrist, supplying the skin (see Fig. 50.1). It connects with the medial cutaneous nerve of the arm, the posterior cutaneous nerve of the forearm and the dorsal branch of the ulnar nerve.

Ulnar nerve

The ulnar nerve (seventh and eighth cervical ventral rami and first thoracic ventral ramus) is the continuation of the medial cord (see Fig. 48.12). It usually has no branches in the arm, but occasionally may give a branch to the medial head of triceps. The nerve runs distally through the axilla, medial to the axillary artery and between it and the vein, and continues distally medial to the brachial artery as far as the mid-arm. Here it inclines posteromedially to perforate the medial intermuscular septum about 10 cm proximal to the medial epicondyle and passes through a fibrous canal, the arcade of Struthers, which is between 5 and 6 cm long. The walls of the canal include the medial intermuscular septum and the fascial sheath which invests the medial head of triceps brachii. The nerve passes behind the medial epicondyle in a groove where it is easily palpable (see Fig. 50.29) and runs through the cubital tunnel, between the capsule of the humero-ulnar joint and the overlying arcuate ligament of Osborne (joining the two heads of flexor carpi ulnaris). It gives off articular branches to the elbow as it lies between the medial epicondyle and the olecranon. The ulnar nerve enters the forearm between the two heads of flexor carpi ulnaris, which it supplies by two neurovascular pedicles, the first arising just distal to the cubital tunnel and the second about one-quarter of the way down the forearm: it is superficial to the posterior and oblique parts of the ulnar collateral ligament and deep to the tough deep fascia of flexor carpi ulnaris (Osborne's fascia). The nerve descends on the medial side of the forearm on flexor digitorum profundus, to which it sends several branches (see Fig. 50.32). Proximally, it runs with the ulnar vessels in a well-defined sheath deep to the anterior margin of flexor carpi ulnaris; distally, it lies lateral to the muscle and is covered only by skin and fasciae. In the upper third of the forearm, the ulnar nerve is distant from the ulnar artery but it comes to lie close to the medial side of the artery more distally. Some 5–6 cm proximal to the ulnar styloid it gives off the dorsal cutaneous branch which winds around the ulna, at first deep to flexor carpi ulnaris, and then subcutaneously, and innervates the skin of the dorsum of the hand and little finger, and the medial side of the ring finger. At the wrist the ulnar nerve passes under the superficial part of the flexor retinaculum (in Guyon's canal) with the ulnar artery and divides into superficial and deep branches (see Fig. 51.10). The superficial division innervates the skin of the medial two digits and palmaris brevis. The deep branch passes, with the deep branch of the ulnar artery, between abductor and flexor digiti minimi, pierces opponens digiti minimi and then runs across the deep palmar space with the deep palmar arch. It innervates all the muscles of the hand, except for the first and second (index and middle) lumbricals, abductor pollicis brevis, opponens pollicis and part of flexor pollicis brevis.

The ulnar nerve is accompanied by the superior collateral ulnar vessels in the lower third of the arm as far as the entrance to the cubital tunnel, and then by the posteroinferior ulnar collateral vessels. The anastomosis between these vessels permits the use of most of the ulnar nerve as a free vascularized graft, in cases where the parent roots, the seventh and eighth cervical ventral rami and the first thoracic ventral ramus, are irreparable.. The ulnar nerve is palpable in the lower arm and behind the medial epicondyle, where it is subcutaneous. There is an important relation here: a posterior branch of the medial cutaneous nerve of the forearm sweeps across the cubital tunnel and gets in the way of medial surgical exposures. Inadvertent injury may cause severe pain. The ulnar nerve is palpable at the wrist where it emerges from under flexor carpi ulnaris. The dorsal cutaneous branch can be palpated in those of slender physique where it crosses the subcutaneous ulna.

Muscular branches

There are two main muscular branches of the ulnar nerve in the forearm. They arise near the elbow and supply flexor carpi ulnaris and the medial half of flexor digitorum profundus.

Dorsal branch

The dorsal branch arises approximately 5 cm proximal to the wrist (see Fig. 51.9). It passes distally and dorsally, deep to flexor carpi ulnaris, perforates the deep fascia, descends along the medial side of the dorsum of the wrist and hand, and then divides into two, or often three, dorsal digital nerves. The first supplies the medial side of the little finger; the second, the adjacent sides of the little and ring fingers; while the third, when present, supplies adjoining sides of the ring and middle fingers. The latter may be replaced, wholly or partially, by a branch of the radial nerve, which communicates with it on the dorsum of the hand. In the little finger, the dorsal digital nerves extend only to the base of the distal phalanx; in the ring finger, they extend only to the base of the middle phalanx. The most distal parts of the little finger and of the ulnar side of the ring finger are supplied by dorsal branches of the proper palmar digital branches of the ulnar nerve. The most distal part of the lateral side of the ring finger is supplied by dorsal branches of the proper palmar digital branch of the median nerve.

Superficial terminal branch

The superficial terminal branch supplies palmaris brevis and the medial palmar skin. It divides into two palmar digital nerves. One supplies the medial side of the little finger; the other (a common palmar digital nerve) sends a branch to the median nerve and divides into two proper digital nerves to supply the adjoining sides of little and ring fingers. The proper digital branches within the digit are distributed like those derived from the median nerve.

Deep terminal branch

The deep terminal branch accompanies the deep branch of the ulnar artery as it passes between abductor digiti minimi and flexor digiti minimi, and then perforates opponens digiti minimi to follow the deep palmar arch dorsal to the flexor tendons. At its origin, it supplies the three short muscles of the little finger. As it crosses the hand, it supplies the interossei and the third and fourth lumbricals. It ends by supplying adductor pollicis, the first dorsal interosseous and, usually, flexor pollicis brevis.

The medial part of flexor digitorum profundus is supplied by the ulnar nerve, as are the third and fourth lumbricals, which are connected with the tendons of this part of the muscle. Similarly, the lateral part of flexor digitorum profundus and the first and second lumbricals are supplied by the median nerve. The third lumbrical is often supplied by both nerves. The deep terminal branch gives branches to some intercarpal, carpometacarpal and intermetacarpal joints; precise details are uncertain. Vasomotor branches, arising in the forearm and hand, supply the ulnar and palmar arteries.

Palmar cutaneous branch

The palmar cutaneous branch of the ulnar nerve arises in mid-forearm, descends on the ulnar artery, which it supplies, and then perforates the deep fascia. It communicates with the palmar branch of the median nerve and ends in the palmar skin. It sometimes supplies palmaris brevis.

Lesions of the ulnar nerve

The ulnar nerve is a mixed nerve and so patients may present with sensory or motor symptoms or a combination of the two, sometimes with additional physical signs of autonomic disturbance. There may be tenderness and a positive Tinel's sign over the nerve at the point of compression. Numbness and paraesthesiae occur early, followed, in more severe cases, by weakness of power grip and, ultimately, atrophy of the lumbricals and interossei with clawing of ring and little fingers.

The ulnar nerve may be compressed by the arcade of Struthers at the level of the medial intermuscular septum; at the level of the flexor/pronator aponeurosis as it enters the forearm between the heads of flexor carpi ulnaris; or deep to the deep fascia of flexor carpi ulnaris which exhibits tough condensations extending up to 9 cm from the medial epicondyle (Siemionow et al 2007). The nerve is most often compressed at the level of the cubital tunnel by the Osborne's arcuate ligament; this is the most common nerve compression syndrome after that of the median nerve in the carpal tunnel.

The cross-sectional area of the cubital tunnel has been shown to narrow by almost 55% in full flexion. Ultrasound studies have suggested that the ratio of the cross-sectional area of radial nerve : cubital tunnel is most strongly linked to reduced conduction velocity (Yoon et al 2007). Combining elbow flexion with direct pressure over the cubital tunnel for 60 seconds will elicit symptoms in most affected patients (Novak et al 1994). Other contributory factors are previous trauma, especially supracondylar and medial epicondyle fractures in childhood, valgus instability of the elbow in athletes involved in throwing sports, and degenerative disease.

The most reliable treatment for patients who fail to respond to non-surgical remedies is a simple release of the cubital tunnel. The release should be complete and include release of Osborne's ligament and the deep fascia of flexor carpi ulnaris; care should be taken to avoid damage to branches of the medial cutaneous nerve of the forearm that usually cross the line of incision approximately 2 cm above the medial epicondyle and a mean 3.1 cm distal to the medial epicondyle in all patients (Lowe et al 2004). Anconeus epitrochlearis should be excised if present because it is a potential cause for recurrent symptoms. The ulnar nerve should not be circumferentially denuded of its retinaculum because this contains its intrinsic blood supply. Transposition of the nerve should be reserved for cases of persistent subluxation or of failure of a simple release to achieve symptomatic relief. This is relatively unusual and is said to occur in only 7% of cases.

The ulnar nerve can be compressed as it passes through Guyon's canal at the wrist. Causes of compression at this site include a ganglion from the piso-triquetral joint, prolonged compression from a cyclist's handlebars, hook of hamate fracture, and proximity of aberrant or accessory muscles. The symptoms depend on the precise level at which the ulnar nerve and its branches are compressed. Altered sensation is noted in the palmar aspect of the little finger and ulnar half of the ring finger; sensation on the ulnar aspect of the dorsum of the hand is normal due to preservation of the dorsal cutaneous branch. If the motor branch fibres are affected, there is weakness and wasting of the intrinsic muscles of the hand supplied by the ulnar nerve, with clawing posture in severe compression. Weakness of adductor pollicis and first dorsal interosseous substantially degrades pinch strength; if a slip of paper is held in the key pinch position between the pulp of the thumb and the radial side of the index proximal interphalangeal joint, the tip of the thumb involuntarily flexes as flexor pollicis longus contracts to compensate for the absent adductor pollicis and first dorsal interosseous (Froment's sign). Surgical treatment involves decompression of the nerve by division of the roof of Guyon's canal and removal of any causative lesion, such as a ganglion. Ulnar tunnel syndrome can be difficult to distinguish from more proximal causes of ulnar nerve compression, of which the most common is entrapment of the nerve in the cubital canal at the elbow. In this condition, sensory changes would include the dorso-ulnar aspect of the hand and motor changes would involve flexor carpi ulnaris and flexor digitorum profundus to the little and ring fingers. Clawing is less apparent with a more proximal failure of the ulnar nerve (the 'ulnar paradox') because flexor digitorum profundus also fails so there is less flexion force to expose the absent extensor moment of the paralysed intrinsics. In the absence of obvious clinical indicators, an unpleasant tingling sensation (Tinel's sign) over the site of compression, electrophysiological studies and MRI scans may aid diagnosis.

Ulnar nerve division at the wrist paralyses all the intrinsic muscles of the hand (apart from the radial two lumbricals, abductor pollicis brevis, and part of flexor pollicis brevis and opponens pollicis). The intrinsic muscle action of flexing the metacarpophalangeal joint and extending the interphalangeal joints is lost. The unopposed action of the long extensors and flexors of the fingers cause clawing, with extension of the metacarpophalangeal joints and flexion of the interphalangeal joints. The clawing is less intense in the index and middle fingers because their lumbricals are supplied by the median nerve. There is sensory loss over the little finger and the ulnar half of the ring finger. The skin over the ulnar aspect of the dorsum of the hand is spared because the dorsal branch of the ulnar nerve is given off approximately 5 cm proximal to the wrist joint. A combined median and ulnar nerve palsy at the wrist results in a full claw hand with thenar and hypothenar flattening and thumb adduction and flexion (a simian hand).

Median nerve

The median nerve is formed by the union of the lateral root from the lateral cord (sixth and seventh cervical ventral rami), and the medial root from the medial cord (eighth cervical and first thoracic ventral rami), which meet anterior or lateral to the third part of the axillary artery (see Figs 48.7, 48.10, 49.29, 49.35, 49.44). Some fibres from C7 often leave the lateral root in the lower part of the axilla, pass distomedially posterior to the medial root, and usually anterior to the axillary artery, to join the ulnar nerve. Clinically, they are believed to be mainly motor and to supply flexor carpi ulnaris. If the lateral root is small, the musculocutaneous nerve (fifth, sixth and seventh cervical ventral rami) connects with the median nerve in the arm.

The first branch of the median nerve, to pronator teres, arises 2–3 cm above the medial epicondyle. A second branch, or leash of branches, arises at the level of the tip of the medial epicondyle and innervates palmaris longus, flexor carpi radialis and flexor digitorum superficialis. In the cubital fossa, the median nerve lies medial to the brachial artery, deep to the bicipital aponeurosis and anterior to brachialis. It usually enters the forearm between the heads of pronator teres, although, occasionally, it may pass posterior to both heads of the muscle, or it may pass through its humeral head (see Fig. 50.31; see also Figs 50.21–50.22). The nerve crosses to the lateral side of the ulnar artery, from which it is separated by the deep head of pronator teres, passes behind a tendinous bridge between the humero-ulnar and radial heads of flexor digitorum superficialis, and descends through the forearm posterior and adherent to flexor digitorum superficialis and anterior to flexor digitorum profundus. Just proximal to the tendinous arcade of flexor digitorum superficialis, the median nerve gives off the anterior interosseous nerve. Accompanied by the anterior interosseous vessels, this large branch dives deeply to pass down along the interosseous membrane and supplies flexor pollicis longus, the radial half of flexor digitorum profundus and pronator quadratus. There is no cutaneous distribution.

The main nerve continues in the plane between the superficial and deep digital flexors, supplying two or three branches to the former. About 5 cm proximal to the flexor retinaculum, the median nerve emerges from behind the lateral edge of flexor digitorum superficialis and becomes superficial just proximal to the wrist. Just proximal to the flexor retinaculum the median nerve is lateral and superficial to the tendons of flexor digitorum superficialis and lies between the tendons of flexor carpi radialis and palmaris longus (see Fig. 50.31). It passes under the retinaculum in the ‘carpal tunnel’, where it may be compressed in carpal tunnel syndrome, and enters the palm. Distal to the retinaculum, the nerve enlarges and flattens, and usually divides into five or six branches; the mode and level of division are variable. The recurrent (motor) nerve to the thenar muscles arises within, or just distal to, the carpal tunnel, usually on the lateral side of the main nerve. The palmar digital nerves are formed within the palm of the hand and pass distally, deep to the superficial palmar arch and its digital vessels, at first anterior to the tendons of the long flexors, to supply the palmar skin of the thumb, index and middle fingers and the lateral side of the ring finger. The palmar cutaneous branch arises 3.5–6 cm proximal to the most proximal wrist crease, and passes lateral to the main nerve and superficial to the flexor retinaculum to innervate the skin of the proximal palm.

Within the carpal tunnel and hand, the median nerve has been shown to glide by up to 3 mm, depending on the position of the elbow and the attitude of the forearm in pronation or supination (Echigo et al 2008). The greatest longitudinal excursion of the median nerve (15.5 mm) is seen just proximal to the carpal tunnel; similar excursion of the ulnar nerve has been recorded as 14.8 mm in cadavers (Wilgis and Murphy 1986).

The median nerve is palpable along its course in the arm, where it is covered by deep fascia and skin, after emerging from deep to coracobrachialis; on the flexor aspect of the elbow, deep to the bicipital aponeurosis; and at the wrist where it emerges from behind the superficial flexor tendons, just lateral to palmaris longus. It is closely related to the brachial artery in the anterior aspect of the elbow, where it courses anterior to brachialis and medial to the artery.

The median nerve has muscular, anterior interosseous, palmar cutaneous and palmar digital branches.

Muscular branches

Muscular branches are given off near the elbow to all the superficial flexor muscles except flexor carpi ulnaris. The branch to the part of flexor digitorum superficialis that serves the index finger is given off near the mid-forearm and may be derived from the anterior interosseous nerve.

Anterior interosseous nerve

The anterior interosseous nerve arises from the posterior aspect of the median nerve between the two heads of pronator teres, just distal to the branches to the superficial forearm flexors and proximal tendinous arch of flexor digitorum superficialis (see Figs 50.10, 50.22). It descends with the anterior interosseous artery anterior to the interosseous membrane, between and deep to flexor pollicis longus and flexor digitorum profundus (see Fig. 50.32), supplying flexor pollicis longus and the lateral part of flexor digitorum profundus (to the index and middle fingers). Terminally, the anterior interosseous nerve lies posterior to pronator quadratus, which it supplies via its deep surface. It also supplies articular branches to the distal radio-ulnar, radiocarpal and carpal joints.

Palmar cutaneous branch

The palmar cutaneous branch emerges from the radial side of the median nerve 3.5 cm to 6 cm proximal to the flexor retinaculum. It runs in a small tunnel alongside the ulnar edge of the sheath of flexor carpi radialis, radial and deep to palmaris longus, before piercing the deep fascia to enter the palm either through or superficial to the flexor retinaculum (see Fig. 51.27B). It usually ends in medial and lateral terminal branches that supply a patch of skin over and just beyond the anterior surface of the palm overlying the scaphoid tubercle and anterior aspect of the carpometacarpal joint of the thumb (Hobbs et al 1990, da Silva et al 1996). The lateral branches connect with the lateral cutaneous nerve of the forearm and the medial branches connect with the palmar cutaneous branch of the ulnar nerve (see Fig. 51.27B).

Muscular branch (recurrent motor branch)

The recurrent motor branch is short and thick, and arises from the lateral side of the nerve; it may be the first palmar branch or a terminal branch that arises level with the digital branches. It runs laterally, just distal to the flexor retinaculum and with a slight recurrent curve beneath the part of the palmar aponeurosis covering the thenar muscles (see Fig. 51.27B). It turns round the distal border of the retinaculum to lie superficial to flexor pollicis brevis, which it usually supplies, and either continues superficial to the muscle or traverses it. It gives a branch to abductor pollicis brevis that enters the medial edge of the muscle, and then passes deep to it to supply opponens pollicis, entering its medial edge. Its terminal part occasionally gives a branch to the first dorsal interosseous, and may be its sole or partial supply. The muscular branch may arise in the carpal tunnel and pierce the flexor retinaculum. Anomalies of the median nerve occur in approximately 10% of patients undergoing a carpal tunnel release. These branches usually arise from the ulnar side of the nerve and may be motor or sensory.

Palmar digital branches

The median nerve supplies palmar cutaneous digital branches to the radial three and a half digits (thumb, index, middle and the lateral side of the ring); sometimes, the radial side of the ring finger is supplied by the ulnar nerve. Occasionally, there is a communicating branch between the common digital nerve to the middle and ring fingers (derived from the median nerve) and the common digital nerve to the ring and little fingers (derived from the ulnar nerve); this may explain variations in sensory patterns that do not conform to the classic pattern.

Various patterns of termination of the palmar digital nerves have been described: the branches are commonly arranged as follows. Distal to the flexor retinaculum, the median nerve splits into a smaller lateral portion and a larger medial portion. The lateral portion gives rise to a recurrent motor branch and divides into three proper digital nerves that supply the thumb and radial index finger. The branch that supplies the radial side of the index finger also supplies the first lumbrical. The medial portion divides into two common palmar digital nerves which each further divide into two proper digital nerves that supply the adjacent sides of the index, middle and ring fingers. The lateral common digital nerve supplies the second lumbrical, and the medial receives a communicating twig from the common palmar digital branch of the ulnar nerve and may supply the third lumbrical. In the distal part of the palm, the digital arteries pass deeply between the divisions of the digital nerves; the nerves lie anterior to the arteries on the sides of the digits.

The digital nerves pass distally, deep to the superficial palmar arch and its digital vessels, at first anterior to the tendons of the long flexors. Together with the lumbricals and palmar digital arteries, they pass dorsal to the superficial transverse metacarpal ligament and ventral to the deep transverse metacarpal ligament. In the digits, the nerves run distally beside the long flexor tendons (outside their fibrous sheaths), level with the anterior phalangeal surfaces and anterior to the digital arteries, between Grayson’s and Cleland’s ligaments. Each nerve gives off several branches to the skin on the volar and lateral aspects of the digit and sends branches to the metacarpophalangeal and interphalangeal joints.

The digital nerves supply the fibrous sheaths of the long flexor tendons, blood vessels (vasomotor) and sweat glands (sudomotor).

Distal to the base of the distal phalanx, each digital nerve gives off a branch that passes dorsally to the nail bed (see Fig. 51.9). The main nerve frequently trifurcates to supply the pulp and skin of the terminal part of the digit. Distal to the base of the proximal phalanx, each proper digital nerve also gives off a dorsal branch to supply the skin over the dorsum of the middle and distal phalanges. The proper palmar digital nerves to the thumb and the lateral side of the index finger emerge with the tendons of the long flexors from under the lateral edge of the palmar aponeurosis. They are arranged in the digits as described above, except that, in the thumb, small distal branches supply the skin on the dorsum of the distal phalanx only.

Other branches

In addition to the branches of the median nerve described above, variable vasomotor branches supply the radial and ulnar arteries and their branches. Some of the intercarpal, carpometacarpal and intermetacarpal joints are said to be supplied by the median nerve or its anterior interosseous branch; the precise details are uncertain.

Martin–Gruber nerve connection

A motor communicating branch between the median and ulnar nerves in the forearm occurs in approximately one-quarter of patients. The most common variant has a branch passing from the anterior interosseous to the ulnar nerve. A number of patterns have been described where branches pass between flexors digitorum superficialis and profundus, deep to the ulnar artery, to join the ulnar nerve; such branches may explain the variations in innervation of the intrinsic muscles.

Lesions of the median nerve

The median nerve may be compressed at four sites in the elbow and forearm. The most proximal is the ligament of Struthers, where, if the median nerve is accompanied by the brachial artery, vascular symptoms and signs may also be present. More distally, it may become entrapped by a thickened bicipital aponeurosis. The other sites of compression are between the superficial and deep heads of pronator teres, and the proximal fibrous arch of flexor digitorum superficialis.

Median nerve division at the wrist leads to paralysis of the lumbricals to the index and middle fingers and of the thenar muscles (apart from flexor pollicis brevis and adductor pollicis), as well as loss of sensation to the thumb, index, middle and radial half of the ring fingers. The thenar muscles waste, and the adductor pollicis, which is no longer antagonized by flexor pollicis brevis and opponens pollicis, produces an adducted posture of the thumb. Division of the median nerve distal to the origin of its palmar cutaneous branch, which arises somewhere between 3.5 and 6 cm proximal to the proximal edge of the flexor retinaculum and the distal transverse wrist crease, will leave the branch intact to supply the skin over the thenar eminence and radial side of the proximal part of the hand. Careful clinical examination of the sensibility of the skin in this region should help to clarify the level of the lesion. High division of the nerve will, as with compressive lesions at this level, result in weakness of pronation of the forearm, radial flexion of the wrist and the lateral two fingers.

Patients essentially present with one of two syndromes. The anterior interosseous nerve syndrome presents as a failure of pinch grip due to weakness of flexor pollicis longus and the radial portion of flexor or digitorum profundus. This reduces the flexion power of the interphalangeal joint of the thumb and the distal interphalangeal joint of the index finger. The pronator syndrome presents with symptoms and signs that mimic carpal tunnel syndrome. Patients present with pain and altered sensation in the radial three and a half fingers of the hand that are aggravated by activity. However, a Tinel's sign will be positive over the proximal forearm, and sensation over the thenar eminence may be diminished, because the palmar cutaneous branch of the nerve arises above the carpal tunnel. The clinical presentation may vary in the presence of a Martin–Gruber anastomosis (Rodriguez-Niedenführ et al 2002).

Most patients will respond to non-operative treatment but those who fail to do so usually respond well to surgical decompression. Exploration and decompression should address all the potential areas of compression.

Carpal tunnel syndrome

Carpal tunnel syndrome is the most common entrapment mononeuropathy. It is caused by compression of the median nerve as it passes through the fibro-osseous tunnel beneath the flexor retinaculum (see Fig. 51.38).

Carpal tunnel syndrome is usually idiopathic, however, certain diagnoses may predispose to the condition. The carpal tunnel may be narrowed by arthritic changes in the wrist joint, by thickening of the synovium (especially in rheumatoid disease) by soft tissue thickening, as may occur in myxoedema and acromegaly; it is associated with diabetes, oedema, obesity, pregnancy and vibration. The association with repetitive use is controversial and has probably been overestimated. Normally, the median nerve slides smoothly in and out of the carpal tunnel during flexion and extension of the wrist, but when the nerve is compressed this sliding is restricted by traction that aggravates the conduction block. Typically, the syndrome produces painful paraesthesia and numbness in the thumb, index, middle and medial side of the ring fingers, which is worse at night and when performing manoeuvres such as holding a book or telephone. The palmar branch of the median nerve is spared because it does not pass through the carpal tunnel. With time, the compression leads to wasting and weakness of abductor pollicis brevis and loss of sweating in the cutaneous territory of the median nerve, sparing the patch overlying the scaphoid tubercle and palmar side of the carpometacarpal joint which is supplied by the palmar cutaneous nerve. Treatment depends on the cause. If present just at night, due to involuntary flexion of the wrist (which increases pressure in the carpal canal) then a splint may suffice. If the syndrome is of recent onset, especially in association with pregnancy or synovial thickening, then a steroid injection can be curative. For more persistent symptoms, and especially if there is evidence of axonal failure (numbness, loss of sweating, wasting of abductor pollicis brevis) then surgery is recommended. This involves dividing the flexor retinaculum. The most common hazards of decompression are inadequate decompression because of failure to divide the most distal or most proximal part of the flexor retinaculum, damage to the motor branch causing weakness, or palmar cutaneous branch or one or more terminal sensory branches causing scar tenderness and a patch of numbness and damage to the superficial palmar arch causing a haematoma.

Anatomical anomalies of the median nerve in the carpal tunnel are very common (Henry et al 2015) and occur in up to 12% of hands. The most common are variations in the course of the recurrent motor branch in relation to the flexor retinaculum. These may be transligamentous (11.3%), subligamentous (13.5%) or extraligamentous (75.2%). Damage may also occur to the palmar cutaneous branch of the median nerve and to the superficial connections between the median and ulnar nerves (Martin et al 1996), (the Berrettini branch, division of which will leave the patient with numbness in the middle and ring fingers). Stancič et al (1999) noted that this connection was present in 81% of dissected hands and proposed that it should be regarded as a normal anatomical finding.

Radial nerve

The radial nerve (fifth, sixth, seventh and eighth cervical and first thoracic ventral rami) is the terminal branch of the posterior cord (see Fig. 48.9). It is the largest nerve in the upper limb and the most commonly damaged. Between its origin at the level of the base of the coracoid and its entrance into the spiral groove, where it is accompanied by the profunda brachii artery, the radial nerve is supplied by fewer arteries than elsewhere along its course. The first 8–10 cm of the nerve may not have a nutrient artery and will, therefore, be relatively avascular if the nerve is transected at its origin. The nerve lies closest to the bone where it pierces the lateral intermuscular septum to pass through a short tunnel bounded by bone and unyielding fascia. The nerve is tethered here, a common level of rupture, entrapment or compression.

The radial nerve descends behind the third part of the axillary artery and the upper part of the brachial artery, anterior to subscapularis above and the tendons of latissimus dorsi and teres major below, giving branches to the medial head of triceps at this level. With the profunda brachii artery, it inclines dorsally, passing through the lower triangular space below the lower border of teres major, between the long head of triceps and the humerus. It then spirals obliquely across the posterior shaft of the humerus, lying posterior to the uppermost fibres of the medial head of triceps, which separate the nerve from the bone in the first part of the spiral groove. The nerve(s) to the lateral head of triceps arise(s) within the spiral groove; that to the lateral head just before the radial nerve re-enters the anterior compartment. Two cutaneous nerves, the lower lateral cutaneous nerve of the arm and the posterior cutaneous nerve of the forearm, pass away from the main nerve in the final part of the spiral groove and course along the anterior face of the lateral head of triceps to perforate the deep fascia about four fingers' breadths above the lateral epicondyle. They innervate the skin of the lower lateral arm and the posterior aspect of the forearm, respectively. The radial nerve at the elbow lies in the deep groove between brachialis medially and brachioradialis and extensor carpi radialis longus laterally (see Fig. 50.21). The nerve to brachioradialis arises about three fingers' breadths proximal to the lateral epicondyle; the nerve to extensor carpi radialis longus about one finger's breadth more distal; and the nerve to extensor carpi radialis brevis about one finger's breadth above the epicondyle. These branches arise from the main radial nerve as it runs between brachialis anteriorly and brachioradialis posteriorly; the nerve may be palpable at this level. On reaching the lateral side of the humerus, the radial nerve pierces the lateral intermuscular septum to enter the anterior compartment of the arm. At the level of the tip of the lateral epicondyle, the nerve divides into the posterior interosseous and superficial radial nerves. Another branch to extensor carpi radialis brevis is usually given off here. There is some variation in the level at which branches of the radial nerve arise from the main trunk in different individuals. Branches to extensor carpi radialis brevis and supinator may arise from the main trunk of the radial nerve or from the proximal part of the posterior interosseous nerve, but almost invariably above the arcade of Frohse.

The superficial radial nerve innervates the skin over the dorsum of the radial half of the ring, middle and index fingers, and that of the thumb as far as the distal interphalangeal joint. It often provides important sensation on the skin of the thumb web space and the skin on the adjacent sides of the thumb and index finger.

The branches of the radial nerve are: muscular, cutaneous, articular, superficial radial and posterior interosseous.

Muscular branches

Muscular branches supply triceps, anconeus, brachioradialis, extensor carpi radialis longus and brachialis in medial, posterior and lateral groups. Medial muscular branches arise from the radial nerve on the medial side of the arm and supply the medial and long heads of triceps. The branch to the medial head is a long, slender filament that lies close to the ulnar nerve as far as the distal third of the arm, and is often termed the ulnar collateral nerve. A large posterior muscular branch arises from the nerve as it lies in the humeral groove and divides to supply the medial and lateral heads of triceps and anconeus. The branch to anconeus is a long nerve that descends in the medial head of triceps and partially supplies it; the nerve is accompanied by the middle collateral branch of the profunda brachii artery and passes behind the elbow joint to end in anconeus. Lateral muscular branches arise anterior to the lateral intermuscular septum and supply the lateral part of brachialis, brachioradialis and extensor carpi radialis longus.

Cutaneous branches

Cutaneous branches are the posterior and lower lateral cutaneous nerves of the arm and the posterior cutaneous nerve of the forearm.

Posterior cutaneous nerve of the arm The small posterior cutaneous nerve of the arm arises in the axilla and passes medially to supply the skin on the dorsal surface of the arm nearly as far as the olecranon. It crosses posterior to, and communicates with, the intercostobrachial nerve.

Lower lateral cutaneous nerve of the arm The lower lateral cutaneous nerve of the arm perforates the lateral head of triceps distal to the deltoid tuberosity, passes to the front of the elbow close to the cephalic vein, and supplies the skin of the lateral part of the lower half of the arm.

Posterior cutaneous nerve of the forearm The posterior cutaneous nerve of the forearm arises with the lower lateral cutaneous nerve of the arm. Perforating the lateral head of triceps, it descends first lateral in the arm, then along the dorsum of the forearm to the wrist, supplying the skin in its course. It supplies the central forearm skin along its course and, near its termination, joins the dorsal branches of the lateral cutaneous nerve of the forearm.

Superficial radial nerve

The superficial radial nerve descends from the lateral epicondyle anterolaterally in the proximal two-thirds of the forearm, initially lying on supinator, lateral to the radial artery and behind brachioradialis. In the middle third of the forearm, it lies behind brachioradialis, close to the lateral side of the artery. It runs anterior to pronator teres, the radial head of flexor digitorum superficialis and flexor pollicis longus, and usually leaves the artery 7 cm proximal to the wrist and passes deep to the tendon of brachioradialis. It curves round the lateral side of the radius as it descends, pierces the deep fascia and divides into five, sometimes four, dorsal digital nerves. On the dorsum of the hand, it usually communicates with the posterior and lateral cutaneous nerves of the forearm.

Dorsal digital nerves

There are usually four or five small dorsal digital nerves (see Fig. 51.9). The first supplies the skin of the radial side of the thumb and the adjoining thenar eminence, and communicates with branches of the lateral cutaneous nerve of the forearm. The second supplies the medial side of the thumb; the third, the lateral side of the index finger; the fourth, the adjoining sides of the index and middle fingers. The fifth communicates with a ramus of the dorsal branch of the ulnar nerve and supplies the adjoining sides of the middle and ring fingers, where it is frequently replaced by the dorsal branch of the ulnar nerve. The digital nerves of the thumb reach only to the root of the nail; those in the index finger, midway along the middle phalanx; and those to the middle and the lateral part of the ring finger may reach no further than the proximal interphalangeal joints. The remaining distal dorsal areas of the skin in these digits are typically supplied by palmar digital branches of the median and ulnar nerves. However, the superficial terminal branch of the radial nerve may supply the whole dorsum of the hand.

Posterior interosseous nerve

The posterior interosseous nerve is the deep terminal branch of the radial nerve (see Figs 48.9, 50.21). It reaches the back of the forearm by passing round the lateral aspect of the radius between the two heads of supinator (see Figs 50.25–50.26). It supplies supinator both before entering the muscle and as it passes through it. As it emerges from supinator posteriorly, the nerve gives off three short branches to extensor digitorum, extensor digiti minimi and extensor carpi ulnaris, and two longer branches, a medial branch to extensor pollicis longus and extensor indicis, and a lateral branch that supplies abductor pollicis longus and extensor pollicis brevis. The nerve at first lies between the superficial and deep extensor muscles, but at the distal border of extensor pollicis brevis, it passes deep to extensor pollicis longus and, diminished to a fine thread, descends on the interosseous membrane to the dorsum of the carpus. Filaments arising from its flattened termination supply the carpal ligaments and articulations. Articular branches from the posterior interosseous nerve supply carpal, distal radio-ulnar and some intercarpal and intermetacarpal joints. Digital branches supply the metacarpophalangeal and proximal interphalangeal joints.

The distal portion of the nerve lies in a separate fascial sheath in the radial, deep, aspect of the fourth dorsal compartment of the extensor retinaculum of the wrist, where it is located deep to extensor digitorum and extensor indicis.

Branches of the superficial branch of the radial nerve reach the hand by curving around the wrist over the tendons of abductor pollicis longus and extensor pollicis brevis, and dividing into dorsal digital nerves (see Fig. 51.37). They usually communicate with the posterior and lateral cutaneous nerves of the forearm on the dorsum of the hand.

Lesions of the radial nerve

Radial nerve compression may occur at several sites in the elbow and forearm. The most proximal of these is within the radial tunnel which starts where the deep branch of the radial nerve lies over the radiohumeral joint and ends at the point where the deep branch becomes the posterior interosseous nerve at the distal border of supinator. At the level of the radial head, the nerve may be compressed by fibrous bands. More distally, it has been suggested that branches of the radial recurrent artery may compress the posterior interosseous nerve. Other sites of compression are the tendinous edge of the deep surface of extensor carpi radialis brevis and the point at which the nerve passes under the arcade of Frohse and between the two heads of supinator. Rarely, the nerve can be compressed at the level of the distal border of supinator.

Patients present with one of two syndromes: the radial tunnel syndrome, in which the presentation is that of pain along the lateral border of the elbow and upper forearm (Roles and Maudsley 1972), or the posterior interosseous nerve syndrome, which presents with motor weakness in the distribution of the nerve particularly affecting the extensors digitorum and carpi ulnaris. Primary treatment is non-operative and involves the avoidance of activities that cause pain, aided by appropriate splintage. In resistant cases, surgical decompression may be necessary. A complete release of all potential areas of compression is essential.

The elbow is a notorious site for nerve injuries, especially in children. The close proximity of all the major nerve trunks to bone makes them vulnerable. The ulnar nerve is particularly at risk in elbow dislocation, especially when the medial epicondyle is displaced into the joint. All three nerves are at risk of displacement into a dislocated joint. The posterior interosseous and radial nerves are particularly at risk from a Monteggia fracture-dislocation. Any nerve may become entrapped within a fracture, e.g. the median nerve is often accompanied by the brachial artery in cases of supracondylar fracture. Pain that persists, or worsens, after reduction of a fracture suggests impending critical ischaemia, continuing irritation of the nerve, or both. The nerves are at risk during operations or other medical interventions, particularly so when normal anatomical planes are distorted by haematoma, fibrosis or bone fragments.

Lumbar and sacral plexuses

Nerves derived from the lumbar and sacral plexuses innervate the lower limb (see Fig. 76.11). The lumbar plexus lies deep within psoas major, anterior to the transverse processes of the first three lumbar vertebrae. The sacral plexus lies in the pelvis on the anterior surface of piriformis, external to the pelvic fascia, which separates it from the inferior gluteal and internal pudendal vessels. The lumbosacral trunk (fourth and fifth lumbar ventral rami) emerges medial to psoas major on the posterior abdominal wall and lies on the ala of the sacrum before crossing the pelvic brim to join the first sacral ventral ramus. Contributions to the lumbosacral trunk may also be derived from the third lumbar nerve (Apaydin 2016).

Lesions of the lumbar and sacral plexuses

The deep and protected situation of the plexuses means that lesions are not common. The lumbar plexus may be involved in retroperitoneal pathology and the sacral plexus may be invaded by pelvic malignancies and both may be involved in the reticuloses, affected by plexiform neuromas, or damaged in fractures of the lumbar spine and pelvis or in other conditions that cause severe retroperitoneal and pelvic haemorrhage. Temporary lesions may occur after pregnancy and childbirth, e.g. after difficult forceps delivery of a large baby. Pain, which may be diffuse, is the most common feature. Iatrogenic injury can occur during surgical approaches to the abdomen and pelvis, particularly when operating within the retroperitoneal space and also during the lateral approach to spine.

Sciatica is pain in the lower back and hip region, radiating inferiorly along the posterior thigh to the leg. It is often caused by a herniated intervertebral disc, compressing the fifth lumbar or first sacral ventral rami. The so-called piriformis syndrome, which may result from a variant or anomalous relationship between piriformis and the sciatic nerve, may also produce hip pain that radiates inferiorly along the course of the sciatic nerve. Diagnosis of specific nerve injuries relies on the distribution and characteristics of clinical findings in combination with supportive electrophysiological studies and/or MRI and CT scans. The clinical presentation of lesions can vary as a result of anatomical variation and overlapping innervation patterns. Generally, loss of hip flexion and knee extension indicates a lumbar lesion; loss of hip abduction, knee flexion and plantarflexion and dorsiflexion are symptoms of sacral lesions (Ahmadian et al 2015).

Lumbar plexus

The lumbar plexus is formed by the first three and most of the fourth lumbar ventral rami, usually together with a contribution from the twelfth thoracic ventral ramus (see Fig. 61.16). The lumbar ventral rami pass laterally into the posterior part of psoas major, anterior to the transverse processes of the lumbar vertebrae (Moro et al 2003, Benglis et al 2009). Although there are many variations, the most common arrangement of the plexus is described here (Tubbs et al 2018).

The first lumbar ventral ramus is often joined by a branch from the twelfth thoracic ventral ramus, and these roots contribute to the formation of the iliohypogastric and ilioinguinal nerves, which run laterally on the posterior abdominal wall. A branch from the first lumbar ventral ramus unites with a branch from the second lumbar ventral ramus to form the genitofemoral nerve. The second, third and most of the fourth lumbar ventral rami divide into ventral and dorsal divisions; the ventral divisions unite to form the obturator nerve, while most of the nerve fibres in the dorsal divisions form the femoral nerve. The remaining fibres from the fourth lumbar ventral ramus join the fifth lumbar ventral ramus to form the lumbosacral trunk, which descends to join the sacral plexus. Branches from the dorsal divisions of the second and third lumbar ventral rami unite to form the lateral femoral cutaneous nerve. The accessory obturator nerve, when present, usually arises from the third and fourth ventral rami. The lumbar plexus is supplied by branches from the lumbar vessels that supply psoas major.

The division of constituent ventral rami into ventral and dorsal branches is not as clear in the lumbar and sacral plexuses as it is in the brachial plexus. Lateral cutaneous branches of the twelfth thoracic and first lumbar ventral rami are drawn into the gluteal skin, but otherwise these nerves are similar to intercostal nerves. The second lumbar ventral ramus is more complex. It contributes substantially to the femoral and obturator nerves, and also has an anterior terminal branch (the genital branch of the genitofemoral) and a lateral cutaneous branch that contributes to the lateral femoral cutaneous nerve and the femoral branch of the genitofemoral nerve. Anterior terminal branches of the third to fifth lumbar and first sacral ventral rami are suppressed, but the corresponding branches of the second and third sacral ventral rami supply the perineal skin.

The furcal nerve is an independent nerve with its own ventral and dorsal rootlets most commonly arising alongside the fourth lumbar spinal nerve. Its branches contribute to the femoral and obturator nerves arising from the lumbar plexus and to the lumbosacral trunk (Harshavardhana and Dabke 2014). The term ‘furcal’ refers to its forked nature, since it links the lumbar and sacral plexuses. Occasionally, the furcal nerve arises at the level of either the third or the fifth lumbar spinal nerves, in which case the sacral plexus is considered prefixed or postfixed, respectively.

Inflammatory processes, such as retrocaecal appendicitis on the right and diverticular abscess on the left, can occur in the posterior abdominal wall in the tissues immediately anterior to psoas major. These may irritate one or more branches of the lumbar plexus, causing pain or sensory disturbance in the distribution of the affected nerves, e.g. the skin of the thigh, hip or buttock.

Terminal branches of the lumbar plexus

Muscular branches

Small branches from the lumbar ventral rami supply adjacent muscles such as psoas major and quadratus lumborum (Mahan et al 2017).

Iliohypogastric nerve

The iliohypogastric nerve usually originates from the first lumbar ventral ramus but may arise wholly or in part from the twelfth thoracic ventral ramus (Klaassen et al 2011). It emerges from the upper lateral border of psoas major and crosses obliquely posterior to the inferior pole of the kidney on the anterior surface of quadratus lumborum. Above the iliac crest it enters the posterior part of transversus abdominis and then runs anteriorly between transversus abdominis and internal abdominal oblique, which it supplies. It gives off a lateral cutaneous branch that pierces internal and external abdominal oblique above the iliac crest and supplies the posterolateral gluteal skin. It continues forwards, pierces internal abdominal oblique approximately 3 cm medial and 1 cm inferior to the anterior superior iliac spine (in adults), and then penetrates the external abdominal oblique aponeurosis approximately 3 cm above and medial to the superficial inguinal ring to supply the skin of the hypogastric region. The iliohypogastric nerve frequently connects with the ilioinguinal nerve and less commonly with the subcostal nerve. Motor branches of the iliohypogastric nerve innervate transversus abdominis and internal abdominal oblique. Cutaneous branches innervate the posterolateral gluteal and skin of the hypogastric region.

Lesions of the iliohypogastic nerve

The iliohypogastric nerve is occasionally injured by a surgical incision in the right inguinal region, e.g. during an inguinal hernia repair, open appendicectomy or abdominal wall trocar placement, but there is rarely any noticeable sensory loss because the skin of the hypogastric region is innervated from several sources. Division of the iliohypogastric nerve above the anterior superior iliac spine may weaken the posterior wall of the inguinal canal and predispose to formation of a direct inguinal hernia.

Ilioinguinal nerve

The ilioinguinal nerve usually originates from the first lumbar ventral ramus but may receive a contribution from the twelfth thoracic or second lumbar ventral rami (Klaassen et al 2011). It emerges from the lateral border of psoas major, with or just inferior to the iliohypogastric nerve, passes obliquely across the anterior aspect of quadratus lumborum and the superior part of iliacus and enters transversus abdominis about 3 cm medial and 4 cm inferior to the anterior superior iliac spine (in the adult); at this site, it is readily blocked by local anaesthetic. In this region, a branch may connect with the iliohypogastric or lateral femoral cutaneous nerve. It pierces internal abdominal oblique more inferiorly, supplies it and then traverses the remainder of the inguinal canal superficial to the spermatic cord or round ligament of the uterus. It emerges with the spermatic cord from the superficial inguinal ring and divides into terminal cutaneous branches.

Numerous anatomical variations have been described (Al-dabbagh 2002, Ndiaye et al 2007). The ilioinguinal and genitofemoral nerves may interconnect within the inguinal canal, so that each innervates the skin of the genitalia to a variable extent (Rab et al 2001, Cesmebasi et al 2015). The ilioinguinal nerve may pierce the aponeurosis of external abdominal oblique proximal to the superficial inguinal ring or divide into terminal branches within the inguinal canal. It may form a common trunk with the iliohypogastric nerve as far as the midpoint of the inguinal canal or may be very small or absent, in which case the iliohypogastric nerve and genital branch of the genitofemoral nerve supply its territory. Rarely, it arises as a branch of the genitofemoral nerve. Motor branches of the ilioinguinal nerve supply transversus abdominis and internal abdominal oblique; the fibres are given off before the nerve enters the lateral aspect of the inguinal canal. Sensory branches innervate the skin of the proximal medial thigh and the skin over the root of the penis and proximal part of the scrotum in males (anterior scrotal nerve), or the skin covering the mons pubis and the adjoining labium majus in females (anterior labial nerve).

Lesions of the ilioinguinal nerve

The ilioinguinal nerve may be injured or entrapped during inguinal surgery, particularly for inguinal hernia repair, leading to sensory disturbances including pain from the external genitalia and proximal medial thigh (Ndiaye et al 2007).

Genitofemoral nerve

The genitofemoral nerve originates from the first and second lumbar ventral rami and is formed within the substance of psoas major. It descends obliquely anteriorly through the muscle to emerge on its anterior surface nearer the medial border, opposite the third or fourth lumbar vertebra (Moro et al 2003). It then descends deep to the posterior parietal peritoneum overlying psoas major, crosses obliquely posterior to the ureter, and divides into genital and femoral branches; it may divide close to its origin such that its branches emerge separately from psoas major. The genital branch crosses the distal part of the external iliac artery, enters the inguinal canal through the deep ring and accompanies the spermatic cord or round ligament of the uterus. It exits the superficial inguinal ring, usually posterior to the spermatic cord or round ligament of the uterus, and supplies cremaster and the skin of the external genitalia. The femoral branch descends lateral to the external iliac artery before crossing the deep circumflex iliac artery to pass deep to the inguinal ligament (occasionally, through it) (Rab et al 2001) and enter the femoral sheath lateral to the femoral artery. It pierces the anterior aspect of the femoral sheath and fascia lata and supplies the skin over the proximal part of the femoral triangle. It may connect with the lateral femoral cutaneous nerve and anterior femoral cutaneous branches of the femoral nerve. Motor branches of the genitofemoral nerve innervate cremaster via its genital branch. Sensory fibres travelling in the genital branch innervate the skin of the scrotum in males and of the mons pubis and labium majus in females; there is considerable variability and overlap with the cutaneous distribution of the ilio-inguinal nerve (Cesmebasi et al 2015).

Lesions of the genitofemoral nerve

The genital branch of the genitofemoral nerve may be injured during inguinal hernia repair (open or laparoscopic), leading to neuralgia (Cesmebasi et al 2015).

Lateral femoral cutaneous nerve

The lateral femoral cutaneous nerve (lateral femoral cutaneous nerve of the thigh) is usually derived from the dorsal branches of the second and third lumbar ventral rami, but variable contributions from the first to the third lumbar ventral rami have been described (de Ridder et al 1999). The nerve emerges from the posterolateral border of psoas major and crosses iliacus obliquely, running towards the anterior superior iliac spine. It supplies sensory fibres to the parietal peritoneum in the iliac fossa. On the right, the nerve passes posterolateral to the caecum, from which it is separated by the iliac fascia and peritoneum; on the left, it passes posterior to the inferior part of the descending colon. Both nerves usually pass posterior to the inguinal ligament about 1–2 cm medial to the anterior superior iliac spine; occasionally they pass through or, rarely, anterior to the ligament (Tubbs et al 2016): a separate fascial canal for this nerve has been described (Hanna 2017). Occasionally, the nerve lies anterior or superior to the anterior superior iliac spine as it enters the thigh, where it usually passes anterior or lateral to sartorius, but may also pierce the muscle. It divides into anterior and posterior branches. The anterior branch becomes superficial approximately 10 cm distal to the anterior superior iliac spine and supplies the skin of the anterior and lateral thigh as far distally as the knee. It connects terminally with the cutaneous branches of the anterior division of the femoral nerve and the infrapatellar branch of the saphenous nerve, forming the peripatellar plexus. The posterior branch pierces the fascia lata higher than the anterior, and divides to supply the skin on the lateral surface from the greater trochanter to about mid-thigh. It may also supply skin of the gluteal region.

Lesions of the lateral femoral cutaneous nerve

The lateral femoral cutaneous nerve may become entrapped at three sites along its course: close to the vertebral column; within the abdominal cavity as the nerve travels across the pelvis; and as it leaves the pelvis. This last site is where the nerve is most commonly damaged, and entrapment is thought to occur as the nerve passes through or deep to the inguinal ligament just medial to the anterior superior iliac spine. The angulation of the nerve as it crosses the iliac crest means that it is vulnerable to compression during movement, e.g. hip extension may increase angulation and tension on the nerve.

Injury produces an area of impaired sensation, often with pain and paraesthesia on the anterolateral aspect of the thigh (meralgia paraesthetica) in the distal cutaneous distribution of the nerve. This area does not extend across the midline anteriorly, it does not extend below the knee and it does not extend behind the hamstring tendons laterally. Symptoms may be exacerbated when wearing tight belts or tight-waisted clothes or as a result of a recent weight gain or pregnancy. Exceptionally, the posterior branch of the lateral femoral cutaneous nerve, which supplies a thin strip from the greater trochanter of the femur down about two-thirds of the way to the knee, may be affected separately. This branch leaves the main trunk of the nerve, usually distal to the inguinal ligament, and it then turns laterally to pierce tensor fasciae latae, where it may become entrapped.

Accessory obturator nerve

The accessory obturator nerve is sometimes present, more often on the left (Turgut et al 2017). It arises from the ventral branches of the third and fourth lumbar ventral rami, emerges from the medial border of psoas major, lateral to the obturator nerve, descends along the medial border of psoas major, crosses the superior pubic ramus behind pectineus and divides into branches; one branch enters the deep surface of pectineus, another supplies the hip joint, and a third connects with the anterior branch of the obturator nerve. Sometimes the accessory obturator nerve is very small and only supplies pectineus. Any branch may be absent and others may occur; an additional branch sometimes supplies adductor longus.

Femoral nerve

The femoral nerve is the largest branch of the lumbar plexus and is the nerve of the anterior compartment of the thigh. It has motor branches to iliacus, pectineus, sartorius and quadriceps femoris; articular branches to the hip, knee and ankle joints; cutaneous branches that supply most of the skin covering the anterior thigh, medial leg and medial foot and branches to the femoral artery (see Fig. 61.16). It arises from the dorsal branches (posterior divisions) of the second to fourth lumbar ventral rami (see Figs 76.11A, 77.44, 77.49) and descends through psoas major, emerging on or deep to its lateral border, about 4 cm above the inguinal ligament (Moore and Stringer 2011). It next passes between psoas major and iliacus deep to the iliac fascia, lying lateral to the femoral artery and sheath. As it passes behind the inguinal ligament into the thigh, the femoral nerve is split into anterior and posterior divisions by the lateral circumflex femoral artery. The branches of the anterior division are the intermediate and medial femoral cutaneous nerves and the nerve to sartorius. The branches of the posterior division are the saphenous nerve, muscular branches to quadriceps femoris and articular branches to the hip and knee joint. The terminal branches of the femoral nerve form in the femoral triangle about 2 cm distal to the inguinal ligament.

Nerve to pectineus

The nerve to pectineus branches from the medial side of the femoral nerve near the inguinal ligament. It passes behind the femoral sheath and enters the anterior aspect of the muscle.

Medial femoral cutaneous nerve of the thigh

The medial femoral cutaneous nerve (medial cutaneous nerve of the thigh) is at first lateral to the femoral artery. It crosses anterior to the artery at the apex of the femoral triangle and divides into anterior and posterior branches. Before doing so, it sends a few fibres through the fascia lata to supply the skin of the medial side of the thigh, near the long saphenous vein; one branch emerges via the saphenous opening, while another becomes subcutaneous about mid-thigh. The anterior branch descends on sartorius, perforates the fascia lata beyond mid-thigh, and divides into a branch that supplies the skin as low as the medial side of the knee, and another that runs lateral to the former and connects with the infrapatellar branch of the saphenous nerve. The posterior branch descends along the posterior border of sartorius to the knee, pierces the fascia lata, connects with the saphenous nerve and gives off several cutaneous rami, some as far as the medial side of the leg. The nerve contributes to the subsartorial plexus (see below).

Intermediate cutaneous nerve of the thigh

The intermediate femoral cutaneous nerve (intermediate cutaneous nerve of the thigh) usually pierces the fascia lata some 8 cm below the inguinal ligament, either as two branches or as one trunk that quickly divides into two. These descend on the anterior thigh, supplying the skin as far as the knee and ending in the peripatellar plexus. The lateral branch of the intermediate cutaneous nerve communicates with the femoral branch of the genitofemoral nerve, frequently piercing sartorius and sometimes supplying it.

Nerve to sartorius

The main nerve to sartorius arises from the femoral nerve in common with the intermediate femoral cutaneous nerve.

Saphenous nerve

The saphenous nerve is the largest and longest cutaneous branch of the femoral nerve and the longest nerve in the body (see Figs 76.11, 77.48). It descends lateral to the femoral artery in the femoral triangle and enters the adductor canal, where it crosses anterior to the artery to lie medial to it. At the distal end of the canal, it leaves the artery and emerges through the aponeurotic covering with the saphenous branch of the descending genicular artery. As it leaves the adductor canal, the saphenous nerve gives off an infrapatellar branch that contributes to the peripatellar plexus and then pierces the fascia lata between the tendons of sartorius and gracilis, becoming subcutaneous to supply the skin anterior to the patella. It descends along the medial border of the tibia with the long saphenous vein and divides distally into a branch that continues along the tibia to the ankle and a branch that passes anterior to the ankle to supply the skin on the medial side of the foot, often as far as the first metatarsophalangeal joint. The saphenous nerve connects with the medial branch of the superficial fibular nerve. Near the mid-thigh, it contributes a branch to the subsartorial plexus. The nerve may become entrapped as it leaves the adductor canal.

Muscular branches

The muscular branches of the posterior division of the femoral nerve supply quadriceps femoris. A branch to rectus femoris enters its proximal posterior surface and also supplies the hip joint. A larger branch to vastus lateralis forms a neurovascular bundle with the descending branch of the lateral circumflex femoral artery in its distal part and also supplies the knee joint. A branch to vastus medialis descends through the proximal part of the adductor canal, lateral to the saphenous nerve and femoral vessels, and enters the muscle at about its midpoint, sending a long articular filament distally along the muscle to the knee. Two or three branches to vastus intermedius enter its anterior surface about mid-thigh, and a small branch from one of these descends through the muscle to supply articularis genus and the knee joint.

Vascular branches

Vascular branches of the femoral nerve supply the femoral artery and its branches.

Lesions of the femoral nerve

Partial or complete injury can occur during surgery directed to the hip, pelvis or spine; with femoral artery catheterization; from trauma; or as a result of a retroperitoneal haematoma or mass. The most striking feature of femoral neuropathy is wasting and weakness of quadriceps femoris, resulting in difficulty in walking and a tendency for the leg to collapse. Pain and paraesthesia may occur on the anterior and medial aspect of the thigh, extending down the medial aspect of the leg in the distribution of the saphenous branch of the femoral nerve.

Obturator nerve

The obturator nerve is the nerve of the medial compartment of the thigh: it arises from the ventral branches of the second to fourth lumbar ventral rami. The branch from the third is the largest while that from the second is often very small. The nerve descends within the substance of psoas major, emerging from its posteromedial border near the fifth lumbar vertebra (Kirchmair et al 2008). It passes posterior to the common iliac vessels and lateral to the internal iliac vessels, descends on the lateral wall of the pelvis attached to the obturator fascia, and lies anterosuperior to the obturator vessels before running into the obturator canal to enter the thigh. Near the foramen, it divides into anterior and posterior branches, separated initially by part of obturator externus and further distally by adductor brevis.

The obturator nerve is said to have no branches in the abdomen or pelvis, although it has been reported to send articular branches to the anterior aspect of the sacroiliac joint. Its sensory branches innervate the hip and knee joints, and a small, variable patch of skin on the proximal medial thigh, and its motor branches innervate obturator externus, adductor longus, adductor brevis, adductor magnus, gracilis and sometimes pectineus (see Fig. 61.16) (Tubbs et al 2016).

Anterior branch

The anterior branch (see Fig. 77.49) leaves the pelvis anterior to obturator externus, and descends anterior to adductor brevis, behind pectineus and adductor longus. At the lower border of adductor longus it communicates with the medial cutaneous and saphenous branches of the femoral nerve, to form a subsartorial plexus that supplies the skin on the medial side of the thigh. It descends on, and supplies, the femoral artery. Near the obturator foramen, the anterior branch supplies the hip joint. Behind pectineus it supplies adductor longus, gracilis, usually adductor brevis and often pectineus, and connects with the accessory obturator nerve (when present). Occasionally the communicating branch to the femoral medial cutaneous and saphenous branches continues as a cutaneous branch to the thigh and leg. When this occurs the nerve emerges from behind the distal border of adductor longus to descend along the posterior margin of sartorius to the knee, where it pierces the deep fascia and connects with the saphenous nerve to supply the skin halfway down the medial side of the leg.

Subsartorial nerve plexus The medial cutaneous nerve of the thigh forms a subsartorial plexus with branches of the saphenous and obturator nerves, deep to the fascia lata, at the lower border of adductor longus. When the communicating branch of the obturator nerve is large and reaches the leg, the posterior branch of the medial cutaneous nerve is small, and ends in the plexus from which it gives rise to a few cutaneous filaments.

Posterior branch

The posterior branch pierces obturator externus anteriorly, supplies it and passes behind adductor brevis to the front of adductor magnus, dividing into branches to this and adductor brevis when the latter is not supplied by the anterior division. It usually sends an articular filament to the knee joint, which either perforates adductor magnus distally or traverses its opening with the femoral artery to enter the popliteal fossa. Within the fossa, the nerve descends on the popliteal artery to the back of the knee, pierces its oblique posterior ligament and supplies the articular capsule. It gives filaments to the popliteal artery.

Lesions of the obturator nerve

Isolated lesions of the obturator nerve are rare. However, it may be injured together with other nerves in retroperitoneal lesions that occur close to the origins of the lumbar plexus, or by an acetabular fracture, pelvic tumour, obturator hernia, prolonged labour or direct trauma. It can be damaged iatrogenically following manipulation, transection or retraction during pelvic surgery and can become entrapped within the fascia overlying adductor brevis. Compression of the nerve by herniated bowel loops at the obturator foramen can result in pain referred to the hip, medial thigh and knee, the so-called Howship–Romberg sign. A more distal nerve entrapment syndrome causing chronic medial thigh pain has been described in athletes with large adductor muscles.

Sacral plexus

The sacral plexus is formed by the lumbosacral trunk, the first to third sacral ventral rami, and part of the fourth sacral ventral ramus (the remainder of the fourth sacral ventral ramus joins the coccygeal plexus). The lumbar part of the lumbosacral trunk contains part of the fourth and all of the fifth lumbar ventral rami; it appears at the medial margin of psoas major and descends over the linea terminalis, at first medial to and then distally crossing anterior to the sacroiliac joint, to join the first sacral ventral ramus. The greater parts of the second and third sacral rami converge on the inferomedial aspect of the lumbosacral trunk in the greater sciatic foramen to form the sciatic nerve. The ventral and dorsal divisions of the nerves do not separate physically from each other but their fibres remain separate within the rami; the ventral and dorsal divisions of each contributing root join within the sciatic nerve. The fibres of the dorsal divisions will go on to form the common fibular nerve, and the fibres of the ventral division form the tibial nerve. Occasionally, the sciatic nerve divides into common fibular and tibial nerves inside the pelvis; when this occurs, the common fibular nerve usually runs through piriformis.

The sacral plexus lies against the posterior pelvic wall anterior to piriformis, posterior to the internal iliac vessels and ureter, and posterior to the sigmoid colon on the left. The superior gluteal vessels run either between the lumbosacral trunk and first sacral ventral ramus, or between the first and second sacral rami, while the inferior gluteal vessels lie between either the first and second, or the second and third, sacral ventral rami.

The sacral plexus is not commonly involved in malignant tumours of the pelvis because it lies behind the relatively dense presacral fascia, which resists all but locally very advanced malignant infiltration. When it occurs, there is intractable pain in the distribution of the branches of the plexus, which can be very difficult to treat. The plexus can also be involved in reticuloses or be affected by plexiform neuromas. The branches of the sacral plexus are shown in Table 77.1.

Sacral visceral and muscular branches

Visceral branches, the pelvic splanchnic nerves, arise from the second to fourth sacral verntral rami and innervate the pelvic viscera.

Several muscular branches arise from the fourth sacral ventral ramus to supply the superior surface of levator ani and the upper part of the external anal sphincter. The branches to levator ani enter the superior surface of the muscle. The branch to the external anal sphincter (also referred to as the perineal branch of the fourth sacral nerve) reaches the ischio-anal fossa by running either through ischiococcygeus or between ischiococcygeus and iliococcygeus: it also supplies the skin between the anus and coccyx.

Superior gluteal nerve

The superior gluteal nerve arises from the dorsal branches of the fourth and fifth lumbar and first sacral ventral rami. Accompanied by the superior gluteal vessels, the nerve leaves the pelvis via the greater sciatic foramen above piriformis, and divides into superior and inferior branches (see Fig. 77.47). The superior branch accompanies the upper branch of the deep division of the superior gluteal artery to supply gluteus medius and occasionally gluteus minimus. The inferior branch runs with the lower ramus of the deep division of the superior gluteal artery across gluteus minimus, supplies the glutei medius and minimus, and ends in tensor fasciae latae.

Inferior gluteal nerve

The inferior gluteal nerve arises from the dorsal branches of the fifth lumbar and first and second sacral ventral rami. It leaves the pelvis via the greater sciatic foramen below piriformis, and divides into branches that enter the deep surface of gluteus maximus (see Fig. 77.47).

Lesions of the superior and inferior gluteal nerves

Focal lesions of the superior and inferior gluteal nerves usually occur concurrently with those of the sciatic nerve, posterior femoral cutaneous nerve and/or pudendal nerve. However, both gluteal nerves are vulnerable to injury during total hip replacement, and less commonly due to blunt trauma or misplaced gluteal injections. Injury to the superior gluteal nerve causing paralysis of gluteus medius and minimus can result in Trendelenburg's sign, where the pelvis drops on the unsupported side (in the coronal plane) when standing on the affected limb. Injury to the inferior gluteal nerve results in weakness of gluteus maximus causing impaired hip extension (Kretschmer and Heinen 2015).

Pudendal nerve

The pudendal nerve arises from the ventral divisions of the second, third and fourth sacral ventral rami and is formed just above the superior border of the sacrotuberous ligament and the upper fibres of ischiococcygeus (Klink 1953, Sato 1980). It leaves the pelvis via the greater sciatic foramen between piriformis and ischiococcygeus (see Fig. 71.10), enters the gluteal region and passes dorsal to the sacrospinous ligament, close to its attachment to the ischial spine, where it lies medial to the internal pudendal vessels. It accompanies the internal pudendal artery through the lesser sciatic foramen into the pudendal canal on the lateral wall of the ischio-anal fossa. In the posterior part of the canal, it gives rise to the inferior anal (rectal) and perineal nerves; the dorsal nerve of the penis or clitoris continues anteriorly from this origin.

The course of the branches of the pudendal nerve parallels that of the pudendal vessels (see Figs 74.24, 75.4). Muscular branches that arise directly from the pudendal nerve supply the superficial transverse perineal muscles, bulbospongiosus, ischiocavernosus, the external urethral sphincter and the anterior parts of the external anal sphincter and levator ani. In males, the branch to bulbospongiosus pierces this muscle to supply the corpus spongiosum penis, and ends in the urethral mucosa. For the innervation of the female genitalia, see Table 75.2.

The pudendal nerve occupies a constant position over the ischial spine and it can be 'blocked' by infiltration with a local anaesthetic applied via a needle passed through the lateral wall of the vagina to anaesthetize the perineal and anal skin. It can also be palpated over the ischial spine through the lateral wall of the rectum.

Inferior anal nerve

The inferior anal (rectal) nerve runs either through the medial wall of the pudendal canal with the inferior anorectal vessels, or behind the sacrospinous ligament directly from the fourth sacral ventral ramus without passing through the pudendal canal (Maldonado et al 2015), or occasionally it arises directly from the sacral plexus and crosses the sacrospinous ligament or rejoins the pudendal nerve. The nerve crosses the ischio-anal fossa to supply the external anal sphincter, the lining of the distal part of the anal canal and the skin around the anus. It frequently breaks into terminal branches before reaching the lateral border of the external anal sphincter. Its cutaneous branches distributed around the anus overlap the branches of the perineal branch of the posterior femoral cutaneous nerve and of the posterior scrotal or labial nerves. In females, the inferior anal nerve can supply sensory branches to the distal part of the vagina.

Perineal nerve

The perineal nerve is the inferior and larger terminal branch of the pudendal nerve in the pudendal canal. It runs anteriorly, inferior to the internal pudendal artery and accompanies the perineal artery, dividing into posterior scrotal or posterior labial and muscular branches. The posterior scrotal or labial nerves are usually double; they have medial and lateral branches that run over the perineal membrane and pass anteriorly in the lateral part of the urogenital triangle with the posterior scrotal or posterior labial branches of the perineal artery. They supply the skin of the scrotum or labia majora, respectively, overlapping the distribution of the perineal branch of the posterior femoral cutaneous nerve and inferior anal nerve. In females, the posterior labial branches also supply sensory fibres to the skin of the distal vagina.

Dorsal nerve of the penis or clitoris

The dorsal nerve of the penis or clitoris runs anteriorly above the internal pudendal artery along the ischiopubic ramus, deep to the perineal membrane. It supplies the corpus cavernosum and accompanies the dorsal artery of the penis or clitoris between the layers of the suspensory ligament of the penis or clitoris. The dorsal nerve of the penis runs on the dorsum of the penis to end in the glans penis.

Perforating cutaneous nerve

The perforating cutaneous nerve usually arises from the posterior aspects of the second and third sacral ventral spinal rami. It pierces the sacrotuberous ligament, curves round the inferior border of gluteus maximus and supplies the skin over the inferomedial aspect of this muscle. The nerve may arise from the pudendal nerve or it may be absent, in which case it may be replaced either by a branch from the posterior femoral cutaneous nerve or from the third and fourth, or fourth and fifth, sacral ventral rami.

Nerve to quadratus femoris

The nerve to quadratus femoris arises from the ventral branches of the fourth lumbar to the first sacral ventral rami. It leaves the pelvis via the greater sciatic foramen below piriformis, descends on the ischium deep to the sciatic nerve, the gemelli and the tendon of obturator internus, and supplies gemellus inferior, quadratus femoris and the hip joint.

Nerve to obturator internus

The nerve to obturator internus arises from the ventral branches of the fifth lumbar and first and second sacral ventral rami. It leaves the pelvis via the greater sciatic foramen below piriformis, supplies a branch to the upper posterior surface of gemellus superior, crosses the ischial spine lateral to the internal pudendal vessels, re-enters the pelvis via the lesser sciatic foramen, and enters the pelvic surface of obturator internus.

Posterior femoral cutaneous nerve (posterior cutaneous nerve of the thigh)

The posterior femoral cutaneous nerve (posterior cutaneous nerve of the thigh) arises from the dorsal branches of the first and second, and the ventral branches of the second and third sacral rami. It leaves the pelvis via the greater sciatic foramen below piriformis and descends under gluteus maximus with the inferior gluteal vessels, lying posterior or medial to the sciatic nerve (see Fig. 77.47). It descends in the back of the thigh superficial to the long head of biceps femoris, deep to the fascia lata. It pierces the deep fascia behind the knee and accompanies the short saphenous vein to mid-calf, its terminal twigs connecting with the sural nerve. Its branches are cutaneous and are distributed to the gluteal region, perineum, posterior thigh and proximal posterior leg.

Three or four gluteal branches (inferior clunial nerves) curl round the lower border of gluteus maximus to supply the skin over the inferolateral portion of the muscle. The perineal branch supplies the superomedial skin in the thigh, curves forwards across the hamstrings below the ischial tuberosity, pierces the fascia lata and then runs in the superficial perineal fascia to the scrotal or labial skin. It communicates with the inferior anal (rectal) and posterior scrotal or labial branches of the perineal nerve, and gives numerous branches to the skin of the back and medial side of the thigh, the popliteal fossa and the proximal part of the back of the leg. One study found the perineal branch of the posterior cutaneous nerve of the thigh in about one-half of specimens (Tubbs et al 2009).

Nerve to piriformis

The nerve to piriformis usually arises from the dorsal branches of the first and second sacral ventral rami (sometimes only the second) and enters the anterior surface of piriformis.

Sciatic nerve

The sciatic nerve is typically 2 cm wide at its origin and is the thickest nerve in the body. It travels in the posterior compartment of the thigh and supplies the leg and foot. It leaves the pelvis via the greater sciatic foramen, usually inferior to piriformis, and descends between the greater trochanter and ischial tuberosity, along the back of the thigh, dividing into the tibial and common fibular nerves at a varying level proximal to the knee (see Fig. 77.50; see also Fig. 76.11B). Superiorly, it lies deep to gluteus maximus, resting first on the posterior ischial surface with the nerve to quadratus femoris between them. It then crosses posterior to obturator internus, the gemelli and quadratus femoris, separated by the latter from obturator externus and the hip joint. It is accompanied medially by the posterior femoral cutaneous nerve and the inferior gluteal artery. More distally, it lies behind adductor magnus and is crossed posteriorly by the long head of biceps femoris. Its course corresponds to a line drawn from just medial to the midpoint between the ischial tuberosity and greater trochanter to the apex of the popliteal fossa. Articular branches arise proximally to supply the hip joint through its posterior capsule; these are sometimes derived directly from the sacral plexus. Muscular branches are distributed to biceps femoris, semitendinosus, semimembranosus and the ischial part of adductor magnus.

The point of division of the sciatic nerve into its tibial and common fibular components is very variable: the two large nerves are only loosely held together as the sciatic nerve and the level of their separation in the thigh is variable. The common site is at the junction of the middle and lower thirds of the thigh, near the apex of the popliteal fossa, but the division may occur at any level above this point and, rarely, may occur below it: the common variations of the sciatic nerve have been classified into six types (Beaton and Anson 1937). The tibial nerve is derived from the anterior divisions of the sacral plexus and the common fibular nerve is derived from the posterior divisions of the plexus. The medial (tibial) component innervates the posterior thigh muscles, including the ischial part of adductor magnus, but not the short head of biceps femoris, which is supplied by the lateral (common fibular) component.

Blood supply to the sciatic nerve In the gluteal region, the sciatic nerve is supplied by the inferior gluteal artery and cruciate anastomosis (the medial and lateral circumflex femoral arteries, inferior gluteal artery and the first perforating branch of the profunda femoris artery) (see Fig. 77.47). On rare occasions, it is supplied by branches from the superior gluteal or internal pudendal arteries, which reach the nerve on its medial side. Lower in the thigh, arterial branches derived from the perforating branches of the profunda femoris artery or the anastomotic chain between them or, occasionally, from the popliteal artery, enter the nerve on its lateral or anterolateral side (Sunderland 1945). The numerous arterial branches to the sciatic nerve anastomose with each other to form extraneural and intraneural arterial chains (Sunderland 1945, Ugrenovic et al 2013).

Lesions of the sciatic nerve

The sciatic nerve supplies the posterior thigh muscles and all the muscles below the knee, which means that a complete palsy of the sciatic nerve results in a flail foot and severe difficulty in walking. Fortunately, complete sciatic nerve palsy is very rare. The nerve is vulnerable in posterior dislocation of the hip. As it leaves the pelvis, it passes either inferior to piriformis or sometimes through the muscle, and at that point it may very rarely become entrapped or tethered; the piriformis syndrome is a controversial condition in which an anomalous relationship between piriformis and the sciatic nerve is thought to cause pain in the buttocks and along the course of the sciatic nerve. External compression over the buttock, e.g. in patients who lie immobile on a hard surface for a considerable length of time, can injure the nerve. However, the most common cause of serious sciatic nerve injury (and of the resulting major medicolegal claims) is iatrogenic (Dillow et al 2013). The nerve may be iatrogenically damaged in misplaced therapeutic injections into gluteus maximus. Sciatic nerve palsy occurs after total hip replacement or similar surgery in 1% of cases, and may be caused by sharp injury, burning from bone cement, traction from instruments, manipulation of the hip, inadvertent lengthening of the femur, or haematoma surrounding the nerve. For some reason, possibly anatomical, the common fibular component of the sciatic nerve is more usually affected, resulting in a foot drop and a high-stepping gait.

Tibial nerve

The tibial nerve, the larger component of the sciatic nerve, is derived from the ventral branches (anterior divisions) of the fourth and fifth lumbar and first to third sacral ventral rami. It descends along the posterior thigh and popliteal fossa to the distal border of popliteus. It then passes anterior to the arch of soleus with the popliteal artery and continues into the leg. In the thigh, it is overlapped proximally by the hamstring muscles but it becomes more superficial in the popliteal fossa, where it is lateral to the popliteal vessels. At the level of the knee, the tibial nerve becomes superficial to the popliteal vessels and crosses to the medial side of the artery. In the distal popliteal fossa, it is overlapped by the junction of the two heads of gastrocnemius.

In the leg, the tibial nerve is the nerve of the posterior compartment. It descends with the posterior tibial vessels to lie between the heel and the medial malleolus (see Fig. 78.4). Proximally, it is deep to soleus and gastrocnemius, but in its distal third is covered only by skin and fasciae, and overlapped sometimes by flexor hallucis longus. At first medial to the posterior tibial vessels, it crosses behind them and descends lateral to them until it bifurcates. It lies on tibialis posterior for most of its course except distally, where it adjoins the posterior surface of the tibia. The tibial nerve ends under the flexor retinaculum by dividing into the medial and lateral plantar nerves.

The branches of the tibial nerve are articular, muscular (to gastrocnemius, plantaris, soleus, popliteus, tibialis posterior, flexor digitorum longus and flexor hallucis longus), sural, medial calcaneal and medial and lateral plantar nerves.

Articular branches

Articular branches to the knee joint accompany the superior and inferior medial genicular arteries and the middle genicular artery; they form a plexus with a branch from the obturator nerve and also supply the oblique popliteal ligament. The branches accompanying the superior and inferior medial genicular arteries supply the medial part of the capsule. A branch of the nerve to popliteus (tibial nerve) supplies the posterior portion of the superior tibiofibular joint. Just before the tibial nerve bifurcates, it gives off branches that supply the ankle joint.

Muscular branches

Proximal muscular branches arise between the heads of gastrocnemius and supply gastrocnemius, plantaris, soleus and popliteus. The nerve to soleus enters its superficial aspect. The branch to popliteus descends obliquely across the popliteal vessels, curling round the distal border of the muscle to its anterior surface. It also supplies tibialis posterior, the superior tibiofibular joint and the tibia, and gives off an interosseous branch that descends near the fibula to reach the distal tibiofibular joint.

Muscular branches in the leg, either independently or by a common trunk, supply soleus (on its deep surface), tibialis posterior, flexor digitorum longus and flexor hallucis longus. The branch to flexor hallucis longus accompanies the fibular vessels.

Sural nerve

The sural nerve descends between the heads of gastrocnemius, pierces the deep fascia proximally in the leg, and is joined at a variable level by the sural communicating branch of the common fibular nerve. Some authors term this branch the lateral sural cutaneous nerve, and call the main trunk (from the tibial nerve) the medial sural cutaneous nerve. The sural nerve descends lateral to the calcaneal tendon, near the short saphenous vein, to the region between the lateral malleolus and the calcaneus, and supplies the posterior and lateral skin of the distal third of the leg. It then passes distal to the lateral malleolus along the lateral side of the foot and fifth toe, supplying the overlying skin. It connects with the posterior femoral cutaneous nerve in the leg and with the superficial fibular nerve on the dorsum of the foot.

The sural nerve is often used as an autologous peripheral nerve graft on the grounds that it is easily harvested, readily identified and exclusively cutaneous.

Medial calcaneal nerve

The medial calcaneal nerve arises from the tibial nerve and perforates the flexor retinaculum to supply the skin of the heel and medial side of the sole.

Medial plantar nerve

The medial plantar nerve is the larger terminal division of the tibial nerve, and lies lateral to the medial plantar artery. From its origin under the flexor retinaculum, it passes deep to abductor hallucis, then appears between it and flexor digitorum brevis, gives off a medial proper digital nerve to the great toe, and divides near the metatarsal bases into three common plantar digital nerves (see Fig. 79.27; see also Fig. 79.22).

Cutaneous branches pierce the plantar aponeurosis between abductor hallucis and flexor digitorum brevis to supply the skin of the sole of the foot. Muscular branches supply abductor hallucis, flexor digitorum brevis, flexor hallucis brevis and the first lumbrical. The first two arise near the origin of the nerve and enter the deep surfaces of the muscles. The branch to flexor hallucis brevis is from the hallucal medial digital nerve, and that to the first lumbrical from the first common plantar digital nerve. Articular branches supply the joints of the tarsus and metatarsus.

Three common plantar digital nerves pass between the slips of the plantar aponeurosis, each dividing into two proper digital branches. The first supplies adjacent sides of the great and second toes; the second supplies adjacent sides of the second and third toes; and the third supplies adjacent sides of the third and fourth toes, and also connects with the lateral plantar nerve. The first gives a branch to the first lumbrical. Each proper digital nerve has cutaneous and articular branches: near the distal phalanges, a dorsal branch supplies structures around the nail. Abductor hallucis, flexor hallucis brevis and the first lumbrical are all supplied by the medial plantar nerve.

Lateral plantar nerve

The lateral plantar nerve supplies the skin of the fifth toe, the lateral half of the fourth toe, and most of the deep muscles of the foot (see Fig. 79.22). It is located medial to the lateral plantar artery and courses anteriorly towards the tubercle of the fifth metatarsal. Next, it passes between flexor digitorum brevis and flexor accessorius, and ends between flexor digiti minimi brevis and abductor digiti minimi by dividing into superficial and deep branches. Before division, it supplies flexor accessorius and abductor digiti minimi, and gives rise to small branches that pierce the plantar aponeurosis to supply the skin of the lateral part of the sole (see Fig. 79.27). The superficial branch splits into two common plantar digital nerves: the lateral supplies the lateral side of the fifth toe, flexor digiti minimi brevis and the two interossei in the fourth intermetatarsal space; the medial connects with the third common plantar digital branch of the medial plantar nerve and divides into two to supply the adjoining sides of the fourth and fifth toes. The deep branch accompanies the lateral plantar artery deep to the flexor tendons and adductor hallucis, and supplies the second to fourth lumbricals, adductor hallucis and all the interossei (except those of the fourth intermetatarsal space). Branches to the second and third lumbricals pass distally deep to the transverse head of adductor hallucis, and travel around its distal border to reach them (see Video 79.1).

Lesions of the tibial nerve

The tibial nerve is vulnerable to direct injury in the popliteal fossa, where it lies superficial to the popliteal vessels at the level of the knee, or to compression at the tendinous arch of the soleus. It may be damaged in compartment syndrome that affects the deep flexor compartment of the calf. All nerves of the foot can be affected by entrapment, leading classically to a burning sensation in the distribution of that nerve. Tarsal tunnel syndrome is much less common than carpal tunnel syndrome. The flexor retinaculum may compress the tibial nerve or either of its branches (medial and lateral plantar nerves); entrapment at this level is most commonly due to a space-occupying lesion, e.g. a ganglion, or to compression by either a leash of vessels or the deep fascia associated with abductor hallucis. Compression of the first branch of the lateral plantar nerve (Baxter's nerve) by the deep fascia that covers abductor hallucis has been implicated as a possible cause of chronic heel pain and of plantar fasciitis. (Plantar fasciitis, often caused by repetitive high-impact injury to the foot, may be associated with pain, especially over the medial calcaneal process, which may be exacerbated by passive ankle or great toe flexion.) The medial plantar nerve can be compressed at the 'knot of Henry', which is the point where the tendon of flexor hallucis longus crosses deep to the tendon of flexor digitorum longus, to reach its medial side in the sole of the foot. It may also be compressed between abductor hallucis and the navicular bone ('jogger's foot'). Sural nerve entrapment is usually not due to compression by fascial elements. Entrapment of the third common digital nerve as it passes deep to the intermetatarsal ligament of the third (or less commonly the second) web space can result in a Morton's neuroma, which is probably the most common form of nerve entrapment in the foot.

Depending on the level of the injury, damage to the tibial nerve can produce weakness of knee flexion, plantarflexion, inversion and toe flexion, accompanied by sensory loss in the lower lateral leg, heel and sole of the foot.

Common fibular nerve

The common fibular nerve (common peroneal nerve) is the nerve of the anterior and lateral compartments in the leg. It is approximately half the size of the tibial nerve and is derived from the dorsal (posterior) branches of the fourth and fifth lumbar and first and second sacral ventral rami. It descends obliquely along the lateral side of the popliteal fossa to the fibular head, medial to biceps femoris. It lies between the tendon of biceps femoris, to which it is bound by fascia, and the lateral head of gastrocnemius (see Fig. 78.41). The nerve then passes into the anterolateral compartment of the leg through a tight opening in the thick fascia overlying tibialis anterior. It curves lateral to the neck of the fibula, lying on the bone deep to fibularis longus, and divides into superficial and deep fibular nerves; an articular trunk, derived from the deep fibular nerve, provides an articular branch that travels with the anterior tibial recurrent artery and a proximal branch to tibialis anterior.

The common fibular nerve supplies the anterolateral part of the knee joint capsule and the proximal tibiofibular joint and the skin on the anterior, posterior and lateral surfaces of the proximal leg. The superficial peroneal nerve supplies fibulares longus and brevis and the skin of the lower leg before dividing into medial and intermediate dorsal cutaneous nerves. The deep fibular nerve supplies muscular branches to tibialis anterior, extensors hallucis longus and digitorum longus and fibularis tertius, and an articular branch to the ankle joint, before dividing into lateral and medial terminal branches.

The common fibular nerve has articular and cutaneous branches, and terminates as the superficial and deep fibular nerves.

Articular branches

There are three articular branches. Two accompany the superior and inferior lateral genicular arteries; they may arise in common. The third, the recurrent articular branch, arises near the termination of the common fibular nerve. It ascends with the anterior recurrent tibial artery through tibialis anterior and supplies the anterolateral part of the knee joint capsule and the proximal tibiofibular joint.

Cutaneous branches

The two cutaneous branches, often from a common trunk, are the lateral sural and sural communicating nerves. The lateral sural cutaneous nerve (lateral cutaneous nerve of the calf) supplies the skin on the anterior, posterior and lateral surfaces of the proximal leg. The sural communicating nerve arises near the head of the fibula and crosses the lateral head of gastrocnemius to join the sural nerve. It may descend separately as far as the heel.

Lesions of the common fibular nerve

The common fibular nerve is relatively unprotected as it traverses the lateral aspect of the neck of the fibula and is easily compressed at this site, e.g. by plaster casts or ganglia. The nerve may also become entrapped by a fascial band beneath fibularis longus within the so-called fibular tunnel, between the attachments of fibularis longus to the head and shaft of the fibula. Traction lesions can accompany dislocations of the lateral compartment of the knee, and are most likely to occur if the distal attachments of biceps femoris and the ligaments that insert on to the fibular head are avulsed, possibly with a small part of the fibular head; the nerve is tethered to the tendon of biceps femoris by dense fascia and so is pulled proximally. Severe traction lesions may produce longitudinal injuries affecting a long segment of the common fibular nerve. Torsional injury following ankle injury (sprain or fracture) may result in common fibular neuropathy; the injury is transmitted from the ankle along the interosseous membrane to the proximal leg (Lalezari et al 2012). Patients with such injury present with a foot drop. Physical examination reveals weakness or paralysis of ankle dorsiflexion, toe extension and eversion of the foot, but inversion and plantar flexion are normal. Sensation on the dorsum of the foot, including the first dorsal web space, is diminished. The ankle reflex is preserved. Since the common fibular nerve divides at the fibular neck into the superficial and deep fibular nerves, injuries to the nerve at this level may damage either the main trunk or its branches. Electrodiagnostic studies can help localize a common fibular nerve injury to the fibular neck region. At this level, nerve conduction studies may show slowed velocities and electromyography would demonstrate denervation in the muscles innervated by the common fibular nerve (such as tibialis anterior or fibularis longus), whereas more proximally innervated muscles (particularly the short head of biceps femoris) would be normal. Injury specifically to the superficial fibular nerve will result in paralysis of eversion and sensory loss in the lower lateral aspect of the leg extending onto the dorsum of the foot. Damage to the deep fibular nerve results in paralysis of dorsiflexion and toe extension with sensory loss in the first interdigital web space.

Superficial fibular nerve

The superficial fibular nerve (superficial peroneal nerve) begins at the bifurcation of the common fibular nerve. It lies deep to fibularis longus at first, then passes anteroinferiorly between fibularis longus and brevis and extensor digitorum longus, and pierces the deep fascia in the distal third of the leg (see Fig. 78.41). It divides into a large medial dorsal cutaneous nerve and a smaller, more laterally placed, intermediate dorsal cutaneous nerve, usually after piercing the deep fascia, but sometimes while it is still deep to the fascia. As the nerve lies between the muscles it supplies fibularis longus, fibularis brevis and the skin of the lower leg. The deep course, i.e. the compartmental localization, and the peripheral digital distribution of the superficial fibular nerve are subject to considerable variation (see Kosinksi's classification; Kosinski 1926, Solomon et al 2001).

Cutaneous branches

The medial dorsal cutaneous nerve passes in front of the ankle joint and divides into two dorsal digital branches; one of these supplies the medial side of the hallux and the other supplies the adjacent side of the second and third toes. It communicates with the saphenous and deep fibular nerves. The smaller intermediate branch crosses the dorsum of the foot laterally. It divides into dorsal digital branches that supply the contiguous sides of the third to fifth toes and the skin of the lateral aspect of the ankle, where it connects with the sural nerve. Both branches, especially the intermediate, are at risk during the placement of portal skin incisions for arthroscopy and during surgical approaches to the lateral malleolus. Branches of the superficial fibular nerve supply the skin of the dorsum of all the toes except that of the lateral side of the fifth toe (supplied by the sural nerve) and the adjoining sides of the great and second toes (supplied by the medial terminal branch of the deep fibular nerve). Some of the lateral branches of the superficial fibular nerve are frequently absent and are replaced by sural nerve branches.

Accessory fibular nerves

An accessory superficial fibular nerve and an accessory deep fibular nerve have been described as variant branches of the superficial fibular nerve; both are probably the product of atypical branching of the parent nerve deep to the deep fascia (see above).

Lesions of the superficial fibular nerve

A lesion of the superficial fibular nerve causes weakness of foot eversion and sensory loss on the lateral aspect of the leg that extends onto the dorsum of the foot. The nerve can be subject to entrapment as it penetrates the deep fascia of the leg, be involved in compartment syndrome that affects the lateral compartment of the leg, or be damaged in severe inversion injuries of the ankle.

Deep fibular nerve

The deep fibular nerve (deep peroneal nerve) begins at the bifurcation of the common fibular nerve, between the fibula and the proximal part of fibularis longus. It passes obliquely forwards deep to extensor digitorum longus to the front of the interosseous membrane and reaches the anterior tibial artery in the proximal third of the leg. It descends with the artery to the ankle, where it divides into lateral and medial terminal branches. As it descends, the nerve is first lateral to the artery, then anterior, and finally lateral again at the ankle.

Cutaneous and muscular branches

The deep fibular nerve supplies muscular branches to tibialis anterior, extensor hallucis longus, extensor digitorum longus and fibularis tertius, and an articular branch to the ankle joint.

The lateral terminal branch crosses the ankle deep to extensor digitorum brevis, enlarges as a pseudoganglion and supplies extensor digitorum brevis. From the enlargement, three minute interosseous branches supply the tarsal and metatarsophalangeal joints of the middle three toes.

The medial terminal branch runs distally on the dorsum of the foot lateral to the dorsalis pedis artery, and connects with the medial branch of the superficial fibular nerve in the first interosseous space. It divides into two dorsal digital nerves, which supply adjacent sides of the great and second toes. Before dividing, it gives off an interosseous branch, which supplies the first metatarsophalangeal joint. The deep fibular nerve may end as three terminal branches.

Lesions of the deep fibular nerve

Isolated injury to the deep fibular nerve may result from compartment syndrome that affects the anterior compartment of the leg or from an intraneural ganglion cyst (mucinous cyst within the nerve derived from the superior tibiofibular joint via the articular branch that travels with the anterior tibial recurrent artery (Spinner et al 2003)). The nerve is sometimes compressed by osteophytes in the region of the second tarsometatarsal joint.

Individuals with lesions of the deep fibular nerve have weakness of ankle dorsiflexion and extension of all toes but normal foot eversion. Sensory impairment is confined to the first interdigital web space.

Coccygeal plexus

The coccygeal plexus is formed by a small descending branch from the fourth sacral ventral ramus and by the fifth sacral and coccygeal ventral rami. The fifth sacral ventral ramus emerges from the sacral hiatus, curves round the lateral margin of the sacrum inferior to its cornu, and pierces ischiococcygeus inferiorly to reach its pelvic surface. Here it is joined by a descending branch of the fourth sacral ventral ramus; the small trunk so formed descends on the pelvic surface of ischiococcygeus, joins the minute coccygeal ventral ramus that emerges from the sacral hiatus, and curves round the lateral coccygeal margin, piercing ischiococcygeus to reach the pelvis. The small trunk that is formed in this way is the coccygeal plexus. Anococcygeal nerves arise from it and form a few fine filaments that pierce the sacrotuberous ligament to supply the adjacent skin.

AUTONOMIC NERVOUS SYSTEM

The autonomic nervous system represents the visceral component of the nervous system. It consists of neurones located within the CNS and the PNS that are concerned with the control of the internal environment, through the innervation of secretory glands and cardiac and smooth muscle. Its functions are, however, closely integrated with those of the somatic nervous system.

Visceral efferent pathways differ from their somatic equivalents in that the former are interrupted by peripheral synapses, there being a sequence of at least two neurones between the CNS and the target structure (see Fig. 24.11). These are referred to as preganglionic and postganglionic neurones, respectively. The somata of preganglionic neurones are located in the visceral efferent nuclei of the brainstem and in the lateral horn of the spinal cord. Their axons, which are usually finely myelinated, exit from the CNS in certain cranial and spinal nerves, and then pass to peripheral ganglia, where they synapse with postganglionic neurones. The axons of postganglionic neurones are usually unmyelinated. Postganglionic neurones are more numerous than preganglionic ones; one preganglionic neurone may synapse with 15–20 postganglionic neurones, which permits the wide distribution of many autonomic effects.

The autonomic nervous system is traditionally divided into the sympathetic and parasympathetic systems that coordinate the neural regulation of visceral and homeostatic functions. In general, sympathetic activity results in the constriction of cutaneous arteries (increasing blood supply to the heart, muscles and brain), cardiac acceleration, an increase in blood pressure, contraction of sphincters and depression of peristalsis, all of which mobilize body energy stores for dealing with increased activity. Parasympathetic activity results in cardiac slowing and an increase in intestinal glandular and peristaltic activities, which may be considered to conserve body energy stores.

SYMPATHETIC NERVOUS SYSTEM

Preganglionic sympathetic axons originate from neuronal somata in the intermediolateral nucleus (lateral horn) of the spinal cord from the first thoracic to the second lumbar spinal segments (T1–L2) (see Fig. 24.12). Postganglionic sympathetic axons arise from neuronal somata in the sympathetic (paravertebral) trunk or in a more peripheral plexus. There are between 10 and 12 (usually 11) thoracic ganglia, four lumbar ganglia, and four or five ganglia in the sacral region. Cervical sympathetic ganglia are usually reduced to three by fusion.

Preganglionic axons are myelinated with diameters of 1.5–4 μm and release acetylcholine as their principal neurotransmitter. They travel initially with the corresponding ventral roots and leave the latter as white rami communicantes to enter the adjacent sympathetic ganglion in the sympathetic trunk (see Fig. 24.13). Their targets vary; some synapse in the sympathetic ganglion that they enter, whereas others ascend or descend in the sympathetic trunk to synapse in cervical or lumbar ganglia, respectively. Axons destined for the cervical ganglia are mainly derived from preganglionic neurones in the first thoracic spinal nerve. Many of the preganglionic axons that originate in the lower thoracic spinal segments (T5–T12) do not synapse locally but enter the abdominal cavity as the thoracic splanchnic nerves. These nerves pass through the posterior mediastinum and respiratory diaphragm to enter the abdominal cavity where they synapse either in prevertebral ganglia that surround the origin of the major visceral arteries arising from the abdominal aorta, e.g. the coeliac and superior mesenteric ganglia, or around the medullary chromaffin cells of the suprarenal gland.

The axons of postganglionic neurones are unmyelinated and generally longer than those of preganglionic neurones, an exception being some of those that innervate pelvic viscera. Postganglionic axons are distributed to target organs in various ways. Those from a ganglion of the sympathetic trunk may return to the spinal nerve of preganglionic origin through a grey ramus communicans, which usually joins the nerve just proximal to the white ramus, and are then distributed through ventral and dorsal spinal rami to blood vessels, sweat glands, hairs, etc., in their zone of supply. Segmental areas vary in extent and overlap considerably and the extent of innervation of different effector systems, e.g. vasomotor, sudomotor, etc., by a particular nerve may differ (a single preganglionic fibre probably synapses with the postganglionic neurones in only one effector system). Alternatively, postganglionic fibres can pass in a medial branch of a ganglion direct to particular viscera, or innervate adjacent blood vessels, or pass along them externally to their peripheral distribution. They may ascend or descend before leaving the sympathetic trunk as described above. Many fibres are distributed along arteries and ducts as plexuses to distant effectors, e.g. the internal carotid nerve, a continuation of the sympathetic trunk, issues from the cranial pole of the superior ganglion and accompanies the internal carotid artery through its canal into the cranial cavity.

The principal neurotransmitter released by postganglionic sympathetic neurones is noradrenaline (norepinephrine). The sympathetic system has a much wider distribution than the parasympathetic system: it innervates all sweat glands, the arrector pili muscles, the muscular walls of many blood vessels, the heart, lungs and respiratory tree, the abdominopelvic viscera, the oesophagus, the muscles of the iris, and the non-striated muscle of the urogenital tract, eyelids and elsewhere. Postganglionic sympathetic fibres that return to the spinal nerves are vasoconstrictor to blood vessels, secretomotor to sweat glands and motor to the arrector pili muscles within their dermatomes. Most, if not all, peripheral nerves contain postganglionic sympathetic fibres. Those reaching the viscera are concerned with general vasoconstriction, bronchial and bronchiolar dilation, modification of glandular secretion, pupillary dilation, inhibition of gastrointestinal muscle contraction, etc.

Sympathetic trunk

The sympathetic trunk is a ganglionated nerve cord that extends on the side of the vertebral column from the cranial base to the coccyx. The ganglia are joined to spinal nerves by short connecting nerves called white and grey rami communicantes. Preganglionic axons join the trunk through the white rami communicantes, while postganglionic axons leave the trunk in the grey rami. In the thorax, the trunks are anterior to the heads of the ribs, in the abdomen they lie anterolateral to the bodies of the lumbar vertebrae, and in the pelvis they are anterior to the sacrum and medial to the anterior sacral foramina. Anterior to the coccyx the two trunks meet in a single, median, terminal ganglion.

Cervical sympathetic system

In the neck, each sympathetic trunk lies posterior to the carotid sheath and anterior to the transverse processes of the cervical vertebrae. The cervical sympathetic trunk lies on the prevertebral fascia behind the carotid sheath and contains three interconnected ganglia: the superior, middle and inferior (stellate or cervicothoracic) (see Figs 35.17–35.18). There may occasionally, however, be two or four ganglia. The cervical sympathetic ganglia send grey rami communicantes to all the cervical spinal nerves but receive no white rami communicantes from them. Their spinal preganglionic fibres emerge in the white rami communicantes of the upper five thoracic spinal nerves (mainly the upper three), and ascend in the sympathetic trunk to synapse in the cervical ganglia. In their course, the grey rami communicantes may pierce longus capitis or scalenus anterior.

Superior cervical ganglion

The superior cervical ganglion is the largest of the three ganglia (see Fig. 35.17). It lies on the transverse processes of the second and third cervical vertebrae and is probably formed from four fused ganglia, judging by its grey rami communicantes to the upper four cervical spinal nerves. The internal carotid artery within the carotid sheath is anterior, and longus capitis is posterior. The lower end of the ganglion is united by a connecting trunk to the middle cervical ganglion. Postganglionic branches are distributed in the internal carotid nerve, which ascends with the internal carotid artery into the carotid canal to enter the cranial cavity, and in lateral, medial and anterior branches. They supply vasoconstrictor and sudomotor nerves to the face and neck, dilator pupillae and smooth muscle in the eyelids and orbitalis.

Lateral branches

The lateral branches of the superior cervical ganglion are grey rami communicantes to the upper four cervical spinal nerves and to some of the cranial nerves. Branches pass to the inferior vagal ganglion, the hypoglossal nerve, the superior jugular bulb and associated jugular glomus or glomera, and to the meninges in the posterior cranial fossa. Another branch, the jugular nerve, ascends to the cranial base and divides into two; one part joins the inferior glossopharyngeal ganglion and the other joins the superior vagal ganglion.

Medial branches

The medial branches of the superior cervical ganglion are the laryngopharyngeal and cardiac branches. The laryngopharyngeal branches supply the carotid body and pass to the side of the pharynx, joining glossopharyngeal and vagal rami to form the pharyngeal plexus. A cardiac branch arises by two or more filaments from the lower part of the superior cervical ganglion and occasionally receives a twig from the trunk between the superior and middle cervical ganglia. It is thought to contain only efferent fibres, the preganglionic outflow being from the upper thoracic segments of the spinal cord, and to be devoid of pain fibres from the heart. It descends behind the common carotid artery, anterior to longus colli, and crosses anterior to the inferior thyroid artery and recurrent laryngeal nerve. The courses on the two sides then differ. The right cardiac branch usually passes posterior, but sometimes anterior, to the subclavian artery and runs posterolateral to the brachiocephalic trunk to join the deep (dorsal) part of the cardiac plexus behind the aortic arch. It has other sympathetic connections. About mid-neck, it receives filaments from the external laryngeal nerve. Inferiorly, one or two vagal cardiac branches join it. As it enters the thorax, it is joined by a filament from the recurrent laryngeal nerve. Filaments from the nerve also communicate with the thyroid branches of the middle cervical ganglion. The left cardiac branch, in the thorax, is anterior to the left common carotid artery and crosses anterior to the left side of the aortic arch to reach the superficial (ventral) part of the cardiac plexus. It may descend on the right of the aorta to end in the deep (dorsal) part of the cardiac plexus. It communicates with the cardiac branches of the middle and inferior cervical sympathetic ganglia and sometimes with the inferior cervical cardiac branches of the left vagus nerve, and forms a plexus on the ascending aorta with branches from these mixed nerves

Anterior branches

The anterior branches of the superior cervical ganglion ramify on the common and external carotid arteries and the branches of the external carotid, and form a delicate plexus around each, in which small ganglia are occasionally found. The plexus around the facial artery supplies a filament to the submandibular ganglion; the plexus on the middle meningeal artery sends one ramus to the otic ganglion and another, the external petrosal nerve, to the facial ganglion. Many of the fibres coursing along the external carotid and its branches ultimately leave them to travel to facial sweat glands via branches of the trigeminal nerve.

Middle cervical ganglion

The middle cervical ganglion is the smallest of the three cervical sympathetic ganglia and is occasionally absent, in which case it may be replaced by minute ganglia in the sympathetic trunk or may be fused with the superior ganglion. It is usually found at the level of the sixth cervical vertebra, anterior or just superior to the inferior thyroid artery, or it may adjoin the inferior cervical ganglion. It probably represents a coalescence of the ganglia of the fifth and sixth cervical segments, judging by its postganglionic rami, which join the fifth and sixth cervical spinal nerves (but sometimes also the fourth and seventh). It is connected to the inferior cervical ganglion by two or more very variable cords. The posterior cord usually splits to enclose the vertebral artery, while the anterior cord loops down anterior to, and then below, the first part of the subclavian artery, medial to the origin of its internal thoracic branch, and supplies rami to it. This loop is the ansa subclavia and is frequently multiple, lies in close contact with the cervical pleura, and typically connects with the phrenic nerve, and sometimes with the vagus nerve (see Fig. 35.18).

The middle cervical ganglion gives off thyroid and cardiac branches. The thyroid branches accompany the inferior thyroid artery to the thyroid gland. They communicate with the superior cardiac, external laryngeal and recurrent laryngeal nerves, and send branches to the parathyroid glands. Fibres to both glands are largely vasomotor but some reach the secretory cells. The cardiac branch, the largest sympathetic cardiac nerve, arises either from the ganglion itself or more often from the sympathetic trunk cranial or caudal to it. On the right side, it descends behind the common carotid artery and anterior or posterior to the subclavian artery, to the trachea, where it receives a few filaments from the recurrent laryngeal nerve before joining the right half of the deep (dorsal) part of the cardiac plexus. In the neck, it connects with the superior cardiac and recurrent laryngeal nerves. On the left side, the cardiac nerve enters the thorax between the left common carotid and subclavian arteries to join the left half of the deep (dorsal) part of the cardiac plexus. Fine branches from the middle cervical ganglion also pass to the trachea and oesophagus.

Inferior (cervicothoracic/stellate) ganglion

The inferior cervical ganglion (cervicothoracic/stellate) is irregular in shape and much larger than the middle cervical ganglion (see Figs 35.18, 48.16). It is probably formed by a fusion of the lower two cervical and first thoracic segmental ganglia, sometimes including the second and even third and fourth thoracic ganglia. The first thoracic ganglion may be separate, leaving an inferior cervical ganglion above it. The sympathetic trunk turns backwards at the junction of the neck and thorax, and so the long axis of the cervicothoracic ganglion becomes almost anteroposterior. The ganglion lies on or just lateral to the lateral border of longus colli between the base of the transverse process of the seventh cervical vertebra and the neck of the first rib (which are both posterior to it). The vertebral vessels are anterior, and the ganglion is separated from the posterior aspect of the cervical pleura inferiorly by the suprapleural membrane. The costocervical trunk of the subclavian artery branches near the lower pole of the ganglion, and the supreme intercostal artery is lateral.

A small vertebral ganglion may be present on the sympathetic trunk anterior or anteromedial to the origin of the vertebral artery and directly superior to the subclavian artery. When present, it may provide the ansa subclavia. It is also joined to the inferior cervical ganglion by fibres enclosing the vertebral artery and is usually regarded as a detached part of the middle cervical or inferior cervical ganglion. Like the middle cervical ganglion, it may supply grey rami communicantes to the fourth and fifth cervical spinal nerves. The inferior cervical ganglion sends grey rami communicantes to the seventh and eighth cervical and first thoracic spinal nerves, and gives off a cardiac branch, branches to nearby vessels and sometimes a branch to the vagus nerve.

The grey rami communicantes to the seventh cervical spinal nerve vary from one to five (two being the usual number). A third often ascends medial to the vertebral artery in front of the transverse process of the seventh cervical vertebra. It connects with the seventh cervical nerve, and sends a filament upwards through the transverse foramen of the sixth cervical vertebra in company with the vertebral vessels to join the sixth cervical spinal nerve as it emerges from the intervertebral foramen. An inconstant ramus may traverse the transverse foramen of the seventh cervical vertebra. Grey rami to the eighth cervical spinal nerve vary from three to six in number.

The cardiac branch descends behind the subclavian artery and along the anterior aspect of the trachea to the deep cardiac plexus. Behind the artery, it connects with the recurrent laryngeal nerve and the cardiac branch of the middle cervical ganglion (the latter is often replaced by fine branches of the inferior cervical ganglion and ansa subclavia).

The branches to blood vessels form plexuses on the subclavian artery and its branches. The subclavian supply is derived from the inferior cervical ganglion and ansa subclavia, and typically extends to the first part of the axillary artery, although a few fibres may extend further. An extension of the subclavian plexus to the internal thoracic artery may be joined by a branch of the phrenic nerve.

Within the foramina transversaria and intertransverse spaces, the cervical grey rami communicantes form intersegmental arcades as they communicate with one another and the ventral rami of the upper five or six cervical spinal nerves. These arcades accompany the second part of the vertebral artery and create the appearance of a long nerve known as the vertebral nerve. Fine filaments from this nerve and the grey rami communicantes form the vertebral plexus on the surface of the vertebral artery. This plexus contains not only sympathetic efferent fibres but also somatic sensory fibres from the adventitia of the artery with cell bodies in the cervical dorsal root ganglia. The vertebral nerve sends filaments to the posterolateral corners of the cervical intervertebral discs (Bogduk et al 1988), and gives rise to the meningeal branches (sinuvertebral nerves) at each cervical segment. The vertebral plexus, which contains some neuronal cell bodies, continues into the skull along the vertebral and basilar arteries and their branches as far as the posterior cerebral artery, where it meets a plexus from the internal carotid artery. The plexus on the inferior thyroid artery reaches the thyroid gland and connects with the recurrent and external laryngeal nerves, the cardiac branch of the superior cervical ganglion and the common carotid plexus.

Horner's syndrome Any condition or injury that destroys the sympathetic trunk ascending from the thorax through the neck into the face results in Horner's syndrome (Bernard–Horner syndrome, oculosympathetic palsy), characterized by a drooping eyelid (ptosis), sunken globe (enophthalmos), narrow palpebral fissure, contracted pupil (meiosis), and vasodilation and lack of thermal sweating (anhydrosis) of the face on the affected side. Classically, this is seen in patients with bronchial carcinomas that have invaded the sympathetic trunk and it is a recognized complication of cervical sympathectomy or a radical neck dissection. Avulsion of the first thoracic nerve from the spinal cord may be diagnosed by development of the syndrome after closed traction lesion of the supraclavicular brachial plexus. Congenital Horner's syndrome has been reported in association with ipsilateral internal carotid artery agenesis (Fons et al 2009). Special features of congenital Horner's syndrome are unilateral straight hair and abnormalities of iris pigmentation in one or both eyes (heterochromia iridis or heterochromia iridum), usually inherited as an autosomal dominant trait and attributed to disruption of the postganglionic sympathetic pathway producing a neurotropic dysgenesis of iris melanocytes (Rennie 2011). Connections between the recurrent laryngeal nerve, the vagus and cervical sympathetic have been linked with Horner's syndrome complicating thyroidectomy.

Thoracic sympathetic system

The left and right thoracic sympathetic trunks and associated ganglia (commonly 11 in number) sit posterior to the costal part of the parietal pleura on either side of the vertebral column. The majority of the thoracic sympathetic ganglia lie anterior to the head of a rib; the first thoracic and inferior cervical ganglia are fused, and the inferior two or three thoracic ganglia are often located lateral to their correspondingly numbered vertebral bodies (see Fig. 56.6). A tumour of the superior pulmonary sulcus (apex of lung) may compress the ventral ramus of the first thoracic spinal nerve, the cervicothoracic ganglion or the sympathetic trunk (see Fig. 54.2) resulting in a loss of sympathetic innervation to the ipsilateral side of the head (Horner's syndrome) (Nikolaos et al 2014) and pain radiating to the medial aspect of the ipsilateral forearm (Bruzzi et al 2008).

Preganglionic sympathetic axons originate from neuronal somata in the intermediolateral nucleus (lateral horn) of the spinal cord from T1 to L2. They travel initially with the corresponding ventral roots (rami) and leave the latter as white rami communicantes to enter the adjacent sympathetic ganglion in the sympathetic trunk. Their targets vary; some synapse in the sympathetic ganglion that they enter, whereas others ascend or descend in the sympathetic trunk to synapse in cervical or lumbar ganglia, respectively. Many of the preganglionic axons that originate in the lower thoracic spinal segments (T5–T12) do not synapse locally but enter the abdominal cavity as the thoracic splanchnic nerves. These nerves pass through the posterior mediastinum and respiratory diaphragm to enter the abdominal cavity where they synapse either in prevertebral ganglia that surround the origin of the major visceral arteries arising from the abdominal aorta, e.g. the coeliac and superior mesenteric ganglia, or around the medullary chromaffin cells of the suprarenal gland. Axons destined for the cervical ganglia are mainly derived from preganglionic neurones in the first thoracic spinal nerve.

Greater thoracic splanchnic nerve

On each side, the greater thoracic splanchnic nerve is derived from the medial, branches of the fifth to ninth thoracic ganglia. It gives off branches to the descending thoracic aorta and enters the abdomen through the fibres of the ipsilateral crus of the respiratory diaphragm, on which it descends anteroinferiorly. The main trunk of the nerve enters the superior aspect of the coeliac ganglion, where most of the preganglionic fibres synapse (but not those destined for the medulla of the suprarenal gland).

Lesser thoracic splanchnic nerve

On each side, the lesser thoracic splanchnic nerve is derived from the medial branches of the tenth and eleventh (or ninth and tenth) thoracic ganglia. It enters the abdomen running through the most inferior fibres of the ipsilateral crus of the respiratory diaphragm or under the medial arcuate ligament, and then lies on the crus as it runs anteroinferiorly. The trunk of the nerve joins the aorticorenal ganglion and may give branches to the lateral aspect of the coeliac ganglion. It occasionally joins the greater and least splanchnic nerves as a single splanchnic nerve.

Least thoracic splanchnic nerve

On each side, the least thoracic splanchnic nerve is derived from the medial branches of the eleventh and/or twelfth thoracic ganglion. It enters the abdomen medial to the sympathetic trunk under the medial arcuate ligament of the respiratory diaphragm and runs inferiorly to join the renal plexus. The trunk of the nerve enters the aorticorenal ganglion and may give branches to the lateral aspect of the coeliac ganglion. It is sometimes part of the lesser splanchnic nerve, when it forms a twig that enters the renal plexus just below the aorticorenal ganglion.

The thoracic splanchnic nerves show considerable individual variation in their origin and distribution (Loukas et al 2010). For example, the greater splanchnic nerve can receive a contribution from the fourth or tenth thoracic ganglion of the sympathetic trunk or originate only from the sixth to ninth ganglia.

Lumbar sympathetic system

The lumbar part of each sympathetic trunk usually contains four ganglia lying on the anterolateral aspects of the lumbar vertebrae along the medial margin of psoas major (see Figs 59.2–59.4) (Murata et al 2003). Superiorly, it is continuous with the thoracic part of the sympathetic trunk posterior to the medial arcuate ligament. Inferiorly, it passes posterior to the common iliac vessels and is continuous with the sacral part of the sympathetic trunk. On the right side, it lies posterior to the inferior vena cava; on the left, it is posterior to the lateral aortic nodes. It is anterior to most of the lumbar vessels but may pass behind some lumbar veins.

On each side, the first, second and sometimes the third lumbar ventral rami are connected to the lumbar part of the sympathetic trunk by white rami communicantes. All lumbar ventral rami are joined near their origins by long, slender, grey rami communicantes from the four lumbar ganglia. Their arrangement is irregular: one ganglion can give rami to two or three lumbar ventral rami, one lumbar ventral ramus can receive rami from two ganglia, or grey rami can leave the sympathetic trunk between ganglia (Murata et al 2003).

Somatic and vascular branches

Sympathetic nerve branches accompany the lumbar arteries round the sides of the vertebral bodies, medial to the fibrous arches to which psoas major is attached, to provide sympathetic innervation to the segmental distribution of the lumbar arteries. Branches from the lumbar ganglia innervate the abdominal aorta and common, external and internal iliac arteries, forming delicate nerve plexuses that extend along the vessels. Other postganglionic sympathetic nerves to vessels and skin travel with somatic nerves. Thus, the femoral nerve carries vasoconstrictor sympathetic nerves to the femoral artery and its branches in the thigh, as well as sympathetic fibres in its cutaneous branches. Postganglionic fibres travelling with the obturator nerve supply the obturator artery and a variable patch of skin of the medial thigh. Sympathetic denervation of vessels in the lower limb can occur by removing or ablating the proximal three lumbar ganglia and intervening parts of the sympathetic trunk; this procedure can be useful for treating some varieties of vascular insufficiency of the lower limb.

Lumbar splanchnic nerves

Four lumbar splanchnic nerves pass as medial branches from the ganglia to join the coeliac, inferior mesenteric and superior hypogastric plexuses (see Fig. 59.4). The first lumbar splanchnic nerve, from the first ganglion of the lumbar part of the sympathetic trunk, gives branches to the coeliac, renal and inferior mesenteric plexuses. The second lumbar splanchnic nerve joins the inferior part of the intermesenteric or inferior mesenteric plexus. The third lumbar splanchnic arises from the third or fourth ganglion and joins the superior hypogastric plexus. The fourth lumbar splanchnic nerve from the lowest ganglion joins the distal part of the superior hypogastric plexus, or the hypogastric nerves. It is important to note that lumbar splanchnic nerves contribute to the superior and inferior hypogastric plexuses and therefore to the innervation of the neck of the urinary bladder, ductus deferens and prostate, among other structures. Injury to these nerves, e.g. during aortoiliac surgery, can result in sexual dysfunction.

Pelvic sympathetic system

The sacral part of the sympathetic trunk supplies the pelvic organs and vascular system. It usually consists of four or five interconnected ganglia located medial or anterior to the anterior sacral foramina beneath the presacral fascia (Oh et al 2004) (see Fig. 71.11). Occasionally, one or two coccygeal ganglia are present. The first sacral ganglion is the largest and succeeding ganglia become progressively smaller (Blaszczyk 1981). The sacral sympathetic trunk is often asymmetric, with absent or fused ganglia, and cross-communications between sides are frequent. Each ganglion sends at least one grey ramus communicans to its adjacent spinal nerve but up to eleven such branches from a single ganglion have been reported (Potts 1925).

Superiorly, the sacral part of the sympathetic trunk is continuous with the lumbar part of the sympathetic trunk, and preganglionic fibres descend from the distal lumbar spinal cord segments via this route. The right and left trunks converge distal to the most inferior ganglia and unite to form a solitary retroperitoneal structure, the ganglion impar (ganglion of Walther), which lies at a variable level between the sacrococcygeal joint and the tip of the coccyx; it is occasionally paired, unilateral or absent (Oh et al 2004). Grey rami communicantes pass from the ganglia to sacral and coccygeal spinal nerves and there are no white rami communicantes. Medial branches connect across the midline, and twigs from the first two ganglia join the inferior hypogastric plexus or the hypogastric nerve. Other branches form a plexus on the median sacral artery.

Nociceptive afferents from the perineum and terminal urogenital regions pass to the ganglion impar and the sacral parasympathetic trunks: anaesthetic blockade of the ganglion impar can be used to treat intractable perineal pain carried by visceral afferent fibres in patients with pelvic cancers (Toshniwal et al 2007).

Vascular branches

Preganglionic fibres for the vessels supplying the pelvis and lower limb are derived from the lower three thoracic and upper two or three lumbar spinal cord segments. They reach the lower thoracic and upper lumbar ganglia through white rami communicantes and descend through the sympathetic trunk to synapse in the lumbar ganglia. Postganglionic fibres pass from these ganglia via grey rami communicantes to the second, third and fourth lumbar ventral rami and then to the femoral nerve, which carries them to the femoral artery and its branches. Some fibres descend through the lumbar ganglia to synapse in the upper two or three sacral ganglia, from which postganglionic axons pass through grey rami communicantes to the roots of the sacral plexus. Those in the pudendal and superior and inferior gluteal nerves accompany the arteries of the same name to the gluteal and perineal tissues; branches can also supply the pelvic nodes. Those joining the tibial nerve are carried to the popliteal artery and are distributed via its branches to the leg and foot.

Sympathetic denervation of vessels in the lower limb is used, rarely, for treating vascular insufficiency of the lower limb; it can be effected by removing or ablating the upper three lumbar sympathetic ganglia and the intervening parts of the sympathetic trunk.

Sacral splanchnic nerves

Sacral splanchnic nerves pass directly from the ganglia of the sacral part of the sympathetic trunk to the inferior hypogastric plexus and, from there, to pelvic viscera; they usually arise from the first two sacral ganglia.

Autonomic innervation of the limbs

The autonomic nerve supply to the limbs is exclusively sympathetic. The preganglionic sympathetic inflow to the upper limb is derived from neurones in the intermediolateral nucleus of spinal cord segments from T2 to T6/7. Myelinated preganglionic axons pass from the spinal nerves to the thoracic sympathetic trunk via white rami communicates and pass up the trunk to the middle cervical and inferior cervical (stellate or cervicothoracic) ganglia, where they relay. The unmyelinated postganglionic fibres are distributed by grey rami communicantes to the nerves of origin of the brachial plexus; innervation is particularly rich in the palmar skin of the hand and in the skin of the axilla. C5 and C6 receive grey rami from the middle cervical ganglion; C7 and C8 receive grey rami from the inferior cervical ganglion; T1 not only receives a grey ramus from the inferior cervical ganglion but also contributes a white ramus to it (see Fig. 48.16). Interruption of this white ramus is one cause of Horner's (Bernard–Horner) syndrome.

The preganglionic sympathetic outflow to the lower limb is derived from neurones in the intermediolateral nucleus of spinal cord segments T10–T12 and L1, L2. Fibres pass in white rami communicantes to the sympathetic trunk and synapse in the lumbar and sacral ganglia. Postganglionic fibres pass in grey rami communicantes to enter the lumbar and sacral plexuses; many are distributed to the skin via the cutaneous branches of the nerves derived from these plexuses. Blood vessels to the lower limb receive their sympathetic nerve supply via adjacent peripheral nerves. Postganglionic fibres accompanying the iliac arteries are destined mainly for the pelvis but may supply vessels in the proximal thigh

PARASYMPATHETIC NERVOUS SYSTEM

Preganglionic parasympathetic neurones are located in the Edinger–Westphal and superior and inferior salivatory nuclei in the brainstem (see Fig. 28.3) and in the intermediate grey matter of the second to fourth sacral segments of the spinal cord. Their axons, which are myelinated, emerge from the CNS only in the oculomotor, facial, glossopharyngeal and vagus nerves, and as the pelvic splanchnic nerves in the second to fourth sacral spinal nerves. Preganglionic parasympathetic neurones are cholinergic. The somata of postganglionic parasympathetic neurones are mostly sited distant from the CNS, either in discrete ganglia located near the structures innervated, or dispersed in the walls of viscera.

Cranial part of the parasympathetic system

The cranial part of the parasympathetic system contains four small paired peripheral ganglia, ciliary, pterygopalatine, submandibular and otic, in which preganglionic axons relay. (These efferent parasympathetic ganglia are unlike the trigeminal, facial, glossopharyngeal and vagal sensory ganglia, all of which are concerned exclusively with afferent impulses and contain the cell bodies of sensory neurones.) The cranial parasympathetic ganglia are also traversed by afferent fibres, postganglionic sympathetic fibres and, in the case of the otic ganglion, by branchial efferent fibres; however, none of these fibres synapses in the ganglia. Postganglionic parasympathetic fibres are usually unmyelinated and shorter than their counterparts in the sympathetic system because the ganglia in which the parasympathetic fibres synapse are either in or near the viscera they supply. Postganglionic parasympathetic neurones are cholinergic. In the head, parasympathetic fibres are secretomotor to the lacrimal and parotid, submandibular and sublingual salivary glands and innervate intraocular smooth muscle (sphincter pupillae and the ciliary muscle).

Otic ganglion

The otic ganglion is a small (major diameter 3–4 mm), oval, flat reddish-grey ganglion situated just below the foramen ovale. It is a peripheral parasympathetic ganglion related topographically to the mandibular nerve but connected functionally with the glossopharyngeal nerve (see Fig. 42.11). Near its junction with the trigeminal motor root, the mandibular nerve lies lateral to the ganglion, tensor veli palatini lies medially, separating the ganglion from the cartilaginous part of the pharyngotympanic tube, and the middle meningeal artery is posterior to the ganglion. The otic ganglion usually surrounds the origin of the nerve to medial pterygoid. It has three roots, parasympathetic motor, sympathetic and sensory: only the parasympathetic fibres relay in the ganglion (see Fig. 33.7). The parasympathetic fibres arise from cell bodies in the inferior salivatory nucleus and travel in the lesser petrosal branch of the glossopharyngeal nerve. The lesser petrosal nerve runs intracranially in the middle cranial fossa on the anterior surface of the petrous temporal bone and passes through either the foramen ovale or the sphenopetrosal fissure or the innominate canal of Arnold (a canal in the greater wing of the sphenoid close to the foramen spinosum), to join the otic ganglion where it synapses. Postganglionic fibres pass by a communicating branch to the auriculotemporal nerve to reach the parotid gland. The sympathetic root arises from a plexus on the middle meningeal artery. It contains postganglionic vasomotor fibres from the superior cervical sympathetic ganglion that pass through the otic ganglion and join the parasympathetic fibres to travel via the auriculotemporal nerve to the parotid gland. Sensory fibres from the parotid gland are derived from the auriculotemporal nerve. Clinical observations suggest that in humans the parotid gland also receives secretomotor parasympathetic fibres through the chorda tympani.

Branches

The otic ganglion is connected by branches to the chorda tympani nerve and the nerve of the pterygoid canal. These branches may form an additional pathway by which gustatory fibres from the anterior two-thirds of the tongue reach the geniculate ganglion without passing through the middle ear: they do not synapse in the otic ganglion. Motor branches to tensor veli palatini and tensor tympani, derived from the nerve to medial pterygoid, pass through the ganglion without synapsing. (For further reading, see Senger et al (2014).)

Ciliary ganglion

The ciliary ganglion is a parasympathetic ganglion concerned with the innervation of the ciliary muscle and sphincter pupillae. It is a small, flat, reddish-grey swelling, 1–2 mm in diameter, connected to the nasociliary nerve, and located near the apex of the orbit in loose fat approximately 1 cm in front of the medial end of the superior orbital fissure. It lies between the optic nerve and lateral rectus, usually lateral to the ophthalmic artery. Its neurones, which are multipolar, are larger than those found in typical autonomic ganglia; a very small number of more typical neurones are also present.

Its connections or roots (motor, sensory and sympathetic) enter or leave the ganglion posteriorly (see Fig. 44.18). Eight to ten delicate filaments, termed the short ciliary nerves, emerge anteriorly from the ganglion, arranged in two or three bundles, the lower being larger. They run forwards sinuously with the ciliary arteries, above and below the optic nerve, and divide into 15–20 branches that pierce the sclera around the optic nerve and run in small grooves on the internal scleral surface. They convey parasympathetic, sympathetic and sensory fibres between the eyeball and the ciliary ganglion; only the parasympathetic fibres synapse in the ganglion.

The parasympathetic root, derived from the branch of the oculomotor nerve to the inferior oblique, consists of preganglionic fibres from the Edinger–Westphal nucleus, which relay in the ganglion. Postganglionic fibres travel in the short ciliary nerves to the sphincter pupillae and ciliary muscle. More than 95% of these fibres supply the ciliary muscle, which is much the larger muscle in volume.

The sympathetic root contains fibres from the plexus around the internal carotid artery within the cavernous sinus. These postganglionic fibres, derived from the superior cervical ganglion, form a fine branch that enters the orbit through the superior orbital fissure inside the common tendinous ring. The fibres may pass directly to the ganglion, or may join the nasociliary nerve and travel to the ganglion in its sensory root; either way, they traverse the ganglion without synapsing to emerge into the short ciliary nerves and are distributed to the blood vessels of the eyeball. Sympathetic fibres innervating dilator pupillae may sometimes travel via the short ciliary nerves (rather than the more usual route via the ophthalmic, nasociliary and long ciliary nerves).

The sensory fibres that pass through the ciliary ganglion are derived from the nasociliary nerve. They enter the short ciliary nerves and carry sensation from the cornea, the ciliary body and the iris.

Pterygopalatine ganglion

The pterygopalatine ganglion, known colloquially as the 'ganglion of hay fever', is the largest of the peripheral parasympathetic ganglia, and is well protected, deep in the pterygopalatine fossa. Immediately anterior to the pterygoid canal, the ganglion lies below and medial to the foramen rotundum and the maxillary nerve and lateral to the sphenopalatine foramen (see Fig. 38.30B). It is flattened and reddish-grey in colour and lies just below the maxillary nerve as it crosses the pterygopalatine fossa. The majority of the 'branches' of the ganglion are connected with it morphologically but not functionally, because they are primarily sensory branches of the maxillary nerve and so pass through the ganglion without synapsing to enter the ganglionic branches of the maxillary nerve.

The deep petrosal nerve (postganglionic sympathetic fibres) and the greater petrosal nerve (preganglionic parasympathetic fibres) converge to form the nerve of the pterygoid canal (the Vidian nerve in the Vidian canal). This nerve is an important landmark to the petrous portion of the internal carotid artery, and rarely can be transected to treat intractable rhinorrhoea. The pterygoid canal enters the pterygopalatine fossa, where the nerve of the pterygoid canal joins the pterygopalatine ganglion posteriorly and the parasympathetic fibres synapse on postganglionic neurones.

Some postganglionic parasympathetic fibres may join the maxillary nerve via a ganglionic branch and then travel via its zygomatic and zygomaticotemporal branches to the lacrimal gland, but most are thought to travel by orbital branches to the gland. The parasympathetic supply to the preocular part of the central artery of the retina is believed to be derived mainly from the pterygopalatine ganglion and is vasodilatory. Preganglionic secretomotor fibres of uncertain origin also travel in the nerve of the pterygoid canal and synapse in the pterygopalatine ganglion: postganglionic fibres are distributed to palatine, pharyngeal and nasal mucous glands via palatine and nasal branches of the maxillary nerve.

Postganglionic sympathetic fibres pass through the ganglion without synapsing. They arise in the superior cervical ganglion and travel via the internal carotid plexus and deep petrosal nerve to enter the pterygopalatine ganglion within the nerve of the pterygoid canal: they supply blood vessels and orbitalis. General sensory fibres destined for distribution via orbital, nasopalatine, superior alveolar, palatine and pharyngeal branches of the maxillary division of the trigeminal nerve also run through the ganglion without synapsing.

Orbital branches of the pterygopalatine ganglion

Several rami orbitales arise dorsally from the pterygopalatine ganglion and enter the orbit through the inferior orbital fissure. Branches leave the orbit through the posterior ethmoidal air sinus. There is strong experimental evidence from animal studies that postganglionic parasympathetic branches pass directly to the lacrimal gland, ophthalmic artery and choroid.

Lacrimation reflex The lacrimal gland is innervated by secretomotor postganglionic parasympathetic fibres from the pterygopalatine ganglion. They reach the gland either via zygomatic and lacrimal branches of the maxillary nerve, or by passing directly from the ganglion (Ruskell 2004). Postganglionic sympathetic fibres from the superior cervical ganglion supply the lacrimal gland and may be involved in the regulation of blood flow and the modulation of gland secretion (Dartt 2009). The lacrimation reflex produces a significant increase in tear volume and is elicited by thermal, mechanical or chemical stimulation of polymodal nociceptors in the conjunctiva and cornea (Situ and Simpson 2010). The afferent limb of the reflex involves branches of the ophthalmic nerve, with an additional contribution from the infraorbital nerve if the conjunctiva of the lower eyelid is involved. Corneal afferents travelling in these nerves terminate in the nucleus of the spinal tract of the trigeminal nerve: experimental tract tracing studies in animals have implicated the transition between the trigeminal subnuclei caudalis and interpolaris as an important area that projects to preganglionic parasympathetic neurones lying close to or within the superior salivatory nucleus and to the facial motor nucleus, both regions involved in the efferent limb of the blinking reflex (Meng and Kurose 2013). The neural mechanism for controlling and maintaining basal tear production is less clear. Lacrimation may also occur in response to emotional triggers without any irritation of ocular structures, when it may be accompanied by alterations in the mimetic facial muscles, vocalizations and sobbing (Gračanin et al 2014): emotional lacrimation is thought to be mediated by limbic projections to the superior salivatory nucleus.

Submandibular ganglion

The submandibular ganglion is a small, fusiform body that lies on the upper part of hyoglossus, superior to the deep part of the submandibular gland and inferior to the lingual nerve, to which it is connected by several filaments. The posterior filament is the motor, parasympathetic root that conveys preganglionic fibres from the superior salivatory nucleus in the brainstem via the facial, chorda tympani and lingual nerves to the ganglion, where they synapse. Five or six postganglionic secretomotor branches from the ganglion supply the submandibular gland and its duct, and the sublingual and anterior lingual glands, by travelling either through the anterior filaments that connect the submandibular gland to the lingual nerve or along adjacent blood vessels to their targets. Neuronal cell bodies and small ganglia have been described in the interlobular connective tissue stroma of human submandibular ganglia, close to salivary parenchymal cells and blood vessels (Tosios et al 2010). The sympathetic root is derived from the plexus on the facial artery and consists of postganglionic fibres from the superior cervical ganglion that traverse the submandibular ganglion without synapsing. These fibres are vasomotor to the blood vessels of the submandibular and sublingual glands. Sensory fibres derived from the lingual nerve may also pass through the ganglion.

Parasympathetic components of the vagus nerve

Preganglionic parasympathetic axons destined for the thoracic viscera travel in the pulmonary, cardiac and oesophageal branches of the vagus nerve (see Fig. 56.7) and synapse in minute ganglia in the walls of the target viscera. Axons travelling in cardiac branches join the cardiac plexuses and synapse in ganglia distributed over both atria, the interatrial septum and perinodal subepicardial tissue: when stimulated, they normally slow the cardiac cycle and constrict coronary arteries, although low-level stimulation may increase heart rate. Pulmonary branches contain axons that synapse in ganglia of the pulmonary plexuses: they are motor (bronchoconstrictor) to the circular non-striated muscle fibres of the bronchi and bronchioles, and secretomotor to the mucous glands of the respiratory epithelium.

The parasympathetic neurones that innervate viscera in the abdomen and pelvis lie either in the dorsal nucleus of the vagus nerve or in the intermediolateral grey matter of the second, third and fourth sacral spinal cord segments. The vagus supplies preganglionic parasympathetic innervation to the abdominal viscera as far as the distal transverse colon, i.e. it supplies derivatives of the foregut and midgut. Derivatives of the hindgut are supplied by parasympathetic fibres travelling via the pelvic splanchnic nerves; the overlap between these two supplies is variable. The vagal trunks are derived from the oesophageal plexus and enter the abdomen via the oesophageal hiatus, closely related to the anterior and posterior walls of the abdominal part of the oesophagus (see Fig. 56.6). The anterior vagal trunk is mostly derived from the left vagus and the posterior vagal trunk from the right vagus. The nerves supply the abdominal part of the oesophagus and stomach directly. The anterior vagal trunk gives off a hepatic branch, which innervates the liver and its vasculature, including the gallbladder and bile ducts, and the other structures in the free edge of the lesser omentum (hepatoduodenal ligament). The posterior vagal trunk supplies branches to the coeliac plexus and these fibres frequently constitute the largest portion of the fibres that contribute to the plexus. They arise directly from the posterior vagal trunk and from its gastric branch, and run beneath the peritoneum, deep to the posterior wall of the superior part of the omental bursa, to reach the coeliac plexus. Their synaptic relays with postganglionic neurones are situated in the myenteric (Auerbach's) and submucosal (Meissner's) plexuses in the wall of the hollow viscera.

Pelvic splanchnic nerves

Pelvic splanchnic nerves (nervi erigentes) travel in the ventral rami of the second, third and fourth sacral spinal nerves. They leave the nerves as they exit the anterior sacral foramina and pass in the presacral tissue as a fine network of branches distributed to three principal destinations. Most pass anterolaterally into the inferior hypogastric plexus (see below). Some join the hypogastric nerves and ascend out of the pelvis as far as the superior hypogastric plexus, from where they are distributed with branches of the inferior mesenteric artery. A few run superolaterally in the presacral fascia, over the linea terminalis anterior to the left iliac vessels, and pass directly into the tissue of the retroperitoneum toward the sigmoid and descending colons. The pelvic splanchnic nerves are motor to the smooth muscle of the derivatives of the hindgut and the wall of the urinary bladder, are vasodilator to the erectile tissues of the penis and clitoris, and are secretomotor to the derivatives of the hindgut.

An experimental study of the differential expression of transcription factors in embryonic mice has argued that thoracic and sacral pools of preganglionic neurones share a common sympathetic identity and that the sacral autonomic outflow should therefore be regarded as sympathetic (Espinosa-Medina et al 2016). This controversial view has been challenged (Horn 2018).

AUTONOMIC PLEXUSES

The autonomic nervous system in the thorax consists of the right and left sympathetic trunks and left and right vagus nerves, and the cardiac, oesophageal and pulmonary plexuses (see Figs 56.6–56.7). The autonomic supply to the abdominal and pelvic viscera is via the abdominopelvic part of the sympathetic trunk and the greater, lesser and least splanchnic nerves (sympathetic), and the vagus and pelvic splanchnic nerves (parasympathetic).

The somata of preganglionic sympathetic neurones are located in the intermediolateral grey matter (lamina VII) of the thoracolumbar segments of the spinal cord; those destined for the smooth muscle of the wall of the hollow viscera mostly pass through the sympathetic trunk without synapsing and relay in prevertebral ganglia (coeliac, mesenteric and pelvic). Postganglionic sympathetic fibres are distributed with the branches of the coeliac trunk and mesenteric arteries to three principal targets: the myenteric and submucosal ganglia (causing inhibition); blood vessels (inducing vasoconstriction); and sphincter muscles (inducing contraction). The neuronal somata of preganglionic parasympathetic axons are found in the dorsal nucleus of the vagus nerve in the medulla oblongata and in the second to fourth sacral segments of the spinal cord.

Their main targets in the wall of the hollow viscera are the enteric neurones of the myenteric plexus. The vagus nerve plays a major role in oesophageal propulsion, gastric acid secretion and emptying of the stomach, gallbladder contraction and pancreatic exocrine secretion. Pelvic splanchnic nerves innervate the distal colon and rectum.

There are numerous interconnections between plexuses and ganglia, particularly in the major plexuses around the abdominal aorta and therefore descriptions, as here, are simplifications based on the 'main' supply to each organ (see Fig. 59.2).

Thoracic plexuses

Cardiac plexus

The cardiac plexus has a superficial component inferior to the aortic arch, lying between the arch and the pulmonary trunk, and a deep part between the aortic arch and tracheal bifurcation (see Fig. 57.61). The plexus has coronary, pulmonary, atrial and aortic extensions. The superficial (ventral) part is formed by the cardiac branch of the left superior cervical sympathetic ganglion and the inferior of the two cervical cardiac branches of the left vagus nerve. The deep (dorsal) part is formed by the cardiac branches of the cervical and upper thoracic sympathetic ganglia and of the vagus and recurrent laryngeal nerves. The only cardiac nerves that do not join it are those that join the superficial part of the plexus. Branches from the cardiac plexuses subsequently form the left and right coronary and atrial plexuses.

Pulmonary plexus

The autonomic nervous system (either by direct axonal innervation or circulating neurotransmitter) controls many aspects of airway function, including regulation of airway smooth muscle tone, mucus secretion from submucosal glands and surface epithelial goblet cells, vascular permeability and blood flow (Belvisi 2002). The trachea and bronchi are innervated by branches of the vagus nerves, recurrent laryngeal nerves and sympathetic trunks via the anterior and posterior pulmonary plexuses. The plexuses are interconnected and lie anterior and posterior to the structures of the lung root and hilum (see Figs 56.6–56.7, 57.61). The posterior plexus provides the majority of the autonomic innervation to the lung and is formed by approximately 12 (8–18) branches from the vagus nerve (Weijs et al 2015) and cardiac branches from the second to fifth (or sixth) thoracic sympathetic ganglia. The smaller anterior plexus is formed by 3 (2–4) branches of the vagus nerve and cervical sympathetic cardiac nerves via the superficial and deep parts of the cardiac plexus. Branches of the recurrent laryngeal nerves form a plexus on the membranous posterior wall of the trachea; the plexus primarily innervates the trachea and proximal parts of the main bronchi, with branches to the oesophagus.

Efferent preganglionic parasympathetic nerves from the vagus nerve synapse on small ganglia within the walls of the tracheobronchial tree, likely acting as sites of integration and/or modulation of the input from extrinsic nerves or permitting local control of aspects of airway function by local reflex mechanisms. The predominant contractile innervation of airway smooth muscle is parasympathetic cholinergic, while the primary relaxant innervation of the airways is non-cholinergic (parasympathetic nerves containing nitric oxide synthase and vasoactive intestinal peptide). These parasympathetic nerves are anatomically and physiologically distinct from one another and differentially regulated by reflexes. Stimulation of cholinergic nerves also results in mucus secretion and bronchial vasodilation. Sympathetic-adrenergic nerves play little, if any, role in directly regulating smooth muscle tone in the human airways, although they may control constriction of tracheobronchial blood vessels. Circulating noradrenaline (norepinephrine) can bring about bronchodilation through activation of β-adrenergic receptors in the airways. Extrapulmonary afferents may modulate neurally mediated regulation of airway smooth muscle tone (Canning and Fischer 2001). Vagal innervation is involved in the cough reflex, mucous production and control of bronchial diameter; inadvertent transection of the pulmonary vagal nerves during oesophagectomy may be related to the high incidence of postoperative pneumonia and pulmonary complications following oesophagectomy (Weijs et al 2017); preservation of vagal pulmonary branches is therefore desirable (Weijs et al 2016).

Oesophageal plexus

The oesophageal plexus surrounds the oesophagus below the level of the hila of the lungs (see Fig. 56.6). Preganglionic parasympathetic axons from the vagus and recurrent laryngeal nerves travel to ganglia in the oesophageal wall, either directly or through the oesophageal plexus, and are motor to the smooth muscle in the lower oesophagus and secretomotor to mucous glands in the oesophageal mucosa. Vasomotor sympathetic axons arise from the first to sixth (sometimes fewer) thoracic segments of the spinal cord. Those passing from the more superior cord segments often synapse in the middle and inferior cervical sympathetic ganglia; their postganglionic axons are vasomotor to the vessels of the cervical and superior part of the thoracic oesophagus. Preganglionic axons from the fifth or sixth thoracic spinal cord segments pass directly to the oesophageal plexus or to the coeliac ganglion, where they synapse; postganglionic axons innervate the vessels of the distal oesophagus.

Abdominopelvic autonomic plexuses and ganglia

The abdominopelvic autonomic plexuses are somewhat variable and often fuse or are closely interrelated. The following descriptions encompass their main features (see Figs 59.3–59.4, 73.8).

Coeliac plexus

The coeliac plexus is located at the level of the twelfth thoracic and first lumbar vertebrae. It is a dense network that unites the coeliac ganglia, and surrounds the coeliac trunk and the proximal superior mesenteric artery. It is posterior to the stomach and omental bursa and anterior to the crura of the respiratory diaphragm and the beginning of the abdominal aorta, and lies medial to the suprarenal glands. The plexus and ganglia receive the greater and lesser splanchnic nerves and branches from the vagal trunks. The plexus is in continuity with small branches along adjacent arteries and is connected to the phrenic, splenic, hepatic, superior mesenteric, suprarenal, renal and ovarian/testicular plexuses. Visceral afferent fibres in the coeliac plexus convey pain and other sensations from proximal abdominal viscera. Anaesthesia or ablation of these nerves (coeliac plexus blockade) is sometimes undertaken to treat medically intractable pain from pancreatic disorders.

Coeliac and aorticorenal ganglia

The coeliac ganglia are irregular neural masses, measuring approximately 2 cm across, located between the origin of the coeliac trunk and superior mesenteric artery, medial to the suprarenal glands and anterior to the crura of the respiratory diaphragm (Zhang et al 2006). They vary in number, size, shape and precise location; there are often two, one on each side. The right ganglion is frequently posterior to the inferior vena cava, and the left ganglion often lies posterior to the origin of the splenic artery. The ipsilateral greater splanchnic nerve joins the superior part of each ganglion and the lesser splanchnic nerve joins the inferior part. The most inferior part of each ganglion usually forms a distinct subdivision, the aorticorenal ganglion, which receives the ipsilateral lesser splanchnic nerve and gives origin to most of the renal plexus.

Phrenic plexus

The phrenic plexus is a periarterial extension of the coeliac plexus around the right inferior phrenic artery, adjacent to the right crus of the respiratory diaphragm (Rusu 2006). It contains one or two phrenic ganglia and a definable nerve trunk that connects the coeliac plexus and phrenic nerve: the phrenic ganglion is probably sympathetic (Tubbs et al 2008). The phrenic plexus supplies branches to the suprarenal glands and the respiratory diaphragm.

Superior mesenteric plexus and ganglion

The superior mesenteric plexus lies in the pre-aortic connective tissue posterior to the pancreas, around the origin of the superior mesenteric artery. It is an inferior continuation of the coeliac plexus and includes branches from the posterior vagal trunk and coeliac plexus. Its branches accompany the superior mesenteric artery and its branches. The superior mesenteric ganglion lies superiorly in the plexus, usually above the origin of the superior mesenteric artery.

Intermesenteric plexus

Like other parts of the abdominal aortic autonomic plexus, the intermesenteric plexus is not a discrete structure but is part of a continuous periarterial nerve plexus connected to the ovarian/testicular, inferior mesenteric, iliac and superior hypogastric plexuses. It lies on the lateral and anterior aspects of the aorta, between the origins of the superior and inferior mesenteric arteries, and consists of numerous fine, interconnected nerve fibres and a few ganglia continuous superiorly with the superior mesenteric plexus and inferiorly with the superior hypogastric plexus. It is not well characterized but receives parasympathetic and sympathetic branches from the coeliac plexus and additional sympathetic contributions from the first and second lumbar splanchnic nerves.

Inferior mesenteric plexus

The inferior mesenteric plexus lies around the origin of the inferior mesenteric artery and is distributed along its branches. It is formed predominantly from the aortic plexus, supplemented by sympathetic fibres from the first and second lumbar splanchnic nerves and ascending pelvic parasympathetic fibres from the inferior hypogastric plexus (via the hypogastric nerves and superior hypogastric plexus). Disruption of the inferior mesenteric plexus alone rarely causes clinically significant disturbances of autonomic function.

Superior hypogastric plexus

The superior hypogastric plexus lies anterior to the aortic bifurcation, the left common iliac vein, median sacral vessels, fifth lumbar vertebral body and sacral promontory, and between the common iliac arteries. It lies within extraperitoneal connective tissue in the midline, extending a little to the left. The breadth of the plexus and its constituent nerves varies; appearances range from a reticular-like arrangement to a band-like structure or one or two distinct nerve trunks (Paraskevas et al 2008). The medial attachment of the sigmoid mesocolon and superior limit of the mesorectum lie anterior to the distal part of the plexus, separated from it by a thin layer of loose connective tissue. The plexus is formed by branches from three main sources: the abdominal aortic plexus (sympathetic and parasympathetic), lumbar splanchnic nerves (sympathetic) and pelvic splanchnic nerves (parasympathetic), which ascend from the inferior hypogastric plexus via the right and left hypogastric nerves (Kraima et al 2015). Visceral sensory fibres also pass through the plexus. The hypogastric nerves lie in loose connective tissue just posterolateral to the proximal mesorectum and pass over the linea terminalis medial to the internal iliac vessels. The superior hypogastric plexus conveys branches to the inferior mesenteric plexus and to the ureteric, ovarian/testicular and common iliac nerve plexuses; additional small branches turn abruptly forwards into the proximal mesorectum to travel with the superior anorectal artery.

Inferior hypogastric plexus

The inferior hypogastric plexus lies in the thin extraperitoneal connective tissue on the pelvic side wall anterolateral to the mesorectum. The internal iliac vessels and the attachments of levator ani and obturator internus lie laterally, and the superior vesical and occluded part of the umbilical arteries superiorly. In males, the inferior hypogastric plexus lies posterolaterally, on each side of the seminal glands, prostate and the fundus of the urinary bladder: the point where the ductus deferens crosses the ureter provides an approximate guide to the superior limit of the plexus (Mauroy et al 2003). The proximal border of the plexus lies beneath the peritoneum of the rectovesical pouch and is in contact with the lateral aspect of the fundus of the urinary bladder. The anterior border reaches the posterior aspect of the prostate; at its inferior limit, the cavernous nerves of the penis pass forwards to reach the posterolateral aspect of the prostate (see Fig. 73.8). In females, each plexus lies lateral to the cervix of the uterus, vaginal fornix and the fundus of the urinary bladder, often extending into the broad ligament of the uterus; the proximal limit of the plexus corresponds approximately to the level where the uterine artery crosses the ureter (Azaïs et al 2013).

The inferior hypogastric plexus is formed mainly from pelvic splanchnic (parasympathetic) and sacral splanchnic (sympathetic) branches; a smaller contribution is derived from sympathetic fibres (from the inferior lumbar ganglia) that descend into the plexus from the superior hypogastric plexus via the hypogastric nerves. It gives origin to a complex network of small pelvic branches that supply the pelvic viscera either directly or indirectly via periarterial plexuses. The branches of the inferior hypogastric plexus supply the ductus deferens, seminal glands, prostate, bulbo-urethral glands and penis in males; the ovary, uterine tubes, uterus, cervix of the uterus and vagina in females; and the urinary bladder and distal ureter in both sexes. The plexus plays a key role in continence and sexual function.

Hypogastric nerves

The hypogastric nerves are usually paired nerve bundles but can consist instead of multiple filaments. They contain sympathetic fibres (mostly descending from the superior hypogastric plexus) and parasympathetic fibres (ascending from the inferior hypogastric plexus). The nerves run between the superior and inferior hypogastric plexuses on each side posterior to the presacral fascia, medial to the internal iliac vessels, and lateral to the anterior sacral foramina.

Other autonomic plexuses and ganglia

Additional plexuses are described for abdominopelvic viscera, such as the hepatic and ovarian/testicular plexuses. Each plexus tends to lie around the main arterial supply to the named organ, receive both sympathetic and parasympathetic fibres from one or more of the major autonomic plexuses, and contain at least one ganglion. For example, autonomic ganglia supplying the testis are found around the origin of the testicular arteries from the abdominal aorta and have connections with the renal and intermesenteric plexuses and the first and second lumbar splanchnic nerves (Motoc et al 2010).

ENTERIC NERVOUS SYSTEM

The walls of the hollow viscera are densely innervated by both the enteric nervous system (intrinsic control) and the autonomic nervous system (extrinsic control). The latter is not essential for function, as evidenced by intestinal activity after transplantation of the extrinsically denervated part of the gastrointestinal tract. In contrast, neuropathies affecting the enteric nervous system, such as Hirschsprung's disease, are potentially life-threatening. For a detailed description of the enteric nervous system, see Furness et al (2014).

Intrinsic innervation

The intrinsic innervation of the gastrointestinal tract is derived from enteric neurones distributed throughout its wall in thousands of small ganglia, each consisting of neuronal cell bodies supported by enteric glial cells; it is estimated that there are between 200 and 600 million neurones in the human enteric nervous system. Enteric neurones are derived from neural crest cells and innervate the hollow viscera from oesophagus to anus, together with the pancreas and bile ducts.

Most of the enteric neurones in the wall of the gastrointestinal tract are found in two ganglionated plexuses (see Fig. 59.9). The most extensive of these is the myenteric (Auerbach's) plexus, which consists of a network of nerve fibres and small ganglia lying between the circular and longitudinal layers of the muscularis externa. It runs in continuity from the oesophagus to the anus. The submucosal (Meissner's) plexus has outer and inner components and is present throughout the intestines but is absent or minimal in the oesophagus and stomach (Nagy and Goldstein 2017). Interconnecting, non-ganglionated nerve plexuses lie at various levels in the wall of the gastrointestinal tract, including the lamina propria (mucosal plexus); at the interface between the submucosa and muscularis externa; between the circular and longitudinal muscles (the non-ganglionated part of the myenteric plexus); and within the serosa.

Individual enteric neurones function in one of several ways: as afferent (sensory) nerves responding to mechanical and chemical stimuli; as efferent (motor) nerves innervating epithelial cells (influencing absorption, secretion and/or the release of hormones), smooth muscle (excitatory or inhibitory), arterioles (vasoconstriction or vasodilatation) and lymphoid tissue; or as interneurones that relay and integrate signals. Collectively, they are involved in a hierarchy of enteric reflexes that include local reflexes within the wall of the hollow viscera; reflexes mediated through prevertebral ganglia; and reflexes mediated through the central nervous system (the gut–brain axis). The functions of enteric neurones can be further modulated by local environmental factors, e.g. enteric glia, gut microbiota and feeding state, and by general factors in the host, e.g. the immune system, stress and disease (Brierley and Linden 2014). Pathological states become manifest by abnormal secretion, impaired absorption, disordered gastrointestinal motility and pain.

References

Ahmadian A, Abel N, Dakwar E 2015 Injuries to the nerves of the abdominopelvic region. In: Tubbs RS, Rizk E, Shoja MM et al (eds) Nerves and Nerve Injuries: Volume 2: Pain, Treatment, Injury, Disease and Future Directions. Elsevier Science; Ch. 35, pp. 545–55.

Al-dabbagh AK 2002 Anatomical variations of the inguinal nerves and risks of injury in 110 hernia repairs. Surg Radiol Anat 24:102–7.

Apaydin N 2016 Lumbosacral plexus. In: Tubbs RS, Shoja MM, Loukas M (eds) Bergman's Comprehensive Encyclopedia of Human Anatomical Variation. Hoboken: John Wiley & Sons; Ch. 92, pp. 1114–19.

Aronson AE, Bless DM 2009 Clinical Voice Disorders, 4th ed. New York: Thieme.

Azaïs H, Collinet P, Delmas V et al 2013 Uterosacral ligament and hypogastric nerve anatomical relationship. Application to deep endometriotic nodules surgery. Gynecol Obstet Fertil 41:179–83.

Barnes G, Liang J, Hall S et al 2001 Development of the Fallopian canal in humans – a morphologic and radiologic study. Otol Neurotol 22:931–7.

Beaton LE, Anson BJ 1937 The relationship of the sciatic nerve and of its subdivisions to the piriformis muscle. Anat Rec 70:1–5.

Belvisi MG 2002 Overview of the innervation of the lung. Curr Opin Pharmacol 2:211–15.

Benglis DM, Vanni S, Levi AD 2009 An anatomical study of the lumbosacral plexus as related to the minimally invasive transpsoas approach to the lumbar spine. J Neurosurg Spine 10:139–44.

Benninger B, McNeil J 2010 Transitional nerve: a new and original classification of a peripheral nerve supported by the nature of the accessory nerve (CN XI). Neurol Res Int 2010(2):476018:1–15.

Bielefeldt K, Gebhart GF 2013 Visceral pain: basic mechanisms. In: McMahon SB, Koltzenburg M, Tracey I et al (eds) Wall and Melzack's Textbook of Pain, 6th ed. Philadelphia: Elsevier, Saunders; Ch. 51, pp. 703–17.

Blaszczyk B 1981 Variation of ganglia of the pelvic segment of the sympathetic trunk in human fetuses. Folia Morphol (Warsz) 39:313–26.

Blitzer A, Brin MF, Ramig LO 2009 Neurologic Disorders of the Larynx, 2nd ed. New York: Thieme.

Bogduk N, Windsor M, Inglis A 1988 The innervation of the cervical intervertebral discs. Spine 13:2–8.

Bridger MW, Farkashidy J 1980 The distribution of neuroglia and Schwann cells in the 8th nerve of man. J Laryngol Otol 94:1353–62.

Brierley SM, Linden DR 2014 Neuroplasticity and dysfunction after gastrointestinal inflammation. Nat Rev Gastroenterol Hepatol 11:611–27.

Brown H 2002 Anatomy of the spinal accessory nerve plexus: relevance to head and neck cancer and atherosclerosis. Exp Biol Med 227:570–8.

Bruzzi JF, Komaki R, Walsh GL et al 2008 Imaging of non-small cell lung cancer of the superior sulcus. Part 2: Initial staging and assessment of resectability and therapeutic response. Radiographics 28:561–72.

Camp SJ, Birch R 2011 Injuries to the spinal accessory nerve: a lesson to surgeons. J Bone Joint Surg Br 93:62–7.

Canning BJ, Fischer A 2001 Neural regulation of airway smooth muscle tone. Respir Physiol 125:113–27.

Carpenter MB, Sutin J 1983 Human Neuroanatomy, 8th ed. Baltimore, MD: Williams & Wilkins.

Cernea CR, Ferraz AR, Nishio S et al 1992 Surgical anatomy of the external laryngeal branch of the external laryngeal nerve. Head Neck 14:380–83.

Cesmebasi A, Yadav A, Gielecki J et al 2015 Genitofemoral neuralgia: a review. Clin Anat 28:128–35.

Dartt DA 2009 Neural regulation of lacrimal gland secretory processes: relevance in dry eye diseases. Prog Retin Eye Res 28:155–77.

DaSilva MF, Moore DC, Weiss AP et al 1996 Avoidance of transection of the palmar cutaneous branch of the median nerve in carpal tunnel release. J Hand Surg Am 21(4):644–50.

Davis RA, Anson BJ, Budinger JM et al 1956 Surgical anatomy of the facial nerve and parotid gland based upon a study of 350 cervicofacial halves. Surg Gynecol Obstet 102:385–412.

de Ridder VA, de Lange S, Popta JV 1999 Anatomical variations of the lateral femoral cutaneous nerve and the consequences for surgery. J Orthop Trauma 13:207–11.

Demer JL 2016 Optic nerve sheath as a novel mechanical load on the globe in ocular duction. Invest Ophthalmol Vis Sci 57:1826–38.

Dillow JM, Rosett RL, Petersen TR et al 2013 Ultrasound-guided parasacral approach to the sciatic nerve block in children. Paediatr Anaesth 23:1042–7.

Durham FC, Harrison TS 1962 The surgical anatomy of the superior laryngeal nerve. Surg Gynecol Obstet 118:33–44.

Echigo A, Aok M, Ishiai S et al 2008 The excursion of the median nerve during nerve gliding exercise: an observation with high-resolution ultrasonography. J Hand Ther 21:221–8.

Espinosa-Medina I, Saha O, Boismoreau F et al 2016 The sacral autonomic outflow is sympathetic. Science 354:893–7.

Felix H, Hoffman V, Wright A, Gleeson MJ 1987 Ultrastructural findings on human Scarpa's ganglion. Acta Otolaryngol Suppl 436:85–92.

Fitzgerald MJ, Law ME 1958 The peripheral connexions between the lingual and hypoglossal nerves. J Anat 92:178–88.

Fons C, Vasconcelos M, Vidal M 2009 Agenesis of internal carotid artery in a child with ipsilateral Horner's syndrome. J Child Neurol 24:101–4.

Friedman M, Toriumi DM, Grybauskas V et al 1986 Nonrecurrent laryngeal nerves and their clinical significance. Laryngoscope 96:87–90.

Furlan JC, Brandão LG, Ferraz AR 2002 Prevalence of Galen's anastomosis: an anatomical and comparative study. J Laryngol Otol 116:823–5.

Furness JB, Callaghan BP, Rivera LR et al 2014 The enteric nervous system and gastrointestinal innervation: integrated local and central control. Adv Exp Med Biol 817:39–71.

Garcia-Cosamalon J, del Valle ME, Calavia MG et al 2010 Intervertebral disc, sensory nerves and neurotrophins: who is who in discogenic pain? J Anat 217:1–15.

Gračanin A, Bylsma LM, Vingerhoets AJ 2014 Is crying a self-soothing behavior? Front Psychol 28:502.

Haines DE, Mihailoff GA 2017 Fundamental Neuroscience for Basic and Clinical Applications. 5th ed Elsevier.

Hanna A 2017 The lateral femoral cutaneous nerve canal. J Neurosurg 126:972–8.

Harshavardhana NS, Dabke HV 2014 The furcal nerve revisited. Orthop Rev (Pavia) 6:5428.

Henry BM, Zwinczewska H, Roy J et al 2015 The prevalence of anatomical variations of the median nerve in the carpal tunnel: a systematic review and meta-analysis PLoS One 10:e0136477.

Henry BM, Vikse J, Graves MJ et al 2016. Extralaryngeal branching of the recurrent laryngeal nerve: a meta-analysis of 28,387 nerves. Langenbecks Arch Surg 401:913–923.

Henry BM, Pękala PA, Sanna B et al 2017 The anastomoses of the recurrent laryngeal nerve in the larynx: a meta-analysis and systematic review. J Voice. 31:495–503.

Hobbs RA, Magnussen PA, Tonkin MA 1990 Palmar cutaneous branch of the median nerve. J Hand Surg Am 15(1):38–43.

Holstein GR 2012 The vestibular system. In: Mai JK, Paxinos G (eds) The Human Nervous System, 3rd ed. Amsterdam: Elsevier, Academic Press; Ch. 35, pp. 1239–69.

Horn JP 2018 The sacral autonomic outflow is parasympathetic: Langley got it right. Clin Auton Res 28:181–185.

Iaconetta G, de Notaris M, Cavallo LM et al 2010 The oculomotor nerve: microanatomical and endoscopic study. Neurosurgery 66:593–601.

Joo W, Yoshioka F, Funaki T et al 2012 Microsurgical anatomy of the abducens nerve. Clin Anat 25:1030–1042.

Joo W, Rhoton AL Jr 2015 Microsurgical anatomy of the trochlear nerve. Clint Anat 28:857–64.

Kerr FW, Hollowell OW 1964 Location of pupillomotor and accommodation fibres in the oculomotor nerve: experimental observations on paralytic mydriasis. J Neurol Neurosurg Psychiat 27473–81.

Kierner AC, Aigner M, Burian M 1998 The external branch of the superior laryngeal nerve: its topographical anatomy as related to surgery of the neck. Arch Otolaryngol Head Neck Surg 124:301–3.

Kirchmair L, Lirk P, Colvin J et al 2008 Lumbar plexus and psoas major muscle: not always as expected. Reg Anesth Pain Med 33:109–14.

Klaassen Z, Marshall E, Tubbs RS et al 2011 Anatomy of the ilioinguinal and iliohypogastric nerves with observations of their spinal nerve contributions. Clin Anat 24:454–61.

Klink EW 1953 Perineal nerve block: an anatomic and clinical study in the female. Obstet Gynecol 1:137–46.

Kochilas X, Bibas A, Xenellis J et al 2008 Surgical anatomy of the external branch of the superior laryngeal nerve and its clinical significance in head and neck surgery. Clin Anat 21:99–105.

Kosinski C 1926 The course, mutual relations and distribution of the cutaneous nerves of the metazonal regions of the leg and foot. J Anat Physiol 60:274–97.

Kozicz T, Bittencourt JC, May PJ et al 2011 The Edinger–Westphal nucleus: a historical, structural, and functional perspective on a dichotomous terminology. J Comp Neurol 519:1413–34.

Kraima AC, van Schaik J, Susan S et al 2015 New insights in the neuroanatomy of the human adult superior hypogastric plexus and hypogastric nerves. Auton Neurosci 189:60–7.

Krammer EB, Lischka MF, Egger TP et al 1987 The motoneuronal organization of the spinal accessory nuclear complex. Advances in Anatomy, Embryology and Cell Biology 103. Berlin: Springer.

Kretschmer T, Heinen C 2015 Iatrogenic injuries of the nerves. In: Tubbs RS, Rizk E, Shoja MM et al (eds) Nerves and Nerve Injuries: Volume 2: Pain, Treatment, Injury, Disease and Future Directions. Elsevier Science; Ch. 36, pp. 557–85.

Kubik S, Müntener M 1969 [Topography of the spinal nerve roots. II. The influence of the growth of the dural sac as well as of the curvatures and of the movements of the vertebral column upon the course of spinal nerve roots]. Acta Anatomica 74:149–68. [Article in German.]

Kwak HH, Park HD, Youn KH et al 2004 Branching patterns of the facial nerve and its communication with the auriculotemporal nerve. Surg Radiol Anat 26:494–500.

Lachman N, Acland RD, Rosse C 2002 Anatomical evidence for the absence of a morphologically distinct cranial root of the accessory nerve in man. Clin Anat 15:4–10.

Lalezari S, Amrami KK, Tubbs RS et al 2012 Interosseous membrane: the anatomic basis for combined ankle and common fibular (peroneal) nerve injuries. Clin Anat 25:401–6.

Lee MW, McPhee RW, Stringer MD 2008 An evidence-based approach to human dermatomes. Clin Anat 21:363–73.

Lineaweaver W, Rhoton A, Habal MB 1997 Microsurgical anatomy of the facial nerve. Craniofac Surg 8:6–10.

Liu HF, Won HS, Chung IH et al 2014 Variable composition of the internal and external branches of the accessory nerve. Clin Anat 27:97–101.

Loukas M, Du Plessis M, Louis RG Jr et al 2016 The subdiaphragmatic part of the phrenic nerve – morphometry and connections to the autonomic ganglia. Clin Anat 29:120–8.

Loukas M, Klaassen Z, Merbs W et al 2010 A review of the thoracic splanchnic nerves and celiac ganglia. Clin Anat 23:512–22.

Lowe JB, Maggi SP, MacKinnon SE 2004 The position of the crossing branches of the medial antebrachial cutaneous nerve during cubital tunnel surgery in humans. Plast Reconstr Surg 114:692–6.
Lucas GDA, Laudanna A, Chopard RP et al 1994 Anatomy of the lesser occipital nerve in relation to cervicogenic headache. Clin Anat 7:90–6.
Mahan MA, Sanders LE, Guan J et al 2017 Anatomy of psoas muscle innervation: cadaveric study. Clin Anat 30:479–86.
Maldonado PA, Chin K, Garcia AA et al 2015 Anatomic variations of pudendal nerve within pelvis and pudendal canal: clinical applications. Am Obstet Gynecol 213:727.e1–6.
Maranillo E, Leon X, Orus C 2005 Variability in nerve patterns of the adductor muscle group supplied by the recurrent laryngeal nerve. Laryngoscope. 115:358–362.
Maranillo E, Vazquez T, Ibanez M et al 2008 Anatomic study of human laryngeal ganglia: number and distribution. Clin Anat 21:641–6.
Martin CH, Seiler JG 3rd, Lesesne JS 1996 The cutaneous innervation of the palm: an anatomic study of the ulnar and median nerves. J Hand Surg Am 21:634–8.
Mauroy B, Demondion X, Drizenko A et al 2003 The inferior hypogastric plexus (pelvic plexus): its importance in neural preservation techniques. Surg Radiol Anat 25:6–15.
Meng ID, Kurose M 2013 The role of corneal afferent neurons in regulating tears under normal and dry eye conditions. Exp Eye Res 117:79–87.
Monfared A, Gorti G, Kim D 2002 Microsurgical anatomy of the laryngeal nerves as related to thyroid surgery. Laryngoscope 112:386–92.
Moore AE, Stringer MD 2011 Iatrogenic femoral nerve injury: a systematic review. Surg Radiol Anat 33:649–58.
Moro T, Kikuchi S, Konno S et al 2003 An anatomic study of the lumbar plexus with respect to retroperitoneal endoscopic surgery. Spine (Phila Pa 1976) 28:423–8.
Motoc A, Rusu MC, Jianu AM 2010 The spermatic ganglion in humans: an anatomical update. Rom J Morphol Embryol 51:719–23.
Mu L, Sanders I 2009 The human cricothyroid muscle: three muscle bellies and their innervation patterns. J Voice 23:21–28.
Mu L, Sanders I 2010 Human tongue neuroanatomy: nerve supply and motor endplates. Clin Anat 23:777–791.
Murata Y, Takahashi K, Yamagata M et al 2003 Variations in the number and position of human lumbar sympathetic ganglia and rami communicantes. Clin Anat 16:108–13.
Mussa BM, Verberne AJ 2013 The dorsal motor nucleus of the vagus and regulation of pancreatic secretory function. Exp Physiol 98:25–37.
Nagy N, Goldstein AM 2017 Enteric nervous system development: a crest cell's journey from neural tube to colon. Semin Cell Dev Biol 66:94–106.
Naidich TP, Duvernoy HM, Delman BN et al 2009 Duvernoy's Atlas of the Human Brain Stem and Cerebellum. High-Field MRI: Surface Anatomy, Internal Structure, Vascularization and 3D Sectional Anatomy. Heidelberg: Springer Verlag.
Naidu L, Lazarus L, Partab P et al 2014 Laryngeal nerve 'anastomoses'. Folia Morphol (Warsz) 73:30–6.
Ndiaye A, Diop M, Ndoye JM et al 2007 Anatomical basis of neuropathies and damage to the ilioinguinal nerve during repairs of groin hernias (about 100 dissections). Surg Radiol Anat 29:675–81.
Neidre A, MacNab I 1983 Anomalies of the lumbosacral nerve roots. Review of 16 cases and classification. Spine 8:294–9.
Nieuwenhuys R, Voogd J, van Huijzen C 2008 The Human Central Nervous System, 4th ed. Berlin: Heidelberg Springer.
Nikolaos P, Vasilios L, Efstratios K et al 2014 Therapeutic modalities for Pancoast tumors. J Thorac Dis Suppl 1:S180–93.
Novak CB, Lee GW, MacKinnon SE et al 1994 Provocative testing for cubital tunnel syndrome. J Hand Surg [Am] 19:817–20.
Oh CS, Chung IH, Ji HJ et al 2004 Clinical implications of topographic anatomy on the ganglion impar. Anesthesiology 101:249–50.
Owens WA, Gladstone DJ, Heylings DJ 1994 Surgical anatomy of the phrenic nerve and internal mammary artery. Ann Thorac Surg 58:843–4.
Paraskevas G, Tsitsopoulos P, Papaziogas B et al 2008 Variability in superior hypogastric plexus morphology and its clinical applications: a cadaveric study. Surg Radiol Anat 30:481–8.
Paraskevas GK, Raikos A, Chouliaras K et al 2011 Variable anatomical relationship of phrenic nerve and subclavian vein: clinical implication for subclavian vein catheterization. Br J Anaesth 106(3):348–51.
Park HK, Rha HK, Lee KJ et al 2017 Microsurgical anatomy of the oculomotor nerve. Clin Anat 30:21–31.
Potts TK 1925 The main peripheral connections of the human sympathetic nervous system. J Anat 59:129–35.
Proctor B, Nager GT 1982 The facial canal: normal anatomy, variations and anomalies. Ann Otol Rhinol Laryngol 91:33–61.
Proctor B 1991 The anatomy of the facial nerve. Otolaryngol Clin North Am 24:479–504.
Pu YM, Tang EY, Yang XD 2008 Trapezius muscle innervation from the spinal accessory nerve and branches of the cervical plexus. Int J Oral Maxillofac Surg 37:567–72.
Rab M, Ebmer J, Dellon AL 2001 Anatomic variability of the ilioinguinal and genitofemoral nerve: implications for the treatment of groin pain. Plast Reconstr Surg 108:1618–23.
Rajanna MJ 1947 Anatomical and surgical considerations of the phrenic and accessory phrenic nerves. J Int Coll Surg 60:42–52.
Ray B, Roy TS, Wadhwa S et al 2005 Development of the human fetal cochlear nerve. Hearing Res 202:74–86.
Rennie IG 2011 Don't it make my blue eyes brown: heterochromia and other abnormalities of the iris. Eye (Lond) 26:29-50.
Renton T 2011 Minimising and managing iatrogenous trigeminal nerve injuries in relation to dental procedures. In: Birch R (ed) Surgical Disorders of the Peripheral Nerves. Berlin: Springer. Ch. 11, pp. 501–25.
Rodriguez-Niedenführ M, Vazquez T, Parkin I et al 2002 Martin–Gruber anastomosis revisited. Clin Anat 15:129–34.
Roles NC, Maudsley RH 1972 Radial tunnel syndrome: resistant tennis elbow as a nerve entrapment. J Bone Joint Surg Br 54:499–508.
Rozen WM, Ashton MW, Taylor GI 2008 Reviewing the vascular supply of the anterior abdominal wall: redefining anatomy for increasingly refined surgery. Clin Anat 21:89–98.
Ruskell GL 2004 Distribution of pterygopalatine ganglion efferents to the lacrimal gland in man. Exp Eye Res 78:329–35.
Rusu MC 2006 Considerations on the phrenic ganglia. Ann Anat 188:85–92.
Ryan S, Blyth P, Duggan N et al 2007 Is the cranial accessory nerve really a portion of the accessory nerve? Anatomy of the cranial nerves in the jugular foramen. Anat Sci Int 82:1–7.
Sanders I, Mu L 1998 Anatomy of the human internal superior laryngeal nerve. Anat Rec 252:646–56.
Sanudo J-R, Maranillo E, León X et al 1999 An anatomical study of anastomoses between the laryngeal nerves. Laryngoscope 109:983–7.
Sato K 1980 Amorphological analysis of the nerve supply of the sphincter ani externus, levator ani and coccygeus. Kaibogaku Zasshi 55:187–223.
Senger M, Stoffels HJ, Angelov DN 2014 Topography, syntopy and morphology of the human otic ganglion: a cadaver study. Ann Anat 196:327–35.
Shechtman DL, Woods AD, Tyler JA 2007 Pupil sparing incomplete third nerve palsy secondary to a cavernous sinus meningioma: challenges in management. Clin Exp Optom 90:132–38.
Shepherd G 2006 Smells, brains and hormones. Nature 439:149–151.
Shoja MM, Oyesiku NM, Shokouhi G et al 2014 A comprehensive review with potential significance during skull base and neck operations, Part II: Glossopharyngeal, vagus, accessory, and hypoglossal nerves and cervical spinal nerves 1–4. Clin Anat 27:131–44.
Siemionow M, Agaoglu G, Hoffmann R 2007 Anatomic characteristics of a fascia and its bands overlying the ulnar nerve in the proximal forearm: a cadaver study. J Hand Surg [Eur Vol] 32:302–7.
Situ P, Simpson TL 2010 Interaction of corneal nociceptive stimulation and lacrimal secretion. Invest Ophthalmol Vis Sci 51:5640–5.
Skinner SA 2011 Neurophysiologic monitoring of the spinal accessory nerve, hypoglossal nerve, and the spinomedullary region. J Clin Neurophysiol 28:587–98.
Solomon LB, Ferris L, Tedman R et al 2001 Surgical anatomy of the sural and superficial fibular nerves with an emphasis on the approach to the lateral malleolus. J Anat 199:717–23.
Spinner RJ, Atkinson JL, Tiel RL 2003 Peroneal intraneural ganglia: the importance of the articular branch. A unifying theory. J Neurosurg 99:330–43.
Stancič MF, Mičovič V, Potocnjak M 1999 The anatomy of the Berrettini branch: implications for carpal tunnel release. J Neurosurg 91:1027–30.
Sun SQ, Chang RW 1991 The superior laryngeal nerve loop and its surgical implications. Surg Radiol Anat 13:175–80.
Sunderland S 1945 Blood supply of the sciatic nerve and its popliteal divisions in man. Arch Neurol Psychiatry 54:283–9.
Toshniwal GR, Dureja GP, Prashanth SM 2007 Trans-sacrococcygeal approach to ganglion impar block for management of chronic perineal pain: a prospective observational study. Pain Physician 10:661–6.
Tosios KI, Nikolakis M, Prigkos AC et al 2010 Nerve cell bodies and small ganglia in the connective tissue stroma of human submandibular glands. Neurosci Lett 475:53–5.
Tubbs RS, Stetler W, Kelly DR et al 2008 Immunohistochemical study of the phrenic ganglion. Anat Sci Int 83:159–61.
Tubbs RS, Miller J, Loukas M et al 2009 Surgical and anatomical landmarks for the perineal branch of the posterior femoral cutaneous nerve: implications in perineal pain syndromes. Laboratory investigation. J Neurosurg 111:332–5.
Tubbs RS, Shoja MM, Loukas M et al 2011 Study of the cervical plexus innervation of the trapezius muscle. J Neurosurg Spine 14:626–9.
Tubbs RS, Benninger B, Loukas M et al 2014 Cranial roots of the accessory nerve exist in the majority of adult humans. Clin Anat 27:102–7.
Tubbs RS, Shoja M, Loukas M 2016 Bergman's Comprehensive Encyclopedia of Human Anatomic Variation. Hoboken: Wiley Blackwell.

Tubbs RS, Loukas M, Hanna AS et al 2018 Surgical Anatomy of the Lumbar Plexus. New York: Thieme.
Turgut M, Protas M, Gardner B et al 2017 The accessory obturator nerve: an anatomical study with literature analysis. Anatomy 11:121–27.
Ugrenovic SZ, Jovanovic ID, Kovacevic P et al 2013 Similarities and dissimilarities of the blood supplies of the human sciatic, tibial, and common peroneal nerves. Clin Anat 26:875–82.
Vanelderen P, Lataster A, Levy R et al 2010 8. Occipital neuralgia. Pain Pract 10:137–44.
Voogd J 2016 Deiters' nucleus: its role in cerebellar ideogenesis: The Ferdinando Rossi Memorial Lecture. Cerebellum 15:54–66.
Wadie M, Adam SI, Sasaki CT 2013 Development, anatomy and physiology of the larynx. In: Shaker R, Belafsky PC, Postma GN et al (eds) Principles of Deglutition: A Multidisciplinary Text for Swallowing and Its Disorders. New York: Springer Science+Business Media.
Warr WB 1992 Organization of olivocochlear efferent systems in mammals. In: Webster DB, Popper AN, Fay RR (eds) Mammalian Auditory Pathway: Neuroanatomy. New York: Springer; pp. 410–448.
Weijs TJ, Ruurda JP, Luyer MD et al 2015 Topography and extent of pulmonary vagus nerve supply with respect to transthoracic oesophagectomy. J Anat 227:431–9.
Weijs TJ, Ruurda JP, Luyer MD et al 2016 Preserving the pulmonary vagus nerve branches during thoracoscopic esophagectomy. Surg Endosc 30:3816–22.
Weijs TJ, Ruurda JP, Luyer MDP et al 2017 New insights into the surgical anatomy of the esophagus. J Thorac Dis Suppl 8:S675–S680.
Wiles CC, Wrigley B, Greene JR 2007 Re-examination of the medullary rootlets of the accessory and vagus nerves. Clin Anat 20:19–22.
Wilgis ES, Murphy R 1986 The significance of longitudinal excursion in peripheral nerves. Hand Clin 2:761–6.
Xanthos DN, Sandkühler J 2014 Neurogenic neuroinflammation: inflammatory CNS reactions in response to neuronal activity. Nature Rev Neurosci 15:43–53.
Yoon JS, Kim BJ, Kim SJ et al 2007 Ultrasonographic measurements in cubital tunnel syndrome. Muscle Nerve 36:853–5.
Yousry I, Morrigl B, Schmid UD et al 2002 Detailed anatomy of the hypoglossal nerve: neurovascular relationships and landmarks on magnetic resonance imaging sequences. J Neurosurg 96:1113–22.
Zandian A, Osiro S, Hudson R et al 2014 The neurologist's dilemma: a comprehensive clinical review of Bell's palsy, with emphasis on current management trends. Med Sci Monit 20:83–90.
Zhang XM, Zhao QH, Zeng NL et al 2006 The celiac ganglia: anatomic study using MRI in cadavers. Am J Roentgenol 186:1520–3.
Zur KB, Mu L, Sanders I 2004 Distribution pattern of the human lingual nerve. Clin Anat 17:88–92.

CHAPTER
81

The anatomy of the vascular and lymphatic systems

This chapter brings together the regional descriptions of the arteries, veins and lymphatic vessels and their draining nodes that appear in the relevant sections of chapters 24–79. The text is not illustrated: all cross-referenced figures and videos are HTML-linked to the corresponding figure or video in the appropriate chapter in the eBook.

ARTERIAL SUPPLY OF THE HEAD AND NECK

The head and neck and the brain are supplied by the carotid system of arteries and by many, but not all, of the branches of the subclavian arteries. The carotid system is described here. The subclavian artery is described on pages 1464.e83 et seq.

Carotid system of arteries

The right and left common carotid arteries supply the head and neck Both ascend to just above the level of the upper border of the thyroid cartilage, where each divides into an external carotid artery that supplies the external head, face and most of the neck, and an internal carotid artery that supplies the cranial and orbital contents.

Common carotid arteries

The right and left common carotid arteries differ in their length and origin. The right is exclusively cervical and usually arises from the brachiocephalic trunk posterior to the superior part of the right sternoclavicular joint, or immediately superior to the joint, but it may be a separate branch from the aorta. The left originates directly from the aortic arch immediately posterolateral to the brachiocephalic trunk and therefore has both thoracic and cervical parts (see Figs 35.8, 57.4, 58.1). Its thoracic part (2.0–2.5 cm long) lies initially anterior and then to the left side of the trachea as it ascends to enter the neck by passing through the superior thoracic aperture, posterior to the left sternoclavicular joint.

In the neck, the right and left common carotid arteries follow a similar course. They ascend, diverging laterally from behind the sternoclavicular joint to the level of the upper border of the thyroid cartilage of the larynx (C3–C4 junction), where each divides into external and internal carotid arteries. This bifurcation can sometimes be at a higher or lower level (see Fig. 35.7B). The angle of bifurcation remains unchanged from infancy to adulthood. However, there is a significant change in the angle of the split between the internal and the external carotid arteries relative to the common carotid artery (Seong et al 2005). The artery may be compressed against the prominent transverse process of the sixth cervical vertebra (Chassaignac's tubercle); above this level it is superficial, and its pulsation can be easily felt.

In the lower part of the neck, the common carotid arteries are separated by a narrow gap that contains the trachea. Above this, the arteries are separated by the thyroid gland, larynx and pharynx. Each artery is contained within the carotid sheath of deep cervical fascia, which also encloses the internal jugular vein and vagus nerve, the vein lying lateral to the artery, and the nerve lying between them and posterior to both.

Relations At the level of the cricoid cartilage the common carotid artery is crossed anterolaterally by the intermediate tendon, or sometimes the superior belly, of omohyoid. Below omohyoid, it is sited deeply, and covered by skin, superficial fascia, platysma, deep cervical fascia and sternocleidomastoid, sternohyoid and sternothyroid. Above omohyoid, it is more superficial, and covered merely by skin, superficial fascia, platysma, deep cervical fascia and the medial margin of sternocleidomastoid; it is crossed obliquely from its medial to lateral side by the sternocleidomastoid branch of the superior thyroid artery. The superior root of the ansa cervicalis, joined by its inferior root from the second and third cervical spinal nerves, lies anterior to, or embedded within, the carotid sheath as it crosses it obliquely. The superior thyroid vein usually crosses near the upper border of the thyroid cartilage, and the middle thyroid vein crosses a little below the level of the cricoid cartilage. The anterior jugular vein crosses the common carotid artery above the clavicle, separated from it by sternohyoid and sternothyroid. Posterior to the carotid sheath are the transverse processes of the fourth to sixth cervical vertebrae, to which are attached longus colli, longus capitis and tendinous slips of scalenus anterior. The sympathetic trunk and ascending cervical branch of the inferior thyroid artery lie between the common carotid artery and the muscles. Below the level of the sixth cervical vertebra, the artery is in an angle between scalenus anterior and longus colli, anterior to the vertebral vessels, inferior thyroid and subclavian arteries, sympathetic trunk and, on the left, the thoracic duct. The oesophagus, trachea, inferior thyroid artery, recurrent laryngeal nerve and, at a higher level, the larynx and pharynx are medial to the sheath and its contents. The thyroid gland overlaps it anteromedially. The internal jugular vein lies lateral and, in the lower neck, also anterior to the artery, while the vagus nerve lies posterolaterally in the angle between the artery and vein.

On the right side, low in the neck, the recurrent laryngeal nerve crosses obliquely behind the artery. The right internal jugular vein diverges from it below but the left vein approaches and often overlaps its artery.

Although the common carotid artery usually has no branches, it may occasionally give rise to the vertebral, superior thyroid, superior laryngeal, ascending pharyngeal, inferior thyroid or occipital arteries.

Variants The origin of the arteries may vary: both common carotid arteries may emerge from the brachiocephalic trunk (Panagouli et al 2018), or separately from the aorta, or from a common trunk (Akgun et al 2016). The left common carotid artery varies in origin more than the right. Either common carotid artery may bifurcate higher, near the level of the hyoid bone, or, more rarely, at a lower level alongside the larynx. Very rarely, the common carotid artery ascends without division, so that either the external or internal carotid artery is absent, or separate external and internal carotid arteries may arise directly from the aorta, unilaterally or bilaterally.

Carotid sinus and carotid body

The common carotid artery has two specialized organs near its bifurcation: the carotid sinus and the carotid body. They relay information concerning the pressure and chemical composition of the arterial blood, respectively, and are innervated principally by the carotid branch(es) of the glossopharyngeal nerve, with small contributions from the cervical sympathetic trunk and the vagus nerve.

The carotid sinus usually appears as a dilation of the lower end of the internal carotid in late adolescence (Seong et al 2005) and functions as a baroreceptor.

The carotid body is a reddish-brown, oval structure, 5–7 mm in height and 2.5–4 mm in width. It lies either posterior to the carotid bifurcation or between its branches, and is attached to, or sometimes partly embedded in, their adventitia. Occasionally it takes the form of a group of separate nodules. Aberrant miniature carotid bodies, microstructurally similar but with diameters of 600 μm or less, may appear in the adventitia and adipose tissue near the carotid sinus.

The carotid body is surrounded by a fibrous capsule, from which septa divide the enclosed tissue into lobules. Each lobule contains glomus (type I) cells, which are separated from an extensive network of fenestrated sinusoids by sustentacular (type II) cells (see Fig. 35.10). Glomus cells store a number of peptides, particularly enkephalins, bombesin and neurotensin, and amines including dopamine, serotonin (5-hydroxytryptamine, 5-HT), adrenaline (epinephrine) and noradrenaline (norepinephrine), and are therefore regarded as paraneurones. Unmyelinated axons lie in a collagenous matrix between the sustentacular cells and the sinusoidal endothelium, and many synapse on the glomus cells. They are visceral afferents, which travel in the carotid sinus nerve to join the glossopharyngeal nerve. Preganglionic sympathetic axons and fibres from the carotid sinus synapse on parasympathetic and sympathetic ganglion cells, which lie either in isolation or in small groups near the surface of each carotid body. Postganglionic axons travel to local blood vessels; the parasympathetic efferent fibres are probably vasodilatory and the sympathetic ones are vasoconstrictor.

The carotid body receives a rich blood supply from branches of the adjacent external carotid artery, which is consistent with its role as an arterial chemoreceptor. When stimulated by hypoxia, hypercapnia or increased hydrogen ion concentration (low pH) in the blood flowing through it, it elicits reflex increases in the rate and volume of ventilation via connections with brainstem respiratory centres. The bodies are most prominent in children and normally involute in older age, when they are infiltrated by lymphocytes and fibrous tissue. Individuals with chronic hypoxia, or who live at high altitude or suffer from lung disease, may have enlarged carotid bodies as a result of hyperplasia. Disrupted carotid body maturation may play a role in sudden infant death syndrome (Porzionato et al 2013). Benign and malignant paragangliomas develop in association with succinyl dehydrogenase mutations (SDH).

Other small bodies, resembling carotid bodies and also considered to be chemoreceptors, are present near the arteries of the fourth and sixth pharyngeal arches and hence are found near the aortic arch, ligamentum arteriosum and right subclavian artery; they are supplied by the vagus nerve.

External carotid artery

The external carotid artery (see Figs 35.7A, 35.8) begins lateral to the upper border of the thyroid cartilage, level with the intervertebral disc between the third and fourth cervical vertebrae. A little curved and with a gentle spiral, it first ascends slightly forwards and then inclines backwards and a little laterally, to pass midway between the tip of the mastoid process and the angle of the mandible. Here, in the substance of the parotid gland behind the neck of the mandible, it divides into its terminal branches, the superficial temporal and maxillary arteries. As it ascends, it gives off several large branches and diminishes rapidly in calibre. In children the external carotid is smaller than the internal carotid, but in adults the two are of almost equal size. At its origin, it is in the carotid triangle and lies anteromedial to the internal carotid artery. It later becomes anterior, then lateral, to the internal carotid as it ascends. At mandibular levels, the styloid process and its attached structures intervene between the vessels; the internal carotid is deep, and the external carotid superficial, to the styloid process. A fingertip placed in the carotid triangle perceives a powerful arterial pulsation, which represents the termination of the common carotid, the origins of external and internal carotids, and the stems of the initial branches of the external carotid.

Relations The skin and superficial fascia, the loop between the cervical branch of the facial nerve and the transverse cutaneous nerve of the neck, the deep cervical fascia and the anterior margin of sternocleidomastoid all lie superficial to the external carotid artery in the carotid triangle. The artery is crossed by the hypoglossal nerve and its vena comitans, and by the lingual, facial and, sometimes, the superior thyroid veins. Leaving the carotid triangle, the external carotid artery is crossed by the posterior belly of digastric and by stylohyoid; it ascends between these muscles and the posteromedial surface of the parotid gland, which it next enters. Within the parotid, the artery lies medial to the facial nerve and the junction of the superficial temporal and maxillary veins. The pharyngeal wall, superior laryngeal nerve and ascending pharyngeal artery are the initial medial relations of the artery. At a higher level, it is separated from the internal carotid artery by the styloid process, styloglossus and stylopharyngeus, glossopharyngeal nerve, pharyngeal branch of vagus nerve and part of the parotid gland. The artery is equally likely to lie medial to the parotid gland, or within it.

The external carotid artery has eight named branches distributed to the head and neck. The superior thyroid, lingual and facial arteries arise from its anterior surface, the occipital and posterior auricular arteries arise from its posterior surface, and the ascending pharyngeal artery arises from its medial surface. The maxillary and superficial temporal arteries are its terminal branches within the parotid gland.

Ascending pharyngeal artery

The ascending pharyngeal artery is the first and smallest branch of the external carotid artery. It is a long, slender vessel that arises from the medial (deep) surface of the external carotid artery near the origin of that artery. It is important that it is identified and preserved if the external carotid is being ligated because of its potential to supply to a compromised internal carotid circulation.

The ascending pharyngeal artery ascends between the internal carotid artery and the pharynx to the base of the cranium, crossed by styloglossus and stylopharyngeus; longus capitis is posterior. It gives off numerous small branches to supply longus capitis and longus colli, the sympathetic trunk, the hypoglossal, glossopharyngeal and vagus nerves, and some of the cervical lymph nodes. It anastomoses with the ascending palatine branch of the facial artery and the ascending cervical branch of the inferior thyroid artery.

The ascending pharyngeal artery has the following named branches: pharyngeal, inferior tympanic and meningeal arteries.

Pharyngeal artery

The pharyngeal artery gives off three or four branches to supply the constrictor muscles of the pharynx and stylopharyngeus. A variable ramus supplies the palate and may replace the ascending palatine branch of the facial artery. The artery descends forwards between the superior border of the superior constrictor and levator veli palatini to the soft palate, and also supplies a branch to the palatine tonsil and the pharyngotympanic tube.

Inferior tympanic artery

The inferior tympanic artery is a small branch that traverses the temporal canaliculus with the tympanic branch of the glossopharyngeal nerve and supplies the medial wall of the tympanic cavity.

Meningeal arteries

The meningeal arteries are small vessels that supply the nerves that traverse the foramen lacerum, jugular foramen and hypoglossal canal, and the associated dura mater and adjoining bone. One branch, the posterior meningeal artery, reaches the cerebellar fossa via the jugular foramen and is usually regarded as the terminal branch of the ascending pharyngeal artery.

Superior thyroid artery

The superior thyroid artery is the second branch of the external carotid artery. It arises from the anterior surface of the external carotid just below the level of the greater cornu of the hyoid bone (see Figs 35.7A, 35.8). It descends along the lateral border of thyrohyoid to reach the apex of the lobe of the thyroid gland. The inferior constrictor muscle and the external laryngeal nerve are medial. The nerve is often posteromedial, and therefore at risk when the artery is being ligated, and occasionally it may issue directly from the common carotid.

The superior thyroid artery supplies the thyroid gland and some adjacent skin. Branches to the gland are anterior, running along the medial side of the upper pole of the lateral lobe to supply mainly the anterior surface; a branch that crosses above the isthmus to anastomose with its contralateral fellow; and posterior, descending on the posterior border to supply the medial and lateral surfaces and anastomose with the inferior thyroid artery. A lateral branch sometimes supplies the lateral surface. The superior thyroid artery is often accompanied by the external branch of the superior laryngeal nerve: care should be taken to preserve this nerve when ligating the superior thyroid artery during surgery because it supplies cricothyroid, and iatrogenic damage affects vocal cord function.

Named branches of the superior thyroid artery are the infrahyoid, superior laryngeal, sternocleidomastoid and cricothyroid.

Infrahyoid artery

The infrahyoid artery is a small branch that runs along the lower border of the hyoid bone deep to thyrohyoid and anastomoses with its fellow of the opposite side to supply the infrahyoid strap muscles.

Superior laryngeal artery

The superior laryngeal artery accompanies the internal laryngeal nerve. Deep to thyrohyoid, it pierces the lower part of the thyrohyoid membrane to supply the tissues of the upper part of the larynx. It anastomoses with its fellow of the opposite side and with the inferior laryngeal branch of the inferior thyroid artery.

Sternocleidomastoid artery

The sternocleidomastoid artery descends laterally across the carotid sheath and supplies the middle region of sternocleidomastoid. Like the parent artery itself, it may arise directly from the external carotid artery.

Cricothyroid artery

The cricothyroid artery crosses high on the anterior cricothyroid ligament, anastomoses with its fellow of the opposite side and supplies cricothyroid.

Lingual artery

The lingual artery provides the chief blood supply to the tongue and the floor of the mouth (see Fig. 35.8). It arises anteromedially from the external carotid artery opposite the tip of the greater cornu of the hyoid bone, between the superior thyroid and facial arteries. It often arises with the facial or, less often, with the superior thyroid artery. It may be replaced by a ramus of the maxillary artery. Ascending medially at first, it loops down and forwards, passes medial to the posterior border of hyoglossus and then runs horizontally forwards deep to it, accompanied by the lingual veins and the glossopharyngeal nerve. At the anterior border of hyoglossus, the lingual artery bends sharply upwards (see Fig. 37.11A). It is covered by the mucosa of the tongue and lies between genioglossus medially and the inferior longitudinal muscle laterally. Near the tip of the tongue, it anastomoses with its contralateral fellow; this contribution is important in maintaining the blood supply to the tongue in any surgical resection of the tongue. The branches of the lingual artery form a rich anastomotic network, which supplies the musculature of the tongue, and a very dense submucosal plexus. Named branches of the lingual artery in the floor of the mouth are the dorsal lingual, sublingual and deep lingual arteries.

Relations Its relationship to hyoglossus naturally divides the lingual artery into descriptive 'thirds'. In its first part, the lingual artery is in the carotid triangle. Skin, fascia and platysma are superficial to it, while the middle pharyngeal constrictor muscle is medial. The artery ascends a little medially, then descends to the level of the hyoid bone, and the loop so formed is crossed externally by the hypoglossal nerve. The second part passes along the upper border of the hyoid bone, deep to hyoglossus, the tendons of digastric and stylohyoid, the lower part of the submandibular gland and the posterior part of mylohyoid. Hyoglossus separates it from the hypoglossal nerve and its vena comitans. Here, its medial aspect adjoins the middle constrictor muscle and it crosses the stylohyoid ligament accompanied by lingual veins. The third part is the arteria profunda linguae, which turns upwards near the anterior border of hyoglossus and then passes forwards close to the inferior lingual surface near the frenulum, accompanied by the lingual nerve. Genioglossus is a medial relation, and the inferior longitudinal muscle of the tongue lies lateral to it below the lingual mucous membrane. Near the tip of the tongue, the lingual artery anastomoses with its fellow of the opposite side. Its named branches are the suprahyoid, dorsal lingual and sublingual arteries.

Suprahyoid artery

The suprahyoid artery is a small branch that runs along the upper border of the hyoid bone to anastomose with the contralateral artery and supply adjacent structures.

Dorsal lingual arteries

There are usually two or three small dorsal lingual arteries. They arise medial to hyoglossus and ascend to the posterior part of the dorsum of the tongue. They supply its mucous membrane and the palatoglossal arch, tonsil, soft palate and epiglottis and anastomose with their contralateral fellows.

Sublingual artery

The sublingual artery arises at the anterior margin of hyoglossus. It passes forwards between genioglossus and mylohyoid to the sublingual gland, and supplies the gland, mylohyoid and the buccal and gingival mucous membranes. One branch pierces mylohyoid and joins the submental branches of the facial artery. Another branch courses through the mandibular gingivae to anastomose with its contralateral fellow. A single artery arises from this anastomosis and enters a small foramen (lingual foramen) on the mandible, situated in the midline on the posterior aspect of the symphysis immediately above the genial tubercles.

Deep lingual artery

The deep lingual artery is the terminal part of the lingual artery and is found on the inferior surface of the tongue near the lingual frenulum.

In addition to the lingual artery, the tonsillar and ascending palatine branches of the facial and ascending pharyngeal arteries also supply tissue in the root of the tongue. In the region of the valleculae, epiglottic branches of the superior laryngeal artery anastomose with the inferior dorsal branches of the lingual artery.

Facial artery

The facial artery (see Figs 35.7–35.8, 36.25) arises anteriorly from the external carotid in the carotid triangle, above the lingual artery and immediately above the greater cornu of the hyoid bone. In the neck, at its origin, it is covered only by the skin, platysma, fasciae and often by the hypoglossal nerve. It runs up and forwards, deep to digastric and stylohyoid. At first on the middle pharyngeal constrictor, it may reach the lateral surface of styloglossus, separated there from the palatine tonsil only by this muscle and the lingual fibres of the superior constrictor. Medial to the mandibular ramus, it arches upwards and grooves the posterior aspect of the submandibular gland. It then turns down and descends to the lower border of the mandible in a lateral groove on the submandibular gland, between the gland and medial pterygoid. It initially lies beneath platysma and passes onto the face at the anteroinferior border of masseter, where its pulse can be felt as it crosses the mandible. The artery is deep to skin, the fat of the cheek and, near the angle of the mouth, zygomaticus major and risorius, and superficial to buccinator and levator anguli oris. It may pass over or through levator labii superioris and pursues a tortuous course along the side of the nose towards the medial corner of the eye. At its termination, it is embedded in levator labii superioris alaeque nasi.

Occasionally the facial artery barely extends beyond the angle of the mouth, in which case its normal territory beyond this region is taken over by an enlarged transverse facial branch from the superficial temporal artery and by branches from the contralateral facial artery. The facial vein is posterior to the artery and runs a more direct course across the face. At the anterior border of masseter, the two vessels are in contact, whereas in the neck the vein is superficial to the artery. The facial artery supplies branches to the muscles and skin of the face (see Fig. 36.20). The part of the artery distal to its terminal branch is called the angular artery.

The facial artery is very sinuous throughout its extent. In the neck, this may be so that the artery is able to adapt to the movements of the pharynx during deglutition, and similarly on the face, so that the artery can adapt to movements of the mandible, lips and cheeks. Facial artery pulsation is most palpable where the artery crosses the mandibular base, and again near the corner of the mouth. There are four branches within the neck and four on the face. The named branches in the neck are the ascending palatine, tonsillar, submental and glandular arteries. The named branches on the face are the premasseteric, inferior and superior labial, and lateral nasal arteries.

Ascending palatine artery

The ascending palatine artery arises close to the origin of the facial artery. It passes up between styloglossus and stylopharyngeus to reach the side of the pharynx, along which it ascends between the superior constrictor of the pharynx and medial pterygoid towards the cranial base. It bifurcates near levator veli palatini. One branch follows this muscle, winding over the upper border of the superior constrictor of the pharynx to supply the soft palate and to anastomose with its fellow of the opposite side and the greater palatine branch of the maxillary artery. The other branch pierces the superior constrictor muscle to supply the tonsil and pharyngotympanic tube, and to anastomose with the tonsillar and ascending pharyngeal arteries (see Fig. 40.7).

Tonsillar artery

The tonsillar artery provides the main blood supply to the palatine tonsil. It ascends between medial pterygoid and styloglossus, penetrates the superior constrictor of the pharynx at the upper border of styloglossus, and enters the inferior pole of the tonsil. Its branches ramify in the tonsil and in the musculature of the posterior part of the tongue. The tonsillar artery may sometimes arise from the ascending palatine artery.

Submental artery

The submental artery is the largest cervical branch of the facial artery (see Fig. 35.7A). It arises as the facial artery separates from the submandibular gland and turns forwards on mylohyoid below the mandible. It supplies the overlying skin and muscles, and anastomoses with a sublingual branch of the lingual and mylohyoid branch of the inferior alveolar artery. At the chin, it ascends over the mandible and divides into superficial and deep branches that anastomose with the inferior labial and mental arteries to supply the chin and lower lip.

Glandular branches

Three or four large vessels supply the submandibular salivary gland and associated lymph nodes, adjacent muscles and skin.

Premasseteric artery

The premasseteric artery is small and inconstant. When present, it passes upwards along the anterior border of masseter and supplies the surrounding tissues.

Inferior labial artery

The inferior labial artery arises near the angle of the mouth, passes upwards and forwards under depressor anguli oris, and then penetrates orbicularis oris to run sinuously near the margin of the lower lip, between the muscle and the mucous membrane. It supplies the inferior labial glands, mucous membrane and muscles, and anastomoses with its contralateral fellow and with the mental branch of the inferior alveolar artery.

Superior labial artery

The superior labial artery is larger and more tortuous than the inferior labial artery. It pursues a similar course along the superior labial margin, between the mucous membrane and orbicularis oris, anastomoses with its contralateral fellow, and supplies the upper lip. It gives off an alar branch and a septal branch that ramifies anteroinferiorly in the nasal septum.

Lateral nasal artery

The lateral nasal artery is given off by the side of the nose, supplies the dorsum and ala of the nose, and anastomoses with its contralateral fellow. The lateral nasal artery can be replaced by a branch from the superior labial artery.

Occipital artery

The occipital artery arises posteriorly from the external carotid artery, approximately 2 cm from its origin (see Figs 35.7A, 35.8). At its origin, the artery is crossed superficially by the hypoglossal nerve, which winds round it from behind. The artery next passes backwards, up and deep to the posterior belly of digastric, and crosses the internal carotid artery, internal jugular vein, and hypoglossal, vagus and accessory nerves. Between the transverse process of the atlas and the mastoid process, the occipital artery reaches the lateral border of rectus capitis lateralis. It then runs in the occipital groove of the temporal bone, medial to the mastoid process and attachments of sternocleidomastoid, splenius capitis, longissimus capitis and digastric, and lies successively on rectus capitis lateralis, obliquus superior and semispinalis capitis. Accompanied by the greater occipital nerve, it finally turns upwards to pierce the investing layer of the deep cervical fascia that connects the cranial attachments of trapezius and sternocleidomastoid. Accompanied by the greater occipital nerve, the occipital artery enters the posterior scalp by piercing the investing layer of deep cervical fascia that connects the cranial attachments of trapezius and sternocleidomastoid. It gives off many tortuous branches that run between the skin and the occipital belly of occipitofrontalis, anastomosing with the contralateral occipital, posterior auricular and superficial temporal arteries, as well as with the transverse cervical branch of the subclavian artery. These branches supply the occipital belly of occipitofrontalis and the skin and pericranium associated with the scalp as far forwards as the vertex. The artery may give off a meningeal branch that traverses the parietal foramen.

The occipital artery has two main branches (superior and inferior) to the upper part of sternocleidomastoid in the neck. The inferior branch arises near the origin of the occipital artery and may sometimes arise directly from the external carotid artery. It descends backwards over the hypoglossal nerve and internal jugular vein, enters sternocleidomastoid and anastomoses with the sternocleidomastoid branch of the superior thyroid artery. The superior branch arises as the occipital artery crosses the accessory nerve and runs down and backwards superficial to the internal jugular vein. It enters the deep surface of sternocleidomastoid with the accessory nerve.

Posterior auricular artery

The posterior auricular artery is a small vessel that branches posteriorly from the external carotid just above digastric and stylohyoid. It ascends between the parotid gland and the styloid process to the groove between the auricular cartilage and mastoid process. It supplies the cranial surface of the auricle via its auricular branch, and the occipital belly of occipitofrontalis and the scalp behind and above the auricle via its occipital branch and anastomoses with the occipital artery.

In the neck, it provides branches that supply digastric, stylohyoid, sternocleidomastoid and the parotid gland. It also gives origin to the stylomastoid artery (described as an indirect branch of the posterior auricular artery in about a third of subjects) that enters the stylomastoid foramen to supply the facial nerve, tympanic cavity, mastoid antrum air cells and semicircular canals. In the young, its posterior tympanic ramus forms a circular anastomosis with the anterior tympanic branch of the maxillary artery.

Superficial temporal artery

The superficial temporal artery is the smaller terminal branch of the external carotid artery (see Figs 33.1A, 36.20). It arises in the parotid gland behind the neck of the mandible, where it is crossed by temporal and zygomatic branches of the facial nerve. Initially deep, it becomes superficial as it passes over the posterior root of the zygomatic process of the temporal bone, where its pulse can be felt. It then ascends in the scalp for approximately 4 cm and divides into frontal (anterior) and parietal (posterior) branches. The artery is accompanied by corresponding veins, and by the auriculotemporal nerve that usually lies just posterior to it.

The superficial temporal artery supplies the skin and muscles at the side of the face and in the scalp, the parotid gland and the temporomandibular joint. It is occasionally biopsied when a histological diagnosis of giant cell arteritis is required. The named branches of the superficial temporal artery are the transverse facial, auricular, zygomatico-orbital, middle temporal, frontal and parietal arteries. The relative sizes of the frontal, parietal and transverse facial branches vary: the frontal and parietal branches may be absent, whereas the transverse facial branch may replace a shortened transverse facial artery arising from the facial artery.

Transverse facial artery

The transverse facial artery arises before the superficial temporal artery emerges from the parotid gland. It traverses the gland, crosses masseter between the parotid duct and the zygomatic arch (accompanied by one or two facial nerve branches), and divides into numerous branches that supply the parotid gland and duct, masseter and adjacent skin. The branches anastomose with the facial, masseteric, buccal, lacrimal and infraorbital arteries, and can have a direct origin from the external carotid artery.

Auricular artery

The branches of the auricular artery are distributed to the lobule and lateral surface of the auricle and to the external acoustic meatus.

Zygomatico-orbital artery

The zygomatico-orbital artery may arise independently from the superficial temporal artery or from its middle temporal or parietal branches. It runs close to the upper border of the zygomatic arch, between the two layers of temporal fascia, to the lateral orbital angle. It supplies orbicularis oculi and anastomoses with the lacrimal and palpebral branches of the ophthalmic artery. A well-developed zygomatico-orbital artery can be associated with a delayed division of the superficial temporal artery into frontal and parietal branches.

Middle temporal artery

The middle temporal artery arises just above the zygomatic arch and perforates the temporal fascia to supply temporalis. It anastomoses with the deep temporal branches of the maxillary artery.

Frontal (anterior) branch

The frontal branch passes upwards towards the frontal tuberosity and supplies the muscles, skin and pericranium in this region. It anastomoses with its contralateral fellow and with the supraorbital and supratrochlear branches of the ophthalmic artery.

Parietal (posterior) branch

The parietal branch is larger than the frontal branch of the superficial temporal artery. It curves upwards and backwards, remains superficial to the temporal fascia, and anastomoses with its contralateral fellow and with the posterior auricular and occipital arteries.

Maxillary artery

The maxillary artery is the larger terminal branch of the external carotid artery. It arises behind the neck of the mandible and is at first embedded in the parotid gland, then crosses the infratemporal fossa to enter the pterygopalatine fossa through the pterygomaxillary fissure. Within the pterygopalatine fossa, the maxillary artery and its branches lie in a plane anterior to the maxillary nerve, pterygopalatine ganglion and the nerve of the pterygoid canal: this spatial arrangement is particularly relevant in endoscopic approaches to the pterygopalatine fossa (see Video 38.2). The veins accompanying the third (pterygopalatine) part of the maxillary artery, in common with those accompanying the second (pterygoid) part, are in the form of a venous plexus and profuse haemorrhage may be encountered from this pterygopalatine venous plexus. The maxillary artery has a variable and tortuous course in its short passage through the pterygopalatine fossa, where it gives off numerous named branches, including the posterior superior alveolar and infraorbital arteries and the artery of the pterygoid canal (Vidian artery), and terminates in the sphenopalatine and greater palatine arteries.

The maxillary artery is widely distributed to the mandible, maxilla, teeth, muscles of mastication, palate, nasal cavity and cranial dura mater (see Figs 38.20–38.21). It is conventionally described in three parts: mandibular, pterygoid and pterygopalatine.

The mandibular part runs horizontally by the medial surface of the ramus and passes between the neck of the mandible and the sphenomandibular ligament, parallel with and slightly below the auriculotemporal nerve. It next crosses the inferior alveolar nerve and skirts the lower border of lateral pterygoid. The pterygoid part ascends obliquely forwards medial to temporalis and is usually superficial to the lower head of lateral pterygoid. When it runs deep to lateral pterygoid, it lies between the muscle and branches of the mandibular nerve and may project as a lateral loop between the two parts of lateral pterygoid. Asymmetry in this pattern of distribution may occur between the right and left infratemporal fossae. Where the maxillary artery runs superficial to the lower head of lateral pterygoid, the most common pattern is that the artery passes lateral to the inferior alveolar, lingual and buccal nerves. Less frequently, only the buccal nerve crosses the artery laterally, and rarely the artery can pass deep to all the branches of the mandibular nerve. The pterygopalatine part passes between the two heads of lateral pterygoid to reach the pterygomaxillary fissure before it passes into the pterygopalatine fossa, where it terminates as the third part of the maxillary artery.

The mandibular part of the maxillary artery has five branches that all enter bone. The named branches are the deep auricular, anterior tympanic, middle meningeal, accessory meningeal and inferior alveolar arteries.

The pterygoid part of the maxillary artery has five branches that do not enter bone but supply muscle, and include the deep temporal, pterygoid, masseteric and buccal arteries.

The branches of the pterygopalatine part of the artery accompany similarly named branches of the maxillary nerve (including those associated with the pterygopalatine ganglion) and include the posterior superior alveolar and infraorbital arteries, the artery of the pterygoid canal (Vidian artery), and the pharyngeal, greater (descending) palatine and sphenopalatine arteries.

Deep auricular artery

The deep auricular artery pierces the osseous or cartilaginous wall of the external acoustic meatus and supplies the skin of the external acoustic meatus and part of the tympanic membrane. A small branch contributes to the arterial supply of the temporomandibular joint.

Anterior tympanic artery

The anterior tympanic artery passes through the petrotympanic fissure to supply part of the lining of the middle ear and accompanies the chorda tympani nerve.

Middle meningeal artery

The middle meningeal artery is the main source of blood to the calvaria (see Fig. 38.22). It may arise either directly from the first part of the maxillary artery or from a common trunk with the inferior alveolar artery. When the maxillary artery lies superficial to lateral pterygoid, the middle meningeal artery is usually the first branch of the maxillary artery: this is not usually the case when the maxillary artery takes a deep course in relation to the muscle. The middle meningeal artery ascends between the sphenomandibular ligament and lateral pterygoid, passes between the two roots of the auriculotemporal nerve, and leaves the infratemporal fossa through the foramen spinosum to enter the cranial cavity medial to the midpoint of the zygomatic bone. It then runs in an anterolateral groove on the squamous part of the temporal bone, dividing into frontal and parietal branches (see Fig. 25.10A). The larger frontal (anterior) branch crosses the greater wing of the sphenoid and enters a groove or canal in the sphenoidal angle of the parietal bone (the sphenoparietal canal). It divides into branches between the dura mater and cranium; some branches ascend to the vertex. The parietal (posterior) branch curves back on the squamous temporal bone, reaches the lower border of the parietal bone anterior to its mastoid angle and divides to supply the posterior parts of the dura mater and cranium. These frontal and parietal branches anastomose with their fellows and with the anterior and posterior meningeal arteries.

Ganglionic branches supply the trigeminal ganglion and associated roots. The petrosal branch enters the hiatus for the greater petrosal nerve, supplies the facial nerve, geniculate ganglion and tympanic cavity, and anastomoses with the stylomastoid artery (El Khouly et al 2008). The superior tympanic artery runs in the canal for tensor tympani and supplies the muscle and the mucosa that lines the canal. Temporal branches traverse minute foramina in the greater wing of the sphenoid and anastomose with deep temporal arteries that supply temporalis. An anastomotic branch enters the orbit laterally in the superior orbital fissure, and anastomoses with a recurrent branch of the lacrimal artery; enlargement of this anastomosis is believed to account for the occasional origin of the lacrimal artery from the middle meningeal artery.

Accessory meningeal artery

The accessory meningeal artery may arise from the maxillary artery or the middle meningeal artery. It enters the cranial cavity through the foramen ovale and supplies the trigeminal ganglion, dura mater and bone. Its main distribution is extracranial, principally to medial pterygoid, lateral pterygoid (upper head), tensor veli palatini, the greater wing and pterygoid processes of the sphenoid bone, the mandibular nerve and the otic ganglion. It is sometimes replaced by separate small arteries.

Inferior alveolar artery

The inferior alveolar (dental) artery descends in the infratemporal fossa posterior to the inferior alveolar nerve. Here, it lies between the ramus of the mandible laterally and the sphenomandibular ligament medially. Before entering the mandibular foramen it gives off a mylohyoid branch, which pierces the sphenomandibular ligament to descend with the mylohyoid nerve in its groove on the inner surface of the ramus of the mandible. The mylohyoid artery ramifies superficially on the muscle and anastomoses with the submental branch of the facial artery. The inferior alveolar artery then traverses the mandibular canal with the inferior alveolar nerve to supply the mandibular molars and premolars, and divides into the incisive and mental arteries near the first premolar.

The incisive artery continues below the incisor teeth (which it supplies) to the midline, where it anastomoses with its fellow, although few anastomotic vessels cross the midline. In the canal, the arteries supply the mandible, tooth sockets and teeth via branches that enter the minute hole at the apex of each root to supply the pulp. The mental artery emerges onto the face from the mandibular canal at the mental foramen, supplies muscles and skin in the chin region, and anastomoses with the inferior labial and submental arteries. Near its origin, the inferior alveolar artery has a lingual branch, which descends with the lingual nerve to supply the lingual mucous membrane. The pattern of branching of the inferior alveolar artery reflects that of the nerves of the same name.

Arterial supply of periodontal ligaments

The periodontal ligaments supporting the teeth are supplied by dental branches of the alveolar arteries. One branch enters the alveolus apically and sends two or three small rami into the dental pulp through the apical foramen, and other rami into the periodontal ligament. Interdental arteries ascend in the interdental septa, sending branches at right-angles into the periodontal ligament, and terminate by communicating with gingival vessels that also supply the cervical part of the ligament. The periodontal ligament therefore receives its blood from three sources: from the apical region; ascending interdental arteries; and descending vessels from the gingivae. These vessels anastomose with each other, which means that when the pulp of a tooth is removed during endodontic treatment, the attachment tissues of the tooth remain vital.

Deep temporal arteries

The arterial supply to the temporalis in the coronal plane is concentrated mainly on its medial and lateral aspects. The anterior and posterior branches of the deep temporal arteries pass between temporalis and the pericranium, producing shallow grooves in the bone. They anastomose with the middle temporal branch of the superficial temporal artery situated laterally (Cheung 1996). The anterior deep temporal artery anastomoses with the lacrimal artery by small branches that perforate the zygomatic bone and greater wing of the sphenoid.

Masseteric artery

The masseteric artery is small and accompanies the masseteric nerve as it passes through the mandibular incisure (notch), posterior to the tendon of temporalis, to enter the deep surface of masseter (see Fig. 38.20). Its branches can also supply the temporomandibular joint. The masseteric artery anastomoses with the masseteric branches of the facial artery and with the transverse facial branch of the superficial temporal artery. This vessel is at risk and may cause considerable bleeding if damaged when the sigmoid notch is entered or split surgically.

Pterygoid arteries

The pterygoid arteries are irregular in number and origin, and are distributed to lateral and medial pterygoid.

Buccal artery

The buccal artery emerges onto the face from the infratemporal fossa. It runs obliquely forwards between medial pterygoid and the attachment of temporalis, accompanying the lower part of the buccal branch of the mandibular nerve, to supply the skin and mucosa over buccinator (see Fig. 38.21A). It anastomoses with branches of the facial and infraorbital arteries. A small lingual branch may be given off to accompany the lingual nerve and supply structures in the floor of the mouth.

Posterior superior alveolar artery

The posterior superior alveolar artery usually arises from the maxillary artery within the pterygopalatine fossa and runs through the pterygomaxillary fissure onto the maxillary tuberosity. It gives off branches that penetrate the bone here to supply the maxillary molar and premolar teeth and the maxillary air sinus, and other branches that supply the buccal mucosa. Occasionally the posterior superior alveolar artery arises from the infraorbital artery.

Infraorbital artery

The infraorbital artery often arises with the posterior superior alveolar artery. It enters the orbit posteriorly through the inferior orbital fissure. Accompanying the infraorbital nerve, it passes along the infraorbital groove of the maxilla in the floor of the orbit before entering the infraorbital canal, and emerges onto the face through the infraorbital foramen. On the face the infraorbital artery supplies the lower eyelid, the lateral aspect of the nose and the upper lip.

While in the infraorbital groove, it gives off branches that supply inferior rectus and inferior oblique, the nasolacrimal sac and, occasionally, the lacrimal gland.

Within the infraorbital canal it gives off the anterior superior alveolar artery which curves through the canalis sinuosus to supply the upper incisor and canine teeth and the mucous membrane in the anterior part of the maxillary sinus. The canalis sinuosus swerves laterally from the infraorbital canal and inferomedially below it in the wall of the maxillary sinus, following the rim of the anterior nasal aperture, between the alveoli of canine and incisor teeth and the nasal cavity. It ends near the nasal septum where its terminal branch emerges. The canal may be up to 55 mm long.

A middle superior alveolar artery is often described. When present, it branches from the infraorbital artery within the infraorbital canal and runs inferiorly along the lateral wall of the maxillary sinus towards the region of the canine and lateral incisor teeth, forming anastomotic arcades with the anterior and posterior superior alveolar arteries, and terminating near the canine tooth.

The infraorbital artery has extensive anastomoses with the transverse facial and buccal arteries and with branches of the ophthalmic and facial arteries.

Artery of the pterygoid canal

The artery of the pterygoid canal (Vidian artery) usually arises as a branch of the distal part of the maxillary artery or sometimes as a branch of the petrous segment of the internal carotid artery. It passes through the pterygoid canal and anastomoses with the pharyngeal, ethmoidal and sphenopalatine arteries in the pterygopalatine fossa and with the ascending pharyngeal, accessory meningeal, ascending palatine and descending palatine arteries in the oropharynx and around the pharyngotympanic tube. Through these complex anastomoses, the artery of the pterygoid canal contributes to the supply of part of the pharyngotympanic tube, the tympanic cavity and the upper part of the pharynx. It can also anastomose with the artery of the foramen rotundum and so communicate with branches of the cavernous portion of the internal carotid artery.

The communication between the internal and external carotid arteries via the artery of the pterygoid canal is one of a number of collateral vascular pathways that exist between the external carotid artery and branches of the petrous and intracavernous segments of the internal carotid artery. Albeit small and difficult to demonstrate angiographically, these vascular connections may nevertheless provide the arterial supply for arteriovenous malformations, dural-based fistulae and skull base tumours, and may also compensate for occlusion of the internal carotid artery. They also pose a risk of inadvertent embolization of the brain parenchyma during interventional angiography of the external carotid artery system.

There are extensive communications between the artery of the pterygoid canal and the highly vascular nasopharyngeal mucosa. Embolization of branches of the external carotid artery can result in incomplete obliteration of a vascular nasopharyngeal lesion when the artery of the pterygoid canal arises from the internal carotid artery. The collateral circulation provided by the artery of the pterygoid canal can help to maintain cerebral circulation if there is stenosis of the petrous internal carotid artery proximal to the point where the artery of the pterygoid canal joins it, because blood flow in the post-stenotic segment of the internal carotid artery will be supplemented from the external carotid artery via the artery of the pterygoid canal (see Fig. 38.29) (Allen et al 2005, Takeuchi et al 2005, Tubbs et al 2007).

Pharyngeal artery

The pharyngeal branch of the maxillary artery passes through the palatovaginal canal, accompanying the nerve of the same name, and is distributed to the mucosa of the nasal roof, nasopharynx, sphenoidal air sinus and pharyngotympanic tube.

Greater (descending) palatine artery

The greater palatine artery leaves the pterygopalatine fossa through the greater (anterior) palatine canal, within which it gives off two or three lesser palatine arteries. The greater palatine artery supplies the inferior meatus of the nasal cavity, then passes onto the roof of the hard palate at the greater (anterior) palatine foramen and runs forwards to supply the hard palate and the palatal gingivae of the maxillary teeth. It gives off a branch that runs up into the incisive canal to anastomose with the nasopalatine artery and so contribute to the arterial supply of the nasal septum. The lesser palatine arteries emerge on to the palate through the lesser (posterior) palatine foramen, or foramina, and supply the soft palate.

As the greater palatine artery runs the length of the hard palate, it permits axial mucoperiosteal flaps to be raised, if necessary bilaterally, for the reconstruction of local defects. It is also possible to pedicle the entire mucoperiosteum of the hard palate on a single greater palatine artery. The vascular supply to the denuded palatal bone is sufficient, presumably from its nasal surface, to permit regeneration of the palatal soft tissue. Contracture of the regenerated tissue does not occur because the defect lies over the palatal bone (Gullane and Arena 1977, Gullane and Arena 1985, Salins and Benjamin 2009).

Sphenopalatine artery

The sphenopalatine artery and the greater palatine artery are the terminal branches of the maxillary artery. The sphenopalatine artery is the principal artery that supplies the mucosa of the nasal cavity. It passes through the sphenopalatine foramen posterior to the superior meatus. From here, its posterior lateral nasal branches ramify over the turbinates and meatuses and anastomose with the ethmoidal arteries and nasal branches of the greater palatine artery to supply the frontal, maxillary, ethmoidal and sphenoidal air sinuses. The sphenopalatine artery next crosses anteriorly on the inferior surface of the sphenoid and ends on the nasal septum in a series of posterior septal branches that anastomose with the ethmoidal arteries (see Fig. 39.9).

Ligation of the sphenopalatine artery may be necessary in the control of refractory epistaxis. It is usually located endoscopically at the postero-inferior end of the middle turbinate. Multiple branches may be encountered. The sphenopalatine artery provides the axial blood supply to the nasal septal mucosal flap (nasoseptal flap) used in endoscopic skull-base repair, a reflection of its contribution to the vascular supply to the nasal cavity (Hadad et al 2006).

Internal carotid artery

The internal carotid artery supplies most of the ipsilateral cerebral hemisphere, eye and accessory organs, the forehead and, in part, the nose. From its origin at the carotid bifurcation, approximately at the level of T4 (see Figs 35.8–35.9) where there is usually a carotid sinus, it ascends in front of the transverse processes of the upper three cervical vertebrae to the inferior aperture of the carotid canal in the petrous part of the temporal bone. Here, it enters the cranial cavity and turns anteriorly through the cavernous sinus in the carotid groove on the side of the body of the sphenoid bone. It terminates below the anterior perforated substance by division into the anterior and middle cerebral arteries.

The internal carotid artery may be divided conveniently into cervical, petrous, cavernous and cerebral parts (see Video 26.1). Rarely, persistent embryonic branches to the basilar artery from the cervical part of the internal carotid artery may be encountered at the C1–C2 (persistent hypoglossal artery) and C2–C3 (pro-atlantal intersegmental artery) levels.

Occlusive atherosclerotic disease within either the internal carotid or common carotid arteries may cause strokes or transient ischaemic attacks (TIAs) characterized by weakness of the contralateral side. Visual disturbances experienced in the ipsilateral eye and classically described as a ‘curtain’ falling down over the visual field (amaurosis fugax) may also occur.

Cervical part

The cervical part begins at the carotid bifurcation and ascends anterior to the transverse processes of the upper three cervical vertebrae and enters the cranial cavity via the carotid canal in the petrous part of the temporal bone. The artery has no branches in the neck and so is easily distinguishable from the external carotid artery, should the latter require ligation, e.g. to control haemorrhage from a penetrating injury to the neck (Nowinski et al 2015).

Relations The internal carotid artery is initially superficial in the carotid triangle, and then passes deeper, medial to the posterior belly of digastric. Except near the skull, the internal jugular vein and vagus nerve are lateral to it within the carotid sheath. The external carotid artery is first anteromedial, but then curves back to lie superficial. Posteriorly, the internal carotid adjoins longus capitis, and the superior cervical sympathetic ganglion lies between them. The superior laryngeal nerve crosses obliquely behind it. The pharyngeal wall lies medial to the artery, which is separated by fat and pharyngeal veins from the ascending pharyngeal artery and superior laryngeal nerve. Anterolaterally, the internal carotid artery is covered by sternocleidomastoid. Below the posterior belly of digastric, the hypoglossal nerve and superior root of the ansa cervicalis and the lingual and facial veins are superficial to the artery. At the level of the digastric, the internal carotid is crossed by stylohyoid and the occipital and posterior auricular arteries. Above the digastric, it is separated from the external carotid artery by the styloid process, styloglossus and stylopharyngeus, the glossopharyngeal nerve and the pharyngeal branch of the vagus, and the deeper part of the parotid gland. At the base of the skull, the glossopharyngeal, vagus, accessory and hypoglossal nerves lie between the internal carotid artery and the internal jugular vein, which here has become posterior. The length of the artery varies with the length of the neck and the point of the carotid bifurcation. It may arise from the aortic arch, in which case it lies medial to the external carotid as far as the larynx, where it crosses behind it. The cervical portion is normally straight but may be very tortuous, when it lies closer to the pharynx than usual, very near the tonsil. In children, the tonsillocarotid distance increases with growth to a maximum value of 25 mm (Deutsch et al 1995). The internal carotid artery enters the cranium without giving off any branches. It may occasionally be absent.

Petrous part

The petrous part of the internal carotid artery ascends in the carotid canal, curves anteromedially and then superomedially above the cartilage that fills the foramen lacerum, and enters the cranial cavity. It lies at first anterior to the cochlea and tympanic cavity, and is separated from the latter and the pharyngotympanic tube by a thin, bony lamella that is cribriform in the young and partly absorbed in old age. Further anteriorly, it is separated from the trigeminal ganglion by the thin roof of the carotid canal, although this is often deficient. The artery is surrounded by a venous plexus and by the carotid autonomic plexus, derived from the internal carotid branch of the superior cervical ganglion. The petrous part of the artery gives rise to two branches. The caroticotympanic artery is a small, occasionally double, vessel that enters the tympanic cavity by a foramen in the carotid canal and anastomoses with the anterior tympanic branch of the maxillary artery and the stylomastoid artery. The pterygoid artery is inconsistent; when present, it enters the pterygoid canal with the nerve of the same name, and anastomoses with a (recurrent) branch of the greater palatine artery.

Cavernous part

The cavernous part of the internal carotid artery ascends to the posterior clinoid process. It turns anteriorly to the side of the body of the sphenoid within the cavernous sinus and then curves superiorly and medial to the anterior clinoid process, to emerge through the dural roof of the sinus. The oculomotor, trochlear, ophthalmic and abducens nerves are lateral to it within the cavernous sinus. The abducens nerve is closely related to the lateral wall of the internal carotid artery, whilst the oculomotor and trochlear nerves are situated in the lateral wall of the cavernous sinus (see Figs 25.8–25.9). This explains the higher risk of abducens nerve injury secondary to pathology such as aneurysms of the cavernous part of the carotid artery. Occasionally the caroticoclinoid ligament between the anterior and middle clinoid processes becomes ossified, forming a bony ring (caroticoclinoid foramen) around the artery (Ray and Gupta 2006).

The cavernous part of the artery gives off a number of small vessels. Branches supply the trigeminal ganglion, the walls of the cavernous and inferior petrosal sinuses, and the nerves contained therein. A minute meningeal branch passes over the lesser wing of the sphenoid to supply the dura mater and bone in the anterior cranial fossa, and also anastomoses with a meningeal branch of the posterior ethmoidal artery. Numerous small hypophysial branches supply the neurohypophysis, and are of particular importance because they form the pituitary portal system (see Fig. 23.11).

Intracranial part

After piercing the dura mater, the internal carotid artery turns back below the optic nerve to run between it and the oculomotor nerve. It reaches the anterior perforated substance at the medial end of the lateral fissure and terminates by dividing into the anterior and middle cerebral arteries (see Fig. 26.3).

Several preterminal vessels leave the cerebral portion of the internal carotid. The ophthalmic artery arises from the anterior part of the internal carotid as it leaves the cavernous sinus, often at the point of piercing the dura, and enters the orbit through the optic canal. The posterior communicating artery (see Fig. 26.3) runs back from the internal carotid above the oculomotor nerve, and anastomoses with the posterior cerebral artery (a terminal branch of the basilar artery), thereby contributing to the circulus arteriosus around the interpeduncular fossa. The posterior communicating artery is usually very small. However, sometimes it is so large that the posterior cerebral artery is supplied via the posterior communicating artery rather than from the basilar artery ('fetal posterior communicating artery'); it is often larger on one side only. Small branches from its posterior half pierce the posterior perforated substance together with branches from the posterior cerebral artery. Collectively they supply the medial thalamic surface and the walls of the third ventricle. The anterior choroidal artery leaves the internal carotid just distal to its posterior communicating branch and passes back above the medial part of the uncus. It crosses the optic tract to reach and supply the crus cerebri of the midbrain, then turns laterally, recrosses the optic tract, and gains the lateral side of the lateral geniculate body, which it supplies with several branches. It finally enters the inferior horn of the lateral ventricle via the choroidal fissure and ends in the choroid plexus. This small, but important, vessel also contributes to the blood supply of the globus pallidus, caudate nucleus, amygdala, hypothalamus, tuber cinereum, red nucleus, substantia nigra, posterior limb of the internal capsule, optic radiation, optic tract, hippocampus and the fimbria of the fornix.

The combination of the petrous, cavernous and intracranial parts of the internal carotid artery is called the 'carotid siphon' because of its sigmoid course (see Fig. 26.1 and Video 26.1). However, in infants, the parasellar region of the internal carotid artery does not form a siphon but takes a relatively straight course (Weninger and Muller 1999). The cranial and sympathetic nerves therefore have different topographical relationships with the artery in the infant compared with that found in older children and adults.

The initial millimetres of the intracranial part lie between two rings (proximal and distal rings) of dense connective tissue that surround the carotid artery where the ophthalmic artery usually branches. In cases of surgical clipping of ophthalmic artery aneurysms, it is of surgical relevance for neurosurgeons to expose this part of the artery by removing the anterior clinoid process and exposing this segment of the internal carotid artery (see Video 26.1).

Ophthalmic artery

The ophthalmic artery leaves the internal carotid artery as it exits the cavernous sinus medial to the anterior clinoid process. It enters the orbit by the optic canal, inferolateral to the optic nerve and continues forwards for a short distance before turning medially by crossing (almost always) over or under the optic nerve (see Fig. 44.13A). The main trunk of the artery continues along the medial wall of the orbit between the superior oblique and lateral rectus, and divides into supratrochlear (frontal) and dorsal nasal branches at the medial end of the upper eyelid. Although the order of branches from the ophthalmic artery is quite variable, there are several consistent branches, including the central retinal artery, muscular branches, ciliary arteries, lacrimal artery, supraorbital artery, anterior and posterior ethmoidal arteries, meningeal branch, medial palpebral arteries, supratrochlear artery and dorsal nasal artery (Hayreh and Dass 1962a). Many of the branches of the ophthalmic artery accompany sensory nerves with the same name and have a similar distribution to these nerves. Variations in the origin and course of the ophthalmic artery have been described (Huynh-Le et al 2005, Hayreh 2006, Bertelli et al 2017).

Central retinal artery

The small central artery of the retina is the first branch of the ophthalmic artery. It begins below the optic nerve and, for a short distance, lies in the dural sheath of the nerve. It enters the inferomedial surface of the nerve 6.4–15.2 mm behind the eyeball, and runs to the retina (accompanying the central retinal vein) along its axis (Kocabiyik et al 2005). It travels within the optic nerve to its head, where it passes through the lamina cribrosa. At this level, the ophthalmic artery divides into equal superior and inferior branches, each of which, after a few millimetres, give off nasal and temporal branches that supply the 'quadrants' of the retina (see Fig. 45.27). Although similar retinal veins unite to form the central retinal vein, the courses of the arteries and veins do not correspond exactly. These vessels mainly run within the nerve fibre and ganglion cell layers of the retina, a course that accounts for their clarity when seen through an ophthalmoscope (see Fig. 45.20A), and explains why they can serve as an easily accessible indicator of cardiovascular disease. Arteries often cross veins, usually lying superficial to them; in severe hypertension, the arteries may press on the veins and cause visible dilations distal to these crossings. The vitreal location of arteries, their lighter, bright red coloration and smaller diameter in comparison to veins allow the two vessel types to be distinguished ophthalmoscopically. The detailed pattern of the inner retinal vessels is unique and therefore can be used as a source of biometric information for individual recognition.

From the four major arteries within the inner retina, dichotomous branches run from the posterior pole to the periphery, supplying the whole retina (Zhang 1994). Arteries and veins ramify in the nerve fibre layer, near the internal limiting membrane, and arterioles pass deeper into the retina to supply capillary beds. Venules return from these beds to larger superficial veins that converge towards the disc to form the central retinal vein.

Retinal capillary networks are often in three different layers, the number of layers depending on location. Radial peripapillary capillaries are the most superficial of the capillary networks and lie within the inner nerve fibre layer. A layer of inner capillaries runs within the nerve fibre and ganglion cell layers, and an outer capillary layer is located in the inner plexiform and inner nuclear layers (see Fig. 45.29). Approaching the fovea, capillaries are restricted to two layers, and terminal capillaries eventually join to form a single-layered macular capillary ring, producing a capillary-free zone 450–500 μm in diameter at the fovea. This avascular region is clearly visible in a fluorescein angiogram (see Fig. 45.20B). Capillaries become less numerous in the peripheral retina and are absent from a zone approximately 1.5 mm wide adjoining the ora serrata.

The territories of the arteries that supply a particular quadrant do not overlap, nor do the branches within a quadrant anastomose with each other, which means that a blockage in a retinal artery causes loss of vision in the corresponding part of the visual field. The only exception to this end-arterial pattern is in the vicinity of the optic disc. Here, the posterior ciliary arteries enter the eye near the disc and their rami not only supply the adjacent choroid, but also form an anastomotic circle in the sclera around the head of the optic nerve (circle of Zinn/Haller) (see Fig. 45.30). Branches from this ring join the pial arteries of the nerve (see below). Small cilioretinal arteries derived from any arteries in this region may enter the eye in up to 50% of individuals and contribute to the central retinal vasculature; they may possibly preserve visual function following occlusion of the central retinal artery. Small retinociliary veins may sometimes be present.

The structure of retinal blood vessels resembles that of vessels elsewhere, except that the arteries lack an internal elastic lamina, and their adventitia may contain muscle cells. Capillaries are non-fenestrated; endothelial cells are joined by complex tight junctions, fulfilling the requirements of a blood–retinal barrier. Perivascular cells, including pericytes and glia, play key roles in the development and maintenance of the blood–retinal barrier (Bharadwaj et al 2013). Selective loss of pericytes happens early in the development of diabetic retinopathy and has been linked to the characteristic pathological changes seen in this condition (Park et al 2017). Within the optic nerve, the central artery is innervated by sympathetic and parasympathetic nerves; this innervation does not extend to the retinal vessels. The cholinergic parasympathetic supply is derived mainly from the pterygopalatine ganglion and is vasodilatory. The adrenergic postganglionic sympathetic supply originates in the superior cervical ganglion and travels via a plexus around the internal carotid and ophthalmic arteries; it is unclear whether it elicits vasoconstriction or dilation (Bergua et al 2013).

Although inner retinal blood vessels lie between the incoming light and the photoreceptors, they are not perceived because their location is constant. In marked contrast, the growth of new retinal vessels (neovascularization) is one of the major sight-threatening complications of diseases such as diabetes and retinopathy of prematurity.

Muscular arteries

Branches to the extraocular muscles frequently spring from a common trunk to form superior and inferior groups, most of which accompany branches of the oculomotor nerve. The inferior branch contains most of the anterior ciliary arteries. Other muscular vessels branch from the lacrimal and supraorbital arteries or from the trunk of the ophthalmic artery.

Ciliary arteries

The ciliary arteries are distributed in long and short posterior, and in anterior groups (see Fig. 44.13A). Long posterior ciliary arteries, usually two, pierce the sclera near the optic nerve, pass anteriorly along the horizontal meridian and join the major arterial circle of the iris (see Fig. 45.8). About seven short posterior ciliary arteries pass close to the optic nerve to reach the eyeball, where they divide into 15–20 branches. They pierce the sclera around the optic nerve to supply the choroid, and anastomose with twigs of the central retinal artery at the optic disc (see Fig. 45.30). Anterior ciliary arteries arise from muscular branches of the ophthalmic artery. They reach the eyeball on the tendons of the recti, form a circumcorneal subconjunctival vascular zone, and pierce the sclera near the sclerocorneal junction to end in the major arterial circle of the iris.

Lacrimal artery

The lacrimal artery is a large branch that usually leaves the ophthalmic artery near its exit from the optic canal (see Fig. 44.13A), although it occasionally arises before the ophthalmic artery enters the orbit. It accompanies the lacrimal nerve along the upper border of lateral rectus, supplies and traverses the lacrimal gland, and ends in the eyelids and conjunctiva as the lateral palpebral arteries. The latter run medially in the upper and lower lids and anastomose with the medial palpebral arteries. The lacrimal artery gives off one or two zygomatic branches. The zygomaticofacial artery passes through the lateral wall of the orbit to emerge onto the face at the zygomaticofacial foramen, supplies the region overlying the prominence of the cheek foramen and anastomoses with transverse facial and zygomatico-orbital branches of the facial artery. The zygomaticotemporal artery also passes through the lateral wall of the orbit, via the zygomaticotemporal foramen, supplies the skin over the non-beard part of the temple and anastomoses with the deep temporal branches of the maxillary artery. A recurrent meningeal branch, usually small, passes back via the lateral part of the superior orbital fissure to anastomose with the middle meningeal artery. This branch is sometimes large and replaces the lacrimal artery, in which case it becomes a more significant contributor to the orbital blood supply (Hayreh and Dass 1962b, Uchino et al 2013).

Supraorbital artery

The supraorbital artery leaves the ophthalmic artery where it crosses the optic nerve (see Fig. 44.13A), and ascends medial to superior rectus and levator palpebrae superioris. It accompanies the supraorbital nerve between the periosteum and levator palpebrae superioris, passes through the supraorbital foramen or notch, and divides into superficial and deep branches. These supply the skin, muscles and frontal periosteum, and anastomose with the supratrochlear artery and with the frontal branch of the superficial temporal artery and its contralateral fellow (see Fig. 36.20). The supraorbital artery supplies superior rectus and levator palpebrae superioris, sends a branch across the trochlea to the medial canthus, and often sends a branch to the diploë of the frontal bone at the supraorbital margin; it may also supply the mucoperiosteum in the frontal sinus.

Anterior ethmoidal artery

The anterior ethmoidal artery passes with its accompanying nerve through the anterior ethmoidal canal to supply the ethmoidal and frontal air sinuses. Entering the cranium, it gives off a meningeal branch to the dura mater, and nasal branches that descend into the nasal cavity with the anterior ethmoidal nerve (see Fig. 39.9). It runs in a groove on the deep surface of the nasal bone to supply the lateral nasal wall and septum. A terminal branch emerges at the junction of the nasal bone and the lateral nasal cartilage and supplies the skin covering the external nose.

Posterior ethmoidal artery

The posterior ethmoidal artery runs through the posterior ethmoidal canal and supplies the posterior ethmoidal air sinuses. Entering the cranium, it gives off a meningeal branch to the dura mater, and nasal branches that descend into the nasal cavity via the cribriform plate and anastomose with branches of the sphenopalatine artery (see Fig. 39.9).

Meningeal branch

A meningeal branch, usually small, passes back through the superior orbital fissure or its own foramen to the middle cranial fossa, where it anastomoses with the middle meningeal artery. It is sometimes large, in which case it becomes a major contributor to the orbital blood supply.

Medial palpebral arteries

Superior and inferior medial palpebral arteries arise from the ophthalmic artery below the trochlea. They descend behind the nasolacrimal sac to enter the eyelids, where each divides into two branches that course laterally along the edges of the tarsal plates, forming the superior and inferior arches and supplying the eyelids. They anastomose with branches of the supraorbital, zygomatico-orbital and lacrimal arteries. The inferior arch also anastomoses with the facial artery.

Supratrochlear artery

The supratrochlear artery is a terminal branch of the ophthalmic artery. It emerges onto the face from the orbit superomedially with the supratrochlear nerve at the frontal notch and ascends on the forehead to supply the medial parts of the upper eyelid, forehead and scalp, muscles and pericranium. It anastomoses with the supraorbital artery and with its contralateral fellow.

Dorsal nasal artery

The dorsal nasal artery is the other terminal branch of the ophthalmic artery and emerges from the orbit between the trochlea and medial palpebral ligament. It gives a branch to the upper part of the nasolacrimal sac and then divides into two branches. One branch anastomoses with the terminal part of the facial artery, and the other runs along the dorsum of the nose, supplies its outer surface and anastomoses with its contralateral fellow and the lateral nasal branch of the facial artery.

Anterior cerebral artery

The anterior cerebral artery is the smaller of the two terminal branches of the internal carotid artery (see Fig. 26.1).

Surgical nomenclature divides the vessel into three parts: A1, from the termination of the internal carotid artery to the junction with the anterior communicating artery; A2, from the junction with the anterior communicating artery to the origin of the callosomarginal artery; and A3, distal to the origin of the callosomarginal artery, this segment is also known as the pericallosal artery.

The anterior cerebral artery starts at the medial end of the stem of the lateral fissure. It passes anteromedially above the optic nerve to the great longitudinal fissure where it connects with its contralateral fellow by a short transverse anterior communicating artery. The anterior communicating artery is about 4 mm in length and may be double. It gives off numerous anteromedial central branches that supply the optic chiasma, lamina terminalis, hypothalamus, para-olfactory areas, anterior columns of the fornix and the cingulate gyrus (see Fig. 26.2C).

The two anterior cerebral arteries travel together in the great longitudinal fissure. They pass around the curve of the genu of the corpus callosum and then along its upper surface to its posterior end, where they anastomose with posterior cerebral arteries. They give off cortical and central branches.

The cortical branches of the anterior cerebral artery are named according to their distribution. Two or three orbital branches ramify on the orbital surface of the frontal lobe and supply the olfactory cortex, gyrus rectus and medial orbital gyrus. Frontal branches supply the corpus callosum, cingulate gyrus, medial frontal gyrus and paracentral lobule. Parietal branches supply the precuneus, while the frontal and parietal branches both send twigs over the superomedial border of the hemisphere to supply a strip of territory on the superolateral surface (see Fig. 26.2B). Cortical branches of the anterior cerebral artery, therefore, supply the areas of the motor and somatosensory cortices that represent the lower limb.

Central branches of the anterior cerebral artery arise from its proximal portion and enter the anterior perforated substance (see Fig. 26.3) and lamina terminalis. Collectively, they supply the rostrum of the corpus callosum, the septum pellucidum, the anterior part of the putamen, the head of the caudate nucleus and adjacent parts of the internal capsule. Immediately proximal or distal to its junction with the anterior communicating artery, the anterior cerebral artery gives rise to the medial striate artery, which supplies the anterior part of the head of the caudate nucleus and adjacent regions of the putamen and internal capsule.

Middle cerebral artery

The middle cerebral artery is the larger terminal branch of the internal carotid artery. Surgical nomenclature divides the vessel into four parts: M1, from the termination of the internal carotid artery to the bi-/trifurcation, this segment also being known as the sphenoidal; M2, the segment running in the lateral (Sylvian) fissure, also known as the insular; M3, coming out of the lateral fissure, also known as the opercular; and M4, cortical portions.

The middle cerebral artery runs at first in the lateral fissure, then posterosuperiorly on the insula, and divides into branches distributed to the insula and the adjacent lateral cerebral surface (see Figs 26.2–26.4). Like the anterior cerebral artery, it has cortical and central branches.

Cortical branches send orbital vessels to the inferior frontal gyrus and the lateral orbital surface of the frontal lobe. Frontal branches supply the precentral, middle and inferior frontal gyri. Two parietal branches are distributed to the postcentral gyrus, the lower part of the superior parietal lobule and the whole inferior parietal lobule. Two or three temporal branches supply the lateral surface of the temporal lobe. Cortical branches of the middle cerebral artery therefore supply the motor and somatosensory cortices that represent the whole of the body (other than the lower limb), the auditory area and the insula.

Small central branches of the middle cerebral artery, the lateral striate or lenticulostriate arteries, arise at its origin and enter the anterior perforated substance together with the medial striate artery. Lateral striate arteries ascend in the external capsule over the lower lateral aspect of the lentiform complex, then turn medially, traverse the lentiform complex and the internal capsule and extend as far as the caudate nucleus.

Circulus arteriosus cerebri

The circulus arteriosus cerebri (cerebral arterial circle, circle of Willis) is a large arterial anastomosis that unites the internal carotid and vertebrobasilar systems (see Fig. 26.3). It lies in the subarachnoid space within the basal cisterns that surround the optic chiasma and infundibulum. The anterior cerebral arteries are derived from the internal carotid arteries and are linked by a small, but functionally important, anterior communicating artery. Posteriorly, the two posterior cerebral arteries, formed by the division of the basilar artery, are joined to the ipsilateral internal carotid artery by a posterior communicating artery.

There is considerable individual variation in the pattern and calibre of vessels that make up the circulus arteriosus (Puchades-Orts et al 1976). Although a complete circular channel almost always exists, one vessel is usually sufficiently narrowed to reduce its role as a collateral route and the circle is rarely functionally complete. Cerebral and communicating arteries individually may all be absent, variably hypoplastic, double or even triple. The haemodynamics of the circle are influenced by variations in the calibre of communicating arteries and in the segments of the anterior and posterior cerebral arteries that lie between their origins and their junctions with the corresponding communicating arteries. The greatest variation in calibre between individuals occurs in the posterior communicating artery, which is normally very small, so that only limited flow is possible between the anterior and posterior circulations. Commonly, the diameter of the pre-communicating part of the posterior cerebral artery is larger than that of the posterior communicating artery, in which case the blood supply to the occipital lobes is mainly from the vertebrobasilar system. However, sometimes the diameter of the pre-communicating part of the posterior cerebral artery is smaller than that of the posterior communicating artery, in which case the blood supply to the occipital lobes is mainly from the internal carotids via the posterior communicating arteries. Since the primary purpose of the vascular circle is to provide anastomotic channels if one vessel is occluded, it is important to note that a normal-sized posterior communicating artery cannot usually fulfil this role. Agenesis or hypoplasia of the initial segment of the anterior cerebral artery is more frequent than anomalies in the anterior communicating artery and contribute to defective circulation in about one-third of individuals.

Central or perforating arteries

Numerous small central (perforating or ganglionic) arteries arise from the circulus arteriosus or from vessels near it (see Fig. 26.3). Many of these enter the brain through the anterior and posterior perforated substances. Central branches supply nearby structures on or near the base of the brain together with the interior of the cerebral hemisphere, including the internal capsule, basal ganglia and thalamus. These branches form four principal groups. The anteromedial group arises from the anterior cerebral and anterior communicating arteries, and passes through the medial part of the anterior perforated substance. These arteries supply the optic chiasma, lamina terminalis, anterior, preoptic and supraoptic areas of the hypothalamus, septum, para-olfactory areas, anterior columns of the fornix, cingulate gyrus, rostrum of the corpus callosum and the anterior part of the putamen and the head of the caudate nucleus. The posteromedial group comes from the entire length of the posterior communicating artery and from the proximal portion of the posterior cerebral artery. Anteriorly, these arteries supply the hypothalamus and pituitary gland, and the anterior and medial parts of the thalamus via thalamo-perforating arteries. Caudally, branches of the posteromedial group supply the mammillary bodies, subthalamus, the lateral wall of the third ventricle, including the medial thalamus, and the globus pallidus. The anterolateral group is mostly comprised of branches from the proximal part of the middle cerebral artery that are also known as striate, lateral striate or lenticulostriate arteries. They enter the brain through the anterior perforated substance and supply the posterior striatum, lateral globus pallidus and the anterior limb, genu and posterior limb of the internal capsule. The medial striate artery, derived from the middle or anterior cerebral arteries, supplies the rostral part of the caudate nucleus and putamen, and the anterior limb and genu of the internal capsule. The posterolateral group is derived from the posterior cerebral artery distal to its junction with the posterior communicating artery, and supplies the cerebral peduncle, colliculi, pineal gland and, via thalamogeniculate branches, the posterior thalamus and medial geniculate body.

ARTERIAL SUPPLY OF THE BRAIN AND MENINGES

Meningeal arteries

Despite their names, the cranial meningeal arteries are predominantly periosteal (see Fig. 25.10A). Their main targets are bone and haemopoietic marrow, and only some arterial branches are distributed to the cranial dura mater *per se*.

The branches of the meningeal vessels lie mainly in the endosteal layer of dura. In the anterior cranial fossa, the dura is supplied by the anterior meningeal branches of the anterior and posterior ethmoidal and internal carotid arteries and a branch of the middle meningeal artery. In the middle cranial fossa, the dura is supplied by the middle and accessory meningeal branches of the maxillary artery; a branch of the ascending pharyngeal artery (entering via the foramen lacerum); branches of the internal carotid artery; and a recurrent branch of the lacrimal artery. In the posterior fossa, the dura is supplied by meningeal branches of the occipital artery which enter the skull by the jugular and mastoid foramina; the posterior meningeal branches of the vertebral artery; occasional small branches of the ascending pharyngeal artery which enter the skull by the jugular foramen and hypoglossal canal; and dorsal meningeal and tentorial branches from the meningohypophysial trunk. The anatomy of the meningeal arteries explains the vascular supply of tumours arising from the meninges (meningiomas) and the architecture of dural arteriovenous fistulae and malformations. (For detailed information on the surgical anatomy of the meningeal arteries, see Lasjaunias et al (2001), Martins et al (2005).)

Brainstem

The medulla oblongata is supplied by branches of the vertebral, anterior and posterior spinal, posterior inferior cerebellar and basilar arteries, entering along the ventral median fissure and the dorsal median sulcus. Vessels that supply the central substance enter along the rootlets of the glossopharyngeal, vagus and hypoglossal nerves. There is an additional supply via a pial plexus from the same main arteries. The choroid plexus of the fourth ventricle is supplied by the posterior inferior cerebellar arteries. The pons is supplied by the basilar artery and the anterior inferior and superior cerebellar arteries. Direct branches from the basilar artery enter the pons along the basilar sulcus. Other vessels enter along the trigeminal, abducens, facial and vestibulocochlear nerves and from the pial plexus. The midbrain is supplied by the posterior cerebral, superior cerebellar and basilar arteries. The crura cerebri are supplied by vessels entering on their medial and lateral sides. The medial vessels enter the medial side of the crus and also supply the superomedial part of the tegmentum, including the oculomotor nucleus. Lateral vessels supply the lateral part of the crus and the tegmentum. The colliculi are supplied by three vessels on each side from the posterior cerebral and superior cerebellar arteries. An additional supply to the crura, and the colliculi and their peduncles, comes from the posterolateral group of central branches of the posterior cerebral artery.

Cerebellum

The cerebellum is supplied by the posterior inferior, anterior inferior and superior cerebellar arteries. The cerebellar arteries form superficial anastomoses on the cortical surface. Anastomoses between deeper, subcortical, branches have been postulated (Duvernoy et al 1983).

Optic chiasma, tract and radiation

The blood supply to the optic chiasma, tract and radiation is of considerable clinical importance. The chiasma is supplied in part by the anterior cerebral arteries but its median zone depends upon rami from the internal carotid arteries reaching it via the stalk of the hypophysis. The anterior choroidal and posterior communicating arteries supply the optic tract, and the optic radiation receives blood through deep branches of the middle and posterior cerebral arteries.

Diencephalon

The thalamus is supplied chiefly by branches of the posterior communicating, posterior cerebral and basilar arteries (Plets et al 1970). A contribution from the anterior choroidal artery is often noted but this has been disputed. The medial branch of the posterior choroidal artery supplies the posterior commissure, habenular region, pineal gland and medial parts of the thalamus, including the pulvinar. Small central branches, which arise from the circulus arteriosus and its associated vessels, supply the hypothalamus. The pituitary gland is supplied by hypophysial arteries derived from the internal carotid artery, and the anterior cerebral and anterior communicating arteries supply the lamina terminalis.

The choroid plexuses of the third and lateral ventricles are supplied by branches of the internal carotid and posterior cerebral arteries.

Basal ganglia

The majority of the arterial supply to the basal ganglia comes from the striate arteries, which are branches from the roots of the anterior and middle cerebral arteries. They enter the brain through the anterior perforated substance and also supply the internal capsule. The caudate nucleus receives blood additionally from the anterior and posterior choroidal arteries. The posteroinferior part of the lentiform complex is supplied by the thalamostriate branches of the posterior cerebral artery. The anterior choroidal artery, a preterminal branch of the internal carotid artery, contributes to the blood supply of both segments of the globus pallidus and the caudate nucleus. Famously, the ligation of this vessel during a neurosurgical procedure on a patient suffering from Parkinson's disease led to alleviation of the parkinsonian symptoms, presumably as a consequence of infarction of the globus pallidus. This chance observation led to the initiation of pallidal surgery (pallidotomy) for this condition.

Internal capsule

The internal capsule is supplied by central, or perforating, arteries that arise from the circulus arteriosus and its associated vessels. These include the lateral and medial striate arteries that come from the middle and anterior cerebral arteries and also supply the basal ganglia. The lateral striate arteries supply the anterior limb, genu and much of the posterior limb of the internal capsule and are commonly involved in ischaemic and haemorrhagic stroke. One of the larger striate branches of the middle cerebral artery is anachronistically known as 'Charcot's artery of cerebral haemorrhage'. The medial striate artery, a branch of the proximal part of either the middle or anterior cerebral artery, supplies the anterior limb and genu of the internal capsule and the basal ganglia. The anterior choroidal artery also contributes to the supply of the ventral part of the posterior limb and the retrolenticular part of the internal capsule.

Cerebral cortex

The entire blood supply of the cerebral cortex comes from cortical branches of the anterior, middle and posterior cerebral arteries (see Figs 26.1–26.2, 26.4–26.5, Video 26.1; Duvernoy et al 1981). In general, long branches traverse the cortex and penetrate the subjacent white matter for 3 or 4 cm without communicating. Short branches are confined to the cerebral cortex and form a compact network in the middle zone of the grey matter, whereas the outer and inner zones are sparingly supplied. Although adjacent vessels anastomose on the surface of the brain, they become end arteries as soon as they enter it. In general, superficial anastomoses only occur between microscopic branches of the cerebral arteries, and there is little evidence that they can provide an effective alternative circulation after the occlusion of larger vessels.

The lateral surface of the hemisphere is mainly supplied by the middle cerebral artery. This includes the territories of the motor and somatosensory cortices, which represent the whole of the body, apart from the lower limb, and also the auditory cortex and language areas. The anterior cerebral artery supplies a strip next to the superomedial border of the hemisphere, as far back as the parieto-occipital sulcus. The occipital lobe and most of the inferior temporal gyrus (excluding the temporal pole) are supplied by the posterior cerebral artery.

Medial and inferior surfaces of the hemisphere are supplied by the anterior, middle and posterior cerebral arteries. The area supplied by the anterior cerebral artery is the largest; it extends almost to the parieto-occipital sulcus and includes the medial part of the orbital surface. The rest of the orbital surface and the temporal pole are supplied by the middle cerebral artery, and the remaining medial and inferior surfaces are supplied by the posterior cerebral artery.

Near the occipital pole, the junctional zone between the territories of the middle and posterior cerebral arteries corresponds to the visual (striate) cortex, which receives information from the macula. When the posterior cerebral artery is occluded, a phenomenon known as 'macular sparing' may occur, in which vision with the central part of the retina is preserved. Collateral circulation of blood from branches of the middle cerebral artery into those of the posterior cerebral artery may account for this phenomenon. In addition, in some individuals, the middle cerebral artery may itself supply the macular area.

ARTERIAL SUPPLY OF THE SPINAL CORD, ROOTS AND NERVES

The spinal cord and its roots and nerves are supplied with blood by both longitudinal and segmental vessels (see Fig. 47.11). Three major longitudinal vessels, a single anterior and two posterior spinal arteries (each of which is sometimes doubled to pass on either side of the dorsal rootlets) originate intracranially from the vertebral artery and terminate in a plexus around the conus medullaris. The anterior spinal artery forms from the fused anterior spinal branches of the vertebral artery, and descends in the ventral median fissure of the cord. Each posterior spinal artery originates either directly from the ipsilateral vertebral artery or from its posterior inferior cerebellar branch, and descends in a posterolateral sulcus of the cord. The segmental arteries are derived in craniocaudal sequence from spinal branches of the vertebral, deep cervical, intercostal and lumbar arteries. These vessels enter the vertebral canal through the intervertebral foramina and anastomose with branches of the longitudinal vessels to form a pial plexus on the surface of the cord. The segmental spinal arteries send anterior and posterior radicular branches to the spinal cord along the ventral and dorsal roots. Most anterior radicular arteries are small and end in the ventral nerve roots or in the pial plexus of the cord. The small posterior radicular arteries also supply the dorsal root ganglia; branches enter at both ganglionic poles to be distributed around ganglion cells and nerve fibres (see also Crock (1996).)

Segmental radiculomedullary feeder arteries

Some radicular arteries, mainly situated in the lower cervical, lower thoracic and upper lumbar regions, are large enough to reach the ventral median fissure, where they divide into slender ascending and large descending branches. These are the anterior radiculomedullary feeder arteries (Dommisse 1975). They anastomose with the anterior spinal arteries to form a single or partly double longitudinal vessel of uneven calibre along the ventral median fissure. The largest anterior medullary feeder, the great anterior radiculomedullary artery of Adamkiewicz, varies in level, arising from a spinal branch of either one of the lower posterior intercostal arteries (T9–T11), or of the subcostal artery (T12), or less frequently of the upper lumbar arteries (L1 and L2). It most often arises on the left side (Carmichael and Gloviczki 1999). Reaching the spinal cord, it sends a branch to the anterior spinal artery below and another to anastomose with the ramus of the posterior spinal artery, which lies anterior to the dorsal roots. It may be the main supply to the lower two-thirds of the cord. Central branches of the anterior spinal artery enter the ventral median fissure, and then turn right or left to supply the ventral grey column, the base of the dorsal grey column, including the dorsal nucleus, and the adjacent white matter (see Fig. 47.12).

Each posterior spinal artery contributes to a pair of longitudinal anastomotic channels, anterior and posterior to the dorsal spinal roots. These are reinforced by posterior medullary feeders from the posterior radicular arteries. The latter are variable in number and size, but smaller, more numerous and more evenly distributed than the anterior medullary feeders. The anterior channel is joined by a ramus from the descending branch of the great anterior segmental medullary artery of Adamkiewicz. In all longitudinal spinal arteries the width of the lumen is uneven and complete interruptions may occur. At the conus medullaris they communicate by anastomotic loops. Anastomoses other than those between the pial or peripheral spinal arterial branches may be important, e.g. a posterior spinal series of anastomoses between rami of the dorsal divisions of segmental arteries near the spinous processes.

Intramedullary arteries

The central branches of the anterior spinal artery supply about two-thirds of the cross-sectional area of the cord. The rest of the dorsal grey and white columns and peripheral parts of the lateral and ventral white columns are supplied by numerous small radial vessels that branch from posterior spinal arteries and the pial plexus. In a microangiographic study of the human cervical spinal cord, up to six anterior, and eight posterior, radicular spinal arteries were described, and up to eight central branches arose from each centimetre of the anterior spinal artery (Turnbull et al 1966). Abnormalities of blood vessels in the spinal cord can result in clinically significant haemorrhages and neurological events (see Fig. 47.13).

Spinal cord ischaemia

The spinal cord can rely for neither its transverse nor its longitudinal blood supply entirely on the longitudinal arteries. The anterior longitudinal artery and the intramedullary arteries are functional end-arteries, although overlap of territories of supply has been described (Backes and Nijenhuis 2008). Damage to the anterior longitudinal artery can result in loss of function of the anterior two-thirds of the cord (see Fig. 47.14). The longitudinal arteries cannot supply the whole length of the cord, and the input of the segmental medullary feeder vessels is essential. This is especially true of the artery of Adamkiewicz, which may effectively carry the major supply for the lower cord; damage to this individual artery compromises perfusion of the distal cord and may be responsible for paraplegia following aortic bypass procedures. For many years it was assumed that the anterior spinal artery system provided the dominant supply to the cord, but clinical evidence implies that the posterior spinal arteries may be as important as the anterior system in protecting the cord. The mid-thoracic cord, distant from the main anterior medullary feeders, is particularly liable to become ischaemic after periods of hypotension; T4–T9 has been described as the critical vascular zone of the spinal cord, where interference with the circulation is most likely to result in paraplegia.

ARTERIAL SUPPLY OF THE THORAX, ABDOMEN AND PELVIS

Pulmonary trunk

The pulmonary trunk conveys deoxygenated blood from the right ventricle to the lungs (see Figs 57.4, 57.10). About 5 cm in length and 3 cm in diameter, it is the most anterior of the cardiac vessels and arises from the pulmonary anulus surrounding the subpulmonary conus arteriosus (infundibulum) at the base of the right ventricle, superior and to the left of the supraventricular crest. The pulmonary trunk inclines posterosuperiorly and divides into right and left pulmonary arteries, of almost equal size, at the level of the body of the sixth thoracic vertebra (range, bodies of the fourth to the eighth thoracic vertebrae), 2–3 cm inferior to the sternal plane and inferior to the aortic arch to the left of the midline (see Table 52.2). The bifurcation of the pulmonary trunk commonly lies anteroinferior and to the left of the tracheal bifurcation and the associated subcarinal (inferior tracheobronchial) lymph nodes and deep cardiac plexus. In the fetus, at the level of the tracheal bifurcation, the left pulmonary artery is connected to the aortic arch by the ductus arteriosus, the obliterated remnant of which forms the ligamentum arteriosum in the adult (Ch. 13).

Relations The pulmonary trunk is located entirely within the pericardium, enclosed with the ascending aorta in a common sheath of visceral pericardium (see Figs 57.1, 58.1). The fibrous pericardium gradually blends with and disappears within the adventitia of the pulmonary arteries. Anteriorly, it is separated from the sternal end of the left second intercostal space, and/or the third costal cartilage, by the pericardium, pleura, left lung and the superior part of transversus thoracis. Posterior relations of the proximal part near to its origin are the ascending aorta and left coronary artery, and superiorly, the left atrium. Moving superiorly, the ascending aorta spirals around the pulmonary trunk and comes to lie to the right of its more superior part. The atrial auricles and left and right coronary arteries lie on each side of its origin. The superficial cardiac plexus lies between the branching of the pulmonary trunk and the aortic arch (see Fig. 57.61). The tracheal bifurcation and subcarinal lymph nodes are superior and to the right (see Fig. 52.7).

Variants and congenital anomalies The pulmonary trunk is a relatively constant structure and there are minimal variations in healthy individuals. Congenital anomalies include pulmonary atresia and truncus arteriosus (common truncus).

The coronary arteries usually originate from the aortic sinuses, but occasionally may arise from ectopic locations. Most commonly, an ectopic left coronary artery arises from the pulmonary trunk or one of its branches (Bland–White–Garland syndrome) (see Fig. 58.2). This potentially fatal condition requires urgent surgical correction because the myocardium is supplied with deoxygenated pulmonary blood instead of systemic blood (Loukas et al 2009). Infantile symptoms include pallor, fatigue, irritability, weak cry, cough, dyspnoea, and signs of ischaemia and cardiac failure precipitated during or after feeding, or during defecation or crying. The electrocardiogram may reveal deep narrow Q waves, left ventricular hypertrophy and left axis deviation. Radiologically, cardiomegaly is present with left ventricular and left atrial enlargement. Colour flow imaging can identify the anomalous origin of the left coronary artery. The pulmonary trunk may also give rise to the right coronary artery, the left anterior interventricular branch of the left coronary artery, or even both coronary arteries. Typically, there is an extensive development of collateral vessels in the heart (see Fig. 58.3).

Pulmonary atresia is caused by a complete obstruction of pulmonary outflow and may be due to an absence or defect of the pulmonary valvular leaflets. It is associated with a blind-ending pulmonary trunk that causes right ventricular hypoplasia. Reduced flow may render the pulmonary trunk atretic, small or even normal in size, making diagnosis challenging. A diminished pulmonary flow is supplied through a patent ductus arteriosus (Smith and McKay 2004), and a concomitant ventricular septal defect may permit outflow from the right ventricle. Surgical repair is necessary to allow adequate oxygenation of blood throughout the body.

In truncus arteriosus (common truncus), a single common arterial trunk exits the heart and subsequently divides into the pulmonary trunk and the ascending aorta. Early neonatal life is possible because there is usually a coexisting ventricular septal defect; expedited surgical repair is necessary to avoid congestive heart failure, failure to thrive and death.

Right pulmonary artery

The right pulmonary artery divides into two large branches posterior to the superior vena cava, or immediately lateral to its right side (see Fig. 54.13). This intimate relationship facilitates the cavopulmonary anastomosis (the Glenn shunt) conceived to bypass the defective right heart chambers in various congenital cardiac disorders. A lymph node usually lies adjacent to the bifurcation. The smaller branch to the superior lobe usually divides again, supplying the majority of that lobe. The inferior branch descends anterior to the bronchus intermedius and posterior to the superior pulmonary vein. It provides a small recurrent branch to the superior lobe, and then, at the point where the horizontal fissure meets the oblique fissure, it gives off the branch to the middle lobe anteriorly, and a branch to the superior segment of the inferior lobe posteriorly. It then continues a short distance before dividing to supply the rest of the inferior lobe segments.

Left pulmonary artery

The left pulmonary artery emerges from under the concavity of the aortic arch and descends anterior to the descending thoracic aorta to enter the oblique fissure. The ligamentum arteriosum passes between the superior aspect of the left pulmonary artery and the proximal descending thoracic aorta; the aorta is relatively fixed in position by the ligament, and so may be ruptured in this region in cases of major trauma associated with rapid deceleration. The left recurrent laryngeal nerve branches from the left vagus nerve, passes inferior to the aorta to the left of the ligamentum arteriosum, and then courses superiorly posterior to the aortic arch; it is a close relation of the superior part of the left lung root and hilum, where it may be compressed or invaded by lung tumour. The branches of the left pulmonary artery are variable (Sivrikoz 2016). The first and largest branch is usually given off to the anterior segment of the left superior lobe. Before reaching the oblique fissure, the artery gives off a variable number of other branches to the superior lobe; it usually supplies a large branch to the superior segment of the inferior lobe as it enters the fissure. Lingular branches arise within the fissure, and the rest of the lower lobe is supplied by many varied branching patterns. It was a surgical aphorism of the late Lord Brock that when performing a left upper lobectomy, 'there was always one more branch of the pulmonary artery than you thought!'

Unilateral absence of a pulmonary artery is a rare congenital anomaly characterized by normal lung volume and anatomy at birth. Revascularization before the age of 6 months avoids the development of lung hypoplasia (Alison et al 2011). The left pulmonary artery sling is a congenital anomaly where the left pulmonary artery arises from the right pulmonary artery, travels posteriorly over the right main bronchus and then passes between the trachea and oesophagus: it is associated with significant tracheobronchial stenosis (Zhong et al 2010).

Pulmonary sequestration

When a portion of lung exists without the appropriate bronchial and vascular connections, it is usually supplied by the systemic vasculature (descending thoracic or abdominal aorta or its branches) and drains into either the atria, superior vena cava or azygos venous system (Clements 1999) (see Figs 54.14–54.15). Extralobar pulmonary sequestration segments are covered by visceral pleura and usually found below the left inferior lobe, whereas intralobar anomalies are usually embedded in normal lung, classically, in the posterior basal segment of the left inferior lobe. Extralobar pulmonary sequestration is normally asymptomatic but often associated with other congenital anomalies such as pulmonary hypoplasia, congenital diaphragmatic hernia, congenital cystic adenomatoid malformation and congenital heart disorders (Stocker et al 1978, Kravitz 1994). A fistula into the oesophagus may also develop. Consideration of differential diagnoses that include mediastinal or pulmonary tumours is mandatory.

Pulmonary embolism and arteriography

A thrombus that has developed in the deep venous system (usually in the lower limb or pelvis) may embolize and travel in the right side of the circulation through the right atrium and right ventricle and lodge in the pulmonary vasculature. The clinical abnormalities observed depend on the size of the embolus and on the number and frequency of embolic episodes. Large emboli may lodge in branches of the main pulmonary artery and cause right ventricular dysfunction and hypoxia, representing a medical emergency. Smaller emboli may lodge in segmental pulmonary arteries and cause pleuritic chest pain, shortness of breath and haemoptysis, although the clinical picture is rarely pathognomonic. Pulmonary emboli cause a ventilation/perfusion ratio mismatch that can have serious physiological implications leading to a significant reduction in the oxygenation of blood. Ventilation/perfusion scans with radiolabelled xenon and technetium usually demonstrate segmental abnormalities in perfusion with normal ventilation in the corresponding regions. Pulmonary emboli may also be evaluated by contrast-enhanced spiral CT or pulmonary angiograms and appear as filling defects. Repetitive embolization may eventually lead to a dramatic reduction of the pulmonary vascular bed and chronic cor pulmonale. Thrombolysis, anticoagulation or inferior vena caval filters prevent progression or recurrence of embolism. A clot may also traverse a patent foramen ovale and lodge in the arterial system (paradoxical embolism), most severely in the cerebral circulation resulting in stroke (Kent and Thaler 2011).

Aorta

For descriptive purposes, the aorta is divided into ascending, arch, descending thoracic and abdominal parts.

Ascending aorta

The ascending aorta is typically about 5 cm in length. It originates at the base of the left ventricle, commonly level with the inferior border of the third left costal cartilage, and initially ascends whilst curving anteriorly and to the right. It passes from posterior to the left half of the sternum to become the aortic arch posterior to the right half of the inferior part of the manubrium sterni, or the manubriosternal joint (level with the right second costal cartilage), or the superior part of the right side of the sternal body (level with the right second intercostal space). In children, the diameter of the thoracic aorta correlates most closely with body surface area (Kervancioglu et al 2006, Kaiser et al 2008).

Relations The ascending aorta lies within the fibrous pericardium, enclosed in a tube of visceral serous pericardium together with the pulmonary trunk (see Figs 57.1, 57.4, 58.1). The conus arteriosus of the right ventricle, initial segment of the pulmonary trunk and right auricle are anterior to its lower part. Superiorly, it is separated from the sternum by the pericardium, the pleura and the anterior border of the right lung, loose areolar tissue and the thymus or its remnants. The left atrium, right pulmonary artery and right main bronchus are posterior. The superior vena cava (also partly posterior) and the right atrium are to the right. The left atrium and, more superiorly, the pulmonary trunk are to the left. At least two para-aortic bodies (aortopulmonary paraganglia) lie between the ascending aorta and the pulmonary trunk. Relative to the ascending aorta, the inferior para-aortic body is located on its anterior surface near to the heart, and the middle para-aortic body is located on its right side.

The aortopulmonary window is a space between the pulmonary trunk and aortic arch, bordered by the ascending aorta anteriorly, the descending aorta posteriorly, the mediastinal part of the parietal pleura laterally and the left main bronchus medially (Deutsch and Savides 2005) (see Figs 58.1, 58.4). It contains lymph nodes, fatty tissue, the ligamentum arteriosum, the superficial cardiac plexus, cardiac nerves and the left recurrent laryngeal nerve.

Coronary arteries

The right coronary artery arises from the right aortic sinus and the left coronary artery from the left aortic sinus of the proximal ascending aorta (see Figs 57.21, 57.24, 57.41); the level of the opening of each artery is variable. The two arteries form an oblique inverted crown (hence their name) within the atrioventricular sulcus. They also form a variable and often insignificant anastomosis (in the non-pathological state) via marginal and interventricular loops that intersect at the cardiac apex. The main arteries and major branches are usually subepicardial, but those in the atrioventricular and interventricular sulci are often deeply sited, and occasionally hidden by or embedded in overlapping myocardium (myocardial bridging). The left or right coronary artery is classed as being dominant if it gives off the inferior interventricular branch, which supplies the inferior part of the ventricular septum and often part of the inferolateral wall of the left ventricle. The right coronary artery is dominant in around 60% of hearts. Anastomoses between right and left coronary arteries are abundant in the fetus but are much reduced by one year of age. Anastomoses providing collateral circulation may become prominent in conditions of chronic hypoxia and in coronary artery disease. An additional collateral circulation is provided by small branches from mediastinal, pericardial and bronchial vessels.

Normal coronary arterial calibre, based on arterial casts or angiogram measurements, ranges between 1.5 and 5.5 mm. The calibre of the left origin exceeds the right in 60% of hearts, the right being larger in 17%, and both vessels being of approximately equal calibre in 23%. The external diameter of the left coronary artery increases from 2.1 mm at the age of 1 year to 3.3 mm at the age of 15 years (Pesonen et al 1991) and the diameters of the coronary arteries may increase up to the 30th year. A significant association has been found between the diameters of the right and left coronary arteries at 0 (birth), 1 and 6 months of age and birth weight, height and body surface area (Karagol et al 2012).

A wide range of coronary artery anomalies or variants may occur, and are categorized according to the origin (connection), course, area of termination of the artery, or the presence of anastomoses, bridging, fistula or atresia (Muresian 2016).

Congenital anomalies of the coronary arteries are found rarely in children. The two most common anomalies are coronary arteriovenous fistula and anomalous left coronary artery arising from the pulmonary trunk (Uysal et al 2014). Other congenital anomalies include ectopic origin of circumflex artery (normally a branch of the left coronary artery) from right coronary artery, single coronary artery arising from right aortic sinus, ectopic right coronary artery arising from the left aortic sinus, left or right coronary artery arising from the ascending aorta (Clemente et al 2010).

Right coronary artery

The right coronary artery arises from the right aortic sinus; its opening is usually below the sinutubular junction (see Fig. 57.23). The artery is usually single, although up to four openings have been observed, reflecting the independent origins of the conal, sinuatrial nodal and ventricular arteries (see Figs 57.42–57.43). The right coronary artery passes at first anteriorly and slightly to the right between the right atrial auricle and pulmonary trunk. On reaching the atrioventricular sulcus, it descends almost vertically to the right side of the inferior cardiac border, curving around it into the inferior part of the sulcus in which it passes towards the cardiac crux (the junction of the atrioventricular, interatrial and interventricular sulci) (see Fig. 57.4B). The artery ends a little to the left of the crux, often by anastomosing with the circumflex branch of the left coronary artery. The right coronary artery may end near the right cardiac border, between this and the crux, or more often it reaches the left border, replacing the more distal part of the circumflex artery. Its branches supply the right and variable parts of the left chambers and atrioventricular septum. Usually, the first branch is the conal branch of the right coronary artery (Loukas et al 2014). This vessel arises independently from the right aortic sinus in approximately 33% of hearts and is sometimes termed the third coronary artery, but this is an inappropriate term because a similarly named vessel arises from the left coronary circulation. The conal branch of the right coronary artery branches anteroinferiorly over the conus arteriosus (infundibulum) and over the superior aspect of the right ventricle, sometimes anastomosing with a similar branch from the anterior interventricular (left anterior descending) artery to form Vieussens arterial ring, an inconstant anastomosis around the right ventricular outflow tract that may provide an important collateral circulation in cases of arterial occlusion (see Figs 57.44–57.45) (Loukas et al 2009).

The first segment of the right coronary artery (between its origin and the right side of the inferior cardiac margin) gives off anterior atrial and ventricular branches that diverge widely. The ventricular arteries arise at almost 90° from the right coronary artery, an arrangement that is in marked contrast to the more acutely angled origins of the ventricular branches of the left coronary artery. The anterior ventricular branches, usually two or three, ramify towards the cardiac apex, but they rarely reach the apex unless the right marginal artery is included within this group. The right marginal artery is greater in calibre than the other anterior ventricular arteries and reaches the cardiac apex in most hearts. When it is very large, there may be no additional anterior ventricular branch. Two, sometimes three, small inferior ventricular branches, arise from the second segment of the right coronary artery between the right side of the inferior cardiac margin and cardiac crux to supply the inferior aspect of the right ventricle. Their size is inversely proportional to that of the right marginal artery, which usually extends to the inferior cardiac surface. On approaching the cardiac crux, the right coronary artery normally produces up to three inferior interventricular branches (occasionally none). The actual inferior interventricular artery sits within the interventricular sulcus, and may be flanked either to the right or left, or on both sides, by these parallel branches. When these flanking vessels exist, branches of the inferior interventricular artery are small and sparse. The inferior interventricular artery is occasionally replaced by a branch of the left coronary artery. Although the atrial branches of the right coronary artery are sometimes described as part of anterior, lateral (right or marginal) and posterior groups, they are usually small single vessels, 1 mm in diameter (see Figs 57.46–57.48). The right anterior and lateral branches (occasionally double, and very rarely triple) mainly supply the right atrium. The posterior branch is usually single and supplies both atria.

The artery of the sinuatrial node is an atrial branch of variable origin, distributed largely to right atrial myocardium. Its origin is variable: most commonly, it arises as the first atrial branch of the right coronary artery, less often from its right lateral atrial branch, and least often from its inferior atrioventricular part. It may sometimes originate from the circumflex branch of the left coronary artery. It usually passes posteriorly in the groove between the right atrial auricle and ascending aorta, and branches around the junction of the superior vena cava and right atrium, typically as an arterial loop from which small branches supply the right atrium. A large branch, the ramus cristae terminalis, traverses and supplies the sinuatrial node: it would seem more appropriate to name this branch the nodal artery, given that the vessel currently bearing this name is predominantly atrial in distribution.

Septal perforating branches of the right coronary artery are relatively short and leave the inferior interventricular branch to supply the inferior part (about one-third) of the interventricular septum. They are numerous but do not usually reach the apical region of the septum. The largest inferior septal perforating artery, usually the first branch, commonly arises from the inverted loop said to characterize the right coronary artery at the crux and it almost always supplies the atrioventricular node. Small, recurrent atrioventricular branches originate from the ventricular branches of the right coronary artery as they cross the atrioventricular sulcus and supply adjacent atrial myocardium.

Left coronary artery

The left coronary artery is usually larger in calibre than the right. It supplies a greater volume of myocardium, including almost all of the left ventricle and atrium, and most of the interventricular septum (see Figs 57.42, 57.49–57.51). In hearts with right dominance, the right coronary artery supplies a variable amount of the inferior region of the left ventricle (see Fig. 57.41A–C).

The left coronary artery arises from the left aortic sinus. The opening of the artery sometimes lies inferior to the margin of the valve leaflets and may be double, usually leading into the circumflex and anterior interventricular (left anterior descending) branches of the left coronary artery. Its initial portion, between its opening and first branches, varies in length from a few millimetres to a few centimetres. The artery lies between the pulmonary trunk and the left atrial auricle, emerging into the atrioventricular sulcus, where it turns left. This part is loosely embedded in subepicardial fat and usually has no branches, but may give off a small atrial branch and, rarely, the sinuatrial nodal artery. Reaching the atrioventricular sulcus, the left coronary artery divides into its two main branches: the circumflex and anterior interventricular arteries.

The anterior interventricular artery is commonly described as the continuation of the left coronary artery. It descends obliquely forwards and to the left in the interventricular sulcus (see Fig. 57.52), sometimes deeply embedded in or crossed by myocardial tissue (myocardial bridges), and by the great cardiac vein and its tributaries.

Myocardial bridges are reported to have a frequency varying from 0.5 to 40% when identified clinically and from 15 to 85% when found at autopsy (see Fig. 57.53). The wide variation in frequency indicates that many bridges may be asymptomatic during life. The major clinical conditions produced by a myocardial bridge are cardiac ischaemia, atherosclerosis and sudden cardiac death. The incidence of atherosclerosis is increased when the right coronary artery is bridged. Although a relationship between myocardial bridges and sudden cardiac death has not been established, autopsy series have shown histological evidence of otherwise unexplained ischaemia in individuals with myocardial bridges; many died during exercise and had no other risk factors for coronary arterial disease.

Almost invariably, the anterior interventricular artery reaches the cardiac apex, where it terminates in around 33% of hearts. More frequently, it curves around the notch of the cardiac apex into the inferior interventricular sulcus and passes one-third to one-half of the way along its length, meeting the terminal parts of the inferior interventricular branches of the right coronary artery.

The anterior interventricular artery gives off right and left anterior ventricular and anterior septal branches, and a variable number of corresponding posterior branches. Anterior right ventricular branches are small and rarely number more than one or two; the right ventricle is supplied almost entirely by the right coronary artery. Up to nine large left anterior ventricular arteries branch at acute angles from the anterior interventricular artery, crossing the anterior aspect of the left ventricle diagonally, with the largest reaching the rounded left (obtuse) cardiac border. One, termed the left diagonal artery, often dominates, sometimes arising separately from the left coronary artery, which then ends by trifurcation. It is reported in at least 33–50% of hearts, and may be doubled in around 20%. A small left conal artery frequently leaves the anterior interventricular artery near its origin, and anastomoses on the conus arteriosus with its counterpart from the right coronary artery and with the vasa vasorum of the pulmonary trunk and aorta. The anterior septal perforating branches leave the anterior interventricular artery almost perpendicularly, and pass posteroinferiorly within the septum, usually supplying its anterior two-thirds. The first septal perforator artery usually supplies the atrioventricular bundle at the point of its division. Small inferior septal branches from the same source supply the inferior third of the septum for a variable distance from the cardiac apex (Loukas et al 2009).

The circumflex branch of the left coronary artery, comparable to the anterior interventricular artery in calibre, curves leftwards in the atrioventricular sulcus, and continues around the left cardiac border into the posterior and then inferior part of the sulcus, terminating to the left of the cardiac crux in most hearts, although sometimes continuing as the inferior interventricular artery. Proximally, the left atrial auricle usually overlaps it. A large ventricular branch, the left marginal artery, normally arises from the left circumflex artery at a 90° angle and branches over the rounded left border, supplying much of the adjacent left ventricle, typically to its apex. Smaller anterior and inferior branches of the circumflex artery also supply the left ventricle. Anterior ventricular branches (from one to five, commonly two or three) course parallel to the diagonal artery when it is present, and replace it when it is absent. Inferior ventricular branches are smaller and fewer because the left ventricle is partly supplied by the inferior interventricular artery. When this artery is small or absent, it is accompanied or replaced by often doubled or tripled interventricular continuations of the circumflex artery.

The artery to the sinuatrial node is often derived from the first 1–2 cm of the circumflex artery after its origin from the left coronary artery (anterior circumflex segment) and less often from the remaining length of the circumflex artery. It passes over and supplies the left atrium, encircles the superior vena cava (similar to a right coronary sinuatrial nodal branch) and sends a large branch through the node; despite its name, it is predominantly atrial in distribution. The artery to the atrioventricular node, sometimes the terminal branch of the circumflex artery (20%), arises near the cardiac crux. When this occurs, the circumflex artery usually gives off the inferior interventricular artery, an example of left dominance.

Coronary arterial distribution

Details of coronary arterial distribution should be integrated into a concept of total cardiac supply. Most commonly, the right coronary artery supplies all of the right ventricle (except a narrow strip to the right of the anterior interventricular sulcus); a variable part of the inferior aspect of the left ventricle; the inferior one-third of the interventricular septum; the right atrium and part of the left atrium; the conduction system as far as the proximal parts of the right and left bundles (branches of the atrioventricular bundle). Left coronary distribution is reciprocal and includes most of the left ventricle; a narrow strip of right ventricle; the anterior two-thirds of the interventricular septum; most of the left atrium. Variations in the coronary arterial system mainly affect the inferior aspect of the ventricles and reflect the relative dominance of coronary arterial supply (see Fig. 57.41). The term dominance is misleading because the left artery almost always supplies a greater volume of tissue than the right. In right dominance, the inferior interventricular artery is derived from the right coronary artery, and in left dominance it is derived from the left coronary artery. In the balanced pattern of supply, branches of both the left and right coronary arteries run in or near the inferior interventricular sulcus.

Less is known about variations in atrial supply because the small vessels involved are not easily preserved in the corrosion casts that are used for analysis. In more than 50% of individuals, the right atrium is supplied by the right coronary artery alone. More than 62% of left atria are supplied mainly by the left coronary artery, 27% by the right coronary artery (in each group a small accessory supply from the other coronary artery exists), and 11% are supplied almost equally by both arteries. Arterial supply to the sinuatrial and atrioventricular nodes also varies: the sinuatrial node is supplied more often by the right coronary artery and fewer than 10% of sinuatrial nodes receive a bilateral supply. The atrioventricular node is usually supplied by the right coronary artery.

Uncommonly, variants of coronary arteries may be present and are the second most common cause of sudden cardiac death in young athletes. Anomalous origins of the coronary artery, particularly from the contralateral aortic sinus, is the variant that is most commonly associated with sudden cardiac death. Other anomalies include left coronary artery origin from the pulmonary trunk, coronary fistula and left main stem atresia (Kastellanos et al 2018).

Coronary anastomoses

The cardiac collateral circulation represents a built-in system for coronary arterial bypass. The first few centimetres of the main stems of the left and right coronary arteries are devoid of anastomotic branches. Collateral channels are abundant further distally, exhibiting variable calibres and occupying numerous locations, allowing for bidirectional flow between most arteries. Approximately 30 different sites of collateral extramural vessels have been described, the most frequent being at the cardiac apex; the anterior aspect of the right ventricle; the inferior aspect of the left ventricle; the cardiac crux; the interatrial and interventricular sulci; between the sinuatrial nodal and other atrial vessels (see Figs 57.44–57.45). Anastomoses between branches of the coronary arteries, both subepicardial and myocardial, and between these arteries and extracardiac vessels, are of great clinical importance. Clinical studies suggest that anastomoses cannot rapidly provide collateral routes sufficient to circumvent sudden coronary obstruction (see Figs 57.44–57.45, 57.54). Nevertheless, it has long been established that anastomoses do occur, particularly between fine subepicardial branches, and they may increase during the life of an individual by both angiogenesis and arteriogenesis. The Vieussens arterial ring is a collateral vessel that crosses the conus arteriosus inferior to the pulmonary trunk, and provides an anastomosis between the conal branches of the right coronary artery and the anterior interventricular artery. The artery to the sinuatrial node commonly provides a communication between the proximal parts of the left and right coronary arteries. The apical collateral artery joins the interventricular arteries. The frequent enlargement of the first septal branch of the anterior interventricular artery, Kugel's anastomotic artery (arteria anastomotica auricularis magna), has been described as running between the proximal parts of the coronary arteries along the anterosuperior margin of the fossa ovalis to anastomose with the distal part of the right coronary artery. Clinical imaging (catheter angiography and colour Doppler ultrasound) has led to the development of a grading system to describe the overall pattern of cardiac collateral arteries (see Table 57.1).

Extracardiac anastomoses

Extracardiac anastomoses connect various coronary arterial branches with other intrathoracic vessels, most commonly involving the bronchial and internal thoracic arteries (see Fig. 57.54). To a much lesser degree, anastomoses between coronary arteries and pericardiacophrenic branches of the internal thoracic, anterior mediastinal, intercostal and oesophageal arteries also exist.

The posterior pericardium also receives a direct supply from the bronchial arteries: extracardiac coronary anastomoses involving bronchial arteries are typically found at the pericardial reflections, such as the points of entry of the superior and inferior venae cavae. The most common anastomoses are with the circumflex branch of the left coronary artery via the posterior pericardial reflections and reflect the close proximity of the bronchial arteries within the root of the lung. In pathological conditions, notably those resulting in pericardial adhesions, it is also possible for extracardiac anastomoses to develop through trans-pericardial vascularization. Extracardiac communications also exist with coronary atrial branches, especially the sinuatrial nodal artery. The effectiveness of any of these connections as collateral routes in coronary occlusion is not well quantified. Coronary arteriovenous anastomoses and numerous connections between the coronary circulation and cardiac cavities, producing so-called 'myocardial sinusoids' and 'arterioluminal vessels', have been reported, but their importance in coronary disease remains uncertain.

Coronary angiography

Coronary angiography may be performed by introducing a catheter through the femoral, radial or brachial artery. The femoral artery is punctured with a needle 3 cm below the inguinal ligament while the leg is held adducted and slightly externally rotated. The exact position is guided by palpation of the femoral arterial pulse, and the needle is inserted at an angle of 45° to the artery. After arterial puncture, a fine guidewire is inserted through the needle and fed into the artery. The catheter is then inserted over the guidewire and passed through the external and common iliac arteries into the abdominal aorta, then through the descending thoracic aorta, aortic arch and ascending aorta.

The brachial or radial artery may be used for percutaneous access to the circulation. Once the catheter is located in the ascending aorta, a variety of guidewires may be used to enter the coronary vessels for selective arteriography and interventions. Angiography is performed with standard high osmolality contrast medium and cine-angiography. In selected patients, new-generation, low osmolality contrast medium may be used. All the coronary arteries are catheterized and visualized in a variety of views to obtain a full evaluation of their anatomy and to determine the location and degree of any stenosis (see Figs 57.55–57.56). The opening of the left coronary artery arises from the left aortic sinus and is best viewed in the direct frontal and left anterior oblique projections. The right anterior oblique view is useful in demonstrating the diagonal and anterior interventricular branches of the left coronary artery. The right coronary artery originates from the right aortic sinus and is usually visualized in the right anterior oblique view. Pressure and oxygen saturations can be measured via the catheter; changes in pressure across valves allow the degree of stenosis to be measured. Coronary blood flow and relative flow reserve can also be calculated. Significant stenosis may be treated initially by balloon angioplasty followed by stent insertion. The balloon exerts pressure against the plaque in the arterial wall, fracturing and splitting the plaque. The splinting effect of the plaque and elastic recoil are reduced, resulting in an increase in the arterial lumen. Stent insertion reduces the rate of re-stenosis.

Coronary revascularization

Atherosclerosis causing more than 60% stenosis of the terminal diameter of the coronary arteries is likely to cause significant reduction in myocardial perfusion. Patients with high-grade lesions, left main stem coronary artery or triple-vessel disease with impaired left ventricular function are usually considered for coronary artery bypass grafting. The common grafts that are used are the internal thoracic (mammary) and radial arteries. The left internal thoracic artery and radial artery grafts have a greater patency rate than saphenous vein grafts. Approximately 15% of saphenous vein grafts occlude in 1 year and, from then on, at an annual rate of 1–2% in the first 6 years and 4% thereafter; between 40% and 50% of saphenous vein grafts have occluded by 10 years, whereas only about 10% of left internal thoracic or radial artery grafts will have occluded over this time. The common surgical approach is via a midline sternotomy. If the internal thoracic artery is used as a donor graft, it is divided distally (maintaining its proximal origin from the subclavian artery) and anastomosed to the coronary artery distal to the stenosis. If radial artery grafts are used, they must bridge the stenosis via both proximal and distal anastomoses. In selected cases, minimally invasive direct coronary artery bypass grafting is performed, but the approach is dependent on the vessel being grafted. The anterior approach, via a mini-thoracotomy through the fourth intercostal space, is used for grafting the left anterior interventricular and diagonal arteries. The anterolateral approach, via an incision in the third intercostal space from the mid-clavicular to anterior axillary lines, is used for grafting early marginal branches of the circumflex branch of the left coronary artery. The lateral approach, via a lateral thoracotomy measuring only 10 cm in size through the fifth or sixth intercostal spaces, allows grafting of the circumflex vessels. Extrathoracic approaches that are occasionally used include the subxiphoid approach for the distal part of the right coronary artery and inferior interventricular artery. The vast majority of patients are treated with stent placement (see Fig. 57.57). Port access surgery allows for full revascularization with cardiopulmonary bypass and obviates the need for midline sternotomy.

Coronary artery fistula

A coronary artery fistula is an abnormal connection that directly links one or more coronary arteries to a heart chamber or to major thoracic vessels without an interposed capillary bed.

Coronary artery fistulae are rare (see Fig. 57.58); those that arise from a coronary artery and then terminate in a chamber of the heart are known as coronary cameral fistulae, while those terminating in a vein are coronary arteriovenous fistulae. Fistulae may be congenital or may develop later in life. Congenital fistulae are more common and account for 50% of paediatric coronary vascular aberrations: they are believed to be derived from the smallest cardiac (Thebesian) veins. Acquired coronary artery fistulae are most commonly iatrogenic in aetiology but may also occur after traumatic injury. The most commonly seen are of the coronary cameral type, from the right coronary artery into the right side of the heart.

Aortic arch

The aortic arch continues from the ascending aorta and lies mainly within the superior mediastinum (see Figs 57.4A–C). Its origin, slightly to the right of the midline, is level typically with either the right first intercostal space, the second costal cartilage or the second intercostal space. The arch initially ascends obliquely and posteriorly to the left over the anterior surface of the trachea, and then posteriorly across its left side. It ascends superiorly to the midlevel of the manubrium sterni, and curves around the hilum of the left lung. Posteriorly it descends to the left of the body of the fourth thoracic vertebra: at around the level of the sternal plane, posterior to the second left sternocostal joint, it continues as the descending thoracic aorta. The concavity of the aortic arch may lie superior, on or inferior to the sternal plane: most commonly it is inferior to the plane (see Fig. 52.7).

The shadow of the aortic arch is easily identified in frontal chest radiographs, where it is seen as a rounded leftward projection (aortic knuckle) to the left of the manubrium (see Fig. 56.17). The shadow of the adjacent left superior intercostal vein crossing its left side, from posterior to anterior, may form an additional small rounded shadow termed the 'aortic nipple'. The aortic arch is best visualized in left anterior oblique views on angiography and with equivalent computed tomography (CT) reconstruction planes, when the pulmonary trunk and its left branch will be seen inferiorly occupying the concavity of the arch.

The concavity of the aortic arch is the upper curved limit through which structures gain access to, or leave, the hilum of the left lung. The diameter of the aortic arch initially matches that of the ascending aorta but is significantly reduced distal to the origin of the three large branches to the head, neck and upper limbs. The aortic isthmus, a small stricture at the border of the aortic arch with the descending thoracic aorta, may be followed by a dilation; in the fetus, the isthmus lies between the origin of the left subclavian artery and the opening of the ductus arteriosus (Ch. 13).

Relations The left mediastinal part of the parietal pleura is located anterior and to the left of the arch. Deep to the pleura, the arch is crossed, in anteroposterior order, by the left phrenic nerve, left lower cervical cardiac branch of the vagus nerve, left superior cervical cardiac branch(es) of the sympathetic trunk, and the left vagus nerve (see Figs 56.7B, 57.61). As the latter crosses the aortic arch, its recurrent laryngeal branch hooks inferior to the vessel, to the left posterior aspect of the ligamentum arteriosum, and then ascends on the right of the aortic arch. The left superior intercostal vein ascends obliquely anteriorly on the arch, anterolateral to the left vagus nerve and posteromedial to the left phrenic nerve and pericardiacophrenic vessels. The left lung and pleura separate all these structures from the thoracic wall. Posterior and to the right are the trachea and the deep cardiac plexus, the left recurrent laryngeal nerve, the oesophagus, thoracic duct and vertebral column. Superiorly, the brachiocephalic trunk, left common carotid and subclavian arteries arise from its convexity (from left-to-right), and are crossed anteriorly near their origins by the left brachiocephalic vein. The branching of the pulmonary trunk, left main bronchus, ligamentum arteriosum, superficial cardiac plexus and the left recurrent laryngeal nerve are typically inferior.

Variants The most superior level of the aortic arch is typically about 2.5 cm inferior to the jugular notch, although this may vary. It is located more superiorly, closer to the jugular notch, in infants and again in senescence when it is a result of vascular ectasia.

In a right-sided aortic arch, the aorta curves over the hilum of the right lung and descends to the right of the vertebral column: this is usually associated with transposition of the thoraco-abdominal viscera (situs inversus) (Akgun et al 2016). Less often, after arching over the hilum of the right lung, the aorta may pass posterior to the oesophagus to gain a left-sided position, and this is not accompanied by visceral transposition. The presence of a right-sided aortic arch is of relevance when planning the repair of oesophageal atresia in neonates.

The aorta may divide into ascending and descending trunks, the former dividing into three branches to supply the head and upper limbs. Alternatively, it may divide near its origin, producing a double aortic arch; the two branches soon reunite and the oesophagus and trachea usually pass through the interval between them. Entrapment of the oesophagus and/or trachea by the aorta, ductus arteriosus or descending aorta is referred to as a vascular ring.

There are several variants of this arrangement. The most common are when a right-sided aortic arch and the upper part of the descending thoracic aorta pass anterior to the oesophagus and trachea, and the ductus arteriosus passes posterior to the oesophagus into an aortic diverticulum; a right-sided aortic arch and the upper part of the descending thoracic aorta pass anteriorly, and the ductus arteriosus is inserted into the left subclavian artery that arises as a fourth branch from the aortic arch; a left-sided descending thoracic aorta is attached to a left-sided ductus arteriosus anterior to the oesophagus, and a right-sided aortic arch passes posteriorly; the right superior part of the descending thoracic aorta wraps around the oesophagus and the ductus arteriosus is right-sided; the right upper part of the aorta wraps around the oesophagus and the ductus arteriosus is left-sided (Akgun et al 2016).

From right to left, the brachiocephalic trunk, left common carotid and left subclavian arteries arise from the convex aspect of the aortic arch (see Figs 57.4, 58.1). These vessels may branch from the beginning of the aortic arch or the superior part of the ascending aorta. The distance between their origins varies, the most frequent being apposition of the left common carotid artery to the brachiocephalic trunk. Multiple variants of their branching pattern have been observed; other branches may arise from the aortic arch, including the inferior thyroid, thyroidea ima, thymic, left coronary and bronchial arteries (Akgun et al 2016). The left vertebral artery may arise between the left common carotid and the left subclavian arteries.

The left common carotid artery may arise from the brachiocephalic trunk, when it is known as a bovine arch (7%), although this does not represent the morphology seen in bovines. Rarely the left common carotid and subclavian arteries may arise from a left brachiocephalic trunk or from the right common carotid artery, with the right subclavian artery arising separately (Akgun et al 2016). The right common carotid and subclavian arteries may arise separately, in which case the right subclavian artery often branches from the left part of the aortic arch distal to the left subclavian artery, and usually passes posterior to the oesophagus as an aberrant right subclavian artery (sometimes referred to as a lusoria artery). A diverticular outpouching (diverticulum of Kommerell) may be present at the origin of an aberrant left or right subclavian artery from a right or left aortic arch, respectively (see Fig. 58.6). It can become aneurysmal and cause fatal haemorrhage during endoscopy and can form a vascular ring around the oesophagus and trachea, presenting in the neonate as a feeding disorder with failure to thrive.

Rare avian forms of branching have been reported. For example, the right common carotid and right subclavian arteries arise from the aortic arch, and the left common carotid and left subclavian arteries arise from the descending aorta (Akgun et al 2016). Alternatively, two common arterial trunks arise from the aortic arch, the right trunk branching into the left and right common carotid arteries, and the left trunk branching into the left and right subclavian arteries. Another rare order of the branching from the aortic arch is (from right to left): the right subclavian artery, left subclavian artery, followed by the right common carotid, and left common carotid arteries, with the latter two arising close together and almost forming a common carotid trunk.

The aortic arch may curve posterior to the oesophagus and trachea, instead of passing anteriorly, and may show variation in its branching. For example, another rare avian form reported is with both carotid arteries originating from the same common trunk, and a left subclavian artery originating from the arch, while the right subclavian artery arises from the descending thoracic aorta. One or more of the ductus arteriosi may remain patent.

Very rarely, the external and internal carotid arteries arise separately from the aortic arch and the common carotid artery is absent on one or both sides, or both carotid arteries and one or both vertebral arteries can be separate branches. When a right aortic arch and aorta occur, the arrangement of its three branches is reversed and the common carotid arteries may have a single trunk. Other arteries may branch from it; most commonly, these are one or both bronchial arteries and the thyroidea ima artery.

Pneumomediastinum and aortic nipple

Pneumomediastinum is an overarching term that describes the presence of air in the mediastinum. It may arise from a wide range of pathological conditions or physiological states, e.g. penetrating trauma, ruptured major airways or oesophagus, hyperventilation or distressed ventilation such as acute asthma, periparturition or diabetic ketoacidosis.

The aortic nipple is the radiographic term used to describe a lateral nipple-like projection located on the aortic knuckle. It corresponds to the end-on appearance of the left superior intercostal vein coursing anteriorly and is not observed in all individuals. It may be mistaken radiologically for lymphadenopathy or an intrapulmonary nodule or neoplasm. Despite their relative independence, the aortic nipple is defined by new contours in cases of pneumomediastinum, taking on an 'inverted aortic nipple' appearance (see Fig. 58.5). In this position, the inverted aortic nipple may facilitate radiographic discrimination of pneumomediastinum from similar conditions. The presence of an aortic nipple has also been shown to precede pathological conditions such as venous obstruction in the superior and inferior vena cavae or left brachiocephalic vein, and has been identified in conditions where venous flow through the left superior intercostal vein is increased (e.g. portal venous hypertension and certain congenital venous anomalies).

Coarctation of the thoracic aorta

The aortic lumen is occasionally partly or completely obliterated, either above (preductal or infantile type), opposite or just beyond (postductal or adult type), the entry of the ductus arteriosus. In the preductal type, the length of coarctation is variable, aortic arch hypoplasia is common, and the left subclavian and even the brachiocephalic trunk may be involved. Severe forms of infantile coarctation and its extreme form (aortic interruption) may be patent ductus arteriosus-dependent, as there is no time for effective collateral circulation to develop. Prostaglandin infusion prior to transfer, and surgery at a tertiary centre, often provide a good mid- to long-term outlook for such infants.

The postductal type of coarctation has been attributed to abnormal extension of tissue of the ductus arteriosus into the aortic wall, stenosing both vessels as the duct contracts after birth. This form may permit years of normal life, allowing the development of an extensive collateral circulation to the aorta distal to the stenosis (see Figs 58.7–58.8). High vascularity of the thoracic wall is important and clinically characteristic. Many arteries that arise indirectly from the aorta proximal to the region of coarctation anastomose with vessels that are connected to the aorta distal to the region of coarctation; these vessels form a bypass route and become greatly enlarged. Thus, in the thoracic wall, the thoraco-acromial, lateral thoracic and subscapular arteries (from the axillary artery), the suprascapular artery (from the subclavian artery) and the supreme intercostal artery (from the costocervical trunk) anastomose with other posterior intercostal arteries and the internal thoracic artery and its terminal branches (e.g. the musculophrenic artery) anastomose with many of the posterior intercostal arteries and the inferior epigastric arteries (from the external iliac artery). Posterior intercostal arteries are always involved, and enlargement of their dorsal branches may eventually groove (notch) the inferior margins of the ribs. The radiographic shadow of an enlarged left subclavian artery is also increased. Enlargement of the scapular vessels and anastomoses may lead to widespread interscapular pulsation which is palpated easily with the palm of the hand, and is sometimes heard on auscultation.

Aortic aneurysm formation

Degeneration of the aortic tunica media and intimal dissection play a major role in the pathogenesis of aneurysms affecting the ascending aorta and aortic arch. Smooth muscle cells are lost and elastic fibres degenerate, producing cystic spaces in the media that then fill with mucoid material. The loss of these structural cells leads to weakening of the wall with progressive dilation. Ageing and hypertension are major predisposing factors to cystic medial degeneration and there is a strong link with cigarette smoking. Thoracic aortic aneurysms are categorized by their location. A particular pattern of aortic root involvement, anulo-aortic ectasia, is seen in Marfan syndrome (Baliga et al 2007). Descending aortic aneurysms are generally caused by atherosclerosis (90%) and the remainder result from mycotic disease or trauma.

Associations also exist between thoracic aortic aneurysm and other connective tissue diseases such as homocysteinuria and Ehlers–Danlos syndrome. A genetic relation is seen in familial thoracic aortic aneurysm syndrome (Baliga et al 2007). Rarely, aneurysms may occur as a result of Takayasu's arteritis, or infections within the aortic wall. Some aortic aneurysms are incidental findings on chest films or CT studies. Symptomatic cases present with breathlessness, unbearable chest and back pain, hoarse voice, cough and haemoptysis. Early diastolic murmurs caused by aortic regurgitation may be audible. Repair is carried out in patients with symptoms or fusiform dilation measuring more than 5 cm in diameter. Aneurysms may also occur in an aberrant right subclavian artery and may involve the diverticulum of Kommerell, leading to dysphagia and even tracheal compression. Inadvertent rupture may occur during endoscopy because of the retro-oesophageal location.

Aortic dissection

Aortic dissection occurs as a result of degeneration of the tunica media of the aortic wall and is associated with senescence, persistent hypertension or collagen vascular diseases such as Marfan syndrome. Many patients with aortic dissection have a pre-existing aneurysm. Other associations include aortic coarctation, Turner's syndrome, cocaine abuse (<1%) and trauma during surgical procedures. There is a higher prevalence in males than females, but after 75 years of age there is no sex difference in prevalence (Baliga et al 2007). In a classic aortic dissection, an intimal tear may occur, producing a split into the tunica media that creates a false lumen (see Fig. 58.9). If another tear occurs, connection can be made once again with the true lumen (double-barrel aorta). Additional aetiopathologies include penetrating atherosclerotic ulceration, where an atherosclerotic plaque ruptures into the aortic tunica media, and aortic intramural haematoma, where the vasa vasorum haemorrhage into the wall of the aorta (Baliga et al 2007).

Aortic dissections are classified as types I, II, IIIa and IIIb (DeBakey classification), or types A and B (Stanford classification). Dissections that include the aorta proximal to the left subclavian artery, with or without distal extension, are classified as type I, II or A. Type I involves up to the entire aorta (ascending, arch and descending), whereas type II involves the ascending aorta only. Dissections that are distal to the left subclavian artery are classified as type IIIa (extend to the respiratory diaphragm), IIIb (extend below the respiratory diaphragm) or B. These cases present acutely with severe retrosternal, neck or interscapular chest pain. Depending on the extent of the dissection, they may be associated with neurological signs, diarrhoea or leg weakness. Extension into the pericardium causes cardiac tamponade and circulatory collapse. Diagnosis is established by echocardiography and on contrast-enhanced CT or magnetic resonance imaging (MRI). Medical management is possible for descending aortic dissections, while surgical repair is essential for ascending aortic or aortic arch dissection.

Para-aortic bodies

Para-aortic bodies (aortopulmonary paraganglia) belong to the branchiomeric category of paraganglia. They are chemoreceptors and respond to changes in arterial gas concentrations such as lowered pO_2, increased pCO_2 and increased hydrogen ion concentration. These microscopic structures occur in several locations within the thorax. Coronary paraganglia lie between the ascending aorta and pulmonary trunk, either anteriorly or posteriorly, adjacent to the proximal aorta (aortic root); pulmonary paraganglia lie in the groove between the ductus arteriosus and the pulmonary trunk; subclavian–supra-aortic paraganglia lie between either the right subclavian and right common carotid arteries, or the left subclavian and left common carotid arteries, or caudal to the left subclavian artery, adjacent to the aortic arch.

Rarely, tumours may arise within the para-aortic bodies (e.g. mediastinal paragangliomas that originate in the pulmonary trunk and aortic arch). Generally, these tumours are asymptomatic and are discovered incidentally, but they may occasionally lead to feelings of pressure and hoarseness (Rooke et al 2007).

The major blood vessels of the thorax include the pulmonary trunk, the thoracic aorta and its branches, and the superior and inferior venae cavae and their tributaries (see Fig. 58.1).

Brachiocephalic trunk

The brachiocephalic (innominate) trunk, the largest diameter branch of the aortic arch, is 4–5 cm in length (see Figs 57.4A–B, 58.1). It arises from the convexity of the aortic arch posterior to the centre of the manubrium sterni, and ascends posterolaterally to the right, initially located anterior to the trachea, then on its right. It divides into the right common carotid and right subclavian arteries level with the superior border of the right sternoclavicular joint. The brachiocephalic trunk and left common carotid artery may share a common origin (Osborn 1998). A thymic, bronchial or thyroidea ima artery can arise from the brachiocephalic trunk (see Fig. 58.1). The thyroidea ima artery is a small and inconstant artery that may also arise from the aortic arch, common carotid, subclavian, pericardiacophrenic or internal thoracic arteries; most commonly it arises from right-sided vessels (Tunali 2016, Yalcin 2016) and ascends on the trachea to the thyroid isthmus, where it terminates.

Relations The anterior surface of the brachiocephalic trunk is separated from the manubrium by sternohyoid and sternothyroid, thymic remnants, the left brachiocephalic and right inferior thyroid veins (crossing its root), and sometimes by the right cardiac branches of the vagus nerve. Posterior relations are the trachea (inferiorly) and the right mediastinal part of the parietal pleura (superiorly). The right vagus nerve is posterolateral (superiorly) and sits lateral to the trachea (inferiorly) (see Fig. 56.7). On its right side are the right brachiocephalic vein and the upper part of the superior vena cava and mediastinal part of the parietal pleura, and on its left side are thymic remnants, the origin of the left common carotid artery, the inferior thyroid veins and the trachea (superiorly).

Left common carotid artery

The left common carotid artery originates directly from the aortic arch immediately posterolateral to the brachiocephalic trunk and therefore has both thoracic and cervical parts. Its course and relations are described on page 1464.e56.

Left subclavian artery

In the majority of individuals, the left subclavian artery originates independently from the aortic arch after the origins of the brachiocephalic and left common carotid arteries. Its course and relations are described on page 1464.83.

Descending thoracic aorta

The descending thoracic aorta is located within the posterior mediastinum (see Figs 52.3, 56.1, 56.6, 56.7B, 56.13, 56.14A, 56.20D–E). It is continuous with the aortic arch, beginning level with the lower border of the body of the fourth thoracic vertebra (typically at the sternal plane, although the level of the plane may vary), and ending anterior to the lower border of the body of the twelfth thoracic vertebra at the aortic hiatus, through which it passes. It is left of the vertebral column at its origin, and reaches the midline, anterior to the vertebral bodies, as it descends.

Relations Anterior to the descending thoracic aorta, from superior to inferior, are the hilum of the left lung, the pericardium separating it from the left atrium, oesophagus and the lumbar part of the respiratory diaphragm. The vertebral column and accessory hemiazygos (superiorly) and hemiazygos (inferiorly) veins are posterior. To the right is the thoracic duct and the azygos vein, and inferiorly, to both the left and right sides, are the pleura-covered parts of the mediastinal surfaces of the respective lungs. The oesophagus with its associated plexus of nerves is closely related to the descending thoracic aorta; it is located to the right of the descending aorta in the upper thorax, anterior to it in the lower thorax, and anterolaterally to the left at the level of the diaphragm. Occasionally the aorta traverses the diaphragm to the left and posterior to the oesophagus (Berdjas and Turina 2011).

The descending thoracic aorta provides visceral branches to the pericardium, lungs, bronchi and oesophagus, and parietal branches to the thoracic wall and vertebral column.

Pericardial branches

A variable number of small vessels are distributed to the posterior aspect of the pericardium.

Bronchial arteries

Bronchial arteries vary in number, size and origin. There is usually only one right bronchial artery that arises from either the right third posterior intercostal artery, or the superior left bronchial artery, or various right posterior intercostal arteries, and runs posteriorly on the right principal main bronchus. The left bronchial arteries, usually two, arise from the thoracic aorta, the superior near the fifth thoracic vertebra, the inferior below the left principal main bronchus, and run posterior to the left main bronchus. The bronchial arteries supply the pulmonary areolar tissue, bronchopulmonary lymph nodes, pericardium and oesophagus.

Oesophageal branches

Two or three bronchial arteries supply the thoracic oesophagus. Two or three oesophageal arteries that arise either anteriorly or from the right side of the descending thoracic aorta supply the distal oesophagus (Norton et al 2008).

Mediastinal branches

Numerous small vessels supply lymph nodes and areolar tissue in the posterior mediastinum.

Superior phrenic branches

Superior phrenic arteries arise from the distal descending thoracic aorta and are distributed posteriorly to the superior (thoracic) surface of the respiratory diaphragm, anastomosing with the musculophrenic and pericardiacophrenic arteries (see Fig. 55.6).

Posterior intercostal arteries

There are usually nine pairs of posterior intercostal arteries. They arise from the posterior aspect of the descending thoracic aorta and are distributed to the lower nine intercostal spaces (third to eleventh spaces). The right posterior intercostal arteries are longer because the aorta deviates to the left (see Fig. 53.18): they cross the vertebral bodies posterior to the oesophagus, thoracic duct and azygos vein, and the parietal pleura covering the right lung. The left posterior intercostal arteries travel posteriorly across the vertebral bodies and are in contact with the parietal pleura covering the left lung; the first and second are crossed by the left superior intercostal vein, and those located inferiorly are crossed by the hemiazygos and accessory hemiazygos veins. The sympathetic trunk and ganglia lie anterior to all of the arteries, and the thoracic splanchnic nerves are anterior to the more inferiorly located arteries.

Each artery crosses its intercostal space obliquely towards the angle of the rib above and continues forwards in its costal groove. It runs between the costal parietal pleura and associated endothoracic fascia, and the internal intercostal membrane as far as the angle of the rib, then passes between the internal and innermost intercostal muscles (see Fig. 53.17) and anastomoses with an anterior intercostal branch from either the internal thoracic or musculophrenic artery. Each artery is accompanied by a vein above and a nerve below, except in the upper spaces, where the nerve is initially superior to the artery. The third posterior intercostal artery anastomoses with the supreme intercostal artery and may provide the major supply to the second intercostal space. The inferior two posterior intercostal arteries continue anteriorly into the abdominal wall, where they anastomose with the subcostal, superior epigastric and lumbar arteries (see Fig. 52.3). Each posterior intercostal artery has dorsal, collateral, muscular and cutaneous branches (see Fig. 53.18).

Dorsal branch

Each dorsal branch passes posteriorly in the space between the necks of adjacent ribs (superiorly and inferiorly), the adjacent vertebral body (medially) and the superior costotransverse ligament (laterally) (see Fig. 53.11). Each dorsal branch gives off a spinal branch that enters the vertebral canal via the intervertebral foramen and supplies the vertebra, spinal cord and meninges, anastomosing with the spinal arteries located immediately superior, inferior, and contralateral (see Fig. 53.18). It then divides into a medial and a lateral dorsal musculocutaneous branch; occasionally, these arise separately from the posterior intercostal artery rather than from a common trunk. The medial branch crosses the transverse process of a vertebra with the medial dorsal branch of a thoracic spinal nerve to supply spinalis, longissimus thoracis and an area of overlying skin. The lateral branch supplies longissimus thoracis and iliocostalis, and the medial aspects of latissimus dorsi and trapezius, in addition to an area of overlying skin.

Collateral intercostal branch

A collateral intercostal branch arises near the angle of a rib and descends to the upper border of the subjacent rib, along which it courses to anastomose with its partner branch from the anterior intercostal branch of the internal thoracic or musculophrenic artery.

Muscular branches

Muscular branches supply the intercostal and pectoral muscles and serratus anterior, and anastomose with the superior and lateral thoracic branches of the axillary artery. Mammary branches from the anterior intercostal vessels in the second to fourth spaces supply the pectoral muscles, breast tissue and covering skin, and enlarge during lactation.

Lateral cutaneous branch

The lateral cutaneous branch arises in the posterior part of the intercostal space and travels anteriorly for a few centimetres with an accompanying vein and the lateral cutaneous branch of the accompanying intercostal nerve (see Fig. 53.21). This neurovascular bundle pierces the intercostal muscles and passes slightly inferiorly to emerge between the interdigitations of serratus anterior and external abdominal oblique. It divides into anterior and posterior rami that contribute to the blood supply of the skin of the lateral trunk; these vessels are less significant in the upper three intercostal spaces.

Unnamed branches

Unnamed branches supply tissues of the thoracic wall, including the costal periosteum, bone and bone marrow of the ribs, tissues of the synovial and synarthrodial joints, and the parietal pleura and tissues of the extrapleural space.

Clinical significance of the posterior intercostal arteries

Catheter embolization is an interventional radiology technique that can be used to block branches of the posterior intercostal arteries when they are bleeding, e.g. secondary to blunt trauma usually associated with rib fractures, or when there is an abnormality of the vertebrae supplied by the dorsal branch of the posterior intercostal artery. In such cases, the posterior intercostal artery may be accessed by placing a catheter in the thoracic aorta, usually by puncturing the femoral artery in the femoral triangle. A smaller catheter (referred to as a superselective catheter) may then be placed in the posterior intercostal artery and embolic material (metallic coils or glue) is injected to block the artery. This can cause cessation of bleeding in cases of trauma and provide pain relief when, for example, the vertebral body is infiltrated with tumour (see Fig. 53.20).

Subcostal arteries

The subcostal arteries are the last paired branches of the descending thoracic aorta, in series with the posterior intercostal arteries and inferior to the twelfth ribs. Each runs laterally anterior to the body of the twelfth thoracic vertebra and posterior to the thoracic splanchnic nerves, sympathetic trunk, costal part of the parietal pleura and lumbar part of the respiratory diaphragm. The right subcostal artery is also posterior to the thoracic duct and azygos vein, while the left is posterior to the hemiazygos vein. Each artery enters the abdomen at the lower border of the twelfth rib, accompanied by the twelfth thoracic (subcostal) nerve, lying posterior to the lateral arcuate ligament and kidney, and anterior to quadratus lumborum. The right artery courses posterior to the ascending colon, and the left courses posterior to the descending colon. The subcostal arteries pierce the aponeurosis of transversus abdominis to become more superficial, and continue toward the anterior midline in the plane between transversus abdominis and internal abdominal oblique; they anastomose with the superior epigastric, lower posterior intercostal and lumbar arteries. Each has a dorsal branch, distributed like those of the posterior intercostal arteries.

Aberrant artery (right dorsal aorta vestige)

A small artery sometimes leaves the descending thoracic aorta from its right side near the origin of the right bronchial artery. It ascends to the right behind the trachea and oesophagus and may anastomose with the right supreme intercostal artery.

Aortic rupture in trauma

Rupture of the ascending aorta is usually associated with a high immediate mortality (Baliga et al 2007). Blunt aortic rupture commonly occurs in road traffic accidents and has a 20% survival rate. There is usually a transverse tear involving the tunica intima and tunica media of the aortic wall; systemic circulatory pressure may cause the formation of a false aneurysm. Rupture of the isthmus region of the descending thoracic aorta is more common, probably because it marks the junction between the mobile and fixed parts of the aorta. Other sites include the ascending aorta proximal to the origin of the brachiocephalic trunk, the aortic arch and the abdominal aorta. Rupture is likely to be the result of a number of factors, including torsion, shear and stretching forces, possibly compounded by hydrostatic pressure.

Aortic atherosclerosis or calcification

Echocardiography, particularly transoesophageal, allows detailed assessment of proximal aortic atherosclerosis implicated in systemic embolic events and strokes, and the extent of turbulent flow. MRI can allow accurate assessment of the composition and size of atherosclerotic plaques and flow dynamics, permitting assessment of the risk of plaque rupture and thrombus formation.

Abdominal aorta

The abdominal aorta begins at the aortic hiatus of the respiratory diaphragm anterior to the twelfth thoracic vertebra. It descends anterior to the lumbar vertebrae and bifurcates into two common iliac arteries anterior to the fourth lumbar vertebra or the intervertebral disc between the fourth and fifth lumbar vertebrae, slightly to the left of the midline (Mirjalili et al 2012a, 2012b, Moussallem et al 2012) (see Figs 61.8–61.11). The angle of bifurcation is very variable (Moussallem et al 2012). The mean adult diameter of the aorta inferior to the origin of the renal arteries measured by computed tomography is 19–21 mm (males) and 16–18 mm (females) (Rogers et al 2013), but there are ethnic variations (Jasper et al 2014). Measured by ultrasound, equivalent values are 20± 2.5 mm (males) and 17±1.5 mm (females) (Needleman 2006). The mean calibre of the abdominal aorta decreases slightly from proximal to distal. With advancing age, there is a progressive increase in abdominal aortic diameter in both sexes and the tapering becomes more pronounced (Fleischmann et al 2001). In the elderly, the abdominal aorta frequently becomes ectatic and tortuous, changing the angle and position of the bifurcation and rotating the origins of the major branches.

Approximately 80% of abdominal aortic aneurysms occur in the aorta inferior to the origin of the renal arteries. Males with atherosclerosis are most at risk of developing the condition, particularly from the sixth decade onwards (Takayama and Yamanouchi 2013). The high mortality risk from spontaneous rupture has prompted the development of ultrasound screening programmes to detect aneurysms and repair them electively. Overall, surgery is performed in patients with an aneurysm greater than 5.0 cm in diameter (females) and 5.5 cm (males) (Groeneveld et al 2018). Repair is most commonly performed by open surgery or endovascular stenting (endovascular aneurysm repair).

Relations The proximal abdominal aorta is directly related anteriorly to the coeliac trunk and its branches, autonomic nerve plexuses and lymphatics. Inferior to the coeliac trunk, the superior mesenteric artery leaves the aorta and descends anterior to the left renal vein. The body of the pancreas is anterior to these vessels; the splenic vein is on its posterior surface and extends obliquely up and to the left. Further anteriorly, the omental bursa separates the proximal abdominal aorta from the lesser omentum, stomach and left lobe of the liver. Inferior to the pancreas, the horizontal third part of the duodenum crosses the aorta anteriorly.

The twelfth thoracic vertebra, the upper four lumbar vertebrae, intervening intervertebral discs and the anterior longitudinal ligament lie posterior to the abdominal aorta. Lumbar arteries arise from its dorsal aspect, and the third and fourth (and sometimes the second) left lumbar veins cross posterior to it to reach the inferior vena cava. The abdominal aorta can overlap the medial border of psoas major on the left.

On the right, the abdominal aorta is related superiorly to the cisterna chyli and thoracic duct, the azygos vein and the right crus of the respiratory diaphragm, which overlaps and separates it from the inferior vena cava and right coeliac ganglion. Below the second lumbar vertebra it is closely applied to the left side of the inferior vena cava. This close relationship allows a fistula to develop between the aorta and adjacent inferior vena cava, a rare complication of aneurysmal disease or trauma. On the left, the aorta is related superiorly to the left crus of the respiratory diaphragm and left coeliac ganglion. Level with the second lumbar vertebra, it is related to the ascending part of the duodenum, the left sympathetic trunk and the inferior mesenteric vein.

The branches of the abdominal aorta are described as anterior, lateral and dorsal (see Fig. 61.9). The anterior (unpaired) branches are the coeliac trunk and superior and inferior mesenteric arteries and the lateral (paired) branches are the inferior phrenic, middle suprarenal, renal and gonadal (ovarian or testicular) arteries: both groups are distributed to the viscera. The dorsal branches are the lumbar and median sacral arteries which supply the body wall, vertebral column and the vertebral canal and its contents.

Coeliac trunk

The coeliac trunk is the first anterior branch and arises just inferior to the aortic hiatus, usually at the level of the vertebral body of the twelfth thoracic vertebra. It is 1–3 cm long and passes almost horizontally anteriorly and slightly to the right superior to the body of the pancreas and splenic vein. In most individuals it trifurcates into the left gastric, common hepatic and splenic arteries. Variations occur and include a separate origin of the left gastric artery from the abdominal aorta, one or both inferior phrenic arteries arising from the coeliac trunk, and the superior mesenteric artery or one or more of its branches arising in common with the coeliac trunk (Panagouli et al 2013). Anterior to the coeliac trunk lies the omental bursa. The coeliac plexus surrounds the coeliac trunk, sending extensions along its branches. On the right lie the right coeliac ganglion, right crus of the respiratory diaphragm and the caudate lobe of the liver. To the left lie the left coeliac ganglion, left crus of the respiratory diaphragm and the cardia of the stomach. Rarely the coeliac trunk can be compressed by the median arcuate ligament (Dunbar's syndrome), resulting in visceral ischaemia and abdominal pain (Ho et al 2017).

Left gastric artery

The left gastric artery is the smallest branch of the coeliac trunk. It ascends to the left of the midline and crosses over the distal end of the left crus of the respiratory diaphragm beneath a fold of peritoneum in the upper posterior wall of the omental bursa (the gastropancreatic fold). Here, it lies adjacent to the left inferior phrenic artery and medial or anterior to the left suprarenal gland. It runs forwards into the superior portion of the lesser omentum adjacent to the proximal end of the lesser curvature, and then it turns anteroinferiorly to run along the lesser curvature between the two peritoneal leaves of the lesser omentum. At the highest point of its course it gives off one or more oesophageal branches. In its course along the lesser curvature it gives off multiple branches that run on to the anterior and posterior surfaces of the stomach, after which it anastomoses with the right gastric artery in the region of the angular incisure.

Rarely the left gastric artery (replaced or accessory) arises from the common hepatic or left hepatic arteries, or directly from the abdominal aorta (Panagouli et al 2013). The most common of these variations is an origin from the left hepatic artery, when the left gastric artery passes between the peritoneal layers of the proximal lesser omentum to reach the lesser curvature of the stomach. However, a replaced/accessory left hepatic artery arising from the left gastric artery is more common than a replaced/accessory left gastric artery origin.

Hepatic artery

During fetal and early postnatal life the common hepatic artery is the largest branch of the coeliac trunk, whereas in adults it is intermediate in size between the left gastric and splenic arteries. The common hepatic artery gives off the right gastric and gastroduodenal arteries (see Fig. 66.9A). After originating from the coeliac trunk, it passes anteriorly and laterally, above the superior border of the pancreas, to the superior aspect of the first part of the duodenum. It is subdivided into the common hepatic artery, from the coeliac trunk to the origin of the gastroduodenal artery, and the proper hepatic artery, from that point to its bifurcation. Both parts ascend anterior to the hepatic portal vein and medial to the bile duct within the free margin of the hepatoduodenal ligament in the anterior wall of the omental foramen. The left and right hepatic arteries arise at a variable level below the porta hepatis. The right hepatic artery typically crosses posterior (occasionally anterior) to the common hepatic duct (see Fig. 66.9B). Its usual course is toward the common hepatic duct: it bends inferiorly before crossing posterior to the duct and then bends back up toward the right hepatic duct lateral to the common hepatic duct and hepatic portal vein. Its close proximity to the bifurcation of the bile duct means that it is often involved or encased by bile duct cancers that arise at the bifurcation (hilar cholangiocarcinoma): the right hepatic artery is more frequently involved than the left hepatic artery in bile duct cancers of the porta hepatis. Occasionally the right hepatic artery crosses anterior to the common hepatic duct and is more vulnerable to injury during biliary surgery. It almost always divides into an anterior branch supplying segments V and VIII and a posterior branch supplying segments VI and VII. The anterior division also often supplies a branch to segment I and the gallbladder. The proper hepatic artery sometimes divides at a more inferior level close to its origin, and occasionally it divides at a superior level, well to the left of the porta hepatis. The main significance of an early division is that the right hepatic artery can pass posterior to the hepatic portal vein (Launois and Jamieson 1993). The segmental arteries of the liver are macroscopically end arteries, although some collateral circulation occurs between segments via fine terminal branches.

Anatomical variants of the normal arrangement of the hepatic arteries are found in about one-third of individuals and are important to recognize because they are relevant to surgical and interventional radiological procedures (Michels 1966, Covey et al 2002, López-Andújar et al 2007, Saba and Mallarini 2011). An artery that supplies a part of the liver in addition to the normal artery supplying that part is defined as an accessory artery. A replaced hepatic artery is an artery that does not originate from an orthodox position and provides the sole supply to that part of the liver.

A replaced proper hepatic artery can arise from the superior mesenteric artery (see Fig. 66.10) and can be suspected at surgery by a relatively superficial hepatic portal vein (reflecting the absence of a hepatic artery that would normally ascend in front of the vein). More commonly, a replaced or accessory right hepatic artery arises from the superior mesenteric artery (see Figs 66.10–66.11). In such cases, the variant artery runs in the lesser omentum posterior to the hepatic portal vein and bile duct and can usually be identified at surgery by palpable pulsation posterior to the hepatic portal vein. An accessory right hepatic artery can be injured during resection of the pancreatic head because it lies close to the hepatic portal vein. Occasionally a replaced or accessory left hepatic artery arises from the left gastric artery, entering the liver through the umbilical fissure; this artery provides a source of collateral supply in cases where the arteries at the porta hepatis are occluded, but it can also be injured during mobilization of the stomach as it lies in the superior portion of the lesser omentum. Rarely an accessory left or right hepatic artery arises from the gastroduodenal artery or directly from the aorta. The presence of replaced arteries can be life-saving in patients with bile duct cancer; because they are further away from the bile duct they tend to be spared from infiltration by the cancer, making excision of the tumour feasible. Knowledge of these variations is also essential when whole and split liver transplantation is performed, and their presence often requires reconstruction.

The most common anatomical variants are a replaced or accessory left hepatic artery that arises from the left gastric artery, or a replaced or accessory right hepatic artery that arises from the superior mesenteric artery, both occurring in 10–20% of individuals.

Variations in the intrahepatic arteries are common and can be important surgically. For example, the segment IV artery most commonly arises from the left hepatic artery, but in up to 30% of cases it arises from the right hepatic artery or the proper hepatic artery (Onishi et al 2000). The segment IV artery never arises to the right of the common hepatic duct, which means that if the right hepatic artery is divided to the right of the common hepatic duct, the arterial supply to segment IV is not endangered. Failure to recognize this variation can compromise the blood supply to segment IV following right hepatectomy, and it is especially important during right liver donation for live donor liver transplantation.

Right gastric artery

The right gastric artery is a relatively small artery that usually arises from the proper hepatic artery and runs forwards into the lesser omentum just above the superior part of the duodenum. It then travels within the lesser omentum along the lesser curvature of the stomach, giving off multiple branches to the anterior and posterior surfaces of the stomach, before anastomosing with the left gastric artery. Less commonly, the right gastric artery arises from the common hepatic, left hepatic or gastroduodenal arteries (Tubbs et al 2016).

Gastroduodenal artery

The gastroduodenal artery usually arises from the common hepatic artery posterior or superior to the superior part of the duodenum. It descends posterior to the retroperitoneal portion of the superior part of the duodenum to the left of the bile duct. At the inferior border of the superior part of the duodenum, it is commonly described as dividing into the right gastro-omental and superior pancreaticoduodenal arteries, but this anatomical arrangement is rare (Bradley 1973, Bertelli et al 1995, Bertelli et al 1996a) and its usual branching pattern is as follows. As it descends posterior to the superior part of the duodenum it usually gives off the posterior superior pancreaticoduodenal artery, several retroduodenal branches that supply the superior part and the proximal portion of the descending part of the duodenum, and a supraduodenal artery that supplies the anterosuperior part of the proximal duodenum (Bianchi and Albanèse 1989). As the gastroduodenal artery emerges inferior to the superior part of the duodenum it usually gives off the right gastro-omental artery and several pyloric branches. It then descends on the anterior surface of the pancreas, where it divides into the anterior superior pancreaticoduodenal artery and pancreatic branches. Although the gastroduodenal artery usually branches from the common hepatic artery, it occasionally originates from other sources including the coeliac trunk, the superior mesenteric artery, as a trifurcation with the right and left hepatic arteries, or from the right or left hepatic artery. The gastroduodenal artery or one of its branches can be a source of haemorrhage from a penetrating posterior duodenal ulcer (see above) or a site of aneurysm or pseudoaneurysm formation, and for these reasons, it is an important vessel for interventional radiologists.

Posterior superior pancreaticoduodenal artery The posterior superior pancreaticoduodenal artery usually arises as the first branch of the gastroduodenal artery at the superior edge of the superior (first) part of the duodenum. It runs to the right, anterior to the supraduodenal segment of the bile duct, before spiralling posteriorly around the pancreatic segment of the bile duct and descending on the posterior surface of the head of the pancreas. It gives branches to the duodenum, head of the pancreas and bile duct before anastomosing with the posterior inferior pancreaticoduodenal artery to form the posterior pancreaticoduodenal arcade. The posterior superior pancreaticoduodenal artery can also give origin to the retroduodenal and supraduodenal arteries that supply the duodenum (Bertelli et al 1996a). The spiral course of the posterior superior pancreaticoduodenal artery reflects its embryonic development: it is the artery to the anterior aspect of the ventral pancreatic bud and the bile duct that subsequently rotate clockwise posterior to the duodenum and dorsal pancreatic bud (Bertelli et al 1997).

Anterior superior pancreaticoduodenal artery The anterior superior pancreaticoduodenal artery usually arises as the smaller terminal branch of the gastroduodenal artery, together with the right gastro-omental artery. It originates posterior to the superior portion of the duodenum and runs inferiorly on the anterior aspect of the head of the pancreas at a variable distance medial to the groove between the descending duodenum and head of the pancreas. It passes inferiorly around the right or inferior border of the head of the pancreas, often piercing the gland to reach the posterior surface of the uncinate process, where it joins the anterior inferior pancreaticoduodenal artery to form the anterior pancreaticoduodenal arcade (Bertelli et al 1995).

Right gastro-omental artery The right gastro-omental artery usually originates from the gastroduodenal artery behind the superior part of the duodenum, anterior to the head of the pancreas. It passes inferiorly towards the midline just below the pylorus and then runs laterally along the greater curvature between the layers of the greater omentum about 1–2 cm from the greater curvature of the stomach. It ends by anastomosing with the left gastro-omental artery (although this anastomosis is variably developed (Ndoye et al 2006) and can be absent). The right gastro-omental artery gives off gastric branches that ascend onto the anterior and posterior surfaces of the pyloric antrum and distal body of the stomach, omental branches that descend into the greater omentum, and duodenal branches that contribute to the supply of the inferior aspect of the superior part of the duodenum. The course of the right gastro-omental artery can vary: it can pass down into the greater omentum before arching back towards the greater curvature; it is important that the surgeon appreciates this anatomical variation if relying on the right gastro-omental artery to supply a surgically fashioned gastric conduit during reconstruction following oesophagectomy.

Splenic artery

The artery almost always arises from the coeliac trunk, in common with the left gastric and common hepatic arteries. However, it can originate from the common hepatic artery or the left gastric artery, or, rarely, directly from the abdominal aorta either in isolation or as a splenomesenteric trunk (Tubbs et al 2016). From its origin, the artery runs a little way inferiorly before turning to the left behind the stomach to run horizontally anterior to the left kidney and left suprarenal gland and behind or above the tail of the pancreas in the splenorenal ligament (see Fig. 68.6A). Multiple loops or even coils of the artery appear above the superior border of the pancreas (McFee et al 1995, Pandey et al 2004). The splenic artery gives off multiple small branches along its course that penetrate and supply the pancreas, including the dorsal pancreatic artery, the great pancreatic artery, arising approximately two-thirds of the way along the gland, and the artery to the tail of the pancreas, arising near the tail. These branches lie on or within the posterior aspect of the gland and often anastomose with the inferior pancreatic artery. Anatomical variations are not unusual, and the dorsal, great or inferior pancreatic arteries can be dominant in any one individual (Wu et al 2011). Near its termination, the splenic artery gives off the short gastric arteries and the left gastro-omental artery (Skandalakis et al 1993). Additional variant branches include a posterior gastric artery and small retroperitoneal branches.

The splenic artery is one of the most tortuous arteries in the body (see Fig. 69.6). The reason for the tortuosity, which can become more pronounced with advancing age, is not understood, although there have been several proposals (Cortés and Pellico 1988, García-Porrero and Lemes 1988, Borley et al 1995, Sylvester et al 1995, Liu et al 1996, Pandey et al 2004). The artery is 8–32 cm long and its calibre usually exceeds that of the common hepatic and left gastric arteries, which range from 3 to 12 mm. Splenic arterial blood flow is approximately 3 ml/sec/100 g, corresponding to approximately 7% of cardiac output (Trubel et al 1985, Cortés and Pellico 1988, García-Porrero and Lemes 1988, Nakamura et al 1989, Skandalakis et al 1993, Romero-Torres 1998, Pandey et al 2004).

The splenic artery usually divides into two, or occasionally three, branches before entering the splenic hilum. The superior and inferior branches are sometimes known as superior and inferior polar arteries; as they enter the hilum they divide into four or five segmental arteries, each of which supplies a segment of splenic tissue. There is relatively little arterial collateral circulation between segments, which means that occlusion of a segmental vessel often leads to infarction of part of the spleen. Segmental arteries divide within the splenic trabeculae, becoming trabecular arteries. These leave the trabeculae and give rise to central arterioles that are surrounded by thick lymphoid sheaths of white pulp. Central arterioles ramify into several penicillar arterioles that feed the sinusoids of the red pulp. There is considerable communication among arterioles (Mikhail et al 1979, García-Porrero and Lemes 1988, Trubel et al 1988, Sow et al 1991, Liu et al 1996).

Dorsal pancreatic artery

The dorsal pancreatic artery commonly arises from the initial 2 cm of the splenic artery, although it can also take origin from the common hepatic or superior mesenteric arteries or the coeliac trunk (Horiguchi et al 2008). It is short and gives off numerous branches, including a terminal left branch near the inferior border of the gland. Several right-sided branches run to the head of the pancreas, passing either posterior or anterior to the superior mesenteric vein to supply the posterior or anterior surface of the head of the pancreas, respectively; they anastomose with arteries of the pancreaticoduodenal arcade (Tsutsumi et al 2014). The terminal left branch anastomoses with the inferior pancreatic artery.

The length and course of the dorsal pancreatic artery depend primarily on its site of origin. When it arises from the splenic artery, common hepatic artery or coeliac trunk, it runs inferiorly on the dorsal surface of the pancreas, whereas if it arises from the superior mesenteric artery, it runs superiorly. These variations should be taken into account during organ procurement because injury to the dorsal pancreatic artery, including at its origin, can jeopardize the pancreatic graft as a result of inadequate perfusion of the tail of the pancreas (Baranski et al 2016). The artery uniformly terminates near the inferior border of the pancreas close to the confluence of the splenic and superior mesenteric veins (Bertelli et al 1998).

Kirk's arcade is formed by a right branch of the dorsal pancreatic artery that emerges on to the anterior surface of the head of the gland and anastomoses with a branch of either the gastroduodenal artery or the anterior pancreaticoduodenal arcade (Woodburne and Olsen 1951). It supplies the ventral surface of the head and neck of the gland.

Inferior pancreatic artery The inferior (transverse) pancreatic artery commonly originates from the left terminal branch of the dorsal pancreatic artery. It runs to the left on the posterior surface of the gland close to its inferior border, gives multiple branches to the body and tail, and anastomoses with other pancreatic branches of the splenic artery. Occasionally the inferior pancreatic artery originates from the gastroduodenal artery or the anterior superior pancreaticoduodenal artery, crossing the anterior surface of the head of the pancreas to reach the inferior border of the neck of the gland and then the tail. In such cases it may be the dominant artery to the body of the pancreas, and its injury or deliberate ligation during pancreaticoduodenectomy can cause ischaemia of the pancreas.

Short gastric arteries

For practical purposes, the short gastric arteries can be defined as those arteries arising above the level of the splenic artery and supplying the fundus of the stomach on its greater curvature. The short gastric arteries vary in number, commonly between five and seven. They arise from the splenic artery or its terminal divisions, or from the proximal left gastro-omental artery, and pass between the layers of the gastrosplenic ligament to supply the fundus of the stomach and cardiac orifice. They anastomose with branches of the left gastric and left gastro-omental arteries. Rarely an accessory left gastric artery arises with these vessels from the distal splenic artery.

Left gastro-omental artery

The left gastro-omental artery is the largest branch of the splenic artery. It arises near the splenic hilum and runs anteroinferiorly between the layers of the gastrosplenic ligament into the proximal gastrocolic part (gastrocolic ligament) of the greater omentum. Here, it descends between the layers of peritoneum close to the greater curvature and often anastomoses with the right gastro-omental artery. It gives off gastric branches to the fundus of the stomach through the gastrosplenic ligament, and to the body of the stomach through the gastrocolic ligament. These are necessarily longer than the gastric branches of the right gastro-omental artery and can be up to 8 cm long. Omental branches arise along the course of the vessel and descend between the layers of the greater omentum. A particularly large omental branch commonly originates close to the origin of the left gastro-omental artery, descends in the lateral portion of the greater omentum and provides a large arterial supply to this part.

Posterior gastric artery

A posterior gastric artery supplying the posterior wall of the upper part of the body of the stomach is commonly present but there has been a lack of consensus regarding its origin, course and distribution. When present, it usually arises from the splenic artery (typically from its midsection) posterior to the body of the stomach (see Fig. 63.11) and ascends behind the peritoneum of the omental bursa towards the fundus to reach the posterior surface of the stomach. It can also arise from the left gastric artery or coeliac trunk (Loukas et al 2007a).

Superior mesenteric artery

The superior mesenteric artery is the artery of the midgut. It originates from the abdominal aorta approximately 1–2 cm below the coeliac trunk, at the level of the body of the first lumbar vertebra (Mirjalili et al 2012b) (see Figs 64.13–64.14).

The angle of the origin of the superior mesenteric artery from the aorta is acute (mean value 45°, range 38–60° and greater in individuals with a greater body mass index; Ozkurt et al 2007). Among the major branches of the descending aorta, the superior mesenteric artery typically has the most acute take-off angle. The result is less turbulent flow, which makes embolic events more likely than in the other visceral arterial branches of the abdominal aorta. The acuteness of the angle between the aorta and superior mesenteric artery can make intravascular cannulation via the transfemoral route somewhat difficult. The artery is usually surrounded by fat, lymphatics and neural tissue at its origin, which helps to increase the angle and the distance between it and the aorta, thereby preventing compression of the duodenum where it is crossed by the artery. The artery runs steeply downwards, anterior to the uncinate process of the pancreas and the horizontal part of the duodenum and posterior to the splenic vein and the body of the pancreas. The left renal vein lies posterior to it and separates it from the aorta (see Fig. 64.15B). Within the small intestine mesentery, the superior mesenteric artery crosses anterior to the inferior vena cava, right ureter and right psoas major. Its calibre progressively decreases as successive branches are given off to the jejunum and ileum, and its terminal branch anastomoses with the termination of the ileocolic artery.

Anatomical variations in the origin and branching pattern of the superior mesenteric artery are well described (Winston et al 2007, Horton and Fishman 2010, Tubbs et al 2016), the most common being an accessory or replaced right hepatic artery arising near the origin of the superior mesenteric artery. Present in about 15% of individuals, the accessory or replaced right hepatic artery courses posterior to the hepatic portal vein and ascends posterolateral to the bile duct (Winston et al 2007). It can be the source of the common hepatic, gastroduodenal, accessory or replaced right hepatic, accessory pancreatic, splenic or rarely the inferior mesenteric artery. Also rare is a superior mesenteric artery arising from a common coeliacomesenteric trunk (Rountas et al 2013). The remnant of the omphalomesenteric artery (vitelline artery) (the embryonic artery that originally connected the intestinal circulation to the yolk sac) is usually obliterated; when present, it forms the artery supplying a congenital ileal diverticulum. It is occasionally represented in the mesentery by a fibrous strand from the termination of the superior mesenteric artery to the ileum.

Branches from the superior mesenteric artery supply the jejunum and ileum. The arteries divide as they approach the mesenteric border of the intestine (see Fig. 64.5), giving off numerous branches that extend between the muscular layers before forming a submucosal arterial plexus that supplies the mucosa. Although there is a rich anastomotic network of arteries within the intestinal mesentery, there are few anastomoses between the terminal branches close to the intestinal wall. The intramural and submucosal arterial networks consist of small-calibre vessels only. Consequently, division or occlusion of several consecutive straight arteries can produce segmental ischaemia of the intestine, while division of more proximal arterial branches in the small intestine mesentery might not cause ischaemia because of collateral flow through vascular arcades.

The superior mesenteric artery usually gives off the inferior pancreaticoduodenal, middle colic, right colic and ileocolic arteries from its right side, and jejunal and ileal arteries from its left side. Its jejunal and ileal arteries form vascular arcades within the small intestine mesentery. The last of these arcades forms an irregular and incomplete marginal artery (of Drummond) of the small intestine. Straight arteries are given off from the most distal arcades and pass directly to the small intestine.

Inferior pancreaticoduodenal artery

An inferior pancreaticoduodenal artery is present in most individuals. It usually arises either directly from the superior mesenteric artery at the inferior border of the pancreas or as a common vessel with the first jejunal artery (a pancreaticoduodenojejunal trunk) from the posterior or left aspect of the superior mesenteric artery (Bertelli et al 1996b, Horiguchi et al 2008). It runs to the right, posterior to the superior mesenteric vein, to reach the posterior surface of the uncinate process, where it divides into anterior and posterior inferior pancreaticoduodenal arteries. The smaller anterior pancreaticoduodenal artery passes to the right, immediately inferior and then anterior to the inferior border of the head of the pancreas, and runs superiorly to anastomose with the anterior superior pancreaticoduodenal artery and form the anterior pancreaticoduodenal arcade. The larger posterior branch runs posteriorly and to the right, posterior to the head of the pancreas, parallel and superior to the anterior inferior pancreaticoduodenal artery, and anastomoses with the posterior superior pancreaticoduodenal artery to form the posterior pancreaticoduodenal arcade (Bertelli et al 1997). Both branches supply the head of the pancreas, its uncinate process and the superior and descending parts of the duodenum. Occasionally the anterior and posterior pancreaticoduodenal arteries arise separately from the superior mesenteric or first jejunal artery. Multiple small arteries run between the anterior and posterior pancreaticoduodenal arcades, either via the pancreaticoduodenal groove or through the substance of the gland. The largest and most consistent of these is the communicating artery (sometimes known as the middle pancreaticoduodenal arcade) that passes between the pancreatic duct and accessory pancreatic duct and connects the anterior pancreaticoduodenal arterial arcade and the posterior superior pancreaticoduodenal artery (Yamaguchi et al 2001; see Fig. 68.6C). This artery gives rise to most of the small arteries that supply the major duodenal papilla (Mirjalili and Stringer 2011).

When it arises as a pancreaticoduodenojejunal trunk, the inferior pancreaticoduodenal artery gives off a jejunal branch and then runs posterior to both the superior mesenteric artery and vein before dividing into its terminal branches. The inferior pancreaticoduodenal artery is at risk of bleeding during the retroperitoneal dissection of a Whipple procedure. Occasionally it is absent and the anterior and posterior inferior pancreaticoduodenal arteries arise separately from the superior mesenteric artery.

Jejunal branches

Usually, 4–6 jejunal branches arise from the left side of the proximal portion of the superior mesenteric artery (see Figs 64.13–64.14). They are distributed to the jejunum via 1–3 tiers of arterial arcades, the most distal of which gives rise to straight arteries. The latter run almost parallel in the mesentery before being distributed alternately to either side of the small intestine, forming two distinct 'leaves' of vessels within the mesentery separated by a relatively avascular plane (see Fig. 64.5A). This vascular arrangement allows a dilated segment of small intestine to be bisected longitudinally and tubularized to double its length, a potentially useful technique for achieving small intestine lengthening in short bowel syndrome (Bianchi 1984). Small twigs from the jejunal arteries supply regional mesenteric nodes.

Branches from the first jejunal branch of the superior mesenteric artery supply the ascending part of the duodenum and frequently anastomose with a terminal branch of the anterior superior pancreaticoduodenal artery. The ascending part of the duodenum therefore receives a potential collateral supply from the coeliac trunk and superior mesenteric artery, which means that it is not commonly affected by ischaemia.

Ileal branches

Ileal branches are more numerous (around 8–12) and slightly smaller in calibre than jejunal branches. They arise from the left and anterior aspects of the superior mesenteric artery. The length of the mesentery from the superior mesenteric artery to the mesenteric border of the intestine is greater in the ileum, and so the branches form between two and six arcades before giving rise to multiple straight arteries that run directly towards the ileal wall (see Fig. 64.10B). These branches run parallel in the mesentery and are distributed to both aspects of the ileum. They are shorter and thinner than their jejunal counterparts, particularly in the distal ileum, and do not form such distinct parallel 'leaves' of vessels. The terminal ileal arcades are supplied by the ileal branch of the ileocolic artery and the last ileal branch of the superior mesenteric artery (see Fig. 64.13). Few other vessels connect the ileocolic and superior mesenteric artery territories, and this makes surgical dissection of the ileocolic artery up to its origin relatively simple.

Ileocolic artery

The ileocolic artery arises from the superior mesenteric artery near the root of the mesentery of the small intestine, descending within that mesentery to the right towards the caecum, and crossing anterior to the right ureter, gonadal vessels and psoas major. It usually divides into superior and inferior branches, the superior branch running up along the left side of the ascending colon to anastomose with the right colic artery (or right branch of the middle colic artery) (Veeresh et al 2012). The inferior branch runs to the ileocaecal junction and divides into anterior and posterior caecal arteries, the appendicular artery, and an ileal branch that passes to the left in the ileal mesentery to anastomose with a terminal ileal branch of the superior mesenteric artery (see Fig. 65.23). The latter therefore provides a collateral arterial supply to the caecum. The ileocolic artery provides the major arterial supply to the caecum; traction on the caecum in the direction of the anterior superior iliac spine will cause the artery to tent up the mesentery, allowing the vessel to be easily identified.

The appendicular artery usually arises directly from the ileocolic artery and descends posterior to the terminal ileum to enter the meso-appendix a short distance from the base of the appendix (see Fig. 65.23). Here, it gives off a recurrent branch that anastomoses at the proximal appendix with a branch of the posterior caecal artery. The appendicular artery approaches the distal end of the organ, at first near to and then in the edge of the meso-appendix. Its terminal part lies on the wall of the appendix and can become thrombosed in appendicitis, resulting in distal gangrene or necrosis. Less commonly, the appendicular artery arises from the posterior caecal artery or an ileal artery (Ouattara et al 2007) (see Fig. 65.12). Accessory appendicular arteries are common; two or more arteries may supply the appendix.

Right colic artery

The right colic artery is relatively small and variable in its anatomy (Batra et al 2013). It usually arises as a common trunk with the middle colic artery, but can originate directly from the superior mesenteric artery or from the ileocolic artery (when it is referred to as an accessory right colic artery) (see Fig. 65.24). It passes to the right, across the right psoas major and quadratus lumborum, crossing the right gonadal vessels and ureter. Near the left side of the ascending colon it divides into a descending branch, which runs down to anastomose with the superior branch of the ileocolic artery, and an ascending branch, which passes up across the inferior pole of the right kidney to the right colic flexure, where it anastomoses with a branch of the middle colic artery. Together, these anastomoses form the marginal artery at the right colic flexure.

Middle colic artery

The middle colic artery arises from the right side of the superior mesenteric artery, either separately or in common with the right colic artery, just inferior to the neck of the pancreas, and passes anteriorly and superiorly within the transverse mesocolon, just to the right of the midline. As it approaches the colon, it usually divides into right and left branches. The right branch anastomoses with the ascending branch of the right colic artery. The left branch supplies the terminal part of midgut derivatives and anastomoses with a branch of the left colic artery near the left colic flexure. The marginal artery thus formed lies a few centimetres from the mesenteric edge of the transverse colon. Sometimes, the middle colic artery divides into three or more branches within the transverse mesocolon, in which case the most lateral branches form the arterial anastomoses. An accessory, or rarely a replaced, middle colic artery can arise directly from the abdominal aorta (Yoshida et al 1993), dorsal pancreatic, hepatic, inferior mesenteric or left colic arteries (see Fig. 65.25). In addition, an accessory middle colic artery is occasionally found arising from the superior mesenteric artery proximal to the origin of the actual middle colic artery (Turmezei and Cockburn 2009).

Inferior mesenteric artery

The inferior mesenteric artery is smaller than the superior mesenteric artery. It arises from the anterior or left anterolateral aspect of the abdominal aorta at about the level of the body of the third lumbar vertebra, 3–4 cm proximal to the aortic bifurcation and posterior to the inferior border of the horizontal part of the duodenum. It runs obliquely down to the linea terminalis (pelvic brim) initially anterior to and then to the left of the abdominal aorta. It gives off the left colic and sigmoid arteries and crosses the origin of the left common iliac artery medial to the ureter, with the inferior mesenteric vein lying between. Beyond the linea terminalis it continues in the root of the sigmoid mesocolon as the superior anorectal artery.

Left colic artery

The left colic artery usually arises from the inferior mesenteric artery shortly after its origin, ascends within the left colic mesentery and divides into an ascending and a descending branch (see Figs 65.38–65.39). The ascending branch passes upwards across the left psoas major, gonadal vessels, ureter and left kidney, and is crossed by the inferior mesenteric vein; its terminal branches anastomose with those of the left branch of the middle colic artery within the transverse mesocolon. The descending branch passes laterally and inferiorly and anastomoses with branches from the ascending branch and the most proximal sigmoid artery to form part of the marginal artery. The arterial arcades thus formed supply the distal third of the transverse and the descending colon. The left colic artery can originate from or in common with a sigmoid artery (Murono et al 2015). Occasionally an accessory, or rarely a replaced, left colic artery originates from the trunk of the superior mesenteric artery or its middle colic or first jejunal artery. When present, it runs laterally in the upper left colic mesentery just inferior to the duodenojejunal flexure to supply the proximal descending colon, and forms all or part of the marginal artery in the region of the distal transverse colon. The left colic artery can itself give rise to an accessory left middle colic artery. Occasionally it gives rise to a branch shortly after its origin, which ascends in the mesentery and anastomoses directly with a similar descending branch of the left branch of the middle colic artery (the so-called arc of Riolan; van Gulik and Schoots 2005).

The dominant arterial supply of the left colic flexure is usually from the left colic artery but can be from the left branch of the middle colic artery. The marginal artery in this region may be absent or small, but it can enlarge considerably if the inferior mesenteric artery is stenosed or occluded.

Vascular ligation in left colonic resections

During resection of the distal descending and sigmoid colon, ligation of the inferior mesenteric artery close to its origin preserves the bifurcation of the left colic artery and helps to maintain the arterial supply to the proximal descending colon via the anastomosis between the left branch of the middle colic artery and the ascending branch of the left colic artery. Ligation of the left colic artery close to its bifurcation can interfere with this supply and render the proximal descending colon ischaemic. Similarly, if the inferior mesenteric vein is ligated, then the bifurcation of the left colic vein forms the route of venous drainage from the proximal descending colon to the middle colic vein.

Sigmoid arteries

The inferior mesenteric artery gives rise to between two and five sigmoid arteries, which descend obliquely in the sigmoid mesocolon anterior to the left psoas major, ureter and gonadal vessels. They supply the distal descending colon and sigmoid colon and anastomose superiorly with the left colic artery and inferiorly with the superior anorectal artery. Unlike the arrangement in the small intestine, arterial arcades do not form until the arteries are close to the wall of the colon, when small branches arise to supply the sigmoid colon directly. A true marginal artery is less obvious in the sigmoid colon. There is often a significant interval in the mesentery between the highest sigmoid artery and the descending branch of the left colic artery; this forms a useful guide to the arterial territories during surgical dissection.

Superior anorectal artery

The principal arterial supply to the upper two-thirds of the rectum is via the superior anorectal artery (see Fig. 65.41). The inferior mesenteric artery crosses the left common iliac vessels medial to the ureter and descends in the medial limb of the sigmoid mesocolon, straddled by the hypogastric nerves on either side. As it crosses the linea terminalis it becomes the superior anorectal artery. At the level of the third sacral vertebra, where the rectum begins, the artery enters the proximal mesorectum in the midline and divides into two branches that descend, initially posterolaterally and then on each side of the rectum. Terminal branches pierce the rectal wall and anastomose with branches of the middle rectal and inferior anorectal arteries within the rectal submucosa.

The middle anorectal arteries arise from the internal pudendal, inferior gluteal, internal iliac arteries and less frequently from other internal iliac artery branches (DiDio et al 1986, Bilhim et al 2013). When present, they enter the mesorectum anterolaterally in the 'lateral ligaments' and provide some additional supply to the middle third of the rectum.

Inferior phrenic artery

The inferior phrenic arteries usually arise either from the aorta, just superior to the level of the coeliac trunk, or directly from the coeliac trunk; occasionally, they originate from the renal artery (Loukas et al 2005a, Gwon et al 2007). They contribute to the arterial supply of the respiratory diaphragm. Each artery ascends laterally, anterior to the crus of the respiratory diaphragm, near the medial border of the ipsilateral suprarenal gland and then divides into an ascending and a descending branch. The left ascending branch passes behind the oesophagus and runs anteriorly on the left side of the oesophageal hiatus, where it bifurcates; one branch curves anteriorly to anastomose with its counterpart anterior to the central tendon of the respiratory diaphragm and the other approaches the thoracic wall to anastomose with the musculophrenic and pericardiacophrenic arteries. The right ascending branch passes posterior to the inferior vena cava and then bifurcates; one branch runs anteriorly on the right side of the caval foramen before anastomosing with its counterpart anterior to the central tendon of the respiratory diaphragm, and the other passes laterally on the inferior surface of the diaphragm. The descending branches on each side supply the respiratory diaphragm and anastomose with the lower posterior intercostal and musculophrenic arteries. Each inferior phrenic artery gives off two or three small superior suprarenal arteries. The abdominal part of the oesophagus, fibrous capsule of the liver and the superior border of the spleen may also receive small arterial twigs from this vessel.

The inferior phrenic artery may be a source of significant collateral blood flow to large hepatocellular cancers and is sometimes specifically occluded, along with the relevant hepatic artery, when such tumours are treated by arterial embolization.

Superior suprarenal artery

The superior suprarenal artery usually arises from the ipsilateral inferior phrenic artery and passes to the gland as four or five small branches. It occasionally arises from the abdominal aorta.

Middle suprarenal arteries

The right and left middle suprarenal arteries often arise from the lateral aspect of the abdominal aorta at around the level of the superior mesenteric artery and ascend slightly over the crura of the respiratory diaphragm to anastomose with the suprarenal branches of the ipsilateral inferior phrenic and renal arteries (Toni et al 1988): each is usually single, but can be multiple or absent. The right middle suprarenal artery passes posterior to the inferior vena cava near the right coeliac ganglion. The left middle suprarenal artery passes close to the left coeliac ganglion, splenic artery and the superior border of the pancreas. The middle suprarenal arteries can originate from either the ipsilateral inferior phrenic or renal artery.

Renal artery

The paired renal arteries take about 20% of the cardiac output to supply organs that represent less than 1% of total body weight. They branch laterally from the aorta at right-angles just below the origin of the superior mesenteric artery (see Figs 59.5A, 72.10A). Both cross the corresponding crus of the respiratory diaphragm. The right renal artery is longer and often slightly higher, passing posterior to the inferior vena cava, right renal vein, head of the pancreas, and descending part of the duodenum. The left renal artery is often a little lower and passes behind the left renal vein, the body of the pancreas and the splenic vein. It may be crossed anteriorly by the inferior mesenteric vein.

A single renal artery to each kidney is present in approximately 70% of individuals (see Fig. 72.11). The arteries vary in their level of origin and in their calibre, obliquity and precise relations. In its extrarenal course, each renal artery gives off one or more inferior suprarenal arteries, ureteric and capsular branches, and branches that supply perirenal tissue and the renal pelvis. Near the hilum of the kidney, each artery divides into an anterior and a posterior branch, and these divide into segmental arteries supplying the renal vascular segments. Accessory renal arteries are common (in approximately 30% of individuals) and usually arise from the abdominal aorta above or below (most commonly below) the renal artery and follow it to the hilum (see Fig. 72.10B–D). Accessory vessels to the inferior pole cross anterior to the ureter and can, by obstructing the ureter, cause hydronephrosis. In children with ureteropelvic junction obstruction, a crossing vessel is found in 28% of cases (Veyrac et al 2003). Three anatomical variants of aberrant lower pole crossing vessels have been described: either anterior to the dilated renal pelvis or ureteropelvic junction, or inferior to the ureteropelvic junction, causing kinking of the ureter (Schneider et al 2013). Rarely accessory renal arteries arise from the coeliac or superior mesenteric arteries near the aortic bifurcation, or from the common iliac arteries.

The subdivisions of the renal arteries are described sequentially as segmental, lobar, interlobar, arcuate and interlobular (cortical radiate) arteries, and afferent and efferent glomerular arterioles (see Fig. 72.13).

Segmental arteries

Renal vascular segmentation was originally recognized by John Hunter in 1794, but the first detailed account of the primary pattern was produced in the 1950s from casts and radiographs of injected kidneys. Five arterial segments of the kidney have been identified (see Fig. 72.14). The superior segment occupies the anteromedial region of the superior pole. The anterior superior segment includes the rest of the superior pole and the central anterosuperior region. The inferior segment encompasses the whole inferior pole. The anterior inferior segment lies between the anterior and inferior segments. The posterior segment includes the whole posterior region between the superior and inferior segments. This is the pattern most commonly seen, and although there can be considerable variation, it is the pattern that clinicians most frequently encounter when performing partial nephrectomy. Recent anatomical and radiological analyses have suggested that there could be up to nine arterial segments for each kidney (Macchi et al 2019). Whatever pattern is present, it is important to emphasize that vascular segments are supplied by virtual end arteries. In contrast, the larger intrarenal veins have no segmental organization and anastomose freely.

Brödel described a relatively avascular longitudinal zone (the 'bloodless' line of Brödel) along the convex renal border, which was proposed as the most suitable site for surgical incision (Brödel 1911). However, many vessels cross this zone and it is far from 'bloodless'; planned radial or intersegmental incisions are therefore preferable (Macchi et al 2018). Knowledge of the vascular anatomy of the kidney is important when partial nephrectomy is undertaken for renal cell carcinoma. In this surgery, the branches of the renal artery are defined so that the surgeon can safely excise the tumour while not compromising the vascular supply to the remaining renal tissue (Novick 1998).

Lobar, interlobar, arcuate and interlobular arteries

The initial branches of segmental arteries are lobar, usually one to each renal pyramid. Before reaching the renal pyramid they subdivide into two or three interlobar arteries, extending towards the cortex around each pyramid. At the junction of the renal cortex and medulla, interlobar arteries dichotomize into arcuate arteries, which diverge at right angles. As they arch between the renal cortex and medulla, each divides further, ultimately supplying interlobular arteries that diverge radially into the cortex. The terminations of adjacent arcuate arteries do not anastomose but end in the renal cortex as additional interlobular arteries. Though most interlobular arteries come from arcuate branches, some arise directly from arcuate, or even terminal, interlobar arteries (see Fig. 72.13). Interlobular arteries ascend towards the superficial cortex or can branch occasionally en route. Some are more tortuous and recurve towards the renal medulla at least once before proceeding towards the renal surface. Others traverse the surface as perforating arteries to anastomose with the capsular plexus (which is also supplied from the inferior suprarenal, renal and gonadal arteries).

Afferent and efferent glomerular arterioles Afferent glomerular arterioles are mainly the lateral rami of interlobular arteries. A few arise from arcuate and interlobar arteries when they vary their direction and angle of origin: deeper ones incline obliquely back towards the renal medulla, the intermediate pass horizontally, and the more superficial approach the surface of the kidney obliquely before ending in a glomerulus (see Fig. 72.13). Efferent glomerular arterioles from most glomeruli (except at juxtamedullary and, sometimes, intermediate cortical levels) soon divide to form a dense peritubular capillary plexus around the proximal and distal convoluted tubules; there are therefore two sets of capillaries – glomerular and peritubular – in series in the main renal cortical circulation, linked by efferent glomerular arterioles. The vascular supply of the renal medulla is largely from efferent arterioles of juxtamedullary glomeruli, supplemented by some from more superficial glomeruli, and 'aglomerular' arterioles (probably from degenerated glomeruli). Efferent glomerular arterioles passing into the renal medulla are relatively long, wide vessels, and contribute side branches to neighbouring capillary plexuses before entering the renal medulla, where each divides into 12–25 descending vasa recta. As their name suggests, these run straight to various depths in the renal medulla, contributing side branches to a radially elongated capillary plexus applied to the descending and ascending limbs of renal loops and to collecting ducts. The venous ends of capillaries converge to the ascending vasa recta, which drain into arcuate or interlobular veins. An essential feature of the vasa recta (particularly in the outer medulla) is that both descending and ascending vessels are grouped into vascular bundles, within which the external aspects of both types are closely apposed, bringing them close to the limbs of the nephron loops (of Henle) and collecting ducts. As these bundles converge centrally into the renal medulla, they contain fewer vessels; some terminate at successive levels in neighbouring capillary plexuses. This proximity of descending and ascending vessels to each other and to adjacent collecting ducts provides the structural basis for the countercurrent exchange and multiplier phenomena (see Fig. 72.15). These complex renal vascular patterns show regional specializations that are closely adapted to the spatial organization and functions of renal corpuscles, tubules and ducts (see below).

The renal arteries are two of the largest branches of the abdominal aorta and arise laterally just inferior to the origin of the superior mesenteric artery at about the level of the body of the first lumbar vertebra (Mirjalili et al 2012b). When the arteries arise at different cranio-caudal levels, the right ostium is usually superior to the left. The right renal artery is longer and passes posterior to the inferior vena cava, right renal vein, head of the pancreas and descending part of the duodenum. The left renal artery passes behind the left renal vein, the body of the pancreas and the splenic vein. Variations in the number, origin, course and branching patterns of the renal arteries are common.

Inferior suprarenal arteries

The inferior suprarenal arteries often contribute most of the arterial supply to the suprarenal gland. One or two arteries usually arise from the ipsilateral renal artery, but the inferior suprarenal arteries can originate from either the abdominal aorta or the ipsilateral gonadal artery.

Testicular artery

The testicular artery usually arises from the abdominal aorta, inferior to the origin of the renal artery, and courses inferolaterally under the parietal peritoneum, along psoas major towards the pelvis. On the right, it courses anterior to the inferior vena cava and posterior to the middle colic and ileocolic arteries and the terminal ileum. On the left, it courses posterior to the inferior mesenteric vein, left colic artery and the descending colon. As the right and left testicular arteries enter the pelvis they lie anterior to the genitofemoral nerves, ureters and external iliac arteries. Both arteries then enter the deep inguinal ring and travel within the ipsilateral spermatic cord in the inguinal canal to the scrotum (see Figs 74.2, 74.5). The origin, number and course of the testicular arteries can vary (Asala et al 2001, Pai et al 2008, Kotian et al 2016, Kayalvizhi et al 2017).

Proximally, the testicular artery supplies the upper and middle parts of the ureter (Daniel and Shackman 1952). Distally, in its course to the testis the testicular artery gives off one or more internal testicular arteries (MacLennan 2012), an inferior testicular artery and branches supplying the head, body and tail of the epididymis (Macmillan 1954). The level at which this branching occurs is variable; in 31–88% of cases it occurs within the inguinal canal (Beck et al 1992, Jarow et al 1992). At the level of the testis, branches of the testicular artery enter the tunica albuginea in the mediastinum of the testis and ramify in the vascular layer before reaching their distribution. The testicular arteries ramify primarily in the anterior, medial and lateral portions of the inferior pole of the testis and in the anterior segment of the superior pole (Jarow 1991, Mostafa et al 2008), which has important implications for planning testicular biopsies.

Ovarian artery

The ovarian artery originates below the renal artery and descends behind the peritoneum, crossing the external iliac artery and vein at the linea terminalis to enter the lesser pelvis. Here, the artery turns medially in the suspensory ligament of the ovary and splits into a branch to the mesovarium that supplies the ovary and a branch that continues into the broad ligament, below the uterine tube, and supplies the tube. There are variations in the site of the division to the ovary and tube (see Fig. 75.21). On each side a branch passes lateral to the uterus to unite with the uterine artery. Other branches accompany the round ligaments through the inguinal canal to the skin of the labium majus and the inguinal region. Early in intrauterine life, the ovaries flank the vertebral column inferior to the kidneys and so the ovarian arteries are relatively short; they gradually lengthen as the ovaries descend into the pelvis.

Lumbar arteries

There are usually four lumbar arteries on each side, in series with the posterior intercostal arteries. They arise from the posterolateral aspect of the abdominal aorta, opposite the lumbar vertebrae. A fifth, smaller, pair occasionally arises from the median sacral artery, but lumbar branches of the iliolumbar arteries often take their place. The lumbar arteries run posterolaterally on the first to the fourth lumbar vertebral bodies, passing behind the sympathetic trunk and tendinous arches formed by the attachments of psoas major to the vertebral bodies. The right lumbar arteries pass posterior to the inferior vena cava. The superior two right lumbar arteries and the first left lumbar artery lie behind the corresponding crus of the respiratory diaphragm. Just beyond the intervertebral foramina, each lumbar artery divides into a medial branch, which gives off spinal and ganglionic branches; a middle branch, from which dorsal and anastomotic branches arise; and a lateral branch, which supplies the abdominal wall (Arslan et al 2011). Of particular importance is the spinal branch known as the great radicular artery (artery of Adamkiewicz), which frequently originates from an upper lumbar artery, particularly on the left side (Biglioli et al 2004). Injury to this vessel, e.g. during thoracoabdominal aortic surgery, can cause spinal cord infarction.

The lateral branch of each lumbar artery runs posterior to psoas major and the lumbar plexus, then across the anterior surface of quadratus lumborum, before piercing the posterior aspect of transversus abdominis to run forwards between it and internal abdominal oblique. Perforating branches pass posteriorly to supply the muscles and skin of the posterior abdominal wall (Kiil et al 2009). The lumbar arteries anastomose with one another and the lower posterior intercostal, subcostal, iliolumbar, deep circumflex iliac and inferior epigastric arteries.

The dorsal branch of each lumbar artery passes backwards between the adjacent transverse processes to supply the back muscles, vertebrae and their joints and the skin of the back.

Median sacral artery

The median sacral artery is a small branch that usually arises from the posterior aspect of the aorta a little above its bifurcation. It descends close to the midline, anterior to the fourth and fifth lumbar vertebrae, sacrum and coccyx. At the level of the fifth lumbar vertebra it is crossed by the left common iliac vein and often gives off a small lumbar artery (arteriae lumbales imae), whose small branches reach the anus and rectum via the anococcygeal ligament. Anterior to the fifth lumbar vertebra, the median sacral artery anastomoses with a lumbar branch of the iliolumbar artery. Anterior to the sacrum, it anastomoses with the lateral sacral arteries and sends branches into the anterior sacral foramina.

Common iliac arteries

The abdominal aorta bifurcates into the right and left common iliac arteries anterolateral to the left side of the body of the fourth lumbar vertebra (Roberts and Krishingner 1967). These arteries diverge as they descend and they divide at the level of the sacro-iliac joint into external and internal iliac arteries. The anteroposterior diameters of the common, external and internal iliac arteries are strongly correlated to body surface area (BSA) in children, in contrast to adults, where the relation is inconsistent. Vessel diameters measured by ultrasonography are significantly larger in boys than in girls (Munk et al 2002).

Each common iliac artery also gives small branches to the peritoneum, psoas major, ureter, adjacent nerves and surrounding areolar tissue. The common iliac artery occasionally gives rise to the iliolumbar artery and accessory or replaced renal arteries if the kidney is low-lying.

Right common iliac artery

The right common iliac artery is approximately 5 cm long. It passes obliquely across part of the bodies of the fourth and the fifth lumbar vertebrae, and is crossed anteriorly by the sympathetic rami to the pelvic plexus and, at its division into internal and external iliac arteries, by the ureter. It is covered by the parietal peritoneum, which separates it from the small intestine. Posteriorly, it is separated from the bodies of the fourth and fifth lumbar vertebrae and the intervening intervertebral disc by the right sympathetic trunk, the terminal parts of the common iliac veins and the start of the inferior vena cava, the obturator nerve, lumbosacral trunk and iliolumbar artery. Laterally, the inferior vena cava and the right common iliac vein lie superiorly and the right psoas major lies inferiorly. The left common iliac vein is medial to the proximal part of the right common iliac artery.

Left common iliac artery

The left common iliac artery is shorter than the right and is approximately 4 cm long. Lying anteriorly are branches of the sympathetic trunk that contribute to the superior hypogastric plexus, the superior anorectal artery and, at its terminal bifurcation, the ureter. The sympathetic trunk, the bodies of the fourth and fifth lumbar vertebrae and the intervening intervertebral disc, the obturator nerve, lumbosacral trunk and iliolumbar artery are all posterior. The left common iliac vein is posteromedial and the left psoas major is lateral.

Internal iliac arteries

The internal iliac arteries provide the principal supply to the walls and viscera of the pelvis, the perineum and the gluteal region. Each internal iliac artery is approximately 4 cm long and begins at the common iliac bifurcation, level with the lumbosacral intervertebral disc and anterior to the sacroiliac joint (see Fig. 71.5). It descends posteriorly to the superior margin of the greater sciatic foramen, where it divides into an anterior division, which continues in the same line towards the ischial spine, and a posterior division, which passes back to the greater sciatic foramen.

The ureter and, in females, the ovary and distal end of the uterine tube, are anterior to the artery. The internal iliac vein, lumbosacral trunk and sacroiliac joint are posterior. Laterally are the external iliac vein, between the artery and psoas major, and the obturator nerve lying inferior to the vein. Medially, the parietal peritoneum and tributaries of the internal iliac vein separate the artery from the terminal ileum on the right and the sigmoid colon on the left. For details of the considerable variation in the anatomy of the internal iliac artery see Tubbs et al (2016).

In the fetus, the internal iliac artery is twice the size of the external iliac artery and is the direct continuation of the common iliac artery. The main trunk ascends on the anterior abdominal wall to the umbilicus, converging on the contralateral artery, and the two arteries run through the umbilicus to enter the umbilical cord as the umbilical arteries. At birth, when placental circulation ceases, only the pelvic segment remains patent as the internal iliac artery and part of the superior vesical artery and the remainder becomes a fibrous medial umbilical ligament. Persistence of the umbilical artery has been described and can cause extrinsic obstruction of the distal ureter (Gupta et al 1999). In males, the patent part (commonly, the superior vesical artery) usually gives off the artery to the ductus deferens.

The anterior division of the internal iliac arteries primarily supply the pelvic organs via the superior and inferior vesical, middle anorectal, vaginal, obturator, uterine, internal pudendal and inferior gluteal arteries (see Fig. 71.5). It should be noted that there is significant variation in the branching patterns of the anterior division and therefore only the general principles will be considered here. The posterior division of the internal iliac arteries primarily supply muscles in the hip and back via the iliolumbar, lateral sacral and superior gluteal arteries.

Superior vesical artery

The superior vesical artery is the first large branch of the anterior division. It lies on the lateral wall of the pelvis, just inferior to the linea terminalis, and runs anteroinferiorly, medial to the periosteum of the posterior surface of the pubis. It supplies the distal end of the ureter, the fundus of the urinary bladder, the proximal end of the ductus deferens and the seminal glands. It also gives origin to the umbilical artery in the fetus, which remains as a fibrous cord – the medial umbilical ligament – in the adult. This vessel occasionally remains patent as a small artery supplying the umbilicus.

The artery to the ductus deferens often originates from one of the branches of the superior vesical artery to the fundus of the urinary bladder: it accompanies the ductus deferens to the testis, where it anastomoses with the testicular artery.

Inferior vesical artery

The inferior vesical artery sometimes arises as a common branch with the middle anorectal artery from the internal iliac artery. In the male, it supplies the fundus of the urinary bladder, prostate, seminal glands and distal ureter and sometimes provides the artery to the ductus deferens. Branches to the prostate communicate across the midline. In the female it supplies the urinary bladder, and is often replaced by the vaginal artery (de Treigny et al 2017).

Middle anorectal artery

The middle anorectal artery runs into the lateral fascial coverings of the mesorectum. It often consists of multiple branches, can be small, and occasionally arises either close to or in common with the origin of the inferior vesical artery in males.

Vaginal artery

In females, the vaginal artery sometimes replaces the inferior vesical artery. It can arise from the uterine artery close to its origin as either a single vessel or multiple branches.

Obturator artery

The obturator artery arises from the anterior division of the internal iliac artery and runs anteroinferiorly on the lateral pelvic wall to the upper part of the obturator foramen. In the pelvis, it is related laterally to the obturator fascia and is crossed on its medial aspect by the ureter and, in the male, by the ductus deferens. The obturator nerve is superior to the artery, the obturator vein inferior to it. The obturator artery provides iliac branches to the iliac fossa that supply the underlying bone and iliacus and anastomose with the iliolumbar artery. It gives off a branch that runs medially to the urinary bladder and sometimes replaces the inferior vesical artery. In the female, the ovary lies medial to the obturator artery. A pubic branch usually arises just before the obturator artery leaves the pelvis and ascends over the pubis to anastomose with the contralateral artery and the pubic branch of the inferior epigastric artery.

The obturator artery leaves the pelvis via the obturator canal. It divides into anterior and posterior branches that encircle the obturator foramen between obturator externus and the obturator membrane. The anterior branch curves anteriorly on the membrane and then inferiorly along its anterior margin to supply branches to obturator externus, pectineus, adductors longus, brevis and magnus and gracilis. It anastomoses with the posterior branch and the medial circumflex femoral artery. The posterior branch follows the posterior margin of the obturator foramen, turning anteriorly on the ischial part to anastomose with the anterior branch. It supplies the muscles attached to the ischial tuberosity and anastomoses with the inferior gluteal artery. An acetabular branch enters the hip joint at the acetabular notch, ramifies in the fat of the acetabular fossa and sends a branch along the ligament of the head of the femur.

The obturator artery is occasionally replaced by an enlarged pubic branch of the inferior epigastric artery that descends almost vertically to the obturator foramen. It usually lies near the external iliac vein, lateral to the femoral ring, and is rarely injured during inguinal or femoral hernia surgery. It may curve along the edge of the lacunar ligament, partly encircling the neck of a hernia sac, and can be cut inadvertently during enlargement of the femoral ring in reducing a femoral hernia.

Uterine artery

The uterine artery is large and it usually arises inferior to the obturator artery on the lateral wall of the pelvis, running inferomedially within the cardinal ligament. It may arise directly from the internal iliac artery, the superior gluteal artery, obturator artery or from a common trunk with the internal pudendal artery (Chantalat et al 2014).

From its origin, the uterine artery crosses the ureter anteriorly in the broad ligament before branching as it reaches the uterus at the level of the cervico-isthmic junction (see Fig. 75.21). One major branch ascends the uterus tortuously within the broad ligament until it reaches the region of the hilum of the ovary, where it anastomoses with branches of the ovarian artery. Another branch descends to supply the cervix and anastomoses with branches of the vaginal artery to form two median longitudinal vessels, the azygos arteries of the vagina, which descend anterior and posterior to the vagina. Although there are anastomoses with the ovarian and vaginal arteries, the dominance of the uterine artery is indicated by its marked hypertrophy during pregnancy.

The tortuosity of the vessels as they ascend in the broad ligaments is repeated in their branches within the uterine wall. Each uterine artery gives off numerous branches. These enter the uterine wall, divide and run circumferentially as groups of anterior and posterior arcuate arteries. They ramify and narrow as they approach the anterior and posterior midline so that no large vessels are present in these regions. However, the left and right arterial trees anastomose across the midline and unilateral ligation can be performed without serious effects. Terminal branches in the uterine muscle are tortuous and are called helicine arterioles. They provide a series of dense capillary plexuses in the myometrium and endometrium. From the arcuate arteries, many helical arteriolar rami pass into the endometrium. Their detailed appearance changes during the menstrual cycle. Helical arterioles are less prominent during the proliferative phase, whereas they grow in length and calibre, becoming even more tortuous, during the secretory phase.

Internal pudendal artery

The internal pudendal artery is the smaller terminal branch of the anterior division of the internal iliac artery. Close to its origin it crosses anterior to piriformis, the sacral plexus and the inferior gluteal artery. It descends laterally to the inferior aspect of the greater sciatic foramen, where it leaves the pelvis between piriformis and ischiococcygeus and enters the gluteal region (see Fig. 75.4). It next curves around the posterior aspect of the ischial spine and enters the ischio-anal fossa via the lesser sciatic foramen. This course effectively allows the nerve to wrap around the posterior limit of levator ani at its attachment to the ischial spine. Posterior to the ischial spine, the artery is covered by gluteus maximus, the pudendal nerve is medial, and the nerve to obturator internus is lateral. The artery passes through the ischio-anal fossa in the pudendal canal (Alcock's canal) in the fascia covering obturator internus, giving off the inferior anorectal artery early in its course through the fossa (see Fig. 71.12). It gives off several muscular branches in the pelvis and the gluteal region to supply adjacent muscles and nerves. The internal pudendal artery enters the perineum around the posterior aspect of the ischial spine and runs on the lateral wall of the ischio-anal fossa in the pudendal canal with the internal pudendal veins and the pudendal nerve. The canal lies about 4 cm superior to the inferior limit of the ischial tuberosity and is formed by connective tissue binding the internal pudendal vessels and pudendal nerve to the medial surface of the fascia covering obturator internus. As the artery approaches the margin of the ischial ramus, it proceeds superficial or deep to the perineal membrane, along the medial margin of the inferior pubic ramus, en route to its target structures.

In the male, the internal pudendal artery distal to the perineal artery gives a branch to the bulb of the penis before it divides into the deep and dorsal arteries of the penis (see Fig. 71.12). In the female, a similar branch of the internal pudendal artery is distributed to the corpus spongiosum and vagina. The deep arteries supply the corpora cavernosa of the clitoris; the dorsal arteries supply the glans and prepuce of the clitoris.

Branches of the internal pudendal artery are sometimes derived from an accessory pudendal artery, which is usually a branch of the internal pudendal artery before its exit from the pelvis.

Inferior anorectal artery

The inferior anorectal artery is a terminal branch of the internal pudendal artery and supplies the internal and external anal sphincters, the anal canal and perianal skin. It arises just after the internal pudendal artery enters the pudendal canal on the lateral wall of the ischio-anal fossa and runs anteromedially through the adipose tissue of the fossa to enter the proximal anal canal laterally. Ascending branches supply the distal third of the rectum, anastomosing with terminal branches of the superior anorectal artery in the rectal submucosa to reach the external anal sphincter: the artery often branches before reaching the sphincter. During dissections of the anal canal, particularly during perineal excisions of the anus or rectum, the inferior anorectal vessels are encountered in the ischio-anal fossa and must be ligated before division, otherwise they tend to retract laterally, where they can cause troublesome bleeding.

Perineal artery

The perineal artery is a branch of the internal pudendal artery that arises near the anterior end of the pudendal canal and runs through the perineal membrane. In the male, it approaches the scrotum in the superficial perineal space, between bulbospongiosus and ischiocavernosus (see Fig. 74.24). A small transverse branch passes medially, inferior to the superficial transverse perineal muscle, to anastomose with the contralateral artery and with the posterior scrotal and inferior anorectal arteries. It supplies the transverse perinei, the perineal body and the posterior attachment of the bulb of the penis. The posterior scrotal arteries are usually terminal branches of the perineal artery but can also arise from its transverse branch. They are distributed to the scrotal skin and dartos in the male and supply the perineal muscles. In the female, the perineal artery runs an almost identical course to that in the male and gives off posterior labial branches (see Fig. 75.4).

Artery to the bulb of the penis

The artery to the bulb of the penis penetrates the perineal membrane to enter the corpus spongiosum from above its posterolateral border and supplies the bulb of the penis and the urethra, in addition to the corpus spongiosum and glans penis.

Dorsal artery of the penis

The dorsal artery of the penis passes between the crus of the penis and the pubis to reach the dorsal surface of the corpus cavernosum. It runs alongside the deep dorsal vein of the penis and the dorsal nerve of the penis and is attached, together with these structures, to the underside of the deep fascia of the penis. As it courses to the glans penis it gives off circumferential branches to the corpus spongiosum and spongy urethra. The rich blood supply to the corpus spongiosum allows the urethra to be divided safely during stricture repair.

Deep artery of the penis

The deep artery of the penis is often a paired vessel that pierces the tunica albuginea of the corpora cavernosa proximally and then travels near the centre of the corporal bodies in the direction of the glans penis. Along its course it gives off several straight and helicine branches at regular intervals; they open directly into the cavernous spaces of the corporal bodies.

Variations in penile vascular anatomy are common and can include a single or absent cavernous artery or the presence of accessory pudendal arteries (Bare et al 1994, Matin 2006). While the penile arterial supply is commonly derived from both accessory and internal pudendal arteries, it can be derived exclusively from either the internal pudendal arteries or the accessory pudendal arteries (Droupy et al 1997). Recognizing such variation is extremely important for any surgeon contemplating penile revascularization surgery.

The artery to the bulb of the penis supplies the corpus spongiosum, and the deep artery of the penis supplies the corpus cavernosum on each side. The dorsal artery runs on the dorsal aspect of the penis and supplies circumflex branches to the corpora cavernosa and corpus spongiosum that end by anastomosing near the corona of the glans and supplying the glans and prepuce of the penis.

Inferior gluteal artery

The inferior gluteal artery is the larger terminal branch of the anterior division of the internal iliac artery. It descends posteriorly, anterior to the sacral plexus and piriformis but posterior to the internal pudendal artery. It passes between either the first and second, or the second and third, sacral ventral rami, then between piriformis and ischiococcygeus, before running through the inferior aspect of the greater sciatic foramen to reach the gluteal region. It next runs inferiorly with the sciatic and posterior femoral cutaneous nerves, deep to gluteus maximus and between the greater trochanter and ischial tuberosity, and continues down the thigh, supplying the skin and anastomosing with branches of the perforating arteries. The inferior gluteal and internal pudendal arteries often arise as a common stem from the internal iliac artery, sometimes with the superior gluteal artery. In the pelvis, the inferior gluteal artery gives branches to piriformis, ischiococcygeus and iliococcygeus, and occasionally gives rise to the middle anorectal artery. It can supply vessels to the seminal glands and prostate.

Arteria comitans nervi ischiadici (artery to sciatic nerve)

The arteria comitans nervi ischiadici is a direct or indirect branch of the internal iliac artery, and runs on the surface of, or within, the sciatic nerve. It represents the primitive axial artery of the lower limb. The artery is usually a very small vessel; occasionally, it persists as a large vessel, in which case the femoral artery is correspondingly reduced in size. The artery may participate in collateral circulatory pathways.

Iliolumbar artery

The iliolumbar artery is the first branch of the posterior division of the internal iliac artery and ascends laterally anterior to the sacro-iliac joint and lumbosacral trunk. It lies posterior to the obturator nerve and external iliac vessels, and reaches the medial border of psoas major, dividing behind it into the lumbar and iliac branches. The lumbar branch supplies psoas major and quadratus lumborum, and anastomoses with the fourth lumbar artery. It sends a small spinal branch through the intervertebral foramen between the fifth lumbar and first sacral vertebrae to supply radicular branches to the cauda equina. The iliac branch supplies iliacus; between the muscle and bone it anastomoses with the iliac branches of the obturator artery. A large nutrient branch enters an oblique canal in the ilium. Other branches run around the iliac crest, contribute to the supply of gluteal and abdominal muscles, and anastomose with the superior gluteal, circumflex iliac and lateral circumflex femoral arteries.

Lateral sacral arteries

The lateral sacral arteries are usually double. If they are single, they soon divide into superior and inferior branches. The superior and larger branch passes medially into the first or second anterior sacral foramen, supplies the sacrum and contents of the sacral canal, and then leaves the sacrum via the corresponding dorsal foramen to supply the skin and muscles posterior to the sacrum. The inferior branch crosses obliquely anterior to piriformis and the sacral ventral rami, and then descends lateral to the sympathetic trunk to anastomose with its fellow and the median sacral artery anterior to the coccyx. Its branches enter the anterior sacral foramina and are distributed in the same way as the branches of the superior artery.

Superior gluteal artery

The superior gluteal artery is the largest branch of the internal iliac artery and effectively forms the main continuation of its posterior division. It runs posteriorly between the lumbosacral trunk and the first sacral ventral ramus, or between the first and second sacral ventral rami, and then turns slightly inferiorly, leaving the pelvis via the greater sciatic foramen above piriformis and dividing into superficial and deep branches. In the pelvis, it supplies piriformis, obturator internus and a nutrient artery to the ilium. The superficial branch enters the deep surface of gluteus maximus. Its numerous branches supply the muscle and anastomose with the inferior gluteal branches (see Fig. 77.47), while others perforate the tendinous medial attachment of the muscle to supply the skin over the sacrum, where they anastomose with the posterior branches of the lateral sacral arteries. The deep branch of the superior gluteal artery passes between gluteus medius and the ilium, soon dividing into superior and inferior branches. The superior branch skirts the superior border of gluteus minimus to the anterior superior iliac spine and anastomoses with the deep circumflex iliac artery and the ascending branch of the lateral circumflex femoral artery. The inferior branch runs through gluteus minimus obliquely, supplies it and gluteus medius, and anastomoses with the lateral circumflex femoral artery. A branch enters the trochanteric fossa to join the inferior gluteal artery and ascending branch of the medial circumflex femoral artery; other branches run through gluteus minimus to supply the hip joint.

The superior gluteal artery occasionally arises directly from the internal iliac artery with the inferior gluteal artery and sometimes from the internal pudendal artery.

External iliac arteries

The external iliac arteries are the principal arteries of the lower limbs. They are larger than the internal iliac arteries (see Figs 71.5–71.6). Each artery descends laterally along the medial border of psoas major, from the common iliac bifurcation to a point midway between the anterior superior iliac spine and the pubic symphysis, and enters the thigh posterior to the inguinal ligament to become the femoral artery.

The parietal peritoneum and extraperitoneal tissue separate the right external iliac artery from the terminal ileum and, usually, the appendix, and the left external iliac artery from the sigmoid colon and coils of small intestine anteromedially. The external iliac artery can be crossed at its origin by the ureter and it is subsequently crossed by the gonadal vessels, the genital branch of the genitofemoral nerve, the deep circumflex iliac vein, and the ductus deferens or round ligament of the uterus. Posteriorly, the artery is separated from the medial border of psoas major by the iliac fascia. The external iliac vein lies partly posterior to its upper part but is more medial below. Laterally, it is related to psoas major, which is covered by the iliac and psoas fasciae. Numerous lymph vessels and nodes lie on its anterior and lateral aspects. The external iliac artery primarily supplies the lower limb and as such has few branches in the pelvis. It gives off very small vessels to psoas major and neighbouring lymph nodes, but has no other branches until it gives off the deep circumflex iliac and inferior epigastric arteries, near to where it passes deep to the inguinal ligament.

Deep circumflex iliac artery

The deep circumflex iliac artery branches laterally from the external iliac artery almost opposite the origin of the inferior epigastric artery (see Fig. 76.4A). It ascends and runs laterally to the anterior superior iliac spine deep to the inguinal ligament in a sheath formed by the union of the transversalis and iliac fasciae. There, it anastomoses with the ascending branch of the lateral circumflex femoral artery, pierces the transversalis fascia and skirts the inner lip of the iliac crest. About halfway along the iliac crest, it runs through transversus abdominis, and then between transversus abdominis and internal abdominal oblique, to anastomose with the iliolumbar and superior gluteal arteries. It gives off a large ascending branch at the anterior superior iliac spine that runs between internal abdominal oblique and transversus abdominis, supplies both muscles, and anastomoses with the lumbar and inferior epigastric arteries.

Inferior epigastric artery

The inferior epigastric artery originates from the external iliac artery posterior to the inguinal ligament. It curves forwards in the anterior extraperitoneal tissue, ascends obliquely along the medial margin of the deep inguinal ring, and continues as an artery of the anterior abdominal wall.

The inferior epigastric artery (often referred to as the deep inferior epigastric artery in clinical practice in order to distinguish it from the superficial (inferior) epigastric artery) originates from the medial aspect of the external iliac artery just proximal to where the vessels pass deep to the inguinal ligament (see Figs 60.1–60.3). Its accompanying veins, usually two, unite to form a single vein that drains into the external iliac vein (Rozen et al 2009). The vessel curves forwards in the extraperitoneal tissue and ascends obliquely along the medial margin of the deep inguinal ring. It lies posterior to the spermatic cord, separated from it by the transversalis fascia. It pierces the transversalis fascia and enters the posterior layer of the rectus sheath by passing anterior to the arcuate line. In this part of its course it is visible through the parietal peritoneum of the anterior abdominal wall and with this covering forms the lateral umbilical fold. Disruption of the artery by surgical incisions (e.g. insertion of laparoscopic ports, surgical tacks or abdominal drains) can cause a haematoma, which can expand to considerable size because there is no adjacent tissue against which the bleeding can be tamponaded.

The ductus (vas) deferens in males or the round ligament of the uterus in females, pass medially after hooking around the inferior epigastric artery at the deep inguinal ring. The inferior epigastric vessels form the lateral border of the inguinal triangle (Hesselbach's triangle). The boundaries of this anatomical region are seen during laparoscopic inguinal hernia repair: the inferior border of the triangle is formed by the iliopubic tract/inguinal ligament and the medial border by the lateral margin of rectus abdominis. Hernias occurring within the triangle are termed direct inguinal hernias.

The inferior epigastric arteries ascend and anastomose with their superior counterparts as a single vessel in only about 30% of cases (El-Mrakby and Milner 2002). Branching into two vessels before anastomosing is the most common pattern, accounting for almost 60%, with a trifurcation in the remainder. The inferior epigastric arteries have an average diameter of approximately 3 mm at their origin, compared to an average diameter of 1.6 mm at the origin of the superior epigastric arteries, presumably explaining why the inferior epigastric arteries provide the 'dominant' blood supply to rectus abdominis. Preliminary ligation of the inferior epigastric artery is often performed when preparing a myocutaneous flap from the mid or lower rectus abdominis based on the superior epigastric artery; this encourages augmentation of the superior epigastric arterial supply.

Branches of the inferior epigastric artery anastomose with branches of the superior epigastric artery within rectus abdominis at a variable level proximal to the umbilicus (Rozen et al 2008). Other branches anastomose with terminal branches of the distal five posterior intercostal, subcostal and lumbar arteries at the lateral border of the rectus sheath. Inferolaterally, branches anastomose with the deep circumflex iliac artery. The inferior epigastric artery also gives off the cremasteric artery, a pubic branch, and muscular and cutaneous branches.

Cremasteric artery

The cremasteric artery is a branch of the inferior epigastric artery. It accompanies the spermatic cord and supplies cremaster and other coverings of the cord and anastomoses with the testicular artery. Both the artery to the ductus deferens and the cremasteric artery enter the inguinal canal at the deep inguinal ring and travel the length of the spermatic cord alongside the testicular artery. The testicular artery and pampiniform plexus lie within the internal spermatic fascia, whereas the ductus deferens and its vessels, as well as cremaster and its vessels, lie outside the internal spermatic fascia but within the external spermatic fascia. In the scrotum, there is a rich vascular anastomosis at the head of the epididymis, between the testicular artery and the epididymal artery, and at the tail of the epididymis between the testicular, epididymal, and cremasteric arteries and the artery to the ductus deferens.

In females, the homologous artery is small and accompanies the round ligament of the uterus.

Pubic branch

A pubic branch, near the femoral ring, descends posterior to the pubis and anastomoses with the pubic branch of the obturator artery. The pubic branch of the inferior epigastric artery can be larger than the obturator artery and supply most of the territory of the obturator artery in the thigh, in which case it is referred to as the aberrant obturator artery (Pai et al 2009). It lies close to the medial border of the femoral ring and can be injured during medial dissection of the ring in femoral hernia repair, laparoscopic inguinal hernia repair, or with pelvic fractures.

Muscular and cutaneous branches

Muscular branches supply the abdominal muscles and peritoneum and anastomose with the circumflex iliac and lumbar arteries. Cutaneous branches arise within rectus abdominis, and perforate the aponeurosis of external abdominal oblique to supply the overlying skin; they anastomose with branches of the superficial epigastric artery, contributing to the 'periumbilical perforator vessels'. These perforating vessels have been mapped in detail because they are particularly important in creating large lipocutaneous flaps on the abdominal wall: if this requires ligation of these vessels, the flap is at risk of necrosis (Rozen et al 2008).

Occasionally the inferior epigastric artery arises from the femoral artery. It then ascends anterior to the femoral vein, passing deep to the inguinal ligament and into the abdominal cavity before following its usual abdominal course. Rarely it arises from the external iliac artery in common with an aberrant obturator artery or from the obturator artery itself.

The superior and inferior epigastric arteries are important sources of collateral blood flow between the internal thoracic artery, the external iliac artery and the lumbar vessels when aortic blood flow is compromised. Additionally, small tributaries of the inferior epigastric vein draining the skin around the umbilicus anastomose with terminal branches of the umbilical vein that drain into the liver via the falciform ligament. These portosystemic communications can dilate substantially in patients with portal hypertension, resulting in portal venous blood draining into the systemic circulation via the inferior epigastric veins. Back pressure to the level of the skin leads to a pattern of dilated, serpiginous superficial veins radiating out from the umbilicus, referred to as the 'caput medusae'.

SUBCLAVIAN ARTERY AND ARTERIAL SUPPLY OF THE UPPER LIMB

The stem artery of the upper limb is single as far as the elbow, but its name changes as it traverses different regions. From its origin to the outer border of the first rib it is the subclavian artery. From the outer border of the first rib to the tendon of teres major it is the axillary artery and from the tendon of teres major to its division at the elbow it is the brachial artery.

Subclavian artery

The right subclavian artery arises from the brachiocephalic trunk, the left from the aortic arch (see Figs 35.14, 35.18).

For description, each is divided into a first part, from its origin to the medial border of scalenus anterior; a second part posterior to scalenus anterior; and a third part from the lateral margin of scalenus anterior to the outer border of the first rib, where the subclavian artery becomes the axillary artery. The subclavian artery gives off the vertebral, internal thoracic, thyrocervical, costocervical and dorsal scapular arteries. On the left, all the branches except the dorsal scapular artery arise from the first part. On the right, the costocervical trunk usually arises from the second part. The suprascapular artery (usually a branch of the thyrocervical trunk) may arise from the third part of the subclavian artery.

Each subclavian artery arches over the cervical pleura and pulmonary apex. The first parts differ on the right and left sides, whereas the second and third parts are almost identical.

First part of right subclavian artery

The right subclavian artery arises from the brachiocephalic trunk either posterior to the right sternoclavicular joint or immediately superior to it (level with the body of the second thoracic vertebra or T1–T2 intervertebral disc (Badshah et al 2017)) (see Fig. 52.3). It ascends superolaterally to the level of the first rib, where it is located posterior to both the sternal end of the clavicle and scalenus anterior; it has a minimal intrathoracic presence. The vessel then passes inferolaterally across the superior surface of the first rib, and at the external border of the rib becomes the right axillary artery (see Fig. 48.3). It usually ascends 2 cm above the clavicle but this varies.

Relations The artery is deep to the skin, superficial fascia, platysma, supraclavicular nerves, deep fascia, clavicular attachment of sternocleidomastoid, sternohyoid and sternothyroid. It is at first behind the origin of the right common carotid artery; more laterally, it is crossed by the vagus nerve, the cardiac branches of the vagus and the sympathetic trunk, and by internal jugular and vertebral veins; the subclavian sympathetic loop encircles it. The anterior jugular vein diverges laterally in front of it, separated by sternohyoid and sternothyroid. Below and behind the artery are the pleura and pulmonary apex; they are separated from the artery by the suprapleural membrane, the ansa subclavia, a small accessory vertebral vein and the right recurrent laryngeal nerve, which winds round the lower and posterior part of the vessel.

First part of left subclavian artery

In the majority of individuals, the left subclavian artery originates independently from the aortic arch after the origins of the brachiocephalic and left common carotid arteries. It ascends into the neck posterior to scalenus anterior, then passes inferolaterally towards the external border of the first rib, where it becomes the left axillary artery. A common origin occasionally exists between the left subclavian and vertebral arteries. Bilateral brachiocephalic trunks are rare: they divide on both sides into common carotid and subclavian arteries.

Relations In the thorax, the left subclavian artery is related anteriorly to the left common carotid artery and left brachiocephalic vein (and sometimes the inferior thyroid vein), from which it is separated by the left vagus, cardiac and phrenic nerves. Sternothyroid and sternohyoid lie between the vessel and the upper left aspect of the posterior surface of the manubrium sterni. On the left side of the oesophagus, the thoracic duct and longus colli are posterior. The left subclavian artery is in contact posterolaterally with the left lung and pleura. The trachea, left recurrent laryngeal nerve, oesophagus and thoracic duct are medial. Laterally, the artery grooves the mediastinal surface of the left lung and pleura, which also encroach on its anterior and posterior aspects. In the neck, near the medial border of scalenus anterior the artery is crossed anteriorly by the left phrenic nerve and the termination of the thoracic duct. Otherwise, anterior relations are the same as those of the first part of the right subclavian artery. Posteriorly and inferiorly, the relations of both vessels are identical but the left recurrent laryngeal nerve, medial to the left subclavian artery in the thorax, is not directly related to its cervical part.

Second part of subclavian artery

The second part of the subclavian artery lies behind scalenus anterior; it is short and constitutes the highest part of the vessel (see Fig. 35.18).

Relations The skin, superficial fascia, platysma, deep cervical fascia, sternocleidomastoid and scalenus anterior are anterior. The right phrenic nerve is often described as being separated from the second part of the subclavian artery by scalenus anterior, whereas it crosses the first part of the left subclavian artery. However, both nerves may sometimes lie anterior to the muscle. The suprapleural membrane, pleura and lung, and the lower trunk of the brachial plexus are posteroinferior; the upper and middle trunks of the plexus are superior; and the subclavian vein is anteroinferior, separated by scalenus anterior.

Third part of subclavian artery

The third part of the subclavian artery descends laterally from the lateral margin of scalenus anterior to the outer border of the first rib, where it becomes the axillary artery. It is the most superficial part of the artery and lies partly in the supraclavicular triangle, where its pulsations may be felt and it may be compressed. The third part of the subclavian artery is the most accessible segment of the artery. Since the line of the posterior border of sternocleidomastoid approximates to the (deeper) lateral border of scalenus anterior, the artery can be felt in the anteroinferior angle of the posterior triangle. It can only be effectively compressed against the first rib: with the shoulder depressed, pressure is exerted down, back and medially in the angle between sternocleidomastoid and the clavicle. The palpable trunks of the brachial plexus may be injected with local anaesthetic allowing major surgical procedures to the arm.

Relations The skin, superficial fascia, platysma, supraclavicular nerves and deep cervical fascia are anterior. The external jugular vein crosses its medial end and here receives the suprascapular, transverse cervical and anterior jugular veins, which collectively often form a venous plexus. The nerve to subclavius descends between the veins and the artery; the latter is terminally behind the clavicle and subclavius, where it is crossed by the suprascapular vessels. The subclavian vein is anteroinferior and the lower trunk of the brachial plexus is posteroinferior, between the subclavian artery and the scalenus medius (and on the first rib). The upper and middle trunks of the brachial plexus (which are palpable here) and the inferior belly of omohyoid are superolateral. The first rib is inferior.

The right subclavian artery may arise above or below sternoclavicular level; it may be a separate aortic branch and be the first or last branch of the arch. When it is the first branch, it is in the position of a brachiocephalic trunk. When it is the last branch, it arises from the left end of the arch, and ascends obliquely to the right behind the trachea, oesophagus and right common carotid to the first rib. When this happens, the right recurrent laryngeal nerve hooks round the common carotid artery. Sometimes, when the right subclavian artery is the last aortic branch, it passes between the trachea and oesophagus and can cause dysphagia, a condition known as dysphagia lusoria. It may perforate scalenus anterior, and very rarely may pass anterior to it. Sometimes, the subclavian vein accompanies the artery behind scalenus anterior. The artery may ascend as high as 4 cm above the clavicle or it may reach only its upper border. The left subclavian artery is occasionally combined at its origin with the left common carotid artery.

Branches The branches of the subclavian artery are the vertebral, internal thoracic, thyrocervical, costocervical and dorsal scapular arteries. On the left, all the branches except the dorsal scapular arise from the first part. On the right, the costocervical trunk usually arises from the second part. The suprascapular artery (usually a branch of the thyrocervical trunk) may arise from the third part of the subclavian artery.

Vertebral artery

The vertebral arteries and their major branches (sometimes referred to as the ‘vertebrobasilar system’) essentially supply blood to the upper spinal cord, the brainstem and cerebellum, and a significant but variable part of the posterior cerebral hemispheres (see Figs 26.4–26.5).

The vertebral artery arises from the superoposterior aspect of the first part of the subclavian artery. It passes through the foramina in the transverse processes of all of the cervical vertebrae except the seventh; occasionally, it may enter the cervical vertebral column via the fourth, fifth or seventh cervical vertebra (see Fig. 35.12). The artery curves medially behind the lateral mass of the atlas and enters the cranium via the foramen magnum (see Fig. 35.11). The right and left vertebral arteries converge medially as they ascend the medulla and unite to form the midline basilar artery at approximately the level of the junction between the medulla and pons.

Relations The first part, V1, passes back and upwards between longus colli and scalenus anterior, behind the common carotid artery and the vertebral vein. It is crossed by the inferior thyroid artery, and by the thoracic duct on the left side and the right lymphatic duct on the right side. The seventh cervical transverse process, the inferior cervical ganglion and ventral rami of the seventh and eighth cervical spinal nerves lie posterior to the artery. The second part, V2, ascends through the transverse foramina of the remaining cervical vertebrae, accompanied by a large branch from the inferior cervical ganglion and a plexus of veins that form the vertebral vein low in the neck. It lies anterior to the ventral rami of the cervical spinal nerves (C2–C6) and ascends almost vertically to pass through the transverse process of the axis, where it turns laterally to gain access to the transverse foramen of the atlas (see Fig. 35.11). The third part, V3, issues medial to rectus capitis lateralis, and curves backwards and medially behind the lateral mass of the atlas, with the first cervical ventral spinal ramus lying on its medial side. In this position, it lies in a groove on the upper surface of the posterior arch of the atlas, and it enters the vertebral canal below the inferior border of the posterior atlanto-occipital membrane. This part of the artery, covered by semispinalis capitis, lies in the suboccipital triangle. The first cervical dorsal spinal ramus separates the artery from the posterior arch. The fourth part, V4, pierces the dura and arachnoid mater, and ascends anterior to the hypoglossal roots. It inclines anterior to the medulla oblongata and unites with its contralateral fellow to form the midline basilar artery at the lower border of the pons.

Cervical branches of the vertebral artery

Spinal branches

The spinal branches enter the vertebral canal via the intervertebral foramina and supply the spinal cord and its membranes. They fork into ascending and descending rami, which unite with those above and below, to form two lateral anastomotic chains on the posterior surfaces of the vertebral bodies near the attachment of their pedicles. Branches from these chains supply the periosteum and vertebral bodies, and others communicate with similar branches across the midline; from these connections small rami join similar ones above and below, to form a median anastomotic chain on the posterior surfaces of the vertebral bodies.

Muscular branches

Muscular branches arise from the vertebral artery as it curves round the lateral mass of the atlas. They supply the deep muscles of the suboccipital region and anastomose with the occipital, ascending and deep cervical arteries.

Cranial branches of the vertebral artery

Meningeal branches

One or two meningeal branches arise from the vertebral artery near the foramen magnum and ramify between the bone and dura mater in the posterior cranial fossa. They supply bone, diploë and the falx cerebelli.

Posterior spinal artery

A posterior spinal artery usually arises from the posterior inferior cerebellar artery, but may originate directly from the vertebral artery near the medulla oblongata. It passes posteriorly and descends as two branches that lie anterior and posterior to the dorsal roots of the spinal nerves. These are reinforced by spinal twigs from the vertebral, ascending cervical, posterior intercostal and first lumbar arteries, all of which reach the vertebral canal by the intervertebral foramina, and sustain the posterior spinal arteries to the lower spinal levels.

Anterior spinal artery

A small anterior spinal artery arises near the end of the vertebral artery, and descends anterior to the medulla oblongata to unite with its contralateral fellow at mid-medullary level. The single trunk then descends on the ventral midline of the spinal cord, and is reinforced sequentially by small spinal rami from the vertebral, ascending cervical, posterior intercostal and first lumbar arteries, which all enter the vertebral canal via intervertebral foramina. Branches from the anterior spinal arteries and the beginning of their common trunk are distributed to the medulla oblongata. Minute medullary arteries are distributed widely to the medulla oblongata.

Posterior inferior cerebellar artery

The largest branch of the vertebral artery (although sometimes absent), the posterior inferior cerebellar artery arises near the lower end of the olive and then ascends behind the roots of the glossopharyngeal and vagus nerves to reach the inferior border of the pons. Here it curves and descends along the inferolateral border of the fourth ventricle before it turns laterally into the cerebellar vallecula between the hemispheres, and divides into medial and lateral branches. The medial branch runs back between the cerebellar hemisphere and inferior vermis, and supplies both. The lateral branch supplies the inferior cerebellar surface as far as its lateral border and anastomoses with the anterior inferior and superior cerebellar arteries (from the basilar artery). The trunk of the posterior inferior cerebellar artery supplies the medulla oblongata dorsal to the olivary nucleus and lateral to the hypoglossal nucleus and its emerging nerve roots. It also supplies the choroid plexus of the fourth ventricle and sends a branch lateral to the cerebellar tonsil to supply the dentate nucleus.

Basilar artery

The basilar artery is a large median vessel formed by the union of the vertebral arteries at the junction of the medulla and pons (see Figs 26.3, 26.5). It lies in the pontine cistern, and follows a shallow median groove on the ventral pontine surface, extending to the upper border of the pons. It ends by dividing into two posterior cerebral arteries at a variable level behind the dorsum sellae, usually in the interpeduncular cistern.

Pontine branches

Numerous small pontine branches arise from the front and sides of the basilar artery along its course and supply the pons.

Labyrinthine artery

The long and slender labyrinthine (internal auditory) artery has a variable origin. It usually arises from the anterior inferior cerebellar artery, but variations in its origin include the lower part of the basilar artery, the superior cerebellar artery or, occasionally, the posterior inferior cerebellar artery. The labyrinthine artery accompanies the facial and vestibulocochlear nerves into the internal acoustic meatus and is distributed to the internal ear.

Anterior inferior cerebellar artery

The anterior inferior cerebellar artery is given off from the lower part of the basilar artery and runs posterolaterally, usually ventral to the abducens, facial and vestibulocochlear nerves. It commonly exhibits a loop into the internal acoustic meatus below the nerves, and when this occurs, the labyrinthine artery may arise from the loop. The anterior inferior cerebellar artery supplies the inferior cerebellar surface anterolaterally and anastomoses with the posterior inferior cerebellar branch of the vertebral artery. A few branches supply the inferolateral parts of the pons and occasionally also supply the upper medulla oblongata.

Superior cerebellar artery

The superior cerebellar artery (see Figs 26.3, 26.5) arises near the distal portion of the basilar artery, immediately before the formation of the posterior cerebral arteries. It passes laterally below the oculomotor nerve, which separates it from the posterior cerebral artery, and curves round the cerebral peduncle below the trochlear nerve to gain the superior cerebellar surface. Here it divides into branches that ramify in the pia mater and supply this aspect of the cerebellum, and also anastomose with branches of the inferior cerebellar arteries. The superior cerebellar artery supplies the pons, pineal body, superior medullary velum and tela choroidea of the third ventricle.

Posterior cerebral artery

The paired posterior cerebral arteries are the terminal branches of the basilar artery (see Figs 26.3–26.5). Surgical nomenclature divides the vessel into three parts: P1 – from the basilar bifurcation to the junction with the posterior communicating artery; P2 – from the junction with the posterior communicating artery to the portion in the perimesencephalic cistern; and P3 – the portion that runs in the calcarine fissure.

The posterior cerebral artery is larger than the superior cerebellar artery, from which it is separated near its origin by the oculomotor nerve and, lateral to the midbrain, by the trochlear nerve. It passes laterally, parallel with the superior cerebellar artery, and receives the posterior communicating artery. It then winds round the cerebral peduncle and reaches the tentorial cerebral surface, where it supplies the temporal and occipital lobes. Like the anterior and middle cerebral arteries, the posterior cerebral artery has cortical and central branches.

The cortical branches of the posterior cerebral artery are named according to their distribution. Temporal branches, usually two, are distributed to the uncus and parahippocampal, medial occipitotemporal and lateral occipitotemporal gyri. Occipital branches supply the cuneus, lingual gyrus and posterolateral surface of the occipital lobe. Parieto-occipital branches supply the cuneus and precuneus. The posterior cerebral artery supplies the visual areas of the cerebral cortex and other structures in the visual pathway.

The central branches supply subcortical structures. Several small posteromedial central branches arise from the beginning of the posterior cerebral artery (see Fig. 26.3) and, together with similar branches from the posterior communicating artery, pierce the posterior perforated substance to supply the anterior thalamus, subthalamus, lateral wall of the third ventricle and globus pallidus. One or more posterior choroidal branches pass over the lateral geniculate body and supply it before entering the posterior part of the inferior horn of the lateral ventricle via the lower part of the choroidal fissure. Branches also curl round the posterior end of the thalamus and pass through the transverse fissure, or go to the choroid plexus of the third ventricle, or traverse the upper choroidal fissure. Collectively these branches supply the choroid plexuses of the third and lateral ventricles and the fornix. Small posterolateral central branches arise from the posterior cerebral artery beyond the cerebral peduncle, and supply the peduncle and the posterior thalamus, superior and inferior colliculi, pineal gland and medial geniculate body.

Internal thoracic artery

The internal thoracic (mammary) artery arises inferiorly from the first part of the subclavian artery, approximately 2 cm superior to the sternal end of the clavicle and opposite the root of the thyrocervical trunk (see Fig. 52.3). It descends posterior to the first six costal cartilages and intervening intercostal spaces, about 1 cm lateral to the lateral sternal border and divides at the level of the sixth intercostal space into musculophrenic and superior epigastric branches.

Both the right and left internal thoracic arteries are used as standard in coronary artery bypass grafting (CABG) reflecting successful long-term outcomes. Variations are rare, however when present, they must be imaged prior to harvesting for CABG: morphologically abnormal internal thoracic arteries have been shown to supply major parts of the gastrointestinal tract (Mashhour et al 2018).

Relations From its origin, the internal thoracic artery descends anteromedially, passing posterior to the sternal end of the clavicle, the internal jugular and brachiocephalic veins, and the first costal cartilage. As it enters the thoracic cavity, the phrenic nerve crosses it obliquely from its lateral side either superior or inferior to the nerve. The artery then descends almost vertically to its bifurcation, lying anterior to transversus thoracis and posterior to the first six costal cartilages, internal intercostals and terminations of the upper six intercostal nerves. Down to the second or third cartilage it is separated from the costal parietal pleura and associated endothoracic fascia by a strong layer of fascia, and below this transversus thoracis intervenes. The artery is accompanied by the parasternal lymph nodes (see Fig. 56.4A) and by venae comitantes that unite at about the third costal cartilage into a single vein medial to the artery. Its intermediate branches are sternal, anterior intercostal and perforating.

Sternal branches

Sternal branches are distributed to transversus thoracis, the periosteum of the posterior sternal surface and the sternal red bone marrow. These branches, together with small branches of the pericardiacophrenic artery, anastomose with branches of the posterior intercostal and bronchial arteries to form a subpleural mediastinal plexus.

Anterior intercostal branches

Anterior intercostal arteries are distributed to the upper six intercostal spaces. They usually arise from the internal thoracic artery as single vessels that promptly divide into two branches (anterior and collateral intercostal arteries) that pass laterally along the superior and inferior borders of each space and anastomose with the posterior intercostal arteries and their collateral branches (see Figs 53.17, 53.19). Occasionally, separate branches of the anterior intercostal artery pass to the intercostal space located superiorly and/or inferiorly and the two branches of an anterior intercostal may sometimes arise separately from the internal thoracic artery. At first, the arteries lie between the endothoracic fascia and associated costal parietal pleura posteriorly, and the internal intercostals anteriorly. As they pass posteriorly within a space they lie between the innermost and internal intercostals. They supply the intercostal muscles and send branches through them to the pectoral muscles, breast and skin.

Perforating branches

Perforating branches traverse the upper five or six intercostal spaces with the anterior cutaneous branches of the corresponding intercostal nerves. They pierce and supply pectoralis major, and then curve laterally to become direct cutaneous vessels that supply the skin (see Fig. 53.19). These cutaneous vessels provide the anatomical basis for surgically raising the deltopectoral skin flap that is used for reconstructing areas of missing tissue in the head and neck. The second to fourth branches supply the breast and become enlarged during lactation (see Fig. 53.22).

Musculophrenic artery

The musculophrenic artery passes inferolaterally posterior to the seventh to ninth costal cartilages, close to the costal arch, then traverses the respiratory diaphragm and terminates near the eleventh (last) intercostal space (see Fig. 55.2). It anastomoses with the inferior phrenic and lower two posterior intercostal arteries and ascending branches of the deep circumflex iliac arteries. Two anterior intercostal arteries branch from it for each of the seventh to ninth intercostal spaces, and are distributed similarly to their counterparts in other intercostal spaces. The musculophrenic artery also supplies the lower part of the pericardium and the abdominal muscles.

Superior epigastric artery

The superior epigastric artery arises at the level of the sixth costal cartilage and descends between the costal and sternal parts of the respiratory diaphragm, accompanied by two or more veins that drain to the internal thoracic vein (see Figs 60.1–60.2). The vessels pass anterior to the distal fibres of transversus thoracis and the proximal fibres of transversus abdominis before entering the rectus sheath, where they run inferiorly behind rectus abdominis. They anastomose with the inferior epigastric arteries within rectus abdominis in one of several potential branching patterns (Rozen et al 2008).

Vascular branches supply rectus abdominis itself and perforate the anterior layer of the rectus sheath to supply the abdominal skin and subcutaneous fat. These vessels generally penetrate rectus abdominis within a 10 cm circle around the umbilicus and are referred to clinically as 'peri-umbilical perforator' vessels. A branch given off in the proximal rectus sheath passes anterior to the xiphoid process of the sternum and anastomoses with a corresponding contralateral branch. This vessel can give rise to bleeding during surgical incisions that extend up to and alongside the xiphoid process. The superior epigastric artery also gives small branches to the anterior part of the respiratory diaphragm. On the right, small branches reach the falciform ligament, where they anastomose with branches from the hepatic artery.

Clinical significance of the internal thoracic artery

The internal thoracic artery has a number of clinical uses but perhaps most significant is that it is the vessel of choice for coronary artery bypass grafting. It has become a popular recipient vessel for free flap transfers to the chest wall, principally for breast reconstruction (Ninković et al 1995), and has largely superseded the thoracodorsal vessels for this purpose. It is routinely accessed by removing a portion of the third costal cartilage (see Fig. 53.18), although some surgeons prefer to dissect the vessels between the ribs, with a rib-sparing approach (Parrett et al 2008, Malata et al 2011) or even utilizing the anterior perforating branches as they pierce pectoralis major (Park et al 2003, Munhoz et al 2004). The anterior perforating branches form the vascular pedicles for fasciocutaneous flaps raised from the anterior chest wall that have been used for many decades in head and neck reconstruction (Bakamjian et al 1971, Neligan et al 2007). The superior epigastric artery is the main vascular pedicle for the superiorly based rectus abdominis flap, a muscle or myocutaneous flap useful in breast, sternal and chest wall reconstruction (Hartrampf et al 1982). During CT-guided lung and mediastinal biopsies, the internal thoracic vessels must be avoided; exsanguination has been reported following Tru-Cut needle trauma: the approach must be at least 2 cm lateral to the sternal margin. The vessels are not seen easily on non-contrast fluoroscopic CT images.

Thyrocervical trunk

The thyrocervical trunk is a short, wide artery that arises from the first part of the subclavian artery near the medial border of scalenus anterior, and divides almost at once into the inferior thyroid, suprascapular and superficial cervical arteries.

Inferior thyroid artery

The inferior thyroid artery loops upwards anterior to the medial border of scalenus anterior, turns medially just below the sixth cervical transverse process, and then descends on longus colli to the lower border of the thyroid gland (see Fig. 35.17). It passes anterior to the vertebral vessels and posterior to the carotid sheath and its contents (and usually the sympathetic trunk, whose middle cervical ganglion frequently adjoins the vessel). On the left, near its origin, the artery is crossed anteriorly by the thoracic duct as the latter curves inferolaterally to its termination. Relations between the terminal branches of the artery and recurrent laryngeal nerve are very variable and of considerable surgical importance. The artery usually passes behind the nerve as it nears the gland. However, very close to the gland, the right nerve is equally likely to be anterior, posterior or amongst the branches of the artery, and the left nerve is usually posterior. Together with the inferior thyroid and common carotid arteries, the recurrent laryngeal nerve forms one of the sides of Beahr's triangle. Since the nerve winds around the artery of the sixth branchial arch (aortic arch) on the left side, it is 45° to the midline in its ascent from the chest to the neck. However, on the right side it is slightly more superficial and lateral because it goes around the fourth branchial arch artery (subclavian) in the neck: these variations are important in thyroid surgery and are reversed in dextrocardia. The artery is not accompanied by the inferior thyroid vein.

Muscular branches

These supply the infrahyoid muscles, longus colli, scalenus anterior and the inferior pharyngeal constrictor.

Ascending cervical artery

The ascending cervical artery is a small branch that arises as the inferior thyroid turns medially behind the carotid sheath and ascends on the anterior tubercles of the cervical transverse processes between scalenus anterior and longus capitis. It supplies the adjacent muscles and gives off one or two spinal branches that enter the vertebral canal through the intervertebral foramina to supply the spinal cord and membranes and vertebral bodies, and thereby supplement the spinal branches of the vertebral artery. The ascending cervical artery anastomoses with the vertebral, ascending pharyngeal, occipital and deep cervical arteries.

Inferior laryngeal artery

The inferior laryngeal artery ascends on the trachea with the recurrent laryngeal nerve, enters the larynx at the lower border of the inferior constrictor and supplies the laryngeal muscles and mucosa. It anastomoses with its contralateral fellow, and with the superior laryngeal branch of the superior thyroid artery.

Pharyngeal branches

These supply the lower part of the pharynx. Tracheal branches supply the trachea and anastomose with the bronchial arteries; oesophageal branches supply the oesophagus and anastomose with the oesophageal branches of the thoracic aorta; inferior and ascending glandular branches supply the posterior and inferior regions of the thyroid gland and anastomose with the contralateral inferior and ipsilateral superior thyroid arteries. The ascending branch also supplies the parathyroid glands.

Suprascapular artery

The suprascapular artery usually arises from the thyrocervical trunk of the subclavian artery, although it may arise from the third part of the subclavian artery. It first descends laterally across scalenus anterior and the phrenic nerve, posterior to the internal jugular vein and sternocleidomastoid (see Fig. 35.7A), then crosses anterior to the subclavian artery and brachial plexus, posterior and parallel with the clavicle, subclavius and the inferior belly of omohyoid, to reach the superior border of the scapula. Here, it passes above (sometimes, under) the superior transverse ligament, separating it from the suprascapular nerve, and enters the supraspinous fossa (see Figs 49.31, 49.33), where it lies on the bone, and supplies supraspinatus. It descends behind the scapular neck, and passes through the spinoglenoid notch deep to the inferior transverse ligament to gain the deep surface of infraspinatus, where it anastomoses with the circumflex scapular and deep branch of the transverse cervical artery. Its muscular branches supply sternocleidomastoid, subclavius and infraspinatus. It also gives off a suprasternal branch that crosses the sternal end of the clavicle to supply the skin of the upper thorax, and an acromial branch that pierces trapezius to supply the skin over the shoulder. This last branch anastomoses with the thoracoacromial and posterior circumflex humeral arteries.

As the suprascapular artery passes over the superior transverse ligament, it gives off a branch that enters the subscapular fossa beneath subscapularis and anastomoses with the subscapular artery and the deep branch of the transverse cervical artery. It also supplies the acromioclavicular and glenohumeral joints, the clavicle and the scapula.

Superficial cervical artery

The superficial cervical artery is given off at a higher level than the suprascapular artery. It crosses anterior to the phrenic nerve, scalenus anterior and the brachial plexus, and is covered by the internal jugular vein, sternocleidomastoid and platysma. It crosses the floor of the posterior triangle to reach the anterior margin of levator scapulae and ascends deep to the anterior part of the trapezius, which it supplies, together with the adjoining muscles and the cervical lymph nodes. It anastomoses with the superficial ramus of the descending branch of the occipital artery. About a third of the superficial cervical and dorsal scapular arteries arise in common from the thyrocervical trunk, with a superficial (superficial cervical artery) and a deep (dorsal scapular artery) branch (see Figs 33.1A, 33.2A). The latter passes laterally anterior to the brachial plexus and then posterior to levator scapulae.

Costocervical trunk

On the right, this short vessel arises posteriorly from the second part of the subclavian artery, and, on the left, from its first part. It arches back above the cervical pleura to the neck of the first rib, where it divides into supreme intercostal and deep cervical branches.

Supreme intercostal artery

The supreme (highest) intercostal artery arises from the costocervical trunk. It descends between the parietal pleura and associated endothoracic fascia, and the neck of the first and second ribs, and anastomoses with the third posterior intercostal artery. Crossing the neck of the first rib, it lies medial to the ventral ramus of the first thoracic nerve (crossing it at a lower level), and lateral to the stellate ganglion (see Fig. 55.10). In the first intercostal space it gives off the first posterior intercostal artery, which has a similar distribution to the more inferiorly located posterior intercostal arteries. It descends to become the second posterior intercostal artery, usually joining a branch from the third. The artery is not constant, and is more common on the right: when absent, it is replaced by a direct branch from the aorta.

Deep cervical artery

The deep cervical artery usually arises from the costocervical trunk (see Fig. 33.1A). It is analogous in its first segment to a posterior branch of a posterior intercostal artery, and occasionally is a separate branch of the subclavian artery. It passes back above the eighth cervical spinal nerve between the transverse process of the seventh cervical vertebra and the neck of the first rib (sometimes between the transverse processes of the sixth and seventh cervical vertebrae). It then ascends between semispinales capitis and cervicis to the level of the second cervical vertebra. It supplies adjacent muscles and anastomoses with the deep branch of the descending branch of the occipital artery and branches of the vertebral artery. A spinal branch enters the vertebral canal between the seventh cervical and first thoracic vertebrae.

Dorsal scapular artery

In the majority of cases, the dorsal scapular artery arises from the third, or less often the second, part of the subclavian artery. It passes laterally through the trunks of the brachial plexus in front of scalenus medius and then deep to levator scapulae to reach the superior scapular angle. Here, it descends with the dorsal scapular nerve under the rhomboids along the medial border of the scapula to the inferior angle. It supplies the rhomboids, latissimus dorsi and the inferior portion of trapezius and the skin over the inferomedial aspect of trapezius via musculocutaneous perforators. It anastomoses with the suprascapular and subscapular arteries and with posterior branches of some posterior intercostal arteries. It sends a small branch to scalenus anterior; sometimes, this arises directly from the subclavian artery.

Variants About one-third of the superficial cervical and dorsal scapular arteries arise as a common vessel, the transverse cervical artery, from the thyrocervical trunk, which then divides into a superficial and a deep branch (superficial cervical and dorsal scapular arteries, respectively) (see Figs 33.1A, 49.31). In this case, the dorsal scapular artery arises near the superior border of the scapula; it passes laterally, anterior to the brachial plexus and then posterior to levator scapulae.

Axillary artery

The axillary artery, a continuation of the subclavian artery, begins at the outer border of the first rib and ends nominally at the inferior border of teres major, where it becomes the brachial artery (see Fig. 49.31). Its direction varies with the position of the limb; it is almost straight when the arm is raised at right-angles, concave upwards when the arm is elevated above this level, and convex upwards and laterally when the arm is by the side (see Fig. 49.32). At first deep, it subsequently becomes superficial, when it is covered only by the skin and fasciae. Pectoralis minor crosses it and so divides it into three parts, which are proximal, posterior and distal to the muscle.

The branches of the axillary artery are the superior thoracic artery (first part), thoraco-acromial and lateral thoracic arteries (second part), and subscapular, and anterior and posterior circumflex humeral arteries (third part) (see Fig. 49.47).

Relations of the first part The skin, superficial fascia, platysma, supraclavicular nerves, deep fascia, clavicular fibres of pectoralis major and the clavipectoral fascia, lateral pectoral nerve and the loop of communication between the lateral and medial pectoral nerves, and the thoraco-acromial and cephalic veins are all anterior. The first intercostal space and external intercostal, first and second digitations of serratus anterior, long thoracic and medial pectoral nerves, and the medial cord of the brachial plexus are all posterior. The posterior cord of the brachial plexus is lateral and the axillary vein is anteromedial. The first part is enclosed with the axillary vein and brachial plexus in a fibrous axillary sheath, which is continuous with the prevertebral layer of the deep cervical fascia.

Relations of the second part The skin, superficial and deep fascia, and pectoralis major and minor are all anterior. The posterior cord of the brachial plexus and the areolar tissue between it and subscapularis are posterior. The axillary vein is medial, separated from the artery by the medial cord of the brachial plexus and the medial pectoral nerve. The lateral cord of the brachial plexus is lateral, separating the artery from coracobrachialis. The cords of the brachial plexus thus surround the second part on three sides, with the dispositions implied by their names, and separate it from the vein and adjacent muscles.

Relations of the third part Pectoralis major and, distal to the muscle, skin and fasciae are anterior. The lower part of subscapularis and the tendons of latissimus dorsi and teres major are posterior. Coracobrachialis is lateral and the axillary vein is medial. Branches of the brachial plexus are arranged as follows: laterally, the lateral root and then trunk of the median nerve and, for a short distance, the musculocutaneous nerve; medially, the medial cutaneous nerve of the forearm between the axillary artery and vein anteriorly, and the ulnar nerve between these vessels posteriorly; anteriorly, the medial root of the median nerve; and posteriorly, the radial and axillary nerves, the latter only to the distal border of subscapularis. The dispositions of the branches of the brachial plexus around the axillary artery have, therefore, altered: there has been a rotation such that the nerves derived from the lateral cord are now more anterior, those from the medial cord more posterior, and those of the posterior cord come to lie more laterally.

Variants The branches of the axillary artery exhibit considerable variation. An alar thoracic artery, often from the second part, may supply fat and lymph nodes in the axilla. The lateral thoracic artery may be absent, in which case it is replaced by lateral perforating branches of the intercostal arteries; alternatively, it may become, or give off, a direct cutaneous vessel (named the superficial thoracic artery by some sources) that supplies the skin over the lateral border of pectoralis major. In up to one-third of cases, the subscapular artery can arise from a common trunk with the posterior circumflex humeral artery. Occasionally the subscapular, circumflex humeral and profunda brachii arteries arise in common, and in this case, branches of the brachial plexus surround this common vessel instead of the axillary artery. The posterior circumflex humeral artery may arise from the profunda brachii artery and pass back below teres major, instead of passing through the quadrangular space. Sometimes the axillary artery divides into radial and ulnar arteries (anomalous 'high division') and is, occasionally, the source of the anterior interosseous artery.

Superior thoracic artery

The superior thoracic artery is a small vessel that arises from the first part of the axillary artery near the lower border of subclavius; it sometimes arises from the thoraco-acromial artery (see Fig. 49.47). It runs anteromedially above the medial border of pectoralis minor, then passes between it and pectoralis major to gain the thoracic wall. It supplies these muscles and the thoracic wall, and anastomoses with the internal thoracic and upper intercostal arteries.

Thoraco-acromial (acromiothoracic) artery

The thoraco-acromial artery is a short branch that arises from the second part of the axillary artery (see Figs 49.27, 49.47). It is initially overlapped by pectoralis minor, skirting its medial border; it next pierces the clavipectoral fascia and divides into pectoral, acromial, clavicular and deltoid branches, which supply pectoralis major and minor, an area of skin over the clavipectoral fascia, and the anterior portion of deltoid.

Pectoral branch

The pectoral branch is the largest branch. It descends between the pectoral muscles, gives a branch to pectoralis minor, and then continues on the deep surface of pectoralis major. It enters the muscle and anastomoses with the intercostal branches of the internal thoracic and lateral thoracic arteries. It gives off perforating branches to the breast, and musculocutaneous perforators to the skin over pectoralis major.

Acromial branch

The acromial branch crosses the coracoid process under deltoid, which it supplies, then pierces the muscle and ends on the acromion. It anastomoses with branches of the suprascapular artery, the deltoid branch of the thoraco-acromial artery and the posterior circumflex humeral arteries.

Clavicular branch

The clavicular branch ascends medially between the clavicular part of pectoralis major and the clavipectoral fascia. It supplies the sternoclavicular joint and subclavius.

Deltoid branch

The deltoid branch often arises with the acromial branch. It crosses pectoralis minor to accompany the cephalic vein between pectoralis major and deltoid, and supplies both muscles.

Lateral thoracic artery

The lateral thoracic artery arises from the second part of the axillary artery. Following the lateral border of pectoralis minor, it passes to the deep surface of pectoralis major as far distally as the fifth intercostal space (see Fig. 49.45). It supplies serratus anterior and the pectoral muscles, the axillary lymph nodes and subscapularis. It anastomoses with the internal thoracic, subscapular and intercostal arteries, and with the pectoral branch of the thoraco-acromial artery. In females, it is large and has lateral mammary branches, which curve round the lateral border of pectoralis major to the breast. In both males and females, it gives off cutaneous branches that pass around the lateral border of pectoralis major to supply the skin in this region.

Subscapular artery

The subscapular artery is the largest branch of the axillary artery (see Figs 49.31, 49.47). It usually arises from the third part of the axillary artery at the distal (inferior) border of subscapularis, which it follows to the inferior scapular angle where it anastomoses with the lateral thoracic and intercostal arteries and the deep branch of the transverse cervical artery. It supplies adjacent muscles and the thoracic wall. It is accompanied distally by the nerve to latissimus dorsi. Approximately 4 cm from its origin the subscapular artery divides into the circumflex scapular and thoracodorsal arteries.

Circumflex scapular artery

The circumflex scapular artery, the larger of the two terminal branches of the subscapular artery, curves backwards around the lateral border of the scapula, traversing a triangular space between subscapularis above, teres major below and the long head of the triceps laterally (see Fig. 49.33). It enters the infraspinous fossa under teres minor and then divides. One branch (infrascapular) enters the subscapular fossa deep to subscapularis, and anastomoses with the suprascapular and dorsal scapular arteries (or deep branch of the transverse cervical artery). The other branch continues along the lateral border of the scapula between teres major and minor, then, dorsal to the inferior angle, anastomoses with the dorsal scapular artery. Small branches supply the posterior part of deltoid and the long head of triceps, and anastomose with an ascending branch of the profunda brachii artery.

Two significant cutaneous branches arise from the circumflex scapular artery as it emerges through the upper triangular space. The superior, or horizontal, branch is a direct cutaneous artery that passes medially at the level of the deep fascia parallel with the spine of the scapula and supplies a band of skin overlying the spine of the scapula. The lower branch (parascapular branch) is also a direct cutaneous vessel that passes in an inferomedial direction, again at the level of the deep fascia, and supplies an area of skin overlying the lateral border of the scapula. Both of these cutaneous vessels provide the anatomical basis of skin flaps that can be surgically raised in this region (scapular flap based on the horizontal branch and parascapular flap based on the lower, parascapular branch) to reconstruct areas of missing tissue elsewhere in the body.

Thoracodorsal artery

The other terminal branch of the subscapular artery, the thoracodorsal artery, follows the lateral margin of the scapula, posterior to the lateral thoracic artery, between latissimus dorsi and serratus anterior. Before entering the deep surface of latissimus dorsi, it supplies teres major and the intercostals, and sends one or two branches to serratus anterior. It enters latissimus dorsi with the thoracodorsal nerve; this constitutes the principal neurovascular pedicle to the muscle. It provides numerous musculocutaneous perforators that supply the skin over the superior part of latissimus dorsi. The intramuscular portion of the artery anastomoses with intercostal arteries and lumbar perforating arteries.

Anterior circumflex humeral artery

The anterior circumflex humeral artery arises from the lateral side of the axillary artery at the distal border of subscapularis (see Fig. 49.31). It runs horizontally behind coracobrachialis and the short head of biceps, anterior to the surgical neck of the humerus. Reaching the intertubercular sulcus, it sends an ascending branch to supply the humeral head and shoulder joint (Brooks et al 1993), continues laterally under the long head of biceps and deltoid, and anastomoses with the posterior circumflex humeral artery.

Posterior circumflex humeral artery

The posterior circumflex humeral artery is larger than the anterior (see Fig. 49.31). It branches from the third part of the axillary artery at the distal border of subscapularis and runs backwards with the axillary nerve through a quadrangular space bounded by subscapularis, the capsule of the shoulder joint and teres minor above, teres major below, the long head of triceps medially, and the surgical neck of the humerus laterally (see Fig. 49.22B). It curves round the humeral neck and supplies the shoulder joint, deltoid, teres major and minor, and long and lateral heads of triceps (Gerber et al 1990). It gives off a descending branch that anastomoses with the deltoid branch of the profunda brachii artery and with the anterior circumflex humeral and acromial branches of the suprascapular and thoraco-acromial arteries.

Potential vascular anastomoses around the shoulder girdle: clinical relevance

The potential vascular anastomoses around the shoulder girdle are numerous, which means that collateral perfusion of the upper limb is possible in occlusion of the axillary artery or vein. In acute occlusion of the axillary artery, these potential anastomoses are not reliable and clinicians should not rely on anastomotic perfusion of the acutely ischaemic limb. The axillary artery is most ‘at risk’ of occlusion as a result of intimal separation and dissection in its second part, behind pectoralis minor, an injury associated with infraclavicular brachial plexus traction lesions (Birch 2011). Although magnetic resonance imaging with angiography is recommended for the diagnosis of the poorly perfused limb after distraction trauma, the site of intimal rupture is so consistent as to make urgent surgical exploration without imaging a reasonable clinical decision.

Angiomyosomes

The axillary artery supplies the muscles of the ventral compartments of the shoulder, including the pectoral–deltoid muscle sheet, the scapulohumeral muscles (other than the posterosuperior rotator cuff) and the shoulder joint, including the scapula (with the serratus muscles) and proximal humerus. Its terminal branch, the brachial artery, supplies the muscles of the anterior compartment of the arm. The profunda brachii artery, the major proximal branch of the brachial artery, supplies the muscles of the posterior compartment of the arm and the shaft of the humerus.

Brachial artery

The brachial artery is a continuation of the axillary artery. It begins at the distal (inferior) border of the tendon of teres major and ends about a centimetre distal to the elbow joint (at the level of the neck of the radius) by dividing into the radial and ulnar arteries (see Figs 49.33, 49.44, 50.21–50.22). At first, it is medial to the humerus, but gradually spirals anterior to it until it lies midway between the humeral epicondyles, medial to the tendon of biceps brachii and deep to the bicipital aponeurosis. The latter separates the artery from the anterior structures, namely the skin, superficial fascia and the median cubital vein. The artery divides into its terminal branches, the radial and ulnar arteries, at the level of the radial neck (see Fig. 50.27A).

The branches of the brachial artery are the profunda brachii, nutrient, superior, middle and inferior ulnar collateral, deltoid, muscular, radial and ulnar arteries.

Relations The brachial artery is wholly superficial, covered anteriorly only by skin and superficial and deep fascia: its pulsation can be felt throughout the arm. The bicipital aponeurosis crosses it anteriorly at the elbow, separating it from the median cubital vein; the median nerve crosses it lateromedially near the distal attachment of coracobrachialis. Posterior to the artery are the long head of triceps, separated initially by the radial nerve and profunda brachii artery, and then successively by the medial head of triceps, the attachment of coracobrachialis and brachialis. Proximally, the median nerve and coracobrachialis lie laterally and the medial cutaneous nerve of the forearm and ulnar nerve lie medially. Distally, biceps brachii overlaps the artery laterally and the median nerve and basilic vein lie medially. The artery is accompanied by two venae comitantes, connected by transverse and oblique branches. At the elbow, the brachial artery sinks deeply into the triangular intermuscular cubital fossa. Posteriorly, brachialis separates it from the elbow joint. The median nerve passes close to the medial side of the artery.

Variants The brachial artery, with the median nerve, may diverge from the medial border of biceps brachii and descend towards the medial humeral epicondyle, usually behind a supracondylar process from which a fibrous arch crosses the artery, and which then runs behind or through pronator teres to the elbow. Occasionally the artery divides proximally into two trunks that reunite. Frequently it divides more proximally than usual into radial, ulnar and common interosseous arteries. Most often the radial branches arise proximally, leaving a common trunk for the ulnar and common interosseous arteries. Sometimes the ulnar artery arises proximally and the radial and common interosseous arteries form the other division, or the common interosseous may also arise proximally. Slender vasa aberrantia may connect the brachial artery to the axillary artery or to one of the forearm arteries, usually the radial. The brachial artery may be crossed by muscular or tendinous slips from coracobrachialis, biceps brachii, brachialis or pronator teres. Rarely the median nerve crosses posterior, rather than anterior, to the brachial artery near the insertion of coracobrachialis.

Profunda brachii artery

The profunda brachii artery (see Figs 49.31, 49.33) is a large branch from the posteromedial aspect of the brachial artery, distal to teres major. It follows the radial nerve closely, at first posteriorly between the long and medial heads of triceps, then in the spiral groove covered by the lateral head of triceps. It supplies muscular branches, and the nutrient artery of the humerus, and finally divides into terminal radial and middle collateral branches. The radial collateral branch pierces the lateral intermuscular septum to reach the anterior aspect of the epicondyle of the humerus in the groove between brachioradialis and brachialis, and takes part in the anastomosis around the elbow. The middle collateral branch runs posterior to the septum and epicondyle.

The profunda brachii may originate from a common origin with the posterior circumflex humeral artery, from the axillary artery proximal to the tendon of latissimus dorsi, or from the distal portion of the axillary artery.

Middle collateral (posterior descending) branch

The middle collateral artery is the larger terminal branch of the profunda brachii artery. It arises posterior to the humerus and descends along the posterior surface of the lateral intermuscular septum to the elbow. Proximally, the artery lies between brachialis (anteriorly) and the lateral head of triceps (posteriorly). Distally, it lies between brachioradialis (anteriorly) and the lateral head of triceps (posteriorly). It may pierce the deep fascia and become cutaneous, or remain deep to the fascia, forming an arch with the inferior ulnar collateral artery proximal to the olecranon fossa before anastomosing with the interosseous recurrent artery behind the lateral epicondyle; it gives off about five small fasciocutaneous perforators and often has a small branch that accompanies the nerve to anconeus.

Radial collateral (anterior descending) branch

The radial collateral artery accompanies the radial nerve through the lateral intermuscular septum, descending between brachialis and brachioradialis anterior to the lateral epicondyle and anastomosing with the radial recurrent artery. It supplies brachialis, brachioradialis, the radial nerve and a few fasciocutaneous perforators.

Nutrient artery of humerus

The nutrient artery of the humerus arises near the mid-level of the upper arm and enters the nutrient canal near the attachment of coracobrachialis, posterior to the deltoid tuberosity; it is directed distally.

Superior ulnar collateral artery

The superior ulnar collateral artery arises a little distal to the mid-level of the upper arm, usually from the brachial artery (see Fig. 48.3), but often as a branch from the profunda brachii. It accompanies the ulnar nerve, piercing the medial intermuscular septum to descend in the posterior compartment and supply the medial head of triceps. It passes between the medial epicondyle and olecranon, ending deep to flexor carpi ulnaris by anastomosing with the posterior ulnar recurrent and inferior collateral arteries. A branch sometimes passes anterior to the medial epicondyle and anastomoses with the anterior ulnar recurrent artery.

Middle ulnar collateral artery

If present, the middle ulnar collateral artery arises from the brachial artery between the superior and inferior ulnar collateral arteries. It passes anterior to the medial epicondyle, anastomoses with the anterior ulnar recurrent artery, supplies triceps and sends small fasciocutaneous perforators to the skin.

Inferior ulnar collateral (supratrochlear) artery

The inferior ulnar collateral artery begins approximately 5 cm proximal to the elbow. It passes medially between the median nerve and brachialis, pierces the medial intermuscular septum and curls round the humerus between triceps and bone (see Figs 48.3, 49.33). It forms an arch proximal to the olecranon fossa with the middle collateral branch of the profunda brachii artery. As it lies on brachialis, it gives off branches that descend anterior to the medial epicondyle to anastomose with the anterior ulnar recurrent artery. Behind the epicondyle, a branch anastomoses with the superior ulnar collateral and posterior ulnar recurrent arteries.

Muscular branches

Muscular branches are distributed to coracobrachialis, biceps and brachialis.

Deltoid (ascending) branch

The deltoid branch ascends between the lateral and long heads of triceps, and anastomoses with a descending branch of the posterior humeral circumflex artery.

Radial artery

The radial artery is smaller than the ulnar artery, yet appears a more direct continuation of the brachial artery (see Figs 50.21–50.22). It may occasionally arise from a continuation of a superficial brachial artery, or as a high proximal division of an otherwise normal brachial artery and it can give rise to the common interosseous artery.

The radial artery passes deep to brachioradialis and gives off the radial recurrent artery before continuing into the forearm. It descends along the lateral side of the forearm, accompanied by paired venae comitantes, from the medial side of the neck of the radius to the wrist. The artery is medial to the radial shaft proximally, and anterior to it distally. Proximally, it is overlapped anteriorly by the belly of brachioradialis, but elsewhere in its course it is covered only by the skin and superficial and deep fasciae. Its posterior relations in the forearm are, successively, the tendon of biceps, supinator, the distal attachment of pronator teres, the radial head of flexor digitorum superficialis, flexor pollicis longus, pronator quadratus and the lower end of the radius (where its pulsation is most accessible). Brachioradialis is lateral to the artery throughout its length. Pronator teres is medial to the proximal part of the artery, and the tendon of flexor carpi radialis is medial to the distal portion. The superficial radial nerve lies lateral to the middle third of the radial artery; multiple branches from the artery supply the nerve throughout its length.

At the wrist, the radial artery passes on to the dorsal aspect of the carpus between the lateral carpal ligament and the tendons of abductor pollicis longus and extensor pollicis brevis (see Fig. 51.37). It crosses the scaphoid bone and trapezium (in the anatomical snuff-box), where again, its pulsation is obvious; as it passes between the heads of the first dorsal interosseous, it is crossed by the tendon of extensor pollicis longus. Between the thumb extensors, it is crossed by the start of the cephalic vein and the branches of the radial nerve that pass to the thumb and index finger. Occasionally it gives off a distal superficial dorsal branch that crosses the radial extensor tendons at the wrist, together with the superficial radial nerve. Branches of the lateral cutaneous nerve of the forearm run along its distal part as it curves round the carpus.

In the hand, the radial artery passes through the first interosseous space between the heads of the first dorsal interosseous and crosses the palm. At first, it lies deep to the oblique head of adductor pollicis and then passes between its oblique and transverse heads or through the transverse head. At the fifth metacarpal base, it anastomoses with the deep branch of the ulnar artery, completing the deep palmar arch (see Fig. 51.36).

Radial recurrent artery

The radial recurrent artery is given off by the radial artery just distal to the elbow joint (see Figs 50.21–50.22, 50.27). It passes between the superficial radial nerve and the posterior interosseous nerve before ascending beneath brachioradialis, anterior to supinator and brachialis. It supplies these muscles and then anastomoses with the radial collateral branch of the profunda brachii artery. The radial recurrent artery also gives branches to extensor carpi radialis longus, extensor digitorum, extensor digiti minimi and extensor carpi ulnaris.

Muscular branches

Muscular branches are distributed to the muscles on the radial side of the forearm. Direct branches from the radial artery supply the radial insertion of pronator teres, the anterolateral aspect of flexor carpi radialis, the lateral surface of flexor digitorum superficialis, the lateral half of flexor pollicis longus, and the distal sections of extensor carpi radialis longus and extensor carpi radialis brevis.

Palmar carpal branch

The palmar carpal branch arises near the distal border of pronator quadratus (see Fig. 50.9B). It crosses the anterior surface of the distal end of the radius, near the palmar carpal surface, and passes medially to anastomose behind the long flexor tendons with the palmar carpal branch of the ulnar artery. This transverse anastomosis is joined by longitudinal branches from the anterior interosseous artery and recurrent branches from the deep palmar arch, forming a cruciate palmar radiocarpal arch that supplies the carpal articulations and bones by descending branches.

Superficial palmar branch

The superficial palmar branch arises from the radial artery just before it curves round the carpus. It passes through, and occasionally over, the thenar muscles, which it supplies, and usually anastomoses with the end of the ulnar artery to complete a superficial palmar arch (see Fig. 51.36). The superficial arch is complete in about 80% of cases (Zarzecki et al 2018).

First dorsal metacarpal artery

The first dorsal metacarpal artery arises from the radial artery just before it passes between the heads of the first dorsal interosseous. It divides, almost at once, into two branches that supply the adjacent sides of the thumb and index finger as far distally as the proximal interphalangeal joint. The radial side of the thumb receives a branch direct from the radial artery proper. In most cases, the first dorsal metacarpal artery follows a fascial course overlying the first dorsal interosseous and parallel to the second metacarpal. Occasionally it may follow an intramuscular course. Distally, it anastomoses with the dorsal branches of the radiopalmar digital artery of the index finger over the proximal phalanx.

Dorsal carpal branch

The dorsal carpal branch of the radial artery arises deep to the tendons of the thumb extensors. It runs medially across the dorsal carpal surface under the tendons and anastomoses with the ulnar dorsal carpal branch, and also with the anterior and posterior interosseous arteries, to form a dorsal radiocarpal arch (see Figs 50.9A, 50.9C, 51.37). The carpal arches are both close to bone and supply the distal epiphysial parts of the radius and ulna. Three dorsal metacarpal arteries descend from the dorsal intercarpal arch on the second to fourth dorsal interossei, and bifurcate into dorsal digital branches to supply the adjacent sides of all four fingers.

Second, third and fourth dorsal metacarpal arteries

The second to fourth dorsal metacarpal arteries arise from the dorsal carpal arch. Near their origins, they anastomose with the deep palmar arch by proximal perforating arteries and, near their bifurcation, with dorsal perforating branches from the palmar metacarpal arteries that pass between the metacarpal necks. They also anastomose distally at the level of the web spaces with dorsal perforating branches from the palmar digital arteries from the superficial palmar arch. The third and fourth dorsal metacarpal arteries are much smaller than the first and second. Cutaneous branches from the dorsal metacarpal arteries supply the dorsal skin as far distally as the proximal interphalangeal joint. At the level of the neck of the second, third and fourth metacarpals, a direct cutaneous branch is given off that passes proximally and supplies an area of skin between the two adjacent metacarpals.

Arteria princeps pollicis

The arteria princeps pollicis (Miletin et al 2017) arises from the radial artery as it turns into the palm to form the deep palmar arch (see Fig. 51.2A). It descends on the palmar aspect of the first metacarpal under the oblique head of adductor pollicis lateral to the first palmar interosseous. At the base of the proximal phalanx, deep to the tendon of flexor pollicis longus, the artery divides into two branches that appear between the medial and lateral attachments of the oblique head of adductor pollicis and run along both sides of the thumb. On the palmar surface of the distal phalanx, the branches form a pollicial arch that supplies the skin and subcutaneous tissue. The arteria princeps pollicis is the usual nutrient of supply to the first metacarpal.

Arteria radialis indicis

The arteria radialis indicis is often a proximal branch of the arteria princeps pollicis, or may arise from the superficial arch or from the first dorsal metacarpal artery, or may combine with the arteria princeps pollicis to form the first palmar metacarpal artery. It descends between the first dorsal interosseous and transverse head of adductor pollicis, and runs along the lateral side of the index finger to its tip (see Fig. 51.27B). It anastomoses with the index medial digital artery and with the arteria princeps pollicis and the superficial palmar arch at the distal border of the transverse head of adductor pollicis.

Deep palmar arch

The deep palmar arch is formed by anastomosis of the end of the radial artery with the deep palmar branch of the ulnar artery (see Figs 51.2A, 51.35G, 51.36). It crosses the bases of the metacarpals and interossei, covered by the oblique head of adductor pollicis, the tendons of the digital flexors and the lumbricals. In its concavity, running laterally, is the deep branch of the ulnar nerve. The deep palmar arch is incomplete in about 5% (Zarzecki et al 2018).

Palmar metacarpal artery

The three palmar metacarpal arteries run distally from the convexity of the deep palmar arch on the interossei of the second to fourth spaces, and join the common digital branches of the superficial arch at the digital clefts (see Fig. 51.36). They supply nutrient branches to the medial four metacarpals.

Perforating branches

Three perforating branches from the deep palmar arch cross the second to fourth interosseous spaces between the heads of the corresponding dorsal interossei and anastomose with the dorsal metacarpal arteries.

Recurrent branches

Recurrent branches ascend proximally from the deep palmar arch anterior to the carpus to supply the carpal bones and intercarpal articulations. They end in the palmar carpal arch.

Ulnar artery

The ulnar artery arises from the brachial artery just distal to the flexion crease of the elbow at the level of the radial neck, and reaches the medial side of the forearm in its upper third (see Figs 50.21–50.22). It is larger than the radial artery and is accompanied throughout its length by venae comitantes. In the forearm, the ulnar artery initially lies on brachialis before passing deep to pronator teres, flexor carpi radialis, palmaris longus and flexor digitorum superficialis. It then lies on flexor digitorum profundus, between flexor carpi ulnaris and flexor digitorum superficialis. At the wrist, the ulnar artery (see Fig. 51.10) is covered by skin, fascia and palmaris brevis. It lies between the superficial and main parts of the flexor retinaculum, lateral to the ulnar nerve and pisiform bone, and enters the hand. The median nerve is a medial relation for approximately 2.5 cm distal to the elbow, and then crosses the artery, from which it is separated by the ulnar head of pronator teres. The ulnar nerve lies medial to the distal two-thirds of the ulnar artery, which supplies the nerve throughout its length; the palmar cutaneous branch of the ulnar nerve descends along the ulnar artery to reach the hand.

The ulnar artery may arise above the elbow, when it can lie superficial to the forearm flexors under the deep fascia; only rarely is it subcutaneous. When this occurs, the brachial artery supplies the common interosseous and the ulnar recurrent arteries.

Anterior ulnar recurrent artery

The anterior ulnar recurrent artery arises from the ulnar artery distal to the elbow and close to the origin of the ulnar artery itself. It ascends between brachialis and pronator teres, which it supplies, then anastomoses with the inferior ulnar collateral artery anterior to the medial epicondyle (see Fig. 50.27A). It limits distal extension of the medial Hotchkiss approach to the coronoid process.

Posterior ulnar recurrent artery

The posterior ulnar recurrent artery arises from the ulnar artery distal to the anterior ulnar recurrent artery, passes dorsomedially between flexor digitorum profundus and flexor digitorum superficialis, and ascends between the posterior aspect of the medial epicondyle and the olecranon. It is deep to flexor carpi ulnaris, ascending between its heads with the ulnar nerve. It supplies flexor digitorum profundus, flexor digitorum superficialis, flexor carpi ulnaris, the ulnar nerve, underlying bone and the elbow joint, and anastomoses with the ulnar collateral artery and interosseous recurrent artery. The posterior ulnar recurrent artery and ulnar nerve are both vulnerable to injury behind the medial epicondyle (see Figs 50.28–50.29).

Common interosseous artery

The common interosseous artery is a short branch of the ulnar artery (see Figs 50.10, 50.22). It arises just distal to the radial tuberosity and passes back to the proximal border of the interosseous membrane, where it divides into the anterior and posterior interosseous arteries. Occasionally the common interosseous artery is a branch of the radial artery.

Anterior interosseous artery

The anterior interosseous artery arises from the common interosseous artery and descends on the anterior aspect of the interosseous membrane with the anterior interosseous branch of the median nerve (see Figs 50.10, 50.22, 50.27, 50.32A). It is overlapped by contiguous sides of flexor digitorum profundus and flexor pollicis longus. Shortly after its origin, it usually gives off a slender median artery. This accompanies and supplies the median nerve as far as the palm, where it may join the superficial palmar arch or end as one or two palmar digital arteries. The median artery can also arise from the ulnar or the common interosseous artery. Muscular and nutrient branches from the anterior interosseous artery pierce the interosseous membrane to supply deep extensor muscles and the radius and ulna, respectively. A branch descends deep to pronator quadratus before piercing the interosseous membrane to join the anterior ‘carpal’ arch.

The anterior interosseous artery leaves the anterior compartment by piercing the interosseous membrane proximal to pronator quadratus. It anastomoses with the posterior interosseous artery in the posterior compartment of the forearm, and travels through a tunnel under the extensor retinaculum with the tendons of the digital extensors before joining the dorsal carpal arch. Three small cutaneous perforating branches supply the skin over the lower lateral border of the forearm.

Posterior interosseous artery

The posterior interosseous artery arises from the common interosseous artery and is usually smaller than the anterior interosseous artery (see Figs 50.10, 50.27A). It passes dorsally between the oblique cord and proximal border of the interosseous membrane, and then between supinator and abductor pollicis longus. It descends deep in the groove between extensor carpi ulnaris and the extensor digiti minimi component of extensor digitorum. While in the groove, it gives rise to multiple muscular branches that supply these muscles and fasciocutaneous perforators that travel in the intermuscular septum between extensor carpi ulnaris and extensor digiti minimi. The posterior interosseous artery accompanies the deep branch of the radial nerve (posterior interosseous nerve) on abductor pollicis longus. Distally, it anastomoses with the terminal part of the anterior interosseous artery and the dorsal carpal arch.

Sometimes, the posterior interosseous artery disappears halfway down the forearm, in which case the anterior interosseous artery pierces the interosseous membrane more proximally to anastomose with it. Occasionally the two vessels do not anastomose.

Posterior interosseous recurrent artery

The posterior interosseous recurrent artery leaves the posterior interosseous artery near its origin and ascends between the lateral epicondyle and olecranon, either on or through supinator, and deep to anconeus. It anastomoses with the middle collateral branch of the profunda brachii artery, posterior ulnar recurrent artery and ulnar collateral artery. Occasionally the artery is absent.

Dorsal cutaneous branch

A constant dorso-ulnar perforator vessel is given off distally. It arises 2–5 cm proximal to the pisiform and accompanies the dorsal cutaneous branch of the ulnar nerve. It emerges between flexor carpi ulnaris and extensor carpi ulnaris.

Palmar carpal branch

The palmar carpal branch crosses the distal ulna deep to the tendons of flexor digitorum profundus and anastomoses with the palmar carpal branch of the radial artery to make a palmar radiocarpal arch.

Dorsal carpal branch

The dorsal carpal branch arises just proximal to the pisiform. It curves deep to the tendon of flexor carpi ulnaris to reach the carpal dorsum, which it crosses laterally beneath the extensor tendons. It anastomoses with the dorsal carpal branch of the radial artery to complete the dorsal carpal arch. Near its origin, it sends a small digital branch along the ulnar side of the fifth metacarpal to supply the medial side of the dorsal surface of the fifth finger.

Deep palmar branch

The deep palmar branch is often double. It passes between abductor and flexor digiti minimi, through or deep to opponens digiti minimi, and anastomoses with the radial artery, completing the deep palmar arch. The deep palmar branch accompanies the deep branch of the ulnar nerve.

Superficial palmar arch

The superficial palmar arch is an anastomosis fed mainly by the ulnar artery (see Figs 51.2A, 51.10, 51.36). The latter enters the palm with the ulnar nerve, anterior to the flexor retinaculum and lateral to the pisiform. It passes medial to the hook of the hamate, then curves laterally to form an arch that is convex distally and level with a transverse line through the distal border of the fully extended base of the thumb. About one-third of superficial palmar arches are formed by the ulnar artery alone, a further third are completed by the superficial palmar branch of the radial artery, and a third by the arteria radialis indicis, or a branch of either arteria princeps pollicis or the median artery. The superficial palmar arch is covered by palmaris brevis and the palmar aponeurosis, and it is superficial to flexor digiti minimi, branches of the median nerve and the tendons of the long flexors and the lumbricals.

Common and proper palmar digital arteries

Three common palmar digital arteries arise from the convexity of the superficial palmar arch (see Fig. 51.2A, 51.36). They pass distally on the second to fourth lumbricals, each joined by a corresponding palmar metacarpal artery from the deep palmar arch, and divide into two proper palmar digital arteries. These run along the contiguous sides of all four fingers, dorsal to the digital nerves, between Grayson’s and Cleland’s ligaments, anastomosing in the subcutaneous tissue of the fingertips and near the interphalangeal joints. Each digital artery has two dorsal branches that anastomose with the dorsal digital arteries and supply the soft parts dorsal to the middle and distal phalanges, including the matrices of the nails (see Fig. 51.2B). The palmar digital artery for the medial side of the little finger leaves the arch under palmaris brevis. Palmar digital arteries supply the metacarpophalangeal and interphalangeal joints and nutrient rami to the phalanges. They are the main digital supply because the dorsal digital arteries are minute. The origins of the palmar digital arteries of the thumb are quite variable. Both may arise from a single arteria princeps pollicis or they may arise separately from the superficial palmar arch. The ulnar digital artery may arise from the first dorsal metacarpal artery.

The terminal branches of the digital arteries contribute to a number of vascular arcades that provide a rich vascular supply for the distal elements of each digit (see Fig. 51.2A, 51.5). Three distal phalangeal dorsal arterial arcades anastomose with each other and with those from the other side of the digit. The superficial arcade occurs at the level of the proximal nail fold and is supplied primarily by a dorsal branch from the palmar digital artery, which is given off at the level of the middle phalanx. The proximal subungual arcade is at the level of the lunula and is supplied by a terminal branch of the digital artery, which passes dorsally. The distal subungual arcade occurs more distally in the nail bed. It is supplied by a dorsal vessel that emerges from the point of confluence of the ‘H’-shaped anastomosis between the terminal portions of both digital arteries, and passes from the volar to the dorsal aspect of the digit under the interosseous ligament connecting the proximal and distal parts of the distal phalanx.

Variants

The ulnar and radial arteries to the hand may occasionally be supplemented by a median artery that contributes to, or supplies, the superficial palmar arch and by the anterior interosseous artery, which may make a contribution to the deep palmar arch. The median artery may persist in two different forms, palmar and antebrachial (Rodriguez-Niedenführ et al 1999). The palmar type arises from the junction of the ulnar artery and its common interosseous trunk; it is long and large, and reaches the palm, usually ending as the first or second common digital artery, or both. The antebrachial type is slender and short, usually arising from the anterior interosseous artery and finishing in the forearm. These variations are seen in about 20% of individuals and tend to be unilateral. Ulnar artery dominance in all digits is rare, complete radial artery dominance has been described in 28% of hands (Kleinert et al 1989).

Collateral circulation at the elbow

The collateral circulation at the elbow is more robust than that at the knee. Alternative pathways include the profunda brachii artery, which accompanies the radial nerve through the lateral intermuscular septum to become the radial collateral artery. The superior ulnar collateral artery accompanies the ulnar nerve: in the adult, it may be as wide as 1.5 mm at its origin; hence its regular use as the artery to a free vascularized ulnar nerve graft. The inferior ulnar collateral artery is regularly seen during medial approaches to the elbow as a vessel that pierces the intermuscular septum to curl around the humerus between triceps and bone. On occasion, there is a substantial artery running with the median nerve. These vessels anastomose with recurrent branches from the ulnar and radial arteries to form a network that may maintain perfusion of the hand and the extensor muscles in cases where the brachial artery has been divided in the lower third of the arm (when there is no associated fracture or dislocation). Collateral circulation will diminish or cease altogether if the ulnar or radial nerve is entrapped within the fracture or compressed by haematoma (Blakey et al 2009, Birch 2011).

Cutaneous vascular supply of the upper limb

The skin over the lateral end of the clavicle is supplied by the supraclavicular artery, which pierces the deep fascia superior to the clavicle and anterior to trapezius. In most cases, this artery arises from the superficial cervical/transverse cervical artery, but it occasionally arises from the suprascapular artery. The area over deltoid is supplied by the anterior and posterior circumflex humeral arteries. The deltoid branch of the thoraco-acromial axis contributes to the blood supply of the anterior aspect of the shoulder via musculocutaneous perforators through deltoid.

The blood supply to the skin of the upper arm may be divided into three regions with separate supplies. The deltoid region is supplied by musculocutaneous perforators, and the medial and lateral regions are supplied by fasciocutaneous perforators (Cormack and Lamberty 1994, Salmon, in Taylor and Razaboni 1994).

The deltoid region is supplied by the posterior circumflex humeral artery via musculocutaneous perforators. After exiting from the quadrangular space, it gives off a descending branch that runs down to the insertion of deltoid and the overlying skin, and an ascending branch that passes superiorly towards the acromion and pierces the edge of deltoid and the deep fascia to fan out and supply the overlying skin.

The medial side of the upper arm is supplied by five or six fasciocutaneous perforators that arise from the brachial artery, the superior ulnar collateral artery and, if present, the single artery to biceps brachii. These perforators pass along the medial intermuscular septum to spread out in the deep fascia and anastomose with perforating vessels superiorly and inferiorly, and from the lateral side. There are virtually no musculocutaneous perforators through biceps or triceps.

The lateral side of the upper arm below deltoid is supplied by perforating vessels from the middle collateral and radial collateral arteries (the terminating bifurcation of the profunda brachii). The middle collateral artery sends perforators to the skin via the lateral intermuscular septum between brachioradialis and triceps, while the radial collateral artery gives off cutaneous perforators via the intermuscular septum between brachialis and brachioradialis. These cutaneous vessels anastomose with those from the medial side.

The skin of the elbow and forearm receives its blood supply from muscle perforators, fasciocutaneous networks and direct cutaneous vessels. The skin of the anterolateral cubital fossa is supplied by muscle perforators arising from the radial collateral and radial recurrent arteries. The skin of the medial cubital fossa receives branches from an anastomosis between the inferior ulnar collateral and the ulnar recurrent arteries. Small direct cutaneous vessels spring from the brachial artery. The skin of the posterolateral aspect of the elbow is supplied by branches of the posterior interosseous recurrent artery and a rich plexus of collateral and anastomosing arteries. The skin of the posteromedial aspect is supplied by branches of the superior and inferior ulnar collateral arteries and the posterior ulnar recurrent artery feeding into the plexus.

The skin of the anterior forearm is supplied by fasciocutaneous perforators; the largest is the inferior cubital artery, which arises from the radial artery at the distal apex of the cubital fossa and extends to midway down the forearm. Fasciocutaneous perforators from the radial artery supply the lateral two-thirds of the anterior surface of the forearm (see Fig. 48.5). The vessels pass in the intermuscular septa between brachioradialis and flexor carpi radialis, and between flexor carpi radialis and flexor digitorum superficialis. Fasciocutaneous perforators from the ulnar artery supply skin over the ulnar side of the anterior forearm and the medial quarter of the posterior forearm from the cubital fossa to the wrist. A small contribution comes from musculocutaneous perforators that pass through brachioradialis and flexor carpi ulnaris.

The skin of the distal third of the lateral forearm is supplied by the terminal perforating branches of the anterior interosseous artery. The central half of the posterior surface of the forearm, from the lateral edge of extensor digitorum, just below the lateral epicondyle of the humerus, to the wrist, is supplied by fasciocutaneous perforators from the posterior interosseous artery that pass along the intermuscular fascia between extensor carpi ulnaris and extensor digiti minimi.

Arterial Supply of the Lower Limb

The femoral artery provides the principal arterial supply to the lower limb distal to the inguinal ligament and the gluteal fold. It courses within the subsartorial (adductor) canal, which is located on the anteromedial aspect of the thigh, passes through the adductor hiatus and becomes the popliteal artery on entering the posterior compartment of the thigh. The popliteal artery soon divides into the anterior and posterior tibial arteries which supply the leg, ankle and foot.

The obturator and inferior gluteal vessels also contribute to the supply of the proximal part of the lower limb. In the embryo, the inferior gluteal artery supplies the main axial artery of the limb, which is represented in the adult by the artery to the sciatic nerve.

The bones of the lower limb receive their arterial supply from nutrient vessels, metaphysial arterial branches of the peri-articular anastomoses, and the arteries supplying the muscles that attach to their periosteum. The pattern of arterial supply is particularly relevant to fracture healing, the spread of infection and malignancy, and the planning of reconstructive surgical procedures. For further details, consult Cormack and Lamberty (1994), Taylor and Razaboni (1994) and Crock (1996).

Ischaemia of the lower limb due to peripheral arterial disease is a tremendous burden on healthcare resources. Obesity and smoking and diseases including diabetes, hypertension and atherosclerosis, contribute to this pathology. Symptoms include intermittent claudication and wounds that do not heal well (see Sampson et al 2017). Physical examination of such patients may reveal decreased distal pulses (e.g. of the posterior tibial artery), pallor or a cool extremity.

Pulses The pulsation of the femoral artery is palpable as it enters the femoral triangle. Posterior to the knee joint, the popliteal pulse is difficult to identify due to the depth of the popliteal artery, and is best assessed with the knee in slight flexion. Distally, the posterior tibial artery is palpable just posterior to the medial malleolus and the dorsalis pedis pulse is located over the tarsal bones, immediately lateral to the tendon of extensor hallucis longus. Clinical signs of decreased or absent peripheral pulses, particularly the pedal pulses (posterior tibial artery and dorsalis pedis) bilaterally may be indicative of peripheral artery disease (Londero et al 2016).

Femoral artery

The femoral artery (see Figs 77.2, 77.43–77.44, 77.48) is a continuation of the external iliac artery (Benninger 2014) and provides the principal arterial supply to the lower limb distal to the inguinal ligament and the gluteal fold (see Figs 76.4–76.5). It begins posterior to the inguinal ligament, midway between the anterior superior iliac spine and the pubic symphysis, descends along the anteromedial part of the thigh in the femoral triangle, enters and passes through the adductor (subsartorial) canal, and becomes the popliteal artery as it passes through an opening in adductor magnus near the junction of the middle and distal thirds of the thigh. Its first 3 or 4 cm are enclosed, with the femoral vein, in the femoral sheath. The femoral artery gives off several branches in the proximal thigh, including the superficial epigastric, superficial circumflex iliac, superficial external pudendal, deep external pudendal and the profunda femoris artery. It gives off the descending genicular artery within the adductor canal.

Rarely the femoral artery divides, distal to the origin of the profunda femoris artery, into two trunks that reunite near the adductor opening. The inferior gluteal artery, accompanying the sciatic nerve to the popliteal fossa and representing a persistence of the original axial artery, may replace it. The external iliac artery is then small, ending as the deep artery of the thigh.

Relations Anterior to the artery in the femoral triangle are the skin, subcutaneous tissue, superficial inguinal lymph nodes, fascia lata, femoral sheath, superficial circumflex iliac vein (crossing in the subcutaneous tissue) and the femoral branch of the genitofemoral nerve (which is at first lateral and then anterior). Near the apex of the triangle, the medial femoral cutaneous nerve crosses in front of the artery from the lateral to the medial side. Posteriorly, the posterior wall of the femoral sheath separates the artery from the tendons of psoas, pectineus and adductor longus. The artery is separated from the hip joint by the tendon of psoas major, from pectineus by the femoral vein and deep femoral vessels, and from adductor longus by the femoral vein. Proximally, the nerve to pectineus passes medially behind the artery. The femoral nerve lies lateral to the artery, outside the femoral sheath. The femoral vein is medial to the artery in the proximal part of the triangle and becomes posterior distally at the apex.

Within the adductor canal, the artery is covered by skin, subcutaneous tissue, deep fascia, sartorius and the fibrous roof (subsartorial fascia) of the canal. The saphenous nerve lies at first lateral, then anterior and finally medial to the artery. Adductor longus and adductor magnus are posterior, vastus medialis and its nerve are anterolateral, and the femoral vein is also posterior proximally but it becomes lateral distally (see Figs 77.48–77.49).

Compression of the femoral artery is most effective just distal to the inguinal ligament, where it is superficial and separated from the bone (iliopubic ramus) only by the psoas major tendon. For this reason, arterial injury proximal to the inguinal ligament, such as laceration by a knife, cannot be controlled simply by compression. Gaining proximal control of bleeding involves major exposure of the more proximal arteries as a life-saving manoeuvre.

The branches of the femoral artery include the superficial epigastric, superficial circumflex iliac, superficial external pudendal, deep external pudendal arteries, muscular branches, the profunda femoris artery and the descending genicular artery (see Fig. 76.4).

Superficial epigastric artery

The superficial epigastric artery arises anteriorly from the femoral artery approximately 1 cm distal to the inguinal ligament, and traverses the cribriform fascia to ascend anterior to the ligament and run in the abdominal subcutaneous tissue almost to the umbilicus. It supplies the superficial inguinal lymph nodes, subcutaneous tissue and skin, and anastomoses with branches of the inferior epigastric artery and its contralateral fellow.

Superficial circumflex iliac artery

The superficial circumflex iliac artery is the smallest superficial branch of the femoral artery and arises near or with the superficial epigastric artery. It usually emerges through the fascia lata, lateral to the saphenous opening, and turns laterally distal to the inguinal ligament towards the anterior superior iliac spine. It supplies the skin, subcutaneous tissue and superficial inguinal lymph nodes, anastomosing with the deep circumflex iliac, superior gluteal and lateral circumflex femoral arteries.

The superficial circumflex iliac artery is the basis for the important axial-pattern pedicled groin skin flap. Free flaps based on the vessel may also be raised.

Superficial external pudendal artery

The superficial external pudendal artery arises medially from the femoral artery, close to the preceding branches. Emerging from the cribriform fascia, it passes medially, usually deep to the long saphenous vein, across the spermatic cord (or round ligament) to supply the lower abdominal, penile, scrotal or labial skin, and anastomoses with branches of the internal pudendal artery. The anterior scrotal wall is supplied primarily by branches of the external pudendal artery, which run parallel to the rugae and do not cross the raphe of the scrotum; this anatomical detail is important for planning appropriate incisions during scrotal surgery.

Deep external pudendal artery

The deep external pudendal artery passes medially across pectineus and anterior or posterior to adductor longus, covered by fascia lata, which it pierces to supply the skin of the perineum and scrotum or labium majus. Its branches anastomose with the posterior scrotal or labial branches of the internal pudendal artery.

Muscular branches

Muscular branches supply sartorius, vastus medialis and the adductors.

Profunda femoris artery (deep artery of the thigh)

The profunda femoris artery (see Figs 77.40B, 77.43A, 77.48–77.49) is a large branch that arises posterolaterally from the femoral artery about 3.5 cm distal to the inguinal ligament. At first lateral to the femoral artery, it spirals posterior to this and the femoral vein to reach the medial side of the femur. It passes between pectineus and adductor longus, then between the latter and adductor brevis, before it descends between adductor longus and adductor magnus. It pierces adductor magnus and anastomoses with the upper muscular branches of the popliteal artery. This terminal part is sometimes named the fourth perforating artery.

The profunda femoris artery is the main supply to the adductor, extensor and flexor muscles, and also anastomoses with the internal and external iliac arteries above and with the popliteal artery below. It is a major collateral artery of the lower limb in patients with femoropopliteal arterial occlusive disease (see Fig. 77.49) (Shakeri et al 2010).

The profunda femoris artery sometimes arises from the posterior aspect of the femoral artery, and more rarely from the medial aspect. If it arises posteriorly, it may cross anterior to the femoral vein and then pass backwards around its medial side.

The profunda femoris artery gives off the lateral and medial circumflex arteries in the proximal thigh, and perforating and muscular branches more distally.

Relations Posteriorly, in proximodistal order, lie iliacus, pectineus, adductor brevis and adductor magnus. Anteriorly, the femoral and deep femoral veins, and distally, adductor longus, separate the profunda femoris artery from the femoral artery. Laterally, vastus medialis separates the proximal part of the artery from the femur.

Lateral circumflex femoral artery

The lateral circumflex femoral artery (see Figs 77.48–77.49) is a laterally running branch given off near the root of the profunda femoris artery. It passes between the divisions of the femoral nerve, posterior to sartorius and rectus femoris, and divides into ascending, transverse and descending branches. The ascending branch ascends along the intertrochanteric line, under tensor fasciae latae, lateral to the hip joint. It anastomoses with the superior gluteal and deep circumflex iliac arteries, supplying the greater trochanter, and, with branches of the medial circumflex femoral, forms an anastomotic ring round the femoral neck, from which the femoral neck and head are supplied. The ascending branch forms the pedicle of the tensor fasciae latae musculocutaneous flap. The descending branch descends posterior to rectus femoris, along the anterior border of vastus lateralis, which it supplies; a long branch descends in vastus lateralis to the knee (Tayfur et al 2010), anastomosing with the superior lateral genicular branch of the popliteal artery, accompanied by the nerve to vastus lateralis. The fasciocutaneous perforators that arise from the descending branch supply the anterolateral thigh fasciocutaneous flap. The transverse branch, the smallest, passes laterally anterior to vastus intermedius and pierces vastus lateralis to wind round the femur, just distal to the greater trochanter. It anastomoses with the medial circumflex, inferior gluteal and first perforating arteries, forming a cruciate anastomosis.

The lateral circumflex femoral artery may arise from the femoral artery or as a common trunk with the profunda femoris artery and the medial circumflex femoral artery. The ascending and descending branches may occasionally arise separately (Siddharth et al 1985).

Medial circumflex femoral artery

The medial circumflex femoral artery (see Figs 77.48–77.49) usually originates from the posteromedial aspect of the profunda femoris artery, but sometimes originates from the femoral artery itself or as a common trunk with either the profunda femoris artery or the lateral circumflex femoral artery or both (Siddharth et al 1985). It supplies the adductor muscles and curves medially round the femur between pectineus and psoas major and then obturator externus and adductor brevis, finally appearing between quadratus femoris and the upper border of adductor magnus, dividing into transverse and ascending branches. The transverse branch takes part in the cruciate anastomosis. The ascending branch ascends on the tendon of obturator externus, anterior to quadratus femoris, to the trochanteric fossa, where it anastomoses with branches of the gluteal and lateral circumflex femoral arteries. An acetabular branch at the proximal edge of adductor brevis enters the hip joint under the transverse acetabular ligament with one from the obturator artery. It supplies the fat in the fossa and reaches the femoral head along its ligament. For details of the blood supply of the proximal end of the femur consult Crock (1996).

Perforating arteries

The perforating arteries (see Fig. 77.40A) perforate the femoral attachment of adductor magnus to reach the flexor aspect of the thigh. There are three perforating branches, and the terminal part of the profunda femoris artery itself becomes the fourth perforator. They pass close to the linea aspera under small tendinous arches and give off muscular, cutaneous and anastomotic branches. Diminished, they pass deep to the short head of biceps femoris (the first usually through the attachment of gluteus maximus), traverse the lateral intermuscular septum and enter vastus lateralis. The first arises proximal, the second anterior and the third distal to adductor brevis. The first perforating artery passes back between pectineus and adductor brevis (sometimes through the latter), pierces adductor magnus near the linea aspera to supply adductor brevis, adductor magnus, biceps femoris and gluteus maximus, and anastomoses with the inferior gluteal, medial and lateral circumflex femoral and second perforating arteries. The larger second perforating artery, often arising with the first, pierces the attachments of adductor brevis and magnus, divides into the ascending and descending branches supplying the posterior thigh muscles and anastomoses with the first and third perforating arteries. The femoral nutrient artery usually arises from it. When two nutrient arteries exist, they usually arise from the first and third perforators. The third perforating artery starts distal to adductor brevis, pierces the attachment of adductor magnus and divides into branches to the posterior thigh muscles. It anastomoses proximally with the perforating arteries, and distally with the end of the profunda femoris artery and muscular branches of the popliteal. The femoral nutrient artery may arise from it. Side branches of the diaphysial nutrient and other branches of the profunda femoris artery provide subsidiary cortical arteries.

The perforating arteries form a double chain of anastomoses, initially in the adductor muscles and subsequently near the linea aspera.

Muscular branches

Numerous muscular branches arise from the profunda femoris artery. Some end in the adductors, and others pierce adductor magnus, supply the flexors and anastomose with the medial circumflex femoral artery and superior muscular branches of the popliteal artery. The profunda femoris artery is thus the main supply to the thigh muscles.

Descending genicular artery

The descending genicular artery (see Figs 77.48–77.49, 78.1), the distal branch of the femoral artery, arises just proximal to the adductor opening and immediately supplies a saphenous branch. It then descends in vastus medialis, anterior to the tendon of adductor magnus, to the medial side of the knee, where it anastomoses with the superior medial genicular artery. Muscular branches supply vastus medialis and adductor magnus, and give off articular branches that anastomose around the knee joint. One articular branch crosses above the femoral patellar surface, forming an arch with the superior lateral genicular artery and supplying the knee joint. The saphenous branch (saphenous artery) emerges distally through the roof of the adductor canal to accompany the saphenous nerve to the medial side of the knee. It passes between sartorius and gracilis, and supplies the skin of the proximomedial area of the leg; it anastomoses with the inferior medial genicular artery.

Arterial anastomoses around the hip and thigh

In the fetus, a peri-acetabular vascular circle formed by the superior and inferior gluteal, internal pudendal and obturator arteries reduces the risk of bony necrosis of this region in children. However, there is a zone at the anterior portion of the acetabulum where the blood supply is less abundant (Damsin et al 1992).

An important chain of anastomoses extends on the back of the thigh from the gluteal region to the popliteal fossa. It is formed in proximodistal order by anastomoses between the gluteal arteries and terminal branches of the medial circumflex femoral artery; the circumflex femoral arteries and the first perforating artery; the perforating arteries themselves; and between the fourth perforating artery and the superior muscular branches of the popliteal artery (see Fig. 76.4). The trochanteric and cruciate anastomoses are the proximal elements of this chain.

Trochanteric anastomosis

The so-called trochanteric anastomosis lies near the trochanteric fossa of the femur and is an anastomosis between the ascending branch of the medial circumflex femoral artery and descending branches of the superior and inferior gluteal arteries. The lateral circumflex femoral artery and the first perforating artery from the profunda femoris artery may also contribute, creating an extracapsular 'arterial ring of the femoral neck' (Crock 1996). Branches from this ring, the retinacular vessels, pierce the capsule and ascend along the femoral neck to give the main blood supply to the head of the femur.

Cruciate anastomosis

The cruciate anastomosis lies at the level of the lesser trochanter, near the lower edge of the femoral attachment of quadratus femoris, and is an anastomosis between the transverse branches of the medial and lateral circumflex femoral arteries, a descending branch of the inferior gluteal artery and an ascending branch from the first perforating artery.

Collateral circulation in proximal femoral artery occlusion

After occlusion of the femoral artery proximal to the origin of the profunda femoris artery, five main anastomotic channels are available. These are between branches of the superior and inferior gluteal arteries, the medial and lateral circumflex femoral arteries and the first perforating branch of the profunda femoris artery; the obturator branch of the internal iliac artery and the medial circumflex femoral artery; the internal pudendal branch of the internal iliac artery and the superficial and deep external pudendal branches of the femoral artery; a deep circumflex iliac branch of the external iliac artery, the lateral circumflex femoral branch of the deep artery of the thigh and the superficial circumflex iliac branch of the femoral artery; and the inferior gluteal branch of the internal iliac artery and perforating branches of the profunda femoris artery.

Popliteal artery

The popliteal artery is the continuation of the femoral artery and crosses the popliteal fossa (see Figs 78.1B, 78.2, 78.4). It descends laterally from the opening in adductor magnus to the femoral intercondylar fossa, inclining obliquely to the distal border of popliteus, where it divides into the anterior and posterior tibial arteries. This division usually occurs at the proximal end of the interosseous space between the wide tibial metaphysis and the slender fibular metaphysis. The artery is relatively tethered at the adductor hiatus and again distally by the fascia related to soleus, and is therefore susceptible to damage following knee injuries, e.g. dislocation. Aneurysms of the popliteal artery are not uncommon.

The popliteal artery may occasionally bifurcate more superiorly and divide into its terminal branches proximal to popliteus, or it may trifurcate into anterior and posterior tibial and fibular arteries. Either the anterior tibial or the posterior tibial artery may be reduced or increased in size. The size of the fibular artery is usually inversely related to the size of the anterior and posterior tibial arteries. Rarely the anterior tibial artery is the source of the fibular artery, a variation that is almost always associated with a high bifurcation of the popliteal artery. The popliteal and inferior gluteal arteries may be joined by a large anastomotic vessel; in such cases, the femoral artery is hypoplastic (Kawashima and Sasaki 2010). When this occurs, the popliteal artery usually has an abnormal relationship to popliteus, running deep to the muscle before dividing into its terminal branches. The popliteal artery may pass medially beneath the medial head of gastrocnemius, or may pass beneath an aberrant band of muscle in the popliteal fossa; in either case, contraction of the muscles may occlude the artery, a condition that may present with claudication on exertion. The popliteal vein is usually superficial and adjacent to the artery, but it may run deep to the artery, or be separated from it by a slip of muscle derived from the medial head of gastrocnemius.

Relations Anteriorly, from proximal to distal, are fat covering the femoral popliteal surface, the capsule of the knee joint, and the fascia of popliteus. Posteriorly are semimembranosus (proximally) and gastrocnemius and plantaris (distally). In between, the artery is separated from the skin and fasciae by fat and crossed from its lateral to its medial side by the tibial nerve and popliteal vein; the vein lies between the nerve and artery and is adherent to the latter. Laterally are biceps femoris, the tibial nerve, popliteal vein and lateral femoral condyle (all proximal), and plantaris and the lateral head of gastrocnemius (distal). Medially are semimembranosus and the medial femoral condyle (proximal), and the tibial nerve, popliteal vein and medial head of gastrocnemius (distally). The relations of the popliteal nodes are described below.

Superior genicular arteries

The superior genicular arteries branch from the popliteal artery, curving round proximal to both femoral condyles to reach the anterior aspect of the knee. The superior medial genicular artery lies under semimembranosus and semitendinosus, proximal to the medial head of gastrocnemius and deep to the tendon of adductor magnus. It divides into a branch to vastus medialis that anastomoses with the descending genicular and inferior medial genicular arteries, and a branch that ramifies on the femur and anastomoses with the superior lateral genicular artery. Its size varies inversely with that of the descending genicular artery. The superior lateral genicular artery passes under the tendon of biceps femoris, pierces the lateral intermuscular septum and divides into superficial and deep branches. The superficial branch supplies vastus lateralis and anastomoses with the descending branch of the lateral circumflex femoral and inferior lateral genicular arteries, while the deep branch anastomoses with the superior medial genicular artery, forming an anterior arch across the femur with the descending genicular artery. The superficial branch is vulnerable if the lateral patellar retinaculum is divided surgically.

Middle genicular artery

The middle genicular artery is small. It arises from the popliteal artery near the midpoint of the posterior aspect of the knee joint. It pierces the oblique popliteal ligament to supply the cruciate ligaments and synovial membrane.

Inferior genicular arteries

The inferior medial and lateral genicular arteries arise from the popliteal artery deep to gastrocnemius. The inferior medial genicular artery is deep to the medial head of gastrocnemius. It descends along the proximal margin of popliteus, which it supplies; passes inferior to the medial tibial condyle, under the tibial collateral ligament; and then ascends anteromedial to the knee joint at the anterior border of the tibial collateral ligament. It supplies the joint and the tibia, and anastomoses with the inferior lateral and superior medial genicular arteries and with the anterior tibial recurrent artery and saphenous branch of the descending genicular artery. The inferior lateral genicular artery runs laterally across popliteus and forwards over the head of the fibula to the front of the knee joint, passing under the lateral head of gastrocnemius, the fibular collateral ligament and the tendon of biceps femoris. Its branches anastomose with the inferior medial and superior lateral genicular arteries; anterior and posterior tibial recurrent arteries; and the circumflex fibular branch of the posterior tibial artery.

Cutaneous branches: the superficial sural arteries

The superficial sural arteries are three vessels that leave the popliteal artery, or its side branches, descend between the heads of gastrocnemius and perforate the deep fascia to supply the skin on the back of the leg. The central or median vessel is usually larger than the medial or lateral vessels, and usually accompanies the sural nerve.

Fasciocutaneous free and pedicled flaps may be raised on the superficial sural arteries.

Superior muscular branches

The superior muscular branches are two or three vessels that arise proximally and pass to adductor magnus and the posterior thigh muscles. They anastomose with the termination of the profunda femoris artery.

Sural arteries

The two sural arteries are large and arise behind the knee joint to supply gastrocnemius, soleus and plantaris. They are used in gastrocnemius musculocutaneous flaps.

Genicular anastomosis

There is an intricate arterial anastomosis around the patella and femoral and tibial condyles (see Fig. 78.1). A superficial network spreads between the fascia and skin around the patella and in the fat deep to the patellar ligament. A deep network lies on the femur and tibia near their adjoining articular surfaces, and supplies the bone, articular capsule and synovial membrane. The vessels involved in this anastomosis are the superior medial and lateral genicular; inferior medial and lateral genicular; descending genicular; descending branch of the lateral circumflex femoral; circumflex fibular; and anterior and posterior tibial recurrent arteries.

Anterior tibial artery

The anterior tibial artery arises at the distal border of popliteus (see Figs 76.4A–B, 78.1, 78.4, 78.36, 78.39, 78.40, 79.10A). At first in the flexor compartment, it passes between the heads of tibialis posterior and through the oval aperture in the proximal part of the interosseous membrane to reach the extensor (anterior) compartment, passing medial to the fibular neck; it is vulnerable here during tibial osteotomy. Descending on the anterior aspect of the membrane, it approaches the tibia and, distally, lies anterior to it. At the ankle, the anterior tibial artery is located approximately midway between the malleoli, and it continues on the dorsum of the foot, lateral to extensor hallucis longus, as the dorsalis pedis artery.

The anterior tibial artery may, on occasion, be small but it is rarely absent. Its function may be replaced by perforating branches from the posterior tibial artery or by the perforating branch of the fibular artery. It occasionally deviates laterally, regaining its usual position at the ankle. It may also be larger than normal, in which case its territory of supply in the foot may be increased to include the plantar surface.

The named branches of the anterior tibial artery are the posterior and anterior tibial recurrent, muscular, perforating, and anterior medial and lateral malleolar arteries.

Relations In its proximal two-thirds the anterior tibial artery lies on the interosseous membrane, and in its distal third it is anterior to the tibia and ankle joint. Proximally, it lies between tibialis anterior and extensor digitorum longus, then between tibialis anterior and extensor hallucis longus. At the ankle it is crossed superficially from the lateral side by the tendon of extensor hallucis longus and then lies between this tendon and the first tendon of extensor digitorum longus. Its proximal two-thirds are covered by adjoining muscles and deep fascia, its distal third by the skin, fasciae and extensor retinacula. It is accompanied by venae comitantes. The deep fibular nerve, curling laterally round the fibular neck, reaches the lateral side of the artery where it enters the extensor region, is then anterior to the artery in the middle third of the leg, and becomes lateral again distally.

Posterior tibial recurrent artery

The posterior tibial recurrent artery is an inconstant branch that arises before the anterior tibial artery reaches the extensor compartment of the leg. It ascends anterior to popliteus, anastomosing with the inferior genicular branches of the popliteal artery. It supplies the superior tibiofibular joint.

Anterior tibial recurrent artery

The anterior tibial recurrent artery arises near the posterior tibial recurrent artery. It ascends in tibialis anterior, ramifies on the front and sides of the knee joint, and joins the patellar anastomosis, which interconnects with the genicular branches of the popliteal and circumflex fibular arteries.

Muscular branches

Numerous branches supply the adjacent muscles. Some then pierce the deep fascia to supply the skin, while others traverse the interosseous membrane to anastomose with branches of the posterior tibial and fibular arteries.

Perforating branches

Most of the fasciocutaneous perforators pass along the anterior fibular fascial septum behind extensor digitorum longus before penetrating the deep fascia to supply the skin.

Anterior medial malleolar artery

The anterior medial malleolar artery arises approximately 5 cm proximal to the ankle. It passes posterior to the tendons of extensor hallucis longus and tibialis anterior medial to the joint, where it joins branches of the posterior tibial and medial plantar arteries.

Anterior lateral malleolar artery

The anterior lateral malleolar artery runs posterior to the tendons of extensor digitorum longus and fibularis tertius to the lateral side of the ankle and anastomoses with the perforating branch of the fibular artery and ascending branches of the lateral tarsal artery.

Posterior tibial artery

The posterior tibial artery begins at the distal border of popliteus, between the tibia and fibula (see Figs 76.4B, 78.4, 78.40). It descends medially in the flexor compartment and divides under abductor hallucis, midway between the medial malleolus and the calcaneal tubercle, into the medial and lateral plantar arteries. In its course, the posterior tibial artery gives off a communicating branch that runs posteriorly across the tibia approximately 5 cm above its distal end, deep to flexor hallucis longus, and joins a communicating branch of the fibular artery; calcaneal branches that arise just proximal to the termination of the posterior tibial artery, pierce the flexor retinaculum and supply the skin and fat behind the calcaneal tendon; and the artery of the tarsal canal. The posterior tibial artery may be much reduced in length or in calibre, in which case, the fibular artery then takes over its distal territory of supply and may consequently be increased in size.

The named branches of the posterior tibial artery are the circumflex fibular, nutrient, muscular, perforating, communicating, medial malleolar, calcaneal, fibular and medial and lateral plantar arteries.

Relations The posterior tibial artery is successively posterior to tibialis posterior, flexor digitorum longus, the tibia and the ankle joint. Proximally, gastrocnemius, soleus and the transverse intermuscular septum of the leg are superficial to the artery, and distally, it is covered only by skin and fascia. It is parallel with and approximately 2.5 cm anterior to the medial border of the calcaneal tendon; terminally, it is deep to the flexor retinaculum. The artery is accompanied by two veins and the tibial nerve. The nerve is at first medial to the artery but soon crosses behind it and subsequently becomes largely posterolateral in position.

Circumflex fibular artery

The circumflex fibular artery, which sometimes arises from the anterior tibial artery, passes laterally round the neck of the fibula through the soleus to anastomose with the inferior medial and lateral genicular and anterior tibial recurrent arteries. It supplies bone and related articular structures.

Nutrient artery of the tibia

The nutrient artery of the tibia is one of the largest of the nutrient arteries. It arises from the posterior tibial artery near its origin. After giving off a few muscular branches, it descends into the bone immediately distal to the soleal line.

Muscular branches

Muscular branches are distributed to soleus and the deep flexors of the leg.

Perforating branches

Approximately five fasciocutaneous perforators emerge between flexor digitorum longus and soleus, and pass through the deep fascia, often accompanying the perforating veins that connect the deep and superficial venous systems. The arterial perforators then divide into anterior and posterior branches to supply the regional periosteum and skin. These vessels are utilized in raising medial fasciocutaneous perforator flaps in the leg.

Communicating branch

The communicating branch runs posteriorly across the tibia approximately 5 cm above its distal end, deep to flexor hallucis longus, to join a communicating branch of the fibular artery.

Medial malleolar branches

The medial malleolar branches pass round the medial malleolus to the medial malleolar network, which supplies the skin.

Calcaneal branches

Calcaneal branches arise just proximal to the terminal division of the posterior tibial artery. They pierce the flexor retinaculum to supply fat and skin behind the calcaneal tendon and in the heel, and muscles on the tibial side of the sole; the branches anastomose with medial malleolar arteries and calcaneal branches of the fibular artery.

Fibular artery

The fibular artery arises from the posterior tibial artery approximately 2.5 cm distal to popliteus and passes obliquely to the fibula, descending along its medial crest either in a fibrous canal between tibialis posterior and flexor hallucis longus or within flexor hallucis longus (see Figs 76.4B, 78.4). Reaching the inferior tibiofibular syndesmosis, it divides into calcaneal branches that ramify on the lateral and posterior surfaces of the calcaneus. Proximally, it is covered by soleus and the transverse intermuscular septum between soleus and the deep muscles of the leg, and distally it is overlapped by flexor hallucis longus.

The fibular artery may branch high from the posterior tibial artery or may even branch from the popliteal artery separately, resulting in a true 'trifurcation'. It may also branch more distally from the posterior tibial artery, sometimes 7 or 8 cm distal to popliteus. Its size tends to be inversely related to the size of the other arteries of the leg. It may be reduced in size but is more often enlarged, when it may join, reinforce or even replace the posterior tibial artery in the distal leg and foot.

The fibular artery has muscular, nutrient, perforating, communicating and calcaneal branches.

Muscular branches

Multiple short branches supply soleus, tibialis posterior, flexor hallucis longus and the fibular muscles.

Nutrient artery

The nutrient artery branches from the main trunk approximately 7 cm from its origin and enters the fibula 14–19 cm from the apex of the head of the fibula.

Perforating branches

The main perforating branch traverses the interosseous membrane approximately 5 cm proximal to the lateral malleolus to enter the extensor compartment, where it anastomoses with the anterior lateral malleolar artery. Descending anterior to the inferior tibiofibular syndesmosis, it supplies the tarsus and anastomoses with the lateral tarsal artery. This branch is sometimes enlarged and may replace the dorsalis pedis artery.

Fasciocutaneous perforators from the lateral muscular branches pass along the posterior fibular fascial septum to penetrate the deep fascia and reach the skin. These vessels are utilized in raising fasciocutaneous posterolateral leg flaps.

Communicating branch

The communicating branch connects to a communicating branch of the posterior tibial artery approximately 5 cm proximal to the ankle.

Calcaneal branches

Calcaneal (terminal) branches anastomose with the anterior lateral malleolar and calcaneal branches of the posterior tibial artery.

Medial plantar artery

The medial plantar artery is the smaller terminal branch of the posterior tibial artery and passes distally along the medial side of the foot, medial to the medial plantar nerve (see Figs 76.4B, 79.26). At first deep to abductor hallucis, it runs distally between this muscle and flexor digitorum brevis, and supplies both. Near the first metatarsal base, its size, already diminished by muscular branches, is further reduced to a superficial stem that divides to form three superficial digital branches. These accompany the digital branches of the medial plantar nerve and join the first to third plantar metatarsal arteries. The main trunk of the medial plantar artery then runs on to reach the medial border of the hallux, where it anastomoses with a branch of the first plantar metatarsal artery.

Lateral plantar artery

The lateral plantar artery is the larger terminal branch of the posterior tibial artery (see Fig. 79.26). It passes distally and laterally to the fifth metatarsal base; the lateral plantar nerve is medial. (The medial and lateral plantar nerves lie between the corresponding plantar arteries.) Turning medially with the deep branch of the nerve, the lateral plantar artery reaches the interval between the first and second metatarsal bases, and unites with the dorsalis pedis artery to complete the deep plantar arch. As it passes laterally, it is first between the calcaneus and abductor hallucis, then between flexor digitorum brevis and flexor accessorius. Running distally to the fifth metatarsal base, it passes between flexor digitorum brevis and abductor digiti minimi, and is covered by the plantar aponeurosis, superficial fascia and skin.

Muscular branches supply the adjoining muscles. Superficial branches emerge along the intermuscular septum to supply the skin and subcutaneous tissue over the lateral part of the sole. Anastomotic branches run to the lateral border and join branches of the lateral tarsal and arcuate arteries. Sometimes, a calcaneal branch pierces abductor hallucis to supply the skin of the heel. Anastomosis between the medial and lateral plantar arteries superficial to the flexor digitorum brevis is sometimes present and is termed the superficial plantar arch.

Dorsalis pedis artery

The dorsalis pedis artery (see Figs 79.1, 79.25) is usually the continuation of the anterior tibial artery distal to the ankle. It passes to the proximal end of the first intermetatarsal space, where it turns into the sole between the heads of the first dorsal interosseous to complete the deep plantar arch, and provides the first plantar metatarsal artery.

The artery may be larger than normal, to compensate for a small lateral plantar artery. It often diverges laterally from its usual route. It may rarely be absent (Robertson et al 1990), in which event it is replaced by a large perforating branch of the fibular artery.

The dorsalis pedis artery gives rise to the tarsal, arcuate and first dorsal metatarsal arteries (see Figs 79.1, 79.10, 79.25).

Relations The dorsalis pedis artery crosses, successively, the talocrural articular capsule, talus, navicular and intermediate cuneiform and their ligaments; superficial to it are the skin, fasciae, inferior extensor retinaculum and, near its termination, extensor hallucis brevis. Medial to it is the tendon of extensor hallucis longus and lateral to it are the medial tendon of extensor digitorum longus and medial terminal branch of the deep fibular nerve. The tendons and navicular tuberosity are useful landmarks in palpation, or the planning of safe anatomical approaches in surgery of the ankle and foot.

Tarsal arteries

There are two tarsal arteries, lateral and medial (see Fig. 79.25). They arise as the dorsalis pedis artery crosses the navicular. The lateral tarsal artery runs laterally under extensor digitorum brevis; it supplies this muscle and the tarsal articulations, and anastomoses with branches of the arcuate, anterior lateral malleolar and lateral plantar arteries, and the perforating branch of the fibular artery. Two or three medial tarsal arteries ramify on the medial border of the foot and join the medial malleolar arterial network.

Arcuate artery

The arcuate artery (see Fig. 79.25) arises near the medial cuneiform, passes laterally over the metatarsal bases, deep to the tendons of the digital extensors, and anastomoses with the lateral tarsal and plantar arteries. It supplies the second to fourth dorsal metatarsal arteries, running distally superficial to the corresponding dorsal interossei, and divides into two dorsal digital branches for the adjoining toes in the interdigital clefts. Proximally, these branches receive proximal perforating branches from the deep plantar arch. Distally, they are joined by distal perforating branches from the plantar metatarsal arteries. The fourth dorsal metatarsal artery sends a branch to the lateral side of the fifth toe.

The frequency of the arcuate artery has been reported to range from 10% to 67%, depending on the precise definition of the artery (DiLandro et al 2001).

First dorsal metatarsal artery

The first dorsal metatarsal artery (see Fig. 79.25) arises just before the dorsalis pedis artery enters the sole. It runs distally on the first dorsal interosseous and divides at the cleft between the first and second toes. One branch passes under the tendon of extensor hallucis longus and supplies the medial side of the great toe; the other bifurcates to supply the adjoining sides of the great and second toes.

Cutaneous branches

The dorsalis pedis artery and its first dorsal metatarsal branch give rise to small direct cutaneous branches that supply the dorsal foot skin between the extensor retinaculum and the first web space. This vessel provides the basis for a fasciocutaneous flap raised from this region, and which may be used to cover superficial defects elsewhere.

Deep plantar arch

The deep plantar arch (see Fig. 79.26) is deeply situated, extending from the fifth metatarsal base to the proximal end of the first intermetatarsal space. Convex distally, it is plantar to the bases of the second to fourth metatarsals and corresponding interossei, but dorsal to the oblique part of adductor hallucis.

The deep plantar arch gives rise to three perforating and four plantar metatarsal branches, and numerous branches that supply the skin, fasciae and muscles in the sole. Three perforating branches ascend through the proximal ends of the second to fourth intermetatarsal spaces, between the heads of dorsal interossei, and anastomose with the dorsal metatarsal arteries. Four plantar metatarsal arteries extend distally between the metatarsals in contact with the interossei (see Fig. 79.26). Each divides into two plantar digital arteries, supplying the adjacent digital aspects. Near its division, each plantar metatarsal artery sends a distal perforating branch dorsally to join a dorsal metatarsal artery. The first plantar metatarsal artery springs from the junction between the lateral plantar and dorsalis pedis arteries, and sends a digital branch to the medial side of the great toe. The lateral digital branch for the fifth toe arises directly from the lateral plantar artery near the fifth metatarsal base. Haemorrhage from the deep plantar arch is difficult to control because of the depth of the vessel and its important close relations.

Surface anatomy The lateral plantar artery begins between the heel and medial malleolus, and crosses obliquely to a point 2.5 cm medial to the tuberosity of the fifth metatarsal. With a slight distal convexity, it reaches the proximal end of the first intermetatarsal space.

Arterial perforators of the lower limb and surgical flaps

Achieving adequate and aesthetically satisfactory skin and soft tissue cover for large, superficial tissue defects is a perennial challenge in the field of plastic and reconstructive surgery, and accounts for a substantial part of a plastic surgeon's workload. Generally, split-thickness and full-thickness skin grafts are suitable only for very superficial defects. To achieve tissue coverage for deeper and larger tissue defects, one of a variety of autologous tissue flaps may be used. A fasciocutaneous flap is composed of skin, fat and deep fascia (fascia musculorum); a lower-extremity fasciocutaneous flap (Pontén 1981) is very useful in the repair of soft tissue defects of the leg.

The viability of a flap transplanted from one part of the body to another is crucially dependent on the blood supply of the flap. An appreciation of the angiosome concept (Chs 6, 7), coupled with technological advances in reconstructive microsurgery, has stimulated the development and use of perforator (or perforator-based) flaps. These are flaps of skin or subcutaneous tissue supplied by one or more fascial 'perforators', i.e. arteries, which reach the suprafascial plexus either directly from a source vessel, or indirectly from some other neighbouring tissue (Harry et al 2009) (see Fig. 76.6). Perforator-based flaps are typically harvested with sparing of underlying muscle tissue and minimal trauma; their use is said to reduce postoperative pain, donor site morbidity and functional loss.

The lower limb is the largest donor site in the body for perforator-based flaps. Commonly used flaps include anterolateral thigh flaps, which provide a large amount of skin; superior and inferior gluteal artery perforator flaps used in breast reconstruction; vascularized fibular flaps for reconstruction of deficient bone; vascularized tensor fasciae latae flaps for tendon reconstruction; vascularized sural nerve flaps for nerve reconstruction; and the gracilis muscle flap, used for example in the reanimation of paralysed muscle.

In the context of perforator flap surgery, the lower limb may be considered in terms of four anatomic regions: gluteal; anterior hip and thigh; knee and leg; ankle and foot. Each lower limb accounts for approximately 23% of the total body surface area (thigh 10.5%, leg 6.5%, buttock 2.5% and foot 3.5%) and contains an average of 90 arterial perforators.

Gluteal region

The gluteal region of the lower limb has an average of 21 perforators, which arise from three main source arteries: namely, the superior and inferior gluteal and the internal pudendal arteries (see Fig. 76.7). The flaps based on these perforators are used as free flaps for breast reconstruction and as local flaps for covering defects in the sacral and perineal region.

Hip and thigh region

The hip and thigh region has six source arteries and an average of 50 arterial perforators. The thigh can be divided into four areas: anteromedial; anterolateral and trochanteric; posteromedial; and posterolateral. The perforators that supply the anteromedial thigh are derived from the femoral artery, and those for the anterolateral thigh are derived from branches of the lateral circumflex femoral artery. Perforators that supply the skin over the posteromedial and posterolateral thigh regions are derived from the profunda femoris artery and the popliteal arteries. Skin flaps based on the superficial circumflex iliac, superficial external pudendal and superficial inferior epigastric arteries have been used as local flaps, tube pedicles and free tissue transfers. Other popular skin flaps are TFL (tensor fasciae latae) perforator flaps, ALT (anterolateral thigh) and AMT (anteromedial thigh) flaps, the gracilis perforator flap and posterior thigh flaps.

Knee and leg region

The perforators, which arise from the rich vascular anastomosis around the patella, generally traverse the tendon of quadriceps femoris to supply the skin over the patella and the peripatellar region (see Fig. 76.7). The skin flaps based on these perforators may be used as distally based or proximally based flaps to cover defects over the knee and popliteal region. The direct cutaneous branch of the popliteal artery and a superficial sural artery, which accompanies the sural nerve, provide additional perforators to the skin over the back of the knee. The posterior tibial artery gives off an average of ten perforators to the skin covering the anteromedial and posterior parts of the leg. In the upper third of the leg, the perforating vessels are predominantly muscular and periosteocutaneous, while in the lower third, the perforating vessels are mainly direct subcutaneous types. They anastomose with the perforating branches of the anterior tibial artery anteriorly and fibular artery posteriorly. Inferiorly, the posterior tibial artery forms a rich anastomotic ring around the ankle joint with the fibular and anterior tibial arteries. Perforators from these vessels supply the calcaneal tendon and the overlying skin. The posterior tibial artery gives off three direct cutaneous perforators in the lower part of the leg; a distally based skin or adipofascial flap based on one of these perforators may be used to reconstruct a defect over the anterior or the posterior aspect of the lower leg. The anterior tibial artery gives off an average of six perforators, which supply the anterolateral part of the leg. They emerge in two longitudinal rows; one perforator is fairly large and accompanies the superficial fibular nerve. A small skin flap based on any one of these perforators may be used to cover small defects over the tibia, and a neurocutaneous flap that includes the superficial fibular nerve may be used.

The fibular artery has an average of five perforators. A constant perforator pierces the deep fascia approximately 5 cm above the lateral malleolus and divides into an ascending and a descending branch. A vascularized fibula graft based on the fibular artery is now the standard graft used in reconstruction of the mandible, while small fasciocutaneous and adipofascial flaps based on the perforators of the fibular artery are useful in covering soft tissue defects over the heel and proximal part of the foot.

Ankle and foot region

The arteries around the ankle and in the foot are the medial and lateral calcaneal arteries, medial and lateral plantar arteries and the dorsalis pedis artery (see Fig. 76.7). In the foot, the two plantar arteries with communicating arteries from the dorsalis pedis artery give rise to multiple small perforators. In the sole of the foot, the perforators emerge on either side of the plantar aponeurosis, and also pass through it, to supply the skin. 'Island flaps' from these perforators may be advanced to reconstruct small defects in the weight-bearing area. The skin of the sole of the foot is highly specialized and therefore, ideally, defects in this region should be reconstructed using local skin.

VENOUS DRAINAGE OF THE HEAD AND NECK

The veins of the head and neck can be subdivided into three groups: veins of the exterior of the head and face; veins of the neck; diploic, meningeal, intracranial veins and dural venous sinuses.

Venous drainage of the face

The veins of the face are subject to considerable variations; the following description concerns those that are relatively constant (see Fig. 36.20).

Ophthalmic veins

Superior and inferior ophthalmic veins link the facial and intracranial veins. The superior ophthalmic vein forms posteromedial to the upper eyelid from tributaries that connect anteriorly with the facial and supraorbital veins. It runs with the ophthalmic artery, receiving corresponding tributaries and traverses the superior orbital fissure to end in the cavernous sinus. The inferior ophthalmic vein begins in a network near the anterior region of the orbital floor and medial wall, receiving veins from inferior rectus and inferior oblique, the lacrimal sac and eyelids. It runs back above inferior rectus and often joins the superior ophthalmic vein or may reach the cavernous sinus independently. It is connected with the pterygoid plexus via small branches that pass through the inferior orbital fissure.

Central retinal vein

The central retinal vein traverses the optic nerve then leaves it to pursue a long course in the subarachnoid space before entering the cavernous sinus or the superior ophthalmic veins. It receives a central vein from within the optic nerve.

Supratrochlear vein

The supratrochlear vein starts on the forehead from a venous network connected to the frontal tributaries of the superficial temporal vein. Veins from this network form a single trunk that descends to the bridge of the nose, near the midline and parallel with its contralateral fellow. The veins are joined by a nasal arch across the nose and then diverge, each joining a supraorbital vein to form the facial vein near the medial canthus of the eye.

Supraorbital vein

The supraorbital vein begins near the zygomatic process of the frontal bone, connecting with branches of the superficial and middle temporal veins. It passes medially above the orbital opening, pierces orbicularis oculi and unites with the supratrochlear vein near the medial canthus of the eye to form the facial vein. A branch passes through the supraorbital notch, where it receives veins from the frontal sinus and frontal diploë, and subsequently connects with the superior ophthalmic vein.

Facial vein

The facial vein is the main vein draining the face. After receiving the supratrochlear and supraorbital veins, it travels obliquely downwards by the side of the nose, passes under zygomaticus major, risorius and platysma, descends to the anterior border of masseter and then passes over the surface of the muscle. The facial vein initially lies behind the more tortuous facial artery but it crosses the artery at the lower border of the mandible and enters the neck, where it runs obliquely back under platysma. Here it lies superficial to the submandibular gland, digastric and stylohyoid (see Fig. 35.13). Just anteroinferior to the mandibular angle, it is joined by the anterior division of the retromandibular vein, and then descends superficial to the loop of the lingual artery, the hypoglossal nerve and external and internal carotid arteries, to enter the internal jugular vein near the greater cornu of the hyoid bone, i.e. in the upper angle of the carotid triangle. Near its end, a large branch often descends along the anterior border of sternocleidomastoid to join the anterior jugular vein. Its uppermost segment, above its junction with the superior labial vein, is often termed the angular vein.

Near its origin, the facial vein connects with the superior ophthalmic vein, both directly and via the supraorbital vein, and so is linked to the cavernous sinus. On the face, the facial vein receives tributaries from the side of the nose and, below this, an important deep facial vein from the pterygoid venous plexus. It also receives the inferior palpebral, superior and inferior labial, buccinator, parotid and masseteric veins. The portion of the facial vein that lies below the mandible receives submental, tonsillar, external palatine (paratonsillar) and submandibular veins, vena comitans of the hypoglossal nerve (sometimes), and the pharyngeal and superior thyroid veins.

Superficial temporal vein

A widespread venous network across the scalp receives branches from the supratrochlear, supraorbital, posterior auricular and occipital veins. Anterior and posterior tributaries from this network unite above the zygomatic arch to form the superficial temporal vein on each side. The vein accompanies its artery, usually lying behind it, crosses the posterior root of the zygoma and enters the parotid gland. In its course it receives the parotid veins, rami draining the temporomandibular joint, and the anterior auricular, transverse facial and middle temporal veins. The middle temporal vein receives the orbital vein (formed by the lateral palpebral veins), pierces the temporal fascia and then passes back between the layers of the fascia to join the superficial temporal vein just above the level of the zygomatic arch. The superficial temporal vein joins the maxillary vein in the parotid gland to form the retromandibular vein.

Buccal, mental and infraorbital veins

The buccal, mental and infraorbital veins drain the cheek and chin regions and pass into the pterygoid venous plexus.

Pterygoid venous plexus

The pterygoid plexus is found partly between temporalis and lateral pterygoid and partly between lateral and medial pterygoid. Sphenopalatine, deep temporal, pterygoid, masseteric, buccal, dental, greater palatine and middle meningeal veins and a branch or branches from the inferior ophthalmic vein are all tributaries. The plexus is connected by the deep facial vein with the facial vein and with the cavernous sinus through the sphenoidal emissary foramen, foramen ovale and foramen lacerum. Its deep temporal tributaries are often connected with tributaries of the anterior diploic vein and thus with the middle meningeal veins.

Maxillary vein

The maxillary vein is a short trunk that accompanies the first part of the maxillary artery. It is derived from the confluence of veins from the pterygoid plexus, and passes back between the sphenomandibular ligament and the neck of the mandible, joining the superficial temporal vein to form the retromandibular vein.

Retromandibular vein

The retromandibular vein descends in the parotid gland, between the external carotid artery and, superficially, the facial nerve. It divides into an anterior branch going forwards to join the facial vein and a posterior branch that joins the posterior auricular vein to form the external jugular vein. Occasionally it is not connected to the external jugular vein, which is then small and the anterior jugular is often enlarged.

Posterior auricular vein

The posterior auricular vein arises in a parieto-occipital network that also drains into tributaries of the occipital and superficial temporal veins. It descends behind the auricle to join the posterior division of the retromandibular vein in, or just below, the parotid gland, to form the external jugular vein. It receives a stylomastoid vein and tributaries from the cranial surface of the auricle, drains the region of the scalp behind the ear and drains into the external jugular vein.

Occipital vein

The occipital vein begins in a posterior network in the scalp, pierces the cranial attachment of trapezius, turns into the suboccipital triangle and joins the deep cervical and vertebral veins. It may be joined by a vein draining the diploë in the occipital bone and then passes to either the internal jugular, posterior auricular, deep cervical or vertebral veins. Emissary veins connect the occipital vein to the intracranial venous sinuses via the mastoid and parietal foramina and through the posterior condylar canal and occipital protuberances.

Venous drainage of the neck

Veins in the neck show considerable variation. They are superficial or deep to the deep fascia but are not entirely separate systems. Superficial veins are tributaries – some with specific names, given below – of the anterior, external and posterior jugular veins (see Figs 35.13–35.14). They drain a much smaller volume of tissue than the deep veins. The latter drain all but the subcutaneous structures, mostly into the internal jugular vein and also into the subclavian vein.

External jugular vein

The external jugular vein mainly drains the scalp and face, although it also drains some deeper parts. The vein is formed by the union of the posterior division of the retromandibular vein with the posterior auricular vein and begins near the mandibular angle just below or in the parotid gland (see Fig. 33.3A). It descends from the angle to the mid-clavicle, running obliquely, superficial to sternocleidomastoid, to the root of the neck. Here, it crosses the deep fascia and ends in the subclavian vein, lateral or anterior to scalenus anterior. There are valves at its entrance into the subclavian but they do not prevent regurgitation. Its wall is adherent to the rim of the fascial opening. It is covered by platysma, superficial fascia and skin, and is separated from sternocleidomastoid by deep cervical fascia. The vein crosses the transverse cutaneous nerve and lies parallel with the great auricular nerve, posterior to its upper half. In size, the external jugular vein is inversely proportional to the other veins in the neck and may be double. Between the entrance into the subclavian vein and a point approximately 4 cm above the clavicle, the vein is often dilated, producing a so-called sinus. In addition to formative tributaries, the external jugular receives the posterior external jugular and, near its end, transverse cervical, suprascapular and anterior jugular veins. In the parotid gland, it is often joined by a branch from the internal jugular vein. The occipital vein occasionally joins it.

Posterior external jugular vein

The posterior external jugular vein begins in the occipital scalp and drains the skin and the superficial muscles that lie posterosuperior in the neck. It usually joins the middle part of the external jugular vein.

Anterior jugular vein

The anterior jugular vein arises near the hyoid bone from the confluence of the superficial submandibular veins. It descends between the midline and the anterior border of sternocleidomastoid. Turning laterally, low in the neck, deep to sternocleidomastoid but superficial to the infrahyoid strap muscles, it either joins the end of the external jugular vein or may enter the subclavian vein directly (see Fig. 33.3A). In size, it is usually inverse to the external jugular vein. It communicates with the internal jugular vein and receives the laryngeal veins and sometimes a small thyroid vein. There are usually two anterior jugular veins, united just above the manubrium by a large transverse jugular arch, receiving the inferior thyroid tributaries. They have no valves and may be replaced by a midline trunk.

Internal jugular vein

The internal jugular vein collects blood from the skull, brain, superficial parts of the face and much of the neck. It begins at the cranial base in the posterior compartment of the jugular foramen, where it is continuous with the sigmoid sinus. At its origin, it is dilated as the superior bulb, which lies below the posterior part of the tympanic floor. The internal jugular vein descends in the carotid sheath, and unites with the subclavian vein, posterior to the sternal end of the clavicle, to form the brachiocephalic vein (see Fig. 35.14). Near its termination, the vein dilates into the inferior bulb, above which is a pair of valves. The jugular bulb is a dynamic structure; it forms after 2 years of age and its size stabilizes in adulthood (Friedmann et al 2011).

The tributaries are the inferior petrosal sinus, facial, lingual, pharyngeal, superior and middle thyroid veins, and occasionally the occipital vein. The internal jugular vein may communicate with the external jugular vein. The thoracic duct opens near the union of the left subclavian and internal jugular veins, and the right lymphatic duct opens at the same site on the right.

Relations From above, rectus capitis lateralis, the transverse process of the atlas, levator scapulae, scalenus medius, scalenus anterior, the cervical plexus, the phrenic nerve, thyrocervical trunk, vertebral vein and the first part of the subclavian artery all lie posterior to the vein. On the left, the internal jugular crosses anterior to the thoracic duct. The internal and common carotid arteries and the vagus nerve are medial to the vein, the vagus lying between and posterior to the vessels. The accessory nerve is sometimes found posterior to the vein. Superficially, the internal jugular vein is overlapped above, then covered below, by sternocleidomastoid, and is crossed by the posterior belly of digastric and the superior belly of omohyoid. The parotid gland, styloid process, accessory nerve (almost always), and the posterior auricular and occipital arteries cross the vein superior to the posterior belly of digastric. Between digastric and omohyoid, the sternocleidomastoid arteries and the inferior root of the ansa cervicalis cross the internal jugular vein, the nerve often passing between the vein and the common carotid artery. Below omohyoid, the vein is covered by the infrahyoid muscles and sternocleidomastoid and is crossed by the anterior jugular vein. Deep cervical lymph nodes lie along the internal jugular, mainly on its superficial aspect. At the root of the neck, the right internal jugular vein is separated from the common carotid artery, but the left usually overlaps its artery. At the base of the skull, the internal carotid artery is anterior to the vein, separated from it by the ninth to twelfth cranial nerves.

Tympanic body The tympanic body (glomus jugulare) is ovoid, 0.5 mm long and 0.25 mm broad, and lies in the adventitia of the upper part of the superior bulb of the internal jugular vein. It is similar in structure to the carotid body and is presumed to have a similar function. The predominant cell type has morphological similarities to adrenal chromaffin cells, being derived from the neural crest. Cells obtained from glomus jugulare paragangliomas show spontaneous neurite outgrowth in culture and have vasoactive intestinal peptide (VIP)-like activity. The tympanic body may be present as two or more parts near the tympanic branch of the glossopharyngeal nerve or the auricular branch of the vagus as they lie within their canals in the petrous part of the temporal bone. Tumours of tympanic bodies often involve the adjacent cranial nerves and present with pulsatile tinnitus and a husky voice. These tumours grow into the hypotympanum of the middle ear; intraluminal growth, both proximally and distally, is well recognized.

Inferior petrosal sinus

The inferior petrosal sinus leaves the skull through the anterior part of the jugular foramen, crosses lateral or medial to the ninth to eleventh cranial nerves, and joins the superior jugular bulb.

Lingual veins

The lingual veins follow two routes. The dorsal lingual vein drains the dorsum and side of the tongue, joins the lingual vein accompanying the lingual artery between hyoglossus and genioglossus, and enters the internal jugular vein near the greater cornu of the hyoid bone. The deep lingual vein begins near the tip of the tongue and runs back, lying near the mucous membrane on the inferior surface of the tongue. Near the anterior border of hyoglossus, it joins a sublingual vein from the sublingual salivary gland to form the vena comitans nervi hypoglossi, which runs back between mylohyoid and hyoglossus with the hypoglossal nerve to join either the facial, internal jugular or lingual vein (see Fig. 33.3A).

Pharyngeal veins

The pharyngeal veins begin in a pharyngeal plexus external to the pharynx. They receive meningeal veins and a vein from the pterygoid canal, and usually end in the internal jugular vein, but may sometimes end in the facial, lingual or superior thyroid vein.

Superior thyroid vein

The superior thyroid vein is formed by deep and superficial tributaries corresponding to the arterial branches in the upper part of the thyroid gland (see Figs 35.13–35.14). It accompanies the superior thyroid artery, receives the superior laryngeal and cricothyroid veins, and ends in the internal jugular or facial vein.

Middle thyroid vein

The middle thyroid vein drains the lower part of the thyroid gland and receives veins from the larynx and trachea. It crosses anterior to the common carotid artery to join the internal jugular vein behind the superior belly of omohyoid. The middle thyroid vein is encountered early in thyroid, parathyroid and pharyngeal pouch surgery and usually ligated. It is one of only two structures that lie within the paracarotid tunnel, the other being a non-recurrent laryngeal nerve.

Vertebral vein

Numerous small tributaries from internal vertebral plexuses leave the vertebral canal above the posterior arch of the atlas and join small veins from local deep muscles in the suboccipital triangle. Their union produces a vessel that enters the foramen in the transverse process of the atlas, forms a plexus around the vertebral artery, and descends through successive transverse foramina to end as the vertebral vein. The vein emerges from the sixth cervical transverse foramen, and descends, at first anterior, then anterolateral, to the vertebral artery. It may join the deep cervical vein before it opens superoposteriorly into the brachiocephalic vein (see Fig. 33.4); the opening has a paired valve. As it descends, it passes behind the internal jugular vein and anterior to the first part of the subclavian artery. A small accessory vertebral vein usually descends from the vertebral plexus, traverses the seventh cervical transverse foramen and turns forwards between the subclavian artery and the cervical pleura to join the brachiocephalic vein. The vertebral artery or vein can be encountered deep in Chassaignac's triangle and care should be taken when dissecting this area.

The vertebral vein is connected with the sigmoid sinus by a vessel in the posterior condylar canal, when the latter exists. It also receives branches from the occipital vein, the veins draining the prevertebral muscles, and the internal and external vertebral plexuses. It is joined by the anterior vertebral and deep cervical veins and sometimes, near its end, by the first intercostal vein.

Anterior vertebral vein

The anterior vertebral vein starts in a plexus around the upper cervical transverse processes, descends near the ascending cervical artery between the attachments of scalenus anterior and longus capitis, and opens into the end of the vertebral vein.

Deep cervical vein

The deep cervical vein accompanies its artery between semispinales capitis and cervicis. It is formed in the suboccipital region by the union of communicating branches of the occipital vein, the veins draining the suboccipital muscles, and veins from plexuses around the cervical spines. It passes forwards between the transverse process of the seventh cervical vertebra and the neck of the first rib to end in the inferior part of the vertebral vein.

Subclavian vein

The subclavian vein is the central continuation of the axillary vein (see Fig. 48.4). It starts at the outer border of the first rib, which it crosses. Initially deep to the clavicular head of pectoralis major and then to subclavius, which is a buffer between it and the overlying medial portion of the clavicle, the vein then runs deep to the insertion of sternocleidomastoid. Only the superior margins of the vein may rise above the medial end of the clavicle, or the entire vein may do so. The phrenic nerve and the inferior part of scalenus anterior lie posteriorly. The subclavian vein joins the internal jugular vein to form the brachiocephalic vein at the medial border of scalenus anterior, behind the sternoclavicular joint (see Fig. 35.14). A pair of valves usually lies within 2 cm of this junction. The subclavian vein receives, as tributaries, the external jugular, dorsal scapular and, sometimes, the anterior jugular veins. The trifurcation of subclavian, external and internal jugular veins is demonstrable by a forced expiration (Valsalva) manoeuvre, when the distended veins rise up above the sternoclavicular joint, filling the fossa above the jugular notch of the sternum. Main lymphatic vessels join the subclavian veins at, or very close to, this junction with the internal jugular vein. The left subclavian vein receives the thoracic duct; the right receives the right lymphatic duct (see Fig. 35.16). There is a risk of air embolism after wounding of the subclavian, external or internal jugular veins.

Dural venous sinuses, emissary veins and diploic veins

Dural venous sinuses form a complex network of venous channels that drain blood from the brain and cranial bones (see Figs 25.2, 25.4, 26.10–26.11, 26.13). They lie between the endosteal and meningeal layers of dura mater, are lined by endothelium, lack valves and their walls are devoid of muscular tissue (Kılıç and Akakın 2008). They develop initially as venous plexuses and, to a variable degree, most adult sinuses retain that form. Plexiform arrays of small veins adjoin the superior and inferior sagittal and straight sinuses, and, less frequently, the transverse sinuses. Ridges of 'spongy' venous tissue, venous lacunae, often project into the lumina of the superior sagittal and transverse sinuses (Browder and Kaplan 1976, Kaplan and Browder 1976).

The plexiform nature of the cranial venous sinuses and their wide connections with cerebral and cerebellar veins vary considerably, particularly in earlier years, e.g. in infancy, the falx cerebelli may contain large plexiform channels and venous lacunae that augment the occipital sinus. These variations must be established for each patient by catheter-based angiography, magnetic resonance (MR) venography or computed tomographic (CT) venography, when clinical necessity arises. The existence of arteriovenous shunts has been inferred from the demonstration of a connection between the middle meningeal arteries and the superior sagittal sinus (Browder and Kaplan 1976). Dural arteriovenous fistulae are thought to be acquired lesions that form in an area of thrombosis within a sinus. If the sinus remains completely thrombosed, venous drainage from these lesions takes place through cortical veins: when the sinus remains closed, the elevated pressure within the cortical veins receiving the arterial flow carries the risk of haemorrhage. If the sinus is partially open, venous drainage is usually into the involved sinus.

The named sinuses are the superior and inferior sagittal, straight, transverse, sigmoid, occipital, cavernous, intercavernous, superior and inferior petrosal, sphenoparietal, basilar and marginal.

Superior sagittal sinus

The superior sagittal sinus runs in the attached convex margin of the falx cerebri. It grooves the internal surface of the frontal bone, the adjacent margins of the two parietal bones and the squamous part of the occipital bone (see Figs 25.2, 25.5, 26.10). It begins near the crista galli, a few millimetres posterior to the foramen caecum, and receives primary tributaries from the cortical veins draining the superior part of the frontal, parietal and occipital lobes, and the anterior part of the orbital surface of the frontal lobe. The sinus is triangular in cross-section, with the apex directed downwards, and is continuous with the falx cerebri. Its lumen is invaded in its intermediate third by projections from its dural walls that may divide the lumen into superior and inferior channels. It is narrow anteriorly, and widens gradually to approximately 1 cm in diameter as it runs posteriorly to enter the confluence of the sinuses, situated to one side (usually the right) of the internal occipital protuberance (see Fig. 25.4). (The confluence of the sinuses is also known as the torcular Herophili or the torcula, although the term actually describes the bony gutter in which the confluence lies.) At the confluence of the sinuses, the superior sagittal sinus usually deviates to become continuous with the right transverse sinus, but also usually connects with the occipital and contralateral transverse sinuses. The size and degree of communication of the channels meeting at the confluence are highly variable; any sinus involved may be duplicated, narrowed or widened near the confluence.

There are usually two or three lateral venous lacunae on each side of the midline, named frontal (small), parietal (large) and occipital (intermediate) lacunae; they tend to become confluent in the elderly, producing a single elongated lacuna on each side. Fine fibrous bands cross the lacunae, and numerous arachnoid granulations project into them (see Fig. 25.6). The lacunae mainly drain diploic and meningeal veins. The cortical veins typically pass beneath the lacunae on their way to the sinus. The superior anastomotic vein (of Trolard), the largest cortical vein that connects the superficial Sylvian (middle cerebral) vein and the superior sagittal sinus, often runs in the precentral, central or postcentral sulci. Near its posterior end, the superior sagittal sinus receives veins from the pericranium that pass through parietal foramina. Acute and complete thrombosis of the superior sagittal sinus is an extremely severe condition causing acute elevation of the intracranial pressure and herniation. Slow and progressive occlusion of the sinus, as is typical for sagittal meningiomas, may be compensated by the development of collateral venous drainage with no clinical consequences.

Inferior sagittal sinus

The inferior sagittal sinus is located in the posterior half or two-thirds of the free margin of the falx cerebri (see Fig. 25.2). It increases in size posteriorly, ends in the straight sinus, and receives veins from the falx and sometimes from the medial surfaces of the cerebral hemispheres (anterior pericallosal veins).

Straight sinus

The straight sinus lies in the junction of the falx cerebri and the tentorium cerebelli (see Figs 25.2, 26.10). It runs posteroinferiorly as a continuation of the inferior sagittal sinus and drains into the transverse sinus, most commonly into the left sinus. It is not (or is only tenuously) continuous with the superior sagittal sinus. Its tributaries include the great cerebral vein (of Galen), formed by the convergence of the internal cerebral and basal veins, and some superior cerebellar veins which may drain initially into the medial tentorial sinus (a short sinus within the tentorium).

Transverse sinus

The transverse sinuses are attached to the internal occipital protuberance (see Figs 25.2, 25.4). They begin at the confluence of the sinuses: one, usually the right, is directly continuous with the superior sagittal sinus, and the other is directly continuous with the straight sinus. The right transverse sinus is typically larger and drains blood from the superficial parts of the brain. The left transverse sinus mainly drains blood from the deep parts of the brain. On each side, the sinuses run in the attached margin of the tentorium cerebelli, first on the squama of the occipital bone, then on the mastoid angle of the parietal bone. Each follows a gentle anterolateral curve, increasing in size as it does so, to the posterolateral part of the petrous temporal bone, where it turns down as a sigmoid sinus that ultimately becomes continuous with the internal jugular vein. The transverse sinuses receive tributaries from the lateral temporal surface and basal surface of the temporal and occipital lobes. The inferior anastomotic vein (of Labbé) is the largest vein that connects the veins of the Sylvian fissure with the transverse sinus. All tributaries of each transverse sinus may drain first into a lateral tentorial sinus. The superior petrosal sinuses drain into the transition between the transverse and sigmoid sinuses on each side (see Figs 25.2, 25.4).

Sigmoid sinus

The sigmoid sinuses are continuations of the transverse sinuses, beginning where these leave the tentorium cerebelli (see Figs 25.4, 25.7). Each sigmoid sinus curves inferomedially in a groove on the mastoid process of the temporal bone, crosses the jugular process of the occipital bone and turns forwards to the superior jugular bulb, lying posteriorly in the jugular foramen. Anteriorly, a thin plate of bone separates its upper part from the mastoid antrum and mastoid air cells. The sigmoid sinus is connected with pericranial veins via mastoid and condylar emissary veins. Neurosurgical approaches to the lateral aspect of the posterior fossa (cerebellopontine angle) are classified as retrosigmoid, when the craniectomy is located just behind the sigmoid sinus, and presigmoid, when the mastoid bone in front of the sinus is drilled away to provide a more anterior corridor into the posterior fossa.

Superior petrosal sinus

The superior petrosal sinuses are small, narrow sinuses that drain the cavernous sinus into the transverse sinus on each side (see Figs 25.2, 25.4, 25.8–25.9). Each leaves the posterosuperior part of the cavernous sinus and runs posterolaterally in the attached margin of the tentorium cerebelli, crosses superior to the trigeminal nerve to lie in a groove on the superior border of the petrous part of the temporal bone, and ends by joining the transverse sinus at the point where this curves down to become the sigmoid sinus. The superior petrosal sinuses may receive cerebellar and brainstem veins, such as the superior petrosal vein, and, rarely, the inferior cerebral and tympanic veins; they are connected with the inferior petrosal sinuses and the basilar plexus.

Inferior petrosal sinus

The inferior petrosal sinuses drain the cavernous sinus into the internal jugular veins (see Figs 25.4, 26.10). They begin at the posteroinferior aspect of the cavernous sinus and run back in the petroclival fissure (a groove between the petrous part of the temporal bone and the basilar part of the occipital bone). On each side, the inferior petrosal sinus then passes through the anteromedial part of the jugular foramen, accompanied by a meningeal branch of the ascending pharyngeal artery, and descends obliquely backwards to drain into the superior jugular bulb. It sometimes drains via a vein in the hypoglossal canal to the suboccipital vertebral plexus.

The inferior petrosal sinuses are often plexiform. Each receives labyrinthine veins via the cochlear canaliculus and the vestibular aqueduct, and tributaries from the medulla oblongata, pons and inferior cerebellar surface. The venous spaces in the sphenopetroclival area, which are filled anteriorly by blood from the cavernous sinus, medially by blood from the basilar plexus, and laterally by blood from the superior petrosal sinus, typically drain into the inferior petrosal sinuses (Iaconetta et al 2003).

Cavernous sinus

The cavernous sinuses are two large venous plexuses that lie on either side of the body of the sphenoid bone (see Fig. 25.4). They extend from the superior orbital fissure to the apex of the petrous temporal bone, with an average length of 2 cm and width of 1 cm. The cavity of the cavernous sinus is formed when the two layers of dura that cover the anterior aspect of the pituitary gland separate from each other at the lateral margin of the sella: the outer (endosteal) layer continues laterally to form the anterior (sphenoidal) wall of the cavernous sinus, and the inner (meningeal) layer remains attached to the pituitary gland and runs back towards the dorsum sellae to form the medial (sellar) wall of the cavernous sinus. The posterior dural wall is posterior to the dorsum sellae and upper clivus, and is shared with the basilar plexus. The lateral wall extends from the superior orbital fissure to the petrous apex, and separates the cavernous sinus from Meckel's cave, which is inferior and posterior to the sinus. The roof of the cavernous sinus is formed by the clinoidal triangle (the dura lining the lower margin of the anterior clinoid process anteriorly), and the oculomotor triangle (the patch of dura between the anterior and posterior clinoids and the petrous apex).

Each sinus contains the cavernous segment of the internal carotid artery which is associated with a perivascular sympathetic plexus. From proximal to distal, the cavernous carotid artery has several portions, named short ascending, posterior genu, horizontal, anterior genu. The anterior genu of the cavernous carotid artery continues as the paraclinoidal segment of the carotid artery, which typically protrudes into the cavity of the sphenoidal sinus. The cavernous carotid gives off two major arterial branches: the meningohypophysial and inferolateral trunks (see Fig. 25.9B). The meningohypophysial trunk typically arises from the posterior genu and gives off the inferior hypophysial, tentorial and dorsal meningeal arteries. The inferolateral trunk arises a few millimetres distal to the meningohypophysial and is distributed around the nerves on the lateral wall of the sinus. (For more detailed descriptions of these branches, including their main variations, see Krisht et al (1994), Reisch et al (1996), Tekdemir et al (1998).)

Several cranial nerves run forwards through the cavernous sinus to enter the orbit via the superior orbital fissure (see Fig. 25.9). The oculomotor and trochlear nerves and the ophthalmic division of the trigeminal nerve all lie in the lateral wall of the sinus. The abducens nerve enters the cavernous sinus by passing inferior to the petrosphenoidal ligament within a dural tunnel (Dorello's canal) just posterior to the short ascending portion of the cavernous carotid artery, and then runs on the inferolateral side of the horizontal portion of the cavernous carotid artery, just medial to the ophthalmic nerve. The space between the trochlear and ophthalmic nerves at the lateral wall of the sinus, known as the infratrochlear or Parkinson's triangle, gives access to the horizontal and posterior genu portions of the cavernous carotid and the meningohypophysial trunk, and the abducens nerve. Unlike the ophthalmic division of the trigeminal nerve, the maxillary division of the trigeminal nerve does not run through the cavernous sinus or its lateral wall, but courses beneath the dura of the middle cranial fossa below the level of the cavernous sinus (Abhinav et al 2017).

Several major venous spaces or compartments can be identified within the sinus in relation to the cavernous carotid artery: superior, posterior, inferior and lateral (Fernandez-Miranda et al 2017, modified from Harris and Rhoton 1976). The superior and inferior ophthalmic veins drain into the inferior space; the basilar plexus and inferior petrosal sinus drain into the posterior space; the superior petrosal sinus opens into the superior space; and the superficial middle cerebral vein, the inferior cerebral veins and the sphenoparietal sinus may drain into the lateral compartment. Veins traversing the emissary sphenoidal foramen, foramen ovale and foramen lacerum and, less frequently, the central retinal vein and frontal tributary of the middle meningeal vein, also drain into the cavernous sinus.

Tumours (meningiomas, haemangiomas, schwannomas) can arise within the cavernous sinus or extend into the cavernous sinus from adjacent regions, typically, these are pituitary adenomas that invade the medial wall of the sinus. Transcranial microsurgical approaches enter the cavernous sinus through the lateral wall (infratrochlear triangle) or roof (oculomotor triangle) of the sinus. Recently introduced endoscopic endonasal approaches facilitate access to the cavernous sinus from its anterior (sphenoidal) and medial (sellar) walls and provide access to the posterior clinoids (Fernandez-Miranda et al 2014). (For more detailed descriptions of the microsurgical anatomy of the cavernous sinus, see Dolenc (1987), Umansky et al (1994), Seoane et al (1998), Yasuda et al (2004), Dolenc and Rogers (2009), Fernandez-Miranda et al (2014, 2017).)

Caroticocavernous sinus fistula and cavernous sinus thrombosis

Direct communication between the intracavernous portion of the internal carotid artery and the cavernous sinus, creating a caroticocavernous sinus fistula (CCF), may occur as a result of either severe head trauma or aneurysmal vessel disease. The classic signs are ptosis, proptosis (which may be pulsatile), chemosis, periorbital oedema, and extraocular dysmotility causing diplopia secondary to a combination of third, fourth and sixth cranial nerve palsies. Hypo- or hyperaesthesia in the distribution of the ophthalmic division of the trigeminal nerve and a decreased corneal reflex may also be detected. There may be evidence of dilated, tortuous retinal veins and papilloedema. These changes can cause permanent blindness. CCFs are most commonly treated by passing a catheter up the carotid into the fistula, and then occluding it with dilatable balloons or flexible metal coils. Any spreading infection involving the upper nasal cavities, paranasal sinuses, cheek (especially near the medial canthus), upper lip, anterior nares, or even an upper incisor or canine tooth, may very rarely lead to septic thrombosis of the cavernous sinuses; infected thrombi pass from the facial vein or pterygoid venous complex into the sinus via either ophthalmic veins or emissary veins that enter the cranial cavity through the foramen ovale. This is a critical medical emergency with a high risk of disseminated cerebritis and cerebral venous thrombosis.

Intercavernous sinuses

The two cavernous sinuses are connected by superior, inferior and posterior intercavernous sinuses, and the basilar plexus (see Figs 25.4, 25.8). The superior and posterior intercavernous sinuses lie in the anterior and posterior attached borders of the diaphragma sellae and they thus form a complete circular venous sinus. The inferior intercavernous sinuses are irregular and plexiform in nature, and commonly encountered in a surgical transnasal approach to the pituitary gland. Obliteration of any intercavernous sinus has no clinical consequences because all connections are valveless and the direction of flow in them is reversible.

Basilar venous plexus

The basilar sinus and plexus consist of interconnecting channels between the two layers of dura mater on the clivus (see Fig. 25.4). The basilar venous plexus interconnects the cavernous sinuses and inferior and superior petrosal sinuses, and joins the internal vertebral venous plexus.

Sphenoparietal sinus

The sphenoparietal sinuses are inconstant dural venous channels that lie under the lesser wings of the sphenoid bone, near their posterior edge (see Fig. 25.4). Each sinus curves medially to open into the anterior part of the cavernous sinus, and receives small veins from the adjacent dura mater and sometimes from the frontal ramus of the middle meningeal vein. In its middle course, each may also receive connecting rami from the superficial middle cerebral vein, temporal lobe veins and the anterior temporal diploic vein. When these connections are well developed, the sphenoparietal sinus is a large channel. It has been suggested that the term sphenoparietal sinus should be abandoned on the basis that it is not an anatomical entity, but an artificial combination of two independent meningeal vessels, namely the parietal portion of the anterior branch of the middle meningeal veins and the sinus of the lesser wing of the sphenoid (Ruíz et al 2004).

Occipital sinus

The occipital sinus is the smallest of the sinuses and is typically larger in children. It lies in the attached margin of the falx cerebelli (see Fig. 25.4) and is occasionally paired. It starts near the foramen magnum in several small channels, one of which joins the end of the sigmoid sinus and connects with the internal vertebral plexuses. It ends in the confluence of the sinuses.

Marginal sinus

The marginal sinus encircles the foramen magnum. It communicates anteriorly with the basilar plexus and posteriorly with the occipital sinus. It typically drains to the sigmoid sinus or jugular bulb by small sinuses and may connect extracranially to the internal vertebral venous plexus or the paravertebral or deep cervical veins in the suboccipital region.

Emissary veins

Emissary veins traverse cranial apertures and connect intracranial venous sinuses and extracranial veins. Some are relatively constant, others may be absent. These connections are of clinical significance in determining the spread of infection from extracranial foci to venous sinuses, e.g. the spread of infection from the mastoid to the venous sinuses or from the paranasal sinuses to the cavernous sinus, and they may provide alternative drainage pathways in cases of venous sinus thrombosis.

The following emissary veins have been recognized. A mastoid emissary vein in the mastoid foramen connects the sigmoid sinus with the posterior auricular or occipital veins. A parietal emissary vein in the parietal foramen connects the superior sagittal sinus with the veins of the scalp. The venous plexus of the hypoglossal canal (occasionally a single vein) connects the sigmoid sinus and the internal jugular vein. A supracondylar emissary vein connects the sigmoid sinus and veins in the suboccipital triangle via the posterior condylar canal. A plexus of emissary veins (venous plexus of the foramen ovale) connects the cavernous sinus to the pterygoid plexus via the foramen ovale. Two or three small veins traverse the foramen lacerum and connect the cavernous sinus and the pharyngeal veins and pterygoid plexus. A vein in the emissary sphenoidal foramen (of Vesalius) connects the cavernous sinus with the pharyngeal veins and pterygoid plexus. The internal carotid venous plexus, which passes through the carotid canal, connects the cavernous sinus and the internal jugular vein. A vein may traverse the foramen caecum and connect nasal veins with the superior sagittal sinus. An occipital emissary vein usually connects the confluence of the sinuses with the occipital vein through the occipital protuberance, and also receives the occipital diploic vein. The occipital sinus connects with variably developed veins around the foramen magnum (marginal sinuses) and thus with the vertebral venous plexuses; this pathway provides an alternative venous drainage when the jugular vein is blocked or tied. The ophthalmic veins are potentially emissary because they connect intracranial and extracranial veins. The petrosquamous sinus arises from the dorsolateral portion of the transverse sinus before its confluence with the superior petrosal sinus, courses over the lateral superior surface of the petrous part of the temporal bone, and drains anteroinferiorly into the retromandibular vein and anteromedially into the pterygoid venous plexus. It usually disappears during the development of adult venous patterns in the last three months of prenatal life.

Meningeal veins

Meningeal veins include the middle meningeal and diploic veins. They begin from plexiform vessels in the dura mater and drain into efferent vessels in the outer dural layer that connect with lacunae associated with some of the cranial sinuses. Intracranial veins also communicate with extracranial veins via emissary veins.

Middle meningeal vein

The frontal (anterior) branch of the middle meningeal vein crosses the floor of the middle cranial fossa, from either the foramen ovale or foramen spinosum, to the pterion, usually in the form of two parallel channels that accompany the middle meningeal artery. The vein subsequently passes cranially along the anterior margin of the parietal squama to empty into the venous lakes of the superior sagittal sinus. As they course under the most lateral aspect of the lesser sphenoidal wing, the anterior branches of the middle meningeal vessels are contained for a short distance within a bony canal, the sphenoparietal canal (of Trolard), which they leave to enter a groove on the internal surface of the parietal squama. The veins lie closer to the bone than the artery, sometimes occupying separate grooves, and are particularly liable to tear in cranial fractures. Before it enters the sphenoparietal canal, the anterior branch of the middle meningeal vein usually connects with the sinus of the lesser sphenoidal wing, which is connected medially with the anterior and superior aspect of the cavernous sinus by a channel that crosses over the superior ophthalmic vein to reach the sinus. The parietal (posterior) trunk of the middle meningeal vein may traverse the foramen spinosum to end in the pterygoid venous plexus. The frontal trunk may also reach this plexus via the foramen ovale, or it may end in the sphenoparietal or cavernous sinus (see Fig. 25.4). The middle meningeal vein receives meningeal tributaries and small inferior cerebral veins, and connects with the diploic and superficial middle cerebral veins. It frequently bears arachnoid granulations.

Diploic veins

The diploic veins are large, thin-walled vessels that occupy channels in the diploë of the cranial bones (see Fig. 25.10B). Four main trunks are usually described: the frontal, anterior and posterior temporal, and occipital diploic veins. The frontal vein opens into the supraorbital vein and the superior sagittal sinus; the anterior temporal vein is confined mainly to the frontal bone, and opens into the sphenoparietal sinus and one of the deep temporal veins through an aperture in the greater wing of the sphenoid; the posterior temporal vein lies in the parietal bone and empties into the transverse sinus either through an opening at the mastoid angle of the parietal bone or through the mastoid foramen; the occipital vein, the largest of the four, is confined to the occipital bone and may open externally into the occipital vein or internally into either the transverse sinus or the confluence of the sinuses.

VENOUS DRAINAGE OF THE BRAIN AND SPINAL CORD

Cerebral hemispheres

Superficial and deep cerebral veins drain the surfaces and the interior of the cerebral hemisphere, respectively. The superficial veins may be divided into three groups, namely superior, middle and inferior. Eight to 12 superior cerebral veins drain the superolateral and medial surfaces of each hemisphere. They mainly follow the sulci, although some pass across gyri. They ascend to the superomedial border of the hemisphere, where they receive small veins from the medial surface, and then open into the superior sagittal sinus. Superior cerebral veins in the anterior part of the hemisphere join the sinus almost at right angles. The larger posterior veins are directed obliquely forwards, against the direction of flow in the sinus, an arrangement which may resist their collapse when intracranial pressure is raised.

Middle cerebral veins

The superficial middle cerebral vein drains most of the lateral surface of the hemisphere, and follows the lateral fissure to end in the cavernous sinus. A superior anastomotic vein runs posterosuperiorly between the superficial middle cerebral vein and the superior sagittal sinus, thus connecting the superior sagittal and cavernous sinuses. An inferior anastomotic vein courses over the temporal lobe and connects the superficial middle cerebral vein to the transverse sinus. The deep middle cerebral vein drains the insular region and joins the anterior cerebral and striate veins to form a basal vein. Regions drained by the anterior cerebral and striate veins correspond approximately to those supplied by the anterior cerebral artery and the central branches which enter the anterior perforated substance. The basal veins pass back alongside the interpeduncular fossa and midbrain, receive tributaries from this vicinity and join the great cerebral vein.

Inferior cerebral veins

Inferior cerebral veins on the orbital surface of the frontal lobe join the superior cerebral veins and thus drain to the superior sagittal sinus. Those on the temporal lobe anastomose with basal veins and middle cerebral veins, and drain to the cavernous, superior petrosal and transverse sinuses.

Basal vein

The basal vein begins at the anterior perforated substance by the union of a small anterior cerebral vein, which accompanies the anterior cerebral artery, a deep middle cerebral vein, which receives tributaries from the insula and neighbouring gyri and runs in the lateral cerebral fissure, and striate veins, which emerge from the anterior perforated substance. The basal vein passes back round the cerebral peduncle to the great cerebral vein and receives tributaries from the interpeduncular fossa, inferior horn of the lateral ventricle, parahippocampal gyrus and midbrain.

Internal cerebral vein

The internal cerebral vein drains the deep parts of the hemisphere and the choroid plexuses of the third and lateral ventricles. It is formed near the interventricular foramen, behind the column of the fornix, primarily by union of the thalamostriate and choroidal veins, although numerous smaller veins from surrounding structures also converge here.

Thalamostriate vein

The thalamostriate vein runs anteriorly, between the caudate nucleus and thalamus, and receives many tributaries from both.

Choroidal vein

The choroidal vein runs a convoluted course along the whole choroid plexus, and receives veins from the hippocampus, fornix, corpus callosum and adjacent structures. After their formation, the two internal cerebral veins travel back parallel to one another beneath the splenium of the corpus callosum, where they unite to form the great cerebral vein.

Great cerebral vein

The great cerebral vein is a short median vessel which curves sharply up around the splenium of the corpus callosum and opens into the anterior end of the straight sinus after receiving the right and left basal veins.

Brainstem

The veins of the brainstem form a superficial venous plexus deep to the arteries. Veins of the medulla oblongata drain into the veins of the spinal cord or the adjacent dural venous sinuses, or into variable radicular veins that accompany the last four cranial nerves to either the inferior petrosal or occipital sinuses, or to the superior bulb of the jugular vein. Anterior and posterior median medullary veins may run along the ventral median fissure and dorsal median sulcus, to become continuous with the spinal veins in corresponding positions. Pontine veins, which may include a median vein and a lateral vein on each side, drain into the basal vein, cerebellar veins, the petrosal or transverse sinuses or the venous plexus of the foramen ovale. Veins of the midbrain join the great cerebral vein (of Galen) or the basal vein.

The veins of the cerebellum drain mainly into sinuses adjacent to them or, from the superior surface, into the great cerebral vein. The cerebellar veins course on the cerebellar surface, and consist of superior and inferior groups. Superior cerebellar veins either run anteromedially across the superior vermis to the straight sinus or great cerebral vein, or they run laterally to the transverse and superior petrosal sinuses. Inferior cerebellar veins include a small median vessel that runs backwards on the inferior vermis to enter the straight or sigmoid sinus. Laterally coursing vessels join the inferior petrosal and occipital sinuses.

Spinal cord

Intramedullary veins within the substance of the spinal cord drain into a circumferential plexus of surface veins, the coronal plexus (venous plexus of the pia mater). Six tortuous longitudinal channels are usually identified within this plexus: anterior and posterior spinal veins (anterior and posterior median veins) and four others that run on either side of the ventral and dorsal nerve roots (see Fig. 47.15). Only the anterior spinal vein, which drains the central grey matter, is consistently complete. It receives sulcal veins and small pial veins from the coronal plexus and is largest in calibre in the lumbosacral region. The posterior spinal vein is frequently variable, appearing plexiform in some segments and as a single channel in others. These vessels connect freely and drain superiorly into the cerebellar veins and cranial sinuses, and segmentally into medullary veins mainly. The segmental veins drain into the intervertebral veins and thence into the external vertebral venous plexuses (see Fig. 46.21), the caval and azygos systems.

Segmental veins

Anterior and posterior radiculomedullary veins run along some of the ventral and dorsal roots. Like the medullary feeder arteries, they are largest in the cervical and lumbar regions of the cord, but do not necessarily occur in the same segments as the medullary feeders. They drain the cord but not the roots themselves. Very small anterior and posterior radicular veins occur in most spinal segments, accompanying and draining the ventral and dorsal roots and some of the cord at the points of entry and exit of the rootlets; they usually drain into the intervertebral veins.

VENOUS DRAINAGE OF THE VERTEBRAL COLUMN

Veins draining the vertebral column form intricate plexuses along the entire column, external and internal to the vertebral canal (see Fig. 46.21) (Groen et al 2004). Both groups are devoid of valves, anastomose freely with each other, and join the intervertebral veins. Interconnections are widely established between these plexuses and longitudinal veins early in fetal life. When development is complete, the plexuses drain into the caval and azygos/ascending lumbar systems via named veins that accompany the arteries described above.

The veins also communicate with cranial dural venous sinuses and with the deep veins of the neck and pelvis. The venous complexes associated with the vertebral column can dilate considerably, and can form alternative routes of venous return in patients with major venous obstruction in the neck, chest or abdomen. The absence of valves allows pathways for the wide and sometimes paradoxical spread of malignant disease and sepsis. Pressure changes in the body cavities are transmitted through these venous plexuses and thus to the cerebrospinal fluid, though the cord itself may be protected from such congestion by valves in the small veins that drain from the cord into the internal vertebral plexus.

External vertebral venous plexuses

The external vertebral venous plexuses are anterior and posterior. They anastomose freely, and are most developed in the cervical region. Anterior external plexuses are anterior to the vertebral bodies, communicate with basivertebral and intervertebral veins, and receive tributaries from vertebral bodies. Posterior external plexuses lie posterior to the vertebral laminae and around spines and transverse and articular processes. They anastomose with the internal plexuses and join the vertebral, posterior intercostal and lumbar veins.

Internal vertebral venous plexuses

The internal vertebral venous plexuses are embedded in epidural fat, supported by a network of collagenous fibres (Chaynes et al 1998). These thin-walled channels receive tributaries from the bones, red bone marrow and spinal cord. They form a denser network than the external plexuses and are arranged vertically as four interconnecting longitudinal vessels: two anterior and two posterior.

The anterior internal plexuses are large plexiform veins on the posterior surfaces of the vertebral bodies and intervertebral discs. They flank the posterior longitudinal ligament, beneath which they are connected by transverse vessels into which the large basivertebral veins open. The posterior internal plexuses, on each side in front of the vertebral arches and ligamenta flava, anastomose with the posterior external plexuses via veins that pass through and between the ligaments. The internal plexuses interconnect by venous rings near each vertebra. Around the foramen magnum, they form a dense network connecting with vertebral veins, occipital and sigmoid sinuses, the basilar plexus, the venous plexus of the hypoglossal canal and the condylar emissary veins.

Basivertebral veins

The basivertebral veins are paired valveless veins that drain the pars spongiosa of the vertebral bodies into the internal and external vertebral venous plexuses. In each segment, they emerge horizontally from foramina in the vertebral bodies. Posteriorly, they drain into the transverse branches of the anterior internal vertebral plexuses. Anteriorly, they drain directly into the anterior external vertebral venous plexus. The basivertebral veins enlarge in advanced age.

Intervertebral veins

Branches of the anterior internal plexuses drain into retrocorporal veins that join the posterior internal venous plexuses to form intervertebral veins. As their name suggests, these veins accompany the spinal nerves through intervertebral foramina; they drain in craniocaudal sequence into the vertebral, posterior intercostal, lumbar and lateral sacral veins. Upper posterior intercostal veins may drain into the caval system via brachiocephalic veins, whereas the lower intercostals drain into the azygos system. Lumbar veins are joined longitudinally in front of the transverse processes by the ascending lumbar veins, in which they may terminate. Alternatively, they may proceed around the vertebral bodies to drain into the inferior vena cava. Whether the basivertebral or intervertebral veins contain effective valves is uncertain but experimental evidence strongly suggests that their blood flow can be reversed (Batson 1957). This may explain how pelvic neoplasms, e.g. carcinoma of the prostate, may metastasize in vertebral bodies: the cells spread into the internal vertebral plexuses via their connections with the pelvic veins when blood flow is temporarily reversed by raised intra-abdominal pressure or postural alterations (Pearce 2006).

VENOUS DRAINAGE OF THE UPPER LIMB

The upper limb is drained by widely interconnected superficial and deep groups of vessels. The superficial veins are subcutaneous and lie in the superficial fascia. The deep group of veins drains the tissues beneath the deep fascia of the upper limb and is connected to the superficial system by perforating veins. The deep veins accompany the arteries, usually as venae comitantes, becoming the axillary vein, and ultimately the subclavian vein. Both groups have valves, which are more numerous in the deep group.

Superficial veins

The superficial group starts as an irregular dorsal arch on the back of the hand and includes the cephalic, basilic, median cubital and additional antebrachial veins and their tributaries.

Dorsal and palmar digital veins

Dorsal digital veins pass along the sides of the fingers, joined by oblique branches (see Fig. 51.4). They unite from the adjacent sides of the digits into three dorsal metacarpal veins that form a dorsal venous network over the metacarpus (see Fig. 51.3). This is joined laterally by a dorsal digital vein from the radial side of the index finger and both dorsal digital veins of the thumb, and is prolonged proximally as the cephalic vein. Medially, a dorsal digital vein from the ulnar side of the little finger joins the network, which ultimately drains proximally into the basilic vein. A vein often connects the central parts of the network to the cephalic vein near the mid-forearm. Palmar digital veins connect to their dorsal counterparts by oblique veins that pass between metacarpal heads. They also drain to a plexus superficial to the palmar aponeurosis, extending over both thenar and hypothenar regions. The venous drainage of the hand is predominantly dorsal: flexion and extension of the digits compresses the veins within the tight dorsal skin envelope, promoting venous return.

Cephalic vein

The cephalic vein usually forms over the anatomical snuff-box on the radial side of the wrist from the radial end of the dorsal venous plexus (see Fig. 48.4). It curves proximally around the radial side of the forearm, receiving tributaries from both radial and ulnar aspects of the forearm, and continues anterior to the elbow, superficial to a groove between brachioradialis and biceps brachii. It crosses superficial to the lateral cutaneous nerve of the forearm, and ascends along the lateral aspect of the arm within the superficial fascia, lateral to biceps and between pectoralis major and deltoid, where it adjoins the deltoid branch of the thoraco-acromial artery (see Fig. 49.34). It enters the infraclavicular fossa, passes posterior to the clavicular head of pectoralis major, pierces the clavipectoral fascia, crosses the axillary artery and enters the axillary vein near the tip of the coracoid (see Fig. 48.4). It may connect with the external jugular vein by a branch anterior to the clavicle.

Accessory cephalic vein

The accessory cephalic vein may arise either from a dorsal forearm plexus or from the ulnar side of the dorsal venous network in the hand. It joins the cephalic vein distal to the elbow. A large oblique vein often connects the basilic and cephalic veins dorsally in the forearm.

Median cubital vein

The median cubital vein links the cephalic and basilic veins on the flexor aspect of the elbow. It receives a number of tributaries from the flexor aspect of the forearm and gives off the deep median vein, which pierces the fascial roof of the antecubital fossa to join the venae comitantes of the brachial artery. When the median cubital vein is large, so that it transfers most blood from the cephalic to the basilic vein, the proximal cephalic vein is either absent or much diminished.

Basilic vein

The basilic vein arises medially in the dorsal venous network of the hand (see Fig. 48.4). It ascends posteromedially in the forearm, inclining forwards to the anterior surface distal to the elbow, where it pierces the deep fascia and is joined by the median cubital vein. It then ascends superficially between biceps and pronator teres, and is crossed by filaments of the medial cutaneous nerve of the forearm that pass both superficial and deep to the vein. The basilic vein joins the venae comitantes of the brachial artery to form the axillary vein at the lower border of teres major.

Median vein of the forearm

The median vein of the forearm drains the superficial palmar venous plexus and ascends through the anterior part of the forearm to join either the basilic or the median cubital vein (see Figs 49.34, 50.30). It may divide distal to the elbow to join both veins.

Deep veins

Venae comitantes run with the radial and ulnar arteries to drain the deep and superficial palmar venous arches, respectively, and unite near the elbow as paired brachial veins. The radial veins are smaller and receive the deep dorsal veins of the hand. The ulnar veins are larger and drain the deep palmar venous arch. They connect with superficial veins near the wrist and receive the venae comitantes of the anterior and posterior interosseous arteries near the elbow. A large branch connects them to the median cubital vein.

Superior and deep palmar venous arches

Superficial and deep palmar venous arches accompany their arterial counterparts and receive correspondingly named tributaries; common palmar digital veins drain to the superficial arch and palmar metacarpal veins join the deep arch.

Palmar and dorsal metacarpal veins

Deep veins accompanying the dorsal metacarpal arteries receive perforating tributaries from the palmar metacarpal veins and end in the radial veins and the dorsal venous network over the metacarpus. This network is joined laterally by a dorsal digital vein from the radial side of the index finger and by both digital veins of the thumb, and is prolonged proximally as the cephalic vein.

Brachial veins

The brachial veins flank the brachial artery, as venae comitantes with tributaries similar to the arterial branches; they join the axillary vein near the lower margin of subscapularis. The medial branch often joins the basilic vein before it becomes the axillary vein.

Axillary vein

The axillary vein is the continuation of the basilic vein (see Fig. 48.4). It begins at the lower border of teres major and ascends to the outer border of the first rib, where it becomes the subclavian vein. It is joined by the brachial vein near subscapularis, and by the cephalic vein near its costal end; other tributaries follow the branches of the axillary artery. It lies medial to the axillary artery, which it partly overlaps. The medial pectoral nerve, medial cord of the brachial plexus, ulnar nerve and medial cutaneous nerve of the forearm lie between the artery and the vein. The medial cutaneous nerve of the arm is medial to the vein; the lateral group of axillary lymph nodes is posteromedial. There are a pair of valves near the distal end of the vein, and valves near the ends of the cephalic and subscapular veins.

VENOUS DRAINAGE OF THE THORAX

Pulmonary veins

There are usually four pulmonary veins, two from each lung. They originate from capillary networks in the alveolar walls and return oxygenated blood to the left atrium: they are devoid of valves. All the main tributaries of the pulmonary veins receive smaller tributaries, both intra- and intersegmental. By serial junctions, tributaries ultimately form a single lobar trunk (one for each lobe). Usually, there are three trunks in the right lung and two in the left: variations reflect the lobar arrangement of an individual. The right middle and superior lobar veins usually unite so that two veins, superior and inferior, leave each lung at the hilum: the superior pulmonary vein is anteroinferior to the pulmonary artery, and the inferior pulmonary vein is the most inferior hilar structure and slightly posterior (see Fig. 54.3). The right superior pulmonary vein is formed by the union of apical, anterior and posterior veins (draining the upper lobe) with a middle lobar vein formed by lateral and medial tributaries. The right inferior pulmonary vein is formed in the hilar region by the union of superior (apical) and common basal veins from the lower lobe. The union of superior and inferior basal tributaries forms the common basal vein. Occasionally the three right lobar veins remain separate. The right superior pulmonary vein passes posterior to the superior vena cava, and the inferior passes posterior to the right atrium.

The left superior pulmonary vein is formed by the union of apicoposterior, anterior and lingular veins. The left inferior pulmonary vein is formed by the union of the superior (apical) and common basal veins, the latter formed by the union of the superior and inferior basal veins. Both left superior and inferior pulmonary veins pass anterior to the descending thoracic aorta. Sometimes, the two left pulmonary veins form a single trunk, or they may be augmented by an accessory lobar vein from each lobe that unite to form a third left pulmonary vein.

The right and left pulmonary veins pass through the pericardia and open separately in the posterosuperior aspect of the left atrium (see Figs 57.3, 57.4B). Their terminations are separated medially by the oblique pericardial sinus, and laterally by smaller and variable pulmonary venous pericardial recesses that are directed superomedially.

The variable incorporation of the primitive pulmonary vein into the left atrium during development (Ch. 13) means that the number of main pulmonary veins may differ. Pulmonary vein atresia is a rare congenital anomaly (Kozak et al 2011). The left atrium is the heart chamber most posterior and median in position, and so the length of the left and right pulmonary veins is relatively equal, unlike the arteries and bronchi, where there are obvious left–right differences in length. The terminal parts of the pulmonary veins are surrounded by atrial myocardium; these areas represent potential accessory re-entrant circuits responsible for the initiation or maintenance of supraventricular tachycardias or atrial fibrillation and may be percutaneously ablated.

Cardiac veins

The cardiac venous system is divided into two major parts. The greater system consists of large vessels that lie within the subepicardial myocardium and drain most of the outer myocardium. These veins extend over the myocardial surface and do not adhere to topographical borders, although the larger collecting vessels lie within the interventricular sulci before draining into the coronary sinus (see Figs 57.4, 57.59). The intercommunicating parts of this system are the coronary sinus and its tributaries, the anterior cardiac venous system and the ventricular septal and atrial veins. The coronary sinus and its tributaries return blood to the right atrium from the entire heart (including its septa), except for the anterior region of the right ventricle and small, variable parts of both atria and the left ventricle. The anterior cardiac veins drain an anterior region of the right ventricle; this expands to include a region around the right cardiac border when the right marginal vein joins this group.

The smaller system functions primarily to return venous blood from the inner myocardial walls into the right atrium and ventricle and, to a lesser extent, into the left atrium and sometimes the left ventricle. It contains the smallest cardiac (Thebesian) veins that drain the subendocardial myocardium either directly, via connecting intramural arteries and veins, or indirectly, via subendocardial sinusoidal spaces.

Variants Attempts to categorize variations in cardiac venous circulation into types have not produced any accepted pattern. The coronary sinus may receive all the cardiac veins, except the smallest (Thebesian) veins, including the anterior cardiac veins, which may be reduced by diversion into the small cardiac vein and then to the coronary sinus.

Coronary sinus

Most cardiac veins drain into the wide coronary sinus, 2 or 3 cm long, lying in the inferior atrioventricular (coronary) sulcus between the left atrium and ventricle (see Fig. 57.4B,E). The sinus opens into the right atrium between the opening of the inferior vena cava and the right atrioventricular orifice. The opening may be guarded by the valve of the coronary sinus (Thebesian valve) a fold of endocardium (see Fig. 57.13); the fold may be absent or may cover completely the opening of the sinus. The tributaries of the coronary sinus are the great, small and middle cardiac veins, the posterior vein of the left ventricle and the oblique vein of the left atrium; all except the oblique vein have valves at their openings. Isolated absence of the coronary sinus has been reported, with coronary venous drainage into the pulmonary trunk (Ogawa et al 2013).

Great cardiac vein

The great cardiac vein begins at the cardiac apex, and ascends in the anterior interventricular sulcus to the atrioventricular sulcus, which it follows, passing to the left and posteriorly to enter the coronary sinus at its origin. It receives tributaries from the left atrium and both ventricles, including the large left marginal vein that ascends the left (obtuse) border of the heart. It usually courses superior to the arterial branches. The valve of Vieussens normally sits at the opening of the great cardiac vein at its junction with the oblique vein of the left atrium (this junction often representing the start of the coronary sinus); smaller diminutive valves may occur. The valve of Vieussens can impede the passage of a catheter into the great cardiac vein.

Small cardiac vein

The small cardiac vein lies in the anterior part of the inferior atrioventricular sulcus between the right atrium and ventricle, receiving blood from the inferior parts of each chamber and opening into the atrial end of the coronary sinus. The right marginal vein passes right, along (or near) the inferior cardiac border, and sometimes joins the small cardiac vein in the atrioventricular sulcus, typically opening directly into the right atrium.

Middle cardiac vein

The middle cardiac vein begins at the cardiac apex and runs posteriorly in the inferior interventricular sulcus to end in the coronary sinus near its atrial end. The vein is also described as meeting the great cardiac vein at the cardiac apex, and so forming, with the coronary sinus, a complete venous circle.

Inferior vein of the left ventricle

The inferior vein of the left ventricle (previously named the posterior vein of the left ventricle) lies on the inferior surface of the left ventricle, a little to the left of the middle cardiac vein. It usually opens into the middle of the coronary sinus, but may sometimes empty into the great cardiac vein. Rarely the inferior vein of the left ventricle is absent, in which case the left marginal vein drains most of the left ventricular wall.

Oblique vein of the left atrium

The diminutive oblique vein of the left atrium descends obliquely on the posterior aspect of the left atrium to join the coronary sinus. Its junction with the great cardiac vein marks the start of the coronary sinus and, often, the location of the valve of Vieussens. It is continuous above with the ligament of the left superior vena cava.

Left marginal vein

The left (obtuse) marginal vein courses over or near the left border of the heart, draining much of the left ventricular myocardium. It runs superficial to the marginal branch of the left coronary artery and usually drains into the great cardiac vein, although it may sometimes drain directly into the coronary sinus.

Anterior cardiac veins

The anterior cardiac veins drain the anterior part of the right ventricle. Usually two or three, and up to five, they ascend in subepicardial tissue to cross the anterior part of the atrioventricular sulcus, passing deep or superficial to the right coronary artery. They drain into the right atrium, near the atrioventricular sulcus, separately or in variable combinations. A subendocardial collecting channel, into which all may open, has been described.

Right marginal vein

The right marginal vein courses along the inferior (acute) border of the heart, draining adjacent parts of the right ventricle, and usually opens separately into the right atrium, although it may join the anterior cardiac veins or, less often, the coronary sinus. It is often grouped with the small cardiac veins, but it is larger in calibre, being comparable to or even wider than the anterior cardiac veins.

Smallest cardiac veins

The smallest cardiac (venae cordis minimae, Thebesian) veins, opening into all heart chambers, are difficult to demonstrate; their existence is not disputed. Their numbers and size are highly variable: vessels up to 2 mm in diameter open into the right atrium and vessels as small as 0.5 mm in diameter open into the right ventricle, all with valveless openings. Numerous smallest cardiac veins have been identified in the right atrium and ventricle but they are rarely found in the left side. Four types of smallest cardiac veins have been described. Venoluminal veins drain directly into the cardiac chambers; venosinusoidal veins drain into subendocardial sinusoids (which, in turn, drain into the cardiac chambers); arterioluminal veins connect small arteries and arterioles directly with the cardiac chambers; and arteriosinusoidal veins connect thin arteries or arterioles with subendocardial sinusoidal spaces.

Cardiac venous anastomoses

Widespread anastomoses occur at all levels of the cardiac venous circulation, on a scale exceeding that of the arteries and amounting to a venous plexus. Not only are adjacent veins often connected, but connections also exist between tributaries of the coronary sinus and those of the anterior cardiac veins. Abundant anastomoses occur at the cardiac apex and its anterior and posterior aspects. Like the coronary arteries, cardiac veins are connected with extracardiac vessels, particularly the vasa vasorum of the large vessels that are continuous with the heart.

Brachiocephalic veins

The right and left internal jugular and subclavian veins join to form the right and left brachiocephalic veins, respectively. The right and left brachiocephalic veins join to form the superior vena cava (see Figs 35.14, 52.7, 57.12).

In children, the length and diameter of the left brachiocephalic vein are closely related to height; the diameter reaches adult dimensions at around 10–12 years of age (Sanjeev and Karpawich 2006).

Right brachiocephalic vein

The right brachiocephalic vein is about 2.5 cm long. It is commonly formed posterior to the right sternoclavicular joint, although this may vary with study population. It descends almost vertically to join the left brachiocephalic vein, forming the superior vena cava posterior to the right second costal cartilage or first intercostal space and the associated part of the sternum. It is anterolateral to the brachiocephalic trunk and right vagus nerve; the right pleura, phrenic nerve and internal thoracic artery are initially posterolateral, becoming lateral inferiorly (see Figs 35.14, 56.7A). Its tributaries are the right vertebral, right internal thoracic and right inferior thyroid veins, and sometimes the right supreme intercostal (first right posterior intercostal) vein.

Left brachiocephalic vein

The left brachiocephalic vein is about 6 cm long. It arises posterior to left sternoclavicular joint, although this may vary with study population (see Fig. 52.7). It is anterior to the cervical part of the parietal pleura, and descends obliquely and to the right, posterior to the superior half of the manubrium sterni, reaching the right second costal cartilage or first intercostal space and the associated part of the sternum where it joins the right brachiocephalic vein to form the superior vena cava (see Figs 35.14, 57.12, 58.1). It is separated from the left sternoclavicular joint and manubrium by sternohyoid and sternothyroid, the thymus or its remnants, and areolar tissue. Near its junction with the right brachiocephalic vein it is partly covered by mediastinal right parietal pleura. It crosses anterior to the left internal thoracic, left subclavian, left common carotid and brachiocephalic arteries, the left phrenic and left vagus nerves, and the trachea (see Fig. 55.10B). The aortic arch is normally inferior to it. Its tributaries are the left vertebral, left internal thoracic, left inferior thyroid and left superior intercostal veins, and sometimes the left supreme intercostal (first left posterior intercostal), thymic and left pericardiacophrenic veins.

In children, the length and diameter of the left brachiocephalic vein are closely related to height; the diameter reaches adult dimensions at around 10–12 years of age (see Figs 58.10–58.11) (Sanjeev and Karpawich 2006).

Internal thoracic veins

The internal thoracic veins are formed by the union of the venae comitantes associated with the inferior half of the internal thoracic artery. Near the third costal cartilage, the veins unite and ascend medial to the artery to drain into the ipsilateral brachiocephalic vein. The internal thoracic veins have several valves. Their tributaries correspond to the branches of the internal thoracic artery and include the pericardiacophrenic veins, which run parallel to the phrenic nerves. The phrenic nerves are surrogate markers of the thymic border but are difficult to detect on CT: the pericardiacophrenic veins can be used in their place as an important landmark when differentiating thymic versus nonthymic tumours (Ozawa et al 2018).

Left superior intercostal vein

The left superior intercostal vein drains the second and third (sometimes fourth) left posterior intercostal veins (see Fig. 56.7B). It ascends obliquely anteriorly across the left aspect of the aortic arch, lateral to the left vagus nerve and medial to the left phrenic nerve, to open into the left brachiocephalic vein. It usually receives the left bronchial veins and sometimes the left pericardiacophrenic vein, and connects inferiorly with the accessory hemiazygos vein. It may be seen on a chest X-ray as the 'aortic nipple', not to be confused with a small lung nodule.

Superior vena cava

The superior vena cava returns blood to the heart from the tissues above the respiratory diaphragm. It is approximately 7 cm in length and is formed by the junction of the left and right brachiocephalic veins. According to conventional anatomical descriptions, the superior vena cava forms posterior to the right first costal cartilage. However, the majority of *in vivo* CT-based studies show that it forms posterior to the right second costal cartilage or first intercostal space and the associated part of the sternum. It descends vertically, being slightly convex to the right, and drains into the right atrium either posterior to the right third costal cartilage, or the third intercostal space, or the region posterior to the right fourth to fifth costal cartilages (see Fig. 52.4). Its inferior half is within the fibrous pericardium and it is covered anterolaterally by the visceral layer of serous pericardium (from which the retrocaval recess projects) (see Figs 57.1, 57.4A–B, 57.12). In children, the length and diameter of the superior vena cava are closely related to height; the diameter reaches adult dimensions at around 10-12 years of age (see Figs 58.10–58.11) (Sanjeev and Karpawich 2006). The superior vena cava is valveless.

Tributaries of the superior vena cava are the azygos vein and small veins from the pericardium and other mediastinal structures such as the thymus (see Figs 56.7A, 58.1).

Relations The anterior margins of the right lung and pleura are anterior and the pericardium intervenes inferiorly; these structures separate the superior vena cava from the right internal thoracic artery, transversus thoracis and the associated region of the anterior thoracic wall (see Figs

55.10A, 56.7A). The trachea and right vagus nerve are located posteromedially, the pleura and right lung are posterolateral, and the hilum of the right lung is posterior. The right phrenic nerve is an immediate right lateral relation, the brachiocephalic trunk and ascending aorta sit to the left of the superior part, and the aorta sits anteromedial to the inferior part, of the superior vena cava (see Fig. 57.4A).

Superior vena cava obstruction Superior vena cava obstruction is characterized by headaches, facial and neck venous congestion, and oedema, reflecting impaired venous drainage of the head, neck and upper limbs, and of the collateral circulation, resulting in chest wall telangiectasia. Several of the symptoms may subside with recumbency, or may be aggravated by standing up. The obstruction may be either partial or complete, and may occur suddenly or gradually. It is usually caused by mediastinally invasive right upper lobe primary bronchogenic carcinoma, metastatic involvement of the right paratracheal lymph nodes or non-Hodgkin lymphoma.

Haemorrhagic intrathoracic goitre, mediastinitis (either benign, malignant or fibrous), mediastinal haematoma, constrictive pericarditis, mediastinal cyst, thrombosis of the superior vena cava and sarcoidosis are less common aetiologies. Radiographic findings might include widening of the upper mediastinum on the frontal film or obliteration of the retrosternal space on the lateral film. Other correlative findings may include pulmonary or mediastinal masses, lymphadenopathy, an enlarged or obliterated azygos venous system, pleural effusion or rib notching. This is usually considered to be an oncological emergency and symptoms are often completely and promptly relieved by insertion of a vascular stent via the femoral vein or by radiotherapy to the affected region after a tissue diagnosis is established.

Variants of the brachiocephalic veins and superior vena cava The left and right brachiocephalic veins may enter the right atrium separately, the right vein descending like a normal superior vena cava. During embryological development, if the cardinal vein does not obliterate, it will persist as a left-sided superior vena cava. A left superior vena cava may have a slender connection with the right superior vena cava and subsequently cross the left side of the aortic arch to pass anterior to the hilum of the left lung before turning to enter the right atrium. It replaces the oblique vein of the left atrium (of Marshall) and coronary sinus, and receives all the normal tributaries of the coronary sinus. Other variations include drainage of the hemiazygos vein directly into the persistent left superior vena cava (Liu et al 2019). The left brachiocephalic vein sometimes projects above the manubrium (more frequently in childhood) and crosses the midline superior to the jugular notch, immediately anterior to the trachea. A left-sided superior vena cava may cause difficulties when placing a cardiac catheter, pacing or defibrillating electrodes because the angle between the left superior vena cava and the left subclavian vein is more acute than that normally found between the left subclavian and left brachiocephalic vein. Its calibre may also be smaller than that of the right. Even if insertion of a catheter into a left superior vena cava is possible, the angle at which the catheter enters the right atrium causes difficulty when attempting to place it into the right ventricle and pulmonary trunk; this generally leaves the catheter tip against the coronary sinus, making it difficult to obtain blood samples. In the majority of cases of persistent left superior venae cava, blood drains into the right atrium via the coronary sinus. When this does not happen, the coronary sinus is absent, and the persistent left superior vena cava drains directly into the right atrium. Cyanosis reflects a persistent right-to-left shunt and affected individuals have a higher risk for paradoxical embolism. Radiographically, there is a paramediastinal bulge anterior to the aortic arch. Electrocardiograms show a left P-wave axis. Diagnosis can be confirmed by cardiac catheterization and angiography. Persistent left superior vena cava may be associated with extracardiac conditions such as VACTERL association (vertebral defects, anal atresia, cardiac malformations, tracheo-oesophageal fistula with oesophageal atresia, radial and renal dysplasia, and limb anomalies); trisomy 21; 22q11; CHARGE association (coloboma, heart defects, choanal atresia, mental retardation, genital and ear anomalies); and 45 XO karyotype (Turner syndrome).

If the superior vena cava is duplicated, the right superior vena cava may drain into the right atrium and the left superior vena cava into the left atrium. Although double superior vena cava is largely asymptomatic, it is usually (along with a sole left-sided superior vena cava) associated with congenital cardiac anomalies, such as pulmonary stenosis, coarctation of the aorta, tetralogy of Fallot and atrial septal defects.

Azygos vein

The azygos vein has a variable origin at or below the level of the renal veins (see Figs 56.2–56.3, 56.14B). When present, the azygos lumbar vein ascends anterior to the bodies of the upper lumbar vertebrae and passes either posterior to, or through, the right diaphragmatic crus or traverses the aortic hiatus to the right of the cisterna chyli. Anterior to the body of the twelfth thoracic vertebra, it is joined by a venous trunk, formed by the union of the right ascending lumbar and subcostal veins, to form the azygos vein. In the absence of a lumbar azygos vein, this common venous trunk continues as the azygos vein. The azygos vein passes to the right, posterior to the right crus of the respiratory diaphragm, and ascends in the posterior mediastinum to the level of the body of the fourth thoracic vertebra, where it arches anteriorly, superior to the right pulmonary hilum, and joins the posterior aspect of the superior vena cava, just superior to the point where it passes into the pericardium.

In its course, the azygos vein lies anterior to the anterior longitudinal ligament covering the bodies of the lower eight thoracic vertebrae and the intervening intervertebral discs, and the right posterior intercostal arteries. Right lateral relations include the right sympathetic trunk and associated ganglia, the right greater thoracic splanchnic nerve, lung, and parietal pleura. Left lateral relations include the thoracic duct, descending thoracic aorta and, where the vein arches anteriorly, the oesophagus, trachea and right vagus nerve. Aortic pulsations may assist venous return in the azygos and hemiazygos veins, although only a small and variable number of imperfect valves are present. Inferiorly, the azygos vein lies posterior to the oesophagus, from which it is separated by a right-sided pleural recess, the azygo-oesophageal recess. There are age-related differences in the appearance of the contour of this recess on computed tomography (CT); the recess is dextroconvex below the age of 6 years of age, non-concave (equally divided between straight and convex) between 6 and 12 years of age and concave, as in adults, after the age of 12 years of age (Miller et al 1993).

The major tributaries of the azygos vein are the right intercostal veins (excluding the right supreme (first) intercostal vein that drains into the right brachiocephalic vein), the right superior intercostal vein (usually formed by the union of the second to fourth intercostal veins), the right ascending lumbar and subcostal veins, mediastinal, oesophageal, superior phrenic, pericardial and right bronchial veins, and the hemiazygos and accessory hemiazygos veins.

Numerous anastomoses exist between the tributaries and the main trunks of the azygos, hemiazygos and accessory hemiazygos veins, the inferior vena cava and the vertebral venous plexuses. These allow for alternate drainage pathways in case of segmental agenesis ('interruption') or thrombosis of the inferior vena cava.

Hemiazygos vein

The hemiazygos vein represents the left-sided equivalent of the more inferior part of the azygos vein. It originates in a similar fashion, from the union of the left lumbar ascending and subcostal veins, but exhibits greater variability, and may also connect with the left renal vein via the equivalent of the lumbar azygos vein. The hemiazygos vein crosses the midline anterior to the body of the eighth or ninth thoracic vertebra, passing posterior to the aorta and oesophagus, and either anterior or posterior to the thoracic duct, to join the azygos vein (see Figs 56.2, 56.5B). It receives mediastinal, oesophageal and the ninth to eleventh left posterior intercostal veins.

Accessory hemiazygos vein

The accessory hemiazygos vein functions as the left-sided mirror image of the superior portion of the azygos vein. It drains the left fifth to eighth posterior intercostal veins and occasionally the left bronchial veins, and usually crosses the midline anterior to the body of the seventh thoracic vertebra to join the azygos vein. The first left posterior intercostal vein drains directly into the left brachiocephalic vein, while the second to the fourth may connect indirectly to the accessory hemiazygos vein via the left superior intercostal vein (see Fig 56.7). The accessory hemiazygos vein typically joins the azygos vein directly, but it can join the hemiazygos vein before draining into the azygos vein. One or more prevertebral transversal anastomoses can be present.

Variants of the azygos venous system The origin, course, tributaries, anastomoses and termination of the azygos system of veins are all highly variable (Loukas and Tubbs 2016). The arrangement shown in Fig. 56.2 represents the most common pattern with a right-sided azygos vein. The left sided hemiazygos vein can be absent or underdeveloped, allowing direct drainage of the left intercostal veins into the azygos vein and/or the termination of the accessory hemiazygos vein into the left brachiocephalic vein either directly or by joining the left superior intercostal vein. In such cases, the azygos vein is located in a median position. In cases of common cardinal or anterior cardinal vein malformation, the azygos vein may enter the right atrium, right brachiocephalic vein or right subclavian vein rather than joining the superior vena cava.

In congenital interruption of the inferior vena cava or acquired thrombosis, the azygos system provides an alternative pathway for venous drainage. A higher than usual azygos arch may travel over the apical region of the right upper lobe within an accessory azygos fissure, covered by four pleural layers (two parietal and two visceral), and isolate a portion of the superior lobe of the right lung medially: the 'azygos lobe' (Loukas and Tubbs 2016). If present, the azygos fissure can be identified on chest radiograph as a fine radiopaque line. The azygos vein located within the azygos fissure often presents as a lung 'pseudo-nodule' on a chest radiograph; it is typically comma-shaped and should not be confused with a more rounded early lung carcinoma or metastasis.

Posterior intercostal veins

The 11 pairs of posterior intercostal veins accompany their respective arteries (see Fig. 52.4). Approaching the vertebral column, each vein receives a posterior tributary that returns blood from the dorsal musculature and skin and the external vertebral venous plexuses, and an intervertebral vein that drains the internal vertebral venous plexus. On both sides, the first posterior (supreme) intercostal vein ascends anterior to the neck of the first rib, then arches anteriorly, superior to the suprapleural membrane to drain into the ipsilateral brachiocephalic or vertebral vein. On the right side, the second, third and often the fourth veins form a right superior intercostal vein that drains into the arch of the azygos vein. The more inferior intercostal spaces drain directly into the azygos vein. On the left side, the second, third and sometimes the fourth veins form a left superior intercostal vein. Veins from the fifth (sometimes fourth) to eighth intercostal spaces drain into the accessory hemiazygos vein, and veins from the ninth to the eleventh intercostal spaces drain into the hemiazygos vein; it should be remembered that the azygos system is highly variable.

Posterior intercostal veins are so called to distinguish them from small anterior intercostal veins, which are tributaries of the internal thoracic and musculophrenic veins.

VENOUS DRAINAGE OF THE ABDOMEN AND PELVIS

External iliac vein

The external iliac vein is the proximal continuation of the femoral vein (see Figs 76.8, 77.49). It begins posterior to the inguinal ligament, ascends along the linea terminalis, and ends anterior to the sacro-iliac joint by joining the internal iliac vein to form the common iliac vein. On the right, it lies medial to the external iliac artery, gradually inclining behind it as it ascends. On the left, it is wholly medial. Disease of the external iliac artery can cause it to adhere closely to the vein at the point where it is in contact, and, particularly on the right side, the walls of the vessels can become fused, making dissection hazardous. The external iliac vein is crossed medially by the ureter and internal iliac artery and by the ductus deferens (males) or the round ligament of the uterus and ovarian vessels (females). Psoas major lies laterally, except where the artery intervenes. The vein is usually valveless but sometimes contains a single valve. Its tributaries are the inferior epigastric, deep circumflex iliac and pubic veins. Agenesis of the external iliac vein has been reported in association with Klippel–Trenaunay syndrome (Doğan et al 2003).

Inferior epigastric vein

One or two inferior epigastric veins accompany the inferior epigastric artery and drain into the external iliac vein just proximal to the inguinal ligament.

Deep circumflex iliac vein

The deep circumflex iliac vein is formed from venae comitantes of the corresponding artery. It joins the external iliac vein a little above the inferior epigastric vein after crossing anterior to the external iliac artery.

Pubic vein

The pubic vein connects the external iliac and obturator veins. It ascends on the pelvic surface of the pubis with the pubic branch of the inferior epigastric artery and occasionally replaces the normal obturator vein.

Internal iliac vein

The internal iliac vein is formed by the convergence of several veins above the greater sciatic foramen. It does not have the predictable trunks and branches of the internal iliac artery but its tributaries drain the same territories. It ascends posteromedial to the internal iliac artery to join the external iliac vein, forming the common iliac vein at the linea terminalis, anterior to the lower part of the sacro-iliac joint. It is covered anteromedially by parietal peritoneum. Its tributaries are the gluteal, internal pudendal and obturator veins, which originate outside the pelvis; the lateral sacral veins, which run from the anterior surface of the sacrum; and the middle anorectal, vesical, uterine and vaginal veins, which originate in the venous plexuses of the pelvic viscera (see Fig. 71.8).

The venous drainage of the leg can be blocked by thrombosis involving the external iliac systems and the inferior vena cava. Under these circumstances, the pelvic veins, particularly the internal iliac tributaries, enlarge and provide a major avenue of venous return from the femoral system. Surgical interference with these veins can seriously compromise venous drainage and precipitate oedema of one or both lower limbs.

Superior gluteal veins

The superior gluteal veins are the venae comitantes of the superior gluteal artery. They receive tributaries that correspond to the branches of the superior gluteal artery and enter the pelvis via the greater sciatic foramen, superior to piriformis. They join the internal iliac vein, frequently as a single trunk.

Inferior gluteal veins

The inferior gluteal veins are venae comitantes of the inferior gluteal artery. They begin proximally and posteriorly in the thigh, where they anastomose with the medial circumflex femoral and first perforating veins, and they enter the pelvis low in the greater sciatic foramen, joining to form a vessel that opens into the distal part of the internal iliac vein. The inferior gluteal and superficial gluteal veins connect by perforating veins (Doyle 1970). The gluteal veins probably have a venous 'pumping' role, and provide collaterals between the femoral and internal iliac veins.

Internal pudendal veins

The internal pudendal veins are venae comitantes of the internal pudendal artery and unite as a single vessel that drains into the internal iliac vein. They receive veins from the inferior anorectal veins and either the bulb of the penis and scrotum, or the clitoris and labia. The scrotal vessels are arranged in a dense subcutaneous network, which facilitates heat loss and regulation of scrotal temperature: simple arteriovenous anastomoses are common.

Obturator vein

The obturator vein begins in the proximal adductor region and enters the pelvis via the obturator foramen. It runs posteriorly and superiorly on the lateral pelvic wall below the obturator artery and between the ureter and internal iliac artery, and ends in the internal iliac vein. It is sometimes replaced by an enlarged pubic vein that joins the external iliac or the inferior epigastric veins (Sanna et al 2018).

Lateral sacral veins

The lateral sacral veins accompany the lateral sacral arteries and are interconnected by a sacral venous plexus.

Middle anorectal vein

The middle anorectal vein begins in the rectal venous plexus and drains the rectum and mesorectum. Variable in size, it runs laterally on the pelvic surface of levator ani to end in the internal iliac vein. The middle anorectal vein often receives tributaries from the urinary bladder and either the prostate and seminal gland (males) or the posterior aspect of the vagina (females).

Vesical plexus

The vesical plexus envelops the lower bladder and, in males, the prostatic base. It communicates with the prostatic plexus in males and the vaginal plexus in females and is drained by several vesical veins that usually unite to drain into the internal iliac vein.

Prostatic venous plexus

The prostatic venous plexus is posterior to the arcuate pubic ligament and the lower part of the pubic symphysis, and anterior to the urinary bladder and prostate. Its chief tributary is the deep dorsal vein of the penis and it drains into vesical and internal iliac veins.

Dorsal veins of the penis

Blood leaving the penis is drained by one of three venous systems: superficial, intermediate or deep (see Figs 74.22B, 74.23). The superficial veins are contained within the superficial fascia of the penis and on its dorsolateral surface. They receive blood from the skin of the body of the penis and prepuce and coalesce to form a single superficial dorsal vein that drains into the long saphenous vein via the superficial external pudendal veins.

The intermediate drainage system contains the circumflex and deep dorsal veins, which lie within and beneath the deep fascia of the penis. This system receives blood from the glans penis, corpus spongiosum and distal two-thirds of the penis. Circumflex veins originate in the corpus spongiosum and course around the corpora cavernosa to meet the deep dorsal vein of the penis perpendicularly. They are only present in the distal two-thirds of the body of the penis and there are 3–10 of them. Intermediate venules in the erectile tissue of the corpora cavernosa arise from the cavernous spaces and drain into a subtunical capillary plexus. This plexus gives rise to emissary veins that course obliquely through the tunica albuginea and drain either into the circumflex veins or directly into the deep dorsal vein. The deep dorsal vein lies in the midline groove between the two corpora cavernosa. It passes inferior to the pubic symphysis at the level of the suspensory ligament of the penis, leaving the body of the penis at the crus, and drains into the prostatic venous plexus.

Deep venous drainage occurs via the crural and cavernous veins of the penis, the latter travel almost the entire length of the corpus cavernosum and ultimately drain independent of the deep dorsal vein of the penis into the prostatic venous plexus (Hsu et al 2003). The emissary veins consolidate into 2–5 veins on the dorsomedial surface of the corpora cavernosa.

Uterine plexuses

The uterine plexuses extend lateral to the uterus in the broad ligaments, and communicate with the ovarian and vaginal plexuses. They are drained by uterine veins to the internal iliac veins.

Vaginal plexuses

The vaginal plexuses flank the vagina and connect with uterine, vesical and anorectal plexuses. They drain by vaginal veins to the internal iliac veins.

Common iliac veins

The common iliac vein is formed by the union of the external and internal iliac veins, anterior to the sacro-iliac joints (see Fig. 76.8). It ascends obliquely to end at the right side of the fifth lumbar vertebra, uniting at an acute angle with the contralateral vessel to form the inferior vena cava. The right common iliac vein is shorter and more nearly vertical, lying posterior and then lateral to its artery; the right obturator nerve passes posteriorly. The left common iliac vein is longer and more oblique and lies first medial, then posterior, to its artery. It is crossed anteriorly by the attachment of the sigmoid mesocolon and superior anorectal vessels. Each vein receives iliolumbar and, sometimes, lateral sacral veins. The left common iliac vein usually drains the median sacral vein. There are no valves in these veins.

The left common iliac vein occasionally ascends to the left of the aorta to the level of the kidney, where it receives the left renal vein and then crosses anterior to the aorta to join the inferior vena cava; this vessel represents the persistent caudal half of the left postcardinal or supracardinal vein.

Median sacral veins

The right and left medial sacral veins accompany the corresponding arteries anterior to the sacrum, where they unite to form a single vein that usually ends in the left common iliac vein, but sometimes ends at the common iliac junction.

Inferior vena cava

The inferior vena cava returns blood to the heart from infradiaphragmatic tissues. It is formed by the junction of the left and right common iliac veins anterior to the body of the fifth lumbar vertebra, about 1 cm to the right of the midline. It ascends anterior to the vertebral column, to the right of the aorta, and lies in a deep groove on the posterior surface of the liver, sometimes completely surrounded by liver tissue. It passes through the caval foramen of the respiratory diaphragm between the right folia and central area of the central tendon of the diaphragm at the level of the superior half of the body of the eleventh thoracic vertebra (see Fig. 55.1), and drains into the inferoposterior part of the right atrium (see Fig. 57.4B). The thoracic part is short, and is partly within and partly outside the pericardial sac. The extrapericardial part is separated from the pleura and right lung by the right phrenic nerve and associated pericardiacophrenic vessels, and the intrapericardial part is covered, except posteriorly, by the visceral layer of serous pericardium (see Fig. 57.4E). Its abdominal portion is devoid of valves.

The inferior vena cava can be encircled and controlled between the renal veins inferiorly and the hepatic veins superiorly, e.g. during operations on a renal cell carcinoma extending into the inferior vena cava. Obstruction of the inferior vena cava from thrombosis, embolism, extrinsic compression (e.g. tumour or pregnancy) or intrinsic disease results in the development of an extensive venous collateral circulation via tributaries that ultimately connect to the superior vena cava. These include the azygos–hemiazygos venous system, the vertebral venous plexuses, and the superficial veins of the thoracic and abdominal walls. The lumbar veins contribute significantly to these pathways (Golub et al 1992).

The inferior vena cava usually receives the common iliac veins at its origin and the lumbar, right gonadal, renal, right suprarenal, hepatic and inferior phrenic veins throughout its course (see Fig. 61.12).

Relations of the abdominal part of the inferior vena cava The inferior vena cava lies behind the parietal peritoneum lining the posterior abdominal wall. At its origin it is related anteriorly to the right common iliac artery. From below upwards, its anterior surface is crossed obliquely by the root of the mesentery of the small intestine and its contained vessels and nerves, the right gonadal artery and the horizontal part of the duodenum. Further cranially, it lies posterior to the head of the pancreas and superior (first) part of the duodenum, separated from those structures by the bile duct and hepatic portal vein. Superior to the duodenum, its anterior surface is covered by the parietal peritoneum lining the posterior abdominal wall, which forms the posterior wall of the omental foramen and separates the inferior vena cava from the right free border of the lesser omentum, i.e. the hepatoduodenal ligament and its contents. Superior to this, it is intimately related to the liver anteriorly.

The posterior relations of the inferior vena cava include the lower three lumbar vertebral bodies and their intervertebral discs, the anterior longitudinal ligament, sympathetic trunk, right third and fourth lumbar arteries, and psoas major on the right. Superior to these structures, it is related posteriorly to the right renal and middle suprarenal arteries, the medial part of the right suprarenal gland, the right coeliac ganglion and the right inferior phrenic arteries.

The right ureter, medial border of the right kidney, descending part of the duodenum and the right lobe of the liver are all lateral to the right side of the inferior vena cava. The abdominal aorta, right crus of the respiratory diaphragm and the caudate lobe of the liver are on its left side.

The normal diameter of an adult inferior vena cava is up to 30 mm (Moeller and Reif 2000); its cross-sectional shape and calibre reflect the degree of venous filling. Anatomical variants, related to its complex embryogenesis, are well described. Among these are a double inferior vena cava (the left-sided vessel usually joins the left renal vein); azygos continuation of the inferior vena cava; a left-sided inferior vena cava (which may exist in isolation or as part of situs inversus) (Ang et al 2013, Spentzouris et al 2014).

Collateral venous channels In obstruction of the superior part of the inferior vena cava, the azygos and hemiazygos veins and vertebral venous plexuses are the main collateral channels that maintain venous circulation. They connect the superior and inferior venae cavae and communicate with the common iliac vein via the ascending lumbar veins and with multiple tributaries of the inferior vena cava.

Variants The inferior vena cava may be congenitally interrupted, duplicated, left-sided or even absent.

Embryologically, if the right subcardinal vein fails to anastomose with the hepatic sinusoids, the hepatic segment of the inferior vena cava fails to develop. When this occurs, the hemiazygos or azygos veins, both of which originate from the cranial supracardinal veins, return blood to the heart. Azygos continuation of the inferior vena cava, characterized by a prominent azygos vein, is a variant that the paediatric surgeon should be aware of when undertaking repair of oesophageal atresia and tracheo-oesophageal atresia in neonates. The azygos vein, which is commonly ligated and divided during this procedure, should be spared because ligation of this vessel in neonates with azygos continuation of the inferior vena cava leads to intraoperative circulatory collapse and death. Double inferior vena cava (right side usually dominant) is a result of the persistence of all or any segments of the subcardinal veins. One of the most common variations is a left-sided inferior vena cava, which is formed if the right supracardinal vein regresses and the left supracardinal vein persists (Spratt 2016). There may also be a duplication of the inferior vena cava, which typically occurs inferior to the level of the renal veins, and is the result of persistence of the left lumbar and thoracic supracardinal veins and left suprasubcardinal anastomosis as well as malformation of the right subcardinal–hepatic anastomosis. Abnormalities associated with duplication of the inferior vena cava include congenital heart disease, congenital absence of the right kidney, cloacal extrophy, renal ectopia with abdominal aneurysm, right retrocaval ureter, left retrocaval ureter and congenital absence of the iliac anastomosis, abnormal left upper limb drainage and transcaval ureter.

In situs inversus with dextrocardia, the inferior vena cava passes inferiorly along the left side instead of the right. In situs inversus with levocardia, the inferior vena cava remains on the right side. In situs ambiguus (heterotaxy) the major organs are arranged ambiguously within the body. Prominent azygos veins with interrupted inferior vena cava are associated with heterotaxy (Punn and Olson 2010). Situs ambiguus with polysplenia is associated with an absence of parts of the inferior vena cava on the right side (with continuation through the azygos or hemiazygos vein), transposition of the inferior vena cava to the left side, or duplication of the inferior vena cava with one on the right and one on the left. Situs inversus with asplenia is similar to that of polysplenia, in that the inferior vena cava may be absent with azygos continuation or with the inferior vena cava to the left of the midline. In situs inversus totalis, transposition of the inferior vena cava consists of a right-sided inferior vena cava. The inferior vena cava may have an abnormally high insertion into the right atrium.

Scimitar syndrome, a form of anomalous pulmonary venous drainage, occurs when there is an abnormal connection between the right pulmonary vein(s) and the inferior vena cava. This often involves hypoplasia of the pulmonary veins and the pulmonary trunk and arteries, as well as abnormal ipsilateral lung parenchyma. This creates a left-to-right shunt and increases the risk of right ventricular failure as a result of ventricular hypertrophy. Typical symptoms include respiratory insufficiency such as recurrent respiratory infections, heart failure, or pulmonary hypertension.

Congenital agenesis of the inferior vena cava may occur and may be completely asymptomatic because venous drainage of the lower limbs occurs through anastomosed channels of the azygos and hemiazygos veins. However, this condition may be associated with a higher risk for deep vein thrombosis.

Lumbar veins

Four pairs of lumbar veins collect blood from the territories supplied by the corresponding lumbar arteries, including the posterior, lateral and anterior abdominal walls. These branches anastomose posteriorly with tributaries of the azygos and hemiazygos veins, and anteriorly with branches of the epigastric, circumflex iliac and lateral thoracic veins. These superficial anastomoses provide alternative routes of venous drainage from the pelvis and lower limbs to the heart when the inferior vena cava is obstructed. The lumbar veins communicate with the external and internal vertebral venous plexuses, providing an additional collateral pathway for venous return.

The paired longitudinal ascending lumbar veins connect the individual ipsilateral lumbar veins. The third and fourth lumbar veins usually pass anteriorly on the sides of the corresponding vertebral bodies to enter the posterior aspect of the inferior vena cava; the left lumbar veins pass posterior to the abdominal aorta and are therefore longer. The first and second lumbar veins are much more variable and may drain into the inferior vena cava or the ascending lumbar, lumbar azygos or renal veins (on the left); they are often connected to each other. The first lumbar vein often passes inferiorly to join the second lumbar vein or, less commonly, drains either directly into the ascending lumbar vein or passes anteriorly over the body of the first lumbar vertebra to join the lumbar azygos vein. The second lumbar vein may join the inferior vena cava at or near the level of the renal veins or, less commonly, join the third lumbar or ascending lumbar vein.

Ascending lumbar veins

The paired ascending lumbar veins run medial to psoas major and connect the ipsilateral common iliac, iliolumbar and lumbar veins. They are variable in their course and connections; rarely, the whole vein or a segment is absent on one side (Lolis et al 2011). An ascending lumbar vein commonly joins the subcostal vein to form the azygos vein on the right and the hemiazygos vein on the left. The azygos and hemiazygos veins run anteriorly over the body of the twelfth thoracic vertebra and pass deep to or through the right and left crura of the respiratory diaphragm, respectively, into the thoracic cavity. The ascending lumbar vein is usually joined by a small vein, the lumbar azygos vein, from the back of the inferior vena cava or left renal vein. Sometimes, the ascending lumbar vein ends in the first lumbar vein, which then joins the lumbar azygos vein at the level of the first lumbar vertebra. Blood can flow in either direction in the ascending lumbar veins (Morita et al 2007).

Testicular veins

Testicular veins emerge posteriorly from the testis, drain the epididymis, and unite to form several highly anastomotic channels surrounding the testis known as the pampiniform plexus, a major component of the spermatic cord (see Fig. 74.2). This vascular arrangement means that counterflowing arteries and veins are separated only by the thickness of their vascular walls, permitting the exchange of heat and small molecules (Harrison 1949) and facilitating the maintenance of lower testicular temperatures. The pampiniform plexus ascends anterior to the ductus deferens and is drained by three or four veins in the inguinal canal. The veins enter the abdomen through the deep inguinal ring, ascend anterior to psoas major and the ureter on each side, and coalesce into a single testicular vein that drains into the inferior vena cava on the right and the renal vein on the left.

The right testicular vein enters the inferior vena cava directly on its right anterolateral aspect at an acute angle about 2 cm inferior to the left renal vein in adults; occasionally, it drains into the right renal vein (Tubbs et al 2016). The left testicular vein joins the left renal vein at a right-angle (see Fig. 74.8). Both veins may be replaced by multiple vessels in the lower abdomen and sometimes remain double as far as their termination.

The testicular veins contain valves. Varicocele, which is almost always on the left, may be a consequence of the greater length of the left testicular vein and its orthogonal junction with the left renal vein. The testicular veins can anastomose with the external pudendal and cremasteric veins and veins of the ductus deferens, allowing varicoceles to persist or recur after ablative procedures that do not address these potential collaterals.

Ovarian veins

The ovarian veins emerge from the ovary as a plexus (pampiniform plexus) in the mesovarium and suspensory ligament of the ovary (see Fig. 75.3A). Two veins emerge from the plexus and ascend with the ovarian artery, anterior to psoas major and the ureter. They usually merge into a single vessel before entering either the inferior vena cava on the right side or the renal vein on the left.

Renal veins

Fine radicles from the venous ends of the peritubular plexuses converge to join interlobular veins, one with each interlobular artery. Many interlobular veins begin beneath the fibrous capsule of the kidney by the convergence of several stellate veins, which drain the most superficial zone of the renal cortex and so are named from their surface appearance. Interlobular veins pass to the corticomedullary junction and also receive some ascending vasa recta before ending in arcuate veins (which accompany arcuate arteries), and anastomose with neighbouring veins. Arcuate veins drain into interlobar veins, which anastomose and form the renal vein.

The large renal veins lie anterior to the renal arteries and open into the inferior vena cava almost at right-angles (see Figs 59.7, 72.16). The left renal vein is three times longer than the right (7.5 cm and 2.5 cm, respectively): the left kidney is the preferred side for live donor nephrectomy for this reason. However, the left renal vein can also be double, one vein passing posterior and the other anterior to the aorta before draining into the inferior vena cava, an arrangement that is sometimes referred to as persistence of the ‘renal collar’. The anterior vein can be absent, in which case there is a single retro-aortic left renal vein. These variations could negate any advantage of using the left kidney as a donor (Phelan et al 2009). The left renal vein runs from its origin in the hilum of the kidney, posterior to the splenic vein and the body of the pancreas, and then across the anterior aspect of the abdominal aorta, just below the origin of the superior mesenteric artery. Anterior nutcracker syndrome, characterized by left renal vein hypertension secondary to compression of the vein between the ventral surface of the abdominal aorta and the dorsal surface of the superior mesenteric artery, has been associated with haematuria and varicocele in children (Kurklinsky and Rooke 2010). The left gonadal vein enters the left renal vein from below, and the left suprarenal vein, usually receiving one of the left inferior phrenic veins, enters it above but nearer the midline. The left renal vein enters the inferior vena cava slightly superior to the right renal vein. The right renal vein lies posterior to the descending part of the duodenum and, sometimes, the head of the pancreas. It can be extremely short (less than 1 cm), such that safe nephrectomy can require excision of a cuff of the inferior vena cava.

The left renal vein may have to be ligated during surgery for aortic aneurysm because it has such a close relationship with the aorta; this seldom results in any harm to the kidney, provided that the ligature is placed medial to the draining gonadal and suprarenal veins, since these usually provide adequate collateral venous drainage. The right renal vein has no significant collateral drainage and cannot be ligated with impunity.

Suprarenal vein

Most commonly, a single vein drains each suprarenal gland. The short right suprarenal vein drains directly into the inferior vena cava at the level of the twelfth thoracic vertebra; the longer left vein usually joins the left renal vein and may receive the left inferior phrenic vein. Numerous anatomical variations of this vein have been described (Cesmebasi et al 2014).

Inferior phrenic veins

The inferior phrenic veins usually originate on the superior surface of the respiratory diaphragm but run mostly on its inferior surface to drain into the posterolateral aspect of the inferior vena cava. Both veins receive several diaphragmatic tributaries. The left vein runs to the left of the oesophageal hiatus, whereas the right courses to the right of the caval foramen; each receives a venous tributary from the oesophagus (Loukas et al 2005b). The left inferior phrenic vein frequently communicates with the left gastric vein and may therefore become prominent in portal hypertension. Both inferior phrenic veins usually drain directly into the inferior vena cava just inferior to the respiratory diaphragm, sometimes joining anteriorly to form a short common trunk. The right occasionally drains into the right hepatic vein or inferior vena cava superior to the respiratory diaphragm, whereas the left frequently drains into the left suprarenal, left renal or left hepatic vein.

Hepatic veins

The liver drains by three major hepatic veins into the suprahepatic part of the inferior vena cava and via numerous minor hepatic veins that drain into the retrohepatic inferior vena cava. The adult retrohepatic inferior vena cava is 6–7 cm long and is surrounded to a variable extent by segment I (Camargo et al 1996). The three major veins are located between the four sectors of the liver (see Figs 66.6A, 66.14–66.15). Thus, the right hepatic vein lies between the right anterior and posterior sectors, the middle hepatic vein lies between the right and left hemilivers, and the left hepatic vein lies between the left medial and lateral sectors. During hepatic resection, the surgeon should transect the liver parenchyma slightly to the left or right of the particular fissure that is being opened to avoid the main trunk of a hepatic vein.

Right hepatic vein

The right hepatic vein is the longest and largest hepatic vein. It is usually single, but occasionally remains as two trunks until it terminates by draining into the inferior vena cava. It runs in the right portal fissure between the right medial and lateral sectors. It drains the whole of segments VI and VII and variable proportions of segments V and VIII, depending on the extent to which these segments drain into the middle hepatic vein. The right hepatic vein is formed anteriorly near the inferior border of the liver and lies in a coronal plane through most of its course. It drains into the inferior vena cava near the superior border of the caudate lobe. Of the three major hepatic veins, the right hepatic vein is most variable in calibre, reflecting the variable contribution of the middle hepatic vein to the drainage of segments V and VIII and the existence of an accessory right inferior (30%) and/or middle hepatic vein (10%) (Fang et al 2012). The hepatic venous anatomy is particularly important in right lobe living donation and can be assessed preoperatively by computed tomography (CT) or magnetic resonance imaging (MRI), and/or by intraoperative ultrasound.

Middle hepatic vein

The middle hepatic vein lies in the main portal fissure between the right and left hemilivers. It usually joins the left hepatic vein and terminates in the inferior vena cava as a short common trunk (about 5 mm long); it ends as a single trunk in the inferior vena cava in fewer than 10% of individuals. The middle hepatic vein drains the central part of the liver and receives constant tributaries from segments IV, V and VIII. The vein from segment IV lies in a sagittal plane and enters the middle hepatic vein on its left side. The vein from segment VIII runs transversely into the right side of the middle hepatic vein and is sometimes large enough to be mistaken for the middle hepatic vein. Anteriorly, the middle hepatic vein drains some of segment V; the calibres of the tributaries draining segments V and VIII are variable. Intrahepatic venous anastomoses between the middle and right hepatic veins, particularly in segment VIII, have been reported in up to one-third of adult livers (Hribernik and Trotovšek 2014).

Left hepatic vein

The left hepatic vein lies between the left medial and left lateral sectors of the liver and drains segments II, III and occasionally IV. Small veins draining segment II and occasionally the superior part of segment IV, can drain directly into the inferior vena cava. The umbilical fissure vein, a major tributary of the left hepatic vein, usually runs between segments III and IV and contributes to their drainage. Occasionally the vein draining segment III ends separately in the confluence of the left and middle hepatic veins. These variations in venous drainage are significant in split liver transplantation and live donor liver transplantation.

Minor hepatic veins

Segment I veins, ranging in number from one to five, drain directly into the inferior vena cava. Since this segment has a venous drainage independent of the rest of the liver, segment I often continues to drain effectively and undergoes compensatory hypertrophy in patients with Budd–Chiari syndrome, where the major hepatic veins are blocked. There can be an accessory inferior or middle right hepatic vein, and several smaller 'retrohepatic' veins that drain the right lobe directly into the inferior vena cava. When present, these veins are surgically important, especially if they exceed 5 mm in diameter. They drain segments V and VI independently of the three major hepatic veins, which means that a tumour involving the latter can be resected safely as long as venous drainage from the accessory veins is preserved. In live donor and split liver transplantation, larger accessory veins must be individually anastomosed to the recipient inferior vena cava to ensure adequate venous drainage.

Hepatic portal system

The liver has two venous systems. The portal venous system conveys blood from the majority of the gastrointestinal tract and its associated organs to the liver and the hepatic venous system drains blood from the liver parenchyma into the inferior vena cava.

Portal vein

The hepatic portal vein is formed posterior to the neck of the pancreas, usually from the convergence of the superior mesenteric and splenic veins (see Figs 59.7, 66.12). Its origin lies in the transpyloric plane between the inferior border of the body of the first lumbar vertebra and the superior border of the body of the second lumbar vertebra (Mirjalili et al 2012c). The hepatic portal vein is approximately 8 cm long and ascends obliquely to the right, posterior to the superior (first) part of the duodenum, bile duct and gastroduodenal artery, and anterior to the inferior vena cava. It enters the hepatoduodenal ligament and ascends anterior to the omental foramen to reach the right end of the porta hepatis, where it divides into right and left main branches that enter the liver. In the lesser omentum, the hepatic portal vein lies posterior to both the bile duct and the hepatic artery. It is surrounded by the hepatic nervous plexus and accompanied by numerous lymphatics and some lymph nodes. The hepatic portal vein contains smooth muscle in its wall and, in experimental animals at least, has well-developed spontaneous contractions with frequencies between 0.01 and 1 Hz (Burt 2003). It is typically valveless.

The hepatic portal vein divides into right and left branches at the porta hepatis of the liver (see Fig. 66.13). The left branch of the hepatic portal vein has a longer extrahepatic course (4–5 cm) than the right branch of the hepatic portal vein, tends to lie more horizontally, and is often smaller in calibre. The horizontal portion runs along the inferior surface of segment IV and invariably gives branches to segment I and sometimes to segment IV. The left branch of the hepatic portal vein continues within the liver, giving off a segment II branch laterally before taking a more anterior and vertical course in the umbilical fissure, where it gives off branches to segments III and IV and receives the obliterated left umbilical vein (round ligament of the liver). Most of the portal venous supply to segment IV comes from the left branch of the hepatic portal vein and only occasionally from either the right branch of the hepatic portal vein or its branches to segments V or VIII. The right branch of the hepatic portal vein is only 2–3 cm in length and usually divides into a right medial (anterior) sectoral division supplying segments V and VIII, and a right lateral (posterior) sectoral division supplying segments VI and VII. The medial division can give a branch to segment I.

The main extrahepatic tributaries of the hepatic portal vein are the left gastric vein, which ends in the left margin of the hepatic portal vein, and the posterior superior pancreaticoduodenal vein near the head of the pancreas.

Variants Hepatic portal vein variations usually involve the right branch (Covey et al 2004). When this branch is absent (10–15% of livers), the hepatic portal vein usually trifurcates into left portal, right anterior and right posterior sectoral veins. Absence of the right branch of the hepatic portal vein might be considered as a relative contraindication for split liver and live donor liver transplantation because this variation is often associated with a similar variation in biliary anatomy. The right anterior sectoral portal vein can arise from the hepatic portal vein, or the right posterior sectoral portal vein can originate from the left branch of the hepatic portal vein, variations that are important to remember during left-sided liver resection. When the bifurcation of the hepatic portal vein is absent, the hepatic portal vein enters the liver, giving off the right sectoral branches, and then turns left to supply the left lobe, a variation that presents an added complexity in major liver surgery (Chaib 2009).

Left gastric vein

The left gastric vein drains the proximal body and fundus of the stomach. It ascends along the lesser curvature to the gastro-oesophageal junction, where it receives several distal oesophageal veins. It then curves posteriorly and medially behind the posterior wall of the omental bursa. It usually passes anterior or posterior to the common hepatic artery and drains into the hepatic portal vein at the level of the proximal border of the superior part of the duodenum (which corresponds to 1–2 cm from the origin of the portal vein) (Rebibo et al 2012). In up to one-third of individuals, it passes anterior or posterior to the common hepatic artery and terminates in the splenic vein. On rare occasions it drains into the left branch of the hepatic portal vein within the liver (Ohkubo 2000), a variant that may be clinically important in portal hypertension. Knowledge of these venous variations is important during lymphadenectomy for gastric cancer to avoid unexpected venous bleeding.

Right gastric vein

The right gastric vein is typically small and runs along the medial end of the lesser curvature, passing under the peritoneum as it is reflected from the posterior aspect of the pylorus and superior part of the duodenum on to the posterior wall of the omental bursa. It drains directly into the hepatic portal vein at the level of the superior part of the duodenum. It receives the prepyloric vein as it ascends anterior to the pylorus at the level of the pyloric orifice. Rarely the right gastric vein drains directly into a branch of the hepatic portal vein within the liver.

Pancreaticoduodenal veins

The pancreaticoduodenal veins accompany their corresponding arteries. The posterior superior pancreaticoduodenal vein courses adjacent to the distal part of the common bile duct within the pancreatic head. It is the major draining vein of the posterior pancreatic head and adjacent duodenum and usually joins the portal vein just superior to the pancreas.

Cystic veins and venous plexuses draining biliary tract

The venous drainage of the gallbladder is rarely by a single cystic vein and there are usually multiple small veins. Those arising from the superior surface of the body and neck lie in loose connective tissue between the gallbladder and liver and drain into the branches of the hepatic portal vein within the liver. The remainder of the organ drains by one or two small cystic veins into either branches of the hepatic portal vein within the liver or portal venous tributaries draining the hepatic ducts and proximal bile duct (Sugita et al 2000). Only rarely does a single or double cystic vein drain directly into the right branch of the hepatic portal vein.

A delicate epicholedochal venous plexus covers the surface of the bile ducts. A fine paracholedochal venous plexus runs parallel with the bile ducts and typically forms two distinct marginal veins (3 o'clock and 9 o'clock marginal veins). The plexuses and the marginal veins communicate with gastric veins, the posterior superior pancreaticoduodenal vein, the gastrocolic trunk and with the hilar venous plexus that ultimately drains into branches of the portal vein (Vellar 2001, Ramesh Babu and Sharma 2014).

Splenic vein

Blood from the spleen is collected by trabecular veins that join to form segmental veins that drain individual splenic segments. In general, there are no anastomoses between intrasegmental venous tributaries. The segmental veins join to form two (superior and inferior) or three (superior, middle and inferior) 'lobar' veins that emerge from the length of the splenic hilum and unite to form the splenic vein within the splenorenal ligament (see Fig. 69.2). Communicating veins may interconnect lobar veins (Par et al 1965, DeLand 1970, Gupta et al 1980, Sow et al 1991, Liu et al 1996).

The splenic vein most commonly runs posterior to the splenic artery and tail and body of the pancreas (Par et al 1965, Gürleyik et al 2000, Skandalakis et al 2004). It crosses the posterior abdominal wall anterior to the left kidney and abdominal aorta, separated from the left sympathetic trunk and left crus of the respiratory diaphragm by the left renal vessels, and from the abdominal aorta by the superior mesenteric artery and left renal vein (Par et al 1965, Gupta et al 1976, Gupta et al 1980, Liu et al 1996). It ends posterior to the neck of the pancreas, where it joins the superior mesenteric vein to form the hepatic portal vein. Along its course it receives the short gastric veins, left gastro-omental veins, pancreatic veins and the posterior gastric vein. It may also receive the left gastric vein and inferior mesenteric veins in approximately 30% of individuals (Gerber et al 1951). Anastomoses between the splenic vein and left renal vein have been reported, particularly in cases of portal hypertension (Bowdler 2002). Approximately 60% of hepatic portal vein blood flow is derived from the gut and the remainder from the spleen and pancreas (Par et al 1965, Gupta et al 1980, Dawson et al 1986, Oguro et al 1993, Liu et al 1996, Gürleyik et al 2000). Obstruction of the hepatic portal or splenic veins can lead to reversed venous flow through the splenic vein and its tributaries, resulting in splenomegaly and widespread varices (Re et al 1985, Skandalakis et al 1993, Petroianu 2011).

Short gastric veins

Three to five short gastric veins drain the fundus and the upper part of the greater curvature of the stomach into the splenic vein or one of its large tributaries: they travel within the gastrosplenic ligament (Power et al 2001).

Left gastro-omental vein

The left gastro-omental vein drains both the anterior and posterior surfaces of the body of the stomach and the adjacent greater omentum via multiple tributaries. It runs superolaterally along the greater curvature, between the layers of the gastrocolic ligament, and drains into the splenic vein within the gastrosplenic ligament.

Pancreatic veins

Multiple veins drain the pancreas into the hepatic portal, superior mesenteric and splenic veins (Mourad et al 1994; Fig. 68.7). Although variations are common, the anterior superior pancreaticoduodenal vein typically joins either the confluence of the right gastro-omental and right colic veins (the gastrocolic trunk of Henle) or the right gastro-omental vein alone, to drain into the superior mesenteric vein at the inferior border of the neck of the pancreas (Mourad et al 1994, Lange et al 2000). The posterior superior pancreaticoduodenal vein drains cranially into the hepatic portal vein. Both anterior and posterior inferior pancreaticoduodenal veins usually drain directly into the dorsal aspect of the superior mesenteric vein inferior to the uncinate process. These veins can be a major source of blood loss when the uncinate process is dissected off the superior mesenteric vein during a pancreaticoduodenectomy procedure. In most individuals the first and second jejunal veins form a single vein known as the first jejunal trunk that drains into the superior mesenteric vein (Ishikawa et al 2017). Veins from the body and tail of the gland drain directly into the splenic vein. An inferior (transverse) pancreatic vein sometimes runs along the inferior border of the pancreas to join the inferior mesenteric vein. A few pancreatic veins communicate with systemic veins in the retroperitoneum (veins of Retzius), and can form retroperitoneal varices in portal hypertension.

Posterior gastric veins

One or more distinct posterior gastric veins can be present, draining the middle of the posterior surface of the stomach into the splenic vein: they can become particularly prominent in portal hypertension (Kimura et al 1990).

Inferior mesenteric vein

The inferior mesenteric vein drains the rectum and the sigmoid, descending and distal transverse colon (see Figs 65.15, 65.42). It begins as the continuation of the superior anorectal vein from the anorectal plexus, through which it connects with the middle anorectal and inferior anal veins. The inferior mesenteric vein lies to the left of the inferior mesenteric artery in the retroperitoneum and ascends anterior to the left psoas major and left ureter; it may cross the gonadal vessels or ascend medial to them. It lies just lateral or occasionally posterior to the duodenojejunal flexure, where it can be located intraoperatively. The inferior mesenteric vein receives the superior anorectal vein, several sigmoid veins and the left colic vein. It usually passes posterior to the lower border of the body of the pancreas and anterior to the left renal vein to drain into the splenic vein, but it can also drain into the confluence of the splenic and superior mesenteric veins or directly into the superior mesenteric vein (Graf et al 1997).

Superior anorectal vein

Venous tributaries from the rectal venous plexus ascend in the rectal submucosa and pierce the rectal wall to form the superior anorectal vein. This runs in the upper mesorectum and root of the sigmoid mesocolon to the left of the superior anorectal artery, crossing the linea terminalis and left common iliac vessels to form the inferior mesenteric vein (see Figs 65.15, 65.44).

Rectal venous plexus

The rectal venous plexus surrounds the rectum and connects anteriorly with the vesical plexus in males or the uterine and vaginal venous plexuses in females. It consists of internal veins beneath the mucosa of the rectum and proximal anal canal, and external veins lying outside the muscular wall. The upper two-thirds of the rectum and the internal part of the rectal venous plexus drain mainly to the superior anorectal vein and, from there, to the inferior mesenteric vein; the middle third of the rectum drains via one or more middle anorectal veins into the internal iliac vein; and the lower third of the rectum and anal canal drains via inferior anal veins into the internal pudendal veins. The rectal venous plexus is therefore a site of communication between the portal and systemic venous systems.

Left colic vein

The left colic vein is formed from several tributaries, including ascending and descending branches that correspond to the similarly named arteries. The left colic vein usually lies superior to its corresponding artery, and has a shorter course because the inferior mesenteric vein lies lateral to the inferior mesenteric artery (see Fig. 65.42). Occasionally there are two left colic veins that both drain into the inferior mesenteric vein (Tubbs et al 2016).

Superior mesenteric vein

The superior mesenteric vein drains the small intestine, caecum, ascending and transverse parts of the colon, and parts of the stomach and greater omentum (see Figs 59.8, 64.16). It is formed in the mesentery of the small intestine by the union of tributaries from the terminal ileum, caecum and appendix. It ascends in the mesentery to the right of the superior mesenteric artery, passing anterior to the right ureter, inferior vena cava, horizontal part of the duodenum and uncinate process of the pancreas. It joins the splenic vein posterior to the neck of the pancreas in the transpyloric plane (inferior border of L1 vertebra) to form the hepatic portal vein.

The superior mesenteric vein receives jejunal, ileal, ileocolic, right colic, middle colic, right gastro-omental and inferior pancreaticoduodenal veins. A major proximal jejunal branch usually runs transversely posterior to the superior mesenteric artery to enter the right posterolateral aspect of the superior mesenteric vein (Kim et al 2007). The right colic vein is highly variable. When present, it can drain directly into the superior mesenteric vein or join the right gastro-omental or inferior pancreaticoduodenal vein to form a ‘gastrocolic trunk’, which then drains into the superior mesenteric vein (Yamaguchi et al 2002). Although the inferior mesenteric vein usually drains into the splenic vein, it can join the superior mesenteric vein directly or its confluence with the splenic vein (Graf et al 1997).

Right gastro-omental vein

The right gastro-omental vein drains the greater omentum, distal body of the stomach and pyloric antrum. It runs medially along the greater curvature in the upper part of the gastrocolic omentum. Just proximal to the pylorus, it passes posteriorly to drain into the superior mesenteric vein posterior to the neck of the pancreas. The right gastro-omental vein can receive the right colic vein (forming a ‘gastrocolic trunk’) and/or the superior pancreaticoduodenal vein close to its entry into the superior mesenteric vein (Yamaguchi et al 2002, Stefura et al 2018).

Porto-systemic shunts

Increased pressure within the portal venous system can result in dilation of portal venous tributaries and reversed flow at sites of porto-systemic anastomoses. Common sites of porto-systemic shunts are listed in Table 66.1.

In cases of extreme chronic portal hypertension, a large calibre anastomosis between the portal and systemic circulations can be created within the liver parenchyma by inserting a stent between a large hepatic portal vein and an intrahepatic vein (transjugular intrahepatic portosystemic shunt). The stent is introduced through a catheter inserted into the internal jugular vein and guided into the liver under radiological control (Siramolpiwat 2014). This large shunt relieves the severe portal hypertension but tends to worsen incipient hepatic encephalopathy.

Oesophageal and gastric varices

Blood from the oesophageal mucosa normally drains into a submucosal venous plexus, then into a deeper intrinsic venous plexus and finally into oesophageal veins via perforating veins. In the abdominal part of the oesophagus, the perforating veins drain into tributaries of the left gastric vein, whereas in the distal thoracic part of the oesophagus, they drain into tributaries of the azygos and hemiazygos venous systems. Bidirectional flow is possible in this region and accommodates pressure changes during breathing and Valsalva manoeuvres.

Oesophageal and gastric varices are abnormally dilated veins that occur in the submucosal plexus of the distal oesophagus and fundus of the stomach when portal venous pressure is chronically elevated (typically greater than 15 mmHg). This can arise as a consequence of liver fibrosis or cirrhosis, or hepatic portal vein thrombosis, or from a variety of other causes. Portal hypertension leads to the recanalization of occluded embryonic venous channels connecting tributaries of the portal system and the systemic venous circulation (e.g. the round ligament of the liver), and progressive dilation of small, naturally occurring venous anastomoses between portal and systemic venous tributaries (Paquet 2000). The raised pressure causes the valves within these veins to become incompetent, permitting retrograde flow and the development of varices. Varices in the distal oesophagus are readily visible at endoscopy because they are situated superficially and protrude into the lumen of the oesophagus (see Fig. 63.13A); they are vulnerable to rupture and are a source of major gastrointestinal bleeding. Gastric varices can also be present on the inferior aspect of the cardiac orifice and isolated gastric varices can develop as a result of splenic vein thrombosis. The close anatomical relationship between the splenic vein and the pancreas means that inflammation or cancers of the pancreas can result in the formation of a thrombus in the splenic vein. Because the short gastric veins drain into the splenic vein, thrombosis of that vein will result in increased pressure and engorgement, leading to varices in the fundus of the stomach.

VENOUS DRAINAGE OF THE LOWER LIMB

The veins of the lower limb can be subdivided into a superficial group lying in the subcutaneous tissue and vessels that lie deep to the deep fascia and accompany the major arteries and their branches (see Figs 76.8–76.9). Valves are present in both groups, but are more numerous in the deep veins. (They are also more numerous than in the veins of the upper limb). Venous plexuses occur within and between some of the lower limb muscles. The two principal superficial veins are the long and short saphenous veins; their numerous tributaries are mostly unnamed, however, changes in clinical practice are driving a revision of the terminology (Caggiati et al 2002, 2005). The long saphenous vein can be harvested and used as a graft for peripheral vascular surgery, including coronary artery bypass (Kosinski 1926).

Plantar digital veins arise from plexuses in the plantar regions of the toes, connect with dorsal digital veins and unite to form four plantar metatarsal veins. These run in the intermetatarsal spaces and connect first with dorsal veins by means of perforating veins and then connect with each other to constitute a deep plantar venous arch adjacent to the deep plantar arterial arch. Medial and lateral plantar veins from the venous arch run near the corresponding arteries and communicate with the long and short saphenous veins before forming the posterior tibial veins posterior to the medial malleolus.

The posterior tibial veins accompany the posterior tibial artery. They receive veins from the calf muscles, especially the venous plexus in soleus, and connect with superficial veins and with the fibular veins. The latter accompany the fibular artery and receive tributaries from both soleus and superficial veins. The anterior tibial veins are continuations of the venae comitantes of the dorsalis pedis artery. They leave the extensor region between the tibia and fibula, pass through the proximal end of the interosseous membrane and unite with the posterior tibial veins at the distal border of popliteus to form the popliteal vein.

Venous (muscle) pumps

While standing, venous return from the lower limb depends largely on muscular activity, especially contraction of the calf and foot muscles, known as the 'muscle pump', aided by the tight sleeve of deep fascia (Ricci 2017). 'Perforating' veins connect the long saphenous vein with the deep veins, particularly near the ankle, distal calf and knee. Their valves are arranged so as to prevent flow of blood from the deep to the superficial veins. At rest, pressure in a superficial vein is equal to the height of the column of blood extending from that vein to the heart. When the posterior leg muscles contract, blood is pumped proximally into the deep veins and is normally prevented from flowing into the superficial veins by the valves in the perforating veins. During muscular relaxation, blood is drawn into the deep veins from the superficial veins. If the valves in the perforating veins become incompetent, these veins become sites of 'high-pressure leaks' during muscular contraction, and the superficial veins become dilated and varicose. There are similar perforating connections in the anterolateral region, where varicosities may also occur. Incompetence of the valves in the connecting veins between the long saphenous vein and femoral vein in the adductor canal may predispose to superficial varicosities along the medial aspect of the thigh (Dodd and Cockett 1976). Venous plexuses, which may be intramuscular (soleus) or intermuscular (in the foot and gluteal region), communicate with the axially running deep veins and are components of the 'muscle pump' mechanism.

Venous disease

Chronic venous disease is common. Sustained overdistension of the superficial veins of the lower limb may result in the development of short, dilated venous segments or varicosities. Varicose veins can occur as a consequence of venous valve failure at the proximal end of the long saphenous vein at the saphenofemoral junction, or in the perforating veins that pass from the superficial system to the high-pressure deep veins. Varicose veins have thin walls and 'leak' red blood cells into adjacent soft tissues. As these cells are broken down, haemosiderin is deposited in the soft tissues, resulting in a brown pigmentation. This phenomenon, together with the fact that venous stasis produces oedema, renders the soft tissues of the leg unhealthy and prone to ulceration, particularly after minor trauma.

Acute venous disease occurs most commonly in the posterior compartment of the leg. This is attributed to the sluggish blood flow that occurs, at times, in the deep veins of the calf. This relative stasis predisposes to the formation of venous thrombi. Fragments of these thrombi may become dislodged and carried in the venous return to the heart to cause a life-threatening pulmonary embolism. Blockage of the normal venous system may contribute to increased local venous pressure and oedema.

Superficial veins

Superficial veins of the foot

As occurs in the upper limb, the vessels are described centripetally from peripheral to major drainage channels.

Dorsal digital veins receive rami from the plantar digital veins in the clefts between the toes and then join to form dorsal metatarsal veins, which are united across the proximal parts of the metatarsals in a dorsal venous arch. Proximal to this arch, an irregular dorsal venous network receives tributaries from deep veins and is continuous proximally with a venous network in the leg. At each side of the foot, this network connects with medial and lateral marginal veins, which are both formed mainly by veins from more superficial parts of the sole. In the sole, superficial veins form a plantar cutaneous arch across the roots of the toes and also drain into the medial and lateral marginal veins.

Long saphenous vein

The long (great) saphenous vein (see Fig. 76.9A), the longest vein in the body, starts distally as a continuation of the medial marginal vein of the foot, and ends in the femoral vein a short distance distal to the inguinal ligament. It ascends immediately anterior to the medial malleolus, crosses the distal third of the medial surface of the tibia obliquely in an anteroposterior direction to reach its medial border, and then ascends a little behind the border to the knee. Proximally, it is posteromedial to the medial tibial and femoral condyles and then ascends the medial aspect of the thigh. It passes through the saphenous opening and finally opens into the femoral vein. The 'centre' of the opening is often said to be 2.5–3.5 cm inferolateral to the pubic tubercle, and the vein is then represented by a line drawn from this point to the adductor tubercle. However, the saphenous opening varies greatly in size and disposition so that this 'centre' is not a reliable surface marking for the saphenofemoral junction.

In its course through the thigh, the long saphenous vein is accompanied by the medial branches of the anterior cutaneous branches of the femoral nerve. At the knee, the saphenous branch of the descending genicular artery (the saphenous artery) and, in the leg and foot, the saphenous nerve all lie anterior to the vein. The vein is often duplicated, especially distal to the knee. It has 10–20 valves, which are more numerous in the leg than in the thigh. One is present just before the vein pierces the cribriform fascia, another at its junction with the femoral vein. In almost its entire extent the vein lies in subcutaneous tissue, but it has many connections with the deep veins, especially in the leg.

At the ankle, the long saphenous vein drains the sole of the foot by medial marginal veins. In the leg, it often connects with the short saphenous vein and with deep veins via perforating veins. Just distal to the knee it usually receives three large tributaries from the front of the leg, the medial malleolar region (connecting with some of the 'perforating' veins) and the calf (communicating with the short saphenous vein). The tributary draining the medial malleolar region is formed distally from a fine network or 'corona' of delicate veins just over the medial malleolus, and then ascends the medial aspect of the calf as the posterior arch vein. This vein was first illustrated by Leonardo da Vinci, whose name is sometimes given to it. It connects with posterior tibial venae comitantes by a series of perforating (communicating) veins. There are usually three, equally spaced between the medial malleolus and the mid-calf. More than three such perforators are uncommon, and an arch vein perforator above mid-calf is only very rarely found.

Above the posterior crural arch vein, perforating veins join the long saphenous vein or one of its main tributaries at two main sites. The first is at a level in the upper calf indicated by its name, the tibial tubercle perforator; the second is in the lower/intermediate third of the thigh, where it perforates the deep fascia roof of the subsartorial canal to join the femoral vein.

In the thigh, the long saphenous vein receives many tributaries. Some open independently, while others converge to form large named channels that frequently pass towards the basal half of the femoral triangle before joining the long saphenous near its termination. These may be grouped as follows: one or more large posteromedial tributaries, one or more large anterolateral tributaries, and four or more peri-inguinal veins. The posteromedial vein of the thigh, large and sometimes double, drains a large superficial region indicated by its name; it has (as have the other tributaries) radiological and surgical significance. One of its lower radicles is often continuous with the short saphenous vein. The posteromedial vein is sometimes named the accessory saphenous vein, though some restrict the term accessory to a lower (more distal) posteromedial tributary when two (or more) are present. Another large vessel, the anterolateral vein of the thigh (anterior femoral cutaneous vein), usually commences from an anterior network of veins in the distal thigh and crosses the apex and distal half of the femoral triangle to reach the long saphenous vein. As the latter traverses the saphenous opening, it is joined by the superficial epigastric, superficial circumflex iliac and superficial external pudendal veins. Their mode of union varies. Superficial epigastric and circumflex iliac veins drain the inferior abdominal wall, the latter also receiving tributaries from the proximolateral region of the thigh. The superficial epigastric or the femoral vein may connect with the lateral thoracic veins by means of a thoraco-epigastric vein that runs superficially on the anterolateral aspect of the trunk. This vein connects the inferior and superior caval areas of drainage and may be dilated and visible in cases of inferior caval obstruction. Superficial external pudendal veins drain part of the scrotum/labia; one is joined by the superficial dorsal vein of the penis/clitoris. The deep external pudendal veins join the long saphenous vein at the saphenous opening.

The long saphenous vein is often harvested for grafts used in both peripheral and coronary arterial surgery.

Short saphenous vein

The short saphenous vein (small saphenous vein) begins posterior to the lateral malleolus as a continuation of the lateral marginal vein (see Fig. 76.9B). In the lower third of the calf, it ascends lateral to the calcaneal tendon, lying on the deep fascia and covered only by subcutaneous tissue and skin. Inclining medially to reach the midline of the calf, it penetrates the deep fascia, within which it ascends on gastrocnemius, only emerging between the deep fascia and gastrocnemius gradually at about the junction of the middle and proximal thirds of the calf (usually well below the lower limit of the popliteal fossa). Continuing its ascent, it passes between the heads of gastrocnemius and proceeds to its termination in the popliteal vein, 3–7.5 cm above the knee joint.

The short saphenous vein connects with deep veins on the dorsum of the foot, receives many cutaneous tributaries in the leg, and sends several communicating branches proximally and medially to join the long saphenous vein. Sometimes a communicating branch ascends medially to the accessory saphenous vein: this may be the main continuation of the short saphenous vein. In the leg, the short saphenous vein lies near the sural nerve and contains 7–13 valves, with one near its termination. Its mode of termination is variable: it may join the long saphenous vein in the proximal thigh or it may bifurcate, one branch joining the long saphenous vein and the other joining the popliteal or deep posterior femoral veins. Sometimes it drains distal to the knee in the long saphenous or sural veins.

Deep veins

The deep veins draining the knee and leg correspond in name to the arteries and run with them; the named smaller veins drain into the popliteal and femoral veins.

Deep veins of the foot

Plantar digital veins arise from plexuses in the plantar regions of the toes. They connect with dorsal digital veins to form four plantar metatarsal veins, which run proximally in the intermetatarsal spaces and connect via perforating veins with dorsal veins, then continue to form the deep plantar venous arch, which is situated alongside the deep plantar arterial arch. From this venous arch, medial and lateral plantar veins run near the corresponding arteries and, after communicating with the long and short saphenous veins, form the posterior tibial veins behind the medial malleolus. Proximal to the deep plantar arch there is a plantar cutaneous venous plexus, especially dense in the fat of the heel. It connects with the plantar cutaneous venous arch and other deep veins, but drains mainly into the marginal veins. The veins of the sole are an important part of the lower limb 'venous pump' system aiding propulsion of blood up the limb (Broderick et al 2008). Intermittent foot compression devices are available to enhance this flow and so reduce the risk of deep vein thrombosis during periods of increased risk, e.g. after surgery.

Posterior tibial veins

The posterior tibial veins accompany the posterior tibial artery (see Fig. 76.8). They receive tributaries from the calf muscles (especially from the venous plexus in the soleus) and connections from superficial veins and the fibular veins.

Fibular veins

The fibular veins, running with their artery, receive tributaries from soleus and from superficial veins.

Anterior tibial veins

The anterior tibial veins, continuations of the venae comitantes of the dorsalis pedis artery, leave the anterior compartment between the tibia and fibula, and pass through the proximal end of the interosseous membrane. They unite with the posterior tibial veins to form the popliteal vein at the distal border of popliteus.

Popliteal vein

The popliteal vein ascends through the popliteal fossa to the opening in adductor magnus, where it becomes the femoral vein (see Figs 76.8, 76.9B, 77.47). Its relationship to the popliteal artery changes as the vein ascends: distally, it is medial to the artery; between the heads of gastrocnemius, it is superficial (posterior) to the artery; and proximal to the knee joint, it is posterolateral to the artery. Its tributaries are the short saphenous vein; veins corresponding to branches of the popliteal artery; and muscular veins, including a large branch from each head of gastrocnemius. There are usually four or five valves in the popliteal vein.

Femoral vein

The femoral vein accompanies its artery, beginning at the adductor opening as the continuation of the popliteal vein, and ending posterior to the inguinal ligament as the external iliac vein (see Figs 76.8, 77.1–77.2, 77.44). The vein is posterolateral to the femoral artery in the distal adductor canal. More proximally in the canal, and in the distal femoral triangle (i.e. at its apex), the vein lies posterior to the artery and proximally, at the base of the triangle, the vein lies medial to the artery. The vein occupies the middle compartment of the femoral sheath, between the femoral artery and femoral canal; fat in the canal permits expansion of the vein.

The femoral vein has numerous muscular tributaries. The profunda femoris vein (deep vein of the thigh, deep femoral vein) joins the femoral vein posteriorly 4–12 cm distal to the inguinal ligament, and the long saphenous vein then enters anteriorly. Veins accompanying the superficial epigastric, superficial circumflex iliac and external pudendal arteries join the long saphenous vein before it enters the saphenous opening. Lateral and medial circumflex femoral veins are usually tributaries of the femoral vein. There are usually four or five valves in the femoral vein; the two most constant are just distal to the entry of profunda femoris and near the inguinal ligament.

Profunda femoris vein (deep vein of the thigh)

The profunda femoris vein lies anterior to its artery and receives tributaries corresponding to the branches of the artery. Through these tributaries it connects distally with the popliteal vein and proximally with the inferior gluteal veins. It sometimes drains the medial and lateral circumflex femoral veins and has a valve just before it empties into the femoral vein.

LYMPHATIC DRAINAGE

Lymphocytes are located in many sites in the body, most obviously at strategic sites that are liable to infection, e.g. the oropharynx. The main areas of lymphocyte concentration are classified as primary or secondary lymphoid organs, according to whether they are involved in *de novo* lymphocyte generation (primary lymphoid organs, e.g. bone marrow, thymus) or are the site of mature lymphocyte activation and initiation of an immune response (secondary lymphoid organs, e.g. lymph nodes, spleen).

All lymphocytes arise from pluripotent haemopoietic stem cells in the bone marrow. The B lymphocyte lineage develops through a series of differentiation stages within the bone marrow. The newly formed B cells then leave through the circulation and migrate to peripheral sites. In contrast, T-lymphocyte development requires the thymus; the bone marrow-derived stem cells must therefore migrate via the blood circulation to the thymus. After their differentiation and maturation into immunocompetent T cells that have survived thymic selection processes (1–3%), they re-enter the circulation and are transported to peripheral sites where they join the pool of naïve lymphocytes that recirculate through the secondary lymphoid organs via blood and lymphatic circulation systems.

The secondary or peripheral lymphoid organs are the specialized sites where B and T lymphocytes and antigen-presenting cells come together to initiate immune responses to foreign antigens (Malhotra et al 2013). They include lymph nodes, spleen, lymphoid tissue associated with epithelial surfaces (mucosa-associated lymphoid tissue, MALT), e.g. the palatine and nasopharyngeal tonsils; Peyer's patches in the small intestine; lymphoid nodules in the respiratory and urogenital systems; the skin. The microstructure of lymph nodes and of MALT in general is described in Chapter 4.

Thoracic duct

The thoracic duct conveys the lymph from the entire body back to the venous circulation, except lymph from the right part of the head, neck and heart, right upper limb, parts of the left and right lung and part of the convex surface of the liver. It usually originates anterior to the body of the first or second lumbar vertebra, where the intestinal and two lumbar lymphatic trunks join to form the cisterna chyli. Both the thoracic duct and the cisterna chyli are variable in their origin, course and length; the latter is even more variable in width and shape than the thoracic duct (Song 2016) (see page 1464.e120 for a description of the cisterna chyli). From the superior aspect of the cisterna chyli, the thoracic duct passes through the aortic hiatus and enters the posterior mediastinum, lying to the right of the midline, between the aorta and the azygos vein, up to the level of the body of the fifth or sixth thoracic vertebra, where it typically crosses over the vertebral column posterior to the oesophagus (see Fig. 56.7B). It may branch or even have duplicate trunks that eventually form a single thoracic duct (Song 2016). It continues superiorly, first posterior to the aortic arch adjacent to the left side of the oesophagus, then posterior to the left subclavian artery in the superior mediastinum. It subsequently arches over the left subclavian artery and descends anteriorly to empty into the venous circulation in the region of the left internal jugular and subclavian veins, either at their very confluence or in proximity, or sometimes into the left brachiocephalic vein (see Fig. 56.5). In the space between longus colli, scalenus anterior and the suprapleural membrane, the duct usually arches 3–4 cm superior to the clavicle, crossing anterior to the vertebral vessels, the left sympathetic trunk, the vertebral ganglion, the left thyrocervical trunk and the left phrenic nerve. The course and position of the thoracic duct determines the location of the effusion seen with duct injury or obstruction.

Two thoracic ducts are sometimes present within the mediastinum and may terminate in veins on their respective side of the body. Occasionally a single thoracic duct may empty into right-sided venous structures, a disposition that is more frequent in individuals with an aberrant right subclavian artery originating from the distal aortic arch ascending posterior to the oesophagus.

The thoracic duct is commonly 36–45 cm in length; its external diameter varies according to region (Song 2016). When present as a single channel it is 5–8 mm in diameter at its origin, narrows to 2–3 mm at mid-thoracic level and then widens again at its termination: the diameter may fluctuate with lymph flow rate (Smith et al 2013). Alternatively, the thoracic duct may divide into two or three branches that eventually reunite or drain into both the left and right venous systems. The duct appears sinuous and has valves throughout its length; a bicuspid valve at its termination may prevent the backflow of blood. As it passes through the mediastinum, the thoracic duct also receives non-chylous lymph from tributaries that drain regions of the pulmonary parenchyma and parietal pleura. The sum of these sources accounts for a total lymphatic flow through the thoracic duct of 1500–2400 ml per day in proportion to the dietary intake of fat, particularly long-chain triglycerides.

The thoracic duct crosses the mediastinum at, or at about, the level of the body of the fifth thoracic vertebra which means that lymphatic injury or obstruction above or below this level results in a left- or right-sided pleural effusion (chylothorax), respectively (Doerr et al 2001). Anomalies and sites of injury to the duct are identified by lymphangiography, with or without post-procedure CT scanning, or lymphoscintigraphy. Lymphangiography is performed after bilateral localization of pedal lymphatics with a subcutaneous injection of methylene blue, followed by a minor surgical procedure to cannulate the lymphatic vessels, and injection of Lipiodol contrast agent. Conventional X-ray and CT imaging (without intravenous contrast) are then undertaken. Lymphangiography can identify areas of chyle leakage and lymphangiectasia in the majority of patients (Deso et al 2012).

Tributaries Some tributaries of the thoracic duct may terminate directly in the venous system. There are numerous anastomoses between visceral, parietal, limb and mammary lymphatics, as is apparent from observed multiple patterns of dissemination of cancer cells (see Figs 56.4–56.5). As well as the cisterna chyli and its tributaries, bilateral ascending lumbar lymphatic trunks from the upper lateral aortic (abdominal part) nodes pierce the corresponding diaphragmatic crus and eventually join the thoracic duct in the posterior mediastinum. The inferior six or seven intercostal lymphatic trunks from the corresponding bilateral intercostal nodes descend to terminate in the duct, either directly or by variable common trunks. The left upper intercostal lymphatics may join the cervical portion of the duct or the subclavian trunk. The left subclavian trunk usually joins the thoracic duct but may open independently into the left subclavian vein. These mediastinal trunks provide lymph drainage paths to the thoracic duct from the convex diaphragmatic aspect of the liver, the respiratory diaphragm, the pericardium, heart and oesophagus; many possess terminal bicuspid valves. The left bronchomediastinal trunk occasionally joins the thoracic duct but usually has an independent venous termination. The left jugular trunk usually joins the thoracic duct but may open independently into the left internal jugular vein (see Fig. 35.16).

LYMPHATIC DRAINAGE OF THE HEAD AND NECK

Lymph nodes in the head and neck are arranged in two horizontal rings and two vertical chains on either side of the neck (see Figs 35.1, 35.15). The superficial ring consists of the occipital, preauricular (parotid), submandibular and submental nodes, and the inner, deep, ring is formed by clumps of mucosa-associated lymphoid tissue (MALT) located primarily in the nasopharynx and oropharynx (Waldeyer's ring). The vertical chain consists of superior and inferior groups of nodes related to the carotid sheath, and known collectively as the deep cervical lymph nodes. All lymph vessels of the head and neck drain into the deep cervical nodes, either directly from the tissues or indirectly via nodes in the outlying groups. Efferents of the deep cervical nodes form the jugular trunk on either side. The right jugular trunk collects lymph from the right head and neck, the right arm and the right half of the thorax, and may end in the jugulosubclavian junction or the right lymphatic duct. The left jugular trunk usually enters the thoracic duct, but it may join the internal jugular or subclavian vein. A summary of the widely used surgical neck lymph node classification system is shown in Table 81.1. (For a concise description of the main anatomical boundaries of each nodal group, the normal structures juxtaposed to these nodes, and the main tumour sites at risk for harbouring metastases in each level, see Grégoire et al 2014.)

TABLE 81.1 Surgical levels of the neck

Level	Boundaries
Level Ia	The submental triangle, bounded by the anterior bellies of the digastric and mylohyoid muscles
Level Ib	The submandibular triangle, formed by the anterior and posterior bellies of digastric and the body of the mandible
Level IIa	The region anterior to the accessory nerve, bounded by the digastric muscle superiorly and either the hyoid bone (clinical landmark) or the carotid bifurcation (surgical landmark) inferiorly, down to the prevertebral fascia
Level IIb	The region above and posterior to the accessory nerve, extending to the skull base
Level III	Extends from the carotid bifurcation superiorly either to the cricothyroid notch (clinical landmark) or to omohyoid (surgical landmark). Note that the position of omohyoid moves with head position and so the inferior extent of this level can be arbitrary
Level IV	Contains the lower jugular nodes extending from omohyoid superiorly to the clavicle inferiorly
Level V	The posterior triangle, bounded posteriorly by the anterior border of trapezius, anteriorly by the posterior border of sternocleidomastoid, and inferiorly by the clavicle. It is divided into level Va (above) and Vb (below) by the accessory nerve as it crosses the posterior triangle
Level VI	The anterior neck compartment, extending from the level of the hyoid bone superiorly to the suprasternal notch inferiorly. On each side the lateral boundary is the medial border of the carotid sheath

Face and scalp

Lymph vessels from the frontal region above the root of the nose drain to the submandibular nodes (see Fig. 36.21). Vessels from the rest of the forehead, temporal region, upper half of the lateral auricular aspect and anterior wall of the external acoustic meatus drain to the superficial parotid nodes that lie just anterior to the tragus, either on or deep to the parotid fascia. These nodes also drain lateral vessels from the eyelids and skin of the zygomatic region, and their efferent vessels pass to the upper deep cervical nodes. A strip of scalp above the auricle, the upper half of the cranial aspect and margin of the auricle, and the posterior wall of the external acoustic meatus all drain to the upper deep cervical and posterior auricular nodes. The posterior auricular nodes are superficial to the mastoid attachment of sternocleidomastoid and deep to auricularis posterior and drain to the upper deep cervical nodes. The auricular lobule, floor of the external acoustic meatus and skin over the mandibular angle and lower parotid region all drain to the superficial cervical or upper deep cervical nodes. Superficial cervical nodes lie along the external jugular vein superficial to sternocleidomastoid. Some efferents pass round the anterior border of sternocleidomastoid to the upper deep cervical nodes, while others follow the external jugular vein to the lower deep cervical nodes in the subclavian triangle.

The occipital region of the scalp drains partly to the occipital nodes, and partly to a vessel that runs along the posterior border of sternocleidomastoid to the lower deep cervical nodes. Occipital nodes are commonly superficial to the upper attachment of trapezius but occasionally lie in the superior angle of the posterior triangle.

There are usually three submandibular nodes, internal to the deep cervical fascia in the submandibular triangle. One lies at the anterior pole of the submandibular gland, and two flank the facial artery as it reaches the mandible. Other nodes are often embedded in the gland or deep to it. Submandibular nodes drain a wide area, including vessels from the submental, buccal and lingual groups of nodes, and their efferents pass to the upper and lower deep cervical nodes. The external nose, cheek, upper lip and lateral parts of the lower lip drain directly to the submandibular nodes; the afferent vessels may have a few buccal nodes along their course and near the facial vein. The mucous membrane of the lips and cheek drains to the submandibular nodes, and the lateral part of the cheek drains to the parotid nodes. The central part of the lower lip, buccal floor and tip of the tongue all drain to the submental nodes lying on mylohyoid between the anterior bellies of the digastric muscles. These nodes receive afferents bilaterally, some decussating across the chin and their efferents pass to the submandibular and jugulo-omohyoid nodes.

The posterior aspect of the auricle (pinna) drains to nodes at the mastoid tip. The tragus and upper part of the pinna drain into preauricular nodes, while the remainder of the pinna drains to upper deep cervical lymph nodes. Lymphatic vessels of the tympanic and antral mucosae drain to the parotid or upper deep cervical lymph nodes. Vessels draining the tympanic end of the pharyngotympanic tube probably end in the deep cervical nodes. Lymphatic vessels from the conjunctiva drain into pre-auricular and submandibular lymph nodes. The infratemporal and temporal fossae drain to the superior deep cervical nodes. Lymphatics from the temporomandibular joint drain deeply to the upper cervical lymph nodes surrounding the internal jugular vein.

Mouth

Gingivae and teeth

The lymph vessels of the labial and buccal gingivae of the maxillary and mandibular teeth unite to drain into the submandibular nodes; they may drain into the submental lymph nodes in the labial region of the mandibular incisors. The lingual and palatal gingivae drain into the jugulodigastric group of nodes, either directly or indirectly through the submandibular nodes.

The lymph vessels from the teeth usually run directly into the ipsilateral submandibular lymph nodes. Lymph from the mandibular incisors drains into the submental lymph nodes and lymph from the molars may occasionally pass directly into the jugulodigastric group of nodes.

Tongue

The mucosa of the pharyngeal part of the dorsal surface of the tongue contains many lymphoid follicles aggregated into dome-shaped groups: the lingual tonsils. Each group is arranged around a central deep crypt, or invagination, which opens on to the surface epithelium. The ducts of mucous glands open into the bases of the crypts. Small isolated follicles also occur beneath the lingual mucosa. The lymphatic drainage of the tongue can be divided into three main regions: marginal, central and dorsal. The anterior region of the tongue drains into marginal and central vessels, and the posterior part of the tongue behind the circumvallate papillae drains into the dorsal lymph vessels. The more central regions may drain bilaterally, and this must be borne in mind when planning to remove malignant tumours of the tongue that are approaching the midline. If the tumour has a propensity for lymphatic spread, both cervical chains may be involved.

Marginal vessels

Marginal vessels from the apex of the tongue and the lingual frenulum area descend under the mucosa to widely distributed nodes. Some vessels pierce mylohyoid as it contacts the mandibular periosteum to enter either the submental or anterior or middle submandibular nodes, or else to pass anterior to the hyoid bone to the jugulo-omohyoid node. Vessels arising in the plexus on one side may cross under the frenulum to end in contralateral nodes. Efferent vessels of median submental nodes pass bilaterally. Some vessels pass inferior to the sublingual gland and accompany the companion vein of the hypoglossal nerve to end in jugulodigastric nodes. One vessel often descends further to reach the jugulo-omohyoid node, and passes either superficial or deep to the intermediate tendon of digastric.

Vessels from the lateral margin of the tongue cross the sublingual gland, pierce mylohyoid and end in the submandibular nodes. Others end in the jugulodigastric or jugulo-omohyoid nodes. Vessels from the posterior part of the lingual margin traverse the pharyngeal wall to the jugulodigastric lymph nodes (see Fig. 37.12).

Central vessels

The regions of the lingual surface draining into the marginal or central vessels are not distinct. Central lymphatic vessels ascend between the fibres of the two genioglossi; most pass between the muscles and diverge to the right or left to follow the lingual veins to the deep cervical nodes, especially the jugulodigastric and jugulo-omohyoid nodes. Some pierce mylohyoid to enter the submandibular nodes.

Dorsal vessels

Vessels draining the postsulcal region and the circumvallate papillae run posteroinferiorly. Those near the median plane may pass bilaterally. They turn laterally, joining the marginal vessels, and all pierce the pharyngeal wall, passing around the external carotid arteries to reach the jugulodigastric and jugulo-omohyoid lymph nodes. One vessel may descend posterior to the hyoid bone, perforating the thyrohyoid membrane to end in the jugulo-omohyoid node.

Neck

The lymphatics of the skin in the suprahyoid region drain to level I nodes (submental and submandibular lymph nodes). The lymphatics of the skin of the rest of the neck drain to levels II, III and IV, apart from the posterior lateral neck skin lymphatics, which drain into the spinal accessory nodes in the posterior triangle.

Thyroid gland

Lymphatic vessels communicate within the thyroid gland and the tracheal plexus, passing onwards to prelaryngeal nodes just above the thyroid isthmus and then to pretracheal and paratracheal nodes (level VI). Some may also drain into the brachiocephalic nodes related to the thymus in the superior mediastinum (level VII). Laterally, the gland is drained to the deep cervical nodes (level IV) by vessels lying along the superior thyroid veins. Thyroid lymphatics may drain directly, with no intervening node, to the thoracic duct. In summary, the major lymphatic drainage of the thyroid is to the middle and lower jugular lymph nodes in levels III and IV and to the posterior triangle nodes in level VB, supplemented by minor drainage to the pretracheal and paratracheal nodes in level VI and to the superior mediastinal nodes in level VII.

Larynx

The vocal folds, with their paucity of lymphatics at their edges, provide a clear demarcation between the upper and lower areas of the larynx. Above the vocal folds, the rich network of lymph vessels draining the supraglottic part of the larynx accompany the superior laryngeal artery, pierce the thyrohyoid membrane, and end in the upper deep cervical lymph nodes, often bilaterally. The supraglottic lymphatics also communicate with those at the base of the tongue. Below the vocal folds, some of the lymph vessels of the infraglottic cavity pass through the conus elasticus to reach the prelaryngeal (Delphian) and/or pretracheal and paratracheal lymph nodes, while others accompany the inferior laryngeal artery and join the lower deep cervical nodes (Welsh et al 1983, Werner et al 2003).

Nodal spread of laryngeal tumours

The upper deep cervical lymph nodes act as pathways for the spread of malignant tumours of the supraglottic larynx. Up to 40% of these tumours will have undergone such spread at the time of clinical presentation. The glottis is very poorly endowed with lymphatic vessels; some 95% of malignant tumours confined to the glottis will present only with a change in voice or airway obstruction, but will not show signs of spread to adjacent lymph nodes at presentation. Tumours of the subglottic larynx will often spread to the paratracheal lymph node chain prior to clinical presentation. The presenting symptoms are usually voice change and airway obstruction rather than a mass in the neck. The paratracheal lymph nodes occupy a deep-seated position in the root of the neck and so their enlargement may remain occult. They must be looked for carefully at surgery and included in any radiation field.

LYMPHATIC DRAINAGE OF THE THORAX

Thoracic wall

Superficial lymphatic vessels of the thoracic wall ramify subcutaneously and converge on the axillary nodes (see Figs 46.5, 53.22). Lymphatic vessels from breast tissue drain mainly to axillary nodes, with some passing initially to parasternal, interpectoral and supraclavicular nodes (see Fig. 53.24). Those superficial to trapezius and latissimus dorsi unite to form up to 12 trunks that end in the subscapular (posterior axillary) nodes. Those in the pectoral region, including vessels from the skin covering the periphery of the breast and its subareolar plexus, run back, collecting those superficial to serratus anterior, to reach the pectoral (anterior axillary) nodes. Vessels near the lateral sternal margin pass between the costal cartilages to the parasternal nodes and anastomose across the sternum, providing a route for contralateral nodal spread in medially located breast carcinoma. A few vessels from the upper pectoral region ascend over the clavicle to the inferior deep cervical nodes. Lymph from the deeper tissues of the thoracic walls drains mainly to the parasternal, intercostal or diaphragmatic (phrenic) nodes.

Parasternal nodes

There are four or five parasternal nodes along each internal thoracic artery at the anterior ends of the intercostal spaces. They drain afferents from the breast, deeper structures of the supra-umbilical anterior abdominal wall, the superior hepatic surface (through a small anterior group of nodes posterior to the xiphoid process) and deeper parts of the anterior thoracic wall. Their efferents usually unite with those from the paratracheal (tracheobronchial) and brachiocephalic (prevascular) nodes to form the bronchomediastinal trunk (see Fig. 56.5). On either side, the bronchomediastinal trunk may either open directly into the jugulosubclavian junction; into either the internal jugular or subclavian vein near their junction; into the subclavian trunk; or into the lymphatic duct on the right or the thoracic duct on the left.

Intercostal nodes

Intercostal nodes occupy the intercostal spaces near the heads and necks of the ribs. They receive deep lymph vessels from the posterolateral aspects of the chest wall and breast, some of which are interrupted by small more laterally placed intercostal nodes. Efferent vessels from nodes in the lower intercostal spaces unite into a trunk that descends to the abdominal confluence of lymph trunks or to the start of the thoracic duct. Efferent vessels from nodes in the left upper intercostal spaces end in the thoracic duct; those of the right upper intercostal spaces end in one of the right lymphatic trunks.

Breast

The lymphatic drainage of the breast is of great clinical significance because metastatic dissemination occurs principally by the lymphatic routes (the breasts are the site of malignant change in as many as 1 in 8 women; see Commentary 7.1). The dominant lymphatic drainage of the breast is derived from the dermal network (see Fig. 53.24). Breast lymphatics branch extensively; the smallest valveless superficial lymph capillaries (20–70 μm diameter) drain into larger lymph pre-collecting vessels (~300 μm diameter) that contain valves and smooth muscle. These pre-collectors unite to form a subcutaneous network between skin and breast tissue and drain almost always to at least one sentinel node, usually near the lateral border of pectoralis minor (Suami et al 2008). Lymphatic blockage through tumour occlusion may therefore result in reverse flow through the lymphatic channels, resulting in oedema. The direction of lymphatic flow within the breast parallels the major venous tributaries and enters the regional lymph nodes via an extensive periductal and perilobular network of lymphatic channels. Most of these lymphatics drain into the axillary group of regional lymph nodes either directly or through the retro-areolar lymphatic plexus (see Fig. 49.48). Dermal lymphatics also penetrate pectoralis major to join channels that drain the deeper parenchymal tissues, and then follow the vascular channels to terminate in the regional lymph nodes below the level of the clavicle.

Lymphatics from the left breast ultimately terminate in the thoracic duct and, subsequently, the left subclavian vein. On the right, the lymphatics ultimately drain into the right subclavian vein near its junction with the internal jugular vein. Part of the medial sides of the breasts drain to the parasternal nodes, lying along the internal thoracic vessels. These may anastomose across the sternum, providing a route for contralateral nodal spread in medially located breast carcinoma. Parasternal nodes and vessels may drain inferiorly via the superior and inferior epigastric lymphatic routes to the superficial and deep inguinal nodes in the femoral triangle.

Axillary nodes receive more than 75% of the lymph from the breast. There are 20–40 axillary nodes, grouped somewhat artificially as pectoral (anterior), subscapular (posterior), central and apical. Surgically, the nodes are described in relation to pectoralis minor; those lying lateral or inferior to pectoralis minor are the low nodes (level 1), those lying posterior to pectoralis minor are the middle group (level 2), and those lying between the upper border of pectoralis minor and the lower border of the clavicle are the upper or apical axillary nodes (level 3) (see Fig. 53.24). There may be one or two interpectoral (Rotter's) nodes lying between pectoralis minor and major. Efferent vessels may pass directly from the breast around the anterior axillary border and through the axillary fascia to the pectoral (anterior axillary) lymph nodes; some may pass directly to the subscapular (posterior axillary) nodes. A few vessels pass from the superior part of the breast to the apical axillary nodes, sometimes interrupted by the infraclavicular nodes or by small, inconstant, interpectoral nodes. Most of the remainder drain to parasternal nodes from the medial and lateral parts of the breast and accompany perforating branches of the internal thoracic artery. Lymphatic vessels occasionally follow lateral cutaneous branches of the posterior intercostal arteries to the intercostal nodes (see Fig. 56.4A).

Axillary surgery in breast cancer

Axillary lymph node dissection may be performed for diagnostic and therapeutic reasons. The presence of metastases within axillary lymph nodes has strong prognostic significance and may influence decisions on adjuvant therapy. Axillary lymph node dissection can lead to chronic postoperative problems such as pain, seroma formation, reduced mobility of the arm, impaired sensation and lymphoedema.

Nerves and lymph vessels in the axillary region must be considered as anatomical landmarks at surgery and carefully identified and preserved. Chronic neuropathic pain is a common consequence of surgery, with a prevalence of 25–60% (Jung et al 2003). Chronic pain exacerbates the stress associated with the already burdensome management of breast cancer and in many patients adversely impacts their daily life. Complete resection, stretch or compression of the lateral cutaneous branch of the second thoracic ventral ramus (intercostobrachial nerve) may result in numbness or pain in the ipsilateral axilla, medial arm and upper anterior chest. Symptoms are more common and longer lasting when the origin of the nerve is injured as opposed to its peripheral branches (Jung et al 2003). Resection or compression of the long thoracic nerve, which passes below the clavicle through the axillary sheath and then down the chest wall to innervate serratus anterior, can result in palsy (with scapular winging): shoulder pain may be exacerbated by shoulder instability and reduced abduction.

Lymphatic drainage in breast cancer and role of sentinel lymph node biopsy

Lymphatic mapping with sentinel lymph node biopsy has become an important technique in the staging of patients with early breast cancer. Based upon the assumption that the majority of the lymphatic drainage of the breast occurs through the subareolar plexus (Suami et al 2009), a radiolabelled colloid is injected into either the subareolar tissue of the index quadrant of the breast or into the peritumoural and intradermal tissue overlying the primary breast cancer. At the time of surgery, a vital blue dye is injected after general anaesthesia is established. The combination of radioisotope and dye provides the most accurate means of localizing the sentinel node (Tanis et al 2001). The latter represents the first draining node within the axilla and is surgically removed for careful histopathological analysis to detect the presence of metastases. There is a 5–10% false-negative rate for this procedure that can be partly attributed to anatomical differences in lymphatic drainage (Tanis et al 2005, Suami et al 2008).

If the histopathological results prove negative, the morbidity associated with axillary dissection can be avoided. Where metastases to the axillary nodal group are found, axillary completion dissection or radiotherapy is offered. The majority of sentinel nodes are found in the low axilla (level 1) (see Fig. 53.24). Higher-level 'skip' nodes are involved in 5–10% of cases. Occasionally the sentinel node is identified in an extra-axillary position, either within the breast parenchyma as an intramammary lymph node, or as a parasternal (internal thoracic) lymph node or in the supraclavicular fossa.

Deeper thoracic tissues

Collecting vessels of the deeper thoracic tissues include lymphatics that drain the muscles attached to the ribs. Most end in axillary nodes but some from pectoralis major also drain to the parasternal nodes. Intercostal vessels drain the intercostal muscles, tissues of the extrapleural space (e.g. endothoracic fascia) and the costal parietal pleura; those from the anterior thoracic wall end in the parasternal nodes and their posterior counterparts drain to intercostal nodes.

Vessels from the respiratory diaphragm form a thoracic and an abdominal plexus, which anastomose freely, especially in areas covered by diaphragmatic parietal pleura and peritoneum, respectively. The thoracic plexus unites with lymph vessels draining the costal and mediastinal parts of the parietal pleura. Its efferents are anterior, draining to the anterior diaphragmatic nodes near the junctions of the seventh rib and costal cartilage; middle, draining to nodes on the oesophagus (paraoesophageal) and around the intrathoracic part of the inferior vena cava; and posterior, draining to nodes around the aorta at the point where it leaves the thorax. The abdominal plexus anastomoses with the hepatic lymphatics and peripherally with those of the subperitoneal tissue. Efferents from its right half pass to a group of nodes close to the inferior phrenic artery, or in the right lateral aortic nodes. Those from the left half of the abdominal diaphragmatic plexus pass to the pre-aortic, lateral aortic and paraoesophageal nodes.

Heart

Cardiac lymphatic vessels form subendocardial, myocardial and subepicardial plexuses. Efferent vessels from the subepicardial plexuses form the left and right cardiac collecting trunks; two or three left-sided trunks ascend the anterior interventricular sulcus, receiving vessels from both ventricles. On reaching the atrioventricular sulcus, they are joined by a large vessel from the inferior surface of the left ventricle that first ascends in the inferior interventricular sulcus and then turns left along the atrioventricular sulcus. The vessel formed by this union ascends between the pulmonary trunk and the left atrium and usually ends in a subcarinal (inferior tracheobronchial) node. The right cardiac collecting trunk receives efferents from the right atrium and the right border and inferior surface of the right ventricle. It ascends in the atrioventricular sulcus, near the right coronary artery, and then anterior to the ascending aorta, and ends in a brachiocephalic or prevascular node, usually on the left (see Fig. 57.60) (Loukas et al 2011).

Cardiac lymphatics play a crucial role in cardiac function, such as maintaining fluid balance, removal of extravasated proteins and transport of immune cells (Vuorio et al 2016). The developed lymphatic network of the heart traverses all its layers, including those of the atria and ventricles and extends to the mitral valve. Most lymph drainage of the pericardium is to the thoracic and the right lymphatic ducts; upper mediastinal (e.g. para-aortic, subaortic, retrotracheal, prevascular) and parasternal internal thoracic lymph nodal groups also receive efferents (see Fig. 54.12B). There are two layers of pericardial lymphatic vessels, contacting and surrounding the parietal pericardium and also within the fat and loose areolar tissue. The anterior (sternocostal) part of the pericardium either drains laterally towards the phrenic nerves as they enter the respiratory diaphragm (superior phrenic nodes), or travels along the ventral border of the pericardium to enter the prepericardial lymph nodes located at the pericardio-diaphragmatic junction. Drainage from the lateral pericardium is more variable. Inferiorly, it drains towards the phrenic nerves and the pericardiacophrenic vessels as they reach the respiratory diaphragm, and includes the lateral pericardial nodes; superiorly, it drains into the tracheobronchial (subcarinal) and paratracheal lymph nodes. The posterior pericardium, including the posterior aspect of the associated dome of the respiratory diaphragm and extending as far as the pulmonary veins, drains superiorly to the superior and inferior tracheobronchial (upper and lower paratracheal, and subcarinal) lymph nodes. The portion of the pericardium that adheres to the diaphragm drains via short channels to the lymph nodes at the right border of the inferior vena caval opening in the central diaphragmatic tendon.

Lymphangiogenesis, the formation of new lymphatics, is beneficial in delaying atherosclerotic plaque formation in coronary arteries. In patients with myocardial infarction, lymphangiogenesis is therapeutic during the healing process, reflecting their ability to reduce fluid retention and aid the clearance of inflammatory cells within the cardiac tissues.

Pleura and lungs

Lymph from the costal part of the parietal pleura drains into the parasternal nodes anteriorly and intercostal chains posteriorly, while that from the diaphragmatic pleura drains into the mediastinal, parasternal, para-aortic (phrenic) and coeliac nodes (see Figs 56.4–56.5). The lymphatic drainage of the visceral pleura is initially via the subpleural lymphatic plexus. Lymph can pass via segmental or intersegmental lymphatic pathways, and sometimes peribronchial lymphatic pathways; the exact pattern of drainage varies depending on lobe, segment, side and individual (Fourdrain et al 2018).

The pulmonary lymphatics originate in superficial and deep plexuses. The walls of the alveoli and the alveolar ducts have no lymph vessels, these only start at the bronchioles. The superficial plexus lies deep to the visceral pleura; its efferents pass around the margins of the lung and its fissures, eventually reaching the bronchopulmonary (hilar) nodes (see Fig. 54.12). The deep lymphatics originate at bronchiolar level and follow the bronchial tree divisions and pulmonary vessels to the hilum, ending in the same nodes as the superficial plexus. In larger bronchi, the deep plexus has submucosal and peribronchial parts, but in smaller bronchi there is only a single plexus that extends to the bronchioles. Lymph node groups (stations) sit alongside the bronchi and are classified according to their location, specifically; subsegmental, segmental, lobar and hilar (Rusch et al 2009). Lymph from the hilar nodes drains into subcarinal (inferior tracheobronchial) and lower paratracheal (superior tracheobronchial) node groups (stations).

No free anastomoses exist between the two superficial and deep plexuses, except at the hilum and peripherally, where small but dilatable channels connect superficial and deep lymphatic vessels; these connections direct lymph from the deep to the superficial channels when outflow from deep vessels is obstructed by pulmonary disease. There is a tendency for vessels from the superior lobes to pass to the superior tracheobronchial (lower paratracheal) nodes, and those from the inferior lobes to pass to the inferior tracheobronchial (subcarinal) group. However, lymphatic vessels of adjoining lobes connect deep in the fissures and so these connections are not exclusive. At the level of pulmonary lobation, the arrangement of lymphatic vessels follows the central artery of a lobule and its peripheral veins. Lymphoid aggregations, non-follicular in appearance, occur in peribronchial sites and in ‘placoid’ formations deep to the visceral pleura.

Pulmonary nodes within the lung parenchyma are continuous with the bronchopulmonary node groups (in order, these include subsegmental, segmental, lobar, interlobar and hilar nodes) (see Figs 54.12, 56.4B). Bronchopulmonary node groups are continuous with inferior tracheobronchial (subcarinal) nodes located inferior to the tracheal bifurcation and the superior tracheobronchial (lower paratracheal) nodes. In turn, these groups are continuous with the upper paratracheal groups of nodes that drain the lungs, bronchi, the thoracic part of the trachea, heart, pericardium and also receive efferent vessels from prevertebral nodes that receive lymph from the posterior respiratory diaphragm, thoracic oesophagus, and intercostal lymph nodes. Efferent vessels ascend on the trachea to unite with efferents from the parasternal and brachiocephalic nodes to become the right and left bronchomediastinal trunks. The right trunk may occasionally join a right lymphatic duct or another right-sided lymph trunk, and the left trunk may join the thoracic duct, but usually they open independently in or near the ipsilateral junction of the internal jugular and subclavian vein (see Fig. 35.16).

Oesophagus

The oesophagus has an extensive, longitudinally continuous submucosal lymphatic system within which flow may be bidirectional: this is pertinent to lymphatic spread in oesophageal carcinoma. Efferent vessels from the cervical oesophagus drain to the deep cervical nodes either directly or through the paratracheal nodes. Vessels from the cervical oesophagus drain to paraoesophageal, deep cervical and supraclavicular nodes; those from the thoracic oesophagus drain directly to the thoracic duct or to paratracheal, retrotracheal, subcarinal and right recurrent laryngeal nodes; and those from the abdominal oesophagus drain to the nodes associated with the left gastric artery or other arteries originating from the coeliac trunk, including those associated with the lesser curvature of the stomach (Wang et al 2018).

The lymphatics of the oesophagus are concentrated into submucosal and intermuscular plexuses. Both of these plexuses receive lymph from all layers of the oesophageal wall (Kuge et al 2003, Rice et al 2016). Terminology is not straightforward. In general, lymphatic drainage from the oesophagus communicates with nodes in the adventitia, para-oesophageal nodes or the thoracic duct directly (Wang et al 2018). However, the lymphatics of the distal third of the oesophagus do not drain to para-oesophageal nodes of the same level but distally to the left gastric nodes and nodes around the cardia, and then to coeliac nodes (Tachimori 2017). Therefore, cancer of the lower thoracic oesophagus tends to metastasize to nodes of the upper abdominal area (Tamaki et al 2012).

Mediastinum

There are multiple groups of lymph nodes throughout the mediastinum. Conventionally they have been named according to their position relative to the nearest mediastinal structure (which they often drain): parietal node groups drain the thoracic wall and visceral groups drain the thoracic viscera (see Figs 54.12, 56.4A). However, this naming system implies that the mediastinal node groups are separate and distinct, whereas in reality they are part of a continuum. To better reflect their regional disposition, and for the purposes of cancer staging and management, mediastinal lymph node groups are categorized into regional lymph node stations and zones (Rusch et al 2009) (see Fig. 56.4B, Table 56.1).

Metastatic involvement of mediastinal lymph nodes has important prognostic implications and influences the choice of treatment (Mountain and Dresler 1997, Rusch et al 2009). The staging system for lung cancer classifies node involvement using a nodal descriptor (N-‘Stage’), where N0 indicates no regional lymph node metastases; N1 indicates involvement of ipsilateral peribronchial or hilar lymph nodes and intrapulmonary nodes; N2 indicates involvement of ipsilateral mediastinal and/or subcarinal nodes; and N3 indicates involvement of contralateral mediastinal or hilar nodes, and ipsilateral or contralateral scalene or supraclavicular nodes/scalene nodes (Goldstraw et al 2016, Chansky et al 2017, Lim et al 2018).

Mediastinoscopy

The decision to proceed with mediastinoscopic biopsy depends on whether suitable nodal stations (zones) seem involved on CT scanning and whether there is a history of prior neck and mediastinal surgical procedures. Complications of mediastinoscopy include haemorrhage, iatrogenic injury to the trachea or left recurrent laryngeal nerve, and pneumothorax. Mediastinoscopy can be performed with video-assisted or direct optic visualization. A transverse incision is made at the level of the suprasternal notch; sternohyoid and sternothyroid within the superficial lamina of deep cervical fascia are retracted; the deep lamina of the deep cervical fascia is incised. The pretracheal plane is dissected and a space is created between the anterior aspect of the trachea and the brachiocephalic trunk inferior to the carina and along both sides of the trachea and main bronchi. This space facilitates biopsy of the upper paratracheal 2R and 2L stations, the right lower paratracheal 4R station and higher nodes from the left lower paratracheal 4L station superior to the aortic arch (see Table 56.1). The anterior part of subcarinal station 7 and bilateral hilar stations 10R and 10L may be accessible but are technically challenging. Lymph nodes can be sampled or removed entirely for histological evaluation.

The anterior part of the superior mediastinum is more difficult to assess by mediastinoscopy and usually requires an anterior mediastinotomy (Chamberlain procedure). This is performed to biopsy nodes from the more inferior aspect of the left lower paratracheal 4L station, subaortic station 5, para-aortic station 6 and subcarinal station 7, and also facilitates anterior mediastinal mass biopsy. Endobronchial ultrasound can be performed to biopsy lymph nodes in stations 1–4, 7 and 10–12, using fine needle aspiration through the tracheal or bronchial walls. In a similar way, transoesophageal ultrasound may help during biopsy of subcarinal station 7, para-oesophageal station 8 and pulmonary ligament station 9.

Respiratory diaphragm

The respiratory diaphragm is drained by anterior, middle and posterior groups of lymph nodes that lie on its thoracic (superior) surface (see Fig. 56.4). These nodes also drain the superior portion of the liver, the gastro-oesophageal junction and the abdominal surface of the respiratory diaphragm. Lymph drains anterosuperiorly to the parasternal and anterior mediastinal nodes, and posterosuperiorly to the posterior mediastinal and brachiocephalic nodes.

Anterior group

The anterior group consists of two or three small nodes posterior to the base of the xiphoid process, draining the convex diaphragmatic surface of the liver, and one or two nodes on each side near the junction of the seventh rib and costal cartilage that receive anterior lymph vessels from the respiratory diaphragm. The anterior group drains to the parasternal nodes.

Lateral groups

The lateral groups each contain two or three nodes and lie close to the point where the phrenic nerves enter the respiratory diaphragm. On the right, some nodes lie within the fibrous pericardium anterior to the intrathoracic part of the inferior vena cava. Their afferents drain the central part of the respiratory diaphragm; those on the right also drain the convex (diaphragmatic) surface of the liver, and their efferents pass to the paraoesophageal (posterior mediastinal), parasternal and brachiocephalic nodes.

Posterior group

The posterior group consists of a few nodes that lie on the posterior aspect of the crura of the respiratory diaphragm and connect with the lateral and posterior aortic (prevertebral) and para-oesophageal (posterior mediastinal) nodes.

LYMPHATIC DRAINAGE OF THE ABDOMEN AND PELVIS

Lymph from the skin and subcutaneous tissues of the abdominal wall drains via small calibre superficial lymphatics to axillary and inguinal nodes (Tourani et al 2013). The midline and the level of the umbilicus form inconstant and variable watershed boundaries for these drainage territories. Lymphatics from the deeper layers of the body wall and the abdominal and pelvic viscera drain almost exclusively to the cisterna chyli and thoracic duct. The former drains via ipsilateral nodes in the retroperitoneum concentrated around the external iliac and common iliac vessels and along the lateral aspects of the aorta and inferior vena cava. There is considerable overlap between the lymphatic drainage of individual viscera. At certain sites there is a cranio-caudal sequence of lymph nodes, e.g. lateral aortic nodes; and parasternal and inferior epigastric nodes. Some lymphatic drainage from the bare area of the liver occurs directly across the respiratory diaphragm to the thoracic cavity. The highest concentration of lymphatic vessels in the anterior abdominal wall is found in the dermis (Friedman et al 2015). Lymphatic vessels from the lumbar and gluteal regions run with the superficial circumflex iliac vessels, and those from the abdominal skin distal to the umbilicus run with the superficial epigastric vessels. Both drain into superficial inguinal nodes. Lymphatic vessels from the proximal umbilical region drain to axillary and parasternal nodes. Enlargement of a lymph node in the umbilical region is rare but can herald an abdominal or pelvic malignancy.

The deep lymphatic vessels accompany the deeper arteries. Laterally, they run either with the lumbar arteries to drain into the lateral aortic nodes, or with the posterior intercostal and subcostal arteries to nodes in the posterior mediastinum. Lymphatics in the proximal anterior abdominal wall run with the superior epigastric vessels to parasternal nodes while those in the distal abdominal wall run with the deep circumflex iliac and inferior epigastric arteries to external iliac nodes.

The paired viscera of the retroperitoneum drain to lateral aortic nodes around the origin of their arterial supply. Thus, the kidneys and suprarenal glands drain to nodes around the hilum of the kidney and to lateral aortic nodes around the origin of the renal arteries (first and second lumbar vertebral levels). The testes drain to lateral aortic and lateral, precaval and retrocaval nodes (approximately second lumbar vertebral level); the pattern of lymphatic spread from a testicular malignancy suggests that lymph from the left testis drains to left lateral aortic nodes en route to the cisterna chyli, whereas lymph from the right testis drains to right and then left lateral aortic nodes before reaching the cisterna chyli. Lymph from the ovary may drain via lymphatics in the broad ligament of the uterus and round ligament of the uterus to internal iliac and inguinal nodes, respectively. Lymphatic drainage of the ureters is less well defined but follows a regional pattern to nearby nodes.

The pancreas drains to numerous pancreatic nodes (Ch. 68) and to nodes between the hepatic portal vein and inferior vena cava (clinically referred to as portacaval nodes), splenic, superior mesenteric and coeliac nodes. The lymphatic drainage of the duodenum is not well described but the lymphatics generally drain to nodes related to local arteries (Ch. 64). Whilst the clinical pattern of nodal metastases usually reflects normal lymphatic drainage pathways, lymphatic obstruction may lead to metastases at unusual nodal sites.

Cisterna chyli and abdominal lymph trunks

The abdominal origin of the thoracic duct usually lies to the right of the midline at the level of the body of the twelfth thoracic vertebra or the intervertebral disc between the twelfth thoracic and first lumbar vertebrae. It receives almost all the lymph from below the respiratory diaphragm via the cisterna chyli, a localized saccular or fusiform lymphatic dilation formed most commonly by the union of the intestinal trunk and the left lumbar trunk (Phang et al 2014). The cisterna chyli is approximately 1 cm wide and 2 cm long in the cadaver (Loukas et al 2007b): studies using magnetic resonance imaging (MRI) *in vivo* have shown that it expands considerably during movement from supine to sitting and again from sitting to standing (Niggemann et al 2010).

The formation of the cisterna chyli is variable and it may be absent. When present, it usually lies anterior to the first and second lumbar vertebrae, posterior to the right crus of the respiratory diaphragm and to the right of the abdominal aorta, but it may be located at a more proximal vertebral level (see Fig. 61.14). The most common configuration, found in approximately two-thirds of individuals, is a single structure formed from the union of the intestinal trunk and the left (or, less commonly, the right) lumbar trunk (Loukas et al 2007b). In most other individuals it is formed by the confluence of the intestinal and both lumbar trunks, with additional small branches from intercostal lymphatics (intercostal trunks) and retro-aortic nodes (Skandalakis et al 2004). The proximal two right lumbar arteries and the right lumbar azygos vein lie between the cisterna chyli and the vertebral column.

The paired lumbar trunks are formed by lymphatic vessels draining lateral aortic nodes. The intestinal trunk (which may be double) receives vessels draining from coeliac, superior and inferior mesenteric nodes that collectively drain the entire abdominal gastrointestinal tract down to the anal canal. The thoracic duct leaves the superior end of the cisterna chyli and passes through the aortic hiatus of the respiratory diaphragm posterolateral to the right side of the aorta. Its thoracic continuation is described on page 1464.e115.

The major lymphatic vessels adjacent to the abdominal aorta are at risk of injury during surgical procedures that involve peri-aortic dissection and/or lymphadenectomy. Injury to these lymphatic vessels or their obstruction by malignant disease can cause leakage of lymph manifesting as chylous ascites or chylothorax.

Retroperitoneal lymph node groups

The lymphatic drainage of the rectum, colon, stomach, pancreas, oesophagus and other organs is often described in terms of lymph node stations and levels of dissection that relate to the management of malignant disease. The terminology and classification of retroperitoneal lymph nodes are based on their location. In classic anatomical descriptions, the lymph nodes of the retroperitoneum around the abdominal aorta are grouped into pre-aortic, lateral and retro-aortic nodes, but adjacent nodal groups merge into one another with no clear demarcating boundaries. Normal lymph node dimensions are very variable. Cross-sectional imaging frequently uses 10 mm as an approximate measurement for the upper limit of normal lymph node dimensions in the adult (Moeller and Reif 2000): some normal retroperitoneal nodes such as the portacaval nodes are typically larger.

Pre-aortic nodes

Pre-aortic nodes drain the gastrointestinal viscera including the pancreas, liver and spleen. They lie anterior to the aorta clustered around its anterior unpaired visceral branches and can be subdivided into coeliac, superior mesenteric and inferior mesenteric nodes. Their efferent lymphatics contribute to the formation of the intestinal lymph trunk.

Coeliac nodes

Coeliac nodes drain lymph from nodes around the stomach, splenic hilum, porta hepatis, cystic duct, lesser omentum, portacaval nodes, pancreatic nodes and pancreaticoduodenal nodes. They also receive lymph from superior and inferior mesenteric nodes and their efferent lymphatics drain to the intestinal trunks.

Superior mesenteric nodes

Superior mesenteric nodes share an extensive overlap with the drainage territory of coeliac nodes, with subsidiary nodal groups that include pancreatic, pancreaticoduodenal, portacaval, ileocolic, mesenteric and inferior mesenteric nodes. Efferent lymphatics drain to the intestinal trunks either directly or via coeliac nodes.

Inferior mesenteric nodes

Inferior mesenteric nodes such as the superior rectal nodes drain lymph from derivatives of the hindgut, including the distal transverse, descending and sigmoid colon, and the rectum.

Lateral aortic groups

Lateral aortic (para-aortic) nodes lie on either side of the abdominal aorta and inferior vena cava anterior to the medial margins of psoas major, the crura of the respiratory diaphragm and the sympathetic trunks. Constituent nodal groups that are recognized clinically include the retrocrural (posterior to the diaphragmatic crura at the aortic hiatus); left and right hilar (of the kidney); aortocaval, lateral caval, retrocaval and precaval groups. Retro-aortic nodes are sometimes included within the lateral aortic group. The latter drain into the paired intestinal trunks that terminate directly or indirectly in the cisterna chyli and thoracic duct. There are lymphatic connections between lateral aortic, pre-aortic, retro-aortic and contralateral lateral aortic nodes. The lateral aortic nodes drain the deep layers of the body wall, the retroperitoneal paired viscera (including the gonads) and tributaries from the iliac nodes. Lymph from the right ovary or testis drains via lymphatics travelling with the gonadal vessels to the right lateral aortic and pre-aortic nodes at the level of the second lumbar vertebra, whereas lymph from the left ovary or testis drains to the left lateral aortic nodes just inferior to the left renal vein (Morton and Thomas 2008, Paño et al 2011).

Iliac nodes

Paired iliac nodes are distributed around the common, external and internal iliac arteries and veins. Constituent groups include the common iliac, external iliac, internal iliac and obturator nodes. The latter are located near the obturator foramen and, together with the iliac nodes, are a common site of lymph node metastasis in prostate cancer. ‘Pelvic side-wall’ nodes, lying adjacent to the ilium but not associated with a large artery or vein, are also described in the clinical literature. The iliac nodes drain the pelvic viscera and walls, except for the ovaries and those parts of the rectum drained by superior rectal nodes. They also drain lymph from the inguinal nodes and lower limbs.

Lymphatic drainage of viscera

Duodenum

Duodenal lymphatics run to nodes associated with the superior and inferior pancreaticoduodenal arteries, and from there to nodes related to the common hepatic and superior mesenteric arteries and coeliac trunk and to nodes in supra- and infra-pyloric positions and within the hepatoduodenal ligament. Lymphatic drainage to lateral aortic nodes has also been described (Hirai et al 2001).

Stomach

The stomach has a rich network of lymphatics that connect with lymphatics draining other viscera within the proximal abdomen. At the gastro-oesophageal junction the lymphatics are continuous with those draining the distal oesophagus; in the region of the pylorus they are continuous with those draining the duodenum and pancreas. In general, lymphatics follow the course of the arteries supplying the stomach. However, many separate groups of nodes are now recognized (see Fig. 63.14A) and their relationship to the specific regions and vascular territories of the stomach is of great importance during resection of the stomach, particularly for malignancy. Pancreatic and hepatic lymphatics are significant in draining the stomach during disease.

Gastrectomy and gastric lymphadenectomy

Surgery for gastro-oesophageal malignancy involves various degrees of radical resection of lymph nodes that drain the tumour. Locoregional lymphatic spread can occur in the absence of haematogenous spread and gastric cancer can therefore remain a localized disease, even when lymph nodes are involved (Brierley et al 2017). Hence, gastrectomy with meticulous lymphadenectomy can be curative in a proportion of patients with gastric cancer and lymph node involvement.

The extent of potential/actual lymph node involvement by the tumour is classified as N1 (locoregional nodes specific to the tumour site); N2 (regional and major named vessel nodes draining the tumour); and N3 (wider-draining nodes, including lateral aortic nodes). Gastrectomies can be classified according to the node groups excised with the tumour: D1 (removal of the affected portion of the stomach and *en bloc* resection of N1 nodes); D2 (total gastrectomy, including all N1 and N2 nodes); and D3 (total gastrectomy plus extensive lymphadenectomy that includes the associated proximal abdominal lymph nodes, namely: pancreatic, superior mesenteric, coeliac, hepatic and middle colic) (Japanese Gastric Cancer Association 2011).

Pancreas

The lymphatic drainage of the pancreas is extensive (see Fig. 63.14B), which partly explains the poor prognosis of individuals with pancreatic cancer. Lymphatic vessels start within the connective tissue septa within the gland and join to form larger lymphatics that follow the paths of local arteries (Deki and Sato 1988, O’Morchoe 1997). Lymphatics from the tail and body of the pancreas drain mostly into nodes along the splenic artery and inferior border of the gland, and from there to pre-aortic nodes between the coeliac trunk and superior mesenteric artery. Lymphatics from the neck and head drain more widely into nodes along the pancreaticoduodenal, superior mesenteric and hepatic arteries, and ultimately into pre-aortic nodes (Donatini and Hidden 1992, Cesmebasi et al 2015). There is no evidence of lymphatic channels within the pancreatic islets.

Hepatobiliary system

Lymph from the gallbladder and cystic duct drains via several pathways: to the cystic node, which usually lies above the cystic duct in the cystohepatic triangle, and from there via nodes in the hepatoduodenal ligament and along the common hepatic artery to coeliac nodes; via lymphatics that descend along the bile duct to the superior retropancreaticoduodenal node (which communicates with lateral aortic nodes); and directly to superior mesenteric nodes (Sato et al 2013). Lymphatics on the deep aspect of the gallbladder connect directly with intrahepatic lymph vessels.

Lymphatic vessels accompanying the hepatic ducts and proximal bile duct drain to hepatic nodes at the porta hepatis and then via lymph nodes in the hepatoduodenal ligament to coeliac nodes. Lymphatics from the distal bile duct also drain to the latter but some pass directly to pancreatic and superior mesenteric nodes. Lymph from the liver is rich in protein and is mostly a product of the hepatic sinusoids (Ohtani and Ohtani 2008). It passes via deep and superficial pathways to nodes superior and inferior to the respiratory diaphragm (Trutmann and Sasse 1994). Obstruction of hepatic venous drainage increases the flow of lymph in the thoracic duct.

Superficial hepatic lymphatics

Superficial lymphatics run in subserosal areolar tissue over the surface of the liver and drain in four directions. Lymphatics from most of the posterior surface, including the caudate lobe, drain into nodes alongside the inferior vena cava; a few lymphatics from the posterior surface of the left lobe pass towards the oesophageal hiatus and nodes around the cardia of the stomach. Lymphatics in the coronary and right triangular ligaments can pass directly to the thoracic duct. Lymphatics from most of the inferior, anterior and superior surfaces drain into hepatic nodes at the porta hepatis. A few lymphatics from the right superior surface accompany the inferior phrenic artery across the right diaphragmatic crus to drain into coeliac nodes.

Deep hepatic lymphatics

Fine lymphatics within the portal triads and around interlobular veins merge to form larger vessels. Some ascend through the parenchyma to pass through the caval foramen in the respiratory diaphragm and drain into inferior mediastinal nodes, but most drain to lymph nodes at the porta hepatis.

Small intestine

The lymphatic system of the small intestine regulates tissue fluid homeostasis, participates in immune surveillance and transports dietary fat and fat-soluble vitamins from the gut lumen. It is organized into two networks. First, lacteals from the villi drain into a plexus of lymphatics in the submucosa and are joined by vessels from lymph spaces at the bases of solitary lymphoid follicles; these lymphatic vessels have few if any valves. Second, a coarse plexus of lymphatics also runs in the muscularis externa between the two muscle layers. The submucosal and muscular networks share few connections but both communicate freely with larger valved collecting lymphatics at the mesenteric border of the small intestine (Miller et al 2010). Mesenteric lymphatics pass between the layers of the mesentery and drain via a series of mesenteric nodes concentrated around the regional mesenteric vessels. Individual segments of small intestine have a relatively wide field of lymphatic drainage, which makes radical surgical resection of draining lymph nodes difficult if the blood supply to the remaining unaffected small intestine is to be preserved. Mesenteric nodes drain into superior mesenteric nodes around the proximal part of the superior mesenteric artery.

Large intestine

Lymph drainage from the large intestine follows the course of the arteries. Thus, lymphatic vessels of the caecum and the ascending and proximal transverse colon drain ultimately into lymph nodes related to the superior mesenteric artery, while those of the distal transverse colon, descending colon, sigmoid colon and rectum drain into nodes following the course of the inferior mesenteric artery (see Fig. 65.16). In cases where the distal transverse colon or left colic flexure is predominantly supplied by vessels from the middle colic artery, most of the lymphatic drainage of this area may be to superior mesenteric nodes.

Lymph nodes related to the colon form four groups: epicolic, paracolic, intermediate colic and preterminal colic. Epicolic nodes are minute whitish nodules on the serosal surface of the colon, sometimes within the omental appendices. Paracolic nodes lie along the medial borders of the ascending and descending colon and along the mesenteric borders of the transverse and sigmoid colon. Intermediate colic nodes lie along the named colic vessels (the ileocolic, right colic, middle colic, left colic, sigmoid and superior anorectal arteries). Preterminal colic nodes lie along the main trunks of the superior and inferior mesenteric arteries and drain into pre-aortic nodes at the origin of these vessels.

Ascending mesocolic nodes are significantly larger than sigmoid mesocolic ones; this is relevant to lymph node retrieval and examination after resection for colonic cancer (Ahmadi et al 2015).

Lymphatic vessels originate from both anterior and posterior aspects of the colon. Lymph drainage from the midgut follows the course of the superior mesenteric artery. Thus, lymph from the caecum and appendix drains to nodes associated with the ileocolic artery, and lymph from the distal ascending colon and right colic flexure drains to nodes along the right colic artery (see Fig. 65.16). When the distal transverse colon and left colic flexure are predominantly supplied by the middle colic artery, lymph drainage of this segment is also largely to superior mesenteric nodes. Lymphatic vessels in the appendix are numerous and combine to form vessels that ascend in the mesoappendix, occasionally interrupted by one or more nodes. They unite to form three or four larger vessels that anastomose with lymphatic vessels draining the ascending colon into ileocolic nodes.

Small lymphoid aggregates measuring no more than a few millimetres are occasionally visible on the surface of the large intestine (epicolic and epirectal nodes). Lymph from the descending colon drains to paracolic nodes in the mesentery adjacent to the colon and from there to intermediate nodes along the left colic artery (Jamieson and Dobson 1909). Lymphatics from the sigmoid colon follow a similar pathway from paracolic to intermediate nodes in the sigmoid mesocolon. Intramural lymph from the rectum and anal canal above the pectinate line drains predominantly to pararectal nodes in the adipose tissue of the mesorectum and then along lymphatics accompanying the superior anorectal artery (see Fig. 65.43). These intermediate nodes then drain to lymph nodes along the inferior mesenteric artery and from there to pre-aortic nodes. Some lymphatics from the distal rectum travel with the middle and inferior anorectal arteries to internal iliac nodes and along the median sacral artery to sacral nodes. The clinical significance of such drainage for the spread of malignancy from the distal rectum is debated (Bell et al 2009).

Radical lymphadenectomy during resection of colorectal cancer requires removal of the highest possible lymph nodes draining the region of colon in which the tumour is located. In cases of cancer of the rectum or sigmoid colon, this usually involves excision of the preterminal colic nodes along the inferior mesenteric artery with ligation of the artery at its root or just below the origin of the left colic artery. At least 12 lymph nodes must be excised in an oncologically resected partial colectomy for cancer.

Kidney, urinary bladder, prostate and urethra

Renal lymphatic vessels begin in three plexuses: around the renal tubules, under the renal capsule and in the perirenal fat (the latter two connect freely). Collecting vessels from the intrarenal plexus form four or five trunks that follow the renal vein to end in the lateral aortic nodes; the subcapsular collecting vessels join them as they leave the hilum of the kidney. The perirenal plexus drains directly into the same nodes.

Lymphatics that drain the bladder begin in mucosal, intermuscular and adventitial plexuses. There are three sets of collecting vessels; most end in the external iliac nodes (see Fig. 75.3B). Vessels from the trigone emerge on the exterior of the bladder to run superolaterally. Vessels from the superior surface of the bladder converge to the posterolateral angle and pass superolaterally to the external iliac nodes (some might drain to the internal or common iliac nodes). Vessels from the inferolateral surface of the bladder ascend to join those from the superior surface or run to the lymph nodes in the obturator fossa. Minute nodules of lymphoid tissue can occur along the lymph vessels of the bladder. In the male, vessels from the posterior urethra pass mainly to the internal iliac nodes; a few end in the external iliac nodes. Vessels from the membranous urethra accompany the internal pudendal artery. Vessels from the anterior urethra accompany those of the glans penis, most ending in the deep inguinal nodes; some can end in superficial inguinal nodes, while others traverse the inguinal canal to end in the external iliac nodes. Lymphatic vessels from the ductus deferens drain into the external iliac nodes, while those from the seminal glands drain to the internal and external iliac nodes. Lymphatic vessels from the prostate end mainly in the internal iliac, sacral and obturator nodes. A vessel from the posterior surface of the prostate accompanies the urinary bladder vessels to the external iliac nodes, and another from the anterior surface of the prostate reaches the internal iliac nodes by joining vessels that drain the membranous urethra. In the female the lymphatics of the distal urethra drain into the internal and external iliac nodes, while those of the proximal urethra drain into the iliac, obturator and sacral nodes.

Uterus, ovaries

There are uterine lymphatics in the superficial (subperitoneal) and deep parts of the uterine wall. Collecting vessels from the body of the uterus and cervix pass laterally in the parametrium to three main groups of lymph nodes, namely the external and internal iliac and the obturator nodes (see Table 75.1). The external and internal iliac nodes surround their corresponding arteries. The obturator nodes lie in the 'obturator fossa' between the external and internal iliac vessels, and the obturator nerve passes through the lower part of this group of lymph nodes. Lymph vessels from the fundus of the uterus and the uterine tubes can accompany the lymph drainage of the ovaries to lateral aortic nodes (see Fig. 75.3B). The region surrounding the isthmus of the uterine tube can drain along the round ligament of the uterus to the superficial inguinal nodes. Lymph drainage from the uterine (Fallopian) tubes is via ovarian vessels to the lateral aortic nodes and uterine vessels to the internal iliac nodes: it is possible for lymph to reach the inguinal nodes via the round ligament of the uterus. The main lymphatic drainage of the ovaries is along vessels that follow the ovarian veins to lateral aortic nodes situated near the origin of the renal arteries. There can also be drainage via pelvic nodes into lower lateral aortic nodes and, less commonly, via the round ligament of the uterus to the inguinal nodes (Kleppe et al 2015).

External genitalia: female

A meshwork of connecting vessels from the skin of the labia, clitoris and perineum join to form three or four collecting trunks that drain to superficial inguinal nodes lying on the cribriform fascia covering the femoral artery and vein; these nodes drain through the cribriform fascia to the deep inguinal nodes lying medial to the femoral vein (Corton 2012). The deep inguinal nodes drain via the femoral canal to the pelvic nodes (see Table 75.1). The last of the deep inguinal nodes lies under the inguinal ligament within the femoral canal and is often called Cloquet's node. Lymph vessels from the clitoris drain directly to the deep inguinal nodes, and direct clitoral lymphatics may pass to the internal iliac nodes (see Fig. 75.3B). Lymph vessels in the perineum and lower part of the labia majora drain primarily to inguinal nodes.

Vaginal lymphatic vessels link with those of the cervix, rectum and vulva. They form three groups but the regions drained are not sharply demarcated. Upper vessels accompany the uterine artery to the internal and external iliac nodes; intermediate vessels accompany the vaginal artery to the internal iliac nodes; and vessels draining the vagina below the hymen, and from the vulva and perineal skin, pass to the superficial inguinal nodes.

External genitalia: male

The penile and perineal skin is drained by lymphatic vessels that accompany the external pudendal veins to the superficial inguinal nodes. Lymphatics from the glans penis pass to the deep inguinal and external iliac nodes, and those from the erectile tissue and spongy urethra pass to the internal iliac nodes. Scrotal lymphatics do not cross the raphe of the scrotum and therefore lymphatic drainage from the scrotum is always routed to the ipsilateral superficial inguinal nodes.

Testicular lymphatic flow is abundant and consistent and follows the general retroperitoneal scheme of vertical drainage, with lateral flow from right to left. Lymphatic vessels from the right testis drain primarily into the right lateral aortic and lateral caval nodes, with some drainage into the left lateral aortic nodes. Lymphatic vessels from the left testis drain into the left and right lateral aortic and lateral caval nodes.

LYMPHATIC DRAINAGE OF THE VERTEBRAL COLUMN

Little is known in detail about the lymphatic drainage of the vertebral column and its associated soft tissues. In general, deep lymphatic vessels tend to follow the arteries. The cervical vertebral column drains to deep cervical nodes, the thoracic to (posterior) intercostal nodes and the lumbar column to lateral aortic and retroaortic nodes. The pelvic part of the column drains to lateral sacral and internal iliac nodes.

LYMPHATIC DRAINAGE OF THE LIMBS

The subcutaneous tissues of the upper and lower limbs can be divided into five layers: skin (layer 1); subcutaneous fat (2); superficial fascia (3); loose areolar tissue (4); and deep fascia (5). Layer 2 can be subdivided into a superficial (2a) and deep layer (2c) by a thin transparent horizontal septum (2b) (Tourani et al 2014). The main superficial veins and the superficial nerves are found in layer 4 and the lymphatic collectors in layer 2c and layer 4.

Upper limb

Superficial tissues

Superficial lymphatic vessels begin in cutaneous plexuses: in the hand, the palmar plexus is denser than the dorsal plexus. Digital plexuses drain along the digital borders to their webs, where they join the distal palmar vessels, which pass back to the dorsal aspect of the hand. The proximal palm drains towards the carpus, medially by vessels that run along its ulnar border, and laterally to join vessels draining the thumb. Several vessels from the central palmar plexus form a trunk that winds round the second metacarpal bone to join the dorsal vessels that drain the index finger and thumb.

In the forearm and arm, superficial vessels run with the superficial veins. Collecting vessels from the hand pass into the forearm on all carpal aspects. Dorsal vessels, after running proximally in parallel, curve successively round the borders of the limb to join the ventral vessels. Anterior carpal vessels run through the forearm parallel with the median vein of the forearm to the cubital region, then follow the medial border of biceps brachii before piercing the deep fascia at the anterior axillary fold to end in the lateral axillary lymph nodes.

Lymph vessels that lie laterally in the forearm receive vessels that curve round the lateral border from the dorsal aspect of the limb. They follow the cephalic vein to the level of the tendon of deltoid, where most incline medially to reach the lateral axillary nodes; a few continue with the vein and drain into the infraclavicular nodes. Vessels lying medially in the forearm are joined by vessels that curve round the medial border of the limb and follow the basilic vein. Proximal to the elbow, some end in supratrochlear lymph nodes whose efferents, together with the medial vessels that have bypassed them, pierce the deep fascia with the basilic vein and end in the lateral axillary nodes or deep lymphatic vessels.

Collecting vessels from the deltoid region pass round the anterior and posterior axillary folds to end in the axillary nodes. The scapular skin drains either to subscapular axillary nodes or by channels that follow the transverse cervical vessels to the inferior deep cervical nodes.

Deeper tissues

Deep lymph vessels follow the main neurovascular bundles (radial, ulnar, interosseous and brachial) to the lateral axillary nodes. They are less numerous than the superficial vessels and communicate with them at intervals. A few lymph nodes occur along the vessels. Scapular muscles drain mainly to the subscapular axillary nodes, and pectoral muscles drain mainly to the pectoral, central and apical nodes.

One or two supratrochlear nodes are superficial to the deep fascia proximal to the medial epicondyle and medial to the basilic vein; their efferents accompany the vein to join the deep lymph vessels. Small, isolated nodes sometimes occur along the radial, ulnar and interosseous vessels, in the cubital fossa near the bifurcation of the brachial artery, or in the arm medial to the brachial vessels.

Lower limb

Most lymph from the lower limb traverses a large intermediary inguinal group of nodes (see Fig. 76.10). Peripheral nodes are few and are all deeply sited in the popliteal fossa except for an inconsistent node lying proximally on the interosseous membrane near the anterior tibial vessels. Enlarged popliteal nodes, often as a result of inflammation, malignancy or injury to the lateral side of the foot, may be palpated along the line of the popliteal vessels while the passively supported knee is gradually moved from extension to semi-flexion. Inguinal lymph nodes are found superficial and deep to the deep fascia. The superficial nodes may be divided into a lower vertical group that clothe the proximal part of the long saphenous vein, and an upper group that lie parallel to, but below, the inguinal ligament and which are related laterally to the superficial circumflex iliac and medially to the superficial external pudendal vessels. The deep nodes are few and lie alongside the medial aspect of the femoral vein. Lymph from the lower limb passes from the inguinal lymph nodes to the external and common iliac nodes, and ultimately drains to the lateral aortic nodes. Deep gluteal lymph reaches the same group through the internal and common iliac lymphatic vessels.

Superficial tissues

The superficial lymph vessels begin in subcutaneous plexuses. Collecting vessels leave the foot either medially with the long saphenous vein, or laterally with the short saphenous vein. Medial vessels are larger and more numerous. They start on the medial side of the dorsum of the foot, ascend anterior or posterior to the medial malleolus, accompany the long saphenous vein and drain to the distal superficial inguinal nodes. Lateral vessels begin on the fibular side of the dorsum of the foot. Some cross anteromedially in the leg to join the medial vessels and so pass to the distal superficial inguinal lymph nodes, while others accompany the short saphenous vein and drain to the popliteal nodes. Superficial lymph vessels from the gluteal region run anteriorly to the proximal superficial inguinal nodes.

Deeper tissues

The deep lymph vessels accompany the anterior and posterior tibial, fibular, popliteal and femoral vessels. Popliteal nodes interrupt the deep vessels from the foot and leg; deep vessels from the thigh pass to the deep inguinal nodes. The deep lymphatic vessels of the gluteal region follow their corresponding blood vessels. Those accompanying the superior gluteal vessels end in a node near the intrapelvic part of the superior gluteal artery, adjacent to the superior border of the greater sciatic foramen, while those that follow the inferior gluteal vessels traverse one or two of the small nodes inferior to piriformis and then pass to the internal iliac nodes.

References

Abhinav K, Panczykowski D, Wang WH et al 2017 Endoscopic endonasal interdural middle fossa approach to the maxillary nerve: anatomical considerations and surgical relevance. Oper Neurosurg (Hagerstown) 13:522–8.

Ahmadi O, McCall JL, Stringer MD 2015 Mesocolic lymph node number, size, and density: an anatomical study. Dis Colon Rectum 58:726–5.

Akgun V, Hamcan S, Bozkurt Y et al 2016 Thoracic aorta. In: Tubbs RS, Shoja MM, Loukas M Bergman's Comprehensive Encyclopedia of Human Anatomic Variation, 2nd ed. Hoboken: Wiley–Blackwell; Ch. 49, pp. 501–29.

Alison M, Garel L, Bigras JL et al 2011 Unilateral absence of pulmonary artery in children: bronchovascular anatomy, natural course and effect of treatment on lung growth. Pediatr Radiol 41:459–68.

Allen JW, Alastra JG, Nelson PK 2005 Proximal intracranial internal carotid artery branches: prevalence and importance for balloon occlusion test. J Neurosurg 102:45–52.

Ang WC, Doyle T, Stringer MD 2013 Left-sided and duplicate inferior vena cava: a case series and review. Clin Anat 26:990–1001.

Arslan M, Comert A, Acar HI et al 2011 Surgical view of the lumbar arteries and their branches: an anatomical study. Neurosurgery 68:16–22.

Asala S, Chaudhary SC, Masumbuko-Kahamba N et al 2001 Anatomical variations in the human testicular blood vessels. Ann Anat 183:545–9.

Backes WH, Nijenhuis RJ 2008 Advances in spinal cord MR angiography. AJNR Am J Neuroradiol 29:619–31.

Badshah M, Soames R, Ibrahim M et al 2017 Surface anatomy of major anatomical landmarks of the neck in an adult population: a CT evaluation of vertebral level. Clin Anat 30:781–7.

Bakamjian VY, Long M, Rigg B 1971 Experience with the medially based deltopectoral flap in reconstructive surgery of the head and neck. Br J Plast Surg 24:174.

Baliga RR, Neinaber CA, Isselbacher EM et al 2007 Aortic Dissection and Related Syndromes. Ann Arbor, MI: Springer.

Baranski AG, Lam HD, Braat AE et al 2016 The dorsal pancreatic artery in pancreas procurement and transplantation: anatomical considerations and potential implications. Clin Transplant 30:1360–4.

Bare RL, DeFranzo A, Jarow JP 1994 Intraoperative arteriography facilitates penile revascularization. J Urol 151:1019–21.

Batra A, Kaur J, Parihar D et al 2013 Variations in origin of right colic artery supplying the colon. CIBTech J Surg 2:14–20.

Batson OV 1957 The vertebral vein system. Caldwell Lecture, 1956. Am J Roentgenol Radium Ther Nuclear Med 78:195–212.

Beck EM, Schlegel PN, Goldstein M 1992 Intraoperative varicocele anatomy: a macroscopic and microscopic study. J Urol 148:1190–4.

Bell S, Sasaki J, Sinclair G et al 2009 Understanding the anatomy of lymphatic drainage and the use of blue-dye mapping to determine the extent of lymphadenectomy in rectal cancer surgery: unresolved issues. Colorectal Dis 11:443–9.

Benninger B 2014 Novel femoral artery terminology: integrating anatomy and clinical procedures leading to standardized intuitive nomenclature. Clin Anat 27:1085–8.

Berdjas D, Turina MI 2011 Operative Anatomy of the Heart. Berlin: Springer.

Bergua A, Kapsreiter M, Neuhuber WL et al 2013 Innervation pattern of the preocular human central retinal artery. Exp Eye Res 110:142–7.

Bertelli E, Di Gregorio F, Bertelli L et al 1995 The arterial blood supply of the pancreas: a review. I. The superior pancreaticoduodenal and the anterior superior pancreaticoduodenal arteries: an anatomical and radiological study. Surg Radiol Anat 17:97–106.

Bertelli E, Di Gregorio F, Bertelli L et al 1996a The arterial blood supply of the pancreas: a review. II. The posterior superior pancreaticoduodenal artery. An anatomical and radiological study. Surg Radiol Anat 18:1–9.

Bertelli E, Di Gregorio F, Bertelli L et al 1996b The arterial blood supply of the pancreas: a review. III. The inferior pancreaticoduodenal artery: an anatomical review and a radiological study. Surg Radiol Anat 18:67–74.

Bertelli E, Di Gregorio F, Bertelli L et al 1997 The arterial blood supply of the pancreas: a review. IV. The anterior inferior and posterior pancreaticoduodenal aa., and minor sources of blood supply for the head of the pancreas. An anatomical review and radiologic study. Surg Radiol Anat 19:203–12.

Bertelli E, Di Gregorio F, Mosca S et al 1998 The arterial blood supply of the pancreas: a review. V. The dorsal pancreatic artery: an anatomic review and a radiologic study. Surg Radiol Anat 20:445–52.

Bertelli E, Regoli M, Bracco S 2017 An update on the variations of the orbital blood supply and hemodynamic. Surg Radiol Anat 39(5):485–96.

Bharadwaj AS, Appukuttan B, Wilmarth PA et al 2013 Role of the retinal vascular endothelial cell in ocular disease. Prog Retinal Eye Res 32:102–80.

Bianchi A 1984 Intestinal lengthening: an experimental and clinical review. J R Soc Med 77(Suppl 3):35–41.

Bianchi HF, Albanèse EF 1989 The supraduodenal artery. Surg Radiol Anat 11:37–40.

Biglioli P, Roberto M, Cannata A et al 2004 Upper and lower spinal cord blood supply: the continuity of the anterior spinal artery and the relevance of the lumbar arteries. J Thorac Cardiovasc Surg 127:1188–92.

Bilhim T, Pereira JA, Tinto HR et al 2013 Middle rectal artery: myth or reality? Retrospective study with CT angiography and digital subtraction angiography. Surg Radiol Anat 35:517–22.

Birch R 2011 Surgical Disorders of the Peripheral Nerves, 2nd ed. London: Springer-Verlag.

Blakey CM, Biant LC, Birch R 2009 Ischaemia and the pink, pulseless hand complicating supracondylar fractures of the humerus in childhood: long-term follow-up. J Bone Joint Surg Br 91:1487–92.

Borley NR, McFarlane JM, Ellis H 1995 A comparative study of the tortuosity of the splenic artery. Clin Anat 8:219–21.

Bowdler AJ (ed) 2002 The Complete Spleen: Structure, Function, and Clinical Disorders. Totowa: Humana Press.

Bradley RL 1973 Surgical anatomy of the gastroduodenal artery. Int Surg 58:393–6.

Brierley JD, Gospodarowicz MK, Wittekind C (eds) 2017 TNM Classification of Malignant Tumours, 8th ed. Hoboken: Wiley Blackwell.

Brödel M 1911 The intrinsic blood-vessels of the kidney and their significance in nephrotomy. Bull Johns Hopkins Hosp 12:10–13.

Broderick BJ, Corley GJ, Quondamatteo F et al 2008 A haemodynamic study of the physiological mechanisms of the venous pump in the healthy human foot. Conf Proc IEEE Eng Med Biol Soc 2008:1411–14.

Brooks CH, Revell WJ, Heatley FW 1993 Vascularity of the humeral head after proximal humeral fractures. An anatomical cadaver study. J Bone Joint Surg Br 75B:132–6.

Browder J, Kaplan HA 1976 Cerebral Dural Sinuses and their Tributaries. Springfield, IL: Thomas.

Burt RP 2003 Phasic contractions of the rat portal vein depend on intracellular Ca^{2+} release stimulated by depolarization. Am J Physiol Heart Circ Physiol 284:H1808–17.

Caggiati A, Bergan JJ, Gloviczki P et al 2002 Nomenclature of the veins of the lower limbs: an international interdisciplinary consensus statement. J Vasc Surg 36:416–22.

Caggiati A, Bergan JJ, Gloviczki P et al 2005 Nomenclature of the veins of the lower limb: extensions, refinements, and clinical application. J Vasc Surg 41:719–24.

Camargo AM, Teixeira GG, Ortale JR 1996 Anatomy of the ostia venae hepaticae and the retrohepatic segment of the inferior vena cava. J Anat 188:59–64.

Carmichael S, Gloviczki P 1999 Anatomy of the blood supply to the spinal cord: the artery of Adamkiewicz revisited. Perspect Vasc Surg 12:113–22.

Cesmebasi A, Du Plessis M, Iannatuono M et al 2014 A review of the anatomy and clinical significance of adrenal veins. Clin Anat 27:1253–63.

Cesmebasi A, Malefant J, Patel SD et al 2015 The surgical anatomy of the lymphatic system of the pancreas. Clin Anat 28:527–37.

Chaib E 2009 Absence of bifurcation of the portal vein. Surg Radiol Anat 31:389–92.

Chansky K, Detterbeck FC, Nicholson AG et al 2017 The IASLC Lung Cancer Staging Project: External Validation of the Revision of the TNM Stage Groupings in the Eighth Edition of the TNM Classification of Lung Cancer. J Thorac Oncol 12(7):1109–21.

Chantalat E, Merigo, O, Chaynes P et al 2014 Radiological anatomical study of the origin of the uterine artery. Surg Radiol Anat 36:1093–9.

Chaynes P, Verdie JC, Moscovici J et al 1998 Microsurgical anatomy of the internal vertebral venous plexuses. Surg Radiol Anat 20:47–51.

Cheung LK 1996 The vascular anatomy of the human temporalis muscle: implications for surgical splitting techniques. Int J Oral Maxillofac Surg 25:414–21.

Clemente A, Del Borrello M, Greco P et al 2010 Anomalous origin of the coronary arteries in children: diagnostic role of three-dimensional coronary MR angiography. Clin Imaging 34:337–43.

Clements BS 1999 Congenital malformations of the lungs and airways. In: Taussig LM , Landau LI (eds) Pediatric Respiratory Medicine. St Louis: Mosby, p. 1106.

Cormack G, Lamberty B 1994 The arterial anatomy of skin flaps. Edinburgh: Churchill Livingstone.

Cortés JA, Pellico LG 1988 Arterial segmentation in the spleen. Surg Radiol Anat 10:323–32.

Corton MM 2012 Anatomy. In: Hoffman B, Schorge JO, Schaffer JI et al (eds) Williams Gynecology, 2nd ed. New York: McGraw Hill.

Covey AM, Brody LA, Getrajdman GI et al 2004 Incidence, patterns, and clinical relevance of variant portal vein anatomy. AJR Am J Roentgenol 183:1055–64.

Covey AM, Brody LA, Maluccio MA et al 2002 Variant hepatic arterial anatomy revisited: digital subtraction angiography performed in 600 patients. Radiology 224:542–7.

Crock H 1996 An Atlas of Vascular Anatomy of the Skeleton and Spinal Cord. London: Martin Dunitz.

Damsin JP, Lazennec JY, Gonzales M et al 11992 Arterial supply of the acetabulum in the fetus: application to periacetabular surgery in childhood. Surg Radiol Anat 4:215–21.

Daniel O, Shackman R 1952 The blood supply of the human ureter in relation to ureterocolic anastomosis. Br J Urol 24:549–50.

Dawson DL, Molina ME, Conner CES 1986 Venous segmentation of the human spleen. Am Surg 52:253–6.

de Treigny OM, Roumiguie M, Deudon R et al 2017 Anatomical study of the inferior vesical artery: is it specific to the male sex? Surg Radiol Anat 39:961–5.

Deki H, Sato T 1988 An anatomic study of the peripancreatic lymphatics. Surg Radiol Anat 10:121–35.

DeLand FH 1970 Normal spleen size. Radiology 97:589–592.

Deso S, Ludwig B, Kabutey NK et al 2012 Lymphangiography in the diagnosis and localization of various chyle leaks. Cardiovasc Intervent Radiol 35:117.

Deutsch J, Savides TJ 2005 Normal Thoracic Anatomy in Digital Human Anatomy and Endoscopic Ultrasonography. Hamilton, ON: BC Decker.

Deutsch MD, Kriss VM, Willging JP 1995 Distance between the tonsillar fossa and internal carotid artery in children. Arch Otolaryngol Head Neck Surg 121:1410–2.

Deutsch MD, Kriss VM, Willging JP 1995 Distance between the tonsillar fossa and internal carotid artery in children. Arch Otolaryngol Head Neck Surg 121:1410–2.

DiDio LJ, Diaz-Franco C, Schemainda R et al 1986 Morphology of the middle rectal arteries: a study of 30 cadaveric dissections. Surg Radiol Anat 8:229–36.

DiLandro AC, Lilja EC, Lepore FL et al 2001 The prevalence of the arcuate artery: a cadaveric study of 72 feet. J Am Podiatr Med Assoc 91:300–5.

Dodd H, Cockett FB 1976 The Pathology and Surgery of the Veins of the Lower Limb, 2nd ed. Edinburgh: Churchill Livingstone.

Doerr CH, Miller DL, Ryu JH 2001 Chylothorax. Semin Respir Crit Care Med 22:617.

Doğan R, Doğan OF, Oç M et al 2003 A rare vascular malformation, Klippel–Trenaunay syndrome. Report of a case with deep vein agenesis and review of the literature. J Cardiovasc Surg 44:95–100.

Dolenc VV 1987 The Cavernous Sinus. Vienna: Springer.

Dolenc VV, Rogers L 2009 Cavernous Sinus: Developments and Future Perspectives. Vienna: Springer.

Dommisse G 1975 The Arteries and Veins of the Human Spinal Cord from Birth. Edinburgh: Churchill Livingstone.

Donatini B, Hidden G 1992 Routes of lymphatic drainage from the pancreas: a suggested segmentation. Surg Radiol Anat 14:35–42.

Doyle JF 1970 The perforating veins of the gluteus maximus. Ir J Med Sci 3:285–8.

Droupy S, Benoît G, Giuliano F et al 1997 Penile arteries in humans. Origin–distribution–variations. Surg Radiol Anat 19:161–7.

Duvernoy H, Delon S, Vannson JL 1983 The vascularization of the human cerebellar cortex. Brain Res Bull 11:419–80.

Duvernoy HM, Delon S, Vannson JL 1981 Cortical blood vessels of the human brain. Brain Res Bull 7:519–79.

El Khouly H, Fernandez-Miranda JC, Rhoton AL Jr 2008 Blood supply of the facial nerve in the middle fossa: the petrosal artery. Neurosurgery 62:ONS297–303.

El-Mrakby HH, Milner RH 2002 The vascular anatomy of the lower anterior abdominal wall: a microdissection study on the deep inferior epigastric vessels and the perforator branches. Plast Reconstr Surg 109:539–543; discussion 44–7.

Fang CH, You JH, Lau WY et al 2012 Anatomical variations of hepatic veins: three-dimensional computed tomography scans of 200 subjects. World J Surg 36:120–4.

Fernandez-Miranda JC, Gardner PA, Rastelli MM Jr et al 2014 Endoscopic endonasal transcavernous posterior clinoidectomy with interdural pituitary transposition. J Neurosurg 121:91–9.

Fernandez-Miranda JC, Zwagerman NT, Abhinav K et al 2017 Cavernous sinus compartments from the endonasal endoscopic approach: anatomical considerations and surgical relevance to adenoma surgery. J Neurosurg 1:1–12.

Fleischmann D, Hastie TJ, Dannegger FC et al 2001 Quantitative determination of age-related geometric changes in the normal abdominal aorta. J Vasc Surg 33:97–105.

Fourdrain A, Lafitte S, Iquille J et al 2018 Lymphatic drainage of lung segments in the visceral pleura: a cadaveric study. Surg Radiol Anat 40:15–19.

Friedman T, Coon D, Kanbour-Shakir A 2015 Defining the lymphatic system of the anterior abdominal wall: an anatomical study. Plast Reconstr Surg 135:1027–32.

Friedmann DR, Eubig J, McGill M et al 2011 Development of the jugular bulb: a radiologic study. Otol Neurotol 32:1389–95.

García-Porrero JA, Lemes A 1988 Arterial segmentation and subsegmentation in the human spleen. Acta Anat 131:276–83.

Gerber AB, Lev M, Goldberg SL 1951 The surgical anatomy of the splenic vein. Am J Surg 82:339–43.

Gerber C, Schneeberger AG, Vinh TS 1990 The arterial vascularization of the humeral head. An anatomical study. J Bone Joint Surg Am 72:1486–94.

Gerber C, Schneeberger AG, Vinh TS 1990 The arterial vascularization of the humeral head. An anatomical study. J Bone Joint Surg Am 72:1486–94.

Goldstraw P, Chansky K, Crowley J et al 2016 The IASLC Lung Cancer Staging Project: Proposals for revision of the TNM stage groupings in the forthcoming (eighth) edition of the TNM classification for lung cancer J Thorac Oncol 11(1):39–51.

Golub RM, Parsons RE, Sigel B et al 1992 A review of venous collaterals in inferior vena cava obstruction. Clin Anat 5:441–51.

Graf O, Boland GW, Kaufman JA et al 1997 Anatomic variants of mesenteric veins: depiction with helical CT venography. AJR Am J Roentgenol 168:1209–13.

Grégoire V, Ang K, Budach W et al 2014 Delineation of the neck node levels for head and neck tumors: A 2013 update. DAHANCA, EORTC, HKNPCSG, NCIC CTG, NCRI, RTOG, TROG consensus guidelines. Radiother Oncol 110:172–81.

Groen RJ, du Toit DF, Phillips FM et al 2004 Anatomical and pathological considerations in percutaneous vertebroplasty and kyphoplasty: a re appraisal of the vertebral venous system. Spine 29:1465–71.

Groeneveld ME, Meekel JP, Rubinstein SM et al 2018 Systematic review of circulating, biomechanical, and genetic markers for the prediction of abdominal aortic aneurysm growth and rupture. J Am Heart Assoc 7:e007791.

Gullane PJ, Arena S 1977 Palatal island flap for reconstruction of oral defects. Arch Otolaryngol 103:598–603.

Gullane PJ, Arena S 1985 Extended palatal island mucoperiosteal flap. Arch Otolaryngol 111:330–5.

Gupta CD, Gupta SC, Arora AK et al 1976 Vascular segments in the human spleen. J Anat 121:613–16.

Gupta NP, Kumar M, Karan SC et al 1999 Lower ureteral obstruction due to a persistent umbilical artery. Urol Int 63:249–51.

Gupta SB, Gupta SC, Gupta CD 1980 Venous segments in the human spleen. Indian J Med Res 72:465–9.

Gürleyik E, Gürleyik G, Bingöl K et al 2000 Perfusion and functional anatomy of the splenic remnant supplied by short gastric vessels. Excerpta Med 179:490–3.

Gwon DI, Ko GY, Yoon HK et al 2007 Inferior phrenic artery: anatomy, variations, pathologic conditions, and interventional management. Radiographics 27:687–705.

Hadad G, Bassagasteguy L, Carrau RL 2006 A novel reconstructive technique after endoscopic expanded endonasal approaches: vascular pedicle nasoseptal flap. Laryngoscope 116:1882–6.

Harris FS, Rhoton AL 1976 Anatomy of the cavernous sinus: a microsurgical study. J Neurosurg 45:169–80.

Harrison RJ 1949 The vascular supply to the human testis. J Anat 83:61.

Harry LE, Sandison A, Pearse MF et al 2009 Comparison of the vascularity of fasciocutaneous tissue and muscle for coverage of open tibia fracture. Plast Reconstr Surg 124:1211–9.

Hartrampf CR, Scheflan M, Black PW 1982 Breast reconstruction with a transverse abdominal island flap. Plast Reconstr Surg 69:216–25.

Hayreh SS 2006 Orbital vascular anatomy. Eye (Lond) 20:1130–44.

Hayreh SS, Dass R 1962a The ophthalmic artery. II. Intra-orbital course. Br J Ophthal 46:165–85.

Hayreh SS, Dass R 1962b The ophthalmic artery: I. Origin and intra-cranial and intra-canalicular course. Br J Ophthalmol 46:65–98.

Hirai I, Murakami G, Kimura W et al 2001 Long descending lymphatic pathway from the pancreaticoduodenal region to the para-aortic nodes: its laterality and topographical relationship with the celiac plexus. Okajimas Folia Anat Jpn 77:189–99.

Ho KKF, Walker P, Smithers BM et al 2017 Outcome predictors in median arcuate ligament syndrome. J Vasc Surg 65:1745–52.

Horiguchi A, Ishihara S, Ito M et al 2008 Multislice CT study of pancreatic head arterial dominance. J Hepatobil Pancreat Surg 15:322–6.

Horton KM, Fishman EK 2010 CT angiography of the mesenteric circulation. Radiol Clin North Am 48:331–45, viii.

Hribernik M, Trotovšek B 2014 Intrahepatic venous anastomoses with a focus on the middle hepatic vein anastomoses in normal human livers: anatomical study on liver corrosion casts. Surg Radiol Anat 36:231–7.

Hsu GL, Hsieh CH, Wen HS et al 2003 Penile venous anatomy: an additional description and its clinical implication. J Androl 24:921–27.

Huynh-Le P, Natori Y, Sasaki T 2005 Surgical anatomy of the ophthalmic artery: its origin and proximal course. Neurosurgery 57(4 Suppl):236–41.

Iaconetta G, Fusco M, Samii M 2003 The sphenopetroclival venous gulf: a microanatomical study. J Neurosurg 99:366–75.

Ishikawa Y, Ban D, Matsumura S et al 2017 Surgical pitfalls of jejunal vein anatomy in pancreaticoduodenectomy. J Hepatobiliary Pancreat Sci 24:394–400.

Jamieson JK, Dobson JF 1909 The lymphatics of the colon. Ann Surg 50:1077–90.

Japanese Gastric Cancer Association 2011 Japanese Classification of Gastric Carcinoma – 3rd English edition. Gastric Cancer 14:101–12.

Jarow JP 1991 Clinical significance of intratesticular arterial anatomy. J Urol 145:777–9.

Jarow JP, Ogle A, Kaspar J et al 1992 Testicular artery ramification within the inguinal canal. J Urol 147:1290–2.

Jasper A, Harshe G, Keshava SN et al 2014 Evaluation of normal abdominal aortic diameters in the Indian population using computed tomography. J Postgrad Med 60:57–60.

Jung BF, Ahrendt GM, Oaklander AL et al 2003 Neuropathic pain following breast cancer surgery: proposed classification and research update. Pain 104:1–13.

Kaiser T, Kellenberger CJ, Albisetti M et al 2008 Normal values for aortic diameters in children and adolescents – assessment in vivo by contrast-enhanced CMR-angiography. J Cardiovasc Magn Reson 10:56.

Kaplan HA, Browder J 1976 Neurosurgical consideration of some features of the cerebral dural sinuses and their tributaries. Clin Neurosurg 23:155–69.

Karagol BS, Orun UA, Zenciroglu A et al 2012 The diameter of coronary arteries in healthy newborns at birth, 1 and 6 months of ages. J Matern Fetal Neonatal Med 25:2729–34.

Kastellanos S, Aznaouridis K, Vlachopoulos C et al 2018. Overview of coronary artery variants, aberrations and anomalies. World J Cardiol 10:127–40.

Kawashima T, Sasaki H 2010 Reasonable classical concepts in human lower limb anatomy from the viewpoint of the primitive persistent sciatic artery and twisting human lower limb. Okajimas Folia Anat Jpn 87:141–9.

Kayalvizhi I, Narayan RK, Kumar P 2017 Anatomical variations of testicular artery: a review. Folia Morphol 76:541–50.

Kent DM, Thaler DE 2011 The Risk of Paradoxical Embolism (RoPE) study: developing risk models for application to ongoing randomized trials of percutaneous patent foramen ovale closure for cryptogenic stroke. Trials 12:185.

Kervancioglu P, Kervancioglu M, Tuncer CM 2006 Echocardiographic study of aortic root diameter in healthy children. Saudi Med J 27:27–30.

Kiil BJ, Rozen WM, Pan WR et al 2009 The lumbar artery perforators: a cadaveric and clinical anatomical study. Plast Reconstr Surg 123:1229–38.

Kılıç T, Akakın A 2008 Anatomy of cerebral veins and sinuses. In: Caso V, Agnelli G, Paciaroni M (eds) Handbook on Cerebral Venous Thrombosis. Front Neurol Neurosci 23:4–15.

Kim HJ, Ko YT, Lim JW et al 2007 Radiologic anatomy of the superior mesenteric vein and branching patterns of the first jejunal trunk: evaluation using multi-detector row CT venography. Surg Radiol Anat 29:67–75.

Kimura K, Ohto M, Matsutani S et al 1990 Relative frequencies of portosystemic pathways and renal shunt formation through the ‘posterior’ gastric vein: portographic study in 460 patients. Hepatology 12:725–8.

Kleinert JM, Fleming SG, Smith Abel C et al 1989 Radial and ulnar artery dominance in normal digits. J Hand Surg Am 14A:504–8.

Kleppe M, Kraima AC, Kruitwagen RF et al 2015 Understanding lymphatic drainage pathways of the ovaries to predict sites for sentinel nodes in ovarian cancer. Int J Gynecol Cancer 25:1405–14.

Kocabiyik N, Yalcin B, Ozan H 2005 The morphometric analysis of the central retinal artery. Ophthal Physiol Opt 25:375–8.

Kosinski C 1926 Observations on the superficial venous system of the lower extremity. J Anat 60:131–42.

Kotian SR, Pandey AK, Padmashali S et al 2016 A cadaveric study of the testicular artery and its clinical significance. J Vasc Bras 15:280–6.

Kozak MF, Kozak AC, Souza AS et al 2011 Left pulmonary vein atresia: the contribution of multislice computed tomography. Pediatr Cardiol 32:108–10.

Kravitz RM 1994 Congenital malformations of the lung. Pediatr Clin North Am 41:453.

Krisht A, Barnett DW, Barrow DL et al 1994 The blood supply of the intracavernous cranial nerves: an anatomic study. Neurosurgery 34:275–9.

Kuge K, Murakami G, Mizobuchi S et al 2003 Submucosal territory of the direct lymphatic drainage system to the thoracic duct in the human esophagus. J Thorac Cardiovasc Surg 125:1343–9.

Kurklinsky AK, Rooke TW 2010 Nutcracker phenomenon and nutcracker syndrome. Mayo Clin Proc 85:552–9.

Lange JF, Koppert S, van Eyck CH et al 2000 The gastrocolic trunk of Henle in pancreatic surgery: an anatomo-clinical study. J Hepatobil Pancreat Surg 7:401–3.

Lasjaunias P, Berenstein A, ter Brugge KG 2001 Surgical Neuroangiography. Berlin: Springer.

Launois B, Jamieson GG 1993 Modern operative techniques in liver surgery. Clinical Surgery International 18. Edinburgh: Elsevier, Churchill Livingstone.

Lim W, Ridge CA, Nicholson AG et al 2018 The 8th lung cancer TNM classification and clinical staging system: review of the changes and clinical implications. Quant Imaging Med Surg 8:709–18.

Liu DL, Xia S, Xu W et al 1996 Anatomy of vasculature of 850 spleen specimens and its application in partial splenectomy. Surgery 119:27–33.

Liu F, Ruze A, Amuti S et al 2019 A rare variation of the hemiazygos vein draining into the persistent left superior vena cava. Anat Sci Int 94(3):269–73.

Lolis E, Panagouli E, Venieratos D 2011 Study of the ascending lumbar and iliolumbar veins: surgical anatomy, clinical implications and review of the literature. Ann Anat 193:516–29.

Londero LS, Lindholt JS, Thomsen MD et al 2016 Pulse palpation is an effective method for population-based screening to exclude peripheral arterial disease. J Vasc Surg 63:1305–10.

López-Andújar R, Moya A, Montalvá E et al 2007 Lessons learned from anatomic variants of the hepatic artery in 1,081 transplanted livers. Liver Transpl 13:1401–4.

Loukas M, Tubbs RS 2016 Adrenal, renal, gonadal, azygos, hemiazygos, lumbar, and ascending lumbar veins. In: Tubbs RS, Shoja MM, Loukas M (eds) Bergman’s Comprehensive Encyclopedia of Human Anatomic Variation, 2nd ed. Hoboken: Wiley Blackwell; Ch. 69, pp. 890–3.

Loukas M, Hullett J, Wagner T 2005a Clinical anatomy of the inferior phrenic artery. Clin Anat 18:357–65.

Loukas M, Louis RG Jr, Hullett J et al 2005b An anatomical classification of the variations of the inferior phrenic vein. Surg Radiol Anat 27:566–74.

Loukas M, Wartmann CT, Louis RG Jr et al 2007a The clinical anatomy of the posterior gastric artery revisited. Surg Radiol Anat 29:361–6.

Loukas M, Wartmann CT, Louis RG Jr et al 2007b Cisterna chyli: a detailed anatomic investigation. Clin Anat 20:683–8.

Loukas M, Groat C, Khangura R et al 2009 The normal and abnormal anatomy of the coronary arteries. Clin Anat 22:114–28.

Loukas M, Abel N, Tubbs RS et al 2011 The cardiac lymphatic system. Clin Anat 24:684–91.

Loukas M, Patel S, Cesmebasi A et al 2014 The clinical anatomy of the conal artery. Clin Anat 29:371–9.

Macchi V, Picardi E, Inferrera A et al 2018 Anatomic and radiologic study of renal avascular plane (Brödel’s line) and its potential relevance on percutaneous and surgical approaches to the kidney. J Endourol 32:154–9.

Macchi V, Picardi EEE, Porzionato A et al 2019 Integration of anatomical and radiological analysis suggests more segments in the human kidney. Clin Anat 32:46–52.

MacLennan GT 2012 Hinman’s Atlas of UroSurgical Anatomy, 2nd ed. Philadelphia: Elsevier.

Macmillan EW 1954 The blood supply of the epididymis in man. Br J Urol 26:60–71.

Malata CM, Moses M, Mickute Z et al 2011 Tips for successful microvascular abdominal flap breast reconstruction utilizing the ‘total rib preservation’ technique for internal mammary vessel exposure. Ann Plast Surg 66:36–42.

Malhotra D, Fletcher AL, Turley SJ 2013 Stromal and hematopoietic cells in secondary lymphoid organs: partners in immunity. Immunol Rev 251:160–76.

Martins C, Yasuda A, Campero A et al 2005b Microsurgical anatomy of the dural arteries. Neurosurgery 56:211–51.

Mashhour A, Thabet A, Easo J et al 2018 The left internal thoracic artery supplying a major part of the gastrointestinal tract. J Thorac Cardiovasc Surg 155:e25–7.

Matin SF 2006 Recognition and preservation of accessory pudendal arteries during laparoscopic radical prostatectomy. Urology 67:1012–15.

McFee RB, Musacchio T, Gorgescu D et al 1995 Wandering spleen with torsion in a geriatric patient. Dig Dis Sci 40:2656–9.

Michels NA 1966 Newer anatomy of the liver and its variant blood supply and collateral circulation. Am J Surg 112:337–47.

Mikhail Y, Kamel R, Nawar NN et al 1979 Observations on the mode of termination and parenchymal distribution of the splenic artery with evidence of splenic lobation and segmentation. J Anat 128:253–8.

Miletin J, Sukop A, Baca V et al 2017 Arterial supply of the thumb: systematic review. Clin Anat 30:963–73.

Miller FH, Fitzgerald SW, Donaldson JS 1993 CT of the azygoesophageal recess in infants and children. Radiographics 13:623–34.

Miller MJ, McDole JR, Newberry RD 2010 Microanatomy of the intestinal lymphatic system. Ann N Y Acad Sci 1207(Suppl 1):E21–E28.

Mirjalili SA, Hale SJ, Buckenham T et al 2012a A reappraisal of adult thoracic surface anatomy. Clin Anat 25:827–34.

Mirjalili SA, McFadden SL, Buckenham T et al 2012b A reappraisal of adult abdominal surface anatomy. Clin Anat 25:844–50.

Mirjalili SA, McFadden SL, Buckenham T et al 2012c Anatomical planes: are we teaching accurate surface anatomy? Clin Anat 25:819–26.

Mirjalili SA, Stringer MD 2011 The arterial supply of the major duodenal papilla and its relevance to endoscopic sphincterotomy. Endoscopy 43:307–11.

Moeller TB, Reif E 2000 Normal Findings in CT and MRI. New York: Thieme.

Morita S, Kimura T, Masukawa A et al 2007 Flow direction of ascending lumbar veins on magnetic resonance angiography and venography: would 'descending lumbar veins' be a more precise name physiologically? Abdom Imaging 32:749–53.

Morton GC, Thomas GM 2008 Testis. In: Halperin EC, Perez C, Brady LW (eds) Perez and Brady's Principles and Practice of Radiation Oncology, 5th ed. Wolters Kluwer.

Mostafa T, Labib I, el-Khayat Y et al 2008 Human testicular artery supply: gross anatomy, corrosion case, and radiologic study. J Androl 90:2226–30.

Mountain CF, Dresler CM 1997 Regional lymph node classification for lung cancer staging. Chest 111:1718–23.

Mourad N, Zhang J, Rath AM et al 1994 The venous drainage of the pancreas. Surg Radiol Anat 16:37–45.

Moussallem CD, Abou Hamad I, El-Yahchouchi CA et al 2012 Relationship of the lumbar lordosis angle to the abdominal aortic bifurcation and inferior vena cava confluence levels. Clin Anat 25:866–71.

Munhoz AM, Ishida LH, Montag E et al 2004 Perforator flap breast reconstruction using the internal mammary perforator branches as a recipient site: an anatomical and clinical analysis. Plast Reconstr Surg 114:62–8.

Munk A, Darge K, Wiesel M et al 2002 Diameter of the infrarenal aorta and the iliac arteries in children: ultrasound measurements. Transplantation 73:631–5.

Muresian H 2016 Coronary arteries. In Tubbs RS, Shoja MM, Loukas M Bergman's comprehensive encyclopedia of human anatomic variation, 2nd ed. Hoboken: Wiley–Blackwell; Ch. 50, pp. 530–68.

Murono K, Kawai K, Kazama S et al 2015 Anatomy of the inferior mesenteric artery evaluated using 3-dimensional CT angiography. Dis Colon Rectum 58:214–19.

Nakamura T, Moriyasu F, Ban N et al 1989 Quantitative measurement of abdominal arterial blood flow using image-directed Doppler ultrasonography. J Clin Ultrasound 17:261–8.

Ndoye JM, Dia A, Ndiaye A et al 2006 Arteriography of three models of gastric oesophagoplasty: the whole stomach, a wide gastric tube and a narrow gastric tube. Surg Radiol Anat 28:429–37.

Needleman L 2006 Measurements of the abdominal aorta. In: Goldberg BB, McGahan JP (eds) Atlas of Ultrasound Measurements, 2nd ed. Boston: Elsevier, Mosby.

Neligan PC, Gullane PJ, Vesely M et al 2007 The internal mammary artery perforator flap: new variation on an old theme. Plast Reconstr Surg 119:891–3.

Niggemann P, Förg A, Grosskurth D et al 2010 Postural effect on the size of the cisterna chyli. Lymphat Res Biol 8:193–7.

Ninković M, Anderl H, Hefel L et al 1995 Internal mammary vessels: a reliable recipient system for free flaps in breast reconstruction. Br J Plast Surg 48:533–9.

Norton JA, Barie PS, Bollinger RR et al 2008 Surgery: Basic Science and Clinical Evidence, 2nd ed. New York: Springer.

Novick AC 1998 Anatomic approaches in nephron-sparing surgery for renal cell carcinoma. Atlas Urol Clin North Am 6:39.

Nowinski W, Chua B, Johnson A et al 2013 Three-dimensional stereotactic atlas of head muscles and glands correlated with cranial nerves and surface sectional neuroanatomy. J Neurosci Methods 215:12–18.

Nowinski WL, Shoon Let Thaung T, Choon Chua B et al 2015 Three-dimensional stereotactic atlas of the extracranial vasculature correlated with the intracranial vasculature, cranial nerves, skull and muscles. Neuroradiol J. 28:190–197.

O'Morchoe CC 1997 Lymphatic system of the pancreas. Microsc Res Tech 37:456–77.

Ogawa K, Hishitani T, Hoshino K 2013 Absence of the coronary sinus with coronary venous drainage into the main pulmonary artery. Cardiol Young 23:759–62.

Oguro A, Taniguchi H, Koyama H et al 1993 Relationship between liver function and splenic blood flow. Ann Nucl Med 7:251–255.

Ohkubo M 2000 Aberrant left gastric vein directly draining into the liver. Clin Anat 13:134–7.

Ohtani O, Ohtani Y 2008 Lymph circulation in the liver. Anat Rec 291:643–52.

Onishi H, Kawarada Y, Das BC et al 2000 Surgical anatomy of the medial segment (S4) of the liver with special reference to bile ducts and vessels. Hepatogastroenterology 47:143–50.

Osborn AG 1998 Diagnostic Cerebral Angiography. Philadelphia: Lippincott, Williams & Wilkins.

Ouattara D, Kipré YZ, Broalet E et al 2007 Classification of the terminal arterial vascularization of the appendix with a view to its use in reconstructive microsurgery. Surg Radiol Anat 29:635–41.

Ozawa Y, Suzuki R, Hara M et al 2018 Identification of the pericardiacophrenic vein on CT. Cancer Imaging 18:1.

Ozkurt H, Cenker MM, Bas N et al 2007 Measurement of the distance and angle between the aorta and superior mesenteric artery: normal values in different BMI categories. Surg Radiol Anat 29:595–9.

Pai MM, Krishnamurthy A, Prabhu LV et al 2009 Variability in the origin of the obturator artery. Clinics (São Paulo) 64:897–901.

Pai MM, Vadgaonkar R, Rai R et al 2008 A cadaveric study of the testicular artery in the South Indian population. Singapore Med J 49:551–5.

Panagouli E, Venieratos D, Lolis E et al 2013 Variations in the anatomy of the celiac trunk: a systematic review and clinical implications. Ann Anat 195:501–11.

Panagouli E, Tsoucalas G, Papaioannou T et al 2018 Right and left common carotid arteries arising from the brachiocephalic, a rare variation of the aortic arch. Anat Cell Biol 51:215–17.

Pandey SK, Bhattacharya S, Mishra RN et al 2004 Anatomical variations of the splenic artery and its clinical implications. Clin Anat 17:497–502.

Paño B, Sebastià C, Buñesch L et al 2011 Pathways of lymphatic spread in male urogenital pelvic malignancies. Radiographics 31:135–60.

Paquet KJ 2000 Causes and pathomechanisms of oesophageal varices development. Med Sci Monit 6:915–28.

Par MM, Barry P, Autissier JM et al 1965 Considérations sur la morphologie de la veine splénique et de ses affluents. Soc Nac Med 1:539–47.

Park KA, Oh SY 2013 Choroidal thickness in healthy children. Retina 33:1971–6.

Park MC, Lee JH, Chung J et al 2003 Use of internal mammary vessel perforator as a recipient vessel for free TRAM breast reconstruction. Ann Plast Surg 50:132–7.

Park DY, Lee J, Kim J et al 2017 Plastic roles of pericytes in the blood–retinal barrier. Nat Commun 8:15296.

Parrett BM, Caterson SA, Tobias AM et al 2008 The rib-sparing technique for internal mammary vessel exposure in microsurgical breast reconstruction. Ann Plast Surg 60:241–3.

Pearce JMS 2006 The craniospinal venous system. Eur Neurol 56:136–8.

Pesonen E, Hirvonen J, Karkola K et al 1991 Dimensions of the coronary arteries in children. Ann Med 23:85–8.

Petroianu A 2011 The Spleen. London: Bentham Science.

Phang K, Bowman M, Phillips A et al 2014 Review of thoracic duct anatomical variations and clinical implications. Clin Anat 27:637–44.

Phelan PJ, Shields W, O'Kelly P et al 2009 Left versus right deceased donor renal allograft outcome. Transpl Int 22:1159–63.

Plets C, De Reuck J, Vander Eecken H et al 1970 The vascularization of the human thalamus. Acta Neurol Belg 70:687–770.

Pontén B 1981 The fasciocutaneous flap: its use in soft tissue defects of the lower leg. Br J Plast Surg 34:215–20.

Porzionato A, Macchi V, Stecco C et al 2013 The carotid body in sudden infant death syndrome. Respir Physiol Neurobiol 185:194–201.

Power D, Forshaw M, Birch J et al 2001 The distribution and clinical anatomy of the short gastric veins. Internet J Surg 3:1–3.

Puchades-Orts A, Nombela-Gomez M, Ortu-o-Pacheco G 1976 Variation in form of the circle of Willis. Some anatomical and embryological considerations. Anat Rec 185:119–23.

Punn R, Olson I 2010 Anomalies associated with a prominent azygos vein on echocardiography in the pediatric population. J Am Soc Echocardiogr 23:282–5.

Ramesh Babu CS, Sharma M 2014 Biliary tract anatomy and its relationship with venous drainage. J Clin Exp Hepatol 4 (Suppl 1):S18–S26.

Ramesh Babu CS, Sharma M 2014 Biliary tract anatomy and its relationship with venous drainage. J Clin Exp Hepatol 4 (Suppl 1):S18–S26.

Ray B, Gupta N 2006 Caroticoclinoid foramen with interclinoid osseous bar. Clin Anat 19:732–3.

Re G, Casali A, Cavalli D et al 1985 Morphological bases of splenic circulation in congestive splenomegaly. Haematologica 70:283–90.

Rebibo L, Chivot C, Fuks D et al 2012 Three-dimensional computed tomography analysis of the left gastric vein in a pancreatectomy. HPB (Oxford) 14:414–21.

Reisch R, Vutskits L, Patonay L et al 1996 The meningohypophyseal trunk and its blood supply to different intracranial structures. An anatomical study. Minim Invasive Neurosurg 39:78–81.

Ricci S 2017 Anatomy. In: Goldman MP, Guex J-J, Weiss RA (eds) Sclerotherapy: Treatment of Varicose and Telangiectatic Leg Veins, 6th ed. Elsevier; Ch. 1, pp. 1–26.

Rice TW, Ishwaran H, Ferguson MK et al 2016 Cancer of the esophagus and esophagogastric junction: an eighth edition staging primer. J Thorac Oncol 12:36–42.

Roberts WH, Krishingner GL 1967 Comparative study of human internal iliac artery based on Adachi classification. Anat Rec 158:191–196.

Robertson GS, Ristic CD, Bullen BR 1990 The incidence of congenitally absent foot pulses. Ann R Coll Surg Engl 72:99–100.

Rodriguez-Niedenführ M, Sanudo JR, Vazquez T et al 1999 Median artery revisited. J Anat 195:57–63.

Rogers IS, Massaro JM, Truong QA et al 2013 Distribution, determinants, and normal reference values of thoracic and abdominal aortic diameters by computed tomography (from the Framingham Heart Study). Am J Cardiol 111:1510–16.

Romero-Torres R 1998 The true splenic blood supply and its surgical applications. Hepatogastroenterology 45:885–8.

Rooke TW, Sullivan TM, Jaff MR 2007 Unusual Vascular Diseases in Vascular Medicine and Endovascular Interventions. Columbia, MD: Blackwell Futura, pp. 134–5.

Rountas CH, Fanariotis M, Vlychou M et al 2013 Celiomesenteric trunk demonstrated by multi-detector computed tomography angiography: two cases of a rare vascular variation. Folia Morphol (Warsz) 72:171–5.

Rozen WM, Ashton MW, Taylor GI 2008 Reviewing the vascular supply of the anterior abdominal wall: redefining anatomy for increasingly refined surgery. Clin Anat 21:89–98.

Rozen WM, Pan WR, Le Roux CM et al 2009 The venous anatomy of the anterior abdominal wall: an anatomical and clinical study. Plast Reconstr Surg 124:848–53.

Ruíz DSM, Fasel JHD, Rüfenacht DA et al 2004 The sphenoparietal sinus of Breschet: does it exist? An anatomic study. Am J Neuroradiol 25:112–20.

Rusch VW, Asamura H, Watanabe H et al 2009 The IASLC lung cancer staging project: a proposal for a new international lymph node map in the forthcoming seventh edition of the TNM classification for lung cancer. J Thorac Oncol 4(5):568–77.

Saba L, Mallarini G 2011 Anatomic variations of arterial liver vascularization: an analysis by using MDCTA. Surg Radiol Anat 33:559–68.

Salins P, Benjamin P 2009 Anatomic basis for reconstruction of retromolar region: significance of palatal flap. J Oral Maxillofac Surg 67:1141–8.

Sampson UKA, Fowkes FGR, Naidoo NG et al 2017 Peripheral artery disease. In: Prabhakaran D, Anand S, Gaziano TA et al (eds) Cardiovascular, Respiratory, and Related Disorders, 3rd ed (Disease Control Priorities Vol 5). Washington, DC: The International Bank for Reconstruction and Development/The World Bank; Ch. 14, pp. 253–62.

Sanjeev S, Karpawich PP 2006 Superior vena cava and innominate vein dimensions in growing children: an aid for interventional devices and transvenous leads. Pediatr Cardiol 27:414–19.

Sanna B, Henry BM, Vikse J et al 2018 The prevalence and morphology of the corona mortis (crown of death): a meta-analysis with implications in abdominal wall and pelvic surgery. Injury 49:302–8.

Sato T, Ito M, Sakamoto H 2013 Pictorial dissection review of the lymphatic pathways from the gallbladder to the abdominal para-aortic lymph nodes and their relationships to the surrounding structures. Surg Radiol Anat 35:615–21.

Schneider A, Ferreira CG, Delay C et al 2013 Lower pole vessels in children with pelviureteric junction obstruction: laparoscopic vascular hitch or dismembered pyeloplasty? J Pediatr Urol 9:419–23.

Seoane E, Rhoton AL Jr, de Oliveira E 1998 Microsurgical anatomy of the dural collar (carotid collar) and rings around the clinoid segment of the internal carotid artery. Neurosurgery 42:869–84.

Seong J, Lieber BB, Wakhloo AK 2005 Morphological age-dependent development of the human carotid bifurcation. J Biomech 38:453–65.

Shakeri A, Tubbs RS, Shoja MM et al 2010 Analysis of the profunda femoris artery with superficial femoral artery occlusive disease. Biomed Int 1:62–5.

Siddharth P, Smith NL, Mason RA et al 1985 Variational anatomy of the deep femoral artery. Anat Rec 212:206–9.

Siramolpiwat S 2014 Transjugular intrahepatic portosystemic shunts and portal hypertension-related complications. World J Gastroenterol 20:16996–7010.

Sivrikoz MC 2016 Pulmonary arteries. In: Tubbs RS, Shoja MM, Loukas M (eds) Bergman's Comprehensive Encyclopedia of Human Anatomic Variation, 2nd ed. Hoboken: Wiley Blackwell; Ch. 51, pp. 569–74.

Skandalakis PN, Colborn GL, Skandalakis LJ et al 1993 The surgical anatomy of the spleen. Surg Clin North Am 73:747–68.

Skandalakis JE, Coborn GL, Weidman TA et al 2004 Spleen. In: Skandalakis JE (ed.) Skandalakis' Surgical Anatomy. Athens: Paschalidis Medical Publications; Ch. 22, pp. 1231–87.

Smith A, McKay R 2004 A Practical Atlas of Congenital Heart Disease. London: Springer.

Smith ME, Riffat F, Jani P 2013 The surgical anatomy and clinical relevance of the neglected right lymphatic duct: review. J Laryngol Otol 127:128–33.

Song Y-B 2016 Thoracic duct, chyle cistern and right lymphatic duct. In: Tubbs RS, Shoja MM, Loukas M (eds) Bergman's Comprehensive Encyclopedia of Human Anatomic Variation, 2nd ed. Hoboken: Wiley Blackwell; Ch 75, pp. 921–34.

Sow ML, Dia A, Ouedraogo T 1991 Anatomic basis for conservative surgery of the spleen. Surg Radiol Anat 13:81–7.

Spentzouris G, Zandian A, Cesmebasi A et al 2014 The clinical anatomy of the inferior vena cava: a review of common congenital anomalies and considerations for clinicians. Clin Anat 27:1234–43.

Spratt J 2016 Inferior vena cava, portal and hepatic venous systems. In: Tubbs RS, Shoja MM, Loukas M Bergman's Comprehensive Encyclopedia of Human Anatomic Variation, 2nd ed. Hoboken: Wiley–Blackwell; Ch. 68, pp. 877–89.

Stefura T, Kacprzyk A, Droś J et al 2018 The venous trunk of Henle (gastrocolic trunk): a systematic review and meta-analysis of its prevalence, dimensions, and tributary variations. Clin Anat 31:1109–21.

Stocker JT, Drake RM, Madewell JE 1978 Cystic and congenital lung disease in the newborn. Perspect Pediatr Pathol 4:93.

Suami H, Pan WR, Mann GB et al 2008 The lymphatic anatomy of the breast and its implications for sentinel lymph node biopsy: a human cadaver study. Ann Surg Oncol 15:863–71.

Suami H, Pan WR, Taylor GI 2009 Historical review of breast lymphatic studies. Clin Anat 22:531–6.

Sugita M, Ryu M, Satake M et al 2000 Intrahepatic inflow areas of the drainage vein of the gallbladder: analysis by angio-CT. Surgery 128:417–21.

Sylvester PA, Stewart R, Ellis H 1995 Tortuosity of the human splenic artery. Clin Anat 8:214–18.

Tachimori Y 2017 Pattern of lymph node metastases of squamous cell esophageal cancer based on the anatomical lymphatic drainage system: efficacy of lymph node dissection according to tumor location. J Thorac Dis 9:S724–S730.

Takayama T, Yamanouchi D 2013 Aneurysmal disease: the abdominal aorta. Surg Clin North Am 93:877–91.

Takeuchi M, Kuwayama N, Kubo M et al 2005 Vidian artery as a collateral channel between the external and occluded internal carotid arteries. Neuro Med Chir (Tokyo) 45:470–1.

Tamaki Y, Sasaki R, Ejima Y et al 2012 Efficacy of intraoperative radiotherapy targeted to the abdominal lymph node area in patients with esophageal carcinoma. J Rad Res 53:882–91.

Tanis PJ, Nieweg OE, Valdes Olmos RA et al 2001 Anatomy and physiology of lymphatic drainage of the breast from the perspective of sentinel node biopsy. J Am Coll Surg 192:399–409.

Tanis PJ, van Rijk MC, Nieweg OE 2005 The posterior lymphatic network of the breast rediscovered. J Surg Oncol 91:195–8.

Tayfur V, Magden O, Edizer M, Atabey A. 2010 Anatomy of vastus lateralis muscle flap. J Craniofac Surg 21:1951–3.

Taylor GI, Razaboni RM (eds) 1994 Michel Salmon: Anatomic Studies. Book 1, Arteries of the Muscles of the Extremities and the Trunk. Book 2, Arterial Anastomotic Pathways of the Extremities. St Louis: Quality Medical Publishing.

Tekdemir I, Tuccar E, Cubuk HE et al 1998 Branches of the intracavernous internal carotid artery and the blood supply of the intracavernous cranial nerves. Ann Anat 180:343–8.

Toller PA 1974 Temporomandibular arthropathy. Proc R Soc Med 67:153–9.

Toni R, Mosca S, Favero L et al 1988 Clinical anatomy of the suprarenal arteries: a quantitative approach by aortography. Surg Radiol Anat 10:297–302.

Tourani SS, Taylor GI, Ashton MW 2013 Anatomy of the superficial lymphatics of the abdominal wall and the upper thigh and its implications in lymphatic microsurgery. J Plast Reconstr Aesthet Surg 66:1390–5.

Tourani SS, Taylor GI, Ashton MW 2014 Understanding the three-dimensional anatomy of the superficial lymphatics of the limbs. Plast Reconstr Surg 134:1065–74.

Trubel W, Turkof E, Rokitansky A et al 1985 Incidence, anatomy and territories supplied by the posterior gastric artery. Acta Anat 124:26–30.

Trubel W, Rokitansky A, Turkof E et al 1988 Correlations between posterior gastric artery and superior polar artery in human anatomy. Anat Anz 167:219–23.

Trutmann M, Sasse D 1994 The lymphatics of the liver. Anat Embryol (Berl) 190:201–9.

Tsutsumi M, Arakawa T, Terashima T et al 2014 Morphological analysis of the branches of the dorsal pancreatic artery and their clinical significance. Clin Anat 27:645–52.

Tubbs RS, Hansasuta A, Loukas M et al 2007 Branches of the petrous and cavernous segments of the internal carotid artery. Clin Anat 20:596–601.

Tubbs RS, Shoja M, Loukas M 2016 Bergman's Comprehensive Encyclopedia of Human Anatomic Variation. Hoboken: Wiley Blackwell.

Tunali S 2016 Subclavian artery. In: Tubbs RS, Shoja MM, Loukas M Bergman's Comprehensive Encyclopedia of Human Anatomic Variation, 2nd ed. Hoboken: Wiley–Blackwell; Ch. 52, pp. 575–82.

Turmezei TD, Cockburn JF 2009 Digital subtraction angiography of the superior mesenteric artery: identifying arterial branches. Clin Anat 22:777–9.

Turnbull IM, Brieg A, Hassler O 1966 Blood supply of cervical spinal cord in man. A microangiographic cadaver study. J Neurosurg 24:951–65.

Uchino A, Saito N, Takahashi M et al 2013 Persistent dorsal ophthalmic artery and ophthalmic artery arising from the middle meningeal artery diagnosed by MR angiography at 3 T. Surg Radiol Anat 35:775–82.

Umansky F, Valarezo A, Elidan J 1994 The superior wall of the cavernous sinus: a microanatomical study. J Neurosurg 81:914–20.

Uysal F, Bostan OM, Semizel E et al 2014 Congenital anomalies of coronary arteries in children: the evaluation of 22 patients. Pediat Cardiol 35:778–84.

van Gulik TM, Schoots I 2005 Anastomosis of Riolan revisited: the meandering mesenteric artery. Arch Surg 140:1225–9.

Veeresh H, Halasagi SS, Shakuntala RP et al 2012 A study of arterial supply of caecum in humans. J Evol Med Dent Sci 1:811–16.

Vellar ID 2001 Preliminary study of the anatomy of the venous drainage of the intrahepatic and extrahepatic bile ducts and its relevance to the practice of hepatobiliary surgery. ANZ J Surg 71:418–22.

Veyrac C, Baud C, Lopez C et al 2003 The value of colour Doppler ultrasonography for identification of crossing vessels in children with pelvi-ureteric junction obstruction. Pediatr Radiol 33:745–51.

Vuorio T, Tirronen A, Yla-Herttuala S 2016 Cardiac lymphatics – a new avenue for therapeutics? Trends Endocrinol Metabol 28:2327–37.

Wang C, Zhang R, Luo P et al 2018 Reconstruction of extensive thoracic wall defect using the external oblique myocutaneous flap: an analysis on 20 Chinese patients with locally advanced soft tissue sarcoma. J Surg Oncol 117:130–6.

Welsh LW, Welsh JJ, Rizzo TA 1983 Laryngeal spaces and lymphatics: current anatomic concepts. Ann Otol Rhinol Laryngol Suppl 105:19–31.

Weninger WJ, Muller GB 1999 The parasellar region of infants: cavernous sinus topography and surgical approaches. J Neurosurg 90:484–90.

Werner JA, Dünne AA, Myers JN 2003 Functional anatomy of the lymphatic drainage system of the upper aerodigestive tract and its role in metastasis of squamous cell carcinoma. Head Neck 25:322–32.

Winston CB, Lee NA, Jarnagin WR et al 2007 CT angiography for delineation of celiac and superior mesenteric artery variants in patients undergoing hepatobiliary and pancreatic surgery. AJR Am J Roentgenol 189:W13–19.

Woodburne RT, Olsen LL 1951 The arteries of the pancreas. Anat Rec 111:255–70.

Wu ZX, Yang XZ, Cai JQ et al 2011 Digital subtraction angiography and computed tomography angiography of predominant artery feeding pancreatic body and tail. Diabetes Technol Ther 13:537–41.

Yalcin B 2016 Thyroid gland. In: Tubbs RS, Shoja MM, Loukas M Bergman's Comprehensive Encyclopedia of Human Anatomic Variation, 2nd ed. Hoboken: Wiley–Blackwell; Ch. 99, pp. 1189–204.

Yamaguchi H, Wakiguchi S, Murakami G et al 2001 Blood supply to the duodenal papilla and the communicating artery between the anterior and posterior pancreaticoduodenal arterial arcades. J Hepatobil Pancreat Surg 8:238–44.

Yamaguchi S, Kuroyanagi H, Milson JW et al 2002 Venous anatomy of the right colon: precise structure of the major veins and gastrocolic trunk in 58 cadavers. Dis Colon Rectum 45:1337–40.

Yasuda A, Campero A, Martins C et al 2004 The medial wall of the cavernous sinus: microsurgical anatomy. Neurosurgery 55:179–89.

Yoshida T, Suzuki S, Sato T 1993 Middle mesenteric artery: an anomalous origin of a middle colic artery. Surg Radiol Anat 15:361–3.

Zarzecki MP, Popieluszko P, Zayachowski A et al 2018 The surgical anatomy of the superficial and deep palmar arches: a meta-analysis. J Plast Reconstr Aesthet Surg 71:1577–92.

Zhang HR 1994 Scanning electron-microscopic study of corrosion casts on retinal and choroidal angioarchitecture in man and animals. Prog Retinal Eye Res 13:243–70.

Zhong YM, Jaffe RB, Zhu M et al 2010 CT assessment of tracheobronchial anomaly in left pulmonary artery sling. Pediatr Radiol 40:1755–62.

COMMENTARY

I.1

A note on anatomy from an imaging perspective

Tom Turmezei

In recent years there have been reciprocal, reinforcing developments between the disciplines of human anatomy and clinical radiology. Most medical schools include medical imaging as a core component of their anatomy syllabus. Ongoing developments in medical technology have enabled us to visualize living anatomy with far greater detail. Higher-field magnetic resonance imaging (e.g. 3 Tesla MRI) is perhaps the best known of these advances, but there have been contributing improvements across all imaging modalities. From a clinical perspective, the ability to see greater detail can be a blessing in disguise: radiologists have had to develop interpretive skills alongside their anatomical knowledge to ensure that they understand what they are seeing.

Limitations on visualization remain, often defined by the modality used to image a particular body region, which means that the wealth of information now available to us must be considered in the context of how the images were acquired. Imaging such as MRI and ultrasound can be pre-arranged for educational purposes, whereas modalities that involve exposure to ionizing radiation such as computed tomography (CT) and radiography cannot. Therefore we must rely on clinical imaging acquisitions to be furnished with as close to ideal anatomy as possible. Patient positioning, physiology and individual anatomical variation all come into the mix, factors that challenge radiologists daily.

Fig. I.1.1 shows how a small change in the axis of multiplanar reformatting through a CT image volume of the thorax can subtly change the anatomy displayed. In the top row, the axial, sagittal and coronal slices are taken with respect to the gantry, while in the bottom row these planes are set with respect to the vertebral body of T5. There are distinct topographical differences within each pair of images. Taking the axial plane as an example, note how the aortic arch (red arrow) is present in the top image, but is not seen in bottom image. Likewise, the carina (green arrow) is not seen in the top image, but is just seen in the bottom image. Finally, the whole chest seems wider (in the anteroposterior dimension) in the bottom image, also with a different configuration of the ribs. If the same patient were to get up and lie down again on the gantry for a second examination just moments later, would they be in the same position and would a slice at T5 axial to the plane of the gantry show the same information? (The answer is no.) Since image plane acquisitions are routinely standardized with respect to the gantry, individual anatomical variations between patients mean that body positioning also affects imaging planes. But as this exercise shows, it is possible to manipulate orthogonal imaging planes with multiplanar reformats to overcome this effect when reviewing an image set at workstation. This at least means that we can attempt to review imaging with some anatomical consistency across individuals.

Physiology also significantly affects the visualization of living anatomy in medical imaging. For example, a different depth of inspiration would give a different lung volume (similar to the effect seen above with respect to the anteroposterior chest diameter) and a different respiratory diaphragm level, shifting mobile abdominal organs to a different position. A hyperdynamic state might also push intravenous contrast medium through the heart and lungs more quickly, meaning

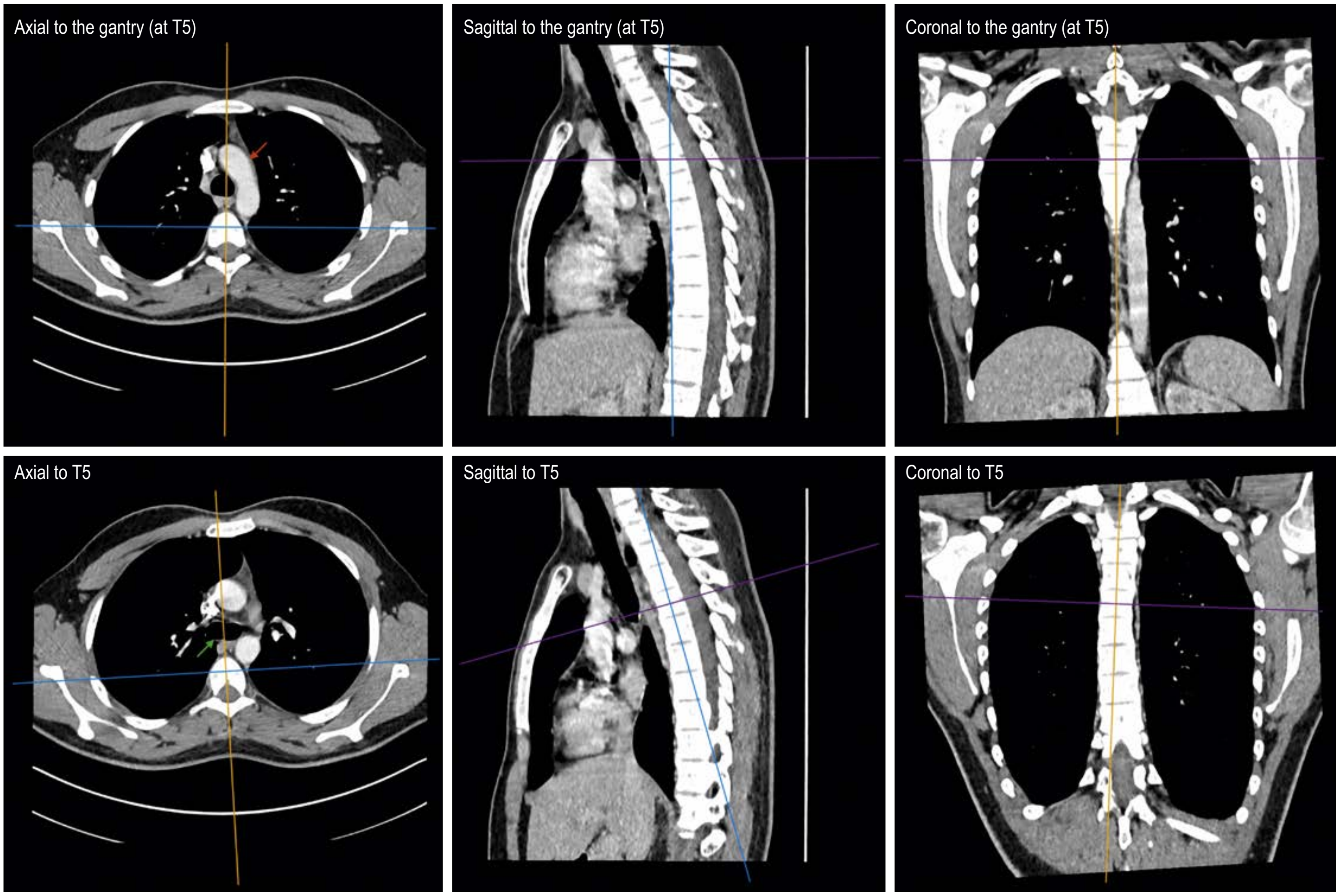
Axial to the gantry (at T5)
Sagittal to the gantry (at T5)
Coronal to the gantry (at T5)
Axial to T5
Sagittal to T5
Coronal to T5

Fig. I.1.1 CT scan of the thorax with intravenous contrast medium. Top row: axial, sagittal and coronal image planes (purple, orange and blue planes, respectively) with respect to CT machine gantry at the level of T5. Bottom row: axial, sagittal and coronal image planes with respect to the T5 vertebral body. Red arrow = aortic arch; green arrow = carina.

that the scan would have to be acquired earlier after injection to achieve the same contrast opacification of the pulmonary vasculature. This is a key skill that radiographers develop in order to see meaningful patterns of contrast opacification in different vessels and perfused tissues. For example, in choosing a protocol in order to visualize the pulmonary arterial system to exclude a pulmonary embolism, if an acquisition is too early, then the contrast medium will sit in the peripheral venous system or right side of the heart, whereas if acquisition is too late, contrast medium will have passed beyond the left side of the heart: both will lead to a non-diagnostic scan from inadequate opacification of the pulmonary arterial tree.

Fig. I.1.2 demonstrates another visualization challenge for radiologists, namely how to see all tissue types in the same image. A feature of most medical imaging is that it can contain more grayscale information than the human eye can process. As a result, information is lost when displayed on screen. In this figure, the same underlying image information has simply been viewed with different brightness and contrast settings, but note how different structures stand out in each. The 'soft tissue' window clearly shows greater definition between fat, muscle, lymph nodes and the vascular structures of the mediastinum; the 'lung' window shows vessels, airways and the septal/lobular structure of the lungs; the 'bone' window shows greater skeletal detail. Each must be reviewed according to the clinical question at hand. In the same way, an appropriate window must be chosen to review certain anatomical structures.

Advances in digital data handling have been essential in making imaging available for anatomical education. They have placed tools for 3D image reconstruction, manipulation and navigation (such as seen in Figs I.1.1–I.1.2) in the hands of anatomists and their students, and have greatly enhanced an understanding of important structural relationships in the human body. However, it is important to remember that a *single* image rarely holds all the necessary cues for learning these relationships and therefore, whenever possible, many slices in different planes should be examined.

One near-certain means to improve educational experiences will be to continue to collaborate in imaging projects and publications. In this way, hopefully the skills of experts in anatomy and medical imaging will continue to bear fruit for the students of both disciplines.

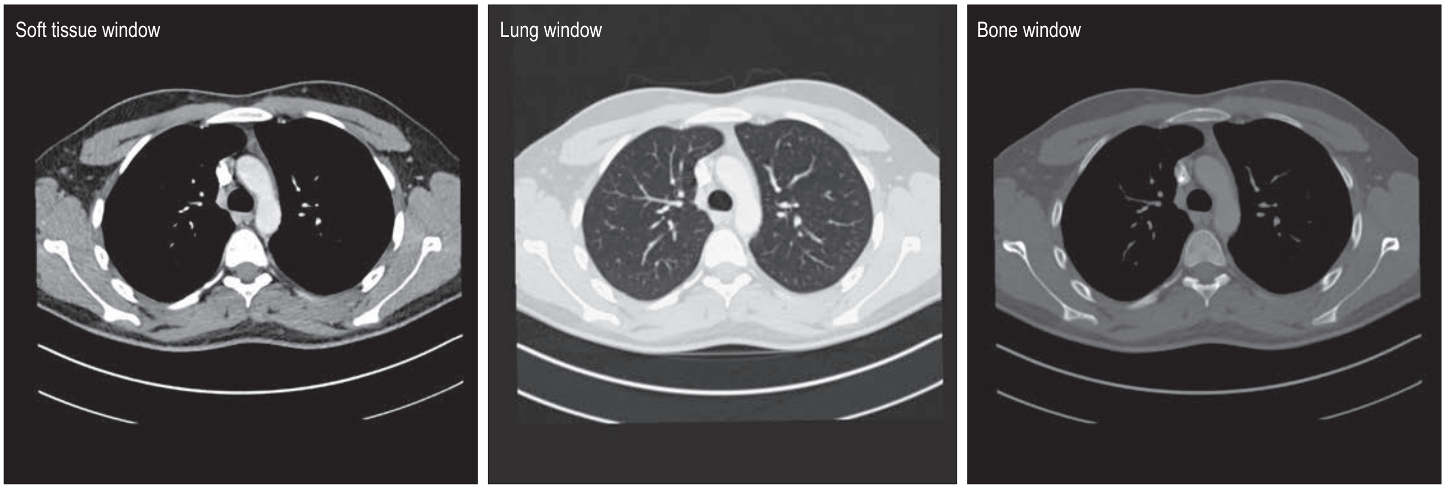

Fig. I.1.2 CT scan of the thorax with intravenous contrast medium at the level of T5. Three different window settings commonly used for looking at the thorax: from left to right these are 'soft tissue', 'lung' and 'bone', each making specific tissue types more apparent.

COMMENTARY

I.2

Technical aspects and applications of diagnostic radiology

Jonathan Spratt

MAGNETIC RESONANCE IMAGING

Magnetic resonance imaging (MRI) produces images by first magnetizing a patient in the bore of a powerful magnet and then broadcasting short pulses of radiofrequency (RF) energy at 46.3 MHz that resonate mobile protons (hydrogen nuclei) in the fat, protein and water of the patient's soft tissues and bone marrow. The protons produce RF echoes when their resonant energy is released; their density and location can be exactly correlated into an image matrix by complex mathematical algorithms.

The spinning proton of the hydrogen nucleus acts like a tiny bar magnet, aligning either with or against the magnetic field, and producing a small net magnetic vector. RF energy from various types of coil, either built into the scanner or attached to specific body parts, generates a second magnetic field perpendicular to the static magnetic field that rotates or 'flips' the protons away from the static magnetic field. When the RF pulse is switched off, the protons flip back (relax) to their original position of equilibrium, emitting the RF energy they had acquired into the antenna around the patient. This information is then amplified, digitized and spatially encoded by the array processor.

MRI systems are graded according to the strength of the magnetic field they produce. Routine high-field systems are those capable of producing a magnetic field strength of 3–7 T (Tesla), using a superconducting electromagnet immersed in liquid helium. Open magnets for claustrophobic patients and limb scanners use permanent magnets of 0.2–0.75 T. For comparison, Earth's magnetic field varies from 30 to 60 μT. MRI does not present any recognized biological hazard. Patients who have any ferromagnetic intracranial aneurysm clips, certain types of cardiac valve replacement or intraocular metallic foreign bodies must never be examined because there is a high risk of death or blindness. Patients with implanted electronic devices such as a cardiac pacemaker or spinal cord stimulator must be screened carefully if MRI is being considered. Many new devices are now MRI-compatible, but the precise product details must be made available to the MRI team to ensure the patient's safety (e.g. the need to induce a 'scanner mode' in the device, or establishing definitive MRI-incompatibility). Many extracranial vascular clips and orthopaedic prostheses are now 'MRI-friendly' but may cause local artefacts; newer sequences exist to reduce artefact. Loose metal items, 'MR-unfriendly' anaesthetic equipment and credit cards must be excluded from the examination room. Pillows containing metallic coiled springs have been known nearly to suffocate patients, and heavy floor-buffing equipment has been found wedged in the magnet bore because domestic staff had been suboptimally informed.

New methods of analysing normal and pathological brain anatomy are now at the forefront of research. These are MR spectroscopy (MRS); functional MRI (fMRI); diffusion tensor imaging (DTI); high angular resolution diffusion imaging (HARDI) for MR tractography (MRT, see below); and molecular MRI (mMRI), which has taken on a new direction since the description of the human genome.

MRS assesses function within the living brain. It capitalizes on the fact that protons residing in differing chemical environments possess slightly different resonant properties (chemical shift). For a given volume of brain, the distribution of these proton resonances can be displayed as a spectrum. Discernible peaks can be seen for certain neurotransmitters: *N*-acetylaspartate varies in multiple sclerosis, stroke and schizophrenia while choline and lactate levels have been used to evaluate certain brain tumours.

fMRI depends on the fact that haemoglobin is diamagnetic when oxygenated but paramagnetic when deoxygenated. These different signals can be weighted to the smaller vessels, and hence closer to the active neurones, by using larger magnetic fields. mMRI uses biomarkers that interact chemically with their surroundings and alter the image according to molecular changes occurring within the area of interest, potentially enabling early detection and treatment of disease and basic pharmaceutical development and quantitative testing.

High-field-strength magnets give significant improvement in spatial resolution and contrast. MR images of the microvasculature of the live human brain that allow close comparison with the detail seen in histological slides have been acquired at 8 T. This has significant implications for the treatment of reperfusion injury and research into the physiology of solid tumours and angiogenesis. There is every reason to believe that continued efforts to push the envelope of high-field-strength applications will open new vistas in what appears to be a never-ending array of potential clinical applications.

T1-weighted images best accentuate fat and other soft tissues, whereas fluid is low-signal; these images are nicknamed the 'anatomy weighting' amongst radiologists who publish or teach anatomy. T2-weighted images reveal fluid as high signal as well as fat. Fat suppression sequences using T2 'fat sat' (T2FS) or short tau inversion recovery (STIR) are very sensitive in highlighting the soft tissue or bone marrow oedema that almost invariably accompanies pathological states such as inflammation or tumours. Contrast-enhanced images with gadolinium, when used with T1 fat saturation (T1FS) sequences, also exquisitely highlight hypervascularity, particularly that associated with tumours and inflammation, especially in pathologies where the blood–brain barrier is compromised. Metallic artefact reduction sequences (MARS) are superior in imaging periprosthetic soft tissues after joint replacement or other orthopaedic metalwork implantation.

MR tractography

MR tractography (MRT) is a three-dimensional modelling technique used to represent neural tracts visually using data collected by DTI or, more recently, by HARDI, with results presented in two- and three-dimensional images (Nucifora et al 2007) (see Chapter 32).

The MRI sequences used look at the symmetry of water diffusion in the brain. Bundles of fibre tracts make the water diffuse asymmetrically in a 'tensor', the major axis parallel to the direction of the fibres. There is a direct relationship between the number of fibres and the degree of anisotropy. DTI assumes that the direction of least restriction corresponds to the direction of white matter tracts. Diffusion MRI was introduced in 1985. In the more recent evolution of the technique into diffusion tensor MRI (DTI), the relative mobility of the water molecules from the origin is modelled as an ellipsoid rather than a sphere. This allows full characterization of molecular diffusion in the three dimensions of space and the formation of tractograms. Barriers cause uneven anisotropic diffusion. In white matter, the principal barrier is the myelin sheath, whereas bundles of axons provide a barrier to perpendicular diffusion and a path for parallel diffusion along the orientation of the fibres. Anisotropic diffusion is expected to be increased overall in areas of high mature axonal order. Conditions where barriers offered by the myelin sheaths or the axons are disrupted, e.g. in trauma, tumours and inflammation, reduce anisotropy and yield DTI data used to seed various tractographic assessments of the brain. Data sets may be rotated continuously into various planes in order to appreciate the structure better; colour may be assigned based on the dominant direction of the fibres. A leading clinical application of MRT is in the presurgical mapping of eloquent regions. Intraoperative electrical stimulation (IES) provides a clinical gold standard for the existence of functional motor pathways that can be used to determine the accuracy and sensitivity of fibre-tracking algorithms.

Intersecting tracts or partial volume averaging of adjacent pathways with different fibre orientations are the reasons why DTI does not accurately describe the microstructure in complex white matter voxels that contain more than one fibre population, e.g. in the centrum semiovale, where major white matter tracts such as the pyramidal tract, the superior longitudinal fasciculus and the corpus callosum intersect. This has hindered preoperative mapping of the pyramidal tract in brain tumour patients. HARDI permits more accurate delineation of pathways within complex regions of white matter. The q-ball reconstruction of HARDI data provides an orientation distribution function (ODF) that can be used to determine the orientations of multiple fibre populations contributing to a voxel's diffusion MR signal, mapping fibre trajectories through regions of complex tissue architecture in a clinically feasible timeframe.

ULTRASOUND

Uniquely, ultrasound images do not depend on the use of electromagnetic wave forms. The properties of high-frequency sound waves (longitudinal waves) and their interaction with biological tissues are responsible for the production of 'echograms' (Desser and Jeffrey 2001). A sound wave of appropriate frequency (diagnostic range 3.5–20 MHz) is produced by piezo-electric principles. Image production is determined by attenuation and reflection as the beam passes through tissues. Attenuation is caused by the loss of energy due to absorption, reflection and refraction in soft tissues, resulting in a reduction in signal intensity. Reflection of sound waves within the range of the receiver produces the image, and the echotexture is dependent on tiny differences in acoustic impedance between different tissues. Blood flow and velocity can be measured (using the Doppler principle) in duplex mode.

Techniques such as harmonic imaging and the use of ultrasound contrast agents (stabilized microbubbles) have enabled non-invasive determination of myocardial perfusion. These contrast agents also clearly improve the detection of metastases in the liver and spleen. Ultrasound is the most common medical imaging technique for producing elastograms, in which stiffness or strain images of soft tissue are used to detect or classify tumours. Cancer is 5–28 times stiffer than the background of normal soft tissue; when a mechanical compression or vibration is applied, a tumour deforms less than the surrounding tissue. Elastography may be used, for example, to measure the stiffness of the liver *in vivo* or in the detection of breast or thyroid tumours. A correlation between liver elasticity and the cirrhosis score has been shown (Yeh et al 2002, Foucher et al 2006).

Interpretation of anatomy and pathology from static ultrasound images is more difficult than that from other imaging modalities: compare the real-time nature ultrasound in Video 23.1 with the static images in Fig. 23.5. The technique is highly operator-dependent and provides unique information on tissue structure and form not obtained from other imaging techniques.

NUCLEAR MEDICINE

Historically, the field of nuclear medicine began in 1946 when radioactive iodine was administered as an 'atomic cocktail' to treat thyroid cancer. Since that time, nuclear medicine has advanced to the point where it was recognized in the early 1970s as a diagnostic subspecialty.

Unlike diagnostic radiology, where an image is created by passing energy through the body from an external source, nuclear medicine creates an image by measuring the radiation emitted from tracers taken internally. Overall, the radiation dosages are comparable with CT and vary depending on the examination. Nuclear medicine also differs from most other imaging modalities in that the tests demonstrate the physiological function of a specific area of the body. In some instances, this physiological information may be fused with the more anatomical imaging of CT or MRI, combining the strengths of anatomy and function for diagnosis (e.g. Dewey et al 2020).

Nuclear medicine uses pharmaceuticals that have been labelled with a radionuclide (radiopharmaceuticals) and which are administered to patients by intravenous injection, ingestion or inhalation (the method of administration depends on the type of examination and the organ or organ process to be imaged). Emitted radiation is detected and imaged with specialized equipment such as gamma cameras, positron emission tomography (PET) or single photon emission computed tomography (SPECT). Radiation may be measured from parts of the body by the use of probes, or samples may be taken from patients and measured in counters.

Radiopharmaceuticals may be used to image a disease process or to treat diseases. Those used for imaging emit a gamma ray (γ) and those used for treatment emit a beta (β) particle. Gamma rays are of higher energy in order to pass through the body and be detected by a detection camera, whereas β particles travel only short distances and emit their radiation dose to the target organ. For example, ^{99m}technetium or ^{123}iodine may be used to detect thyroid disease, but certain thyroid diseases or thyroid cancer may be treated solely or in part with ^{131}iodine. The difference in the agent used depends on the type and energy levels of the radiation particle that the radioisotope emits.

Radionuclides used in nuclear medicine are often chemically bound to a complex called a tracer. The way the body handles a tracer may differ in disease or pathological processes. For example, the tracer used in bone imaging is methylene-diphosphonate (MDP) bound to ^{99m}technetium. MDP attaches to hydroxyapatite in bone; altered bone physiology, such as occurs in a fracture, metastatic bone disease or arthritic change, produces an increase in biochemical bone activity and an accumulation of MDP that is seen as a focal 'hot spot' of the radiopharmaceutical on a bone scan.

^{99m}Technetium is the major workhorse radioisotope of nuclear medicine. It can be eluted from a molybdenum/technetium generator stored within a nuclear medicine department, allowing for easy access. It has a short half-life (6 hours), which allows for ease of medical imaging and disposal. Its pharmacological properties allow it to be easily bound to various tracers and it emits gamma rays that are of suitable energy for medical imaging. In addition to ^{99m}technetium, the most common intravenous radionuclides used in nuclear medicine are ^{123}iodine and ^{131}iodine, ^{201}thallium, ^{67}gallium, ^{18}fluorodeoxyglucose (FDG) and ^{111}indium-labelled leukocytes. The most common gaseous/aerosol radionuclides used are ^{133}xenon, ^{81m}krypton, ^{99m}technetium (Technegas) and ^{99m}technetium diethylene triamine pentaacetic acid (DTPA).

The images obtained from nuclear medicine imaging can be single or multiple. Image sets may be represented by time sequence imaging (e.g. cine), such as dynamic imaging or cardiac gated sequences, or by spatial sequence imaging, where the gamma camera is moved relative to the patient, e.g. in SPECT imaging. Spatial sequence imaging allows the images to be presented as a slice-stack much in the way that CT or MRI images are displayed. It may also be fused with concomitant CT or MRI to provide combined physiological and anatomical imaging.

A PET scan is a specialized type of nuclear medicine imaging that measures important body functions, such as blood flow, oxygen use or glucose metabolism. It involves short-lived radioactive tracer isotopes that emit positrons (positively charged subatomic particles with the same mass and magnitude of charge as electrons). The radioisotopes are chemically incorporated into biologically active molecules: most commonly, the sugar FDG (2-deoxy-2-[fluorine-18]fluoro-D-glucose). An hour after injection, FDG becomes concentrated into the tissues of interest; images are obtained as the isotope undergoes positron emission decay. A positron travels only a few millimetres before reacting with an electron by annihilation, producing a pair of gamma photons that move in opposite directions. The PET scan detectors process only those photon pairs that are detected simultaneously (coincident detection) to create an image of tissue activity with respect to that particular isotope. These images may subsequently be fused with CT or MR images. The short half-life of the isotopes limits PET imaging; close access to a cyclotron for generation of the isotopes plays an important role in the feasible location of a PET scanner. Typical isotopes used in medical imaging and their half-lives are: ^{11}carbon (about 20 min), ^{13}nitrogen (about 10 min), ^{13}oxygen (about 2 min) and ^{18}fluorine (about 110 min).

ANGIOGRAPHY/INTERVENTIONAL RADIOLOGY

Angiographic imaging was first described in 1927, when Egas Moniz, a physician and neurologist, introduced contrast X-ray cerebral angiography. (Moniz was awarded the Nobel Prize for his work in 1949.) In 1953, the field was revolutionized by the Seldinger technique, in which no sharp needles remained inside the vascular lumen during imaging. Although angiography initially involved X-ray and fluoroscopic imaging of blood vessels and organs of the body after injecting radiopaque contrast agents into the blood stream, it has evolved to encompass so much more. Many of the procedures currently performed by angiography may be diagnostic; following the advent of minimally invasive procedures performed with image guidance, the name of the discipline changed to interventional radiology (or vascular and interventional radiology).

Angiograms are typically performed by gaining access to the blood vessels, through either the femoral artery, femoral vein or jugular vein, depending on the area of interest to be imaged (e.g. cerebral, coronary or pulmonary angiograms). Following vascular access, catheters are directed to the specific location to be imaged by the use of guidewires, and contrast agents are injected through these catheters to visualize the vessels or the organ with X-ray imaging. Imaging of the arterial and venous circulation of the arms and legs may demonstrate peripheral vascular disease.

Treatment and/or interventions can often be performed through similar catheter-based examinations. Such procedures might involve angioplasties, where a balloon mechanism is placed across an area of narrowing (stenosis) in a vessel or lumen. With controlled inflation of the balloon, the area of narrowing can be widened.

Imaging in diagnostic or interventional procedures may produce still or motion (cine) images. The technique often used, digital subtraction angiography (DSA), involves taking images at 2–30 frames per second to allow imaging of the flow of blood through vessels. A preliminary image of the area is taken before the contrast is injected; this ‘mask’ image is then electronically subtracted from all subsequent images, leaving only the vessels filled with contrast. For optimal subtraction, the patient must remain motionless.

Angiograms of the heart may be performed to visualize the size and contractility of the chambers and the anatomy of the coronary vessels. The thorax may also be studied to evaluate the pulmonary arteries and veins for vascular malformations, blood clots and possible origins of haemoptysis. In the investigation of atherosclerotic disease, vascular malformations or tumoral vascularization, the neck is often imaged in order to visualize the vessels that supply the brain in their entirety, from the points at which they arise from the aortic arch to their termination as cerebral vessels. Renal artery imaging may elucidate the cause of hypertension in selected patients, and imaging of the mesenteric vessels may identify the origin of gastrointestinal bleeding or mesenteric angina.

In addition to angiograms and venograms, the field of interventional radiology also includes such procedures as coil embolization of aneurysms and vascular malformations; balloon angioplasty and stent placement, even now for the endovascular repair of aortic aneurysms; chemoembolization directly into tumours; drainage catheter insertion; embolization (e.g. uterine artery for treatment of fibroids); thrombolysis to dissolve blood clots; tissue biopsy (percutaneous or transvascular); radiofrequency ablation and cryoablation of tumours; line insertions for specialized vascular access; inferior vena cava filter placements; vertebroplasty; nephrostomy placement; gastrostomy tube placement for feeding; dialysis access; transjugular intrahepatic portosystemic shunt (TIPS) placement; biliary interventions; and, most recently, endovenous laser ablation of varicose veins.

COMPUTED TOMOGRAPHY

The limitation of all plain radiographic techniques is the two-dimensional representation of three-dimensional structures; the linear attenuation coefficient of all the tissues in the path of the X-ray beam form the image. CT obtains a series of different angular X-ray projections that are processed by a computer to give a section of specified thickness. The CT image comprises a regular matrix of picture elements (pixels). All of the tissues contained within the pixel attenuate the X-ray projections and result in a mean attenuation value for the pixel. This value is compared with the attenuation value of water and is displayed on a scale (the Hounsfield scale). Water is said to have an attenuation of 0 Hounsfield units (HU); air typically has a HU number of −1000; fat is approximately −100 HU; soft tissues are in the range +20 to +70 HU; and bone is usually greater than +400 HU.

Modern multislice helical CT scanners can obtain images in subsecond times, and imaging of the whole body from the top of the head to the thighs can take as little as a single breath-hold of only a few seconds. The fast scan times allow dynamic imaging of arteries and veins at different times after the injection of intravenous contrast agents. The continuous acquisition of data from a helical CT scanner allows reconstruction of an image in any plane (multiplane reconstruction, MPR), commonly sagittal and coronal, as may be seen in many of the images throughout this forty-second edition of *Gray's Anatomy*. This orthogonal imaging greatly improves the understanding of the three-dimensional aspects of radiological anatomy and now forms part of the standard practice of assessing disease.

No specific preparation is required for most CT examinations of the brain, spine or musculoskeletal system. Studies of the chest, abdomen and pelvis, and those of the brain with complex histories, usually require intravenous contrast medium that contains iodine because this defines vascular relationships and differentiates normal and pathological soft tissues more effectively. Opacification of the bowel in CT studies of the abdomen and pelvis may be accomplished by oral ingestion of a water-soluble contrast medium from 24 hours prior to the examination, in order to outline the colon, combined with further oral intake 0–60 minutes prior to the scan, in order to outline the stomach and small bowel. This procedure is much less frequently performed with the latest generation of scanners, which exquisitely differentiate various enhancing layers within the bowel wall. Occasionally, direct insertion of rectal contrast to show the distal large bowel may be required.

Generally, most studies are performed with the patient supine with images obtained in the transverse or axial plane. Some CT scanners allow up to 25° of gantry angulation, which is particularly valuable in spinal imaging, but multidetector technology and the ability to reconstruct imaging in virtually any plane from the acquired 3D imaging block has obviated this need. Occasionally, direct coronal images are obtained in the investigation of cranial and maxillofacial abnormalities; in these cases, the patient lies prone with the neck extended and the gantry appropriately angled, but this technique has largely been superseded by the orthogonal imaging described above. The ability to acquire time-gated images at the same point in the cardiac cycle with multidetector scanners has also revolutionized ‘cold’ coronary artery assessment with the detail that is now achievable from these CT coronary angiograms.

References

Desser TS, Jeffrey RB 2001 Tissue harmonic imaging techniques: physical principles and clinical applications. Semin Ultrasound CT MR 22:1–10.

Dewey M, Siebes M, Kachelrieß M et al 2020 Clinical quantitative cardiac imaging for the assessment of myocardial ischaemia. Nature Rev Cardiol 17:427–450.

Foucher J, Chanteloup E, Vergniol J et al 2006 Diagnosis of cirrhosis by transient elastography (FibroScan): a prospective study. Gut 55:403–8.

Nucifora PG, Verma R, Lee SK et al 2007 Diffusion-tensor MR imaging and tractography: exploring brain microstructure and connectivity. Radiology 245:367–84.

Yeh WC, Li PC, Jeng YM et al 2002 Elastic modulus measurements of human liver and correlation with pathology. Ultrasound Med Biol 28:467–74.

COMMENTARY

I.3

Imaging the ageing musculoskeletal system

Andoni P. Toms

How long is a generation? This is a debate that simmers in the disciplines of anthropology, genetics and genealogy. Generations can be very short, with both males and females becoming parents in their early teens, or very long, with men fathering children in their 10th decade, but these variations are uncommon. It is probable that the average male generation is somewhere between 30 and 35 years and that female generations are shorter, at between 25 and 30 years. Despite a long-held assumption that generations were shorter in prehistoric societies there is now evidence to suggest that these mean generational gaps have been stable for millennia (Tremblay and Vézina 2000, Helgason et al 2003).

For genealogists these figures are used as a rule of thumb to assess the integrity of a family tree. Too few generations in a given century alerts them to the possibility of missing data. For geneticists these figures are used to estimate the rate at which mutations have occurred in our genome. And in evolutionary terms these figures may determine the age at which our bodies begin to fail.

It seems reasonable to argue that the child of a parent who remains healthy, until their offspring are independent, is more likely to survive and propagate their genes than the progeny of a weak and feeble parent. The traits of good health in parenthood would therefore be passed on to subsequent generations whereas the weaker phenotype would be less likely to endure. Assuming that the age of independence is 15, then the evolutionary driver is a parent who is healthy until the age of 45. After that a healthy parent is much less likely to contribute to the survival of the offspring; evolution has selected a human phenotype that remains strong until the age of 45 and then starts to fall apart.

While the estimate of intervals between generations has an evidence base, my subsequent argument is a hypothesis. One that is supported by a number of facts: at 45 we go grey (Van Neste and Tobin 2004), we become short sighted (Michael and Bron 2011) and we suffer a peak in short-term musculoskeletal pain (Claus et al 2019). At age 45 the production of new collagen in cartilage and bone falls to the lowest level in our lifetimes (Mouritzen et al 2003) and we start to shrink (Sorkin et al 1999).

Cartilage

Normal hyaline cartilage in a young adult has a laminar appearance on magnetic resonance (MR) imaging (**Fig. I.3.1**). The vertical and oblique zones of type 1 collagen fibres that make up the parabolic arcades of Benninghoff (Benninghoff 1925), and the armour-plated surface layer can be differentiated because the orientation of collagen fibres influences the signal generated by radiofrequency pulses. The extracellular matrix of cartilage, consisting mainly of glycosaminoglycan, is hygroscopic; as water is absorbed the cartilage expands until limited by the collagen arcades. This balanced tension between expanding extracellular matrix and restraining collagen is often referred to as a hydrostatic cushion, implying that hyaline articular cartilage plays a significant role in load distribution. As we shall see later this may not be the case, and the main role of hydrostatic cartilage may be to resist shearing forces.

As we age, our chondrocytes die. Those that survive synthesize less glycosaminoglycan which means that less water is bound into the cartilage, which gets thinner and loses its compressive stiffness (Lotz and Loeser 2012). This age-related biological degeneration is commonly seen in routine clinical practice (Fig. I.3.1) where, paradoxically, many musculoskeletal radiologists will resist describing them as degenerative. This is because in clinical practice the terms ‘degeneration’ and ‘osteoarthritis’ are often used interchangeably. An alternative approach is to describe uncomplicated thinning of articular cartilage as normal age-related change, the assumption being that this does not contribute to symptoms. Once the integrity of the articular cartilage has been breached, or there is reactive subchondral bone marrow signal, this may then be described as being ‘degenerative’. When the clinical history or secondary signs of inflammation support the diagnosis, then these findings can be interpreted as ‘osteoarthritis’.

All these assumptions and tortuous semantic manipulations illustrate one of the principal difficulties that clinicians and scientists have when approaching the ageing musculoskeletal system. We do not have a language that allows us to differentiate normal ageing from degenerative disease and the imaging phenotypes do not allow us to separate the two with any certainty.

For the purpose of clinical practice most clinicians consider diffuse thinning of articular cartilage to be a predictable asymptomatic feature of the ageing musculoskeletal system. This does not mean that it is entirely benign. The thin, soft and collagen-depleted cartilage is less resistant to shearing injuries and is therefore a risk factor for developing osteoarthritis (OA). The knee joint in particular is dependent on the integrity of the cruciate and collateral ligaments, rather than the profile of the articular surfaces, for its stability. As the joint space narrows so these ligaments become redundant and the joint becomes intrinsically less stable; there is a view that the redundancy of stabilizing ligaments caused by joint space narrowing is a significant source of symptoms (Hunter et al 2008).

Bone

The ability of bone to resist fracture is defined by two characteristics: strength, a measure of maximum load without failure, and toughness, the ability to flex under a deforming force. While bone mineral density contributes to both of these functions it appears that ageing type 1 collagen is an important contributor to bone fragility (Boskey and Coleman 2010). The mechanical properties of collagen in bone are determined

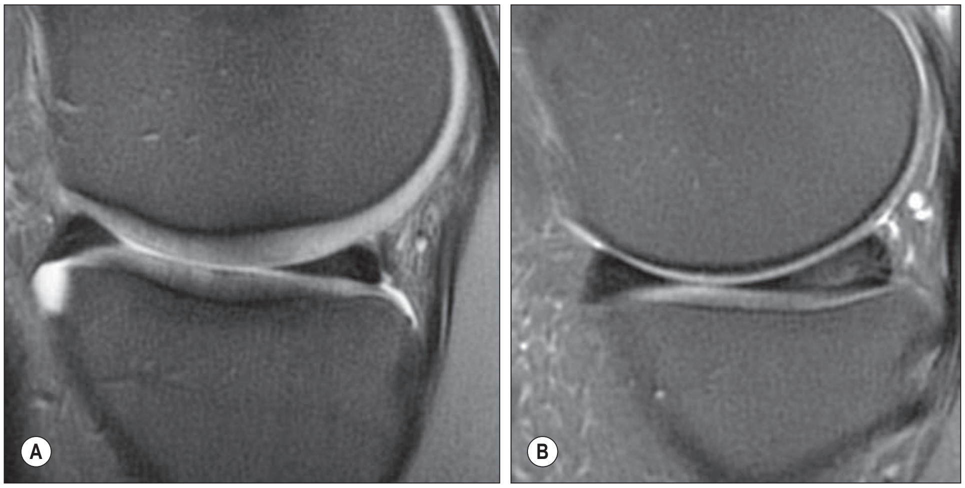

Fig. I.3.1 Sagittal fat-saturated proton density MR images through the medial tibiofemoral compartment of the knee of a 24-year-old (**A**) and a 62-year-old (**B**) male patient.

by the type of cross-link between fibrils. New collagen is connected by cross-links that result from a specific enzymatic reaction. As collagen persists in tissues the method of cross-linkage changes to glycation or oxidation. With increasing age, the production of new collagen slows down and these non-enzymatic cross-links predominate, with a concomitant decrease in bone strength and a reduction in toughness (Saito and Marumo 2010).

The effect of these changes in stiffness can be seen on radiographs in the form of subchondral sclerosis (MacKay et al 2014). This has long been recognized as one of the hallmarks of OA, together with irregular joint space loss, osteophytes and subchondral cysts, but there is evidence that sclerosis can develop in the absence of any of the other features of OA. High resolution MRI of the subchondral bone in asymptomatic middle-aged volunteers demonstrates increased subchondral sclerosis but also significant differences in trabecular architecture when compared to young asymptomatic volunteers (**Fig. I.3.2**) (MacKay et al 2016).

One explanation for this is that bone is a major contributor to the dissipation of loads through a weight-bearing joint, i.e. it is an important shock absorber. Bone has been estimated to account for up to 40% of the load-damping capacity of a limb in some animal models (Dodge et al 2012). One consequence of the increased stiffness of non-enzymatic cross-linked collagen is that these loads will not be as efficiently dissipated along the length of a weight-bearing bone. Therefore loading will become more localized and increased over smaller volumes of bone. According to Wolff's law, that volume of bone will then adapt by laying down more bone and the result will be subchondral sclerosis.

Osteoporosis is reduced bone mineral density that is most commonly related to age and in particular to postmenopausal females. It is an independent risk factor for developing fragility fractures, but it is not the only variable that contributes to bone fragility; ageing collagen also contributes to reduced bone toughness. The anatomical distribution of bone loss is an important independent predictor of fragility fractures. The cross-sectional cortical morphology of bones, their curvature and the cortico-medullary distribution of mineralized osteoid and trabecular organization, all change with increasing age (**Fig. I.3.3**). Which of these traits contribute to disease, and which do not, is only partly understood.

An example of changing anatomy that appears to relate simply to age is 'cortical drift'. This is a process that describes the changing cross-sectional profile of long bones that occurs with increasing age and refers

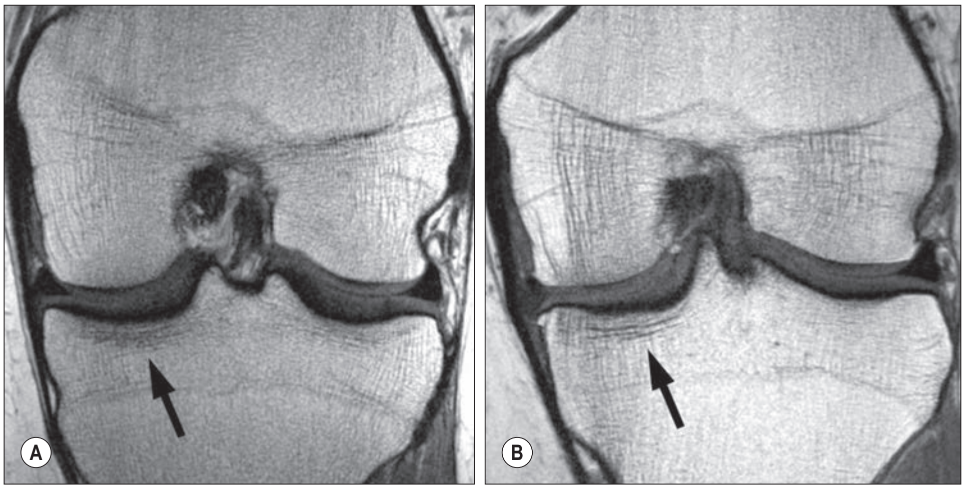

Fig. I.3.2 Coronal high resolution T1-weighted trabecular maps of subchondral bone in (**A**) 27-year-old and (**B**) 46 year-old asymptomatic male volunteers demonstrating changes in the conspicuity and texture of subchondral trabecular bone with age (arrows). (Courtesy of Dr James MacKay, University of East Anglia.)

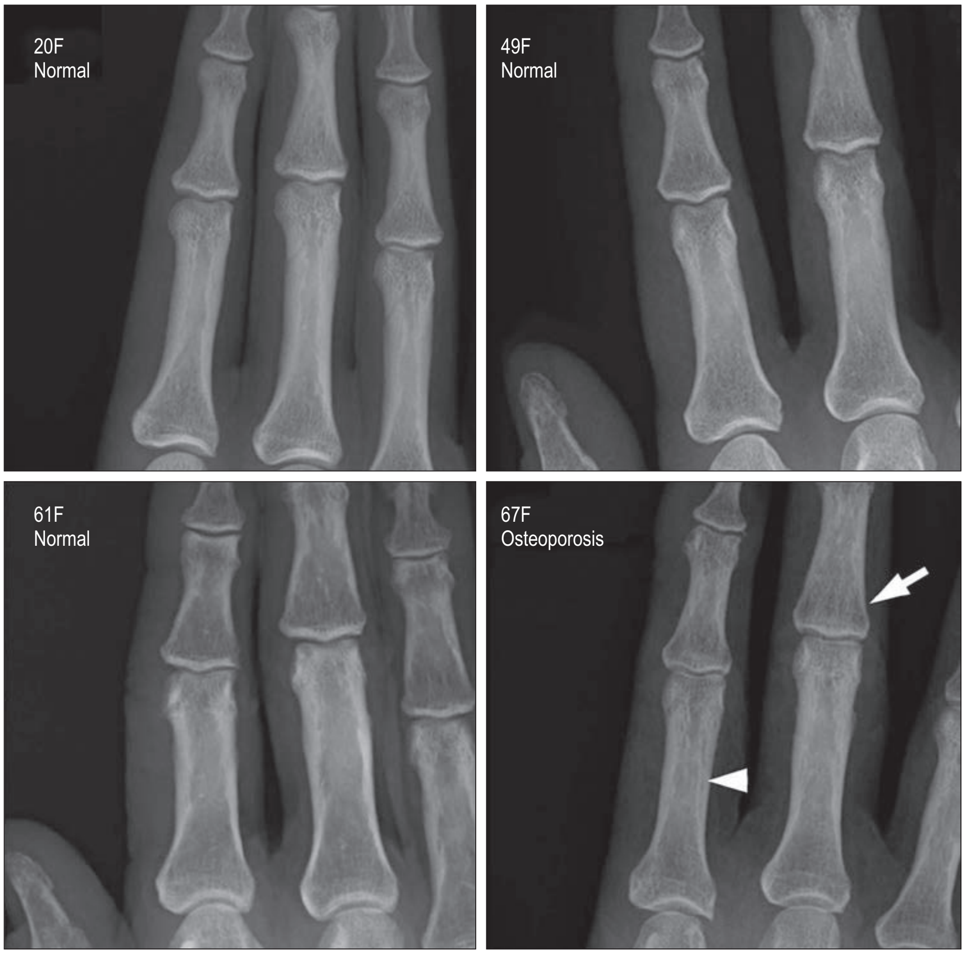

Fig. I.3.3 Conventional dorsopalmar radiographs of the proximal and middle phalanges of the right index and middle fingers of a 20-year-old female (20F) demonstrating the normal proportions of 1/3 cortex, 1/3 medulla and 1/3 cortex at the mid-diaphysis. With increasing age (49F, 61F), and with normal bone mineral density, the width of the medulla increases and the cortex decreases. In osteoporosis these normal age-related changes are accompanied by cortical tunnelling, illustrated by a longitudinal lucency in the ulnar cortex of the proximal phalanx of the index finger, and patchy secondary trabecular bone loss, best seen here at the base of the middle phalanx of the middle finger (arrows).

to the drift away from a perfect circle. During adolescence, remodelling occurs rapidly so that in the femur of a young adult the cross-section looks like a polygon closely fitted to a circle. With increasing years the cross-section becomes more ellipsoid resulting in a wider diameter bone with relatively thinner cortices (**Fig. I.3.4**) (Goldman 2009). What causes this change in shape is not understood, neither has it been associated with any adverse outcomes. This is an example of an age-related anatomical feature that, for the moment, we assume to be a 'normal' finding in the absence of evidence to the contrary.

When it comes to trabecular bone, males tend to lose bone mass diffusely across the struts that comprise the secondary trabeculae, whereas bone loss in females leads to greatly reduced trabecular connectivity (**Fig. I.3.5**) (Aaron et al 1987). The secondary trabeculae are stabilizers of the longitudinal load-bearing primary trabeculae and contribute to the toughness of bone by allowing the longitudinal trabeculae to flex without fracture under increased load. Bone loss in the secondary trabeculae has a disproportionately higher impact on fragility than loss of bone in the primary trabeculae (Pathria et al 2016) which means that it is not only the severity of bone loss, but also the distribution of that loss, that predicts the increased risk of fragility fractures in females.

Tendon

Changes in the prevalence of non-enzymatic cross-links in type 2 collagen might also account for the observation that buckling of the patellar tendon changes with age. The distal patellar tendon in particular buckles during extension of the knee; it has been suggested that this reflects a property that protects the extensor mechanism during sudden extreme contraction. The proposed effect is similar to that seen in crimping of ligament fibrils. Patellar tendon buckling is usually demonstrable at any age but the tendons of the middle-aged and elderly buckle less, and unbuckle more slowly, than those of young adults (**Fig. I.3.6**) (Slane et al 2018).

Muscle

The loss of muscle (sarcopaenia) that occurs with age has been well documented. There is a slow steady decline in muscle volume until the age of 70 and a rapid decline in the 9th and 10th decades of life (Siparsky et al 2014). This decline in muscle volume is accompanied by a loss of strength but this loss is not proportionate; the loss of strength with increasing age is greater than the loss of muscle bulk (Stenholm et al 2008). This mismatch between form and function is one of the limitations of conventional cross-sectional imaging that may be addressed by novel functional imaging techniques (**Fig. I.3.7**) (Yoon et al 2017).

Sarcopaenia is commonly seen in patients with cachexia; related to cancer, cardiovascular disease or inflammatory arthritis; or from disuse as a result of chronic pain. In all these cases, the loss of muscle volume and fatty atrophy may be indistinguishable from the effects of age, especially if combined with obesity (**Fig. I.3.8**).

It is difficult to define the limits of what constitutes a normal ageing musculoskeletal system. In fact, it may be a redundant question. Some might argue that osteoarthritis is so prevalent in old age that OA is 'normal'. Functional impairment in the musculoskeletal system is more strongly associated with psychological profiles than with any degree of joint disruption. In other words, the happier an individual is, the less likely their ageing joints will hurt. Therefore it seems rather insular to

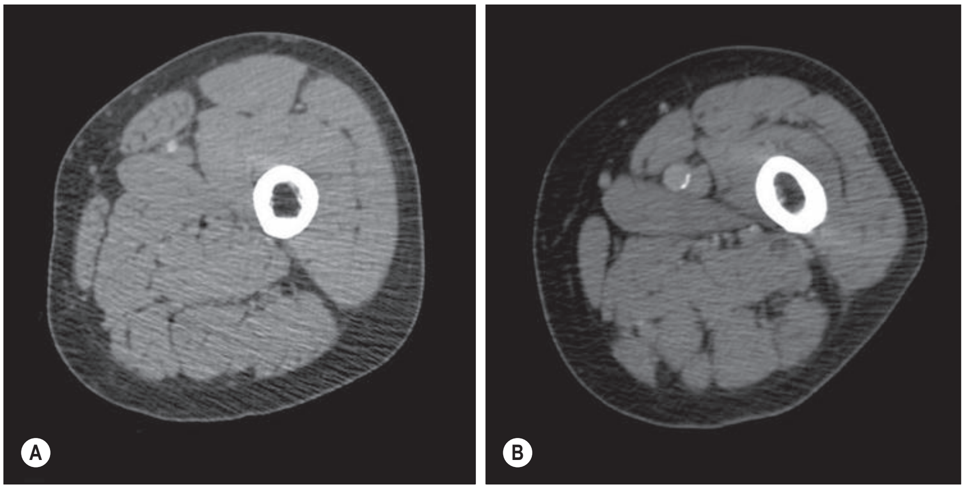

Fig. I.3.4 Axial CT through the left femur of (**A**) a 20-year-old male in whom the cross-section of the femoral diaphysis is roughly circular. In a 76-year-old male (**B**) the left femur is oval in cross-section as a result of progressive cortical drift.

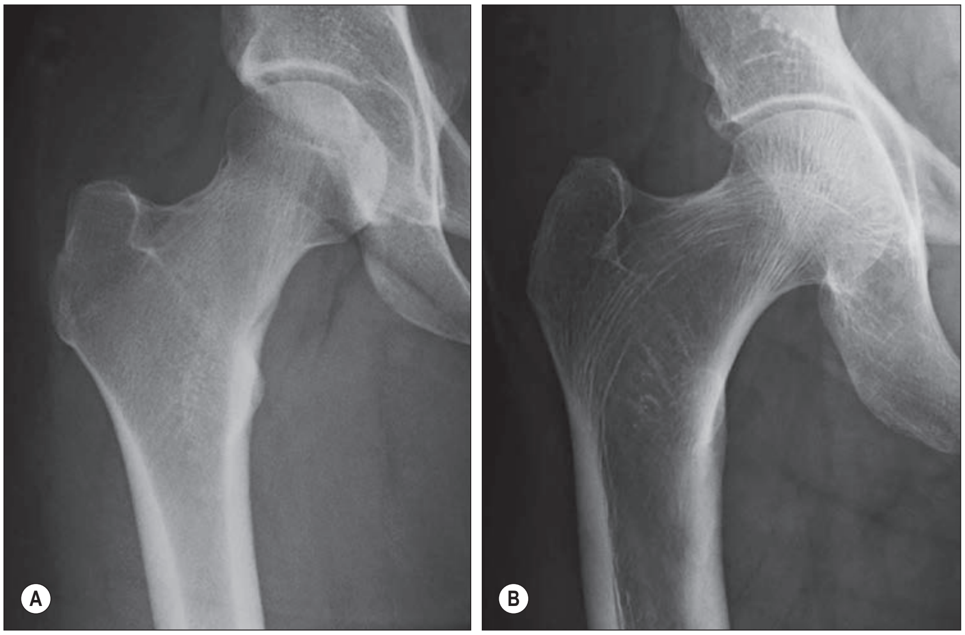

Fig. I.3.5 Anteroposterior radiographs in (**A**) 23-year-old and (**B**) 69-year-old females. The principal tensile and compressive trabeculae are easier to see in the older patient because the small horizontal secondary trabeculae have been resorbed.

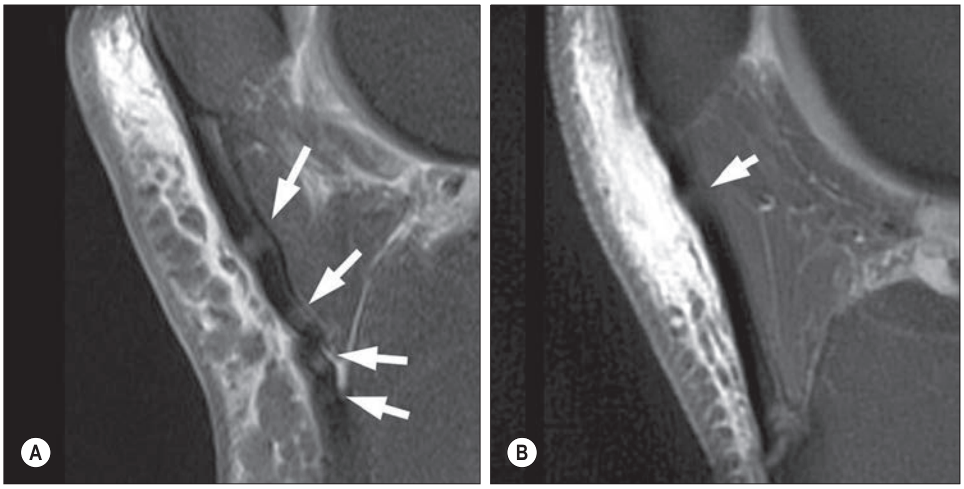

Fig. I.3.6 Sagittal fat-saturated proton density MR images in two patients with acute complete tears of the anterior cruciate ligament that produce anterior translation of the tibia and redundancy of the extensor mechanism. In the 24-year-old male patient (**A**) multiple foci of buckling of the patellar tendon (arrows) are demarcated by high signal generated by the magic-angle phenomenon. In the 46-year-old male (**B**) there is a single barely visible buckle that may reflect stiffer non-enzymatic cross-linking of collagen.

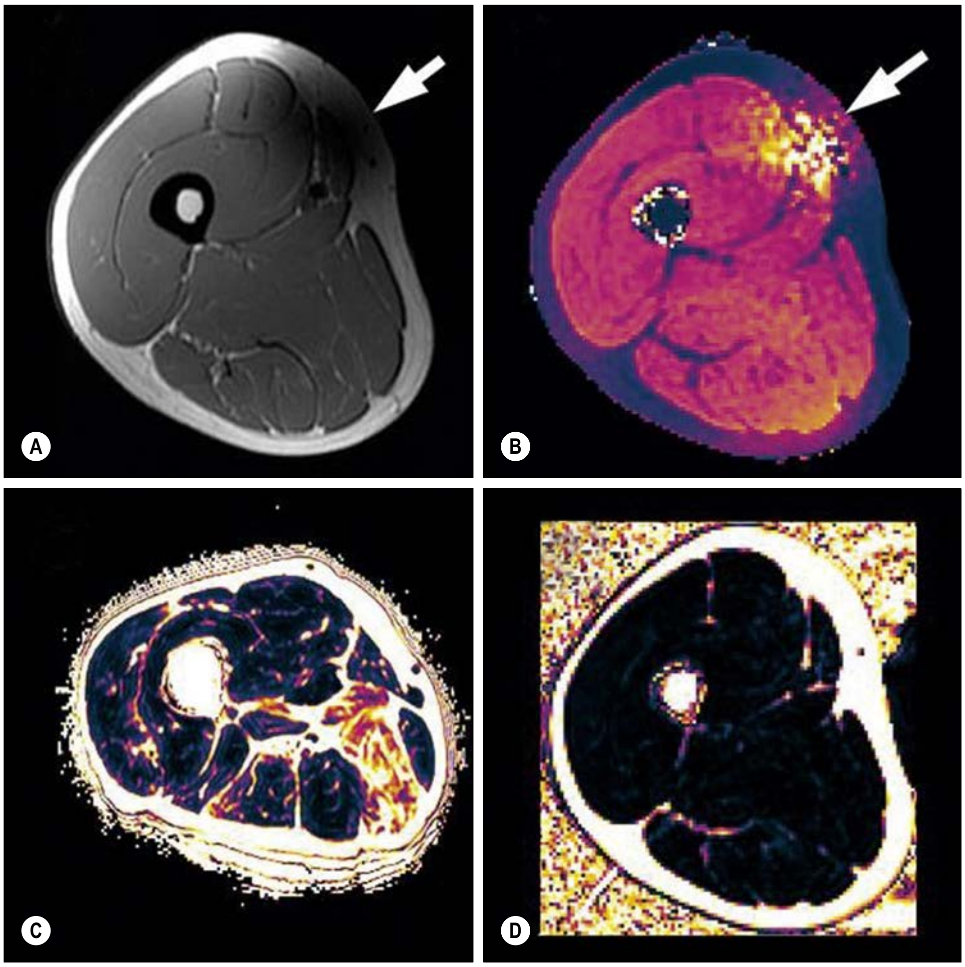

Fig. I.3.7 Axial MR images through the right thigh demonstrating (**A**) anatomy of muscle compartments using T1W, (**B**) T2 map demonstrating muscle activation and (**C–D**) fat fractionation using modified 2-point Dixon techniques. The dark area in the anteromedial thigh (arrow) in **A** and the corresponding bright area in image **B** are the result of inhomogeneity in the magnetic field of the MRI machine caused by the presence of the volunteer. (Courtesy of Dr Donnie Cameron, University of East Anglia.)

define normal anatomical appearances in the elderly without considering the context of their life experience (Creamer et al 2000). Interestingly, strength training in the very elderly has a reassuringly wide range of positive impacts on function and happiness (Marcos-Pardo et al 2018). This is a two-way street: the function of the musculoskeletal system can be dictated by our psychology and the health of the musculoskeletal system can influence our outlook on life.

The linear narrative of the ageing musculoskeletal system in which most of us progress inexorably from health to frailty does not do justice to the heterogeneity of the ageing phenotype. If evolution has selected for relatively homogeneous good health until the age of 45, progress thereafter is increasingly variable. The genes that code for good health in later years probably do not offer an evolutionary advantage and so are not propagated through future generations in favour of genes that code for poor health. Some individuals degenerate rapidly in middle age and present early in their life to radiologists with images demonstrating failure of articular cartilage, and the consequences of degenerating ligaments and tendons. A fortunate few maintain youthful joint alignment, hyaline cartilage integrity, muscle mass and connective tissue elasticity (Fig. I.3.9).

An often-cited challenge to clinicians is to define 'healthy ageing' (Mount et al 2016). The corollary for radiologists and anatomists is to try to define what constitutes a 'healthy' older human body. What does a normal old musculoskeletal system look like on imaging? How is that different from a patient in pain, or from someone with functional impairment, or from someone with limited quality of life scores? These are almost impossible questions to answer. Some of the strongest predictors of pain and quality of life, in a patient with a degenerative joint, are psychological status, education and wealth. An absence of pain in old age can be attributable not to 'good health' but rather to decent schooling, a good pension and a close circle of family and friends. The available measurable endpoints of healthy ageing, with which we can correlate anatomical imaging features, are multiple, variable and confounded.

For now, the available scientific methods limit us to hypothesis testing. We can compare quantitative measures of morphology on

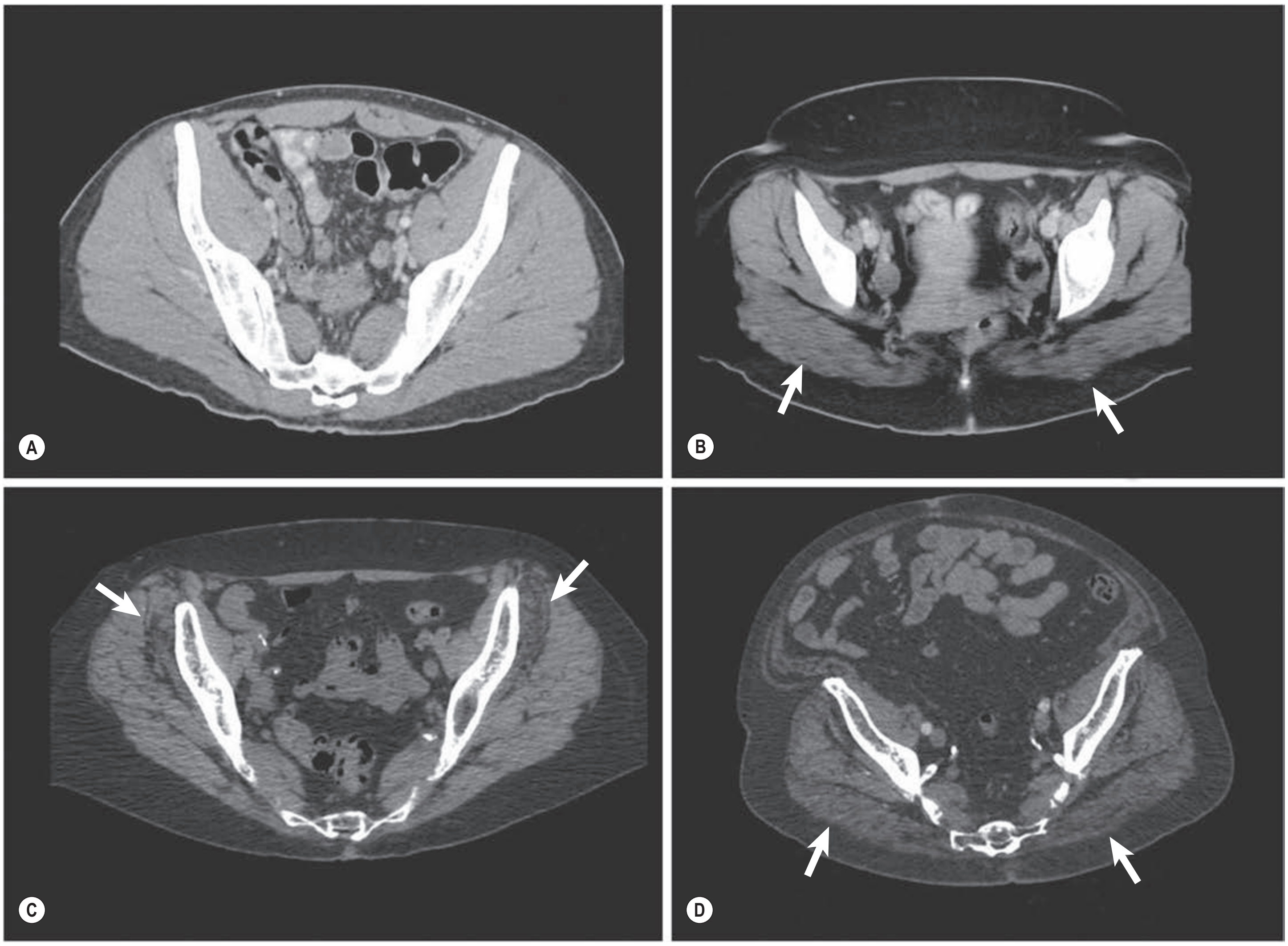

Fig. I.3.8 Axial CT images through the pelvis of a 26-year-old male (**A**) demonstrating normal homogeneous gluteal muscles as intermediate grey with thin dark lines of intermuscular fat. In a 21-year-old obese female (**B**) the gluteus maximus muscles retain their volume but are marbled with fat (arrows). In a 73-year-old female (**C**) there is fatty atrophy of the gluteus minimus muscles (arrows) associated with disuse caused by osteoarthritis of the hips. In a 72-year-old male arteriopath (**D**) with bilateral lower limb arterial claudication, there is diffuse reduction in muscle mass and fatty replacement (arrows).

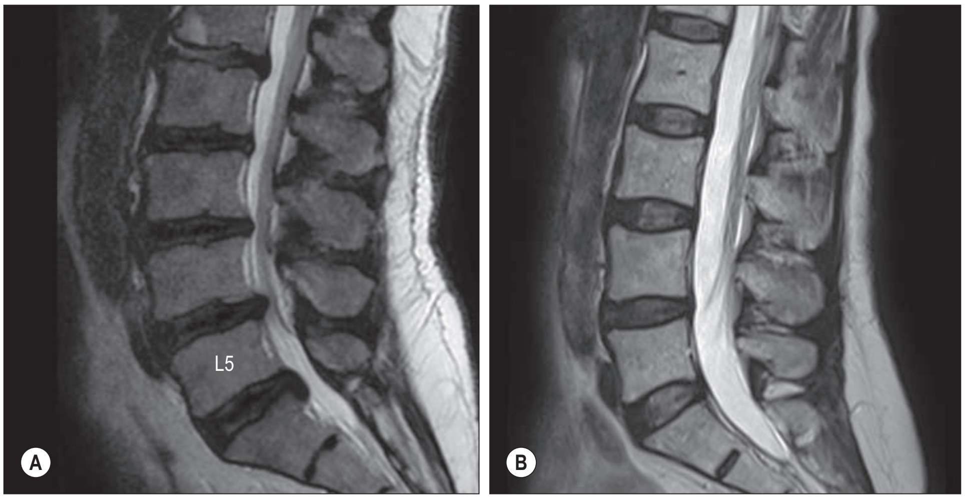

Fig. I.3.9 Sagittal T2-weighted MR images of the lumbar spine in 45-year-old (**A**) and 63-year-old (**B**) male patients. While the 45-year-old has a congenitally narrow vertebral canal and dark black degenerative intervertebral discs with herniations protruding into the canal, the older patient has normal discs and a wide, patent canal.

radiological images against measures of what the scientific community considers to be useful measures of health. We can do these in defined samples of individuals from whom we hope to extrapolate generalizable results. Each study will result in a one-dimensional outcome. In the future we may be able to take a more sophisticated approach to defining normal anatomy in the healthy ageing human. Picture Archiving and Communication Systems (PACS) are now vast archives of anatomical information in digital form. Full integration of healthcare records, including primary and secondary care clinic notes, pharmacy prescriptions and pathology reports, will allow us to data mine whole populations using machine learning algorithms overcoming the one dimensional limitations of hypothesis testing. Of course, this will only succeed if we can decide what it means to be healthy and old.

References

Aaron JE, Makins NB, Sagreiya K 1987 The microanatomy of trabecular bone loss in normal aging men and women. Clin Orthop 215:260–71.

Benninghoff A 1925 Spaltlinien am knochen. Eine methodoe zur ermittlung der architektur platter knochen. Anat Ann 60:189–206.

Boskey AL, Coleman R 2010 Aging and bone. J Dent Res 89:1333–48.

Claus M, Schuster M, Webendörfer S et al Prevalence of back pain in employees of a German chemical company: results of a large cross-sectional study. J Occup Med Toxicol 14:16.

Creamer P, Lethbridge–Cejku M, Hochberg MC 2000 Factors associated with functional impairment in symptomatic knee osteoarthritis. Rheumatology 39:490–6.

Dodge T, Wanis M, Ayoub R et al 2012 Mechanical loading, damping, and load-driven bone formation in mouse tibiae. Bone 51:810–18.

Goldman H 2009 Ontogenetic patterning of cortical bone microstructure and geometry at the human mid-shaft femur. Anat Rec Hoboken 292:48–64.

Helgason A, Hrafnkelsson B, Gulcher JR et al 2003 Populationwide coalescent analysis of Icelandic matrilineal and patrilineal genealogies: evidence for a faster evolutionary rate of mtDNA lineages than Y chromosomes. Am J Hum Genet 72:1370–88.

Hunter DJ, McDougall JJ, Keefe FJ 2008 The symptoms of osteoarthritis and the genesis of pain. Rheum Dis Clin North Am 34:623–43.

Lotz M, Loeser RF 2012 Effects of aging on articular cartilage homeostasis. Bone 51:241–8.

MacKay JW, Godley KC, Toms AP 2014 MRI signal-based quantification of subchondral bone at the tibial plateau: a population study. Skeletal Radiol 43:1567–75.

MacKay JW, Murray PJ, Kasmai B et al 2016 MRI texture analysis of subchondral bone at the tibial plateau. Eur Radiol 26:3034–45.

Marcos-Pardo PJ, Martínez-Rodríguez A, Gil-Arias A 2018 Impact of a motivational resistance-training programme on adherence and body composition in the elderly. Sci Rep 8:1370.

Michael R, Bron AJ 2011 The ageing lens and cataract: a model of normal and pathological ageing. Philos Trans R Soc B Biol Sci 366:1278–92.

Mount S, Lara J, Schols AMWJ et al 2016 Towards a multidimensional healthy ageing phenotype. Curr Opin Clin Nutr Metab Care 19:418–26.

Mouritzen U, Christgau S, Lehmann H-J et al 2003 Cartilage turnover assessed with a newly developed assay measuring collagen type II degradation products: influence of age, sex, menopause, hormone replacement therapy, and body mass index. Ann Rheum Dis 62:332–6.

Pathria MN, Chung CB, Resnick DL 2016 Acute and stress-related injuries of bone and cartilage: pertinent anatomy, basic biomechanics, and imaging perspective. Radiology 280:21–38.

Saito M, Marumo K 2010 Collagen cross-links as a determinant of bone quality: a possible explanation for bone fragility in aging, osteoporosis, and diabetes mellitus. Osteoporos Int 21:195–214.

Siparsky PN, Kirkendall DT, Garrett WE 2014 Muscle changes in aging: understanding sarcopenia. Sports Health 6:36–40.

Slane LC, Dandois F, Bogaerts S et al 2018 Patellar tendon buckling is altered with age. Med Eng Phys 59:15–20.

Sorkin JD, Muller DC, Andres R 1999 Longitudinal change in height of men and women: implications for interpretation of the Body Mass Index: the Baltimore Longitudinal Study of Aging. Am J Epidemiol 150:969–77.

Stenholm S, Harris TB, Rantanen T et al 2008 Sarcopenic obesity – definition, etiology and consequences. Curr Opin Clin Nutr Metab Care 11:693–700.

Tremblay M, Vézina H 2000 New estimates of intergenerational time intervals for the calculation of age and origins of mutations. Am J Hum Genet 66:651–8.

Van Neste D, Tobin DJ 2004 Hair cycle and hair pigmentation: dynamic interactions and changes associated with aging. Micron 35:193–200.

Yoon MA, Hong S-J, Ku MC et al 2017 Multiparametric MR imaging of age-related changes in healthy thigh muscles. Radiology 287:235–46.

COMMENTARY
I.4

Cinematic rendering offers entirely new possibilities for studying human anatomy

Andrea Hofbauer, Klaus Engel

Medical images constitute a source of information essential for disease diagnosis, treatment and follow-up. In addition, because of its patient-specific nature, imaging information represents an important component required for advancing patient-tailored precision medicine into clinical practice. By characterizing patient anatomy, physiology and metabolism, medical imaging can enable precise, personalized procedures and predictive, patient-specific therapy selection and delivery. For this reason it is important to continue to develop means of handling image information. Cinematic rendering, a 3D visualization technology, is capable of producing high-quality photorealistic images from traditional computed tomography (CT) or magnetic resonance (MR) volume data, thus potentially enhancing the ease of viewing anatomical structures and their pathologies. These striking new visualizations could simplify communication between physicians and patients or between radiologists and referring clinicians, help surgeons select the most appropriate surgical strategy, and open up new horizons in medical training.

Medical imaging plays an increasingly important role in moving precision medicine, the science of delivering care tailored to each individual patient, into clinical practice. Efficient clinical decisions and procedures require rapid appreciation of relevant information contained within medical images. Although medical image viewing based on multiplanar reconstruction is still dominant in diagnostic imaging, the significance of 3D visualization of medical data is increasing: the methods allow a much faster understanding of the spatial relationships between anatomical structures and they have the potential to increase the sensitivity and specificity of medical image interpretation (Comaniciu et al 2016). Drs Klaus Engel and Robert Schneider (Siemens Healthineers) have developed a visualization technology, cinematic rendering (CR), that provides unprecedented photorealistic clinical images by leveraging the physics of light. Refined in collaboration with Professor Franz Fellner (Head of the Central Radiology Institute at Kepler University Hospital, Linz, Austria and extraordinary professor at the Friedrich-Alexander University Erlangen-Nuremberg (FAU)), CR is a physically based volume rendering method that provides hyper-realistic representations of, for example, fractures, organs or the structure of fine blood vessels (Berger et al 2018, Ebert et al 2017) (Fig. I.4.1).

Physically based volume visualization techniques reproduce complex illumination effects in computer-generated images by mimicking the real-world interaction of light with matter. The results are physically plausible images that are often easier for the human brain to interpret, since the brain is trained to interpret the slightest shading cues to reconstruct shape and depth information (Fig. I.4.2). Shading cues are often missing from computer-generated images based on simpler geometric calculations such as ray casting, which produce images without precisely depicted tissue depth and structure and hence less realistic 3D volume visualization (Comaniciu et al 2016) (Fig. I.4.2).

Photorealistic clinical images obtained by leveraging the physics of light

As its name suggests, CR owes its origins to film technology that enables characters to appear entirely lifelike on screen despite having been digitally added to the scenes in which they appear. Although a character is digitally modelled and post-edited into the film, its lifelike appearance is achieved via a technique known as image-based lighting, where a

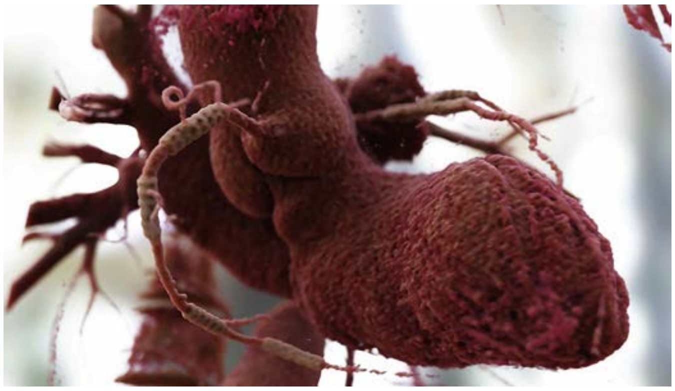

Fig. I.4.1 Blood in the left ventricle and coronary arteries, which have been stented; image produced with cinematic rendering. (Source: Hospital do Coração, São Paulo, Brazil.)

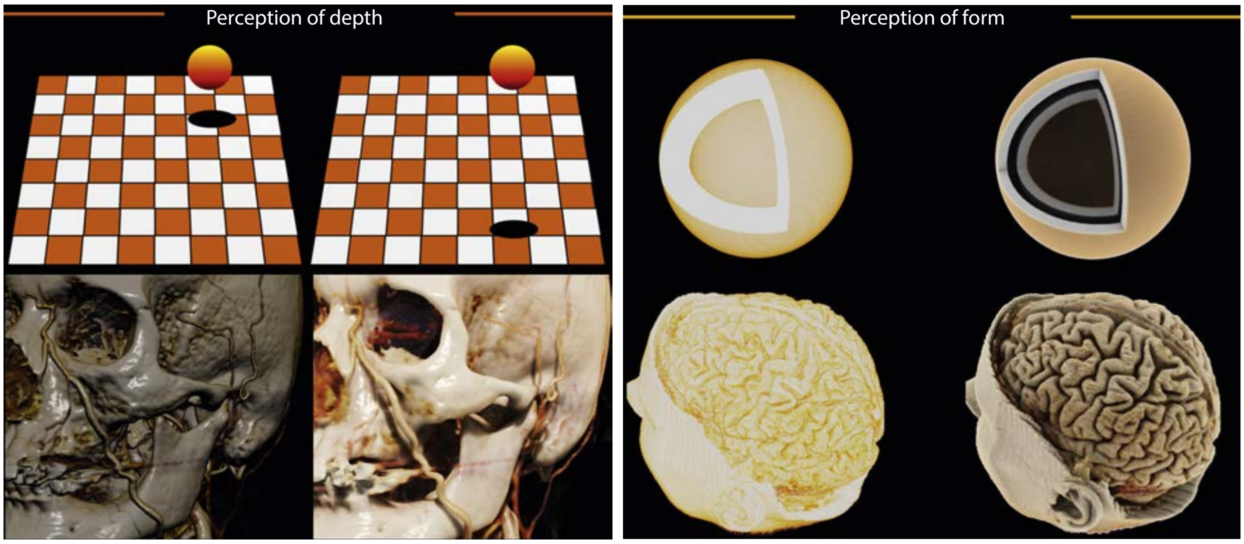

Fig. I.4.2 Traditional versus cinematic rendering. Left: Shadow effects (top) illustrate the distances between cranial bones and blood vessels (bottom). Right: Ambient light masking effects enhance the impression of cortical gyri and sulci (bottom). (Source: Stanford volume data archive/Siemens Healthineers.)

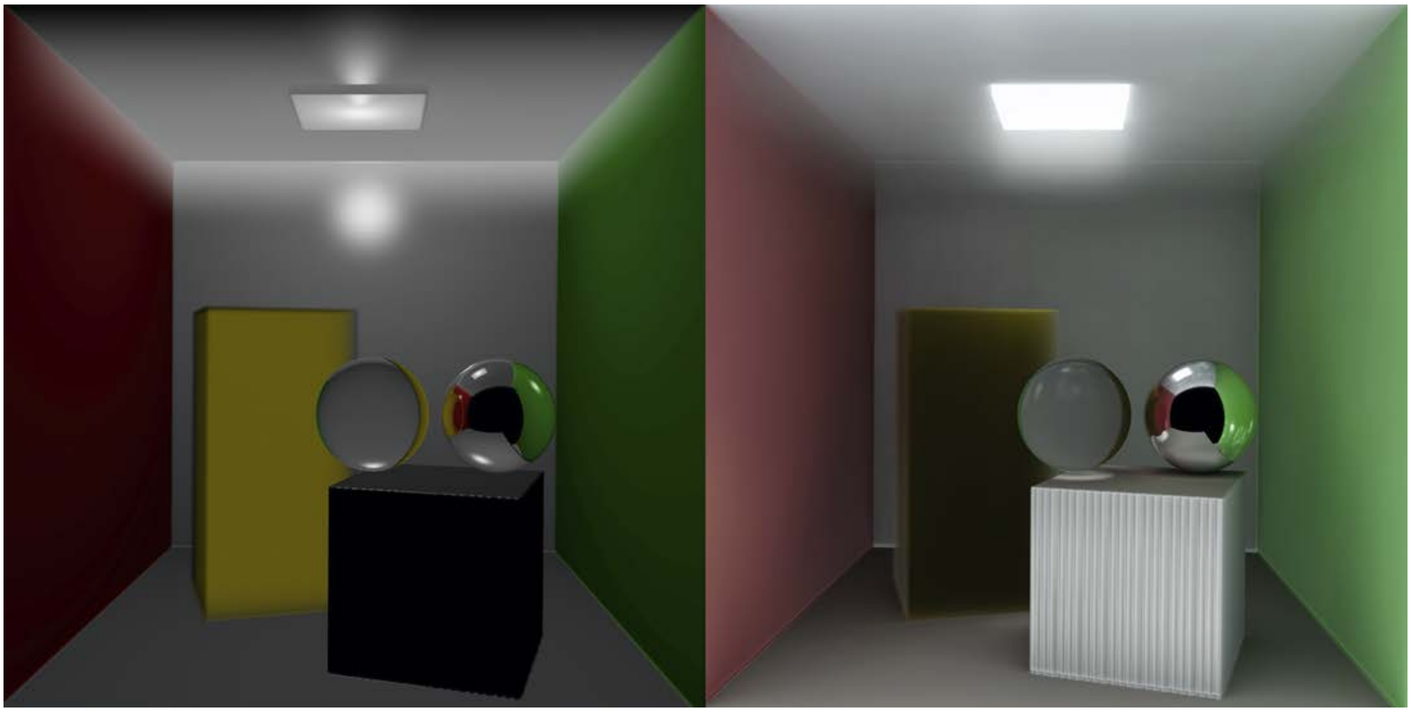

Fig. I.4.3 Volumetric Cornell Box: traditional volume rendering technology (left) versus cinematic rendering (right)**.** The consideration of light shafts, scattering, caustic reflections, ambient occlusion, colour bleeding and soft shadows enables photorealistic representations. (Source: Siemens Healthineers.)

spherical panorama is captured using a reflective sphere. The sphere records the current light environment for subsequent application to image datasets. To understand how these images are rendered, we must turn to the physics of light. Rays of light are made up of particles called photons that interact with their environment. When light encounters matter, it is reflected, bouncing off the surface in various directions: in some places it is absorbed, producing shadows. CR mimics this behaviour.

In the case of CT and MRI images, a physical rendering algorithm which uses a Monte Carlo path tracing method simulates the complex interactions between photons and the scanned images of a patient's body (Comaniciu et al 2016). Unlike the digital modelling used in cinema, CR not only calculates how light is reflected off the surface of the body but also takes into account how light penetrates tissue and is then scattered in different directions. CR generates photorealistic images by calculating realistic lighting by light transport simulation along hundreds or thousands of photon paths per pixel through the anatomical structure using a stochastic process (Fig. I.4.3). In this way, even complex effects such as ambient occlusion (the effect of how hidden a surface is from the ambient lighting) can be modelled. For example, when the depth of a fracture is fed into the calculations, the deeper the fracture, the less light is able to penetrate, resulting in a range of shadows and a more realistic depiction. Diagnostic 3D medical imaging has not previously leveraged these special characteristics of light (Comaniciu et al 2016, Eid et al 2017, Dappa et al 2016). The result is an enhanced depiction of fractures, ivory-coloured bones, and clearly defined organs and blood vessels, all of which can be more easily discerned as a result of the inclusion of shadows and the impression of depth (Fig. I.4.4A). The process requires vast amounts of computing power: depending on the image resolution, hundreds or even thousands of light paths per pixel must be calculated (Novák et al 2018). The images can be rotated on the screen as desired or zoomed in for greater detail (Fig. I.4.4B). Since rendering occurs in the postprocessing stage, the patient is not exposed to additional radiation.

Cinematic rendering in anatomical practice and education

An appreciation of spatial relationships is crucial to understand human topographical anatomy: gaining this understanding not only takes time but also differs from individual to individual (Garg et al 2001, Pandey and Zimitat 2007). CR offers new opportunities for integrating medical imaging into anatomical education from the earliest stages of medical training. Including visualization technology within a blended medical curriculum has the potential to enhance the learning experience, enabling students to gain a clearer understanding of, for example, the bronchial tree, coronary circulation, or skeletal anatomy (Fig. I.4.5) and enhancing self-study away from lecture theatres and cadaveric labs on an electronic device such as a portable tablet. By using augmented reality, virtual dissection offers the opportunity to relive and revise the whole dissection course (Binder et al 2019).

CR has been tested in the setting of an interactive anatomy lecture with first-year undergraduate medical and dental students at the Friedrich-Alexander University Erlangen-Nürnberg (FAU), Institute of Functional and Clinical Anatomy; the majority of students (95.9%) found it enhanced their understanding of anatomy (Binder et al 2019). Commenting on the didactic potential of CR, Professor Dr Michael Scholz (Anatomical Institute at FAU Erlangen) was '*…convinced that this application must and will find its way into the anatomy education in the near future*'. Since 2016, CR has also been used for anatomical teaching at the Ars Electronica Center in Linz, Austria, installed in a high-definition 8K 3D projection space, demonstrating how the study of anatomy can embrace technological learning tools in the 'dissecting theatre of the future' (Fellner et al 2017).

Cinematic rendering has the potential to become an important tool for enhancing the visualization of anatomical structures, and for facilitating the understanding of spatial relationships required in clinical practice, particularly for specialties such as surgery, radiology, orthopaedics and cardiology.

Footnote

Cinematic rendering has been used to produce the cover image of this edition of *Gray's Anatomy,* and is also demonstrated in the context of computed tomography of coronary angiography in the mapping of anomalous coronary artery circulation (see Commentary 7.2).

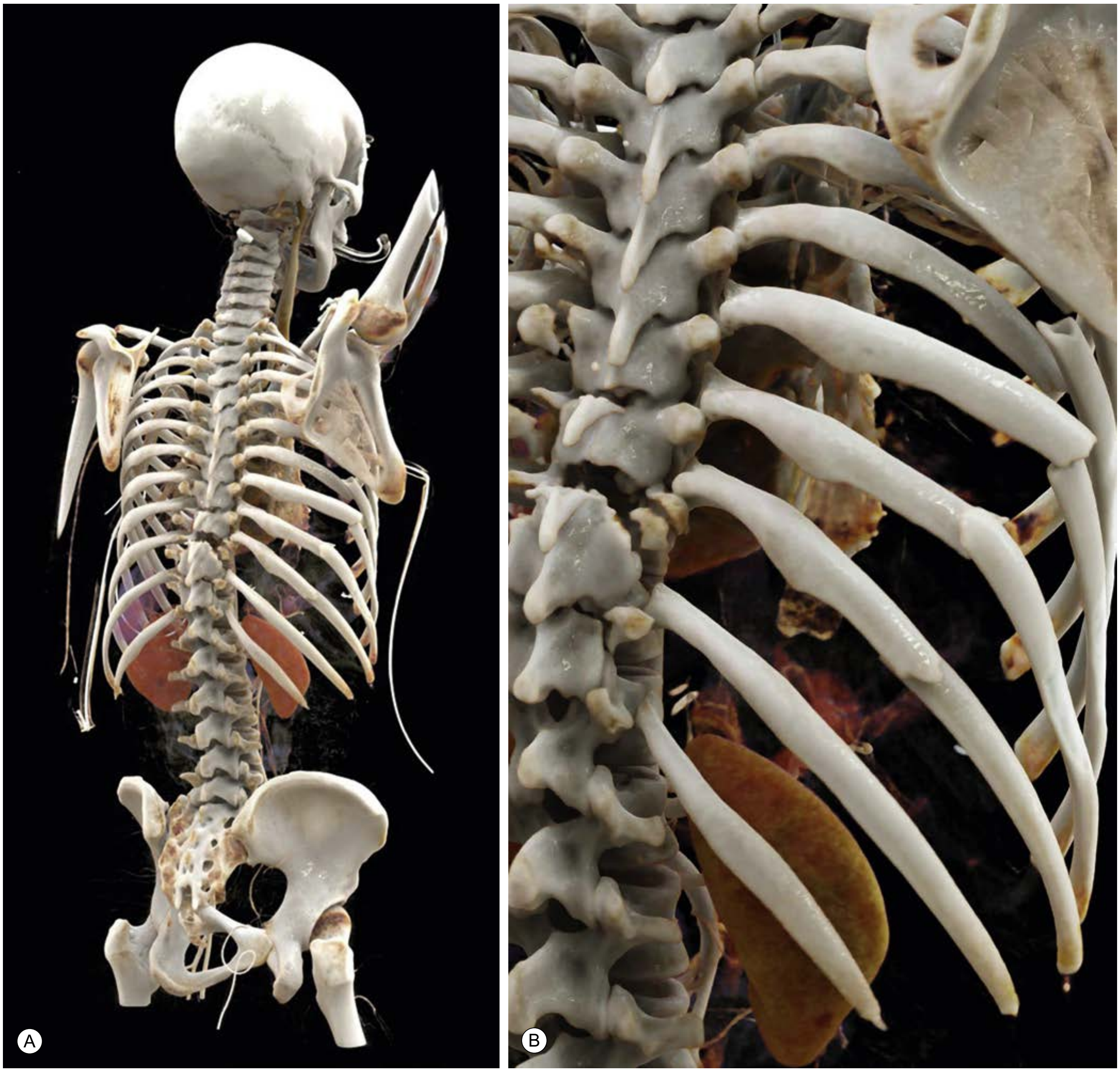

Fig. I.4.4 **A**, Cinematic rendering of a CT, head to pelvis. The patient has multiple fractures of the ribs and spine, as demonstrated in the zoomed view (**B**). (Source: General Hospital of Vancouver, Canada.)

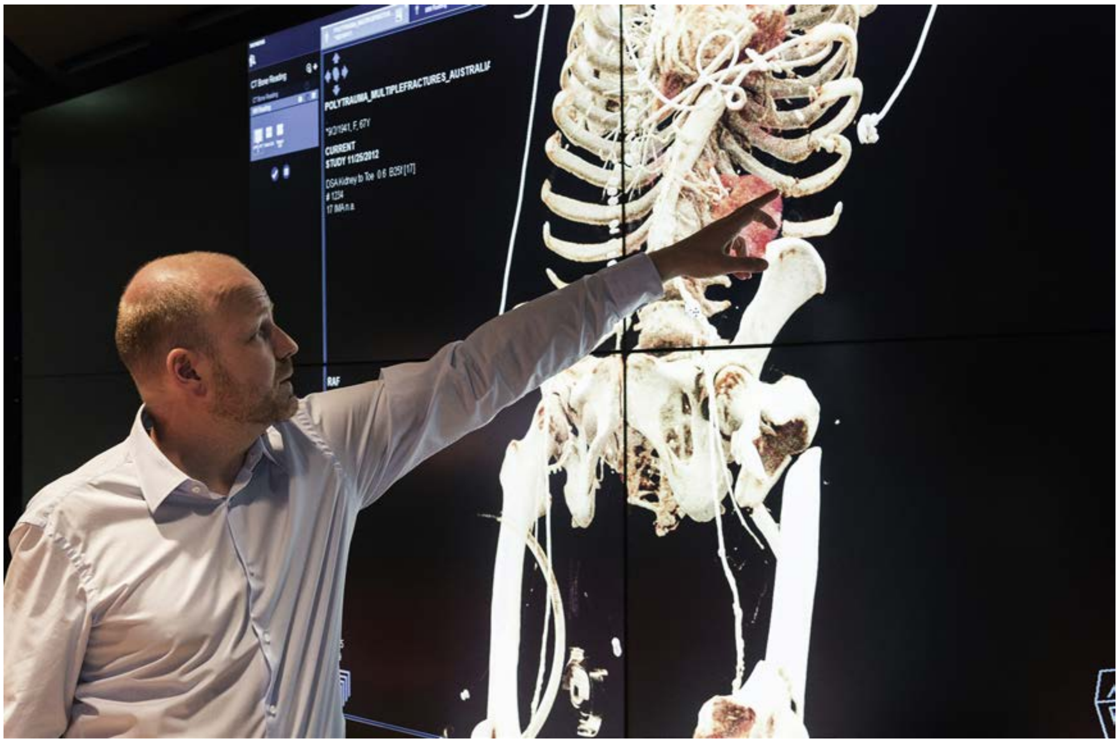
POLYTRAUMA_MULTIPLEFRACTURES_AUSTRALIA
CURRENT
STUDY 11/25/2012

Fig. I.4.5 Cinematic rendering in use for educational purposes. (Source: Deutscher Zukunftspreis/Ansgar Pudenz.)

References

Berger F, Ebert LC, Kubik-Huch RA et al 2018 Application of cinematic rendering in clinical routine CT examination of ankle sprains. AJR Am J Roentgenol 211:887–90.

Binder J, Krautz C, Engel K et al 2019 Leveraging medical imaging for medical education – a cinematic rendering-featured lecture. Ann Anat 222:159–65.

Comaniciu D, Engel K, Georgescua B et al 2016 Shaping the future through innovations: From medical imaging to precision medicine. Med Image Anal 33:19–26.

Dappa E, Higashigaito K, Fornaro J et al 2016 Cinematic rendering – an alternative to volume rendering for 3D computed tomography imaging. Insights Imag 7:849–56.

Ebert LC, Schweitzer W, Gascho D et al 2017 Forensic 3D visualization of CT data using cinematic volume rendering: a preliminary study. AJR Am J Roentgenol 208:233–40.

Eid M, De Cecco CN, Nance JW Jr et al 2017 Cinematic rendering in CT: a novel, lifelike 3D visualization technique. Am J Roentgen 209:370–79.

Fellner F, Engel K, Kremer C 2017 Virtual anatomy: the dissecting theatre of the future— implementation of cinematic rendering in a large 8 K high-resolution projection environment. J Biomed Sci Eng 10:367–75.

Garg AX, Norman G, Sperotabl L 2001 How medical students learn spatial anatomy. Lancet 357:363–64.

Novák J, Georgiev I, Hanika J et al 2018 Monte Carlo methods for physically based volume rendering. In: ACM SIGGRAPH 2018 Courses, 1. SIGGRAPH '18

Pandey P, Zimitat C 2007 Medical students' learning of anatomy: memorisation, understanding and visualisation. Med Ed 41:7–14.

EPONYMS

An annotated list of eponyms, edited by Harold Ellis, was first published in the 39th edition. That list has now been updated by Susan Standring. An appropriate reference has been cited when it has not proved possible to source biographical information.

Achilles tendon: the calcaneal tendon.
Achilles, in Greek mythology, was slain by a wound in his vulnerable heel, inflicted by Paris in the Trojan War.

Adam's apple: a protrusion in the front of the throat that is part of the larynx.
According to the Old Testament, Adam was the first man.

Adamkiewicz, artery of: the largest anterior medullary feeder artery to the anterior spinal artery. It varies in level, arising from the lower (T9–11) posterior intercostal, the subcostal or, less frequently, the upper, lumbar (L1–2) arteries. Most often occurs on the left side.
Albert Adamkiewicz (1850–1921), Professor of Pathology, University of Cracow, Poland.

Addison's disease: a disease resulting from progressive destruction of the suprarenal gland with deficiency in the secretion of adrenocortical hormones.
Thomas Addison (1795–1860), English physician.

Alcock's canal: canalis pudendalis.
Benjamin Alcock (1801–1833), British anatomist who published an article in 1836 on the iliac arteries.

Allen's test: a test of sufficiency of the blood supply to the hand by compression and release of the ulnar and radial arteries, and observation of the colour change of the hand.
EV Allen (1901–1961), Professor of Medicine, Mayo Clinic, Rochester, Minnesota, USA.

Alport's syndrome: a rare hereditary condition characterized by progressive renal failure.
Arthur Cecil Alport (1880–1959), South African physician.

Alzheimer's disease: the most common form of dementia, characterized at postmortem by neurofibrillary tangles and amyloid plaques.
Alois Alzheimer (1864–1915), neurologist, Breslau, Poland.

Ammon's horn: the hippocampus. Cornu Ammonis, or Ammon's horn, describes the whorled, chambered shells of a fossil genus of Cephalopods. It also refers to the ram-shaped horns on the head of the Egyptian god Amun.

Andresen lines: structural lines within dentine, representing incremental lines that run more or less perpendicular to the direction of the tubules. They represent an incremental period of about 1 week and are best visualized when longitudinal ground sections are viewed between crossed polars.
Viggo Andresen (1870–1950), Norwegian orthodontist.

Angelman syndrome: a chromosome 15 disorder comprising microcephaly with mental and motor retardation, epilepsy, ataxic gait or complete inability to walk, muscle hypotonia, EEG abnormalities and peculiar facies marked by a protruding jaw and tongue, occipital depression and blue eyes.
Harry Angelman (1915–1996), English paediatrician.

Apert's syndrome: a complex of craniofacial abnormalities caused by premature craniosynostosis, usually of the coronal suture, leading to turribrachycephaly, associated with syndactyly and polydactyly.
Eugène Charles Apert (1868–1940), French paediatrician.

Arantius, nodule of: a small nodule in the free border of the aortic valves.
Julio Caesar Aranzio (Arantius) (1530–1589), pupil of Vesalius. Professor of Medicine and Surgery, Bologna, Italy.

Argyll Robertson pupil: a pupil that reacts to accommodation but not light. A highly specific sign in neurosyphilis but may also occur in other conditions such as sarcoidosis, multiple sclerosis, and, occasionally, diabetes mellitus.
Douglas Moray Cooper Lamb Argyll Robertson (1837–1909), ophthalmic surgeon, Edinburgh, UK. Worked in Berlin, Germany, with the German ophthalmologist Albrecht von Graefe.

Arnold: Arnold's bundle – frontopontine fibres;

innominate canal of – the canal in the petrous portion of the temporal bone that transmits the auricular branch of the vagus;

Arnold's nerve – the auricular branch of the vagus.
Friedrich Arnold (1803–1890), German anatomist.

Arnold–Chiari malformation: a congenital brainstem and cerebellar herniation through the foramen magnum.
Julius Arnold (1835–1915), Professor of Pathology, Heidelberg, Germany; Hans Chiari (1851–1916), Austrian pathologist.

Auerbach's plexus: the autonomic nervous plexus between the circular and longitudinal layers of muscle of the intestinal wall.
Leopold Auerbach (1828–1897), Professor of Neuropathology, Breslau, Poland.

Axenfeld–Rieger syndrome: an autosomal dominant disorder characterized by bilateral abnormalities of the anterior segment of the eye in association with extraocular anomalies.
Karl Theodor Paul Polykarpus Axenfeld (1867–1930), German ophthalmologist; Herwigh Rieger (1898–1986), Austrian ophthalmologist.

Babinski reflex, response, sign: an upgoing plantar response in pyramidal tract disturbances.
Joseph Babinski (1857–1922), pupil of Charcot, neurologist, Hôpital Pitié, Paris, France.

Bachmann's bundle: the intra-auricular bundle.
Jean George Bachmann (1877–1959), German–American physiologist, Professor of Physiology, Atlanta College of Physicians and Surgeons 1910–1915, USA.

Baillarger, bands, lines, striae, stripe of: inner and outer white striations on the cerebral cortex.
Jules Gabriel Baillarger (1815–1890), French neurologist and psychiatrist.

Bardet–Biedl syndrome: an autosomal recessive ciliopathy characterized by retinal dystrophy, obesity, postaxial polydactyly, renal dysfunction, learning difficulties and hypogonadism.
Georges Louis Bardet (1885–1966), French physician;
Artur Biedl (1869–1933), Hungarian pathologist and endocrinologist.

Barkow, ligament of: the anterior and posterior portions of the fibrous capsule of the elbow joint.
Hans KL Barkow (1798–1873), German anatomist.

Barr body: the inactive X-chromatin mass in the nucleus of female cells.
Murray Llewellyn Barr (1908–1995), Professor of Anatomy, University of Western Ontario, Canada.

Barrett's oesophagus: abnormal columnar mucosa (Barrett's mucosa) that covers a variable length of the distal oesophagus.
Norman Rupert Barrett (1903–1979), consultant thoracic surgeon, Royal Brompton Hospital, London, UK.

Bartholin's: ducts and gland – the sublingual salivary gland and its ducts;

glands – the greater vestibular glands on either side of the vaginal orifice.
Casper Bartholin (1655–1738), Professor of Medicine, Anatomy and Physics, Copenhagen, Denmark.

Bartons' adductor cord: a dense cord on the ulnar side of the little finger that runs from the medial edge of the insertion of abductor digiti minimi (Barton NJ 1984 Dupuytren's disease arising from the abductor digiti minimi. J Hand Surg (Brit & Europ) 9:265–70).

Bassett's ligament: an accessory anterior–inferior tibiofibular ligament that presents as a low-lying slip inserted so far distally on the fibula that it may cause irritation of the lateral aspect of the talus.
Frank H. Bassett III (1928–2007), American orthopaedic surgeon.

Batson's vertebral venous plexus: the valveless vertebral venous veins that communicate with the prostatic venous plexus and explain the readiness of carcinoma of the prostate to spread to the pelvic bones and vertebrae.
Oscar Batson (1894–1979), Professor of Anatomy, University of Philadelphia, USA.

Battle's sign: bruising over the mastoid process developing 2 or 3 days after fracture of the posterior cranial fossa.
William Battle (1855–1936), surgeon, St Thomas Hospital, London, UK.

Baxter's nerve: the first branch of the lateral plantar nerve (Baxter DE, Thigpen CM 1989 Heel pain: operative results. Foot Ankle 5:16–25).
Donald E Baxter, American orthopaedic surgeon.

Beahrs' triangle: otherwise known as Riddle's triangle, the triangle is delimited by the recurrent laryngeal nerve in the tracheo-oesophageal groove, the inferior thyroid artery and the common carotid artery.
Oliver Howard Beahrs (1914–2006), American surgeon.

Bechterew, nucleus of: the nucleus centralis tegmenti superior.
Vladimir M Bekhterev (Bechterew) (1857–1927), Russian neurologist.

Becker muscular dystrophy: muscular dystrophy of the pelvis girdle type.
Peter Emil Becker (1908–2000), German human geneticist.

Beck's triad: a combination of three symptoms that characterize cardiac tamponade: high central venous pressure, low arterial pressure and a small, quiet heart.
Claude Schaeffer Beck (1894–1971), American surgeon.

Beckwith–Wiedemann syndrome: an overgrowth syndrome – main symptoms are gigantism, macroglossia and umbilical abnormalities in the newborn, enlarged liver and spleen, hyperplasia of the kidney, congenital abnormalities of the urinary tract, slight microcephaly, clonic seizures.
John Bruce Beckwith (1933–), American paediatric pathologist; Hans-Rudolf Wiedemann (1915–2006), German paediatrician.

Beighton Scoring System: a system that measures joint hypermobility on a 9-point scale.
Peter H Beighton (1934–), British medical geneticist.

Bell's muscle: a band of muscular fibres forming a slight fold in the wall of the bladder, running from the uvula vesicae to the opening of the ureter on either side, and bounding the trigonum (Fuss FK 1992 Contribution to the trigone musculature in the case of ureteral duplication. J Urol 147:1363–4).

Bell's: nerve – the long thoracic nerve;

palsy – paresis or paralysis, usually unilateral, of the facial muscles, caused by dysfunction of the facial nerve.
Sir Charles Bell (1774–1842), surgeon, Middlesex Hospital, London, UK.

Bennett shift, movement: the lateral shift of the working mandibular condyle during a laterotrusive movement.

Norman Bennett (1870–1947), British dentist.

Bergmann cells, glia: the glial cells of the cerebellum.
Gottlieb Heinrich Bergmann (1781–1861), neurologist and anatomist, Medical Director, Hildersheim Asylum, Germany.

Bernard–Horner syndrome: *see* ***Horner's syndrome****.*

Bernoulli effect: the phenomenon in which fluid flowing through a tube of varying diameter travels fastest and exerts the largest lateral pressure at its narrowest point.
Jakob Bernoulli (1654–1705), mathematician, Switzerland. Shares with Isaac Newton the invention of calculus.

Berrettini branch: a superficial connection between the median and ulnar nerves, apparently displayed in an anatomical plate by Pietro Berrettini di Cortona in 1741. Similar communications are said to be shown in a print from Charles Estienne dated 1545 (Berrettini P, Petrioli CR 1741 Tabulae Anatomicae. Rome: Typographia Antonii de Rubeis: 1–4).

Berry's ligament: the thickened elastic bundle connecting the superior horn of the thyroid cartilage to the tip of the greater horn of the hyoid cartilage (synonyms: lateral thyrohyoid ligament; ligamentum thyrohyoideum laterale).
Sir James Berry (1860–1946), Canadian surgeon.

Betz cells: large pyramidal cells of the cerebral cortex.
Vladimir Aleksandrovich Betz (1834–1894), Professor of Anatomy, Kiev, Ukraine.

Bezold's abscess: subperiosteal temporal bone abscess.
Friedrich Bezold (1842–1908), otologist, Munich, Germany.

Bichat, buccal fat pad of: a variable, but usually considerable, amount of adipose tissue in the cheek. It is often encapsulated to form a biconcave mass, that is particularly evident in infants (the suctorial fat pad).
Marie-François Xavier Bichat (1771–1802), Professor of Anatomy and physician, Hôtel Dieu, Paris, France.

Bielschowsky stain: a silver stain for nerve fibres.
Max Bielschowsky (1869–1940), German neuropathologist.

Billroth, cords of: splenic cords found in the red pulp between the sinusoids.
Christian Albert Theodor Billroth (1829–1894), German-Austrian surgeon, considered to be the founder of modern abdominal surgery.

Bill's bar: a vertical crest that separates the superior fundus above the crista falciformis into anterior and posterior portions containing the facial nerve (and nervus intermedius) and the superior vestibular nerve, respectively. It is usually described as a thin layer of arachnoid tissue that may have an osseous medial component.
William Fouts House (1923–2012), American otologist, physician and medical researcher. Developed and invented the cochlear implant.

Birbeck granules: small, cross-striated granules first reported in the Langerhans cells of the epidermis.
Michael S Birbeck (1925–2005), cancer researcher, Institute of Cancer Research, London, UK.

Bland–White–Garland syndrome: an anomalous origin of the left coronary artery arising from the pulmonary artery (ALCAPA) – a rare, but serious, congenital anomaly. The first clinical description in conjunction with autopsy findings was given by Bland and colleagues in 1933 (Bland EF 1933 Congenital anomalies of the coronary arteries: report of an unusual case associated with cardiac hypertrophy. Am Heart J 8:787–801).

Blake's pouch: a temporary outpouching of the posterior membranous area continuous with the fourth ventricle; its neck becomes the foramen of Magendie (Blake JA 1900 The roof and lateral recesses of the fourth ventricle, considered morphologically and embryologically. J Comp Neurol 10:79–108).
Joseph A Blake (1864–1937), American physician.

Blaschko's lines: a pattern of cutaneous mosaicism that can be observed in a range of congenital and acquired skin conditions.
Alfred Blaschko (1858–1892), German dermatologist, Berlin, Germany.

Bloom's syndrome: an inherited disorder characterized by short stature, sun-sensitive skin changes, an increased risk of cancer, and other health problems (Bloom D 1954 Congenital telangiectatic erythema resembling lupus erythematosus in dwarfs; probably a syndrome entity. AMA Am J Dis Child 88:754–8).
David Bloom, American dermatologist.

Bochdalek, triangle of: when present, the lumbocostal triangle of Bochdalek represents a developmental defect resulting from an incomplete formation of the pleuroperitoneal membrane, located in the posterolateral respiratory diaphragm between the lumbar and costal parts, superior to the lateral arcuate ligament;

Bochdalek's hernia: a congenital diaphragmatic hernia due to failure of closure of the pleuroperitoneal hiatus.
Vincent Alexander Bochdalek (1801–1883), Czech anatomist.

Boerhaave's syndrome: spontaneous rupture of the oesophagus, first described in 1723; the patient was Baron Jan von Wassenaer, Grand Admiral of the Dutch Fleet and Prefect of Rhineland.
Herman Boerhaave (1668–1738), Dutch physician, anatomist, botanist, chemist and humanist.

Bolk's ansiform lobules: formerly known as the superior and inferior semilunar lobules in the cerebellum.
Lodewijk Bolk (1866–1930), Dutch anatomist.

Bowman's: anterior limiting lamina, layer – the anterior elastic membrane of the cornea;

capsule – the sheath surrounding the renal glomerulus;

glands – glands in the olfactory mucosa.

space – the space between the two walls of Bowman's capsule, also called the urinary space.
Sir William Bowman (1816–1892), surgeon, Birmingham General Hospital, then Professor of Anatomy and Physiology, King's College Hospital, London, UK.

Braille text: a system of writing consisting of raised dots and points, which can be interpreted by touch as letters of the alphabet.
Louis Braille (1809–1852), French teacher of the blind.

Brissaud's sulcus: the transverse parietal sulcus.
Édouard Brissaud (1852–1909), French physician and pathologist.

Broca lesion: anteroinferior detachment of the glenoid labrum (Broca A, Hartman H 1890 Contribution à l'étude des luxations de l'épaule (luxations anciennes, luxations recidivantes). Bulletins de La Société Anatomique de Paris 5, serie IV, 312–36. June 1890).
Auguste Broca (1859–1924), French orthopaedic surgeon.

Broca's: area – the speech area of the cerebral cortex;

diagonal band – a fibre tract in the basal forebrain;

plis de passage moyen de Broca – Broca described several passages or bridges connecting the frontal and parietal lobes in the vicinity of the central sulcus. The pli de passage fronto-parietal moyen is an elevation in the floor of the central sulcus at its midpoint, constant and occasionally duplicated.
Pierre Paul Broca (1824–1880), Professor of Clinical Surgery, Paris, France.

Brödel, bloodless line of: the line of division between the areas of kidney supplied by the anterior and posterior branches of the renal artery.

Max Brödel (1870–1941), medical artist, Leipzig, Germany, then Director of Institute of Art as Applied to Medicine, Baltimore, USA.

Brodmann's area 17, area 18: the primary visual cortex.

Korbinian Brodmann (1868–1918), Professor of Anatomy, Tübingen, Germany.

Brown-Séquard syndrome: an incomplete spinal cord lesion, characterized by ipsilateral upper motor neurone paralysis and loss of proprioception, as well as contralateral loss of pain and temperature sensation.

Charles E Brown-Séquard (1817–1894), French physiologist and neurologist.

Broyles ligament: the anterior commissure, commissural tendon. A band of fibrous tissue that extends from the vocal ligaments to the midline of the inner surface of the upper thyroid cartilage.

Edwin N Broyles (1894–1977), American laryngologist.

Bruch's choroidal basal lamina, membrane: the basal membrane of the choroid.

Karl Wilhelm Ludwig Bruch (1819–1884), Professor of Anatomy at Basle, Switzerland, and then Giessen, Germany.

Brunner's glands: duodenal glands lying deep to the muscularis mucosae.

Johann Konrad Brunner (1653–1727), Professor of Anatomy successively at Heidelberg, Germany, and Strasbourg, France.

Buck's fascia: the penile fascial sheath.

Gordon Buck (1807–1877), surgeon, New York, USA.

Budd–Chiari syndrome: spontaneous thrombosis (complete or partial) of the hepatic veins, with or without additional inferior vena caval thrombosis.

George Budd (1808–1882), Professor of Medicine, King's College Hospital, London, UK; Hans Chiari (1851–1916), Austrian pathologist.

Budge (and Waller), ciliospinal centre of: neurones located in the intermediolateral cell columns of the spinal cord (C8–T2) that receive a pretectal input and project to the superior cervical ganglion, and are involved in controlling the operation of the ciliary muscle. Associated with a reflex identified by Augustus Volney Waller and Ludwig Julius Budge in 1852.

Buerger's disease: thromboangiitis obliterans (an inflammatory vasculopathy).

Leo Buerger (1879–1943), Austrian-born American physician and urologist.

Buford complex: a combination of an absent anterior superior labrum and a cord-like middle glenohumeral ligament (Williams MM, Snyder SJ, Buford D 1994 The Buford complex – the cordlike middle glenohumeral ligament and absent anterosuperior labrum complex: a normal anatomic capsulolabral variant. Arthroscopy 10:241–7).

Don Buford Jr, American orthopaedic surgeon.

Büngner, bands of: columns of denervated Schwann cells

Otto von Büngner (1858–1905), German surgeon. Studied in Dorpat, Estonia and Halle, Germany, from 1877 to 1883 as a student of Eduard von Wahl (1833–1890) and Richard von Volkmann (1830–1889).

Bunnell tightness test: tests the tightness of the intrinsic muscles of the hand. The metacarpophalangeal joint is held extended by the examiner and the proximal interphalangeal joint is passively flexed. An inability to flex the latter indicates that the intrinsic muscle is foreshortened.

Sterling Bunnell, (1882–1957), American surgeon who is considered to be the 'founding father' of American hand surgery.

Burns, suprasternal space of: a slit-like interval between two layers of the deep investing fascia of the neck that are attached to the anterior and posterior borders of the manubrium. The space contains a small amount of areolar tissue, the lower parts of the anterior jugular veins and the jugular venous arch, the sternal heads of the sternocleidomastoid muscles and sometimes a lymph node.

Allan Burns (1781–1813), Scottish anatomist.

Cajal: **interstitial cells of –** cells in the muscularis externa of the gut wall active as pacemakers in gut motility;

interstitial nucleus of – group of neurones lateral to the Edinger–Westphal nucleus and ventrolateral to the periaqueductal grey in the rostral part of the midbrain within the medial longitudinal fasciculus involved in the vestibulo-ocular response, smooth pursuit and optokinetic eye movements and vertical eye movement during saccades (Cajal, S Ramón Y 1911 Histologie du système nerveux de l'homme et des vertébrés. Paris: Maloine, pp. 263–266).

Cajal–Retzius cell: 'CR cell', a class of neurones with different morphotypes that express Reln in the MZ/layer I.

Santiago Ramón y Cajal (1852–1934), Professor of Anatomy, Valencia, then Barcelona, then Professor of Histology and Morbid Anatomy, Madrid, Spain; Cajal shared the Nobel Prize in Physiology or Medicine (1906) with Camillo Golgi for their work on the structure of the nervous system. Gustav Magnus Retzius (1842–1919), Professor of Anatomy, Karolinska Institute, Stockholm, Sweden. Son of Andreas Adolf Retzius.

Caldwell–Luc procedure: an operation that involves opening the maxillary sinus by way of an incision into the supradental fossa opposite the premolar teeth, usually done to remove tooth roots or abnormal tissue.

George W Caldwell (1867–1946), American physician, writer and painter; Henri Luc (1855–1925), French laryngologist.

Calleja, islands of: aggregations of very small, densely packed granule cell neurones located in the basal forebrain of most vertebrate species. They are found in all layers of the olfactory tubercle and between the tubercle and the ventral striatum.

Julián Calleja y Sánchez (1836–1913), Spanish physician and anatomist.

Calot's triangle: an isosceles triangle based on the common hepatic duct with the cystic artery and cystic duct forming its sides.

Jean-François Calot (1861–1914), surgeon, Rothschild Hospital, Berck-sur-Mer, France. Specialized in the treatment of surgical tuberculosis in children.

Campbell's lines: five lines that should be traced when assessing a coronal radiograph of the facial skeleton (McGrigor B, Campbell W 1950 The radiology of war injuries. IV. Wounds of the face and jaw. Br J Radiol 23:685–96).

Camper's: angle – the line running from the inferior border of the ala of the nose to the superior border of the tragus of the ear;

chiasm(a) – the passage of the tendons of flexor digitorum profundus (flexor digitorum longus in the foot) through the interval left by the decussation of the fibres of the tendons of flexor digitorum superficialis (flexor digitorum brevis in the foot);

fascia – the layer of fascia extending between the ischiopubic rami inferior to sphincter urethrae and the deep transverse perineal muscle;

plane – a plane defined by the inferior border of the right or left ala of the nose and the superior border of the tragus of both ears.

Petrus Camper (1722–1789), Dutch physician and anatomist.

Cantlie's line: a line that separates the right and left lobes of the liver, drawn from the inferior vena cava to just left of the gallbladder fossa.

Sir James Cantlie (1851–1926), Scottish physician, a pioneer of First Aid, and co-founder of the Hong Kong College of Medicine for Chinese (subsequently, the University of Hong Kong).

Cantrell, pentalogy of: a syndrome of congenital defects involving the abdominal wall, sternum, diaphragm, pericardium and heart (Cantrell JR, Haller JA, Ravitch MM 1958 A syndrome of congenital defects involving the abdominal wall, sternum, diaphragm, pericardium, and heart. Surg Gynecol Obstet 107:602–14).

Carabelli's cusp, cusplet, tubercle: an occasional fifth tubercle lingual to the anteromedial cusp of the first upper molar tooth.

Edler Carabelli (1787–1842), Professor of Dental Surgery, Vienna, Austria.

Carnegie stage: not an eponym but a standardized system of 23 stages used to provide a unified developmental chronology of the vertebrate embryo.

Carnegie Institution for Science, organization established to support scientific research, Washington, DC, USA.

Carpenter's syndrome: mental retardation, acrocephaly and syndactyly related to, but genetically distinct from, Alpert's syndrome.

George Carpenter (1859–1910), physician, UK.

Carus, curve of: the lower end of the pelvic curve.

Karl (Carl) Gustav Carus (1789–1869), German anatomist, physiologist and painter.

Chamberlain procedure: anterior mediastinotomy.

J Maxwell Chamberlain (1906–1968), American thoracic surgeon.

Charcot's artery of cerebral haemorrhage: the lenticulostriate branch of the middle cerebral artery.

Jean-Martin Charcot (1825–1893), neurologist and physician, Salpêtrière, Paris, France.

Charcot–Marie–Tooth disease: an inherited disorder of nerves that is characterized by loss of muscle tissue and touch sensation, predominantly in the feet and legs.

Jean-Martin Charcot (1825–1893), French neurologist and physician, Salpêtrière, Paris, France; Pierre Marie (1853–1940), French neurologist, assistant to Charcot; Howard Henry Tooth (1856–1925), British neurologist.

Chassaignac's carotid tubercle: the prominent anterior tubercle of the transverse process of the sixth cervical vertebra, against which the carotid artery can be compressed.

Charles-Marie Édouard Chassaignac (1805–1879), surgeon, Paris, France.

Cheyne–Stokes respiration: breathing pattern characterized by alternating periods of apnoea and hyperpnoea.

John Cheyne (1777–1836), Scottish physician; William Stokes (1804–1878), Irish physician, Regius Professor of Physic at the University of Dublin.

Chiari malformation, Chiari's network: *see* ***Arnold–Chiari malformation.***

Hans Chiari (1851–1916), Austrian pathologist.

Chilaiditi's syndrome: the presence of a long mesentery related to the distal ascending and proximal transverse colon, resulting in the presence of either or both becoming interposed between the right lobe of the liver and the diaphragm, with or without abdominal symptoms.

Demetrius Chilaiditi (1883–1975), Greek radiologist in Vienna, Austria.

Chopart: joint – the transverse tarsal joint or midtarsal joint formed by the calcaneocuboid and talonavicular joints;

Chopart's ligament – the bifurcate ligament (calcaneonavicular ligament and calcaneocuboid ligament).

François Chopart (1743–1795), French surgeon. Professor of Practical Surgery at the École Pratique, Paris, France, from 1771; in 1782, he succeeded Toussaint Bordenave (1728–1782) as Chair of Physiology.

Clara cells: bronchiolar cells secreting surfactant. This is now regarded as a 'tainted eponym'. Max Clara acknowledged that the sample on which he based his work 'was obtained from a prisoner executed by the Nazi justice system'.

Max Clara (1899–1966), Professor of Anatomy, Leipzig, Germany.

Clarke's column: the basal nucleus in the posterior horn of spinal grey matter.

Jacob Augustus Lockhart Clarke (1817–1880), neurologist, Hospital for Epilepsy and Paralysis, London, UK.

Claudius' cells: supporting cells on the floor of the cochlear canal of the inner ear.

Friedrich Matthias Claudius (1822–1869), Professor of Anatomy successively in Kiel and Marburg, Germany.

Cleland's ligament, transverse retrovascular ligament: thin fibres passing from the lateral surfaces of the interphalangeal joints to the skin of the fingers.

John Cleland (1835–1925), Professor of Anatomy, Glasgow, UK.

Cloquet's node, gland: a lymph node in the femoral canal.

Jules-Germain Cloquet (1790–1883), Professor of Anatomy and Surgery, Paris, France.

Colles': fascia – a continuation of Scarpa's layer of abdominal fascia;

fracture – a fracture of the lower end of the radius with dorsal displacement.

Abraham Colles (1773–1843), Professor of Anatomy and Surgery, Royal College of Surgeons of Ireland, Dublin, Ireland.

Conn syndrome: a disorder of excessive aldosterone production.

Jerome W Conn (1907–1994), American endocrinologist.

Cooper's: pectineal ligament – thickened periosteum on the pecten pubis;

suspensory ligaments – suspensory ligaments of the breast.

Sir Astley Pastor Cooper (1768–1841), surgeon, Guy's Hospital, London, UK.

Corti: organ of, rods of – auditory hair cells of the cochlea;

tunnel of – the tunnel between the internal and external pillar cells in the inner ear.

Alfonso Corti (1822–1888), histologist. Held no academic post but worked in Vienna, Austria; Berlin, Germany; Utrecht, Netherlands; and Turin, Italy.

Cowper's glands: the bulbo-urethral glands.

William Cowper (1666–1709), British surgeon and anatomist.

Crouzon's syndrome: craniofacial dysostosis. Premature closures of cranial vault sutures, maxillary hypoplasia and ocular and aural anomalies.

Octave Crouzon (1874–1938), neurologist, Salpêtrière, Paris, France.

Cullen's sign: bluish discoloration at the umbilicus from extravasated blood in ruptured ectopic pregnancy and pancreatitis – an uncommon physical sign.

Thomas Cullen (1869–1953), Professor of Gynaecology, Johns Hopkins Hospital, Baltimore, USA.

Cunningham, sulcus precentralis medialis of: the medial precentral sulcus in the cerebral cortex.

Daniel John Cunningham (1850–1909), Scottish anatomist.

Cupid's bow: the upper curl of the lip, which resembles Cupid's bow.

Cupid, the Roman god of love, pictured as a winged boy with a bow.

Cusco's speculum: a bivalved, self-retaining speculum used to inspect the cervix.

Edward Gabriel Cusco (1819–1894), French surgeon.

Cushing's syndrome: the syndrome produced by glucocorticosteroid excess.

Harvey Cushing (1869–1939), Professor of Surgery, Harvard University, Cambridge, Massachusetts; neurosurgeon, Peter Bent Brigham Hospital, Boston, USA.

Cuvier, duct of: the termination of the cardinal vein in the fetus.

Baron Georges Cuvier (1760–1832), zoologist and palaeontologist, Paris, France.

Dandy–Walker malformation: a variant of Arnold–Chiari syndrome involving the fourth ventricle and cerebellum.

Walter Edward Dandy (1886–1946), American neurosurgeon, pioneer in surgery of the posterior skull cavity and intracranial vascular surgery; Arthur Earl Walker (1907–1995), American neurologist.

Danon disease: a condition characterized by cardiomyopathy, myopathy and intellectual disability; attributed to mutations in the *LAMP2 gene* (Danon MJ, Oh SJ, DiMauro S et al 1981 Lysosomal glycogen storage disease with normal acid maltase. Neurology 31:51–7).

Darkschewitsch, nucleus of: the posterior commissural nucleus.

Liverij Osipovich Darkschewitsch (1858–1925), neuroanatomist, University of Moscow, Russia.

Darwin's tubercle: a slight projection that may be present on the posterior superior aspect of the helix of the pinna (auricle) of the external ear.

Charles Robert Darwin (1809–1882), English naturalist, author of On the Origin of Species by Means of Natural Selection.

DeBakey classification: a system used to classify aortic dissections based upon the site of origin of the dissection. Dissections that include the aorta proximal to the left subclavian artery, with or without distal extension, are classified as type I or II. Dissections distal to the left subclavian artery are classified as type IIIa (extend to the respiratory diaphragm) or IIIb (extend below the respiratory diaphragm).

Michael Ellis DeBakey (1908–2008), American cardiovascular surgeon and pioneer in surgical procedures for treatment of defects and diseases of the cardiovascular system.

Deiters': nucleus – the lateral vestibular nucleus of the vestibulocochlear nerve;

phalangeal supporting cells – outer hair cells in the organ of Corti.

Otto Friedrich Karl Deiters (1834–1863), Professor of Anatomy and Histology, Bonn, Germany.

Delphian node: prelaryngeal (anterior to larynx) lymph node(s), located just above the thyroid isthmus. They may harbour metastatic disease and should be routinely removed as part of a central neck dissection.

Greek Oracle of Delphi, who could predict the future, because the presence of metastatic disease in these lymph nodes predicted that further nodal disease was present in the neck and that the patient had a worse cancer prognosis.

Denonvilliers' fascia: the fascia separating the prostate from the rectum.

Charles-Pierre Denonvilliers (1808–1872), Professor of Anatomy, Paris, France.

de Quervain's tenovaginitis, tenosynovitis: stenosing tenovaginitis of the tendon sheath of abductor pollicis longus and extensor pollicis brevis.
Fritz de Quervain (1868–1940), Professor of Surgery, Berne, Switzerland.

Descemet's posterior limiting lamina, layer, membrane: the posterior membrane of the cornea.
Jean Descemet (1732–1810), Professor of Anatomy and Surgery, Paris, France.

Dieulafoy lesion: rare cause of recurrent gastrointestinal bleeding from ectatic submucosal vessels in the intestinal mucosa.
Paul Georges Dieulafoy (1839–1911), French physician.

DiGeorge syndrome: a congenital disorder in which defective development of the third and fourth pharyngeal pouches results in hypoplasia or aplasia of the thymus and parathyroid glands.
Angelo Mario DiGeorge (1921–2009), American paediatrician.

Dingman approach: a popular method for repairing zygomatic complex fractures (Dingman RO, Natvig P 1964 Surgery of Facial Fractures. Philadelphia: WB Saunders).

Disse, perisinusoidal space of: the space between the venous sinusoid and the hepatic cells.
Josef Disse (1852–1912), German anatomist.

Doppler effect: a change in frequency of an incident sound (or light) wave related to the difference in velocity between the sender and receiver (Doppler CA 1843 Über das farbige Licht der Doppelsterne und einiger anderer Gestirne des Himmels. Abh Königl Böhm Ges Wiss 2:465–82).
Christian Andreas Doppler (1803–1853), Austrian mathematician and physicist.

Dorello's canal: the invagination of the dura in the petroclival region from the petroclival entrance point to the posterior end of the cavernous sinus. It conveys the mid portion of the abducens nerve.
Primo Dorello, Italian anatomist is credited with the discovery of the canal that bears his name in 1905, although it had been described in 1859 by Wenzel Leopold Gruber. Dorello was Professor of Human Anatomy at Peruggia (1926–1946).

Douglas: arcuate line of – the arcuate line of the sheath of rectus abdominis;

pouch of – the rectouterine peritoneal pouch.
James Douglas (1675–1742), anatomist and obstetrician, London, UK.

Down's syndrome: trisomy 21, producing mental retardation and a characteristic facies with variable additional abnormalities.
John Langdon Haydon Down (1828–1896), Cornish physician, UK.

Drummond, marginal artery of, arch of: the anastomoses between the ileocolic, right colic, middle colic, left colic and sigmoid arteries (the arc of Riolan is the part of this arch between the middle and left colic artery).
Hamilton Drummond (1882–1925), surgeon, Newcastle upon Tyne, UK.

Duchenne muscular dystrophy: chronic progressive muscular atrophy due to mutations in the dystrophin gene.
Guillaume Benjamin Amand Duchenne de Boulogne (1806–1875), French neurologist.

Dunbar syndrome: external compression of the coeliac trunk by the median arcuate ligament. The symptoms include abdominal pain, nausea and vomiting (aka median arcuate ligament syndrome (MALS), coeliac artery compression syndrome, coeliac axis syndrome, coeliac trunk compression syndrome, Harjola–Marable syndrome, Marable syndrome) (Dunbar JD, Molnar W, Beman FF, Marable SA 1965 Compression of the celiac trunk and abdominal angina. Am J Roentgenol Radium Ther Nucl Med 95:731–44).

Dupuytren's disease, contracture: contraction and fibrosis of the palmar (and, occasionally, the plantar) fascia.
Baron Guillaume Dupuytren (1777–1835), surgeon, Hôtel Dieu, Paris, France.

Eagle's syndrome: an elongated and/or calcified styloid process and/or a calcified stylohyoid ligament impinge on local structures, triggering sudden sharp pain, e.g. when swallowing.
Watt Weems Eagle (1898–1980), American otorhinolaryngologist.

Eberstaller: sulcus precentralis medialis of, diagonal sulcus of: (Eberstaller, O 1884 Zür Oberflachen Anatomie der Grosshirn Hemisphären. Vienna: Med. 7. Eberstaller O 1890 Das Stirnhirn. Vienna: Urban & Schwartzenberg).

Ebstein malformation: a rare congenital cardiac malformation where the septal and inferior tricuspid valve leaflets are attached abnormally deep into the right ventricular chamber.
Wilhelm Ebstein (1836–1912), German physician.

Ecker: gyrus descendens of – a gyrus that encircles the retrocalcarine sulcus;

paracentral lobule of – a division of the medial aspect of the cerebral cortex formed by the anterior and the posterior paracentral gyri. It lies above the cingulate sulcus and is bounded by the paracentral sulcus anteriorly and the marginal part of the cingulate sulcus posteriorly.
Johann Alexander Ecker (1816–1887), German anthropologist and anatomist.

Edinger–Westphal nucleus: the midbrain nucleus containing preganglionic neurones destined to synapse in the ciliary ganglion; it lies close to the nucleus of the oculomotor nerve.
Ludwig Edinger (1855–1918), Professor of Anatomy, Frankfurt-am-Main, German; Karl Westphal (1833–1890), Professor of Psychiatry, Berlin, Germany.

Ehlers–Danlos syndrome: a group of rare genetic disorders affecting humans and domestic animals, caused by a defect in collagen synthesis.
Edward Ehlers of Denmark (1863–1937) and Henri-Alexandre Danlos of France (1844–1912) identified the syndrome at the turn of the twentieth century.

Eisenmenger complex: the combination of ventricular septal defect with pulmonary hypertension and consequent right-to-left shunt through the defect, with or without an associated overriding aorta.
Victor Eisenmenger (1864–1932), German physician.

Elliot Smith, paramesial sulcus of: paramesial sulcus, certebral cortex.
Sir Grafton Elliot Smith (1871–1937), Australian anatomist.

Ellis–van Creveld syndrome: a very rare autosomal recessive skeletal dysplasia, with inter- and intra-familial variability, characterized by short ribs, short limbs, postaxial polydactyly, and dysplastic teeth and nails. Congenital heart defects occur in 60% of the individuals (Ellis RWB, van Crefeld S 1940 A syndrome characterized by ectodermal dysplasia, polydactyly, chondro-dysplasia and congenital morbus cardis. Arch Dis Child 15:65–84).

Elschnig's layer: the astroglial membrane at the optic nerve head, continuous with the internal limiting membrane of the retina.
Anton Elschnig (1863–1939), Professor, University of Prague Eye Clinic, Czech Republic.

Emery–Dreifuss muscular dystrophy: an X-linked form of muscular dystrophy (Emery AE, Dreifuss FE 1966 Unusual type of benign X-linked muscular dystrophy. J Neurol Neurosurg Psychiatr 29:338–42).

Epley's manoeuvre: canalith repositioning for benign paroxysmal positional vertigo (Epley JM 1980 New dimensions of benign paroxysmal positional vertigo. Otolaryngol Head Neck Surg 88:599–605).

Erb's point: a point on the side of the neck 2–3 cm above the clavicle and in front of the transverse process of the sixth cervical vertebra. Pressure over this point elicits Duchenne–Erb paralysis, and electrical stimulation over this area causes various arm muscles to contract.
Wilhelm Erb (1840–1921), Professor of Neurology, Heidelberg, Germany.

Erb–Duchenne paralysis: the result of injury to the C5 and C6 roots of the brachial plexus.
Wilhelm Erb (1840–1921), Professor of Neurology, Heidelberg, Germany; Guillaume Benjamin Amand Duchenne de Boulogne (1806–1875), French neurologist.

Essex–Lopresti injury: fractures of the radial head with distal radio-ulnar dislocation (Essex-Lopresti P 1951 Fractures of the radial head with distal radio-ulnar dislocation: report of two cases. J Bone Joint Surg Br 33:244–247).

Eustachian: tube – the pharyngotympanic tube;

valve – the inferior vena caval valve in the right atrium.
Bartolomeo Eustachi (1513–1574), Professor of Anatomy, Rome, Italy, and physician to the Pope.

Fallopian: aqueduct, canal – the canal for the facial nerve in the temporal bone;

tube – the uterine tube.

Gabrielle Fallopio (1523–1562), Professor of Anatomy, Padua, Italy. A pupil of Vesalius.

Fallot's tetralogy: a congenital heart disease comprising pulmonary stenosis, right ventricular hypertrophy, ventricular septal defect and overriding of the aorta.
Étienne-Louis Fallot (1850–1911), Professor of Medicine, Marseilles, France.

Fañanas cells: astroglial subtypes in the deeper molecular layer of the cerebellum (Fañanas JRY 1916 Contribucion al estudo de la neuroglia del cerebelo. Trab Lab Invest Biol (Madrid) 14:163–179).

Jorge Ramon y Cajal Fananas (1886–?) Spanish physician.

Ferguson reflex: enhancement of uterine activity due to mechanical stretching of the lower uterine segment and cervix (Ferguson JKW 1941 A study of the motility of the intact uterus at term. Surg Gynecol Obstet 73:359–66).
James Ferguson, Canadian obstetrician.

Fitz-Hugh–Curtis syndrome: a rare complication of pelvic inflammatory disease involving the liver capsule and leading to the creation of adhesions. Thomas Fitz-Hugh, Jr and Arthur Hale Curtis first reported this condition in 1934 and 1930, respectively.
Arthur Hale 'Art' Curtis (1881–1955), American football player, coach and gynaecologist.
Thomas Fitz-Hugh (1894–1963), American haematologist.

Fleschig's temporal knee: *see* ***Meyer's loop***.

Fordyce spots: small mucosal cysts of the cheeks, lips and tongue.
John Addison Fordyce (1858–1925), dermatologist, New York, USA.

Forel, H field of: ventral tegmental decussation between the red nuclei.
August Forel (1848–1931), anatomist and neurologist, Zurich, Switzerland.

Foville, quadrangular lobule of: the precuneus (part of the medial portion of the parietal lobe), delineated anteriorly by the marginal branch of the cingulate sulcus, posteriorly by the parieto-occipital sulcus, and inferiorly by multiple Y-shaped sulcal segments that constitute the subparietal sulcus.
Achille Louis François Foville (1799–1878), French neurologist.

Fox's sign: ecchymosis of the inguinal ligament due to blood tracking from the retroperitoneum and collecting at the inguinal ligament in haemorrhagic pancreatitis.
George Henry Fox (1846–1937), American dermatologist.

Fox–Fordyce disease: a chronic, papular disease involving apocrine sweat duct obstruction, e.g. in the axilla.
George Henry Fox (1846–1937), American dermatologist; John Addison Fordyce (1858–1925), American dermatologist (see ***Fordyce spots****).*

Freiberg's infraction: osteochondrosis of a metatarsal head, usually the second (more rarely, third or fourth) metatarsal bone of the foot, presenting the picture of subchondral cancellous bone necrosis. Characterized by localized pain and swelling over the metatarsal head, red overlying skin and limitation of movement in an adolescent. X-rays show the head to be crushed and fragmented.
Albert Henry Freiberg (1868–1940), American surgeon.

Frey's syndrome: sweating in the distribution of the auriculotemporal nerve, triggered by eating ('auriculo-gustatory sweating') after injury to the facial nerve.
Lucja Frey (1889–1944), neurologist, Warsaw, Poland.

Frohse (Fröhse), arcade of: an arcade between the two layers of supinator, that transmits the posterior interosseous nerve.
Fritz Frohse (1871–1916), German anatomist.

Fröhlich's syndrome: adiposogenital dystrophy.

Alfred Fröhlich (1871–1953), Austrian pharmacologist in the USA.

Froment's sign: weakness of adductor pollicis and the first dorsal interosseous substantially degrades pinch strength. Froment's sign is positive when a slip of paper is held in the key pinch position between the pulp of the thumb and the radial side of the index proximal interphalangeal joint, and the tip of the thumb involuntarily flexes as flexor pollicis longus contracts to compensate for the absent adductor pollicis and first dorsal interosseous.
Jules Froment (1878–1946), French neurologist.

Fruchaud, myopectineal orifice of: the surgical name given to the inferomedial aspect of the anterior abdominal wall.
Henri Rene Fruchaud (1894–1960), Professor of Clinical Surgery, Angers.

Fuchs, crypts of: large depressions often found on the anterior surface of the iris.
Ernst Fuchs (1851–1930), Austrian ophthalmologist.

Furnas' ligament: retaining ligaments of the cheek (Furnas DW 1989 The retaining ligaments of the cheek. Plast Reconstr Surg 83:11–16).

Futcher's lines: *see* ***Voigt's lines***.

Galeazzi fracture-dislocation: a fracture of the distal part of the radius with dislocation of distal radio-ulnar joint and an intact ulna.
Riccardo Galeazzi (1866–1952), Italian orthopaedic surgeon.

Galen's: nerve, anastomosis (ansa galeni) – the anastomosis between the internal branch of the superior laryngeal nerve and the recurrent laryngeal nerve in the wall of the laryngopharynx;

vein (deep galenic venous system) – the great cerebral vein.
Claudius Galen (130–200 AD), born Pergamum, Asia Minor, studied there and in Smyrna, Corinth and Alexandria. Physician to Marcus Aurelius and teacher of anatomy and medicine in Rome. Author of numerous texts on anatomy, surgery and medicine.

Gans, fissure of: a structure that lies on the undersurface of the right lobe of the liver behind the gallbladder fossa; it often marks the variable site of division of the portal pedicle to the right posterior sector.
Henry Gans (1925–2017), Dutch surgeon.

Gartner's: cyst – usually a benign cyst in the anterolateral wall of the vaginal remnant of Gartner's duct;

duct – the paravaginal duct; a mesonephric duct remnant.
Hermann Treschow Gartner (1785–1827), surgeon in the Norwegian and then Danish armies.

Gasserian ganglion: sensory ganglion of the trigeminal nerve. The ganglion was described in 1765 by Antonius Hirsh, who named it after his teacher.
Johann Lorentz Gasser (1723–1765), Austrian anatomist.

Gennari, stria of, white line of: a white band or stripe in the occipital cortex.
Francesco Gennari (1750–1797), anatomist, Parma, Italy.

Gerdy's tubercle: the attachment of the iliotibial tract to the proximal tibia.
Pierre Nicolas Gerdy (1797–1856), surgeon and pathologist, Paris, France.

Gerota's fascia: the renal fascia, which encapsulates the perinephric fat.
Dumitru Gerota (1867–1939), Professor of Surgery, Bucharest, Romania.

Geschwind's area/territory/region: a region in the inferior parietal lobule.
Norman Geschwind (1926–1984), American behavioural neurologist.

Giacomini, band of: the band on the surface of the uncus.
Carlo Giacomini (1840–1898), Professor of Anatomy, Turin, Italy.

Giemsa staining: a solution containing azure-II, glycerin and methanol. Stained elements appear pink, purple or blue.
Gustav Giemsa (1867–1948), German chemist and bacteriologist.

Gillies approach, flap, operation: a procedure in which the instrument is inserted deep to the deep lamina of temporalis fascia through a scalp incision and used to elevate depressed zygomatic complex fractures.
Sir Harold Delf Gillies (1882–1960), British plastic surgeon.

Giraldes, organ of: a vestige of the Wolffian body on the posterior aspect of the testicle.
Joaquim Albino Cardoso Casado Giraldes (1808–1875), Portuguese anatomist and surgeon.

Glanzmann's thrombasthenia: a hereditary platelet abnormality characterized by defective clot retraction, prolonged bleeding time, and related symptoms such as epistaxis and inappropriate bleeding.
Eduard Glanzmann (1887–1959), Swiss paediatrician.

Glenn shunt: a surgical operation for children born with cyanotic heart disease, in which the superior vena cava is anastomosed to the right pulmonary artery so that blood bypasses the malformed right chambers of the heart and is shunted directly into the lungs to be oxygenated.

William WL Glenn (1914–2003), Chief of Cardiovascular Surgery, Yale University, New Haven, Connecticut, USA.

Glisson's (Glissonian) capsule, sheath: the fibrous capsule of the liver.
Francis Glisson (1597–1677), Regius Professor of Medicine, Cambridge, UK. Described rickets in 1671.

Goethe, ossicle of: the incus (an auditory ossicle).
Johann Wolfgang Goethe (1749–1832), German poet, philosopher and scientist.

Goldenhaar's syndrome: hemifacial microsomia. A syndrome of dermoid cysts, auricular appendices, asymmetrical malformations of the face, and vertebral abnormalities.
Maurice Goldenhaar (1924–2001), American physician.

Golgi: cells, neurones – GABAergic cerebellar interneurones;

complexes, apparatus, bodies – membranous cellular organelles or vesicles;

corpuscles – tactile end organs in skin and muscle;

staining technique – a silver staining method for neurones;

tendon organ – a proprioceptive sensory nerve ending embedded among the fibres of a tendon.
Camillo Golgi (1844–1926), Professor of Histology and Anatomy successively in Padua and then Siena, Italy; shared the Nobel Prize in Physiology or Medicine (1906) with Ramon Santiago y Cajal for their work on the structure of the nervous system.

Goodpasture's syndrome: an autoimmune condition in which autoantibodies damage basal laminae, primarily affecting renal and lung function.
Ernest William Goodpasture (1886–1960), pathologist, Tennessee, USA.

Gorlin syndrome: nevoid basal-cell carcinoma syndrome (NBCC syndrome).
Robert J Gorlin (1923–2006), American oral pathologist and human geneticist.

Graafian follicle: the mature ovarian follicle.
Regnier de Graaf (1641–1673), Dutch anatomist and physician, Delft, Netherlands.

Grapow, vertical bands of: vertical connections between the palmar skin and palmar aponeurosis (Grapow M 1887 Die Anatomie und physiologische Anatomie der Palmaraponeurose. Arch Anat Physiol 2–3:143–58).

Gratiolet, 'pli de passage' of: Gratiolet introduced the term plis de passage for some interconnecting gyri in the cerebral cortex.
Louis-Pierre Gratiolet (1815–1865), anatomist and zoologist, became Professor of Zoology, Paris, France.

Graves' disease: a disorder of the thyroid, usually of autoimmune aetiology, characterized by at least two of the following: hyperthyroidism, goitre and exophthalmos.
Robert James Graves (1796–1853), Irish physician.

Grayson's ligament: fascial fibres that pass from the lateral sides of the phalanges volar to the neurovascular bundle (Grayson J 1941 The cutaneous ligaments of the digits. J Anat 75:164–75).
J Grayson, Professor of Anatomy, Manchester, UK.

Grey Turner's sign: bluish discoloration in the left loin caused by extravasated blood in acute pancreatitis – an uncommon physical sign.
George Grey Turner (1877–1951), surgeon, Royal Victoria Infirmary, Newcastle upon Tyne, and Professor of Surgery, Royal Postgraduate Medical School, Hammersmith, London, UK.

Gruber, petrosphenoidal ligament of: a ligament that spans between the petrous apex and the posterior clinoid process, between the meningeal and periosteal layers of the dura mater; the insertion and thickness of the ligament may vary *(see also* ***Dorello's canal****)*.
Wenzel Leopold Gruber (1814–1890), Russian anatomist.

Guérin's fracture: a Le Fort I level fracture of the maxilla.
Alphonse Guérin (1816–1895), surgeon, Paris, France.

Guillain–Barré syndrome: acute idiopathic polyneuritis.
Georges Guillain (1876–1951), French neurologist; Jean Alexandre Barré (1880–1967), French neurologist.

Guillain-Mollaret triangle: dentato-rubro-olivary circuit.
Georges Charles Guillain (1876–1961), French neurologist; Pierre Mollaret (1898–1987), French physician.

Guyon's canal: the canal for the ulnar nerve and vessels; defined medially by the pisiform, and posteriorly by the flexor retinaculum.
Jean Casimir Guyon (1831–1920), surgeon, Paris, France.

Haglund's disease, syndrome, deformity: an abnormal prominence of the posterior superior lateral aspect of the os calcis.
Sims Emil Patrik Haglund (1870–1937), Swedish orthopaedic surgeon.

Haller's: arches – the medial and lateral arcuate ligaments (or lumbocostal arches);

cells – infraorbital ethmoidal cells (synonym: orbitoethmoidal cells), which may be specified as either anterior or posterior and which may lie lateral to the infundibulum and then open into the middle meatus. They grow into the bony orbital floor and may obstruct the ostia of either the ethmoidal infundibulum or the maxillary sinus during endonasal procedures;

circle of, zonula of – *see* ***Zinn, circle of, zonula of;***

layer: a layer of large blood vessels in the choroid derived from the short posterior ciliary arteries.
Victor Albrecht von Haller (1708–1777), Professor of Anatomy, Physiology, Surgery and Botany, University of Göttingen, Germany.

Hallermann–Streiff syndrome: oculomandibulofacial syndrome.
Wilhelm Hallermann (1909–2005), German ophthalmologist; Enrico Bernardo Streiff (1908–1988), Italian-Swiss ophthalmologist.

Hallgren syndrome: *see* ***Usher syndrome*** (Hallgren B 1959 Retinitis pigmentosa combined with congenital deafness; with vestibulo-cerebellar ataxia and mental abnormality in a proportion of cases: a clinical and genetico-statistical study. Acta Psychiat Neurol Scand 138:5–101).

Harris's growth lines: transverse juxta-epiphyseal lines of long bones seen on X-ray, which represent temporary growth arrest.
Henry Harris (1886–1951), Professor of Anatomy, Cambridge, UK.

Hartmann's pouch: dilation above the neck of the gallbladder – a pathological entity produced by a contained gallstone.
Henri Hartmann (1860–1952), Professor of Surgery, Faculty of Medicine, Paris, France.

Hasner's valve: otherwise known as the plica lacrimalis, a fold of mucous membrane that forms an imperfect cover at the lower opening of the nasolacrimal duct into the inferior nasal meatus.
Joseph Hasner, Ritter von Artha (1819–1892), Austrian ophthalmologist.

Hassall's corpuscles: spherical or ovoid bodies found in the medulla of the thymus, composed of concentric arrays of epithelial cells that contain keratohyalin and bundles of cytoplasmic filaments.
Arthur Hill Hassall (1817–1894), English chemist and physician.

Haversian: canals – central vascular channels in Haversian systems;

systems – cylindrical units of tissue (osteons) in compact bone.
Clopton Havers (1817–1894), physician practising first in London, then in the Isle of Wight, UK.

Hawkins sign: subchondral lucency of the talar dome, occurring secondary to subchondral atrophy 6–8 weeks after a fracture of the talar neck (Hawkins LG 1970 Fractures of the neck of the talus. J Bone Joint Surg Am 52:991–1002).

Heidenhain's trichrome stain: a stain for connective tissue.
Rudolf Peter Heinrich Heidenhain (1834–1897), Polish physiologist, Breslau.

Heller's myotomy, cardiomyotomy: a surgical procedure in which the muscles of the cardia (lower oesophageal sphincter) are cut, allowing food and liquids to pass to the stomach; the procedure may be open or closed (laparoscopic) (Heller E 1914 Extramuköse Kardioplastik beim chronischen Kardiospasmus mit Dilatation des Oesophagus. Mitt Grenzgeb Med Chir 27:141–9).
Ernest Heller (1877–1964), German surgeon.

Henle's: accessory paraflocculus of Henle – the dorsal leaf of the cerebellar flocculus;

conjunctival crypts of Henle – infoldings of the conjunctiva;

fibres – the 'axons' of foveal retinal cones running parallel to the retinal surface;

gastrocolic trunk of Henle – the confluence of the right superior colic and right superior gastroepiploic veins, draining into the superior mesenteric vein at the inferior border of the neck of the pancreas;

layer – the outer layer of cells in the root sheath of a hair;

loop of Henle – the looped portion of the renal tubule.
Friedrich Gustav Henle (1808–1885), Professor of Anatomy in Zurich, Switzerland, then Heidelberg and Göttingen, Germany.

Henry: anterior approach of – an approach that provides exposure to the volar aspect of the radial shaft;

knot of – the crossing of the tendon of flexor hallucis longus deep to the tendon of flexor digitorum longus in the sole of the foot;

mobile wad of – three muscles, brachioradialis, extensor carpi radialis longus and extensor carpi radialis brevis, that are palpable below the lateral epicondyle of the humerus, lying on the lateral aspect of the radius.
Arnold Kirkpatrick Henry (1886–1962), Professor of Anatomy, Royal College of Surgeons in Ireland, Dublin, Ireland.

Hensen's: cells, stripe – in the ***organ of Corti*** *(see above)* to the outer side of the ***cells of Deiters*** *(see above)*;

node – thickening at the site of the first formation of the primitive streak.
Viktor Hensen (1834–1924), Professor of Physiology, Kiel, Germany.

Hering–Breuer reflex: a lung stretch reflex mediated by the vagus.
Carl Ewald Hering (1834–1918), physiologist, Academy of Military Medicine, Vienna, Austria, and then Leipzig, Germany; Josef Breuer (1842–1925), psychiatrist and physiologist, Vienna, Austria, where he collaborated with Hering.

Hering, canals of: fine terminal ductules lined by cuboidal epithelium, linking the intralobular bile canaliculi with bile ducts in the portal canals.
Carl Ewald Hering (see above).

Heschl: sulcus of – the anterior border of the planum temporale;

Heschl's transverse temporal gyri – gyri on the temporal lobe of the brain.
Richard Heschl (1824–1881), Professor of Pathology, Cracow, Poland, then Professor of Clinical Medicine, Graz, Austria.

Hesselbach's: fascia – the cribriform fascia;

ligament – the interfoveolar ligament;

triangle – the inguinal triangle.
Franz Kaspar Hesselbach (1759–1816), German surgeon and anatomist.

Heubner's artery: the artery that supplies the anteromedial part of the head of the caudate nucleus and the anteroinferior internal capsule.
Johann Otto Leonhard Heubner (1843–1926), German paediatrician.

Heuser's membrane: the parietal hypoblast layer.
Chester Heuser (1885–1965), American embryologist.

Hill–Sachs lesion: cortical depression of the posterolateral head of the humerus related to impaction of the humeral head with the inferior glenoid fossa in anterior shoulder dislocation.
Harold Arthur Hill (1901–1973), American radiologist; Maurice David Sachs (1909–1987), American radiologist.

Hilton's law: nerves crossing a joint supply the joint, the muscles acting on the joint and the skin overlying the joint.
John Hilton (1805–1878), surgeon, Guy's Hospital, London, UK.

Hirschsprung's disease: megacolon resulting from congenital absence of autonomic ganglion cells in the distal contracted segment.
Harald Hirschsprung (1830–1916), physician, Queen Louise Children's Hospital, Copenhagen, Denmark.

His: angle of – the normally acute angle between the abdominal oesophagus and the fundus of the stomach at the oesophagogastric junction;

bundle of – the atrioventricular bundle of the heart;

furcula of – an inverted U that appears in the central wall of the developing pharynx;

sinus of – the caudal portion of the second branchial arch, as well as the third and fourth arches, which becomes submerged in the cervical sinus of His, a shallow ectodermal pit.
Wilhelm His (Junior) (1863–1934), Professor of Anatomy successively at Leipzig, Germany; Basle, Switzerland; and Göttingen and Berlin, Germany. Son of Wilhelm His (Senior).

Hitselberger's sign: loss of sensation in the posterosuperior part of the external acoustic meatus (external auditory canal) that may be an early sign of an acoustic tumour.
William E Hitselberger (1930–2014), American neurosurgeon, a pioneer in developing the auditory brainstem implant.

Hjortsjö's crook: in the biliary tract, the right posterior sectional duct normally hooks over the origin of the right anterior sectional portal vein, forming 'Hjortsjö's crook' (Hjortsjö CH 1951 The topography of the intrahepatic duct system. Acta Anat (Basel) 11:599–615).

Hoboken, valves of: constrictions of the contours of the umbilical arteries along their course through the umbilical cord.
Nicolas van Hoboken (1632–1678), Professor of Anatomy, Harderwyk, then Professor of Medicine and Mathematics, Steinfurt, Netherlands.

Hodgkin's lymphoma: a haematopoietic neoplasm characterized by cancerous Hodgkin and Reed–Sternberg cells (HRS cells) in an inflammatory background. The aetiology of the disease is not well understood.
Thomas Hodgkin (1798–1866), English physician and pathologist.

Hofbauer cells: placental macrophages in the chorionic villi.
J Isfred Hofbauer (1878–1961), American gynaecologist.

Holden, line of: the transverse skin crease at the groin caused by flexion of the hip.
Luther Holden (1815–1905), surgeon, St Bartholomew's Hospital, London, UK.

Holmes tremor: a tremor that is usually slow and large in amplitude, and may be present at rest, with movement, and often with sustained posture.
Gordon Morgan Holmes (1876–1965), British neurologist.

Holmes–Adie syndrome: a disorder characterized by one eye with a pupil that is larger than normal and constricts slowly in bright light (tonic pupil), and absence of deep tendon reflexes, usually in the Achilles tendon.
Gordon Morgan Holmes (1876–1965), Irish neurologist; William John Adie (1886–1935), British physician and neurologist.

Hopkinson squeeze test: a test to assess the inferior tibiofibular joint, by compressing the fibula to the tibia at the midpoint of the leg: an injured syndesmosis will result in pain felt in the area of the inferior tibiofibular joint (Hopkinson WJ, St Pierre P, Ryan JB et al 1990 Syndesmosis sprains of the ankle. Foot Ankle 10:325–30).

Horner's syndrome, Bernard–Horner syndrome: ptosis and pupillary constriction following interruption of the sympathetic supply to the eyelid and pupil, respectively (hemifacial anhidrosis may also occur).
Johann Horner (1831–1886), Professor of Ophthalmology, Zurich, Switzerland; Claude Bernard (1813–1878), French physiologist, considered one of the founders of experimental medicine.

Hotchkiss approach: anteromedial 'over the top' surgical approach to the elbow performed between flexor carpi ulnaris and flexor carpi radialis (or palmaris longus, when present); it provides good access to the tip of the coronoid process and the whole anterior elbow joint (Hotchkiss R 1998 Surgical technique. In: Hotchkiss R (ed) Compass Universal Hinge. Surgical Technique. Memphis: Smith & Nephew, 8–12).
Robert N Hotchkiss, American orthopaedic surgeon.

Houston, valves of: three intraluminal folds in the wall of the rectum.
John Houston (1802–1845), Irish surgeon and anatomist.

Howship's lacunae: absorption spaces in bone.
John Howship (1781–1841), surgeon, St George's and Charing Cross Hospitals, London, UK. Suffered from osteomyelitis of the tibia and made a special study of bone pathology.

Howship–Romberg sign: *see* ***Romberg sign.***

Humphrey, ligament of: meniscofemoral ligament – Humphrey described this ligament as running from the lateral meniscus to the posterior cruciate ligament.
George Murray Humphrey (1820–1896), Professor of Anatomy and then of Surgery, Cambridge, UK. Founder of Journal of Anatomy.

Hunter's canal: the subsartorial canal.
John Hunter (1728–1793), surgeon, St George's Hospital, London, UK. Described ligation of the femoral artery in the subsartorial canal for popliteal aneurysm. John Hunter is often described as the Founder of Scientific Surgery.

Huntington's disease, chorea: an autosomal dominant disease characterized by chronic progressive chorea and mental deterioration.
George Sumner Huntington (1850–1916), American physician.

Hurler's syndrome: a genetic disorder resulting in a deficiency in breakdown of mucopolysaccharides in the extracellular matrix.
Gertrud Hurler (1889–1965), German paediatrician.

Huschke: foramen of – otherwise known as the foramen tympanicum. An uncommon developmental defect in the anteroinferior aspect of the bony external acoustic meatus. which usually closes by the fifth year but may persist throughout life;

inferior longitudinal sulcus of – (synonym: collateral sulcus) a structure that separates the fusiform gyrus from the parahippocampal gyrus of the limbic lobe.
Emil Huschke (1797–1858), German anatomist and embryologist.

Hutchinson's incisors: pegged lateral incisors and notched central incisors, seen in congenital syphilis.
Sir Jonathan Hutchinson (1828–1913), British surgeon, pathologist, pioneer in the study of congenital syphilis.

Huxley's layer: the inner layer of cells of the root sheath of a hair.
Thomas Henry Huxley (1825–1895), lecturer in Natural History, Royal School of Mines, UK. An early supporter of Darwinism.

Hyrtl's anastomosis: an occasional anastomosis between umbilical arteries in the placenta.
Joseph Hyrtl (1811–1894), Austrian anatomist.

Jackson's membrane: a peritoneal fold between the caecum or ascending colon and the lateral abdominal wall.
Jabez North Jackson (1868–1935), Professor of Anatomy and Surgery, Kansas City, USA.

Jacobson's organ: otherwise known as the vomeronasal organ. A bilateral structure in the anteroinferior wall of the nasal septum just dorsal to the paraseptal cartilages, presumed to be analogous to the vomeronasal organ of other vertebrates: function in humans not yet established, but might be involved in the detection of pheromones.
Ludwig Lewin Jacobson (1783–1843), Danish surgeon.

Jacoby, border tissue of: a posterior extension of astrocytes from the intermediary tissue of Kuhnt, located internal to the border tissue of Elschnig at the optic nerve head (Jacoby E 1905 Über die Neuroglia des Sehnerven. Klin Mbl Augenheilk 43:129–37).

Jadassohn–Lewandowsky syndrome: an autosomal dominant skin disorder characterized predominantly by thickened nails, palmoplantar hyperkeratosis, keratosis pilaris, hyperkeratotic follicular papules on the sites of friction, hair abnormalities and hyperhidrosis of the palms and soles (Jadassohn J, Lewandowsky F 1906 Jacob's Ikonographia Dermatologica. Berlin: Urban & Schwarzenberg).

Jensen, intermediate sulcus of: a downward-projecting side branch of the intraparietal sulcus that descends across the inferior parietal lobule. It starts at the dorsal hemispheric margin and divides the area between the posterior ascending ramus of the Sylvian gyrus and the angular gyrus as it courses ventrally (Jensen J 1870 Die Furchen und Windungen der menschlichen Grosshirn-Hemisphären. Berlin: Georg Reimer).

Jeune syndrome: asphyxiating thoracic dystrophy (Jeune M, Carron R, Beraud C et al 1954 Polychondrodystrophie avec blocage thoracique d'évolution fatale. Pediatrie, Lyon 9:390–2).
Mathis Jeune (1910–1983), French paediatrician.

Joll's triangle: otherwise known as the sternothyrolaryngeal triangle and used to identify the external laryngeal branch of the superior laryngeal nerve during thyroid surgery, the triangle is formed laterally by the upper pole of the thyroid gland and the superior thyroid vessels, superiorly by the attachment of the strap muscles to the thyroid cartilage and medially by the midline.
Cecil Augustus Joll (1885–1945), English surgeon.

Joubert's syndrome: a ciliopathy, one of a group of rare genetic disorders characterized by decreased muscle tone, difficulties with coordination, abnormal eye movements, abnormal breathing pattern and cognitive impairment (Joubert M, Eisenring JJ, Robb JP et al 1969 Familial agenesis of the cerebellar vermis. A syndrome of episodic hyperpnea, abnormal eye movements, ataxia, and retardation. Neurology 19:813–25).
Marie Joubert, paediatric neurologist.

Kager's fat pad: (synonym: pre-Achilles fat pad) a structure located in Kager's triangle between the Achilles tendon, the superior cortex of the calcaneus and flexor hallucis longus (both muscle and tendon) (Kager H 1939 Zur Klinik und Diagnostik des Achillessehnenrisses. Der Chirurg 11:691–5).

Kartagener's syndrome: a genetic disorder (immotile cilia syndrome) affecting axonemal dynein function.
Manes Kartagener (1897–1975), Swiss physician.

Kawase's triangle of the middle fossa: an area that lies between the lateral margin of the greater petrosal nerve (medial border), the lateral edge of the trigeminal nerve behind the point where the greater petrosal nerve passes below its lateral surface to the crest of the petrous apex (lateral border), and a line along the connection of the posterior border of the mandibular division of the trigeminal nerve and the trigeminal ganglion (the crest of petrous apex) to the centre of the geniculate ganglion (Kawase T, van Loeren HR, Keller JT et al 1996 Meningeal architecture of the cavernous sinus: clinical and surgical implications. Neurosurg 39:527–36).

Keen approach: Keen categorized zygomatic fractures as those of the arch, the body or the sutural disjunction. He was the first to introduce an intraoral approach to the zygomatic arch, in which an incision is made in the gingivobuccal sulcus (Keen WW 1909 Surgery: Its Principles and Practice. Philadelphia: WB Saunders).

Kehr's sign: the occurrence of acute pain in the tip of the shoulder due to the presence of blood or other irritants in the peritoneal cavity when an individual is lying down and the legs are elevated. Kehr's sign in the left shoulder is considered a classic symptom of a ruptured spleen.
Johannes Otto Kehr (1862–1916), German surgeon.

Kerckring: valves of – the plicae circulares;

Kerckring's centre – an occasional independent centre of ossification in the occipital bone.
Theodor Kerckring (1640–1693), Dutch anatomist.

Kienböck's disease: slowly progressing degeneration of the lunate bone of the wrist.
Robert Kienböck (1871–1953), Austrian radiologist.

Kiesselbach's plexus: a site of haemorrhage on the nasal septum.
Wilhelm Kiesselbach (1839–1902), ear, nose and throat surgeon, Erlangen, Germany.

Killian's: dehiscence – a gap between the attachments of the inferior constrictor of the pharynx to the cricoid and thyroid cartilages. Site of origin of a pharyngeal pouch;

sling – the cricopharyngeal sphincter;

triangle – a triangular area in the wall of the pharynx between the oblique fibres of the inferior constrictor muscle and the transverse fibres of cricopharyngeus, through which a Zenker's diverticulum may occur.
Gustav Killian (1860–1921), Professor of Laryngorhinology, successively in Freiburg and Berlin, Germany.

Kindler's syndrome: congenital poikiloderma with bullae and progressive cutaneous atrophy.
Theresa Kindler (1890–1975), Austrian-born dermatologist.

Kirk's arcade: an anastomosis between branches of the dorsal pancreatic artery and the right gastro-epiploic artery (Kirk E 1931 Untersuchungen über die gröbere und feinere topographische Verteilung der Arterien, Venen und Ausführungsgänge in der menschlichen Bauchspeicheldrüse. Z Ges Anat 94:822–75).

Klingler's method/technique: a method of brain fixation and dissection based on freezing and thawing the brain and subsequently peeling away tissues to expose white matter tracts (Agrawal A, Kapfhammer JP, Kress A et al 2011 Josef Klingler's models of white matter tracts: influences on neuroanatomy, neurosurgery, and neuroimaging. Neurosurgery 69:238–52).
Josef Klingler (1888–1963), Swiss neuroanatomical 'technician'.

Klippel–Feil syndrome: congenital fusion or reduction in number of the cervical vertebrae.
Maurice Klippel (1858–1942), neurologist, Salpêtrière, Paris, France; André Feil (1884–1955), French neurologist.

Klippel–Trenaunay syndrome: a rare congenital condition where blood vessels and/or lymph vessels fail to form properly.
Maurice Klippel (1858–1942), French physician; Paul Trénaunay (1875–?), French neurologist.

Klumpke's paralysis: injury to lowest root of brachial plexus (T1).
Augusta Déjerine-Klumpke (1859–1927), neurologist, Paris, France. Married to another neurologist, Joseph Déjerine.

Koch, triangle of: a triangular area in the wall of the right atrium that marks the site of the atrioventricular node.
Walter Karl Koch (1880–1962), physician and pathologist, Berlin and Freiburg, Germany.

Kocher's manoeuvre, method: an invagination method for radical operation for an inguinal hernia.
Theodor Kocher (1841–1917), made numerous contributions to surgery. Awarded Nobel Prize in Medicine or Physiology (1909) for his pioneering work on physiology, pathology and surgery of the thyroid gland.

Köhler's disease: avascular necrosis of the tarsal navicular bone and, less frequently, the patella, possibly due to repetitive compressive forces that cause a loss of blood supply and fragmentation in a

bone that is not fully ossified. More common in males; onset at 3–8 years of age. Asymptomatic or painful on the medial side of the foot; tenderness on palpation and swelling over area of navicular bone; slight, usually unilateral, limp.
Alban Köhler (1874–1947), German radiologist.

Kohn, interalveolar pores of: pores that link adjacent alveolar air spaces of the lung.
Hans Kohn (1866–1935), pathologist, Berlin, Germany.

Kölliker–Fuse nucleus: the substantia intermedia centralis in the spinal cord.
Rudolf Albert von Kölliker (1817–1905), Swiss anatomist.

Kommerell, diverticulum of: an aortic diverticulum associated with an aberrant right subclavian artery.
Burckhard Friedrich Kommerell (1901–1990), German radiologist.

Kooy, dorsal cap of – a subnucleus of the inferior olive: processes optokinetic information and projects to the contralateral flocculus and nodulus (Kooy FH 1916 The inferior olive in vertebrates. Thesis, Haarlem: Erven Bohn; Kooy FH 1917 The inferior olive in vertebrates. Folia Neurabiol 10:205–369).

Körner's septum: a dense bony plate in the mastoid process that represents the persistence of the petrosquamous suture line. The septum divides the mastoid process into a superficial squamous portion and a deep petrous portion (Korner O 1926 Das Septum petrosquamosum (mastoideum) und seine klinische Bedeutung. Arch Ohren Nasen Kehlkopfheilk 17:137).

Korsakoff psychosis, syndrome: a syndrome of anterograde and retrograde amnesia with confabulation, associated with alcoholic or non-alcoholic polyneuritis, described as 'cerebropathia psychica toxaemia' by Korsakoff; currently used synonymously with 'amnestic syndrome'.
Sergei Sergeievich Korsakoff (1854–1900), Russian neuropsychiatrist.

Kraissl's lines: the lines of greatest tension in the skin.
Cornelius Kraissl (1902–1999), plastic surgeon, New Jersey, USA.

Krause, glands of: accessory lacrimal glands in the subconjunctival tissue of the upper fornix.
Karl Friedrich Theodor Krause (1797–1868), Professor of Anatomy, Hanover, Germany.

Krebs' cycle: the citric acid cycle – the oxidative energy production pathway in mitochondria.
Sir Hans Adolf Krebs (1900–1981), German-born British biochemist.

Kugel's anastomotic artery: the arteria anastomotica auricularis magna (synonym: atrial anastomotic branch of circumflex branch of left coronary artery) (Kugel MA 1927 Anatomical studies on the coronary arteries and their branches. I. Arteria anastomotica auricularis magna. Am Heart J 3:260–70).

Kuhn classification: a classification of frontal ethmoidal cells into types 1 to 4 (Kuhn FA 1996 Chronic frontal sinusitis: the endoscopic frontal recess approach. Oper Techn Otolaryngol Head Neck Surg 7:222–9).

Kuhnt: central tissue meniscus of – a thickening of the astroglial membrane (of Elschnig) covering the optic nerve head at the centre of the disc;

intermediary layer of, intermediary tissue of – a collar of astrocytes that separates the optic nerve head from the retina.
Hermann Kuhnt (1850–1925), German ophthalmologist.

Kulchitsky cells: neuroendocrine cells in the lung and gut.
Nicholas Kulchitsky (1856–1925), Professor of Histology, Kharkov, Russia. After the Russian Revolution, went to London, UK, to continue his work in neuropathology at University College.

Kuntz, nerve of: an inconstant intrathoracic ramus that joins the second intercostal nerve to the ventral ramus of the first thoracic nerve, proximal to the point where the latter gives a branch to the brachial plexus.
Albert Kuntz (1879–1957), American anatomist.

Kupffer cells: resident liver macrophages.
Karl Wilhelm von Kupffer (1829–1902), Professor of Anatomy successively at Kiel, Königsberg and Munich, Germany.

Labbé, inferior anastomotic vein of: a vein that connects the superficial middle cerebral vein to the transverse sinus.
Léon Labbé (1832–1916), French surgeon.

Ladd's bands: congenital bands across the duodenum in volvulus neonatorum.
William Edward Ladd (1880–1967), surgeon, Boston Children's Hospital, USA.

Laimer's: diverticulum – a pulsion diverticulum located below cricopharyngeus;

triangle – *see* ***Killian's triangle.***
Eduard Laimer (1857–1934), anatomist, Graz, Austria.

Lancisi, muscle of: the main medial papillary muscle of the right ventricle (quoted in: Tandler J 1913 Anatomie des Herzens. In: Bardeleben's Handbuch der Anatomie des Menschen. Jena: Gustav Fischer).
Giovanni Maria Lancisi (1654–1720), Italian physician, epidemiologist and anatomist.

Landsmeer's ligaments: the transverse and oblique retinacular ligaments of the fingers.
Johan Landsmeer (1919–1999), Professor of Anatomy, Leiden, Netherlands.

Langer's lines: cleavage or crease lines in the skin produced by the arrangement of the subcutaneous fibrous tissues.
Karl Ritter von Edenberg Langer (1819–1887), Professor of Anatomy, Hungary, and then Vienna, Austria.

Langerhans: cells – dendritic cell of haemopoietic origin, in the epidermis and other epithelia;

islets of – clumps of insulin- and other hormone-secreting cells of the pancreas.
Paul Langerhans (1847–1888), Professor of Pathology, Freiburg, Germany. Described the islet cells in his doctoral thesis in 1869, at the age of 22.

Langhans cells: cells of the villous cytotrophoblast.
Theodor Langhans (1839–1915), pathologist, Berne, Switzerland.

Laplace's equation: the prototypical elliptic partial differential equation.
Pierre-Simon Laplace (1749–1827), French mathematician and astronomer.

Ledderhose's disease: plantar fascial fibromatosis.
Georg Ledderhose (1855–1925), German surgeon. Discovered glucosamine while working on cartilage with Ernst Felix Immanuel Hoppe-Seyler (1825–1895) in Strasbourg, France.

Le Fort I, II and III fractures: a system of classification of facial fractures.
René Le Fort (1869–1951), surgeon, Lille, France.

Legueu and Juvara, vertical septa of: vertical septa that pass from the transverse fibres of the palmar aponeurosis to the underlying deep transverse metacarpal ligament, forming fibro-osseous compartments (Legueu F, Juvara E 1892 Des aponévroses de la paume de la main. Bull Soc Anat Paris 6:383–400).

Leydig cells: the interstitial testosterone-secreting cells of the testis.
Franz von Leydig (1821–1908), Professor of Histology successively at Würzburg, Tübingen and Bonn, Germany.

Lieberkühn, crypts of: tubular glands of the small intestine.
Johann Nathaniel Lieberkühn (1711–1756), physician and anatomist, Berlin, Germany. These glands were described in 1688 by Marcello Malpighi (1628–1694), Italian physician and biologist, often cited as 'the father of microscopical anatomy and histology'.

Li Fraumeni syndrome: a rare autosomal dominant cancer predisposition syndrome first reported in 1969 by Frederick Li and Joseph Fraumeni from the National Cancer Institute, Rockville, Maryland, USA (Li FP, Fraumeni JF Jr, Mulvihill JJ et al 1988 A cancer family syndrome in twenty-four kindreds. Cancer Res 48:5358–62).

Liliequist's membrane: an arachnoid membrane passing from the dorsum sellae to the anterior edge of the mammillary body. Described by Key and Retzius in 1875 and 'rediscovered' in 1956 in Liliequist's cadaveric pneumoencephalographic studies. (Liliequist B 1956 The anatomy of the subarachnoid cisterns. Acta Radiol 46:61–71).

Lisfranc: **joint –** the tarsometatarsal joint;

Lisfranc's ligament – an interosseous ligament between the second metatarsal and first cuneiform bone of the foot.
Jacques de St Martin Lisfranc (1790–1847), Professor of Surgery, Paris, France.

Lissauer, fasciculus of, tract of: the ascending tract in the spinal cord.
Heinrich Lissauer (1861–1891), neurologist, Breslau, Poland.

Lister's tubercle: a prominence on the posterior surface of the distal radius, ulnar to the groove for the tendon of extensor pollicis longus.

Lord Joseph Lister (1827–1912), successively Professor of Surgery at Glasgow, Edinburgh and King's College, London, UK.

Little's area: a site of haemorrhage on the nasal septum.

James Laurence Little (1836–1885), Professor of Surgery, University of Vermont, USA.

Littre, glands of: small mucous glands of the male urethra.

Alexis Littre (1658–1726), French anatomist and surgeon.

Lockwood, suspensory ligament of: the thickened area of contact between Tenon's capsule and the sheaths of inferior rectus and inferior oblique in the orbit.

Charles Barrett Lockwood (1856–1914), British surgeon and anatomist, St Bartholomew's Hospital, London, UK.

Louis, angle of: the sternal angle – the angle formed on the anterior surface of the sternum at the junction of its body and manubrium.

Antoine Louis (1723–1792), Maître de Chirurgie and later Professor of Physiology, Royal College of Surgeons, Paris, France. He designed the prototype of the guillotine, which was originally nicknamed the 'Louison' or 'Louisette'.

Lower, intervenous tubercle of: a structure that lies between the fossa ovalis and the superior vena cava. *Richard Lower (1631–1691), English physician.* (Lower R 1669 Tractatus de corde. Item de motu, colore sanguinis et chyli in eum transitum. London: J Redmayne & J Allestry, p. 22).

Ludwig's angina: a potentially life-threatening, rapidly expanding, diffuse inflammation of the submandibular and sublingual spaces, occurring most often in young adults with dental infections.

Wilhelm Friedrich von Ludwig (1790–1865), German surgeon and obstetrician.

Lugaro cell: an inhibitory interneurone in the cerebellum.

Ernesto Lugaro (1870–1940), Italian neuropsychiatrist.

Luschka: bursa of (lateral Luschka aperture) – an accessory pharyngeal recess in front of the anterior arch of the atlas;

duct of – small, gland-like tubular structures in the wall of the gallbladder adjacent to the liver, especially in the part covered with peritoneum;

foramen of – the lateral aperture in the roof of the fourth cerebral ventricle;

uncovertebral joints of – small synovial joints on either side of the intervertebral cartilaginous joint in cervical vertebrae C3–C7 (between the uncinate process of the inferior vertebral body and the bevelled lateral border of the superior body at each level).

Hubert Luschka (1820–1875), Professor of Anatomy, Tübingen, Germany.

McBurney's point: the reputed site of maximal tenderness in appendicitis.

Charles McBurney (1845–1913), American surgeon.

Macewen's triangle: the surface marking of the mastoid antrum.

Sir William Macewen (1848–1924), Scottish surgeon. Established the treatment of intracranial complications of middle ear suppuration.

McGregor's patch: an area of fibrous attachment between the anterior edge of the parotid fascia and the dermis of the skin of the cheek (Rossell-Perry P 2013 The zygomatic ligament of the face: a critical review. OA Anat 1:3).

McLaughlin lesion: reverse ***Hill–Sachs lesion*** – an impaction fracture of the anteromedial aspect of the humeral head following posterior dislocation of the humerus.

Harrison Lloyd McLaughlin (1906–1970), American orthopaedic surgeon.

Mackenrodt, ligament of: the transverse cervical (or cardinal) ligament of the uterus.

Alwin Mackenrodt (1859–1925), Professor of Gynaecology, Berlin, Germany.

McKenzie branch of first cervical nerve: a communicating branch between the (spinal) accessory nerve and the anterior root of the first cervical nerve (McKenzie KG 1955 The surgical treatment of spasmodic torticollis. Clin Neurosurg 2:37–43).

Magendie, foramen of, aperture of: the median aperture in the roof of the fourth ventricle.

François Magendie (1783–1855), physician to the Hôtel Dieu, Paris, France.

Malassez, rests of: epithelial remnants of the enamel organ found in the periodontal ligament.

Louis Charles Malassez (1842–1909), French surgeon and physiologist.

Mallory's triple stain: Mallory's acid fuchsin, orange G and aniline blue stain for connective tissue.

Frank Burr Mallory (1862–1941), pathologist, Boston, USA.

Marfan: aortic dissection – *see below;*

syndrome – an autosomal genetic disorder of the connective tissue characterized by a long body and extended limbs and fingers, often associated with cardiovascular abnormalities such as dissecting aortic aneurysms and valve defects, as well as subluxated ocular lenses.

Antoine Bernard-Jean Marfan (1858–1942), Professor of Infantile Hygiene, Paediatric Clinic, University of Paris, France.

Marshall, vein of: the left atrial oblique vein, an embryonic remnant of the left superior caval vein which is enclosed within the Marshall ligament (Marshall J 1850 On the development of the great anterior veins in man and mammalia: including an account of certain remnants of fetal structure found in the adult, a comparative view of these great veins in the different mammalia, and an analysis of their occasional peculiarities in the human subject. Philos Trans R Soc Lond 140:133–69).

John Marshall (1818–1891), English surgeon and anatomist.

Martin–Gruber anastomosis: an anomalous connection between the median and ulnar nerves in the forearm (Martin R 1763 Om nervernas allmänna egenskaper i menniskans kropp jemte nervernas särskilda anatomiska beskrifning. Stockholm: Lars Silvius. Gruber W 1870 Über die Verbindung des Nervus medianus mit dem Nervus ulnaris am Unterarme des Menschen und der Säugethiere. Archiv für pathologische Anatomie und Physiologie und für klinische Medizin 37:501–22); *see* ***Gruber*** *above*.

Martinotti cell, neurone: a fusiform neurone in the deepest layer of the cerebral cortex.

Giovanni Martinotti (1857–1928), pathologist, Bologna, Italy.

Martius fat pad flap: a procedure used for complex fistula repair and as an interposition graft with vaginal reconstructive surgery (Martius H 1928 Die operative Wiederherstellung der vollkommen fehlenden Harnrohre und des Schlessmuskels derselben. Zentralbi Gynakol 52:480–6).

Masson's trichrome stain: a stain for connective tissue.

Claude Laurent Pierre Masson (1880–1959), French-born Canadian pathologist.

Mattox manoeuvre: a left medial visceral rotation – a surgical step to explore and handle Zone 1 and 2 retroperitoneal injuries (aorta, left iliac and pelvic vessels).

Kenneth L Mattox (1938–) American surgeon.

Maubrac, ansa of: an obsolete term for an anastomosis between the lateral deep branches of the cervical plexus and the accessory nerve (Maubrac G 1883 Recherches anatomiques et physiologiques sur le nerf SCM. Thesis, Bordeaux University (no. 38)).

Mayer–Rokitansky–Küster–Hauser syndrome: a syndrome characterized by congenital absence of the vagina, primary amenorrhoea, rudimentary cornua uteri and morphologically normal ovaries and Fallopian tubes situated on the side wall of the pelvis.

August Franz Joseph Karl Mayer (1787–1865), German anatomist and physiologist; Karl Freiherr von Rokitansky (1804–1878), Austrian pathologist; Hermann Küster (1879–1964), German gynaecologist; Georges André Hauser (1921–2009), Swiss gynaecologist.

Mayo, prepyloric vein of: a tributary of the right gastric vein that passes anterior to the pylorus at the gastroduodenal junction, also called vena prepylorica [TA], and Latarget's vein.

William James Mayo (1861–1939), American physician and surgeon, one of the founders of the Mayo Clinic.

Meckel's: cartilage – the cartilage of the first branchial arch;

cave – a cerebrospinal fluid-containing arachnoidal pouch protruding from the posterior cranial fossa. Located near the apex of the petrous part of the temporal bone, it houses the trigeminal ganglion and extends forwards, rather like an open-ended, three-fingered glove, enveloping the rootlets of the trigeminal nerve, the trigeminal ganglion and the ophthalmic, maxillary and mandibular divisions of the trigeminal nerve;

diverticulum – the remains of the vitellointestinal duct.

Johann Meckel (1781–1833), Professor of Anatomy, Halle, Germany. His grandfather was Professor of Anatomy in Berlin and described the pterygopalatine ganglion and the dural sac, which contains the ganglion of the trigeminal nerve. His father was also Professor of Anatomy in Halle.

Meibomian glands: the tarsal glands of the eyelid. If blocked, they become distended into Meibomian cysts.

Heinrich Meibom (1638–1700), Professor of Medicine, History and Poetry, Helmstadt, Germany.

Meissner's: corpuscles – tactile nerve endings in skin;

plexus – the submucosal autonomic plexus of the intestine.
George Meissner (1829–1905), Professor of Anatomy and Physiology, Basle, Switzerland; Zoology and Physiology, Freiburg, Germany; and Physiology, Göttingen, Germany.

Mendel's laws: the laws of inheritance of single-gene traits that form the basis of the science of genetics, first described by Gregor Mendel in 1865.
Gregor Johann Mendel (1822–1884), abbot and pioneer of genetics from Brno, Czech Republic.

Ménière's disease: aural or auditory vertigo.
Prosper Ménière (1799–1862), French otorhinolaryngologist.

Mercier's bar: a curved fold of mucous membrane extending across the bladder between the two ureteric orifices, produced by a transverse bundle of muscle fibres.
Louis Auguste Mercier (1811–1882), French urologist.

Merkel: cells, corpuscles – sensory cells in the skin;

disc – a slowly adapting type I receptor, which lies in the basal epidermis of glabrous skin and is sensitive to sustained pressure.
Friedrich Sigmund Merkel (1845–1919), Professor of Anatomy successively at Rostock, then Göttingen, Germany.

Meyer's loop: the fibres of the geniculocalcarine tract that loop forwards in the temporal lobe.
Adolf Meyer (1866–1950), American psychiatrist.

Meynert, basal nucleus of: part of the 'substantia innominata' of the basal forebrain; contains large cholinergic neurones that project to the cerebral cortex, amygdala and thalamus.
Theodore Herman Meynert (1833–1892), Professor of Neurology, Vienna, Austria.

Mikulicz angle: the angle formed between the head and neck of the femur and its shaft.
Johann (Jan) Freiherr von Mikulicz-Radecki (1850–1905), Polish surgeon in Germany.

Minor's syndrome: dehiscence of the roof of the superior semicircular canal (Minor LB 2000 Superior canal dehiscence syndrome. Am J Otol 21:9–19).

Mirizzi syndrome: partial obstruction to the flow of bile and the appearance of mild jaundice as a result of biliary stones.
Pablo Mirizzi (1893–1964), Argentinian physician.

Moll, glands of: modified sweat glands associated with the eyelashes.
Jacob Antonius Moll (1832–1914), ophthalmologist, The Hague, Netherlands.

Monro, foramen of: the foramen between the lateral and third ventricles of the brain.
Alexander Monro (1733–1817), Professor of Anatomy, Edinburgh, UK. The chair was also held by his father and his son – both also named Alexander.

Monteggia injury: a fracture of the upper portion of the ulna combined with dislocation of the radial head.
Giovanni Battista Monteggia (1762–1815), Italian physician and surgeon.

Montgomery, glands of, tubercles of: sebaceous glands situated in the areola of the breast (previously described by Morgagni; *see below*).
William Montgomery (1797–1859), Professor of Midwifery, Dublin, Ireland.

Morgagni: columns of – the columns of the anal canal;

concha – otherwise known as concha nasalis suprema, superior nasal choncha;

hernia – a congenital diaphragmatic hernia between the sternal and costal attachments of the diaphragm;

hydatid of – (synonyms: appendix testis, appendices vesiculosae epoophori) a cyst-like remnant of the Müllerian duct attached to a testis;

sinus – a sinus that lies between the superior pharyngeal constrictor and the base of the skull. Internally it is covered by mucosa and posteriorly by the pharyngobasilar fascia and is a route for the spread of neoplasms and infection from the nasopharynx to the base of the skull;

triangle(s) of – the right and left sternocostal triangles of Morgagni are openings in the anterior part of the respiratory diaphragmatic muscle, between the sternal and costal parts;

Morgagni's tubercle – otherwise known as the tuberculum septi nasi or the septal tubercle, it is a focal bulge of the anterior nasal septum at the level of the middle turbinate.
Giovanni Battista Morgagni (1682–1771), Professor of Anatomy, Padua, Italy, for 59 years. Described as the founder of modern morbid anatomy.

Morgenstern, 'criminal' fold of: a constant peritoneal fold attached to the lower pole of the spleen near to the splenic flexure but distinct from the splenocolic ligament. It is most commonly responsible for iatrogenic injuries to the lower pole of the spleen during operation on the left upper quadrant.
Leon Morgenstern (1919–2012), American surgeon.

Morison, hepatorenal pouch of: the right subhepatic space.
James Rutherford Morison (1853–1939), Professor of Surgery, Durham, UK.

Moro reflex: the startle reflex.
Ernst Moro (1874–1951), German physician.

Morquio syndrome: mucopolysaccharidosis type IV (MPS IV), an autosomal recessive disorder in which there is an inability to process keratan sulphate.
Luis Morquio (1867–1935), Uruguayan physician.

Morton's neuroma: a disease of the foot characterized by a sudden cramp-like pain in the metatarsal area radiating to the fourth and fifth toes, and sometimes to the calf of the leg. Compression of the plantar nerve by a tumour, arthritic changes or bursitis is the common cause.
Thomas George Morton (1835–1903), American surgeon.

Müller: cells – neuroglial cells in the retina;

orbital muscle of – a collection of smooth muscle fibres spanning the infraorbital fissure. Its functions are uncertain;

superior tarsal muscle of – a thin lamina of smooth muscle that passes from the underside of levator palpebrae superioris to the upper margin of the superior tarsus.
Heinrich Müller (1820–1864), Professor of Anatomy, Würzburg, Germany.

Müllerian duct (also Müllerian duct syndrome)**:** paramesonephric ducts. Persistent Müllerian duct syndrome is a disorder of sexual development that affects males. Males with this disorder have normal male reproductive organs but also have a uterus and uterine tubes.
Heinrich Müller (1820–1864), Professor of Anatomy, Würzburg, Germany.

Müller–Weiss disease: spontaneous osteonecrosis of the navicular in the adult.
Walther Müller (1888–1949), German orthopaedic surgeon; Konrad Weiss (1891–1976), Austrian radiologist.

Nabothian cyst, follicle: a retention cyst of the uterine cervix.
Martin Naboth (1675–1721), Professor of Medicine, Leipzig, Germany.

Newton: Newtonian equations – equations using the SI unit of force (N), which, when applied in a vacuum to a body having a mass of 1 kg, accelerates it at the rate of 1 m/sec^2;

Newton's second law of motion – applied force = mass × acceleration.
Sir Isaac Newton (1643–1727), English mathematician and physicist.

Nissl: bodies, granules – basophilic granules in the cytoplasm of neuronal somata;

staining technique – a specific stain for Nissl granules.
Franz Nissl (1860–1919), neurologist successively at Frankfurt, Heidelberg and Munich, Germany.

Nitabuch's layer, stria: a layer of fibrinoid matrix between the basal plate of the placenta and the endometrium.
Raissa Nitabuch, nineteenth-century German physician.

Noonan syndrome: autosomal dominant RASopathy. Clinical features are short stature, low-set ears and minor skeletal deformities of which the commonest are pectus excavatum and cubitus valgus.
Jacqueline Anne Noonan (1928–), American paediatric cardiologist.

Nuck, canal of: a diverticulum of the peritoneal membrane extending into the inguinal canal, accompanying the round ligament in the female, or the testis in its descent into the scrotum in the male; usually completely obliterated in the female.
Anton Nuck (1650–1692), Dutch anatomist.

Nuel, spaces of: spaces between the outer rods of Corti and hair cells.
Jean Pierre Nuel (1847–1920), Professor of Otology, Louvain and later Liège, Belgium.

Oddi, sphincter of: the sphincter at the termination of the common bile duct. The sphincter had already been described by Glisson *(see above)* in the seventeenth century.
Ruggero Oddi (1845–1906), surgeon, Rome, Italy.

Odland bodies: small, lamellated structures (keratinosomes) in the granular layer of the epidermis, containing hydrophobic phospholipid.
George Fisher Odland (1922–1997), American dermatologist and electron microscopist.

Ondine's curse: primary alveolar hypoventilation.
Ondine, a sea nymph in German mythology, who cursed an unfaithful human lover by abolishing the automaticity of his bodily functions.

Onodi cell: a sphenoethmoidal cell formed by lateral and posterior pneumatization of the most posterior ethmoid cells over the sphenoid sinus.
A Onodi, twentieth-century Hungarian laryngologist.

Onuf, nucleus of: neurones in lamina IX of the sacral spinal cord involved in the maintenance of micturition and defecatory continence.
Bronislaw Onuf-Onufrowicz (1863–1928), Russian-born American neurologist of Polish descent.

Oort, anastomosis of: a link between the saccular and cochlear nerves at the bottom of the internal auditory meatus (Oort H 1918 Über die Verästelung des Nervus octavus bei Säugetieren (Modell des Utriculus und Sacculus des Kainchens). Anat Anz 851:272–80).
H Oort, Dutch anatomist, Utrecht.

Oppenheim's dystonia: Oppenheim described dystonia musculorum deformans (DMD), a movement disorder characterized by twisting or turning movements and abnormal postures. Now called early-onset primary torsion dystonia, this condition is an autosomal dominant disorder most commonly associated with deletion of GAG in the coding region of the DYT1 gene encoding torsinA. It has been suggested that the condition should be referred to as 'Oppenheim's dystonia'.
Hermann Oppenheim (1858–1919), German neurologist.

Osborne, arcuate ligament: otherwise known as the cubital tunnel retinaculum, Osborne's fascia, Osborne's band, or the tendinous arch. A band of fibrous tissue that spans between the humeral and ulnar heads of flexor carpi ulnaris and forms the roof of the cubital tunnel.
Geoffrey Vaughan Osborne (1918–2005), Welsh surgeon.

Osgood–Schlatter disease: osteochondrosis of the tibial tuberosity.
Robert Bayley Osgood (1873–1956), Professor of Orthopaedic Surgery, Harvard University, Cambridge, Massachusetts, USA; Carl Schlatter (1864–1934), Professor of Surgery, Zurich, Switzerland.

Ostmann's fat pads: two small fat deposits medial and lateral in the membranous part of the Eustachian tube.
Paul Ostmann (1859–1945), German otologist.

Owen, contour lines of: accentuated incremental lines in the dentine, thought to be due to disturbances in the mineralization process. Defined by parallel deviations of neighbouring dentinal tubules.
Sir Richard Owen (1804–1892), English anatomist and palaeontologist.

Pacchionian bodies: arachnoid granulations.
Antoine Pacchion (1665–1726), physician and anatomist, Rome, Italy.

Pacinian corpuscle: a pressure-sensitive mechanoreceptor.
Filippo Pacini (1812–1883), Professor of Anatomy and Physiology, successively at Pisa and then Florence, Italy.

Paget's disease: chronic localized disorder of bone remodelling, with increased bone formation and resorption, often resulting in major long-bone and skull deformities.
Sir James Paget (1814–1899), British surgeon and physiologist.

Palomo procedure: retroperitoneal ligation of the internal spermatic vein between the anterior superior iliac spine and the renal vein (Palomo A 1949 Radical cure of varicocele by a new technique: preliminary report. J Urol 61:604–7).

Pancoast tumour: an apical carcinoma of the lung involving C8 and T1 nerves, the cervical sympathetic chain and upper ribs.
Henry Pancoast (1875–1939), Professor of Radiology, University of Pennsylvania, USA.

Paneth cells: bacteriocidal lysozyme-secreting cells.
Joseph Paneth (1857–1890), Professor of Physiology, first at Breslau, Poland, then Vienna, Austria.

Papez circuit: a neuroanatomical circuit mediating emotion, involving the hippocampal formation, mammillary body, anterior nuclei of the thalamus and cingulate gyrus.
James Wenceslas Papez (1883–1958), American neurologist.

Parkinson's syndrome, disease: the main symptoms of tremor, rigidity and slowness of movement caused by degeneration of dopaminergic neurones in the substantia nigra, usually occcur in late life and are more common in men.
James Parkinson (1755–1824), English physician and paleontologist. In his Essay on the Shaking Palsy (1817), Parkinson established the disease that now bears his name as a clinical entity.

Parkinson's triangle: the infratrochlear triangle. Defined by the inferior margin of the trochlear nerve from its beginning in the lateral wall of the cavernous sinus to its transit through the superior orbital fissure (medial border); the superior margin of the ophthalmic division of the trigeminal nerve (lateral border); and a line connecting the entry points of these nerves into the cavernous sinus (base) (Parkinson D 1965 A surgical approach to the cavernous portion of the carotid artery. Anatomical studies and case report. J Neurosurg 23:474–83).

Parks, mucosal suspensory ligament of: a condensation of fibres at the level of the dentate line (Parks AG 1954 A note on the anatomy of the anal canal. Proc R Soc Med 47:997–8).

Passavant's: muscle – the upper fibres of palatopharyngeus;

ridge, bar – a projecting ridge, or bar, on the posterior wall of pharynx, which appears during swallowing.
Phillip Gustav Passavant (1815–1893), surgeon, Frankfurt, Germany.

Petit's triangle, lumbar triangle of Petit: the inferior lumbar triangle bounded inferiorly by the iliac crest, anteriorly by external oblique and posteriorly by latissimus dorsi.
Jean L Petit (1640–1750), French surgeon.

Peyer's patches: lymphoid aggregates in the ileum.
Johann Conrad Peyer (1653–1712), Professor of Logic, Rhetoric and Medicine in Schaffhausen, Switzerland.

Peyronie's disease: induration of the corpora cavernosa of the penis, producing a fibrous chordee.
François de la Peyronie (1678–1747), French surgeon.

Pfannenstiel incision: a transverse curved abdominal incision with downward convexity, above the symphysis pubis.
Hermann Johann Pfannenstiel (1862–1909), German gynaecologist.

Pfeiffer's syndrome: a congenital syndrome characterized by craniostenosis, abnormal skull shape, facial anomalies, syndactyly of hands and feet, and broad thumbs and great toes.
Rudolf Arthur Pfeiffer (1931–2012), human geneticist, Saarbrücken, Germany.

Pierre Robin sequence: micrognathia, U-shaped cleft palate and glossoptosis.
Pierre Robin (1867–1950), French dentist.

Poirier, space of: a discrete interval between the inferior margin of the fibres of the radioscaphocapitate ligament that attach to the body of the capitate and the palmar horn of the lunate.
Paul Poirier (1853–1907), French surgeon.

Poiseuille's law: a mathematical expression of the flow rate for the laminar (nonturbulent) flow of fluids in circular tubes.
Jean-Louis-Marie Poiseuille (1799–1869), French physician and physiologist.

Poland's syndrome: a condition that is comprised of ipsilateral breast and nipple hypoplasia and/or aplasia, deficiency of subcutaneous fat and axillary hair, absence of the sternal head of pectoralis major, hypoplasia of the rib cage, and hypoplasia of the upper extremity, including cutaneous syndactyly.
Sir Alfred Poland (1822–1872), English surgeon.

Poswillo approach: a percutaneous closed reduction technique for management of fractures of the zygoma.
David Ernest Poswillo (1927–2003), maxillofacial surgeon, New Zealand.

Potter's syndrome: a rare condition combining a characteristic facial appearance with renal agenesis or hypoplasia and other defects.
Edith Louise Potter (1901–1993), early twentieth-century American paediatric surgeon.

Pott's abscess: a tuberculous abscess of the spine.
Sir Percivall Pott (1713 or 1714–1788), British surgeon.

Prader–Willi syndrome: a rare genetic condition that causes a wide range of physical symptoms, learning difficulties and behavioural problems.
Andrea Prader (1919–2001), Swiss paediatrician and endocrinologist; Heinrich Willi (1900–1971), Swiss paediatrician.

Pringle manoeuvre: the application of digital or mechanical pressure across the entire free edge of the lesser omentum, resulting in complete, temporary occlusion of the hepatic portal vein, hepatic artery and common bile duct.
J Pringle the Elder (1863–1941), Australian surgeon.

Prinzmetal's angina: variant angina occurring at rest, manifesting on electrocardiography as episodic ST segment elevations, and caused by coronary artery spasms with or without superimposed coronary artery disease.
Myron Prinzmetal (1908–1987), American cardiologist.

Probst, commissure of, Probst bundle: a callosal longitudinal bundle, seen in agenesis of the corpus callosum, when callosal fibres from the hemispheres fail to cross the midline and, instead, form thick bundles.
Moriz Probst (1867–1923), Austrian psychiatrist.

Prussak's: fibres – elastic and connective tissue fibre bounding the pars flaccida membranae tympani;

space – the superior recess of the tympanic membrane.
Alexander Prussak (1839–1897), Russian otologist.

Purkinje: cells, neurones – large neurones forming a single eponymous layer in the cerebellar cortex;

fibres – subendocardial muscle fibres.
Johannes Purkinje (1787–1869), Professor of Physiology, Breslau, Poland, and then Prague, Czech Republic.

Ramsay Hunt syndrome: herpes zoster involvement of the geniculate ganglion associated with facial paresis, hyperacusis, unilateral loss of taste, decrease in lacrimation and salivation, and otalgia.
James Ramsay Hunt (1874–1937), Professor of Neurology, Columbia University, New York, USA.

Ranvier, nodes of: short (~1 µm) gaps between adjacent myelin sheaths that are essential for the propagation of action potentials via saltatory conduction along myelinated axons.
Louis-Antoine Ranvier (1835–1922), French anatomist and histopathologist, Paris, France.

Raschkow's plexus: a plexus of myelinated nerve fibres located between the core of the pulp of the tooth and the cell-rich zone; axons lose their myelin sheath (but not their Schwann cells) as they penetrate the cell-rich and cell-free zones to make synaptic contact with the odontoblast cell body in the pulp or odontoblastic process within the dentinal tubule; responsible for transmitting pain sensation from the pulp of the tooth.
I *Raschkow (1811–1872), German physician.*

Rasmussen: bundle of – the olivocochlear tract;

Rasmussen's encephalitis – a rare, progressive, inflammatory disorder of the central nervous system.
Theodore Brown Rasmussen (1910–2002), neurologist, Utah, USA.

Rathke's pouch: a diverticulum of the roof of the stomodeum, which forms the anterior pituitary gland.
Martin Heinrich Rathke (1793–1860), Professor of Zoology and Anatomy, Königsberg, Germany.

Rayleigh scatter: the scattering of light or other electromagnetic radiation by particles much smaller than the wavelength of the light.
John William Strutt, 3rd Baron Rayleigh OM (1842–1919), Cavendish Professor of Physics, University of Cambridge, UK.

Raynaud's disease: idiopathic paroxysmal bilateral cyanosis of the digits due to arterial and arteriolar contraction, caused by cold or emotion.
Maurice Raynaud (1834–1881), French physician.

Reichert's cartilage: a cartilage in the mesenchyme of the second branchial arch in the embryo, from which the stapes, styloid processes, stylohyoid ligaments and lesser cornua of the hyoid bone develop.
Karl Bogislaus Reichert (1811–1883), German anatomist.

Reid's baseline: a plane that passes through the inferior margin of the orbit and the superior margin of the external acoustic meatus (external auditory canal).
Robert William Reid (1851–1939), Scottish surgeon and anatomist. He proposed a method of cerebral localization where the topography of the brain could be related to a system of lines drawn between large and easily felt landmarks on the surface of the head.

Reil: **circular sulcus of** – the peri-insular sulcus (synonym: sulcus circularis insulae); the insular surface is delineated peripherally by the peri-insular sulcus, which is interrupted by the transverse insular gyrus running across the limen insulae;

island of – the insular lobe.
Johann Christian Reil (1759–1813), German physician.

Reinke's: crystals – rod-shaped crystals in the interstitial cells of the testis and hilus cells of the ovary;

oedema – chronic laryngitis with swelling of the membranous part of the vocal cords;

space – a potential space between the vocal ligament and the overlying mucosa.
Friedrich Berthold Reinke (1862–1919), French anatomist.

Reissner's membrane: the vestibular membrane of the cochlea.
Ernst Reissner (1824–1878), Professor of Anatomy, Tartu, Estonia, and then Breslau, Poland.

Renshaw's cells: inhibitory interneurones modulating the response of anterior horn cells.
Birdsy Renshaw (1911–1948), American neurologist.

Retzius: space of, cave of – the prevesical space or retropubic space;

veins of, retroperitoneal venous plexus of – porto-caval anastomoses formed from veins in the walls of the retroperitoneal viscera, forming communications between the mesenteric veins and the inferior vena cava.
Andreas Adolf Retzius (1796–1860), Professor of Anatomy, Karolinska Institute, Stockholm, Sweden.

Retzius: cell – see ***Cajal–Retzius cell***;

gyrus – two small bulges on the medial segment of the hippocampal tail that consist of a CA1 subfield and the subiculum (Ziogas IA, Triarhou L 2016 Anders Retzius and his gyri. Neurol Sci 37:1861–6);

inferior sagittal sulcus of the cuneus of – a structure that lies superior to the posterior part of the calcarine sulcus;

lines of, striae of – brown lines in the dental enamel;

superior sagittal sulcus of – a paracalcarine sulcus (Retzius G 1896 Das Menschenhirn. Königliche Buchdruckerei PA Norstedt und Söner, Stockholm).

Gustav Magnus Retzius (1842–1919), Professor of Anatomy, Karolinska Institute, Stockholm, Sweden. Son of Andreas Adolf Retzius.

Rexed's lamina: subdivisions of cells of spinal cord grey matter.
Bror Rexed (1914–2002), Swedish neuroanatomist.

Riolan, arc of: the anastomosis between the middle and left colic arteries.
Jean Riolan (Secondus) (1577–1657), Professor of Anatomy and Botany, Paris, France.

Rives–Stoppa–Wantz technique: a technique that involves incising the posterior layer of the rectus sheath just lateral to the linea alba, allowing a retromuscular dissection to the lateral edge of the rectus sheath.
Jean Rives (1922–2012), Rene Stoppa (1921–2006), French-Algerian surgeons; George E. Wantz (1923–2000), American surgeon.

Rolando: cruciform sulcus of – the H-shaped orbital sulcus;

Rolandic fissure – the central fissure of the cerebral hemisphere.
Luigi Rolando (1773–1831), Italian anatomist.

Romberg sign: swaying of the body or falling when standing with the feet close together and the eyes closed.
Moritz Heinrich Romberg (1795–1873), German physician.

Rosenmüller, fossa of: the pharyngeal recess.
Johann Christian Rosenmüller (1779–1820), Professor of Anatomy and Surgery, Leipzig, Germany.

Rosenthal: basal vein of – a vein that courses from the premesencephalic cistern, through the ambient cistern, and terminates in the quadrigeminal cistern;

Rosenthal's canal – the spiral canal in the modiolus of the cochlea.

Isidor Rosenthal (1836–1915), physiologist, Greifswald, Germany.

Roser–Nelaton's line: a line drawn from the anterior superior iliac spine to the ischial tuberosity.
Auguste Nélaton (1807–1873), French physician and surgeon; Wilhelm Roser (1817–1888), German surgeon and ophthalmologist.

Rotter's node: the lymph node between pectoralis major and minor.
Josef Rotter (1857–1924), German surgeon.

Rouvière's sulcus: the incisura hepatis dextra (synonym: Gans incisura) (see Stringer MD 2009 Eponyms in Surgery and Anatomy of the Liver, Bile Ducts and Pancreas. London: Royal Society of Medicine).

Ruffini endings, bodies, corpuscles: sensory nerve endings, originally described in the skin of the fingers.

Angelo Ruffini (1887–1929), Professor of Histology, Bologna, Italy.

Russell, **hook bundle of:** uncinate fasciculus, where the crossed fibres from the fastigial nucleus pass dorsal to the superior cerebellar peduncle.

James Samuel Risien Russell (1863–1939), Guyanese-British neurologist.

Sachs, sagittal striata of: extrastriate thalamocortical projections (internal sagittal stratum of Sachs); association fibres of the inferior longitudinal fasciculus (external sagittal stratum of Sachs).

Heinrich Sachs (1863–1928), German neurologist and a student of Carl Wernicke in Breslau.

Saethre–Chotzen syndrome: acrocephalosyndactyly type III. A very rare disorder characterized by the fusion of cranial structures, which sometimes produces an asymmetric head and face; low-set hairline; ptosis and/or widely spaced eyes; 'beaked' nose and possible deviated septum; and, sometimes, brachydactyly and syndactyly.

Haakon Saethre (1891–1945), Norwegian psychiatrist; F. Chotzen (1932), German psychiatrist.

Santorini: duct of – the accessory pancreatic duct;

fissures of – two fissures in the anterior cartilaginous wall of the external acoustic meatus;

plexus of – the retropubic venous plexus giving rise to the pudendal vein.

Giovanni Domenico Santorini (1681–1737), Professor of Medicine and Anatomy, Venice, Italy.

Satiro's ear: usually known as Stahl's syndrome or Satyr's ear. A common congenital deformity of the auricle in which the helix is flattened and the upper crus of the antihelix is duplicated.

Friedrich Stahl (1811–1879), German physician.

Sattler's layer: a layer of medium-sized blood vessels in the choroid, derived from the short posterior ciliary arteries.

Hubert Sattler (1844–1928), Professor of Ophthalmology, Leipzig University Eye Hospital, Germany.

Scarpa's: fascia – the fibrous layer of the superficial fascia of the lower abdomen;

ganglion – the vestibular ganglion.

Antonio Scarpa (1747–1832), Professor of Anatomy, Padua, Italy.

Schaffer collaterals: the projections from pyramidal cells of fields CA3 and CA2 to CA1 in the hippocampus.

Max Schaffer (1852–1923), German neurologist.

Scheuermann's osteochondritis, disease, kyphosis: osteochondrosis of the vertebrae.

Holger Werfel Scheuermann (1834–1915), German biochemist.

Schiff's stain, reagent: a stain for aldehydes, used with periodic acid (PAS) to detect carbohydrates.

Hugo Schiff (1834–1915), German biochemist.

Schirmer test: a test that measures lacrimal gland secretory capacity; used principally to diagnose dry eye syndrome.

Otto Schirmer (1864–1918), German ophthalmologist.

Schlemm, canal of: a canal at the junction of the cornea and sclera.

Freidrich Schlemm (1795–1858), Professor of Anatomy, Berlin, Germany.

Schmidt–Lanterman incisures, cleft: a helical inclusion of glial cytoplasm within the myelin sheaths of central and peripheral nerves.

Henry Schmidt (1823–1888), pathologist, Charity Hospital, New Orleans, USA; AJ Lanterman, nineteenth-century anatomist, Strasbourg, France.

Schütz, fasciculus of: the dorsal longitudinal fasciculus.

Hugo Schütz (1859–1923), neurologist, Leipzig, Germany.

Schwalbe: **line of, ring of –** the anterior border ring of the cornea;

nucleus of – the vestibular nucleus;

pocket – a depression between the tendinous arch of levator ani and the lateral wall of the pelvis.

Gustav Albert Schwalbe (1844–1916), German anatomist and anthropologist.

Schwann cell: the major glial cell of the peripheral nervous system.

Theodor Schwann (1810–1882), Professor of Anatomy first in Louvain and then Liège, Belgium. One of the instigators of the cell theory.

Seessel's pouch: a small endodermal diverticulum that projects towards the brain from the cranial end of the foregut, immediately caudal to the buccopharyngeal membrane.

Albert Seessel (1850–1910), American embryologist.

Segond fracture: an avulsion fracture of the lateral margin of the lateral tibial plateau, with a significant association with anterior cruciate ligament and meniscal injuries.

Paul Ferdinand Segond (1851–1912), French orthopaedic surgeon.

Semon's law: an obsolete 'law' stating that injury to the recurrent laryngeal nerve results in paralysis of the abductor muscles of the vocal cords before paralysis of the adductor muscles.

Sir Felix Semon (1849–1921), German laryngologist in the UK.

Sertoli cells: the supporting cells of the testicular tubules.

Enrico Sertoli (1842–1910), Professor of Experimental Physiology, Milan, Italy.

Sever's disease: inflammation of the calcaneal apophysis in children and adolescents.

James Warren Sever (1878–1964), American orthopaedic surgeon.

Sharpey's fibres: connective tissue joining periosteum to bone.

William Sharpey (1802–1880), Professor of Anatomy successively at Edinburgh and University College, London, UK.

Sibson's fascia: the suprapleural membrane.

Francis Sibson (1814–1846), English surgeon.

Simmonds–Thompson test: a diagnostic tool for Achilles tendon rupture: absence of foot plantar flexion on calf compression is interpreted as a positive test result.

Franklin Adin Simmonds (1910–1983), English orthopaedic surgeon; Theodore Campbell Thompson (1902–1986), American orthopaedic surgeon.

Sistrunk's procedure: a procedure for removal of a thyroglossal duct cyst. It involves resection of the entire cyst, the central portion of the hyoid bone, and the thyroglossal duct tract that terminates at the foramen caecum. Several modifications of the procedure have been described.

Walter Ellis Sistrunk (1880–1933), American surgeon; originally described this operation in 1920.

Sjögren's connective tissue disease: a chronic autoimmune disease characterized by keratoconjunctivitis sicca and many other symptoms.

Henrik Samuel Conrad Sjögren (1899–1986), Swedish ophthalmologist.

Skene's glands: the paraurethral ducts of the female urethra.

Alexander Johnston Chalmers Skene (1838–1900), gynaecologist, New York, USA.

Skoog, fibres of: transverse fibres of the palmar aponeurosis of the hand.

Tord Skoog (1915–1977), Foundation Professor of Plastic Surgery, University of Uppsala, Sweden.

Sly syndrome: mucopolysaccharidosis type VII (MPS-VII), an autosomal recessive lysosomal storage disease caused by a deficiency of β-glucuronidase.

William S Sly (1932–), American physician.

Sondergaard: see ***Waterston, groove of.***

Tyge Sondergaard (1914–1990), Danish cardiac surgeon. The first surgeon to use cold chemical cardioplegia in open heart surgery.

Spence, tail of: the projection of mammary glandular tissue extending into the axillary region, sometimes forming a visible mass that may enlarge premenstrually or during lactation.

James Spence (1812–1882), Scottish surgeon.

Spiegel, Spigelian, Spieghel: **hernia –** (1–2% of all hernias – the protrusion of extraperitoneal fat, peritoneal sac or organ(s) through a congenital or acquired defect in the Spiegelian aponeurosis (i.e. the aponeurosis of transversus abdominis limited by the semilunar line laterally and the lateral edge of rectus muscle medially). Although named after Adriaan van der Spieghel, the semilunar line (linea Spiegeli) was only described by Spieghel in 1645. Josef Klinkosch first defined the Spiegelian hernia as a defect in the semilunar line in 1764. Defects in the aponeurosis of transversus abdominis (mainly distal to the arcuate line and more often in obese individuals) have been considered the principal aetiological factor;

line – the linea semilunaris (semilunar line);

lobe – the caudate lobe of the liver.

Adriaan van den Spiegel (1578–1625), Flemish anatomist and botanist. Name also written as Spieghel, Spigel, Adrianus Spigelius, Spiegelius, Adriano Spigeli.

Sprengel deformity: congenital elevation of the scapula with rotation of its lower angle towards the spine.

Otto Gerhard Karl Sprengel (1852–1915), German surgeon.

Stahl's deformity: congenital deformity of the ear characterised by a broad helix, absence of the fossa of the antihelix and upper scaphoid fossa.
Friedrich Stahl (1811–1879), German physician.

Stanford classification: a widely used system of classifying aortic dissections first proposed by a group of cardiovascular surgeons at Stanford University, in which dissections that involve the ascending aorta are classified as type A, regardless of the site of the primary intimal tear, and all other dissections as type B (Daily PO, Trueblood HW, Stinson EB et al 1970 Management of acute aortic dissections. Ann Thorac Surg 10:237–47).

Stener lesion: the ulnar collateral ligament is normally covered by the aponeurotic fibres of the tendon of adductor pollicis. Following avulsion, the proximal end of the ligament can become superficially displaced around the proximal free edge of the aponeurotic insertion of adductor pollicis, producing a Stener lesion (Stener B 1962 Displacement of the ruptured ulnar collateral ligament of the metacarpo-phalangeal joint of the thumb. J Bone Joint Surg Br 44:869–79).
Bertil Stener, Swedish orthopaedic surgeon.

Sternberg's canal: otherwise known as the lateral craniopharyngeal canal. Originally described as a membranous space in the lateral wall of the sphenoid sinus, this rare small canal was once believed to be the primary cause of spontaneous lateral sphenoid CSF leaks.
Maximilian Sternberg (1863–1934), Austrian physician.

Stickler syndrome: hereditary progressive arthro-ophthalmodystrophy, characterized by a distinctive flattened facial appearance, numerous ocular abnormalities, sensorineural or conductive hearing loss, and skeletal abnormalities that affect the joints.
Gunnar B Stickler (1925–2010), German paediatrician.

Stieda's process: the lateral tubercle of the talus, when elongated.
Christian Hermann Ludwig Stieda (1837–1918), German anatomist.

Struthers: arcade of – a thickening of the anteromedial aspect of the medial intermuscular septum, forming a myofibrous sheath around the ulnar nerve after it passes from the anterior to the posterior compartment of the arm;

ligament of – a ligamentous or muscular structure (often an extension of the humeral head of pronator teres), passing between the medial epicondyle and supracondylar processes of the humerus in approximately 1% of individuals.
Sir John Struthers (1823–1899), Scottish anatomist, professor and surgeon.

Sylvian: aqueduct – the midbrain channel connecting the third and fourth cerebral ventricles;

cistern – the subarachnoid space associated with the lateral cerebral sulcus (Sylvian fissure). It contains the M1 segment of the middle cerebral artery, the origin of the lenticulostriate arteries, and proximal parts of the middle cerebral artery;

fissure – the lateral cerebral fissure;

vein – the superficial middle cerebral vein.
François de la Boe Sylvius (1614–1672), Professor of Medicine, Leiden, Netherlands.

Takayasu's arteritis: a granulomatous vasculitis with massive intimal fibrosis and vascular narrowing mainly affecting the aorta and its large branches (aka aortic arch syndrome, nonspecific aortoarteritis, pulseless disease).
Mikito Takayasu (1860–1938), Japanese ophthalmologist.

Tamm–Horsfall protein: the most abundant protein in normal urine.
Igor Tamm (1922–1995), virologist, New York, USA; Frank Lappin Horsfall (1906–1971), American clinician and virologist.

Tanner's stages: scales for stages of sexual development in puberty.
James Mourilyan Tanner (1920–2010), British paediatric endocrinologist.

Taussig–Bing anomaly, syndrome, disease: transposition of the aorta to the right ventricle and malposition of the pulmonary artery with subpulmonary ventricular septal defect.
Helen B Taussig (1898–1986), American paediatrician; Richard Bing (1909–2010), American physician.

Tay–Sachs disease: a lysosomal storage disorder affecting neurones.
Warren Tay (1843–1927), ophthalmologist, London, UK; Bernard Sachs (1858–1944), neurologist, New York, USA.

Tenon's capsule: the fascial sheath of the eyeball.
Jacques René Tenon (1724–1816), Professor of Pathology, Academy of Sciences, Paris. Chief Surgeon, Salpêtrière, Paris, France. Specialized in ophthalmology.

Testut, ligament of: a radio-scaphoid-lunate connection.
Leo Testut (1849–1925), Professor of Anatomy, Lyons, France.

Thebesian: valve – the valve at the orifice of the coronary sinus;

veins – venae cordis minimae of the heart.
Adam Christian Thebesius (1686–1732), anatomist and pathologist, Leiden, Netherlands.

Thomine, retrovascular cord of: a pathological cord formed from the retrovascular fascia or band of Thomine (longitudinally oriented fibres dorsal to the neurovascular bundle) (Thomine JM 1985 The development and anatomy of the digital fascia. In: Hueston JT, Tubiana R eds, Dupuytren's Disease, 2nd ed. New York: Churchill Livingstone, pp. 3–12).

Thompson, posterior (dorsal) approach of: a surgical approach to treat fractures of the proximal and middle thirds of the radius and to address injury to the proximal radioulnar joint (Thompson JE 1918 Anatomical methods of approach in operations on the long bones or extremities. Ann Surg 68:309–29).

Thornwaldt cyst: a benign cyst located in the upper posterior nasopharynx, covered by mucosa anteriorly and bounded by longus muscles posteriorly.
Gustav Ludwig Tornwaldt/Thornwaldt (1843–1910), German physician.

Tinel's sign: the fact that lightly tapping (percussing) over a nerve trunk that has been damaged or is regenerating following trauma causes a sensation of tingling and pain in its distribution up to the site of regeneration. In closed injuries, percussion of the skin over a nerve in which axons have been ruptured evokes sensations that are usually described as a wave or surge of pins and needles into the cutaneous distribution of the nerve.
Jules Tinel (1879–1952), French neurologist.

Todaro, tendon of: a variable tendinous strand attached to the valvular fold at the termination of the inferior vena cava. It forms the superior border of the triangle of Koch.
Francesco Todaro (1839–1918), Professor of Anatomy at Messina and then Rome, Italy.

Toldt's fascia, fusion fascia of Toldt: an avascular fascial plane posterior to the ascending or descending colon and mesocolon, kidney and tail of the pancreas.
Carl Toldt (1840–1920), Austrian anatomist.

Towne's projection: positioning of the head in the radiological examination of the foramen magnum and posterior cranial fossa.
Edward Towne (1883–1957), neurosurgeon, Stanford Medical School, California, USA.

Treacher Collins syndrome: mandibulofacial dysostosis.
Edward Treacher Collins (1862–1932), English surgeon.

Treitz: fascia of, fusion fascia of – the fascia behind the head of the pancreas;

ligament of – a fold of peritoneum over the suspensory muscle of the duodenum;

muscle of – the suspensory muscle of the duodenum (musculus suspensorius duodenii).
Václav (Wenzel) Treitz (1819–1872), Professor of Pathological Anatomy, Jagellonian University, Prague, Czech Republic.

Trendelenburg's sign, gait: a dipping gait due to hip abductor dysfunction, e.g. in congenital dislocation of the hip or paralysis of gluteus medius and minimus.
Friedrich Trendelenburg (1844–1924), Professor of Surgery successively at Rostock, Bonn and Leipzig, Germany.

Treves, bloodless fold of: a peritoneal fold adjacent to the mesoappendix.
Sir Frederick Treves (1853–1923), surgeon, London Hospital, UK. Drained the appendicular abscess of King Edward VII in 1902.

Trolard: canal of – the sphenoparietal canal: a short bony canal that contains the anterior branches of the middle meningeal vessels;

superior anastomotic vein of – the vein that connects the superior sagittal sinus and the superficial middle cerebral vein (of Sylvius).
Paulin Trolard (1842–1910), French anatomist.

Tsai, ventral tegmental area of: the ventral tegmental area.
Tsai Chiao (1897–1990), Chinese physiologist.

Tuffier's line: a line that may be drawn between the highest points of the iliac crests on which the spine of L4 usually lies in adults.

Théodore Tuffier (1857–1929), French surgeon.

Türk, bundle of: corticopontine fibres that originate from parietal, occipital and temporal lobes.

Ludwig Türck (1810–68), Austrian neurologist.

Turner syndrome: a disorder of gonadal differentiation, marked by short stature, undifferentiated (streak) gonads and variable anomalies that may include webbing of the neck, low posterior hair line and cardiac defects.

Henry Hubert Turner (1892–1970), American endocrinologist.

Twining's line: the line between the tuberculum sellae and the torcular.

Edward Wing Twining (1887–1939), often cited as the 'father of British neuroradiology'.

Urbach–Wiethe syndrome: lipoid proteinosis, an autosomal recessive multisystem genodermatosis that primarily affects the skin, oral cavity and larynx, with the deposition of an amorphous hyaline material as a consequence of mutation of extracellular matrix protein 1 (ECM1). Neurological complications include basal ganglia calcification, usually bilaterally symmetrical.

Erich Urbach (1893–1946), Austrian dermatologist; Camillo Wiethe (1889–1949), Austrian otorhinolaryngologist.

Usher syndrome, Usher–Hallgren syndrome: a condition characterized by hearing loss or deafness and progressive loss of vision caused by retinitis pigmentosa. The three major types of Usher syndrome (types I, II and III) are distinguished by their severity and the age at which signs and symptoms appear (synonyms: Hallgren syndrome, dysacusis syndrome, dystrophia retinae dysacusis syndrome).

Charles Howard Usher (1865–1942), Scottish ophthalmologist.

Valoean sheath: the connective tissue capsule surrounding the liver.

Valoeus, an anatomist from the Middle Ages, who first described the liver capsule.

Valsalva: aortic sinuses of – the aortic sinuses;

manoeuvre – any forced expiratory effort ('strain') against a closed airway, whether at the nose and mouth or at the glottis.

Antonio Maria Valsalva (1666–1723), Professor of Anatomy, Bologna, Italy.

van de Woude's syndrome: an autosomal dominant syndrome characterized by a cleft lip or cleft palate, and/or distinctive pits of the lower lips, the most common syndrome associated with cleft lip or cleft palate (Van der Woude A 1954 Fistula labii inferioris congenita and its association with cleft lip and palate. Am J Hum Genet 6:244–56).

van Gieson technique, elastic van Gieson technique: a solution of trinitrophenol and acid fuchsin used to stain connective tissue elastin on histological sections.

Ira Thompson van Gieson (1866–1913), American neuropathologist, New York, USA.

Vater, ampulla of: the ampulla at the junction of the common hepatic and pancreatic ducts.

Abraham Vater (1684–1751), Professor of Anatomy, Botany, Pathology and Therapeutics, Wittenburg, Germany.

Velpeau, space of: (quadrangular space, quadrilateral space, foramen humerotricipitale): a space bounded by subscapularis, the capsule of the shoulder joint and teres minor superiorly, teres major inferiorly, the long head of triceps medially and the surgical neck of the humerus laterally. The axillary nerve and the posterior circumflex humeral artery and vein pass obliquely through the space.

Alfred-Armand-Louis-Marie Velpeau (1795–1867), French anatomist and surgeon.

Vesalius, foramen of: a small foramen for the emissary vein immediately anterior and medial to the foramen ovale in the sphenoid bone.

Andreas Vesalius (1514–1564), Professor of Anatomy, Padua, Italy.

Vicq d'Azyr, band or stripe of: a white band or stripe in the occipital cortex; also described by Gennari in 1782.

Félix Vicq d'Azyr (1748–94), French physician, anatomist, historian and social reformer who is often described as the greatest comparative anatomist of the eighteenth century before Cuvier.

Vidian: canal – the pterygoid canal;

nerve – the nerve of the pterygoid canal.

Guido Guidi Vidius (1500–1561), Professor of Medicine, Pisa, Italy.

Vieussens: anulus of – the ansa subclavia of sympathetic nerves; a tenuous anastomosis around the right ventricular outflow tract

arterial ring – an inconstant anastomosis around the right ventricular outflow tract that may provide an important collateral circulation in cases of arterial occlusion.

Raymond de Vieussens (1641–1715), physician and anatomist, Montpellier, France.

Virchow–Robin space: a perivascular space in the central nervous system.

Rudolf Ludwig Virchow (1821–1902), Professor of Pathological Anatomy, Würzburg, and then Berlin, Germany; Charles-Philippe Robin (1821–1885), Professor of Histology, Paris, France.

Vogt, palisades of: crests of epithelial folds at the limbus that run radially towards the cornea from the bulbar conjunctiva.

Alfred Vogt (1879–1943), Swiss ophthalmologist.

Voigt's lines, Voigt–Futcher lines: pigmentary demarcation lines or hair tracts (synonym: Futcher's lines).

Christian August Voigt (1809–1890), Professor of Anatomy, Vienna, Austria; Palmer Howard Futcher (1910–2004), US–Canadian physician.

Volkmann's: canals – osseous canals carrying blood vessels from the periosteum and between osteons;

ischaemic contracture – a permanent flexion contracture of the hand at the wrist, resulting in a claw-like deformity of the hand and fingers.

Alfred Wilhelm Volkmann (1800–1877), Professor of Anatomy and Physiology, first at Dorpat, Estonia, and later Halle, Germany.

von Brunn's nests: ectopic (subepithelial) urothelial masses in the urinary tract.

Albert von Brunn (1849–1872), Professor of Anatomy, Göttingen, Germany.

von Ebner's: fissure – in the development of the back, sclerotomal populations form from the ventral half of the epithelial somite. An intrasegmental boundary (fissure or cleft, sometimes termed von Ebner's fissure), which is initially filled with extracellular matrix and a few cells, appears within the sclerotome and divides it into loosely packed cranial, and densely packed caudal, halves;

glands – serous glands of the tongue, located beneath the circumvallate and foliate papillae;

lines – incremental lines of dentine.

Anton Gilbert Viktor von Ebner (also commonly called Viktor von Ebner-Rofenstein) (1842–1925), Professor of Histology and Embryology, Innsbruck, Austria.

Von Economo neurone: spindle neurone characterized by a single apical dendrite, a single basal dendrite and a long projection axon.

Constantin von Economo (1876–1931), Austrian psychiatrist and neurologist.

von Hippel–Lindau disease: an autosomal dominant genetic condition with high penetrance resulting from a deletion or mutation in the VHL tumour suppressor gene on chromosome 3p25.3. Characterized by retinal and CNS haemangioblastomas, pheochromocytomas, multiple cysts in the pancreas and kidneys. Benign tumours have an increased potential for malignant transformation.

Eugen Adolf Arthur von Hippel (1867–1939), German ophthalmologist; Arvid Vilhelm Lindau (1892–1958), Swedish pathologist and bacteriologist.

von Willebrand factor: the factor released from endothelial cells and platelets, promoting platelet adhesion and blood clotting. Deficient or defective factor production (usually inherited as an autosomal dominant trait) causes von Willebrand disease.

Erik Adolf von Willebrand (1870–1949), Finnish haematologist. Described the eponymous hereditary clotting disorder in 1926.

Waardenburg type II syndrome: a deafness syndrome associated with pigmentary disturbances. A group of heterogeneous entities distinguished from Waardenburg type I syndrome by the absence of dystopia canthorum.

Petrus Johannes Waardenburg (1886–1979), Dutch ophthalmologist and geneticist.

Waldeyer: presacral fascia of – the floor of the retrorectal space (Jin ZM, Peng JY, Zhu QC et al 2011 Waldeyer's fascia: anatomical location and relationship to neighboring fasciae in retrorectal space. Surg Radiol Anat 33:851–4);

Waldeyer's ring – a ring of lymphoid tissue that includes the palatine, pharyngeal, tubal and lingual tonsils;

Waldeyer's sheath – adventitia of distal segments of the ureter.

Heinrich Wilhelm Waldeyer (1836–1921), Professor of Pathology at Breslau, Poland, and then Berlin, Germany.

Wallenberg's syndrome: a lesion of the lateral medullary region of the brainstem.
Adolf Wallenberg (1862–1949), German physician.

Wallerian degeneration: degeneration of myelinated and unmyelinated axons distal to any injury that transects the axons and separates their distal segments from their centrally placed neuronal cell bodies.
Augustus Volney Waller (1816–1870), British neurophysiologist.

Walther, ganglion of: the solitary, retroperitoneal median ganglion impar or sacrococcygeal ganglion, which lies anterior to the sacrococcygeal junction; it represents the distal termination of the sympathetic chains.
August F Walther (1688–1746), German anatomist.

Wartenberg's disease, sign, symptom: radial sensory nerve entrapment.
Robert Wartenberg (1866–1956), American neurologist.

Warwick's foramen: a foramen located between the inferior end of the superior orbital fissure and the foramen rotundum.
Roger Warwick (1912–1991), English anatomist.

Waterston, groove of/interatrial sulcus of: the sulcus separating the right and left atria of the heart (aka Sondergaard's groove).
David Waterston (1910–1985), Scottish cardiothoracic surgeon.

Weigert–Meyer rule: the rule that, when complete, duplicated ureters insert separately into the bladder; the upper pole ureter is the ectopic ureter and its orifice inserts inferomedially in the bladder; the lower pole ureter is the normal ureter
Carl Weigert (1845–1904), German pathologist; Robert Meyer (1864–1947), German gynaecologist and pathologist.

Weigert, staining technique of: histological stains for myelin and for elastic fibres. The former uses a solution of ferric chloride and haematoxylin that stains myelin sheaths deep blue and degenerated tissue a pale yellow; the latter uses a resorcin–fuchsin solution that stains elastic fibres blue–black.
Carl Weigert (1845–1904), German histopathologist, Frankfurt-am-Main, Germany.

Werner's syndrome: a rare, autosomal recessive progeroid syndrome, characterized by the appearance of premature ageing.
Carl Wilhelm Otto Werner (1879–1936), German physician.

Wernicke: frontomarginal sulcus of – frontomarginal sulcus in the cerebral cortex;

Wernicke's speech area – the motor speech area in the superior temporal lobe of the cerebral cortex;

Wernicke's syndrome – a syndrome characterized by mental and ocular disorders and ataxia. Mental disturbances include listlessness, disorientation, confusion, hallucinations, Korsakoff psychosis and other behavioural symptoms.
Karl (or Carl) Wernicke (1848–1904), German physician, anatomist, psychiatrist and neuropathologist. Breslau, Poland, and then Halle, Germany.

Wharton's: duct – a duct of the submandibular salivary gland;

jelly – a homogenous intercellular substance of the umbilical cord; gives a reaction for mucin and contains thin collagenous fibres that increase in number with fetal age.
Thomas Wharton (1614–1673), physician and anatomist, St Thomas's Hospital, London, UK. Remained on duty there during the Great Plague of 1665.

Whipple procedure: pancreaticoduodenectomy.
Allen Oldfather Whipple (1881–1963), American surgeon.

Whitnall: transverse ligament of – a ligament that originates from the trochlea and inserts into the lateral orbital wall, approximately 10 mm above Whitnall's tubercle;

Whitnall's tubercle – a tubercle on the orbital surface of the zygomatic bone.
Samuel Ernest Whitnall (1876–1950), Professor of Anatomy, successively at McGill University, Montreal, Canada, and Bristol, UK.

Wiebel–Palade bodies: rod-shaped storage granules in endothelial cells.
Euald Wiebel, Swiss physician; George Emil Palade (1912–2008), Romanian cytologist, Rockefeller Institute, New York, USA, awarded the Nobel Prize for Medicine or Physiology in 1974.

Williams–Campbell syndrome: a rare form of congenital cystic bronchiectasis, in which distal bronchial cartilage is defective (Williams H, Campbell P 1960 Generalized bronchiectasis associated with deficiency of cartilage in the bronchial tree. Arch Dis Child 35:182–91).
Howard Williams, twentieth-century Australian physician; Peter E Campbell, twentieth-century Australian physician.

Willis, circle of: circulus arteriosus cerebri (cerebral arterial circle); the arterial anastomosis at the base of the brain.
Thomas Willis (1621–1675), physician to King James II, practised first in Oxford, then London, UK.

Wilson's pencils, pencil fibres of Wilson: the striatopallidal fibres (Wilson SAK 1914 An experimental research into the anatomy and physiology of the corpus striatum. Brain 36:427–92).
Samuel Kinnier Wilson (1878–1937), American-born British neurologist.

Winslow, foramen of: the epiploic foramen leading to the lesser sac.
Jacob B Winslow (1669–1760), Professor of Anatomy and Surgery, Paris, France.

Wirsung, duct of: the main pancreatic duct.
Johann Georg Wirsung (1589–1643), German physician, Prosector in Anatomy, Padua, Italy.

Wiskott–Aldrich syndrome: primary immunodeficiency resulting from an X-linked recessive mutation.
Alfred Wiskott (1898–1978), German paediatrician; Robert Anderson Aldrich (1917–1998), American paediatrician.

Wolffian: body – the mesonephros;

duct – the mesonephric duct.
Caspar Wolff (1733–1794), born in Berlin, Professor of Anatomy, St Petersburg, Russia, one of the pioneers of embryology.

Wolff's law: states that changes in the stresses on bones are reflected in their internal structure.
Julius Wolff (1836–1902), orthopaedic surgeon, Berlin, Germany.

Wolff–Parkinson–White syndrome: bundle-branch block with short P–R interval in healthy young people prone to paroxysmal tachycardia.
Louis Wolff (1898–1972), American cardiologist; John Parkinson (1885–1976), English cardiologist; Paul Dudley White (1886–1973), American cardiologist.

Wolfring, glands of: small tubuloalveolar glands in the subconjunctival tissue above the upper border of the tarsal plate.
Emilij Franzevic von Wolfring (1832–1906), Polish ophthalmologist.

Wormian bones: small bones that occasionally occur along the lambdoid suture of the human skull (synonym: sutural bones).
Ole Worm (1588–1654), physician, Professor of Medicine, University of Copenhagen, Denmark.

Wright's stain: a mixture of eosin and methylene blue, used for demonstrating blood corpuscles and malarial parasites on histological sections or blood smears.
James Homer Wright (1869–1928), pathologist, Harvard University, Cambridge, Massachusetts, USA.

Wrisberg, ligament of: a band attached to the posterior cruciate ligament of the knee.
Heinrich August Wrisberg (1739–1808), Professor of Anatomy, Göttingen, Germany.

Yakovlev's circuit: one of the divisions of the limbic system, a circuit involving the orbitofrontal, insular and anterior temporal lobe cortex, the amygdala and the dorsomedial nucleus of the thalamus, involved in emotion, reward and social behaviour.
Paul Ivan Yakovlev (1894–1983), Russian-born neurologist and neuropathologist who worked in the USA from 1925.

Young's modulus: sometimes called Young's modulus of elasticity: a measure of the ability of a material to withstand changes in length when under lengthwise tension or compression.
Thomas Young (1773–1829), British physician and physicist.

Zeis, glands of: modified rudimentary sebaceous glands attached directly to the follicles of the eyelashes.
Edward Zeis (1807–1868), German ophthalmologist.

Zellweger's syndrome: an inherited defect in peroxisome biogenesis and functioning.
Hans Ulrich Zellweger (1909–1990), Swiss–American paediatrician.

Zencker's diverticulum: a posteromedial pulsion diverticulum through Killian's dehiscence that causes debilitating dysphagia and regurgitation.
Friedrich Albert von Zenker (1825–1898), German physician and pathologist.

Zinn: anulus of – otherwise known as the common tendinous ring, it is a fibrous ring that surrounds the optic canal and part of the superior orbital fissure at the apex of the orbit and gives origin to the four recti;

circle of, zonula of – an (often incomplete) vascular circle within the sclera, formed by branches of the short posterior ciliary arteries, whose centripetal branches supply the laminar region of the optic nerve head (synonym: circle of Haller, zonula of Haller).

Johann Gottfried Zinn (1727–1759), Professor of Medicine and Director of Botanical Gardens, Göttingen, Germany.

Zuckerkandl: fascia of – the fascia posterior or anterior to the kidney;

organ of – the para-aortic bodies (also known as paraganglia) are collections of neural crest-derived chromaffin tissue found in close relation to the abdominal aortic plexus;

tuberculum of, tubercle of – a projection of normal thyroid tissue from the posterior or lateral lobes of the thyroid gland.

Emil Zuckerkandl (1849–1910), Professor of Anatomy at Graz and then Vienna, Austria.

Many of the eponyms in this list are described in more detail in Firkin BG, Whitworth JA 2001 Dictionary of Medical Eponyms. London: Parthenon. A concise illustrated account of the derivation and individuals behind the more common eponyms associated with liver anatomy and surgery is provided in Stringer MD 2009 Eponyms in Surgery and Anatomy of the Liver, Bile Ducts and Pancreas. London: Royal Society of Medicine.